Available online at www.sciencedirect.com
SCIENCE DIRECT®
Polyhedron 24 (2005) 1–39
POLYHEDRON
www.elsevier.com/locate/poly

Polyhedron Report No. 71

The coordination chemistry of tripodal tetraamine ligands

Allan G. Blackman *

Department of Chemistry, University of Otago, P.O. Box 56, Dunedin, New Zealand

Received 27 July 2004; accepted 26 October 2004
Available online 8 December 2004

Abstract

The coordination chemistry of tripodal tetrammine ligands is reviewed. These ligands contain a tertiary N atom bonded to three arms, each of which contains an N-donor atom, via at least one methylene group on each arm, and generally bind to a single transition metal or lanthanide ion using all four N-donor atoms. Fifty-four such ligands, not including substituted derivatives, are described. References are given to methods for the synthesis of these, and the coordination chemistry of each ligand with both transition metals and lanthanide ions is detailed, with emphasis being placed on structural features of the resulting metal complexes.
© 2004 Elsevier Ltd. All rights reserved.

Keywords: Tripodal; Tetraamine; Ligands; Coordination chemistry; Review

1. Introduction

Tetradentate tripodal ligands have the general structure depicted in Fig. 1 and consist of a central donor atom X attached to three arms, each of which also contains at least one methylene group and a donor atom Y.

A large number of such ligands containing identical sets or combinations of the donor atoms N, S, O and P are known, but this paper will discuss only those ligands having four N donor atoms and which normally bind to a single metal ion using all of these. These tetradentate tripodal tetraamine ligands thus contain a single tertiary N atom, which 'caps' the tripod, and one N-donor atom on each arm. The ligands can differ both in the lengths of the arms and in the nature of the N-donor atoms on each arm and there are at least 54 such ligands (not including their alkylated and substituted derivatives) known. The majority of these ligands have been prepared only in the last 20 years and much of their coordination chemistry remains to be explored in detail. This paper presents a review of the chemistry of tripodal tetraamine ligands. It aims not to be comprehensive in terms of a discussion of every known complex containing a tripodal tetraamine ligand (such a task would fill a book for the complexes of tris(2-aminoethyl)amine (tren) alone!); rather, it aims to provide the reader some idea of the range of chemistry that has been carried out (and indeed remains still to do) with these ligands. Each section details the synthesis of the ligand, and discusses some of its more important transition metal and (where applicable) lanthanide complexes, with particular emphasis being placed on structural aspects of these.

2. General remarks

2.1. Nomenclature

As is the case with many organic ligands, most tripodal tetraamine ligands are known by an abbreviation, usually of three or four letters, nominally derived from the full name of the ligand. Thus, the systematically named ligand *N*,*N*-bis(2-aminoethyl)ethane-1,2-diamine is better known as tren (Section 3.1.1), the abbreviation being derived from the non-systematic name

* Tel.: +64 3 479 7931; fax: +64 3 479 7906.
E-mail address: blackman@alkali.otago.ac.nz.

0277-5387/$ - see front matter © 2004 Elsevier Ltd. All rights reserved.
doi:10.1016/j.poly.2004.10.012

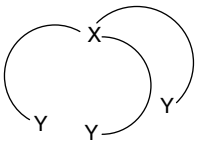


Fig. 1. General structure of a tetradentate tripodal ligand.

tris(2-aminoethyl)amine, and the name tren is in fact part of the 2004 provisional IUPAC recommendations on ligand abbreviations. However, this is the only tripodal tetraamine ligand for which IUPAC has proposed such a recommendation, and the abbreviations of other tripodal tetraamine ligands are somewhat haphazard and confusing. For example, the common ligand tris(2-pyridylmethyl)amine (Section 3.2.9) is variously abbreviated as tpa or tmpa, while the abbreviation bppa has been used for both bis(1-pyrazolylmethyl)(2-pyridylmethyl)-amine (Section 4.2.8) and bis(2-(3,5-dimethylpyrazol-1-yl)ethyl)(pyrazol-1-yl)methyl)amine (Section 4.2.9). Obviously, this is an unsatisfactory situation and ideally a systematic abbreviation system should be developed. However, in what follows, the ligand abbreviations given are those used most commonly in the literature (in some cases, more than one), and, where no abbreviation exists, a suitable one is proposed.

2.2. Synthesis

While the majority of tripodal tetraamine ligands discussed herein have been synthesised in the laboratory, some have been found in natural systems. Trpn (Section 3.1.4) and abbp (Section 3.1.8) have been found in the aquatic plants *Potamogeton distinctus* and *Sagittaria trifolia* L. [1], and also in the thermophilic eubacteria *T. thermophilus* HB8, *T. filoformis* Wai33 A1, *T. flavus* AT-62 and *T. caldophilus* GK24 [2].

Various methods are available for the synthesis of tripodal tetraamine ligands, with the route of choice generally dictated by the nature of the donor atoms on the three arms. All routes have in common the alkylation of the N atom of ammonium ion, or a primary or secondary amine precursor, with this N atom becoming the tertiary N atom of the resulting tripodal ligand. Bromo- and chloroalkylphthalimides are useful for the synthesis of ligands having aliphatic donor atoms as these can alkylate both primary and secondary N atoms at elevated temperatures, and deprotection using acid then gives the amine directly. Aliphatic N-donor atoms can also result from reduction of nitrile precursors with such reagents as $LiAlH_4/H_2SO_4$ or $NaBH_4$/Raney nickel, with the nitrile precursors generally being prepared from the reaction of acrylonitrile with the appropriate protected amine. Ligands having aromatic amine donor atoms are often prepared using haloalkylpyridines, imidazoles or pyrazoles as alkylating agents, while 2-vinylpyridine has proven useful as a reagent for the introduction of 2-(pyridylethyl) arms and 1-hydroxymethylpyrazole has been used in the synthesis of a number of pyrazole-containing tripodal ligands. The Mannich reaction has also been used in the synthesis of a number of tripodal tetraamine ligands.

2.3. Stereochemistry

The so-called "symmetric" tripodal ligands, in which all three arms are identical, usually have nominal C_{3v} symmetry about the central N atom, providing all the arms have the same conformations about the C–C and C–N bonds. Ligands in which the lengths of the arms differ, or which have N-donors of different types on each arm, are usually termed "asymmetric" and are of C_s symmetry or lower. Crystal structures of the free ligands show a variety of geometries, ranging from a "splayed" arrangement of the three arms, to internally H-bonded structures in which the three arms are folded to form a cavity into which an anion can bind. The latter arrangement is often found in protonated salts of the ligands.

Coordination to a metal ion generally results in a complex having a lower symmetry than the free ligand, depending on the coordination number of the metal ion. Four-coordinate complexes of tripodal amine ligands, in which all four N atoms are coordinated to a single metal ion, are relatively rare, as the ligands are often too constrained to be able to accommodate the square planar or tetrahedral geometries preferred by such complexes. Thus, four-coordinate complexes of tripodal tetradentate ligands often display either a very distorted tetrahedral geometry, or a trigonal pyramidal geometry, with the tertiary N atom occupying the apical position. Five-coordinate complexes are much more common, and the geometries of these occupy a continuum between the idealised trigonal bipyramidal and square pyramidal geometries. Such complexes are characterised by their τ value, where $\tau = 1$ for perfect trigonal bipyramidal geometry and $\tau = 0$ for perfect square pyramidal geometry [3]. It has been found that complexes having trigonal bipyramidal geometries are significantly more numerous than those having square pyramidal geometries. Indeed, five-coordinate complexes containing ligands such as tren (Section 3.1.1) and tpa (Section 3.2.9), almost invariably display trigonal bipyramidal geometries with the tertiary N atom at an apical position, reflecting the low-energy conformation of the ligand in such complexes. However, when the ligand arm lengths differ, such that a mixture of five- and six-membered chelate rings are present in the complex, square pyramidal geometries become more common, due presumably to the increased strain resulting from the accommodation of larger chelate rings in a trigonal bipyramidal geometry. Six-coordinate complexes containing tripodal amine ligands usually adopt distorted octahedral geometries, while seven coordinate

and above complexes appear to have no preferred stereochemistries, with a variety of geometries having been found.

2.4. Isomerism

The isomeric possibilities available to complexes of tripodal amine ligands is an oft-overlooked feature of such complexes. Most investigations have centred on six-coordinate complexes of symmetric ligands of the type outlined in Fig. 2. The two coordination sites labelled *p* and *t* are chemically inequivalent, being trans to a primary and tertiary amine N atom, respectively, and thus complexes such as $[M(tren)(X)(Y)]^{n+}$ can exist as geometric isomers.

When the arms of the tripodal ligands are of unequal lengths, then further isomeric possibilities exist, depending on the orientation of the tripodal ligand with respect to the two remaining coordination sites not occupied by this ligand. Thus a six-coordinate complex of baep (Section 3.1.2), a ligand which forms one six-membered and two five-membered chelate rings on coordination to a metal ion, can exist as either a 5-isomer or a 6-isomer, in which a five-membered or six-membered chelate ring lies in the same plane as the remaining two coordination sites, respectively (Fig. 3).

Should these sites be occupied by two monodentate ligands, or an asymmetric bidentate ligand, then *p*- and *t*-isomerism is also possible in addition to this. The 5- and 6-terminology is simple, unambiguous, and can be adapted to any type of asymmetric tetradentate tripodal tetraamine ligand. Note that a somewhat more rigorous nomenclature system which is applicable to all multidentate amine ligands has also been recently proposed [4]. Six-coordinate complexes of symmetric tripodal ligands are potentially chiral, owing to the different possible conformations of the chelate rings, and complexes such as $[Co(tren)(DL\text{-leucinato})]X_2$ ($X = ClO_4^-$, BF_4^-, PF_6^-, N atom of the amino acid *trans* to the tertiary N atom of tren) [5] and $[Co(tren)(N_3)_2]Br$ [6] have been found to undergo conglomerate crystallisation from solutions of the racemates. More remarkable is the behaviour of $[Co(tren)(N_3)_2]I$, which crystallises as a racemate in the space group $P2_1/n$ at room temperature, but which undergoes a phase change to the space group $P2_1$ upon cooling the crystal [6]. Six-coordinate complexes of asymmetric tripodal ligands are also chiral and the complexes $[Co(abap)(NO_2)_2]Cl$ and $[Co(abap)(NO_2)_2]ClO_4 \cdot H_2O$ crystallise as conglomerates [7]. Donor atoms of different types on the arms of the tripodal ligand, even when the arms are the same length, can lead to geometric isomerism, in that a choice of donor atom in the same plane as the two remaining coordination sites can exist (Fig. 4), and such possibilities have been realised in, for example, complexes of the uns-penp ligand (Section 4.1.7).

While isomerism in six-coordinate systems is well recognised, the same cannot be said of five-coordinate complexes. Square pyramidal complexes containing asymmetric tetradentate tripodal ligands can potentially exist as geometric isomers, as outlined in Fig. 5. In cases where the tertiary N atom lies in the square plane, the size of the chelate ring involving the apical N atom can differ (**A** and **B**), while complexes in which the tertiary N atom occupies the apical position can have different sized chelate rings situated *cis* and *trans* to the fifth coordination site (**C** and **D**). These types of isomerism have not been well documented, and a simple nomenclature system has yet to be proposed.

Polymetallic complexes containing more than one tripodal ligand have numerous isomeric possibilities resulting from the relative orientations of the tertiary N atoms with respect to each other and also, in the case of asymmetric tripodal ligands, from the relative positioning of the different sized chelate rings or the different types of N-donor atoms. Such possibilities are rarely remarked on, and it is certain that the solution chemistry of these complexes is more complicated than might be suggested by the crystallisation and structural characterisation of a single isomer from solutions of such complexes.

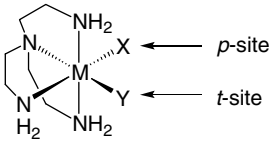


Fig. 2. The inequivalence of *p*- and *t*-coordination sites in six-coordinate complexes.

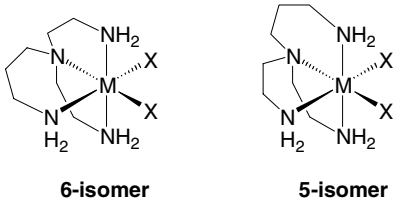


Fig. 3. Isomeric possibilities for six-coordinate complexes containing the asymmetric tripodal ligand baep.

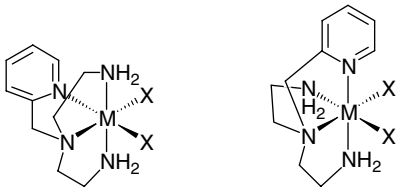


Fig. 4. Isomeric possibilities in six-coordinate complexes of tripodal ligands containing different N-donor atoms.

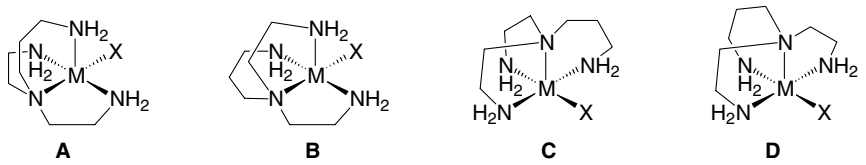
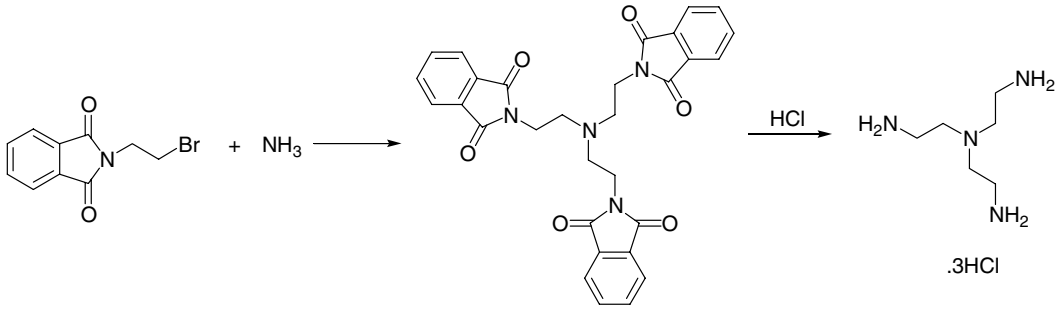


Fig. 5. Isomeric possibilities in square-pyramidal complexes of the asymmetric tripodal ligand baep.

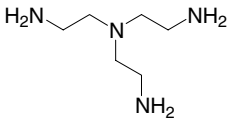


Scheme 1. Original synthesis of tren.

3. Ligands containing identical N-donor atoms on each arm

3.1. Ligands containing three aliphatic N-donor atoms

3.1.1. Tris(2-aminoethyl)amine



Tren was the first tripodal tetraamine ligand to be synthesised, and dates from 1896 when Ristenpart [8] prepared it as the trihydrochloride salt from the reaction of 2-bromoethylphthalimide with dry ammonia, and subsequent deprotection of the formed tris(2-phthalimidoethyl)amine using HCl (Scheme 1). This method was slightly modified by Mann and Pope in 1925 [9] and these workers also studied the coordination chemistry of the ligand with a number of metals.

An alternative method for the synthesis of tris(2-phthalimidoethyl)amine starting from triethanolamine was published by Collman and coworkers in 1970 involving reaction of triethanolamine with $SOCl_2$ to give tris(2-chloroethyl)amine hydrochloride, which is then reacted with potassium phthalimide [10]. [1] Tris(2-phthalimidoethyl)amine can also be deprotected using aqueous hydrazine and this gives the free base ligand directly. There are also numerous reports in the Patent literature of the synthesis of tren by reduction of tris(cyanomethyl)amine. The free base ligand is now commercially available.

Tren may be derivatised at either the terminal N atoms or a methylene carbon to give a variety of ligands having different steric and electronic properties from the parent. Exhaustive methylation at the terminal N atoms using formic acid/formaldehyde gives hexamethyltren [11], while the hexaethyl and hexa(isopropyl) derivatives are obtained from the reaction of tris(2-chloroethyl)amine with *N*,*N*-diethylethylenediamine and diisopropylamine, respectively [11]. *N*,*N*′,*N*″-trimethyltren has been prepared by reaction of tren with ethylchloroformate and subsequent reduction with $LiAlH_4$ [12] while the corresponding triethyl derivative is formed on reaction of tritosyltren with ethyl iodide [11]. Two isomeric monomethylated tren derivatives are known. Reaction of phthalimido-protected diethylenetriamine with phenylsulfonylaziridine, methylation with MeI and deprotection with HCl gives monomethyltren with the methyl group on a primary N atom [13], while monomethylation at the tertiary N atom can be achieved by methylation of tris(2-phthalimidoethyl)amine or triBoc-protected tren and deprotection [14,15]. The resulting cation is a poor ligand towards transition metal ions. The preparation of tren-based ligands having substituents on the carbon atoms of the ethyl chain is less facile, and there are consequently fewer examples of these than their *N*-alkyl congeners. The synthesis of homochiral tris(2-methyl-2-aminoethyl)amine has been reported, involving reaction of commercially available *N*-Boc-

[1] Tris(2-chloroethyl)amine hydrochloride is a powerful vesicant, while the free base form is a Schedule 1 Chemical Weapons Convention chemical. Indeed, the author's own laboratory was subject to a search by a three-person United Nations Chemical Weapons Inspection Team in 1997, owing to the large amounts of the hydrochloride salt stored therein. The synthesis of tren via this method is thus not recommended.

Table 1
Measured pK_a values for tren in aqueous solution

pK_a (1)	pK_a (2)	pK_a (3)	pK_a (4)	Conditions	References
	8.94	9.89	10.44	25.0 °C, 1.00 M $NaClO_4$	[324]
				25.0 °C, 1.00 M $LiClO_4$	
	8.89	9.81	10.39	25.0 °C, 1.0 M $NaNO_3$	[324]
	9.03	10.02	10.51	25.0 °C, 1.0 M NaBr	[324]
	8.41	9.43	10.14	25.0 °C, 0.1 M KCl	[325]
	8.43	9.45	10.15	25.0 °C, 0.1 M KNO_3	[326]
	8.39	9.46	10.18	25.0 °C, 0.1 M 2,4,6-Me_3PhSO_3Na	[326]
	8.42	9.41	10.12	25.0 °C, 0.1 M $NaClO_4$	[326]
	8.43	9.47	10.17	25.0 °C, 0.1 M KCl	[326]
	8.383	9.453	10.123	25.0 °C, 0.1 M R_4NX	[327]
2.60	8.45	9.43	10.14	25.0 °C, 0.1 M KNO_3	[328]
	8.56	9.59	10.29	20.0 °C, 0.1 M KCl	[329]
1.57	8.94	9.89	10.42	25.0 °C, 1.0 M NaCl	[330]
	9.17	10.26	11.00	20 °C, D_2O	[331]

Table 2
Formation constants for the reaction $M^{n+}(aq) + tren \rightleftharpoons [M(tren)]^{n+}(aq)$

M	log K	Conditions	References
Cu^{2+}	18.5	25.0 °C, $I = 0.1$ M	[326]
	18.86	25.0 °C, 0.1 M KNO_3	[332]
Ni^{2+}	14.6	25.0 °C, $I = 0.1$ M	[326]
	14.50	25.0 °C, 0.1 M KNO_3	[332]
Zn^{2+}	14.5	25.0 °C, $I = 0.1$ M	[326]
	13.76	20.0 °C, 0.1 M KNO_3	[333]
Ag^{+}	7.8	20.0 °C, 0.1 M $NaNO_3$	[329]
Cd^{2+}	11.72	25.0 °C, 0.1 M R_4NX	[327]
	12.3	20,0 °C, 0.1 M KCl	[329]
Co^{2+}	12.7	25.0 °C, $I = 0.1$ M	[326]
	12.69	25.0 °C, 0.1 M KNO_3	[328]
Fe^{2+}	8.8	20.0 °C, 0.1 M KCl	[329]
Mn^{2+}	5.77	25.0 °C, 0.1 M R_4NX	[327]

alanal with NH_4OAc and subsequent deprotection [16].

Tren and its derivatives have been used as the basis for the synthesis of a variety of Group 12, 13, 14, and 15 atranes [17], and tren has also been used in the synthesis of a large number of cryptate and cryptand species [18]. Both mono- [19–21] and diprotonated [22] derivatives of tren have been structurally characterised, and there are over 30 reported X-ray structures containing tri- and tetraprotonated tren. The tetraprotonated derivatives tend to adopt a ''splayed'' arrangement of the ligand arms, while the triprotonated congeners often have the three arms wrapping around to form a cleft which can bind an anion. The acid/base chemistry of tren has been extensively studied, and pK_a values obtained in various studies are given in Table 1.

As can be seen from these data, protonation of the tertiary N atom is more difficult than for similar ligands having longer arms, due to the relatively close proximity of the three primary N atoms. Likewise, there are many studies in which formation constants for 1:1 M^{n+}/tren species have been measured and some representative data from these are given in Table 2.

Tren generally binds as a tetradentate ligand to a single metal ion, but it is also found as a monodentate ligand bound through a primary N atom in $[Co(NH_3)_5(trenH_3)]Cl_6 \cdot 3H_2O$ and *p*-$[Co(tren)(NH_3)(trenH_3)]Cl_6 \cdot 2H_2O$ [23], a bidentate ligand (presumably through the tertiary and a primary N atom) in *trans*-$[ReO_2(tren)_2]I$ [24] and the $[Cr(trenH_2)(H_2O)_2(ox)]^{3+}$ cation [25], and a tridentate ligand bound through the tertiary and two primary N atoms in $[Ni(tren)_2]X$ (X = Cl_2, WS_4, [26] $(BF_4)_2$ [27]) and $[Co(tren)_2][Co(CO)_4]_2$ [28]. Tren has also been found as a bridging ligand between both two [29–31] and three [32,33] metal ions. An aesthetically pleasing example of the latter is $[Cd_7(tren)_{12}]$

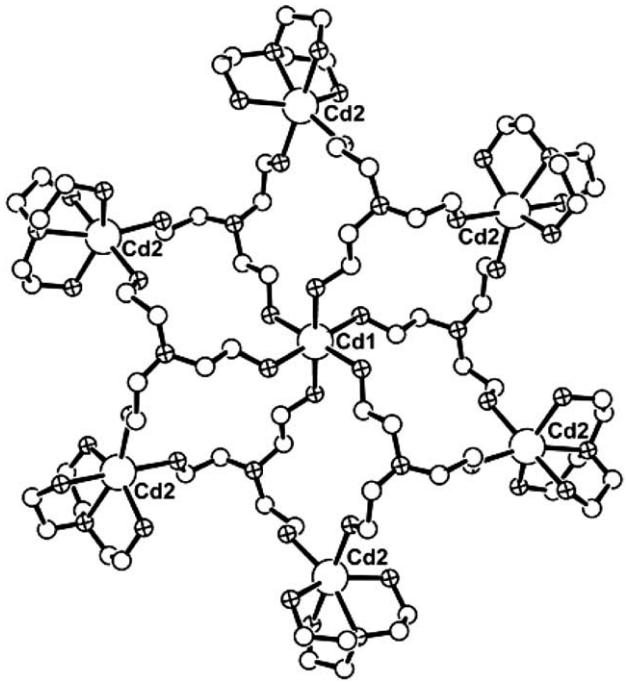


Fig. 6. The X-ray structure of the $[Cd_7(tren)_{12}]^{14+}$ cation. Hydrogen atoms are omitted for clarity.

$(ClO_4)_{14}$, the cation of which is shown in Fig. 6, in which tren acts both as a tetradentate ligand towards six separate Cd^{2+} ions and as a triply bridging monodentate ligand [34].

There are no crystallographically characterised examples of four-coordinate $[M(tren)]^{n+}$ complexes, owing presumably to the inability of the ligand to accommodate a suitable geometry. There are numerous examples of monomeric five-coordinate complexes containing tren, and those for which X-ray structures are available are listed in Table 3.

It can be seen that the majority of such complexes adopt some type of distorted trigonal bipyramidal geometry, with the only two having τ values less than 0.50, namely $[Cu(4,5\text{-diazafluorene-9-hydrazine})](ClO_4)_2$ [35] and $[Cu(4,5\text{-diazafluoren-9-one})](ClO_4)_2$ [36], containing ligands having a potential donor N-atom situated ~3 Å from the metal ion in a possible sixth coordination site. Six-coordinate complexes containing tren are numerous but, in contrast to other tripodal ligands having longer arms, there are surprisingly few crystallographically characterised examples of tren complexes containing a metal ion with a coordination number greater than six, with a seven-coordinate Cd^{2+} coordination polymer [37], and the nine-coordinate lanthanide complexes $[Nd(tren)_2(MeCN)](ClO_4)_3$ [38] and $[Pr(tren)(trien)(OSO_2CF_3)](CF_3SO_3)_2$ [39] apparently being the only examples [40,41].

Of the many metal ions with which tren forms complexes, undoubtedly the best studied is Co(III). Over five hundred complexes of the type $[Co^{III}(tren)(L)_2]^{n+}$ ($(L)_2$ = one bidentate or two monodentate ligands) are known (it is interesting to note that a previous review of tripodal amine ligands in 1977 listed fewer than fifty

Table 3
Structurally characterised monomeric five-coordinate $[M(tren)X]^{n+}$ complexes

M	X	τ	References
Zn^{2+}	Cl^-	0.96	[334]
Cu^{2+}	NH_3	1.01	[335]
Cu^{2+}	Cl^-	0.90	[336]
Cu^{2+}	NCS^-	0.80	[337]
Cu^{2+}	NCO^-	0.88	[336]
Cu^{2+}	N-acetylhistamine	0.80	[338]
Cu^{2+}	2-methylimidazole	0.66	[338]
Cu^{2+}	MeCN	1.01	[339]
Cu^{2+}	adenine (bound through N-7)	0.91	[340]
Cu^{2+}	3,4-bis(cyanamide)cyclobutane-1,2-dione	0.78	[341]
Cu^{2+}	4,5-diazafluorene-9-hydrazine	0.43	[35]
Cu^{2+}	pyridine	0.95	[342]
Cu^{2+}	4-dimethylaminopyridine	0.80	[343]
Cu^{2+}	imidazole	0.98, 0.61[a]	[344]
Cu^{2+}	CN^-	0.92	[345]
Mn^{2+}	NCO^-	0.83	[346]
Mn^{2+}	NCS^-	0.73	[346]
Cu^{2+}	NCS^-	0.92	[336]
Cu^{2+}	1-benzylimidazole	0.91	[347]
Zn^{2+}	Cl^-	0.96	[348]
Cu^{2+}	4-aminopyridine	0.85, 0.90[a]	[349]
Cu^{2+}	adenine	0.83	[350]
Zn^{2+}	NCS^-	0.97	[351]
Cu^{2+}	4,5-diazafluoren-9-one	0.42	[36]

[a] More than one independent molecule in the asymmetric unit.

such complexes [42]) and X-ray structures of nearly one hundred of these are available. Much of the interest in these complexes has stemmed from their utilility in assisting the determination of the stereochemical course of ligand substitution reactions at Co(III) centres. The diastereoisomeric *p*- and *t*-isomers possible in bis(monodentate) complexes of the type $[Co(tren)(X)(Y)]^{n+}$ often have quite different physical properties; for example, *p*-$[Co(tren)(NH_3)Cl]^{2+}$ is red, while *t*-$[Co(tren)(NH_3)Cl]^{2+}$ is purple [43]. Such isomers can often be easily separated, and analysis of the products obtained in either hydrolysis or anation reactions of these complexes readily shows the presence of any stereochemical change during such reactions [44–47]. In addition, tren has the ideal geometry to stabilise putative trigonal bipyramidal 5-coordinate intermediates which may be formed in these reactions. Ligands in the *p*- and *t*-positions can also be distinguished by a variety of NMR techniques, and an elegant example of this is the ^{17}O NMR study of a number of Co(III) aquo and hydroxo tren complexes by Buckingham and Clark and coworkers [48]. The two ^{17}O NMR peaks observed for $[Co(tren)(OH_2)_2]^{3+}$ at −95 ppm and −131 ppm (relative to solvent $H_2{}^{17}O$) were assigned to the *p*- and *t*-aquo ligands, respectively, and all other tren complexes studied were found to have the *p*-aquo or hydroxo resonance at a less negative chemical shift than the corresponding *t*-resonance. This study also showed that solvent exchange at the *p*-site was faster than at the *t*-site under all pH conditions, and that solvent exchange in $[Co(tren)(OH_2)(OH)]^{2+}$ was much faster than in either the diaqua or dihydroxo complexes.

Despite the large number of Co(III) complexes of tren, it is interesting to note that there are currently no known Co(III) complexes containing hexamethyltren, with the five-coordinate Co(II) complex $[Co(Me_6tren)(OH_2)]^{2+}$ being unreactive towards air-oxidation [49]. Notable amongst recent Co(III) complexes of tren is $[Co(tren)(L^{ISQ})](ClO_4)_2 \cdot 0.5CH_3OH \cdot 0.5H_2O$, where L^{ISQ} is the chelated *o*-iminobenzosemiquinonate radical anion derived from 2-anilino-4,6-di-*tert*-butylphenol

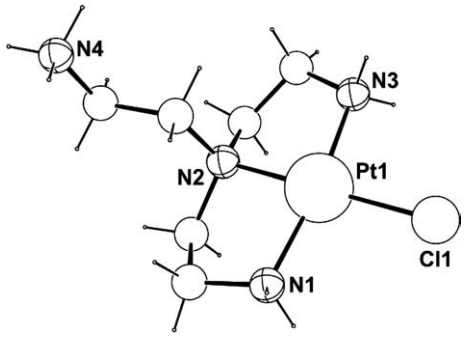


Fig. 7. Hypodentate coordination of tren in the $[Pt(trenH)Cl]^{2+}$ cation.

[50]. This complex is prepared by air oxidation of a methanolic solution of $Co(OAc)_2 \cdot 4H_2O$, tren and 2-anilino-4,6-di-*tert*-butylphenol in the presence of Et_3N, with subsequent addition of $LiClO_4$, and displays a temperature independent magnetic moment of 1.7 μ_B, indicating the presence of an O,N-coordinated radical anion with an $S_{rad} = 1/2$ ground state, and a diamagetic low-spin d^6 Co(III) ion.

Complexes of tren with all first row transition metals except vanadium are known, but complexes of the second and third row transition metals are less numerous. While there are over 20 known tren complexes of Rh(III), surprisingly there are only two examples of tren complexes of ruthenium, and both *fac*-$[RuCl_3(trenH)]Cl \cdot 0.5H_2O$ and *fac*-$[RuCl(ox)(trenH)]Cl \cdot 1.5H_2O$ feature hypodentate tridentate coordination of the tren ligand [51]. Equally surprisingly, there are no known examples of either osmium or iridium complexes. Metal ions such as Pd^{2+} and Pt^{2+} which prefer square planar geometries also, of necessity, form hypodentate complexes with tren. For example, the structurally characterised complex $[Pt(trenH)Cl]Cl_2$ contains monoprotonated tren coordinated as a tridentate ligand, with one arm remaining unbound (Fig. 7) [52].

$[Ag(tren)]PF_6$ is polymeric and again features tridentate coordination of the tren ligand to a single Ag^+ ion, but in this case one arm of the tren ligand bridges to a neighbouring silver ion [53]. The binding geometry of the tren ligand is ideal for the formation of molecular squares from six-coordinate monomers, owing to the *cis* configuration of the remaining two ligand binding sites, and this has been exploited in the heterometallic complex $K_2\{[Co(tren)]_2[W(CN)_8]_2\} \cdot 9H_2O$, the anion of which features a tetranuclear square of alternating Co(III) and W(IV) ions bridged by cyanide ligands [54].

Iron provides a number of examples of polynuclear complexes containing the tren ligand. The tetranuclear complex $[\{Fe_2(tren)_2(\mu\text{-}O)\}_2(\mu_4\text{-}PO_4)](ClO_4)_5 \cdot 2.5H_2O$, in which the four Fe(III) ions are bridged by a single phosphate ligand, is formed from the reaction of $Fe(ClO_4)_3 \cdot 9H_2O$ with 4-nitrophenylphosphate and tren in MeOH (Fig. 8) [55], hexanuclear $[Fe_6(\mu_4\text{-}O)_2(\mu_2\text{-}OMe)_8(OMe)_4(tren)_2](CF_3SO_3)_2 \cdot 2MeOH$ results from the solvolytic aggregation of the $[Fe_3O_2(OH)(tren)_3]^{4+}$ ion in MeOH [56], and the octanuclear iron complex $[Fe_8O_5(OAc)_8(tren)_4](CF_3SO_3)_6 \cdot 5MeCN$, which features a four-coordinate square planar oxo bridge, is obtained from air oxidation of a mixture of $[Fe(tren)(OAc)_2]$ and $Fe(CF_3SO_3)_2 \cdot 2MeCN$ in butyronitrile [57].

In all these complexes, the tren ligand acts as a type of capping ligand which mediates the otherwise uncontrolled polymerisation of Fe-oxo species. Similarly, the dodecanuclear mixed-valence manganese complex $[Mn_{10}O_{14}(tren)_6](CF_3SO_3)_8 \cdot 6MeCN$ forms on air oxidation of a solution of $Mn(CF_3SO_3)_2$ and tren in MeCN

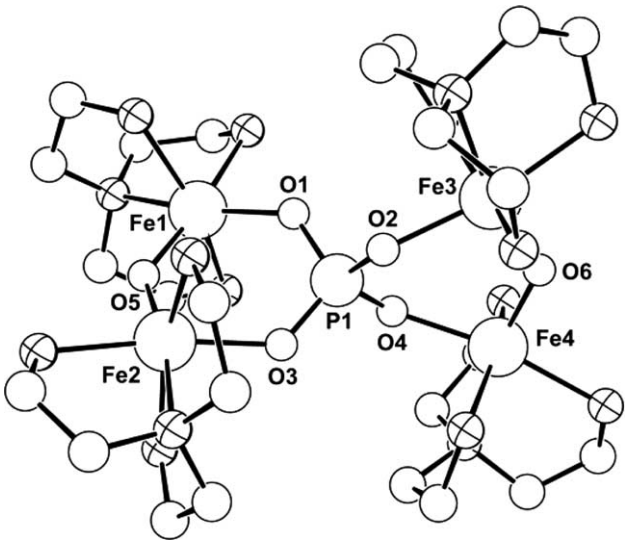


Fig. 8. X-ray structure of the tetranuclear $[\{Fe_2(tren)_2(\mu\text{-}O)\}_2(\mu_4\text{-}PO_4)]^{5+}$ cation. Hydrogen atoms are omitted for clarity.

[58]. Other multinuclear tren complexes, based on hexacyanometallates, include heptanuclear $[\{Cu(tren)CN\}_6Fe](ClO_4)_8 \cdot 10H_2O$ (Fig. 9), which is obtained from a mixture of $Cu(ClO_4)_2 \cdot 6H_2O$, tren and $K_3[Fe(CN)_6]$ [59], while the pentanuclear cation $[\{Cu(tren)CN\}_4Fe(CN)_2]^{4+}$, in which the non-bridging cyanide ligands are mutually *trans*, is present in $[\{Cu(tren)CN\}_6Fe][\{Cu(tren)CN\}_4Fe(CN)_2][Fe(CN)_6]_4 \cdot 6DMSO \cdot 21H_2O$ [59]. The analogous heptanuclear $[\{Cu(tren)CN\}_6Cr]^{9+}$ and $[\{Cu(tren)CN\}_6Co]^{9+}$ complexes have also been structurally characterised [33].

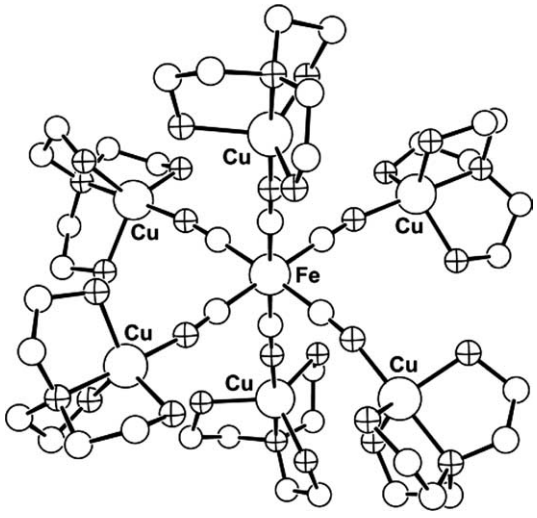
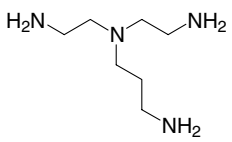


Fig. 9. X-ray structure of the $[\{Cu(tren)CN\}_6Fe]^{8+}$ cation. Hydrogen atoms are omitted for clarity.

3.1.2. 3-Aminopropylbis(2-aminoethyl)amine (baep)

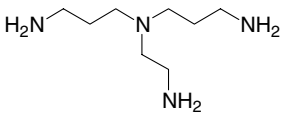


The free base form of baep was first reported in 1966 as the product of a multistep synthesis involving reaction of acrylonitrile with a protected diethylenetriamine derivative and subsequent reduction [60] but its use as a ligand was not investigated at this time. A more convenient synthesis of $baep \cdot 4HCl \cdot 2H_2O$ was detailed by Sargeson and coworkers in 1993 from the reaction of phthaloyl-protected diethylenetriamine with 3-bromopropylphthalimide followed by deprotection with HCl [61], while Hahn and coworkers reported an alternative synthesis in 1996 involving synthesis of the trinitrile and reduction with $LiAlH_4/H_2SO_4$ [62]. Two independent studies under identical conditions (potentiometric titration, 0.1 M KCl, 25.0 °C) have given successive pK_a values of 10.22, 9.51, 8.78 and 1.60 [63] and 10.14, 9.72, 8.40 and 2.1 [64] while formation constants (log *K*) for the 1:1 complexes of baep with Co^{2+}, Ni^{2+}, Cu^{2+}, Zn^{2+} and Cd^{2+} are 12.15, 14.17, 16.55, 13.35 and 9.74, respectively [63].

Only three complexes of baep have been structurally characterised; the cation of the 5-coordinate complex $[Cu(baep)(NH_3)](PF_6)_2$ displays a distorted trigonal bipyramidal geometry ($\tau = 0.58$) [62], while both $[Ni(baep)(ONO_2)_2]$ and dimeric $[(baep)Ni(\mu\text{-}Cl)_2Ni(baep)]Cl_2 \cdot 2CH_3OH$ contain approximately octahedral Ni^{2+} [65]. Geometric isomeric possibilities exist for the Ni^{2+} complexes, although both appear to crystallise as the 5-isomer in which a 5-membered chelate ring lies in the same plane as the nitrate and chloride ligands. This is particularly interesting in the case of the dimeric complex, where a total of at least eight isomers are possible, due to the different relative positionings of both the tertiary N atoms and the six-membered chelate rings. Solution studies of the Cu^{2+}(aq)/baep system have given evidence for the formation of the hypodentate complex $[Cu(baepH)(OH_2)_2]^{3+}$ in which the tripodal ligand binds in a tridentate fashion. This species in fact predominates in aqueous solution over the pH range 4–6 and similar behaviour is observed in both the Cu^{2+}(aq)/abap and Cu^{2+}(aq)/trpn systems. Log *K* values for the formation of the 1:1 complexes of Cu^{2+} with tren, baep, abap and trpn are 18.5, 17.1, 16.0 and 13.21, respectively, with the observed decrease in stability being ascribed to the decreasing number of 5-membered chelate rings in the complexes. Attempts to measure the rate of ligand substitution in Cu^{2+} complexes of baep, abap and trpn using T-jump techniques were unsuccessful, indicating

that ligand exchange in these species occurs orders of magnitude more rapidly than in $[Cu(tren)(OH_2)]^{2+}$ [64]. The Co(III) complexes $[Co(baep)(NO_2)_2]Cl$ and $[Co(baep)(O_2SOCF_3)_2]CF_3SO_3$ have been reported. Dissolution of the latter in aqueous solution and adjustment to neutral pH gave in situ formation of $[Co(baep)(OH_2)(OH)]^{2+}$, which was found to hydrolyse metal-bound pyrophosphate at rates comparable to the corresponding tren complex [61].

3.1.3. 2-Aminoethylbis(3-aminopropyl)amine (abap)

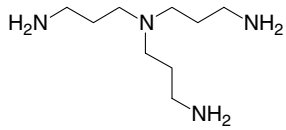


The preparation of abap from the reaction of dipropylenetriamine with aziridine in acidic solution was first described in a 1972 patent. However, this synthesis gave an inseparable mixture of abap and the straight chain product obtained from alkylation at the primary N atom in a 65:35 ratio [66]. Over 20 years elapsed before independent syntheses of the pure ligand were reported in the literature almost simultaneously by two separate groups [62,67]. These syntheses both involve alkylation at the secondary N atom of a dipropylenetriamine derivative. Reaction of phthalimido-protected dipropylenetriamine with 2-bromoethylphthalimide and subsequent deprotection with HCl gives $abap \cdot 4HCl \cdot 2.5H_2O$, while reaction of $HN(CH_2CH_2CN)_2$ with formaldehyde and KCN in the presence of $Na_2S_2O_5$ gives the trinitrile, which is then reduced to the free-base amine using $LiAlH_4/H_2SO_4$. It has been suggested that free base abap may have been prepared as early as 1964 when attempts to prepare the linear ligand 3-2-3-tet following a published procedure [68] involving cyanoethylation of ethylenediamine and subsequent reduction resulted in isolation of a product which was not identical to authentic 3-2-3-tet prepared by an alternative route [69]. The authors thus proposed that the unknown amine was abap, although frustratingly, no ^{13}C NMR data, which would allow an unambiguous distinction between the two amines to be made, were reported.

Potentiometric titration of abap (0.1 M KCl, 25.0 °C) in two independent studies reveals successive pK_a values of 10.38, 9.68, 8.95 and 3.81 [70] and 10.4, 9.87, 8.85 and 3.86 [64], while formation constants (log *K*) for the 1:1 complexes of abap with Co^{2+}, Ni^{2+}, Cu^{2+}, Zn^{2+} and Cd^{2+} are 9.26, 11.95, 15.98, 12.01 and 8.33, respectively [70]. Several complexes of abap have been structurally characterised and these are listed in Table 4.

While it may appear from this table that the 5-isomer is formed exclusively in complexes where the remaining two coordination sites are occupied by monodentate ligands, this is not the case in solution where, for example, the 5- and 6-forms of $[Co(abap)(OH_2)_2]^{3+}$ exist in equilibrium [71]. There appears to be no isomeric preference for the complexes containing bidentate CO_3^{2}, PO_4^{3-} and NO_3^{-}, indicating that the metal ion can accommodate bond angles of significantly less than 90° without requiring expansion of the opposite angle in the same plane. The low symmetry of the abap ligand leads to a large number of isomeric possibilities in binuclear complexes, and ^{31}P NMR spectroscopy has been used to identify 9 of the 12 possible isomers of $[(abap)CoO_2P(O)OCo(abap)(OH/H)]^{2+/3+}$ in which the bridging phosphate ligand is chelated to one Co centre and binds monodentate to the other, and all three possible isomers of the doubly chelated dimer $[(abap)Co(O_2PO_2)Co(abap)]^{3+}$ [71].

3.1.4. Tris(3-aminopropyl)amine (trpn)



The trpn ligand was first prepared as the tetrahydrochloride hemihydrate by Mann and Pope in 1926, from the reaction of molten 3-(bromopropyl)phthalimide with $NH_3(g)$ followed by deprotection with HCl, and this paper also described the first metal complexes of trpn, namely $[Ni(trpn)](SCN)_2$ (which was thought to contain four-coordinate Ni^{2+}, but is most likely six-coordinate $[Ni(trpn)(NCS)_2]$) $[Ni(trpn)]I_2 \cdot 1.5H_2O$ and $[Ni(trpn)]I(OH) \cdot 2H_2O$ [72]. Modifications of this synthesis of trpn have since been published, involving reaction of phthaloyl-protected dipropylenetriamine with *N*-(3-bromopropyl)phthalimide and subsequent deprotection in acid [73,74]. Alternative routes involving formation of tris(2-cyanoethyl)amine or tris(3-acetamidopropyl)amine and reduction of these to the amine have also been reported. Thus, reaction of acrylonitrile with ammonia gives the trinitrile [75] and this can be reduced using Raney nickel/H_2 to the triamide, which can then undergo acid hydrolysis to give trpn [76,77]. Use of Raney nickel/hydrazine as reductant has also been reported to give trpn in good yield [62]. Tris(3-acetamidopropyl)amine can also be prepared directly from acrylamide and ammonia, and reduction of this with either $LiAlH_4$ [78] or B_2H_6 [79] gives trpn. Trpn is also commercially available. Some N-substituted derivatives of trpn have been reported. Thus tris(3-(*N*-methylamino)propyl)amine, in which each pendant-arm N atom is monomethylated can be prepared by either $LiAlH_4$ reduction of tris(3-(ethoxycarbonylamino)propyl)amine or treatment of tris(3-bromopropyl)amine with methylamine [80] while the hexamethylated ligand is obtained on reaction of trpn with HCOOH/HCHO [81]. The trpn ligand generally crystallises as the tetrahydrochloride

Table 4
Structurally characterised complexes containing the abap ligand

Complex	Isomer	References
$[Co(abap)(NO_2)_2]Cl$	5	[7]
$[Co(abap)(NO_2)_2]ClO_4 \cdot H_2O$	5	[7]
$[Co(abap)(NO_2)_2]PF_6 \cdot H_2O$	5	[7]
$[Co(abap)(NO_2)_2]I \cdot H_2O$	5	[7]
$[Ni(abap)(O_2NO)]NO_3 \cdot MeCN$	6	[65]
$[Ni(abap)(OH_2)Cl]Cl$	5 (*t*-OH_2, *p*-Cl)	[65]
$[Cu_2(abap)_2(ONO_2)_2](NO_3)_2 \cdot 2H_2O$	an aminopropyl arm from each abap ligand bridges the Cu ions	[64]
$[Co(abap)Cl_2]Cl$	5	[352]
$[Co(abap)(O_2NO)](ClO_4)_2$	6	[67]
$[Cu(abap)(NH_3)](PF_6)_2$	five-coordinate ($\tau = 0.35$)	[62]
$[Co(abap)(O_2PO)] \cdot 6H_2O$	6	[71]
$[Co(abap)(O_2CO)]ClO_4 \cdot 0.5H_2O$[a]	5	[353]

[a] Structure determined in solution by ^{13}C NMR.

salt from solutions of HCl, and pK_a values of 5.615, 9.129, 9.824 and 10.511 ($I = 0.1$ M, KCl) [82,83], 5.62, 9.13, 9.97 and 10.52 ($I = 0.1$ M, Me_4NCl) [79] and 5.80, 9.28, 9.92 and 10.58 ($I = 0.1$ M, KCl) [64] have been measured in separate studies.

Despite its long pedigree, there are surprisingly few studies of simple metal complexes of trpn, with the majority of work in this area concentrating on the metal-assisted condensation reactions of trpn with a variety of carbonyl compounds to give aminopropyl-appended Schiff-base macrocycles, or cryptates. Formation constants (log *K*) for the 1:1 complexes of trpn with Co(II), Ni(II), Cu(II) and Zn(II) in aqueous solution are 6.360, 8.702, 13.117 and 10.702, respectively and these values are some 4–6.5 log units smaller than the corresponding values for tren, reflecting the lower stability of six-membered chelate rings when compared to their five-membered congeners [82]. This is further emphasised by potentiometric measurements which show that the predominant Cu(II) complex between pH 6 and 8 is the hypodentate cation $[Cu(Htrpn)(OH_2)_2]^{3+}$ in which one arm of the tripodal ligand is protonated and uncoordinated [64]. Likewise, $[Cu(trpn)(N_3)]ClO_4$, prepared by reaction of $Cu(ClO_4)_2 \cdot 6H_2O$ with trpn and azide in $MeOH/H_2O$, is not, as might be expected, a simple five-coordinate mononuclear complex, but a polymeric species in which one arm of the tripodal ligand bridges two Cu ions, and a similar bridging motif is also observed in the dimeric complex $[(tren)Cu(trpn)Cu(ONO)(OH_2)](ClO_4)_3$ (Fig. 10) [84].

Thermodynamic data suggested that the 1:1 Zn^{2+}/trpn complex was four-coordinate [83] and this was subsequently confirmed by the isolation from aqueous solution and structural characterisation of both $[Zn(trpn)]Cl_2 \cdot 2H_2O$ [85] and $[Zn(trpn)](ClO_4)_2$ [81] in which the Zn ion displays a trigonal pyramidal geometry, although it should be noted that, in the former complex, a water oxygen atom lies in an ideal apical coordination site 2.91 Å from the Zn ion (Fig. 11).

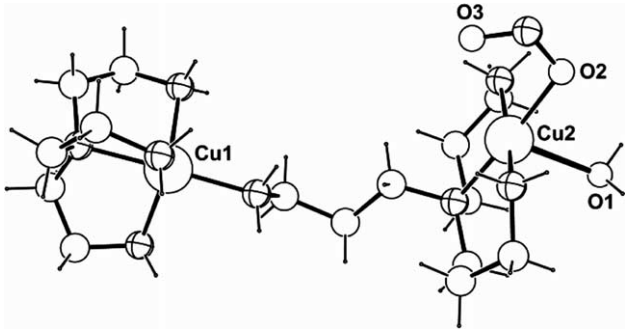


Fig. 10. X-ray structure of the $[(tren)Cu(trpn)Cu(ONO)(OH_2)]^{3+}$ cation.

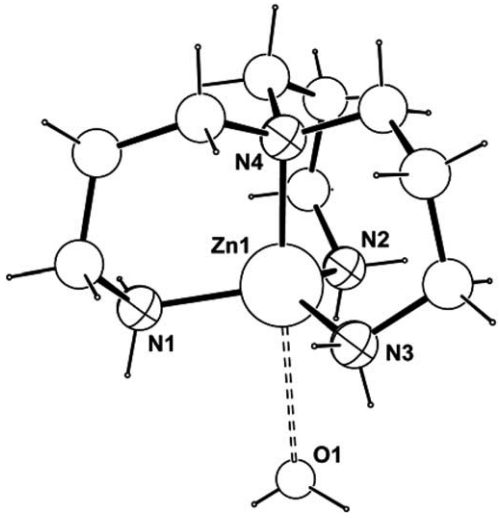
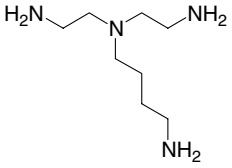


Fig. 11. X-ray structure of the cation of $[Zn(trpn)]Cl_2 \cdot 2H_2O$, showing the long Zn–O interaction.

$[Zn(trpn)](ClO_4)_2$ reacts with potassium *O*,*O*-diethylthiophosphate (DETP) to give five-coordinate $[Zn(trpn)(DETP)](ClO_4)$ in which the thiophosphate acts as a monodentate ligand to give a distorted trigonal bipyramidal geometry about the metal ion ($\tau = 0.91$). Other five-coordinate trpn complexes to have been structurally characterised include $[Co(trpn)Br]Br \cdot 0.5\text{-}C_2H_5OH$ [86], $[Cu(trpn)(NH_3)](PF_6)_2$ [62] and $[Cu(trpn)(MeCN)](ClO_4)_2$ [87]; the cation of the latter has $\tau = 0.46$, while $[Co(trpn)Br]^+$ and $[Cu(trpn)(NH_3)]^{2+}$ ($\tau = 0.81$) are distorted trigonal bipyramidal. The axial Co–Br bond distance of 2.658(3) Å in $[Co(trpn)Br]^+$ is very long and invites comparison with the complex $[Zn(trpn)]Cl_2 \cdot 2H_2O$ discussed above.

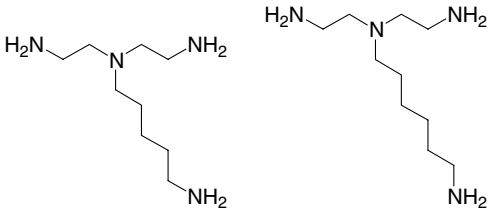
The chemistry of Co(III) complexes of trpn has been extensively studied and a large number of these complexes have been prepared [88,89]. Crystal structures of mononuclear $[Co(trpn)(OH_2)_2][Na(CF_3SO_3)_4(H_2O)]$ [90], $[Co(trpn)(O_2SO_2)]ClO_4 \cdot H_2O$ [91], $[Co(trpn)(O_2CCMe_3)](ClO_4)_2$ [92] and binuclear $[(trpn)CoO_2PO_2Co(trpn)](ClO_4)_3 \cdot 3H_2O$ [93] are available. Interestingly, $[Co(trpn)(O_2SO_2)]ClO_4 \cdot H_2O$ was the first authenticated example of sulfate chelated to Co(III). The $[Co(trpn)(OH_2)(OH)]^{2+}$ ion has been found to be particularly effective as a hydrolytic agent for ADP [94], ATP [95], AMP [96], RNA [97], and a variety of other phosphate esters [93,98,99], as well as organic esters [100] and nitriles [101], and its high reactivity, when compared to the analogous tren complex, has been ascribed to the greater flexibility of the trpn ligand which is thought to facilitate intramolecular nucleophilic attack of coordinated hydroxide ion at the coordinated substrate. However, $[Co(trpn)(OH_2)(OH)]^{2+}$ was shown under acidic conditions to be unstable with respect to oxidative N-dealkylation of the trpn ligand and concomitant reduction of the metal ion to Co(II) [102,103] and this hence limits the use of this complex as a hydrolytic agent. Ni^{2+} forms six-coordinate complexes with trpn, and both $[Ni(trpn)(O_2NO)]NO_3 \cdot CH_3OH$ and $[Ni(trpn)(OH_2)_2]Cl_2 \cdot H_2O$ have been structurally characterised [65]. It is interesting to note that no complexes of trpn with second or third row transition metal ions have yet been isolated, as it may well be that these larger metal ions are better able to accommodate three six-membered chelate rings.

3.1.5. 4-Aminobutylbis(2-aminoethyl)amine (bee, abba)



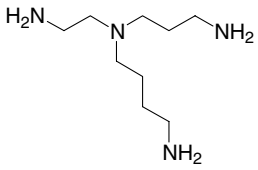
Two syntheses of the tetrahydrochloride salt of this ligand have been reported, both involving reaction of phthalimido-protected diethylenetriamine with *N*-(4-bromobutyl)phthalimide in a melt, followed by deprotection with HCl [104,105]. Reaction of abba · 4HCl with $CuCO_3 \cdot Cu(OH)_2$ gives the 5-coordinate complex $[Cu(abbaH)Cl_2]Cl \cdot 2H_2O \cdot CH_3OH$ in which the abba ligand coordinates as a tridentate ligand, with the protonated aminobutyl arm remaining unbound.

3.1.6. 5-Aminopentylbis(2-aminoethyl)amine (apba) and 6-aminohexylbis(2-aminoethyl)amine (ahba)



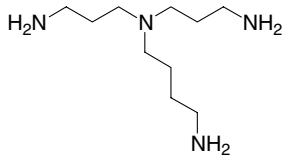
These ligands have been prepared by reaction of phthalimido-protected diethylenetriamine with *N*-(5-bromopentyl)phthalimide and *N*-(6-bromohexyl)phthalimide, respectively [105]. Their coordination chemistry has not been extensively investigated and is limited to the Cu(II) complexes $[Cu(apbaH)Cl(ClO_4)]ClO_4$ and $[Cu(ahbaH)Cl(ClO_4)]ClO_4$ in which the longest arms of the tripodal ligands are presumably protonated and not coordinated to the metal ion.

3.1.7. (4-Aminobutyl)-(3-aminopropyl)-(2-aminoethyl)amine (epb)



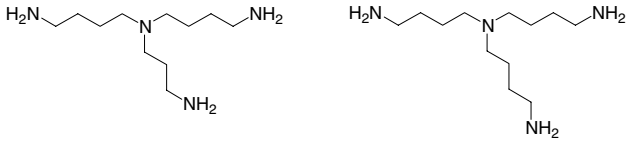
The first example of a tetradentate aliphatic tripodal amine ligand with all arms of different lengths, the tetrahydrochloride salt of epb was prepared by fusing 2,3′-diphthalimidoethylpropylamine and *N*-(4-bromobutyl)phthalimide at 160 °C, with subsequent deprotection using HCl [106]. The coordination chemistry of this ligand has not yet been investigated, but condensation of epb with 2,6-diacetylpyridine in the presence of Cu(II) and Ni(II) salts gives 5-coordinate macrocyclic Schiff-base complexes in which all three arms of the tripodal amine are coordinated to the metal ion.

3.1.8. 4-Aminobutylbis(3-aminopropyl)amine (abbp)



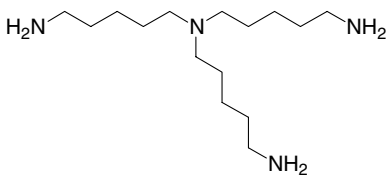
The first reported synthesis of this ligand involved reaction of phthaloyl-protected dipropylenetriamine with *N*-(4-bromopropyl)phthalimide in refluxing MeCN followed by deprotection using hydrazine hydrate and purification on Dowex cation exchange resin with HCl as eluent to give the ligand as the tetrahydrochloride salt [107]. More recently, a synthesis of the tetra(hydrogenperchlorate) salt from melts of either phthaloyl-protected dipropylenetriamine and *N*-(4-bromobutyl)phthalimide or 3,4-diphthalimidopropylbutylamine and *N*-(3-bromopropyl)phthalimide and subsequent deprotection have been reported [108]. Reaction of the perchlorate salt with copper(II) chloride gives the 5-coordinate complex $[Cu(abbpH)Cl_2]ClO_4$ in which the protonated aminobutyl arm is not coordinated to the metal ion.

3.1.9. 3-Aminopropylbis(4-aminobutyl)amine (apbb) and tris(4-aminobutyl)amine (trbn)



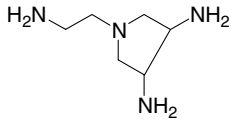
The tetrahydrochloride salts of these ligands have been prepared by treatment of phthaloyl-protected dibutylenetriamine with either *N*-(3-bromopropyl)phthalimide or *N*-(4-bromobutyl)phthalimide respectively in refluxing MeCN followed by deprotection using hydrazine hydrate and purification on Dowex cation exchange resin with HCl as eluent [107]. No metal complexes of either ligand have been reported.

3.1.10. Tris(5-aminopentyl)amine (trpa)



The free base ligand is formed from the reaction of ammonia with 1-cyanobutadiene and subsequent hydrogenation over Raney nickel [109]. Although first prepared in 1978, the coordination chemistry of this ligand remains to be investigated.

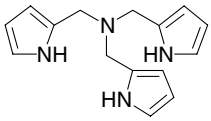
3.1.11. N-(2-aminoethyl)pyrrolidine-3,4-diamine (aepd)



The synthesis of this ligand has not been reported, but the ligand was in fact found as an impurity in commercial 96% tren, during the serendipitous synthesis of $[Ni_2(tren)_2(aepd)][ClO_4]_4 \cdot 2H_2O$ [110]. In this complex, aepd acts as a bridging ligand, binding in a bidentate fashion to the two Ni^{2+} ions.

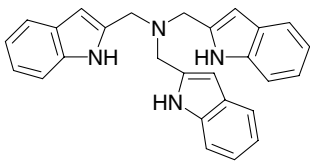
3.2. Ligands containing three aromatic N-donor atoms

3.2.1. Tris((2-pyrrolyl)methyl)amine (H_3tpa)



This ligand was prepared in 84% yield by a triple Mannich reaction involving 1 equivalent of NH_4Cl, 3 equivalents of formaldehyde and 3 equivalents of pyrrole [111]. The coordination chemistry of this ligand has thus far been restricted to complexes of Ti(IV) and Zr(IV). Treatment of $[Ti(NMe_2)_4]$ with one equivalent of H_3tpa gives trigonal bipyramidal $[Ti(tpa)(NMe_2)]$ which has been structurally characterised, while the analogous reaction with $[Zr(NMe_2)_4]$ and subsequent addition of either pyridine or 4,4′-*t*-Bu_2-2,2′-bipy gives the seven-coordinate complexes $[Zr(tpa)(NMe_2)(py)_2]$ and $[Zr(tpa)(NMe_2)(4,4'\text{-}Bu_2bipy)]$, respectively, the latter of which has also been structurally characterised. The triply deprotonated ligand can be isolated as the lithium salt Li_3tpa by treatment with BuLi, and reaction of this with $[ZrCl_4(THF)_2]$ gives $[Zr(tpa)(THF)_2Cl]$.

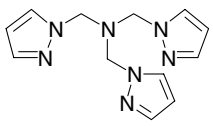
3.2.2. Tris((2-indolyl)methyl)amine ($N(CH_2in)_3$)



Reaction of 2-bromomethyl-1-indolecarboxylate with NH_3 and subsequent deprotection with NaOMe/NaOH gives $N(CH_2in)_3$ [112]. The syntheses of several tantalum complexes of this ligand have been reported, in all cases starting with dimethylamido tantalum species. Reaction

of $[Ta(Me_2N)_3(NAr)]$ $(Ar = 2,6\text{-}C_6H_3Pr^i_2)$ with $N(CH_2in)_3$ gives the structurally characterised 6-coordinate complex $[Ta(N(CH_2in)_3)(NAr)(NMe_2H)]$, while reaction of $[Ta(NMe_2)_5]$ with $N(CH_2in)_3$ gives the hypodentate complex $[Ta((N(CH_2in)_3)(NMe_2)_3]$ in which the tripodal ligand is tridentate, with one indole N atom remaining protonated and unbound to the metal centre. Reaction of this complex with MeLi leads to deprotonation of the non-coordinated indole and eventual formation of $[Ta((N(CH_2in)_3)(NMe_2)_2]$ in which the tripodal ligand is tetradentate.

3.2.3. Tris(2-(1-pyrazolyl)methyl)amine (amtp)



The 3,5-dimethylpyrazolyl derivative of amtp was first prepared in 1980 from the reaction of potassium 3,5-dimethylpyrazolate with $N(CH_2Cl)_3$ in THF [113] while amtp itself was first reported in 1982 as the product of the reaction of 1-hydroxymethylpyrazole with ammonium acetate [114], and this latter method has also been adapted for the synthesis of the 3,5-dimethylpyrazolyl derivative [115]. Reaction of the amtp ligand with hydrated MX_2 salts (M = Co, Cu, Zn, X = Cl, NCS) in ethanol gives five-coordinate $[M(amtp)X]X \cdot nH_2O$ or six-coordinate $[M(amtp)X_2] \cdot nH_2O$ when excess ligand is used, whereas five-coordinate $[M(amtp)X]_2(MX_4)$ complexes are obtained under conditions of excess metal salt [116]. The amtp ligand, but not its 3,5-dimethylpyrazolyl derivative, is found to hydrolyse in the presence of some metal salts [117,118], with loss of a pyrazolylmethyl arm resulting in formation of a tridentate ligand, and this reactivity has been ascribed to the three small bite angles of the amtp ligand (~80°) which leads to highly strained complexes on coordination of a metal ion to all four N donor atoms. This strain appears to be exemplified in the complex $[Zn(amtp)(NCS)_2]$, where the X-ray structure (Fig. 12) shows the amtp ligand to bind in a hypodentate fashion through only two pyrazole N atoms (the Zn–N_{tert} distance is 2.599 Å), to give a four-coordinate trigonal pyramidal geometry about the Zn ion [119].

Hypodentate coordination of amtp is also proposed in the Rh(I) and Ir(I) complexes $[Ir(coe)(amtp)]BF_4$, $[M(cod)(amtp)]BF_4$ (M = Ir, Rh) and $[Rh(CO)_2(amtp)]BF_4$, although no X-ray structural data are available [120]. In contrast to the analogous trpyn ligand (Section 3.2.5), the 3,5-dimethylpyrazolyl derivative of amtp readily forms five-coordinate complexes. Thus treatment of the ligand with the appropriate metal salt gives five-coordinate $[M(amtpMe_6)X]BPh_4$ complexes (M = Fe, Co; X = Cl, Br, I), and Ni complexes of the formula $[Ni_2(amtpMe_6)_2X_2](BPh_4)_2$ (X = Cl, Br) are thought to be halo-bridged dimers with each Ni ion six-coordinate [113]. The five-coordinate complexes $[Co(amtpMe_6)(OH_2)](ClO_4)_2$ [121], $[Co(amtpMe_6)(OH_2)][Co(amtpMe_6)F](BF_4)_3 \cdot 1.5EtOH$ [115], and $[Cu(amtpMe_6)(ONO_2)](NO_3)$ [122] have been structurally characterised and display approximate trigonal bipyramidal geometries about the metal ion ($\tau > 0.60$) with the aliphatic N atom and the ancillary ligand occupying the apical positions. Six-coordinate $[Ni(amtpMe_6)(O_2NO)]NO_3$ [122], $[Co(amtpMe_6)(OH_2)(OAc)]ClO_4$ [123], $[Fe(amtpMe_6)(NO)(ClO_4)]ClO_4$ [124] and $[Fe(amtpMe_6)(NO)Cl]BPh_4$ [124,125], and seven coordinate $[Cd(amtpMe_6)(ONO_2)(O_2NO)]$ [122] have also been structurally characterised, as has dimeric $[(amtpMe_6)Fe(Cl)_2Fe(amtpMe_6](BPh_4)_2$ in which both Fe ions are six-coordinate [126]. The latter complex displays weak ferromagnetic coupling between the high-spin Fe(II) centres. Both blue $[Co(amtpMe_6)(N_3)](ClO_4)$ and red-purple $[Co(amtpMe_6)(N_3)_2]$ can be prepared, with the latter formed only under conditions of excess azide $(Co^{2+} : N_3^- = 1 : 5)$ [127]. X-ray structures show an approximate trigonal bipyramidal geometry about the five-coordinate Co(II) ion in the blue complex ($\tau = 1.01$), while the red-purple complex displays a distorted octahedral geometry, with an angle of 95.93° between the *cis* azide ligands. Potentiometric titration of $[Co(amtpMe_6)(OH_2)](ClO_4)_2$ reveals two pK_a values (7.4 and 8.9) with the latter ascribed to deprotonation of coordinated water and the former to proton loss from the tertiary N atom [128,129]. Two further derivatives of amtp, the chiral camphor-derived ligand L^1 [130] and the bulky *p*-methoxyphenyl-substituted ligand L^2 (Fig. 13) [131] have recently been reported. Cu(I) and Cu(II) complexes of the latter ligand have been structurally characterised, with five-coordinate $[CuL^2Cl_2]$ displaying hypodentate coordination through three N donor atoms, while both $[CuL^2Cl](SbF_6)$ and

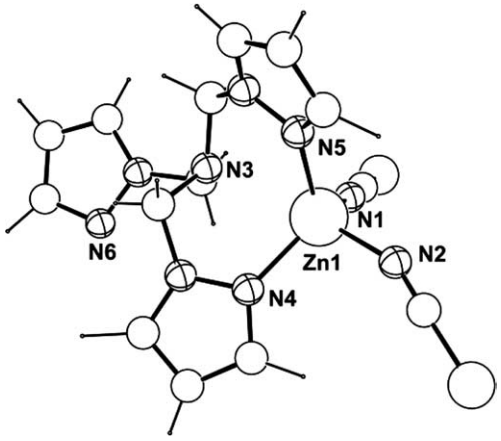
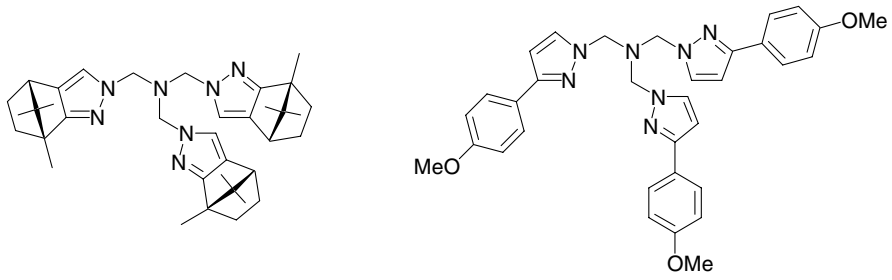


Fig. 12. X-ray structure of $[Zn(amtp)(NCS)_2]$.

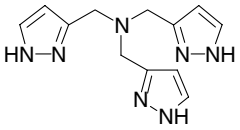


L^1 L^2

Fig. 13. Sterically demanding ligands derived from amtp.

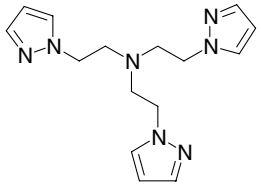
$[CuL^2(OH_2)](SbF_6)_2 \cdot MeOH$ show square pyramidal geometries about the Cu(II) ion ($\tau = 0.16$ and 0.17, respectively). All three complexes are reduced by BPh_4^- to give the $[CuL^2]^+$ ion, and the X-ray structure of $[CuL^2](CuCl_2)$ shows a trigonal pyramidal geometry about the Cu(I) ion in the cation. This complex is unreactive towards both O_2 and CO.

3.2.4. Tris(2-(3-pyrazolyl)methyl)amine (L^3)



The synthesis of this ligand and its 1-methylpyrazolyl and 1-benzylpyrazolyl derivatives from the appropriate 3-pyrazolyl esters was reported in 1985 [132], but there has been no further mention of this ligand in the literature.

3.2.5. Tris(2-(1-pyrazolyl)ethyl)amine (trpyn)

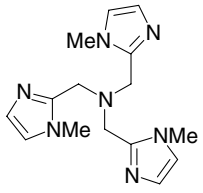


The preparation of the 3,5-dimethylpyrazolyl derivative of trpyn was first reported in 1981 [133,134] while the synthesis of trpyn and its 3,5-di-*t*-butylpyrazolyl derivative was published the following year [135]. The ligands were prepared by the reaction of the appropriate deprotonated pyrazole with tris(2-chloroethyl)amine, and metal complexes of each have been reported. Reaction of all three ligands with $[Cu(MeCN)_4]BF_4$ in MeCN gives the air-stable four-coordinate complexes $[Cu(L)]BF_4$, and the X-ray structure of $[Cu(trpynMe_6)]BF_4$ shows a distorted trigonal pyramidal geometry about the Cu(I) ion with the aliphatic N atom occupying the apical position. In THF solution, the Cu(I) complexes emit in the visible region between 433 and 453 nm on excitation in the UV (255–273 nm), with the excited state lifetimes for these processes being much longer than those found in Cu(I) polypyridyl complexes [136]. Reaction of both trpyn and $trpynMe_6$ with $[Cu(H_2O)_6](BF_4)_2$ in MeOH gives the five-coordinate Cu(II) complexes $[Cu(L)(OH_2)](BF_4)_2$, but the same reaction with $trpynBu_6$ results in isolation of the Cu(I) complex $[Cu(trpynBu_6)](BF_4)_2$ only, and the Cu(II) complex of this ligand cannot be prepared chemically, although cyclic voltammetry experiments show a one-electron oxidation at high potential (+0.94 V vs. SCE) which is chemically reversible only at scan rates of 5 $V\,s^{-1}$ or above [135]. The X-ray structure of $[Cu(trpyn)(OH_2)](BF_4)_2$ shows a distorted square pyramidal geometry about the Cu(II) ion with the aliphatic N atom in the square plane *trans* to the aquo ligand. Reaction of trpyn with hydrated $CuBr_2$ gives the green Cu(II) complex $[Cu(trpyn)Br]_3(CuBr_3)Br \cdot 3H_2O$, which contains three crystallographically non-equivalent $[Cu(trpyn)Br]^+$ moieties. The X-ray structure of this complex shows the three cations adopt distorted square pyramidal structures ($\tau = 0.36$–0.42) with the aliphatic N atom at the apical position [137]. A larger distortion towards trigonal bipyramidal geometry is found in $[Cu(trpyn)(NCS)][Cu(NCS)_2]$ ($\tau = 0.59$), with the tertiary N atom and NCS^- ligand being pseudo axial [138]. Neither $[Cu(trpyn)(OH_2)]^{2+}$ nor $[Cu(trpyn)Cl]^+$ were found to oxidise 3,5-di-*t*-butylcatechol, in contrast to a number of other Cu(II) complexes of tripodal amine ligands containing pyrazole or pyridine donors, and this was ascribed to a combination of both steric and electronic effects [139].

Several Co(II) complexes of trpyn and its 3,5-dimethylpyrazolyl derivative have been prepared. The trpyn complexes [Co(trpyn)X]Y (X = F, Cl, Br, I, NCS, NCO, N_3, ClO_4, acac, bzac, thbz, $(NCS)_2$, Y = BF_4, BPh_4, ClO_4) are five- and six-coordinate [140], but the $trpynMe_6$ ligand gives predominantly the four-coordinate cation $[Co(trpynMe_6)]^{2+}$, with the five coordinate

isothiocyanato complex $[Co(trpynMe_6)(NCS)]BPh_4$ being the only apparent exception [141]. The pink to magenta $[Co(trpyn)X]BPh_4$ complexes (X = F, Cl, Br, N_3) change colour to violet on heating, and the X-ray structure of the magenta form of the bromide complex shows this to be dimeric $[(trpyn)Co(Br)_2Co(trpyn)](BPh_4)_2$ with two bromide ligands bridging the six-coordinate metal ions. Six-coordinate $[Co(trpyn)(Me_2CO)_2](BPh_4)_2$ has also been structurally characterised [142]. The crystal structure of $[Co(trpynMe_6)](BPh_4)_2$ shows a tetrahedrally distorted trigonal pyramidal geometry about the metal ion with the aliphatic N atom in the apical position, and the methyl groups effectively shielding the remaining apical coordination site, thus preventing binding of further ligands [133]. This complex displays an unusual UV–Vis spectrum, with four d–d transitions at very high energy (7000–21,500 cm^{-1}) when compared to those of typical tetrahedral complexes, and this has been ascribed to the high ligand-field strength of the pyrazole donors [143]. In contrast to Co(II), the Ni(II) cations $[Ni(trpynMe_6)L]^{+/2+}$ (L = Cl, Br, NCS, OH_2) are five-coordinate, and yellow and emerald forms of the bromo complexes can be isolated. Crystal structures of yellow $[Ni(trpyn)Br]BPh_4 \cdot C_2H_5OH$ and emerald $[Ni(trpyn)Br]BPh_4 \cdot CH_3COCH_3$ show both cations to be five coordinate, with the yellow isomer displaying a significant distortion towards a trigonal bipyramidal geometry about the metal ion ($\tau = 0.44$) whereas the emerald isomer is essentially square pyramidal ($\tau = 0.12$) [141]. The extremely air-sensitive blue Cr(II) complex $[Cr(trpyn)(NCS)]BPh_4$ can be prepared from in situ-generated $[Cr(NCS)_2]$ in ethanol, and air-oxidation of this gives the green oxo-bridged dimer $[(trpyn)(NCS)Cr(O)Cr(NCS)(trpyn)](BPh_4)_2$ containing an essentially linear (176.5°) Cr–O–Cr bridge which is thought to mediate a strong antiferromagnetic coupling between the Cr ions (μ_{eff} (300 K) = 1.63 μ_B per Cr ion) [144]. A Ru(II) complex containing the trpyn ligand has also been reported [145].

3.2.6. Tris(2-(1-methylimidazolyl)methyl)amine (tmima)



The first reference to tmima in the literature came in 1990 in a study of alkane functionalisation by iron complexes in the presence of H_2O_2 [146] and the synthesis of the ligand was detailed shortly thereafter from the reaction of 1-methyl-2-aminomethylimidazole with two equivalents of 2-chloromethyl-1-methylimidazole [147]. While the free ligand is hygroscopic and cannot be easily crystallised, it can be co-crystallised with boric acid and the crystal structure of this assembly shows the ligand to have approximate three-fold symmetry, with a paddle-wheel-like arrangement of the imidazole rings (Fig. 14) [148].

pK_a values for triprotonated tmima are 4.57, 6.00 and 7.30 [149]. Reaction of tmima with $CuCl_2 \cdot 2H_2O$ in MeOH and addition of $NaPF_6$ gives five-coordinate $[Cu(tmima)Cl]PF_6 \cdot MeCN$ (crystallised from MeOH/MeCN) which adopts a trigonal bipyramidal geometry ($\tau = 0.94$), and reaction of this complex with 1-methylimidazole gives $[Cu(tmima)(1\text{-}Meim)](PF_6)_2$. Electrochemical and UV/vis spectral data for these complexes suggest that the tmima ligand exerts a weaker ligand field than tpa (Section 3.2.9) [147]. Reaction of tmima with anhydrous $FeCl_3$ in ethanol and addition of $NaClO_4$ gives monomeric six-coordinate $[Fe(tmima)Cl_2]ClO_4 \cdot 0.5MeCN$ [150] while dimeric $[(tmima)(OH_2)Fe\text{-}OFe(OH_2)(tmima)](ClO_4)_4$ is obtained on reaction of tmima with $Fe(ClO_4)_3 \cdot 9H_2O$ [151]. The asymmetric dimer $[(temima)Fe(O)(OAc)Fe(tmima)](ClO_4)_3$ (the structure of temima is depicted in Fig. 15) has also been reported [152].

The Mn(III,III) dimer $[(tmima)Mn(O)(OAc)Mn(tmima)](ClO_4)_3 \cdot 2MeCN$ is obtained on reaction of tmima with $Mn(OAc)_3 \cdot 2H_2O$ in ethanol, addition of $NaClO_4$ and crystallisation from MeCN, and the Mn ions in this complex display weak ferromagnetic coupling ($J = 1.33$ cm^{-1}) [153]. Three Hg(II) complexes of tmima, namely eight-coordinate $[Hg(tmima)_2](ClO_4)_2$, five-coordinate $[Hg(tmima)(NCCH_3)](ClO_4)_2$ and five-coordinate $[Hg(tmima)Cl]_2(HgCl_4)$, have been prepared and structurally characterised [154]. The latter complexes display trigonal bipyramidal geometries ($\tau = 1.15$ and 0.85, respectively) and both show Hg–H coupling at −40 °C in CD_3CN. Tmima binds Zn^{2+} strongly as a 1:1 complex in aqueous solution (log $K = 11.98$) and the pK_a for the so formed $[Zn(tmima)(OH_2)]^{2+}$ cation is 8.72 [149].

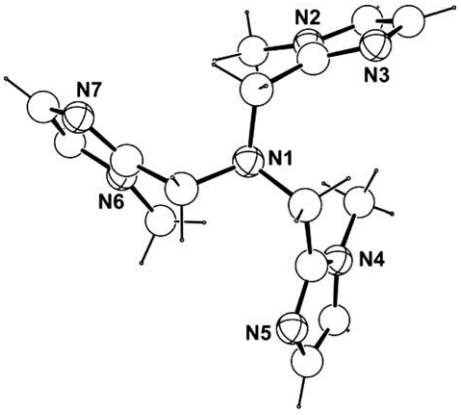
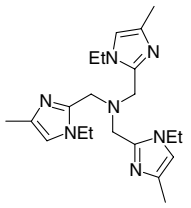


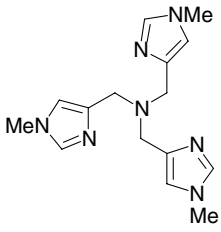
Fig. 14. X-ray structure of the tmima ligand (co-crystallised H_3BO_3 molecule not shown).



38

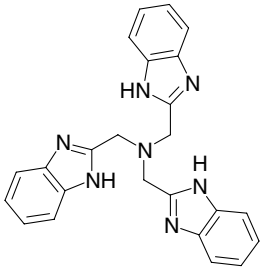
Fig. 15. Structure of the temima ligand.

3.2.7. Tris(4-(1-methylimidazolyl)methyl)amine (T4IA)



This ligand was first reported in 2003, from the reaction of 1-methylimidazole-4-carboxaldehye with ammonium chloride and subsequent hydrogenation (Pd/C) [149]. pK_a values for the triprotonated ligand are 5.26, 5.79 and 8.36. The only complex thus far reported is $[Zn(T4IA)OH_2]^{2+}$ generated in aqueous solution ($\log K = 12.47$), which has a pK_a of 9.11.

3.2.8. Tris(2-benzimidazolylmethyl)amine (ntb)



The benzimidazole derived ligand ntb and its complexes have been studied extensively since the first report of the synthesis of ntb in 1977 [155]. The ligand was originally prepared in over 50% yield by fusion of either nitrilotriacetonitrile or nitrilotriacetic acid with *o*-phenylenediamine at ~200 °C, while a more recent synthesis involves heating a mixture of nitrilotriacetic acid and *o*-phenylenediamine in ethylene glycol at 140–200 °C [156]. Reaction of the appropriately substituted *o*-phenylenediamine with nitrilotriacetic acid also allows synthesis of ntb derivatives having substituents on the benzene ring and both the tris(5,6-dimethyl)-substituted [157] and tris(6-sulfonato)-substituted [158] ntb ligands have been prepared by this route. The free ntb ligand can be crystallised as a monohydrate, and the crystal structure shows the water molecule to sit in the cleft formed by the aliphatic N atom and the three arms of the tripodal ligand, where it is hydrogen-bonded in an approximately tetrahedral fashion to three imidazole N donors of one ligand molecule, and one of a neighbouring molecule [159]. The free ligand also forms a 1:2 inclusion compound with 4-nitrobenzoic acid in which one acid molecule is hydrogen-bonded in the same cleft [160]. The ligand can be deprotonated with potassium, and subsequent reaction with alkylating agents gives the tris-alkylated products. Thus the tris(N-methyl) [161], tris(N-ethyl), tris(benzyl), tris(*o*-methylbenzyl) [162] and tris(N-propyl) [163] derivatives of ntb have been prepared by this method. Ntb can also be selectively alkylated at a benzimidazole N atom and the mono(*N*-carboxymethyl) derivative HAcntb has been reported [164]. Similarly, ntb derivatives having a methyl, isobutyl or isopropyl group in place of a methylene proton on only one of the tripodal arms can be prepared by condensation of *o*-phenylenediamine with an asymmetric nitrilotriacetic acid derivative, which is itself prepared from the reaction of alanine, leucine or valine with two equivalents of chloroacetic acid [165].

The ntb ligand forms predominantly five- and six-coordinate complexes, a significant number of which have been structurally characterised. Table 5 lists the mononuclear five-coordinate complexes of ntb for which X-ray structures are available, and it can be seen that these almost exclusively exhibit trigonal bipyramidal geometries about the metal ion.

The notable exception to this is $[Cu(ntb)Cl]Cl \cdot 3H_2O$ [166] ($\tau = 0.34$) which is distorted square pyramidal with the chloride ligand and three N atoms constituting the square plane (Fig. 16).

τ values slightly greater than unity are obtained for some ntb complexes owing to the fact that the metal ion generally sits slightly below the plane of the three imidazole donor N atoms, and this arrangement results in the bond between the metal ion and the aliphatic N atom usually being significantly longer than those to the imidazole N atoms. In some cases, this results in hypodentate tridentate coordination of the ligand, with binding to the metal ion through the imidazole N atoms only. Examples of this include $[Zn(ntb)(SPh)]BPh_4 \cdot MeCN \cdot 2CH_3OH$ [167] ($Zn–N_{tert} = 2.590$ Å), $[Mn(ntb)Cl]Cl \cdot 2H_2O$ [168] ($Mn–N_{tert} = 2.483$, 2.498 Å), $[Mn(ntb)Cl]Cl \cdot 2CH_3OH \cdot 0.5H_2O$ [169] ($Mn–N_{tert} = 2.502, 2.519$ Å), $[Mn(ntb)(sal)]ClO_4$ [170] ($Mn–N_{tert} = 2.507$ Å), [Mn(ntb)(terephthalate)]$0.5CH_3OH \cdot 0.5H_2O \cdot DMF$ [171] ($Mn–N_{tert} = 2.526$ Å) and $[Mn(ntb)Cl][Mn(ntb)Cl_2]Cl \cdot EtOH \cdot 3H_2O$ [172] ($Mn–N_{tert} = 2.516$ Å). The latter complex contains both four- and five-coordinate cations in which the metal ion is formally not bound to the tertiary N atom. $[Cu(ntb)(PPh_3)]NO_3 \cdot 1.5H_2O$ provides a crystallographically characterised example of a hypodentate ntb com-

Table 5
Structurally characterised monomeric five-coordinate $[M(ntb)X]^{n+}$ complexes

M	X	τ	References
Co^{2+}	ClO_4^-	0.92	[354]
Co^{2+}	Cl^-	1.03, 1.00[a]	[355]
Co^{2+}	Cl^-	1.02	[356]
Co^{2+}	OH_2	1.08	[357]
Co^{2+}	NCS^-	0.81	[358]
Co^{2+}	NCS^-	0.97	[358]
Cu^{2+}	Cl^-	0.34	[166]
Cu^{2+}	imidazole	0.55	[359]
Cu^{2+}	imidazole	0.55	[360]
Zn^{2+}	N_3^-	0.99, 0.96[a]	[361]
Zn^{2+}	NCS^-	1.04, 0.98[a]	[361]
Zn^{2+}	Cl^-	0.94	[362]
Zn^{2+}	Cl^-	1.01	[363]
Zn^{2+}	Cl^-	1.06	[364]
Zn^{2+}	OH_2	1.08	[357]
Zn^{2+}	OH_2	0.88	[365]
Zn^{2+}	$C_6H_5COO^-$	0.82	[366]
Zn^{2+}	$(p\text{-}CH_3C_6H_4)P_2O_7^{2-}$	0.93, 0.90[a]	[367]
Zn^{2+}	$(p\text{-}ClC_6H_4)_2P_2O_7^{2-}$	0.97	[367]
Zn^{2+}	salicylate	0.88	[368]
Zn^{2+}	NCS^-	1.02	[369]
Hg^{2+}	Cl^-	1.06	[363]

[a] More than one independent molecule in the asymmetric unit.

plex in which one of the benzimidazole arms is not coordinated to the metal centre, presumably due to the steric bulk of the PPh_3 ligand [166].

Complexes of ntb with the first row transition metals from V–Zn and some second and third row transition metals have been reported. Of particular note are the complexes $[Cd(ntb)X]^+$ (X = Cl^-, Br^-, I^-, CN^-, PhS^-, L-cysteinate) which, unusually, display slow exchange ^{113}Cd NMR spectra in d^6-Me_2SO solution [173]. A number of lanthanide and actinide complexes of ntb have also been synthesised and studied. The eight-coordinate lanthanide complexes have the stoichiometry $[Ln(ntb)_2]^{3+}$ (Ln = Eu, Pr, Tb, La, Nd, Lu) [174–177] when prepared by reaction of the metal perchlorate with the ligand, even in the presence of excess metal ion, and this has been ascribed to strong intramolecular π–π interactions between the two ntb ligands both in the solid state and in solution (Fig. 17) [176].

Reaction of $LuCl_3 \cdot 6H_2O$ with 2 equivalents of ntb also gives the bis ligand cation $[Lu(ntb)_2]^{3+}$, but reaction of a number of lanthanide nitrates with ntb in a 1:1 ratio gives ten-coordinate $[Ln(ntb)(O_2NO)_3] \cdot H_2O$ complexes (Ln = La, Ce, Nd, Sm, Eu, Gd, Tb, Dy, Er) which undergo dissociation of the ntb ligand in DMSO solution [178]. The U(III) bis ligand complex $[U(ntb)_2]I_3$ can also

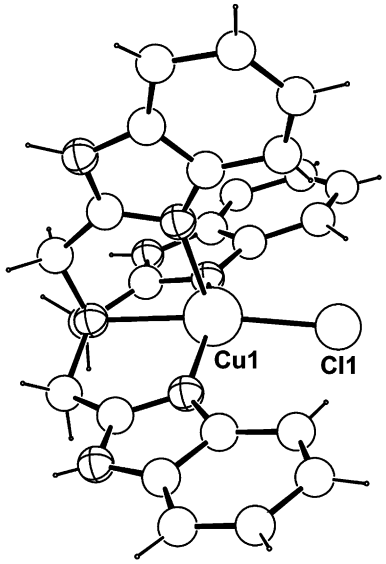


Fig. 16. X-ray structure of the $[Cu(ntb)Cl]^+$ cation.

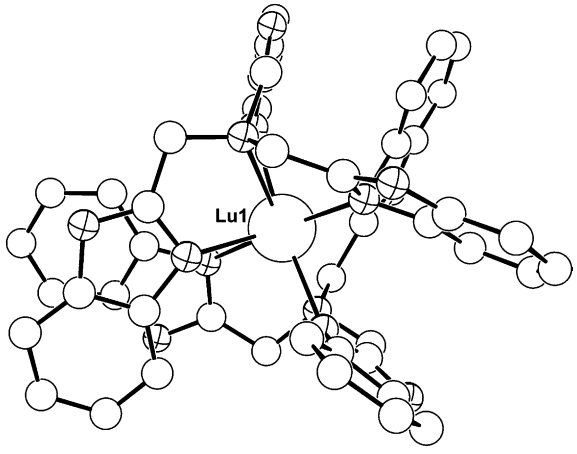
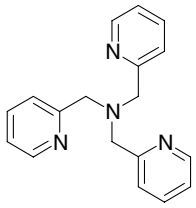


Fig. 17. View of the $[Lu(ntb)_2]^{3+}$ cation emphasising the π–π interactions between the ntb ligands.

be prepared from reaction of $[UI_3(THF)_4]$ with two equivalents of ntb [174]. The ntb ligand and its N-alkylated derivatives display a rich coordination chemistry with Ag(I), with mono-, di-, tri- and tetranuclear complexes having been reported. Thus reaction of $AgCF_3SO_3$ with ntb in a 3:2 molar ratio gives the trinuclear complex $[Ag_3(ntb)_2](CF_3SO_3)_3$ [179] while reaction of $AgCF_3CO_2$ with ntb in a 2:1 molar ratio gives tetranuclear $[Ag_4(ntb)_2(CF_3CO_2)_2(MeCN)_2](CF_3CO_2)_2 \cdot 2H_2O$ [163]. The sodium salt of the HAcntb ligand (vide supra) reacts with $Cu(ClO_4)_2 \cdot 6H_2O$ to give the hexameric cation $[Cu_6(Acntb)_6]^{6+}$, the perchlorate salt of which crystallises to give a nanoporous network containing large octahedral voids [164].

3.2.9. Tris(2-pyridylmethyl)amine (tpa, tmpa)



Tpa was first prepared by Anderegg and Wenk in 1967 from the reaction of 2-(aminomethyl)pyridine with two equivalents of 2-(chloromethyl)pyridine in aqueous solution [180] and this, or slight modifications thereof, appears to be the method of choice for the synthesis of this ligand to the present day [181]. Derivatives of tpa substituted on either the pyridine rings or at a methylene carbon can be prepared by adaptation of this method and use of the appropriately substituted starting materials. Particular interest has centred on the synthesis of tpa derivatives having substituents at the 6-positions of the pyridyl rings and the ligands of this type that have been prepared are detailed in Table 6.

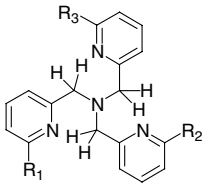
While the free base of tpa is an oil, the triprotonated ligand has been crystallographically characterised as the $\cdot 3HClO_4$ [182], $\cdot (SO_4)(NO_3)$ [183], $\cdot (CF_3SO_3)_2(PF_6)$, $\cdot (Br)(PF_6)_2$ and $\cdot (Cl)(PF_6)_2$ [184] salts, and in all cases, the ligand adopts a similar conformation to that which obtains when it coordinates to a metal ion, with the three protonated N atoms positioned to form a cleft into which the anion is hydrogen-bonded. The pK_a values for the triprotonated ligand have been measured in a number of studies, with values of 2.55, 4.35 and 6.17 (20 °C, 0.1 M KNO_3) [180,185] and 2.73, 4.49 and 6.28 (25 °C, 0.1 M $NaClO_4$) [186] having been measured by potentiometric titration. Observation of peaks over the range chemical shift range $\delta = 200$–300 ppm in ^{14}N and ^{15}N NMR studies of the protonation of tpa in both MeOH and 1 M HNO_3 confirm the pyridine N atoms as the most basic in the molecule, with the failure to observe a signal for the aliphatic N atom even at high acidity being ascribed to the long relaxation times typical of unprotonated N atoms [187].

Tpa is one of the two most studied tripodal tetradentate amine ligands (tren being the other), with complexes of all first row metals except Ti having been reported, along with most second and third row metals, as well as the majority of lanthanide ions. Formation constants for the formation of 1:1 $[M(tpa)]^{n+}$ complexes with a number of metal ions have been measured, and these are given in Table 7.

Various 1:2 $[M(tpa)_2]^{n+}$ complexes have also been prepared and a study of these has shown that the ionic radius of the metal ion is crucial in determining the stoichiometry of the complexes obtained from the reaction of the metal ion with tpa, with 1:2 complexes being formed for metal ions having ionic radii greater than 0.9 Å, while smaller ions give 1:1 complexes [183]. There are no crystallographically characterised examples of four-coordinate transition metal complexes of the type $[M(tpa)]^{n+}$, although the thallium complex $[Tl(tpa)]_2(H_3O)(NO_3)_3$ has been shown to contain a $[Tl(tpa)]^+$ cation [188]. Monomeric five-coordinate complexes containing tetradentate tpa are relatively common, and those that have been structurally characterised are listed in Table 8.

These complexes display, without exception, trigonal bipyramidal geometries in which the aliphatic N atom occupies an axial site, with the smallest τ value being 0.74. Numerous six-coordinate complexes have been structurally characterised, while $[Cd(tpa)(O_2NO)OH_2](NO_3) \cdot 3H_2O$ (seven-coordinate) [189], $[Fe(tpa)_2](BPh_4)_2$ [190], $[Hg(tpa)_2](ClO_4)_2$ [191], $[Cd(tpa)_2](ClO_4)_2 \cdot C_7H_8$ [192], $[La(tpa)(py)(I)_3]$ [174] and $[Mn(tpa)_2](ClO_4)_2$ [193] (eight coordinate) providing examples of structurally characterised high coordinate tpa complexes. Iron complexes of tpa have received particular attention, most notably due to their reactivity in alkane hydroxylation reactions [194]. Thus, complexes such as $[Fe(tpa)Cl_2]ClO_4$ [195], $[Fe(tpa)Br_2]ClO_4$ [196], $[Fe_2O(OAc)(tpa)_2](ClO_4)_3$ [197] and $[Fe_2O(tpa)_2(H_2O)_2](CF_3SO_3)_4$ [198] have been found to catalyse alkane functionalisation reactions in the presence of *t*-BuOOH, purportedly via a mechanism involving production of a high valent Fe(IV)-oxo species, although an alternative mechanism involving H-atom abstraction by hydroperoxide-derived alkoxyl radicals has also been proposed [199,200]. However, the reaction of $[Fe(tpa)(MeCN)_2]^{2+}$ with one equivalent of peracetic acid in MeCN at −40 °C has recently been shown to give the pale green Fe(IV) complex $[Fe(O)(tpa)]^{2+}$, which is stable for several days at −40 °C, and which was characterised by ES-MS, Mössbauer spectroscopy, XANES and EXAFS spectroscopy [201], thus demonstrating that high valent oxo species can indeed be accessed in Fe/tpa systems. Reaction of $Fe(CF_3SO_3)_2 \cdot 2MeCN$ with tpa in a variety of solvents affords a

Table 6
Known 6-substituted tpa derivatives



R_1	R_2	R_3	References
F	F	F	[370]
Br	Br	Br	[371]
NH_2	NH_2	NH_2	[372]
NH–CH_2–CMe_3	NH–CH_2–CMe_3	NH–CH_2–CMe_3	[373]
NH–C(O)–CMe_3	NH–C(O)–CMe_3	NH–C(O)–CMe_3	[374]
COOH	COOH	COOH	[375]
$C(O)NEt_2$	$C(O)NEt_2$	$C(O)NEt_2$	[375]
CH_2OH	CH_2OH	CH_2OH	[376]
(4-$OCH_2OCH_2CH_2OMe)C_6H_4$	(4-$OCH_2OCH_2CH_2OMe)C_6H_4$	(4-$OCH_2OCH_2CH_2OMe)C_6H_4$	[371]
C_6H_5	C_6H_5	C_6H_5	[377]
Me	Me	Me	[378]
Br	Br	Cl	[371]
Me	Me	C_6H_5	[379]
Me	Me	CH_2-OH	[380]
NH_2	NH_2	H	[186]
3,5-$Me_2C_6H_3$	3,5-$Me_2C_6H_3$	H	[381]
NH–CH_2–CMe_3	NH–CH_2–CMe_3	H	[382]
NH–C(O)–(2-$C_{10}H_7$)	NH–C(O)–(2-$C_{10}H_7$)	H	[383]
CH_2OH	CH_2OH	H	[376]
NH–C(O)–CMe_3	NH–C(O)–CMe_3	H	[384]
Br	Br	H	[371]
C_6H_5	C_6H_5	H	[385]
Me	Me	H	[378]
NH_2	H	H	[386]
C_6H_4(2-NH-SO_2-(4-MeC_6H_4))	H	H	[387]
2,5-$(HO)_2C_6H_3$	H	H	[388]
2,5-$(O$-(2-$C_5H_9O))_2C_6H_3$	H	H	[388]
2,5-$(MeO)_2C_6H_3$	H	H	[388]
2-HOC_6H_4	H	H	[379]
2-DC_6H_4	H	H	[379]
3-(OMe)C_6H_4	H	H	[379]
3-MeC_6H_4	H	H	[379]
3-ClC_6H_4	H	H	[379]
3-$F_3CC_6H_4$	H	H	[379]
3-$O_2NC_6H_4$	H	H	[379]
4-$OMeC_6H_4$	H	H	[389]
NH–CH_2CMe_3	H	H	[382]
NH–$C(O)CMe_3$	H	H	[382]
CH_2Cl	H	H	[376]
CHO	H	H	[376]
CH_2OH	H	H	[376]
(4-$OCH_2OCH_2CH_2OMe)C_6H_4$	H	H	[371]
Cl	H	H	[371]
Br	H	H	[371]
4-(benzo-18-crown-6)	H	H	[371]
C_6H_5	H	H	[385]
Me	H	H	[264]

range of products having different stoichiometries, coordination numbers and spin states. Reaction with one equivalent of tpa in MeCN gives low-spin [Fe(tpa)-$(MeCN)_2$]$(CF_3SO_3)_2$ but dissolution of this complex in $CHCl_3$ and addition of pentane gives high-spin [Fe(tpa)-$(OSO_2CF_3)_2$]. Reaction of $Fe(CF_3SO_3)_2 \cdot 2MeCN$ with two equivalents of tpa in MeOH gives eight-coordinate $[Fe(tpa)_2](BPh_4)_2$ (Fig. 18) on addition of $NaBPh_4$,

Table 7
Formation constants for the reaction $M^{n+}(aq) + tpa \rightleftharpoons [M(tpa)]^{n+}(aq)$

M	log *K*	Conditions	References
Zn^{2+}	11.06	H_2O, 25 °C, I = 0.1 M ($NaClO_4$)	[186]
	11.00	H_2O, 20 °C, I = 0.1 M (KNO_3)	[185]
Mn^{2+}	5.62	H_2O, 20 °C, I = 0.1 M (KNO_3)	[185]
Fe^{2+}	8.65	H_2O, 20 °C, I = 0.1 M (KNO_3)	[185]
Co^{2+}	11.38	H_2O, 20 °C, I = 0.1 M (KNO_3)	[185]
Ni^{2+}	14.60	H_2O, 20 °C, I = 0.1 M (KNO_3)	[185]
Cu^{2+}	16.15	H_2O, 20 °C, I = 0.1 M (KNO_3)	[185]
Cd^{2+}	9.9	H_2O, 20 °C, I = 0.1 M (KNO_3)	[185]
Pb^{2+}	8.58	H_2O, 20 °C, I = 0.1 M (KNO_3)	[185]
Ag^{+}	7.92	H_2O, 20 °C, I = 0.1 M (KNO_3)	[185]
Hg^{2+}	17.15	H_2O, 20 °C, I = 0.1 M (KNO_3)	[185]
Na^{+}	3.41	MeCN, 25 °C, I = 0.1 M (NEt_4ClO_4)	[390]

Table 8
Structurally characterised monomeric five-coordinate $[M(tpa)X]^{n+}$ complexes

M	X	τ	References
Cu^{2+}	CN^-	0.94	[213]
Cu^{2+}	Cl^-	1.00	[202]
Cu^{2+}	Cl^-	0.90	[391]
Cu^{2+}	MeCN	0.96	[209]
Cu^{+}	MeCN	1.03	[209]
Co^{2+}	Cl^-	1.00, 1.05, 1.01[a]	[392]
Cu^{2+}	F^-	0.92	[204]
Co^{2+}	Cl^-	1.01, 1.05[a]	[393]
Zn^{2+}	Cl^-	0.93	[229]
Zn^{2+}	$C_6H_5COO^-$	0.90	[229]
Cu^{2+}	$C_6H_5C(O)COO^-$	0.78	[394]
Cu^{2+}	OH_2	0.97	[395]
Hg^{2+}	Cl^-	1.05, 1.01[a]	[191]
Co^{2+}	MeCN	0.99	[396]
Cu^{2+}	ONO^-	0.74	[397]
Zn^{2+}	$(p\text{-}NO_2C_6H_4O)_2PO_2^-$	0.84	[230]
Cu^{2+}	CN^-	0.96, 0.95[a]	[205]
Fe^{2+}	2,4,6-$Me_3C_6H_2S^-$	0.90	[398]
Cu^{2+}	NO_2^-	0.99	[397]
Zn^{2+}	Cl^-	0.99, 0.94[a]	[189]
Zn^{2+}	I^-	0.99, 0.99[a]	[189]
Cu^{2+}	Br^-	0.95, 0.90[a]	[189]

[a] More than one independent molecule in the aysmmetric unit.

while the same reaction in acetone in the absence of $NaBPh_4$ gives $[Fe(tpa)_2](CF_3SO_3)_2$ which contains six-coordinate Fe(II), with one arm of each ligand remaining uncoordinated to the metal centre (Fig. 19) [190].

Reaction of $CuCl_2$ with tpa in MeOH and subsequent addition of $NaPF_6$ gives $[Cu(tpa)Cl]PF_6$ [202] while addition of the ligand to $[Cu(MeCN)_4]X$ (X = ClO_4, PF_6) in MeCN under argon gives [Cu(tpa)(MeCN)]X [203]. $[Cu(tpa)(MeCN)]PF_6$ is extremely reactive towards O_2 at −85 °C, initially giving a transient monomeric superoxo complex which then reacts further to give the peroxo-bridged dimer $[(tpa)Cu(O_2)Cu(tpa)](PF_6)_2 \cdot 5Et_2O$ which has been structurally characterised. The same reaction at room temperature gives a mixture of the fluoride-bridged dimer $[Cu(tpa)F]_2(PF_6)_2$ and monomeric $[Cu(tpa)F](PF_6)_2 \cdot CH_2Cl_2$, with the coordi-

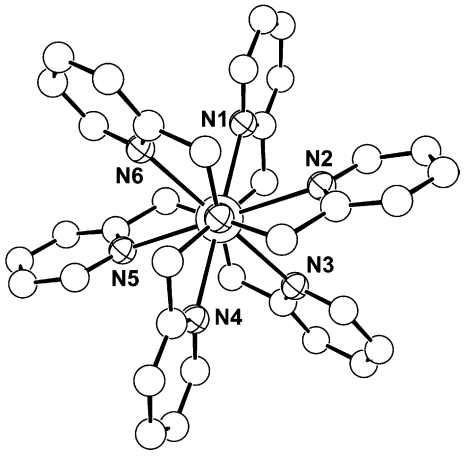


Fig. 18. Eight coordinate Fe(II) in the cation of $[Fe(tpa)_2](BPh_4)_2$, viewed down the N_{tert}–Fe–N_{tert} axis.

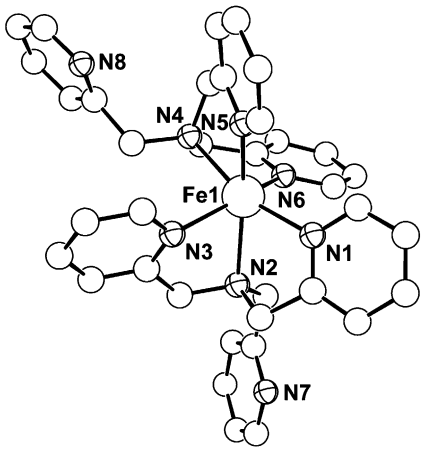


Fig. 19. Six-coordinate Fe(II) in the cation of $[Fe(tpa)_2](CF_3SO_3)_2$.

nated fluoride ligands being derived from the PF_6^- counterion [204]. $[Cu(tpa)(MeCN)]PF_6$ also reacts with PPh_3 to give the four coordinate complex $[Cu(tpa)(PPh_3)]PF_6$, which contains hypodentate tridentate tpa, presumably due to the steric bulk of the PPh_3 ligand. A number of polynuclear complexes containing multiple $[Cu(tpa)]^{n+}$ units have been prepared. In addition to the peroxo- and bis(fluoro)-bridged dimers mentioned above, dimeric $[(tpa)CuCNCu(tpa)](ClO_4)_3$ [205,206], $[(tpa)Cu(S_2)Cu(tpa)](ClO_4)_2 \cdot 3Et_2O$ [207], $[(tpa)Cu(\mu_2\text{-}CO_3)Cu(tpa)](ClO_4)_2 \cdot 2EtCN$ [208] and $[(tpa)CuCNCu(tpa)]ClO_4$ [209] have been reported; the latter features two tridentate tpa ligands, in keeping with the preference of Cu(I) for four-coordination. The tricopper complexes $[(tpaCu)_3(\mu_3\text{-}CO_3)](ClO_4)_4$ [210], containing a triply-bridging carbonate ligand, and $[(tpaCu)_3(\mu_3\text{-}1,3,5\text{-benzenetricarboxylate})](ClO_4)_3 \cdot 4H_2O$ are also known [211]. The trinuclear complex $[((tpa)Cu(NC))_2Fe(CN)_4]ClO_4 \cdot 6H_2O$ [212], in which the two Cu(tpa) units are situated *trans* with respect to the octahedral Fe centre, and the related complex $[(tpa)Cu(\mu\text{-}NC)(F_8\text{-}TPPFe)(\mu\text{-}CN)Cu(tpa)](PF_6)_3 \cdot 4CH_2Cl_2$ [213], which contains two $[Cu(tpa)NC]^+$ units coordinated in the *trans* axial positions of an iron porphyrin, have also been structurally characterised. The heptanuclear complex $[Fe((CN)Cu(tpa))_6](ClO_4)_8 \cdot 3H_2O$ is prepared by reaction of $K_3[Fe(CN)_6]$ with six equivalents of $[Cu(tpa)(OH_2)](ClO_4)_2$ in water, while reaction of $[Cu_6((PhSiO_2)_6)_2(n\text{BuOH})_{6-x}(H_2O)_x]$ with $[Cu(tpa)(CN)]PF_6$ gives the decacopper complex $[Cu_6((PhSiO_2)_6)_2(NCCu(tpa))_4](PF_6)_4$ [214].

The chemistry of tpa with chromium is dominated by dimeric species, and monomeric complexes are relatively rare. Reaction of $CrCl_2$ with one equivalent of tpa in THF gives $[Cr(tpa)Cl_2]$, while treatment of $[Cr(THF)_3Cl_3]$ with one equivalent each of tpa and $NaBPh_4$ in THF gives $[Cr(tpa)Cl_2]BPh_4$ [215]. The Cr(II) complex is tetragonally distorted, with the axial Cr–N and Cr–Cl bond distances significantly longer than their equatorial counterparts, and magnetic measurements confirm the high-spin nature of the metal ion which gives rise to this Jahn–Teller distortion. Reaction of the Cr(III) complex with the appropriate Grignard reagent gives the cationic Cr(III) alkyl species $[Cr(tpa)(Me)_2]BPh_4$ and $[Cr(tpa)(Ph)_2]BPh_4$, and all the complexes studied were found to be active catalysts for the polymerisation of ethene in the presence of MAO. Routes to other monomeric Cr/tpa complexes often utilise cleavage of dimeric Cr(III) species, which are themselves generally obtained from treatment of a Cr(II) salt with tpa and subsequent air oxidation, or reaction of the ligand with a Cr(III) salt. Thus the dihydroxy-bridged dimer $[(tpa)Cr(OH)_2Cr(tpa)](ClO_4)_4 \cdot 4H_2O$ results from treatment of aqueous $Cr(ClO_4)_2$ with tpa in EtOH and subsequent air oxidation, and can also be prepared by reaction of $tpa \cdot 3HClO_4$ with $Cr(NO_3)_3 \cdot 9H_2O$ [216]. Treatment of this with a twenty-fold excess of NaSCN gives the linear μ-oxo dimer $[(tpa)(NCS)CrOCr(NCS)(tpa)](ClO_4)_2 \cdot 0.5H_2O$ [217,218]. Other dimeric species to have been structurally characterised are $[(tpa)Cr(\mu\text{-}O)(\mu\text{-}CO_3)Cr(tpa)](ClO_4)_2 \cdot 2H_2O$ [219], $[(tpa)Cr(\mu\text{-}Cl)_2Cr(tpa)]X_2$ ($X = BPh_4$, $BAr^F{}_4$) [215] and $[(tpa)Cr(\mu\text{-}O)(\mu\text{-}CH_3CO_2)Cr(tpa)](ClO_4)_3 \cdot 0.7H_2O$ [220], while the tetranuclear malonate ($n = 1$) and succinate ($n = 2$) complexes $[(\mu\text{-}O_2C(CH_2)_nCO_2)(tpa)Cr(\mu\text{-}O)Cr(tpa)_2](ClO_4)_6 \cdot 4H_2O$ have also been isolated [221]. Monomeric Ru(II) and Ru(III) complexes of tpa have been investigated as catalysts for the *m*-CPBA-mediated functionalisation of various alkanes [222,223], and it is of note that the two geometric isomers of $[Ru(tpa)(Me_2SO)Cl]^+$ show different catalytic activities in the reaction with adamantane. Mono-oxo ruthenium species have been suggested to be the active agents in such reactions. The crystal structure of $[Ru(tpa)(bipy)](PF_6)_2$ indicates steric congestion manifested by elongated Ru–N bond distances, and NMR studies in CD_3CN show this complex relieves the steric strain by undergoing thermal dissociation of one arm of the tpa ligand to give the hypodentate complex $[Ru(tpa)(bipy)(NCCD_3)]^{2+}$. This reaction can also be initiated by photoirradiation and was found to be reversible under these conditions [224].

Rhodium alkene complexes of tpa have been found to react with oxidants such as H_2O_2 and O_2 to give unusual metallacyclic products. For example, while the Rh(I) complex $[Rh(tpa)(CH_2CH_2)]BPh_4$ is oxidised by air in solution to give unidentified products, reaction of the solid complex with air leads to the formation of only one of two possible isomeric 3-rhoda-1,2-dioxolanes (Fig. 20), whereas the PF_6^- salt gives a 1:1 mixture of both isomers [225]. The analogous Ir complex reacts similarly. $[Rh(tpa)(CH_2CH_2)]^+$ is also oxidised by H_2O_2 to give the rhodaoxetane [226,227].

Given the extensive chemistry of Co(III) with tren, it is remarkable that there have been so few Co(III)

complexes of tpa reported. Of these very few, the most interesting are the complexes $[Co(tpa)(CH_2NH_2)](ClO_4)_2$ and $[Co(tpa)(CH_2NHMe)](ClO_4)_2 \cdot H_2O$ containing three-membered metallacycles, which are prepared by photolysis of the amino acid chelates $[Co(tpa)(AA)]^{2+}$ (AA = gly, sar), respectively [228]. Mono- [189,229, 230], di- [229,231–233] and trinuclear (Fig. 21) [210, 231] Zn complexes of tpa have been structurally characterised, and nickel tpa complexes also exhibit a variety of nuclearities.

A variety of bridging ligands have been found in structurally characterised complexes containing the dimeric cations $[(tpa)Ni(\mu\text{-}X)_2Ni(tpa)]^{2+}$ (X = OH [234–236], Cl [237,238], Br [239], $O_2P(OPh)_2$ [240]) and the X-ray structures of analogous dimers containing the bidentate bridging ligands CO_3^{2} [234] and $C_2O_4^{2}$ [241] have also been reported. The tpa ligand can stabilise Re in both low and high oxidation states, with the Re(I) and Re(II) dinitrogen complexes $[Re(tpa)(PPh_3)(N_2)](CF_3SO_3)$ and $[Re(tpa)(PPh_3)(N_2)](CF_3SO_3)_2$ [242], and the Re(VII) oxo complex $[Re(O)_3(tpa)]PF_6$ [243] having been structurally characterised. X-ray structures of the Re(V)-oxo complexes $[Re(tpa)(O)L]PF_6$ (L = chelated 2-amidophenolate, catecholate, 1,2-ethanediolate) show hypodentate tridentate coordination of the tpa ligand, while it is tetradentate in the analogous complex $[Re(tpa)(O)(OMe)](PF_6)_2$, which contains a monodentate methanoate ligand [243,244]. Oxo-complexes are also found in vanadium complexes of tpa, with the (IV/V) mixed-valence oxo-bridged dimer $[(tpa)(O)VOV(O)(tpa)](ClO_4)_3 \cdot MeCN$ being notable amongst these [245], while the mixed valence manganese (III,IV) dimer $[(tpa)Mn(\mu\text{-}O)_2Mn(tpa)](S_2O_6)_{1.5} \cdot 7H_2O$ has also been structurally characterised [246]. Reaction of $LnCl_3 \cdot 6H_2O$ with one equivalent of tpa in MeOH gives seven- or eight-coordinate $[Ln(tpa)(MeOH)_nCl_3]$ species (n = 0 for Eu, Tb, Lu, n = 1 for La, Nd), and X-ray structures of the Eu, Tb and Lu complexes are available [247].

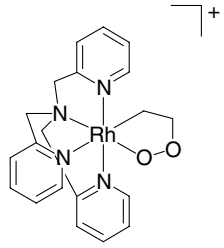


Fig. 20. The dioxolone obtained from air oxidation of solid $[Rh(tpa)(CH_2CH_2)]BPh_4$.

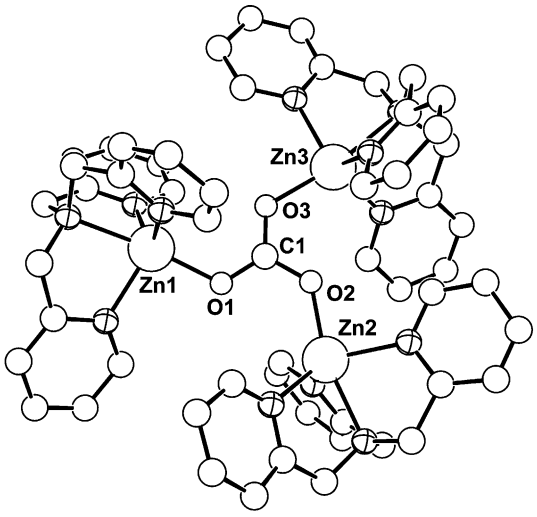
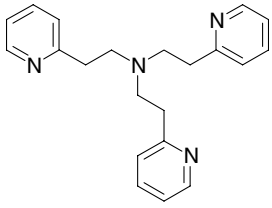


Fig. 21. X-ray structure of the trinuclear $[(tpaZn)_3(\mu_3\text{-}CO_3)]^{4+}$ cation.

3.2.10. Tris(2-(2-pyridyl)ethyl)amine (tepa)



Tepa was first reported by Karlin and coworkers in 1982, from the reaction of 2-vinylpyridine with ammonium acetate in methanol [248], and although another partial synthesis was subsequently reported [249], a detailed synthesis of the ligand was not published until 1994 [250]. Two further syntheses have since been reported [139,251], and the ligand can also be isolated as the mono(hydrogenperchlorate) [251] and tetrahydrochloride [250] salts. The crystal structure of the former (Fig. 22) shows the proton to reside on the aliphatic N atom, which is presumably the most basic centre in the free base ligand [251]. This is in contrast to the aliphatic tripodal tetraamine ligands, where this N atom is the least basic centre, and indeed cannot be protonated in some instances. Measured pK_a values for tepa in aqueous solution (25.0 °C, I = 0.10) are 8.21, 3.94, 3.51 and <2 [252].

The majority of investigations into the coordination chemistry of the tepa ligand have involved complexes of Cu(I) and Cu(II), owing to the importance of such complexes as possible models for the active sites of various copper-containing metalloproteins. Reaction of tepa with cupric nitrate in MeOH and subsequent addition of $NaBPh_4$ gives the four-coordinate Cu(I) complex $[Cu(tepa)]BPh_4$ in which the metal ion adopts a distorted tetrahedral geometry, while Cu(II) complexes of tepa are almost exclusively five-coordinate. The crystallographically characterised five-coordinate complexes $[Cu(tepa)(ONO_2)]NO_3$ [253], $[Cu(tepa)Cl]PF_6 \cdot CH_2Cl_2$

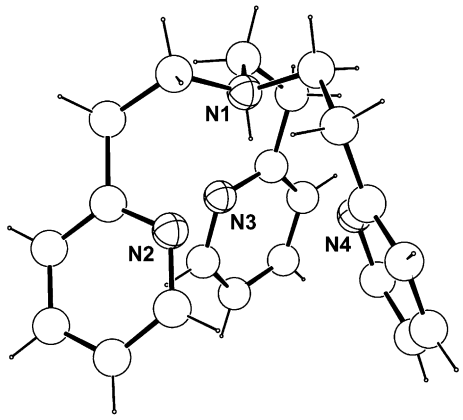


Fig. 22. X-ray structure of the monoprotonated tepa cation in tepa · $HClO_4$.

[202], [Cu(tepa)(OH_2)](CF_3SO_3)$_2$ · H_2O [254] and [Cu(tepa)($OC(O)CH_3$)]PF_6 [254] all display approximate square pyramidal geometries about the metal ion (τ values of 0.07, 0.19, 0.12 and 0.04, respectively), with a pyridyl N atom occupying the apical site, while the 1-methylimidazole complex [Cu(tepa)(1-Meim)](PF_6)$_2$ lies exactly halfway between square pyramidal and trigonal bipyramidal geometry ($\tau = 0.50$) [248]. The six-coordinate complex [Cu(tepa)(ONO)]PF_6 contains an asymmetrically chelated nitrite ligand with one short (2.012 Å) and one long (2.633 Å) Cu–N bond and a resulting distorted octahedral geometry about the Cu ion [255]. Rate data for the reaction of both free base and monoprotonated tepa with $[Cu(H_2O)_6]^{2+}$ in aqueous solution suggest that initial Cu–N bond formation with a pyridyl nitrogen atom is probably rate-determining in the case of the free base ligand, whereas the monoprotonated ligand reacts such that proton loss from the tertiary N atom following initial coordination of a pyridine nitrogen atom becomes rate determining [256]. Despite the aforementioned rationale for the synthesis of Cu/tepa complexes, the oxygen chemistry of such species is virtually non-existent. $[Cu(tepa)]^+$ is unreactive towards dioxygen in both acetone and propionitrile solution [251] which is surprising given the measured reduction potentials for the $[Cu(tepa)]^{2+/+}$ couple of 0.51 V [252] and 0.315 V [257] obtained in two separate studies, although these values do refer to aqueous solution. Stopped flow studies of the reaction of [Cu(tepa)(ClO_4)]ClO_4 with H_2O_2 in MeOH at −90 °C have given evidence for the formation of a Cu^{II}-hydroperoxo intermediate which rapidly decays to give $[Cu(tepa)]^+$ [258].

Few other transition metal complexes containing tepa have been reported. Four-coordinate [Zn(tepa)](ClO_4)$_2$ displays a distorted tetrahedral geometry about the metal ion [259] and a very similar overall structure to [Cu(tepa)]BPh_4. The Co(III) complex [Co(tepa)(O_2CO)]ClO_4 can be protonated in aqueous solution to give the structurally characterised complex [Co(tepa)O_2COH](ClO_4)$_2$ · $3H_2O$ which contains a rare example of chelated bicarbonate [260]. Interestingly, [Co(tepa)(O_2CO)]ClO_4 cannot be prepared by air oxidation of a Co(II) precursor in the presence of the ligand, and PbO_2 must be used as the oxidant in this reaction. ^1H and ^{13}C NMR data show that tepa forms an adduct with Li^+ but not with Na^+ in D_2O and deuterioacetone [250], while qualitative ESI-MS experiments suggest that tepa binds Li^+ with high selectivity in MeOH/H_2O mixtures containing equimolar Li^+, Na^+, K^+, Rb^+ and Cs^+. No peaks corresponding to K^+, Rb^+ or Cs^+ binding were observed, and the Li/Na selectivity was 10:1, compared to 8:1 found for tpa [261]. [Ru(tepa)Cl_2]Cl has been prepared by reaction of K_2[Ru(H_2O)Cl_5] with tepa in refluxing ethanol. Treatment of this with silver *p*-toluenesulfonate and subsequent addition of H_2O_2 and NaClO_4 results in the formation of [Ru(N_4O)(OH_2)](ClO_4)$_2$ (Fig. 23), in which C–H bond activation at the methylene carbon adjacent to the pyridyl ring of one arm of the tripodal ligand has occurred to give the formally pentadentate N_4O ligand [249,262]. Remarkably, the same reaction occurs in the absence of H_2O_2, indicating the possible involvement of the Ru(III) centre in the oxidation process. Treatment of [Ru(N_4O)(H_2O)](ClO_4)$_2$ with $(NH_4)_2$[Ce(NO_3)$_6$] in cold water gives the Ru(V)-oxo complex [Ru(N_4O)O](ClO_4)$_2$ which exhibits a strong Ru=O stretch at 872 cm^{-1} in its IR spectrum. This complex is stable for several days in the solid state at 0 °C and is found to oxidise a wide variety of organic substrates in good yield. Its oxidising strength is attested to by the fact that it can oxidise chloride ion to molecular chlorine.

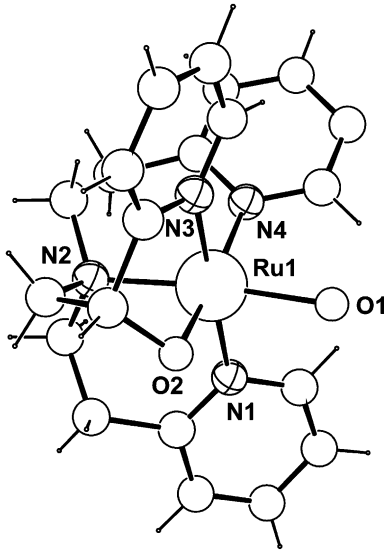
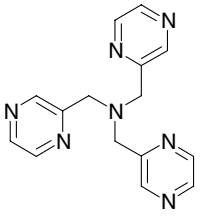


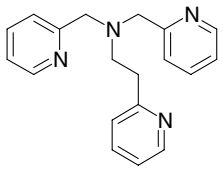
Fig. 23. X-ray structure of the $[Ru(N_4O)OH_2]^{2+}$ cation.

3.2.11. Tris((2-pyrazinyl)methyl)amine (tpza)



Tpza was first reported in 1998, from the reaction of two equivalents of 2-(chloromethyl)pyrazine with 2-(methylamino)pyrazine in THF [247]. Only a single pK_a value for this ligand can be measured over the pH range 0.9–6.5, and this presumably corresponds to deprotonation of the aliphatic N atom. Thus far, the coordination chemistry of this ligand is restricted to a number of lanthanide and actinide complexes. The ten-coordinate complex $[Nd(tpza)(MeCN)_3(OH_2)_3](ClO_4)_3 \cdot 3H_2O$ is obtained on reaction of the ligand with $Nd(ClO_4)_3 \cdot 6H_2O$ in MeCN and other less well-characterised high coordinate complexes are obtained for La^{3+} and Eu^{3+}. The isostructural eight-coordinate complexes $[La(tpza)I_3(MeCN)] \cdot MeCN$ and $[U(tpza)I_3(MeCN)] \cdot MeCN$ are obtained on treatment of the appropriate $MI_3(THF)_4$ complex with one equivalent of ligand in THF/MeCN, while the same reaction in solely THF as solvent gives the isostructural complexes $[La(tpza)I_3(THF)] \cdot THF$ and $[U(tpza)I_3(THF)] \cdot THF$. All four complexes have been structurally characterised [263].

3.2.12. Bis((2-pyridyl)methyl)-2-((2-pyridyl)-ethyl)amine (pmea)



Pmea was first prepared in 1983 from the reaction of (2-(2-pyridyl)ethyl)amine with 2-(chloromethyl)pyridine [264]. Although this procedure gave only a 10% yield of ligand, subsequent improvements have now allowed yields approaching 50% to be obtained [251,265].

Both Fe(II) and Fe(III) complexes of pmea have been reported. In contrast to the analogous tpa complex, $[Fe(pmea)(NCS)_2]$ does not show spin-crossover behaviour, with effective magnetic moments of 4.33 BM at 80 K and 4.59 BM at 300 K indicative of an equal mixture of $^5T_2$ and $^3T_1$ phases. The 5- and 6-isomeric possibilities in this complex were recognised, but the presence of only one isomer was assumed [264]. $[Fe(pmea)Cl_2]Cl$ and a number of similar Fe(III) complexes containing tripodal tetradentate amine ligands have been studied as functional models for the enzyme catechol 1,2-dioxygenase. $[Fe(pmea)Cl_2]Cl$ is high-spin at room temperature and catalyses the oxidative cleavage of 3,5-di-*t*-butylcatechol by molecular oxygen, but no attempt was made at the characterisation of possible 5- and 6-isomers of this complex [266]. The diferric complex $[(pmea)Fe(O)(OAc)Fe(pmea)](ClO_4)_3$ catalyses the ^{t}BuOOH-promoted oxidation of cyclohexane to a variety of products, but is not as effective as the analogous tpa complex [197]. The Cu(I) and Cu(II) complexes $[Cu(pmea)]PF_6$ and $[Cu(pmea)Cl]ClO_4 \cdot H_2O$ have been prepared from the reaction of $[Cu(MeCN)_4]PF_6$ and $Cu(ClO_4)_2 \cdot 6H_2O$/$CuCl_2 \cdot 2H_2O$, respectively with pmea. X-ray crystallographic analysis shows that $[Cu(pmea)]PF_6$ adopts an unusual 4-coordinate pyramidal geometry about the metal ion (Fig. 24), with the Cu ion essentially coplanar with the three pyridyl donor atoms. The complex is very reactive towards dioxygen, giving formation of a transient purple species at −90 °C thought to be a peroxo-bridged dimer, while the same reaction at room temperature gives formation of the Cu(II) complex $[Cu(pmea)F]PF_6$.

Five-coordinate $[Cu(pmea)Cl]ClO_4 \cdot H_2O$ ($\tau = 0.12$ and 0.14 for the two independent molecules in the asymmetric unit) and $[Cu(pmea)F]PF_6$ ($\tau = 0.14$) both adopt an essentially square pyramidal geometry with a pyridyl N atom of the unique pyridylethyl arm occupying the axial position. Five-coordinate complexes of tepa and pmap are also square pyramidal, in contrast to analogous $[Co(tpa)X]^{+/2+}$ complexes ($X = Cl^-$, MeCN, F^-, H_2O, CN^-) which are uniformly trigonal bipyramidal with the aliphatic N atom and the X ligand occupying the apical positions, and the introduction of additional methylene units into the ligand arms obviously disfavours this geometry. The bis(μ-oxo) dimer $[(pmea)Mn(O)_2Mn(pmea)](ClO_4)_3 \cdot MeCN$ has been prepared by H_2O_2 oxidation of an equimolar aqueous mixture of

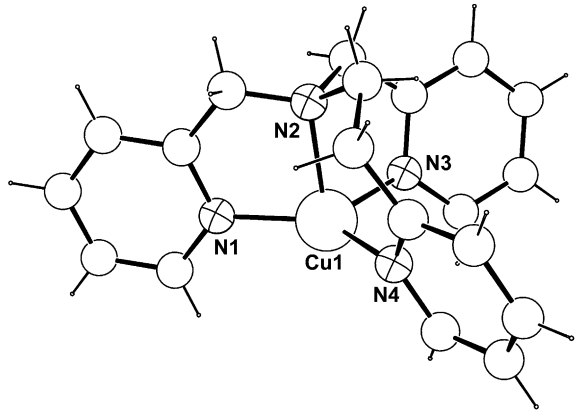


Fig. 24. X-ray structure of the $[Cu(pmea)]^+$ cation.

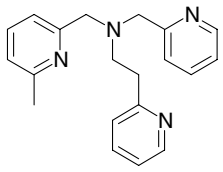


Fig. 25. Structure of the pmea derivative L^4.

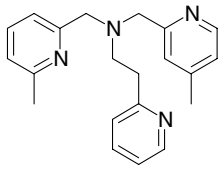
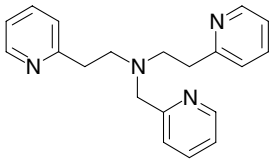


Fig. 26. Structure of the pmea derivative L^5.

$Mn(ClO_4)_2 \cdot 6H_2O$ and pmea [265]. The complex was proposed to contain discrete localised Mn(III) and Mn(IV) ions, although these could not be distinguished by X-ray crystallography at room temperature due to disorder in the crystal which led to the observation of an apparent centre of inversion. The six-membered chelate rings lie in the same plane as the bridging oxo ligands and the tertiary N atoms lie mutually trans to each other, as required by the apparent centre of inversion. A similar synthetic strategy was used to prepare the Mn(III,IV) dimer of the related ligand L^4 (Fig. 25), and this complex was able to be oxidised to the Mn(IV,IV) dimer by treatment with NaOCl.

X-ray structural analysis of this (IV,IV) complex again showed the six membered chelate rings to lie in the same plane as the bridging oxo ligands. The Mn(III,III) dimer of the dimethyl analogue L^5 (Fig. 26) has also been prepared by H_2O_2 oxidation of a methanolic solution of $Mn(ClO_4)_2 \cdot 6H_2O$ and ligand, and the complex shows similar structural features to those discussed above [267].

3.2.13. Bis(2-(2-pyridyl)ethyl)-((2-pyridyl)-methyl)amine (pmap)



Pmap was first prepared in 1999 from the reaction of 2-vinylpyridine with 2-(aminomethyl)pyridine in MeOH/HOAc [268], and a subsequent preparation using a similar method has also been reported [251]. The coordination chemistry of pmap has been little studied, and only complexes of Zn, Cu and Mn have been reported. Reaction of pmap with $Zn(ClO_4)_2 \cdot 6H_2O$ in the presence of Et_3N and CO_2 gives the dimeric complex $[(pmap)Zn(CO_3)Zn(pmap)](ClO_4)_2 \cdot 7H_2O$ in which the bridging carbonate ligand chelates to both Zn ions. The unique five-membered chelate rings are situated perpendicular to the plane containing the Zn ions and the carbonate ligand, and the tertiary N atoms lie mutually *cis* [268]. The Mn(III,IV) dimer $[(pmap)Mn(O)_2Mn(pmap)](ClO_4)_3 \cdot MeCN$ is prepared in a similar fashion to the analogous pmea complex (Section 3.2.12) and the X-ray structure again shows the cation to contain an apparent centre of inversion for the same reasons as discussed for the pmea complex. The Mn···Mn separation of 2.7379(13) Å is longer than that found in the tpa (2.643(1) Å) and pmea (2.693(1) Å) complexes, and the unsuccessful attempts to prepare the analogous tepa complex were attributed to the Mn···Mn separation in such a complex being too long to accommodate a bis (μ-oxo) bridge [269]. The methyl-substituted pmap ligand L^6 (Fig. 27) forms the distorted octahedral monomeric Mn(II) complex $[Mn(L^6)(MeCN)(OH_2)](ClO_4)_2$ on reaction with $Mn(ClO_4)_2 \cdot 6H_2O$ under aerobic conditions, with X-ray analysis confirming production of the 6-isomer [267]. Addition of H_2O_2 to a MeOH solution of this complex did not produce the expected bis(μ-oxo) dimer.

$[Cu(pmap)]PF_6$ adopts a similar structure to $[Cu(pmea)]PF_6$, with a pseudo trigonal pyramidal geometry about the Cu(I) ion and the aliphatic N atom occupying the apical position [251]. The complex reacts rapidly with O_2 at −90 °C in propionitrile and no superoxo or peroxo intermediate can be observed, while at room temperature the same reaction in MeCN gives $[Cu(pmap)F]PF_6$ as also found for the analgous pmea complex. $[Cu(pmap)Cl]ClO_4$ can be obtained either anhydrous or as the monohydrate, and both show similar structures. The five-coordinate Cu(II) ion adopts a square pyramidal geometry ($\tau = 0.08$) with both the chloride ligand and the five-membered chelate ring in the basal plane.

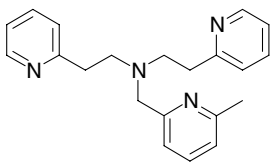
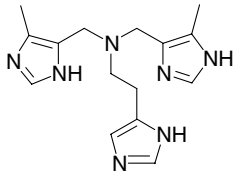


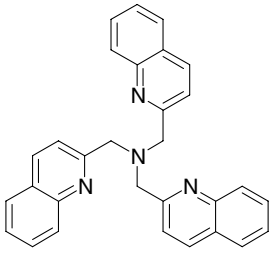
Fig. 27. Structure of the pmap derivative L^6.

3.2.14. N,N′-bis(imidazole-4-ylmethyl-5-methyl)histamine (bimhm)



Bimhm · 4HCl was first prepared in 2002 from the reaction of histamine with 4-methyl-5-imidazolecarboxaldehyde and subsequent reduction with sodium borohydride [270]. pK_a values of 5.86, 6.59 and 8.61 (I = 0.1 M, T = 25 °C) were obtained by potentiometric titration, while the pK_a corresponding to deprotonation of the tertiary N atom could not be measured by this method. Reaction of the ligand with Cu(II) and Zn(II) up to pH ~ 9 was studied potentiometrically, and log K values for the $[M(bimhm)]^{2+}$ complexes were 16.06 and 12.73 for Cu and Zn, respectively. Evidence for hypodentate coordination of the ligand was found for both metals, with log K values for $[Cu(bimhmH)]^{3+}$ (20.15) and $[Cu(bimhmH_2)]^{4+}$ (22.10) complexes being significantly greater than those for $[Cu(bimhm)]^{2+}$. The formation of dinuclear complexes was also observed for Cu^{2+} but not for Zn^{2+}.

3.2.15. Tris(2-quinolylmethyl)amine (tmqa)

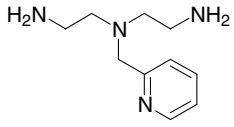


The synthesis of tmqa from the reaction of 2-(bromomethyl)quinoline and ammonium hydroxide in THF was reported in 1994 [271], and the coordination chemistry of this ligand has thus far been limited to some copper complexes. [Cu(tmqa)]X (X = PF_6, ClO_4) results from reaction of $[Cu(MeCN)_4]X$ with the ligand in CH_2Cl_2 under argon. The complex adopts a trigonal pyramidal geometry with the tertiary N atom occupying the apical position, and the three quinolyl moieties provide a binding pocket for another axial ligand. Both the PF_6^- and ClO_4^- salts are unreactive towards O_2 in the solid state, and the PF_6^- salt decomposes only very slowly under oxygen in MeCN solution. [Cu(tmqa)Cl]P-F_6 · MeCN · 0.5Et_2O, formed from the reaction of Cu-Cl_2 · 2H_2O with tmqa in MeOH, addition of $NaPF_6$ and crystallisation from MeCN/Et_2O, is nearly perfectly square pyramidal, with τ = 0.06, and this geometry has been rationalised on the basis that adoption of a trigonal bipyramidal structure would lead to unfavourable steric interactions between the Cl^- ligand and the protons at the 8-position of the three quinolyl rings [272].

4. Ligands containing non-identical N-donor atoms on each arm

4.1. Ligands containing mixed aliphatic and aromatic N-donor atoms

4.1.1. N,N-bis(aminoethyl)-2-(aminomethyl)pyridine (pdt)



The pdt ligand was first mentioned in the literature in 1985 in a paper describing the template synthesis of a macrocycle derived from this, although the synthesis of pdt was not detailed [273]. The first reported synthesis dates from 1990 and involves the reaction of phthalimido-protected diethylenetriamine with 2-(chloromethyl)pyridine (although it should be noted that the experimental section of this paper refers to reaction with a "bromoalkane" to effect substitution at the central N atom) in refluxing ethanol followed by deprotection with HCl [274]. This, and some subsequent [275–277], papers dealt solely with the formation of macrocycles derived from tripodal ligands and thus the coordination chemistry of free pdt was not investigated. Similarly, pdt was reported as an intermediate in the construction of a tetraaminetetracarboxylic acid ligand, but no metal complex of the pdt ligand itself was reported [278]. A recent alternative synthesis of pdt involves reaction of 2-(aminomethyl)pyridine with two equivalents of tosylaziridine in ethanol, followed by detosylation with H_2SO_4 [279], and the X-ray structure of the tosylated intermediate has been reported [280]. Surprisingly, there is only one reference to a metal complex of pdt in the literature, namely $[Zn(pdt)(OH_2)]^{2+}$, which was generated in aqueous solution by reaction of a Zn(II) salt with pdt · 3HCl [149]. This study also reported the pK_a values of pdt · 3HCl as 4.00, 9.27 and 10.04, while the pK_a of $[Zn(pdt)(OH_2)]^{2+}$ was given as 9.63. Reaction of pdt with Me_3SiCl or t-BuMe_2SiCl and subsequent reaction with BuLi gives the trialkylsilyl-substituted pdt derivatives shown in Fig. 28 and some Ti, Ta, Zr, Hf and Y amido complexes of these ligands have been reported [279,280].

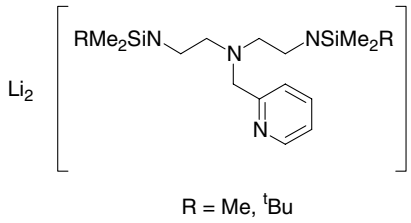
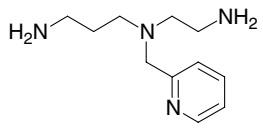


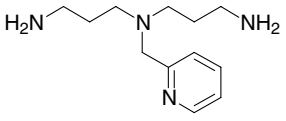
Fig. 28. Silylated derivatives of pdt.

4.1.2. N-(3-aminopropyl)-N-(2-aminoethyl)-2(aminomethyl)pyridine (TO-PY)



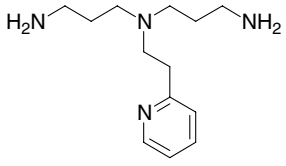
The synthesis of this ligand was described in 2001 from the reaction of phthalimido protected *N*-(2-aminoethyl)-1,3-propanediamine with 2-(chloromethyl)pyridine [281], but its coordination chemistry appears not to have been investigated to date.

4.1.3. N,N-bis(aminopropyl)-2-(aminomethyl) pyridine (dapp)



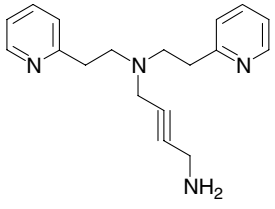
Three methods for the synthesis of dapp have been reported. The first, dating from 1990, is very similar to that used for the synthesis of pdt (Section 4.1.1), involving reaction of phthalimido-protected dipropylenetriamine with 2-(chloromethyl)pyridine followed by deprotection with HCl [274]. The other syntheses both use 2-(aminomethyl)pyridine as the starting material, in one case reacting it with two equivalents of 3-(bromopropyl)phthalimide and deprotecting with HCl [282], or reacting it with two equivalents of acrylonitrile and subsequent reduction with $NaBH_4$/Raney nickel [283]. Dapp has been mostly used to synthesise pyridyl-appended macrocyclic ligands [274,277,283,284] and there are few reports of discrete metal complexes of dapp. $[Zn(dapp)](ClO_4)_2$, $[Co(dapp)Br_2]Br$, $[Cr(dapp)Cl_2]Cl$, $[Ni(dapp)(MeCN)_2](ClO_4)_2$ and $[Cu(dapp)Cl]ClO_4$ have all been reported [285], and the two latter complexes have been structurally characterised. $[Ni(dapp)(MeCN)_2](ClO_4)_2$ adopts a distorted octahedral geometry about the metal ion, and crystallises as the 5-isomer, while $[Cu(dapp)Cl]ClO_4$ is distorted square pyramidal ($\tau = 0.24$) with an aliphatic N atom in the apical position. This paper is in fact one of the first to specifically detail the isomeric possibilities available in five-coordinate complexes containing asymmetric tripodal ligands. The Fe(II) spin-crossover complex [Fe(dapp)(abpt)] (abpt = 4-amino-3,5-bis(pyridin-2-yl)-1,2,4-triazole) has also been structurally characterised at 293, 183 K (both high spin) and 123 K (low spin) [282]. The complex crystallises in the same space group at all temperatures to give the 6-isomer in which a pyridyl N atom of the triazole ligand lies *trans* to the tertiary N atom of the tripodal ligand. The low spin form of the complex shows the expected diminution of the Fe–N bond distances by amounts between 0.127 and 0.224 Å. The obtained hysteresis loop is unusually wide (10 K) for a mononuclear complex.

4.1.4. N,N-bis(aminopropyl)-2-(aminoethyl)pyridine (L^7)



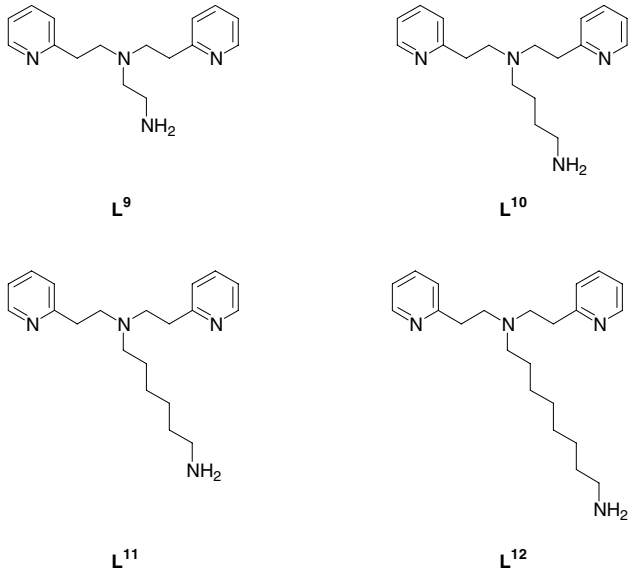
This ligand was prepared in an analogous fashion to dapp (Section 4.1.3) by reaction of 2-(2-aminoethyl)pyridine with acrylonitrile and reduction of the resulting nitrile with $NaBH_4$/Raney nickel [284]. The coordination chemistry of this ligand has yet to be studied.

4.1.5. N,N-bis(2-(2-pyridyl)ethyl)-1,4-diamino-2-butyne (L^8)



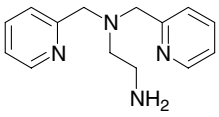
This ligand provides a rare example of a tripodal tetraamine ligand containing unsaturation in one of the arms. The tetrahydrochloride salt of this ligand was first reported in 2003 from the reaction of 1-chloro-4-phthalimido-2-butyne with bis(2-(2-pyridyl)ethyl)amine) in MeCN, followed by deprotection with aqueous hydrazine [286]. No metal complexes of this ligand have yet been reported.

4.1.6. N,N-bis(2-(2-pyridyl)ethyl)-1,2-diaminoethane (L^9), N,N-bis(2-(2-pyridyl)ethyl)-1,4-diaminobutane (L^{10}), N,N-bis(2-(2-pyridyl)ethyl)-1,6-diaminohexane (L^{11}) and N,N-bis(2-(2-pyridyl)ethyl)-1,8-diaminooctane (L^{12})



These ligands were first reported in 1962 from the reaction of the reaction of the appropriate α,ω-diamine with 2-vinylpyridine [287]. Their coordination chemistry remains to be studied.

4.1.7. N,N-bis(2-pyridylmethyl)ethylenediamine (uns-penp, dpea, N,N-bispicen, bpen)



The synthesis of this ligand as the hydrochloride salt was first reported in 1988 from the reaction of *N*-acetylethylenediamine with 2-(chloromethyl)pyridine followed by deprotection with HCl [288]. The free base ligand can also be prepared by reaction of bis(2-pyridylmethyl)amine with *N*-(2-bromoethyl)phthalimide, deprotection with HCl and ether extraction of the basified solution [289], reaction of mono Boc-protected ethylenediamine with 2-(chloromethyl)pyridine, deprotection with TFA and CH_2Cl_2 extraction of the basified solution [290], or reductive amination of *N*-acetylethylenediamine with 2-pyridinecarbaldehyde using $NaBH(OAc)_3$, deprotection with HCl, basification and extraction with CH_2Cl_2 [291]. The triprotonated ligand displays pK_a values of 3.17, 5.22 and 9.93, and a formation constant (log *K* of 12.48 for the 1:1 Zn^{2+} complex, which exhibits a pK_a of 9.14 [149]. The coordination chemistry of uns-penp has not been extensively studied, and the ligand has more often been used as an intermediate in the synthesis of various multidentate ligands [290,292–295]. Reaction of the hydrochloride salt of the ligand with copper chloride in water and addition of $NaClO_4$ results in crystallisation of the hypodentate complex $[Cu(uns\text{-}Hpenp)Cl_2](ClO_4)$ in which the aminoethyl arm is protonated and not coordinated to the metal ion [288,296], while reaction of the monoprotonated ligand with $Cu(ClO_4)_2 \cdot 6H_2O$ and $CuCl_2 \cdot 2H_2O$ in water gives the hypodentate chloride-bridged dimer $[(Cu(uns\text{-}Hpenp)Cl)_2Cl](ClO_4)_3$ in which both copper ions are square pyramidal ($\tau = 0.05$) and which contains two uncoordinated protonated aminoethyl arms [291]. However, use of the free base ligand ensures coordination of all four N atoms, and thus reaction of this with $Cu(ClO_4)_2 \cdot 6H_2O$ and $CuCl_2 \cdot 2H_2O$ in water/MeOH gives $[Cu(uns\text{-}penp)Cl]ClO_4$, which exhibits trigonal bipyramidal geometry ($\tau = 0.84$). Reaction of free base uns-penp with $[Cu(MeCN)_4]ClO_4$ in MeCN gives the dimeric Cu(I) species $[Cu_2(uns\text{-}penp)_2](ClO_4)_2 \cdot MeCN$, in which the two extremely distorted four-coordinate metal centres are bridged by the aminoethyl arms from the two tripodal ligands (Fig. 29). This complex reacts with O_2 at −89.9 °C to give formation of both superoxo and peroxo complexes, although the exact nature of these was unable to be determined.

Interestingly, the dimethyl-substituted derivative of uns-penp, in which the amine protons are replaced by methyl groups, reacts quite differently to uns-penp with both Cu(I) and Cu(II) starting materials. Reaction with $[Cu(MeCN)_4]ClO_4$ gives the monomeric five-coordinate Cu(I) product $[Cu(Me_2\text{-}uns\text{-}penp)(MeCN)]ClO_4$ ($\tau = 0.81$) while reaction with $Cu(ClO_4)_2 \cdot 6H_2O$ and $CuCl_2 \cdot 2H_2O$ in water/MeOH gives five-coordinate $[Cu(Me_2\text{-}uns\text{-}penp)Cl]ClO_4$ which is square pyramidal

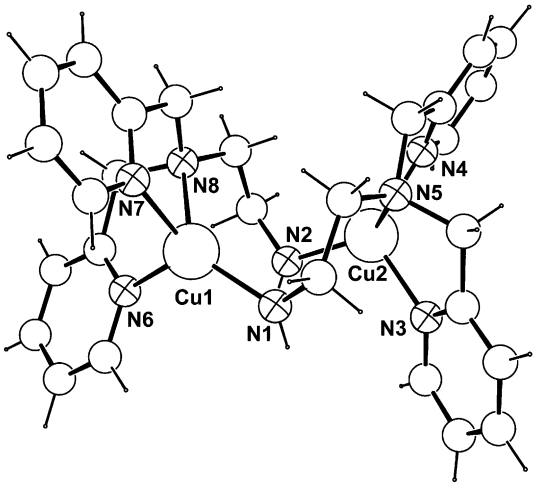


Fig. 29. X-ray structure of the $[Cu_2(uns\text{-}penp)_2]^{2+}$ cation.

($\tau = 0.26$) with the aliphatic N atom in the apical position [297].

Two spin-crossover Fe(II) complexes containing uns-penp have been reported. [Fe(uns-penp)$(NCS)_2$] crystallises with the thiocyanate ligands in the same plane as the chelate ring formed by the two aliphatic N atoms, and undergoes an abrupt HS–LS transition centred at 138 K [289]. [Fe(uns-penp)(bim)]$(ClO_4)_2 \cdot 0.5H_2O$ (bim = 2,2′-bisimidazole) undergoes a two-step HS–LS transition, with centres at 218 and 171 K. Structural characterisation of the complex at 293 and 123 K showed the expected shortening of the Fe–N bond lengths in the LS form, and in both cases, the bim ligand was found to lie in the same plane as the two aliphatic N atoms [298]. The Mn(III,IV) dimer [Mn_2O_2(uns-penp)$_2$]$(ClO_4)_3 \cdot$ MeCN was prepared from reaction of the free base ligand with $Mn(OAc)_3 \cdot 2H_2O$ in EtOH, addition of $NaClO_4$ and crystallisation from MeCN [299]. A number of isomeric possibilities exist for this dimer, but it crystallises as the single isomer depicted in Fig. 30. The X-ray structure shows localised Mn(III) and Mn(IV) centres which are strongly antiferromagnetically coupled ($J = -316$ cm^{-1}), and a Mn–Mn distance of 2.646(2) Å which is typical of bis-μ-oxo bridged manganese dimers.

The Co(III) complex [Co(uns-penp)(OH_2)Cl]-$(ClO_4)_2 \cdot H_2O$ was prepared from the reaction of $Na_3[Co(NO_2)_6]$ with the ligand hydrochloride in water followed by anation in concentrated HCl and purification on Sephadex cation exchange resin [288]. The stereochemistry of the complex was determined by NMR, with the Cl and OH_2 ligands lying in the same plane as the aliphatic N atoms of the uns-penp ligand.

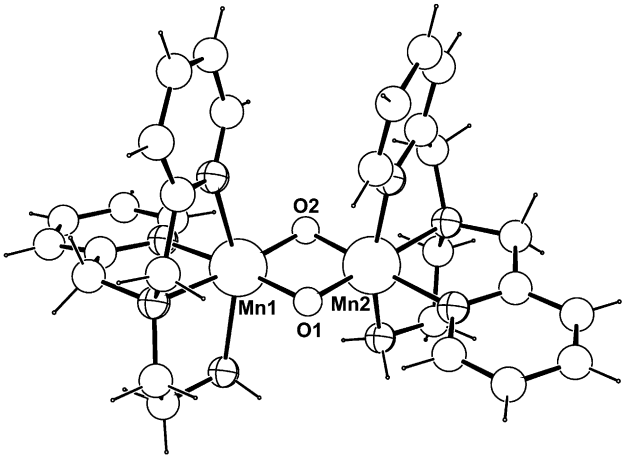
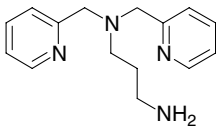


Fig. 30. X-ray structure of the mixed-valence [Mn_2O_2(uns-penp)$_2$]$^{3+}$ cation.

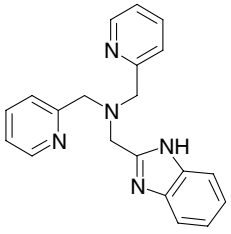
4.1.8. 3-Aminopropylbis(2-pyridylmethyl)amine (dppa, bptn)



Dppa was first reported in 1997 as the product of the reaction between bis(2-pyridylmethyl)amine and *N*-(3-bromopropyl)phthalimide in refluxing toluene [300]. An alternative synthesis involves reaction of bis(2-pyridylmethyl)amine with acrylonitrile and subsequent reduction of the dinitrile with $NaBH_4$/Raney nickel [301]. Few complexes of dppa have been prepared, with only [Fe(dppa)$(NCS)_2$], [Co(dppa)$(NO_2)_2$]-$NO_3 \cdot 0.5H_2O$ and [Co(dppa)Cl_2]ClO_4 having been reported. Three polymorphs of [Fe(dppa)$(NCS)_2$] have been structurally characterised, and each shows a distinctive variable temperature magnetic behaviour. Polymorph A undergoes a gradual HS–LS transition at 176 K without hysteresis, polymorph B is paramagnetic over the temperature range 4.5–295 K, and polymorph C undergoes an abrupt HS–LS transition around 116 K, with a 8 K wide hysteresis loop [300]. The three polymorphs crystallise in different space groups, but in all cases the 5-isomer is obtained. The differing magnetic behaviour is explained on the basis of different crystal packing within the three-dimensional assemblies. [Co(dppa)$(NO_2)_2$]$NO_3 \cdot 0.5H_2O$ was prepared by air oxidation of a solution of $Co(NO_3)_2 \cdot 6H_2O$ and dppa in the presence of $NaNO_2$, and reaction of this complex with HCl followed by addition of $NaClO_4$ gave the dichloro complex [Co(dppa)Cl_2]ClO_4. The observation of five methylene signals in the ^{13}C NMR of these complexes shows that both were obtained as the 5-isomer, and this was confirmed for the dichloro complex by X-ray structural characterisation [228].

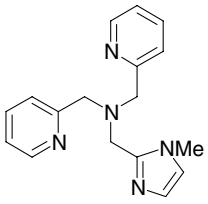
4.2. Ligands containing three aromatic N-donor atoms

4.2.1. ((Benzimidazol-2-yl)methyl)bis((2-pyridyl)-methyl)amine (bpba)



The asymmetric tripodal ligand bpba was first prepared in 2001 from the reaction of excess 2-(chloromethyl)pyridine with ((benzimidazol-2-yl)methyl)amine in CH_2Cl_2 [302]. Bpba reacts with $Fe(ClO_4)_3 \cdot 9H_2O$ and deprotonated tetrachlorocatechol (tcc) in acetone to give the catecholate chelate complex [Fe(bpba)(tcc)]-$ClO_4 \cdot (CH_3)_2CO$ in which the benzimidazole and catecholate rings are essentially coplanar. This, and a number of other Fe(III) catecholate complexes of bpba react with oxygen to give cleavage of the catecholate ligand [302]. The ten-coordinate lanthanide complexes $[Ln(bpba)(O_2NO)_2]$ (Ln = La, Eu, Gd, Tb) have been prepared and the Eu, Gd and Tb complexes have been structurally characterised [303], as has the silver dimer $[Ag_2(bpba)(dppm)](BF_4)_2 \cdot MeOH$ [304].

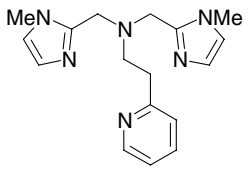
4.2.2. Bis(2-(pyridyl)methyl)(2-(1-methylimidazolyl)-methyl)amine (bpia)



The mixed donor tripodal ligand bpia was first reported in 1990 [147]. The original synthesis involved reaction of 1-methyl-2-aminomethylimidazole with two equivalents of 2-(chloromethyl)pyridine in acetonitrile, although bpia has also been prepared by an alternative method from the reaction of 2-(chloromethyl)-1-methylimidazole with bis(2-pyridylmethyl)amine in CH_2Cl_2 [305]. Reaction of bpia with $CuCl_2 \cdot 2H_2O$ and addition of $NaPF_6$ gives five-coordinate trigonal bipyramidal $[Cu(bpia)Cl]PF_6$ ($\tau = 0.79$) [306], which reacts further with 1-methylimidazole to give [Cu(bpia)(1-Meim)]$(PF_6)_2$ [147]. The dimeric Cu(I) complex $[(bpia)_2Cu_2](CF_3SO_3)_2$ can be prepared from reaction of the ligand with $[Cu(MeCN)_4]CF_3SO_3$ in MeCN [305]. The crystal structure shows two four-coordinate Cu centres (Cu···Cu = 3.329 Å) bridged by the two imidazole-appended arms of the two tripodal ligands. This complex reacts rapidly with dioxygen at −80 °C in a Cu:O_2 ratio of ~2:1 to give a peroxo-bridged dimer which is EPR-silent.

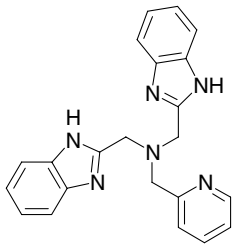
Several mono- and binuclear manganese complexes of bpia have been described in studies aimed at preparing catalase mimics [307] and oxidation catalysts [308]. The mononuclear Mn(III) complexes $[Mn(bpia)(OAc)(OCH_3)]PF_6$ and $[Mn(bpia)Cl_2]ClO_4$ both crystallise as a single isomer having the imidazole ring essentially coplanar with the monodentate ligands. The structurally characterised binuclear complexes $[(bpia)Mn(\mu\text{-}OAc)_2Mn(bpia)](ClO_4)_2$, $[(bpia)Mn(\mu\text{-}O)(\mu\text{-}OAc)Mn(bpia)](ClO_4)_3 \cdot MeCN$, $[(bpia)Mn(\mu\text{-}O)_2Mn(bpia)](ClO_4)_2(PF_6) \cdot 2MeCN$ and $[(bpia)ClMn(\mu\text{-}O)MnCl(bpia)](ClO_4)_2 \cdot 2MeCN$ form an interesting set of complexes having differing oxidation states ((II,II), (III,III), (III,IV) and (III,III), respectively) and differing bridging ligands. All except the (II,II) complex have the imidazole ring coplanar with the bridging ligand(s), although the relative orientations of the two bpia ligands vary. Fe(III) complexes of bpia have been studied as models for catechol dioxygenases, and a number of in situ-generated Fe(III)/bpia complexes are found to cleave catechols in the presence of O_2. $[Fe(bpia)Cl_2][FeCl_4]$, $[(bpia)ClFe(\mu\text{-}O)FeCl(bpia)]Cl_2 \cdot 4MeOH$ [309] and $[Fe(bpia)(tcc)]ClO_4$ [302] have been structurally characterised and all three complexes have the imidazole ring in the same plane as the two coordination sites not occupied by the bpia ligand. The Fe(III) dithiolato complex $[Fe(bpia)(dtc)](ClO_4)$ has also been structurally characterised, and exhibits a similar ligand geometry to the three complexes discussed above [310].

4.2.3. Bis(1-methylimidazol-2-yl)methyl)(2-(pyridyl-2-yl)ethyl)amine (L^{13})



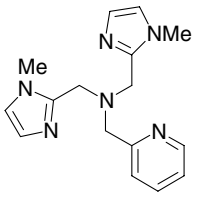
This ligand was first reported in 2004, as the product of the reaction of 1-methyl-2-imidazolecarboxaldehyde with 2-(2-aminoethyl)pyridine in CH_3OH [311]. Reaction of the ligand with $K_2[Ru(OH_2)Cl_5]$ in EtOH and addition of $NaClO_4$ gives the structurally characterised 5-isomer of $[Ru(L^{13})Cl_2]ClO_4$, which can be chemically reduced (Zn(Hg) or Eu^{2+}) to the diaqua species $[Ru\text{-}(L^{13})(OH_2)_2]^{2+}$ in aqueous solution. The five-coordinate complex $[Cu(L^{13})Cl]ClO_4$ is formed on reaction of the ligand with $CuCl_2 \cdot 2H_2O$ in EtOH, and this reacts with one equivalent of $NaNO_2$ to give the distorted square-pyramidal complex $[Cu(L^{13})(ONO)]ClO_4$ ($\tau = 0.27$) which has an imidazole in the apical position [312].

4.2.4. Bis(2-benzimidazolylmethyl)(2-pyridylmethyl)-amine (pb2)



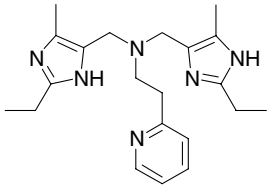
This ligand was first mentioned in the literature in 1991, although no preparative details were given [313]. A subsequent paper by different authors detailed two methods for the synthesis of pb2, both starting from iminodiacetic acid and differing only in the order of addition of reactants [314]. Reaction of iminodiacetic acid with *o*-phenylenediamine gives bis(2-benzimidazolylmethyl)amine which is then reacted with 2-(chloromethyl)pyridine in MeOH to give the ligand in low yield. Conversely, reaction of iminodiacetic acid with 2-(chloromethyl)pyridine under alkaline conditions gives dipotassium *N*-(2-pyridylmethyl)iminodiacetate, and condensation of this with *o*-phenylenediamine in acidic aqueous solution gives the ligand in moderate (42%) yield. The nitrate salt of the diprotonated (at the imidazole N atoms) ligand has been structurally characterised [303], and thus far, only lanthanide complexes of this ligand have been prepared. Thus, reaction of either $Ln(NO_3)_3$ (Ln = La, Sm, Eu, Gd, Tb, Tm) or $LnCl_3$ (Ln = La, Sm, Eu, Tb, Ho) with one equivalent of ligand in ethanol gives $[Ln(pb2)(NO_3)_3]\cdot C_2H_5OH$ and $[Ln(pb2)Cl_3(H_2O)]\cdot C_2H_5OH$, respectively [314]. Structural characterisation of $[Sm(pb2)(NO_3)_3]\cdot C_2H_5OH$ and $[Gd(pb2)(NO_3)_3]\cdot C_2H_5OH$ show the metal ions in these complexes to be ten-coordinate, while the samarium ion in $[Sm(pb2)Cl_3(H_2O)]\cdot C_2H_5OH$ is eight-coordinate. The antipyrine complexes $[Ln(pb2)(antipyrine)_3](ClO_4)_3$ (Ln = La, Pr, Eu, Gd, Tb, Y) and $[Ln(L)(antipyrine)Cl(H_2O)_2]Cl_2\cdot 2H_2O$ (Ln = Eu, Gd, Tb) have also been prepared; structural characterisation (Pr, Y) shows the former to be seven-coordinate, while the latter (Eu) are eight-coordinate [303].

4.2.5. Bis(2-(1-methylimidazolyl)methyl)(2-(pyridyl)-methyl)amine (bipa)



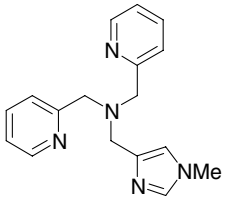
The synthesis of bipa was first reported in 1990, from the reaction of bis(2-(1-methylimidazolyl)methyl)amine with 2-(chloromethyl)pyridine in dry acetonitrile [147], while a subsequent alternative synthesis involves reaction of 2-(chloromethyl)imidazole with 2-(methylamino)pyridine in CH_2Cl_2 [305]. The trigonal bipyramidal Cu(II) complex $[Cu(bipa)Cl]PF_6\cdot MeCN$ ($\tau = 0.85$) is prepared by reaction of the ligand with $CuCl_2\cdot 2H_2O$ and this reacts further with 1-methylimidazole to give $[Cu(bipa)(1\text{-}Meim)](PF_6)_2$ [147]. The dimeric Cu(I) complex $[(bipa)_2Cu_2](ClO_4)_2\cdot 1/2Et_2O$ results from the reaction of the ligand with $[Cu(MeCN)_4]ClO_4$, and this reacts rapidly with O_2 at −80 °C to give an unidentified red product which decomposes rapidly [305]. Reaction of $Fe(ClO_4)_3\cdot 9H_2O$ and $FeCl_3$ with bipa in MeOH/EtOH gives the red complex $[Fe(bipa)Cl_2](ClO_4)$ and this crystallises as a single isomer with an imidazole in the same plane as the chloride ligands [309]. The analogous Mn(III) complex $[Mn(bipa)Cl_2](ClO_4)$ is essentially isostructural while the mononuclear complex $[Mn(bipa)(OAc)(OCH_3)](PF_6)$ also adopts the same ligand configuration [308].

4.2.6. N,N-bis(2-ethyl-5-methyl-imidazolyl 4-methyl)amino-2-ethylpyridine (biapy)



The ligand biapy was first reported in 2003 [315], and was prepared from the Mannich reaction of 2-ethyl-4-methylimidazole, 2-(aminoethyl)pyridine and formaldehyde in aqueous solution. The coordination chemistry of this ligand remains to be studied.

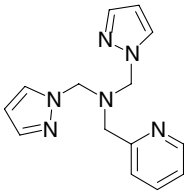
4.2.7. ((1-Methyl-4-imidazolyl)methyl)bis(2-pyridylmethyl)amine (MeIm(Py)$_2$)



This ligand was first prepared in 2000 from the reaction of bis(2-pyridylmethyl)amine with 1-methylimidazole-4-aldehyde and subsequent reduction of the generated imine with $NaBH_3CN$ [316]. Reaction of the ligand with $Cu(ClO_4)_2\cdot 6H_2O$ in MeOH and subsequent crystallisation of the obtained crystals from MeCN gives five-coordinate $[Cu(MeIm(Py)_2)MeCN](ClO_4)_2\cdot MeCN$, which is trigonal bipyramidal ($\tau = 0.96$). Methylation of the pyridine rings at the carbon adjacent to the N-donor atom affects the geometry of the obtained Cu(II) complexes markedly; the complex $[Cu(MeIm(Me)_1)(MeCN)](ClO_4)_2$, in which one pyridyl ligand is methylated is square pyramidal ($\tau = 0.15$) while the analogous complex of the dimethylated ligand,

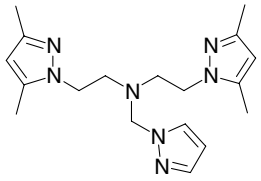
$[Cu(MeIm(Me)_2)(MeCN)](ClO_4)_2$ has $\tau = 0.65$ [317]. The three complexes react with H_2O_2 at −80 °C to give Cu(II)-hydroperoxo complexes. Five-coordinate $[Zn(MeIm(Py)_2)(MeCN)](ClO_4)_2$ may be prepared from $Zn(ClO_4)_2 \cdot 6H_2O$ in an analogous fashion to the Cu(II) complexes described above [318], and this reacts with superoxide ion in EtCN to give $[Zn(MeIm(Py)_2)(O_2)]^+$ which can be detected by ESR.

4.2.8. Bis(1-pyrazolylmethyl)(2-pyridylmethyl)amine (bppa)



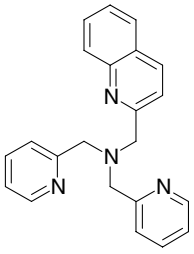
The synthesis of the bppa ligand was first reported in 1996, and used a modification of the method used to prepare the amtp ligand (Section 3.2.3) [319]. Reaction of the ligand with CuI in MeCN gives the polymeric species $[Cu_2(\mu\text{-BPPA})(\mu\text{-I})_2]_n$ in which each bppa ligand binds bidentate to two Cu ions.

4.2.9. Bis(2-(3,5-dimethylpyrazol-1-yl)ethyl)(pyrazol-1-yl)methyl)amine (bppa)



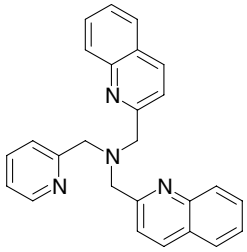
The synthesis of the asymmetric ligand bppa from reaction of bis(2-(3,5-dimethylpyrazol-1-yl)ethyl)amine with (1-hydroxymethyl)pyrazole was reported in 2001 [320]. The crystal structure of the five-coordinate complex $[Co(bppa)Cl]BPh_4 \cdot C_2H_5OH$ shows a distorted trigonal bipyramidal geometry ($\tau = 0.80$) about the Co(II) ion, with the tertiary N atom and Cl ligand occupying the apical positions.

4.2.10. Bis(2-pyridylmethyl)(2-quinolylmethyl)amine (bpqa)



The synthesis of this ligand was first reported in 1994, from the reaction of 2-(bromomethyl)quinoline with one equivalent of dipicolylamine [271]. Reaction of $[Cu(MeCN)_4]PF_6$ with bpqa in MeCN under argon gives $[Cu(bpqa)]PF_6$, which reacts rapidly with dioxygen at −80 °C to give an intensely purple complex formulated as a *trans*-(μ-1,2-peroxo)-bridged dimer. The Cu(II) complex $[Cu(bpqa)Cl]PF_6 \cdot 0.5CH_2Cl_2$ is obtained on reaction of $CuCl_2 \cdot 2H_2O$ with bpqa in MeOH, addition of $NaPF_6$ and crystallisation from MeCN/Et_2O [272]. The cation displays a distorted square-pyramidal geometry ($\tau = 0.16$). Reaction of $Fe(CF_3SO_3)_2 \cdot 2MeCN$ with bpqa in THF under argon gives six-coordinate $[Fe(bpqa)(OSO_2CF_3)_2]$, in which the triflate ligands lie in the same plane as a pyridyl ring [321]. This complex is active as a catalyst in H_2O_2-promoted alkane hydroxylation reactions. The Fe(III) complex $[Fe(bpqa)(tcc)]ClO_4 \cdot EtOH$ is formed from reaction of $Fe(ClO_4)_3 \cdot 9H_2O$ with bpqa and $H_2tcc \cdot H_2O$ in EtOH, and in situ-generated Fe(III) complexes of bpqa are reactive with respect to air-oxidation of various catechol substrates [302].

4.2.11. Bis(2-quinolylmethyl)(2-pyridylmethyl)amine (bqpa)



Bqpa was first reported in 1994, resulting from the reaction between 2-(bromomethyl)quinoline and 2-(methylamino)pyridine in THF [271], while a more recent synthesis utilises 2-(chloromethyl)quinoline and MeCN as solvent [322]. The Cu(I) complex $[Cu(bqpa)]PF_6$ is obtained from reaction of $[Cu(MeCN)_4]PF_6$ with a slight excess of ligand in propionitrile under argon, and reacts with dioxygen at −80 °C to give a brown EPR-silent species with a $Cu:O_2$ ratio of 1:1, formulated as a superoxo complex. $[Cu(bqpa)]ClO_4$ reacts with PPh_3 in MeCN to give $[Cu(bqpa)PPh_3]ClO_4$, and the crystal structure of this shows that the bqpa ligand coordinates in a tridentate fashion with a dangling quinolyl group. Reaction of $CuCl_2 \cdot 2H_2O$ with bqpa in MeOH, addition of $NaPF_6$ and crystallisation from CH_2Cl_2 gives the Cu(II) complex $[Cu(bqpa)Cl]PF_6$ [272]. The dimeric Fe(III) complex $[Fe_2O(OH)(bqpa)_2](ClO_4)_3 \cdot MeCN$ is obtained from the reaction of $Fe(ClO_4)_3 \cdot 10H_2O$ with bqpa in MeOH and subsequent crystallisation from MeCN/THF. This complex crystallises as a single isomer having both pyridine rings in the same plane as

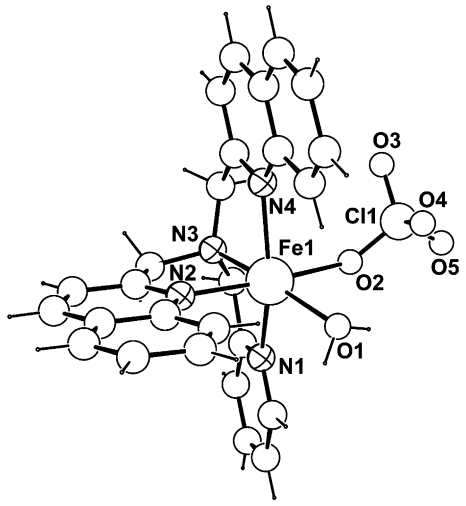


Fig. 31. X-ray structure of the $[Fe(bqpa)(H_2O)(ClO_4)]^+$ cation.

the oxo and hydroxo bridging ligands [323]. The Fe(III) catecholate complex $[Fe(bqpa)(dbc)]BPh_4$ (dbc = the dianion of 3,5-di-*tert*-butylcatechol) has been prepared by reaction of anhydrous $FeCl_3$ with bqpa and $dbcH_2$ in EtOH, and addition of $NaBPh_4$. Bubbling O_2 through a DMF solution of this complex for 24 h results in complete degradation of the catechol ligand to mostly 3,5-di-*tert*-butyl-5-(carboxymethyl)-2-furanone [322]. Reaction of equimolar amounts of $Fe(ClO_4)_2 \cdot 6H_2O$ with bqpa in MeCN gives the Fe(II) complex $[Fe(bqpa)(H_2O)(ClO_4)]$-ClO_4, with the presence of the coordinated perchlorate ligand confirmed by X-ray crystallography (Fig. 31) [321]. This complex crystallises such that a quinoline moiety lies in the same plane as the H_2O and ClO_4^- ligands. The bis (μ-oxo) mixed valence manganese dimer $[(bqpa)Mn(\mu\text{-}O)_2Mn(bqpa)]^{3+}$ has also been reported [399].

5. Conclusions

It is obvious from the preceding pages that, just over a century since the first synthesis of a tripodal tetraamine ligand, the coordination chemistry of such ligands is an expanding field of great current interest. This area of research will undoubtedly continue to expand, given the relatively recent nature of the majority of references in this paper, and the numerous synthetic methods now documented for the synthesis of tripodal tetraamines. Obvious areas for further investigation include the chemistry of second and third row transition metals with such ligands, the use of hypodentate tripodal amine complexes in supramolecular systems, and further studies of the chemistry of tripodal amine ligands with the generally oxophilic lanthanide ions. The results of such future investigations will, in all probability, be collated by another chronicler.

References

[1] K. Hamana, M. Niitsu, K. Samejima, Can. J. Botany 78 (2000) 266.
[2] K. Hamana, M. Niitsu, K. Samejima, S. Matsuzaki, J. Biochem. (Tokyo) 109 (1991) 444.
[3] A.W. Addison, T.N. Rao, J. Reedijk, J. VanRijn, G.C. Verschoor, J. Chem. Soc., Dalton Trans. (1984) 1349.
[4] R.M. Hartshorn, D.A. House, J. Chem. Soc., Dalton Trans. (1998) 2577.
[5] X. Hu, J. Cai, C. Chen, X.-M. Chen, L.-N. Ji, Cryst. Eng. 4 (2001) 141.
[6] M.K. Saha, F.R. Fronczek, L.H. Rees, I. Bernal, Inorg. Chem. Commun. 6 (2003) 983.
[7] I. Bernal, X. Xia, F. Somoza, Fundamental Principles of Molecular Modeling [Proceedings of an International Workshop on Fundamental Principles of Molecular Modeling], Skukuza, Southern Africa, August 20–25, 1995 (1996) Meeting Date 1995, pp. 223–244.
[8] E. Ristenpart, Berichte 29 (1896) 2526.
[9] F.G. Mann, W.J. Pope, Proc. Roy. Soc. (London) 109A (1925) 444.
[10] E. Kimura, S. Young, J.P. Collman, Inorg. Chem. 9 (1970) 1183.
[11] R.H. Mizzoni, M.A. Hennessey, C.R. Scholz, J. Am. Chem. Soc. 76 (1954) 2414.
[12] H. Schmidt, C. Lensink, S.K. Xi, J.G. Verkade, Z. Anorg. Allg. Chem. 578 (1989) 75.
[13] D.A. Buckingham, J.D. Edwards, G.M. McLaughlin, Inorg. Chem. 21 (1982) 2770.
[14] N. Ghanem, J. Martinez, D. Stien, Tetrahedron Lett. 43 (2002) 1693.
[15] A.G. Blackman, Aust. J. Chem. 55 (2002) 263.
[16] S.P. Hajela, A.R. Johnson, J. Xu, C.J. Sunderland, S.M. Cohen, D.L. Caulder, K.N. Raymond, Inorg. Chem. 40 (2001) 3208.
[17] J.G. Verkade, Coord. Chem. Rev. 137 (1994) 233.
[18] J. Nelson, V. McKee, G. Morgan, Prog. Inorg. Chem. 47 (1998) 167.
[19] C. Glidewell, G. Ferguson, R.M. Gregson, C.F. Campana, Acta Crystallogr., Sect. B 56 (2000) 68.
[20] J.C.M. Rivas, L. Brammer, Acta Crystallogr., Sect. C 54 (1998) 1799.
[21] C.A. Ilioudis, K.S.B. Hancock, D.G. Georganopoulou, J.W. Steed, New J. Chem. 24 (2000) 787.
[22] C. Naether, S. Scherb, W. Bensch, Acta Crystallogr., Sect. E 59 (2003) m280.
[23] R.L. Fanshawe, A. Mobinikhaledi, C.R. Clark, A.G. Blackman, Inorg. Chim. Acta 307 (2000) 26.
[24] J. Gancheff, C. Melian, C. Kremer, S. Dominguez, A. Mederos, O.N. Ventura, E. Kremer, J. Coord. Chem. 54 (2001) 285.
[25] M.J. Saliby, S.K. Madan, Inorg. Chem. 20 (1981) 289.
[26] J. Ellermeier, R. Staehler, W. Bensch, Acta Crystallogr., Sect. C 58 (2002) m70.
[27] G.J. Colpas, M. Kumar, R.O. Day, M.J. Maroney, Inorg. Chem. 29 (1990) 4779.
[28] J.C.M. Rivas, L. Brammer, Acta Crystallogr., Sect. C 54 (1998) 757.
[29] M. Zehnder, U. Thewalt, S. Fallab, Helv. Chim. Acta 62 (1979) 2099.
[30] K.S. Hagen, W.H. Armstrong, H. Hope, Inorg. Chem. 27 (1988) 967.
[31] S.S. Massoud, H. Chun, I. Bernal, J. Coord. Chem. 55 (2002) 619.
[32] I.P.Y. Shek, T.-C. Lau, W.-T. Wong, J.-L. Zuo, New J. Chem. 23 (1999) 1049.
[33] V. Marvaud, C. Decroix, A. Scuiller, C. Guyard-Duhayon, J. Vaissermann, F. Gonnet, M. Verdaguer, Chem. Eur. J. 9 (2003) 1677.

[34] P. Klufers, P. Mayer, Acta Crystallogr., Sect. C 54 (1998) 722.
[35] Z.-L. Lu, C.-Y. Duan, Y.-P. Tian, X.-Z. You, H.-K. Fun, B.-C. Yip, E. Hovestreydt, Polyhedron 16 (1996) 187.
[36] Z.-L. Lu, C.-Y. Duan, Y.-P. Tian, X.-Z. You, X.-Y. Huang, Inorg. Chem. 35 (1996) 2253.
[37] H. Zhang, J. Cai, X.-L. Feng, B.-H. Ye, X.-Y. Li, L.-N. Ji, J. Chem. Soc., Dalton Trans. (2000) 1687.
[38] C.W. Eigenbrot Jr., K.N. Raymond, Inorg. Chem. 21 (1982) 2867.
[39] P.H. Smith, Z.E. Reyes, C.W. Lee, K.N. Raymond, Inorg. Chem. 27 (1988) 4154.
[40] X-ray structures are also available for the eight-coordinate main group species $[Pb(tren)_2]Cl_2$. See H. Miyamae, K. Yoshinari, G. Hihara, M. Nagata, Acta Crystallogr., Sect. C 44 (1988) 1528.
[41] X-ray structures are also available for the eight-coordinate main group species $[Sr(tren)(thd)_2]$. See J.W. Park, J.T. Kim, S.M. Koo, C.G. Kim, Y.S. Kim, Polyhedron 19 (2000) 2547.
[42] S.G. Zipp, A.P. Zipp, S.K. Madan, J. Indian. Chem. Soc. 54 (1977) 149.
[43] D.A. Buckingham, P.J. Cresswell, A.M. Sargeson, Inorg. Chem. 14 (1975) 1485.
[44] D.A. Buckingham, C.R. Clark, T.W. Lewis, Inorg. Chem. 18 (1979) 2041.
[45] D.A. Buckingham, C.R. Clark, W.S. Webley, Aust. J. Chem. 33 (1980) 263.
[46] D.A. Buckingham, C.R. Clark, W.S. Webley, J. Chem. Soc., Dalton Trans. (1980) 2255.
[47] M.J. Gaudin, C.R. Clark, D.A. Buckingham, Inorg. Chem. 25 (1986) 2569.
[48] N.E. Brasch, D.A. Buckingham, C.R. Clark, A.J. Rogers, Inorg. Chem. 37 (1998) 4865.
[49] Z-L. Lu, M.S.A. Hamza, R. van Eldik, Eur. J. Inorg. Chem. (2001) 503.
[50] K.S. Min, T. Weyhermüller, K. Wieghardt, Dalton Trans. (2003) 1126.
[51] K. Sakai, Y. Yamada, T. Tsubomura, Inorg. Chem. 35 (1996) 3163.
[52] M.S. Davies, R.R. Fenton, F. Huq, E.C.H. Ling, T.W. Hambley, Aust. J. Chem. 53 (2000) 451.
[53] E.C. Plappert, D.M.P. Mingos, S.E. Lawrence, D.J. Williams, J. Chem. Soc., Dalton Trans. (1997) 2119.
[54] R. Kania, K. Lewinski, B. Sieklucka, Dalton Trans. (2003) 1033.
[55] B.-H. Ye, X.-Y. Li, F. Xueb, T.C.W. Mak, J. Chem. Soc., Chem. Commun. (1997) 2407.
[56] V.S. Nair, K.S. Hagen, Inorg. Chem. 31 (1992) 4048.
[57] V.S. Nair, K.S. Hagen, Inorg. Chem. 33 (1994) 185.
[58] K.S. Hagen, W.H. Armstrong, M.M. Olmstead, J. Am. Chem. Soc. 111 (1989) 774.
[59] R.J. Parker, L. Spiccia, S.R. Batten, J.D. Cashion, G.D. Fallon, Inorg. Chem. 40 (2001) 4696.
[60] V.F. Vasil'eva, O.Y. Lavrova, N.M. Dyatlova, V.G. Yashunskii, Zh. Obshch. Khim. 36 (1966) 674.
[61] R.J. Geue, A.M. Sargeson, R. Wijesekera, Aust. J. Chem. 46 (1993) 1021.
[62] A.M. Dittler-Klingemann, F.E. Hahn, Inorg. Chem. 35 (1996) 1996.
[63] H. Keypour, M. Dehdari, S. Salehzadeh, K.P. Wainwright, Transit. Metal Chem. 28 (2003) 425.
[64] A.M. Dittler-Klingemann, C. Orvig, F.E. Hahn, F. Thaler, C.D. Hubbard, R. van Eldik, S. Schindler, I. Fabian, Inorg. Chem. 35 (1996) 7798.
[65] C. Ochs, F.E. Hahn, T. Lugger, Eur. J. Inorg. Chem. (2001) 1279.
[66] Selective alkylation of polyalkylene-polyamines. Dow Chemical Corporation. French Patent 2112697 (1972).
[67] R.L. Fanshawe, A.G. Blackman, Inorg. Chem. 34 (1995) 421.
[68] M. Israel, J.S. Rosenfield, E.J. Modest, J. Med. Chem. 7 (1964) 710.
[69] S.A. McCormack, B.J. Zimmerman, M. Israel, P. Blanner, L.R. Johnson, Mol. Pharmacol. 48 (1995) 724.
[70] H. Keypour, M. Dehdari, S. Salehzadeh, Asian J. Chem. 14 (2002) 856.
[71] R.L. Fanshawe, A.G. Blackman, C.R. Clark, Inorg. Chim. Acta 342 (2003) 114.
[72] F.G. Mann, W.J. Pope, J. Chem. Soc. (1926) 489.
[73] H. Keypour, D.A. Stotter, Inorg. Chim. Acta 33 (1979) L149.
[74] M. Streater, P.D. Taylor, R.C. Hider, J. Porter, J. Med. Chem. 33 (1990) 1749.
[75] O.F. Wiedeman, W.H. Montgomery, J. Am. Chem. Soc. 67 (1945) 1994.
[76] J.L. Van Winkle, J.D. McClure, P.H. Williams, J. Org. Chem. 31 (1966) 3300.
[77] J.A. Laurino, S. Knapp, H.J. Schugar, Inorg. Chem. 17 (1978) 2027.
[78] F.E. Hahn, M. Tamm, Angew. Chem., Int. Ed. Engl. 30 (1991) 203.
[79] B. Dietrich, D.L. Fyles, T.M. Fyles, J.M. Lehn, Helv. Chim. Acta 62 (1979) 2763.
[80] F. Renaud, C. Decurnex, C. Piguet, G. Hopfgartner, J. Chem. Soc., Dalton Trans. (2001) 1863.
[81] M.M. Ibrahim, K. Ichikawa, M. Shiro, Inorg. Chim. Acta 353 (2003) 187.
[82] P. Paoletti, A. Dei, A. Vacca, Inorg. Chem. 7 (1968) 865.
[83] A. Vacca, P. Paoletti, J. Chem. Soc. A (1968) 2378.
[84] S.S. Massoud, F.A. Mautner, M.A.M. Abu-Youssef, N.M. Shuaib, Polyhedron 18 (1999) 2061.
[85] E.V. Rybak-Akimova, A.Y. Nazarenko, S.S. Silchenko, Inorg. Chem. 38 (1999) 2974.
[86] K.N. Raymond, J.L. Shafer, Inorg. Chem. 10 (1971) 1799.
[87] A.M. Dittler-Klingemann, F.E. Hahn, C. Orvig, S.J. Rettig, Acta Crystallogr., Sect. C 52 (1996) 1957.
[88] S.S. Massoud, Transit. Metal Chem. 22 (1997) 583.
[89] S.S. Massoud, R.M. Milburn, Polyhedron 8 (1989) 2389.
[90] G.H. Rawji, V.M. Lynch, Acta Crystallogr., Sect. C 48 (1992) 1667.
[91] M. Banaszczyk, J.J. Lee, F.M. Menger, Inorg. Chem. 30 (1991) 1972.
[92] J.A. Connolly, J.-H. Kim, M. Banaszczyk, M. Drouin, J. Chin, Inorg. Chem. 34 (1995) 1094.
[93] J.A. Connolly, M. Banaszczyk, R.C. Hynes, J. Chin, Inorg. Chem. 33 (1994) 665.
[94] G. Rawji, M. Hediger, R.M. Milburn, Inorg. Chim. Acta 79 (1983) 247.
[95] F. Tafesse, S.S. Massoud, R.M. Milburn, Inorg. Chem. 24 (1985) 2591.
[96] J. Chin, M. Banaszczyk, J. Am. Chem. Soc. 111 (1989) 4103.
[97] M. Komiyama, Y. Matsumoto, H. Takahashi, T. Shiiba, H. Tsuzuki, H. Yajima, M. Yashiro, J. Sumaoka, J. Chem. Soc., Perkin Trans. 2 (1998) 691.
[98] J. Chin, M. Banaszczyk, V. Jubian, X. Zou, J. Am. Chem. Soc. 111 (1989) 186.
[99] R.W. Hay, N. Govan, Transit. Metal Chem. 23 (1998) 721.
[100] J. Chin, M. Banaszczyk, J. Am. Chem. Soc. 111 (1989) 2724.
[101] J. Chin, J.H. Kim, Angew. Chem. Int. Ed. Engl. 29 (1990) 523.
[102] A.M. Calafat, L.G. Marzilli, Inorg. Chem. 32 (1993) 2906.
[103] A.M. Calafat, L.G. Marzilli, Inorg. Chem. 31 (1992) 1719.
[104] H. Keypour, S. Salehzadeh, Transit. Metal Chem. 25 (2000) 205.
[105] N.J. Lundin, I.G. Hamilton, A.G. Blackman, Polyhedron 23 (2004) 97.
[106] H. Keypour, S. Salehzadeh, R.G. Pritchard, R.V. Parish, Inorg. Chem. 39 (2000) 5787.
[107] M. Niitsu, H. Sano, K. Samejima, Chem. Pharm. Bull. 40 (1992) 2958.

[108] H. Keypour, R.G. Pritchard, R.V. Parish, Transit. Metal Chem. 23 (1998) 121.
[109] F.J. Weigert, J. Org. Chem. 43 (1978) 622.
[110] V.M. Masters, P.V. Bernhardt, L.R. Gahan, B. Moubaraki, K.S. Murray, K.J. Berry, J. Chem. Soc., Dalton Trans. (1999) 2323.
[111] Y. Shi, C. Cao, A.L. Odom, Inorg. Chem. 43 (2004) 275.
[112] J.M. Tanski, G. Parkin, Inorg. Chem. 42 (2003) 264.
[113] F. Mani, G. Scapacci, Inorg. Chim. Acta 38 (1980) 151.
[114] W.L. Driessen, Recl. Trav. Chim. Pays-Bas 101 (1982) 441.
[115] G.J. van Driel, W.L. Driessen, J. Reedijk, Inorg. Chem. 24 (1985) 2919.
[116] W.L. Driessen, W.G.R. Wiesmeijer, M. Schipper-Zablotskaja, R.A.G. De Graaff, J. Reedijk, Inorg. Chim. Acta 162 (1989) 233.
[117] W.L. Driessen, R.A.G. De Graaff, W.G.R. Wiesmeijer, Acta Crystallogr., Sect. C 43 (1987) 2319.
[118] A.L. Spek, A.J.M. Duisenberg, W.L. Driessen, W.G.R. Wiesmeijer, Acta Crystallogr., Sect C 44 (1988) 623.
[119] A.L. Spek, W.L. Driessen, W.G.R. Wiesmeijer, Acta Crystallogr., Sect. C 44 (1988) 1567.
[120] M.J. Fernandez, M.J. Rodriguez, L.A. Oro, Polyhedron 10 (1991) 1595.
[121] C. Benelli, I. Bertini, M. Di Vaira, F. Mani, Inorg. Chem. 23 (1984) 1422.
[122] G.J. Kleywegt, W.G.R. Wiesmeijer, G.J. van Driel, W.L. Driessen, J. Reedijk, J.H. Noordik, J. Chem. Soc., Dalton Trans. (1985) 2177.
[123] W.L. Driessen, R.A.G. de Graaff, J. Ochocki, J. Reedijk, Inorg. Chim. Acta 150 (1988) 41.
[124] C.R. Randall, L. Shu, Y.-M. Chiou, K.S. Hagen, M. Ito, N. Kitajima, R.J. Lachicotte, Y. Zang, L. Que Jr., Inorg. Chem. 34 (1995) 1036.
[125] C.R. Randall, Y. Zang, A.E. True, L. Que Jr., J.M. Charnock, C.D. Garner, Y. Fujishima, C.J. Schofield, J.E. Baldwin, Biochemistry 32 (1993) 6664.
[126] Y. Zang, H.G. Jang, Y.-M. Chiou, M.P. Hendrich, L. Que Jr., Inorg. Chim. Acta 213 (1993) 41.
[127] Z.-H. Zhang, H.-L. Yang, Z.-H. Ma, A.-D. Qi, Chinese J. Chem. 18 (2000) 842.
[128] I. Bertini, G. Canti, C. Luchinat, F. Mani, Inorg. Chem. 20 (1981) 1670.
[129] I. Bertini, G. Canti, C. Luchinat, F. Mani, Inorg. Chim. Acta 46 (1980) L91.
[130] A.A. Watson, D.A. House, P.J. Steel, Aust. J. Chem. 48 (1995) 1549.
[131] Z. Chen, N. Karasek, D.C. Craig, S.B. Colbran, J. Chem. Soc., Dalton Trans. (2000) 3445.
[132] O. Juanes, J. De Mendoza, J.C. Rodriguez-Ubis, J. Chem. Soc., Chem. Commun. (1985) 1765.
[133] F. Mani, C. Mealli, Inorg. Chim. Acta 54 (1981) L77.
[134] F. Mani, Inorg. Nucl. Chem. Lett. 17 (1981) 45.
[135] T.N. Sorrell, D.L. Jameson, Inorg. Chem. 21 (1982) 1014.
[136] T.N. Sorrell, A.S. Borovik, Inorg. Chem. 26 (1987) 1957.
[137] A. Bencini, F. Mani, Inorg. Chim. Acta 87 (1984) L9.
[138] M. Di Vaira, F. Mani, J. Chem. Soc., Dalton Trans. (1985) 2327.
[139] M.R. Malachowski, H.B. Huynh, L.J. Tomlinson, R.S. Kelly, J.W. Furbee Jr., J. Chem. Soc., Dalton Trans. (1995) 31.
[140] M. Di Vaira, F. Mani, Inorg. Chim. Acta 70 (1983) 99.
[141] F. Mani, C. Mealli, Inorg. Chim. Acta 63 (1982) 97.
[142] M. Di Vaira, P. Stoppioni, F. Mani, J. Organomet. Chem. 247 (1983) 95.
[143] L. Banci, C. Benelli, D. Gatteschi, F. Mani, Inorg. Chem. 21 (1982) 1133.
[144] M. Di Vaira, F. Mani, Inorg. Chem. 23 (1984) 409.
[145] A.D. Shukla, A. Das, Polyhedron 19 (2000) 2605.
[146] R.H. Fish, M.S. Konings, K.J. Oberhausen, R.H. Fong, W.M. Yu, G. Christou, J.B. Vincent, D.K. Coggin, R.M. Buchanan, Inorg. Chem. 30 (1991) 3002.
[147] K.J. Oberhausen, R.J. O'Brien, J.F. Richardson, R.M. Buchanan, Inorg. Chim. Acta 173 (1990) 145.
[148] M.S. Mashuta, L. Cheruzel, R.M. Buchanan, Acta Crystallogr., Sect. C 58 (2002) o629.
[149] Y.-H. Chiu, J.W. Canary, Inorg. Chem. 42 (2003) 5107.
[150] L.E. Cheruzel, J. Wang, M.S. Mashuta, R.M. Buchanan, Chem. Commun. (2002) 2166.
[151] R.M. Buchanan, S. Chen, J.F. Richardson, M. Bressan, L. Forti, A. Morvillo, R.H. Fish, Inorg. Chem. 33 (1994) 3208.
[152] J. Wang, M.S. Mashuta, Z. Sun, J.F. Richardson, D.N. Hendrickson, R.M. Buchanan, Inorg. Chem. 35 (1996) 6642.
[153] K.J. Oberhausen, R.J. O'Brien, J.F. Richardson, R.M. Buchanan, R. Costa, J.-M. Latour, H.L. Tsai, D.N. Hendrickson, Inorg. Chem. 32 (1993) 4561.
[154] D.C. Bebout, M.M. Garland, G.S. Murphy, E.V. Bowers, C.J. Abelt, R.J. Butcher, Dalton Trans. (2003) 2578.
[155] L.K. Thompson, B.S. Ramaswamy, E.A. Seymour, Can. J. Chem. 55 (1977) 878.
[156] L.-F. Jin, F.-P. Xiao, W.-X. Chen, Huaxue Shiji 25 (2003) 233.
[157] M. Pascaly, C. Nazikkol, F. Schweppe, A. Wiedemann, K. Zurlinden, B. Krebs, Z. Anorg. Allg. Chem. 626 (2000) 50.
[158] K. Nakata, N. Shimomura, N. Shiina, M. Izumi, K. Ichikawa, M. Shiro, J. Inorg. Biochem. 89 (2002) 255.
[159] W.-H. Zhou, Z.-W. Mizo, X.-L. Liu, F.-M. Miao, H.-G. Wang, X.-K. Yao, Jiegou Huaxue 18 (1999) 204.
[160] B. Ji, C. Du, Y. Zhu, K. Ding, J. Chem. Crystallogr. 30 (2001) 783.
[161] H.M.J. Hendriks, P.J.M.W.L. Birker, G.C. Verschoor, J. Reedijk, J. Chem. Soc., Dalton Trans. (1982) 623.
[162] Y. Nakao, M. Onoda, T. Sakurai, A. Nakahara, I. Kinoshita, S. Ooi, Inorg. Chim. Acta 151 (1988) 55.
[163] C.-Y. Su, B.-S. Kang, C.-X. Du, Q.-C. Yang, T.C.W. Mak, Inorg. Chem. 39 (2000) 4843.
[164] C.-Y. Su, X.-P. Yang, B.-S. Kang, T.C.W. Mak, Angew. Chem., Int. Ed. Engl. 40 (2001) 1725.
[165] T. Sakurai, H. Oi, A. Nakahara, Inorg. Chim. Acta 92 (1984) 131.
[166] C.-Y. Su, B.-S. Kang, T.-B. Wen, Y.-X. Tong, X.-P. Yang, C. Zhang, H.-Q. Liu, J. Sun, Polyhedron 18 (1999) 1577.
[167] R. Burth, H. Vahrenkamp, Z. Anorg. Allg. Chem. 624 (1998) 381.
[168] F.-M. Miao, Z. Fan, W.-H. Zhou, L.-N. Qi, A.-X. Li, X.-L. Liu, Wuli Huaxue Xuebao 15 (1999) 775.
[169] M.S. Lah, H. Chun, Inorg. Chem. 36 (1997) 1782.
[170] D.-F. Xiang, C.-Y. Duan, X.-S. Tan, Q.-W. Hang, W.-X. Tang, J. Chem. Soc., Dalton Trans. (1998) 1201.
[171] D.-F. Xiang, X.-S. Tan, Q.-W. Hang, W.-X. Tang, B.-M. Wu, T.C.W. Mak, Inorg. Chim. Acta 277 (1998) 21.
[172] A.R. Oki, P.R. Bommarreddy, H.-M. Zhang, N. Hosmane, Inorg. Chim. Acta 231 (1995) 109.
[173] M.F. Summers, J. Van Rijn, J. Reedijk, L.G. Marzilli, J. Am. Chem. Soc. 108 (1986) 4254.
[174] R. Wietzke, M. Mazzanti, J.-M. Latour, J. Pecaut, J. Chem. Soc., Dalton Trans. (2000) 4167.
[175] C.-Y. Su, B.-S. Kang, Q.-C. Yang, T.C.W. Mak, J. Chem. Soc., Dalton Trans. (2000) 1857.
[176] R. Wietzke, M. Mazzanti, J.-M. Latour, J. Pecaut, Jacques. Chem. Commun. (1999) 209.
[177] C.-Y. Su, Q.-C. Wang, T.C.W. Mak, C.-Y. Su, B.-S. Kang, H.-Q. Liu, Chem. Commun. (1998) 1551.
[178] C.-Y. Su, B.-S. Kang, X.-Q. Mu, J. Sun, Y.-X. Tong, Z.-N. Chen, Aust. J. Chem. 51 (1998) 565.
[179] C.-Y. Su, B.-S. Kang, Q.-G. Wang, T.C.W. Mak, J. Chem. Soc., Dalton Trans. (2000) 1831.
[180] G. Anderegg, F. Wenk, Helv. Chim. Acta 50 (1967) 2330.
[181] J.W. Canary, Y. Wang, R. Roy Jr., L. Que Jr., H. Miyake, Inorg. Synth. 32 (1998) 70.

[182] D. Britton, R.E. Norman, L. Que Jr., Acta Crystallogr., Sect. C 47 (1991) 2415.
[183] A. Hazell, J. McGinley, H. Toftlund, J. Chem. Soc., Dalton Trans. (1999) 1271.
[184] H. Sugimoto, H. Miyake, H. Tsukube, J. Chem. Soc., Dalton Trans. (2002) 4535.
[185] G. Anderegg, E. Hubmann, N.G. Podder, F. Wenk, Helv. Chim. Acta 60 (1977) 123.
[186] J.C. Mareque-Rivas, R. Prabaharan, R.T. Martin de Rosales, Chem. Commun. (2004) 76.
[187] G. Anderegg, K. Popov, P.S. Pregosin, Helv. Chim. Acta 69 (1986) 329.
[188] A. Hazell, J. McGinley, H. Toftlund, Inorg. Chim. Acta 323 (2001) 113.
[189] C.S. Allen, C.-L. Chuang, M. Cornebise, J.W. Canary, Inorg. Chim. Acta 239 (1995) 29.
[190] A. Diebold, K.S. Hagen, Inorg. Chem. 37 (1998) 215.
[191] D.C. Bebout, D.E. Ehmann, J.C. Trinidad, K.K. Crahan, M.E. Kastner, D. Parrish, Inorg. Chem. 36 (1997) 4257.
[192] D.C. Bebout, S.W. Stokes, R.J. Butcher, Inorg. Chem. 38 (1999) 1126.
[193] Y. Gultneh, A. Farooq, K.D. Karlin, S. Liu, J. Zubieta, Inorg. Chim. Acta 211 (1993) 171.
[194] M. Costas, K. Chen, L. Que Jr., Coord. Chem. Rev. 200–202 (2000) 517.
[195] R.A. Leising, R.E. Norman, L. Que Jr., Inorg. Chem. 29 (1990) 2553.
[196] J. Kim, R.G. Harrison, C. Kim, L. Que Jr., J. Am. Chem. Soc. 118 (1996) 4373.
[197] R.A. Leising, J. Kim, M.A. Perez, L. Que Jr., J. Am. Chem. Soc. 115 (1993) 9524.
[198] J. Kim, E. Larka, E.C. Wilkinson, L. Que Jr., Angew. Chem., Int. Ed. Engl. 34 (1995) 2048.
[199] I.W.C.E. Arends, K.U. Ingold, D.D.M. Wayner, J. Am. Chem. Soc. 117 (1995) 4710.
[200] P.A. MacFaul, I.W.C.E. Arends, K.U. Ingold, D.D.M. Wayner, J. Chem. Soc., Perkin Trans. 2 (1997) 135.
[201] M.H. Lim, J.-U. Rohde, A. Stubna, M.R. Bukowski, M. Costas, R.Y.N. Ho, E. Munck, W. Nam, L. Que Jr., Proc. Natl. Acad. Sci. USA 100 (2003) 3665.
[202] K.D. Karlin, J.C. Hayes, S. Juen, J.P. Hutchinson, J. Zubieta, Inorg. Chem. 21 (1982) 4106.
[203] Z. Tyeklár, R.R. Jacobson, N. Wei, N.N. Murthy, J. Zubieta, K.D. Karlin, J. Am. Chem. Soc. 115 (1993) 2677.
[204] R.R. Jacobson, Z. Tyeklár, K.D. Karlin, J. Zubieta, Inorg. Chem. 30 (1991) 2035.
[205] R.J. Parker, L. Spiccia, B. Moubaraki, K.S. Murray, B.W. Skelton, A.H. White, Inorg. Chim. Acta 300–302 (2000) 922.
[206] A. Rodríguez-Fortea, P. Alemany, S. Alvarez, E. Ruiz, A. Scuiller, C. Decroix, V. Marvaud, J. Vaissermann, M. Verdaguer, I. Rosenman, M. Julve, Inorg. Chem. 40 (2001) 5868.
[207] M.E. Helton, P. Chen, P.P. Paul, Z. Tyeklár, R.D. Sommer, L.N. Zakharov, A.L. Rheingold, E.I. Solomon, K.D. Karlin, J. Am. Chem. Soc. 125 (2003) 1160.
[208] Z. Tyeklár, P.P. Paul, R.R. Jacobson, A. Farooq, K.D. Karlin, J. Zubieta, J. Am. Chem. Soc. 111 (1989) 388.
[209] B.S. Lim, R.H. Holm, Inorg. Chem. 37 (1998) 4898.
[210] S. Yan, J. Cui, X. Liu, P. Cheng, D. Liao, Z. Jiang, G. Wang, H. Wang, X. Yao, Sci. China, Ser. B 42 (1999) 535.
[211] H. Oshio, H. Ichida, J. Phys. Chem. 99 (1995) 3294.
[212] R.J. Parker, K.D. Lu, S.R. Batten, B. Moubaraki, K.S. Murray, L. Spiccia, J.D. Cashion, A.D. Rae, A.C. Willis, J. Chem. Soc., Dalton Trans. (2002) 3723.
[213] D.M. Corsi, N.N. Murthy, V.G. Young Jr., K.D. Karlin, Inorg. Chem. 38 (1999) 848.
[214] G.L. Abbati, A. Caneschi, A. Cornia, A.C. Fabretti, Y.A. Pozdniakova, O.I. Shchegolikhina, Angew. Chem., Int. Ed. Engl. 41 (2002) 4517.
[215] N.J. Robertson, M.J. Carney, J.A. Halfen, Inorg. Chem. 42 (2003) 6876.
[216] D.J. Hodgson, M.H. Zietlow, E. Pedersen, H. Toftlund, Inorg. Chim. Acta 149 (1988) 111.
[217] B.G. Gafford, R.A. Holwerda, H.J. Schugar, J.A. Potenza, Inorg. Chem. 27 (1988) 1126.
[218] B.G. Gafford, R.A. Holwerda, Inorg. Chem. 28 (1989) 60.
[219] N.K. Dalley, X. Kou, C.J. O'Connor, R.A. Holwerda, Inorg. Chem. 35 (1996) 2196.
[220] B.G. Gafford, R.E. Marsh, W.P. Schaefer, J.H. Zhang, C.J. O'Connor, R.A. Holwerda, Inorg. Chem. 29 (1990) 4652.
[221] R.A. Holwerda, Polyhedron 13 (1994) 737.
[222] T. Kojima, Chem. Lett. (1996) 121.
[223] M. Yamaguchi, H. Kousaka, T. Yamagishi, Chem. Lett. (1997) 769.
[224] T. Kojima, T. Sakamoto, Y. Matsuda, Inorg. Chem. 43 (2004) 2243.
[225] M. Krom, T.P.J. Peters, R.G.E. Coumans, T.J.J. Sciarone, J. Hoogboom, S.I. ter Beek, P.P.J. Schlebos, J.M.M. Smits, R. de Gelder, A.W. Gal, Eur. J. Inorg. Chem. (2003) 1072.
[226] B. De Bruin, M.J. Boerakker, J.J.J.M. Donners, B.E.C. Christiaans, P.P.J. Schlebos, R. De Gelder, J.M.M. Smits, A.L. Spek, A.W. Gal, Angew. Chem., Int. Ed. Engl. 36 (1997) 2064.
[227] B. De Bruin, M.J. Boerakker, J.A.W. Verhagen, R. De Gelder, J.M.M. Smits, A.W. Gal, Chem. Eur. J. 6 (2000) 298.
[228] C.A. Otter, R.M. Hartshorn, Dalton Trans. (2004) 150.
[229] H. Adams, N.A. Bailey, D.E. Fenton, Q.-Y. He, J. Chem. Soc., Dalton Trans. (1997) 1533.
[230] M. Ito, K. Fujita, F. Chitose, T. Takeuchi, K. Yoshida, Y.-S. Takita, Chem. Lett. (2002) 594.
[231] N.N. Murthy, K.D. Karlin, J. Chem. Soc., Chem. Commun. (1993) 1236.
[232] H. Adams, N.A. Bailey, D.E. Fenton, Q.-Y. He, J. Chem. Soc., Dalton Trans. (1995) 697.
[233] Z.-W. Mao, Q.-W. Hang, W.-X. Tang, S.-X. Liu, Z.-M. Wang, J.-L. Huang, Polyhedron 15 (1996) 321.
[234] M. Ito, Y. Takita, Chem. Lett. (1996) 929.
[235] M. Ito, K. Sakai, T. Tsubomura, Y. Takita, Bull. Chem. Soc. Jpn. 72 (1999) 239.
[236] R.E. Marsh, M. Kapon, S. Hu, F.H. Herbstein, Acta Crystallogr., Sect. B 58 (2002) 62.
[237] B. Tong, R.E. Norman, S.-C. Chang, Acta Crystallogr., Sect. C 55 (1999) 1236.
[238] S.-P. Yan, L. Zhang, H.-L. Yan, D.-Z. Liao, Z.-H. Jiang, G.-L. Wang, H.-G. Wang, X.-K. Yao, Huaxue Xuebao 57 (1999) 583.
[239] B. Tong, S.-C. Chang, E.E. Carpenter, C.J. O'Connor, J.O. Lay Jr., R.E. Norman, Inorg. Chim. Acta 300–302 (2000) 855.
[240] M. Ito, H. Kawano, T. Takeuchi, Y.-S. Takita, Chem. Lett. (2000) 372.
[241] L. Yang, Y. Peng, F. Bian, S.-P. Yan, D.-Z. Liao, P. Cheng, Z.-H. Jiang, J. Coord. Chem. 56 (2003) 961.
[242] R.M. Chin, R.H. Dubois, L.E. Helberg, M. Sabat, T.Y. Bartucz, A.J. Lough, R.H. Morris, W.D. Harman, Inorg. Chem. 36 (1997) 3553.
[243] H. Sugimoto, Y. Sasaki, Chem. Lett. (1997) 541.
[244] H. Sugimoto, Y. Sasaki, Chem. Lett. (1998) 197.
[245] R.A. Holwerda, B.R. Whittlesey, M.J. Nilges, Inorg. Chem. 37 (1998) 64.
[246] D.K. Towle, C.A. Botsford, D.J. Hodgson, Inorg. Chim. Acta 141 (1988) 167.
[247] R. Wietzke, M. Mazzanti, J.-M. Latour, J. Pecaut, P.-Y. Cordier, C. Madic, Inorg. Chem. 37 (1998) 6690.
[248] K.D. Karlin, J.C. Hayes, J.P. Hutchinson, J.R. Hyde, J. Zubieta, Inorg. Chim. Acta 64 (1982) L219.

[249] C.M. Che, V.W.W. Yam, T.C.W. Mak, J. Am. Chem. Soc. 112 (1990) 2284.
[250] S.K. Brownstein, P.-Y. Plouffe, C. Bensimon, J. Tse, Inorg. Chem. 33 (1994) 354.
[251] M. Schatz, M. Becker, F. Thaler, F. Hampel, S. Schindler, R.R. Jacobson, Z. Tyeklár, N.N. Murthy, P. Ghosh, Q. Chen, J. Zubieta, K.D. Karlin, Inorg. Chem. 40 (2001) 2312.
[252] E.A. Ambundo, M.-V. Deydier, A.J. Grall, N. Aguera-Vega, L.T. Dressel, T.H. Cooper, M.J. Heeg, L.A. Ochrymowycz, D.B. Rorabacher, Inorg. Chem. 38 (1999) 4233.
[253] K.D. Karlin, P.L. Dahlstrom, J.C. Hayes, R.A. Simon, J. Zubieta, Cryst. Struct. Commun. 11 (1982) 907.
[254] E.H. Alilou, A.E. Hallaoui, H.E. Ghadraoui, M. Giorgi, M. Pierrot, M. Réglier, Acta Crystallogr., Sect. C 53 (1997) 559.
[255] F. Jiang, R.R. Conry, L. Bubacco, Z. Tyeklár, R.R. Jacobson, K.D. Karlin, J. Peisach, J. Am. Chem. Soc. 115 (1993) 2093.
[256] E.A. Ambundo, M.-V. Deydier, L.A. Ochrymowycz, D.B. Rorabacher, Inorg. Chem. 39 (2000) 1171.
[257] H.K. Baek, K.D. Karlin, R.A. Holwerda, Inorg. Chem. 25 (1986) 2347.
[258] T. Osako, S. Nagatomo, Y. Tachi, T. Kitagawa, S. Itoh, Angew. Chem., Int. Ed. Engl. 41 (2002) 4325.
[259] X. Xu, C.S. Allen, C.-L. Chuang, J.W. Canary, Acta Crystallogr., Sect C 54 (1998) 600.
[260] K.E. Baxter, L.R. Hanton, J. Simpson, B.R. Vincent, A.G. Blackman, Inorg. Chem. 34 (1995) 2795.
[261] C.-L. Chuang, M. Frid, J.W. Canary, Tetrahedron Lett. 36 (1995) 2909.
[262] C.M. Che, V.W.W. Yam, J. Am. Chem. Soc. 109 (1987) 1262.
[263] M. Mazzanti, R. Wietzke, J. Pécaut, J.-M. Latour, P. Maldivi, M. Remy, Inorg. Chem. 41 (2002) 2389.
[264] F. Højland, H. Toftlund, S. Yde-Andersen, Acta Chem. Scand., Ser. A 37 (1983) 251.
[265] A.R. Oki, J. Glerup, D.J. Hodgson, Inorg. Chem. 29 (1990) 2435.
[266] R. Viswanathan, M. Palaniandavar, T. Balasubramanian, T.P. Muthiah, Inorg. Chem. 37 (1998) 2943.
[267] Y. Gultneh, T.B. Yisgedu, Y.T. Tesema, R.J. Butcher, Inorg. Chem. 42 (2003) 1857.
[268] J. Dietrich, F.W. Heinemann, A. Schrodt, S. Schindler, Inorg. Chim. Acta 288 (1999) 206.
[269] S. Schindler, O. Walter, J.Z. Pedersen, H. Toftlund, Inorg. Chim. Acta 303 (2000) 215.
[270] A. Jancso, I. Toeroek, L. Korecz, A. Rockenbauer, T. Gajda, J. Chem. Soc., Dalton Trans. (2002) 2601.
[271] N. Wei, N.M. Murthy, Q. Chen, J. Zubieta, K.D. Karlin, Inorg. Chem. 33 (1994) 1953.
[272] N. Wei, N.M. Murthy, K.D. Karlin, Inorg. Chem. 33 (1994) 6093.
[273] D.E. Fenton, G. Rossi, Inorg. Chim. Acta 98 (1985) L29.
[274] H. Adams, N.A. Bailey, W.D. Carlisle, D.E. Fenton, G. Rossi, J. Chem. Soc., Dalton Trans. (1990) 1271.
[275] R. Dohno, J.-I. Satho, A. Shimura, Oriental J. Chem. 12 (1996) 109.
[276] R. Dohno, S. Goto, A. Tanigawa, T. Hakushi, Nippon Kagaku Kaishi (1994) 435.
[277] H. Adams, M.R.J. Elsegood, D.E. Fenton, S.L. Heath, S.J. Ryan, J. Chem. Soc., Dalton Trans. (1999) 2031.
[278] T.-H. Cheng, Y.-M. Wang, W.-T. Lee, G.-C. Liu, Polyhedron 19 (2000) 2027.
[279] M.E.G. Skinner, D.A. Cowhig, P. Mountford, Chem. Commun. (2000) 1167.
[280] M.E.G. Skinner, Y. Li, P. Mountford, Inorg. Chem. 41 (2002) 1110.
[281] T-.H. Cheng, Y.-M. Wang, K.-T. Lin, G.-C. Liu, J. Chem. Soc., Dalton Trans. (2001) 3357.
[282] G.S. Matouzenko, A. Bousseksou, S.A. Borshch, M. Perrin, S. Zein, L. Salmon, G. Molnar, S. Lecocq, Inorg. Chem. 43 (2004) 227.
[283] S.J. Grant, P. Moore, H.A.A. Omar, N.W. Alcock, J. Chem. Soc., Dalton Trans. (1994) 485.
[284] M.L. Turonek, P. Moore, H.J. Clase, N.W. Alcock, J. Chem. Soc., Dalton Trans. (1995) 3659.
[285] R.W. Hay, T. Clifford, P. Lightfoot, Polyhedron 17 (1998) 4347.
[286] H.-B. Jeon, Y. Lee, C. Qiao, H. Huang, L.M. Sayre, Bioorg. Med. Chem. 11 (2003) 4631.
[287] E. Profft, S. Lojack, Rev. Chim., Acad. Rep. Populaire Roumaine 7 (1962) 405.
[288] J.B. Mandel, C. Maricondi, B.E. Douglas, Inorg. Chem. 27 (1988) 2990.
[289] G.S. Matouzenko, A. Bousseksou, S. Lecocq, P.J. van Koningsbruggen, M. Perrin, O. Kahn, A. Collet, Inorg. Chem. 36 (1997) 2975.
[290] K. Hanaoka, K. Kikuchi, Y. Urano, T. Nagano, J. Chem. Soc., Perkin Trans. 2. (2001) 1840.
[291] M. Schatz, M. Leibold, S.P. Foxon, M. Weitzer, F.W. Heinemann, F. Hampel, O. Walter, S. Schindler, Dalton Trans. (2003) 1480.
[292] J.M. Rowland, M. Olmstead, P.K. Mascharak, Inorg. Chem. 40 (2001) 2810.
[293] C. Incarvito, M. Lam, B. Rhatigan, A.L. Rheingold, C.J. Qin, A.L. Gavrilova, B. Bosnich, J. Chem. Soc., Dalton Trans. (2001) 3478.
[294] D.S. Marlin, M.M. Olmstead, P.K. Mascharak, Eur. J. Inorg. Chem. (2002) 859.
[295] A.K. Patra, M.M. Olmstead, P.K. Mascharak, Inorg. Chem. 41 (2002) 5403.
[296] J.B. Mandel, B.E. Douglas, Inorg. Chim. Acta 155 (1989) 55.
[297] M. Weitzer, M. Schatz, F. Hampel, F.W. Heinemann, S. Schindler, J. Chem. Soc., Dalton Trans. (2002) 686.
[298] G.S. Matouzenko, J.-F. Letard, S. Lecoeq, A. Bousseksou, L. Capes, L. Salmon, M. Perrin, O. Kahn, A. Collet, Eur. J. Inorg. Chem. (2001) 2935.
[299] O. Horner, M.-F. Charlot, A. Boussac, E. Anxolabehere-Mallart, L. Tchertanov, J. Guilhelm, J.-J. Girerd, Eur. J. Inorg. Chem. (1998) 721.
[300] G.S. Matouzenko, A. Bousseksou, S. Lecocq, P.J. van Koningsbruggen, M. Perrin, O. Kahn, A. Collet, Inorg. Chem. 36 (1997) 5869.
[301] S. Yamanaka, H. Okawa, K. Motoda, M. Yonemura, D.E. Fenton, M. Ebadi, A.B.P. Lever, Inorg. Chem. 38 (1999) 1825.
[302] M. Pascaly, M. Duda, F. Schweppe, K. Zurlinden, F.K. Muller, B. Krebs, J. Chem. Soc., Dalton Trans. (2001) 828.
[303] X.-P. Yang, B.-S. Kang, W.-K. Wong, C.-Y. Su, H.-Q. Liu, Inorg. Chem. 42 (2003) 169.
[304] L. Zhang, J. Liu, L.-R. Deng, H.-X. Zhang, Y.-P. Cai, H.-Q. Liu, B.-S. Kang, Huaxue Xuebao 60 (2002) 566.
[305] N. Wei, N.N. Murthy, Z. Tyeklár, K.D. Karlin, Inorg. Chem. 33 (1994) 1177.
[306] J. Wang, M.S. Mashuta, J.F. Richardson, R.M. Buchanan, Acta Crystallogr., Sect. C 51 (1995) 50.
[307] M.U. Triller, W.-Y. Hsieh, V.L. Pecoraro, A. Rompel, B. Krebs, Inorg. Chem. 41 (2002) 5544.
[308] M.U. Triller, D. Pursche, W.-Y. Hsieh, V.L. Pecoraro, A. Rompel, B. Krebs, Inorg. Chem. 42 (2003) 6274.
[309] M. Pascaly, M. Duda, A. Rompel, B.H. Sift, W. Meyer-Klaucke, B. Krebs, Inorg. Chim. Acta 291 (1999) 289.
[310] M. Merkel, M. Pascaly, M. Wieting, M. Duda, A. Rompel, Z. Anorg. Allg. Chem. 629 (2003) 2216.
[311] M. Scarpellini, J.C. Toledo, A. Neves, J. Ellena, E.E. Castellano, D.W. Franco, Inorg. Chim. Acta 357 (2004) 707.
[312] M. Scarpellini, A. Neves, E.E. Castellano, E.F. de Almeida Neves, D.W. Franco, Polyhedron 23 (2004) 511.

[313] Y. Nishida, T. Akamatsu, Chem. Lett. (1991) 2013.
[314] X.-P. Yang, C.-Y. Su, B.-S. Kang, X.-L. Feng, W.-L. Xiao, H.-Q. Liu, J. Chem. Soc., Dalton Trans. (2000) 3253.
[315] W.L. Driessen, D. Rehorst, J. Reedijk, I. Mutikainen, U. Turpeinen, Inorg. Chim. Acta 355 (2003) 64.
[316] H. Ohtsu, Y. Shimazaki, A. Odani, O. Yamauchi, W. Mori, S. Itoh, S. Fukuzumi, J. Am. Chem. Soc. 122 (2000) 5733.
[317] H. Ohtsu, S. Itoh, S. Nagatomo, T. Kitagawa, S. Ogo, Y. Watanabe, S. Fukuzumi, Inorg. Chem. 40 (2001) 3200.
[318] H. Ohtsu, S. Fukuzumi, Chem. Eur. J. 7 (2001) 4947.
[319] S.-C. Sheu, G.-H. Lee, T.-I. Ho, Y.-C. Lin, S.-M. Peng, Acta Crystallogr., Sect. C. 52 (1996) 56.
[320] J.-W. Lim, M. Mikuriya, H. Sakiyama, Bull. Chem. Soc. Jpn. 74 (2001) 2131.
[321] K. Chen, L. Que Jr., J. Am. Chem. Soc. 123 (2001) 6327.
[322] P. Mialane, L. Tchertanov, F. Banse, J. Sainton, J.-J. Girerd, Inorg. Chem. 39 (2000) 2440.
[323] H. Zheng, Y. Zang, Y. Dong, V.G. Young Jr., L. Que Jr., J. Am. Chem. Soc. 121 (1999) 2226.
[324] G. Anderegg, Inorg. Chim. Acta 111 (1986) 25.
[325] R.J. Motekaitis, A.E. Martell, D.A. Nelson, Inorg. Chem. 23 (1984) 275.
[326] R.J. Motekaitis, A.E. Martell, J.M. Lehn, E. Watanabe, Inorg. Chem. 21 (1982) 4253.
[327] R.M. Jellish, L.C. Thompson, J. Coord. Chem. 4 (1975) 199.
[328] G. McLendon, A.E. Martell, J. Coord. Chem. 4 (1975) 235.
[329] J.E. Prue, G. Schwarzenbach, Helv. Chim. Acta 33 (1950) 963.
[330] A. De Robertis, C. Foti, O. Giuffre, S. Sammartano, J. Chem. Eng. Data 46 (2001) 1425.
[331] S.P. Dagnall, D.N. Hague, A.D. Moreton, J. Chem. Soc., Dalton Trans. (1986) 1505.
[332] G. Anderegg, N.G. Podder, P. Blaeuenstein, M. Hangartner, H. Stuenzi, J. Coord. Chem. 4 (1975) 267.
[333] G. Anderegg, F. Wenk, Helv. Chim. Acta 54 (1971) 216.
[334] A. Zalkin, R.J. Sime, R.P. Dodge, D.H. Templeton, Inorg. Chem. 10 (1971) 537.
[335] M. Duggan, N. Ray, B. Hathaway, G. Tomlinson, P. Brint, K. Pelin, J. Chem. Soc., Dalton Trans. (1980) 1342.
[336] E.J. Laskowski, D.M. Duggan, D.N. Hendrickson, Inorg. Chem. 14 (1975) 2449.
[337] P.C. Jain, E.C. Lingafelter, J. Am. Chem. Soc. 89 (1967) 6131.
[338] C.C. Su, W.S. Lu, T.Y. Hui, T.Y. Chang, S.L. Wang, F.L. Liao, Polyhedron 12 (1993) 2249.
[339] M.J. Scott, S.C. Lee, R.H. Holm, Inorg. Chem. 33 (1994) 4651.
[340] M.A. Salam, K. Aoki, Inorg. Chim. Acta 314 (2001) 71.
[341] P.-L. Fabre, A.M. Galibert, B. Soula, F. Dahan, P. Castan, J. Chem. Soc., Dalton Trans. (2001) 1529.
[342] Y.-J. Liu, Z.-H. Liu, Jiegou Huaxue 17 (1998) 94.
[343] Z.-L. Lu, C.-Y. Duan, Y.-P. Tian, X.-Z. You, Polyhedron 15 (1996) 1769.
[344] H.-K. Fun, B.-C. Yip, Z.-L. Lu, C.-Y. Duan, Y.-B. Tian, X.-Z. You, Transit. Metal Chem. 21 (1996) 193.
[345] D.M. Duggan, D.N. Hendrickson, Inorg. Chem. 13 (1974) 1911.
[346] E.J. Laskowski, D.N. Hendrickson, Inorg. Chem. 17 (1978) 457.
[347] R.T. Stibrany, J.A. Potenza, H.J. Schugar, Acta Crystallogr., Sect. C 49 (1993) 1561.
[348] A. Marzotto, D.A. Clemente, G. Valle, Acta Crystallogr., Sect. C 50 (1994) 1451.
[349] Z.-L. Lu, C.-Y. Duan, X.-Z. You, Z.-Y. Zhou, T.C.W. Mak, J. Coord. Chem. 44 (1998) 151.
[350] A. Marzotto, A. Ciccarese, D.A. Clemente, G. Valle, J. Chem. Soc., Dalton Trans. (1995) 1461.
[351] G.D. Andreetti, P.C. Jain, E.C. Lingafelter, J. Am. Chem. Soc. 91 (1969) 4112.
[352] R.L. Fanshawe, C.R. Clark, A.G. Blackman, Acta Crystallogr., E E57 (2001) m17.
[353] L.F. McClintock, A.G. Blackman, unpublished results.
[354] X. Zhang, J.-L. Wang, F.-M. Miao, Huaxue Yanjiu Yu Yingyong 12 (2000) 503.
[355] M.S. Lah, M. Moon, Bull. Korean Chem. Soc. 18 (1997) 406.
[356] W.-H. Zhou, X.-L. Liu, F.-M. Miao, Wuji Huaxue Xuebao 16 (2000) 916.
[357] X. Zhang, J.-L. Wang, M. Yu, F.-M. Miao, Huaxue Xuebao 58 (2000) 1280.
[358] B.S. Hammes, M.T. Kieber-Emmons, R. Sommer, A.L. Rheingold, Inorg. Chem. 41 (2002) 1351.
[359] Z. Fan, X. Wen, W.-H. Zhou, X.-L. Liu, F.-M. Miao, Wuji Huaxue Xuebao 15 (1999) 601.
[360] W.-H. Zhou, X.-L. Liu, F.-M. Miao, H.-G. Wang, X.-K. Yao, Jiegou Huaxue 15 (1996) 288.
[361] J.-L. Tian, W. Gu, S.-P. Yan, D.-Z. Liao, Z.-H. Jiang, P. Cheng, J. Coord. Chem. 56 (2003) 275.
[362] N. Matsumoto, T. Akui, A. Ohyoshi, H. Okawa, Bull. Chem. Soc. Jpn. 61 (1988) 2250.
[363] E. Quiroz-Castro, S. Bernes, N. Barba-Behrens, R. Tapia-Benavides, R. Contreras, H. Noth, Polyhedron 19 (2000) 1479.
[364] R. Gregorzik, U. Hartmann, H. Vahrenkamp, Chem. Ber. 127 (1994) 2117.
[365] T. Brandsch, F.A. Schell, K. Weis, M. Ruf, B. Mueller, H. Vahrenkamp, Chem. Ber. 130 (1997) 283.
[366] D.E. Fenton, H. Adams, Q.-Y. He, Acta Crystallogr., Sect. C 54 (1988) 286.
[367] A. Muller-Hartmann, H. Vahrenkamp, Eur. J. Inorg. Chem. (2000) 2371.
[368] R.E. Marsh, Acta Crystallogr., Sect. B 55 (1999) 931.
[369] C. Nazikkol, R. Wegner, J. Bremer, B. Krebs, Z. Anorg. Allg. Chem. 622 (1996) 329.
[370] A. Machkour, D. Mandon, M. Lachkar, R. Welter, Inorg. Chem. 43 (2004) 1545.
[371] C.-L. Chuang, O. dos Santos, X. Xu, J.W. Canary, Inorg. Chem. 36 (1997) 1967.
[372] K. Jitsukawa, M. Harata, H. Arii, H. Sakurai, H. Masuda, Inorg. Chim. Acta 324 (2001) 108.
[373] S. Ogo, S. Wada, Y. Watanabe, M. Iwase, A. Wada, M. Harata, K. Jitsukawa, H. Masuda, H. Einaga, Angew. Chem., Int. Ed. Engl. 37 (1998) 2102.
[374] M. Harata, K. Jitsukawa, H. Masuda, H. Einaga, Chem. Lett. (1995) 61.
[375] Y. Bretonniere, M. Mazzanti, J. Pecaut, F.A. Dunand, A.E. Merbach, Chem. Commun. (2001) 621.
[376] Z. He, P.J. Chaimungkalanont, D.C. Craig, S.B. Colbran, J. Chem. Soc., Dalton Trans. (2000) 1419.
[377] C.-L. Chuang, K. Lim, Q. Chen, J. Zubieta, J.W. Canary, Inorg. Chem. 34 (1995) 2562.
[378] M.M. Da Mota, J. Rodgers, S.M. Nelson, J. Chem. Soc. A (1969) 2036.
[379] M.P. Jensen, S.J. Lange, M.P. Mehn, E.L. Que, L. Que Jr., J. Am. Chem. Soc. 125 (2003) 2113.
[380] H. Hayashi, K. Uozumi, S. Fujinami, S. Nagatomo, K. Shiren, H. Furutachi, M. Suzuki, A. Uehara, T. Kitagawa, Chem. Lett. (2002) 416.
[381] M.M. Makowska-Grzyska, E. Szajna, C. Shipley, A.M. Arif, M.H. Mitchell, J.A. Halfen, L.M. Berreau, Inorg. Chem. 42 (2003) 7472.
[382] K. Jitsukawa, Y. Oka, H. Einaga, H. Masuda, Tetrahedron Lett. 42 (2001) 3467.
[383] T. Kojima, K.-I. Hayashi, Y. Matsuda, Chem. Lett. (2000) 1008.
[384] M. Harata, K. Hasegawa, K. Jitsukawa, H. Masuda, H. Einaga, Bull. Chem. Soc. Jpn. 71 (1998) 1031.
[385] C.-L. Chuang, K. Lim, J.W. Canary, Supramol. Chem. 5 (1995) 39.
[386] J.C. Mareque Rivas, E. Salvagni, R.T. Martin de Rosales, S. Parsons, Dalton Trans. (2003) 3339.

[387] M.P. Jensen, M.P. Mehn, L. Que Jr., Angew. Chem., Int. Ed. Engl. 42 (2003) 4357.
[388] Z. He, S.B. Colbran, D.C. Craig, Chem. Eur. J. 9 (2003) 116.
[389] D. Mandon, A. Nopper, T. Litrol, S. Goetz, Inorg. Chem. 40 (2001) 4803.
[390] H. Toftlund, S. Ishiguro, Inorg. Chem. 28 (1989) 2236.
[391] S. Yan, C. Li, P. Cheng, D. Liao, Z. Jiang, G. Wang, X. Yao, H. Wang, J. Chem. Crystallogr. 29 (1999) 1085.
[392] M. Nieger, G. Hilt, E.Steckhan, Private communication to Cambridge Crystallographic Database (Refcode IGUZUF), 2002.
[393] T.M. Kooistra, K.F.W. Hekking, Q. Knijnenburg, B. de Bruin, P.H.M. Budzelaar, R. de Gelder, J.M.M. Smits, A.W. Gal, Eur. J. Inorg. Chem. (2003) 648.
[394] H. Zheng, L. Que Jr., Inorg. Chim. Acta 263 (1997) 301.
[395] H. Nagao, N. Komeda, M. Mukaida, M. Suzuki, K. Tanaka, Inorg. Chem. 35 (1996) 6809.
[396] A. Nanthakumar, S. Fox, N.N. Murthy, K.D. Karlin, J. Am. Chem. Soc. 119 (1997) 3898.
[397] N. Komeda, H. Nagao, Y. Kushi, G. Adachi, M. Suzuki, A. Uehara, K. Tanaka, Bull. Chem. Soc. Jpn. 68 (1995) 581.
[398] Y. Zang, L. Que Jr., Inorg. Chem. 34 (1995) 1030.
[399] T. Tzedakis, Electrochim. Acta 46 (2000) 99.

Available online at www.sciencedirect.com
SCIENCE DIRECT®
Polyhedron 24 (2005) 41–48
POLYHEDRON
www.elsevier.com/locate/poly

Bis(μ-alkoxo)-bridged dinuclear iron(III) complexes of pyrazole-based ligands as models for iron-oxo proteins

Stefania Tanase [a], Elisabeth Bouwman [a], Gary J. Long [b], Ahmed M. Shahin [b], René de Gelder [c], Allison M. Mills [d], Anthony L. Spek [d], Jan Reedijk [a,*]

[a] Leiden Institute of Chemistry, Gorlaeus Laboratories, Leiden University, P.O. Box 9502, 2300 RA Leiden, The Netherlands
[b] Department of Chemistry, University of Missouri-Rolla, Rolla, MO 65409-0010, USA
[c] Institute for Molecules and Materials, Radboud University, Nijmegen, Toernooiveld 1, 6525 ED Nijmegen, The Netherlands
[d] Bijvoet Center for Biomolecular Research, Utrecht University, Padualaan 8, 3584 CH Utrecht, The Netherlands

Received 19 May 2004; accepted 27 July 2004
Available online 21 November 2004

Abstract

The synthesis and characterization of two new bis(μ-alkoxo)-bridged dinuclear iron(III) complexes with the ligands 1-(2-hydroxyethyl)-pyrazole (Hnhep) and 1-(2-hydroxyethyl)-3,5-dimethylpyrazole (Hnhed), $[Fe(nhep)Cl_2(EtOH)]_2$ (**1**) and $[Fe(nhed)Cl_2]_2$ (**2**) are reported. The crystal structures of both complexes reveal the presence of centrosymmetric dinuclear units. In compound **1**, the iron(III) center has a coordination number of six, with a slightly distorted octahedral geometry. In compound **2**, the bulkier nhed ligand, with methyl groups at the 3- and 5-positions of the pyrazole ring, leads to a coordination number of five at the iron(III) center in a distorted square pyramidal geometry. The magnetic properties of both complexes have been investigated in the range 2–300 K and indicate the presence of fairly weak antiferromagnetic exchange interactions between iron(III) ions ($J_1 = -10.04$ cm^{-1} for **1** and $J_2 = -12.5$ cm^{-1} for **2**). The inactivity of both complexes in the cyclohexane hydroxylation appears to be partly due to the presence of the strong iron(III)–chloride bond that does not allow exchange with the reactant molecules.
© 2004 Published by Elsevier Ltd.

Keywords: Iron; Pyrazole; Alkoxo-bridged; Model compounds

1. Introduction

Over the past few decades, considerable progress has been made in the development of oxo-bridged dinuclear iron(III) complexes that can reproduce both the structural and the functional properties of the metallic cores of the non-heme proteins including hemerytin (Hr) [1], ribonucleotide reductase (RR) [2], methane monooxygenase (MMO) and purple acid phosphatase (PAPs) [3]. In particular, the ability of the MMO enzyme to activate inert C–H bonds under ambient conditions has received special attention over the past 20 years. The enzyme is known to catalyze the conversion of methane into methanol (Eq. (1)). Substrate oxidation occurs at the diiron centre of the hydroxylase component of the enzyme, which receives two electrons from NADH via reductase to activate the dioxygen molecule [4].

$$2NADH + CH_4 + O_2 \rightarrow 2NAD^+ + CH_3OH + H_2O + 2e^- \quad (1)$$

In the oxidized state of methane monooxygenase (MMO_{ox}), the positive charge of the two high-spin iron(III) ions is balanced by four glutamate and two bridging hydroxide ligands; two additional histidine ligands complete the octahedral coordination spheres of the iron ions [5]. Because of the rather elaborate synthesis

* Corresponding author. Tel.: +31 715274450; fax: +31 715274671.
E-mail address: reedijk@chem.leidenuniv.nl (J. Reedijk).

0277-5387/$ - see front matter © 2004 Published by Elsevier Ltd.
doi:10.1016/j.poly.2004.07.026

of imidazole-based ligands, aliphatic amines, imine or pyridines are commonly used to synthesize model compounds [3,6–11]. Pyrazole-based ligands have been less well investigated for the purpose of synthesizing model complexes that can mimic the active site of those metalloenzymes and metalloproteins which are known to contain imidazole groups from histidine bound to the iron center in the active site [12,13]. This type of ligands might be preferred in the field of biomimetic chemistry, both because they are good structural analogues for the size and electronic properties of histidine and because of their relative ease of preparation as compared to imidazole ligands.

Although a large number of oxygen-bridged dinuclear iron(III) complexes have been synthesized and characterized as structural and functional models for the MMO enzyme, the most efficient models for alkane hydroxylation remain μ-oxo dinuclear iron(III) complexes with didentate (bipyridine, bpy) [10,14], or tetradentate (tris(2-pyridylmethyl)amine, tpa) pyridine-like ligands [7,15–17] and exchangeable μ-acetato or terminal aquo ligands. In these cases, both *tert*-butylhydroperoxide and H_2O_2 have proven to be the most widely studied oxidants in association with these catalysts. In a programme to search for more adequate synthetic models for the active site of MMO, we report herein the synthesis, characterization, magnetic properties and the reactivity studies of two new bis(μ-alkoxo)-bridged dinuclear iron(III) complexes, $[Fe(nhep)Cl_2(EtOH)]_2$ (**1**) (Hnhep = 1-(2-hydroxyethyl)-pyrazole) and $[Fe(nhed)Cl_2]_2$ (**2**) (Hnhed = 1-(2-hydroxyethyl)-3,5-dimethylpyrazole).

2. Experimental

2.1. Synthesis

Chemicals were purchased from Aldrich and were used as received. The ligands 1-(2-hydroxyethyl)-pyrazole (Hnhep) [18] and 1-(2-hydroxyethyl)-3,5-dimethylpyrazole (Hnhed) [19] were synthesized as previously reported.

2.1.1. $Fe(nhep)Cl_2(EtOH)]$ (**1**)

The complex was obtained by slow diffusion, in an H-shaped tube, of two ethanolic solutions, one containing 1 mmol (0.2 g) $FeCl_2 \cdot 4H_2O$ and the other one containing 1 mmol (0.15 g) of 1-(2-hydroxyethyl)-pyrazole. Dark orange crystals were obtained in one week. The crystals were collected by filtration, washed with diethyl ether and dried in vacuum. Yield: 0.32 g (60%) *Anal.* Calc. for $C_{14}H_{26}Cl_4Fe_2N_4O_4$: C, 29.57; H, 4.57; N, 9.85. Found: C, 29.89; H, 4.62; N, 9.48%. IR (ν_{max}/cm^{-1}): 3288m, 2938m, 2873w, 1624w, 1546m, 1421s, 1280m, 1188s, 1060s, 1028s, 1004m, 893s, 765s, 611m, 562s, 467s, 386m. UV–Vis (λ_{max}/nm): 411, 639, 1050.

2.1.2. $Fe(nhed)Cl_2]$ (**2**)

The complex was prepared by adding 2 mmol (0.3 g) of the ligand 1-(2-hydroxyethyl)-3,5-dimethylpyrazole (Hnhed) dissolved in 10 ml of tetrahydrofuran to a solution of 2 mmol (0.4 g) $FeCl_2 \cdot 4H_2O$ in 20 ml tetrahydrofuran. Slow diffusion of hexane into the resulting orange solution over 3 days yielded orange crystals that were collected by filtration, washed with hexane and dried in air. Yield: 0.45 g (78%) *Anal.* Calc. for $C_{14}H_{22}Cl_4Fe_2N_4O_2$: C, 30.45; H, 3.98; N, 10.15. Found: C, 31.07; H, 3.74; N, 10.48%. IR (ν_{max}/cm^{-1}): 2925m, 2865w, 1636w, 1558m, 1473s, 1364m, 1227m, 1133s, 1084m, 1049s, 895s, 798s, 627m, 570s, 513m, 450s, 356m. UV–Vis (λ_{max}/nm): 407, 589, 1018.

2.2. Physical measurements

Elemental analyses of C, H, and N were performed on a Perkin Elmer 2400 Series II analyzer. Infrared spectra (4000–300 cm^{-1}) were recorded using the reflectance technique on a Perkin–Elmer Paragon 1000 FTIR spectrometer equipped with a Golden Gate ATR device. Ligand field spectra were obtained on a Perkin-Elmer Lambda 900 spectrophotometer using the diffuse reflectance technique, with MgO as a reference. Magnetic susceptibility measurements (2–300 K) were carried out at 1 T using a Quantum Design MPMS-5 5T SQUID magnetometer. Data were corrected for the magnetization of the sample holder and for diamagnetic contributions, the latter of which were calculated from the Pascal constants [20]. The GC–MS measurements were carried out on a Hewlett–Packard 5890 Series II gas chromatograph, equipped with WCOT fused silica column (stationary phase: CP-Was 58 (FFAP) CB) and coupled to a Hewlett–Packard 5971 series mass spectrometer with a mass-selective detector. Standard oxidation reactions were carried out under ambient conditions. The Mössbauer spectra were measured on a constant-acceleration spectrometer which utilized a room temperature rhodium matrix cobalt-57 source and was calibrated at room temperature with α-iron foil.

2.3. X-ray crystallography and data collection

Intensity data for a single crystals of **1** and **2** were collected using Mo Kα radiation (λ = 0.71073 Å) on a Nonius KappaCCD diffractometer. A correction for absorption was considered unnecessary in the case of compound **1**. In the case of compound **2**, an empirical absorption correction was made using PLATON/DELABS (0.600–0.800 transmission) [21]. The structures were solved by automated Patterson methods using DIRDIF99 (**1**) or direct methods using SHELX-97 (**2**) and were refined on F^2 by least-squares procedures using SHELXL-97 [22–24]. All non-hydrogen atoms were refined with anisotropic displacement parameters. In the

case of compound **1**, all hydrogen atoms were independently refined. For compound **2**, all hydrogen atoms were constrained to idealized geometries and allowed to ride on their carrier atoms with an isotropic displacement parameter related to the equivalent displacement parameter of their carrier atoms. Structure validation and molecular graphics preparation were performed with the PLATON package [21].

2.4. Oxidation reactions

2.4.1. Procedure I

In a typical run, 10 equiv. of H_2O_2 (30%) were added to a methanol solution (10 ml) containing 1 mM catalyst (stock solution) and 1 M cyclohexane at room temperature with a final catalyst:substrate:H_2O_2 ratio of 1:1000:10.

2.4.2. Procedure II

The complexes (0.05 mmol) were dissolved in methanol (10 ml) containing 2.5 mmol of substrate. The reaction was started by adding 5 mmol of 30% H_2O_2. The final catalyst:substrate:H_2O_2 ratio was 1:50:100. In both procedures, after 3 h of reaction at 25 °C, aliquots were taken from the reaction mixtures and analyzed twice by GC–MS: both with and without the addition of an excess of triphenylphosphane for the quantification of the amount of hydroperoxide [25]. Chlorobenzene was used as internal standard.

3. Results and discussions

3.1. Synthesis and spectroscopic studies

The reaction of Hnhep or Hnhed with either $FeCl_2$ or $FeCl_3$ affords two new bis(μ-alkoxo)-bridged dinuclear iron(III) complexes (**1** and **2**), as confirmed by their X-ray structure determinations (vide infra).

The infrared spectra of the complexes **1** and **2** exhibit the bands expected for the deprotonated ligands 1-(2-oxyethyl)-pyrazole and 1-(2-oxyethyl)-3,5-dimethylpyrazole. The most significant effect of the coordination of the pyrazole-based ligands to the iron(III) center is observed in the range 1500–1650 cm^{-1}. In this spectral range, both free ligands exhibit two characteristic bands, ν(C=N) (at 1636 cm^{-1} for Hnhep and 1642 cm^{-1} for Hnhed) and ν(C–O) (at 1508 cm^{-1} for Hnhep and 1512 cm^{-1} for Hnhed). Upon coordination of these ligands to iron(III), the energy of the ν(C=N) band decreases (to 1624 cm^{-1} for **1** and 1632 cm^{-1} for **2**) and that of ν(C–O) increases (to 1546 cm^{-1} for **1** and 1558 cm^{-1} for **2**), suggesting the presence of an alkoxo bridge. Both the symmetric and the asymmetric Fe–O–Fe vibrations have associated bands in the infrared spectra of complexes **1** and **2** [26]. The asymmetric stretching vibrations at 611 cm^{-1} for **1** and 627 cm^{-1} for **2** and the symmetric stretching vibrations at 562 cm^{-1} for **1** and 570 cm^{-1} for **2** are in the range of those observed for similar $Fe_2(OR)_2$ dimers [3,6–11]. A sharp peak at 3288 cm^{-1} observed in the infrared spectrum of **1** indicates the presence of moderately strong hydrogen bonds.

The ligand field spectra of both **1** and **2** display the features typical of bis(μ-alkoxo)-bridged iron(III) compounds: an intense absorption band (at 411 nm for **1** and 407 nm for **2**) with a lower energy shoulder (at 639 nm for **1** and 589 nm for **2**), assigned to the ligand-to-iron(III) charge-transfer transitions [27]. In the ligand field spectrum of complex **2**, a medium intensity absorption band that occurs at 1018 nm is attributed to the d–d transitions involving forbidden states of high-spin iron(III). The unusually high intensity of this band may be due either to the exchange coupling between the iron(III) centers that engenders a relaxation of the spin selection rules or to the low symmetry of the iron(III) coordination [28]. For complex **1**, a weak poorly-resolved absorption band at 1050 nm is observed.

3.2. Description of crystal structures

The structures of complexes **1** and **2** were determined by X-ray crystallography. Crystallographic data and selected bond lengths and angles are listed in Tables 1 and 2.

A Pluton projection of the centrosymmetric dinuclear unit of **1** is depicted in Fig. 1. Each iron center, coordinated to two bridging alkoxo-groups, two terminal chloride ions, one nitrogen atom of the Hnhep pyrazole ring and one oxygen atom of an ethanol molecule, has a Cl_2NO_3 donor set in a pseudo-octahedral geometry. The two metal-centred octahedra share an edge in the dinuclear complex. The anionic Hnhep ligand is found in a didentate coordination mode forming the alkoxo-bridges of a planar $Fe_2(OR)_2$ core. The O6–Fe1–N1 bite angle (87.78(5)°) is smaller than that found in a related copper compound [29]. The Fe1–O_{alkoxo} bond distances of 1.9707(10) and 2.0026(10) Å are nearly equivalent to those observed in other bis(μ-alkoxo)-iron complexes [30–33]. The Fe–O–Fe angle (105.69(5)°) and the Fe···Fe separation (3.1670(5) Å) are within the range of values found in bis(μ-alkoxo)-bridged iron(III) complexes [26,30,31,33]. The positions of *trans* coordinating ligands deviate slightly from linearity (161.75(5)°–175.67(4)°), and the iron(III) ion is lifted from the basal plane by 0.17 Å in the direction of the ethanol molecule. The two chloride ions are *cis* to each other (Cl1–Fe1–Cl2 = 93.936(19)°) with Fe–Cl bond distances of 2.2667(5) and 2.3400(5) Å that are close to the values generally observed for iron(III) complexes [34–38]. An interesting feature of the crystal structure of **1** is the presence of two intramolecular hydrogen bonds (Fig. 1) that are established between the chloride ions

Table 1
Crystal and structure refinement data

	$[Fe(nhep)Cl_2(EtOH)]_2$ (**1**)	$[Fe(nhed)Cl_2]_2$ (**2**)
Chemical formula	$C_{14}H_{26}Cl_4Fe_2N_4O_4$	$C_{14}H_{22}Cl_4Fe_2N_4O_2$
Molecular weight	567.89	531.86
Crystal system	monoclinic	monoclinic
Space group	$P2_1/c$	$P2_1/c$
a (Å)	8.9777(11)	11.1114(3)
b (Å)	11.7553(11)	9.4134(2)
c (Å)	12.7193(14)	10.8790(2)
β (°)	125.156(7)	112.1261(9)
V (Å^3)	1097.5(2)	1054.10(4)
Z	2	2
D_{calc} (Mg m^{-3})	1.7185(3)	1.6757(1)
μ(Mo Kα) (mm^{-1})	1.836	1.899
Crystal size (mm)	$0.23 \times 0.21 \times 0.19$	$0.24 \times 0.24 \times 0.12$
T (K)	293(2)	150
Data collected	38 599	11 672
Unique data	2527	2391
R_{int}	0.0371	0.0412
$R(F)$ [$I > 2\sigma(I)$]	0.0216	0.0270
$R_w(F^2)$	0.0496	0.0621
S	1.03	1.03
$\Delta\rho_{min}$, $\Delta\rho_{max}$ (e Å^{-3})	0.284, −0.245	0.285, −0.313

Table 2
Selected bond distances (Å) and angles (°)

$[Fe(nhep)Cl_2(EtOH)]_2$ (**1**)		$[Fe(nhed)Cl_2]_2$ (**2**)	
Bond distances			
Fe1–Cl1	2.3400(5)	Fe1–Cl1	2.2490(6)
Fe1–Cl2	2.2667(5)	Fe1–Cl2	2.2183(6)
Fe1–O6	2.0026(10)	Fe1–O10	1.9384(13)
Fe1–O9	2.1796(13)	Fe1–N12	2.1059(16)
Fe1–N1	2.1106(13)	Fe1–O10a	2.0157(13)
Fe1–O6a	1.9707(10)	Fe···Fe	3.184
Fe···Fe	3.167		
Bond angles			
Cl1–Fe1–Cl2	93.936(19)	Cl1–Fe1–Cl2	112.05(2)
Cl1–Fe1–O6	95.46(4)	Cl1–Fe1–O10	132.86(5)
Cl1–Fe1–O9	175.67(4)	Cl1–Fe1–N12	94.86(5)
Cl1–Fe1–N1	91.71(4)	Cl1–Fe1–O10a	91.75(4)
Cl1–Fe1–O6a	93.44(4)	Cl2–Fe1–O10	113.38(5)
Cl2–Fe1–O6	169.78(4)	Cl2–Fe1–N12	102.45(5)
Cl2–Fe1–O9	89.43(4)	Cl2–Fe1–O10a	94.74(5)
Cl2–Fe1–N1	95.96(4)	O10–Fe1–N12	87.23(6)
Cl2–Fe1–O6a	101.14(3)	O10–Fe1–O10a	72.75(6)
O6–Fe1–O9	81.39(5)	N12–Fe1–O10a	157.64(6)
O6–Fe1–N1	87.78(5)		
O6–Fe1–O6a	74.31(5)		
O9–Fe1–N1	85.22(5)		
O9–Fe1–O6a	88.58(5)		
N1–Fe1–O6a	161.75(5)		

Symmetry operations: x, y, z; $-x$, 1/2 + y, 1/2−z; $-x$, $-y$, $-z$; x, −1/2 + y, −1/2 + z.

and the ethanol molecules of the adjacent iron(III) centers (O9–H9···Cl1a = 3.163(2) Å). The observed O-H stretching vibration of the ethanol molecule (3288 cm^{-1}) and the O–H···Cl distance fit fairly well the relationship developed by Bellamy et al. (O9–H9···Cl1a = 3.158 Å) [39]. No evidence was found for strong intermolecular contacts between dinuclear units.

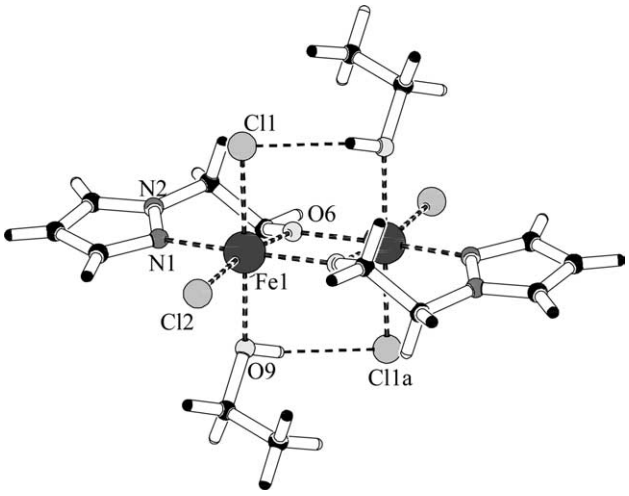


Fig. 1. Pluton projection and numbering scheme of the dinuclear structure of **1**.

The crystal structure of compound **2** (Fig. 2) reveals a centrosymmetric dinuclear unit, similar to that observed for compound **1**. The presence of the methyl groups at the 3- and 5-positions of the pyrazole ring of the Hnhed ligand in **2** results in a change of the coordination geometry around the iron(III) ions. Each iron(III) center is now five-coordinate and has a distorted square pyramidal geometry (as ascertained by the factor $\tau = 0.4$; $\tau = 0$ for a square pyramid and $\tau = 1$ for trigonal bipyramid) [40]. One chloride ion, the two bridging O_{alkoxo} ligands and the nitrogen donor of the pyrazole ring constitute the basal plane of the square pyramid, and the other chloride ion occupies the apical position of the square pyramid. As a result, the dinuclear complex consists of two square pyramids sharing a basal edge (Fig. 2). The largest distortion from the square pyramidal geometry is evidenced by the angles N12–Fe1–O10a = 157.64(6)° and O10–Fe1–Cl1 = 72.75(6)°. The O10–Fe1–N12 = 87.23(6)° bite angle of the didentate ligand is similar to that observed for Hnhep in compound **1**.

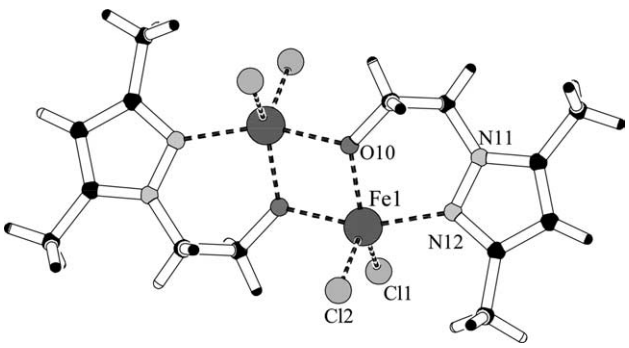


Fig. 2. Pluton projection and numbering scheme of the dinuclear structure of **2**.

The Fe–O–Fe angle (107.25(6)°), Fe–O distances (1.9384(14) and 2.0157(16) Å) and Fe···Fe separation (3.184 Å) are within the range of values found for related bis(μ-alkoxo) bridged iron(III) complexes [30–32,41]. The angle between the two chloride ions is Cl1–Fe1–Cl2 = 112.05(2)°; the average Fe–Cl bond distance of 2.2336(5) Å, is significantly shorter than in compound **1**, but still within the range of the values observed for other iron(III) complexes [34–38]. No stacking interactions or classical hydrogen bonds are observed in the crystal structure of compound **2**.

3.3. Magnetic properties

The variable temperature solid-state magnetic susceptibilities of **1** and **2** have been investigated in the range 2–300 K in an applied magnetic field of 1 T. The values of the $\chi_m T$ product at room temperature are 8.761 $cm^3\,K\,mol^{-1}$ for **1** and 8.749 $cm^3\,K\,mol^{-1}$ for **2**, in agreement with the expected value for two independent spins $S = 5/2$ (8.754 $cm^3\,K\,mol^{-1}$). The $\chi_m T$ versus T curves of both compounds are similar and show a continuous decrease, as the temperature is lowered from 300 to 2 K indicating that the two iron(III) ions are antiferromagnetically coupled. Fig. 3 shows the $\chi_m T$ versus T plot for compound **1**; a very similar behaviour was observed for **2** (not shown).

The six possible states for a dinuclear Fe(III)–Fe(III) complex have total spins of $S = 0, 1, 2, 3, 4, 5$. These spin states are split in energy and produce a spin ladder that can be modeled by the Heisenberg–Dirac–van Vleck phenomenological Hamiltonian: $H = -2JS_1S_2$ [20]. The value of the exchange interaction J can be obtained from the fit of the $\chi_m T$ versus T curve, where the measured magnetic susceptibility is a sum of three terms without zero field splitting (Eq. (2)):

$$\chi_{exp} = \chi_{para} + \chi_{dia} + \chi_{TIP} \tag{2}$$

in which χ_{para} is the paramagnetic (temperature-dependent) contribution, χ_{dia} is the diamagnetic contribution and χ_{TIP} is the temperature-independent paramagnetism, arising from mixing of the excited states into the ground state by the magnetic field. Typically J is determined from a fit of the magnetic susceptibility data using the Van Vleck equation evaluated for an exchange-coupled high-spin dinuclear Fe(III)Fe(III) complex (Eq. (3)) [20]:

$$\chi = \frac{2Ng^2\beta^2}{kT} \times \frac{e^x + 5e^{3x} + 14e^{6x} + 30e^{10x} + 55e^{15x}}{1 + 3e^x + 5e^{3x} + 7e^{6x} + 9e^{10x} + 11e^{15x}}, \tag{3}$$

with $x = J/kT$. The temperature-independent paramagnetism (TIP = 400×10^{-6} $cm^3\,K\,mol^{-1}$ for each iron ion) was taken into account. Using this approach, the best fit parameters were $J_1 = -10.04$ cm^{-1}, $g_1 = 2.02$, for compound **1** and $J_2 = -12.5$ cm^{-1}, $g_2 = 2.03$, for compound **2**. The values obtained are in the range of those observed for other weak antiferromagnetically coupled alkoxo-iron complexes. A correlation between the experimental and calculated magnetic data together with structural parameters is shown in Table 3 [42].

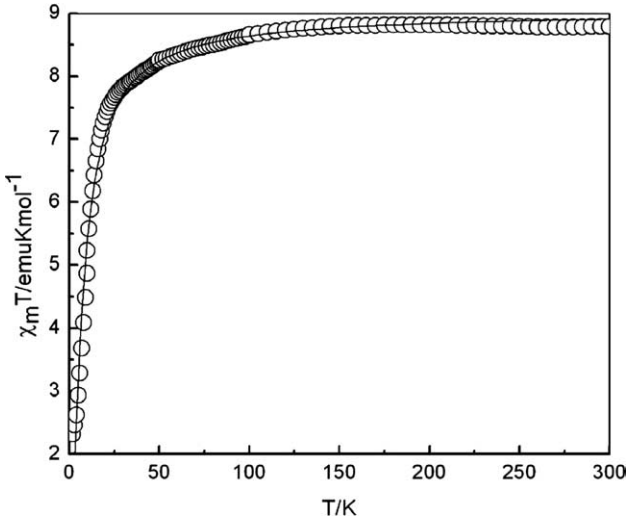


Fig. 3. Plot of the χ_mT vs. T for compound **1**: circles experimental values; (—) calculated values.

3.4. Mössbauer spectral studies

The Mössbauer spectra of **1** and **2** have been measured at 295 and 78 K and show the expected single quadrupole doublet. The hyperfine parameters resulting from quadrupole doublet fits are given in Table 4 and the 78 K spectra are shown in Fig. 4. The 295 K spectra are essentially identical to the 78 K spectra. The hyperfine parameters are typical of iron(III) [43–45] in a somewhat distorted five- or six-coordinate environment and, as expected, the isomer shifts increase slightly upon cooling as a result of the second-order Doppler shift. Rather surprisingly there is little difference in the isomer shift between the six-coordinate iron(III) in **1** and the

Table 3
Magnetic and structural parameters

Complex	P (Å)[a]	d(Fe···Fe) (Å)	α (°)[b]	J_{calc} (cm^{-1})[c]	J_{exp} (cm^{-1})
1	1.9708	3.167	105.69	−12.7	−10
2	1.9384	3.184	107.25	−19.5	−12.5

[a] P corresponds to the half of the length of the shortest Fe–O–Fe bridge.
[b] α = Fe–O–Fe angle.
[c] Calculated after Gorun and Lippard [42] ($-J = Ae^{BP}$) with $A = -1.08 \times 10^{13}$ cm^{-1} and $B = -13.9$ $Å^{-1}$.

Table 4
Mössbauer spectral hyperfine parameters

Compound	T (K)	δ (mm/s[a])	ΔE_Q (mm/s)	Γ (mm/s)	Area ((%ε)/(mm/s))
$[Fe(nhep)Cl_2(EtOH)]_2$ (**1**)	295	0.314(6)	0.40(2)	0.31(1)	0.45(2)
	78	0.409(3)	0.47(1)	0.25(1)	1.64(1)
$[Fe(nhed)Cl_2]_2$ (**2**)	295	0.320(6)	0.51(2)	0.31(1)	1.54(2)
	78	0.412(4)	0.54(1)	0.31(1)	2.33(1)

[a] The isomer shifts are given relative to room temperature α-iron foil.

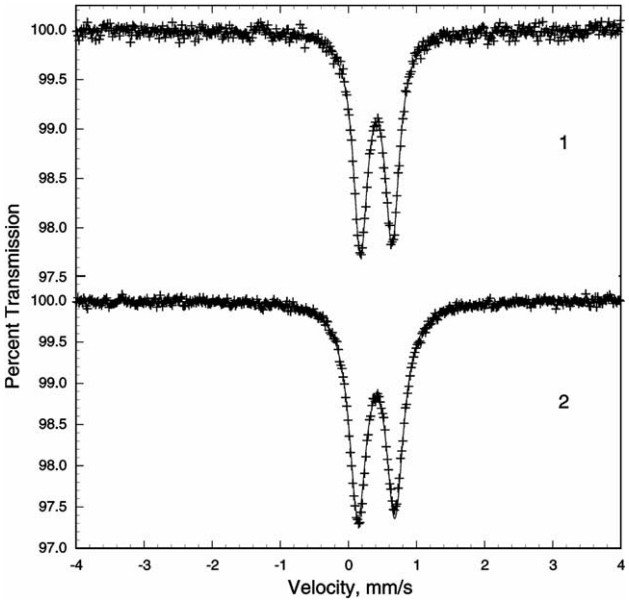


Fig. 4. The Mössbauer spectra of **1** and **2** obtained at 78 K.

five-coordinate iron(III) in **2**, but the five-coordinate **2** does exhibit a slightly larger quadrupole splitting.

3.5. Reactivity studies

The monooxygenase-like activity of complexes **1** and **2** has been tested in the oxidation of cyclohexane using H_2O_2 as oxidant, in methanol as solvent, and under ambient conditions. However, by using either one of the procedures described in the experimental part, no cyclohexane conversion was observed. Several additives (*N*-methylimidazole, acetic acid, benzoic acid, pyridine 2-carboxylic acid, pyridine 2,6-dicarboxylic acid, 3,5-pyrazoledicarboxylic acid, 4,5-imidazoledicarboxylic acid, 2-pyrazinecarboxylic acid) have been screened for possible improvement of the catalytic efficiency, however, no improvement was observed. The inactivity of the complexes **1** and **2** in cyclohexane oxidation is most probably due to the presence of iron(III)–chloride bonds that are too strong to allow exchange with solvent molecules or reactants.

Fontecave et al. [46] have reported that the activation of the C-H bond by hydroperoxides requires the presence of exchangeable coordination sites, in order to allow the binding of the oxidant to the metal centre. Therefore, it was decided to evaluate the corresponding in situ $CF_3SO_3^-$ salts of compounds **1** and **2** (obtained by addition of $AgCF_3SO_3$ to the methanol solution of **1** or **2**, followed by stirring and filtration through Celite to remove the silver salt) for the oxidation of cyclohexane. Using the procedure II, the maximum catalytic activity is reached after 3 h and it results in the formation of 3.2 equiv. cyclohexanol and 1.4 equiv. cyclohexanone in the reaction catalyzed by **1** and 1.8 equiv. cyclohexanol and 1.2 equiv. cyclohexanone in the reaction catalyzed by **2**. The use of the procedure I does not lead to any catalytic activity. Also, H_2O_2 dismutation has not been observed in both complexes.

By using a large excess of H_2O_2 (100 to 1000 equiv. in procedure II) neither cyclohexane conversion nor H_2O_2 dismutation activity was observed. In order to gain insight into the total lack of activity of complexes **1** and **2** under these conditions, the oxidation attempts were also followed by UV–Vis and ES-MS spectroscopy. The UV–Vis spectra of both compounds in methanol solution show similar features and no significant changes are observed when the solutions are kept at room temperature for several days. In both cases, the UV–Vis spectrum is dominated by a broad band at about 360 nm which is assigned to the iron-to-oxygen charge transfer transition. When H_2O_2 is added, the alkoxo-to-iron(III) LMCT band at 360 nm of **1** (356 nm for **2**) starts to decrease in intensity and to shift to higher energy; however in the presence of 10–20 equiv. H_2O_2, only insignificant changes are observed. When the amount of H_2O_2 added is increased, the intensity of the band decreases progressively and the band disappears completely after addition of 1000 equiv. of H_2O_2. The observed spectroscopic changes observed for compound **1** are presented in Fig. 5. This behaviour suggests a change in, or loss of, the coordination of the pyrazole ligand. Indeed, after addition of 1000 equiv. of H_2O_2, the ES-MS mass spectrum of complex **1** shows a peak at $m/z = 113$ with an abundance of 100% corresponding to the free Hnhep ligand and some other peaks of low intensity (abundance <10%) that could not be clearly assigned. A similar ES-MS mass spectrum was observed for complex **2** after addition of H_2O_2 (m/z = 141 $[Hnhed + H]^+$, 176 $[(H_2nhed)Cl + H]^+$).

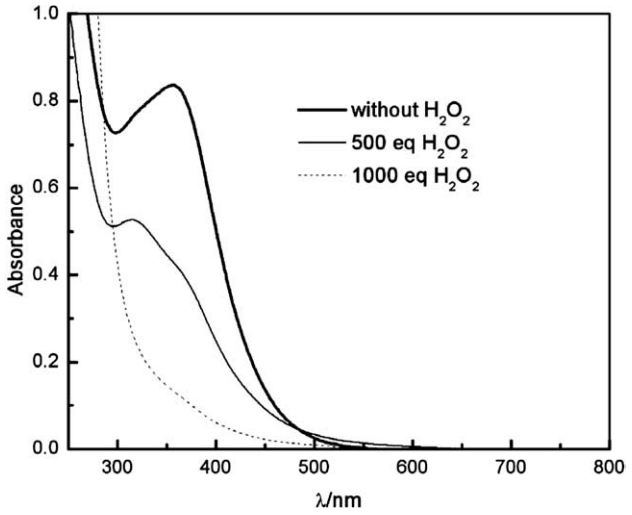


Fig. 5. Spectroscopic changes observed for a methanol solution of compound **1** upon the addition of H_2O_2.

4. Conclusions

We have synthesized and characterized two new bis(μ-alkoxo)diiron(III) complexes, $[Fe(nhep)Cl_2(EtOH)]_2$ (**1**) and $[Fe(nhed)Cl_2]_2$ (**2**) which have been inspired by the methane monooxygenase enzyme. The structural analysis of both complexes demonstrates the ability of the 1-(2-hydroxyethyl)pyrazole ligands to form dinuclear iron(III) compounds with a coordination number of five or six at the metal centre. A detailed characterization of complexes **1** and **2** including structural, spectroscopic and magnetic studies has been carried out. Replacing chloride ions with non-coordinating anions ($CF_3SO_3^-$) in compounds **1** and **2**, results in apparent catalytic activity in the oxidation of cyclohexane. This observation suggests that the inactivity of these complexes appears to be partly due to the presence of iron(III)-chloride bonds that are too strong to allow exchange with solvent molecules or reactants. Further optimization of the reaction conditions and the investigation of other substrates are in progress.

5. Supplementary material

Crystallographic data (excluding structure factors) have been deposited with the Cambridge Crystallographic Data Centre as supplementary publication no. CCDC 216734 (for **1**) and CCDC 223689 (for **2**). Copies of the data can be obtained free of charge on application to The Director, CCDC, 12 Union Road, Cambridge, CB2 1EZ, UK (fax: +44-1223-336-033; e-mail: deposit@ccdc.cam.ac.uk or www.ccdc.cam.ac.uk).

Acknowledgements

This work was in part financially supported by the Dutch Economy, Ecology, Technology (EET) programme, a joint programme of the Ministry of Economic Affairs, the Ministry of Education, Culture and Science, and the Ministry of Housing, Spatial Planning and the Environment. We thank Dr. R. Hage (Unilever, The Netherlands) for useful discussions.

References

[1] J.B. Vincent, G.L. Olivier-Lilley, B.A. Averill, Chem. Rev. 90 (1990) 1447.
[2] L. Que, A.E. True, Prog. Inorg. Chem., Bioinorg. Chem. 38 (1990) 97.
[3] B. Meunier, W. Adam, Metal-oxo and Metal-peroxo Species in Catalytic Oxidations, Springer, Berlin, 2000.
[4] J. Reedijk, E. Bouwman, Bioinorganic Catalysis, Marcel Dekker, New York, 1999.
[5] M.H. Baik, M. Newcomb, R.A. Friesner, S.J. Lippard, Chem. Rev. 103 (2003) 2385.
[6] D. Riley, M. Stern, J. Ebner, The Activation of Dioxygen and Homogeneous Catalytic Oxidation, Plenum, New York, 1993.
[7] R.A. Leising, J.H. Kim, M.A. Perez, L. Que, J. Am. Chem. Soc. 115 (1993) 9524.
[8] M. Costas, K. Chen, L. Que, Coord. Chem. Rev. 200 (2000) 517.
[9] R.A. Sheldon, J.K. Kochi, Metal-Catalyzed Oxidations of Organic Compounds, Academic Press, New York, 1981.
[10] J.B. Vincent, J.C. Huffman, G. Christou, Q.Y. Li, M.A. Nanny, D.N. Hendrickson, R.H. Fong, R.H. Fish, J. Am. Chem. Soc. 110 (1988) 6898.
[11] L. Que, Y.H. Dong, Accounts Chem. Res. 29 (1996) 190.
[12] H. Toftlund, Coord. Chem. Rev. 94 (1989) 67.
[13] R. Mukherjee, Coord. Chem. Rev. 203 (2000) 151.
[14] R.H. Fish, M.S. Konings, K.J. Oberhausen, R.H. Fong, W.M. Yu, G. Christou, J.B. Vincent, D.K. Coggin, R.M. Buchanan, Inorg. Chem. 30 (1991) 3002.
[15] R.A. Leising, R.E. Norman, L. Que, Inorg. Chem. 29 (1990) 2553.
[16] R.A. Leising, B.A. Brennan, L. Que, E. Munck, J. Am. Chem. Soc. 113 (1991) 3988.
[17] R.A. Leising, Y. Zang, L. Que, J. Am. Chem. Soc. 113 (1991) 8555.
[18] I.L. Finar, K. Utting, J. Chem. Soc. (1960) 5272.
[19] W.L. Driessen, E. Bouwman, Inorg. Synth. 32 (1998) 82.
[20] O. Kahn, Molecular Magnetism, VCH Publishers, New York, 1993.
[21] A.L. Spek, PLATON, A Multi-purpose Crystallographic Tool, Utrecht University, The Netherlands, 2003.
[22] P.T. Beurskens, G. Beurskens, R. de Gelder, S. García-Granda, R.O. Gould, R.I. Israel, J.M.M. Smits, The DIRDIF99 Program System, Technical Report of the Crystallography Laboratory, University of Nijmegen, The Netherlands, 1999.
[23] G.M. Sheldrick, SHELXL-97. Program for Crystal Structure Refinement, University of Göttingen, Germany, 1997.
[24] G.M. Sheldrick, SHELXL-97. Program for Crystal Structure Solution, University of Göttingen, Germany, 1997.
[25] G.B. Shul'pin, The Chemistry Preprint Server (www.chemceb.com/orgchem/0106001).
[26] E.I. Solomon, T.C. Brunold, M.I. Davis, J.N. Kemsley, S.K. Lee, N. Lehnert, F. Neese, A.J. Skulan, Y.S. Yang, J. Zhou, Chem. Rev. 100 (2000) 235.

[27] J.A. Bertrand, P.G. Eller, Inorg. Chem. 13 (1974) 927.
[28] A.B.P. Lever, Inorganic Electronic Spectroscopy, Elsevier Science, Amsterdam, 1986.
[29] S. Tanase, E. Bouwman, W.L. Driessen, J. Reedijk, R. de Gelder, Inorg. Chim. Acta 355 (2003) 458.
[30] H. Aneetha, K. Panneerselvam, T.F. Liao, T.H. Lu, C.S. Chung, J. Chem. Soc., Dalton Trans. 16 (1999) 2689.
[31] J.M. Clemente-Juan, C. Mackiewicz, M. Verelst, F. Dahan, A. Bousseksou, Y. Sanakis, J.P. Tuchagues, Inorg. Chem. 41 (2002) 1478.
[32] N.S. Goncalves, L.M. Rossi, L.K. Noda, P.S. Santos, A.J. Bortoluzzi, A. Neves, I. Vencato, Inorg. Chim. Acta 329 (2002) 141.
[33] A. Neves, L.M. Rossi, I. Vencato, W. Haase, R. Werner, J. Chem. Soc., Dalton Trans. 5 (2000) 707.
[34] H. Duval, V. Bulach, J. Fischer, M.W. Renner, J. Fajer, R. Weiss, J. Biol. Inorg. Chem. 2 (1997) 662.
[35] R.C. Finn, J. Zubieta, J. Clust. Sci. 11 (2000) 461.
[36] A. Horn, A. Neves, A.J. Bortoluzzi, V. Drago, W.A. Ortiz, Inorg. Chem. Commun. 4 (2001) 173.
[37] M. Pawlicki, L. Latos-Gralynski, Inorg. Chem. 41 (2002) 5866.
[38] J. Simaan, S. Poussereau, G. Blondin, J.J. Girerd, D. Defaye, C. Philouze, J. Guilhem, L. Tchertanov, Inorg. Chim. Acta 299 (2000) 221.
[39] L.J. Bellamy, A.J. Owen, Spectrochim. Acta A 25 (1969) 329.
[40] A.W. Addison, T.N. Rao, J. Reedijk, J. van Rijn, G.C. Verschoor, J. Chem. Soc., Dalton Trans. 7 (1984) 1349.
[41] E. Rentschler, G.A. Timco, T. Weyhermuller, V.B. Arion, A.S. Batsanov, J. Inorg. Biochem. 86 (2001) 398.
[42] S.M. Gorun, S.J. Lippard, Inorg. Chem. 30 (1991) 1625.
[43] J.A. Bertrand, J.L. Breece, A.R. Kalyanaraman, G.J. Long, W.A. Baker, J. Am. Chem. Soc. 92 (1970) 5233.
[44] G.J. Long, J.T. Wrobleski, R.V. Thundathil, D.M. Sparlin, E.O. Schlemper, J. Am. Chem. Soc. 102 (1980) 6040.
[45] W.M. Reiff, G.J. Long, W.A. Baker, J. Am. Chem. Soc. 90 (1968) 6347.
[46] S. Menage, J.M. Vincent, C. Lambeaux, M. Fontecave, J. Mol. Catal. A Chem. 113 (1996) 61.

Available online at www.sciencedirect.com
SCIENCE DIRECT®
Polyhedron 24 (2005) 49–55
POLYHEDRON
www.elsevier.com/locate/poly

Synthesis, crystal structure and spectroscopic characterization of a novel bis (oxo-bridged) dinuclear vanadium(V)–dipicolinic acid complex

A.C. Gonzalez-Baró [a], E.E. Castellano [b], O.E. Piro [c], Beatriz S. Parajón-Costa [a,*]

[a] Centro de Química Inorgánica (CEQUINOR, CONICET/UNLP), Facultad de Ciencias Exactas, Universidad Nacional de La Plata, C.Correo 962, 1900 La Plata, Argentina
[b] Instituto de Física de São Carlos, Universidade de São Paulo, C.P. 369, 13560 São Carlos (SP), Brazil
[c] Departamento de Física, Facultad de Ciencias Exactas, Universidad Nacional de La Plata and Institute IFLP (CONICET), C. C. 67, 1900 La Plata, Argentina

Received 28 May 2004; accepted 29 September 2004
Available online 24 November 2004

Abstract

The reaction of $[VO(dipic)(H_2O)_2]\cdot H_2O$ with creatinine in a H_2O–CH_3OH mixture yields yellow crystals of a bis(oxo-bridged) binuclear vanadium(V) compound of stoichiometry $[CH_3NHC(NH_2)_2]_2[V_2O_4(dipic)_2]$, ($dipic^{2-}$ = pyridine 2,6 dicarboxylate; $CH_3NHC(NH_2)_2^{+}$) = methylguanidinum). The molecular structure of the compound was determined by X-ray diffraction methods. The binuclear complex crystallizes in the monoclinic space group $P2_1/c$ with $a = 9.557(1)$, $b = 12.363(1)$, $c = 10.466(1)$ Å, $\beta = 101.56(2)°$ and $Z = 2$. It sits at a crystallographic inversion center with the pair of V(V) atoms in an edge-sharing distorted octahedral environment. In the $[VO_2(dipic)]^-$ halves of the dimer, the VO_2^+ cation is coordinated to a dipicolinate group acting as a tridentate planar ligand through one oxygen of each carboxylic group and the hetereocyclic nitrogen atom. The oxo ligand lying near the coordination plane bridges through a weak axial V–O bond to the other half of the dimer. This gives rise to a V=O2 bond length slightly longer than the other terminal V=O1 bond. The infrared and Raman spectra of the compound were recorded and discussed on the basis of its structural data and compared with those of the free acid. The results are also compared with the corresponding results of related structures.
© 2004 Elsevier Ltd. All rights reserved.

Keywords: Vanadium(V); Dipicolinic acid; Pyridine dicarboxylic acid; Oxo-bridge compounds; X-ray structure; IR and Raman spectra

1. Introduction

Vanadium coordination chemistry constitutes a field of increasing interest and has been the subject of extensive studies during recent decades by many different authors. A great number of ligands have been employed in the study of biologically relevant vanadium systems with the aim of finding a possible correlation between activity and coordination geometry. Diverse aspects related to its biological and pharmacological activity have been reviewed [1–4].

Vanadium(III, IV and V) has a high affinity for N, O and/or S donor groups. It reacts with many naturally occurring species, including pyridine carboxylic acids, forming stable complexes of diverse stoichiometries. Metal complexes of pyridine carboxylic acids and some of their derivatives have recently received considerable attention as model systems for the design of new metallopharmaceutical compounds. Furthermore, several vanadium complexes were investigated as antidiabetic agents,

* Corresponding author. Tel./fax: +54 221 4259485.
E-mail address: beatrizp@quimica.unlp.edu.ar (B.S. Parajón-Costa).

0277-5387/$ - see front matter © 2004 Elsevier Ltd. All rights reserved.
doi:10.1016/j.poly.2004.09.032

most of them involving vanadium(IV) as the metal center [5–9]. Among others, oxovanadium(IV) associated with picolinate and other related ligands appear as very promising insulin-mimetic oral active drugs [7–9].

Dipicolinic acid (H_2dipic – Fig. 1) is a versatile N–O chelating agent that can act as a bidentate, tridentate, meridian or bridging ligand with different metal ions as well as with oxometal cations [10–14]. It is present in many natural compounds as an oxidative degradation product of vitamins, coenzymes and alkaloids and is also a component of fulvic acids. It shows various biological functions including activation-inactivation of some metalloenzymes and inhibition of electron transport and of LDL oxidation [15]. Lately, it has become one of the more suitable ligands for modeling potential pharmacological active compounds because of its low toxicity and amphophilic nature. It was also determined that vanadium complexes of this bio-ligand are more effective than the ligand alone in the treatment of diabetes [16]. The insulin-like properties of the V(V) dipicolinate compound, $[VO_2dipic]^-$, originally prepared by Wieghard [17,18], and its 4-hydroxydipicolinate derivative, $[VO_2dipic\text{-}OH]^-$, have been recently determined [16,19,20].

The structural chemistry of vanadium(V), like that of other transition metals in high oxidation states, is mainly related to the oxo complexes. Although a great number of oxo-bridged vanadium(IV and V) and mixed valence complexes are described in the literature, these compounds are less abundant than those of Ti(IV) or Mo(V,VI). Moreover, only few examples of bis-oxo-bridged compounds have been reported [21–24]. In the present paper, we report the synthesis, crystal structure and spectroscopic characterization of $[CH_3NHC(NH_2)_2]_2[V_2O_4(dipic)_2]$, a new vanadium(V) bis-oxo-bridged dimer complex. The dimeric complex anion has two methyl-guanidinium counterions.

Methylguanidine (MG) is a metabolic product of creatinine oxidation in living organisms. However, it is uncertain which enzymes are involved in its biosynthesis [25]. Clinical studies led to the conclusion that MG is adsorbed in the gastrointestinal tract and is not converted into other products. It has been also determined that MG is formed by incubation of creatinine, at 38 °C in the presence of oxygen, indicating that the conversion can take place non-enzymatically [26].

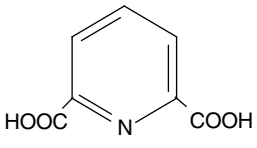


Fig. 1. Schematic structure of the protonated ligand H_2dipic.

2. Experimental

2.1. Reagents and instrumentation

All chemicals were of analytical grade. $VOSO_4 \cdot 5H_2O$ (Merck), Dipicolinic acid (Sigma) and Creatinine (Merck) were used without further purification.

IR spectra were recorded on a Bruker 113 v FTIR instrument, using the KBr pellet technique. Raman spectra were obtained with a Brucker IFS 66 FTIR spectrophotometer, using the FRA 106 Raman accessory and the 1064 nm line of a Nd:YAG solid state laser for excitation. The electronic absorption spectra were recorded on a Hewlett–Packard 8453 diode – array spectrophotometer using 1 cm quartz cells. Elemental analysis (C, H, N) was performed using a Carlo Erba EA 1108 analyzer.

2.2. Synthesis of complexes

*$[VO(dipic)(H_2O)_2]H_2O$ (**1**).* The complex was prepared according to the reported procedure [12]. 0.5 g of $VOSO_4.5H_2O$ (1.75 mmol) and 0.4 g of dipicolinic acid (2.45 mmol) were dissolved in 20 ml of hot water. The bright green solution obtained was then cooled to 5 °C and the precipitated ligand excess was filtered off. The filtrate was kept overnight in a refrigerator. The blue crystalline product obtained was filtered, washed with absolute ethanol and dried in air. (yield: 66%). *Anal.* Calc. for $C_7H_9NO_8V$: C, 29.3; H, 3.2; N, 4.7. Found: C, 28.9; H, 3.1; N, 4.5%.

*$[CH_3NHC(NH_2)_2]_2[V_2O_4(dipic)_2]$ (**2**).* 0.207 g (0.72 mmol) of complex **1** was dissolved in 12 ml of hot water and added dropwise to 25 ml of a methanolic solution of creatinine (0.168 g, 1.49 mmol), kept under continuous stirring. After 30 min stirring of the resulting solution, its color changed from bright deep green to pale light green. The solution was then kept at room temperature for 24 h before storing it in a refrigerator. After several months, yellow crystals of the complex, suitable for X–ray structural analysis, were obtained. During this period the color of the solution changed to yellow. The crystalline product obtained was filtered out, washed with small portions of 1:1 methanol:water mixture and dried in air. The low yield of the reaction (28%) can be improved by further precipitation from the filtrate at 5 °C. *Anal.* Calc. for $C_{18}H_{22}N_8O_{12}V_2$: C, 33.5; H, 3.4; N, 17.4. Found: C, 32.9; H, 3.3; N, 17.1%.

2.3. Crystal structure determination

The measurements were performed at 120 K on an Enraf-Nonius Kappa-CCD diffractometer with graphite monochromated Mo Kα ($\lambda = 0.71073$ Å) radiation. The temperature was controlled employing an Oxford

Cryosystems low-temperature device. Diffraction data were collected (φ and ω scans with κ offsets) with COLLECT [27]; integration and scaling of the reflections were performed with the HKL DENZO-SCALEPACK [28] suite of programs. The unit cell parameters were obtained by least-squares refinement based on the angular settings for all collected reflections using HKL SCALEPACK [28]. Absorption correction was not applied as μ times the largest crystal size was less than 0.103. The structure was solved by Patterson (SHELXS-97 [29]) and Fourier (SHELXL-97 [30]) methods and the molecular model refined by full-matrix least-squares procedure on F^2 with SHELXL-97. The H-atoms were positioned stereochemically and refined with the riding model. The data for publication were prepared with SHELXL-97. Crystal data, data collection procedure, structure determination methods and refinement results are summarized in Table 1.

Table 1
Crystal data and structure solution methods and refinement results for $[CH_3(NH)C(NH_2)_2]_2$ $[(VO_2)(dipic)]_2$

Empirical formula	$C_{18}H_{22}N_8O_{12}V_2$
Formula weight	644.32
Temperature (K)	120(2)
Wavelength (Å)	0.7107
Crystal system	monoclinic
Space group	$P2_1/c$
Unit cell dimensions	
a (Å)	9.557(2)
b (Å)	12.363(2)
c (Å)	10.466(2)
β (°)	101.56(2)
Volume (Å^3)	1211.5(4)
Z, calculated density (Mg/m^3)	2, 1.766
Absorption coefficient (mm^{-1})	0.853
F(000)	656
Crystal size (mm)	$0.12 \times 0.10 \times 0.10$
Crystal color/shape	pale yellow/polyhedral
ϑ range for data collection (°)	2.73 to 25.00
Index ranges	$-11 \leqslant h \leqslant 11$, $-14 \leqslant k \leqslant 14$, $-11 \leqslant l \leqslant 12$
Reflections collected/unique [R_{int}]	10728/2130 [0.0574]
Completeness (%)	99.8 (to $\vartheta = 25.00°$)
Observed reflections [$I > 2\sigma(I)$]	1941
Maximum and minimum transmission	0.919 and 0.905
Refinement method	full-matrix least-squares on F^2
Weights, w	$[\sigma^2(F_o^2) + (0.0309P)^2 + 0.99P]^{-1}$, where $P = [\mathrm{Max}(F_o^2, 0) + 2F_c^2]/3$
Data/restraints/parameters	2130/0/182
Goodness-of-fit on F^2	1.099
Final R indices [$I > 2(I)$]	$R_1 = 0.0280$, $wR_2 = 0.0722$
R indices (all data)	$R_1 = 0.0315$, $wR_2 = 0.0749$
Largest peak and hole (e Å^{-3})	0.275 and −0.363

3. Results and discussion

3.1. Structure of the complex

Fractional coordinates and equivalent isotropic displacement parameters are presented in Table 2. Bond distances and angles around the metal ion are given in Table 3. An ORTEP [31] drawing of the binuclear vanadium(V) complex with the atom numbering scheme is shown in Fig. 2.

The $[(VO_2)(dipic)]^-$ ions are arranged in the lattice as centrosymmetric oxo-bridged binuclear complexes. The pair of vanadium(V) atoms in a dimer are in an edge-sharing octahedral environment, with the dioxo vanadium(V) cation coordinated to a dipicolinate molecule acting as a tridentate ligand through one oxygen of each carboxylic group [V–O distances of 1.984(1) and 1.995(1) Å] and the heterocyclic nitrogen atom [d(V–N) = 2.097(2) Å]. The dipicolinate group defines an equatorial ligand plane [with a rms deviation of atoms from the least-squares plane of 0.025 Å] with the metal lying close to this plane [at 0.144(1) Å]. The bridging oxo ligand [d(V–O2) = 1.684(1) Å] is much closer to this plane [at 0.486(2) Å] than the terminal oxo atom [at 1.739(2) Å] which shows a slightly shorter V=O bond distance [d(V–O1) = 1.606(1) Å] and occupies an axial position. The O1–V–O2 angle is 105.36(7)°. The octahedral bonding structure around the metal is completed at the other axial position by the weak interaction with the bridging oxo ligand of the inversion related VO_2^+ group in the dimer [d(V–O2′) = 2.370(1) Å]. The bonding structure around vanadium(V) agrees well with other

Table 2
Atomic coordinates (×10^4) and equivalent isotropic displacement parameters (Å$^2 \times 10^3$) for $[CH_3(NH)C(NH_2)_2]_2[(VO_2)(dipic)]_2$

Atom	X	Y	Z	U_{eq}
C(1)	1497(2)	458(2)	1063(2)	13(1)
C(2)	652(2)	965(2)	1813(2)	18(1)
C(3)	618(2)	2091(2)	1815(2)	19(1)
C(4)	1424(2)	2680(2)	1087(2)	18(1)
C(5)	2243(2)	2110(2)	359(2)	14(1)
C(6)	3205(2)	2546(2)	−491(2)	14(1)
C(7)	1713(2)	−737(2)	892(2)	13(1)
C(10)	2479(2)	−1098(2)	5227(2)	24(1)
O(1)	2248(1)	152(1)	−2156(1)	16(1)
O(2)	4889(1)	−387(1)	−1159(1)	14(1)
O(3)	3883(1)	1785(1)	−991(1)	15(1)
O(4)	3326(2)	3512(1)	−674(1)	21(1)
O(5)	2641(1)	−933(1)	140(1)	14(1)
O(6)	1100(1)	−1424(1)	1394(1)	18(1)
N	2251(2)	1036(1)	366(2)	12(1)
N(1)	4438(2)	−2343(1)	2944(2)	17(1)
N(2)	4037(2)	−545(1)	3325(2)	15(1)
N(3)	3152(2)	−1869(1)	4492(2)	16(1)
C(8)	3872(2)	−1586(2)	3593(2)	14(1)
V	3427(1)	223(1)	−828(1)	11(1)

U_{eq} is defined as one third of the trace of the orthogonalized U_{ij} tensor.

Table 3
Bond lengths [Å] and angles [°] around the vanadium(V) ion in $[CH_3(NH)C(NH_2)_2]_2$ $[(VO_2)(dipic)]_2$[a]

Bond distances	
O(1)–V	1.606(1)
O(2)–V	1.684(1)
O(3)–V	1.995(1)
O(5)–V	1.984(1)
N–V	2.097(2)
V–O(2)′	2.370(1)
Bond angles	
O(1)–V–O(2)	105.36(7)
O(1)–V–O(5)	97.54(6)
O(2)–V–O(5)	101.38(6)
O(1)–V–O(3)	96.11(6)
O(2)–V–O(3)	102.19(6)
O(5)–V–O(3)	148.46(5)
O(1)–V–N	100.08(7)
O(2)–V–N	154.56(6)
O(5)–V–N	74.80(6)
O(3)–V–N	74.90(6)
O(1)–V–O(2)′	177.61(6)
O(2)–V–O(2)′	76.89(6)
O(5)–V–O(2)′	82.72(5)
O(3)–V–O(2)′	82.54(5)
N–V–O(2)′	77.68(5)

[a] Primed atoms are related to unprimed ones through the inversion symmetry operation: $-x+1,-y,-z$.

binuclear dioxovanadium(V) complexes of tridentate ligands reported in the literature [22,23].

To rationalize the changes in the bonding structure of $[(VO_2)(dipic)]^-$ upon dimerization we can compared the above structural data with that reported for the monomeric complex, $Cs[(VO_2)(dipic)]\cdot H_2O$ [18]. Here the V=O double bond distances are equal to within experimental accuracy [1.610(6) and 1.615(6) Å], while in our dimeric complex the V–O2 bond involving the bridging oxygen atom is 0.078(2) Å longer than the terminal V–O1 distance. This slight bond asymmetry within the dioxovanadium(V) ion is due to the formation of the weak intermolecular V···O bond bridging the halves of the binuclear complex.

As expected, significant bond localization is also observed in the carboxylic groups of the dipicolinate ligand. In fact, the terminal C–O bond lengths are about 0.1 Å shorter than the C–O distances involving the coordinated-to-vanadium oxygen atoms.

The C–N geometrical parameters of the methylguanidinium cation (MG) are in good accord with those found in related structures [32]. It has a singular planar CN_3 skeleton with a strong electronic delocalization that makes it able to participate in nets of H-bonding.

The $[(VO_2)(dipic)]^-$ monomeric units and the $CH_3NHC(NH_2)_2^+$ ions are arranged in the lattice along layers parallel to (101) crystallographic planes. Adjacent layers in the crystal are linked by the dimer-bridging bond. These layers are stabilized by a net of medium to strong N–H...O bonds involving the methylguanidinium NH and NH_2 groups and the oxo-bridge and the carboxylic oxygen atoms of the dipicolinate ligand [N···O distances are in the range 2.858–2.964 Å and N–H···O angles from 156.0° to 176.6°]. Each methylguanidinium has two N–H groups, from different N atoms, linked to one monomeric $[(VO_2)(dipic)]^-$ unit through an oxo-bridge atom and the carboxylate oxygen coordinated to the metal. The structural feature of this pattern is similar to that described for the interaction of phosphate, sulfonate and nitrate with the guanidinium cation [32]. The other N–H groups of the same MG ion bond to adjacent monomer units through N–H···O hydrogen bonds, forming a layer structure. Fig. 3 is a PLUTON [33] view of the crystal packing showing the layered and H-bonding structures.

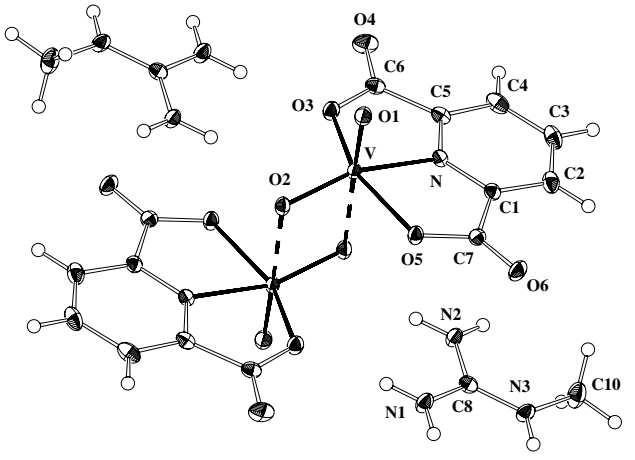


Fig. 2. Molecular plot of the centrosymmetric binuclear $[CH_3NHC(NH_2)_2]_2[(VO_2)(dipic)]_2$ vanadium(V) complex showing the labelling of the non-H atoms and their displacement ellipsoids at the 50% probability level. Full lines indicate vanadium-ligand bonds within the monomeric units and dashed lines indicate bridging bonds.

3.2. Vibrational spectra

The solid-state properties of the compound were examined by infrared and Raman spectroscopy. The spectra were compared with those of the free ligand and of methyl guanidine hydrochloride. Assignments of the spectroscopic bands are given in Table 4.

The dipicolinic acid spectra were coincident with those previously reported [34]. The IR spectrum of the free ligand shows a strong absorption in the 3100–2500 cm^{-1} region due to the O–H stretching mode of the COOH group, overlapped with the C–H stretching bands. The broad and irregular shape of this signal is indicative of the hydrogen bonded dimer structure of the acid. The corresponding C–OH in-plane bending and out-of-plane OH···O deformation modes are observed at 1417 cm^{-1} and 927 cm^{-1}, respectively. These modes are not present in the $[VO_2(dipic)]^-$ units, hence revealing the deprotonation of the carboxylic group

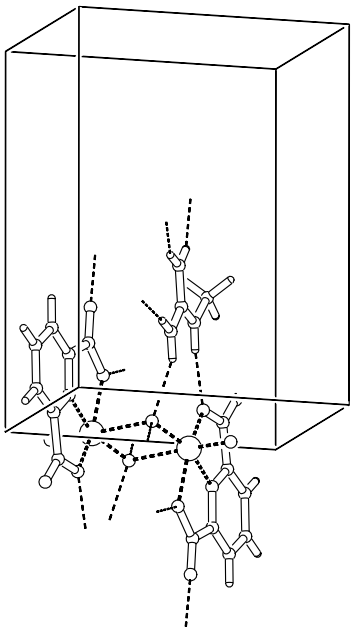


Fig. 3. Partial view showing the crystal packing in the $[CH_3NHC(NH_2)_2]_2[(VO_2)(dipic)]_2$ solid. Thick dashed lines indicate vanadium(V)–ligand bonds and thin dashed lines H-bonds. The crystal unique *b*-axis is along the vertical and the *a*-axis is horizontal.

upon complex formation. The typical ν(C=O) stretch is observed as a broad and very strong IR band centered at 1705 cm^{-1} due to the out-of-phase vibrations of the monomeric units in the dipicolinic acid dimer. The respective in-phase mode appears at 1644 cm^{-1} in the Raman spectra [35]. Two strong IR bands are observed at 1332 and 1301 cm^{-1} (Ra: 1325, 1296) that corresponds to the ν(C–O) vibration. Ring modes were also observed in the expected range [34].

The IR spectrum of the complex shows additional rather broad bands in the 3400–3200 cm^{-1} region that can be attributed to N–H stretching modes of the methylguanidinum, which is involved in hydrogen bonds. Characteristic bands of this cation related to C–NH_2 stretching and N–CH_3 deformation are also present in the compound's spectra [35,36]. After complex formation the carboxylate ν(C=O) and ν(C–O) bands are transformed into the symmetric and antisymmetric stretching vibrations of the carboxylate anion. The antisymmetric mode should be located at the same spectral zone as expected for the ν(C=N) and $\delta(NH_2)$ modes of guanidinium. The three strong IR bands present in the 1700–1620 cm^{-1} region can be assigned to these modes. The symmetric stretch vibration leads to a characteristic strong Raman line at 1329 cm^{-1}, with the corresponding IR band at 1327 cm^{-1}. The frequency difference between these two vibrations in the IR spectrum $[\Delta\nu = \nu_{as}(COO^-) - \nu_s(COO^-)]$ is higher than that reported for the calcium dipicolinate compound [34]. This value ($\Delta\nu > 300$ cm^{-1}) is in accordance with monodentate coordination of the carboxylate group [37]. Coordination of the heterocyclic nitrogen of dipicolinate to vanadium is indicated by an upward shift of some ring modes: skeletal vibration and in plane deformation [11,37]. These observations were confirmed by the X-ray crystallographic study.

Upon chelation, changes in intensity and position of some of the ligand bands were also observed in the 1000–200 cm^{-1} region. The strong IR absorption at 957 cm^{-1} and the intense Raman dispersion at 965 cm^{-1} are assigned to a Davydov split asymmetric VO_2 stretching mode. The first one is due to the IR-active crystal anti-symmetric optic mode and the second, to the Raman-active centrosymmetric optic vibration. The ordering of the IR and Raman wavenumbers agrees with that expected for transition dipole-dipole coupling between the $\nu_{asym}(VO_2)$ mode of the close VO_2 groups in the dimer (V–V distance of 3.2 Å), where the interacting dipoles are nearly parallel to the vanadium-vanadium direction. The other VO_2 stretching vibration, namely the $\nu_{sym}(VO_2)$ mode, appears as a strong doublet, both in the IR (at 862 and 849 cm^{-1}) and the Raman (at 837 and 817 cm^{-1}) spectra. The doublet can be interpreted as a Fermi resonance between the IR- and Raman-active VO_2 symmetric stretching vibration and the first overtone of the also active and symmetric $\delta(VO_2)$ bending mode. It is to be noted that the ordering of the IR and Raman doublets is inverse to that observed for the asymmetric VO_2 stretching mode. Again, this can be rationalized in terms of the correlation (Davydov) interaction between the transition dipole moments localized on the neighboring VO_2 groups of the dimer. Now, however, the coupling constant is of opposite sign to the one of the optical VO_2 asymmetric mode because the transition dipole moments are nearly perpendicular, rather than parallel, to the coupling V–V direction.

Furthermore, new bands were found at 457 and 366 cm^{-1} which are assigned to the stretching modes of the metal-to-ligand bonds, ν(V–O) and ν(V–N), respectively, as they lie in similar ranges to other V(V) compounds with N–O donor ligands (reviewed in [38]).

3.3. Electronic spectra

The electronic spectrum of the pale yellow aqueous solution of the complex shows two bands. The very strong absorption with a maximum at 194 nm can be assigned to intramolecular transitions as both the dipicolinic acid and the N-methylguanidinium salt spectra show strong bands in this region.

The second absorption, centered at 276 nm, denotes the presence of three components (approximate maxima at 268, 276 and 284 nm). It can be interpreted as an intraligand band (located at 274 nm in the free ligand spectrum) overlapped with ligand-to-metal charge transfer transitions. The higher energy component could

Table 4
Assignment of some of the characteristic IR and Raman bands of dipicolinic acid (H_2dipic), methylguanidine hydrocloride (MG) and the dimer complex

H_2dipic		MG		Dimer		Assignment
IR	Ra	IR	Ra	IR	Ra	
				3388 s		
		3340 s		3338 s		ν(NH),
		3270 s		3257 s		H-bonds,
		3170 s		3199 s		(See text)
3070 m	3097 w			3078 m	3085 w	ν(CH)
	3069 w					
2800* s, b	2600* vw					ν(OH)
1705* vs, b	1644 m, b					ν(C=O)
				1699 vs	1705w	$\nu_{as}(COO^-)$+
		1664 vs, b	1667 vw	1664 vs		δ (NH_2)+
		1621 s	1650 vw	1632 s		ν(C=N)
		1614 w	1617 vw			
			1583 vw			
1576 s	1576 m			1601 m	1605 w	ν(ring)
1460 m	1460 sh			1470 m	1585 m	
		1458 m	1467 w	1435 m		$\delta_a(N–CH_3)$
		1428 w	1433 vw	1420 w		
1417 m						δ(OH)
		1378 w		1352 m		$\delta_s(N–CH_3)$
1332 s	1325 w					ν(C–O)
1301 s	1296 w					
				1327 vs	1329 s	$\nu_s(COO^-)$
				1286 sh		
1268 s	1257 w			1250 w		δ(ring)
		1178 w, b	1190 vw	1211 w		ν(C–NH_2)
1177 m	1185 vw			1170 sh	1175 vw	δ(CH)
1162 m	1154 w+			1161 s		
1151 w						
1082 m	1086 vw			1078 s		
997 m	998 vs				1034s	Ring modes
				957 s	965 s	$\nu_{asym}(VO_2)$
		913 vw	917 vs	922 m	940w	$\nu_s(CN_3)$
					916w	
927 m, b						γ(OH)
				862 s	837 s	$\nu_{sym}(VO_2)$+
				849 s	817 s	2$\delta(VO_2)$
855 m	854 w			816 m		
783 w	802 w			795 vw		
753 s				771 s		γ(CH)
701 s	762 s			750 s		δ(OCO)
649 s	647 w			679 m		δ(ring)
		600* m, vb	683 vw	577 m, b		
			600 w			
			517 m			
				457 m	455 s	ν(V–O)carb
				440 w	440 m	$\delta(VO_2)$
				367 s		ν(V–N)
333 w						δ(C–COOH)
				295 w		
				260 w		

Band positions are in cm^{-1}.
vs, very strong; s, strong; m, medium; w, weak; sh, shoulder, b, broad; δ, in plane deformation; γ, out of plane deformation; *centered.

essentially involve the oxygen of the carboxylate moiety, whereas the lower energy one can be related to the nitrogen of the heterocycle. This pattern has been described for vanadium(V) complexes with other N, O-donor ligands [38]. According to MO calculations on related compounds the $O \rightarrow V$ charge transfer involving the double bonded oxo group is expected to appear at shorter wavelength than the ligand-to-metal bands [39]. In our compound this absorption is probably superimposed with the band at 194 nm.

Acknowledgements

This work was supported by CONICET and ANPCyT (PICT 06-06148) of Argentina and by FAPESP of Brazil. A.G.B, O.E.P and B.S.P.C are members of the Research Career from CONICET. The authors thank Professor Dr. E.J. Baran, Dr. P.A.M Williams and Dr. S.E. Ulic for valuable comments.

Appendix A. Supplementary data

Tables of full intra-molecular bond distances and angles (Table S1), atomic anisotropic displacement parameters (Table S2), hydrogen atoms positions (Table S3), H-bond distances and angles (Table S4) and observed and calculated structure factor amplitudes (Table S5) have been deposited with the Cambridge Crystallographic Data Centre, CCDC N°. 238652. Copies of this information are available free of charge from The Director, CCDC, 12 Union Road, Cambridge, CB2 1EZ, UK (Fax: +44 1223 336 033; e-mail: deposit@ccdc.cam.ac.uk or http://www.ccdc.cam.ac.uk).

Supplementary data associated with this article can be found, in the online version, at doi:10.1016/j.poly.2004.09.032.

References

[1] A. Butler, C.J. Carrano, Coord. Chem. Rev. 109 (1991) 61.
[2] H. Siegel, A. Siegel (Eds.), Metal Ions in Biological Systems, Vanadium and its Role in Life, vol. 31, Marcel Dekker, New York, 1995.
[3] D. Rehder, Coord. Chem. Rev. 182 (1999) 297.
[4] E.J. Baran, J. Inorg. Biochem. 80 (2000) 1.
[5] V.G. Yuen, C. Orvig, J.H. McNeill, Can. J. Physiol. Pharmacol. 73 (1995) 55.
[6] L.C.Y. Woo, V.G. Yuen, K.H. Thompson, J.H. McNeill, C. Orvig, J. Inorg. Biochem. 76 (1999) 251.
[7] K. Fukui, Y. Fujisawa, H. Ohya-Nishiguchi, H. Kamada, H. Sakurai, J. Inorg. Biochem. 77 (1999) 215.
[8] H. Sakurai, K. Fujii, H. Watanabe, H. Tamura, Biochem. Biophys. Res. Commun. 214 (1999) 1095.
[9] H. Sakurai, Y. Koyima, Y. Yoshikawa, K. Kawabe, H. Yasui, Coord. Chem. Rev. 226 (2002) 187, and references therein.
[10] M. Chatterjee, M. Maji, S. Ghosh, T.C.W. Mak, J. Chem. Soc., Dalton Trans. (1998) 3641.
[11] S.K. Sengupta, S.K. Shani, R.N. Kapoor, J. Indian Chem. Soc. LX (1983) 821.
[12] M. Chatterjee, M. Maji, S. Ghosh, B.M. Wu, T.C.W. Mak, Polyhedron 17 (1998) 1369.
[13] L. Yang, D.C. Crans, S.M. Miller, A. la Cour, O.P. Anderson, P.M. Kaszynski, M.E. Godzala III, L.D. Austin, G.R. Willsky, Inorg. Chem. 41 (2002) 4859.
[14] P. Lainé, A. Gourdon, J.P. Launay, Inorg. Chem. 34 (1995) 5129, 5138; 5150; 5156.
[15] K. Murakami, Y. Tanemura, M. Yoshino, J. Nutr. Biochem. 14 (2003) 99, and references therein.
[16] D.C. Crans, M. Mahroof-Tahir, M.D. Johnson, P.C. Wilkins, L. Yang, K. Robbins, A. Johnson, J.A. Alfano, M.E. Godzala, L.T. Austin, G.R. Willsky, Inorg. Chim. Acta 356 (2003) 365.
[17] K. Wieghardt, Inorg.Chem. 17 (1978) 57.
[18] B. Nuber, J. Weiss, K. Wieghardt, Z. Naturforsch. 33b (1978) 265.
[19] D.C. Crans, L. Yang, T. Jakusch, T. Kiss, Inorg. Chem. 39 (2000) 4409.
[20] D.C. Crans, L. Yang, J.A. Alfano, L.H. Chi, W. Jing, M. Mahroof-Tahir, K. Robbins, M.M. Toloue, L.K. Chan, A.J. Plante, R.Z. Grayson, G.R. Willsky, Coord. Chem. Rev. 237 (2003) 13.
[21] H. Mimoum, L. Saussini, E. Daire, M. Postel, J. Fischer, R. Weiss, J. Am. Chem. Soc. 105 (1983) 3101.
[22] X. Li, M.S. Lah, V.L. Pecoraro, Inorg. Chem. 27 (1988) 4657.
[23] C.A. Rooth, J.D. Hoeschele, C.R. Cornman, J.W. Kampf, V.L. Pecoraro, Inorg. Chem. 32 (1993) 3855.
[24] I. Cavaco, J. Costa Pessoa, M.T. Duarte, R.T. Henriques, P.M. Matias, R.D. Gillard, J. Chem. Soc., Dalton Trans. (1996) 1989.
[25] K. Takemura, K. Aoyagi, S. Nagase, M. Gotoh, A. Hirayama, A. Ueda, C. Tomida, A. Koyama, Nephron 78 (1998) 82.
[26] M. Gonella, G. Barsotti, S. Lupetti, S. Giovannetti, Clin. Sci. Mol. Med. 48 (1975) 341.
[27] Enraf-Nonius COLLECT, Nonius BV, Delft, The Netherlands (1997–2000).
[28] Z. Otwinowski, W. Minor, in: C.W. CarterJr., R.M. Sweet (Eds.), Methods in Enzymology, vol. 276, Academic Press, New York, 1997, pp. 307–326.
[29] G.M. Sheldrick, SHELXS-97. Program for Crystal Structure Resolution, University of Göttingen, Göttingen, Germany, 1997.
[30] G.M. Sheldrick, SHELXL-97. Program for Crystal Structures Analysis, University of Göttingen, Göttingen, Germany, 1997.
[31] C.K. Johnson, ORTEP-II. A Fortran Thermal-Ellipsoid Plot Program, Report ORNL-5318, Oak Ridge National Laboratory, Oak Ridge, TN, 1976.
[32] (a) F.A. Cotton, V.W. Day, E.E. Hazen Jr., S. Larsen, J. Am. Chem. Soc. 95 (1973) 4834;
(b) V.A. Russell, M.C. Etter, M.D. Ward, J. Am. Chem. Soc. 116 (1994) 1941;
(c) A. Katrusiak, M. Szafrański, J. Mol. Struct. 378 (1996) 205.
[33] A.L. Spek, PLATON, A Multipurpose Crystallographic Tool, Utrecht University, Utrecht, The Netherlands, 1998.
[34] P. Carmona, Spectrochim. Acta 36 (1979) 705.
[35] D. Lin-Vien, N.B. Colthup, W.G. Fately, J.G. Grasselli, Infrared and Raman Characteristic Frequencies of Organic Molecules, Academic Press, Boston, MA, 1991.
[36] Z. Biresak, W.T.A. Harrison, Inorg. Chem. 37 (1998) 3204.
[37] K. Nakamoto, Infrared and Raman Spectra of Inorganic and Coordination Compounds, 5th ed., Wiley, New York, 1997.
[38] E.J. Baran, J. Coord. Chem. 54 (2001) 215.
[39] A.H. Jubert, A.C. González Baró, R. Pis Diez, E.J. Baran, J. Raman Spectrosc. 23 (1992) 273.

Available online at www.sciencedirect.com
SCIENCE DIRECT®
Polyhedron 24 (2005) 57–63
POLYHEDRON
www.elsevier.com/locate/poly

Some *trans*-chlorobis(triphenylphosphine)ruthenium(II) complexes with N,N,O-donor *N*-(aroyl)-*N*′-(picolinylidene)hydrazines

Raji Raveendran, Samudranil Pal *

School of Chemistry, University of Hyderabad, Hyderabad 500 046, India

Received 25 August 2004; accepted 30 September 2004
Available online 18 November 2004

Abstract

The reactions of $[Ru(PPh_3)_3Cl_2]$ and *N*-(aroyl)-*N*′-(picolinylidene)hydrazines (HL), derived from 2-pyridinecarbaldehyde and 4-substituted aroylhydrazines in boiling methanol provide mixed-ligand complexes having the general formula *trans*-$[RuL(PPh_3)_2Cl]$. The complexes were characterized by analytical, spectroscopic and electrochemical measurements. The +2 oxidation state of the metal ions in these complexes is confirmed by their diamagnetic nature in the solid state and electrically non-conducting behavior in solution. The X-ray structure of a representative complex has been determined. The metal ion is in a distorted octahedral N_2OP_2Cl coordination sphere. The monoanionic pyridine-N, imine-N and deprotonated amide-O donor ligand and the chlorine atom form an N_2OCl square-plane around the metal centre and the P-atoms of the PPh_3 molecules occupy the remaining two axial sites. The ^{31}P NMR spectra of all the complexes in $CDCl_3$ solutions are consistent with the *trans* orientation of the PPh_3 molecules. Electronic spectra of the complexes in dichloromethane solution display several bands in the range 590–261 nm due to metal-to-ligand charge transfer and intraligand transitions. Cyclic voltammograms of the complexes in dimethylformamide solution display the reversible Ru(III)/Ru(II) couple in the potential range 0.40–0.52 V (versus saturated calomel electrode). The trend in these potential values reflects the polar effect of the substituents on the aroyl moiety of the ligand (L^-).
© 2004 Elsevier Ltd. All rights reserved.

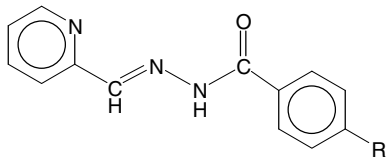
Keywords: Ruthenium(II); Aroylhydrazone; Mixed-ligand; Crystal structure; Redox property

1. Introduction

The interest in coordination complexes of ruthenium stems from their versatile electron-transfer and energy-transfer properties [1–20]. As a result these complexes exhibit a wide range of reactivities. Due to these characteristics a large variety of ruthenium complexes have found applications in diverse types of research areas. These include artificial photosynthesis, photomolecular devices, elucidation of structural and electron transfer properties of proteins and DNA, catalytic oxidation of water and organic substrates, and stoichiometric as well as catalytic reactions for organic synthesis [12–20]. Due to such a wide range of applications, new ruthenium complexes with different types of ligands are of particular interest. The purpose is to alter the metal ion coordination environment, which is primarily responsible for the properties exhibited by the complex. The Schiff bases derived from aroyl- or acylhydrazines can provide an amide oxygen for metal coordination. Such ligands also give the scope to scrutinize the effect of the amide protonation state on the structural and physical properties of the complex.

* Corresponding author. Tel.: +91 40 2313 4756; fax: +91 40 2301 2460.
E-mail address: spsc@uohyd.ernet.in (S. Pal).

0277-5387/$ - see front matter © 2004 Elsevier Ltd. All rights reserved.
doi:10.1016/j.poly.2004.09.027



Hpabh(R = H) Hpadh (R = NMe_2)
Hpath (R = Me) Hpach (R= Cl)
Hpamh (R= OMe) Hpanh (R = NO_2)

(I)

Prior to our reports on ruthenium(II) bis complexes with *N*-(aroyl)-*N*′-(picolinylidene)hydrazines (HL, **I**) [21] and ruthenium(III) bis complexes with *N*-(acetyl)-*N*′-(salicylidene)hydrazine (H_2L') [22], there were no examples of ruthenium complexes with aroyl- or acylhydrazones. In the former, the ligand (L^-) coordinates the metal ion via pyridine-N, imine-N and deprotonated amide-O atoms and in the latter the monoanionic (HL'^-) or dianionic ligand (L'^{2-}) coordinates the metal ion via phenolate-O, imine-N and amide-O atoms of the protonated or deprotonated amide functionality. For the ruthenium(II) complexes, spectroscopic and electrochemical studies suggest that the energy gap between the metal-dπ and the ligand-π* levels remains constant despite the variation in the polar effect of the substituent on the aroyl fragment of the ligand [21]. On the other hand, electrochemical measurements with the ruthenium(III) complexes of L'^{2-} indicate that the +4 oxidation state of the metal ion can be accessed and the potential of the Ru(IV)/Ru(III) couple is dependent on the protonation state of the coordinated amide functionalities [22]. In the present work, we have described the synthesis and characterization of a new series of mixed-ligand ruthenium(II) complexes having the general formula *trans*-$[RuL(PPh_3)_2Cl]$ obtained from *N*-(aroyl)-*N*′-(picolinylidene)hydrazines (HL) and $[Ru(PPh_3)_3Cl_2]$. In solution, electron transfer and spectroscopic properties have been investigated. An X-ray structure of a representative complex has been determined.

2. Experimental

2.1. Materials

The Schiff bases were prepared in 80–90% yield by condensation of one mole equivalent of 2-pyridinecarbaldehyde and one mole equivalent of the corresponding aroylhydrazine by following a reported procedure [21,23]. All other chemicals and solvents were of analytical grade, available commercially and were used as received.

2.2. Physical measurements

Microanalytical (C, H, N) data were obtained with a Thermo Finnigon Flash EA1112 series elemental analyzer. Infrared spectra were collected using KBr pellets on a Jasco-5300 FT-IR spectrophotometer. A Shimadzu 3101-PC UV/vis/NIR spectrophotometer was used to record the electronic spectra. ^1H and ^{31}P NMR spectra were recorded on a Bruker 200 MHz spectrometer. A Sherwood Scientific balance was used for magnetic susceptibility measurements. Solution electrical conductivities were measured with a Digisun DI-909 conductivity meter. A CH-Instruments model 620A electrochemical analyzer was used for cyclic voltammetric experiments with dimethylformamide solutions of the complexes containing tetrabutylammonium perchlorate (TBAP) as supporting electrolyte. The three electrode measurements were carried out at 298 K under a dinitrogen atmosphere with a platinum working electrode, a platinum wire auxiliary electrode and a saturated calomel reference electrode (SCE). The potentials reported in this work are uncorrected for junction contributions.

2.3. Synthesis of $[Ru(pabh)(PPh_3)_2Cl]$

To a yellow methanol solution (30 ml) of Hpabh (50 mg, 0.22 mmol) and KOH (12 mg, 0.22 mmol), solid $[Ru(PPh_3)_3Cl_2]$ (213 mg, 0.22 mmol) was added and the mixture was refluxed to boiling for 24 h and then cooled to room temperature. The complex, precipitated as a brown solid, was collected by filtration, washed with ether and dried in vacuum. Recrystallization was performed by dissolving the complex in a 1:1 dichloromethane–hexane mixure. Yield, 80 mg (41%).

The other five complexes reported in this work were synthesized from a methanolic medium using one mole equivalent each of $[Ru(PPh_3)_3Cl_2]$, the corresponding Schiff base and KOH in 40–70% yields by following similar procedures as described above.

2.4. X-ray crystallography

Single crystals of *trans*-$[Ru(pamh)(PPh_3)_2Cl]$ were grown by slow evaporation of its dichloromethane–hexane (1:1) solution. A crystal of dimensions $0.50 \times 0.15 \times 0.03$ mm was used for the structure determination. Unit cell parameters and the intensity data were obtained on a Bruker-Nonius SMART APEX CCD single crystal diffractometer, equipped with a graphite monochromator and a Mo Kα fine-focus sealed tube ($\lambda = 0.71073$ Å) operated at 2.0 kW. The detector was placed at a distance of 6.0 cm from the crystal. Data were collected at 100 K with a scan width of 0.3° in ω and an exposure time of 15 s/frame. The SMART software was used for data acquisition and the SAINT-Plus software was used for data extraction [24]. The absorp-

tion correction was performed with the help of the SADABS program [25]. The structure was solved by direct methods in the C_2/c space group and refined on F^2 by full-matrix least-squares procedures. The asymmetric unit contains a molecule of *trans*-[Ru(pamh)(PPh_3)$_2$Cl] and a water molecule. All non-hydrogen atoms were refined using anisotropic thermal parameters. The hydrogen atoms of the water molecule located in a difference map and the rest of the hydrogen atoms obtained by using a riding model were included in the structure factor calculation at idealized positions, but not refined. The SHELX-97 programs [26] were used for structure solution and refinement. The ORTEX6a package [27] was used for molecular graphics. Selected crystallographic data are listed in Table 1.

Table 1
Crystallographic data for *trans*-[Ru(pamh)(PPh_3)$_2$Cl] · H_2O

Chemical formula	$RuP_2ClC_{50}H_{44}N_3O_3$
Formula weight	933.34
Crystal system	monoclinic
Space group	C_2/c
a (Å)	39.643(4)
b (Å)	9.5984(10)
c (Å)	23.526(2)
β (°)	98.038(2)
V (Å^3)	8863.9(16)
Z	8
μ (mm^{-1})	0.532
Reflections collected	50801
Unique reflections	10426
Reflections [$I \geqslant 2\sigma(I)$]	8219
R_1, wR_2 [$I \geqslant 2\sigma(I)$]	0.0648, 0.1229
R_1, wR_2 [all data]	0.0889, 0.1316
Goodness-of-fit on F^2	1.135
Largest peak and hole (e Å^{-3})	1.713, −0.996

3. Results and discussion

3.1. Synthesis and some properties

The Schiff bases (HL) were obtained by the condensation of 2-pyridinecarbaldehyde and 4-substituted aroylhydrazines (1:1 mole ratio) in methanol. Reactions of one mole equivalent each of [Ru(PPh_3)$_3$Cl$_2$], HL and KOH in boiling methanol afforded the complexes in moderate to good yields. The elemental analysis data of the complexes are consistent with the general formula [RuL(PPh_3)$_2$Cl] (Table 2). The complexes are more soluble in less polar solvents such as dichloromethane and chloroform than polar solvents such as methanol and acetonitrile. In dimethylformamide solutions, the complexes are electrically non-conducting. Thus the chloride ion is coordinated to the metal ion in each complex. All the complexes are diamagnetic and NMR active. Thus the oxidation state of the metal ion is +2 and it is in a low-spin state in each complex.

3.2. Spectroscopic characteristics

Infrared spectra of the complexes do not display the characteristic bands associated with the N–H and C=O bonds of the amide functionality present in the free Schiff bases [28,29]. Thus in each complex the amide functionality is deprotonated and exists in the enolate form (**II**). A medium to strong band observed in the range 1585–1606 cm^{-1} is most likely associated with the conjugated —C=N—N=C— fragment of the ligands [21–23,30]. The presence of the {Ru(PPh_3)$_2$} unit in all the complexes has been indicated by three strong bands at ~743, ~694 and ~515 cm^{-1}. Similar bands are displayed by [Ru(PPh_3)$_3$Cl$_2$] and complexes containing the {Ru(PPh_3)$_2$} unit [31].

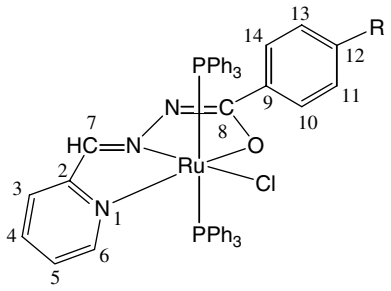
Dichloromethane solutions of the complexes are brown in colour. These solutions have been used to record the electronic spectra. All the complexes display several absorptions in the visible and ultraviolet region. The spectroscopic data are listed in Table 2. The intense absorptions in the higher energy region are most likely due to transitions involving the ligand orbitals only [21]. The absorptions in the visible region are attributed to metal-to-ligand charge-transfer transitions. Multiple absorptions in this region for these types of mixed-ligand ruthenium(II) complexes are not unusual considering the possibilities of several closely spaced acceptor levels, lower symmetry splitting of the metal orbitals

Table 2
Elemental analysis and electronic spectroscopic[a] data

Complex	Found (Calc.) (%)			λ_{max} (nm) ($10^{-3} \times \varepsilon$ (M^{-1} cm^{-1}))
	C	H	N	
trans-[Ru(padh)(PPh_3)$_2$Cl]	65.73 (65.98)	4.59 (4.88)	5.88 (6.03)	580[b] (0.9), 482[b] (5.7), 415 (20.8), 378[b] (15.7), 308[b] (12.6), 270 (32.3)
trans-[Ru(pamh)(PPh_3)$_2$Cl]	65.86 (65.61)	4.66 (4.62)	4.37 (4.59)	577[b] (0.7), 484 (3.3), 393[b] (13.1), 364 (16.8), 331 (17.8), 261 (32.4)
trans-[Ru(path)(PPh_3)$_2$Cl]	66.58 (66.77)	4.69 (4.71)	4.42 (4.67)	580[b] (0.9), 489 (3.4), 389[b] (12.1), 362 (16.7), 329 (17.5), 262 (36.2)
trans-[Ru(pabh)(PPh_3)$_2$Cl]	66.63 (66.47)	4.45 (4.55)	4.58 (4.75)	575[b] (0.8), 494 (3.3), 390[b] (7.4), 367[b] (11.1), 325 (17.7), 263 (33.5)
trans-[Ru(pach)(PPh_3)$_2$Cl]	63.81 (63.99)	4.51 (4.27)	4.67 (4.57)	570[b] (0.9), 493 (3.9), 391[b] (10.7), 365[b] (16.9), 323 (21.8), 263 (41.6)
trans-[Ru(panh)(PPh_3)$_2$Cl]	63.44 (63.26)	4.42 (4.22)	6.26 (6.02)	590[b] (0.8), 500 (3.1), 394[b] (13.7), 341 (22.9), 261 (41.4)

[a] In dichloromethane solution.
[b] Shoulder.

and singlet–triplet transitions made allowed by spin–orbit coupling [21,31–33].



(II)

The proton NMR spectra of the complexes (**II**) in $CDCl_3$ are consistent with the presence of one tridentate ligand and two PPh_3 molecules. Significant NMR data are listed in Table 3. In all the spectra, a broad peak corresponding to a single proton is observed in the range δ 7.95–8.10 ppm. This signal is assigned to the azomethine hydrogen (H7) of the ligand. For the complexes of $padh^-$, $pamh^-$ and $path^-$ the methyl protons of the substituent on the aroyl fragment of the ligands are observed as singlets at δ 2.96, 3.77 and 2.30 ppm, respectively. The *ortho* proton (H6) of the pyridyl ring appears as a doublet in the range δ 6.77–6.84 ppm. A multiplet observed within δ 6.56–6.62 ppm is assigned to the *para* proton (H4) of the pyridyl unit. A doublet corresponding to two protons is observed in all the spectra except in that of the complex of $pach^-$. This doublet shows a down-field shift with the progressive increase in the electron withdrawing ability of the R group on the aroyl moiety (Table 3). For the complex of $padh^-$ (R = NMe_2) this signal appears at δ 6.41 ppm and for the complex of $panh^-$ (R = NO_2) it appears at δ 7.99 ppm. This doublet is attributed to the two protons (H11 and H13) that are *ortho* to the R group. In each spectra, broad signals observed in the range δ 7.1–7.8 ppm correspond to the phenyl ring protons of the two PPh_3 ligands. The signal due to the H11 and H13 protons for the complex of $pach^-$ and the signals due to the H3, H5, H10 and H14 protons for all the complexes are buried under these broad signals.

Two geometrical isomers are possible for each of these complexes with respect to the arrangement of the two PPh_3 molecules in the coordination sphere. To probe whether the two PPh_3 molecules are a *cis* or *trans* pair we have recorded the ^{31}P NMR spectrum of each of the six complexes. All the complexes display a singlet in the range δ 26.34–27.62 ppm. Thus the $\{Ru(PPh_3)_2\}$ unit in these complexes exists in the *trans* configuration.

3.3. X-ray structure of *trans*-$[Ru(pamh)(PPh_3)_2Cl]\cdot H_2O$

The structure of the complex molecule is illustrated in Fig. 1. Selected bond lengths and angles are listed in Table 4. The ruthenium(II) centre is in a distorted octahedral N_2OP_2Cl coordination sphere constituted by pyridine-N, imine-N and amide-O donor $pamh^-$, two PPh_3 molecules and the chloride ion. The *trans* and *cis* angles are in the ranges 156.77(10)°–179.38(9)° and 77.29(10)°–102.21(6)°, respectively. As observed in solution the PPh_3 molecules are *trans* to each other. The P1–Ru–P2 angle is 169.05(3)°. The tridentate ligand forms two five-membered chelate rings. The bite angles are 79.61(11)° and 77.29(10)°. The N–N, N–C and C–O bond lengths in the =N–N=C(O^-)– fragment of $pamh^-$ are consistent with the enolate form of the amide functionality [21–23]. The Ru(II)–N(pyridine) and Ru(II)–N(imine) bond lengths are within the range reported for ruthenium(II) complexes containing the same coordinating atoms [21,34–36]. The two Ru(II)–P bond lengths are very similar and comparable to that reported for other PPh_3 coordinated ruthenium(II) complexes [31,35]. The Ru(II)–Cl bond length is unexceptional [34,35].

The tridentate ligand is not planar due to the twisting of the anisoyl ring plane (C8–C14, O2; mean deviation 0.019 Å) and the plane containing the rest of the atoms (N1–N3, C1–C7, O1; mean deviation 0.073 Å) along the C7–C8 bond. The angle between these two planes is

Table 3
^1H and ^{31}P NMR spectroscopic[a] data

Complex	δ (ppm) (J (Hz))[b]					
	H(4)	H(6)	H(7)	H(11)/H(13)	CH_3	P
trans-[Ru(padh)(PPh_3)$_2$Cl]	6.56m	6.78d (8)	7.95br,s	6.41d (6)	2.96s	26.66s
trans-[Ru(pamh)(PPh_3)$_2$Cl]	6.58m	6.77d (6)	8.04br,s	6.62d (8)	3.77s	26.71s
trans-[Ru(path)(PPh_3)$_2$Cl]	6.56m	6.80d (8)	8.02br,s	6.92d (8)	2.30s	26.66s
trans-[Ru(pabh)(PPh_3)$_2$Cl]	6.59m	6.78d (8)	7.92br,s	7.04d (7)		27.62s
trans-[Ru(pach)(PPh_3)$_2$Cl]	6.58m	6.82d (8)	8.05br,s			26.53s
trans-[Ru(panh)(PPh_3)$_2$Cl]	6.62m	6.84d (8)	8.10br,s	7.99d (8)		26.34s

[a] In $CDCl_3$ solution.
[b] Symbols: s, singlet; d, doublet; m, multiplet; br, broad.

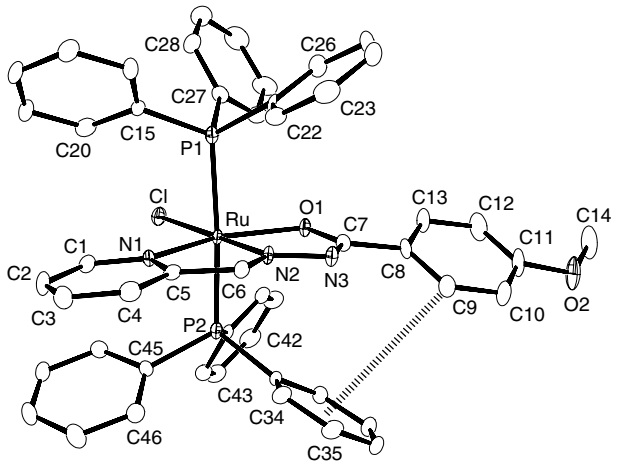


Fig. 1. Molecular structure of *trans*-[Ru(pamh)(PPh_3)$_2$Cl] with the atom labelling scheme. All atoms are represented by their 50% probability thermal ellipsoids. Hydrogen atoms are omitted and selected carbon atoms of the PPh_3 phenyl rings are labelled for clarity. The C–H···π interaction is shown by the dashed bond.

Table 4
Selected bond lengths (Å) and angles (°) for *trans*-[Ru(pamh)(PPh_3)$_2$Cl] · H_2O

Bond lengths			
Ru–N(1)	2.065(3)	Ru–N(2)	1.933(3)
Ru–O(1)	2.144(2)	Ru–P(1)	2.3649(10)
Ru–P(2)	2.3607(10)	Ru–Cl	2.4620(8)
C(6)–N(2)	1.308(4)	N(2)–N(3)	1.375(4)
C(7)–N(3)	1.327(4)	C(7)–O(1)	1.294(4)
Bond angles			
N(1)–Ru–N(2)	79.61(11)	N(1)–Ru–O(1)	156.77(10)
N(1)–Ru–P(1)	93.47(8)	N(1)–Ru–P(2)	91.34(8)
N(1)–Ru–Cl	100.87(8)	N(2)–Ru–O(1)	77.29(10)
N(2)–Ru–P(1)	94.72(9)	N(2)–Ru–P(2)	95.82(9)
N(2)–Ru–Cl	179.38(9)	O(1)–Ru–P(1)	90.84(7)
O(1)–Ru–P(2)	88.60(7)	O(1)–Ru–Cl	102.21(6)
P(1)–Ru–P(2)	169.05(3)	P(1)–Ru–Cl	85.64(3)
P(2)–Ru–Cl	83.79(3)		

30.34(10)°. As a consequence one of the aromatic C–H bonds of the anisoyl ring (C9) is directed toward a phenyl ring plane (C33–C38) of one PPh_3 ligand (Fig. 1). The C9···cg (centroid of the phenyl ring) and H9···cg distances are 3.914 and 3.475 Å, respectively. The C9–H9···cg angle is 110.77°. These parameters indicate the possibility of a C–H···π interaction [37]. Perhaps this intramolecular C–H···π interaction is responsible for the twisting of the anisoyl ring of pamh$^-$ along the C7–C8 vector. However, the existence of any such interaction in solution could not be verified due to non-appearance of the NMR signal corresponding to this proton of the anisoyl ring (vide supra).

The water molecule is hydrogen bonded to the uncoordinated amide nitrogen atom (N3) of pamh$^-$. The O3···N3 distance and the O3–H3A···N3 angle are 3.034(5) Å and 168.69°, respectively. It also participates in another weak hydrogen bonding interaction with the methoxy O-atom of a symmetry related complex molecule. The O3···O2 distance and the O3–H3B···O2 angle are 3.233(6) Å and 140.68°, respectively. Thus the *trans*–[Ru(pamh)(PPh_3)$_2$Cl] · H_2O units form discrete dimers in the crystal lattice. Two complex molecules are bridged by two water molecules via the above mentioned two hydrogen bonds. The second hydrogen bonding interaction may also contribute to the twisting of the anisoyl ring of pamh$^-$ along the C7–C8 vector.

3.4. Redox properties

Dimethylformamide solutions of the complexes have been used to study the redox properties with the help of cyclic voltammetry. A representative voltammogram has been depicted in Fig. 2 and the potential data are listed in Table 5. The complexes display the Ru(III)/Ru(II) couple in the potential range 0.40–0.52 V (versus

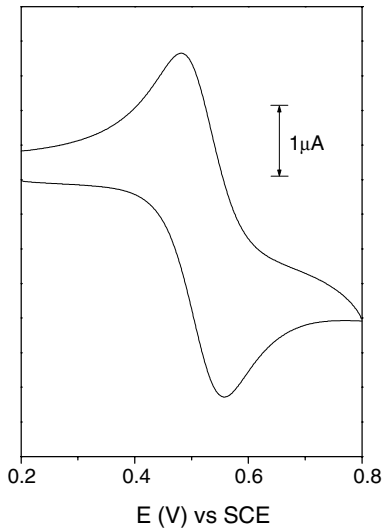


Fig. 2. Cyclic voltammogram (scan rate 50 mV s^{-1}) of *trans*-[Ru(panh)(PPh_3)$_2$Cl] in dimethylformamide solution (0.1 M TBAP) at a platinum electrode at 298 K.

Table 5
Cyclic voltammetric[a,b] data

Complex	$E_{1/2}$ (V)	ΔE_p (mV)
trans-[Ru(padh)(PPh_3)$_2$Cl]	0.40	70
trans-[Ru(pamh)(PPh_3)$_2$Cl]	0.43	70
trans-[Ru(path)(PPh_3)$_2$Cl]	0.45	70
trans-[Ru(pabh)(PPh_3)$_2$Cl]	0.46	80
trans-[Ru(pach)(PPh_3)$_2$Cl]	0.48	70
trans-[Ru(panh)(PPh_3)$_2$Cl]	0.52	80

[a] In dimethylformamide solution at 298 K at a scan rate of 50 mV s^{-1}.

[b] $E_{1/2} = (E_{pa} + E_{pc})/2$, where E_{pa} and E_{pc} are anodic and cathodic peak potentials, respectively; $\Delta E_p = E_{pa} - E_{pc}$.

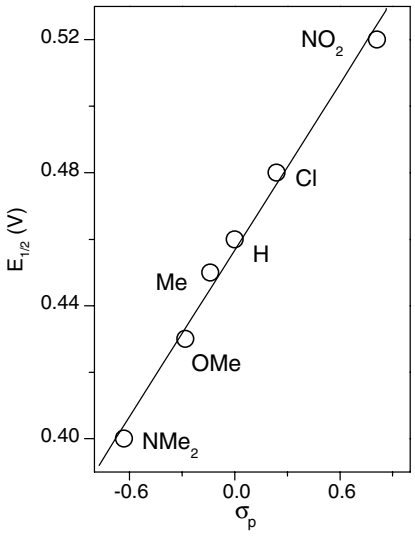


Fig. 3. Correlation between the $E_{1/2}$ values for the Ru(III)/Ru(II) couple and the Hammett substituent constants. The straight line represents a linear least-squares fit.

SCE). The peak-to-peak separations are in the range 70–80 mV. The cathodic and anodic peak currents are essentially identical for all the complexes. The one-electron stoichiometry of this response is confirmed by comparing the current heights with known one-electron redox processes under identical experimental conditions [21,22,30,31,34]. The trend in the $E_{1/2}$ values reflects the influence of the electronic nature of the substituents (R) at the *para* position of the O-coordinating deprotonated amide functionality present in the ligands. For the most electron releasing substituent (R = NMe_2) the oxidation of the metal ion occurs at the lowest potential and for the most electron withdrawing substituent (R = NO_2) it occurs at the highest potential. When these $E_{1/2}$ values are plotted against the Hammett substituent constants (σ_p) [38] a linear correlation is observed (Fig. 3). Thus, as the σ-bonding ability of the O-atom of the deprotonated amide functionality decreases with the increasing electron withdrawing ability of the substituent, the Ru(II) to Ru(III) oxidation becomes more difficult.

4. Conclusion

The synthesis and physical properties of a new series of ruthenium(II) complexes with the general formula *trans*-[RuL(PPh_3)$_2$Cl] have been described. The ligands used are pyridine-N, imine-N and amide-O donor deprotonated Schiff bases *N*-(aroyl)-*N*′-(picolinylidene)hydrazines (HL). These Schiff bases differ by the substituent present in the aroyl fragment. The *trans* configuration of the {Ru(PPh_3)$_2$} unit in each complex molecule has been confirmed by NMR spectroscopic measurements. The solid state structure of a representative complex has been determined by X-ray crystallography. The molecular structure indicates the possibility of an intramolecular C–H···π interaction involving an aroyl ring C–H and a PPh_3 phenyl ring. All the complexes exhibit low-energy metal-to-ligand charge transfer bands. The complexes are redox active and display a reversible one electron metal centred oxidation. The potential of this Ru(II) to Ru(III) oxidation is sensitive to the electronic nature of the substituent on the aroyl moiety of the ligand.

5. Supplementary material

Crystallographic data for *trans*-[Ru(pamh)(PPh_3)$_2$Cl]·H_2O have been deposited with the Cambridge Crystallographic Data Centre (deposition number CCDC-240872). Copies of this information may be obtained from The Director, CCDC, 12 Union Road, Cambridge, CB2 1EZ, UK (fax: +44 1233 336033; email: deposit@ ccdc.cam.ac.uk; or the web: http://www.ccdc.cam.ac. uk).

Acknowledgements

Financial support provided by the Council of Scientific and Industrial Research, New Delhi (Grant No. 01(1880)/03/EMR-II) is gratefully acknowledged. X-ray crystallographic data were obtained from the National Single Crystal Diffractometer Facility (established by the Department of Science and Technology, New Delhi) at the School of Chemistry, University of Hyderabad. We thank the University Grants Commission, New Delhi for the facilities provided under the University with Potential for Excellence program.

References

[1] E.A. Seddon, K.R. Seddon, The Chemistry of Ruthenium, Elsevier, New York, 1984.
[2] G. Wilkinson, R.D. Gillard, J.A. McCleverty, Comprehensive Coordination Chemistry, vol. 4, Pergamon, Oxford, 1987, p. 277.
[3] B.K. Ghosh, A. Chakravorty, Coord. Chem. Rev. 95 (1989) 239.
[4] A.B.P. Lever, H. Masui, R.A. Metcalfe, D.J. Stufkens, E.S. Dodsworth, P.R. Auburn, Coord. Chem. Rev. 125 (1993) 317.
[5] V. Balzani, A. Juris, M. Venturi, S. Campagna, S. Serroni, Chem. Rev. 96 (1996) 759.
[6] S.-M. Lee, W.-T. Wong, Coord. Chem. Rev. 164 (1997) 415.
[7] A. Juris, V. Balzani, F. Barigelletti, S. Campagna, P. Belser, A. Zefewsky, Coord. Chem. Rev. 84 (1998) 85.
[8] D.B. Grotjahn, Coord. Chem. Rev. 190–192 (1999) 1125.
[9] K. Szaciowski, W. Macyk, G. Stochel, Z. Stasicka, S. Sostero, O. Traverso, Coord. Chem. Rev. 208 (2000) 277.
[10] B.-Z. Shan, Q. Zhao, N. Goswami, D.M. Eichhorn, D.P. Rillema, Coord. Chem. Rev. 211 (2001) 117.
[11] M.J. Clarke, Coord. Chem. Rev. 232 (2002) 69.
[12] L. Sun, L. Hammarström, B. Åkermark, S. Styring, Chem Soc. Rev. 30 (2001) 36.

[13] C. Joachim, J.K. Gimzewski, A. Aviram, Nature 408 (2000) 541.
[14] N. Sardesai, S.C. Lin, K. Zimmermann, J.K. Barton, Bioconjugate Chem. 6 (1995) 302.
[15] H.B. Gray, J.R. Winkler, Annu. Rev. Biochem. 65 (1996) 537.
[16] P. Lincoln, E. Tuite, B. Nordén, J. Am. Chem. Soc. 119 (1997) 1454.
[17] S. Goswami, A.R. Chakravarty, A. Chakravorty, J. Chem. Soc., Chem. Commun. (1982) 1288.
[18] J.A. Gilbert, D.S. Eggleston, W.R. Murphy Jr., D.A. Geselowitz, S.W. Gersten, D.J. Hodgson, T.J. Meyer, J. Am. Chem. Soc. 107 (1985) 3855.
[19] C.-M. Che, Pure Appl. Chem. 67 (1995) 225.
[20] T. Naota, H. Takaya, S.-I. Murahashi, Chem. Rev. 98 (1998) 2599.
[21] S.N. Pal, S. Pal, J. Chem. Soc., Dalton Trans. (2002) 2102.
[22] S.N. Pal, S. Pal, Eur. J. Inorg. Chem. (2003) 4244.
[23] N.R. Sangeetha, S.N. Pal, S. Pal, Polyhedron 19 (2000) 2713.
[24] SMART version 5.630 and SAINT-plus version 6.45, Bruker-Nonius Analytical X-ray Systems Inc., Madison, WI, USA, 2003.
[25] G.M. Sheldrick, SADABS, Empirical Absorption Correction Program, University of Göttingen, Göttingen, Germany, 1997.
[26] G.M. Sheldrick, SHELX-97, Structure Determination Software, University of Göttingen, Göttingen, Germany, 1997.
[27] P. McArdle, J. Appl. Crystallogr. 28 (1995) 65.
[28] R.M. Silverstein, F.X. Webster, Spectrometric Identification of Organic Compounds, 6th ed., Wiley, New York, 1998, p. 101.
[29] K. Nakamoto, Infrared and Raman Spectra of Inorganic and Coordination Compounds, 4th ed., Wiley, New York, 1986, p. 242.
[30] S.N. Pal, S. Pal, Inorg. Chem. 40 (2001) 4807.
[31] F. Basuli, A.K. Das, G. Mostafa, S.-M. Peng, S. Bhattacharya, Polyhedron 19 (2000) 1663.
[32] A. Ceulemans, L.G. Vanquickenborne, J. Am. Chem. Soc. 103 (1981) 2238.
[33] E.M. Kober, T.J. Meyer, Inorg. Chem. 21 (1982) 5645.
[34] S.N. Pal, S. Pal, Polyhedron 22 (2003) 867.
[35] L.A. Ortiz-Frade, L. Ruiz-Ramírez, I. González, A. Marín-Becerra, M. Alcarazo, J.G. Alvarado-Rodriguez, R. Moreno-Esparza, Inorg. Chem. 42 (2003) 1825.
[36] C.-Y. Lai, W.-L. Mak, E.Y.Y. Chan, Y.-K. Sau, Q.-F. Zhang, S.M.F. Lo, I.D. Williams, W.-H. Leung, Inorg. Chem. 42 (2003) 5863.
[37] M. Nishio, Cryst. Eng. Commun. 6 (2004) 130.
[38] J. March, Advanced Organic Chemistry, 4th ed., Wiley, New York, 1992, p. 280.

Available online at www.sciencedirect.com
SCIENCE DIRECT®
Polyhedron 24 (2005) 65–73
POLYHEDRON
www.elsevier.com/locate/poly

Luminescence study of Ru(II) bipyridine–acridine spaced by amide and proline bridges

Idalina M.M. de Carvalho [a,*], Ícaro de Sousa Moreira [a], Marcelo H. Gehlen [b]

[a] *Departamento de Química Orgânica e Inorgânica, Universidade Federal do Ceará, Cx Postal 12200, Campus do Pici s/n, 60455760 Fortaleza-CE, Brazil*
[b] *Instituto de Química de São Carlos, Universidade de São Paulo, Cx Postal 780, São Carlos-SP, Brazil*

Received 31 May 2004; accepted 30 September 2004
Available online 18 November 2004

Abstract

Complexes containing polypyridyl Ru(II) and the organic chromophore acridine (as the acridinium ion) separated by an amide, proline and diproline groups attached to one of the pyridyl ligands were prepared, and their photophysical properties, including electronic absorption and emission spectra, luminescence quantum yields and lifetimes, were determined in different solvents. Generally, the inductive effect of the carbonyl group from the amide or from the proline as well as the solvent interactions cause a decrease of the energy level of the metal-to-ligand charge transfer excited state, with energy stabilization of about 5 kJ/mol in polar solvents when compared with the properties of $[Ru(bpy)_3]^{2+}$. The excited state dynamics of the dyads is more favorable for triplet–triplet energy transfer between the Ru(II) donor and the acridine acceptor than for electron transfer and photoreduction of the dye, but the efficiency of the energy transfer is low in all compounds. However, the luminescence decay of the dyad with a diproline bridge is biexponential, displaying a fast component of low weight percent. This result has been ascribed to a presence of a *cis* conformer in which the diproline peptide is folded allowing a more close contact of the donor and acceptor species, and therefore a fast triplet–triplet energy transfer process. This assumption is supported by the ^{13}C NMR spectrum analysis which indicates the presence of about 11% of the *cis* conformation in solution.
© 2004 Elsevier Ltd. All rights reserved.

Keywords: Intramolecular energy transfer; Ru(II) complexes; Excited-state kinetics; Luminescence; Supramolecular systems

1. Introduction

The study of photoinduced electron or energy transfer between donor and acceptor molecules that are spatially separated by a molecular bridge is an interesting subject for learning about the factors controlling primarily photochemical events in chemistry and biology [1–4], and for designing of new artificial systems for photonic applications [5–7]. Among several types of molecular bridges, the separation of donor and acceptor species by a peptide spacer has been used in many experimental systems [8–13]. In this sense, we have designed and characterized molecular systems composed of a single amide, one and two prolines as spacers for the separation of donor and acceptor chromophores, which under favorable conditions may undergo a photoinduced energy transfer reaction.

The system described herein utilizes polypyridyl Ru(II) as the donor and an acridinium ion as the acceptor. The tris-bipyridine Ru(II) complex was chosen because of its lowest electronic excited state, which is based on a metal-to-ligand charge transfer (MLCT) transition that is able to transfer energy to aromatics

* Corresponding author. Tel.: +55031852889844; fax: +55031852889784.
E-mail addresses: idalina@dqoi.ufc.br (I.M.M. de Carvalho), marcelog@iqsc.usp.br (M.H. Gehlen).

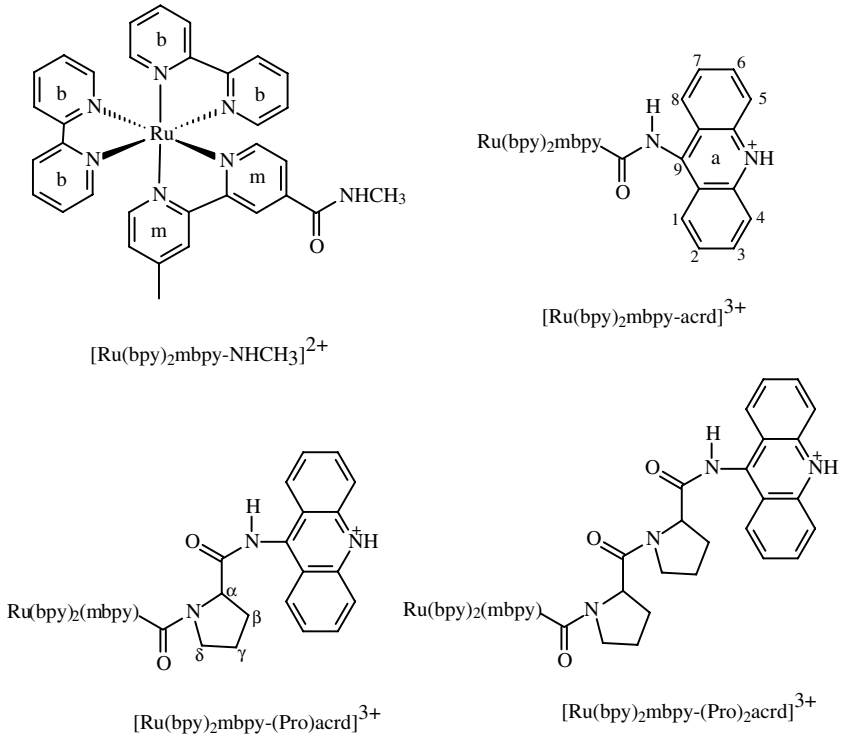
0277-5387/$ - see front matter © 2004 Elsevier Ltd. All rights reserved.
doi:10.1016/j.poly.2004.09.030

or dyes by a Dexter type mechanism [14–26]. The ^{3}MLCT electronic excited state is a long lived and luminescent species, allowing easy measurement of excited state kinetics by using the conventional time resolved emission techniques. Compounds derived from the tris-bipyridine Ru(II) complex with amide, $[Ru(bpy)_2mbpy–acrd]^{3+}$, one proline, $[Ru(bpy)_2mbpy–(Pro)acrd]^{3+}$, and two prolines, $[Ru(bpy)_2mbpy–(Pro)_2acrd]^{3+}$, as spacers, all of them molecular bridged to acridine (in the acridinium ion form), were carefully prepared (Scheme 1). The solvent effect and the role of the molecular structure of the spacer on the donor–acceptor energy transfer process are discussed.

2. Experimental

2.1. Equipments

Absorption spectra were measured with a Hitachi U-2000 spectrophotometer and the corrected steady state emission and excitation spectra were recorded using a CD-900 Edinburgh spectrofluorimeter. Emission quantum yields (Φ_{em}) were calculated relatively to $[Ru(bpy)_3]^{2+}$ in CH_3CN, assuming a standard value of $\Phi_{em} = 0.062$. Luminescence decays were measured by a time-correlated single photon counting technique using a CD-900 Edinburgh spectrometer operating with a hydrogen-filled nanosecond flash lamp at 40 kHz pulse frequency and a cooled PMT Hamamatsu R955 as photon detector. The decays were analyzed by monoexponential or biexponential fittings using reconvolution of the δ-function with the instrument response function (pulse width of 1.5 ns FWHM). Absorption transients with excitation at 532 nm from the second harmonic of the Surelite I-10 Nd:YAG laser were determined using an Edinburgh LP 900 laser flash photolysis system. Oxygen was removed from the samples by repeated freeze–pump–thaw cycles. ^{1}H and ^{13}C NMR spectra were obtained in the designated solvents on a Bruker (400 MHz) spectrometer. Syntheses were accompanied by the HPLC (column: μ-Bondapak C18 Waters Associates −10μ, 3.9 mm × 30 cm) technique using a Shimadzu LC-10AD chromatograph with a SPD-10A UV–VIS detector. Electrochemical data were obtained by cyclic voltammetry with a BAS 100W. The experiments were performed in CH_3CN solutions degassed with an argon flow, with Pt-bead work, Au-wire auxiliary and Ag/AgCl reference electrodes in a single compartment cell. The tetra-*n*-butylammonium perchlorate, TBAP (0.1 M) was used as a supporting electrolyte throughout the experiment. All the potentials reported in this study are quoted versus the Ag/AgCl electrode, which under the experimental conditions gave a value of 0.37 V for the ferrocene/ferrocenium couple.



Scheme 1. Bichromophoric compounds.

2.2. Reagents

Acetonitrile (AN), 9-aminoacridine, tetrafluorborate acid, 1,3-diisopropilcarbodiimide (DIC), 1-hydroxybenzotriazole hydrate (HOBT) and *N*-methylmorpholine (NMM) were obtained from Aldrich Co. HCl, dichloromethane, ethanol, ammonium hydroxide, sodium hydroxide and methanol were obtained from Mallinckrodt. Trifluoracetic acid (HTFA) and silver nitrate were obtained from Merck. These reagents, as well as Boc-proline (Peptides International), ammonium carbonate (Reagen), ruthenium trisbipyridine chloride (G. Frederick Smith Chemical Co.) and cobalt nitrate (Carlo Erba), were all used as received. Acetone (Mallinckrodt) was treated with sodium sulfate and then distilled and stored with 4 Å molecular sieves. Dimethylformamide (DMF, Merck) was distilled under reduced pressure at 75 °C and dried with 4 Å molecular sieves. Diethyl ether (Synth) was treated with sodium and then distilled twice before use.

2.3. Synthesis $[Ru(bpy)_2mbpy–acrd](BF_4)_2$

This compound was prepared according to the method described in the literature [21].

2.4. $[(NH_3)_5CoCO_3]NO_3$ and $[(NH_3)_5CoOH_2](ClO_4)_3$

These precursor compounds were prepared by following the procedures previously published in the literature [27].

2.5. $[ProCo(NH_3)_5](BF_4)_3$ and $[Pro_2Co(NH_3)_5](BF_4)_3$

These compounds were prepared following the procedures described by Isied and Kuehn [28].

2.6. $[Ru(bpy)_2mbpy–(Pro)Co](BF_4)_5$

The active ester was prepared by the reaction of 0.23 g (0.29 mmol) $[Ru(bpy)_2mbpy–OH](BF_4)_2$, 70 μL (0.44 mmol) DIC and 0.051 g (0.38 mmol) HOBT in 400 μL DMF. After 15 min, 0.30 g (0.60 mmol) of the compound $[ProCo(NH_3)_5](BF_4)_3$ and 20 μL (0.18 mmol) NMM were mixed with the active ester, and the system was stirred at room temperature for 1 h. The reaction mixture was filtered, the solvent was removed by rotary evaporation and the residue was dissolved in a minimum amount of water and loaded on a BIO-GEL P2 column. The column was washed with the same solvent and the fractions were collected and analyzed by HPLC. The first and major orange fraction was dried by rotary evaporation and the solid obtained was dissolved in a minimum amount of ethanol. The compound was precipitated by addition of a few drops of concentrated HBF_4 and diethyl ether. The precipitate was filtered off, washed with an excess of anhydrous diethyl ether and dried under vacuum. (0.31 g, 82% yield). *Anal*. Calc. for $C_{37}H_{47}N_{12}O_3CoRuB_5F_{20}$: C, 34.14; H, 3.64; N, 12.91. Found: C, 34.16; H, 3.67; N, 12.92%.

2.7. $[Ru(bpy)_2mbpy–(Pro)_2Co](BF_4)_5$

The procedure followed was the same as that described before, but substituting $[Pro_2Co(NH_3)_5](BF_4)_3$ for $[ProCo(NH_3)_5](BF_4)_3$ (0.32 g, 79% yield). *Anal*. Calc. for $C_{42}H_{54}N_{13}O_4CoRuB_5F_{20}$: C, 36.06; H, 3.89; N, 13.02. Found: C, 36.01; H, 3.85; N, 13.00%.

2.8. $[Ru(bpy)_2\ mbpy–(Pro)](BF_4)_2$

0.28 g (0.22 mmol) $[Ru(bpy)_2mbpy–(Pro)Co](BF_4)_5$ was dissolved in a degassed aqueous 0.2 M solution of HTFA. A pellet of Zn/Hg was added and an argon flow was maintained through the solution for 4 h. The reaction mixture was concentrated by rotary evaporation, dissolved in a minimum amount of ethanol–water (20:80) mixture and purified by using reversed-phase liquid chromatography in a low pressure column loaded with a reversed phase C_{18} resin (Yamamura Chemical Lab Co.). The column was slowly washed with the same solvent mixture. The first orange fraction was collected and concentrated by rotary evaporation and dissolved in a minimum amount of ethanol. A few drops of a concentrated solution of HBF_4 were added followed by a minimal amount of diethyl ether to precipitate the final product (0.15 g, 75% yield). *Anal*. Calc. for $C_{37}H_{33}N_7O_3RuB_2F_8$: C, 49.47; H, 3.70; N, 10.91. Found: C, 49.41; H, 3.68; N, 10.88%.

2.9. $[Ru(bpy)_2mbpy–(Pro)_2\ ](BF_4)_2$

The complex was prepared by following the same procedure used to synthesize the $[Ru(bpy)_2mbpy–(Pro)](BF_4)_2$ complex, but using $[Ru(bpy)_2mbpy–(Pro)_2-Co](BF_4)_5$ instead of $[Ru(bpy)_2mbpy–(Pro)Co](BF_4)_5$. (0.15 g, 73% yield). *Anal*. Calc. for $C_{42}H_{40}N_8O_4RuB_2F_8$: C, 50.67; H, 4.05; N, 11.26. Found: C, 50.64; H, 4.02; N, 11.23%.

2.10. $[Ru(bpy)_2mbpy–(Pro)acrd](BF_4)_2$

A solution of 0.100 g (0.11 mmol) $[Ru(bpy)_2mbpy–(Pro)](BF_4)_2$ dissolved in 250 μL DMF was mixed with 22 μL (0.14 mmol) DIC and 0.013 g (0.11 mmol) HOBT to prepare the active ester. After 15 min, 0.069 g (0.28 mmol) 9-aminoacridrine and 15 μL (0.14 mmol) NMM were added, and the coupling reaction mixture was allowed to proceed for 3 h, under stirring at room temperature. At the end of the reaction, a small amount of water was added and the reaction mixture was filtered to remove an excess of organic starting materials. The

solvent was removed by rotary evaporation. The resulting slurry was dissolved in a minimum amount of water and loaded on a Bio-Gel P2 (45–90 μm, from Bio-Rad laboratories) column. The elution was performed by washing the column with water. The collected fractions were concentrated and their purity level was evaluated by HPLC (μ-Bondapak C18 Waters Associates – 10μ, 3.9 mm × 30 cm). The first and major orange fraction, containing the desired complex, was dried by rotary evaporation, dissolved in a minimum amount of ethanol and precipitated by adding a few drops of an aqueous solution of HBF_4 followed by anhydrous diethyl ether. The precipitate was filtered off, washed with an excess of ethanol and diethyl ether, and dried under vacuum (0.095 g, 80% yield). Spectral data: ^{1}H NMR ($(CD_3)_2SO$): δ 1.29–1.37 (m, 4H, β–γ Pro), 2.50 (3H, m4′-CH_3), 3.31–3.32 (2H, δ Pro), 4.70 (1H, α Pro), 7.40–7.41 (2H, a2 and a7), 7.44–7.46 (2H, a4 and a5), 7.52–7.58 (7H, a1, a8, m5′ and b5), 7.68–7.76 (7H, m5, m6′, b6 and m6), 7.78–7.80 (2H, a3 and a6), 8.12–8.18 (4H, b4), 8.70–8.74 (1H, m3′) and 8.82 (5H, b3 and m3). ^{13}C NMR: δ 13.93 (γ Pro), 20.56 (4′-CH_3), 36.52 (β Pro), 46.39 (δ Pro), 63.71 (α Pro), 121.03 (a1′ and a8′), 121.54 (a2 and a7), 121.89 (a4 and a5), 122.64 (m5′), 124.38 (b5), 125.30 (m5), 125.89 (m6′), 126.08 (a1 and a8), 127.78 (b6), 128.79 (a3 and a6), 129.01 (m6), 137.89 (b4), 140.6 (a4′ and a5′), 144.70 (m4′), 150.04 (m3′), 150.95 (b3), 151.59 (m3), 152.35 (a9), 155.17 (m2′), 156.26 (m2), 156.39 (b2), 156.70 (m4), 160.0 (CO-Pro) and 164.54 (m4-CO_2H). *Anal.* Calc. for $C_{50}H_{42}N_9O_2RuB_2F_8$: C 55.83; H 3.94; N 11.72. Found: C 55.91; H 3.99; N 11.81%.

2.11. *[Ru(bpy)$_2$ mbpy–(Pro)$_2$acrd](BF$_4$)$_2$*

The procedure used here was the same as that described in the preparation of [Ru(bpy)$_2$mbpy–(Pro)-acrd](BF$_4$)$_2$, except the complex [Ru(bpy)$_2$mbpy–(Pro)$_2$]-(BF$_4$)$_2$ was the coupling reagent for 9-aminoacridine (0.086 g, 72% yield). Spectral data: ^{1}H NMR (D_2O): δ 1.25–1.28 (3H, m4′-CH_3), 1.87–1.92 (2H, γ-p2), 1.99–2.01 (2H, γ-p1), 2,13–2.23 (4H, β-p2 and p1), 3.51–3.60 (2H, δ-p2), 3.68–3.71 (2H, -p1) 4.38–4.39 (1H, α-p2), 4.54–4.55 (1H, α-p1), 7.18–7.21 (2H, a2 and a7), 7.28–7.29 (4H, a4, a5, a1 and a8), 7.30–7.33 (5H, m5′ and b5), 7.55–7.56 (2H, m5 and m6′), 7.67–7.73 (5H, b6 and m6), 7.88–7.89 (2H, a3 and a6) 7.95–7.98 (4H, b4), 8.35 (1H, m3′) 8.43–8.47 (4H, b3) and 8.85 (1H, m3). ^{13}C NMR: δ 23.52 (4′-CH_3), 29.01(γ-p2), 29.58 (γ-p1), 33.04 (β-p2), 33.75 (β-p1), 46.12 (δ-p2), 47.22 (δ-p1), 56.05 (α-p2), 58.83 (α-p1), 120.02 (a1′ and a8′), 121.84 (a2 and a7), 123.05 (a4 and a5), 125.55 (m5′), 126.91 (b5), 127.89 (m5), 125.89 (m6′), 129.08 (a1 and a8), 129.93 (b6), 130.03 (a3 and a6), 130.98 (m6), 138.23 (b4), 140.17 (a4′ and a5′), 141.90 (m4′), 152.92 (m3′), 154.78 (b3), 155.56 (m3), 157.60 (a9), 159.01 (m2′), 159.96 (m2), 156.39 (b2), 161.35 (m4), 164.96 (CO-Pro) and 171.02 (m4-CO_2H). *Anal.* Calc. for $C_{55}H_{49}N_{10}O_3RuB_2F_8$: C 56.33; H 4.21; N 11.94. Found: C 56.40; H 4.27; N 11.98%.

3. Results and discussion

The electronic absorption spectra for all of the studied complexes were similar to the $[Ru(bpy)_3]^{2+}$ spectrum, especially in the visible region (see Fig. 1). The relatively intense and broad absorption band in the visible region (around 450 nm) is due to the spin-allowed metal-to-ligand charge transfer (MLCT) transition. The MLCT band displays a small red shift in the dyads compared to the precursor complex.

When the complexes are excited at the maximum wavelength of the MLCT absorption spectrum, broad emission bands, similar in shape to the luminescence band of the $[Ru(bpy)_3]^{2+}$ complex, are obtained (see Fig. 2). However, the luminescence spectra of the model compounds show a bathochromic shift when compared to that of the precursor complex. The change in electronic energy of the ^{3}MLCT excited state of the new complexes and that of the $[Ru(bpy)_3]^{2+}$ complex are

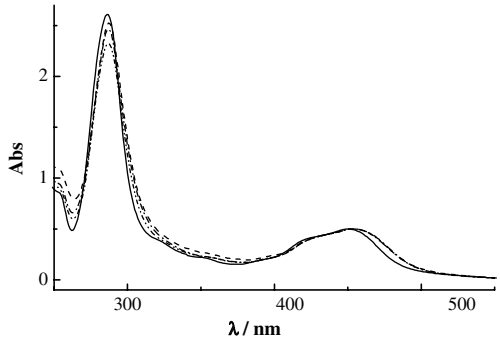


Fig. 1. Electronic spectra of the complexes: (—) $[Ru(bpy)_3]^{2+}$, (– –) $[Ru(bpy)_2mbpy\text{-}acrd]^{3+}$, (–·–) $[Ru(bpy)_2mbpy\text{-}(Pro)acrd]^{3+}$, and (–··–) $[Ru(bpy)_2mbpy\text{-}(Pro)acrd]^{3+}$, in methanol ($10^{-5}$ M) at 293 K.

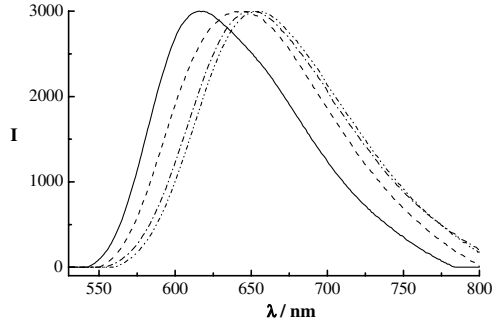


Fig. 2. Luminescence spectra of the compounds in methanol at 293 K. (—) $[Ru(bpy)_3]^{2+}$, (– –) $[Ru(bpy)_2mbpy–acrd]^{3+}$, (–·–) $[Ru(bpy)_2mbpy–(Pro)acrd]^{3+}$ and (–··–) $[Ru(bpy)_2mbpy–(Pro)_2acrd]^{3+}$.

Table 1
Difference in triplet energy level (ΔE_{0-0}, kJ/mol) of the MLCT transition of the complexes at 293 K in different solvents compared to $[Ru(bpy)_3]^{2+}$

Compound	Acetonitrile	methanol	Dichloromethane
$[Ru(bpy)_2mbpy–acrd]^{3+}$	−4.6	−2.5	−0.4
$[Ru(bpy)_2mbpy–(Pro)acrd]^{3+}$	−4.6	−4.6	0.4
$[Ru(bpy)_2mbpy–(Pro)_2acrd]^{3+}$	−6.3	−6.3	0.0

summarized in Table 1. The spectral shift indicates a more stable ^{3}MLCT state, which could be the result of the enhanced solvation at the mbpy ligand due to the presence of the polar groups, in addition to an inductive effect of the amide or proline groups of the molecular bridge. Proline has a permanent dipole moment and its orientation and solvation would affect the charge distribution, and therefore the energy of the ^{3}MLCT state.

The inclusion of the spacers causes a symmetry breakdown among the bipyridyl ligands. The energy stabilization in acetonitrile and methanol, calculated from the spectral shift, is in the range of 4.6–6.3 kJ/mol, when compared to the energy of the ^{3}MLCT of the $[Ru(bpy)_3]^{2+}$ complex of 205 kJ/mol [29].

The ^{3}MLCT state of the Ru complexes may be deactivated by energy or electron transfer to the acridinium acceptor. The possibility of deactivation of the ^{3}MLCT excited state by electron transfer to the acridinium derivative (dye photoreduction) was evaluated from $\Delta G^0 \approx E_{1/2}(Ru^{2+}/Ru^{3+}) - E_{1/2}(dye/dye^-) - E_{0,0}(^3MLCT)$. According to the data of $E_{1/2}$ reported in Table 2, and assuming the excitation energy of the ^{3}MLCT corresponds to 2.12 eV, photoinduced electron transfer will be an endothermic process. On the other hand, the free-energy change for triplet–triplet energy transfer ($\Delta G^0 \approx E_{0,0}{}^3MLCT + E_{0,0}{}^3Dye$) is negative (exothermic process), and therefore is a more favorable process than electron transfer.

The numerical values for the driving force in T–T energy transfer or electron transfer in acetonitrile are reported in Table 3. These results are consistent with those reported in the early studies in which acridine dyes were more capable to have T–T energy transfer with $*[Ru(bpy)3]^{2+}$ than oxidative quenching [23–26].

Table 2
Redox Potentials for the one-electron processes on the complexes in 0.1 M TBAP/AN solution at 298 K

Complex	$E_{1/2}$[b] (V)	
	Oxidation	Reduction[a]
$[Ru(bpy)_2mbpy–acrd]^{3+}$	1.31	−0.87; −1.15
$[Ru(bpy)_2mbpy–(Pro)acrd]^{3+}$	1.31	−0.88; −1.22
$[Ru(bpy)_2mbpy–(Pro)_2acrd]^{3+}$	1.28	−0.88; −1.22

[a] The first reduction potential refers to the reduction of the acrd group while the second value listed is the reduction of the first bpy ligand. The non-complexing dye 9-aminoacridine has a reduction potential of −0.92 V [30].

[b] All the potentials are quoted against the Ag/AgCl electrode with $E_{1/2}$ = 0.37 V for the F_c/F_c^+ couple.

Table 3
Free-energy change ΔG^0 (acetonitrile solution at 298 K) considering T–T Energy transfer and electron-transfer processes

Complex	ΔG^0 (kJ/mol)	
	Energy transfer*	Electron transfer
$[Ru(bpy)_2mbpy–acrd]^{3+}$	−6.4	5.8
$[Ru(bpy)_2mbpy–(Pro)acrd]^{3+}$	−6.4	6.7
$[Ru(bpy)_2mbpy–(Pro)_2acrd]^{3+}$	−4.7	5.8

(*) Values calculated assuming the energy values of the ^{3}MLCT of $[Ru(bpy)_3]^{2+}$ = 205 kJ/mol [29], ^{3}acrd = 194 kJ/mol [31,32], and the differences observed in the energy of the compounds given in Table 1.

The lifetimes and luminescence quantum yields of the systems prepared are reported in Table 4. The data for the $[Ru(bpy)_3]^{2+}$ complex and for its derivative with 2-aminonaphthalene ($[Ru(bpy)_2mbpy–naph]^{2+}$) were enclosed for a comparative purpose with those containing the spacers and acridine. An ideal reference is a compound which carriers the isolated properties (lifetime and quantum yield) of the donor part of the supramolecule. Thus, the difference in lifetime and quantum yield of the reference compound (τ_0,ϕ_0) and of the donor–acceptor system (τ,ϕ) would be ascribed to the presence of an energy transfer process in an ideal situation. $[Ru(bpy)_2mbpy–naph]^{2+}$ approaches to a reference compound [21], the triplet energy of the naphthalene is much higher than the triplet energy of the Ru complex, which precludes an energy transfer process from the metal complex to the peripheral naphthalene. The value of the rate constant for energy transfer (k_{et}) in the case of irreversible energy transfer can be estimated by the difference of lifetimes of the dyad and the reference compound

$$k_{et} = \tau^{-1} - \tau_0^{-1}. \quad (1)$$

Assuming the experimental values of τ_0 and τ reported in Table 3, the k_{et} values of $[Ru(bpy)_2mbpy–acrd]^{3+}$ are 4.0×10^4, 3.6×10^4 and 1.5×10^5 s^{-1} in acetonitrile, methanol and dichloromethane, respectively [21].

In the case of the $[Ru(bpy)_2mbpy–(Pro)acrd]^{3+}$ complex, the rate constants are 1.6×10^4 and 1.5×10^5 s^{-1} in methanol and dichloromethane, respectively. For the system with two prolines, the difference in the luminescence quantum yield between the reference and dyad indicates a very low efficiency of energy transfer. In general, the results indicate the tendency of an increase of

Table 4
Lifetime (τ), and quantum yield (Φ_{em}) of the complexes in different solvents at 293 K

Compound	τ (ns), Φ_{em}					
	Acetonitrile		Methanol		Dichloromethane	
$[Ru(bpy)_3]^{2+}$	836	0.061	813	0.045	485	0.091
$[Ru(bpy)_2$ mbpy–naph$]^{2+}$	1321	0.078	941	0.034	792	0.124
$[Ru(bpy)_2$mbpy–acrd$]^{3+}$	1255	0.064	910	0.029	707	0.101
$[Ru(bpy)_2$mbpy–(Pro)acrd$]^{3+}$	1343	0.068	927	0.037	708	0.105
$[Ru(bpy)_2$mbpy–$(Pro)_2$acrd$]^{3+}$	1350; 90 (0.89; 0.11)	0.076	977; 306 (0.95; 0.05)	0.038	678; 63 (0.85; 0.15)	0.114

Excitation of the samples was performed at 450 nm. The normalized pre-exponential factors of the biexponential decay of the compound $[Ru(bpy)_2$mbpy–$(Pro)_2$acrd$]^{3+}$ are show in parentheses. The $[Ru(bpy)_2$ mbpy–naph$]^{2+}$ complex was used as a reference (see text for details and [21]).

the energy transfer efficiency with the decrease of the solvent polarity, reflecting the effect of the solvent reorganization in the process [26]. Moreover, the lifetime of the dyad compounds get larger as the spacer increases in size, which is qualitatively in agreement with the effect of distance in the energy transfer by an exchange mechanism. Laser excitation at 532 nm for the $[Ru(bpy)_2$mbpy–acrd$]^{3+}$ complex in methanol resulted in an absorption transient in the region of 700–800 nm (see Fig. 3). The decay was exponential with a lifetime of 904 ns, which agrees quite well with the parameters determined by luminescence decay (910 ns) given in Table 4.

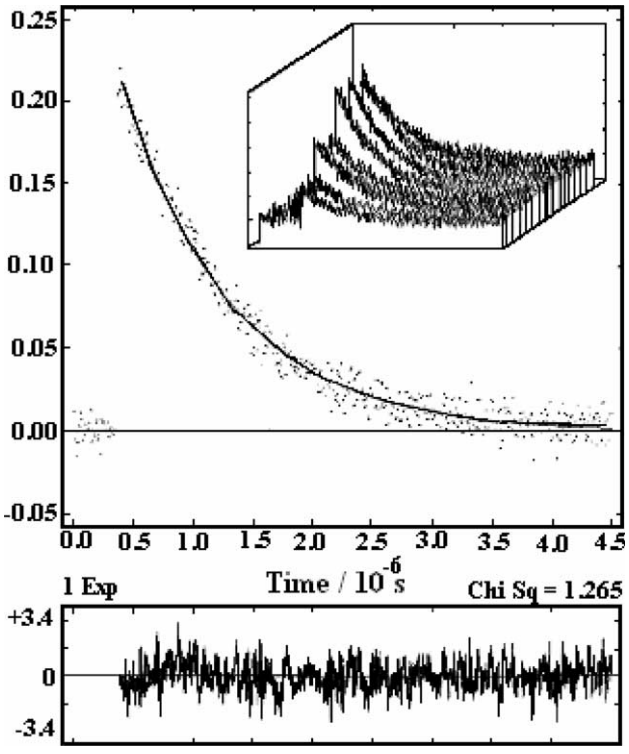


Fig. 3. Absorption transient (760 nm) of the $[Ru(bpy)_2$mbpy–acrd$]^{3+}$ complex in methanol from laser excitation at 532 nm. Inset: Decay traces in the region 700 800 nm.

The rate constants of energy transfer in these compounds are considerably low, deserving a discussion about the factors that control the process. In polar solvents, the energy difference between the triplet levels of the Ru complex and the acceptor is 6 kJ/mol. In acetonitrile and methanol, the intrinsic dipolar nature of the ^{3}MLCT excited state accounts for the solvent reorganization energy, 23 kJ/mol, and the inner contribution concerning bond rearrangement of the reactant is about 20 kJ/mol [26]. Thus, the total reorganization energy is seven times higher than the driving force, decreasing the rate of the energy transfer.

The energy transfer rate in an exchange or super-exchange (via bridge) mechanism in weakly coupled systems is given by [2],

$$k_{et} = \frac{2\pi}{\hbar} \mid V\mid^2 \mathrm{FC}, \tag{2}$$

where V is the electronic coupling matrix element and FC is the Franck–Condon weighted density of states. The extent of the electronic coupling in the model compounds investigated should be dictated by the geometry attained by the ligand–amide–acridine. The electronic coupling matrix element, V, is enhanced when the π systems of donor and acceptor are coplanar. An affect that reduces the energy transfer rate is the unfavorable Franck–Condon factors related to the low frequency conformational change of the amide bridge (torsional motion) necessary for the donor and acceptor π systems to approach a coplanar alignment. When the bridge is extended with one and two prolines, not only the center-to-center distance between donor and acceptor is increased, but also more degrees of freedom and conformations are introduced, and both factors are expected to decrease the rate of energy transfer.

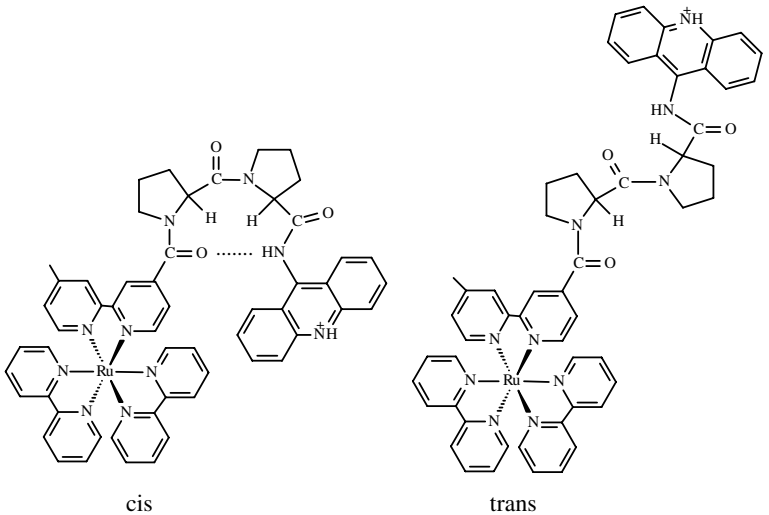
An unexpected result in the present study, however, was the biexponential character of the decay of the system with two prolines, contrasting with the monoexponential decay of the other systems (within the time resolution of the performed experiments). Solutions of proline oligomers are known to exist in either *cis*- or *trans*-helical structures, depending on solvent polarity and ionic strength of the solution [33–35]. Proline-con-

taining dipeptides may have several types of rotamers and conformers in solution that are stabilized by specific intramolecular hydrogen bonding between carbonyl oxygen and amide hydrogen atoms of the molecule [36–41]. Therefore, the fast decay component of the biexponential fitting could be ascribed to the presence of a molecular conformer allowing a more efficient energy transfer pathway. An analysis of the molecular geometry of the donor–acceptor system with two prolines in *trans* and *cis* conformations (related to the carbonyl position) is draw in Scheme 2.

The *cis* conformer would allow a close contact between the bpy ligand with the acridine acceptor, while the distance between the donor and acceptor moieties are bigger in the *trans* conformer, and therefore hinder the T–T energy transfer. In the *cis* geometry the energy transfer would be mediated by a solvent shell between donor and acceptor centers, while in the *trans* geometry the process would occur through the diproline bridge. The decay time and weight of the short-lived component depends on the solvent used. In methanol, there is a very weak contribution of 5% of the decay time of 306 ns. In acetonitrile, a short-lived component (90 ns and 11% weight) was observed, while in dichloromethane the decay time is 63 ns with 15%. These results could be ascribed to the presence of a *cis* conformer. In oligoprolines, the *cis* conformer increases its fraction with the decrease of the solvent polarity [13].

The decay time decreases due to the solvent effect in the energy transfer process as discussed before. Considering these short-lived components, the rate constant of T–T energy transfer of the *cis* conformer is estimated to be in the range $(0.2–1.4) \times 10^7\ s^{-1}$, being larger (a factor of 10–100) than that of the previous values found for the donor–acceptor system with amide or one proline as spacers. This difference should not be ascribed only to a distance effect in the T–T energy transfer process. The diproline bridge in the *cis* conformer is a folded structure that may allow a closest contact and more efficient electronic coupling between donor and acceptor orbitals, maximizing the electronic coupling matrix element V of the donor–acceptor interaction. A second factor that could account for the enhancement of the energy transfer rate is a contribution of a predicted hydrogen bonding involving the C=O of the mbpy and the NH of 9-amido-acridine (see the *cis* conformer structured in Scheme 2). Note that this kind of geometry of the diproline bridge resembles the intramolecular hydrogen bond structure of the classical 10-member β-turn present in model peptides [35–40]. In the dynamics of the excited state, this interaction will promote a high frequency mode that may contribute favorably in the Franck–Condon factors, thus increasing the rate constant of energy transfer.

In order to extend the investigation of the intramolecular T–T energy transfer process, the compound $[Ru(bpy)_2mbpy–(Pro)_2acrd]^{3+}$ was studied in dioxane–water mixtures, and the results obtained are summarized in Table 5. These results in solvents with different polarities evidence the importance of the molecular structure and the presence of conformers in the process of energy transfer as well as the effect of the solvent in the whole process of T–T energy transfer. If the isomerization of the oligoprolines is considered a slow process [42], then the decay observed may be related to each type of conformer and its fraction in solution. The formation of a fraction of the *cis* conformer in water may result from the hydrophobic character of the complex that drives it to a more packed structure. In aqueous solution, the normalized amplitude of the fast decay component is 0.18, which would indicate 18% of the *cis* conformer in solution (see Table 5).



Scheme 2. *cis* and *trans* conformers of the proline bridge in $[Ru(bpy)_2mbpy–(Pro)_2acrd]^{3+}$.

Table 5
Decay times of $[Ru(bpy)_2mbpy–(Pro)_2acrd]^{3+}$ in dioxane–water mixtures at 293 K

% Dioxane	ε*	τ_1 (ns)	τ_2 (ns)	$\tilde{b}_1$	χ^2	$\tau_2^{-1} - \tau_2^{-1}$ (s^{-1})
0	80.4	540 ± 2	97 ± 10	0.819	1.069	8.5×10^6
20	62.1	689 ± 5	168 ± 14	0.780	1.084	4.5×10^6
40	44.2	841 ± 17	359 ± 36	0.744	1.087	1.6×10^6
60	26.6	867 ± 6	242 ± 49	0.915	0.972	3.0×10^6
80	11.0	871 ± 6	148 ± 30	0.917	1.033	5.6×10^6
100	2.1	805 ± 3	43 ± 9	0.809	1.052	2.2×10^7

(*) Dielectric constant is from [43]. Emission lifetimes (±5%) at the emission maximum following excitation at 450 nm. $b_1 + b_2 = 1$. χ^2 is the chi-square of biexponential fitting.

The fraction of conformers of proline peptides has been determined from the analysis of NNMR data [13]. Our analysis of the ^{13}C NMR spectrum of the dyad with respect to the signals of β and γ carbons of the proline rings indicated that the percent of the *cis* conformer is near to 11%. The ^{13}C NMR spectrum of the dyad with two prolines is shown in Fig. 4. Proceeding similar analysis with the compound $[Pro_2Co(NH_3)_5](BF_4)_3$ in D_2O, the fraction of the *cis* conformer was calculated as 10%. These values are not far from the results of 14–16% of the *cis* conformer found for $[Pro_2Co(NH_3)_5]^{3+}$ by ^{13}C and ^1H NMR spectra analysis in a 0.01 M DCl solution [13].

The difference in the inverse of the decay time of the two components is a measure of the rate constant k_{et}, considering that the ET process is irreversible and the *trans* conformer is almost inactive for energy transfer. Under these conditions, the values of k_{et} of the *cis* conformer in different solvent compositions are calculated within the range of $(0.16–2.20) \times 10^7$ s^{-1} (see Table 5). Thus, the folded structure, here defined as the *cis* conformer of the proline bridge in $[Ru(bpy)_2mbpy–(Pro)_2acrd]^{3+}$, presents a faster rate of T–T energy transfer when compared to similar reported systems [21].

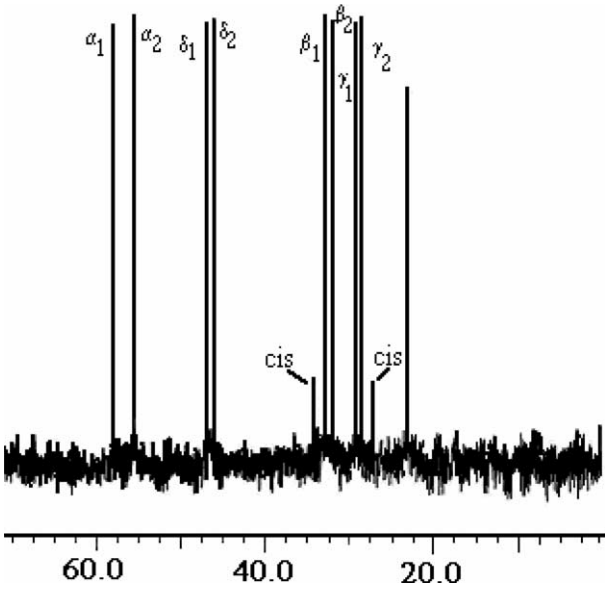


Fig. 4. ^{13}C NMR spectrum of the dyad $[Ru(bpy)_2mbpy–(Pro)_2acrd]^{3+}$ in D_2 O, illustrating the signal of the α, β, γ and δ carbons of the proline rings and the indication of the signal from the *cis* conformer.

Acknowledgements

I.M.M.C. thanks to CAPES and CNPq (Brazil) for a fellowship. Financial support by CAPES, FAPESP and CNPq (Brazil) is gratefully acknowledged. We thank Professor Frank H. Quina for the laser flash photolysis measurements.

References

[1] V. Balzani, F. Scandola, Supramolecular Photochemistry, Ellis Horwood, Chichester, 1991.
[2] M.E. Sigman, G.L. Closs, J. Phys. Chem. 95 (1991) 5012.
[3] S.S. Isied, Adv. Chem. Ser. 253 (1997) 331.
[4] K.S. Schanze, L.A. Lucia, M. Cooper, K.A. Walters, H.F. Ji, O. Sabina, J. Phys. Chem. A 102 (1998) 5577.
[5] D. Gust, T.A. Moore, A.L. Moore, Acc. Chem. Res. 26 (1993) 198.
[6] A.A. Krasnovsky Jr., M.E. Bashtanov, N.N. Drozdova, P.A. Liddell, A.L. Moore, T.A. Moore, D. Gust, J. Photochem. Photobiol. A: Chem. 102 (1997) 157.
[7] D. Gust, T.A. Moore, A.L. Moore, D. Kuciauskas, P.A. Liddell, B.D. Halbert, J. Photochem. Photobiol. B: Biol. 43 (1998) 209.
[8] L. Stryer, R.P. Haugland, Proc. Natl. Acad. Sci. USA 58 (1967) 719.
[9] S.S. Isied, A. Vassilian, J. Am. Chem. Soc. 106 (1984) 1726.
[10] S.S. Isied, A. Vassilian, J. Am. Chem. Soc. 106 (1984) 1732.
[11] K.S. Schanze, K. Sauer, J. Am. Chem. Soc. 110 (1988) 1180.
[12] M.Y. Ogawa, I.S. Moreira, J.F. Wishart, S.S. Isied, Chem. Phys. 176 (1993) 589.
[13] A. Vassilian, J.F. Wishart, B. van Hemelryck, H. Schwarz, S.S. Isied, J. Am. Chem. Soc. 112 (1990) 7278.
[14] S. Boyde, G.F. Strouse, W.E. Jones Jr., T.J. Meyer, J. Am. Chem. Soc. 111 (1989) 7448.
[15] W.E. Ford, M.A.J. Rodgers, J. Phys. Chem. 96 (1992) 2917.
[16] G.J. Wilson, W.H.F. Sasse, A.W.H. Mau, Chem. Phys. Lett. 250 (1996) 583.
[17] G.J. Wilson, A. Launikonis, W.H.F. Sasse, A.W.H. Mau, J. Phys. Chem. A 101 (1997) 4860.
[18] J.A. Simon, S.L. Curry, R.H. Schmehl, T.R. Schatz, P. Piotrowiak, P.X.Q. Jin, R.P. Thummel, J. Am. Chem. Soc. 119 (1997) 11012.
[19] D.S. Tyson, F.N. Castellano, J. Phys. Chem. A 103 (1999) 10955.
[20] D.S. Tyson, K.B. Henbest, J. Bialecki, F.N. Castellano, J. Phys. Chem. A 105 (2001) 8154.

[21] I.M.M. de Carvalho, I.S. Moreira, M.H. Gehlen, Inorg. Chem. 42 (2003) 1525.
[22] D.L. Dexter, J. Chem. Phys. 21 (1953) 866.
[23] M. Wrighton, J. Markham, J. Phys. Chem. 26 (1973) 3042.
[24] W.E. Ford, M.A.J. Rodgers, J. Photochem. Photobiol. A: Chem. 59 (1991) 73.
[25] R. Wang, Y. Liang, R.H. Schmehl, Inorg. Chim. Acta 225 (1994) 275.
[26] I.M.M. Carvalho, M.H. Gehlen, J. Photochem. Photobiol. A: Chem. 122 (1999) 109.
[27] H. Taube, E.S. Gould, J. Am. Chem. Soc. 85 (1963) 3706.
[28] S.S. Isied, C.G. Kuehn, J. Am. Chem. Soc. 100 (1978) 6752.
[29] S.L. Murov, Handbook of Photochemistry, Marcel Dekker, New York, 1999.
[30] M. Chan Sze, J.R. Bolton, Solar Energy 24 (1980) 561.
[31] K. Kasama, K. Kikuchi, Y. Nishida, H. Kokubun, J. Phys. Chem. 85 (1981) 4148.
[32] K. Kikuchi, C. Sato, M. Watabe, H. Ikeda, Y. Takahashi, T. Miyashi, J. Am. Chem. Soc. 115 (1993) 5180.
[33] C. Grathwohl, K. Wuthrich, Biopolymers 15 (1976) 2025.
[34] S.S. Isied, A. Vassilan, R.H. Magnuson, H.A. Schwartz, J. Am. Chem. Soc. 107 (1985) 7432.
[35] S.S. Isied, A. Vassilan, J.F. Wishart, C. Creutz, H.A. Schwarz, N.J. Sutin, J. Am. Chem. Soc. 110 (1988) 635.
[36] G. Boussard, M. Marraud, J. Am. Chem. Soc. 107 (1985) 1825.
[37] G.B. Liang, C.J. Rito, S.H. Gellman, Biopolymers 32 (1992) 293.
[38] M.S. Prachand, S. Singh, M.M. Dhingra, U. Singh, S.K. Ghosh, V.R. Mamdapur, M.S. Chadha, Magn. Res. Chem. 31 (1993) 944.
[39] G.B. Liang, C.J. Rito, S.H. Gellman, J. Am. Chem. Soc. 114 (1992) 4440.
[40] D.Q. McDonald, W.C. Still, J. Org. Chem. 61 (1996) 1385.
[41] L. Halab, W.D. Lubell, J. Org. Chem. 64 (1999) 3312.
[42] H.N. Cheng, F.A. Bovey, Biopolymers 16 (1977) 1465.
[43] G. Åkerlöf, O.A. Short, J. Am. Chem. Soc. 58 (1936) 1241.

Available online at www.sciencedirect.com
SCIENCE DIRECT®
Polyhedron 24 (2005) 75–87
POLYHEDRON
www.elsevier.com/locate/poly

Synthesis spectroscopic and structural properties of transition metal complexes of the *o*-xylyl diphosphine *o*-$C_6H_4(CH_2PPh_2)_2$

Michael D. Brown, William Levason, Gillian Reid *, Rebecca Watts

School of Chemistry, University of Southampton, Highfield, Southampton SO17 1BJ, UK

Received 20 September 2004; accepted 11 October 2004
Available online 8 December 2004

Abstract

The systematic coordination chemistry of the wide-angle diphosphine *o*-$C_6H_4(CH_2PPh_2)_2$ (L^1) has been investigated with metal ions from Groups 9–11 in order to explore the consequences of the steric demands of the phosphine and its flexibility towards different oxidation states and coordination geometries. The products isolated include the tetrahedral $[CoX_2(L^1)]$ (X = Cl, Br or I), the very distorted square planar $[Rh(L^1)_2]^+$, $[M(cod)(L^1)]^+$ (M = Rh or Ir), square planar $[NiX_2(L^1)]$ (X = Cl or Br), $[M'Cl_2(L^1)]$ (M′ = Pd or Pt), the chloro-bridged $[Pd_2Cl_2(L^1)_2]^{2+}$, $[Pd(L^1)_2]^{2+}$, the tetrahedral $[M''(L^1)_2]^+$ (M″ = Cu, Ag or Au) and the dinuclear $[(AuCl)_2(L^1)]$. Chemical oxidation of some of the complexes are described, giving examples of Co(III), Ni(III) and Pt(IV) species. Where possible the products have been characterised by IR, UV–vis, NMR (^1H, ^{31}P, ^{63}Cu and ^{195}Pt as appropriate) spectroscopies, mass spectrometry and microanalysis. Crystal structures of six representative examples confirm the coordination environments in particular species and illustrate the steric demands of L^1. L^1 is a versatile ligand which can readily alter its chelate bite angle to accommodate a range of coordination geometries (the P···P distances within the chelate rings varies by >0.5 Å), and the presence of the rigid aromatic ring in the C_4 backbone leads to some preorganisation favouring *cis* chelation. It also shows a preference for low coordination numbers and this results in some unexpected products.
© 2004 Elsevier Ltd. All rights reserved.

Keywords: Diphosphine; Metal complexes; X-ray structures

1. Introduction

The reaction chemistry of sterically demanding wide-angle diphosphines is attracting great interest at present owing to the remarkably high catalytic activities exhibited by some transition metal complexes involving these ligands. Major reactions of interest are Rh-catalysed hydroformylation of alkenes, Ni-catalysed hydrocyanation and Pd-catalysed copolymerisation of CO and alkenes. In particular, the P–M–P bite angle plays an important role in determining the selectivity and rates in these catalytic reactions [1,2]. In previous studies platinum metal complexes incorporating the xylyl diphosphine *o*-$C_6H_4(CH_2PPh_2)_2$ have been shown to be active catalysts for several different transformations, e.g., platinum-tin catalysed hydroformylation [3], rhodium-catalysed hydrogenation of CO_2 [4] and iridium-catalysed hydrogenation of aldehydes [5]. Given the level of interest in these systems, it is surprising that the systematic coordination chemistry of L^1 with transition metal ions has been rather neglected. Initial studies on the complexation of L^1 with medium and low valent late transition metal centres were conducted by Venanzi and co-workers [6,7] who reported the preparations of some mononuclear derivatives and dinuclear halide- and hydride-bridged complexes. Example, include the structurally characterised $[Ag_2X_2(L^1)_2]$ (X = Cl or I) which involve distorted tetrahedral coordination at Ag(I) via two halides and a chelating L^1, and the Pt(0) complex, $[Pt(H_2C{=}CH_2)(L^1)]$ [8]. Werner et al. [9–11]

* Corresponding author. Tel.: +44 2380593609; fax: +44 2380593781.
E-mail address: gr@soton.ac.uk (G. Reid).

0277-5387/$ - see front matter © 2004 Elsevier Ltd. All rights reserved.
doi:10.1016/j.poly.2004.10.008

have reported a number of other platinum metal complexes of L^1 with various organic co-ligands, while sulfido- and selenido-Ru and Fe carbonyl clusters, which result from chalcogen transfer from the phosphine sulfide or selenide derivatives of L^1 to the metal centre, have also been reported [12,13].

In this paper we describe a systematic study of the coordination of L^1 with metal ions from Groups 9–11, including their syntheses and spectroscopic properties. The transition metal ions studied adopt square planar, tetrahedral, linear and octahedral coordination geometries and thus allow the ligating properties of the *o*-xylyl diphosphine to be probed. Comparisons are drawn with the ligating properties of the related flexible C_4-diphosphine, $Ph_2P(CH_2)_4PPh_2$ (dppb), and the more rigid *o*-phenylene derivative *o*-$C_6H_4(PPh_2)_2$.

2. Results and discussion

The diphosphine L^1 was prepared in high yield as a white solid by a slight modification of the literature method [8] involving reaction of Ph_2PLi with *o*-$C_6H_4(CH_2Br)_2$ in thf solution. In solution L^1 is quite air-sensitive, hence all measurements and subsequent reactions used deoxygenated solutions and Schlenk techniques.

2.1. Co, Rh and Ir complexes

Treatment of an isopropanol solution of CoX_2 (X = Cl, Br or I) with one mol equiv. of L^1 under N_2 affords the distorted tetrahedral $[CoX_2(L^1)]$ as brightly coloured blue, green or brown-green solids, respectively, in good yield. The formulation follows from the microanalytical data, [1] while magnetic measurements are consistent with high spin Co(II) species. The UV–vis spectra show absorptions consistent with tetrahedral Co(II) [14,15], and the spectra are the same in the solid state and in CH_2Cl_2 solution. The far IR spectrum of $[CoCl_2(L^1)]$ shows a broad peak at 318 cm^{-1}, consistent with ν(Co–Cl). The distorted tetrahedral coordination with one chelating L^1 is confirmed in the solid state by a structure determination on a very small crystal of $[CoCl_2(L^1)]$ (Fig. 1, Table 1). The Co–P bond distances are 2.3795(16) and 2.4034(16) Å, while *d*(Co–Cl) = 2.2045(15) and 2.2165(15) Å.

[1] We note that microanalytical data for several of the complexes are consistent with there being some CH_2Cl_2 solvent associated with the compounds even after drying in vacuo. For the diamagnetic complexes, there is evidence for CH_2Cl_2 in the ^1H NMR spectra, and indeed four of the crystal structures show two molecules of CH_2Cl_2 (or $CHCl_3$) solvent per metal ion. Thus, we conclude that the steric bulk of the coordinated L^1 probably leaves considerable voids in the lattice which can accommodate solvent molecules.

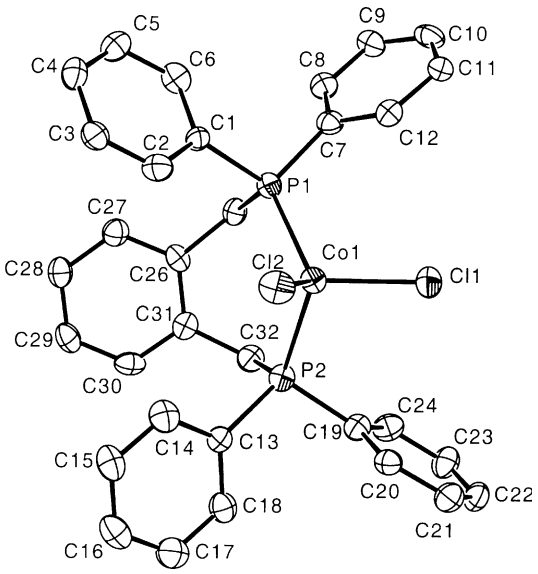


Fig. 1. View of the structure of $[CoCl_2(L^1)]$ with numbering scheme adopted. H atoms are omitted for clarity. Ellipsoids are shown at the 50% probability level.

Table 1
Selected bond lengths (Å) and angles (°) for $[CoCl_2(L^1)]$

Bond lengths	
Co1–Cl2	2.2045(15)
Co1–Cl1	2.2165(15)
Co1–P2	2.3795(16)
Co1–P1	2.4034(16)
P1–C7	1.810(5)
P1–C1	1.811(5)
P1–C25	1.851(5)
P2–C19	1.815(5)
P2–C13	1.817(5)
P2–C32	1.840(5)
Bond angles	
Cl2–Co1–Cl1	109.50(6)
Cl2–Co1–P2	111.52(6)
Cl1–Co1–P2	103.26(5)
Cl2–Co1–P1	114.64(6)
Cl1–Co1–P1	111.13(6)
P2–Co1–P1	106.18(5)
C7–P1–C1	106.1(2)
C7–P1–C25	103.1(2)
C1–P1–C25	102.0(2)
C7–P1–Co1	115.43(17)
C1–P1–Co1	115.45(16)
C25–P1–Co1	113.18(17)
C19–P2–C13	104.7(2)
C19–P2–C32	105.1(2)
C13–P2–C32	103.7(2)
C19–P2–Co1	107.68(16)
C13–P2–Co1	119.13(16)
C32–P2–Co1	115.25(17)

The related, but more rigid *o*-phenylene diphosphine, *o*-$C_6H_4(PPh_2)_2$, gives planar cations $[Co\{o\text{-}C_6H_4(PPh_2)_2\}_2][CoX_4]$ and 5-coordinate $[Co\{o\text{-}C_6H_4(PPh_2)_2\}_2X]^+$ on reaction with Co(II) halides, reflecting

both the stronger ligand field imposed and the 5-membered chelate rings present [15], whereas larger chelate rings give tetrahedral Co(II) (as in $[CoX_2(L^1)]$ above) [16]. We note that an early assignment [16] of the product from reaction of $CoCl_2$ with dppe (Ph_2PCH_2-CH_2PPh_2) as $[CoCl_2(dppe)]$ was in error and the compound was subsequently shown to be the phosphine oxide complex [17].

Low temperature oxidation of a CH_2Cl_2 solution of $[CoCl_2(L^1)]$ with NOCl gives the Co(III) species $[CoCl_3(L^1)]$ as a deep blue-green solid. The electronic spectrum of this product is characteristic of the rare 5-coordinate geometry and the Cl_3P_2 donor set [18]. The far IR spectrum shows the three Co–Cl bands expected. The Co(III) compound decomposes slowly in CH_2Cl_2 solution at room temperature.

In an attempt to explore the coordination chemistry of rhodium with L^1 we reacted $RhCl_3 \cdot 3H_2O$ with two molar equivalents of L^1 in EtOH solution in the presence of a few drops of 40% aqueous HBF_4. Stirring at room temperature for approximately 30 min gave an orange solution and concentration of this solution in vacuo afforded an orange solid. The IR spectrum shows peaks associated with coordinated L^1 and BF_4^- anion. Inspection of the far IR region did not reveal any significant peaks due to Rh–Cl bonds. The electrospray mass spectrum (MeCN) shows peaks with the correct isotope distribution for $[Rh(L^1)_2]^+$ and $[Rh(L^1)]^+$, however again there is no evidence for any Cl containing species or significant higher mass peaks.

The ^1H NMR spectrum shows the ligand resonances shifted to high frequency upon coordination, while the $^{31}P\{^1H\}$ NMR spectrum of this product is a sharp doublet at +11.6 ppm, indicative of one P environment, with $^1J_{RhP} = 140$ Hz. This large coupling constant, together with the mass spectrometry data were unexpected for a Rh(III) species, but more in line with the values expected for a planar Rh(I) derivative with more s-orbital character in the Rh(I)–P bond (sp^2d hybridisation). This result prompted us to seek X-ray structural data to authenticate our assignment of the product as $[Rh(L^1)_2]BF_4$.

Orange single crystals were obtained by layering a $CHCl_3$ solution of the complex with hexane. The structure shows (Fig. 2, Table 2) two chelating L^1 units bound to the Rh centre in a distorted square planar arrangement, with no evidence for other co-ligands. One BF_4^- anion and two $CHCl_3$ solvent molecules also occupy general positions in the asymmetric unit, consistent with a Rh(I) complex. The Rh–P bond distances are in the range 2.31–2.34 Å. These are in accord with *d*(Rh–P) in other Rh(I) phosphine complexes, e.g., $[RhCl(PPh_3)_3]$ *d*(Rh–P_{trans}P) = 2.304–2.338 Å [19,20]. The sum of the P–Rh–P angles is 370°, indicating a significant tetrahedral distortion, which probably results from the significant steric requirements of the two bulky L^1 ligands. The P1···P2 and P3···P4 distances within the chelates are 3.28 and 3.37 Å, and the P1–Rh–P2 and P3–Rh–P4 angles are 90.05(3) and 92.31(3) Å, respectively.

The formation of the bis-diphosphine Rh(I) cation under these reaction conditions is unexpected as this is the method used to obtain the Rh(III) species $[RhCl_2(L\text{-}L)_2]^+$ (L-L = $Ph_2PCH_2CH_2PPh_2$, *o*-C_6H_4-$(PPh_2)_2$) [21,22]. The different reaction course may also be a consequence of the steric bulk imposed by the wide angle diphosphine L^1, which disfavours formation of the 6-coordinate Rh(III) dichloro derivative. The preparation of the very well known Wilkinson's compound, $[RhCl(PPh_3)_3]$, is however readily achieved by reaction of $RhCl_3 \cdot 3H_2O$ with excess PPh_3 in ethanol [23].

We note also that a CCl_4 suspension of the $[Rh(L^1)_2]BF_4$ is not oxidised when treated with Cl_2 saturated CCl_4 at room temperature (monitored by ^{31}P NMR spectroscopy).

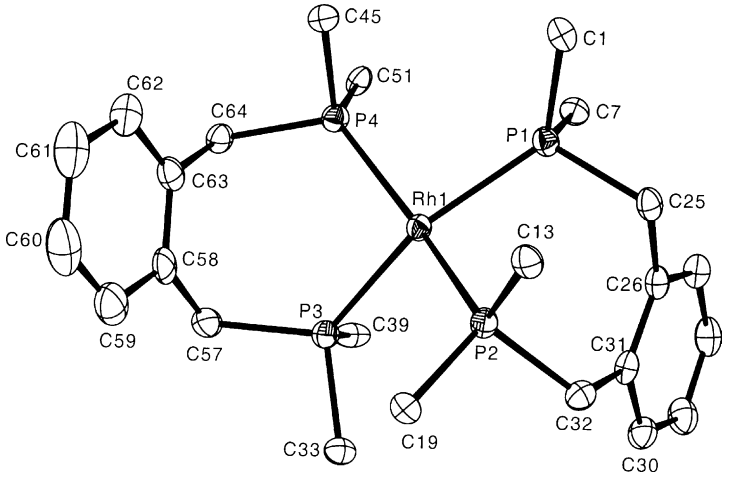


Fig. 2. View of the structure of the $[Rh(L^1)_2]^+$ cation with numbering scheme adopted. H atoms and phenyl rings (except the *ipso* C atoms) are omitted for clarity. Ellipsoids are shown at the 50% probability level.

Table 2
Selected bond lengths (Å) and angles (°) for $[Rh(L^1)_2]BF_4 \cdot 2CHCl_3$

Bond lengths	
Rh1–P2	2.3099(10)
Rh1–P1	2.3269(10)
Rh1–P4	2.3352(10)
Rh1–P3	2.3427(10)
P1–C7	1.818(4)
P1–C1	1.833(4)
P1–C25	1.855(4)
P2–C19	1.830(4)
P2–C32	1.837(4)
P2–C13	1.847(4)
P3–C39	1.840(4)
P3–C33	1.842(4)
P3–C57	1.855(4)
P4–C45	1.828(4)
P4–C51	1.833(4)
P4–C64	1.854(4)
Bond angles	
P2–Rh1–P1	90.05(3)
P2–Rh1–P4	158.54(3)
P1–Rh1–P4	92.70(3)
P2–Rh1–P3	93.98(3)
P1–Rh1–P3	155.45(4)
P4–Rh1–P3	92.31(3)
C7–P1–C1	102.58(17)
C7–P1–C25	97.91(17)
C1–P1–C25	102.09(17)
C7–P1–Rh1	115.19(12)
C1–P1–Rh1	122.96(12)
C25–P1–Rh1	112.54(12)
C19–P2–C32	103.10(16)
C19–P2–C13	95.41(16)
C32–P2–C13	105.02(17)
C19–P2–Rh1	116.97(12)
C32–P2–Rh1	119.44(12)
C13–P2–Rh1	113.61(12)
C39–P3–C33	98.12(16)
C39–P3–C57	103.34(19)
C33–P3–C57	102.59(17)
C39–P3–Rh1	104.85(13)
C33–P3–Rh1	121.61(12)
C57–P3–Rh1	122.25(12)
C45–P4–C51	105.85(17)
C45–P4–C64	96.21(17)
C51–P4–C64	99.38(17)
C45–P4–Rh1	112.34(13)
C51–P4–Rh1	121.99(12)
C64–P4–Rh1	117.36(12)

The reaction of L^1 with 0.5 mol equiv. of the Rh(I) dimer $[Rh_2Cl_2(cod)_2]$ in CH_2Cl_2 solution in the presence of NH_4PF_6 yields, after work-up, the Rh(I) species $[Rh(cod)(L^1)]PF_6$ as an orange solid in good yield. The IR spectrum confirms the presence of the anionic PF_6^- as well as coordinated L^1. Phosphorus-31 NMR spectroscopy of this species shows a sharp doublet at +10.3 ppm ($^1J_{RhP}$ = 146 Hz) and a septet at −145 ppm from the PF_6^- anion. Evidence for the cod ligation comes from the ^{1}H NMR spectrum which also confirms a 1:1 L^1:cod ratio. The Rh–P coupling constant is comparable to that for $[Rh(L^1)_2]^+$ described above, and the ^{31}P NMR shift is also similar, further supporting the earlier assignments.

The analogous reaction using $[Ir_2Cl_2(cod)_2]$ with 0.5 mol equiv. of L^1 in CH_2Cl_2 and NH_4PF_6 gives the corresponding Ir(I) complex $[Ir(cod)(L^1)]PF_6$ as an orange-red solid in good yield ($\delta^{31}P = -1.8$ (L^1); electrospray MS *m/z* 775 $[Ir(cod)(L^1)]^+$.

2.2. Ni, Pd and Pt complexes

The hydrated Ni(II) halides $NiX_2 \cdot xH_2O$ (X = Cl or Br) react with one mol equiv. of L^1 in isopropanol to give deep red solids with formation $[NiX_2(L^1)]$ in good yield. These are similar to the species described previously by Venanzi and co-workers, who assigned them as tetrahedral apparently on the basis that they did not give NMR spectra [7,8]. However, from the diffuse reflectance electronic spectra which show one d–d transition, we assign them as square planar compounds. The far IR spectra show two peaks which are assigned as Ni–X stretching vibrations, indicative of a *cis*-NiX_2 unit. These data, together with ^{1}H NMR and microanalyses, confirm the assignment of these compounds as square planar Ni(II) species with a chelating L^1 and mutually *cis* halides.

The square planar geometry identified for $[NiX_2(L^1)]$ is somewhat unexpected given that the corresponding Ni(II) complexes with the flexible dppb ligand, $[NiX_2(dppb)]$ (also incorporating a 7-membered chelate ring) [24] adopt tetrahedral geometries. Therefore, it appears that the increased rigidity of L^1 over dppb results in a preference for square planar coordination. The *o*-phenylene diphosphine in $[NiX_2\{o\text{-}C_6H_4(PPh_2)_2\}]$ (5-membered chelate ring) which exerts a strong ligand field, leads to square planar coordination at Ni(II) [25].

An attempt to generate the 5-coordinate Ni(II) species $[NiI(L^1)_2](ClO_4)$ through reaction of NiI_2 and $Ni(ClO_4)_2 \cdot 6H_2O$ with four mol equiv. of L^1, using the method described by Meek and co-workers [26] for other diphosphines was unsuccessful. Similarly, we were unable to isolate the square planar bis-L^1 species $[Ni(L^1)_2](ClO_4)_2$.

The deep orange-brown, unstable Ni(III) species $[NiCl_3(L^1)]$ was obtained by NOCl oxidation of $[NiCl_2(L^1)]$. The formulation follows from the electronic spectrum, which is characteristic of the 5-coordinate molecule, and the IR spectrum which shows *v*(Ni–Cl) in the same region as previously reported Ni(III) species [27].

Dissolution of $Na_2[PdCl_4]$ in EtOH followed by addition of one mol equiv. of L^1 results in formation of a cream coloured precipitate with formulation $[PdCl_2(L^1)]$. The far IR spectrum of this compound shows two peaks in the region expected for *v*(Pd–Cl), indicative of a *cis*-$PdCl_2$ unit. The ^{1}H NMR spectrum is unexceptional, showing small high frequency shifts

upon coordination of L^1, while the $^{31}P\{^1H\}$ NMR spectrum shows a singlet at 16.4 ppm, in accord with the data obtained by Venanzi and co-workers [8] and assigned as $[PdCl_2(L^1)]$. The crystal structure of this compound (Fig. 3, Table 3) confirms a distorted square planar coordination environment at Pd(II) through one chelating L^1 ligand and mutually *cis* Cls. The molecule has crystallographic *m* symmetry, with *d*(Pd–P) = 2.2572(11) and *d*(Pd–Cl) = 2.3536 Å. The P1–Pd–P1′ angle in the chelate of 100.04(6)° is much more obtuse than those seen in the Rh(I) species described above, reflecting the considerable reduction in steric demand when the metal centre only needs to accommodate one L^1 rather than two. The P1···P1′ distance of 3.46 Å is larger than in $[Rh(L^1)_2]^+$ above.

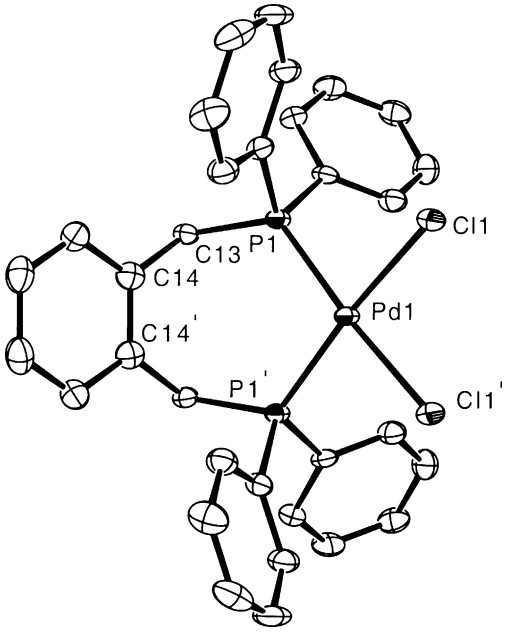


Fig. 3. View of the structure of $[PdCl_2(L^1)]$ with numbering scheme adopted. Ellipsoids are drawn at 50% probability and H atoms are omitted for clarity (symmetry operation: ′, *x*, 1/2 − *y*, *z*).

Table 3
Selected bond lengths (Å) and angles (°) for $[PdCl_2(L^1)]$

Bond lengths	
Pd1–P1	2.2572(11)
Pd1–Cl1	2.3536(11)
P1–C1	1.813(4)
P1–C7	1.818(4)
P1–C13	1.835(4)
Bond angles	
P1–Pd1–P1′	100.04(6)
P1–Pd1–Cl1′	174.91(4)
P1–Pd1–Cl1	84.95(4)
Cl1–Pd1–Cl1′	90.04(5)
C1–P1–C7	108.26(19)
C1–P1–C13	102.1(2)
C7–P1–C13	103.3(2)
C1–P1–Pd1	111.79(14)
C7–P1–Pd1	109.05(14)
C13–P1–Pd1	121.43(14)

Symmetry operation: ′, *x*, 1/2 − *y*, *z*.

Attempts to abstract both the Cl's from $[PdCl_2(L^1)]$ in MeCN solution using 2.1 mol equiv. of $TlPF_6$ were not successful – the only identifiable Pd-containing species after work-up being the dinuclear $[Pd_2Cl_2(L^1)_2](PF_6)_2$. This complex was prepared in good yield by reaction of $[PdCl_2(NCMe)_2]$ with one mol equiv. of L^1 and one mol equiv. of $TlPF_6$ in $MeCN/CH_2Cl_2$. Removal of the TlCl precipitate left a light yellow solution from which the complex was obtained as a yellow solid following work-up. The IR, ^1H NMR spectroscopic and microanalytical data are consistent with the formulation $[Pd_2Cl_2(L^1)_2](PF_6)_2$. The $^{31}P\{^1H\}$ NMR spectrum of this compound shows a singlet at 27.3 ppm, significantly to high frequency of the mononuclear $[PdCl_2(L^1)]$ above.

The structure of $[Pd_2Cl_2(L^1)_2](PF_6)_2 \cdot 2CH_2Cl_2$ shows (Fig. 4, Table 4) a dinuclear $(\mu^2\text{-}Cl)_2$ palladium dication with a chelating L^1 bound to each Pd centre to give a distorted square planar geometry. The dication is centrosymmetric, the centre of inversion in the middle of the Pd_2Cl_2 core. The Pd–P bond distances are 2.2481(10) and 2.2657(10) Å, very similar to *d*(Pd–P) in the mononuclear complex above. The P1–Pd–P2 angle in this species is 98.00(4)° and *d*(P1···P2) is 3.41 Å.

The homoleptic bis-ligand ion $[Pd(L^1)_2]^{2+}$ was subsequently prepared by addition of an aqueous solution of $Pd(NO_3)_2$ to two mol equiv. of L^1 in $EtOH/CH_2Cl_2$ solution, followed by addition of aqueous HBF_4. The IR spectrum of the yellow solid isolated shows peaks consistent with coordinated L^1 and ionic BF_4^-, with no evidence for any remaining nitrate or H_2O/OH^- in the product. The ^1H NMR spectrum only shows resonances due to L^1. These are shifted to high frequency of the 'free' ligand. The $^{31}P\{^1H\}$ NMR spectrum of this

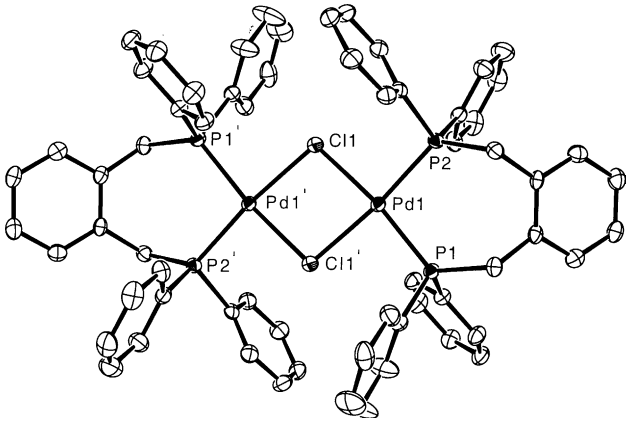


Fig. 4. View of the structure of the centrosymmetric $[Pd_2Cl_2(L^1)_2]^{2+}$ cation with numbering scheme adopted. H atoms are omitted for clarity. Ellipsoids are drawn at 50% probability (symmetry operation: ′, − *x*, 2 − *y*, 1 − *z*).

Table 4
Selected bond lengths (Å) and angles (°) for $[Pd_2Cl_2(L^1)_2](PF_6)_2 \cdot 2CH_2Cl_2$

Bond lengths	
Pd1–P1	2.2481(10)
Pd1–P2	2.2657(10)
Pd1–Cl1	2.3917(10)
P1–C1	1.818(4)
P1–C7	1.821(4)
P1–C25	1.821(4)
P2–C13	1.802(4)
P2–C19	1.818(4)
P2–C32	1.830(4)
Bond angles	
P1–Pd1–P2	98.00(4)
P1–Pd1–Cl1	168.73(4)
P2–Pd1–Cl1	90.93(4)
P1–Pd1–Cl1′	88.11(4)
P2–Pd1–Cl1′	172.66(4)
Cl1–Pd1–Cl1′	83.52(4)
Pd1–Cl1–Pd1′	96.48(3)
C1–P1–C7	106.36(19)
C1–P1–C25	108.45(19)
C7–P1–C25	100.83(18)
C1–P1–Pd1	108.46(14)
C7–P1–Pd1	109.03(13)
C25–P1–Pd1	122.51(14)
C13–P2–C19	107.65(19)
C13–P2–C32	104.80(18)
C19–P2–C32	104.87(18)
C13–P2–Pd1	114.78(14)
C19–P2–Pd1	103.67(13)
C32–P2–Pd1	120.10(13)

Symmetry operation: ′, $2-x$, $2-y$, $1-z$.

P_4-coordinated species shows a singlet at 7.1 ppm. These data, together with microanalyses, are consistent with the formulation $[Pd(L^1)_2](BF_4)_2$. The Pd(II) centre is likely to be rather crowded, however this formulation is not unreasonable given the structural evidence for distorted planar $[Rh(L^1)_2]^+$ cation described above.

The Pt(II) species $[PtCl_2(L^1)]$ is formed in high yield by addition of a solution of $K_2[PtCl_4]$ to one mol equiv. of L^1 in CH_2Cl_2/EtOH. Acetone was then added to give a homogeneous solution which was stirred for 72 h before filtering and concentrating the filtrate in vacuo to give a white solid. The ^1H NMR spectrum is unexceptional and the far IR spectrum shows two peaks, indicating a *cis*-$PtCl_2$ unit. The $^{31}P\{^1H\}$ NMR spectrum shows a singlet at −1.8 ppm with ^{195}Pt satellites (J = 3584 Hz), consistent with the literature data [8]. Confirmation that the product is indeed the neutral $[PtCl_2(L^1)]$ and not the dinuclear $[Pt_2Cl_2(L^1)_2]Cl_2$ (cf. the Pd analogue above) comes from conductivity measurements which show that in $MeNO_2$ solution the complex is a non-electrolyte. The ^{195}Pt NMR spectrum shows a triplet at −4503 ppm, in accord with a P_2Cl_2 donor set at Pt(II) [28].

Treatment of a CCl_4 suspension of $[PtCl_2(L^1)]$ with excess Cl_2 saturated CCl_4 gives the Pt(IV) species $[PtCl_4(L^1)]$ as a yellow solid. This formulation follows from the far IR spectrum and the microanalysis. The Pt(IV) complex readily reverts to $[PtCl_2(L^1)]$ in solution (as observed by ^{31}P NMR spectroscopy), and the $^{31}P\{^1H\}$ NMR spectrum measured in CH_2Cl_2 solution in the presence of Cl_2 shows δ −4.8, $^1J_{PtP}$ = 2170 Hz, consistent with a $PtCl_4(L^1)$ composition [28,29]. Similar treatment of $[PdCl_2(L^1)]$ did not result in a colour change, and the $^{31}P\{^1H\}$ NMR spectrum is unchanged.

2.3. Cu, Ag and Au complexes

Reaction of $[Cu(NCMe)_4]BF_4$ or $AgBF_4$ with two molar equivalents of L^1 in CH_2Cl_2 solution in the dark affords colourless solutions from which the homoleptic phosphine complexes $[Cu(L^1)_2](BF_4)$ and $[Ag(L^1)_2](BF_4)$ were obtained in high yield. The 2:1 L^1:M composition follows from microanalyses and from the magnitude of the $^{107/109}Ag$–^{31}P coupling constants in the $^{31}P\{^1H\}$ NMR spectra – below. Electrospray mass spectrometry (MeCN) shows the only significant species in each case is $[M(L^1)_2]^+$, with much weaker fragment peaks corresponding to $[M(L^1)]^+$. The ^1H NMR spectra for these compounds each show small high frequency shifts in the CH_2 resonance compared to L^1 itself, and the aromatic protons appear as a broad overlapping multiplet. The $^{31}P\{^1H\}$ NMR spectrum of the Cu(I) complex shows a single broad resonance at −8.7 ppm, giving a small high frequency coordination shift. A *pseudo*-tetrahedral bis-L^1 coordination environment at Cu(I) is confirmed by the observation of a broad ^{63}Cu NMR resonance at +193 ppm which does not change significantly upon cooling. Phosphorus–copper coupling is not observed in either the $^{31}P\{^1H\}$ or ^{63}Cu NMR spectra. This chemical shift is typical of a P_4-donor set at Cu(I) and compares with +150 ppm for $[Cu(Ph_2PCH_2CH_2PPh_2)_2]^+$ and +231 ppm for $[Cu(dppp)_2]^+$, although no ^{63}Cu NMR resonance has been observed for $[Cu(dppb)_2]^+$ between 300 and 175 K, probably due to reversible chelate ring-opening [30]. The $^{31}P\{^1H\}$ NMR spectrum of the Ag(I) complex reveals two overlapping doublets at room temperature at −1.5 ppm, giving $^1J(^{107}Ag$–$^{31}P) = 226$ Hz and $^1J(^{109}Ag$–$^{31}P) = 257$ Hz, indicating that ligand exchange and/or dissociation are slow on the NMR time-scale. Furthermore, the magnitude of the coupling constants provides a good indication of the coordination environment at Ag. In this species the coupling constants are consistent with tetrahedral P_4-coordination in solution (compare for example the tetrahedral $[Ag(dppe)_2]^+$ $J(^{107}Ag$–$^{31}P) = 231$ and $J(^{109}Ag$–$^{31}P) = 266$ Hz) [31]. The dihalo-bridged complexes $[Ag_2Cl_2(L^1)_2]$ (distorted tetrahedral P_2Cl_2 coordination) give $J(^{107}Ag$–$^{31}P) = 359$ and $J(^{109}Ag$–$^{31}P) = 413$ Hz, small reductions in the J values occur as the Cl is replaced by Br or I [6].

The coordination environment at Ag(I) was subsequently confirmed by a crystal structure determination on $[Ag(L^1)_2](BF_4)\cdot CH_2Cl_2$. The structure of the cation shows (Fig. 5, Table 5) two L^1 ligands coordinated in a bidentate manner to Ag(I), giving a distorted tetrahedral coordination environment, consistent with the solution spectroscopic studies. The Ag–P bond distances are in the range 2.47–2.54 Å, while the P1–Ag–P2 and P3–Ag–P4 chelate angles are 102.88(3)° and 104.21(3)°, only slightly larger than those observed in the 1:1 Pd:L^1 complexes above, but some 10°–12° larger than in the bis-L^1 complex $[Rh(L^1)_2]BF_4$. The obtuse angles within the chelate rings in $[Ag(L^1)_2]^+$ are also confirmed by the P1···P2 and P3···P4 distances of 3.90 and 3.96 Å, respectively. These are over 0.5 Å larger than in $[Rh(L^1)_2]^+$, reflecting the structural flexibility of the 7-membered chelate ring incorporating the somewhat rigid *o*-xylyl unit.

The structures of the Ag(I) complexes $[Ag_2X_2(L^1)_2]$ (X = Cl or I) have been described previously. These both show distorted tetrahedral coordination at Ag(I) via two bridging X ligands and a chelating L^1, with *d*(Ag–P) very similar to those seen here for $[Ag(L^1)_2]^+$ (X = Cl: *d*(Ag–P) = 2.446(1), 2.450(2) Å; X = I: *d*(Ag–P) = 2.487(1), 2.493(2) Å), although the P–Ag–P angles within the chelate rings are closer to the ideal tetrahedral value in the halo-bridged complexes. Again, this probably reflects the reduction in steric bulk when only one L^1 is present on the Ag centre [6].

The analogous Au(I) complex $[Au(L^1)_2]PF_6$ was obtained in good yield as a white solid by reaction of [AuCl(tht)] with two mol equiv. of L^1 and one mol equiv. of $TlPF_6$ in CH_2Cl_2 solution. The electrospray mass spectrum reveals a cluster of peaks with the correct isotope distribution at ca. 1145, consistent with $[Au(L^1)_2]^+$, with a lower intensity cluster corresponding to a fragment ion derived from loss of one L^1, while the IR spectrum shows the presence of ionic PF_6^-, but no

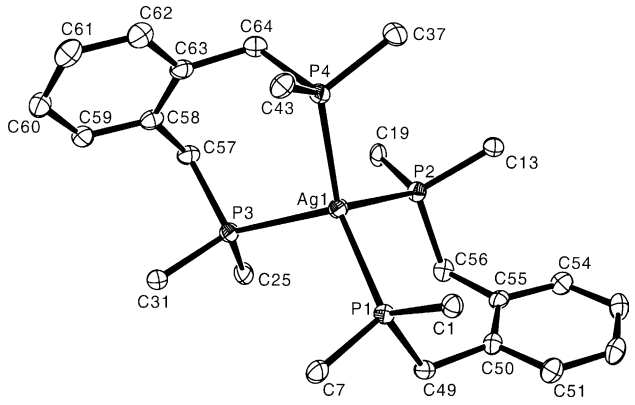


Fig. 5. View of the structure of the $[Ag(L^1)_2]^+$ cation with numbering scheme adopted. Ellipsoids are drawn at 50% probability and H atoms and phenyl rings (except the *ipso* C atoms) are omitted for clarity.

Table 5
Selected bond lengths (Å) and angles (°) for $[Ag(L^1)_2]BF_4$

Bond lengths	
Ag1–P1	2.4691(9)
Ag1–P4	2.4787(9)
Ag1–P2	2.5222(9)
Ag1–P3	2.5385(9)
P1–C1	1.821(4)
P1–C7	1.827(4)
P1–C49	1.856(4)
P2–C13	1.825(4)
P2–C19	1.829(4)
P2–C56	1.856(4)
P3–C25	1.830(4)
P3–C31	1.833(4)
P3–C57	1.857(4)
P4–C43	1.821(4)
P4–C37	1.826(4)
P4–C64	1.863(4)
Bond angles	
P1–Ag1–P4	124.76(3)
P1–Ag1–P2	102.88(3)
P4–Ag1–P2	108.32(3)
P1–Ag1–P3	110.69(3)
P4–Ag1–P3	104.21(3)
P2–Ag1–P3	104.37(3)
C1–P1–C7	101.21(17)
C1–P1–C49	104.64(16)
C7–P1–C49	104.40(17)
C1–P1–Ag1	117.74(12)
C7–P1–Ag1	114.77(12)
C49–P1–Ag1	112.52(12)
C13–P2–C19	102.14(17)
C13–P2–C56	102.08(16)
C19–P2–C56	105.35(17)
C13–P2–Ag1	123.17(13)
C19–P2–Ag1	112.89(12)
C56–P2–Ag1	109.45(12)
C25–P3–C31	101.35(17)
C25–P3–C57	104.86(17)
C31–P3–C57	100.45(17)
C25–P3–Ag1	112.36(12)
C31–P3–Ag1	124.87(13)
C57–P3–Ag1	110.74(12)
C43–P4–C37	104.34(17)
C43–P4–C64	102.05(16)
C37–P4–C64	102.88(17)
C43–P4–Ag1	119.38(12)
C37–P4–Ag1	116.37(12)
C64–P4–Ag1	109.72(12)

Au–Cl unit. The $^{31}P\{^1H\}$ NMR spectrum shows a singlet at +0.8 ppm due to coordinated L^1 and a septet (PF_6^-) at −143.9 ppm with a 4:1 integral ratio. The coordination environment is confirmed from a crystal structure of the complex. The structure of $[Au(L^1)_2]PF_6\cdot 2CH_2Cl_2$ shows a distorted tetrahedral cation (Fig. 6, Table 6) derived from two chelating L^1 ligands and giving Au–P bond lengths in the range 2.40–2.43 Å. These bond distances compare very well with the range 2.39–2.42 Å reported for $[Au(Ph_2PCH_2CH_2PPh_2)_2]^+$ (flattened tetrahedron) [32].

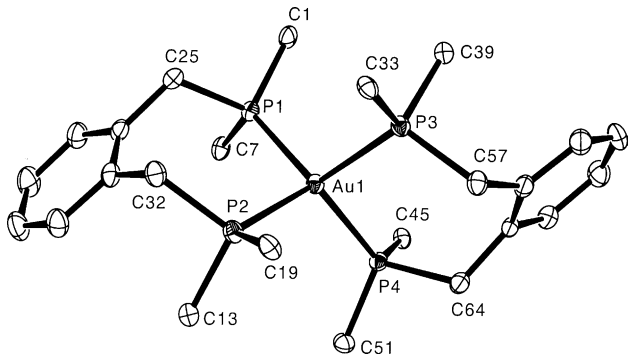


Fig. 6. View of the structure of the $[Au(L^1)_2]^+$ cation with numbering scheme adopted. Ellipsoids are drawn at 50% probability and H atoms and phenyl rings (except the *ipso* C atoms) are omitted for clarity.

The chelate angles subtended at Au are 103.62(2)° and 103.65(2)°, with d(P1···P2) and d(P3···P4) = 3.78 Å. Comparison of this structure with the Ag(I) analogue above reveals a small but significant shortening of the metal–phosphorus bond distances in the 5d Au(I) complex. Similar observations have been made on other related systems [33].

A similar reaction between [AuCl(tht)] and L^1 in a 2:1 ratio and in the absence of $TlPF_6$ also gives a white, light sensitive solid. The IR spectrum of this compound clearly indicates the presence of terminal Au–Cl units (319 cm^{-1}), and its $^{31}P\{^1H\}$ NMR spectrum is a singlet at 30.5 ppm, very significantly to high frequency of the PF_6^- salt above. The $^{31}P\{^1H\}$ NMR spectrum of the related $[Au_2Cl_2(Ph_2PCH_2CH_2PPh_2)]$ displays a similar coordination shift, giving $\delta(^{31}P)$ = +31.5 [32]. These data together with ^1H NMR data confirm the formulation as $[(AuCl)_2(L^1)]$, probably involving linear Au–Cl coordination at each P atom of a bridging diphosphine.

3. Conclusions

These results show that L^1 is an effective ligand for a range of late transition metal ions, functioning routinely as a chelating bidentate. The steric demands of L^1 favour the formation of lower coordination numbers, and indeed the only bis-L^1 complexes we have isolated involve either distorted square planar or tetrahedral coordination environments and are sterically quite hindered. This factor may also be responsible for formation of the unusual Cl-bridged dimer $[Pd_2Cl_2(L^1)_2]^{2+}$, as the Pd(II) centre can more readily accommodate one L^1 and two relatively small Cl ligands rather than two chelating L^1's. The presence of the aromatic unit in the ligand backbone leads to increased rigidity relative to the aliphatic dppb, a greater tendency to chelate, and promotes coordination chemistry more akin to the rigid *o*-phenylene analogue *o*-$C_6H_4(PPh_2)_2$. The flexibility of L^1 is also evident from the wide range of P···P distances measured within the chelate rings from the six crystal structures.

Table 6
Selected bond lengths (Å) and angles (°) for $[Au(L^1)_2]PF_6 \cdot 2CH_2Cl_2$

Bond lengths	
Au1–P4	2.4006(7)
Au1–P1	2.4086(7)
Au1–P2	2.4255(7)
Au1–P3	2.4301(7)
Cl1–C65	1.756(4)
Cl2–C65	1.746(4)
Cl3–C66	1.726(6)
Cl4–C66	1.745(5)
P1–C1	1.822(3)
P1–C7	1.824(3)
P1–C25	1.853(3)
P2–C19	1.826(3)
P2–C13	1.830(3)
P2–C32	1.855(3)
P3–C33	1.820(3)
P3–C39	1.828(3)
P3–C57	1.862(3)
P4–C45	1.827(3)
P4–C51	1.830(3)
P4–C64	1.849(3)
Bond angles	
P4–Au1–P1	116.16(2)
P4–Au1–P2	115.81(2)
P1–Au1–P2	103.62(2)
P4–Au1–P3	103.65(2)
P1–Au1–P3	114.22(2)
P2–Au1–P3	102.94(2)
C1–P1–C7	105.50(14)
C1–P1–C25	101.16(13)
C7–P1–C25	102.43(13)
C1–P1–Au1	116.95(9)
C7–P1–Au1	114.35(9)
C25–P1–Au1	114.61(9)
C19–P2–C13	101.77(13)
C19–P2–C32	104.33(13)
C13–P2–C32	100.13(13)
C19–P2–Au1	112.74(10)
C13–P2–Au1	122.67(10)
C32–P2–Au1	112.98(10)
C33–P3–C39	102.42(13)
C33–P3–C57	105.29(13)
C39–P3–C57	101.65(13)
C33–P3–Au1	114.18(9)
C39–P3–Au1	117.67(10)
C57–P3–Au1	113.96(9)
C45–P4–C51	103.92(13)
C45–P4–C64	101.18(13)
C51–P4–C64	100.63(13)
C45–P4–Au1	118.84(9)
C51–P4–Au1	117.08(10)
C64–P4–Au1	112.58(9)

4. Experimental

Infrared spectra were recorded as either Nujol mulls between CsI plates or as CsI disks using a Perkin–Elmer

983G spectrometer over the range 4000–200 cm^{-1}. UV/vis spectra were recorded either as solids by diffuse reflectance or in CH_2Cl_2 solution using 1 cm path length quartz cells using a Perkin–Elmer Lambda19 spectrometer. Mass spectra were run by electron impact on a VG-70-SE Normal geometry double focusing spectrometer or by positive ion electrospray (MeCN solution) using a VG Biotech platform. ^1H NMR spectra were recorded using a Bruker AC300 spectrometer. $^{13}C\{^1H\}$, $^{31}P\{^1H\}$, ^{63}Cu and $^{195}Pt\{^1H\}$ NMR spectra were recorded using a Bruker DPX400 spectrometer operating at 100.6, 162.0, 106.11 or 85.62 MHz, respectively, and are referenced to TMS, external 85% H_3PO_4, $[Cu(NCMe)_4]BF_4$ and 1 mol dm^{-3} $Na_2[PtCl_6]$, respectively. Microanalyses were undertaken by the University of Strathclyde microanalytical service.

Solvents were dried prior to use and all preparations were undertaken using standard Schlenk techniques under a N_2 atmosphere. The ligand L^1 was prepared as described previously [8].

4.1. $[CoCl_2(L^1)]$

$CoCl_2 \cdot 6H_2O$ (0.075 g, 0.316 mmol) was dissolved in isopropanol (20 cm^3). One molar equivalent of L^1 (0.150 g, 0.316 mmol) dissolved in CH_2Cl_2 (10 cm^3) was added and the reaction mixture was stirred for ca. 30 min. to give a turquoise solid. The solvent was concentrated to ca. 5 cm^3 in vacuo and the solid was collected by filtration, washed with isopropanol and dried in vacuo (yield 67%). Required for $[C_{32}H_{28}Cl_2CoP_2] \cdot 1/4CH_2Cl_2$: C, 61.9; H, 4.6. Found: C, 62.4; H, 4.3%. UV/vis (diffuse reflectance): ν 6120, 7750, 13460, 15080, 16155, 25700 sh cm^{-1}; (CH_2Cl_2 solution): ν 13590 (ε_{mol} 1000 cm^{-1} mol^{-1} dm^3), 15625 (900), 16920 (1060) cm^{-1}. IR (Nujol mull): ν 318 br cm^{-1}. Magnetic moment = 4.68 μ_B.

4.2. $[CoCl_3(L^1)]$

Treatment of a CH_2Cl_2 solution of $[CoCl_2(L^1)]$ with a stream of NOCl at ca. −15 °C leads to immediate formation of a deep green-blue solution which, upon pumping to dryness in vacuo affords a green-blue solid. IR (Nujol mull): ν 349, 321, 311 cm^{-1}. UV/vis (CH_2Cl_2 solution): ν 6580, 16130, 16530 sh, 28570 cm^{-1}.

4.3. $[CoBr_2(L^1)]$

Method as above, but using $CoBr_2 \cdot 6H_2O$. Green solid (yield 62%). Required for $[C_{32}H_{28}Br_2CoP_2]$: C, 55.4; H, 4.1. Found: C, 55.4; H, 3.7%. UV/vis (diffuse reflectance): ν 6540, 7605, 13265, 15130, 15875 cm^{-1}; (CH_2Cl_2 solution): 13280 (ε_{mol} 1580 cm^{-1} mol^{-1} dm^3), 15040 (1560), 16050 (1460) cm^{-1}. IR (Nujol mull): ν 243 br cm^{-1}. Magnetic moment = 4.41 μ_B.

4.4. $[CoI_2(L^1)]$

Method as above, but using CoI_2. Brown-green solid (yield 55%). Required for $[C_{32}H_{28}CoI_2P_2] \cdot 1.5CH_2Cl_2$: C, 44.0; H, 3.4. Found: C, 43.7; H, 3.1%. UV/vis (diffuse reflectance): ν 6610, 7350, 12770, 14045, 14730, 20830 sh, 2500 sh cm^{-1}; (CH_2Cl_2 solution): 12805 (ε_{mol} 920 cm^{-1} mol^{-1} dm^3), 13965 (885), 14840 (770) cm^{-1}. Magnetic moment = 4.84 μ_B.

4.5. $[Rh(L^1)_2]BF_4$

$RhCl_3 \cdot 3H_2O$ (0.0416 g, 0.158 mmol) was dissolved in EtOH (20 cm^3). Two equivalents of L^1 (0.15 g, 0.316 mmol) dissolved in CH_2Cl_2 (10 cm^3) was then added, together with 40% aqueous HBF_4 (1 cm^3). The resulting mixture was stirred at room temperature for 30 min. Concentrating the mixture in vacuo gave an orange precipitate, which was filtered, washed with diethyl ether and dried in vacuo (yield 52%). Required for $[C_{64}H_{56}BF_4P_4Rh] \cdot 2CHCl_3$: C, 57.5; H, 4.2. Found: C, C, 58.3; H, 4.6%. ^1H NMR ($CDCl_3$): 7.00–7.40 (m) [40H] (Ph), 6.90 (m) [4H] (*o*-C_6H_4), 6.35 (m) [4H] (*o*-C_6H_4), 3.65 (br s) [8H] (CH_2). $^{31}P\{^1H\}$ NMR ($CH_2Cl_2/CDCl_3$): 11.6 ppm (d, $^1J_{RhP} = 140$ Hz). IR spectrum (Nujol mull): ν 1060 s, 506 s cm^{-1}. Electrospray MS (MeCN): *m/z* 1051 $[Rh(L^1)_2]^+$, 557 $[Rh(L^1)]^+$, 475 $[L^1 + H]^+$.

4.6. $[Rh(cod)(L^1)]PF_6$

$[RhCl(cod)]_2$ (0.077 g, 0.158 mmol) was dissolved in a degassed solution of CH_2Cl_2 (20 cm^3). NH_4PF_6 (0.057 g, 0.35 mmol) and L^1 (0.15 g, 0.316 mmol) were added to the mixture and the reaction was stirred under nitrogen for 30 min. The reaction mixture changed from yellow to red and the white precipitate (NH_4Cl) was filtered off. The solution was reduced in volume to ~5 cm^3 in vacuo. Upon addition of diethyl ether (10 cm^3) an orange precipitate formed which was filtered and washed with diethyl ether (2×10 cm^3). The orange solid (0.145 g, 55%) was dried in vacuo. Required for $[C_{40}H_{40}F_6P_3Rh] \cdot 1/2CH_2Cl_2$: C, 55.7; H, 4.7. Found: C, 56.1; H, 3.9%. ^1H NMR ($CDCl_3$): δ 7.70–7.50 (m) [20H] (Ph), 6.85 (m) [2H] (*o*-C_6H_4), 6.40 (m) [2H] (*o*-C_6H_4), 4.40 (br m) [4H] (cod CH), 3.90 (br m) [4H] (L^1CH_2), 2.0–2.2 (m) [8H] (cod CH_2). $^{31}P\{^1H\}$ NMR ($CH_2Cl_2/CDCl_3$): 10.3 ppm (d, $^1J_{RhP} = 146$ Hz) [2P], −143.8 (septet, PF_6^-) [1P]. IR (Nujol mull): 840 s, 557 s cm^{-1}.

4.7. $[Ir(cod)(L^1)]PF_6$

Method as above, using $[Ir_2Cl_2(cod)_2]$, giving an orange-red solid (yield 55%).

Required for $[C_{40}H_{40}F_6IrP_3]\cdot CH_2Cl_2$: C, 49.0; H, 4.2. Found: C, 48.3; H, 3.7%. ^{1}H NMR ($CDCl_3$): δ 7.70–7.30 (m) [20H] (Ph), 6.85 (m) [2H] (*o*-C_6H_4), 6.40 (m) [2H] (*o*-C_6H_4), 4.18 (br m) [4H] (cod CH), 3.92 (br m) [4H] (L^1CH_2), 1.7–2.0 (m) [8H] (cod CH_2). $^{31}P\{^1H\}$ NMR ($CH_2Cl_2/CDCl_3$): −1.8 ppm (s) [2P], −143.8 (septet, PF_6^-) [1P]. IR (Nujol mull): 841 s, 557 s cm^{-1}. Electrospray MS (MeCN): *m*/*z* 775 $[Ir(cod)(L^1)]^+$.

4.8. $[NiCl_2(L^1)]$

$NiCl_2\cdot 6H_2O$ (0.075 g, 0.316 mmol) was dissolved in isopropanol (20 cm^3) and one mol equiv. of L^1 (0.15 g, 0.316 mmol) was added. Stirring the reaction mixture for 1 h afforded a deep pink solid which was filtered and dried in vacuo. Recrystallisation from CH_2Cl_2 gave a deep pink solid (yield 76%). Required for $[C_{32}H_{28}Cl_2NiP_2]\cdot 1.5CH_2Cl_2$: C, 55.0; H, 4.3. Found: C, 55.5; H, 5.0%. ^{1}H NMR ($CDCl_3$): δ 6.90–7.40 (br m) [20H] (Ph), 6.70 (br m) [2H] (*o*-C_6H_4), 6.30 (br m) [2H] (*o*-C_6H_4), 3.40 (br m) [4H] (CH_2) ppm. UV/vis (diffuse reflectance): 20325, 29415, 37310 cm^{-1}; (CH_2Cl_2 solution): 20410 (ε_{mol} 510 cm^{-1} mol^{-1} dm^3). IR (Nujol mull): *v* 337 m, 322 m cm^{-1}.

4.9. $[NiCl_3(L^1)]$

Treatment of a CH_2Cl_2 solution of $[NiCl_2(L^1)]$ with a stream of NOCl at ca. −50 °C gave a deep orange-brown solution, from which an orange brown solid was obtained upon pumping to dryness in vacuo. IR (Nujol mull): *v* 340, 312, 300 sh cm^{-1}. UV/vis (CH_2Cl_2 solution): 12900 v br, 21050, 28570 cm^{-1}.

4.10. $[NiBr_2(L^1)]$

Prepared as above with $NiBr_2\cdot 3H_2O$ (0.086 g, 0.316 mmol) and L^1 (0.15 g, 0.316 mmol) to afford a brick red solid (yield 87%). Required for $[C_{32}H_{28}Br_2NiP_2]\cdot 1.5CH_2Cl_2$: C, 49.0; H, 3.8. Found: C, 48.3; H, 4.9%. ^{1}H NMR ($CDCl_3$): δ 6.70–7.50 (br m) [24H] (Ar–CH), 3.80 (br m) [4H] (CH_2) ppm. UV/vis (diffuse reflectance): 19600, 24040, 29240 cm^{-1}; (CH_2Cl_2 solution): 19920 (ε_{mol} 450 cm^{-1} mol^{-1} dm^3), 25000 (1485), 30675 (3140) cm^{-1}. IR (Nujol mull): 282 w, 262 cm^{-1}.

4.11. $[PdCl_2(L^1)]$

Na_2PdCl_4 (0.093 g, 0.316 mmol) was dissolved in EtOH (20 cm^3). One equivalent of L^1 (0.15 g, 0.316 mmol) was added in EtOH (~5 cm^3). The reaction mixture was stirred overnight, and a pale cream precipitate formed. After filtering and drying in vacuo a cream solid (yield 58%) was recovered. Required for $[C_{32}H_{28}Cl_2P_2Pd]\cdot CH_2Cl_2$: C, 53.8; H, 4.1. Found: C, 54.2; H, 4.2%. ^{1}H NMR ($CDCl_3$): δ 7.85–7.98 (m), 7.44–7.60 (m) [20H] (Ph), 6.88 (m) [2H] (*o*-C_6H_4), 6.15 (m) [2H] (*o*-C_6H_4), 3.75 (br d, J = 10 Hz) [4H] (CH_2). $^{31}P\{^1H\}$ NMR ($CH_2Cl_2/CDCl_3$): δ 16.4 ppm. IR (CsI disk): *v* 3064 w, 2971 w, 2933 w, 1586 w, 1481 m, 1433 s, 1360 m, 1188 w, 1103 s, 1073 w, 1027 w, 1000 m, 867 w, 837 m, 746 s, 700 s, 504 s, 452 w, 316 m, 304 m cm^{-1}.

4.12. $[Pd_2Cl_2(L^1)_2](PF_6)_2$

$PdCl_2$ (0.056 g, 0.316 mmol) was dissolved in MeCN (20 cm^3), by refluxing for 1 h. One equivalent of L^1 (0.15 g, 0.316 mmol) was added to the reaction mixture, followed by, one equivalent of $TlPF_6$ (0.11 g, 0.316 mmol). The resulting reaction mixture was stirred overnight and then filtered. The yellow filtrate was reduced to ~5 cm^3. Cold diethyl ether (~10 cm^3) was added dropwise to precipitate a yellow solid, which was filtered and dried in vacuo (yield 44%). Required for $[C_{64}H_{56}Cl_2F_{12}P_6Pd_2]$: C, 50.5; H, 3.7. Found: C, 50.9; H, 3.8%. ^{1}H NMR ($CDCl_3$): δ 7.40–7.90 (m) [40H], (Ph), 6.80 (m) [4H] (*o*-C_6H_4), 6.20 (m) [4H] (*o*-C_6H_4), 3.90 (br d, J = 12 Hz) [8H], (CH_2). $^{31}P\{^1H\}$ NMR ($CH_2Cl_2/CDCl_3$): δ 27.3 (s) [4P] (–P–Ph), −143.7 (septet) [2P] (PF_6^-) ppm. IR (CsI disk): *v* 3082 w, 3067 w, 3031 w, 2932 w, 1587 w, 1485 w, 1437 s, 1356 m, 1185 w, 1167 w, 1106 m, 1068 w, 1002 m, 843 br s, 777 m, 746 m, 696 m, 561 s, 501 m, 457 m, 374 w, 315 m cm^{-1}. Electrospray MS (MeCN): *m*/*z* 617 $[PdCl(L^1)]^+$, 658 $[PdCl(L^1)(MeCN)]^+$.

4.13. $[Pd(L^1)_2](BF_4)_2$

L^1 (0.15 g, 0.316 mmol) was dissolved in a mixture of EtOH (20 cm^3) and CH_2Cl_2 (10 cm^3). $Pd(NO_3)_2$ (0.036 g, 0.158 mmol) was dissolved in deionised H_2O (~10 cm^3) and added forming an orange solution. An excess of 40% aqueous HBF_4 (2 cm^3) was then added, and the reaction was stirred for 1 h. The solution was reduced in volume until a yellow precipitate formed which was filtered and dried in vacuo (yield 69%). Required for $[C_{64}H_{56}B_2F_8P_4Pd]$: C, 62.5; H, 4.6. Found: C, 63.0; H, 4.9%. ^{1}H NMR ($CDCl_3$): δ 7.30–7.80 (m) [40H] (Ph), 6.20–6.80 (m) [8H] (*o*-C_6H_4), 3.70 (br m) ppm [8H] (CH_2). $^{31}P\{^1H\}$ NMR ($CH_2Cl_2/CDCl_3$): δ 7.1 ppm. IR (Nujol mull): *v* 1067 s, 505 s cm^{-1}.

4.14. $[PtCl_2(L^1)]$

K_2PtCl_4 (0.13 g, 0.316 mmol) was dissolved in deionised H_2O (10 cm^3) and added to EtOH (20 cm^3) whilst stirring. One equivalent of L^1 (0.15 g, 0.316 mmol) dissolved in CH_2Cl_2 (10 cm^3) was added. The reaction mixture was stirred for 3 h, and the subsequent two layers were combined with the addition of acetone (10 cm^3). After stirring for 72 h, the mixture was filtered and then reduced in volume until a cream precipitate formed

which was filtered and dried in vacuo (yield 98%). Required for $[C_{32}H_{28}Cl_2P_2Pt]$: C, 51.9; H, 3.8. Found: C, 51.1; H, 3.9%. ^{1}H NMR ($CDCl_3$): δ 7.90–8.00 (m), 7.45–7.60 (m) [20H] (Ph), 6.90 (m) [2H] (*o*-C_6H_4), 6.20 (m) [2H] (*o*-C_6H_4), 3.95 (br d, $J = 11$ Hz) [4H] (CH_2) ppm. $^{31}P\{^1H\}$ NMR ($CH_2Cl_2/CDCl_3$): δ −1.8 ppm, $^1J_{Pt-P} = 3584$ Hz. ^{195}Pt NMR: −4503 (t, $^1J_{PtP} = 3584$ Hz). IR (Nujol mull): *v* 326 w, 304 w cm^{-1}. Conductivity Λ_M/Ω^{-1} cm^2 mol^{-1} (10^{-3} mol dm^{-3} $MeNO_2$): 11.0. Electrospray MS (MeCN): *m*/*z* 745 $[PtCl(L^1)(MeCN)]^+$.

4.15. $[PtCl_4(L^1)]$

Treatment of a CH_2Cl_2 solution of $[PtCl_2(L^1)]$ with Cl_2 in CCl_4 gave a bright yellow solution, which upon concentrating in vacuo gave a bright yellow solid. Required for $[C_{32}H_{28}Cl_4P_2Pt]\cdot CH_2Cl_2$: C, 44.2; H, 3.4. Found: C, 44.8; H, 3.4%. $^{31}P\{^1H\}$ NMR ($CH_2Cl_2/CDCl_3$): δ −4.8 ppm, $^1J_{Pt-P} = 2160$ Hz. IR (Nujol mull): *v* 344, 299, 288 cm^{-1}.

4.16. $[Cu(L^1)_2](BF_4)$

$[Cu(NCMe)_4](BF_4)$ (0.044 g, 0.158 mmol) was dissolved in CH_2Cl_2 (20 cm^3) and stirred. Two equivalents of L^1 (0.15 g, 0.316 mmol) were added, and the reaction was stirred for 2 h. The solution was reduced in volume to ~5 cm^3 and hexane (15 cm^3) was added to precipitate a solid. This was filtered and the white solid (yield 92%) was dried in vacuo. Required for $[C_{64}H_{56}BCuF_4P_4]\cdot 2CH_2Cl_2$: C, 62.5; H, 4.8. Found: C, 62.5; H, 4.9%. ^{1}H NMR ($CDCl_3$): δ 7.70–6.80 (br m) [44H] (Ar–CH), 6.30 (br m) [4H] (*o*-C_6H_4) 3.65 (br m) [8H] (CH_2). $^{31}P\{^1H\}$ NMR: δ −8.7 (s) ppm. ^{63}Cu NMR: δ +193 ppm. Electrospray MS (MeCN): *m*/*z* 1011 $[Cu(L^1)_2]^+$, 578 $[Cu(L^1)](MeCN)]^+$, 537 $[Cu(L^1)]^+$. IR (CsI disk): *v* 3059 w, 2964 w, 2927 w, 1590 w, 1482 m, 1437 s, 1359 w, 1272 w, 1186 m, 1159 w, 1096 s, 1062 br s, 1003 w, 865 m, 842 m, 766 m, 735 s, 700 s, 504 s, 486 s, 445 w, 342 w cm^{-1}.

4.17. $[Ag(L^1)_2](BF_4)$

$AgBF_4$ (0.031 g, 0.158 mmol) was dissolved in CH_2Cl_2 (20 cm^3) in a foil wrapped reaction vessel to exclude light, at 0 °C. Two equivalents of L^1 (0.15 g, 0.316 mmol) were dissolved in CH_2Cl_2 (10 cm^3) and added dropwise whilst stirring to the reaction mixture, keeping the temperature at 0 °C. After stirring for 2 h, the white precipitate was recovered by filtration, and dried in vacuo to afford a white solid (yield 82%). The solid was stored in a foil wrapped container to exclude light. Required for $[C_{64}H_{56}AgBF_4P_4]\cdot 1.5CH_2Cl_2$: C, 61.9; H, 4.7. Found: C, 62.4; H, 5.1%. ^{1}H NMR ($CDCl_3$): δ 6.95–7.30 (m) [40H] (Ph), 6.65 (br m) [4H] (*o*-C_6H_4), 6.20 (br m) [4H] (*o*-C_6H_4), 3.65 (br s) [8H] (CH_2) ppm. $^{31}P\{^1H\}$ NMR ($CH_2Cl_2/CDCl_3$): δ −1.5 (2 × d, $^1J_{^{107}Ag-^{31}P} = 226$ Hz, $^1J_{^{109}Ag-^{31}P} = 257$ Hz). Electrospray MS (MeCN): *m*/*z* 1055 $[^{107}Ag(L^1)_2]^+$, 1057 $[^{109}Ag(L^1)_2]^+$. IR (Nujol mull): *v* 1059 m, 504 m cm^{-1}.

4.18. $[Au(L^1)_2]PF_6$

L^1 (0.15 g, 0.316 mmol) was dissolved in CH_2Cl_2 (20 cm^3). AuCl(tht) (0.051 g, 0.158 mmol) was added to the reaction vessel, followed by $TlPF_6$ (0.055 g, 0.158 mmol). The vessel was wrapped in foil to exclude light. This was stirred for 1 h, and filtered to remove TlCl. The volume was reduced to ~5 cm^3 and a white precipitate formed, which was filtered and dried in vacuo. The resulting fine white powder (yield 66%) was stored in a sample bottle excluding light. Required for $[C_{64}H_{56}AuF_6P_5]\cdot CH_2Cl_2$: C, 56.7; H, 4.2. Found: C, 57.3; H, 3.9%. ^{1}H NMR ($CDCl_3$): δ 7.10–7.35 (m) [40H] (Ph), 6.40 (m) [4H] (*o*-C_6H_4), 5.83 (m) [4H] (*o*-C_6H_4), 3.75 (br s) [8H], (CH_2) ppm. $^{31}P\{^1H\}$ NMR ($CH_2Cl_2/CDCl_3$): δ 0.8 (s) [4P] (P–Ph), −143.9 (sep) [1P] (PF_6) ppm. Electrospray MS (MeCN): *m*/*z* 1145 $[Au(L^1)_2]^+$, 671 $[Au(L^1)]^+$. IR (Nujol mull): *v* 850 br s, 560 s cm^{-1}.

4.19. $[(AuCl)_2(L^1)]$

L^1 (0.072 g, 0.152 mmol) was dissolved in CH_2Cl_2 (20 cm^3). AuCl(tht) (0.098 g, 0.304 mmol) was added and the vessel was wrapped in foil to exclude light. The reaction mixture was stirred for 30 min at room temperature, and then reduced in volume to ~5 cm^3. The resulting white precipitate was filtered and dried in vacuo to afford a fine white powder (yield 23%), which was placed in a foil wrapped container. ^{1}H NMR ($CDCl_3$): δ 7.30–7.60 (m) [20H] (Ph), 6.86 (m) [2H] (*o*-C_6H_4), 6.35 (m) [2H] (*o*-C_6H_4), 3.92 (br) [4H] (CH_2) ppm. $^{31}P\{^1H\}$ NMR ($CH_2Cl_2/CDCl_3$): δ 30.5 (s) ppm. IR (Nujol mull): *v* 319 m cm^{-1}.

5. X-ray crystallography

Details of the crystallographic data collection and refinement parameters are given in Table 7. Small blue crystals of $[CoCl_2(L^1)]$ were obtained by vapour diffusion of diethyl ether into a CH_2Cl_2 solution of the complex. Orange crystals of $[Rh(L^1)_2]BF_4\cdot 2CHCl_3$ were obtained by liquid diffusion of hexane into a solution of the complex in $CHCl_3$, while yellow crystals of $[PdCl_2(L^1)]\cdot 2CH_2Cl_2$ and $[Pd_2Cl_2(L^1)_2](PF_6)_2$ and colourless crystals of $[Ag(L^1)_2]BF_4\cdot 2CH_2Cl_2$ and $[Au(L^1)_2]PF_6\cdot 2CH_2Cl_2$ were grown by liquid diffusion of hexane into a CH_2Cl_2 solution of the appropriate complex. Data collection used a Nonius Kappa CCD diffractometer ($T = 120$ K) and with graphite-monochromated

Table 7
Crystallographic parameters

Complex	$[CoCl_2(L^1)]$	$[Rh(L^1)_2]BF_4\cdot 2CHCl_3$	$[PdCl_2(L^1)]\cdot 2CH_2Cl_2$	$[Pd_2Cl_2(L^1)_2](PF_6)_2$	$[Ag(L^1)_2]BF_4\cdot 2CH_2Cl_2$	$[Au(L^1)_2]PF_6\cdot 2CH_2Cl_2$
Formula	$C_{32}H_{28}Cl_2CoP_2$	$C_{66}H_{58}BCl_6F_4P_4Rh$	$C_{34}H_{32}Cl_6P_2Pd$	$C_{64}H_{56}Cl_2F_{12}P_6Pd_2$	$C_{66}H_{60}AgBCl_4\ F_4P_4$	$C_{66}H_{60}AuCl_4F_6P_5$
M	604.31	1377.42	821.72	1522.61	1313.50	1460.76
Crystal system	monoclinic	monoclinic	monoclinic	triclinic	triclinic	monoclinic
Space group	$P2_1/c$	$P2_1/c$	$P2_1/m$	$P\bar{1}$	$P\bar{1}$	$P2_1/n$
a (Å)	8.431(3)	12.5675(2)	10.0854(7)	9.6898(4)	11.8886(3)	11.32970(10)
b (Å)	18.217(3)	24.5759(7)	17.7620(15)	13.1151(7)	14.8588(3)	24.0180(3)
c (Å)	18.075(5)	20.1428(6)	10.5702(7)	13.8233(7)	17.5104(4)	22.8978(2)
α (°)	90	90	90	66.043(2)	85.0570(10)	90
β (°)	93.54(2)	100.595(2)	115.727(4)	86.115(3)	89.6220(10)	93.7570(10)
γ (°)	90	90	90	75.645(3)	86.0290(10)	90
U (Å^3)	2770.8(13)	6115.2(3)	1705.8(2)	1554.17(13)	3074.28(12)	6217.48(11)
Z	4	4	2	1	1	4
μ(Mo Kα) (cm^{-1})	9.49	7.00	11.32	8.96	6.58	2.726
Unique reflections	6330	13925	3756	7038	14004	14231
Number of parameters	334	739	202	388	721	739
R_1 [$I_o > 2\sigma(I_o)$]	0.0692	0.0570	0.0539	0.0512	0.0571	0.0301
R_1 [all data]	0.1668	0.1041	0.0746	0.0751	0.0775	0.0425
wR_2 [$I_o > 2\sigma(I_o)$]	0.1172	0.1082	0.1116	0.1041	0.1393	0.0642
wR_2 [all data]	0.1464	0.1236	0.1202	0.1142	0.1527	0.0694

$R_1 = \sum ||F_o| - |F_c||_i / \sum |F_o| \quad wR_2 = [\sum_w (F_o^2 - F_c^2)^2 / \sum wF_{oi}^4]^{1/2}$.

Mo Kα X-radiation (λ = 0.71073 Å). Structure solution and refinement were routine [34,35]. Selected bond lengths and angles are given in Tables 1–6.

6. Supplementary material

Crystallographic data for the structural analyses have been deposited with the Cambridge Crystallographic Data Centre, CCDC nos. 240478 (Co), 240479 (Rh), 240480 (Pd monomer), 240481 (Pd dimer), 240482 (Ag), 240483 (Au). Copies of this information may be obtained free of charge from The Director, CCDC, 12 Union Road, Cambridge CD2 1EZ, UK (fax: +44 1223 336033; email: deposit@ccdc.cam.ac.uk or www: http://www.ccdc.cam.ac.uk).

Acknowledgements

We thank the EPSRC for support and Johnson-Matthey plc for loans of precious metal salts. We also thank Professor M.B. Hursthouse for access to the Nonius Kappa CCD diffractometer.

References

[1] See Z. Freixa, P.W.N.M. van Leeuwen, Dalton Trans. (2003) 1890, and references therein.
[2] P.W.N.M. van Leeuwen, P.C.J. Kamer, J.N.H. Reek, P. Dierkes, Chem. Rev. 100 (2000) 2741.
[3] K. Angermund, W. Bauman, E. Dinjus, R. Fornika, H. Gorls, M. Kessler, C. Kruger, W. Leitner, F. Lutz, Chem. Eur. J. 3 (1997) 755.
[4] T. Hayashi, Y. Kawabata, T. Isoyama, I. Ogata, Bull. Chem. Soc. Jpn. 54 (1981) 3438.
[5] R.-X. Li, X.-J. Li, N.-B. Wong, K.-C. Tin, Z.-Y. Zhou, T.C.W. Mak, J. Mol. Catal. A 178 (2002) 181.
[6] F. Caruso, M. Camalli, H. Rimml, L.M. Venanzi, Inorg. Chem. 34 (1995) 673.
[7] H. Rimml, L.M. Venanzi, Phosphorus Sulfur 30 (1987) 297.
[8] M. Camalli, F. Caruso, S. Chaloupka, E.M. Leber, H. Rimml, L. Venanzi, Helv. Chim. Acta 73 (1990) 2263.
[9] M. Ebner, H. Otto, H. Werner, Angew. Chem. Int. Ed. Eng. 24 (1985) 518.
[10] H. Werner, M. Ebner, H. Otto, J. Organomet. Chem. 350 (1988) 257.
[11] H. Werner, M. Ebner, W. Bertleff, U. Schubert, Organometallics 2 (1983) 891.
[12] D. Belletti, C. Graiff, C. Massera, A. Minarelli, G. Predieri, A. Tiripicchio, D. Acquotti, Inorg. Chem. 42 (2003) 8509.
[13] D. Belletti, C. Graiff, V. Lostao, R. Pattacini, G. Predieri, G. Tiripicchio, Inorg. Chim. Acta 347 (2003) 137.
[14] A.B.P. Lever, Inorganic Electronic Spectrsocopy, 2nd ed., Elsevier, Amsterdam, 1984.
[15] W. Levason, C.A. McAuliffe, Inorg. Chim. Acta 14 (1975) 127.
[16] W. De, W. Horrocks, G.R. van Hecke, D. De, W. Hall, Inorg. Chem. 6 (1966) 694.

[17] R. Jones, P. Warrens, D.J. Williams, D.J. Woollins, J. Chem. Soc., Dalton Trans. (1987) 907.
[18] W. Levason, M.D. Spicer, J. Chem. Soc., Dalton Trans. (1990) 719.
[19] M.J. Bennett, P.B. Donaldson, Inorg. Chem. 16 (1977) 659.
[20] P.B. Hitchcock, M. McPartlin, R. Mason, Chem. Commun. (1969) 1367.
[21] W. Levason, C.A. McAuliffe, Inorg. Chim. Acta 16 (1976) 167.
[22] W. Levason, C.A. McAuliffe, J. Chem. Soc., Dalton Trans. (1974) 2238.
[23] J.A. Osborn, G. Wilkinson, Inorg. Synth. 10 (1967) 67.
[24] L. Sacconi, J. Gelsomini, Inorg. Chem. 7 (1968) 290.
[25] W. Levason, C.A. McAuliffe, Inorg. Chim. Acta 11 (1974) 33.
[26] T.D. DuBois, D.W. Meek, Inorg. Chem. 6 (1967) 1395.
[27] L.R. Gray, S.J. Higgins, W. Levason, M. Webster, J. Chem. Soc., Dalton Trans. (1984) 459.
[28] E.G. Hope, W. Levason, N.A. Powell, Inorg. Chim. Acta 115 (1986) 187.
[29] D.J. Gulliver, W. Levason, K.G. Smith, J. Chem. Soc., Dalton Trans. (1981) 2153.
[30] J.R. Black, W. Levason, M.D. Spicer, M. Webster, J. Chem. Soc., Dalton Trans. (1993) 3129.
[31] S.J. Berners Price, C. Brevard, A. Pagelot, P.J. Sadler, Inorg. Chem. 24 (1985) 4278.
[32] S.J. Berners Price, M.A. Mazid, P.J. Sadler, J. Chem. Soc., Dalton Trans. (1984) 969.
[33] A. Bayler, A. Schier, G.A. Bowmaker, H. Schmidbauer, J. Am. Chem. Soc. 118 (1996) 7006.
[34] G.M. Sheldrick, SHELXS-97, program for crystal structure solution, University of Göttingen, 1997.
[35] G.M. Sheldrick, SHELXL-97, program for crystal structure refinement, University of Göttingen, 1997.

Available online at www.sciencedirect.com
SCIENCE DIRECT®
Polyhedron 24 (2005) 89–95
POLYHEDRON
www.elsevier.com/locate/poly

Dialkyldithiocarbamate derivatives of toluene-3,4-dithiolato arsenic(III) and -bismuth(III): synthetic, spectral and single crystal X-ray structural studies

H.P.S. Chauhan [*,a], Kavita Kori [a], Nagulu Meera Shaik [a], Sanjay Mathur [b,*], Volker Huch [b]

[a] School of Chemical Sciences, Devi Ahilya University, Takshshila Campus, Khandwa Road, Indore 452017, India
[b] Institute of Inorganic Chemistry, Saarland University, D-66123 Saarbruecken, Germany

Received 15 July 2004; accepted 13 October 2004
Available online 24 November 2004

Abstract

We report here on dialkyldithiocarbamates complexes of the type $[C_6H_3(CH_3)S_2MS_2CNR_2]$ (M = As and Bi; R = CH_3, C_2H_5 and CH_2–CH_2), prepared by the reaction of toluene-3,4-dithiolatoarsenic(III) and -bismuth(III) chlorides $[C_6H_3(CH_3)S_2MCl]$ (M = As and Bi) with sodium/ammonium salts of dialkyldithiocarbamates $[XS_2CNR_2]$ (X = Na and NH_4; R = CH_3, C_2H_5 and CH_2–CH_2). The new derivatives were characterized by melting point, elemental analysis (C, H, N, S and As/Bi) and spectroscopic studies (IR, ^1H and ^{13}C NMR). Single crystal X-ray diffraction analyses of toluene-3,4-dithiolatoarsenic(III) dimethyldithiocarbamate and toluene-3,4-dithiolatoarsenic(III) pyrrolidine-dithiocarbamate revealed a monodentate chelating mode of the dimethyl as well as the pyrrolidine-dithiocarbamate moieties in these complexes.
© 2004 Elsevier Ltd. All rights reserved.

Keywords: Arsenic(III); Bismuth(III); Toluene-3,4-dithiol; Dialkyldithiocarbamate derivatives

1. Introduction

Dialkyldithiocarbamate [1–5] groups are versatile ligands that exhibit different types of coordination patterns towards metals [1–10]. A number of arsenic(III) [8,11–15] and bismuth(III) [15–20] complexes with these ligands have been described and some of them have also been characterized by X-ray crystal structure determination [11–13,15–17,21–27]. However, the heteroleptic complexes of toluene-3,4-dithiolatoarsenic(III) and -bismuth(III) complexes with dialkyl-dithiocarbamate ligands have not been investigated so far. Recently we have reported on toluene-3,4-dithiolatoantimony(III) complexes based on these ligands [6]. Our continuing interest in the group 15 metal derivatives of dithiolato ligands [6–10,15,28,29] has prompted us to investigate the mixed toluene-3,4-dithiolatodialkyldithiocarbamates of arsenic(III) and bismuth(III) of the type $[C_6H_3(CH_3)S_2MS_2CNR_2]$ (M = As and Bi; R = CH_3, C_2H_5 and CH_2–CH_2).

2. Experimental

2.1. Reagents and general procedures

All the preparative reactions were performed under strictly moisture-free conditions due to hydrolysable nature of the reactants and the products. Solvents were

* Corresponding author. Present address: Leibniz Institute of New Materials, CVD Division, Saarland University Campus, Build 43A, In Stadtwald, D-66123 Saarbruecken, Germany. Tel.: +49 681 9300 338; fax: +49 681 9300 279.
E-mail address: smathur@inm-gmbh.de (S. Mathur).

0277-5387/$ - see front matter © 2004 Elsevier Ltd. All rights reserved.
doi:10.1016/j.poly.2004.10.007

dried by standard methods [30]. Bismuth trichloride (Fluka), toluene-3,4-dithiol (Merck), the sodium salt of dimethyldithiocarbamate (Fluka), the sodium salt of diethyldithiocarbamate (BDH) and the ammonium salt of pyrrolidinedithiocarbamate (Merck) were used as received. Toluene-3,4-dithiolato arsenic(III) and bismuth(III) chlorides were prepared by reacting equimolar ratios of toluene-3,4-dithiol with arsenic trichloride and bismuth trichloride, respectively in anhydrous benzene. Sulfur was determined gravimetrically as barium sulfate [31], while arsenic was determined iodometrically [32]. Bismuth was titrated complexometrically against a standard EDTA solution using xylenol orange as an indicator [33]. Carbon, hydrogen and nitrogen were analysed at the Sophisticated Analytical Instrument Facility (SAIF) of the Central Drug Research Institute (CDRI), Lucknow. The IR spectra of these complexes were recorded as Nujol mulls on a Perkin–Elmer 557 spectrophotometer in the range 4000–200 cm^{-1}. The ^{1}H and ^{13}C NMR spectra were recorded in $CDCl_3$ solutions on a Bruker DRX-300 spectrophotometer using TMS as an internal standard. The single crystal X-ray diffraction analysis was performed on a STOE IPDS (imaging plate system) diffractometer at 25 °C, using graphite-monochromated Mo Kα X-ray radiation ($\lambda = 0.71073$ Å). A suitable crystal, grown from a toluene–isopropyl alcohol solution, was sealed in a glass capillary under dry nitrogen atmosphere and mounted on the goniometer head. The data collection was performed at room temperature using the ω–θ scan technique. The crystal structure was solved by direct methods and refined by full-matrix least squares on F^2 using the SHELXS software package for crystal structure solution and refinement. All non-hydrogen atoms were refined with anisotropic thermal parameters in the later cycles of refinement. The hydrogen atoms were placed in idealized positions and refined using the riding model with general isotropic temperature factors. One of the crystals ($[C_6H_3(CH_3)S_2AsS_2CN(CH_2–CH_2)_2]$) showed gradual decay during measurements as inferred from the intensity of the diffraction data. The data collection was therefore performed only up to 22.50°.

2.2. Syntheses of complexes

2.2.1. Synthesis of toluene-3,4-dithiolatoarsenic(III) dimethyldithiocarbamate

A mixture of toluene-3,4-dithiolatoarsenic(III) chloride (0.59 g, 2.23 mmol) and sodium dimethyldithiocarbamate (0.40 g, 2.23 mmol) was refluxed in ~30 mL benzene for ~4 h. The precipitated sodium chloride (0.13 g) was filtered off. The solvent was removed from the filtrate under reduced pressure. The yellow solid compound thus obtained was crystallized in dichloromethane (Yield: 0.74 g, 95%).

2.2.2. Synthesis of toluene-3,4-dithiolatobismuth(III) diethyldithiocarbamate

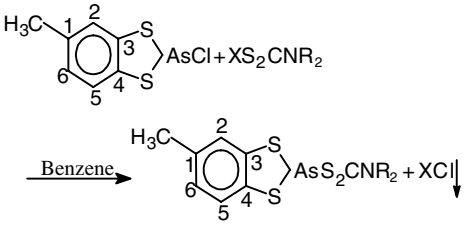
Toluene-3,4-dithiolatobismuth(III) chloride (0.34 g, 0.86 mmol) and sodium diethyldithiocarbamate (0.19 g, 0.86 mmol) in ~30 mL acetone were refluxed for ~4 h. The precipitated sodium chloride (0.05 g) was filtered off. The solvent was removed under reduced pressure from the filtrate, and the orange–red solid compound thus obtained was crystallized in acetone (Yield: 0.34 g, 77%).

The other derivatives were prepared by adopting the above methods. Pertinent analytical and physico-chemical data for these complexes are listed in Table 1.

3. Results and discussion

3.1. Synthesis of arsenic(III) complexes

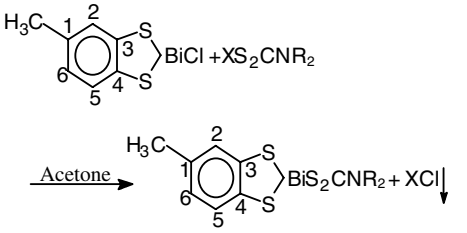
Toluene-3,4-dithiolatodialkyldithiocarbamate derivatives of arsenic(III) have been prepared by the reaction of toluene-3,4-dithiolatoarsenic(III) chloride with sodium/ammonium dialkyldithiocarbamates in 1:1 molar ratios in anhydrous benzene.



(where, R= CH_3,$C_2H_5$and CH_2-CH_2;X= Na and NH_4)

3.2. Synthesis of bismuth(III) complexes

The mixed-ligand toluene-3,4-dithiolatobismuth(III) dialkyldithiocarbamate derivatives were obtained by refluxing the mixture of toluene-3,4-dithiolatobismuth(III) chloride and sodium/ammonium dialkyldithiocarbamates in equimolar ratios in anhydrous acetone.



(where, R= CH_3,$C_2H_5$and CH_2-CH_2;X= Na and NH_4)

Table 1
Reactions of toluene-3,4-dithiolato chlorides of arsenic(III) and bismuth(III) with sodium/ammonium dialkyldithiocarbamates

S. No.	$C_6H_3(CH_3)S_2MCl$ M (g)	XS_2CNR_2X, R (g)	$C_6H_3(CH_3)S_2MS_2CNR_2$ colour (yield %)	XCl Found (calcd)	M.p. (°C)	Empirical formula (Formula weight)	Elemental analysis found/(calculated)				
							C	H	N	S	Metal As or Bi
1	As (0.59)	Na, CH_3 (0.40)	Yellow (95)	0.13 (0.13)	144	$C_{10}H_{12}NS_4As$ (349.40)	34.95 (34.37)	3.45 (3.46)	3.60 (4.00)	36.58 (36.70)	21.79 (21.44)
2	As (0.56)	Na, C_2H_5 (0.47)	Yellow (96)	0.12 (0.12)	103	$C_{12}H_{16}NS_4As$ (377.44)	38.14 (38.18)	4.65 (4.27)	3.37 (3.71)	33.79 (33.98)	19.77 (19.84)
3	As (0.57)	NH_4, CH_2–CH_2 (0.35)	Yellow (93)	0.11 (0.11)	116	$C_{12}H_{14}NS_4As$ (375.42)	38.73 (38.39)	4.07 (3.75)	3.57 (3.73)	34.05 (34.16)	19.99 (19.95)
4	Bi (0.51)	Na, CH_3 (0.23)	Orange–red (82)	0.07 (0.07)	121	$C_{10}H_{12}NS_4Bi$ (483.44)	24.58 (24.84)	2.30 (2.50)	2.71 (2.89)	26.32 (26.52)	43.35 (43.22)
5	Bi (0.34)	Na, C_2H_5 (0.19)	Orange–red (77)	0.05 (0.05)	86	$C_{12}H_{16}NS_4Bi$ (511.49)	28.30 (28.17)	2.84 (3.15)	3.06 (2.73)	24.99 (25.07)	40.52 (40.85)
6	Bi (0.46)	NH_4, CH_2–CH_2 (0.19)	Orange–red (81)	0.06 (0.06)	108	$C_{12}H_{14}NS_4Bi$ (509.48)	28.68 (28.29)	2.83 (2.76)	2.94 (2.74)	25.32 (25.17)	41.50 (41.01)

Derivatives of arsenic(III) (compounds **1**, **2** and **3** (Table 1)) are yellow crystalline solids and those of bismuth(III) (compounds **4**, **5** and **6** (Table 1)) are orange–red crystalline solids. These compounds are soluble in common organic solvents such as benzene, acetone, chloroform and dichloromethane. They tend to decompose in carbon tetrachloride.

3.3. ^1H NMR spectra

The ^1H NMR spectra of these compounds have been recorded in $CDCl_3$ solutions using TMS as internal standard. These compounds exhibit characteristic signals without any appreciable shifts from reported values [6,8,13,28].

In these compounds the protons on the ring C(2) appear as a single proton singlet in the region 6.90–7.21 ppm and those on the rings C(6) and C(5) appear as single proton doublets in the region 6.44–6.87 and 6.98–7.26 ppm, respectively. A sharp singlet corresponding to three protons appears in the region 2.21–2.28 ppm due to methyl protons on the ring. In addition, these compounds also show expected proton resonances due to alkyl protons of dithiocarbamate moieties [34,35] (Table 2). The dimethyldithiocarbamate derivatives (**1** and **4**) show a sharp singlet around 3.28–3.35 ppm due to the methyl protons thus suggesting the magnetic equivalence of these protons. The ethyl protons in the diethyldithocarbamate derivatives (**2** and **5**) appear as a triplet at 1.24–1.34 ppm and a quartet at 3.66–3.75 ppm due to methyl and *N*-methylene protons, respectively. The pyrrolidine dithiocarbamate derivatives (**3** and **6**) appear as multiplets in the region 1.97–2.08 and 3.66–3.86 ppm due to CH_2 and NCH_2 protons of the heterocyclic pyrrolidine ring, respectively.

3.4. ^{13}C NMR spectra

The proton decoupled ^{13}C NMR spectra of these compounds ($CDCl_3$) exhibit signals in the region 135.1–137.1, 137.5–139.2 and 141.1–142.8 ppm assignable to the resonances of ring carbon no. C (2,5,6); C (1) and C (3,4), respectively. A sharp signal is observed in the region 20.1–20.8 ppm due to ring the methyl carbon. A weak signal in the region 190.3–201.2 ppm is observed due to NCS_2 carbon atoms of the dithiocarbamate moieties. In addition, these derivatives also exhibit the expected signals due to *N*-alkyl carbons of the dithiocarbamate moieties [6,8] (Table 2). The dimethyldithiocarbamate derivatives (**1** and **4**) show a signal at 43.1–44.5 δ ppm for the methyl carbon. The ethyl carbon in diethyldithiocarbamate derivatives (**2** and **5**) appear as two signals one at 23.6–25.9 ppm due to the methyl group carbons and the other at 48.5–58.6 ppm due to the *N*-methylene carbons. The pyrrolidine dithiocarbamate derivatives (**3** and **6**) exhibit two signals

Table 2
^{1}H and ^{13}C NMR spectral data of toluene-3,4-dithiolato dialkyldithiocarbamates of arsenic(III) and bismuth(III)

S. No.	Compound	^{1}H Chemical shift (ppm)	^{13}C Chemical shift (ppm)
1	$[C_6H_3(CH_3)S_2AsS_2CN(CH_3)_2]$	2.28 (3H, s, ring CH_3) 3.35 (6H, s, CH_3N) 6.87 (1H, d (J = 8.1 Hz), ring-CH(6)) 7.21 (1H, s, ring-CH(2)) 7.26 (1H, d (J = 8.1 Hz), ring–CH(5))	20.6 (ring-CH_3) 43.1 (NCH_3) 135.1 (C-2,5,6) 138.1 (C-1) 141.7 (C-3,4) 197.6 (NCS_2)
2	$[C_6H_3(CH_3)S_2AsS_2CN(C_2H_5)_2]$	1.24 (6H, t (J = 6.5 Hz), CH_3) 2.28 (3H, s, ring-CH_3) 3.75 (4H, q (J = 6.5 Hz), CH_2N) 6.87 (1H, d (J = 8.1 Hz), ring-CH(6)) 7.21 (1H, s, ring-CH(2)) 7.26 (1H, d (J = 8.1 Hz), ring CH(5))	20.6 (ring CH_3) 23.6 (CH_3) 48.5 (NCH_2) 135.2 (C-2,5,6) 138.2 (C-1) 141.7 (C-3,4) 190.3 (NCS_2)
3	$[C_6H_3(CH_3)S_2AsS_2CN(CH_2–CH_2)_2]$	1.97–2.02 (4H, m, $CH_2–CH_2N$) 2.28 (3H, s, ring CH_3) 3.66–3.79 (4H, m, CH_2N) 6.87 (1H, d (J = 8.1 Hz), ring-CH(6)) 7.21 (1H, s, ring-CH(2)) 7.26 (1H, d (J = 8.1 Hz), ring CH(5))	20.6 (ring CH_3) 25.6 (CH_2) 52.8 (NCH_2) 135.1 (C-2,5,6) 137.5 (C-1) 141.1 (C-3,4) 191.4 (NCS_2)
4	$[C_6H_3(CH_3)S_2BiS_2CN(CH_3)_2]$	2.21 (3H, s, ring-CH_3) 3.28 (6H, s, CH_3N) 6.49 (1H, d (J = 8.7 Hz), ring-CH(6)) 6.90 (1H, s, ring-CH(2)) 6.98 (1H, d (J = 8.7 Hz), ring CH(5))	20.1 (ring-CH_3) 44.5 (NCH_3) 137.1 (C-2,5,6) 139.1 (C-1) 142.8 (C-3,4) 201.1 (NCS_2)
5	$[C_6H_3(CH_3)S_2BiS_2CN(C_2H_5)_2]$	1.34 (6H, t (J = 7.1 Hz), CH_3) 2.25 (3H, s, ring-CH_3) 3.66 (4H, q (J = 7.1 Hz), CH_2N) 6.44 (1H, d (J = 8.1 Hz), ring CH(6)) 6.96 (1H, s, ring-CH(2)) 7.03 (1H, d (J = 8.1 Hz), ring CH(5))	20.1 (ring CH_3) 25.9 (CH_3) 58.6 (NCH_2) 137.1 (C-2,5,6) 139.2 (C-1) 142.8 (C-3,4) 201.2 (NCS_2)
6	$[C_6H_3(CH_3)S_2BiS_2CN(CH_2–CH_2)_2]$	2.00–2.08 (4H, m, $CH_2–CH_2N$) 2.24 (3H, s, ring CH_3) 3.80–3.86 (4H, m, CH_2N) 6.50 (1H, d (J = 8.1 Hz), ring-CH(6)) 6.95 (1H, s, ring-CH(2)) 7.03 (1H, d (J = 8.1 Hz), ring CH(5))	20.8 (ring CH_3) 25.8 (CH_2) 54.2 (NCH_2) 137.0 (C-2,5,6) 139.2 (C-1) 142.8 (C-3,4) 201.0 (NCS_2)

s = singlet, d = doublet, q = quartet, sep = septet, m = multiplet.

around 25.6–25.8 and 52.8–54.2 ppm due to the CH_2 group and NCH_2 group carbons, respectively.

3.5. Crystal structure

The solid-state structures of two compounds, $[C_6H_3(CH_3)S_2AsS_2CN(CH_3)_2]$ and $[C_6H_3(CH_3)S_2AsS_2CN(CH_2–CH_2)_2]$ have been established by single crystal X-ray analysis, which revealed monomeric units in both cases.

3.6. Crystal structure of $[C_6H_3(CH_3)S_2AsS_2CN(CH_3)_2]$

The molecular structure of $[C_6H_3(CH_3)S_2AsS_2CN(CH_3)_2]$ is shown in Fig. 1 and selected interatomic parameters are collected in Table 3. The arsenic atom forms three close contacts, two to the toluene-3,4-dithiolato sulfur atoms at As(1)–S(5) (2.266 Å) and As(1)–S(2) (2.235 Å) and one to the dithiocarbamato sulfur atom

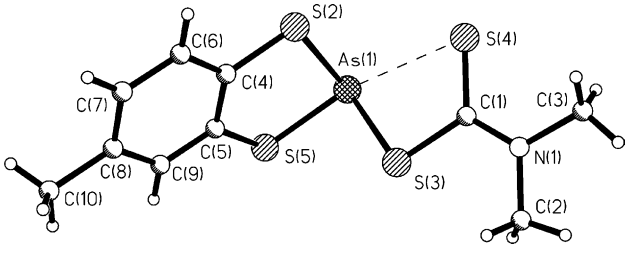


Fig. 1. Molecular structure of $[C_6H_3(CH_3)S_2AsS_2CN(CH_3)_2]$.

Table 3
Crystal data and refinement details for $[C_6H_3(CH_3)S_2AsS_2CN(R)_2]$, R = CH_3 and CH_2–CH_2

Compound	$[C_6H_3(CH_3)S_2AsS_2CN(CH_3)_2]$	$[C_6H_3(CH_3)S_2AsS_2CN(CH_2–CH_2)_2]$
Formula	$C_{10}H_{12}AsNS_4$	$C_{12}H_{14}AsNS_4$
Formula weight	349.37	375.40
Crystal system	triclinic	monoclinic
Space group	$P\bar{1}$	$P2_{(1)}/c$
a (Å)	9.108(2)	16.034(3)
b (Å)	9.312(2)	7.774(2)
c (Å)	9.650(2)	12.354(2)
α (°)	80.98(3)	90
β (°)	61.91(3)	91.25(3)
γ (°)	77.22(3)	90
V (A^3)	702.8(3)	1539.5(5)
Z	2	4
Crystal size (mm)	$0.44 \times 0.32 \times 0.28$	$0.34 \times 0.29 \times 0.17$
D_c ($Mg m^{-3}$)	1.651	1.620
$F(000)$	352	760
Reflection collected	2477	2013
θ max (°)	2.25–25.00	2.54–22.49
Maximum and minimum transmission	0.9972 and 0.4706	0.98 and 0.63
Final R indices [$I > 2\sigma(I)$]	$R_1 = 0.0356$	$R_1 = 0.0687$
	$wR_2 = 0.0923$	$wR_2 = 0.1627$
R indices (all data)	$R_1 = 0.0414$	$R_1 = 0.0885$
	$wR_2 = 0.0973$	$wR_2 = 0.1798$
Residual ρ_{max} (e$Å^3$)	0.749	0.897
Residual ρ_{min} (e$Å^3$)	−0.426	−0.780

Table 4
Selected bond distances (Å) and angles (°) for $[C_6H_3(CH_3)S_2AsS_2CN(R)_2]$, R = CH_3 and CH_2–CH_2

$[C_6H_3(CH_3)S_2AsS_2CN(CH_3)_2]$		$[C_6H_3(CH_3)S_2AsS_2CN(CH_2–CH_2)_2]$	
Bond distances			
As(1)–S(2)	2.2345(13)	As–S(3)	2.233(3)
As(1)–S(5)	2.2663(14)	As–S(4)	2.279(3)
As(1)–S(3)	2.2983(12)	As–S(1)	2.276(2)
S(2)–C(4)	1.761(4)	S(3)–C(7)	1.756(9)
S(3)–C(1)	1.767(4)	S(1)–C(1)	1.768(7)
S(4)–C(1)	1.689(4)	S(2)–C(1)	1.697(7)
S(5)–C(5)	1.777(4)	S(4)–C(6)	1.754(10)
N(1)–C(1)	1.317(5)	N–C(1)	1.302(9)
N(1)–C(3)	1.471(5)	N–C(5)	1.472(10)
N(1)–C(2)	1.479(5)	N–C(2)	1.478(9)
Bond angles			
S(2)–As(1)–S(5)	91.36(5)	S(3)–As–S(4)	90.98(10)
S(2)–As(1)–S(3)	103.23(4)	S(3)–As–S(1)	103.62(9)
S(5)–As(1)–S(3)	93.79(5)	S(1)–As–S(4)	92.03(10)
C(4)–S(2)–As(1)	102.05(13)	C(7)–S(3)–As	101.3(3)
C(1)–S(3)–As(1)	96.40(13)	C(1)–S(1)–As	95.6(2)
C(5)–S(5)–As(1)	100.76(13)	C(6)–S(4)–As	100.5(3)
C(1)–N(1)–C(3)	121.3(3)	C(1)–N–C(5)	124.0(6)
C(1)–N(1)–C(2)	122.0(3)	C(1)–N–C(2)	125.4(6)
C(3)–N(1)–C(2)	116.7(3)	C(5)–N–C(2)	110.6(6)
N(1)–C(1)–S(4)	124.0(3)	N–C(1)–S(2)	124.6(6)
N(1)–C(1)–S(3)	116.8(3)	N–C(1)–S(1)	116.8(5)
S(4)–C(1)–S(3)	119.1(2)	S(2)–C(1)–S(1)	118.6(4)

As(1)–S(3) (2.298 Å). If these close contacts were considered to define the coordination geometry, the dithiocarbamate ligand behaves in a monodentate fashion. Considering the observed As–S interactions, the environment about the arsenic atom would be best described as pyramidal with the lone pair of electrons being stereochemically active, but with non-equivalent S–As–S bond angles (91.36(5)°, 93.79(5)° and 103.23(4)°) (Table 4)

[26]. The remaining sulfur atom (S(4)) is in proximity to the arsenic atom with an As ··· S(4) distance of 2.984 Å. This interaction is possibly responsible for the observed distortion from the ideal pyramidal geometry. This distance is significantly shorter than the sum of the van der Waal's radii of arsenic and sulfur (3.74 Å). Based on the relationship between bond order and bond distances suggested by Pauling [36], the As ··· S distances correspond to a bond order of 0.0532 for As–S(4) suggesting the interactions to be rather weak.

It is noticeable that in dithiocarbamate ligands the C–S bond associated with the strong As–S bonds is significantly longer (1.767(4) Å) than that associated with the weaker As ··· S bond (1.689(4) Å), showing clearly the localization of the double bond. The disparity in the associated C–S distances indicate that the As ··· S interaction present would be weak [22]. A remarkable feature concerns the N–C–S angles of the two sets of N–C–S angles (viz. 124.0(3)° and 116.8(3)°), the larger value is as expected owing to the mutual repulsion between the double bond and the adjacent electronegative "N" atom [22]. Similar coordination behaviour of dithiocarbamate ligands towards arsenic was also found in (i) [$RAsS_2CNEt_2$], R = Me and Ph [21], As–S = 2.344–2.323 Å and As ··· S = 2.943–2.840 Å, (ii) [$As\{S_2CNEt_2\}_3$], As–S = 2.34(9) Å and As ··· S = 2.84(9) Å [23], (iii) [$As\{S_2CN(Me)CH_2–CH_2OH\}_3$], As–S = 2.320(3) Å and As ··· S = 2.927(2) Å [24], (iv) [$As\{S_2CN(CH_2–CH_2OH)_2\}_3$], As–S = 2.34(2) Å and As ··· S = 2.84(2) Å [22].

3.7. Crystal structure of $[C_6H_3(CH_3)S_2AsS_2CN(CH_2–CH_2)_2]$

The coordination environment of the arsenic atom (Fig. 2) in $[C_6H_3(CH_3)S_2AsS_2CN(CH_2–CH_2)_2]$ is similar to that described for $[C_6H_3(CH_3)S_2AsS_2CN(CH_3)_2]$. The selected interatomic parameters are listed in Table 3. The arsenic atom is coordinated by the two sulfur atoms of the toluene-3,4-dithiol group and one sulfur atom derived from the dithiocarbamate ligand. The As–S(3) and As–S(4) separations of 2.233(3) and 2.279(3) Å, respectively, are equivalent to As(1)–S(2) and As(1)–S(5) distances observed in $[C_6H_3(CH_3)S_2AsS_2CN(CH_3)_2]$ (Table 4). Similarly, the As–S(1) and As–S(2) separations of 2.276(2) and 2.931 Å, respectively, are comparable to the As(1)–S(3) and As(1)–S(4) contacts found in the $[C_6H_3(CH_3)S_2AsS_2CN(CH_3)_2]$. The bonding situation suggests that substitution of the nitrogen-bound CH_2 groups of the pyrrolidine moiety, does not have any profound influence on the coordination geometry about the arsenic atom. The non-equivalent S–As–S angles (90.98(10)°, 103.62(9)° and 92.03(10)°) indicate a distorted pyramidal geometry about the central arsenic atom.

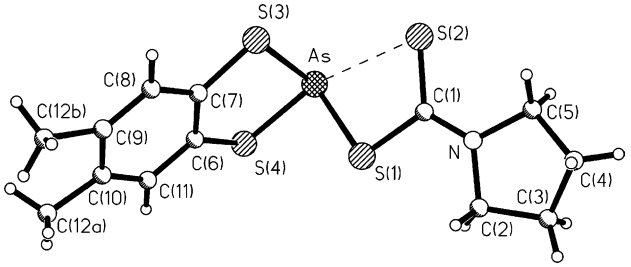


Fig. 2. Molecular structure of $[C_6H_3(CH_3)S_2AsS_2CN(CH_2–CH_2)_2]$.

3.8. Infrared spectra

These newly synthesized compounds show medium to strong intensity bands in the regions 920–1030 and 1442–1480 cm^{-1} due to C---S and C---N stretching vibrations, respectively. The bands of weak intensities at 310–320 and 340–360 cm^{-1} are due to As–S and Bi–S stretching vibrations, respectively. The characteristic bands observed in the region 680–695 cm^{-1} may be attributed to an asymmetric tri-substituted benzene ring [6,28].

4. Supplementary materials

Crystallographic data, tables of atomic coordinates, thermal parameters, bond lengths and bond angles of the structures have been deposited with the Cambridge Crystallographic Data Center, with the deposition numbers: CCDC 245175 and 245176. Copies of this information are available free of charge from the Director, CCDC, 12 Union Road, Cambridge, CB2 1EZ, UK (Fax: +44 1223 336 033; e-mail: deposit@ccdc.cam.ac.uk or http://www.ccdc.cam.ac.uk).

Acknowledgements

Financial assistance from UGC, New Delhi is gratefully acknowledged. The elemental analyses (C, H and N) and spectral (IR, ^1H and ^{13}C NMR) data were recorded at the Sophisticated Analytical Instrument Facility (SAIF), Central Drug Research Institute (CDRI), Lucknow.

References

[1] D. Coucouvanis, Prog. Inorg. Chem. 11 (1970) 233.
[2] D. Coucouvanis, Prog. Inorg. Chem. 22 (1979) 301.
[3] G.E. Manoussakis, M. Lalia-Kantouri, R.B. Huff, J. Inorg. Nucl. Chem. 37 (1975) 2330.
[4] G.E. Manoussakis, C.A. Tsipis, A.G. Christophides, Z. Anorg. Allg. Chem. 417 (1975) 235.
[5] C.L. Raston, A.H. White, J. Chem. Soc., Dalton Trans. 791 (1976).

[6] S. Chourasia, B. Nahar, H.P.S. Chauhan, Phosphorus, Sulfur Silicon 119 (1996) 77.
[7] H.P.S. Chauhan, B. Nahar, Phosphorus, Sulfur Silicon 128 (1997) 119.
[8] H.P.S. Chauhan, S. Chourasia, B. Nahar, R.K. Singh, Phosphorus, Sulfur Silicon 134/135 (1999) 345.
[9] H.P.S. Chauhan, B. Nahar, R.K. Singh, Synth. React. Inorg. Met-Org. Chem. 28 (9) (1998) 1541.
[10] H.P.S. Chauhan, R.K. Singh, Kavita Kori, Main Group Metal Chem. 25 (8) (2002) 511.
[11] R. Cea-Olivares, R.A. Toscano, M. Lopez, P. Garcia, Monatsh Chem. 124 (1993) 177.
[12] R. Cea-Olivares, R.A. Toscano, M. Lopez, P. Garcia, Heteroatom Chem. 4 (1993) 313.
[13] R. Cea-Olivares, R.A. Toscano, C. Silvestru, P. Garcia, M.L. Cardoso, G.B. Amador, H. Noth, J. Organomet. Chem. 493 (1995) 61.
[14] C.A. Tsipis, G.E. Manoussakis, Inorg. Chem. Acta 18 (1976) 35.
[15] H.P.S. Chauhan, Coord. Chem. Rev. 173 (1998) 1.
[16] S.L. Lawton, C.J. Fuhrmeister, R.G. Hass, C.S. Jarman, F.G. Lothmeyer, Inorg. Chem. 13 (1974) 135.
[17] M. Wieber, M. Schroff, Phosphorus, Sulfur Silicon 102 (1995) 265.
[18] H.P.S. Chauhan, G. Srivastava, R.C. Mehrotra, Phosphorus, Sulfur Silicon 17 (1983) 161.
[19] H.P.S. Chauhan, G. Srivastava, R.C. Mehrotra, Polyhedron 3 (1984) 1337.
[20] R. Bohra, H.P.S. Chauhan, G. Srivastava, R.C. Mehrotra, Phosphorus, Sulfur Silicon 60 (1991) 167.
[21] S.S. Garje, V.K. Jain, E.R.T. Tiekink, J. Organomet. Chem. 538 (1997) 129.
[22] V. Venkatachalam, K. Ramalingam, U. Casellato, R. Grazian, Polyhedron 16 (1997) 1211.
[23] C.L. Raston, A.H. White, J. Chem. Soc., Dalton Trans. 2425 (1975).
[24] V. Venkatachalam, K. Ramalingam, T.C.W. Mak, B.S. Luo, J. Chem. Crystallorg. 26 (1996) 467.
[25] R. Karra, Y.P. Singh, R. Bohara, A.K. Rai, J. Cryst. Spectrosc. Res. 22 (1992) 721.
[26] R.K. Gupta, A.K. Rai, R.C. Mehrotra, V.K. Jain, B.F. Hoskins, E.R.T. Tiekink, Inorg. Chem. 24 (1985) 3280.
[27] E.R.T. Tiekink, Main Group Metal Chem. 15 (1992) 161.
[28] H.P.S. Chauhan, B. Porwal, R.K. Singh, Phosphorus, Sulfur Silicon 160 (2000) 93.
[29] H.P.S. Chauhan, B. Porwal, R.K. Singh, Indian J. Chem. A 39 (2000) 880.
[30] J.A. Riddick, W.B. Bunger, Techniques of Chemistry, Organic Solvents, vol. 2, Wiley Interscience, New York, 1970.
[31] Practical Organic Chemistry textbook of Vogel's Edition, Addison Wesley Longman (First ISE Reprint), 1998.
[32] H.P.S. Chauhan, G. Srivastava, R.C. Mehrotra, Polyhedron 2 (1983) 359.
[33] A.I. Vogel, Quantitative Inorganic Analysis, 3rd ed., Longman, London, 1961.
[34] C.P. Sharma, N. Kumar, M.C. Khandpal, S. Sharma, V.G. Bhinde, J. Inorg. Nucl. Chem. 43 (1981) 923.
[35] R. Nomura, A. Takabe, H. Matsuda, Polyhedron 6 (1987) 411.
[36] L. Pauling, The Nature of Chemical Bond, 3rd ed., Cornell University Press, Ithaca, NY, 1960.

Available online at www.sciencedirect.com
SCIENCE DIRECT®
Polyhedron 24 (2005) 97–111
POLYHEDRON
www.elsevier.com/locate/poly

The inside and outside protonation of a 15-membered O_2N_2-macrocycle. Synthesis and structural characterization of the protonated ligand salts

Ljerka Tušek-Božić [a,*], Aleksandar Višnjevac [a,*], Ester Marotta [b,1], Biserka Kojić-Prodić [a]

[a] Division of Physical Chemistry, Ruđer Bošković Institute, P.O. Box 180, Bijenička 54, HR-10002 Zagreb, Croatia
[b] CNR, Istituto di Scienze e Tecnologie Molecolari, Sezione di Padova, Corso Stati Uniti 4, 35100 Padova, Italy

Received 23 September 2004; accepted 15 October 2004

Abstract

Reactions of a mixed dioxa-diaza macrocycle 5,6,14,15-dibenzo-1,4-dioxa-8,12-diazacyclopentadeca-5,14-diene (**L**) and various sodium salts NaX (X = picrate, ClO_4, BF_4, PF_6, SCN and BPh_4) in methanol afford the ion-pair compounds containing the protonated macrocyclic ligand as the cation, with the anion from the sodium salt as a counterion. The new compounds were identified and characterized on the basis of elemental analysis, spectroscopic studies (IR, ^{1}H NMR and MS), conductivity data and X-ray structure analysis. The mode of ligand protonation, as well as the hydrogen bond network which stabilizes the binding site of the proton in the protonated macrocyclic species, depend on the sodium salt used. It was found that the proton-to-ligand ratio is 1:1 in the picrate salt (**1**), 1:2 in the perchlorate (**2**), tetrafluoroborate (**3**), hexafluorophosphate (**4**) and thiocyanate (**5**) salts, and 2:3 in the tetraphenylborate salt (**6**), which was converted by recrystallization in acetonitrile into the 1:1 salt (**7**). In the 1:1 proton:ligand compounds, [H(**L**)]X, the intraligand monoprotonation occurs in two modes: the proton is either bound to one of the nitrogen atoms (**1**) or is disordered between two nitrogen atoms (**7**). In the compounds with 1:2, $[H(\mathbf{L})_2]X$, and 2:3, $[H_2(\mathbf{L})_3](X)_2$, proton-to-ligand ratios, there is interligand protonation where one proton is located between nitrogen atoms from two macrocyclic molecules (**2**–**5**) or two protons are shared between nitrogens from three ligand moieties (**6**). Crystallographic and infrared spectroscopic data indicate some differences in location of the proton between the nitrogen atoms in the monoprotonated ligand salts **2**–**5**.
© 2004 Elsevier Ltd. All rights reserved.

Keywords: Dioxa-diaza macrocycle; Protonation; Spectroscopy; Crystal structures; Hydrogen bonding

1. Introduction

The chemistry of oxygen–nitrogen mixed-donor macrocycles has attracted continuous attention due to their ability to bind selectively different chemical species. With an appropriate combination of the macrocyclic cavity size, shape and topology, substituent effects as well as the number, type and arrangement of donor atoms, these polydentate ligands are able to bind a wider variety of both cations and anions than single heteroatom ligands such as oxygen-containing or nitrogen-containing macrocycles [1,2]. Although these ligands favour transition and post-transition metal ions [3–7], the selected derivatives also form complexes with alkali [8], alkaline earth [9] and lanthanide cations [10], as well as with ammonium [2,11] and oxonium [12]

* Corresponding authors. Tel.: +385 1 4571217; fax: +385 1 4680245 (L. Tušek-Božić), Tel.: +385 1 4571203; fax: +385 1 4680245 (A. Višnjevac).
E-mail addresses: tusek@rudjer.irb.hr (L. Tušek-Božić), aleksandar.visnjevac@irb.hr (A. Višnjevac).
[1] Present address: CNR, INTM, Sezione di Padova, Dipartimento di Scienze Chimiche, Università di Padova, Via Marzolo 1, 35131 Padova, Italy.

0277-5387/$ - see front matter © 2004 Elsevier Ltd. All rights reserved.
doi:10.1016/j.poly.2004.10.013

ions. In the case of the interaction with some anionic and neutral organic and biological substrates, supramolecular compounds of specific properties and applications were prepared [12,13]. The presence of basic amino sites in the macrocyclic molecule also enables diffusion of a proton inside the molecular cavity, followed by ligand protonation and formation of the protonated derivatives [14–16]. In general, the proton transfer reaction is of great importance in chemistry and biology. It plays a fundamental role in numerous processes including acid–base neutralization and electrophilic addition, and it is involved in transport phenomena, photosynthesis, enzyme reactions, etc. [17]. In general, the problem of proton transfer is important but very complex and far from resolution although there is significant progress due to the application of new theoretical methods using powerful computers [18] and experimental findings on ultrafast reactions involving proton transfers that are induced by lasers [19]. The proton transfer properties of macrocyclic compounds are connected with the number of amino groups in the molecular skeleton, their type (secondary and tertiary) and nature (aliphatic and aromatic), the length of the linkers, the presence of different donor groups in the ligand frame as well as the flexibility/rigidity and the overall structure of the macrocyclic molecule [15]. In addition, the protonated macrocycles can interact with simple as well as with more complex inorganic and organic anions, and their complexation properties are based on the solvation and hydrogen bonding capabilities of both the protonated moiety and the accompanying anion.

In the present work, we investigate the protonation behaviour of 5,6,14,15-dibenzo-1,4-dioxa-8,12-diazacyclopentadeca-5,14-diene (**L**) in the interaction with various sodium salts in methanol solution, since it was shown that this dioxa-diaza macrocycle forms the protonated species and does not bind the sodium ion in these reactions. In general, protonation of aza macrocycles would be expected in acidic medium. Thus, the dihydronitrate salt $[H_2(\mathbf{L})](NO_3)_2$ was obtained by the hydrogenation with sodium tetrahydroborate of the structurally related macrocyclic diimine, which was used as a precursor for the synthesis of **L**, and the successive reaction with HNO_3 in a methanol–water solution [16]. In previous studies, it was demonstrated that this mixed-donor ligand binds some transition metal ions in reactions with the corresponding metal salts in methanol solution. Complexes of the type $M(\mathbf{L})X_2$, where M = Ni, Co, Zn or Cd; X = Cl, Br, I or NCS, were synthesized and examined [4,5,20,21]. Interactions between **L** and alkali metal ions have not been studied yet. We report here the preparation and structural characterization of the protonated ligand salts obtained by reactions of this 15-membered macrocycle with a series of sodium salts.

2. Experimental

2.1. Materials and instrumentation

5,6,14,15-Dibenzo-1,4-dioxa-8,12-diazacyclopentadeca-5,14-diene (**L**) was used directly as supplied (Aldrich). Sodium perchlorate, tetrafluoroborate, hexafluorophosphate, tetraphenylborate and thiocyanate salts were commercial chemicals of the highest purity available and used without further purification except for vacuum drying over P_4O_{10} and storing in a dry-box prior to use. Sodium picrate was prepared and purified as described. Solvents used (AR grade) were purified and dried by standard procedures.

Melting points were determined on a hot stage microscope and are uncorrected. FTIR spectra were recorded on an ABB Bomen MB102 spectrometer using KBr pellets. ESI mass measurements were performed on a Finnigan LCQ DECA instrument (ThermoFinnigan, Palo Alto, CA) operating in the positive ion mode. Compounds were dissolved in methanol or acetonitrile (10^{-6} M solutions) and directly injected by a syringe pump at a flow of 5 μL min^{-1}. LDI mass spectra were performed on a Voyager-DE PRO instrument (Applied Biosystems, Foster City, CA), operating in the linear positive ion mode. External mass calibration was done using the Calibration Mixture 1 of Sequazyme Peptide Mass Standards Kit, based on the monoisotopic values of $[M + H]^+$ of des-arg-bradykinin, angiotensin, glu-fibrinopeptide B and neurotensin at *m/z* 905, 1297, 1571 and 1673, respectively. The ^1H NMR spectra were recorded with Varian 300 Gemini and Bruker XWIN-600 Fourier-transform spectrometers in DMSO-d_6 at 300 K. Chemical shifts were referred to the residual solvent signal at 2.51 ppm. The two-dimensional experiments were performed by standard pulse sequences, using Gemini Data System software Version 6.3 Revision A and Bruker XWIN-NMR software Version 3.5. Conductance measurements were carried out at room temperature using a CD 7A Tacussel conductance bridge for 10^{-3} mol^{-1} solutions in DMF. Elemental analyses (CHNS) were performed on a Perkin–Elmer Analyser PE 2400 Series 2 and thermogravimetric analyses with a Cahn RG electromicrobalance in air atmosphere.

2.2. Preparations of the compounds

2.2.1. *[H(**L**)](picrate) (**1**)*

A mixture of 5,6,14,15-dibenzo-1,4-dioxa-8,12-diazacyclopentadeca-5,14-diene (**L**) (0.110 g, 0.35 mmol) and sodium picrate (0.108 g, 0.40 mmol) in dry MeOH (10 cm^3) was refluxed for 1–2 h with continuous stirring. The yellow-orange microcrystalline product, which precipitated immediately after cooling to room temperature was collected by filtration, washed with cold MeOH,

and dried overnight in vacuo under P_4O_{10}. Yield: 0.172 g, 91%; m.p. 205–207 °C. *Anal.* Calc. for $C_{25}H_{27}N_5O_9$: C, 55.65; H, 5.03; N, 12.93. Found: C, 55.55; H, 5.02; N, 12.68%. Molar conductance Λ_M (DMF, 22 °C) 56.3 S cm^2 mol^{-1}. Selected IR data (KBr, cm^{-1}) 3297 s [ν(NH)], 2812 m–s br [$\nu(NH_2^+)$], 1634 s, 1621 m, 1590 s, 1562 s and 1552 s [ν(C═C), $\nu_{as}(NO_2)$, δ(NH), $\delta(NH_2^+)$], 1309 vs [$\nu_s(NO_2)$], 1264 s br and 1249 vs [ν_s(ArCOC), ν(CNC)], 949 m–s, 924 m–s and 913 w [$\omega,\tau,\rho(CH_2)$, ν(aliphCC)], 762 s, 753 m–s, 734 w and 712 m [δ(NH) and δ(ArCH) out-of-plane, $\gamma(NO_2)$]. ^{1}H NMR (300 MHz, DMSO-d$_6$, δ ppm) 1.73 (2H, m, CH_2-CH_2-CH_2), 2.82 (4H, t, J = 5.1 Hz, NH-CH_2-CH_2), 3.41 (3H, br s, NH, NH_2^+), 3.84 (4H, s, Ar–CH_2–NH), 4.41 (4H, s, O-CH_2), 6.95 (2H, t, J = 7.4 Hz, ArH-c), 7.08 (2H, d, J = 8.1 Hz, ArH-a), 7.29 (2H, d, J = 6.0 Hz, ArH-d), 7.36 (2H, t, J = 8.0 Hz, ArH-b), 8.59 (2H, s, ArH-picrate). MS (+ ESI, MeCN) m/z 313 ([LH]$^+$, 100%). MS (+LDI) m/z 542 ([MH]$^+$, 3%), 313 ([LH]$^+$, 100%). Crystals for X-ray analysis were obtained by very slow overnight cooling of the methanolic reaction solution to room temperature. Single crystals of **1** were also grown from acetonitrile solution.

2.2.2. *[H(**L**)$_2$]ClO$_4$ (**2**)*

A mixture of **L** (0.105 g, 0.34 mmol) and $NaClO_4$ (0.022 g, 0.18 mmol) in dry MeOH (5 cm^3) was stirred at ca. 50 °C for 6 h. The solution was allowed to stand for 6 days at 4 °C and the crystalline solid was isolated by filtration, washed with cold MeOH, and dried in vacuo over P_4O_{10}. A certain amount of single crystals were grown from the mother liquor. Although no problems were encountered in the preparation of this compound, a precaution should be taken when handling such potentially hazardous compounds. Yield: 0.088 g, 71%; m.p. 198–201 °C. *Anal.* Calc. for $C_{38}H_{49}ClN_4O_8$: C, 62.93; H, 6.81; N, 7.73. Found: C, 62.71; H, 6.82; N, 7.69%. Molar conductance Λ_M (DMF, 22 °C) 71.7 S cm^2 mol^{-1}. Selected IR data (KBr, cm^{-1}) 3337 w–m, 3328 w–m and 3183 m–s [ν(NH)], 2600–1900 w–m br [ν(HN···H$^+$)], 1634 w [δ(NH)], 1601s and 1592 s [ν(C═C)], 1248 s br [ν_{as}(ArCOC), ν(CNC)], 1087 s br [$\nu_{as}(ClO_4^-)$], 982 m, 942 m and 914 m [$\omega,\tau,\rho(CH_2)$, ν(aliphCC)], 762 s and 732 m [δ(NH) and δ(ArCH) out of plane], 622s [$\nu_s(ClO_4^-)$]. ^{1}H NMR (300 MHz, DMSO-d$_6$, δ ppm) 1.64 (4H, m, CH_2-CH_2-CH_2), 2.67 (8H, t, J = 5.4 Hz, NH-CH_2-CH_2), 3.72 (8H, s, Ar-CH_2-NH), 4.38 (8H, s, O-CH_2), 5.13 (5H, br s, NH, NH_2^+), 6.92 (4H, t, J = 7.4 Hz, ArH-c), 7.05 (4H, d, J = 8.3 Hz, ArH-a), 7.23 (4H, d, J = 6.6 Hz, ArH-d), 7.31 (4H, t, J = 7.7 Hz, ArH-b). MS (+ ESI, MeOH) m/z 313 ([LH]$^+$, 100%); MS (+ LDI) m/z 625 ([L$_2$H]$^+$, 10%), 313 ([LH]$^+$, 100%).

2.2.3. *[H(**L**)$_2$]BF$_4$ (**3**)*

A mixture of **L** (0.115 g, 0.37 mmol) and $NaBF_4$ (0.022 g, 0.20 mmol) was refluxed for 3 h in dry MeOH (10 cm^3). The rod-like single crystals, gradually grown on cooling over a few days at 4 °C, were collected after removing the solvent with a syringe, washed with cold MeOH, and dried under reduced pressure. Yield: 0.101 g, 77%; m.p. 196–197 °C. *Anal.* Calc. for $C_{38}H_{49}BF_4N_4O_4$: C, 64.04; H, 6.93; N, 7.86%. Found: C, 64.15; H, 6.79; N, 7.68%. Molar conductance Λ_M (DMF, 22 °C) 74.4 S cm^2 mol^{-1}. Selected IR data (KBr, cm^{-1}) 3339 m, 3331 sh and 3185 m [ν(NH)], 2600–1900 w–m br [ν(HN···H$^+$)], 1636 w [δ(NH)], 1601 s and 1592 s [ν(C═C)], 1233 s br [ν_{as}(ArCOC), ν(CNC)], 1073 s vbr [$\nu_{as}(BF_4^-)$], 985 m, 941 s and 916 m [$\omega,\tau,\rho(CH_2)$, ν(aliph(CC))], 760 vs and 731 s [$\nu_s(BF_4^-)$, δ (NH) and δ(ArCH) out of plane]. ^{1}H NMR (300 MHz, DMSO-d$_6$, δ ppm) 1.61 (4H, m, CH_2-CH_2-CH_2), 2.63 (8H, br s, NH-CH_2-CH_2), 3.69 (8H, s, Ar-CH_2-NH), 4.20 (5H, br s, NH, NH_2^+), 4.35 (8H, s, O-CH_2), 6.90 (4H, t, J = 7.1 Hz, ArH-c), 7.03 (4H, d, J = 8.1 Hz, ArH-a), 7.21 (4H, d, J = 7.0 Hz, ArH-d), 7.29 (4H, t, J = 7.6 Hz, ArH-b). MS (+ ESI, MeOH) m/z 313 ([LH]$^+$, 100%). MS (+ LDI) m/z 625 ([L$_2$H]$^+$, 5%), 313 ([LH]$^+$, 100%).

2.2.4. *[H(**L**)$_2$]PF$_6$ (**4**)*

A mixture of **L** (0.121 g, 0.39 mmol) and $NaPF_6\cdot H_2O$ (0.040 g, 0.22 mmol) in dry MeOH (5 cm^3) was refluxed for 8 h with vigorous stirring. The filtered solution was subjected to slow evaporation, first overnight at room temperature then at 4 °C for two days. The solvent was removed with a syringe and the remaining white single crystals were washed with cold MeOH, and dried under reduced pressure over P_4O_{10} at room temperature. Yield: 0.122 g, 82%; m.p. 208–210 °C. *Anal.* Calc. for: $C_{38}H_{49}F_6N_4O_4P$: C, 59.21; H, 6.41; N, 7.27. Found: C, 59.33; H, 6.48; N, 7.31%. Molar conductance Λ_M (DMF, 22 °C) 66.2 S cm^2 mol^{-1}. Selected IR data (KBr, cm^{-1}) 3338 w–m and 3184 w–m [ν(NH)], 2600–2000 w–m br [ν(HN···H$^+$)], 1654 w [δ(NH)], 1601 s and 1591 s [ν(C═C)], 1249 m–s br [ν_{as}(ArCOC), ν(CNC)], 986 w, 937 s and 918 m [$\omega,\tau,\rho(CH_2)$, ν(aliphCC)], 830 s br [$\nu_{as}(PF_6^-)$], 759 s and 735 s [δ(NH) and δ(ArCH) out of plane], 557 s [$\nu_s(PF_6^-)$]. ^{1}H NMR (300 MHz, DMSO-d$_6$, δ ppm) 1.63 (4H, m, CH_2-CH_2-CH_2), 2.67 (8H, t, J = 5.2 Hz, NH-CH_2-CH_2), 3.72 (8H, s, Ar-CH_2-NH), 4.03 (5H, br s, NH, NH_2^+), 4.31 (8H, s, O-CH_2), 6.92 (4H, t, J = 7.3 Hz, ArH-c), 7.05 (4H, d, J = 8.0 Hz, ArH-a), 7.23 (4H, d, J = 7.3 Hz, ArH-d), 7.31 (4H, t, J = 7.8 Hz, ArH-b). MS (+ ESI, MeCN) m/z 625 ([L$_2$H]$^+$, 4%), 313 ([LH]$^+$, 100%); MS (+ LDI) m/z 313 ([LH]$^+$, 100%).

*2.2.5. [H(**L**)$_2$]SCN (**5**)*

A mixture of **L** (0.118 g, 0.38 mmol) and NaSCN (0.018 g, 0.22 mmol) in dry MeOH (5 cm^3) was refluxed for 5 h with continuous stirring under a stream of nitrogen. The clear solution was filtered hot and allowed to stand first overnight at 4 °C and then at −10 °C for two weeks. The crystalline precipitate that gradually formed during that time was filtered off, washed with a minimum of ice-cold MeOH, and dried in a desicator under reduced pressure over P_4O_{10}. Yield: 0.085 g, 66%; m.p. 180–181 °C. *Anal.* Calc. for $C_{39}H_{49}N_5O_4S$: C, 68.49; H, 7.22; N, 10.24; S, 4.69. Found: C, 68.72; H, 7.32; N, 10.34; S, 4.80%. Molar conductance Λ_M (DMF, 22 °C) 72.7 S cm^2 mol^{-1}. Selected IR data (KBr, cm^{-1}) 3339 w, 3330 vw and 3183 w–m [ν(NH)], 2600–2100 w br [ν(HN···H$^+$)], 2057 s [ν(SCN$^-$)], 1649 w [δ(NH)], 1599 s and 1587 m [ν(C=C)], 1245 s and 1239 sh [ν_{as}(ArCOC), ν(CNC)], 978 w–m, 937 s and 920 sh [ω,τ,ρ(CH$_2$), ν(aliphCC)], 761 vs and 732 m–s [δ(NH) and δ(ArCH) out of plane]. ^{1}H NMR (300 MHz, DMSO-d$_6$, δ ppm) 1.63 (4H, m, CH$_2$-C*H*$_2$-CH$_2$), 2.65 (8H, s br, NH-C*H*$_2$-CH$_2$), 3.45 (5H, br s, NH, NH$_2^+$), 3.71 (8H, s, Ar-C*H*$_2$-NH), 4.37 (8H, s, O-C*H*$_2$), 6.91 (4H, t, J = 7.3 Hz, Ar*H*-c), 7.05 (4H, d, J = 7.8 Hz, Ar*H*-a), 7.22 (4H, d, J = 7.5 Hz, Ar*H*-d), 7.30 (4H, t, J = 7.7 Hz, Ar*H*-b). MS (+ESI, MeCN) *m/z* 625 ([L$_2$H]$^+$, 1%), 313 ([LH]$^+$, 100%); MS (+ LDI) *m/z* 313 ([HL]$^+$, 100%). Good quality crystals were grown by very slow evaporation from MeCN solution in a desicator over silica gel.

*2.2.6. [H$_2$(**L**)$_3$](BPh$_4$)$_2$ (**6**)*

An equimolar amount of **L** (0.101 g, 0.32 mmol) and NaBPh$_4$ (0.111 g, 0.32 mmol) was dissolved in dry MeOH (10 cm^3) and refluxed for 6 h with continuous stirring. Solvent was partly removed from the filtered solution to give, on gradual cooling at 4 °C, a pale-ochre precipitate. The crystalline compound was filtered off, washed with cold MeOH and dried in vacuo over P_4O_{10}. Yield: 0.145 g, 85%; m.p. 150–151 °C. *Anal.* Calc. for $C_{105}H_{114}B_2N_6O_6$: C, 79.93; H, 7.28; N, 5.33. Found: C, 80.05; H, 7.20; N, 5.27%. Molar conductance Λ_M (DMF, 22 °C) 96.5 S cm^2 mol^{-1}. Selected IR data (KBr, cm^{-1}) 3292 vw, 3160 w br and 3121 w [ν(NH)], 2600–2150 w br [ν(HN···H$^+$)], 1643 w [δ(NH)], 1602 m–s, 1591 m, 1580 m and 1561 w [ν(C=C)], 1247 vs br and 1228 m [ν_{as}(ArCOC), ν(CNC)], 983 w, 943 m and 934 m [ω,τ,ρ(CH$_2$), ν(aliphCC)], 752 vs, 734 vs and 705 vs [δ(NH) and δ(ArCH) out of plane]. ^{1}H NMR (600 MHz, DMSO-d$_6$, δ ppm) 1.67 (6H, m, CH$_2$-C*H*$_2$-CH$_2$), 2.73 (12H, t, J = 5.2 Hz, NH-C*H*$_2$-CH$_2$), 3.77 (12H, s, Ar-C*H*$_2$-NH), 4.38 (12H, s, O-C*H*$_2$), 5.10 (8H, br s, NH, NH$^+$), 6.94 (6H, t, J = 7.2 Hz, Ar*H*-c), 7.08 (6H, d, J = 8.2 Hz, Ar*H*-a), 7.27 (6H, d, J = 7.3 Hz, Ar*H*-d), 7.34 (6H, t, J = 7.8 Hz, Ar*H*-b); tetraphenylborate: 6.80 (16H, t, J = 7.1 Hz, Ar*H*-c′), 6.93 (16H, t, J = 7.3 Hz, Ar*H*-b′), 7.19 (8H, br s, Ar*H*-a′). MS (+ESI, MeOH) *m/z* 945 ([(LH)$_2$BPh$_4$]$^+$, 2%), 313 ([LH]$^+$, 100%); MS (+ LDI) *m/z* 945 ([(LH)$_2$BPh$_4$]$^+$, 5%), 937 ([L$_3$H]$^+$, 5%), 867 ([(L$_2$H)BPh$_3$]$^+$, 5%), 789 ([(L$_2$)BPh$_2$]$^+$, 14%), 625 ([L$_2$H]$^+$, 50%), 555 ([(LH)-BPh$_3$]$^+$, 20%), 477 ([(L)BPh$_2$]$^+$, 12%), 313 ([LH]$^+$, 100%). It is worth noting that regardless of the proportion of macrocycle and sodium salt used, only compound with a 2:3 proton to ligand ratio was observed.

*2.2.7. [H(**L**)]BPh$_4$ (**7**)*

Recrystallization of **6** from MeCN yielded the compound **7**. It was also obtained by reaction of **L** and NaBPh$_4$ in MeCN.

A mixture of **L** (0.095 g, 0.30 mmol) and NaBPh$_4$ (0.104 g, 0.30 mmol) was dissolved in MeCN (10 cm^3) and refluxed for 3 h with continuous stirring. The reaction solution was filtered hot to remove some impurities and allowed to stand first at room temperature for 2 days and then it was left at 4 °C. The crystalline precipitate gradually formed was filtered off, washed with cold MeCN and dried under vacuum overnight over P_4O_{10}. Yield: 0.114 g, 60%; m.p. 160–162 °C. *Anal.* Calc. for $C_{43}H_{45}BN_2O_2$: C, 81.63; H, 7.17; N, 4.43. Found: C, 81.45; H, 7.22; N, 4.26%. Molar conductance Λ_M (DMF, 22 °C) 56.5 S cm^2 mol^{-1}. Selected IR data (KBr, cm^{-1}) 3344 vw br, 3280 vw br, 3145 w-m and 3120 sh [ν(NH)], 1653 w–m [δ(NH)], 1602 m–s, 1592 m–s and 1579 m [ν(C=C)], 1247 s br [ν_{as}(ArCOC), ν(CNC)], 984 w and 934 w–m [ω,τ,ρ(CH$_2$), ν(aliphCC)], 753 vs, 734 vs and 706 vs [δ(NH) and δ(ArCH) out of plane]. ^{1}H NMR (600 MHz, DMSO-d$_6$, δ ppm) 1.73 (2H, m, CH$_2$-C*H*$_2$-CH$_2$), 2.82 (4H, t, J = 5.2 Hz, NH-CH$_2$-C*H*$_2$), 3.85 (4H, s, Ar-C*H*$_2$-NH), 4.41 (4H, s, O-C*H*$_2$), 6.10 (3H, s br, NH, NH$^+$), 6.97 (2H, t, J = 7.2 Hz, Ar*H*-c), 7.10 (2H, d, J = 8.2 Hz, Ar*H*-a), 7.30 (2H, d, J = 7.3 Hz, Ar*H*-d), 7.37 (2H, t, J = 7.8 Hz, Ar*H*-b); tetraphenylborate: 6.80 (8H, t, J = 7.1 Hz, Ar*H*-c′), 6.94 (8H, t, J = 7.4 Hz, Ar*H*-b′), 7.19 (4H, s br, Ar-a′). MS (+ESI, MeCN) *m/z* 633 ([MH]$^+$, 1%), 313 ([LH]$^+$, 100%); MS (+ LDI) *m/z* 633 ([MH]$^+$, 2%), 555 ([(LH)BPh$_3$]$^+$, 3%), 313 ([LH]$^+$, 100%). Single crystals of poor quality were grown by slow evaporation from a mixture of MeOH, MeCN and CHCl$_3$ (1:2:1) in a desicator over silica gel after a few weeks.

2.3. X-ray diffraction

X-ray data were collected on an Enraf Nonius CAD4 diffractometer using Cu Kα radiation (λ = 1.54178 Å) at room temperature, except for compound **4** (measured at 100 K). The WINGX [22] data reduction procedure was applied. The structures were solved by direct methods with SIR97 [23], and refined by full-matrix least square refinement on F^2 using all reflections, with SHELXL [24]. All non-hydrogen atoms were refined anisotropi-

cally. The hydrogen atoms were located according to the relevant established geometry, and refined as a riding model, except those included in hydrogen bonding (attached to N8 and/or N12) that were located in the Fourier map and refined freely. Poor crystal quality and sensitivity to air of **4** affected the accuracy of data (Table 1) and consequently N–H bond distances (Table 2). Details of the crystal data and refinement are listed in Table 1.

3. Results and discussion

3.1. Preparation of the compounds

Reactions of a series of sodium salts with a mixed dioxa-diaza macrocycle 5,6,14,15-dibenzo-1,4-dioxa-8,12-diazacyclopentadeca-5,14-diene (**L**) in methanol yielded the ion-pair compounds shown in Scheme 1. The microanalytical, conductance, spectroscopic and X-ray structure analysis confirmed formation of the protonated ligand salts with different modes of inside and outside protonation, and hydrogen bonding systems. The proton-to-ligand ratio depends on the sodium salt and in the case of sodium tetraphenylborate also on the solvent used: 1:1 for the picrate salt (**1**), 1:2 for the perchlorate (**2**), tetrafluoroborate (**3**), hexafluorophosphate (**4**) and thiocyanate (**5**) salts, and 2:3 or 1:1 for the tetraphenylborate salt obtained from methanol (**6**) or acetonitrile (**7**) solution, respectively. A transformation of compound **6** to **7** in acetonitrile solution was confirmed by the ^{1}H NMR measurements. There are many effects influencing the formation of the protonated species, although the hole size of **L**, defined by the N_2O_2-donor set, of 2.06–2.26 Å would be suitable for complexation of Na^+ [25]. The main effects are related to the structural properties of the ligand. Since **L** as a diamine is a moderately strong base ($\log K_1 = 9.81$ and $\log K_2 = 6.84$, determined potentiometrically in 95% methanol) [20], it gives rise to competition between the protonation and metal complexation reactions. The presence of nitrogen donors having a low affinity for alkali metal cations and the presence of oxygen donor atoms next to the benzene rings having a reduced basicity and flexibility, are in favour of proton binding. In addition, the solvation power of Na^+ is strong due to its high charge density, and the formation of a protonated macrocycle is preferred. On the other hand, the dioxa-diaza macrocycle **L**, which contains both a hydrogen bond donor atom (the hydrogen on the nitrogen atom) and hydrogen bond acceptors (oxygen atom and the lone pair on the nitrogen atom) must also be strongly solvated in methanol, disrupting the hydrogen bonds which were shown to exist between the amine hydrogens and the ether oxygens [26]. This fact presumably gives rise to favourable outside ligand protonation in methanol solution, which is supported by the X-ray structure of **L** determined on crystals obtained from a mixture of methanol and water [25]. It was found that the water of hydration is placed between two ligand molecules and forms with each of them N–H···O(s) and N···H(s)–O hydrogen bonds. A similar interligand position of the proton is in compounds **2**–**6**. The exception is the picrate salt **1** with inside protonation, which is stabilized by a hydrogen bonding network with the picrate anion.

In the case of compounds **6** and **7**, with the bulky tetraphenylborate anion, the solvent media effects are shown to be important for the type of ligand protonation, which may arise from a difference in the ion and ligand solvation in methanol and acetonitrile solution. In general, methanol causes extensive solvation of both cations and anions, while acetonitrile shows moderate cation solvating ability and a rather weak anion solvating ability, which decreases with the anion size [13,27]. The ligand solvation in acetonitrile is also expected to be small.

The prepared protonated ligand salts **1**–**7** are crystalline compounds, insoluble in water, slightly soluble in alcohols and other common organic solvents, and very soluble in dimethylformamide and dimethylsulfoxide. The molar conductance measurements are consistent with the proposed structure of the ion-pair compounds and their stoichiometry. Thus, all compounds except **6**, which behaves as an 1:2 electrolyte ($\Lambda_M = 96.5$ S cm^2 mol^{-1} in DMF), exhibit conductivity comparable to that of 1:1 electrolytes ($\Lambda_M = 56$ to 75). The anhydrous character of the compounds was checked by thermogravimetric analyses. Crystals suitable for X-ray structural determination were obtained for all compounds, apart of **6**, under conditions outlined in Section 2.

3.2. IR spectra

The infrared spectra of the compounds support a different mode of ligand protonation and different hydrogen bond networks in the various types of protonated ligand salts, which is in agreement with the X-ray crystal structure data. The protonation of the macrocyclic moiety is evident by the characteristic changes in the ligand bands arising from various stretching and deformation modes of the NH vibrations present in the 3400–1500 (see Fig. 1) and 790–730 cm^{-1} regions. In the free macrocycle, the absorption of the antisymmetric and symmetric ν(NH) vibrations occurs as two strong bands at 3295 and 3185 cm^{-1} as well as a weak absorption at 3259 cm^{-1} [28], indicating different hydrogen bonding behaviour of the two amine protons. This is in accordance with the X-ray data, which show that the NH groups are involved in intra- and intermolecular hydrogen bonding with the ether oxygens [26]. The δ(NH) vibrations are displayed along with the aromatic

Table 1
Crystallographic data, crystallisation details, structure solution and refinement

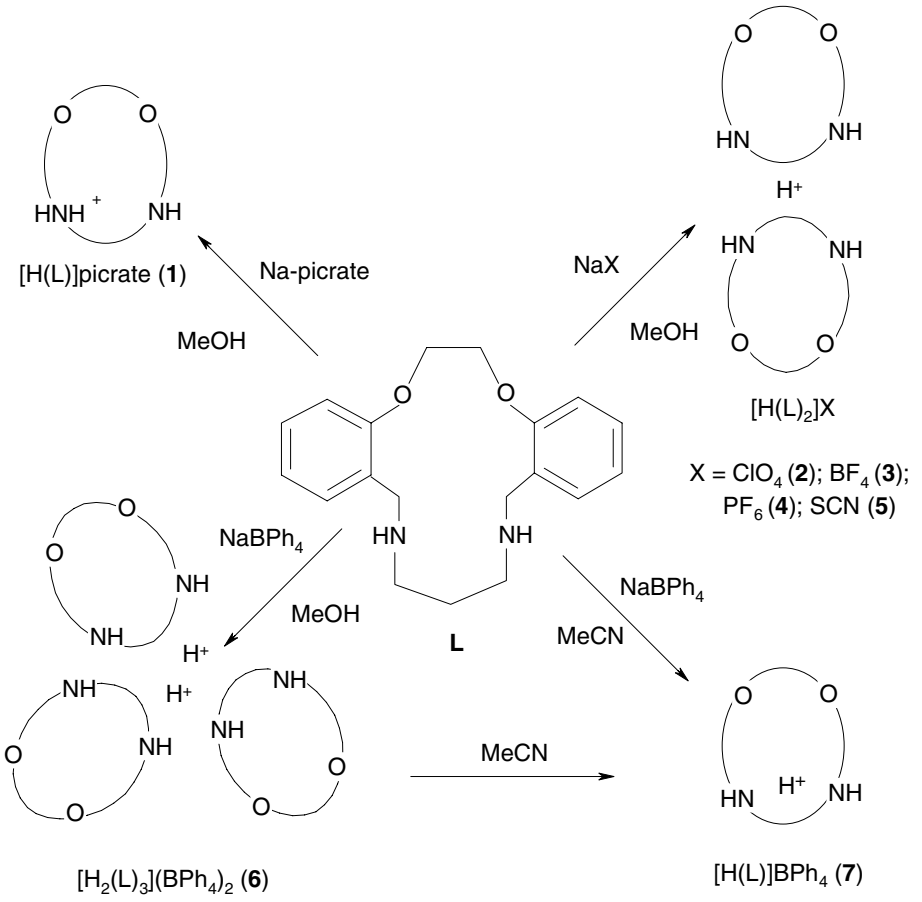
Compound	**1**	**2**	**3**	**4**	**5**	**7**
Formula	$C_{19}H_{25}N_2O_2 \cdot C_6H_2N_3O_7$	$C_{19}H_{24.5}N_2O_s1/2(ClO_4)$	$C_{19}H_{24.5}N_2O_21/2(BF_4)$	$C_{19}H_{25}N_2O_21/2(PF6) \cdot 1/2(CH_3OH)$	$C_{19}H_{24.5}N_2O_21/2SCN$	$C_{19}H_{25}N_2O_2 \cdot C_{24}H_{20}B \cdot CHCl_3 \cdot CH_3CN$
Anion	picrate	perchlorate	tetrafluoroborate	hexafluorophosphate	thiocyanate	tetraphenylborate
M_r	541.52	362.63	356.82	401.70	341.95	792.11
Crystal system	orthorhombic	monoclinic	monoclinic	triclinic	triclinic	triclinic
Space group	*Pbca*	*C*2/*c*	*C*2/*c*	$P\bar{1}$	$P\bar{1}$	$P\bar{1}$
a (Å)	14.1604(4)	16.9981(7)	16.8322(7)	8.712(5)	9.2595(3)	11.779(3)
b (Å)	16.2683(7)	12.3519(7)	12.1597(5)	10.543(5)	10.8116(5)	11.820(4)
c (Å)	21.9411(7)	19.2964(8)	19.4592(8)	12.080(5)	11.1690(6)	18.697(4)
α (°)				72.77 (1)	66.426(4)	75.56(2)
β (°)		111.280(10)	110.14(1)	70.38(1)	86.196(4)	71.94 (2)
γ (°)				81.34(1)	65.452(3)	60.93(3)
V (Å^3)	5054.5(3)	3775.2(3)	3739.1(3)	996.62(17)	925.48(7)	2148(1)
Z	8	8	8	2	2	2
D_x (Mg m^{-3})	1.423	1.276	1.304	1.324	1.227	1.226
Crystallization solvent(s)	methanol	methanol	methanol	methanol	acetonitrile	methanol, chloroform, acetonitrile
Crystal colour	orange	colourless	colourless	colourless	colourless	colourless
Crystal shape	prismatic	prismatic	prismatic	prismatic	prismatic	prismatic
Crystal dimensions (mm)	0.18 × 0.198 × 0.20	0228 × 0.158 × 0.15	0.25 × 0.15 × 0.10	0.178 × 0.158 × 0.12	0.158 × 0.128 × 0.10	0.408 × 0.258 × 0.20
Total data	5881	4374	4303	4277	4141	9259
Unique data	5304	3964	3897	4074	3890	8973
R_{int}	0.00	0.0257	0.0177	0.0712	0.0355	0.0464
R_σ	0.0516	0.0211	0.0346	0.0263	0.0995	0.0521
Observed data	2749 [$I > 2\sigma(I)$]	2819 [$I > 2\sigma(I)$]	2165 [$I > 2\sigma(I)$]	3692 [$I > 2\sigma(I)$]	1596 [$I > 2\sigma(I)$]	4254 [$I > 2\sigma(I)$]
θ_{max}	76.40 (Cu Kα)	76.42 (Cu Kα)	76.40 (Cu Kα)	75.85 (Cu Kα)	76.52 (Cu Kα)	77.45 (Cu Kα)
Range of *h*, *k*, *l*	−17, 0; −20, 0; −27, 0	19, 21; −15, 0; −24, 0	−21, 19; 0, 15; 0, 24	−10, 10; −13, 12; −15, 0	0, 11; −12, 13; −14, 14	−14, 14; −14, 14; −23, 0
μ (mm^{-1})	0.928	1.358	0.813	1.245	1.144	2.24
Absolute corrections	Ψ-scan (7)	none	Ψ-scan (7)	Ψ-scan (7)	Ψ-scan (8)	Ψ-scan (7)
T_{min}	0.8025		0.9377	0.9473	0.7404	0.6177
T_{max}	0.8460		0.9737	0.9913	0.8403	0.9113
R_1 [$F_o > \sigma(F_o)$]	0.0500	0.0439	0.0545	0.1207	0.0678	0.1063
$wR_2(F^2)$ (all)	0.1371	0.1269	0.1643	0.3230	0.1994	0.3810
S	1.087	1.056	1.029	1.110	1.038	1.171
Number of parameters	478	261	262	266	244	433
$\Delta\rho_{max}$ [e Å^{-3}]	0.16	0.16	0.16	0.63	0.35	0.53
$\Delta\rho_{min}$ [e Å^{-3}]	−0.21	−0.19	−0.15	−0.70	−0.19	−0.53

Table 2
Hydrogen bonding

	D–H (Å)	H···A (Å)	D···A (Å)	D–H···A (°)	Symmetry operation on A
Compound ***1***					
N12–H12A···O30	0.96(3)	1.84(3)	2.735(3)	153(3)	
N12–H12A···O38	0.96(3)	2.50(3)	3.219(4)	132(2)	
N12–H12B···N8	0.93(3)	2.17(3)	2.829(3)	127(2)	
N12–H12B···O1	0.93(3)	2.54(3)	3.002(3)	111(2)	
N8-H8···O30	0.90(3)	2.39(3)	3.191(3)	149(3)	
Compound ***2***					
N8–H8···O4	0.84(3)	2.47(3)	2.987(2)	121(2)	
N8–H8···N12	0.84(3)	2.43(3)	2.984(3)	124(2)	
N12–H12A···O1	0.82(3)	2.44(3)	2.929(2)	119(2)	
N12–H12A···N8	0.82(3)	2.41(3)	2.984(3)	128(2)	
N12–H12B···N8	1.46(4)	1.51(3)	2.963(1)	174(1)	$-x+1, -y, -z+1$
Compound ***3***					
N8–H8A···N12	0.79(4)	2.38(4)	2.839(4)	119(3)	
N8–H8A···O4	0.79(4)	2.48(4)	3.005(3)	126(3)	
N12–H12···N8	0.78(4)	2.46(4)	2.839(4)	112(3)	
N12–H12···O1	0.78(4)	2.35(4)	2.935(3)	133(3)	
N12–H12B···N8	1.55(4)	1.48(3)	3.03(1)	171(1)	$-x+1, -y, -z+1$
Compound ***4***					
N8–H8···O4	0.64(5)	2.70(8)	2.98(8)	110(3)	
N12–H12A···O1	0.69(5)	2.41(5)	2.95(8)	136(4)	
N12–H12A···N8	0.69(5)	2.64(6)	3.05(9)	120(1)	
N12–H12B···N8*i*	1.33(4)	1.81(5)	2.94(8)	139(2)	$1-x, 1-y, 1-z$
Compound ***5***					
N8–H8···O4	0.67(3)	2.49(3)	2.965(5)	130(1)	
N8–H8···N12	0.67(3)	2.63(5)	3.024(6)	121(2)	
N12–H12···O1	0.87(2)	2.36(4)	2.952(6)	126(2)	
N12–H12···N8	0.87(2)	2.47(3)	3.024(6)	122(4)	
N12–H12A···N8	1.23(2)	1.74(6)	2.961(7)	170(1)	$1-x, -y, -z$
Compound ***7***					
N8–H8···N12	0.86(5)	2.08(6)	2.880(7)	156(2)	
N12–H12···O1	0.85(5)	2.49(6)	3.092(8)	128(4)	
N12–H12···N8	0.85(5)	2.41(5)	2.880(7)	115(1)	

ν(C=C) vibrations within 1600 and 1500 cm^{-1}. The most prominent feature in the spectrum of **L** is the appearance of a series of sharp bands of strong to medium intensity within 2800–2600 cm^{-1}, assigned to the perturbed ν_s(CH) vibrations as a result of α-CH_2 hydrogens being *trans*-anti-parallel to N lone-pairs (Bohlmann bands) [14]. In all the protonated ligand salts, great changes may be noticed in this region due to electronic redistribution in the macrocycle molecule caused by various types of intra- or inter-ligand protonation and hydrogen-bonding interactions. In the 1:1 proton-to-ligand compounds, the proton is located inside the macrocyclic cavity either on one of the nitrogen atoms as in **1** or is disordered between two nitrogen atoms as in **7**. For this reason, their spectra are significantly different. In the picrate salt, in the ν(NH) region one strong sharp band at 3297 cm^{-1} is present which is associated with the unprotonated amino group, while a medium band at 2182 cm^{-1}, partly superimposed upon the alkane ν(CH) absorptions on the higher frequency side and with shoulders on its lower side, could be ascribed to the $\nu(NH_2^+)$ absorption [29]. The broadness and position of the later absorption can be rationalized with the additional hydrogen bonding not only to the second nitrogen atom but also to oxygens of the macrocyclic and picrate moieties. On the other hand, in the tetraphenylborate salt **7**, the presence of two very small absorptions at 3344 and 3280 cm^{-1} and a broader band of medium intensity at 3140 cm^{-1}, associated with the NH stretching vibrations, indicates a proton disordering inside the macrocyclic cavity and no association with the counterion. Hence, a completely different hydrogen bond network could be proposed to that observed in **1**. A weak band at 1653 cm^{-1} could be assigned to the NH bending mode. It is known that these absorptions are shifted towards higher frequencies under associated conditions [29]. In **1**, δ(NH) is overlapped with the strong absorptions of the picrate anion in the 1635–1550 cm^{-1} region.

In the compounds with 1:2 and 2:3 proton-to-ligand ratios, there is interligand protonation in which a proton is dislocated between nitrogen atoms from two macrocyclic



Scheme 1. The protonated ligand salts formed by the reactions of **L** with sodium salts.

molecules (**2**–**5**) or two protons are shared among nitrogens from three ligand molecules (**6**). In general, the spectral features of the monoprotonated ligand salts **2**–**5** are similar, but the presence of extra bands attributed to the anion moiety [30], gives a different profile of their spectra (Fig. 2, see c and d and data in Section 2). Some variations observed in the position and intensity of the NH stretching vibrations may arise from some differences in location of the proton in the $N\cdots H^{+}\cdots N$ bonds between two ligand molecules. Two ν(NH) bands appear at about 3338 (mostly split) and 3185 cm^{-1}, while a very broad complex progression of absorptions displayed in the 2600–1900 cm^{-1} region could be assigned to the $HN\cdots H^{+}$ bonding system. It was found that the absorption region arisen from this type of hydrogen bonding shifts towards smaller wave numbers and gains more in intensity with increasing symmetry in the $N\cdots H^{+}\cdots N$ bond [14,31,32]. In the perchlorate and tetrafluoroborate salts, which were shown to be isostructural compounds, this absorption is the most intense and is centred around 2250 cm^{-1}, suggesting the symmetrical position of the proton between two nitrogen atoms. In the hexafluorophosphate and thiocyanate salts, this absorption is less intense and is centred at higher frequencies at about 2280 and 2300 cm^{-1}, respectively, indicating that the proton is placed asymmetrically between the two nitrogen atoms. In addition, it could be concluded that it is closer to one of the nitrogen atoms in the thiocyanate than in the hexafluorophosphate salt. A series of bands of less intensity between 2000 and 1800 cm^{-1} arises from overtones and a number of combination bands enhanced by Fermi resonance and is visible both in the spectrum of the **L** and in all its protonated derivatives [32]. The δ(NH) vibration in **2**–**5** appears as a weak band between 1654 and 1634 cm^{-1}. In general, the spectral pattern associated with the NH vibrations is also similar in the tetraphenylborate salt **6**, although some variation in position and intensity of these absorptions could be observed. Both bands over 3100 cm^{-1} are split and display at lower frequencies (around 3292 and 3140 cm^{-1}), while a broad complex band occurs at a narrow frequency region within 2600–2150 cm^{-1}. All these absorptions are less intense than those in the 1:2 (proton to ligand) compounds.

Compared to the free macrocycle, in the spectra of the protonated species considerable changes can be noticed also in the NH deformation region between 800 and 700 cm^{-1}. Overlap of the out of plane bending of

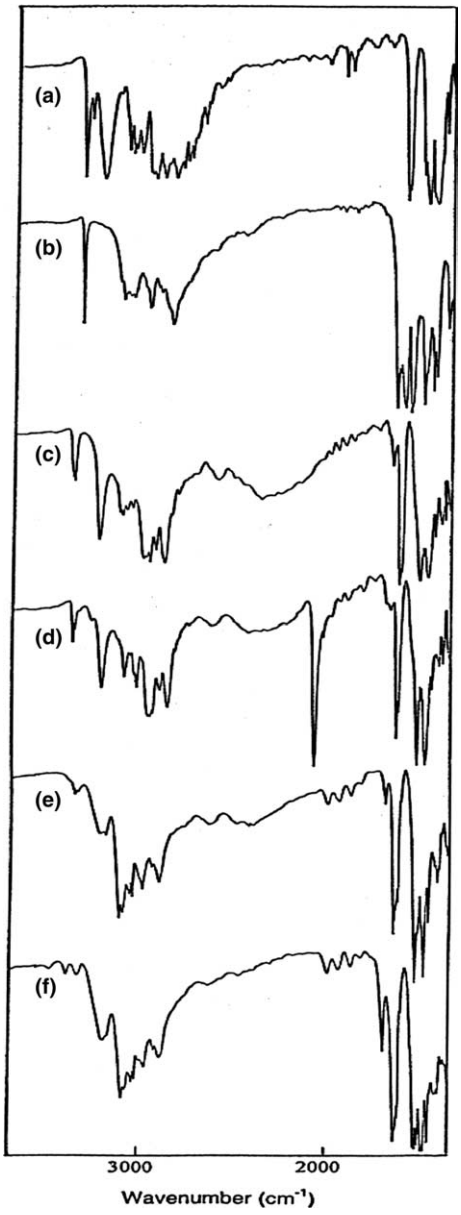


Fig. 1. Part of the infrared spectra of **L** and its salts: (a) **L**, (b) **1**, (c) **2**, (d) **5**, (e) **6** and (f) **7**.

the NH and ArCH vibrations gives a very complex spectral pattern of **L** with two strong split bands at 768 and 730 cm^{-1} and a very strong band at 753 cm^{-1}. Compounds **2**–**5** in this region show a strong to very strong band at 760 and a medium to strong band at 732 cm^{-1}. The situation is more complicated in compounds **1**, **6** and **7** due to overlapping with absorptions of the picrate or tetraphenylborate anions. In addition, some changes could be observed in the ligand vibration region around 1250 cm^{-1} ascribed to the stretching Ar-COC and CNC vibrations as well as between 1000 and 900 cm^{-1} where wagging, twisting and rocking modes of vibration of the methylene groups occur [33].

3.3. Mass spectra

The mass spectra (ESI and LDI) of all the compounds show the base peak at *m*/*z* 313, corresponding to the protonated ligand ion $[LH]^+$. The weak peak corresponding to $[MH]^+$ (1–2%) is only visible in the 1:1 proton-to-ligand compounds (**1** and **7**), while $[L_2H]^+$ (4–10%) is visible in the 1:2 compounds (**2**–**5**). In **6**, besides $[LH]^+$, $[L_2H]^+$ and $[L_3H]^+$ peaks, there is a series of ions which also contains tetraphenylborate fragments.

3.4. ^1H NMR spectra

The ^1H NMR spectra of the protonated macrocyclic species show a set of four resonant signals for the methylene protons and a set of four resonances for the ligand aromatic protons. In free **L**, an unresolved quintet at 1.54 and a triplet at 2.49 ppm are found for the methylene protons of the $NHCH_2CH_2CH_2NH$ group, whereas two singlets at 3.58 and 4.34 ppm are assigned to methylene protons of the Ar-CH_2NH and OCH_2 groups, respectively [28]. Two partly split doublets and two triplets appear in the aromatic region. In compounds **6** and **7**, these absorptions are overlapped with those arising from the tetraphenylborate anion and their relationship confirms the 2:3:2 proton–ligand–anion ratio in **6** as well as 1:1:1 in **7** (Fig. 2). Signal assignments were ascertained by 2D NMR spectra. It could be presumed that protonation of the macrocycle in solution is kinetically labile in all compounds, as evidenced by the averaging of the free and the protonated NH signal. The NH proton in **L** appears as a single absorption at 1.94 ppm. Upon ligand protonation, it broadens and moves to lower fields by 1.5–4.5 ppm due to a dynamic process involving fast intra- or inter-ligand proton exchange between the amino groups. Furthermore, the protonation of the basic site in the macrocycle leads to a deshielding of the adjacent methylene groups. A downfield shift of 0.11–0.26 ppm is observed in the salts for the Ar-CH_2-NH protons as well as that of 0.14–0.33 ppm for the NH-CH_2-CH_2 protons. The resonances for OCH_2 protons and of the aromatic protons undergo quite small shifts of 0.01–0.07 and 0.03–0.14 ppm, respectively. All these changes are more pronounced in compounds with the intraligand protonation.

3.5. X-ray structure analysis

The crystal structures solved (**1**–**5** and **7**, Table 1) revealed intra- (compounds **1** and **7**) and inter-macrocycle protonated compounds (compounds **2**–**5**) (Scheme 1). For the interligand protonated compounds (**2**–**5**), the proton is statistically distributed between two nitrogen atom pairs of two macrocyclic ligands as defined by crystallographic symmetry: each ligand molecule involves two N···N pairs but only one shares the proton.

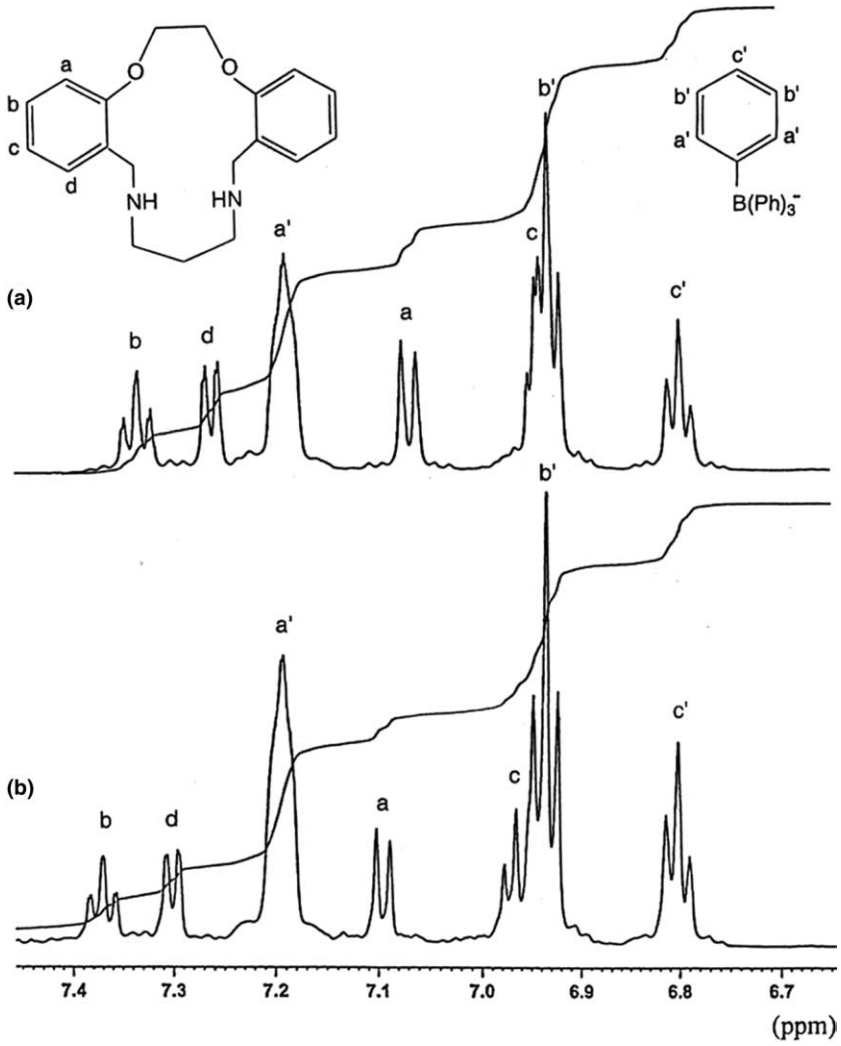


Fig. 2. The aromatic part of the ^{1}H NMR spectra of tetraphenylborate salts: (a) **6** and (b) **7**.

The proton locations in the electron density maps can be recognized using good quality intensity data. However, the crystal quality does not always permit the required experimental standards to be met, as for compounds **4** and **7** (Table 1). Sometimes, it is not possible to produce crystals at all (as for **6**). But for the structures of **1**–**5**, the proton locations were identified and the assignment of the correct structural formula was possible. Thus, in the [H(**L**)]picrate salt (**1**, Fig. 3) the proton attached to the nitrogen atom forms a $N12^+H_2$-cation (Fig. 4). The crystal structure of **7** (Fig. 5) also reveals an intraligand protonation. In the structure of **7**, the non-covalent intraligand distances N···N, N···O and O···O can be interpreted as possible hydrogen bonds upon distance criteria defined by Jeffrey (1997) but without the exact proton location, a particular hydrogen bond cannot be assigned [34]. The compounds **2**–**5**, with the ligand-to-proton ratio of 2:1, revealed intermacrocycle protonation as well as for compound **6** with a 3:2 ratio (deduced from ^{1}H NMR measurements, see Section 2 and Scheme 1). The crystal structure of **2** clearly reveals that the proton H12B (with a population parameter value of 0.5) participates in hydrogen bonding N···H^+···N (Table 2) involving N12 and N8 of two ligands, forming a centrosymmetric ring dimer of two macrocycles (Fig. 6). The distances from nitrogen to hydrogen are somewhat longer and can be related to the quality of the crystals: 1.46(4) and 1.51(4) Å. In addition to N···H^+···N hydrogen bonds, N8H and N12H also realise intraligand hydrogen bonds to O1 and O4 (Table 2), generating bifurcated hydrogen bonds. The isostructural relationship between **2** and **3** [perchlorate and tetrafluoroborate tetrahedral analogues (Fig. 7), respectively] is obvious from crystallographic evidence (both crystallise in the monoclinic space group *C*2/*c*, Table 1) and the protonation type is identical. The interligand N···N separation as donor to acceptor distances of hydrogen bonds are similar to intraligand ones involving nitrogen atoms: 2.963 and 2.984 Å, respectively (in **2**). The analogous protonation model is

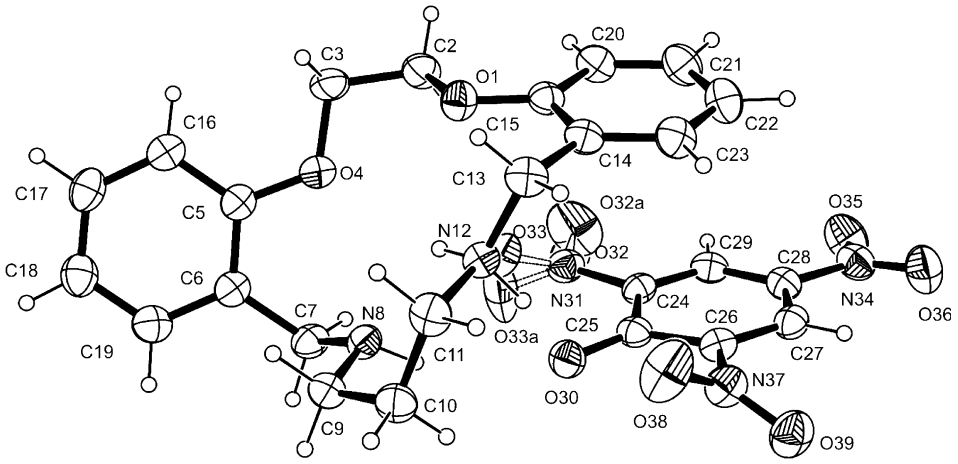


Fig. 3. ORTEP [38] drawing of **1**. The thermal parameters are scaled at the 30% probability level. The bonds to the disordered atoms are dashed.

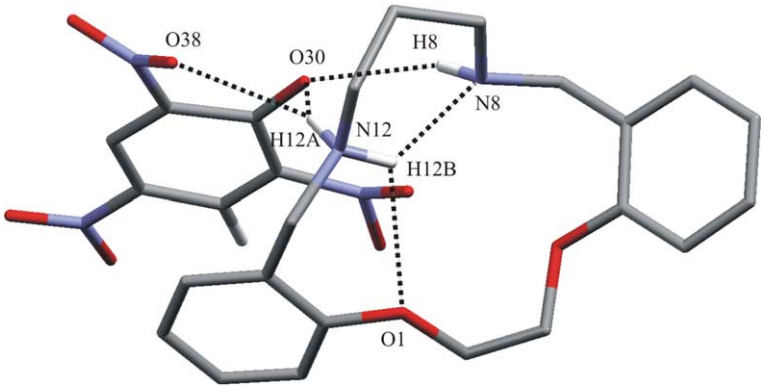


Fig. 4. Hydrogen bonding in **1**. Hydrogen atoms are omitted for clarity, except those included in hydrogen bonding. Donor, acceptor and hydrogen atoms involved in hydrogen bonds are labelled. The protonated $N^{+}12H_2$ of the macrocycle is involved in two bifurcated hydrogen bonds: to picrate via N12–HA···O30 and N12–HA···O38, and with the same ligand through N12–HB···N8, and N12–H12B···O1. The additional hydrogen bond between the ligand and the anion is through N8–H···O30.

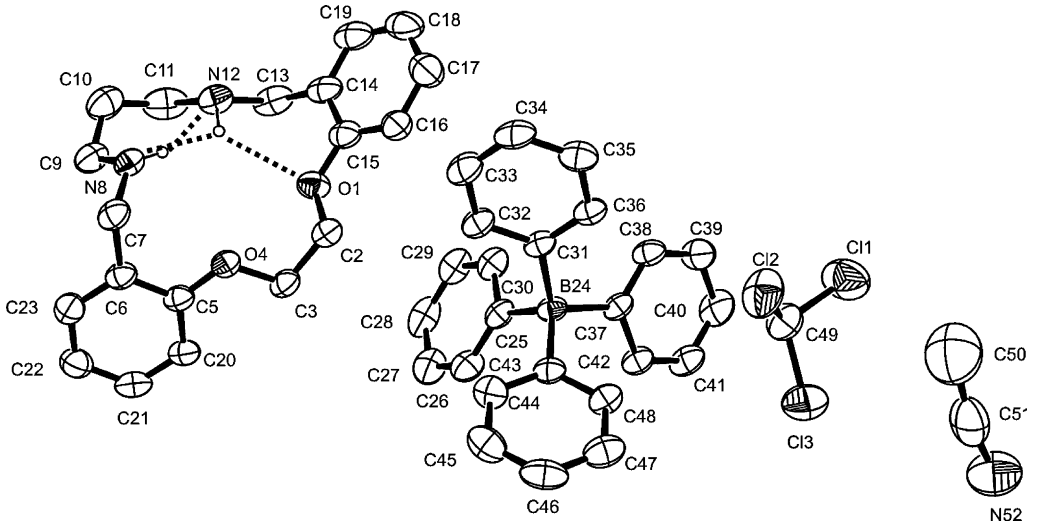


Fig. 5. ORTEP drawing of **7** with the hydrogen bonds marked by dashed lines. The thermal parameters are scaled to the 30% probability level. The hydrogen atoms are omitted for clarity except those included in hydrogen bonding.

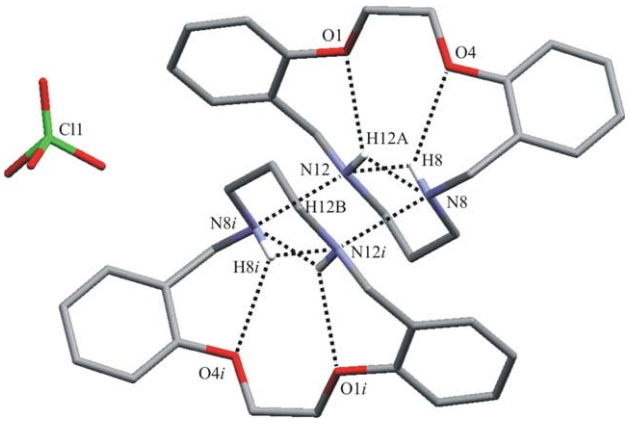


Fig. 6. Hydrogen bonding scheme in **2**. Hydrogen atoms are omitted for clarity, except those included in hydrogen bonding. Only non-hydrogen atoms included in hydrogen bonding are labelled.

present in the crystal structure of $[H(\mathbf{L})_2]PF_6$ salt (**4**, Fig. 8, Scheme 1). From the values of nitrogen to proton distances involved in hydrogen bonding, 1.33 (4) and 1.81(5) Å, the asymmetrical position of the proton is obvious but less pronounced than in the structure of **5** which exhibits the proton located on N12. Crystals of **4** include methanol as a solvent and they are sensitive to air. The low temperature data were collected but they were not of high quality. Disorder of a methanol molecule with two orientations and a partly occupied position (pp ~ 0.5) affects the data. In spite of these problems, protons were located in a difference Fourier map and interligand protonation, as observed in **2** and **3**, was confirmed with hydrogen bonding in **4** (Table 2). In the crystal of $[H(\mathbf{L})_2]SCN$, compound **5** (Fig. 9), the interligand protonation mode is analogous to that

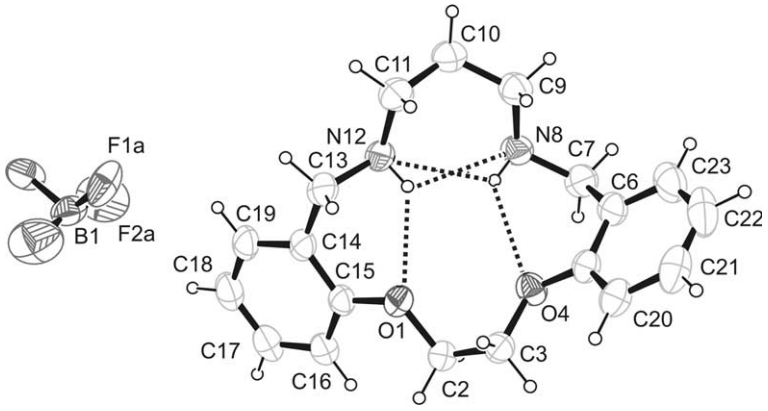


Fig. 7. ORTEP drawing of **3** with the hydrogen bonds. The thermal parameters are scaled at the 30% probability level.

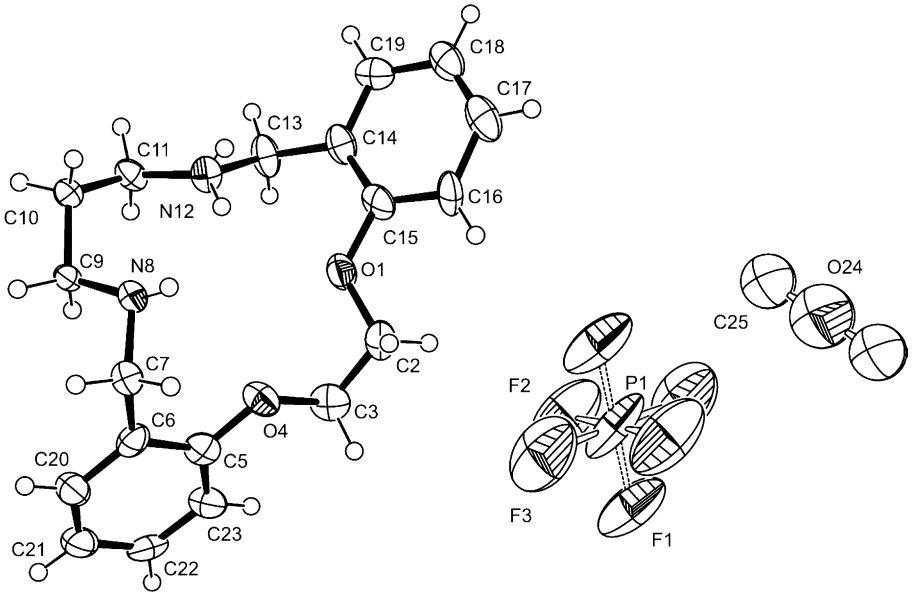


Fig. 8. ORTEP drawing of **4**. The thermal parameters are scaled to the 50% probability level.

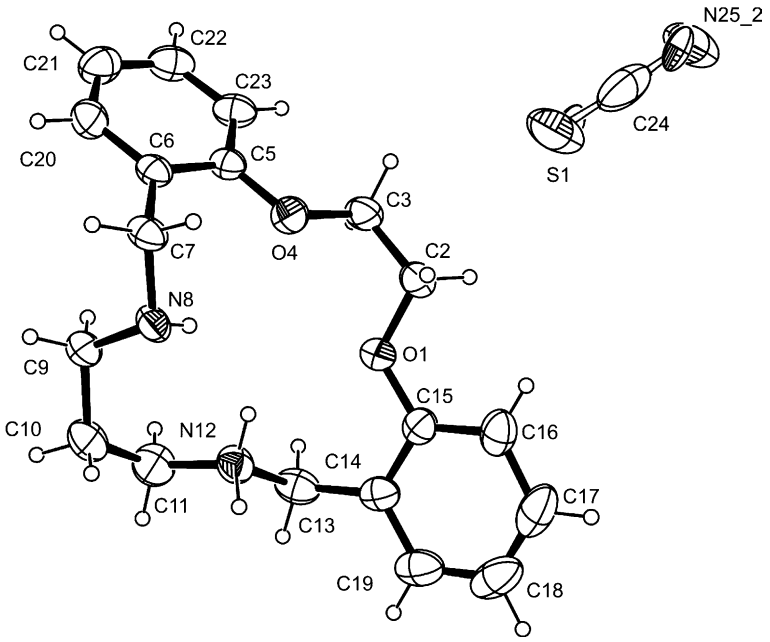


Fig. 9. ORTEP drawing of **5**. Thermal ellipsoids are scaled to the 30% probability level.

already described for **2**, also including the formation of the centrosymmetric hydrogen bonded macrocycle dimer (Scheme 1). However, the geometrical parameters of the hydrogen bonds are slightly different; the proton is located at N12 as can be seen from asymmetrical nitrogen to proton distances: N12–H12A, 1.23 (2) Å and N8···H12A, 1.74 (6) Å. The acceptor to donor distance $N^{+}12\cdots N8$ of 2.961 Å (Table 2) of two centrosymmetrically related ligands is shorter than the intraligand $N^{+}12\cdots N8$ distance of 3.025 Å.

The conformation of the macrocyclic rings defined as *anti–gauche–anti* for the sequence O–C–C–O and *anti–gauche–gauche–anti* for the N–C–C–C–N fragment is preserved in all the compounds studied. Different modes of protonation observed in the compounds and the presence of tetrahedral or octahedral anions of different polarity and the completely different thiocyanate anion do not affect the overall conformations of the O_2N_2-macrocycle (Fig. 10). The comparison with two transition metal complexes (Ni and Cu) coordinated by this type of ligand reveals significant differences in two torsion angles for the sequence C–N–C–C_{ar} due to the coordination of nitrogen to the metal [3,4]. The intraligand N···N, N···O and O···O distances are close to the sum of van der Waals radii in all the structures analysed. The optimization of the macrocycle ring conformation explains its stability under various steric and electronic influences. The same type of ring puckering is related to the narrow range of values of the dihedral angles between the two aromatic rings (from 59.7° to 69.7°).

The intraligand protonation in structures **1** and **7** results in intraligand hydrogen bonding (Table 2); however there are no common features in the crystal packing of **1** and **7**. The crystal structure of the picrate salt reveals interactions between the cation and anion via N–H···O hydrogen bonds (Table 2, Fig. 4). On the contrary, the crystal packing of **7** is dominated by van der Waals interactions, whereas hydrogen bonds only occur within the ligand (Fig. 5).

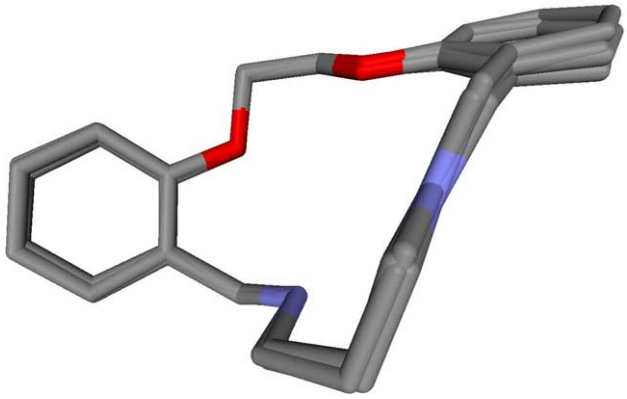


Fig. 10. Overlap of the O_2N_2-15-membered ring observed in the structures **1**–**5** and **7**.

The interligand protonation is characterized by formation of dimers via hydrogen bonds between two macrocycles (**2**–**5**). Channels occupied by anions separate these dimers. In the crystal structure of **2**, the perchlorate anion is involved in C2–H2B···O1A interactions [H···O1A, 2.54 Å, C2···O1A, 3.501(8) Å, C–H···O, 169°] using the methylene group (carbon attached to the macrocycle oxygen atom) creating an interaction between the cation and anion. According to the geometry

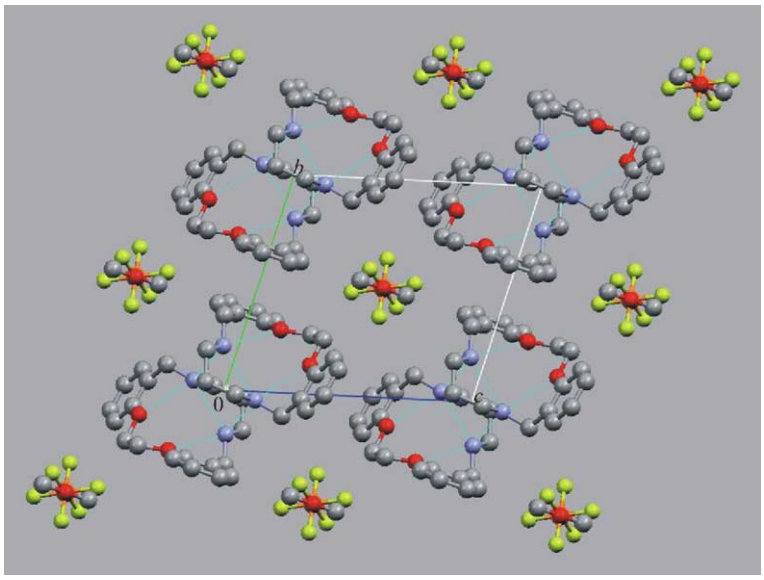


Fig. 11. The crystal packing of **4** with cation dimers arranged around the inversion centres of the corners of the triclinic unit cell and the channels between them occupied by PF_6 anions. Methanol molecules are in disorder.

observed this is the classical example of a C–H···O hydrogen bond [38]. The structures of **2** and **3** are isostructural, where the tetrahedral anions realize either C–H···O (**2**) or C–H···F (**3**) interactions connecting the macrocycle and the anion. In (**3**), the interaction with the cation is via C2–H2B···F1A [H2B···F1A ($1 + x$, y, $1 + z$), 2.39 Å, C2···F1A, 3.351(10) Å, C2–H2B···F1A 169°; H19···F1A, 2.53 Å, C19···F1A, 3.244(1) Å, C19–H19···F1A, 134°]. Anionic fluorine acts as the acceptor of the C–H donor group. There are controversial comments on the acceptor function of the covalently bound fluorine in organic compounds [35–37], whereas the fluoride acceptor function is well documented. The geometry of the observed contacts in the structure containing BF_4 (**3**) and PF_6 (**4**) anions can be characterized as the C–H···F interaction. However, the crystal packing of **4** reveals no contacts between cations and anions but involves the PF_6 anion and a solvent. The ligands arranged around the inversion centres at the corners of the triclinic unit cell leave the channel that is occupied by PF_6 anions (Fig. 11). A disordered methanol solvent molecule is located between two anions, realizing C–H···F contacts [C24–H24B···F3 ($1 - x$, y, z) with H···F3, 2.45 Å, C24···F3, 3.31(2) Å, C24–H···F3, 149° and C24–H24B···F2 ($1 - x$, $1 - y$, $1 - z$) with H···F2 2.39 Å, C24···F2, 3.29(2) Å, C24–H···F2, 154°]. Because of the disorder of the methanol, it was not possible to locate the hydrogen atom of the hydroxy group. Thus the hydrogen bond involving the OH group cannot be specified, but from the O25···F1 distance of 3.34 Å, a hydrogen bond can be expected. In the crystal structure of **5**, two dimeric cations are connected by a weak interaction of C–H···SCN^- generating a large ring. As usual, the thiocyanate anion is in disorder and unambiguous specification of S or N in the interaction with the cations is not possible.

4. General conclusions

The results of an investigation on the interaction of a 15-membered macrocycle containing an O_2N_2-donor set with a number of sodium salts in methanol show that affinity of this macrocycle for protons is much larger than for the sodium ion. This is primarily connected with the stereochemistry of this ligand. The type, number and arrangement of the donor atoms in the macrocyclic cavity are shown to have a great influence on the cation binding selectivity. The choice of anion in a salt-ligand system, along with the choice of solvent (methanol or acetonitrile) in the case of the tetraphenylborate compound, is important on the resulting inter- or intraligand protonation. The position of the proton depends on the size, shape and polarizability of the anion, which ranged from planar SCN^-, tetrahedral ClO_4^- and BF_4^-, octahedral PF_6^-, inorganic anions to bulky Pic^- and BPh_4^- organic anions. Transfer of proton either inside or outside the molecular cavity imposes different hydrogen bond networks in the various types of protonated macrocyclic salts.

5. Supplementary material

CCDC-243426, CCDC-243427, CCDC-243428, CCDC-243429, CCDC-243430 and CCDC-243431 contain the supplementary crystallographic data for this pa-

per. This data can be obtained free of charge via www.ccdc.cam.ac.uk/conts/retreiving.html (or from the Cambridge Crystallographic Data Centre, 12 Union Road, Cambridge CB2 1EZ, UK, Fax: +44 1223 336033; or deposit@ccdc.cam.ac.uk).

Acknowledgements

The financial support granted by the Croatian Ministry of Science, Education and Sports (Grants No. 0098035 and 0098036) is gratefully acknowledged. The authors thank Mr. Ž. Marinić (Ruđer Bošković Institute) for recording the NMR spectra and Prof. P. Traldi for valuable discussions.

References

[1] (a) For examples, see: G.W. Gokel, Crown Ethers and Cryptands, The Royal Society of Chemistry, London, 1991;
(b) R.M. Izatt, K. Pawlak, J.S. Bradshaw, Chem. Rev. 95 (1995) 2529.
[2] B. Dietrich, P. Viout, J.-M. Lehn, Macrocyclic Chemistry, Aspects of Organic and Inorganic Supramolecular Chemistry, VCH, Weinheim, 1993.
[3] K.R. Adam, G. Anderegg, L.F. Lindoy, H.C. Lip, M. McPartlin, J.H. Rea, R.J. Smith, P.A. Tasker, Inorg. Chem. 19 (1980) 2956.
[4] L.P. Battaglia, A. Bonamartini Corradi, A. Mangia, Inorg. Chem. 39 (1980) 211.
[5] L.F. Lindoy, H.C. Lip, J.H. Rea, R.J. Smith, K. Henrick, M. McPartlin, P.A. Tasker, Inorg. Chem. 19 (1980) 3360.
[6] (a) N.A. Bailey, D.E. Fenton, M.G. Williams, D.J. Winter Soc., J. Chem. Dalton Trans. (1989) 1727;
(b) L. Tei, A.J. Blake, A. Bencini, B. Valtancoli, C. Wilson, M. Schröder, Inorg. Chim. Acta 337 (2002) 59;
(c) G. Crisponi, F. Cristiani, V.M. Nurchi, R. Pinna, T. Pivetta, V. Fusi, M. Micheloni, Inorg. Chim. Acta 323 (2001) 62;
(d) D. Baldvin, L.F. Lindoy, D.P. Graddon, Aust. J. Chem. 41 (1988) 1347;
(e) J.C. Aguilar, E.R. de San Miguel, J. de Gyves, R.A. Bartsch, M. Kim, Talanta 54 (2001) 1195.
[7] Y. Gok, S.Z. Yildiz, Z. Anorg. Allg. Chem. 620 (1994) 959.
[8] (a) R.M. Izatt, K. Pawlak, J.S. Bradshaw, Chem. Rev. 91 (1991) 1721;
(b) I. Saraoka, S. Kato, T. Chujo, H. Sato, K. Fukuhara, H. Matsura, J. Incl. Phenom. Mol. Recogn. Chem. 22 (1995) 59.
[9] (a) S. Chaves, A. Cerva, R. Delgado, Polyhedron 17 (1998) 93;
(b) H.-J. Buschmann, E. Cleve, S. Torkler, E. Schollmeyer, Talanta 51 (2000) 145.
[10] M.I. Saleh, A. Salhin, B. Saad, H.-K. Fun, J. Mol. Struct. 475 (1999) 93.
[11] A.R. Kausar, Inorg. Chim. Acta 86 (1984) 61.
[12] L.R. MacGillivray, J.L. Atwood, J. Org. Chem. 60 (1995) 4972.
[13] (a) For example, see: B.A. Moyer, P.V. Bonnesen, in: A. Bianchi, K. Bowman-James, E. Garcia-Espana (Eds.), Supramolecular Chemistry of Anions, Wiley-VCH, New York, 1996, p. 1 (Chapter 1);
(b) A. Bianchi, E. Garcia-Espana, in: A. Bianchi, K. Bowman-James, E. Garcia-Espana (Eds.), Supramolecular Chemistry of Anions, Wiley-VCH, New York, 1996, p. 217 (Chapter 6).
[14] H.J. Brüge, D. Carboo, K. von Deuten, A. Knöchel, J. Kopf, W. Dreissig, J. Am. Chem. Soc. 108 (1986) 107.
[15] (a) P.B. Smith, J.L. Dye, J. Cheney, J.-M. Lehn, J. Am. Chem. Soc. 103 (1981) 6044;
(b) A. Bencini, A. Bianci, E. Garcia-Espana, M. Micheloni, J.A. Ramirez, Coord. Chem. Rev. 188 (1999) 97;
(c) S. Balalaie, A. Kunze, R. Gleiter, F. Rominger, S. Geis, T. Oeser, Eur. J. Org. Chem. (2003) 3378.
[16] A. Mangia, A. Tiripicchio, Cryst. Struct. Comm. 8 (1979) 699.
[17] E.F. Caldin, V. Gold (Eds.), Proton-Transfer Reactions, Chapman & Hall, London, 1975.
[18] (a) T. Bountis (Ed.), Proton Transfer in Hydrogen-Bonded Systems, NATO ASI Series B, Physics, vol. 291, Plenum Press, New York, 1992;
(b) J.E. del Bene, M.J.T. Jordan, Theochem. 573 (2001) 11.
[19] T.E. Elsaesser, H.J. Bakker (Eds.), Ultrafast Hydrogen Bonding Dynamics and Proton Transfer Processes in the Condensed Phase, Kluwer Academic Press, Dordrecht, 2002.
[20] G. Anderegg, A. Ekstrom, L.F. Lindoy, R.J. Smith, J. Am. Chem. Soc. 102 (1980) 2670.
[21] (a) L.G. Amstrong, P. Grimsley, L.F. Lindoy, H.C. Lip, V.A. Norris, R.J. Smith, Inorg. Chem. 17 (1978) 2350;
(b) A. Ekstrom, L.F. Lindoy, H.C. Lip, R.J. Smith, H.J. Goodwin, M. McPartlin, P.A. Tasker, J. Chem. Soc., Dalton Trans. (1979) 1027;
(c) A. Ekstrom, L.F. Lindoy, R.J. Smith, Inorg. Chem. 19 (1980) 724.
[22] L.J. Farrugia, J. Appl. Crystallgr. 32 (1999) 837.
[23] A. Altomare, M.C. Burla, M. Camalli, G.L. Cascaranno, C. Giacovazzo, A. Guagliardi, A.G.G. Moliterni, G. Plidor, R. Spagna, J. Appl. Crystallogr. 32 (1999) 115.
[24] G.M. Sheldrick, SHELXL97: Program for the Refinement of Crystal Structures, Universität Göttingen, Germany, 1997.
[25] P.A. Tasker, J. Trotter, J. Chem. Res. (1981) 3834.
[26] I. Matijašić, G. Bocelli, Lj. Tušek- Božić, in: Presented at the 2nd Croatian-Slovenian Crystallographic Meeting, Stubičke Toplice, Croatia, 1993.
[27] (a) R.C. West (Ed.), Handbook of Chemistry and Physics, 67th ed., CRC Press, Boca Raton, FL, 1987;
(b) V. Gutmann, The Donor–Acceptor Approach to Molecular Interactions, Plenum, New York, 1978.
[28] P.G. Grimsley, L.F. Lindoy, H.C. Lip, R.J. Smith, J.T. Baker, Aust. J. Chem. 30 (1977) 2095.
[29] R.M. Silverstein, F.X. Webster, Spectrometric Identification of Organic Compounds, 6th ed., Wiley, New York, 1998.
[30] K. Nakamoto, Infrared and Raman Spectra of Inorganic and Coordination Compounds, Part B: Applications in Coordination Organometallic and Bioinorganic Chemistry, 5th ed., Willey-Interscience, New York, 1997.
[31] (a) J. Cheney, J.-M. Lehn, Nouv. J. Chim. 2 (1978) 411;
(b) R.L. Dean, J.L. Wood, J. Mol. Struct. 26 (1975) 215.
[32] B. Brzezinski, G. Zundel, J. Chem. Soc., Faraday Trans. 2 (72) (1976) 2127.
[33] (a) S.V. Trepalin, A.V. Yarkov, A.F. Solotnov, O.A. Raevsky, Spectrochim. Acta A 55 (1999) 1715;
(b) H. Matsura, K. Fukuhara, K. Kaneko, H. Yoshida, J. Mol. Struct. 265 (1992) 269.
[34] G.A. Jeffrey, An Introduction to Hydrogen Bonding, Oxford University Press, Oxford, 1997.
[35] G.R. Desiraju, T. Steiner, The Weak Hydrogen Bond in Chemistry and Biology, Oxford University Press, Oxford, 1999.
[36] J. Dunitz, R. Taylor, Chem. Eur. J. 3 (1997) 89.
[37] L. Shimoni, J.P. Glusker, Struct. Chem. 5 (1994) 383.
[38] L.J. Farrugia, J. Appl. Crystallogr. 30 (1997) 565.

Available online at www.sciencedirect.com
SCIENCE DIRECT®
Polyhedron 24 (2005) 113–120
POLYHEDRON
www.elsevier.com/locate/poly

Coordination properties of a dicompartmental ligand with tetra- and hexadentate coordination sites towards copper (II) and nickel (II) ions

K.R. Krishnapriya, M. Kandaswamy *

Department of Inorganic Chemistry, University of Madras, Guindy Campus, Chennai 600 025, India

Received 25 August 2004; accepted 18 October 2004

Abstract

A new dicompartmental ligand, *N*,*N*′-bis[2-iminomethyl-4-methyl-6-(4-methylpiperazin-1-ylmethyl)1-hydroxybenzene]1,8,naphthalene (H_2L) possessing contiguous tetra- and hexadentate coordination sites has been synthesized in simple route by the Schiff's base condensation of the precursor compound (PC) 2-formyl-4-methyl-6[4-methyl-6-(4-methylpiperazin-1-yl)methyl]phenol with 1,8-diaminonaphthalene.The mononuclear and binuclear Cu(II) and Ni(II) complexes of this ligand have been prepared and characterized by elemental analysis, IR, NMR and UV–Vis spectra.The electronic spectra of the mono- and binuclear Cu(II) complexes and mononuclear Ni(II) complex revealed one d–d transition in the region 570–600 nm, whereas the binuclear Ni(II) complex showed three d–d transitions at 800 nm ($\varepsilon \sim 95\ M^{-1}\ cm^{-1}$), 620 nm ($\varepsilon \sim 140\ M^{-1}\ cm^{-1}$) and 560 nm ($\varepsilon \sim 250\ M^{-1}\ cm^{-1}$), which were assigned to $^3A_{2g} \rightarrow {}^3T_{2g}$, $^3A_{2g} \rightarrow {}^3T_{1g}$, $^3A_{2g} \rightarrow {}^3T_{1g}(P)$, and these spin allowed electronic transitions are characteristic of an octahedral Ni^{2+} centre.The electrochemical studies evidenced for the mononuclear Cu(II) complex shows a single quasireversible one electron wave at −0.83 V (E_{pc}).The binuclear Cu(II) complex shows two quasireversible one electron reduction waves at −0.68 V (E^1_{pc}) and − 1.35 V (E^2_{pc}) in the cathodic region.The mononuclear Ni(II) complex shows one quasireversible reduction potential at −0.80 V (E_{pc}) and the binuclear Ni(II) complex shows two irreversible reduction potentials at −1.10 V (E^1_{pc}) and − 1.40 V (E^2_{pc}) in the cathodic region.The room-temperature magnetic moment value for the mononuclear Cu(II) complex is $1.72\mu_B(\mu_{eff})$ and for the binuclear Cu(II), $2.05\mu_B(\mu_{eff})$. The mononuclear Ni(II) complex is square planar and diamagnetic whereas the binuclear Ni(II) complex has a magnetic moment value of 3.05 μ_B (μ_{eff}). Kinetic studies on the oxidation of pyrocatechol to *o*-quinone using the copper (II) complexes and hydrolysis of 4-nitrophenyl phosphate using the nickel (II) complexes as catalysts showed that the binuclear complexes have higher rate constant values than that of the corresponding mononuclear complexes.
© 2004 Elsevier Ltd. All rights reserved.

Keywords: Compartmental ligands; Copper (II) and Nickel (II) complexes

1. Introduction

The term ''dinucleating ligands'' was first introduced in 1970 by Robson [1] to describe the class of polydentate chelating ligands, able to bind simultaneously two metal ions. Since then, a very large number of such ligands have been designed, and their coordination compounds have been thoroughly investigated.

Among the many different types of dinucleating ligands, the phenol-based compartmental ligands attracted particularly wide attention of scientists. The term ''compartmental'' was introduced to indicate a

* Corresponding author. Tel./fax: +91 44 22300488.
E-mail address: mkands@yahoo.com (M. Kandaswamy).

0277-5387/$ - see front matter © 2004 Elsevier Ltd. All rights reserved.
doi:10.1016/j.poly.2004.10.010

ligand containing two adjacent, but dissimilar coordination sites [2]. Particular interest in this type of ligand resulted from the recent recognition of the asymmetric nature of a number of dimetallic biosites [3,4]. Understanding of the ability of individual metal ions to play possibly different functions in dinuclear sites in metalloenzymes led to the design of a great number of asymmetric ligands where two compartments would provide a different coordination surrounding for the two metal ions.

Complexes of dicompartmental ligands with hexa- and tetradentate coordination sites were sparse; only three types of ligands have been reported in the literature (**I**–**III**, Fig. 1) [5–8]. Thus, in the present work, we have synthesized a new dicompartmental ligand (H_2L) by the Mannich base reaction followed by the Schiff's base condensation in a simple route, which contains a hexa-(N_4O_2) and tetradentate (N_2O_2) coordination site. Using this dicompartmental ligand (H_2L), mono- and homobinuclear Cu(II) and Ni(II) complexes were synthesized and their spectral, magnetic, electrochemical and catalytic properties were studied.

2. Experimental

2.1. Physical measurements

Elemental analysis was carried out on a Carlo Erba model 1106 elemental analyzer. ^{1}H NMR and ^{13}C NMR spectra were recorded using a model FX-80-Q Fourier transition NMR spectrometer. IR spectra were recorded on a Hitachi model 270-50 spectrophotometer on KBr discs in the wavenumber range of 4000–250 cm^{-1}. Electronic spectral studies were conducted on a Hitachi model 320, spectrophotometer in the wavelength range of 200–800 nm. Molar conductivity was measured with an Elico model SX 80 conductivity bridge, using a freshly prepared solution of the complex in DMF. Cyclic voltammograms were obtained on CHI600A electrochemical analyzer. The measurements were carried out under oxygen free conditions using a three-electrode cell, in which a glassy carbon electrode was the working electrode, a saturated Ag/AgCl electrode was the reference electrode and a platinum wire was used as the auxiliary electrode. A ferrocene/ferrocenium(1+) couple was used as an internal standard and $E_{1/2}$ of the ferrocene/ferrocenium (Fc/Fc^+) couple, under the experimental conditions, is 470 mV in dimethylformamide (DMF) and the ΔE_p value for Fc/Fc^+ is 70 mV. Tetra(*n*-butyl) ammonium perchlorate was used as the supporting electrolyte. The catalytic studies of the copper (II) and nickel (II) complexes were studied by taking 10^{-3} M solutions of the complexes in DMF and treating them with 10^{-1} M solutions of pyrocatechol and 4-nitrophenyl phosphate respectively in the presence of air. The reaction was followed spectrophotometrically by choosing the strongest absorbance of the *o*-quinone for the Cu(II) complexes at 390 nm and the 4-nitrophenolate anion for the Ni(II) complexes at 420 nm, and monitoring the increase in the absorbance at these wavelengths as a function of time. A plot of $\log(A_\infty/A_\infty - A_t)$ versus time was made for mono- and binuclear Cu(II) and Ni(II) complexes and the initial rate constant values were calculated.

2.2. Materials

5-Methylsalicylaldehyde was prepared by the literature method [9]. Tetra(*n*-butyl) ammonium perchlorate (TBAP), used as the supporting electrolyte in the electrochemical measurements, was purchased from Fluka and recrystallized from hot methanol. (*Caution!* TBAP is potentially explosive; hence, care should be taken in the handling of the compound). All other chemicals and solvents were of analytical grade and used as received.

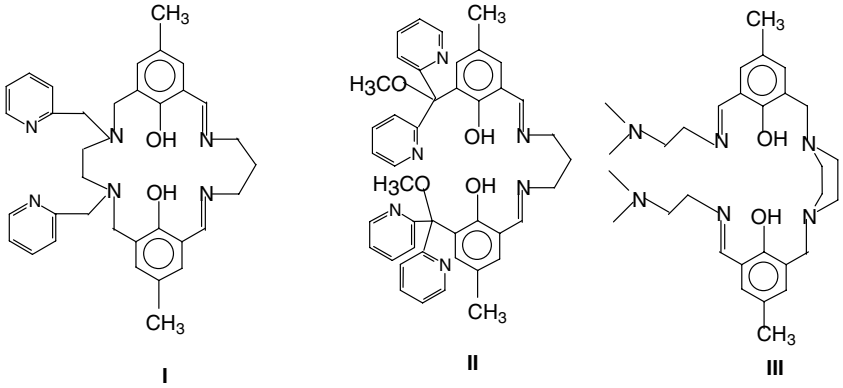


Fig. 1. (**I**)–(**III**) Examples of dicompartmental ligands reported in the literature.

2.3. Synthesis of 2-formyl-4-methyl-6[4-methyl-6-(4-methylpiperazin-1-yl)methyl] phenol (precursor compound PC)

Precursor compound PC was prepared by following the procedure in the literature [10].

2.4. Synthesis of N,N′-bis[2-iminomethyl-4-methyl-6-(4-methylpiperazin-1-yl methyl)1-hydroxybenzene]1,8, naphthalene (the dicompartmental ligand, H_2L)

The dicompartmental ligand (H_2L) was prepared by the dropwise addition of a solution of the precursor compound, PC (2.48 g, 0.01 mol) in ethanol (30 ml) to a stirred solution of 1,8-diaminonaphthalene (0.79 g, 0.005 mol) in ethanol (30 ml). After the addition was completed, the stirring was continued for a further hour. The solution was then refluxed on a water bath for 6 h and was allowed to cool by standing at room temperature. A brown coloured compound was recovered after removing the solvent by distillation under reduced pressure, which was then recrystallised from chloroform. (Scheme 1). Yield: 4.2 g (68%). M.p. 170 °C. *Anal*. Calc. for $C_{38}H_{46}N_6O_2$: C, 73.78; H, 7.44; N, 13.59. Found: C, 73.75; H, 7.46; N, 13.58%. ^{1}H NMR ($CDCl_3$, δ ppm): 2.56–2.74 (m, 16H, methylene protons), 2.59 (s, 4H, benzylic protons), 2.3 (s, 6H, Ar–CH_3), 2.06(s, 6H, –N–CH_3) 7.01–7.12 (m, 10H, Ar–H), 8.12 (s, 2H, CH=N), 10.1 (s, 2H, Ar–OH). Selected IR data (KBr, ν cm^{-1}): 3378, 1615, 1582. UV–Vis (λ_{max}, nm) (ε, M^{-1} cm^1) (CH_3CN): 345(45 000), 310(31 500), 275(23 500).

2.5. Synthesis of complexes

2.5.1. Synthesis of the [CuL](ClO$_4$) complex

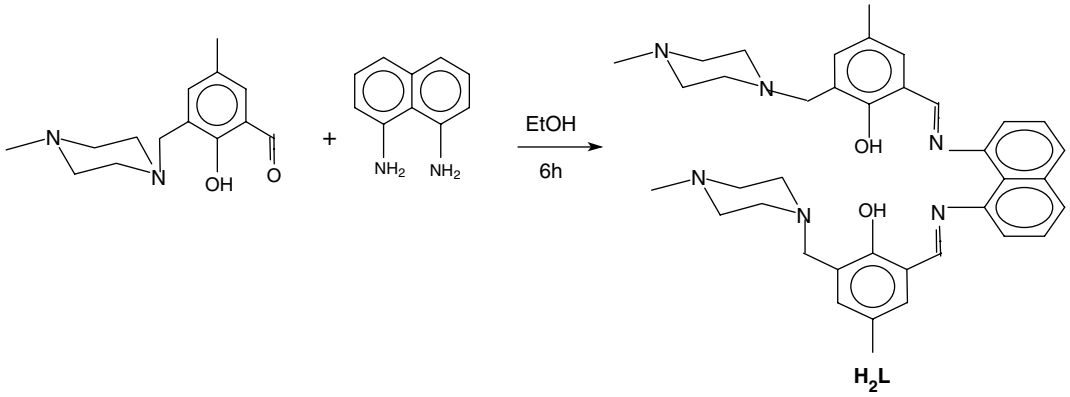
To ligand H_2L (0.618 g, 1 mmol) dissolved in MeOH (30 ml) was added $Cu(ClO_4)_2\cdot 6H_2O$ (0.37 g, 1 mmol) dissolved in MeOH (20 ml), and the mixture was refluxed for 6 h. The resulting solution was evaporated to half the volume and then allowed to cool by standing at room temperature (25 °C). After the slow evaporation of the solvent at 25 °C, the brown coloured compound obtained was recrystallised from ethanol. Yield: 0.60 g (77%). *Anal*. Calc. for $C_{38}H_{45}N_6O_2Cu(ClO_4$: C, 58.46; H, 5.77; N, 10.77; Cu, 8.16. Found: C, 58.45; H, 5.79; N, 10.76; Cu, 8.17%. Selected IR data (KBr, ν cm^{-1}): 1625, 1561, 1096, 626. Conductance in CH_3CN was given as $\Lambda_m = 82\ \Omega^{-1}\,mol^{-1}\,cm^2$. UV–Vis ($\lambda_{max,}$ nm) (ε, M^{-1} cm^1) (DMF): 600(141), 345(19 000), 275(10 400). $\mu_{eff} = 1.72\mu_B$.

2.5.2. Synthesis of the [NiL](ClO$_4$) complex

This Ni(II) complex was prepared by following the above procedure using the ligand H_2L (0.618 g, 1 mmol) and $Ni(ClO_4)_2\cdot 6H_2O$ (0.365 g, 1 mmol). An orange red compound was obtained on recrystallisation from ethanol. Yield: 0.56 g (72%). *Anal*. Calc. for $C_{38}H_{45}N_6O_2$-$Ni(ClO_4)$: C, 58.83; H, 5.80; N, 10.84; Ni, 7.57. Found: C, 58.82; H, 5.81; N, 10.83; Ni, 7.58%. ^{1}H NMR (DMSO-d_6, δ ppm): 2.06 (s, 6H, N–CH_3), 2.35 (s, 6H, Ar–CH_3), 3.40 (s, 2H, benzylic protons attached to $^+$NH), 2.59 (s, 2H, benzylic protons attached to N), 2.23–2.46 (m, 16H, methylene protons) 7.20–7.32 (m, 10H, Ar–H), 8.24 (s, 2H, CH=N). ^{13}C NMR (DMSO-d_6, δ ppm): 160 (s, 2C, CH=N), 110–140 (m, 22C, aromatic carbons), 46 (s, 1C, benzylic carbon attached to $^+$NH), 52 (s, 1C, benzylic carbon attached to N), 30 (s, 2C, methylene carbons attached to $^+$NH), 28 (s, 6C, methylene carbons attached to N–CH_3 and N–CH_2). Selected IR data (KBr, ν cm^{-1}): 1632, 1556, 1092, 628. Conductance in CH_3CN was given as $\Lambda_m = 87\ \Omega^{-1}\,mol^{-1}\,cm^2$. UV–Vis: ($\lambda_{max}$, nm) ($\varepsilon$, M^{-1} cm^{-1}) (DMF): 570(110), 345(12 100), 270(18 200).

2.5.3. Synthesis of the [Cu$_2$L](ClO$_4$)$_2$ complex

The binuclear Cu(II) complex was prepared by taking the ligand H_2L (0.618 g, 1 mmol) dissolved in MeOH (30



Scheme 1.

ml) and adding $Cu(ClO_4)_2 \cdot 6H_2O$ (0.74 g, 2 mmol) dissolved in MeOH (20 ml) and refluxing for 6 h. A brown precipitate was collected on evaporation of the resulting solution to half the volume and then allowing cooling by standing at room temperature (25 °C). A brown coloured compound was obtained on recrystallisation from ethanol. Yield: 0.60 g (64%). *Anal.* Calc. for $C_{38}H_{44}N_6O_2Cu_2(ClO_4)_2$: C, 48.42; H, 4.67; N, 8.92; Cu, 13.47. Found: C, 48.40; H, 4.69; N, 8.91; Cu, 13.48%. Selected IR data (KBr, ν cm^{-1}): 1630, 1580, 1100, 625. Conductance in CH_3CN was given as $\Lambda_m = 128\ \Omega^{-1}mol^{-1}\,cm^2$. UV–Vis: ($\lambda_{max}$, nm) ($\varepsilon$, $M^{-1}\,cm^{-1}$) (DMF): 575(257), 350(28 200), 275(21 000). $\mu_{eff} = 2.05\mu_B$.

2.5.4. Synthesis of the $[Ni_2L](ClO_4)_2$ complex

The $[Ni_2L](ClO_4)_2$ complex was prepared by following the above procedure using $Ni(ClO_4)_2 \cdot 6H_2O$ (0.73 g, 2 mmol). An orange red coloured compound was obtained on recrystallisation from ethanol. Yield: 0.70 g (75%). *Anal.* Calc. for $C_{38}H_{44}N_6O_2Ni_2(ClO_4)_2$: C, 48.91; H, 4.72; N, 9.01; Ni, 12.59. Found: C, 48.90; H, 4.74; N, 9.00; Ni, 12.58%. Selected IR data (KBr, ν cm^{-1}): 1630, 1554, 1100, 622. Conductance in CH_3CN was given as $\Lambda_m = 140\ \Omega^{-1}\,mol^{-1}\,cm^2$. UV–Vis: ($\lambda_{max}$, nm) ($\varepsilon$, $M^{-1}\,cm^{-1}$) (DMF): 800(95), 620(140), 560(250), 350(19 000), 280(25 200). $\mu_{eff} = 3.05\mu_B$.

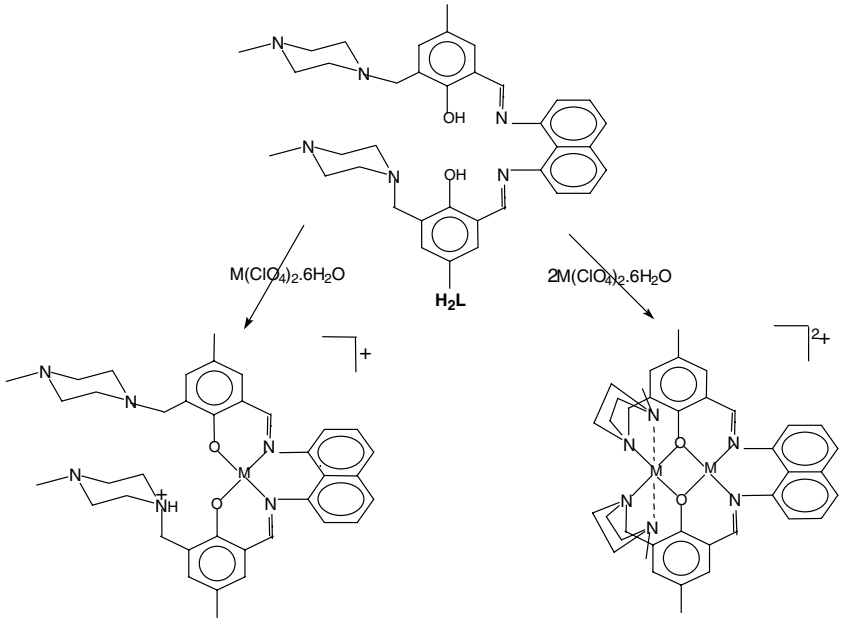
3. Results and discussion

A novel dicompartmental ligand (H_2L) with tetra- and hexadentate coordination sites has been synthesized (Scheme 1) and characterized. Using this dicompartmental ligand (H_2L) mono- and binuclear Cu(II) and Ni(II) complexes were prepared as shown in Scheme 2. The complexes were characterized by spectral studies. Their magnetic, electrochemical and catalytic behaviors are discussed.

3.1. Spectral studies

The IR spectrum of the dicompartmental ligand (H_2L) shows a ν(C=N) peak at 1625 cm^{-1}, and the absence of a ν(C=O) peak around 1700 cm^{-1} is indicative of Schiff's base condensation. The IR spectra of all the complexes show ν(C=N) bands at 1620–1640 cm^{-1} [11] and it is found that the ν(C=N) bands in the complexes are shifted by about 15–20 cm^{-1} to the lower energy regions compared to the free ligand (H_2L). This phenomenon appears to be due to the coordination of the azomethine nitrogens to the metal ion [12–14]. Also, a broad ν(OH) band of free ligand at 3378 cm^{-1} disappears on complexation. The peaks around 1100 and 620 cm^{-1} indicates the presence of perchlorate ions in the complexes. Furthermore, there is no splitting of the 1100 cm^{-1} peak. This indicates that the perchlorate ions are not coordinated to the metal ions.

^1H NMR and ^{13}C NMR of the mononuclear Ni(II) complex in DMSO-d_6 solution shows that it is NMR active. The ^1H NMR spectrum of the free ligand shows a multiplet in the range 7.01–7.12 ppm due to aromatic protons, and O–H protons of the two phenolic groups are at 10.1 ppm. The azomethine protons in the free ligand appear at 8.12 ppm. The mononu-



Scheme 2.

clear Ni(II) complex shows the aromatic protons as a multiplet in the range 7.20–7.32 ppm and the azomethine protons are shifted downfield at about 8.24 ppm, and the phenolic O–H disappears. These observations suggest that the dicompartmental ligand coordinates to the Ni(II) atom through the charged phenolic oxygen and the nitrogen atoms of azomethine groups of the N_2O_2 compartment in its mononuclear complex.

3.2. Electronic absorption spectroscopy

The electronic spectrum of the dicompartmental ligand (H_2L) in CH_3CN shows absorption bands at 345, 310 and 275 nm. These bands are indicative of naphthalene and other chromophore moieties present in the ligand. The electronic spectra of the mono- and binuclear Cu(II) complexes and the mononuclear Ni(II) complex showed three main transitions. The electronic spectra of the Cu(II) complexes show a d–d transition in the region 570–600 nm and the mononuclear Ni(II) complex shows one d–d transition at 570 nm. A moderately intensive band observed in the range of 340–350 nm is due to a ligand-to-metal charge transfer transition, and the strong band observed in the range of 270–280 nm is due to an intraligand charge transfer transition [15] for these complexes. The binuclear Ni(II) complex shows three d–d transitions at 800 nm ($\varepsilon \sim 95$ $M^{-1}\,cm^{-1}$), 620 nm ($\varepsilon \sim 140$ $M^{-1}\,cm^{-1}$) and 560 nm ($\varepsilon \sim 250$ $M^{-1}\,cm^{-1}$), assigned to $^3A_{2g} \rightarrow {}^3T_{2g}$, $^3A_{2g} \rightarrow {}^3T_{1g}$, $^3A_{2g} \rightarrow {}^3T_{1g}(P)$ spin allowed electronic transitions, which are characteristic of Ni^{2+} in an octahedral site [16,17].

3.3. Magnetic studies

The room-temperature magnetic studies of the mononuclear Cu(II) complex resulted in a magnetic moment value of $1.72\mu_B$, which is very close to the spin-only value ($1.73\mu_B$) for complexes that have one Cu(II) ion [18] with a single unpaired electron sited in an essentially $d_{x^2-y^2}$ orbital. The observed room-temperature magnetic moment value for the binuclear Cu(II) complex is found to be $2.05\mu_B$ for the binuclear entity, suggesting the presence of antiferromagnetic coupling between the two Cu(II) ions [7]. The mononuclear Ni(II) complex has a square planar geometry and is diamagnetic [18]. The binuclear Ni(II) complex has a magnetic moment value of $3.05\mu_B$ (μ_{eff}), characteristic of Ni^{2+} in an octahedral site [16,19].

3.4. Electrochemistry

Conductivity measurements [20] of the mononuclear Cu(II) and Ni(II) complexes in DMF resulted in Λ_m values in the range of 80–90 $\Omega^{-1}\,mol^{-1}\,cm^2$, which indicates that they are of the 1:1 electrolyte type, and the binuclear complexes show Λ_m values in the range of 125–140 $\Omega^{-1}\,mol^{-1}\,cm^2$ indicating that they are of 2:1 electrolyte type. The electrochemical properties of all the complexes reported in the present work were studied by cyclic voltammetry in DMF containing 10^{-1} M TBAP as a supporting electrolyte and the reduction potentials are summarized in Table 1. The cyclic voltammograms of the complexes are shown in Figs. 2 and 3.

3.4.1. Reduction process at negative potential

Reduction at negative potential is the usual trend observed for phenoxo copper and nickel complexes because of the electronegativity and hard nature of the phenoxide atoms in the ligand [21–23]. The cyclic voltammograms of mononuclear complexes at negative potential show a single electron transfer. The redox process

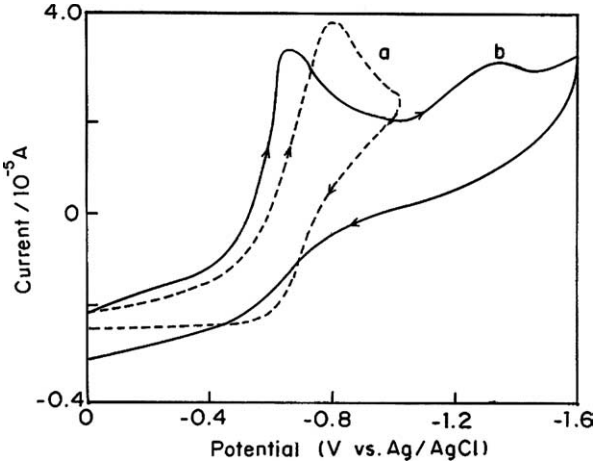


Fig. 2. Cyclic voltammograms of the copper (II) complexes: (a) $[CuL](ClO_4)$ and (b) $[Cu_2L](ClO_4)_2$.

Table 1
Electrochemical data for the complexes (reduction at the cathodic potential region)

Complexes	E^1_{pc} (V)	E^1_{pa} (V)	$E^1_{1/2}$ (V)	ΔE (mV)	E^2_{pc} (V)	E^2_{pa} (V)	$E^2_{1/2}$ (V)	ΔE (mV)
$[CuL](ClO_4)$	−0.83	−0.60	−0.72	170				
$[Cu_2L](ClO_4)_2$	−0.68	−0.50	−0.59	180	−1.35	−1.15	−1.25	200
$[NiL](ClO_4)$	−0.80	−0.64	−0.72	160				
$[Ni_2L](ClO_4)_2$	−1.10				−1.40			

Measured by CV at 100 mV s^{-1}. E vs. Ag/AgCl conditions: GC working and Ag/AgCl reference electrodes; supporting electrolyte, TBAP; concentration of complex, 1×10^{-3} M, concentration of TBAP, 1×10^{-1} M.

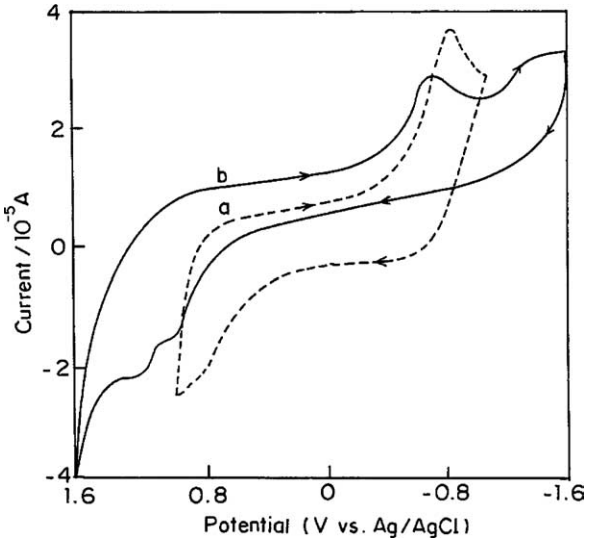


Fig. 3. Cyclic voltammograms of the nickel (II) complexes: (a) $[NiL](ClO_4)$ and (b) $[Ni_2L](ClO_4)_2$.

is quasireversible in nature as is evident from the criteria: the $E_{1/2}$ values are independent of scan rate; E_P increases with increasing scan rate (25, 50, 75 and 100 mV s^{-1}) and is always greater than 60 mV; i_{pc}/i_{pa} are not the same at different scan rates.

The reduction potential of mononuclear Cu(II) is −0.83 V (E_{pc}) and the reduction process is found to be quasireversible. The binuclear Cu(II) complex is associated with two quasireversible reduction waves. The reduction potentials are found to be −0.68 V (E^1_{pc}) and − 1.35 V (E^2_{pc}). Controlled potential electrolysis also carried out for the complexes at 100 mV s^{-1} more negative consumed one electron per molecule ($n = 0.95$), which reports that each couple corresponds to a one electron transfer process. So, the two redox processes are assigned as follows:

$$Cu^{II}Cu^{II} \rightleftharpoons Cu^{II}Cu^{I} \rightleftharpoons Cu^{I}Cu^{I}$$

The mononuclear Ni(II) complex of the same ligand undergoes a quasireversible reduction at −0.80 V and the binuclear Ni(II) complex shows irreversible reduction potentials at −1.10 V (E^1_{pc}) and − 1.40 V (E^2_{pc}).

The reduction potentials of the mononuclear complexes are comparable to those observed for the $[M(salen)]^{2+}$ complexes and may suggest that the couple observed for the mononuclear complexes refers to the reduction of the metal (II) ion in the naphthalene (N_2O_2) compartment.

The electrochemical studies of similar types of complexes with hexa- and tetradentate coordination sites reported in the literature [24] suggest that the formal reduction potentials of the binuclear complexes may be assigned to the metal ion in the first binding site, that is the naphthalene compartment. The second reduction potentials are comparable to that of the metal in the 6-coordination (N_4O_2) site.

3.4.2. Oxidation process at anodic potential

The mononuclear Ni(II) complex shows an irreversible oxidation wave in positive potentials at +0.85 V (E_{pa}). The binuclear Ni(II) complex shows two step single electron transfer processes in the potential range +1.0 V (E^1_{pa}) and + 1.2 V (E^2_{pa}) and both are found to be irreversible in nature.

3.5. Kinetic studies

3.5.1. Oxidation of pyrocatechol

A great interest has developed in the investigation of the catechol oxidase activity of copper complexes using suitable model substrates, which can serve as functional mimics for catechol oxidases or as new biomimetic catalysts for oxidation reactions [25–32]. The catecholase activity of mono- and binuclear copper (II) complexes synthesized in the present work were carried out using pyrocatechol as the model substrate. The course of the reaction was followed spectrophotometrically for nearly 45 min at regular time intervals of 5 min. The slope was determined by the method of initial rates by monitoring the growth of the 390 nm band of the product *o*-quinone. A linear relationship for initial rate and the complex concentration obtained for the copper complexes shows a first order dependence on the complex concentration for the systems. The rate constants for the mono- and binuclear copper complexes were found to be 4.6×10^{-3} and 1.52×10^{-2} min^{-1}, respectively. The kinetic plot of $\log(A_\infty/A_\infty - A_t)$ versus time of catecholase activity is shown in Fig. 4. It is found that the binuclear

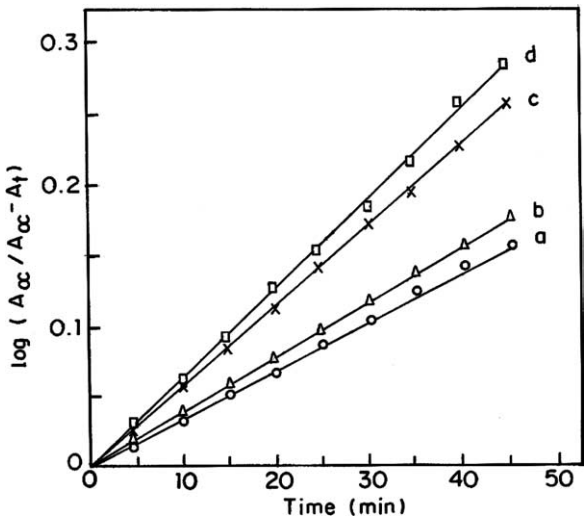


Fig. 4. The kinetic plot for the oxidation of pyrocatechol and hydrolysis of 4-nitrophenyl phosphate: (a) $[NiL](ClO_4)$, (b) $[CuL](ClO_4)$, (c) $[Ni_2L](ClO_4)_2$ and (d) $[Cu_2L](ClO_4)_2$.

Cu(II) complex show higher reactivity than its mononuclear complex. This is due to the fact that the oxidation of pyrocatechol to *o*-quinone requires the presence of two metal ions in close proximity [26]; hence the rate constant for the binuclear copper complex is high.

3.5.2. Hydrolysis of 4-nitrophenyl phosphate

The catalytic activity of the mono- and binuclear Ni(II) complexes on the hydrolysis of 4-nitrophenyl phosphate was determined spectrophotometrically by monitoring the increase of the 4-nitrophenolate anion characteristic absorption at 420 nm over time in DMF at 25 °C. The nickel (II) complexes were able to hydrolyze *p*-nitrophenyl phosphate to the 4-nitrophenolate anion. The rate constants were calculated by the initial rate method. The rate constants for the catalytic hydrolysis of 4-nitrophenyl phosphate catalyzed by the mono- and binuclear nickel (II) complexes were found to be 8.8×10^{-3} and 1.3×10^{-2} min^{-1}, respectively. The kinetic plot of $\log(A_\infty/A_\infty - A_t)$ versus time for the nickel (II) complexes is shown in Fig. 4.

Upon comparing the kinetics of the mononuclear and binuclear nickel (II) complexes, the rate constants were found to be higher for the binuclear analogue. This is due to the fact that the mononuclear complex proceeds via a SN_1 type of reaction followed by deprotonation of the OH group and formation of an intermediate with the phosphate group and then cleavage of the bond to form the phenolate anion, along with hydroxylation of the phosphate group.

The binuclear nickel (II) complex followed a concerted SN_2 type of mechanism where the nucleophile OH adds to one of the nickel ions and the phosphate group simultaneously gets bounded to another nickel ion. Here, bond formation and bond breakage occurs at the same time. This kind of mechanism requires two metal ions in close proximity. Convincingly, the rate constants are also higher than the corresponding mononuclear complexes. The mechanism of action has already been explained with the help of model complexes [33,34].

From the above studies we conclude that, in the mononuclear complexes, the metal ions prefer the tetradentate compartmental site rather than the hexadentate site. This may be due to the stronger coordination behaviour of azomethine nitrogens in the tetradentate site than the tertiary nitrogens in the hexadentate compartmental site.

Acknowledgement

KRK thanks the University Grants Commission (India) for financial assistance through Major Research Project sanctioned to MK.

References

[1] R. Robson, Inorg. Nucl. Chem. Lett. 6 (1970) 125.
[2] D.E. Fenton, Inorg. Chem. Commun. 5 (2002) 537.
[3] T. Klabunde, C. Eicken, J.C. Sacchettini, B. Krebs, Nat. Struct. Biol. 5 (1998) 1084.
[4] E.I. Solomon, U.M. Sundaram, T.E. Machonkin, Chem. Rev. 96 (1996) 2563.
[5] C. Jin qin, A. Gavrilova, B. Bosnich, Pure Appl. Chem. 73 (2001) 221.
[6] E.V. Rybak-Akimova, N.W. Alcock, D.H. Busch, Inorg. Chem. 37 (1998) 1563.
[7] L.M. Liable-sands, C. Incarvito, A.L. Rheingold, C. Jin Qin, A. Gavrilova, B. Bosnich, Inorg. Chem. 40 (2001) 2147.
[8] R. Thirumurugan, K. Vengadesan, S. Shanmuga Sudara Raj, G. Shanmugam, H.K. Fun, Cryst. Res. Tech. 35 (2000) 987.
[9] J.C. Duff, J. Chem. Soc. (1941) 547.
[10] M. Lubben, R. Hage, A. Meetsma, K. Byma, B.L. Feringa, Inorg. Chem. 34 (1995) 2217.
[11] G. Das, R. Shukala, S. Mandal, R. Singh, P.K. Bharadwaj, J.V. Singh, K.H. Whitmire, Inorg. Chem. 36 (1997) 323.
[12] F.M. Ashmawy, R.M. Issa, S.A. Amer, C.A. Mc Auliffe, R.V. Parish, J. Chem. Soc., Dalton Trans. (1987) 2009.
[13] B.G. Jeong, C.P. Rim, S.K. Kook, K.H. Chjo, Y.K. Choi, Chem. Soc. Bull. Korean 17 (1996).
[14] M. Thirumavalavan, P. Akilan, M. Kandaswamy, Supramol. Chem. (2004) (in press).
[15] J. Manonmani, M. Kandaswamy, V. Narayanan, R. Thirumurugan, S. Shanmuga Sundara Raj, G. Shanmugam, M.N. Ponnuswamy, H.K. Fun, Polyhedron 20 (2001) 3039.
[16] T.C. Higgs, C.J. Carrano, Inorg. Chem. 36 (1997) 298.
[17] M.F. Cabral, B. Murphy, J. Nelson, Inorg. Chim. Acta 90 (1984) 169.
[18] A. Bottcher, H. Elias, E. Jager, H. Lanffelderova, M. Mazur, L. Mullor, H. Paulus, P. Pelikan, M. Rudolph, M. Valko, Inorg. Chem. 32 (1993) 4131.
[19] M.P. Suh, B.Y. Shim, T.S. Yoon, Inorg. Chem. 33 (1994) 5509.
[20] K.R. Adam, G. Anderegg, L.F. Lindoy, H.C. Lip, M. McPartlin, J.H. Rea, R.J. Smith, P.A. Tasker, Inorg. Chem. 19 (1980) 2956.
[21] M. Thirumavalavan, P. Akilan, M. Kandaswamy, Inorg. Chem. 42 (2003) 3308.
[22] (a) A. Benzekeri, P. Dubourdeaux, J.M. Latour, P. Rey, J. Langier, J. Chem. Soc., Dalton Trans. (1991) 3359;
(b) P. Zanello, S. Tamburini, P.A. Vigato, G.A. Mazzocchin, Coord. Chem. Rev. 77 (1987) 165.
[23] F. Azevedo, C.T. Carrondo, B. Caseto, M. Convery, D. Domingues, C. Freire, T. Durate, K. Neilson, C. Santos, Inorg. Chim. Acta 219 (1994) 43.
[24] C. Fraser, B. Bosnich, Inorg. Chem. 41 (2002) 1788.
[25] K. Selmeczi, M. Reglier, M. Giorge, G. Speier, Coord. Chem. Rev. 245 (2003) 191.
[26] A. Neves, L.M. Rossi, A.J. Bortoluzzi, B.S. Szpoganicz, C. Wiezbicki, E. Schwingel, W. Haase, S. Ostrovsky, Inorg. Chem. 41 (2002) 1788.
[27] C. Fernandes, A. Neves, A.J. Bortoluzzi, A.S. Mangrich, E. Rentschler, B. Szpoganicz, E. Schwingel, Inorg. Chim. Acta 320 (2001) 12.
[28] P. Gentschev, N. Moller, B. Krebs, Inorg. Chim. Acta 300–302 (2000) 442.
[29] A. Neves, L.M. Rossi, A.J. Bortoluzzi, A.S. Mangrich, W. Haase, R. Werner, J. Braz. Chem. Soc. 12 (2001) 747.
[30] S. Torelli, C. Belle, I. Gautier-Luneau, J.L. Pierre, E. Saint-aman, J.M. Latour, L. Le Pape, D. Luneau, Inorg. Chem. 39 (2000) 3256.

[31] J. Kaizer, J. Pap, G. Speier, L. Parkanyi, L. Korecz, A. Rockenbauer, J. Inorg. Biochem. 91 (2002) 190.
[32] P. Akilan, M. Thirumavalavan, M. Kandaswamy, Polyhedron 22 (2003) 1407.
[33] C.D. Toia, S. Menage, J.M. Vincent, M.T.V. Pouchot, M. Fontecave, Inorg. Chem. 36 (1997) 6148.
[34] M. Yamami, H. Furutachi, T. Yokohama, H. Okawa, Inorg. Chem. 37 (1998) 6832.

Available online at www.sciencedirect.com
SCIENCE DIRECT®
Polyhedron 24 (2005) 121–128
POLYHEDRON
www.elsevier.com/locate/poly

Synthesis, spectroscopic and structural properties of an unusual series of homoleptic phosphine oxide complexes of the alkaline earth dications

Michael B. Hursthouse [a], William Levason [a], Raju Ratnani [b], Gillian Reid [a,*], Holly Stainer [a], Michael Webster [a]

[a] School of Chemistry, University of Southampton, Highfield, Southampton SO17 1BJ, UK
[b] Department of Pure and Applied Chemistry, M. D. S. University, Ajmer 305 009, India

Received 27 September 2004; accepted 22 October 2004
Available online 15 December 2004

Abstract

The distorted tetrahedral $[M(OPPh_3)_4](SbCl_6)_2$ (M = Mg, Ca, Sr) are obtained from MCl_2, $OPPh_3$ and $SbCl_5$ in suitable solvent conditions, while Ba^{2+} gives $[Ba(OPPh_3)_5](SbCl_6)_2$. The chelating o-$C_6H_4(P(O)Ph_2)_2$ gives the tris complexes $[M\{o\text{-}C_6H_4(P(O)Ph_2)_2\}_3](SbCl_6)_2$, while under similar conditions the stoichiometries of the products obtained using $Ph_2P(O)CH_2P(O)Ph_2$ vary with M; and products include the five-coordinate $[Mg\{Ph_2P(O)CH_2P(O)Ph_2\}_2(H_2O)](SbCl_6)_2$, the distorted octahedral $[M\{Ph_2P(O)CH_2P(O)Ph_2\}_3](SbCl_6)_2$ (M = Ca or Sr) and the seven-coordinate $[Sr\{Ph_2P(O)CH_2P(O)Ph_2\}_3(EtOH)](SbCl_6)_2$. Strontium is unusual in that both six- and seven-coordinate species are evident and may be isolated depending upon the reaction conditions. These are the first reported Group 2 complexes with bidentate phosphine oxides and there are no other phosphine oxide complexes with Sr or Ba. Crystal structures are reported for $[Mg(OPPh_3)_4](SbCl_6)_2\cdot CH_2Cl_2$, $[Ca\{Ph_2P(O)CH_2P(O)Ph_2\}_3](SbCl_6)_2\cdot 2CH_2Cl_2$ and $[Sr\{Ph_2P(O)CH_2P(O)Ph_2\}_3(EtOH)](SbCl_6)_2\cdot 0.45CH_2Cl_2$ The compounds isolated show significant dependence upon the charge:radius ratio of the metal and the steric bulk and rigidity of the ligand.
© 2004 Elsevier Ltd. All rights reserved.

Keywords: Homoleptic phosphine oxide complexes; Alkaline earth dications

1. Introduction

The coordination chemistry of especially the heavier alkaline earth cations is among the least studied of the metal ions in the periodic table. Examples of complexes involving these closed shell dications with neutral ligands are dominated by those with crown ethers and their derivatives while complexes with anionic diamine tetracarboxylate ligands are also well known [1,2], although these are hugely outnumbered by crown ether complexes of the Group 1 metal ions. The role of the lighter Mg^{2+} ion in chlorophyll has been the stimulus for the majority of studies of Mg-containing complexes, many of which have been prepared as model compounds [1,2].

In recent work, we have shown that homoleptic phosphine oxide complexes involving the Group 3 metal ions Sc^{3+}, Y^{3+} and La^{3+}, also closed shell ions, exhibit a surprisingly wide speciation, with considerable dependence upon both the steric bulk of the ligand and the charge: radius ratio of the metal [3–6]. There are some early reports of phosphine oxide complexes with Mg^{2+} and Ca^{2+}, including $[M(OPPh_3)_4]^{2+}$, although these are mainly part of wider compilations and characterisation

* Corresponding author. Tel.: +44 2380593609; fax: +44 2380593781.
E-mail address: gr@soton.ac.uk (G. Reid).

0277-5387/$ - see front matter © 2004 Elsevier Ltd. All rights reserved.
doi:10.1016/j.poly.2004.10.009

data are very limited [7,8], while Rodley and co-workers [9,10] have reported crystal structure analyses for the magnesium cations $[Mg(OPMe_3)_5]^{2+}$ and $[Mg(OPMe_3)_5(OH_2)]^{2+}$.

In order to probe further the effect of the charge:radius ratio upon the M-phosphine oxide coordination we have synthesised and spectroscopically characterised a systematic series of Group 2 metal (Mg, Ca, Sr and Ba) complexes with the phosphine oxide ligands $OPPh_3$, $Ph_2P(O)CH_2P(O)Ph_2$ and o-$C_6H_4(P(O)Ph_2)_2$. The results are reported here together with crystal structures of representative examples, including the first structure of a strontium phosphine oxide complex and the first structure of a homoleptic phosphine oxide complex of calcium. The structures confirm the conclusions from the spectroscopic assignments.

2. Results and discussion

The tetrakis complexes $[M(OPPh_3)_4](SbCl_6)_2$ were obtained in good yield by treatment of dehydrated MCl_2 (M = Mg or Ca) with four molar equivalents of $OPPh_3$ in anhydrous CH_2Cl_2 solution, with addition of two molar equivalents of $SbCl_5$ to abstract chlorine. There is no indication that these compounds take up solvent molecules or water into the coordination sphere, suggesting that despite the unusually low coordination number for Ca^{2+}, they are coordinatively saturated. This contrasts with the previously studied $Mg^{2+}/OPMe_3$ system where both the five-coordinate $[Mg(OPMe_3)_5]^{2+}$ and the six-coordinate $[Mg(OPMe_3)_5(OH_2)]^{2+}$ have been structurally characterised (see below) even with the small Mg(II) ion [9,10]. While the ionic radii of Ca^{2+} and Y^{3+} are the same (approximately 106 pm), [1] we have shown previously that with Y^{3+} we can obtain the six-coordinate $[YCl(OPPh_3)_5]^{2+}$, hence it is possible to accommodate more ligands on size grounds [4]. It is therefore likely that the lower charge:radius ratio of Ca^{2+} disfavours higher coordination numbers. The corresponding strontium and barium complexes cannot be obtained by direct addition of $SrCl_2$, $OPPh_3$ and $SbCl_5$ in CH_2Cl_2. Under these conditions the major product is $[SbCl_5(OPPh_3)]$ on the basis of IR and ^{31}P NMR spectroscopic measurements [11]. This difficulty was alleviated by forming $Sr(SbCl_6)_2$ in MeCN solution initially (from anhydrous $SrCl_2$ and $SbCl_5$) [12] with subsequent addition of $OPPh_3$ giving $[Sr(OPPh_3)_4](SbCl_6)_2$. Using $Ba(SbCl_6)_2$ gave the 5:1 species $[Ba(OPPh_3)_5](SbCl_6)_2$, probably as a consequence of the much larger radius of Ba(II). Unlike the lighter Group 2 analogues, this barium compound is poorly soluble in CH_2Cl_2, but dissolves readily in MeCN in the presence of added $OPPh_3$ (without incorporation of solvent into the coordination sphere). These formulations follow from microanalysis and from the IR spectra which show a small low frequency shift in the P=O stretching vibration (ca. 10 cm^{-1}) and a single strong absorption at ca. 345 cm^{-1}, attributed to the octahedral $SbCl_6^-$ anion. The ^{31}P NMR spectra show a single resonance in each with a small high frequency coordination shift ($\delta^{31}P$ for $OPPh_3$ = +28).

Crystals of $[Mg(OPPh_3)_4](SbCl_6)_2 \cdot CH_2Cl_2$ were obtained by diffusion of diethyl ether into a solution of the complex in CH_2Cl_2. The structure shows (Fig. 1, Table 1) four O-bonded $OPPh_3$ ligands coordinated in an almost regular tetrahedral arrangement to the central Mg^{2+} cation. The Mg–O distances are in the range 1.890(2)–1.919(2) Å, while the P–O distances are 1.507(2)–1.513(2) Å. The only other crystallographically characterized Mg(II) phosphine oxide complexes are the five-coordinate $[Mg(OPMe_3)_5](ClO_4)_2$ (d(Mg–O) = 1.94(2)–2.06(2) Å) and the six-coordinate, distorted octahedral $[Mg(OPMe_3)_5(OH_2)](ClO_4)_2$ (d(Mg–O(P)) = 2.06(3)–2.11(3) Å, d(Mg–O(H_2)) = 2.19(2) Å) [9,10]. The significantly shorter Mg–O bond distances in the $[Mg(OPPh_3)_4]^{2+}$ cation almost certainly reflect the lower coordination number in this species. The Mg–O–P angles show surprising variation, taking values in the range 139.41(15)°–163.08(16)°, probably mainly due to the steric influence and packing of the phenyl rings.

We have also examined the coordination chemistry of the diphosphine dioxides $Ph_2P(O)CH_2P(O)Ph_2$ and o-$C_6H_4(P(O)Ph_2)_2$ with the alkaline earth chlorides. Using $MgCl_2$, three molar equivalents of $Ph_2P(O)CH_2$-

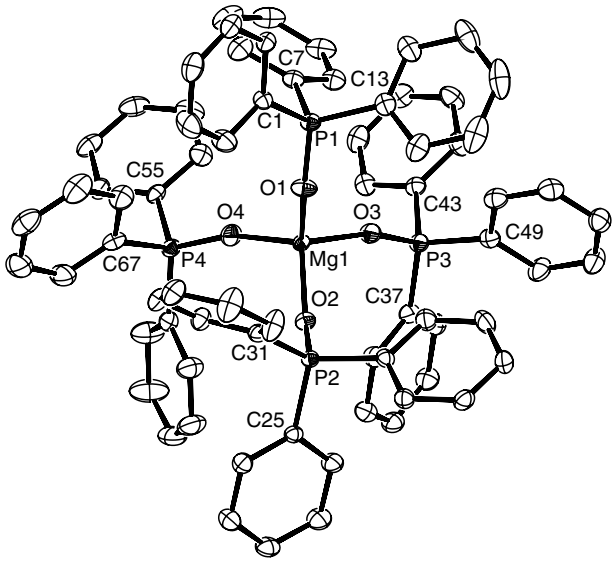


Fig. 1. View of the structure of the $[Mg(OPPh_3)_4]^{2+}$ cation with numbering scheme adopted. H atoms are omitted for clarity. Ellipsoids are shown at the 50% probability level.

[1] The ionic radius of Ca^{2+} does vary with coordination number and with the nature of the compound, hence these are illustrative values only.

Table 1
Selected bond lengths (Å) and angles (°) for $[Mg(OPPh_3)_4](SbCl_6)_2\cdot CH_2Cl_2$

Bond lengths	
Mg1–O1	1.919(2)
Mg1–O2	1.914(2)
Mg1–O3	1.900(2)
Mg1–O4	1.890(2)
P1–O1	1.508(2)
P2–O2	1.513(2)
P3–O3	1.509(2)
P4–O4	1.507(2)
Bond angles	
O4–Mg1–O3	111.50(12)
O4–Mg1–O2	109.19(11)
O3–Mg1–O2	106.41(11)
O4–Mg1–O1	112.48(11)
O3–Mg1–O1	109.74(11)
O2–Mg1–O1	107.26(10)
P1–O1–Mg1	139.41(15)
P2–O2–Mg1	146.69(15)
P3–O3–Mg1	163.08(16)
P4–O4–Mg1	161.45(17)

$P(O)Ph_2$ and two molar equivalents of $SbCl_5$ in CH_2Cl_2 solution, followed by precipitation with Et_2O gives the five-coordinate $[Mg\{Ph_2P(O)CH_2P(O)Ph_2\}_2(OH_2)](SbCl_6)_2\cdot Et_2O$ with a coordinated water molecule (presumably arising from traces of adventitious water in the solvent during recrystallisation). The IR spectrum shows ν(P=O) at 1179 cm^{-1} and ionic $SbCl_6^-$ at 346 cm^{-1}, as well as confirming the presence of the coordinated water, while the ^1H NMR spectrum shows 1 mol of Et_2O solvent per two diphosphine dioxide ligands. The $^{31}P\{^1H\}$ NMR spectrum is a singlet at 34.0 ppm, consistent with a small high frequency coordination shift ($\delta^{31}P$ for $Ph_2P(O)CH_2P(O)Ph_2$ itself is +25). The six-coordinate, tris-chelated calcium complex $[Ca\{Ph_2P(O)CH_2P(O)Ph_2\}_3](SbCl_6)_2$ is obtained similarly, with precipitation achieved using ethanol. The ^1H NMR and IR spectra, as well as microanalysis indicate that there is no incorporation of EtOH in this product, and $\delta(^{31}P)$ is 32.6 ppm. For strontium both the six-coordinate $[Sr\{Ph_2P(O)CH_2P(O)Ph_2\}_3](SbCl_6)_2$ and the seven-coordinate $[Sr\{Ph_2P(O)CH_2P(O)Ph_2\}_3(EtOH)](SbCl_6)_2$ (see crystal structure below) can be obtained, the former by concentrating the CH_2Cl_2 solution until precipitation occurs, the latter by adding EtOH to initiate precipitation. The $^{31}P\{^1H\}$ NMR spectra are very slightly different, however the presence of EtOH is clearly evident in the ^1H NMR and IR spectra of the latter. No product could be isolated from reaction of $Ba(SbCl_6)_2$ with $Ph_2P(O)CH_2P(O)Ph_2$ in either MeCN or CH_2Cl_2 solution, consistent with a much reduced affinity of Ba^{2+} for the phosphine oxide compared to the lighter metals. This series of compounds reveals a clear variation in coordination number as Group 2 is descended, with Sr^{2+} representing a cross-over point were both six- and seven-coordinate species are accessible with this ligand.

The coordination environment at Ca^{2+} was confirmed from a crystal structure determination on $[Ca\{Ph_2P(O)CH_2P(O)Ph_2\}_3](SbCl_6)_2\cdot 2CH_2Cl_2$, the first structural study on a homoleptic phosphine oxide complex of Ca^{2+}. The crystals obtained were very small and hence the diffraction data weak. However, the structure shows (Fig. 2, Table 2) the Ca atom coordinated to all six O atoms of three chelating diphosphine dioxide ligands to give a distorted octahedral geometry. The Ca–O bond distances of 2.283(6)–2.332(6) Å are markedly longer (by ca. 0.4 Å) than d(Mg–O) in the $[Mg(OPPh_3)_4]^{2+}$ described earlier, reflecting both the increase in radius on going down Group 2 and the increase in coordination number. The O–Ca–O angles within the chelate rings are ca. 85°, while the Ca–O–P angles are all in the range 130°–136°. The distorted octahedral tris chelate observed here contrasts with that observed for $[Na\{Ph_2P(O)CH_2P(O)Ph_2\}_3]X$ which is precisely trigonal prismatic (X = Cl: d(Na–O) = 2.4566(14), d(P–O) = 1.4883(13) Å) [13–15]. The only other reported structure of a Ca^{2+} phosphine oxide species is the organometallic cation $[Ca(\eta^5\text{-}C_5Me_5)(OPPh_3)_3]^+$ which shows similar Ca–O bond lengths, d(Ca–O) = 2.254(2), 2.282(1), 2.300(2) Å [16].

Crystals of $[Sr(EtOH)\{Ph_2P(O)CH_2P(O)Ph_2\}_3](SbCl_6)_2\cdot 0.45CH_2Cl_2$ were obtained by layering a CH_2Cl_2 solution of the complex with EtOH and cooling to ca. −18 °C in the freezer. The structure shows (Fig. 3, Table 3) the Sr atom coordinated to three chelating diphosphine dioxide ligands, with the EtOH ligand completing the coordination sphere. The Sr–O distances

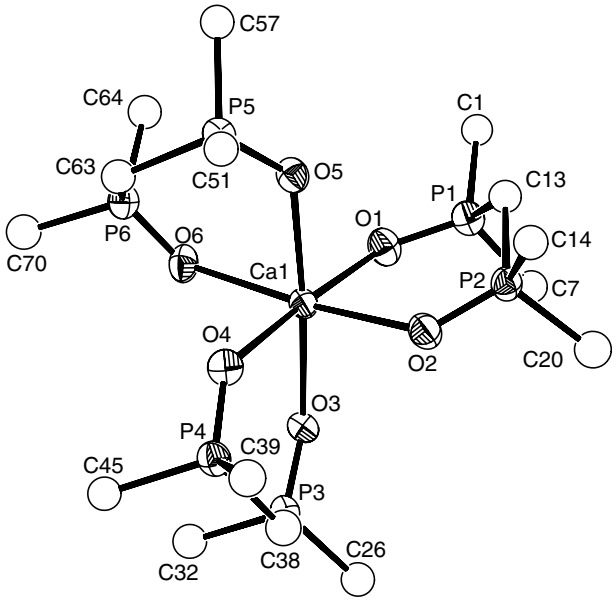


Fig. 2. View of the structure of the $[Ca\{Ph_2P(O)CH_2P(O)Ph_2\}_3]^{2+}$ cation with numbering scheme adopted. Ellipsoids are drawn at 50% probability. H atoms and phenyl rings (except the *ipso* C atoms) are omitted for clarity.

Table 2
Selected bond lengths (Å) and angles (°) for $[Ca\{Ph_2P(O)CH_2P(O)Ph_2\}_3](SbCl_6)_2\cdot 2CH_2Cl_2$

Bond lengths	
Ca1–O1	2.283(6)
Ca1–O2	2.309(6)
Ca1–O3	2.291(6)
Ca1–O4	2.332(6)
Ca1–O5	2.327(6)
Ca1–O6	2.308(6)
P1–O1	1.507(6)
P2–O2	1.495(6)
P3–O3	1.488(6)
P4–O4	1.490(6)
P5–O5	1.495(6)
P6–O6	1.476(7)
Bond angles	
O1–Ca1–O2	85.2(2)
O1–Ca1–O3	95.9(2)
O1–Ca1–O4	174.0(2)
O1–Ca1–O5	89.6(2)
O1–Ca1–O6	97.8(2)
O2–Ca1–O4	88.9(2)
O2–Ca1–O5	89.3(2)
O3–Ca1–O2	92.3(2)
O3–Ca1–O4	85.2(2)
O3–Ca1–O5	174.4(2)
O3–Ca1–O6	95.6(2)
O5–Ca1–O4	89.5(2)
O6–Ca1–O2	171.2(2)
O6–Ca1–O4	87.9(2)
O6–Ca1–O5	82.5(2)
P1–O1–Ca1	132.9(4)
P2–O2–Ca1	133.0(3)
P3–O3–Ca1	135.7(4)
P4–O4–Ca1	134.6(4)
P5–O5–Ca1	130.2(3)
P6–O6–Ca1	131.7(4)

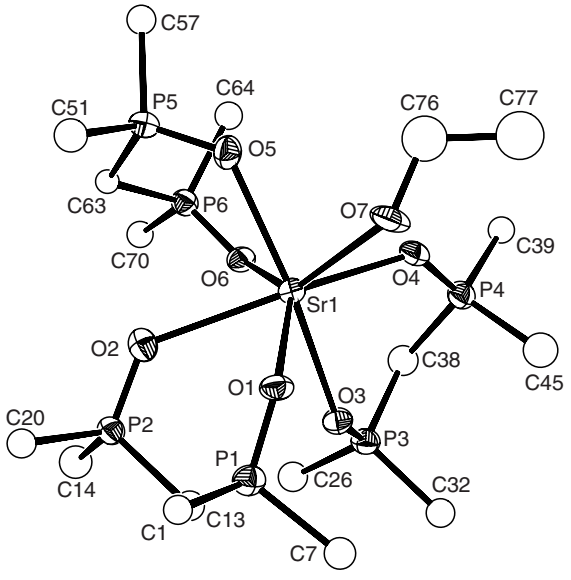


Fig. 3. View of the structure of the $[Sr(EtOH)\{Ph_2P(O)CH_2P(O)Ph_2\}_3]^{2+}$ cation with numbering scheme adopted. H atoms and phenyl rings (except the *ipso* C atoms) are omitted for clarity. Ellipsoids are drawn at 50% probability.

Table 3
Selected bond lengths (Å) and angles (°) for $[Sr(EtOH)\{Ph_2P(O)CH_2P(O)Ph_2\}_3](SbCl_6)_2\cdot 0.45CH_2Cl_2$

Bond lengths	
Sr1–O1	2.557(6)
Sr1–O2	2.597(6)
Sr1–O3	2.540(6)
Sr1–O4	2.509(6)
Sr1–O5	2.502(6)
Sr1–O6	2.560(6)
Sr1–O7	2.573(6)
P1–O1	1.498(6)
P2–O2	1.496(7)
P3–O3	1.477(6)
P4–O4	1.475(7)
P5–O5	1.487(7)
P6–O6	1.481(7)
Bond angles	
O1–Sr1–O2	72.19(19)
O1–Sr1–O6	146.06(19)
O1–Sr1–O7	76.8(2)
O3–Sr1–O1	81.16(19)
O3–Sr1–O2	90.18(19)
O3–Sr1–O6	85.52(19)
O3–Sr1–O7	117.8(2)
O4–Sr1–O1	128.7(2)
O4–Sr1–O2	151.5(2)
O4–Sr1–O3	76.46(19)
O4–Sr1–O6	77.1(2)
O4–Sr1–O7	74.1(2)
O5–Sr1–O1	114.0(2)
O5–Sr1–O2	84.9(2)
O5–Sr1–O3	161.5(2)
O5–Sr1–O4	99.7(2)
O5–Sr1–O6	76.0(2)
O5–Sr1–O7	77.6(2)
O6–Sr1–O2	76.80(19)
O6–Sr1–O7	136.51(19)
O7–Sr1–O2	134.0(2)
P1–O1–Sr1	129.1(3)
P2–O2–Sr1	130.0(4)
P3–O3–Sr1	135.9(4)
P4–O4–Sr1	133.5(3)
P5–O5–Sr1	130.9(4)
P6–O6–Sr1	129.5(3)
C76–O7–Sr1	123.0(6)

within the phosphine oxide coordination lie in the range 2.502(6)–2.597(6) Å, with the Sr–O(EtOH) distance being 2.573(6) Å . These are ca. 0.2 Å longer than *d*(Ca–O) in the six-coordinate $[Ca\{Ph_2P(O)CH_2P(O)Ph_2\}_3]^{2+}$ above. As expected on the basis of the seven-coordination, the O–Sr–O angles reveal much greater variation compared to the corresponding Ca species, those within the chelate rings are 72.2(2)°, 76.0(2)° and 76.5(2)°. The coordination environment approximates to a capped octahedron. This represents the first structural study of a Sr^{2+} phosphine oxide complex.

Similar reactions using the more rigid *o*-phenylene diphosphine dioxide, $o\text{-}C_6H_4(P(O)Ph_2)_2$, gives the compounds $[M\{o\text{-}C_6H_4(P(O)Ph_2)_2\}_3](SbCl_6)_2$ (M = Mg, Ca

or Sr), all of which are six-coordinate, with no coordinated solvent. The spectroscopic properties parallel those for the compounds described earlier, with a small (ca. 10 cm^{-1}) low frequency shift in ν(P=O) and a small high frequency shift in $\delta(^{31}P)$ upon coordination ($\delta^{31}P$ for o-$C_6H_4(P(O)Ph_2)_2$ is +33). The compounds were also characterised by ^1H NMR spectroscopy and microanalysis. The occurrence of only the six-coordinated tris-chelates with this ligand may be a consequence of the increased rigidity of the o-phenylene-based ligand (we have shown that this plays a significant role in dictating the coordinating properties of other related 7-membered chelate ligands e.g. involving o-xylylene linkages which also show a greater tendency for chelation than their analogues with saturated aliphatic (C4) linkages) [17–19]. Using o-$C_6H_4(P(O)Ph_2)_2$ we were also able to obtain the Ba^{2+} complex, $[Ba\{o\text{-}C_6H_4(P(O)Ph_2)_2\}_3](SbCl_6)_2$, although the poor affinity of Ba^{2+} for the phosphine oxide ligands is reflected in the tendency of this species to dissociate with loss of ligand in CH_2Cl_2 solution, readily precipitating Ba species with lower barium:phosphine oxide ratios. Hence recrystallisation was carried out in the presence of a small amount of added ligand. While the spectroscopic properties are in line with those of the lighter Group 2 analogues, the need for added ligand during recrystallisation meant that the microanalytical data were slightly higher in C, H than predicted.

3. Experimental

Infrared spectra were recorded as Nujol mulls between CsI plates using a Perkin–Elmer 983G spectrometer over the range 4000–200 cm^{-1}. ^1H NMR spectra were recorded at 300 K using a Bruker AM300 spectrometer. $^{31}P\{^1H\}$ NMR spectra were recorded using a Bruker DPX400 spectrometer operating at 162.0 MHz and are referenced to external 85% H_3PO_4. Microanalyses were undertaken by the University of Strathclyde microanalytical service.

Solvents were dried prior to use and all preparations were undertaken using standard Schlenk techniques under a N_2 atmosphere. The alkaline earth dichlorides were obtained from Aldrich and were dehydrated by strong heating in vacuo prior to use. The diphosphine dioxide ligands were obtained by oxidation of the parent diphosphines by either I_2/OH^- or SnI_4/O_2 according to the literature methods [20,21]. The CH_2Cl_2 was dried by distilling from CaH_2 prior to use.

3.1. $[Mg(OPPh_3)_4](SbCl_6)_2$

$MgCl_2$ (0.025 g, 0.26 mmol) was added to CH_2Cl_2 (10 cm^3). Four molar equivalents of $OPPh_3$ (0.297 g, 1.10 mmol) dissolved in CH_2Cl_2 (2 cm^3) was added, together with two molar equivalents of $SbCl_5$ (0.168 g, 0.56 mmol) in CH_2Cl_2 (5 cm^3). The reaction mixture was stirred for 72 h. The solvent was concentrated to ca. 3 cm^3 in vacuo to give a white solid which was collected by filtration and washed with diethyl ether. The product was then recrystallised from CH_2Cl_2/diethyl ether (yield 0.34 g, 70%). *Anal.* Calc. for $[C_{72}H_{60}Cl_{12}MgO_4P_4Sb_2]$: C, 47.9; H, 3.5. Found: C, 47.8; H, 3.2%. IR (Nujol mull): 1156 (P=O), 339 ($SbCl_6^-$) cm^{-1}. ^1H NMR ($CDCl_3$): 7.30–7.75 ppm (m, aromatic H). $^{31}P\{^1H\}$ NMR ($CH_2Cl_2/CDCl_3$): 41.6 ppm.

3.2. $[Ca(OPPh_3)_4](SbCl_6)_2$

Method as above, but using $CaCl_2$. A white solid was obtained upon addition of EtOH to a concentrated solution of the product in CH_2Cl_2 (yield 70%). *Anal.* Calc. for $[C_{72}H_{60}CaCl_{12}O_4P_4Sb_2]$: C, 47.5; H, 3.3. Found: C, 48.6; H, 3.0%. ^1H NMR ($CDCl_3$): 7.00–8.00 ppm (m, aromatic H). $^{31}P\{^1H\}$ NMR ($CDCl_3$): 36.2 ppm. IR (Nujol mull): 1169 (P=O), 342 ($SbCl_6^-$) cm^{-1}.

3.3. $[Sr(OPPh_3)_4](SbCl_6)_2$

$SrCl_2$ (0.027 g, 0.17 mmol) was suspended in stirred MeCN (3 cm^3) and $SbCl_5$ (0.11 g, 0.37 mmol) was added, when the suspended strontium salt dissolved to give a clear solution. After 1 h, a solution of $OPPh_3$ (0.19 g, 0.68 mmol) in CH_2Cl_2 (5 cm^3) was added and the mixture stirred overnight. The solvent was removed in vacuo, and the white product recrystallised from CH_2Cl_2/diethyl ether. White solid (yield 0.28 g, 86%). *Anal.* Calc. for $[C_{72}H_{60}Cl_{12}O_4P_4Sb_2Sr]$: C, 46.2; H, 3.2. Found: C, 45.4; H, 3.3%. ^1H NMR ($CDCl_3$): 7.2–7.7 ppm (m, aromatic H). $^{31}P\{^1H\}$ NMR ($CDCl_3$): 37.9 ppm. IR (Nujol mull): 1162 (P=O), 344 ($SbCl_6^-$) cm^{-1}.

3.4. $[Ba(OPPh_3)_5](SbCl_6)_2$

$BaCl_2$ (0.052 g, 0.25 mmol) was suspended in dry MeCN (15 cm^3), $SbCl_5$ (0.15 g, 0.5 mmol) added and the solution boiled gently until all the $BaCl_2$ had dissolved to give a clear solution. A solution of $OPPh_3$ (0.39 g, 1.5 mmol) in MeCN (10 cm^3) was added and the mixture stirred overnight. The solution was concentrated to ca. 5 cm^3, and the white solid filtered off, rinsed with MeCN (2 cm^3) and dried in vacuo. White solid (yield 0.35 g, 65%). *Anal.* Calc. for $[C_{90}H_{75}BaCl_{12}O_5P_5Sb_2]$: C, 49.2; H, 3.5. Found: C, 50.0; H, 3.5%. ^1H NMR ($CDCl_3$): 7.2–7.8 ppm (m, aromatic H). $^{31}P\{^1H\}$ NMR (MeCN): 31.0 (br) ppm. IR (Nujol mull): 1162sh, 1156 (P=O), 341 ($SbCl_6^-$) cm^{-1}.

3.5. $[Mg\{Ph_2P(O)CH_2P(O)Ph_2\}_2(H_2O)](SbCl_6)_2 \cdot Et_2O$

Anhydrous $MgCl_2$ (0.015 g, 0.15 mmol) was suspended in CH_2Cl_2 (10 cm^3), $SbCl_5$ (0.09 g, 0.3 mmol)

added and the mixture stirred for 30 min. A solution of the diphosphine dioxide (0.19 g, 0.45 mmol) in CH_2Cl_2 (5 cm^3) was added, and the mixture stirred overnight. The solution was concentrated to about 5 cm^3 in vacuo, diethyl ether (5 cm^3) added dropwise, and the mixture refrigerated. The white precipitate was filtered off, rinsed with diethyl ether and dried in vacuo (yield 0.15 g, 65%). *Anal*. Calc. for $[C_{54}H_{56}Cl_{12}O_6MgP_4Sb_2]$: C, 40.5; H, 3.5. Found: C, 41.1; H, 3.4%. ^1H NMR ($CDCl_3$): 7.2–7.7 (m, Ph, 20H), 3.58 (t, 2H, PCH_2), 3.41 (q, 2H, CH_2), 1.23 (t, 3H, CH_3) ppm. $^{31}P\{^1H\}$ NMR ($CDCl_3$): 34.0 ppm. IR (Nujol mull): ca. 3400 (OH), 1630 (HOH), 1179 (P=O), 346 ($SbCl_6^-$) cm^{-1}.

3.6. $[Ca\{Ph_2P(O)CH_2P(O)Ph_2\}_3](SbCl_6)_2$

Anhydrous calcium chloride (0.013 g, 0.12 mmol) was suspended in CH_2Cl_2 (10 cm^3) and a solution of $SbCl_5$ (0.075 g, 0.25 mmol) in CH_2Cl_2 (1 cm^3) added, followed immediately by powdered $Ph_2P(O)CH_2P(O)Ph_2$ (0.15 g, 0.36 mmol). The mixture was stirred for 3d. then concentrated in vacuo to ca. 5 cm^3. Ethanol (10 cm^3) was added and the white precipitate allowed to settle and the ethanol decanted off. The white solid was washed with a further quantity of ethanol (5 cm^3), separated, and dried in vacuo. White solid (yield 0.13 g, 79%). *Anal*. Calc. for $[C_{75}H_{66}CaCl_{12}O_6P_6Sb_2]$: C, 46.0; H, 3.4. Found: C, 45.9; H, 2.6%. ^1H NMR ($CDCl_3$): 7.05–7.65 (m, Ph, 10H), 3.55 (t, CH_2, 1H) ppm. $^{31}P\{^1H\}$ NMR ($CDCl_3$): 32.6 ppm. IR (Nujol mull): 1175 (P=O), 345 ($SbCl_6^-$) cm^{-1}.

3.7. $[Sr(EtOH)\{Ph_2P(O)CH_2P(O)Ph_2\}_3](SbCl_6)_2$

Method as for the calcium salt above, but using $SrCl_2$. Pale cream solid (yield 17%). *Anal*. Calc. for $[C_{77}H_{72}Cl_{12}O_7P_6Sb_2Sr]$: C, 45.1; H, 3.5. Found: C, 45.6; H, 3.6%. ^1H NMR ($CDCl_3$): 7.10–7.60 (m, Ph, 60H), 3.55 (t, CH_2P, 6H), 3.65 (q, CH_2O, 2H), 1.22 (t, CH_3, 3H) ppm. $^{31}P\{^1H\}$ NMR ($CDCl_3$): 31.3 ppm. IR (Nujol mull): 1174 (P=O), 341 ($SbCl_6^-$) cm^{-1}.

3.8. $[Sr\{Ph_2P(O)CH_2P(O)Ph_2\}_3](SbCl_6)_2$

Made in the same way except that the addition of ethanol in the work up was omitted. White solid (yield 38%). *Anal*. Calc. for $[C_{75}H_{66}Cl_{12}O_6P_6Sb_2Sr]$: C, 44.9; H, 3.3. Found: C, 44.5; H, 3.2%. ^1H NMR ($CDCl_3$): 7.10–7.60 (m, Ph, 60H), 3.56 (t, CH_2, 6H) ppm. $^{31}P\{^1H\}$ NMR ($CDCl_3$): 31.5 ppm. IR (Nujol mull): 1177 (P=O), 346 ($SbCl_6^-$) cm^{-1}.

3.9. $[Mg\{o\text{-}C_6H_4(P(O)Ph_2)_2\}_3](SbCl_6)_2$

Method as described above for $[Mg(OPPh_3)_4](SbCl_6)_2$ using $MgCl_2$: o-$C_6H_4(P(O)Ph_2)_2$ mol. ratio of 1:2. The reaction mixture was taken to dryness in vacuo, the white solid stirred with ethanol (5 cm^3) for 20 min., filtered off and dried in vacuo (yield 37%). *Anal*. Calc. for $[C_{90}H_{72}Cl_{12}MgO_6P_6Sb_2]$: C, 50.7; H, 3.4. Found: C, 49.9; H, 3.5%. ^1H NMR ($CDCl_3$): 7.2–7.7 (m, aromatic H) ppm. $^{31}P\{^1H\}$ NMR ($CDCl_3$): 40.1 ppm. IR (Nujol mull): 1170 (P=O), 341 ($SbCl_6^-$) cm^{-1}.

3.10. $[Ca\{o\text{-}C_6H_4(P(O)Ph_2)_2\}_3](SbCl_6)_2$

Method as described above for $[Ca\{Ph_2P(O)CH_2P(O)Ph_2\}_3](SbCl_6)_2$, White solid (yield 47%). *Anal*. Calc. for $[C_{90}H_{72}CaCl_{12}O_6P_6Sb_2]$: C, 50.4; H, 3.4. Found: C, 49.6; H, 3.0%. ^1H NMR ($CDCl_3$): 6.90–7.80 (m, aromatic H) ppm. $^{31}P\{^1H\}$ NMR ($CDCl_3$): 36.7 ppm. IR (Nujol mull): 1185, 1169(sh) (P=O), 343 ($SbCl_6^-$) cm^{-1}.

3.11. $[Sr\{o\text{-}C_6H_4(P(O)Ph_2)_2\}_3](SbCl_6)_2$

Method as described for $[Sr(OPPh_3)_4](SbCl_6)_2$ using a $SrCl_2$: ligand mol. ratio of 1:3. The solution was concentrated to ca. 5 cm^3, and refrigerated for 48 h. The white solid was filtered off, rinsed with diethyl ether, dried in vacuo (yield 55%). *Anal*. Calc. for $[C_{90}H_{72}Cl_{12}O_6P_6Sb_2Sr]$: C, 49.3; H, 3.3. Found: C, 48.2; H, 3.2%. ^1H NMR ($CDCl_3$): 7.2–7.7 (m, aromatic H) ppm. $^{31}P\{^1H\}$ NMR ($CDCl_3$): 36.5 ppm. IR (Nujol mull): 1169, 1156(sh) (P=O), 347 ($SbCl_6^-$) cm^{-1}.

3.12. $[Ba\{o\text{-}C_6H_4(P(O)Ph_2)_2\}_3](SbCl_6)_2$

Was made similarly to the calcium salt. The white solid was obtained by concentrating the CH_2Cl_2 solution in vacuo to a small volume. The solid was only partially soluble in CH_2Cl_2 but dissolved on warming after addition of more diphosphine dioxide, and was recrystallised twice from CH_2Cl_2/diethylether in the presence of added ligand. White powder (yield 45%). *Anal*. Calc. for $[C_{90}H_{72}BaCl_{12}O_6P_6Sb_2]$: C, 48.2; H, 3.2. Found: C, 49.9; H, 3.5%. ^1H NMR ($CDCl_3$): 7.2–7.7 (m, aromatic H) ppm. $^{31}P\{^1H\}$ NMR ($CDCl_3$): 36.4 ppm. IR (Nujol mull): 1186, 1172(sh) (P=O), 343 ($SbCl_6^-$) cm^{-1}.

3.13. X-ray crystallography

Details of the crystallographic data collection and refinement parameters are given in Table 4. Colourless crystals of $[Mg(OPPh_3)_4](SbCl_6)_2 \cdot CH_2Cl_2$ were obtained by liquid diffusion of diethyl ether into a solution of the complex in CH_2Cl_2, while small crystals of $[Ca\{Ph_2P(O)CH_2P(O)Ph_2\}_3](SbCl_6)_2 \cdot 2CH_2Cl_2$ and $[Sr(EtOH)\{Ph_2P(O)CH_2P(O)Ph_2\}_3](SbCl_6)_2 \cdot 0.45CH_2Cl_2$ were obtained by liquid diffusion of EtOH into a solution of the appropriate complex in CH_2Cl_2. Data collection used a Nonius Kappa CCD diffractometer ($T = 120$ K) and with graphite-monochromated Mo Kα X-radiation

Table 4
Crystallographic parameters

Complex	$[Mg(OPPh_3)_4](SbCl_6)_2\cdot CH_2Cl_2$	$[Ca\{Ph_2P(O)CH_2P(O)Ph_2\}_3](SbCl_6)_2\cdot 2CH_2Cl_2$	$[Sr(EtOH)\{Ph_2P(O)CH_2P(O)Ph_2\}_3](SbCl_6)_2\cdot 0.45CH_2Cl_2$
Formula	$C_{73}H_{62}Cl_{14}MgO_4P_4Sb_2$	$C_{77}H_{70}CaCl_{16}O_6P_6Sb_2$	$C_{77.45}H_{72.90}Cl_{12.90}O_7P_6Sb_2Sr$
M	1891.22	2127.93	2089.90
Crystal system	triclinic	monoclinic	orthorhombic
Space group	$P\bar{1}$ (no. 2)	$P2_1/c$ (no. 14)	$Pca2_1$ (no. 29)
a (Å)	15.9687(10)	25.127(3)	37.116(4)
b (Å)	16.7069(10)	13.043(2)	12.7960(10)
c (Å)	16.9441(15)	27.262(4)	19.2794(15)
α (°)	90.020(6)	90	90
β (°)	89.426(5)	91.128(8)	90
γ (°)	62.759(5)	90	90
U (Å^3)	4018.9(5)	8933(2)	9156.5(13)
Z	2	4	4
μ(Mo Kα) (cm^{-1})	12.71	12.97	16.95
Total number of reflections	59756	54993	40384
Unique reflections	18170	15559	15485
R_{int}	0.0495	0.1500	0.0778
Number of parameters	879	445	440
R_1 ($I_o > 2\sigma(I_o)$)	0.0404 (14260 reflections)	0.0699 (6981 reflections)	0.0593 (10600 reflections)
R_1 (all data)	0.0600	0.1942	0.1035
wR_2 ($I_o > 2\sigma(I_o)$)	0.0882	0.1413	0.1413
$wR2$ (all data)	0.0946	0.1814	0.1589

$R_1 = \sum\|F_o| - |F_c\|/\sum|F_o|$; $wR2 = [\sum w(F_o^2 - F_c^2)^2/\sum wF_{oi}^4]^{1/2}$.

($\lambda = 0.71073$ Å). Structure solution and refinement were routine [22–24]. Selected bond lengths and angles are given in Tables 1–3.

4. Conclusions

We have successfully prepared and isolated an unusual series of homoleptic phosphine oxide complexes involving Group 2 metal dications, including the first examples with bidentate phosphine oxides and the first examples with Sr^{2+} and Ba^{2+}. The M–L interactions in these complexes are weaker than those involving the Group 3 metal ions, a consequence of the reduction in charge:radius ratio in the alkaline earth systems. The affinity of Ba^{2+} for phosphine oxide coordination is very low. There is also a clear dependence upon the metal ion radius and the spectroscopic and structural results from the $Sr^{2+}/Ph_2P(O)CH_2P(O)Ph_2$ system show that this represents a crossover point where both the six- and seven-coordinate species may be isolated. As expected the coordination number at the metal centre is dependent upon the steric requirements, denticity and the rigidity of the phosphine oxide as well as the metal ion radius. However, the coordination numbers identified in this work (4–6) are much lower than those seen typically for Ca^{2+} and Mg^{2+} complexes with neutral O-donor ligands [25,26] Comparisons with the literature show that for Ca^{2+} coordination numbers below six are extremely rare, while for Mg^{2+} six-coordination is dominant, although a small number of lower coordination species are known.

5. Supplementary material

Crystallographic data for the structural analyses have been deposited with the Cambridge Crystallographic Data Centre, CCDC Nos. 250370 (Mg), 250371 (Ca), 250372 (Sr). Copies of this information may be obtained free of charge from The Director, CCDC, 12 Union Road, Cambridge CD2 1EZ, UK (Fax: +44-1223-336033; email: deposit@ccdc.cam.ac.uk or www: http://www.ccdc.cam.ac.uk).

Acknowledgements

R.R. thanks the Commonwealth Scholarship Commission, UK (INCF-2003-85) for funding and M. D. S. University, Ajmer (India) for granting a leave of absence. We thank the EPSRC for provision of X-ray crystallographic facilities.

References

[1] D. Fenton, in: G. Wilkinson, R.D. Gillard, J.A. McCleverty (Eds.), Comprehensive Coordination Chemistry, 3, Pergamon, Oxford, 1989.

[2] T.P. Hanusa, in: J.A. McCleverty, T.J. Meyer (Eds.), Comprehensive Coordination Chemistry II, 3, Elsevier, Amsterdam, 2003, and references therein.
[3] L. Deakin, W. Levason, M.C. Popham, G. Reid, M. Webster, J. Chem. Soc., Dalton Trans. (2000) 2439.
[4] W. Levason, B. Patel, M.C. Popham, G. Reid, M. Webster, Polyhedron 20 (2001) 2711.
[5] N.J. Hill, W. Levason, M.C. Popham, G. Reid, M. Webster, Polyhedron 21 (2002) 445.
[6] N.J. Hill, L.-S. Leung, W. Levason, M. Webster, Inorg. Chim. Acta 343 (2003) 169.
[7] M.W.G. de Bolster, I.E. Kortram, W.L. Groeneveld, J. Inorg. Nucl. Chem. 34 (1972) 575.
[8] N.M. Karayannis, C.M. Mikulski, M.J. Strocko, L.L. Pytlewski, M.M. Labes, J. Inorg. Nucl. Chem. 32 (1970) 2629.
[9] Y.S. Ng, G.A. Rodley, W.T. Robinson, Acta Crystallogr., Sect. B 34 (1978) 2835.
[10] Y.S. Ng, G.A. Rodley, W.T. Robinson, Acta Crystallogr., Sect. B 34 (1978) 2837.
[11] S.M. Corcoran, W. Levason, R. Patel, G. Reid, Inorg. Chim. Acta, in press.
[12] A.P. Zuur, W.L. Groeneveld, Rec. Trav. Chim. Pays Bas 86 (1967) 1089.
[13] Y. Ding, P.E. Fanwick, R.A. Walton, Inorg. Chim. Acta 309 (2000) 159.
[14] W. Hewertson, B.T. Kilbourn, R.H.B. Mais, Chem. Commun. (1970) 952.
[15] A.E. Kalinin, V.G. Andrianov, Y.T. Struchkov, J. Struct. Chem. 17 (1976) 127.
[16] K.C. Jayaratne, L.S. Fitts, T.P. Hanusa, V.G. Young Jr., Organometallics 20 (2001) 3638.
[17] W. Levason, M.L. Matthews, G. Reid, M. Webster, Dalton Trans. (2004) 51.
[18] W. Levason, M.L. Matthews, G. Reid, M. Webster, Dalton Trans. (2004) 554.
[19] M.D. Brown, W. Levason, G. Reid, R. Watts, Polyhedron, 24 (2005), in press.
[20] A.R.J. Genge, W. Levason, G. Reid, Inorg. Chim. Acta 288 (1999) 142.
[21] W. Levason, R. Patel, G. Reid, J. Organomet. Chem. 688 (2003) 280.
[22] G.M. Sheldrick, SHELXS-97, Program for Crystal Structure Solution, University of Göttingen, 1997.
[23] G.M. Sheldrick, SHELXL-97, Program for Crystal Structure Refinement, University of Göttingen, 1997.
[24] H.D. Flack, Acta Crystallogr., Sect. A 39 (1983) 876.
[25] O. Carugo, K. Djinovic, M. Rizzi, J. Chem. Soc., Dalton Trans. (1993) 2127.
[26] C.W. Bock, A. Kaufman, J.P. Glusker, Inorg. Chem. 33 (1994) 419.

Available online at www.sciencedirect.com
SCIENCE DIRECT®
Polyhedron 24 (2005) 129–136
POLYHEDRON
www.elsevier.com/locate/poly

Pseudotetrahedral cobalt(II) complexes with thiazoline and thiazine derivative ligands: synthesis and characterization

F.J. Barros-García, A. Bernalte-García *, A.M. Lozano-Vila, F. Luna-Giles, E. Viñuelas-Zahínos

Departamento de Química Inorgánica, Facultad de Ciencias, Universidad de Extremadura, 06071 Badajoz, Spain

Received 7 September 2004; accepted 25 October 2004
Available online 8 December 2004

Abstract

The cobalt(II) complexes dichloro[2-(3,4-dichlorophenyl)imino-κN-N-(2-thiazolin-κN-2-yl)thiazolidine]cobalt(II) (**1**) and dichloro[2-(3,4-dichlorophenyl)imino-κN-N-(2-thiazin-κN-2-yl)thiazolidine]cobalt(II) (**2**) have been isolated and characterized in the solid state by X-ray diffraction, elemental analysis, IR spectra, magnetic measurements and UV–Vis–NIR diffuse reflectance spectroscopy. In both complexes, the environment around the cobalt(II) ion may be described as a distorted tetrahedral geometry, with the metallic atom coordinated to two chlorine atoms [Co–Cl(1) = 2.213(1) Å; Co–Cl(2) = 2.226(1) Å], one imino nitrogen [Co–N(3) = 1.992(2) Å] and one thiazoline nitrogen [Co–N(1) = 1.974(2) Å] in complex **1** and to two chlorine atoms [Co–Cl(1) = 2.244(2) Å; Co–Cl(2) = 2.226(1) Å], one imino nitrogen [Co–N(3) = 1.970(4) Å] and one thiazine nitrogen [Co–N(1) = 1.946(4) Å] in complex **2**.
© 2004 Elsevier Ltd. All rights reserved.

Keywords: Crystal structures; Cobalt(II) complexes; Thiazoline; Thiazolidine; Thiazine

1. Introduction

Multidentate ligands containing N,N donors are extensively used in coordination chemistry with the aim of obtaining new frameworks having potential bioactivity [1]. Among these ligands, thiazoline and thiazine derivative ligands have attracted our attention due to their biological and pharmaceutical activity. The use of compounds containing thiazine, thiazoline or/and thiazolidine rings as antitumoral, analgesic, antibiotic, antiviral, antihistamine, anti-HIV, antiinflammatory and sedative agents, is well known [2–9]. In some cases, the structural and biological properties of the corresponding coordination compounds are more noteworthy than those of the ligands [10].

The synthesis of new siderophore analogues constitutes another pharmacological application example. Microbial siderophores are relatively low molecular weight compounds synthesized in order to solubilize and transport iron (III) into the procariotes cells in the necessary concentrations. New siderophore analogues are prototypes for the synthesis of chelating agents employed for clinical use [11]. Thus, there have been characterized siderophores containing thiazoline and thiazine rings that have been used in the treatment of acute iron poisoning and in chronic iron overload resulting from transfusion therapy of β-thalasemia [12].

Because of the aforementioned, recently we have been investigating the coordination chemistry of compounds containing these heterocycles [13–17]. As a continuation of this research, we report here the synthesis and characterization by elemental analysis, infrared spectra (IR), ultraviolet and visible spectra (UV–Vis), proton nuclear

* Corresponding author. Tel.: +34 924 289394; fax: +34 924 289395.
E-mail address: alberga@unex.es (A. Bernalte-García).

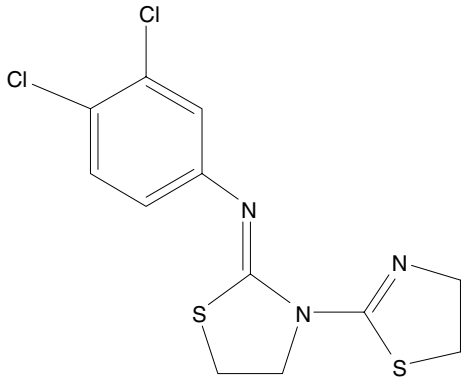
0277-5387/$ - see front matter © 2004 Elsevier Ltd. All rights reserved.
doi:10.1016/j.poly.2004.10.011

magnetic resonance (^{1}H NMR) and carbon nuclear magnetic resonance (^{13}C NMR) of the ligand TdTz [TdTz = 2-(3,4-dichlorophenyl)imino-N-(2-thiazin-2-yl)-thiazolidine]. Likewise, the cobalt(II) complexes [$CoCl_2$(TdTn)] [TdTn = 2-(3,4-dichlorophenyl)imino-N-(2-thiazolin-2-yl)thiazolidine] and [$CoCl_2$(TdTz)] have been isolated and their characterization has been carried out by means of single crystal X-ray diffraction, elemental analysis, spectroscopic and magnetic measurements.

2. Experimental

2.1. Preparation of 2-(3,4-dichlorophenyl)imino-N-(2-thiazolin-2-yl)thiazolidine (TdTn)

The preparation of TdTn has been carried out as described by Outcalt et al. [18]. ^{1}H NMR (deuteriochloroform): δ 7.37 (d, J = 8.49 Hz, 1H), 7.10 (d, J = 2.45 Hz, 1H), 6.85 (dd, J = 2.45, 2.49 Hz, 1H), 4.33 (t, J = 7.05 Hz, 2H), 4.01 (t, J = 8.28 Hz, 2H), 3.28 (t, J = 7.05 Hz, 2H), 3.23 (t, J = 8.16 Hz, 2H); ^{13}C NMR (deuteriochloroform): δ 157.58, 155.68, 148.73, 132.47, 130.53, 127.29, 123.30, 120.89, 57.27, 51.30, 33.87, 26.74. *Anal.* Calc. for $C_{12}H_{11}Cl_2N_3S_2$: C, 43.38; H, 3.34; N, 12.64; S, 19.30. Found: C, 43.44; H, 3.36; N, 12.71; S, 18.95%. UV–Vis (EtOH): λ_{max}, nm; (ε, l mol^{-1} cm^{-1}) 205 (35 087), 239 (17 542), 289 (12 351).

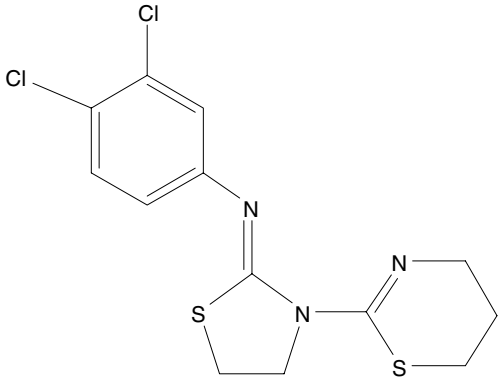


TdTn

2.2. Preparation of 2-(3,4-dichlorophenyl)imino-N-(2-thiazin-2-yl)thiazolidine (TdTz)

A solution of 2.01 g (8.1 mmoles) of 2-(3,4-dichlorobenzylamino)-2-thiazoline (that was obtained by the method of Fanta and Deutsch [19] and by the method of Outcalt et al. [18]) and 1.38 g (10.2 mmoles) of 3-chloropropylisothiocyanate [20] in 30 ml of toluene was stirred and heated to reflux for 4 h. At this point, a white precipitate had separated out and the reaction mixture was allowed to cool to room temperature. A solution of 1.62 g (15.3 mmoles) of sodium carbonate in 20 ml of water was added and the mixture was stirred until dissolution of the solid was complete. The phases were separated and the aqueous layer was extracted with dichloromethane. The combined organic layers were dried over anhydrous magnesium sulfate and concentrated under reduced pressure to give a solid that was recrystallized from ethanol 96% (1.5 g; 53%).

^{1}H NMR (deuteriochloroform): δ 7.32 (d, J = 8.76 Hz, 1H), 7.07 (d, J = 2.24 Hz, 1H), 6.80 (dd, J = 2.24, 8.76 Hz, 1H), 4.19 (t, J = 7.04 Hz, 2H), 3.72 (t, J = 5.62 Hz, 2H), 3.15 (t, J = 7.01 Hz, 2H), 2.95 (t, J = 6.01 Hz, 2H), 1.90 (m, J = 5.88 Hz, 2H); ^{13}C NMR (deuteriochloroform): δ 156.48, 149.61, 148.31, 132.32, 130.42, 126.86, 123.37, 121.03, 51.42, 46.46, 27.07, 26.46, 20.64. *Anal.* Calc. for $C_{13}H_{13}Cl_2N_3S_2$: C, 45.09; H, 3.78; N, 12.13; S, 18.52. Found: C, 45.26; H, 3.78; N, 11.82; S, 18.07%. UV–Vis (EtOH): λ_{max}, nm; (ε, l mol^{-1} cm^{-1}) 205 (35 140), 247 (19 059), 292 (10 833).



TdTz

2.3. Preparation of [$CoCl_2$(TdTn)]

This complex was isolated from a freshly prepared ethanol solution (1 ml) of $CoCl_2 \cdot 6H_2O$ (71.6 mg, 0.3 mmol) that was added to an ethanol solution (15 ml) of TdTn (100 mg, 0.3 mmol). The resulting solution was allowed to evaporate slowly at room temperature. After a few days, blue crystals were isolated from the solution (124 mg, 89.2%). The crystals were separated by filtration, washed with cold ether and air-dried. *Anal.* Calc. for $C_{12}H_{11}Cl_4CoN_3S_2$: C, 31.19; H, 2.40; N, 9.09; S, 13.88. Found: C, 31.33; H, 2.42; N, 8.97; S, 14.37%.

2.4. Preparation of [$CoCl_2$(TdTz)]

This complex was prepared by reacting an ethanol solution (1 ml) of $CoCl_2 \cdot 6H_2O$ (68.7 mg, 0.3 mmol)

with an ethanol solution (15 ml) of TdTz (100 mg, 0.3 mmol), blue crystals being obtained after a slow evaporation of the solution at room temperature (96.5 mg, 67.5%). The crystals were filtered, washed with cold ether and air-dried. *Anal.* Calc. for $C_{13}H_{13}Cl_4CoN_3S_2$: C, 32.79; H, 2.75; N, 8.82; S, 13.47. Found: C, 32.76; H, 2.74; N, 8.58; S, 12.93%.

2.5. Instrumental procedures

Chemical analyses of carbon, hydrogen, nitrogen and sulfur were performed by microanalytical methods using a Leco CHNS-932 microanalyser. IR spectra were recorded on a Perkin–Elmer FT-IR 1720 spectrophotometer, from KBr pellets in the 4000–370 cm^{-1} range and on a Perkin–Elmer FT-IR 1700X spectrophotometer, from polyethylene pellets in the 500–150 cm^{-1} range. Electronic spectra of the ligands in solution were measured on a Shimadzu UV-3101 PC using a 10 mm quartz cell. UV–Vis–NIR reflectance spectra for complexes in the 200–2000 nm range were obtained from a pellet of the samples, using a Shimadzu UV-3101 PC spectrophotometer and $BaSO_4$ as a reference. Magnetic measurements were made at room temperature on a magnetometer with a pendulum MANICS DSM8, equipped with a helium continuous-flow cryostat and an electromagnetometer DRUSCH EAF 16 UE. Data were corrected for temperature-independent paramagnetism and diamagnetic contributions, which were estimated from Pascal constants. ^1H and ^{13}C NMR spectra were obtained with a Bruker AM 400 instrument at 400 and 100 MHz, respectively, in $CDCl_3$ using Me_4Si as internal standard.

2.6. Crystal structure determinations

Experimental details of the crystal structure determinations including crystal data, data collection, structure determination and refinement for complexes **1** and **2** are listed in Table 1. X-ray diffraction measurements were

Table 1
Crystal data, data collection and refinement details for $[CoCl_2(TdTn)]$ (**1**) and $[CoCl_2(TdTz)]$ (**2**)

	$[CoCl_2$ (TdTn)] (**1**)	$[CoCl_2(TdTz)]$ (**2**)
Crystal shape	prism	prism
Colour	blue	blue
Size (mm)	$0.34 \times 0.18 \times 0.14$	$0.50 \times 0.32 \times 0.13$
Chemical formula	$C_{12}H_{11}Cl_4CoN_3S_2$	$C_{13}H_{13}Cl_4CoN_3S_2$
Formula weight	462.09	476.11
Crystal system	monoclinic	monoclinic
Space group	$P2_1/a$	Cc
Unit cell dimensions		
a (Å)	9.699(1)	7.637(1)
b (Å)	17.336(1)	18.273(2)
c (Å)	10.825(1)	13.709(1)
β (°)	104.06(1)	101.54(1)
Cell volume (Å^3)	1765.4(2)	1874.3(3)
Z	4	4
T (K)	298(2)	298(2)
D_{calc} (g cm^{-3})	1.739	1.687
μ (mm^{-1})	1.810	1.708
F (0 0 0)	924	956
Diffractometer	Bruker SMART CCD	Bruker SMART CCD
Radiation	Mo-Kα (λ = 0.71073Å)	Mo-Kα (λ = 0.71073 Å)
Collection method	ϕ–ω	ϕ–ω
2θ Range	3.8–56.6	5.4–51.4
Index ranges	$-10 \leqslant h \leqslant 12$, $-22 \leqslant k \leqslant 22$, $-12 \leqslant l \leqslant 14$	$-6 \leqslant h \leqslant 9$, $-22 \leqslant k \leqslant 21$, $-16 \leqslant l \leqslant 14$
Independent reflections	4222	2298
Observed reflections	3220 [$F > 4.0\sigma(F)$]	2230 [$F > 4.0\sigma(F)$]
Absorption correction	empirical	empirical
Maximum/minimum transmission	0.7857/0.5781	0.8085/0.4822
Number of refined parameters	199	208
R [$I > 2\sigma(I)$][a]	0.0347	0.0317
wR [all data][b]	0.0875	0.0844
GOF[c]	1.027	1.060
ρ_{max}, ρ_{min} (e Å^{-3})	0.824, −0.679	0.267, −0.260

[a] $R = \sum\|F_o| - |F_c\|/\sum|F_o|$.

[b] $wR = \left\{\sum[w(F_o^2 - F_c^2)^2]/\sum[w(F_o^2)^2]\right\}^{1/2}$.

[c] The goodness-of-fit (GOF) equals $\left\{\sum[w(F_o^2 - F_c^2)^2]/(N_{rf\,ln\,s} - N_{params})\right\}^{1/2}$.

performed using a Bruker SMART CCD diffractometer. The first fifty frames were recollected at the end of the data collection to monitor for decay. Absorption corrections were applied using the program SADABS. The structures were solved by direct methods and subsequent Fourier differences using the WINGX package [21] and refined by full-matrix least-squares. The H atoms were placed from a differential Fourier synthesis and included in the final refinement cycles in calculated positions.

3. Results and discussion

3.1. Description of the crystal structures

3.1.1. [$CoCl_2$(TdTn)] (1)

The structure of **1** consists of discrete neutral monomeric units in which the environment around the cobalt(II) atom may be described as a distorted tetrahedral geometry. The metallic atom is coordinated by two chlorine atoms [Co–Cl(1) = 2.213(1) Å; Co–Cl(2) = 2.226(1) Å], one thiazoline nitrogen [Co–N(1) = 1.974(2) Å] and one imino nitrogen [Co–N(3) = 1.992(2) Å]. A diagram of the molecular structure and the atom numbering system used is shown in Fig. 1. The most relevant bond lengths and angles are given in Table 2.

The Co–Cl bond lengths are similar and comparable to the calculated average value [2.240(26) Å] for 100 tetrahedral cobalt(II) complexes with a chromophore group $CoCl_2N_2$, obtained from CONQUEST software [22] from the Cambridge Structural Database (CSD) [23]. Likewise, the Co–N_{imino} bond distance is slightly shorter than the mean value [2.027(24) Å] calculated for 16 cobalt(II) complexes with an Cl_2N_2 environment collected in the CSD. The Co–$N_{thiazoline}$ bond distance is closer to that found in [$CoCl_2$(PyTT)] (1.982 Å) [13], but shorter than those observed in [Co(2,2′-bithiazoline)-$(N_3)_2]_n$ (average 2.155 Å) [24]. The ligand–metal–ligand bite angles differ from the ideal value of 109.5°, varying between 116.6(1)° [Cl(1)–Co–N(3)] and 90.8(1)° [N(3)–Co–N(1)].

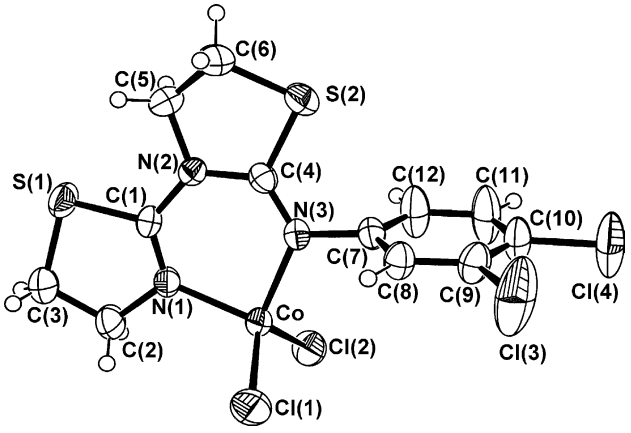


Fig. 1. Molecular structure of [$CoCl_2$(TdTn)] (**1**), showing the atom numbering scheme. The thermal ellipsoids are drawn at the 50% level.

Table 2
Selected bond lengths (Å) and bond angles (°) for [$CoCl_2$(TdTn)] (**1**)

Bond lengths			
Co–Cl(1)	2.213(1)	Co–Cl(2)	2.226(1)
Co–N(1)	1.974(2)	Co–N(3)	1.992(2)
C(1)–N(1)	1.280(3)	N(2)–C(4)	1.381(3)
N(2)–C(1)	1.382(3)	C(7)–N(3)	1.445(3)
C(4)–N(3)	1.292(3)		
Bond angles			
Cl(1)–Co–Cl(2)	114.4(4)	Cl(1)–Co–N(3)	116.6(1)
Cl(2)–Co–N(3)	109.4(1)	Cl(1)–Co–N(1)	108.7(1)
Cl(2)–Co–N(1)	114.8(1)	N(3)–Co–N(1)	90.8(1)
C(4)–N(2)–C(1)	126.4(2)	N(2)–C(4)–N(3)	124.5(2)
Co–N(3)–C(4)	126.3(2)	Co–N(3)–C(7)	115.5(2)
C(4)–N(3)–C(7)	118.1(2)	Co–N(1)–C(1)	126.9(2)
C(1)–N(1)–C(2)	112.6(2)	N(2)–C(1)–N(1)	125.0(2)
N(3)–C(4)–N(2)	124.5(2)		

The six-membered chelate ring Co–N(1)–C(1)–N(2)–C(4)–N(3) is essentially planar with maximum mean-plane deviation for C(4) (0.020 Å). In the organic ligand, the values of the puckering parameters for the 2-thiazoline ring, calculated according to Cremer and Pople [25], are q = 0.143 Å and ϕ = 251.2°, whereas for the thiazolidine ring these are q = 0.330 Å and ϕ = 289.3°. These values indicate that both five-membered rings show a conformation near to envelope, with the apex at C(3) [deviating 0.230 Å from the plane formed by S(1)–C(1)–N(1)–C(2), maximum mean plane deviation for N(1) = 0.001 Å] for the 2-thiazoline ring, and at C(6) [deviating 0.514 Å from the plane formed by S(2)–C(4)–N(2)–C(5), maximum mean plane deviation for N(2) = 0.004 Å] for the thiazolidine ring.

3.1.2. [$CoCl_2$(TdTz)] (2)

The X-ray study revealed that the crystals of **2** are made up of monoclinic unit cells, each containing four complex molecules. A diagram of the molecular structure and the atom numbering system used is shown in Fig. 2. Selected bond lengths and angles are given in Table 3.

The cobalt(II) is bound to two chlorine atoms [Co–Cl(1) = 2.244(2) Å; Co–Cl(2) = 2.226(1) Å], one thiazine nitrogen [Co–N(1) = 1.946(4) Å] and one imino nitrogen [Co–N(3) = 1.970(4) Å] in a distorted tetrahedral geometry. The distortion of the tetrahedral environment of the cobalt(II) ion is smaller than in complex **1**, being indicated by the ligand–metal–ligand bite angles that vary between 115.1(2)° [Cl(1)–Co–N(1)] and 92.5(2)° [N(3)–Co–N(1)]. This compound is the first structurally characterized compound having a 1,3-thiazine link to cobalt(II). The Co-ligand bond lengths were compared with the same values collected from the CSD used during discussion of complex **1**. Thus, the Co–Cl bond

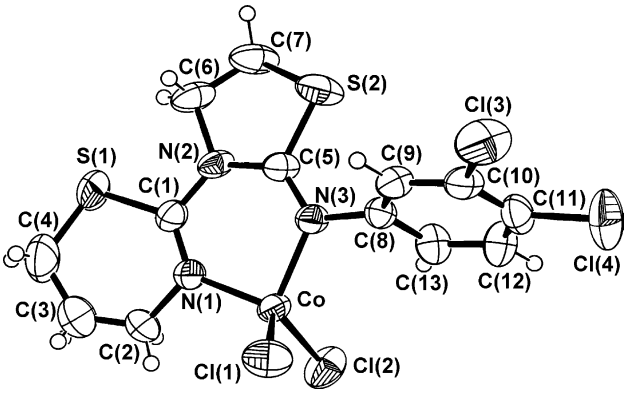


Fig. 2. Molecular structure of $[CoCl_2(TdTz)]$ (**2**), showing the atom numbering scheme. The thermal ellipsoids are drawn at the 50% level.

Table 3
Selected bond lengths (Å) and bond angles (°) for $[CoCl_2(TdTz)]$ (**2**)

Bond lengths			
Co–Cl(1)	2.244(2)	Co–Cl(2)	2.226(1)
Co–N(1)	1.946(4)	Co–N(3)	1.970(4)
C(1)–N(1)	1.284(6)	N(2)–C(5)	1.384(6)
N(2)–C(1)	1.403(6)	C(8)–N(3)	1.433(6)
C(5)–N(3)	1.288(6)		
Bond angles			
Cl(1)–Co–Cl(2)	112.8(1)	Cl(1)–Co–N(3)	108.2(1)
Cl(2)–Co–N(3)	115.0(1)	Cl(1)–Co–N(1)	115.1(2)
Cl(2)–Co–N(1)	111.7(1)	N(3)–Co–N(1)	92.5(2)
C(5)–N(2)–C(1)	127.0(4)	N(2)–C(5)–N(3)	125.6(4)
Co–N(3)–C(5)	124.4(3)	Co–N(3)–C(8)	117.1(3)
C(5)–N(3)–C(8)	118.5(4)	Co–N(1)–C(1)	127.8(3)
C(1)–N(1)–C(2)	119.2(4)	N(2)–C(1)–N(1)	122.1(4)
N(3)–C(5)–N(2)	125.6(4)		

lengths are similar to those collected, whereas the Co–N_{imino} bond length is shorter to those collected.

The six membered chelate ring Co–N(1)–C(1)–N(2)–C(5)–N(3), similarly to complex **1**, is essentially planar with maximum mean-plane deviation for C(1) (0.047 Å). The 1,3-thiazine ring shows a conformation near to boat with S(1) and C(2) deviating 0.350 and 0.215 Å, respectively, above the plane formed by C(1), N(1), C(3), C(4) [maximum mean-plane deviation for N(1) = 0.051 Å]. This geometry is proved by the puckering parameters $q = 0.336$ Å, $\phi = 303.4°$ and $\theta = 82.9°$ [25]. For the thiazolidine ring, the puckering parameters $q = 0.356$ Å and $\phi = 303.4°$ [25] indicate a conformation near to envelope with the apex at C(7), deviating 0.546 Å from the plane formed by C(5), N(2), C(6), S(2) [maximum mean-plane deviation for N(2) = 0.038 Å].

Finally, it should be pointed out that the organic moiety in both complexes presents a different degree of rotation of the 3,4-dichlorophenyl ring around the N(3)–C(7) [or N(3)–C(8)] bond, which could be due to the molecular packing of the crystal structures [torsion angle C(4)–N(3)–C(7)–C(12) = −78.5° in complex **1**; torsion angle C(5)–N(3)–C(8)–C(13) = −119.2° in complex **2**].

3.2. Physical measurements

A pseudotetrahedral stereochemistry may be assigned to the two complexes reported in this paper on the basis of their diffuse reflectance spectra, which closely resemble those of other Co(II) tetrahedral complexes.

Complex **1** exhibits one intense band at 34 720 cm^{-1} (288 nm), which is assigned to the $\pi \rightarrow \pi^*$ transition of the organic ligand. Moreover, the spectrum shows two multicomponent absorptions in the near infrared and visible regions with intensities consistent with spin-allowed d–d transitions. These bands may be assigned to ν_2 [$^4A_2(F) \rightarrow {}^4T_1(F)$] (10 800, 8300, 6930 cm^{-1}) and ν_3 [$^4A_2(F) \rightarrow {}^4T_1(P)$] (18 870 and 16 290 cm^{-1}) transitions, respectively, in an idealized T_d symmetry.

The very large splitting for these bands suggests a marked effect of a low symmetry component of the crystal field, C_1, prevailing on the spin-orbit coupling effects, although such a mechanism may contribute [26].

The ligand field parameters, 10 Dq and B, were calculated from the average values of the ν_2 and ν_3 bands taking the centre of gravity of the total intensity, using the following known relationships [27] for tetrahedral d^7 complexes:

$$\nu_2[^4A_2(F) \rightarrow {}^4T_1(F)] = 15Dq + (15/2)B - 1/2[(-6Dq + 15B)^2 + 64(Dq)^2]^{1/2} \quad (1)$$

$$\nu_3[^4A_2(F) \rightarrow {}^4T_1(P)] = 15Dq + (15/2)B + 1/2[(-6Dq + 15B)^2 + 64(Dq)^2]^{1/2} \quad (2)$$

The calculated values of the ligand field parameters 10 Dq = 4870 cm^{-1} and B = 746 cm^{-1} are in fair agreement with the predicted values for tetrahedral complexes and are consistent with the presence of a chromophore group $[CoCl_2N_2]$ [13,28–30].

The electronic spectra of **1** and **2** resemble each other closely. Thus, complex **2** shows one intense band at 34 480 cm^{-1} (290 nm) which can be assigned to the $\pi \rightarrow \pi^*$ transition of the organic ligand.

Likewise, in a similar form to **1**, the electronic spectrum exhibits a splitting of the ν_2 and ν_3 transitions. Thus, the bands at 18 670 and 16 500 cm^{-1} are assigned to the ν_3 [$^4A_2(F) \rightarrow {}^4T_1(P)$] transition, whereas the bands at 11 130 cm^{-1}, 8200 cm^{-1} and 7130(sh) cm^{-1} are assigned to the ν_2 [$^4A_2(F) \rightarrow {}^4T_1(F)$] transition.

Attention is now given to the splitting of the ν_2 transition of **2** (two bands and a shoulder) that is smaller than that of **1** (three bands). This fact may possibly be explained in terms of geometrical effects, since in accordance with the X-ray crystallographic results, the distortion of the coordination polyhedron around the cobalt(II) atom in **1** is greater than that in **2** [31].

The ligand field parameters, 10 Dq and B, were collected in the same way as for **1** using the Eqs. (1) and (2). Likewise, the calculated values of the ligand field

parameters, 10 Dq = 4861 cm^{-1} and B = 754 cm^{-1}, are consistent with the presence of the chromophore group $[CoCl_2N_2]$ [13,28–30].

The observed molar magnetic susceptibilities for **1** and **2** were corrected for diamagnetism and temperature-independent paramagnetism to provide the fully corrected magnetic moments at room temperature of 4.37 and 4.44 MB, respectively. These values are consistent with an ion with an $e^4t_2^3$ electronic configuration in a tetrahedral field [32,33].

It should be pointed out that the magnetic moment of **2** is a little higher than that of **1**, this fact can be explained by considering, according to Cotton [34,35], that the orbital contribution to the spin only value of the magnetic moment varies inversely with the strength of the ligand field, and that is lower for **2** than for **1**.

The IR spectra of TdTn and TdTz in the 4000–370 cm^{-1} region show the presence of bands due to thiazolidine ring vibrations at 1027 (νn_1), 906 (νn_2), 828 (νn_3), 704 (νn_4), 673 (νn_5) and 477 cm^{-1} (δn_2) for TdTn, and at 1024 (νn_1), 923 (νn_2), 891 (νn_3), 701 (νn_4), 675 (νn_5) and 475 cm^{-1}(δn_2) for TdTz [36,37].

Likewise, the spectrum of TdTn exhibits bands assignable to the thiazoline ring vibrations at 1602 (W_1), 985 (W_2), 937 (W_3), 799 (W_4), 733 (W_5), 644 (W_6), 593 (W_8), 526 (W_7) and 445 cm^{-1} (Γ_1) [38], whereas the spectrum of TdTz shows bands assignable to the thiazine ring vibrations at 1604 (Ψ_1), 1010 (Ψ_2), 947 (Ψ_3), 823 (Ψ_4), 765 (Ψ_5), 710 (Ψ_6), 628 (Ψ_7), 592 (Ψ_8) and 528 cm^{-1} (ϕ_1) [14,39,40].

Moreover, the bands of 3,4-dichlorophenyl ring vibrations are detected at 1586 (8b), 1550 (8a), 1470 (19b), 1384 (19a), 1253 (14), 1131 (1) and 433 cm^{-1} (16b) for TdTn, and at 1585 (8b), 1548 (8a), 1466 (19b), 1372 (19a), 1244 (14), 1136 (1) and 428 cm^{-1} (16b) for TdTz [41].

Other relevant bands are registered at 1635 [$\nu(C{=}N)_{imine}$] and 1035 cm^{-1} [$\nu(C–Cl)_{orto}$] for TdTn, and at 1631 [$\nu(C{=}N)_{imine}$], 1358 [$\nu(C–N)$] and 1048 cm^{-1} [$\nu(C–Cl)_{orto}$] for TdTz [42,43].

Table 4
Infrared bands (cm^{-1}) due to ring vibrations of TdTn, $[CoCl_2(TdTn)]$ (**1**), TdTz and $[CoCl_2(TdTz)]$ (**2**)

Assignment		TdTn	**1**	TdTz	**2**
Thiazoline	W_1	1602 (vs)	1540 (s)		
	W_2	985 (w)	1001 (w)		
	W_3	937 (w)	949 (m)		
	W_4	799 (w)	774 (w), 753 (vw)		
	W_5	733 (vw)	730 (w), 717 (w)		
	W_6	644 (m)	631 (w)		
	W_8	593 (m)	588 (w)		
	W_7	526 (w)	542 (w)		
	Γ_1	445 (w)	444 (w)		
Thiazine	Ψ_1			1604 (vs)	1598 (vs)
	Ψ_2			1010 (m)	1022 (m)
	Ψ_3			947 (w)	942 (w)
	Ψ_4			823 (m)	839 (m)
	Ψ_5			765 (w)	760 (w), 746 (w)
	Ψ_6			710 (w)	721 (w)
	Ψ_7			628 (w)	631 (w)
	Ψ_8			592 (w)	594 (w)
	ϕ_1			528 (w)	545 (w)
Thiazolidine	νn_1	1027 (m)		1024 (m)	1031 (m)
	νn_2	906 (m)	912 (w)	923 (m)	912 (w)
	νn_3	828 (m)	830 (w)	891 (m)	893 (m)
	νn_4	704 (m)	696 (w)	701 (w)	702 (w)
	νn_5	673 (m)	672 (w)	675 (w)	673 (w)
	δn_2	477 (w)	484 (w)	475 (w)	478 (w)
	Γ_1	445 (w)	444 (w)		
3,4-Dichlorophenyl	8b	1586 (s)	1606 (vs)	1585 (s)	1563 (m)
	8a	1550 (m)	1558 (m)	1548 (m)	1538 (m)
	19b	1470 (s)	1463 (m)	1466 (s)	1467 (m)
	19a	1384 (s)	1391 (s)	1372 (m)	1377 (s)
	14	1253 (m)	1237 (m)	1244 (m)	1233 (m)
	1	1131 (m)	1121 (m)	1136 (m)	1147 (w)
	6a				686 (w)
	16a		550 (w)		584 (w)
	16b	433 (w)	435 (w)	428 (w)	425 (w)

Abbreviations: (s) strong; (m) medium; (w) weak; (v) very.

The IR spectra of **1** and **2** in the 4000–370 cm^{-1} region show the presence of bands due to the organic moiety ring vibrations as is shown in Table 4.

The two complexes showed a strong $\nu(C{=}N)_{imine}$ absorption, at 1606 cm^{-1} in **1** and at 1598 cm^{-1} in **2**, suffering a shift to a lower wavenumber when compared with that for the uncoordinated imine function of the respective ligands. Likewise, the in-plane stretching vibrations corresponding to $\nu(C{=}N)$ skeletal vibrations of the heterocyclic rings (W_1 of **1** and ψ_1 of **2**), were also shifted to lower wavenumbers compared with that for the respective free ligands (Table 4). From this a coordination via the imino nitrogens of the ligands can be deduced [44–47].

In the low-frequency region, the C_1 symmetry of both complex cations predicts the appearance of four bands assignable to metal–ligand stretching vibrations. The IR spectrum of **1** shows three such bands at 345, 322 and 226 cm^{-1}. The band at 345 cm^{-1} could include the $\nu(Co–N_{imino})$ vibration [13,44–46,48] and one $\nu(Co–Cl)$ vibration [13,49–52], whereas the band at 322 cm^{-1} is assigned to the other $\nu(Co–Cl)$ vibration [13,49–52]. Finally, the band at 226 cm^{-1} is assignable to $\nu(Co–N_{thiazoline})$ [13,29,30]. In a similar form, only three such bands are observed for **2**. Of these, the band at 337 cm^{-1} can include the $\nu(Co–N_{imino})$ vibration [13,44–46,48] and one $\nu(Co–Cl)$ vibration [13,49–52], whereas the band at 320 cm^{-1} is assigned to the other $\nu(Co–Cl)$ vibration [13,49–52]. The last band at 230 cm^{-1} is tentatively assigned to $\nu(Co–N_{thiazine})$, in good accord with literature data for several complexes containing thiazoline or thiazine derivative ligands [13,29,30].

4. Supplementary material

CCDC 247453, corresponding to $[CoCl_2(TdTn)]$, and CCDC 247454, to $[CoCl_2(TdTz)]$ contain the supplementary crystallographic data for this paper. These data can be obtained free of charge via www.ccdc.cam.ac.uk/conts/retrieving.html (or from the CCDC, 12 Union Road, Cambridge CB2 1EZ, UK; fax: +44 1223 336033; e-mail: deposit@ccdc.cam.ac.uk).

Acknowledgements

We would like to thank the Spanish Ministerio de Ciencia y Tecnología, [Project BQU01-0374], the Junta de Extremadura (Consejería de Educación, Ciencia y Tecnología) and the FEDER [Project 2PR02A098] for financial support. A.M. Lozano-Vila thanks the Spanish Ministerio de Ciencia y Tecnología and E. Viñuelas-Zahínos thanks the Junta de Extremadura (Consejería de Educación, Ciencia y Tecnología) and the FEDER for their Ph.D. fellowships.

References

[1] W.Y. Sun, J. Fan, T. Okamura, N. Ueyama, Inorg. Chem. Commun. 3 (2000) 541.
[2] A. Korolkovas, J.H. Burckhalter, in: Compendio Esencial de Química Farmacéutica, Reverte, Barcelona, 1983.
[3] R.F. Schinazi, R.A. Floyd, PCT Int. Appl. WO 90 13,296 (Cl. A61K31/54) (1991) Chem. Abstr. 115 (1991) 105989.
[4] D. Bozsing, P. Sohar, G. Gigler, G. Kovacs, Eur. J. Med. Chem. 31 (1996) 663.
[5] I.A. Shehata, H.I. Elsubbagh, A.M. Abdelal, M.A. Elsherbeny, A.A. Alobaid, Med. Chem. Res. 6 (1996) 148.
[6] B. Tozkoparan, G. Aktay, E. Yesilada, Il Farmaco 57 (2002) 145.
[7] P. Wipf, P. Fritch, Tetrahedron Lett. 35 (1994) 5377.
[8] M. Premanathan, R. Arakaki, S. Ramanan, S. Jinno, M. Baba, S. Yamashita, H. Nakashima, Antiviral Chem. Chemother. 9 (1998) 423.
[9] C. Della Monica, A. Randazzo, G. Bifulco, P. Cimino, M. Aquino, I. Izzo, F. De Riccardis, L. Gomez-Paloma, Tetrahedron Lett. 43 (2002) 5707.
[10] C.A. Bolos, K.T. Papazisis, A.H. Kortsaris, S. Voyatzi, D. Zambouli, D.A. Kyziakidis, J. Inorg. Biochem. 88 (2002) 25.
[11] M.L. Guerinot, Annu. Rev. Microbil. 48 (1994) 743.
[12] R.J. Bergeron, C.Z. Liu, J.S. McManis, M.X.B. Xia, S.E. Algee, J. Wiegand, J. Med. Chem. 37 (1994) 1411.
[13] A. Bernalte García, F.J. García Barros., F.J. Higes Rolando, F. Luna Giles, Polyhedron 20 (2001) 3315.
[14] A. Bernalte García, F.J. García Barros, F.J. Higes Rolando, F. Luna Giles, R. Pedrero Marín, J. Inorg. Biochem. 98 (2004) 15.
[15] F.J. Barros García, A. Bernalte García, F.J. Higes Rolando, F. Luna Giles, R. Pedrero Marín, Polyhedron 23 (2004) 1453.
[16] F.J. Barros García, A. Bernalte García, F.J. Higes Rolando, F. Luna Giles, R. Pedrero Marín, E. Viñuelas-Zahínos, Inorg. Chim. Acta 357 (2004) 1457.
[17] F.J. Barros García, A. Bernalte García, F.J. Higes Rolando, F. Luna Giles, M.A. Maldonado Rogado, E. Viñuelas-Zahínos, Inorg. Chim. Acta 357 (2004) 3574.
[18] R.J. Outcalt, J. Heterocyclic Chem. 24 (1987) 1425.
[19] A.S. Deutsch, P.E. Fanta, J. Org. Chem. 21 (1956) 892.
[20] H.W. Schubert, O. Behner, Arch. Pharm. 301 (1968) 752.
[21] L.J. Farrugia, J. Appl. Cryst. 32 (1999) 837.
[22] F.H. Allen, Acta Cryst. B58 (2002) 380.
[23] I.J. Bruno, J.C. Cole, P.R. Edington, M. Kessler, C.F. Macrae, P. McCabe, J. Pearson, R. Taylor, Acta Cryst. B58 (2002) 389.
[24] T.F. Liu, D. Fu, S. Gai, Y.Z. Zhang, H.L. Sun, G. Su, Y.J. Liu, J. Am. Chem. Soc. 124 (2003) 13976.
[25] D. Cremer, J.A. Pople, J. Am. Chem. Soc. 97 (1975) 1354.
[26] B.B. Garrett, V.L. Goedken, J.V. Quagliano, J. Am. Chem. Soc. 11 (1970) 489.
[27] D.K. Rastogi, K.C. Sharma, S.K. Dua, M.P. Teotia, J. Inorg. Nucl. Chem. 37 (1975) 685.
[28] Y.J. Weaver, J.A. Weaver, J. Inorg. Nucl. Chem. 37 (1975) 1309.
[29] J.A. Weaver, P. Hambright, P.T. Talbert, E. Kang, A.N. Thorpe, Inorg. Chem. 9 (1970) 268.
[30] A.C. Fabretti, G. Peyronel, G.C. Franchini, Inorg. Chim. Acta 35 (1979) 49.
[31] G. Marcotrigiano, L. Menabue, G.C. Pellacani, Inorg. Chim. Acta 26 (1978) 57.
[32] B.N. Figgis, J. Lewis, Prog. Inorg. Chem. 6 (1964) 37.
[33] R.L. Carlin, Transit. Metal Chem. 1 (1965) 21.
[34] F.A. Cotton, O.D. Fant, D.M.L. Goodgame, R.H. Holm, J. Am. Chem. Soc. 83 (1961) 1780.
[35] F.A. Cotton, D.M.L. Goodgame, M. Goodgame, J. Am. Chem. Soc. 83 (1961) 4690.
[36] M. Guiliano, G. Mille, J. Choteau, J. Mol. Struct. 50 (1978) 233.

[37] M. Guiliano, G. Mille, T. Avignon, J. Chouteau, J. Raman Spectrosc. 7 (1978) 214.
[38] G. Mille, J.L. Meyer, J. Choteau, J. Mol. Struct. 50 (1978) 247.
[39] A.I. Meyers, J. Org. Chem. 26 (1961) 218.
[40] A. Pastura, K. Thewalt, J. Prakt. Chem. 38 (1968) 177.
[41] G. Varsanyi, in: Vibrational Spectra of Benzene Derivatives, Academic Press, New York, 1969.
[42] R.T. Conley, in: Espectroscopía Infrarroja, Alhambra, Madrid, 1979.
[43] E. Pretsch, T. Clerc, J. Seibl, W. Simon, in: Tablas para la determinación estructural por métodos espectroscópicos, Springer-Verlag Ibérica, Barcelona, 2000.
[44] M. Shakir, S.P. Varkey, F. Firdaus, P.S. Hameed, Polyhedron 13 (1994) 2319.
[45] B. Singh, R.N. Singh, R.C. Aggarwal, Polyhedron 4 (1985) 401.
[46] M.M. Mostafa, M.A. Khattab, K.M. Ibrahim, Polyhedron 2 (1983) 583.
[47] J. Nelson, S. Martin Nelson, W.D. Perry, J. Chem. Soc., Dalton Trans. (1976) 1282.
[48] N.K. Singh, S. Agrawal, R.C. Aggarwal, Polyhedron 3 (1984) 1271.
[49] E.J. Duff, M.N. Hughes, K.J. Rutt, J. Chem. Soc. (1969) 2101.
[50] C.E. Taylor, A.E. Underhill, J. Chem. Soc. A (1969) 368.
[51] W.J. Eilbeck, F. Holmes, C.E. Taylor, A.E. Underhill, J. Chem. Soc. A (1968) 128.
[52] W.J. Eilbeck, F. Holmes, C.E. Taylor, A.E. Underhill, J. Chem. Soc. A (1969) 1189.

Available online at www.sciencedirect.com
SCIENCE DIRECT®
Polyhedron 24 (2005) 137–142
POLYHEDRON
www.elsevier.com/locate/poly

Synthesis, crystal structure and luminescence properties of a saturated dimeric Er(III)-chelated complex based on benzoate and bipyridine ligands

Soo-Gyun Roh [a], Min-Kook Nah [a], Jae Buem Oh [a], Nam Seob Baek [a], Ki-Min Park [b], Hwan Kyu Kim [a,*]

[a] *Center for Smart Light-Harvesting Materials and Department of Polymer Science and Engineering, Hannam University, 133 Ojung-dong, Daeduck-gu, Daejeon 306-791, South Korea*
[b] *Research Institute of Natural Sciences, Gyeongsang National University, 900 Gazwa-dong, Chinju 600-701, South Korea*

Received 9 September 2004; accepted 27 October 2004
Available online 15 December 2004

Abstract

New saturated dimeric Er(III)-chelated model complexes based on benzoate and bipyridine ligands were synthesized through a ligand-exchange reaction in the presence of the Er(III) ion and potassium benzoate salts. The crystal structure of the novel 8-coordinated dimeric complex, $[Er_2(benzoate)_6(bipyridine)_2]$, involving four bridging and two chelating benzoate ligands and two bipyridine ligands, was determined by X-ray crystal structure analysis. The dimeric Er(III)-chelated complex has an asymmetric unit with a Er(1)–Er(2) distance of 4.33 Å and its crystal exhibited a very strong intensity near-IR emission, taking place from the first excited state ($^4I_{13/2}$) to the ground state ($^4I_{15/2}$) in the region of 1.53 μm.
© 2004 Elsevier Ltd. All rights reserved.

Keywords: Crystal structure; Erbium complex; Dimeric lanthanide complex; Photophysical properties; Planar waveguide amplifiers

1. Introduction

Very recently, the development of integrated planar waveguide optical amplifiers has been extremely essential to achieve photonic devices in super high speed communication systems [1]. In particular, wavelength division multiplexing (WDM)-integrated planar waveguide amplifiers are recognized to be essential for successfully realizing photonic devices in WDM technology. Despite such needs, the problem still remains to be the materials for the use in the real optical amplifiers. At present, erbium-doped silica amplifiers are widely used, but the poor solubility of the erbium ion (Er^{3+}) in conventional inorganic/organic media leads to low amplification properties. When the higher doping concentration of the erbium ion was introduced, clustered Er^{3+} species can be formed, which in turn have a limited amplification property. It is ascribed to the cooperative energy-transfer processes between the clustered Er^{3+} species. For critical problems of erbium-doped silica, the optical amplification gain is currently not enough for amplifying the optical signals in small sized photonic devices. In order to enhance the amplified luminescence intensity, the development of luminescent lanthanide complexes based on energy transfer mechanisms by using supramolecular complexes as organic ligands has been extensively studied [1–7]. Luminescent lanthanide complexes consist of lanthanide ions and chelating luminescent ligands as a sensitizer. They efficiently absorb and transfer lights to the central lanthanide ion through energy transfer. Their supramolecular

* Tel.: +82 42 629 7865; fax: +82 42 629 8325.
E-mail address: hwankkim@mail.hannam.ac.kr (H.K. Kim).

0277-5387/$ - see front matter © 2004 Elsevier Ltd. All rights reserved.
doi:10.1016/j.poly.2004.10.014

complexes contain well-known antenna chromophores to photoexcite the lanthanide ions via the energy transfer process, but crystal structural studies of their complexes are rare [7b]. Crystal structures of dimeric Eu(III)-chelated complexes based on *p*-methoxybenzoate [8a], *o*- or *p*-aminobenzoate [8b,c], and *p*-methylbenzoate [8d] with bipyridine are well known. Recently, dimeric and polymeric Ln(III) complexes (Ln = Eu, Gd, Tb) based on benzoic acid and its derivatives have been studied [10]. Even more recently, dimeric Eu, Nd and Sm(III) lanthanide complexes based on bis-diketonate ligands have been reported [9]. However, structural studies and photophysical properties of these dimeric Er(III)-chelated complexes are not known. Also, even though the structure of the Er(III)-chelated complexes are similar to Eu(III)-chelated complexs, the Er(III)-chelated complexes have quite different features with regards to their optophysical properties and applications, in comparison with the Eu(III) complexes [1,11].

Recently, we studied the synthesis and photophysical properties of luminescent lanthanide complexes based on coumarin [12a], benzoate and pentafluorobenzoate [12b], porphyrin [13,14b] and naphthalene [14] derivatives for advanced photonic applications such as planar waveguide amplifiers and light-emitting diodes, in order to get highly efficient lanthanide emission via energy transfer between the luminescent ligands and the lanthanide ions. In this paper, a novel dimeric Er(III)-chelated complex, through a ligand exchange reaction using $ErCl_3$ in the presence of bipyridine and potassium benzoate salt, has been synthesized and its molecular structure and photophysical properties have been investigated.

2. Experimental

2.1. Synthesis of $[Er_2(benzoate)_6(bipyridine)_2]$

A mixture of benzoic acid (0.500 g, 4.094 mmol), bipyridine (0.469 g, 3.002 mmol) and KH (0.167 g, 4.163 mmol) was dissolved in 150 mL of dried THF. This suspension was stirred at room temperature overnight. A suspension was formed with gas evolution during the reaction. After the complete formation of the salt, a methanol solution of anhydrous $ErCl_3$ (0.373 g, 1.365 mmol) in 10 mL of methanol was added dropwise to the reaction solution. After stirring at room temperature for one day, the resulting solution was filtered and solvents were removed to give a pinkish solid. The solid was washed with diethylether and *n*-hexane, and dried under vacuum. This pinkish solid was dissolved in hot methanol, filtered, and then the filtrate was left at room temperature. $[Er_2(benzoate)_6(bipyridine)_2]$ (0.629 g, 0.458 mmol, 67%) was obtained over a period of several weeks. *Anal.* Calc. (%) for $C_{31}H_{23}ErN_2O_6$: C, 54.21; H, 3.38; N, 4.08; Er, 24.35. Found: C, 54.15; H, 3.37; N, 4.05; Er, 24.34%. UV–Vis. (λ nm (%), reflectance) 306 (37.8), 380 (91.5), 490 (94.5), 523 (90.7). FT-IR (KBr pellet, cm^{-1}) 3115, 3089, 3059, 3024, 2928, 1641, 1597, 1537, 1406, 1311, 1179, 1155, 1065, 1014, 854, 764, 720, 687, 669, 642, 570, 429.

2.2. X-ray structure determination

A pinkish crystal of the erbium complex, suitable for X-ray structure analysis, was obtained by slow evaporation of methanol over a period of several weeks. All data were collected on a Bruker SMART diffractometer equipped with a graphite monochromated Mo Kα (λ = 0.71073 Å) radiation source and a CCD detector; 45 frames of two-dimensional diffraction images were collected and processed to obtain the cell parameters and orientation matrix [15a]. The two-dimensional diffraction images were collected, each of which was measured for 30 s. The frame data were processed to give structure factors using the program SAINT [15a]. The molecular structure was solved by a direct method and refined by full-matrix least-squares against F^2, for all data using SHELXTL software [15b]. All non-hydrogen atoms were refined with anisotropic displacement parameters. The final cycle of the refinement gave $R = 0.0244$ with 12774 reflections in the θ range of 1.85°–28.27° ($-18 \leqslant h \leqslant 14$, $-20 \leqslant k \leqslant 19$, $-22 \leqslant l \leqslant 34$) at −100 °C. A summary of the crystallographic data is given in Table 1.

2.3. Measurements and apparatus

FT-IR spectra, in the region of 4000–400 cm^{-1}, were recorded on a Perkin–Elmer 1000 FT-IR spectrometer using the conventional KBr pellet method. UV–Vis spectra were measured with a Shimazu UV–Vis spectrophotometer using UV-2401PC. A TGA curve was carried out with a Dupont 9900 Model 951 thermogravimetric analyzer with a heat rate of 10 °C/min under N_2 atmosphere. Photoluminescence spectra were measured on a steady-state fluorimeter (Edinburgh Instruments. FS920) with a 450W Xe lamp. A He–Cd laser (325 nm) and an Ar-ion laser (488 nm) were used as an excitation light source when the emission was measured. The emission from the sample was collected and refocused to the emission monochrometer with 300 nm focal length. The emission spectra in the visible region were taken with a PMT system (Hamamatsu R955) and in the near infrared region with a liquid nitrogen cooled Ge-detector (Edinburgh Instruments. EI-L). All spectra were taken at room temperature. The excitation laser powers were adjusted to the same power (about 16 mW) at the sample.

Table 1
Crystal data and structure refinement for $[Er_2(benzoate)_6(bipyridine)_2]$

Empirical formula	$C_{62}H_{46}Er_2N_4O_{12}$
Formula weight	1373.55
T (K)	173(2)
Crystal system	monoclinic
Space group	$P2_1/n$
a (Å)	14.1075(4)
b (Å)	15.2676(5)
c (Å)	25.7442(8)
β (°)	103.5340(10)
V (Å^3)	5391.0(3)
Z	4
$F(000)$	2712
D_{calc} (Mg/m^3)	1.692
Absorption coefficient (mm^{-1})	3.162
Crystal size (mm)	$0.40 \times 0.30 \times 0.30$
Range hkl collected	$-18 \leqslant h \leqslant 14$, $-20 \leqslant k \leqslant 19$, $-22 \leqslant l \leqslant 34$
Reflections collected	34239
Independent reflections	12774 [$R_{int} = 0.0296$]
Completeness to θ (=28.27 °C)	95.5%
Absorption correction	SADABS [11c]
Maximum and minimum transmission	0.509488 and 0.414415
Data/restraints/parameters	12774/0/721
Goodness-of-fit on F^2	1.068
Final R indices [$I > 2\sigma(I)$]	$R_1 = 0.0244$, $wR_2 = 0.0539$
R indices (all data)	$R_1 = 0.0334$, $wR_2 = 0.0572$
Largest difference peak and hole (e Å^{-3})	1.066 and −0.725

3. Results and discussion

3.1. Synthesis

The synthesis of the dimeric Er(III)-chelated complex was verified by elementary analysis, TGA, FT-IR, absorption and emission spectroscopies, and X-ray crystal analysis. The paramagnetic nature of the Er complex does not permit NMR characterization. The FT-IR spectrum of the Er(III)-chelated complex exhibited the vibration modes of the carbonyl moieties of two bidentate-like carboxylate bands in the region of 1640 and 1410 cm^{-1}. According to previous studies for acetate complexes [16], the difference between asymmetric and symmetric vibration modes shows that the values of unidentate complexes have a significant difference in comparison with those of bridging bidentate and/or chelating complexes. But, the two different modes of benzoate ligand coordination, by X-ray structure analysis, are almost not distinguished in the IR spectrum of the dimeric Er-chelated complex. As seen from Fig. 1, the 8-coordinated dimeric Er(III)-chelated complex shows two obvious weight loss processes in the TGA curve. The first one, with a weight loss of 23%, is assigned to the releasing of bipyridine from 180 to 237 °C, and the second one is assigned to the loss of six benzoate ligands up to ca. 550 °C. There is no obvious weight loss process before 180 °C in the TGA trace, indicating that the 8-coordinated dimeric Er(III)-chelated complex has no coordinated H_2O molecules.

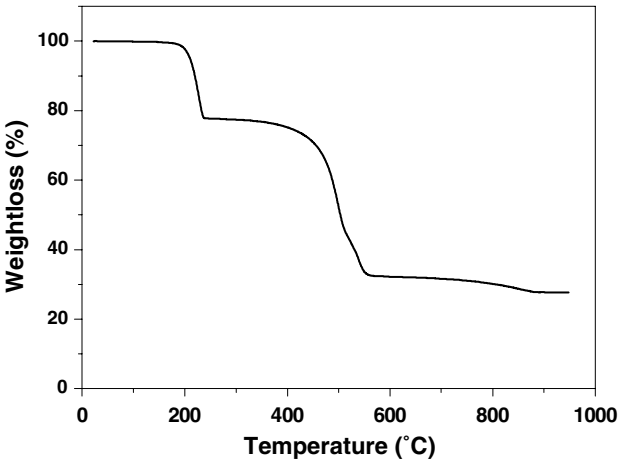


Fig. 1. TGA trace of $[Er_2(benzoate)_6(bipyridine)_2]$.

3.2. Crystal structure

In order to clarify the exact structure of the novel dimeric Er(III)-chelated complex, we have carried out an X-ray structure analysis for the pinkish white crystals of the dimeric Er(III)-chelated complex.

The molecular structure, as shown in Fig. 2, shows that the crystal structure consists of two Er(III) ions, having 8-coordinated asymmetric units, remarkably bridged by four benzoate groups, and chelated by two benzoate and two bipyridine groups to give the dimeric $[Er_2(benzoate)_6(bipyridine)_2]$. It is similar to {[Eu(*o*-aminobenzoate)$_3$(bipyridine)]bipyridine}$_2$ [8b], but the former complex, having a more distorted coordination mode due to a higher trans influence and asymmetry, has a greater steric effect than the latter complex.

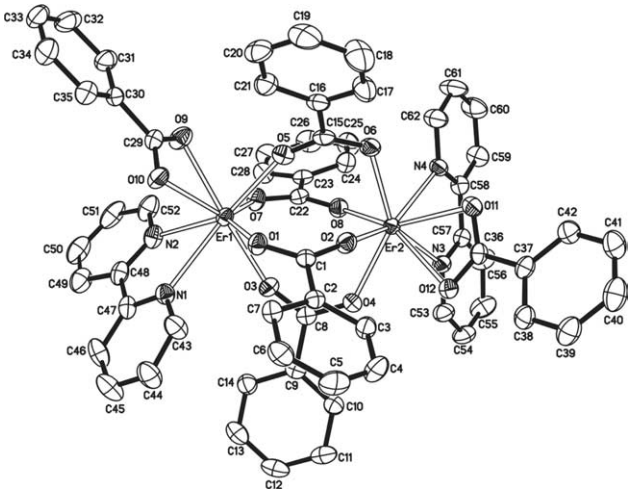


Fig. 2. ORTEP drawing of the molecular structure for $[Er_2(benzoate)_6(bipyridine)_2]$. Hydrogen atoms are omitted for clarity.

The coordination geometries of the Er(1) and Er(2) centers are distorted square antiprisms consisting of O(1), O(3), O(5), O(7), O(9), O(10), N(1) and N(2), and of O(2), O(4), O(6), O(8), O(11), O(12), N(3) and N(4), respectively. Selected bond distances and bond angles are given in Tables 2 and 3. The bond distances of Er(1)–O are in the range 2.258(2)–2.4370(19) Å and those of Er(1)–N are in the range 2.437(2)–2.533(2) Å, while the bond distances of Er(2)–O are 2.2742(19)–2.4289(19) Å and those of Er(2)–N are in the range 2.516(2)–2.573(2) Å. The average distances of Er–O [2.404 Å] for the bridged benzoate groups are shorter than those of Er–O [2.2899 Å] for chelated benzoate groups and the average distance Er–N [2.552 Å] for bipyridine groups are longer than those of Er–O for benzoate groups. The average distances of Er–O and Er–N in this work are somewhat longer than those of $Er(C_{23}H_{20}N_5O_2)](H_2O)(NO_3)]$ ($C_{23}H_{20}N_5O_2$ = bis(2,6-diacetylpyridine-bis-(phenylhydrazone) [17], while the average distances of Er–O are similar to $[Er_2(Acc^6)_4(H_2O)_8](ClO_4)_6(H_2O)_{11}$ (Acc = 1-amino cyclohexane-1-carboxylic acid) [18]. The distance of Er(1)–Er(2) (4.33 Å) is relatively long. Therefore, there are no significant intermolecular interactions in the crystal.

Table 2
Selected bond lengths (Å) for $[Er_2(benzoate)_6(bipyridine)_2]$

Er(1)–O(1)	2.3262(19)	Er(1)–O(3)	2.265(2)
Er(1)–O(5)	2.258(2)	Er(1)–O(7)	2.2965(19)
Er(1)–O(9)	2.437(2)	Er(1)–O(10)	2.3570(19)
Er(1)–N(1)	2.586(2)	Er(1)–N(2)	2.533(2)
Er(2)–O(2)	2.2800(19)	Er(2)–O(4)	2.3205(19)
Er(2)–O(6)	2.2989(19)	Er(2)–O(8)	2.2742(19)
Er(2)–O(11)	2.395(2)	Er(2)–O(12)	2.4289(19)
Er(2)–N(3)	2.516(2)	Er(2)–N(4)	2.573(2)
O(1)–C(1)	1.266(3)	O(1)–C(2)	1.255(3)
O(3)–C(8)	1.252(3)	O(4)–C(8)	1.253(3)
O(5)–C(15)	1.252(4)	O(6)–C(15)	1.259(4)
O(7)–C(22)	1.259(3)	O(8)–C(22)	1.257(3)
O(9)–C(29)	1.262(3)	O(10)–C(29)	1.266(3)
O(11)–C(36)	1.272(3)	O(12)–C(36)	1.256(3)

Table 3
Selected bond angles (°) for $[Er_2(benzoate)_6(bipyridine)_2]$

O(1)Er(1)O(3)	78.32(7)	O(1)Er(1)O(5)	77.38(7)
O(1)Er(1)O(7)	137.77(7)	O(1)Er(1)O(9)	126.29(7)
O(1)Er(1)O(10)	81.64(7)	O(3)Er(1)O(5)	108.26(7)
O(3)Er(1)O(7)	76.63(7)	O(3)Er(1)O(9)	154.39(7)
O(3)Er(1)O(10)	147.44(7)	O(5)Er(1)O(7)	78.92(7)
O(5)Er(1)O(9)	74.81(8)	O(5)Er(1)O(10)	91.89(7)
O(7)Er(1)O(9)	79.17(7)	O(7)Er(1)O(10)	133.65(7)
O(9)Er(1)O(10)	54.71(7)	N(1)Er(1)O(1)	76.32(7)
N(1)Er(1)O(3)	73.45(7)	N(1)Er(1)O(5)	152.67(7)
N(1)Er(1)O(7)	126.63(7)	N(1)Er(1)O(9)	115.90(7)
N(1)Er(1)O(10)	77.04(7)	N(2)Er(1)O(1)	139.00(7)
N(2)Er(1)O(3)	93.21(8)	N(2)Er(1)O(5)	141.99(8)
N(2)Er(1)O(7)	76.01(7)	N(2)Er(1)O(9)	72.77(8)
N(2)Er(1)O(10)	85.31(7)	N(1)Er(1)N(2)	62.88(8)
O(2)Er(2)O(4)	74.90(7)	O(2)Er(2)O(6)	74.03(7)
O(2)Er(2)O(8)	111.08(7)	O(2)Er(2)O(11)	92.34(7)
O(2)Er(2)O(12)	77.26(7)	O(4)Er(2)O(6)	137.52(7)
O(4)Er(2)O(8)	78.91(7)	O(4)Er(2)O(11)	129.25(7)
O(4)Er(2)O(12)	75.04(7)	O(6)Er(2)O(8)	86.01(7)
O(6)Er(2)O(11)	80.26(7)	O(6)Er(2)O(12)	124.22(7)
O(8)Er(2)O(11)	148.41(7)	O(8)Er(2)O(12)	149.43(7)
O(11)Er(2)O(12)	54.21(6)	N(3)Er(2)O(2)	144.10(7)
N(3)Er(2)O(4)	76.24(7)	N(3)Er(2)O(6)	141.33(7)
N(3)Er(2)O(8)	83.52(7)	N(3)Er(2)O(11)	89.63(7)
N(3)Er(2)O(12)	75.02(7)	N(4)Er(2)O(2)	150.88(7)
N(4)Er(2)O(4)	133.06(7)	N(4)Er(2)O(6)	77.78(7)
N(4)Er(2)O(8)	73.66(7)	N(4)Er(2)O(11)	75.68(7)
N(4)Er(2)O(12)	113.93(7)	N(3)Er(2)N(4)	63.55(7)

3.3. UV–Vis absorption and emission spectra

The absorption spectrum of the dimeric Er(III)-chelated complex shows a very intense absorption band at 306 nm, indicating a π–π* electronic transition. Also, some absorption bands at 380, 490 and 523 nm were observed with relatively narrow bandwidths, as shown Fig. 3. These bands are in good agreement with the absorption spectrum of the trivalent Er ion itself. Upon photoexcitation with a wavelength of 325 nm, the emission spectrum of the dimeric Er(III)-chelated complex was observed, the emission band in the UV–Vis region around 335 nm corresponding to the organic ligand emission. Interestingly, three spectral hollow points at 357, 365 and 378 nm were explicitly observed in the crystal state. These hollow points are consistent with the absorption bands ($^2G_{7/2}$, $^4G_{9/2}$ and $^4G_{11/2}$) of the Er ion itself. It should be noted to spectrally visualize that the energy transfer between the exited organic ligands and trivalent Er ion takes place at the three corresponding bands. It reduces the PL intensity of the organic ligand, thus yielding stronger near IR emission bands.

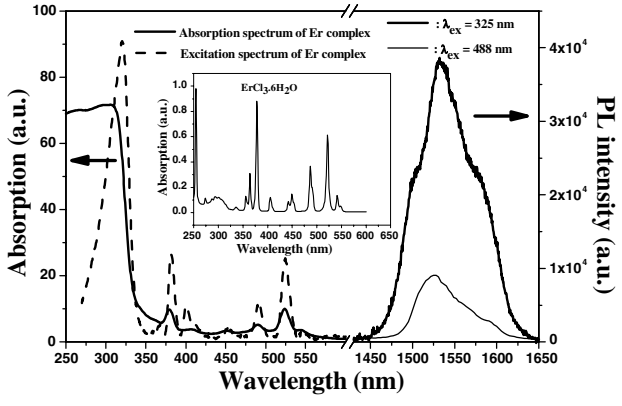


Fig. 3. Absorption (reflectance) and excitation (at λ_{em} = 1.53 μm) spectra of $[Er_2(benzoate)_6$ (bipyridine)$_2]$; and emission spectra of $[Er_2(benzoate)_6(bipyridine)_2]$ in the crystal state at λ_{ex} = 325 (He–Cd laser) and 488 (Ar ion laser) nm with a power of about 16 mW. The inset shows the UV–Vis spectrum of the Er(III) salt (H_2O, 0.1 M). Here, λ_{ex} means the excitation wavelength, while λ_{em} means the the emission wavelength.

Fig. 3 shows a strong near IR emission band, corresponding to the characteristic $^4I_{13/2} \rightarrow {}^4I_{15/2}$ transition of trivalent erbium ions at 1.53 μm, of the dimeric Er(III)-chelated complex using a photoexcitation wavelength of 325 and 488 nm. The near IR emission band, obtained with a photoexcitation wavelength of 325 nm, which excited through the organic ligands, exhibited a much stronger emission intensity in the crystal state than the direct excitation of Er ions at 488 nm. The maximum emission band of the dimeric Er-chelated complex was observed at 1.53 μm, at which the excitation spectrum exhibits the maximum excitation band at 335 nm. Several additional excitation bands, corresponding to the Er ion itself, were exhibited in the region of 350–550 nm. These results are very similar to the absorption spectrum of the dimeric Er-chelated complex. Thus, we think that the major factor for the effect of the emission bands is the ligands coordinated to the central metal ion. With these results, it should be considered that an energy transfer process from the excited organic ligands to the erbium ions takes place. Fig. 3 shows the near IR emission spectra of the Er-chelated complex at a photoexcitation wavelength of 325 and 488 nm. Here, using a photoexcitation wavelength of 325 nm, the energy transfer process between the excited ligand and the Er ion takes place possibly to generate the emission of the central lanthanide ion (Er ion), while using a photoexcitation wavelength of 488 nm, the emission of the inherent lanthanide ion (Er ion) was obtained through the direct excitation of the Er ion without an energy transfer process between the excited ligand and the Er ion. The PL intensity of the Er complex by photoexcitation at 325 nm shows a much stronger PL intensity than that at 488 nm, as shown in Fig. 3 in which the stronger emission band of the Er(III) complex was obtained by the indirect photoexcitation of the ligands rather than by the direct photoexcitation of the Er(III) ions. This could be explained by an energy transfer between the PL emission band of the ligands and the absorption band of the erbium ion. Thus, these results could be attributed to the efficient energy transfer process between the organic ligands and the Er ion, since spectral overlap between the PL band of the organic ligands and the absorption bands of the Er ion at 357, 365 and 379 nm occurs.

4. Supplementary material

Supplementary data are available from the Cambridge Crystallographic Data Centre, 12 Union Road, Cambridge CB2 1EZ, UK (fax: +44-1233-336033; e-mail: deposit@ccdc.cam.ac.uk or http://www.ccdc.cam.ac.uk) on request, quoting the Deposit No. CCDC 233294.

Acknowledgements

The authors acknowledge that this research was financially supported from the National Creative Research Initiatives Program of Ministry of Science and Technology of Korea at Hannam University.

References

[1] H.K. Kim, S.-G. Roh, K.-S. Hong, J.-W. Ka, N.S. Baek, J.B. Oh, M.K. Nah, S.M. Ma, Y.H. Cha, J. Ko, Macromol. Res. 11 (2003) 133, and references cited therein.
[2] F.J. Steemers, W. Verboom, D.N. Reinhoudt, E.B. van der Tol, J.W. Verhoeven, J. Am. Chem. Soc. 117 (1995) 9408.
[3] M.P. Oude Wolbers, F.C.J.M. van Veggel, F.G.A. Peters, E.S.E. van Beelen, J.W. Hofstraat, F.A.J. Guerts, D.N. Reinhoudt, Chem. Eur. J. 4 (1998) 772.
[4] L.H. Slooff, A. Polman, M.P. Oude Wolbers, F.C.J.M. van Veggel, D.N. Reinhoudt, J.W. Hofstraat, J. Appl. Phys. 83 (1998) 497.
[5] S.I. Klink, G.A. Hebbink, L. Grave, F.C.J.M. van Veggel, D.N. Reinhoudt, L.H. Slooff, J. Appl. Phys. 86 (1999) 1181.
[6] C. Pitois, R. Vestberg, M. Rodlert, E. Malmström, A. Hult, M. Lindgren, Opt. Mater. 21 (2002) 499.
[7] (a) S. Destri, W. Porzio, F. Meinardi, R. Tubino, G. Salerno, Macromolecules 36 (2003) 273;
(b) P.R. Selvin, J. Jancarik, M. Li, L.-W. Hung, Inorg. Chem. 35 (1996) 700.
[8] (a) L. Jin, R. Wang, L. Li, S. Lu, S. Huang, Polyhedron 18 (1999) 487;
(b) L. Jin, S. Lu, S. Lu, Polyhedron 15 (1996) 4069;
(c) X. Zheng, L. Jin, M. Wang, J. Zhang, S. Liu, Chem. J. Chin. Univ. (in Chinese) 16 (1995) 1007;
(d) R. Wang, L. Jin, M. Wang, S. Huang, Chem. J. Acta. Chim. Sin. (in Chinese) 53 (1995) 39.
[9] A.W.-H. Lam, W.-T. Wong, S. Gao, G. Wen, X.-X. Zhang, Eur. J. Inorg. Chem. (2003) 149.
[10] A.P. Bassett, S.W. Magennis, P.B. Glover, D.J. Lewis, N. Spencer, S. Parsons, R.M. Williams, L. De Cola, Z. Pikramenou, J. Am. Chem. Soc. 126 (2004) 9413.
[11] J. Kido, Y. Okamoto, Chem. Rev. 102 (2002) 2357.
[12] (a) S.-G. Roh, N.S. Baek, K.-S. Hong, H.K. Kim, Bull. Korean Chem. Soc. 25 (2004) 343;
(b) S.-G. Roh, J.B. Oh, M.-K. Nah, N.S. Baek, Y.L. Lee, H.K. Kim, Bull. Korean Chem. Soc. 25 (2004) 1503.
[13] (a) J.B. Oh, K.L. Paik, J.-W. Ka, S.-G. Roh, M.-K. Nah, H.K. Kim, Mater. Sci. Eng. C. 24 (2004) 257;
(b) J.B. Oh, M.-K. Nah, Y.H. Kim, H.K. Kim, J. Lumin. (2004), in press.
[14] (a) N.S. Baek, M.-K. Nah, Y.H. Kim, S.-G. Roh, H.K. Kim, Bull. Korean Chem. Soc. 25 (2004) 443;
(b) H.K. Kim, J.B. Oh, N.S. Baek, J.-W. Ka, S.-G. Roh, Y.H. Kim, M.K. Nah, K.-S. Hong, B.J. Song, G.J. Zhou, J. Nonlinear Opt. Phys. Mater. (2004), in press.
[15] (a) Siemens: Area Detector Control and Integration Software, Version 5.0, SMART and SAINT, Siemens Analytical X-ray Instruments, Madison, WI, 1998;
(b) Siemens: Structure Determination Programs, Version 5.03, SHELXTL, Siemens Analytical X-ray Instruments, Madison, WI, 1998;
(c) G.M. Sheldrick, SADABS: Empirical Absorption and Correction Software, University of Göttingen, Institüt für Anorganische

Chemie der Universität, Tammanstrasse 4, D-3400 Göttingen, Germany, 1999.
[16] G.B. Deacon, R.J. Phillips, Coord. Chem. Rev. 33 (1980) 27.
[17] F.B. Tamboura, P.M. Haba, M. Gaye, A.S. Sall, A.H. Barry, T. Jouini, Polyhedron 23 (2004) 1191.
[18] K. Aparna, S.S. Krishnamurthy, M. Nethaji, P. Balaram, Polyhedron 16 (1997) 507.

Available online at www.sciencedirect.com
SCIENCE DIRECT®
Polyhedron 24 (2005) 143–150
POLYHEDRON
www.elsevier.com/locate/poly

Magnetic measurements, UV–Vis spectroscopy, and XAS of dinuclear nickel(II) complexes of bistetraazamacrocycles

Mathieu Soibinet [a], Isabelle Déchamps-Olivier [a], Emmanuel Guillon [a,*], Jean-Pierre Barbier [a], Michel Aplincourt [a], Françoise Chuburu [a,*], Michel Le Baccon [b], Henri Handel [b]

[a] *GRECI, Université de Reims Champagne-Ardenne, Moulin de la Housse, BP 1039, 51687 Reims Cedex 2, France*
[b] *UMR CNRS 6521, Université de Bretagne Occidentale, BP 809, 29285 Brest Cedex, France*

Received 11 June 2004; accepted 29 October 2004
Available online 19 November 2004

Abstract

The nickel(II) complexes of *N*,*N*′-xylylenebis(tetraazamacrocycles) have been isolated. The description of these dinuclear bismacrocyclic complexes have been carried out by means of magnetic measurements and spectrophotometric experiments (UV–Vis). The metal environment and the ligand shape have been specified by XANES and EXAFS experiments, since attempts to obtain suitable crystals failed.
© 2004 Elsevier Ltd. All rights reserved.

Keywords: Bistetraazamacrocycles; Nickel(II) complexes; Magnetic measurements; UV–visible spectroscopy; XANES; EXAFS

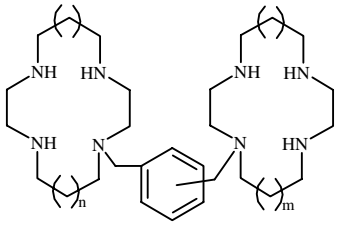
1. Introduction

Over the last 10 years, numerous polyamine ligands that are able to bind increasing number of metallic ions have been described in the literature. For this purpose, macrocyclic polyamines are often involved because of their strong ligating properties towards metallic ions, and then for the thermodynamic and kinetic stability of the corresponding complexes [1,2]. According to the design of the macrocyclic framework, these ligands may particularly be able to hold two or more metal centres in relatively close proximity [3].

There have been few reports on the X-ray structures of bistetrazamacrocyclic complexes [4,5] because they often failed to crystallize. In this study, besides magnetic measurements and UV–visible spectroscopy of Ni(II) dinuclear bistetraazamacrocyclic complexes formed with various ligands (Scheme 1), X-ray absorption spectroscopy is used as alternative technique to crystallography. X-ray absorption near edge structure (XANES) and extended X-ray absorption fine structure (EXAFS) are well known to provide reliable information about the geometry, the oxidation state of metal ions and the structure of the metallic complexes including tetraazamacrocyclic complexes [4,6]. Moreover, in dinuclear complexes with symmetrical ligands $\mathbf{L}^{1-4}$, the XAS spectroscopy is expected to give an average of the two metal environments, since the few known X-ray structures of bistetraazamacrocyclic complexes [4,5] indicated that the two metallic sites are almost identical.

* Corresponding authors. Tel.: +33 326 91 33 30/31 42; fax: +33 326 91 32 43.
E-mail addresses: emmanuel.guillon@univ-reims.fr (E. Guillon), francoise.chuburu@univ-reims.fr (F. Chuburu).

0277-5387/$ - see front matter © 2004 Elsevier Ltd. All rights reserved.
doi:10.1016/j.poly.2004.10.005



n = m = 0 { m – xylyl = $\mathbf{L^1}$; p – xylyl = $\mathbf{L^2}$ } **Bis-cyclen**

n = m = 1 { m – xylyl = $\mathbf{L^3}$; p – xylyl = $\mathbf{L^4}$ } **Bis-cyclam**

n = 1, m = 0 p – xylyl = $\mathbf{L^5}$: **Bis-cyclencyclam**

Scheme 1.

2. Results and discussion

2.1. Magnetic measurements and UV–Vis spectroscopy

Magnetic and spectroscopic data for complexes $[Ni_2\mathbf{L}^{1-5}]^{4+}$ are listed in Table 1. The molar magnetic susceptibilities of cyclen complexes $[Ni_2\mathbf{L}^{1,2}(ClO_4)_4]$ (respectively, 7793 and 7160×10^{-6} cgs unit at 293 K) indicate that the two d^8 nickel ions are held in an octahedral geometry (this value is calculated if one assume that there is no strong interaction between the two metal centers). On the contrary, the diamagnetism of cyclam complexes $[Ni_2\mathbf{L}^{3,4}(ClO_4)_4]$ indicate that the metal ions included in the macrocyclic cavity are held in a square planar geometry. Nevertheless, when the counter anion is chloride, the biscyclam complex $[Ni_2\mathbf{L}^{3}Cl_4]$ becomes again paramagnetic (7670×10^{-6} cgs unit) indicating that two chloride anions are coordinated to each nickel(II) center whose geometry becomes octahedral. Finally, the low-magnetic susceptibility of $[Ni_2\mathbf{L}^{5}(ClO_4)_2](ClO_4)_2$ is, as expected for a complex based on a dissymmetrical cyclen–cyclam ligand, an average of the magnetic susceptibility of a square planar Ni(II) ion (in the cyclam cavity, Ni(II) is diamagnetic) and an octahedral Ni(II) ion (in the cyclen moiety, Ni(II) is then paramagnetic).

The UV–visible absorbance spectra are also indicative of coordination of the nickel ions (Table 1). Solid spectra of the dinuclear cyclen complexes $[Ni_2\mathbf{L}^{1}(ClO_4)_4]$ and $[Ni_2\mathbf{L}^{2}(ClO_4)_4]$ present several similar bands (respectively, 390–392, 571–588, 950–980 nm) typical of Ni(II) d^8 ions in an octahedral geometry. Electronic spectra of the biscyclam complexes $[Ni_2\mathbf{L}^{3}](ClO_4)_4$ and $[Ni_2\mathbf{L}^{4}](ClO_4)_4$ are simplest since they exhibit a single band at 460 nm characteristic of Ni(II) ions in a square planar geometry. On the other hand, the solid spectrum of the dinuclear complex $[Ni_2\mathbf{L}^{3}Cl_4]$ exhibits several bands at 364, 448(sh), 558, 741(sh) and 1240 nm. These values can be attributed to the transitions of nickel(II) ions d^8 in a weak D_{4h} field, i.e., an octahedral environment, in accordance with magnetic measurements. At last, the electronic spectrum of $[Ni_2\mathbf{L}^{5}(ClO_4)_2](ClO_4)_2$ exhibits either the bands of the octahedral Ni ion in the cyclen moiety (392, 588, 799(sh), 950(br) nm) and the band of a square planar nickel(II) ion in a cyclam moiety (460 nm).

2.2. XANES and EXAFS studies

As Ni(II) complexes of $\mathbf{L^1}$ to $\mathbf{L^5}$ bismacrocycles failed to crystallize, XANES and EXAFS spectra were recorded. The Ni K-edge XANES spectra of nickel(II)

Table 1
Magnetic susceptibilities and electronic spectra of nickel(II) complexes, in solid state

Complexes	Magnetic susceptibilities $\chi_{Mcorr.}$ (10^{-6} cgs unit) at 293 K	λ_{max} (nm)
$[Ni_2\mathbf{L}^{1}(ClO_4)_4]$	7793	390–571–792(sh)–950(br)
$[Ni_2\mathbf{L}^{2}(ClO_4)_4]$	7160	392–588–799(sh)–980(br)
$[Ni_2\mathbf{L}^{3}Cl_4]$	7670	364–448(sh)–558–741(sh)–1240
$[Ni_2\mathbf{L}^{3}](ClO_4)_4$	diamagnetic	460
$[Ni_2\mathbf{L}^{4}](ClO_4)_4$	diamagnetic	460
$[Ni_2\mathbf{L}^{5}(ClO_4)_2](ClO_4)_2$	4600	392–460–588–799(sh)–950(br)

complexes, gathered in Fig. 1, display a very small peak around 8330 eV (α) assigned to 1s → 3d transition, a main edge resonance around 8350 eV (β) and a multiple scattering feature above 8353 eV (γ). This last feature is related to the geometry of the medium range structure around the investigated element. The absence of a shift for this feature in all the spectra indicates a similar organization around Ni(II) ions. In Fig. 1(a), the XANES spectra of cyclam complexes $[Ni_2\mathbf{L}^3Cl_4]$, $[Ni_2\mathbf{L}^3](ClO_4)_4$, $[Ni_2\mathbf{L}^4](ClO_4)_4$ are reported. For the $[Ni_2\mathbf{L}^3Cl_4]$ spectrum, the low intensity of the pre-edge peak (α) near 8330 eV and the high intensity of the shape resonance (β) indicate that Ni(II) ions may be closed to an octahedral environment, since the intensity of this latter peak decreases with the cation coordination number [7]. The Ni(II) geometry is confirmed by the absence of splitting for the main edge resonance (β). On the contrary, $[Ni_2\mathbf{L}^3](ClO_4)_4$ and $[Ni_2\mathbf{L}^4](ClO_4)_4$ spectra exhibit a splitting of the main edge peak (β) associated with $1s \rightarrow 4p_z$ and $1s \rightarrow 4p_{x,y}$ transitions, which means that nickel ions may be closed to a square planar geometry. One should notice that the comparison of $[Ni_2\mathbf{L}^3Cl_4]$ and $[Ni_2\mathbf{L}^3](ClO_4)_4$ spectra illustrates the influence of the anion on the signal for these cyclam complexes, depending on whether the anion is coordinated (Cl^-) or not (ClO_4^-).

The XANES spectra of the cyclen complexes $[Ni_2\mathbf{L}^1(ClO_4)_4]$, $[Ni_2\mathbf{L}^2(ClO_4)_4]$ (Fig. 1(b)) are similar to the $[Ni_2\mathbf{L}^3Cl_4]$ one, i.e., without splitting of the main-edge resonance. Consequently, nickel ions display an octahedral mode of coordination, which means that in these cyclen complexes, the perchlorate ions are coordinated.

Finally, in Fig. 1(c), the XANES spectrum of the $[Ni_2\mathbf{L}^5(ClO_4)_2](ClO_4)_2$ complex and those of $[Ni_2\mathbf{L}^2(ClO_4)_4]$ and $[Ni_2\mathbf{L}^4](ClO_4)_4$ complexes are reported. The dissymmetrical ligand $\mathbf{L}^5$ involves both a cyclen and a cyclam cavity. The intensity of the $1s \rightarrow 4p_z$ transition around 8335 eV, intermediate between a D_{4h} and an O_h symmetry, may significate that the nickel ion is held in two different geometries according to the macrocyclic cavity.

The k^3-weighted experimental and least-squares fitted EXAFS spectra of nickel(II) compounds are shown in Fig. 2 and the results of least-squares fitting reported in Table 2. Two kinds of EXAFS spectra are obtained depending on the shape of the sinusoidal signal. For the perchlorate complexes based on the cyclam cavity, no beating is noticed between 6 and 8 $Å^{-1}$ (spectra 2 and 3, Fig. 2) whereas for the complexes based on the cyclen moiety (spectra 4 and 5, Fig. 2) a splitting of the second sinusoid is observed. This discrepancy is due to the metal environment and, for the first two complexes, the nickel is held in a square-planar environment whereas, for the latter, the metal is held in an octahedral system. One-coordination shell is therefore found for square planar compounds, whereas, for the octahedral ones, two-coordination shells are determined. In all cases, the first coordination sphere around the Ni(II) is

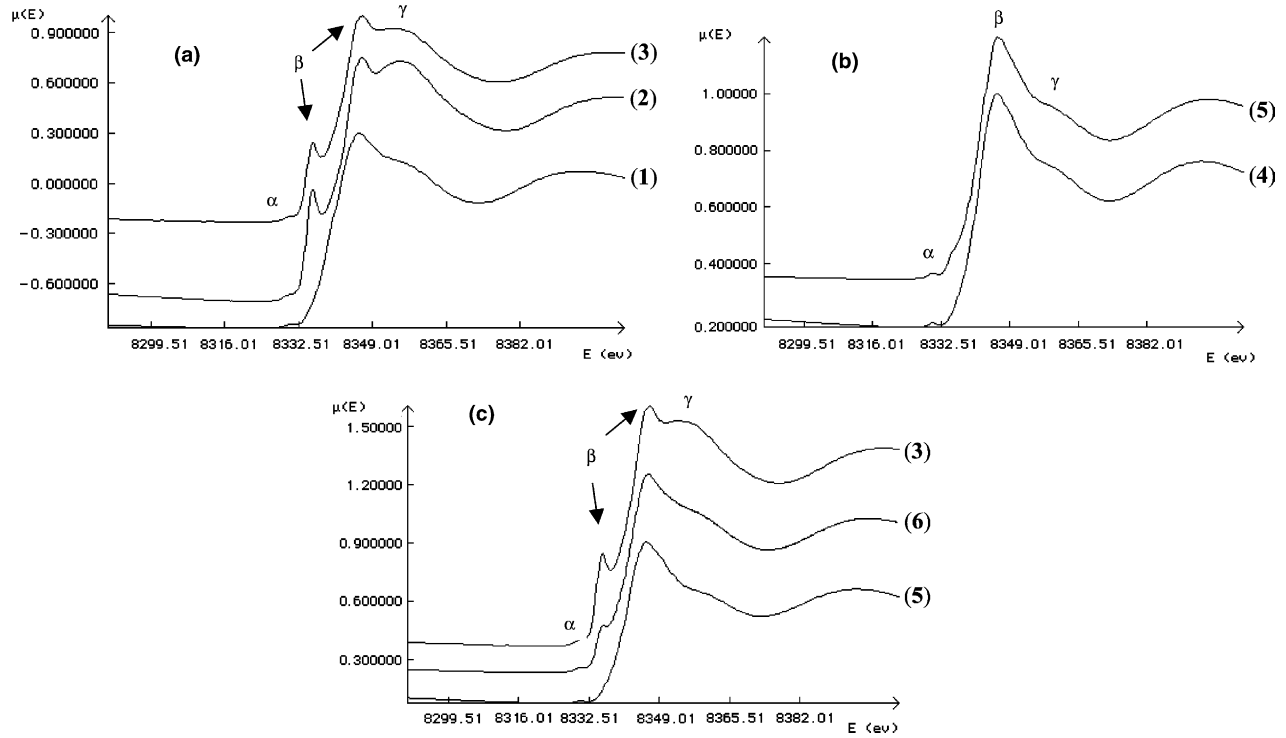


Fig. 1. XANES spectra of nickel compounds. (**1**): $[Ni_2\mathbf{L}^3Cl_4]$; (**2**): $[Ni_2\mathbf{L}^3](ClO_4)_4$; (**3**): $[Ni_2\mathbf{L}^4](ClO_4)_4$; (**4**): $[Ni_2\mathbf{L}^1(ClO_4)_4]$; (**5**): $[Ni_2\mathbf{L}^2(ClO_4)_4]$; (**6**): $[Ni_2\mathbf{L}^5(ClO_4)_2](ClO_4)_2$.

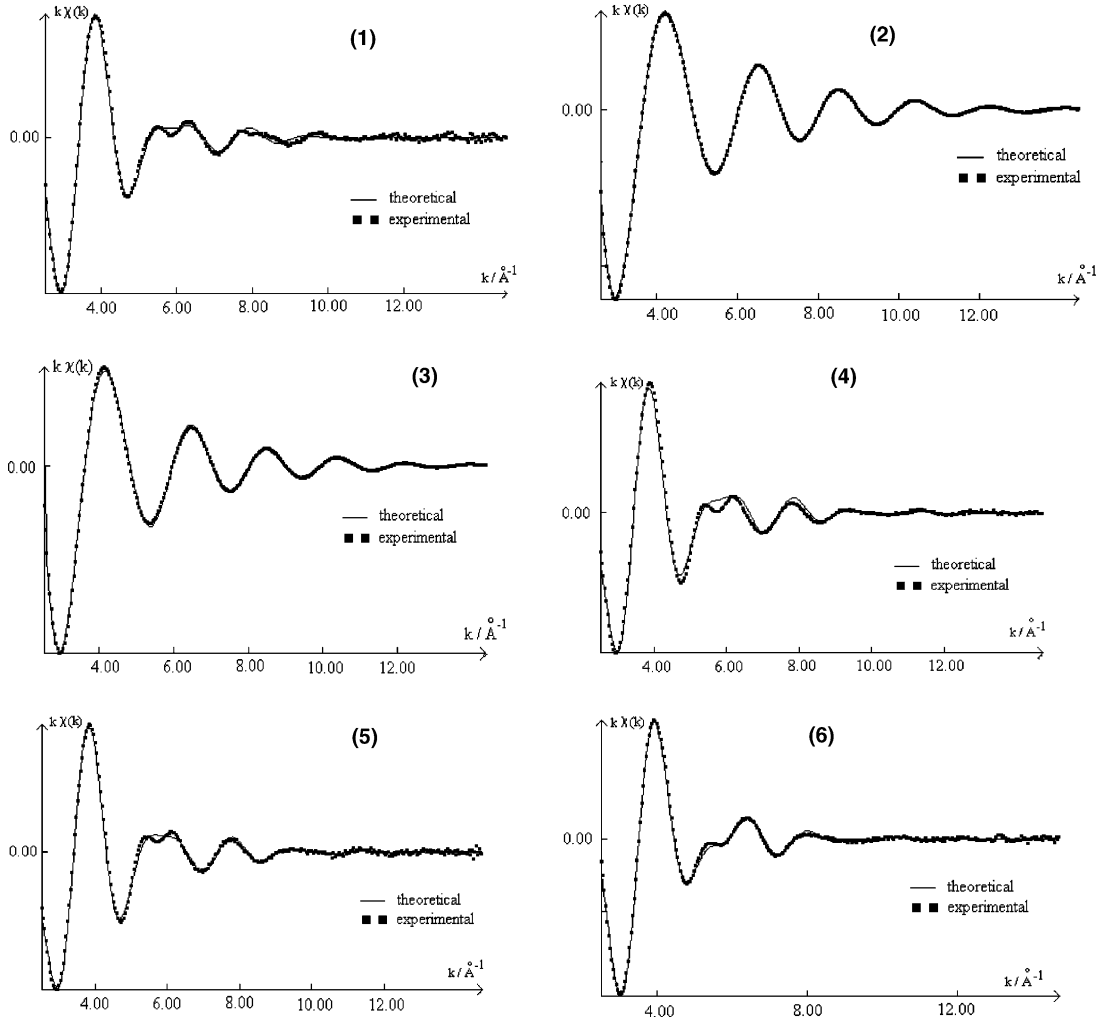


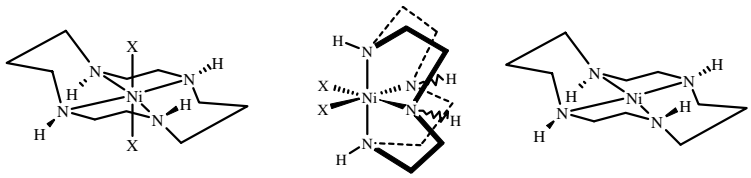
Fig. 2. k^3-weighted experimental and least-squares fitted EXAFS spectra of nickel(II) complexes. The broken line shows the experimental data and the solid line represents the calculated EXAFS spectrum (see Table 2). (**1**): $[Ni_2\mathbf{L}^4](ClO_4)_4$; (**2**): $[Ni_2\mathbf{L}^3](ClO_4)_4$; (**3**): $[Ni_2\mathbf{L}^3Cl_4]$; (**4**): $[Ni_2\mathbf{L}^2(ClO_4)_4]$; (**5**): $[Ni_2\mathbf{L}^1(ClO_4)_4]$; (**6**): $[Ni_2\mathbf{L}^5(ClO_4)_2](ClO_4)_2$.

Table 2
EXAFS data[a]

Compound	N (±20%)	$M^{n+} - X$	r (Å) (±0.02 Å)	σ^2 (Å^{-2})	ΔE (eV)	R-factor[b]: (error square sum)/(sum of data values)
$[Ni_2\mathbf{L}^1(ClO_4)_4]$	4	Ni–N	2.10	0.0050	−0.29	0.0192
	2	Ni–O	2.88	0.0010	1.84	
$[Ni_2\mathbf{L}^2(ClO_4)_4]$	4	Ni–N	2.12	0.0050	−0.21	0.0073
	2	Ni–O	2.89	0.0015	1.84	
$[Ni_2\mathbf{L}^3Cl_4]$	4	Ni–N	2.08	0.0096	−1.26	0.0135
	2	Ni–Cl/O	2.84	0.0037	−0.38	
$[Ni_2\mathbf{L}^3](ClO_4)_4$	4	Ni–N	1.96	0.0015	−0.09	0.0037
$[Ni_2\mathbf{L}^4](ClO_4)_4$	4	Ni–N	1.98	0.0027	−0.04	0.0042
$[Ni_2\mathbf{L}^5(ClO_4)_2](ClO_4)_2$	4	Ni–N	2.03	0.0035	−1.12	0.0056
	2[c]	Ni–O	2.86	0.0062	1.6	

[a] Ni, absorber; X, backscatterer; N, coordination number; σ, Debye-Waller factor; ΔE, shift of the energy threshold.
[b] Final statistical fits were against raw EXAFS data.
[c] There are two different chromophores (N_4 and N_4O_2) for this complex. The value corresponds to the N_4O_2 chromophore.

adequately fitted by a shell of four nitrogen scattering atoms at an average distance of 2.11 Å for the cyclen derivatives $[Ni_2\mathbf{L}^1(ClO_4)_4]$ and $[Ni_2\mathbf{L}^2(ClO_4)_4]$, 1.97 Å for the cyclam derivatives $[Ni_2\mathbf{L}^3](ClO_4)_4$ and $[Ni_2\mathbf{L}^4](ClO_4)_4$. For $[Ni_2\mathbf{L}^3Cl_4]$, an average Ni–N distance of 2.08 Å, which suggests a different metal environment



Trans-III-[Ni-cyclamX$_2$] *cis*-V-[Ni-cyclenX$_2$] *Trans*-III-[Ni-cyclam]

Octahedral compounds Square-planar compound

Scheme 2.

than in the case of $[Ni_2\mathbf{L^3}](ClO_4)_4$, is in accordance with the octahedral geometry proposed from the XANES spectrum. Finally, for the dissymmetrical complex $[Ni_2\mathbf{L^5}(ClO_4)_2](ClO_4)_2$, the best fit is in accordance with an average bond around 2.03 Å, since the shells between the Ni–N_{cyclen} and Ni–N_{cyclam} bonds cannot be distinguished.

In tetraazamacrocyclic complexes, the metal–N bond lengths can generally be correlated to the conformation of the macrocyclic cavity. The comparison between these distances determined either by X-ray or by EXAFS can give an estimation of the shape of the ligand in the $[Ni_2\mathbf{L^{1-5}}]^{4+}$ complexes. For instance, the X-ray characterisation of mononuclear perchlorate Ni cyclam complexes [8] demonstrates that the Ni–N length is 1.96–1.98 Å in average. The Ni(II) ion is then in a square planar geometry and the ligand adopts the *trans*-III conformation [8] (Scheme 2). The comparison between these distances and the ones determined by EXAFS for bis-cyclam complexes $[Ni_2\mathbf{L^3}](ClO_4)_4$ and $[Ni_2\mathbf{L^4}](ClO_4)_4$ (Ni–N lengths of 1.96 and 1.98 Å, respectively) seems to indicate that in these dinuclear complexes, the macrocyclic cavities can be considered as similar and exhibit a *trans-III* conformation with a Ni(II) ion in a square planar environment.

Furthermore, in Ni cyclam complexes with halide [9,10] as counter-ions, the X-ray structures of complexes show that Ni–N length are 2.05 Å in average, with the Ni(II) ion in a distorted octahedral geometry and the ligand in a *trans-III* conformation. The Ni–N distances determined by EXAFS for $[Ni_2\mathbf{L^3}Cl_4]$ (2.08 Å) leads to propose, by comparison, a distorted octahedral environment for the nickel ion with a *trans-III* conformation for each cyclam subunit. The determination by EXAFS of a second coordination shell around the nickel ion on the radial distribution function, corroborates this analysis since it indicates that the nickel coordination sphere is probably completed with two chloride ions at a distance of approximately 2.84–2.90 Å. This long distance between Ni(II) and chloride ions is in agreement with a tetragonal distortion along the *z*-axis in $[Ni_2\mathbf{L^3}Cl_4]$. Since it is well known that N (or O) atom presents quite out of phase signals (for the same inter-atomic distance) with Cl, we can not rule out by EXAFS that oxygen atoms from solvent molecules complete the Ni coordination sphere. But, the chemical analysis of the $[Ni_2\mathbf{L^3}Cl_4]$ complex clearly indicates the presence of four chloride atoms (see Section 4).

In the case of the mononuclear Ni cyclen complexes, the known crystal structures [11,12] show that the nickel(II) ion is six coordinated. The macrocyclic cavity is in a *cis-V* conformation (Scheme 2) which leads to the extrusion of the metal ion from the macrocyclic nitrogen plane and to Ni–N lengths of 2.10 Å in average [12]. The distances determined by EXAFS for the complexes $[Ni_2\mathbf{L^1}(ClO_4)_4]$ and $[Ni_2\mathbf{L^2}(ClO_4)_4]$ are, respectively, of 2.10 and 2.12 Å. They seem then to indicate that in these complexes, each cyclen cavity is in a *cis-V* conformation and the Ni(II) ion held in an octahedral geometry. This is strengthened by the determination in the radial distribution function, of a second coordination shell with two oxygen atoms (Ni–O distance of 2.88–2.89 Å coming probably from the perchlorate counter-ion, as already observed for Ni(II) Schiff base macrocycle [13]).

Finally, for $[Ni\mathbf{L^5}(ClO_4)_2](ClO_4)_2$ complex, according to the counter-ions and the Ni–N distances one can assume that the cyclam cavity is in a *trans-III* conformation with a Ni(II) in a square planar environment (N_4 chromophore), while the cyclen cavity is in a *cis-V* conformation with a six-coordinated nickel(II) (N_4O_2 chromophore).

These structural data implicate that the metal is situated over the cyclen cavity in each biscyclen complex whereas for the biscyclam ones, the nickel is held inside the cyclam cavity.

3. Conclusion

X-ray absorption spectroscopy represents an alternative technique for the characterisation of the metallic environment in bismacrocyclic complexes. The nature of the surrounding chromophore can be specified by XANES, confirmed by UV–Vis spectrospcopy and magnetic measurements, especially for Ni (II) complexes. The determination of bond lengths between the nickel

atom and its closest neighbours was achieved by EXAFS. The good agreement between Ni–N EXAFS distances in dinuclear macrocycles and the distances obtained by crystallography for the mononuclear complexes, allowed the description of the complex stereochemistry. Consequently, these methods may be useful for the knowledge of the metal coordination polyhedron in bistetraazamacrocyclic complexes, especially when these compounds failed to crystallize.

4. Experimental

4.1. Materials

The metal salts and the ion exchanger resin "Amberlite IRA-900" were purchased from Aldrich.

4.2. Synthesis of the ligands and their complexes

The ligands were synthesised following a new three-step method [14] that used a macrocyclic bisaminal as an intermediate. The bismacrocycles are obtained in good yields as hydrochloride salts for the cyclam derivatives and neutral powders for the cyclen ones. When necessary, the products were eluted with water on an anionic exchange resin.

4.2.1. Synthesis of complexes $[Ni_2\mathbf{L}](ClO_4)_4$, $\mathbf{L} = \mathbf{L^1}$ to $\mathbf{L^5}$

The neutral ligand (10^{-4} mol) was dissolved in methanol (20 mL) and the nickel(II) perchlorate in methanolic solution (2.1×10^{-4} mol) was added dropwise. The yellow solution was refluxed for 2 h, and evaporated under vacuum. The solid obtained was filtered and washed twice with absolute ethanol. The presence of ethyl alcohol in complexes was revealed by NMR spectroscopy, the perchlorate by IR. *Caution*: The perchlorate compounds must be handled with care due to their tendency to explode.

$[Ni_2\mathbf{L^1}(ClO_4)_4] \cdot EtOH$: *Anal*. Calc. for $C_{26}H_{52}N_8O_{17}Cl_4Ni_2$ (1007,93 g. mol^{-1}): C, 30.97; H, 5.16; N, 11.12. Found: C, 30.95; H, 5.15. N, 11.11%. IR (KBr pellet, ν/cm^{-1}): 1088. Yield: 70%.

$[Ni_2\mathbf{L^2}(ClO_4)_4] \cdot EtOH$: *Anal*. Calc. for $C_{26}H_{52}N_8O_{17}Cl_4Ni_2$ (1007,93 g. mol^{-1}): C, 30.97; H, 5.16; N, 11.12. Found: C, 30.91; H, 4.92; N, 11.14%. IR (KBr pellet, ν/cm^{-1}): 1089. Yield: 74%.

$[Ni_2\mathbf{L^3}](ClO_4)_4 \cdot EtOH$: *Anal*. Calc. for $C_{30}H_{60}N_8O_{17}Cl_4Ni_2$ (1064,04 g. mol^{-1}): C, 33.85; H, 5.64; N, 10.53. Found: C, 33.62; H, 5.50; N, 10.65%. IR (KBr pellet, ν/cm^{-1}): 1095. Yield: 94%.

$[Ni_2\mathbf{L^4}](ClO_4)_4 \cdot 0.5EtOH$: *Anal*. Calc. for $C_{29}H_{57}N_8O_{16.5}Cl_4Ni_2$ (1041,01 g. mol^{-1}): C, 33.45; H, 5.48; N, 10.77. Found: C, 33.20; H, 5.23; N, 10.85%. IR (KBr pellet, ν/cm^{-1}): 1093. Yield: 72%.

$[Ni_2\mathbf{L^5}](ClO_4)_4 \cdot EtOH$: *Anal*. Calc. for $C_{28}H_{56}N_8O_{17}Cl_4Ni_2$ (1035.99 g. mol^{-1}): C, 32.45; H, 5.41; N, 10.81. Found: C, 32.60; H, 5.55; N, 11.05%. IR (KBr pellet, ν/cm^{-1}): 1095. Yield: 40%.

4.2.2. Synthesis of $[Ni_2\mathbf{L^3}Cl_4] \cdot H_2O$

A methanolic nickel(II) chloride solution (2.1×10^{-4} mol) was added dropwise to the neutral $\mathbf{L^3}$ ligand (10^{-4} mol, 20 mL MeOH). The yellow solution was refluxed for 2 h, and evaporated under vacuum. The purple solid obtained was filtered and washed twice with absolute ethanol.

Anal. Calc. for $C_{28}H_{56}N_8OCl_4Ni_2$ (779.99 g. mol^{-1}): C, 43.11; H, 7.19; N, 14.37. Found: C, 43.43; H, 7.38; N, 14.54%. Yield: 30%.

4.3. UV–Vis spectroscopy

Electronic spectra were measured in the 300–1100 nm range on a Shimadzu UV 160A spectrophotometer. Solid spectra were obtained by depositing the product on a "Schleicher and Schul" paper. IR spectra were obtained in KBr pellets with a Nicolet Avatar 320 spectrometer.

4.4. Magnetic susceptibility measurements

Magnetic susceptibilities were determined at room temperature (293 K) using $HgCo(SCN)_4$ as a calibrant. Diamagnetic susceptibility corrections were calculated from Pascal's constants.

4.5. X-ray absorption data collection and processing

Experiments were made at room temperature on the beam line D44 of the LURE-DCI storage ring (Orsay, France), with a double crystal Si(1 1 1) for EXAFS and Si(3 1 1) for XANES mono-chromator. The DCI storage ring was operating at 1.85 GeV, with a 300 mA positron current. Nickel K-edge spectra were obtained in transmission mode with two low-pressure (≈0.2 atm) air-filled ionisation chambers. The compounds were dispersed in cellulose pellets. The weight of the samples was calculated in order to have an absorption edge equal to 1. XANES spectra were recorded with an energy step of 0.3 eV and 2 s per step, from the beginning of the spectrum to 100 eV after the edge (E_K = 8333 eV). EXAFS spectra were recorded with a 2 eV energy step and an accumulation time of 2 s per step. For each compound, three spectra were averaged to improve the signal-to-noise ratio for both XANES and EXAFS regions. A nickel metallic foil was used for energy calibration. All XANES spectra were normalised using the Galaad software from the "EXAFS pour le Mac" package [15].

The EXAFS data analysis was performed by means of the "EXAFS pour le Mac" package. The $\chi(k)$ functions were extracted from the data [16–18] with a linear

pre-edge background, a combination of polynomials and spline atomic-absorption background, and normalised by using the Lengeler–Eisenberg method [19]. The energy threshold, E_0, was taken at the middle of the absorption edge. E_0 was corrected for each spectrum in the fitting procedure. The experimental XAFS signal $\chi(k)$ was multiplied by a factor k^3 to compensate for the decrease in its amplitude with the increase in the wave-vector value. The k^3 weighted $\chi(k)$ function was Fourier transformed by means of a Kaiser-Bessel window with a smoothness parameter τ equal to 2.5 (k is the photoelectron wave number). In this work, all Fourier transforms were calculated and presented without phase correction; therefore, the position of the peaks differs about 0.4 Å from the true crystallographic values. In all the FTs of the experimental spectra, there is one main peak located at 1.6 Å, a second peak at 2.4 Å, and a third one at 2.7 Å. The lower peaks located above 3.0 Å were attributed to multiple-scattering contributions [6a]. Only the two first peaks, which correspond to the atoms directly bound to the metal (first coordination shell), were analysed using a single scattering approach which is suitable for the first shell, since multiple scattering is negligible under 2.8 Å [6a]. The latest, corresponding to carbon atoms, is not analysed because of the low interest of this coordination shell for our purpose.

The peaks corresponding to the first-coordination shell were then isolated and back-Fourier transformed into k space to determine the mean coordination number, N, the bond length, R, and the Debye-Waller factor, σ, by a fitting procedure realised in the framework of single scattering using the standard EXAFS formula

$$\chi(k) = -S_0^2 \sum_i \left[\frac{N_i}{R_i^2} A_i(k)\, \mathrm{e}^{-2\sigma_i^2 k^2}\, \mathrm{e}^{-2R_i/\lambda(k)} \sin(2kR_i + \Phi_i(k)) \right].$$

The number of fitting parameters did not exceed the number of independent points (N_{IDP}) throughout the fitting process, where $N_{IDP} = 2\Delta k(\Delta R/\pi)$, where Δk is the range fit and ΔR is the width of the R-space Fourier window [18]. Optimization of the parameters was performed with the E_0 shift constrained, and the amplitude reduction factor, S_0^2, fixed at 0.90.

The experimental XAFS signals of the first coordination shell of Cu were singled out by the back FT procedure in the range 0.7–2.6 Å. The back-scattering phase, $\Phi_i(k, R_i)$, and amplitude, $A_i(k, R_i)$, functions were extracted from the EXAFS data of the model compounds of known crystallographic structure: [Ni(cyclam)$(ClO_4)_2$] [8], and $Ni(NO_3)_2 \cdot 6H_2O$ [20]. The XAFS signal was Fourier transformed in the k range from 2.0 to 15.0 $Å^{-1}$ and filtered in the 0.8–2.1 Å range (see ESI1). Theoretical approach, using the ab-initio code FEFF 7.02 [21], was used to check the back-scattering amplitude and phase-shift functions, and if multiple scattering was effectively negligible under 2.8 Å. These functions were calculated assuming the following local structure around the metallic cation in [Ni(cyclam)$(ClO_4)_2$] [8]: NiN_4C_{10} ($R_{Ni-N} = 1.98$ Å, $R_{Ni-C} = 2.77$, 2.95, and 3.29 Å). The phase and amplitude functions for the Ni–Cl pair were extracted from the Ni(cyclam)Cl_2 compound [9] using the FEFF 7.02 code. Coordination numbers, N, were kept constant during each optimization although different coordination numbers were tested to find the best fit. During the final fitting procedure, coordination numbers, N, were fixed, while distance R, Debye-Waller factor σ^2, and energy shift ΔE_0 were varied. Interatomic distances and coordination numbers derived from fitting of model compounds are in close agreement with those obtained by X-ray diffraction (XRD) in limit of ±0.02 Å and ±20% atoms for the first atomic shell (Table 2).

Acknowledgements

We thank Dr. S. Belin (Université Paris Sud, LURE, France) for her help in XAS data recording and for helpful discussions. M.S. acknowledges the Region Champagne-Ardenne for research grant.

Appendix A. Supplementary data

Supplementary data associated with this article can be found, in the online version, at doi:10.1016/j.poly.2004.10.005.

References

[1] Th.A. Kaden, Coord. Chem. Rev. 190–192 (1999) 371.
[2] J.D. Chartres, L.F. Lindoy, G.V. Meehan, Coord. Chem. Rev. 216–217 (2000) 249.
[3] A. McAuley, S. Subramanian, Coord. Chem. Rev. 200–202 (2000) 75.
[4] (a) H. Ohtaki, H. Seki, J. Macromol. Sci. Chem. A 27 (1990) 1305;
(b) M. Soibinet, I. Déchamps-Olivier, E. Guillon, J.P. Barbier, M. Aplincourt, M. Le Baccon, F. Chuburu, H. Handel, Eur. J. Inorg. Chem. 10 (2003) 1984.
[5] R. Schneider, A. Riesen, Th.A. Kaden, Helv. Chim. Acta 66 (1983) 53.
[6] (6) S. Bénazeth, J. Purans, M.C. Chalbot, M.K. Nguyen-van-Duong, L. Nicolas, F. Keller, A. Gaudemer, Inorg. Chem. 37 (1998) 3667;
(b) G. Moreau, L. Burai, L. Helm, J. Purans, A.E. Merbach, J. Phys. Chem. A 107 (2003) 758;
(c) J. Moreau, E. Guillon, P. Aplincourt, J.C. Pierrard, J. Rimbault, M. Port, M. Aplincourt, Eur. J. Inorg. Chem. 16 (2003) 3007.
[7] J. Garcia, J. Phys. 47 (1986) 49.

[8] L. Prasad, S.C. Nyburg, A. Mc. Auley, Acta Crystallogr., Sect. C 43 (1987) 1038.
[9] B. Bosnich, M.L. Tobe, G.A. Webb, Inorg. Chem. 4 (1965) 1109.
[10] T. Kajiwara, T. Yamaguchi, H. Kido, S. Kawataba, R. Kuroda, T. Ito, Inorg. Chem. 32 (1993) 4990.
[11] R. Smierciak, J. Passariello, E.L. Blinn, Inorg. Chem. 16 (1977) 2646.
[12] A. Bencini, A. Bianchi, E. Garcia-España, Y. Jeannin, M. Julve, V. Marcelino, M. Philoche-Levisalles, Inorg. Chem. 29 (1990) 963.
[13] A.M. Herrera, R.J. Staples, S.V. Kryatov, A.Y. Nazarenko, E.V. Rybak-Akimova, J. Chem. Soc., Dalton Trans. 5 (2003) 846.
[14] M. Le Baccon, F. Chuburu, L. Toupet, H. Handel, M. Soibinet, I. Déchamps-Olivier, J.-P. Barbier, M. Aplincourt, New J. Chem. 25 (2001) 1168.
[15] A. Michalowicz, EXAFS pour le Mac, Logiciel pour la Chimie, Société Française de Chimie Paris, 1991, p. 102.
[16] B.K. Teo, in: Inorganic Chemistry Concepts, EXAFS: Basic Principles and Data Analysis, Springer, Berlin, 1986, p. 9.
[17] D.C. Königsberger, R. Prins, in: X-ray Absorption Principles, Applications, Techniques of EXAFS, SEXAFS and XANES, Wiley, New York, 1988.
[18] F.W. Lytle, D.E. Sayers, E.A. Stern, Physica B 158 (1989) 701.
[19] B. Lengeler, P. Eisenberg, Phys. Rev. B 21 (1980) 4507.
[20] F. Bigoli, A. Braibanti, A. Tiripicchio, M. Tiripicchio-Camellini, Acta Crystallogr., Sect. B 27 (1971) 1427.
[21] J.J. Rehr, J. Mustre de Leon, S.I. Zabinski, R.C. Albers, J. Am. Chem. Soc. 113 (1991) 5135.

Available online at www.sciencedirect.com
SCIENCE DIRECT®
Polyhedron 24 (2005) 151–156
POLYHEDRON
www.elsevier.com/locate/poly

Synthesis and catalytic activity of dinuclear imido titanium complexes: the molecular structure of $[Ti(NPh)Cl(\mu\text{-}Cl)(THF)_2]_2$

Dale A. Pennington [a], Peter N. Horton [b], Michael B. Hursthouse [b], Manfred Bochmann [a,*], Simon J. Lancaster [a,*]

[a] *Wolfson Materials and Catalysis Centre, School of Chemical Sciences and Pharmacy, University of East Anglia, Earlham Road, Norwich NR4 7TJ, UK*
[b] *School of Chemistry, University of Southampton, Highfield, Southampton SO17 1BJ, UK*

Received 4 October 2004; accepted 29 October 2004
Available online 21 November 2004

Abstract

Reaction of $TiCl_4$ with the reagents $RN(SiMe_3)_2$ in dichloromethane precipitates red to black powders (R = 1-adamantyl, phenyl, pentafluorophenyl, 3,5-bis(trifluoromethyl)phenyl), which on treatment with tetrahydrofuran gives the new THF adducts $[Ti(NR)Cl(\mu\text{-}Cl)(THF)_2]_2$. The complexes are dimeric in the solid state with bridging chloride and terminal imido ligands. Activation with MAO (methylaluminoxane) gives ethene polymerisation catalysts with productivities of up to 31 kg PE [(mol complex) h bar]$^{-1}$.
© 2004 Elsevier Ltd. All rights reserved.

Keywords: Titanium; Imido; Catalysis; Polymerisation; Methylaluminoxane

1. Introduction

Metal imido complexes are known to adopt a number of structural motifs [1]. For example, titanium forms complexes in which imido ligands adopt either bridging (for example **I**, Chart 1) [2] or terminal (**II**) [3] bonding modes [4]. We recently reported the synthesis and structure of $[Ti(\mu\text{-}NAr^P)Me_2(THF)]_2$ (**III**) (Ar^P = *m*-$C_6H_4P(3,5\text{-}(CF_3)_2C_6H_3)_2$) in which the imido ligand is bridging [5]. This result contrasts with Nielson's 2-*tert*-butyl- (**IV**) and 2-phenyl-phenylimido complexes which form chloride-bridged dimers [6] and Carmalt's exclusively chloride-bridged tetramer (**V**) [7]. In the absence of basic co-ligands structures with even higher nuclearity have been observed [8–10]. We continue to be interested in the factors dictating whether the imido ligand adopts a bridging or terminal bonding mode and the implications for alkene polymerisation catalysis using titanium imido precatalysts [6,11]. We report here the synthesis, structure and polymerisation activity of compounds of the type $[Ti(NR)Cl_2(THF)_2]$.

2. Results and discussion

Most commonly imidotitanium complexes are prepared through an imido exchange reaction between $[Ti(NBu^t)Cl_2(L)_x]$ and the corresponding primary amine [6]. We chose to employ an alternative dehalosilylation methodology in order to access the base-free compounds [12]. The ligand precursors $RN(SiMe_3)_2$ (**1a**–**g**) were readily prepared by the step-wise deprotonation of the parent amine and reaction with trimethylsilylchloride (Scheme 1). Treating $TiCl_4$ with **1a**–**d** in dichloromethane solution led to the precipitation of sparingly soluble red to black solids (Scheme 2). Unfortunately the poor solubility of these crude materials in non-basic

* Corresponding authors. Tel./fax: +44 1603 592009.
E-mail address: S.Lancaster@uea.ac.uk (S.J. Lancaster).

0277-5387/$ - see front matter © 2004 Elsevier Ltd. All rights reserved.
doi:10.1016/j.poly.2004.10.006

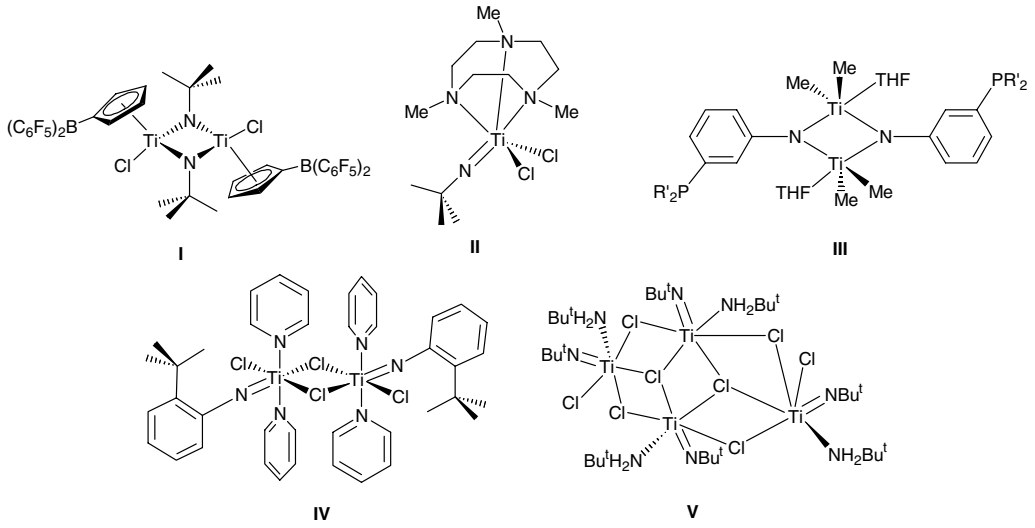
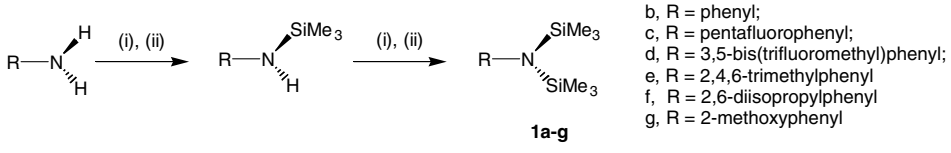


Chart 1.

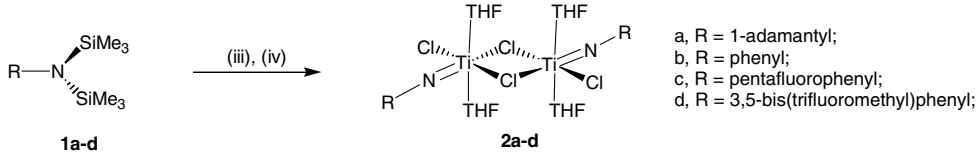
solvents, which presumably reflects high nuclearity, precluded spectroscopic characterisation or attempts to obtain X-ray quality crystals. However, the solids reacted exothermically on dissolution in tetrahydrofuran and could be isolated as THF adducts **2a**–**d** on crystallisation from THF/light petroleum mixtures. ^{1}H NMR spectroscopy of **2a**–**d** confirmed that quantitative dehalosilylation had taken place and indicated a ligand RN:THF ratio of 1:2, which was supported by the elemental analysis. This composition differs from that observed for $[Ti(\mu\text{-}NAr^P)Cl_2(THF)]_2$ where the ligand RN:THF ratio is 1:1 [5], but is consistent with a formulation analogous to complex **IV**, which has a chloride-bridged structure with terminal imido ligands. While the dehalosilylation route is effective for the introduction of *meta*-substituted aryl imido ligands, the *ortho* disubstituted reagents **1e** and **1f** failed to react with $TiCl_4$, even after refluxing in toluene, presumably as a consequence of steric encumbrance. However, the mononuclear complex $[Ti(NAr'')Cl_2(py)_3]$ (Ar″ = 2,6-diisopropylphenyl, py = pyridine) is accessible through an imido exchange reaction [3c]. The *o*-OMe compound **1g** reacted with $TiCl_4$ but the resulting product was intractable and could not be isolated even after treatment with THF.

The structure of **2b** (Fig. 1) was determined by X-ray crystallography and confirmed as a chloride-bridged dimer with two edge-sharing octahedral metal coordination spheres. Each distorted octahedron is completed by terminal chloride and imido ligands opposite the bridging chlorides and two mutually *trans* THF ligands. The geometry resembles the 2-*tert*-butylphenyl imido complex **IV**, which has *trans* pyridine ligands.

Selected bond lengths and angles for complex **2b** are shown in Table 1. While the terminal imido bond length is insensitive to the differences between **2b**, **IV** and the mononuclear complex $[Ti(NC_6H_5)Cl_2(py)_3]$ at 1.710(2), 1.702(2) and 1.714(2) Å, respectively, the C1–N1–Ti1 angle decreases from the almost linear, 177.5(2)°, in $[Ti(NC_6H_5)Cl_2(py)_3]$ to 167.5(2)° in **2b** and 165.9(2)° in **IV**, which reflects the increase in steric crowding.



Scheme 1. *Reagents and conditions*: (i) *n*-BuLi, THF, −78 °C to room temperature; (ii) $SiClMe_3$, THF, −78 °C to room temperature.



Scheme 2. *Reagents and conditions*: (iii) $TiCl_4$, CH_2Cl_2, room temperature; (iv) tetrahydrofuran, room temperature.

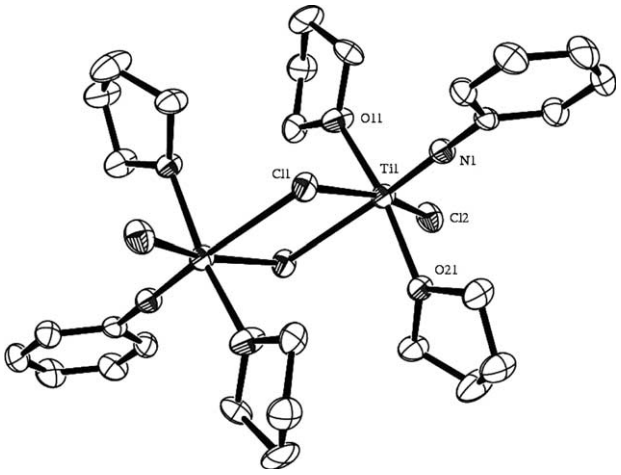


Fig. 1. The molecular structure of **2b** with thermal ellipsoids at 50% probability and the hydrogen atoms, the solvent THF and one half of the co-ordinated disordered THF removed for clarity.

Table 1
Selected bond lengths (Å) and angles (°) for **2b**

Bond lengths			
Cl1–Ti1	2.4845(9)	Cl2–Ti1	2.3734(9)
Cl1–Ti1	2.6408(8)	Ti1–N1	1.710(2)
Ti1–O11	2.085(2)	Ti1–O21	2.114(2)
Ti1–Cl1^{i}	2.6408(8)	C1–N1	1.387(3)
Bond angles			
Ti1–Cl1–Ti1^{i}	103.21(3)	N1–Ti1–O11	97.18(10)
N1–Ti1–Cl2	103.90(9)	O11–Ti1–O21	168.94(8)
O21–Ti1–Cl2	87.87(6)	O11–Ti1–Cl2	87.96(7)
O11–Ti1–Cl1	89.54(7)	N1–Ti1–Cl1	90.84(9)
Cl2–Ti1–Cl1	165.24(3)	O21–Ti1–Cl1	91.90(6)
O11–Ti1–Cl1^{i}	85.18(6)	N1–Ti1–Cl1^{i}	167.42(9)
Cl2–Ti1–Cl1^{i}	88.51(3)	O21–Ti1–Cl1^{i}	84.48(6)
C1–N1–Ti1	167.5(2)	Cl1–Ti1–Cl1^{i}	76.79(3)

Symmetry transformations used to generate equivalent atoms: (i) $-x + 3/2, -y + 1/2, -z + 1$.

Since complexes **2b**, **IV** and $[Ti(NCMe_3)Cl(\mu\text{-}Cl)(NH_2CMe_3)_2]_2$ [6] all adopt similar dimeric structures with bridging chlorides, its seems likely that the remaining examples **2a,c,d,** which all have two THF ligands per metal centre, have a similar structure. Our complexes are consistent with the pattern illustrated by **II** and **IV**, whereas bridging imido ligands are preferred to bridging chloride ligands only in relatively electron rich complexes, with low steric hindrance.

We reasoned that exchanging the chloride for methyl ligands in complexes **2a**–**2d** might result in structural analogues to **III**. Unfortunately, attempts to isolate the products of treating **2a**–**d** with the alkylating agents LiMe, MgClMe and $ZnMe_2$ were unsuccessful, yielding only black tars. [1] This is in sharp contrast to the reaction of $[Ti(\mu\text{-}NAr^{P})Cl_2(THF)]_2$ with LiMe which proceeds smoothly in diethyl ether at 0 °C to give **III**. Nevertheless, it remains possible that dinuclear imido-bridged complexes are formed during the reaction of **2a**–**d** with the catalyst activator methylaluminoxane (MAO).

[1] Similar difficulties were reported in [6].

3. Polymerisation studies

Complexes **2a**–**d** were screened as ethene polymerisation pre-catalysts in combination with MAO (methylaluminoxane) and the results are presented in Table 2. The productivities are in the region of 10 kg [(mol complex) h bar]$^{-1}$, and there is no suggestion of mass transport limitation. The gel permeation chromatography (GPC) traces indicated bi- or polymodal distributions preventing the assignment of meaningful polydispersities and implying the formation of more than one active species. In each of the systems studied increasing the polymerisation temperature from 20 to 60 °C resulted in significantly lower molecular weight polymer. The effect of raising the polymerisation temperature on the productivity appears to be highly dependent on the nature of the imido substituent, such that **2a** and **2d** showed a modest increase in productivity, while in contrast **2b** and **2c** showed a decrease, possibly as a result of catalyst decomposition. Mountford has recently reported a dramatic productivity dependence on polymerisation temperature for imido titanium catalysts of the type illustrated by **II** [11b]. Our results are broadly comparable with those observed for $[Ti(NC_6H_4\text{–}Ph\text{-}2)Cl(\mu\text{-}Cl)(tmeda)]_2$ (12.7 kg PE [(mol complex) h bar]$^{-1}$ at 20 °C) [6] but they do not approach the 1.1×10^6 g PE [(mol complex) h bar]$^{-1}$ we obtained with **III**/MAO [5].

4. Conclusion

Titanium tetrachloride undergoes a facile dehalosilylation reaction with the relatively unhindered bis(silyl)amines **1a**–**1d** but fails to react with 2,6-substituted silyl anilines (**1f, 1g**). The resulting products react with tetrahydrofuran to give the adducts $[Ti(NR)Cl(\mu\text{-}Cl)(THF)_2]_2$ (**2a**–**2d**). **2a**–**d** are chloride-bridged dimers with terminal imido ligands. Activation of **2a**–**2d** with MAO (methylaluminoxane) gives ethene polymerisation catalysts with moderate productivity.

5. Experimental

5.1. General

Syntheses were performed under nitrogen using standard Schlenk techniques. Solvents were distilled over sodium–benzophenone (diethyl ether, tetrahydrofuran), sodium (toluene), sodium–potassium alloy

Table 2
Ethene polymerisation results for **2a**–**d**/MAO[a]

Run	Complex (μmol)	MAO (mmol)	T (°C)	t (min)	Polymer yield (g)	Productivity[b]	M_w
1	**2a**(10)	10	20	30	0.078	16	370 000
2	**2a**(10)	10	60	30	0.150	30	23 000
3	**2b**(10)	10	20	30	0.040	8	270 000
4	**2b**(10)	10	60	30	0.004	0.7	150 000
5	**2c**(10)	10	20	10	0.052	31	220 000
6	**2c**(10)	10	60	10	0.013	8	83 000
7	**2d**(10)	10	20	10	0.009	5.5	270 000
8	**2d**(10)	10	60	10	0.028	17	23 000

[a] In 50 cm^3, 1 bar ethene pressure.
[b] In kg PE [(mol complex) h bar]$^{-1}$.

(light petroleum, b.p. 40–60 °C), or CaH_2 (dichloromethane). NMR solvent ($CDCl_3$) was dried over activated 4 Å molecular sieves and degassed by several freeze thaw cycles. NMR spectra were recorded using a Bruker DPX300 spectrometer. Data are reported in ppm and referenced to residual solvent resonances (^1H, ^{13}C); ^{19}F is relative to $CFCl_3$. IR spectra were measured as nujol mulls on a Perkin–Elmer Spectrum 1000 FT IR spectrometer in the range of 600–4000 cm^{-1}. Nitrogen and ethene (BOC, 99.5%) were purified by passing through columns of supported P_2O_5 with moisture indicator, and activated 4 Å molecular sieves. MAO was purchased from Witco as a 10% solution in toluene and used as received. GPC analyses were performed on a Polymer Labs PL-GPC-220 chromatograph. Elemental analyses were performed by the School Microanalysis Service.

5.2. Ligand synthesis

5.2.1. *(1-Adamantyl)N(SiMe$_3$)$_2$ (**1a**)*

To a stirred solution of 1-adamantylamine (4.6 cm^3, 50 mmol) in tetrahydrofuran (100 cm^3), held at −78 °C, was slowly added *n*-butyllithium (31.3 cm^3 of a 1.6 M hexane solution, 50 mmol). The reaction was stirred for 2 h at room temperature before slow addition of trimethylsilylchloride (6.4 cm^3, 50 mmol). The resulting mixture was stirred for 2 h at room temperature before cooling to −78 °C and treatment with a second portion of *n*-butyllithium (31.3 cm^3 of a 1.6 M hexane solution, 50 mmol). This suspension was stirred for 2 h at room temperature before adding further trimethylsilylchloride (6.4 cm^3, 50 mmol) and stirring for 2 h to ensure complete reaction. The volatiles were removed under reduced pressure and the product extracted with light petroleum (2×50 cm^3). The product was purified by vacuum distillation, 65 °C at 0.1 mbar to give a colourless oil in 80% yield. ^1H NMR (300 MHz, 293 K, $CDCl_3$): δ 0.51 (br m, 3H, $(CH)_3$), 0.18 (br m, 6H $(CH_2)_3$), 0.1 (br m, 6H $(CH_2)_3$), 0.08 (s, 18H, $Si(CH_3)_3$). ^{13}C NMR (75.5 MHz, 293 K, $CDCl_3$): δ 36.7 (CH), 30.4 (CH_2), 30.1 (CH_2), 3.3 ($Si(CH_3)_3$).

5.2.2. *C$_6$H$_5$N(SiMe$_3$)$_2$ (**1b**)*

1b was prepared from aniline following the procedure outlined for **1a**. The product was purified by vacuum distillation, 81 °C at 15 mbar giving the product as a colourless oil in 80% yield. ^1H NMR (300 MHz, 293 K, $CDCl_3$): δ 7.26 (t, 2H, $J = 7.0$ Hz, Ar), 7.11 (t, 1H, $J = 7.3$ Hz, Ar), 6.96 (d, 2H, $J = 6.9$ Hz, Ar), 0.14 (s, 18H, $Si(CH_3)_3$). ^{13}C NMR (75.5 MHz, 293 K, $CDCl_3$): δ 148.4, 130.6, 128.7, 123.9 (Ar), 2.5 ($Si(CH_3)_3$).

5.2.3. *C$_6$F$_5$N(SiMe$_3$)$_2$ (**1c**)*

1c was prepared from pentafluoroaniline following the procedure outlined for **1a**. The product was purified by vacuum distillation, 75 °C at 15 mbar to give a colourless oil in 90% yield. ^1H NMR (300 MHz, 293 K, $CDCl_3$): δ 0.13 (s, 18H, $Si(CH_3)_3$). ^{13}C NMR (75.5 MHz, 293 K, $CDCl_3$): δ 146.4 (d, $J_{C-F} = 242$ Hz, *o*-C), 138.0 (d, $J_{C-F} = 249$ Hz, *m*-C), 127.9 (*i*-C), 1.6 ($Si(CH_3)_3$). ^{19}F NMR (283.4 MHz, 293 K, $CDCl_3$): δ −147.5 (d, 2F, $J_{F-F} = 20$ Hz, *o*-F), −162.5 (tr, 1F, $J_{F-F} = 20$ Hz, *p*-F), −165.0 (tr, 2F, $J_{F-F} = 20$ Hz, *m*-F).

5.2.4. *C$_6$H$_3$(CF$_3$)$_2$N(SiMe$_3$)$_2$ (**1d**)*

1d was prepared from 3,5-bis(trifluoromethyl)aniline following the procedure outlined for **1a**. The product was purified by vacuum distillation, 70 °C at 20 mbar to give a colourless oil in 80% yield. ^1H NMR (300 MHz, 293 K, $CDCl_3$): δ 7.60 (s, 1H, *p*-H), 7.34 (s, 2H, *o*-H), 0.12 (s, 18H, $Si(CH_3)_3$). ^{13}C NMR (75.5 MHz, 293 K, $CDCl_3$): δ 150.9 (*p*-C), 132.2 (q, $J_{C-F} = 33$ Hz, *m*-C(CF_3)), 130.2 (*o*-C), 123.7 (q, $J_{C-F} = 273$ Hz, CF_3), 117.5 (*i*-C), 2.2 ($Si(CH_3)_3$). ^{19}F NMR (283.4 MHz, 300 K, $CDCl_3$): δ −63.5 (s, 6F, CF_3).

5.2.5. *C$_6$H$_2$Me$_3$N(SiMe$_3$)$_2$ (**1e**)*

1e was prepared from 2,4,6-trimethylaniline following the procedure outlined for **1a**. The product was purified by vacuum distillation, 95 °C at 15 mbar to give a colourless oil in 80% yield. ^1H NMR (300 MHz, 293 K, $CDCl_3$): δ 6.89 (s, 2H, *m*-H), 2.31 (s, 6H, *o*-CH_3), 2.31 (s, 3H, *p*-CH_3), 0.18 (s, 18H, $Si(CH_3)_3$). ^{13}C NMR (75.5 MHz, 293 K, $CDCl_3$): δ 143.5 (*p*-C), 136.8

(*m*-C), 132.7 (*i*-C), 129.5 (*o*-C), 21.2 (*p*-CH_3), 20.8 (*o*-CH_3), 2.9 ($Si(CH_3)_3$).

5.2.6. $C_6H_3{}^iPr_2N(SiMe_3)_2$ (**1f**)

1f was prepared from 2,6-di(isopropyl)aniline following the procedure outlined for **1a**. The product was purified by crystallisation from light petroleum at −30 °C to give white crystals in 90% yield. ^{1}H NMR (300 MHz, 293 K, $CDCl_3$): δ 7.07 (m, 3H, Ar), 3.49 (sep, 2H, $J = 6.9$, $CH(CH_3)_2$), 1.21 (d, 12H, $J = 6.9$ Hz, $CH(CH_3)_2$), 0.11 (s, 18H, $Si(CH_3)_3$). ^{13}C NMR (75.5 MHz, 293 K, $CDCl_3$): δ 147.4 (*m*-C), 143.6 (*p*-C), 124.5 (*i*-C), 123.9 (*o*-C), 27.9 ($CH(CH_3)_2$), 25.5 ($CH(C_3)_2$), 2.9 ($Si(CH_3)_3$).

5.2.7. $C_6H_4OMeN(SiMe_3)_2$ (**1g**)

1g was prepared from 2-methoxyaniline following the procedure outlined for **1a**. The product was purified by vacuum distillation, 85 °C at 15 mbar to give a colourless oil in 80% yield. ^{1}H NMR (300 MHz, 293 K, $CDCl_3$): δ 7.09 (t, 1H, $J = 6.0$ Hz, Ar), 6.98 (d, 1H, $J = 6.3$ Hz, Ar), 6.88 (m, 2H, $J = 6.2$ Hz, Ar), 3.80 (s, 1H, OCH_3), 0.12 (s, 18H, $Si(CH_3)_3$). ^{13}C NMR (75.5 MHz, 293 K, $CDCl_3$): δ 157.5, 137.4, 131.5, 124.8, 120.6, 110.9 (Ar), 55.2 (OCH_3), 2.3 ($Si(CH_3)_3$).

5.3. Complex synthesis

5.3.1. $[Ti(N\text{-}1\text{-}adamantyl)Cl(\mu\text{-}Cl)(THF)_2]_2$ (**2a**)

To a stirred solution of $TiCl_4$ (0.54 cm^3, 5 mmol) in dichloromethane (40 cm^3), **1a** (1.4 g, 5 mmol) was added drop wise and stirred for 2 h. The volatiles were removed under reduced pressure and the resulting red solid was washed with light petroleum (2×20 cm^3). The product was crystallised from a tetrahydrofuran (20 cm^3)/light petroleum (5 cm^3) solvent mixture at −30 °C to give yellow needle-shaped crystals in 65% yield. ^{1}H NMR (300 MHz, 293 K, $CDCl_3$): δ 4.57 (m, 4H, THF), 2.10 (m, 4H, THF), 1.88 (br m, 3H, $(CH)_3$), 1.66 (br m, 6H, $(CH_2)_3$), 1.44 (br m, 6H, $(CH_2)_3$). ^{13}C NMR (75.5 MHz, 293 K, $CDCl_3$): δ 75.6 (THF), 45.2 ($(CH)_3$), 41.4 ($(CH_2)_3$), 29.9 ($(CH_2)_3$), 26.0 (THF). IR (cm^{-1}): 1278s, 1170m, 1039m, 1024s, 926w, 864m, 698w, 682w. *Anal.* Calc. for $C_{34}H_{62}N_2Cl_4O_4Ti_2$: C, 51.02; H, 7.81; N, 3.50; Cl, 17.72. Found: C, 50.81; H, 7.30; N, 3.42; Cl, 17.56%.

5.3.2. $[Ti(NPh)Cl(\mu\text{-}Cl)(THF)_2]_2$ (**2b**)

2b was prepared following a similar procedure to **2a** from $TiCl_4$ (1.1 cm^3, 10 mmol) and **1b** (2.4 g, 10 mmol) giving a black powder. Tetrahydrofuran (20 cm^3) was added and stirred for 5 min. An exothermic reaction took place to give a red solution. The product was crystallised from a tetrahydrofuran (20 cm^3)/light petroleum (5 cm^3) mixture at −30 °C to give red block crystals suitable for X-ray crystallography in 95% yield. ^{1}H NMR (300 MHz, 293 K, $CDCl_3$): δ 7.05 (t, 2H, $J = 7.7$ Hz, Ar), 6.80–6.88 (m, 3H, Ar), 4.47 (m, 8H, THF), 2.11 (m, 8H, THF). ^{13}C NMR (75.5 MHz, 293 K, $CDCl_3$): δ 128.0 (Ar), 123.5 (Ar), 123.1 (Ar), 75.3 (THF), 25.5 (THF). IR (cm^{-1}): 1576m, 1342m, 1315s, 1246m, 1172w, 1066m, 1042m, 1017s, 970m, 825m, 860s, 772s, 684m, 649w, 619w. *Anal.* Calc. for $C_{28}H_{42}N_2Cl_4O_4Ti_2$: C, 47.48; H, 5.98; N, 3.96; Cl, 20.02. Found: C, 46.20; H, 6.02; N, 3.40; Cl, 19.31%.

5.3.3. $[Ti(NC_6F_5)Cl(\mu\text{-}Cl)(THF)_2]_2$ (**2c**)

2c was prepared following a similar procedure to **2a** from $TiCl_4$ (0.54 cm^3, 5 mmol) and **1c** (1.6 g, 5 mmol) giving a red solid. The product was crystallised from a tetrahydrofuran (20 cm^3)/petroleum (5 cm^3) mix at −30 °C to give dark red block crystals in 70% yield. ^{1}H NMR (300 MHz, 293 K, $CDCl_3$): δ 4.50 (m, 4H, THF), 2.15 (m, 4H, THF). ^{13}C NMR (75.5 MHz, 293 K, $CDCl_3$): δ 76.4 (THF), 26.0 (THF). ^{19}F NMR (283.4 MHz, 293 K, $CDCl_3$): δ −152.8 (d, 2F, *o*-F), −164.7 (t, 1F, *p*-F), −165.5 (d, 2F, *m*-F). IR (cm^{-1}): 1525m, 1505s, 1334m, 1216w, 1171w, 1377w, 1350s, 1014m, 988m, 949w, 920w, 852m. *Anal.* Calc. for $C_{28}H_{32}F_{10}N_2Cl_4O_4Ti_2$: C, 37.87; H, 3.63; N, 3.15; Cl, 15.97. Found: C, 37.26; H, 3.66; N, 3.10; Cl, 15.53%.

5.3.4. $[Ti(NC_6H_3(CF_3)_2\text{-}3,5)Cl(\mu\text{-}Cl)(THF)_2]_2$ (**2d**)

2d was prepared following a similar procedure to **2a** from $TiCl_4$ (1.1 cm^3, 10 mmol) and **1d** (3.7 g, 10 mmol) giving a red solid. The product was crystallised from a tetrahydrofuran (20 cm^3)/petroleum (5 cm^3) mix at −30 °C to give bright red/orange needle-shaped crystals in 75% yield. ^{1}H NMR (300 MHz, 293 K, $CDCl_3$): δ 7.29 (s, 1H, *o*-H), 7.25 (s, 2H, *p*-H), 4.44 (m, 4H, THF), 2.09 (m, 4H, THF). ^{13}C NMR (75.5 MHz, 293 K, $CDCl_3$): δ 158.7 (Ar), 132.0 (q, $J_{C-F} = 33$ Hz, *m*-$C(CF_3)$), 129.0 (Ar), 123.8 (Ar), 123.5 (q, $J_{C-F} = 271$ Hz, CF_3), 116.2 (Ar), 76.0 (THF), 26.0 (THF). ^{19}F NMR (283.4 MHz, 300 K, $CDCl_3$): δ −63.5 (s, 6F, CF_3). IR (cm^{-1}): 1229m, 1089m, 1021s, 920w, 864m, 672w. *Anal.* Calc. for $C_{32}H_{38}F_{12}N_2Cl_4O_4Ti_2$: C, 39.21; H, 3.91; N, 2.86; Cl, 14.47. Found: C, 39.31; H, 3.97; N, 3.60; Cl, 14.72%.

5.4. Polymerisation procedure

A solution of MAO in toluene (50 cm^3) was saturated with ethene (1 bar) at the given temperature. Polymerisation was initiated by addition of a toluene solution of pre-catalyst into the reactor under vigorous stirring (1000 rpm). Methanol (1 cm^3) was added to terminate the polymerisation. The polymeric product was precipitated and separated from aluminium residues by addition of methanol (~300 cm^3) and 2 M HCl (~5 cm^3). The polymer was collected by filtration, washed with methanol, 2 M HCl, distilled water and

again with methanol before drying until constant mass at 80 °C. Each run is the average of at least two polymerisations.

6. Crystal structure analysis

Intensity data were recorded at the EPSRC National Crystallography Service at the University of Southampton on a Nonius Kappa CCD diffractometer (with Mo Kα radiation and graphite monochromator).

From a sample of orange block crystals of **2b** under oil, one, $0.44 \times 0.38 \times 0.22$ mm was mounted on a glass fibre and fixed in the cold nitrogen stream.

The cell was determined using DirAx [13]. Data were collected using Collect [14] and processed using the DENZO program [15]. The absorption was correction using SORTAV [16]. The structure was determined by the direct methods routines in the SHELXS [17] program and refined by full-matrix least-squares methods, on F^2's, in SHELXL [18]. The non-hydrogen atoms were refined with anisotropic thermal parameters. Hydrogen atoms were included in idealised positions and their U_{iso} values were set to ride on the U_{eq} values of the parent carbon atoms.

Crystal data for **2b**: $C_{32}H_{50}Cl_4N_2O_5Ti_2$, Mr = 780.34, $T = 120(2)$ K, monoclinic, space group $C2/c$, $a = 19.5782(8)$ Å, $b = 9.0622(4)$ Å, $c = 31.5335(9)$ Å, $\beta = 107.507(2)°$, $V = 3643.5(3)$ Å^3, $\rho_{(calc)} = 1.423$ Mg/m^3, $\mu = 0.772$ mm^{-1}, $Z = 4$, reflections collected: 19 476, independent reflections: 4079 ($R_{int} = 0.0554$), completeness (to $\theta = 27.48°$) = 97.8%, final R indices [$I > 2\sigma(I)$]: $R_1 = 0.0461$, $wR_2 = 0.1148$, R indices (all data): $R_1 = 0.0638$, $wR_2 = 0.1248$.

7. Supplementary material

Crystallographic data (excluding structure factors) for structure **2b** have been deposited with the Cambridge Crystallographic Data Centre as Supplementary Publication No. CCDC-251697. Copies of the data can be obtained free of charge on application to CCDC, 12 Union Road, Cambridge CB2 1EZ, UK [fax: (internat.) +44 1223 336 033, e-mail: deposit@ccdc.cam.ac.uk, or www at http://www.ccdc.cam.ac.uk].

Acknowledgements

The support of the Engineering and Physical Sciences Research Council and the University of East Anglia are gratefully acknowledged. The authors thank Dr. Fuquan Song for his assistance with polymer molecular weight determinations.

References

[1] (a) D.E. Wigley, Prog. Inorg. Chem. 42 (1994) 239;
(b) P. Mountford, Chem. Commun. (1997) 2127;
(c) L.H. Gade, P. Mountford, Coord. Chem. Rev. 216 (2001) 65.
[2] (a) C.T. Vroegop, J.H. Teuben, F. van Bolhuis, J.G.M. van der Linden, J. Chem. Soc., Chem. Commun. (1983) 550;
(b) Y. Bai, H.W. Roesky, H.-G. Schmidt, M. Noltemeyer, Z. Naturforsch. B 47B (1992) 603;
(c) W.J. Grigsby, M.M. Olmstead, P.P. Power, J. Organomet. Chem. 513 (1996) 173;
(d) F.-Q. Liu, A. Herzog, H.W. Roesky, I. Usón, Inorg. Chem. 35 (1996) 741;
(e) S.J. Lancaster, S. Al-Benna, M. Thornton-Pett, M. Bochmann, Organometallics 19 (2000) 1599;
(f) G. Bai, H.W. Roesky, H. Hao, M. Noltemeyer, H.-G. Schmidt, Inorg. Chem. 40 (2001) 2424.
[3] (a) S.C. Dunn, A.S. Batsanov, P. Mountford, J. Chem. Soc., Chem. Commun. (1994) 2007;
(b) P.E. Collier, S.C. Dunn, P. Mountford, O.V. Shishkin, D. Swallow, J. Chem. Soc., Dalton Trans. (1995) 3743;
(c) A.J. Blake, P.E. Collier, S.C. Dunn, W.-S. Li, P. Mountford, O.V. Shishkin, J. Chem. Soc., Dalton Trans. (1997) 1549;
(d) S.C. Lawrence, M.E.G. Skinner, J.C. Green, P. Mountford, Chem. Commun. (2001) 705;
(e) A.J. Blake, P.E. Collier, L.H. Gade, P. Mountford, J. Lloyd, S.M. Pugh, M. Schubart, M.E.G. Skinner, D.J.M. Trösch, Inorg. Chem. 40 (2001) 870.
[4] For examples of both bridging and terminal imido ligands see: T.S. Lewkebandara, P.H. Sheridan, M.J. Heeg, A.L. Rheingold, C.H. Winter, Inorg. Chem. 33 (1994) 5879.
[5] M. Said, D.L. Hughes, M. Bochmann, Dalton Trans. (2004) 359.
[6] A.J. Nielson, M.W. Glenny, C.E.F. Rickard, J. Chem. Soc., Dalton Trans. (2001) 232.
[7] C.J. Carmalt, A.C. Newport, I.P. Parkin, A.J.P. White, D.J. Williams, J. Chem. Soc., Dalton Trans. (2002) 4055.
[8] Base-free oligomeric or polymeric complexes are obtained from the reaction of $N(H)(SiMe_3)_2$ or $N(SiMe_3)_3$ and $TiCl_4$: N.W. Alcock, M. Pierce-Butler, G.R. Willey, J. Chem. Soc., Dalton Trans. (1976) 707.
[9] R. Schlichenmaier, J. Straehle, Z. Anorg. Allg. Chem. 619 (1993) 1526.
[10] R. Bettenhausen, W. Milius, W. Schnick, Chem. Eur. J. 3 (1997) 1337.
[11] (a) For examples of alkene polymerization with titanium imido complexes see: N.A.H. Male, M.E.G. Skinner, S.Y. Bylikin, P.J. Wilson, P. Mountford, M. Schröder, Inorg. Chem. 39 (2000) 5483;
(b) N. Adams, H.J. Arts, P.D. Bolton, D. Cowell, S.R. Dubberly, N. Friederichs, C.M. Grant, M. Kraneburg, A.J. Sealey, B. Wang, P.J. Wilson, A.R. Cowley, P. Mountford, M. Schröder, Chem. Commun. (2004) 434.
[12] For an example of the dehalosilylation route to imido complexes see: I. Dorado, A. Garcés, C. López-Mardomingo, M. Fajardo, A. Rodríguez, A. Antinolo, A. Otero, J. Chem. Soc., Dalton Trans. (2000) 2375.
[13] A.J.M. Duisenberg, J. Appl. Crystallogr. 25 (1992) 92.
[14] R. Hooft, Nonius B.V., Data collection software, 1998.
[15] Z. Otwinowski, W. Minor, Meth. Enzymol. 276 (1997) 307.
[16] (a) R.H. Blessing, Acta Crystallogr. A 51 (1995) 33;
(b) R.H. Blessing, J. Appl. Crystallogr. 30 (1997) 421.
[17] G.M. Sheldrick, Acta Crystallogr. A 46 (1990) 467.
[18] G.M. Sheldrick, University of Göttingen, Germany, 1997.

Available online at www.sciencedirect.com
SCIENCE DIRECT®
Polyhedron 24 (2005) 157–163
POLYHEDRON
www.elsevier.com/locate/poly

Synthesis, structure and electrochemical properties of tris-picolinate complexes of rhodium and iridium

Semanti Basu [a], Shie-Ming Peng [b], Gene-Hsiang Lee [b], Samaresh Bhattacharya [a,*]

[a] *Inorganic Chemistry Section, Department of Chemistry, Jadavpur University, Kolkata 700 032, India*
[b] *Department of Chemistry, National Taiwan University, Taipei, Taiwan, ROC*

Received 25 August 2004; accepted 29 October 2004
Available online 13 December 2004

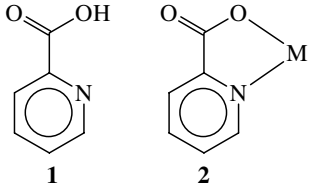
Abstract

Reaction of picolinic acid (Hpic) with rhodium trichloride or iridium trichloride affords tris-picolinate complexes of the type $[M(pic)_3]$ (M = Rh, Ir). The crystal structures of both complexes have been determined by X-ray diffraction. In both complexes, the picolinate ligands are coordinated to the metal center as bidentate N,O-donors forming five-membered chelate rings. There is one molecule of water of crystallization per molecule of each $[M(pic)_3]$ complex. The water molecule is hydrogen bonded to the carboxylate fragments of two adjacent $[M(pic)_3]$ molecules and thus acts as a bridge between the individual complex molecules. The complexes are diamagnetic (low-spin d^6, $S = 0$) and show intense MLCT transitions in the visible region. Cyclic voltammetry on the $[M(pic)_3]$ complexes shows a M(III)–M(IV) oxidation near 1.0 V versus SCE and a ligand-centered reductive response near −1.0 V versus SCE.
© 2004 Elsevier Ltd. All rights reserved.

Keywords: Rhodium and iridium tris-picolinate complexes; Crystal structures; Electronic spectra; Electrochemical properties

1. Introduction

The chemistry of rhodium and iridium has been receiving considerable current attention [1], largely because of the interesting properties exhibited by the complexes of these two metals. As the properties of the complexes are dictated primarily by the coordination environment around the metal center, complexation of these metals by ligands of selected types has been of significant importance, and the present work has originated from our interest in this area [2]. For the complexation of rhodium and iridium, picolinic acid (**1**) has been chosen as the ligand in the present study. Picolinic acid (abbreviated as Hpic, where H stands for the dissociable carboxylic proton) is known to bind to metal ions as a bidentate N,O-donor forming a stable five-membered chelate ring (**2**) [3]. It is interesting to note that the two donor sites of the picolinate ligand are of significantly different nature.



1 **2**

The pyridine nitrogen is a soft donor and a recognized stabilizer of the lower oxidation states of transition metals, whereas the carboxylate oxygen is a hard donor and is known to stabilize transition metals in their higher oxidation states. Hence, coordination of rhodium and iridium by the picolinate ligand may be expected to have an interesting effect on the redox properties of the complexes. The main objective of the present work has been to synthesize the tris-picolinate complexes of rhodium

* Corresponding author. Tel.: +91 33 24146223; fax: +91 33 24146584.
E-mail address: samaresh_b@hotmail.com (S. Bhattacharya).

0277-5387/$ - see front matter © 2004 Elsevier Ltd. All rights reserved.
doi:10.1016/j.poly.2004.10.015

and iridium, and to study their physicochemical properties. It may be mentioned here that though tris-picolinate complexes of many transition metals have been studied well [4], those of rhodium and iridium appear to have remained unexplored. It may also be mentioned here that the tris-picolinate complexes of several transition metals have important applications in the biological field [4c,4e–4g]. Reaction of picolinic acid with the trichlorides of rhodium and iridium has afforded the targeted $[M(pic)_3]$ (M = Rh, Ir) complexes and the chemistry of these two complexes is reported in this paper with special reference to their synthesis, structure and, spectroscopic and electrochemical properties.

2. Experimental

2.1. Materials and measurements

Rhodium trichloride and iridium trichloride were obtained from Arora Matthey, Kolkata, India. Picolinic acid was purchased from Merck, India. All other chemicals and solvents were reagent grade commercial materials and were used as received. Purification of acetonitrile and preparation of tetrabutylammonium perchlorate (TBAP) for electrochemical work were performed as reported in the literature [5]. Microanalyses (C, H, N) were performed using a Heraeus Carlo Erba 1108 elemental analyzer. Magnetic susceptibilities were measured using a PAR 155 vibrating sample magnetometer fitted with a Walker Scientific L75FBAL magnet. ^{1}H NMR spectra were obtained on a Bruker AV300 NMR spectrometer using TMS as the internal standard. Thermogravimetric analyses were carried out on a Shimadzu DT-30 thermal analyzer. IR spectra were obtained on a Perkin–Elmer spectrometer with samples prepared as KBr pellets. Electronic spectra were recorded on a JASCO V-570 spectrophotometer. Electrochemical measurements were made using a CH Instruments Model 600A electrochemical analyzer. A platinum disc working electrode, a platinum wire auxiliary electrode and an aqueous saturated calomel reference electrode (SCE) were used in the cyclic voltammetry experiments. All electrochemical experiments were performed under a dinitrogen atmosphere. All electrochemical data were collected at 298 K and are uncorrected for junction potentials.

2.2. Synthesis

2.2.1. $[Rh(pic)_3] \cdot H_2O$

Picolinic acid (0.4 g, 3.25 mmol) was dissolved in ethanol (40 ml) and to it was added triethylamine (0.1 g, 0.99 mmol) followed by $RhCl_3.3H_2O$ (0.1 g, 0.38 mmol). The solution was heated at reflux for 4 h to produce a bright yellow solution. Upon cooling the solution to room temperature, a white precipitate separated, which was removed by filtration. Upon partial evaporation of the filtrate, yellow crystals of $[Rh(pic)_3] \cdot H_2O$ separated,

Table 1
Selected crystallographic data for $[Rh(pic)_3] \cdot H_2O$ and $[Ir(pic)_3] \cdot H_2O$

Compound	$[Rh(pic)_3] \cdot H_2O$	$[Ir(pic)_3] \cdot H_2O$
Empirical formula	$C_{18}H_{14}N_3O_7Rh$	$C_{18}H_{14}N_3O_7Ir$
Formula weight	487.23	576.52
T (K)	295(2)	295(2)
λ(Mo Kα) (Å)	0.71073	0.71073
Crystal system	monoclinic	monoclinic
Space group	*C2/c*	*C2/c*
Unit cell dimensions		
a (Å)	30.3514(11)	30.4463(13)
b (Å)	8.5072(3)	8.4725(4)
c (Å)	13.9537(5)	13.9589(6)
β (°)	95.311(1)	95.0621(11)
V (Å^3)	3587.5(2)	3586.7(3)
Z	8	8
D_{calc} (Mg m^{-3})	1.804	2.135
Absorption coefficient (mm^{-1})	1.002	7.495
F(000)	1952	2208
Crystal size (mm)	$0.20 \times 0.10 \times 0.03$	$0.30 \times 0.14 \times 0.03$
θ Range for data collection (°)	1.35–27.50	1.34–27.50
Index ranges	$-39 \leqslant h \leqslant 39$, $-11 \leqslant k \leqslant 11$, $-18 \leqslant l \leqslant 18$	$-39 \leqslant h \leqslant 39$, $-11 \leqslant k \leqslant 10$, $-18 \leqslant l \leqslant 16$
Number of reflections collected (R_{int})	20525 (0.0583)	17398 (0.0442)
Final R indices [$I > 2\sigma(I)$]	$R_1 = 0.0544$, $wR_2 = 0.1138$	$R_1 = 0.0320$, $wR_2 = 0.0772$
Number of parameters refined	270	262
Maximum and minimum transmission	0.9706 and 0.8248	0.8064 and 0.2120
Goodness-of-fit on F^2	1.289	1.174
Largest difference peak and hole (e Å^{-3})	0.887 and −0.984	1.480 and −0.789

which were collected by filtration, washed with water and dried in vacuo over P_4O_{10}. (~70% yield). *Anal.* Calc. for $C_{18}H_{14}N_3O_7Rh$: C, 44.35; H, 2.87; N, 8.62. Found: C, 45.01; H, 2.83; N, 8.64%. FT-IR (KBr phase), cm^{-1}: 3522m, 1676s, 1604s, 1472m, 1329s, 1285m, 1149m, 1098w, 1057m, 862m, 766m, 716m, 689m, 475m (s, strong; m, medium; w, weak).

2.2.2. $[Ir(pic)_3] \cdot H_2O$

Sodium acetate (1 g, 12.2 mmol) and $IrCl_3.3H_2O$ (0.1 g, 0.28 mmol) were taken in glacial acetic acid (40 ml). The solution was warmed and picolinic acid (0.4 g, 3.25 mmol) was added to it. The solution was heated at reflux for 4 h to produce a bright yellow solution. Upon partial evaporation of this solution, yellow crystals of $[Ir(pic)_3] \cdot H_2O$ separated, which were collected by filtration, washed with water and dried in vacuo over P_4O_{10} (~75% yield). *Anal.* Calc. for $C_{18}H_{14}N_3O_7Ir$: C, 37.50; H, 2.43; N, 7.29; Found: C, 37.83; H, 2.37; N, 7.28%. FT-IR (KBr phase), cm^{-1}: 3529m, 1684s, 1608s, 1472m, 1326s, 1282m, 1148m, 1099w, 1059m, 864m, 770m, 718m, 688m, 471m (s, strong; m, medium; w, weak).

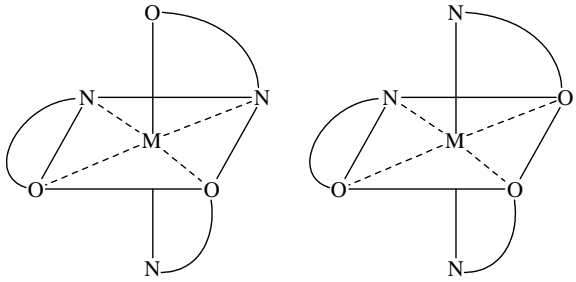
2.3. X-ray crystallography

Single crystals of both $[Rh(pic)_3] \cdot H_2O$ and $[Ir(pic)_3] \cdot H_2O$ were obtained directly from the synthetic reactions. Selected crystal data and data collection parameters are given in Table 1. Data were collected on a Bruker SMART CCD diffractometer using graphite monochromated Mo Kα radiation ($\lambda = 0.71073$ Å) by ω scans. X-ray data reduction and, structure solution and refinement were done using SHELXS-97 and SHELXL-97 programs [6,7]. The structures were solved by direct methods.

3. Results and discussion

3.1. Syntheses and crystal structures

Reaction of picolinic acid with rhodium trichloride proceeds smoothly in refluxing ethanol in the presence of triethylamine to afford the targeted tris-picolinate rhodium(III) complex, $[Rh(pic)_3]$, in a decent yield. The analogous iridium complex, $[Ir(pic)_3]$, has been obtained in a similar yield from the reaction of picolinic acid with iridium trichloride using slightly different experimental conditions. Such differences in experimental procedure is often required for the synthesis of analogous complexes of rhodium and iridium [8]. An excess of picolinic acid has been used in both synthetic reactions to optimize the yield of the $[M(pic)_3]$ (M = Rh, Ir) complexes. The observed elemental (C, H, N) analytical data of the two complexes agree well with their compositions. As the picolinate anion is an unsymmetrical bidentate ligand, the tris-picolinate complexes of rhodium and iridium may exist, in principle, in two different isomeric forms, viz. facial (**3**) and meridional (**4**). Chromatographic experiments have shown that these $[M(pic)_3]$ complexes are isomerically pure.



To find out the stereochemistry of these complexes, structure of both the complexes has been determined by X-ray crystallography. Both the structures have been found to be very similar. The structure of the $[Rh(pic)_3]$ complex is shown in Fig. 1 and structure of the $[Ir(pic)_3]$ complex is deposited as Fig. S1. Some selected bond parameters are listed in Table 2. In each complex the picolinate ligands are coordinated to the metal center in the usual fashion (**2**), with a bite angle of ~81°. In both complexes, the central metal ion is thus sitting in an N_3O_3 coordination sphere, which is distorted from an ideal octahedral geometry as reflected in all the bond parameters around the metal centers. The relative

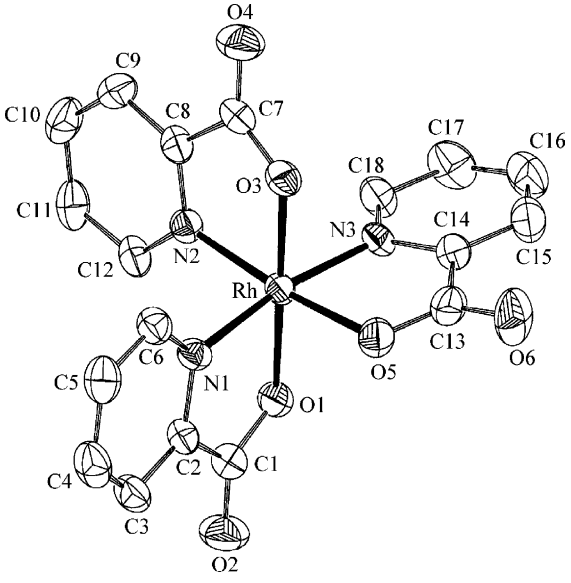


Fig. 1. View of the $[Rh(pic)_3]$ complex. The $[Ir(pic)_3]$ complex is visually identical to the $[Rh(pic)_3]$ complex and the same atom numbering scheme has been used for both structures.

Table 2
Selected bond distances (Å) and angles (°) for $[Rh(pic)_3]\cdot H_2O$ and $[Ir(pic)_3]\cdot H_2O$

$[Rh(pic)_3]\cdot H_2O$		$[Ir(pic)_3]\cdot H_2O$	
Bond distances			
Rh–N(1)	2.011(4)	Ir–N(1)	2.014(4)
Rh–N(2)	2.017(4)	Ir–N(2)	2.026(5)
Rh–N(3)	2.028(4)	Ir–N(3)	2.039(4)
Rh–O(1)	2.022(3)	Ir–O(1)	2.033(4)
Rh–O(3)	2.013(3)	Ir–O(3)	2.042(4)
Rh–O(5)	2.025(3)	Ir–O(5)	2.037(4)
C(1)–O(1)	1.306(6)	C(1)–O(1)	1.309(6)
C(1)–O(2)	1.203(6)	C(1)–O(2)	1.207(7)
C(7)–O(3)	1.303(6)	C(7)–O(3)	1.289(7)
C(7)–O(4)	1.208(6)	C(7)–O(4)	1.206(7)
C(13)–O(5)	1.267(6)	C(13)–O(5)	1.286(7)
C(13)–O(6)	1.222(6)	C(13)–O(6)	1.220(7)
Bond angles			
N(1)–Rh–O(1)	81.15(14)	N(1)–Ir–O(1)	80.44(15)
N(2)–Rh–O(3)	81.90(14)	N(2)–Ir–O(3)	81.27(17)
N(3)–Rh–O(5)	81.75(15)	N(3)–Ir–O(5)	80.72(16)
N(1)–Rh–N(3)	170.73(16)	N(1)–Ir–N(3)	170.95(17)
N(2)–Rh–O(5)	172.48(15)	N(2)–Ir–O(5)	172.52(18)
O(1)–Rh–O(3)	179.07(14)	O(1)–Ir–O(3)	179.46(15)

disposition of the nitrogen and oxygen atoms shows that both $[M(pic)_3]$ (M = Rh, Ir) complexes have the meridional stereochemistry (**4**), which is quite common in trischelates of rhodium and iridium [1]. The M–N and M–O distances are all quite normal and so are the C–O distances in the carboxylate fragments [2,3]. There is one molecule of water of crystallization per molecule of both $[M(pic)_3]$ complexes. A closer look at the packing pattern of the crystals reveals that the water molecule is hydrogen bonded to the carboxylate fragments of two adjacent $[M(pic)_3]$ molecules, which is illustrated in Fig. 2. One hydrogen of the water molecule is hydrogen-bonded to a carboxylate oxygen, which is coordinated to the metal center. The other hydrogen of the same water molecule is hydrogen-bonded to another carboxylate oxygen of an adjacent $[M(pic)_3]$ molecule, which is not coordinated to the metal center. The water molecule thus acts as a bridge between individual complex molecules. The $[M(pic)_3]\cdot H_2O$ complex molecules, when viewed along the *b*-axis, exhibit an extended spiral of M(pic)···H–O–H···(pic)M chains, which run along the *c*-axis and thus the $[M(pic)_3]$ complexes have acquired a chain supramolecular structure (Fig. 2). This extended intermolecular hydrogen-bonding has resulted in poor solubility of these $[M(pic)_3]$ complexes (vide infra). To assess the strength of the observed hydrogen-bonding, both the $[M(pic)_3]\cdot H_2O$ complexes have been subjected to thermogravimetric analysis. Within 120–150 °C each complex shows a mass loss, which corresponds well with the loss of one molecule of water per molecule of the $[M(pic)_3]\cdot H_2O$ complexes. This shows that the water molecule is held fairly tightly in the crystal lattice of both the complexes through hydrogen bonding.

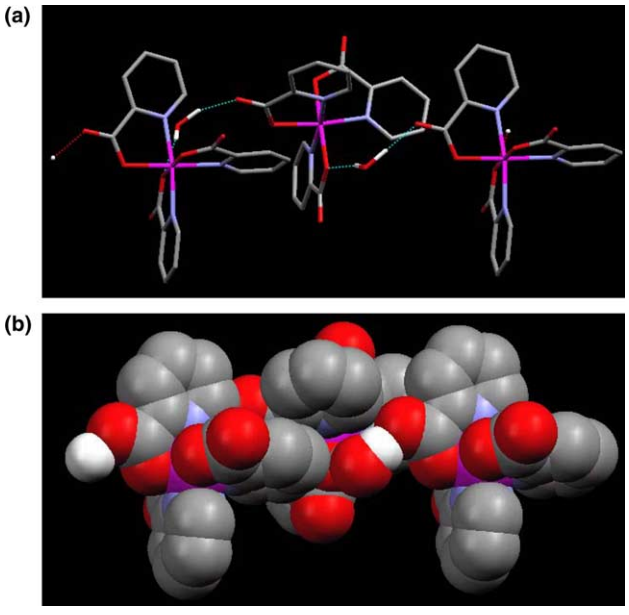


Fig. 2. Chain structure of $[Rh(pic)_3]\cdot H_2O$ through intermolecular hydrogen-bonding in (a) the stick style and (b) the space-filling model.

3.2. Spectral and electrochemical properties

Magnetic susceptibility measurements show that the $[M(pic)_3]$ complexes are diamagnetic, which corresponds to the +3 state of rhodium and iridium (low-spin d^6, $S = 0$) in these complexes. ^1H NMR spectra of both the complexes have been recorded in DMSO-d_6 solution. Each complex shows several overlapping signals within 7.7–8.6 ppm. The spectra clearly show the absence of any C_3 symmetry in the complex molecules and thus indicate that the meridional stereochemistry (**4**) also prevails in solution for both the complexes. The infrared spectra of both the $[M(pic)_3]$ complexes are very similar. Each complex shows a broad band around 3520 cm^{-1} due to the water of crystallization and several bands of different intensities in the 1700–400 cm^{-1} region. Assignment of each individual band to a specific vibration has not been attempted. However, a broad and strong band observed at 1676 cm^{-1} in $[Rh(pic)_3]$ and at 1684 cm^{-1} in $[Ir(pic)_3]$ is attributable to the coordinated carboxylate fragment [9].

The $[M(pic)_3]$ complexes are poorly soluble in methanol, ethanol and acetonitrile, and moderately soluble in dimethylformamide and dimethylsulfoxide, producing light yellow solutions. Electronic spectra of these complexes have been recorded in acetonitrile solution. Each complex shows several intense absorptions below 400 nm (Table 3). The lowest energy absorption, displayed near 370 nm by both the complexes, is probably due to a metal-to-ligand charge-transfer transition. The other absorptions at higher energies are believed to be due to transitions within the ligand orbitals. To have a better in-

Table 3
Electronic spectral[a] and cyclic voltammetric[b] data

Compound	λ_{max}/nm (ε/M^{-1} cm^{-1})	*E*/V	
		Oxidation[d]	Reduction[e]
$[Rh(pic)_3]$	366[c] (2100), 328[c] (9000), 266 (9900), 218[c] (22200)	1.06	−1.03
$[Ir(pic)_3]$	378[c] (1900), 296 (9200), 270 (9800), 236 (20700)	1.13	−1.07

[a] In acetonitrile.
[b] Solvent, acetonitrile; supporting electrolyte, TBAP; scan rate 50 mV s^{-1}.
[c] Shoulder.
[d] Anodic peak potential (E_{pa}).
[e] Cathodic peak potential (E_{pc}).

sight into the nature of the absorption near 370 nm, qualitative EHMO calculations have been performed [10] on computer generated models of both $[M(pic)_3]$ complexes. Results of these calculations have been found to be similar for both the complexes. A partial MO diagram of the $[Rh(pic)_3]$ complex is shown in Fig. 3, and that of the $[Ir(pic)_3]$ complex is deposited as supporting information (Fig. S2). Compositions of some selected molecular orbitals are given in Table 4. The highest occupied molecular orbital (HOMO) and the next two filled orbitals (HOMO − 1 and HOMO − 2) are relatively close and have major (⩾74%) contributions from the metal d_{xy}, d_{yz} and d_{zx} orbitals, and hence they may be regarded as the metal t_2 orbitals. The lowest unoccupied molecular orbital (LUMO) and next two vacant orbitals (LUMO + 1 and LUMO + 2) are also close in energy and they are delocalized almost entirely (⩾95%) on the picolinate ligands. The intense absorption near 370 nm may therefore be assigned to the charge-transfer transition taking place from the filled metal t_2-orbital (HOMO) to the vacant π*-orbital (LUMO) of the picolinate ligand.

Electrochemical properties of both the complexes have been studied by cyclic voltammetry in acetonitrile solution (0.1 M TBAP). Each complex shows an oxidative response on the positive side and one reductive response on the negative side. Voltammetric data are given in Table 3. Keeping the results of the EHMO calculations in view, the oxidation is assigned to the M(III)–M(IV) oxidation and the reduction is attributable to reduction of the coordinated picolinate ligands.

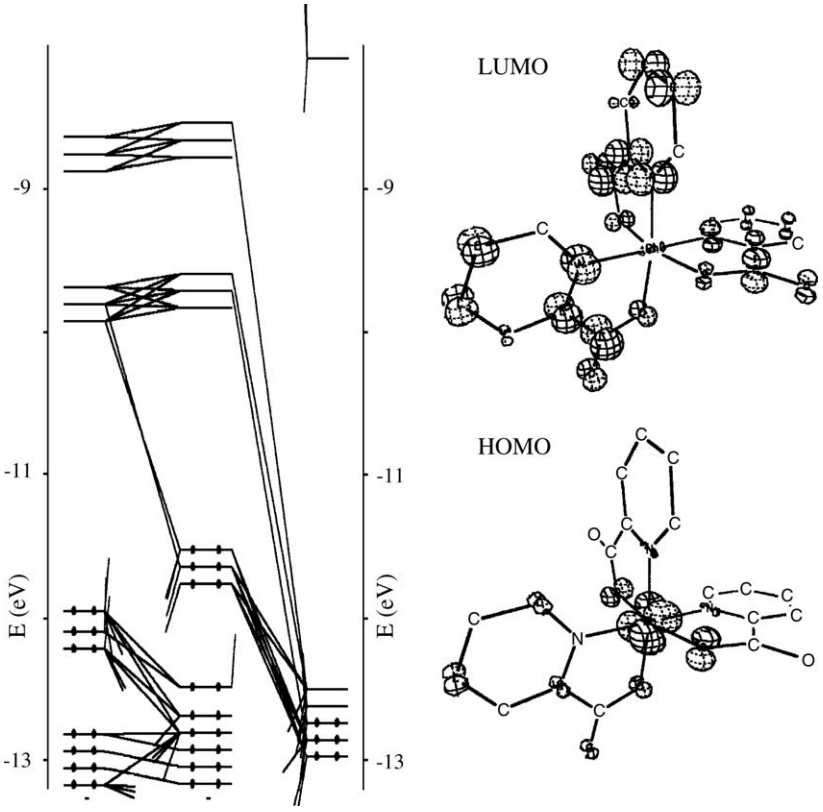


Fig. 3. Partial molecular orbital diagram of $[Rh(pic)_3]$.

Table 4
Composition of molecular orbitals

Compound	Contributing fragment	Percentage contribution of fragments to					
		HOMO	HOMO − 1	HOMO − 2	LUMO	LUMO + 1	LUMO + 2
$[Rh(pic)_3]$	Rh	76	74	76	1	3	5
	pic	24	26	24	99	97	95
$[Ir(pic)_3]$	Ir	77	84	88	1	2	4
	pic	23	16	12	99	98	96

Both the redox responses are irreversible in nature, which indicates that the oxidized $[M(pic)_3]^+$ and reduced $[M(pic)_3]^-$ species are unstable in nature and undergo rapid decomposition.

4. Conclusion

The present study shows that coordination by picolinic acid (**1**), in the usual bidentate fashion (**2**) via dissociation of the carboxylic proton, can stabilize the higher oxidation states of a transition metal. This is manifested in the stabilization of the trivalent state of rhodium and iridium in the $[M(pic)_3]$ (M = Rh, Ir) complexes. This study also shows that simple water of crystallization may give rise to an interesting supramolecular chain structure through intermolecular hydrogen-bonding.

Acknowledgements

The authors thank the referees for their constructive criticisms, which have been very helpful in preparing the revised version of the manuscript. The authors also thank the Department of Science and Technology, New Delhi, for providing the Bruker AV300 NMR spectrometer to the Department of Chemistry, Jadavpur University, under the FIST program. Thanks are also due to Prof. Samiran Mitra and Dr. Asok Nath Mandal of the Department of Chemistry, Jadavpur University, for their help with the IR and NMR spectral measurements, respectively. Semanti Basu thanks the Council of Scientific and Industrial Research, New Delhi, for her fellowship [Grant No. 9/96(378)/2002-EMR-I].

Appendix A. Supplementary data

Crystallographic data for $[Rh(pic)_3] \cdot H_2O$ and $[Ir(pic)_3] \cdot H_2O$ complexes in the CIF format have been deposited with the Cambridge Crystallographic Data Center, CCDC Nos. 248414 and 248413, respectively. A view of the $[Ir(pic)_3]$ complex has been deposited as Fig. S1 and a partial MO diagram of the $[Ir(pic)_3]$ complex has been deposited as Fig. S2. Copies of this information may be obtained free of charge from The Director, CCDC, 12 Union Road, Cambridge, CB2 1EZ (fax: +44 1223 336033; e-mail: deposit@ccdc.cam.ac.uk or at www: http://www.ccdc.cam.ac.uk). Supplementary data associated with this article can be found, in the online version at doi:10.1016/j.poly.2004.10.015.

References

[1] (a) C.E. Housecroft, Coord. Chem. Rev. 115 (1992) 163;
(b) C.E. Housecroft, Coord. Chem. Rev. 115 (1992) 191;
(c) C.E. Housecroft, Coord. Chem. Rev. A 134 (1994) 307;
(d) C.E. Housecroft, Coord. Chem. Rev. 146 (1995) 235;
(e) C.E. Housecroft, Coord. Chem. Rev. 146 (1995) 269;
(f) C.E. Housecroft, Coord. Chem. Rev. 152 (1996) 107;
(g) C.E. Housecroft, Coord. Chem. Rev. 152 (1996) 141;
(h) M.J. Hannon, Coord. Chem. Rev. 152 (1996) 393;
(i) M.C. Simpson, D.J.C. Hamilton, Coord. Chem. Rev. 155 (1996) 163;
(j) M.J. Hannon, Coord. Chem. Rev. 162 (1997) 477;
(k) A.M. Trezeciak, J.J. Ziolkowski, Coord. Chem. Rev. 190–192 (1999) 883;
(l) M.A. Esteruelas, L.A. Oro, Coord. Chem. Rev. 193–195 (1999) 557;
(m) I.M. Dixon, J.-P. Collin, J.-P. Sauvage, L. Flamigni, S. Encinas, F. Barigelletti, Chem. Soc. Rev. (2000) 385;
(n) J. Chen, R.J. Angelici, Coord. Chem. Rev. 206–207 (2000) 63;
(o) C. Slugovc, I. Padilla-Martnez, S. Sirol, E. Carmona, Coord. Chem. Rev. 213 (2001) 129;
(p) C.E. Webster, M.B. Hall, Coord. Chem. Rev. 238–239 (2003) 315;
(q) N. Pinault, D.W. Bruce, Coord. Chem. Rev. 241 (2003) 1;
(r) E. Baranoff, J.-P. Collin, L. Flamigni, J.-P. Sauvage, Chem. Soc. Rev. (2004) 147.
[2] (a) S. Dutta, S.-M. Peng, S. Bhattacharya, Inorg. Chem. 39 (2000) 2231;
(b) S. Dutta, S.-M. Peng, S. Bhattacharya, J. Chem. Soc., Dalton Trans. (2000) 4623;
(c) A. Das, F. Basuli, S.-M. Peng, S. Bhattacharya, Inorg. Chem. 41 (2002) 440;
(d) S. Dutta, F. Basuli, S.-M. Peng, G.-H. Lee, S. Bhattacharya, New J. Chem. 26 (2002) 1607;
(e) I. Pal, S. Dutta, F. Basuli, S. Goverdhan, S.-M. Peng, G.-H. Lee, S. Bhattacharya, Inorg. Chem. 42 (2003) 4338;
(f) R. Acharyya, F. Basuli, G. Rosair, S. Bhattacharya, New J. Chem. 28 (2004) 115;
(g) R. Acharyya, F. Basuli, R.Z. Wang, T.C.W. Mak, S. Bhattacharya, Inorg. Chem. 43 (2004) 704;

(h) R. Acharyya, S. Basu, S.-M. Peng, G.-H. Lee, S. Bhattacharya, unpublished results.

[3] (a) M.C. Barral, R.J. Aparicio, P.C. Royer, M.J. Saucedo, F.A. Urdanos, E.G. Pueblo, C.R. Valero, J. Chem. Soc., Dalton Trans. (1991) 1609;
(b) M. Chatterjee, M. Maji, S. Ghosh, T.C.W. Mak, J. Chem. Soc., Dalton Trans. (1998) 3641.

[4] (a) R.W. Green, J. Am. Chem. Soc. 79 (1957) 5608;
(b) O. Bekaroglu, B. Erdem, S. Fallab, Fen Fak. Mecmuasi., Seri C 29 (1964) 16;
(c) K.S. Yamaguchi, L. Spencer, D.T. Sawyer, FEBS Lett. 197 (1986) 249;
(d) N. Ghatak, J. Chakravarty, S. Bhattacharya, Polyhedron 14 (1995) 3591;
(e) J.K. Speetjens, R.A. Collins, J.B. Vincent, S.A. Woski, Chem. Res. Toxicol. 12 (1999) 483;
(f) K. Sahin, O. Ozbey, M. Onderci, G. Cikim, M.H. Aysondu, J. Nutr. 132 (2002) 1265;
(g) S.J. Brinovec, M. Golob, A. Plaper, P. Raspor, Farmacevtski Vestnik 54 (2003) 533.

[5] (a) M. Walter, L. Ramaley, Anal. Chem. 45 (1973) 165;
(b) D.T. Sawyer, J.L. Roberts Jr., Exp. Electrochem. Chemists (1974) 167.

[6] G.M. Sheldrick, SHELXS-97: Program for Solution of Crystal Structures, University of Göttingen, Göttingen, Germany, 1997.

[7] G.M. Sheldrick, SHELXL-97: Program for Refinement of Crystal Structures, University of Göttingen, Göttingen, Germany, 1997.

[8] (a) $[Rh(bpy)_3]^{3+}$: B. Martin, G.M. Waind, J. Chem. Soc. (1958) 4284;
(b) $[Ir(bpy)_3]^{3+}$: C.M. Flynn Jr., J.N. Demas, J. Am. Chem. Soc. 96 (1974) 1959;
(c) $[Rh(en)_2X_2]^{+}$: S.A. Johnson, F. Basolo, Inorg. Chem. 1 (1962) 925;
(d) $[Ir(en)_2X_2]^{+}$: R.A. Bauer, F. Basolo, Inorg. Chem. 8 (1969) 2231;
(e) $[Rh(PPh_3)_3Cl]$: J.A. Osborn, G. Wilkinson, Inorg. Synth. 10 (1967) 67;
(f) $[Ir(PPh_3)_3Cl]$: M.A. Bennett, J.L. Latten, Inorg. Synth. 26 (1989) 200;
(g) $[Rh(quinolin\text{-}8\text{-}olate)_3]$ and $[Ir(quinolin\text{-}8\text{-}olate)_3]$: W. Cheng, J. Coord. Chem. 13 (1983) 57.

[9] K. Nakamoto, Infrared and Raman Spectra of Inorganic and Coordination Compounds, 3rd ed., Wiley, New York, 1978.

[10] (a) C. Mealli, D.M. Proserpio, J. Chem. Educ. 67 (1990) 399;
(b) C. Mealli, D.M. Proserpio, CACAO Version 4.0, July, Firenze, Italy, 1994.

Available online at www.sciencedirect.com
SCIENCE DIRECT®
Polyhedron 24 (2005) 165–171
POLYHEDRON
www.elsevier.com/locate/poly

Supramolecular structures of $Co^{(III)}$ and $Cu^{(II)}$ complexes of a novel alcohol and phenol containing polyamine ligand H_2L (H_2L = *N*,*N*′-bis(2-hydroxybenzyl)-1,3-bis[(2-aminoethyl)amino]-2-propanol)

Yong-Shu Xie, Xue-Ting Liu, Min Zhang, Kai-Ju Wei, Qing-Liang Liu *

Department of Chemistry, University of Science and Technology of China, Hefei 230026, PR China

Received 3 August 2004; accepted 2 November 2004
Available online 15 December 2004

Abstract

A novel alcohol and phenol containing polyamine ligand H_2L (H_2L = *N*,*N*′-bis(2-hydroxybenzyl)-1,3-bis[(2-aminoethyl) amino]-2-propanol) and its $Co^{(III)}$ and $Cu^{(II)}$ complexes, $[CoL]ClO_4$ (**1**) and $[Cu(H_2L)Cl]ClO_4 \cdot CH_3OH \cdot H_2O$ (**2**) have been synthesized and characterized. Single crystal X-ray diffraction analyses indicate that both of the complexes are mononuclear. The $Co^{(III)}$ center in complex **1** has a distorted octahedral geometry, with four N atoms of L^{2-} situated in the equatorial plane, and two deprotonated phenoxo O atoms strongly coordinated at the axial positions. Along the *c*-axis, the $[CoL]^+$ cations are connected alternatively by double ClO_4^- and double alkoxyl hydrogen-bonding bridges, affording a 1D supramolecular structure. In **2**, the $Cu^{(II)}$ center has a similar coordination geometry, whereas the axial positions are weakly coordinated by Cl^- and a protonated phenolic O atom. Approximately along the *ab*-plane, a 2D structure is assembled via multiple hydrogen bonds involving the alkoxyl, phenoxyl, amino, Cl^- and the lattice water molecules. In this work, the structures of the supramolecular coordination assemblies are shown to be tuned by various factors, such as the donor sets of the ligands, the central metal atoms and the counteranions.
© 2004 Elsevier Ltd. All rights reserved.

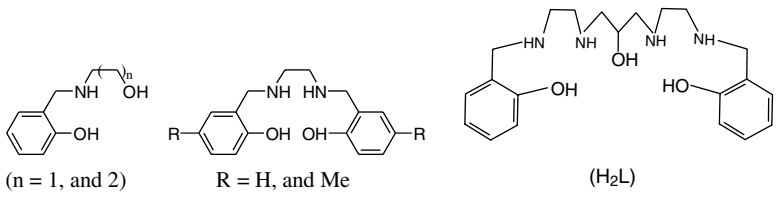
Keywords: Crystal structures; Co(III) complexes; Cu(II) complexes; Supramolecular structures; Hydrogen bonds

1. Introduction

In the past decades, great efforts have been devoted to the self-assembly of supramolecular coordination structures, due to its appealing potential applications in various fields, such as catalysis and molecular electronics [1,2]. Hydrogen bonds, as specific and strong non-covalent forces, have shown their great versatility in constructing these assemblies [3–8]. The structures of supramolecular coordination assemblies can be tailored by varying the functional groups of the organic ligands with various hydrogen bonding donor sets [9–11]. In this respect, we have demonstrated that various supramolecular structures can be obtained starting from tridentate and tetradentate ligands containing amino, alcoholic and phenolic groups (Scheme 1) [12–15]. In the complexes of the tridentate ligands, the phenolic and alcoholic groups are readily deprotonated and act as bridges, yielding binuclear, tetranuclear and hexanuclear complexes [15–17]. While in the complexes of the tetradentate ligands, the deprotonated phenolates can act as either terminal or bridging groups, yielding binuclear or mononuclear complexes.

* Corresponding author. Tel.: +86 551 360 3214; fax: +86 551 360 3388.
E-mail address: qliu@ustc.edu.cn (Q.-L. Liu).

0277-5387/$ - see front matter © 2004 Elsevier Ltd. All rights reserved.
doi:10.1016/j.poly.2004.11.009



Scheme 1. Polydentate ligand H_2L and related tridentate and tetradentate ligands.

Herein, we report the design and synthesis of a novel polydentate alcohol and phenol containing polyamine ligand, *N*,*N*′-bis(2-hydroxybenzyl)-1,3-bis[(2-aminoethyl)amino]-2-propanol (H_2L) (Scheme 1), and the crystal structures of its mononuclear $Co^{(III)}$ and $Cu^{(II)}$ complexes, $[CoL]ClO_4$ (**1**) and $[Cu(H_2L)Cl]ClO_4 \cdot CH_3OH \cdot H_2O$ (**2**). In these complexes, the deprotonation and coordination of the phenol groups are modified by the metal ions, affording 1D and 2D supramolecular structures, respectively. H_2L has up to seven donor atoms. It tends to form mononuclear complexes, as compared with the previously reported tridentate and tetradentate ligands (Scheme 1). The tuning of the supramolecular structures by the ligand, the central metal atoms, and the counteranions are discussed. The results herein provide further insight into the design and synthesis of hydrogen-bonded supramolecular coordination assemblies.

2. Experimental

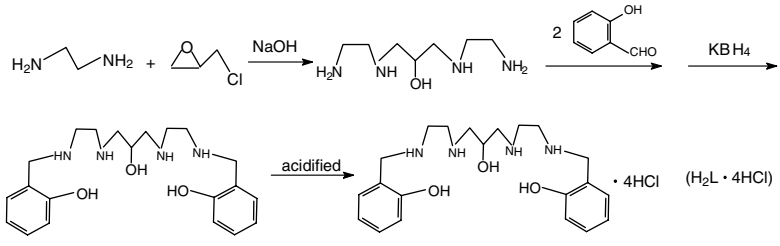
2.1. Safety note and materials

Perchlorate salts of metal complexes with organic ligands are potentially explosive. Only a small amount of the materials should be used and handed with extreme care. All of the chemicals were analytical grade and used as received without further purification.

2.2. Preparation of $H_2L \cdot 4HCl$ (H_2L = *N*,*N*′-bis(2-hydroxybenzyl)-1,3-bis[(2-aminoethyl) amino]-2-propanol)

The synthetic procedure of ligand $H_2L \cdot 4HCl$ is shown in Scheme 2. With continuous stirring, epichlorohydrin (23.2 ml, 0.296 mol) was added slowly to ethylenediamine (200 ml, 2.96 mol) cooled in an ice-bath. Several hours later, water (60 ml) was added. After stirring for 24 h at room temperature, the solution was refluxed for 10 h. The colorless solution gradually changed to light orange. Then, solid NaOH (14.2 g, 0.35 mol) was added in portions. One hour later, the solution was concentrated by rotary evaporation to give an orange-red oil. Upon adding a small amount of ethanol, solid NaCl was precipitated. After filtration, the resulting orange solution was distilled in vacuo, yielding a light yellow oil of 1,3-bis[(2-aminoethyl) amino]-2-propanol. b.p. 172–176 °C/30 mmHg.

To the methanol solution of the oil (29.1 g, 0.17mol) was added salicylaldehyde (42.5 g, 0.34 mol). After stirring for 2 h, KBH_4 (21 g) was added in small portions to the yellow-orange solution. The solution gradually faded to nearly colorless. Six hours later, the pH of the solution was adjusted to about 5 with hydrochloric acid, and then to about 9 with NaOH. The solvent was removed in vacuo, and the residue was dissolved in water and extracted with CH_2Cl_2. The CH_2Cl_2 layers were combined, dried overnight with Na_2SO_4, and concentrated in vacuo. The oily residue was dissolved in ethanol. Upon introduction of hydrochloric acid, a white precipitate formed, which was collected, washed with cooled ethanol and dried. Yield: 24 g, 15.2% (based on epichlorohydrin). *Anal.* Calc. for: $C_{21}H_{36}Cl_4N_4O_3$: C, 47.29; H, 6.79; N, 10.51. Found: C, 47.07; H, 6.83; N, 10.38%. IR (KBr disc, cm^{-1}): 2942(s), 2769(br, vs), 2694(br, vs), 2420(m), 1615(w), 1584(m), 1492(s), 1458(s), 1321(w), 1213(s), 1165(m), 1149(m), 1037(m), 897(w), 811(w), 755(s), 478(w). ^1H NMR (D_2O): δ 6.98–7.41 (8H, m, Ar–H), 4.33 (4H, s, Ar–CH_2), 4.33 (1H, s, CHOH), 3.52 (8H, s, $N(CH_2)_2N$), 3.14–3.34 (4H, m, NCH_2C).



Scheme 2. Synthesis of ligand $H_2L \cdot 4HCl$.

2.3. Preparation of [CoL]ClO_4 (1)

To a methanol solution of $H_2L \cdot 4HCl$ (0.1602 g, 0.3 mmol) was added $Co(OAc)_2 \cdot 4H_2O$ (0.1494 g, 0.6 mmol), followed by addition of aqueous NaOH (4.0 N, 0.40 ml). After refluxing for an hour, $NaClO_4 \cdot H_2O$ (0.1734 g, 1.2 mmol) was added. Three hours later, the residue was filtered off. The resulting solution was concentrated in vacuo to 6 ml and left undisturbed at room temperature for three weeks, yielding plate-like dark red single crystals of **1** suitable for X-ray diffraction analysis. Yield: 0.0510 g, 31.2%. *Anal*. Calc. for $C_{21}H_{30}Cl$- CoN_4O_7: C, 46.29; H, 5.55; N, 10.28. Found: C, 46.50; H, 5.32; N, 10.03%. IR (KBr, cm^{-1}): 3223.1(s), 2923.0(w), 1593.3(s), 1565.5(w), 1479.0(vs), 1446.1(s), 1290.1(s), 1270.6(s), 1204.3(w), 1108.5(br, vs), 1071.6(vs), 1030.1(s), 972.5(w), 877.3(m), 760.1(m), 624.0(s), 487.8(w).

2.4. Preparation of [Cu(H_2L)Cl]$ClO_4 \cdot CH_3OH \cdot H_2O$ (2)

To a methanol solution of $H_2L \cdot 4HCl$ (0.1067 g, 0.20 mmol) was added $Cu(ClO_4)_2 \cdot 6H_2O$ (0.1482 g, 0.40 mmol), followed by addition of aqueous NaOH (4.0 N, 0.35 ml). After refluxing for two hours, the resulting dark blue solution was concentrated in vacuo and left undisturbed at room temperature for over two months, yielding X-ray quality of needle-like violet-red single crystals of **2**. Yield: 0.014 g, 11%. *Anal*. Calc. for $C_{21}H_{32}Cl_2CuN_4O_7$: C, 42.97; H, 5.50; N 9.54. Found: C, 42.65; H, 5.32; N, 9.78%. IR (KBr, cm^{-1}): 3279.9(w), 3233.9(w), 1612.0(w), 1594.9(w), 1461.4(s), 1356.6(w), 1273.0(w), 1250.9(m), 1194.5(w), 1120.2(vs), 1042.7(s), 1016.6(s), 964.2(w), 888.6(w), 773.0(s), 759.3(s), 727.0(w), 624.0(m).

2.5. X-ray data collection and structural determination

All measurements on single crystals of **1** and **2** were made at 18 °C on a Rigaku RAXIS-IV image plate area detector with graphite monochromated Mo Kα radiation. The structure was solved by direct methods and the non-hydrogen atoms were refined anisotropically. Hydrogen atoms were included but not refined. The final cycle of full-matrix least-squares refinement was based on observed reflections ($I > 2.00\sigma(I)$) and variable parameters. All calculations were performed using the SHELX-97 software package [18]. Crystallographic data as well as details of data collection and refinement for complexes **1** and **2** are listed in Table 1.

Table 1
Summary of crystallographic data for **1** and **2**

Empirical formula	$C_{21}H_{30}ClCoN_4O_7$	$C_{22}H_{38}Cl_2CuN_4O_9$
Formula weight	544.87	637.00
Colour	red	purple
Temperature (K)	291(2)	291(2)
Wavelength (Å)	0.71073	0.71073
Crystal system	triclinic	monoclinic
space group	$P\bar{1}$	$P2(1)/n$
Unit cell dimensions		
a (Å)	11.044(2)	7.8666(16)
b (Å)	11.469(2)	14.524(3)
c (Å)	11.493(2)	25.050(5)
α (°)	100.90(3)	90
β (°)	114.34(3)	93.99(3)
γ (°)	105.52(3)	90
Volume ($Å^3$)	1201.4(4)	2855.0(10)
Z, D_{calc} ($Mg\ m^{-3}$)	2, 1.506	4, 1.482
Absorption coefficient (mm^{-1})	0.875	1.006
F(0 0 0)	568	1332
Crystal size (mm)	0.22 × 0.20 × 0.20	0.22 × 0.20 × 0.20
θ Range for data collection (°)	1.96–25.00	1.62–25.00
h/*k*/*l*	−11, 13/−13, 13/−12, 0	0, 9/−17, 17/−29, 29
Reflections collected/unique [R_{int}]	3611/3611 [0.0000]	7887/4543 [0.0255]
Completeness to $2\theta = 25.00$ (%)	88.5	90.2
Maximum and minimum transmission	0.8445 and 0.8309	0.8241 and 0.8089
Refinement method	full-matrix least-squares on F^2	full-matrix least-squares on F^2
Data/restraints/parameters	3611/0/328	4543/0/374
Goodness-of-fit on F^2	1.076	1.082
Final R indices [$I > 2\sigma(I)$]	$R_1 = 0.0468$, $wR_2 = 0.1349$	$R_1 = 0.0495$, $wR_2 = 0.1414$
R indices (all data)	$R_1 = 0.0569$, $wR_2 = 0.1389$	$R_1 = 0.0649$, $wR_2 = 0.1469$
Extinction coefficient	0.0072(19)	0.0009(7)
Largest difference peak and hole ($e\ Å^{-3}$)	0.960 and −0.601	0.986 and −0.830

2.6. Other physical measurements

The FT-IR spectra were recorded on a Bruker Vector-22 Spectrometer (KBr disc). The ^{1}H NMR measurements were carried out on a Bruker 300 Ultrashield NMR Spectrometer in D_2O (99.85%). Elemental analyses (C, H and N) were performed on an Elementar Vario EL-III Elemental analyzer. Electronic spectra were obtained on an UV-2401PC spectrophotometer in DMSO.

3. Results and discussion

3.1. Synthesis and spectroscopic characterization of *1* and *2*

In the IR spectrum of **1**, the strong band at 3223 cm^{-1} can be assigned to ν(N–H), while the medium band at 877 cm^{-1} and the weak band at 972 cm^{-1} correspond to staggering vibrations of CH_2 groups of the ligand with four amine N atoms coordinating in a coplanar fashion [19]. The strong bands at 1108–1030 cm^{-1} and one sharp band at 624 $cm^{-1}$are characteristic of ClO_4^- [20,21]. For **2**, free ClO_4^- exhibits similar absorption bands. The strong band at 1461 cm^{-1} is ascribed to δ (CH_2), with two absorption bands at 3280 and 3234 cm^{-1} of ν(NH). It is noted that the band at 1038 cm^{-1} for ν(C–O) of the isopropanol moiety [22] in $H_2L \cdot 4HCl$ shifts to 1043 cm^{-1} in **2**, but to 1030 cm^{-1} in **1**.

The electronic spectra of **1** show two weak transition bands at 816 nm ($\varepsilon = 6.86\ l\,cm^{-1}\,mol^{-1}$) and 560 nm ($\varepsilon = 128\ l\,cm^{-1}\,mol^{-1}$), which can be assigned to $^1A_{1g} \rightarrow {}^1T_{1g}$, and $^1A_{1g} \rightarrow {}^1T_{2g}$ ligand field transitions, respectively. The appearance of two d–d transitions is consistent with the pseudo-octahedral geometry of low spin $Co^{(III)}$ complexes [23]. For **2**, the d–d transition appears at 637 nm ($\varepsilon = 168\ l\,cm^{-1}\,mol^{-1}$).

3.2. Description of the structures

Selected bond angles and lengths for **1** and **2** are collected in Table 2.

In complex **1**, $Co^{(III)}$ has a distorted octahedral coordination geometry (Fig. 1). The *cis* angles around $Co^{(III)}$ vary in the range of 86.5(1)°–95.8(1)°, indicating the distortion of the octahedron. Despite the relatively short Co(1)–N(4) bond (1.943(3) Å), the other three Co–N bond lengths are very similar (1.968(3)–1.973(3) Å), and lie in the normal range [24,25]. The short Co–O bond lengths of 1.904(3) and 1.909(3) Å indicate the strong coordination of the deprotonated phenoxo groups. In complex **2** (Fig. 2), the $Cu^{(II)}$ center is coordinated by four N atoms and a protonated phenolic oxygen atom, O3, from a neutral H_2L ligand. The other protonated phenol group is left uncoordinated. The positive charge of $Cu^{(II)}$ is balanced by Cl^- and ClO_4^-.

Table 2
Selected bond lengths (Å) and bond angles (°) for **1** and **2**

Complex **1**			
Bond lengths			
Co(1)–O(1)	1.904(3)	Co(1)–O(3)	1.909(3)
Co(1)–N(4)	1.943(3)	Co(1)–N(1)	1.968(3)
Co(1)–N(3)	1.971(3)	Co(1)–N(2)	1.973(3)
Bond angles			
O(1)–Co(1)–O(3)	175.1(1)	O(1)–Co(1)–N(4)	90.8(1)
O(3)–Co(1)–N(4)	93.7(1)	O(1)–Co(1)–N(1)	88.8(1)
O(3)–Co(1)–N(1)	88.8(1)	N(4)–Co(1)–N(1)	94.6(1)
O(1)–Co(1)–N(3)	86.5(1)	O(3)–Co(1)–N(3)	95.8(1)
N(4)–Co(1)–N(3)	86.6(2)	N(1)–Co(1)–N(3)	175.2(2)
O(1)–Co(1)–N(2)	88.3(1)	O(3)–Co(1)–N(2)	87.3(1)
N(4)–Co(1)–N(2)	178.4(2)	N(1)–Co(1)–N(2)	86.6(1)
N(3)–Co(1)–N(2)	92.0(1)		
Complex **2**			
Bond lengths			
Cu(1)–N(2)	2.016(3)	Cu(1)–N(3)	2.035(4)
Cu(1)–N(4)	2.040(3)	Cu(1)–N(1)	2.054(3)
Bond angles			
N(2)–Cu(1)–N(3)	93.1(1)	N(2)–Cu(1)–N(4)	176.8(1)
N(3)–Cu(1)–N(4)	85.5(2)	N(2)–Cu(1)–N(1)	85.2(1)
N(3)–Cu(1)–N(1)	175.8(2)	N(4)–Cu(1)–N(1)	96.5(1)
O(3)–Cu(1)–N(1)	86.9(4)	O(3)–Cu(1)–N(4)	85.3(2)
O(3)–Cu(1)–N(2)	92.0(7)	O(3)–Cu(1)–N(3)	97.0(6)

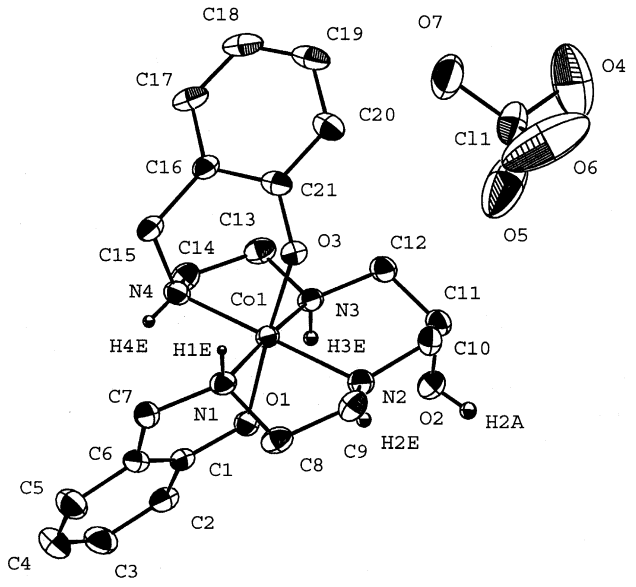


Fig. 1. View of complex **1** showing the numbering scheme.

For complex **1**, Along the *c*-axis, the $[Co^{(III)}L]^+$ cations are connected alternatively by double ClO_4^- and double alcoholic hydrogen bonding bridges in the complementary mode, forming a 1D supramolecular structure (Fig. 3 and Table 3). The 2D supramolecular structure of **2**, approximately along the *ab*-plane, is shown in Fig. 4. In detail, along the *a*-axis, a rather weak Cu–Cl coordination bond with the a bond length of 2.892 Å occurs between $Cu^{(II)}$ and the Cl^- from a neighboring molecule. Thus, the coordination geometry of $Cu^{(II)}$ can be viewed as an axially elongated octahe-

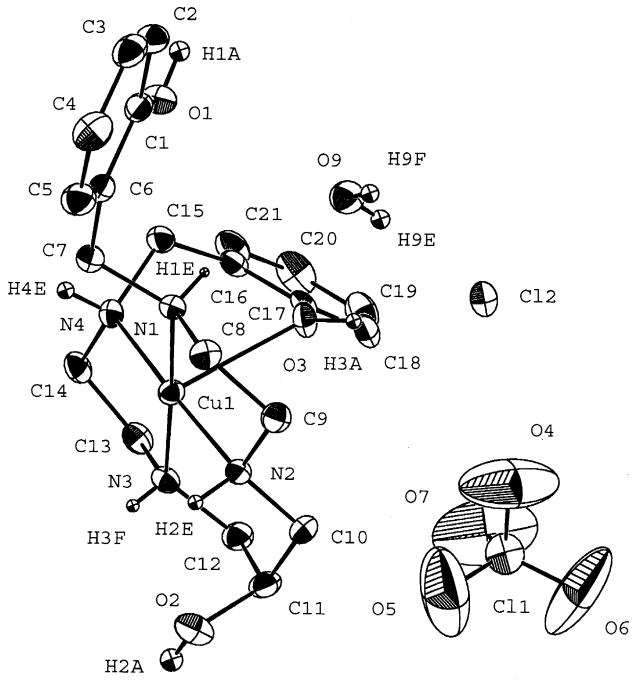


Fig. 2. View of complex **2** showing the numbering scheme (the methanol molecule is omitted for clarity).

dron. Along the *a*-axis, the adjacent $[Cu(H_2L)]^{2+}$ cations are connect by hydrogen bonds involving Cl^- (Table 3). Approximately along the *b*-axis, the $[Cu(H_2L)]^{2+}$ cations are connected by hydrogen bonds containing double water bridges and two sets of N1–H1E and O1–H1A groups. Furthermore, the alcoholic group O2–H2A is involved in intermolecular hydrogen bonds with N2–H2E, also in the complementary mode. Thus, approximately along the *ab*-plane, each molecule is connected to adjacent ones through multiple hydrogen bonds involving the alcoholic, phenolic and amino groups, as well as the Cl^- and the lattice water molecules, affording the 2D structure.

In both complexes of **1** and **2**, four amino groups are coordinated in the equatorial plane. The deprotonation and coordination of the phenol groups are related to the central metal atoms. In complex **1**, the cobalt atom has a high oxidation state of +3. It promotes the deprotonation and the subsequent coordination of the phenol groups, thus, both of the phenol groups are deprotonated and coordinated. In contrast, in complex **2**, $Cu^{(II)}$ coordinates to H_2L without deprotonating its phenolic groups. This may be ascribed to the weak axial coordination due to the Jahn–Teller effect and the lower oxidation

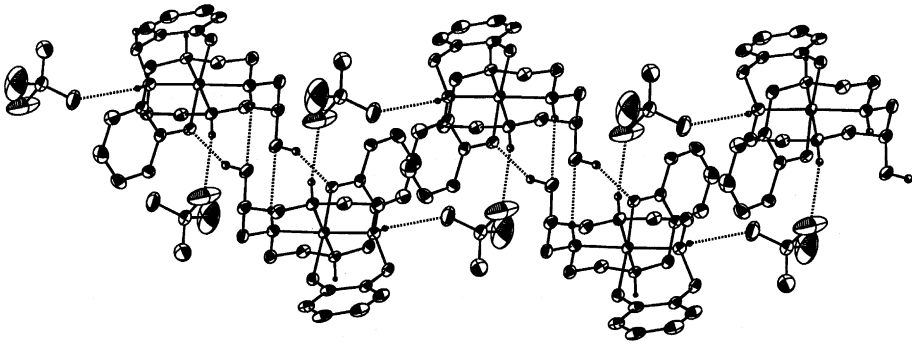


Fig. 3. 1D supramolecular structure of complex **1** (along the *c*-axis).

Table 3
Hydrogen bond lengths (Å) and angles (°) for **1** and **2** complex **1**

D–H	*d*(H...A)	∠DHA	*d*(D...A)	A (symmetry operations)
Complex **1**				
N3–H3E	2.32	150	3.09	O6 [$x-1, y-1, z-1$]
N2–H2E	2.58	169	3.38	O2 [$-x+2, -y+2, -z+1$]
N4–H4E	2.41	135	2.99	O7 [$-x+3, -y+3, -z+1$]
O2–H2A	2.01	152	2.78	O1 [$-x+2, -y+2, -z+1$]
Complex **2**				
O1–H1A	1.96	151	2.71	O9 [$-x-2, -y+1, -z+2$]
O2–H2A	2.37	134	3.00	O4 [$x-1, y, z$]
O2–H2A	2.45	175	3.27	O6 [$x-1, y, z$]
O8–H8	1.96	169	2.77	O9
N2–H2E	2.50	133	3.15	O2 [$-x-3, -y, -z+2$]
N1–H1E	2.56	147	3.20	O9
N3–H3F	2.85	125	3.29	Cl2 [$x-1, y, z$]
O3–H3A	2.30	165	3.07	Cl2
O9–H9E	2.45	174	3.15	Cl2
O9–H9F	1.63	162	2.77	O8

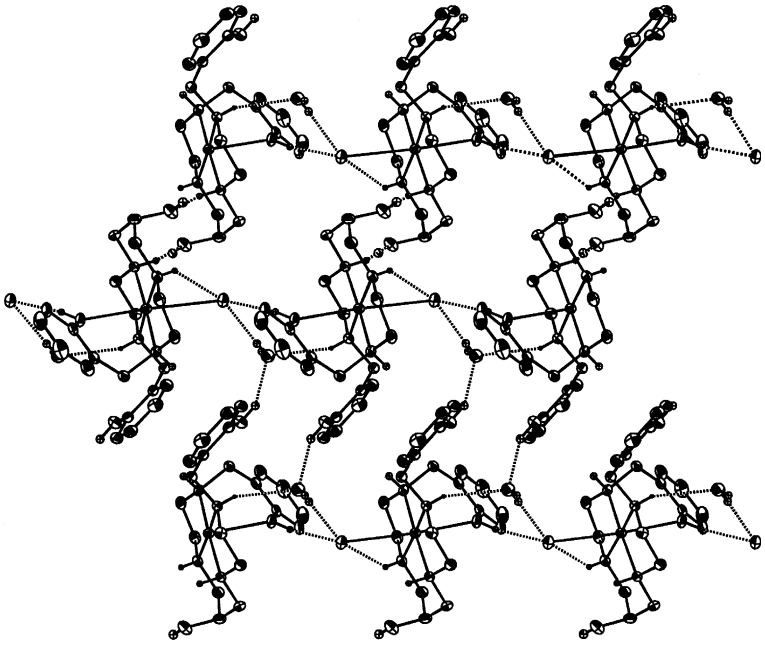


Fig. 4. 2D supramolecular structure of complex **2** (along the *ab*-plane).

state of $Cu^{(II)}$, as compared with $Co^{(III)}$. Thus, the $Cu^{(II)}$ atom has an axial elongated octahedral geometry, with a weak coordination of one of the protonated phenolic groups. The alcoholic group remains non-coordinated in the protonated form, directed outwards for intermolecular hydrogen bonding interactions. The coordination behavior of the phenolic and alcoholic groups are different from the corresponding groups in the previously reported complexes of the tridentate and tetradentate ligands (Scheme 1). In the latter complexes [15–17], these groups tend to deprotonate and act as bridges to form binuclear and polynuclear complexes, which may be related to the unsaturated coordination sphere in the supposed mononuclear 1:1 (M:L) complexes, due to the relatively fewer donor atoms. Whereas in **1** and **2** the ligand H_2L has more coordination atoms, so in the 1:1 mononuclear complexes the coordination spheres of the metal atoms are relatively more saturated. Therefore, the alkoxyl groups remain non-coordinated in the protonated form. The deprotonation and coordination of the phenolic groups are more difficult, and they can be tuned by varying the metal centers.

As for the roles of the anions ClO_4^- and Cl^- in **1** and **2**, apart from acting as the counteranions to balance the positive charge, they also form various multiple hydrogen bonds to assist in the formation of the supramolecular structures.

4. Conclusion

A polydentate ligand H_2L and its $Co^{(III)}$ and $Cu^{(II)}$ complexes are reported. The coordination environment of $Co^{(III)}$ in **1** can be described as a distorted octahedron, with four N atoms of the ligand H_2L defining the equatorial plane and two deprotonated phenoxo O atoms strongly coordinating at the axial positions. Along the *c*-axis, a 1D supramolecular structure is constructed by multiple hydrogen bonds. The $Cu^{(II)}$ center in **2** also has a distorted octahedral geometry, with the axial positions occupied by weakly coordinating Cl^- and a protonated phenolic O atom. Approximately along the *ab*-plane, the molecules are assembled to form a 2D structure by multiple hydrogen bonds.

In both **1** and **2**, the four amino N atoms of the ligand H_2L coordinate in the equatorial positions. The deprotonation and coordination of the phenolic groups are dependent on the metal centers. The high oxidation state of $Co^{(III)}$ facilitates the deprotonation and coordination of the phenolic groups in **1**, while the phenolic groups in **2** are not deprotonated.

The results in this work indicate that the new polydentate ligand H_2L is promising for the construction of novel hydrogen-bonded supramolecular coordination assemblies, which can be tailored by controlling the deprotonation and the coordination of the phenol groups with various metal ions, and also by varying the counteranions.

5. Supplementary material

The crystal structure data of complexes **1** and **2** have been deposited at the Cambridge Crystallographic Data Centre and allocated the deposition numbers 237180 (**1**) and 237181 (**2**). Copies of this information can be ob-

tained free of charge from The Director, CCDC, 12 Union Road, Cambridge, CB2 IEZ, UK (fax: +44-1223-336033; e-mail: deposit@ccdc.cam.ac.uk or www.ccdc.cam.ac.uk).

Acknowledgements

This work was financially supported by the National Science Foundation of China (No. 30270321) and the Natural Science Foundation of Anhui Province (No. 01045408).

References

[1] Z. Tang, A.M. Guloy, J. Am. Chem. Soc. 121 (1999) 452.
[2] M. Fujita, S. Nagao, K. Ogura, J. Am. Chem. Soc. 117 (1995) 1649.
[3] J. Dai, M. Yamamoto, T. Kuroda-Sowa, M. Mackawa, Y. Suenaga, M. Munakata, Inorg. Chem. 36 (1997) 2688.
[4] A.D. Burrows, C.W. Chan, M.M. Chowdhry, J.E. Mcgrady, D.M.P. Mingos, Chem. Soc. Rev. (1995) 329.
[5] A.D. Burrows, D.M.P. Mingos, A.J.P. White, D.J. Williams, Chem. Commun. (1996) 97.
[6] A.D. Burrows, D.M.P. Mingos, A.J.P. White, D.J. Williams, J. Chem. Soc., Dalton Trans. (1996) 149.
[7] M.P. Suh, K.S. Min, J.W. Ko, H.J. Choi, Eur. J. Inorg. Chem. (2003) 1373.
[8] P. Brunet, M. Simard, J.D. Wuest, J. Am. Chem. Soc. 119 (1997) 2737.
[9] D. Bose, S.H. Rahaman, G. Mostaha, R.D.B. Walsh, M.J. Zaworotko, B.K. Ghosh, Polyhedron 23 (2004) 545.
[10] X.J. Zheng, L.P. Jin, Polyhedron 22 (2003) 2617.
[11] S.B. Raj, P.T. Muthiah, G. Bocelli, A. Cantoni, Inorg. Chem. Commun. 6 (2003) 748.
[12] Y.S. Xie, W.M. Bu, A.S.C. Chan, X.L. Xu, Q.L. Liu, Z.D. Zhang, J. Yu, Y.G. Fan, Inorg. Chim. Acta 310 (2000) 257.
[13] Y.S. Xie, H. Jiang, M.G. Yu, C.X. Du, Q.L. Liu, X.L. Xu, Y. Zhu, J. Mol. Struct. 608 (2002) 169.
[14] Y.S. Xie, J. Ni, X.T. Liu, Q.L. Liu, X.L. Xu, C.X. Du, Y. Zhu, Transit. Metal Chem. 28 (2003) 367.
[15] Y.S. Xie, Q.L. Liu, H. Jiang, J. Ni, Eur. J. Inorg. Chem. (2003) 4010.
[16] Y.S. Xie, H. Jiang, A.S.C. Chan, Q.L. Liu, X.L. Xu, C.X. Du, Y. Zhu, Inorg. Chim. Acta. 333 (2002) 138.
[17] Y.S. Xie, X.T. Liu, J. Ni, Q.L. Liu, J. Mol. Struct. 655 (2003) 279.
[18] G.M. Sheldrick, SHELX 97, Program for Crystal Structure Refinement, University of Göttingen, Germany, 1997.
[19] K. Nakamoto, Infrared and Raman Spectra of Inorganic and Coordination Compounds, 4th ed., p. 205.
[20] X.T. Liu, Y.S. Xie, Q.L. Liu, C.X. Du, Y. Zhu, X.L. Xu, J. Mol. Struct. 654 (2003) 235.
[21] A. Mitra, T. Banerjee, P. Roychowdhury, S. Chaudhuri, P. Bera, N. Saha, Polyhedron 21 (1997) 3735.
[22] A. Karadag, V.T. Yilmaz, C. Thoene, Polyhedron 20 (2001) 635.
[23] N.C. Saha, R.J. Butcher, S. Chaudhuri, N. Saha, Polyhedron 22 (2003) 383.
[24] R.L. Fanshawe, A. Mobinikhaledi, C.R. Clark, A.G. Blackman, Inorg. Chim. Acta 26 (2000) 307.
[25] G.A. Amadei, M.H. Dickman, R.A. Wazzeh, P. Dimmock, J.E. Earley, Inorg. Chim. Acta 40 (1999) 288.

Available online at www.sciencedirect.com
SCIENCE DIRECT®
Polyhedron 24 (2005) 173–180
POLYHEDRON
www.elsevier.com/locate/poly

Synthesis and structural characterization of (pyrazolyl)alkenyl Fischer carbene complexes of chromium and tungsten

Kai-Chun Gu [a], Jin-Zhu Chen [a], Zhao-Yan Zheng [a], Si-Zhong Wu [a], Xiao-Wei Wu [a], Xiu-Wen Han [b], Zheng-Kun Yu [a,*]

[a] *Dalian Institute of Chemical Physics, Chinese Academy of Sciences, 457 Zhongshan Road, Dalian, Liaoning 116023, P.R. China*
[b] *State Key Laboratory of Catalysis, Dalian Institute of Chemical Physics, Chinese Academy of Sciences, 457 Zhongshan Road, Dalian, Liaoning 116023, P.R. China*

Received 11 October 2004; accepted 3 November 2004
Available online 18 December 2004

Abstract

Michael addition of substituted pyrazoles **2** to 1-alkynyl Fischer carbene complexes $(CO)_5M{=}C(OEt)(C{\equiv}CPh)$ (**1**) (**a**, M = Cr and **b** M = W) afforded (pyrazolyl)alkenyl Fischer carbene complexes $(CO)_5M{=}C(OEt)(CH{=}C(R^1R^2R^3pz)Ph)$ ($R^1R^2R^3pz$ = pyrazolyl) **3** (M = Cr) and **4** (M = W), respectively, with an exclusive (*E*)-configuration in mild to excellent yields. The reaction of **1a** and 3,5-dimethylpyrazole (**2b**) was monitored to demonstrate the formation and decomposition of complex **3b** by ^1H NMR measurements in $CDCl_3$ at 23 °C. Complexes **3** and **4** were characterized with ^1H, $^{13}C\{^1H\}$ NMR, IR spectroscopies and elemental analysis. When the substituted pyrazoles were 3-methylpyrazole (**2a**) and 3,5-di-*tert*-butylpyrazole (**2d**), molecular structures of the corresponding (pyrazolyl)alkenyl Fischer carbene complexes **3a** and **4d** were characterized by X-ray crystallographic study.
© 2004 Elsevier Ltd. All rights reserved.

Keywords: Fischer carbene; Pyrazole; Michael addition; Chromium; Tungsten

1. Introduction

Fischer carbene complexes were first synthesized by Fischer and Maasböl in 1964 [1,2] and have been paid much attention in the last two decades because they can be rather readily prepared and manipulated to demonstrate diverse reactivity in organic synthesis [3]. Transformations from alkynyl carbene to alkenyl carbene complexes have been extensively investigated. Michael addition of dimethylamine to Fischer alkynylcarbene complexes was reported by Fischer and Kreissl [4] as early as 1972, followed by several other groups [5]. Michael-type addition of amines or N–H bond-containing compounds to α,β-unsaturated Fischer carbene complexes to form β-aminovinyl-substituted products has been considered a useful methodology for certain preparative organic synthesis because the resultant Michael-type adducts are usually reactive intermediates [6–18]. A rich chemistry of pyrazoles [19] and pyrazolato ligands [20–22] has been evolved since pyrazoles were first prepared in 1968 [23], due to the presence of pyrazolyl-containing compounds in nature and potential bioactivity of pyrazole derivatives as well as their good coordination ability as ligands. Pyrazole contains a reactive N–H bond which can be easily deprotonated to proceed a lot of reactions. However, up to date no β-pyrazolyl subsitituted alkenyl Fischer carbene complexes have been synthesized, although 1-methoxy-1-(5-pyrazole) Fischer carbene complexes were reportedly generated in the reactions of 1-alkynyl Fischer carbene

* Corresponding author. Tel./fax: +86 411 8437 9227.
E-mail address: zkyu@dicp.ac.cn (Z.-K. Yu).

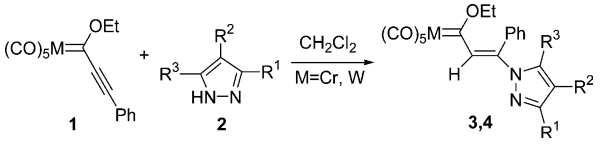
0277-5387/$ - see front matter © 2004 Elsevier Ltd. All rights reserved.
doi:10.1016/j.poly.2004.11.012

complexes with Me_3SiCHN_2 [24a] and $(CO)_5W$-C(OEt)(CH=C($C_3H_3N_2$)Ph) was detected by UV spectroscopy [24b]. Herein, we report the synthesis of (pyrazolyl)alkenyl Fischer carbene complexes **3** and **4** by the reactions of substituted pyrazoles **2** with 1-alkynyl Fischer carbene complexes **1a**,**b** (**a**, M = Cr; **b**, M = W) under mild conditions, as well as their structural characterization.

2. Results and discussion

2.1. Synthesis of (pyrazolyl)alkenyl carbene complexes 3 and 4

Treatment of the 1-alkynyl Fischer carbene complexes **1a** and **1b** with an equivalent amount of substituted pyrazole in dichloromethane at ambient temperature afforded (pyrazolyl)alkenyl Fischer carbene complexes **3** and **4** in mild to excellent yields (Eq. (1)). The reaction temperature was elevated to 38 °C due to the poor solubility of 3,5-di-*tert*-butylpyrazole and 3,5-di-phenylpyrazole in CH_2Cl_2. 3-Methylpyrazole exhibited very low reactivity to both complexes **1a** and **1b** and only 32.2% and 17.6% yields of the desired products were achieved over a period of 77–85 h for **1a** and **1b**, respectively.



(1)

2	R^1	R^2	R^3	3 (M = Cr), %	4 (M = W), %
2a	Me	H	H	**3a**, 32.2	**4a**, 17.6
2b	Me	H	Me	**3b**, ~77[a]	**4b**, 99.6
2c	Ph	H	Ph	**3c**, 60.5	**4c**, 90.4
2d	*t*-Bu	H	*t*-Bu	**3d**, 65.8	**4d**, 80.5
2e	Me	Me	Me	**3e**, 65.8	**4e**, 93.0
2f	Me	$PhCH_2$	Me	**3f**, 88.5	**4f**, 93.1

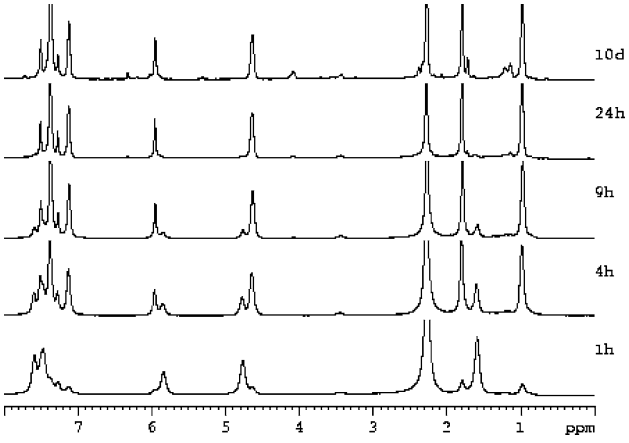
[a] Containing small amounts of decomposition products.

In the other cases, the tungsten carbene complex **1b** demonstrated higher reactivity (shorter reaction time) to the investigated substituted pyrazoles than its chromium analogue, leading to higher yields for the tungsten products (80.5–99.6%) and lower isolated yields for their chromium analogues (60.5–88.5%). It was observed that the chromium products were subject to decomposition on silica gel when the crude products were purified by column chromatography.

It is noteworthy that complex **4b** was obtained in 99.6% isolated yield while its chromium analogue, i.e., complex **3b** underwent decomposition under mild conditions to form some unidentified products when 3,5-dimethyl pyrazole was used. In order to understand the behavior of complex **3b**, Fischer carbene complex **1a** was treated with an equivalent amount of 3,5-dimethyl pyrazole (**2b**) in $CDCl_3$ in a 5-mL NMR tube at ambient temperature and the reaction was monitored by ^1H NMR measurements over a period of ten days (Scheme 1). The ^1H NMR measurements revealed that the reaction exclusively proceeded to form **3b** and the reaction was completed in 24 h at ambient temperature. It was noticed that the product, i.e., **3b**, gradually decomposed when the reaction solution was kept at ambient temperature for a longer time (e.g., 10 days). It was also observed that the reaction of **1a** with an excess of the pyrazole (2.0 equiv.) in $CDCl_3$ at ambient temperature did not lead to any formation of the de-ethoxy product, i.e., the 2,4-dipyrazolyl alkenylcarbene complex. Due to its decomposition at ambient temperature, the full characterization data for complex **3b** could not be collected, but its NMR data was tentatively assigned.

2.2. Spectroscopy of (pyrazolyl)alkenyl carbene complexes 3 and 4

The strong bands in the region 2069–1902 cm^{-1} of the IR spectra are characteristic of the typical patterns expected for a $M(CO)_5$ moiety in Fischer carbene complexes. The proton resonances of HC=C($R^1R^2R^3$pz)Ph in complexes **3** and **4** in $CDCl_3$ are shown in the region 8.20–7.31 ppm as singlets and those of the alkenyl complexes of chromium, **3**, are slightly shifted downfield as compared with their tungsten analogues. The ^{13}C resonances of the carbene carbons, i.e., Cr=C in complexes **3** are at 331.4–338.4 ppm and those of W=C in complexes **4** are at 310.5–304.6 ppm, while the ^{13}C NMR signals of typical β-aminoalkenyl Fischer carbene complexes exhibiting some conjugation between the metal carbene M=C and the alkenyl moiety are in the region ~270–290 ppm [7,10], and those of metal carbene M=C in $(OC)_5M$=



Scheme 1. Formation and decomposition of **3b** from the reaction of **1a** and 3,5-dimethylpyrazole (**2b**) monitored by ^1H NMR measurements in $CDCl_3$ at 23 °C.

C(OMe)Me showing no conjugation between the M=C and methyl moieties are at ~320 ppm (M = Cr) to 361 ppm (M = W) [25]. These results indicate that only little (or even no) π-conjugation is expected to operate within the (pyrazolyl)alkenyl unit and the metal carbene bond M=C. The ^{13}C resonance signals of the $M(CO)_5$ moieties are always shown at about 224 ppm/216 ppm for the chromium complexes **3** and at about 204 ppm/197 ppm for the tungsten complexes **4** with a 1:4 intensity ratio. The proton signals of the 4′-H in the pyrazolyl ring appear at 7.00–5.96 ppm as singlets, and the ^{13}C resonance signals of the C4′ and C3′ (i.e., C=N) carbons are shown in the region 102.8–119.5 and 150.5–161.5 ppm, respectively, corresponding to those of an NH deprotonated pyrazolyl ring [22].

2.3. Crystal structure analyses of complexes *3a* and *4d*

Fig. 1 is a perspective SCHAKAL-97 drawing of complex **3a** showing the labelling scheme. The molecular structure is in line with the assignment by IR and NMR spectra of the complex. The pyrazolyl ring is situated at an (*E*)-configuration with respect to the $(CO)_5Cr$=C moiety. The distances Cr–C6, C6–C7 and C7–C8 are 2.057(3), 1.456(4) and 1.344(4) Å, respectively, corresponding to a typical Cr=C bond in alkenyl Fischer carbene complexes, single and double carbon–carbon bonds, indicating little or even no π-conjugation in the metal butadienyl system. The pyrazolyl ring is bound to C8 atom via the N1 atom of the pyrazolyl moiety and the methyl substituent on the pyrazolyl ring is arranged in a position separated far away from the phenyl group to reduce the steric hindrance. The lengths N2–C19 (1.321(3) Å) and C17–C18 (1.336(4) Å) are in

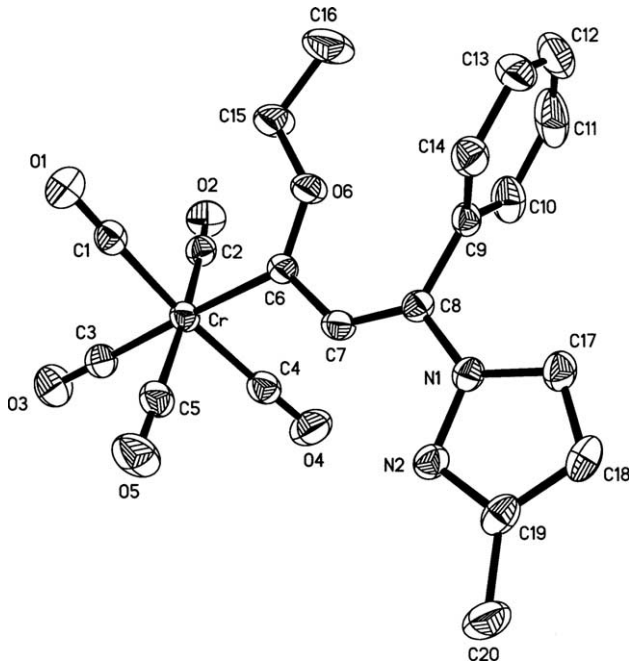


Fig. 1. Molecular structure of complex **3a**.

accordance with C=N and C=C bonds, respectively, revealing no structural change for the pyrazolyl ring. All the structural data confirms a Michael addition product from the 1-alkynylcarbene complex **1a**. No obvious difference is observed between the molecular structures of **3a** and **4d** (Fig. 2). The W–C6 bond length is 2.150(5) Å and C7–C8 bond length in **4d** is 1.342(7) Å. The N1–C8 bond (1.405(6) Å) is longer than its analogue in **3a** (1.395(3) Å), presumably due to bigger steric hindrance from the *tert*-butyl groups. The angle C17–N1–C8 (133.9(4)°) in **4d** is bigger than that in **3a**

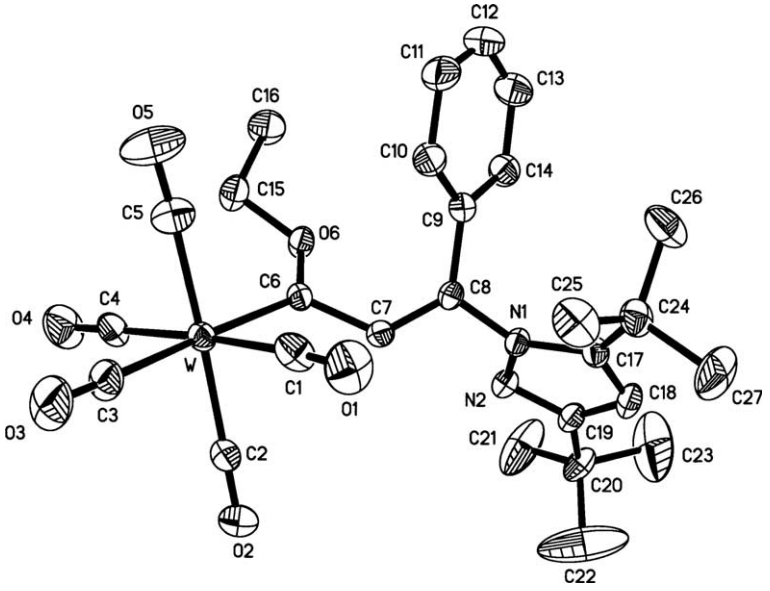


Fig. 2. Molecular structure of complex **4d**.

(127.7(3)°) and N1–C8 (1.405(6) Å) in **4d** is longer than that in **3a** (1.395(3) Å), demonstrating that the 3,5-di-*tert*-butylpyrazolyl ring is separated farther away from the backbone of the alkenyl carbene complex than the less steric ring, i.e., 3-methylpyyrazolyl.

3. Experimental

Dried solvents were used in all experiments. Melting points are not corrected. Instrumentation: ^{1}H and ^{13}C NMR spectra were obtained with Bruker DRX-400 spectrometer (chemical shifts refer to $\delta_{TMS} = 0.00$ ppm); IR spectra were obtained on a Bruker Tensor 27 spectrophotometer. Elemental analysis was achieved by the Analysis Center, Shanghai Institute of Organic Chemistry, Chinese Academy of Sciences. Substituted pyrazoles were prepared as reported [23]. 3,4,5-Trimethylpyrazole [26] and 3,5-dimethyl-4-benzyl-pyrazole [27] were synthesized by reported procedures, respectively.

*General procedure for the synthesis of the (pyrazolyl)alkenyl carbene complexes **3** and **4***. A mixture of 1-alkynylcarbene complex **1** (1.0 mmol) and substituted pyrazole (1.0 mmol) in 3 mL of dichloromethane was stirred in a 5-mL screwtop vessel at ambient temperature (23 °C) or elevated temperature as stated. The reaction was monitored by TLC analysis on silica gel. After the reaction was completed, the resultant mixture was subject to column chromatography on silica gel to collect the product **3** or **4**. Recrystallization at −20 °C afforded single crystals suitable for X-ray crystallographic study. The crystal color of complexes **3** and **4** are red and dark red, respectively.

*2-Ethoxy-4-phenyl-4-(3′-methylpyrazol-1′-yl)-1,1,1,1,1-pentacarbonyl-1-chroma-1,3-butadiene (**3a**):* 23 °C, 85 h, 139 mg (32.2%). M.p. 89–91 °C. Single crystals suitable for X-ray determination were grown in CH_2Cl_2/pentane (v/v, 1/4) at −20 °C. ^{1}H NMR ($CDCl_3$, 23 °C, 400 MHz): δ 8.20 (br, 1H, 3-H), 7.42 and 7.20 (br each, 3:2 H, 4-Ph), 7.00 (br, 1H, 4′-H), 6.12 (br, 1H, 5′-H), 4.57 (q, 2H, OCH_2), 2.35 (s, 3H, 3′-CH_3), 0.81 (br, 3H, CH_2CH_3); ^{13}C{^{1}H} NMR ($CDCl_3$, 23 °C, 400 MHz): δ 331.40 (s, Cq, Cr=C), 224.39 and 216.84 (s each, Cq, 1:4, *trans*- and *cis*-CO, $Cr(CO)_5$), 153.49 (s, Cq, C=N, C3′), 134.70 (s, Cq, *i*-C of Ph), 132.70 and 109.32 (s each,1:1 CH, C5′ and C4′), 129.83 and 128.67 (s each, aromatic CH, 4-Ph), 129.54 (s, CH, C4), 129.34 (s, CH, C3), 75.99 (s, OCH_2), 14.15 (s, 4′-CH_3), 13.96 (s, CH_2CH_3); IR (KBr) cm^{-1}: 2050.2 (90), 1924.0 (100), 1903.6 (100) [ν(C≡O)], 1537.2 (80), 1490.9 (60), 1444.6 (50) [ν(C=C, C=N)]. *Anal.* Calc. for $C_{20}H_{16}N_2O_6Cr$: C, 55.56; H, 3.73; N, 6.48. Found: C, 55.51; H, 3.76; N, 6.45%.

*2-Ethoxy-4-phenyl-4-(3′-methylpyrazol-1′-yl)-1,1,1,1,1-pentacarbonyl-1-tungsta-1,3-butadiene (**4a**):* 23 °C, 77 h, 99 mg (17.6%). M.p. 121–122 °C; ^{1}H NMR ($CDCl_3$, 23 °C, 400 MHz): δ 8.03 (s, 1H, 3-H), 7.30 and 7.10 (m each, 3:2 H, 4-Ph), 6.86 and 6.00 (dd each, J = 1.9 Hz, 1:1H, 4′- and 5′-H), 4.25 (q, 2H, OCH_2), 2.21 (s, 3H, 3′-CH_3), 0.66 (t, 3H, CH_2CH_3); ^{13}C{^{1}H} NMR ($CDCl_3$, 23 °C, 400 MHz): δ 304.55 (s, Cq, Cr=C), 204.29 and 198.43 (s each, Cq, 1:4, *trans*- and *cis*-CO, $Cr(CO)_5$), 153.77 (s, Cq, C=N, C3′), 137.59 (s, Cq, C4), 134.90 (s, Cq, *i*-C of Ph), 132.63, 129.65 and 128.64 (aromatic CH, 4-Ph), 129.56 (s, CH, C5′), 109.56 (s, CH, C4′), 78.53 (s, OCH_2), 14.24 (s, 3′-CH_3), 13.80 (s, CH_2CH_3); IR (KBr) cm^{-1}: 2057.9 (90), 1947.0 (100), 1924.0 (100), 1899.8 (100) [ν(C≡O)], 1537.2 (90), 1490.9 (70), 1442.7 (60) (ν(C=C, C=N)). *Anal.* Calc. for $C_{20}H_{16}N_2O_6W$: C, 42.58; H, 2.86; N, 4.96. Found: C, 42.59; H, 2.88; N, 4.93%.

*2-Ethoxy-4-phenyl-4-(3′,5′-di-methylpyrazol-1′-yl)-1,1,1,1,1-pentacarbonyl-1-chroma-1,3-butadiene (**3b**):* 23 °C, 10 h, 77.0%. Dec. 23 °C; ^{1}H NMR ($CDCl_3$, 23 °C, 400 MHz): δ 7.58 (s, 1H, 3-H), 7.37 and 7.12 (br each, 3:2 H, 4-Ph), 5.95 (s, 1H, 4′-H), 4.63 (br, 2H, OCH_2), 2.27 and 1.79 (s each, 3:3 H, 3′- and 5′-CH_3), 0.97 (br, 3H, CH_2CH_3); ^{13}C{^{1}H} NMR ($CDCl_3$, 23 °C, 400 MHz): δ 335.50 (s, Cq, Cr=C), 224.14 and 216.58 (s each, Cq each, 1:4, *trans*- and *cis*-CO, $Cr(CO)_5$), 150.71 and 143.70 (s each, Cq each, C3′ and C5′), 135.85 (s, CH, C3), 134.58 (s, Cq, C4), 132.81 (s, Cq, *i*-C of 4-Ph), 129.65, 129.50 and 128.72 (s each, 1:2:2 CH, 4-Ph), 109.54 (s, CH, C4′), 76.34 (s, OCH_2), 14.13, 13.83 and 12.96 (s each, CH_3).

*2-Ethoxy-4-phenyl-4-(3′,5′-di-methylpyrazol-1′-yl)-1,1,1,1,1-pentacarbonyl-1-tungsta-1,3-butadiene (**4b**):* 23 °C, 8 h, 576 mg (99.6%). M.p. 89–90 °C; ^{1}H NMR ($CDCl_3$, 23 °C, 400 MHz): δ 7.43 (s, 1H, 3-H), 7.37 and 7.16 (m each, 3:2 H, 4-Ph), 5.96 (s, 1H, 4′-H), 4.47 (q, 2H, OCH_2), 2.27 and 1.76 (s each, 3:3 H, 3′- and 5′-CH_3), 0.92 (t, 3H, CH_2CH_3); ^{13}C{^{1}H} NMR ($CDCl_3$, 23 °C, 400 MHz): δ 307.55 (s, Cq, W=C), 204.06 and 197.45 (s each, Cq each, 1:4, *trans*- and *cis*-CO, $W(CO)_5$), 150.89 and 142.50 (s each, Cq each, C=N, C3′ and C5′), 139.22 (s, CH, C3), 137.41 (s, Cq, C4), 135.96 (s, Cq, *i*-C of 4-Ph), 129.61 and 128.61 (3:2 CH, 4-Ph), 109.91 (s, CH, C4′), 78.72 (s, OCH_2), 13.85 and 13.09(s, 3′-CH_3 and 5′-CH_3), 13.10 (s, CH_2CH_3); IR (KBr) cm^{-1} : 2059.8 (30), 1931.3 (70), 1901.7 (70) [ν(C≡ O)], 1533.2 (45), 1477.4 (25) [ν(C=C, C=N)]. *Anal.* Calc. for $C_{21}H_{18}N_2O_6W$: C, 43.62; H, 3.14; N, 4.84. Found: C, 43.70; H, 3.16; N, 4.80%.

*2-Ethoxy-4-phenyl-4-(3′,5′-di-phenylpyrazol-1′-yl)-1,1,1,1,1-pentacarbonyl-1-chroma-1,3-butadiene (**3c**):* 38 °C, 48h, 345 mg (60.5%). M.p. 106–107 °C; ^{1}H NMR ($CDCl_3$, 23 °C, 400 MHz): δ 7.92 and 7.41 (m each, 2:3 H, 4-Ph), 7.72 (s, 1H, 3-H), 7.38–6.90 (m, 10H, 3′- and 5′-Ph), 6.76 (s, 1H, 4′-H), 4.64 (br, 2H, OCH_2), 0.96 (br, 3H, CH_3); ^{13}C{^{1}H} NMR ($CDCl_3$,

23 °C, 400 MHz): δ 335.72 (s, Cq, Cr=C), 224.08 and 216.45 (s each, Cq, 1:4, *trans*- and *cis*-CO, $Cr(CO)_5$), 152.72 and 146.97 (s each, Cq, C=N, C3′ and C5′), 137.52 (s, CH, C3), 135.48 (s, Cq, C4), 134.57, 132.58 and 130.40 (s each, Cq each, *i*-C of Ph), 129.60, 129.10, 128.84, 128.73, 128.61, 128.45, 128.16, 127.97 and 126.20 (aromatic CH of 4-, 5′-, and 3′-Ph), 106.72 (s, CH, C4′), 76.45 (s, O*C*H_2), 14.06 (s, *C*H_3); IR (KBr) cm^{-1}: 2057.9 (100), 1986.7 (100), 1911.3 (100) [ν(C≡O)], 1548.7 (80), 1487.0 (70), 1446.5 (60) [ν(C=C, C=N)]. *Anal*. Calc. for $C_{31}H_{22}N_2O_6Cr$: C, 65.26; H, 3.89; N, 4.91. Found: C, 65.26; H, 3.88; N, 4.88%.

*2-Ethoxy-4-phenyl-4-(3′,5′-di-phenylpyrazol-1′-yl)-1,1,1,1,1-pentacarbonyl-1-tungsta-1,3-butadiene (**4c**):* 38 °C, 27 h, 635 mg (90.4%). M.p. 132 °C; ^1H NMR ($CDCl_3$, 23 °C, 400 MHz): δ 7.92, 7.45 and 7.38 (m each, 2:2:1 H, 4-Ph), 7.60 (s, 1H, 3-H), 7.22, 7.15, 7.08 and 6.92 (m each, 2:3:3:2 H, 3′- and 5′-Ph), 6.76 (s, 1H, 4′-H), 4.49 (q, 2H, O*C*H_2), 0.92 (t, 3H, C*H*$_3$); $^{13}C\{^1H\}$ NMR ($CDCl_3$, 23 °C, 400 MHz): δ 308.14 (s, Cq, W=C), 204.00 and 197.29 (s each, Cq, 1:4, *trans*- and *cis*-CO, $W(CO)_5$), 152.78 and 146.98 (s each, Cq each, C=N, C3′ and C5′), 141.14 (s, CH, C3), 137.18, 132.56 and 130.44 (s each, Cq each, *i*-C of Ph), 135.62 (s, Cq, C4), 129.78, 129.09, 128.87, 128.75, 128.65, 128.45, 128.17, 127.86, and 126.21 (aromatic CH of 4-, 3′- and 5′-Ph), 106.96 (s, CH, C4′), 78.87 (s, O*C*H_2), 13.82 (s, *C*H_3); IR (KBr) cm^{-1}: 2065.6 (60), 1986.7 (55), 1903.6 (80) [ν(C≡O)], 1548.7 (40), 1485.1 (40), 1444.6 (40) [ν(C=C, C=N)]. *Anal*. Calc. for $C_{31}H_{22}N_2O_6W$: C, 53.01; H, 3.16; N, 3.99. Found: C, 53.07; H, 3.18; N, 3.96%.

*2-Ethoxy-4-phenyl-4-(3′,5′-di-tert-butylpyrazol-1′-yl)-1,1,1,1,1-pentacarbonyl-1-chroma-1,3-butadiene (**3d**):* 38 °C, 24 h, 349 mg (65.8%). M.p. 118-119 °C; ^1H NMR ($CDCl_3$, 23 °C, 400 MHz): δ 7.40 (s, 1H, 3-H), 7.30 and 6.94 (m each, 3:2 H, 4-Ph), 6.03 (s, 1H, 4′-H), 4.72 (br, 2H, O*C*H_2), 1.33 (9H, s, 5′-C(C*H*$_3$)$_3$), 1.10 (t, 3H, CH_2CH_3), 1.08 (s, 9H, 3′-C(C*H*$_3$)$_3$); $^{13}C\{^1H\}$ NMR ($CDCl_3$, 23 °C, 400 MHz): δ 338.41 (s, Cq, Cr=C), 224.02 and 216.22 (s each, Cq each, 1:4, *trans*- and *cis*-CO, $Cr(CO)_5$), 161.46 and 153.77 (s each, Cq each, C=N, C3′ and C5′), 140.21 (s, CH, C3), 137.14 (s, Cq, C4), 136.36 (s, Cq, *i*-C of 4-Ph), 129.58, 129.40 and 128.41 (1:2:2 CH, 4-Ph), 102.80 (s, CH, C4′), 76.71 (s, O*C*H_2), 32.13 (s, Cq, *C* $(CH_3)_3$), 30.82 and 30.64 (s each, 3′- and 5′-C(*C*H_3)$_3$), 14.22 (s, CH_2CH_3); IR (KBr) cm^{-1}: 2057.9 (60), 1951.8 (60) [ν(C≡O)], 1571.9 (20) [ν(C=C, C=N)]. *Anal*. Calc. for $C_{27}H_{30}N_2O_6Cr$: C, 61.12; H, 5.70; N, 5.28. Found: C, 61.14; H, 5.74; N, 5.18%.

*2-Ethoxy-4-phenyl-4-(3′,5′-di-tert-butylpyrazol-1′-yl)-1,1,1,1,1-pentacarbonyl-1-tungsta-1,3-butadiene (**4d**):* 38 °C, 22 h, 533 mg (80.5%). M.p. 132–133 °C. Single crystals suitable for X-ray study were obtained by recrystallization in pentane at −20 °C. ^1H NMR ($CDCl_3$, 23 °C, 400 MHz): δ 7.31 (s, 1H, 3-H), 7.29 and 7.00 (m each, 3:2 H, 4-Ph), 6.04 (s, 1H, 4′-H), 4.61 (q, 2H, O*C*H_2), 1.34 and 1.08 (s each, 9:9 H, 3′- and 5′-C(C*H*$_3$)$_3$), 1.07 (t, 3H, CH_2CH_3); $^{13}C\{^1H\}$ NMR ($CDCl_3$, 23 °C, 400 MHz): δ 310.50 (s, Cq, W=C), 203.77 and 197.05 (s each, Cq, 1:4, *trans*- and *cis*-CO, $W(CO)_5$), 161.52 and 153.82 (s each, Cq, C=N, C3′ and C5′), 144.08 (s, CH, C3), 139.04 (s, Cq, *i*-C of 4-Ph), 137.19 (s, Cq, C4), 129.74, 129.58 and 128.26 (s each, 2:1:2 CH, 4-Ph), 102.97 (s, CH, C4′), 76.12 (s, O*C*H_2), 32.17 (s, Cq, *C* $(CH_3)_3$), 30.83 and 30.65 (s each, 3′- and 5′-C(*C*H_3)$_3$), 13.92 (s, CH_2CH_3); IR (KBr) cm^{-1}: 2065.6 (50), 1953.8 (80), 1908.0 (70) [ν(C≡O)], 1566.1 (40), 1541.0 (40), 1490.9 (30), 1446.5 (30) [ν(C=C, C=N)]. *Anal*. Calc. for $C_{27}H_{30}N_2O_6W$: C, 48.96; H, 4.56; N, 4.23. Found: C, 48.92; H, 4.57; N, 4.18%.

*2-Ethoxy-4-phenyl-4-(3′,4′,5′-trimethylpyrazol-1′-yl)-1,1,1,1,1-pentacarbonyl-1-chroma-1,3-butadiene (**3e**):* 23 °C, 5 h, 406 mg (88.2%). M.p. 78–79 °C; ^1H NMR ($CDCl_3$, 23 °C, 400 MHz): δ 7.49 (s, 1H, 3-H), 7.37 and 7.11 (br each, 3:2 H, 4-Ph), 4.60 (br, 2H, O*C*H_2), 2.21, 1.89 and 1.70 (s each, 3:3:3 H, 3′-, 4′- and 5′-C*H*$_3$), 0.94 (br, 3H, CH_2CH_3); $^{13}C\{^1H\}$ NMR ($CDCl_3$, 23 °C, 400 MHz): δ 334.47 (s, Cq, Cr=C), 224.76 and 217.24 (s each, Cq, 1:4, *trans*- and *cis*-CO, $Cr(CO)_5$), 151.03 and 139.15 (s each, Cq each, C=N, C3′ and C5′), 136.65 (s, Cq, C4), 135.94 (s, Cq, *i*-C of 4-Ph), 135.71 (s, CH, C3), 130.18 and 129.18 (each, 3:2 CH, 4-Ph), 116.71 (s, CH, C4′), 76.70 (s, O*C*H_2), 14.62 (s, 5′-*C*H_3), 12.85 (s, 3′-*C*H_3), 12.08 (s, CH_2CH_3), 8.84 (s, 4′-*C*H_3); IR (KBr) cm^{-1}: 2054.1 (80), 1982.0 (70), 1938.4 (100) [ν(C≡O)], 1608.5 (40), 1529.5 (80), 1481.2 (60) [ν(C=C, C=N)]. *Anal*. Calc. for $C_{22}H_{20}N_2O_6Cr$ (460.4): C, 57.39; H, 4.38; N, 6.08. Found: C, 55.89; H, 4.65; N, 6.08%.

*2-Ethoxy-4-phenyl-4-(3′,4′,5′-trimethylpyrazol-1′-yl)-1,1,1,1,1-pentacarbonyl-1-tungsta-1,3-butadiene (**4e**):* 23 °C, 2 h, 551 mg (93.0%). M.p. 104 °C; ^1H NMR ($CDCl_3$, 23 °C, 400 MHz): δ 7.43 (s, 1H, 3-H), 7.36 and 7.16 (m each, 3:2 H, 4-Ph), 4.45 (q, 2H, O*C*H_2), 2.21, 1.90 and 1.69 (s each, 3:3:3 H, 3′-, 4′- and 5′-C*H*$_3$), 0.89 (t, 3H, CH_2CH_3); $^{13}C\{^1H\}$ NMR ($CDCl_3$, 23 °C, 400 MHz): δ 306.69 (s, Cq, W=C), 204.11 and 197.56 (s each, Cq each, 1:4, *trans*- and *cis*-CO, $W(CO)_5$), 151.72 and 138.62 (s each, Cq, C=N, C3′ and C5′), 138.44 (s, CH, C3), 138.29 (s, Cq, C4), 136.23 (s, Cq, *i*-C of 4-Ph), 129.70, 129.56 and 128.53 (2:1:2, CH, 4-Ph), 116.52 (s, CH, C4′), 78.55 (s, O*C*H_2), 13.82 (s, 5′-*C*H_3), 12.33 (s, 3′-*C*H_3), 11.66 (s, CH_2CH_3), 8.30 (s, 4′-*C*H_3); IR (KBr) cm^{-1}: 2059.8 (40), 1939.3 (60), 1913.3 (70) [ν(C≡O)], 1604.7 (30), 1529.5 (40), 1481.2 (30) [ν(C=C, C=N)]. *Anal*. Calc. for $C_{22}H_{20}N_2O_6W$:

C, 44.62; H, 3.40; N, 4.73. Found: C, 44.72; H, 3.42; N, 4.67%.

*2-Ethoxy-4-phenyl-4-(3′,5′-dimethyl-4′-benzylpyrazol-1′-yl)-1,1,1,1,1-pentacarbonyl-1-chroma-1,3-butadiene (**3f**):* 23 °C, 10 h, 475 mg (88.5%). M.p. 97–98 °C; ^{1}H NMR ($CDCl_3$, 23 °C, 400 MHz): δ 7.59 (s, 1H, 3-H), 7.44 and 7.35 (br each, 3:2 H, 4-Ph), 7.26 and 7.19 (br each, 2:3 H, 4′-CH_2Ph), 4.70 (br, 2H, OCH_2), 3.78 (br, 2H, 4′-CH_2Ph), 2.23 and 1.81 (s each, 3:3 H, 3′- and 5′-CH_3), 1.03 (br, 3H, CH_2CH_3); ^{13}C{^{1}H} NMR ($CDCl_3$, 23 °C, 400 MHz): δ 334.57 (s, Cq, Cr=C), 224.18 and 216.64 (s each, Cq, 1:4, *trans*- and *cis*-CO, $Cr(CO)_5$), 150.52 and 140.07 (s each, Cq, C=N, C3′ and C5′), 139.43 (s, Cq, C4), 136.04 and 135.09 (s each, Cq each, *i*-C of Ph), 135.58 (s, CH, C3), 129.57, 128.71, 128.18 and 126.23 (aromatic CH of Ph), 119.14 (s, C4′), 76.25 (s, OCH_2), 29.51 (4′-CH_2Ph), 14.11 (s, 5′-CH_3), 12.54 (s, 3′-CH_3), 11.64 (s, CH_2CH_3); IR (KBr) cm^{-1}: 2059.8 (60), 1986.7 (60), 1939.3 (80), 1915.2 (90) [ν(C≡O)], 1560.3 (40), 1490.9 (30) [ν(C=C, C=N)]. *Anal.* Calc. for $C_{28}H_{24}N_2O_6Cr$: C, 62.68; H, 4.51; N, 5.22. Found: C, 62.37; H, 4.52; N, 5.14%.

*2-Ethoxy-4-phenyl-4-(3′,5′-dimethyl-4′-benzylpyrazol-1′-yl)-1,1,1,1,1-pentacar-bonyl-1-tungsta-1,3-butadiene (**4f**):* 23 °C, 4 h, 622 mg (93.1%). M.p. 110 °C; ^{1}H NMR ($CDCl_3$, 23 °C, 400 MHz): δ 7.52 (s, 1H, 3-H), 7.44 and 7.34 (m each, 3:2 H, 4-Ph), 7.24 and 7.16 (m each, 3:2 H, 4′-CH_2Ph), 4.53 (q, 2H, OCH_2), 3.77 (s, 2H, 4′-CH_2Ph), 2.20 and 1.76 (s each, 3:3 H, 3′- and 5′-CH_3), 0.97 (t, 3H, CH_2CH_3); ^{13}C{^{1}H} NMR ($CDCl_3$, 23 °C, 400 MHz): δ 307.00 (s, Cq, W=C), 204.12 and 197.55 (s each, Cq each, 1:4, *trans*- and *cis*-CO, $W(CO)_5$), 150.77 and 140.00 (s each, Cq each, C=N, C3′ and C5′), 139.48 (s, Cq, C4), 138.90 (s, CH, C3), 137.96 and 136.20 (s each, Cq, *i*-C of Ph), 129.66, 128.64, 128.18 and 126.26 (aromatic CH of Ph), 119.52 (s, C4′), 78.66 (s, OCH_2), 29.51 (4′-CH_2Ph), 13.87 (s, 5′-CH_3), 12.59 (s, 3′-CH_3), 11.79 (s, CH_2CH_3); IR (KBr) cm^{-1} : 2069.5 (80), 1986.7 (80), 1909.4 (100) [ν(C≡O)], 1560.3 (50), 1490.9 (40), 1446.5 (40) [ν(C=C, C=N)]. *Anal.* Calc. for $C_{28}H_{24}N_2O_6W$ (668.3): C, 50.32; H, 3.62; N, 4.19. Found: C, 50.37; H, 3.71; N, 4.17%.

*Crystallographic study of complexes **3a** and **4d**.* Single crystals were mounted on a glass fiber and sealed with epoxy glue. Diffraction measurements were made on a Bruker Smart diffractometer (graphite monochromated Mo Kα radiation, λ = 0.71073 Å) at 293 K. The crystal structures were solved by means of the program SHELXS-86 and refined by a full-matrix least-squares procedure on F^2 with the program SHELXL-97. Table 1 lists the crystal data and refinement details for complexes **3a** and **4d**. The selected bond lengths and angles are summarized in Tables 2 and 3. The molecular structures of **3a** and **4d** are given in Figs. 1 and 2.

Table 1
Crystal data and refinement details for complexes **3a** and **4d**

Complex	**3a**	**4d**
Empirical formula	$C_{20}H_{16}N_2O_6Cr$	$C_{27}H_{30}N_2O_6W$
Formula weight	432.35	662.38
T (K)	293(2)	293(2)
Crystal system	monoclinic	monoclinic
Space group	*P*2(1)/*c*	*C*2/*c*
a (Å)	9.255(1)	30.960(2)
b (Å)	13.542(1)	10.715(1)
c (Å)	16.563(1)	22.558(2)
α (°)	90	90
β (°)	103.3(2)	129.9(1)
γ (°)	90	90
V (Å^3)	2020.2(3)	5744.0(7)
Z	4	8
D_{calc} (g cm^{-3})	1.422	1.532
μ (mm^{-1})	0.605	4.062
F(000)	888	2624
Crystal size (mm)	0.37 × 0.37 × 0.27	0.51 × 0.50 × 0.27
θ limits (°)	1.96–28.30	1.71–28.31
Number of data collected	12127	16958
Number of unique data	4693	6657
R_{int}	0.0464	0.0839
Number of data observed [$I > 2\sigma(I)$]	4693	6657
Number of refined parameters	280	323
Goodness-of-fit	0.902	0.960
R (all data/observed data)	0.080/0.047	0.056/0.044
wR_2 (all data/observed data)	0.129/0.105	0.107/0.103
Residual ρ_{max} (ρ_{min}) (e Å^{-3})	0.357 (−0.254)	3.121 (−1.334)

Table 2
Selected bond lengths (Å) and angles (°) for complex **3a**

Cr–C(6)	2.057(3)
O(6)–C(6)	1.313(3)
C(6)–C(7)	1.456(4)
C(7)–C(8)	1.344(4)
C(8)–C(9)	1.474(4)
N(1)–C(8)	1.395(3)
N(1)–N(2)	1.375(3)
N(1)–C(17)	1.363(3)
N(2)–C(19)	1.321(3)
C(17)–C(18)	1.336(4)
C(18)–C(19)	1.418(4)
O(6)–C(6)–Cr	129.8(2)
C(7)–C(6)–Cr	121.4(2)
O(6)–C(6)–C(7)	108.8(2)
C(8)–C(7)–C(6)	128.6(3)
C(7)–C(8)–C(9)	127.0(2)
N(1)–C(8)–C(9)	113.1(2)
C(7)–C(8)–N(1)	119.8(2)
N(2)–N(1)–C(8)	121.1(2)
C(17)–N(1)–C(8)	127.7(3)
C(17)–N(1)–N(2)	111.1(2)
O(6)–C(6)–C(7)–C(8)	−12.1(4)
Cr–C(6)–C(7)–C(8)	169.4(2)
C(6)–C(7)–C(8)–N(1)	−178.9(3)
C(6)–C(7)–C(8)–C(9)	−1.3(5)
N(1)–C(17)–C(18)–C(19)	0.1(3)
N(1)–N(2)–C(19)–C(18)	0.0(3)
C(17)–C(18)–C(19)–N(2)	−0.1(3)

Table 3
Selected bond lengths (Å) and angles (°) for complex **4d**

W–C(6)	2.150(5)
O(6)–C(6)	1.332(6)
C(6)–C(7)	1.468(7)
C(7)–C(8)	1.342(7)
C(8)–C(9)	1.470(7)
N(1)–C(8)	1.405(6)
N(1)–N(2)	1.375(6)
N(1)–C(17)	1.374(6)
N(2)–C(19)	1.320(6)
C(17)–C(18)	1.358(8)
C(18)–C(19)	1.393(8)
O(6)–C(6)–W	132.2(3)
C(7)–C(6)–W	122.2(3)
O(6)–C(6)–C(7)	105.5(4)
C(8)–C(7)–C(6)	126.9(5)
C(7)–C(8)–C(9)	124.9(4)
N(1)–C(8)–C(9)	117.9(4)
C(7)–C(8)–N(1)	117.2(4)
N(2)–N(1)–C(8)	114.9(4)
C(17)–N(1)–C(8)	133.9(4)
C(17)–N(1)–N(2)	111.2(4)
O(6)–C(6)–C(7)–C(8)	44.0(6)
W–C(6)–C(7)–C(8)	−136.4(5)
C(6)–C(7)–C(8)–N(1)	−166.5(4)
C(6)–C(7)–C(8)–C(9)	10.1(8)
N(1)–C(17)–C(18)–C(19)	−0.2(6)
N(1)–N(2)–C(19)–C(18)	0.6(6)
C(17)–C(18)–C(19)–N(2)	−0.2(7)

4. Conclusion

(Pyrazolyl)alkenyl Fischer carbene complexes were synthesized from the reactions of 1-alkynyl Fischer carbene complexes $(CO)_5M{=}C(OEt)(C{\equiv}CPh)$ (M = Cr, W) with substituted pyrazoles under mild conditions. Transformation of these complexes into organic heterocyclic compounds are under way.

5. Supplementary material

The X-ray crystallographic files, in CIF format, are available from the Cambridge Crystallographic Data Centre on quoting the deposition numbers: CCDC 243529 for **3a** and CCDC 243528 for **4d**. Copies of this information may be obtained free of charge from The Director, CCDC, 12 Union Road, Cambridge CB2 IEZ, UK (fax: +44 1223 336 033; e-mail: deposit@ccdc.cam.ac.uk or www: http://www.ccdc.cam.ac.uk).

Acknowledgements

We are grateful for financial support from the Innovation Funding and the "Hundred Talented Program" Funding of the Chinese Academy of Sciences, P.R. China.

References

[1] E.O. Fischer, A. Maasböl, Angew. Chem. 76 (1964) 645.
[2] E.O. Fischer, A. Maasböl, Angew. Chem., Int. Ed. Engl. 3 (1964) 58.
[3] (a) For selected recent reviews, see J. Barluenga, J. Santamaría, M. Tomás, Chem. Rev. 104 (2004) 2259;
(b) J.W. Herndon, Coord. Chem. Rev. 243 (2003) 3;
(c) K.H. Dötz, C. Jakel, W.C. Haase, J. Organomet. Chem. 617–618 (2001) 119;
(d) J. Barluenga, J. Flórez, F.J. Fañanás, J. Organomet. Chem. 624 (2001) 5;
(e) M.A. Sierra, Chem. Rev. 100 (2000) 3591;
(f) A. de Meijere, H. Schirmer, M. Duetsch, Angew. Chem. Int. Ed. 39 (2000) 3964;
(g) J. Barluenga, F.J. Fañanás, Tetrahedron 56 (2000) 4597;
(h) J.W. Herndon, Tetrahedron 56 (2000) 1257;
(i) R. Aumann, Eur. J. Org. Chem. (2000) 17;
(j) K.H. Dötz, P. Tomuschat, Chem. Soc. Rev. 28 (1999) 187;
(k) W.D. Wulff, Organometallics 17 (1998) 3116;
(l) B. Alcaide, L. Casarrubios, G. Domínguez, M.A. Sierra, Curr. Org. Chem. 2 (1998) 551;
(m) L.S. Hegedus, Tetrahedron 53 (1997) 4105;
(n) R. Aumann, H. Nienaber, Adv. Organomet. Chem. 41 (1997) 163.
[4] E.O. Fischer, F.R. Kreissl, J. Organomet. Chem. 35 (1972) C47.
[5] (a) E.O. Fischer, H.J. Kalder, J. Organomet. Chem. 131 (1977) 57;
(b) L. Lattuda, E. Licandro, A. Papagni, S. Maiorana, A.C. Villa, C. Guastini, J. Chem. Soc., Chem. Commun. (1988) 1092;
(c) R. Aumann, P. Hinterding, Chem. Ber. 123 (1990) 611, 2047;
(d) R. Aumann, P. Hinterding, C. Krüger, P. Betz, Chem. Ber. 123 (1990) 1847;
(e) M. Duetsch, R. Lackmann, F. Stein, A. de Meijere, Synlett (1991) 324.
[6] F. Stein, M. Duetsch, R. Lackmann, M. Noltemeyer, A. de Meijere, Angew. Chem., Int. Ed. Engl. 30 (1991) 1658.
[7] M. Duetsch, F. Stein, R. Lackmann, E. Pohl, R. Herbst-Irmer, A. de Meijere, Chem. Ber. 125 (1992) 2051.
[8] F. Stein, M. Duetsch, E. Pohl, R. Herbst-Irmer, A. de Meijere, Organometallics 12 (1993) 2556.
[9] R. Pipoh, R. van Eldik, G. Henkel, Organometallics 12 (1993) 2236.
[10] R. Aumann, P. Hinterding, Chem. Ber. 126 (1993) 421.
[11] R. Pipoh, R. van Eldik, Organometallics 12 (1993) 2668.
[12] A. Rahm, W.D. Wulff, Organometallics 12 (1993) 597.
[13] F. Funke, M. Duetsch, F. Stein, M. Noltemeyer, A. de Meijere, Chem. Ber. 127 (1994) 911.
[14] R. Aumann, Chem. Ber. 127 (1994) 725.
[15] R. Aumann, B. Jasper, M. Läge, B. Krebs, Organometallics 13 (1994) 3502.
[16] J. Barluenga, M. Tomás, E. Rubio, J.A. López-Pelegrín, S. García-Granda, M.P. Priede, J. Am. Chem. Soc. 121 (1999) 3065.
[17] I. Fernández, M.A. Sierra, M.J. Mancheño, M. Gómez-Gallego, S. Ricart, Organometallics 20 (2001) 4304.
[18] A. Spinella, T. Caruso, U. Pastore, S. Ricart, J. Organomet. Chem. 684 (2003) 266.
[19] S. Radi, A. Ramdani, Y. Lekchiri, M. Morcellet, G. Crini, L. Janus, Tetrahedron 60 (2004) 939, and references therein.
[20] For selected recent reviews, see G. La Monica, G.A. Ardizzoia, Prog. Inorg. Chem. 46 (1997) 151.
[21] J.E. Cosgriff, G.B. Deacon, Angew. Chem., Int. Ed. Engl. 37 (1998) 286.
[22] C.T. Sirimanne, J.E. Knox, M.J. Heeg, H.B. Schlegel, C.H. Winter, J. Am. Chem. Soc. 125 (2003) 11152.

[23] J. Elguero, E. Gonzalez, R. Jacquier, Bull. Soc. Chim. Fr. (1968) 707.
[24] (a) K.S. Chan, W.D. Wulff, J. Am. Chem. Soc. 108 (1986) 5229; (b) R. Pipoh, P.P. Martinez, R. van Eldik, Ber. Bunsen-Ges. Phys. Chem. 97 (1993) 1435.
[25] (a) A. Hafner, L.S. Hegedus, G. de Weck, B. Hawkins, K.H. Dötz, J. Am. Chem. Soc. 110 (1988) 8413; (b) R. Aumann, Z.K. Yu, R. Fröhlich, F. Zippel, Eur. J. Inorg. Chem. (1998) 1623.
[26] D. Chamber, W.A. Denny, J. Org. Chem. 50 (1985) 4736.
[27] J.C. Jeffery, S.S. Kurek, J.A. McCleverty, E. Psillakis, R.M. Richardson, M.D. Ward, A. Wlodarczyk, J. Chem. Soc., Dalton Trans. (1994) 2559.

Available online at www.sciencedirect.com
SCIENCE DIRECT®
Polyhedron 24 (2005) 181–187
POLYHEDRON
www.elsevier.com/locate/poly

Silver(I) bis(1,2,4-triazolyl)borate complexes containing bidentate phosphine ligands

Giancarlo Gioia Lobbia [a], Maura Pellei [a,*], Claudio Pettinari [a], Carlo Santini [a], Brian W. Skelton [b], Allan H. White [b]

[a] *Dipartimento di Scienze Chimiche, Università degli Studi di Camerino, Via S. Agostino 1, 62032 Camerino MC, Italy*
[b] *Chemistry M313, The University of Western Australia, Crawley, WA 6009, Australia*

Received 8 October 2004; accepted 4 November 2004

Abstract

New silver(I) derivatives containing bidentate phosphine and anionic bis(triazol-1-yl)borate ligands have been prepared from the reaction of $AgNO_3$ and dppm (bis(diphenylphosphino)methane), dppe (1,2-bis(diphenylphosphino)ethane), or dppf (1,1′-bis(diphenylphosphino)ferrocene) and potassium dihydrobis(1,2,4-triazolyl)borate, $K[H_2B(tz)_2]$; their solid state and solution properties have been investigated through analytical and spectroscopic measurements (IR, ^1H and ^{31}P NMR). All the compounds are soluble in chlorinated solvents and are non-electrolytes in CH_2Cl_2 and acetone solutions. $[\{H_2B(tz)_2\}Ag(dppf)]$ is simple mononuclear array, the silver atom lying in four-coordinate N_2AgP_2 environment. In $[\{H_2B(tz)_2\}_2Ag_3(dppm)_2(NO_3)]$, the silver environment is still four-coordinate but $PAgN_3$, utilizing the coordinating capability of one of the additional ('exo'-) ring nitrogens not only to complete the four-coordinate array about the silver but, necessarily, to link successive asymmetric units into a single-stranded polymer. $[\{H_2B(tz)_2\}_2Ag_3(dppm)_2(NO_3)]$ may be regarded as a hemi-adduct of $[\{H_2B(tz)_2\}Ag(dppm)]$ with silver(I) nitrate, thus $[\{H_2B(tz)_2\}Ag(dppm)]$: $AgNO_3$ (2:1).
© 2004 Elsevier Ltd. All rights reserved.

Keywords: Scorpionate ligands; Triazole; Silver; Diphosphine ligands; X-ray crystal structure

1. Introduction

Since the pioneering work by Trofimenko [1], a very large number of papers has appeared describing the synthesis and the application of poly(pyrazolyl)borate, in an extraordinarily wide range of chemistry, from modelling the active site of metallo-enzymes, through analytical chemistry and organic synthesis, to catalysis and materials science [2]. By contrast, only a few poly(azolyl)borate complexes with azolyl groups other than pyrazole have been investigated, although it has been shown that the chemistry of poly(azolyl)borate complexes may be critically dependent on the pattern of ring substitution [3]. This aspect has induced several researchers to study the behaviour of metal complexes of analogous ligand systems with modified steric and/or electronic properties, such as poly(tetrazolyl)borate [4], poly(1,2,3-benzotriazolyl)borate [5], poly(2-sulfanyl-1-methylimidazolyl)borate [6] and poly(imidazolyl)borate ligands [7]. These modifications have led to new scorpionates capable of bridging different metal centers, yielding dimers or coordination polymers characterized by peculiar spectroscopic and structural features. Two features of triazole-based ligands make them attractive candidates for further examination: (i) they should be electron-withdrawing relative to their pyrazole-based counterparts so that the properties of metal complexes should differ accordingly [8]; (ii) the *exo* ring-nitrogen

* Corresponding author. Tel: +39 0737 402213; fax: +39 0737 637345.
E-mail address: maura.pellei@unicam.it (M. Pellei).

0277-5387/$ - see front matter © 2004 Elsevier Ltd. All rights reserved.
doi:10.1016/j.poly.2004.11.001

atoms of triazole-based ligands may bridge between metal centers, thereby creating coordination polymers with interesting solid-state structures and optical properties, as recently shown by Janiak et al. [9]. Moreover, the exocyclic nitrogen atoms might take part in hydrogen-bond interactions assisting the formation of two-dimensional water-intercalate or water-layer clathrates [10], thus leading to water soluble species [11].

As part of this study, we have been interested in complexes incorporating poly(azolyl)borate and phosphine ligands with different steric and electronic profiles. The different coordination characteristics of poly(triazolyl)borate species offer the prospect of new and interesting chemistry, paralleling that of pyrazolyl and imidazolyl arrays [12]. In our research concerning modifications of the poly(pyrazolyl)borate ligands in which the pyrazolyl rings are replaced by 1,2,4-triazolyl or imidazolyl rings, some interesting single strand silver(I) coordination polymers containing bridging poly(1-imidazolyl) borates have been reported [13].

We have also previously reported that the substitution of triazole for pyrazole in poly(pyrazolyl)alkanes to form poly(triazolyl)alkanes as bis(1,2,4-triazolyl)alkane ligand, extends the capability to coordinate silver(I) salts through the additional nitrogen atoms yielding two- and three-dimensional coordination polymers [14].

We have now decided to extend this work by reporting the synthesis, characterization and reactivity of some new metal complexes obtained from the interaction of dihydrobis(1,2,4-triazolyl)borate, $[H_2B(tz)_2]^-$ (Fig. 1), with $AgNO_3$ and diphosphines, together with the crystal and molecular structures of some representative arrays as determined by X-ray diffraction studies.

2. Experimental

2.1. Materials and methods

All syntheses and handling were carried out under an atmosphere of dry oxygen-free dinitrogen, using standard Schlenk techniques or a glove box. All solvents were dried, degassed and distilled prior to use. All chemicals were purchased from Aldrich and used without further purification. The potassium salt of the donor dihydrobis(1,2,4-triazolyl)borate, $[H_2B(tz)_2]^-$ was prepared in accordance with the procedure first reported by Trofimenko [1]. KBH_4, $AgNO_3$, dppm, dppe, dppf and 1,2,4-triazole were purchased from Aldrich and used without further purification. Elemental analyses (C, H and N) were performed in-house with a Fisons Instruments 1108 CHNS-O Elemental Analyser. IR spectra were recorded from 4000 to 100 cm^{-1} with a Perkin–Elmer System 2000 FT-IR instrument. ^1H and ^{13}P NMR spectra were recorded on a VXR-300 Varian spectrometer (300 MHz for ^1H and 121.4 MHz for ^{31}P). The electrical resistances of acetone, DMSO and CH_2Cl_2 solutions were measured with a Crison CDTM 522 conductimeter at room temperature.

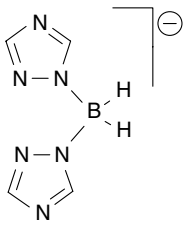


Fig. 1. Structure of the bis(triazolyl)borate ligand.

2.1.1. Syntheses of complexes

*2.1.1.1. [{$H_2B(tz)_2$}Ag(dppm) (**1**).* $K[H_2B(tz)_2]$ (0.188 g, 1.0 mmol) was added at room temperature to a methanol solution (50 ml) of $AgNO_3$ (0.170 g, 1.0 mmol) and $(PPh_2)_2CH_2$ (0.384 g, 1.0 mmol). After the addition, the solution was stirred for 2 h and subsequently the solvent was removed with a rotary evaporator. Chloroform (50 ml) was added. The suspension was filtered and the organic layer was dried over Na_2SO_4, filtered and concentrated under reduced pressure. A colourless precipitate was formed, which was filtered off and washed with diethylether. Re-crystallization from diethylether (1:2) gave complex **1** as a micro-crystalline solid in 60% yield. m.p. 161–163 °C. ^1H NMR ($CDCl_3$, 293 K): δ 3.0 (s br, 2H, C*H*$_2$), 6.97–7.20 (m, 20H, C*H*), 7.44 (s, 2H, 3- or 5-C*H*), 8.07 (s, 2H, 3- or 5-C*H*). $^{31}P\{^1H\}$ NMR ($CDCl_3$, 293 K): δ 3.90 (m, $^1J(^{13}P, Ag) = 330$ Hz; $^{31}P\{^1H\}$ NMR ($CDCl_3$, 218 K): δ 3.56 (m, $^1J(^{13}P, Ag) = 435$ Hz. IR (nujol, cm^{-1}): 3045w (CH), 2430w, 2405m (BH), 1498s (C=C + C=N), 515m, 504m, 473br, 438br, 412br (Ar_3P), 348w. *Anal.* Calc. for $C_{29}H_{28}AgBN_6P_2$: C, 54.32; H, 4.40; N, 13.11. Found: C, 54.64; H, 4.60; N, 13.07%.

*2.1.1.2. [{$H_2B(tz)_2$}$_2$$Ag_3$(dppm)$_2$($NO_3$)]($H_2O$)$_{0.5}$ (**2**).* Compound **2** was prepared similarly to compound **1**, by using $AgNO_3$ (0.255 g, 1.5 mmol), $(PPh_2)_2CH_2$ (0.384 g, 1.0 mmol) and $K[H_2B(tz)_2]$ (0.188 g, 1.0 mmol) in methanol solution (50 ml). Re-crystallisation from dichloromethane gave complex **2** as a micro-crystalline solid in 50% yield. m.p. 160 °C dec. ^1H NMR ($CDCl_3$, 293 K): δ 3.0 (s br, 2H, C*H*$_2$), 6.97–7.20 (m, 20H, C*H*), 7.44 (s, 2H, 3- or 5-C*H*), 8.07 (s, 2H, 3- or 5-C*H*). $^{31}P\{^1H\}$ NMR ($CDCl_3$, 293 K): δ −2.4 (d br $^1J(^{31}P, Ag) = 433$ Hz), 3.90 (m, $^1J(^{13}P, Ag) = 330$ Hz; $^{31}P\{^1H\}$ NMR ($CDCl_3$, 218 K): δ 3.56 (m, $^1J(^{31}P, Ag) = 435$ Hz. IR (nujol, cm^{-1}): 3370 (OH), 3045w (CH), 2430w, 2405m (BH), 1964br, 1895br, 1824wbr, 1732w br (NO_3), 1498s (C=C + C=N), 515m, 504m, 473br, 438br, 412br, 399m, 375m, 351w, 325w, 302w, 278w (Ar_3P), 348w. *Anal.* Calc. for $C_{58}H_{57}Ag_3B_2N_{13}O_{0.5}P_4$:

C, 54.32; H, 4.40; N, 13.11. Found: C, 53.64; H, 4.60; N, 12.67%.

*2.1.1.3. [{$H_2B(tz)_2$}$_2Ag_2(dppe)$] (**3**).* K[$H_2B(tz)_2$] (0.188 g, 1.0 mmol) was added at room temperature to a methanol solution (50 ml) of $AgNO_3$ (0.170 g, 1.0 mmol) and $(PPh_2)_2C_2H_4$ (0.398 g, 1.0 mmol). After the addition, the solution was stirred for 2 h. The colourless precipitate obtained was filtered off and washed with methanol. Re-crystallisation from methanol gave complex **3** as a micro-crystalline solid in 56% yield. mp 130–133 °C. ^{1}H NMR ($CDCl_3$, 293K): δ 2.48 (s, 4H, CH_2), 7.37-7.78 (m, 20H, C*H*), 7.69 (s, 4H, 3- or 5-C*H*), 8.14 (s, 4H, 3- or 5-C*H*). ^{31}P{^{1}H} NMR ($CDCl_3$, 293K): δ 11.05 (d, $^1J(^{13}P, Ag) = 604$ Hz). ^{31}P{^{1}H} NMR ($CDCl_3$, 218K): δ 10.2 (d, $^1J(^{31}P, Ag) = 600$ Hz). IR (nujol, cm^{-1}): 3098w (CH), 2411m (BH), 1514m, 1501m (C═C + C═N), 512s, 474m, 421w (Ar_3P), 343w. *Anal.* Calc. for $C_{34}H_{36}Ag_2B_2N_{12}P_2$: C, 44.78; H; 3.98; N, 18.43. Found: C, 45.23; H, 3.67; N, 17.96%.

*2.1.1.4. [{$H_2B(tz)_2$}$Ag(dppf)$] (**4**).* Compound **4** was prepared similarly to compound **3**, by using $AgNO_3$ (0.170 g, 1.0 mmol), $(PPh_2)_2(C_5H_4)_2Fe$ (0.544 g, 1.0 mmol) and K[$H_2B(tz)_2$] (0.188 g, 1.0 mmol) in methanol solution (50 ml). Re-crystallisation from methanol gave complex **4** as a micro-crystalline solid in 77% yield. m.p. 209–211 °C. ^{1}H NMR ($CDCl_3$, 293.K): δ 4.24 (s, 4H, C*H*), 4.36 (s, 4H, C*H*), 7.29–7.50 (m, 22H, C*H* and 3- or 5-C*H*), 8.17 (s, 2H, 3- or 5-C*H*). ^{31}P{^{1}H} NMR ($CDCl_3$, 293K): δ −5.18 (dd, $^1J(^{31}P,^{107}Ag) = 361$ Hz, $^1J(^{31}P,^{109}Ag) = 415$ Hz). IR (nujol, cm^{-1}): 3039w (CH), 2399m (BH), 1492s (C═C + C═N), 533m, 516m, 487s, 460s, 442m, 425m (Ar_3P), 350w. *Anal.* Calc. for $C_{38}H_{34}AgBFeN_6P_2$: C, 56.26; H, 4.22; N, 10.36. Found: C, 55.88; H, 4.46; N, 10.33%.

2.2. Structure determinations

Full spheres of 'low'-temperature CCD area-detector diffractometer data were measured (Bruker AXS instrument, ω-scans; monochromatic Mo Kα radiation, $\lambda = 0.71073$ Å, T ca. 153 K) yielding $N_{(total)}$ reflections, these merging to N unique (R_{int} cited) after 'empirical'/multiscan absorption correction (proprietary software), N_o with $F > 4\sigma(F)$ considered 'observed' and used in the full-matrix least squares refinements, refining anisotropic displacement parameter forms for the non-hydrogen atoms, (x, y, z, $U_{iso})_H$ being constrained at estimates. Conventional residuals R, R_w (weights: $(\sigma^2(F) + 0.000n_wF^2)^{-1}$) are quoted at convergence; neutral atom complex scattering factors were employed within the context of the XTAL 3.7 program system [15]. Pertinent results are given below and in the tables and figures, the latter showing 50% probability amplitude displacement envelopes for the non-hydrogen atoms, hydrogen atoms where shown having arbitrary radii of 0.1 Å.

3. Results and discussion

3.1. Syntheses

The interaction between $AgNO_3$, K[$H_2B(tz)_2$] and equimolar quantity of diphosphine ligand L in methanol at room temperature readily gave the complexes **1**, **3** and **4** in good yields, in accordance with the following general equation:

$$2K[H_2B(tz)_2] + 2AgNO_3 + xL \rightarrow x[\{H_2B(tz)_2Ag\}_y(L)] + 2KNO_3 \quad (1)$$

1: L = dppm, $x = 2$, $y = 1$;

3: L = dppe, $x = 1$, $y = 2$;

4: L = dppf, $x = 2$, $y = 1$.

It is noteworthy that when the reaction between $AgNO_3$, dppm and K[$H_2B(tz)_2$] was carried out in the presence of an excess of $AgNO_3$, the derivative [{$H_2B(tz)_2$}$_2Ag_3$-(dppm)$_2$(NO_3)](H_2O)$_{0.5}$ (**2**) is obtained, which could be considered as a hemi-adduct of [{$H_2B(tz)_2$}Ag(dppm)] (**1**) with silver(I) nitrate.

All of the colourless compounds **1**–**4** are soluble in $CHCl_3$, acetone and DMSO, in which, with exception of **2**, are non-electrolytes.

3.2. Spectroscopy

The IR spectra (see Section 2) show all the bands expected by the presence of the organic nitrogen donor and the phosphine ligand. For the derivatives of $H_2B(tz)_2$ **1**–**4** the BH stretches generally appear as a series of broad peaks in the expected regions (2399–2430 cm^{-1}). Upon coordination these bands are slightly shifted to higher frequency with respect to the same absorptions observed for free dihydrobis(1,2,4-triazolyl)borate ligands [10]. In the far IR spectra of all the derivatives, we have assigned, on the basis of a previous report on phosphino silver(I) complexes, the broad absorptions near 500 cm^{-1} and those at ca. 450 cm^{-1} to Whiffen's y and t vibrations [16]. In some cases, weak to medium bands at ca. 300 cm^{-1} appeared, similar to those described for silver-azolato complexes [17], which are tentatively assigned to ν(Ag–N) stretching vibrations.

The room temperature proton spectra of **1**–**4** in $CDCl_3$ (see Section 2) are very similar to each other and also to the potassium salt of bis-(1,2,4-triazolyl)borate in respect of their chemical shifts [18].

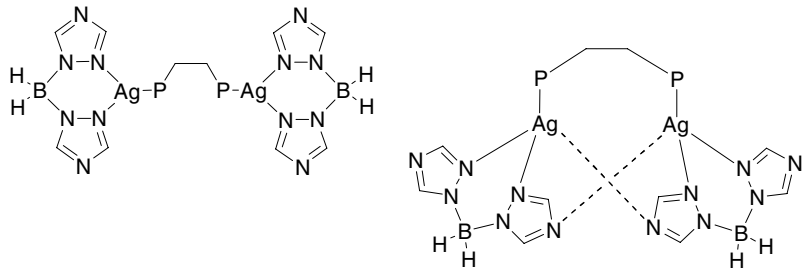


Fig. 2. Hypothetical structures for the dppe adduct **3**.

The BH signal was not observed in any case, presumably due to broadening of the resonance in consequence of quadrupolar coupling and relaxation effects from the boron atom [19].

Compound **1** may have a dinuclear $[Ag(dppm)]_2$ core analogous to that found in other dppm compounds, not only in the solid state but also in solution [20]. The ^{31}P NMR spectra of **1** support this finding. A double triplet has been observed at room temperature whereas the low temperature ^{13}P spectrum consists of an AA′XX′A″A* pattern [21], presumably due to the non-equivalence of the phosphorus atoms in perturbed $[AgX(dppm)]_2$ systems [20].

The δ and the coupling constant values found for the derivative **3** are typical of silver(I) species in AgN_2P or AgN_3P environments [22] suggesting a bridging coordination mode for the dppe ligand (Fig. 2), as expected on the basis of the stoichiometry, but not excluding a bridging coordination also of the $H_2B(tz)_2$ ligand.

Table 1
Crystal/refinement data

Compound[a]	**2**[b] $[L_2Ag_3(dppm)_2](NO_3)$ $1/2H_2O$	**4** [LAg(dppf)]
Formula	$C_{58}H_{57}Ag_3B_2N_{13}O_{7/2}P_4$	$C_{38}H_{34}AgBFeN_6P_2$
M_r	1461.3	811.2
Crystal system	triclinic	triclinic
Space group	$P\bar{1}$ (#2)	$P\bar{1}$ (#2)
a (Å)	10.844(2)	10.6069(6)
b (Å)	13.478(2)	12.8139(9)
c (Å)	21.706(4)	15.3718(9)
α (°)	107.300(3)	69.766(1)
β (°)	96.878(3)	71.458(1)
γ (°)	96.639(3)	66.926(1)
V (Å^3)	2969	1763
D_c (g cm^{-3})	1.63_5	1.52_8
Z (f.u.)	2	2
μ_{Mo} (mm^{-1})	1.15	1.10
Specimen (mm)	$0.10 \times 0.09 \times 0.07$	$0.26 \times 0.24 \times 0.09$
'T'$_{min/max}$	0.85	0.85
$2\theta_{max}$ (°)	53	75
N_t	27 127	36 324
$N(R_{int})$	11 876 (0.050)	18 063 (0.020)
N_o	8290	14 620
R	0.045	0.035
$R_w(n_w)$	0.050(5)	0.043(2)

[a] L = $H_2B(tz)_2$.

[b] Difference map residues were modelled as water molecule oxygen atoms, the site occupancy of that in **2** being set at 0.5 after trial refinement.

3.3. Structure determinations

The results of the 'low'-temperature single crystal X-ray structure determinations are consistent with the above stoichiometries. The $H_2B(tz)_2$ ligand although exhibiting diverse hapticities, in all cases exhibits a chelate interaction with a silver atom through N(11,21), forming a six-membered ring with a 'boat' conformation, B and Ag at the prows, the latter the 'flatter' of the two (Table 1), although there are considerable diversities in detail among the various torsion components for the different complexes. Complex **4** is a simple mononuclear array, the silver atoms lying in four-coordinate N_2AgP_2 environments (Fig. 3). As usual in such species, the Ag–P distances are remarkably constant across a diversity of angular parameters, in particular, that imposed by ligand 'bite' in **4** (Tables 2 and 3), and in all cases P–Ag–N angles span a range of over 20°, with similar diversity in Ag–N, despite a constant N^N 'bite' angle. In each of these cases, one formula unit (devoid of

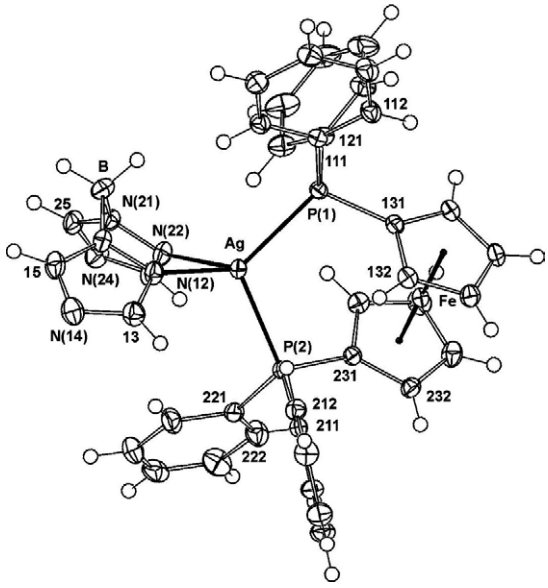


Fig. 3. The mononuclear array of **4**.

Table 2
$H_2B(tz)_2$ descriptors

Compound(/ligand)	**4**	**2**/1,2
Angles (°)		
N(11)–B–N(21)	107.8(1)	109.5(4), 111.1(5)
Chelate ring torsion angles (°)		
N(22)–Ag–N(12)–N(11)	−28.2(1)	13.4(4), −0.2(4)
N(12)–Ag–N(22)–N(21)	35.2(1)	−19.6(4), 3.0(4)
Ag–N(12)–N(11)–B	−17.1(2)	24.8(6), 33.2(6)
Ag–N(22)–N(21)–B	3.6(2)	−13.0(7), −38.9(6)
N(12)–N(11)–B–N(21)	72.0(2)	−64.2(2), −71.6(6)
N(22)–N(21)–B–N(11)	−61.7(2)	57.1(7), 75.5(6)
Interplanar dihedral angles (°)		
θ	70.46(7)	50.3(2), 59.3(2)
Out-of-plane silver atom deviations (Å)		
Ring 1	0.692(3)	0.638(9), 1.047(9)
Ring 2	0.192(3)	0.233(9), 1.257(9) −0.117(9)[a], 2.416(10)[b],

[a] Ag(2) (ring 2).
[b] Ag(3) (ring 2).

Table 3
The silver environment in compound **4**

Distances (Å)	
Ag–N(12)	2.307(1)
Ag–N(22)	2.389(2)
Ag–P(1)	2.4350(5)
Ag–P(2)	2.4634(3)
Angles (°)	
N(12)–Ag–N(22)	84.58(6)
N(12)–Ag–P(1)	123.03(4)
N(12)–Ag–P(2)	116.01(3)
N(22)–Ag–P(1)	116.44(4)
N(22)–Ag–P(2)	100.07(3)
P(1)–Ag–P(2)	111.40(2)
Phosphine Ag–P–C–C (acute) torsion angles	
(Ring) 11n	−30.3(1)
12n	−1.8(1)
13n	−43.9(1)
21n	−9.5(2)
22n	−50.9(1)
23n	−37.1(2)

crystallographic symmetry) comprises the asymmetric unit of the structure.

The last statement is also true of **2**, where the stoichiometry is different, and where difference map residues have been modelled in terms of included solvent. This complex contains three independent silver atoms and may be regarded as a hemi-adduct of [{$H_2B(tz)_2$}Ag (dppm)] (1:1) with silver(I) nitrate, thus {$H_2B(tz)_2$}Ag:- dppm:$AgNO_3$ (2:2:1), one such formula unit, devoid of crystallographic symmetry, comprising the asymmetric unit of the structure (Fig. 4). The complex may be viewed even more appropriately as {$H_2B(tz)_2$}Ag: dppm (2:1)/$AgNO_3$:dppm (1:1). Ag(3) lies close to a crystallographic inversion centre and is linked to its inversion image by a pair of symmetry related bridging dppm ligands, an *O*-nitrato group pendent from each silver atom, thus [(O_2NO)Ag(*P*-dppm-*P*)$_2$Ag(ONO_2)], an array familiar in numerous 1:1 dppm adducts of silver(I) oxyanion salts. In the nitrate adduct of this type, in particular, the form taken is [(ONO_2)Ag(*P*-dppm-*P*)$_2$Ag(O_2NO)]; in the present complex the remainder of the structure impacts by supplanting of one of the chelating nitrato oxygen donors (N(24)) by an exo-nitrogen of a triazine ring, the association of the oxygen in the four-coordinate array about the silver becoming tenuous (Table 4). The second $H_2B(tz)_2$ ligand is associated solely with Ag(2) as a chelate, without further exocyclic interactions. The other diphosphine ligand bridges Ag(1) and Ag(2) which are then bridged further afield by the first $H_2B(tz)_2$ ligand, forming a centrosymmetric 16-membered metallacycle (Fig. 5).

Thus, whereas one $H_2B(tz)_2$ ligand is associated exclusively with Ag(2) as a chelate, the other $H_2B(tz)_2$ ligand not only chelates Ag(1), but its additional 'exo'-nitrogen atoms function as donors, the N(14) enabling the formation of the macro-metallacycle, and the N(24) linking these to the binuclear centrosymmetric eight-membered rings, formed by the second diphosphine ligand and the Ag(3), the totality of the array being a one-dimensional polymer. It should be noted that the Ag(1) are three-coordinate (PAgNP′), the array being essentially planar (angle sum 359.7°) (see Fig. 4).

Table 4
The silver environments in **2**

Atoms	Parameters	Atoms	Parameters
Distances (Å)			
Ag(1)–N(12)	2.273(4)	Ag(2)–N(14)	2.310(5)
Ag(1)–N(22)	2.228(5)	Ag(2)–N(32)	2.390(4)
Ag(1)–P(1)	2.340(2)	Ag(2)–N(42)	2.435(6)
Ag(3)–P(3)	2.435(2)	Ag(2)–P(2^i)	2.368(1)
Ag(3)–P(4^{ii})	2.410(2)	Ag(1)···Ag(2^i)	3.9143(8)
Ag(3)–N(24)	2.456(5)	Ag(3)···Ag(3^{ii})	3.5214(9)
Ag(3)–O(1)	2.654(5)	P(1)···P(2)	3.027(2)
		P(3)···P(4)	3.034(2)
Angles (°)			
P(1)–Ag(1)–N(12)	133.5(1)	P(2^i)–Ag(2)–N(14)	141.8(1)
P(1)–Ag(1)–N(22)	138.3(1)	P(2^i)–Ag(2)–N(32)	117.4(1)
N(12)–Ag(1)–N(22)	87.9(2)	P(2^i)–Ag(2)–N(42)	120.0(1)
P(3)–Ag(3)–P(4^{ii})	153.18(6)	N(14)–Ag(2)–N(32)	88.3(2)
N(24)–Ag(3)–P(3)	94.8(1)	N(14)–Ag(2)–N(42)	85.1(2)
N(24)–Ag(3)–P(4^{ii})	94.8(1)	N(32)–Ag(2)–N(42)	90.3(2)
O(1)–Ag(3)–N(24)	102.0(2)	P(1)–C(10)–P(2)	110.5(2)
O(1)–Ag(3)–P(3)	80.2(1)	P(3)–C(20)–P(4)	111.2(3)
O(1)–Ag(3)–P(4^{ii})	122.0(1)	Ag–O(1)–N	132.7(4)

Transformations of the asymmetric unit: $^i\bar{x},1-y,\bar{z}$; $^{ii}\bar{x},1-y,1-z$.

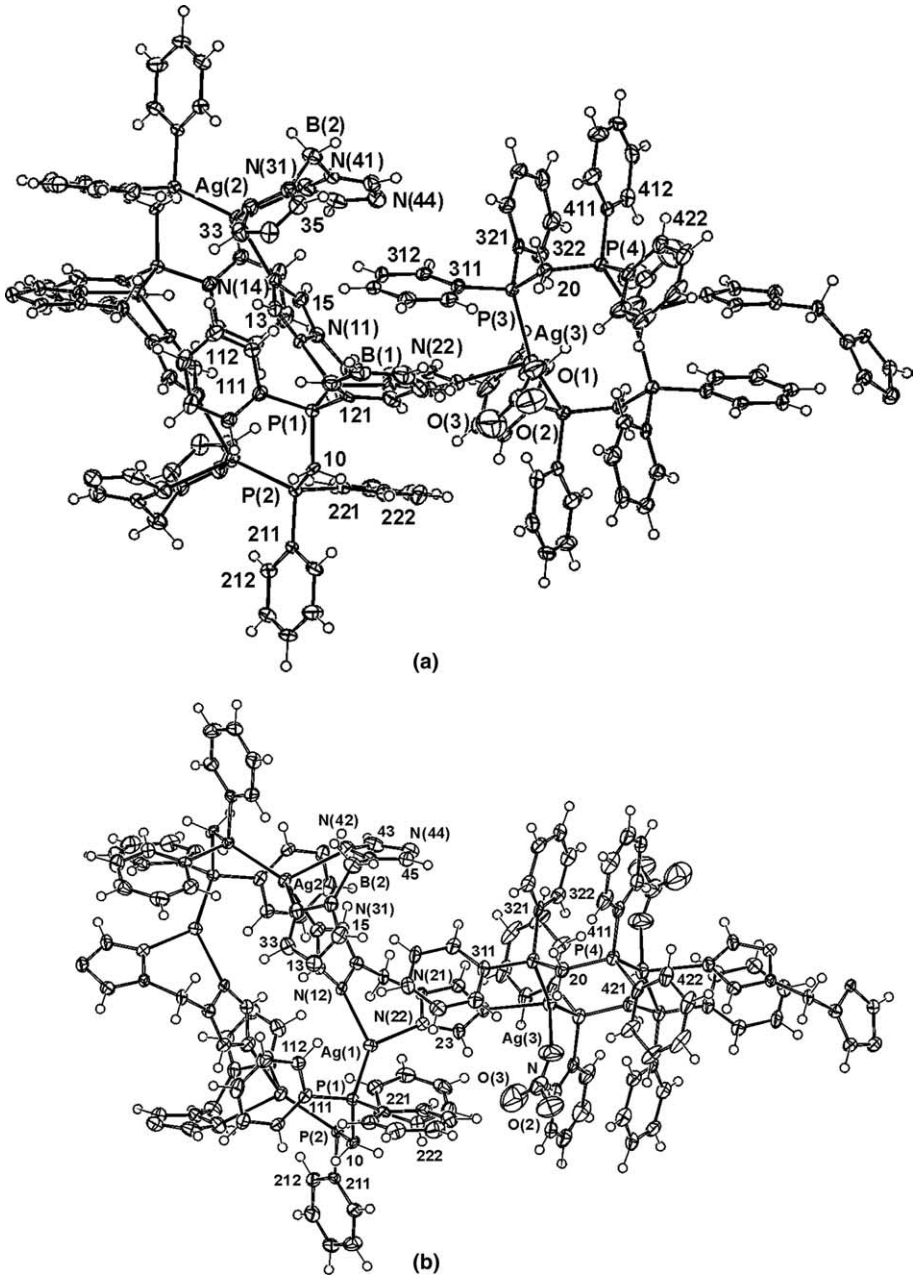


Fig. 4. (a,b) Two views of the single-stranded polymer of **2** (the polymer axis horizontal in the page) showing the alternating eight- and 16-membered metallacycle components.

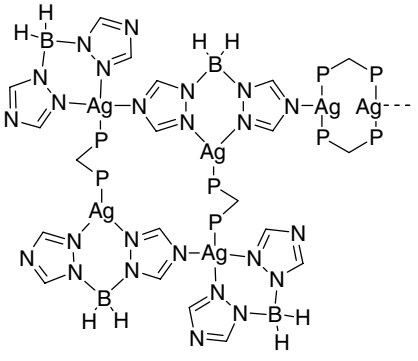


Fig. 5. The centrosymmetric 16-membered metallacycle of **2**.

4. Conclusions

We have here reported the synthesis, spectroscopic and structural characterization of new silver(I) derivatives containing bidentate phosphines and anionic bis(triazol-1-yl)borate ligand and demonstrated the formation of different types of complexes depending on the reaction conditions and nature (basicity and steric hindrance) of the ancillary phosphine ligands. From the interaction of $K[H_2B(tz)_2]$ with diphosphine ligands we have obtained simple mononuclear arrays (L = dppf), (likely) dimeric structures (L = dppe or dppm) or

hemi-adducts of [{$H_2B(tz)_2$}AgL] with silver(I) nitrate (L = dppm).

5. Supporting information available

X-ray crystallographic files, in CIF format, for the structure determinations of **2** and **4** have been deposited with the Cambridge Crystallographic Data Centre, CCDC: 236838 and 236841. Copies of this information may be obtained free of charge from The Director, CCDC, 12 Union Road, Cambridge, CB2 1EZ (fax: +44 1223 336033; e-mail: deposit@ccdc.cam.uk or at www: http://www.ccdc.cam.ac.uk).

Acknowledgements

We are grateful to Unicam (FAR, Progetto Strategico di Ricerca di Ateneo), Fondazione CARIMA, and INTAS (00-469) for funding support.

References

[1] S. Trofimenko, J. Am. Chem. Soc. 88 (1966) 1842.
[2] (a) S. Trofimenko, Scorpionates: The Coordination Chemistry of Polypyrazolylborate Ligand, Imperial College Press, Imperial College Press, London, 1999;
(b) S. Trofimenko, Chem. Rev. 93 (1993) 943.
[3] T. Desmond, F.J. Lalor, G. Ferguson, B. Ruhl, M. Parvez, J. Chem. Soc., Chem. Commun. (1983) 55.
[4] (a) C. Janiak, T.G. Scharmann, T. Bräuniger, J. Holubová, M. Nádvorník, Z. Anorg. Allg. Chem. 624 (1998) 769;
(b) C. Janiak, T.G. Scharmann, J.C. Green, R.P.G. Parkin, M.J. Kolm, E. Riedel, W. Mickler, J. Elguero, R.M. Claramunt, D. Sanz, Chem. Eur. J. 2 (1996) 992.
[5] (a) F. Lalor, S.M. Miller, N. Garvey, J. Organomet. Chem. 356 (1988) C57;
(b) F. Lalor, S.M. Miller, N. Garvey, Polyhedron 9 (1990) 63;
(c) K.-B. Shiu, F.-M. Shen, S.-L. Wang, S.-C. Wei, J. Organomet. Chem. 372 (1989) 251;
(d) P. Cecchi, G. Gioia Lobbia, D. Leonesi, C. Pettinari, C. Sepe, V. Vinciguerra, Gazz. Chim. Ital. 123 (1993) 569;
(e) S. Anderson, A. Harman, A.F. Hill, J. Organomet. Chem. 498 (1995) 251;
(f) J. Cartwright, A. Harman, A.F. Hill, J. Organomet. Chem. 396 (1990) C31.
[6] (a) C. Santini, G. Gioia Lobbia, C. Pettinari, M. Pellei, G. Valle, S. Calogero, Inorg. Chem. 37 (1998) 890;
(b) A.F. Hill, G.R. Owen, A.J.P. White, D.J. Williams, Angew. Chem., Int. Ed. 38 (1999) 2759;
(c) P.A. Slavin, J. Reglinski, M.D. Spicer, A.R. Kennedy, J. Chem. Soc., Dalton Trans. (2000) 239;
(d) C. Santini, C. Pettinari, G. Gioia Lobbia, R. Spagna, M. Pellei, F. Vallorani, Inorg. Chim. Acta 285 (1999) 81;
(e) C. Kimblin, B.M. Bridgewater, T. Hascall, G. Parkin, J. Chem. Soc., Dalton Trans. (2000) 891.
[7] (a) S. Trofimenko, J. Am. Chem. Soc. 89 (1967) 3903;
(b) G.J.A.A. Koolhaas, W.L. Driessen, J. Reedijk, H. Kooijman, A.L. Spek, J. Chem. Soc., Chem. Commun. (1995) 517;
(c) R. Gregorzik, U. Hartmann, H. Vahrenkamp, Chem. Ber. 127 (1994) 2117;
(d) U. Hartmann, R. Gregorzik, H. Vahrenkamp, Chem. Ber. 127 (1994) 2123;
(e) W.E. Lynch, D.M. Kurtz, S. Wang, R.A. Scott, J. Am. Chem. Soc. 116 (1994) 11030;
(f) S. Chen, J.F. Richardson, R.M. Buchanan, Inorg. Chem. 33 (1994) 2376;
(g) W. Klaui, C. Piefer, G. Rheinwald, H. Lang, Eur. J. Inorg. Chem. 1549 (2000);
(h) C. Kimblin, B.M. Bridgewater, D.G. Churchill, G. Parkin, J. Chem. Soc., Dalton Trans. (2000) 2191.
[8] (a) Z. Xiao, R.W. Gable, A.G. Wedd, C.G. Young, J. Chem. Soc., Chem. Commun. (1994) 1295;
(b) I.T. Macleod, E.R.T. Tiekink, C.G. Young, J. Organomet. Chem. 506 (1996) 301;
(c) K.-B. Shiu, J.Y. Lee, Y. Wang, M.-C. Cheng, S.-L. Wang, F.-L. Liao, J. Organomet. Chem. 453 (1993) 211.
[9] (a) C. Janiak, T.G. Scharmann, P. Albrecht, F. Marlow, R. MacDonald, J. Am. Chem. Soc. 118 (1996) 6307;
(b) C. Janiak, S. Temizdemir, T.G. Scharmann, A. Schmalstieg, J. Demtschuk, Z. Anorg. Allg. Chem. 626 (2000) 2053.
[10] (a) I. Goldberg, Top. Curr. Chem. 149 (1988) 2;
(b) F.H. Herbstein, Top. Curr. Chem. 140 (1987) 107;
(c) C. Janiak, J. Chem. Soc., Chem. Commun. (1994) 545.
[11] (a) F.T. Edelmann, Angew. Chem. Int. Ed. 40 (2001) 1656;
(b) B.E. Hanson, Coord. Chem. Rev. 185–186 (1999) 795;
(c) N. Navon, H. Cohen, P. Paoletti, B. Valtancoli, A. Bencini, D. Meyerstein, Ind. Eng. Chem. Res. 39 (2000) 3536.
[12] G. Gioia Lobbia, M. Pellei, C. Pettinari, C. Santini, B.W. Skelton, N. Somers, A.H. White, J. Chem. Soc., Dalton Trans. (2002) 2333.
[13] Effendy, G. Gioia Lobbia, M. Pellei, C. Pettinari, C. Santini, B.W. Skelton, A.H. White, J. Chem. Soc., Dalton Trans. (2001) 528.
[14] Effendy, F. Marchetti, C. Pettinari, R. Pettinari, B.W. Skelton, A.H. White, Inorg. Chem. 42 (2003) 112.
[15] S.R. Hall, D.J. du Boulay, R. Olthof-Hazekamp (Eds.), The XTAL 3.7. System, University of Western Australia, 2001.
[16] (a) G.B. Deacon, R.A. Jones, Aust. J. Chem. 16 (1963) 499;
(b) K. Shobatake, C. Postmus, J.R. Ferraro, K. Nakamoto, Appl. Spectrosc. 12 (1969) 23.
[17] (a) B.C. Cornilsen, K. Nakamoto, J. Inorg. Nucl. Chem. 36 (1974) 2467;
(b) C. Pettinari, F. Marchetti, A. Lorenzotti, G. Gioia Lobbia, D. Leonesi, A. Cingolani, Gazz. Chim. Ital. 124 (1994) 51.
[18] (a) C. Janiak, Chem. Ber. 127 (1994) 1379;
(b) C. Janiak, T.G. Scharmann, J.C. Green, R.P.G. Parkin, M.J. Kolm, E. Riedel, W. Mickler, J. Elguero, R.M. Claramunt, D. Sanz, Chem. Eur. J. 2 (1996) 992.
[19] R.K. Harris, Nuclear Magnetic Resonance Spectroscopy, Pitman, London, 1986, pp. 138–141 (Chapters 5–14).
[20] Effendy, J.V. Hanna, F. Marchetti, D. Martini, C. Pettinari, R. Pettinari, B.W. Skelton, A.H. White, Inorg. Chim. Acta 357 (2004) 1523.
[21] Z. Yuan, N.H. Dryden, J.J. Vittal, R.J. Puddephatt, Can. J. Chem. 72 (1994) 1605.
[22] E.L. Muetterties, C.W. Alegranti, J. Am. Chem. Soc. 94 (1972) 6386.

Available online at www.sciencedirect.com
SCIENCE DIRECT®
Polyhedron 24 (2005) 189–200
POLYHEDRON
www.elsevier.com/locate/poly

Syntheses, photoluminescence and electroluminescence of some new blue-emitting phosphorescent iridium(III)-based materials

Inamur R. Laskar, Shih-Feng Hsu, Teng-Ming Chen *

Department of Applied Chemistry, National Chiao Tung University, Hsinchu 30055, Taiwan

Received 20 August 2004; accepted 29 October 2004
Available online 22 December 2004

Abstract

The cyclometallated ligand 2-(4′,6-difluorophenyl)-4-methoxypyridine (F_2MeOppyH), whose complexes with iridium(III) emit bright blue to green light, was synthesized in five separate steps. Ir(F_2MeOppy)$_2$(acac), (acacH = 2,4-pentanedione), Ir(F_2MeOppy)$_2$(pic) (picH = 2-picolinic acid), *fac*-Ir(F_2MeOppy)$_3$ and *mer*-Ir(F_2MeOppy)$_3$ complexes were synthesized from solution and fully characterized. The structures of Ir(F_2MeOppy)$_2$(acac) and *fac*-Ir(F_2MeOppy)$_3$ were authenticated by X-ray single crystal structure analysis. *fac*-Ir(F_2MeOppy)$_3$ showed a much higher solution photoluminescence (PL) quantum efficiency and blue-shifted emission compared to its counter *mer*-isomer. All of the complexes showed reversible oxidations between 0.3 and 0.7 V versus the ferrocene/ferrocenium ion. The relative thermodynamic stability of the *mer* versus *fac* isomer was investigated and correlated to their corresponding redox and PL properties. Two electroluminescent (EL) devices (D-1 and D-2) were fabricated using the same blue Ir(F_2MeOppy)$_2$(acac) complex as a a dopant but with two different hole blockers, BCP and BAlq, and consequently BCP proved itself a good hole blocker for this type of system. The fabrication of another EL device (D-3) was carried out by using the same dopant, only replacing the host CBP by a wider band gap host, *m*CP which showed improved luminance, luminance yield and power efficiency (D-2: 133 cd m^{-2}, 0.66 cd A^{-1}, 0.22 lm W^{-1}; D-3: 326 cd m^{-2}; 1.63 cd A^{-1}; 0.26 lm W^{-1}).
© 2004 Elsevier Ltd. All rights reserved.

Keywords: Facial; Meridional; Iridium(III) complex; Blue phosphorescent; Photoluminescence; Electroluminescence

1. Introduction

Syntheses of materials based on heavy metal (Ir(III), Pt(II), Os(II), Re(I)) complexes, used as phosphorescent dopants, have attracted a great deal of attention due to their potential applications in organic light emitting devices (OLEDs) [1–4]. Of the above heavy metal-containing phosphor emitters that have been reported in OLEDs, cyclometallated complexes of iridium(III) materials have shown the most promising applications due to their higher stability, higher photoluminescence (PL) efficiency and relatively shorter excited state lifetime. Purely green- and red-emitting phosphorescent complexes of iridium(III) [5] are common, whereas the purely blue-emitting complex dopants [6] are scarcely found. Hence, the current effort of scientists has been focused on the syntheses of blue-emitting iridium(III)-based materials.

Amongst the complexes, the syntheses of Ir(F_2ppy)$_2$(acac) and Ir(F_2ppy)$_2$(pic) (F_2ppy = 2-(2′, 4′-difluorophenyl)pyridine; acacH = 2,4-pentanedione; picH = 2-picolinic acid) [7] are notable examples for blue-emitting materials. Recently, Coppo et al. [8] reported the blue-emitting phenylpyridine iridium(III) complexes using triazolyl pyridine types as ancillary ligands. In this work, we have introduced strong electron donating substituents at the 4-position of the LUMO containing pyridyl moiety in 2-(2′,4′-difluorophenyl)pyridine, which is

* Corresponding author. Tel.: +8865712121x56526; fax: +88635723764.
E-mail address: tmchen@mail.nctu.edu.tw (T.-M. Chen).

0277-5387/$ - see front matter © 2004 Elsevier Ltd. All rights reserved.
doi:10.1016/j.poly.2004.10.016

supposed to further raise the LUMO energy state of the corresponding iridium(III) complex. Hence, the energy gap will be enhanced and consequently result in a more hypsochromic shift when compared to the parent complex. Our first choice was to incorporate a methoxy substituent at the 4-position of the pyridyl moiety in 2-(2,4′-difluorophenyl)pyridine. We have also synthesized both the *fac*-/*mer*-isomers of the same ligand, investigated and differentiated their photoluminescence and redox behaviors as well as their thermal stability. We report on the syntheses of four blue-emitting iridium(III) complex dopants using the same cyclometallated ligand, 2-(2′,4′-difluorophenyl)-4-methoxypyridine, and characterization and detailed studies of their photophysical as well as redox properties, X-ray single-crystal structure analyses of $Ir(F_2MeOppy)_2(acac)$ and *fac*-$Ir(F_2MeOppy)_3$ and the application of $Ir(F_2MeOppy)_2(acac)$ as a dopant in electroluminescent (EL) devices.

2. Experimental

2.1. Materials

$IrCl_3 \cdot 3H_2O$ was purchased from Alfa Aesar, USA, 2,4-difluoroboronic acid, picolinic acid and glycerol from Aldrich Chemicals, USA and the remaining compounds from Tokyo Kasei Kogyo Co. Ltd., Japan, and all were used as received.

2.2. Syntheses

2-Chloropyridine-N-oxide (yield 95%): 2-Chloropyridine was allowed to react with excess *m*-chloroperoxybenzoic acid in dichloromethane at ~0 °C, for 16 h. Then, the volume of the solvent was reduced to half and it was passed through a basic alumina bed using dichloromethane as an eluent, which resulted in pure 2-chloropyridine-N-oxide. ^1H NMR (300 MHz, $CDCl_3$): δ 8.39 (t, 1H, *J* 3.9 Hz), 7.54 (t, 1H, *J* 5.1 Hz), 7.27 (m, 2H). EIMS: *m*/*z* 130, Calc. 130.5.

2-Chloro-4-nitropyridine-N-oxide (yield 70%) [9]: 2-chloropyridine-N-oxide (10 g) was added to conc. sulfuric acid (15 ml) at 0–5 °C. Then, a mixture of conc. sulfuric acid (15 ml) and fuming nitric acid (30 ml) (sp. gr. 1.5) was added dropwise with stirring at 1–2 °C over a 45-min period. The mixture was heated slowly to 90 °C over 1 h and then maintained at 90 °C with stirring for an additional hour after which the mixture was cooled to 10 °C, poured into a stirred ice–water mixture, and neutralized with sodium carbonate. The yellow precipitate was collected, air-dried, and then recrystallized from an ethanol–chloroform mixture. ^1H NMR (300 MHz, $CDCl_3$): δ 8.45 (m, 2H), 8.04 (m, 1H). EIMS: *m*/*z* 176, Calc. 175.5.

2-Chloro-4-nitropyridine (yield 90%) [9]: 2 g of 2-chloro-4-nitropyridine-N-oxide was taken in 30 ml of ethyl acetate and ~3 ml of phosphorous tribromide was added slowly. Then, the mixture was heated with stirring at 70 °C for 10 min. The mixture was cooled, poured into an ice–water mixture, made alkaline to litmus with 10% aqueous sodium hydroxide and extracted with chloroform. The solvent was evaporated and purified by column chromatography. ^1H NMR (300 MHz, $CDCl_3$): δ 8.67 (dd, 1H, *J* 0.5, 5.4 Hz), 8.20 (d, 1H, *J* 1.8 Hz), 7.99 (dd, 1H *J* 1.8, 5.4 Hz). EIMS: *m*/*z* 158, Calc. 158.5.

2-Chloro-4-methoxypyridine (yield 55%): 2-Chloro-4-nitropyridine (1 eq.) was reacted with sodium methoxide (1.3 eq.) in dioxane at 100 °C for 12 h. The reaction mixture was cooled to room temperature and poured into water. Then, the organic layer was separated out and the aqueous layer was washed by ethyl acetate. The combined organic extracts were dried and evaporated to dryness. The compound was purified by column chromatography. ^1H NMR (300 MHz, $CDCl_3$): δ 8.43 (d, 1H, *J* 6 Hz), 7.26 (d, 1H, *J* 2.1 Hz), 7.06 (m, 1H). EIMS: *m*/*z* 143, Calc. 143.5.

2-(2′,4′-Difluorophenyl)-4-methoxypyridine (yield 80%) [10]. 5 g of 2-chloro-4-methoxy pyridine (1 eq.), 8.8 g of 2,4-difluorophenylboronic acid (1.6 eq.) and 1.15 g of triphenylphosphine (0.1 eq.) were dissolved in 1,2-dimethoxyethane (50 ml). 60 ml of 2 M K_2CO_3 (2.7 eq.) aqueous solution was added and the mixture was purged with argon gas. 0.25 g of palladium acetate (0.025 eq.) was added and the mixture was refluxed for 18 h. The two phases were then separated and the aqueous phase was extracted with ethyl acetate. The combined organic phases were washed with water and brine, successively, and then dried over $MgSO_4$. After evaporation of the solvent, the pure product was obtained by column chromatography. ^1H NMR (300 MHz, $CDCl_3$): δ 8.51 (d, 1H, *J* 5.7 Hz), 7.98 (m, 1H), 7.26 (t, 1H, *J* 2.1 Hz), 6.94 (m, 2H), 6.78 (dd, 1H, *J* 2.4, 5.7 Hz), 3.87 (s, 3H). EIMS: *m*/*z* 221, Calc. 221.

$(F_2MeOppy)_2Ir(\mu\text{-}Cl)Ir(F_2MeOppy)_2$ (yield 75%) [5e–5f]. Calc. for $C_{48}H_{32}N_4O_4F_8Cl_2Ir_2$: C, 43.1; H, 2.4; N, 4.2. Found: C, 43.0; H 2.3; N 4.0%. A solution of $IrCl_3 \cdot 3H_2O$ (1 mmol) and 2-(2′,4′-difluorophenyl)-4-methoxypyridine (3 mmol) in 2-ethoxyethanol (30 ml) was refluxed for 24 h. The pale green mixture was cooled to room temperature and 20 ml of 1 M HCl was added to precipitate the product. The mixture was filtered and washed with 100 ml of 1 M HCl followed by 50 ml of methanol, and then dried. The product was obtained as a light green powder. ^1H NMR (300 MHz, $CDCl_3$): δ 8.91 (d, 4H, *J* 6.6 Hz), 7.80 (s, 4H), 6.43 (m, 4H), 6.31 (t, 4H, *J* 9.9 Hz), 5.37 (d, 4H, *J* 9.0 Hz), 4.01 (s, 12H). FABMS: *m*/*z* 1335, Calc. 1335.

$Ir(F_2MeOppy)_2(acac)$ (yield 85%) [5e–5f]. Calc. for $C_{29}H_{23}N_2O_4F_4Ir$: C, 47.6; H, 3.1; N, 3.8. Found: C, 47.3; H 3.1; N 3.6%. $(F_2MeOppy)_2Ir(\mu\text{-}Cl)Ir(F_2MeOp-$

$py)_2$ (1 mmol), acetylacetone (3 mmol) and sodium carbonate (10 mmol) were mixed in 10 ml of 2-ethoxyethanol. The mixture was refluxed under nitrogen for 12 h. The reaction mixture was then cooled and the pale green precipitate was filtered off. The product was washed by methanol several times, followed by hexane. Then it was recrystallised from the mixture of dichloromethane and methanol (1:1). ^{1}H NMR (300 MHz, $CDCl_3$): δ 8.19 (d, 2H, *J* 6.6 Hz), 7.75 (s, 2H), 6.76 (dd, 2H, *J* 2.5, 6.3 Hz), 6.30 (t, 2H, *J* 10.5 Hz), 5.70 (d, 2H, *J* 7.2 Hz), 5.22 (s, 1H), 4.20 (s, 6H), 1.85 (s, 6H). FABMS: *m*/*z* 731, Calc. 731.

$Ir(F_2MeOppy)_2$(pic) (yield 92%) [6d]. Calc. for $C_{30}H_{20}N_3O_4F_4Ir_2$: C, 47.7; H, 2.7; N, 4.8. Found: C, 47.6; H 2.6; N 4.8%. 2.2 mmol of picolinic acid was added to a room temperature solution of 0.8 mmol of $(F_2MeOppy)_2Ir(\mu\text{-}Cl)Ir(F_2MeOppy)_2$ in 60 ml of dichloromethane. The mixture was heated to reflux under nitrogen in an oil bath for 16 h. The reaction mixture was cooled to room temperature and the pale yellow precipitate was filtered off. The pure product was obtained by flash chromatography. ^{1}H NMR (300 MHz, $CDCl_3$): δ 8.48 (d, 1H, *J* 6.9 Hz), 8.32 (d, 1H, *J* 7.2 Hz), 7.92 (t, 1H, *J* 6.6 Hz), 7.76 (m, 3H), 7.40 (td, 1H, *J* 1.5, 5.7 Hz), 7.17 (d, 1H, *J* 6.6 Hz), 6.73 (dd, 1H, *J* 2.7, 6.9 Hz), 6.53 (dd, 1H, *J* 2.7, 6.6 Hz), 6.42 (m, 2H), 5.88 (dd, 1H, *J* 2.3, 8.7 Hz), 5.64 (dd, 1H, *J* 2.6, 8.7 Hz), 4.06 (s, 6H). FABMS: *m*/*z* 754, Calc. 754.

mer-$Ir(F_2MeOppy)_3$ (yield 60%) [6a]. Calc. for $C_{36}H_{24}N_3O_3F_6Ir$: C, 50.7; H, 2.8; N, 4.2. Found: C, 50.5; H 2.7; N 4.0%. 1 equivalent of $(F_2MeOppy)_2Ir(\mu\text{-}Cl)$ $Ir(F_2MeOppy)_2$, 2 equivalents of the cyclometallated ligand ($F_2MeOppyH$) and 10 equivalents of sodium carbonate were mixed and refluxed in 2-ethoxyethanol for 20 h. The reaction was then allowed to cool to room temperature and distilled water was poured down on it. Immediately, the impure product was precipitated out and it was purified by flash chromatography by using dichloromethane as an eluant. ^{1}H NMR (300 MHz, $CDCl_3$): δ 7.77 (m, 3H), 7.64 (m, 2H), 7.31 (t, 1H, *J* 7.5 Hz), 6.64 (td, 1H, *J* 2.1, 7.9 Hz), 6.52 (td, 2H, *J* 3.0, 6.6 Hz), 6.39 (m, 4H), 6.06 (dd, 1H, *J* 2.4, 7.5 Hz), 5.88 (dd, 1H, *J* 2.4, 9.3 Hz), 4.14 (s, 9H). FABMS: *m*/*z* 852, Calc. 852.

fac-$Ir(F_2MeOppy)_3$ (yield 50%) [6a]. Calc. for $C_{36}H_{24}N_3O_3F_6Ir$: C, 50.7; H, 2.8; N, 4.2. Found: C, 50.4; H 2.7; N 4.1%. 1 equivalent of $Ir(F_2MeOppy)_2$(acac) and 1.5 equivalents of the cyclometallated ligand ($F_2MeOppyH$) were refluxed in glycerol for 24 h. Then the reaction mixture was cooled to room temperature and distilled water was added to it. The impure product was separated out and purified by flash chromatography. ^{1}H NMR (300 MHz, $CDCl_3$): δ 7.39 (s, 3H), 7.28 (d, 3H, *J* 6.6 Hz), 6.50 (t, 3H, *J* 4.2 Hz), 6.31 (m, 2H), 4.11 (s, 9H). FABMS: *m*/*z* 852, Calc. 852.

2.3. Crystallography

Single crystal diffraction data for $Ir(F_2MeOppy)_2$(acac) and *fac*-$Ir(F_2MeOppy)_3$ were collected on a Bruker Smart CCD diffractometer equipped with a normal focus, 3kW sealed-tube X-ray source (λ = 0.71073 Å). The intensity data were collected in the ω scan mode (width of 0.3/° frame) and corrected for *Lp* and absorption effects by using the SAINT [11] program. Cell refinement and data reduction were carried out by using the program Bruker SHELXTL [12] and the crystal structure was solved by direct methods using the SHELXTL [12] version 5.1 software packages. The structure was further refined by full-matrix least-squares methods based on F^2 using SHELXTL version 5.1 [12]. Positions of non-hydrogen atoms were refined anisotropically, whereas the hydrogen positions were not refined.

2.4. Optical measurements and compositions analysis

The ultraviolet-visible (UV–Vis) spectra of the phosphorescent Ir(III) complexes were measured on an UV–Vis spectrophotometer (Agilent model 8453) and corrected for background due to solvent absorption. Photoluminescence (PL) spectra were carried out with a spectrophotometer (Jobin-Yvon Spex, model Fluorolog-3). Emission quantum yields were measured by the method of Demas and Crosby [13] using *fac*-$Ir(ppy)_3$ as a reference [14]. NMR spectra were recorded on Varian 300 MHz. MS spectra (EI and FAB) were taken by micromass TRIO-2000. Cyclic voltammetry (CV) analyses were performed by using CHI 2.05; dichloromethane was used as a solvent in an inert atmosphere and 0.1 M tetra(*n*-butyl)ammonium tetrafluoroborate was used as the supporting electrolyte. A glassy carbon rod was used as the working electrode, platinum was used as the counter electrode and a silver wire was used as a pseudo-reference electrode. The TG-DTA analysis was carried out by using a thermal analyzer (SEIKO 1TG/DTA model 200). Emission lifetimes were obtained by exponentially fitting the emission decay curves recorded on Continuum model NY61 spectrofluorometer.

2.5. OLED fabrication and testing

In the fabrication of OLEDs organic layers were thermally evaporated onto a glass substrate precoated with an indium–tin–oxide (ITO) layer with a sheet resistance of 20 Ω under high-vacuum. Prior to use, the ITO surface was ultrasonicated in a detergent solution followed by rinsing with deionized (DI) water, dipped into acetone, trichloroethylene and 2-propanol, and then degreased with a vapor of 2-propanol. After degreasing, the substrate was oxidized and cleaned in a UV-ozone chamber before it was loaded into an evaporator. In a vacuum chamber at a pressure of 10^{-6} Torr, 500 Å of

NPB as the hole transporting layer; 200 Å of the complex doped (7%) CBP as the emitting layer; 100 Å of 2,9-dimethyl-4,7-diphenyl-1,10-phenanthroline (BCP) as a hole and exciton blocking layer (HBL); 650 Å of Alq_3 as the electron transport layer; and a cathode composed of 10 Å lithium fluoride and 2000 Å aluminum were sequentially deposited onto the substrate to give the device structure. The current–voltage (*I–V*) profiles and light intensity characteristics for the above-fabricated devices were measured in a vacuum chamber of 10^{-6} Torr at ambient temperature using a Keithley 2400 Source Meter/2000 Multimeter coupled to a PR 650 Optical Meter.

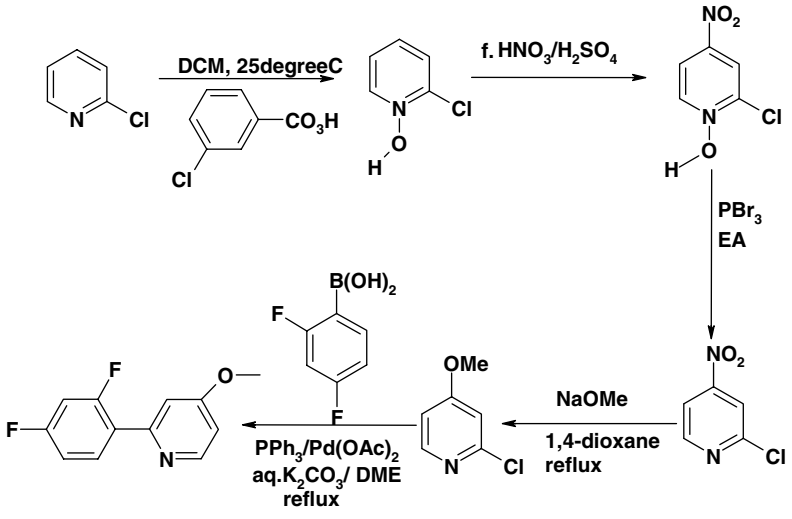
3. Results and discussion

3.1. Synthesis

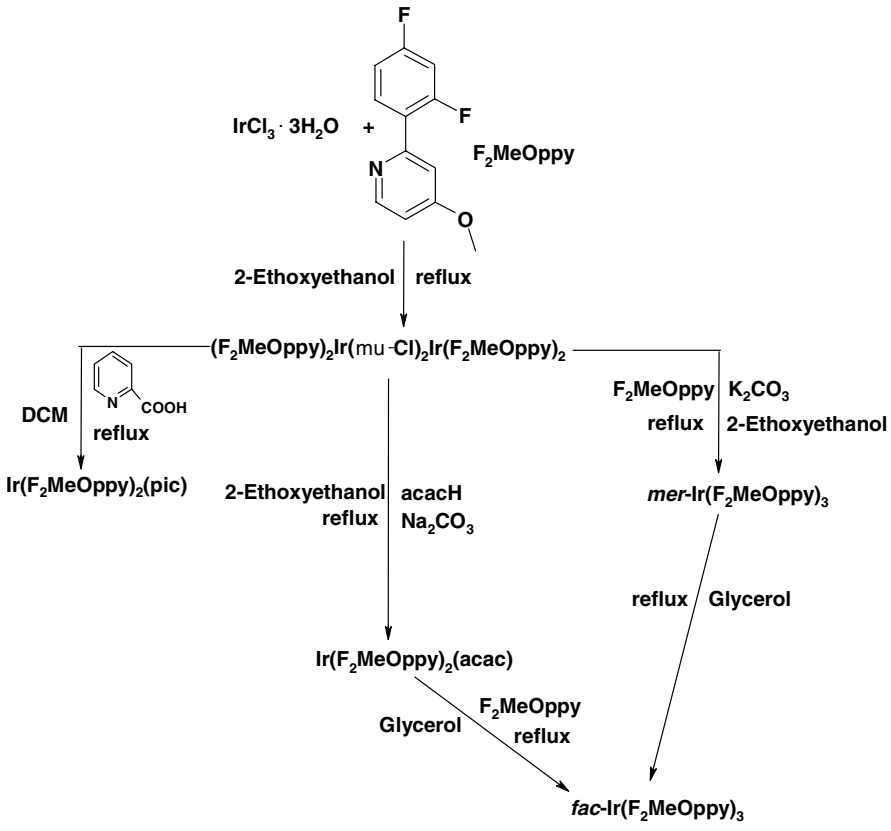
The ligand, 2-(2′,4′-difluorophenyl)-4-methoxypyridine (F_2MeOppyH) has been synthesized in five separate steps smoothly (Scheme 1; see experimental part). The yield of 4-methoxy-2-chloro-pyridine (4th step) is relatively poor (~55%) as compared to the other intermediates and the final compound (F_2MeOppyH). $IrCl_3 \cdot 3H_2O$ was allowed to react with an excess of F_2MeOppyH to give chloride-bridged dinuclear complex [5e,5f]. The mononuclear complexes, Ir(F_2MeOppy)$_2$(acac) and Ir(F_2MeOppy)$_2$(pic) have been synthesized [5e,5f] by replacing the bridging chlorides from the dinuclear species (Scheme 2), with bidentate, monoanionic acetylacetonate and picolinate, respectively. The proton NMR spectra of these complexes are consistent with the heterocyclic rings of the cyclometallated ligand being in a *trans*-disposition. The tris-isomeric complexes (*facial/meridional*) have also been synthesized by varying the temperature and using the cyclometallated ligand, F_2MeOppyH. Thompson et al. [6a] reported the syntheses of the *mer*-isomer at 140 °C and the *fac*-isomer of iridium(III) complexes at 200 °C along with little amount of *mer*-isomer as a by-product. In our case, the *meridional* form has been synthesized at a relatively lower temperature (~120 °C), whereas the synthesis at higher temperature (~200 °C) generates absolutely the *facial* form (Scheme 2). We have always isolated a mixture of *fac* and *mer* isomers at 140 °C. Furthermore, pure *mer*-isomer was taken in glycerol and refluxed for 24 h. It was observed that the *mer*-isomer converted to the *fac*-isomer almost completely, inferring that the *mer*-isomer was a kinetically controlled product, whereas the *fac*-isomer was favored thermodynamically. These isomers could also been differentiated clearly on the TLC plate due to their large polarity differences. ^{1}H NMR and ^{19}F NMR spectra (Fig. 1) clearly distinguished the *fac*-isomer from the *mer*-form. In ^{19}F spectra, we observed two peaks for the inherent-C_3 symmetric *facial* isomer and the six peaks for the asymmetric *mer*-isomer. Furthermore, TGA-DTA studies showed that the complexes are stable up to 340–360 °C and they can be sublimed easily under a pressure of 10^{-3} mm Hg.

3.2. X-ray crystallography

Single crystals of Ir(F_2MeOppy)$_2$(acac) and *fac*-Ir(F_2MeOppy)$_3$ were grown from methanol/dichloromethane (1:1) and chloroform, respectively, and characterized using X-ray crystallography. The ORTEP drawings of Ir(F_2MeOppy)$_2$(acac) and *fac*-Ir(F_2MeOppy)$_3$ are represented in Figs. 2(a) and (b), respectively. The crystal data and the selected bond lengths of both complexes are displayed in Tables 1 and 2, respectively. The dispo-



Scheme 1.



Scheme 2.

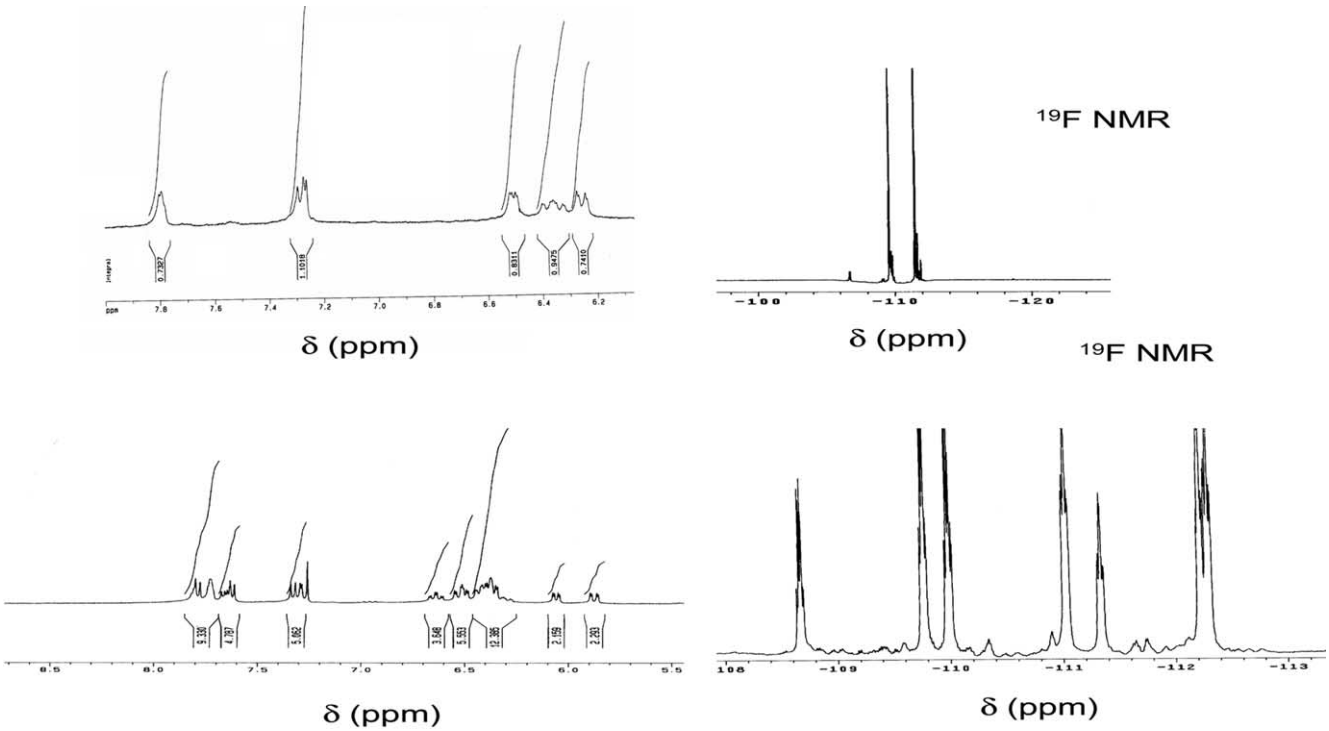


Fig. 1. ^{1}H and ^{19}F NMR spectra of *fac*-Ir(F_2MeOppy)$_3$ (top) and *mer*-Ir(F_2MeOppy)$_3$ (bottom), clearly distinguish the structures.

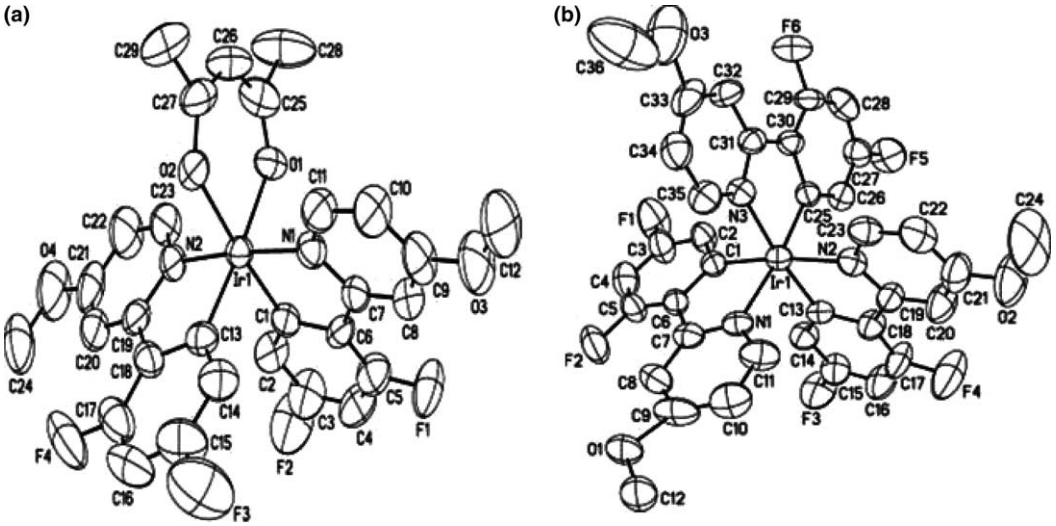


Fig. 2. The ORTEP drawings of (a) $Ir(F_2MeOppy)_2(acac)$ and (b) *fac*-$Ir(F_2MeOppy)_3$; the thermal ellipsoids for the image represent 50% probability.

Table 1
Crystal data and structure refinement for *fac*-$Ir(F_2MeOppy)_3$ and $Ir(F_2MeOppy)_2(acac)$

	fac-Ir($(F_2$ MeOppy$)_3$	Ir(F_2 MeOppy$)_2$ (acac)
Empirical formula	$C_{36}H_{28}F_6IrN_3O_5$	$C_{29}H_{23}F_4IrN_2O_4$
Formula weight	888.81	731.69
Temperature (K)	295(2)	296(2)
Wavelength (Å)	0.71073	0.71073
Crystal system	triclinic	monoclinic
Space group	$P\bar{1}$	$P2_1/c$
Unit cell dimensions		
a (Å)	12.2277(5)	8.1323(7)
b (Å)	12.3887(5)	18.9904(15)
c (Å)	24.4856(10)	17.2636 (14)
α (°)	93.103(1)	
β (°)	103.427(1)	90.777(2)
γ (°)	104.939(1)	
Volume (Å^3)	3460.1(2)	2665.9(4)
Z	4	4
D_{calc} (Mg/m^3)	1.706	1.823
Absorption coefficient (mm^{-1})	3.938	5.075
F(000)	1744	1424
Crystal size (mm)	$0.20 \times 0.20 \times 0.10$	$0.30 \times 0.20 \times 0.20$
θ Range for data collection	0.86–28.33	1.59–28.30
Index ranges	$-16 \leqslant h \leqslant 16$, $-16 \leqslant k \leqslant 16$, $-32 \leqslant l \leqslant 32$	$-10 \leqslant h \leqslant 9$, $-24 \leqslant k \leqslant 24$, $-20 \leqslant l \leqslant 23$
Reflections collected	41 099	17 219
Independent reflections [R_{int}]	17 088 [0.0514]	6331 [0.0432]
Completeness to θ (%)	99.0 (23.33)	95.5 (23.3)
Absorption correction	empirical	empirical
Maximum and minimum transmission	0.97346 and 0.59790	0.93848 and 0.71891
Refinement method	full-matrix least-squares on F^2	full-matrix least-squares on F^2
Data/restraints/parameters	17 088/1/941	6331/0/365
Goodness-of-fit on F^2	0.917	0.892
Final R indices [$I > 2\sigma(I)$]	$R_1 = 0.0443$, $wR_2 = 0.1034$	$R_1 = 0.0378$, $wR_2 = 0.0894$
R indices (all data)	$R_1 = 0.0971$, $wR_2 = 0.1178$	$R_1 = 0.0779$, $wR_2 = 0.958$
Largest differential peak and hole (e Å^{-3})	1.638 and −0.704	2.973 and −2.353

sitions of the ligands in both the complexes exhibit pseudo-octahedral geometry around the metal center. The C–C and C–N intraligand bond lengths and angles are within normal ranges expected for cyclometallated iridium(III) complexes and similar to the values reported for $(C^\wedge N)_2Ir(acac)$ [5e], *fac*-$Ir(C^\wedge N)_3$ [15,16] and

Table 2
Selected bond distances [Å] for *fac*-Ir($(F_2MeOppy)_3$ and Ir$(F_2MeOppy)_2$(acac)

fac-Ir($(F_2MeOppy)_3$		Ir$(F_2MeOppy)_2$(acac)	
Atom (1)–atom (2)	Distance (Å)	Atom (1)–atom (2)	Distance (Å)
Ir(1)–C(1)	2.017(7)	Ir(1)–C(13)	1.976(6)
Ir(1)–C(25)	2.020(6)	Ir(1)–C(1)	1.982(6)
Ir(1)–C(13)	2.021(7)	Ir(1)–N(1)	2.028(5)
Ir(1)–N(3)	2.113(6)	Ir(1)–N(2)	2.043(5)
Ir(1)–N(1)	2.117(6)	Ir(1)–O(1)	2.135(4)
Ir(1)–N(2)	2.131(6)	Ir(1)–O(2)	2.136(4)

$(C^N)_2Ir(\mu\text{-}Cl)Ir(C^N)_2$ [16] complexes. The *mer*-Ir$(F_2MeOppy)_3$ complex should have the same disposition of F_2MeOppy ligand as found in Ir$(F_2MeOppy)_2$(acac). The mutually *trans*-disposed Ir–N bonds in Ir$(F_2MeOppy)_2$(acac) have shorter bond lengths (Table 2) in comparison with those in *fac*-Ir$(F_2MeOppy)_3$ where the bond lies in a *trans* position (Fig. 2(b)) to the strong *trans* influencing phenyl group. Another point to be noted is that the weak *trans* influence of the acetylacetonate ligand leads to shorter Ir–C bonds for the Ir$(F_2MeOppy)_2$(acac) complex than those observed in *fac*-Ir$(F_2MeOppy)_3$, as indicated in Table 2.

3.3. Photophysical properties

The solution UV–Vis absorption and PL spectra of all these complexes have been measured. The UV–Vis absorption spectra of these complexes show intense bands appearing in the ultraviolet part of the spectrum between 240 and 340 nm. The measured energies and the extinction coefficients are comparable to those of the free ligand, which helped us to assign the bands as spin allowed $^1(\pi\text{–}\pi^*)$ transitions of the ligand. These ligand-centered bands are accompanied by weaker transitions with lower energy extending into the visible region from 350 to 400 nm (Fig. 3). With reference to the previous photophysical studies of cyclometallated complexes of the iridium(III) system [17], these absorption features are assigned to intra-ligand (IL) $\pi\text{–}\pi^*$ ($F_2MeOppy^-$) and also spin-allowed metal-to-ligand charge transfer ^{1}MLCT [$d\pi$ (Ir) $\rightarrow \pi$ $F_2MeOppy^-$)] transitions. In addition, spectra of all the complexes exhibit weaker absorption tails toward the further lower energy region (400–470 nm) (Fig. 3), which may be recognized as the spin-forbidden ^{3}MLCT [$d\pi$ (Ir) $\rightarrow \pi^*$ ($F_2MeOppy^-$)] transitions. The high intensity of these MLCT bands (shown by the extinction coefficients in the Table 3) has been attributed to an effective mixing of these charge transfer transitions with higher lying spin-allowed transitions on the cyclometallated ligand, which is facilitated by the strong spin–orbit coupling of the iridium(III) center. The energy of the MLCT transitions for the *fac*-isomer is comparatively higher than those of the rest of the complexes. These MLCT bands in the *fac*-isomer are more prominent and easily distinguishable as compared to its *mer*-counterpart, which is indicated in Fig. 3. The lowest energy transitions show blue-shifted absorption with increasing polarity of the solvents (i.e., toluene → chloroform → acetone → methanol). As shown in Fig. 4, the solution PL emission spectra of all the complexes exhibit structured features. These facts support that the lowest excited states of the complexes have a mixed ligand centered (LC) as well as MLCT character. As shown in Fig. 4, the PL intensity of the *fac*-isomer is much higher and exhibits ~6 nm hypsochromic shift with respect to its *mer*-counterpart. Similarly, the PL intensity of the Ir$(F_2MeOppy)_2$(acac) complex is found to be much higher and its emission spectrum much sharper relative to that of Ir$(F_2MeOppy)_2$(pic), whose spectrum is red-shifted, broad and

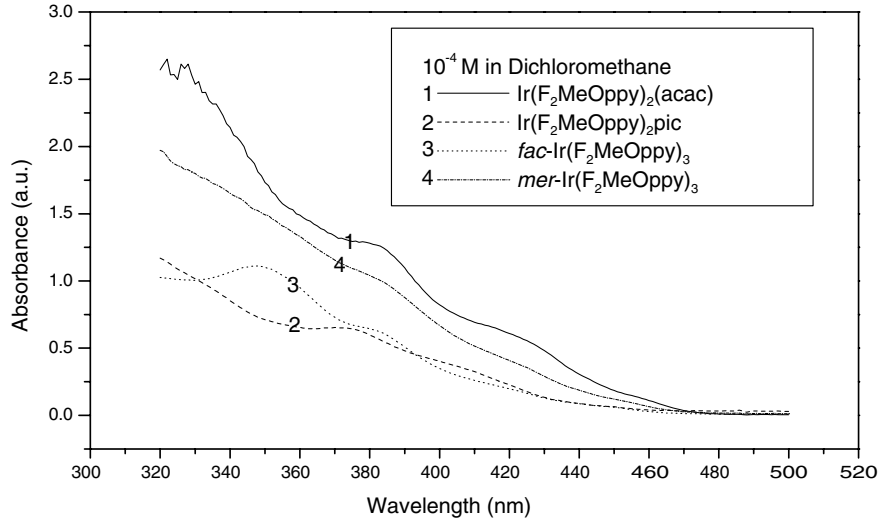


Fig. 3. UV–Vis absorption spectra for bis-and tris-cyclometallated complexes investigated in this work.

Table 3
Photophysical and electrochemical data for the bis and tris-(F_2MeOppy) cyclometallated iridium(III) complexes

Complex	Absorbance[a] λ (nm) (logε)	Emission λ_{max} (nm)		Relative quantum efficiency[a,c]	Redox $E^{ox}_{1/2}$ (V)[a]	HOMO (eV)	Lifetime (μs)
		Solution[a,b]	Film[b]				
Ir(F_2MeOppy)$_2$(acac)	383 (4.1); 419 (3.8)	471	469	0.60	0.508	5.3	0.59
Ir(F_2MeOppy)$_2$(pic)	375 (3.8); 411 (3.5)	509	485	0.82	0.661	5.5	0.84
fac-Ir(F_2MeOppy)$_3$	348 (4.1); 383 (3.8)	471	464	0.95	0.551	5.4	0.74
mer-Ir(F_2MeOppy)$_3$	384 (4.0); 420 (3.6)	477	468	0.41	0.345	5.6	0.68

[a] Solvent used dichloromethane.
[b] Excitations used 384, 374, 378 and 380 nm for solutions and 279, 270, 273 and 276 nm for thin films.
[c] Values are reported relative to Cp_2Fe/Cp_2Fe^+.

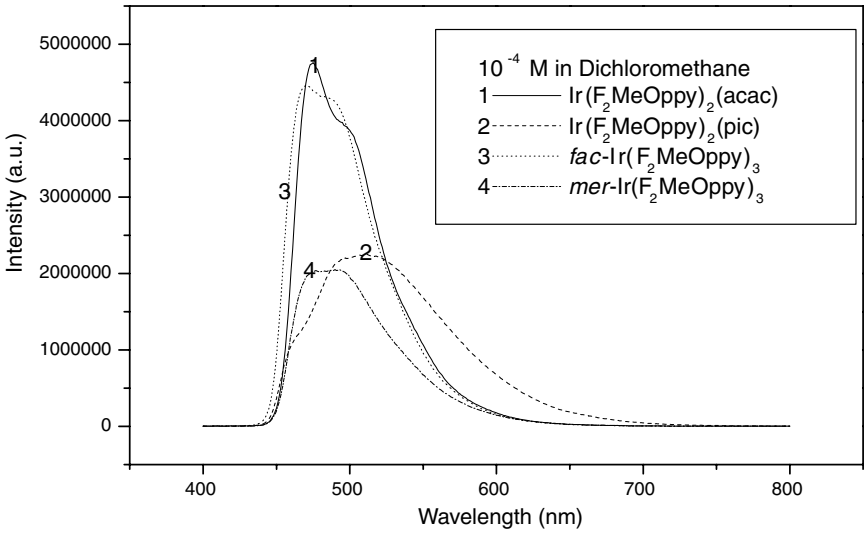


Fig. 4. Room temperature solution PL spectra for all the complexes in CH_2Cl_2.

featureless. The solution spectrum of Ir(F_2MeOppy)$_2$-(pic) also markedly differs from its thin-film emission spectrum (Fig. 5), which shows blue-shifted emission to a larger extent (~30 nm). It has also been observed that the nature of the emission spectra of Ir(F_2MeOppy)$_2$-(pic) is red-shifted in order of increasing polarity of the solvents, which suggest that the energy of the lowest emitting state of Ir(F_2MeOppy)$_2$(pic) is highly solvent dependent. The thin-film spectra for the other complexes, as shown in Fig. 5, exhibit blue-shifted emission to a smaller extent (~5–8 nm) as compared to their respective solution spectra.

The complexes, Ir(F_2ppy)$_2$(acac) and Ir(F_2ppy)$_2$(pic) [F_2ppy = 2-(2,4-difluorophenyl)pyridyine], have been reported [6d,7] and well characterized. The strong electron-donating methoxy substituent was incorporated onto the LUMO containing pyridyl ring of F_2ppy, and, therefore, it raised the LUMO energy and thereby increased the HOMO–LUMO energy gap. Hence, the complex Ir(F_2MeOppy)$_2$(acac) (λ_{max} = 471 nm) shows the expected blue-shifted emission as compared to the reported complex, Ir(F_2ppy)$_2$(acac) (λ_{max} = 476 nm). It is also known that Ir(F_2ppy)$_2$(pic) (λ_{max} = 456 nm) exhibits blue shifted emission compared to its acetylacetonate analogue, Ir(F_2ppy)$_2$(acac) (λ_{max} = 476 nm). But in our case, Ir(F_2MeOppy)$_2$(pic) (λ_{max} = 509 nm) shows a wide red shifted emission compared to its acetylacetonate analogue (λ_{max} = 471 nm). We have measured the solution quantum efficiency of the complexes and the results are shown in Table 3. The *fac*-isomer shows a much higher quantum efficiency as compared to its counter *mer*-isomer. Furthermore, as shown in Table 3, the measured lifetime for thin film samples falls into the microsecond regime, which evidence the lowest excited states are the triplet-emitting states for these complexes. The short life-time also indicates that there is strong spin–orbit coupling in the presence of heavy metal iridium(III).

3.4. Electrochemistry

The electrochemical properties of the bis- and tris-cyclometallated complexes were examined by cyclic voltammetry. Redox potentials, given in Table 3, were measured relative to an internal ferrocene reference (Cp_2Fe/Cp_2Fe^+ = 0.62 versus SCE in dichloromethane solvent). All of these complexes showed reversible oxidation, in

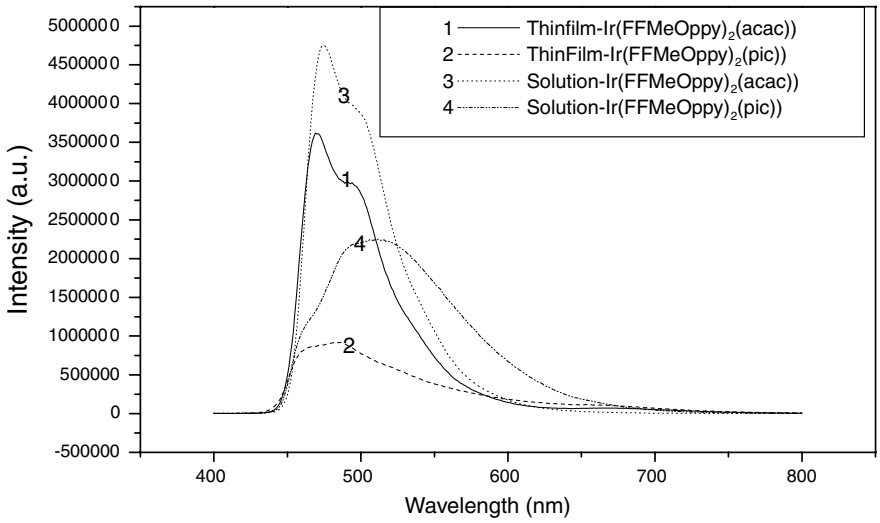


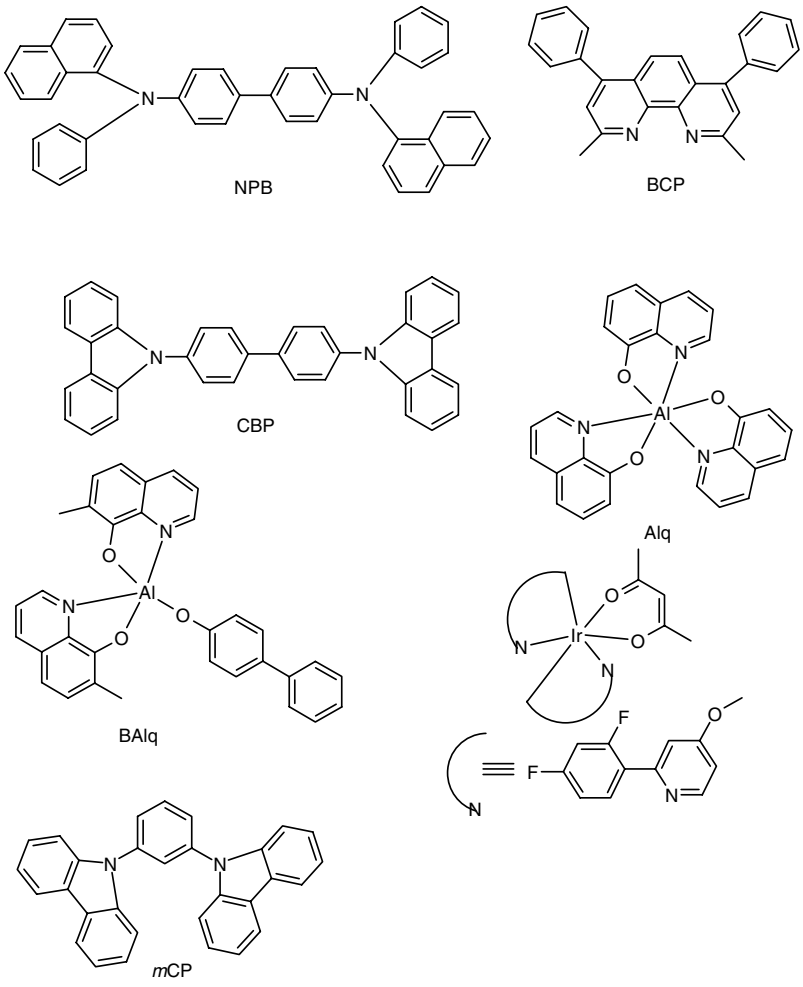
Fig. 5. Comparison of thin-film and solution PL spectra for $Ir(F_2MeOppy)_2X$ (X = acac and pic).

the range from 0.34 to 0.67 V. The *fac*-isomer has oxidation potentials ca. ~200 mV more positive than the corresponding *mer*-form (i.e., fac_{ox}: 0.55 V; mer_{ox}: 0.34 V), whereas the reduction potential for the *fac*-form is slightly more negative than that of the *mer*-isomer (i.e., fac_{red}: −2.67 V; mer_{red}: −2.62 V). It was known that for phenyl-pyridyl based complexes, the oxidation processes involve the Ir–phenyl center (major HOMO contribution), while reduction processes occur primarily on the heterocyclic portion (major LUMO contribution) of the ligand [6]. The difference in electrochemical properties between *facial* and *meridional* isomers can be rationalized by the presence of mutually *trans* phenyl rings of the ligands in the *mer*-isomer, whereas in the *facial* form all the phenyls are *cis* (Fig. 2(b)) with respect to one another. Electron-rich sigma phenyl ligands normally exhibit a very strong *trans* influence and *trans* effect, which results in a lengthening of the *transoid* Ir–C bonds and hence destabilization of the HOMO to a significant extent, which is supported by the HOMO–LUMO energy calculations using redox data and absorption wavelength, summarized in Table 3. Therefore, it is concluded that the *mer*-isomer is easier to oxidize than the *fac*-isomer.

3.5. Description and performance of OLED devices

Initially, we fabricated an electroluminescent device D-1 with structure ITO/CF_x/NPB (300 Å)/CBP + 7% dopant (200 Å)/BAlq (300 Å)/Alq_3 (150 Å)/LiF (10 Å)/Al (2000 Å) (the molecular structures of each compound used in the EL device are shown in Scheme 3) using the complex $Ir(F_2MeOppy)_2(acac)$ as a dopant in the emitting layer. Fig. 6 shows the EL emission spectra of the device where a broad and long tail extending up to 735 nm was observed. Clearly, the emission appearing in the green and red regions is attributed to the leakage of holes into the BAlq and Alq_3 layers and the consequent recombination in those layers infers that BAlq is not an effective hole blocker (HB) for deep-blue electroluminescent material (Scheme 4a). Consequently, we replaced BAlq with BCP, which has a comparatively higher HOMO level (6.5 eV) as compared to BAlq (6.0 eV). Accordingly, we fabricated another device by incorporating the same dopant, $Ir(F_2MeOppy)_2(acac)$ (D-2) into the emitting layer, with BAlq replaced by BCP as a hole blocker. No observation of a broad emission was found in this device, but another extra emission was observed at ca. 425 nm, which was attributed to the NPB hole transport material as shown in Fig. 6. The external luminance efficiency and the power efficiency is found to be 0.66 cd A^{-1} and 0.22 lm W^{-1}, respectively, at a current density of 20 mA cm^{-2}, as indicated in Fig. 7. The lowest triplet energy levels for the dopant, $Ir(F_2MeOppy)_2(acac)$ and the host, CBP are 2.64 [1] and 2.56 eV [12], respectively, which suggests that the endothermic energy transfer [7] is being operated between the host and the dopant. This type of energy transfer in an EL device is not completely favorable for blue-emitting dopants (Scheme 4b) [c]. The fabrication of another EL device was carried out with the host *m*CP, having a wider band gap, i.e., 2.90 eV [18]. The layer sequences and the thicknesses of each layer were kept constant as before. The comparisons of device performance of D-2 and D-3 have been shown in Table 4. As indicated in Fig. 7, in this case the external quantum efficiency and the power efficiency are improved and found to be 1.63 cd A^{-1} and 0.47 lm W^{-1} at 20 mA cm^{-2} current density, respectively, as compared

[1] The triplet emitting state of $Ir(F_2MeOppy)_2(acac)$ has been calculated from the maximum emission wavelength at 298 K.



Scheme 3.

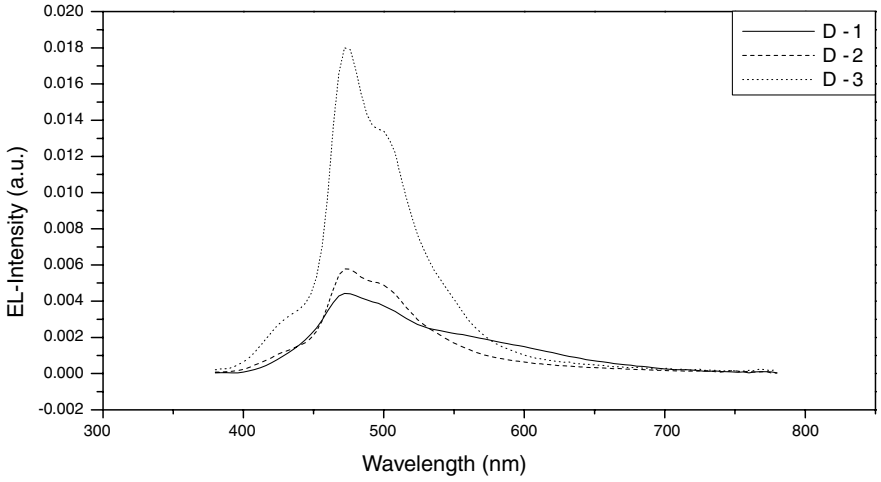
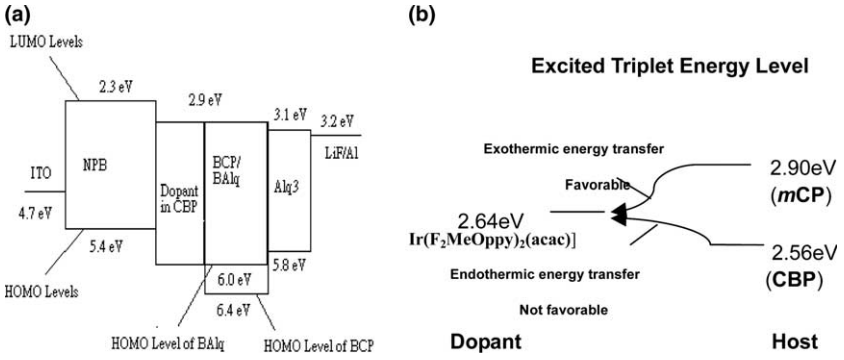


Fig. 6. Comparative electroluminescent emission spectra of devices D-1, D-2 and D-3.

to the previous devices. This device shows a luminance value of 326 cd m^{-2} at 20 mA cm^{-2} current density, that is also higher than that of the former device (133 cd m^{-2} at 20 mA cm^{-2}) (Figs. 8(a) and (b)). Hence the exothermic triplet energy transfer to the blue dopant Ir(F_2-MeOppy)$_2$(acac) is more efficient when using the wider band gap host *m* CP. The comparisons of *I–V* curves have also been shown in Fig. 8(a) and (b).



Scheme 4.

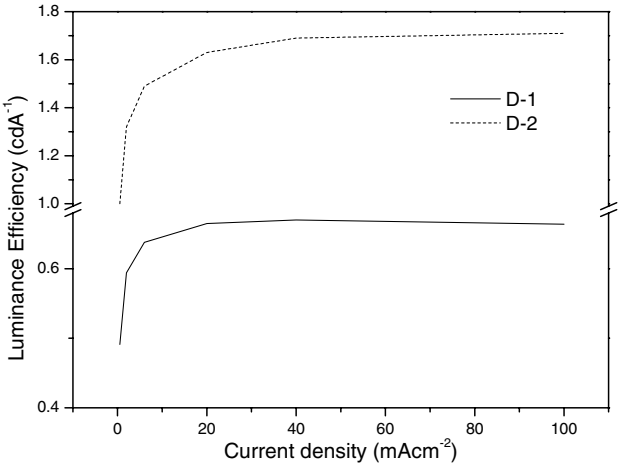


Fig. 7. Comparative plot of luminescent efficiency vs. current density of D-2 and D-3 devices.

Table 4
Comparisons of the EL performances of the devices with structure: ITO/CHF_3/NPB (300 Å)/Host + 7% dopant (200 Å)/BAlq (300 Å)/Alq_3(150 Å)/LiF (10 Å)/Al (2000 Å), Host − CBP for D-2; *m*CP for D-3

	D-2	D-3
EL color	blue	blue
Peak wavelength (nm)	472	472
CIE-x at 20 mA cm^{-2}	0.19	0.17
CIE-y	0.31	0.30
Luminance (cd m^{-2} at 20 mA cm^{-2})	133	327
External quantum efficiency (cd A^{-1} at 20 mA cm^{-2})	0.66	1.63
Power efficiency (lm W^{-1} at 20 mA cm^{-2})	0.22	0.88

All these parameters have been recorded at 20 mA cm^{-2}.

4. Conclusion

We have synthesized four iridium(III)-based phosphorescent dopants that emit in the blue range, using the same cyclometallated ligand, 2-(2′,4′-difluorophenyl)-4-methoxypyridine. These complexes show different maximum emission wavelengths and quantum efficiencies with respect to the ancillary ligands (actylacetonate and picolinate) and the types of isomerism. The strong

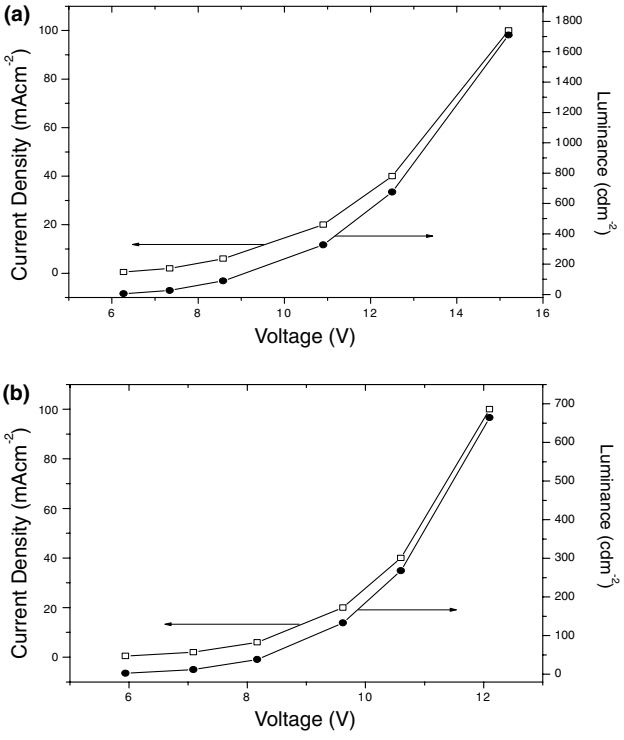


Fig. 8. Comparative plot of current density, voltage and luminance characteristics for the devices 2 (presented in **b**) and 3 (presented in **a**).

trans-influence in the *meridional* isomer leads to less stable, broader, red-shifted and lower quantum efficiencies than the *facial* counterpart. Three EL devices were fabricated. It can be stated that BAlq is not a good hole blocker in the EL device for a blue-emitting phosphorescent dopant. It has also been shown that the wider band gap host *m*CP shows good EL performances with respect to the host CBP having a relatively lower band gap, for the same blue-emitting iridium(III) dopant.

5. Supplementary data

Crystallographic data for the structural analysis have been deposited with the Cambridge Crystallographic

Data Centre, CCDC Nos. 228968 and 228969 for compounds $Ir(F_2MeOppy)_2(acac)$ and *fac*-$Ir(F_2MeOppy)_3$, respectively. Copies of this information may be obtained free of charge from the Director, CCDC, 12 Union Road, Cambridge, CB2 1EZ, UK (fax: +44 1223 336033; email: deposit@ccdc.cam.ac.uk or www:http://www.ccdc.cam.ac.uk).

Acknowledgement

This research is supported by the Program for Promoting University Academic Excellence from the Ministry of Education, Taiwan, Republic of China under the Contract PPAEU91-E-FA04-2-4-(B).

References

[1] (a) J.K. Lee, D. Yoo, M.F. Rubner, Chem. Mater. 9 (1997) 1710;
(b) F.G. Gao, A. Bard, J. Am. Chem. Soc. 122 (2000) 7426.
[2] (a) Y. Li, Y. Liu, J. Guo, F. Wu, W. Tian, B. Li, Y. Wang, Synth. Met. 118 (2001) 175;
(b) K. Wang, L. Huang, L. Gao, L. Jin, C. Huang, Inorg. Chem. 41 (2002) 3353.
[3] F.G. Gao, A.J. Bard, Chem. Mater. 14 (2002) 3465.
[4] (a) C.-L. Lee, K.B. Lee, J.-J. Kim, Appl. Phys. Lett. 77 (2000) 2280;
(b) R.R. Das, C.-L. Lee, J.-J. Kim, Mat. Res. Soc. Symp. Proc. 708 (2002) BB3.39.1;
(c) J.P.J. Markham, S.-C. Lo, S.W. Magennis, P.L. Burn, I.D.W. Samuel, Appl. Phys. Lett. 80 (2002) 2645.
[5] (a) I.R. Laskar, T.-M. Chen, Chem. Mater. 16 (2004) 111;
(b) T. Tsuzuki, N. Shirasawa, T. Suzuki, S. Tokito, Adv. Mater. 15 (2003) 1455;
(c) A. Beeby, S. Bettington, I.D.W. Samuel, Z.J. Wang, Mater. Chem. 13 (2003) 80;
(d) M.K. Nazeeruddin, R. Humphry-Baker, D. Berner, S. Rivier, L. Zuppiroli, M. Graetzel, J. Am. Chem. Soc. 125 (2003) 8790;
(e) S. Lamansky, P. Djurovich, D. Murphy, F. Abdel-Razzaq, R. Kwong, I. Tsyba, M. Bortz, B. Mui, R. Bau, M.E. Thompson, Inorg. Chem. 40 (2001) 1704;
(f) S. Lamansky, P. Djurovich, D. Murphy, F. Abdel-Razzaq, H.-F. Lee, C. Adachi, P.E. Burrows, S.R. Forrest, M.E. Thompson, J. Am. Chem. Soc. 123 (2001) 4304;
(g) M.E. Thompson, S. Lamansky, P. Djurovich, D. Murphy, F. Abdel-Razzaq, R. Kwong, S.R. Forrest, M.A. Baldo, P.E. Burrows, patent US 20020034656A1;
(h) M.A. Baldo, M.E. Thompson, S.R. Forrest, Pure Appl. Chem. 71 (1999) 2095.
[6] (a) A.B. Tamayo, B.D. Alleyne, P.I. Djurovich, S. Lamansky, I. Tsyba, N.N. Ho, R. Bau, M.E. Thompson, J. Am. Chem. Soc. 125 (2003) 7377;
(b) R.J. Holmes, W. D'Andrade, S.R. Forrest, X. Ren, J. Li, M.E. Thompson, Appl. Phys. Lett. 83 (2003) 3818;
(c) S. Tokito, T. Iijima, Y. Suzuri, H. Kita, T. Tsuzuki, F. Sato, Appl. Phys. Lett. 83 (2003) 569;
(d) S. Lamansky, M.E. Thompson, V. Adamovich, P.I. Djurovich, C. Adachi, M.A. Baldo, S.R. Forrest, Kwong, patent US 20020182441A1.
[7] C. Adachi, R.C. Kwong, P. Djurovich, V. Adamovich, M.A. Baldo, M.E. Thompson, S.R. Forrest, Appl. Phys. Lett. 79 (2001) 2082.
[8] P. Coppo, E.A. Plummer, L.D. Cola, Chem. Commun. 15 (2004) 1774.
[9] G.C. Finger, L.D. Starr, J. Am. Chem. Soc. 81 (1959) 2674.
[10] S.J. Connon, A.F. Hegarty, Tetrahedron Lett. 42 (2001) 735.
[11] G.M. Sheldrick, SAINT; Bruker Analytical X-ray Instrument Division, Madison, WI, 1998.
[12] G.M. Sheldrick, SHELXTL Programs, version 5.1; Bruker AXS GmbH, Karlsruhe, Germany, 1998.
[13] J. Demas, G.A. Crosby, J. Phys. Chem. 75 (1971) 991.
[14] K.A. King, P.J. Spellane, R.J. Watts, J. Am. Chem. Soc. 107 (1985) 1431.
[15] V.V. Grushin, N. Herron, D.D. LeCloux, W.J. Marshall, V.A. Petrov, Y. Wang, New Chem. Commun. (2001) 1494.
[16] F.O. Graces, K. Dedian, N.L. Keder, R.J. Watts, Acta Crystallogr. C49 (1993) 1117.
[17] (a) F.O. Graces, K.A. King, R.J. Watts, Inorg. Chem. 27 (1988) 3464;
(b) S. Serroni, A. Juris, S. Campagna, M. Venturi, G. Denti, V. Balgani, J. Am. Chem. Soc. 116 (1994) 9086;
(c) P.M. Griffiths, F. Loiseou, F. Puntoriero, S. Serroni, S. Campagna, Chem. Commun. (2000) 2297.
[18] R.J. Holmes, S.R. Forrest, Y.-J. Tung, R.C. Kwong, J.J. Brown, S. Garon, M.E. Thompson, Appl. Phys. Lett. 82 (2003) 2422.

Available online at www.sciencedirect.com
SCIENCE DIRECT®
Polyhedron 24 (2005) 201–208
POLYHEDRON
www.elsevier.com/locate/poly

Synthesis, spectroscopic and electrochemical properties of some heteroleptic tris-chelates of ruthenium (II) involving 2,2′-bipyridine (bpy) and *N*-(aryl) pyridine-2-aldimine(L): X-ray crystal structures of $[Ru(bpy)(L_2)_2](ClO_4)_2 \cdot H_2O$ and 3-*N*(4-tolyl) imidazo [1,5a] pyridinium perchlorate

Dipankar Mishra [a], Subhendu Naskar [a], Bibhutosh Adhikary [a], Raymond J. Butcher [b], Shyamal Kumar Chattopadhyay [a,*]

[a] *Department of Chemistry, Bengal Engineering and Science University, Shibpur, Howrah 711 103, India*
[b] *Department of Chemistry, University of Howard, 525 College Street, NW, Washington, DC 20059, USA*

Received 28 September 2004; accepted 1 November 2004

Abstract

Four ruthenium (II) complexes of the formulae $[Ru(bpy)(L_1)_2](ClO_4)_2 \cdot H_2O$ (**A1**), $[Ru(bpy)(L_2)_2](ClO_4)_2 \cdot H_2O$ (**A2**), $[Ru(bpy)(L_3)_2](ClO_4)_2 \cdot H_2O$ (**A3**), $[Ru(bpy)(L_4)_2](ClO_4)_2 \cdot H_2O$ (**A4**) (where L_1 = *N*-(2-pyridylmethylene) phenyl amine, L_2 = *N*-(2-pyridylmethylene) 4-(methyl) phenyl amine, L_3 = *N*-(2-pyridylmethylene) 4-(chloro) phenyl amine, L_4 = *N*-(2-pyridylmethylene) 4-(fluoro) phenyl amine and bpy = 2,2′-bipyridyl) have been synthesized. In addition to these ruthenium complexes, we have also been able to isolate four imidazopyridinium perchlorate compounds **B1**–**B4** from the same reactions. The X-ray crystal structures of one representative ruthenium complex (**A2**) and the imidazopyridinium perchlorate compound (**B2**) have been determined. The Ru(II) center in the complex is coordinated by six N donors with a distorted octahedral geometry. The imine ligands (L) act as bidentate N,N donors.
© 2004 Elsevier Ltd. All rights reserved.

Keywords: Ruthenium (II) complexes; Bidentate N,N donors; Imidazopyridinium perchlorate; Synthesis; X-ray structures

1. Introduction

Chemistry of ruthenium with α–α′ diimine ligands is an area of unabated interest during the past two decades [1–16] because of the interesting photophysical and photochemical characteristics of these compounds and their possible applications in energy research [7,17], in electroluminescent devices [18,19], as well as sensors and switches [20,21]. A number of these compounds are also reported to exhibit an interesting non-linear optical response [22,23]. The α–α′ diimine ligands, most commonly investigated in these studies, are those where both the donor nitrogen atoms are part of heterocyclic rings like pyridine, pyrimidine and pyrazine. Comparatively less attention has been devoted [15,16,30] to systems where at least one nitrogen atom is not part of a heterocyclic ring. In this paper, we report on the synthesis and spectroscopic properties of four heteroleptic ruthenium (II) complexes (**A1**–**A4**), where Ru(II) is coordinated by one bipyridyl and two *N*-(aryl) pyridine-2-aldimine ligands (L). We also report here the

* Corresponding author. Tel.: +91 33 2668 4561; fax: +91 33 2668 4564/2916.
E-mail address: shch20@hotmail.com (S.K. Chattopadhyay).

0277-5387/$ - see front matter © 2004 Elsevier Ltd. All rights reserved.
doi:10.1016/j.poly.2004.11.011

synthesis and spectroscopic properties of four 3-*N*(aryl) imidazo [1,5a] pyridinium compounds (**B1**–**B4**), which were obtained as side products during the synthesis of the ruthenium complexes.

2. Experimental

2.1. Materials

Commercial ruthenium trichloride ($RuCl_3 \cdot xH_2O$) purchased from Arora Matthey (Kolkata, India) was processed by repeated evaporation to dryness with conc. HCl. '$Ru(bpy)Cl_3$' was prepared by the published procedure [24]. Acetonitrile used for spectroscopic and electrochemical studies was purified according to a reported method [25]. Tetraethyl ammonium perchlorate (TEAP), used for the electrochemical work, was prepared as reported in the literature [25]. All other chemicals were of analytical grade and used without further purification. The ligands (L) were prepared by reacting pyridine-2-aldehyde with the appropriate aryl amine using the published procedure [8].

2.2. Physical measurements

Elemental analyses were performed on a Perkin–Elmer 240 C, H, N analyzer. UV–Vis spectra were recorded using a JASCO7850 spectrophotometer. Luminescence spectra were obtained using a Perkin–Elmer LS55 fluorescence spectrophotometer. Magnetic susceptibilities were measured with a PAR model 155 vibrating sample magnetometer with $Hg[Co(SCN)_4]$ as the calibrant. Cyclic voltammetry and differential pulse voltammetry experiments were carried out using a PAR Versastat-II instrument driven by E-chem software. A three-electrode configuration with a Pt working and auxiliary electrodes, Ag/AgCl reference electrode and TEAP as the supporting electrolyte were used. The potentials were calibrated against the ferrocene/ferrocenium couple (0.44 V versus Ag/AgCl reference).

2.3. Synthesis of the complexes

CAUTION! Perchlorate salts of organic and metallo-organic species are potentially explosive, and though we have not encountered any problems in our work, nevertheless they should be handled with care.

The complexes **A1**–**A4** and the organic products **B1**–**B4** reported in this work were synthesized by a general procedure in almost similar yields; therefore, details are given for **A2** and **B2** as a representative example.

To a 30 ml methanolic solution of L_2 (1 mmol, 182 mg) solid '$Ru(bpy)Cl_3$' (0.5 mmol, 181.75 mg) was added and the reaction mixture was heated to reflux for 4 h. The solution was allowed to come to room temperature; a saturated methanolic solution (2 ml) of $NaClO_4$ was added and filtered. The filtrate was evaporated to dryness and the crude product was washed with water and dried over fused $CaCl_2$. The crude mass was then dissolved in chloroform and purified by column chromatography using a silica gel (60–120 mesh) column. A pink band was eluted with $CHCl_3$–CH_3CN (4:1), followed by a brown band eluted with $CHCl_3$–CH_3CN (3:2). Evaporation of the pink fraction led to isolation of **B2**, whereas **A2** was obtained from the brown fraction. The pink product **B2** was recrystallized from ethanol–isopropanol (1:1) (yield 70–75 mg, 34–36%). The brown product was recrystallized from dichloromethane to acetonitrile (1:2) solution (yield 175–180 mg, 31%). The elemental analyses data of all the compounds are in good agreement with the calculated values (Calc. values are in parentheses). $RuC_{34}H_{30}N_6O_9Cl_2$ (**A1**): C, 48.87 (48.92); H, 3.52 (3.59); N, 9.98 (10.07)%. $RuC_{36}H_{34}N_6O_9Cl_2$ (**A2**): C, 49.67 (49.88); H, 3.77 (3.92); N, 9.69 (9.70)%; $RuC_{34}H_{28}N_6O_9Cl_4$ (**A3**): C, 44.88 (44.98); H, 2.98 (3.08); N, 9.19 (9.26)%; $RuC_{34}H_{28}N_6O_9F_2Cl_2$ (**A4**): C, 46.53 (46.68); H, 3.13 (3.20); N, 9.54 (9.61)%; $C_{13}H_{11}N_2O_4Cl$ (**B1**): C, 52.89 (52.97); H, 3.66 (3.73); N, 9.43 (9.50)%; $C_{14}H_{13}N_2O_4Cl$ (**B2**): C, 54.41 (54.43); H, 4.17 (4.21); N, 8.97 (9.07)%; $C_{13}H_{10}N_2O_4Cl_2$ (**B3**): C, 47.37 (47.41); H, 2.99 (3.03); N, 8.46 (8.51)%; $C_{13}H_{10}N_2O_4FCl$ (**B4**): C, 49.86 (49.92); H, 3.18 (3.20); N, 8.89 (8.96)%.

2.4. X-ray crystallography

For both **A2** and **B2**, data were collected on a Bruker smart CCD area detector diffractometer at 93(2) K, using graphite monochromated Mo Kα radiation. The data were solved by direct methods [26] and refined by a least square program [27] using SHELX 97. The non-hydrogen atoms were refined with anisotropic displacement parameters. All hydrogen atoms were placed at calculated positions and refined as riding atoms using isotropic displacement parameters. The refinement converged with residuals summarized in Table 1. Corrections for Lorentz polarization effects and semiempirical absorption were applied.

2.4.1. Description of the structures

A2: The molecular structure of **A2** is given in Fig. 1. In this complex, Ru(II) is in an octahedral N_6 donor environment with the average *trans* angles being. ~175°, where as *cis* angles lie between 78° and 101°. The average Ru–N distance is 2.0602 Å (Table 2), which is quite comparable to that observed [28] for $[Ru(bpy)_3]^{2+}$. The average Ru–N distance (2.0585Å) observed for the Ru(II)-bpy fragment is also similar to that of the Ru(II)–$(L_2)_2$ fragment, where it has a value of 2.061 Å. The Ru–N_{imine} distances (2.057 Å) within the Ru(II)–$(L_2)_2$ fragment are shorter than the Ru–N_{py}

Table 1
Crystallographic data for **A2** and **B2**

	A2	**B2**
Empirical formula	$C_{36}H_{34}Cl_2N_6O_9Ru$	$C_{14}H_{13}N_2O_4Cl$
Formula weight	866.66	308.71
Temperature (K)	93(2)	93(2)
Wavelength (Å)	0.71073	0.71073
Crystal system	triclinic	orthorhombic
Space group	$P\bar{1}$	*Pbca*
Unit cell dimensions		
a (Å)	11.5049(11)	10.0776(7)
b (Å)	13.2695(13)	7.7626(5)
c (Å)	13.4267(12)	34.819(3)
α (°)	98.453(2)	90
β (°)	99.652(2)	90
γ (°)	113.044(2)	90
Volume (Å^3)	1807.7(3)	2723.8(3)
Z	2	8
Density (calc.) (g cm^{-3})	1.592	1.489
Absorption coefficient (mm^{-1})	0.646	0.256
F(0 0 0)	884	1272
Crystal size (mm)	0.05 × 0.30 × 0.86	0.45 × 0.5 × 0.99
Index ranges	$-14 \leqslant h \leqslant 14$, $-16 \leqslant k \leqslant 17$, $-18 \leqslant l \leqslant 17$	$-13 \leqslant h \leqslant 13$, $-10 \leqslant k \leqslant 9$, $-46 \leqslant l \leqslant 46$
Reflections collected	13 617	19 578
Independent reflections	8631 [R_{int} = 0.0290]	3494 [R_{int} = 0.0634]
Absorption correction	semi-empirical	semi-empirical
Refinement method	full-matrix least-squares on F^2	full-matrix least-squares on F^2
Data/restraints/parameters	8631/0/516	3494/0/191
Goodness-of-fit on F^2	1.053	1.090
Final *R* indices [$I > 2\sigma(I)$]	R_1 = 0.0407, wR_2 = 0.0857	R_1 = 0.0586, wR_2 = 0.1460
R indices (all data)	R_1 = 0.0542, wR_2 = 0.0907	R_1 = 0.0696, wR_2 = 0.1526
Largest difference peak and hole (e Å^{-3})	0.728 and −0.719	0.794 and −0.433

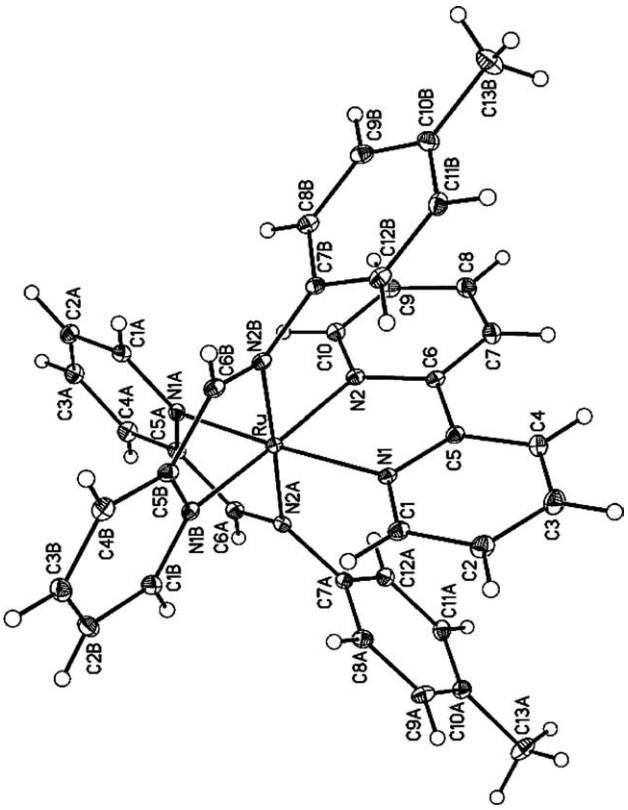


Fig. 1. ORTEP diagram and atom numbering scheme for the cation of **A2**, showing 50% probability ellipsoids.

distances (the average is 2.065 Å). The fact that the Ru–N_{imine} distances are shorter than the Ru–N_{py} distances of Ru-bpy as well as the Ru(II)–$(L_2)_2$ fragment is probably due the greater back bonding acceptor capability of the imine moiety compare to the pyridine moiety. The bite angle of the imine ligand (78.02(9)° (Table 2)) is also very similar to that of bpy (78.61(9)°) and agrees well with the values reported earlier [29,30]. One of the perchlorate ions is disordered in the lattice.

B2: The ORTEP diagram along with the atom numbering scheme for the compound **B2** is shown in Fig. 2. The bond distances within the imidazo pyridine fragment clearly indicate that there is extensive delocalization within the imidazole ring and the C5–C4 and N1–C1 part of the pyridine ring. However the C4–C3 and C1–C2 bonds are more like double bonds. The aryl ring attached to the N2 atom is twisted by about 46° from the plane of the imidazopyridine fragment (Table 3).

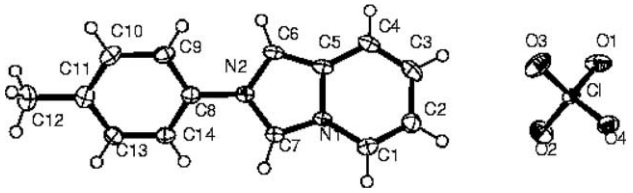


Fig. 2. ORTEP diagram and atom numbering scheme for the compound **B2**, showing 50% probability ellipsoids.

Table 2
Selected bond distances (Å) and bond angles (°) for **A2**

Bond distances			
Ru–N(2)	2.053(2)	Ru–N(2A)	2.059(2)
Ru–N(2B)	2.057(2)	Ru–N(1)	2.064(2)
Ru–N(1B)	2.057(2)	Ru–N(1A)	2.071(2)
Bond angles			
N(2)–Ru–N(2B)	96.38(9)	N(1B)–Ru–N(1)	98.46(9)
N(2)–Ru–N(1B)	174.03(9)	N(2A)–Ru–N(1)	97.99(8)
N(2B)–Ru–N(1B)	78.02(9)	N(2)–Ru–N(1A)	94.23(9)
N(2)–Ru–N(2A)	85.82(9)	N(2B)–Ru–N(1A)	101.60(8)
N(2B)–Ru–N(2A)	177.80(9)	N(1B)–Ru–N(1A)	88.97(9)
N(1B)–Ru–N(2A)	99.79(9)	N(2A)–Ru–N(1A)	78.02(9)
N(2)–Ru–N(1)	78.61(9)	N(1)–Ru–N(1A)	172.11(9)
N(2B)–Ru–N(1)	82.64(8)		

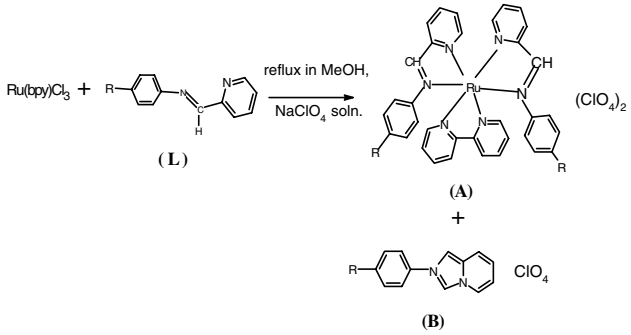
Table 3
Selected bond distances (Å) and bond angles (°) for **B2**

C(1)–C(2)	1.339(3)	C(2)–C(1)–N(1)	118.4(2)
C(1)–N(1)	1.390(3)	C(1)–C(2)–C(3)	121.3(2)
C(2)–C(3)	1.439(3)	C(4)–C(3)–C(2)	120.7(2)
C(3)–C(4)	1.349(3)	C(3)–C(4)–C(5)	119.1(2)
C(4)–C(5)	1.419(3)	C(6)–C(5)–N(1)	106.09(18)
C(5)–C(6)	1.367(3)	C(6)–C(5)–C(4)	135.5(2)
C(5)–N(1)	1.409(3)	N(1)–C(5)–C(4)	118.4(2)
C(6)–N(2)	1.379(3)	C(5)–C(6)–N(2)	106.97(18)
C(7)–N(1)	1.337(3)	N(1)–C(7)–N(2)	107.50(18)
C(7)–N(2)	1.341(3)	C(9)–C(8)–N(2)	119.03(19)
C(8)–C(9)	1.386(3)	C(14)–C(8)–N(2)	119.67(19)
C(8)–C(14)	1.392(3)	C(7)–N(2)–C(6)	110.14(18)
C(8)–N(2)	1.429(3)	C(7)–N(2)–C(8)	124.94(18)
C(9)–C(10)	1.391(3)	C(6)–N(2)–C(8)	124.92(18)
C(10)–C(11)	1.397(3)	C(7)–N(1)–C(1)	128.70(19)
C(11)–C(13)	1.392(3)	C(7)–N(1)–C(5)	109.30(18)
		C(1)–N(1)–C(5)	121.98(19)

3. Results and discussion

Reaction of 'Ru(bpy)Cl_3' with L in refluxing methanol produces a mixture of the Ru(II) complex **A** and the imidazopyridine derivative **B**, both of which can be separated by column chromatography and on recrystallization, crystalline compounds can be isolated for both species. Crystal structure determinations were made for **A2** and **B2** as representative members of **A** and **B**, respectively.

The imidazopyridinium derivatives **B1** to **B4**: The formation of the imidazopyridinium derivatives in the reaction described in Scheme 1 is very interesting. Though imidazopyridine compounds and some of their simple salts are well known [31,32], the 3-*N*(aryl) imidazopyridinium derivatives are rare. Thus a simple single step synthesis of these compounds starting from readily available laboratory chemicals, as described above, is attractive. It has been reported [31] that imidazopyridine is formed in the reaction of 2-picolylamine with formic acid in presence of $POCl_3$. Probably, a similar mechanism is operative here. The 'Ru(bpy)Cl_3' (where the oxidation state of ruthenium is closer to +4 than +3) first

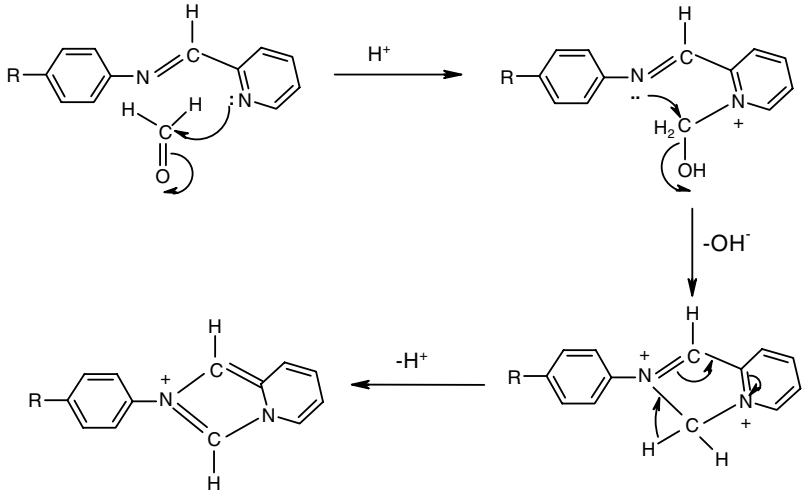


	L	A	B
R = H	L_1	**1**	**1**
R = Me	L_2	**2**	**2**
R = Cl	L_3	**3**	**3**
R = F	L_4	**4**	**4**

Scheme 1.

oxidizes the solvent methanol to formaldehyde, which then reacts with the schiff base in the presence of 'Ru(bpy)Cl_3' to produce **B**, as described in Scheme 2.

The 3-*N*(aryl) imidazo [1,5a] pyridinium compounds (**B1**–**B4**) are deep pink in colour due to a strong absorption at 520–535 nm. The solvatochromism (Fig. 3) exhibited by this band clearly suggests it is a charge transfer transition. It was also observed that for a given solvent the energy of the longest wavelength band followed the order **B3** < **B1** = **B2** < **B4**. The same trend was followed in the E^0 value of the first oxidation peak for the compounds (Table 7). In fact, a plot of energy of the transition (cm^{-1}) versus E^0 value yields a good linear relationship ($R = 0.99$; supplementary Figure. 1). However, this trend is different from that observed for the HOMO–LUMO gap for these compounds (in the gaseous phase) as calculated by the PM3 method [33a,b], which follows the order **B3** < **B4** ≈ **B1** < **B2**. This indicates that solvation plays a very important role in determining the energy of the frontier orbitals of these compounds, which is quite expected because of their charged structures and appreciable ground state dipole moment (Table 5). Interestingly, the transition energy follows a roughly linear relationship (Table 6, supplementary Figure. 2) with the change in dipole moment ($\Delta\mu_{ge} = \mu_e - \mu_g$) between the ground state (μ_g) and the first excited singlet state (μ_e), assuming the excited state has the same geometry as the ground state i.e., a Franck–Condon excited state. It was also observed that the intensity of the first charge transfer transition follows a linear correlation (Table 6, supplementary Figure 3) with $\Delta\mu_{ge}^2$. All the four compounds **B1**–**B4** exhibit luminescence, with a strong emission at ~380 nm (excited at 280 nm or 240 nm) at room temperature (Table 4). These compounds with a strong charge transfer transition near the visible region, appreciable dipole moment in the ground state, moderate value of $\Delta\mu$, as



Scheme 2.

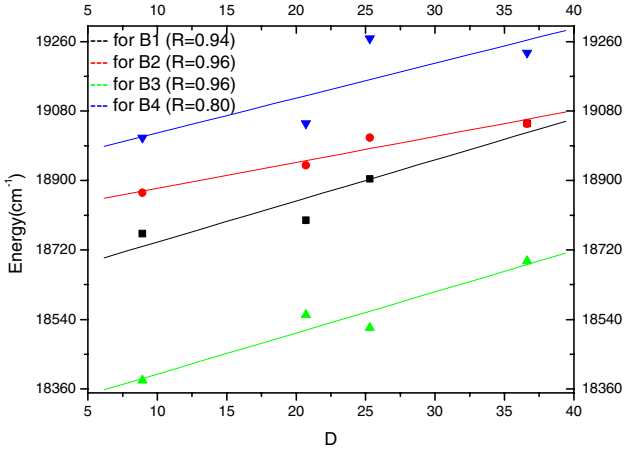


Fig. 3. Plot of energy of CT transition vs. Dielectric constant (*D*) for compounds **B**.

well as stable excited state, are good candidates for screening of their possible non linear optical properties [23]. Besides, the imidazopyridinium cephalosporins are known to exhibit good Gram positive activity, as well as excellent activity against K1 β-lactamase producing *Klebsiella aerogenes* 1082 E strain [34].

Table 5
HOMO and LUMO energies and calculated dipole moments of the imidazopyridinium derivatives

Compounds	B1	B2	B3	B4
E_{HOMO} (eV)	−13.09	−13.23	−12.77	−13.17
E_{LUMO} (eV)	−4.99	−5.05	−5.16	−5.11
E_{LUMO} (eV) − E_{HOMO} (eV)	8.10	8.18	7.61	8.06
μ_g (debye)	2.70	3.70	7.15	6.53
μ_e (debye)	4.29	1.42	2.06	8.36
$\Delta\mu_{ge}$ (i.e., $\mu_e - \mu_g$) (debye)	1.59	−2.28	−5.09	1.83
$(\Delta\mu_{ge})^2$	2.53	5.20	25.91	3.349

The redox behaviors of the pink compounds (**B**) have been investigated using cyclic voltammetry (CV), as well as differential pulse voltammetry (DPV) (Table 7). Both **B1** and **B2** exhibit one quasi reversible oxidative response at around 1.02 V; in the DPV one sharp peak is obtained at the same potential demonstrating that only one redox couple is involved. However for **B3** and **B4** no resolvable peak was observed in the CV,

Table 4
UV–Vis spectra and luminescence spectral data

Compounds	λ_{max}/nm (ε/lit mol^{-1} cm^{-1})[a]	λ_{em}/nm[b]
A1	631 (641), 481 (5938), 440 (5792), 388[c] (1833), 283 (21 994), 235 (13 196)	733
A2	631 (525), 482 (6472), 438 (6220), 315[c](13 448), 282 (23 534), 231[c] (19 331)	725
A3	631 (924), 485 (8375), 440 (7883), 390[c] (3941), 282 (39 413), 240[c] (24 633)	710
A4	631 (957), 481 (10 209), 437 (9444), 387[c] (3190), 283 (36 499), 237 (21 695)	722
B1	525 (886), 285 (6203), 270 (5907), 232 (12 582)	384
B2	525 (1824), 310[c] (6566), 282 (12 787), 245 (23 345)	382
B3	535 (3499), 288 (7607), 265[c] (7150), 237[c] (10 345)	378
B4	520 (759), 285 (7290), 270 (6683), 232 (13 001)	383

[a] Acetonitrile solution.
[b] Qualitative spectra recorded in acetonitrile solutions at room temp., for **A1**, **A2**, **A3**, **A4** the excitation wavelength was 480nm and for **B1**, **B2**, **B3** and **B4** it was 285, 280, 265 and 285 nm, respectively.
[c] Shoulder.

Table 6
Correlation between the lowest energy absorption band and $\Delta\mu_{ge}$ for the imidazopyridinium derivatives

Solvent	Energy (cm^{-1}) vs. $\Delta\mu_{ge}$			Molar extinction coefficient vs. $(\Delta\mu_{ge})^2$		
	Slope	Intercept	R^a	Slope	Intercept	R^a
Dichloromethane	64.19	18 819	0.79	231.52	394.27	0.99
Acetone	46.21	18 879	0.71	59.65	824.40	0.99
Ethanol	74.68	18 999	0.79	94.45	521.39	0.98
Acetonitrile	59.89	19 063	0.87	108.27	740.82	0.95

[a] R = correlation coefficient.

Table 7
Cyclic voltammetry and differential pulse voltammetry (DPV) data

Compounds	E^0/V (ΔE_p/mV) in MeCN solution
A1	1.45 (71), −0.86 (208), −1.61 (CV)/−1.46 (DPV), −1.74 (DPV)
A2	1.45 (90), −0.86 (217), −1.54 (CV)/−1.41 (DPV), −1.69 (DPV)
A3	1.49 (92), −0.83 (145), −1.50 (CV)/−1.41 (DPV), −1.57 (DPV)
A4	1.48 (105), −0.82 (132), −1.56 (CV)/−1.42 (DPV), −1.70 (DPV)
B1	1.02 (145)
B2	1.02 (286)
B3	1.07, 0.91 (DPV)
B4	1.26, 1.06 (DPV)

but in the DPV two well-defined oxidation peaks are observed at 0.91 and 1.07 V for **B3** and at 1.06 and 1.26 V for **B4**.

The ruthenium complexes **A1** to **A4**: The heteroleptic tris chelate complexes are brown in colour with a strong absorption around 480nm. For *tris*-chelate complexes such as these three isomers are possible [16]. However determination of the X-ray crystal structure of one representative complex **A2**, shows that in the isolated complex only one isomer is present in the solid state where the two N_{py} of the two ligands (L) are *cis* to each other, whereas the two N_{imine} are *trans* to each other, which may be called a *cis–trans* isomer. The similarity of spectroscopic, electrochemical and chromatographic behaviors of **A1**, **A3** and **A4** with that of **A2** led us to believe that in these complexes the same isomer also predominates.

The redox behavior of the complexes was studied by cyclic voltammetry (CV) and differential pulse voltammetry (DPV). All the complexes undergo a quasi-reversible oxidation at ~1.3 to 1.4 V which may be assigned to Ru(II) to Ru(III) oxidation. In the reductive side all the complexes show a two-electron quasi-reversible reduction at −0.8 V and two one electron quasi-reversible reductions near −1.4 to −1.7 V. The last two peaks are not resolved in the CV, but they can be well identified in the DPV (supplementary Figure 4). As our PM3 calculations show that the LUMO of the ligand L is about 0.2 eV lower in energy than that of bpy, the first reduction is assigned to electron addition to the π* orbital of coordinated L. In fact the EHMO calculation shows that LUMO and LUMO + 1 have large contributions from $L_{\pi*}$ orbitals and are separated from each other by only 0.03 eV, so that the first two electron reduction is probably due to simultaneous electron addition to LUMO and LUMO + 1. The second and third reductions are probably due to addition of electrons to LUMO + 2 and LUMO + 3, where the former is mainly based on bpy, and the later have contributions from all the three ligands (see supplementary Figure 5 for pictures of the HOMOs and LUMOs).

The visible region of the electronic spectra of the complexes consists of a weak transition at ~630 nm and a broad envelope from 600 to 375 nm consisting of two peaks at ~480 and ~440 nm and a poorly resolved shoulder around 380 nm. The weak intensity of the first transition suggests that it is probably a charge transfer transition to a ^{3}MLCT state [4,35,36]. The bands near 480nm and 440nm are charge transfer transitions to ^{1}MLCT states. Under the C_2 symmetry of the complex, the metal dπ orbitals will transform as $a + 2b$. The lowest energy π* orbital of bpy will transform as b while the lowest energy π* orbitals of the two imine ligands will transform as $a + b$. Thus nine MLCT transitions are possible in principle, six of them are charge transfer from metal to imine ligand Lπ* orbitals, while three of them are charge transfer from metal to bpy π* orbital. Overlapping of these bands is expected to give rise to a broad envelope. As mentioned earlier, the ligand Lπ* orbitals are of lower energy than the bpy π* orbital, so the MLCT transition to the later orbital is expected to be of higher energy than those involving the Lπ* orbital. Earlier workers [15] have assigned the peak around 480 nm to that involving the Lπ* orbital, while the peak near 440 nm to that involving the bpy π* orbital. However the comparable intensity of both the bands precludes such an assignment, as only one bpy ligand is present, compared to two L ligands. Moreover it was pointed out by Lever [37,38] that for a MLCT transition involving the bpy π* orbital, a molar extinction coefficient of ~4000 $M^{-1}\,cm^{-1}$ per bpy ligand is expected. As the molar extinction coefficients of the transition near 440nm for the present complexes are much larger than that predicted by Lever, so the band ~440 nm as well as that ~480 nm are assigned to MLCT transitions involving the Lπ* orbital, while the shoulder around 380nm is probably due to that involving the bpy π* orbital. This is also supported by the large difference of the observed reduction potential in the complexes between the L based reduction and bpy based reduction. The other higher energy transitions are probably intraligand in nature. An EHMO calculation on the compound **A2** supports this conclusion. Since the actual symmetry of the molecule in this case is less than C_2 (it is C_1), all

the orbitals are of 'a' symmetry. The three d orbitals are 106A (−12.25 eV), 105A (−12.31 eV) and 104A (−12.38 eV), where 106A and 105A have appreciable contribution from schiff base ligands and 104A has similarly appreciable contribution from bpy. The LUMO, LUMO + 1 and LUMO + 2 are 107A (−10.01 eV), 108A (−9.97 eV) and 109A (−9.68 eV), respectively; again the first two are schiff base ligand based where as the last one is bpy based. Thus the first two bands are probably due to the transitions between 106A → 107A, 108A and 105A → 107A, 108A, where as the charge transfer to bpy 104A → 109A is expected to lie at higher energy. A preliminary luminescence study shows that all the complexes are luminescent at room temperature. Excitation at 480 nm leads to a broad emission at 700–730 nm.

4. Computations

The PM3 and EHMO calculations were carried out with the HYPERCHEM 7.01 program [39] using the default parameters of the program. Single point PM3 calculations (which includes configuration interaction involving single, excited states arising from the 10 highest occupied and 10 lowest unoccupied orbitals) on the ligands were made on the geometries obtained directly from the crystal structure or when the structure was not available, the geometry was optimized by the MM+ method. An extended Hückel calculation was done on **A2** using the geometry taken directly from the crystal structure after removing the perchlorate counter ions.

Acknowledgments

D.M. and S.N. acknowledge CSIR, UGC respectively, for their fellowships. S.K.C. acknowledges AICTE and UGC, New Delhi, for financial support. We thank Dr. A. Barbieri for her comments and suggestions.

Appendix A. Supplementary data

The structural data for **A2** and **B2** have been deposited at the Cambridge Crystallographic Data Centre with the deposition numbers 240405 and 240406 respectively. Copies of this information may be obtained free of charge from The Director, CCDC, 12 Union Road, Cambridge CB2 IEZ, UK (Fax: +44-1223-336033; e-mail: deposit@ccdc.cam.ac.uk or www: http://www.ccdc.cam.ac.uk). Supplementary data associated with this article can be found, in the online version, at doi:10.1016/j.poly.2004.11.011.

References

[1] V. Balzani, F. Scandola, Supramolecular Photochemistry, Ellis Horwood, Chichester, UK, 1991.
[2] K. Kalyansundaram, Photochemistry of Polypyridine and Porphyrin Complexes, Academic Press, New York, 1992.
[3] A.M.W. Cargill Thompson, M.C.C. Smailes, J.C. Jeffery, M.D. Ward, J. Chem. Soc., Dalton Trans. (1997) 737.
[4] E.C. Constable, R.W. Handel, C.E. Housecroft, A.M. Morales, L. Flamigni, F. Barigelletti, J. Chem. Soc., Dalton Trans. (2003) 1220.
[5] V. Aranyos, J. Hjelm, A. Hagfeldt, H. Grennberg, J. Chem. Soc., Dalton Trans. (2003) 1280.
[6] A. Hagfeldt, M. Gratzel, Acc. Chem. Res. 33 (2000) 269.
[7] H. Durr, S. Bosmann, Acc. Chem. Res. 34 (2001) 905.
[8] E.V. Dose, L.J. Wilson, Inorg. Chem. 17 (1978) 2660.
[9] T.J. Meyer, Acc. Chem. Res. 22 (1989) 163.
[10] M.-a. Haga, T. Takasugi, A. Tomie, M. Ishizuya, T. Yamada, M.D. Hossain, M. Inoue, J. Chem. Soc., Dalton Trans. (2003) 2069.
[11] S. Rau, T. Büttner, C. Temme, M. Ruben, H. Görls, D. Walther, M. Duati, S. Fanni, J.G. Vos, Inorg. Chem. 39 (2000) 1621.
[12] D.P. Rillema, R. Sahai, P. Matthews, A.K. Edwards, R.J. Shaver, L. Morgan, Inorg. Chem. 29 (1990) 167.
[13] X. Xiaoming, M.–a. Haga, T.M. Inoue, Y. Ru, A.W. Addison, K. Kano, J. Chem. Soc., Dalton Trans. (1993) 2477.
[14] M.–a. Haga, T.–a. Ano, K. Kano, S. Yamabe, Inorg. Chem. 30 (1991) 3843.
[15] S. Choudhury, A.K. Deb, S. Goswami, J. Chem. Soc., Dalton Trans (1994) 1305.
[16] P. Byabartta, J. Dinda, P.K. Santra, C. Sinha, K. Panneerselvam, F. Liao, T.H. Lu, J. Chem. Soc., Dalton Trans. (2001) 2825.
[17] M.K. Nazeeruddin, P. Péchy, T. Renouard, S.M. Zakeeruddin, R. Humphrey-Baker, P. Comte, P. Liska, L. Cevey, E. Costa, V. Shklover, L. Spiccia, G. Deacon, C.A. Bignozzi, M. Gratzel, J. Am. Chem. Soc. 123 (2001) 1613.
[18] J. Slinker, D. Bernards, P.L. Houston, H.D. Abruna, S. Bernhard, G.G. Malliaras, Chem. Commun. (2003) 2392.
[19] S. Ranjan, S.Y. Lin, K.C. Hwang, Y. Chi, W.L. Ching, C.S. Liu, Inorg. Chem. 42 (2003) 1248.
[20] A.P. de Silva, B. McCaughan, B.O.F. Mckinney, M. Querol, J. Chem. Soc., Dalton Trans. (2003) 1902.
[21] P.D. Beer, J. Cadman, New. J. Chem. 23 (1994) 347.
[22] H. Sakaguchi, L.A. Gomez-Jahn, M. Prichard, T.L. Penner, D.G. Whitten, T. Nagamura, J. Phys. Chem. 97 (1993) 1474.
[23] S. Di Bella, Chem. Soc. Rev. 30 (2001) 355.
[24] (a) R.A. Krause, Inorg. Chim. Acta 22 (1977) 209;
(b) S. Anderson, K.R. Seddon, J. Chem. Res. (1979) 74.
[25] D.T. Sawyer, A. Sobkowiak, J.L. Roberts Jr., Electrochemistry for Chemists, 2nd ed., Wiley, New York, 1995, pp. 333–336.
[26] G.M. Sheldrick, SHELX97 [Includes SHELXS97, SHELXL97, CIFTAB] – Programs for Crystal Structure Analysis (Release 97-2), Göttingen, Germany, 1998.
[27] G.M. Sheldrick, SHELXS-86. Program for the Solution of Crystal Structures, Univ. of Göttingen, Germany, 1986.
[28] D.P. Rillema, D.S. Jones, H.A. Levy, J. Chem. Soc., Chem. Commun. (1979) 849.
[29] M. Menon, S. Choudhury, A. Pramanik, A.K. Deb, S.K. Chandra, N. Bag, S. Goswami, A. Chakravorty, J. Chem. Soc., Dalton Trans. (1994) 57.
[30] K.N. Mitra, S. Choudhury, S. Goswami, S.-M. Peng, Polyhedron 16 (1997) 1605.
[31] J.D. Bower, G.R. Ramage, J. Chem. Soc. (1955) 2834.
[32] E.G. Glover, L.W. Peck, J. Chem. Soc., Perkin Trans. I (1980) 959.

[33] (a) J.J.P. Stewart, J. Comp. Chem. 12 (1991) 320;
(b) J.J.P. Stewart et al. QCPE# 506.
[34] R. Lattrell, J. Blumbach, W. Duerckheimer, K. Fleischmann, R. Kirrstetter, N. Klessel, B. Mencke, K.H. Scheunemann, W. Schwab, H. Seliger, U. Stache, I. Winkler, J. Antibiotics 41 (1988) 1395.
[35] J.A. Demas, J. Chem. Edu. 60 (1983) 803.
[36] J.A. Demas, G.A. Crossby, J. Am. Chem. Soc. 93 (1971) 2841.
[37] A.B.P. Lever, Inorganic Electronic Spectroscopy, 2nd ed., Elsevier Science Publishers, New York, 1984.
[38] A.B.P. Lever, P.R. Auburn, E.S. Dodsworth, M.–a. Haga, W. Lui, M. Melnik, A. Nevin, J. Am. Chem. Soc. 110 (1988) 8076.
[39] HYPERCHEM for Windows, Release 7.01, Hypercube Inc., 115 NW 4th Street, Gainesville, FL 32601.

Available online at www.sciencedirect.com
SCIENCE DIRECT®
Polyhedron 24 (2005) 209–214
POLYHEDRON
www.elsevier.com/locate/poly

Diorganotin(IV) derivatives containing the 3,5-dimethyl-4-(4′-pyridyl)pyrazole ligand

Qian Cui [a], Xiu-Ying Cao [b], Liang-Fu Tang [a,*]

[a] Department of Chemistry, State Key Laboratory of Elemento-Organic Chemistry, Nankai University, Tianjin 300071, PR China
[b] Tianjin Institute of Scientific and Technical Information, Tianjin 300074, PR China

Received 28 September 2004; accepted 2 November 2004
Available online 19 December 2004

Abstract

3,5-Dimethyl-4-(4′-pyridyl)pyrazole, prepared by the reaction of 3-(4-pyridyl)pentane-2,4-dione with hydrazine hydrate, reacts with R_2SnCl_2 (R = Ph, Et and *n*-Bu) in a 1:1 ratio to yield 2:1 (ligand:tin) adducts. In the crystal structure of the Ph_2SnCl_2 adduct, two 3,5-dimethyl-4-(4′-pyridyl)pyrazole ligands coordinate to the tin atom through the pyridyl nitrogen atom instead of the pyrazolyl nitrogen atom, and the molecules are connected into a linear chain through intermolecular N–H···N hydrogen bonds. The reaction of 3,5-dimethyl-4-(4′-pyridyl)pyrazole with dibromomethane under phase transfer catalytic conditions affords bis[3,5-dimethyl-4-(4′-pyridyl)pyrazol-1-yl]methane. Treatment of this potential polydentate ligand with R_2SnCl_2 yields 1:1 adducts, in which bis[3,5-dimethyl-4-(4′-pyridyl)pyrazol-1-yl]methane coordinates to the tin atom through the pyridyl nitrogen atom to form six-coordinate diorganotin linkage coordination polymers, leading to a bridging instead of a general chelating metal coordination. In all new complexes, the pyridyl nitrogen atom exhibits stronger donating ability than the pyrazolyl nitrogen to the tin atom.
© 2004 Elsevier Ltd. All rights reserved.

Keywords: Bis(pyrazol-1-yl)methane; Organotin(IV); Pyridine; X-ray structure

1. Introduction

For a long time diorganotin complexes containing nitrogen donor ligands have attracted considerable attention due to their potential biological applications [1,2]. Many complexes of the type R_2SnX_2(N–N) have been synthesized and tested for their antitumor activities [3–5]. Poly(pyrazol-1-yl)alkanes, especially bis(pyrazol-1-yl)methanes, have also been found to act as good donors to organotin compounds [6–11]. The interactions between poly(pyrazol-1-yl)alkanes and tin(IV) or organotin(IV) acceptors indicate that the donating ability of the ligands can be easily controlled by varying the substituents of the pyrazolyl ring, leading to a variable coordination geometry of the tin atom. Recently, we have also successfully prepared a variety of five and six-coordinate organotin(IV) complexes with symmetric or asymmetric bis(pyrazol-1-yl)methane [12,13], and bidentate organotin Lewis acid derivatives of bis(pyrazol-1-yl)methane [14,15], as well as novel five and six-coordinate diorganotin(IV) linkage coordination polymers with bis(1,2,4-triazol-1-yl)methane [16]. Poly(pyrazol-1-yl)alkanes containing heteroatoms such as phosphine or sulfur in the pyrazolyl rings display variable coordination modes toward different metals [17,18], which encourages us to investigate the effects of more extensive donor sets on the coordination modes of poly(pyrazol-1-yl)alkanes. Herein, we report the synthesis and structural characterization of diorganotin(IV) derivatives containing 3,5-dimethyl-4-(4′-pyridyl)pyrazole. Treatment of diorganotin(IV) chloride with this ligand yields 1:2 adducts, while employment of its

* Corresponding author. Tel.: +86 22 234 99114; fax: +86 22 235 02458.
E-mail address: lftang@nankai.edu.cn (L.-F. Tang).

0277-5387/$ - see front matter © 2004 Elsevier Ltd. All rights reserved.
doi:10.1016/j.poly.2004.11.016

derivative, bis(3,5-dimethyl-4-(4′-pyridyl)pyrazol-1-yl) methane, gives a 1D linkage coordination polymer.

2. Experimental

Solvents were dried by standard methods and distilled prior to use. NMR spectra (^{1}H, ^{13}C and ^{119}Sn) were recorded on a Bruker AV300 spectrometer, and the chemical shifts were reported in ppm with respect to reference standards (internal $SiMe_4$ for ^{1}H NMR and ^{13}C NMR spectra, external $SnMe_4$ for ^{119}Sn NMR). IR spectral data were obtained from a Bruker Equinox55 spectrometer in KBr pellets. Elemental analyses were carried out on a Perkin–Elmer 240C analyser. Melting points were reported with a PHMK melting-point apparatus and were uncorrected.

2.1. Preparation of 3,5-dimethyl-4-(4′-pyridyl)pyrazole (*1*)

Hydrazine hydrate (4 ml, 85%, 68 mmol) was added to a toluene solution of raw 3-(4-pyridyl)pentane-2,4-dione, obtained by the reaction of 4-methylpyridine (18.2 ml, 186 mmol) with acetyl chloride (10.6 ml, 149 mmol) according to the literature method [19], and then the mixture was stirred at room temperature overnight. After removal of the solvent under reduced pressure, the residue was recrystallized from water to yield 1.6 g of **1** as white plate crystals, m.p. 105–107 °C. ^{1}H NMR ($CDCl_3$): δ 8.63 (d, 2H, α-Py*H*), 7.24 (d, 2H, β-Py*H*), 4.30 (s, br, 1H, N*H*), 2.37 (s, 6H, CH_3). ^{13}C NMR ($CDCl_3$): δ 11.83 (*C*H_3), 100.00, 115.72, 123.71, 142.39, 149.55 (carbons of pyrazolyl and pyridyl rings). IR: ν_{NH} = 3407.0 (m); $\nu_{pyridyl\ ring}$ = 1605.7 (s) cm^{-1}. *Anal.* Calc. for $C_{10}H_{11}N_3$: C, 69.34; H, 6.40; N, 24.26. Found: C, 69.12; H, 6.17; N, 24.43%.

2.2. Reaction of *1* with R_2SnCl_2 (R = Ph, Et or n-Bu)

All reactions were carried out in a similar manner, so a general procedure is described. To a stirred solution of R_2SnCl_2 (1 mmol) in 15 ml ether at room temperature, a solution of **1** (1 mmol) in 15 ml ether was added. The reaction mixture was stirred continuously for 6 h at room temperature, during which time a precipitate gradually formed. The precipitate was filtered off, washed with ether and dried in vacuo. Yields, melting points and analytical data are given below.

2.2.1. [Bis(3,5-dimethyl-4-(4′-pyridyl)pyrazole)] diphenyltin dichloride (*2*)

This compound was obtained by the reaction of **1** with Ph_2SnCl_2. White solid; yield: 82%; m.p. 155–158 °C. ^{1}H NMR (CD_3COCD_3): δ 8.61 (d, 4H, α-Py*H*), 7.50 (d, 4H, β-Py*H*), 8.06, 7.41 (m, m, 4H, 6H, C_6H_5), 2.36 (s, 12H, CH_3). IR: ν_{NH} = 3294.0 (m); $\nu_{pyridyl\ ring}$ = 1612.4 (s) cm^{-1}. *Anal.* Calc. for $C_{32}H_{32}Cl_2N_6Sn$: C, 55.68; H, 4.67; N, 12.18. Found: C, 55.75; H, 4.84; N, 12.49%.

2.2.2. [Bis(3,5-dimethyl-4-(4′-pyridyl)pyrazole)] diethyltin dichloride (*3*)

This compound was obtained by the reaction of **1** with Et_2SnCl_2. Pale-yellow solid; yield: 85%; m.p. 162–165 °C. ^{1}H NMR (CD_3SOCD_3): δ 8.57 (d, 4H, α-Py*H*), 7.36 (d, 4H, β-Py*H*), 2.28 (s, 12H, CH_3), 1.56 (q, 4H, SnCH_2), 1.26 (t, 6H, CH_2 CH_3). IR: ν_{NH} = 3262.3 (m); $\nu_{pyridyl\ ring}$ = 1611.7 (s) cm^{-1}. *Anal.* Calc. for $C_{24}H_{32}Cl_2N_6Sn$: C, 48.52; H, 5.43; N, 14.14. Found: C, 48.34; H, 5.28; N, 14.29%.

2.2.3. [Bis(3,5-dimethyl-4-(4′-pyridyl)pyrazole)] di(n-butyl)tin dichloride (*4*)

This compound was obtained by the reaction of **1** with *n*-Bu_2SnCl_2. Pale-yellow solid; yield: 78%; m.p. 152–154 °C. ^{1}H NMR (CD_3SOCD_3): δ 8.56 (d, 4H, α-Py*H*), 7.35 (d, 4H, β-Py*H*), 2.27 (s, 12H, CH_3), 1.65–1.56 (m, 8H, SnCH_2CH_2), 1.36–1.24 (m, 4H, CH_2CH$_3$), 0.87 (t, 6H, CH_2CH_3). ^{13}C NMR (CD_3SOCD_3): δ 11.37, 13.62, 25.56, 27.76, 37.72 (carbons of butyl and methyl groups), 114.13, 122.41, 142.13, 149.24 (carbons of pyrazolyl and pyridyl rings). ^{119}Sn NMR (CD_3SOCD_3): δ −214 (s, br). IR: ν_{NH} = 3250.0 (m); $\nu_{pyridyl\ ring}$ = 1612.9 (s) cm^{-1}. *Anal.* Calc. for $C_{28}H_{40}Cl_2N_6Sn$: C, 51.72; H, 6.20; N, 12.92. Found: C, 51.96; H, 6.08; N, 12.69%.

2.3. Preparation of bis[3,5-dimethyl-4-(4′-pyridyl) pyrazol-1-yl]methane (*5*)

3,5-Dimethyl-4-(4′-pyridyl)pyrazole (3.25 g, 18.8 mmol), dibromomethane (1.38 ml, 9.4 mmol), tetrabutylammonium bromide (0.5 g, 1.6 mmol) and sodium hydroxide (5.7 g, 142.5 mmol) were added into a mixed solvent of water (10 ml) and benzene (50 ml). The mixture was stirred and refluxed for 48 h. After cooling to room temperature, the benzene layer was separated and the water phase was extracted with benzene (3 × 40 ml). The organic layers were combined and dried by $MgSO_4$. After evaporating the solvent, the residue was recrystallized (charcoal treatment) from benzene to yield 1.35 g of **5** (40%) as white crystals, m.p. 139–140 °C. ^{1}H NMR ($CDCl_3$): δ 8.63 (d, 4H, α-Py*H*), 7.18 (d, 4H, β-Py*H*), 6.21 (s, 2H, CH_2), 2.58, 2.27 (s, s, 6H, 6H, CH_3). ^{13}C NMR ($CDCl_3$): δ 10.55, 12.75 (*C*H_3), 60.58 (*C*H_2), 117.99, 123.95, 138.29, 141.73, 146.72, 149.97 (carbons of pyrazolyl and pyridyl rings). IR: $\nu_{pyridyl\ ring}$ = 1599.7 (s) cm^{-1}. *Anal.* Calc. for $C_{21}H_{22}N_6$: C, 70.37; H, 6.19; N, 23.45. Found: C, 70.12; H, 6.11; N, 23.06%.

2.4. Reaction of **5** with R_2SnCl_2 (R = Ph, Et or n-Bu)

A general procedure was used for all preparations. The solution of **5** (0.5 mmol) in 10 ml CH_2Cl_2 was added to the stirred solution of R_2SnCl_2 (0.5 mmol) in 10 ml CH_2Cl_2 at room temperature. The reaction mixture was stirred continuously for 4 h, during which time a precipitate gradually formed. The precipitate was filtered off, washed and dried in vacuo. Yields, melting points and analytical data are given below.

2.4.1. [Bis(3,5-dimethyl-4-(4′-pyridyl)pyrazol-1-yl) methane]diphenyltin dichloride (**6**)

This compound was obtained by the reaction of **5** with Ph_2SnCl_2. White solid; yield: 90%; m.p. 131–133 °C. ^{1}H NMR (CD_3COCD_3): δ 8.63 (d, 4H, α-Py*H*), 7.39 (d, 4H, β-Py*H*), 7.96, 7.47 (m, m, 4H, 6H, C_6H_5), 6.34 (s, 2H, CH_2), 2.65, 2.23 (s, s, 6H, 6H, CH_3). IR: $\nu_{\text{pyridyl ring}}$ = 1614.7 (s) cm^{-1}. *Anal.* Calc. for $C_{33}H_{32}Cl_2N_6Sn$: C, 56.44; H, 4.59; N, 11.97. Found: C, 56.63; H, 4.73; N, 12.06%.

2.4.2. [Bis(3,5-dimethyl-4-(4′-pyridyl)pyrazol-1-yl) methane]diethyltin dichloride (**7**)

This compound was obtained by the reaction of **5** with Et_2SnCl_2. White solid; yield: 89%; m.p. 138–140 °C. ^{1}H NMR (CD_3SOCD_3): δ 8.59 (d, 4H, α-Py*H*), 7.31 (d, 4H, β-Py*H*), 6.31 (s, 2H, CH_2), 2.56, 2.18 (s, s, 6H, 6H, CH_3), 1.55 (q, 4H, $SnCH_2$), 1.26 (t, 6H, CH_2CH_3). ^{13}C NMR (CD_3SOCD_3): δ 10.14, 10.55, 12.61, 31.79 (carbons of ethyl and methyl groups), 59.30 (CH_2), 116.66, 123.52, 137.96, 141.05, 145.82, 149.61 (carbons of pyrazolyl and pyridyl rings). ^{119}Sn NMR (CD_3SOCD_3): δ −227.06 (s, br). IR: $\nu_{\text{pyridyl ring}}$ = 1612.6 (s) cm^{-1}. *Anal.* Calc. for $C_{25}H_{32}Cl_2N_6Sn$: C, 49.54; H, 5.32; N, 13.86. Found: C, 49.88; H, 5.44; N, 13.87%.

2.4.3. [Bis(3,5-dimethyl-4-(4′-pyridyl)pyrazol-1-yl) methane]di(n-butyl)tin dichloride (**8**)

This compound was obtained by the reaction of **5** with *n*-Bu_2SnCl_2. After the reaction was completed, the solvent was concentrated to ca. 5 ml, then the same volume hexane was slowly added to yield a white solid; yield: 80%; m.p. 105–106 °C. ^{1}H NMR ($CDCl_3$): δ 8.73 (d, 4H, α-Py*H*), 7.29 (d, 4H, β-Py*H*), 6.23 (s, 2H, CH_2), 2.62, 2.29 (s, s, 6H, 6H, CH_3), 1.84–1.66 (m, 8H, $SnCH_2CH_2$), 1.43–1.34 (m, 4H, CH_2CH_3), 0.92 (t, 6H, CH_2CH_3). ^{13}C NMR ($CDCl_3$): δ 10.67, 12.99, 13.53, 26.09, 27.84, 35.93 (carbons of butyl and methyl groups), 117.27, 124.41, 138.92, 144.27, 147.01, 148.16 (carbons of pyrazolyl and pyridyl rings). ^{119}Sn NMR ($CDCl_3$): δ −98.46, −145.68. IR: $\nu_{\text{pyridyl ring}}$ = 1621.1 (s) cm^{-1}. *Anal.* Calc. for $C_{29}H_{40}Cl_2N_6Sn$: C, 52.59; H, 6.09; N, 12.69. Found: C, 52.37; H, 5.89; N, 12.63%.

2.5. Crystal structure determinations

Crystals of complexes **2** and **6** suitable for X-ray analysis were obtained by slowly cooling hot acetone solutions of **2** and **6**. Crystals of complex **2** contain one-half of a co-crystallized acetone molecule. The methyl carbon and oxygen atoms of the acetone molecule as well as the hydrogen atom on the pyrazolyl nitrogen exhibit disorder. Satisfactory results were obtained when they were given occupancy factors of 0.5. Crystals of complex **6** have the stoichiometry **6** · H_2O · $\frac{1}{4}$ acetone, in which the phenyl group of C7–C12, pyrazolyl group of N4–N5–C28 and pyridyl group of N6–C33 are disordered, and their occupancy factors were refined to 0.594 for C7–C12 and 0.406 for C7′–C12′, 0.906 for N4–N5–C28 and 0.094 for N4′–N5′–C28′, and 0.788 for N6–C33 and 0.212 for N6′–C33′, respectively. The N4′ atom was refined to the same position with N4 by EXYZ and EADP. When acetone (occupancy factor of 0.25) appears, the disordered phenyl group locates in the position of C7–C12 (occupancy factor of 0.594). All intensity data were collected with a Bruker SMART CCD diffractometer, using graphite monochromated Mo Kα radiation (λ = 0.71073 Å). The structures were resolved by the direct method and refined by full-matrix least-squares on F^2. All non-hydrogen atoms were refined anisotropically. A summary of the fundamental crystal data for complexes **2** and **6** is listed in Table 1.

Table 1
Crystal data for compounds **2** and **6**

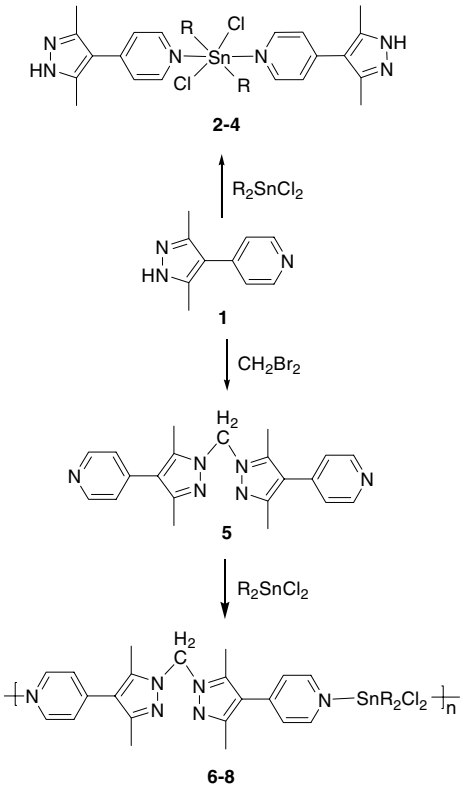
Compound	**2** · $0.5CH_3COCH_3$	**6** · H_2O · $0.25CH_3COCH_3$
Formula	$C_{33.5}H_{35}Cl_2N_6O_{0.5}Sn$	$C_{33.75}H_{35.5}Cl_2N_6O_{1.25}Sn$
Formula weight	719.27	734.77
Crystal size (mm)	0.26 × 0.24 × 0.20	0.30 × 0.25 × 0.20
Crystal class	tetragonal	monoclinic
Space group	*I*-42*d*	*P*2(1)/*c*
Cell parameters		
a (Å)	20.489(4)	7.820(3)
b (Å)	20.489(4)	17.777(6)
c (Å)	15.274(6)	29.97(1)
β (°)	90.00	91.053(6)
V (Å^3)	6412(3)	4166(2)
Z	8	4
T (K)	293(2)	293(2)
D_{calc} (Mg m^{-3})	1.490	1.172
F(000)	2928	1496
λ (Mo Kα) (Å)	0.71073	0.71073
μ (mm^{-1})	0.999	0.772
Number of reflections measured	3294	7072
Number of reflections observed ($I \geqslant 2\sigma(I)$)	3013	4216
Number of parameters	224	524
Residuals *R*, R_w	0.0231, 0.0553	0.0757, 0.2049

3. Results and discussion

3.1. Synthesis and characterization of complexes

Since 3-(4-pyridyl)pentane-2,4-dione is unstable [19], the raw pyridylpentadione was directly reacted with an excess of hydrazine hydrate to give 3,5-dimethyl-4-(4′-pyridyl)pyrazole (**1**) in a reasonable yield. Treatment of this pyrazolyl ligand with R_2SnCl_2 (R = Ph, Et or *n*-Bu) in a 1:1 ratio affords 2:1 (ligand:tin) adducts **2**–**4** (Scheme 1), according to the results of ^1H NMR data and elemental analyses. The ^1H NMR spectra of the complexes are consistent with the formulae of 2:1 adducts, which exhibit the expected proton signals for two equivalent pyridylpyrazole ligands. The chemical shifts of the protons for the ligand in the complexes are similar to those of the free ligand. Complexes **2**–**4** are insoluble in ether, chlorinated solvents, slightly soluble in acetone at room temperature, and moderately soluble in stronger polar organic solvents such as DMF and DMSO.

Reaction of **1** with CH_2Br_2 under phase-transfer conditions gives the new bridging ligand bis(3,5-dimethyl-4-(4′-pyridyl)pyrazol-1-yl)methane (**5**). Treatment of **5** with an equimolar amount of R_2SnCl_2 in CH_2Cl_2 affords 1:1 adducts **6**–**8**. Like complexes **2**–**4**, **6** and **7** are insoluble in ether, chlorinated solvents, and slightly soluble in acetone at room temperature, but complex **8** is soluble in chlorinate solvents possibly because the longer alkyl groups increase its solubility in organic solvents.



Scheme 1. R = Ph (**2**) and (**6**); R = Et (**3**) and (**7**); R = *n*-Bu (**4**) and (**8**).

It is well known that the δ (^{119}Sn) values in the ^{119}Sn NMR spectra are markedly dependent on the coordination environments around the tin atom. Owing to low solubility, only ^{119}Sn NMR spectra of complexes **4**, **7** and **8** can be clearly observed. The ^{119}Sn NMR signals of **4** and **7** in CD_3SOCD_3 occur at −214.0 and −227.1 ppm, respectively, as broad peaks, while complex **8** exhibits two ^{119}Sn NMR signals in $CDCl_3$ at −98.5 and −145.7 ppm. These data indicate that these adducts may partially dissociate in polar solutions. This kind of dissociation equilibrium can often be observed in other diorganotin derivatives containing N-donor ligands [8,12,16,20].

3.2. Crystal structures of complexes 2 and 6

The molecular structure of **2** has been confirmed by X-ray diffraction analysis as shown in Fig. 1, which clearly shows that two 3,5-dimethyl-4-(4′-pyridyl)pyrazole ligands coordinate to the tin atom through the pyridyl nitrogen atom instead of the pyrazolyl nitrogen atom. The pyridylpyrazole acts as a monodentate ligand toward the tin atom, which is six-coordinate with a slightly distorted octahedral geometry, containing two nitrogen atoms of pyridyl groups, two phenyl carbons as well as two chlorine atoms in an all-*trans* configuration. The Sn–Cl and Sn–C bond distances are similar to those in other diorganotin derivatives with monodentate or bidentate N-donor ligands [8,20,21]. The average Sn–N bond distance (2.365(3) Å) in **2** is also close to those in other diorganotin derivatives with monodentate N-donor ligands [8], such as in $Ph_2SnCl_2(Tz)_2$ (2.369(8) Å, Tz = thiazole) [20]. The dihedral angle between the two phenyl planes is 46.2°, larger than that between the two pyridyl planes (40.9°). The pyridyl group is not coplanar with the pyrazolyl ring. The dihedral angle formed by the N(1)–C(1A) pyridyl plane and the N(2)–C(5) pyrazolyl plane is 33.0°, slightly larger than the dihedral angle formed by the N(3)–C(7A) pyridyl plane and the N(4)–C(11) pyrazolyl plane (30.5°).

It is also noteworthy that molecules of complex **2** are linked into a linear chain in the solid state through intermolecular N–H···N hydrogen bond interactions (Fig. 2), while bis(pyrazole) or bis(imidazole) complexes of diorganotin dihalides tend to self-organize into chain polymers by intermolecular N–H···X hydrogen bonding (X = Cl or Br) [22–28].

Bis(3,5-dimethyl-4-(4′-pyridyl)pyrazol-1-yl)methane is a potential multidentate ligand which can act as a chelating multidentate ligand, like original bis(pyrazol-1-yl)methane using the pyrazolyl nitrogens coordinated to metals, as well as a bridging ligand by the exodentate pyridyl nitrogens. In order to confirm the coordination mode of this ligand with diorganotin halides, the

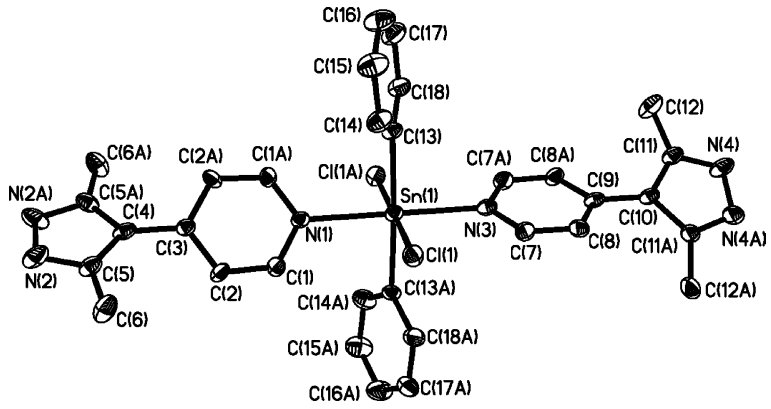


Fig. 1. The molecular structure of complex **2**. The thermal ellipsoids are drawn at the 30% probability. Selected bond distances (Å) and angles (°): Sn(1)–N(1) = 2.352(3), Sn(1)–N(3) = 2.377(3), Sn(1)–C(13) = 2.177(3), Sn(1)–Cl(1A) = 2.534(1), C(3)–C(4) = 1.478(6); C(13)–Sn(1)–C(13A) = 177.0(1), N(1)–Sn(1)–N(3) = 180.0, Cl(1)–Sn(1)–Cl(1A) = 179.11(4), C(13)–Sn(1)–N(3) = 91.50(9), C(13A)–Sn(1)–Cl(1) = 89.5(1), N(1)–Sn(1)–Cl(1A) = 89.55(2); torsion angles: C(2)–C(3)–C(4)–C(5) = 32.7(3); C(2)–C(3)–C(4)–C(5A) = −147.3(3)° (symmetry code: A = x, $-y + 1/2$, $-z + 1/4$).

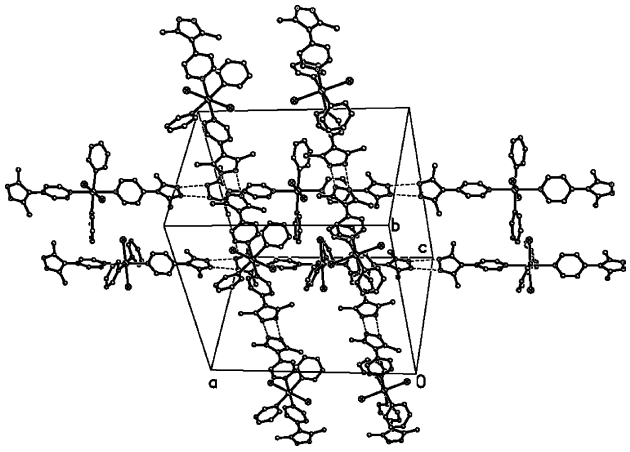


Fig. 2. The crystal packing diagram of complex **2** emphasizing the intermolecular hydrogen bonding interactions (N(2)–H···N(4)^{i} = 2.984 Å, N(4)–H···N(2)^{ii} = 2.984 Å; symmetry code: i = $x - 1$, $-y + 1/2$, $-z + 1/4$, ii = $x + 1$, $-y + 1/2$, $-z + 1/4$) and the one-dimensional chain. The solvent molecule is omitted for clarity.

X-ray diffraction analysis of complex **6** was undertaken. Fig. 3 shows that **6** is a 1D coordination polymer and bis(3,5-dimethyl-4-(4′-pyridyl)pyrazol-1-yl)methane acts as a bridged bidentate ligand by two exodentate pyridyl nitrogen atoms. The coordination environment around the tin atom is similar to that in complex **2**, i.e., a slightly distorted octahedral geometry, as well as an all-*trans* configuration of pyridyl nitrogen atoms, phenyl carbons and chlorine atoms. The Sn–Cl, Sn–C and Sn–N bond distances are also similar to those in complex **2**. The coordination mode of ligand **5** in complex **6** with the tin atom is analogous to those of bis(triazol-1-yl)methane [16] and pyrazine [28]. However, in the diorganotin derivatives of bis(triazol-1-yl)methane and pyrazine, the halide atoms as well as the coordinated nitrogen atoms are in *cis*-positions.

In conclusion, the coordination modes of 4-pyridylpyrazole and bis(4-pyridylpyrazol-1-yl)methane with diorganotin are quite different from those of the original azole and 2-pyridylpyrazole as well as bis(pyrazol-1-yl)methane. In diorganotin derivatives of pyridylpyrazole, the exodentate pyridyl nitrogen atoms have priority in coordinating to the tin atom possibly owing to their stronger donor ability over the pyrazolyl nitrogen. The coordination mode of ligand **5** to the tin atom is similar to those of 4,4-bipyridine and bis(1,2,4-triazol-1-yl)methane.

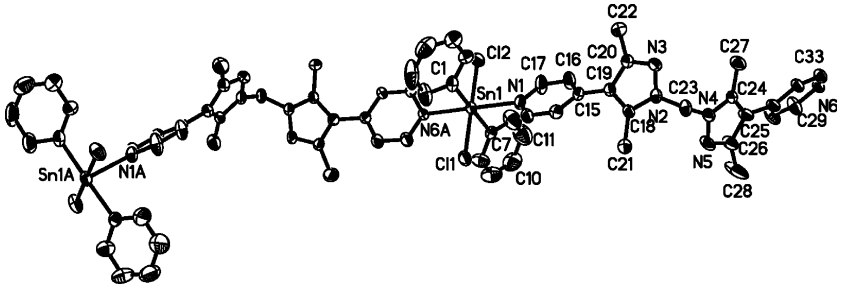


Fig. 3. The molecular structure of complex **6**. The thermal ellipsoids are drawn at 30% probability. The solvent molecules are omitted for clarity. Selected bond distances (Å) and angles (°): Sn1–Cl1 = 2.551(2), Sn1–Cl2 = 2.526(2), Sn1–N1 = 2.371(6), Sn1–N1A = 2.361(6), Sn1–C1 = 2.132(10), C15–C19 = 1.470(10), N2–C23 = 1.452(9), C23–N4 = 1.446(9); C1–Sn1–C7 = 177.0(4), N6A–Sn1–N1 = 178.3(3), Cl1–Sn1–Cl2 = 179.37(8), N6A–Sn1–Cl1 = 89.1(1), C1–Sn1–Cl1 = 90.2(3), C1–Sn1–Cl2 = 89.5(3), C7–Sn1–N1 = 89.0(3), C1–Sn1–N1 = 88.7(3), N4–C23–N2 = 110.9(5); torsion angles: C16–C15–C19–C20 = 40.1(13), C16–C15–C23–C18 = −142.0(10), N3–N2–C23–N4 = −81.5(8)° (symmetry code: A = $x + 1, -y + 1/2, z - 1/2$).

4. Supplementary material

Crystallographic data (CIF files) for the structures of complexes **2** and **6** have been deposited with the Cambridge Crystallographic Data Centre, CCDC No. 248284 for complex **2** and CCDC No. 248283 for complex **6**. Copies of this information may be obtained free of charge from The Director, CCDC, 12 Union Road, Cambridge, CB2 1EZ, UK (fax: +44 1223 336 033; e-mail: deposit@ccdc.cam.ac.uk or www: http://www.ccdc.cam.ac.uk).

Acknowledgements

This work is supported by the National Natural Science Foundation of China (No. 20172029) and the Research Fund for the Doctoral Program of Higher Education.

References

[1] (a) A.J. Crowe, P.J. Smith, G. Atassi, Chem. Biol. Interact. 32 (1980) 171;
(b) A.J. Crowe, P.J. Smith, G. Atassi, Inorg. Chim. Acta 93 (1984) 179.
[2] M. Gielen, Coord. Chem. Rev. 151 (1996) 41.
[3] A.K. Saxena, F. Huber, Coord. Chem. Rev. 95 (1989) 109.
[4] P. Álvarez-Boo, J.S. Casas, A. Castiñeiras, M.D. Couce, E. Freijanes, E. Novoa, J. Sordo, Appl. Organomet. Chem. 17 (2003) 725.
[5] P. Álvarez-Boo, J.S. Casas, A. Castiñeiras, M.D. Couce, E. Freijanes, A. Furlani, U. Russo, V. Scarcia, J. Sordo, M. Varela, Inorg. Chim. Acta 353 (2003) 8.
[6] C. Pettinari, M. Pellei, A. Cingolani, D. Martini, A. Drozdov, S. Troyanov, W. Panzeri, A. Mele, Inorg. Chem. 38 (1999) 5777.
[7] C. Pettinari, A. Cingolani, B. Bovio, Polyhedron 15 (1996) 115.
[8] C. Pettinari, A. Lorenzotti, G. Sclavi, A. Cingolani, E. Rivarola, M. Colapietro, A. Cassetta, J. Organomet. Chem. 496 (1995) 69.
[9] G.G. Lobbia, F. Bonati, A. Cingolani, D. Leonesi, A. Lorenzotti, J. Organomet. Chem. 359 (1989) 21.
[10] G.G. Lobbia, A. Cingolani, D. Leonesi, A. Lorenzotti, F. Bonati, Inorg. Chim. Acta 130 (1987) 203.
[11] R. Visalakshi, V.K. Jain, S.K. Kulshreshtha, G.S. Rao, Inorg. Chim. Acta 118 (1986) 119.
[12] L.-F. Tang, Z.-H. Wang, W.-L. Jia, Y.-M. Xu, J.-T. Wang, Polyhedron 19 (2000) 381.
[13] L.-F. Tang, P.-J. Zhu, J.-T. Wang, J. Chem. Res. (S) (2002) 370.
[14] Z.-H. Wang, L.-F. Tang, W.-L. Jia, J.-T. Wang, H.-G. Wang, Polyhedron 21 (2002) 873.
[15] Z.-H. Wang, L.-F. Tang, J.-F. Chai, J.-T. Wang, H.-G. Wang, Chin. J. Struct. Chem. 21 (2002) 273.
[16] L.-F. Tang, Z.-H. Wang, J.-F. Chai, W.-L. Jia, Y.-M. Xu, J.-T. Wang, Polyhedron 19 (2000) 1949.
[17] A. Antiñolo, F. Carrillo-Hermosilla, E. Díez-Barra, J. Fernández-Baeza, M. Fernández-López, A. Lara-Sánchez, A. Moreno, A. Otero, A.M. Rodriguez, J. Tejeda, J. Chem. Soc., Dalton Trans. (1998) 3737.
[18] L.-F. Tang, W.-L. Jia, Z.-H. Wang, J.-T. Wang, H.-G. Wang, J. Organomet. Chem. 649 (2002) 152.
[19] L.G. Mackay, H.L. Anderson, J.K.M. Sanders, J. Chem. Soc., Perkin Trans. I (1995) 2269.
[20] P. Álvarez-Boo, M.D. Couce, E. Freijanes, J.S. Casas, A. Castiñeiras, A. Sánchez González, J. Sordo, U. Russo, J. Organomet. Chem. 506 (1996) 253.
[21] E. García Martínez, A. Sánchez González, J.S. Casas, J. Sordo, U. Casellato, R. Graziani, U. Russo, J. Organomet. Chem. 463 (1993) 91.
[22] G. Valle, E. Ettore, V. Peruzzo, G. Plazzogna, J. Organomet. Chem. 326 (1987) 169.
[23] B. Alberte, A. Sanchez-Gonzalez, E.R. Garcia, E.E. Castellano, J. Organomet. Chem. 338 (1988) 187.
[24] A. Sanchez-Gonzalez, B. Alberte, J.S. Casas, J. Sordo, A. Castineiras, W. Hiller, J. Strähle, J. Organomet. Chem. 353 (1988) 169.
[25] V. Peruzzo, G.. Plazzogna, G. Valle, J. Organomet. Chem. 375 (1989) 167.
[26] E. Garcia-Martinez, A. Sanchez-Gonzalez, A. Macias, M.V. Castano, J.S. Casas, J. Sordo, J. Organomet. Chem. 385 (1990) 329.
[27] A. Sanchez-Gonzales, J.S. Casas, J. Sordo, G. Valle, J. Organomet. Chem. 435 (1992) 29.
[28] (a) D. Cunningham, J. McManus, M.J. Hynes, J. Organomet. Chem. 393 (1990) 69;
(b) D. Cunningham, P. McArdle, J. McManus, T. Higgins, K. Molloy, J. Chem. Soc., Dalton Trans. (1988) 2621.

Available online at www.sciencedirect.com
SCIENCE DIRECT®
Polyhedron 24 (2005) 215–220
POLYHEDRON
www.elsevier.com/locate/poly

Synthesis, characterization and crystal structures of 2,4-di(2-aminopyridine)-6-methypyrimidine (dapmp), [Cu(dapmp)Cl_2] and [Cu(dapmp)$(CH_3COO)_2$] · H_2O

Hai-Rui Ma [a], Yao-Yu Wang [a,*], Ping Liu [a], Dong-Sheng Li [a], Qi-Zhen Shi [a], Gene-Hsiang Lee [b], Shie-Ming Peng [b]

[a] *Department of Chemistry, Shaanxi Key Laboratory of Physico-inorganic Chemistiy, Northwest University, Xi'an 710069, PR China*
[b] *Department of Chemistry, National Taiwan University, Taipei, Taiwan*

Received 6 September 2004; accepted 3 November 2004
Available online 25 December 2004

Abstract

The new ligand dapmp (**1**) has been synthesized and the reactions of $CuCl_2 \cdot 2H_2O$ and $Cu(CH_3COO)_2 \cdot H_2O$ with the new ligand in methanol afforded two crystalline polymorphic forms: [Cu(dapmp)Cl_2] (**2**) and [Cu(dapmp)$(CH_3COO)_2$] · H_2O (**3**), where dapmp = 2,4-di(2-aminopyridine)-6-methylpyrimidine. Single crystal X-ray diffraction showed that (**1**) and (**2**) are each connected by hydrogen bonding to form a one-dimensional supermolecular compound and (**3**) is connected by hydrogen bonding to form a three-dimensional supermolecular compound.
© 2004 Elsevier Ltd. All rights reserved.

Keywords: New ligand; Copper(II) complex; Cystal structure; One-dimensional supermolecular; Three-dimensional supermolecular; Hydrogen bonds

1. Introduction

In recent years, the synthesis of multidentate N-donor ligands has attracted considerable interest [1,2], mainly because they can be used to design multinuclear metal compounds, coordination polymers and supermolecular compounds, which play a very important role in biological systems, magnetic materials, electronic materials, optical materials and other fields [3–7]. In the present paper, we describe a new multidentate N-donor ligand 2,4-di(2-aminopyridine)-6-methylpyrimidine (dapmp), which can exhibit several coordination modes: anti–anti–anti–anti, syn–syn–syn–syn, anti–syn–syn–anti, anti–syn–syn–syn and syn–syn–syn–anti (see Scheme 1).

Herein we report the anti–anti–anti–anti configuration of dapmp, in which the chain is formed by hydrogen bonding. The crystal structures of its copper(II) complexes with the all-*anti* conformation of the chelating ligand are presented.

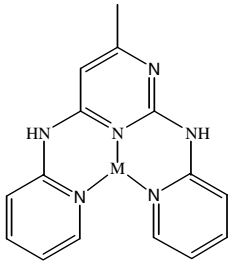
2. Experimental

2.1. Materials and physical measurements

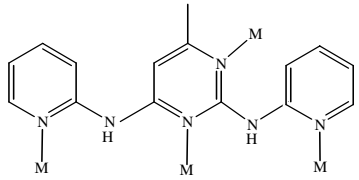
All reagents were commercial grade and were used as received. Infrared spectra on KBr pellets were recorded on a Nicolet 170SX FT-IR spectrophotometer in the range 4000–400 cm^{-1}. NMR spectra were recorded using a VARIAN INOVA400MHZ spectrometer. Electronic spectra were recorded on a Cary 300 Bio UV–visible spectrophotometer. Elemental analyses were determined with a Perkin–Elmer model 240C instrument. FAB-MS

* Corresponding author. Tel.: +86 29 88303097; fax: +86 29 88373398.
E-mail address: wyaoyu@nwu.edu.cn (Y.-Y. Wang).

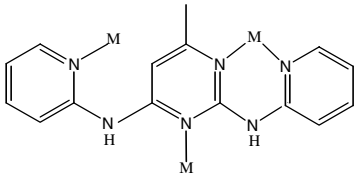
0277-5387/$ - see front matter © 2004 Elsevier Ltd. All rights reserved.
doi:10.1016/j.poly.2004.11.013



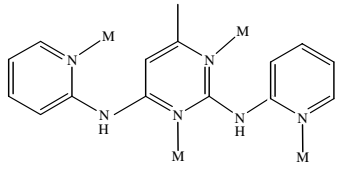
1 anti-anti-anti-anti



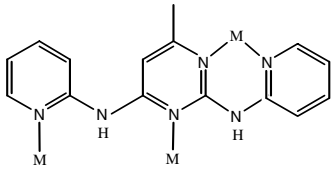
2 syn-syn-syn-syn



3 anti-syn-syn-anti



4 anti-syn-syn-syn



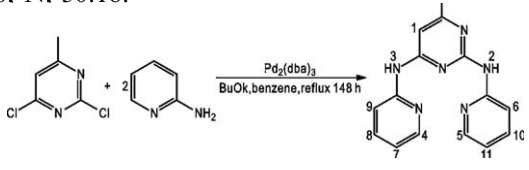
5 syn-syn-syn-anti

Scheme 1. Coordination modes for the ligand dapmp.

mass spectra were obtained with a JEOL HX-110 HF double focusing spectrometer operating in the positive ion detection mode. TGA analyses were recorded with a NETZSCH STA 449C rnicroanalyzer in an atmosphere of nitrogen at a heating rate of 5 °C min^{-1}.

2.2. Synthesis of 2,4-di(2-aminopyridine)-6-methylpyrimidine (dapmp, 1)

2,4-Dichloro-6-methylpyrimidine (5.0 g, 31.1 mmol) and 2-aminopyridine (6.0 g, 72.9 mmol) were added to 100 ml dry benzene in a 200 ml flask. Then BuOK (14.3 g, 127.7 mmol) and tris(dibenzylideneacetone)dipalladium ($Pd_2(dba)_3$) (2.0 g, 2.2 mmol) were added to the solution under nitrogen. The resulting solution was stirred for 148 h under reflux. The product was filtered and washed three times each with methanol and water. Compound **1** was obtained as a white powder in 64% yield (8.7 g). *Anal.* Calc. for $C_{15}H_{14}N_6$: C, 64.47; H, 5.070; N, 30.18.



Found: C, 64.46; H, 4.891; N, 29.56%. IR (KBr, cm^{-1}): v = 3176(w), 3028(w), 1599(s), 1569(m), 1505(m), 1466(m), 1425(s), 1358(s), 1299(m), 1248(vw), 1218(w), 1149(w), 1048(w), 987(m), 773(s), 709(m), 617(vw). MS (FAB) *m/z* (%) 279.2 (dapmp). ^{1}H NMR ($CDCl_3$): δ = 7.14(s, 1H, 1-H), 9.63(s, 1H, 2-H), 9.44(s, 1H, 3-H), 8.37(d, 1H, ^3J = 4.8 Hz, 4-H), 8.37(d, 1H, ^3J = 4.8 Hz, 5-H), 8.33(d, 1H, ^3J = 3.6 Hz 6-H), 6.92(dt, 1H, ^3J = 7.6 Hz, ^4J = 3.6 Hz, 7-H), 6.93(dt, 1H, ^3J = 7.6 Hz, ^4J = 2.4 Hz, 8-H), 7.37(d, 1H, 9-H), 7.68(dt, 1H, ^3J = 7.8 Hz, ^4J = 2.0 Hz, 10-H), 7.62(dt,^4J = 2.0 Hz, 11-H), 2.42(s, 3H, CH_3) ppm.

2.3. Synthesis of [Cu(dapmp)Cl_2] (2)

A solution of the ligand dapmp (61.2 mg, 0.22 mmol) and $CuCl_2 \cdot 2H_2O$ (34.1 mg, 0.2 mmol) in methanol (15 ml) were mixed together and stirred for 3 h. The green solution was filtered. Suitable X-ray quality crystals were obtained by slow evaporation of this green solution. Yield: 42%. *Anal.* Calc. for $[Cu(C_{15}H_{14}N_6)Cl_2]$: C, 43.65; H, 3.419; N, 20.36. Found: C, 43.46; H, 3.485; N, 20.12%.

2.4. Synthesis of [Cu(dapmp)$(CH_3COO)_2$] · H_2O (3)

A solution of the ligand dapmp (61.2 mg, 0.22 mmol) and $Cu(CH_3COO)_2 \cdot H_2O$ (39.9 mg, 0.2 mmol) in methanol (15 ml) were mixed together and stirred for 3 h. The blue-green solution obtained was filtered, from which X-ray quality crystals were obtained by slow evapora-

Table 1
Data collection and processing parameters for dapmp (**1**), [Cu(dapmp)Cl_2] (**2**) and [Cu(dapmp)$(CH_3COO)_2$] · H_2O (**3**)

	(**1**)	(**2**)	(**3**)
Empirical formula	$C_{15}H_{14}N_6$	$C_{15}H_{14}Cl_2CuN_6$	$C_{19}H_{22}CuN_60_5$
Formula weight	278.32	412.76	477.97
Temperature (K)	295(2)	150(1)	150(1)
Wavelength (Å)	0.71073	0.71073	0.71073
Crystal system	monoclinic	monoclinic	monoclinic
Space group	$P2_1/n$	$P2_1/c$	$P2_1/n$
a (Å)	9.8006(4)	10.2639(2)	11.2417(5)
b (Å)	16.2106(6)	18.8819(4)	11.6485(5)
c (Å)	17.2988(7)	8.6769(2)	15.5540(8)
β (°)	91.539(1)	105.233(1)	101.856(1)
Volume (Å^3)	2747.3(2)	1622.52(6)	1996.9(2)
Z	8	4	4
D_{calc} (g/cm^3)	1.346	1.690	1.590
Absorption coefficient (nm^{-1})	0.087	1.685	1.140
$F(000)$	1168	836	988
Crystal size (mm)	$0.20 \times 0.12 \times 0.10$	$0.20 \times 0.15 \times 0.12$	$0.12 \times 0.12 \times 0.08$
θ range for data collection (°)	1.72–27.50	2.06–27.50	2.05–27.50
Limiting indices	$-12 \leqslant h \leqslant 12$, $-21 \leqslant k \leqslant 21$, $-22 \leqslant l \leqslant 18$	$-11 \leqslant h \leqslant 13$, $-24 \leqslant k \leqslant 23$, $-11 \leqslant l \leqslant 10$	$-13 \leqslant h \leqslant 14$, $-14 \leqslant k \leqslant 15$, $-20 \leqslant l \leqslant 20$
Reflections collected	21870	17432	19501
Independent reflections	6307	3716	4579
Absorption correction	semi-empirical	semi-empirical	semi-empirical
Maximum and minimum transmission	0.9914 and 0.9828	0.827 and 0.707	0.9143 and 0.8753
Refinement method	full-matrix least-squares on F^2	full-matrix least-squares on F^2	full-matrix least-squares on F^2
Data/restraints/parameters	6307/0/379	3716/0/218	4579/0/288
Goodness-of-fit on F^2	1.026	1.128	1.068
R_1, wR_2 [$I > 2\sigma(I)$]	0.0667, 0.1503	0.0481, 0.1129	0.0443, 0.1042
R_1, wR_2 (all data)	0.1532, 0.1861	0.0817, 0.1440	0.0584, 0.1108
Largest difference peak and hole (e Å^{-3})	0.243 and −0.253	1.011 and −0.826	0.492 and −0.369

$R = \sum ||F_o| - |F_c|| / \sum |F_o|$; $wR_2 = [\sum[w(F_o^2 - F_c^2)^2] / \sum[(F_o^2)^2]]^{1/2}$.

Table 2
Selected bond lengths (Å) and bond angles (°) of dapmp (**1**), Cu(dapmp)Cl_2 (**2**) and [Cu(dapmp)$(CH_3COO)_2$] · H_2O (**3**)

Dapmp (**1**)		Cu(dapmp)Cl_2 (**2**)		[Cu(dapmp)$(CH_3COO)_2$] · H_2O (**3**)	
Bond lengths					
N(1)–C(1)	1.333(4)	Cu–N(5)	1.9666(3)	Cu–N(5)	1.978(2)
N(1)–C(5)	1.341(3)	Cu–N(3)	2.071(3)	Cu–N(3)	2.067(2)
N(2)–C(6)	1.375(3)	Cu–N(1)	1.974(3)	Cu–N(1)	1.975(2)
N(2)–C(5)	1.384(3)	Cu–Cl(1)	2.369(1)	Cu–O(3)	2.162(2)
N(6)–C(7)	1.350(4)	Cu–Cl(2)	2.417(1)	Cu–O(1)	1.996(2)
N(6)–C(6)	1.359(3)	N(1)–C(1)	1.358(5)	O(1)–C(16)	1.267(3)
N(12)–C(21)	1.367(4)	N(1)–C(5)	1.327(5)	O(2)–C(16)	1.244(3)
N(12)–C(22)	1.372(4)	N(3)–C(9)	1.361(4)	O(3)–C(18)	1.273(3)
N(12′)–C(24)	1.354(4)	N(3)–C(6)	1.352(5)	O(4)–C(18)	1.242(3)
N(12′)–C(22)	1.358(4)	N(5)–C(14)	1.347(5)	N(3)–C(6)	1.362(3)
C(7)–C(8)	1.362(4)	N(5)–C(10)	1.335(5)	N(6)–C(6)	1.343(3)
C(8)–C(9)	1.369(4)	N(6)–C(7)	1.358(5)	N(3)–C(9)	1.352(3)
Bond angles					
C(4)–C(5)–N(2)	124.8(3)	N(5)–Cu–N(1)	172.3(1)	N(5)–Cu–N(1)	172.84(9)
C(6)–N(2)–C(5)	129.9(2)	N(1)–Cu–N(3)	94.1(1)	N(5)–Cu–O(1)	89.80(9)
N(2)–C(6)–N(3)	119.9(2)	N(5)–Cu–N(3)	93.6(1)	N(5)–Cu–N(3)	93.27(9)
N(3)–C(9)–N(4)	118.9(3)	N(1)–Cu–Cl(1)	88.99(9)	N(1)–Cu–O(3)	88.62(8)
C(9)–N(4)–C(10)	128.3(2)	N(5)–Cu–Cl(1)	88.13(9)	O(1)–Cu–O(3)	121.54(8)
N(4)–C(10)–C(11)	123.3(3)	N(5)–Cu–Cl(2)	88.77(9)	N(3)–Cu–O(1)	139.58(8)
C(19)–C(20)–N(8)	124.1(3)	N(1)–Cu–Cl(2)	88.46(9)	N(1)–Cu–O(1)	88.24(8)
C(20)–N(8)–C(21)	130.9(3)	N(3)–Cu–Cl(2)	107.48(8)	N(1)–Cu–N(3)	92.68(9)
N(8)–C(21)–N(9)	119.7(3)	N(3)–Cu–Cl(1)	115.64(8)	N(5)–Cu–O(3)	86.53(8)
C(24)–N(10)–C(25)	129.1(2)	Cl(1)–Cu–Cl(2)	136.88(4)	N(3)–Cu–O(3)	98.88(8)

tion. Yield: 51%. *Anal.* Calc. for $[Cu(C_{15}H_{14}N_6)(CH_3OO)_2]\cdot H_2O$: C, 47.75; H, 4.640; N, 17.58. Found: C, 47.92; H, 4.478; N, 17.71%.

2.5. Crystal structure determination

X-ray diffraction data were collected with graphite-monochromated Mo Kα radiation $\lambda = 0.71073$ Å) on a BRUKER SMART APEXCCD diffractometer for compound **1**, on a NONIUS KaCCD diffractometer for complex **2** and on a BRUKER SMART APEXCCD diffractometer for complex **3**. The structures were solved by direct methods with the SHELXL-93 [8] program and refined by full-matrix least-squares methods on F^2 with SHELXTL-PC V 5.03 [9]. Crystal data and structure refinement details are summarized in Table 1. Selected bond lengths and bond angles are given in Table 2.

3. Results and discussion

3.1. Description of structures

Fig. 1 shows the molecular packing of compound **1**. It can be seen that the ligand dapmp forms *zigzag* chains in the solid state, and the molecules are held together by a series of donor–acceptor (DA) double hydrogen bonds. Each molecule with the *all-anti* conformation is linked via two hydrogen bonds (N(1)···N(10) 3.104 Å, N(2)···N(11) 3.107 Å) with a centrosymmetrically related counterpart to form a dimer as depicted in Fig. 1. The structural characterization of such hydrogen-bonded dimeric compounds linked by self complementary donor–acceptor groups is well documented in organic chemistry [10–13]. The adjacent dapmp dimer units are interlanced and are connected by two hydrogen bonds (N(7)···N(4) 3.147 Å, N(8)···N(5) 3.189 Å), forming a one-dimensional supermolecular compound along the *c* axis (Fig. 1).

The bond length of N(6)–C(7) 1.350(4) Å is shorter than that of N(12C)–C(22B) (1.358(4) Å) while the angle of C(5)–N(2)–C(6) (129.9(2)°) is similar to that of C(9)–N(4)–C(10) (128.3(2)°). The three rings of the dapmp ligand are each planar and the dihedral angle between each pair of neighboring rings is 144.7° and 163.1°.

The crystal structure of complex **2** (Fig. 2) reveals that the coordination geometry around copper(II) is distorted trigonal bipyramidal with the monohelical dapmp ligand existing in an all-*anti* configuration. The equatorial sites consists of N(3), which comes from the pyrimidyl ring of the tridentate dapmp, and two Cl-donors, and the apical sites are occupied by N(1) and N(5) atoms of the pyridal rings. The bond angles Cl(1)–Cu–Cl(2) (136.88(4)°), N(3)–Cu–Cl(1) (115.64(8)°) and N(3)–Cu–Cl(2) (107.48(8)°) sum up to 360° and the Cu(II) atom lies in the equatorial plane. The average Cu–N bond length is observed to be 2.004 Å while the Cu–Cl bond length is 2.393 Å. The dihedral angle between the plane 1 (Cu, Cl(1), Cl(2), N(3)) and the plane 2 (N(3), N(6), C(6), C(7), C(8), C(9)) is 88.9°. The mononuclear unit is connected via two N–H···Cl hydrogen bonds (N(4B)···Cl(2A) 3.225 Å, Cl(2B)···N(4A) 3.225 Å) with a centrosymmetrically related counterpart to form a dimer as depicted in Fig. 3. The structural characterization of such hydrogen-bonded dimeric compounds linked by self complementary donor/acceptor groups is scarce for inorganic compounds. We are aware of only a few transition metal carboxylates of, e.g. zinc [14] and platinum [15] displaying pairs of symmetric C=O···H–N bridges, while here copper displays pairs of symmetric Cl···H–N bridges. The dimer is linked via another two Cl···H–N bridges to form a one-dimensional supermolecular chain along the *c* axis (Fig. 3).

Complex **3** has the same coordination configuration as **2**. The copper(II) atom is 5-coordinated with three N atoms from the ligand dapmp and two monodentate CH_3COO^{-1} ligands in an approximately trigonal bipyramidal environment (Fig. 4). The basal plane is formed by two O atoms from CH_3COO^{-1} and one N atom of the

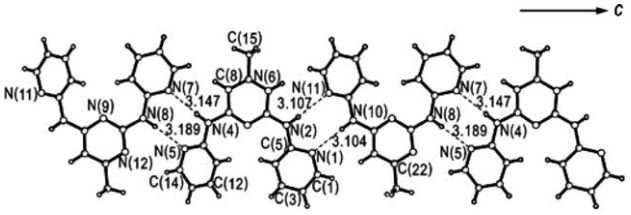


Fig. 1. An ORTEP diagram of dapmp (**1**), showing the interactions among the ligands. Thermal ellipsoids are at the 50% probability level.

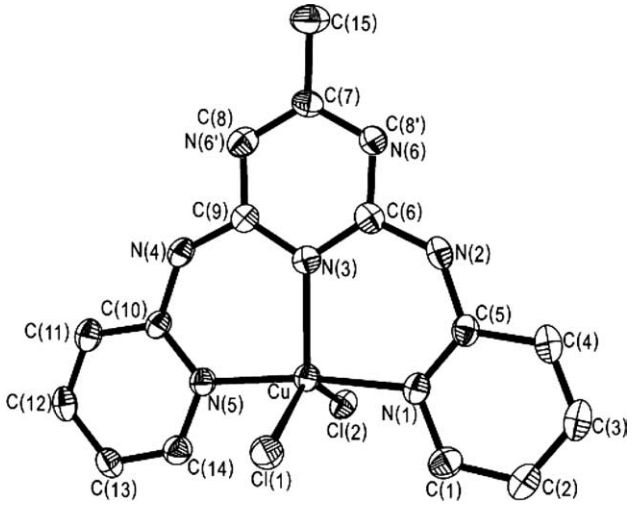


Fig. 2. The ORTEP drawing of $Cu(dapmp)Cl_2$ (**2**). Thermal ellipsoids are drawn at the 50% probability level.

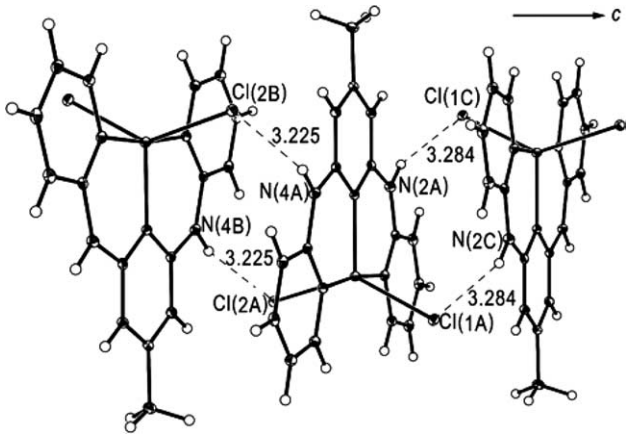


Fig. 3. The one-dimensional chains structure of Cu(dapmp)Cl_2 (**2** formed by hydrogen-bonding interactions (dashed lines).

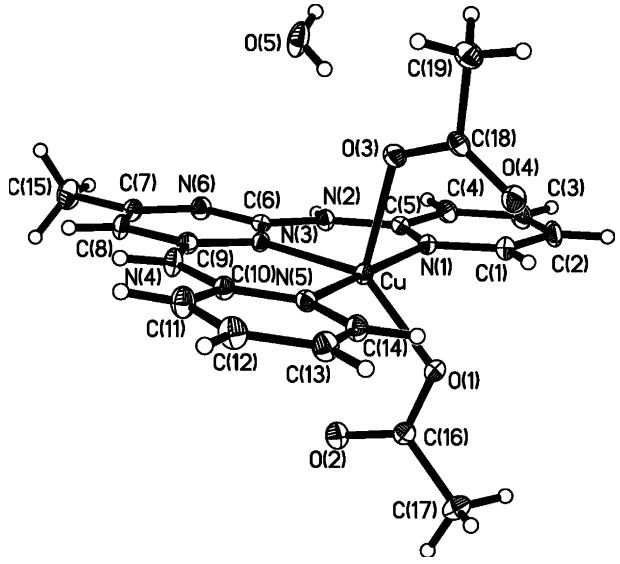


Fig. 4. The ORTEP drawing of [Cu(dapmp)$(CH_3]\cdot H_2O$ (**3**). Thermal ellipsoids are drawn at the 50% probability level.

central pyrimidine, which is indicated by bond angle summation (360°) of O(1)–Cu–O(3) (121.54(8)°), N(3)–Cu–O(1) (139.58(8)°) and N(3)–Cu–O(3) (98.88(8)°). The apical positions are occupied by two N atoms of terminal pyridine groups (N(1)–Cu–N(5) 172.84(9)°). The corresponding Cu–$N_{(dapmp)}$ and Cu–$O_{(CH3COO^-)}$ distances have the same magnitude, ranging from 1.975(2) to 2.067(2) Å. Within the acetate groups the C–O distances are greater for the strongly coordinated O atoms C(18)–O(3) and C(16)–O(1) (average 1.270 Å) than for the non-coordinated O atoms (average 1.243 Å). Intermolecular bonding of O(2) results in an intermediate C(16)–O(2) distance (1.244 Å). Both Cu–N bond lengths are typical of those found for the 5-coordinate Cu(II)-μ-pmea analogues [16]. Buckling of the tridentate dapmp ligand produces a dihedral angle between the two pyridyl rings of 10.5°. The Cu–O(3) bond has the longest distance (2.162(2) Å) in the 5-coordinated unit. The average Cu–N bond length is observed to be 2.006 Å, which is similar to the average Cu–N bond length of **2**. The dihedral angle (84.6°) between the plane (Cu, O(1), O(3), N(3)) and the pyrimidine ring plane is smaller than that of **2** between the plane (Cu, Cl(1), Cl(2), N(3)) and the plane of the pyrimidine ring (88.9°).

The mononuclear units are bridged by two H_2O molecules via four hydrogen bonds to form a dimeric unit (Fig. 5). On the other hand, via two hydrogen bondings ($O_{uncoord}\cdots N(H)$,2.806 Å), adjacent dimers are interconnected, giving rise to a one-dimensional supermolecular chain along the crystallographic *a* axis. It is worthy of note that the H_2O molecule binds the other uncoordinated O atom of CH_3COO^{-1} by hydrogen bonds (O(5)···O(4), 2.744 Å) in the *b*–*c* plane, and the neighboring chains are extended into a three-dimensional supermolecular structure.

3.2. Spectroscopic properties

The IR spectra of the complexes exhibit several characteristic strong bonds. In complex **2**, the bands around 1598 and 1569 cm^{-1} in ligand dapmp (**1**), attributed to the C=N grouping, are shifted to 1651 and 1588cm^{-1}, respectively, confirming the involvement of the ligand dapmp (**1**) in the copper complexation. In complex **3**, the corresponding bands are shifted to 1684 and 1642 cm^{-1}. The bands corresponding to v_{as}(COO) and v_{sym}(-COO) are at 1590 and 1397 cm^{-1} [17,18]. The Δv of the complex are 193 cm^{-1} more than the corresponding values for CH_3COONa (164 cm^{-1}), indicating that the CH_3COO^- group behaves as a monodentate ligand [18]. Other obsorption peaks can also be assigned to the ligand dapmp (**1**). These are in good agreement with the crystallographic results. The electronic spectra of the two complexes in methanol at ambient temperature were measured. On the basis of high extinction coefficient, the bands at 49 505, 46 296 and 47 393 cm^{-1} can be ascribed to a π–π transition of the ligand in **1**, **2** and **3**, respectively. There are two bands 39 370 cm^{-1} (complex **2**)

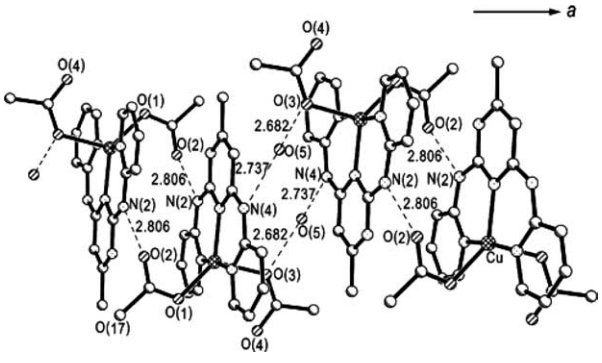


Fig. 5. The molecule packing of [Cu(dapmp)$(CH_3]\cdot H_2O$ (**3**) formed by hydrogen-bonding interactions (dashed lines). For the interest of clarity, the hydrogen atoms are omitted.

and 39063 cm^{-1} (complex **3**) corresponding to a metal–ligand charge transfer transition. The shoulder band 32573 cm^{-1} is due to the d–d transition in **2** and the band 32468 cm^{-1} due to the d–d transition in **3**. In addition, there is a weak unresolved shoulder at 30581 cm^{-1} in **1**.

3.3. Thermogravimetric analysis

Thermogravimetric analysis of complex **3** was carried out to examine its thermal stability. The TGA curve shows that the first weight loss of 3.68%, which occurs between 80 and 105 °C, corresponds to the loss of an uncoordinated water molecule (calc.: 3.77%). Further decomposition begins at 175 °C and ends at 560 °C with residue CuO in 17.5% yield (calc.: 16.6%). Thermogravimetric analysis of complex **2** shows that the decomposition begins at 291 °C and ends at 690.2 °C with residue CuO in 20.2 yield (calc.: 19.4%).

4. Supplementary material

Crystallographic data for the structural analysis have been deposited with the Cambridge Crystallographic Data Center, CCDC No. 236246 for compound **1**, 236245 for compound **2** and 236244 for compound **3**. Copies of this information may be obtained free of charge on application to CCDC, 12 Union Road, Cambridge CB2 1EZ, UK (fax: +44-1223-336-033; e-mail: deposit@ccdc.cam.ac.uk or http://www.ccdc.cam.ac.uk).

Acknowledgments

This work was supported by the National Natural Science Foundation of China 20471048 and IRAPOYT.

References

[1] N.F. Curtis, in: J.A. McCleverty, T.J.M. McCleverty (Eds.), Comprehensive Coordination Chemistry, 1st ed., Elsevier/Pergamon Press, Amsterdam, 2004, p. 447.
[2] J.A. McCleverty, M.D. Ward, in: J.A. McCleverty, T.J.M. McCleverty (Eds.), Comprehensive Coordination Chemistry, 1st ed., Elsevier/Pergamon Press, Amsterdam, 2004, p. 743.
[3] M. FuJita, Y.J. Kwon, S. Washizu, K. Ogura, J. Am. Chem. Soc. 116 (1994) 1151.
[4] R.-G. Xiong, X.-Z. You, B.F. Abrahams, Z. Xue, C.-M. Che, Angew. Chem. Int. Ed. 40 (2001) 4422.
[5] D.M. Bassani, J.-M. Lehn, K. Froman, D. Fenske, Angew. Chem. Int. Ed. 41 (2002) 4041.
[6] N.L. Rosi, J. Eckert, M. Eddaoudi, D.T. Vodak, J. Kim, M. O'keeffe, O.M. Yaghi, Science 300 (2003) 1127.
[7] J.R. Galán-Mascarós, K.R. Dunbar, Angew. Chem. Int. Ed. 42 (2003) 2289.
[8] G.M. Sheldrick, SHELXL-93, Program for the Refinement of Crystal Structure, University of Göttingen, Göttingen, Germany, 1993.
[9] SHELXTL 5.03 (PC-version), Program Library for Structure Solution and Molecular Graphics, Siemens Analytical Instrument Division, Madison, WI, 1995.
[10] Z. Berkovitch-Yelli, L. Leiserowitz, J. Am. Chem. Soc. 102 (1980) 7677.
[11] A.T. Hagler, E. Huler, S. Lifson, J. Am. Chem. Soc. 96 (1974) 5319.
[12] A. Kvick, S.S. Booles, Acta Crystallogr., Sect. B 28 (1972) 3405.
[13] M. Simard, D. Su, J.D. Wuest, J. Am. Chem. Soc. 113 (1991) 4696.
[14] N. Rodier, R. Ceolin, M. Plat, H. Zumbihl, Acta Crystallogr., Sect. C 46 (1990) 324.
[15] A.D. Burrows, D.M.P. Mingos, A.J.P. White, D.J.J. Williams., J. Chem. Soc., Dalton Trans. (1996) 3805.
[16] K.-Y. Choi, Y.-M. Jeon, H. Ryu, J.-J. Oh, H.-H. Lim, M.-W. Kim, Polyhedron 23 (2004) 903.
[17] K. Nakamoto, Infrared and Raman Spectra of Inorganic and Coordination Compounds, 4th ed., Wiley, New York, 1986.
[18] G.B. Deacon, R.J. Phillips, Coord. Chem. Rev. 33 (1980) 227.

Available online at www.sciencedirect.com
SCIENCE DIRECT®
Polyhedron 24 (2005) 221–228
POLYHEDRON
www.elsevier.com/locate/poly

One-dimensional coordination polymer $[Co(H_2O)_4(pyz)](NO_3)_2 \cdot 2H_2O$ (pyz = pyrazine) with intra- and inter-chain H-bonds: structure, electronic spectral studies and magnetic properties

K. Travis Holman [a], Hassan H. Hammud [b,*], Samih Isber [c], Malek Tabbal [c]

[a] Department of Chemistry, Georgetown University, Washingtown, DC 20057-1227, USA
[b] Department of Chemistry, Faculty of Science, Beirut Arab University, 11-5020 Beirut, Lebanon
[c] Department of Physics, American University of Beirut, 11-0236 Beirut, Lebanon

Received 8 July 2004; accepted 4 November 2004
Available online 29 December 2004

Abstract

The synthesis, structure and magnetic properties of the cobalt(II) complex (**1**) $[Co(H_2O)_4(pyz)](NO_3)_2 \cdot 2H_2O$ is reported. The compound crystallizes in the triclinic system, space group $P\bar{1}$, with cell constants: $a = 7.0328(15)$ Å, $b = 7.1255(16)$ Å, $c = 8.4198(19)$ Å, $\alpha = 107.226(4)°$, $\beta = 114.242(4)°$, $\gamma = 90.487(4)°$, $Z = 1$ and $V = 363.35(14)$ Å^3. The structure of **1** consists of elongated octahedral CoO_4N_2 chromophores with bridging pyrazine ligands forming a one-dimensional coordination polymer along the crystallographic *b*-axis. The nitrate ions hydrogen-bond to the water ligands (L) and guest water (G), and form $H_2O(L)\cdots H_2O(G)\cdots NO_3^-\cdots H_2O(G)\cdots H_2O(L)$ chains which flank either side of the coordination polymer chains. Hydrogen-bonding is extended to neighboring chains forming a two-dimensional network. The solvent effect on the electronic spectra of pyrazine and pyrazine cobalt complex **1** has been investigated. The magnetic susceptibility of complex **1** versus temperature data showed a strong antiferromagnetic coupling between Co ions. The best fitting parameters were obtained for $J_1/k_B = -26.4$ K, $J_2/k_B = -2.2$ K and $g = 2.3$.
© 2004 Elsevier Ltd. All rights reserved.

Keywords: Coordination polymer; Cobalt(II) pyrazine complex; H-bond; Magnetic susceptibility

1. Introduction

During the last decade, there has been great interest in the design of various supramolecular self assemblies from basic building blocks. Self assembly concerns the reversible spontaneous association of a limited number of tectons under the intermolecular control of relatively labile coordination, hydrogen-bonds and dipolar interactions. The reversibility is key to the resulting systems ability to sift through the available components to form the thermodynamically most favorable structure. The tectons come together spontaneously in a well defined way to give assemblies in one, two or three dimensions [1,2]. Molecular recognition occurring between host and guest may be an intrinsic part of the operation of the supramolecular device, which might be designed to bind and then signal the presence of a guest [3]. Supramolecular assemblies of the polymer type are of interest in the area of tunable zeolite mimics [4]. Other interests are applications in catalysis and advanced materials such as magnetic, optic and electronic materials [5–8]. In the crystal engineering 'toolbox' [9], hydrogen-bonding moieties are perhaps the most used implements in

* Corresponding author. Tel.: +961 3 381862; fax: +961 1 818402.
E-mail address: h.hammud@bau.edu.lb (H.H. Hammud).

0277-5387/$ - see front matter © 2004 Elsevier Ltd. All rights reserved.
doi:10.1016/j.poly.2004.11.017

the design of such supramolecular systems [10], and have been particularly strongly applied towards the synthesis of molecular magnetic materials [11–16].

Because of its rod like rigidity and length, pyrazine is a good candidate for molecular building blocks. Several factors influence the specific framework structure that is formed: One factor is the role of the solvent, for example a large difference has been obtained between the double-layer structure of the solvent inclusion compound $[Ag(pyz)_2][Ag_2(pyz)_5](PF_6)_3 \cdot 2S$ ($S = CH_2Cl_2$, $CHCl_3$, CCl_4) [17] and the layer structure of the solvent-free compound $[Ag(pyz)_2](PF_6)$ [18]. The counterion can also influence the final structure, replacing the counterion PF_6^- by SbF_6^-, or BF_4^- changes the structure from the two-dimensional undulated sheet structure of $[Ag(pyz)_2](PF_6)$ [18], to the three-dimensional non-interpenetrating cubic framework of $[Ag(pyz)_3](SbF_6)$ [17], or to the interpenetrated three-dimensional structure of $[Ag_2(pyz)_3](BF_4)_2$ [19]. The specific oxidation of the metal cation can also determine the final polymer structure: Cu^{2+} is in a distorted octahedral coordination and forms a square two-dimensional network with pyrazine or substituted pyrazine [20], while Cu^+ adopts a tetrahedral coordination forming three-dimensional networks with substituted pyrazine or 4,4′-bipyridine [21], Cu^+ may also be trigonally coordinated by pyrazine or 4,4′-bipyridine forming three-dimensional networks or two-dimensional layers containing six-membered rings [21–26], where only $[Cu_2(pyz)_3](SiF_6)$ [22] has an interpenetrated structure. In addition the type of metal cation affects the coordination preference and thus the final polymer structure; when bonded to pyrazine, Cu^+ is tetrahedral, or trigonal as just described, whereas Ag^+ is found in a wide range of coordination environments: linear [19,27], trigonal [19], tetrahedral [18,19,28], square-planar, square-pyramidal and octahedral [17].

It is noted from the above discussion that the formation of coordination polymers of group IB and IIB metal ions with pyrazine has been well studied, and that more work needs to be devoted to the study of complexation with other transition metals. In the present work, we report the reaction of $Co(NO_3)_2 \cdot 6H_2O$ with pyrazine. A new polymer compound (**1**) $[Co(pyz)(H_2O)_4](NO_3)_2 \cdot 2H_2O$ is formed, which has a linear chain structure (Fig. 1). There are straight chain polymers, such as (**2**) $[Co(H_2O)_4(pyz)](SO_4) \cdot 2H_2O$ [29] and $[Co(acac)_2(pyz)]$ (**3**) [30], two-dimensional sheets examples are $[CoCl_2(pyz)_2]$ [31] and $[M(pyz)_2(NCS)]$ (M = Co, Fe) [32,33], and a three-dimensional network example is $[M(pyz)(Au(CN)_2)_2]$ (M = Cu, Ni, Co) [34]. Measurement of variable temperature magnetic susceptibilities of various cobalt pyrazine complexes indicated anti-ferromagnetic behaviors [30,32–35]. The conducting properties of pyrazine metal complexes were investigated, with Fe(II) complexes showing higher conductance values compared to other metal complexes [36,37].

One important feature about the structure of compound **1** is that guest water molecules occupy void spaces in the structure and that both intra- and intermolecular hydrogen-bonding interactions are observed involving coordinated water molecules, guest water molecules and the nitrate counterions. The compound also shows weak antiferromagnetic behavior.

2. Experimental

All reagents were obtained from Aldrich and were used as received.

2.1. Synthesis of $[Co(H_2O)_4(pyrazine)](NO_3)_2 \cdot 2H_2O$

An acetonitrile solution (30.0 ml) of pyrazine (0.310 g, 3.87 mmol) was added to an ethanolic solution (20.0 ml) of $Co(NO_3)_2 \cdot 6H_2O$ (0.75 g, 2.58 mmol). The mixture was refluxed for 2 h then left to stand at room temperature. Red block crystals of **1** were formed in one week. The typical yield was 92% based on $Co(NO_3)_2 \cdot 6H_2O$. Calc. for $C_4H_{16}CoN_4O_{12}$: C, 12.94; H, 4.35, N 15.10; Co, 15.88. *Anal.* Found: C, 12.40; H, 4.30; N, 15.30; Co, 15.80.

IR (KBr): 3319.1 (m), 3209.3 (m), 3112.9 (w), 3089.8 (w), 3051.2 (w), 1762.8 (w), 1615.2 (w), 1483.2 (m), 1433.3 (s), 1384.8 (s), 1163.0 (m), 1116.7 (m), 1055.0 (m), 987.5 (w), 825.5 (m), 788.8 (m), 474.5 (m).

2.2. Physical measurements

Elemental analyses of Co, C, H, N were performed by Kanti Labs Ltd., Mississauga, Canada. Infrared data

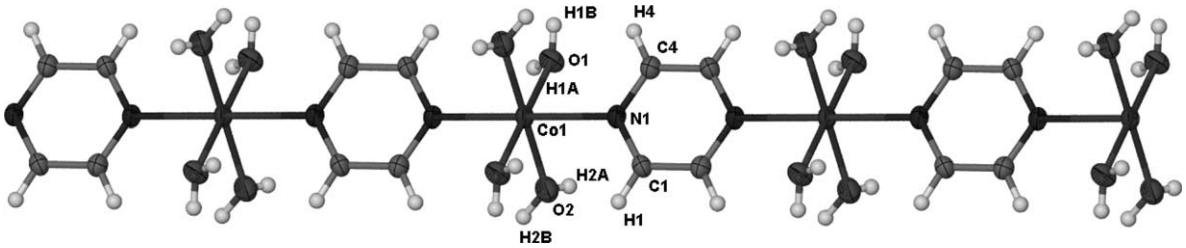


Fig. 1. Thermal ellipsoid plot of the one-dimensional polymer chain of **1**.

were collected on a Schimadzu 8300 FTIR spectrophotometer using the KBr pellet method. The electronic absorption spectra were obtained using a Ciba Corning 2800 spectrophotometer. The magnetic susceptibility of crystalline samples was measured on a Quantum Design Model 6000 Physical Property Measurement System. Diamagnetic corrections were applied using Pascal's constants.

2.3. Crystallography

Experimental parameters pertaining to single crystal X-ray analysis of **1** are given in Table 1. Data were collected on a single prismatic crystal measuring $0.35 \times 0.30 \times 0.20$ mm mounted and centered on a Siemens SMART 1000 CCD platform diffractometer with graphite monochromated Mo Kα radiation (λ = 0.71073 Å) at 173(2) K. The final unit cell was determined from 1222 reflections in the range of $2.8° < \theta < 28.0°$. The data were integrated using the SAINT suite of software. Lorentz and polarisation effects were accounted for using SADABS. The structure was solved by direct methods and refined iteratively via full-matrix least-squares and difference Fourier analysis using the SHELX-97 suite of software [38] and with the assistance of X-SEED [39].

The cell symmetry triclinic $P\bar{1}$ has been preferred over monoclinic $C2/m$ symmetry: The internal R-factor, $R_{(int)}$ for the triclinic setting is 0.036 whereas in the monoclinic setting $R_{(int)}$ it was 0.28. Structure solution and refinement in the monoclinic setting led to very high R-factors as well as unreasonable thermal parameters (and imposed disorder) for both pyrazine ligand and nitrate anions.

All non-hydrogen atoms were refined with anisotropic displacement parameters. The hydrogen atoms of the pyrazine ligand were placed in idealized positions and refined with a riding model whereas those on the coordinated and lattice water molecules were located and fully refined with isotropic displacement parameters. The nitrate anions are disordered and the two orientations are very well resolved, hinting at statistical disorder.

Table 1
Crystal data and refinement for **1**

Formula	$C_4H_{16}O_{12}N_4Co$
Color	red
M (g mol^{-1})	371.14
T (K)	173(2)
Crystal system	triclinic
θ (°)	2.8–28.0
Space group	$P\bar{1}$
Unit cell dimensions	
a (Å)	7.0328(15)
b (Å)	7.1255(16)
c (Å)	8.4198(19)
α (°)	107.226(4)
β (°)	114.242(4)
γ (°)	90.487(4)
V (Å^3)	363.35(14)
Z	2
ρ_{calc} (g cm^{-3})	1.696
μ (mm^{-1})	1.248
# Unique reflections/parameters	1543/140
# Reflections $I > 2\sigma(I)$	1365
R, wR_2 (observed data)	0.0446, 0.1133
Residual (e Å^{-3})	0.801

3. Results and discussion

3.1. Reaction chemistry

The title compound was obtained by the reflux reaction of hydrated cobaltous nitrate in ethanol with pyrazine in acetonitrile. Single crystals suitable for X-ray diffraction were obtained by slow evaporation of the reaction mixture after several days.

3.2. Description of the structure

3.2.1. One-dimensional linear chain structure

The compound has a one-dimensional linear chain structure along the crystallographic b-axis, which is formed by bridging pyrazine ligands connecting the $Co(H_2O)_4$ units. A thermal ellipsoid plot of the one-dimensional polymer chain of **1** is depicted in Fig. 1. The Co atom lies at a center of symmetry and is coordinated by the oxygen atoms of four water molecules and the nitrogen atoms from two pyrazine molecules, forming an elongated octahedral cobalt coordination sphere. The oxygen atoms occupy the equatorial positions forming four short bonds with cobalt (Co(1)–O(1) = 2.073(2) Å, Co(1)–O(2) = 2.064(2) Å). The oxygens form an essentially square planar array around the central cobalt ion; the angles O(1)–Co(1)–O(1) and O(2)–Co(1)–O(2) are ideal 180.08(7)°, and the angles O(2)–Co(1)–O(1) are 89.12(10)° and 90.88(10)° (Fig. 1). The nitrogen atoms are located in axial positions with a perfect angle of 180.00(7)°. They form two long bonds with cobalt (Co(1)–N(1) = 2.173(2) Å) (Fig. 1), with values that are consistent with those found in related linear chain polymers (e.g. Co–N = 2.198 Å in $[Co(H_2O)_4(pyz)]$ $(SO_4) \cdot 2H_2O$ (**2**) [29] and 2.227(2) Å in $[Co(acac)_2(pyz)]$ (**3**) [30]). The cobalt atoms in **1** are bridged by pyrazine ligands with the nearest Co···Co separation of 7.125 Å within the chain (Fig. 1), compared to 7.189 Å in **2** [29]. Each chain is surrounded by six identical chains. The separations of the metal ions between two neighboring chains are 7.033, 8.420 and 8.469 Å (see Fig. 2). This compares separations of 6.308, 7.189 and 8.724 Å in **2** [29], and 6.290 and 6.27 Å in **3** [30]. Other one-dimensional

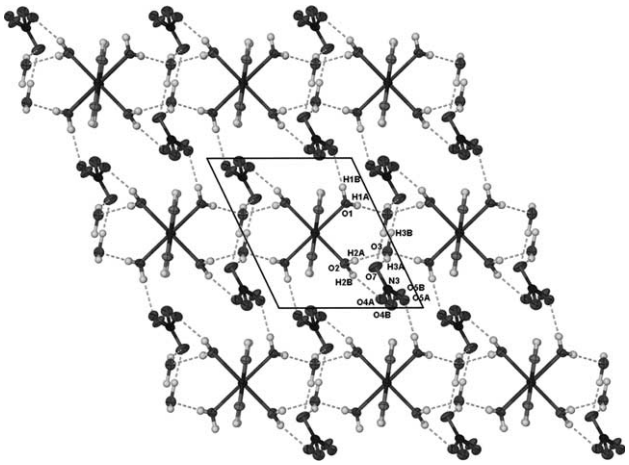


Fig. 2. Cross-sectional view in the *ac*-plane. Two-dimensional network caused by H-bonds between cobalt units in **1**.

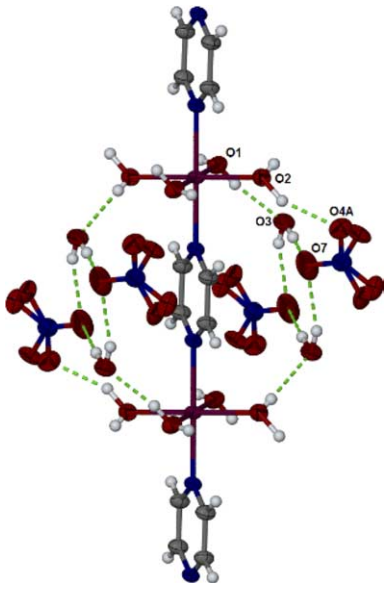


Fig. 3. Intra-chain H-bond interactions in **1**.

straight chain compounds are $[Co(DBSQ)_2(pyz)]$ (DBSQ = 3,6-dibutylbenzocatecholato-*O*,*O*′) [40] and $[Co(WO)_2(pyz)]$ (WO = dimethylglyoximato) [41]. Further bridging of pyrazine ligands can lead to two-dimensional extended structures such as in $[CoCl_2(pyz)_2]$ [31] and $[Co(NCS)_2(pyz)_2]$ [32]. Thus the type of anion greatly affects the final structure of the cobalt pyrazine complex: reaction of cobalt nitrate with pyrazine produces one-dimensional polymer (**1**) $[Co(pyz)(H_2O)_4](NO_3)_2 \cdot 2H_2O$ with two included water molecules and no participation of nitrate in the inner coordination sphere. Notably, the reaction of cobalt nitrate with 4,4′-bipyridine, a linear *N*,*N*′-bidentate spacer similar to pyrazine, produces in the presence of *p*-nitroaniline (PNA) an interpenetrated square grid two-dimensional network $[Co(bipy)_2(NO_3)_2] \cdot 2PNA$ that results from a higher ligand:metal stoichiometry. In this compound, two nitrate ions occupy the axial positions within the inner coordination sphere of Co. The interpenetrated PNA forms planar networks sustained by edge-to-face interactions between the edges formed by NO_2 moieties and the faces formed by the NH_2 moieties [42].

3.2.2. H-Bond

The nitrate ions of **1** hydrogen-bond to the coordinated water ligand (L) and the lattice-included guest water (G) such that each $[Co(pyz)_2(H_2O)_4]$ chain is flanked on either side by two hydrogen-bonded $H_2O(G)$ molecules and two NO_3^- ions. Thus two adjacent cobalt units within the same chain interact on each side by six extended intra-chain H-bond paths: two through $H_2O(L) - NO_3^- - H_2O(G) - H_2O(L)$, and four through $H_2O(L) - H_2O(G) - NO_3^- - H_2O(G) - H_2O(L)$, (Fig. 3). The bonds distances and bond angles involved in the H-bonds labelled in Fig. 3 follow. For $H_2O(L)$ with NO_3^- ions: O(2)···O(4A) = 2.866(6) Å, H(2B)···O(4A) = 2.0 Å, O(2)–H(2B)···O(4A) = 156°; for $H_2O(G)$ molecules with NO_3^- ions: O(3)··· O(5B) = 2.87(1) Å, H(3A)···O(5B) = 2.2 Å, O(3)–H(3A)··· O(5B) = 149°, O(3)···O(7) = 2.907(4) Å, H(3A)··· O(7) = 2.2 Å, O(3)–H(3A)···O(7) = 159° and O(3) ···O(7) = 2.788(4) Å, H(3B)···O(7) = 1.8 Å, O(3)–H(3B) ···O(7) = 177°; for $H_2O(L)$ with $H_2O(G)$ molecules: O(1)···O(3) = 2.740(3) Å, H1(A)···O(3) = 2.1 Å, O(1)–H(1A)···O(3) = 178° and O(2)···O(3) = 2.704(4) Å, H(2A)···O(3) = 1.9 Å, O(2)–H(2A)···O(3) = 170°.

Fig. 2 shows that each linear chain is surrounded by six neighboring chains in a cross-sectional view along the *b*-axis in the *ac*-plane. Each cobalt unit interacts directly by extended inter-chain H-bonds with six neighboring units making a two-dimensional network. Complex **1** thus forms a three-dimensional supramolecular structure due to both coordination bonds (bridging by pyrazine) and H-bonds. Four types of inter-chain H-bonds paths are involved: (1) $H_2O(L) - NO_3^- - H_2O(L)$, (2) $H_2O(L) - H_2O(G) - NO_3^- - H_2O(L)$, (3) $H_2O(L) - H_2O(G) - H_2O(L)$, and (4) $H_2O(L) - H_2O(G) - NO_3^- - H_2O(G) - H_2O(L)$. The extension of intra-chain H-bonds described previously serve also in inter-chain H-bonds. The difference is in the coordinated water molecules whether they belong to the same chains or to two different chains. Thus the bonds distances and bond angles involved in inter-chain H-bonds are the same as before. Only for inter-chain H-bondings between $H_2O(L) - NO_3^- - H_2O(L)$ two additional bondings values should be listed: O(1)···O(4B) = 2.83(1) Å, H(1B)···O(4B) = 2.1 Å, O(1)–H(1B)··· O(4B) = 149° and O(1)···O(5A) = 2.742(8) Å, H(1B)··· O(5A) = 2.0 Å, O(1)–H(1B)···O(5A) = 150°.

Solvent or guest molecules are generally included in the void between chains and hydrogen-bonding interac-

tions have been also observed in related one-dimensional structures such as compound (**2**), $[Co(H_2O)_4(pyz)](SO_4)\cdot 2H_2O$ [29], $[Co(pyz)(H_2O)_4](C_8H_4O_4)$ [43] but not in $[Co(acac)_2(pyz)]$ [30].

3.3. Discussion on IR

The absorbances between 1055.0, 1116.7 and 1163.0 cm^{-1} are assignable to pyrazine bands; the peak at 474.5 cm^{-1}, shifted from 417.0 cm^{-1} in free pyrazine, is particularly diagnostic of bridging bidentate ligands [44–47]. Nitrate group absorbances are observed at 1615.0 cm^{-1} due to an assymmetric stretch, and very strong at 1433.3 and 1384.8 cm^{-1} (symmetric stretch). Broadened O–H stretches are observed for H_2O(G) and H_2O(L) at 3319.1 cm^{-1}.

3.4. Discussion on electronic absorption spectra

Complex **1** shows a d–d transition at 521 nm in DMF, 536 nm in DMSO and 502 nm in pyridine.

The solvent effect on the electronic absorption spectra of pyrazine in the free state and in the complexed state in cobalt pyrazine complex **1** has been investigated, see Table 2. The absorption peak location Y (λ_{max} nm) of the species in a given solvent has been expressed by the following multi-parameter [48,49]:

$$Y = a_0 + a_1X_1 + a_2X_2 + a_3X_3 + a_4X_4.$$

This is amenable to solution for the intercept a_0 and the coefficient a_i by multiple regression techniques. The independent variables X_i are the solvent interaction mechanisms E, K, M and N. The empirical solvent polarity E is sensitive to both solvent–solute hydrogen-bonding and to dipolar interactions. It is related to v, which is the wave number of the absorption maximum in the given solvent, $E = 2.859 \times 10^{-3}v$.

K is a measure of the polarity of the solvent that depends on the solvent dielectric constant D. $K = (D - 1)/(2D + 1)$.

M is a measure of solute permanent dipole–solvent induced dipole interactions that depend on the solvent refractive index n. $M = (n^2 - 1)/(2n^2 + 1)$.

N is a measure of permanent dipole–permanent dipole interactions

$$N = (D - 1)/(D + 2) - (n^2 - 1)/(n^2 + 2).$$

A multiple regression analysis has been performed. In each case fits are obtained as a function of one parameter alone, two parameters or three parameters. The results are summarized in Tables 3 and 4. The λ_{max} studied λ_1 and λ_2 are for B and R bands, respectively, for pyrazine and complex **1**. The values obtained are very close for both species. B bands (λ_1) which originate from π–π* transitions shift to longer wavelengths in the polar solvents DMF and DMSO, while the R bands (λ_2), which are due to n–π* transitions, shift to shorter

Table 2
Solvent parameters and observed λ_{max} (nm) for cobalt pyrazine complex **1** (and pyrazine)

Solvent	E	K	M	N	λ_1	λ_2
Carbon tetrachloride	32.5	0.20	0.22	0.01	is[a] (266.8)	is[a] (313.8)
Diethyl ether	34.6	0.34	0.18	0.30	259.5 (260.0)	ncp[b] (315.6)
Chloroform	39.1	0.36	0.21	0.29	260.8 (261.2)	ns[b] (311.2)
Dimethyl formamide	43.8	0.48	0.20	0.67	271.5 (270.0)	316.2 (316.8)
Dimethyl sulfoxide	45.0	0.48	0.22	0.66	262.8 (265.0)	316.2 (317.0)
Acetonitrile	46.0	0.48	0.18	0.71	260.0 (260.5)	312.5 (313.5)
Ethanol	51.9	0.47	0.18	0.67	259.5 (259.5)	312.0 (312.5)
Methanol	55.5	0.48	0.17	0.71	261.2 (260.0)	310.0 (310.0)
Water	63.1	0.49	0.17	0.76	260.0 (260.6)	300.0 (301.0)

[a] Complex **1** is insoluble.
[b] No characteristic peak observed.

Table 3
Regression analysis for cobalt pyrazine complex **1** (and pyrazine) using E, K, M, N at λ_1

Parameters	a_0	a_1	a_2	a_3	a_4	MCC
E	265.189 (269.238)	−0.069 (−0.145)				0.157 (0.383)
K	253.636 (265.874)	18.495 (−7.743)				0.279 (0.208)
M	245.210 (238.932)	88.492 (123.245)				0.414 (0.676)
N	259.449 (264.195)	4.131 (−2.961)				0.194 (0.209)
EK	252.586 (268.726)	−0.361 (−0.212)	59.035 (8.580)			0.614 (0.409)
EM	241.16 (234.544)	0.042 (0.041)	99.461 (136.301)			0.422 (0.681)
KM	231.787 (232.900)	24.158 (6.736)	102.332 (139.906)			0.548 (0.693)
EKM	242.919 (234.172)	−0.273 (−0.024)	51.726 (8.132)	46.473 (135.856)		0.636 (0.694)
$EKMN$	196.234 (253.723)	−0.298 (−0.196)	362.369 (−516.78)	−110.923 (−547.90)	−102.996 (532.256)	0.691 (0.902)

Table 4
Regression analysis for cobalt pyrazine complex **1** (and pyrazine) using *E*, *K*, *M*, *N* at λ_2

Parameters	a_0	a_1	a_2	a_3	a_4	MCC
E	349.778 (328.657)	−0.759 (−0.356)				0.949 (0.720)
K	599.150 (316.688)	−600.000 (−10.262)				0.634 (0.210)
M	270.019 (287.605)	220.345 (128.874)				0.724 (0.540)
N	413.306 (315.062)	−146.636 (−5.055)				0.925 (0.272)
EK	453.342 (326.066)	−0.669 (−0.698)	−225.304 (43.418)			0.972 (0.912)
EM	345.843 (321.599)	−0.732 (−0.318)	13.772 (27.727)			0.950 (0.726)
KM	516.233 (283.904)	−502.832 (4.134)	194.336 (139.099)			0.894 (0.545)
EKM	456.477 (319.617)	−0.558 (−0.663)	−262.775 (43.335)	49.314 (25.355)		0.978 (0.915)
EKMN	321.726 (336.260)	−0.488 (−0.785)	295.952 (−31.273)	−118.938 (39.824)	−151.569 (32.954)	0.992 (0.941)

wavelengths in hydrogen-bonding solvents. The data for λ_1 shows good dependence of the shift in λ_{max} on *M*, the data indicates improvement in the fit in going from one parameter to two, three and four parameter correlations. The data for λ_2 shows very good dependence of the shift in λ_{max} on *E*, *K*, *M* and *N* parameters. The multiple correlation coefficients MCC in the complex are higher than in the free pyrazine.

3.5. Magnetic study

The temperature dependence of the inverse magnetic susceptibility for compound **1** as a function of the temperature in the range 2–300 K is shown in Fig. 4 (χ_M^{-1} versus *T*). This figure shows that χ_M^{-1} follows the Curie–Weiss law, and decreases linearly as the temperature decreases down to 25 K. The best fitting to a straight line yields a negative Curie–Weiss temperature of −16.8 K, indicative of a strong antiferromagnetic coupling between Co ions. At 300 K $\chi_M T$ versus *T* is equal to 2.985 cm^3 K mol^{-1} which is quite different from the value of 2.1 cm^3 K mol^{-1} reported by Ma et al. [30].

The $\chi_M T$ versus *T* curve exhibits a continuous decrease from 300 to 2 K as the temperature is lowered. Such behavior is characteristic for Co(II) complexes,

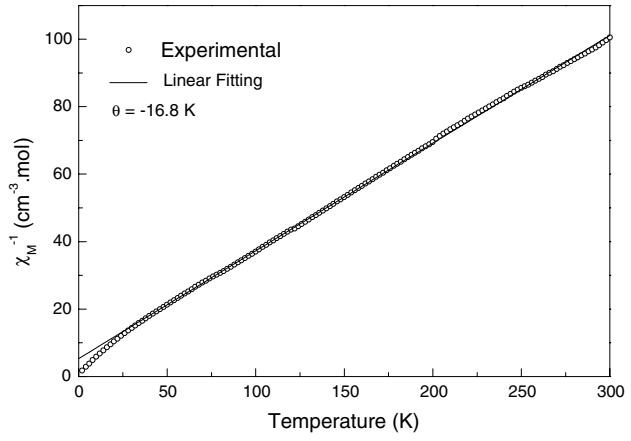


Fig. 4. Inverse of the molar magnetic susceptibility of **1** vs. temperature, the straight line represents the best fit to a Curie–Weiss law obtained for $\theta = -16.8$ K.

due to single ion anisotropy with some contribution of antiferromagnetic exchange between the Co(II) centers. The magnetic coupling can be mediated through extensive intra-chain as well as inter-chain H-bondings interactions between the cobalt atoms. The experimental susceptibility data has been tentatively fitted for $S = 3/2$ using the classical spin model for the magnetic susceptibility of an infinite chain derived by Fisher [50]. Thus, the best fitting gave the following values for the parameters: $J = -1.1$ cm^{-1}, $g = 2.55$. However, the experimental data did not match the calculated ones especially at low temperature, and the Landé factor obtained does not reflect the ground of Co as seen in many systems [51–55]. A three-dimensional magnetic behavior with two exchange couplings rather than one should be considered. Also the analysis of magnetic data for cobalt complexes is complicated by single ions effects such as spin–orbit coupling, distortion from regular stereochemistry, electron delocalization, crystal field mixing of excited states into the ground state and by magnetic exchange interactions [56]. To improve the correlation between the experimental and theoretical data we attempted to include a second exchange coupling constant, thus our model consists of two linear chains corresponding to the shortest Co distances deduced from the X-rays data that are 7.125, 7.033, 8.420 and 8.469 Å. We calculated the spin Hamiltonian and the magnetic susceptibility of the linear chains taking into account two isotropic exchange-coupling constants, J_1 and J_2 [57]. For simplicity reasons each linear chain is considered to be a closed triplet that contains three Co ions interacting among themselves [58]. Thus, the spin Hamiltonian of a closed triplet is given by

$$H = -2J_i(S_1S_2 + S_1S_3 + S_2S_3) \quad i = 1, 2. \tag{1}$$

The magnetic susceptibility was calculated using the expression given by Spasojevic et al. [59]

$$\chi = \left(\frac{g\mu_B}{k_BT}\right)^2 \left(\frac{\sum_{S,m} m^2 \mathrm{Exp}(E(\alpha,S,m)/k_BT)}{\sum_{S,m} \mathrm{Exp}(E(\alpha,S,m)/k_BT)} - \left(\frac{\sum_{S,m} m \mathrm{Exp}(E(\alpha,S,m)/k_BT)}{\sum_{S,m} \mathrm{Exp}(E(\alpha,S,m)/k_BT)}\right)^2\right), \tag{2}$$

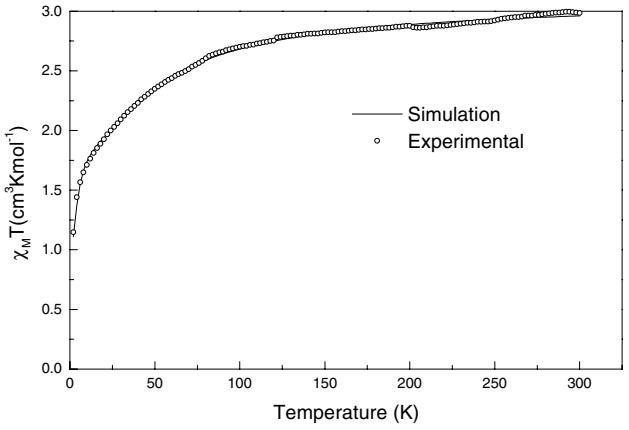


Fig. 5. $\chi_M T$ vs. temperature for **1**, the continuous line represents the best fitting using Eq. (2).

where μ_B is the Bohr magneton k_B is the Boltzman constant, g is the Landé factor and α is a notation for all quantum numbers besides S and m. Using this model the fit has been improved tremendously, as shown in Fig. 5. The best fitting parameters were obtained for $J_1/k_B = -26.4$ K, $J_2/k_B = -2.2$ K and $g = 2.3$.

Appendix A. Supplementary data

CCDC No. 211146 contains the supplementary crystallographic data for this paper. These data can be obtained free of charge at www.ccdc.cam.ac.uk/conts/retrieving.html, or from the Cambridge Crystallographic Data Centre (CCDC), 12 Union Road, Cambridge CB2 1EZ, UK (fax: +44 1223 336033; e-mail: deposit@ccdc.cam.ac.uk). Supplementary data associated with this article can be found, in the online version, at doi:10.1016/j.poly.2004.11.017.

References

[1] J.S. Lindsey, New J. Chem. 15 (1991) 153.
[2] D. Braga, F. Grepioni, G.R. Desiraju, Chem. Rev. 98 (1998) 1375.
[3] J.-M. Lehn, Supramolecular Chemistry: Concept and Perspectives, VCH, Weinheim, 1995, p. 89.
[4] C.J. Jones, Chem. Soc. Rev. 27 (1998) 289.
[5] B.F. Abrahams, B.F. Hoskins, D.M. Michael, R. Robson, Nature 369 (1994) 727.
[6] S. Kitagawa, M. Kondo, Bull. Chem. Soc. Jpn. 71 (1998) 1.
[7] O.M. Yaghi, G. Li, H. Li, Nature 378 (1995) 703.
[8] S.S.Y. Chui, S.M.F. Lo, J.P.H. Charmant, A.G. Orpen, I.D. Williams, Science 283 (1999) 1148.
[9] D. Braga, F. Grepioni, G.R. Desiraju, Chem. Rev. 98 (1998) 1375.
[10] M.J. Zaworotko, Chem. Soc. Rev. (1994) 283.
[11] C.J. O'Connor, E. Sinn, Inorg. Chem. 20 (1981) 545.
[12] A. Lang, Y. Pei, L. Ouahab, O. Khan, Adv. Mater. 8 (1996) 60.
[13] J. Veciana, J. Cirujeda, C. Rovira, E. Molins, J.J. Novoa, J. Phys. I 6 (12) (1996) 1967.
[14] N. Yoshioka, M. Irisawa, Y. Mochizuki, T. Kato, H. Inoue, S. Ohba, Chem. Lett. (1997) 251.
[15] O. Kahn (Ed.), Magnetism: A Supramolecular Function, Kluver, Dordrecht, 1996.
[16] M.M. Matsushita, A. Izuoka, T. Sugawara, T. Kobayashi, N. Wada, N. Takeda, M. Ishikawa, J. Am. Chem. Soc. 119 (1997) 4369.
[17] L. Carlucci, G. Cianni, D.M. Proserpio, A. Sironi, Angew. Chem., Int. Ed. Engl. 34 (1995) 1895.
[18] L. Carlucci, G. Cianni, D.M. Proserpio, A. Sironi, Inorg. Chem. 34 (1995) 5698.
[19] L. Carlucci, G. Cianni, D.M. Proserpio, A. Sironi, J. Am. Chem. Soc. 117 (1995) 4562.
[20] T. Otieno, S.J. Rettig, R.C. Thompson, J. Trotter, Inorg. Chem. 32 (1993) 4384.
[21] P. Halasyamani, K.R. Heier, M.J. Willis, C.L. Stern, K.R. Poppelmeier, Z. Anorg. Allg. Chem. 622 (1996) 479.
[22] L.R. MacGillivray, S. Subramanian, M.J.J. Zaworotko, J. Chem. Soc., Chem. Commun. (1994) 1325.
[23] T. Otieno, S.J. Rettig, R.C. Thompson, J. Trotter, Inorg. Chem. 32 (1993) 1607.
[24] S. Kitagawa, M. Munakata, T. Tanimura, Inorg. Chem. 1714 (1992) 31.
[25] S. Kitagawa, S. Katawa, M. Kondo, Y. Nozaka, M. Munakata, Bull. Chem. Soc. Jpn. 66 (1993) 3387.
[26] M.M. Turnbull, G. Pon, R.D. Willett, Polyhedron 10 (1991) 1835.
[27] O.M. Yaghi, H. Li, J. Am. Chem. Soc. 118 (1996) 295.
[28] L. Carlucci, G. Ciani, D.M. Proserpio, A. Sironi, J. Chem. Soc., Chem. Commun. (1994) 2755.
[29] Th. Fetzer, R. Jooss, A. Lentz, T. Debaerdemaeker, Z. Anorg. Allg. Chem. 620 (1994) 1750.
[30] B.-Q. Ma, S. Gao, T. Yi, G.-X. Xu, Polyhedron 20 (2001) 1255.
[31] P.W. Carreck, M. Goldstein, E.M. McPartlin, W.D. Unsworth, J. Chem. Soc., Dalton Trans. (1971) 1634.
[32] J. Lu, T. Paliwala, S.C. Lim, C. Yu, T. Niu, A.J. Jacobson, Inorg. Chem. 36 (1997) 923.
[33] J.A. Real, G.D. Munno, M.C. Munoz, M. Julve, Inorg. Chem. 30 (1991) 2701.
[34] D.B. Leznoff, B.-Y. Xue, C.L. Stevens, A. Storr, R.C. Thompson, B.O. Patrick, Polyhedron 20 (2001) 1247.
[35] R.L. Carlin, D.W. Carnegie, J. Bartolome, D. Gonzalez, L.M. Floria, Phys. Rev. B: Condens. Matter 32 (11) (1985) 7476.
[36] J. Straehle, F. Kubel, W. Hiller, R. Dantona, Mol. Cryst. Liq. Cryst. 81 (1–4) (1982) 265.
[37] M. Hanak, W. Kobel, J. Metz, M. Mezger, G. Pawlowski, O. Schneider, H.J. Schulze, L.R. Subramanian, Mater. Sci. 7 (2–3) (1981) 185.
[38] G.M. Sheldrick, SHELX-97, University of Göttingen, Germany, 1997.
[39] L.J. Barbour, J. Supramol. Chem. 1 (2001) 189. http://x-seed.net/.
[40] O.-S. Jung, C.G. Pierpont, J. Am. Chem. Soc. 116 (1994) 2229.
[41] F. Kubel, J. Strahle, Z. Naturforsch., Teil B 36 (1981) 441.
[42] B. Moulton, E.B. Rather, M.J. Zaworotko, Cryst. Eng. 4 (2001) 309.
[43] S.-Y. Yang, L.-S. Long, R.-B. Huang, L.-S. Zheng, S.W. Ng, Acta Crystallogr., Sect. E 59 (2003) m961.
[44] J.S. Haynes, J.R. Sams, R.C. Thompson, Inorg. Chem. 25 (1986) 3740.
[45] J.S. Haynes, J.R. Sams, R.C. Thompson, Can. J. Chem. 66 (1988) 2079.
[46] T. Otieno, S.J. Rettig, R.C. Thompson, J. Trotter, Can. J. Chem. 67 (1989) 1964.
[47] T. Otieno, S.J. Rettig, R.C. Thompson, J. Trotter, Can. J. Chem. 68 (1990) 1901.
[48] M.S. Masoud, H.H. Hammud, Ultra Science 12-1 (2000) 12.
[49] M.S. Masoud, H.H. Hammud, Spectrochim. Acta A 57 (2001) 977.
[50] M.E. Fisher, Am. J. Phys. 32 (1964) 343.

[51] A. Abragham, B. Bleaney, Electron Paramagnetic Resonance of Transition Ions, Clarendon Press, Oxford, 1970.
[52] S. Isber, M. Averous, Y. Shapira, V. Bindilatti, A.N. Anisimov, N.F. Olivera, V.M. Orera, M. Demianiuk, Phys. Rev. B 51 (1995) 15211.
[53] V. Bindilatti, Y. Shapira, M. Goiran, F. Yang, S. Isber, M. Averous, M. Demianiuk, Phys. Rev. B 50 (1994) 14464.
[54] 1M. Villeret, S. Rodriguez, E. Kartheuser, Phys. Rev. B 41 (1990) 10028.
[55] A. Lewicki, A.I. Schindler, I. Miotkowski, B.C. Grooker, J.K. Furdyna, Phys. Rev. B 43 (1991) 5713.
[56] S. Emori, M. Inoue, M. Kubo, Coord. Chem. Rev. 21 (1976) 1.
[57] T. Christidis, S. Isber, M. Tabbal, U. Kortz, D. Ravot, J. Magn. Magn. Mater. 242 (2002) 939.
[58] S. Isber, P. Masri, S. Charar, X. Gratens, S.K. Misra, J. Phys. C 9 (1997) 10023.
[59] V. Spasojevic, A. Bojorek, A. Szytula, W. Giriat, D. Mitic, Phys. Stat. Sol. B 165 (1991) 555.

Available online at www.sciencedirect.com
SCIENCE DIRECT®
Polyhedron 24 (2005) 229–237
POLYHEDRON
www.elsevier.com/locate/poly

Uranyl complexes with the pyridine-2,6-dicarboxylato ligand: new dinuclear species with μ-η^2,η^2-peroxide, μ_2-hydroxide or μ_2-methoxide bridges

Bernardo Masci [*,a], Pierre Thuéry [b,*]

[a] Dipartimento di Chimica and IMC-CNR Sezione Meccanismi di Reazione, Università "La Sapienza", Box 34, Roma 62, P.le Aldo Moro 5, 00185 Rome, Italy
[b] CEA/Saclay, DSM/DRECAM/SCM (CNRS URA 331), Bâtiment 125, F91191 Gif-sur-Yvette, France

Received 16 September 2004; accepted 5 November 2004

Abstract

Pyridine-2,6-dicarboxylic acid (LH_2) reacts with uranyl nitrate in the presence of triethylamine to form either mononuclear or new dinuclear complexes, the latter being different from the species obtained up to now with this ligand under different experimental conditions. In all cases, the uranium atom is bound to the pyridine nitrogen atom and to one oxygen atom from each carboxylate group. Its coordination sphere is completed either by a second ligand L^{2-}, giving the 1:2 mononuclear complex **1**, by a water molecule and a bridging μ-η^2,η^2-peroxide ion in the dinuclear complex **2**, by two bridging μ_2-hydroxide ions in **3** and **4** or by two bridging μ_2-methoxide ions in **5**. Complex **5** provides the first example of uranyl-bridging by methoxide ions to be crystallographically characterized. Extended hydrogen bonded networks involving the carboxylate groups, the bridging species and the counter-ions and solvent molecules are formed in all cases, resulting in chain, ribbon or sheet assemblages.
© 2004 Elsevier Ltd. All rights reserved.

Keywords: Uranyl ion; Pyridine-2,6-dicarboxylic acid; Alkoxides; Crystal structures

1. Introduction

We have recently been interested in exploiting the peculiar geometric requirements of the linear uranyl ion in its coordination complexes for the design of new polynuclear cyclic architectures, and polycarboxylate appeared suitable candidate ligands [1]. The tetra-, penta- or hexa-coordinated equatorial planar environment suitable for this ion is well suited, in association with bent ligands, for the design of macrocyclic species. While tri- or tetra-nuclear metallamacrocycles could be obtained with the tetraacid of tetrahydrofuran [1], we turn here our attention to diacids. Among the latter, the planar pyridine-2,6-dicarboxylic acid (dipicolinic acid, denoted LH_2 hereafter) has previously been used as a ligand for UO_2^{2+} [2–5] or U^{IV} [6] ions. In the most usual case, two tridentate ligands encompass one uranyl ion bound to the nitrogen atoms and one oxygen atom from each acid group [2,4], which is also the case with the related ligand pyridine-2,6-bis(monothiocarboxylic)-acid [7]. Polymeric arrangements occur when one acid group is bridging two metal centres through its two oxygen atoms [3,5]. Of particular interest in the prospect of using this ligand to get supramolecular systems is the helical polymeric neutral arrangement found by Immirzi et al. [3] which shows that, although LH_2 is a planar and not a bent molecule, three-dimensional architectures

* Corresponding author. Tel.: +33 1 69 08 63 29; fax: +33 1 69 08 66 40.
E-mail addresses: bernardo.masci@uniroma1.it (B. Masci), thuery@drecam.cea.fr (P. Thuéry).

0277-5387/$ - see front matter © 2004 Elsevier Ltd. All rights reserved.
doi:10.1016/j.poly.2004.11.002

incorporating uranyl ions can be generated. So, we decided to investigate the uranyl complexes formed with LH_2 under experimental conditions different from those used up to now, namely in the presence of triethylamine as a deprotonating agent. On changing the reactant ratio, both a 1:2 mononuclear complex and a 2:2 binuclear dimer including triethylammonium ions could be obtained. Moreover, with the aim of preparing mixed uranyl complexes, a different potential bidentate ligand, namely *N*,*N*,*N*′,*N*′-tetramethylethylenediamine, bis(2-hydroxyphenyl)methane or (1*R*,3*S*)-(+)-camphoric acid, was added together with LH_2. In no such experiment the additional species was included as a ligand, but each mixture allowed a structurally different 2:2 dimeric complex with L^{2-} to be isolated, with a geometry unprecedented in this family of uranyl complexes. The role of the additional species in the formation of the different dimeric complexes has not been rationalized.

2. Experimental

2.1. Synthesis

^{1}H NMR spectra (300 MHz) were taken on a Bruker AC 300 spectrometer in either $CDCl_3$ stored on activated molecular sieves (4 Å) or in $(CD_3)_2SO$.

2.1.1. $[HNEt_3]_2[UO_2L_2]\cdot 2H_2O$ (**1**)

Uranyl nitrate hexahydrate (50 mg, 0.10 mmol) in MeOH (1 ml) was added dropwise to a boiling stirred mixture of LH_2 (33 mg, 0.20 mmol) and triethylamine (200 mg, 2.0 mmol) in MeOH (9 ml). Stirring and heating of the resulting yellow solution were continued for additional 5 min. Greenish yellow single crystals of compound **1**, suitable for X-ray crystallography, deposited on solvent evaporation. The complex (40 mg, 48% yield) was readily soluble in chloroform. ^{1}H NMR ($CDCl_3$) $\delta = 1.47$ (t,18H, $J = 7.1$ Hz), 3.88 (q,12H, $J = 7.1$ Hz), 8.29 (t, 7.6 Hz, 2H), 8.54 (d, 7.6 Hz, 4H), 11.13 (s, 2H). *Anal*. Calc. for $C_{26}H_{42}N_4O_{12}U$: C, 37.15; H, 5.04; N, 6.66. Found: C, 36.96; H, 5.39; N, 6.38%.

2.1.2. $[HNEt_3]_2[(UO_2)_2L_2O_2(H_2O)_2]\cdot 2H_2O$ (**2**)

Uranyl nitrate hexahydrate (50 mg, 0.10 mmol) in MeOH (1 ml) was added dropwise to a boiling stirred mixture of LH_2 (17 mg, 0.10 mmol), (1*R*,3*S*)-(+)-camphoric acid (20 mg, 0.10 mmol) and triethylamine (270 mg, 2.7 mmol) in MeOH (9 ml). Stirring and heating of the resulting yellow solution were continued for additional 5 min. A few yellow single crystals of compound **2**, suitable for X-ray crystallography, deposited on standing.

2.1.3. $[HNEt_3]_2[(UO_2)_2L_2(OH)_2]\cdot 2H_2O$ (**3**)

Uranyl nitrate hexahydrate (110 mg, 0.22 mmol) in MeOH (2 ml) was added dropwise to a boiling stirred mixture of LH_2 (36 mg, 0.22 mmol), bis(2-hydroxyphenyl)methane (46 mg, 0.23 mmol) and triethylamine (350 mg, 3.5 mmol) in MeOH (20 ml). Stirring and heating of the resulting reddish orange solution were continued for additional 5 min. The reddish oil obtained on solvent evaporation was dissolved in acetonitrile and yellow crystals of compound **3**, suitable for X-ray crystallography, deposited on standing. The complex (13 mg, 10% yield) appeared to be insoluble in chloroform, acetone and acetonitrile. ^{1}H NMR [$(CD_3)_2SO$], $\delta = 0.92$ (t, 18H, $J = 7.0$ Hz), 2.42 (q,12H, $J = 7.0$ Hz), 8.50–8.60 (superimposed signals, 8H). *Anal*. Calc. for $C_{26}H_{44}N_4O_{16}U_2$: C, 27.28; H, 3.87; N, 4.89. Found: C, 27.42; H, 3.98; N, 4.42%.

2.1.4. $[HNEt_3][HNMe_2(CH_2)_2NMe_2][(UO_2)_2L_2(OH)_2]\cdot 2H_2O$ (**4**)

Uranyl nitrate hexahydrate (110 mg, 0.22 mmol) in MeOH (2 ml) was added dropwise to a boiling stirred mixture of LH_2 (36 mg, 0.22 mmol), *N*,*N*,*N*′,*N*′-tetramethylethylenediamine (14 mg, 0.12 mmol) and triethylamine (350 mg, 3.5 mmol) in MeOH (9 ml). Stirring and heating of the resulting solution were continued for an additional 5 min. A few yellow crystals of compound **4**, suitable for X-ray crystallography, deposited on standing.

2.1.5. $[HNEt_3]_2[(UO_2)_2L_2(MeO)_2]\cdot MeOH\cdot H_2O$ (**5**)

Uranyl nitrate hexahydrate (50 mg, 0.10 mmol) in MeOH (1 ml) was added dropwise to a boiling stirred mixture of LH_2 (17 mg, 0.10 mmol), and triethylamine (200 mg, 2.0 mmol) in MeOH (7 ml). Stirring and heating of the resulting yellow solution were continued for additional 5 min. Yellow crystals of compound **5**, suitable for X-ray crystallography, deposited on standing. The complex (16 mg, 26% yield) appeared to be slightly soluble in chloroform. ^{1}H NMR ($CDCl_3$) $\delta = 1.41$ (unresolved t, 18H), 3.50 (s, 9H) 3.67 (unresolved q, 12H), 8.37 (t, 7.5 Hz, 2H), 8.62 (d, 7.5 Hz, 4H). *Anal*. Calc. for $C_{29}H_{50}N_4O_{16}U_2$: C, 29.35; H, 4.25; N, 4.72. Found: C, 29.12; H, 4.39; N, 4.50%.

2.2. Crystallography

Data were collected at 100(2) K with a Nonius KappaCCD area detector diffractometer [8] using graphite-monochromated Mo Kα radiation ($\lambda = 0.71073$ Å). The crystals were placed inside glass capillaries with a protecting 'Paratone-N' oil (Hampton Research) coating. The unit cell parameters were determined from ten frames, then refined on all data. A 180° φ-range was scanned with 2° steps during data collection, with a crystal-to-detector distance fixed at 28 mm. The data were processed with DENZO-SMN [9]. The structures were solved by Patterson map interpretation (**1**) or direct methods (**2**–**5**) with SHELXS-97 and subsequent Fou-

rier-difference synthesis and refined by full-matrix least-squares on F^2 with SHELXL-97 [10]. Absorption effects were corrected empirically with the program DELABS from PLATON [11]. In compound **5**, one ethyl group of a triethylammonium ion was found to be disordered over two positions which were refined with occupancy parameters constrained to sum to unity. All non-hydrogen atoms were refined with anisotropic displacement parameters, with a few additional restraints for some badly behaving parts (triethylammonium ion containing N3 in compound **2**, two carbon atoms of a triethylammonium ion and methanol atom O15 in compound **5**). The hydrogen atoms bound to oxygen and nitrogen atoms were found on Fourier-difference maps (those bound to oxygen only in compound **2**) and all the other hydrogen atoms were introduced at calculated positions. All hydrogen atoms were treated as riding atoms with a displacement parameter equal to 1.2 (OH, NH, CH, CH_2) or 1.5 (CH_3) times that of the parent atom. Crystal data and structure refinement details are given in Table 1 and selected bond lengths and angles in Table 2. The molecular plots were drawn with SHELXTL [12].

3. Results and discussion

The compound $[HNEt_3]_2[UO_2L_2] \cdot 2H_2O$ (**1**) contains a 1:2 dianionic complex analogous to those previously obtained under different conditions [2,4] (Fig. 1). The asymmetric unit contains only half a molecule, the other half being generated by the binary axis containing the uranyl ion. The latter is bound, in its equatorial plane, to the two nitrogen atoms and to one oxygen atom from each carboxylate group, resulting in a hexagonal bipyramidal environment for the uranium atom, as usual for small bite polydentate ligands. The U–N bond length [2.626(2) Å] is larger than the mean U–O(carboxylate) bond length [2.459(14) Å] and both values agree with those in the previous mononuclear, hexa-coordinated uranyl complexes with the same ligand [2,4]. The mean value of the N–U–O(carboxylate) and O(carboxylate)–U–O(carboxylate) angles is 60.7(5)°, the O–U–O angle, involving the two ligands, being only about 1° larger than the N–U–O angles. The six equatorial donor atoms define a strongly distorted plane with a rms deviation of 0.26 Å. The atoms O1 and O1′ are little displaced from this plane, by 0.042(2) Å, whereas atoms O3 and N1, and their symmetry equivalents, are located on either side, with deviations of 0.339(2) and −0.298(2) Å, respectively. The environment of the uranyl ion, with two nitrogen atoms in *trans* position and four oxygen atoms, is reminiscent of that found in the complex with diaza-18-crown-6 [13], but the differing charges and ligand rigidity result in much larger U–N and U–O bond lengths in the latter (2.68–2.74 Å). The acid groups in **1** are slightly tilted with respect to the aromatic ring best plane, with deviations of −0.232(4) and 0.122(4) Å for the donor atoms O1 and O3, respectively. The two aromatic rings define a dihedral angle of 37.44(6)°. The triethylammonium counter-ions are located so as to form

Table 1
Crystal data and structure refinement details

Compound	**1**	**2**	**3**	**4**	**5**
Empirical formula	$C_{26}H_{42}N_4O_{12}U$	$C_{26}H_{46}N_4O_{18}U_2$	$C_{26}H_{44}N_4O_{16}U_2$	$C_{26}H_{45}N_5O_{16}U_2$	$C_{29}H_{50}N_4O_{16}U_2$
M (g mol^{-1})	840.67	1178.73	1144.71	1159.73	1186.79
Crystal system	monoclinic	monoclinic	monoclinic	monoclinic	triclinic
Space group	$C2/c$	$P2/c$	$P2_1/c$	$P2_1/c$	$P\bar{1}$
a (Å)	28.4430(11)	20.7844(12)	9.5406(5)	12.0832(4)	12.1243(4)
b (Å)	7.0964(2)	11.5593(4)	11.8115(7)	21.4234(8)	12.4273(7)
c (Å)	16.0520(6)	15.7702(9)	15.4941(9)	14.6526(5)	14.4015(8)
α (°)	90	90	90	90	92.486(3)
β (°)	108.850(2)	98.377(2)	90.779(4)	109.714(2)	112.154(3)
γ (°)	90	90	90	90	105.555(3)
V (Å^3)	3066.22(19)	3748.4(3)	1745.85(17)	3570.7(2)	1910.54(17)
Z	4	4	2	4	2
D_{calc} (g cm^{-3})	1.821	2.089	2.178	2.157	2.063
μ (mm^{-1})	5.361	8.707	9.339	9.135	8.538
$F(000)$	1656	2232	1080	2192	1128
Reflections collected	10062	24365	11303	23502	12906
Independent reflections	2885	7039	3255	6585	6595
'Observed' reflections [$I>2\sigma(I)$]	2797	5161	2787	5682	5862
R_{int}	0.038	0.095	0.058	0.050	0.034
Parameters	199	457	220	449	479
R_1	0.019	0.051	0.026	0.033	0.035
wR_2	0.045	0.119	0.065	0.078	0.083
S	1.078	1.033	1.034	1.020	1.158
$\Delta\rho_{min}$ (e Å^{-3})	−0.63	−1.12	−1.05	−0.88	−1.47
$\Delta\rho_{max}$ (e Å^{-3})	0.47	1.38	0.73	1.07	1.30

Table 2
Selected bond lengths (Å) and angles (°) for compounds **1**–**5**

*Compound **1***			
Bond lengths			
U–N1	2.626(2)		
U–O1	2.444(2)		
U–O3	2.4730(19)		
U–O5	1.780(3)		
U–O6	1.782(3)		
Bond angles			
O1–U–N1	60.33(7)		
N1–U–O3	60.40(7)		
O1–U–O3′	61.36(6)		
O5–U–O6	180		
Symmetry code: ′ = $-x$, y, $1.5 - z$			
*Compound **2***			
Bond lengths			
U1–N1	2.585(9)	U2–N2	2.546(10)
U1–O1	2.432(7)	U2–O5	2.436(8)
U1–O3	2.409(8)	U2–O7	2.416(8)
U1–O9	1.780(8)	U2–O11	1.790(8)
U1–O10	1.788(8)	U2–O12	1.794(8)
U1–O13	2.516(8)	U2–O14	2.467(7)
U1–O15	2.287(7)	U2–O15	2.320(7)
U1–O16	2.404(7)	U2–O16	2.461(7)
Bond angles			
O1–U1–N1	61.7(3)	O5–U2–N2	62.1(3)
N1–U1–O3	62.1(3)	N2–U2–O7	62.7(3)
O3–U1–O13	66.6(3)	O7–U2–O14	68.1(3)
O13–U1–O15	63.6(3)	O14–U2–O16	67.5(2)
O15–U1–O16	36.3(2)	O16–U2–O15	35.5(2)
O16–U1–O1	70.6(2)	O15–U2–O5	64.5(2)
O9–U1–O10	175.6(4)	O11–U2–O12	176.7(4)
*Compound **3***			
Bond lengths			
U–N1	2.544(4)		
U–O1	2.373(4)		
U–O3	2.387(4)		
U–O5	1.784(4)		
U–O6	1.801(4)		
U–O7	2.357(3)		
U–O7′	2.319(3)		
Bond angles			
O1–U–N1	63.11(12)		
N1–U–O3	62.95(12)		
O3–U–O7	78.66(12)		
O7–U–O7′	71.21(13)		
O7′–U–O1	84.65(11)		
O5–U–O6	177.22(15)		
Symmetry code: ′ = $-x$,$-y$, $1 - z$			
*Compound **4***			
Bond lengths			
U1–N1	2.543(5)	U2–N2	2.539(5)
U1–O1	2.375(4)	U2–O5	2.366(4)
U1–O3	2.376(4)	U2–O7	2.368(4)
U1–O9	1.786(5)	U2–O11	1.803(4)
U1–O10	1.781(4)	U2–O12	1.792(4)
U1–O13	2.366(4)	U2–O13	2.360(4)
U1–O14	2.358(4)	U2–O14	2.336(4)
Bond angles			
O1–U1–N1	63.56(15)	O5–U2–N2	63.65(15)
N1–U1–O3	63.25(15)	N2–U2–O7	63.48(15)
O3–U1–O14	79.74(13)	O7–U2–O13	77.03(14)
O14–U1–O13	72.07(14)	O13–U2–O14	72.58(14)
O13–U1–O1	81.78(14)	O14–U2–O5	83.28(14)
O9–U1–O10	178.0(2)	O11–U2–O12	179.0(2)
*Compound **5***			
Bond lengths			
U1–N1	2.549(6)	U2–N2	2.535(5)
U1–O1	2.377(5)	U2–O5	2.375(5)
U1–O3	2.368(5)	U2–O7	2.404(5)
U1–O9	1.789(5)	U2–O11	1.788(4)
U1–O10	1.795(5)	U2–O12	1.792(4)
U1–O13	2.356(5)	U2–O13	2.338(4)
U1–O14	2.338(5)	U2–O14	2.352(5)
Bond angles			
O1–U1–N1	63.44(18)	O5–U2–N2	63.47(17)
N1–U1–O3	63.24(17)	N2–U2–O7	63.25(17)
O3–U1–O14	81.40(16)	O7–U2–O13	85.32(16)
O14–U1–O13	71.56(16)	O13–U2–O14	71.62(16)
O13–U1–O1	80.40(16)	O14–U2–O5	76.37(16)
O9–U1–O10	179.4(2)	O11–U2–O12	178.6(2)

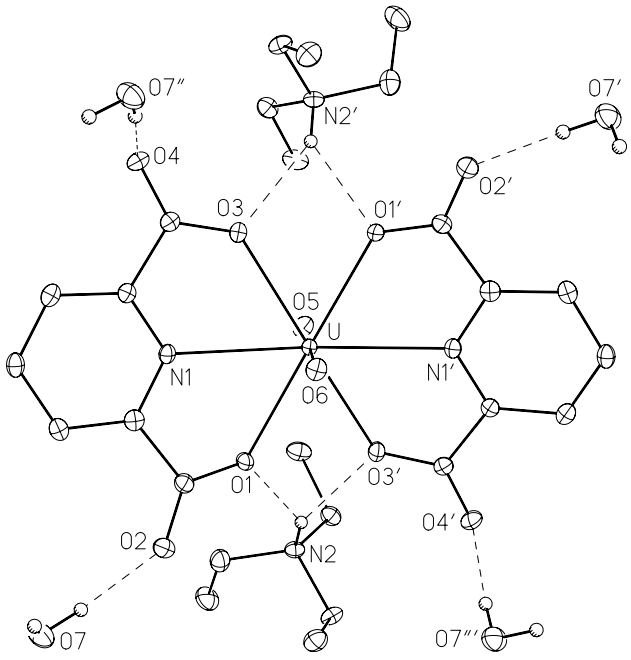


Fig. 1. View of the complex $[HNEt_3]_2[UO_2L_2]\cdot 2H_2O$ (**1**). The hydrogen atoms not involved in hydrogen bonding have been omitted. Hydrogen bonds are shown as dashed lines. Displacement ellipsoids are drawn at the 40% probability level. Symmetry codes: ′ = $-x$, y, $1.5 - z$; ″ = $-x$, $-y$, $1 - z$; ‴ = x, $-y$, $0.5 + z$.

bifurcated hydrogen bonds with the coordinated oxygen atoms O1, O3 and their symmetry equivalents (Table 3), thus resulting in the formation of a 16-membered ring around the uranium atom. The water molecules are hydrogen bonded to the non-coordinated carboxylate oxygen atoms O2 and O4 from different molecules related by a symmetry centre. This results in the formation

Table 3
Hydrogen bonding geometry [distances (Å) and angles (°)] in compounds **1**–**5**

D···A		D–H		H···A		D–H···A	
Compound ***1***							
N2···O1	2.941(3)	N2–H2	0.89	H2···O1	2.18	N2–H2···O1	143
N2···O3′	2.974(3)	N2–H2	0.89	H2···O3′	2.20	N2–H2···O3′	146
O7···O2	2.824(3)	O7–H7A	0.85	H7A···O2	1.98	O7–H7A···O2	174
O7···O4″	2.894(3)	O7–H7B	0.82	H7B···O4″	2.08	O7–H7B···O4″	176
Symmetry codes: ′ = $-x$, y, $1.5-z$; ″ = $-x$,$-y$, $1-z$							
Compound ***2***							
N3···O18	2.94(2)	N3–H3	0.91	H3···O18	2.04	N3–H3···O18	169
N4···O16	2.793(13)	N4–H4	0.91	H4···O16	1.90	N4–H4···O16	165
O13···O5	2.797(11)	O13–H13A	0.92	H13A···O5	1.88	O13–H13A···O5	174
O13···O18	2.821(14)	O13–H13B	0.93	H13B···O18	1.93	O13–H13B···O18	160
O14···O17	2.688(10)	O14–H14A	0.93	H14A···O17	1.77	O14–H14A···O17	174
O14···O4′	2.755(11)	O14–H14B	0.95	H14B···O4′	1.86	O14–H14B···O4′	158
O17···O2″	2.847(11)	O17–H17A	0.89	H17A···O2″	1.96	O17–H17A···O2″	172
O17···O1	2.789(10)	O17–H17B	0.84	H17B···O1	1.97	O17–H17B···O1	166
O18···O3	2.788(14)	O18–H18A	0.94	H18A···O3	2.07	O18–H18A···O3	132
O18···O8‴	2.659(15)	O18–H18B	0.91	H18B···O8‴	1.94	O18–H18B···O8‴	134
Symmetry codes: ′ = x, $1+y$, z; ″ = $1-x$, $1-y$, $1-z$; ‴ = x, $y-1$, z							
Compound ***3***							
N2···O8	2.692(6)	N2–H2	0.91	H2···O8	1.80	N2–H2···O8	167
O7···O2″	2.878(5)	O7–H7	0.97	H7···O2″	1.95	O7–H7···O2″	158
O8···O4	2.674(5)	O8–H8A	0.80	H8A···O4	1.93	O8–H8A···O4	156
O8···O6″	2.871(5)	O8–H8B	0.88	H8B···O6″	2.00	O8–H8B···O6″	167
Symmetry code: ″ = x, $0.5-y$, $z-0.5$							
Compound ***4***							
N3···O13	2.944(7)	N3–H3	0.89	H3···O13	2.10	N3–H3···O13	160
N5···O14	2.697(6)	N5–H5	0.90	H5···O14	1.82	N5–H5···O14	166
O14···N4	2.668(7)	O14–H14	0.88	H14···N4	1.79	O14–H14···N4	173
O13···O16′	2.747(6)	O13–H13	0.88	H13···O16′	1.90	O13–H13···O16′	163
O15···O2	2.968(7)	O15–H15A	0.99	H15A···O2	2.11	O15–H15A···O2	144
O15···O4″	2.870(6)	O15–H15B	0.89	H15B···O4″	1.98	O15–H15B···O4″	176
O16···O8	2.819(6)	O16–H16A	0.92	H16A···O8	1.91	O16–H16A···O8	168
O16···O15′	2.781(6)	O16–H16B	0.85	H16B···O15′	1.95	O16–H16B···O15′	165
Symmetry codes: ′ = $1-x$, $-y$, $-z$; ″ = $2-x$, $y-0.5$, $0.5-z$							
Compound ***5***							
N3···O8	2.760(9)	N3–H3	0.99	H3···O8	1.83	N3–H3···O8	156
N4···O16	2.686(9)	N4–H4	0.91	H4···O16	1.78	N4–H4···O16	173
O15···O6	2.756(10)	O15–H15	1.00	H15···O6	1.96	O15–H15···O6	135
O16···O15	2.661(10)	O16–H16A	0.90	H16A···O15	1.77	O16–H16A···O15	168
O16···O2′	2.811(9)	O16–H16B	0.92	H16B···O2′	1.90	O16–H16B···O2′	173
Symmetry code: ′ = x, $1+y$, z							

of zig-zag chains of doubly hydrogen bonded molecules along the *c*-axis.

Compounds **2**–**5** all contain dianionic complexes comprising two metal ions, two dicarboxylate ligands and one dianionic or two monoanionic bridging species. Complex **2**, $[HNEt_3]_2[(UO_2)_2L_2O_2(H_2O)_2]\cdot 2H_2O$, is an example of a μ-η^2,η^2-peroxide bridged uranyl dinuclear complex (Fig. 2). The occurrence of such $[O_2]^{2-}$ bridges has been discussed previously in the role that they play in the formation of uranyl-containing molecular boxes or cages [14]. Due to the presence of an extra coordinated water molecule, each uranyl ion in **2** retains the hexagonal bipyramidal coordination found in compound **1**, but, since the O–U–O angles defined by the μ-η^2,η^2-peroxide ion [36.3(2)° and 35.5(2)°] are much smaller than the other equatorial bond angles [61.7(3)°–70.6(2)°], this case can be considered as borderline between hexa- and pentagonal coordinations, the μ-η^2,η^2-peroxide ion being considered as a single atom in the latter. The mean plane defined by the six equatorial donor atoms around each uranyl ion is less distorted than in compound **1**, with rms deviations lower than 0.10 Å. The U–N and U–O(carboxylate) bond lengths are also shorter than in **1**, with mean values of 2.57(2) and 2.423(11) Å, respectively, and, as a consequence, the N–U–O(carboxylate) angles are slightly larger [mean value 62.2(4)°]. These differences likely result from the less crowded uranium environment in **2**. The

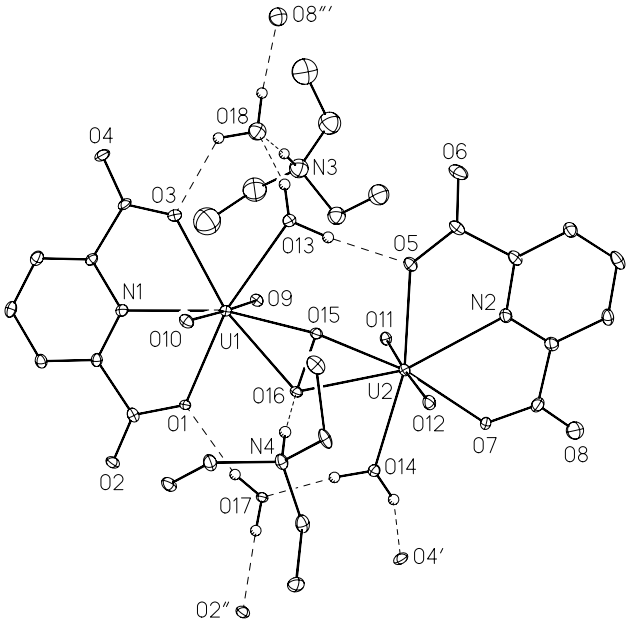


Fig. 2. View of the complex $[HNEt_3]_2[(UO_2)_2L_2O_2(H_2O)_2] \cdot 2H_2O$ (**2**). The hydrogen atoms not involved in hydrogen bonding have been omitted. Hydrogen bonds are shown as dashed lines. Displacement ellipsoids are drawn at the 10% probability level. Symmetry codes: ′ = *x*, 1+*y*, *z*; ″ = 1 − *x*, 1 − *y*, 1 − *z*; ‴ = *x*, *y* − 1, *z*.

O–O and the mean U–O(peroxo) bond lengths, 1.464(9) and 2.37(8) Å, are in fair agreement with the values found in the molecular cages, 1.48(5) and 2.33(3) Å [14a] or 1.541(13) and 2.38(6) Å [14b] as well as with the mean values for the $(UO_2)_2(\mu\text{-}\eta^2,\eta^2\text{-peroxo})$ molecular systems previously reported, 1.478(12) and 2.324(13) Å [15]. However, the bonding of the $\mu\text{-}\eta^2$, η^2-peroxide ion in **2** is slightly asymmetric, with mean values of 2.304(17) and 2.43(3) Å for the U–O15 and U–O16 bond lengths, and 128.9(3)° and 117.4(3)° for the angles U1–O15–U2 and U1–O16–U2, respectively. This may be partly due to the involvement of O16 in a strong hydrogen bond with a triethylammonium counter-ion (see below). The dihedral angle characterizing the folding about the O–O bond in the U_2O_2 central group amounts to 44.2(3)° and the dihedral angle between the mean planes defined by the six donor atoms around each uranyl ion is 39.52(11)°. The mean U–O(water) bond length, 2.49(2) Å, agrees with the mean value of 2.45(3) Å for the similar groups present in the Cambridge Structural Database (CSD, Version 5.25) [16]. The U1···U2 distance of 4.1570(6) Å indicates the absence of any metal–metal bond. The carboxylate donor atoms are closer to the best aromatic mean planes than in compound **1**, with deviations lower than 0.14(2) Å. The two triethylammonium ions are differently bound to the complex unit: one of them, containing N4, forms a hydrogen bond with the peroxide atom O16, as stated above, whereas the other one, containing N3, acts as a hydrogen bond donor towards the water molecule containing O18, which is also an acceptor from the coordinated water molecule containing O13. The latter forms a second bond with the coordinated carboxylate atom O5. The second coordinated water molecule (O14) is a donor towards another water molecule (O17) and the non-coordinated carboxylate atom O4 of a neighbouring complex unit related to the first by a translation along the *b*-axis. The two non-coordinated water molecules are further hydrogen bond donors towards the coordinated carboxylate atoms O1 and O3 in the same unit, and also towards the non-coordinated ones O2 and O8 from different neighbouring complexes related to the first unit by a symmetry centre or a translation along the *b*-axis, respectively. Each asymmetric unit is thus connected to three of its neighbours through six water-carboxylate hydrogen bonds (two per neighbour), which gives rise to the formation of double-stranded ribbons roughly parallel to the *ab*-plane and running along the *b*-axis.

Compounds **3**, **4** and **5** present many common features: all are doubly bridged dianionic dimers in which the uranium atom is in a pentagonal bipyramidal environment. In compounds **3**, $[HNEt_3]_2[(UO_2)_2L_2(OH)_2] \cdot 2H_2O$ (Fig. 3), and **4**, $[HNEt_3][HNMe_2(CH_2)_2\text{-}NMe_2][(UO_2)_2L_2(OH)_2] \cdot 2H_2O$ (Fig. 4), the bridging involves two μ_2-hydroxide groups, whereas it is effected through two μ_2-methoxide groups in compound **5**, $[HNEt_3]_2[(UO_2)_2L_2(MeO)_2] \cdot MeOH \cdot H_2O$ (Fig. 5). The anionic complex in **3** contains an inversion centre, whereas those in **4** and **5** have no crystallographic symmetry.

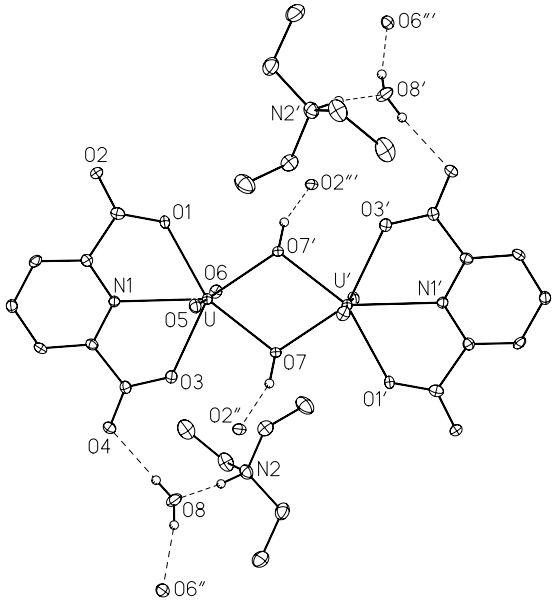


Fig. 3. View of the complex $[HNEt_3]_2[(UO_2)_2L_2(OH)_2] \cdot 2H_2O$ (**3**). The hydrogen atoms not involved in hydrogen bonding have been omitted. Hydrogen bonds are shown as dashed lines. Displacement ellipsoids are drawn at the 30% probability level. Symmetry codes: ′ = −*x*, −*y*, 1 − *z*; ″ = *x*, 0.5 − *y*, *z* − 0.5; ‴ = −*x*, *y* − 0.5, 1.5 − *z*.

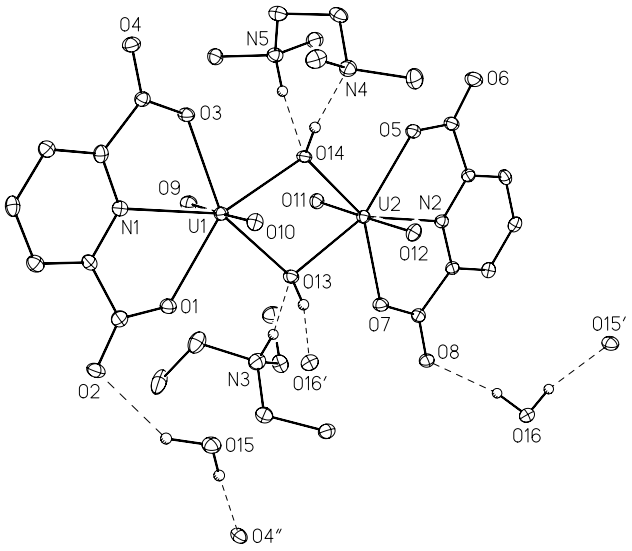


Fig. 4. View of the complex $[HNEt_3][HNMe_2(CH_2)_2NMe_2][(UO_2)_2L_2(OH)_2]\cdot 2H_2O$ (**4**). The hydrogen atoms not involved in hydrogen bonding have been omitted. Hydrogen bonds are shown as dashed lines. Displacement ellipsoids are drawn at the 20% probability level. Symmetry codes: $' = 1-x, -y, -z$; $'' = 2-x, y-0.5, 0.5-z$.

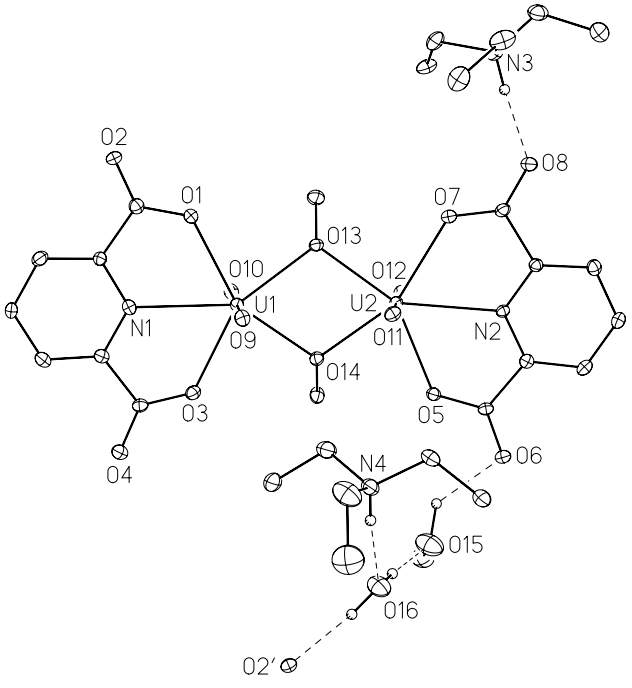


Fig. 5. View of the complex $[HNEt_3]_2[(UO_2)_2L_2(MeO)_2]\cdot MeOH\cdot H_2O$ (**5**). The hydrogen atoms not involved in hydrogen bonding have been omitted. Hydrogen bonds are shown as dashed lines. Only one position of the disordered ethyl group is represented. Displacement ellipsoids are drawn at the 20% probability level. Symmetry code: $' = x, 1+y, z$.

The U–N and U–O(carboxylate) bond lengths, with mean values of 2.542(5) and 2.377(11) Å, respectively, are shorter than in **1** (by about 0.08 Å) and even than in **2** (by about 0.035 Å), as expected from the difference in coordination number and geometry, as previously noticed [7]. The mean U–O(methoxo) bond length in **5**, 2.346(8) Å, is not different from the mean U–O(hydroxo) bond length in **3** and **4**, 2.349(16) Å and both are in good agreement with the mean U–O bond length for dihydroxide bridges in the CSD, 2.345(5) Å. To the best of our knowledge, compound **5** is the first example of a uranyl complex with methoxide bridges to be crystallographically characterized; however, comparable mean U(uranyl)–O(alkoxo) bond lengths have been reported [17–21] and several examples of bridging phenoxide ligands are also found in the CSD, with a mean U–O bond length of 2.44(9) Å. One example only of a terminal methanol/methoxide ligand has been reported for the uranyl ion, in which the hydroxylic proton is distributed over the methanol and methoxide ligands of adjacent units [22]; as expected, the mean U–O bond length in this case, 2.31(5) Å, is shorter than for the bridging species. The central U_2O_2 group in **5** defines a plane with a rms deviation of 0.112 Å, with respect to which the two methoxide carbon atoms are displaced (on the same side) by 1.119(10) and 1.045(10) Å. The N–U–O(carboxylate) angles in all three compounds [mean value 63.3(2)°] are about 3° larger than the corresponding angles in **1**, in keeping with the shorter bond lengths, whereas the O(carboxylate)–U–O(bridge) angles span a wide range [71.21(13)°–85.32(16)°]. The five equatorial donor atoms around each uranium atom define mean planes with rms deviations lower than 0.10 Å. The dihedral angle between the pentagonal mean planes in each dimer is 0°, 8.57(8)° and 12.68(10)° in **3**, **4** and **5**, respectively; all complexes are thus nearly planar. The mean value of the U–O–U angles around the bridging atoms is 107.6(7)° in **3**–**5** and the U···U distances are 3.8015(4), 3.7907(3) and 3.7791(4) Å in **3**, **4** and **5**, respectively. The displacements of the donor carboxylate oxygen atoms with respect to the best mean aromatic planes are in the range 0.008(11)–0.196(8) Å. It may be noted that dinuclear Fe^{III} and Cr^{III} complexes with the ligand L and μ_2-hydroxide double bridges have been reported previously, but the metal ion environment is distorted octahedral in these cases [23].

Compounds **3**–**5** further differ by their counter-ions and/or the features of the hydrogen bonding network. In compound **3**, the two crystallographically equivalent triethylammonium ions are hydrogen bonded to a water molecule, the latter also bridging between the non-coordinated carboxylate atom O4 in the same unit and the uranyl oxo atom O6 in the adjacent unit related by the glide plane perpendicular to the *b*-axis. The hydroxide ion is in its turn bound to the non-coordinated atom O2 of the same neighbouring unit. Each complex is thus linked to four of its neighbours by eight hydrogen bonds, which gives rise to sheets parallel to the *bc*-plane containing molecules tilted with respect to one another. Only in the case of **4** the potential additional bidentate

species was found in the isolated crystalline complex, actually as a counter-ion along with triethylammonium ion, rather than as a ligand. In this case, the triethylammonium ion is simply hydrogen bonded to the hydroxide atom O13, but the behaviour of the mono-protonated *N*,*N*,*N*′,*N*′-tetramethylethylenediammonium counter-ion is more interesting since it is both a donor (through N5) and an acceptor (through N4) with respect to the hydroxide group HO14. This leads to the formation of a seven-membered ring stabilized by cooperative (homodromic) hydrogen bonds [24]. The water molecule H_2O15 links two neighbouring molecules, related by a binary screw axis, through the carboxylate atoms O2 and O4, while H_2O16 is both an acceptor from O13 in an adjacent unit related by a symmetry centre and a donor towards O8 and O15, the latter in the same neighbouring unit. Hence, six hydrogen bonds insure the linking of each unit to three of its neighbours and result in the formation of sheets perpendicular to the $(1\,0\,-2)$ direction. In compound **5**, one of the triethylammonium ions, N3, is bound to the uncoordinated carboxylate oxygen O8 and the other, N4, to a water molecule, O16. The latter acts as a donor towards the solvent methanol molecule, O15, itself bound to the carboxylate oxygen O6, and towards the carboxylate atom O2 of a neighbouring molecule related to the first by a translation along the *b*-axis. This results in a linking of each complex moiety to two of its neighbours by two hydrogen bonds only and the subsequent formation of chains of parallel molecules directed along the *b*-axis.

4. Conclusion

The use of tertiary amines in the synthesis of complexes of uranyl ions with pyridine-2,6-dicarboxylic acid has enabled us to obtain new dinuclear compounds, different from the complexes obtained up to now with this system. These 2:2 dimers present many common features, the differences being apparently due to the presence in the experimental conditions employed, basic and non-water free, of several bridging species currently observed in uranyl chemistry, such as peroxide or hydroxide anions, and also, more surprisingly, methoxide anions, which had never been found before to bridge two uranyl ions. Such roughly planar dinuclear complexes are so readily formed that little can be expected of this system, under the present conditions, as a way to get supramolecular architectures based on coordination bonds. However, extended hydrogen bonding due to the counter-ions and solvent molecules result in the formation of infinite chains, ribbons or sheets. The role of the additional ligand used during the synthesis of the complexes is far from being understood. Although the synthesis of most 2:2 dimeric complexes was not a rational one and a control of the reaction outcome seems very difficult, the variations observed in the crystal structures upon slight changes in the reaction environment points out the versatility of LH_2 as a ligand, at least for the uranyl ion.

Appendix A. Supplementary material

Crystallographic data for the structural analysis have been deposited with the Cambridge Crystallographic Data Centre, CCDC Nos. 250309–250313. Copies of this information may be obtained free of charge from The Director, CCDC, 12 Union Road, Cambridge CB2 1EZ, UK (fax: +44 1223 336033; e-mail: deposit@ccdc.cam.ac.uk or www: http://www.ccdc.cam.ac.uk). Supplementary data associated with this article can be found, in the online version, at doi:10.1016/j.poly.2004.11.002.

References

[1] P. Thuéry, C. Villiers, J. Jaud, M. Ephritikhine, B. Masci, J. Am. Chem. Soc. 126 (2004) 6838.
[2] G. Marangoni, S. Degetto, R. Graziani, G. Bombieri, E. Forsellini, J. Inorg. Nucl. Chem. 36 (1974) 1787.
[3] A. Immirzi, G. Bombieri, S. Degetto, G. Marangoni, Acta Crystallogr., Sect. B 31 (1975) 1023.
[4] A. Cousson, J. Proust, E.N. Rizkalla, Acta Crystallogr., Sect. C 47 (1991) 2065.
[5] A. Cousson, F. Nectoux, M. Pagès, E.N. Rizkalla, Radiochim. Acta 61 (1993) 177.
[6] S.F. Haddad, R.H. Al-Far, F.R. Ahmed, Acta Crystallogr., Sect. C 43 (1987) 453.
[7] M.P. Neu, M.T. Johnson, J.H. Matonic, B.L. Scott, Acta Crystallogr., Sect. C 57 (2001) 240.
[8] Kappa-CCD Software, Nonius BV, Delft, 1998.
[9] Z. Otwinowski, W. Minor, Methods Enzymol. 276 (1997) 307.
[10] G.M. Sheldrick, SHELXS-97 and SHELXL-97, University of Göttingen, Göttingen, Germany, 1997.
[11] A.L. Spek, PLATON, University of Utrecht, The Netherlands, 2000.
[12] G.M. Sheldrick, SHELXTL, Version 5.1, Bruker AXS, Inc., Madison, WI, 1999.
[13] (a) P. Thuéry, N. Keller, M. Lance, J.M. Sabattié, J.D. Vigner, M. Nierlich, Acta Crystallogr., Sect. C 51 (1995) 801;
(b) P. Thuéry, N. Keller, M. Lance, J.D. Vigner, M. Nierlich, New J. Chem. 19 (1995) 619.
[14] (a) P. Thuéry, M. Nierlich, B.W. Baldwin, N. Komatsuzaki, T. Hirose, J. Chem. Soc., Dalton Trans. (1999) 1047;
(b) P. Thuéry, B. Masci, Supramol. Chem. 15 (2003) 95.
[15] (a) R. Haegele, J.C.A. Boeyens, J. Chem. Soc., Dalton Trans. (1977) 648;
(b) P. Charpin, G. Folcher, M. Lance, M. Nierlich, D. Vigner, Acta Crystallogr., Sect. C 41 (1985) 1302;
(c) G.A. Doyle, D.M.L. Goodgame, A. Sinden, D.J. Williams, J. Chem. Soc., Chem. Commun. (1993) 1170;
(d) D. Rose, Y.D. Chang, Q. Chen, J. Zubieta, Inorg. Chem. 33 (1994) 5167;
(e) G.H. John, I. May, M.J. Sarsfield, H.M. Steele, D. Collison, M. Helliwell, J.D. McKinney, Dalton Trans. (2004) 734.
[16] F.H. Allen, Acta Crystallogr., Sect. B 58 (2002) 380.

[17] U. Turpeinen, R. Hämäläinen, I. Mutikainen, O. Orama, Acta Crystallogr., Sect. C 52 (1996) 1169.
[18] I. Farkas, I. Csoregh, Z. Szabo, Acta Chem. Scand. 53 (1999) 1009.
[19] (a) W. Plass, G. Fries, Z. Naturforsch. B 52 (1997) 831;
(b) P.V. Rao, C.P. Rao, A. Sreedhara, E.K. Wegelius, K. Rissanen, E. Kolehmainen, J. Chem. Soc., Dalton Trans. (2000) 1213;
(c) A.K. Sah, C.P. Rao, P.K. Saarenketo, E.K. Wegelius, E. Kolehmainen, K. Rissanen, Eur. J. Inorg. Chem. (2001) 2773.
[20] C.J. Burns, A.P. Sattelberger, Inorg. Chem. 27 (1988) 3692.
[21] M.P. Wilkerson, C.J. Burns, H.J. Dewey, J.M. Martin, D.E. Morris, R.T. Paine, B.L. Scott, Inorg. Chem. 39 (2000) 5277.
[22] U. Abram, E.S. Lang, E. Bonfada, Z. Anorg. Allg. Chem. 628 (2002) 1873.
[23] (a) J.A. Thich, C.C. Ou, D. Powers, B. Vasiliou, D. Mastropaolo, J.A. Potenza, H.J. Schugar, J. Am. Chem. Soc. 98 (1976) 1425;
(b) C.C. Ou, W.J. Borowski, J.A. Potenza, H.J. Schugar, Acta Crystallogr., Sect. B 33 (1977) 3246.
[24] T. Steiner, Angew. Chem. Int. Ed. 41 (2002) 48.

Available online at www.sciencedirect.com
SCIENCE DIRECT®
Polyhedron 24 (2005) 239–247
POLYHEDRON
www.elsevier.com/locate/poly

Anionic dihalotetraacetatodiruthenium(II,III) compounds

M.C. Barral [a], R. González-Prieto [a], S. Herrero [a], R. Jiménez-Aparicio [a,*], J.L. Priego [a], M.R. Torres [b], F.A. Urbanos [a]

[a] *Departamento de Química Inorgánica, Facultad de Ciencias Químicas, Universidad Complutense de Madrid, Ciudad Universitaria, 28040 Madrid, Spain*

[b] *Centro de Asistencia a la Investigación de Rayos X, Facultad de Ciencias Químicas, Universidad Complutense de Madrid, Ciudad Universitaria, 28040 Madrid, Spain*

Received 15 October 2004; accepted 5 November 2004

Abstract

The synthesis and characterization of $Q[Ru_2Cl_2(\mu\text{-}O_2CMe)_4]$ [Q = NEt_4 (**1**), PPh_4 (**2**)], $Q[Ru_2Br_2(\mu\text{-}O_2CMe)_4]$ [Q = NEt_4 (**3**), PPh_4 (**4**), K (**5**)] and $Q[Ru_2I_2(\mu\text{-}O_2CMe)_4]$ [Q = NEt_4 (**6**), PPh_4 (**7**)] are described. All compounds have been characterized by elemental analysis, spectroscopic, mass and magnetic data. The structures of **1–3**, **5** and **7** are determined by the single crystal X-ray diffraction method. The Ru–Ru bond distances vary from 2.2956(5) to 2.312(3) Å, slightly longer than those observed in the corresponding discrete dinuclear complexes $Ru_2X(\mu\text{-}O_2CR)_4(S)$ (S = solvent molecule) with Ru–X terminal and in the polymeric arrangement $[Ru_2X(\mu\text{-}O_2CR)_4]_n$ with Ru–X–Ru bonds. The anionic complexes have two axially coordinated halide ligands. The Ru–X bond distance is in accordance with the size of the axial ligand. Thus, the Ru–Cl bond lengths are 2.5396(15) and 2.5627(10) Å, respectively for **1** and **2**; the Ru–Br distances are 2.6763(14) (**3**) and 2.6779(4) Å (**5**), and the Ru–I length are 2.897(2) and 2.893(2) Å in **7**. The crystal structure determination of complexes **3** and **5** constitutes the first examples of dibromotetracarboxylatodiruthenium(II,III) compounds. The electronic properties of all the compounds are also explored. Their solvatochromism is less accentuated than the corresponding monohalo derivatives.
© 2004 Elsevier Ltd. All rights reserved.

Keywords: Diruthenium compounds; Carboxylate complexes; Multiple bonds; Metal–metal bonds; Solvatochromism

1. Introduction

Numerous halotetracarboxylatodiruthenium(II,III) complexes, and especially chloro derivatives, of the formula $Ru_2X(\mu\text{-}O_2CR)_4$ (X = halide; R = alkyl, aryl) have been described [1,2]. In these compounds the diruthenium atoms are bridged by four carboxylate ligands, having one axial position occupied by one halogen atom. In the solid state, most of them show a polymeric structure where the dinuclear units are linked by the halide ligands giving zigzag or linear chains [3–16]. Discrete dinuclear molecules of the type $Ru_2X(\mu\text{-}O_2CR)_4(S)$ (S = solvent molecule) have also been reported [4,5,17–19]. Several methods to remove the chloride ligand have been used and many cationic compounds with the general formula $[Ru_2(\mu\text{-}O_2CR)_4(L)_2]^+A^-$ (L = neutral ligand; A = BF_4, PF_6, BPh_4) have been isolated [1,2]. In contrast, anionic tetracarboxylatodiruthenium(II,III) complexes have been scarcely reported. Miskowski and Gray studied the species $[Ru_2X_2(\mu\text{-}O_2CPr)_4]^-$ (X = Cl, Br, I) in solution but the corresponding compounds were not isolated [20]. Only the crystal structures of $K[Ru_2Cl_2(\mu\text{-}O_2CH)_4]$, $Cs[Ru_2Cl_2(\mu\text{-}O_2CMe)_4]$ and $[RuCl(MeCN)_4(PPh_3)][Ru_2Cl_2(\mu\text{-}O_2CC_6H_4\text{-}p\text{-}OMe)_4]$ have been described [13,21]. However, anionic units $[Ru_2X_2(\mu\text{-}O_2CR)_4]^-$

* Corresponding author. Tel.: +34 91 394 4334; fax: +34 91 394 4352.
E-mail address: qcmm@quim.ucm.es (R. Jiménez-Aparicio).

0277-5387/$ - see front matter © 2004 Elsevier Ltd. All rights reserved.
doi:10.1016/j.poly.2004.11.018

have been found in some compounds with the formula $Ru_2X(\mu\text{-}O_2CR)_4(H_2O)$ [4,10]. Thus, the crystal of $Ru_2Cl(\mu\text{-}O_2CCH_2OEt)_4(H_2O)$ contains not only $Ru_2Cl(\mu\text{-}O_2CCH_2OEt)_4$ zigzag chains but also $[Ru_2(\mu\text{-}O_2CCH_2OEt)_4(H_2O)_2]^+$ cations and $[Ru_2Cl_2(\mu\text{-}O_2CCH_2OEt)_4]^-$ anions [10]. Recently, we have also published [4] the first crystal structure of a iododiruthenium complex, $[Ru_2(\mu\text{-}O_2CCH_2CH_2OPh)_4(H_2O)_2]$-$[Ru_2I_2(\mu\text{-}O_2CCH_2CH_2OPh)_4]$, which shows a cation–anion arrangement in the solid state.

A few anionic tetracarboxylatodiruthenium(II,III) complexes such as $[Ru_2(\mu\text{-}O_2CC_6H_5)_4(EtOH)_2][Ru_2(\mu\text{-}O_2CC_6H_5)_4(HSO_4)_2]$ [22] and $M_3[Ru_2(\mu\text{-}O_2CR)_4(H_2O)_2]\cdot 4H_2O$ (M = Na, R = *m*-$C_6H_4SO_3$; M = K, R = *p*-$C_6H_4SO_3$) [23] have also been described.

The sole example of a dihalotetracarboxylatodiruthenium(II) complex is $[RuCl(MeCN)_4(PPh_3)]_2[Ru_2Cl_2(\mu\text{-}O_2CC_6H_4\text{-}p\text{-}OMe)_4]$ [21], whereas no example of dihalotetracarboxylatodiruthenium(III) is yet known. Even for diruthenium(III) with other equatorial bridging ligands, very few crystal structures of dihalo complexes have been reported [24].

In a previous paper [5] we have described the influence of the halide axial ligand on the properties of the monohalo complexes $Ru_2X(\mu\text{-}O_2CR)_4(S)$ and we have found a strong solvatochromism in the iododerivatives. In this work we report the synthesis of a series of tetraacetatodiruthenium(II,III) compounds where both axial positions are occupied by halide ligands, and analyse their properties. The comparison with the monohalo complexes is also illustrated.

2. Results and discussion

2.1. Synthesis and characterization of the complexes

In the aim to obtain heterometallic species we carried out the reaction of $[Ru_2(\mu\text{-}O_2CMe)_4]BF_4$ with $(NEt_4)_2[CoX_4]$ (X = Cl, Br) in MeOH. However, instead of the formation of heterometallic compounds, the rupture of the Co–X bonds occurs and the formation of the dihalo complexes $NEt_4[Ru_2X_2(\mu\text{-}O_2CMe)_4]$ is produced. The compounds $Q[Ru_2X_2(\mu\text{-}O_2CMe)_4]$ (Q = NEt_4, PPh_4; X = Cl, Br, I) and $K[Ru_2Br_2(\mu\text{-}O_2CMe)_4]$ were synthesized using QX and KBr, respectively. $NEt_4[Ru_2Cl_2(\mu\text{-}O_2CMe)_4]$ can be also obtained directly by the reaction of $Ru_2Cl(\mu\text{-}O_2CMe)_4$ with an excess of NEt_4Cl.

All compounds are thermally stable and can be manipulated in air without appreciable decomposition for a long period of time. The complexes are soluble in dichloromethane or acetone, but insoluble in diethyl ether, toluene or petroleum ether. The tetraphenylphosphonium compounds are always more soluble than the corresponding triethylammonium derivatives. The conductivity measurements in acetone and acetonitrile (101–138 and 126–160 $\Omega^{-1}cm^2mol^{-1}$, respectively) indicate that these complexes are 1:1 electrolytes [25]. However, the conductivity is higher in methanol solution (232–280 $\Omega^{-1}cm^2mol^{-1}$) because of the dissociation of the axial halide ligands.

The IR spectra show in the COO stretching region the typical pattern of a bridging carboxylate ligand. Complexes **1**–**4** and **6**–**7** exhibit characteristic bands of the corresponding cation, $[NEt_4]^+$ or $[PPh_4]^+$.

The room temperature magnetic moment of complexes **1**–**7** corresponds to the presence of three unpaired electrons for the diruthenium unit, in accordance with the $\sigma^2\pi^4\delta^2(\pi^*\delta^*)^3$ ground-state configuration proposed by Norman et al. [26]. The molar susceptibility χ_M increases continuously with decreasing temperature (300–2 K) and a decrease of the magnetic moment with the temperature is observed for all complexes. A similar behaviour has been noticed in other molecular and zigzag polymeric compounds of diruthenium(II,III) [4,5,11,12,15,27] and has been ascribed to a large zero-field splitting (ZFS) and some degree of antiferromagnetic coupling between the diruthenium units. The model of Cukiernik et al. [11] was successfully used to fit the magnetic data of complexes **1**–**7**, obtaining in all cases similar parameters to those described for other diruthenium(II,III) species [4,5,11,12,15]. The zJ values (from -0.02 to -0.11 cm^{-1}) are almost negligible, in accordance with the presence of isolated anionic dimetallic units in the compounds.

The base peak in all mass spectra corresponds to the cation $[NEt_4]^+$ (**1**, **3**, and **6**) or $[PPh_4]^+$ (**2**, **4**, and **7**) and one peak due to the ion $[Ru_2(\mu\text{-}O_2CMe)_4]^+$ is also detected.

2.2. Electronic properties

The electronic spectral data for complexes **1**–**7** in several solvents are collected in Table 1. These compounds show in methanol solution the same electronic spectra corresponding to the species $[Ru_2(\mu\text{-}O_2CMe)_4(MeOH)_2]^+$. A similar behaviour has been observed for the monohalo complexes $Ru_2X(\mu\text{-}O_2CR)_4$ [5], due to the breaking of the Ru–X bonds and the formation of bis(adducts) units $[Ru_2(\mu\text{-}O_2CR)_4(MeOH)_2]^+$, and for cationic species [28]. However, their electronic spectra in dichloromethane, acetonitrile and acetone are different. The presence of the dihalo species was confirmed by the equality of the spectra registered in neat solvents and solutions saturated with QX ($Q = PPh_4^+, NEt_4^+$). The electronic spectra of these species is consistent with those described by Miskowski and Gray [20] for $Ru_2X(\mu\text{-}O_2CPr)_4$ in an excess of halide ions. As expected, the counterion has no influence in the electronic spectra of the complexes.

However, some important differences have been observed varying the nature of the axial ligands. The main visible band for the chloro derivatives (**1** and **2**) appears

Table 1
UV–Vis data for **1**–**7** in different solvents

λ/nm (ε/dm^3 mol^{-1} cm^{-1})					
Compound	σ(axial ligand) → σ*(Ru_2)	π(axial ligand) → π*(Ru_2)	π(RuO,Ru_2) → π*(Ru_2)	σ(axial ligand) → π*(Ru_2)	δ(Ru_2) → δ*(Ru_2)
MeOH					
1		339 (392)	427 (760)		1001 (23)
2		326sh (352)	427 (657)		986 (17)
3		338 (255)	427 (740)		1001 (15)
4		342 (408)	427 (643)		1025 (20)
5		337sh (445)	426 (807)		1000 (18)
6	343 (363)	427 (498)			1013 (10)
7	340 (420)	427 (641)			1025 (2)
CH_2Cl_2					
1			464 (973)		1123 (41)
2			465 (925)	649sh (42)	1130 (32)
3		343 (8818)	479 (1311)	671sh (60)	1141 (64)
4		344 (8433)	479 (1389)	659sh (197)	1123 (121)
5		343 (6088)	480 (920)	672 (47)	1123 (47)
6		422 (8581)	554 (2883)	778sh (96)	1141 (133)
7		423 (9772)	554 (3268)	788sh (97)	1141 (144)
CH_3CN					
1			464 (937)	627sh (37)	1129 (29)
2			464 (797)	643sh (14)	1131(25)
3		343 (3852)	474 (1185)	630sh (50)	1139 (36)
4		345 (3947)	470 (1243)	631sh (44)	1141 (25)
5		345 (4122)	471 (1314)		1123 (34)
6	333sh (3166)	405 (1996)	546 (1897)	701sh (191)	1129 (46)
7	329sh (3733)	412 (2352)	545 (2418)	701sh (236)	1129 (60)
Acetone					
1	Insoluble				
2			468 (912)	619sh (56)	1174 (36)
3		353 (2266)	480 (468)	703sh (22)	1149 (60)
4		354 (6176)	480 (1324)	648sh (21)	1141 (21)
5		354 (4350)	477 (1104)		1174 (30)
6	336sh (2952)	424 (2300)	566 (1842)	702sh (137)	1141 (23)
7	336sh (3902)	424 (3092)	566 (2461)	701sh (239)	1139 (58)

at 464–468 nm in dichloromethane, acetonitrile and acetone. This absorption has been assigned to a π(RuO,Ru_2) → π*(Ru_2) transition according to Norman et al. [26] and Miskowski et al. [20,29]. In the dibromo derivatives this absorption is very slightly red shifted (474–480 nm) and remains essentially unaltered changing the nature of the solvents. The greatest shift is observed for the iodo complexes, which show this band in the range 545–566 nm. Moreover, this absorption is sensitive to the nature of the solvents: 545–546 nm in acetonitrile, 554 nm in dichloromethane and 566 nm in acetone.

The complexes $Q[Ru_2X_2(\mu\text{-}O_2CMe)_4]$ (Q = PPh_4, NEt_4) also display a shoulder ranging from 619–649 nm for the dichloro derivatives, which is shifted to 631–672 nm in the dibromo complexes, and to 701–788 nm in the diiodo derivatives. This absorption is attributed to a (Ru-axial ligand) → π*(Ru_2) transition, analogous to the monohalo compounds [5]. Two additional absorption bands appear in the ranges 339–427 and 986–1174 nm, which are assigned to LMCT π(axial ligand) → π*(Ru_2) and δ → δ* transitions, respectively. Similarly to the monoiodo derivatives [5] the absorption detected for the $Q[Ru_2I_2(\mu\text{-}O_2CMe)_4]$ compounds in the range 336–343 nm could be assigned to a σ(Ru-axial ligand) → σ*(Ru_2) transition.

As indicated above, the presence of two iodide ligands at the axial positions of the $[Ru_2(\mu\text{-}O_2CMe)_4]^+$ unit shifts the π(RuO,Ru_2) → π*(Ru_2) transition to the visible range, alike to the $Ru_2I(\mu\text{-}O_2CR)_4(S)$ compounds [5]. A strong solvatochromism has been observed for these monoiodo complexes due mainly to the coordination of a solvent molecule at the free axial position of the dimetallic unit. This coordination is not possible for the $[Ru_2I_2(\mu\text{-}O_2CR)_4]^-$ species, however, a significant solvatochromism is still perceived.

2.3. Crystal structures

The structure of complexes **1**–**3**, **5** and **7** have been determined by X-ray crystallography. PLUTO views of complexes **1**, **5** and **7** are depicted in Figs. 1–3. The corresponding figures for complexes **2** and **3** are deposited as supplementary material. Table 2 gives selected bond distances and angles. The anionic unit of these com-

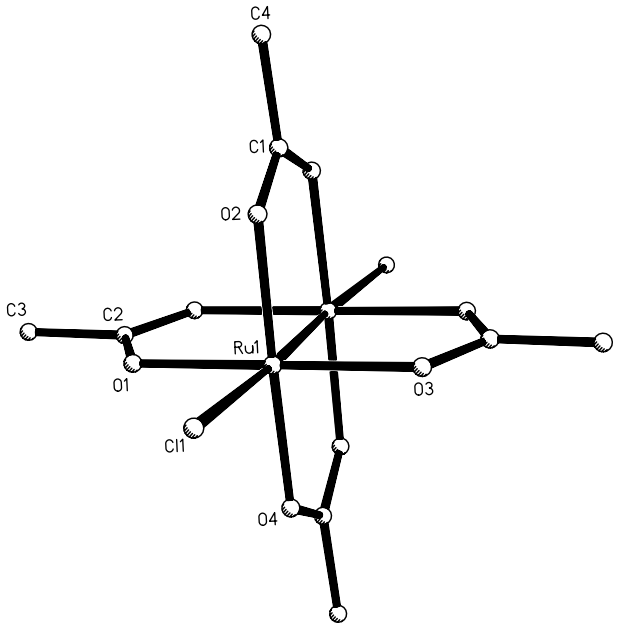


Fig. 1. PLUTO view of the anion $[Ru_2Cl_2(\mu\text{-}O_2CMe)_4]^-$ corresponding to complex **1**. Hydrogen atoms are omitted for clarity.

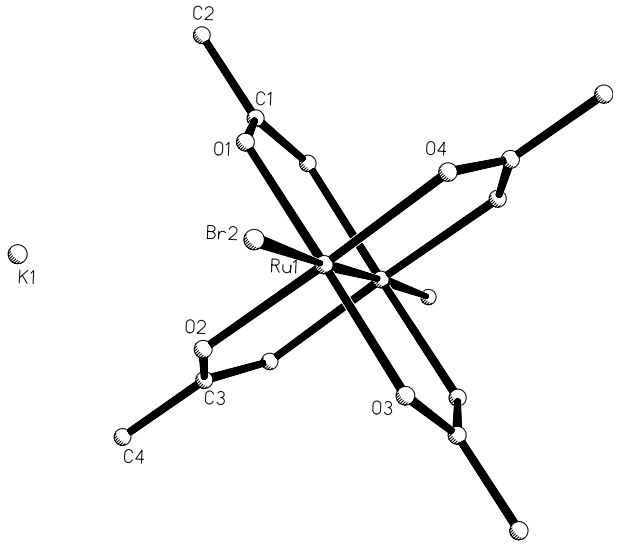


Fig. 2. PLUTO view of $K[Ru_2Br_2(\mu\text{-}O_2CMe)_4]$ (**5**). Hydrogen atoms are omitted for clarity.

pounds have two Ru atoms linked by four acetate bridging ligands and the axial positions are occupied by two halide ligands. The cations in these complexes are NEt_4^+ for **1** and **3**, PPh_4^+ for **2** and **7**, and K^+ in **5**.

The Ru–Ru bond lengths for **1**–**3** and **5** are 2.3069(8), 2.3088(6), 2.2999(16), and 2.2956(5) Å, respectively. The Ru–Ru distances for **7** are 2.312(3) and 2.311(3) Å. The metal–metal distance in these dihalocomplexes are slightly longer than those observed in discrete dinuclear molecules $Ru_2X(\mu\text{-}O_2CR)_4(S)$ [3–5] with Ru–X terminal or in polymeric arrangement $[Ru_2X(\mu\text{-}O_2CR)_4]_n$ [3,5], with the only exception of $Cs[Ru_2Cl_2(\mu\text{-}O_2CMe)_4]$ [13] (Table 3). This tendency is in agreement with the metal-metal distances found in $Ru_2Cl(\mu\text{-}O_2CCH_2OEt)_4(H_2O)$ [10], which contains both anionic (2.294(2) Å) and polymeric (2.277(1) Å) arrangements in the same crystal.

On the other hand, the distance Ru–X varies with the size of the halide ligand. Thus, the Ru–X bond lengths are 2.5396(15) (**1**) and 2.5627(10) (**2**) Å (X = Cl), 2.6763(14) (**3**) and 2.6779(4) (**5**) Å (X = Br), and 2.897(2) and 2.893(2) (**7**) Å (X = I). Only Ru–Cl lengths between $[Ru_2Cl_2(\mu\text{-}O_2CR)_4]^-$ and $[Ru_2Cl(\mu\text{-}O_2CR)_4]_n$ may be compared (Table 3), because there are no other couples of mono- and dihalodiruthenium(II,III) species with the same carboxylate ligand. In contrast to the Ru–Ru bond distance, the metal–chloride length in these complexes are slightly longer in the polymeric arrangements than in the anionic units with two chloride ions at the axial positions. This tendency is illustrated with the Ru–Cl distances in $[Ru_2Cl(\mu\text{-}O_2CCH_2OEt)_4]_n$

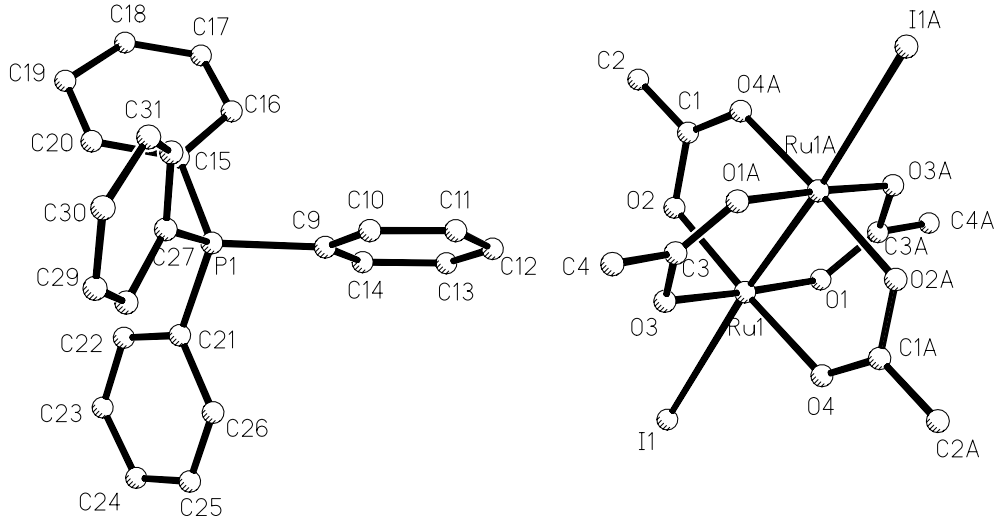


Fig. 3. PLUTO view of $PPh_4[Ru_2I_2(\mu\text{-}O_2CMe)_4]$ (**7**). The complete anionic unit A has been generated by symmetry. Hydrogen atoms and half anionic unit B are omitted for clarity.

Table 2
Selected bond distances (Å) and angles (°) for $NEt_4[Ru_2Cl_2(\mu\text{-}O_2CMe)_4]$ (**1**), $PPh_4[Ru_2Cl_2(\mu\text{-}O_2CMe)_4]$ (**2**), $NEt_4[Ru_2Br_2(\mu\text{-}O_2CMe)_4]$ (**3**), $K[Ru_2Br_2(\mu\text{-}O_2CMe)_4]$ (**5**) and $PPh_4[Ru_2I_2(\mu\text{-}O_2CMe)_4]$ (**7**)

1		**2**		**3**	
Bond distances					
Ru(1)–Ru(1)#1	2.3069(8)	Ru(1)–Ru(1)#1	2.3088(6)	Ru(1)–Ru(1)#2	2.2999(16)
Ru(1)–Cl(1)	2.5396(15)	Ru(1)–Cl(1)	2.5627(10)	Ru(1)–Br(2)	2.6763(14)
Ru(1)–O(1)	2.027(4)	Ru(1)–O(1)	2.020(3)	Ru(1)–O(1)	2.034(5)
Ru(1)–O(2)	2.031(4)	Ru(1)–O(2)	2.034(3)	Ru(1)–O(2)	2.019(5)
Ru(1)–O(3)	2.031(4)	Ru(1)–O(3)	2.024(3)		
Ru(1)–O(4)	2.028(4)	Ru(1)–O(4)	2.026(3)		
Bond angles					
Ru(1)#1–Ru(1)–Cl(1)	177.29(4)	Ru(1)#1–Ru(1)–Cl(1)	178.86(3)	Ru(1)#2–Ru(1)–Br(2)	177.10(6)
O(1)–Ru(1)–Ru(1)#1	88.52(12)	O(1)–Ru(1)–Ru(1)#1	89.59(8)	O(1)–Ru(1)–Ru(1)#2	89.55(15)
O(2)–Ru(1)–Ru(1)#1	88.60(12)	O(2)–Ru(1)–Ru(1)#1	88.68(8)	O(2)–Ru(1)–Ru(1)#2	88.79(15)
O(3)–Ru(1)–Ru(1)#1	89.49(12)	O(3)–Ru(1)–Ru(1)#1	88.76(8)		
O(4)–Ru(1)–Ru(1)#1	92.60(12)	O(4)–Ru(1)–Ru(1)#1	89.09(8)		
5		**7** (unit A)		**7** (unit B)	
Bond distances					
Ru(1)–Ru(1)#1	2.2956(5)	Ru(1)–Ru(1)#1	2.312(3)	Ru(2)–Ru(2)#2	2.311(3)
Ru(1)–Br(2)	2.6779(4)	Ru(1)–I(1)	2.897(2)	Ru(2)–I(2)	2.893(2)
Ru(1)–O(1)	2.022(2)	Ru(1)–O(1)	2.047(14)	Ru(2)–O(5)	2.029(13)
Ru(1)–O(2)	2.028(2)	Ru(1)–O(2)	2.032(14)	Ru(2)–O(6)	2.020(13)
Ru(1)–O(3)	2.033(2)	Ru(1)–O(3)	2.034(13)	Ru(2)–O(7)	2.045(13)
Ru(1)–O(4)	2.025(2)	Ru(1)–O(4)	2.021(14)	Ru(2)–O(8)	2.050(13)
Bond angles					
Ru(1)#1–Ru(1)–Br(2)	177.121(19)	Ru(1)#1–Ru(1)–I(1)	175.78(11)	Ru(2)#2–Ru(2)–I(2)	176.72(11)
O(1)–Ru(1)–Ru(1)#1	89.75(6)	O(1)–Ru(1)–Ru(1)#1	89.4(4)	O(5)–Ru(2)–Ru(2)#2	89.7(4)
O(2)–Ru(1)–Ru(1)#1	89.67(6)	O(2)–Ru(1)–Ru(1)#1	89.8(4)	O(6)–Ru(2)–Ru(2)#2	90.1(4)
O(3)–Ru(1)–Ru(1)#1	88.71(6)	O(3)–Ru(1)–Ru(1)#1	89.1(4)	O(7)–Ru(2)–Ru(2)#2	88.5(4)
O(4)–Ru(1)–Ru(1)#1	88.64(6)	O(4)–Ru(1)–Ru(1)#1	87.5(4)	O(8)–Ru(2)–Ru(2)#2	89.2(4)

Symmetry transformations used to generate equivalent atoms for complexes: **1**: #1 $-x+1/2,-y+1/2,-z$ #2 $-x+1/2,-y+1/2,-z+1$; **2**: #1 $-x+1/2,-y+1/2,-z+1$ #2 $-x,y,-z+1/2$; **3**: #1 $x,y,-z$ #2 $-x+2,-y,-z$ #3 $-x,-y+1,z$ #4 $-x,-y+1,-z+2$ #5 $x,y,-z+2$; **5**: #1 $-x,-y+1,-z+2$ #2 $-y+1,x+1/2,z+1/2$ #3 $-x+1/2,-y+3/2,z$ #4 $y-1/2,-x+1,z-1/2$ #5 $-y+1,x+1/2,z-1/2$; **7**: #1 $-x+2,-y,-z+2$ #2 $-x+1,-y,-z+1$.

Table 3
Comparison of Ru–Ru and Ru–X bond distances (Å) between anionic and molecular or polymeric halotetracarboxylatodiruthenium(II,III) compounds

Dihalodiruthenium(II,III) complexes	d(Ru–Ru)	d(Ru–X)	Monohalodiruthenium(II,III) complexes	d(Ru–Ru)	d(Ru–X)
$K[Ru_2Cl_2(\mu\text{-}O_2CH)_4]$ [13]	2.290(1)	2.517(2)			
			$[Ru_2Br(\mu\text{-}O_2CH)_4]_n$ [3]	2.2897(7)	2.7170(8)
$Cs[Ru_2Cl_2(\mu\text{-}O_2CMe)_4]$ [13]	2.286(2)	2.521(4)	$[Ru_2Cl(\mu\text{-}O_2CMe)_4]_n$ [7]	2.281(3)	2.571(4)
$NEt_4[Ru_2Cl_2(\mu\text{-}O_2CMe)_4]$ (**1**)	2.3069(8)	2.5396(15)	$[Ru_2Cl(\mu\text{-}O_2CMe)_4]_n$ [14]	2.287(2)	2.577(1)
$PPh_4[Ru_2Cl_2(\mu\text{-}O_2CMe)_4]$ (**2**)	2.3088(6)	2.5627(10)	$[Ru_2Cl(\mu\text{-}O_2CMe)_4]_n$ [13]	2.267(1)	2.566(1)
$NEt_4[Ru_2Br_2(\mu\text{-}O_2CMe)_4]$ (**3**)	2.2999(16)	2.6763(14)			
$K[Ru_2Br_2(\mu\text{-}O_2CMe)_4]$ (**5**)	2.2956(5)	2.6779(4)			
$PPh_4[Ru_2I_2(\mu\text{-}O_2CMe)_4]$ (**7**)	2.312(3)	2.897(2)			
	2.311(3)	2.893(2)			
$Q_1[Ru_2Cl_2(\mu\text{-}O_2CCH_2OEt)_4]$ [10]	2.294(2)	2.499(2)	$[Ru_2Cl(\mu\text{-}O_2CCH_2OEt)_4]_n$ [10]	2.277(1) 2.280(1)	2.563(2)
					2.558(2)
$Q_2[Ru_2Cl_2(\mu\text{-}O_2CC_6H_4\text{-}p\text{-}OMe)_4]$ [21]	2.299(1)	2.493(3)	$[Ru_2Cl(\mu\text{-}O_2CC_6H_4\text{-}p\text{-}OMe)_4]_n$ [8]	2.284(1) 2.290(1)	2.554(2)
				2.283(1)	2.583(2)
					2.563(2)
					2.568(3)
			$Ru_2Br(\mu\text{-}O_2C_6H_4\text{-}p\text{-}OMe)_4(H_2O)$ [5]	2.2756(17)	2.671(2)
			$Ru_2I(\mu\text{-}O_2C_6H_4\text{-}p\text{-}OMe)_4(H_2O)$ [5]	2.273(3)	2.831(4)

$Q_1 = [Ru_2(\mu\text{-}O_2CCH_2OEt)_4(H_2O)_2]^+$; $Q_2 = [RuCl(MeCN)_4(PPh_3)]^+$.

(2.563(2) and 2.558(2) Å) and $[Ru_2Cl_2(\mu\text{-}O_2CCH_2OEt)_4]^-$ (2.499(2) Å) [10].

3. Conclusions

In this work, we have reported two routes to the preparation of anionic diruthenium(II,III) complexes with two halide ligands at the axial positions. In spite of the tendency of the halotetraacetatodiruthenium(II,III) compounds to give a polymeric structure, in the presence of an excess of halide ligand the formation of $[Ru_2X_2(\mu\text{-}O_2CMe)_4]^-$ is preferred. The other route demonstrates that the tetraacetatodiruthenium(II,III) unit is even capable of abstracting the halide from another complex, namely $[CoX_4]^{2-}$, in order to form these anionic species. Although the diruthenium(II,III) core remains essentially the same in neutral and anionic species, the ruthenium–ruthenium bond lengths in dihalotetracarboxylatodiruthenum(II,III) are slightly longer than those observed in $Ru_2X(\mu\text{-}O_2CR)_4(S)$ or $[Ru_2X(\mu\text{-}O_2CR)_4]_n$. On the contrary, the Ru–X bond distances are shorter for $[Ru_2X_2(\mu\text{-}O_2CR)_4]^-$ species.

The solvatochromism of the diruthenium(II,III) complexes is associated to the presence of halide ligands at the axial positions and increases with their polarizability. However, this property is more accentuated when an axial position is occupied by a solvent molecule.

Finally, these anionic complexes, which contain three unpaired electrons, could be very useful to be combined with admixed or low spin diruthenium(II,III) cationic species [30] in order to obtain materials with singular magnetic properties. The preparation of this type of complexes is currently being investigated.

4. Experimental

All reactions were carried out in an inert atmosphere, using standard Schlenk techniques. The complexes $Ru_2Cl(\mu\text{-}O_2CMe)_4$, $[Ru_2(\mu\text{-}O_2CMe)_4]BF_4$ and $(NEt_4)_2[CoX_4]$ (X = Cl, Br) were prepared by the literature procedures [31–33]. Unless otherwise stated, other chemical and solvents were obtained from commercial sources and used without further purification.

Elemental analyses were done by the Microanalytical Service of the Complutense University of Madrid. IR spectra were recorded on a Midac prospect FT-IR or on a Shimadzu FT-IR Prestige-21 spectrophotometer using KBr discs. Electronic spectra in the range 250–1300 nm were recorded on a Cary 5G spectrophotometer in solutions 10^{-4} M of methanol, acetone, dichloromethane and acetonitrile. The variable-temperature magnetic susceptibility data were measured on a Quatum Design MPMS*XL* SQUID (Superconducting Quantum Interference Device) susceptometer over a temperature range of 2–300 K. All data were corrected for the diamagnetic contribution of both the sample holder and the compound to the susceptibility. The molar diamagnetic corrections for the complexes were calculated on the basis of Pascal's constants. Mass spectra were obtained on a Bruker Esquire-LC with Electrospray Ionization (ESI) using methanol. Nominal molecular masses and distribution isotopic of all peaks were calculated with the MASAS [34] computer program, using a polynomial expansion based on natural abundances of the isotopes.

4.1. Synthesis of $NEt_4[Ru_2Cl_2(\mu\text{-}O_2CMe)_4]$ (1)

This complex was obtained by two ways: (a) To a solution of $Ru_2Cl(\mu\text{-}O_2CMe)_4$ (0.15 g, 0.32 mmol) in 40 mL of MeOH was added an excess of NEt_4Cl (0.53 g, 3.20 mmol) in 5 mL of MeOH. The reaction mixture was stirred for 30 min. The solution was filtered and the red–brown solid was washed with methanol and diethyl ether, and dried under vacuum to give **1**. Yield: 0.13 g (65%). (b) A suspension of $[Ru_2(\mu\text{-}O_2CMe)_4]BF_4$ (0.15 g, 0.29 mmol) and $(NEt_4)_2[CoCl_4]$ (0.13 g, 0.29 mmol) in 40 mL of dry methanol was stirred for 2 h giving a red–brown solution. This solution was layered with diethyl ether to form red–brown microcrystals of **1** suitable for X-ray study. Yield: 0.09 g (45%). *Anal*. Calc. for $Ru_2O_8NCl_2C_{16}H_{32}$: C, 30.05; H, 5.04; N, 2.19. Found: C, 30.19; H, 5.05; N, 2.28%. IR (KBr, cm^{-1}) = 2984 (m), 2949 (m), 2920 (w), 1642 (w), 1473 (vs), 1450(vs), 1423 (vs), 1409 (vs), 1394 (vs), 1352 (s), 1176 (m), 1056 (s), 1022 (w), 1003 (m), 788 (m), 689 (vs), 631 (m), 604 (w). $\mu_{eff.}$ = 4.06 B.M. at r.t. MS in MeOH (ESI^+): m/z = 440 $[Ru_2(\mu\text{-}O_2CMe)_4 + H]$, 130 $[NEt_4]$.

4.2. Synthesis of $PPh_4[Ru_2Cl_2(\mu\text{-}O_2CMe)_4]$ (2)

To a solution of $Ru_2Cl(\mu\text{-}O_2CMe)_4$ (0.15 g, 0.32 mmol) in 40 mL of MeOH was added an excess of PPh_4Cl (1.20 g, 3.20 mmol) in 15 mL of MeOH. The solution was stirred for 30 min and the volatile components were removed under vacuum. The red–brown solid was washed several times with acetone, dried, and redissolved in 30 mL of MeOH. By slow evaporation of this solution, red crystals of the title compound were obtained. Yield: 0.11 g (40%). *Anal*. Calc. for $Ru_2O_8PCl_2C_{32}H_{32}$: C, 45.29; H, 3.80. Found: C, 45.73; H, 3.84%. IR (KBr, cm^{-1}) = 3060 (w), 2923 (w), 1710 (w), 1637 (w), 1586w (w), 1477 (m), 1439 (vs), 1407 (s), 1351 (w), 1318 (w), 1108 (m), 996 (w), 764 (w), 757 (w), 722 (m), 690 (s), 530 (m). $\mu_{eff.}$ = 4.16 B.M. at r.t. MS in MeOH (ESI^+): m/z = 440 $[Ru_2(\mu\text{-}O_2CMe)_4 + H]$, 474 $[Ru_2Cl(\mu\text{-}O_2CMe)_4]$, 339 $[PPh_4]$.

4.3. Synthesis of $NEt_4[Ru_2Br_2(\mu\text{-}O_2CMe)_4]$ (3)

Two methods were used to obtain this compound: (a) An aqueous solution of $AgNO_3$ (0.05 g, 0.32 mmol) was

Table 4
Crystal data for $NEt_4[Ru_2Cl_2(\mu\text{-}O_2CMe)_4]$ (**1**), $PPh_4[Ru_2Cl_2(\mu\text{-}O_2CMe)_4]$ (**2**) $NEt_4[Ru_2Br_2(\mu\text{-}O_2CMe)_4]$ (**3**), $K[Ru_2Br_2(\mu\text{-}O_2CMe)_4]$ (**5**) and $PPh_4[Ru_2I_2(\mu\text{-}O_2CMe)_4]$ (**7**)

	1	**2**	**3**	**5**	**7**
Empirical formula	$C_{16}H_{32}Cl_2NO_8Ru_2$	$C_{32}H_{32}Cl_2O_8PRu_2$	$C_{16}H_{32}Br_2NO_8Ru_2$	$C_8H_{12}Br_2KO_8Ru_2$	$C_{32}H_{32}I_2O_8PRu_2$
Formula weight	639.47	848.59	728.39	637.24	1031.49
Crystal system	monoclinic	monoclinic	orthorhombic	tetragonal	monoclinic
Space group	*C*2/*c*	*C*2/*c*	*Ibam*	$P4_2/n$	$P2_1/n$
a (Å)	18.6322(19)	16.2015(12)	14.021(2)	12.1472(6)	7.2796(11)
b (Å)	13.8375(14)	7.7469(6)	12.4960(18)	12.1472(6)	30.534(5)
c (Å)	12.2810(12)	27.573(2)	14.020(2)	11.1328(7)	15.773(3)
β (°)	130.8120(10)	101.999(2)	90	90	90.228(3)
Volume (Å^3)	2396.5(4)	3385.1(4)	2456.2(6)	1642.69(15)	3505.9(10)
Z	4	4	4	4	4
$D_{calcd.}$ (g cm^{-3})	1.772	1.665	1.970	2.577	1.954
μ (mm^{-1})	1.522	1.146	4.521	6.986	2.715
F(0 0 0)	1284	1700	1428	1204	1988
Crystal size (mm)	$0.09 \times 0.19 \times 0.26$	$0.04 \times 0.09 \times 0.45$	$0.07 \times 0.14 \times 0.14$	$0.14 \times 0.16 \times 0.17$	$0.08 \times 0.08 \times 0.30$
θ Range (°)	2.06 to 25.00	1.51 to 28.75	2.18 to 29.38	2.37 to 28.75	1.33 to 28.93
Index ranges	$-21 \leqslant h \leqslant 22$, $-16 \leqslant k \leqslant 12$, $-14 \leqslant l \leqslant 14$	$-21 \leqslant h \leqslant 21$, $-10 \leqslant k \leqslant 10$, $-35 \leqslant l \leqslant 26$	$-18 \leqslant h \leqslant 17$, $-7 \leqslant k \leqslant 17$, $-18 \leqslant l \leqslant 18$	$-16 \leqslant h \leqslant 16$, $-16 \leqslant k \leqslant 15$, $-14 \leqslant l \leqslant 8$	$-6 \leqslant h \leqslant 9$, $-39 \leqslant k \leqslant 41$, $-21 \leqslant l \leqslant 21$
Collected reflections	6020	10386	7892	10127	22404
Independent reflections	2107 [R_{int} = 0.0332]	4035 [R_{int} = 0.0448]	1647 [R_{int} = 0.0629]	2030 [R_{int} = 0.0470]	8427 [R_{int} = 0.1380]
Observed reflections ($(I) > 2\sigma(I)$)	1797	2900	1043	1555	3723
Completeness to θ (%)	99.8 to 25.00	91.6 to 25.00	93.7 to 25.00	94.9 to 25.00	91.0 to 28.93
Data/restraints/parameters	2107/10/121	4035/0/206	1647/4/66	2030/0/99	8427/0/406
Goodness-of-fit on F^2	1.076	0.997	0.998	0.923	1.061
Final *R* indices ($I > 2\sigma(I)$)	R_1 = 0.0429 wR_2 = 0.1260	R_1 = 0.0403 wR_2 = 0.1068	R_1 = 0.0506 wR_2 = 0.1516	R_1 = 0.0245 wR_2 = 0.0466	R_1 = 0.1065 wR_2 = 0.2762
R indices (all data)	R_1 = 0.0502 wR_2 = 0.1307	R_1 = 0.0614 wR_2 = 0.1140	R_1 = 0.0852 wR_2 = 0.1715	R_1 = 0.0377 wR_2 = 0.0492	R_1 = 0.2018 wR_2 = 0.3065
Largest different peak/hole (e Å^{-3})	1.273 and −1.044	1.195 and −0.446	1.921 and −1.136	0.585 and −0.585	2.722 and −1.559

added to a suspension of $Ru_2Cl(\mu\text{-}O_2CMe)_4$ (0.15 g, 0.32 mmol) in 10 mL of MeOH. The solution was filtered and treated with an excess of NEt_4Br (0.67 g, 3.20 mmol) in 20 mL of MeOH. The reaction mixture was stirred for 30 min and filtered. The red–brown solid was washed with methanol, and dried under vacuum to give **3**. Yield: 0.14 g (61%). (b) The reaction was carried out following the same procedure described for **1** (method b), using $(NEt_4)_2[CoBr_4]$ (0.19 g, 0.29 mmol) and refluxing the reaction mixture for 4 h. Yield: 0.11 g (48%). Crystals of **3** were obtained similarly to **1**. *Anal*. Calc. for $Ru_2O_8NBr_2C_{16}H_{32}$: C, 26.38; H, 4.43; N, 1.92. Found: C, 26.52; H, 4.42; 1.95 N%. IR (KBr, cm^{-1}) = 2982 (m), 2948 (w), 2919 (w), 1640 (w), 1498 (s), 1442 (vs), 1407 (vs), 1392 (s), 1351 (m), 1174 (m), 1054 (m), 1020 (w), 1002 (m), 786 (m), 688 (vs), 629 (m), 604 (w). $\mu_{eff.}$ = 4.10 B.M. at r.t. MS in MeOH (ESI^+): *m/z* = 440 [$Ru_2(\mu\text{-}O_2CMe)_4$+H], 518 [$Ru_2Br(\mu\text{-}O_2CMe)_4$], 130 [$NEt_4$].

4.4. Synthesis of $PPh_4[Ru_2Br_2(\mu\text{-}O_2CMe)_4]$ (**4**)

Compound **4** was prepared similarly to **3** (method a), using PPh_4Br (1.34 g, 3.20 mmol) and water instead of MeOH, and isolated as red–brown powder. Yield: 0.20 g (67%). *Anal*. Calc. for $Ru_2O_8PBr_2C_{32}H_{32}$: C, 41.00; H, 3.44. Found: C, 40.76; H, 3.37%. IR (KBr, cm^{-1}) = 3010 (w), 2925 (w), 2360 (w), 2342 (w), 1627 (m), 1482 (m), 1471 (m), 1441(vs), 1399 (s), 1350 (m), 1184 (w), 1163 (w), 1108 (s), 1046 (w), 1029 (w), 996 (w), 758 (m), 723 (s), 691 (vs), 605 (w), 527 (s). $\mu_{eff.}$ = 3.94 B.M. at r.t. MS in MeOH (ESI^+): *m/z* = 440 [$Ru_2(\mu\text{-}O_2CMe)_4$+H], 339 [$PPh_4$].

4.5. Synthesis of $K[Ru_2Br_2(\mu\text{-}O_2CMe)_4]$ (**5**)

A solution of KBr (0.35 g, 2.90 mmol) in 10 mL of water was layered with a solution of $[Ru_2(\mu\text{-}O_2CMe)_4]BF_4$ (0.15 g, 0.29 mmol) in 15 mL of ethanol. After two days, a precipitate of $Ru_2Br(\mu\text{-}O_2CMe)_4$ had accumulated at the bottom of the Schlenk tube and crystals of **5**, suitable for X-ray study, were formed at the interface. The crystals were carefully collected and dried. Yield: 0.014 g (7%). *Anal*. Calc. for $Ru_2O_8KBr_2C_8H_{12}$: C, 15.08; H, 1.90. Found: C, 15.02; H, 1.85%. IR (KBr, cm^{-1}) = 2933 (w), 1644 (w), 1440 (vs), 1405 (s), 1346 (s), 1262 (w), 1053 (m), 804 (w), 693 (vs), 629 (m), 609 (w). MS in MeOH (ESI^+): *m/z* = 439 [$Ru_2(\mu\text{-}O_2CMe)_4$].

4.6. Synthesis of $NEt_4[Ru_2I_2(\mu\text{-}O_2CMe)_4]$ (**6**)

Compound **6** was obtained similarly to **3** (method a), using NEt_4I (0.82 g, 3.20 mmol), and isolated as red–brown powder. Yield: 0.16 g (62%). *Anal*. Calc. for $Ru_2O_8NI_2C_{16}H_{32}$: C, 23.37; H, 3.92; N, 1.70. Found: C, 23.42; H, 3.95; N, 1.73%. IR (KBr, cm^{-1}) = 2980 (m), 2914 (m), 1653 (w), 1473 (s), 1460 (vs), 1421 (vs), 1405 (vs), 1356 (s), 1349 (s), 1291 (w), 1173 (m), 1047 (m), 1026 (w), 998 (m), 785 (m), 690 (vs), 630 (m), 604 (w). $\mu_{eff.}$ = 3.79 B.M. at r.t. MS in MeOH (ESI^+): *m/z* = 440 [$Ru_2(\mu\text{-}O_2CMe)_4$ + H], 130 [NEt_4].

4.7. Synthesis of $PPh_4[Ru_2I_2(\mu\text{-}O_2CMe)_4]$ (**7**)

Complex **7** was synthesized similarly to **3** (method a), using PPh_4I (1.49 g, 3.20 mmol). The red–brown solution was allowed to stand at room temperature for 48 h, yielding red–brown crystals of **7**. Yield: 0.18 g (55%). *Anal*. Calc. for $Ru_2O_8PI_2C_{32}H_{32}$: C, 37.26; H, 3.13. Found: C, 37.30; H, 3.13%. IR (KBr, cm^{-1}) = 3052 (w), 3005 (w), 2966 (w), 2923 (w), 2852 (w), 2837(w), 1647 (w), 1583 (w), 1482 (m), 1441 (vs), 1435 (vs), 1395 (s), 1346 (s), 1315 (m), 1184 (w), 1162 (w), 1107 (vs), 1045 (w), 1027 (m), 995 (m), 756 (s), 722 (s), 690 (vs), 627 (w), 526 (vs). $\mu_{eff.}$ = 3.94 B.M. at r.t. MS in MeOH (ESI^+): *m/z* = 439 [$Ru_2(\mu\text{-}O_2CMe)_4$], 339 [$PPh_4$].

4.8. X-ray crystallography

Single crystals of compounds **1**–**3**, **5** and **7** were obtained as described above. Details for data collection and crystal structure refinement for these compounds are summarised in Table 4. Representative crystals were mounted on a Bruker Smart-CCD diffractometer with graphite-monochromated Mo Kα (λ = 0.71073 Å) radiation. In each case data were collected at 293(2) K over a hemisphere of the reciprocal space by a combination of three exposures sets. The cell parameters were determined and refined by a least-squares fit of all reflections collected. The structures were solved by direct methods and refined by the full-matrix least-squares method against F^2 of all data. Calculations were performed with the aid of the SHELXS and SHELXL programs [35,36]. In complexes **1** and **3** a severe disorder of the tetraethylammonium groups was found and the ethyl groups were refined only isotropically; in complex **3** they were refined also with geometrical restraints and a variable common carbon–carbon distance. In addition, in complex **1** the nitrogen atom of the tetraethylammonium ion is located on a centre of symmetry and a conventional draw of the NEt_4 has not been obtained. A similar NEt_4 group has been found, for example, in the cluster complex $(NEt_4)_2[NiRu_2(CO)_{12}]$ [37]. In complexes **3** and **7** the largest residual peaks and holes in the final Fourier difference maps were associated with the nitrogen atom of the tetraethylammonium cation for complex **3** and near to the ruthenium atom for complex **7**. Final mixed refinement for complexes **2**, **5** and **7** was undertaken with anisotropic thermal parameters

for the non-hydrogen atoms. Complex **7** gave only fibrous and polysynthetically twinned crystals, which lead to high R factors.

Acknowledgements

We are grateful to the Ministerio de Ciencia y Tecnología (Dirección General de Investigación, Project No. BQU2000-0643) and the Universidad Complutense de Madrid (Project No. PR3/04-12426) for financial support.

Appendix A. Supplementary data

Crystallographic data for **1**–**3**, **5** and **7** have been deposited at the Cambridge Crystallographic Data Centre as a supplementary publication (CCDC Nos. 251381–251385). These data can be obtained free of charge at www.ccdc.cam.ac.uk/conts/retrieving.html or from the Cambridge Crystallographic Data Centre, 12, Union Road, Cambridge CB2 1EZ, UK [Fax: + 44-1223/336033; e-mail: deposit@ccdc.cam.ac.uk]. PLUTO views of complexes **2** and **3** are deposited as figures S1 and S2. Supplementary data associated with this article can be found, in the online version, at doi:10.1016/j.poly.2004.11.018.

References

[1] F.A. Cotton, R.A. Walton, Multiple bonds between metal atoms, second ed., Oxford University Press, Oxford, UK, 1993.
[2] (a) M.A.S. Aquino, Coord. Chem. Rev. 170 (1998) 141;
(b) M.A.S. Aquino, Coord. Chem. Rev. 248 (2004) 1025.
[3] T. Kimura, T. Sakurai, M. Shima, T. Togano, M. Mukaida, T. Nomura, Bull. Chem. Soc. Jpn. 55 (1982) 3927.
[4] M.C. Barral, R. González-Prieto, R. Jiménez-Aparicio, J.L. Priego, M.R. Torres, F.A. Urbanos, Eur. J. Inorg. Chem. (2003) 2339.
[5] M.C. Barral, R. González-Prieto, R. Jiménez-Aparicio, J.L. Priego, M.R. Torres, F.A. Urbanos, Eur. J. Inorg. Chem. (2004) 4491.
[6] M.J. Bennett, K.G. Caulton, F.A. Cotton, Inorg. Chem. 8 (1969) 1.
[7] T. Togano, M. Mukaida, T. Nomura, Bull. Chem. Soc. Jpn. 53 (1980) 2085.
[8] B.K. Das, A.R. Chakravarty, Polyhedron 10 (1991) 491.
[9] M. McCann, A. Carvill, P. Guinan, P. Higgings, J. Campbell, H. Ryan, M. Walsh, G. Ferguson, J. Gallagher, Polyhedron 10 (1991) 2273.
[10] M.C. Barral, R. Jiménez-Aparicio, J.L. Priego, E.C. Royer, F.A. Urbanos, U. Amador, Inorg. Chem. 37 (1998) 1413.
[11] F.D. Cukiernik, D. Luneau, J.-C. Marchon, P. Maldivi, Inorg. Chem. 37 (1998) 3698.
[12] M.C. Barral, R. Jiménez-Aparicio, D. Pérez-Quintanilla, J.L. Priego, E.C. Royer, M.R. Torres, F.A. Urbanos, Inorg. Chem. 39 (2000) 65.
[13] A. Bino, F.A. Cotton, T.R. Felthouse, Inorg. Chem. 18 (1979) 2599.
[14] D.S. Martin, R.A. Newman, L.M. Vlasnik, Inorg. Chem. 19 (1980) 3404.
[15] F.A. Cotton, Y. Kim, T. Ren, Polyhedron 12 (1993) 607.
[16] M.C. Barral, R. Jiménez-Aparicio, D. Pérez-Quintanilla, E. Pinilla, J.L. Priego, E.C. Royer, F.A. Urbanos, Polyhedron 18 (1998) 371.
[17] M.C. Barral, R. Jiménez-Aparicio, E.C. Royer, C. Ruiz-Valero, M.J. Saucedo, F.A. Urbanos, Inorg. Chem. 33 (1994) 2692.
[18] M.C. Barral, R. Jiménez-Aparicio, J.L. Priego, E.C. Royer, M.J. Saucedo, F.A. Urbanos, U. Amador, J. Chem. Soc., Dalton Trans. (1995) 2183.
[19] M.C. Barral, R. Jiménez-Aparicio, J.L. Priego, E.C. Royer, F.A. Urbanos, U. Amador, J. Chem. Soc., Dalton Trans. (1997) 863.
[20] V.M. Miskowski, H.B. Gray, Inorg. Chem. 27 (1988) 2501.
[21] B.K. Das, A.R. Chakravarty, Inorg. Chem. 31 (1992) 1395.
[22] M. McCann, A. Carvill, C. Cardin, M. Convery, Polyhedron 12 (1993) 1163.
[23] C.E.J. van Rensburg, E. Kreft, J.C. Swarts, S.R. Dalrymple, D.M. MacDonald, M.W. Cooke, M.A.S. Aquino, Anticancer Res. 22 (2002) 889.
[24] (a) J.L. Bear, Y. Li, B. Han, K.M. Kadish, Inorg. Chem. 35 (1996) 1395;
(b) G. Xu, C. Campana, T. Ren, Inorg. Chem. 41 (2002) 3521;
(c) W.Z. Chen, T. Ren, Inorg. Chem. 42 (2003) 8847;
(d) M.C. Barral, R. González-Prieto, S. Herrero, R. Jiménez-Aparicio, J.L. Priego, E.C. Royer, M.R. Torres, F.A. Urbanos, Polyhedron 23 (2004) 2637.
[25] W.J. Geary, Coord. Chem. Rev. 7 (1971) 81.
[26] J.G. Norman, G.E. Renzoni, D.A. Case, J. Am. Chem. Soc. 101 (1979) 5256.
[27] G. Estiú, F.D. Cukiernik, P. Maldivi, O. Poizat, Inorg. Chem. 38 (1999) 3030.
[28] M.C. Barral, R. Jiménez-Aparicio, C. Rial, E. Royer, M.J. Saucedo, F.A. Urbanos, Polyhedron 9 (1990) 1723.
[29] (a) V.M. Miskowski, M.D. Hopkins, J.R. Winkler, H.B. Gray, in: E.I. Solomon, A.B.P. Lever (Eds.), Inorganic Electronic Structure and Spectroscopy, Volume II: Applications and Case Studies, Wiley, New York, 1999, pp. 343–402;
(b) V.M. Miskowski, T.M. Loehr, H.B. Gray, Inorg. Chem. 26 (1987) 1098.
[30] (a) M.C. Barral, S. Herrero, R. Jiménez-Aparicio, M.R. Torres, F.A. Urbanos, Angew. Chem., Int. Ed. 44 (2005) 305;
(b) M.C. Barral, S. Herrero, R. Jiménez-Aparicio, M.R. Torres, F.A. Urbanos, unpublished results.
[31] R.W. Mitchell, A. Spencer, G.J. Wilkinson, J. Chem. Soc., Dalton Trans. (1973) 846.
[32] F.A. Urbanos, M.C. Barral, R. Jiménez-Aparicio, Polyhedron 7 (1988) 2597.
[33] N.S. Gill, F.B. Taylor, Inorg. Synth. 9 (1967) 136.
[34] F.A. Urbanos, Program MASAS V 3.1, 2002.
[35] G.M. Sheldricck, SHELXS-97. Program for the Solution of Crystal Structures, University of Göttingen, Germany, 1997.
[36] G.M. Sheldricck, SHELXL-97. Program for Refinement of Crystal Structures, University of Göttingen, Germany, 1997.
[37] E. Brivio, A. Ceriotti, R.D. Pergola, L. Garlaschelli, M. Manassero, M. Sansoni, J. Cluster Sci. 6 (1995) 271.

Available online at www.sciencedirect.com
SCIENCE DIRECT®
Polyhedron 24 (2005) 249–256
POLYHEDRON
www.elsevier.com/locate/poly

Azido-bridged Cu(II) compounds with asymmetric end-to-end and end-on binding modes: magnetic assignments using a spin dimer model

Young Sin You [a], Chang Seop Hong [a,*], Kwan Mook Kim [b]

[a] Department of Chemistry and Center for Electro-and Photo-Responsive Molecules, Korea University, Seoul 136-701, Korea
[b] Department of Chemistry and Nanoscience Division, Ewha Womans University, Seoul 120-750, Korea

Received 10 September 2004; accepted 8 November 2004

Abstract

Dinuclear $[Cu(aepi)(N_3)_2]_2$ (**1**) [aepi = 1-(2-aminoethyl)piperidine] and 1D chain $[Cu(aepy)(N_3)_2]_n$ (**2**) [aepy = 1-(2-aminoethyl)pyrrolidine] have been prepared and characterized by means of X-ray analysis and magnetic measurements. For **1**, the Cu(II) centers are doubly bridged by end-on (EO) azido units in a basal–apical fashion. The molecular structure of **2** features magnetic centers that are linked by μ-1,1,3 azido groups, forming a 1D chain with alternating EO and end-to-end (EE) azido bridging patterns. The magnetic data for the dinuclear complex **1** were fitted with the Bleaney–Bowers equation derived from the Hamiltonian $\boldsymbol{H} = -JS_1 \cdot S_2$, affording parameters of $g = 2.093(1)$, $J = -3.06(1)$ cm^{-1} and $zJ' = -1.32(3)$ cm^{-1}. This indicates that the EO azido group mediates an antiferromagnetic interaction. Complex **2** has two possible magnetic pathways: one is through the EO azido bridge (J_{eo}) and the other via the EE bridge (J_{ee}). The alternating chain model with ferromagnetic and antiferromagnetic interactions based on the exchange Hamiltonian $\boldsymbol{H} = -\sum_i [J_1 S_{2i} \cdot S_{2i+1} + J_2 S_{2i} \cdot S_{2i-1}]$ was employed, leading to $g = 2.076(2)$, $J_1 = -3.22(5)$ cm^{-1}, $J_2 = 17.0(5)$ cm^{-1} and $zJ' = -1.34(6)$ cm^{-1}. By taking into account structural parameters of **1** and **2**, it is rationally suggested that J_1 and J_2 are ascribed to J_{eo} and J_{ee}, respectively. These assignments are also ascertained by MO calculations using a spin dimer model.
© 2004 Elsevier Ltd. All rights reserved.

Keywords: Copper(II) compounds; Crystal structures; Azide ligand; Magnetic properties

1. Introduction

Coordination materials have received much attention because they have intimate relevance to supramolecular chemistry and molecular magnets [1]. Magnetic coordination materials are devised employing bridging ligands, linking at least two metal ions concurrently, through which spins on paramagnetic centers are coupled to each other. Their magnetic natures are definitely governed by the features of bridging ligands. In this vein, it is essential to choose appropriate bridges to rationally design magnetic systems with desirable properties. Among them, azide is one of the good candidates to construct tailor-made magnetic materials in that the magnetic characters of the complexes bridged by azide are readily predicted in view of its binding pattern. The two main coordination modes for the azido ligand are EE and EO. Generally, the EE mode communicates antiferromagnetic couplings and the EO mode transmits ferromagnetic interactions [2]. In recent years, some exceptional compounds were reported such that even the EE mode enables the mediation of ferromagnetic interactions given large M–N_3–M torsion angles that cause accidental orthogonality between magnetic centers [3–5].

DFT calculations on EO azido-bridged Cu(II) systems revealed that critical regions where the magnetic

* Corresponding author. Tel.: +82232903138; fax: +82232903121.
E-mail address: cshong@korea.ac.kr (C.S. Hong).

0277-5387/$ - see front matter © 2004 Elsevier Ltd. All rights reserved.
doi:10.1016/j.poly.2004.11.022

nature is subject to change are at around 104° for Cu–N(azido)–Cu and about 2.05 Å for Cu–N(azido) [6]. However, the magnetic character for the EO azido bridge can be predestined only in the basal–basal bridging mode. When azido groups bridge Cu(II) centers in a basal–apical fashion, the structural parameters described above did not explain the observed magnetic phenomena. For example, dinuclear EO azido-bridged Cu(II) complexes in basal–apical coordination accompanied magnetic properties ranging from ferromagnetic to antiferromagnetic, regardless of the Cu–N(azido)–Cu angle [7–10]. Likewise, in the basal–apical mode, EE azido bridges in the Cu(II) systems propagate magnetic characters spanning from ferromagnetic to antiferromagnetic interactions [11–14]. Therefore, one should be cautious when attempting to understand magnetic behaviors based on the angles especially in the basal–apical systems.

Several coordination polymers having alternating EO and EE azido bridges were characterized structurally and magnetically, showing that the EO and EE bridges are responsible for ferro- and antiferromagnetic interactions, respectively [15–18]. For Cu(II) systems linked by EO and EE azido groups simultaneously, due to the Jahn–Teller effect of the Cu(II) ion giving rise to a tetragonal elongation, they tend to be coordinated to the metal centers in a basal–apical manner [19]. In this case, it would be a challenge to properly assign the magnetic properties to individual EO and EE pathways owing to the aforementioned reasons.

Herein we report the synthesis, crystal structures and magnetic properties of dinuclear $[Cu(aepi)(N_3)_2]_2$ (**1**) [aepi = 1-(2-aminoethyl)piperidine] and the 1D chain $[Cu(aepy)(N_3)_2]_n$ (**2**) [aepy = 1-(2-aminoethyl)pyrrolidine]. During the course of our studies, compound **2** was reported by others, but their magnetic consequences are different from what we observed in the present work [20]. The magnetic behavior for **1**, with doubly bridged by EO azido ligands in the basal–apical mode, exhibits antiferromagnetic couplings. On the other hand complex **2**, with EO and EE azido bridges in the basal–apical mode, shows dominant ferromagnetic interactions in the high temperature region. Based on structural considerations, the EO azido bridge is responsible for an antiferromagnetic route, while the EE azido bridge provides a ferromagnetic pathway. These assignments are confirmed by MO calculations on spin dimers using the extended Hückel tight binding (EHTB) method.

2. Experimental

2.1. Preparation of $[Cu(aepi)(N_3)_2]_2$ (*1*)

To a methanolic solution (10 ml) of copper(II) perchlorate hexahydrate (0.5 mmol) was slowly added aepi (0.5 mmol) by syringe with stirring. The resulting solution was treated with an aqueous solution (10 ml) of sodium azide (1.0 mmol). After filtration of the solution the filtrate was left undisturbed, giving deep green crystals of **1** suitable for X-ray diffraction. The total yield corresponds to 24% based on Cu. *Anal*. Calc. for $C_7H_{16}CuN_8$ (**1**): C, 30.5; H, 5.85; N, 40.6. Found: C, 30.6; H, 6.15; N, 40.5% Selected IR data (cm^{-1}, KBr pellet): 2051, 2041, 2031 [vs, $\nu_a(N_3^-)$].

2.2. Preparation of $[Cu(aepy)(N_3)_2]_n$ (*2*)

To a methanolic solution (10 ml) of copper(II) perchlorate hexahydrate (0.5 mmol) was slowly added aepy (0.5 mmol) by syringe with stirring. A 10 ml aqueous solution of sodium azide (1.0 mmol) was mixed with the resulting solution. The filtrate of the solution was left to stand for several days, providing deep green crystals of **2**. The product was recrystallized from DMF–ether solvent. The total yield amounts to 25% based on Cu. *Anal*. Calc. for $C_6H_{14}CuN_8$: C, 27.5; H, 5.39; N, 42.8. Found: C, 27.9; H, 5.00; N, 42.3%. Selected IR data (cm^{-1}, KBr pellet): 2057, 2035sh, 2028 [vs, $\nu_a(N_3^-)$].

2.3. Physical measurements

Elemental analyses for C, H and N were performed at the Elemental Analysis Service Center of Sogang University. Infrared spectra were obtained from KBr pellets with a Bomen MB-104 spectrometer. Magnetic susceptibilities for **1** and **2** were carried out using a Quantum Design MPMS-7 SQUID susceptometer. Diamagnetic corrections of **1** and **2** were estimated from Pascal's tables.

2.4. X-ray structural analyses

Data were collected at 293 K using an Enraf-Nonius CAD4TSB diffractometer with graphite monochromated Mo Kα radiation ($\lambda = 0.71073$ Å). The unit cell parameters were calculated by least-squares refinement of 25 well-centered reflections. All data were corrected for Lorentz polarization effects. A total of 2172 (**1**) and 2952 (**2**) reflections with a maximum 2θ of 50.30° (**1**) and 50.40° (**2**) were measured and 1660 (**1**) and 2754 (**2**) reflections were assumed to be observed applying the condition $F_o > 4\sigma(F_o)$. Crystallographic data and details of data collection are listed in Table 1.

The structures were solved and refined by least-squares analysis using anisotropic thermal parameters for non-hydrogen atoms with the WINGX program for **1** and **2** [21]. H atoms were calculated at idealized positions ($d_{CH} = 0.970$ for methylene) and refined riding on the corresponding carbon atoms with isotropic thermal parameters [$U = 1.2U(C_{methylene})$].

Table 1
Crystallographic data for **1** and **2**

	1	2
Chemical formula	$C_7H_{16}N_8Cu$	$C_{12}H_{28}N_{16}Cu_2$
Formular weight	275.82	523.58
Crystal system	monoclinic	monoclinic
Space group	P_1/c	P_1/n
a (Å)	9.206(3)	13.570(3)
b (Å)	10.760(2)	10.957(3)
c (Å)	11.5875(19)	14.823(3)
β (°)	90.27(2)	102.431(17)
V (Å^3)	1147.8(5)	2152.3(8)
Z	4	4
$F(000)$	572	1080
D_{calc} (g cm^{-3})	1.596	1.616
μ (mm^{-1})	1.891	2.013
Radiation, λ (Å)	Mo Kα, 0.71073	Mo Kα, 0.71073
R_1[a]	0.0454	0.0526
wR_2[b]	0.1251	0.1545

[a] $F_o > 4\sigma(F_o)$, $R_1 = \sum||F_o| - |F_c||/\sum|F_o|$.
[b] $wR_2 = [\sum w(F_o^2 - F_c^2)^2/\sum w(F_o^2)^2]^{1/2}$.

3. Results and discussion

3.1. Syntheses and characterization

Compound **1** was prepared by the stoichiometric reaction of Cu(II) ion as a magnetic center, aepi as a capping ligand and azide as a bridge in a methanol–water mixed solution. Three strong $\nu_a(N_3^-)$ peaks were observed in the IR spectrum of **1**, suggesting that there exist different types of azide ligands. The X-ray structure of **1** reveals the presence of terminal and EO azido bridges in a dinuclear Cu(II) compound (see below). To probe the structural variation by altering the capping ligand, we selected aepy with a five-membered ring, instead of aepi with a six-membered ring, using the same reaction conditions. As expected, the less bulky aepy ligand forms 1D chain (**2**) and the copper center is surrounded by six atoms, which is compared with **1** that has a coordination number of five around the central copper ion.

3.2. Description of the structures

The structure of **1**, with the asymmetric unit and symmetry related fragments, is shown in Fig. 1. Selected bond distances and angles are tabulated in Table 2. The Cu1 atom possesses a distorted square pyramidal geometry, based on a geometric parameter τ of 0.15 [22], consisting of two nitrogen atoms from aepi [Cu1–N7 = 2.007(4), Cu1–N8 = 2.090(3) Å], one nitrogen atom from terminal azide [Cu1–N1 = 1.971(4) Å], one nitrogen atom from one azido bridge [Cu1–N4 = 1.971(4) Å], which constitute the basal plane [mean Cu—N distance = 2.02(4) Å], and one apical nitrogen atom [Cu1–N4i = 2.381(4) Å; i = 2 − x, −y, 1 − z]. The longer Cu–N bond length is clearly associated with the Jahn–Teller effect on the Cu(II) ion [23]. The Cu1–N4–Cu1i angle is 98.84(15)° and an inversion center is placed midway between Cu1 and Cu1i. The largest deviation from the basal least-squares plane including N1–N4–N7–N8 atoms is 0.110(2) Å at N7 and the Cu1 atom lies −0.155(2) Å out of the plane toward the apical position (N4i). The six-membered ring of the aepi ligand sits in a chair form, exhibiting that the largest deviation from the C3–C4–C6–C7 least-squares plane is present at C7 with 0.003(4) Å and the C5 and N8 atoms are displaced −0.612(9) and 0.657(8) Å from the plane, respectively. The intradimeric Cu1–Cu1i distance separated by double EO azido bridges in the basal–apical mode is 3.348(1) Å.

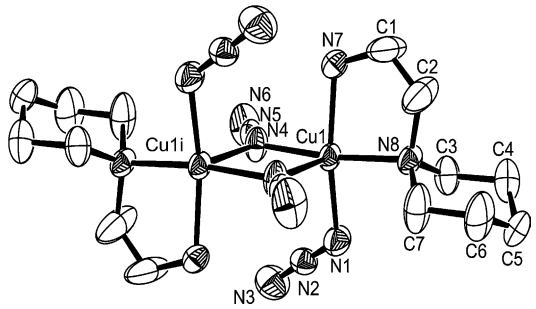


Fig. 1. Molecular structure of **1** showing the asymmetric unit and symmetry-related atoms along with the atom labelling scheme. Symmetry code used to generate equivalent atoms: i = 2 − x, −y, 1 − z.

Table 2
Selected bond distances (Å) and angles (°) for **1**[a]

Bond distances			
Cu1–N1	1.971(4)	Cu1–N7	2.007(4)
Cu1–N4	2.016(4)	Cu1–N8	2.090(3)
Bond angles			
N1–Cu1–N7	164.56(18)	N1–Cu1–N4	94.17(17)
N7–Cu1–N4	88.94(16)	N1–Cu1–N8	91.19(16)
N7–Cu1–N8	84.97(15)	N4–Cu1–N8	173.59(15)
N1–Cu1–N4i	100.20(17)	N7–Cu1–N4i	95.22(16)
N4–Cu1–N4i	81.15(15)	N8–Cu1–N4i	101.36(14)
N2–N1–Cu1	121.3(3)	N3–N2–N1	178.1(5)
N5–N4–Cu1	122.3(3)	N5–N4–Cu1i	138.7(3)
Cu1–N4–Cu1i	98.85(15)	C1–N7–Cu1	108.7(3)
C2–N8–Cu1	104.4(3)	C7–N8–Cu1	111.2(3)
C3–N8–Cu1	109.9(3)		

[a] Symmetry code: i = 2 − x, −y, 1 − z.

The structure of **2** was reported in the literature [20], so we just delineate some structural characteristics related to magnetic behaviors. Fig. 2(a) illustrates an ORTEP diagram showing the asymmetric unit and atom numbering scheme. The Cu atoms (Cu1 and Cu2) adopt distorted octahedral geometries with axial elongations arising from the Jahn–Teller distortion. The torsion angles for Cu1–N11···N9–Cu2 and Cu1–N1···N3–Cu2 are different, 60.1(5)° and 6.2(7)°, respectively. The Cu—N–N angles concerning the EE azido bridges correspond to 123.0(4)° for Cu1–N1–N2, 134.3(4)° for

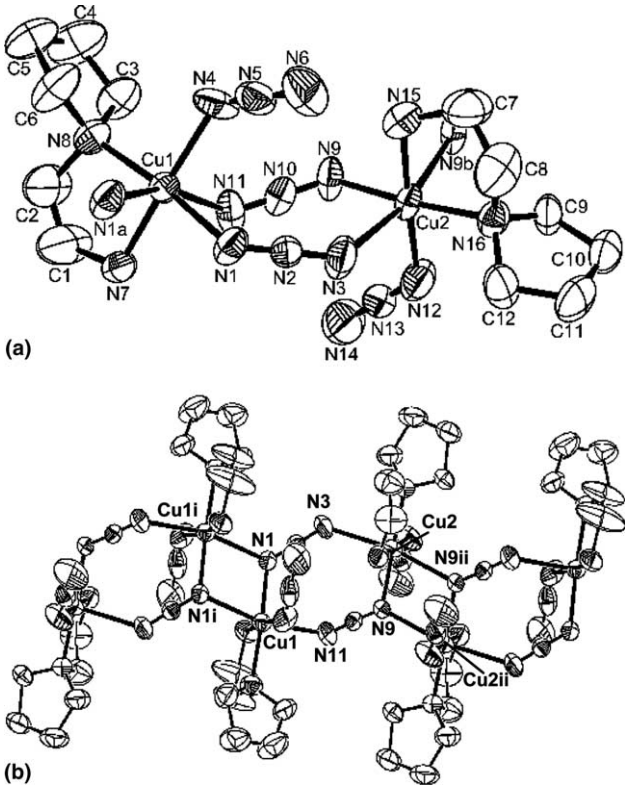


Fig. 2. Perspective molecular representation of **2** showing (a) the asymmetric unit and (b) extended 1D structure. Symmetry code used to generate equivalent atoms: i = 1−*x*, 1−*y*, −*z*; ii = 2−*x*, 1−*y*, −*z*.

Cu2–N3–N2, 122.1(5)° for Cu1–N11–N10 and 123.9(5)° for Cu2–N9–N10. The 1D extended structure is depicted in Fig. 2(b), featuring an alternating EO and EE azido-bridged chain in a basal–apical bridging fashion. The magnetically important Cu–N(azido)–Cu angles with respect to the EO azido bridges are 102.5(2)° for Cu1–N1–Cu1i and 100.0(2)° for Cu2–N9–Cu2ii (i = 1 − *x*, 1 − *y*, −*z* and ii = 2 − *x*, 1 − *y*, −*z*). The intrachain Cu–Cu separations are 3.547(1) Å for Cu1–Cu1i via the EO bridge, 5.342(2) Å for Cu1–Cu2 through the EE bridge and 3.588(1) Å for Cu2–Cu2ii bridged by the EO azide.

3.3. Magnetic results

The magnetic susceptibility data measured in the temperature range 1.8–300 K are shown in Fig. 3. At 300 K, the $\chi_m T$ value is 0.82 cm^3 K mol^{-1}, which falls into the range of two isolated Cu(II) ions ($S = 1/2$). As the temperature is lowered, $\chi_m T$ decreases very slowly and then abruptly at low temperatures, reaching a value of 0.20 cm^3 K mol^{-1} at 1.8 K. This behavior is typical of the existence of antiferromagnetic interactions between Cu(II) centers. The magnetic data for the dinuclear complex **1** were fitted with the Bleaney–Bowers equation derived from the Hamiltonian $\boldsymbol{H} = -JS_1 \cdot S_2$ [24], which is given by

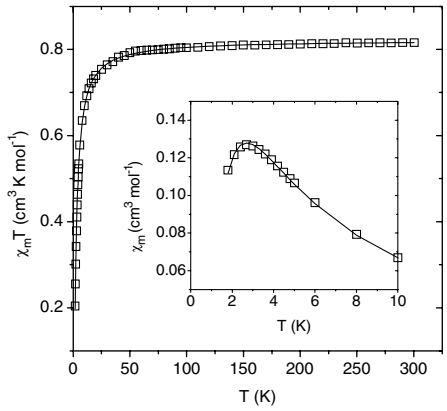


Fig. 3. Plot of $\chi_m T$ vs. T for **1**. The inset shows the temperature dependence of χ_m at low temperatures. The solid lines denote the best theoretical fits.

$$\chi = (2Ng^2\beta^2/kT)/[3 + \exp(-J/kT)]. \quad (1)$$

To take into account interdimer interactions we combined the molecular field correction with Eq. (1). Accordingly, the modified magnetic susceptibility formula can be expressed as [25]

$$\chi_m = \chi/[1 - zJ'\chi/Ng^2\beta^2]. \quad (2)$$

A best fit with this corrected equation provides parameters of $g = 2.093(1)$, $J = -3.06(1)$ cm^{-1} and $zJ' = -1.32(3)$ cm^{-1}. The measure of the goodness of fit R, defined as $R = \Phi/(n-k)$ where n is the number of data points and k the number of parameters, and $\Phi = \sum_i[(\chi_m T)_i^{obs} - (\chi_m T)_i^{calc}]^2$, is equal to 4.0×10^{-6}. The curve calculated with these parameters affords a satisfactory agreement with the experimental points as illustrated in Fig. 3. The inset of Fig. 3 displays the occurrence of a maximum at 2.7 K in χ_m, which is a conspicuous signature of antiferromagnetic coupling. The temperature (T_{max}) of χ_{max} is relevant to the exchange coupling constant (J), i.e., $|J|/kT_{max} = 1.599$ [26]. Using this relation for **1**, J is calculated to be -3.0 cm^{-1}, in good agreement with the above fitting result.

Magnetic properties for complexes with basal–basal EO azido bridges can be predicted depending on the Cu–N(azido)–Cu angle (α) and DFT studies demonstrated that a critical α value for them resides at 104° [6]. From this criterion, **1** should be ferromagnetic because of $\alpha = 98.8°$. However, a number of EO azido-bridged complexes exhibiting antiferromagnetic interactions even at α less than 104° were reported, as given in Table 3. It deserves to be noted that the listed Cu(II) compounds have azide ligands positioned in the basal–apical mode. This suggests that in the case of basal–apical bridging fashion, α is not the determining factor of magnetic nature [7]. It is found that the obtained J value in **1** is consistent with those of Cu(II) compounds in Table 3. On the other hand, the negative zJ' value implies that antiferromagnetic interactions between dimers are

Table 3
Selected magnetostructural parameters for asymmetric double EO bridges

Complex[a]	d_b[b] (Å)	d_a[c] (Å)	α[d] (°)	d[e] (Å)	τ[f]	J (cm^{-1})	Reference
$[Cu(L_1)(N_3)_2]_2$	2.060	2.475	93.6	3.32	0.26	+2.9	[7]
$[Cu(L_2)(N_3)_2]_2$	2.039	2.440	90.5	3.19	0.02	−1.8	[7]
$[Cu(L_3)(N_3)_2]_2$	2.020	2.546	86.8	3.16	0.17	−3.1	[7]
$[Cu(bipy)(N_3)_2]_n$	1.961	2.684	96.8	3.51	0.06	−2.7	[8]
$[Cu(terpy)(N_3)(H_2O)]_2(PF_6)_2$	1.927	2.851	95.7	3.60	0.06	−2.9	[9]
$[Cu_3(dien)_2(N_3)_6]$	1.971	2.490	96.9	3.35		−2.09	[10]
1	2.016	2.381	98.8	3.35	0.15	−3.06	this work
2	2.009	2.583	101.3	3.57		−3.2	this work

[a] L_1 = 8-amino-4-methyl-5-azaoct-3-en-2-one; L_2 = N-(3-aminopropyl)salicylaldimine; L_3 = 7-amino-4-methyl-5-azahept-3-en-2-one; bipy = 2,2′-bipyridine; terpy = 2,2′:6′2″-terpyridine; dien = diethylenetriamine.
[b] The basal Cu–N(azido) bond length.
[c] The apical Cu–N(azido) bond length.
[d] The angle at Cu–N(azido)–Cu.
[e] The Cu–Cu distance through the EO bridge.
[f] The Addison parameter [22].

operating. The field dependence of magnetization at 1.9 K is displayed in Fig. 4 in the field range 0–7 T, showing a dominant antiferromagnetic interaction, compared with the calculated value from the Brillouin function for two independent Cu(II) ions.

For **2**, we repeated magnetic measurements to ensure the observed magnetic data and obtained the same results. The collected magnetic susceptibility data are plotted in Fig. 5, which is quite different from the reported magnetic data [20]. The $\chi_m T$ value of 0.41 cm^3 K mol^{-1} (1.81 BM) at 300 K is slightly larger than the spin-only value (0.38 cm^3 K mol^{-1}; 1.73 BM) derived from an isolated Cu(II) ion. This observed value is more reasonable compared to the reported one (1.98 BM) that is abnormally high, even higher than their fitting result (when $g = 2.15$, $\mu_{eff} = 1.86$ BM), for the overall antiferromagnetic system [20]. On cooling, $\chi_m T$ increases gradually and then reaches a maximum of 0.44 cm^3 K mol^{-1} at 20 K, indicative of a typical dominant ferromagnetic behavior. A sharp drop is encountered on further cooling, which originates from intra- and interchain antiferromagnetic interactions.

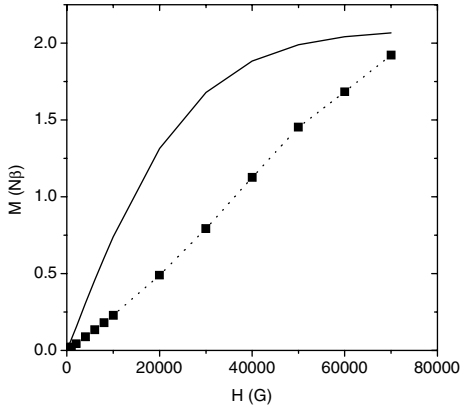


Fig. 4. Field dependence of the magnetization of **1**. The solid line stands for the Brillouin curve for two isolated Cu(II) ions.

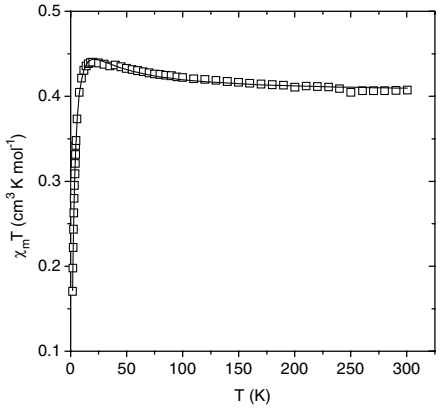


Fig. 5. Plot of $\chi_m T$ vs. T for **2**. The solid line shows the best theoretical fit.

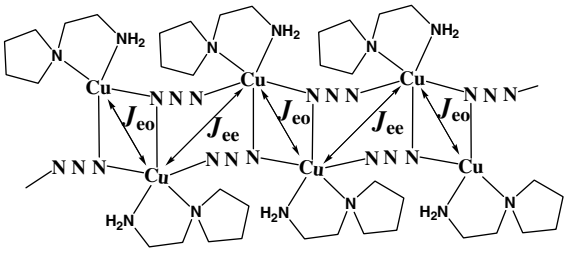


Fig. 6. Schematic view of possible magnetic coupling pathways of **2**.

There are two possible magnetic pathways: one is through the EO azido bridge and the other via the EE bridge. The exchange coupling constants are assigned to J_{eo} for the former route and J_{ee} for the latter, as schematized in Fig. 6. Assuming that one of the couplings is negligible, a best fit with the dimer model using Eqs. (1) and (2) results in $g = 2.07(1)$, $J = 21(2)$ cm^{-1}, $zJ' = -1.57(3)$ cm^{-1} with $R = 2.5 \times 10^{-4}$. If two J are activated in the fitting process, the alternating chain

model with ferromagnetic and antiferromagnetic interactions is applicable on the basis of the exchange Hamiltonian $\boldsymbol{H} = -\sum_i [J_1 S_{2i} \cdot S_{2i+1} + J_2 S_{2i} \cdot S_{2i-1}]$ [27]. The molar magnetic susceptibility is defined as $\chi_m = \chi_r(Ng^2\beta^2/4)/|J_1|$ where χ_r is expressed as Eq. (3).

$$\chi_r = \left[AT_r^3 + BT_r^2 + CT_r + D\right] / \left[T_r^4 + ET_r^3 + FT_r^2 + GT_r + H\right], \quad (3)$$

$$T_r = kT/|J_1|.$$

The parameters A–H are polynominal expressions: $X_i = x_0 + x_1\gamma + x_2\gamma^2 + x_3\gamma^3$ where $\gamma = J_2/|J_1|$. The magnetic data were fitted employing the modified molar magnetic susceptibility formula formed by Eq. (3) incorporated into Eq. (2) to account for interchain interactions. The obtained magnetic parameters are $g = 2.076(2)$, $J_1 = -3.22(5)$ cm^{-1}, $J_2 = 17.0(5)$ cm^{-1} and $zJ' = -1.34(6)$ cm^{-1}, with a significantly improved reliability factor R of 4.9×10^{-6}.

Based on the structural analogy of **2** in the EO mode to **1** and other complexes with asymmetric double EO bridges, as seen in Table 3, it is rationally suggested that J_1 is ascribed to J_{eo}. As exemplified in Table 4, ferromagnetic interactions may take place through EE azido bridges at high torsion angles. In **2**, two EE azido bridges have different values of δ, 6.2° and 60.1°. The larger δ appears to play a role in a ferromagnetic coupling through the EE bridges in **2** [14,28]. The extracted exchange coupling of J_2 is thus assigned to J_{ee}, whose magnitude agrees well with that of a double EE azido-bridged Cu(II) complex [14]. The interchain antiferromagnetic behavior is explained by the negative zJ' in the fitting output. Fig. 7 shows the field dependence of magnetization at 1.9 K and magnetic fields up to 7 T. As seen in the $\chi_m T$ plot of Fig. 5, the global antiferromagnetic coupling occurs at 1.9 K, which is reflected by the $M(H)$ data lower than the Brillouin result for an isolated Cu(II) ion. The magnetization reaches a saturation value at 7 T.

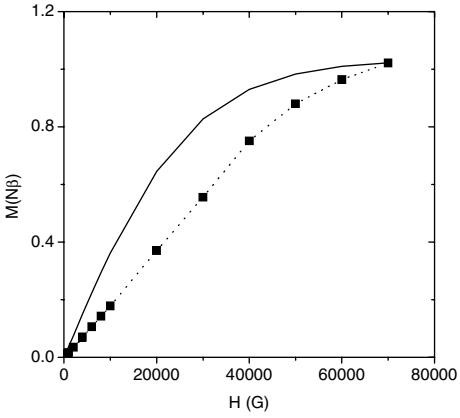


Fig. 7. Field dependence of the magnetization of **2**. The solid line displays the curve calculated from the Brillouin function for an isolated Cu(II) ion.

3.4. MO calculations

To clarify the magnetic nature observed in the alternating ferro- and antiferromagnetic chain system (**2**) we performed MO calculations using the CAESAR program package in which the extended Hückel tight binding (EHTB) method is employed [29–31]. The exchange coupling constant J, contributed from ferromagnetic (J_F) and antiferromagnetic (J_{AF}) components, is mainly dominated by J_{AF}, which is equal to $-(\Delta E)^2/U$. Here $\Delta E = E_2 - E_1$, E_1 and E_2 being the energies of the two singly occupied molecular orbitals (SOMOs) in the triplet state and U the effective on-site repulsion. To assess what magnetic character EE and EO azido bridges belong to, it

Table 4
Selected magnetostructural parameters for asymmetric EE bridges

Complex[a]	d_b[b] (Å)	d_a[c] (Å)	β[d] (°)	δ[e] (°)	d[f] (Å)	J (cm^{-1})	Reference
$[Cu(Me_5dien)(N_3)]_2(ClO_4)_2$	1.996	2.327	122.7, 138.4	15.7	5.29	−7.5	[11][g]
$[Cu(EtMe_4dien)(N_3)]_2(ClO_4)_2$	1.996	2.276	123.3, 137.9	30.4	5.29	−3.6	[11][g]
$[Cu_3(atrz)_2(N_3)_6]$	1.952	2.53	113.1, 120.4	32.3	5.48	+0.86	[12][h]
$[Cu(L_1)(N_3)]_n(ClO_4)_n$	1.991	2.266	134.4, 136.7	31.3	n.a.	+2.69	[13][h]
$[Cu(L_2)(N_3)]_n(ClO_4)_n$	1.946	2.398	122.5, 135.1	102.7	n.a.	+2.02	[13][h]
$[Cu_2(bben)_2(N_3)_4]_n$	2.044	2.373	113.5, 142.6	47.5	5.28	+16.8	[14][g]
2	2.009	2.583	123.0, 134.3	6.2	5.34	+17	this work[g]
			122.1, 123.9	60.1			

[a] Me_5dien = 1,1,4,7,7-pentamethyldiethylenetriamine; $EtMe_4dien$ = 4-ethyl-1,1,7,7-tetramethyldiethylenetriamine; atrz = 4-amino-1,2,4-triazole; bben = 1,2-bis(benzylamino)ethane.
[b] The basal Cu–N(azido) bond length.
[c] The apical Cu–N(azido) bond length.
[d] The angle at Cu–N(azido)–N(azido).
[e] The Cu–N_3–Cu torsion angle.
[f] The Cu–Cu distance through the EE bridge.
[g] Double EE bridge.
[h] Single EE bridge. n.a. = not available.

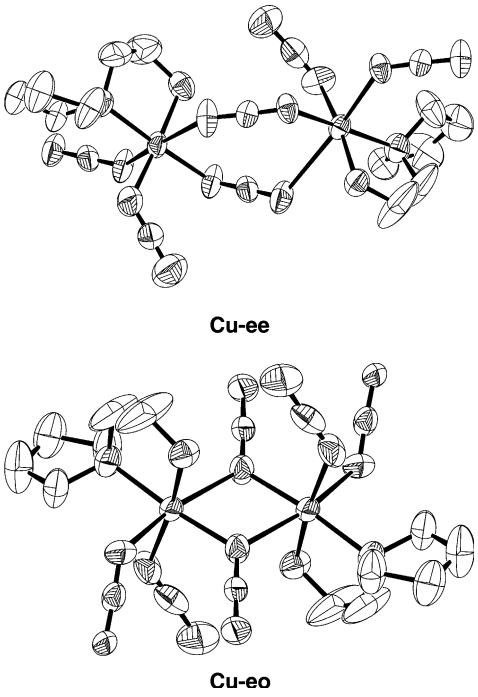


Fig. 8. Molecular representation of the two types of bridging modes between Cu(II) ions in **2**. Cu-ee is the spin dimer $[Cu_2(aepy)_2(N_3)_6]^{2-}$ bridged by double EE azido units and Cu-eo the spin dimer $[Cu_2(aepy)_2(N_3)_6]^{2-}$ linked by double EO azido groups.

is required to estimate the magnitude of ΔE for EE and EO azido bridged spin systems in **2**. To this end, EE azido-bridged Cu(II) dimer, $[Cu_2(aepy)_2(N_3)_6]^{2-}$ (Cu-ee), and EO azido-bridged Cu(II) dimer (Cu-eo) are taken as shown in Fig. 8 [31,32]. MO calculations for each spin dimer were conducted to generate SOMOs at $E_1 = -11.4941$ eV, $E_2 = -11.4863$ eV for Cu-ee, and $E_1 = -11.4938$ eV, $E_2 = -11.4819$ eV for Cu-eo. The ΔE of 0.0119 eV for Cu-eo is larger than that of 0.0078 eV for Cu-ee. Consequently, now that the sign of the J term is basically determined by the magnitude of the J_{AF} term proportional to $(\Delta E)^2$, Cu-eo would undergo an antiferromagnetic interaction when compared with Cu-ee. This result supports that the spins within the Cu-eo dimer are coupled antiferromagnetically in a more significant manner than those in Cu-ee that in contrast experience a ferromagnetic interaction as described above.

4. Conclusion

We have prepared two azido-bridged Cu(II) compounds showing dinuclear and 1D chain structures. The magnetic properties of **1** doubly bridged by the EO azido ligands in a basal–apical pattern demonstrate antiferromagnetic interaction with $J = -3.06$ despite a relatively small α value compared to the critical value of 104° below which ferromagnetic coupling is expected. This suggests that in the basal–apical bridging mode several structural parameters may be taken into consideration to understand the magnetic nature. For **2**, two magnetic pathways, i.e., through EO or EE azido bridges, are possible. To properly assign ferromagnetic/antiferromagnetic couplings to them we examined the structural parameters related to magnetic behavior. From the parameters it is reasonably concluded that magnetic interactions through the EO bridge (J_{eo}) and the EE linkage (J_{ee}) are antiferromagnetic and ferromagnetic, respectively. This result is supported by MO calculations where the ΔE value for the former is rather larger than that for the latter, implicating that J_{eo} should be negative.

5. Supplementary material

Crystallographic data for the structural analysis have been deposited with the Cambridge Crystallographic Data Center, CCDC No. 249816 for complex **1**. Copies of this information may be obtained free of charge from The Director, CCDC, 12 Union Road, Cambridge, CB2 1EZ, UK (fax: +44 1223 336 033; email: deposit@ccdc.cam.ac.uk orwww: http://www.ccdc.cam.ac.uk).

Acknowledgement

This work is financially supported by the CRM-KOSEF. C.S.H. would like to thank an Operation Program on Shared Research Equipment of KBSI and MOST.

References

[1] O. Kahn, Magnetism: A Supramolecular Function, Kluwer Academic Publishers, Dordrecht, The Netherlands, 1996.
[2] J. Ribas, A. Escuer, M. Monfort, R. Vicente, R. Cortes, L. Lezama, T. Rojo, Coord. Chem. Rev. 193–195 (1999) 1027.
[3] C.S. Hong, Y. Do, Angew. Chem. Int. Ed. 38 (1999) 193.
[4] C.S. Hong, J.-e. Koo, S.-K. Son, Y.S. Lee, Y.-S. Kim, Y. Do, Chem. Eur. J. 7 (2001) 4243.
[5] P.S. Mukherjee, S. Dalai, E. Zangrando, F. Lloret, N.R. Chaudhuri, Chem. Commun. (2001) 1444.
[6] E. Ruiz, J. Cano, S. Alvarez, P. Alemany, J. Am. Chem. Soc. 120 (1998) 11122.
[7] M.S. Ray, A. Ghosh, R. Bhattacharya, G. Mukhopadhyay, M.G.B. Drew, J. Ribas, J. Chem. Soc., Dalton Trans. (2004) 252.
[8] G. De Munno, M.G. Lombardi, M. Julve, F. Lloret, J. Faus, Inorg. Chim. Acta 282 (1998) 82.
[9] R. Cortes, M.K. Urtiaga, L. Lezama, J.I.R. Larramendi, M.I. Arriortua, T. Rojo, J. Chem. Soc., Dalton Trans. (1993) 3685.
[10] J. Luo, X.-G. Zhou, S. Gao, L.-H. Weng, Z.-H. Shao, C.-M. Zhang, Y.-R. Li, J. Zhang, R.-F. Cai, Polyhedron 23 (2004) 1243.
[11] A. Escuer, M. Font-Baedia, E. Penalba, X. Solans, R. Vicente, Inorg. Chim. Acta 298 (2000) 195.
[12] J.-C. Liu, D.-G. Fu, J.-Z. Zhuang, C.-Y. Duan, X.-Z. You, J. Chem. Soc., Dalton Trans. (1999) 2337.

[13] S. Dalai, P.S. Mukherjee, M.G.B. Drew, T.-H. Lu, N.R. Chaudhuri, Inorg. Chim. Acta 335 (2002) 85.
[14] Y. Xie, Q. Liu, H. Jiang, C. Du, X. Xu, M. Yu, Y. Zhu, New J. Chem. 26 (2002) 176.
[15] Z. Shen, J.-L. Zuo, S. Gao, Y. Song, C.-M. Che, H.-K. Fun, X.-Z. You, Angew. Chem. Int. Ed. 39 (2000) 3633.
[16] M. Monfort, I. Resino, J. Ribas, H. Stoeckli-Evans, Angew. Chem. Int. Ed. 39 (2000) 191.
[17] E.-Q. Gao, S.-Q. Bai, Y.-F. Yue, Z.-M. Wang, C.-H. Yan, Inorg. Chem. 42 (2003) 3642.
[18] E.-Q. Gao, Y.-F. Yue, S.-Q. Bai, Z. He, S.-W. Zhang, C.-H. Yan, Chem. Mater. 16 (2004) 1590.
[19] G. De Munno, M.G. Lombardi, M. Julve, F. Lloret, J. Faus, Inorg. Chim. Acta 282 (1998) 82.
[20] T.K. Maji, P.S. Mukherjee, S. Koner, G. Mostafa, J.-P. Tuchagues, N.R. Chaudhuri, Inorg. Chim. Acta 314 (2001) 111.
[21] L.J. Farrugia, J. Appl. Crystallogr. 32 (1999) 837.
[22] A.W. Addison, T.N. Rao, J. Reedijk, J. van Rijn, G.C. Verschoor, J. Chem. Soc., Dalton Trans. (1984) 1349.
[23] C.S. Hong, Y.S. You, Inorg. Chim. Acta 357 (2004) 3271.
[24] B. Bleaney, K.D. Bowers, Proc. R. Soc. (Lond.) Ser. A 214 (1952) 451.
[25] C.J. O'Connor, Prog. Inorg. Chem. 29 (1982) 203.
[26] O. Kahn, Molecular Magnetism, VCH, New York, 1993.
[27] J.J. Borras-Almenar, E. Coronado, J. Curley, R. Georges, J.C. Gianduzzo, Inorg. Chem. 33 (1994) 5171.
[28] A. Escuer, R. Vicente, X. Solans, M. Font-Bardia, Inorg. Chem. 33 (1994) 6007.
[29] R. Hoffmann, J. Chem. Phys. 39 (1963) 1397.
[30] R. Hoffmann, Acc. Chem. Res. 4 (1971) 1.
[31] J.L. Manson, J.A. Schlueter, H.-J. Koo, M.H. Whangbo, Inorg. Chem. 43 (2004) 4007.
[32] Y. Zhang, C.J. Warren, R.C. Haushalter, A. Clearfield, D.-K. Seo, M.-H. Whangbo, Chem. Mater. 10 (1998) 1059.

Available online at www.sciencedirect.com
SCIENCE DIRECT®
Polyhedron 24 (2005) 257–265
POLYHEDRON
www.elsevier.com/locate/poly

Dioxomolybdenum(VI) complexes with tri- and tetradentate aminobis(phenolate)s

Ari Lehtonen [a,*], Reijo Sillanpää [b]

[a] Department of Chemistry, University of Turku, FIN-20014, Turku, Finland
[b] Department of Chemistry, University of Jyväskylä, FIN-40351 Jyväskylä, Finland

Received 19 August 2004; accepted 9 November 2004
Available online 8 December 2004

Abstract

The reactions of tridentate ligands, bis(2-hydroxy-3,5-dimethylbenzyl)methylamine (H_2ONO^{Me}) and bis(2-hydroxy-3-*tert*-butyl-5-methylbenzyl)methylamine (H_2ONO^{tBu}) with $[MoO_2(acac)_2]$ (**1**) in methanol lead to the precipitation of monomeric dioxomolybdenum(VI) complexes $[MoO_2(ONO^{Me})(MeOH)] \cdot MeOH$ (**2a**) and $[MoO_2(ONO^{tBu})(MeOH)] \cdot MeOH$ (**2b**), respectively. Identical reactions in acetonitrile provide dimeric complexes $[Mo_2O_2(\mu\text{-}O)_2(ONO^{Me})_2]$ (**3a**) and $[Mo_2O_2(\mu\text{-}O)_2(ONO^{tBu})_2]$ (**3b**). The reactions of **1** with tetradentate ligands, *N*,*N*′-bis(2-hydroxy-3,5-dimethylbenzyl)-*N*,*N*′-dimethylethane-1,2-diamine (H_2ONNO^{Me}) and *N*,*N*′-bis(2-hydroxy-3,5-di-*tert*-butylbenzyl)-*N*,*N*′-dimethylethane-1,2-diamine (H_2ONNO^{tBu}) yield monomeric complexes $[MoO_2(ONNO^{Me})]$ (**4a**) and $[MoO_2(ONNO^{tBu})]$ (**4b**), respectively. All studied complexes catalyse oxotransfer reactions between DMSO and benzoin or triphenyl phosphine. Complexes can also be activated by Et_2AlCl to polymerise norbornene.
© 2004 Elsevier Ltd. All rights reserved.

Keywords: Alkoxide complexes; Phenolate ligands; Molybdenum; Crystal structure

1. Introduction

Coordination compounds of molybdenum can catalyse a variety of industrially important chemical reactions such as olefin epoxidation [1], isomerization of allyl alcohols [2] and olefin metathesis [3]. The useful role of molybdenum is not restricted to artificial catalysis alone, since it is an essential element in diverse biological systems, as nature has made use of molybdenum centre in various redox enzymes [4–6]. Oxidized forms of these molybdoenzymes, e.g., aldehyde and sulfite oxidases, are supposed to contain *cis*-MoX_2 units (X = O, S) coordinated to sulfur, nitrogen and oxygen donor atoms of the protein structure. A large number of dioxomolybdenum(VI) complexes are known, some of which have been investigated as molecular models for these molybdoenzymes. For example, Ghosh and co-workers [7] have demonstrated that certain MoO_2^{2+} complexes of diacidic tridentate Schiff base ligands can oxidise PPh_3, thus they mimic the active sites of oxotransfer enzymes. Barbaro et al. [8] have reported similar results about MoO_2^{2+} complexes with enantiomerically pure tridentate aminodiolato ligands.

Aminobis(phenol)s (potential O, N, O donors) and diaminobis(phenol)s (O, N, N, O donors) are versatile ligands, which have used to make complexes with various transition metal ions [9–13]. For instance, Spence and co-workers [12] and Ng and co-workers [13] have reported several six-coordinate dioxomolybdenum(VI) and -tungsten(VI) complexes of tetradentate N_2O_2 donor ligands with different coordination modes and studied their activity toward oxygen atom transfer reactions. However, to the best of our knowledge, there is no reports on dioxomolybdenum(VI) complexes with tridentate

* Corresponding author. Tel.: +358 2 333 6733; fax: +358 2 333 6700.
E-mail address: ari.lehtonen@utu.fi (A. Lehtonen).

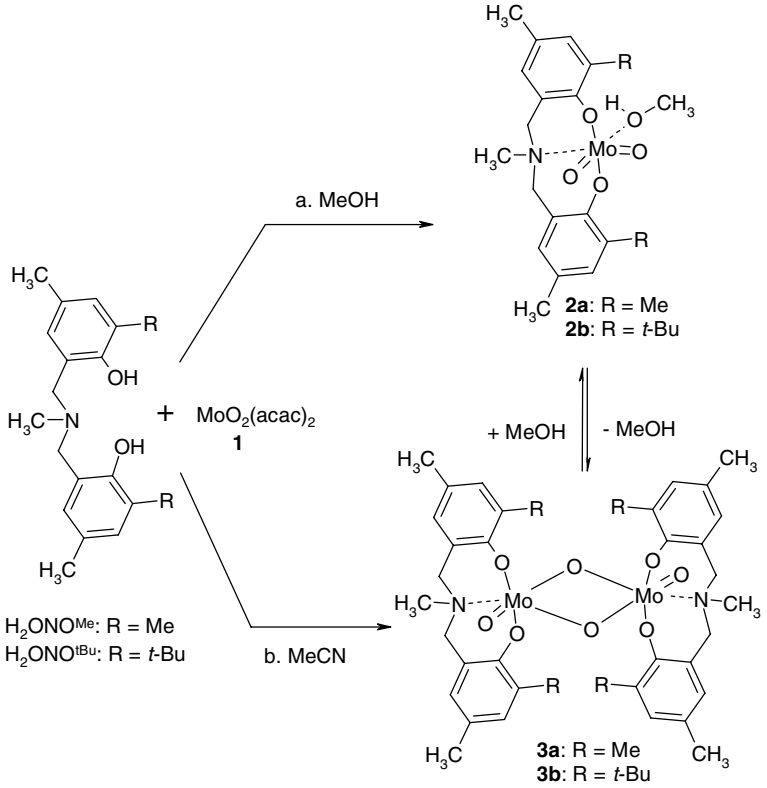
0277-5387/$ - see front matter © 2004 Elsevier Ltd. All rights reserved.
doi:10.1016/j.poly.2004.11.003

aminobis(phenol)s. In principle, tridentate ligands could form five-coordinate complexes when reacting with dioxomolybdenum(VI) moiety, but molybdenum ion usually completes its coordination sphere by abstracting a solvent molecule or though dimerization. As a part of our studies on W(VI) and Mo(VI) complexes with multidentate ligands [14–16], we discuss here the syntheses of new dioxomolybdenum(VI) complexes with linear tri- and tetradentate aminobisphenolate ligands.

2. Results and discussion

2.1. Monomeric $MoO_2(ONO^R)$ and dimeric $Mo_2O_2(\mu\text{-}O)_2(ONO^R)_2$ complexes

The products formed in reactions between $[MoO_2(acac)_2]$ (**1**) and ligand precursors H_2ONO^R were found to depend on the reaction medium (Scheme 1). When methanol solution of **1** was treated with one equivalent of a ligand precursor H_2ONO^{Me}, the reaction initiated and the reaction mixture subsequently turned yellow in colour (Scheme 1a). Solution was stirred overnight at room temperature and then kept at 277 K for 24 h to obtain yellow prismatic crystals, which were characterised as $[MoO_2(ONO^{Me})(MeOH)]\cdot MeOH$ (**2a**) (see below). Intense yellow crystals of analogous complex $[MoO_2(ONO^{tBu})(MeOH)]\cdot MeOH$ (**2b**) precipitated in an equal reaction during few hours at room temperature. When identical reactions between ligand precursors H_2ONO^R and **1** were carried out in acetonitrile solutions, the reaction mixtures turned orange-red and orange crystals started to precipitate (Scheme 1b). Further analyses (see below) verified, that crystals were formed of dimeric complexes $[Mo_2O_2(\mu\text{-}O)_2(ONO^{Me})_2]$ (**3a**) and $[Mo_2O_2(\mu\text{-}O)_2(ONO^R)_2]$ (**3b**), respectively. Air-sensitive crystals of **2a** and **2b** are soluble in DMSO, DMF and hot MeOH, but they decompose slowly in acetonitrile suspensions to form dimeric complexes of type **3** as red powders. Similar decomposition occurs also in open air and particularly in vacuum due to the loss of methanol. Air-stable crystals of **3** dissolve in DMSO to yield yellow solutions, but they are practically insoluble in other common solvents at room temperature. They dissolve also in methanol upon heating, although recrystallization from hot methanol produces complexes **2** in high yields instead of complexes **3**. In conclusion, it is demonstrated that formation of complexes **2** and **3** can be easily adjusted. Particularly, the monomeric complexes **2** are transformed to their dimeric counterparts **3** as a consequence of leaving of methanol in the solid state, whereas complexes **3** can be turned to complexes **2** by recrystallization from MeOH. This solvent-dependent reactivity of above-mentioned ligands resembles reactions of *N*-salicylidene-2-aminoethanol with **1** [17].



Scheme 1. Formation of monomeric and dimeric Mo(VI) complexes with tridentate aminobis(phenolate)s.

The IR spectra of compounds **2** presented two strong bands within 891–932 cm^{-1}, which are distinctive absorption maxims for MoO_2^{2+} moiety [7,15,16]. Broad bands at ~3340 cm^{-1} are due to the presence of coordinated or hydrogen bonded methanol molecules. Complexes **3** have generally similar IR spectra, although they present a strong IR absorption at around 820 cm^{-1}, which is absent in their monomeric counterparts. Furthermore, complexes **3** show only a single stretch at ca. 930 cm^{-1} instead of a characteristic doublet for *cis*-MoO_2 moieties in complexes **2**. ^1H NMR spectra of **2** in DMSO show typical resonances for C_s-symmetric aminobis(phenolate) complexes together with resonances for free methanol, which indicates that DMSO can replace MeOH molecules from the first coordination sphere around Mo(VI) ion. Compounds **3** give similar ^1H NMR resonances for aromatic ligand as their monomeric counterparts.

X-ray analysis of **2a** and **2b** revealed that both complexes are formed of similar mononuclear units, in which the aminobis(phenolate) is coordinated to the dioxomolybdenum(VI) ion as a tridentate ligand. A methanol molecule *trans* to the oxo group completes the distorted octahedral coordination sphere (see Figs. 1 and 2). Another methanol molecule is attached to the complex unit by hydrogen bonds. The O=Mo=O angles and the Mo=O bonds are typical for *cis*-dioxomolybdenum(VI) complexes [7,16–21]. Uncoordinated MeOH molecules

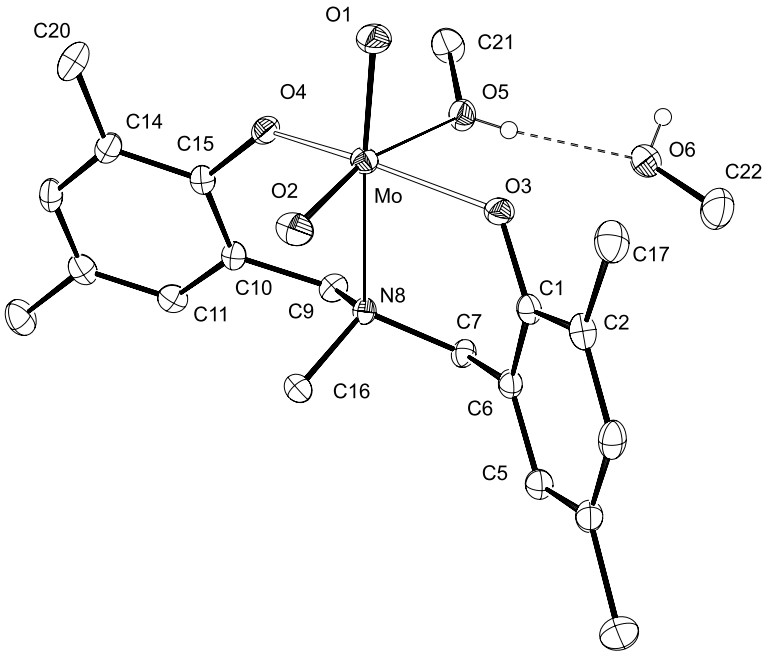


Fig. 1. Molecular structure of $[MoO_2(ONO^{Me})(MeOH)] \cdot MeOH$ (**2a**). Thermal ellipsoids have been drawn at 30% probability level. The CH hydrogen atoms are omitted for the clarity in all ORTEP figures.

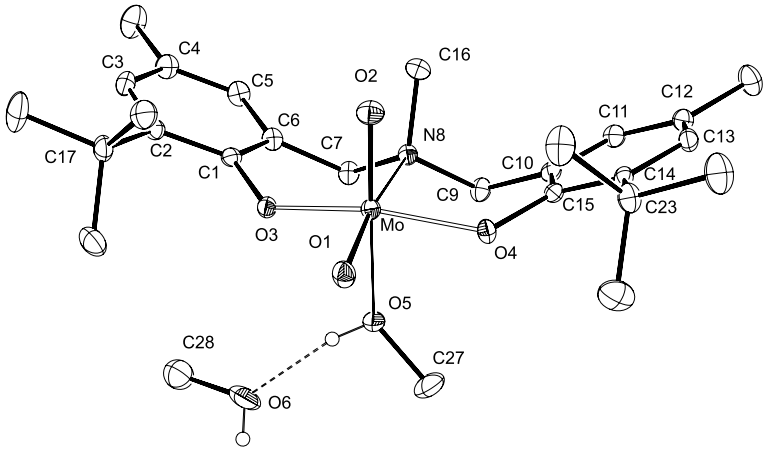


Fig. 2. Molecular structure of $[MoO_2(ONO^{tBu})(MeOH)] \cdot MeOH$ (**2b**). Thermal ellipsoids have been drawn at 30% probability level.

Table 1
Summary of crystallographic data for **2a**, **2b**, **3b**, **4a** and **4b** at 173(2) K.

	2a	**2b**	**3b**	**4a**	**4b**
Formula	$C_{21}H_{31}MoNO_6$	$C_{27}H_{43}MoNO_6$	$C_{50}H_{70}Mo_2N_2O_8$	$C_{22}H_{30}MoN_2O_4$	$C_{34}H_{54}MoN_2O_4$
M_r	489.41	573.56	1018.96	482.42	650.73
Crystal system	triclinic	monoclinic	triclinic	monoclinic	triclinic
Space group (no.)	$P\bar{1}$ (2)	$P2_1/c$ (14)	$P\bar{1}$ (2)	$P2_1/a$ (14)	$P\bar{1}$ (2)
a (Å)	7.1334(2)	12.5240(4)	9.5058(3)	16.1564(4)	14.5335(7)
b (Å)	11.3828(3)	14.7709(5)	10.1004(3)	7.1870(2)	14.7748(9)
c (Å)	14.6798(4)	15.7687(4)	13.7076(3)	18.4291(5)	17.2205(11)
α (°)	99.072(2)	90	73.194(2)	90	109.024(2)
β (°)	95.252(2)	100.992(2)	72.713(2)	97.692(2)	96.865(4)
δ (°)	104.747(2)	90	79.884(2)	90	95.351(4)
V (Å^3)	1127.41(5)	2863.55(15)	1197.17(6)	2120.66(10)	3436.1(3)
Z	2	4	1	4	4
D_c (g cm^{-1})	1.442	1.330	1.413	1.513	1.258
μ(Mo Kα) (cm^{-1})	6.17	4.96	5.78	6.49	4.18
Observed reflections	4943	7041	4188	3729	11 549
R_{int}	0.0561	0.0723	0.0414	0.0396	0.0672
Parameters	307	324	280	262	739
R_1	0.050 (0.036)[a]	0.084 (0.042)	0.032 (0.028)	0.039 (0.028)	0.079 (0.044)
wR_2	0.083 (0.079)	0.093 (0.081)	0.066 (0.064)	0.070 (0.066)	0.099 (0.088)
Peak, hole (e Å^{-3})	0.400, −0.428	0.466, −0.578	0.356, −0.553	1.04, −0.376	0.750, −0.565

[a] Values in parentheses for reflections with $I > 2.0\sigma(I)$: $R_1 = \sum ||F_o| - |F_c|| / \sum |F_o|$, $wR_2 = \{\sum[w(F_o^2 - F_c^2)^2] / \sum[w(F_o^2)^2]\}^{1/2}$ and $w = 1/[\sigma^2(F_o^2) + (aP)^2 + (bP)]$, where $P = (2F_c^2 + F_o^2)/3$.

form H-bonds with terminal oxygen atoms O1, therefore the Mo–O1 bonds are slightly longer than the Mo–O2 bonds. The Mo–$O_{aryloxide}$, Mo–N and Mo–O_{MeOH} distances are as well comparable with previous results [16,18,19]. On the whole these structures resembles to those of dioxomolybdenum(VI) complexes with tridentate Schiff base ligands [16,18]. The bonding parameters around Mo(VI) cations are nearly identical in these compounds (Table 2), though MeOH molecule seems to coordinate more tightly to the Mo(VI) ion in **2a** than in **2b**, as the Mo–O_{MeOH} distance is 2.289(2) Å in **2a** and 2.333(2) Å in **2b**. Furthermore, the alkyl substituents at the *ortho*-positions of the ligand phenyl rings appear to modify the ligand conformation around the metal centre in the solid state. For example, the dihedral angle between the planes C1, C2, ..., C6 and C10, C11, ..., C15 is 54.26(8)° in **2a** and 48.2(1)° in **2b**.

Table 2
Selected bond lengths (Å) and angles (°) for **2a**, **2b** and **3b**

	2a	**2b**	**3b**
Bond lengths			
Mo–O1	1.7161(19)	1.7174(18)	1.7519(16)
Mo–O2	1.6908(18)	1.6877(18)	1.6899(17)
Mo–O3	1.9446(17)	1.9380(18)	1.9203(16)
Mo–O4	1.9281(17)	1.9327(18)	1.9043(16)
Mo–O5	2.289(2)	2.333(2)	2.3901(16)[a]
Mo–N8	2.458(2)	2.436(2)	2.3514(19)
Bond angles			
O1–Mo–O2	104.78(10)	105.05(9)	107.15(8)
O3–Mo–O4	151.59(8)	153.30(8)	158.62(7)
O1–Mo–N8	169.48(8)	165.84(8)	153.16(7)
O2–Mo–O5	164.74(9)	167.25(8)	176.57(7)[b]
O5–Mo–N8	80.02(7)	78.35(7)	76.90(6)[c]
C1–O3–Mo	128.92(15)	134.94(16)	137.42(15)
C15–O4–Mo	136.93(16)	135.97(16)	142.50(15)
C21–O5–Mo	130.85(19)	127.1(2)	

[a] A parameter for a Mo–O1^i, where i = $-x$, $-y + 1$, $-z + 1$.
[b] O2–Mo–O1^i.
[c] O1^i–Mo–N8.

X-ray crystal structure analyses verified that **3b** consist of dinuclear, doubly bridged units of $Mo_2O_2(\mu\text{-}O)_2(ONO^R)_2$. As seen from Fig. 3, each molybdenum ion is bonded to three donor atoms of ONO^R ligand and two bridging and one terminal oxo ligands having a distorted octahedral coordination sphere. Mo(VI) ions and asymmetric oxo bridges form four-membered Mo–O–Mo–O rings, the Mo–O distances being 1.6899(17) and 1.7519(16) Å. Generally, Mo–L (ligand donor atom) distances are shorter in **3b** compared to the relevant bond distances in complexes **2** (Table 2.). Overall structure of **3b** is rather similar to that of dinuclear molybdenum(VI) complex with tridentate *N*-salicylidene-2-amino-4-*tert*-butylphenolate [20].

2.2. Monomeric $MoO_2(ONNO^R)$ complexes

Tetradentate ligand precursors H_2ONNO^R react with **1** in acetonitrile–methanol mixtures at room temperature to produce complexes **4** as intense red crystals (Scheme 2). Air-stable crystals are soluble in $CHCl_3$ and moderately soluble in DMSO. ^{1}H NMR spectra in $CDCl_3$ show expected resonances for octahedral complexes with C_2 rotation axis [13]. The IR absorptions for asymmetric and symmetric Mo=O stretches are seen at 807–903 and 914–916 cm^{-1}, respectively.

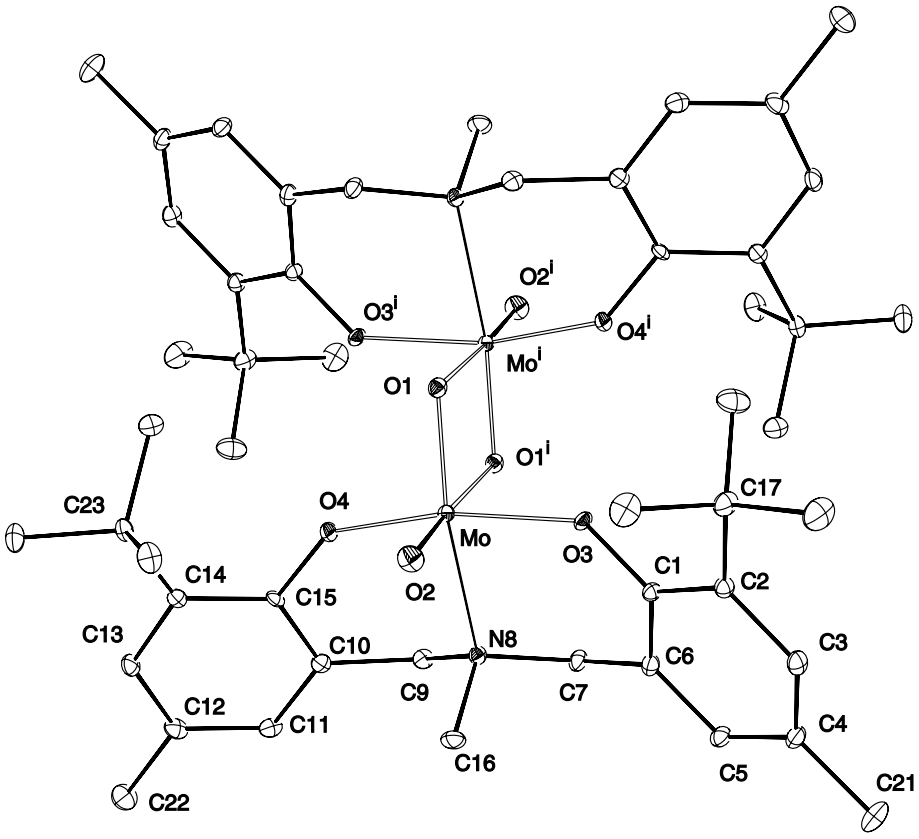
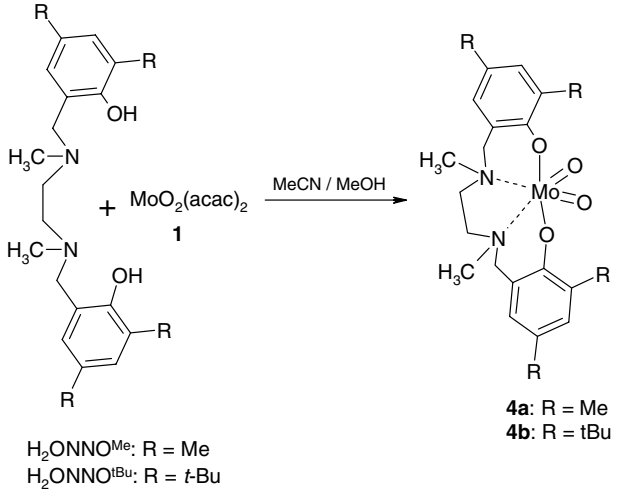


Fig. 3. Molecular structure of $[Mo_2O_4(ONO^{tBu})_2]$ (**3b**). Thermal ellipsoids have been drawn at 30% probability level. Symmetry operation: i = $-x$, $-y + 1$, $-z + 1$.



Scheme 2. Formation of Mo(VI) complexes with diaminobis-(phenolate)s.

X-ray diffraction studies of **4a** (Fig. 4) and **4b** (Fig. 5) revealed the nearly C_2 symmetric distorted octahedral structure of complexes. The bond lengths and angles of both complexes are closely similar and resemble those found in other six-coordinate dioxomolybdenum(VI) complexes [12,13,21]. However, **4b** crystallizes with two independent molecules in the asymmetric unit. A comparison of **4a** and two molecules of **4b** (see Table 3) with other known dioxomolybdenum(VI) complexes reveals, for example, that the O1═Mo═O2 angles are quite flexible. The related Mo complex $[MoO_2(ONNO)]$ (ONNO = *N*,*N*′-bis(2-hydroxybenzyl)-*N*,*N*′-dimethylethane-1,2-diamine) without *ortho*-substituents in the phenyl rings has the C_2 symmetry with the O═Mo═O angle of 108.25(7)° and the Mo═O, Mo–O and Mo–N lengths of 1.702(1), 1.934(1) and 2.390(1) Å, respectively [b]. In solid state, the Mo–O bonds in **4a** are slightly asymmetric (1.923(2) and 1.959(2) Å) and also ligand conformation contradicts C_2 symmetry. In **4b**, the Mo–O bond deviations from the C_2 symmetry are smaller, so it seems that the methyl substituted diaminobis(phenolato) ligand cause more distortions in the coordination sphere of Mo(VI) than the *tert*-butyl substituted analogue.

2.3. Catalytic studies

Oxidation reactions of benzoin and triphenyl phosphine by DMSO were studied as models for oxo-transfer reactions:

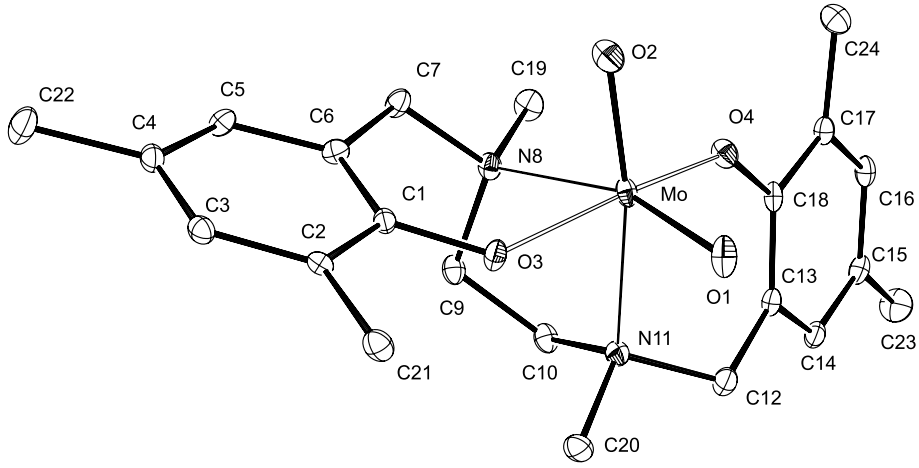


Fig. 4. Molecular structure of $[MoO_2(ONNO^{Me})]$ **(4a)**. Thermal ellipsoids have been drawn at 30% probability level.

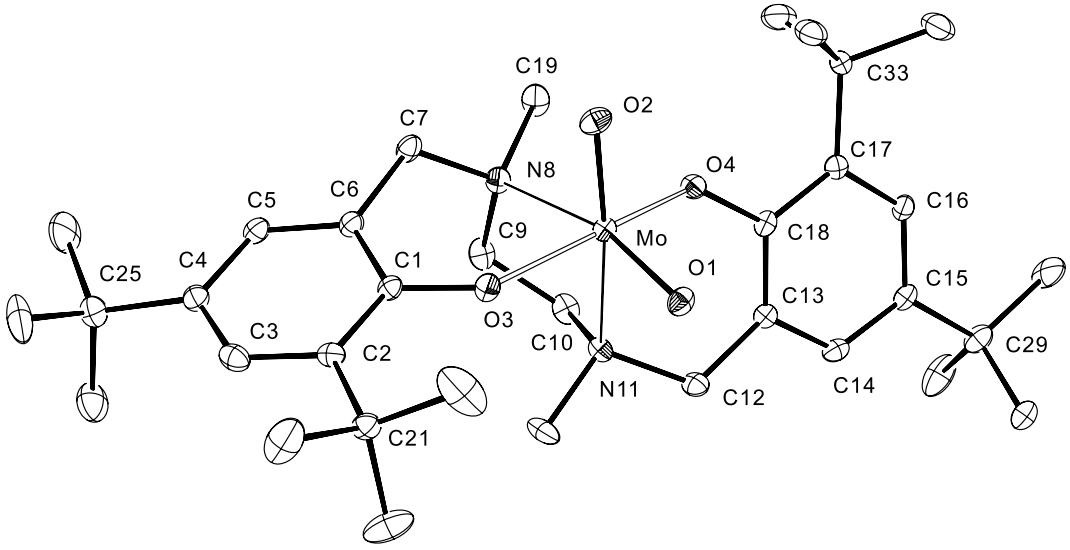


Fig. 5. Molecular structure of $[MoO_2(ONNO^{Bu})]$ (**4b**). Thermal ellipsoids have been drawn at 30% probability level. Only one of the two similar molecules in the asymmetric unit is shown.

Table 3
Selected bond lengths (Å) and angles (°) for **4a**, and **4b**

	4a	4b	4b[a]
Bond lengths			
Mo–O1	1.704(2)	1.713(2)	1.706(2)
Mo–O2	1.713(2)	1.706(3)	1.705(3)
Mo–O3	1.923(2)	1.936(3)	1.943(3)
Mo–O4	1.959(2)	1.944(3)	1.945(3)
Mo–N8	2.420(2)	2.401(3)	2.415(3)
Mo–N11	2.406(2)	2.406(3)	2.424(3)
Bond angles			
O1–Mo–O2	109.06(10)	107.74(12)	108.45(14)
O3–Mo–O4	159.39(8)	157.30(11)	159.06(11)
O1–Mo–N8	161.66(10)	160.96(12)	161.06(12)
O2–Mo–N11	161.59(9)	164.00(11)	162.10(12)
N8–Mo–N11	73.18(7)	73.81(10)	72.81(10)
C1–O3–Mo	135.41(16)	144.5(2)	144.1(2)
C18–O4–Mo	140.92(18)	136.1(2)	137.2(2)

[a] The parameters for the other molecule in the asymmetric unit.

$$C_6H_5CH(OH)C(O)C_6H_5 + Me_2SO \rightarrow C_6H_5C(O)C(O)C_6H_5 + Me_2S + H_2O \quad (1)$$

$$Ph_3P + Me_2SO \rightarrow Ph_3PO + Me_2S \quad (2)$$

Benzoin was dissolved in DMSO and subsequently treated with molybdenum catalyst using a 1:25 catalyst:substrate ratio. The yellow reaction mixture was kept at 120 °C under nitrogen atmosphere, cooled to the room temperature and finally treated with water to precipitate benzil as a white solid. Oxidation of triphenyl phosphine was investigated identically. All complexes **2**–**4** catalysed these oxidation reactions, since in all experiments the isolated yields of oxidized products were within 10% of quantitative, whereas in control experiments without catalysts no reactions between substrates and DMSO were observed. Regrettably, all attempts to

recover catalyst complexes failed. On the grounds of analogous catalyst systems, it is supposed, that the dioxomolybdenum(VI) complexes react with benzoin or Ph_3P to yield oxomolybdenum(IV) complexes and oxidized organic substrates. The Mo(IV) complexes are then rapidly oxidized back to the initial dioxocompounds with DMSO to complete the catalytic cycle [7,8,13].

Catalytic activities of complexes **2** and **4** in ring-opening metathesis polymerization of norbornene [22] were studied in CH_2Cl_2 solutions using a Et_2AlCl cocatalyst, while the overall conversion of monomer to insoluble polymers was used as a measure of activity. Studied molybdenum complexes were dissolved in a CH_2Cl_2/norbornene mixture to form orange solutions, which were subsequently treated with toluene solution of Et_2AlCl. As a result, the solutions changed rapidly dark brown in colour and exothermic polymerization started, which was observed as instantaneous increase in the mixture viscosity. The reactions were carried out at room temperature for 30 min and then quenched by MeOH. Brown colour of the reaction mixtures vanished when exposed to the air. The monomer conversions to solid, rubber-like materials were nearly quantitative. The activation mechanism is not known, but it was found Et_2AlCl activator was required for these polymerizations, as other alkylating main-group organometallics (MeMgI, Me_2Zn or Bu_4Sn) did not activate studied precatalysts in these experimental conditions. The orange to brown colour change of catalyst precursors upon addition of Et_2AlCl is probably related to the reduction of Mo(VI) centres to Mo(V). Similar activation by reducing aluminium compound has earlier used in heterogeneous polymerization of norbornene, which was catalysed by single crystals of $(Bu_4N)_2[W_6O_{19}]$ [23].

3. Conclusion

In conclusion, new series of dioxomolybdenum(VI) complexes with aminobis(phenolate)s have been synthesized. Tridentate aminobis(phenol) ligands can form monomeric dioxomolybdenum(VI) complexes in which the sixth coordination site is occupied by solvent methanol. In the absence of methanol, the coordination sphere around oxophilic Mo(VI) ion is completed by dimerization through oxygen bridges. Tetradentate diaminobis(phenols) form monomeric dioxomolybdenum(VI) complexes, in which the central metal have adopted distorted octahedral coordination. Sterical alteration of the substituents on the *ortho*-position on the bis(phenolato) ligands causes only minor variations on the coordination sphere around central Mo(VI) ion. Synthesised new complexes can catalyse oxotransfer reaction between DMSO and benzoin or triphenyl phosphine. They can also be activated by Et_2AlCl to catalyse ROMP of norbornene.

4. Experimental

Starting compound $[MoO_2(acac)_2]$ (**1**) and ligand precursors H_2ONO^R and H_2ONNO^R were prepared according to the literature [24–26]. Other chemicals were of reagent grade and were used as purchased. ^1H NMR spectra were recorded using a Bruker AM 200 spectrometer in $(CD_3)_2SO$ (**2**, **3**) or $CDCl_3$ (**4**) solutions and were referenced internally to $SiMe_4$. IR spectra were recorded as Nujol mulls using a Mattson Galaxy FTIR spectrometer. Adequate elemental analyses for complexes **3** and **4** were obtained using a Perkin–Elmer CHNS-Analyzer 2400, but analyses for complexes **2** gave insufficient results due to the partial loss of methanol during the process.

4.1. Syntheses

4.1.1. $[MoO_2(ONO^{Me})(MeOH)]\cdot MeOH$ (**2a**)

0.50 mmol of **1** (163 mg) and 0.50 mmol of H_2ONO^{Me} (150 mg) were dissolved in 5 ml of methanol. The orange-yellow reaction mixture was stirred overnight and subsequently stored at 277 °C for 24 h to obtain **2a** as yellow prisms (160 mg, 65%). IR: 3347(m), 3135(m), 1319(m), 1242(vs), 1223(vs), 1157(s), 1096(m), 1034(w), 972(m), 932(m), 892(vs), 868(vs), 833(vs), 735(w), 598(m), 576(w). NMR: δ_H 6.90 (s, 2H, ArH), 6.78 (s, 2H, ArH), 4.40 (d, $J = 14$ Hz, 2H, NCH_2), 4.10 (q, $J = 5$ Hz, CH_3OH), 3.17 (d, $J = 5$ Hz, CH_3OH), 3.07 (d, $J = 14$, 2H, NCH_2), 2.19 (s, 6H, $ArCH_3$), 2.10 (s, 6H, $ArCH_3$), 1.97 (s, 3H, NCH_3).

4.1.2. $[MoO_2(ONO^{tBu})(MeOH)]\cdot MeOH$ (**2b**)

0.50 mmol of **1** (163 mg) and 0.50 mmol of H_2ONO^{tBu} (192 mg) were dissolved in 5 ml of methanol by gentle heating. The yellow reaction mixture was allowed to stand at room temperature for 4 hours to obtain **2b** as yellow blocks 210 mg (73%). IR: 3333(m), 3173 (m), 1314(m), 1289(m), 1240(vs), 1211(s), 1148(s), 1096(m), 1018(vs), 988(m), 941(s), 918(m), 891(vs), 862(vs), 833(vs), 762(m), 573(m), 576(w). NMR: δ_H 6.98 (s, 2H, ArH), 6.82 (s, 2H, ArH), 4.37 (d, $J = 12$ Hz, 2H, NCH_2), 4.10 (q, $J = 5$ Hz, CH_3OH), 3.17 (d, $J = 5$ Hz, CH_3OH), 2.92 (d, $J = 14$, 2H, NCH_2), 2.21 (s, 6H, $ArCH_3$), 2.08 (s, 3H, NCH_3), 1.35 (s, 18H, $C(CH_3)_3$).

4.1.3. $[Mo_2O_2(\mu\text{-}O)_2(ONO^{Me})_2]$ (**3a**)

0.50 mmol of **1** (163 mg) was dissolved in 10 ml of anhydrous acetonitrile. To the solution was added 0.50 mmol of H_2ONO^{Me} (150 mg) in 5 ml of same solvent. The orange-red reaction mixture was allowed to

stand at room temperature for 24 h to obtain **3a** (175 mg, 82%) as orange prisms. IR: 1319(m), 1242(vs), 1221(s), 1155(s), 1094(m), 1034(w), 970(m), 933(s), 874(vs, br), 818(vs, br), 760(m), 733(m), 598(m), 565(m), 511(w). NMR: δ_H 6.92 (s, 2H, ArH), 6.78 (s, 2H, ArH), 4.41 (d, $J = 14$ Hz, 2H, NCH_2), 3.09 (d, $J = 14$, 2H, NCH_2), 2.18 (s, 6H, ArCH_3), 2.10 (s, 6H, ArCH_3), 1.98 (s, 3H, NCH_3). *Anal.* Calc. for $C_{38}H_{46}Mo_2N_2O_8$: C, 53.7; H, 5.55; N, 3.3. Found: C, 53.4; H, 5.6; N, 3.3%.

4.1.4. $[Mo_2O_2(\mu\text{-}O)_2(ONO^{tBu})_2]$ (**3b**)

0.50 mmol of **1** (163 mg) was dissolved in 10 ml of anhydrous acetonitrile. To the solution was added 0.50 mmol of H_2ONO^{tBu} (192 mg) in 5 ml of same solvent. The orange reaction mixture was allowed to stand at room temperature for 24 h to obtain **3b** (220 mg, 86%) as orange prisms. IR: 1418(s), 1294(m), 1240(vs), 1217(s), 1152(s), 1088(m), 984(m), 933(s), 914(m), 851(vs), 822(vs), 800(m), 766(m), 673(m), 571(s). NMR: δ_H 6.98 (s, 2H, ArH), 6.84 (s, 2H, ArH), 4.36 (d, $J = 12$ Hz, 2H, NCH_2), 2.93 (d, $J = 14$, 2H, NCH_2), 2.21 (s, 6H, ArCH_3), 2.10 (s, 3H, NCH_3), 1.35 (s, 18H, C(CH_3)$_3$). *Anal.* Calc. for $C_{50}H_{70}Mo_2N_2O_8$: C, 58.9; H, 6.9; N, 2.8. Found: C, 59.0; H, 6.9; N, 2.9%.

4.1.5. $MoO_2(ONNO^{Me})]$ (**4a**)

0.50 mmol of **1** (163 mg) was dissolved in 10 ml of anhydrous acetonitrile. To the solution was added 0.50 mmol (171 mg) of H_2ONNO^{Me} in 5 ml of methanol. The orange-yellow reaction mixture was allowed to stand at room temperature for 24 h to obtain 200 mg (83%) of **4a** as orange-red crystalline solid. IR: 1317(s), 1271(s), 1252(vs), 1229(vs), 1157(vs), 1146(m), 1065(s), 997(s), 972(s), 949(m), 914(s), 903(vs), 868(m), 841(vs), 808(m), 775(m), 741(w), 687(m), 621(w), 592(w), 559(m). NMR: δ_H 6.93 (2H, ArH), 6.76 (2H, ArH), 4.69 (d, $J = 14$ Hz, 2H, NCH_2), 3.66(d, $J = 14$ Hz, 2H, NCH_2), 3.22 (d, $J = 10$ Hz, 2H, NCH_2), 2.82 (s, 6H, NCH_3), 2.28 (d, $J = 10$ Hz, 2H, NCH_2), 2.20 (s, 6H, ArCH_3), 2.09 (s, 6H, ArCH_3). *Anal.* Calc. for $C_{22}H_{30}MoN_2O_4$: C, 54.8; H, 6.3; N, 5.8. Found: C, 54.5; H, 6.5; N, 5.9%.

4.1.6. $[MoO_2(ONNO^{tBu})]$ (**4b**)

0.50 mmol of **1** (163 mg) was dissolved in 10 ml of anhydrous acetonitrile. To the solution was added 0.50 mmol (255 mg) of H_2ONNO^{tBu} in 10 ml of methanol. The orange-yellow reaction mixture was allowed to stand at room temperature for 24 h to obtain 225 mg (79%) of **4b** as large orange blocks. IR: 1304(vs, br), 1244(vs, br), 1206(s), 1175(s), 1125(s), 1065(m), 1015(m), 984(m), 916(s), 897(vs), 874(s), 845(s), 812(m), 779(m), 756(s), 646(w), 617(w), 557(s), 480(m), 469(m). NMR: δ_H 7.30 (d, $J = 4$ Hz, 2H, ArH), 6.86 (d, $J = 4$ Hz, 2H, ArH), 4.88 (d, $J = 14$ Hz, 2H, NCH_2), 3.61 (d, $J = 14$ Hz, 2H, NCH_2), 3.20 (d, $J = 10$ Hz, 2H, NCH_2), 2.74 (s, 6H, NCH_3), 2.27 (d, $J = 10$ Hz, 2H, NCH_2), 1.42 (s, 18H, C(CH_3)$_3$), 1.29 (s, 18H, C(CH_3)$_3$). *Anal.* Calc. for $C_{34}H_{54}MoN_2O_4$: C, 62.8; H, 8.4; N, 4.3. Found: C, 62.2; H, 8.7; N, 4.3%.

4.2. Catalytic studies

4.2.1. Oxidation of benzoin

106 mg of benzoin (0.50 mmol) and 10 mg (ca. 0.02 mmol) of catalyst were dissolved in 5 ml of DMSO. The yellow mixture was heated at 120 °C under nitrogen atmosphere for 18 h. Solution was cooled to the room temperature and subsequently treated with 5 ml of water to obtain benzil as a white precipitate. Precipitate was filtrated, dried and identified by IR spectroscopy.

4.2.2. Oxidation of PPh_3

131 mg of PPh_3 (0.50 mmol) and 10 mg (ca. 0.02 mmol) of catalyst were dissolved in 5 ml of DMSO. The yellow mixture was heated at 120 °C under nitrogen atmosphere for 4 h. Solution was cooled to the room temperature and subsequently treated with 5 ml of water to obtain a white precipitate. Precipitate was filtrated, dried and analysed by IR spectroscopy.

4.2.3. Polymerization of norbornene

Polymerizations were performed at ambient temperature under a nitrogen atmosphere employing a 1:5:100 precatalyst:activator:monomer ratio. The precatalyst (2×10^{-5} mol) was dissolved in 4 ml of 0.5 M norbornene monomer (2.0 mmol) solution in CH_2Cl_2. The reaction mixture was stirred for 5 min and subsequently treated with 0.05 ml of Et_2AlCl solution (1.8 M in toluene, 9×10^{-5} mol). After 30 min stirring, the solution was exposed to the air and subsequently treated with 10 ml of methanol to precipitate polymer as a white solid. Polymers were swelled in CH_2Cl_2, re-precipitated by methanol and dried in vacuo at 40 °C for 8 h. In all experiments, methanol-insoluble polymers were obtained in 85–95% yield.

4.3. X-ray crystallography

Crystals suitable for X-ray measurements were grown from methanol (**2a**, **2b**), acetonitrile (**3b**) or acetonitrile–methanol mixture (**4a**, **4b**). Crystallographic data for **2a**, **2b**, **3b**, **4a** and **4b** along with other experimental details are summarised in Table 1. The crystal data were collected at 173 K on a Nonius Kappa CCD area-detector diffractometer using graphite monochromatised Mo Kα radiation ($\lambda = 0.71073$ Å). The data collection was performed using φ and ω scans. The data were processed using DENZO-SMN V0.93.0. [27] SHELXA [28] absorption correction was applied for the data of all compounds.

The structures were solved by direct methods using the SHELXS-97 program and full-matrix least-squares refinements on F^2 were performed using the SHELXL-97 program [29]. For all compounds, the heavy atoms were refined anisotropically. The CH hydrogen atoms were included at the fixed distances with fixed displacement parameters from their host atoms. Figures were drawn with *ORTEP-3 for Windows* [30].

5. Supplementary data

Crystallographic data (excluding structure factors) for the structures reported in this paper have been deposited with the Cambridge Crystallographic Data Centre as deposition numbers CCDC 247703–247707 for **2a**, **2b**, **3b**, **4a** and **4b**, respectively. Copies of the data can be obtained free of charge on application to CCDC, 12 Union Road, Cambridge CB2 1EZ, UK [Fax: (internat.) + 44-1223/336-033; E-mail: deposit@ccdc.cam.ac.uk, or on the web: http://www.ccdc.cam.ac.uk].

References

[1] M. Abrantes, A.M. Santos, J. Mink, F.E. Kühn, C.C. Romão, Organometallics 22 (2003) 2112.
[2] F.R. Fronczek, R.L. Luck, G. Wang, Inorg. Chem. Commun. 5 (2002) 384.
[3] R.R. Schrock, J. Mol. Catal. A: Chem. 213 (2004) 21.
[4] D. Collison, C.D. Garner, J.A. Joule, Chem. Soc. Rev. (1996) 25.
[5] R. Hille, Chem. Rev. 96 (1996) 2757.
[6] J.H. Enemark, J.J.A. Cooney, J.-J. Wang, R.H. Holm, Chem. Rev. 104 (2004) 1175.
[7] (a) R. Dinda, P. Sengupta, S. Ghosh, W.S. Sheldrick, Eur. J. Inorg. Chem. (2003) 363;
(b) N.R. Pramanik, S. Ghosh, T.K. Raychaudhuri, S. Ray, R.J. Butcher, S.S. Mandal, Polyhedron 23 (2004) 1595.
[8] P. Barbaro, T.R. Belderrain, C. Bianchini, G. Scapacci, D. Masi, Inorg. Chem. 35 (1996) 3362.
[9] T. Weyhermüller, T.K. Paine, E. Bothe, E. Bill, P. Chaudhuri, Inorg. Chim. Acta 337 (2002) 344.
[10] F. Wolff, C. Lorber, R. Choukroun, B. Donnadieu, Inorg. Chem. 42 (2003) 7839.
[11] S. Groysman, L. Goldberg, M. Kol, E. Genizi, Z. Goldscmidt, Inorg. Chim. Acta 345 (2003) 137.
[12] (a) P. Subramarian, J.T. Spence, R. Ortega, J.H. Enemark, Inorg. Chem. 23 (1984) 2564;
(b) C.J. Hinshaw, G. Peng, R. Singh, J.T. Spence, J.H. Enemark, M. Bruck, J. Kristofzski, S.L. Merbs, R.B. Ortega, P.A. Wexler, Inorg. Chem. 28 (1989) 4483.
[13] (a) Y.-L. Wong, J.-F. Ma, W.-F. Law, Y. Yan, W.-T. Wong, Z.-Y. Zhang, T.C.W. Mak, D.K.P. Ng, Eur. J. Inorg. Chem. (1999) 313;
(b) Y.-L. Wong, Y. Yan, E.S.H. Chan, Q. Yang, T.C.W. Mak, D.K.P. Ng, J. Chem. Soc., Dalton Trans. (1998) 3057.
[14] A. Lehtonen, R. Sillanpää, Inorg. Chem. 43 (2004) 6501.
[15] A. Lehtonen, V.G. Kessler, Inorg. Chem. Commun. 7 (2004) 691.
[16] J. Liimatainen, A. Lehtonen, R. Sillanpää, Polyhedron 19 (2000) 1133.
[17] T. Głowiak, L. Jerzykiewicz, J.M. Sobczak, J.J. Ziółkowski, Inorg. Chim. Acta 356 (2003) 387.
[18] C.P. Rao, A. Sreedhara, P.V. Rao, M.B. Verghese, K. Rissanen, E. Kolehmainen, N.K. Lokanath, M.A. Sridhar, J.S. Prasad, J. Chem. Soc., Dalton Trans. (1998) 2383.
[19] T.A. Hanna, A.K. Ghosh, C. Ibarra, M.A. Mendez-Rojas, A.L. Rheingold, W.H. Watson, Inorg. Chem. 43 (2004) 1511.
[20] S.-J. Mo, B.-K. Koo, Bull. Korean Chem. Soc. 20 (1999) 1105.
[21] H. Elias, F. Stock, C. Röhr, Acta Crystallogr., Sect. C 53 (1997) 862.
[22] K.J. Ivin, J.C. Mol, Olefin Metathesis and Metathesis Polymerization, Academic Press, London, 1997.
[23] M. McCann, D. McDonnell, J. Chem. So., Chem. Commun. (1993) 1718.
[24] G.J.-J. Chen, J.W. McDonald, W.E. Newton, Inorg. Chem. 15 (1976) 2612.
[25] N.V. Timosheva, A. Chandrasekaran, R.O. Day, R.R. Holmes, Inorg. Chem. 37 (1998) 4945.
[26] E.Y. Tshuva, I. Goldberg, M. Kol, J. Am. Chem. Soc. 122 (2000) 10706.
[27] Z. Otwinowski, W. Minor, Methods in Enzymology, in: C.W. CarterJr., R.M. Sweet (Eds.), Macromolecular Crystallography, Part A, vol. 276, Academic Press, New York, 1997, pp. 307–326.
[28] Sheldrick, G.M. (anon) SHELX-97 Release 97-2, 1998.
[29] G.M. Sheldrick, SHELXL-97. Program for Crystal Structure Refinement, University of Göttingen, Germany, 1997.
[30] L.J. Farrugia, J. Appl. Crystallogr. 32 (1999) 837.

Available online at www.sciencedirect.com
SCIENCE DIRECT®
Polyhedron 24 (2005) 267–279
POLYHEDRON
www.elsevier.com/locate/poly

The synthesis, spectroscopic characterisation, crystal and molecular structure of the $[ReCl_3(NO)(OPPh_3)(pyz)]$ complex. DFT calculations for $[ReCl_3(NO)(OPPh_3)(pyz)]$ and $[ReCl_3(NO)(OPPh_3)(PPh_3)]$

B. Machura [a,*], M. Jaworska [b], R. Kruszynski [c,1]

[a] Department of Inorganic and Radiation Chemistry, Institute of Chemistry, University of Silesia, 9th Szkolna St., 40-006 Katowice, Poland
[b] Department of Theoretical Chemistry, Institute of Chemistry, University of Silesia, 9th Szkolna St., 40-006 Katowice, Poland
[c] Department of X-ray Crystallography and Crystal Chemistry, Institute of General and Ecological Chemistry, Lodz University of Technology, 116 Żeromski St., 90-924 Łódź, Poland

Received 8 September 2004; accepted 9 November 2004

Abstract

A new rhenium nitrosyl – $[ReCl_3(NO)(OPPh_3)(pyz)]$ – has been obtained by two different routes: (i) in the substitution reaction of $[ReCl_3(NO)(OPPh_3)(PPh_3)]$ with pyrazine, and (ii) in the nitrosylation reaction of $[ReOCl_3(PPh_3)_2]$ by gaseous nitric oxide in the presence of an excess of pyrazine. The crystal, molecular and electronic structure of the $[ReCl_3(NO)(OPPh_3)(pyz)]$ complex has been determined. The geometric parameters of $[ReCl_3(NO)(OPPh_3)(pyz)]$ have been examined using the density functional theory (DFT) method. The UV–Vis spectrum of the pyrazine complex has been interpreted on the basis of the electronic transitions of $[ReCl_3(NO)(OPPh_3)(pyz)]$ calculated with the time-dependent DFT method (TDDFT). The paper also includes the results of the DFT and TDDFT calculations for $[ReCl_3(NO)(OPPh_3)(PPh_3)]$.
© 2004 Elsevier Ltd. All rights reserved.

Keywords: Rhenium nitrosyl complexes; Pyrazine; X-ray structure; DFT and TDDFT calculations

1. Introduction

For many years nitrosyl compounds of transition metals have been the centre of interest of scientists both engaged in basic research and trying to employ these complexes as catalysts of polymerisation, oligomerisation, metathesis, epoxidation, oxidation and reduction [1–11].

One of the most important aspects of the research on nitrosyl complexes is determination of the bonding nature of NO to the metal center. Terminal NO ligands may adopt either linear or bent geometries. Although the bonding in the M–NO moiety is largely of covalent nature and the electron distribution is more or less evenly distributed in this group, the bonding of the M–NO unit is often described by assigning formal oxidation states to the metal centre and the nitrosyl ligand. In such an assignment nitric oxide can be coordinated as NO^+, NO or NO^-. The M–NO core can be also described using the $\{M(NO)_x\}^n$ formalism proposed by Enemark and Feltham, in which n is taken as the total number of electrons associated with the metal d and π*(NO) orbitals [1,3,9,11].

* Corresponding author. Tel.: +48322582441; fax: +48322599978.
E-mail addresses: bmachura@poczta.onet.pl (B. Machura), mj@tc3.ich.us.edu.pl (M. Jaworska), kruszyna@p.lodz.pl (R. Kruszynski).
[1] A holder of the Foundation for Polish Science (FNP) scholarship.

0277-5387/$ - see front matter © 2004 Elsevier Ltd. All rights reserved.
doi:10.1016/j.poly.2004.11.024

Due to the favourable nuclear properties of ^{186}Re and ^{188}Re nuclides in diagnostic nuclear medicine and applications in radioimmunotheraphy [12,13], the chemistry of nitrosyl rhenium complexes arouses particular interest.

The papers [14–22] present the preparation, structural and spectroscopic characterisation of rhenium mononitrosyls with phosphine and arsine ligands in the coordination sphere.

Here we present the synthesis, crystal, molecular and electronic structure of a new rhenium nitrosyl with pyrazine (pyz) in the coordination sphere – $[ReCl_3(NO)(OPPh_3)(pyz)]$ (**1**). The electronic structure of **1** has been determined on the basis of density functional theory (DFT) calculations. The spin-allowed doublet–doublet electronic transitions of $[ReCl_3(NO)(OPPh_3)(pyz)]$ have been calculated with the time-dependent DFT (TDDFT) method, and the UV–Vis spectrum of the title complex has been discussed on this basis. For comparison, the paper includes also the results of the DFT and TDDFT calculations for $[ReCl_3(NO)(OPPh_3)(PPh_3)]$ (**2**). The crystal, molecular structure and spectroscopic properties of **2** were presented in paper [17].

Recent calculations with the TDDFT method for open- and closed-shell 5d-metal complexes have supported the TDDFT method to be applicable for such systems giving good assignment of experimental spectra [23–29]. Some theoretical investigations have also been carried out on rhenium compounds. The electronic structures of nitrido, oxo, carbonyl and nitrile rhenium complexes, as well as their spectroscopic properties, bonding and reactivity have been theoretically studied at the HF, MP2, EHT and DFT levels of theory using various basis sets [30–37]. Gancheff et al. [32] have performed extended tests of the ability of the B3LYP method in the LANL2DZ basis set for rhenium compounds in a geometry optimisation and calculation of spectral properties. Although this is not a very extended basis set, its use with DFT has been shown to be sufficient for geometry optimisation and calculation of spectral properties. It gives good agreement with the experimental data and its use is especially justified in the case of large molecules.

2. Experimental

2.1. General procedure

The reactions were carried out under an argon atmosphere. All the reagents used for the syntheses of the complexes are commercially available and were used without further purification. $[Re(NO)Cl_3(PPh_3)(OPPh_3)]$ and $[ReOCl_3(PPh_3)_2]$ complexes were prepared according to the literature methods [17,38]. Gaseous NO, obtained in reaction (1)

$$2NaNO_2 + 3H_2SO_4 + FeSO_4 \rightarrow 2NO + 2NaHSO_4 + Fe_2(SO_4)_3 + 2H_2O \quad (1)$$

was purified by passing through washers with concentrated KOH solution and over solid NaOH.

The IR spectrum of **1** was recorded on a Nicolet Magna 560 spectrophotometer in the spectral range 4000–400 cm^{-1} with the sample in the form of a KBr pellet. The electronic spectrum of **1** was measured on a Lab Alliance UV–Vis 8500 spectrophotometer in the range 800–220 nm in deoxygenated dichloromethane solution. Magnetic susceptibility was measured at 296 K by the Faraday method. Elemental analyses (C, H, N) were performed on a Perkin–Elmer CHN-2400 analyzer.

2.2. Preparation of $[ReCl_3(NO)(OPPh_3)(pyz)]$ (1)

2.2.1. Method A

$[Re(NO)Cl_3(OPPh_3)(PPh_3)]$ (1 g, 1.15 mmol) and pyz (0.5 g, 0.62 mmol) in chloroform (100 cm^3) were refluxed for 12 h. The volume was condensed to 20 cm^3 and a dark green microcrystalline solid was formed by addition of 100 cm^3 of diethyl ether. The product was washed with EtOH and cold ether, and dried in vacuo (Yield: 40%).

2.2.2. Method B

NO was passed through a vigorously stirred and refluxing solution of $[ReOCl_3(PPh_3)_2]$ (1.05 g, 1 mmol) and pyz (0.25 g, 3.1 mmol) in acetone (100 cm^3). The reaction was carried out for 4 h. The colour changed gradually from bright green to dark green. Then the resulting solution was evaporated to a volume of 10 cm^3. A green precipitate was formed by an addition of 40 cm^3 of EtOH and after 15 min it was filtered off. The product was washed with cold ether and dried in vacuo. Crystals suitable for X-ray investigation were obtained by recrystallisation from $CHCl_3$–EtOH (Yield: 70%).

IR (KBr, cm^{-1}) 3059 (w), 1762 (s), 1589 (m), 1484 (s), 1440 (s), 1416 (3), 1354 (w), 1316 (w), 1270 (w), 1163(m), 1122 (s), 1060 (s), 1027 (m), 1001 (m), 807 (m), 753 (s), 727 (s), 691 (s), 616 (w), 552 (s), 536 (s), 466(s). Calc. for $C_{21}H_{19}N_3Br_3OAsRe$: C, 38.80; H, 2.81; N, 6.1. Found: C, 38.92; H, 2.75; N, 6.15%.

2.3. Crystal structure determination and refinement

The X-ray intensity data of complex **1** were collected on a KM-4-CCD automatic diffractometer equipped with a CCD detector with 50 s exposure time and all reflections of the Ewald sphere were collected up to $\theta = 25°$. The unit cell parameters were determined from least-squares refinement of the setting angles of 9937 strongest reflections. Details concerning

crystal data and refinement are given in Table 1. Lorentz, polarisation and numerical absorption corrections [39] were applied. The structure was solved by the Patterson method and subsequently completed by difference Fourier recycling. All the non-hydrogen atoms were refined anisotropically using the full-matrix, least-squares technique. The hydrogen atoms of the phenyl rings were treated as "riding" on their parent carbon atoms [d(C–H) = 0.96 Å] and assigned isotropic temperature factors equal to 1.2 times the value of the equivalent temperature factor of the parent carbon atom. SHELXS97 [40], SHELXL97 [41] and SHELXTL [42] programs were used for all the calculations. Atomic scattering factors were those incorporated in the computer programs.

2.4. Computational details

The GAUSSIAN03 program [43] was used in the calculations. The geometry optimisation was carried out with the DFT method with the use of the B3LYP functional [44,45]. The electronic spectra were calculated with the TDDFT method [46].

In the calculations, the LANL2DZ basis set [47] was used on the rhenium atom, 6-31G(d) on the chlorine, nitrogen, phosphorous, oxygen and carbon atoms and 6-31G basis on the hydrogen atoms.

Natural bond orbital (NBO) calculations were performed with the NBO code [48] included in GAUSSIAN03.

3. Results and discussion

3.1. Preparation

Two different routes have been employed for the preparation of **1**. The refluxing of $[ReCl_3(NO)(OPPh_3)(PPh_3)]$ with pyrazine (pyz) (Eq. (2)) in chloroform gives complex **1** in a moderate yield

$$[ReCl_3(NO)(OPPh_3)(PPh_3)] + pyz \rightarrow [ReCl_3(NO)(OPPh_3)(pyz)] + PPh_3 \quad (2)$$

A much higher yield of **1** has been reported for the nitrosylation reaction of $[ReOCl_3(PPh_3)_2]$ by gaseous nitric oxide in the presence of an excess of pyrazine.

3.2. Crystal structure

A thermal ellipsoid plot of **1** is shown in Fig. 1. The rhenium atom of **1** is in a distorted octahedral

Table 1
Crystal data and structure refinement for $[ReCl_3(NO)(OPPh_3)(pyz)]$

Empirical formula	$C_{22}H_{19}Cl_3N_3O_2PRe$
Formula weight	680.92
Temperature (K)	293(2)
Wavelength (Å)	0.71073
Crystal system	orthorhombic
Space group	*Pbcn*
Unit cell dimensions	
a (Å)	29.2078(14)
b (Å)	10.2887(4)
c (Å)	16.6705(7)
Volume (Å^3)	5009.7(4)
Z	8
D_{calc} (Mg/m^3)	1.806
Absorption coefficient (mm^{-1})	5.259
F(0 0 0)	2632
Crystal size (mm)	$0.041 \times 0.180 \times 0.194$
θ Range for data collection	2.81–25.11
Index ranges	$-28 \leqslant h \leqslant 34$; $-2 \leqslant k \leqslant 12$; $-19 \leqslant l \leqslant 19$
Reflections collected	51 246
Independent reflections (R_{int})	4464 (0.0558)
Completeness to 2θ (%)	89.4
Maximum and minimum transmission	0.867 and 0.739
Data/restraints/parameters	4464/0/289
Goodness-of-fit on F^2	1.117
Final *R* indices [$I > 2\sigma(I)$]	$R_1 = 0.0311$; $wR_2 = 0.0473$
R indices (all data)	$R_1 = 0.0486$; $wR_2 = 0.0522$
Largest differential peak and hole (e Å^{-3})	0.918 and −0.660

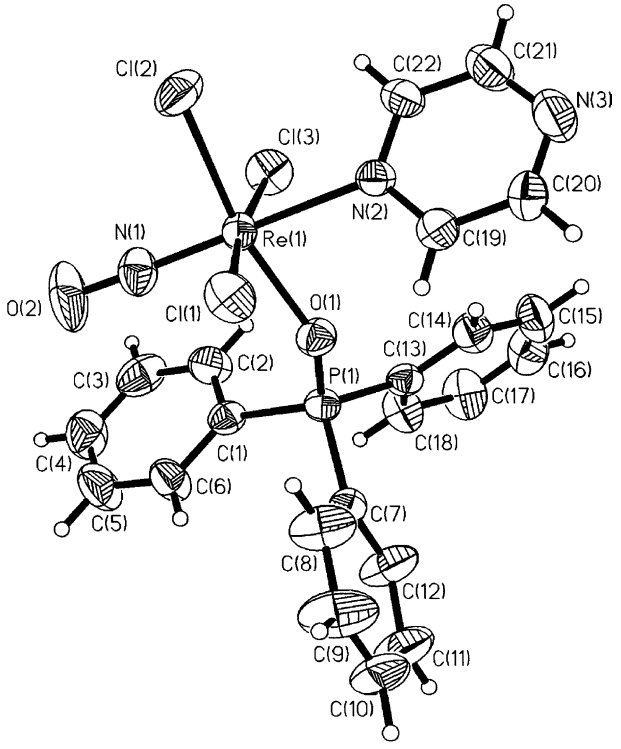


Fig. 1. Thermal ellipsoid plot of $[ReCl_3(NO)(OPPh_3)(pyz)]$ showing the atom numbering scheme (50% probability ellipsoids).

environment with the chloride ligands in *meridional* geometry and the linear N–O group *trans* to the pyrazine molecule and *cis* to the $OPPh_3$ ligand.

The molecules of **1** are linked via one C(12)–H(12)···O2(x, $-y$, $z + 1/2$) intermolecular interaction, which according to Desiraju and Steiner [50] can be considered as a weak hydrogen bond with a D···A distance equal to 3.317(6) Å and a D–H···A angle of 143.9°. The weak intramolecular interaction C(19)–H(19)···Cl(1) with a D···A distance equal to 3.264(4) Å and a D–H···A angle of 112.0° can also be treated as a weak hydrogen bond [49,50]. It provides additional conformational stabilisation of the $[ReCl_3(NO)(OPPh_3)(pyz)]$ molecule.

Table 1 presents the crystal data and structural refinement for complex **1**. The most important experimental bond lengths and angles of **1** are reported in Table 2. The Re–NO (1.740(4) Å) and N–O (1.184(4) Å) bond distances and the Re–N–O angle (176.0(6)°) indicate the nitrosonium character of the NO group. They are well compared with values previously found for other rhenium nitrosyls [14–22]. In comparison with the $[ReCl_3(NO)(OPPh_3)(PPh_3)]$ compound [1.747(5) and 1.165(8) Å] [25], an insignificant shortening of the Re–N distance and elongation of the N–O bond length can be noticed for complex **1**. The Re–$N_{pyrazine}$ distance is affected by the *trans* influence of the nitrosyl group and thus is longer than the Re–$N_{pyrazine}$ distances detected in $[ReO(OEt)Cl_2(pyz)_2]$ (2.152(16) and 2.103(16) Å) with a *trans* arrangement of the N-heterocyclic molecules [51]. The $OPPh_3$ ligand affects the Re–Cl(2) bond length and causes its shortening. A similar trend is observed for the $[ReCl_3(NO)(OPPh_3)_2]$ and $[ReBr_3(NO)(OPPh_3)_2]$ complexes with the halogen ligand in a *trans* position to the $OPPh_3$ molecule. The Re–$OPPh_3$ [2.058(2) Å] and P–O [1.521(3)] bond lengths in **1** are in good agreement with values found for $[ReCl_3(NO)(OPPh_3)_2]$ (Re–O = 2.055(6) Å, P–O = 1.493(6) Å) and $[ReBr_3(NO)(OPPh_3)_2]$ (Re–O = 2.048(4) Å, P–O = 1.505(4) Å) [18,21]. In complex **2**, the Re–$OPPh_3$ distance (2.103(5) Å) is affected by the nitrosyl group and thus is longer than the Re–$OPPh_3$ bond length in **1**.

Table 2
The experimental and optimised bond lengths (Å) and angles (°) for $[ReCl_3(NO)(OPPh_3)(pyz)]$

	Experimental	Optimised
Bond lengths		
Re(1)–N(1)	1.740(4)	1.758
Re(1)–N(2)	2.231(3)	2.245
Re(1)–Cl(1)	2.3656(11)	2.453
Re(1)–Cl(2)	2.3472(11)	2.409
Re(1)–Cl(3)	2.3734(11)	2.458
Re(1)–O(1)	2.058(2)	2.105
N(1)–O(2)	1.184(4)	1.171
P(1)–O(1)	1.521(3)	1.536
Bond angles		
N(1)–Re(1)–O(1)	98.49(14)	99.93
N(1)–Re(1)–N(2)	178.87(15)	177.50
O(1)–Re(1)–N(2)	81.31(11)	82.56
N(1)–Re(1)–Cl(2)	94.00(12)	91.70
O(1)–Re(1)–Cl(2)	167.47(8)	168.36
N(2)–Re(1)–Cl(2)	86.21(9)	85.81
N(1)–Re(1)–Cl(1)	94.03(12)	93.86
O(1)–Re(1)–Cl(1)	86.53(8)	86.09
N(2)–Re(1)–Cl(1)	87.07(9)	86.11
Cl(2)–Re(1)–Cl(1)	91.74(4)	92.66
N(1)–Re(1)–Cl(3)	93.72(12)	95.24
O(1)–Re(1)–Cl(3)	89.52(8)	86.89
N(2)–Re(1)–Cl(3)	85.17(9)	85.04
Cl(2)–Re(1)–Cl(3)	90.55(4)	92.59
Cl(1)–Re(1)–Cl(3)	171.75(4)	169.35
P(1)–O(1)–Re(1)	142.36(16)	141.72
O(2)–N(1)–Re(1)	178.2(3)	176.34

3.3. Infrared data and magnetochemical measurements of complex *1*

The IR spectrum of **1** exhibits a strong band at 1762 cm^{-1}, assignable to ν(NO). The value of ν(NO) corresponds to the linear NO range of Haymore and Ibers [52]. In the IR spectrum of complex **2**, the strong band corresponding to the stretching vibration of the nitrosyl group appears at 1745 cm^{-1}.

The sharp absorption band at 1598 cm^{-1} in the spectrum of **1** is typical of mono-coordinated diaza ligands [53]. The strong bands at 1163 and 1122 cm^{-1} confirm the presence of the coordinated $OPPh_3$ molecule.

The complex **1** is a paramagnetic compound with a room temperature magnetic moment of 1.8 BM, corresponding to one unpaired electron.

3.4. Optimised geometries of *1* and *2*

The geometries of **1** and **2** were optimised in a doublet state by the DFT method with the B3LYP functional. The doublet state agrees well with the experimental values of the effective magnetic moment for complexes **1** and **2**. The geometric parameters of **1** and **2** optimised by the DFT method are gathered in Tables 2 and 3, respectively. For comparison, the experimental bonds and bond angles of **2** are also included in Table 3. The structure and atomic numbering scheme of the complex **2** are shown in Fig. 2. The optimised geometries of **1** and **2** are in good agreement with the experimental ones, and the general trends observed in the experimental data are well reproduced in the calculations.

3.5. Charge distribution and spin densities of *1* and *2*

Table 4 presents the atomic charges from the natural population analysis (NPA) and spin densities for **1** and **2**. For both complexes the calculated charges on the rhenium atoms are considerably lower than the formal

Table 3
The experimental and optimised bond lengths (Å) and angles (°) for $[ReCl_3(NO)(OPPh_3)(PPh_3)]$

	Experimental	Optimised
Bond lengths		
Re(1)–N(1)	1.747(5)	1.751
Re(1)–P(2)	2.5288(18)	2.589
Re(1)–Cl(1)	2.3579(18)	2.425
Re(1)–Cl(2)	2.377(2)	2.453
Re(1)–Cl(3)	2.3502(18)	2.453
Re(1)–O(1)	2.103(5)	2.149
N(1)–O(2)	1.165(8)	1.172
P(1)–O(1)	1.506(5)	1.530
Bond angles		
N(1)–Re(1)–O(1)	176.6(2)	177.66
N(1)–Re(1)–Cl(3)	93.3(2)	94.87
O(1)–Re(1)–Cl(3)	90.05(15)	87.33
N(1)–Re(1)–Cl(1)	91.9(2)	93.17
O(1)–Re(1)–Cl(1)	84.77(15)	84.68
Cl(3)–Re(1)–Cl(1)	174.26(6)	171.18
N(1)–Re(1)–Cl(2)	93.5(2)	91.87
O(1)–Re(1)–Cl(2)	85.74(14)	87.32
Cl(2)–Re(1)–Cl(3)	90.76(8)	90.33
Cl(3)–Re(1)–Cl(1)	91.32(8)	90.33
N(1)–Re(1)–P(2)	93.0(2)	91.44
O(1)–Re(1)–P(2)	87.98(14)	89.53
Cl(3)–Re(1)–P(2)	85.18(7)	85.25
Cl(1)–Re(1)–P(2)	92.14(6)	90.95
Cl(2)–Re(1)–P(2)	171.75(4)	174.69
P(1)–O(1)–Re(1)	150.2(3)	148.76
O(2)–N(1)–Re(1)	176.0(6)	176.63

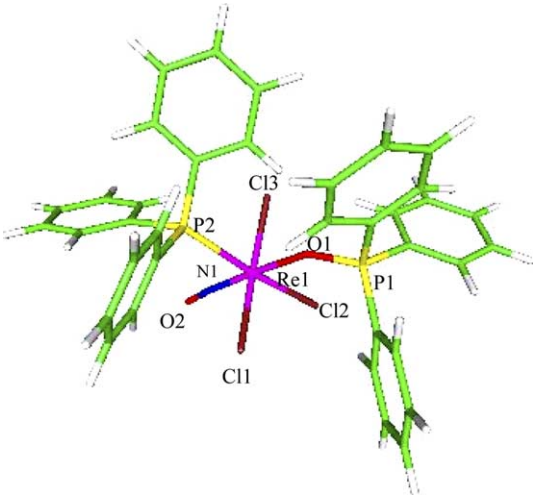


Fig. 2. Atomic numbering scheme of $[ReCl_3(NO)(OPPh_3)(PPh_3)]$.

charge of +2. This is the result of charge donation from Cl^- ions, the charges on the chloride ligands are significantly smaller than −1. The rhenium atom of **2** is less positive than the Re atom of **1**. It results from the presence of triphenylphosphine in the coordination sphere of **2**. The PPh_3 molecule acts as a strong σ-donor; there is a large positive charge on the phosphorus atom of the coordinated triphenylphosphine in complex **2**. The oxygen atoms of the $OPPh_3$ ligands in **1** and **2** are negatively charged. The calculated charges on the nitrogen atoms of the nitrosyl groups are positive, whereas the oxygen atoms are negatively charged. The total charges on the NO groups are positive, being 0.029 and 0.020 for **1** and **2**, respectively.

Table 4
Atomic charges from the natural population analysis (NPA) and spin densities of **1** and **2**

Atom	**1**		**2**	
	Atomic charge	Spin density	Atomic charge	Spin density
Re(1)	0.830	1.079	0.593	1.034
Cl(1)	−0.453	0.036	−0.402	0.080
Cl(2)	−0.380	0.066	−0.441	0.054
Cl(3)	−0.466	0.033	−0.430	0.061
N(1)	0.254	−0.125	0.255	−0.112
O(2)	−0.225	−0.105	−0.235	−0.092
O(1)	−1.097	0.0144	−1.123	−0.001
P(1)	2.339	0.002	2.338	−0.000
N(2)	−0.479	−0.009		
N(3)	−0.400	0.001		
P(2)			1.385	−0.031

For both complexes, there are positive spin densities of about 1 on the rhenium atoms and small negative spin densities of about −0.1 on the nitrogen and oxygen atoms of the nitrosyl ligands. The spin densities on the donor atoms of the other ligands are below 0.1 for complexes **1** and **2**.

3.6. Electronic structure

The energies and characters of several highest occupied and lowest unoccupied molecular orbitals of **1** and **2** are presented in Tables 5 and 6, respectively. Most of the MOs of **1** and **2** have complicated characters. The percent participation of atomic orbitals in the selected HOMO and LUMO orbitals for **1** and **2** are shown in Tables 5 and 6, respectively.

3.7. $[ReCl_3(NO)(OPPh_3)(pyz)]$ (1)

In the molecular orbital approach, the bonding of NO to a metal is considered to be made up of two components. The first involves donation of electron density from a σ-type orbital on NO to the metal, and the second – backdonation from the filled d_{xz} and d_{yz} metal orbitals to the π* orbitals of the NO ligand. Among the MOs of **1** there are no orbitals of pure π_{Re-NO} character. The π_{Re-NO} bonding interaction makes the largest contribution into HOMO − 2 and HOMO − 1 with α-spin and HOMO − 1, HOMO orbitals with β-spin. A substantial contribution of π_{Re-NO} orbitals are also visible in HOMO − 16 and HOMO − 15 with α-spin and HOMO − 15 and HOMO − 12 with β-spin. In

Table 5
The energy and character of the selected occupied molecular orbitals with α- and β-spin for **1** and **2**

	1				**2**			
	α MO		β MO		α MO		β MO	
	E (eV)	Character	*E* (eV)	Character	*E* (eV)	Character	*E* (eV)	Character
HOMO − 19	−9.456	σ_{Cl}, π_{O}, π_{Ph}, π_{pyz}	−9.464	σ_{Cl}, σ_{C-P}, σ_{C-C}	−7.832	$\pi_{Cl}(34.3)$, $\pi_{O}(21.4)$, $\pi_{Ph}(25.2)$, $d_{xz}(10.5) + \pi^{*}_{NO}(5.1)$	−8.202	σ_{Cl}
HOMO − 18	−8.885	$\pi_{Cl}(43.8)$, $\pi_{O}(19.2)$, $d_{xy}(7.8)$	−9.328	$\pi_{Ph}(50.4)$, $\pi_{O}(21.0)$, $\sigma_{Cl}(8.5)$	−7.706	$\pi_{Ph}(35.4)$, $\pi_{Cl}(26.6)$, $\pi_{O}(12.1)$, $d_{yz}(14.7) + \pi^{*}_{NO}(9.1)$	−7.772	$\pi_{Cl}(38.5)$, $\pi_{O}(19.5)$, $d_{yz}(8.7) + \pi^{*}_{NO}(5.7)$
HOMO − 17	−8.709	$\pi_{Cl}(48.4)$, $\pi_{O}(13.7)$, $d_{xy}(12.3)$	−8.841	$\pi_{Cl}(50.1)$, $\pi_{O}(16.6)$	−7.613	$\pi_{Ph}(41.9)$, $\pi_{Cl}(40.0)$, $\pi_{O}(9.8)$	−7.650	$\pi_{Ph}(55.5)$, $\pi_{Cl}(22.4)$, $d_{yz}(7.9) + \pi^{*}_{NO}(6.4)$
HOMO − 16	−8.496	$d_{xz}(32.1) + \pi^{*}_{NO}(16.8)$, $\pi_{Cl}(36.9)$	−8.486	σ_{Cl}, π_{Cl}	−7.527	$\pi_{Ph}(53.5)$, $\pi_{Cl}(37.2)$	−7.579	$\pi_{Cl}(36.7)$, $\pi_{Ph}(36.9)$, $\pi_{O}(12.7)$, $d_{yz}(5.8) + \pi^{*}_{NO}(5.0)$
HOMO − 15	−8.220	$\pi_{pyz}(37.0)$, $\pi_{Cl}(32.8)$, $d_{yz}(14.8) + \pi^{*}_{NO}(8.4)$	−8.362	$d_{xz}(24.1) + \pi^{*}_{NO}(19.1)$, $\pi_{Cl}(47.7)$	−7.475	$\pi_{Ph}(54.6)$, $\pi_{Cl}(33.0)$	−7.496	$\pi_{Ph}(60.5)$, $\pi_{Cl}(33.6)$
HOMO − 14	−8.082	$\sigma_{Cl}(50.1)$, $\pi_{Ph}(19.3)$, $\pi_{O}(11.1)$	−8.168	$\pi_{pyz}(59.4)$, $\pi_{Cl}(25.2)$	−7.421	$\pi_{Ph}(71.2)$, $\pi_{Cl}(15.6)$, $\pi_{O}(8.9)$	−7.418	$\pi_{Ph}(57.1)$, $\pi_{Cl}(27.1)$, $\pi_{O}(6.6)$
HOMO − 13	−8.007	$\pi_{pyz}(30.8)$, $\pi_{Cl}(26.8)$, $d_{yz}(12.6) + \pi^{*}_{NO}(7.1)$	−7.977	$\pi_{Ph}(69.7)$, $\pi_{Cl}(18.3)$	−7.317	π_{Ph}	−7.406	$\pi_{Ph}(71.0)$, $\pi_{Cl}(20.6)$, $\pi_{O}(4.5)$
HOMO − 12	−7.915	$\pi_{Ph}(60.9)$, $\pi_{Cl}(19.4)$, $\pi_{O}(8.3)$	−7.941	$\pi_{Cl}(41.1)$, $\pi_{pyz}(23.0)$, $d_{yz}(13.0) + \pi^{*}_{NO}(9.3)$	−7.277	π_{Ph}	−7.295	π_{Ph}
HOMO − 11	−7.752	$\pi_{Ph}(55.6)$, $\pi_{Cl}(29.6)$	−7.860	$\pi_{Cl}(44.6)$, $\pi_{O}(13.7)$	−7.221	$\pi_{Ph}(68.1)$, $\pi_{Cl}(26.8)$	−7.259	π_{Ph}
HOMO − 10	−7.734	n_{pyz}	−7.728	$\pi_{pyz}(44.6)$, $\pi_{Ph}(43.8)$	−7.156	π_{Ph}	−7.158	π_{Ph}
HOMO − 9	−7.703	π_{Ph}	−7.714	$n_{pyz}(54.4)$, $\pi_{Ph}(35.2)$	−7.073	π_{Ph}	−7.144	π_{Ph}
HOMO − 8	−7.644	π_{Ph}	−7.694	π_{Ph}	−7.013	π_{Ph}	−7.058	π_{Ph}
HOMO − 7	−7.565	$\pi_{Cl}(49.1)$, $\pi_{Ph}(35.7)$	−7.628	π_{Ph}	−6.983	π_{Ph}	−7.004	π_{Ph}
HOMO − 6	−7.564	π_{Ph}	−7.562	π_{Ph}	−6.924	π_{Ph}	−6.951	π_{Ph}
HOMO − 5	−7.489	$\pi_{Cl}(62.9)$, $\pi_{Ph}(29.4)$	−7.535	$\pi_{Cl}(48.5)$, $\pi_{Ph}(33.8)$	−6.918	π_{Ph}	−6.914	π_{Ph}
HOMO − 4	−7.441	$_{Ph}(75.7)$, $\pi_{Cl}(20.0)$	−7.438	$\pi_{Ph}(56.0)$, $\pi_{Cl}(36.1)$	−6.767	$\pi_{Cl}(65.7)$, $\pi_{Ph}(32.0)$	−6.856	$\pi_{Ph}(70.5)$, $\pi_{Cl}(23.5)$
HOMO − 3	−7.094	π_{Cl}	−7.371	π_{Cl}	−6.681	$\pi_{Ph}(54.1)$, $\pi_{Cl}(28.2)$, $n_{p}.(8.7)$	−6.645	$\pi_{Ph}(42.5)$, $\pi_{Cl}(40.6)$, np.(10.8)
HOMO − 2	−6.573	$d_{yz}(30.4) + \pi^{*}_{NO}(20.2)$, $\pi_{Cl}(42.8)$	−6.873	π_{Cl}	−6.425	$d_{yz}(24.9) + \pi^{*}_{NO}(15.4)$, $\pi_{Cl}(44.6)$	−6.569	$\pi_{Cl}(77.7)$, $\pi_{Ph}(19.1)$
HOMO − 1	−6.465	$d_{xz}(30.3) + \pi^{*}_{NO}(19.6)$, $\pi_{Cl}(48.2)$	−6.462	$d_{yz}(25.9) + \pi^{*}_{NO}(30.5)$, $\pi_{Cl}(37.2)$	−6.235	$d_{xz}(30.1) + \pi^{*}_{NO}(22.0)$, $\pi_{Cl}(41.7)$	−6.326	$d_{yz}(23.3) + \pi^{*}_{NO}(23.1)$, $\pi_{Cl}(39.4)$
HOMO	−5.899	$d_{xy}(59.1)$, $\pi_{Cl}(34.9)$	−6.361	$d_{xz}(28.8) + \pi^{*}_{NO}(29.9)$, $\pi_{Cl}(42.6)$	−5.822	$d_{xy}(53.4)$, $\pi_{Cl}(41.8)$	−6.140	$d_{xz}(25.1) + \pi^{*}_{NO}(31.8)$, $\pi_{Cl}(38.9)$

Table 6
The energy and character of the selected unoccupied molecular orbitals with α- and β-spin for **1** and **2**

	1				**2**			
	α MO		β MO		α MO		β MO	
	E (eV)	Character	*E* (eV)	Character	*E* (eV)	Character	*E* (eV)	Character
LUMO	−2.322	$\pi^*_{pyz}(77.8)$, $\pi^*_{NO}(13.5) - d_{yz}(2.3)$	−2.909	$d_{xy}(72.4)$, $\pi_{Cl}(19.4)$	−1.340	$d_{x^2-y^2}(22\%) - \sigma_{Cl}(13.2) - \sigma_P(15.3)$, $\pi^*_{Ph}(36.3)$	−3.096	$d_{xy}(65.4)$, $\pi_{Cl}(25.9)$
LUMO + 1	−1.724	$\pi_P(14.6) + \pi^*_{Ph}(58.1)$, $\pi^*_{NO}(6.4) - d_{yz}(7.9)$	−2.353	$\pi^*_{pyz}(76.6)$, $\pi^*_{NO}(13.1) - d_{yz}(4.2)$	−1.290	$\pi_P(6.6) + \pi^*_{Ph}(56.7), d_{x^2-y^2}(11.8)$	−1.296	$\pi_P(12.7) + \pi^*_{Ph}(72.5)$
LUMO + 2	−1.572	$\pi_P(10.7) + \pi^*_{Ph}(79.2)$	−1.698	$\pi_P(15.1) + \pi^*_{Ph}(61.5)$, $\pi^*_{NO}(5.9) - d_{yz}(6.6)$	−1.200	$\pi^*_{NO}(47.7) - d_{yz}(19.2)$, $\pi^*_{Ph}(18.6)$	−1.211	$\pi^*_{NO}(39.2) - d_{yz}(21.5)$, $\pi^*_{Ph}(22.9)$
LUMO + 3	−1.336	$\pi^*_{NO}(30.3) - d_{xz}(21.2)$, $\pi^*_{Ph}(29.1)$	−1.570	$\pi_P(10.4) + \pi^*_{Ph}(80.2)$	−1.102	$\pi^*_{NO}(45.4) - d_{xz}(22.5)$, $\pi^*_{Ph}(18.1)$	−1.175	$d_{x^2-y^2}(24.0) - \sigma_{Cl}(15.9) - \sigma_P(16.7)$, $\pi^*_{Ph}(34.9)$
LUMO + 4	−1.245	$\pi^*_{NO}(21.4) - d_{xz}(15.3)$, $\pi^*_{Ph}(46.7)$	−1.309	$\pi^*_{NO}(30.6) - d_{xz}(22.4)$, $\pi^*_{Ph}(32.0)$	−0.922	π^*_{Ph}	−1.074	$\pi^*_{NO}(37.9) - d_{xz}(26.3)$, $\pi^*_{Ph}(22.1)$
LUMO + 5	−1.130	$\pi^*_{NO}(29.5) - d_{yz}(22.3)$, $\pi^*_{Ph}(25.4)$	−1.225	$\pi^*_{NO}(13.7) - d_{xz}(10.4)$, $\pi^*_{Ph}(63.9)$	−0.876	$\pi_P(7.7) + \pi^*_{Ph}(82.8)$	−0.909	π^*_{Ph}
LUMO + 6	−1.078	$d_{x^2-y^2}(29.1) - \sigma_{Cl}(23.5)$, $\pi^*_{Ph}(17.9)$, $\pi^*_{pyz}(17.4)$	−1.066	$\pi^*_{NO}(29.3) - d_{yz}(24.8)$, $\pi^*_{Ph}(22.4)$	−0.845	$\pi_P(7.1) + \pi^*_{Ph}(68.4)$	−0.872	$\pi_P(8.5) + \pi^*_{Ph}(85.8)$
LUMO + 7	−1.042	$\pi^*_{pyz}(68.2)$, $d_{x^2-y^2}(9.5)$	−1.047	π^*_{pyz}	−0.801	π^*_{Ph}	−0.803	$\pi^*_{Ph}(68.8)$, $\pi^*_{NO}(9.4) - d_{xz}(10.0)$
LUMO + 8	−0.943	π^*_{Ph}	−0.947	$\pi^*_{Ph}(77.3)$, $\pi^*_{NO}(7.0) - d_{yz}(7.1)$	−0.692	π^*_{Ph}	−0.769	$\pi^*_{Ph}(70.6)$, $\pi^*_{NO}(4.0) - d_{yz}(9.3)$
LUMO + 9	−0.793	π^*_{Ph}	−0.836	$d_{x^2-y^2}(39.7) - \sigma_{Cl}(33.6)$, $\pi^*_{Ph}(16.5)$	−0.511	$d_{z^2}(16.5) - \sigma_N(4.1) - \sigma_{Cl}(18.2)$, $\pi^*_{Ph}(79.8)$	−0.687	π^*_{Ph}
LUMO + 10	−0.579	π^*_{Ph}	−0.788	π^*_{Ph}	−0.474	π^*_{Ph}	−0.482	π^*_{Ph}
LUMO + 11	−0.281	$d_{z^2}(30.5) - \sigma_{Cl}(20.8)$	−0.580	π^*_{Ph}	−0.265	π^*_{Ph}	−0.353	$d_{z^2}(21.3) - \sigma_{Cl}(23.0)$, $\pi^*_{Ph}(39.3)$

HOMO − 16, HOMO − 2 and HOMO − 1 with α-spin and HOMO − 15, HOMO − 1 and HOMO orbitals with β-spin, the π_{Re-NO} orbitals are mixed with π_{Cl} orbitals. HOMO − 15 with α-spin and HOMO − 12 with β-spin have also a significant contribution of π_{pyz} orbitals. The bonding π_{Re-NO} orbitals with α- and β-spin are localised mainly on the rhenium d orbitals. The anti-bonding π^*_{Re-NO} interaction makes the largest contribution into LUMO, LUMO + 3, LUMO + 4 and LUMO + 5 with α-spin and LUMO, LUMO + 4, LUMO + 5 and LUMO + 6 with β-spin. The π^*_{Re-NO} orbitals have prevalent NO character and they are mixed with π^*_{pyz} or π^*_{Ph} orbitals. Considering the molecular orbital composition and positive total charge on the NO group, the character of the nitrosyl ligand in **1** may be described as NO^+.

The d_{xy} rhenium orbital and π orbitals of the chloride ligands in an anti-bonding arrangement make the main contribution into the HOMO with α-spin and LUMO with β-spin. The LUMO with β-spin is mainly localised on the pyrazine ligand with the admixture of π^*_{Re-NO} anti-bonding orbitals. LUMO + 6 with α-spin and LUMO + 9 with β-spin are mainly of $d_{x^2-y^2} - \sigma_{Cl} - \sigma_O$ character with a substantial contribution from π^*_{pyz} and π^*_{Ph} orbitals. The participation of the dz^2 rhenium orbital is visible in LUMO + 11 with α-spin and LUMO + 12 with β-spin.

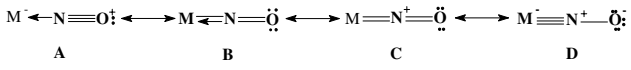
3.8. $ReCl_3(NO)(OPPh_3)(PPh_3)]$ (2)

For complex **2**, the π^*_{NO} orbitals are also distributed among several occupied MOs, and the largest contribution of π_{Re-NO} bonding orbitals is noticed for HOMO − 2 and HOMO − 1 with α-spin and HOMO − 1, HOMO orbitals with β-spin. The percent participations of π^*_{NO} orbitals in HOMO − 20 and HOMO − 18 with α-spin and HOMO − 19 and HOMO − 17 with β-spin do not reach 10%. LUMO + 2 and LUMO + 3 with α-spin and LUMO + 2 and LUMO + 4 are mainly composed of π^*_{Re-NO} orbitals (about 60%). Based on the molecular orbital composition and small spin densities on the nitrogen and oxygen atoms of the nitrosyl ligand, the character of the NO group in **2** may be described as NO^+.

Similar to complex **1**, HOMO with α-spin and LUMO with β-spin are d_{xy} rhenium orbitals with the admixture of chlorine π orbitals. The LUMO with α-spin is mainly of $d_{x^2-y^2} - \sigma_{Cl} - \sigma_P$ character with a substantial contribution from π^*_{Ph} orbitals. The dz^2 rhenium orbital makes a contribution into LUMO + 9 with α-spin and LUMO + 11 with β-spin. HOMO − 3 with α and HOMO − 3 with β-spin are localised on the chloride and phenyl ligands with a substantial contribution from the free electron pair on the phosphorous atom of the PPh_3 molecule.

3.9. NBO analysis

Additional information about the binding in complexes **1** and **2** was obtained by NBO analysis. In open-shell systems, the density operator separates into distinct components for α- and β-spin, leading to the possibility of different NBOs for different spins [54]. Table 7 presents the occupancies and NAO compositions of the selected α- and β-spin NBOs for complexes **1** and **2**. For compound **1**, six natural bond orbitals (three with α-spin and three with β-spin) were detected for the Re–N bond, and two orbitals (one with α-spin and one with β-spin) for the N–O bond. The Re–N bond orbitals of σ-character with α- and β-spins are polarised towards the nitrogen atom (ca. 77% at N) and the s and d orbitals of Re take part in the bonding. The Re–N bond orbitals of π-character are mainly polarised toward the metal atom and only d-orbitals of Re are included in the bonding. The N–O bond orbitals with α- and β-spins are slightly polarised towards the oxygen end. In the valence-bond treatment a linear bonding mode of the nitrosyl group may be represented by the following resonance forms [1]:



The results of the NBO analysis indicate that the resonance structure of D makes a significant contribution to the structure of complex **1**.

For complex **2**, significantly different NBOs for different spins are observed. One natural bond orbital for the Re–N bond and three orbitals for the N–O bond were detected in the case of orbitals with α-spin, whereas three NBOs for the Re–N bond and one orbital for the N–O bond were detected for orbitals with β-spin. For complex **2**, the α and β natural Lewis structure can be represented by the resonance structure of A and D, respectively. The total occupancy number of the natural bond orbitals for the Re–N bond is larger for complex **1**, whereas the total occupancy number of the NBOs for the N–O bond is larger for **2**. It indicates that the π-backdonation is stronger for complex **1**. The changes of Re–N and N–O bond distances, listed in Tables 1 and 2, also confirm the above-discussed results. An insignificant shortening of the Re–N distance and elongation of the N–O bond length can be noticed for complex **1**.

3.10. Electronic spectra

The experimental and calculated electronic spectra of **1** are presented in Fig. 3. Each calculated transition in Fig. 3(b) was represented by a gaussian function with the height equal to the oscillator strength and width equal to 0.06.

Table 7
Results of the NBO analysis of complexes **1** and **2**

Bond orbital		**1**		**2**	
		α-Spin orbitals	β-Spin orbitals	α-Spin orbitals	β-Spin orbitals
Re–N/BD					
σ	occ.	0.986	0.987	0.982	0.982
	%Re	22.96; $sd^{68.73}$	22.14; $sd^{59.14}$	24.79; $sd^{74.11}$	24.23; $sd^{73.96}$
	%N	77.04; $sp^{37.11}$	77.86; $sp^{36.55}$	75.21; $sp^{37.55}$	75.77; $sp^{40.39}$
π	occ.	0.989	0.991		0.990
	%Re	64.20; $d^{99.92}$	53.43; $d^{99.89}$		52.03; $d^{99.32}$
	%N	35.80; $p^{99.90}$	46.57; $p^{99.92}$		47.97; $p^{99.91}$
π	occ.	0.981	0.998		0.983
	%Re	63.14; $d^{98.93}$	44.82; $d^{99.19}$		52.95; $d^{99.21}$
	%N	36.86; $p^{99.88}$	47.24; $p^{99.91}$		47.07; $p^{95.95}$
N–O/BD					
σ	occ.	0.998	0.998	0.998	0.998
	%N	44.84; $sp^{62.92}$	44.82; $sp^{63.43}$	44.95; $sp^{63.07}$	44.89; $sp^{63.45}$
	%O	55.16; $sp^{68.69}$	55.18; $sp^{68.86}$	55.05; $sp^{68.66}$	55.11; $sp^{68.83}$
π	occ.			0.999	
	%N			33.66; $p^{99.47}$	
	%O			66.34; $p^{99.55}$	
π	occ.			0.999	
	%N			34.05; $p^{99.44}$	
	%O			65.95; $p^{99.59}$	
*Re–N/BD**					
σ	occ.	0.144	0.137	0.178	0.136
π	occ.	0.269	0.226		0.230
π	occ.	0.268	0.226		0.237
*N–O/BD**					
σ	occ.	0.007	0.006	0.006	0.006
π	occ.			0.305	
π	occ.			0.295	

The hybridisation of the atoms is indicated with the percent contribution of the metal-centered d or (and) p orbitals as a superscript.

Tables 8 and 9 show the energy and molar absorption coefficients of the experimental absorption bands and the spin-allowed doublet–doublet electronic transitions calculated with the TDDFT method for **1** and **2**, respectively. The positions and molar absorption coefficients of the electronic bands for complex **2** have been taken from paper [17].

The investigated complexes are of large size and the number of basis functions are equal to 510 and 718 for **1** and **2**, respectively. Eighty electron transitions calculated by the TDDFT method do not comprise all the experimental absorption bands. The UV–Vis spectra of **1** and **2** were calculated to ~260 nm, so the shortest wavelength experimental bands cannot be assigned to the calculated transitions. However, considering that the solution spectra of PPh_3, $OPPh_3$ and pyrazine exhibit intense absorption bands in the 260–200 nm region, some additional intraligand and interligand transitions are expected to be found at higher energies in the calculations.

The calculations result in many transitions with very small oscillator strengths. Except for the electronic transitions of $d \rightarrow \pi^*_{NO}$ character and the low energy part of the spectrum, only transitions with oscillator strengths larger than 0.0040 are listed in Tables 7 and 8.

The assignment of the calculated transitions to the experimental bands is based on the criterion of the energy and oscillator strength of the calculated transitions. In the description of the electronic transitions, the main components of the molecular orbital are used. The bonding $\pi_{Re–NO}$ orbitals are assigned as d orbitals, and the antibonding $\pi^*_{Re–NO}$ orbitals as π^*_{NO}.

3.11. *$ReCl_3(NO)(OPPh_3)(pyz)]$ (**1**)*

In the description of the electronic transitions of **1** the main components of the molecular orbital are used: the LUMO with β-spin is assumed as an orbital of d

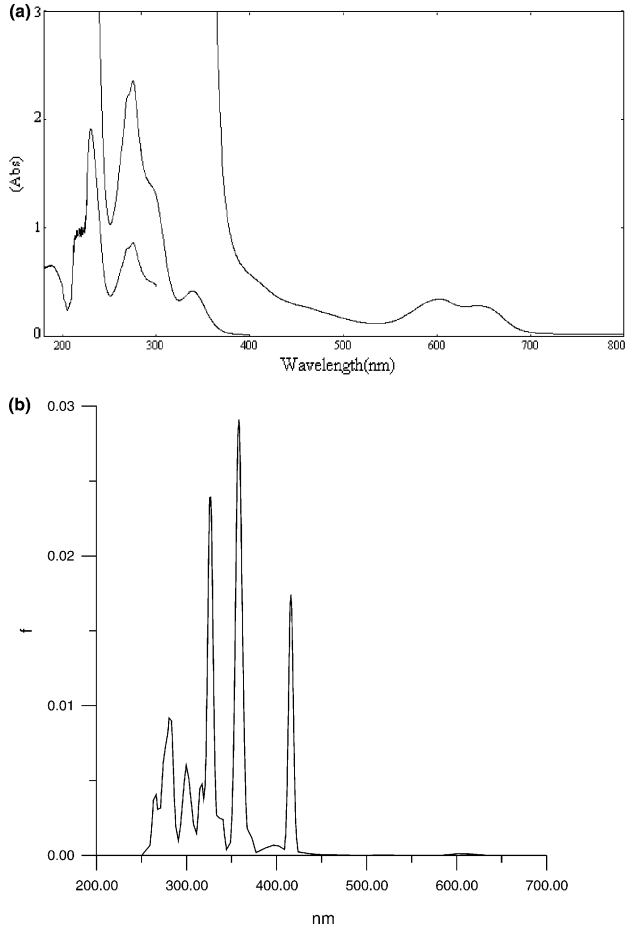


Fig. 3. The experimental (a) and calculated (b) electronic absorption spectrum of **1**.

character, LUMO with α-spin and LUMO + 1 with β-spin are described as π^*_{Ph} orbitals, LUMO + 4 with α-spin and LUMO + 5 with β-spin are treated as π^*_{Ph} orbitals.

The longest wavelength experimental bands at 646.2 and 603.6 nm may be attributed to the transitions of $d_{Re}/\pi_{Cl} \rightarrow d$ character with small oscillator strengths, calculated at 621.3 and 600.9 nm, respectively.

The weak absorption band at 458.9 nm is assigned to the calculated transitions with small oscillator strengths at 526.4 and 463.2 nm. The first one corresponds mainly to the electronic transition from the rhenium d orbitals onto π* orbitals of the nitrosyl group. Considering that the bonding π_{Re-NO} and anti-bonding π^*_{Re-NO} orbitals are mixed with the π chloride and π^*_{Ph} orbitals respectively, the character of the transition at 526.4 nm is determined as $d_{Re}/\pi_{Cl} \rightarrow \pi^*_{NO}/\pi^*_{Ph}$. The transition at 463.2 nm is of $d_{Re}/\pi_{Cl} \rightarrow \pi^*_{pyz}$ origin.

The experimental band at 408.5 nm is also attributed to transitions of $d/\pi_{Cl} \rightarrow \pi^*_{Ph}$ and $d/\pi_{Cl} \rightarrow d/\pi^*_{Ph}/\pi^*_{pyz}$ character with small oscillator strengths, calculated at 449.0 and 437.3 nm, respectively.

The experimental absorption band at 359.4 nm is assigned to the transition calculated between 420 and 335 nm. These transitions are mainly of LMCT ($\pi_{Cl} \rightarrow d$) character. The electronic transitions from the rhenium d orbitals onto π* orbitals of the nitrosyl group calculated in the range 420–335 nm have small oscillator strengths and they do not contribute significantly to the overall shape of the spectrum.

The experimental band at 309.0 nm is attributed to the calculated transition of $\pi_{Cl} \rightarrow \pi^*_{pyz}$ character at 326.7 nm and some LMCT ($\pi_{Cl}/\pi_{Ph}/\pi_O \rightarrow d$) transitions. LUMO + 1 with β-spin has a substantial admixture of the rhenium d orbitals, so the transition from chloride ligand to π^*_{pyz} orbitals are mediated by the metal.

3.12. $ReCl_3(NO)(OPPh_3)(PPh_3)]$ (**2**)

In the description of the electronic transitions of **2** the main components of the molecular orbital are used: the LUMO with β-spin is assumed as an orbital of d character. LUMO + 1 and LUMO + 2 with α-spin and LUMO + 2 and LUMO + 4 with β-spin are described as π^*_{NO} orbitals.

The longest wavelength experimental bands at 719.9 and 656.2 nm may be attributed to transitions of $d/\pi(Cl) \rightarrow d$ character with small oscillator strengths, calculated at 756.8 and 671.3 nm, respectively.

The experimental absorption bands at 421.0 and 356.0 nm are assigned to the LMCT ($\pi_{Cl} \rightarrow d$, $\pi_{Ph} \rightarrow d$ and $n(P) \rightarrow d$) transitions with large oscillator strengths. In comparison with complex **1**, the LMCT ($\pi_{Cl} \rightarrow d$, $\pi_{Ph} \rightarrow d$ and $n(P) \rightarrow d$) electronic transitions are bathochromically shifted. The electronic transitions from the rhenium d orbitals onto π* orbitals of the nitrosyl group have small oscillator strengths and they do not contribute significantly to the overall shape of the bands at 421.0 and 356.0 nm. Similar to complex **1**, they are hidden under the more intense transitions of LMCT character. However, such small values of the oscillator strengths seem to be typical of $d \rightarrow \pi^*_{NO}$ transitions, and they have been supported by the calculations for other metal nitrosyls [55,56].

The experimental band at 279.0 is mainly attributed to the calculated transition of $\pi_{Cl} \rightarrow d$ character at 298.5 nm.

The intense absorption band at 266.0 is assigned to the interligand charge transfer transitions, but this assignment is probably not complete. Similar to complex **1**, some additional intraligand and interligand transitions can be expected at higher energies in the calculated spectrum.

Table 8
The energy and molar absorption coefficients of the experimental absorption bands and the electronic transitions calculated with the TDDFT method for **1**

The most important orbital excitations	Character	λ (nm)	E (eV)	f	Experimental, Λ [nm] (E [eV]) ε
H(β) → L(β)	$d_{xz}/\pi(Cl) \rightarrow d_{xy}$	621.3	2.00	0.0002	646.2 (1.92) 50
H − 1(β) → L(β)	$d_{yz}/\pi(Cl) \rightarrow d_{xy}$	600.9	2.06	0.0001	603.6 (2.05) 60
H − 1(α) → L + 3(α)	$d_{xz}/\pi(Cl) \rightarrow \pi^*(NO)/\pi^*(Ph)$	526.4	2.36	0.0002	
H(β) → L + 4(β)	$d_{xz}/\pi(Cl) \rightarrow \pi^*(NO)/\pi^*(Ph)$				458.9 (2.70) 30
H − 1(β) → L + 6(β)	$d_{yz}/\pi(Cl) \rightarrow \pi^*(NO)/\pi^*(Ph)$				
H(α) → L(α)	$d_{xy}/\pi(Cl) \rightarrow \pi^*(pyz)$	463.2	2.68	0.0002	
H(α) → L + 1(α)	$d_{xy}/(Cl) \rightarrow \pi^*(Ph)$	449.0	2.76	0.0001	
H(α) → L + 6(α)	$d_{xy}/\pi(Cl) \rightarrow d_{x^2-y^2}/\pi^*(Ph)/\pi^*(pyz)$				408.5 (3.04) 70
H(β) → L + 4(β)	$d_{xz}/\pi(Cl) \rightarrow \pi^*(NO)/\pi^*(Ph)$	437.3	2.84	0.0001	
H − 1(β) → L + 1(β)	$d_{yz}/\pi(Cl) \rightarrow \pi^*(pyz)$				
H − 2(β) → L(β)	$\pi(Cl) \rightarrow d_{xy}$	416.1	2.98	0.0175	
H(α) → L + 3(α)	$d_{xy}/\pi(Cl) \rightarrow \pi^*(NO)/\pi^*(Ph)$	399.4	3.10	0.0011	
H − 2(α) → L(α)	$d_{yz}/\pi(Cl) \rightarrow \pi^*(pyz)$	362.4	3.42	0.0080	
H(α) → L + 5(α)	$d_{xy}/\pi(Cl) \rightarrow \pi^*(NO)/\pi^*(Ph)$	358.8	3.45	0.0045	359.4 (3.45) 1040
H − 3(β) → L(β)	$\pi(Cl) \rightarrow d_{xy}$	357.9	3.46	0.0204	
H − 5(β) → L(β)	$\pi(Cl)/\pi(Ph) \rightarrow d_{xy}$	354.4	3.50	0.0061	
H − 2(α) → L + 3(α)	$d_{yz}/\pi(Cl) \rightarrow \pi^*(NO)/\pi^*(Ph)$	339.4	3.65	0.0016	
H − 1(β) → L + 4(β)	$d_{yz}/\pi(Cl) \rightarrow \pi^*(NO)/\pi^*(Ph)$				
H − 2(β) → L + 1(β)	$\pi(Cl) \rightarrow \pi^*(pyz)$	326.7	3.79	0.0143	
H − 11(β) → L(β)	$(Cl)/\pi(O) \rightarrow d_{xy}$				
H(α) → L + 2(α)	$d_{xy}/\pi(Cl) \rightarrow \pi^*(Ph)$	324.7	3.82	0.0042	309.0 (4.01) 3850
H(α) → L + 11(α)	$d_{xy}/\pi(Cl) \rightarrow d_{z^2}$	316.2	3.92	0.0049	
H − 116(β) → L(β)	$\sigma(Cl)/\pi(Cl) \rightarrow d_{xy}$	282.8	4.43	0.0045	
					275.4 (4.51) 9890
					230.4 (5.38) 22000

ε, Molar absorption coefficient ($dm^3\ mol^{-1}\ cm^{-1}$).

Table 9
The energy and molar absorption coefficients of the experimental absorption bands and the electronic transitions calculated with the TDDFT method for **1**

The most important orbital excitations	Character	λ (nm)	E (eV)	f	Experimental, Λ [nm] (E [eV]) ε
H(β) → L(β)	$d_{xz}/\pi(Cl) \rightarrow d_{xy}$	756.8	1.64	0.0001	719.9 (1.72) 17
H − 1(β) → L(β)	$d_{yz}/\pi(Cl) \rightarrow d_{xy}$	671.3	1.85	0.0002	656.2 (1.89) 40
H − 1(α) → L + 3(α)	$d_{xz}/\pi(Cl) \rightarrow \pi^*(NO)$	497.3	2.49	0.0002	
H − 2(β) → L(β)	$\pi(Cl)/\pi(Ph) \rightarrow d_{xy}$	485.9	2.55	0.0093	
H − 3(β) → L(β)	$\pi(Ph)/\pi(Cl)/n(P) \rightarrow d_{xy}$	469.5	2.64	0.0198	421.0 (2.94) 2100
H(α) → L(α)	$d_{xy}/\pi(Cl) \rightarrow d_{x^2-y^2}/\pi^*(Ph)$	426.2	2.91	0.0011	
H(β) → L + 2(β)	$d_{xz}/\pi(Cl) \rightarrow \pi^*(NO)$	415.5	2.98	0.0001	
H − 4(β) → L(β)	$\pi(Ph)/\pi(Cl) \rightarrow d_{xy}$	413.2	3.00	0.0103	
H − 1(β) → L + 2(β)	$d_{yz}/\pi(Cl) \rightarrow \pi^*(NO)$	404.0	3.07	0.0002	
H − 5(β) → L(β)	$\pi(Ph) \rightarrow d_{xy}$	403.1	3.08	0.0022	
H − 6(β) → L(β)	$\pi(Ph) \rightarrow d_{xy}$	383.1	3.24	0.0046	
H(α) → L + 2(α)	$d_{xy}/\pi(Cl) \rightarrow \pi^*(NO)$	371.6	3.34	0.0009	
H(α) → L + 3(α)	$d_{xy}/\pi(Cl) \rightarrow \pi^*(NO)$	366.1	3.39	0.0015	356.0 (3.48) 1793
H − 1(α) → L + 2(α)	$d_{xz}/\pi(Cl) \rightarrow \pi^*(NO)$	352.7	3.51	0.0001	
H(β) → L + 2(β)	$d_{xz}/\pi(Cl) \rightarrow \pi^*(NO)$				
H − 2(α) → L + 2(α)	$d_{yz}/\pi(Cl) \rightarrow \pi^*(NO)$	315.2	3.93	0.0004	
H − 1(α) → L + 3(α)	$d_{xz}/\pi(Cl) \rightarrow \pi^*(NO)$				
H − 2(α) → L + 3(α)	$d_{yz}/\pi(Cl) \rightarrow \pi^*(NO)$	308.6	4.02	0.0002	
H − 21(β) → L(β)	$\pi(Cl) \rightarrow d_{xy}$	298.5	4.15	0.0206	279.0 (4.44) 7 811
H − 2(α) → L + 3(α)	$d_{yz}/\pi(Cl) \rightarrow \pi^*(NO)$	298.1	4.16	0.0057	
H − 2(β) → L + 3(β)	$\pi(Cl)/\pi(Ph) \rightarrow d_{x^2-y^2}/\pi^*(Ph)$	268.2	4.62	0.0071	
H − 3(α) → L + 2(α)	$\pi(Ph)/\pi(Cl)/n(P) \rightarrow \pi^*(NO)/\pi^*(Ph)$	265.5	4.67	0.0134	266.0(4.66)15 800
H − 4(α) → L + 2(α)	$\pi(Cl)/\pi(Ph) \rightarrow \pi^*(NO)$	261.2	4.75	0.0050	

ε, Molar absorption coefficient ($dm^3\ mol^{-1}\ cm^{-1}$).

4. Conclusions

The $[ReCl_3(NO)(OPPh_3)(pyz)]$ (**1**) complex has been obtained by two different routes, and characterised by IR, UV–Vis and magnetic measurements. Its crystal and molecular structure has been determined. Theoretical studies of $[ReCl_3(NO)(OPPh_3)(pyz)]$ and the related complex $[ReCl_3(NO)(OPPh_3)(PPh_3)]$ (**2**) have been performed by the DFT method with the aim to investigate their molecular and electronic structures, spectral properties and bonding. Most of the MOs of **1** and **2** have complicated character. The electronic configuration of the metal center in the investigated complexes is as follows: $(d_{xz})^2(d_{yz})^2(d_{xy})^1$. The d_{xy} rhenium orbital makes the main contributions into the HOMO with α-spin and LUMO with β-spin. The occupied d_{yz} and d_{xz} rhenium orbitals participate in back-donation from the central ion to the NO ligand. However, the d_{yz}/d_{xz} and π^*_{NO} orbitals are distributed among several occupied MOs to give a considerable contribution into several HOMO and LUMO orbitals. For both complexes, the bonding π_{Re-NO} orbitals are localised mainly on the rhenium d orbitals, whereas the π^*_{Re-NO} orbitals have prevalent NO character. The results of the NBO analyses indicate a stronger π-backdonation in complex **1**. A shortening of the Re–N distance and elongation of the N–O bond length observed for complex **1** confirms it. The TDDFT calculations for complexes **1** and **2** reveal that the electronic transitions from the rhenium d orbitals onto the π* orbitals of the nitrosyl group have small oscillator strengths and they do not contribute significantly to the overall shape of the spectrum. They are hidden under the more intense transitions of LMCT character.

5. Supplementary data

Supplementary data for $C_{22}H_{19}Cl_3N_3O_2PRe$ are available from the CCDC, 12 Union Road, Cambridge CB2 1EZ, UK (fax: +44 1223 336033; e-mail: deposit@ccdc.cam.ac.uk or at www: http://www.ccdc.cam.ac.uk) on request, quoting the deposition number: 243040.

Acknowledgements

The GAUSSIAN03 calculations were carried out in the Wrocław Centre for Networking and Supercomputing, WCSS, Wrocław, Poland under calculational Grant No. 51/96.

References

[1] G.B. Richter-Addo, P. Legzdins, Metal Nitrosyls, Oxford University Press, Oxford, 1992.
[2] J.A. McCleverty, Chem. Rev. 79 (1979) 53.
[3] J.N. Kukuškin, Reakcionnaja sposobnost koordinacjonnych soedinienij, Chimija, Leningrad, 1987.
[4] J.H. Enemark, R.D. Feltham, Coord. Chem. Rev. 13 (1974) 339.
[5] K.G. Caulton, Coord. Chem. Rev. 14 (1975) 317.
[6] F. Bottomley, Coord. Chem. Rev. 26 (1978) 7.
[7] K.K. Pandey, Coord. Chem. Rev. 51 (1983) 70.
[8] G. Wilkinson, Comprehensive Coordination Chemistry, vol. 2, Pergamon Press, Oxford, 1987, p. 100.
[9] G.B. Richter-Addo, P. Legzdins, J. Burstyn, Chem. Rev. 102 (2002) 857.
[10] T.W. Hayton, P. Legzdins, W.B. Sharp, Chem. Rev. 102 (2002) 935.
[11] J.A. McCleverty, Chem. Rev. 104 (2004) 403.
[12] W. Volkert, W.F. Goeckeler, G.J. Ehrhardt, A.R. Ketring, J. Nucl. Med. 32 (1991) 174.
[13] E.A. Deutsch, K. Libson, J.L. Vanderheyden, Technetium and Rhenium in Chemistry and Nuclear Medicine, Raven Press, New York, 1990.
[14] J.O. Dzięgielewski, B. Machura, J. Marek, Polyhedron 15 (1996) 3713.
[15] J.O. Dzięgielewski, B. Machura, T.J. Bartczak, Polyhedron 15 (1996) 2813.
[16] T.J. Bartczak, W. Czurak, J.O. Dzięgielewski, B. Machura, Polish J. Chem. 72 (1998) 633.
[17] J.O. Dzięgielewski, B. Machura, T. Kupka, T.J. Bartczak, W. Czurak, Polish J. Chem. 72 (1998) 1009.
[18] J.O. Dzięgielewski, B. Machura, T.J. Bartczak, W. Czurak, J. Kusz, J. Warczewski, J. Coord. Chem. 48 (1999) 125.
[19] T.J. Bartczak, W. Czurak, J.O. Dzięgielewski, B. Machura, A. Jankowska, J. Kusz, J. Warczewski, Polyhedron 18 (1999) 2313.
[20] T.J. Bartczak, W. Czurak, J.O. Dzięgielewski, B. Machura, J. Kusz, J. Warczewski, Polish J. Chem. 74 (2000) 265.
[21] T.J. Bartczak, W. Czurak, J.O. Dzięgielewski, B. Machura, A. Jankowska, J. Kusz, J. Warczewski, J. Coord. Chem. 52 (2001) 361.
[22] B. Machura, J.O. Dzięgielewski, S. Michalik, T.J. Bartczak, R. Kruszynski, J. Kusz, Poyhedron 21 (2002) 2617.
[23] M.C. Aragoni, M. Arca, T. Cassano, C. Denotti, F.A. Devillanova, F. Isaia, V. Lippolis, D. Natali, L. Niti, M. Sampietro, R. Tommasi, G. Verani, Inorg. Chem. Commun. 5 (2002) 869.
[24] P. Romaniello, F. Lelj, Chem. Phys. Lett. 372 (2003) 51.
[25] P. Norman, P. Cronstrand, J. Ericsson, Chem. Phys. 285 (2002) 207.
[26] J. Bossert, N.B. Amor, A. Strich, C. Daniel, Chem. Phys. Lett. 342 (2001) 617.
[27] C.E. Powell, M.P. Cifuentes, A.M. McDonagh, S.K. Hurst, N.T. Lucas, C.D. Delfs, R. Stranger, M.G. Humphrey, S. Houbrechts, I. Asselberghs, A. Persoons, D.C.R. Hockless, Inorg. Chim. Acta 352 (2003) 9.
[28] J.P. Morral, C.E. Powell, R. Stranger, M.P. Cifuentes, M.G. Humphrey, G.A. Heath, J. Organomet. Chem. 670 (2003) 248.
[29] P. Romaniello, F. Lelj, J. Mol. Struct. Theochem. 636 (2003) 23.
[30] A. Voigt, U. Abram, R. Böttcher, U. Richter, J. Reinhold, R. Kirmse, Chem. Phys. 253 (2000) 171.
[31] M. Lipowska, L. Hansen, R. Cini, X. Xu, H. Choi, A.T. Taylor, L.G. Marzilli, Inorg. Chim. Acta 339 (2002) 327.
[32] J. Gancheff, C. Kremer, E. Kremer, O.N. Ventura, J. Mol. Struct. (Theochem) 580 (2002) 107.
[33] M.L. Kuznestov, E.A. Klestova-Nadeeva, A.I. Dement'ev, J. Mol. Struct. (Theochem) 671 (2004) 229.
[34] N. Psaroudakis, K. Mertis, D.G. Liakos, E.D. Simandiras, Chem. Phys. Lett. 369 (2003) 490.
[35] X.-Y. Liu, S. Bouherour, H. Jacobsen, H.W. Schmalle, H. Berke, Inorg. Chim. Acta 330 (2002) 250.
[36] É. Bencze, J. Mink, I. Pápai, I.S. Butler, D. Lafleur, D.F.R. Gilson, J. Organomet. Chem. 616 (2000) 1.

[37] W.-Y. Wong, S.-H. Cheung, X. Huang, Z. Lin, J. Organomet. Chem. 655 (2002) 39.
[38] G. Rouschias, G. Wilkinson, J. Chem. Soc. A (1966) 465.
[39] STOE & Cie (1999), X-RED, Version 1.18, STOE & Cie GmbH, Darmstadt, Germany.
[40] G.M. Sheldrick, Acta Crystallogr. A 46 (1990) 467.
[41] G.M. Sheldrick, SHELXL97. Program for the Solution and Refinement of Crystal Structures, University of Göttingen, Germany, 1997.
[42] G.M. Sheldrick, SHELXTL: Release 4.1 for Siemens Crystallographic Research Systems, 1990.
[43] M.J. Frisch, G.W. Trucks, H.B. Schlegel, G.E. Scuseria, M.A. Robb, J.R. Cheeseman, J.A. Montgomery Jr., T. Vreven, K.N. Kudin, J.C. Burant, J.M. Millam, S.S. Iyengar, J. Tomasi, V. Barone, B. Mennucci, M. Cossi, G. Scalmani, N. Rega, G.A. Petersson, H. Nakatsuji, M. Hada, M. Ehara, K. Toyota, R. Fukuda, J. Hasegawa, M. Ishida, T. Nakajima, Y. Honda, O. Kitao, H. Nakai, M. Klene, X. Li, J.E. Knox, H.P. Hratchian, J.B. Cross, C. Adamo, J. Jaramillo, R. Gomperts, R.E. Stratmann, O. Yazyev, A.J. Austin, R. Cammi, C. Pomelli, J.W. Ochterski, P.Y. Ayala, K. Morokuma, G.A. Voth, P. Salvador, J.J. Dannenberg, V.G. Zakrzewski, S. Dapprich, A.D. Daniels, M.C. Strain, O. Farkas, D.K. Malick, A.D. Rabuck, K. Raghavachari, J.B. Foresman, J.V. Ortiz, Q. Cui, A.G. Baboul, S. Clifford, J. Cioslowski, B.B. Stefanov, G. Liu, A. Liashenko, P. Piskorz, I. Komaromi, R.L. Martin, D.J. Fox, T. Keith, M.A. Al-Laham, C.Y. Peng, A. Nanayakkara, M. Challacombe, P.M.W. Gill, B. Johnson, W. Chen, M.W. Wong, C. Gonzalez, J.A. Pople, GAUSSIAN03, Revision B.03, Gaussian Inc., Pittsburgh, PA, 2003.
[44] A.D. Becke, J. Chem. Phys. 98 (1993) 5648.
[45] C. Lee, W. Yang, R.G. Parr, Phys. Rev. B 37 (1988) 785.
[46] M.E. Casida, in: J.M. Seminario (Ed.), Recent Developments and Applications in Modern Density Functional Theory, Theoretical and Computational Chemistry, vol. 4, Elsevier, Amsterdam, 1996.
[47] P.J. Hay, W.R. Wadt, J. Chem. Phys. 82 (1985) 299.
[48] E.D. Glendening, A.E. Reed, J.E. Carpenter, F. Weinhold, NBO (version 3.1).
[49] G.A. Jeffrey, W. Saenger, Hydrogen Bonding in Biological Structures, Springer-Verlag, New York, 1994.
[50] G.R. Desiraju, T. Steiner, The Weak Hydrogen Bond in Structural Chemistry and Biology, Oxford University Press, Oxford, 1999.
[51] E. Iengo, E. Zangrando, S. Mestroni, G. Fronzoni, M. Stener, E. Alessio, J. Chem. Soc., Dalton Trans. (2001) 1338.
[52] B.L. Haymore, I.A. Ibers, Inorg. Chem. 14 (1975) 3060.
[53] J.P. Collman, J.T. McDevitt, C.R. Leinder, G.T. Yee, J.B. Torrance, W.A. Little, J. Am. Chem. Soc. 109 (1987) 4606.
[54] A.E. Reed, L.A. Curtiss, F. Weinhold, Chem. Rev. 88 (1988) 899.
[55] S.C. da Silva, D.W. Franco, Spectrochim. Acta 55A (1999) 1515.
[56] S.I. Gorelsky, S.C. da Silva, A.B.P. Lever, D.W. Franco, Inorg. Chim. Acta 300–302 (2000) 698.

Available online at www.sciencedirect.com
SCIENCE DIRECT®
Polyhedron 24 (2005) 281–287
POLYHEDRON
www.elsevier.com/locate/poly

Compounds of some alkylamido-substituted cyclic tetraamines with nickel(II); the structure of *trans*-[Ni(L)(OCO_2H)(OH_2)]·*trans*-[Ni(L)(OH_2)$_2$] ClO_4·(HCO_3)$_2$, L = *trans*-6,13-dimethyl-6,13-bis(ethylamido)-1,4,8,11-tetraazacyclotetradecane

Neil F. Curtis [a,*], Horst Puschmann [b]

[a] *School of Chemical and Physical Sciences, Victoria University of Wellington, P.O. Box 600, Wellington, New Zealand*
[b] *Chemical Crystallography Unit, Chemistry Department, Durham University, Durham, DH1 3HP, UK*

Received 19 October 2004; accepted 16 November 2004

Abstract

The amino substituents of (*trans*-6,13-diamino-6,13-dimethyl-1,4,8,11-tetraazacyclotetradecane)nickel(II) are readily acylated by reaction with acetic or propionic anhydrides to form the 6,13-bismethylamido-(acetylamido) or 6,13-bis(propionylamido)-(ethylamido) substituted cations, $[Ni(diamme)]^{2+}$ or $[Ni(diamet)]^{2+}$. The amide substituents, which are resistant towards hydrolysis, show little tendency to coordinate. Square planar salts and octahedral compounds *trans*-[Ni(diamme/et)X_2], X^- = Cl^-, NCS^-, N_3^-, NO_2^-, were prepared. The structure is reported for *trans*-(aquo-κ^1O)-(hydrogen carbonato-κ^1O)-($S^1S^4R^8R^{11}$-*trans*-6,13-bisethylamido-6,13-dimethyl-1,4,8,11-tetraazacyclotetradecane-$\kappa^4N^1N^4N^8N^{11}$)nickel(II) *trans*-di(aquo-κ^1O)-($R^1R^4S^8S^{11}$-*trans*-6,13-bisethylamido-6,13-dimethyl-1,4,8,11-tetraazacyclotetradecane-$\kappa^4N^1N^4N^8N^{11}$)nickel(II) perchlorate bis(hydrogen carbonate), $C_{18}H_{42}N_6NiO_4$·$C_{19}H_{41}N_6NiO_6$·2(CHO_3)·ClO_4. The asymmetric unit has two cations with the macrocycle in square-planar coordination by the endocyclic nitrogen atoms of diamet, one with *trans*-diaqua- and the other with *trans*-aqua-(hydrogen carbonato)-unidentate additional ligands. The two un-coordinated hydrogen carbonate ions are present as a hydrogen-bonded planar dimer.
© 2004 Elsevier Ltd. All rights reserved.

Keywords: Nickel(II) compounds; Cyclic amine compounds; Amido compounds; Methylamido (acetylamino, acetamido) compounds; Ethylamido (propionylamino) compounds; Hydrogen carbonato ligand; Crystal structures

1. Introduction

There have been many studies of the coordinating properties of amides and peptides [1,2] and of azamacrocycles with N-amido [3] or C-amino substituents, but few of azamacrocycles with C-amido substituents.

Compounds of the di-amino-substituted cyclic tetraamine *trans*-6,13-diamino-6,13-dimethyl-1,4,8,11-tetraazacyclotetradecane, diam, have been prepared by reduction of the nitro functions of (*trans*-6,13-diamino-6,13-dinitro-1,4,8,11-tetraazacyclotetradecane)-metal cations, formed by reactions of bis(ethane-1,2-diamine)-metal compounds with methanal plus nitroethane [4–7]. The preparations, properties and structures of compounds of diam with Ni(II) have been described [7].

The amine substituents of $[Cu(diam)]^{2+}$ have been alkylated [8,9] and converted into exo-olefine functions by nitrosation [10]. Reaction of $[Pt(Hdiam)](ClO_4)_3$ with chlorine forms a Pt(IV) compound with dichloroamine substituents [11]. The amine substituents of diam have been converted to the (ferrocenyl-methylamino)-function and Cu(II) and Zn(II) compounds of this ligand

* Corresponding author. Tel.: +64 4463 6514; fax: +64 4 463 5237.
E-mail address: neil.curtis@vuw.ac.nz (N.F. Curtis).

0277-5387/$ - see front matter © 2004 Elsevier Ltd. All rights reserved.
doi:10.1016/j.poly.2004.11.004

prepared [12]. In this communication the facile acylation of the amine substituents of $[Ni(diam)]^{2+}$ to form methyl- and ethyl-amido substituents is described and the structure of one ethylamido compound reported.

2. Results

Reactions of $[Ni(diam)](ClO_4)_2$ with acetic anhydride or propionic anhydride in DMF or DMSO form the 6,13-bis(methylamido) or 6,13-bis(ethylamido) substituted compounds $[Ni(diamme)](ClO_4)_2$ or $Ni(diamet)](ClO_4)_2$, see the Scheme 1. Analogous reactions occur for $[Ni(diam)]Cl_2$ to form the dichloro compounds $[Ni(diamme)Cl_2]$ and $[Ni(diamet)Cl_2]$. The infrared spectra of the compounds all show bands at c. 1650 and 1550 cm^{-1} assignable as the secondary amide bands I and II. The amido formulations are supported by the X-ray crystal structure determination reported below.

The cations $[Ni(diamme)]^{2+}$ and $[Ni(diamet)]^{2+}$ form orange singlet ground state ($S = 1$) square planar perchlorate salts which form orange $S = 1$ solutions in weakly coordinating solvents such as water, alcohols or acetone. They crystallise as triplet ground state ($S = 3$) solvates from DMSO, DMF (blue-violet) and acetonitrile (green), while broad NMR signals from solutions in these solvents indicate the presence of $S = 3$ species. An ammine adduct crystallizes from aqueous ammonia. In strongly basic aqueous solution (e.g. in 1 mol dm^{-3} NaOH) the compounds form lilac coloured solutions, the spectra showing bands attributable to both $S = 1$ and $S = 3$ species. The latter could have coordinated amidato groups, or coordinated hydroxide. The basic solutions on exposure to the atmosphere slowly deposit blue-violet crystals, also formed by addition of sodium hydrogen carbonate to an aqueous solution of the perchlorate salt. Analysis and IR spectra confirm the diamme compound as $\{Ni(diamme)\}\cdot 2(HCO_3)\cdot 4H_2O$ but the crystals obtained from $[Ni(diamet)](ClO_4)_2$ have the composition $2\{Ni(diamet)\}\cdot 3(HCO_3)\cdot ClO_4\cdot 3H_2O$. This has the structure, below, *trans*-$[Ni(diamet)(OH_2)(OCO_2H)]\cdot$ *trans*-$[Ni(diamet)(OH_2)_2]\cdot (HCO_3)_2\cdot ClO_4$, with two distinct cations, one with two *trans*-coordinated water ligands and the other with *trans*-coordinated water and hydrogen carbonato ligands. Other similarly prepared samples did not contain perchlorate, and are presumably analogous to the diamme compound, which could have coordinated water molecules, and/or hydrogen carbonate ions.

Other octahedral $S = 3$ compounds with *trans*-coordinated chloride, thiocyanate, nitrite and azide were prepared.

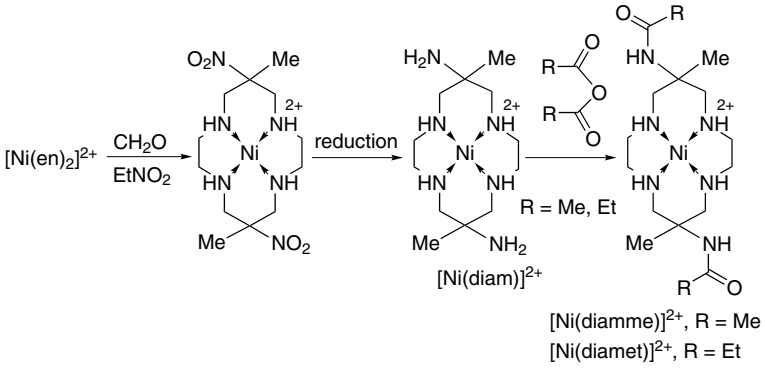
The amide functions of the compounds are resistant to hydrolysis, showing no significant hydrolysis when heated in 2 mol dm^{-3} HCl at 100 °C for 1 h and only slight hydrolysis after 1 h at 100 °C in 2 mol dm^{-3} aqueous NaOH.

3. Structural study

The structure of *trans*-di(aquo-$\kappa^1 O$)-($R^1R^4S^8S^{11}$-*trans*-6,13-bisethylamido-6,13-dimethyl-1,4,8,11-tetraazacyclotetradecane-$\kappa^4N^1N^4N^8N^{11}$)nickel(II) *trans*-(aquo-$\kappa^1 O$)-(hydrogencarbonato-$\kappa^1 O$)-($S^1S^4R^8R^{11}$)-*trans*-6,13-bisethylamido-6,13-dimethyl-1,4,8,11-tetraazacyclotetradecane-$\kappa^4N^1N^4N^8N^{11}$)nickel(II) perchlorate bis(hydrogen carbonate), $C_{18}H_{42}N_6NiO_4\cdot C_{19}H_{41}N_6NiO_6\cdot ClO_4\cdot 2(CHO_3)$, was determined by X-ray diffractometry, see Section 5.2 for details.

The asymmetric unit contains two cations, each with (*trans*-6,13-bisethylamido-6,13-dimethyl-1,4,8,11-tetraazacyclotetradecane)nickel(II) cations with the Ni(II) in square-planar coordination by the four endocyclic secondary amine nitrogen atoms. The cation including Ni1 has O1 of a water molecule and O42 of the hydrogen carbonate ion including C40 coordinated *trans*, see Figs. 1 and 2. The cation including Ni2 has O2 and O3 of water molecules coordinated *trans*. The charges are balanced by two hydrogen carbonate ions (including C50 and C60), which are linked by hydrogen bonding, and a rotationally disordered perchlorate ion.

The macrocyclic ligand cations have nitrogen configurations $\{R^1R^4S^8S^{11}$ for Ni1 and $S^1S^4R^8R^{11}$ for Ni2$\}$



Scheme 1.

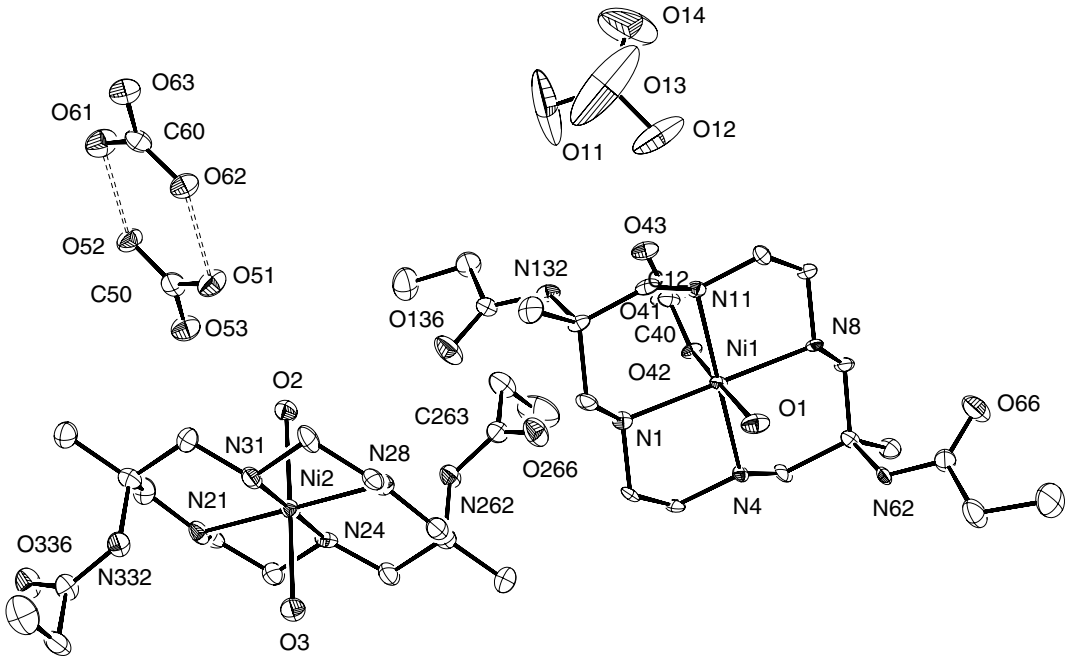


Fig. 1. The asymmetric unit for *trans*-[Ni(diamet)(CO_2OH)(H_2O)]·*trans*-[Ni(diamet)(H_2O)$_2$]·ClO_4·2(CO_2OH), drawn [13] with displacement ellipsoids at the 50% confidence level, with H-atoms omitted for clarity.

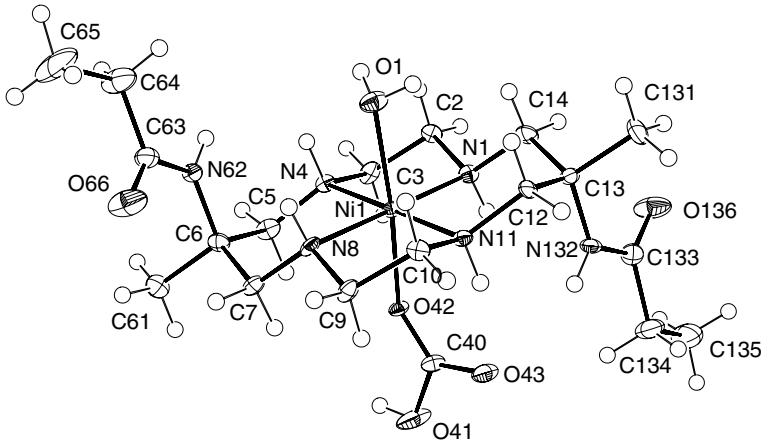


Fig. 2. The cation *trans*-[Ni1(diamet)(CO_2OH)(H_2O)]$^{2+}$, drawn [13] as for Fig. 1, but with H(N) and H(O) atoms shown as circles of arbitrary radius. The cation *trans*-[Ni2(diamet)(H_2O)$_2$]$^{2+}$ is similar.

and conformations with near symmetrical chair and gauche conformations of the chelate rings, similar to compounds with planar coordinated diam [7] or cyclam. The *trans*-diaqua cation including Ni2 is close to centrosymmetrical and the *trans*-aqua-(hydrogen carbonato) cation including Ni1 has near C_2 symmetry and considering only the coordinated oxygen atoms of the *trans* ligands is also close to centrosymmetrical. The ring substituents are arranged *trans*, with the amido substituents axially and the methyl substituents equatorially oriented (cf. *trans*-[Ni(diam)($NCS)_2$] where the un-coordinated amino groups are also axially oriented [9]). The conformations of the two macrocycle cations, as indicated by atomic displacements from the mean N_4 planes are similar (see Table 1), the greatest difference being in the displacement of the terminal methyl groups (C65, C135 and C265, C335).

The mean Ni–N distance is 2.05(1) Å, typical of triplet ground state cyclam-like macrocycles [7]. The Ni–O distances for the diaqua cation are similar, more divergent about the same mean for the aqua (hydrogen carbonato) cation, all slightly longer than usual, see Tables 2 and 3 for significant dimensions. The amide substituents have no interactions with the nickel ions, with Ni–N c. 3.89 Å and Ni–O even longer.

The hydrogen carbonate ion including C40, coordinated to Ni1 by O42, is oriented approximately normal to the NiN_4 plane; aligned 'above' Ni1–N11 (dihedral

Table 1
Displacements of atoms (Å, s.u. < 0.01 Å) from N_4 mean planes for *trans*-[Ni(diamet)(CO_2OH)(H_2O)]·*trans*-[Ni(diamet)(H_2O)$_2$]·ClO_4·2(CO_2OH)

Atom[a]	Ni1 (C2–C7)	Ni1 (C9–C13)	Ni2 (C22–C27)	Ni2 (C29–C33)
C2	−0.42	0.36	0.43	−0.42
C3	0.35	−0.36	−0.33	0.35
C5	0.83	−0.79	−0.79	0.81
C6	0.47	−0.46	−0.46	0.47
C7	0.83	−0.84	−0.79	0.78
C61	1.32	−1.27	−1.31	1.34
N62	−0.95	0.99	0.97	−0.97
C63	−1.69	1.63	1.65	−1.61
C64	−3.07	3.08	2.97	−2.96
C65	−3.80	3.82	2.80	−2.83
O66	−1.28	1.11	1.19	−1.13

The tetrahedral twisting of the N_4 plane for cation Ni1N_4 is ±0.007(3) Å, with Ni1 in the plane and for cation Ni2N_4 is ±0.012(3) Å with Ni2 0.006(3) Å from the plane.

[a] Atom and equivalent atoms, e.g., C2, C9, C22, C29.

Table 2
Selected bond lengths (Å) for *trans*-[Ni(diamet)(CO_2OH)(H_2O)]·*trans*-[Ni(diamet)(H_2O)$_2$]·ClO_4·2(CO_2OH)

Ni1–N1	2.063(5)	Ni2–N21	2.057(6)
Ni1–N4	2.063(5)	Ni2–N24	2.058(4)
Ni1–N8	2.062(5)	Ni2–N28	2.049(6)
Ni1–N11	2.049(5)	Ni2–N31	2.046(5)
Ni1–O1	2.190(4)	Ni2–O2	2.154(5)
Ni1–O42	2.100(4)	Ni2–O3	2.160(5)
C40–O41	1.356(6)	C50–O51	1.340(8)
C40–O42	1.260(6)	C50–O52	1.266(8)
C40–O43	1.247(6)	C50–O53	1.242(9)
C60–O61	1.334(8)	C60–O62	1.256(8)
		C60–O63	1.264(8)

Table 3
Selected bond angles (°) for *trans*-[Ni(diamet)(CO_2OH)(H_2O)]·*trans*-[Ni(diamet)(H_2O)$_2$]·ClO_4·2(CO_2OH)

N1–Ni1–N4	86.2(2)	N21–Ni2–N24	86.4(2)
N1–Ni1–N8	179.8(3)	N21–Ni2–N28	179.6(3)
N1–Ni1–N11	94.0(2)	N21–Ni2–N31	93.5(2)
N4–Ni1–N8	93.8(2)	N24–Ni2–N28	93.5(2)
N4–Ni1–N11	179.4(2)	N24–Ni2–N31	179.0(2)
N8–Ni1–N11	86.0(2)	N28–Ni2–N31	86.6(2)
N11–Ni1–O42	91.8(2)	N21–Ni2–O2	92.7(2)
N8–Ni1–O42	90.0(2)	N24–Ni2–O2	89.2(2)
N1–Ni1–O42	90.2(2)	N28–Ni2–O2	86.9(2)
N4–Ni1–O42	87.6(2)	N31–Ni2–O2	91.8(2)
N1–Ni1–O1	87.7(2)	N21–Ni2–O3	86.7(2)
N4–Ni1–O1	92.4(2)	N24–Ni2–O3	91.6(2)
N8–Ni1–O1	92.1(2)	N28–Ni2–O3	93.6(2)
N11–Ni1–O1	88.1(2)	N31–Ni2–O3	87.4(2)
O1–Ni1–O42	175.0(2)	O2–Ni2–O3	179.1(2)
O43–C40–O42	127.7(5)	O52–C50–O51	118.0(7)
O43–C40–O41	116.2(4)	O53–C50–O51	116.3(6)
O42–C40–O41	116.1(5)	O53–C50–O52	125.7(6)
Ni1–O42–C40	134.9(4)	O63–C60–O61	116.5(6)
O62–C60–O61	119.3(6)	O62–C60–O63	124.2(7)

angle N11–Ni–O42···O43 = −8.3°) with an N11–H11···O43 hydrogen bond, see Table 4 for hydrogen bond parameters.

The macrocylic cations including Ni1 and Ni2 are arranged in stacks of like cations, linked by hydrogen bond N1–H1···O266, normal to the 100 plane, with the Ni1N_4 and Ni2N_4 planes inclined at 46.1(1)°, see Fig. 1. The Ni1(macrocycle) stacks are linked by hydrogen bond O1–H1D···O43 ($x + 1$, y, z) between the coordinated hydrogen carbonate ion of one cation and the coordinated water of the adjacent cation. The rotationally disordered perchlorate anions form a stack between the Ni1(macrocycle) stacks, with Cl1 aligned approximately midway between the Ni1(macrocycle) layers, linked by hydrogen bonds to the coordinated water [O1–H1···O43 ($x + 1$, y, z)] and the coordinated hydrogen carbonate ion [O41–H41···O13 (x, $y + 1$, z)].

The two un-coordinated hydrogen carbonate ions are close to coplanar (mean displacement of C and O atoms from the C_2O_6 mean plane = 0.006(5) Å) and linked by symmetrical hydrogen bonds O51–H51···O62 and O61–H61···O52. These hydrogen carbonate ions form stacks between the Ni2(macrocycle) stacks, with the N_4 and C_2O_6 planes inclined at 47.4(1)°. The atoms O53 and O63 are interlaced between the stacked Ni2(macrocycle)s, with O53 intruding above bond N31–C32 and O63 intruding above bond N24–C25. Hydrogen bonds [O2–H2C···O53, O2–H2D···O63, O3–H3D···O53 and O3–H3C···O63] link the coordinated water molecules and these hydrogen carbonato ions, to form a chain linking the Ni2(macrocycle) macrocycle stacks normal to the 100 plane.

Table 4
Hydrogen-bond parameters (Å, °) for *trans*-[Ni(diamet) (CO_2OH)-(H_2O)]·*trans*- [Ni(diamet)(H_2O)$_2$]· ClO_4 ·2(CO_2OH)

Atoms	D–H	H···A	D···A	D–H···A
N1–H1···O266	0.91	2.18	2.985(7)	147
N4–H4···O41^{iv}	0.91	2.19	3.008(6)	150
N8–H8···O336^{i}	0.91	2.23	3.018(7)	145
N11–H11···O43	0.91	2.07	2.924(6)	155
N132–H132···O43	0.86	2.38	3.134(6)	146
N21–H21···O66^{ii}	0.84	2.26	2.944(8)	138
N24–H24···O62^{iii}	0.91	2.25	3.015(6)	141
N31–H31···O52^{iv}	0.91	2.24	2.995(7)	140
N262–H262···O62^{iii}	0.86	2.17	2.994(7)	161
N332–H332···O52^{iv}	0.86	2.19	2.991(7)	155
O1–H1D···O43^{Iv}	0.83	1.97	2.725(5)	151
O2–H2C···O53	0.81	1.91	2.696(6)	162
O2–H2D···O63^{iii}	0.81	2.08	2.800(7)	148
O3–H3C···O63^{v}	0.84	2.05	2.722(6)	138
O3–H3D···O53^{iv}	0.83	1.97	2.774(7)	163
O41–H41···O13^{iii}	0.80	2.00	2.779(8)	164
O51–H51···O62	0.82	1.79	2.596(7)	167
O61–H61···O52	0.82	1.77	2.584(8)	171

Symmetry codes: (i) x, y, $1 + z$; (ii) x, y, $-1 + z$; (iii) x, $1 + y$, z; (iv) $1 + x$, y, z; (v) $1 + x$, $1 + y$, z.

4. Discussion

The ring secondary amine groups of $[Ni(diam)]^{2+}$ are non-labile, while the substituent primary amine groups are either un-coordinated, or coordinated but labile [7], and therefore accessible for acylation, which occurs readily with acyl anhydrides in DMF or DMSO. The resulting amido compounds are resistant to hydrolysis. Developments of this reaction should provide a convenient synthetic pathway for the incorporation of (azamacrocycle)metal cations into more complex systems.

Coordination of the amino substituents of $[Ni(diam)]^{2+}$ requires the associated six-membered chelate ring to adopt a strained boat conformation, which reduces the coordinating ability. However, the amine substituents for $[Ni(diam)]^{2+}$generally coordinate, unless a more competitive ligand, such as thiocyanate is present, or they are protonated [7].

Simple amides are moderately strong ligands, usually coordinating through the nitrogen [1–3], but the amido groups of $[Ni(diamme)]^{2+}$ and $[Ni(diamet)]^{2+}$show no indication of coordination. Deprotonated (amidato) groups are generally stronger ligands and spectra suggest that in base the amidato groups of diamme and diamet *may* coordinate to Ni(II). However, the displacement of the possible amidate ligands by the hydrogen carbonate ion indicates that these amidate functions can have only weak coordinating abilities (see Section 5.1.5). Molecular mechanics calculations indicate that for coordination of the amidate function the strain energy would be less for *O*-coordination than for *N*-coordination.

5. Experimental

The compounds $[Ni(diam)](ClO_4)_2$ and $[Ni(diam)]Cl_2$ [7] were prepared as hydrates, as previously described, and dehydrated by heating at 100 °C. DMSO can be substituted for DMF in the preparations; commercial anhydrous DMF and DMSO were used; these solvents need not be rigorously dried.

The perchlorate salts described were not observed to be shock sensitive and decomposed non-violently if strongly heated. They should still be treated with the caution due to any perchlorate compound.

5.1. Synthesis of compounds

5.1.1. (trans-6,13-bis-Ethylamido-6,13-dimethyl-1,4,8,11-tetraazacyclotetra-decane)nickel(II) perchlorate, [Ni(diamet)](ClO4)2

$[Ni(diam)](ClO_4)_2$ (1 g) was dissolved in DMF (1 g) by warming. Propionic anhydride (1 g) was added and the solution heated at c. 100 °C for 30 min. The colour slowly darkened, and orange crystals deposited. Propan-2-ol (20 cm^3) was added and after 1 h the orange crystals were filtered off, yield 90+%. The product crystallised from hot DMF (in which it is very soluble)/propan-2-ol, or rapidly from hot water (in which it is sparingly soluble) as orange crystals (a), while yellow crystals (b) formed on slow crystallization from water; mixtures were often observed. The interconversion was inhibited by acid, more rapid in base, suggesting the forms are isomers with different nitrogen configurations. *Anal.* Calc. for $C_{18}H_{38}Cl_2N_6NiO_{10}$: C, 34.4; H, 6.1; N, 13.4. Found for (a): C, 34.4; H, 6.3; N, 13.5%. Spectra: infrared {ν_{max} (cm^{-1})} (a): *v*(NH) 3341sp, 3197sp, 3087w; amide bands 1672, 1542; (b): (NH) 3281, (3194, 3177), 3087w; amide bands 1649, 1553; visible spectra (same for both forms) {λ_{max} (nm) (ε) (mol dm^{-3} cm^{-1})} in water; 446 (48); in 1 mol dm^{-3} NaOH; 450 (14), 524 (22), 696 (8).

5.1.2. trans-Dichloro-(trans-6,13-bis-ethylamido-6,13-dimethyl-1,4,8,11-tetraazacyclotetradecane)nickel(II), trans-[Ni(diamet)Cl2]

$[Ni(diam)]Cl_2$ (1 g), DMF (1 g) and propionic anhydride (1 g) were heated at c. 100 °C for 1 h. Ethanol (10 cm^3) was added and the insoluble blue-violet product filtered off and washed with ethanol. Alternatively, a few drops of conc. hydrochloric acid were added to a solution of the perchlorate salt in DMF or water, when the product precipitated and was treated as before. The compound is slow to dissolve in hot water, but ultimately quite soluble. It can be recovered as blue crystals by evaporation of this solution. *Anal.* Calc. for $C_{18}H_{38}Cl_2N_6NiO_2$: C, 43.2; H, 7.7; N, 16.8. Found: C, 42.8; H, 7.7; N, 16.8%. Infrared spectrum {ν_{max} (cm^{-1})} *v*(NH) 3307, 3279, 3245, 3064w; amide bands 1676, 1545.

5.1.3. trans-Diazido-(trans-6,13-bis-ethylamido-6,13-dimethyl-1,4,8,11-tetraazacyclotetradecane)nickel(II) Hydrate, trans-[Ni(diamet)(N3)2]·H2O

Sodium azide was added to a hot aqueous solution of $[Ni(diamet)](ClO_4)_2$ when the lilac coloured product slowly crystallized. This was filtered off and washed with a small volume of water and then ethanol. *Anal.* Calc. for $C_{18}H_{40}N_{12}NiO_3$: C, 42.1; H, 7.5; N, 32.7. Found: C, 42.0; H, 7.5; N, 32.8%. Infrared spectrum {ν_{max} (cm^{-1})} *v*(NH) 3333, (3271, 3257), 3069w; *v*(N_3^-) 2045vs; amide bands 1685, 1546.

5.1.4. trans-(trans-6,13-bis-Ethylamido-6,13-dimethyl-1,4,8,11-tetraazacyclotetradecane)dithiocyanatonickel(II), trans-[Ni(diamet)(NCS-N)2]

This sparingly soluble blue-violet compound was prepared as for the azide, by using sodium thiocyanate. *Anal.* Calc. for $C_{20}H_{38}N_8NiO_2S_2$: C, 44.0; H, 7.0; N, 20.5. Found: C, 44.2; H, 6.9; N, 20.9%. Infrared spectrum {ν_{max} (cm^{-1})} *v*(NH) 3307, 3272; *v*(C≡N) 2086vs; amide bands 1675, 1530.

5.1.5. trans-diaqua-{trans-(6,13-Dimethyl-6,13-bisethylamido-1,4,8,11-tetraazacyclotetradecane)}nickel(II) trans-aqua-(hydrogen carbonato)-{trans-(6,13-dimethyl-6,13-bisethylamido-1,4,8,11-tetraazacyclotetradecane)}-nickel(II) bis(hydrogen carbonate) perchlorate, trans-[Ni(diamet)(HCO$_3$)(H$_2$O)]·trans-[Ni(diamet)(H$_2$O)$_2$]·ClO$_4$·2(HCO$_3$)

The pale blue-violet compound crystallized when $NaHCO_3$ was added to an aqueous solution of [Ni(diamet)](ClO$_4$)$_2$. It was filtered off and washed with cold water. *Anal.* Calc. for $C_{39}H_{85}ClN_{12}Ni_2O_{20}$: C, 39.2; H, 7.2; N, 14.1. Found: C, 39.2; H, 7.2; N, 14.1%. Infrared spectrum {ν_{max} (cm^{-1})}: ν(OH), ν(NH), 3384w, 3246, 3205, 3159, 3065, 2967, 2937, 2875w, (HCO$_3$) 2630br, 1670vs, 1634sh, amide band 1551. The crystals used for the structural determination grew slowly when a solution of [Ni(diamet)](ClO$_4$)$_2$ in 0.1 mol dm^{-3} NaOH solution was exposed to the atmosphere. The yellow perchlorate salt crystallized when a sample was heated in methanol.

5.1.6. (trans-6,13-bis-Methylamido-6,13-dimethyl-1,4,8,11-tetraazacyclotetradecane)nickel(II) perchlorate, [Ni(diamme)](ClO$_4$)$_2$

The orange compound was prepared as for the propionyl homologue by using acetic anhydride. *Anal.* Calc. for $C_{16}H_{34}Cl_2N_6NiO_{10}$: C, 32.0; H, 5.7; N, 14.0. Found: C, 32.3; H, 5.8; N, 14.2%. When crystallized slowly from water an orange trihydrate formed (weight loss at 100 °C: 8.22%. Calc. for loss of 3H$_2$O: 8.26%). Infrared spectrum {ν_{max} (cm^{-1})}: ν(NH) 3344, 3200, 3070w; amide bands 1675, 1547; hydrate: ν(OH) 3400br, ν(NH) 3246, 3202, 3159, 3068w; amide bands 1676, 1555. The IR spectrum of the hydrate after heating was the same as that of the unhydrated compound.

5.1.7. trans-Diazido-(trans-6,13-bis-methylamido-6,13-dimethyl-1,4,8,11-tetraazacyclotetradecane)nickel(II) Dihydrate, [Ni(diamme)(N$_3$)$_2$]·2H$_2$O

This lilac coloured compound was prepared as for the propionyl homologue. *Anal.* Calc. for $C_{16}H_{38}N_{12}NiO_4$: C, 36.9; H, 7.3; N, 32.2. Found: C, 37.0; H, 7.4; N, 32.6%. Infrared spectrum {ν_{max} (cm^{-1})} ν(OH) 3514, 3471; δ(HOH) 1627; ν(NH) 3351, 3226; ν(N$_3$) (2061, 2055, 2039sh)vs; amide bands 1676, 1556.

5.1.8. trans-(trans-6,13-bis-Methylamido-6,13-dimethyl-1,4,8,11-tetraazacyclotetradecane)dithiocyanatonickel(II), [Ni(diamme)(NCS-N)$_2$]

This blue-violet compound was prepared as for the propionyl homologue. *Anal.* Calc. for $C_{18}H_{34}N_8NiO_1S_2$: C, 41.8; H, 6.6; N, 21.7. Found: C, 41.8; H, 6.7; N, 21.8%. Infrared spectrum {ν_{max} (cm^{-1})} ν(NH) 3302, 3296, 3252; ν(NCS) (2086sh, 2079, 2073)vs; amide bands 1679, 1536.

5.1.9. trans-(6,13-Dimethyl-6,13-bisethylamido-1,4,8,11-tetraazacyclotetradecane)}bis(hydrogen carbonato)nickel(II) Tetrahydrate, trans-[Ni(diamme)(HCO$_3$)$_2$]·4H$_2$O

The blue-violet compound was prepared as for the related diamet homologue. The IR spectrum showed no bands assignable to perchlorate. *Anal.* Calc. for $C_{18}H_{44}N_6NiO_{18}$: C, 36.3; H, 7.5; N, 14.1. Found: C, 36.4; H, 7.6; N, 14.2%.

5.1.10. trans-(trans-6,13-bis-Methylamido-6,13-dimethyl-1,4,8,11-tetraazacyclotetradecane)dinitronickel(II), trans-[Ni(diamme)(NO$_2$)$_2$]

This pale brown compound crystallised when sodium nitrite was added to an aqueous solution of [Ni(diamme)](ClO$_4$)$_2$. it was filtered off and washed with a little cold water, then ethanol. *Anal.* Calc. for $C_{18}H_{34}N_8NiO_2S_2$: C, 39.0; H, 6.9; N, 22.7. Found: C, 38.8; H, 7.0; N, 22.7%. Infrared spectrum {ν_{max} (cm^{-1})} ν(NH) (3290, 3253), 3082; amide bands 1681, 1557, ν(NO$_2^-$) (1455, 1285).

5.2. Structural study

The structure of *trans*-[Ni(L)(CO$_2$OH)(H$_2$O)]·*trans*-[Ni(L)(H$_2$O)$_2$]·ClO$_4$·(CO$_2$OH)$_2$ (L = *trans*-(6,13-dimethyl-6,13-bisethylamido-1,4,8,11-tetraazacyclotetradecane)); *trans*-[Ni(diamet)(CO$_2$OH)(H$_2$O)]·*trans*-[Ni(diamet)(H$_2$O)$_2$]·ClO$_4$·2(CO$_2$OH)) was determined by X-ray diffractometry.

5.2.1. Crystal data [14]

$C_{18}H_{42}N_6NiO_4\cdot C_{19}H_{41}N_6NiO_6\cdot 2(CHO_3)\cdot ClO_4$, M_r = 1195.02, blue-violet needle grown from water (see 5.15), 0.8 × 0.02 × 0.02 mm. Triclinic, space group *P*1, a = 7.8940(4), b = 9.6549(4), c = 18.0054(8) Å, α = 86.917(2)°, β = 84.154(2)°, γ = 83.695(2)°, V = 1355.6(1) Å^3, Z = 1. Cell parameters from 5012 reflections.

5.2.2. Data collection [14]

Bruker SMART 1K CCD area detector diffractomer, ω scans, Mo Kα radiation, multi-scan absorption correction (based on symmetry-related measurements [15]), T_{min} = 0.495, T_{max} = 0.992, twinned crystal, 22241 measured reflections, 14372 independent reflections, 9857 reflections with $I > 2\sigma(I)$, R_{int} = 0.034, θ_{max} = 29.1°, h = −15 → 15, k = −19 → 19, l = −24 → 23.

5.2.3. Refinement [16]

Refinement on F^2, $R[F^2 > 2\sigma(F^2)]$ = 0.056 (8437 reflections), $wR(F^2)$ = 0.147 ($w = 1/[\sigma^2(F_o^2) + (0.092P^2)]$) where $P = (F_o^2 + 2F_c^2)/3$, 683 parameters. Flack parameter = 0.02(2) [17].

H(C) and H(N) atoms are in calculated positions, H(O) atoms for the water molecules and hydrogen

carbonate ions were located from difference syntheses and the positions refined with the OH distances and HOH angles constrained (O–H = 0.82(2), H···H = 1.40(2) Å). All H-atoms are riding. Modeling of the rotationally disordered perchlorate ion with two sets of O atoms, with occupancies of 0.6 and 0.4, led to a solution with a small reduction in *R*-values.

A solution of the structure in space group $P\bar{1}$ was investigated. This has essentially the same structure, but with the H_2O and HCO_3 ligands on Ni2 disordered about an inversion centre at Ni2, and the perchlorate ion oxygen atoms disordered about an inversion centre. This solution is less satisfactory, with larger *R*-values, thermal ellipsoids and positional s.u. values than that in space group $P\bar{1}$.

Appendix A. Supplementary data

Crystallographic data has been deposited with the Cambridge Crystallographic Data Centre; CCDC 253370. Copies may be obtained free of charge from the Director, CDCC, 12 Union Road, Cambridge, CBZ 1EZ, UK (fax: +44-1223-336-033; e-mail: deposit@ccdc.cam.ac.uk or www.http://www.ccdc.cam.uk). Supplementary data associated with this article can be found, in the online version, at doi:10.1016/j.poly.2004.11.004.

References

[1] O. Clement, B.M. Rapko, B.P. Hay, Coord. Chem. Rev. 170 (1998) 203.
[2] H. Sigel, R.B. Martin, Chem. Rev. 82 (1982) 385.
[3] R.D. Hancock, H. Maumela, A.S. de Sousa, Coord. Chem. Rev. 148 (1996) 315.
[4] G.A. Lawrance, M. Maeder, E.N. Wilkes, Rev. Inorg. Chem. 13 (1993) 199.
[5] A.V. Bordunov, J.S. Bradshaw, V.N. Pastushok, R.M. Izatt, Synlett (1996) 933.
[6] P. Comba, N.F. Curtis, G.A. Lawrance, A.M. Sargeson, B.W. Skelton, A.H. White, Inorg. Chem. 25 (1986) 4260.
[7] N.F. Curtis, G.J. Gainsford, A. Siriwardena, D.C. Weatherburn, Aust. J. Chem. 46 (1993) 755.
[8] P.V. Bernhardt, J.M. Harrowfield, D.C.R. Hockless, A.M. Sargeson, Inorg. Chem. 33 (1994) 5659.
[9] P.V. Bernhardt, J.C. Hetherington, L.A. Jones, J. Chem. Soc., Dalton Trans. (1996) 4325.
[10] P.V. Bernhardt, P. Comba, J. Chem. Soc., Chem. Commun. (1993) 113.
[11] P.V. Bernhardt, G.A. Lawrance, T.W. Hambley, Inorg. Chem. 31 (1992) 631.
[12] P.D. Beer, P.V. Bernhardt, J. Chem. Soc., Dalton Trans. (2001) 1428.
[13] L.J. Farrugia, J. Appl. Crystallogr. 30 (1997) 565.
[14] Bruker SMART, (Version 5.054), SADABS (Version 2.03) and Saint (Version 6.02A), Bruker AXS Inc., Madison, WI, USA, 1997.
[15] R.H. Blessing, Acta Crystallogr., Sect. A 51 (1995) 33.
[16] G.M. Sheldrick, SHELXTL, (Version 5.10). Programs for the solution and refinement of crystal structures, Bruker AXS Inc., Madison, WI, USA, 1997.
[17] H.D. Flack, Acta Crystallogr., Sect. A 39 (1983) 876.

Available online at www.sciencedirect.com
SCIENCE DIRECT®
Polyhedron 24 (2005) 289–294
POLYHEDRON
www.elsevier.com/locate/poly

Barium(II) thiocyanate templating Schiff-base lateral macrobicycles derived from 1,10-diaza-15-crown-5

David Esteban, Carlos Platas-Iglesias, Fernando Avecilla, Andrés de Blas *, Teresa Rodríguez-Blas *

Departamento de Química Fundamental, Facultad de Ciencias, Universidade da Coruña, Campus da Zapateira s/n 15071 A Coruña, Spain

Received 7 August 2004; accepted 16 November 2004
Available online 9 December 2004

Abstract

Previously we have proved that barium perchlorate is a highly effective template agent in the formation of the Schiff-base lateral macrobicycles $\mathbf{L^1}$ and $\mathbf{L^2}$ (receptors derived from the condensation of *N*,*N*′-bis(2-aminobenzyl)-1,10-diaza-15-crown-5 with 2,6-diformylpyridine and 2,6-diformyl-4-methylphenol, respectively). Aiming to understand the effect that the nature of the counteranion present in the reaction medium has on the barium template potential, we have carried out the corresponding template synthesis in the presence of barium thiocyanate. We have found that considerably longer reaction times are required to obtain both receptors when barium thiocyanate is employed. The barium template remains trapped into the formed macrobicyclic cavity and compounds of formula $Ba(L^1)(SCN)_2 \cdot H_2O$ (**1**) and $Ba(L^2)(SCN)_2 \cdot 2H_2O$ (**2**) were isolated. The X-ray crystal structure of **1** shows the metal ion coordinated to the eight donor atoms of the receptor and to the nitrogen atom of a isothiocyanate group, the coordination polyhedron being best described as a monocapped distorted dodecahedron. In **1**, the metal ion is nearly centred inside the macrobicyclic cavity of $\mathbf{L^1}$, whereas NMR studies in solution indicate that in **2** the barium ion is asymmetrically situated in the macrobicyclic cavity of $\mathbf{L^2}$. This asymmetric coordination is attributed to the proton transfer from the phenol group to the nitrogen atom of one of the imine groups.
© 2004 Elsevier Ltd. All rights reserved.

Keywords: Lateral macrobicycle; X-ray crystal structures; Template synthesis; Barium; Thiocyanate

1. Introduction

The coordination chemistry of macrocyclic ligands [1,2] is a fascinating area of intense study for inorganic chemists. One aspect of the interest that macrocyclic ligands have promoted steams from the fact that depending on features such as the nature, number and arrangement of the ligand donors, as well as ligand conjugation, substitution and flexibility, it is possible to tailor-make different types of macrocyclic molecules for specific uses. In particular, the cyclic framework of crown ethers and cryptands affords an interesting platform for the complexation of metal ions [3]. Likewise, according to the number of connecting bridges used for their construction as well as to the nature of the subunits used as building blocks, a variety of macropolycyclic structures may be envisaged. Lateral macrobicycles (described as dissymmetrical molecules structurally based on the combination of two different binding units, a chelating one and a macrocyclic one) are one of them [4]. Taking into account the peculiar structural features that the lateral macrobicycles show, it is easy to understand that this type of macropolycyclic architectures exhibit a range of interesting and potentially useful molecular recognition properties [5]. However, to date the coordinative properties of lateral macrobicycles remain considerably unexplored.

* Corresponding authors. Tel.: +34981167000; fax: +34981167065.
E-mail address: mayter@udc.es (A. de Blas).

0277-5387/$ - see front matter © 2004 Elsevier Ltd. All rights reserved.
doi:10.1016/j.poly.2004.11.005

In the recent past a great attention has been devoted to the design and synthesis of Schiff bases with enhanced ability to selectively encapsulate given metal ions [6]. In particular, macrocyclic Schiff bases and Schiff-base derived cryptands and cryptates have successfully been proposed as excellent systems in the complexation of metal ions. However, no example of a Schiff-base lateral macrobicycle was reported until 1999 when we described, at the first time, examples of Schiff-base lateral macrobicycles [7]. These macrobicycles, shown in Scheme 1, structurally derive from bibracchial lariat ethers incorporating pendant aniline moieties. Subsequent studies demonstrated that these systems posses promising coordinating properties [8–10]. We have found that these Schiff-base lateral macrobicycles cannot be prepared by direct reaction between the organic precursors; but barium perchlorate can act as a template, thereby facilitating the formation of the desired macrobicycles in high yields. In fact, it is known that the direct synthesis of a free macrocycle from its organic precursors often results in a low yield of the desired cyclic product, with side reactions such as polymerisation predominating. Consequently, some synthetic strategies such as the use of high dilution conditions, the incorporation of a rigid group in the open chain precursors, and the use of template agents have been developed. Particularly, template Schiff base condensations between dicarbonyl compounds and diamines are among the simplest and most popular methods for macrocycle synthesis [11].

Previously, we have demonstrated that the effectiveness of barium(II) perchlorate to template the macrobicycles $\mathbf{L^1}$ to $\mathbf{L^4}$ comes from its ability to arrange the pendant arms of the diamine precursor [*N*,*N*′-bis(2-aminobenzyl)-1,10-diaza-15-crown-5 (for $\mathbf{L^1}$ and $\mathbf{L^2}$) or *N*,*N*′-bis(2-aminobenzyl)-4,13-diaza-18-crown-6 (for $\mathbf{L^3}$ and $\mathbf{L^4}$)] in a *syn* conformation (Fig. 1) [12]. Aiming to understand the effect that the nature of the counteranion present in the medium reaction had on the barium template potential, we also carried out the corresponding template synthesis in the presence of barium thiocyanate under the same experimental conditions used with barium perchlorate, finding that whereas barium thiocyante can also template the formation of the largest macrobicycles $\mathbf{L^3}$ and $\mathbf{L^4}$, it was not able to do it with the smallest $\mathbf{L^1}$ and $\mathbf{L^2}$ [7]. We have now slightly modified the synthetic conditions, and in this paper we discuss the formation of macrobicycles $\mathbf{L^1}$ and $\mathbf{L^2}$ in the presence of barium thiocyanate. We also describe the structures of the corresponding barium complexes both in solution and in the solid state, and we compare them to those previously described for their perchlorate analogues [7,13].

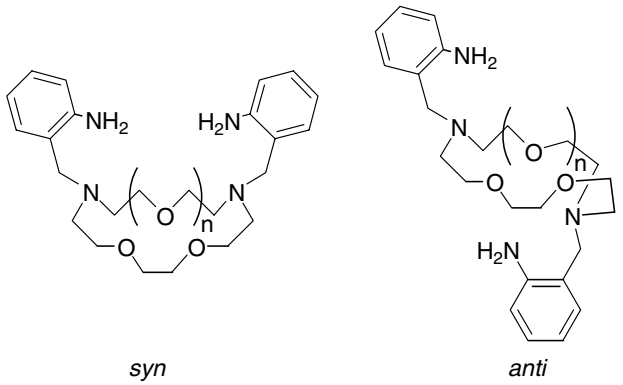
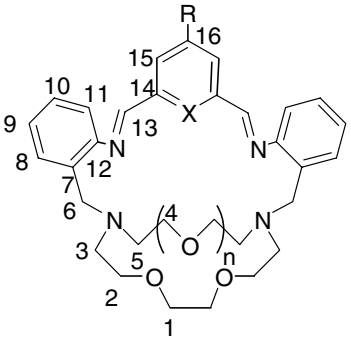


Fig. 1. The *syn* and *anti* conformations of the diamine precursors used for the preparation of macrobicycles $\mathbf{L^1}$ and $\mathbf{L^2}$ ($n = 1$) or $\mathbf{L^3}$ and $\mathbf{L^4}$ ($n = 2$).



$\mathbf{L^1}$: n = 1, R = H, X = N
$\mathbf{L^2}$: n = 1, R = CH_3, X = C-OH
$\mathbf{L^3}$: n = 2, R = H, X = N
$\mathbf{L^4}$: n = 2, R = CH_3, X = C-OH

Scheme 1.

2. Experimental

2.1. Reagents

2,6-Diformylpyridine and 2,6-diformyl-4-methyl-phenol were synthesised according to literature methods [14–16]. The diamine *N*,*N*′-bis(2-aminobenzyl)-1,10-diaza-15-crown-5 was prepared as previously described by us [8]. All other chemicals were purchased from commercial sources and used without further purification. Solvents were of reagent grade purified by the usual methods.

2.2. Template synthesis

2.2.1. $Ba(L^1)(SCN)_2 \cdot H_2O$ (1)

A solution of $Ba(SCN)_2 \cdot H_2O$ (0.072 g; 0.266 mmol) in absolute ethanol (50 mL) was added with stirring to a solution of the diamine *N*,*N*′-bis(2-aminobenzyl)-1,10-diaza-15-crown-5 (0.114 g; 0.266 mmol) also in absolute ethanol (120 mL). The mixture was vigorously stirred

and heated while a solution of 2,6-diformylpyridine (0.036 g; 0.266 mmol) in absolute ethanol (60 mL) was added dropwise over one day. After the addition was complete, the resulting pale yellow solution was stirred and refluxed for 26 h. The solution was filtered while hot and the filtrate rotary-evaporated to 30 mL. Upon cooling the filtrate to room temperature, a pale yellow microcrystalline precipitate formed, which was collected by filtration. Yield: 0.085 g (41%). *Anal.* Calc. for $C_{33}H_{37}N_7O_3BaS_2 \cdot H_2O$: C, 49.6; H, 4.9; N, 12.2. Found: C, 49.9; H, 4.9; N, 12.0%. FAB-MS: $m/z = 723$ $[Ba(L^1)(SCN)]^+$, 665 $[Ba(L^1)]^+$. IR (KBr discs): 1631 $\nu(C{=}N)_{imine}$; 1579 $\nu(C{=}N)_{pyridine}$; 2048, 2038 (SCN) cm^{-1}. ^1H NMR (acetonitrile-d_3), δ: 2.3–4.2 (m, 24H); 7.37(m, 4 H); 7.52(t, 2H); 7.18(d, 2H); 8.63(s, 2H); 8.08(d, 2H); 8.32(t, 1H). ^{13}C NMR (acetonitrile-d_3), δ: 165.6; 153.7; 152.7; 141.0; 133.6; 131.6; 131.1; 130.6; 128.1; 121.5; 69.9; 69.6; 69.4; 60.2; 51.9. X-ray quality crystals of formula $[Ba(L^1)(NCS)](SCN) \cdot CH_3CN$ were grown by slow diffusion of diethyl ether into a solution of **1** in acetonitrile.

2.2.2. $Ba(L^2)(SCN)_2 \cdot 2H_2O$ (2)

The orange complex was prepared as described for **1** by using 2,6-diformyl-4-methylphenol (0.043 g; 0.266 mmol). After the addition was complete, the resulting orange solution was stirred and refluxed for 48 h. Yield: 0.094 g (57%). *Anal.* Calc. for $C_{35}H_{40}N_6O_4BaS_2 \cdot 2H_2O$: C, 49.7; H, 5.2; N, 9.9. Found: C, 49.6; H, 5.1; N, 9.5%. FAB-MS: $m/z = 693$ $[Ba(L^1)]^+$. IR (KBr discs): 3430 $\nu(O{-}H)_{phenol}$ 1620 ($\nu(C{=}N)_{imine}$); 2057 (SCN) cm^{-1}. ^1H NMR (acetonitrile-d_3), δ: 2.40 (s, 3H), 4.24 (d, 2H); 3.73–2.96 (m, 22H); 7.60–7.37 (m, 10H); 7.67 (s, 1H); 8.57(s, 1H), 17.15 (b, 1H). ^{13}C NMR (acetonitrile-d_3), δ: 134.10; 131.01; 130.58; 129.08; 121.99; 69.77; 69.09; 68.52; 55.46; 19.80.

2.3. Measurements

Elemental analyses were carried out on a Carlo Erba 1180 elemental analyser. FAB mass spectra were recorded on a Fisons Quatro mass spectrometer with a Cs ion gun using 3-nitrobenzyl alcohol as matrix. ^1H and ^{13}C NMR spectra were run on a Bruker AC 200F using acetonitrile-d_3 as solvent. IR spectra were recorded, as KBr discs, using a Bruker Vector 22 spectrophotometer. Conductivity measurements were carried out with a Crison Micro CM 2201 conductivimeter using ca. 10^{-3} M solutions of the complexes in acetonitrile.

2.4. X-ray crystallography

Three dimensional X-ray data for compound **1** were collected on a Bruker Smart 1000 CCD operating at 25 °C. Data were corrected for Lorentz and polarisation effects and for absorption by semi-empirical methods. Complex scattering factors were taken from the program package SHELXTL [17]. The structure was solved by direct methods and refined by full-matrix least-squares on F^2. Refinement converged with anisotropic displacement parameters for all non-hydrogen atoms. Hydrogen atoms were included in calculated positions and refined in riding mode. The crystal presents a disorder of both the sulfur atom of one isothiocyanate group and the nitrogen atom of the acetonitrile molecule, and 45 restrains were impossed. The site occupancy factors were 0.55(5) for S(2SA) and 0.4(2) for N(1WA). Crystal data and details on data collection and refinement are summarised in Table 1.

Table 1
Crystal data and structure refinement for **1**

	1
Formula	$C_{35}H_{40}BaN_8O_3S_2$
Molecular weight	822.21
Crystal system	monoclinic
Space group	$P2_1/n$
T/K	293(2)
a (Å)	20.7033(14)
b (Å)	8.4256(6)
c (Å)	22.1063(15)
β (°)	106.3670(10)
V (Å^3)	3699.9(4)
F_{000}	1672
Z	4
D_{calc} (g cm^{-3})	1.476
μ (mm^{-1})	1.232
θ	2.05–28.34
R_{int}	0.0499
Reflections measured	23 308
Reflections observed	5856
Goodness-of-fit on F^2	1.003
R_1[a]	0.0426
wR_2 (all data)[b]	0.0860
Largest differences peak and hole (e Å^{-3})	0.459 and −0.529

[a] $R_1 = \|F_o| - |F_c\|/\sum|F_o|$.
[b] $wR_2 = \{\sum[w(|F_o|^2 - |F_c|^2|)^2]/\sum[wF_o^4]\}^{1/2}$.

3. Results and discussion

Under similar experimental conditions used to prepare the barium perchlorate derivative (2–3 h of reaction after complete addition of the precursors), the expected Schiff-base lateral macrobicycles $\mathbf{L^1}$ and $\mathbf{L^2}$ are not formed when barium thiocyanate is used as template agent [7]. As previously stated, in this case the template effectiveness of barium (II) or any other metal ion comes from its ability to orient the pendant arms of the diamine precursor [*N*,*N*′-bis(2-aminobenzyl)-1,10-diaza-15-crown-5] to a *syn* conformation [12]. Experimental evidences for this conformation were found both in solid state and in solution for the corresponding barium

intermediate in the presence of both perchlorate [7] and thiocyanate anions [18], what suggests that the presence of thiocyanate in the reaction medium instead perchlorate should not be an obstacle to the template effectiveness of the barium ion. So, we decided to modify the initial conditions and the experiments here described show that longer reaction times are necessary to get the expected macrobicycles ($\mathbf{L^1}$ and $\mathbf{L^2}$) when barium thiocyanate is used as template. There so, the reaction of the diamine precursor *N*,*N*′-bis(2-aminobenzyl)-1, 10-diaza-15-crown-5 and the corresponding dialdehyde (2,6-diformylpyridine or 2,6-diformyl-4-methylphenol) in the presence of barium(II) thiocyanate requires a minimum of one day of refluxing and stirring after complete addition of the dialdehyde to get the formation of $\mathbf{L^1}$ and 2 days to get $\mathbf{L^2}$.

Also in the presence of thiocyanate the barium(II) ion remains trapped in the formed macrobicyclic cavity (so acting as a permanent template), and the corresponding macrobicycles $\mathbf{L^1}$ and $\mathbf{L^2}$ were isolated as the corresponding barium complexes of formulas $Ba(L^1)(SCN)_2 \cdot H_2O$ (**1**) and $Ba(L^2)(SCN)_2 \cdot 2H_2O$ (**2**). In any case, the use of barium thiocyanate leads to lower yields (41% and 57%) than the use of the perchlorate salt (88% and 65%; see [7]). The presence of an absorption, attributable to the ν(C=N) stretching frequency, at 1631 cm^{-1} for **1** and 1620 cm^{-1} for **2** in their IR spectra (KBr discs), as well as the absence of carbonyl and amine bands confirms that condensation and cyclization has occurred. Further evidence for the formation of the Schiff-base lateral macrobicycles comes from the FAB mass spectra, which show peaks at *m*/*z* 723 and 665 (**1**) due to $[Ba(L^1)(SCN)]^+$ and $[Ba(L^1)]^+$ and at *m*/*z* 693 (**2**) due to $[Ba(L^2)]^+$.

Recrystallisation of **1** from acetonitrile gave colourless crystals suitable for single crystal X-ray diffraction. Crystals contain the cation $[Ba(L^1)(NCS)]^+$, a thiocyanate group and an acetonitrile molecule. Fig. 2 illustrates the structure of the complex cation, while selected bond lengths and angles of the coordination sphere are compiled in Table 2. The barium ion is nine-coordinate, bound to the eight heteroatoms of the macrobicycle $\mathbf{L^1}$ and to the nitrogen atom of a thiocyanate group. This is in agreement with the IR spectrum (KBr disc) that displays two bands corresponding to the (CN) stretching mode of the thiocyanate groups at 2048 and 2038 cm^{-1}, suggesting the presence of thiocyanate groups with different binding modes. Like in the analogous previously described perchlorate complex, $[Ba(L^1)(ClO_4)_2]$ [7], the metal ion is almost symmetrically placed with respect to the cavity of the macrobicyclic receptor. The barium–donor atom distances fall within the range found in the literature and they are slightly shorter (about 0.1 Å) than those found for the analogous perchlorate complex [7]. The donors O(1), O(3), N(3) and N(4) of the crown moiety are essentially coplanar, with a deviation from planarity of 0.069 Å, and the barium ion lies 1.3353 Å above it.

In the light of the dihedral angles N(5)–C(1)–C(31)–N(1) (7.7(5)°) and N(5)–C(5)–C(6)–N(2) (3.8(5)°), it follows that both imine groups are not coplanar with the pyridine ring. Probably, the presence of the barium

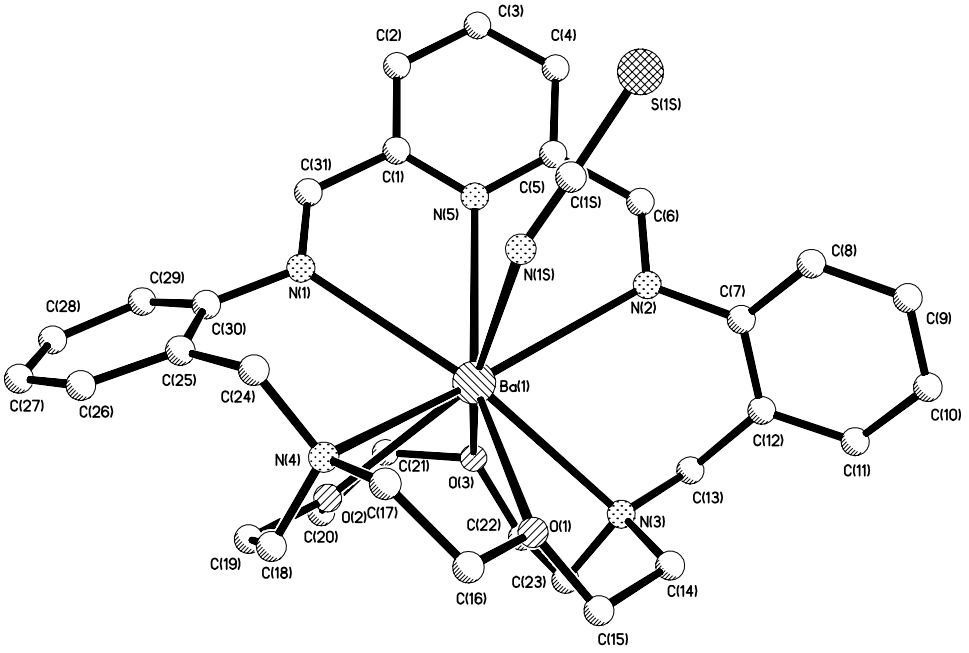


Fig. 2. X-ray crystal structure of the cationic complex $[Ba(L^1)(NCS)]^+$ showing the atomic numbering scheme; hydrogen atoms are omitted for the sake of clarity.

Table 2
Selected bond lengths (Å) and angles (°) for **1**

Bond lengths			
Ba–O(1)	2.750(2)	Ba–N(1)	2.943(3)
Ba–O(2)	2.792(2)	Ba–N(2)	2.930(3)
Ba–O(3)	2.767(2)	Ba–N(3)	2.922(3)
Ba–N(1S)	2.806(3)	Ba–N(4)	2.886(3)
		Ba–N(5)	2.897(3)
Bond angles			
O(1)–Ba–O(3)	106.89(7)	N(1S)–Ba–N(3)	116.32(9)
O(1)–Ba–O(2)	88.93(7)	N(4)–Ba–N(3)	116.62(8)
O(3)–Ba–O(2)	58.86(7)	N(5)–Ba–N(3)	119.75(8)
O(1)–Ba–N(1S)	84.31(9)	O(1)–Ba–N(2)	104.95(7)
O(3)–Ba–N(1S)	160.43(9)	O(3)–Ba–N(2)	88.60(7)
O(2)–Ba–N(1S)	138.99(9)	O(2)–Ba–N(2)	147.31(7)
O(1)–Ba–N(4)	62.41(8)	N(1S)–Ba–N(2)	72.80(9)
O(3)–Ba–N(4)	116.80(8)	N(4)–Ba–N(2)	153.55(8)
O(2)–Ba–N(4)	58.88(8)	N(5)–Ba–N(2)	57.66(8)
N(1S)–Ba–N(4)	82.50(9)	N(3)–Ba–N(2)	68.45(8)
O(1)–Ba–N(5)	154.04(7)	O(1)–Ba–N(1)	133.21(8)
O(3)–Ba–N(5)	92.70(7)	O(3)–Ba–N(1)	98.14(8)
O(2)–Ba–N(5)	116.17(7)	O(2)–Ba–N(1)	71.00(7)
N(1S)–Ba–N(5)	72.44(9)	N(1S)–Ba–N(1)	84.64(9)
N(4)–Ba–N(5)	123.62(8)	N(4)–Ba–N(1)	71.12(8)
O(1)–Ba–N(3)	60.64(7)	N(5)–Ba–N(1)	57.20(8)
O(3)–Ba–N(3)	59.66(7)	N(3)–Ba–N(1)	157.79(8)
O(2)–Ba–N(3)	94.65(7)	N(2)–Ba–N(1)	114.72(8)

ion into the macrobicyclic cavity interacting with all the heteroatoms of the macrobicycle host forces it to fold, so diminishing the π conjugation degree. The pyridine ring forms a dihedral angle of 48.9° with the plane containing the benzyl ring attached to N3 and of 49.1° with the plane containing the other aromatic ring. These angles are about 20° smaller than those found in $[Ba(L^1)(ClO_4)_2]$. Both benzyl rings intersects at 87°, a value substantially different than the one found in the perchlorate complex (49°). Therefore, the presence of a thiocyanate group in the coordination sphere of the barium ion instead semi-coordinated perchlorate groups [7] causes a different fold on the organic receptor. This comes because the angle between both benzyl rings opens in order to enable the entrance of the thiocyanate group, which also causes shorter bond distances. The coordination polyhedron, shown in Fig. 3, may be best described as a monocapped distorted dodecahedron. Distance between both pivotal nitrogen atoms, N(3) and N(4), is 4.941(4) Å, 0.38 Å shorter than that found in the barium intermediate [(*N*,*N*′-bis(2-aminobenzyl)-1,10-diaza-15-crown-5)di(isothiocyanate)barium(II)] prevously described,[18] whereas distance between both imine nitrogen atoms, N(1) and N(2) amounts 4.945(4) Å, around 1 Å longer than the distance between the two precursor amine nitrogen atoms in the intermediate.

Conductivity measurements for 10^{-3} M solution in acetonitrile at 20 °C ($\Lambda_M = 259$ cm^2 Ω^{-1} mol^{-1} for **1** and 107 cm^2 Ω^{-1} mol^{-1} for **2**) reveal that both compounds behave as 1:1 electrolyte in this solvent [19], which confirms the presence of one thiocyanate group

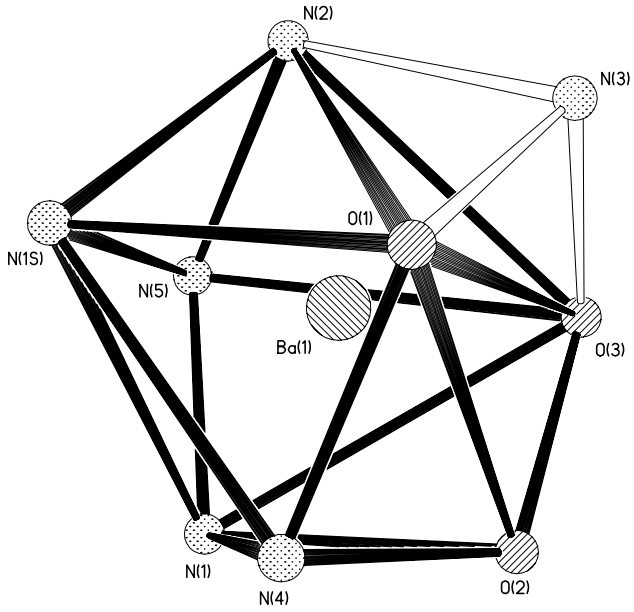


Fig. 3. The coordination polyhedron around the metal ion in the $[Ba(L^1)(NCS)]^+$ complex.

in the coordination sphere of barium(II) in acetonitrile solution as it does in the solid state (vide supra).

The ^{1}H and NMR spectrum of **1** recorded in CD_3CN solution (Table 3, Scheme 1) is also quite similar to that of the analogous perchlorate complex. The spectrum confirms the integrity of the ligand in this solvent; resonances attributable to amino or aldehyde functions are absent. The imine resonances appear as a singlet at 8.63 ppm, which indicates that both imine groups of the macrobicycle are magnetically equivalent. The spectrum shows a group of complicated signals in the region 2.4–4.2 ppm due to the ethylenic and methylenic protons, while the aromatic protons appear between 7.1 and 8.4 ppm. The corresponding ^{13}C NMR spectrum

Table 3
^{1}H and ^{13}C NMR data for compound **1**[a]

Proton	1[b]	Carbon	1[b,c]
H1–H6	2.3–4.2(m), 24H	C1, C2, C4	69.4, 69.6, 69.9
H8, H9	7.37(m), 4H	C3, C5	51.9
H10	7.52(t), 2H	C6	60.2
H11	7.18(d), 2H	C7	130.6
H13	8.63(s), 2H	C8	133.6
H15	8.08(d), 2H	C9	128.1
H16	8.32(t), 1H	C10	131.1
		C11	121.5
		C12	152.7
		C13	165.6
		C14	153.7
		C15	131.6
		C16	141.0

[a] See Scheme 1 for labeling.
[b] Conditions: $T = 293$ K, 200 MHz. $^3J_{16,15} = {}^3J_{15,16} = 7.57$ Hz; $^3J_{11,10} = 7.32$ Hz; $^3J_{10,9}$ 7.81 Hz; $^4J_{11,9} = 2.44$ Hz.
[c] Assignment supported by DEPT experiments.

shows 16 signals for the 33 carbon nuclei of the ligand backbone (Table 3). This points to an effective C_s symmetry of the complexes in acetonitrile solution. The ^1H NMR spectrum of **2** recorded in acetonitrile solution is more complicated. It shows two peaks due to the imine protons at 8.57 and 7.67 ppm, which suggests an unsymmetrical coordination of the metal ion in the macrobicyclic cavity. In particular, this agrees with the barium(II) cation asymmetrically situated in the macrobicyclic cavity of $\mathbf{L^2}$ due to the proton transfer that happens from the phenol group to the nitrogen atom of one of the imine groups as observed in the crystal structure of the perchlorate analogue, $[BaL^2(ClO_4)(CH_3CN)](ClO_4)\cdot 0.5CH_3CH$, previously reported [13]. The spectrum of **2** also shows the signals of the methyl and –OH protons at 2.40 and 17.15 ppm, the latter appearing as a broad resonance as expected.

4. Supplementary material

Crystallographic data for crystal structure of **1** have been deposited at the Cambridge Crystallographic Data Centre as CCDC 246436. Copies of the data can be obtained free of charge upon application to The Director, CCDC, 12 Union Road, Cambridge, CB2 1EZ, UK (Fax: +44-1223-336033; e-mail: deposit@ccdc.cam.ac.uk or http://www.ccdc.cam.ac.uk).

Acknowledgements

The authors thank Xunta de Galicia (PGIDIT03TAM10301PR) for generous financial support.

References

[1] R.M. Izatt, J.J. Christensen (Eds.), Synthesis of Selective Agents (Progress in Macrocyclic Chemistry), vol. 3, Wiley, New York, 1987.
[2] Y. Inoue, G.W. Gokel (Eds.), Cation Binding by Macrocycles, Marcel Dekker, New York, 1990.
[3] G.W. Gokel, Crown Ethers and Cryptands, The Royal Society of Chemistry, Cambridge, 1991.
[4] J.-M. Lehn, Pure Appl. Chem. 52 (1980) 2441.
[5] J.M. Mahoney, J.P. Davis, A.M. Beatty, B.D. Smith, J. Org. Chem. 68 (2003) 9819.
[6] P. Guerriero, S. Tamburini, P.A. Vigato, Coord. Chem. Rev. 139 (1995) 17.
[7] D. Esteban, D. Bañobre, R. Bastida, A. de Blas, A. Macías, A. Rodríguez, T. Rodríguez-Blas, D.E. Fenton, H. Adams, J. Mahía, Inorg. Chem. 38 (1999) 1937.
[8] D. Esteban, D. Bañobre, A. de Blas, T. Rodríguez-Blas, R. Bastida, A. Macías, A. Rodríguez, D.E. Fenton, H. Adams, J. Mahía, Eur. J. Inorg. Chem. (2000) 1445.
[9] D. Esteban, F. Avecilla, C. Platas-Iglesias, J. Mahía, A. de Blas, T. Rodríguez-Blas, Inorg. Chem. 41 (2002) 4337.
[10] D. Esteban, F. Avecilla, C. Platas-Iglesias, A. de Blas, T. Rodríguez-Blas, Polyhedron 22 (2003) 2709.
[11] S.R. Collinson, D.E. Fenton, Coord. Chem. Rev. 148 (1996) 19.
[12] C. Platas-Iglesias, D. Esteban, V. Ojea, F. Avecilla, A. de Blas, T. Rodríguez-Blas, Inorg. Chem. 42 (2003) 4299.
[13] F. Avecilla, D. Esteban, C. Platas-Iglesias, A. de Blas, T. Rodríguez-Blas, Acta Crystallogr. C 59 (2003) m93.
[14] E.P. Papadoupoulus, A. Jarrar, C.H. Issidorides, J. Org. Chem. 31 (1966) 615.
[15] D. Jerchel, J. Heider, H. Wagner, Liebigs Ann. Chem. 613 (1958) 153.
[16] S. Taniguchi, Bull. Chem. Soc. Jpn. 57 (1984) 2683.
[17] G.M. Sheldrick, SHELXTL Bruker Analytical X-ray System, release 5.1, Madison, WI, 1997.
[18] F. Avecilla, D. Esteban, C. Platas-Iglesias, A. de Blas, T. Rodríguez-Blas, Acta Crystallogr. C 59 (2003) m16.
[19] W.J. Geary, Coord. Chem. Rev. 7 (1971) 81.

Available online at www.sciencedirect.com
SCIENCE DIRECT®
Polyhedron 24 (2005) 295–303
POLYHEDRON
www.elsevier.com/locate/poly

Novel inorganic–organic hybrids based on oxo-bridged $M_6(M)$ centered octahedral cage

Chong Lei [a], Jiang-Gao Mao [a,*], Yan-Qiong Sun [a], Zhen-Chao Dong [b]

[a] State Key Laboratory for Structure Chemistry, Fujian Institute for Research on the Structure of Matter, Chinese Academy of Sciences, Fuzhou 350002, People's Republic of china
[b] National Institute for Materials Science, 1-2-1 Sengen, Tsukuba, Ibaraki 305-0047, Japan

Received 10 August 2004; accepted 17 November 2004
Available online 8 December 2004

Abstract

Three new polyoxometalates with *N*-(phosphonomethyl)-*N*-methyl glycine ($MeN(CH_2CO_2H)(CH_2PO_3H_2)$, H_3L), namely, $Cd_9L_6(H_2O)_{12}\cdot 19H_2O$ (**1**), $\{Zn_7L_6\}\{Ni(bipy)(H_2O)_4\}_2\cdot 16H_2O$ (**2**) (bipy = 4,4-bipyridine) and $[H_3O]\{Zn_7L_6\}$ $\{Ni(H_2O)_2(bipy)_2\}_{1.5}\cdot 12H_2O$ (**3**), have been synthesized and structurally determined.The structures of all three compounds are built from oxo-bridged $M_6(M)L_6$(M = Zn or Cd) centered octahedral cages.In compound **1**, the $[Cd_6(Cd)L_6]$ cages are interconnected by Cd_2O_2 dimeric units into a novel $\langle 2\,0\,0\rangle$ layer.Packing of such 2D layers results in cavities that are occupied by lattice water molecules.The structure of compound **2** is composed of $\{Zn_6(Zn)L_6\}^{4-}$ cluster anions and 1D cationic chains of $\{Ni(bipy)(H_2O)_4\}^{2+}$.The lattice water molecules are located in the tunnels created by the above two types of building blocks which are interlinked via hydrogen bonds.In compound **3**, the $\{Zn_6(Zn)L_6\}^{4-}$ cluster anion cages are located at the tunnels formed by the 3D cationic network of$\{Ni(bipy)_2(H_2O)_2\}^{2+}$.
© 2004 Elsevier Ltd. All rights reserved.

Keywords: Metal phosphonates; Hydrothermal synthesis; Open frameworks; Crystal structures; Cage compounds

1. Introduction

The chemistry of metal phosphonates has been an area of interest to both inorganic and materials chemists in recent years due to their potential applications in the areas of catalysis, ion exchange, proton conductivity, intercalation chemistry, photochemistry, and materials chemistry [1]. In addition to the layered species, metal phosphonates also exhibit a variety of open framework and microporous structures [1–3]. Materials with open-framework and microporous structures are expected to find their use as hybrid composite materials in electro-optical and sensing application in the future [4–8]. However, reports on metal phosphonates with a molecular cluster unit are relatively rare [9–14]. Synthesis of multi-zinc clusters is of considerable contemporary interest, as exemplified by the potential application of the trinuclear clusters in biological systems such as phospholipase C and P1 nuclease [15]. Phosphonic acid attached with a carboxylate group can function as multidentate chelating and bridging ligand, hence we deem it can also form cluster cage compounds in addition to compounds with layered or 3D structures. Two zinc(II) cage compounds have been obtained by reactions of zinc(II) acetate with *N*-(phosphonomethyl)proline or *N*-(phosphonomethyl)-*N*-methyl glycine [16]. The structures of both zinc(II) amino-carboxylate-phosphonates are composed of a $Zn_6(Zn)(ligand)_6$ cluster anion and two hexahydrated zinc(II) cations [16]. We deem that these hexahydrated zinc(II) cations should be exchangeable by other

* Corresponding author. Tel.: +86 591 3704836; fax: +86 591 3714946.
E-mail address: mjg@ms.fjirsm.ac.cn (J.-G. Mao).

0277-5387/$ - see front matter © 2004 Elsevier Ltd. All rights reserved.
doi:10.1016/j.poly.2004.11.007

transition metal ions, such as Co(II) and Ni(II) ions for whom an octahedral geometry is more favored. Furthermore, it is possible for these isolated hexahydrated divalent metal ions to be interconnected into a 1D array, a 2D layer or 3D network if a suitable metal linker such as 4,4′-bipyridine (bipy) is added. Another possibility is that these isolated cluster cages may be interconnected into a 2D layer by a suitable linker. Our such research initiatives afforded three new inorganic–organic hybrids based on $M_6(M)(L)_6(H_3L = CH_3N(CH_2CO_2H)(CH_2PO_3H_2))$ cluster cages, namely, $Cd_9L_6(H_2O)_{12} \cdot 19H_2O$ (**1**), $\{Zn_7L_6\}$ $\{Ni(bipy)(H_2O)_4\}_2 \cdot 16H_2O$ (**2**) (bipy = 4,4′-bipyridine) and $[H_3O]\{Zn_7L_6\}$ $\{Ni(H_2O)_2(bipy)_2\}_{1.5} \cdot 12H_2O$ (**3**). All three compounds belong to a new type of polyoxometalates. Herein we reported their syntheses, characterizations and crystal structures.

2. Experimental

2.1. Materials and methods

N-(phosphonomethyl)-*N*-methyl glycine (H_3L) was prepared by a Mannich type reaction according to procedures previous described [16b]. All other chemicals of reagent grade were obtained from commercial sources and used without further purification. Elemental analyses for C, H, N were performed on a Vario EL III elemental analyzer. Ni and Zn elemental analyses for compounds **2** and **3** were carried out with an ICPQ-100 spectrometer. The FT-IR spectra were recorded on a Nicolet Magna 750 FT-IR spectrometer using KBr pellets in the range of 4000–400 cm^{-1}. Thermogravimetric analysis was carried out with a TGA/SBTA851 unit at a heating rate of 15 °C/min under a nitrogen atmosphere. The XRD powder patterns were collected on a Philips X'Pert-MPD diffractometer using graphite-monochromated Cu Kα radiation in the angular range $2\theta = 5-70°$ with a step size of 0.02° and a counting time of 3 seconds per step. Magnetic susceptibility measurements were performed with a Quantum Design SQUID magnetometer at a field of 1 T over the range of 6–300 K. The diamagnetic contributions of the samples were corrected using Pascal's constants.

2.2. Synthesis of $Cd_9L_6(H_2O)_{12} \cdot 19H_2O$ (*1*)

Compound **1** was synthesized by reacting 1.0 mmol of $CdCl_2$ with 0.5 mmol of H_3L in 10 ml of deionized water. Then the pH value of the resultant solution was adjusted to approximately 5 by adding 20 wt% tetrabutylammonium hydroxide solution. The reaction mixture was stirred at room temperature for 24 h and then filtered. Slow diffusion of ethanol into the filtrate afforded colorless crystals of **1** in a ca. 33% yield based on Cd. The final pH value is close to 5.0. Elemental analysis for **1**, $Cd_9C_{24}H_{106}N_6O_{61}P_6$: *Anal.* Calc.: C, 10.85; H, 4.03; N, 3.17. Found: C, 10.45; H, 3.87; N, 3.43%. IR data (KBr, cm^{-1}): 3383 (br), 2924(w), 2814(w), 2175(w), 1579(s), 1452(m), 1431(m), 1406(s), 1346(m), 1317(s), 1317(m), 1288(m), 1244(w), 1186(m), 1128(s), 1061(s), 972(s), 937(m), 895(m), 854(m), 787(m), 719(m), 590(m), 546(m), 526(w), 496(m).

2.3. Synthesis of $\{Zn_7L_6\}$ $\{Ni(bipy)(H_2O)_4\}_2 \cdot 16H_2O$ (*2*)

Compound **2** was prepared by hydrothermal reactions. A mixture of 1.0 mmol of zinc(II) acetate, 0.5 mmol of nickel(II) acetate, 1.0 mmol of H_3L and 1.0 mmol of 4,4′-bipy in 10 ml of deionized water was heated at 130 °C for 4 days. Green crystals of **2** were obtained in a 42.5% yield based on zinc. The initial and final pH values are 4.0 and 5.5, respectively. Elemental analysis for **2**, $C_{44}H_{106}N_{10}O_{54}P_6$ Zn_7Ni_2: *Anal.* Calc.: C, 22.02; H, 4.45; N, 5.84; Zn, 19.06; Ni, 4.89. Found: C, 21.81; H, 4.23; N, 5.67; Zn, 18.3; Ni, 4.5%. IR data (KBr, cm^{-1}): 3660(m), 3438(br), 2918(w), 2818(w), 1606(s), 1535(m), 1493(w), 1466(w), 1406(s), 1331(s), 1279(m), 1223(w), 1173(s), 1119(s), 1082(s), 999(s), 985(s), 933(m), 891(s), 852(s), 818(s), 791(s), 733(m), 634(m), 588(m), 553(m), 503(w), 469(w).

2.4. Synthesis of $[H_3O]\{Zn_7L_6\}\{Ni(H_2O)_2(bipy)_2\}_{1.5} \cdot 12H_2O$ (*3*)

The method for the preparation of compound **3** is similar to that of compound **2** except that the molar ratio of bipy/Ni was increased to 4:1. Green crystals of **3** were isolated in a 47.0% yield based on zinc. The initial and final pH values are 4.5 and 5.0, respectively. Elemental analysis for **3**, $C_{54}H_{99}N_{12}O_{46}P_6Zn_7Ni_{1.5}$: *Anal.* Calc.: C, 27.18; H, 4.19; N, 7.05; Zn, 19.2; Ni, 3.69. Found: C, 26.43; H, 4.33; N, 6.87; Zn, 18.6; Ni, 3.4%. IR data (KBr, cm^{-1}): 3419(br), 1601(s), 1537(m), 1491(w), 1450(w), 1408(s), 1335(m), 1286(w), 1225(w), 1182(m), 1120(s), 1090(s), 1072(s), 997(s), 982(s), 935(w), 895(m), 854(m), 823(s), 793(m), 733(w), 634(s), 555(s), 515(m), 467(w).

2.5. X-ray crystallography

Intensity data of compounds **1**, **2** and **3** were collected on a Siemens Smart CCD diffractometer with graphite-monochromated Mo Kα radiation ($\lambda = 0.71073$ Å) at 293 K. The data sets were corrected for absorption by the SADABS program [17]. All structures were solved by the direct methods and refined by full-matrix least-squares fitting on F^2 by SHELX-97 [17]. For compound **3**, O(wh) located at a position of three-fold position is assumed to be a H_3O^+ cation, and its occupancy factor

is reduced to 1/6 for the sake of charge balance. O2w and O3w of compound **3** are disordered and each has two orientations (O2w, O2w′, O3w, O3w′). The O2w...O2w′ and O3w...O3w′ separations are 1.94(3) and 1.96(3) Å, respectively, and the occupancy factors for these four atoms were assigned to be 50% each. All non-hydrogen atoms, except for O(14w), O(15w) and O(16w) for compound **1**, and O(2w), O(2w′), O(3w) and O(3w′) atoms for compound **3**, were refined with anisotropical thermal parameters. Hydrogen atoms except those for the water molecules were located at the geometrically calculated positions. Crystallographic data and refinement residuals are summarized in Table 1. Important bond distances are listed in Table 2. Further details on the crystallographic studies as well as atomic parameters are given in Section 4.

3. Results and discussion

The structure of compound **1** features a unusual 2D layer built from $[Cd_6(Cd)L_6]$ centered octahedral cluster units interconnected by Cd(2) dimeric units. As shown in Fig. 1, the asymmetric unit of compound **1** contains five independent Cd(II) ions. Cd(1) lies on a position of −1 symmetry, and it is octahedrally coordinated by six phosphonate oxygen atoms from six phosphonate groups. The Cd–O distances are 2.243(7) and 2.296(7) Å, respectively. Cd(2), Cd(3) and Cd(4) have similar coordination geometry, and each is 6-coordinated by a tridentate chelating carboxylate-phosphonate ligand (1 N, 1 carboxylate O and 1 phosphonate O), an aqua ligand and two phosphonate oxygen atoms from two neighboring [CdL] units. The Cd–O and Cd–N distances are in the range of 2.163(8) to 2.43(1) Å, and 2.326(9) to 2.356(9) Å, respectively. Cd(5) forms five normal bonds with two carboxylate oxygen atoms from two ligands and three aqua ligands. The Cd–O distances range from 2.584(9) to 2.631(9) Å, which are much larger than the Cd–O distances for Cd(1), Cd(2), Cd(3) and Cd(4) atoms. Cd(5) also forms two slightly longer Cd–O bonds with two carboxylate oxygen atoms (O3a, O4a, symmetry operator: $1-x$, $2-y$, $-z$) from a neighboring [Cd(2)L] unit. Cd(5)–O(3a) and Cd(5)–O(4a) contacts are 2.662(9) and 2.674(9) Å, respectively. These Cd–O distances are comparable to those reported in other Cd(II) phosphonates [18]. One Cd(1), two Cd(2)L, two Cd(3)L and two Cd(4)L units form an unusual centered $Cd_6(Cd)L_6$ octahedral cluster unit with Cd(1) at its center, and six of its eight Cd_3 triangle phases are each capped by a phosphonate group. This type of cluster cage is similar to that reported in the Zn(II) carboxylate-phosphonates [16]. However, due to a higher coordination number for the Cd(II) ion than that for the Zn(II) ion, all Cd(II) ions in the cage are octahedrally coordinated, whereas in the zinc cages, only the central atom is six-coordinated and the other six are in trigonal bipyramidal geometry [16]. The coordination of the Cd(II) ions in a M_6 octahedron is saturated by an additional aqua ligand. The distances from the central Cd(II) ion to the octahedral ones are in the range of 3.765(5) to 3.790(5) Å. Similar to those in $Zn_6(Zn)L_6$ [16], each phosphonate group bridges with four Cd(II) ions, with one phosphonate oxygen atom acting as a μ_2 metal linker. In addition to the unidentate coordination mode for the carboxylate group (O(5), O(6)) as that in its zinc(II) cluster compounds, two other types of coordination modes are also found in the cadmium(II) compound: the one containing O(1) and O(2) atoms adopts a bidentate bridging coordination mode, whereas the other one containing O(3) and O(4) atoms adopts a tetradentate chelating and bridging mode, connecting with three Cd(II) ions. Two Cd(5)

Table 1
Crystal data and structure refinements for compounds **1**, **2** and **3**

	Compound **1**	Compound **2**	Compound **3**
Formula	$Cd_9C_{24}H_{106}N_6O_{61}P_6$	$C_{44}H_{106}N_{10}O_{54}P_6Zn_7Ni_2$	$C_{54}H_{99}N_{12}O_{46}P_6Zn_7Ni_{1.5}$
Formula weight	2652.57	2400.22	2383.93
Space group	*Pccn*	P_1/nPn-3	
a (Å)	21.6855(3)	11.559(1)	22.59(1)
b (Å)	17.9669(2)	30.8788(8)	22.59(1)
c (Å)	20.6144(3)	13.5549(3)	22.59(1)
α (°)	90.0	90.0	90
β (°)	90.0	108.135(1)	90
γ (°)	90.0	90.0	90
V (Å^3)	8031.8(2)	4597.9(2)	11531(1)
Z	4	2	4
D_{calc} (g cm^{-3})	2.194	1.734	1.373
μ (mm^{-1})	2.566	2.399	1.830
Goodness-of-fit on F^2	1.057	1.131	1.087
R_1, wR_2 ($I > 2\sigma(I)$)	0.0696/0.1796	0.0711/0.1290	0.0570/0.1488
R_1, wR_2 (all data)	0.0909/0.1979	0.1149/0.1491	0.1180/0.1890

$R_1 = \sum||F_o| - |F_c||/\sum|F_o|$, $wR_2 = \{\sum w[(F_o)^2 - (F_c)^2]^2/\sum w[(F_o)^2]^2\}^{1/2}$.

Table 2
Selected bond lengths [Å] for compounds **1**, **2** and **3**

*Compound **1***			
Cd(1)–O(13)	2.243(7)	Cd(1)–O(31)	2.296(7)
Cd(1)–O(23)	2.362(7)	Cd(2)–O(32)	2.186(8)
Cd(2)–O(12)#1	2.207(8)	Cd(2)–O(23)	2.326(7)
Cd(2)–O(4)	2.327(8)	Cd(2)–N(2)	2.356(9)
Cd(2)–O(1W)	2.38(1)	Cd(3)–O(11)	2.163(8)
Cd(3)–O(21)#1	2.205(8)	Cd(3)–N(3)	2.347(9)
Cd(3)–O(6)	2.374(9)	Cd(3)–O(31)	2.382(7)
Cd(3)–O(2W)	2.421(9)	Cd(4)–O(22)	2.172(8)
Cd(4)–O(33)#1	2.222(8)	Cd(4)–N(1)	2.326(9)
Cd(4)–O(13)	2.329(8)	Cd(4)–O(1)	2.349(8)
Cd(4)–O(3W)	2.43(1)	Cd(5)–O(6W)	2.584(9)
Cd(5)–O(3)	2.595(9)	Cd(5)–O(2)#2	2.598(9)
Cd(5)–O(4W)	2.61(1)	Cd(5)–O(5W)	2.63(1)
Hydrogen bonds:			
O(5)...O(5w)#3	2.74(2)	O(5)...O(6w)#3	2.81(2)
O(1w)...O(15w)	2.68(3)	O(2w)...O(11w)#3	2.86(2)
O(3w)...O(3w)	2.70(3)	O(3w)...O(15w)	2.63(3)
O(4w)...O(5w)#4	2.74(2)	O(4w)...O(9w)#5	2.71(2)
O(4w)...O(12w)#5	2.72(2)	O(6w)...O(13w)#2	2.78(2)
O(8w)...O(10w)	2.81(2)	O(8w)...O(11w)#6	2.82(2)
O(9w)...O(13w)#7	2.84(2)	O(10w)...O(14w)#8	2.79(2)
O(11w)...O(12w)#8	2.74(2)	O(12w)...O(16w)#9	2.63(4)
*Compound **2***			
Zn(1)–O(13)	1.965(6)	Zn(1)–O(22)#1	1.982(5)
Zn(1)–O(6)	2.144(6)	Zn(1)–N(3)	2.149(7)
Zn(1)–O(33)	2.188(5)	Zn(2)–O(21)	2.132(5)
Zn(2)–O(12)	2.133(5)	Zn(2)–O(33)	2.137(5)
Zn(3)–O(23)#1	1.989(6)	Zn(3)–O(31)#1	1.999(5)
Zn(3)–O(1)	2.124(6)	Zn(3)–N(1)	2.167(7)
Zn(3)–O(12)	2.186(5)	Zn(4)–O(32)	1.965(6)
Zn(4)–O(11)	1.991(6)	Zn(4)–O(4)	2.135(6)
Zn(4)–N(2)	2.143(7)	Zn(4)–O(21)	2.229(5)
Ni(1)–O(3W)	2.097(6)	Ni(1)–O(2W)	2.102(6)
Ni(1)–O(1W)	2.106(6)	Ni(1)–O(4W)	2.122(6)
Ni(1)–N(4)#2	2.163(7)	Ni(1)–N(5)	2.180(7)
Hydrogen bonds:			
O(1W)...O(5W)	2.75(1)	O(2W) ...O(7W)	2.75(1)
O(2W) ...O(12W)	2.770(9)	O(3W) ...O(8W)	2.775(9)
O(9W) ...O(11W)#3	2.78(2)		
*Compound **3***			
Zn(1)–O(13)	2.116(5)	Zn(2)–O(12)#1	1.946(5)
Zn(2)–O(11)#2	1.952(5)	Zn(2)–O(1)	2.094(5)
Zn(2)–N(1)	2.144(6)	Zn(2)–O(13)	2.206(5)
Ni(1)–O(1W)	2.059(7)	Ni(1)–N(3)	2.113(7)
Ni(1)–N(2)	2.136(7)		
Hydrogen bonds:			
O(2) ...O(1W)	2.673(7)	OWH...O(2W′)	2.71(3)
O(2W) ...O(3W)#3	2.78(5)		

Symmetry transformations used to generate equivalent atoms:
For **1**: #1 $-x+1, -y+1, -z$; #2 $-x+1, y+1/2, -z+1/2$; #3 $1/2+x, -1/2+y, -z$; #4 $1-x, 2-y, -z$; #5 $x, 3/2-y, 1/2+z$; #6 $3/2-x, 1/2-y, z$; #7 $x, 3/2-y, -1/2+z$; #8 $3/2-x, y, 1/2+z$; #9 $3/2-x, y, -1/2+z$.
For **2**: #1 $-x+2, -y+1, -z+2$; #2 $x+1, y, z$; #3 $-x+1, -y+1, -z+1$.
For **3**: #1 $-z, x+1/2, y-1/2$; #2 $-y+1/2, -z+1/2, x$; #3 $-z+1/2, -x+1/2, y$.

atoms are bridged by a pair of carboxylate groups to form a dimeric unit (Fig. 1).

Unlike the isolated $Zn_6(Zn)L_6$ unit in the zinc(II) phosphonates [16b], the $Cd_6(Cd)L_6$ cluster anions of compound **1** are further interconnected by Cd(5) dimers, resulting in a novel $\langle 2\,0\,0\rangle$ metal carboxylate-phosphonate layer (Fig. 2). Each $Cd_6(Cd)L_6$ unit connects with four dimeric units of Cd(5) by using its four bridging car-

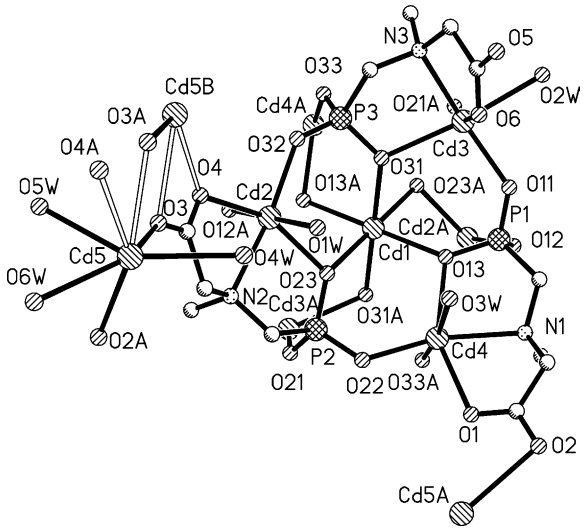


Fig. 1. The asymmetric unit of compound **1**. The open lines represent the weak Cd–O bonds. The lattice water molecules have been omitted for clarity.

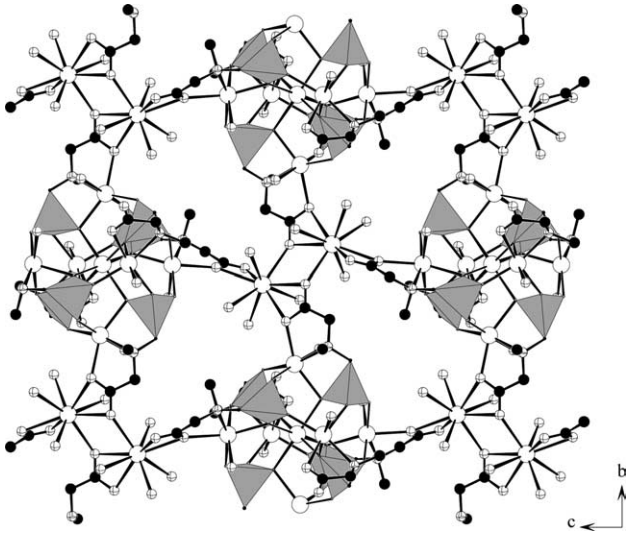


Fig. 2. A ⟨2 0 0⟩ layer of compound **1**. C–PO_3 tetrahedra are shaded in light gray. Cd, N, C and O atoms are represented as open, octand, black and crossed circles, respectively.

boxylate groups, and each dimer is also bridged to four octahedral cluster units. This type of connection creates big voids within the layer. Packing of such layers along the *a*-axis produces micropores that are occupied by the lattice water molecules (Fig. 3), which form a complicated hydrogen bond network with the aqua ligands as well as the non-coordinated carboxylate oxygen atoms (Table 2). In the zinc(II) cluster complex, the four negative charges on a cluster unit are balanced by two hexahydrated Zn(II) cations, which are located in the micropores formed by packing of the cluster cages [16].

Compounds **2** and **3** were obtained in our attempt to replace the two hexahydrated zinc(II) cations by Ni(II)-

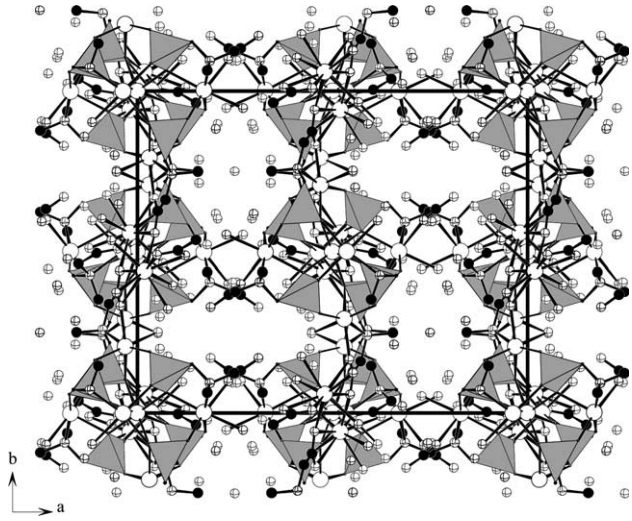


Fig. 3. View of the structure of compound **1** down the *c*-axis. C–PO_3 tetrahedra are shaded in light gray. Cd, N, C and O atoms are represented as open, octand, black and crossed circles, respectively.

bipy complex moieties. Both compounds contain two types of building blocks, a cluster cage and a Ni-bipy complex moiety. This type of compounds is, to some extent, similar to the inorganic-organic hybrids built from polyoxomolybdates with diphosphonates, in which the transition metal complex moieties play a structure directing role [19,20].

The structure of compound **2** is built from anionic $\{Zn_6(Zn)L_6\}^{4-}$ cluster cages and the cationic 1D chains of $\{Ni(H_2O)_4(bipy)\}^{2+}$ (Fig. 4). The $\{Zn_6(Zn)L_6\}$ cluster cage is essentially same as those we reported previously [16]. However, its symmetry is much lowered, and thus a cluster cage contains four independent zinc atoms instead of two as in other $\{Zn_6(Zn)L_6\}$ cluster cages previously reported [16]. Each zinc(II) ion of the Zn_6 cluster unit (Zn1, Zn3 and Zn4) is five-coordinated by a carboxylate phosphonate ligand in a tridentate chelating fashion together with two phosphonate oxygens from two neighboring ZnL chelating units. The zinc(II) ion (Zn2) located at the center of the Zn_6 cluster is octahedrally coordinated by six phosphonate oxygens from six neighboring ZnL chelating units. The coordination mode of the carboxylate-phosphonate ligand is the same as those in other $\{Zn_6(Zn)L_6\}$ cluster cages reported by us [16], but here the four negative charges of the cluster cage are compensated by two $\{Ni(H_2O)_4(bipy)\}^{2+}$ cations. Each nickel(II) ion is octahedrally coordinated by two N atoms from two bipy ligands and four aqua ligands. These nickel octahedra are crosslinked via bridging bipy ligands to form a 1D chain (Fig. 4(b)). The Ni–O, Zn–O, Ni–N and Zn–N distances are comparable to those reported in zinc phosphonates and nickel(II) complexes [6,16,19,20].

The cluster cage anions and 1D chains of $\{Ni(H_2O)_4(bipy)\}^{2+}$ cations are interconnected via electrostatic forces as well as hydrogen bonds. The hydrogen

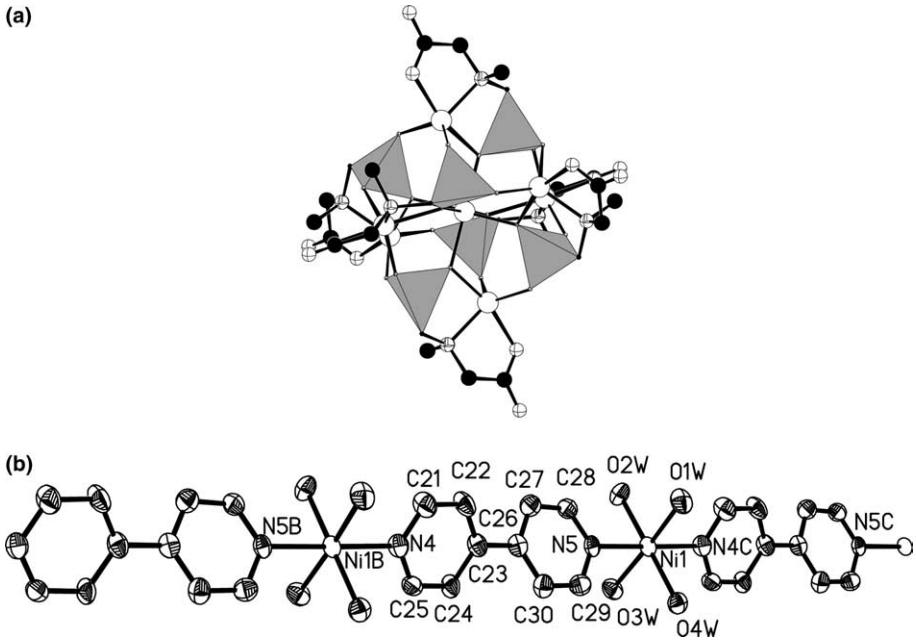


Fig. 4. Building blocks in compound **2**: (a) a $\{Zn_6(Zn)L_6\}^{4-}$ anionic cluster cage; (b) a 1D cationic chain of $\{Ni(bipy)(H_2O)_4\}^{2+}$.

bonds are formed between non-coordinated carboxylate oxygen atoms of the cluster cage and the aqua ligands of the nickel complex chain (Table 2). Interconnection of the above two types of building blocks result in hydrophilic tunnels that accommodate the lattice water molecules (Fig. 5), which are also involved in hydrogen bonding with aqua ligands as well as non-coordinated carboxylate oxygen atoms of the phosphonate ligands (Table 2).

The structure of compound **3** is significantly different from that of compound **2**. It contains two types of building blocks, $\{Zn_6(Zn)L_6\}^{4-}$ cage anion and the $\{Ni(H_2O)_2(bipy)_2\}^{2+}$ cation. Its $\{Zn_6(Zn)L_6\}^{4-}$ cage is similar to those in zinc carboxylate-phosphonates reported previously and that in compound **2**. Unlike that in compound **2**, there are only two unique zinc atoms (central atom, Zn(1) with 222 site symmetry, Zn(2) in a general position). The coordination mode of the carboxylate-phosphonate ligand is same as that in compound **2**. The Ni(II) atom located at a position of a -3 symmetry is octahedrally coordinated by four N atoms from four different bipy ligands and two aqua ligands. The Ni–O and Ni–N bond distances are comparable to those in compound **2**. The NiO_2N_4 octahedra are interconnected by bridging bipy ligands into a novel 3D network with large channels (Fig. 6). It is interesting to note that the square plane defined by NiN_4 is perpendicular to its four neighboring ones generated through symmetry operations and bridged by bipy ligands (Fig. 6). This type of interconnection is unusual and different from the normal two dimensional $\{Ni(H_2O)_2(bipy)_2\}^{2+}$ cation in which the neighboring NiN_4 square planes which are parallel to each other. The size of such a cavity is estimated to be 11.1×11.9 Å^2 after deduction of the van der Waals radius for carbon atoms. The tunnels are occupied by the $\{Zn_6(Zn)L_6\}^{4-}$ cage anions as well as lattice water molecules (Fig. 7). Similar to those in compound **2**, the above two types of building blocks are held together via electrostatic forces as well as hydrogen bonds between non-coordinated carboxylate oxygen of the cluster cage (O2) and the aqua ligand of the $\{Ni(H_2O)_2(bipy)_2\}^{2+}$ cation (O1w) (Table 2).

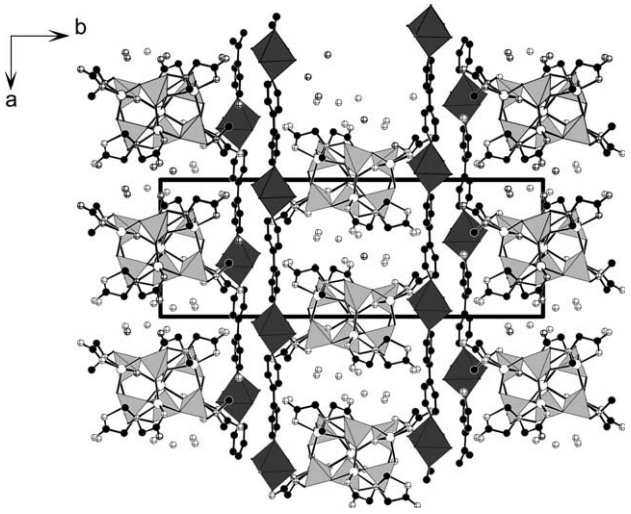


Fig. 5. View of structure of compound **2** down the *c*-axis. Nickel octahedra and C–PO_3 tetrahedra are shaded in dark and light gray, respectively. N, C and O atoms are represented as octand, black and crossed circles, respectively.

It is interesting to note that the ratio of cage anion to nickel complex moiety in compound **2** is 1:2, whereas

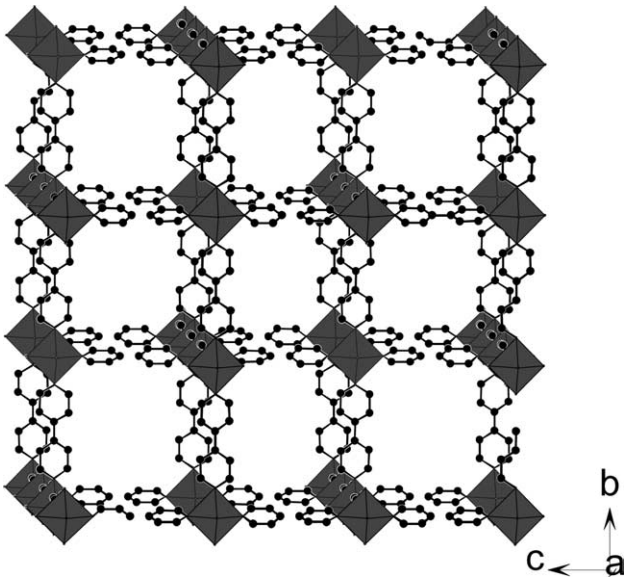


Fig. 6. A 3D cationic network of $\{Ni(bipy)_2(H_2O)_2\}^{2+}$ in compound **3**. The nickel octahedra are shaded in dark grey and the C atoms are drawn as black circles.

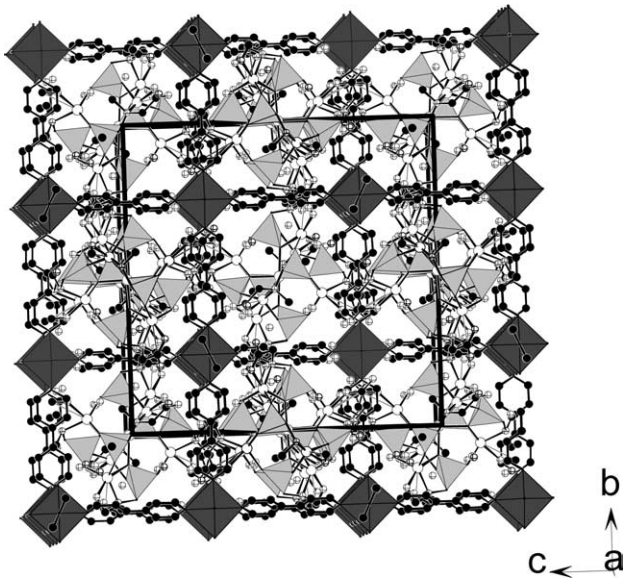


Fig. 7. View of the structure of compound **3** down the *a*-axis. The nickel octahedral and C–PO_3 tetrahedra are shaded in dark and light gray, respectively. The Zn, N, C and O atoms are drawn as open, octand, black and crossed circles, respectively.

that in compound **3** is only 1:1.5, thus an additional positive charge per cluster unit is needed for the sake of charge balance. Therefore, we assign O(wh) to be a $(H_3O)^+$ cation.

The IR spectra of both compounds **1**, **2** and **3**were measured. The broad bands at 3383 (for **1**), 3438 (for **2**) and 3419 cm^{-1} (for **3**) are due to the water molecules. The strong bands at 1579 cm^{-1} (for **1**), 1606 and 1535 cm^{-1} (for **2**) or 1601 and 1537 cm^{-1} (for **3**) correspond to the antisymmetric stretching bands of the carboxylate groups. The symmetric stretching bands of the carboxylate group appeared around 1452, 1466, and 1450 cm^{-1}, respectively for compounds **1**, **2** and **3**. The bands from 900 to 1100 cm^{-1} are due to the stretching vibrations of the tetrahedral CPO_3 group.

The different structures of compounds **2** and **3** are also indicated by their experimental XRD powder patterns. The diffraction peaks from their XRD powder patterns are in good agreement with the ones simulated from single crystal structure data, and thus both compounds **2** and **3** exist as a single phase.

The plots of effective magnetic moments (μ_{eff}) as a function of temperature for compounds **2** and **3** are shown in Fig. 8. At 300 K, μ_{eff} values for compounds **2** and **3** are 4.1 and 3.6 μ_B, respectively, corresponding to 2 and 1.5 isolated nickel(II) ions with S = 1 per formula unit, which is in good agreements with the results from X-ray structure analysis. Upon cooling, the μ_{eff} values for both compounds increase slightly and reach a maximum at about 14 K (4.21 and 4.05 μ_B for compounds **2** and **3**, respectively), which indicates the ferromagnetic behavior for both compounds. Then it decreases slightly upon further cooling, and the μ_{eff} values at 6 K are 4.15 and 3.9 μ_B, respectively for compounds **2** and **3**, indicating that both paramagnetic compounds order antiferromagnetically below 14 K. Non-linear fitting of the data in the range of 50–300 K according to Curie–Weiss law: $\chi_M = C/(T-\theta) + \chi_0$ gave C of 1.96(2) $cm^3\,mol^{-1}\,K$, θ of 5.2(5) K and χ_0 of $-7.4(1)\times10^{-4}$ emu/mol, respectively for compound **2**, and C of 1.72(4) $cm^3\,mol^{-1}\,K$, θ of 7.9(9) K and χ_0 of $-2.3(2)\times10^{-4}$ emu/mol, respectively for compound **3**, indicating mainly a weak ferromagnetic interaction between nickel(II) ions for both compounds. The distances between two nickel(II) ions bridged by a bipy ligand are 11.559(1) and 11.296(1) Å for compounds **2** and **3**, respectively. Thus it is expected that the magnetic interaction in compound **3** will be slightly stronger than that

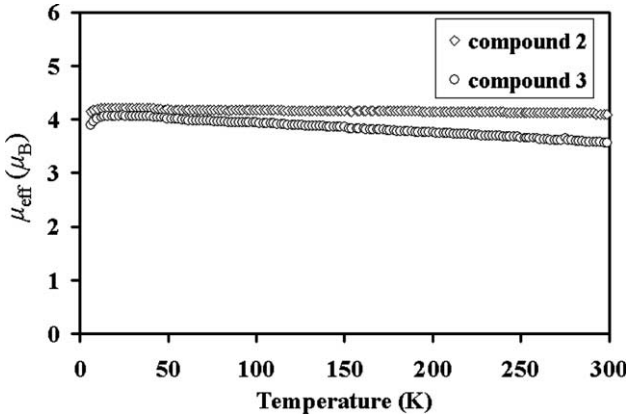


Fig. 8. Plot of effective magnetic moments (μ_{eff}) for compounds **2** and **3** as a function of temperature.

in compound **2**. This may also result from the different structures for the Ni-bipy complex moieties in both compounds. As discussed earlier, the Ni-bipy complex moiety in compound **2** has a 1D chain structure, whereas that in compound **3** features a 3D network structure.

The TGA diagram of compound **1** shows two main steps of weight loss. The first step corresponds to the loss of twenty lattice water molecules and twelve aqua ligands, which started at 61 °C and completed at 255 °C, and the weight loss of 12.2% is in good agreement with the calculated value (13.5%). The second step covering a temperature range of 280–760 °C corresponds to the combustion of the organic group. The final residual is a mixture of $Cd_2P_2O_7$ and CdO in a molar ratio of 1:1 based on XRD powder patterns. The total weight loss of 42.0% is close to the theoretical value (40.7%). The TGA diagram for compound **2** also shows two steps of weight losses. The first weight loss from 40 to 240 °C is the release of the lattice water molecules and aqua ligands, and the observed weight loss of 17.0% is close to the calculated one (18.0%). The second step covers a temperature range from 360 to 650 °C, which corresponding to the burning of organic groups. The third weight loss started from 700 °C and continued up to 1000 °C, corresponding to further decomposing of the compound. The final residual is a mixture of $Zn_2P_2O_7$, ZnO and NiO based on X-ray powder diffraction. The total weight loss of 53.1% is close to the calculated value (52.3%) if we assume the molar ratio of $Zn_2P_2O_7$:ZnO:NiO is 3:1:2. TGA curves of compound **3** also indicate three steps of weight losses. The first step and the second one overlaps and the weight losses cover a temperature range from 37 to 680 °C, during which two processes were undertaking: first, the release of all kinds of water molecules; and second, the burning of organic groups. The combined weight loss is 53.7%, which is good agreement with the calculated value (53.5%) if we assume the residual contains a mixture of $Zn_2P_2O_7$:ZnO:NiO in a molar ratio of 3:1:1.5. The third step started at 720 °C and continued up to 1000 °C, corresponding to partial decomposing of $Zn_2P_2O_7$ to ZnO. The final product is also a mixture of $Zn_2P_2O_7$, ZnO and NiO based on X-ray powder diffraction.

In summary, the reaction of *N*-(phosphonomethyl)-*N*-methyl glycine with divalent metal salts afforded four new divalent metal carboxylate-phosphonate hybrid compounds. The zinc compound contains an isolated heptanuclear $Zn_6(Zn)(ligand)_6$ cluster anion, the packing of which forms micropores which are occupied by hexahydrated zinc(II) cations and lattice water molecules. In the cadmium(II) complex, $Cd_9L_6(H_2O)_{12}\cdot 20H_2O$ (**1**), such heptanuclear $[Cd_6(Cd)(ligand)_6]^{4-}$ cluster anions are no longer isolated, but are interconnected by Cd_2O_2 dimeric units into a hybrid 2D layer. In compounds **2** and **3**, the nickel-bipy complex moieties replace the two hexahydrated zinc(II) cations in the parent Zn compound, and the structure of the nickel(II)-bipy complex depends on the Ni/bipy ratio. These three metal phosphonates resemble a new type of polyoxometalates: the layered compound **1** is homonuclear whereas compounds **2** and **3** are heteronuclear. *N*-(phosphonomethyl)-*N*-methyl glycine contains an aminocarboxylate group and a phosphonate group, so that it can function as a chelating and a bridging ligand simultaneously, and hence cage compounds can be formed. We believe that additional types of polyoxometalates based on metal phosphonates can be obtained by using the present synthetic strategy.

4. Supplementary materials

Crystallographic data for complexes **1**, **2**, and **3** have been deposited with the Cambridge Crystallographic Center, CCDC No. 207759, 231328 and 231329. Copies of this information may be obtained free of charge from The Director, CCDC, 12 Union Road, Cambridge, CB2, 1EZ, UK (fax: +44-1233-336-033, email: deposit@ccdc.cam.ac.uk or www:http://www.ccdc.cam.ac.uk).

Acknowledgements

This work was supported by the National Natural Science Foundation of China (20371047). We thank Prof. Abraham Clearfield for his helpful suggestions.

References

[1] (a) E.W. Stein Sr, A. Clearfield, M.A. Subramanian, Solid State Ionics 83 (1986) 113;
(b) G. Alberti, U. Costantino, in: J.M. Lehn (Ed.), Comprehensive Supramolecular Chemistry, Pergamon–Elsevier Science Ltd, London, 1996, p. 1;
(c) A. Clearfield, Curr. Opin. Solid State Mater Sci. 1 (1996) 268;
(d) A. Clearfield, in: K.D. Karlin (Ed.), Metal Phosphonate Chemistry in Progress in Inorganic Chemistry, 47, Wiley, New York, 1998, p. 371 (and references therein).
[2] M.E. Thompson, Chem. Mater. 6 (1994) 1168.
[3] G. Alberti, U. Costantino, in: J.M. Lehn (Ed.), Comprehensive Supramolecular Chemistry, Pergamon–Elsevier Science Ltd, London, 1996, p. 151.
[4] (a) A.K. Cheetham, G. Ferey, T. Loiseau, Angew.Chem. Int. Ed. 38 (1999) 3268;
(b) J. Zhu, X. Bu, P. Feng, G.D. Stucky, J. Am. Chem. Soc. 122 (2000) 11563.
[5] (a) M. Riou-Cavellec, M. Sanselme, M. Nogues, J.M. Greneche, G. Ferey, Solid State Sci. 4 (2002) 619;
(b) M. Sanselme, M. Riou-Cavellec, J.M. Greneche, G. Ferey, J. Solid State Chem. 164 (2002) 354;
(c) M. Riou-Cavellec, M. Sanselme, N. Guillou, G. Ferey, Inorg. Chem. 40 (2001) 723;
(d) M. Riou-Cavellec, M. Sanselme, J.M. Greneche, G. Ferey, Solid State Sci. 2 (2000) 717;

(e) M. Riou-Cavellec, M. Sanselme, G. Ferey, J. Mater. Chem. 10 (2000) 745;
(f) F. Serpaggi, G. Ferey, Inorg. Chem. 38 (1999) 4741.
[6] (a) J.G. Mao, Z.K. Wang, A. Clearfield, Inorg. Chem. 41 (2002) 6106;
(b) J.G. Mao, Z.K. Wang, A. Clearfield, New J. Chem. 26 (2002) 1010;
(c) J.G. Mao, A. Clearfield, Inorg. Chem. 41 (2002) 2319;
(d) J.L. Song, H.H. Zhao, J.G. Mao, K.R. Dunbar, Chem. Mater. 16 (2004) 1884.
[7] (a) F. Fredoueil, M. Evain, D. Massiot, M. Bujoli-Doeuff, P. Janvier, A. Clearfield, B. Bujoli, J. Chem. Soc., Dalton Trans. (2002) 1508;
(b) P. Rabu, P. Janvier, B. Bujoli, J. Mater. Chem. 9 (1999) 323;
(c) S. Drumel, P. Janvier, M. BujoliDoeuff, B. Bujoli, J. Mater. Chem. 6 (1996) 1843.
[8] (a) N. Stock, Solid State Sci. 4 (2002) 1089;
(b) N. Stock, S.A. Frey, G.D. Stucky, A.K. Cheetham, J. Chem. Soc., Dalton Trans. (2000) 4292;
(c) N. Stock, G.D. Stucky, A.K. Cheetham, Chem. Commun. (2000) 2277.
[9] (a) M.I. Khan, J. Zubieta, Prog. Inorg. Chem. 43 (1995) 1 (and references therein);
(b) M.G. Walawalker, H.W. Roesky, R. Murugavel, Acc. Chem. Res. 32 (1999) 117 (and references therein).
[10] (a) W.F. Ruettinger, D.M. Ho, G.C. Dismukes, Inorg. Chem. 38 (1999) 1036;
(b) W.F. Ruettinger, G.C. Dismukes, Inorg. Chem. 39 (2000) 1021.
[11] (a) V. Chandrasekhar, S. Kingsley, B. Rhatigan, M.K. Lam, A.L. Rheingold, Inorg. Chem. 41 (2002) 1030;
(b) V. Chandrasekhar, S. Kingsley, Angew. Chem. Int. Ed. 39 (2000) 2320.
[12] E.K. Brechin, R.A. Coxall, A. Parkin, S. Parsons, P.A. Tasker, R.E.P. Winpenny, Angew. Chem. Int. Ed. 40 (2001) 2700.
[13] E. Dumas, C. Sassoye, K.D. Smith, S.C. Sevov, Inorg. Chem. 41 (2002) 4029.
[14] Y. Yang, J. Pinkas, M. Noltemeyer, H.-G. Schmidt, H.W. Roesky, Angew. Chem. Int. Ed. 38 (1999) 664.
[15] H. Vahrenkamp, Acc. Chem. Res. 32 (1999) 589 (and references therein).
[16] (a) B.P. Yang, J.G. Mao, Y.Q. Sun, H.H. Zhao, A. Clearfield, Eur. J. Inorg. Chem. (2003) 4211;
(b) C. Lei, J.G. Mao, Y.Q. Sun, H.Y. Zeng, A. Clearfield, Inorg. Chem. 42 (2003) 6157.
[17] (a) G.M. Sheldrick, Program SADABS, Universität Göttingen, 1995;
(b) G.M. Sheldrick, SHELXTL, Crystallographic Software Package, SHELXTL, Version 5.1, Bruker-AXS, Madison, WI, 1998.
[18] (a) J.G. Mao, Z. Wang, A. Clearfield, J. Chem. Soc., Dalton Trans. (2002) 4457;
(b) J.-G. Mao, Z. Wang, A. Clearfield, Inorg. Chem. 41 (2002) 3713.
[19] (a) R.C. Finn, R.S. Rarig, J. Zubieta, Inorg. Chem. 41 (2002) 2109;
(b) R.C. Finn, E. Burkholder, J. Zubieta, Chem. Commun. (2001) 1852;
(c) R.C. Finn, J. Zubieta, Inorg. Chem. 40 (2001) 2466.
[20] (a) E. Burkholder, V. Golub, C.J. O'Connor, J. Zubieta, Chem. Commun. (2003) 2128;
(b) E. Burkholder, V. Golub, C.J. O'Connor, J. Zubieta, Inorg. Chem. 42 (2003) 6729;
(c) R.-B. Fu, X.-T. Wu, S.-M. Hu, J.-J. Zhang, Z.-Y. Fu, W.-X. Du, S.-Q. Xia, Eur. J. Inorg. Chem. (2003) 1798.

Available online at www.sciencedirect.com
SCIENCE DIRECT®
Polyhedron 24 (2005) 305–309
POLYHEDRON
www.elsevier.com/locate/poly

X-ray diffraction study of bisphosphonate metal complexes: Mg and Ca complexes of (dichloromethylene)bisphosphonic acid *P*,*P*′-diisopropyl ester

Mervi Kontturi [a,*], Sirpa Peräniemi [b], Jouko J. Vepsäläinen [b], Markku Ahlgrén [a]

[a] *Department of Chemistry, University of Joensuu, P.O. Box 111, FI-80101 Joensuu, Finland*
[b] *Department of Chemistry, University of Kuopio, P.O. Box 1627, FI-70211 Kuopio, Finland*

Received 11 August 2004; accepted 18 November 2004
Available online 8 December 2004

Abstract

Mg(II) and Ca(II) complexes of a (dichloromethylene)bisphosphosphonic acid *P*,*P*′-diisopropyl ester: $[Na_2Mg\{Cl_2C(PO_3iPr)_2\}_2(H_2O)_4]_n$ (**1**) and $[\{Ca_2[Cl_2C(PO_3iPr)_2]_2(EtOH)_2(H_2O)_2\}\cdot H_2O]_2$ (**2**) were prepared and characterised by X-ray crystallography. Compound **1** contains two independent octahedral Mg atoms at the centres of symmetry and two five-coordinated Na atoms between them, connected to polymeric chains along the *c*-direction by chelating and bridging bisphosphonato ligands. Compound **2** is a tetramer possessing a centre of symmetry; the Ca atoms are connected to each other by chelating and bridging bisphosphonato ligands. Compounds **1** and **2** form layers through hydrogen bonds.
© 2004 Elsevier Ltd. All rights reserved.

Keywords: Bisphosphonate; Clodronate; Magnesium (II); Calcium (II); Crystal structures

1. Introduction

Due to the chemical applications of metal bisphosphonates in, for example, ion exchange, sorption and catalysis, the recent expansion in research on the chemistry of metal bisphosphonates is focused on the properties of solid materials. The effectiveness of the materials is related to the degree of porosity; and the structures consist of chains, layers, pillared layers or three-dimensional networks. The dimensionality is dependent on the number of donor atoms of the ligand, but also on the length of the organic chain between the phosphonate groups and on the degree of protonation of the phosphonate group [1–4].

In order to study the properties of the solid materials, several metal complexes of medronate, $H_2C(PO_3H)_2^{2-}$ [5–15] and etidronate $(CH_3)(OH)C(PO_3H)_2^{2-}$ [16–27], have already been reported. Clodronate, $Cl_2C(PO_3H)_2^{2-}$, which is one of the best-documented bisphosphonates used effectively in medical applications [28], is similar to these compounds; and recently, some metal complexes of clodronate have also been prepared to study the properties of the solid materials: monomeric Ca and Sr complexes [29,30] and three new, polymeric and porous calcium complexes of clodronate [31]. On the other hand, we have also reported alkaline earth metal complexes of the symmetrical diethyl ester derivative of clodronate in which one O atom of both phosphonate groups of clodronate is masked by an ethyl group; these compounds were either dimers or polymeric chains [32].

Now we have prepared metal complexes of another alkyl ester derivative of clodronate, *P*,*P*′-diisopropyl-(dichloromethylene)bisphosphonate, in order to study the effect of the larger alkyl groups on the complexing properties of the ligand and on the dimensionalities of its metal complexes. Two metal complexes of Cl_2C

* Corresponding author. Tel.: +358 13 251 3377; fax: +358 13 251 3390.
E-mail address: mervi.kontturi@joensuu.fi (M. Kontturi).

0277-5387/$ - see front matter © 2004 Elsevier Ltd. All rights reserved.
doi:10.1016/j.poly.2004.11.006

$(PO_3iPr)_2^{2-}$, $[Na_2Mg\{Cl_2C(PO_3iPr)_2\}_2(H_2O)_4]_n$ (**1**) and $[\{Ca_2Cl_2C(PO_3iPr)_2\}_2(EtOH)_2(H_2O)_2\}\cdot H_2O]_2$ (**2**) were crystallized by the gel method; and the structures of the complex crystals were determined by single crystal X-ray diffraction methods.

2. Experimental

2.1. General

Reagents used for the synthesis and characterisation of compounds **1** and **2** were analytical reagent grade. Infrared spectra were recorded on a Nicolet Magna-IR™ Spectrometer 750 by the KBr pellet technique. Synthesis of the disodium-*P*,*P*′-diisopropyl(dichloromethylene)-bisphosphonate $Na_2Cl_2C(PO_3iPr)_2$ is described elsewhere [33]. Metal complexes **1** and **2** were crystallized by a gel method. Carefully weighed amounts of bisphosphonate and the metal salt were dissolved separately in water. The solutions were then mixed together, tetramethoxy silane (TMOS) was added, and the two-phase system was shaken until homogenous. The emulsion was left to form a gel, after which a precipitant was added above the gel to induce crystallisation. The crystals for X-ray diffraction analyses were collected from the gel, purified with pure precipitant and dried in air.

2.2. Preparation of $[Na_2Mg\{Cl_2C(PO_3iPr)_2\}_2(H_2O)_4]_n$ (*1*)

In the preparation of **1**, $Na_2Cl_2C(PO_3iPr)_2$ (0.12 mmol) and $MgCl_2$ (0.24 mmol) were dissolved in water (0.9 ml); and TMOS (0.1 ml) was added. After gel formation, acetone (1.0 ml) was placed above the gel as precipitant. Compound **1** crystallised above the gel as small, colourless cubic crystals. *Anal.* Calc. for $C_{14}H_{36}Cl_4MgNa_2O_{16}P_4$: C, 21.1; H, 4.56; Mg, 3.05; Na, 5.77. Found: C, 21.1; H, 4.60; Mg, 2.97; Na, 6.06%. IR/cm^{-1}: 2990 (w), 2982 (m), 2941 (w), 2877 (vw), 1385 (s), 1230 (b, vs), 1177 (m), 1143 (s), 1129 (vs), 1115 (s), 1093 (vs), 1006 (vs), 995 (vs), 895 (s), 859 (s), 770 (m), 756 (m), 742 (m).

2.3. Preparation of $[\{Ca_2[Cl_2C(PO_3iPr)_2]_2(EtOH)_2(H_2O)_2\}\cdot H_2O]_2$ (*2*)

In the preparation of **2**, $Na_2Cl_2C(PO_3iPr)_2$ (0.15 mmol) and $CaCl_2\cdot 2H_2O$ (0.15 mmol) were dissolved in water (0.9 ml); and ethanol (3 drops) and TMOS (0.1 ml) were added. After gelation, an acetone-ethanol solution (1:1, 1.0 ml) was added above the gel as precipitant. Large, colourless cubic crystals of **2** formed in and above the gel. *Anal.* Calc. for $C_{36}H_{92}Ca_4Cl_8O_{34}P_8$: C, 24.6; H, 5.27; Ca, 9.11. Found: C, 24.2; H, 5.52; Ca, 9.25%. IR/cm^{-1}: 2976 (s), 2939 (m), 2875 (w), 1380 (s), 1372 (s), 1235 (b, vs), 1175 (s), 1140 (s), 1125 (vs, b), 1089 (s), 1065 (s), 1000 (vs, b), 995 (s), 895 (s), 859 (s), 770 (m), 755 (m), 741 (m).

2.4. X-ray diffraction measurements

Experimental data were collected on a Nonius Kappa CCD diffractometer using Mo Kα-radiation (λ = 0.71073 Å) at 120 K. Denzo and Scalepack [34] programs were used for cell refinements and data reduction. Crystal data, details of data collection and refinement of the crystal structures of **1** and **2** are given in Table 1. The structures were solved using direct methods with SHELXS-97 and structural refinements were carried out with SHELXL-97 [35]. The hydrogen atoms of the water molecules in **1**, and of the water molecules and hydroxyl groups in **2** were placed from the difference maps with $U_{iso}(H) = 1.5U_{eq}(O)$; and the hydrogen atoms of the isopropyl groups were on calculated positions with $U_{iso}(H) = 1.2U_{eq}(CH)$ and $U_{iso}(H) = 1.5U_{eq}(CH_3)$.

3. Results and discussion

3.1. Crystal structures

The structures of the Mg and Ca complex of some methylenebisphosphonates [5,16,17,29,31] and the symmetrical diethyl ester derivative of clodronate [32] contain both monomeric [16,29] and dimeric structures [32] as well as one-dimensional chains [5,17,31,32] and two-dimensional layers [31]. In the monomers, the bisphosphonato ligands are chelated to the metal atom, forming one six-membered chelate ring [16,29]. In the dimer, the ligand forms six-membered chelate rings with both metal atoms and triatomic bridges between them, providing four O atoms for the metal atoms [32]. The chain and layered structures also contain chelating and bridging bisphosphonato ligands, and the ligands donate four O atoms to the metals in chains [5,17,31,32] and six O atoms in layers [31]. In the one-dimensional structure of **1**, both independent bisphosphonato ligands, $Cl_2C(PO_3iPr)_2^{2-}$, are chelated to metal atoms forming four- or six-membered chelate rings; and they also form monoatomic bridges between the metal atoms. Four of the six O atoms of both $Cl_2C(PO_3iPr)_2^{2-}$ ligands are coordinated to Mg and Na atoms, and one O atom, O33 with the isopropyl substituent is also coordinated to a metal, Na1. Similar but unexpected coordination was observed in the case of the Ba complex of the symmetrical diethyl ester derivative of clodronate [32]. In the tetrameric structure of **2**, the $Cl_2C(PO_3iPr)_2^{2-}$ ligands form six-membered chelate rings and bridge the metals by mono- and triatomic bridges. One $Cl_2C(PO_3iPr)_2^{2-}$ ligand provides three and the other provides four O atoms to Ca atoms.

Table 1
Experimental data for the crystallographic analyses (Kappa CCD) of compounds **1**–**4**

	1	**2**
Formula	$C_{14}H_{36}Cl_4MgNa_2O_{16}P_4$	$C_{36}H_{92}Ca_4Cl_8O_{34}P_8$
Crystal system	triclinic	monoclinic
Space group	$P\bar{1}$	$P2(1)/n$
a (Å)	8.9895(2)	14.2477(2)
b (Å)	13.3668(4)	12.4150(2)
c (Å)	13.8883(4)	21.7214(2)
α (°)	91.963(2)	90
β (°)	102.832(2)	94.525(1)
γ (°)	90.438(2)	90
Z	2	2
Crystal size (mm)	$0.25 \times 0.25 \times 0.10$	$0.25 \times 0.20 \times 0.20$
θ Range for data collection (°)	1.50–26.00	1.78–25.00
Reflections collected/unique	26727/6350	29389/6704
Data/restraints/parameters	6350/0/381	6704/0/413
Goodness-of-fit on F^2	1.101	1.064
Final R indices [$I > 2\sigma(I)$]	$R_1 = 0.0254$, $wR_2 = 0.0593$	$R_1 = 0.0294$, $wR_2 = 0.0780$
R indices (all data)	$R_1 = 0.0325$, $wR_2 = 0.0625$	$R_1 = 0.0328$, $wR_2 = 0.0802$
Largest difference peak and hole (e Å^{-3})	0.448 and −0.304	0.803 and −0.667

The overall structure of compound **1** $[Na_2Mg\{Cl_2C(PO_3iPr)_2\}_2(H_2O)_4]_n$ is polymeric, consisting of chains in the direction of the *c*-axis. The chains contain two independent, octahedral Mg atoms in the centres of symmetry [Mg–O_{av} 2.07(1) Å] and two independent, five-coordinated Na atoms [Na–O_{av} 2.39(13) Å] between the Mg atoms, connected to chains by four bridging aqua- and two bridging $Cl_2C(PO_3iPr)_2^{2-}$ ligands (Fig. 1(a)). There are two chelating $Cl_2C(PO_3iPr)_2^{2-}$ ligands in *trans*-positions around both Mg atoms, and the coordination spheres are filled with two aqua ligands. One of the aqua ligands of Mg1 bridges it to the Na2 atom, and the remaining coordination sites around Na2 are occupied by three $Cl_2C(PO_3iPr)_2^{2-}$ ligands and one aqua ligand. Na1, on the other hand, carries one aqua ligand and two chelating $Cl_2C(PO_3iPr)_2^{2-}$ ligands, forming one 4- and one 6-membered chelate ring. The chains of **1** are connected to a layered structure parallel to the (0 1 0) plane through hydrogen bonds [O...O 2.720(2)–2.861(2) Å, 145°–173°]. Isopropyl groups and chlorine atoms point to the interlayer section in the direction of the *b*-axis (Fig. 1(b)).

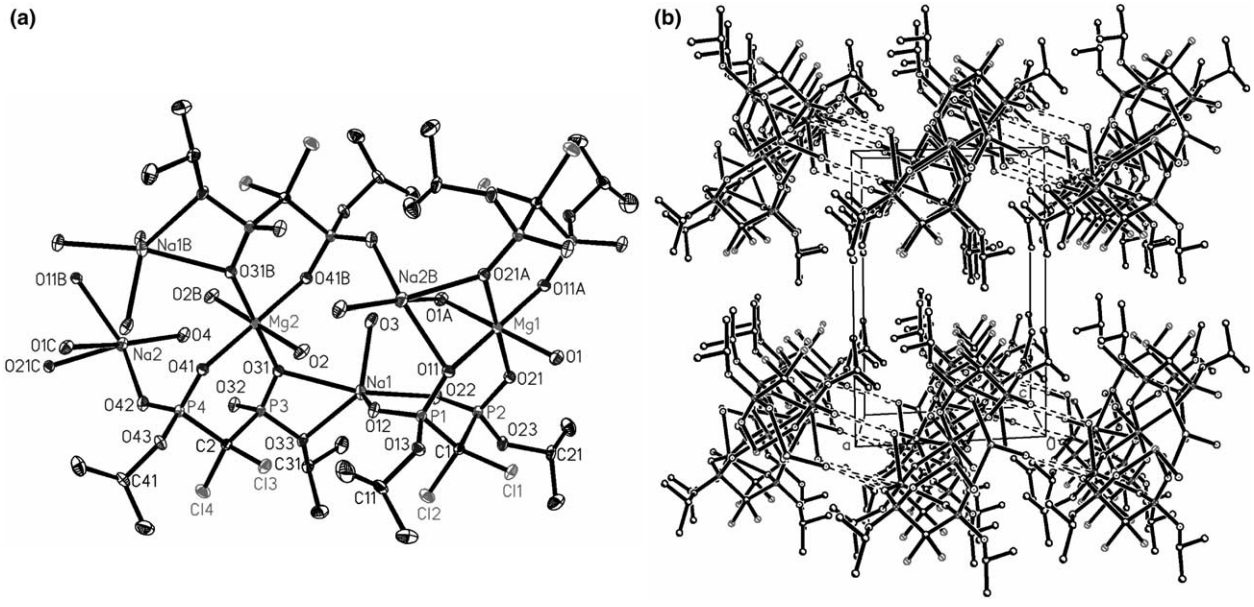


Fig. 1. (a) Part of the chain structure of 1 with numbering scheme and thermal ellipsoids (50%) and (b) packing of the chains. For clarity, hydrogen atoms are omitted. Selected bond distances (Å): Mg1–O11a 2.0558(11), Mg1–O11 2.0558(11), Mg1–O21a 2.0748(11), Mg1–O21 2.0748(11), Mg1–O1 2.0964(12), Mg1–O1a 2.0964(11), Mg2–O31b 2.0640(11), Mg2–O31 2.0640(11), Mg2–O2b 2.0732(12), Mg2–O2 2.0732(12), Mg2–O41b 2.0789(11), Mg2–O41 2.0789(11), Na1–O12 2.2574(13), Na1–O22 2.3021(13), Na1–O3 2.3065(14), Na1–O33 2.4205(13), Na1–O31 2.5420(13), Na2–O4 2.2855(14), Na2–O42 2.3179(14), Na2–O21 2.3577(13), Na2–O11b 2.4102(13), Na2–O1c 2.7112(14). In the figure, A refers to atoms at $(1 - x, -y, 1 - z)$, B at $(1 - x, -y, -z)$, C at $(x, y, z - 1)$.

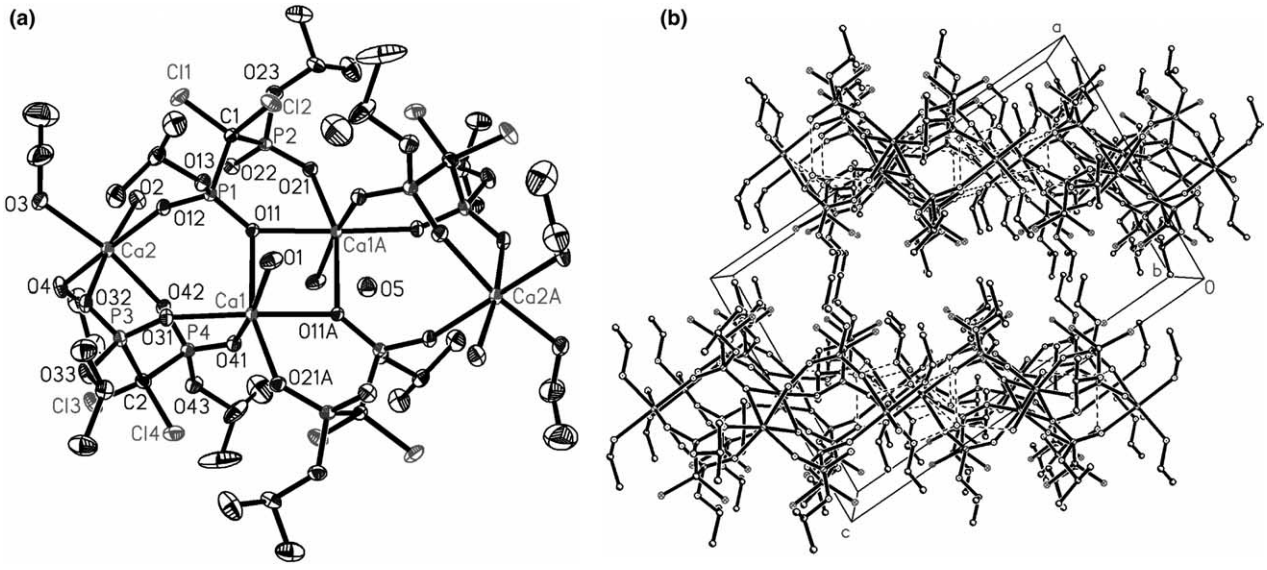


Fig. 2. (a) Structure of the asymmetric unit with numbering scheme and thermal ellipsoids (50%) and (b) packing of compound **2**. For clarity, hydrogen atoms are omitted. Selected bond distances (Å): Ca1–O31 2.2678(14), Ca1–O21a 2.2716(14), Ca1–O41 2.3092(14), Ca1–O1 2.3785(15), Ca1–O11a 2.3830(14), Ca1–O11 2.4574(14), Ca2–O12 2.2862(15), Ca2–O42 2.3092(15), Ca2–O4 2.3458(15), Ca2–O32 2.3479(15), Ca2 O3 2.3528(16), Ca2–O2 2.3603(15). In the figure, A refers to atoms at $(1-x, 1-y, -z)$.

The overall structure of **2** $[\{Ca_2[Cl_2C(PO_3iPr)_2]_2(EtOH)_2(H_2O)_2\}\cdot H_2O]_2$ consists of tetramers connected to layers by hydrogen bonds. There are two crystallographically independent, octahedral Ca atoms [Ca–O_{av} 2.34(5) Å] in the asymmetric unit of **2**, connected to each other by three triatomic bridges formed by $Cl_2C(PO_3iPr)_2^{2-}$ ligands. There are two chelating $Cl_2C(PO_3iPr)_2^{2-}$ ligands around Ca1, forming six-membered chelate rings in *cis*-positions. The fifth coordination site is occupied by a μ-phosphonate O atom that connects Ca1 to the adjacent Ca1 atom, and the sixth site is occupied by an aqua ligand (Fig. 2(a)). The Ca1 atoms form a square plane around a centre of symmetry with two bridging phosphonate O atoms, and the Ca2 atoms lie above and below this plane. The coordination sphere of Ca2 contains one chelating $Cl_2C(PO_3iPr)_2^{2-}$ ligand, forming a six-membered chelate ring, and one $Cl_2C(PO_3iPr)_2^{2-}$ ligand, which provides only one O atom to Ca2. One aqua ligand and two ethanol molecules occupy the rest of the coordination sites. Hydrogen bonds [O...O 2.739(2)–2.972(2) Å, 137°–176°] hold the tetramers together, forming a layered structure parallel to the (−1 0 1) plane. Isopropyl groups and chlorine atoms of the $Cl_2C(PO_3iPr)_2^{2-}$ ligands and ethanol ligands point to the interlayer section (Fig. 2(b)).

3.2. Spectroscopic properties

The characteristic absorption region and characteristic absorption bands of compounds **1** and **2** were determined by IR-spectroscopy. A very strong, broad band attributed to ν(P=O) appeared at ca. 1235–1230 cm^{-1}. The symmetric stretching vibration of the monoanionic, fully ionised PO_2^- group appeared at ca. 1090 cm^{-1}. Bands at 1177–1115 cm^{-1} were assigned to C–O–(P) vibrations and bands at 1065–995 cm^{-1} to P–O–(C) vibrations. Additional features of all the spectra were the bands at ca. 860 and 770 cm^{-1}, which were assigned to the asymmetric and symmetric P–C–P vibrations, respectively. In addition, the metal complexes exhibited bands demonstrating the presence of water molecules: $\nu(H_2O)$ ca. 3400 cm^{-1}, δ(H–O–H) ca. 1640–1630 cm^{-1}; and in both spectra there were bands demonstrating the isopropyl groups (bands in the 2990–2875 cm^{-1} and 1385–1372 cm^{-1} regions). Asymmetric and symmetric stretching vibrations of CCl_2 groups were presented at ca. 755–740 cm^{-1}. The spectra were similar to the spectra of the metal complexes of the diethyl ester derivative of clodronate [32].

4. Conclusion

Magnesium and calcium complexes of the symmetrical diisopropyl ester derivative of clodronic acid are good examples of the ability of bisphosphonates to form different compounds: Mg forms a polymeric chain with the bisphosphonato ligand, while Ca forms a tetramer. In the case of the diethyl ester derivative of clodronate, the Mg complex $[MgCl_2C(PO_3Et)_2(H_2O)_3]_n$ is also a polymeric chain, while the Ca complex $[Ca\{Cl_2C(PO_3Et)_2\}(H_2O)_3]_2$ is a dimer [32]. The esterified bisphosphonato ligands are capable of acting similarly to clodronate in all metal complexes; they are both chelating and bridging ligands, despite the fact that they have two O atoms masked with alkyl groups, which also

cause steric effect. In addition, the esterified compounds are capable of forming polymeric structures and porous materials that can be utilized in chemical applications.

5. Supplementary data

Crystallographic data for the structural analysis have been deposited with the Cambridge Crystallographic Data Centre, CCDC Nos. 244607 (**1**) and 244608 (**2**). Copies of this information may be obtained from The Director, CCDC, 12 Union Road, Cambridge, CB2 1EZ, UK (fax: +44-1233-336033; e-mail: deposit@ccdc.cam.ac.uk or www: http://www.ccdc.cam.ac.uk). Structure factors for **1** and **2** are available from the authors on request.

References

[1] A. Clearfield, Progress in Inorganic Chemistry: Metal-Phosphonate Chemistry, Wiley, New York, 1998, pp. 371–510.
[2] B. Zhang, A. Clearfield, J. Am. Chem. Soc. 119 (1997) 2751.
[3] G. Alberti, M. Casciola, U. Constantino, R. Vivani, Adv. Mater. 8 (1996) 291.
[4] J.L. Snover, H. Byrd, E.P. Suponeva, E. Vicenzi, M.E. Thompson, Chem. Mater. 8 (1996) 1490.
[5] A. Distler, D.L. Lohse, S.C. Sevov, J. Chem. Soc., Dalton Trans. (1999) 1805.
[6] K. Barthelet, C. Merlier, C. Serre, M. Riou-Cavellec, D. Riou, G. Férey, J. Mater. Chem. 12 (2002) 1132.
[7] K. Barthelet, D. Riou, G. Férey, Solid State Sci. 4 (2002) 841.
[8] K. Barthelet, C. Jouve, D. Riou, G. Férey, Solid State Sci. 2 (2000) 871.
[9] C. Serre, G. Férey, J. Mater. Chem. 12 (2002) 2367.
[10] Qiuming Gao, N. Guillou, M. Nogues, A.K. Cheetham, G. Férey, Chem. Mater. 11 (1999) 2937.
[11] K. Barthelet, M. Nogues, D. Riou, G. Férey, Chem. Mater. 14 (2002) 4910.
[12] R.C. Finn, R. Lam, J.E. Greedan, J. Zubieta, Inorg. Chem. 40 (2001) 3745.
[13] R.C. Finn, J. Zubieta, J. Chem. Soc., Dalton Trans. (2000) 1821.
[14] R.C. Finn, R.S. Rarig Jr., J. Zubieta, Inorg. Chem. 41 (2002) 2109.
[15] R.C. Finn, J. Zubieta, Inorg. Chem. 40 (2001) 2466.
[16] V.S. Sergienko, E.G. Afonin, G.G. Aleksandrov, Russ. J. Inorg. Chem. 43 (1998) 916.
[17] V.A. Uchtman, J. Phys. Chem. 76 (1972) 1304.
[18] H.-H. Song, L.-M. Zheng, Z. Wang, C.-H. Yan, X.-Q. Xin, Inorg. Chem. 40 (2001) 5024.
[19] H.-H. Song, P. Yin, L.-M. Zheng, J.D. Korp, A.J. Jacobson, S. Gao, X.-Q. Xin, J. Chem. Soc., Dalton Trans. (2002) 2752.
[20] L.-M. Zheng, H.-H. Song, C.-H. Lin, S.-L. Wang, Z. Hu, Z. Yu, X.-Q. Xin, Inorg. Chem. 38 (1999) 4618.
[21] H.-H. Song, L.-M. Zheng, G. Zhu, Z. Shi, S. Feng, S. Gao, Z. Hu, X.-Q. Xin, J. Solid State Chem. 164 (2002) 367.
[22] H.-H. Song, L.-M. Zheng, C.-H. Lin, S.-L. Wang, X.-Q. Xin, S. Gao, Chem. Mater. 11 (1999) 2382.
[23] L.-M. Zheng, H.-H. Song, C.-Y. Duan, X.-Q. Xin, Inorg. Chem. 38 (1999) 5061.
[24] P. Yin, L.-M. Zheng, S. Gao, X.-Q. Xin, Chem. Commun. (2001) 2346.
[25] H.-H. Song, L.-M. Zheng, Y.-J. Liu, X.-Q. Xin, A.J. Jacobson, S. Decurtins, J. Chem. Soc., Dalton Trans. (2001) 3274.
[26] P. Yin, Y. Peng, L.-M. Zheng, S. Gao, X.-Q. Xin, Eur. J. Inorg. Chem. (2003) 726.
[27] L.-M. Zheng, S. Gao, H.-H. Song, S. Decurtins, A.J. Jacobson, X.-Q. Xin, Chem. Mater. 14 (2002) 3143.
[28] P.P. Major, A. Lipton, J. Berenson, G.H. Hortobagyi, Cancer 88 (2000) 6.
[29] M. Nardelli, G. Pelizzi, G. Staibano, E. Zucchi, Inorg. Chim. Acta 80 (1983) 259.
[30] M. Kontturi, S. Peräniemi, J.J. Vepsäläinen, M. Ahlgrén, Acta Cryst. E 60 (2004) m1060.
[31] M. Kontturi, S. Peräniemi, J.J. Vepsäläinen, M. Ahlgrén, Eur. J. Inorg. Chem. (2004) 2627.
[32] M. Kontturi, E. Vuokila-Laine, S. Peräniemi, T.T. Pakkanen, J.J. Vepsäläinen, M. Ahlgrén, Dalton Trans. (2002) 1969.
[33] J.J. Vepsäläinen, J. Kivikoski, M. Ahlgrén, H.E. Nupponen, E.K. Pohjala, Tetrahedron 51 (1995) 6805.
[34] Z. Otwinowski, W. Minor, in: Methods in Enzymology, in: C.W. Carter, R.M. Sweet (Eds.), Macromolecular Crystallography, Part A, vol. 276, Academic Press, New York, 1997, pp. 307–326.
[35] G.M. Sheldrick, SHELXS-97 and SHELXL-97, University of Göttingen, Germany, 1997.

Available online at www.sciencedirect.com
SCIENCE DIRECT®
Polyhedron 24 (2005) 311–317
POLYHEDRON
www.elsevier.com/locate/poly

Synthesis, characterization and extraction behaviour of calix[4]arene with four propylene phosphonic acid groups on the lower rim

Irena Matulková *, Jan Rohovec

Department of Inorganic Chemistry, Faculty of Science, Charles University, Hlavova 2030, Albertov 2030, 128 42 Prague 2, Czech Republic

Received 30 July 2004; accepted 22 November 2004

Abstract

A new calix[4]arene based ligand bearing four phosphonic acid groups was prepared by modification of *p-tert*-butylcalix[4]arene on the lower rim by bonding with four $(CH_2)_3PO(OH)_2$ groups. The compound was characterized by NMR spectroscopy. The compound obtained was used as an extractant for certain lanthanide ions (La^{3+}, Eu^{3+}, Yb^{3+}). The extraction experiments were carried out at 25 ± 2 °C and pH 5.5 for 2 h. The formation of the complexes with lanthanide ions was revealed by NMR experiments and luminescence spectroscopy. The extraction efficiencies of the prepared ligand decrease with decreasing radius of the lanthanide ions.
© 2004 Elsevier Ltd. All rights reserved.

Keywords: Calixarenes; Extraction efficiencies; Lanthanide ions; NMR spectroscopy

1. Introduction

Nuclear waste is treated by a process based on the separation of its main components. The elements present vary in abundance, toxicity, type and energy of the emitted radiation, life-times and especially in reprocessing and storage.

In industry, the plutonium uranium extraction (PUREX) [1] industrial process is used to separate plutonium/uranium or the transuranium extraction (TRUEX) [2] process is used to extract minor actinides and lanthanides from nuclear waste solutions. The extracting agent is a mixture of (*N*,*N*-diisobutylcarbamoylmethyl)octyl phenyl phosphine oxide (CMPO) [3] (Fig. 1) and tri-*n*-butyl phosphate (TBP) in paraffin diluents. These compounds display high complexing ability for these metal ions and transfer them to the organic phase. The complexing ability of CMPO can be improved by grafting it on the calixarene platform. Actinide and lanthanide ions complex three CMPO molecules, which are not preorganized to form a coordination site. Preorganization of the coordination site could improve the complexing abilities of the ligand. For this reason, a variety of compounds and technologies are now being explored in an attempt to achieve better selectivity and efficiency of the extracting processes.

The highly lipophilic nature of metal–ion complexes of many calixarenes suggests their potential use in solvent extraction. Calixarenes may improve the extraction selectivity because of their hydrophilic properties. Furthermore, ligands based on calixarenes are capable of saturating the relatively high coordination number of f-block elements (8, 9 or higher). The cone conformation of calix[4]arene has the advantage of forming an organized coordination environment. Consequently, the lipophilic calixarene moiety can transfer a metal ion into the organic phase as a complex.

* Corresponding author. Tel.: +420221951258; fax: +420221952378.
E-mail address: irena.mat@atlas.cz (I. Matulková).

0277-5387/$ - see front matter © 2004 Elsevier Ltd. All rights reserved.
doi:10.1016/j.poly.2004.11.008

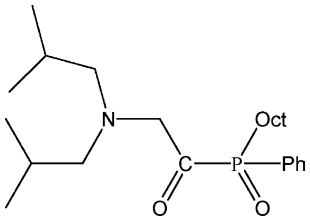


Fig. 1. CMPO (*N*,*N*-diisopropylcarbamoylmethyl)octyl phenyl phosphine oxide.

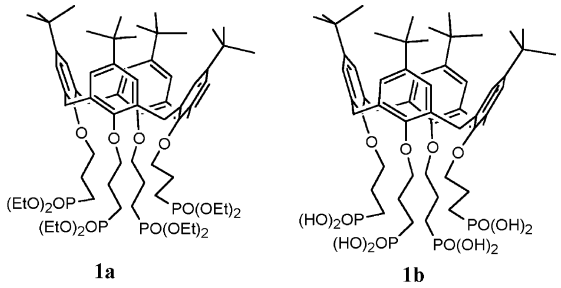


Fig. 3. Compounds studied.

Calixarenes are suitable for chemical modification at the upper or lower rim. The phenolic hydroxy groups on the lower rim can be modified more easily. Thus, a wide range of synthetic receptors for metal cations based on calixarene have been prepared [4]. Earlier work in this area described calixarenes with lower rim carbonyl-containing groups, such as esters, ketones, amides [5], thioamides, carboxylic acids [6] or phosphorus atom-containing groups, such as phosphine oxide [7], phosphate esters (double-bridge alkoxyphosphoryl substituents) [8], phosphine [9] and hydroxamates [10]. Phosphorus-containing extracting agents [11], such as the commonly used tri-*n*-butyl phosphate, have broad utilization in lanthanide (rare earth) and actinide extraction from acidic media, where the phosphoryl oxygen provides a donor atom capable of protonation. Calixarenes bearing phosphoryl groups are more efficient extraction agents for lanthanides and actinides than CMPO itself and also exhibit better actinide/lanthanide selectivity.

Recently, three bis(phosphonic)acid-containing calixarenes (distal disubstitution of calixarene) were described in the literature [12] (Fig. 2). The phosphonic acid groups are connected to the calixarene by a methylene, ethylene or propylene bridge. The phosphonic acid groups are relatively strong and hard acids according to the Hard-Soft-Acid-Base theory, with an affinity for lanthanides and actinides and, therefore, they can form relatively stable complexes with rare-earth elements even in highly acidic media. Unexpected selectivity in the extraction experiments on heavy lanthanides was found for distal disubstitution in the case of the (3-dihydroxyphosphoryl)propoxy ligand. This result corresponds to the presence of a group that can be deprotonated. The extraction power of these three ligands decreases as the acidity of the groups increases, but this dependence is not as obvious as that for carboxylate. High selectivity was observed for Yb^{3+}. The diethoxy esters of this compound exhibit comparable extraction efficiency to CMPO.

In this work, we describe the synthesis and extraction properties of compound **1b**, bearing four PO_3H_2 moieties. These groups are expected to form a preorganized site for the lanthanide ion. They can display a high extraction efficiency and even extra selectivity for lanthanide ions, Fig. 3.

2. Experimental

The starting compounds *p*-*tert*-butylcalix[4]arene and phosphonate ester, $Br(CH_2)_3PO(OEt)_2$, were prepared and purified by the procedures described in the literature [13,14]. All the solvents used in the syntheses were dried and purified by standard methods [15]. The syntheses were performed under an argon atmosphere.

Column chromatography was performed using Merck silica gel 60 (230-400 mesh) and thin layer chromatography (TLC) of the octa-esters using Merck silica 60 F_{254} plates. A chromogenic spray reagent was used for detection of phosphonate groups (a solution

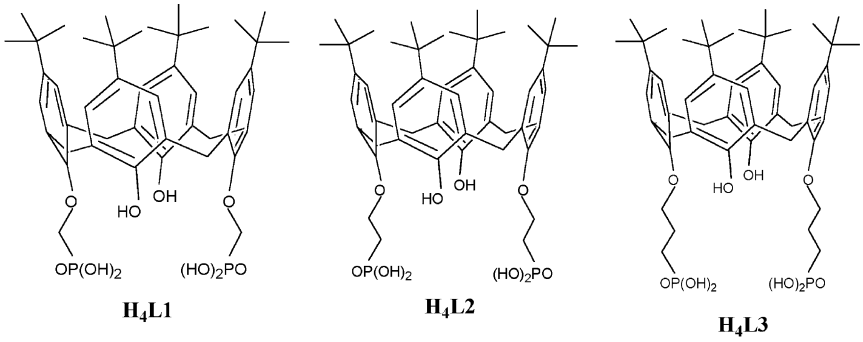


Fig. 2.

of 10 g $Ce(SO_4)_2$, 12 g $(NH_4)_6Mo_7O_{24} \cdot 4H_2O$ in 250 ml of 10% H_2SO_4), usually applied after detecting the plate under ultraviolet light, and exposing it to iodine vapour. The nitrates of Ln^{3+} (La^{3+}, Eu^{3+}, Yb^{3+}) were used in the extraction experiments. The metal concentrations in the aqueous phases were determined by complexometric titrations with DTPA (DTPA = diethylene triamine pentaacetic acid, xylenol orange, pH 5.5 acetate buffer) [16]. All the compounds were characterized by the ^1H, ^{13}C and ^{13}P NMR spectra (recorded on a 400 MHz Unity Varian spectrometer, solvent = $CDCl_3$, reference TMS, ^1H frequency = 399.951 MHz) and MS spectra (recorded on an ESQUIRE 3000 Bruker Mass Spectrometer, ESI electrospray ionization, ionic trap detection). The calix[4]-arene compounds were dried for several hours in vacuo before characterization, as they show a tendency to form inclusion complexes of organic solvents and water. The luminescence spectrum of the complex of **1b** with Eu^{3+} was recorded on LS 50B Perkin–Elmer spectrometer in a 1 cm cuvette with an excitation wavelength of 256 nm in a methanol solution. Elemental analyses were not performed.

3. Syntheses

*3.1. Synthesis of compound **1a**: 5,11,17,23-tetra-tert-butyl-25,26,27,28-tetrakis[(3-diethoxyphosphoryl)-propoxy]calix[4]arene*

A suspension of 5 g of *p-tert*-butylcalix[4]arene (1:1 complex with toluene, 6.7 mmol) and 1.3 g of sodium hydride (53.9 mmol) in 120 ml of dry toluene was stirred and heated to 90 °C (in an oil bath) for 21 h. Then a solution of 14 g of diethyl (3-brompropyl)phosphonate (54 mmol) in 20 ml of dry toluene was added to the reaction mixture. The reaction mixture was stirred and heated to 90 °C for 9 days. An argon atmosphere was maintained during the reaction. The reaction was followed by TLC (mobile phase chloroform/ethyl acetate in a 1:1 ratio) and mass spectrometry in common solvents (methanol).

The reaction mixture was extracted twice with 50 ml of water, and dried over anhydrous $MgSO_4$. After removal of most of the solvent, the resulting yellow oil was purified by column chromatography. A mixture of $CHCl_3/CH_3COOC_2H_5$ in a ratio of 1:1 was used as the first mobile phase. This mixture removed the phosphonate ester, *p-tert*-butylcalix[4]arene and products of mono- or di-substitution of *p-tert*-butylcalix[4]arene. Compound **1a** was eluted from the column by a $CH_3COOC_2H_5/CH_3OH$ mixture in 2:1 ratio. The purity of compound **1a** was 70–75% (from ^{13}P NMR) and the reaction yield was 6.7 g of yellow oil (73%).

The negative mode spectrum did not exhibit any peaks. The positive mode spectrum contained a peak at m/z = 1383.9 (compound **1a**).

*3.2. Synthesis of compound **1b**: 5,11,17,23-tetra-tert-butyl-25,26,27,28-tetrakis[(3-dihydroxyphosphoryl)-propoxy]calix[4]arene*

Compound **1b** was prepared from **1a** following a procedure similar to the one described in the literature [17].

A solution of 4.7 g of **1a** (3.4 mmol) and 10.6 ml of trimethyl silyl bromide (82 mmol) in 40 ml of dry acetonitrile was stirred and refluxed for 6 h. Methanol (20 ml) was added very slowly (after cooling the reaction mixture below the boiling point of methanol). The reaction mixture was then stirred and refluxed for 2 h.

The solvents were removed and the residue was evaporated twice with 20 ml of dry toluene and filtered. The yield of the reaction was 1.8 g of compound **1b** (47%) in the form of an orange oil.

The negative mode spectrum revealed a peak at m/z = 1138 (compound **1b**). The positive mode spectrum included peaks at m/z = 1137.8 (compound **1b**); 1016.6.

3.3. General procedure for the extraction experiments

The following conditions were used for the extraction experiments with compounds **1a** and **1b**: the experiments were performed at pH 2 and 5.5, the temperature was maintained at 25 ± 2 °C (water bath), the extraction time was 2 h (this time is sufficient to achieve extraction equilibrium). Aqueous solutions of the metal nitrates ($c_M = 5 \times 10^{-3}$ M, pH 2) and solution of the ligand ($c_L = 5 \times 10^{-3}$ M) in chloroform were prepared for the extraction experiments. Two milliliters of each solution were mixed and shaken for 2 h in ratios of 1:1, 1:2 and 2:1. After separation of the phases (after 6 h), 1 ml of the water phase and 1 ml of the organic phase were analyzed for the metal content. The organic phase had to be evaporated and dissolved in an aqueous solution of concentrated HNO_3 and evaporated three times with water and then dissolved in an aqueous solution of acetate buffer (pH 5.5). The amounts of metal ion were analyzed by complexometric micro-titration. 0.04 M DTPA was used as the complexing agent with xylenol orange as indicator in acetate buffer solution (pH 5.5, acetic acid and sodium acetate).

4. Discussion

4.1. Syntheses

The general method for synthesizing lower-rim calix[4]arene derivatives is based on the alkylation of the phenolic groups with a strong alkylation agent. This

strategy was used to prepare compound **1a**, which was converted into phosphonic acid (Scheme 1). Careful choice of the reaction conditions is necessary – the temperature, type of base, solvent and type of the alkylation agent are important. It was very difficult to choose an alkylation agent with a good leaving group for preparation of compound **1a** directly in one-step synthesis. Acceptable results were obtained for $Br(CH_2)_3PO_3Et_2$.

A variety of conditions were examined for the synthesis of compound **1a**, for example reaction in refluxing acetonitrile and sodium hydride as the base or performance of the reaction under the conditions of phase-transfer catalysis (PTC), utilizing tetrabutyl ammonium bromide and K_2CO_3 as a base in dry acetonitrile. These reactions yielded a mixture of partially substituted compounds containing one to four phosphonic groups. The best solvent for this reaction appeared to be toluene. The reagent with bromide as a suitable leaving group can be used as an alkylation agent, because the phosphonic group is bound to the calix[4]arene molecule by a relatively long propylene spacer.

Ligand **1b** was obtained by a well-known method using transesterification with trimethyl silyl bromide in refluxing acetonitrile and subsequent hydrolysis of the trimethyl silyl ester in methanol. The yield of compound **1b** was 47%.

The identity and purity of all the compounds were checked by NMR spectroscopy and mass spectrometry. Elemental analyses were not performed due to the large relative molecular weights of the prepared compounds in comparison with common impurities (traces of solvents, etc.). Elemental analyses are unsuitable for the types of compounds prepared, because the compounds were prepared in the form of an oil or glass. It is not possible to evaporate all of the solvents during long drying under the vacuum of an oil pump.

4.2. Extraction experiments

Extraction experiments were designed to compare the results obtained from the measurements for compounds **1a** and **1b** to the data published in the literature and to investigate the potential industrial applicability of the prepared ligands (low concentration of Ln^{3+}, cheap organic solvent, high acidic nitrate solutions, appropriate concentration of the ligands used). The activities and extraction properties of compounds **1b** in the extraction of the lanthanide ion from its nitrate solution (pH 2 or 5.5) into the chloroform solution at concentration ($c_L = 5 \times 10^{-3}$ M) are depicted in Fig. 4. The concentration of the nitrate solution of lanthanide ions used in the extraction experiments is acceptable for the complexometric titration measurements.

Compound **1a** did not transport Ln^{3+} into the chloroform phase. The extraction conditions were changed in the various extraction experiments, for example, the concentration, the duration of the extraction experiment, the pH (2; 5.5), the temperature (25; 30 °C) and the molar ratios. This result is very interesting, because the literature describes a similar ligand, *p-tert*-butylcalix[4]arene, distally disubstituted with the same group on the lower rim as compound **1a**. The extraction efficiency was published %E = 42 for the extraction experiment of Eu^{3+} from aqueous medium (pH 5.8) into a

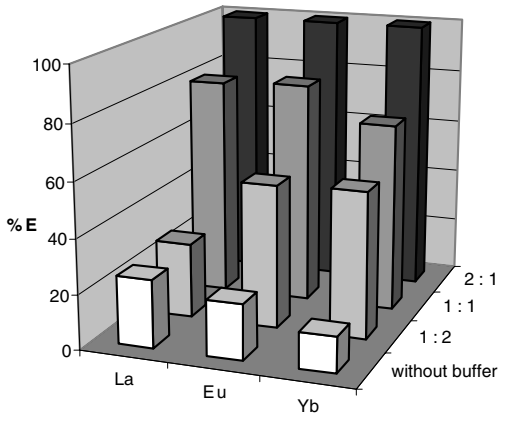
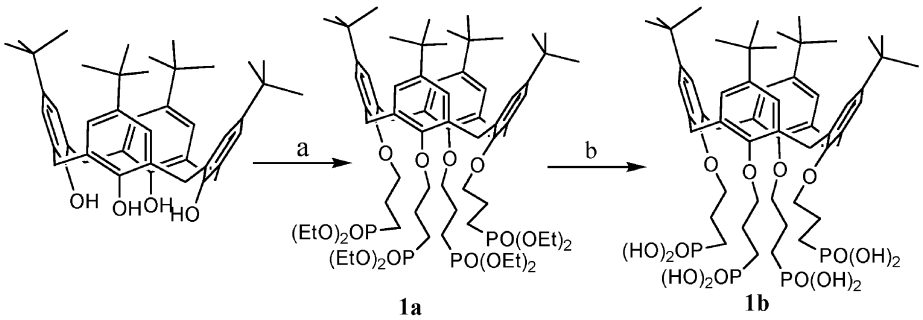


Fig. 4. Extraction efficiencies (%E) for the extraction of chosen lanthanide ions, using molar ratio (ligand **1b**/lanthanide ions), different pH (2 or 5.5) with compound **1b**. The signature without buffer means that the experiment was done with pH 2 in the aqueous phase.



Scheme 1. Synthesis of compounds **1a** and **1b**. (a) NaH, $Br(CH_2)_3PO(OEt)_2$, toluene, 100 °C. (b) (1) $(CH_3)_3SiBr$, CH_3CN, reflux, (2) MeOH.

chloroform phase. The concentrations of Eu^{3+} and of the ligand were the same.

The oxygen atoms in **1a** probably do not form a suitable cavity for the lanthanide ions. The steric requirements for the bulky propylene phosphonic groups entail orienting the non-bonding electron pairs of the oxygen atoms toward the lanthanide ions.

In the series of extraction experiments on compound **1b**, the dependence on the type of lanthanide ion, the pH of the water phase and the molar ratio for compound **1b** and lanthanide ions were observed, Fig. 4.

The extraction efficiencies (%E) for compound **1b** under these conditions are satisfactory and comparable to those for the ligand based on calix[4]arene with (*N*,*N*-diisobutylcarbamoyl)octyl phenyl phosphine oxide (CMPO) groups and better than CMPO itself. The extraction properties for the experiment at pH ≅ 2 increase for charged molecules and the extraction properties were better if an aqueous phase with pH 5.5 (acetate buffer) was used. The differences for the individual lanthanide ions may be caused by an additional protonisation of the molecule in the presence of various large lanthanide ions. We can confirm a higher extraction efficiency for the large lanthanum(III) ion than for the smaller ytterbium(III) ion. The dependence of the extraction properties for the large lanthanum(III) ion and the smaller ytterbium(III) ion is inverse with respect to the dependence which was published in the literature for distally dialkylated compounds bearing the same group $(CH_2)_3PO(OEt)_2$, Fig. 5. This difference is very similar for the calix[4]arene-based diphenyl phosphinoxides with two or four groups on the lower rim, described in the literature [3,18].

The cavity formed from four phosphonic groups on the lower rim is larger than the one formed from two groups, and therefore prefers the larger lanthanum(III) ion to the smaller ytterbium(III) ion.

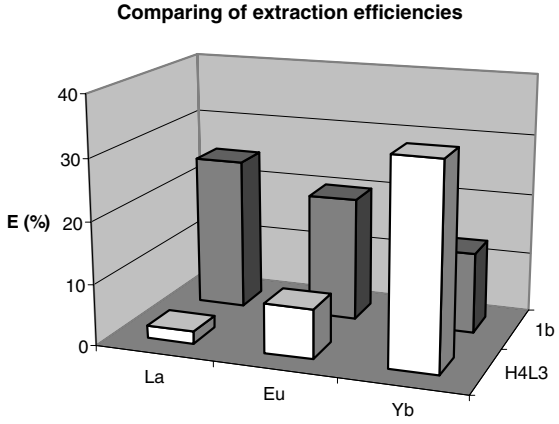


Fig. 5. Comparison of extraction efficiencies compound **1b** presented in this paper and the compound **H_4L3** in the literature [12].

Table 1
Comparison of extraction efficiencies with in the literature described compounds

	Organic phase	Aqueous phase	Th (IV)	Eu (III)	La (III)	Yb (III)
Phosphonate						
1a	$CHCl_3$ ($c_L = 5\times10^{-3}$ M)	$c_{Ln} = 5\times10^{-3}$ M (pH about 2)		0	0	0
1b	$CHCl_3$ ($c_L = 5\times10^{-3}$ M)	$c_{Ln} = 5\times10^{-3}$ M (pH about 2)		20.2 ± 2.7[a]	24.8 ± 2.7[a]	13.1 ± 1.3[a]
		$c_{Ln} = 5\times10^{-3}$ M (pH 5.5)		81.8 ± 3.6[b]	80.5 ± 1.8[b]	69.5 ± 3.6[b]
				52.8 ± 2.4[c]	27.6 ± 0.8[c]	53.7 ± 1.5[c]
				100[d]	100[d]	100[d]
H_4L1 [12]	$CHCl_3$ ($c_L = 1\times10^{-4}$ M)	$c_{Ln} = 1\times10^{-4}$ M HNO_3 (pH 1)		48 ± 4	35 ± 3	52 ± 4
H_4L2 [12]	$CHCl_3$ ($c_L = 1\times10^{-4}$ M)	$c_{Ln} = 1\times10^{-4}$ M HNO_3 (pH 1)		14 ± 3	8 ± 4	26 ± 3
H_4L3 [12]	$CHCl_3$ ($c_L = 1\times10^{-4}$ M)	$c_{Ln} = 1\times10^{-4}$ M HNO_3 (pH 1)		8 ± 2	2	33 ± 4
CMPO [3] itself	CH_2Cl_2 ($c_L = 5\times10^{-3}$ M)	0.6 mM $Ln(ClO_4)_3$	1.6			
	CH_2Cl_2 ($c_L = 1\times10^{-2}$ M)	$c_{Eu} = 1\times10^{-4}$ M, 1 M HNO_3		12.2		
Phosphine oxide [17]	1,2-dichlorethane	1×10^{-3} M La, Pr, Nd, Sm, Eu, Gd,		D approximately		
	($c_L = 2\times10^{-3}$ M)	Ho, Er, Yb, Y, 0.9 M $Al(NO_3)_3$		0.11	0.11	0.11
Derivates of CMPO						
3a [20]	CH_2Cl_2 ($c_L = 1\times10^{-3}$ M)	1 M HNO_3	76 ± 1	16 ± 1	19 ± 1	2.6 ± 0.7
3b [20]	CH_2Cl_2 ($c_L = 1\times10^{-3}$ M)	1 M HNO_3	81 ± 2	12.5 ± 0.8	13 ± 2	2
3c [20]	CH_2Cl_2 ($c_L = 1\times10^{-3}$ M)	1 M HNO_3	96 ± 1	68 ± 1	70 ± 3	37 ± 2
4 [20]	CH_2Cl_2 ($c_L = 1\times10^{-3}$ M)	1 M HNO_3	61 ± 1	58 ± 1	98 ± 1	3 ± 2
Carboxylate **5** [21]	$CHCl_3$ 4% oktan-1-ole	1×10^{-3} M Nd, Eu, Tb, Dy, Yb, Er,		D in interval 0.1–10		
	($c_L = 3\times10^{-3}$ M)	pH 1.5–3.0 ($HClO_4$)				
Hydroxamate **6** [10]	$CHCl_3$ ($c_L = 2\times10^{-3}$ M)	$c_{Th} = 0.18\times10^{-3}$ M, 0.1 M NaCl, pH 2		% E for Th^{4+} 94.6		
Iminocarboxylate **7** [22]	$CHCl_3$ 5 equiv.	0.1 M NaCl, pH 1		2		
	of ligand to metal ions					

[a] Extraction experiment with molar ratio lanthanide/ligand 1:1 with pH 2 in aqueous phase.
[b] The molar ratio 2:1.
[c] The molar ratio 1:2.
[d] Experiment with $c_L = 10^{-2}$ M and $c_{Ln} = 10^{-4}$ M.

For the ratio 1:2 (compound:lanthanide ions), 100% extraction efficiency can be seen in Fig. 4 for all of the studied lanthanide ions.

The extraction of Ln^{3+} for the studied ligand depended on the ionic radii of the lanthanide cations. The value of %E increases significantly with increasing ionic radius. Ligands with two groups on the lower rim are harder in the Pearson classification than calixarenes with carboxylic groups. Other known selective lanthanide extraction agents are also based on the calixarene moiety. In contrast to most CMPO-based calixarenes [18], the extraction efficiency for compound **1b** is highest for low concentrations of nitric acid and decreases sharply as the acidity increases. This trend is close to the behaviour of CMPO itself. The lower acidity constants of alkyl phosphonic acids indicate that the decrease is not as rapid as for carboxylates or hydroxamates. These results are illustrated in Table 1 and Fig. 6.

We attempted to elucidate the chemical form in which Ln^{3+} is transported from the aqueous phase to the organic chloroform phase. We followed the formation of complexes of the diamagnetic La^{3+} and Y^{3+} ions by ^{13}P NMR (molar ratio 1:1 (Ln^{3+}/**1b**), solvent = methanol, room temperature to −10 °C). For the La^{3+} system in the temperature range given, we observed three wide signals in the range 26.8–29.0 ppm, probably caused by quadrupolar interaction or by the dynamic nature of the ^{139}La and ^{13}P NMR spectra (shift to lower chemical shift values; from 32.7 ppm for **1b** to 26.8 ppm). Then we studied the smaller diamagnetic lanthanide Y^{3+} ion in order to check whether the dynamic nature is retained. In the most favourable case, when no diamagnetic effects occur, $^2J_{YP}$ interaction could be observed (about 5 Hz [19]). For the Y^{3+} experiments (molar ratio 1:1, 1:2, 1:4), we observed three wide signals for a molar ratio of 1:1, but these signals arose from very fast changes between the complex of compound **1b** with Y^{3+} and the free compound **1b**, in contrast to La^{3+}. The experiment for the 1:2 molar ratio resulted in two wide signals at 25.0 and 26.5 ppm and we found only one signal at 27.1 ppm for the 1:4 molar ratio. None of them was split into a doublet. Thus, both experiments (for La^{3+} and Y^{3+}) for a molar ratio of 1:1 yielded the same results. NMR measurements revealed that the complexes possessed dynamic behaviour within the NMR time scale.

The other experiment for description of the complex of compound **1b** and lanthanide ions consisted in estimation of the stability constant. This experiment was performed to compare the formation and stability of the complex of Ln^{3+} with DTPA to the complex of Ln^{3+} with compound **1b**. Two samples were prepared for this experiment. One consisted of Eu^{3+} and compound **1b** and the second one consisted of Eu^{3+}, DTPA and compound **1b** (both in methanol). The samples were measured by luminescence spectroscopy [20]. The excitation line at 256 nm was used, exciting the aromatic system in compound **1b**, and the energy was then transferred to the Eu^{3+} ion, probably via intersystem crossing. A characteristic luminescence spectrum was observed for sample 1 (Fig. 7 and Table 2) while

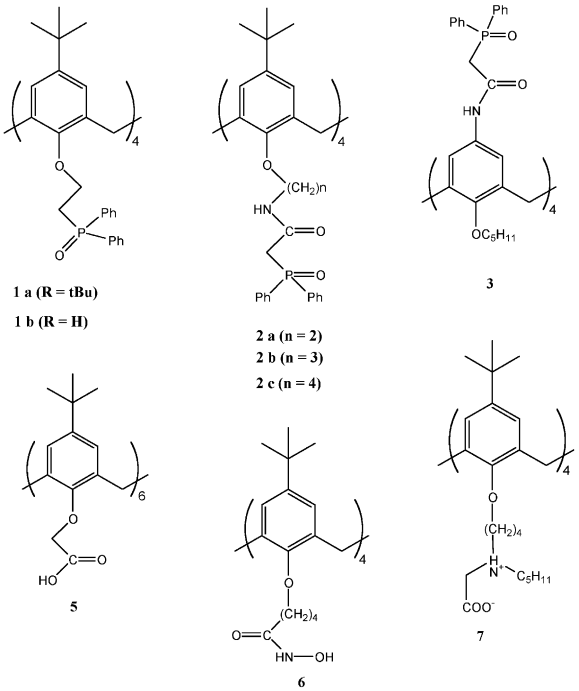


Fig. 6. Formulae of compounds (from the literature) using in Table 1.

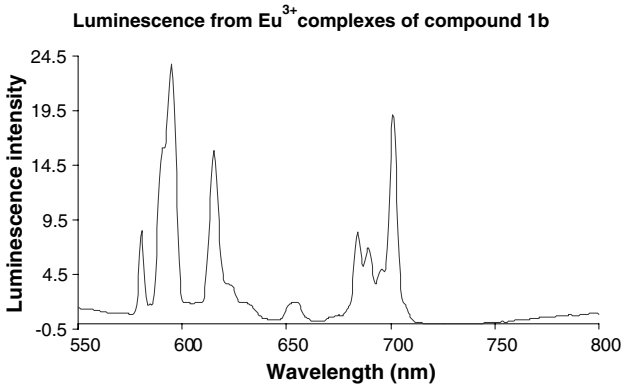


Fig. 7. Europium luminescence emission spectrum (293 K, MeOH, λ_{exc} = 256 nm).

Table 2
Characteristics of the luminescence spectrum of europium(III) complexes

Wavelength (nm)	Characteristics of the $^5D_0$–^7F_j transitions for Eu^{3+} complexes in methanolic solution	
580.5	$^5D_0$–$^7F_0$ $\Delta J = 0$	
594.5	$^5D_0$–$^7F_1$ $\Delta J = 1$	
615.0	$^5D_0$–$^7F_2$ $\Delta J = 2$	hypersensitive
654.5	$^5D_0$–$^7F_3$ $\Delta J = 3$	forbidden
701.0	$^5D_0$–$^7F_4$ $\Delta J = 4$	

sample 2 did not yield a spectrum for this excitation line. It can thus be concluded that there is close contact between Eu^{3+} and the aromatic calixarene system. According to the luminescence spectra, the stability constant of complexes **1b** with the lanthanide ions is lower than that of the DTPA complexes with the lanthanide ions ($pK = 23$) [16,23]. However, the stability constant for compound **1b** and Ln^{3+} is higher than the stability constant for Ln^{3+} and xylenol orange ($pK = 14$) [24]. The solution of Ln^{3+} in methanol can be titrated by a solution of the ligand in methanol (the changes in the colour of the titrimetric solution can be observed). The Job plot experiment revealed simultaneous formation of complexes with Ln^{3+} in various stoichiometries in the solution.

5. Conclusion

A new calix[4]arene with four pendant arms $(CH_2)_3PO(OEt)_2$, used as an extraction agent for lanthanides, was prepared by Williamson alkylation of *p-tert*-butyl calix[4]arene. The extraction studies showed that the ligand is an efficient extraction agent for larger lanthanides, and much more efficient than CMPO and the extraction agent based on calixarene with carboxylic or diphenyl phosphinoxide groups. Because of the presence of groups that can be deprotonated, the extraction behaviour of ligand **1b** decreases with increasing acidity, but not as significantly as in the case of carboxylates, which enables the efficient extraction of lanthanides from 1 M nitric acid. Compound **1a** did not extract Ln^{3+} ions into chloroform solutions from the aqueous phases (pH 2–5.5). NMR measurements revealed that the complexes possessed dynamic behaviour within the NMR time scale. The Job plot result indicated simultaneous formation of complexes **1b** and Ln^{3+} in various stochiometries in the solution. The affinity for Ln^{3+} was reflected in the luminescence spectrum, which revealed energy transfer from the aromatic ring to the lanthanide ion.

Acknowledgement

This work was supported by Grant GAČR 42 201506.

References

[1] A. Naylor, P.D. Wilson, in: T.C. Lo, M.H.I. Brain, C. Hanson (Eds.), Recovery of Uranium and Plutonium from Irradiated Nuclear Fuel, Handbook of Solvent Extraction, Wiley, New York, 1983.
[2] D.B. Chamberlain, R.A. Leonard, J.C. Hoh, E.C. Gay, D.G. Kalina, G.F. Vandegrift, Truex Hot Demonstration: Final Report, Report ANL-89/37, Argonne, IL, 1990.
[3] F.A. Neu, V. Böhmer, J.-F. Dozol, C. Gruttner, R.A. Jakobi, D. Kraft, O. Mauprivez, H. Rouguette, M.J.S. Weill, N. Simon, W. Vogt, J. Chem. Soc., Perkin Trans. 2 (1996) 1175.
[4] F. Arnauld-Neu, M.-J. Schwing-Weill, J.-F. Dozol, in: Z. Asfari, V. Böhmer, J. Harrowfield, J. Vicens (Eds.), Calixarenes, Kluwer, Dordrecht, 2001, p. 642.
[5] O.I. Kalchenko, F. Perret, N. Morel-Desrosiers, A.W. Coleman, J. Chem. Soc., Perkin Trans. 2 (2001) 258.
[6] R. Ludwig, Fresen. J. Anal. Chem. 367 (2000) 103.
[7] C. Dieleman, C. Loeber, D. Matt, A. De Cian, J. Fischer, J. Chem. Soc., Dalton Trans. (1995) 3097.
[8] J.M. Harrowfield, M. Mocerino, B.J. Peachey, B.W. Skelton, A.H. White, J. Chem. Soc., Dalton Trans. (1996) 1687.
[9] (a) J.F. Malone, D.J. Marrs, M.A. McKervey, P. O'Hagan, N. Thompson, A. Walker, F.A. Neu, O. Mauprivez, M.-J. Schwing-Weill, J.-F. Dozol, H. Rouquette, N. Simon, J. Chem. Soc., Chem. Commun. (1995) 2151;
(b) C.B. Dieleman, D. Matt, I. Neda, R. Schmutzler, H. Thonnessen, P.G. Jones, A. Harrimann, J. Chem. Soc., Dalton Trans. (1998) 2115.
[10] R. Ludwig, K. Kunogi, N. Dung, S. Tachimori, Chem. Commun. (1997) 1985.
[11] (a) C. Wieser-Jeunesse, D. Matt, M.R. Yaftian, M. Burgard, J.M. Harrowfield, C.R. Acad. Sci., t1, Série IIc (1998) 479;
(b) I. Neda, T. Kaukorat, R. Schmutzler, Main Group Chem. News 6 (1998) 4.
[12] (a) P. Jurečka, P. Vojtíšek, K. Novotný, J. Rohovec, I. Lukeš, J. Chem. Soc., Perkin Trans. 2 (2002) 1370;
(b) S.K. Máté, G. Nagy, P. Jurečka, L. Kollár, Tetrahedron 58 (2002) 5119.
[13] (a) D. Parker, L.M. Harwood, C.J. Moody, Macrocycle Synthesis, Oxford University Press, Oxford, 1996, p. 145;
(b) C.D. Gutsche, J.F. Stoddart, Calixarenes, Washington University, St. Louis, MO, 1989.
[14] (a) D.G. Hewitt, G.L. Newland, Aust. J. Chem. 30 (1977) 579;
(b) M.J.P. Harger, R. Sreedharan-Menon, J. Chem. Soc., Perkin Trans. 1 (1998) 211.
[15] D.D. Perrin, W.L.F. Armarego, Purification of Laboratory Chemicals, Pergamon Press, Oxford, 1988.
[16] P. Caravan, J.J. Ellison, T.J. McMurry, R.B. Lauffer, Chem. Rev. 99 (1999) 2293.
[17] S. Freeman, J. Irwin, C.H. Schwalbe, J. Chem. Soc., Perkin Trans. 2 (1991) 263.
[18] S. Barboso, A.G. Carrera, S.E. Matthews, F.A. Neu, V. Bohmer, J.-F. Dozol, H. Rouquette, M.J.S. Weill, J. Chem. Soc., Perkin Trans. 2 (1999) 719.
[19] P.S. Pregosin, Transition Metal Nuclear Magnetic Resonance, Elsevier, Amsterdam, 1991.
[20] J.I. Bruce, M.P. Lowe, D. Parker, Photophysical Aspects of Lanthanide (III) Complexes, in: A.E. Merbach, E. Toth (Eds.), The Chemistry of Contrast Agents in Medical Magnetic Resonance Imaging, Wiley, 2001.
[21] M.R. Yaftian, M. Burgard, D. Matt, C.B. Dieleman, F. Rastegar, Solv. Extr. Ion Exch. 15 (1997) 975.
[22] L. Dasaradhi, P.C. Stark, V.J. Huber, P.H. Smith, G.D. Jarvinen, A.S. Gopalan, J. Chem. Soc., Perkin Trans. 2 (1997) 1187.
[23] (a) R. Přibil, Komplexometrie, SNTL, Praha, 1977;
(b) G. Schwarzenbach, H. Flaschka, Die komplexometrische Titration, Stuttgart, 1965.
[24] (a) V.I. Kornev, G.I. Manasheva, Koordinats. Khim. 4 (1978) 1539;
(b) N.V. Kumok, Zh. Neorgan. Khim. 11 (1966) 90.

Available online at www.sciencedirect.com
SCIENCE DIRECT®
Polyhedron 24 (2005) 327–332
POLYHEDRON
www.elsevier.com/locate/poly

Structural and spectral studies of nickel(II), copper(II) and cadmium(II) complexes of 3-furaldehyde thiosemicarbazone

El Mostapha Jouad [a], Magali Allain [b], Mustayeen A. Khan [a], Gilles M. Bouet [a,*]

[a] *Chimie de coordination, SONAS, E.A. 921, Faculté de Pharmacie, 16 Boulevard Daviers, F-49045 Angers Cedex 01, France*
[b] *CIMMA, CNRS UMR 6200, Faculté des Sciences, 2 Boulevard Lavoisier, F-49045 Angers Cedex, France*

Received 8 November 2004; accepted 24 November 2004
Available online 15 December 2004

Abstract

The synthesis and characterisation of Ni(II), Cu(II) and Cd(II) complexes of 3-furaldehyde thiosemicarbazone (3FTSC) are reported. Elemental analysis, molar conductance and spectral (IR, UV and ^{1}H NMR) measurements have been used to characterise the complexes. In addition, the structure of the complex $[Cu(3FTSC)_2]$ has been determined by X-ray diffraction methods. In Cu(II) and Ni(II) complexes, the metal ion is coordinated through the sulfur atom and the azomethine nitrogen atom while in the Cd(II) complexes the coordinating atoms are sulfur and furanic oxygen ones.
© 2004 Elsevier Ltd. All rights reserved.

Keywords: Furan thiosemicarbazone; 3d metals complexes; Spectroscopic studies; Crystal structures

1. Introduction

Thiosemicarbazones, their derivatives, as well as their transition metal complexes have aroused considerable interest in the areas of chemistry and biology. These compounds present a wide variety of biological activity such as antitumoral [1–5], fungicidal [6,7], bactericidal [8] or antiviral [3]. They have been used for metals analyses [9], for device applications relative to telecommunications, optical computing, storage and information processing [10].

As part of our continuous research work about synthesis and biological activity, mainly with thiosemicarbazones and semicarbazones deriving from furaldehyde and their metal complexes [11–16], we describe in this work a new series of transition metal complexes obtained from 3-furaldehyde thiosemicarbazone 3FTSC (Fig. 1) as ligand and the chlorides and bromides of Ni(II), Cu(II) and Cd(II). All structures are determined on the basis of elemental analyses and spectroscopic techniques. In addition, the crystal structure of the copper complex $[Cu(3FTSC)_2]$ is described.

2. Experimental

2.1. Reactants

All reactants and solvents were analytical grade. Thiosemicarbazide and 3-furaldehyde were purchased from Merck and Aldrich, respectively. Nickel, copper and cadmium hydrated salts were used as received (Prolabo).

2.2. Preparation of ligand

The 3-furaldehyde thiosemicarbazone was synthesised as previously described [11] by refluxing 3-furaldehyde and thiosemicarbazone (1:1 molar ratio) in absolute ethanol in the presence of pure acetic acid.

* Corresponding author. Tel.: +33 241 226 600; fax: +33 241 486 733.
E-mail address: gilles.bouet@univ-angers.fr (G.M. Bouet).

0277-5387/$ - see front matter © 2004 Elsevier Ltd. All rights reserved.
doi:10.1016/j.poly.2004.11.010

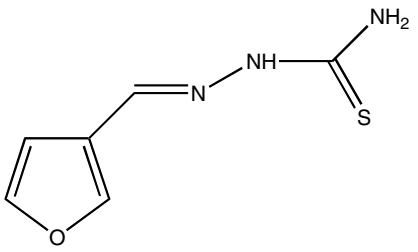


Fig. 1. Chemical structure of 3-furaldehyde thiosemicarbazone (3FTSC).

The mixture was refluxed for 1 h and then cooled, filtered and recrystallised from a mixture of ethanol (75% V/V) and water. Yellow microcrystalline products are obtained. (Elemental *Anal.* Calc. for $C_6H_7N_3OS$: C, 42.59; H, 4.17; N, 24.83. Found: C, 42.90; H, 4.19; N, 24.70%). M.P. = 154 to 155 °C.

2.3. Preparation of complexes

2.3.1. Bis(3-furaldehydethiosemicarbazone)nickel (II) [Ni(3FTSC)$_2$]

The hexahydrated nickel chloride, $NiCl_2 \cdot 6H_2O$ (2.5×10^{-3} mol, 0.59 g), was dissolved in distilled water. An ethanolic solution of FTSC (5×10^{-3} mol; 0.85 g, 10 mL) was added slowly while stirring. The mixture was refluxed for 3 h. After cooling at room temperature, a green precipitate appeared. It was filtered, washed with small amounts of absolute ethanol and finally dried in vacuum over silicagel. All the compounds were washed and dried in the same way.

2.3.2. Dichloro bis(3-furaldehydethiosemicarbazone) copper (II) [CuCl$_2$(3FTSC)$_2$]

This complex was prepared from a mixture of ethanolic solution (10 mL) of 3FTSC (0.42 g, 2.5×10^{-3} mol) and $CuCl_2 \cdot 2H_2O$ (1.25×10^{-3} mol) after 1 h reflux.

2.3.3. Bis(3-furaldehydethiosemicarbazone)copper (II) [Cu(3FTSC)$_2$]

When 2×10^{-3} g of complex [$CuCl_2$(3FTSC)$_2$] was dissolved in ethanol (20 mL), a dark-green crystalline product of formula [Cu(3FTSC)$_2$] was isolated after several days at room temperature. As the crystal structure of this compound was fully solved by X-ray diffraction, its analytical and infrared data are not given in Tables 2 and 4.

2.3.4. Bis(chloro(3-furaldehydethiosemicarbazone) copper (II)) [CuCl(3FTSC)]$_2$

$CuCl_2 \cdot 2H_2O$ (0.24 g, 1.25×10^{-3} mol, 5 mL) was added to 3FTSC (0.21 g, 1.25×10^{-3} mol, 10 mL) in EtOH. The complex is obtained after refluxing EtOH for 1 h.

2.3.5. Bis(bromo(3-furaldehyde thiosemicarbazone) copper (II)) [CuBr(3FTSC)]$_2$

The bromo complex was obtained as the chloro complex starting from 3FTSC (0.21 g, 1.25×10^{-3} mol, 10 mL) and $CuBr_2$ (0.28 g, 1.25×10^{-3} mol, 5 mL).

2.3.6. Dichloro(3-furaldehyde thiosemicarbazone) cadmium (II) [CdCl$_2$(3FTSC)]

This complex was prepared from a mixture of ethanolic solution of 3FTSC (0.21 g, 1.25×10^{-3} mol, 5 mL) and $CdCl_2$ (0.23 g, 1×25.10^{-3} mol, 5 mL) after a 1 h reflux.

2.3.7. Dibromo(3-furaldehyde thiosemicarbazone) cadmium (II) [CdBr$_2$(3FTSC)]

$CdBr_2 \cdot 4H_2O$ (0.34 g, 1.25×10^{-3} mol, 5 mL EtOH) was added to 3FTSC (0.21 g, 1.25×10^{-3} mol, 10 mL) in EtOH. The mixture was refluxed for 1 h.

2.4. Measurements

Elemental analysis were carried out by the Service Central d'Analyses (C.N.R.S. Vernaison, France). Melting points were determined with a digital melting point apparatus using a capillary technique. Conductance values were obtained with a Tacussel CD6NG conductometer at 298 K from 10^{-3} mol L^{-1} solutions of complexes in absolute EtOH. The solvent had a conductance of 10^{-8} S cm^2 mol^{-2}.

The IR spectra were recorded with a Shimadzu FTIR-8010M spectrometer between 4600 and 400 cm^{-1} (KBr disks) and with a Nicolet FTIR 20F in the range 400–50 cm^{-1} using polyethylene disks (Institut des Matériaux Jean Rouxel, UMR 6502, Nantes, France). Electronic spectra were recorded with a Perkin–Elmer Lambda 19 spectrometer from ethanolic solutions (10^{-3} mol L^{-1}). The ^{1}H NMR spectra were recorded on a Bruker Advance DRX 500 spectrometer in DMSO-D6 operating at 500 MHz. The chemical shifts, δ, are given in parts per million (relative to TMS) and coupling constants in hertz.

2.5. Crystal data collection and processing

Crystals of [Cu(3FTSC)$_2$] are monoclinic with space group $P2_{1/c}$. The crystal and instrumental parameters used in the unit-cell determination and data collection are summarised in Table 1. X-ray diffraction data were collected at 293 K on an Enraf Nonius MACH3 four-circles diffractometer ($\lambda_{Mo\ K\alpha} = 0.71073$ Å) equipped with a graphite monochromator (IMMO, UMR, C.N.R.S, 6501 Angers). The structure was solved by direct methods (SIR) using MOLEN package programs [17] and the structure was refined on F by full-matrix least-squares techniques.

Table 1
Crystallographic data for copper complex

Compound	[Cu(3FTSC)$_2$]
Formula	$C_{12}H_{12}N_6CuO_2S_2$
Molecular weight	394
Crystal system	monoclinic
Space group	$P2_{1/c}$
a (Å)	9.871(2)
b (Å)	4.417(1)
c (Å)	17.283(4)
α (°)	90
β (°)	100.08(2)
γ (°)	90
V (Å^3)	741.9(5)
Z	2
Color	dark-green
D_{calc} (g cm^{-3})	2.07
F(0 0 0)	464
μ (mm^{-1})	3.168
hkl limits	−9.9 −4.0 0.16
θ_{min}, θ_{max}	2.5, 20
Number of data with $I > 3\sigma(I)$	494
Weighting scheme	$4F_o^2/[\sigma^2(F_o^2) + (0.06F_o^2)^2]$
Number of variables	82
R	0.045
R_w	0.059

The small size of the crystal did not allow us to obtain enough data and carbon atoms were refined isotropically. Oxygen and nitrogen atoms were refined anisotropically. Hydrogen atoms attached to nitrogen atom (N) were located from Fourier difference synthesis [17]. The remaining hydrogen atoms were located using HYDRO program [17].

3. Results and discussion

The analytical and physical data for the ligand and the metal complexes are listed in Table 2. All the analytical data are in good agreement with the empirical formulae as given in Table 2. The complexes are stable in air. However, the cadmium complexes showed an hygroscopic character. Their molar conductivities are in a range corresponding to a non-electrolytic nature. These results agreed with measurements of the conductivity carried out with their homologous thiosemicarbazones and semicarbazones [13,18–20]. On heating, all the complexes decomposed and did not present a clear melting point.

3.1. Crystal structure of [Cu(3FTSC)$_2$]

The main crystal parameters are reported in Table 1. The bond distances and their angles for this crystal are shown in Table 3. Fig. 2 shows a view of the molecule of [Cu(3FTSC)$_2$] with numbering scheme.

The centrosymmetric structure consists in the neutral molecules Cu(3FTSC)$_2$, with copper at the centre of symmetry. The coordination results in a square planar configuration, which involves the thiolato sulfur atoms and the imine nitrogen atom N3 of the two ligands in *cis*-configuration.

In the complex, the monodeprotonated bidentate ligand shows a *cis*-configuration for the nitrogen N3 and sulfur S atoms. In the free ligand, however, these

Table 3
Bond lengths (Å) and angles (°) for the free ligand and complex

Bond lengths (Å)		Bond angles (°)	
Cu–S	2.180(3)	S–Cu–N3	85.2(2)
Cu–N3	1.911(6)	Cu–S–C1	96.4(3)
S–C1	1.726(8)	C5–O–C6	105.2(7)
O–C5	1.32(1)	N3–N2–C1	112.2(6)
O–C6	1.36(1)	Cu–N3–N2	121.8(5)
N2–N3	1.39(1)	Cu–N3–C2	125.6(6)
N2–C1	1.30(1)	N2–N3–C2	112.6(6)
N3–C2	1.30(1)	S–C1–N2	123.2(7)
C2–C3	1.45(1)	N3–C2–C3	127.8(8)
C3–C4	1.43(1)	C2–C3–C4	123.5(8)
C3–C6	1.32(1)	C2–C3–C6	132.8(9)
C4–C5	1.33(1)	C4–C3–C6	103.7(8)
		C3–C4–C5	106(1)
		O–C5–C4	111.6(9)
		O–C6–C3	112.9(8)

Table 2
Analytical data

Compound	Color	Yield (%)	M.p (°C)	Elemental analysis found (Calc.)				Λ (S cm^2 mol^{-1})
				C (%)	H (%)	X (%)	M (%)	
3FTSC	yellow	43	154–155	42.90 (42.59)	4.19 (4.17)			
[Ni(3FTSC)$_2$]	green	20	238 d	36.39 (36.29)	3.14 (3.55)		14.81 (14.78)	0.3
[CuCl$_2$(3FTSC)$_2$]	green	19	213 d	30.35 (30.48)	2.82 (2.98)	15.07 (14.99)	13.17 (13.44)	39.5
[(CuCl(3FTSC))$_2$]	green	37	210 d	26.57 (26.87)	2.73 (2.63)	12.58 (13.22)	22.84 (23.69)	9.2
[(CuBr(3FTSC))$_2$]	black	26	223 d	23.10 (23.05)	2.22 (2.26)	25.27 (25.56)	19.41 (20.32)	11.3
[CdCl$_2$(3FTSC)]	clear brown	40	241 d	20.26 (20.44)	2.09 (2.00)	19.63 (20.11)	29.71 (31.89)	7.9
[CdBr$_2$(3FTSC)]	clear brown	65	237 d	16.50 (16.33)	1.60 (1.60)	35.86 (36.20)	24.06 (25.47)	5.2

Table 4
Main IR spectral vibrations (cm^{-1})

	$\nu(NH_2)$	ν(C=S)	ν(C=N)	ν(N–N)	Ring Breath.	ν(C–O–C)	ν(M–X)	ν(M–N)	ν(M–S)	ν(M–O)
3FTSC	3421a, 3290s	837	1587	936	1009	1289				
[Ni(3FTSC)$_2$]	3439a, 3344s	829	1608		1010	1290		232	390	
[CuCl$_2$(3FTSC)$_2$]	3389a, 3260s	800	1610	945	1010	1293	240, 255	440	380	
[CuCl(3FTSC)]$_2$	3398a	799	1608	948	1015	1289	260	436	390	
[CuBr(3FTSC)]$_2$	3397a, 3272s	819	1601	944	1014	1289	263	435	388	
[CdCl$_2$(3FTSC)]	3441a, 3329s	832	1599	942	999	1300	245, 255		381	490
[CdBr$_2$(3FTSC)]	3449a, 3329s	829	1594	940	1000	1298	247, 258		380	485

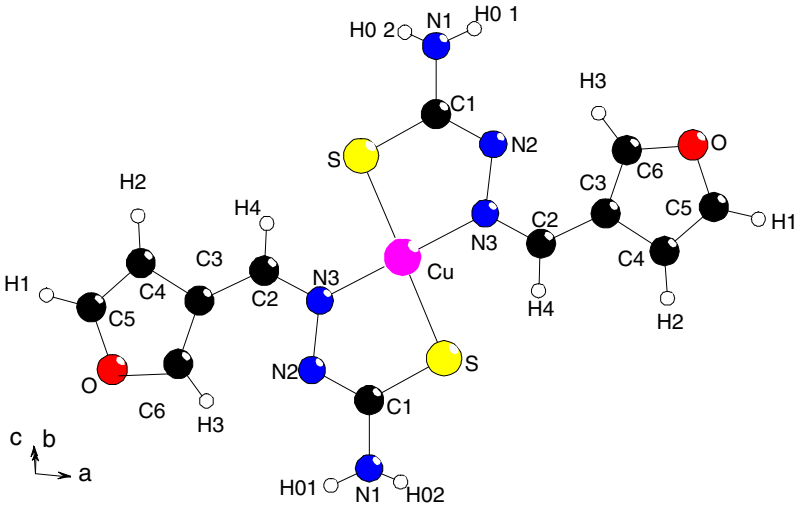


Fig. 2. Perspective view of complex and atom numbering of [Cu(3FTSC)$_2$].

centres present a *trans*-configuration [11], indicating that the complexation occurs after a 180° rotation around the C1–N2 bond.

As the ligand is deprotonated on N2 atom, a negative charge appears and is delocalized along the thiosemicarbazone moiety. This fact is confirmed by the difference between the bond distances in the deprotonated ligand of copper complex: S1–C1 = 1.726(8) Å (thiolato form); C1–N2 = 1.30(1) Å and C2–N3 = 1.30(1) Å, and the same bond distances in the free ligand: S1–C1 = 1.690(2) Å (thione form); C1–N2 = 1.338(2) Å and C2–N3 = 1.271(2) Å [11–13].

The configuration of the complex [Cu(3FTSC)$_2$] is planar, while the carbon atom, C1, is slightly out of this plane, with 0.12 Å deviation.

It is not very easy to compare the S–Cu and N3–Cu bonds lengths with the distances reported in the literature for the same bonds in thiosemicarbazones copper (II) complexes. Generally, these complexes are formulated as [CuLX$_2$] or [CuLX] (X = halogen, L = ligand) with tridentate ligands, whereas the complex [Cu(3FTSC)$_2$] should be written [CuL$_2$] with L being a bidentate ligand.

The molecular arrangement in the unit-cell shows that the neutral molecules Cu(3FTSC)$_2$ in the complex [Cu(3FTSC)$_2$] are stacked, one above the other, so that their main planes are parallel and the copper atoms occupy the apexes and the mid-point of the *c* edges. This is shown by the projection of the structure on the plane (0 1 0) presented in Fig. 3.

The packing is governed by hydrogen bonds between the hydrogen H1 of the amino group N1 and the oxygen atom in furanic ring. This hydrogen bond shows a bond distance of 2.45 Å and a bond angle of 147°. The coordinates of N1 and O are, respectively, $(2 - x, 0.5 + y, 1.5 - z)$ and $(1 - x, 1 - y, 1 - z)$.

3.2. Infrared spectra

Selected vibration bands of 3FTSC and of its metal complexes are given in Table 4.

The vibration ν(C=S) in the spectrum of the ligand shows a band around 837 cm^{-1} [11]. This band is shifted to lower wavenumbers in all the complexes [21,22]. On the other hand, the bands in the region 3421–3290 cm^{-1} attributed to symmetrical and asymmetrical stretching modes $\nu(NH_2)$ in the spectra of the ligand, undergo a change in the spectra of the complexes. This is explained by the coordination of sulfur from the C=S (NH_2) group as reported earlier [23]. In addition, this

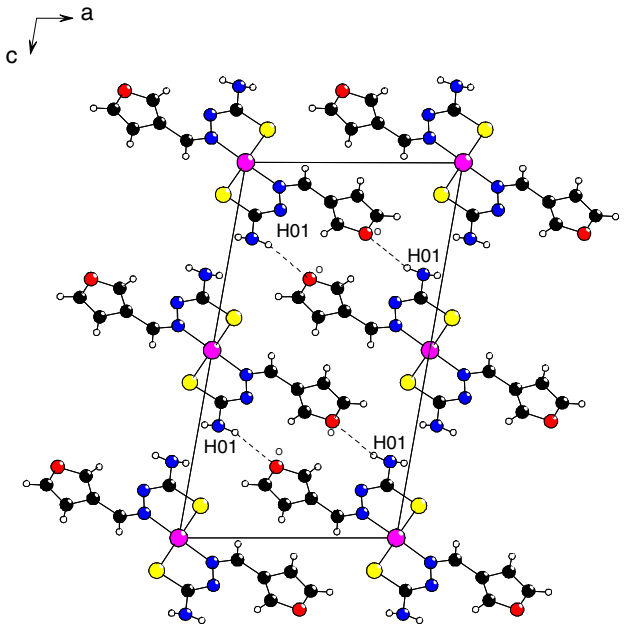


Fig. 3. Packing arrangement and hydrogen bonding in [Cu(3FTSC)2] X-ray structure.

coordination is confirmed by the presence in all complexes of a new band at 380–390 cm^{-1} [5,24], relative to ν(M–S) vibration.

In the ligand spectra, the strong band observed at 1587 cm^{-1} is assigned to (C=N) stretching vibration [11]. This band shifts to higher wavenumbers in the spectra of all metal complexes, indicating the coordination of nitrogen of the azomethine group to the central metal atoms [21,23]. In the case of the cadmium complex, this shift is very feeble. The presence of a new band in the region 430–440 cm^{-1} due to ν(M–N) is an other indication of the involvement of nitrogen of the azomethine group in the coordination [5,24]. However, we did not observe any shifts of frequency of the ν(Cd–N) vibration for the complexes of Cd(II). On the opposite side, we noted a significant displacement of the frequency of the ring breathing and ν(C–O–C) vibrations, and this shows that the coordination occurs through the furanic oxygen atom (instead of the azomethine nitrogen) [25]. This coordination is also supported by the appearance of the ν(Cd–O) vibration for [$CdCl_2$(3FTSC)] and [$CdBr_2$(3FTSC)] at 490 and 485 cm^{-1}, respectively [18,19,25,26].

In the literature, the bands appearing between 160 and 300 cm^{-1} are allotted to the vibration of the M–X bonds, where M = metal and X = Cl or Br [18,26–29]. In our case, the ν(M–X) frequencies appearing between 240 and 260 cm^{-1} (Table 4) are in good agreement with the reported values in the literature.

Generally, the infrared spectra of copper complexes such as [$CuCl_2(L)_2$] or [$CuCl_2$(L)] present two bands between 240 and 280 cm^{-1}, due to ν(Cu–Cl) vibration [27,28]. Billing et al. [30] showed that, when copper(II) complexes present only one vibration band in this range, their structures show halogenide bridges in these compounds. This is observed in the case of the binuclear complexes [CuCl(3FTSC)]$_2$ and [CuBr(3FTSC)]$_2$.

3.3. Electronic spectra

The study of the electronic spectra in ethanol allowed us to determine the geometry of the polyhedrons of coordination for copper complexes. The binuclear complexes [CuCl(3FTSC)]$_2$ and [CuBr(3FTSC)]$_2$ showed only one band around 13 700 cm^{-1}. This band was also observed in the spectrum of the binuclear complex [Cu(TTSC)Cl]$_2$ described by Nair et al. [31], where TTSC is 2-thiophene carboxaldehyde thiosemicarbazone. It is typical of a d–d transition in a square planar environment.

The electronic spectrum of the complex [$CuCl_2$-(3FTSC)$_2$] presents an asymmetrical band with a maximum around 15 410 cm^{-1}. According to Raising [32], the asymmetry of this band is a characteristic of octahedral copper (II) compounds, where a lengthening of the bonds located along the $z'Oz$-axis is often observed. At the outset, this lengthening can lead to an ionic complex with square planar geometry. This fact is confirmed by the high value of the conductivity of [$CuCl_2$(3FTSC)$_2$] (Table 2) and the loss of the two chlorine atoms during the formation of the monocrystals of [Cu(3FTSC)$_2$]. We conclude that the geometry of this complex is closer to square planar rather than regular octahedral geometry.

3.4. NMR spectra

Theoretically, the complexation by azomethine nitrogen should affect the chemical shift of the C=N protons [5]. The recording of spectra ^{1}H NMR for the cadmium complexes did not show any shift of this signal. This confirms our earlier hypothesis, formulated from infrared data, that the second coordinating atom is the oxygen of the furanic ring for the Cd(II) complexes. In addition, no signals appeared around 11.4 ppm (field of appearance of the signal of a NH group next to C=S) and this confirms that the coordination occurs through the thiolato form.

4. Supplementary data

Crystallographic data have been deposited with the CCDC (12 Union Road. Cambridge, CB2 IEZ, UK (fax: +44 1223 336033; e-mail: deposit@ccdc.cam.ac.uk or at www: http://www.ccdc.cam.ac.uk)), and are available on request quoting the deposition numbers CCDC 252861.

References

[1] Y. Kang, N. Yang, S.O. Kang, J. Ko, C.H. Lee, Y.H. Lee, Organometallics 16 (1997) 5522.
[2] D.X. West, J.K. Swearingen, J. Valdès-Martinez, S. Hernandez-Ortega, A.K. El-Sawaf, F. van Meurs, A. Castiñeiras, I. Garcia, E. Bermejo, Polyhedron 18 (1999) 2919.
[3] P. Tarasconi, S. Capacchi, G. Pelosi, M. Cornia, R. Albertini, A. Bonati, P.P. Dall'Aglio, P. Lunghi, S. Pinelli, Bioorg. Med. Chem. 8 (2000) 157.
[4] A. Kumar, U. Chandra, S. Chandra, Synth. React. Inorg. Met. Org. Chem. 23 (1993) 671.
[5] L.J. Ackerman, P.E. Fanwick, M.A. Green, E. John, W.E. Running, J.K. Swearingen, J.W. Webb, D.X. West, Polyhedron 18 (1999) 2759.
[6] S.G. Teoh, S.H. Ang, H.K. Fun, C.W. Ong, J. Organomet. Chem. 580 (1999) 17.
[7] E. Bermejo, R. Carballo, A. Castiñeiras, R. Dominguez, C. Maichle-Mössmer, J. Strähle, D.X. West, Polyhedron 18 (1999) 3695.
[8] S. Abram, C. Maichle-Mössmer, U. Abram, Polyhedron 17 (1998) 131.
[9] H. Nishioka, T. Kumagai, T. Nagahiro, Microchem. J. 50 (1994) 88.
[10] Y. Tian, C. Duan, C. Zhao, X. You, Inorg. Chem. 36 (1997) 1247.
[11] E.M. Jouad, M. Allain, M.A. Khan, G.M. Bouet, J. Mol. Struct. 604 (2002) 205.
[12] E.M. Jouad, G. Larcher, M. Allain, A. Riou, G.M. Bouet, M.A. Khan, X.D. Thanh, J. Inorg. biochem. 86 (2001) 565.
[13] E.M. Jouad, A. Riou, M. Allain, M.A. Khan, G.M. Bouet, Polyhedron 20 (2001) 67.
[14] I.H. Hall, C.B. Lackey, T.D. Kistler, R.W. Durham Jr., El.M. Jouad, M. Khan, X. Do Thanh, S. Djebbar-Sid, O. Benali-Baitich, G.M. Bouet, Die Pharmazie 12 (2000) 937.
[15] E.M. Jouad, X. Do Thanh, G. Bouet, S. Bonneau, M.A. Khan, Anticancer Res. 22 (2002) 1713.
[16] E.M. Jouad, X.D. Thanh, G. Bouet, N. Ménard, M.A. Khan, Biol. Rhyt. Res. 33 (2002) 513.
[17] Crystal Structure Analysis, Molecular Enraf-Nonius (MOLEN), 1990, Delft Instruments X-ray Diffraction B.V. Rontnenweg 1 2624 BD Delft, The Netherlands.
[18] I. Ghassan, M.A. Khan, E. Chebli, G.M. Bouet, Transition Met. Chem. 24 (1999) 294.
[19] G. Ibrahim, Thesis, University of Angers, France, 1997.
[20] G. Ibrahim, M.A. Khan, G.M. Bouet, Transition Met. Chem. 27 (2002) 34.
[21] M. Rodriguez-Argüelles, M.B. Ferrari, G.G. Fava, C. Pelizzi, G. Pelosi, R. Albertini, A. Bonati, P.P. Dall'Aglio, P. Lunghi, S. Pinelli, J. Inorg. Biochem. 66 (1997) 7.
[22] L. Lima, L.R. Teixeira, T.G. Carneiro, H. Beraldo, J. Braz. Chem. Soc. 10 (1999) 184.
[23] P. Bindu, M.R.P. Kurup, T.R. Satyakeerty, Polyhedron 18 (1999) 321.
[24] J. Garcia-Tojal, L. Lezama, J.L. Pizarro, M. Insausti, M.I. Arriortua, T. Rojo, Polyhedron 18 (1999) 3703.
[25] G. Ibrahim, M.A. Khan, P. Richomme, O. Benali-Baïtich, G. Bouet, Polyhedron 16 (1997) 3455.
[26] M.P. Swami, D. Gupta, M. Mohan, A.K. Srivastava, Prog. Nat. Acad. Sci. India A 50 (III) (1980) 176.
[27] A.K. El-Sawaf, D.X. West, F.A. El-Saied, R.M. El-Bahnasawy, Transition Met. Chem. 23 (1998) 565.
[28] D.X. West, H. Beraldo, A.A. Nassar, F.A. El-Saied, M.I. Ayad, Transition Met. Chem. 24 (1999) 421.
[29] A. Castiñeiras, I. Garcia, E. Bermejo, D.X. West, Polyhedron 19 (2000) 1873.
[30] D.E. Billing, A.E. Underhill, D.M. Adams, D.M. Morris, J. Chem. Soc. A (1966) 902.
[31] C.G.R. Nair, K.K. Aravindakshan, J. Inst. Chemists (India) 53 (1981) 295.
[32] A.B.P. Lever, Inorganic Electronic Spectroscopy, 1st ed., Elsevier, Amsterdam, 1968.

Available online at www.sciencedirect.com
SCIENCE DIRECT®
Polyhedron 24 (2005) 333–342
POLYHEDRON
www.elsevier.com/locate/poly

Tetrazine derived mononuclear $Ru^{II}(acac)_2(L)$ (**1**), $[Ru^{II}(bpy)_2(L)](ClO_4)_2$ (**2**) and $[Ru^{II}(bpy)(L)_2](ClO_4)_2$ (**3**) (L = 3-amino-6-(3,5-dimethylpyrazol-1-yl)-1,2,4,5-tetrazine, acac = acetylacetonate, bpy = 2,2′-bipyridine): syntheses, structures, spectra and redox properties

Animesh Nayak [a], Srikanta Patra [a], Biprajit Sarkar [b], Sandeep Ghumaan [a], Vedavati G. Puranik [c], Wolfgang Kaim [b,*], Goutam Kumar Lahiri [a,*]

[a] *Department of Chemistry, Indian Institute of Technology – Bombay, Powai, Mumbai 400 076, India*
[b] *Institut für Anorganische Chemie, Universität Stuttgart, Pfaffenwaldring 55, D-70550 Stuttgart, Germany*
[c] *Center for Materials Characterization, National Chemical Laboratory, Pune, Maharashtra 411 008, India*

Received 13 October 2004; accepted 24 November 2004

Abstract

Mononuclear ruthenium complexes of tetrazine derived L, $Ru^{II}(acac)_2(L)$ (**1**), $[Ru^{II}(bpy)_2(L)](ClO_4)_2$ (**2**) and $[Ru^{II}(bpy)(L)_2](ClO_4)_2$ (**3**) (L = 3-amino-6-(3,5-dimethylpyrazol-1-yl)-1,2,4,5-tetrazine, acac = acetylacetonate and bpy = 2,2′-bipyridine) were prepared. The free L exists as a dimeric entity in the solid state via hydrogen bonding interactions involving L and water molecules present in the crystal lattice. **1** exhibits unusually strong bonds from Ru^{II} to coordinating pyrazolyl-N (2.040(2) Å) and especially to tetrazine-N (1.913(2) Å). The Ru^{III}/Ru^{II} couples of **1**–**3** appeared at 0.28, 1.34 and 1.50 V versus SCE, respectively. The tetrazine and bpy-based reductions were observed at −1.33 (**1**); −0.55 and −1.55/−1.75/−1.98 (**2**); −0.47/−0.78 and −1.80/−2.02 V (**3**), respectively. **1**, **2** and **3** displayed two MLCT bands each, corresponding to $d\pi(Ru^{II}) \rightarrow \pi^*$ (L, tetrazine) and $d\pi(Ru^{II}) \rightarrow \pi^*$ (acac or bpy or L) transitions. $\mathbf{1}^+$ and $\mathbf{2}^+$ showed rhombic EPR spectra at 110 and 4 K, respectively and $\mathbf{1}^-$, $\mathbf{2}^-$ and $\mathbf{3}^-$ exhibited multiple line EPR spectra at 300 K. **1**–**3** exhibited moderately strong emission spectra in EtOH–MeOH glass at 77 K.
© 2004 Elsevier Ltd. All rights reserved.

Keywords: Ruthenium–tetrazine; Synthesis; Structure; Electrochemistry; Redox; Spectra

1. Introduction

Among the well established polynucleating ligands in coordination chemistry are the 3,6-disubstituted 1,2,4,5-tetrazines [1]. During the last decade these ligands have become more and more popular because of their special electronic and structural properties. The electronic properties are related to the strong π-accepting nature of the tetrazine moiety due to the low-lying π* MO, while the structural features are essentially based on the efficient metal–metal bridging capacity.

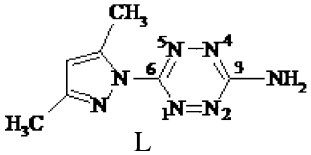
The ability of tetrazine ligand systems to function as efficient electronic spacers between individual metal centers is reflected in a series of diruthenium complexes

* Corresponding authors. Tel.: +91 22 2576 7159; fax: +91 22 2572 3480.
E-mail addresses: kaim@iac.uni-stuttgart.de (W. Kaim), lahiri@chem.iitb.ac.in (G.K. Lahiri).

0277-5387/$ - see front matter © 2004 Elsevier Ltd. All rights reserved.
doi:10.1016/j.poly.2004.11.019

encompassing a variety of 3,6-disubstituted tetrazine derivatives [2]. Their structural, spectroelectrochemical, EPR, magnetic and luminescence aspects have been thoroughly investigated. However, only a limited number of *mononuclear* ruthenium–tetrazine derivatives are known so far, e.g., $[(trpy)Ru(bphtz)](PF_6)_2$ [3a], $[(CO)(PPh_3)_2(H)Ru(bptz)]PF_6$ [3b], $[(NH_3)_4Ru(bptz)](PF_6)_2$ [3c,d], $[(bpy)_2Ru(bptz)](PF_6)_2$ [3d], $[\{(CH_3)_2SO\}_2(Cl)_2Ru(bptz)]\cdot mH_2O$ [3e] and $[(bpz)_2Ru(bptz)](PF_6)_2$ [3d,f] [bptz = 3,6-bis(2-pyridyl)-1,2,4,5-tetrazine; bphtz = 3,6-bis(1,10-phenanthroline)-1,2,4,5-tetrazine; trpy = 2,2′:6′,2″-terpyridine; bpz = 2,2′-bipyrazine].

This situation has prompted the present program of exploring the metallation aspects of 3-amino-6-(3,5-dimethylpyrazol-1-yl)-1,2,4,5-tetrazine (L), comprising of a five-membered pyrazolyl ring on one side of the tetrazine and an $-NH_2$ group on the other side. Although L has been synthesized previously [4], its structural and metallation aspects have not been investigated so far. As part of our systematic approach, we report in this paper the synthesis of three ruthenium complexes, viz., $[Ru^{II}(acac)_2(L)]$ (**1**), $[Ru^{II}(bpy)_2(L)](ClO_4)_2$ (**2**) and $[Ru^{II}(bpy)(L)_2](ClO_4)_2$ (**3**), incorporating ancillary ligands such as σ-donating acetylacetonato ($acac^-$) or π-acidic 2,2′-bipyridine (bpy). The crystal structures of L, **1** and **2**, their spectro-electrochemical and luminescence behavior, and the EPR characteristics of the in situ generated Ru^{III} derivatives ($\mathbf{1}^+$, $\mathbf{2}^+$, $\mathbf{3}^+$) and the reduced radical species ($\mathbf{1}^-$, $\mathbf{2}^-$, $\mathbf{3}^-$) are being reported here.



L

2. Experimental

2.1. Materials

The starting complexes $Ru(acac)_2(CH_3CN)_2$ [5], $Ru(bpy)_2Cl_2\cdot 2H_2O$ [6] and $Ru(bpy)Cl_3$ [7] were prepared according to the reported procedures. The ligand 3-amino-6-(3,5-dimethylpyrazol-1-yl)-1,2,4,5-tetrazine was prepared via a modification of the procedure developed by Glidewell et al. [4]. Other chemicals and solvents were reagent grade and were used as received. For spectroscopic and electrochemical studies HPLC grade solvents were used. Commercial tetraethylammonium bromide was converted into pure tetraethylammonium perchlorate following a published procedure [8].

2.2. Physical measurements

UV–Vis spectra were recorded with a JASCO V-570 spectrophotometer. FT-IR spectra were taken on a Nicolet spectrophotometer with samples prepared as KBr pellets. Solution electrical conductivity was checked using a Systronic 305 conductivity bridge. Magnetic susceptibility was checked with a CAHN electrobalance 7550 model sample magnetometer. ^1H NMR spectra were obtained with a 300 MHz Varian FT spectrometer. The elemental analyses were carried out with a Perkin–Elmer 240C elemental analyzer. The EPR measurements were made in a two-electrode capillary tube [9] with an X-band Bruker system ESP300, equipped with a Bruker ER035M gaussmeter and a HP 5350B microwave detector. Cyclic voltammetric, differential pulse voltammetric and coulometric measurements were carried out using a PAR model 273A electrochemistry system. Platinum wire working and auxiliary electrodes and an aqueous saturated calomel reference electrode (SCE) were used in a three-electrode configuration. The supporting electrolyte was $[NEt_4]ClO_4$ and the solute concentration was $\sim 10^{-3}$ M. The half-wave potential E^0_{298} was set equal to $0.5(E_{pa} + E_{pc})$, where E_{pa} and E_{pc} are anodic and cathodic cyclic voltammetric peak potentials, respectively. A platinum wire-gauze working electrode was used in coulometric experiments. All experiments were carried out under a dinitrogen atmosphere and were uncorrected for junction potentials. Electrospray mass spectra were recorded on a Micromass Q-ToF mass spectrometer. Steady state emission experiments were made using a Perkin–Elmer LS 55 luminescence spectrometer fitted with a cryostat. The quantum yields of the complexes were with reference to the reported quantum yield of $[Ru(bpy)_3](PF_6)_2$ in EtOH–MeOH (4:1) solution ($\Phi_{em,77\ K} = 0.35$) [10].

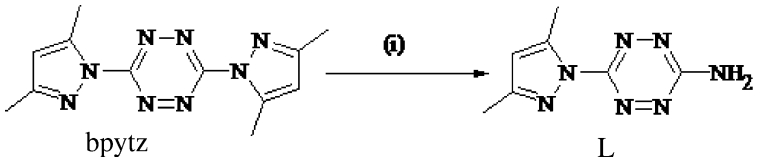
2.3. Preparation of L and complexes *1*, *2* and *3*

2.3.1. Preparation of L, [3-amino-6-(3,5-dimethyl pyrazol-1-yl)-1,2,4,5-tetrazine]

The ligand L was synthesized via a modification (Scheme 1) of the method reported by Glidewell et al. [4]. The ligand bpytz (300 mg, 1.11 mmol) in 20 ml toluene was treated dropwise with 0.3 ml of ammonia at 298 K. The stirring was continued for 2.5 h. The orange solid thus obtained was filtered and washed with toluene and then dried in vacuum. Yield: 170 mg (80%). ^1H NMR in $(CD_3)_2SO$ δ (ppm), 2.20 (s, CH_3), 2.37 (s, CH_3), 6.17 (s, CH), 8.2 (s, NH_2).

2.3.2. $[Ru^{II}(acac)_2(L)]$ (*1*)

The starting complex $Ru(acac)_2(CH_3CN)_2$ (100 mg, 0.26 mmol) and the ligand L (50 mg, 0.26 mmol) were dissolved in 20 ml of ethanol, and the mixture was heated under reflux for 8 h in air. The initially orange



Scheme 1. NH_3, toluene.

solution gradually changed to blue. The solvent was evaporated to dryness under reduced pressure and the solid mass thus obtained was purified by using a silica gel column. Initially, a red compound corresponding to $Ru(acac)_3$ was eluted by CH_2Cl_2–CH_3CN (5:1). With CH_2Cl_2–CH_3CN (1:1), a blue compound corresponding to **1** was separated later. Evaporation of solvent under reduced pressure yielded complex **1**. Yield: **1** (52 mg, 40%). *Anal.* Calc. for complex **1**: C, 41.54; H, 4.69; N, 19.96. Found: C, 41.14; H, 4.33; N, 19.81%. IR, ν/cm^{-1}: 3432 and 3293 ($-NH_2$).

2.3.3. $[Ru^{II}(bpy)_2(L)](ClO_4)_2$ (2)

A mixture of $[Ru(bpy)_2Cl_2]\cdot 2H_2O$ (100 mg, 0.19 mmol) and $AgClO_4$ (100 mg, 0.5 mmol) in 20 ml ethanol was heated with constant stirring for 2 h. The removal of the AgCl precipitate using a sintered-glass funnel resulted in a clear solution containing $[Ru(bpy)_2(EtOH)_2](ClO_4)_2$. To this solution the ligand (L) (39 mg, 0.21 mmol) was added and the mixture was heated under reflux for 5 h in air. The initially red solution gradually changed to purple. The volume of the solution was reduced to about 5 ml under reduced pressure and kept overnight at 268 K. A dark precipitate thus obtained was filtered and washed with cold water followed by cold ethanol. The dried product was then purified by using an alumina column. The purple compound **2** was eluted by CH_3CN. Evaporation of solvent under reduced pressure yielded complex **2**. Yield: **2** (100 mg, 60%). *Anal.* Calc. for complex **2**: C, 40.35; H, 3.14; N, 19.18. Found: C, 40.68; H, 2.87; N, 19.55%. Λ_M/Ω^{-1} ($cm^2\,mol^{-1}$) in MeCN at 298 K: 210. IR, ν/cm^{-1}: 3436/3322 ($-NH_2$) and 1088/618 ClO_4^-.

2.3.4. $[Ru^{II}(bpy)(L)_2](ClO_4)_2$ (3)

A mixture of $Ru(bpy)Cl_3$ (100 mg, 0.27 mmol) and the ligand (L) (130 mg, 0.68 mmol) in ethanol was heated to reflux in air for 12 h. The initially brownish solution gradually changed to purple. The solvent of the reaction mixture was then evaporated to dryness under reduced pressure and the solid mass thus obtained was purified by using a silica gel column. A purple compound containing $[Ru(bpy)(L)_2](ClO_4)_2$ was eluted with 4:1 acetonitrile–methanol mixture. The solvent was evaporated to dryness under reduced pressure, the solid mass was dissolved in the minimum volume of acetonitrile, and an aqueous solution of excess $NaClO_4$ was added to the solution. The dark complex **3** was filtered and washed thoroughly with ice-cold water. Yield: (80 mg, 43%). *Anal.* Calc. for complex **3**: C, 34.38; H, 3.13; N, 26.73. Found: C, 34.53; H, 3.59; N, 22.27%. (Repeated measurements showed the lower 'N' value, typical of compounds containing tetrazine). Λ_M/Ω^{-1} ($cm^2\,mol^{-1}$) in MeOH at 298 K: 220. IR, ν/cm^{-1}: 3429/3318 ($-NH_2$) and 1097/629 (ClO_4^-).

2.4. X-ray structure determination

Single crystals for L and **1** were grown by slow diffusion of a dichloromethane solution into *n*-hexane, followed by slow evaporation. For **2**, an acetonitrile solution was allowed to diffuse slowly into benzene, followed by slow evaporation. X-ray data of L and **1/2** were collected on a PC-controlled Enraf–Nonius CAD-4 (MACH-3) and on a Bruker SMART APEX CCD single crystal X-ray diffractometer, respectively. The structures were solved and refined by full-matrix least-squares techniques on F^2 using the SHELX-97 (SHELXTL program package) [11]. SADABS correction was applied for **1** and **2**. All the data were corrected for Lorentz, polarization and absorption effects.

3. Results and discussion

3.1. Synthesis and characterization of L, 1, 2 and 3

The formation of L was authenticated by its single crystal X-ray structure (Fig. 1). The asymmetric unit contains two molecules of L and two water molecules, all crystallographically independent. The crystal structure of L reveals that it crystallizes as a dimer which is held together via hydrogen bonding interactions involving L and H_2O molecules present in the lattice. Important crystallographic data are summarized in Table 1. Selected bond distances and bond angles for one molecule (molecule A) are listed in Table 2, as bond distances and angles of molecule B are close to those for molecule A. The bond parameters are comparable with standard values [2b,12].

In order to synthesize ruthenium complexes of L incorporating ancillary ligands of a differing electronic nature we chose metal precursors encompassing σ-donating acetylacetonate $\{Ru(acac)_2\}$ and π-acidic bipyridine $\{Ru(bpy)_2^{2+}\}$ and $\{Ru(bpy)^{3+}\}$ cores. The reaction of L and $Ru^{II}(acac)_2(CH_3CN)_2$ in ethanol, followed by chromatographic purification using a silica gel

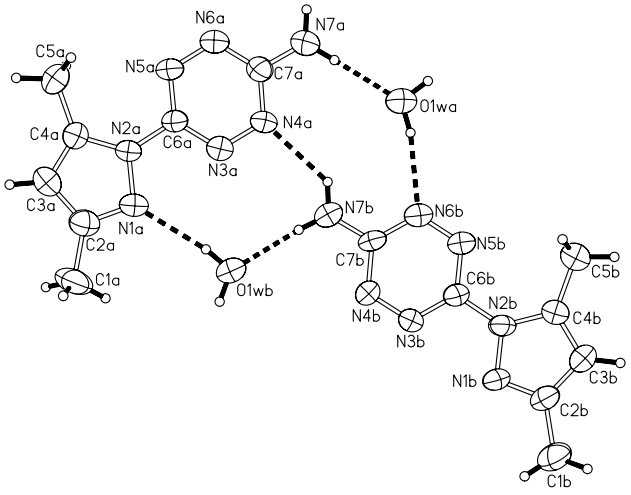


Fig. 1. Asymmetric unit of L.

column, yielded the blue diamagnetic complex $[Ru^{II}(acac)_2L]$ (**1**) (Scheme 2).

Similarly, the reactions of L with $[Ru^{II}(bpy)_2(EtOH)_2]^{2+}$ and $Ru^{III}(bpy)Cl_3$ in ethanol under atmospheric conditions, followed by chromatographic purification, afforded the 1:2 conducting diamagnetic complexes $[Ru^{II}(bpy)_2L](ClO_4)_2$ (**2**) and $[Ru^{II}(bpy)(L)_2](ClO_4)_2$ (**3**), respectively (Scheme 2). During the course of the reaction the +3 oxidation state of the metal ion in the precursor complex $Ru^{III}(bpy)Cl_3$ was reduced to the Ru^{II} state in **3**, even under atmospheric conditions. The replacement of electron rich Cl^- ligands by the strongly π-acidic L stabilizes the metal ion in the +2 state, reflected also by the high redox potential of **3** (see later).

All our attempts to bind a second metal complex fragment via the other tetrazine nitrogen donor center (N4) and the pendant NH_2 group or its anionic form failed altogether. On all occasions the monomeric species **1**–**3** were obtained.

The neutral compound **1** is soluble in non-polar solvents such as CH_2Cl_2 or $CHCl_3$ whereas **2** and **3** are soluble in polar solvents such as CH_3CN and CH_3OH. The NH_2 vibrations of coordinated L and the ClO_4^- vibrations appear near 3300 and 1100/630 cm^{-1}, respectively (see Section 2). The electrospray mass spectra of **1** in CH_2Cl_2 and of **2** and **3** in CH_3CN show maximum molecular ion peaks (*m*/*z*) at 492.23, 704.24 and 739.12, respectively (Fig. S1), corresponding to $[\mathbf{1}]^+$ (calculated molecular mass: 491.08), $\{[\mathbf{2}]\text{-}ClO_4\}^+$ (calculated molecular mass: 704.09) and $\{[\mathbf{3}]\text{-}ClO_4\}^+$ (calculated molecular mass: 739.10).

3.2. Crystal structures of the complexes

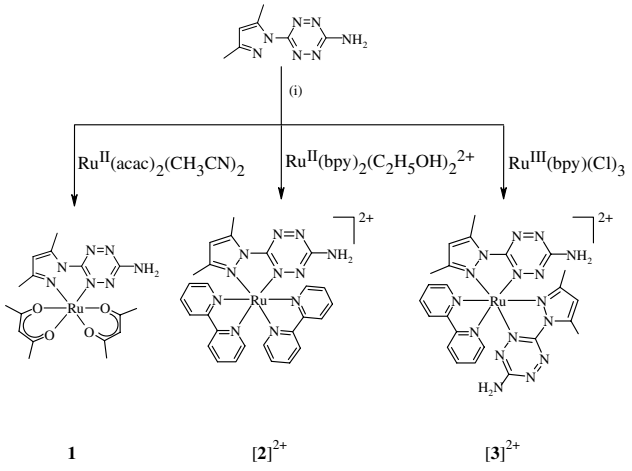
The formation of **1** and **2** was confirmed by single crystal X-ray structures (Figs. 2 and 3). Important crystallographic parameters are given in Table 1, selected bond distances and bond angles are listed in Table 2. The single crystal of **1** contains 0.5 equivalents of H_2O of crystallization. The RuO_4N_2 coordination sphere is slightly distorted octahedral as can be seen from the angles at the metal (Table 2). Although the bite angles involving the acac ligands in **1** are close to the ideal value at 90.95(8)° and 93.19(8)°, the bite angle involving L is only 80.11(9)°, reflecting the smaller chelate ring size. The average *trans* angle is 177.41(11)°. The Ru^{II}–O distances vary between 2.0312(19) and 2.048(2) Å. These are comparable to reported Ru^{II}–O(acac) distances [2d]. The Ru^{II}–N(1)(pyrazolyl) and Ru^{II}–N(4)(tetrazine) distances in **1** are 2.040(2) and 1.913(2) Å, respectively, showing the expected stronger bonding to the better π-accepting tetrazine ring. The Ru^{II}–N(pyrazolyl) distance in **1** is distinctly shorter than that found in

Table 1
Crystallographic data for $L \cdot H_2O$, $[Ru^{II}(acac)_2L] \cdot 0.5H_2O$ (**1**) and $[Ru^{II}(bpy)_2L](ClO_4)_2$ (**2**)

	L	**1**	**2**
Formula	$2(C_7H_9N_7) \cdot 2H_2O$	$RuC_{17}H_{24}N_7O_{4.50}$	$RuC_{27}H_{25}Cl_2N_{11}O_8$
M	418.46	499.50	803.55
Radiation	Mo Kα	Mo Kα	Mo Kα
T (K)	298(2)	293(2)	293(2)
Crystal symmetry	monoclinic	monoclinic	monoclinic
Space group	$P2_1/n$	$C2/c$	$P2_1/n$
a (Å)	8.791(1)	18.624(6)	14.6380(13)
b (Å)	16.992(2)	17.083(6)	15.5770(14)
c (Å)	13.516(1)	15.571(5)	14.8802(13)
β (°)	91.201(9)	123.557(4)	108.968(2)
V (Å^3)	2018.5(4)	4128(2)	3208.7(5)
Z	4	8	4
μ (mm^{-1})	0.102	0.801	0.723
D_{calc} (g cm^{-3})	1.377	1.607	1.663
R_1	0.062	0.0275	0.0680
wR_2	0.118	0.0678	0.1446
Goodness-of-fit	0.912	1.099	1.039

Table 2
Selected bond distances (Å) and bond angles (°) and their standard deviation for L, $[Ru^{II}(acac)_2L]\cdot 0.5H_2O$ (**1**) and $[Ru^{II}(bpy)_2L](ClO_4)_2$ (**2**)

L		**1**		**2**	
Bond distances (Å)					
N(1a)–N(2a)	1.384(4)	Ru–N(1)	2.040(2)	Ru(1)–N(1)	2.077(6)
N(2a)–C(6a)	1.398(5)	Ru–N(4)	1.913(2)	Ru(1)–N(4)	1.996(5)
N(3a)–C(6a)	1.336(5)	Ru–O(1)	2.0346(19)	Ru(1)–N(8)	2.060(6)
N(3a)–N(4a)	1.311(5)	Ru–O(2)	2.0419(18)	Ru(1)–N(9)	2.048(6)
N(4a)–C(7a)	1.348(5)	Ru–O(3)	2.048(2)	Ru(1)–N(10)	2.074(5)
N(6a)–C(7a)	1.342(6)	Ru–O(4)	2.0312(19)	Ru(1)–N(11)	2.055(6)
N(5a)–N(6a)	1.336(5)	N(3)–N(4)	1.345(3)	N(3)–N(4)	1.334(7)
N(5a)–C(6a)	1.319(5)	N(5)–N(6)	1.357(3)	N(5)–N(6)	1.302(8)
Bond angles (°)					
C(2a)–N(1a)–N(2a)	104.5(4)	N(4)–Ru–N(1)	80.11(9)	N(4)–Ru(1)–N(11)	97.8(2)
C(4a)–N(2a)–N(1a)	111.3(4)	N(4)–Ru–O(4)	89.95(8)	N(9)–Ru(1)–N(11)	94.9(2)
C(4a)–N(2a)–C(6a)	131.0(4)	N(1)–Ru–O(4)	92.42(9)	N(4)–Ru(1)–N(8)	87.1(2)
N(1a)–N(2a)–C(6a)	117.7(4)	N(4)–Ru–O(3)	178.61(8)	N(9)–Ru(1)–N(8)	79.3(2)
N(4a)–N(3a)–C(6a)	117.5(4)	N(1)–Ru–O(3)	98.79(8)	N(11)–Ru(1)–N(8)	172.7(2)
N(3a)–N(4a)–C(7a)	116.9(4)	O(4)–Ru–O(3)	90.95(8)	N(4)–Ru(1)–N(10)	173.3(2)
C(6a)–N(5a)–N(6a)	116.8(4)	N(4)–Ru–O(2)	95.82(8)	N(9)–Ru(1)–N(10)	91.8(2)
N(5a)–N(6a)–C(7a)	117.0(4)	O(4)–Ru–O(2)	86.24(8)	N(11)–Ru(1)–N(10)	78.2(2)
N(1a)–C(2a)–C(3a)	111.3(4)	O(3)–Ru–O(2)	85.29(8)	N(8)–Ru(1)–N(10)	97.4(2)
N(1a)–C(2a)–C(1a)	120.3(5)	N(4)–Ru–O(1)	92.40(8)	N(4)–Ru(1)–N(1)	78.4(2)
C(3a)–C(2a)–C(1a)	128.4(5)	N(1)–Ru–O(1)	88.30(8)	N(9)–Ru(1)–N(1)	170.7(2)
C(4a)–C(3a)–C(2a)	107.3(5)	N(1)–Ru–O(2)	175.73(8)	N(11)–Ru(1)–N(1)	91.4(2)
C(3a)–C(4a)–N(2a)	105.6(4)	O(4)–Ru–O(1)	177.62(7)	N(8)–Ru(1)–N(1)	94.9(2)
C(3a)–C(4a)–C(5a)	129.6(5)	O(3)–Ru–O(1)	86.70(8)	N(10)–Ru(1)–N(1)	96.2(2)
N(2a)–C(4a)–C(5a)	124.9(4)	O(2)–Ru–O(1)	93.19(8)	N(4)–Ru(1)–N(9)	93.9(2)



Scheme 2. (i) EtOH, Δ.

$[(bpy)_2Ru^{II}(\mu\text{-bpytz})Ru^{II}(bpy)_2]^{4+}$ at 2.114(16) Å [2b]. The Ru^{II}–N(tetrazine) distances found in dinuclear complexes such as $[(bpy)_2Ru^{II}(\mu\text{-bpytz})Ru^{II}(bpy)_2]^{4+}$ [2b] and $[(acac)_2Ru^{II}(\mu\text{-bptz})Ru^{II}(acac)_2]$ [2d] are 1.976(14)/1.993(11) and 1.946(6)/1.943(6) Å, respectively, which is appreciably longer than the 1.912(3) Å observed for **1**.

The RuN_6 center in **2** is more distorted octahedral. The distortion of the coordination sphere is primarily caused by the small bite angles, viz., 79.3(2)° (bpy), 78.2(2)° (bpy) and 78.5(2)° (L). The average *trans* angle is 172.23(2)°. The Ru^{II}–N(bpy) distances lie between 2.048(6) and 2.074(5) Å which is comparable with reported data of similar species [13]. The Ru^{II}–N(1)(pyrazolyl) and Ru^{II}–N(4)(tetrazine) distances are at 2.077(6) and 1.996(5) Å, respectively. Thus, the back bonding

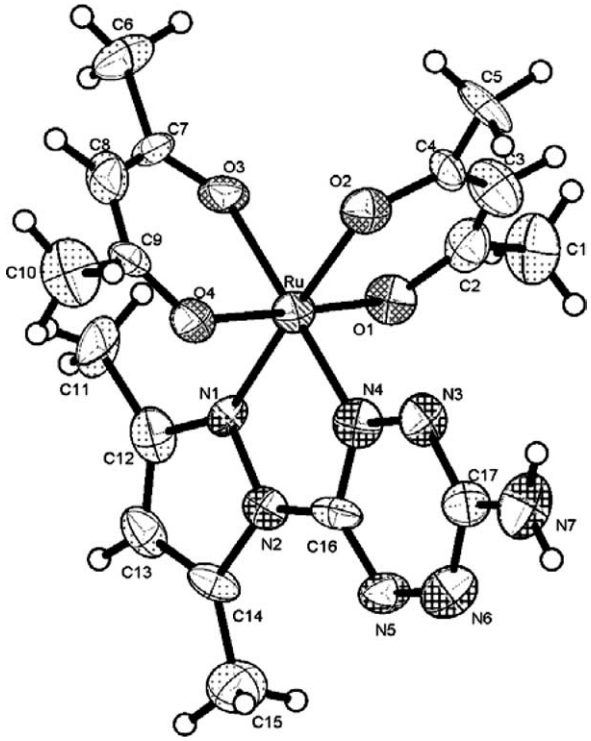


Fig. 2. ORTEP diagram of the complex $[Ru^{II}(acac)_2L]\cdot 0.5H_2O$ (**1**). Ellipsoids are drawn at 50% probability. Water of crystallization has been removed for clarity.

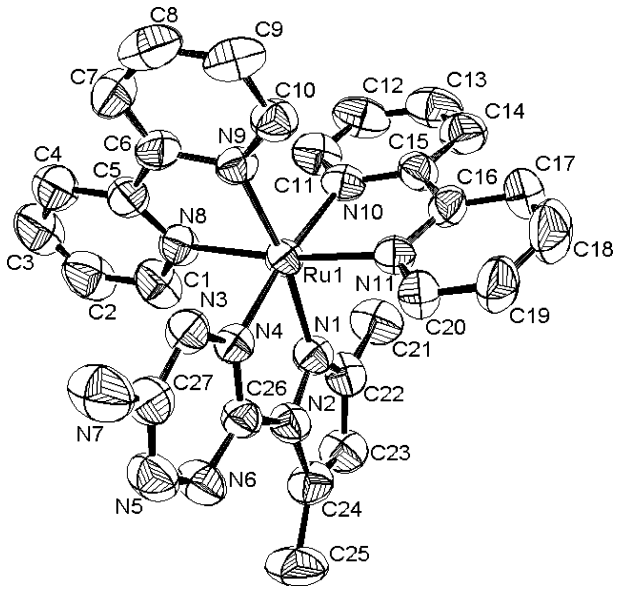


Fig. 3. ORTEP diagram of the complex cation $[Ru^{II}(bpy)_2L]^{2+}$ of (**2**). Ellipsoids are drawn at 50% probability.

effect $d\pi(Ru^{II}) \rightarrow \pi^*$(tetrazine) is also reflected in the structure of **2**. The presence of π-acidic bpy ancillary ligands competing with L in **2** is held responsible for the observed Ru–N bond lengthening, leading to appreciable decreasing $Ru^{II} \rightarrow \pi^*$ back donation on moving from **1** to **2**.

The strong $Ru^{II} \rightarrow \pi^*$(tetrazine) back bonding in **1** is also reflected in the appreciable lengthening of the tetrazine bond lengths involving the coordinated nitrogen donor center [N(4)], C(16)–N(4) 1.377(7) and N(3)–N(4) 1.345(3) Å, as compared to those of the free ligand (L), C(6)–N(3), 1.336(5) and N(3)–N(4), 1.311(5) Å. However, in the case of the corresponding bipyridine complex (**2**) only a slight increase in bond distances has been observed [C(26)–N(4), 1.340(8) and N(3)–N(4), 1.334(7) Å], which is certainly due to the existence of much weaker $Ru^{II} \rightarrow \pi^*$(tetrazine) back bonding in **2** compared to **1** as stated above.

3.3. ^1H NMR spectra

^1H NMR spectra of the complexes **1**, **2** and **3** were recorded in $CDCl_3$ (**1**) and $(CD_3)_2SO$. The spectra are shown in Fig. 4. The unsymmetrical nature of L makes the protons associated with the chelate rings magnetically different. Therefore, the ^1H NMR spectrum of **1** displays three distinct singlets corresponding to two acac CH protons (δ, 5.57 and 5.20 ppm) and one CH proton associated with L (δ, 5.92 ppm) (Fig. 4(a)). The NH_2 protons of L appear as a slightly broad singlet at 4.92 ppm. In addition, six singlets are observable in the upfield region at 2.85, 2.24, 2.18, 2.16, 2.11 and 1.92 ppm, corresponding to four and two CH_3 groups associated with acac and L, respectively.

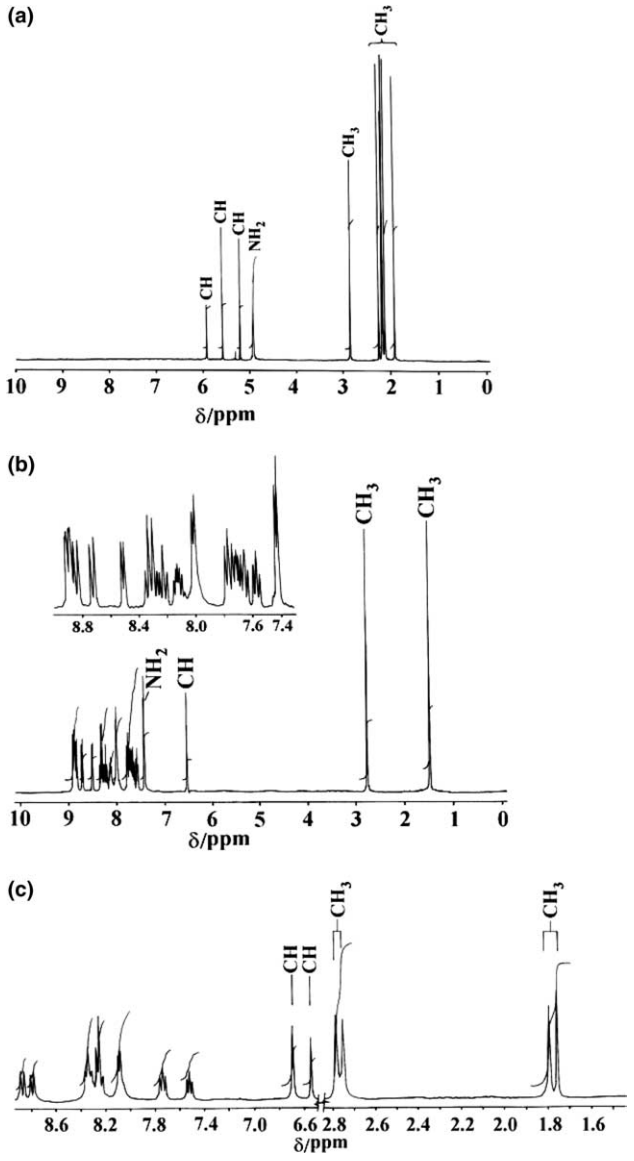


Fig. 4. ^1H NMR spectra of (a) $[Ru^{II}(acac)_2L]$ (**1**) in $CDCl_3$, (b) $[Ru^{II}(bpy)_2L](ClO_4)_2$ (**2**) in $(CD_3)_2SO$, inset shows the expanded aromatic region (δ, 7.4–9.0 ppm), (c) $[Ru^{II}(bpy)(L)_2](ClO_4)_2$ (**3**) in $(CD_3)_2SO$ (solvent peaks are substracted for clarity).

Similarly, the four pyridine rings of two bpy ligands in **2** are inequivalent. Complex **2** should thus exhibit 16 non-equivalent ''aromatic'' proton signals. Since the electronic environment of many such hydrogen atoms is similar, their signals may appear in a narrow chemical shift range. In fact, the ''aromatic region'' of the spectrum of **2** is complicated due to the overlapping of several signals, which has essentially precluded the identification of individual resonances (Fig. 4(b)). However, a direct comparison of the intensity of these signals with that of the clearly observable CH (6.53 ppm) and CH_3 (2.76 and 1.47 ppm) protons of coordinated L in the upfield region revealed the presence of the expected 16 aromatic protons. The NH_2 protons of L appear at 7.4 ppm.

In **3** two distinct CH signals at 6.69 and 6.54 ppm and four CH_3 signals at 2.77, 2.74, 1.79 and 1.47 ppm, corresponding to two L, were observed (Fig. 4(c)). The eight protons of bpy and the NH_2 protons of L appear between 7.4 and 9.0 ppm as partially overlapping signals.

3.4. Metal oxidation

Compounds **1**–**3** exhibit one quasi-reversible Ru^{III}/Ru^{II} couple each at $E_{1/2}$ = 0.28, 1.34 and 1.50 V versus SCE, respectively (Table 3, Fig. 5). The data reveal that a redox potential shift of >1.0 V has taken place on switching from the acac ancillary ligands in $[Ru(acac)_2(L)]$ (**1**) to the bpy co-ligands in $[Ru(bpy)_2(\mathbf{L})](ClO_4)_2$ (**2**). The presence of electron-rich acac ligands in **1** clearly stabilizes the Ru^{III} state [14].

The combination of two bpy ligands and one L ligand around the Ru^{II} center in **2** shifted the Ru^{III}/Ru^{II} couple to 1.34 V which is even higher than that of $[Ru^{II}(bpy)_3]^{2+}$ ($E_{1/2}$ = 1.29 V versus SCE) [15]. This implies that the donor strength of L is lower than that of bpy. It may be noted that the first Ru^{III}/Ru^{II} couple of the related diruthenium complex $[(bpy)_2Ru(\mu\text{-bpytz})Ru(bpy)_2]^{4+}$ appears at 1.25 V [2b].

On the other hand, the replacement of two bpy ligands from $[Ru^{II}(bpy)_3]^{2+}$ by two ligands L in **3** increases the $Ru^{II} \rightarrow Ru^{III}$ oxidation potential further to 1.50 V. Thus, successive exchange of bpy by L from $Ru(bpy)_3^{2+}$ via $Ru(bpy)_2(L)^{2+}$ to $Ru(bpy)(L)_2^{2+}$ enhances the stability of the Ru^{II} state.

3.5. Ligand reduction

Complex **1** shows one reversible reduction at −1.33 V versus SCE. Since tetrazines are known to undergo facile reduction at relatively low potentials due to the low lying π* orbital [1–3], the observed reduction is therefore considered to involve the tetrazine function of coordinated L.

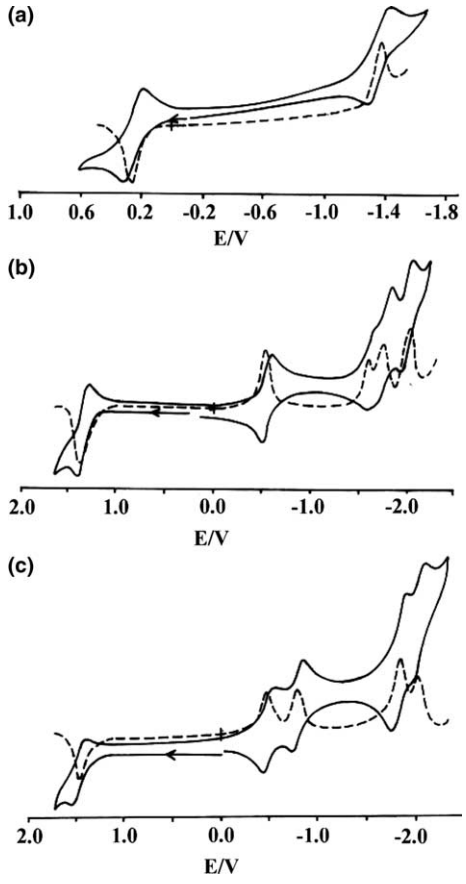


Fig. 5. Cyclic (—) and differential pulse (------) voltammograms of (a) $[Ru^{II}(acac)_2L]$ (**1**) in CH_2Cl_2, (b) $[Ru^{II}(bpy)_2L](ClO_4)_2$ (**2**) and (c) $[Ru^{II}(bpy)(L)_2](ClO_4)_2$ (**3**) in CH_3CN at 298 K.

Table 3
Electrochemical,[a] electronic spectra[a] and spectroelectrochemical correlation data[b]

Compound	Ru^{III}–Ru^{II} couple, E^0_{298}/V (ΔE_p, mV)	Ligand reductions, E^0_{298}/V (ΔE_p, mV)		$\Delta E_{1/2}$[c] (V)	UV–Vis, λ/nm (ε/M^{-1} cm^{-1})	ν(MLCT) (cm^{-1})	
		L-based	bpy-Based			Observed	Calculated[d]
1	0.28(110)	−1.33(110)		1.61	600 (13 650), 366 (9700), 268 (71 250), 218 (30 100)	16 666	15 984
2	1.34(80)	−0.55(100)		1.89	538 (8000), 400 (4800),	18 587	18 242
			−1.55(60)	2.89	278 (52 400), 214 (23 000)	25 000	26 307
			−1.75(100)				
			−1.98(60)				
3	1.50(70)	−0.47(100)		1.97	540 (10 380), 480 (7230),	18 518	18 888
		−0.78(100)		2.28	276 (47 260), 206 (56 400)	20 833	21 388
			−1.80(60)				
			−2.02(60)				

[a] **1** in CH_2Cl_2 and **2**/**3** in CH_3CN.
[b] As stated in the text.
[c] Calculated by Eq. (2) in the text.
[d] Calculated by Eq. (1) in the text.

Similarly, the reduction of the tetrazine in **2** appears at −0.55 V. This substantial increase in the reduction potential by 0.78 V on moving from strongly σ-donating acac as a co-ligand in **1** to π-acidic bpy in **2** parallels to some extent the stabilization of the Ru^{II} state in **2** as compared to **1**.

In addition to the tetrazine-based reduction of L, **2** also shows three more bpy-based quasi-reversible one-electron reduction processes in the range from −1.55 to −1.98 V. Each bpy can accommodate two electrons, therefore, a total of four such reduction waves is expected. Three such waves are detected within the experimental potential limit (−2.0 V versus SCE). The potentials at which the bpy reductions of **2** are observed is consistent with the reduction range of $Ru(bpy)_3^{2+}$ (−1.3 to −1.8 V versus SCE) [16].

Compound **3** contains two tetrazine units from two L ligands, therefore the expected two tetrazine-based one-electron reduction waves were observed at −0.47 and −0.78 V. Two bpy-based reductions appear at −1.80 and −2.02 V. The first tetrazine reduction potential in **3** is slightly less negative relative to **2**, which correlates with the enhanced stabilization of the Ru^{II} state in **3**.

3.6. Spectral properties

Electronic absorption spectra of **1**, **2** and **3** were recorded in CH_2Cl_2 (**1**) and CH_3CN. The spectral data are given in Table 3 and the spectra are shown in Fig. 6. The complexes exhibit strong ligand-based π − π* transitions in the UV region. In the visible region, **1** and **2** display two well separated broad bands at 600/366 and 538/400 nm, respectively, whereas **3** exhibits one main transition at 540 nm with a high-energy shoulder at 480 nm. The lowest energy bands for all the three complexes are attributed to MLCT transitions $d\pi(Ru^{II}) \rightarrow \pi_1^*L$ (where π_1^*L is essentially dominated by the tetrazine moiety) [2]. The higher energy transitions are assigned as $d\pi(Ru^{II}) \rightarrow \pi^*$ (acac), $d\pi(Ru^{II}) \rightarrow \pi^*$(bpy) and $d\pi(Ru^{II}) \rightarrow \pi^*$ L for **1**, **2** and **3**, respectively. This is based on the observation that the reduction of L takes place at a much lower potential than that of bpy. The above assignments find justification through the spectro-electrochemical correlations stated below.

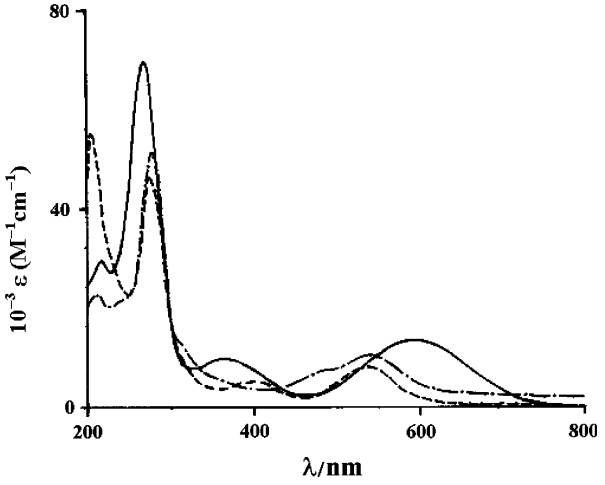


Fig. 6. Electronic spectra of (a) $[Ru^{II}(acac)_2L]$ (**1**) (——), (b) $[Ru^{II}(bpy)_2L](ClO_4)_2$ (**2**) (------) and (c) $[Ru^{II}(bpy)(L)_2](ClO_4)_2$ (**3**) (-·-·-·-) in CH_3CN.

3.7. Spectro-electrochemical correlation

The energies of the MLCT transitions at the band maximum can be reproduced with the help of empirical Eqs. (1) and (2) [17]:

$$\nu(\text{MLCT}) = 8065(\Delta E_{1/2}) + 3000\ \text{cm}^{-1}, \quad (1)$$

$$\Delta E_{1/2} = E_{1/2}(Ru^{III}/Ru^{II}) - E_{1/2}(L). \quad (2)$$

Here $E_{1/2}(Ru^{III}/Ru^{II})$ is the potential of the reversible Ru^{III}/Ru^{II} couple, $E_{1/2}(L)$ is that of the first ligand-based reduction and ν(MLCT) is the wave number of the charge transfer band in cm^{-1}. The factor 8065 is used to convert the potential difference ΔE from V into cm^{-1} and the term 3000 cm^{-1} is of empirical origin (reorganization energy of polypyridine ruthenium MLCT transitions). The calculated and experimentally observed MLCT energies are given in Table 3. Using Eqs. (1) and (2) and $\Delta E_{1/2}$ values of 1.61, 1.89/2.89 and 1.97/2.28, for **1**, **2** and **3**, respectively, the calculated ν(MLCT) values agree rather well with the experimental values (Table 3).

3.8. EPR spectra

The in situ generated species $\mathbf{1}^+$ in CH_2Cl_2 at 110 K exhibits a rhombic EPR signal ($g_1 = 2.260$, $g_2 = 2.170$, $g_3 = 1.880$, Fig. 7(a)), typical of low-spin Ru^{III}. The g anisotropy $g_1 - g_3 = 0.380$ and the average g factor of $\langle g \rangle = 2.11$), derived from $\langle g \rangle = [1/3(g_1^2 + g_2^2 + g_3^2)]^{1/2}$ indicate a slightly distorted octahedral arrangement around the ruthenium center [18] as consistent with the molecular structure of **1**. The electrochemically generated $\mathbf{2}^+$ in CH_3CN failed to show any EPR signals at 110 K, however, at 4 K it displays a poorly resolved rhombic type EPR signal with $g_1 = 2.50$, $g_2 = 2.360$ and an undetectable g_3 component (probably < 1.8). On the other hand, the in situ generated $\mathbf{3}^+$ did not show any EPR response even at 4 K, which signifies rapid relaxation due to excited paramagnetic states lying close to the doublet ground state.

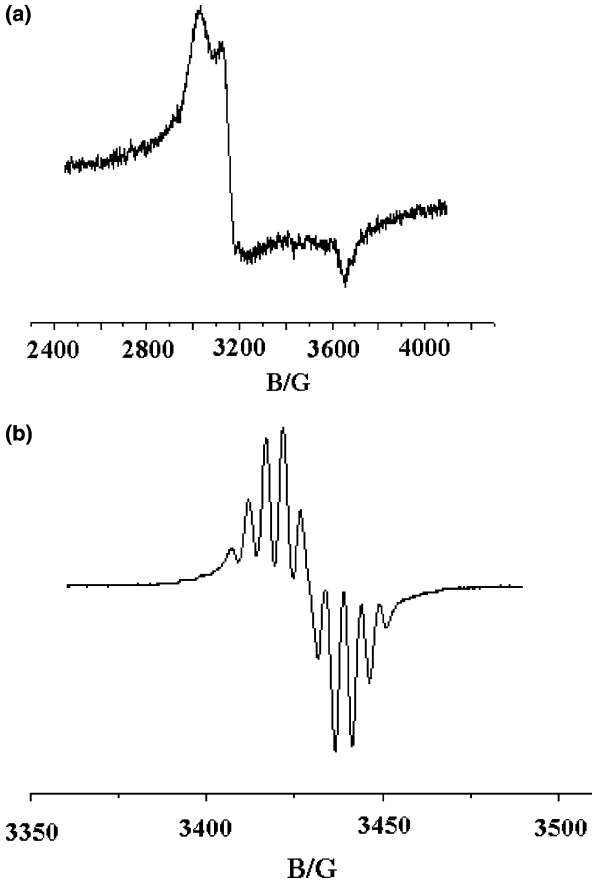


Fig. 7. EPR spectra of (a) $\mathbf{1}^+$ in CH_2Cl_2 at 100 K and (b) $\mathbf{1}^-$ in CH_2Cl_2 at 300 K.

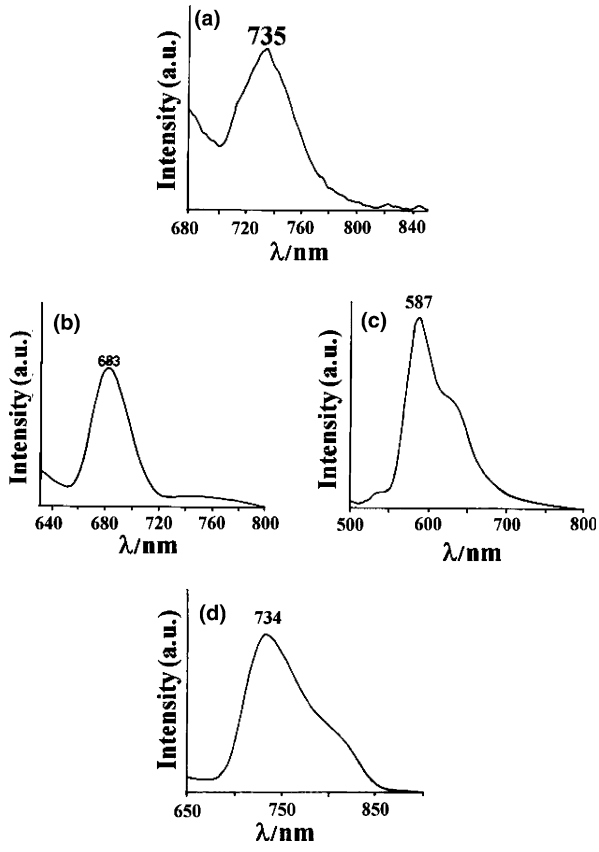


Fig. 8. Emission spectra of (a) **1** ($\lambda_{excitation}$, 592 nm), (b) **2** ($\lambda_{excitation}$, 530 nm), (c) **2** ($\lambda_{excitation}$, 413 nm) and (d) **3** ($\lambda_{excitation}$, 524 nm) in ethanol–methanol (4:1) glass at 77 K.

In situ generated reduced species $\mathbf{1}^-$ (in CH_2Cl_2), $\mathbf{2}^-$ and $\mathbf{3}^-$ (in CH_3CN) exhibit multiple line EPR spectra at 300 K due to hyperfine coupling from four different ^{14}N atoms of the tetrazine ring of L, the signals are centered at $g = 1.9962$, 1.9991 and 1.9984, respectively (Fig. 7(b)) [2,19].

3.9. Emission spectra

Emission properties of the complexes were studied in EtOH–MeOH (4:1) at 77 K. The spectra are shown in Fig. 8. Excitations of the complexes **1**, **2** and **3** at 592, 530/413 and 534 nm, respectively, result in emissions with maxima at 735 nm (quantum yield, $\Phi = 0.65 \times 10^{-2}$), 682/586 nm (quantum yield, $\Phi = 1.8 \times 10^{-1}$, 1.1×10^{-1}) and 734 nm (quantum yield, $\Phi = 1.15 \times 10^{-2}$), respectively, with vibrational structures characteristic of emissions from a ^{3}MLCT excited state [20]. The origin of the emissions was further confirmed by the excitation spectra of the same solutions in each case. The observed moderately strong emissions for **1** and **3** presumably involve primarily L. On the other hand, **2** appears to exhibit strong emissions from both the bpy and L-based MLCT transitions.

4. Conclusion

Although tetrazine based ligands are quite popular in developing polynuclear complexes for varying perspectives, rather rare mononuclear complexes **1**, **2** and **3** have been synthesized using hitherto unexplored tetrazine derived ligand, 3-amino-6-(3,5-dimethylpyrazol-1-yl)-1,2,4,5-tetrazine (L) in combination with σ-donating acetylacetonate and π-accepting bipyridine co-ligands. Structural studies reveal that the presence of electron-rich acetylacetonate co-ligands attributes to a strong $Ru^{II} \rightarrow \pi^*$ (tetrazine) back bonding in **1** which is much stronger than that in the corresponding mononuclear bipyridine derivative (**2**) as well as that in the analogous dinuclear complexes $[(bpy)_2Ru^{II}(\mu\text{-bpytz})Ru^{II}(bpy)_2]^{4+}$ and $[(acac)_2Ru^{II}(\mu\text{-bptz})Ru^{II}(acac)_2]$.

Acknowledgements

Financial support received from the Council of Scientific and Industrial Research, New Delhi (India), the DAAD, the DFG and the FCI (Germany) is gratefully acknowledged. We are grateful to Professor Seik

Weng Ng, Institute of Postgraduate Studies, University of Malaya, Kuala Lumpur, Malaysia for solving the crystal structure of L. Special acknowledgement is made to the Sophisticated Analytical Instrument Facility, Indian Institute of Technology, Bombay, for providing the NMR facility. X-ray structural studies of L were carried out at the National Single Crystal Diffractometer Facility, Indian Institute of Technology, Bombay.

Appendix A. Supplementary data

Crystallographic data for the structural analysis have been deposited with the Cambridge Structural Database, CCDC Nos. 242646, 242644 and 242645, for compounds L, **1** and **2**, respectively. Supplementary data are available from CCDC, 12 Union Road Cambridge CB2 1EZ, UK (fax: +44 1223 336033; E-mail: deposit@ccdc.cam.ac.uk or http://www.ccdc.cam.ac.uk) on request, quoting the deposition numbers. Electrospray mass spectral data of **1** (Fig. S1a), **2** (Fig. S1b) and **3** (Fig. S1c). Supplementary data associated with this article can be found, in the online version at doi:10.1016/j.poly.2004.11.019.

References

[1] W. Kaim, Coord. Chem. Rev. 230 (2002) 127.
[2] (a) B. Sarkar, W. Kaim, A. Klein, B. Schwederski, J. Fiedler, C. Duboc-Toia, G.K. Lahiri, Inorg. Chem. 42 (2003) 6172;
(b) B. Sarkar, R.H. Laye, B. Mondal, S. Chakraborty, R.L. Paul, J.C. Jeffery, V.G. Puranik, M.D. Ward, G.K. Lahiri, J. Chem. Soc., Dalton Trans. (2002) 2097;
(c) A. Singh, N. Singh, D.S. Pandey, J. Organomet. Chem. 642 (2002) 48;
(d) S. Chellamma, M. Lieberman, Inorg. Chem. 40 (2001) 3177;
(e) M. Glockle, W. Kaim, J. Fiedler, Z. Anorg. Allg. Chem. 627 (2001) 1141;
(f) S. Roche, L.J. Yellowlees, J.A. Thomas, Chem. Commun. (1998) 1429;
(g) V. Kasack, W. Kaim, H. Binder, J. Jordanov, E. Roth, Inorg. Chem. 34 (1995) 1924;
(h) J. Poppe, M. Moscherosch, W. Kaim, Inorg. Chem. 32 (1993) 2640;
(i) W. Kaim, V. Kasack, Inorg. Chem. 29 (1990) 4696;
(j) M.H. Zaghal, H.A. Qaseer, Inorg. Chim. Acta 163 (1989) 193;
(k) S. Ernst, V. Kasack, W. Kaim, Inorg. Chem. 27 (1988) 1146.
[3] (a) D. Brown, S. Muranjan, Y. Jang, R. Thummel, Org. Lett. 4 (2002) 1253;
(b) M. Chandra, A.N. Sahay, D.S. Pandey, M.C. Puerta, P. Valerga, J. Organomet. Chem. 648 (2002) 39;
(c) J. Poppe, W. Kaim, A. Ben Altabef, N.E. Katz, J. Chem. Soc., Perkin Trans. (1993) 2105 (1972–1999);
(d) J.E.B. Johnson, C. De Groff, R.R. Ruminski, Inorg. Chim. Acta 187 (1991) 73;
(e) T.S. Akasheh, D. Marji, Z.M. Al-Ahmed, Inorg. Chim. Acta 141 (1988) 125;
(f) T.S. Akasheh, Z.M. El-Ahmed, Chem. Phys. Lett. 152 (1988) 414.
[4] C. Glidewell, P. Lightfoot, B.J.L. Royles, D.M. Smith, J. Chem. Soc., Perkin Trans. (1997) 1167.
[5] T. Kobayashi, Y. Nishina, K. Shimizu, G.P. Satô, Chem. Lett. (1988) 1137.
[6] B.P. Sullivan, D.J. Salmon, T.J. Meyer, Inorg. Chem. 17 (1978) 3334.
[7] S. Anderson, K.R. Seddon, J. Chem. Res. (S) (1979) 74.
[8] D.T. Sawyer, A. Sobkowiak, J.L. Roberts Jr., Electrochemistry for Chemists, Wiley, New York, 1995.
[9] W. Kaim, S. Ernst, V. Kasack, J. Am. Chem. Soc. 112 (1990) 173.
[10] (a) E.F. Godefroi, E.L. Little, J. Org. Chem. 21 (1956) 1163;
(b) P. Chen, R. Duesing, D.K. Graff, T.J. Meyer, J. Phys. Chem. 95 (1991) 5850.
[11] G.M. Sheldrick, SHELX-97 Program for Crystal Structure Solution and Refinement, University of Göttingen, Göttingen, Germany, 1997.
[12] N. Chanda, B. Mondal, V.G. Puranik, G.K. Lahiri, Polyhedron 21 (2002) 2033.
[13] (a) S. Chakravorty, R.H. Laye, P. Munshi, R.L. Paul, M.D. Ward, G.K. Lahiri, J. Chem. Soc., Dalton Trans. (2002) 2348;
(b) S. Chakraborty, R.H. Laye, R.L. Paul, R.G. Gonnade, V.G. Puranik, M.D. Ward, G.K. Lahiri, J. Chem. Soc., Dalton Trans. (2002) 1172;
(c) S. Chakraborty, M.G. Walawalkar, G.K. Lahiri., J. Chem. Soc., Dalton Trans. (2000) 2875.
[14] (a) S. Patra, B. Sarkar, S.M. Mobin, W. Kaim, G.K. Lahiri, Inorg. Chem. 42 (2003) 6469;
(b) S. Patra, T.A. Miller, B. Sarkar, M. Niemeyer, M.D. Ward, G.K. Lahiri, Inorg. Chem. 42 (2003) 4707;
(c) S. Patra, B. Mondal, B. Sarkar, M. Niemeyer, G.K. Lahiri, Inorg. Chem. 42 (2003) 1322.
[15] (a) A. Ceulemansm, L.G. Vanquickenborne, J. Am. Chem. Soc. 103 (1981) 2238;
(b) M.J. Root, E. Deutsch, Inorg. Chem. 24 (1985) 1464;
(c) R. Alsfasser, R.V. Eldik, Inorg. Chem. 35 (1996) 628;
(d) B.J. Coe, T.J. Meyer, P.C. White, Inorg. Chem. 34 (1995) 593.
[16] (a) S. Bhattacharya, Polyhedron 12 (1993) 235;
(b) C.M. Elliott, J. Chem. Soc., Chem. Commun. (1980) 261;
(c) N.E. Tokel-Takvoryan, J. Am. Chem. Soc. 95 (1973) 6583;
(d) D.E. Morris, K.W. Hanck, M.K. DeArmond, Inorg. Chem. 24 (1985) 977.
[17] (a) B.K. Ghosh, A. Chakravorty, Coord. Chem. Rev. 95 (1989) 239;
(b) B.K. Santra, G.K. Lahiri, J. Chem. Soc., Dalton Trans. (1997) 129;
(c) E.S. Dosworth, A.B.P. Lever, Chem. Phys. Lett. 124 (1986) 152.
[18] (a) S. Patra, B. Sarkar, S. Ghumaan, J. Fiedler, W. Kaim, G.K. Lahiri, J. Chem. Soc., Dalton Trans. (2004) 754;
(b) N. Chanda, B. Sarkar, J. Fiedler, W. Kaim, G.K. Lahiri, J. Chem. Soc., Dalton Trans. (2003) 3550;
(c) S. Kar, T.A. Miller, B. Sarkar, B. Pradhan, T. Kundu, M.D. Ward, G.K. Lahiri, J. Chem. Soc., Dalton Trans. (2003) 2591;
(d) B.K. Santra, M. Menon, C.K. Pal, G.K. Lahiri, J. Chem. Soc., Dalton Trans. (1997) 1387.
[19] (a) W. Kaim, S. Kohlmann, Inorg. Chem. 25 (1986) 3442;
(b) W. Kaim, S. Ernst, S. Kohlmann, P. Welkering, Chem. Phys. Lett. 118 (1985) 431.
[20] A. Juris, V. Balzani, F Barigelletti, S. Campagna, P. Belser, A. von Zelewski, Coord. Chem. Rev. 84 (1988) 85.

Available online at www.sciencedirect.com
SCIENCE DIRECT®
Polyhedron 24 (2005) 343–350
POLYHEDRON
www.elsevier.com/locate/poly

Synthesis, crystal structure, and magnetic properties of binuclear Mn^{III}-azido and 1D polymeric Mn^{II}-$\mu_{1,3}$-thiocyanato novel species based on a neutral hexadentate Schiff base

Soma Deoghoria [a], Sujit K. Bera [a], Brian Moulton [b], Michael J. Zaworotko [b], Jean-Pierre Tuchagues [c], Golam Mostafa [d], Tian-Huey Lu [d], Swapan K. Chandra [a,*]

[a] *Department of Chemistry, The University of Burdwan, Burdwan 713104, India*
[b] *Department of Chemistry, University of South Florida, 4202 E. Fowler Avenue, SCA 400, Tampa, FL 33620, USA*
[c] *Laboratoire de Chimie de Coordination du CNRS, UPR 8241, 205 route de Narbonne, 31077 Toulouse Cedex, France*
[d] *Physics Department, National Tsing Hua University, Hsinchu 300, Taiwan, ROC*

Received 18 October 2004; accepted 30 November 2004
Available online 29 December 2004

Abstract

A binuclear manganese(III) complex $[Mn_2(L^1)(N_3)_6]$ (**2**) and an unprecedented 1D chain of manganese(II) binuclear units bridged by two end-to-end thiocyanato anions $\{[Mn_2^{II}(L^1)(NCS)_4]\cdot 2CH_3CN\}_n$ (**3** · $2CH_3CN$) have been prepared from *N*-(1-pyridin-2-ylbenzylidene)-*N*′-[2-({2-[(1-pyridin-2-ylbenzylidene)amino]ethyl}amino)ethyl]ethane-1,2-diamine (L), manganese(II) salts and azide/thiocyanate anions in air. L^1, *N*-(1-pyridin-2-ylbenzylidene)-*N*-[2-(4-{2-[(1-pyridin-2-ylbenzylidene)amino]ethyl}piperazin-1-yl)ethyl]amine, results from an alkylating cyclization of the flexible hexadentate Schiff base L occurring along the course of the complexation reactions. Both complexes have been characterized by single crystal X-ray diffraction studies. The Mn centres of complexes **2** and **3** are in distorted octahedral (**2**: $Mn^{III}N_6$, **3**: $Mn^{II}N_5S$) coordination environments with intramolecular Mn···Mn distance (**2**: 6.473(2) Å, **3**: 6.437(1) Å) consistent with the absence of intramolecular magnetic interactions. Compound **3**, exhibits weak intermolecular antiferromagnetic interactions ($J = -1.5$ cm^{-1}) between pairs of Mn^{II} ions bridged via two $\mu_{1,3}$-NCS.
© 2004 Elsevier Ltd. All rights reserved.

Keywords: Schiff bases; Alkylating cyclization; Pseudo-halide bridges; Manganese polynuclear complexes; 1D Chains; Magnetic exchange interactions

1. Introduction

Coordination chemistry of manganese compounds is an area of considerable interest [1]. These complexes are significant not only for their redox active role in several biochemical processes, but also for the diversity of their magnetic properties [2–4]. Bridging ligands play an important role in the magnetic exchange pathways between paramagnetic centres: pseudo-halides (N_3^-, NCS^-, NCO^-) have been well documented for their numerous bonding abilities leading to various species [5]. End-on ($\mu_{1,1}$-N_3/NCS/NCO) [6] and end-to-end ($\mu_{1,3}$-N_3/NCS/NCO) [7] bridged complexes are known to mediate ferromagnetic [8] and antiferromagnetic [9] exchange interactions, respectively. The use of polydentate ligands, especially polynucleating ones, is an efficient way for assembling metal centres in close proximity, thus ensuring electronic communication. Coordination compounds including both polydentate ligands and suitable bridging anions such as

* Corresponding author. Tel.: +91 342 2557814; fax: +91 342 2557938.
E-mail address: dr_swapan@sify.com (S.K. Chandra).

0277-5387/$ - see front matter © 2004 Elsevier Ltd. All rights reserved.
doi:10.1016/j.poly.2004.11.014

pseudo-halide ions capable of propagating magnetic interactions between paramagnetic centres play an important role in the area of molecular magnetism [3–10].

We report here on the unusual behaviour of a flexible hexadentate ligand, *N*-(1-pyridin-2-ylbenzylidene)-*N*′-[2-({2-[(1-pyridin-2-ylbenzylidene)amino]ethyl}amino)ethyl] ethane-1,2-diamine, (L, Scheme 1) resulting from the bis-condensation reaction of 2-benzoylpyridine and triethylenetetramine. While $[Mn^{II}L](ClO_4)_2$ (**1**) resulted from the reaction of L with manganese(II) perchlorate, the binuclear complex $[Mn_2^{III}(L^1)(N_3)_6]$ (**2**) and the 1D polymer $\{[Mn_2^{II}(L^1)(NCS)_4]\cdot 2CH_3CN\}_n$ (**3** · $2CH_3CN$) resulted from the reaction of L and manganese(II) salts, in the presence of sodium azide (**2**) or ammonium thiocyanate (**3**), respectively. L^1, *N*-(1-pyridin-2-ylbenzylidene)-*N*-[2-(4-{2-[(1-pyridin-2-ylbenzylidene)amino]-ethyl}piperazin-1-yl)ethyl]amine, results from an alkylating cyclization of L. The synthesis, characterization including X-ray structure, and magnetic properties of the novel compounds **2** and **3** are described in this report.

2. Experimental

2.1. Materials

Triethylenetetramine, 2-benzoylpyridine, sodium azide and ammonium thiocyanate were purchased from Lancaster and used as received. All other solvents and chemicals were of analytical grade. The hexadentate ligand (L) was prepared as reported previously and gave satisfactory elemental analysis [11].

2.2. Synthesis of complexes

2.2.1. $[Mn^{II}L](ClO_4)_2$ (*1*)

A methanolic solution (4 cm^3) of the L ligand (0.239 g, 0.5 mmol) was added dropwise to a methanolic solution (4 cm^3) of $Mn(ClO_4)_2\cdot 6H_2O$ (0.181 g, 0.5 mmol) with constant stirring for 1 h at room temperature. The orange-red compound of composition $[MnL](ClO_4)_2$ (**1**) was filtered off, washed with methanol and dried under vacuum. Yield: 0.220 g, ~60%. *Anal.* Calc. for $C_{30}H_{32}N_6O_8Cl_2Mn$: C, 49.33; H, 4.42; N, 11.51, Mn, 7.52. Found : C, 49.28; H, 4.53; N, 11.39; Mn, 7.37%.

2.2.2. $[Mn_2^{III}(L^1)(N_3)_6]$ (*2*)

To a methanolic solution (5 cm^3) of $MnCl_2\cdot 4H_2O$ (0.396 g, 2.0 mmol) was added 0.477 g (1.0 mmol) of the L ligand in methanol (15 cm^3) over a period of 15 min. To the resulting deep orange solution, an aqueous solution of sodium azide (0.260 g, 6.0 mmol, 8 cm^3 H_2O) was added slowly. The solution was then filtered and the filtrate was left to stand. Within 2–3 days of slow evaporation a black compound was obtained. This resulting compound was dissolved in dichloromethane (~12 cm^3) and layered with hexane (~36 cm^3). After about 5 days black prismatic crystals suitable for X-ray analysis were obtained. Yield: 0.225 g, ~27%. *Anal.* Calc. for $C_{32}H_{34}N_{24}Mn_2$: C, 44.41; H, 3.96; N, 38.88, Mn, 12.70. Found: C, 44.48; H, 3.82; N, 38.76; Mn, 12.62%.

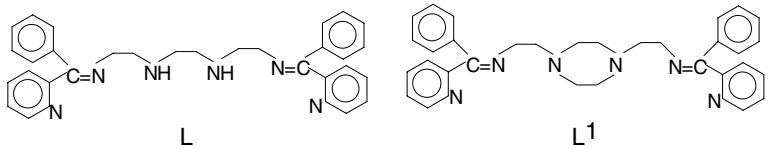
2.2.3. $\{[Mn_2^{II}(L^1)(NCS)_4]\cdot 2CH_3CN\}_n$ ($3\cdot 2CH_3CN$)

Compound **3** was synthesized by slow addition of an acetonitrile solution (12 cm^3) containing the L ligand (0.239 g, 0.5 mmol) to an acetonitrile solution (16 cm^3) of $Mn(ClO_4)_2\cdot 6H_2O$ (0.362 g, 1.0 mmol) with constant stirring for 30 min. To the resulting solution, an aqueous solution of ammonium thiocyanate (0.152 g, 2.0 mmol, 12 cm^3 H_2O) was added slowly with constant stirring for 15 min. The resulting solution was left to stand at room temperature and after several days, orange, prismatic, X-ray quality single-crystal were obtained. Due to solvent loss when the crystals are taken out of the mother solution, the fully desolvated (under vacuum) sample subjected to elemental analyses had the formulation $[Mn_2^{II}(L^1)(NCS)_4]_n$ (**3**). Yield: 0.138 g, ~17%. *Anal.* Calc. for $C_{36}H_{34}N_{10}S_4Mn_2$: C, 51.18; H, 4.06; N, 16.58, Mn, 13.0. Found: C, 51.06; H, 3.92; N, 16.39; Mn, 12.74%.

CAUTION: *Perchlorate salts and azido compounds are potentially explosive especially in the presence of organic compounds. They must be prepared and handled in small amounts, and with special care.*

2.3. Physical measurements

Elemental analyses for C, H and N were performed using a Perkin Elmer 2400II elemental analyzer. Manganese contents were determined by titrimetric methods. IR spectra (4000–400 cm^{-1}) were recorded on KBr pellets at 298 K using a JASCO FT/IR-420 spectrometer. Magnetic data were obtained with a Quantum Design MPMS SQUID susceptometer. Magnetic susceptibility



Scheme 1. The hexadentate Schiff base ligands L and L^1.

measurements were performed in the 2–300 K temperature range in a 1 T applied magnetic field, and diamagnetic corrections were applied by using Pascal's constants [12]. The magnetic susceptibility has been computed by exact calculation of the energy levels associated to the spin Hamiltonian through diagonalization of the full matrix with a general program for axial symmetry [13]. Least-squares fittings were accomplished with an adapted version of the function-minimization program MINUIT [14].

2.4. Crystal structures determination and refinement

Single-crystals suitable for X-ray crystallographic analysis were selected following examination under a microscope. X-ray data of **2** were collected at 293 K with a Siemens SMART CCD diffractometer. Crystals of $\{[Mn_2^{II}(L^1)(NCS)_4]\cdot 2CH_3CN\}_n$ ($\mathbf{3}\cdot 2CH_3CN$) were quickly coated with an inert oil to prevent solvent loss and the X-ray data were collected at 200 K on a Bruker-AXS SMART APEX/CCD diffractometer. Both data collections were carried out using Mo Kα radiation ($\lambda = 0.71073$ Å) in an $\omega - 2\theta$ scan mode. 11 942 reflections were collected for **2**, of which 4434 were independent ($R_{int} = 0.056$) and 14195 reflections for **3**, of which 5227 were independent ($R_{int} = 0.039$). In both cases, intensity data were corrected for Lorentz and polarization effects. Empirical absorption corrections were made based on ψ-scans for **2** [15] and using the SADABS program [16] for **3**. The structures were solved by direct methods and the structure solution and refinement was based on $|F|^2$. All non-hydrogen atoms were refined with anisotropic displacement parameters except those of the disordered acetonitrile which were refined isotropically. Even when located in the Fourier map, hydrogen atoms were placed in calculated positions and given isotropic U values 1.2 times that of the atom to which they are bonded. Acetonitrile hydrogen atoms were neither located nor placed in calculated positions. The atomic scattering factors and anomalous dispersion terms were taken from the standard compilation [17]. All crystallographic calculations were carried out using SHELX-97 [18] and ORTEP-3 [19] program packages. The crystal data and data collection details are gathered in Table 1.

Table 1
Crystallographic data for **2** and $\mathbf{3}\cdot 2CH_3CN$

Compound	**2**	$\mathbf{3}\cdot 2CH_3CN$
Formula	$C_{32}H_{34}N_{24}Mn_2$	$C_{40}H_{40}N_{12}S_4Mn_2$
Formula weight	864.71	926.96
Space group	$P2_1/c$ (no. 14)	$P\bar{1}$ (no. 2)
Temperature (K)	293	200
a (Å)	8.8709(19)	7.8187(12)
b (Å)	9.770(2)	12.0249(18)
c (Å)	25.036(5)	12.1189(18)
α (°)	90	81.291(2)
β (°)	109.482(7)	87.416(2)
γ (°)	90	86.716(2)
V (Å^3)	2045.6(7)	1123.7(3)
Z	2	1
λ (Å)	0.71073	0.71073
$\rho_{calc.}$ (g cm^{-3})	1.404	1.361
μ (Mo Kα) (mm^{-1})	0.675	0.791
R^a	0.0527	0.0413
wR^b	0.0798	0.1005

[a] $R = \sum||F_o| - |F_c||/\sum|F_o|$.
[b] $R_w = [\sum w(|F_o|^2 - |F_c|^2)^2/\sum w|F_o^2|^2]^{1/2}$.

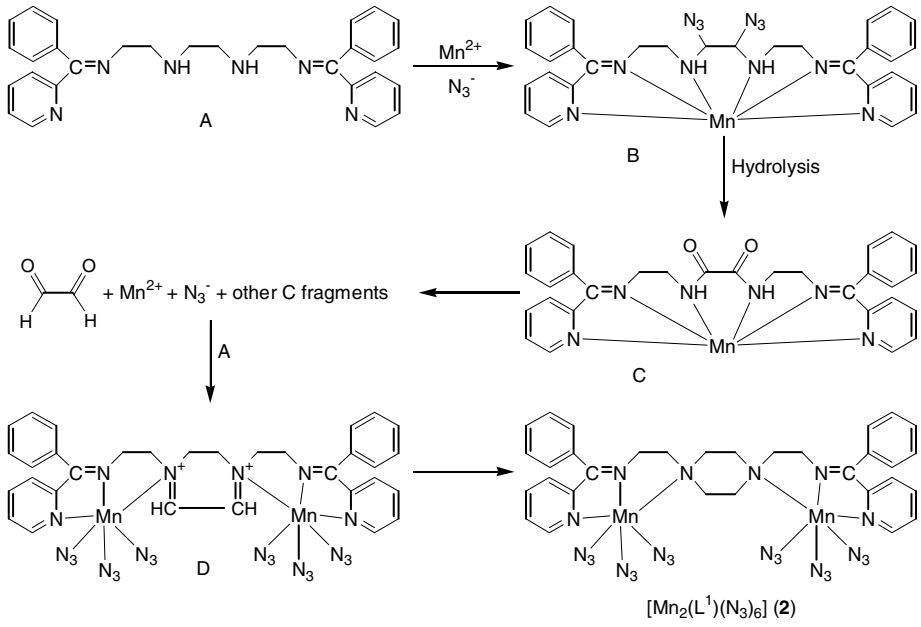
3. Results and discussion

3.1. Synthesis

The reaction of L with manganese(II) perchlorate hexahydrate using a 1:1 molar ratio in methanol/water or acetonitrile/water mixtures yielded an orange-red compound (**1**) formulated $[Mn^{II}L](ClO_4)_2$ on the basis of elemental analyses and IR data. The crystal structure of the nickel analogue $[NiL](ClO_4)_2$, prepared by a similar synthetic route evidenced a monomeric Ni^{II} compound where the hexadentate N_6 ligand is L (no L to L^1 rearrangement) [20].

On the other hand, a manganese(III) binuclear crystalline complex, $[Mn_2^{III}(L^1)(N_3)_6]$ (**2**) has been prepared in methanol/water from manganese(II) salts, L, and sodium azide (2:1:6 (or 2:1:4) molar ratio) in air. The same reactions carried out in acetonitrile/water instead of methanol/water yielded compound **1**, i.e., no L to L^1 rearrangement. Reaction of manganese(II) salts, L, and ammonium thiocyanate (2:1:4 (or 2:1:6) molar ratio) in acetonitrile/water yielded orange crystals of an unprecedented 1D chain of manganese(II) binuclear units bridged by $\mu_{1,3}$-NCS anions, $\{[Mn_2^{II}(L^1)(NCS)_4]\cdot 2CH_3CN\}_n$ ($\mathbf{3}\cdot 2CH_3CN$). The same reactions carried out in methanol/water instead of acetonitrile/water yielded compound **1**, i.e., no L to L^1 rearrangement.

The rearrangement from L to L^1 (Scheme 2), consisting in an alkylating cyclization centred on the two secondary amine functions of L, occurred exclusively along the course of complexation reactions where a pseudo-halide was involved in addition to L and a metal salt in the required solvent (methanol/water for **2**, and acetonitrile/water for **3**). L^1 could not be identified from reaction media devoid either of pseudo-halide or of metal salt, or carried out in different solvent mixtures. Similar rearrangement reactions also occurred with nickel(II) salts and pseudo-halides [11]. However, replacement of pseudo-halides by halides did not yield rearrangement of L to L^1. In addition, the poor yields of **2** and **3** suggest that the extra $-CH_2-CH_2-$ fragment present in L^1 compared to L most probably originates from the L ligand itself. A plausible mechanism for this



Scheme 2. A plausible mechanism for the alkylating cyclization of L to L^1 (case of complex **2**).

alkylating cyclization of L to L^1 may involve the following steps: (a) pseudo-halides in the presence of manganese ions may undergo a nucleophilic attack on the $–CH_2–CH_2–$ bridge located between the two secondary amine functions of L (A), producing a di-azido (-thiocyanato) (B) intermediate which on subsequent hydrolysis would generate an oxamido-like derivative (C) [21]; (b) this oxamido-like derivative would break down, producing glyoxal and C fragments; (c) glyoxal would then react, most possibly through a metal assisted concerted route, with the two secondary amine functions of another L ligand molecule, producing a di-imminium-like intermediate (D) [22], that would be subsequently reduced to L^1.

The role of the solvent with regard to the formation of compounds **2** or **3** is also remarkable. Indeed, while formation of **3** only requires the L to L^1 rearrangement, formation of **2** requires manganese oxidation from the +2 to the +3 state, in addition to the L to L^1 rearrangement. A possible explanation is that the stronger σ donor ability of the azido anion favours oxidation of the manganese centres in the presence of methanol, allowing formation of the $[Mn_2^{III}(L^1)(N_3)_6]$ (**2**) species. This oxidation may be further assisted by coordination of two extra azido ligands per binuclear unit, yielding the neutral hexacoordinated complex **2**. On the other hand, while the weaker σ donor ability of NCS does not favour oxidation of manganese centres, the presence of the very weakly coordinating acetonitrile solvent allows bridging of manganese(II) binuclear units into the 1D chain of **3** through $\mu_{1,3}$-NCS anions. Finally, formation of **1** in the reaction conditions of **2** or **3**, but in the absence of the required solvent (MeOH for **2** and CH_3CN for **3**), i.e. absence of L to L^1 rearrangement, indicates that at least one intermediate in this ligand rearrangement results from an equilibrium reaction: precipitation of the resulting complex (**2** or **3**) is most probably the driving force allowing the L to L^1 rearrangement.

3.2. IR spectroscopy

The IR spectrum of **2** exhibits a very strong absorption at 2040 cm^{-1} corresponding to the azido asymmetric stretching vibrations [6b,6c]. The IR spectrum of **3** exhibits strong absorptions at 2098 and 2053 cm^{-1} corresponding to the N,S-bonded thiocyanate ions [10a,10f]. The absorptions corresponding to the ν(C=N) stretches of L^1 are located at 1639 and 1590 cm^{-1} and 1633 and 1588 cm^{-1} for compounds **2** and **3**, respectively [10a,10f].

4. X-ray structures

4.1. $[Mn_2^{III}(L^1)(N_3)_6]$ (2)

The molecular structure of **2** consists of isolated binuclear molecules. The ORTEP drawing of the centrosymmetric binuclear unit with atom labeling scheme is shown in Fig. 1 and selected bond distances and angles are listed in Table 2.

Each manganese atom is located in a distorted octahedral N_6 coordination environment, with three nitrogen atoms from L^1 (N1, N2 and N3) and three nitrogen donors from terminal azido groups (N4, N7 and N10). The Mn–N(L^1) distances are in the

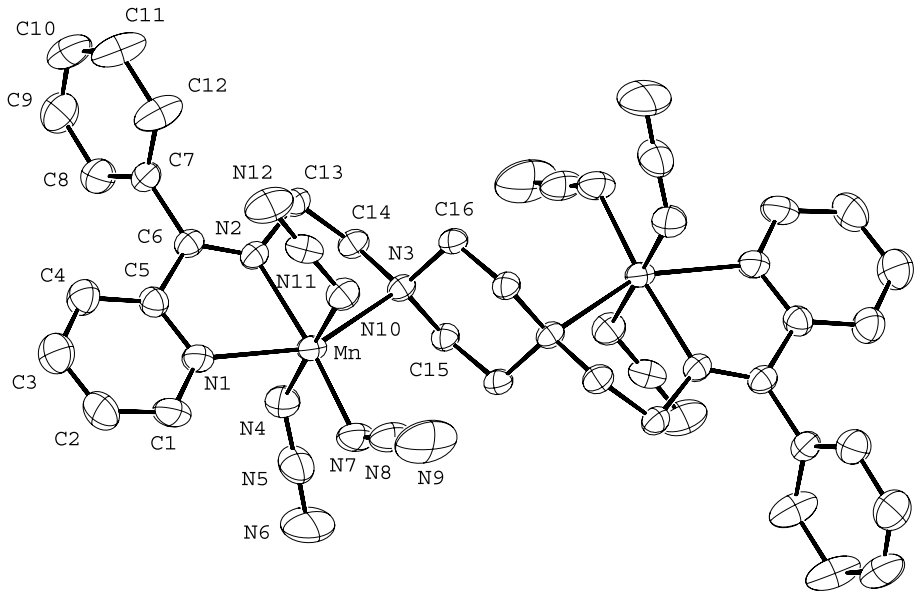


Fig. 1. ORTEP plot with atom labeling scheme for $[Mn_2(L^1)(N_3)_6]$ (**2**). For clarity the hydrogen atoms are omitted.

Table 2
Selected bond lengths (Å) and angles (°) for $[Mn_2(L^1)(N_3)_6]$ (**2**)

Bond lengths			
Mn–N1	2.249(3)	Mn–N2	2.094(3)
Mn–N3	2.395(3)	Mn–N4	1.949(3)
Mn–N7	1.955(4)	Mn–N10	1.962(3)
Bond angles			
N1–Mn–N2	73.76(10)	N1–Mn–N3	152.01(10)
N1–Mn–N4	90.74(12)	N1–Mn–N7	99.93(12)
N1–Mn–N10	90.41(13)	N2–Mn–N3	78.35(10)
N2–Mn–N4	91.24(12)	N2–Mn–N7	173.59(12)
N2–Mn–N10	89.01(12)	N3–Mn–N4	87.46(11)
N3–Mn–N7	108.00(11)	N3–Mn–N10	91.48(10)
N4–Mn–N7	89.94(13)	N4–Mn–N10	178.84(12)
N7–Mn–N10	89.94(13)	N4–N5–N6	177.8(5)
N7–N8–N9	174.8(5)	N10–N11–N12	177.9(4)

2.094(3)–2.395(3) Å range, while the Mn–N(azido) distances are almost equal (1.949(3)–1.962(3) Å range). It is worth noting that none of the azido anions behaves as a bridging ligand: this unusual azido coordination mode [6,7] may originate from the L to L^1 rearrangement. Due to the presence of the central –N(–CH_2–CH_2–)$_2$N– cycle in L^1, the intramolecular Mn···Mn distance in complex **2** is quite large (6.473(2) Å).

4.2. $\{[Mn_2^{II}(L^1)(NCS)_4]\cdot 2CH_3CN\}_n$ (**3**)

The structure of $\mathbf{3}\cdot 2CH_3CN$ (Fig. 2) consists of centrosymmetric binuclear $[Mn_2^{II}(L^1)(NCS)_4]$ repeat units doubly $\mu_{1,3}$-NCS bridged into 1D chains extending along a. Selected bond distances and angles are listed in Table 3.

The octahedral coordination sphere around each manganese(II) consists of three nitrogen donors from L^1 (N3, N4 and N5, 2.183(2)–2.390(2) Å), two nitrogen donors from thiocyanate anions (N1 (2.090(2) Å) from an end-to-end NCS bridge and N2 (2.097(2) Å) from a terminal NCS), and one sulfur donor (S2) (3.084(1) Å) from another end-to-end NCS. This end-to-end thiocyanato bridging mode has already been observed, with corresponding M–S distances either in the 2.6–2.9 Å range [23], or in the longer 3.11–3.18 Å range [10f], the latter suggesting weak M···S interactions rather than the covalent bonding suggested by the former. The intermediate 3.084 Å value observed for 3 is close to the lower limit for weak M···S interactions preventing us to qualify this Mn···S interaction as a covalent bonding. The N_5S coordination sphere is severely distorted from octahedral symmetry, with quite large deviations from the regular *cis* and *trans* angles and large axial distortion evidenced by the quite long Mn–S distance. The intradimer $Mn^{II}\cdots Mn^{II}$ separation (6.437(1) Å), originating from the presence of the central –N(–CH_2–CH_2–)$_2$N– cycle in L^1, is understandably quite similar to that in complex **2**, and slightly longer than the interdimer $Mn^{II}\cdots Mn^{II}$ distance (6.203(1) Å).

4.3. Magnetic properties

As expected from the large intramolecular $Mn^{III}\cdots Mn^{III}$ separation and nature of the polyatomic bridge, and absence of intermolecular contacts in compound **2**, there are no pathways for intra- and/or intermolecular magnetic interactions, as indicated by the paramagnetic behaviour of this binuclear compound. Its $\chi_M T$ product of 5.97 $cm^3\,K\,mol^{-1}$, close to the spin-only value for two non-interacting $S = 2$ ions, is constant over the whole 300–25 K temperature range and decreases from 5.78 (25 K) to 2.44 $cm^3\,K\,mol^{-1}$ (1.95 K) due to single-ion zero fields splitting (ZFS) of

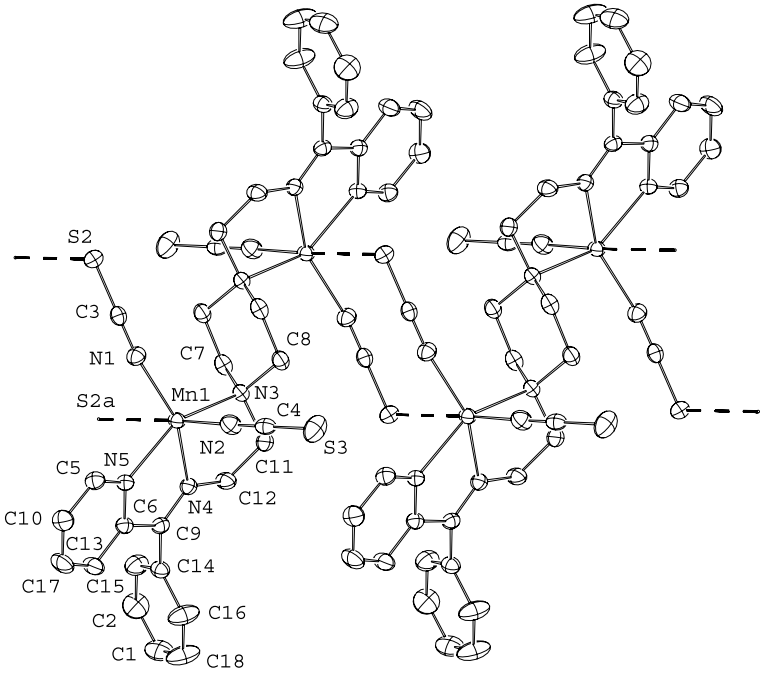


Fig. 2. ORTEP plot with atom labelling scheme of the $[Mn_2^{II}(L^1)(NCS)_4]_n$ 1D polymeric chain of ($\mathbf{3} \cdot 2CH_3CN$). For clarity the hydrogen atoms and solvent molecules are omitted.

Table 3
Selected bond lengths (Å) and angles (°) for $\mathbf{3} \cdot 2CH_3CN$

Bond lengths			
Mn–N1	2.0897(18)	Mn–N2	2.097(2)
Mn–N3	2.3897(18)	Mn–N4	2.1832(18)
Mn–N5	2.2436(17)	Mn···S2a	3.084(1)
Bond angles			
N1–Mn–N2	99.60(7)	N1–Mn–N3	108.00(7)
N1–Mn–N4	152.62(7)	N1–Mn–N5	100.46(7)
N2–Mn–N3	90.76(7)	N2–Mn–N4	107.50(7)
N2–Mn–N5	97.54(7)	N3–Mn–N4	76.02(6)
N3–Mn–N5	148.56(6)	N4–Mn–N5	72.55(6)
N1–Mn–S2a	82.90(6)	N2–Mn–S2a	177.41(7)
N3–Mn–S2a	89.08(5)	N4–Mn–S2a	69.96(5)
N5–Mn–S2a	81.30(4)	N1–C3–S2	179.2(2)
N2–C4–S3	179.3(2)		

Symmetry operation *a*: $1 - x$, $1 - y$, $-z$.

high-spin Mn^{III}. This result being perfectly consistent with the severe distortion of the MnN_6 octahedron evidenced by the crystal structure, we did not attempt to fit these data.

The experimental $\chi_M T$ product of **3** (desolvated crystals) smoothly decreases from 8.48 cm^3 K mol^{-1} at 300 K (slightly below the spin-only value for two non-interacting $S = 5/2$ ions) to 7.61 cm^3 K mol^{-1} at 80 K, and then sharply, down to 0.67 cm^3 K mol^{-1} at 1.96 K, clearly indicating operation of antiferromagnetic interactions in **3**. While no intramolecular magnetic interaction is expected between the Mn^{II} centres of **3** (same rationale as for **2**), weak intermolecular interactions are expected to be mediated by the double end-to-end thiocyanate bridges between binuclear $[Mn_2^{II}(L^1)\ (NCS)_4]$ repeat units along the 1D chains [9]. Taking into account the absence of intramolecular magnetic interaction between the Mn^{II} ions of binuclear constituting units, the overall magnetic behaviour of **3** can not result from extended magnetic interactions along 1D chains, but from pairwise interactions between Mn^{II} bridged by two NCS anions; in other words, the structural constituting units of complex **3** do not correspond to the magnetically interacting pairs.

The experimental magnetic susceptibility data (χ_M, lozenges in Fig. 3) were thus fitted by using the theoretical magnetic susceptibility calculated by exact diagonalization of the effective spin Hamiltonian for a pair of interacting $S_1 = S_2 = 5/2$ ions, taking into account single-ion ZFS: $\hat{H} = -2J\hat{S}_1\hat{S}_2 + D\hat{S}_Z^2$. The best fit (solid lines in

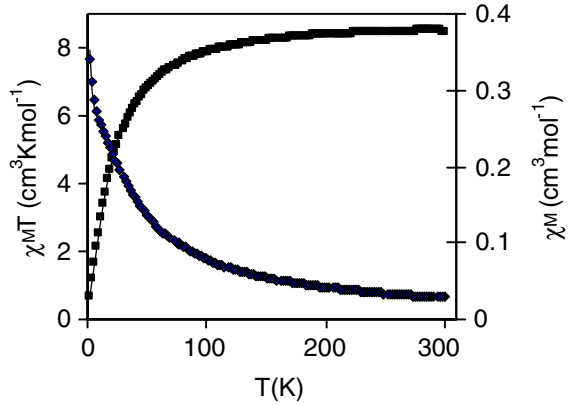


Fig. 3. χ_M and $\chi_M T$ vs. T data for complex **3**. Solid lines represent the best fit of the data with the model described in the text.

Fig. 3) was obtained for the following set of parameters: $J = -1.5\,cm^{-1}$, $D = -2 \times 10^{-4}\,cm^{-1}$, $g = 1.996$, and 1.4% of paramagnetic impurity. This result is in good agreement with the presence of a weak antiferromagnetic interaction between the binuclear $[Mn_2^{II}(L^1)(NCS)_4]$ repeat units along the 1D chains of **3**. The negligible single Mn^{II} ion ZFS value, D, is in agreement with the expectation for a d^5 shell. The fit evidenced as well a low contribution from temperature independent paramagnetism (TIP = 1.2×10^{-4}). Finally, attempts made to take into account additional inter-pair interactions (molecular field approximation according to Ginsberg and Lines' approach [24]) also yielded a negligible value of the intermolecular interaction parameter zj', thus confirming that the magnetic behaviour of **3** does not result from extended magnetic interactions along 1D chains, but from pairwise interactions between Mn^{II} ions.

5. Concluding remarks

Upon reaction with metal salts the Schiff base L, resulting from the bis-condensation of triethylenetetramine and 2-benzoylpyridine, behaves as a straightforward hexadentate ligand, yielding mononuclear complexes where the metal centre is coordinated to the six nitrogen donors of L. On the other hand, when such reactions are conducted in suitable solvents and in the presence of pseudo-halides (N_3^-, NCS^-) a rearrangement from L to L^1, consisting in an alkylating cyclization centred on the two secondary amine functions of L, systematically occurs. In the case of manganese(II), the reaction between the product L^1 and the metal assisting this rearrangement depends on the pseudo-halide and solvents used: while a binuclear manganese(III) complex, $[Mn_2(L^1)(N_3)_6]$ (**2**) is obtained in the case of azido anions in methanol/water mixtures, a polymeric manganese(II) compound, $\{[Mn_2^{II}(L^1)(NCS)_4] \cdot 2CH_3CN\}_n$ ($3.2CH_3CN$), is obtained with thiocyanato anions in acetonitrile/water mixtures.

The Mn centres of complexes **2** and **3** are in distorted octahedral coordination environments (**2**: $Mn^{III}N_6$, **3**: $Mn^{II}N_5S$) with intramolecular Mn···Mn distance (**2**: 6.473(2) Å, **3**: 6.437(1) Å) consistent with the absence of intramolecular magnetic interactions. Compound **3**, the first example of manganese(II) 1D chain where binuclear units are bridged via two $\mu_{1,3}$-NCS anions, exhibits weak intermolecular antiferromagnetic interactions ($J = -1.5\ cm^{-1}$) between pairs of Mn^{II} ions.

Acknowledgements

The authors thank the Council of Scientific and Industrial Research, New Delhi (S.K.C.: Grant No. 01(1836)/03/EMR-II) and University Grants Commission (under DSA program), New Delhi, for financial support. S.D. thanks The University of Burdwan for a fellowship.

Appendix A. Supplementary data

X-ray crystallographic files in CIF format for complexes **2** and **3**, CCDC Reference Nos. 172397 and 187481, respectively. This material is available free of charge via www.ccdc.cam.ac.uk/conts/retrieving.html (or from the Cambridge Crystallographic Data Centre, 12 Union Road, Cambridge CB2 1EZ, UK; fax: +44 1223 336 033; or deposit@ccdc.ca.ac.uk). Supplementary data associated with this article can be found, in the online version, at doi:10.1016/j.poly.2004.11.014.

References

[1] (a) V.L. Pecoraro, W.-Y. Hsieh, in: A. Sigel, H. Sigel (Eds.), Metal Ions in Biological Systems: Manganese and its Role in Biological Processes, vol. 37, Marcel Dekker, New York, 2000, pp. 431–444;
(b) V.L. Pecoraro, Manganese Redox Enzymes, VCH, New York, 1992.
[2] (a) K. Weighardt, Angew. Chem., Int. Ed. Engl. 28 (1989) 1153;
(b) G.C. Dismukes, Chem. Rev. 96 (1996) 2909;
(c) W. Ruttinger, G.C. Dismukes, Chem. Rev. 97 (1997) 1.
[3] (a) O. Kahn, Molecular Magnetism, VCH, New York, 1993;
(b) D. Gatteschi, O. Kahn, J.S. Miller, F. Palacio, Magnetic Molecular Materials, NATO ASI, Kluwer, Dordrecht, 1991.
[4] (a) M.A.M. Abu-Youssef, M. Drillon, A. Escuer, M.A.S. Goher, F.A. Mautner, R. Vicente, Inorg. Chem. 39 (2000) 5022;
(b) J.-P. Costes, F. Dahan, B. Donnadieu, M.-J. Rodriguez Douton, A. Bousseksou, J.-P. Tuchagues, Inorg. Chem. 43 (2004) 2736;
(c) N. Matsumoto, Y. Sunatsuki, H. Miyasaka, Y. Hashimoto, D. Luneau, J.-P. Tuchagues, Angew. Chem., Int. Ed. Eng. 38 (1999) 171;
(d) K.R. Reddy, M.V. Rajasekharan, J.-P. Tuchagues, Inorg. Chem. 37 (1998) 5978;
(e) R. Sessoli, H.-L. Tsai, A.R. Schake, S. Wang, J.B. Vincent, K. Folting, D. Gatteschi, G. Christou, D.N. Hendrickson, J. Am. Chem. Soc. 115 (1993) 1804;
(f) R. Sessoli, D. Gatteschi, A. Caneschi, M. Novak, Nature 365 (1993) 141;
(g) C. Palopoli, B. Chansou, J.-P. Tuchagues, S. Signorella, Inorg. Chem. 39 (2000) 1458.
[5] K. Vrieze, G. van Koten, in: G. Wilkinson, R.D. Gillard, J.A. McLeverty (Eds.), Comprehensive Coordination Chemistry, vol. 2, Oxford, England, 1987, p. 225.
[6] (a) A. Escuer, R. Vicente, J. Ribas, X. Solans, Inorg. Chem. 34 (1995) 1793;
(b) R. Cortes, J.I. Ruiz de Larramendi, L. Lezama, T. Rojo, K. Urtiaga, M.I. Arriortua, J. Chem. Soc., Dalton Trans. (1992) 2723;
(c) M.G. Barandika, R. Cortes, L. Lezama, M.K. Urtiaga, M.I. Arriortua, T. Rojo, J. Chem. Soc., Dalton Trans. (1999) 2971;
(d) J. Cano, G.D. Munno, F. Lloret, M. Julve, Inorg. Chem. 39 (2000) 1611;
(e) M.I. Arriortua, R. Cortes, J.L. Mesa, L. Lezama, T. Rojo, G. Villeneuve, Trans. Met. Chem. 13 (1988) 371.

[7] (a) A. Escuer, I. Castro, F. Mautner, M.S. El Fallah, R. Vicente, Inorg. Chem. 36 (1997) 4633;
(b) A. Escuer, R. Vicente, M.S. El Fallah, X. Solans, M. Font-Bardia, Inorg. Chim. Acta 278 (1998) 43;
(c) A. Escuer, R. Vicente, M.S. El Fallah, X. Solans, M. Font-Bardia, J. Chem. Soc., Dalton Trans. (1996) 1013.
[8] E. Ruiz, J. Cano, S. Alvarej, P. Alemany, J. Am. Chem. Soc. 120 (1998) 11122.
[9] F.F. de Biani, E. Ruiz, J. Cano, J.J. Novoa, S. Alvarej, Inorg. Chem. 39 (2000) 3221.
[10] (a) M.G. Borandika, M.L. Hernandez-Pino, M.K. Urtiaga, R. Cortes, L. Lezama, M.I. Arriortua, T. Rojo, J. Chem. Soc., Dalton Trans. (2000) 1469;
(b) M.J. Plater, M.R.J. Foreman, R.A. Howie, J.M.S. Skakle, Inorg. Chim. Acta 318 (2001) 175;
(c) T.K. Maji, P.S. Mukherjee, S. Koner, G. Mostafa, J.-P. Tuchagues, N.R. Chaudhuri, Inorg. Chim. Acta 314 (2001) 111;
(d) J.M. Clemente-Juan, C. Mackiewicz, M. Verelst, F. Dahan, A. Bousseksou, Y. Sanakis, J.-P. Tuchagues, Inorg. Chem. 41 (2002) 1478;
(e) S. Koner, S. Saha, K.-I. Okamoto, J.-P. Tuchagues, Inorg. Chem. 42 (2003) 4668;
(f) A.K. Boudalis, J.M. Clemente-Juan, F. Dahan, J.-P. Tuchagues, Inorg. Chem. 43 (2004) 1574;
(g) A.K. Boudalis, B. Donnadieu, V. Nastopoulos, J.M. Clemente-Juan, A. Mari, Y. Sanakis, J.-P. Tuchagues, S.P. Perlepes, Angew. Chem., Int. Ed. Eng. 43 (2004) 2266.
[11] S. Deoghoria, S. Sain, M. Soler, W.T. Wong, G. Christou, S.K. Bera, S.K. Chandra, Polyhedron 22 (2003) 257.
[12] P. Pascal, Ann. Chim. Phys. 19 (1910) 5.
[13] B. Mabad, P. Cassoux, J.-P. Tuchagues, D.N. Hendrickson, Inorg. Chem. 25 (1986) 1420.
[14] F. James, M. Roos, Comput. Phys. Commun. 10 (1975) 345.
[15] A.C.T. North, D.C. Phillips, F.S. Mathews, Acta Crystallogr. A 24 (1968) 351.
[16] SAINT+ v6.02. Bruker AXS, Madison, WI, USA, 1999.
[17] International Tables for Crystallography, vol. C, Kluwer Academic Publishers, Dordrecht, The Netherlands, 1992.
[18] G.M. Sheldrick, SHELX-97, Program for Solution of Crystal Structure, University of Göttingen, Germany, 1997.
[19] ORTEP-3 for Windows: L.J. Farrugia, J . Appl. Crystallogr. 30 (1997) 565.
[20] S. Deoghoria, S.K. Chandra, Unpublished results.
[21] P.A. Manis, M.W. Rathke, J. Org. Chem. 45 (1980) 4952.
[22] S.J. Benkovic, P.A. Benkovic, D.R. Comfort, J. Am. Chem. Soc. 91 (1969) 1860.
[23] (a) R. Vicente, A. Escuer, E. Peñalba, X. Solans, M. Font-Bardia, Inorg. Chim. Acta 255 (1997) 7;
(b) P. Gómez-Saiz, J. García-Tojal, F.J. Arnáiz, M.J. Maestro, L. Lezama, T. Rojo, Inorg. Chem. Commun. 6 (2003) 558;
(c) T.K. Maji, G. Mostafa, J.M. Clemente-Juan, J. Ribas, F. Lloret, K. Okamoto, N.R. Chaudhuri, Eur. J. Inorg. Chem. (2003) 1005.
[24] A.P. Ginsberg, M.E. Lines, Inorg. Chem. 11 (1972) 2289.

Available online at www.sciencedirect.com
SCIENCE DIRECT®
Polyhedron 24 (2005) 351–358
POLYHEDRON
www.elsevier.com/locate/poly

Linking thione-ligated copper(I) centres with *trans*-1,2-bis(diphenylphosphino)ethene (*trans*-dppen): crystal structures of the pyrimidine-2-thione derivatives $[CuBr(\mu_2\text{-}trans\text{-dppen})(pymtH)]_2$ and $[CuI(\mu_2\text{-}trans\text{-dppen})(pymtH)]_2$

S. Divanidis [a], P.J. Cox [*,b], P. Karagiannidis [a], P. Aslanidis [a,*]

[a] *Inorganic Chemistry Laboratory, Faculty of Chemistry, Aristotle University of Thessaloniki, P.O. Box 135, GR-541 24 Thessaloniki, Greece*
[b] *School of Pharmacy, The Robert Gordon University Schoolhill, Aberdeen AB 10 1FR, Scotland, UK*

Received 16 July 2004; accepted 30 November 2004
Available online 25 December 2004

Abstract

Several mixed-ligand complexes of the composition [CuX(*trans*-dppen)(L)] (X = Br, I) have been prepared by treatment of copper(I) halide with equimolar amounts of *trans*-1,2-bis(diphenylphosphino)ethene (*trans*-dppen) in acetonitrile followed by the addition of a methanolic solution of one equivalent of a heterocyclic thione (L). The novel complex compounds have been characterized by ^{1}H NMR and IR spectroscopy as well as by elemental analyses and melting points. The X-ray structures of two representative examples, namely the pyrimidine-2-thione complexes of copper(I) bromide and iodide confirm that the compounds are dimers of type $[CuX(\mu_2\text{-}trans\text{-dppen})(L)]_2$ containing two tetrahedral coordination units joined by two diphosphine bridges.
© 2004 Elsevier Ltd. All rights reserved.

Keywords: Copper(I) halide complexes; Heterocyclic thione complexes; *trans*-1,2-Bis(diphenylphosphino)ethene complexes; Crystal structures

1. Introduction

Due to their relevance in biological systems, the use of heterocyclic thiones as ligands in transition metal complexes has drawn much attention in the recent past [1]. Among others, an impressive amount of thione-ligated copper(I) halide complexes have been obtained over the years, that display a rich diversity of stoichiometries and structural prototypes. For some time the focus of our research in this field was directed towards incorporation of tertiary arylphosphines as bulky soft donors. This produced a large amount of mixed-ligand Cu(I) complexes with a variety of structures ranging from mononuclear three- or four-coordinate species with trigonal planar and tetrahedral Cu(I), respectively, to double bridged dimers. In all these complexes the thione molecules were always found to bind the metal exclusively through the exocyclic sulfur atom in either a μ_2-S bridging [2–4] or in a terminal [2,5] fashion, with the preference for each of these two modes of coordination strongly dependent on the nature of the halide ligand. As for the coordination number of the complexes being formed, only the influence of the bulkiness of the phosphine, but not of that of the thione ligands used, could be definitively stated so far [6].

Sometime ago, we started comparative studies into the substitution of unidentate arylphosphines with oligomethylene-backboned symmetric diphosphines of the type $Ph_2P(CH_2)_nPPh_2$ (n = 1–6), whereby we demonstrated that, dependent on the nature of the phosphorus

* Corresponding author. Tel.: +32310997694; fax: +32310997738.
E-mail addresses: p.j.cox@rgu.ac.uk (P.J. Cox), aslanidi@chem.auth.gr (P. Aslanidis).

0277-5387/$ - see front matter © 2004 Elsevier Ltd. All rights reserved.
doi:10.1016/j.poly.2004.11.015

donors, it is possible to prepare and isolate diphosphine complexes of copper(I) of different nuclearity and stoichiometry. Thus, 1,3-bis(diphenylphosphino)propane (dppp), but also *cis*-1,2-bis(diphenylphosphino)ethylene (*cis*-1,2-dppen), were found to chelate at a single metal centre yielding mononuclear pseudo-tetrahedral copper (I) species [7,8] or halide bridged dimers [8], whereby cyclic dimeric compounds in which the two copper(I) centres are linked together by two bidentate phosphine ligands have been obtained when a longer methylene chain connects the two P atoms, but surprisingly also in the case of 1,2-bis(diphenylphosphino)ethane (dppe) [9]. The most recent step within the aforementioned studies deals with the coordination capability of the rigid diphosphine *trans*-1,2-bis(diphenylphosphino)ethene (*trans*-dppen) toward Cu(I) chloride, in the presence of heterocyclic thione donor groups [10]. There, we described the preparation and crystallographic characterization of some examples of complexes of the formula $[CuCl(\mu_2\text{-}trans\text{-dppen})L]_2$ (L = heterocyclic thione), in which the metal centres are spanned by two diphosphine molecules to afford a 10-membered dimetallacyclic ring. In continuation of our efforts in this area, we now extend the use of this diphos ligand to obtain mixed ligand complexes of copper(I) bromide and iodide. This seems necessary, since the Cu(I) halide complexes, depending on the halide present, often show very different structural properties. Thus, to fully define the prepared compounds and to gain additional information concerning trends in the copper–thione and copper–phosphine interactions, the structures of two examples, representative for each type of halide, have been determined by single-crystal X-ray analysis.

2. Experimental

2.1. Materials and instruments

Commercially available copper(I) halides and *trans*-1,2-bis(diphenylphosphino)ethene were used as received while the thiones (Fig. 1) were recrystallized from hot ethanol prior to their use. All the solvents were purified by respective suitable methods and allowed to stand over molecular sieves. Infra-red and electronic absorption spectra, melting points, molar conductivities, magnetic susceptibility measurements and elemental analyses for carbon, nitrogen and hydrogen were performed as described previously [11]. ^{1}H NMR spectra were recorded on a Bruker AM 300 spectrometer at 25 °C; chemical shifts in ppm are quoted relative to internal TMS.

2.2. X-ray crystallographic study

Single crystals suitable for crystal structure analysis were obtained by slow evaporation of acetonitrile/methanol solutions of the complexes at room temperature. X-ray diffraction data were collected on an Enraf-Nonius Kappa CCD area-detector diffractometer. The programs DENZO [12] and COLLECT [13] were used in data collection and cell refinement. Details of crystal and structure refinement are shown in Table 1. The structures were solved using program SIR 97 [14] and refined with program SHELX-97 [15]. Molecular plots were obtained with program ORTEP-3 [16].

2.3. Synthesis of complexes *1–16*

The complexes were prepared according to the following general procedure. To a suspension of copper(I) bromide or iodide (0.5 mmol) in 30 cm^3 of dry acetonitrile, *trans*-1,2-bis(diphenylphosphino)ethene (198.2 mg, 0.5 mmol) was added and the mixture was stirred for 2 h at ambient temperature during which time a white precipitate was formed. A solution of the appropriate thione (0.5 mmol) in 30 cm^3 methanol was added dropwise into the reaction mixture whereupon the white precipitate gradually disappeared. After heating at 50 °C for 2 h followed by stirring at ambient temperature overnight, the resulting clear solution was filtered off and left to evaporate. The microcrystalline solid, which was

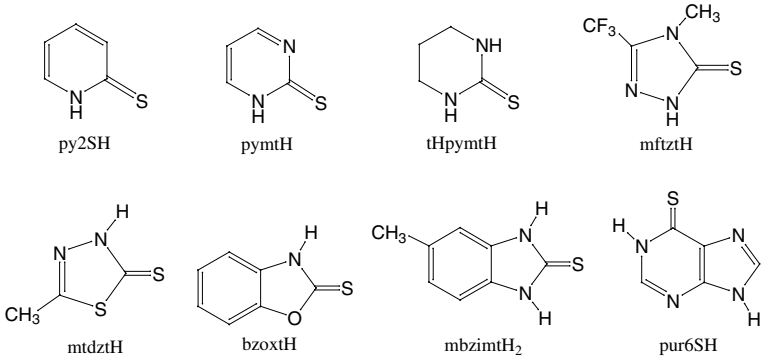


Fig. 1. The heterocyclic thione ligands used with their abbreviations.

Table 1
Crystal data and structure refinements for **1** and **2**

	2	**10**
Chemical formula	$C_{60}H_{50}Br_2Cu_2N_4P_4S_2$	$C_{60}H_{52}Cu_2I_2N_4P_2S_2 \cdot 2CH_3CN$
Formula weight	1201.94	1480.04
Temperature (K)	120(2)	120(2)
Wavelength (Å)	0.71073	0.71073
Crystal system	monoclinic	triclinic
Space group	$P2_1/n$	$P\bar{1}$
Unit cell dimensions		
a (Å)	12.059(5)	11.4866(7)
b (Å)	15.621(5)	12.6464(9)
c (Å)	15.603(5)	12.6960(9)
α (°)	90	92.605(3)
β (°)	95.001(5)	110.561(5)
γ (°)	90	111.982(4)
Volume (Å^3)	2928.0(18)	1567.66(18)
Z	2	1
D_{calc} (Mg/m^3)	1.477	1.568
Absorption coefficient (mm^{-1})	2.313	1.876
F (000)	1316	740
Crystal size (mm)	$0.20 \times 0.10 \times 0.02$	$0.45 \times 0.40 \times 0.20$
θ Range for data collection (°)	3.11–27.49	3.02–27.47
Index ranges	$-15 \leqslant h \leqslant 15$	$-14 \leqslant h \leqslant 14$
	$-20 \leqslant k \leqslant 20$	$-16 \leqslant k \leqslant 16$
	$-20 \leqslant l \leqslant 20$	$-16 \leqslant l \leqslant 16$
Reflections collected	12851	12688
Independent reflections [R_{int}]	6713 [0.0695]	6905 [0.0379]
Completeness to theta = 27.50°	99.7%	96.1%
Maximum and minimum transmission	0.9552 and 0.6548	0.7054 and 0.4856
Refinement method	full-matrix least-square on F^2	full-matrix least-square on F^2
Data/restraints/parameters	6713/16/425	6905/1/402
Goodness-of-fit on F^2 (S)	1.171	1.056
Final R indices [$(I) > 2\sigma(I)$]	$R_1 = 0.0713$, $wR_2 = 0.1399$	$R_1 = 0.0593$, $wR_2 = 0.1483$
R indices (all data)	$R_1 = 0.1121$, $wR_2 = 0.1513$	$R_1 = 0.1065$, $wR_2 = 0.1754$
Extinction coefficient	none	0.0091(12)
Final weighting scheme	Calc $w = 1/[\sigma^2(F_o^2) + 11.8312P]$, where $P = (F_o^2 + 2F_c^2)/3$	Calc $w = 1/[\sigma^2(F_o^2) + 0.0820P^2 + 3.3512P]$, where $P = (F_o^2 + 2F_c^2)/3$
Largest difference in peak and hole (e Å^{-3})	0.417 and −0.444	1.380 and −2.736 (close to iodine)

deposited upon standing for several days was filtered off and dried in vacuo.

2.3.1. [CuBr(trans-dppen)(py2SH)]$_2$ (**1**)

Yellow crystals. Yield: 163 mg (25%), m.p. 241 °C; *Anal.* Calc. for $C_{31}H_{27}NBrCuP_2S$: C, 57.19; H, 4.18; N, 2.15. Found: C, 57.05; H, 4.12; N, 2.08%. IR (cm^{-1}): 3447.4m, 3053.2w, 1617.0s, 1573.8vs, 1435.6vs, 1365.2s, 1186.0vs, 1134.2vs, 1100.6s, 990.4s, 772.5vs, 750.0vs, 722.7vs, 695.4vs, 539.5vs, 520.0vs, 470.0s; UV–Vis [λ_{max} (nm), log ε]: ($CHCl_3$); 246.0 (4.17), 291.0 (3.99), 378.0 (3.65); ^{1}H NMR ($CDCl_3$, δ ppm): 14.28 (b, 1H, NH), 7.47 (m, 12H, PC_6H_5), 7.21 (m, 8H, PC_6H_5), 7.62 (m, 1H, H^6_{py2SH}), 7.37 (dd, 1H, H^4_{py2SH}, $J_{3,5} = 5$ Hz), 7.06 (t, 1H, H^3_{py2SH}), 7.09 (m, 2H, –CH=CH–), 6.51 (dd, 1H, H^5_{py2SH}, $J_6 = 6$ Hz, $J_4 = 5$ Hz).

2.3.2. [CuBr(trans-dppen)(pymtH)]$_2$ (**2**)

Orange crystals. Yield: 339 mg (52%), m.p. 255 °C; *Anal.* Calc. for $C_{30}H_{26}N_2BrCuP_2S$: C, 55.26; H, 4.02; N, 4.30. Found: C, 54.94; H, 3.65; N, 4.25%. IR (cm^{-1}): 3448.12w, 3048.0w, 1604.9vs, 1588.8vs, 1478.0vs, 1433.2vs, 1325.4vs, 1213.7s, 1175.4vs, 1097.3s, 739.5vs, 694.7vs, 509.7s, 463.2s; UV–Vis [λ_{max} (nm), log ε]: ($CHCl_3$); 246.0 (4.05), 284.5 (4.10), 408.0 (2.15); ^{1}H NMR ($CDCl_3$, δ ppm): 12.20 (s, 1H, NH), 7.70 (m, 12H, PC_6H_5), 7.50 (m, 8H, PC_6H_5), 7.60 (m, 2H, $H^{4,6}_{pymtH}$), 7.02 (m, 2H, –CH=CH–), 6.82 (m, 1H, H^5_{pymtH}, $J_4 = 5$ Hz, $J_6 = 6$ Hz).

2.3.3. [CuBr(trans-dppen)(tHpymtH)]$_2$ (**3**)

Pale yellow crystals. Yield: 210 mg (32%), m.p. 236 °C; *Anal.* Calc. for $C_{30}H_{30}N_2BrCuP_2S$: C, 54.92; H, 4.61; N, 4.27. Found: C, 54.76; H, 4.80; N, 4.26%. IR (cm^{-1}): 3214.2m, 2965.5m, 1559.8vs, 1481.5m, 1435.7vs, 1364.5s, 1186.3vs, 1120.0vs, 1099.2s, 744.7vs, 694.5vs, 539.4vs, 418.0s; UV–Vis [λ_{max} (nm), log ε]: ($CHCl_3$); 255.0 (4.24), 282.5 (4.03), 357.5(3.08); ^{1}H NMR ($CDCl_3$, δ ppm): 8.26 + 7.87 (s, 1H, NH), 7.70 (m, 12H, PC_6H_5), 7.53 (m, 8H, PC_6H_5), 3.37 (dt, 4H,

$H^3_{tHpymtH}$, J_4 = 4 Hz, $J_{1,5}$ = 2 Hz), 1.84 (q, 2H, $H^4_{tHpymtH}$, J = 4 Hz), 7.39 (m, 2H, –CH=CH–).

*2.3.4. [CuBr(trans-dppen)(mftztH)]$_2$ (**4**)*

White crystals. Yield: 282 mg (39%), m.p. 280 °C; *Anal*. Calc. for $C_{30}H_{26}N_3BrCuF_3P_2S$: C, 49.84; H, 3.62; N, 5.81. Found: C, 49.55; H, 3.50; N, 5.65%. IR (cm^{-1}): 3447.8m, 3048.5w, 1586.5m, 1480.5vs, 1434.5vs, 1177.8s, 1096.0vs, 1026.0s, 973.5s, 738.0vs, 692.8vs, 510.8vs; UV–Vis [λ_{max} (nm), log ε]: ($CHCl_3$); 255.0 (4.17), 282.5 (3.96), 312.0 (3.18); ^{1}H NMR ($CDCl_3$, δ ppm): 13.8 (br, 1H, NH), 7.67 (m, 12H, PC_6H_5), 7.52 (m, 8H, PC_6H_5), 6.76 (m, 2H, –CH=CH–), 3.34 (s, 3H, N–CH_3).

*2.3.5. [CuBr(trans-dppen)(mtdztH)]$_2$ (**5**)*

Yellow crystals. Yield: 276 mg (41%), m.p. 241 °C; *Anal*. Calc. for $C_{29}H_{26}N_2BrCuP_2S_2$: C, 51.83; H, 3.90; N, 4.17. Found: C, 51.54; H, 3.69; N, 4.10%. IR (cm^{-1}): 3426.0m, 3027.8w, 2964.0w, 1610.2m, 1546.5m, 1479.4vs, 1459.2vs, 1434.2vs, 1280.8vs, 1178.6s, 1101vs, 1052.5s, 969.3s, 809m, 740.0vs, 692.5vs, 508.5vs, 481.0vs, 464.2s 431.7m; UV–Vis [λ_{max} (nm), log ε]: ($CHCl_3$); 245.5 (4.09), 306.0 (4.11), 335.0 (3.59); ^{1}H NMR ($CDCl_3$, δ ppm): 14.02 (s, 1H, NH), 7.50 (m, 12H, PC_6H_5), 7.06 (m, 8H, PC_6H_5), 6.60 (m, 2H, –CH=CH–), 2.60 (s, 3H, C–CH_3).

*2.3.6. [CuBr(trans-dppen)(bzoxtH)]$_2$ (**6**)*

Pale yellow crystals. Yield: 263 mg (38%), m.p. 263 °C; *Anal*. Calc. for $C_{33}H_{27}NBrCuOP_2S$: C, 57.36; H, 3.94; N, 2.03. Found: C, 57.55; H, 4.03; N, 4.06%. IR (cm^{-1}): 3426.2m, 3043.8m, 1615.3s, 1504.9vs, 1480.7s, 1434.3vs, 1428.5vs, 1282.0s, 1251.0s, 1186.3vs, 1140.6vs, 1098.0vs, 971.6s, 935.4s, 738.5vs, 693.5vs, 605.5s, 499.1vs, 483.0vs, 425.9m; UV–Vis [λ_{max} (nm), log ε]: ($CHCl_3$); 244.5 (4.04), 265.5 (3.92), 295.0 (3.91), 344.5 (3.17); ^{1}H NMR ($CDCl_3$, δ ppm): 14.22 (br, 1H, NH), 7.51 (m, 12H, PC_6H_5), 7.18 (m, 8H, PC_6H_5), 7.26 + 7.03 (m, 4H, CH_{bzoxtH}), 6.70 (br, 2H, –CH=CH–).

*2.3.7. [CuBr(trans-dppen)(mbzimtH$_2$)]$_2$ (**7**)*

Pale yellow crystals. Yield: 451 mg (64%), m.p. 295 °C; *Anal*. Calc. for $C_{34}H_{30}N_2BrCuP_2S$: C, 58.00; H, 4.29; N, 3.98. Found: C, 57.62; H, 4.19; N, 3.85%. IR (cm^{-1}): 3450.0w, 3043.8w, 1615.0m, 1515.7vs, 1481.2vs, 1434.5vs, 1383.5s, 1326.6s, 1178.5vs, 1099.8s, 973.1m, 796.5vs, 741.5vs, 693.2vs, 544.9s, 511.8vs, 482.9s, 430.2m; UV–Vis [λ_{max} (nm), log ε]: ($CHCl_3$); 252.5 (4.31), 305.0 (4.39), 349.5 (3.44); ^{1}H NMR ($CDCl_3$, δ ppm): 12.51 (s, 1H, NH), 7.48 (m, 12H, PC_6H_5), 7.13 (m, 8H, PC_6H_5), 7.04 (d, 2H, $H^7_{mbzimtH}$, J = 5 Hz), 6.97 (s, 1H, $H^4_{mbzimtH}$), 6.96 (d, 2H, $H^6_{mbzimtH}$, J = 5 Hz), 6.97 (m, 2H, –CH=CH–), 2.39 (s, 3H, C–CH3).

*2.3.8. [CuBr(trans-dppen)(pur6SH)]$_2$ (**8**)*

Yellow crystals. Yield: 401 mg (58%), m.p. 280 °C; *Anal*. Calc. for $C_{31}H_{26}N_4BrCuP_2S$: C, 53.80; H, 3.78; N, 8.10. Found: C, 53.41; H, 3.65; N, 8.01%. IR (cm^{-1}): 3426.2m, 3043.8m, 1609.9vs, 1556.9vs, 1480.1s, 1433.6vs, 1393.5vs, 1212.3s, 1098.3s, 997s, 860.5s, 739.5vs, 694.7vs, 510.4vs, 483.4m; UV–Vis [λ_{max} (nm), log ε]: ($CHCl_3$); 246.5 (4.12), 282.5 (4.09), 362.0 (3.63); ^{1}H NMR ($CDCl_3$ + DMSO-d_6, δ ppm): 14.14 (s, 2H, NH), 8.28 + 8.16 (s, 2H, CH_{pur6SH}), 7.40 (m, 12H, PC_6H_5), 7.24 (m, 8H, PC_6H_5), 6.98 (m, 2H, –CH=CH–).

*2.3.9. [CuI(trans-dppen)(py2SH)]$_2$ (**9**)*

Yellow crystals. Yield: 189 mg (27%), m.p. 224 °C; *Anal*. Calc. for $C_{31}H_{27}NCuIP_2S$: C, 53.34; H, 3.90; N, 2.00. Found: C, 53.28; H, 3.81; N, 1.95%. IR (cm^{-1}): 3442.1w, 3053.2m, 1607.4vs, 1559.8s, 1481.9vs, 1432.6vs, 1330.2vs, 1186.4s, 1097.8s, 982.8s, 793.4s, 738.2vs, 695.5vs, 509.9vs, 485.9s, 470.4s; UV–Vis [λ_{max} (nm), log ε]: ($CHCl_3$); 245.5 (4.01), 292.5 (4.10), 377.5 (3.64).

*2.3.10. [CuI(trans-dppen)(pymtH)]$_2$ (**10**)*

Orange crystals. Yield: 287 mg (41%), m.p. 251 °C; *Anal*. Calc. for $C_{30}H_{26}N_2CuIP_2S$: C, 51.55; H, 3.75; N, 4.01. Found: C, 51.22; H, 3.65; N, 4.05%. IR (cm^{-1}): 3448.5m, 3054.0m, 1601.7vs, 1583.6vs, 1480.0vs, 1433.5vs, 1325.9vs, 1211.5s, 1174.3vs, 1097.5s, 1049.9s, 975.9s, 739.2vs, 694.0vs, 511.6vs, 472.1s; UV–Vis [λ_{max} (nm), log ε]: ($CHCl_3$); 246.5 (4.10), 284.5 (4.09), 410.0 (3.60); ^{1}H NMR ($CDCl_3$, δ ppm): 15.02 (s, 1H, NH), 7.81 (m, 2H, $H^{4,6}_{pymtH}$), 7.70 (m, 12H, PC_6H_5), 7.52 (m, 8H, PC_6H_5), 7.23 (m, 2H, –CH=CH–), 6.82 (m, 1H, H^5_{pymtH}).

*2.3.11. [CuI(trans-dppen)(tHpymtH)]$_2$ (**11**)*

White crystals. Yield: 267 mg (38%), m..p 215 °C; *Anal*. Calc. for $C_{30}H_{30}N_2CuIP_2S$: C, 51.25; H, 4.30; N, 3.98. Found: C, 51.10; H, 4.38; N, 3.91%. IR (cm^{-1}): 3215.7w, 3074.5w, 2956.2m, 1552.2vs, 1479.0m, 1433.5vs, 1314.3vs, 1204.4vs, 1099.6s, 749.8vs, 694.5vs, 511.5s, 499.5s, 413.4m; UV–Vis [λ_{max} (nm), log ε]: ($CHCl_3$); 254.5 (4.14), 281.5 (3.43), 353.0 (2.90); ^{1}H NMR ($CDCl_3$, δ ppm): 7.84 + 7.76 (s, 2H, NH), 7.68 (m, 12H, PC_6H_5), 7.47 (m, 8H, PC_6H_5), 6.69 (m, 2H, –CH=CH–), 3.28 (dt, 4H, $H^3_{tHpymtH}$, J_4 = 4 Hz, $J_{1,5}$ = 2 Hz), 1.94 (q, 2H, $H^4_{tHpymtH}$, J = 4 Hz).

*2.3.12. [CuI(trans-dppen)(mftztH)]$_2$ (**12**)*

White crystals. Yield: 485 mg (63%), m.p. 237 °C; *Anal*. Calc. for $C_{30}H_{26}N_3CuIF_3P_2S$: C, 46.81; H, 3.38; N, 5.46. Found: C, 46.57; H, 3.30; N, 5.41%. IR (cm^{-1}): 3094.2w, 1480.5s, 1435.4vs, 1342.7s, 1284.7vs, 1200.5vs, 1150.0vs, 1091.8vs, 965.7s, 783.3s, 692.5vs, 611.8s, 556.5s, 500.0m, 351.5s; UV–Vis [λ_{max} (nm),

log ε]: ($CHCl_3$); 264.5 (4.40), 271.5 (4.39), 314.5 (3.24); ^1H NMR ($CDCl_3$, δ ppm): 7.72 (m, 12H, PC_6H_5), 7.54 (m, 8H, PC_6H_5), 7.43 (m, 2H, –CH=CH–), 3.54 (s, 3H, N–CH_3).

2.3.13. [CuI(trans-dppen)(mtdztH)]$_2$ (13)

Yellow crystals. Yield: 338 mg (47%), m.p. 188 °C; *Anal.* Calc. for $C_{29}H_{26}N_2ICuP_2S_2$: C, 48.44; H, 3.64; N, 3.90. Found: C, 48.40; H, 3.50; N, 3.75%. IR (cm^{-1}): 3458.2w, 3043.8m, 2947.5m, 1610.0m, 1554.2s, 1450.5vs, 1378.8.vs, 1272.2vs, 1199.5vs, 1131.7s, 1066.2vs, 974.5s, 763.0vs, 743.5vs, 623.6s, 538.3s, 510.5s, 433.0vs, 352.3s; UV–Vis [λ_{max} (nm), log ε]: ($CHCl_3$); 246.5 (3.99), 307.5 (4.41), 338.5 (3.05); ^1H NMR ($CDCl_3$, δ ppm): 11.34 (br 1H, NH), 7.48 (m, 12H, PC_6H_5), 7.26 (m, 8H, PC_6H_5), 7.17 (m, 2H, –CH=CH–), 2.49 (s, 3H, C–CH_3).

2.3.14. [CuI(trans-dppen)(bzoxtH)]$_2$ (14)

Brownish crystals. Yield: 332 mg (45%), m.p. 195 °C; *Anal.* Calc. for $C_{33}H_{27}NICuOP_2S$: C, 53.70; H, 3.69; N, 1.90. Found: C, 53.58; H, 3.49; N, 1.82%. IR (cm^{-1}): 3338.8m, 3040.5m, 1617.9.s, 1506.0vs, 1473.8s, 1445.7vs, 1278.9s, 1131.2vs, 1095.4vs, 930.7s, 744.8vs, 645.8s, 607.2s, 476.3s, 427.7s; UV–Vis [λ_{max} (nm), log ε]: ($CHCl_3$); 257.5 (4.28), 300.5 (4.30), 343.5 (3.13); ^1H NMR ($CDCl_3$, δ ppm): 11.23 (br, 1H, NH), 7.77 + 7.50 (m, 4H, CH_{bzoxtH}), 7.36 (m, 12H, PC_6H_5), 7.28 (m, 8H, PC_6H_5), 7.19 (m, 2H, –CH=CH–).

2.3.15. [CuI(trans-dppen)(mbzimtH$_2$)]$_2$ (15)

Pale yellow crystals. Yield: 548 mg (73%), m.p. 275 °C; *Anal.* Calc. for $C_{34}H_{30}N_2ICuP_2S$: C, 54.37; H, 4.03; N, 3.73. Found: C, 54.22; H, 3.91; N, 3.67%. IR (cm^{-1}): 3426.2m, 3121.3vs, 1618.2m, 1520.9s, 1492.5vs, 1467.7vs, 1383.1m, 1327.5s, 1187.4vs, 853.2m, 802.0vs, 720.7vs, 665.6s, 593.3s, 542.8s, 507.6m, 428.2w, 343.8w; UV–Vis [λ_{max} (nm), log ε]: ($CHCl_3$); 251.0 (4.27), 306.0 (4.40), 349.0 (3.08); ^1H NMR ($CDCl_3$, δ ppm): 12.39 (br, 2H, NH), 7.72 (m, 12H, PC_6H_5), 7.48(m, 8H, PC_6H_5), 7.33 (d, 2H, $H^7_{mbzimtH}$, $J_6 = 5$ Hz), 7.22 (s, 1H, $H^4_{mbzimtH}$), 7.17 (d, 2H, $H^6_{mbzimtH}$, $J = 5$ Hz), 7.00 (m, 2H, –CH=CH–), 2.39 (s, 3H, C–CH_3).

2.3.16. [CuI(trans-dppen)(pur6SH)]$_2$ (16)

Yellow crystals. Yield: 451 mg (61%), m.p. 285 °C; *Anal.* Calc. for $C_{31}H_{26}N_4ICuP_2S$: C, 50.38; H, 3.55; N, 7.58. Found: C, 50.15; H, 3.40; N, 7.45%. IR (cm^{-1}): 1434.5m, 3043.8m, 1608.4vs, 1552.3vs, 1479.5vs, 1434.4vs, 1408.6vs, 1210.7s, 1097.8s, 1015.9s, 873.2s, 747.3vs, 694.3vs, 509.0vs, 482.5m; UV–Vis [λ_{max} (nm), log ε]: ($CHCl_3$); 249.5 (4.26), 283.0 (4.19), 366.5 (3.57); ^1H NMR ($CDCl_3$ + DMSO-d_6, δ ppm): 13.72 (br, 2H, NH), 8.25 + 8.13 (s, 2H, CH_{pur6SH}), 7.73 (m, 12H, PC_6H_5), 7.23 (m, 8H, PC_6H_5), 6.96 (m, 2H, –CH=CH–).

3. Results and discussion

3.1. General considerations

The reaction of equimolar quantities of copper(I) bromide or iodide and *trans*-1,2-bis(diphenylphosphino)ethene (*trans*-dppen) followed by the addition of one equivalent of the apropriate thione (L) [L = pyridine-2-thione (py2SH), pyrimidine-2-thione (pymtH), tetrahydropyrimidine-2-thione (tHpymtH), 4-methyl-5-trifluoromethyl-4H-1,2,4-triazoline-3(2H)-thione (mftztH), 5-methyl-1,3,4-thiadiazole-2-thione (mtdztH), benz-1,3-oxazoline-2-thione (bzoxtH), 5-methyl-benz-1,3-imidazole-2-thione (mbzimtH_2), and 6-mercaptopurine (pur6SH) (Fig. 1) in dry acetonitrile/methanol solution at 30 °C afforded microcrystalline air stable solids which, on analysis were found to be of composition [CuX(*trans*-dppen)L].

Our initial use of *trans*-1.2-bis(diphenylphosphino)ethene as ligand in low valent coinage metal chemistry had been in the reaction with copper(I) chloride, which had led to formation of homobridged dinuclear derivatives of the type [CuCl(μ_2-dppen)(L)]$_2$ [10]. This was not surprising in view of the geometrical rigidity of the unsaturated carbon backbone which holds the two phosphorus atoms too far apart to chelate at a single metal centre. In respect of this finding we anticipated that dppen would adopt the same bridging mode upon coordination to copper(I) bromide or iodide. Moreover, the Cu···Cu separation of about 6 Å found in these diphosphine bridged dimers prevents the halide or thione-S donors from participating in additional bridges within the dimeric unit. However, one should additionally take the formation of other frequently observed structure types like thione-free dimers or even coordination polymers into consideration, as the structures of copper(I) halides are often determined by the choice of the halide. In fact, only on the grounds of the aforementioned composition were we able to definitively exclude these latter two possibilities, thus, all the new compounds turned out to be once more diphosphine-bridged dimers. Note that we have performed several additional experiments treating the metal salts with various phosphine/thione ratios or even applying more forcing reaction conditions to definitively conclude that the outcome of this reaction is independent of reaction conditions and ligand-to-metal ratio employed.

All prepared complexes are air-stable, coloured, diamagnetic, microcrystalline materials, slightly soluble in polar solvents such as acetonitrile and dimethylsulfoxide, and only marginally soluble in chloroform,

dichloromethane and acetone. Their solutions in acetonitrile and chloroform are non-conducting.

3.2. Spectroscopic investigations

The infrared spectra of compounds **1**–**16**, recorded over the range 4000–250 cm^{-1} are consistent with the formulations proposed, showing all of the bands required by the presence of the thione ligands. The shifts observed for these bands due to coordination in combination with the lack of ν(SH) bands at ca. 2500–2600 cm^{-1} as well as the characteristic NH stretching vibrations observed in the ~3150 cm^{-1} region, signify the exclusive S-coordination mode of the thione ligands. Moreover, the spectra of compounds under investigation contain distinct strong vibrational bands which are only slightly shifted with respect to those of the free donors.

The electronic absorption spectra of the complexes in chloroform solutions are dominated by two intense sharp main bands in the regions 245–265 and 280–308 nm, accompanied by a third one in the 312–410 region. The two former bands correspond to intraligand π* ← π transitions on the phenyl group of the phosphine ligand, since the uncoordinated *trans*-1,2-bis(diphenylphosphino)ethene reveals two strong absorptions at 258.5 and 296.9 nm which are known not to undergo significant shifts upon coordination to Cu(I), whereby the latter are attributed to thione-originating intraligand excitations.

Unfortunately, the prepared complexes are sparingly soluble in common organic solvents and in strongly polar ones such as DMSO and DMF. In addition, they decompose slowly in DMF even under nitrogen. Therefore, ^1H NMR spectra could be only be recorded in $CDCl_3$ or a mixture of $[D_6]DMSO/CDCl_3$. In most of these spectra the phenyl region is dominated by rather uninformative multiplets. Upon coordination, the signals due to bridging ethene protons of the phosphine ligand show a more complicated pattern with respect to those found for the free donor. In addition, they undergo low-field shifts towards the region of the signals attributable to the aromatic protons of the thione groups as well as to the aromatic phosphine protons. In some cases, the extent of overlapping does not allow to resolution of all these signals, making interpretation of the splitting pattern of the individual thione resonances very difficult. Nevertheless, these spectra confirm at least the existence of the complexes in solution. Moreover, the observation of a broad singlet in the 12–15 ppm region due to NH group, considerably highfield shifted with respect to that of the corresponding free donor, clearly indicates that the ligands bond to the metal in their thionato form.

3.3. Description of the structures

Single crystals of complexes **2** and **10** suitable for X-ray crystallographic study were grown by slow concentration of acetonitrile/methanol solutions of the compounds over several days at ambient temperature. Details regarding the crystal data collection and refinement are reported in Table 1. Bond lengths and angles around the Cu(I) are listed in Tables 2 and 3, and respective drawings of the complexes with the labelling of the atoms are given in Figs. 2 and 3. Complex **2** crystallizes in the monoclinic space group $P2_1/n$ with the unit cell containing two dinuclear species, whereas compound **10** crystallizes in the triclinic space group P. Its structure contains one discrete molecule per unit cell, as well as two lattice CH_3CN molecules; the latter solvate molecules do not interact specifically with the dimer and will not be further discussed. Both structures contain a centre of symmetry and each show some degree of molecular disorder. In **2**, atoms of the bromine and pymtH ligands are each disordered over two separate sites. Similarly three atoms of a phenyl ring are also disordered over two sites. In **10**, the dppen carbon atoms each occupy two sites and there are high displacement parameters associated with some of the phenyl ring carbon atoms.

Table 2
Selected bond lengths (Å) and angles (°) for (**2**)

Bond lengths			
Cu(1)–P(1)#1	2.2434(17)	S(1A)–C(1A)	1.691(9)
Cu(1)–P(2)	2.2757(17)	P(1)–C(6)	1.803(6)
Cu(1)–S(1B)	2.286(6)	P(2)–C(5)	1.818(6)
Cu(1)–Br(1B)	2.586(3)	C(5)–C(6)	1.327(8)
Bond angles			
P(1)#1–Cu(1)–P(2)	120.10(6)	S(1B)–Cu(1)–Br(1B)	109.92(17)
P(1)#1–Cu(1)–S(1A)	112.99(11)	Cu(1)#1–P(1)–C(6)	110.43(19)
P(1)#1–Cu(1)–Br(1B)	101.92(8)	Cu(1)–P(2)–C(5)	116.12(19)
P(2)–Cu(1)–S(1A)	100.87(15)	C(5)–C(6)–P(1)	127.1(4)
P(2)–Cu(1)–Br(1B)	101.75(8)	C(6)–C(5)–P(2)	122.1(4)

Symmetry transformations used to generate equivalent atoms: #1 $-x+1, -y+1, -z$.

Table 3
Selected bond lengths (Å) and angles (°) for (**10**)

Bond lengths			
Cu(1)–P(1)	2.2568(18)	S(1)–C(1)	1.694(6)
Cu(1)–P(2)	2.275(2)	P(1)–C(5A)	1.787(13)
Cu(1)–S(1)	2.3169(16)	P(2)–C(6A)#1	1.842(17)
Cu(1)–I(1)	2.7032(9)	C(5A)–C(6A)	1.316(14)
Bond angles			
P(1)–Cu(1)–P(2)	116.19(7)	S(1)–Cu(1)–I(1)	110.16(5)
P(1)–Cu(1)–S(1)	111.27(6)	Cu(1)–P(1)–C(5A)	121.0(6)
P(1)–Cu(1)–I(1)	104.52(5)	Cu(1)–P(2)–C(6A)#1	106.0(6)
P(2)–Cu(1)–S(1)	108.14(7)	C(6A)–C(5A)–P(1)	118.7(15)
P(2)–Cu(1)–I(1)	106.33(5)	C(5A)–C(6A)–P(2)#1	130.2(13)
Hydrogen bridge			
N(1)–H(1)	0.8800	I(1) ... N(1)	3.4870
NH(1)–I(1)	2.6400	I(1) ... H(1)–N(1)	161.0°

Symmetry transformations used to generate equivalent atoms: # $-x+1, -y+1, -z$.

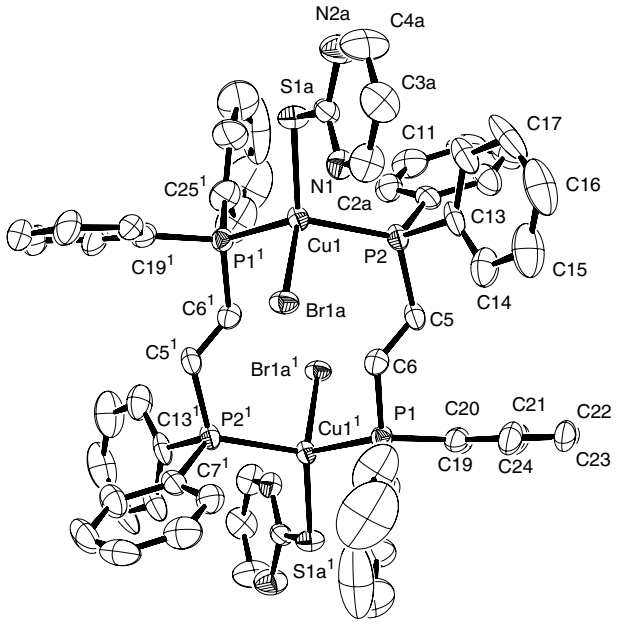


Fig. 2. A view of **2** with disorder removed. Displacement ellipsoids are shown in the 50% probability level.

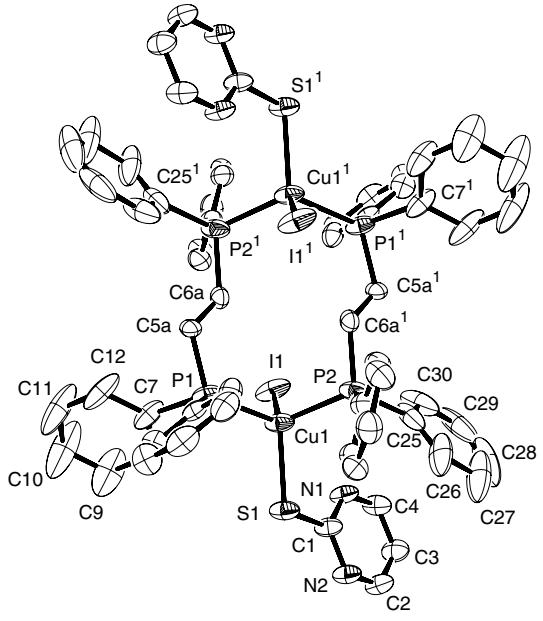


Fig. 3. An ORTEP view of **10** with disorder removed. Displacement ellipsoids are shown in the 50% probability level.

In general, the main structural characteristics of compounds **2** and **10** are very similar. A comparison of the structural parameters of the two compounds with the three previously described copper(I) chloride counterparts $[CuCl(\mu_2\text{-}trans\text{-dppen})(pymtH)]_2$, $[CuCl(\mu_2\text{-}trans\text{-dppen})(tHpymtH)]_2$ and $[CuCl(\mu_2\text{-}trans\text{-dppen})(mftzdtH)]_2$ [10] also reveals strong similarities of their cores. The subsequent comparative discussion will therefore mainly focus on details which underline some of the most interesting fine differences between the two structures under investigation.

In the two dimeric complexes the geometry of each copper(I) involved is a highly distorted tetrahedron, with the metal atom being surrounded by one halogen atom, the S-atom of the pyrimidine-2-thione ligand and two bridging P-atoms belonging to two different diphosphine units. Interestingly, the most regular angle arises even between these two terminally bonded ligands, being in the two complexes almost equal to the ideal tetrahedral value of 109.4°, although this arrangement is accompanied by the formation of the expected strong intramolecular hydrogen bond between the halogen and the hydrogen atom attached to N(1) only within the structure of **10**. Contrary to that, the P–Cu–P angles are markedly larger than the tetrahedral one, with the irregularities being counterbalanced by appropriate smaller P–Cu–Br angles. Particular attention deserve the two S–Cu–P angles around each copper atom, which are in **10** close to the ideal value, against the situation in **2**, where two essential different values are present, one of them being significantly narrowed.

While angular distortions from the ideal tetrahedral geometry around each Cu(I) are considerable, bond distances involving the central metal atom appear normal, generally retaining their values within the range normally observed for tetrahedrally coordinated copper(I) bonded to two phosphorous, one halogen and one sulfur atoms. In detail, the Cu–S bond distances of 2.286(6) and 2.3169(17) Å in **2** and **10**, respectively, remain typical of the usual range of 2.27–2.35 Å observed in other mixed ligand copper(I) complexes bearing terminal bonded pyrimidine-2-thione [17,7]. The Cu(1)–Br(1) bond length of 2.586(3) Å in **2** is quite large for a bromine terminally bonded to a copper(I) centre in a tetrahedral coordination environment, clearly larger than the value of 2.4455 (11) Å found in $[CuBr(py2SH)(PPh_3)]_2$ [18] or that of 2.5369(4) Å found in [CuBr(pymtH)-(dppp)] (dppp = 1,3-bis(diphenylphosphino)propane) [7]. As in the three copper(I) chloride counterparts, each copper atom participates in two inequal Cu–P bonds, with the inequality being particularly marked in **2**. Nevertheless, the values of the individual Cu–P distances remain all within the limits expected for tetrahedrally coordinated Cu(I).

Upon coordination, some significant alterations within the *trans*-dppen geometries appear, which merit special mention. In detail, the P(1)–C(6)–C(5) angle in **2** is very close to the P–C–C angle of 126.9(3)° found in the free *trans*-dppen [19], but the value for the P(2)–C(5)–C(6) angle is suppressed by 5°. At the same time the olefinic C=C double-bond may be considered a little shorter (1.327(8) in **2**, against the value of 1.340(15) found in the non-coordinated *trans*-dppen). Although statistically this difference is not significant, such moderate conformational distortions from the ideal geometry

within the diphosphine units are observed in the three previously described copper(I) chloride counterparts, and are obviously inevitable in order to allow the 10-membered $Cu_2P_4C_4$-ring to be formed. This is strongly supported by the fact that the conformational features of the dppen unit in the dimeric [ClAu(μ-*trans*-dppen)AuCl], where the two metal centres are linked only by one bridging diphosphine unit, which is therefore not forced to lose its favourable conformation, remain practically unaffected [20]. Each of the dppen carbon atoms (C5 and C6) in **10** are disordered over two sites such that the errors associated with the geometries here are high. Finally, another feature of the two molecules under investigation that deserves some interest occurs in respect of the coordination plane of the diphosphine bridges. As indicated by the P(1)–C(6)–C(5)–P(2) torsion angles (169.8 (3)° in **2** and −177.9(10)° in **10**), upon coordination the two P atoms twist about the ethene bridge altering the dihedral angle through the four atoms by about 6.8° and 5.5° respectively with respect to the corresponding value (176.6°) in the free *trans*-dppen, thus significantly modifying the bite size of the diphosphine. Nevertheless, these conformational rearrangements do not affect noticeably the Cu···Cu separation, which remains actually close to the values found in the three already reported copper(I) chloride derivatives.

4. Conclusion

In this paper, we demonstrate the coordination behaviour of copper(I) bromide and iodide in the presence of *trans*-1,2-bis(diphenylphosphino)ethene and a series of heterocyclic thiones. In all the complexes Cu(I) adopts the common distorted pseudo-tetrahedral coordination environment with the neutral thione ligands coordinating to the metal center through the exocyclic sulfur atom. The *trans*-1,2-bis(diphenylphosphino)ethene ligand coordinates in a bidentate manner the two metals exclusively favouring dimeric complexes of the formula $[CuX(\mu_2\text{-}trans\text{-dppet})L]_2$ independent of the reaction stoichiometries and conditions chosen. On the grounds of our hitherto results, this doubly bridging mode of coordination seems to be practically the only possibility for the diphos ligand under investigation to bind Cu(I) centres. Thus, this behaviour supports once more our supposition that for diphosphines inefficient to chelate at a single metal center, but having the appropriate geometrical features to act as bridging ligands, dimerization is on principle favoured over polymerization.

5. Supplementary material

CCDC Nos. 238432 (**2**) and 238433 (**10**) contain the supplementary crystallographic data for this paper. These data can be obtained free of charge at www.ccdc.cam.ac.uk/conts/retrieving.html [or from the Cambridge Crystallographic Data Centre, 12, Union Road, Cambridge CB2 1EZ, UK; fax: (internat.) +44-1223/336-033; e-mail: deposit@ccdc.cam.ac.uk].

Acknowledgement

We thank the EPSRC X-ray crystallography service at the University of Southampton for collecting the X-ray data.

References

[1] (a) E.S. Raper, Coord. Chem. Rev. 129 (1994) 91;
(b) E.S. Raper, Coord. Chem. Rev. 165 (1997) 475.
[2] S.K. Hadjikakou, P. Aslanidis, P.D. Akrivos, P. Karagiannidis, B. Kojic-Prodic, M. Luic, Inorg. Chim. Acta 197 (1992) 31.
[3] P. Aslanidis, S.K. Hadjikakou, P. Karagiannidis, B. Kojic-Prodic, M. Luic, Polyhedron 13 (1994) 3119.
[4] P. Aslanidis, P.J. Cox, S.K. Hadjikakou, C.D. Antoniadis, Eur. J. Inorg. Chem. (2002) 2216.
[5] S.K. Hadjikakou, P. Aslanidis, P. Karagiannidis, A. Hountas, A. Terzis, Inorg. Chim. Acta 184 (1991) 161.
[6] S.K. Hadjikakou, P. Aslanidis, P. Karagiannidis, D. Mentzafos, A. Terzis, Inorg. Chim. Acta 186 (1991) 199.
[7] P. Aslanidis, P.J. Cox, S. Divanidis, A.C. Tsipis, Inorg. Chem. 41 (2002) 6875.
[8] P. Aslanidis, P.J. Cox, S. Divanidis, P. Karagiannidis, Inorg. Chim. Acta 357 (2004) 1063.
[9] P.J. Cox, P. Aslanidis, P. Karagiannidis, Polyhedron 19 (2000) 1615.
[10] P. Aslanidis, P.J. Cox, S. Divanidis, P. Karagiannidis, Inorg. Chim. Acta 357 (2004) 4231.
[11] P. Karagiannidis, S.K. Hadjikakou, P. Aslanidis, A. Hountas, I norg. Chim. Acta 178 (1990) 27.
[12] Z. Otwinowski, W. Minor, in: C.W. CarterJr., R.M. Sweet (Eds.), Macromolecular Crystallography, Part A, vol. 276, Academic Press, New York, 1997, pp. 307–326.
[13] R. Hooft, COLLECT Data Collection Software. Nonius BV, 1998.
[14] A. Altomare, M.C. Burla, M. Camalli, G.L. Cascarano, C. Giacovazzo, A. Guagliardi, A.G.G. Moliterni, G. Polidori, R. Spagna, J. Appl. Cryst. 32 (1999) 115.
[15] G.M. Sheldrick, SHELXL-97. Program for Crystal Structure Analysis (Release 97–2), University of Göttingen, Germany, 1997.
[16] L.J. Farrugia, J. Appl. Crystallogr. 30 (1997) 565.
[17] P. Aslanidis, S.K. Hadjikakou, P. Karagiannidis, M. Gdaniec, Z. Kosturkiewicz, Polyhedron 12 (1993) 2221.
[18] T.S. Lobana, A. Castineiras, Polyhedron 21 (2002) 1603.
[19] H. Schmidbaur, G. Reber, A. Schier, F.E. Wagner, G. Müller, Inorg. Chim. Acta 147 (1988) 143.
[20] D.S. Eggleston, J.V. McArdle, G.E. Zuber, J. Chem. Soc., Dalton Trans. (1987) 677.

Available online at www.sciencedirect.com
SCIENCE DIRECT®
Polyhedron 24 (2005) 359–368
POLYHEDRON
www.elsevier.com/locate/poly

Synthesis, molecular, crystal and electronic structure of $[RuCl_3(NO)(PPh_3)(HPz)]$

J.G. Małecki [a,*], M. Jaworska [b], R. Kruszynski [c,1]

[a] Department of Inorganic and Radiation Chemistry, Institute of Chemistry, University of Silesia, 9th Szkolna Street, 40006 Katowice, Poland
[b] Department of Theoretical Chemistry, Institute of Chemistry, University of Silesia, 9th Szkolna Street, 40006 Katowice, Poland
[c] Department of X-Ray Crystallography and Crystal Chemistry, Institute of General and Ecological Chemistry, Łódź University of Technology, 116 Żeromski Street, 90924 Łódź, Poland

Received 22 October 2004; accepted 5 December 2004
Available online 19 December 2004

Abstract

The reaction of $[RuCl_3(NO)(PPh_3)_2]$ complex with pyrazole has been examined. The new ruthenium complex – $[RuCl_3(NO)(PPh_3)(C_3H_4N_2)]$ has been obtained and characterised by IR and UV–Vis measurements. Crystal, molecular and electronic structures of the complexes have been determined. The electronic spectrum of the complex was calculated by the TDDFT method.
© 2004 Elsevier Ltd. All rights reserved.

Keywords: Ruthenium nitrosyl complexes; Pyrazole; X-ray structure; TDDFT method

1. Introduction

The chemistry of ruthenium nitrosyls is a recent renewed interest in particular in the field of medicinal inorganic chemistry [1–10]. The complexes are investigated as controlled NO-releasing agents for medicinal applications, in particular for the control of high blood pressure (vasodilatation), and as antitumor agents which might perform the release of cytotoxic NO within tumor cells, thus leading to cell death. In other hand the nitrosyl ruthenium complexes have been studied due to their importance as potential catalysts in homogeneous processes [11–16].

In this paper we report the synthesis of the new ruthenium nitrosyl complex with pyrazole ligand. The molecular and crystal structures of the obtained complex are presented. The electronic structure was calculated with the DFT method by using the GAUSSIAN03 program package.

2. Experimental

All reagents used to the synthesis of the complex are commercially available and were used without further purification. The $[RuCl_3(NO)(PPh_3)_2]$ complex was synthesized by publishing procedure [17] from $RuCl_3NO$, which was prepared by passing NO through a solution of $RuCl_3$ in dichloromethane until the solution become red followed by evaporation to dryness. The dried solid obtained was kept in a vacuum desiccator for at least three days before used. Gaseous NO, obtained in the reaction: $2NaNO_2 + 3H_2SO_4 + FeSO_4 \rightarrow 2NO + 2NaHSO_4 + Fe_2(SO_4)_3 + 2H_2O$, was purified by passing through the washers with concentrated KOH solution and over solid NaOH.

* Corresponding author. Tel.: +48 32 255911; fax: +48 32 255911.
E-mail addresses: gmalecki@us.edu.pl (J.G. Małecki), mj@tc3.ich.us.edu.pl (M. Jaworska), kruszyna@p.lodz.pl (R. Kruszynski).
[1] A holder of the Foundation for Polish Science (FNP) scholarship.

0277-5387/$ - see front matter © 2004 Elsevier Ltd. All rights reserved.
doi:10.1016/j.poly.2004.12.001

2.1. Synthesis of $[RuCl_3(NO)(PPh_3)(C_3H_4N_2)]$

A mixture of $[RuCl_3(NO)(PPh_3)_2]$ (0.76 g; 1×10^{-3} mol) and pyrazole (0.42 g; 6×10^{-3} mol) in acetone (100 cm^{-3}) was refluxed for 4 h, cooled and filtered. The yellow-orange crystals suitable for X-ray crystal analysis grew after the reaction mixture was left overnight.

Yield 92%. IR (KBr): 3137 ν_{NH}; 3058 $\nu_{CH-pyrazole}$; 3021, $\nu_{CH-phenyl}$; 1879 ν_{NO}; 1572 ν_{CN}, $\nu_{C=C}$; 1487 $\delta_{(C-CH\ in\ the\ plane)}$; 1436 $\nu_{Ph(P-Ph)}$; 1320 $\delta_{(NH;\ CH)}$; 1095 $\delta_{(C-CH\ in\ the\ plane)}$; 994 $\delta_{(C-C\ out\ of\ the\ plane)}$; 749 $\delta_{(C-C\ out\ of\ the\ plane)}$; 687 $\delta_{(C-C\ in\ the\ plane)}$; 598 ν_{P-Ph}. *Anal*. Calc. for $C_{21}H_{19}Cl_3N_3OPRu$: C, 44.42%; H, 3.37%; Cl, 18.73%; N, 7.40%; O, 2.28%; P, 5.46%; Ru, 17.80%. Found: C, 44.12%; H, 3.35%; N, 7.29%.

2.2. Physical measurements

Infrared spectra were recorded on a Nicolet Magna 560 spectrophotometer in the spectral range 4000–400 cm^{-1} with the sample in the form of KBr pellet. Electronic spectra were measured on a spectrophotometer Lab Alliance UV–Vis 8500 in the range 800–200 nm in dichloromethane solution. Elemental analyses (C, H, N) were performed on a Perkin–Elmer CHN–2400 analyzer.

2.3. DFT calculations

GAUSSIAN03 program [18] was used in the calculations. The geometry optimization was carried out with the DFT method with the use of B3LYP functional [19,20]. The electronic spectrum was calculated with the TDDFT method [21].

Two basis set were used in the calculation. LANL2DZ basis set [22] was used on the ruthenium atom, 6–31G(d) on the chlorine, nitrogen, oxygen and carbon atoms and 6–31G basis on the hydrogen atoms in the first calculations the second one was performed using the SSD basis set on ruthenium atom. The obtained results of calculation were compared.

Natural bond orbital (NBO) analyses was performed using the NBO program as implemented in the GAUSSIAN03 program.

2.4. Crystal structures determination and refinement

A orange crystal of $[RuCl_3(NO)(PPh_3)(C_3H_4N_2)]$ was mounted on a KM–4–CCD automatic diffractometer equipped with CCD detector, and used for data collection. X-ray intensity data were collected with graphite monochromated Mo Kα radiation ($\lambda = 0.71073$ Å) at temperature 293.0(2) K, with ω scan mode. The 21-s exposure time was used and a full Ewald sphere was collected up to $2\theta = 50.28°$. The unit cell parameters were determined from least-squares refinement of the setting angles of 16,950 strongest reflections. Details concerning crystal data and refinement are given in Table 1. During the data reduction above decay correction coefficient was taken into account. Lorentz, polarization, and numerical absorption [23] corrections were applied. The structure was solved by direct methods. All the non-hydrogen atoms were refined anisotropically using full-matrix, least-squares technique on F^2. All the hydrogen atoms were found from difference Fourier synthesis after four cycles of anisotropic refinement, and refined as "riding" on the adjacent atom with individual isotropic temperature factor equal 1.2 times the value of equivalent temperature factor of the parent atom. SHELXS97 [24], SHELXL97 [25] and SHELXTL [26] programs were used for all the calculations. Atomic scattering factors were those incorporated in the computer programs.

3. Results and discussion

Refluxing of the $[RuCl_3(NO)(PPh_3)_2]$ complex with an excess of pyrazole in acetone leads to the new ruthenium nitrosyl $[RuCl_3(NO)(PPh_3)(C_3H_4N_2)]$ complex in high yield. The elemental analysis of the complex is in

Table 1
Crystal data and structure refinement for $[RuCl_3(NO)(PPh_3)(C_3H_4N_2)]$

Empirical formula	$C_{21}H_{19}Cl_3N_3OPRu$
Formula weight	567.78
Crystal system, space group	orthorhombic *Pca*2/1 (No. 29)
Unit cell dimensions	
a (Å)	22.2395(9)
b (Å)	11.8466(5)
c (Å)	17.6351(6)
α (°)	90
β (°)	90
γ (°)	90
Volume ($Å^3$)	4646.2(3)
Z	8
D_{calc} (Mg/m^3)	1.623
Absorption coefficient (mm^{-1})	1.107
F(000)	2272
Crystal size (mm)	$0.249 \times 0.281 \times 0.286$
Theta range for data collection (°)	3.02–25.14
Index ranges	$-26 \leqslant h \leqslant 26$, $-14 \leqslant k \leqslant 13$, $20 \leqslant l \leqslant 20$
Reflections collected/unique	47,979/8274 [$R_{(int)} = 0.0289$]
Completeness to $2\theta = 25.11$	99.6%
Maximum and minimum transmission	0.789 and 0.722
Refinement method	full-matrix least-squares on F^2
Data/restraints/parameters	8274/1/542
Goodness-of-fit on F^2	1.019
Final *R* indices [$I > 2\sigma(I)$]	$R_1 = 0.0206$, $wR_2 = 0.0485$
R indices (all data)	$R_1 = 0.0223$, $wR_2 = 0.0490$
Largest difference between peak and hole (e $Å^{-3}$)	0.318 and −0.453

good agreement with its formulation. The characteristic bands of the pyrazole ligand ν(NH) at 3137 cm^{-1} and ν(CN), ν(C=C) at 1572 cm^{-1} are present in the IR spectrum of the obtained complex. The spectrum of the complex shows ν (NO) at 1879 cm^{-1}, what is consistent with the linear NO range of Haymore and Ibers (ν(NO) above 1620–1610 cm^{-1} were assigned to linear M–N–O systems, while ν(NO) below 1610 cm^{-1} were assigned to bent M–N–O systems) [27].

3.1. Crystal structure

The $[RuCl_3(NO)(PPh_3)(C_3H_4N_2)]$ complex crystallises in the orthorhombic space group *Pca*2/1 The relative orientation of molecules is depicted in Fig. 1 which also shows the displacement vibration ellipsoids (structural drawing of the complex is presented in Fig. 2.). The selected bond lengths and angles are listed in Table 2. The two crystallographically independent molecules are structurally nearly identical (I and II hereafter for molecules containing Ru(1) and Ru(51), respectively). The most different distances are Ru(1)–Cl(1) 2.396(7) Å and Ru(51)–Cl(51) 2.372(7) Å. The most different angles are N(1)–Ru(1)–N(2) 94.68(10)° and N(51)–Ru(51)–N(52) 91.16(10)°. The ruthenium atom is in a distorted octahedral environment with linear N–O group *trans* to one of Cl ligands, two mutually *cis* Cl ligands and the PPh_3 and pyrazole molecules in *trans*. The short bond distances Ru–N (1.735(3) Å), N–O (1.134(3) Å) and particularly the Ru–N–O (176.4(3)°) angle (average values) strongly indicate the nitrosonium character of the NO group, in accordance with the similar data observed for the other ruthenium nitrosyl complexes [28]. The Ru–Cl bond distances (2.372(7)–2.396(7) Å) fall in the range reported in the literature for Ru^{II} complexes, with the exception of the

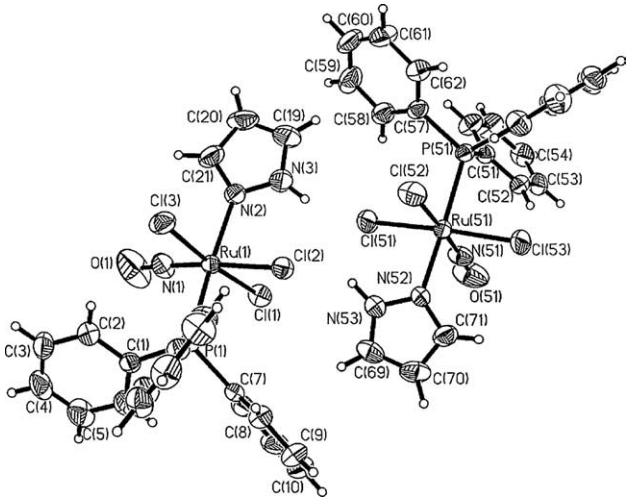


Fig. 1. Relative orientation of the two molecules of the $[RuCl_3(NO)(PPh_3)(C_3H_4N_2)]$ complex in the asymmetric unit. Thermal vibration ellipsoids scaled to include 50% probability.

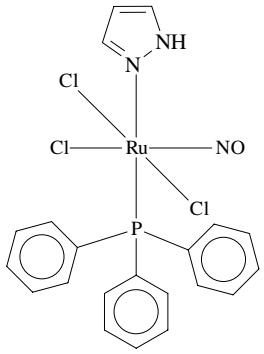


Fig. 2. Structural drawing of $[RuCl_3(NO)(PPh_3)(C_3H_4N_2)]$.

chlorine *trans* to the nitrosyl group (2.342 Å average value). The NO bond length (1.135(3), 1.133(3) Å) is a little longer than the distance 1.06 Å of the free NO^+ group [29]. The pyrazole and triphenylphosphine ligands display Ru–N and Ru–P distances which are in the range of these reported in the literature.

The bond valences were computed as $v_{ij} = \exp[(R_{ij} - d_{ij})/0.37]$ [30–33], where R_{ij} is the bond-valence parameter (in the formal sense R_{ij} is the single-bond length between *i* and *j* atoms) [22]. The R_{Ru-N}, R_{Ru-P}, R_{Ru-Cl} were taken as 1.656 [34], 1.985 [35] and 1.932 [34], respectively. The computed bond valences of the ruthenium are $v_{Ru-N(nitrosyl)} = 0.817$, $v_{Ru-N(pyrazole)} = 0.262$, $v_{Ru-P} = 0.334$; $v_{Ru-Cl} = 0.285, 0.335, 0.300$ v.u. (valence units) for molecule I and $v_{Ru-N(nitrosyl)} = 0.801$, $v_{Ru-N(pyrazole)} = 0.265$, $v_{Ru-P} = 0.325$; $v_{Ru-Cl} = 0.304$, 0.327, 0.300 v.u. which means that Ru–N(nitrosyl) bonds are almost three times stronger than other bonds, and the Ru–N(pyrazole) bonds are the weakest ones. The valence sum rule states that the sum of the valences of the bonds formed by an atom is equal to the valence of the atom. Computed total valence of the Ru atom is 2.332 and 2.323 v.u. for molecules I and II, respectively. Which means that differences in coordination sphere arrangement are local in character and do not influence the molecule.

The three intermolecular hydrogen bond [36–38] linking the Cl ligand and pyrazole ring N(53)–H(53N)···Cl(1) (D···A distance 3.368(2) Å, D–H···A angle 128.0°), C(53)–H(53)···Cl(2) (#1 $x + 1/2, -y - 3, z$) (D···A distance 3.316(3) Å, D–H···A angle 116.7°) and NO with pyrazole C(71)–H(71)···O(1) (#2 $x, y - 1, z$) (D···A distance 3.208(4) Å, D–H···A angle 126.0°) atoms are observed (Table 3). Other intramolecular hydrogen bonds are presented in the structure of the complex: between pyrazole N(3)–H(3A) and Cl(2) (D···A distance 3.092(3) Å, D–H···A angle 115.4°), N(53)–H(53N) and Cl(51) (D···A distance 3.160(2) Å, D–H···A angle 122.6°), between phenyl C(14)–H(14) and Cl(2) (D···A distance 3.372(3) Å, D–H···A angle 140.3°), C(58)–H(58) and Cl(51) (D···A distance 3.268(3) Å, D–H···A angle 112.8°), C(64)–H(64) and

Table 2
Bond lengths (Å) and angles (°) for $[RuCl_3(NO)(PPh_3)(C_3H_4N_2)]$

Bond lengths (Å)	
Ru(1)–Cl(1)	2.396(7)
Ru(1)–Cl(2)	2.337(6)
Ru(1)–Cl(3)	2.378(7)
Ru(1)–N(1)	1.731(2)
Ru(1)–N(2)	2.151(2)
Ru(1)–P(1)	2.391(7)
N(1)–O(1)	1.135(3)
Ru(51)–Cl(51)	2.372(7)
Ru(51)–Cl(52)	2.346(8)
Ru(51)–Cl(53)	2.377(7)
Ru(51)–N(51)	1.738(3)
Ru(51)–N(52)	2.147(2)
Ru(51)–P(51)	2.401(8)
N(51)–O(51)	1.133(3)
Bond angles (°)	
Cl(1)–Ru(1)–Cl(2)	85.68(2)
Cl(1)–Ru(1)–N(1)	88.44(9)
Cl(3)–Ru(1)–N(1)	93.00(9)
Cl(2)–Ru(1)–Cl(3)	93.04(3)
N(1)–Ru(1)–N(2)	94.68(10)
Cl(1)–Ru(1)–N(2)	87.09(6)
Cl(2)–Ru(1)–N(2)	86.89(7)
Cl(3)–Ru(1)–N(2)	87.33(7)
Cl(1)–Ru(1)–P(1)	95.58(2)
Cl(2)–Ru(1)–P(1)	86.16(2)
Cl(3)–Ru(1)–P(1)	89.83(3)
N(1)–Ru(1)–P(1)	92.58(8)
N(2)–Ru(1)–P(1)	172.34(7)
Cl(1)–Ru(1)–Cl(3)	174.33(3)
N(1)–Ru(1)–Cl(2)	173.83(10)
Ru(1)–N(1)–O(1)	176.6(3)
Cl(51)–Ru(51)–Cl(52)	87.31(3)
Cl(51)–Ru(51)–N(51)	89.73(10)
Cl(53)–Ru(51)–N(51)	90.78(9)
Cl(52)–Ru(51)–Cl(53)	92.04(3)
N(51)–Ru(51)–N(52)	91.16(10)
Cl(51)–Ru(51)–N(52)	87.80(6)
Cl(52)–Ru(51)–N(52)	86.70(6)
Cl(53)–Ru(51)–N(52)	88.47(6)
Cl(51)–Ru(51)–P(51)	92.68(3)
Cl(52)–Ru(51)–P(51)	87.47(3)
Cl(53)–Ru(51)–P(51)	90.99(3)
N(51)–Ru(51)–P(51)	94.69(8)
N(52)–Ru(51)–P(51)	174.13(7)
Cl(51)–Ru(51)–Cl(53)	176.24(3)
N(51)–Ru(51)–Cl(52)	176.41(9)
Ru(51)–N(51)–O(51)	176.1(2)

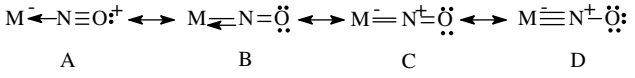
Cl(52) (D···A distance 3.501(3) Å, D–H···A angle 147.1°) and between phenyl C(52)–H(52) and N_{NO}(51) (D···A distance 3.035(4) Å, D–H···A angle 109.0°). In this way infinite three-dimensional hydrogen-bonded net has been created.

3.2. Geometry and electronic structure

The optimized geometry parameters for the complex are given in Table 4. In Table 5 the energies of several HOMO and LUMO orbitals are gathered. The calculated bond lengths agree well with the experiment. The largest difference were found for the ruthenium–chlorine bonds (0.152 Å, 0.056 Å, 0.084 Å – LANL2DZ basis and 0.114 Å, 0.028 Å, 0.045 Å – SSD for Ru–Cl(1), Ru–Cl(2) and Ru–Cl(3), respectively), but the relative differences in these bond lengths are reproduced in the calculations. The N–O distance calculated by using both basis sets are comparable (the difference is 0.005 Å). The SSD basis set has given better $Ru–N_{(NO)}$ and Ru–P distances.

In Table 6 the atomic charges from natural population analysis (NPA) are shown. The formal charge of ruthenium is +2 in this complex. The calculated charge, obtained from NPA, on the ruthenium is close 0.342. This is a result from a charge donation from chloride ions and triphenylphosphine group. There are large positive charges on the phosphorus atom (1.268, total charge on PPh_3 is 1.18), and the charges on the chloride ions are significantly smaller than −1 (Cl1 −0.491, Cl2 −0.409 and Cl3 −0.462). The charge on the pyrazole nitrogen atom bonded with ruthenium is negative (−0.318) – the pyrazole ligands act as electron acceptors (total charge on pyrazole ligand is −0.14). The total charge on the NO group is 0.217 (the charge of $N_{(NO)}$ is 0.370). The π-acceptor nature of NO^+ enhances π-donation by *trans* chlorine ligand, and according to the structural *trans* effect the Ru–Cl(2) distance is shorter than the other ruthenium chlorine ones. The *trans* effect of NO ligand in the complex is presented in Fig. 3.

The linear unit M–NO is usually deemed to coordinate as NO^+ to the metal. In the valence-bond treatment the resulting NO^+ group is considered to involve sp hybridization at the N and O atoms. The following resonance forms may present the linear bonding mode:



A B C D

Taking into consideration the electron population in the Ru–N and N–O bonds, from NBO analysis, (Ru–N/(BD + BD*) = 5.099, N–O/BD = 1.991 and N–O/BD* = 0.018) the resonance structure D becomes more important for the investigated complex.

Table 3
Hydrogen bonds for $[RuCl_3(NO)(PPh_3)(C_3H_4N_2)]$ (Å and °)

D–H···A	*d*(D–H)	*d*(H···A)	*d*(D···A)	∠(DHA)
N(3)–H(3A)···Cl(2)	0.86	2.62	3.092(3)	115.4
N(53)–H(53N)···Cl(51)	0.94	2.55	3.160(2)	122.6
N(53)–H(53N)···Cl(1)	0.94	2.71	3.368(2)	128.0
C(14)–H(14)···Cl(2)	0.93	2.60	3.372(3)	140.3
C(52)–H(52)···N(51)	0.93	2.60	3.035(4)	109.0
C(53)–H(53)···Cl(2)#1	0.93	2.79	3.316(3)	116.7
C(58)–H(58)···Cl(51)	0.93	2.79	3.268(3)	112.8
C(64)–H(64)···Cl(52)	0.93	2.68	3.501(3)	147.1
C(71)–H(71)···O(1)#2	0.93	2.57	3.208(4)	126.0

Symmetry transformations used to generate equivalent atoms: #1 $x + 1/2, -y - 3, z$; #2 $x, y - 1, z$.

Table 4
Optimized geometry parameters for $[RuCl_3(NO)(PPh_3)(C_3H_4N_2)]$

	LANL2DZ	SSD	Experimental
Bond lengths (Å)			
Ru–N1$_{(NO)}$	1.766	1.742	1.734
Ru–N2$_{(HPz)}$	2.174	2.176	2.149
Ru–Cl1	2.500	2.462	2.384
Ru–Cl2	2.398	2.370	2.342
Ru–Cl3	2.462	2.423	2.378
Ru–P	2.459	2.443	2.396
N–O	1.150	1.155	1.134
Bond angles (°)			
Cl(1)–Ru(1)–Cl(2)	87.40	87.32	86.50
Cl(1)–Ru(1)–N(1)	86.79	87.94	89.09
Cl(3)–Ru(1)–N(1)	92.30	92.45	91.89
Cl(2)–Ru(1)–Cl(3)	93.49	92.15	92.54
N(1)–Ru(1)–N(2)	94.57	93.03	92.92
Cl(1)–Ru(1)–N(2)	87.28	87.18	87.45
Cl(2)–Ru(1)–N(2)	85.20	85.15	86.80
Cl(3)–Ru(1)–N(2)	88.53	88.28	87.90
Cl(1)–Ru(1)–P(1)	94.56	94.60	94.13
Cl(2)–Ru(1)–P(1)	85.34	86.86	86.82
Cl(3)–Ru(1)–P(1)	89.79	89.88	90.41
N(1)–Ru(1)–P(1)	95.07	95.11	93.64
N(2)–Ru(1)–P(1)	170.28	171.73	173.24
Cl(1)–Ru(1)–Cl(3)	175.62	175.46	175.29
N(1)–Ru(1)–Cl(2)	174.19	175.00	175.12
Ru(1)–N(1)–O(1)	174.58	175.15	176.35

The structure of the M–NO bond is composed of a σ-bond, using the nitrogen lone pair and two π-interactions involving the filled d_{xz} and d_{yz} orbitals on ruthenium atom and the π* orbitals of the NO (in this complex LUMO and LUMO + 1) [39]. The LUMO and LUMO + 1 orbitals are composed mainly of π^*_{NO} orbitals (about 63%). In the occupied orbitals the π^*_{NO} are distributed among several MOs, but their participation do not excess 15%. On the basis of the molecular orbital composition and the small charge on the NO group (Table 6) the NO^+ character of nitrosyl in this complex can be confirmed.

The HOMO orbital is d_{xy} metal orbital with the admixture of chlorine π orbitals. HOMO − 1, HOMO − 2 and HOMO − 3 are π orbitals of phenyl groups with a contribution from the π Cl atoms. LUMO + 2 and LUMO + 3 are d_z^2 and $d_{x^2-y^2}$ orbitals with an antibonding admixture of the chlorine, phosphorus and pyrazole nitrogen lone pairs orbitals The HOMO − 4, HOMO − 5 and HOMO − 6 orbitals are π type (phenyl and Cl) with a substantial contribution from the appropriate d ruthenium orbitals. The participation of d_{xy}, d_{xz} and d_{yz} orbitals is visible in the lowest HOMO orbitals (H − 15, H − 16, H − 18, H − 19, H − 20, H − 21, H − 22) which are mainly π orbitals of phenyl with contribution of π Cl. The pyrazole ligand participates in lower HOMO orbitals (H − 8, H − 12 and H − 13) with contribution from π phenyl and Cl orbitals. The character of the HOMO and LUMO orbitals calculated by using the SSD basis set on ruthenium are close to these obtained from calculation with LANL2DZ basis. The energy of appropriate HOMO and LUMO orbitals calculated with SSD basis set is

Table 5
The energy and character of upper valence MO for $[RuCl_3(NO)(PPh_3)(C_3H_4N_2)]$

MO	*E* (eV)	Character
LANL2DZ		
H − 21	−9.55	$d_{xz} + \sigma_{Ph} + \sigma_P + \pi_{NO}$
H − 20	−9.45	$d_{yz} + \sigma_{Ph} + \sigma_P + \pi_{NO}$
H − 19	−9.31	$d_{xz} + \sigma_{Ph} + \sigma_P$
H − 18	−9.15	$d_{yz} + \sigma_{Ph} + \sigma_P$
H − 17	−8.96	$\sigma_{Cl} + \pi_{Ph}$
H − 16	−8.83	$d_{xz} + \pi_{Cl} + \sigma_P + \sigma_N + \sigma_{Cl}$
H − 15	−8.77	$d_{yz} + \pi_{Cl} + \sigma_P$
H − 14	−8.29	σ_{Cl}
H − 13	−7.73	$\pi_{Cl} + \pi_{HPz}$
H − 12	−7.57	π_{HPz}
H − 11	−7.52	π_{Cl}
H − 10	−7.40	$\pi_{Ph} + \pi_{HPz}$
H − 9	−7.31	π_{Ph}
H − 8	−7.25	π_{HPz}
H − 7	−7.17	$\pi_{Ph} + \pi_{Cl}$
H − 6	−7.07	π_{Ph}
H − 5	−6.97	$d_{yz} + \pi_{Ph} + \pi_{Cl}$
H − 4	−6.95	π_{Cl}
H − 3	−6.90	π_{Cl}
H − 2	−6.84	π_{Ph}
H − 1	−6.75	$\pi_{Ph} + \pi_{Cl} + n_P$
H	−6.61	$d_{xy} + \pi_{Cl}$
L	−3.08	$d_{xz} + \pi^*_{NO}$
L + 1	−3.05	$d_{yz} + \pi^*_{NO}$
L + 2	−2.49	$d_z^2 + \sigma_{Cl}$
L + 3	−1.95	$d_{x^2-y^2} + \sigma_{Cl} + \sigma_P$
L + 4	−0.99	π_{Ph}
L + 5	−0.78	$\pi_{Ph} + \pi_P$
L + 6	−0.61	$\pi_{Ph} + \pi_P$
L + 7	−0.35	$\pi_{Ph} + \pi_P$
SSD		
H − 18	−9.10	$d_{yz} + \sigma_{Ph} + \sigma_P$
H − 17	−8.93	$d_{xz} + \pi_{Cl} + \sigma_P + \sigma_N$
H − 16	−8.74	$d_{yz} + \pi_{Cl} + \sigma_P$
H − 15	−8.60	$\pi_{Ph} + \pi_{Cl}$
H − 14	−8.21	σ_{Cl}
H − 13	−7.64	π_{HPz}
H − 12	−7.53	$\pi_{Ph} + \pi_{HPz}$
H − 11	−7.38	$\pi_{Ph} + \pi_{Cl}$
H − 10	−7.31	π_{Cl}
H − 9	−7.27	$\pi_{Ph} + \pi_{HPz}$
H − 8	−7.22	π_{HPz}
H − 7	−7.07	$\pi_{Ph} + \pi_{Cl}$
H − 6	−6.99	$d_{yz} + \pi_{Ph} + \pi_{Cl}$
H − 5	−6.93	π_{Ph}
H − 4	−6.87	π_{Ph}
H − 3	−6.76	π_{Cl}
H − 2	−6.70	$\pi_{Cl} + \pi_{Ph}$
H − 1	−6.69	$\pi_{Ph} + \pi_{Cl} + n_P$
H	−6.36	$d_{xy} + \pi_{Cl}$
L	−2.68	$d_{xz} + \pi^*_{NO}$
L + 1	−2.65	$d_{yz} + \pi^*_{NO}$
L + 2	−2.05	$d_z^2 + \sigma_{Cl}$
L + 3	−1.61	$d_{x^2-y^2} + \sigma_{Cl} + \sigma_P$
L + 4	−0.91	$\pi_{Ph} + \pi_N$(HPz)
L + 5	−0.73	π_{Ph}
L + 6	−0.57	$\pi_{Ph} + \pi_P$
L + 7	−0.31	π_{Ph}
L + 8	−0.20	$\pi_{Ph} + \pi_{Cl}$
L + 9	−0.13	$\pi_{Ph} + \pi_{HPz}$
L + 10	0.00	π_{Ph}
L + 11	0.36	π_{Ph}

H denotes HOMO and L denotes LUMO.

Table 6
Atomic charges from the natural population analysis (NPA) of $[RuCl_3(NO)(PPh_3)(C_3H_4N_2)]$

Ru1	0.342
Cl1	−0.491
Cl2	−0.409
Cl3	−0.462
P1	1.268
$N1_{(NO)}$	0.370
$N2_{(HPz)}$	−0.301
O1	−0.153

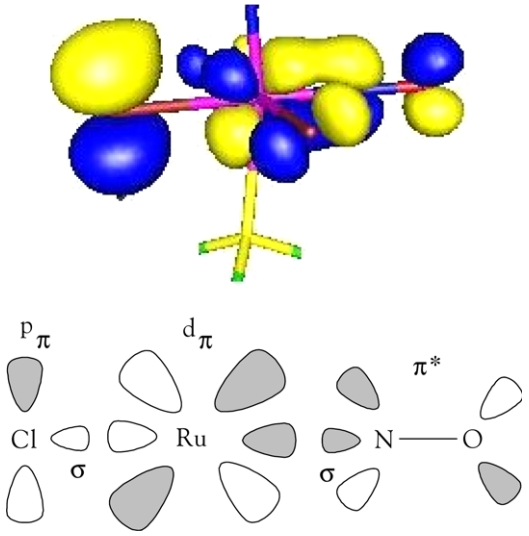


Fig. 3. The structural trans effect of NO ligand in $[RuCl_3(NO)(PPh_3)(C_3H_4N_2)]$.

lower than obtained from calculation with LANL2DZ basis on Ru atom (maximum difference is about 0.4 eV). The HOMO–LUMO gap in both calculations are similar (the difference is 0.15 eV).

3.3. Electronic spectrum

The experimental spectrum of $[RuCl_3(NO)(PPh_3)(C_3H_4N_2)]$ shows bands at 534.6, 468.4, 438.6, 330.8 300.0, 228.8 and 216.8 nm. There is also a shoulder at about 270 nm. The measured electronic spectrum is shown in Fig. 4.

With the use of the TDDFT method 80 electronic transitions were calculated for $[RuCl_3(NO)(PPh_3)(C_3H_4N_2)]$ using the LANL2DZ basis set and 90 transitions with SSD basis set. The calculated electronic transitions are gathered in Tables 7 and 8. Both LANL2DZ and SSD calculation predict the experimental spectra of the complex with similar accuracy. Except for the low energy part of the spectrum, only transitions with oscillator strengths larger than 0.01 are listed. The calculated spectra obtained by both calculations are depicted in Fig. 5. Each calculated transition in Fig. 5 was represented by a gaussian function with the height equal to the oscillator strength and width equal to 0.05.

We ascribe the first experimental bans at 534 nm to the calculated transitions at 517 and 513 nm with small oscillator strengths. These are $d \rightarrow \pi^*_{NO}$ transitions. The transition calculated with SSD basis set is at 502.1 nm. The experimental band at 468 nm is assigned to the transitions calculated between 461 and 429 nm in the case of

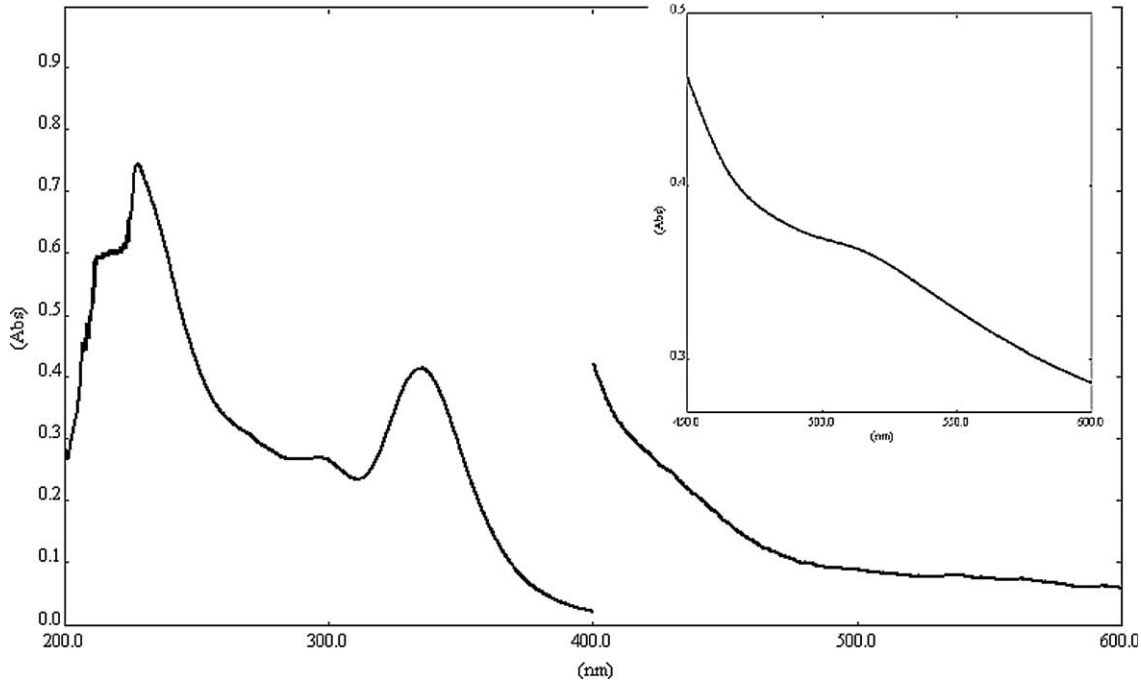


Fig. 4. UV–Vis spectrum of $[RuCl_3(NO)(PPh_3)(C_3H_4N_2)]$.

Table 7
Calculated electronic transitions for $[RuCl_3(NO)(PPh_3)(C_3H_4N_2)]$ with the TDDFT method (LANL2DZ basis set)

Most important configurations			E (V)	λ (nm)	f	Exp. λ (nm) (E (eV))ε
$H(d) \rightarrow L(\pi^*_{NO})$			2.39	517.1	*0.0001*	534.6(2.32)21
$H(d) \rightarrow L + 1(\pi^*_{NO})$			2.41	513.4	*0.0003*	
$H(d) \rightarrow L + 2(d)$			2.68	461.3	*0.0001*	468.4(2.65)67
$H - 4(\pi_{Cl}) \rightarrow L(\pi^*_{NO})$	$H - 1(\pi_{Ph} + \pi_{Cl}) \rightarrow L + 1(\pi^*_{NO})$		2.85	434.7	*0.0001*	
$H - 1(\pi_{Ph} + \pi_{Cl}) \rightarrow L(\pi^*_{NO})$			2.88	429.3	*0.0003*	
$H - 1(\pi_{Ph} + \pi_{Cl}) \rightarrow L(\pi^*_{NO})$			2.96	418.3	*0.0004*	438.6(2.83)120
$H - 2(\pi_{Ph} + \pi_{Cl}) \rightarrow L(\pi^*_{NO})$	$H - 2(\pi_{Ph}) \rightarrow L(+1\pi^*_{NO})$		2.99	414.3	*0.0005*	
$H - 8(\pi_{HPz}) \rightarrow L(\pi^*_{NO})$	$H - 5(d + \pi_{Ph} + \pi_{Cl}) \rightarrow L(\pi^*_{NO})$	$H - 3(\pi_{Cl}) \rightarrow L(\pi^*_{NO})$	3.05	406.3	*0.0012*	
$H - 5(d + \pi_{Ph} + \pi_{Cl}) \rightarrow L(\pi^*_{NO})$	$H - 4(\pi_{Cl}) \rightarrow L + 1(\pi^*_{NO})$		3.09	400.8	*0.0031*	
$H - 7(\pi_{Ph} + \pi_{Cl}) \rightarrow L(\pi^*_{NO})$			3.41	362.9	*0.0092*	
$H - 11(\pi_{Cl}) \rightarrow L(\pi^*_{NO})$	$H - 3(\pi_{Cl}) \rightarrow L + 2(d)$	$H - 2(\pi_{Ph}) \rightarrow L + 2(d)$	3.47	356.9	*0.0111*	330.8(3.75)8660
$H - 5(d + \pi_{Ph} + \pi_{Cl}) \rightarrow L + 2(d)$	$H - 3(\pi_{Cl}) \rightarrow L + 2(d)$		3.67	337.4	*0.0 110*	
$H - 10(\pi_{Ph} + \pi_{Cl} + \pi_{HPz}) \rightarrow L + 1(\pi^*_{NO})$	$H - 8(\pi_{HPz}) \rightarrow L + 1(\pi^*_{NO})$	$H - 2(\pi_{Ph}) \rightarrow L + 2(d)$	3.75	329.9	*0.0137*	
$H - 6(\pi_{Ph}) \rightarrow L + 3(d)$	$H - 1(\pi_{Ph} + \pi_{Cl}) \rightarrow L + 3(d)$		3.97	312.2	*0.0372*	
$H - 5(d + \pi_{Ph} + \pi_{Cl}) \rightarrow L + 3(d)$	$H - 3(\pi_{Cl}) \rightarrow L + 3(d)$	$H - 2(\pi_{Ph}) \rightarrow L + 3(d)$	4.28	289.0	*0.0395*	300.0(4.13)5523
$H - 8(\pi_{HPz}) \rightarrow L + 3(d)$	$H - 6(\pi_{Ph}) \rightarrow L + 3(d)$	$H - 1(\pi_{Ph} + \pi_{Cl}) \rightarrow L + 3(d)$	4.30	287.6	*0.0249*	
$H - 13(\pi_{Cl} + \pi_{HPz}) \rightarrow L + 2(d)$	$H - 4(\pi_{Cl}) \rightarrow L + 3(d)$	$H - 2(\pi_{Ph}) \rightarrow L + 3(d)$	4.32	286.4	*0.0411*	
$H - 13(\pi_{Cl} + \pi_{HPz}) \rightarrow L + 2(d)$	$H - 12(\pi_{HPz}) \rightarrow L + 2(d)$		4.34	285.1	*0.0283*	270sh(4.59)
$H - 8(\pi_{HPz}) \rightarrow L + 3(d)$	$H - 7(\pi_{Ph} + \pi_{Cl}) \rightarrow L + 3(d)$		4.47	277.1	*0.0667*	
$H - 11(\pi_{Cl}) \rightarrow L + 3(d)$	$H - 9(\pi_{Ph}) \rightarrow L + 3(d)$		4.69	263.9	*0.0107*	
$H - 1(\pi_{Ph} + \pi_{Cl}) \rightarrow L + 4(\pi^*_{Ph} + \sigma_P)$	$H(d) \rightarrow L + 5(\pi^*_{Ph} + \pi_P)$		5.15	240.5	*0.0245*	228.8(5.42)11089
$H - 18(d + \sigma_P + \sigma_{Ph}) \rightarrow L(\pi^*_{NO})$	$H - 1(\pi_{Ph} + \pi_{Cl}) \rightarrow L + 4(\pi^*_{Ph} + \sigma_P)$	$H(d) \rightarrow L + 5(\pi^*_{Ph} + \pi_P)$	5.18	238.9	*0.0120*	
$H - 16(d + \sigma_P + \sigma_N + \sigma_{Cl}) \rightarrow L + 2(d)$			5.26	235.6	*0.0122*	
$H - 3(\pi_{Cl}) \rightarrow L + 4(\pi^*_{Ph} + \sigma_P)$			5.27	235.0	*0.0183*	
$H - 4(\pi_{Cl}) \rightarrow L + 4(\pi^*_{Ph} + \sigma_P)$	$H - 3(\pi_{Cl}) \rightarrow L + 4(\pi^*_{Ph} + \sigma_P)$	$H - 1(\pi_{Ph} + \pi_{Cl}) \rightarrow L + 5(\pi^*_{Ph} + \pi_P)$	5.31	233.4	*0.0113*	
$H - 14(\sigma_{Cl}) \rightarrow L + 3(d)$	$H - 4(\pi_{Cl}) \rightarrow L + 4(\pi^*_{Ph} + \sigma_P)$		5.34	231.8	*0.0225*	
						216.8(5.72)9903

Table 8
Calculated electronic transitions for $[RuCl_3(NO)(PPh_3)(C_3H_4N_2)]$ with the TDDFT method (SSD basis set)

Most important configurations			E (V)	λ (nm)	f	Exp. λ (nm) (E (eV))ε
$H(d) \rightarrow L(\pi^*_{NO})$			2.47	502.1	*0.0004*	534.6(2.32)21
$H(d) \rightarrow L + 1(\pi^*_{NO})$			2.49	498.3	*0.0002*	468.4(2.65)67
$H(d) \rightarrow L + 2(d)$	$H - 3(\pi_{Cl}) \rightarrow L(\pi^*_{NO})$		2.80	442.6	*0.0001*	438.6(2.83)120
$H - 4(\pi_{Ph}) \rightarrow L(\pi^*_{NO})$	$H - 1(\pi_{Ph} + \pi_{Cl}) \rightarrow L + 1(\pi^*_{NO})$		2.85	434.7	*0.0001*	
$H - 2(\pi_{Ph} + \pi_{Cl}) \rightarrow L + 1(\pi^*_{NO})$	$H - 3(\pi_{Cl}) \rightarrow L + 1(\pi^*_{NO})$		3.04	407.3	*0.0002*	
$H - 2(\pi_{Ph} + \pi_{Cl}) \rightarrow L(\pi^*_{NO})$	$H - 1(\pi_{Ph} + \pi_{Cl}) \rightarrow L + 1(\pi^*_{NO})$		3.21	385.9	*0.0007*	
$H - 5(\pi_{Ph} + \pi_{Cl}) \rightarrow L(\pi^*_{NO})$	$H - 2(\pi_{Ph} + \pi_{Cl}) \rightarrow L(\pi^*_{NO})$		3.38	366.3	*0.0037*	
$H - 5(\pi_{Cl}) \rightarrow L + 1(\pi^*_{NO})$	$H - 2(\pi_{Ph} + \pi_{Cl}) \rightarrow L + 1(d)$		3.44	360.8	*0.0024*	330.8(3.75)8660
$H - 2(\pi_{Ph} + \pi_{Cl}) \rightarrow L + 2(d)$	$H - 1(\pi_{Ph} + \pi_{Cl}) \rightarrow L + 2(d)$		3.47	357.7	*0.0016*	
$H - 5(\pi_{Cl}) \rightarrow L + 1(\pi^*_{NO})$	$H - 7(\pi_{Ph} + \pi_{Cl}) \rightarrow L + 1(d)$		3.53	351.0	*0.0011*	
$H - 6(d + \pi_{Ph} + \pi_{Cl}) \rightarrow L(d)$	$H - 4(\pi_{Ph}) \rightarrow L(d)$		3.72	333.5	*0.0092*	
$H - 10(\pi_{Ph} + \pi_{Cl} + \pi_{HPz}) \rightarrow L + 1(\pi^*_{NO})$	$H - 8(\pi_{HPz}) \rightarrow L(\pi^*_{NO})$	$H - 3(\pi_{Cl}) \rightarrow L + 2(d)$	3.77	329.0	*0.0133*	
$H - 2(\pi_{Ph}) \rightarrow L + 3(d)$	$H - 3(\pi_{Cl}) \rightarrow L + 3(d)$		3.99	311.0	*0.0051*	300.0(4.13)5523
$H - 11(d + \pi_{Ph} + \pi_{Cl}) \rightarrow L + 1(d)$	$H - 10(\pi_{Cl}) \rightarrow L + 1(d)$	$H - 14(\sigma_{Cl}) \rightarrow L + 1(d)$	4.07	304.4	*0.0121*	
$H - 12(\pi_{HPz}) \rightarrow L(d)$	$H - 1(\pi_{Ph} + \pi_{Cl}) \rightarrow L + 3(d)$		4.14	299.3	*0.0269*	
$H - 13(\pi_{Cl} + \pi_{HPz}) \rightarrow L(d)$	$H - 12(\pi_{Ph} + \pi_{HPz}) \rightarrow L(d)$	$H - 2(\pi_{Ph} + \pi_{Cl}) \rightarrow L + 2(d)$	4.16	298.3	*0.0249*	
$H - 13(\pi_{Cl} + \pi_{HPz}) \rightarrow L(d)$	$H - 12(\pi_{Ph} + \pi_{HPz}) \rightarrow L(d)$	$H - 1(\pi_{Ph} + \pi_{Cl}) \rightarrow L + 3(d)$	4.18	296.9	*0.0102*	270sh(4.59)
$H - 8(\pi_{HPz}) \rightarrow L + 2(d)$	$H - 7(\pi_{Ph} + \pi_{Cl}) \rightarrow L + 2(d)$		4.34	285.4	*0.0096*	
$H - 7(\pi_{Cl}) \rightarrow L + 3(d)$	$H - 6(\pi_{Ph} + \pi_{Cl}) \rightarrow L + 3(d)$		4.59	269.9	*0.0697*	
$H - 15(\pi_{Ph} + \pi_{Cl}) \rightarrow L + 1(\pi^*_{Ph} + \sigma_P)$	$H - 3(\pi_{Cl}) \rightarrow L + 2(d + \sigma_{Cl})$		4.77	259.8	*0.0258*	228.8(5.42)11089
$H - 2(\pi_{Ph} + \pi_{Cl}) \rightarrow L + 4(\pi^*_{NO})$	$H - 3(\pi_{Cl}) \rightarrow L + 4(\pi^*_{Ph} + \pi_{HPz})$		5.19	239.1	*0.0188*	
$H - 2(\pi_{Ph} + \pi_{Cl}) \rightarrow L + 5(\pi_{Ph})$	$H(d) \rightarrow L + 7(\pi_{Ph})$		5.34	232.3	*0.0203*	
$H - 2(\pi_{Ph} + \pi_{Cl}) \rightarrow L + 6(\pi^*_{Ph} + \sigma_P)$			5.51	225.0	*0.0229*	
$H - 7(\pi_{Ph} + \pi_{Cl}) \rightarrow L + 4(\pi^*_{Ph} + \pi_{HPz})$	$H(d) \rightarrow L + 6(\pi^*_{Ph} + \sigma_P)$	$H - 6(\pi_{Ph} + \pi_{Cl}) \rightarrow L + 4(\pi^*_{Ph} + \pi_{HPz})$	5.57	223.2	*0.0117*	
$H - 16(d + \sigma_P + \sigma_{Cl}) \rightarrow L + 2(d)$	$H - 7(\pi_{Ph} + \pi_{Cl}) \rightarrow L + 4(\pi^*_{Ph} + \pi_{HPz})$		5.58	222.2	*0.0044*	
						216.8(5.72)9903

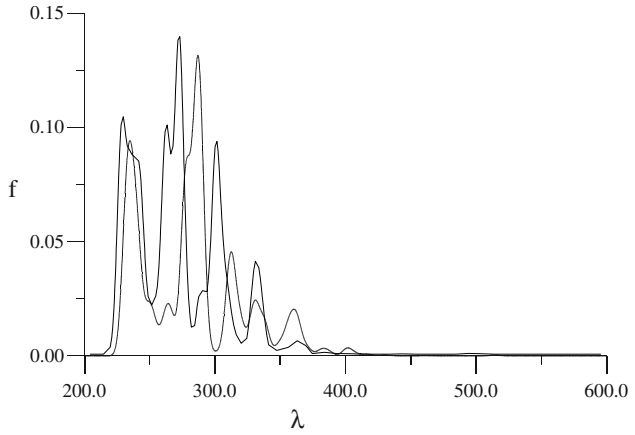


Fig. 5. Calculated electronic spectrum of $[RuCl_3(NO)(PPh_3)(HPz)]$ (solid line – LANL2DZ, dashed line – SSD).

calculation with LANL2DZ basis and with SSD basis set the band we ascribe to the calculated transition at 498.3 nm. These transitions are of d→d and $\pi_{Cl} \rightarrow \pi^*_{NO}$ type (LLCT). In these range of energy transitions the prediction of experimental values with LANL2DZ basis set is better than with using the ECP basis (SSD). The transitions calculated between 418 and 400 nm (442–407 nm SSD) are ascribed to the band at 438 nm. These transitions are again of LCT type and occur from the chlorine, phenyl and pyrazole orbitals to the π^*_{NO} orbitals.

The experimental band at 330 nm is ascribed to the transitions calculated between 356 and 312 nm with medium oscillator strengths and to transitions between 366.3 and 311.0 nm while the SSD basis set was using. These are mainly transitions from the pyrazole, phenyl and chlorine ligands orbitals to the metal d orbitals (LMCT). The transitions 289 and 263 nm (304.4 to 269.9 – SSD) are assigned to the band at 300 nm and shoulder at about 270 nm. These are again transitions of LMCT character.

The transitions between 240 and 231 nm and 259.8 to 222.2 nm in calculation with SSD, respectively, are assigned to the band at 228 nm. They are of LLCT type (interligand transitions) and intraligand ($\pi_{Ph} \rightarrow \pi^*_{Ph}$) (transitions). The experimental band at 216 nm could not be assigned on the basis of the calculated transitions. This band probably corresponds also to $\pi_{Ph} \rightarrow \pi^*_{Ph}$ transitions in the PPh_3 ligand.

As it can be seen from Tables 7 and 8 the UV–Vis spectrum calculated with the SSD basis set on the ruthenium atom gave better results in the higher energy and the LANL2DZ basis set in the lower energy range of the spectrum.

4. Supplementary material

Crystallographic data for the structure of the complex have been deposited at Cambridge Crystallographic Data Center (CCDC 239378). Copies of this information may be obtained free of charge from The Director, CCDC, 12 Union Road, Cambridge CB2 1EZ (fax: +44 1223 336033; e-mail: deposit@ccdc.cam.ac.uk or at www: http://www.ccdc.cam.ac.uk).

Acknowledgements

Crystallographic part was financed by funds allocated by the State Committee for Scientific Research to the Institute of General and Ecological Chemistry, Technical University of Łódź. The GAUSSIAN03 calculations were carried out in the Wrocław Centre for Networking and Supercomputing, WCSS, Wrocław, Poland under calculational Grant No. 51/96.

References

[1] D.S. Bohle, C. Hung, A.K. Powell, B.D. Smith, S. Wocaldo, Inorg. Chem. 36 (1997) 1992.
[2] S.S.S. Borges, C.U. Davanzo, E.E. Castellano, J. Z-Schpector, S.C. Silva, D.W. Franco, Inorg. Chem. 37 (1998) 2670.
[3] M.G. Gomes, C.U. Davanzo, S.C. Silva, L.G. Lopes, P.S. Santos, D.W. Franco, J. Chem. Soc., Dalton Trans. (1998) 601.
[4] H. Nagao, K. Ito, N. Tsuboya, D. Ooyama, N. Nagao, F.S. Howell, M. Mukaida, Inorg. Chim. Acta 290 (1999) 113.
[5] C.W.B. Bezerra, S.C. da Silva, M.T.P. Gambardella, R.H.A. Santos, L.M.A. Plicas, E. Tfouni, D.W. Franco, Inorg. Chem. 38 (1999) 5660.
[6] D.H. Bohle, E.S. Sagan, Eur. J. Inorg. Chem. (2000) 1609.
[7] Y. Chen, F.-T. Lin, R.E. Shepherd, Inorg. Chem. 38 (1999) 973.
[8] C.J. Marmion, T. Murphy, K.B. Nolan, Chem. Commun. (2001) 1870.
[9] L.G.F. Lopes, A. Wieraszko, Y. El-Sherif, M.J. Clarke, Inorg. Chim. Acta 312 (2001) 15.
[10] J.M. Slocik, M.S. Ward, K.V. Somayajula, R.E. Shepherd, Transit. Metal Chem. 26 (2001) 351.
[11] R.A. Sanchez-Delgado, A. Andriollo, O.L. DeOchoa, T. Suarez, N. Valencia, J. Organometal. Chem. 209 (1981) 77.
[12] M.-Y. Park, Y.J. Kim, O.-J. Cho, I.-M. Lee, J. Kor. Chem. Soc. 40 (1996) 445.
[13] F. Joó, J. Kovács, Á. Kathó, A.C. Bényei, T. Decuir, D.J. Darensbourg, Inorg. Synth. 32 (1998) 1.
[14] F. Joó, J. Kovács, A.C. Bényei, Á. Kathó, Angew. Chem. 110 (1998) 1024.
[15] F. Joó, G. Laurenczy, L. Nádasdi, J. Elek, Chem. Commun. (1999) 971.
[16] G. Laurenczy, F. Joó, L. Nádasdi, Inorg. Chem. 39 (2000) 5083.
[17] N. Ahmad, J.J. Levinson, S.D. Robinson, M.F. Uttley, Inorg. Synth. 15 (1974) 51.
[18] M.J. Frisch, G.W. Trucks, H.B. Schlegel, G.E. Scuseria, M.A. Robb, J.R. Cheeseman, J.A. Montgomery Jr., T. Vreven, K.N. Kudin, J.C. Burant, J.M. Millam, S.S. Iyengar, J. Tomasi, V. Barone, B. Mennucci, M. Cossi, G. Scalmani, N. Rega, G.A. Petersson, H. Nakatsuji, M. Hada, M. Ehara, K. Toyota, R. Fukuda, J. Hasegawa, M. Ishida, T. Nakajima, Y. Honda, O. Kitao, H. Nakai, M. Klene, X. Li, J.E. Knox, H.P. Hratchian, J.B. Cross, C. Adamo, J. Jaramillo, R. Gomperts, R.E. Stratmann, O. Yazyev, A.J. Austin, R. Cammi, C. Pomelli, J.W. Ochterski, P.Y. Ayala, K. Morokuma, G.A. Voth, P. Salvador, J.J. Dannenberg, V.G. Zakrzewski, S. Dapprich, A.D. Daniels, M.C. Strain, O. Farkas, D.K. Malick, A.D. Rabuck,

K. Raghavachari, J.B. Foresman, J.V. Ortiz, Q. Cui, A.G. Baboul, S. Clifford, J. Cioslowski, B.B. Stefanov, G. Liu, A. Liashenko, P. Piskorz, I. Komaromi, R.L. Martin, D.J. Fox, T. Keith, M.A. Al-Laham, C.Y. Peng, A. Nanayakkara, M. Challacombe, P.M.W. Gill, B. Johnson, W. Chen, M.W. Wong, C. Gonzalez, J.A. Pople, GAUSSIAN03, Revision 03, Gaussian, Inc, Pittsburgh, PA, 2003.
[19] A.D. Becke, J. Chem. Phys. 98 (1993) 5648.
[20] C. Lee, W. Yang, R.G. Parr, Phys. Rev. B 37 (1988) 785.
[21] M.E. Casida, in: J.M. Seminario (Ed.), Recent Developments and Applications in Modern Density Functional Theory, Theoretical and Computational Chemistry, vol. 4, Elsevier, Amsterdam, 1996.
[22] P.J. Hay, W.R. Wadt, J. Chem. Phys. 82 (1985) 299.
[23] X-RED, Version 1.18, STOE & Cie GmbH, Darmstadt, Germany, 1999.
[24] G.M. Sheldrick, Acta Crystallogr., Sect. A 46 (1990) 467.
[25] G.M. Sheldrick, SHELXL97. Program for the Solution and Refinement of Crystal Structures, University of Göttingen, Germany, 1997.
[26] G.M. Sheldrick, SHELXTL: Release 4.1 for Siemens Crystallographic Research Systems, 1990.
[27] B.L. Haymore, J.A. Ibers, Inorg. Chem. 14 (1975) 3060.
[28] (a) B.L. Wescott, J.H. Enemark, in: E.I. Solomon, A.B.P. Lever (Eds.), Inorganic Electronic Structure and Spectroscopy, Applications and Case Studies, vol. II, Wiley, New York, 1999, pp. 403–450;
(b) I.P. Evans, A. Spencer, W. Wilkinson, J. Chem. Soc., Dalton Trans. (1973) 204;
(c) R.K. Coll, J.E. Fergusson, V. McKee, C.T. Page, W.T. Robinson, T.S. Keong, Inorg. Chem. 26 (1987) 106;
(d) E. Iengo, G. Mestroni, S. Geremia, M. Calligaris, E. Alessio, J. Chem. Soc., Dalton Trans. (1999) 3361;
(e) E. Iengo, B. Milani, E. Zangrando, S. Geremia, E. Alessio, Angew. Chem., Int. Ed. 39 (2000) 1096;
(f) E. Iengo, E. Zangrando, S. Mestroni, G. Fronzoni, M. Stener, E. Alessio, J. Chem. Soc., Dalton Trans. (2001) 1338;
(g) B. Serli, E. Iengo, T. Gianferrara, E. Zangrando, E. Alessio, Met. Based Drugs 8 (2001) 9;
(h) T. Hirano, K. Ueda, M. Mukaida, H. Nagao, T. Oi, J. Chem. Soc., Dalton Trans. (2001) 2341.
[29] J.E. Huheey, E.A. Keiter, R.L. Keiter, Inorganic Chemistry: Principles of Structure and Reactivity, 4th ed., Harper Collins College Publishers, New York, 1993.
[30] I.D. Brown, Acta Crystallogr., Sect. B B48 (1992) 553.
[31] I.D. Brown, Acta Crystallogr., Sect. B 53 (1997) 381.
[32] M. O'Keeffe, N.E. Brese, J. Am. Chem. Soc. 113 (1991) 3226.
[33] L. Sieron, M. Bukowska-Strzyzewska, Acta Crystallogr., Sect. C 55 (1999) 1230.
[34] J.G. Małecki, J.O. Dzigielewski, M. Jaworska, R. Kruszynski, T.J. Bartczak, Polyhedron 23 (5) (2004) 885.
[35] J.F. Bickley, S.J. Higgins, C.A. Stuart, A. Steiner, Inorg. Chem. Commun. 3 (2000) 211.
[36] G.R. Desiraju, T. Steiner, The Weak Hydrogen Bond in Structural Chemistry and Biology, Oxford University Press, Oxford, 1999.
[37] G.A. Jeffrey, W. Saenger, Hydrogen Bonding in Biological Structures, Springer, Berlin, 1994.
[38] R. Taylor, O. Kennard, J. Am. Chem. Soc. 104 (1982) 5063.
[39] J.H. Enemark, R.D. Feltham, Coord. Chem. Rev. 13 (1974) 339.

Available online at www.sciencedirect.com
SCIENCE DIRECT®
Polyhedron 24 (2005) 369–376
POLYHEDRON
www.elsevier.com/locate/poly

Synthesis and characterization of some mono- and dinuclear molybdenum(VI) thiosemicarbazonato complexes

Marina Cindrić *, Višnja Vrdoljak, Neven Strukan, Boris Kamenar

Laboratory of General and Inorganic Chemistry, Chemistry Department, Faculty of Science, University of Zagreb, Ulica kralja Zvonimira 8, 10000 Zagreb, Croatia

Received 3 November 2004; accepted 5 December 2004

Abstract

Mononuclear molybdenum(VI) complexes of the type $[MoO_2\{C_6H_4(O)CH{:}NNC(S)NH_2\}(D)]$ [D = pyridine (**1d**), γ-picoline (**1c**)] and $[MoO_2\{C_6H_4(O)CH{:}NNHC(S)NH\}(CH_3OH)] \cdot CH_3OH \cdot 1/2bpy$ (**1e**) have been prepared by the reaction of $[MoO_2(C_5H_7O_2)_2]$ ($C_5H_7O_2$ = acetylacetonate ion) with salicylaldehyde thiosemicarbazone $[C_6H_4(OH)CH{:}NNC(SH)NH_2]$ and Lewis base in dry methanol. The dinuclear complex $[MoO_2\{C_6H_4(O)CH{:}NNC(S)NH_2\}]_2$ (**1b**) has been prepared by the reaction of $[MoO_2(C_5H_7O_2)_2]$ with salicylaldehyde thiosemicarbazone $[C_6H_4(OH)CH{:}NNC(SH)NH_2]$ in dry dichloromethane. In all complexes, except in the case of complex **1e**, molybdenum is coordinated by two terminal oxo-oxygen atoms, (O_t), by ONS atoms from the salicylaldehyde thiosemicarbazone ligand and by an oxygen atom from the methanol molecule in **1a**, and either by a nitrogen atom from γ-picoline in **1c** or pyridine in **1d**. In $[MoO_2\{C_6H_4(O)CH{:}NNHC(S)NH\}(CH_3OH)] \cdot CH_3OH \cdot 1/2bipy$ (**1e**), salicylaldehyde thiosemicarbazone is coordinated to molybdenum through ONN atoms, while the sixth coordination site around the molybdenum atom is completed by the methanol molecule.

All complexes have been characterized by means of chemical and thermogravimetric analyses and IR spectroscopy. The molecular structures of complexes **1b**, **1c** and **1e** have been determined by a single crystal X-ray diffraction method.
© 2005 Elsevier Ltd. All rights reserved.

Keywords: Molybdenum(VI) complexes; Thiosemicarbazones; X-ray crystal structures; Dinuclear complexes; Polynuclear

1. Introduction

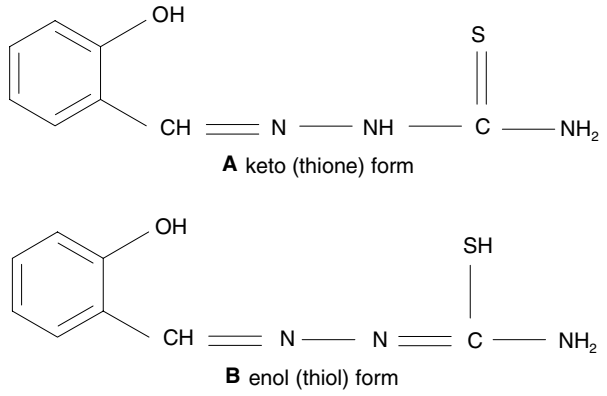
The chemistry of thiosemicarbazones, mixed hard–soft nitrogen–sulfur chelating ligands, has attracted considerable interest primarily due to their biological activities. Those activities have been correlated with their metal-chelating abilities and reductive capacity. Also, such complexes are considered important because of their potential antibacterial, antiviral and antitumor activities [1,2].

Salicylaldehyde thiosemicarbazone [3] can exist in two tautomeric forms A and B (Scheme 1). In form A it can act as a tridentate ligand by coordinating either through hydroxyl–O, after losing its proton, and by imino N and thiocarbonyl S or as a doubly negatively charged tridentate ligand by losing another proton from the mercapto group of tautomeric form B.

Chemistry of nitrogen–sulfur chelating ligands bound to Mo at higher oxidation states is a field of current interest. These studies have been considered even more important after the revelation that several enzymes like DMSO reductase, xanthine oxidase and other oxotransferases in their prosthetic groups contain Mo(IV), Mo(V) or Mo(VI) ions coordinated by nitrogen, oxygen

* Corresponding author. Tel.: +385 1 460 6653; fax: +385 1 461 1191.
E-mail address: marina@chem.pmf.hr (M. Cindrić).

0277-5387/$ - see front matter © 2005 Elsevier Ltd. All rights reserved.
doi:10.1016/j.poly.2004.12.007



Scheme 1.

or sulfur donor atoms of a macromolecular ligand system [4–6].

For some time our laboratory has been active in this field and has already reported syntheses and characterizations of several new Mo(VI) and Mo(V) complexes with ONS, ONO or ONN chelating ligand systems [7–9].

This paper presents a study of the $[MoO_2\{C_6H_4(O)CH{:}NNC(S)NH_2\}(D)]$ and $[MoO_2\{C_6H_4(O)CH{:}NNHC(S)NH\}(D)]$ complexes in which the Mo atom is coordinated by a tridentate ONS salicylaldehyde thiosemicarbazone ligand and one donor molecule D (CH_3OH, γ-picoline, pyridine). To our knowledge the syntheses and structures of $[MoO_2(L)(H_2O)]Cl \cdot H_2O$ [10], $[MoO_2(L)(MeOH)]$ [11] and $[MoO_2(HL')(X)]$-(H_2L' = tridentate ONN salicylaldehyde *S*-methylisothiosemicarbazone and X = MeOH, EtOH and py), and only the synthesis of $[MoO_2(L)(X)]$, where L = salicylaldehyde thiosemicarbazone and X = γ-picoline, imidazole have been reported so far [12].

2. Experimental

The starting complex $[MoO_2(C_5H_7O_2)_2]$ and salicylaldehyde thiosemicarbazone were prepared as described in the literature [13]. 4,4′-Bipyridine, pyridine and γ-picoline were of reagent grade and used as purchased. Methanol was dried over magnesium ethoxide, acetonitrile and dichloromethane over P_2O_5.

C, H and N analyses were provided by the Analytical Services Laboratory of Rudjer Bošković Institute, Zagreb. Molybdenum was determined according to the already known method [14]. Infrared spectra were recorded in KBr with an FTIR 1600 Fourier transform spectrophotometer in the 4500–450 cm^{-1} region. Thermogravimetric analyses were measured on a Mettler TG 50 thermobalance using aluminum crucibles under oxygen atmosphere with a heating rate of 5 °C min^{-1}. For all experiments the temperature ranged from 25 to 600 °C. The results were developed by applying the Mettler STAR^e 6.1 programme.

2.1. Syntheses of molybdenum(VI) complexes

2.1.1. Synthesis of $[MoO_2\{C_6H_4(O)CH{:}NNC(S)NH_2\}]_n$ (1) and $[MoO_2\{C_6H_4(O)CH{:}NNC(S)NH_2\}(CH_3OH)]$ (1a)

A mixture of $[MoO_2(C_5H_7O_2)_2]$ (0.15 g, 0.46 mmol) and salicylaldehyde thiosemicarbazone (0.09 g, 0.46 mmol) in dry acetonitrile (20 cm^3) (**1**) (or dry methanol, 25 cm^3 for **1a**) was warmed up for 4 h for **1** and 2 h for **1a**.

Whereas the yellowish-brown product **1** deposited during warming of the acetonitrile solution, the methanolic solution should be evaporated to one-third of its volume and upon standing at room temperature for few days the orange crystals of **1a** were obtained and filtered off.

(**1**) Yield: 0.09 g, 61%. *Anal.* Calc. for $C_8H_7MoN_3O_3S$: C, 29.9; H, 2.2; Mo, 29.9; N, 13.1; S, 10.0. Found: C, 29.9; H, 2.1; Mo, 29.4; N, 13.1; S, 10.1%.

IR (cm^{-1}): 3452(m), 3339(s), 3185(w), 1619(vs), 1593(s), 915(vs), 812(vs), 760(vs).

(**1a**) Yield: 0.08 g, 49%. *Anal.* Calc. for $C_9H_{11}MoN_3O_4S$: C, 30.6; H, 3.1; Mo, 27.2; N, 11.9; S, 9.1. Found: C, 30.1; H, 2.5; Mo, 26.8; N, 12.1; S, 9.6%.

IR (cm^{-1}): 3460(m), 3323(m), 3179(w), 1609(s), 1598(s), 1553(s), 1518(s), 937(s), 896(vs), 755(vs).

2.1.2. Synthesis of $[MoO_2\{C_6H_4(O)CH{:}NNC(S)NH_2\}]_2$ (1b)

A mixture of $[MoO_2(C_5H_7O_2)_2]$ (0.15 g, 0.46 mmol) and salicylaldehyde thiosemicarbazone (0.09 g, 0.46 mmol) in dry CH_2Cl_2 (150 cm^3) was warmed up for 14 h. The dark red crystals **1b** were deposited during the warming of the reaction mixture. The same product can be obtained by warming of $[MoO_2\{C_6H_4(O)CH{:}NNC(S)NH_2\}(CH_3OH)]$ in dry CH_2Cl_2.

Yield: 0.09 g, 61%. *Anal.* Calc. for $C_{18}H_{22}Mo_2N_6O_8S_2$: C, 29.9; H, 2.2; Mo, 29.9; N, 13.1; S, 10.0. Found: C, 29.9; H, 2.1; Mo, 30.5; N, 13.1; S, 10.1%.

IR (cm^{-1}): 3405(m), 3291(w), 3109(m), 1638(vs), 1598(vs), 1556(vs), 1524(vs), 1439(m), 1274(m), 941(s), 840(vs), 767(s).

2.1.3. Synthesis of $[MoO_2\{C_6H_4(O)CH{:}NNC(S)NH_2\}(\gamma\text{-pic})]$ (1c), $[MoO_2\{C_6H_4(O)CH{:}NNC(S)NH_2\}(py)]$ (1d) and $[MoO_2\{C_6H_4(O)CH{:}NNHC(S)NH\}(CH_3OH)] \cdot CH_3OH \cdot 1/2bipy$ (1e)

A mixture of $[MoO_2(C_5H_7O_2)_2]$ (0.15 g, 0.46 mmol), salicylaldehyde thiosemicarbazone (0.09 g, 0.46 mmol) and γ-picoline (0.22 g, 2.5 mmol) (pyridine 0.20 g, 2.5 mmol or 4,4′- bipyridine 0.035 g, 2.5 mmol) in dry methanol (10 cm^3) was warmed up for 4 h. Upon standing at room temperature for 2–3 days, the solution evap-

Table 1
Crystallographic data for compounds **1b**, **1c** and **1e**

	1b	**1c**	**1e**
Chemical formula	$[MoO_2(C_8H_7N_3OS)]_2$	$[MoO_2(C_8H_7N_3OS)(C_6H_7N)]$	$[MoO_2(C_8H_7N_3OS)(CH_3OH)] \cdot (CH_3OH) \cdot 1/2(C_{10}H_8N_2)$
Formula weight	642.33	414.29	463.34
Crystal system	triclinic	triclinic	triclinic
Space group	$P\bar{1}$	$P\bar{1}$	$P\bar{1}$
a (Å)	7.774(2)	7.892(2)	8.127(1)
b (Å)	7.932(2)	13.950(3)	8.675(1)
c (Å)	8.860(2)	15.222(4)	13.779(2)
α (°)	89.46(2)	98.36(2)	82.37(1)
β (°)	92.27(2)	102.43(2)	87.94(1)
γ (°)	96.35(2)	94.81(2)	74.85(1)
V (Å^3)	542.6(3)	1607.5(7)	929.4(2)
Z	2	4	2
T (K)	295	200	200
ρ_{calc} (g cm^{-3})	1.966	1.712	1.656
μ (mm^{-1})	1.395	0.965	0.852
$F(000)$	316	832	470
Data measured	4354	12567	8874
Unique data	2460	7400	5272
Observed data [$I > 2\sigma(I)$]	1944	5239	4282
Number of variables	153	433	249
Maximum/minimum $\Delta\rho$ (e^3/Å^3)	1.022, −0.904	0.611, −0.758	0.903, −0.869
$R(F_o)$	0.0638	0.0548	0.0335
$R_w(F_o^2)$	0.1257	0.1209	0.0760

orated to one-third of its original volume. The obtained dark red crystals of **1c** (0.08 g) or orange crystals of **1d** (0.09 g) or unstable orange crystals **1e** (0.06 g) were filtered off and washed with tetrachloromethane.

(**1c**) Yield: 0.08 g, 42%. *Anal.* Calc. for $C_{14}H_{14}MoN_4O_3S$: C, 40.6; H, 3.4; Mo, 23.2; N, 13.5; S, 7.7. Found: C, 40.6; H, 3.6; Mo, 23.0; N, 13.5; S, 7.8%.

IR (cm^{-1}): 3452(m), 3287(m), 3132(m), 1620(vs), 1598(s), 1586(m), 1552(s), 1509(s), 1439(m), 918(s), 890(vs), 757(m).

(**1d**) Yield: 0.09 g, 32%. *Anal.* Calc. for $C_{13}H_{12}Mo_2N_4O_3S$: C, 39.0; H, 3.0; Mo, 24.0; N, 14.0; S, 8.0. Found: C, 38.9; H, 3.1; Mo, 24.4; N, 14.1; S, 8.1%.

IR (cm^{-1}): 3460(m), 3283(s), 3118(w), 1626(vs), 1599(s), 1586(m), 1551(s), 1501(s), 1439(s), 926(s), 897(vs), 760(s).

(**1e**) [1] Yield: 0.06 g, 28%. *Anal.* Calc. for $C_{13}H_{11}MoN_4O_3S$: C, 39.1; H, 2.8; Mo, 24.0; N, 14.0; S, 8.0. Found: C, 39.7; H, 3.0; Mo, 23.9; N, 14.7; S, 7.8%.

IR (cm^{-1}): 3437(m), 3295(s), 3138(s), 1636(s), 1600(vs), 1553(vs), 1509(vs), 1438(m), 932(s), 890(vs), 761(vs).

2.2. X-ray crystallography

Single crystals of complexes **1b**, **1c** and **1e** were grown by slow evaporation of solutions obtained from the above described preparations. Intensity data were collected on an Oxford Diffraction Xcalibur CCD diffractometer with graphite-monochromated Mo Kα radiation ($\lambda = 0.7107$ Å), using 1° ω-scans at a crystal to detector distance of 50 mm and 100, 40 and 10 s exposure times per frame for **1b**, **1c** and **1e**, respectively. Data were reduced using the CrysAlis RED program [15].

Crystal data, experimental conditions, details of structure determination and final refinement parameters are summarized in Table 1.

In all structures the molybdenum atoms were located by the Patterson method while the remaining non-hydrogen atoms were found in subsequent difference Fourier maps. In the structure of **1c** two crystallographically independent complex molecules, denoted **A** and **B**, were located in the asymmetric unit. Refinements in which all non-hydrogen atoms were treated anisotropically were performed by the full-matrix least-squares method based on the F^2 values against all reflections. The final Fourier maps revealed positions of all H atoms but some with poor geometry. Therefore, all hydrogen atoms attached to carbon atoms were generated on geometrical grounds. The hydrogen atoms bound to the nitrogen and oxygen atoms were refined isotropically, except H14 attached to oxygen atom O5 of the solvent methanol molecule in **1e**, which was kept fixed during the refinement.

All calculations were performed on an IBM ThinkPad microcomputer (Pentium II processor, 300 MHz) using SHELXS97 [16] and SHELXL97 [17] programs. The molecular structure drawings were prepared using ORTEP [18] and PLATON [19].

[1] The compound was dried before analysis since it loses methanol at room temperature.

3. Results and discussion

3.1. Syntheses of the complexes

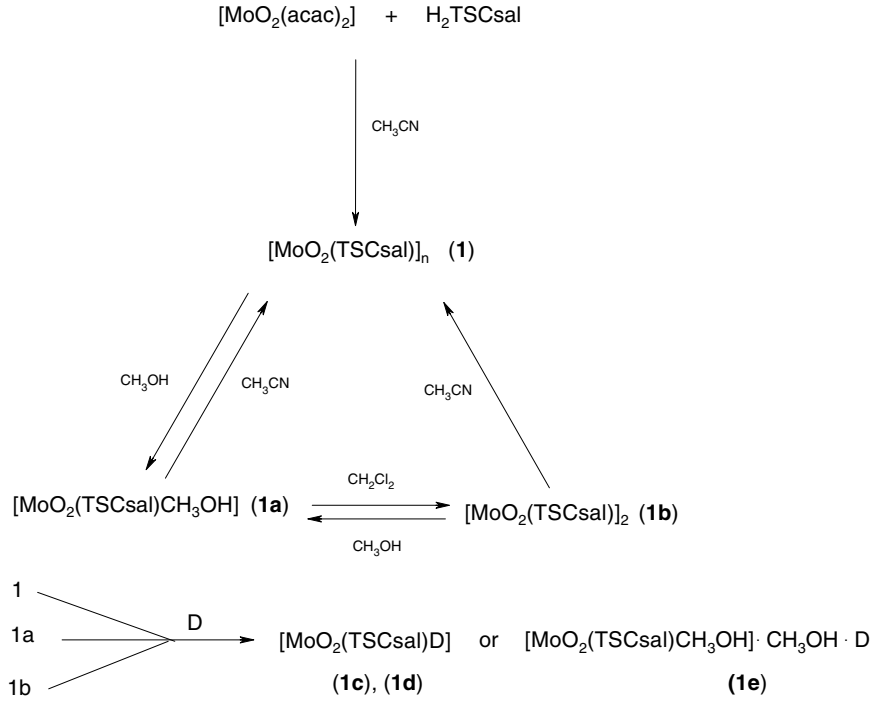
In this paper, we describe syntheses (Scheme 2) and structures of several dioxomolybdenum(VI) complexes coordinated by the tridentate ONS (or ONN) salicylaldehyde thiosemicarbazone ligand.

The yellowish-brown polymeric complex $[MoO_2\{C_6H_4(O)CH{:}NNC(S)NH_2\}]_n$ (**1**) was obtained by the reaction of $[MoO_2(C_5H_7O_2)_2]$ with a stoichiometric amount of salicylaldehyde thiosemicarbazone, L, in dry acetonitrile. Its IR spectrum showed a characteristic strong vibration at 812 cm^{-1} which was absent in the case of $[MoO_2\{C_6H_4(O)CH{:}NNC(S)NH_2\}(D)]$ (D = CH_3OH in **1a**; γ-pic in **1c**; py in **1d**) and in $[MoO_2\text{-}\{C_6H_4(O)CH{:}NNHC(S)NH\}(CH_3OH)]\cdot CH_3OH\cdot$ 1/2bpy (bpy = 4,4′-bipyridine in **1e**). Also, $[MoO_2\text{-}\{C_6H_4(O)CH{:}NNC(S)NH_2\}]_n$ showed a single stretching frequency at 915 cm^{-1} instead of a doublet characteristic of the presence of *cis*-MoO_2 group, as found in $[MoO_2\{C_6H_4(O)CH{:}NNC(S)NH_2\}(D)]$ (at 937 and 896 cm^{-1} in **1a**, at 918 and 890 cm^{-1} in **1c**, at 926 and 898 cm^{-1} in **1d** and at 932 and 890 cm^{-1} in **1e**) so that the stretching frequency at 915 cm^{-1} in (**1**) was assigned to ν(Mo=O) while that at 812 cm^{-1} to the weakened ν(Mo=O) present in the bridging Mo–O → Mo moiety. These observations strongly suggests that the polymerization of $[MoO_2\{C_6H_4(O)CH{:}NNC(S)NH_2\}]$ is realized via oxo bridging as found in $[MoOL(LH)]_n$ (L = diacetyldihydrazone) [20]. If the same reaction was carried out in methanol or in dry dichloromethane we were able to isolate monomeric orange crystals of $[MoO_2\{C_6H_4(O)CH{:}NNC(S)NH_2\}\ (CH_3OH)]$ (**1a**) and the dark red crystalline product of $[MoO_2\text{-}\{C_6H_4(O)CH{:}NNC(S)NH_2\}]_2$ (**1b**), respectively. The dimeric structure of **1b** was confirmed by X-ray analysis. The strong stretching frequency at 840 cm^{-1}, found in its IR spectrum, is characteristic of the presence of a Mo_2O_{2b} group [21]. The behavior of the complex $[MoO_2\{C_6H_4(O)CH{:}NNC(S)NH_2\}(CH_3OH)]$ (**1a**) is different, it undergoes a substitution reaction of the type

$$[MoO_2\{C_6H_4(O)CH\cdot NNC(S)NH_2\}(CH_3OH)] + D \rightarrow [MoO_2\{C_6H_4(O)CH\cdot NNC(S)NH_2\}(D)] + CH_3OH$$

where D is a Lewis base such as pyridine or γ-picoline.

In all complexes (except **1e**) molybdenum is coordinated by two terminal (O_t), by ONS atoms of salicylaldehyde thiosemicarbazone, while the sixth coordination site is occupied by methanol in **1a**, γ-picoline in **1c** and a pyridine molecule in **1d**. Only in $[MoO_2\{C_6H_4(O)CH{:}NNHC(S)NH\}(CH_3OH)]\cdot CH_3OH\cdot$ 1/2bpy (**1e**), is the salicylaldehyde thiosemicarbazone coordinated to molybdenum through ONN atoms, and the sixth coordination site around molybdenum is likewise completed by the methanol molecule. As the deprotonation of the ligand-NH_2 group occurs in alkaline media [22], in our case the presence of acetylacetone,



Scheme 2. TSCsal = salicylaldehyde thiosemicarbazone; D: py = pyridine (**1c**) γ-pic = γ-picoline (**1d**); bpy = 4,4′-bipyridine (**1e**); acac = acetylacetonate ion.

an evidently good proton acceptor and 4,4′-bipyridine as a strong Lewis base, gives favourable conditions for such deprotonation. Most probably this is one of the reasons for obtaining the above mentioned adduct $[MoO_2\{C_6H_4(O)CH{:}NNHC(S)NH\}(CH_3OH)] \cdot CH_3OH \cdot 1/2bpy$.

The thermal analysis data for $[MoO_2\{C_6H_4(O)CH{:}NNC(S)NH_2\}(D)]$ (D = pyridine in **1d** or methanol in **1a**) revealed two main processes: (1) loss of coordinated D molecules [148–182 °C **1d**; 69–100 °C **1a**], and (2) complex decomposition [258–488 °C **1d**; 249–472 °C **1a**]. In the case of complexes $[MoO_2\{C_6H_4(O)CH{:}NNC(S)NH_2\}(\gamma\text{-pic})]$ (**1c**) and $[MoO_2\{C_6H_4(O)CH{:}NNHC(S)NH\}(CH_3OH)] \cdot CH_3OH \cdot 1/2bpy$ (**1e**) loss of γ-picoline or 4,4′-bipyridine was accompanied by the decomposition of the salicylaldehyde thiosemicarbazone ligand without any stable intermediate product (174–492 °C in **1c**; 203–543 °C in **1e**). The compound **1e** was already losing methanol at room temperature.

The thermal analysis of complexes $[MoO_2\{C_6H_4(O)CH{:}NNC(S)NH_2\}(CH_3OH)]_2$ (**1a**) and $[MoO_2\{C_6H_4(O)CH{:}NNC(S)NH_2\}]_n$ (**1**) showed that their ligands were decomposing within the ranges 247–476 and 249–480 °C, respectively.

3.2. Structural studies

Complex molecules found in the crystal structures of $[MoO_2\{C_6H_4(O)CH{:}NNC(S)NH_2\}]_2$ (**1b**), $[MoO_2\{C_6H_4(O)CH{:}NNC(S)NH_2\}(\gamma\text{-pic})]$ (**1c**) and $[MoO_2\{C_6H_4(O)CH{:}NNHC(S)NH\}(CH_3OH)] \cdot (CH_3OH) \cdot 1/2bpy$ (**1e**) are shown in Fig. 1, relevant bond lengths involving non-hydrogen atoms are listed in Table 2, and hydrogen bonding parameters in Table 3.

The crystal structure of complex **1b** is built up of dinuclear centrosymmetric complex molecules $[MoO_2\{C_6H_4(O)CH{:}NNC(S)NH_2\}]_2$, with two dioxomolybdenum–salicylaldehyde thiosemicarbazone units bridged through oxo-oxygen atoms. In such a way a planar asymmetric bridge between Mo atoms is formed. Each bridging oxygen atom is more closely associated with a single molybdenum, with the bond lengths Mo–O1 = 1.741(4) [which is significantly longer than the bond to the terminal oxygen, Mo–O2 = 1.698(5) Å] and Mo–O1^i = 2.516(5) Å, ($i = 1 - x$, $1 - y$, $2 - z$). The Mo–Mo distance of 3.424(1) Å shows that in such a d^0 system there is not any possible metal-to-metal interaction. Octahedral coordination of molybdenum is completed by the tridentate salicylaldehyde thiosemicarbazone ligand bonded to the Mo_2O_4 through the oxygen atom from the deprotonated –OH group [Mo–O3 = 1.895(4) Å], imine nitrogen atom [Mo–N3 = 2.224(5) Å] and sulfur atom from the deprotonated mercapto group [Mo–S1 = 2.410(2) Å]. By chelating the Mo atom, the tridentate ligand forms one six- and one five-membered ring. The bond length values within the Schiff base are as expected and similar to those found in the free ligand [3,10].

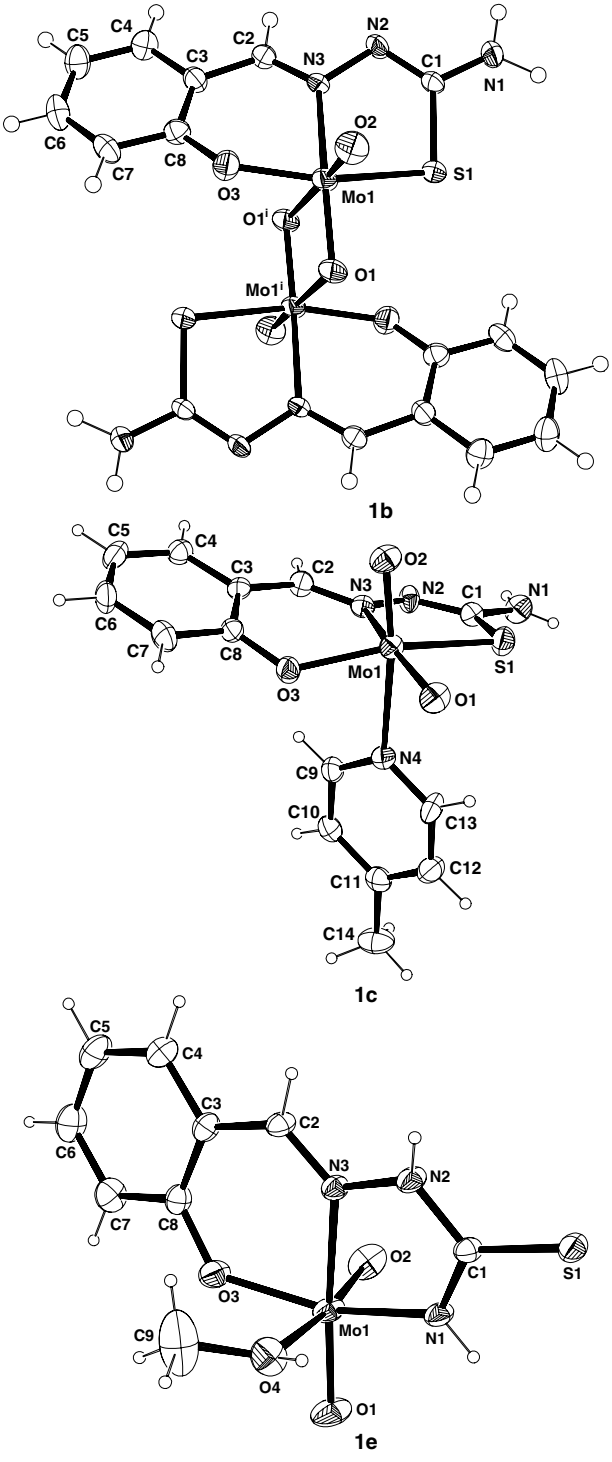


Fig. 1. ORTEP drawings of the complex molecules **1b**, **1c** and **1e** with atom labelling schemes. Ellipsoids are drawn at the 50% probability level.

In the crystal structure, the complex molecules are interconnected through intermolecular N1–H12 ⋯ O2 and N1–H11 ⋯ N2 hydrogen bonds formed between the terminal amide N1–hydrogens and the terminal

Table 2
Selected bond distances (Å) for **1b**, **1c** and **1e**[a]

	1b	**1c**		**1e**
		Molecule (A)	Molecule (B)	
Mo–O1	1.741(4)	1.716(3)	1.714(3)	1.697(2)
Mo–O2	1.698(5)	1.709(3)	1.713(4)	1.717(2)
Mo–O3	1.895(4)	1.953(3)	1.932(3)	1.945(2)
Mo–N3	2.224(5)	2.289(4)	2.284(4)	2.287(2)
Mo–S1	2.410(2)	2.433(1)	2.435(2)	
Mo–N1				2.057(2)
Mo–O1^{i}	2.516(5)			
Mo–N4		2.412(4)	2.431(4)	
Mo–O4				2.325(2)
N1–C1	1.330(7)	1.340(6)	1.339(6)	1.331(3)
N2–C1	1.300(7)	1.318(6)	1.314(6)	1.360(3)
S1–C1	1.763(7)	1.752(5)	1.762(5)	1.707(2)
N2–N3	1.401(6)	1.384(5)	1.398(5)	1.384(2)
N3–C2	1.299(7)	1.312(6)	1.294(6)	1.298(2)
C2–C3	1.445(7)	1.445(6)	1.442(6)	1.449(3)
C8–O3	1.344(7)	1.357(5)	1.369(6)	1.358(3)

Symmetry code: i = $-x + 1$, $-y + 1$, $-z + 2$.
[a] In **1c** two crystallographically independent complex molecules are labelled (A) and (B).

Table 3
Hydrogen bonding geometry in structures **1b**, **1c** and **1e**

D–H ⋯ A	*d*(D–H)	*d*(H ⋯ A)	*d*(D ⋯ A)	∠(DHA)
1b				
N1–H11 ⋯ N2^{ii}	0.83(9)	2.21(9)	3.029(8)	170(8)
N1–H11 ⋯ O2^{iii}	1.01(7)	2.18(7)	3.095(7)	151(6)
1c				
N1a–H1a ⋯ O2a^{iv}	0.76(5)	2.54(6)	3.096(6)	131(5)
N1a–H2a ⋯ N2a^{v}	0.76(6)	2.33(6)	3.069(7)	165(6)
N1b–H1b ⋯ O2b^{vi}	0.86(7)	2.47(7)	3.200(7)	143(5)
N1b–H2b ⋯ N2b^{ii}	0.93(8)	2.12(8)	3.053(6)	177(6)
1e				
N1–H2 ⋯ S1^{vii}	0.76(3)	2.58(3)	3.301(2)	160(3)
N2–H3 ⋯ S1^{ii}	0.85(3)	2.46(3)	3.313(2)	179(3)
O4–H1 ⋯ N4^{viii}	0.77(3)	1.92(3)	2.676(3)	168(3)
O5–H14 ⋯ O1^{vi}	0.91	2.11	2.988(3)	163

Symmetry code: ii = $-x + 1$, $-y + 2$, $-z + 1$; iii = $-x + 1$, $-y + 1$, $-z + 1$; iv = x + 1, *y*, *z*;v = $-x + 3$, $-y + 1$, $-z + 2$; vi = $-x + 1$, *y*, *z*; vii = $-x + 2$, $-y + 2$, $-z + 1$; viii = *x*, $y + 1$, *z*.

oxygen O2 and hydrazinic nitrogen N2 atoms of neighbouring molecules, thus forming sheets of molecules parallel to the crystallographic *bc* plane (Fig. 2).

The complexes $[MoO_2\{C_6H_4(O)CH{:}NNC(S)NH_2\}(\gamma\text{-pic})]$ (**1c**) and $[MoO_2\{C_6H_4(O)CH{:}NNHC(S)NH\}(CH_3OH)] \cdot CH_3OH \cdot 1/2bpy$ (**1e**) are mononuclear molecules with a *cis*-MoO_2 core surrounded by the tridentate salicylaldehyde thiosemicarbazone ligands. However, the molybdenum atoms are differently coordinated. In **1c** the molybdenum atom is octahedrally surrounded by two terminal oxo-oxygen atoms, O1 and O2, and by oxygen O3, imine nitrogen N3 and sulfur atom S1 belonging to the ligand molecule, and finally by nitrogen atom N4 from the coordinated γ-picoline molecule. In **1e** molybdenum is coordinated by the deprotonated amide nitrogen N1 instead of the thiocarbonyl atom S1. Octahedral coordination is completed by oxygen O4 from the methanol molecule. In both structures the values of the Mo = O_t bonds, ranging from 1.697(2) to 1.717(2) Å, are usual for *cis*-MoO_2 complexes. Similarly to **1b** in both independent molecules of **1c** as well as in **1e** the tridentate ligands, occupying meridional positions, form one six- and one five-membered chelate ring, with Mo–O3 bond lengths varying from 1.932(3) to 1.953(3) Å, and Mo–N3 bond lengths, with the imine nitrogen *trans* to the terminal oxo-oxygen ligand, ranging from 2.284(4) to 2.289(4) Å. In **1e** the Mo–N1 bond, *cis* to the oxo ligands, is significantly shorter, amounting to 2.057(2) Å. The longest bonds in the molybdenum coordination sphere in **1c** are those

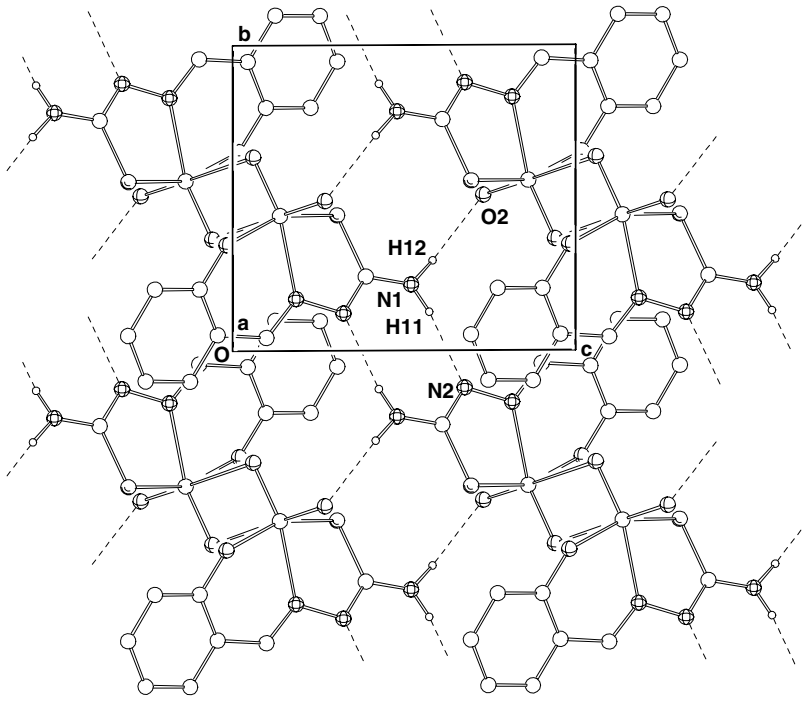


Fig. 2. Hydrogen bonding scheme in **1b** projected along the *a* axis. Sheets of molecules are formed parallel to the *bc* plane.

with sulfur atoms S1, [2.433(1) and 2.435(1) Å], and to the γ-picoline nitrogen atoms [2.412(4) and 2.431(4) Å], while in **1e** the longest bond around Mo is that to the methanol [2.325(2) Å].

Comparing the bond lengths within the thiosemicarbazone ligands it is obvious that the ligand exists in two tautomeric forms. Bond lengths C1–N2, observed in **1b** and **1c**, varying from 1.300(7) to 1.318(6) Å, are significantly shorter than the analogous bond of 1.360(3) Å in **1e**, while the bonds C1–S1, varying from 1.752(5) to 1.763(7) Å (**1b** and **1c**) are longer than that of 1.707(2) Å, observed in **1e**.

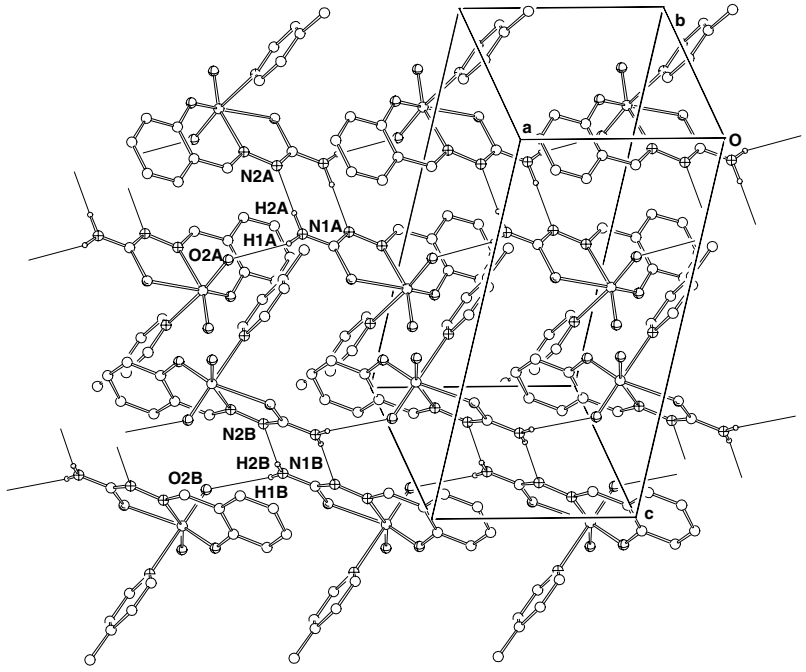


Fig. 3. Hydrogen bonding in **1c**. Symmetry independent double chains of molecules are formed in the *a* axis direction.

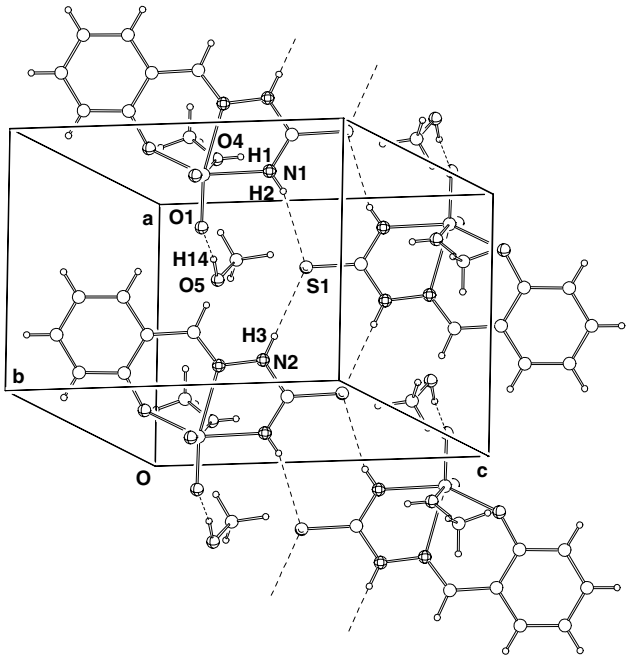


Fig. 4. Hydrogen bonding in **1e**. Chains of molecules are formed along the *a* axis direction, parallel to the (0 1 1) plane, with a solvent methanol hydrogen bonded to a terminal oxo-oxygen atom. The 4,4′-bipyridine solvent molecule is omitted for clarity.

The molecules in **1c** are mutually hydrogen bonded in a similar way as in **1b**, thus forming double chains of molecules in the *a* axis direction (Fig. 3). In **1e** chains of molecules along the *a* axis direction, parallel to the (0 1 1) plane, are formed through intermolecular hydrogen bonds N1–H2 ⋯ S1 and N2–H3 ⋯ S1 between –NH groups and thiocarbonyl sulfur atoms, (Fig. 4). The solvent methanol molecule is hydrogen bonded to a terminal oxo-oxygen atom, O5–H14 ⋯ O1. Additionally, these chains are interconnected through H-bonds O4–H1 ⋯ N4 between the hydroxy group of a coordinated methanol molecule and a 4,4′-bipyridine molecule.

4. Supplementary material

Crystallographic data (excluding structure factors) for the structures reported in this paper have been deposited with the Cambridge Crystallographic Data Centre as supplementary publication nos. CCDC 251692 for compound **1b**, CCDC 251693 for compound **1c** and CCDC 251694 for compound **1e**. Copies of the data can be obtained free of charge on application to CCDC, 12 Union Road, Cambridge CB2 1EZ, UK [fax: (internat.) 144 1223/336 033; e-mail: deposit@ccdc.cam.ac.uk or http://www.ccdc.cam.ac.uk].

Acknowledgement

This research was supported by the Ministry of Science and Technology of the Republic of Croatia Grant 0119631.

References

[1] Z. Afrasiabi, E. Sinn, J. Chen, Y. Ma, A.L. Rheingold, L.N. Zakharov, N. Rath, S. Padhye, Inorg. Chim. Acta 357 (2004) 271.
[2] P. Umapathy, A.P. Budhkar, C.S. Dorai, J. Indian, Chem. Soc. 83 (1986) 714.
[3] D. Chattopadhyay, S.K. Mazamudar, T. Banerjee, S. Ghosh, T.C.W. Mak, Acta Crystallogr. C 44 (1988) 1025.
[4] S.K. Dutta, D.B. McConville, W.J. Youngs, M. Chaudhury, Inorg. Chem. 36 (1997) 2517.
[5] R. Hahn, U. Küsthardt, W. Scherer, Inorg. Chim. Acta 210 (1993) 177.
[6] R. Dinda, P. Sengupta, S. Ghosh, W.S. Sheldrick, Eur. J. Inorg. Chem. (2003) 363.
[7] M. Cindrić, V. Vrdoljak, N. Strukan, P. Tepeš, P. Novak, A. Brbot-Šaranović, G. Giester, B. Kamenar, Eur. J. Inorg. Chem. (2002) 2128.
[8] M. Cindrić, N. Strukan, T. Kajfež, B. Kamenar, Struct. Chem. 13 (2002) 363.
[9] M. Cindrić, N. Strukan, T. Kajfež, G. Giester, B. Kamenar, Z. Anorg. Allg. Chem. 627 (2001) 1.
[10] G. Argay, A. Kalman, V.M. Leovac, V.I. Češljević, B. Ribar, J. Coord. Chem. 37 (1996) 165.
[11] A.B. Ilyukhin, V.L. Abramenko, V.S. Sergienko, Koord. Khim. 20 (1994) 653.
[12] S. Purohit, A.P. Koley, L.S. Prasad, P.T. Manoharan, S. Ghosh, Inorg. Chem. 28 (1989) 3735.
[13] J. Chen, J.W. McDonald, W.E. Newton, Inorg. Chem. 15 (1976) 2612.
[14] G.A. Parker, Analytical Chemistry of Molybdenum, Springer, New York, 1983.
[15] Oxford Diffraction, Oxford Diffraction Ltd., Xcalibur CCD system, CrysAlis Software system, Version 1.170, 2003.
[16] G.M. Sheldrick, SHELXS-97, Program for the Solution of Crystal Structures, University of Göttingen, Germany, 1997.
[17] G.M. Sheldrick, SHELXL-97, Program for the Refinement of Crystal Structures, University of Göttingen, Germany, 1997.
[18] C.K. Johnson, ORTEP-II, Rep. ORNL-5138, Oak Ridge National Laboratory, Oak Ridge, TN, 1976.
[19] A.L. Spek, The EUCLID package, in: D. Sayre (Ed.), Computational Crystallography, Clarendon Press, Oxford, 1982, p. 528.
[20] A. Rana, R. Dinda, S. Ghosh, A.J. Blake, Polyhedron 22 (2003) 3075.
[21] M. Cindrić, N. Strukan, V. Vrdoljak, T. Kajfež, B. Kamenar, Z. Anorg. Allg. Chem. 628 (2002) 2113.
[22] A.F. Petrović, V.M. Leovac, B. Ribar, G. Argay, A. Kalman, Transition Met. Chem. 11 (1986) 207.

Available online at www.sciencedirect.com
SCIENCE DIRECT®
Polyhedron 24 (2005) 377–382
POLYHEDRON
www.elsevier.com/locate/poly

Structural and magnetic characterization of copper(II) halide complexes with 2-(dimethylaminomethyl)-3-hydroxypyridine

Yong-Min Lee [a], Hong-Woo Lee [a], Young-Inn Kim [b,*]

[a] Department of Chemistry, Pusan National University, Pusan 609735, Republic of Korea
[b] Department of Chemistry Education, Chemistry Institute for Functional Materials, Pusan National University, Jangjeon-Dong, Kumjeong-Gu, Pusan 609735, Republic of Korea

Received 6 October 2004; accepted 7 December 2004

Abstract

Dimeric complexes, bis[dihalo(2-dimethylaminomethyl-3-hydroxypyridine)-copper(II)], $[Cu(dmamhp)X_2]_2$, were prepared from the reaction of copper(II) halide (Cl, Br) with 2-dimethylaminomethyl-3-hydroxypyridine (dmamhp) in methanol, and their single crystal structures were determined. The chloro compound was crystallized as green needles in space group $P\bar{1}$ of the triclinic system with $Z = 1$ and unit cell dimensions $a = 7.3420(12)$, $b = 9.196(3)$, $c = 9.817(2)$ Å, $\alpha = 115.16(3)°$, $\beta = 92.433(16)°$ and $\gamma = 111.59(2)°$. The corresponding values for the bromo complex are $a = 7.5652(15)$, $b = 9.191(3)$, $c = 9.7926(13)$ Å, $\alpha = 113.912(14)°$, $\beta = 92.396(14)°$ and $\gamma = 111.24(2)°$. The chloro compound consists of a dimeric molecule $[Cu(dmamhp)Cl_2]_2$, in which copper(II) ions are bridged by chloride ligands. The geometry at the copper is distorted trigonal bipyramidal with the pyridine nitrogen [N9], terminal chloride [Cl1] and the bridging chloride [$Cl2^i$] in the equatorial site; and with the amine nitrogen [N9] and the remaining bridging chloride [Cl2] in the axial site. The dimer units are held through the hydrogen bonding between the hydroxy group in a pyridine ring and the terminal chloride ion. The bromo compound shows a similar structure. The magnetic susceptibility data of both compounds were followed by the Bleaney–Bowers dimer equation with $J = -11.17$ and -21.11 cm^{-1} for the chloro and bromo complexes respectively, indicating that there are antiferromagnetic interactions between the copper(II) ions in the solid state.
© 2004 Elsevier Ltd. All rights reserved.

Keywords: Binuclear 5-coordinated copper(II) complex; Antiferromagnetic interaction; Halide bridging copper(II) complex

1. Introduction

Binuclear five-coordinated copper(II) complexes with monoatomic bridges have been extensively studied, especially those containing halo (chloro and bromo) bridging ligands to develop a correlation between molecular structure and magnetic behavior [1]. The magneto-structural correlations in these kinds of complexes are worthy of constructing molecular-based functional materials [2] and proposing model compounds that mimic the biological active site in copper proteins [3]. This family of compounds show structures ranging from square pyramid to trigonal bipyramid with a variety of bond distances (Cu–X) and bond angles (Cu–X–Cu) in the resulted copper(II) dimer units. However, the structures of these compounds strongly depend on coordinated environments, such as the nature of the coordinated ligand and the crystal packing forces resulting from the existence of the inter- or intra-molecular hydrogen bond in the unit cell. The small changes in structure can have important effects on the magnetic properties of this system [4]. The magnetic behaviors are influenced by the Cu···Cu separation, Cu–X bond distances and Cu–X–Cu angles formed by the bridging CuX moiety in a Cu_2X_2 dimer unit.

* Corresponding author. Tel.: +82 51 510 2695; fax: +82 51 581 2348.
E-mail address: yikim@pusan.ac.kr (Y.-I. Kim).

0277-5387/$ - see front matter © 2004 Elsevier Ltd. All rights reserved.
doi:10.1016/j.poly.2004.12.004

We selected 2-dimethylaminomethyl-3-hydroxypyridine (dmamhp) and reacted it with copper(II) halides since the dmamhp ligand is interesting in that two methyl groups on the amine nitrogen influence the $Cu–N_{amine}$ bond strength and that the hydroxy group on the pyridine ring can form a hydrogen bond with the halide ions in the unit cell. Herein, binuclear copper(II) complexes, $[Cu(dmamhp)X_2]_2$ where X = Cl and Br, were prepared, and the structures were determined. The magnetic properties (EPR and magnetic susceptibility) were examined to investigate the magneto-structural correlation of the prepared compounds.

2. Experimental

2.1. Materials and synthesis

All reagents and solvents were obtained commercially from either Aldrich or Sigma Chemicals. $[Cu(dmamhp)Cl_2]_2$ was prepared from the direct reaction of 2-dimethylaminomethyl-3-hydroxypyridine (dmamhp) with $CuCl_2$. A solution of $CuCl_2$ (0.1 mmol) in 20 ml of absolute methanol was added dropwise to 20 ml of dmamhp (0.1 mmol) absolute methanol solution. The solution changed to a dark blue color immediately. The resulting mixture was stirred for approximately 2 h and then allowed to stand at room temperature. The crystals suitable for X-ray analysis were obtained by slow evaporation from this solution. $[Cu(dmamhp)Br_2]_2$ was obtained by an analogous method using $CuBr_2$.

2.2. Physical measurements

The EPR spectral measurements were carried out both for powered samples and for frozen glass samples (DMF/CH_2Cl_2) at 77 K using an ESP-300S EPR spectrometer at the X-band frequency. The field modulation frequency was 100 kHz, and DPPH was used as a reference. Magnetic susceptibility data was collected from 4 to 300 K by the SQUID method using the Magnetic Property Measurement System (MPMS7) Quantum Design. The data was corrected for the diamagnetism of the constituent atoms using Pascal's constants and for the temperature-independent paramagnetism of the copper estimated to be 60×10^{-6} cgsu/Cu atom.

2.3. X-ray single crystal structure determination

Crystals of $[Cu(dmamhp)Cl_2]_2$ and $[Cu(dmamhp)Br_2]_2$ for X-ray analysis were obtained by slow evaporation from the methanol solution. The crystals were mounted and aligned on a CAD-4 diffractometer [5]. The accurate cell parameters were refined from the setting angles of 21 reflections with $10.0° < \theta < 13.59°$ for $[Cu(dmamhp)Cl_2]_2$ and from the setting angles of 20 reflections with $10.16° < \theta < 14.09°$ for $[Cu(dmamhp)Br_2]_2$.

All non-H atoms were found by the direct method, and their parameters were refined successfully by full matrix least-squares. The weights used for least-squares refinement were $w^{-1} = [\sigma^2(F_o)^2 + (0.0938P)^2]$ for $[Cu(dmamhp)Cl_2]_2$ and $w^{-1} = [\sigma^2(F_o)^2 + (0.0804P)^2]$ for $[Cu(dmamhp)Br_2]_2$, where P is a function of intensity. H atoms were geometrically positioned and fixed. Empirical absorption corrections were applied to the intensity data for the prepared crystals by using ψ-scans. Data collection and cell refinement: CAD4 EXPRESS [6]. Data reduction: XCAD4 [7]. Program used to solve structure and to refine structure: SHELXS97 and SHELXL97 [8]. Molecular graphics: ORTEP-3 for WINDOWS [9].

3. Results and discussion

3.1. Description of the structures

The crystallographic data and structure refinement parameters of the titled compounds are summarized in Table 1. Both compounds consist of dimeric $[Cu(dmamhp)X_2]_2$ where X = Cl and Br, and each dimer unit is connected through the hydrogen bond in the cell. The selected bond distances and bond angles in these two compounds are summarized in Table 2. A typical ORTEP view of $[Cu(dmamhp)Cl_2]_2$ including the atomic numbering scheme is shown in Fig. 1. The Cu–Cl–Cu bridge is formed by atoms Cu, Cl2, $Cl2^i$ and Cu^i (symmetry code: (i) $-x + 1, -y + 1, -z$); and the bridging Cu_2Cl_2 unit is planar with a crystallographic inversion center, which is located in the center of the two copper(II) atoms. The Cu–Cl distances in the bridging unit are 2.298(2) and 2.639(2) Å, and the Cu–Cl–Cu angle is 94.75°. These values are normal as observed in other dimeric copper chloride compounds [1g,10].

The Cu, N1, Cl1 and $Cl2^i$ atoms are quite coplanar, there being a deviation of the Cu atom from the N1–Cl1–$Cl2^i$ plane of only 0.04 Å. This out-of plane deviation value was obtained from the best least-square method. The N9–Cu–Cl2 angle was obtained to be 174.02(19)°. These results indicate that the geometry around the Cu center is the distorted trigonal bipyramid with N1, Cl1 and $Cl2^i$ forming the equatorial site, and N9 and Cl2 occupying the axial one. The crystal structure of $[Cu(dmamhp)Br_2]_2$ complex is similar to that of $[Cu(dmamhp)Cl_2]_2$ with the deviation out of the equatorial plane of the Cu atom being 0.07 Å.

In the $[Cu(dmamhp)Cl_2]_2$ compound, the Cu–N9 bond length of 2.065(6) Å is larger than the Cu–N1 value of 2.035(6) Å. This is not consistent with the expectation that the basicity of the amine nitrogen [N9] is greater than that of the pyridine nitrogen [N1]. Moreover, the electron donating ability of the methyl groups

Table 1
Crystallographic data for the complexes, $[Cu(dmamhp)Cl_2]_2$ and $[Cu(dmamhp)Br_2]_2$

	$[Cu(dmamhp)Cl_2]_2$	$[Cu(dmamhp)Br_2]_2$
Chemical formula	$C_{16}H_{24}Cl_4Cu_2N_4O_2$	$C_{16}H_{24}Br_4Cu_2N_4O_2$
Formula weight (amu)	573.27	751.11
Crystal description	green, block	deep purple, block
Crystal size (mm)	$0.20 \times 0.17 \times 0.13$	$0.28 \times 0.24 \times 0.16$
Crystal system	triclinic	triclinic
Space group	$P\bar{1}$	$P\bar{1}$
T (K)	293(2)	293(2)
Radiation (Mo Kα) (λ/Å)	0.71073	0.71073
Unit cell dimensions		
a (Å)	7.3420(12)	7.5652(15)
b (Å)	9.196(3)	9.191(3)
c (Å)	9.817(2)	9.7926(13)
α (°)	115.16(3)	113.912(14)
β (°)	92.433(16)	92.396(14)
γ (°)	111.59(2)	111.24(2)
Volume (Å^3)	542.1(2)	565.8(2)
Z	1	
D_{calc} (Mg m^{-3})	1.756	2.204
μ (mm^{-1})	2.475	8.961
θ Range (°)	2.36–25.50	2.33–24.97
Absorption correction	ψ-scan	ψ-scan
T_{max}	0.7208	0.5817
T_{min}	0.5375	0.2217
Index ranges	$0 \leqslant h \leqslant 8$, $-11 \leqslant k \leqslant 10$, $-11 \leqslant l \leqslant 11$	$-8 \leqslant h \leqslant 8$, $-10 \leqslant k \leqslant 9$, $0 \leqslant l \leqslant 11$
Independent reflections	2019	1984
Observed reflections	1344	1327
Final R indices [$I > 2\sigma(I)$]	0.0670	0.0575
ωR	0.1484	0.1282
Restraints and parameters	0 and 127	0 and 127
Goodness-of-fit on F^2	1.006	1.015
$(\Delta/\rho)_{max}$	1.000	1.000
$\Delta\rho_{max}$ and $\Delta\rho_{min}$ (e Å^{-3})	1.168 and −1.215	1.450 and −0.940

on N9 presumably leads to the enhancement of electron density at N9 relative to that at N1. This observed longer distance of Cu–N9 than that of Cu–N1 can be explained by the fact that the steric hinderances of the methyl groups at N9 cause a lengthening of the Cu–N9 bond and lead to a smaller angle of C8–N9–Cu [104.4(4)°] than that of C6–N1–Cu [113.1(5)°]. Similar results are found in $[Cu(dmamhp)Br_2]_2$.

A molecular packing diagram for the dimeric $[Cu(dmamhp)Cl_2]_2$ compound is shown in Fig. 2. The distance between the hydrogen atom [HO7] in the hydroxyl group in the dmamhp ligand and the adjacent terminal chloride [Cl1] is 2.32 Å, and the O7···Cl1^{ii} (symmetry code: (ii) $x-1, y-1, z$) separation is 3.061(6) Å, which is smaller than the sum of the van der Waals radii of oxygen [~1.5 Å] and the chlorine [1.7–1.9 Å] atom. Furthermore, the O7–HO7···Cl1^{ii} angle is 151.1°. These results imply that there is a hydrogen bond formation between the hydroxyl group in the dmamhp ligand and the terminal chloride. The dimer units are held together in an one dimensional network through these hydrogen bondings. The hydrogen bond distances and bond angles are summarized in Table 3. The $[Cu(dmamhp)Br_2]_2$ complex shows a similar hydrogen bonded network in the crystal.

Table 2
The selected bond distances (Å) and bond angles (°) of the complexes, $[Cu(dmamhp)Cl_2]_2$ and $[Cu(dmamhp)Br_2]_2$

$[Cu(dmamhp)Cl_2]_2$		$[Cu(dmamhp)Br_2]_2$	
Bond distances			
Cu–N1	2.035(6)	Cu–N1	2.022(8)
Cu–N9	2.065(6)	Cu–N9	2.063(7)
Cu–Cl1	2.257(3)	Cu–Br1	2.3886(19)
Cu–Cl2	2.298(2)	Cu–Br2	2.4389(15)
Cu–Cl2^i	2.639(2)	Cu–Br2^i	2.8048(18)
Cl2–Cu^i	2.639(2)	Br2-Cu^i	2.8048(18)
Bond angles			
N1–Cu–N9	81.0(2)	N1–Cu–N9	81.2(3)
N1–Cu–Cl1	145.2(2)	N1–Cu–Br1	144.4(3)
N9–Cu–Cl1	91.95(19)	N9-Cu–Br1	92.8(2)
N1–Cu–Cl2	94.32(18)	N1–Cu–Br2	94.9(2)
N9–Cu–Cl2	174.02(19)	N9–Cu–Br2	174.0(3)
Cl1–Cu–Cl2	94.02(9)	Br1–Cu–Br2	93.00(6)
N1–Cu–Cl2^i	103.38(19)	N1–Cu–Br2^i	102.2(2)
N9–Cu–Cl2^i	92.20(19)	N9–Cu–Br2^i	91.8(2)
Cl1–Cu–Cl2^i	110.95(9)	Br1–Cu–Br2^i	113.08(6)
Cl2–Cu–Cl2^i	85.25(7)	Br2–Cu–Br2^i	84.57(5)
Cu–Cl2–Cu^i	94.75(7)	Cu–Br2–Cu^i	95.43(5)

Symmetry code: (i) $-x+1, -y+1, -z$.

3.2. EPR and magnetic properties

EPR spectra were obtained both for solid and for frozen glass samples (DMF/CH_2Cl_2) at 77 K. The powdered EPR spectrum of $[Cu(dmamhp)Cl_2]_2$ shows a sharp and symmetric singlet at $\langle g \rangle = 2.007$, whereas the anisotropic g values were well resolved in $[Cu(dmamhp)Br_2]_2$ showing a typical axial symmetry. EPR spectra of frozen solution for both compounds exhibited well-defined hyperfine structure with parallel ($g_\parallel$) and perpendicular ($g_\perp$) components, indicating that no significant inter-dimer interactions are present. The resulted EPR parameters are summarized in Table 4.

The magnetic susceptibilities were collected as a function of temperatures (4–300 K). The magnetic susceptibility data of $[Cu(dmamhp)Br_2]_2$ increases to a maximum at around 18 K and decreases as the temperatures decreases, as shown in Fig. 3. The magnetic susceptibility data of $[Cu(dmamhp)Cl_2]_2$ exhibited a different behavior. The magnetic susceptibility data in the temperature region of 4–300 K increases as the temperatures decreases, but it does not follow the

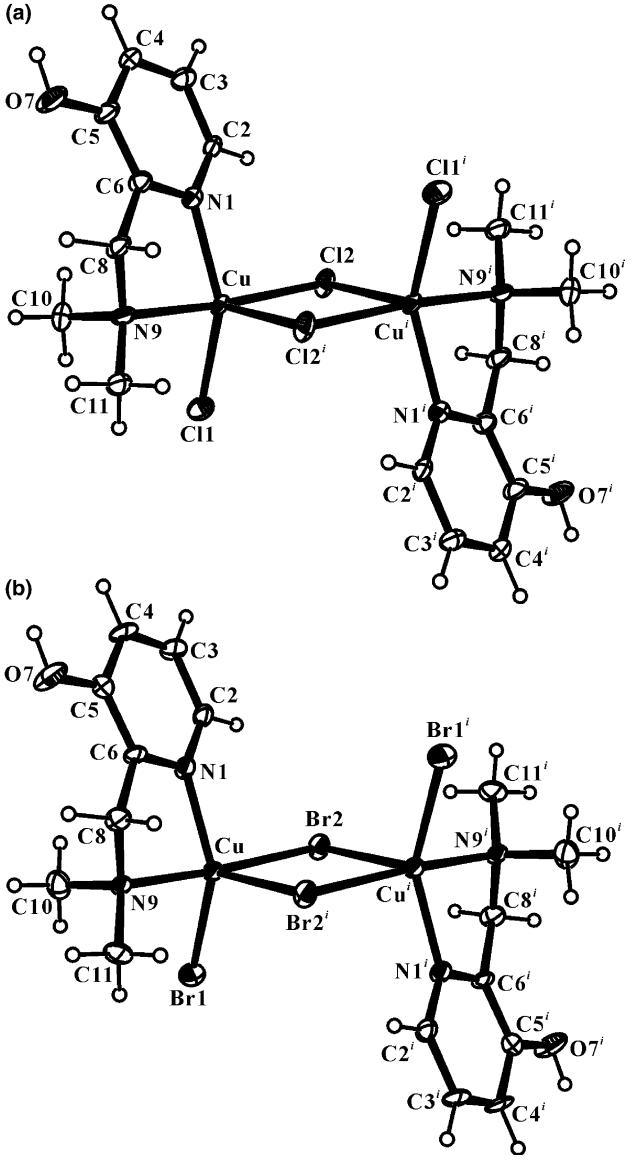


Fig. 1. ORTEP diagrams of $[Cu(dmamhp)Cl_2]_2$ (a) and $[Cu(dmamhp)Br_2]_2$ (b), showing the atom-numbering scheme (Symmetry code: (i) $-x+1, -y+1, -z$).

Curie–Weiss law. However, the data of both compounds can be fit to the Bleaney–Bowers dimer equation [11]

$$\chi_M^{exptl} = \left(\frac{2N\beta^2g^2}{kT}\right)\left\{3+\exp\left(-\frac{J}{kT}\right)\right\}^{-1}(1-\rho) + \left(\frac{N\beta^2g^2}{2kT}\right)\rho + 2N\alpha, \quad (1)$$

where ρ is the mass proportion of uncoupled impurity assumed to follow a Curie law, and the temperature independent paramagnetism $N\alpha$ was taken as 60×10^{-6} cm^3/mol per copper(II) ion. The other symbols have their usual meanings.

The best fit calculated values are $2J = -42.22$ cm^{-1} and $g = 2.134$ for the $[Cu(dmamhp)Br_2]_2$ compound, and $2J = -22.34$ cm^{-1} and $g = 2.130$ for the $[Cu(dmamhp)Cl_2]_2$ compound. The calculated g values are in good agreement with those experimental values obtained by EPR experiments. The calculated singlet–triplet exchange coupling constants ($2J$) clearly show that there are antiferromagnetic interactions between the copper metal ions in both of the compounds in solid state. Fig. 3 shows the excellent agreement between the theoretical Bleaney–Bowers dimer equation and the experimental data in $[Cu(dmamhp)Br_2]_2$.

Hatfield [12] reported the effect of bridge geometry on the singlet–triplet exchange coupling in ligand bridged copper(II) dimers, in which the exchange coupling depended on the angle at the bridging ligand and on the length of the superexchange pathway. In the case of chloro bridged copper(II) dimers, singlet–triplet exchange coupling constant ($2J$) smoothly correlated with the quotient of structure parameters φ/r, where φ is the angle at the bridging chloride atom and r is the long out-of-plane bond distance [12]. Alves et al. [1g] showed this smooth correlation in a variety of the chloro bridged copper(II) dimers. As the quotient φ/r increases from 28 to 40° Å^{-1}, $2J$ values rise from -17 cm^{-1} to a maximum of $+6.3$ cm^{-1} at 32.62° Å^{-1} and fall down to -82.6 cm^{-1} at 40° Å^{-1} of the quotient value. On the ba-

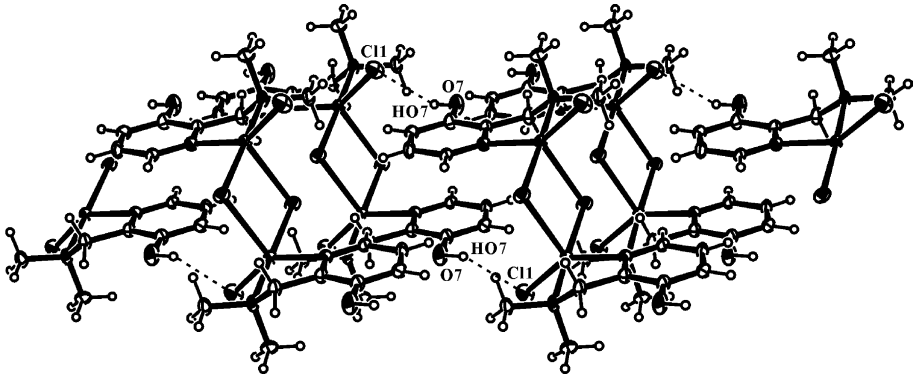


Fig. 2. A molecular packing diagram of $[Cu(dmamhp)Cl_2]_2$. Intermolecular hydrogen bonds are shown with short-dashed lines.

Table 3
The hydrogen bond distances (Å) and bond angles (°) of the complexes, $[Cu(dmamhp)Cl_2]_2$ and $[Cu(dmamhp)Br_2]_2$

Compound	D–H···A	d(D–H)	d(H···A)	d(D···A)	∠(DHA)
$[Cu(dmamhp)Cl_2]_2$	O7–HO7···Cl1^{ii}	0.82	2.32	3.061(6)	151.1
$[Cu(dmamhp)Br_2]_2$	O7–HO7···Br1^{ii}	0.82	2.52	3.240(7)	146.8

Symmetry code: (ii) $x-1, y-1, z$.

Table 4
EPR and magnetic susceptibility parameters for the complexes, $[Cu(dmamhp)Cl_2]_2$ and $[Cu(dmamhp)Br_2]_2$

Compound	Solution[a]		Powder[a]	Magnetic property[b]	
	g Value	A Value ($\times 10^4$ cm^{-1})	g Value	J (cm^{-1})	g Value
$[Cu(dmamhp)Cl_2]_2$	$g_{\parallel} = 2.275$	$A_{\parallel} = 146$	$g_{zz} = 2.254$ $g_{yy} = 2.083$	−11.17	2.130
	$g_{\perp} = 2.053$	$A_{\perp} = 27$	$g_{xx} = 2.029$		
$[Cu(dmamhp)Br_2]_2$	$g_{\parallel} = 2.288$ $g_{\perp} = 2.057$	$A_{\parallel} = 156$ $A_{\perp} = 31$	$\langle g \rangle = 2.007$	−21.11	2.134

[a] EPR parameters were obtained at 77 K.
[b] These values were calculated by the Bleaney–Bowers equation.

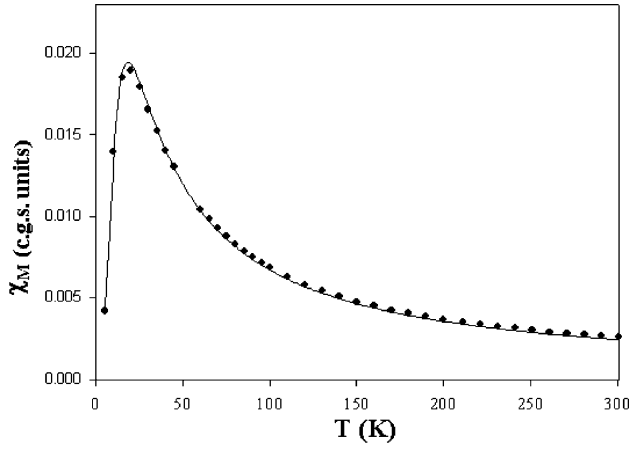


Fig. 3. A plot of magnetic susceptibilities vs. temperature in the temperature region of 4–300 K for $[Cu(dmamhp)Br_2]_2$. Calculated (—) and experimental (•) magnetic data are shown. Calculated curve with $J = -21.11$ cm^{-1}, $g = 2.134$ and $\rho = 0.0205$ was obtained by the Bleaney–Bowers equation, $\chi_M = (2N\beta^2g^2/kT)[3 + \exp(-J/kT)]^{-1}(1-\rho) + (N\beta^2g^2/2kT)\rho + 2N\alpha$.

sis of this correlation, the antiferromagnetic coupling is characterized for the values of the quotient lower than 32.6 and higher than 35.0° Å^{-1}, whereas the ferromagnetic coupling appears when this quotient is between these two values. The calculated antiferromagnetic coupling constants of $[Cu(dmamhp)Cl_2]_2$ ($2J = -22.34$ cm^{-1} and $\varphi/r = 35.90°$ Å^{-1}) fit well in this correlation.

In the bromo bridged copper(II) complexes, $2J$ values do not correlate either with the bridging angle or with the bridged Cu–Br distances. However, in spite of the smaller quotient of $[Cu(dmamhp)Br_2]_2$ ($\varphi/r = 34.02°$ Å^{-1}) than that of the chloro compound and the longer Cu···Cu contact distance of bromo compound in the bridging unit [3.887 Å] than that of chloro compound [3.640 Å], it was found that the exchange coupling constant of $[Cu(dmamhp)Br_2]_2$ ($2J = -42.22$ cm^{-1}) is larger than that of the analogous chloro compound. This relatively larger antiferromagnetic interaction in $[Cu(dmamhp)Br_2]_2$ is explained on the basis of the fact that the magnetic orbital of bromine atom contacts more easily with the copper atom than that of chlorine to provide a superexchange Cu–Br–Cu pathway. Contact of bromine atoms has been discussed in some copper(II) complexes. We have recently reported the magnetic properties of sparteinium tetrahalocuprate(II) compounds and suggested that the antiferromagnetic superexchange in $CuBr_4$ was occurred through a Cu–Br···Br–Cu contact, whereas the magnetic superexchange via a Cu–Cl···Cl–Cu contact was not likely to be observed [13]. A similar Cu–Br···Br–Cu two bromide exchange pathway through Br···Br contact was reported in a bis(cyclophenylammonium) tetrabromocuprate(II) compound [14].

4. Conclusions

2-Dimethylaminomethyl-3-hydroxypyridine (dmamhp) reacts with CuX_2 (X = Cl and Br) to yield the halo-bridged dimeric $[Cu(dmamhp)X_2]_2$ compounds. The geometry around the copper(II) center in the dimeric unit is a distorted trigonal bipyramid, and the Cu–X–Cu bridge provides the magnetic superexchange pathway. There are no magnetic interactions between the dimer units even though the dimers are held together through the hydrogen bondings in the unit cell.

5. Supplementary material

Crystallographic data for the structures reported here have been deposited with the Cambridge Crystallo-

graphic Data Centre (Deposition Nos. CCDC-2244689 and CCDC-244690). The data can be obtained free of charge via www.ccdc.cam.ac.uk/perl/catreq/catreq.cgi (or from the CCDC, 12 Union Road, Cambridge CB2 1EZ, UK; Fax: +44 1223 336033; e-mail: deposit@ccdc.cam.ac.uk).

Acknowledgement

This work was supported by Pusan National University research grant.

References

[1] (a) D.K. Towle, S.K. Hoffmann, W.E. Hatfield, P. Singh, P. Chaudhuri, K. Wieghardt, Inorg. Chem. 24 (1985) 4393;
(b) M. Bukowska-Strzyewska, W. Maniukiewicz, L. Sieron, Acta Crystallogr., Sect. B 53 (1997) 466;
(c) M. Rodriguez, A. Llobet, M. Corbella, A.E. Martell, J. Reibenspies, Inorg. Chem. 38 (1999) 2328;
(d) R.D. Willett, G. Pon, C. Nagy, Inorg. Chem. 40 (2001) 4342;
(e) H. Grove, J. Sletten, M. Julve, F. Llobet, J. Chem. Soc., Dalton Trans. (2001) 2487;
(f) A. Rodriguez–Fortea, P. Alemany, S. Alvarez, E. Ruiz, Inorg. Chem. 41 (2002) 3769;
(g) W.A. Alves, R.H. de Almeida Santos, A. Paduan-Filho, C.C. Becerra, A.C. Borin, A.M. da Costa Ferreira, Inorg. Chim. Acta 357 (2004) 2269.
[2] M. Verdaguer, Polyhedron 20 (2001) 1115.
[3] (a) T.N. Sorrell, Tetrahedron 25 (1989) 3;
(b) E.I. Solomon, U.M. Sundaram, T.E. Machonkin, Chem. Rev. 96 (1996) 2563.
[4] M. Rodriguez, A. Llobet, M. Corbella, Polyhedron 19 (2000) 2483.
[5] Enraf-Nonius, CAD-4 Software: Version 5.0, Delft, The Netherlands, 1989.
[6] Enraf-Nonius, CAD4 EXPRESS, Delft, The Netherlands, 1994.
[7] K. Harms, S. Wocadlo, XCAD4: Program for Processing CAD-4 Diffractometer Data, University of Marburg, Germany, 1995.
[8] G.M. Sheldrick, SHELXL97 and SHELXS97: Program for the Refinement of Crystal Structures, University of Göttingen, Germany, 1997.
[9] L.J. Farrugia, J. Appl. Cryst. 30 (1997) 565.
[10] (a) W.E. Maroh, K.C. Patel, W.E. Hatfield, D.J. Hodgson, Inorg. Chem. 22 (1983) 511;
(b) T. Sekine, T. Okuno, K. Awaga, Chem. Phys. Lett. 249 (1996) 201;
(c) Y. Kani, S. Ohba, S. Ito, Y. Nishida, Acta Crystallogr., Sect. C 56 (2000) 195;
(d) X.-H. Bu, M. Du, L. Zhang, Z.-L. Shang, R.-H. Zhang, M. Shionoya, J. Chem. Soc., Dalton Trans. (2001) 729;
(e) R.D. Kohn, Z. Pan, M.F. Mahon, G. Kociok-Kohn, J. Chem. Soc., Dalton Trans. (2003) 2269.
[11] B. Bleaney, K.D. Bowers, Proc. R. Soc. Lond., Ser. A 214 (1952) 451.
[12] W.E. Hatfield, Comments Inorg. Chem. 1 (1981) 105.
[13] (a) Y.-M. Lee, S.-M. Park, S.K. Kang, Y.-I. Kim, S.-N. Choi, Bull. Kor. Chem. Soc. 25 (2004) 823;
(b) S.K. Kang, Y.-M. Lee, Y.-I. Kim, Y. Kim, K. Seff, S.-N. Choi, Inorg. Chim. Acta 357 (2004) 2602.
[14] R.D. Willett, C. Galeriu, C.P. Landee, M.M. Turnbull, B. Twamley, Inorg. Chem. 43 (2004) 3804.

Available online at www.sciencedirect.com
SCIENCE DIRECT®
Polyhedron 24 (2005) 383–390
POLYHEDRON
www.elsevier.com/locate/poly

Diphenyltin(IV) complexes of the 2-quinolinecarboxaldehyde Schiff bases of *S*-methyl- and *S*-benzyldithiocarbazate (Hqaldsme and Hqaldsbz): X-ray crystal structures of Hqaldsme and two conformers of its diphenyltin(IV) complex

Mohammad Akbar Ali [a,*], A.H. Mirza [a], Malai Haniti S.A. Hamid [a], Paul V. Bernhardt [b]

[a] *Department of Chemistry, Universiti Brunei Darussalam, Jalan Tungku Link, BE 1410, Negara Brunei Darussalam*
[b] *Department of Chemistry, The University of Queensland, Brisbane, Qld 4072, Australia*

Received 2 September 2004; accepted 8 November 2004

Abstract

New organometallic tin(IV) complexes of the empirical formula $Sn(NNS)Ph_2Cl$ (NNS = anionic forms of the 2-quinolinecarboxaldehyde Schiff bases of *S*-methyl- and *S*-benzyldithiocarbazate) have been prepared and characterized by IR, electronic, ^1H NMR and ES mass spectroscopic techniques. The molecular structures of the 2-quinolinecarboxaldehyde Schiff base of *S*-methyldithiocarbazate (Hqaldsme) and its diphenyltin(IV) complex, $Sn(qaldsme)Ph_2Cl$, have been determined by X-ray diffraction. In the solid state, the ligand remains as the thione tautomer in which the dithiocarbazate chain adopts an *E*,*E* configuration and is almost coplanar with the quinoline ring. The $Sn(qaldsme)Ph_2Cl$ complex crystallizes in two distinctly different conformationally isomeric forms, each having the same space group but different lattice parameters. X-ray analysis shows that in each polymorph, the tin atom adopts a distorted octahedral geometry with the Schiff base coordinated to it as a uninegatively charged tridentate chelating agent via the quinoline nitrogen atom, the azomethine nitrogen atom and the thiolate sulfur atom. The two phenyl groups occupy axial positions and the chloride ligand occupies the sixth coordination position of the tin atom. The deprotonated ligand adopts an *E*,*E*,*Z* configuration in the complex.
© 2004 Elsevier Ltd. All rights reserved.

Keywords: Tin(IV) complexes; Dithiocarbazates; 2-Quinolinecarboxaldehyde Schiff bases of *S*-alkyl- and *S*-aryldithiocarbazates; Diphenyltin(IV)complexes of Schiff bases

1. Introduction

There have been a large number of studies on metal complexes of sulfur–nitrogen chelating agents such as Schiff bases derived from *S*-alkyl/aryl esters of dithiocarbazic acid [1–6] and thiosemicarbazones [6–11]. Interest in these compounds has been stimulated by their interesting physical and chemical properties [12–14] and potentially useful biological activities [15–19]. However, the majority of work that has been reported so far involves complexes of these ligands with transition metal ions. Complexes of non-transition metal ions such as tin have received less attention. In recent years, organotin(IV) compounds have received much attention both in academic and applied research because of the ability of tin to afford stable bonds with carbon as well as with other hetero atoms. Since organotin complexes of Schiff base ligands have potential applications in organic synthesis, catalysis, medicinal chemistry and biotechnology [20–23] and as very little work has been done on

* Corresponding author. Tel.: +673 2 2463001x1341; fax: +673 2 461502.
E-mail address: akbar@fos.ubd.edu.bn (M. Akbar Ali).

0277-5387/$ - see front matter © 2004 Elsevier Ltd. All rights reserved.
doi:10.1016/j.poly.2004.11.023

organotin(IV) compounds of Schiff bases derived from *S*-alkyl and *S*-aryldithiocarbazates, we report here the synthesis and characterization of two new diphenyltin(IV) complexes of the 2-quinolinecarboxaldehyde Schiff bases of *S*-methyl- and *S*-benzyl esters of dithiocarbazic acid together with the X-ray crystal structures of the free ligand, Hqaldsme, and two forms of its diphenyltin(IV) complex, Sn (qaldsme)$(Ph)_2Cl$.

2. Experimental

2.1. Reagents

Chemicals and solvents used were of analytical reagent grade and used without any further purification. 2-Quinolinecarboxaldehyde and diphenyltin(IV)dichloride were purchased from the Aldrich Chemical Company and *S*-methyl- and *S*-benzyldithiocarbazates were prepared according to published procedures [24,25].

2.2. Physical measurements

Microanalyses for C, H and N were performed by the Elemental Analysis Laboratory, National University of Singapore, Singapore. Molar conductances of ca. 10^{-3} M solutions of the complexes in DMSO were measured by means of a Jenway 4310 conductivity meter. The IR spectra in KBr discs and the electronic spectra either as Nujol mulls or in solution were recorded on a Perkin–Elmer 2000 FT-IR spectrometer and a Shimadzu MPC-3100 spectrophotometer, respectively. The ^1H NMR spectra of the tin(IV) complexes were run in $CDCl_3$ on a Bruker DPX 300 MHz spectrometer using TMS as an internal standard. The electrospray mass spectra were recorded on a Finnigan Model LCQ mass spectrometer.

2.3. Preparation of the ligands

The Schiff bases were prepared by following procedures similar to those reported previously [26].

2.4. Preparation of the complexes.

2.4.1. Preparation of syn- and anti-[Sn(qaldsme)Ph_2Cl]

Diphenyltin(IV) dichloride (0.51 g; 1.5 mmol) dissolved in boiling absolute ethanol (10 ml) was mixed with a hot solution of Hqaldsme (0.39 g; 1.5 mmol) in a mixture of absolute ethanol (100 ml) and dichloromethane (30 ml). The resulting yellow solution on being heated under reflux for 3 h yielded some yellow crystals (0.26 g) which were filtered off, washed with cold absolute ethanol and dried in a desiccator. X-ray analysis (vide Section 3) showed that this was the *syn*-form of the complex. The filtrate was refluxed for a further period of ca. 72 h during which time the colour of the solution became reddish-brown. On standing overnight, some brown crystals (0.11 g) were obtained. X-ray analysis showed that these were the *anti*-form of the [Sn(qaldsme)Ph_2Cl] complex. Both polymorphs of the complex gave very similar analytical data. *Anal.* Calc.

Table 1
Crystallographic data

	Hqaldsme	*syn*-Sn(qaldsme)Ph_2Cl	*anti*-Sn(qaldsme)Ph_2Cl
Formula	$C_{12}H_{11}N_3S_2$	$C_{24}H_{20}ClN_3S_2Sn$	$C_{24}H_{20}ClN_3S_2Sn$
Formula weight	261.36	568.69	568.69
Temperature (K)	293	293	293
Wavelength (Å)	0.71073	0.71073	0.71073
Crystal system	orthorhombic	monoclinic	monoclinic
Space group	$P2_12_12_1$	$P2_1/n$	$P2_1/n$
Unit cell dimensions			
a (Å)	11.410(2)	13.709(2)	9.071(2)
b (Å)	7.126(3)	10.950(1)	14.839(1)
c (Å)	15.573(8)	15.6877(9)	17.436(1)
β (°)		99.261(7)	95.52(1)
Volume (Å^3)	1266.2(9)	2324.2(4)	2336.1(6)
Z	4	4	4
Absorption coefficient (mm^{-1})	0.400	1.411	1.404
Reflections collected	2516	4259	4363
Independent reflections	2218	4078	4088
R_{int}	0.1077	0.0122	0.0160
Observed reflections [$I > 2\sigma(I)$]	1099	3560	3165
Parameters	154	281	281
Goodness-of-fit on F^2	0.995	1.122	1.026
R_1 [$I > 2\sigma(I)$]	0.0673	0.0228	0.0253
w_2 (all data)	0.1892	0.0644	0.0578
Flack parameter	−0.5(3)		

for [Sn(qaldsme)Ph_2Cl] ($C_{24}H_{20}N_3S_2SnCl$): C, 50.69; H, 3.54; N, 7.39. Found: C, 50.73; H, 3.58; N, 7.16%.

2.4.2. Preparation of [Sn(qaldsbz)Ph_2Cl]

The Schiff base (0.20 g; 0.6 mmol) dissolved in a mixture of absolute ethanol (25 ml) and dichloromethane (15 ml) was mixed with a hot solution of $SnPh_2Cl_2$ (0.20 g; 0.6 mmol) in absolute ethanol (10 ml). The yellow coloured solution on being heated for 30 min yielded a small amount of yellow crystals (0.05 g) which were filtered off. The filtrate was then heated under reflux for ca. 72 h during which time the colour of the solution changed from yellow to brown. Reduction of the volume of the reaction mixture to ca. 30 ml resulted in the deposition of some brown crystals which were filtered off and recrystallized from an acetonitrile–methanol mixture (90:10). Yield, 0.15 g. *Anal.* Calc. for [Sn(Hqaldsbz)Ph_2Cl] ($C_{30}H_{24}N_3S_2SnCl$): C, 55.88; H, 3.75; N, 6.51. Found: C, 55.76; H, 3.49; N, 6.62%.

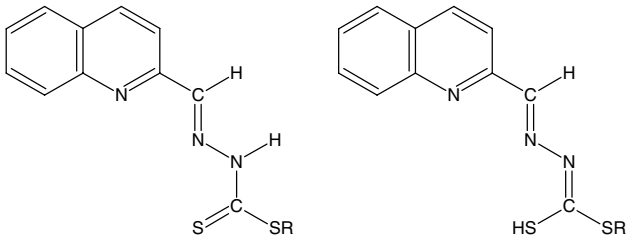
2.5. Crystallography

Cell constants were determined by a least-squares fit to the setting parameters of 25 independent reflections, measured on an Enraf-Nonius CAD 4 four-circle diffractometer using graphite monochromated Mo Kα radiation (0.71073 Å) and operating in the $\omega - 2\theta$ mode within the range $2° < 2\theta < 50°$. Empirical absorption correction (ψ scans) and data reduction were performed with the WINGX [27] suite of programmes. The structures were solved by direct methods with SHELX86 and refined by full-matrix least-squares analysis with SHELXL97 [28]. Non-hydrogen atoms were refined with anisotropic thermal parameters whereas H-atoms were included at estimated positions. Drawings of each molecule were produced with ORTEP3 [29] or PLUTON [30]. A summary of the crystal data, structure solution and refinement parameters are given in Table 1 and selected bond lengths appear in Tables 4 and 5.

3. Results and discussion

Compounds containing the thioamide —N—NH—C(=S) moiety are capable of exhibiting thione-thiol tautomerism and therefore the 2-quinolinecarboxaldehyde Schiff bases of *S*-methyl- and *S*-benzyldithiocarbazate (Fig. 1(a); R = —SCH_3, —$SCH_2C_6H_5$) can exist either as the thione form (**1a**) or the thiol form (**1b**) or as an equilibrium mixture of both forms. However, our previous studies [26] have shown that these ligands remain solely as the thione tautomer both in the solid state as well as in solution.

An X-ray crystal structure determination (see later) of Hqaldsme shows that it remains as an *E* isomer in the solid state but its ^{1}H NMR spectrum in DMSO-d_6 exhibits the sec. –NH– proton resonance at 13.65 ppm indicating that in a DMSO solution it rearranges to the *Z* isomer with the hydrogen atom on N(1) being intra-molecularly hydrogen bonded with the quinoline nitrogen atom, similar to that observed in the closely related 1-quinolinecarboxaldehydethiosemicarbazone [31].



(1a ; R = -CH_3, -$CH_2C_6H_5$) Thione form

(1b ; R=-CH_3, -$CH_2C_6H_5$) Thiol form

Fig. 1. The thione and thiol forms of the Schiff bases; Hqaldsme = the 2-quinolinecarboxaldehyde Schiff base of *S*-methyldithiocarbazate (R = CH_3) and Hqaldsbz = the 2-quinolinecarboxaldehyde Schiff base of *S*-benzyldithiocarbazate (R = $CH_2C_6H_5$).

Although, both in the solid state and in solution, the Schiff bases remain in their thione tautomeric forms, in an ethanolic solution and in the presence of diphenyltin(IV) dichloride, they quickly tautomerize to the thiol forms, deprotonate and coordinate with the tin atom forming stable diphenyltin(IV) complexes of the empirical formula, Sn(NNS)Ph_2Cl (NNS = deprotonated form of the Schiff base). The ready conversion of the Schiff bases from the thione tautomeric forms to the thiol forms in the presence of a metal ion followed by deprotonation and coordination to the metal may be attributed to the extra stability gained by them through π-electron delocalization along the –C–N–N–C–S– chains of the dithiocarbazate moieties. The thione-to-thiol evolution in the presence of metal ions has been found to be common to all Schiff bases derived from *S*-alkyl/aryl dithiocarbazates [1–6,32–34]. The closely related thiosemicarbazone ligand, 1-formylisoquinolinethiosemicarbazone, however, has been shown to react with metal ions in neutral media yielding complexes of both protonated and deprotonated [35] forms. On the other hand, Schiff bases derived from *S*-alkyl esters of dithiocarbazic acid, although they are structurally very similar to thiosemicarbazones, invariably coordinate to metal ions in their deprotonated forms even in the presence of mineral acids.

Reaction of diphenyltin(IV) dichloride with the Schiff bases in boiling absolute ethanol afforded crystalline diphenyltin(IV) complexes of empirical formula, Sn(NNS)Ph_2Cl (NNS = anionic form of the Schiff bases) which are quite stable in the atmosphere and could be stored in a desiccator over silica gel over a long period of time without any sign of decomposition. They are sparingly soluble in acetonitrile, chloroform,

dichloromethane and DMSO, but insoluble in methanol, ethanol and acetone. The complexes Sn(qaldsme)Ph_2Cl and Sn(qaldsbz)Ph_2Cl exhibit molar conductances of 2.5 and 8.6 $ohm^{-1}\,cm^2\,mol^{-1}$, respectively, in DMSO, indicating that they behave essentially as non-electrolytes in this solvent. The low conductance data also support the fact that the Schiff bases are coordinated to the tin atom in their deprotonated anionic forms and that the two phenyl and chloride ligands are also coordinated to the tin atom.

A comparison of the IR spectra of the ligands with those of the two tin complexes indicate that the νNH bands of the free ligands (Table 2) are not present in the spectra of the complexes, supporting deprotonation of the ligands during coordination. The shift of the νC=N bands of the free ligands to lower wavenumbers (Table 2) and the shift of the νN–N bands to higher wavenumbers in the IR spectra of the complexes support coordination of the ligands to the tin atom via the azomethine nitrogen atom. The splitting of the ν_aCSS band of the ligand in the spectra of the complexes indicates coordination of the ligands to tin via one of the sulfur atoms [36,37].

The electronic spectral data of the Schiff bases and their tin(IV) complexes are given in Table 2. The spectra of the ligands exhibit several bands in the 390–247 nm range attributable to the intra-ligand $n \rightarrow \pi^*$ and $\pi \rightarrow \pi^*$ transitions. These bands do not shift much in the spectra of the diphenyltin(IV) complexes but the band ca. 345 nm in the spectra of the ligands disappears in the spectra of the complexes. In addition to the intra-ligand bands, the electronic spectrum of Sn(qaldsme)Ph_2Cl exhibits a strong $S \rightarrow Sn^{IV}$ charge-transfer band at 426 nm. The presence of a $S \rightarrow Sn^{IV}$ LMCT band lends further support to the IR evidence that bonding of the ligands to the tin atom occurs via one of the sulfur atoms. Such LMCT bands are quite common in the electronic spectra of metal complexes of thiosemicarbazones [38] and dithiocarbazates [39–41].

The ESI (positive electrospray ionization) spectra of Sn(qaldsbz)Ph_2Cl and Sn(qalsme)$(Ph)_2Cl$, display base peaks at m/z 610 and 534, which are assigned to the $[Sn(qaldbz)Ph_2]^+$ and $[Sn(qaldsme)Ph_2]^+$ fragment ions, respectively. The simulated isotope patterns of these ions match completely the experimental spectra, supporting assignment of these base peaks to the $[M - Cl]^+$ ions.

The ^1H NMR spectra of the complexes were recorded in $CDCl_3$. Unfortunately, because of inadequate solubilities of these complexes in most non-polar and polar organic solvents, their ^{13}C NMR spectra could not be recorded. The ^1H NMR data of the ligands and their diphenyltin(IV) complexes are shown in Table 3. A comparison of the data for the ligands with those of the complexes shows that the signals due to the sec. –NH protons of the free ligands are absent in the spectra of the complexes, lending further support to the IR and conductance results discussed earlier that the ligands are coordinated to the tin atom in their deprotonated thiolate forms. Also, the signals due to the azomethine protons of the free ligands move downfield in the spectra of the complexes consistent with coordination of the li-

Table 2
IR and electronic spectral data

Compound	IR				UV spectra in CH_2Cl_2
	νNH	νC=N	νN–N	νCSS	λ_{max} (nm)
Hqaldsme[a]	3087br, 2918br,w, 2784br,w	1617m	1050s	899s	[390sh, 360 (4.72), 345 (4.70), 297 (4.52), 247 (4.68)][a]
Hqaldsbz[a]	3087br,w, 2930br, 2806br,	1617m	1047s	901s	[385 (4.90), 362 (5.1), 346 (5.0), ca. 325sh, 298 (5.0), 252 (5.2), 226 (5.1)][a]
Sn(qaldsme)Ph_2Cl	–	1600m	1068s	976s, 961m	390 (4.27), 364 (4.23), 303 (4.10), 250 (4.37), 227 (4.59)
Sn(qaldsbz)Ph_2Cl	–	1594m	1066s	955s, 942m	426 (3.8), ca. 390sh, ca. 360sh, 309 (3.6), ca. 250sh, 228 (5.3)

[a] Data taken from Ref. [26].

Table 3
^1H NMR spectral data for the Schiff bases and their diphenyltin(IV) complexes

Compound	^1H NMR			
	–NH	–CH=N–	Aromatic	$-SCH_2/SCH_3$
Hqaldsme[a]	13.60 (s,1H)	8.42 (s,1H)	7.60–7.70 (m, 1H), 7.75–7.85 (m, 1H), 7.95–8.10 (m, 3H), 8.40 (m, 1H)	2.57 (s, 3H)
Hqaldsbz[a]	13.65 (s, 1H)	8.40 (s, 1H)	7.76–7.97 (t, 1H), 7.61–7.66 (t, 1H), 7.25–7.37 (m, 3H), 7.44–7.46 (m, 2H), 8.00–8.05 (m, 3H), 8.36–8.39 (m, 1H)	4.53 (s, 2H)
Sn(qaldsme)Ph_2Cl	–	9.00 (s, 1H)	6.91 (s, 1H), 7.08–7.10 (m, 3H), 7.52–7.62 (m, 5H), 7.72–7.83 (m, 5H), 8.17–8.20 (m, 2H)	2.74 (s, 3H)
Sn(qaldsbz)Ph_2Cl	–	8.99 (s, 1H)	7.09 (m, 3H), 7.64–7.72 (m, 5H), 7.89 (d, 3H), 7.98 (d, 2H), 8.19 (d, 3H), 8.44 (d, 4H), 8.61 (d, 2H)	4.52 (s, 2H)

[a] Data taken from Ref. [26].

Table 4
Bond lengths (Å) and angles (°) for Hqaldsme

Bond lengths			
C(1)–N(1)	1.346(8)	C(1)–S(1)	1.645(7)
C(1)–S(2)	1.754(7)	C(2)–S(2)	1.803(8)
N(1)–N(2)	1.375(8)	C(3)–N(2)	1.285(9)
C(3)–C(4)	1.476(10)	C(4)–N(3)	1.418(10)
C(4)–C(5)	1.405(10)	C(12)–N(3)	1.377(9)
Bond angles			
N(1)–C(1)–S(1)	121.0(6)	N(1)–C(1)–S(2)	113.1(5)
S(1)–C(1)–S(2)	125.9(4)	N(2)–C(3)–C(4)	118.3(7)
N(3)–C(4)–C(5)	124.2(7)	N(3)–C(4)–C(3)	114.7(7)
C(5)–C(4)–C(3)	121.0(7)	N(3)–C(12)–C(11)	117.6(7)
N(3)–C(12)–C(7)	123.4(7)	C(1)–N(1)–N(2)	120.0(6)
C(3)–N(2)–N(1)	115.2(6)	C(4)–N(3)–C(12)	116.8(6)
C(1)–S(2)–C(2)	101.6(4)		

gands to the tin via the azomethine nitrogen atoms. As has been observed in the ^{1}H NMR spectra of metal complexes of Schiff bases derived from *S*-alkyl- and *S*-aryl esters of dithiocarbazic acid, signals due to the SCH_3/SCH_2 protons of the free ligands do not shift significantly when the ligands coordinate with tin [26].

3.1. The crystal structure of Hqaldsme

The crystal structure of the free ligand Hqaldsme, together with the numbering scheme, is shown in Fig. 2.

The structure shows that the molecule is essentially planar with all non-H atoms lying within 0.009 Å of the least squares plane. The *E*,*E* conformation of the C3–N2 and N1–N2 bonds is apparent, which results in an *anti*-arrangement of both donor atoms pairs S1/N2 and N2/N3. Thus, the ligand must undergo a 180° rotation of the C3–C4 and C1–N1 bonds in order to bind as a tridentate chelate. The bond distances in the dithiocarbazate chain [$NNCSSCH_3$] of Hqaldsme (Table 4) are close to those observed in the *S*-benzyl analogue [26] and in other Schiff bases derived from *S*-alkyl/aryldithiocarbazates [4,42]. The C1-S1 distance [1.645(7) Å] in this compound is by far the shortest value observed in this class of compounds, but the value is still intermediate between a C–S single bond [1.82 Å] and a C═S double bond [1.56 Å] [43,44]. The C1–N1 and C3–N2 bond distances are 1.346(8) and 1.285(9) Å, respectively indicating that the bond order of the former is greater than one but that of the latter is less than two. A comparison of the N–N distance [1.375(8) Å] with that in *S*-methyldithiocarbazate [45] shows that the bond is shorter than a single bond, indicating significant π-charge delocalization along the C(S)NNC moiety. The attachment of the extensively delocalized quinoline group to the imino nitrogen atom is probably responsible for shortening of the N–N distance.

The intermolecular hydrogen bonds, which link the molecules together in the solid state, are shown in Fig. 3. There is only one significant intermolecular H-bonding contact involving the NH group as donor and the quinoline N-atom as acceptor: N1–H1...N3* 2.13 Å, 168°, symmetry operation*: $-x$, $y + 1/2$, $-z + 3/2$, which results in a one-dimensional H-bonded polymer oriented in the direction of the *c* axis.

3.2. Crystal structures of Sn(qaldsme)Ph_2Cl

Interestingly, the complex Sn(qaldsme)Ph_2Cl crystallizes in two distinctly different forms; each having the same space group but with different lattice parameters. In both crystalline forms, the tin atom adopts a distorted octahedral geometry with the Schiff base coordinated to it as a uninegatively charged tridentate chelating agent via the quinoline nitrogen atom, the azomethine nitrogen atom and the thiolate sulfur atom.

Table 5
Selected bond lengths and bond angles for the two conformers of Sn(qaldsme)Ph_2Cl]

	syn	*anti*		*syn*	*anti*
Bond lengths (Å)					
Sn(1)–N(3)	2.670(2)	2.513(3)	Sn(1)–N(2)	2.321(2)	2.322(3)
Sn(1)–Cl(1)	2.5187(8)	2.5316(9)	Sn(1)–C(13)	2.147(3)	2.151(3)
Sn(1)–C(19)	2.151(3)	2.148(3)	Sn(1)– S(1)	2.4986(8)	2.5245(9)
C(3) –C(4)	1.456(4)	1.404(4)	C(2)–N(2)	1.279(4)	1.277(4)
N(2)–N(1)	1.382(3)	1.384(3)	C(1)–N(1)	1.298(4)	1.301(4)
C(1)–S(1)	1.720(3)	1.739(4)	C(1)–S(2)	1.757(3)	1.744(3)
Bond angles (°)					
N(2)–Sn(1)–N(3)	65.95(8)	67.71(8)	C(13)–Sn(1)–C(19)	153.87(10)	164.21(12)
S(1)–Sn(1)– Cl(1)	88.47(3)	93.83(3)	N(2)–Sn(1)–S(1)	77.1(4)	75.48(6)
N(3)–Sn(1)–S(1)	149.1(5)	143.09(6)	C(13)–Sn(1)–N(3)	78. 96(8)	81.39(10)
N(2)–Sn(1)–Cl(1)	164.57(6)	169.22(6)	Cl(1)–Sn(1)–N(3)	129.42(6)	123.03(6)
C(19)–Sn(1)–N(3)	79.15(8)	86.12(10)			
S(1)–Sn(1)–N(3)	142.10(5)	143.09(6)	C(19)–Sn(1)–Cl(1)	90.73(7)	88.59(8)
C(13)–Sn(1)–Cl(1)	92.22(7)	90.14(9)			
C(19)–Sn(1)–N(2)	91.40(9)	91.42(10)	C(19)–Sn(1)–S(1)	102.30(7)	97.68(9)
C(13)–Sn(1)–S(1)	103.73(7)	98.11(9)	C(13)–Sn(1)–N(2)	92.58(9)	92.74(10)

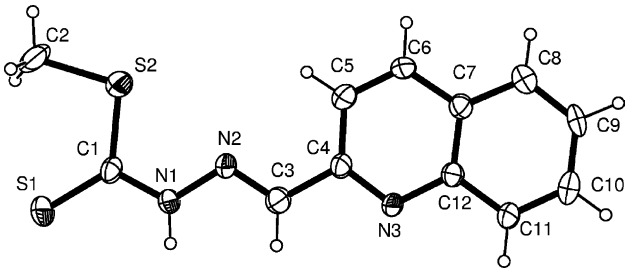


Fig. 2. ORTEP view of Hqaldsme (30% probability ellipsoids).

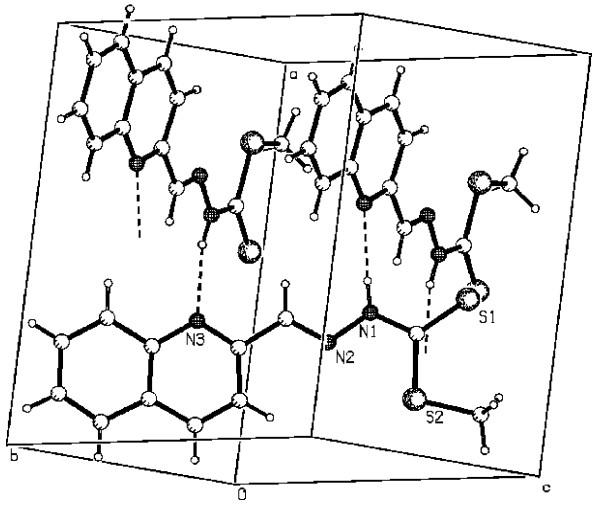


Fig. 3. PLUTON drawing showing the polymeric H-bonded chain in Hqaldsme.

The intrinsic differences in the structures of the two polymorphs lie in the orientation of the *S*-methyl group (C2) with respect to the coordinated S-atom (S1); defined here as *syn* or *anti*.

The structure of the *syn*-conformer (Fig. 4) defines a six coordinate complex with large distortions from an ideal octahedron. The proton attached to N1 in the metal free ligand dissociates upon meridional tridentate coordination of the qaldsme anion. The chloro ligand is formally *trans* to N2, as are the pair of phenyl ligands although there are large deviations from linearity in each pairing (N2–Sn1–Cl1 164.57(6)° and C13–Sn1–C19 153.9(1)°). The shortest coordinate bonds are to the phenyl ligands (~2.15 Å) reflecting the preference of the metal for C-donors over N-donors cf. Sn1–N2 2.321(2) Å. The bond lengths to the Cl- and S-donors are similar. The bond lengths including C1 are greatly affected by deprotonation of N1 and coordination of S1. By a comparison with the bond orders suggested in the structure of Hqaldsme, in the coordinated anion the C1–S1 and C1–S2 bond lengths are similar (1.720(3) and 1.757(2) Å, respectively) and approach that expected for a single bond cf. C2–S2 1.782(4) Å.

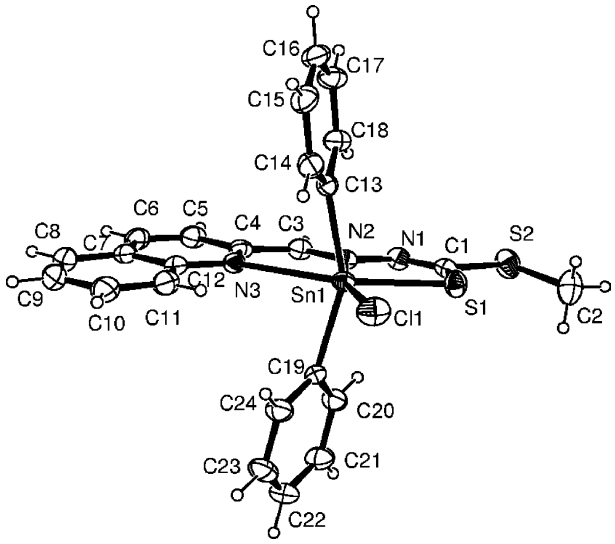


Fig. 4. ORTEP drawing of *syn*-Sn(qaldsme)Ph_2Cl (30% probability ellipsoids).

The C1–N1 bond length (1.298(4) Å) approaches that expected of a true double bond cf. C2–N2 (1.279(4) Å). These observations indicate that upon deprotonation of the ligand, the negative charge, formally on the terminal sulfur atom in the thiolate tautomer, is actually delocalized significantly over the entire —C=N—N=C—S— chain.

The crystal structure of the *anti*-conformational isomer (Fig. 5) reveals a similar coordination environment. The coordinate bond lengths and the internal ligand bond lengths equal the corresponding dimensions found in the *syn*-conformer within experimental error, but

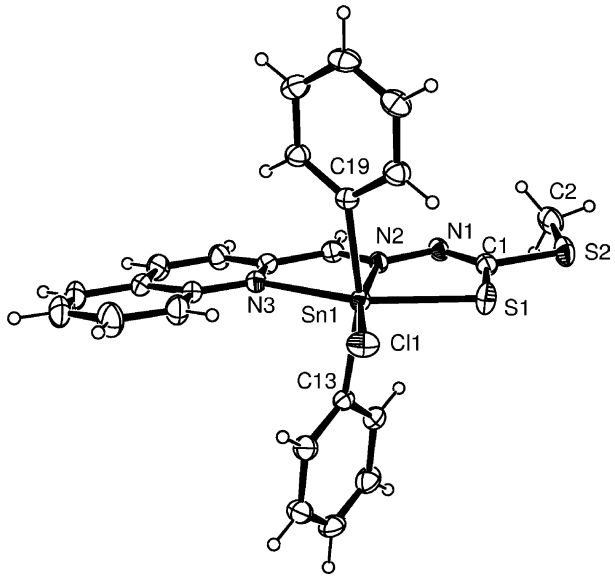


Fig. 5. ORTEP drawing of *anti*-Sn(qaldsme)Ph_2Cl (30% probability ellipsoids).

there is significant variance in the coordination angles. Essentially the *anti*-conformer is less distorted from octahedral geometry.

In both conformers distortions from octahedral geometry are reflected in the 12 bond angles subtended at the tin atom, which show substantial deviations here from 90° or 180°. The largest deviations appear in the ideally 180° angles S1–Sn1–N3 [149.1(5)°/143.09(6)°], and the ideally 90° angles N2–Sn1–S1 [77.1/75.48(6)°], N2–Sn1–N3 [65.95(8)°/67.71(8)°] and Cl1–Sn1–N3 [129.42(6)°/123.03(6)°]. The deviation from octahedral geometry can be attributed to the restricted bite size of the ligand and crystal packing in respect of angles formed by the monodentate ligands.

We recently published the structure of the tri-iodo Sn(IV) complex Sn(qaldsbz)I_3, where a similar tridentate binding mode of the Schiff base was identified [26]. The only other structurally characterized six-coordinated tin complexes of N-heterocyclic thiosemicarbazones and dithiocarbazates are Sn(Hapt)Ph_2Cl (apt = monodeprotonated form of the 2-acetylpyridine thiocarbodiazone) [46] and the carbonato-bridged dimer {Sn(pyaldsme)(*n*-Bu)$_2$}(O-CO-O){Sn(pyaldsme)(*n*-Bu)$_2$} [47]. In the former, similar to that in Sn(qaldsme)Ph_2Cl, the tin atom is also coordinated to a N_2S tridentate ligand, two phenyl groups and a chloride ligand in an approximately octahedral environment, and the latter may be considered as an analogue of the present structures if the *n*-butyl ligands are replaced by phenyls and the carbonato O-donor on each monomeric unit is substituted by a terminal chloro ligand. A comparison of bond lengths of Sn(qaldsme)Ph_2Cl with those in Sn(Hapts)Ph_2Cl indicates while the Sn–S and Sn–$N_{azomethine}$ bond distances have comparable values, the Sn–C, Sn–Cl and Sn–N_{ring} bond lengths differ significantly. The Sn-Cl bond in the present complex is shorter than that found in the Hapt complex but the Sn-C bonds are weaker in both Sn(qaldsme)Ph_2Cl conformers relative to the Sn(Hapt)Ph_2Cl complex. The structural changes that are observed in the structure of the free ligand (Fig. 2) upon coordination with the diphenyltin(IV) cation are similar to those that usually accompany the formation of metal complexes by thiosemicarbazones.

4. Conclusions

In the solid state as well as in solution, the 2-quinolinecarboxaldehyde Schiff bases of *S*-methyl- and *S*-benzydithiocarbazates, like most Schiff bases derived from *S*-alkyl esters of dithiocarbazic acid, remain as thione tautomers. However, in the presence of diphenyltin(IV) dichloride they switch to the iminothiol form, deprotonate and coordinate with the tin atom as uninegatively charged NNS tridentate chelating agents. The ensuing 1:1 diphenyltin(IV) Schiff base complexes adopt a distorted octahedral geometry with the two phenyl groups occupying the apical positions of the coordination sphere.

5. Supplementary material

Crystallographic data in CIF format (CCDC Deposition Nos. 247969-71) have been deposited at the Cambridge Crystallographic Data Centre and are available on request from the Director, CCDC, 12 Union Road, Cambridge, CB2 1EZ, UK (fax: +44 1223 336033 ; e-mail: deposit@ccdc.cam.ac.uk or http://www.ccdc.cam.ac.uk).

Acknowledgements

M. Akbar Ali, A.H. Mirza and Malai Haniti thank Universiti Brunei Darussalam for supporting this work.

References

[1] M. Akbar Ali, A.H. Mirza, L.K. Wei, A.L. Tan, P.V. Bernhardt, Polyhedron 23 (2004) 2037, and references cited therein.
[2] M. Akbar Ali, A.H. Mirza, M. Nazimuddin, R. Ahmed, L.H. Gahan, P.V. Bernhardt, Polyhedron 22 (2003) 1471.
[3] M. Akbar Ali, A.H. Mirza, C.W. Voo, A.L. Tan, P.V. Bernhardt, Polyhedron 22 (2003) 3433, and references cited therein.
[4] M. Akbar Ali, S.E. Livingstone, Coord. Chem. Rev. 13 (1974) 101, and references cited therein.
[5] K.A. Crouse, Kar-Beng Chew, M.T.H. Tarafder, A. Kasbollah, A.M. Ali, B.M. Yamin, H.K. Fun, Polyhedron 23 (2004) 161, and references cited therein.
[6] D.X. West, S.B. Padhye, P.B. Sonawane, Struct. Bond. (Berlin) 76 (1991) 1.
[7] V. Philip, V. Suni, M.R.P. Kurup, M. Nethaji, Polyhedron 23 (2004) 1225, and references cited therein.
[8] I.G. Santos, A. Hagenbach, U. Abram, J. Chem. Soc., Dalton Trans. (2004) 677.
[9] P.J. Blower, T.C. Castle, A.R. Cowley, J.R. Dilworth, P.S. Donnelly, A. Labisbal, F.E. Sowrey, S.J. Teat, M.J. Went, J. Chem. Soc., Dalton Trans. (2003) 4416, and references cited therein.
[10] D.X. West, A.E. Liberta, S.B. Padhye, R.C. Chikate, P.B. Sonawane, A.S. Kumbhar, R.G. Yerande, Coord. Chem. Rev. 123 (1993) 49, and references cited therein.
[11] D.X. West, S.B. Padhye, P.B. Sonawane, R.C. Chikate, Asian J. Chem. Rev. 1 (1990) 125.
[12] Yu-Peng Tian, D. Chung-Ying, Dian Xia-Xeng You, T.C.W. Mak, L. Qing, Z. Jian-Ying, Transition Met. Chem. 23 (1998) 17.
[13] A. Abu-Raqabah, G. Davies, M.A. El- Sayed, A. El-Toukhy, S.N. Shaikh, J. Zubeita, Inorg. Chim. Acta 193 (1992) 43.
[14] S. Al-Shehri, G. Davies, M.A. El-Sayed, A. El-Toukhy, Inorg. Chem. 29 (1990) 1198.
[15] A.E. Liberta, D.X. West, Biometals 5 (1992) 121.
[16] D.H. Petering, in: H. Sigel (Ed.), Carcinostatic Copper Complexes, Marcel Dekker, New York, 1980.
[17] D.X. West, I.H. Hall, K.J. Rajendran, A.E. Liberta, Anticancer Drugs 4 (1993) 231.
[18] M.T.H. Tarafder, Teng-Jin Khoo, K.A. Crouse, A.M. Ali, Polyhedron 25 (2002) 27.

[19] M. Akbar Ali, A.H. Mirza, R.J. Butcher, M.T.H. Tarafder, Tan B. Keat, A.M. Ali, J. Inorg. Biochem. 92 (2002) 141.
[20] I. Belsky, D. Gerther, A. Ziluka, J. Med. Chem. 1 (1968) 92.
[21] R.H. Holm, in: G.L. Eichorn (Ed.), Inorganic Biochemistry, vol. 2, Elsevier, Amsterdam, 1974, p. 1137.
[22] L. Abrams, N.E. Bjorklund, B. Gustafsson, M. Johnson, Acta Pharmacol. Toxicol. Suppl. 36 (1975) 93.
[23] K.C. Joshi, V.N. Pathak, P. Pawar, Agric. Biol Chem. 41 (1977) 543.
[24] G. Bahr, G. Schleitzer, Z. Anorg. Allgem. Chem. 280 (1955) 176.
[25] M. Akbar Ali, M.T.H. Tarafder, J. Inorg. Nucl. Chem. 39 (1977) 1785.
[26] M. Akbar Ali, A.H. Mirza, M.H.S.A. Hamid, F. Hj Bujang, P.V. Bernhardt, Polyhedron 23 (2004) 2405.
[27] L.J. Farrugia, J. Appl. Cryst. 32 (1999) 837.
[28] G.M. Sheldrick, SHELX97. Programs for Crystal Structure Analysis, University of Göttingen, Germany, 1997.
[29] L.J. Farrugia, J. Appl. Cryst. 30 (1997) 565.
[30] A.L. Spek, Acta Cryst., Sect. A 46 (1990) C34.
[31] I. Antonini, F. Claudi, F. Franchetti, S. Martelli, J. Med. Chem. 20 (1970) 447.
[32] M. Akbar Ali, A.H. Mirza, M. Nazimuddin, R. Ahmed, L.H. Gahan, P.V. Bernhardt, Polyhedron 22 (2003) 1471.
[33] M. Akbar Ali, A.H. Mirza, R.J. Butcher, M.T.H. Tarafder, A. Manaf Ali, Inorg. Chim. Acta 320 (2001) 1.
[34] M. Akbar Ali, A.H. Mirza, R.J. Butcher, Polyhedron 20 (2001) 1037.
[35] M. Mohan, P. Sharma, N.K. Jha, Inorg. Chim. Acta 106 (1985) 117.
[36] S. Bonati, S. Cenini, R. Ugo, J. Organomet. Chem. 9 (1967) 395.
[37] M. Akbar Ali, S.E. Livingstone, D.J. Phillips, Inorg. Chim. Acta 23 (1961) 1061.
[38] E.W. Ainscough, A.M. Brodie, J.D. Ranford, J.M. Waters, J. Chem. Soc., Dalton Trans. (1991) 1737.
[39] M. Akbar Ali, K.K. Dey, M. Nazimuddin, F.E. Smith, R.J. Butcher, J.P. Jasinsky, J.M. Jasinski, Polyhedron 15 (1996) 3331.
[40] M.E. Hossain, M.N. Alam, J. Begum, M. Akbar Ali, M. Nazimuddin, F.E. Smith, R.C. Hynes, Inorg. Chim. Acta 249 (1996) 207.
[41] M. Akbar Ali, A.H. Mirza, M. Nazimuddin, H. Rahman, R.J. Butcher, Transition Met. Chem. 27 (2002) 268.
[42] C.-Y. Su, X.-P. Yang, B.-S. Kang, K.-B. Yu, Y.-X. Tong, T.C.W. Mak, Bull. Chem. Soc. Jpn. 72 (1999) 2217.
[43] L.E. Sutton, Tables of Interatomic Distances & Configurations in Molecules and Ion Supplement, The Chemical Society, London, 1965.
[44] R.T. Sanderson, Inorganic Chemistry, Reinhold, New York, 1967, p. 74.
[45] A.M.M. Lanfredi, A. Tiripicchio, M.T. Camellini, A. Monaci, F. Trali, J. Chem. Soc., Dalton Trans. (1977) 417.
[46] M. Carcelli, D. Delledonne, A. Fochi, G. Pelizzi, M.C. Rodriguez-Arguelles, U. Russo, J. Organomet. Chem. 544 (1997) 29.
[47] S. Knoll, F. Tschwatschal, T. Ristau, T. Gelbrich, R. Brordorf, G. Zahn, Z. Anorg. Allg. Chem. 623 (1997) 141.

Available online at www.sciencedirect.com
SCIENCE DIRECT®
Polyhedron 24 (2005) 391–396
POLYHEDRON
www.elsevier.com/locate/poly

Pentamethylcyclopentadienyl ruthenium(II) complexes of *para*-substituted *N*-(pyrid-2-ylmethylene)-phenylamine ligands: syntheses, spectral and structural studies

Keisham Sarjit Singh [a], Patrick J. Carroll [b], Mohan Rao Kollipara [a,*]

[a] *Department of Chemistry, North-Eastern Hill University, Shillong 793022, India*
[b] *Department of Chemistry, University of Pennsylvania, Philadelphia, PA 19104-6323, USA*

Received 8 November 2004; accepted 22 November 2004

Abstract

The reaction of $[(\eta^5\text{-}C_5Me_5)Ru(PPh_3)_2Cl]$ (**1**) with acetonitrile in the presence of excess NH_4PF_6 leads to the formation of the cationic ruthenium(II) complex $[(\eta^5\text{-}C_5Me_5)Ru(PPh_3)_2(CH_3CN)]PF_6$ (**2**). The complex (**2**) reacts with a series of *N*,*N*′ donor Schiff base ligands viz. *para*-substituted *N*-(pyrid-2-ylmethylene)-phenylamines (ppa) in methanol to yield pentamethylcylopentadienyl ruthenium(II) Schiff base complexes of the formulation $[(\eta^5\text{-}C_5Me_5)Ru(PPh_3)(C_5H_4N\text{-}2\text{-}CH{=}N\text{-}C_6H_4\text{-}p\text{-}X)]PF_6$ **[3a]PF$_6$**–**[3f]PF$_6$**, where C_5Me_5 = pentamethylcylopentadienyl, X = H, **[3a]PF$_6$**, Me, **[3b]PF$_6$**, OMe, **[3c]PF$_6$**, NO_2, **[3d]PF$_6$**, Cl, **[3e]PF$_6$**, COOH, **[3f]PF$_6$**. The complexes were isolated as their hexafluorophosphate salts. The complexes were fully characterized on the basis of elemental analyses and NMR spectroscopy. The molecular structure of a representative complex, $[(\eta^5\text{-}C_5Me_5)Ru(PPh_3)(C_5H_4N\text{-}2\text{-}CH{=}N\text{-}C_6H_4\text{-}p\text{-}Cl)]PF_6$ **[3e]PF$_6$**, has been established by X-ray crystallography.
© 2004 Elsevier Ltd. All rights reserved.

Keywords: Ruthenium; Pentamethylcyclopentadienyl; *N*-(pyrid-2-ylmethylene)-phenyl-amines; Pyridine-2-carboxaldehyde

1. Introduction

Half sandwich ruthenium(II) complexes have received great attention in the past few decades owing to their high reactivity ([1] and reference cited in) and catalytic activity [2]. The syntheses, structures and reactivity of half sandwich ruthenium(II) complexes viz., cyclopentadienyl, indenyl and arene have been studied in our laboratory. Our current interest has involved substitution of one triphenylphosphine and a chloride ligand of the complex $[Cp'Ru(PPh_3)_2Cl]$, where Cp′ = ind., Cp*, Cp with N-donor ligands [3,4], which is one of the key routes to explore their chemistry. There exist an extensive study on the chemistry of cyclopentadienyl ruthenium(II) with a variety of ligands [5]. In contrast, the analogous pentamethylcyclopentadienyl ruthenium(II) complexes have not been much studied. The chemistry of the pentamethylcylopentadienyl ruthenium fragment is largely based on the tetramer $[Cp^*RuCl]_4$ [6] and on the tris-acetonitrile $[Cp^*Ru(CH_3CN)_3]PF_6$ adduct [7], which upon addition of monodentate ligands yield octahedral complexes $[Cp^*RuX(L)_2]$ [8,9] and $[Cp^*Ru(L)_2(CH_3CN)]PF_6$ [7], respectively. However, to the best of our knowledge, pentamethylcylopentadienyl ruthenium(II) phosphine complexes chelated with *N*,*N*′ donor Schiff base ligands are not known, although there is an extensive chemistry available on arene and cyclopentadienyl ruthenium(II) [3b,10–12] systems.

* Corresponding author. Tel.: +91 364 272 2620; fax: +91 364 2550076.
E-mail addresses: mrkollipara@yahoo.com, mrkollipara@rediffmail.com, kmrao@nehu.ac.in (M.R. Kollipara).

0277-5387/$ - see front matter © 2004 Elsevier Ltd. All rights reserved.
doi:10.1016/j.poly.2004.11.021

This present work arises from our interest to synthesize various half sandwich ruthenium(II) complexes containing N,N' donor Schiff base ligands. Having this in mind, we have previously described the syntheses of indenyl, cyclopentadienyl and arene [3,10] ruthenium(II) Schiff base complexes. In a continuation of our study, herein we report the syntheses of a series of pentamethylcyclopentadienyl ruthenium(II) Schiff base complexes **[3a]**PF_6–**[3f]**PF_6. The elemental analyses, spectral and structural characterization of the complexes is presented.

2. Experimental

2.1. General remarks

Reactions were carried out in distilled and dried solvents under nitrogen atmosphere. The solvents were purified according to the standard procedures. $RuCl_3\cdot 3H_2O$ was purchased from Arora Matthey (P) Ltd. and used as such. Pyridine-2-carboxaldehyde (Fluka) was used as received. All liquid aromatic amines were reagent grade and were distilled prior to use while solid aromatic amines were used as such. Microanalyses (C, H, N) were done by Regional Sophisticated Instrumentation Centre (RSIC), NEHU using a Perkin–Elmer-2400 CHNS/O analyzer. FT-IR spectra were recorded on a Perkin–Elmer-model 983 spectrophotometer with samples prepared as KBr pellets. Electronic spectra were recorded on a Hitachi-U-2300 spectrophotometer and conductivity measurements were done by Wayne Kerr Automatic Precession Bridge B905 using ca. 10^{-4} M solutions in dry acetonitrile at room temperature (Λ_m value in $S\,cm^2\,mol^{-1}$). The NMR spectra were obtained in $CDCl_3$ solution and recorded on a Bruker ACF-300 MHz spectrometer. Chemical shifts are relative to TMS (^1H, $^{13}C\{^1H\}$) and to 85% H_3PO_4 ($^{31}P\{^1H\}$); coupling constants are given in hertz. The ligands (C_5H_4N-2-CH=N-C_6H_4-*p*-X), (where X = H, Me, OMe, Cl, NO_2, COOH) [13] were prepared by the condensation of pyridine-2-carboxaldehyde with the appropriate amines. The precursor complex [(η^5-C_5Me_5)Ru(PPh_3)$_2$Cl] [14] was prepared by following the literature method.

2.2. Preparation of [(C_5Me_5)Ru(PPh_3)$_2$($NCCH_3$)]PF_6 [2]PF_6

The complex was prepared by following the literature method [15] as delineated here. The complex [Cp*Ru(PPh_3)$_2$Cl] (0.1 g, 0.125 mmol) and NH_4PF_6 (0.041 g, 0.250 mmol) were refluxed in CH_3CN (30 ml) for 2 h. During this time the orange red suspension turned yellow and a white solid appeared. The white solid was filtered off and the filtrate was rotary evaporated. The yellow residue was dissolved in dichloromethane (5 ml) and filtered to remove excess NH_4PF_6. The filtrate on concentration and addition of excess hexane gave a yellow crystalline solid. The yellow solid was collected and washed with hexane to afford 83% yield of complex (**2**).

^1H NMR ($CDCl_3$, δ): 1.32 (s, 15H, Cp), 2.17 (s, 3H, CH_3CN), 6.78–7.83 (m, 30H).

$^{31}P\{^1H\}$ NMR ($CDCl_3$, δ): 45.28 (s. 2P, PPh_3), −143 (septet, PF_6^-).

2.3. Preparation of [(η^5-C_5Me_5)Ru(PPh_3)(C_5H_4N-2-CH=N-C_6H_4-p-X)]PF_6 [X = H [3a]PF_6, Me [3b]PF_6, OMe [3c]PF_6, NO_2 [3d]PF_6, Cl [3e]PF_6, COOH [3f]PF_6

These complexes were prepared by using a general method.

The complex (**2**), (0.1 g, 0.105 mmol) and the appropriate ligand (0.210 mmol) were mixed in 20 ml of methanol. After a few minutes the yellow solution turned into a dark brown suspension. The mixture was refluxed for 1 h under nitrogen atmosphere. The solution was cooled to room temperature and solvent was removed in a rotary-evaporator to dryness. The brown residue was dissolved in dichloromethane (5 ml) and filtered through a short silica gel column. The filtrate on subsequent concentration and addition of excess diethyl ether gave complexes **[3a]**PF_6–**[3f]**PF_6 as dark brown solids in 81–87% yield.

2.4. Analytical and spectroscopic data

2.4.1. [(η^5- C_5Me_5)Ru(PPh_3)(C_5H_4N-2-CH=N-C_6H_5)]-PF_6 [3a]PF_6

Yield: 83% (72 mg). *Anal.* Calc. for $C_{40}H_{40}N_2P_2F_6Ru$: C, 58.13; H, 4.81; N, 3.39. Found: C, 57.6; H, 5.01; N, 3.45%. IR (KBr, cm^{-1}): $\nu_{(C=N)}$ 1600, $\nu_{(PF_6^-)}$ 844.

^1H NMR ($CDCl_3$, *J* Hz): δ 1.31 (s, 15H, C_5Me_5); 7.14 (d, 2H, J_{H-H} = 2.89); 7.18–7.64 (m, 21H); 8.25 (d, 1H, 2.64); 8.92 (d, 1H, 3.38).

$^{13}C\{^1H\}$ NMR ($CDCl_3$): δ 9.31 (s, $C_5Me_5(CH_3)$); 88.73 (s, C_5Me_5 (ring)); 122.46–151.26 (phenyl and pyridyl carbons); 157.83 (N=CH).

$^{31}P\{^1H\}$ NMR: δ 45.26 (s, PPh_3); −141 (septet, PF_6^-).

2.4.2. [(η^5-C_5Me_5)Ru(PPh_3)(C_5H_4N-2-CH=N-C_6H_4-p-Me)]PF_6 [3b]PF_6

Yield: 86% (76 mg). *Anal.* Calc. for $C_{41}H_{42}N_2P_2F_6Ru$: C, 58.59; H, 5.00; N, 3.33. Found: C, 59.35; H, 4.99; N, 3.67%.

IR (KBr, cm^{-1}): $\nu_{(C=N)}$ 1598, $\nu_{(PF_6^-)}$ 844.

^{1}H NMR ($CDCl_3$, J Hz): δ 1.31 (s, 15H, C_5Me_5); 2.38 (s, 3H); 7.07 (d, 2H, J_{H-H} = 5.73); 7.18 (d, 2H, J_{H-H} = 4.82); 7.29–7.62 (m, 18H); 8.22 (d, 1H, J_{H-H} = 3.48); 8.92 (d, 1H, J_{H-H} = 3.38).

$^{13}C\{^1H\}$ NMR ($CDCl_3$): δ 9.23 (s, $C_5Me_5(CH_3)$); 15.29 (s, Me); 88.47 (s, C_5Me_5 (ring)); 123.48–152.01 (phenyl and pyridyl carbons); 160.46 (N=CH).

$^{31}P\{^1H\}$ NMR: δ 46.55 (s, PPh_3); −142 (septet, PF_6^-).

2.4.3. *[(η^5-C_5Me_5)Ru(PPh_3)(C_5H_4N-2-CH=N-C_6H_4-p-OMe)]PF_6 [3c]PF_6*

Yield: 87% (78 mg). *Anal.* Calc. for $C_{41}H_{42}N_2OP_2F_6Ru$: C, 57.49; H, 4.91; N, 3.27. Found: C, 56.29; H, 4.97; N, 3.54%.

IR (KBr, cm^{-1}): $\nu_{(C=N)}$ 1602, $\nu_{(PF_6^-)}$ 844.

^{1}H NMR ($CDCl_3$, J Hz): δ 1.32 (s, 15H, C_5Me_5); 3.84 (s, 3H); 6.77 (d, 2H, J_{H-H} = 5.73); 7.13–7.65 (m, 20H); 8.24 (d, 1H, J_{H-H} = 2.97); 8.87 (d, 1H, J_{H-H} = 5.10).

$^{13}C\{^1H\}$ NMR ($CDCl_3$): δ 9.24 (s, $C_5Me_5(CH_3)$); 88.42 (s, C_5Me_5 (ring)); 113.99 (s, OCH_3); 125.48–151.88 (phenyl and pyridyl carbons); 161.66 (N=CH).

$^{31}P\{^1H\}$ NMR: δ 46.63 (s, PPh_3); −143 (septet, PF_6^-).

2.4.4. *[(η^5- C_5Me_5)Ru(PPh_3)(C_5H_4N-2-CH=N-C_6H_4-p-NO_2)]PF_6 [3d]PF_6*

Yield: 81% (74 mg). *Anal.* Calc. for $C_{40}H_{39}N_3O_2P_2F_6Ru$: C, 55.12; H, 4.47; N, 4.82. Found: C, 55.96; H, 4.73; N, 4.26%.

IR (KBr, cm^{-1}): $\nu_{(C=N)}$ 1608, $\nu_{PF_6^-}$ 844.

^{1}H NMR ($CDCl_3$; J Hz): δ 1.32 (d, 15H, C_5Me_5 J_{P-H} = 1.09); 6.93 (d, 2H, J_{H-H} = 2.89); 7.18–7.96 (m, 18H); 8.15 (d, 2H, J_{H-H} = 6.12); 8.41 (d, 1H, J_{H-H} = 3.34); 8.93 (d, 1H, 3.59).

$^{13}C\{^1H\}$ NMR ($CDCl_3$): δ 9.45 (s, $C_5Me_5(CH_3)$); 88.91 (s, C_5Me_5 (ring)); 124.86–151.99 (phenyl and pyridyl carbons); 162.38 (N=CH).

$^{31}P\{^1H\}$ NMR: δ 47.23 (s, PPh_3); −141 (septet, PF_6^-).

2.4.5. *[(η^5- C_5Me_5)Ru(PPh_3)(C_5H_4N-2-CH=N-C_6H_4-p-Cl)]PF_6 [3e]PF_6*

Yield: 87% (76 mg). *Anal.* Calc. for $C_{40}H_{39}N_2P_2F_6ClRu$: C, 55.84; H, 4.53; N, 3.25. Found: C, 54.20; H, 4.73; N, 3.12%.

IR (KBr, cm^{-1}): $\nu_{(C=N)}$ 1612, $\nu_{(PF_6^-)}$ 844.

^{1}H NMR ($CDCl_3$, J Hz): δ 1.32 (s, 15H, C_5Me_5); 6.83 (d, 2H, J_{H-H} = 3.24); 6.94–7.67 (m, 20H); 8.29 (d, 1H, J_{H-H} = 1.98); 8.90 (d, 1H, J_{H-H} = 4.73).

$^{13}C\{^1H\}$ NMR ($CDCl_3$): δ 9.45 (s, C_5Me_5); 88.73 (s, C_5Me_5 (ring)); 125.19–152.07 (phenyl and pyridyl carbons); 161.83 (N=CH).

$^{31}P\{^1H\}$ NMR: δ 46.53 (s, PPh_3); −143 (septet, PF_6^-).

2.4.6. *[(η^5- C_5Me_5)Ru(PPh_3)(C_5H_4N-2-CH=N-C_6H_4-p-CO_2H)]PF_6 [3f]PF_6*

Yield: 84% (77 mg). *Anal.* Calc. for $C_{41}H_{40}N_2O_2P_2F_6Ru$: C, 55.22; H, 4.60; N, 3.22. Found: C, 54.75; H, 4.83; N, 3.46%.

IR (KBr, cm^{-1}): $\nu_{(C=N)}$ 1610, $\nu_{(PF_6^-)}$ 844.

^{1}H NMR ($CDCl_3$, J Hz): δ 1.31 (s, 15H, C_5Me_5); 6.64 (d, 2H, J_{H-H} = 6.73); 7.37–8.05 (m, 17H); 8.02 (d, 2H, J_{H-H} = 4.02); 8.34 (d, 1H, J_{H-H} = 2.63); 8.62 (s, 1H); 8.95 (d, 1H, J_{H-H} = 5.22).

$^{13}C\{^1H\}$ NMR ($CDCl_3$): δ 9.42 (s, C_5Me_5 (CH_3)); 88.86 (s, C_5Me_5 (ring)); 124.05–155.96 (phenyl and pyridyl carbons); 160.46 (N=CH), 178.26 (C(CO_2H)).

$^{31}P\{^1H\}$ NMR: δ 47.28 (s, PPh_3); −145 (septet, PF_6^-).

2.5. Structure analysis and refinement

X-ray quality crystals of complex **[3e]PF_6** were grown by slow diffusion of hexane into a dichloromethane solution of complex **[3e]PF_6**. The X-ray intensity data were collected on a Rigaku Mercury CCD area detector employing graphite-monochromated Mo Kα radiation (λ = 0.71069 Å) at 143 K. Intensity data were corrected for Lorentz and polarization effects and for absorption correction using REQAB [16]. The structure was solved by direct methods (SIR 97) [17] and refinement was by full matrix least squares based on F^2 using (SHELXL-97) [18]. The weighting scheme used was $W = 1/[\sigma^2(F_0^2) + 0.0822P^2 + 3.3880P]$, where $P = (F_0^2 + 2F_c^2)/3$. The X-ray data were corrected for the presence of disordered solvent using "SQUEEZE" [19]. Non-hydrogen atoms were refined anisotropically and hydrogen atoms were refined using a "riding" model.

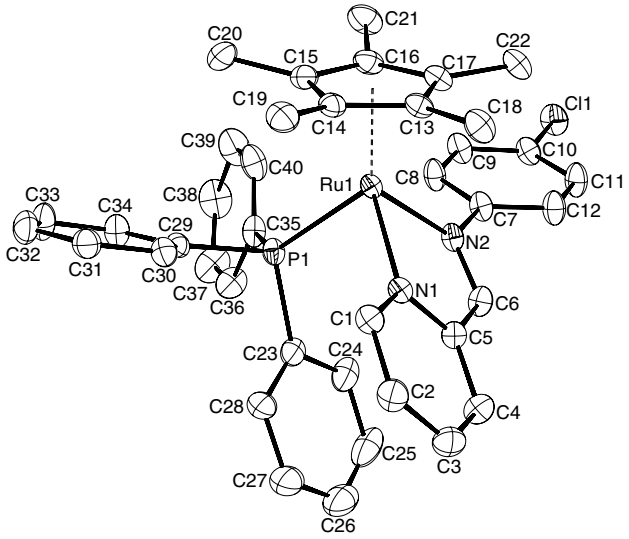


Fig. 1. Molecular structure of complex **[3e]PF_6** with 30% thermal ellipsoids. Hydrogen atoms and the PF_6 ion have been omitted for clarity.

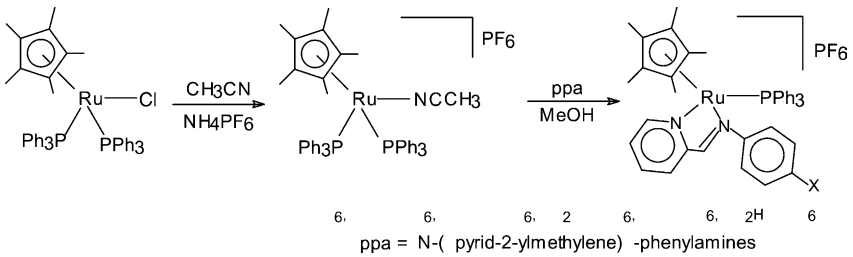
Refinement converged to $R_1 = 0.0444$ and $wR_2 = 0.1267$. Fig. 1 is an ORTEP [20] representation of the molecule with 30% thermal ellipsoids displayed.

3. Results and discussion

While N-chelating cyclopentadienyl ruthenium(II) complexes are well known [3b,5,10], only a few reports about the analogous pentamethylcyclopentadienyl are available in the literature [4]. Here we described the preparation of six new monocationic pentamethylcyclopentadienyl ruthenium(II) phosphine complexes **[3a]PF$_6$**–**[3f]PF$_6$** containing *N*,*N*′ donor Schiff base ligands, and their characterization with the help of elemental analyses, IR and NMR (^{1}H, ^{31}P{^{1}H}, ^{13}C{^{1}H}) spectroscopy. The molecular structure of a representative complex **[3e]PF$_6$** was determined by a single X-ray study. To the best of our knowledge this complex is the first structurally characterized pentamethyl-cyclopentadienyl ruthenium(II) Schiff base complex containing a phosphine ligand. The complexes were obtained in good yield, by reacting complex **[2]PF$_6$** with the appropriate ligands in methanol as depicted in Scheme 1.

We have recently synthesized cyclopentadienyl ruthenium(II) complexes of Schiff base ligands such as $[CpRu(PPh_3)(ppa)]^+$ [3b] by reacting the ligand (ppa) with the complex $[CpRu(PPh_3)_2Cl]$. However, in this present case the complexes are readily obtained in high yields by the reaction of the acetonitrile complex **[2]PF$_6$** with the appropriate ligand. These complexes can also be prepared in lower yield by the reaction of complex (**1**) with the ligand over a longer period of time. This suggests the acetonitrile complex **[2]PF$_6$** is a better precursor than their chloro analog (**1**) for the preparation of these complexes **[3a]PF$_6$**–**[3f]PF$_6$**. This is due to the cationic nature of the complex **[2]PF$_6$** which makes ready coordination of the ligand to the metal atom compared to the neutral chloro complex (**1**). It has been reported that the pentamethylcyclopentadienyl complexes, $[Cp^*Ru(PPh_3)_2Cl]$ are much more reactive than the analogous cyclopentadienyl complexes, which is attributed to the electron rich nature of the Cp* ligand and the presence of five sterically hindered methyl groups associated with these complexes which facilitates ready dissociation of one of the triphenylphosphine ligands. In fact, one triphenylphosphine can be readily substituted by diazonium salts from $[Cp^*Ru(PPh_3)_2Cl]$ irrespective of the solvent used (acetone or toluene), in contrast the same substitution is only possible in the analogous $[CpRu(PPh_3)_2Cl]$ complex using toluene under drastic conditions [21]. It is notable that the Cp* ligand is less stable as compared to the analogous Cp ligand and that prolonged reaction under drastic conditions results in removal of the Cp* ligand from the complex. Very recently we have studied the reaction of $[Cp'Ru(PPh_3)_2Cl]$, [where Cp′ = ind., Cp*, Cp] with sterically demanding the multidentate tetra-2-pyridyl-1,4-pyrazine (tppz) ligand, where attempts to synthesis Cp* and indenyl complexes chelated with the tppz ligand were unsuccessful, instead we isolated complexes of the type $[(tppz)Ru(PPh_3)_2X]$ [22]. However, when the reaction was carried out with $[CpRu(PPh_3)_2Cl]$, the η^5-bonded cyclopentadienyl group remained intact to the metal thus forming a complex of the type $[CpRu(L_2)(PPh_3)]^+$ [5b]. This indicates the more labile nature of the indenyl and Cp* ligands as compared to the cyclopentadienyl ligand.

The complexes **[3a]PF$_6$**–**[3f]PF$_6$** are highly soluble in polar solvents but insoluble in non-polar solvents. The conductivity measurement (10^{-4} in CH_3CN) of the complexes showed the complexes are ionically dissociated into a 1:1 electrolytic system [23]. The microanalyses data of the complexes are in good agreement with that of their formulations. The IR spectra of the complexes exhibit bands corresponding to $\nu_{C=N}$ of the coordinated ligands at 1598–1612 cm^{-1}, while ν_{P-F} of the PF_6^- counter ion appears at 844 cm^{-1}. The IR spectra showed a shift of the C=N stretching frequency towards lower wavenumbers as compared with the free base ligands (1598–1612 versus 1619–1638 cm^{-1}) indicating N-coordination of the C=N group [24]. The complex (**[3d]PF$_6$**) showed a characteristic IR band for symmetric ν_{NO_2} and asymmetric ν_{NO_2} at 1348 and 1458 cm^{-1}, respectively, similar to those observed for other reported compounds. The proton NMR spectra of these complexes displayed a sharp singlet (except **[3d]PF$_6$**) at δ 1.3 for the methyl protons of the pentamethylcyclopentadienyl while for the complex **[3d]PF$_6$** the resonance is observed as a doublet.



Scheme 1. X = H, **[3a]PF$_6$**; Me, **[3b]PF$_6$**; OMe, **[3c]PF$_6$**; NO_2, **[3d]PF$_6$**; Cl, **[3e]PF$_6$**; COOH, **[3f]PF$_6$**.

The doublet observed could be due to the coupling of methyl protons of the Cp* moiety with the phosphorus of the triphenylphosphine. The resonance of ortho proton of the pyridine ring of the ligand appeared as a doublet in the range of δ 8.87–8.95. The doublet observed was probably due to coupling of the methine proton with the proton of the aromatic ring of the coordinated ligands. However, this proton appears as singlet at δ 8.6 in the case of the complex **[3f]PF$_6$**. We did not observe the resonance for the acidic proton CO_2H in the proton NMR spectrum of the complex **[3f]PF$_6$**. The spectra of all these complexes also contained multiple resonances for the aromatic protons in the range of δ 6.94–8.05. The $^{13}C\{^1H\}$ NMR spectra of the complexes contained resonances for C_5Me_5 carbons at around δ 9.49 for the methyl group of Cp* and δ 89.26 for the ring carbons. The resonance observed at around δ 161 could be due to the imine carbon (CH=N) of the Schiff base ligand. The $^{13}C\{^1H\}$ NMR spectrum of complex **[3f]PF$_6$** showed a singlet at δ 178, which is assignable to the carbon of COOH. The spectra also showed resonances in the range of δ 123.48–155.96 for the aromatic carbons and carbons of the pyridyl ring. The $^{31}P\{^1H\}$ NMR spectra of the complexes displayed a singlet in the range of δ 45.26–46.7 due to the triphenylphosphine moiety as compared to δ 38.5, observed in the neutral precursor complex $[Cp^*Ru(PPh_3)_2Cl]$. The spectra also contained a septet in the range of δ −141 to −145 for the PF_6^- counter ion. The electronic spectra of the complexes in dichloromethane exhibited absorption bands in the range of 475–493 nm (Table 1). These low energy absorption bands present in all of these complexes are characteristics of Ru(dπ)–L(π^*), metal to ligand charge transfer transitions (MLCT).

3.1. Crystal structure

The crystal structure determination was carried out for the representative complex **[3e]PF$_6$**. There is a disordered area in the crystal, which was a combination of PF_6's and dichloromethane, the solvent of crystallization. The space group has four symmetry-related positions in the unit cell, of which the PF_6's ions occupy two and the other two by the CH_2Cl_2 molecules. The effect of this disorder was removed from the data using the "SQUEEZE" program, which was written to correct data for the presence of disordered solvents [19]. The perspective view of the cationic part of the complex with the numbering scheme of the atoms is shown in Fig. 1. Details of the crystallographic data collection are given in Table 2. Selected bond lengths and angles are presented in Table 3.

The complex crystallized in the $P2_1/c$ space group and consists of complex cation and PF_6 anions joined by columbic forces. The ruthenium atom presents a pseudo-octahedral environment with the Cp* ligand occupying three facile coordination sites, π-bonded to the metal in η^5-fashion, while the remaining coordination positions are occupied by the P atom of the triphenylphosphine

Table 2
Summary of structure determination of complex **[3e]PF$_6$**

Formula	$C_{40}H_{39}N_2P_2F_6ClRu$
Formula weight	860.19
Crystal class	monoclinic
Space group	$P2_1/c$ (#14)
Z	4
Cell constants	
a (Å)	10.7236(5)
b (Å)	19.9676(9)
c (Å)	18.6390(9)
β (°)	98.3575(4)
V (Å^3)	3948.7(3)
μ (cm^{-1})	6.05
Crystal size (mm)	$0.40 \times 0.35 \times 0.30$
D_c (g/cm^3)	1.447
$F(000)$	1752
Radiation	Mo Kα (λ = 0.71069 Å)
2θ range	5.12–54.96
hkl collected	$-13 \leqslant h \leqslant 13$; $-25 \leqslant k \leqslant 23$; $-23 \leqslant l \leqslant 24$
Number of reflections measured	24 099
Number of unique reflections	8816 (R_{int} = 0.0191)
Number of observed reflections	7696 ($F > 4\sigma$)
Number of reflections used in refinement	8816
Number of parameters	445
R indices ($F > 4\sigma$)	R_1 = 0.0444; wR_2 = 0.1267
R indices (all data)	R_1 = 0.0499; wR_2 = 0.1332
GOF	1.052
Final difference peaks (e/Å^3)	+1.566, −0.656

Table 1
UV–Vis and conductivity data of the complexes at room temperature

No.	Complexes	λ_{max} (nm)	Conductivity Λ_m (S cm^2 mol^{-1})
1.	$[(\eta^5\text{-}C_5Me_5)Ru(PPh_3)(C_5H_4N\text{-}2\text{-}CH{=}N\text{-}C_6H_5)]PF_6$ **[3a]PF$_6$**	486	180
2.	$[(\eta^5\text{-}C_5Me_5)Ru(PPh_3)(C_5H_4N\text{-}2\text{-}CH{=}N\text{-}C_6H_4\text{-}p\text{-}CH_3)]PF_6$ **[3b]PF$_6$**	490	172
3.	$[(\eta^5\text{-}C_5Me_5)Ru(PPh_3)(C_5H_4N\text{-}2\text{-}CH{=}N\text{-}C_6H_4\text{-}p\text{-}OMe)]PF_6$ **[3c]PF$_6$**	475	159
4.	$[(\eta^5\text{-}C_5Me_5)Ru(PPh_3)(C_5H_4N\text{-}2\text{-}CH{=}N\text{-}C_6H_4\text{-}p\text{-}NO_2)]PF_6$ **[3d]PF$_6$**	482	167
5.	$[(\eta^5\text{-}C_5Me_5)Ru(PPh_3)(C_5H_4N\text{-}2\text{-}CH{=}N\text{-}C_6H_4\text{-}p\text{-}Cl)]PF_6$ **[3e]PF$_6$**	493	145
6.	$[(\eta^5\text{-}C_5Me_5)Ru(PPh_3)(C_5H_4N\text{-}2\text{-}CH{=}N\text{-}C_6H_4\text{-}p\text{-}CO_2H)]PF_6$ **[3f]PF$_6$**	478	169

Table 3
Molecular structure of complex [**3e**]PF_6 with 30% thermal ellipsoids

Bond lengths (Å)			
Ru–N(1)	2.106(2)	Ru–P(1)	2.3593(7)
Ru–N(2)	2.097(2)	N(2)–C(6)	1.297(4)
C*–Ru	1.8536(2)		
C* = centroid of C(13), C(14), C(15), C(16), C(17)			
Bond angles (°)			
N(1)–Ru–N(2)	75.67(9)	N(1)–Ru–P(1)	88.79(6)
N(2)–Ru–P(1)	92.84(6)		

Hydrogen atoms and the PF_6 ion have been omitted for clarity.

and N atoms of the Schiff base ligand. The average bond distance of ruthenium to ring carbon is 2.2198 Å, whereas the distance between the ruthenium and the centroid of the ring is 1.8536(2) Å. The Ru–P(1) bond length, 2.3593(7) Å, is within the usual range of Ru–P bond distances (2.20–2.43 Å) [25]. The ruthenium and nitrogen bond distances, 2.106(2) and 2.097(2) Å, are within the range of reported compounds. There is no significant difference in the C–C bond lengths in the cyclopentadienyl ring. The bond lengths falls within the range of 1.418(4)–1.452(4) Å, suggesting the delocalization of π-electrons in the ring. Further, the five-membered ring is planar as evident by the nearly equal bond distances between the ruthenium and ring carbons. The angle between N(1)–Ru(1)–N(2), 75.67(9)°, is very close to those reported for the similar ligand in indenyl ruthenium(II) complexes [3a]. The complex adopts the familiar ''piano stool'' structure as evident by the nearly 90° bond angles for N(1)–Ru–P(1) (88.79(6)°) and N(2)–Ru–P(1) (92.84(6)°).

4. Conclusions

The present study describes the simple synthetic methodology for the preparation of six new monocationic pentamethylcyclopentadienyl ruthenium(II) Schiff base complexes. Complex [**3e**]PF_6 provides a first insight into the structural data of pentamethylcyclopentadienyl ruthenium(II) Schiff base complexes containing a phosphine ligand.

Appendix A. Supplementary data

Crystallographic data for the structural analysis have been deposited at the Cambridge Crystallographic Data Centre (CCDC), CCDC No. 252029 for complex **3e**. Copies of this information may be obtained free of charge from the director, CCDC, 12 Union Road, Cambridge, CB2 1EZ, UK (fax: +44-1223-336033; e-mail: deposit@ccdc.cam.ac.uk or www: http://www.ccdc.cam.ac.uk). Supplementary data associated with this article can be found, in the online version at doi:10.1016/j.poly.2004.11.021.

References

[1] M.A. Bennett, K. Khan, E. Wenger, Comprehensive Organometallic Chemistry, Elsevier, Oxford, 1995, p. 473 (Chapter 8).
[2] (a) C. Standfest-Hauser, C. Slugocv, K. Mereiter, R. Schmid, K. Kirchner, L. Xiao, W. Weissensteiner, J. Chem. Soc., Dalton Trans. (2001) 2989;
(b) A. FÜrstner, M. Picquet, C. Bruneau, P.H. Dixneuf, Chem. Commun. (1998) 1315;
(c) B.C.G. Soderberg, Coord. Chem. Rev. 241 (2003) 147.
[3] (a) S.S. Keisham, Y.A. Mozharrivskyj, P.J. Carroll, M.R. Kollipara, J. Organomet. Chem. 689 (2004) 1249;
(b) P. Govindaswamy, Y.A. Mozharivskyj, M.R. Kollipara, Polyhedron 23 (2004) 1567.
[4] (a) M.R. Kollipara, E.K. Rymmai, Polyhedron 22 (2003) 307;
(b) E.K. Rymmai, M.R. Kollipara, Indian J. Chem. A 42 (2003) 1892.
[5] (a) M.R. Kollipara, C.R.K. Rao, P.S. Zacharias, Polyhedron 16 (1997) 2369;
(b) R. Lalrempuia, P. Govindaswamy, Yurij A. Mozharivskyj, M.R. Kollipara, Polyhedron 23 (2004) 1069.
[6] (a) B. Chaudret, F.A. Jalon, J. Chem. Soc., Chem. Commun. (1988) 711;
(b) P.J. Fagan, M.D. Ward, J.V. Caspar, J.C. Calabrese, P.J. Krusic, J. Am. Chem. Soc. 110 (1988) 2981;
(c) P.J. Fagan, W.S. Mahoney, J.C. Calabrese, I.D. Williams, Organometallics 9 (1990) 1843.
[7] B. Steinmetz, W.A. Schenk, Organometallics 18 (1999) 943.
[8] (a) V. Guerchais, C. Lapinte, J.Y. Thepot, L. Toupet, Organometallics 7 (1988) 604;
(b) R. Le Lagadec, E. Roman, L. Toupet, U. Müller, P.H. Dixneuf, Organometallics 13 (1994) 5030.
[9] W. Lin, S.R. Wilson, G.S. Girolami, Organometallics 16 (1997) 1987.
[10] S. K Mandal, A.R. Chakravarty, Polyhedron 11 (1992) 823.
[11] S. Mandal, A.R. Chakravarty, Polyhedron 10 (1991) 2483.
[12] R. Lalrempuia, M.R. Kollipara, P.J. Carroll, Polyhedron 22 (2003) 605.
[13] (a) R.N. Dominey, B. Hauser, J. Habbard, J. Dunham, Inorg. Chem. 30 (1991) 4754;
(b) E.V. Dose, L.J. Wilson, Inorg. Chem. 17 (1978) 2660.
[14] M.I. Bruce, B.C. Hall, N.N. Zaitseva, B.W. Skelton, A.H. White, J. Chem. Soc., Dalton Trans. (1998) 1793.
[15] P.M. Treichel, D.A. Komar, P.J. Vincenti, Synth. React. Inorg. Met. Org. Chem. 14 (1984) 383.
[16] R.A. Jacobson, Private Communication (1994).
[17] A. Altomare, M. Burla, M. Camalli, G. Cascarano, C. Giacovazzo, A. Guagliardi, A. Moliterni, G. Polidori, R. Spagna, J. Appl. Crystallogr. 32 (1999) 115.
[18] G.M. Sheldrick, SHELXL-97. Program for the Refinement of Crystal structures, University of Göttingen, Göttingen, Germany, 1997.
[19] P.V.D. Sluis, A.L. Spek, Acta Crystallogr., Part A 46 (1990) 194.
[20] ORTEP-II: A Fortran Thermal Ellipsoid Plot Program for Crystal Structure Illustrations, C.K. Johnson, 1976, ORNL-5138.
[21] L. Fan, F.W.B. Einstein, D. Sutton, Organometallics 19 (2000) 684.
[22] K.S. Singh, Yurij A. Mozharivskyj, M.R. Kollipara (unpublished work).
[23] W.J. Geary, Coord. Chem. Rev. 7 (1971) 81.
[24] H. Onoue, I. Moritani, J. Organomet. Chem. 43 (1972) 431.
[25] L.J. Guggenberger, Inorg. Chem. 12 (1973) 1317.

Available online at www.sciencedirect.com
SCIENCE DIRECT®
Polyhedron 24 (2005) 397–406
POLYHEDRON
www.elsevier.com/locate/poly

New α,ω-dicarboxylate coordination polymers with 4,4′-bipyridine: $Cu(bpy)(C_5H_6O_4)$, $Zn(bpy)(C_5H_6O_4)$, $Zn(bpy)(C_6H_8O_4)$ and $Mn(bpy)(C_8H_{12}O_4)\cdot H_2O$

Yue-Qing Zheng *, Er-Bo Ying

Municipal Key Laboratory of Solid Materials Chemistry, Institute of Inorganic Chemistry, Ningbo University, Zheng Ning Xi Li 1211, Ningbo 315211, PR China

Received 18 September 2004; accepted 24 November 2004

Abstract

Four 4,4′-bipyridine α,ω-dicarboxylate coordination polymers $Cu(bpy)(C_5H_6O_4)$ (**1**), $Zn(bpy)(C_5H_6O_4)$ (**2**), $Zn(bpy)(C_6H_8O_4)$ (**3**) and $Mn(bpy)(C_8H_{12}O_4)\cdot H_2O$ (**4**) have been synthesized and structurally characterized by single crystal X-ray diffraction methods (bpy = 4,4-bipyridine, $(C_5H_6O_4)^{2-}$ = glutarate anion, $(C_6H_8O_4)^{2-}$ = adipate anion, $(C_8H_{12}O_4)^{2-}$ = suberate anion). Their crystal structures are featured by dimeric metal units, which are co-bridged by 4,4′-bipyridine ligands and dicarboxylate anions such as glutarate, adipate and suberate anions to generate 2D layers with a (4,4) topology in **1**, **2** and **4** as well as to form 3D frameworks in **3**. Two 3D frameworks in 3 interpenetrate with each other to form a topology identical to the well-known Nb_6F_{15} cluster compound. Over 5–300 K, the paramagnetic behavior of **4** follows the Curie–Weiss law $\chi_m(T-\Theta) = 4.265(5)\ cm^3\ mol^{-1}$ with the Weiss constant $\Theta = -6.3(2)$ K. Furthermore, the thermal behavior of **3** and **4** is also discussed.
© 2005 Elsevier Ltd. All rights reserved.

Keywords: Transition metal; Coordination polymers; Dicarboxylates; X-ray structures; Magnetic properties

1. Introduction

Currently there is considerable interest in metal-organic coordination polymers with fascinating network topologies and specific properties for potential applications in the field of molecular magnetism, electrical conductivity and photoluminescence, as well as in inclusion chemistry, molecular recognition and catalysis [1–4]. One commonly used strategy for designing such materials relies on the utilization of multidentate N- or O-donor ligands which have the capacity to bridge between metal centers to form polymeric structures. For example, benzene polycarboxylic acid ligands are good candidates for this purpose [5–7]. In contrast to the rigid aromatic polycarboxylate anions, the aliphatic α,ω-dicarboxylate ligands as important flexible spacer ligands, due to their conformational and coordination versatility, tend to bridge transition metal ions to form coordination polymers with low dimensionality [8–10]. On the other hand, even the high dimensional α,ω-dicarboxylate coordination polymers normally exhibit little porosity [11]. To avoid such drawbacks, our recent research has been intensively focused on construction of porous α,ω-dicarboxylate coordination polymers by introduction of rigid 4,4′-bipyridine as ancillary ligands [12,13]. Hitherto, however, reports about co-bridging of rigid 4,4′-bipyridine and flexible α,ω-dicarboxylate ligands to construct coordination polymers seem very scarce [14–21].

As part of our ongoing work [12,13], we report here the syntheses and crystal structures of four 4,4′-bipyridine α,ω-dicarboxylate coordination polymers

* Corresponding author. Tel./fax: +86 574 87600747.
E-mail address: zhengcm@nbu.edu.cn (Y.-Q. Zheng).

0277-5387/$ - see front matter © 2005 Elsevier Ltd. All rights reserved.
doi:10.1016/j.poly.2004.11.025

Table 1
Summary of crystal data, data collection, structure solution and refinement details for **1**, **2**, **3** and **4**

	1	**2**	**3**	**4**
Empirical formula	$C_{15}H_{14}CuN_2O_4$	$C_{15}H_{14}N_2O_4Zn$	$C_{16}H_{16}N_2O_4Zn$	$C_{18}H_{22}MnN_2O_5$
Formula weight	349.82	351.65	365.68	401.32
Description	green plate	colorless prism	colorless prism	yellow block
Crystal size (mm)	$0.53 \times 0.11 \times 0.07$	$0.40 \times 0.27 \times 0.24$	$0.220.16 \times 0.09$	$0.51 \times 0.22 \times 0.20$
Crystal system	triclinic	triclinic	triclinic	triclinic
Space group	$P\bar{1}$	$P\bar{1}$	$P\bar{1}$	$P\bar{1}$
Unit cell dimensions				
a (Å)	8.118(2)	7.969(2)	8.584(2)	10.004(2)
b (Å)	9.416(2)	9.501(2)	8.820(2)	10.098(2)
c (Å)	10.535(2)	10.368(2)	10.753(2)	10.400(2)
α(°)	112.18(2)	109.88(3)	109.12(1)	110.66(3)
β(°)	92.35(1)	92.86(3)	95.62(1)	91.42(3)
γ(°)	104.77(1)	104.60(3)	102.51(1)	110.96(3)
Volume (Å^3)	712.5(3)	706.4(2)	737.4	904.2(3)
Z	2	2	2	2
D_{Calc} (g cm^{-3})	1.630	1.653	1.647	1.474
F(0 0 0)	358	360	376	418
Absorption coefficient (mm^{-1})	1.630	1.758	1.688	0.761
Absorption correction	empirical	empirical	empirical	empirical
Transmission range	0.146–0.829	0.399–0.457	0.649–0.817	0.562–0.831
θ Range (°)	0.974–27.50	0.982–27.50	0.973–27.50	0.968–27.50
Refinement method	full-matrix least-squares on F^2	full-matrix least-squares on F^2	full-matrix least-squares on F^2	full-matrix least-squares on F^2
Reflections collected	3867	3884	3956	4722
Unique reflections (R_{int})	3186 (0.0362)	3189 (0.0190)	3292 (0.0303)	4018 (0.0738)
Data	2653	2913	2419	3176
Parameters/restraints	201/0	201/0	214/0	238/0
Goodness-of-fit on F^2	1.038	1.278	1.000	1.020
R_1, wR_2 [$I \geqslant \sigma(I)$][a]	0.0525, 0.1502	0.0448, 0.1135	0.0439, 0.0926	0.0451, 0.1112
R_1, wR_2 (all data)[a]	0.0637, 0.1624	0.0486, 0.1169	0.0726, 0.1062	0.0617, 0.1209
Extinction coefficient	0.000(3)	0.124(8)	0.000(1)	0.002(2)
$\delta\rho_{max}$, $\delta\rho_{min}$ (e Å^{-3})	0.807, −1.307	0.981, −1.143	0.453, −0.463	0.728, −0.552

[a] $wR_2 = [\sum w(F_o^2 - F_c^2)^2 / \sum w(F_o^2)^2]^{1/2}$.

$Cu(bpy)(C_5H_6O_4)$ (**1**), $Zn(bpy)(C_5H_6O_4)$ (**2**), $Zn(bpy)(C_6H_8O_4)$ (**3**) and $Mn(bpy)(C_8H_{12}O_4)\cdot H_2O$ (**4**) along with the magnetic behavior of **4**, in addition to the thermal characterization of **3** and **4**. The title compounds (Table 1) are featured by dimeric metal units, which are co-bridged by 4,4′-bipyridine ligands and dicarboxylate anions into 2D layers with (4,4) topologies in **1**, **2** and **4**, as well as into 3D frameworks in **3**.

2. Results and discussion

2.1. Syntheses and thermal analyses

Systematic investigation showed that hydrothermal reactions of $Cu(NO_3)_2\cdot 3H_2O$, 4,4′-bipyridine and glutaric acid in a methanolic aqueous solution afforded a mixture of $Cu_2(bpy)(C_5H_6O_4)_2\cdot 3H_2O$ [14] and **1** as a minor product. It is very difficult to separate **1** from the mixture in a sufficient quantity for characterization. Much work has been done to suppress the formation of $Cu_2(bpy)(C_5H_6O_4)_2\cdot 3H_2O$ [14]. Unfortunately, all attempts have failed. Complexes **2**–**4** were prepared by reaction of a fresh hydroxo carbonate precipitate of the relevant transition metal and corresponding dicarboxylic acids with 4,4′-bipyridine in methanolic aqueous solutions under ambient conditions. The low synthetic yields of **2** and **3** suggest low reactivity of zinc hydroxo carbonate and dicarboxylic acids with 4,4′-bipyridine at ambient temperature.

When heated up to 600 °C, **3** decomposes in two steps and the DTA curve displays two endothermic peaks centered at 303 and 358 °C. The observed weight loss of 43.3% over 25–320 °C corresponds well to the calculated value of 42.7% for liberation of one mole of bpy per formula unit. Upon further heating up to 395 °C, the sample loses additional weight (35.5%) in good agreement with a value of 35.1% calculated for sublimation of one mole of adipic anhydride ($C_6H_8O_3$). The residue collected at 600 °C was identified to be ZnO according to powder X-ray diffraction patterns.

The DTA curve of **4** exhibits four endothermic peaks centered at 122, 234, 289 and 323 °C. The observed weight loss of 4.6% at 140 °C agrees well with the calculated value of 4.5% for release of one mole of H_2O per formula unit, suggesting complete dehydration. Over

140–465 °C, the observed weight loss of 76.6% is very close to the value of 77.8% calculated for one mole 4,4′-bipyridine and one mole suberic anhydride (“$C_8H_{12}O_3$”). Powder X-ray diffraction patterns confirm the residue of 18.3% at 600 °C to be MnO (Calc. 17.7%).

2.2. Structure of Cu(bpy)($C_5H_6O_4$) (**1**) and Zn(bpy)($C_5H_6O_4$) (**2**)

2.2.1. Cu(bpy)($C_5H_6O_4$) (**1**) and Zn(bpy)($C_5H_6O_4$) (**2**)

Compounds **1** and **2** crystallize isostructurally with Mn(bpy)($C_5H_6O_4$) [12]. As depicted in Fig. 1, the metal atoms (Cu and Zn) are each surrounded by two pyridyl nitrogen atoms (N(1) and N(2)$^{\#4}$) at a mean distance of 2.035 and 2.172 Å for **1** and **2**, respectively, and three carboxylate oxygen atoms (O(1)$^{\#3}$, O(2) and O(3)$^{\#5}$) at distances in the range 1.965–2.223 and 2.020–2.028 Å for **1** and **2**, respectively (Table 2). The next carboxylate oxygen atom (O(4)$^{\#5}$) is at a more remote distance of 2.672 and 2.683 Å for **1** and **2**, respectively, suggesting a negligibly weak interaction between the central metal atom and the O(4)$^{\#5}$ atom. In this sense, the coordination sphere of the metal atoms in **1** and **2** could be regarded as a distorted trigonal bipyramid with the oxygen atoms at the equatorial sites, rather than a severely distorted octahedron as observed in Mn(bpy)($C_5H_6O_4$) [12]. The glutarate anions have normal bond lengths and angles [14], adopting a gauche-gauche conformation with one end carboxylate group bidentately bonded to two metal atoms in a *syn–syn* fashion and the other end monoatomically coordinating one metal atom. Two symmetry-related metal atoms are bridged by two carboxylate groups to form 8-membered rings. Along [1 0 0], the resulting dimeric metal units are linked by the glutarate anions to generate ribbon-like chains with alternative 8- and 16-membered rings. The M···M distances within the former ring are 3.898 and 4.105 Å for **1** and **2**, respectively, and the closest M···M separation within the latter is 6.284 and 6.568 Å for **1** and **2**, respectively. The chains are interconnected by 4,4′-bipyridine ligands to form grid-like layers with a (4,4) topology, showing apertures of dimensions 8.0×11.4 and 8.1×11.2 Å in **1** and **2**, respectively. As illustrated in Fig. 2, the layers are ar-

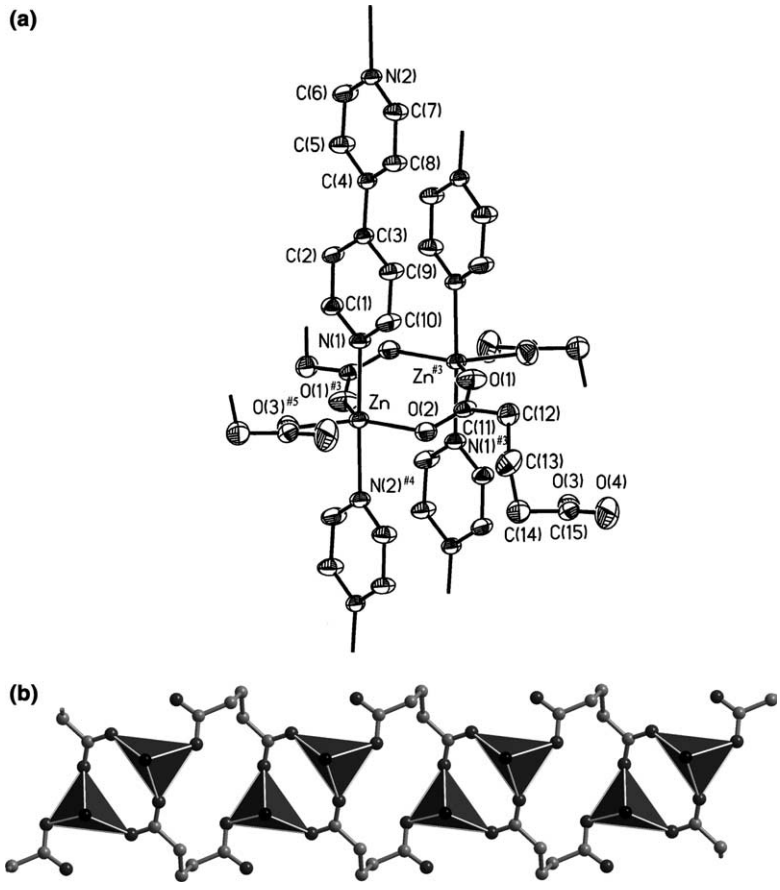


Fig. 1. (a) Coordination environment of the Zn atom along with the atomic labelling for **2**. The displacement ellipsoids are drawn at the 60% probability level (Symmetry transformations used to generate equivalent atoms: #1 = x, $y-1$, $z-1$; #2 = x, y, $z-1$; #3 = $-x+1$, $-y+1$, $-z+1$; #4 = x, $y+1$, $z+1$; #5 = x, y, $z+1$). (b) 1D ribbon-like chains of Zn atoms bridged by glutarato ligands.

Table 2
Selected bond lengths (Å) and angles (°) for **1**–**3**

1[a]					
Bond lengths					
Cu–O(1)$^{\#3}$	2.223(3)	Cu–N(1)	2.035(3)	C(11)–O(2)	1.277(5)
Cu–O(2)	1.965(3)	Cu–N(2)$^{\#4}$	2.035(3)	C(15)–O(3)	1.279(5)
Cu–O(3)$^{\#5}$	1.995(3)	C(11)–O(1)	1.227(5)	C(15)–O(4)	1.238(5)
Cu–O(4)$^{\#5}$	2.672(4)				
Bond angles					
O(1)$^{\#3}$/Cu/O(2)	121.4(1)	O(2)/Cu/O(4)$^{\#5}$	94.1(1)	O(4)$^{\#5}$/Cu/N(1)	87.7(1)
O(1)$^{\#3}$/Cu/O(3)$^{\#5}$	90.3(1)	O(2)/Cu/N(1)	92.9(1)	O(4)$^{\#5}$/Cu/N(2)$^{\#4}$	94.0(1)
O(1)$^{\#3}$/Cu/O(4)$^{\#5}$	144.5(1)	O(2)/Cu/N(2)$^{\#4}$	87.7(1)	N(1)/Cu/N(2)$^{\#4}$	178.2(1)
O(1)$^{\#3}$/Cu/N(1)	90.9(1)	O(3)$^{\#5}$/Cu/O(4)$^{\#5}$	54.3(1)	O(1)/C(11)/O(2)	125.5(4)
O(1)$^{\#3}$/Cu/N(2)$^{\#4}$	87.4(1)	O(3)$^{\#5}$/Cu/N(1)	90.2(1)	O(3)/C(15)/O(4)	123.0(4)
O(2)/Cu/O(3)$^{\#5}$	148.1(1)	O(3)$^{\#5}$/Cu/N(2)$^{\#4}$	90.2(1)		
2[a]					
Bond lengths					
Zn–O(1)$^{\#3}$	2.028(2)	Zn–N(1)	2.167(2)	C(11)–O(2)	1.253(3)
Zn–O(2)	2.024(2)	Zn–N(2)$^{\#4}$	2.175(2)	C(15)–O(3)	1.253(3)
Zn–O(3)$^{\#5}$	2.020(2)	C(11)–O(1)	1.252(3)	C(15)–O(4)	1.223(3)
Bond angles					
O(1)$^{\#3}$/Zn/O(2)	126.29(9)	O(2)/Zn/O(3)$^{\#5}$	136.76(9)	O(3)$^{\#5}$/Zn/N(2)$^{\#4}$	89.83(9)
O(1)$^{\#3}$/Zn/O(3)$^{\#5}$	96.6(1)	O(2)/Zn/N(1)	92.03(8)	N(1)/Zn/N(2)$^{\#4}$	177.21(7)
O(1)$^{\#3}$/Zn/N(1)	91.29(8)	O(2)/Zn/N(2)$^{\#4}$	87.41(8)	O(1)/C(11)/O(2)	126.2(2)
O(1)$^{\#3}$/Zn/N(2)$^{\#4}$	86.84(8)	O(3)$^{\#5}$/Zn/N(1)	92.44(9)	O(3)/C(15)/O(4)	122.2(3)
3[b]					
Bond lengths					
Zn–O(1)	2.017(2)	Zn–N(1)	2.171(3)	O(2)–C(11)	1.248(4)
Zn–O(2)$^{\#2}$	2.023(3)	Zn–N(2)$^{\#3}$	2.201(3)	O(3)–C(14)	1.247(4)
Zn–O(3)	2.197(3)	O(1)–C(11)	1.253(4)	O(4)–C(14)	1.245(4)
Zn–O(4)	2.227(3)				
Bond angles					
O(1)/Zn/O(2)$^{\#2}$	120.4(1)	O(2)$^{\#2}$/Zn/O(4)	147.7(1)	O(4)/Zn/N(1)	90.0(1)
O(1)/Zn/O(3)	149.5(1)	O(2)$^{\#2}$/Zn/N(1)	94.2(1)	O(4)/Zn/N(2)$^{\#3}$	88.3(1)
O(1)/Zn/O(4)	91.3(1)	O(2)$^{\#2}$/Zn/N(2)$^{\#3}$	87.0(1)	N(1)/Zn/N(2)$^{\#3}$	178.2(1)
O(1)/Zn/N(1)	92.8(1)	O(3)/Zn/O(4)	58.4(1)	O(1)/C(11)/O(2)	125.8(3)
O(1)/Zn/N(2)$^{\#3}$	87.7(1)	O(3)/Zn/N(1)	90.9(1)	O(3)/C(14)/O(4)	120.2(4)
O(2)$^{\#2}$/Zn/O(3)	89.4(1)	O(3)/Zn/N(2)$^{\#3}$	87.8(1)		

[a] Symmetry codes: #1 = x, $y-1$, $z-1$; #2 = x, y, $z-1$; #3 = $-x+1$, $-y+1$, $-z+1$; #4 = x, $y+1$, $z+1$; #5 = x, y, $z+1$.
[b] Symmetry codes: #1 = x, $y-1$, $z-1$; #2 = $-x+1$, $-y+2$, $-z+1$; #3 = x, $y+1$, $z+1$; #4 = $-x+2$, $-y+3$, $-z+1$; #5 = $-x+2$, $-y+2$, $-z+2$.

ranged parallel to $(0\,1\,\bar{1})$ and close packed with the bent glutarate anions approaching the apertures of the neighboring layers. Two CH groups from C(8) and C(9) of one 4,4′-bipyridine donate two hydrogen atoms to one uncoordinating carboxylate O(4) atom to form interlayer $R_2^1(7)$ C–H···O hydrogen bonds according to graph set notation [22]. These hydrogen bonding interactions seem essential for supramolecular assembly of the layers.

2.3. Structure of Zn(bpy)($C_6H_8O_4$) (**3**)

This compound is found to be isostructural with Mn(bpy)($C_6H_8O_4$) [12] and Mn(bpe)($C_6H_8O_4$) with bpe = 1,2-bis(4-pyridyl)ethane [19]. Substitution of Zn for Mn brings about no significant variation in the structural features. As shown in Fig. 3, the asymmetric unit cell of **3** contains one Zn atom, one 4,4′-bipyridine molecule and two halves of adipate anions, out of which the twisted one is disordered with the middle two carbon atoms each equally populated over two sites (C(16A) and C(16B)) and the linear one possesses an inversion center at the middle C–C bond. The coordination sphere of the Zn atoms is a considerably distorted octahedron with a ZnN_2O_4 chromophore, where the equatorial oxygen atoms belong to three adipate anions and two nitrogen atoms to different 4,4′-bipyridine ligands. The Zn–O and Zn–N bond distances fall in the ranges 2.017–2.227 and 2.171–2.201 Å, respectively (Table 2), which are comparable

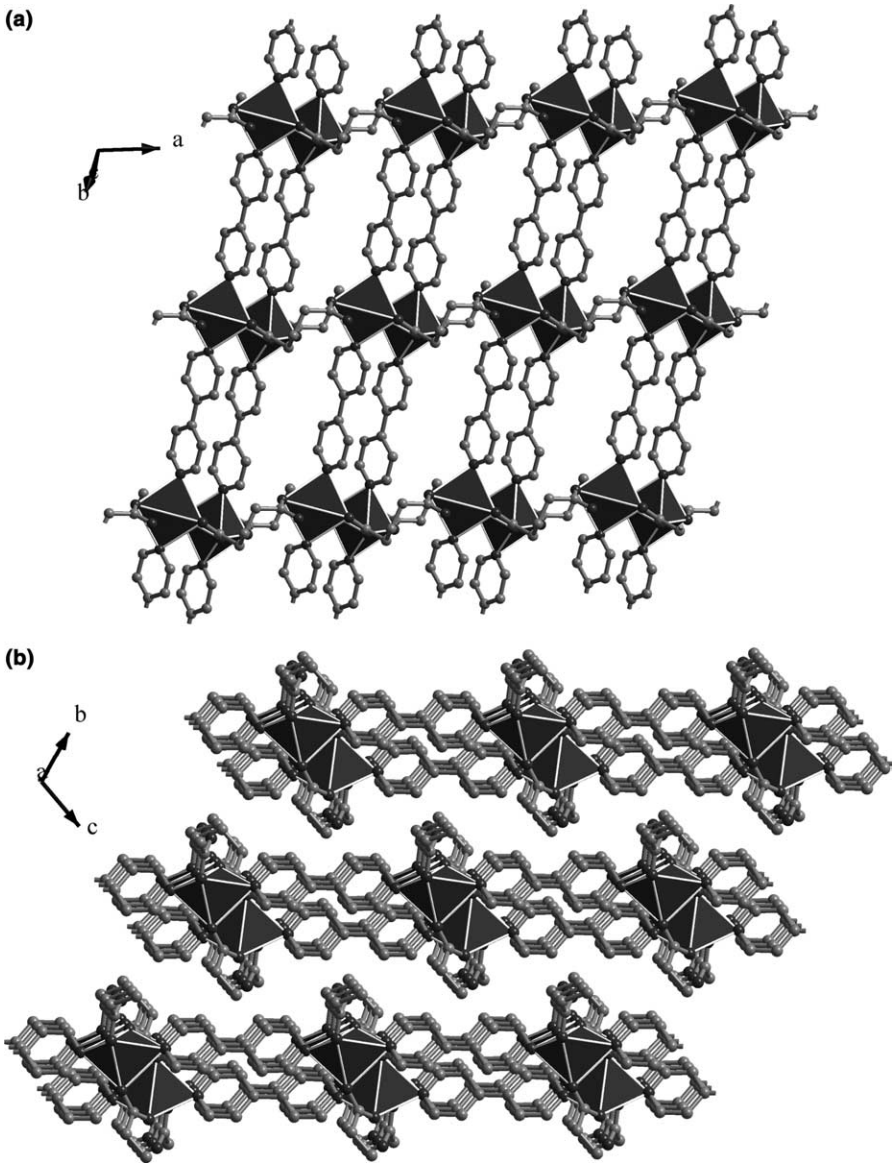


Fig. 2. (a) The ribbon-like chains are pillared by rigid bpy ligands into a 2D layer in **2**. (b) Crystal structure of **2**.

with those reported for Zn(bpy)($C_4H_4O_4$) [21]. The disordered and linear adipate anions function as bischelating and bisbidentate ligands, respectively, to bridge two and four Zn atoms. The dimeric Zn_2 units are interconnected into (4,4) grid-like nets containing 8-membered rings and 36-membered rings of dimension 10.9×13.1 Å (Fig. 3). The 8-membered ring is enclosed by two Zn ions and two carboxylate groups with the Zn···Zn separation being 3.954 Å, substantially less than that in **2**. The resulting nets are pillared by 4,4′-bipyridine ligands to generate 3D frameworks (Fig. 4), which form twofold interpenetration with a topology identical with the well-known Nb_6F_{15} cluster compound containing Nb_6F_{12} clusters [4, 23]. The adipate anions exhibit usual bond distances and angles [24].

2.4. Structure of $Mn(bpy)(C_8H_{12}O_4) \cdot H_2O$ (**4**)

This coordination polymer consists of 2D open layers and hydrogen bonded water molecules. The distorted octahedral coordination sphere of the Mn atoms in **4** is practically identical to those in Mn(bpy)($C_6H_8O_4$) [12] and Mn(bpe)($C_6H_8O_4$), with bpe = 1,2-bis(4-pyridyl)ethane [19]. As shown in Fig. 5, the MnN_2O_4 chromophore is defined by four oxygen atoms from one chelating and two bidentately bridging carboxylate groups of different suberate anions and two nitrogen atoms at the opposite positions from different 4,4′-bipyridine ligands. The Mn–O and Mn–N bond distances fall in the regions 2.110–2.302 and 2.279–2.290 Å, respectively (Table 3). The suberate anions exhibit normal bond distances and angles [24–29] and are

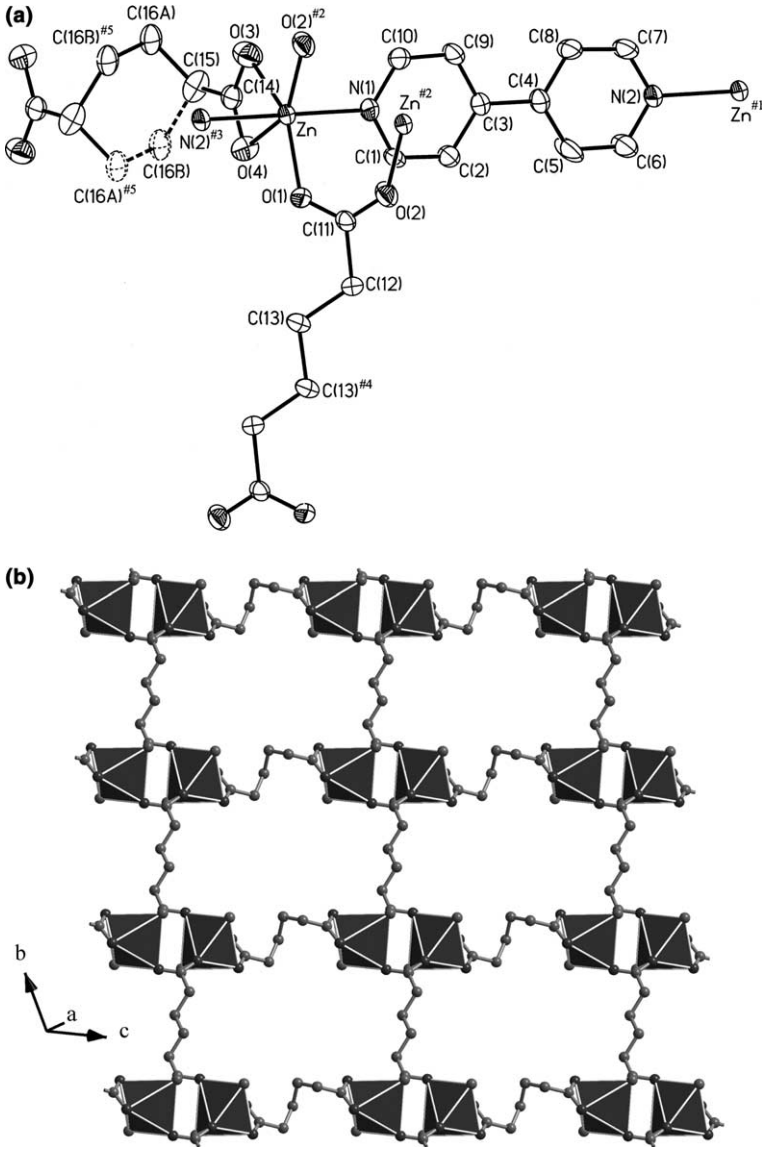


Fig. 3. (a) Coordination environment of the Zn atoms along with the atomic labelling for **3**. The displacement ellipsoids are drawn at the 60% probability level (Symmetry transformations used to generate equivalent atoms: #1 = x, $y-1$, $z-1$; #2 = $-x+1$, $-y+2$, $-z+1$; #3 = x, $y+1$, $z+1$; #4 = $-x+2$, $-y+3$, $-z+1$; #5 = $-x+2$, $-y+2$, $-z+2$). (b) 2D square grid-like network generated from six-coordinate Mn atoms by bis-bidentate and bis-chelating adipato ligands.

each coordinated to three Mn atoms with one end carboxylate group chelating one metal atom and the other bidentately bridging two metal atoms in a syn-anti fashion. This coordination mode of the suberate anion is very similar to the glutarate anions in Mn(bpy)($C_5H_6O_4$) [12], but significantly different from that in $Mn_2(H_2O)(C_8H_{12}O_4)_2$ [10]. The dimeric Mn_2 units are interconnected by suberate anions to generate a 1D ribbon-like chain with alternative 8- and 22-membered rings (Fig. 5). The Mn···Mn distance within the 8-membered ring is 3.914 Å, much less than those in Mn(bpy)($C_5H_6O_4$) (3.973 Å) and Mn(bpy)($C_6H_8O_4$) (4.035 Å) [12]. The resulting chains are interlinked through the 4,4′-bipyridine ligands into grid-like layers with a (4,4) topology (Fig. 6). The formed 2D layers are arranged parallel to (1 0 0) and between them are sandwiched the lattice H_2O molecules, which are hydrogen bonded to both chelating carboxylate oxygen atoms from different layers (Table 3). The 4,4′-bipyridine ligands in **4** are significantly twisted by 23.4(2)° around the middle C–C bonds in comparison with **1**–**3**, where the bpy ligands show nearly perfect coplanarity, with the dihedral angles between both pyridine rings being in the region 4.9(2)°–6.3(3)°. Within the four title coordination polymers, no π-stacking interactions are found between the bpy bridges [30].

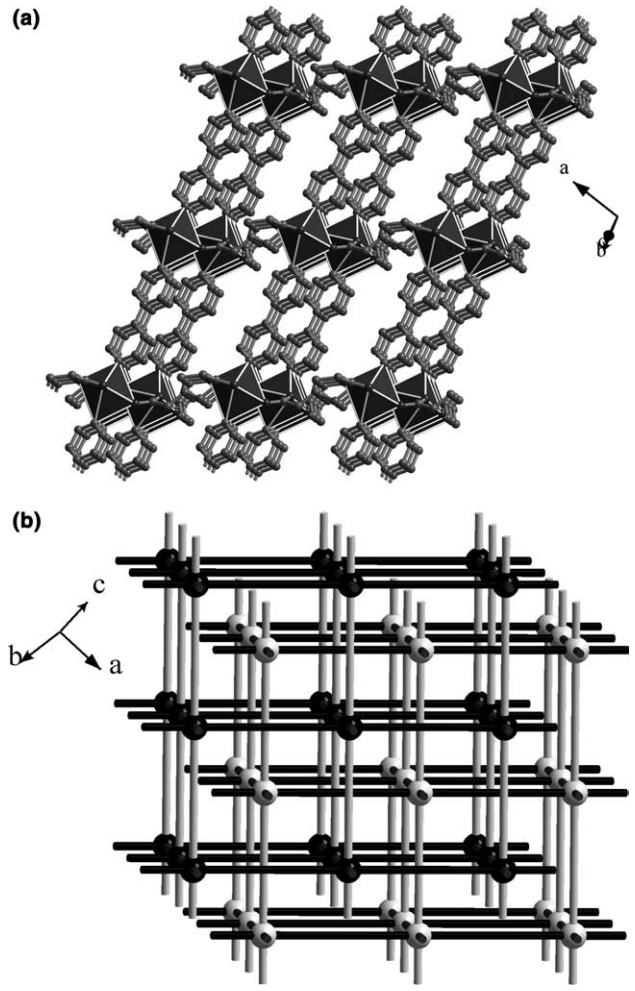


Fig. 4. (a) 3D framework in **3**. (b) The topology of the structure of **3** display twofold interpenetration viewed along the 4,4′-bipyridine ligands (darker and grey rods representing the bis-chelating and bis-bidentate adipato groups, respectively).

2.5. Magnetic properties of $Mn(bpy)(C_8H_{12}O_4)\cdot H_2O$ (**4**)

Fig. 7 demonstrates the temperature dependence of the inverse magnetic susceptibilities (χ_m^{-1}) and effective magnetic moments (μ_{eff}) of **4**, where χ_m is the magnetic susceptibility per molar Mn^{2+} ions and the effective magnetic moments were calculated by the equation $\mu_{eff} = 2.828(\chi_m T)^{1/2}$. The effective magnetic moment at room temperature is $5.77\mu_B$, slightly less than the spin-only value of $5.92\mu_B$ expected for high-spin Mn(II) in an octahedral crystal field [31]. Upon cooling from room temperature to 80 K, the value of μ_{eff} remains essentially constant, then gradually decreases to $3.53\mu_B$ at 5 K, indicative of an overall antiferromagnetic coupling between the Mn^{2+} centers. Over the temperature range 5–300 K, the title complex obeys the Curie–Weiss law $\chi_m(T-\Theta) = 4.265(5)\ cm^3\ mol^{-1}$ with the Weiss constant $\Theta = -6.3(2)$ K.

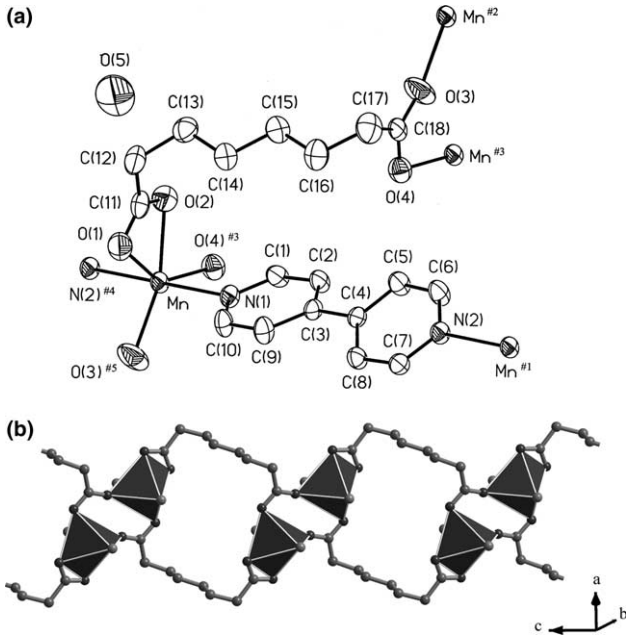


Fig. 5. Coordination environment of the Zn atom along with the atomic labelling for **4**. The displacement ellipsoids are drawn at the 60% probability level (Symmetry transformations used to generate equivalent atoms: #1 = x, $y-1$, $z-1$; #2 = x, y, $z-1$; #3 = $-x+1$, $-y+1$, $-z+1$; #4 = x, $y+1$, $z+1$; #5 = x, y, $z+1$; #6 = $-x+2$, $-y+2$, $-z+2$). (b) 1D ribbon-like chains of Zn atoms bridged by suberato ligands.

3. Experimental

All chemicals of p.a. grade were commercially available and used without further purification. The C, H and N microanalyses were performed with a PE 2400 CHNO/S elemental analyzer. The FT-IR spectra were recorded from KBr pellets in the range 4000–400 cm^{-1} on a Shimadzu FTIR-8900 spectrometer. The combined measurements on thermogravimetric and differential thermal analyses (TG/DTA) were carried out between 25 and 600 °C on powdered samples in a nitrogen stream using Seiko Exstar6000 TG/DTA6300 equipment with a heating rate of 10 °C/min. The magnetic susceptibility of the title complex was measured on a powdered sample (68.86 mg, **4**) using a SQUID magnetometer (Quantum Design Model MPMS-7) in the temperature range $5 \leqslant T\ (K) \leqslant 300$ with an applied field of 10 000 G. Diamagnetic corrections were estimated from Pascal's constants [31].

3.1. Preparation of $Cu(bpy)(C_5H_6O_4)$ (**1**)

The hydrothermal reaction of 0.242 g (1 mmol) $Cu(NO_3)_2\cdot 3H_2O$, 0.132 g (1 mmol) glutaric acid, 0.156 g (1 mmol) 4,4′-bipyridine, 8 ml CH_3OH and 8 ml H_2O in a 23 ml Teflon-lined stainless-steel reactor at 160 °C for 24 h yielded a mixture of green plate-like crystalline

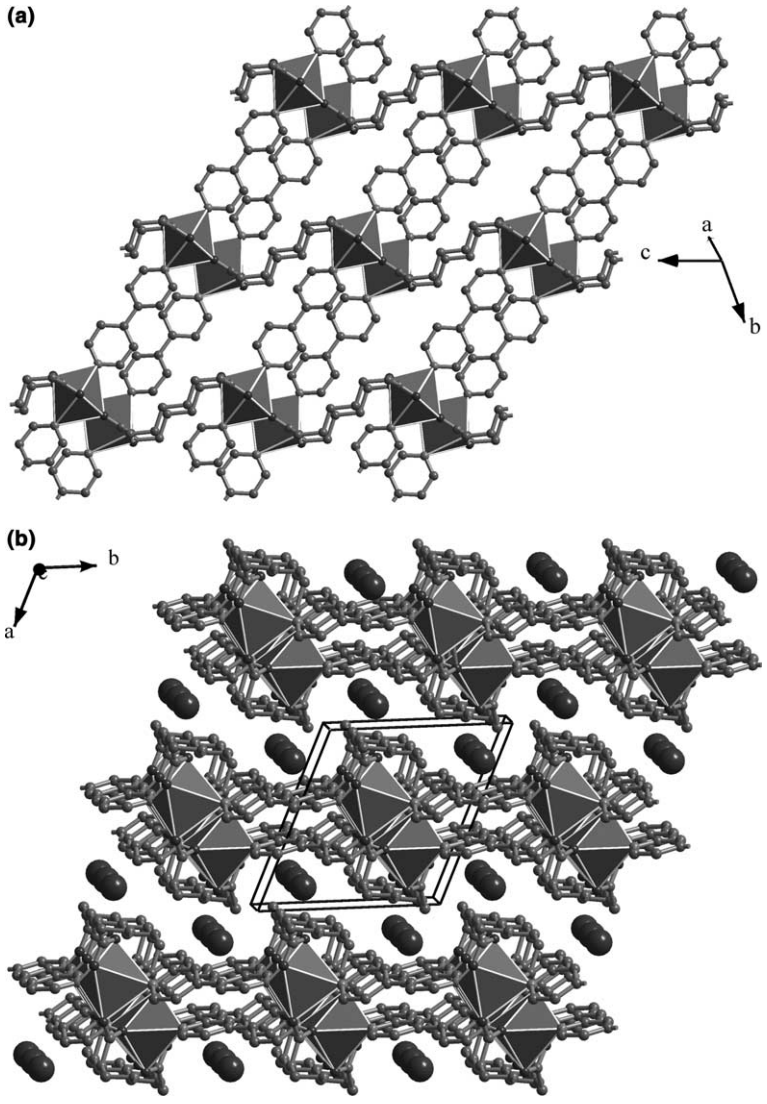


Fig. 6. (a) The ribbon-like chains are pillared by rigid bpy ligands into a 2D layer in **4**. (b) Crystal structure of **4**.

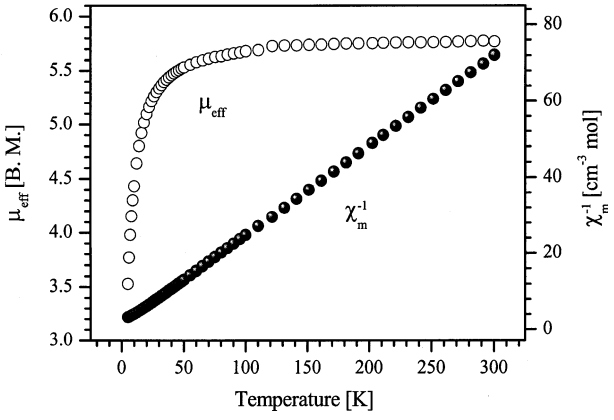


Fig. 7. Temperature dependence of the magnetic susceptibilities of **4** (χ_m being the magnetic susceptibility per Mn(II) ion).

$Cu(bpy)(C_5H_6O_4)$ (**1**) as a minor product and green prismatic crystalline $Cu_2(bpy)(C_5H_6O_4)_2 \cdot 3H_2O$ [14] as the major product.

3.2. Preparation of $Zn(bpy)(C_5H_6O_4)$ (**2**)

Dropwise addition of 1.0 ml Na_2CO_3 (1 M) to a stirred aqueous solution of $ZnSO_4 \cdot 7H_2O$ (0.081 g, 0.50 mmol) in 5.0 ml H_2O produced the white precipitate $Zn(OH)_{2-2x}(CO_3)_x \cdot yH_2O$, which was then centrifuged and washed with double-distilled water until no SO_4^{2-} anions were detectable in the supernatant. The precipitate was subsequently moved to a stirred suspension of glutaric acid (0.066 g, 0.50 mmol) in 20.0 ml CH_3OH–H_2O (v/v = 1:1), and then a methanolic solution of 4,4′-bipyridine (0.078 g, 0.50 mmol) in 5.0 ml CH_3OH was added. The mixture was further stirred for 30 min and the insoluble solid was filtered off. The colorless filtrate (pH 5.33) was allowed to stand at room temperature. Slow evaporation for several days afforded a small amount of colorless prismatic crystals (yield: less than 5% based on the initial $ZnSO_4 \cdot 7H_2O$ input). *Anal.* Calc. for $C_{15}H_{14}N_2O_4Zn$: C, 51.23; N, 7.97; H, 4.01.

Table 3
Selected bond lengths (Å) and angles (°) for **4**

Bond lengths					
Mn–O(1)	2.302(2)	Mn–N(1)	2.290(2)	O(2)–C(11)	1.263(3)
Mn–O(2)	2.254(2)	Mn–N(2)$^{\#4}$	2.279(2)	C(18)–O(3)	1.239(3)
Mn–O(3)$^{\#5}$	2.110(2)	O(1)–C(11)	1.244(4)	C(18)–O(4)	1.248(3)
Mn–O(4)$^{\#3}$	2.203(2)				
Bond angles					
O(1)/Mn/O(2)	57.13(8)	O(2)/Mn/O(3)$^{\#5}$	151.0(1)	O(3)$^{\#5}$/Mn/N(1)	88.61(8)
O(1)/Mn/O(3)$^{\#5}$	93.9(1)	O(2)/Mn/O(4)$^{\#3}$	87.07(8)	O(3)$^{\#5}$/Mn/N(2)$^{\#4}$	91.44(8)
O(1)/Mn/O(4)$^{\#3}$	143.98(8)	O(2)/Mn/N(1)	89.16(8)	O(4)$^{\#3}$/Mn/N(1)	90.24(8)
O(1)/Mn/N(1)	85.84(9)	O(2)/Mn/N(2)$^{\#4}$	90.98(8)	O(4)$^{\#3}$/Mn/N(2)$^{\#4}$	89.41(8)
O(1)/Mn/N(2)$^{\#4}$	94.53(9)	O(3)$^{\#5}$/Mn/O(4)$^{\#3}$	121.9(1)	N(1)/Mn/N(2)$^{\#4}$	179.62(7)
Torsion angles (°)					
C(11)–C(12)–C(13)–C(14)	–76.1(3)	C(12)–C(13)–C(14)–C(15)		176.5(3)	
C(13)–C(14)–C(15)–C(16)	176.1(3)	C(14)–C(15)–C(16)–C(17)		177.9(3)	
C(15)–C(16)–C(17)–C(18)	–63.8(4)				
Hydrogen bonding contacts					
D–H···A	D–H	H···A	D···A	D–H···A	
O(5)–H(A)···O(1)$^{\#6}$	0.91	2.17	3.066	166	
O(5)–H(B)···O(2)	0.86	2.26	3.121	179	

Symmetry codes: #1 = $x, y-1, z-1$; #2 = $x, y, z-1$; #3 = $-x+1, -y+1, -z+1$; #4 = $x, y+1, z+1$; #5 = $x, y, z+1$; #6 = $-x+2, -y+2, -z+2$.

Found: C, 51.31; N 8.03; H, 3.95%. IR (cm^{-1}): 3447w, 2961w, 2922w, 2883vw, 1585s, 1537vs, 1458s, 1448s, 1406s, 1359m, 1340m, 1302m, 1225w, 1209w, 1167vw, 1103vw, 1074m, 1007w, 918w, 885vw, 831m, 768m, 734vw, 687w, 619w, 594vw, 559vw, 517vw.

3.3. Preparation of $Zn(bpy)(C_6H_8O_4)$ (**3**)

3 was prepared analogously to **2** except using 0.073 g (0.50 mmol) adipic acid instead of 0.066 g (0.50 mmol) glutaric acid. The resulting colorless filtrate (pH 3.55) was stood at room temperature. A small amount of colorless prismatic crystals were grown by slow evaporation over several days (yield: less than 5% based on the initial $ZnSO_4 \cdot 7H_2O$ input). *Anal*. Calc. for $C_{16}H_{16}N_2O_4Zn$: C, 52.55; N, 7.66; H, 4.41. Found: C, 52.60; N 7.58; H, 4.28%. IR (cm^{-1}): 3443w, 2955w, 1597s, 1562s, 1487w, 1421m, 1337w, 1298w, 1217w, 1142w, 1065w, 1042w, 1003w, 922w, 818m, 800w, 760w, 735w, 665w, 631m, 471w.

3.4. Preparation of $Mn(bpy)(C_8H_{12}O_4) \cdot H_2O$ (**4**)

Dropwise addition of 1.0 ml (1 M) Na_2CO_3 to a stirred aqueous solution of $MnSO_4 \cdot H_2O$ (0.085 g, 0.50 mmol) in 5.0 ml H_2O produced a pale yellow precipitate of $Mn(OH)_{2-2x}(CO_3)_x \cdot yH_2O$, which was then centrifuged and washed with double-distilled water until no SO_4^{2-} anions were detectable in the supernatant. The precipitate was moved to a stirred suspension of suberic acid (0.087 g, 0.50 mmol) in 20.0 ml H_2O, and then a methanolic solution of 4,4′-bipyridine (0.078 g, 0.50 mmol) in 5.0 ml CH_3OH was added. The mixture was further stirred for 30 min and the insoluble solid was filtered off. The nearly colorless filtrate (pH 6.00) was allowed to stand at room temperature. Slow evaporation over several weeks afforded yellow crystals (Yield: ca. 50% based on the initial $MnSO_4 \cdot H_2O$ input). *Anal*. Calc. for $C_{18}H_{22}MnN_2O_5$: C, 53.82; N, 6.98; H, 5.48. Found: C, 53.77; N 6.99; H, 5.56%. IR (cm^{-1}): 3447m, 3040w, 2924s, 2851m, 1647m, 1601vs, 1568vs, 1555vs, 1489m, 1429vs, 1412vs, 1312s, 1244vw, 1219m, 1173w, 1132w, 1094vw, 1070m, 1045w, 1005w, 887w, 872w, 816vs, 745w, 735w, 691vw, 627vs, 575vw, 536vw, 492w, 419vw.

3.5. Crystal structure determination

The reflection intensities of **1**, **2**, **3** and **4** were collected at 293 K on a Bruker P4 diffractometer with graphite-monochromated Mo Kα radiation ($\lambda = 0.71073$ Å) using the ϑ–2ϑ scan technique. SHELXS-97 [32] and SHELXL-97 [33] programs were used for structure determination and refinements. The structures were solved with direct methods and refined with full-matrix least-squares techniques. Non-hydrogen atoms were refined anisotropically. Hydrogen atoms associated with carbon atoms were generated geometrically, while the water hydrogen atoms were located from the difference Fourier syntheses. Details of crystal data, collection and refinement of the complexes are

summarized in Table 1 and selected interatomic distances and bond angles are listed in Tables 2 and 3.

4. Supplementary data

Supplementary data for the four structures are available from the Cambridge Crystallographic Data Centre, 12, Union Road, Cambridge CB2 1EZ, UK (fax: +44 1223 336033; e-mail: deposit@ccdc.cam.ac.uk, or www: http://www.ccdc.cam.ac.uk), on request quoting the deposition Nos. CCDC 251786, CCDC 251787, CCDC 251788 and CCDC 251789.

Acknowledgments

The project was supported by the National Natural Science Foundation of China (20341006), the Expert Project of Key Basic Research of the Ministry of Science and Technology of China (2003CCA00800), the Zhejiang Provincial Natural Science Foundation (Z203067) and the Ningbo Science and Technology Bureau (2003A62011, 2003A61014, 2003A62026).

References

[1] (a) M. Ruben, J. Rojo, F.J. Romero-Salguero, L.H. Uppadine, J.-M. Lehn, Angew. Chem. Int. Ed. 43 (2004) 3644;
(b) S. Kitagawa, R. Kitaura, S.-I. Noro, Angew. Chem. Int. Ed. 43 (2004) 2334;
(c) L. Carlucci, G. Ciani, D. Proserpio, Coord. Chem. Rev. 246 (2003) 247;
(d) B. Moulton, M.J. Zaworotko, Chem. Rev. 101 (2001) 1629;
(e) P.J. Hagrman, D. Hagrman, J. Zubieta, Angew. Chem. Int. Ed. 38 (1999) 2638;
(f) S.R. Batten, R. Robson, Angew. Chem. Int. Ed. 37 (1998) 1460.
[2] (a) C. Janiak, J. Chem. Soc., Dalton Trans. (2003) 2781;
(b) S.L. James, Chem. Soc. Rev. 32 (2003) 276.
[3] (a) D. Maspoch, D. Ruiz-Molina, J. Veciana, J. Mater. Chem. 14 (2004) 2713;
(b) S.R. Batten, K.S. Murray, Coord. Chem. Rev. 246 (2003) 103.
[4] S.-L. Zheng, X.-M. Chen, Aust. J. Chem. 57 (2004) 703.
[5] H. Li, M. Eddaoudi, M. O'Keeffe, O.M. Yaghi, Nature 402 (1999) 276.
[6] S.S.-Y. Chui, S.M.-F. Lo, J.P.H. Charmant, A.G. Orpen, I.D. William, Science 283 (1999) 1148.
[7] C. Serre, F. Millange, C. Thouvenot, M. Noguès, G. Marsolier, D. Louër, G. Férey, J. Am. Chem. Soc. 124 (2002) 13519.
[8] Y.-Q. Zheng, H.-Z. Xie, J. Solid State Chem. 177 (2004) 1352.
[9] Y.-Q. Zheng, J. Sun, J. Solid State Chem. 172 (2003) 288.
[10] Y.-Q. Zheng, Z.-P. Kong, J. Solid State Chem. 166 (2002) 279.
[11] C.N.R. Rao, S. Natarajan, R. Vaidhyanathan, Angew. Chem. Int. Ed. 43 (2004) 1466.
[12] Y.-Q. Zheng, J.-L. Lin, Z.-P. Kong, Inorg. Chem. 43 (2004) 2590.
[13] Y.-Q. Zheng, Z.-P. Kong, Z. Anorg. Allg. Chem. 629 (2003) 1469.
[14] B. Rather, M.J. Zaworotko, Chem. Commun. (2003) 830.
[15] J.-M. Li, Y.-G. Zhang, J.-H. Chen, L. Rui, Q.-M. Wang, X.-T. Wu, Polyhedron 19 (2000) 1117.
[16] J. Li, H. Zeng, J. Chen, Q. Wang, X. Wu, Chem. Commun. (1997) 1213.
[17] Y. Rodríguez-Martín, M. Hernández-Molina, J. Sanchiz, C. Ruiz-Pérez, F. Lloret, M. Julve, J. Chem. Soc., Dalton Trans. (2003) 2359.
[18] Y. Rodriguez-Martín, C. Ruiz-Pérez, J. Sanchiz, F. Lloret, M. Julve, Inorg. Chim. Acta 318 (2001) 159.
[19] P.S. Mukherjee, S. Konar, E. Zangrando, T. Mallah, J. Ribas, N.R. Chaudhuri, Inorg. Chem. 42 (2003) 2695.
[20] T.K. Maji, S. Sain, G. Mostafa, T.-H. Lu, J. Ribas, M. Monfort, N.R. Chaudhuri, Inorg. Chem. 42 (2003) 709.
[21] S.-M. Ying, J.-G. Mao, Y.-Q. Sun, H.-Y. Zeng, Z.-C. Dong, Polyhedron 22 (2003) 3097.
[22] M.C. Etter, J.C. MacDonald, Acta Crystallogr. B46 (1990) 256.
[23] H. Schäfer, H.G. von Schnering, K.-J. Niehues, H.G. Nieder-Vahrenholz, Less-Common Met. 9 (1965) 95.
[24] Y. Kim, E. Lee, D.-Y. Jung, Chem. Mater. 13 (2001) 2684.
[25] D.-Y. Wei, Y.-Q. Zheng, J.-L. Lin, Z. Anorg. Allg. Chem. 628 (2002) 2005.
[26] M.T. Casey, M. McCann, M. Devereux, M. Curran, C. Cardin, M. Convery, V. Quillet, C. Hardivy, J. Chem. Soc., Chem. Commun. 22 (1994) 2643.
[27] M. McCann, J.F. Cronin, M. Devereux, G. Feruson, Polyhedron 14 (1995) 2379.
[28] Y.-Q. Zheng, J.-L. Lin, Z.-P. Kong, Polyhedron 22 (2003) 2699.
[29] Y.-Q. Zheng, Z.-P. Kong, Inorg. Chem. Commun. 6 (2003) 478.
[30] C. Janiak, J. Chem. Soc., Dalton Trans. (2000) 3885.
[31] E.A. Boudreaux, L.N. Mulay, Theory and Applications of Molecular Paramagnetism, Wiley, New York, 1976.
[32] G.M. Sheldrick, SHELXS-97, Programm zur Lösung von Kristallstrukturen, Göttingen, 1997.
[33] G.M. Sheldrick, SHELXL-97, Programm zur Verfeinerung von Kristallstrukturen, Göttingen, 1997.

Available online at www.sciencedirect.com
SCIENCE DIRECT®
Polyhedron 24 (2005) 407–412
POLYHEDRON
www.elsevier.com/locate/poly

Synthesis and properties of iron (II) quinoline-2-carboxylates, crystal structure of *trans*-diaquabis(quinoline-2-carboxylato)iron (II) bis(dichloromethane) solvate

Danuta Dobrzyńska [a,*], Lucjan B. Jerzykiewicz [b], Marek Duczmal [a]

[a] *Institute of Inorganic Chemistry and Metallurgy of Rare Elements, Wrocław University of Technology, Wybrzeże Wyspiańskiego 27, 50–370 Wrocław, Poland*
[b] *Faculty of Chemistry, University of Wrocław, Joliot–Curie 14, 50-383 Wrocław, Poland*

Received 1 October 2004; accepted 24 November 2004

Abstract

Two mononuclear iron complexes with the quinoline-2-carboxylate ion (quin-2-c ion) have been obtained by the reaction of iron powder with quinoline-2-carboxylic acid in dichloromethane. The compounds $[Fe(quin\text{-}2\text{-}c)_2]$ (**1**), $[Fe(quin\text{-}2\text{-}c)_2(H_2O)_2] \cdot 2CH_2Cl_2$ (**2**) and $[Fe(quin\text{-}2\text{-}c)_2(H_2O)_2] \cdot 2EtOH \cdot 2H_2O$ (**3**) have been investigated by IR and UV–Vis spectroscopy, magnetic susceptibility and field-dependent magnetization measurements. The structure of **2** has been characterised by X-ray diffraction. The 2D bilayered frameworks of **2** and **3** are constructed by extensive hydrogen bonding interactions between water and the organic ligand coordinated to iron (II). The magnetic properties of **2** and **3** were interpreted on the basis of a spin Hamiltonian that included axial and rhombic crystal field components. The weak antiferromagnetic (**2**) and ferromagnetic (**3**) interactions are evident in the low temperature data and possibly occur via strong hydrogen bonds.
© 2005 Published by Elsevier Ltd.

Keywords: Iron (II) complexes; Crystal structure; Magnetic properties; Hydrogen bonds

1. Introduction

The carboxylate group is very common in biological ligands and is often used as the functional group in preparing hybrid materials, ceramic precursors and in systems of catalytic activity. The carboxylate group offers a variety of coordination modes and many types of complexes are known [1]. Examples of catalytic applications of iron carboxylates are Gif [2] and Fenton [3] chemistry. In these experiments, several iron (II/III) picolinate species have been employed as oxidation agents. Some of them have been obtained in the synthetic route starting from the products of the reaction between metallic iron and picolinic acid in dichloromethane [4].

We decided to study the iron/quinoline-2-carboxylic acid/dichloromethane system. Quinoline-2-carboxylic acid, the biological ligand, is the close analogue of picolinic acid (pyridine-2-carboxylic acid) and provides the coordination set characteristic of the PQQ cofactor [5] found in quinoproteins. In our previous study, we have obtained and characterised the complexes of Fe(II) and Co(II) with quinoline-2-carboxylate ion [6]. The structures of quin-2-c complexes with Cu(II) [7], Rh(III) [8], Ga(III) [9], Mn(II) [10–13], Nd(III) [14], Au(III) [15], Fe(II) [16] have also been reported. Here, we describe the amorphous compound $Fe(quin\text{-}2\text{-}c)_2$ and the 2D supramolecular network created by extensive hydrogen

* Corresponding author. Tel.: +48 71 320 3909; fax: +48 71 328 4330.
E-mail address: danuta.dobrzynska@pwr.wroc.pl (D. Dobrzyńska).

0277-5387/$ - see front matter © 2005 Published by Elsevier Ltd.
doi:10.1016/j.poly.2004.11.026

bonding interactions in the crystal of Fe(quin-2-c)$_2$(H$_2$O)$_2$] · 2CH$_2$Cl$_2$. The influence of the system of strong intermolecular hydrogen bonds on the magnetic and spectral properties in **2** and **3** have been studied.

2. Experimental

2.1. Bis(quinoline-2-carboxylato)iron(II) (1)

This compound was obtained by the method described for iron (II) picolinate [4]. A mixture of quinoline-2-carboxylic acid (1 mmol) and Fe powder (0.55 mmol) in dichloromethane was left for three days. The dark-red solution thus obtained was filtered from any remaining Fe and the solvent was removed in a vacuum evaporator to obtain a red-black powder. Yield: 98%. *Anal*. Calc. for C$_{20}$H$_{12}$FeN$_2$O$_4$: C, 60.0; H, 3.0; N, 7.0. Found: C, 60.7; H, 3.3; N, 7.5%.

2.2. trans-Diaquabis(quinoline-2-carboxylato)iron(II) bis dichloromethane solvate (2)

This compound was obtained by the analogous method as for **1**, but with the addition of one drop of water to the reaction mixture. The deep red crystals of **2** which deposited on the wall of the flask were suitable for X-ray analysis. Yield: 95%. *Anal*. Calc. for C$_{22}$H$_{20}$Cl$_4$FeN$_2$O$_6$: C, 43.6; H, 3.3; N, 4.6. Found: C, 43.2; H, 3.1; N, 4.4%

2.3. trans-Diaquabis(quinoline-2-carboxylato)iron(II) bis ethanol bis water (3)

This compound was obtained by the method described by Okabe and Makino [16]. Yield: 94%.

2.4. Physical measurements

The solid-state electronic spectra of the powdered samples were measured in the diffuse reflectance mode on a Carry 500 Scan (Varian) UV–Vis–NIR spectrophotometer. IR spectra were recorded as KBr pellets or nujol mulls using Perkin–Elmer 1600 and Perkin–Elmer 180 spectrophotometers.

Magnetic susceptibility down to 1.9 K and magnetization up to 5 T were measured with a Quantum Design SQUID magnetometer. Diamagnetic corrections were calculated using Pascal's constants [17] and were found to be -215×10^{-6}, -335×10^{-6} and -335×10^{-6} for **1**, **2** and **3**, respectively.

2.5. X-ray diffraction data collection and refinement

Preliminary examinations were carried out on oscillation and Weissenberg photographs. Data collection were performed on a KUMA KM4 κ-axis diffractometer with graphite-monochromated Mo Kα radiation and with a CCD camera. The data were corrected for Lorentz, polarization and absorptions effects (analytical method) [18]. The structures were solved by direct methods and refined by the full-matrix least-squares method on all F^2 data using the SHELXTL (version 5.10) program [19]. Carbon bonded hydrogen atoms were included in calculated positions and refined in the riding mode. Other hydrogen atoms were located in a difference map and refined without any restraints. The crystal data and structure refinement details for **2** are given in Table 1.

Table 1
Crystallographic data and structure refinement for **2**

Formula	C$_{20}$H$_{12}$N$_2$O$_4$Fe
Formula weight	606.04
Crystal system	monoclinic
Space group	$P2_1/c$
Unit cell dimensions	
a (Å)	13.022(3)
b (Å)	12.779(4)
c (Å)	7.212(3)
β (°)	90.39(4)
V (Å^3)	1200.1(7)
Z	2
D_{calc} (g cm^{-1})	1.677
Temperature (K)	100.0(5)
Crystal size (mm)	0.3 × 0.2 × 0.2
F(0 0 0)	616
θ Range for data collection	3.51–28.51
Reflections measured	8114
Unique reflections	2813
R_{int}	0.776
Godness-of-fit	1.121
R_1, wR_2 [$I > 2\sigma(I)$]	0.0468, 0.0671
R_1, wR_2 (all data)	0.1178, 0.1178

3. Results and discussion

3.1. Crystal structure

The studied compounds, Fe(quin-2c)$_2$ (**1**), [Fe(quin-2c)$_2$(H$_2$O)$_2$] · 2CH$_2$Cl$_2$ (**2**) and [Fe(quin-2-c)$_2$(H$_2$O)$_2$] · 2EtOH · 2H$_2$O (**3**), have been obtained under aerobic conditions. The solid complexes are very stable in air, whereas **1**, dissolved in dichloromethane, undergoes oxidation in a few days and yields yellow crystals of the iron (III) complex, which are now under study.

The structure of the Fe(quin-2-c)$_2$(H$_2$O)$_2$ molecule is shown in Fig. 1, the packing in the crystals of **2** and **3** (along with the hydrogen bond system) is shown in Fig. 2. The 2D networks of hydrogen bonds connecting the iron centers in **2** and **3** are presented in Fig. 3. Selected bond lengths and angles are listed in Table 2. The hydrogen bonding parameters for **2** are collected in Table 3.

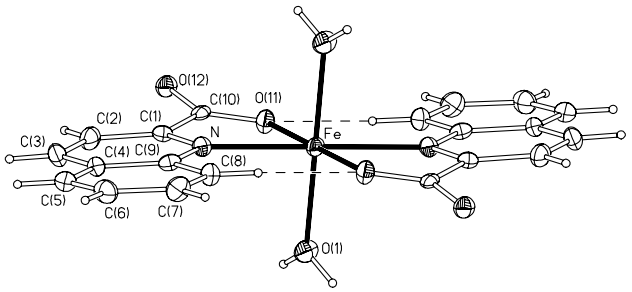


Fig. 1. The molecular structure of **2** with the atom numbering scheme. The displacement ellipsoids are drawn at the 50% probability level.

Table 2
Selected bond lengths (Å) and angles (°) for **2**

Bond distances			
Fe–O(1)	2.087(3)	O(11)–C(10)	1.256(5)
Fe–O(11)	2.115(3)	O(12)–C(10)	1.258(5)
Fe–N	2.254(3)	C(1)–C(10)	1.517(6)
Bond angles			
O(1)–Fe–O(11)(a)	90.65(13)	O(11)–Fe–N	75.92(11)
O(1)–Fe–O(11)	89.35(13)	O(11)–Fe–N(a)	104.08(12)
O(1)–Fe–N(a)	91.65(13)	O(11)–C(10)–O(12)	124.9(4)
O(1)–Fe–N	88.37(13)		

(a) $-x$, $-y$, $-z$.

Table 3
Hydrogen bonds for **2** [Å and °]

D–H···A	*d*(D–H)	*d*(H···A)	*d*(D···A)	∠(DHA)
O(1)–H(1A)···O(12)$^{(i)}$	0.71	2.00	2.7095	172.00
O(1)–H(1B)···O(12)$^{(ii)}$	0.83	1.99	2.8067	168.00
C(8)–H(8)···O(11)$^{(iii)}$	0.93	2.29	3.1721	158.00
C(11)–H(11A)···O(12)$^{(iv)}$	0.97	2.46	3.1168	124.00
C(5)–H(5)···Cl(1)$^{(v)}$	0.93	2.98	3.734	139.00

Symmetry transformations used to generate equivalent atoms: (i) $-x+1$, $-y$, $-z+2$; (ii) $-x+1$, $y-1/2$, $-z+3/2$; (iii) $-x+1$, $-y$, $-z+1$; (iv) $-x+1$, $y+1/2$, $-z+3/2$; (v) x, y, $z+1$.

The crystal of **2** consists of neutral molecules of the iron (II) complex, $[Fe(quin\text{-}2\text{-}c)_2(H_2O)_2]$, and of molecules of dichloromethane. The iron (II) ion is six coordinated with a N_2O_4 donor set. The quin-2-c ions bind to iron in a chelate mode by two *trans* carboxylate O atoms and two *trans* quinoline N atoms, in the equatorial plane. Two water molecules complete the axial positions of the distorted octahedron around the ferrous ion. The Fe(II) ion lies on an inversion centre. Okabe and Makino [16] obtained $[Fe(quin\text{-}2\text{-}c)_2(H_2O)_2] \cdot 2EtOH \cdot 2H_2O$ (**3**) from the ethanolic solution of Hquin-2-c and iron(II) sulfate. Compound **3** comprises a complex molecule almost identical to that found in **2**. The coordination mode and the geometry of the $Fe(quin\text{-}2\text{-}c)_2(H_2O)_2$ moiety is the same in **2** and **3**. Small differences are observed for the coordination bonds length, for example, the Fe–N distance in **2** is equal to 2.254(3) Å, whereas the length of the respective bond found in **3** is 2.270(1) Å. Both values are characteristic for high spin ferrous complexes [20]. The iron-carboxylate oxygen distances in **2** and **3** are very close to the medium value of this bond

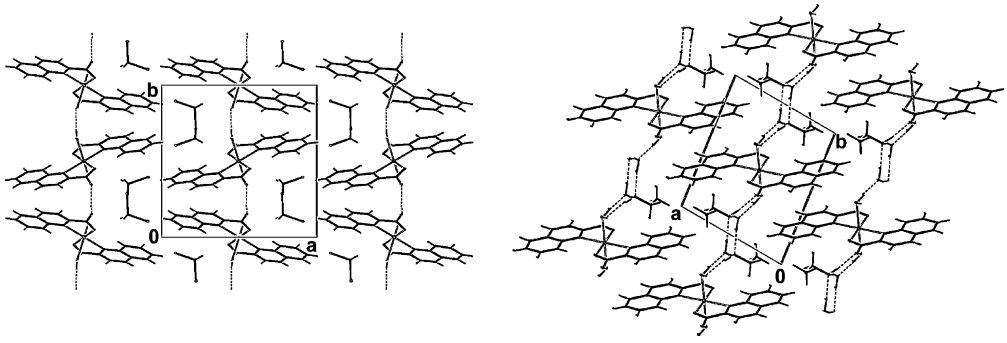


Fig. 2. Projections of the structures **2** (left) and **3** (right) down the *c*-axis, showing the layers comprising of iron ions.

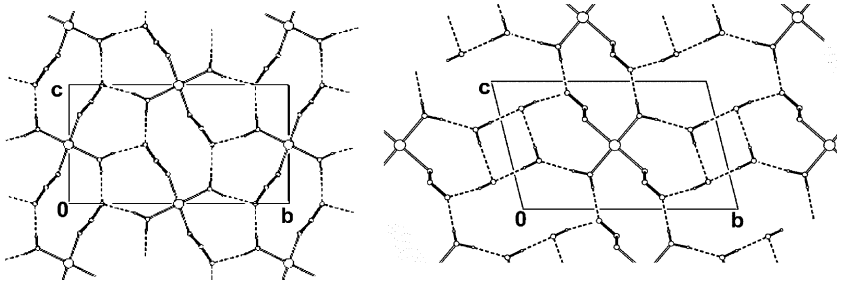


Fig. 3. 2D layers in **2** (left) and **3** (right) constructed by hydrogen bonding interactions between coordination centers (quinoline rings, dichloromethane and C_2H_5 groups of ethanol are omitted for clarity).

(2.10 Å) estimated by Hocking for 68 monodentately coordinated high spin iron (II) carboxylate complexes [21]. However, the structural characteristics of the carboxylate groups in **2** and **3** are very different from the medium parameters estimated for terminal ferrous carboxylates [21,22]. The distances C(10)–O(11) and C(10)–O(12) are surprisingly almost equal (1.257(5) and 1.258(5) Å, respectively) which is mostly observed for the carboxylate group acting in a bridging mode [22].

The organisation of the crystals of **2** and **3** is also very similar, as shown in Fig. 2. The molecules of the complex in **2** and **3** are connected by extensive hydrogen bonding interactions (Table 3). In **2**, each water coordinated to iron makes two strong hydrogen bridges with carbonyl oxygen atoms from the carboxylate group of neighbouring molecules of the complex. In **3**, five strong hydrogen bonds involving the coordinated and lattice water molecules as well as ethanol molecules have been found. The hydrogen bonding networks in **2** and **3** create the 2D, inorganic layers, Fig. 3. The quinoline parts of the quin-2-c ligand form the organic layers in both compounds, in **2** the dichloromethane molecules are also packed in this layer, in **3** the C_2H_5 group of ethanol is located in the organic layer. The organic layers and layers of iron complexes are packed alternately. The shortest Fe–Fe distance within a layer in **2** is equal to 7.212 Å, in the crystal of **3** the closest iron ions are separated by 7.299 Å. In the crystal of **2**, the dichloromethane molecules are involved in hydrogen bonds of C–H···Cl type (Table 3). The weak intramolecular C–H···O interaction (C(8)–H(8)···O(12)^{iii}) stabilize the equatorial plane of the complex in **2** and **3**.

3.2. Spectral and magnetic data

The selected frequencies observed in the IR spectra of **1**, **2**, **3**, Fe(quin-2-c)$_2$(EtOH)$_2$ and of Naquin-2-c are collected in Table 4, together with their assignments. The values of $\Delta\nu$ [$\Delta\nu = \nu_{as}(COO) - \nu_s(COO)$] found for **2** and **3** are equal to 220 and 235 cm^{-1}, respectively. They are smaller than expected for the monodentately coordinated carboxylate group [23]. Such low $\Delta\nu$ values result from the strong hydrogen bonds between the hydroxyl group or water molecules and the carboxylate oxygens. A similar effect was reported earlier for other complexes [24]. The coordination mode in those compounds can be regarded as a "pseudo bridging" arrangement. It is interesting to note that in the case of **1**, $\Delta\nu$ equals 275 cm^{-1} and is in the normal range for terminal carboxylates. On this basis the carboxylates in **1** can be assumed to be monodentately bonded and not involved in any hydrogen bonding. The comparison of the infrared spectra of **1**, **2** and **3** as well as that of [Fe(quin-2-c)$_2$(EtOH)$_2$] [5] and literature data [25] allowed the assignment of the stretching vibrations of coordination bonds in the discussed compounds as shown in Table 4.

The electronic spectra of **1**, **2** and **3** are very similar and feature two bands, representing the transitions to the ^5E_g state, typical of a Fe(II) high-spin chromophore (Table 5). The intense bands with maxima located near 18 000 cm^{-1} are assigned as $t_{2g} \rightarrow \pi^*$ [26].

The magnetic susceptibility of **2** obeys the Curie–Weiss (CW) law above ca. 20 K with the moment $\mu = 5.66\mu_B$ and the Weiss constant $\theta = -1.8$ K, $\mu = 2.828\sqrt{\chi(T-\theta)}$. The effective magnetic moment $\mu_{eff} = 2.828\sqrt{\chi T}$ is almost constant in this temperature range and decreases quickly below it (Fig. 4). The susceptibility of **3** fulfills the CW equation above ca. 100 K with $\mu = 5.30\mu_B$ and $\theta = 8.6$ K. The effective moment increases with temperature in the low temperature range, reaches the rounded maximum around 22 K and then the shallow minimum around 130 K.

While the compounds **2** and **3** may be considered as high-spin Fe(II) complexes, the magnetic properties of **1** cannot be unambiguously categorized. The susceptibility of **1** is low – only 7.7×10^{-3} cm^3 mol^{-1} at 300 K compared to 13.5×10^{-3} and 12.9×10^{-3} for **2** and **3**, respectively. The magnetization of the three compounds also shows similar differences. A more detailed analysis of the magnetic properties of **1** must be postponed until the crystal structure of the compound will be solved.

The shortest Fe–Fe distances in **2** and **3** are greater than 7 Å (7.212 Å for **2** and 7.229 Å for **3**). Thus, their magnetic properties may be calculated using the Hamil-

Table 5
Electronic spectra of **1**, **2** and **3** [cm^{-1}]

Compound	$^5E_g \leftarrow {}^5T_{2g}$	Charge transfer
1	8910, 11 610	17 980
2	9100, 11 510	18 560
3	9500	17 900

Table 4
Selected IR frequencies [cm^{-1}] and $\Delta\nu$ values of **1**, **2**, **3**, [Fe(quin-2-c)$_2$(EtOH)$_2$] and Naquin-2-c (w, water; a, alcohol and carb, carboxylate)

Compound	ν_{as}(COO)	ν_s(COO)	$\Delta\nu$	ν(Fe–O$_{carb}$)	ν(Fe–N)	(Fe–O$_{w,a}$)
1	1652	1377	275	403	227	372
2	1619	1399	220	400	236	369
3	1610	1375	235	399	232	373
[Fe(quin-2-c)$_2$(EtOH)$_2$]	1628	1395	233	398	239	387
Naquin-2-c	1647	1393	254			

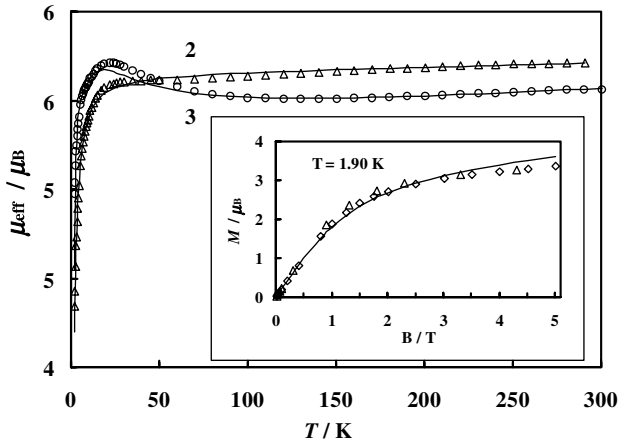


Fig. 4. Effective magnetic moments of **2** and **3**. Inset: Magnetization of **2** as a function of magnetic induction (diamonds – increasing field, triangles – decreasing field). The solid lines are calculated with the parameters quoted in the supplementary material.

tonian of Ginsberg et al. [27], containing the Zeeman effect, crystal field and weak exchange interactions in the molecular field approximation. Details of the calculations are included in the supplementary material and the results are presented in Fig. 4.

The coordination of the Fe(II) ion in **3** is almost identical to that in **2**, but their magnetic properties are quite different. The maximum of the effective moment of **3**, around 22 K, cannot be explained on the ground of pure crystal field theory. Similar effects usually result from ferromagnetic exchange interactions [28]. The theoretical calculations of the magnetic susceptibilities of **2** and **3** seems to justify such an assumption: when the CF interactions in both compounds are comparable ($D = 2.8$ and 3.2 cm^{-1} and $E = -0.3$ and -0.8 cm^{-1} for **2** and **3**, respectively), the exchange parameters zJ' are different (-0.1 and $+0.88$ cm^{-1}, respectively).

The contribution of H-bonds to weak indirect exchange is well documented [29,30]. It has been also suggested that hydrogen bonds can transmit strong exchange interactions, which may result in long-range magnetic ordering [29,31,32]. The former type of interactions were found in compounds **2** and **3**. The monomeric units in **2** and **3** are connected by hydrogen bonds forming extended 2D structures. The bond net is particularly compact in **3**, whereas the interactions involving dichloromethane molecules in **2** are weak. This may explain the differences between the exchange parameters zJ' for both compounds.

4. Conclusions

Two new iron (II) complexes, **1** and **2**, with quinoline-2-carboxylate ion have been obtained in the direct reaction between metallic iron and quinoline-2carboxylic acid in dichloromethane. A spectral and magnetic study has been performed for **1**, **2** and **3**, and the crystal structure of **2** has been found. The high spin state of the ferrous ions in **1**, **2** and **3** has been confirmed by UV–Vis and magnetic data. The strong intermolecular hydrogen bridges found in **2** and **3** create 2D inorganic networks and strongly affect the vibrational characteristic of the carboxylate groups. They are also responsible for the weak, indirect magnetic exchange interactions observed in **2** and **3** at low temperatures.

Appendix A. Supplementary data

Crystallographic data for the structure reported in this paper have been deposited with the Cambridge Crystallographic Data Center as supplementary publication no. CCDC 234055. Copies of the data can be obtained free of charge from The CCDC, 12 Union Road, Cambridge CB2 1EZ, UK (fax: (44) 1223-336-033; e-mail: deposit@ccdc.cam.ac.uk or www: http://www.ccdc.cam.ac.uk). Supplementary data associated with this article can be found, in the online version at doi:10.1016/j.poly.2004.11.026.

References

[1] C. Oldham, Carboxylates, Squarates and Related Species, in: Wilkinson (Ed.), Comprehensive Coordination Chemistry, Pergamon Press, Oxford, 1987.
[2] R. Burton, B. Hu, D.K. Taylor, R.U. Royas Wahl, J. Chem. Soc., Perkin Trans. (1996) 1031.
[3] D.T. Sawyer, A. Sobkowiak, T. Matsushita, Acc. Chem. Res. 29 (1996) 409.
[4] S. Kiani, A. Tapper, R.J. Staples, P. Stavropoulos, J. Am. Chem. Soc. 122 (2000) 7503.
[5] O. Geiger, H. Görisch, Biochem. J. 261 (1989) 415.
[6] D. Dobrzyńska, J.B. Jerzykiewicz, M. Duczmal, K. Drabent, J. Warchulska, Eur. J. Inorg. Chem. (2004) 110.
[7] H.M. Haendler, Acta Crystallogr., Sect. C 42 (1986) 147.
[8] M. Cano, J.V. Heras, M.A. Lobo, E. Pinilla, M.A. Monge, Polyhedron 13 (1994) 1563.
[9] Wei Li, M.M. Olmstead, D. Miggins, R.H. Fish, Inorg. Chem. 35 (1996) 51.
[10] D. Dobrzyńska, L.B. Jerzykiewicz, J. Am. Chem. Soc. 126 (2004) 11118.
[11] M.A.S. Goher, F.A. Mautner, Polyhedron 12 (1993) 1863.
[12] H.M. Haendler, Acta Crystallogr., Sect. C 52 (1996) 801.
[13] N. Okabe, M. Koizumi, Acta Crystallogr., Sect. C 53 (1997) 852.
[14] P. Starynowicz, Acta Crystallogr., Sect. C 46 (1990) 2068.
[15] M.A.S. Goher, A.K. Hafez, Ru-ji Wang, Xiaoming Chen, T.C.W. Mak, Aust. J. Chem. 47 (1994) 1423.
[16] N. Okabe, T. Makino, Acta Crystallogr., Sect. C 54 (1998) 1279.
[17] A. Weiss, H. Witte, Magnetochemie, Verlag Chemie, Weinheim, 1973.
[18] Kuma Diffraction. Kuma KM4 CCD System Software. User's Guide, Version 1.166, Kuma Diffraction, Wrocław, Poland, 1995–2000.

[19] SHELXTL, v. 5.10; Bruker Analytical X-Ray: Madison, WI, 1997.
[20] Y. Zang, J. Kim, Y. Dong, E.C. Wilkinson, E.P. Appelman, L. Que Jr., J. Am. Chem. Soc. 119 (1997) 4197.
[21] R.K. Hocking, T.W. Hambley, Inorg. Chem. 42 (2003) 2833.
[22] A.G. Orpen, L. Brammer, F.H. Allen, O. Kennard, R. Taylor, D.G. Watson, J. Chem. Soc., Dalton Trans. (1989), Supplement.
[23] G.B. Deacon, R.J. Phillips, Coord. Chem. Rev. 33 (1980) 227.
[24] S.T. Warzeska, F. Micciche, M.C. Mimmi, E. Bouwman, H. Kooijman, A.L. Spek, J. Reedijk, J. Chem. Soc., Dalton Trans. (2001) 3507.
[25] K. Nakamoto, Infrared and Raman Spectra of Inorganic and Coordination Compounds, Wiley, New York, 1997.
[26] A.B.P. Lever, Inorganic Electronic Spectroscopy, Elsevier, Amsterdam, 1984.
[27] A.P. Ginsberg, R.L. Martin, R.W. Brookes, R.C. Sherwood, Inorg. Chem. 11 (1972) 2284.
[28] O. Kahn, Molecular Magnetism, VCH, New York, 1993.
[29] C.P. Berlinguette, J.R. Galán-Mascarós, K.R. Dunbar, Inorg. Chem. 42 (2003) 3416.
[30] A.C. Rizzi, C.D. Brondino, R. Calvo, R. Baggio, M.T. Garland, R.E. Rapp, Inorg. Chem. 42 (2003) 4409.
[31] K. Van Langenberg, S.R. Batten, K.J. Berry, D.C.R. Hockless, B. Moubaraki, K.S. Murray, Inorg. Chem. 36 (1997) 5006.
[32] B.R. Müller, G. Leibeling, E.-G. Jäger, Chem. Phys. Lett. 319 (2000) 368.

Available online at www.sciencedirect.com
SCIENCE DIRECT®
Polyhedron 24 (2005) 413–418
POLYHEDRON
www.elsevier.com/locate/poly

New silver(I) coordination architectures of pyridyl dithioether ligands with Ag···Ag, Ag···O, Ag···S and C–H···F weak interactions

Ya-Bo Xie [a,b], Jian-Rong Li [a], Xian-He Bu [a,*]

[a] Department of Chemistry, Nankai University, No. 94, Weijin Road, Tianjin 300071, China
[b] College of Environmental and Energy Engineering, Beijing University of Technology, Beijing 100022, China

Received 12 October 2004; accepted 30 November 2004

Abstract

In our continuous efforts to investigate the coordination architectures of silver(I) complexes with thioethers, we report herein the syntheses and crystal structures of three new silver(I) complexes, a trinuclear complex $[Ag_3L^2_2(NO_3)_2](NO_3)(CH_3CN)$ **2** and two one-dimensional chain complexes $[Ag_2L^1(BF_4)_2(CH_3CN)_2]_\infty$ **1** and $[Ag_2L^3(NO_3)_2]_\infty$ **3**, where L^1, L^2 and L^3 are three structurally related pyridyl dithioether ligands: 1,4-bis(2-pyridylthio)butane (L^1), 1,5-bis(2-pyridylthio)pentane (L^2) and 1,6-bis(2-pyridylthio)hexane (L^3). The structural differences of **1**, **2** and **3** show the influences of the ligand spacers on the coordination modes of the terminal pyridylsulfanyl groups and the coordination geometries of the Ag^I ion. There exist Ag···Ag contacts in the three complexes, C–H···F weak hydrogen bonds in **1**, Ag···S weak coordination bonds in **2** and Ag···O weak interactions in **2** and **3**, and these weak interactions link the low-dimensional complexes into high-dimensional supramolecular structures and further stabilize the crystal structures in the solid states.
© 2005 Elsevier Ltd. All rights reserved.

Keywords: Crystal structure; Pyridyl dithioether; Self-assembly; Silver(I) complexes; Weak interactions

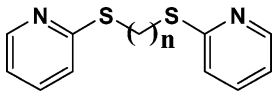
1. Introduction

The self-assembly of supramolecular coordination polymers is the result of combinations of various forces including strong and directional interactions (for example metal–ligand coordination) [1–4] and weak interactions such as π–π stacking [5,6], halogen–halogen [7,8] and C–H···X (X = O, N, Cl or I, etc.) contacts [9,10]. The self-assembly process of metal complexes is quite complicated and the understanding of the factors that affect the process between labile metal ions and flexible multidentate ligands is an interesting and challenging topic in supramolecular and coordination chemistry. Due to the conformational freedom, flexible multidentate bridging ligands show interesting coordination chemistry with transition metal ions and have great possibilities for generating novel coordination frameworks [11,12]. In addition, the flexible bridging ligands are very sensitive to changes of conditions, so they are suitable candidates for investigating the roles of various factors such as solvents, counter anions and weak supramolecular interactions in the aggregation of molecular architectures.

In our previous works, dithioethers as flexible multidentate ligands have been successfully used to construct various structures of complexes including discrete molecules, 1-D, or 2-D network architectures [13–20]. We report herein the synthesis and characterization of three

* Corresponding author. Tel.: +86 22 23502809; fax: +86 22 23502458.
E-mail address: buxh@nankai.edu.cn (X.-H. Bu).

0277-5387/$ - see front matter © 2005 Elsevier Ltd. All rights reserved.
doi:10.1016/j.poly.2004.11.027



L^{n-3} (n =4~6)

Chart 1.

Ag^{I} complexes with three flexible multidentate pyridyl dithioether ligands that are closely related in structure: 1,4-bis(2-pyridylthio)butane ($\mathbf{L^1}$), 1,5-bis(2-pyridylthio) pentane ($\mathbf{L^2}$) and 1,6-bis(2-pyridylthio)hexane ($\mathbf{L^3}$) (see Chart 1), and the roles of weak interactions in the formation of coordination architectures have also been discussed.

2. Experimental

2.1. Materials and general methods

All the reagents for syntheses were commercially available and employed without further purification or purified by standard methods prior to use. Elemental analyses were performed on a Perkin–Elemer 240C analyzer and IR spectra were measured on a 170SX (Nicolet) FT-IR spectrometer with KBr pellets. The three ligands, $\mathbf{L^1} \sim \mathbf{L^3}$, were prepared according to the reported procedures [17].

2.2. Preparation of complexes

2.2.1. $[Ag_2\mathbf{L^1}(BF_4)_2(CH_3CN)_2]_\infty$ (1)

A solution of $AgBF_4 \cdot H_2O$ (21 mg, 0.1 mmol) in CH_3CN (10 mL) was carefully layered on top of a solution of $\mathbf{L^1}$ (28 mg, 0.1 mmol) in $CHCl_3$ (10 mL) in a test-tube. After three days at room temperature, colorless single crystals appeared at the boundary between CH_3CN and $CHCl_3$ (Yield: 25%). IR (KBr pellets, cm^{-1}): 2154w, 1629w, 1581s, 1554s, 1456s, 1416s, 1401m, 1311m, 1127vs, 1043vs, 985s, 766s, 733m, 710m. *Anal*. Calc. for $C_9H_{11}AgBF_4N_2S$: C, 28.91; H, 2.97; N, 7.49. Found: C, 28.31; H, 3.02; N, 7.56%.

2.2.2. $[Ag_3\mathbf{L^2_2}(NO_3)_2](NO_3)(CH_3CN)$ (2)

A solution of $AgNO_3$ (17 mg, 0.1 mmol) in CH_3CN (3 mL) was slowly added to a solution of $\mathbf{L^2}$ (30 mg, 0.1 mmol) in $CHCl_3$ (3 mL). Slow diffusion of ether into the resulting solution yielded colorless single crystals **2** suitable for X-ray analysis (Yield: 34%). IR (KBr pellets, cm^{-1}): 2131w, 1629w, 1578s, 1556m, 1454s, 1414vs, 1384vs, 1124s, 1088m, 1043w, 825w, 757s, 724m. *Anal*. Calc. for $C_{32}H_{39}Ag_3N_8O_9S_4$: C, 33.97; H, 3.47; N, 9.90. Found: C, 33.49; H, 3.23; N, 9.68%.

2.2.3. $[Ag_2\mathbf{L^3}(NO_3)_2]_\infty$ (3)

Colorless crystals of **3** suitable for X-ray analysis (Yield: 31%) were obtained by a similar method as described for **2**. IR (KBr pellets, cm^{-1}): 1578m, 1556w, 1454m, 1414s, 1383vs, 1124m, 757m. *Anal*. Calc. for $C_{16}H_{20}Ag_2N_4O_6S_2$: C, 29.83; H, 3.13; N, 8.70. Found: C, 30.01; H, 3.26; N, 8.51%.

2.3. X-ray crystallographic studies of complexes 1–3

Single-crystal X-ray diffraction measurements were carried out on a Bruker Smart 1000 CCD diffractometer equipped with a graphite crystal monochromator situated in the incident beam for data collection at room temperature. The determination of unit cell parameters and data collections were performed with Mo-Kα radiation ($\lambda = 0.71073$ Å). Unit cell dimensions were obtained with least-squares refinements and all structures were solved by direct methods. Silver atoms in each complex were located from *E*-maps. The other non-hydrogen atoms were located by successive difference Fourier syntheses. The final refinement was performed by full-matrix least-squares methods with anisotropic thermal parameters for non-hydrogen atoms on F^2. The hydrogen atoms were added theoretically and riding on the concerned atoms. In **1**, the BF_4^- ion is disordered and was refined in the occupation ratio of 7:3 in two different positions based on fixing one B–F bond. One C atom of the coordinated CH_3CN molecule is also disordered and refined in two positions with a 1:1 occupation ratio. Crystallographic data and experimental details for structural analyses are summarized in Table 1.

3. Results and discussion

The crystal structure of $[Ag_2\mathbf{L^1}(BF_4)_2(CH_3CN)_2]_\infty$ (**1**) features a one-dimensional (1-D) chain. Fig. 1(a) shows the structure with the atom labelling, and selected bond lengths and angles are listed in Table 2. Each Ag^{I} center is four-coordinated by an N and an S atom from distinct $\mathbf{L^1}$ ligands, an N atom of CH_3CN and an F atom from BF_4^-, showing a distorted tetrahedral coordination geometry. The Ag–N bonds fall in the expected ranges for such coordination bonds [21], while the Ag–S bond is slightly longer than those in the Ag^{I} complexes with thioether ligands [13,15]. The ligands adopt an *N*,*N*,*S*,*S*-tetradentate *anti*-bridging mode to coordinate to the Ag^{I} centers, resulting in an infinite chain. This kind of coordination mode of the ligand is also found in our reported complexes $\{[Ag_2(\mathbf{L^1})_2](ClO_4)_2(CHCl_3)\}_\infty$, $\{[Ag\mathbf{L^1}](ClO_4)(C_3H_6O)\}_\infty$, $\{[Ag_2\mathbf{L^1}](NO_3)_2\}_\infty$ and $[Ag_2\mathbf{L^1}(CF_3SO_3)_2]_\infty$ [17], but is different to that in $\{[Ag\mathbf{L^1}](ClO_4)\}_\infty$ and $\{[Ag\mathbf{L^1}(CH_3CN)](PF_6)\}_\infty$ [19]. Two pyridylsulfanyl groups from two $\mathbf{L^1}$ ligands bridge two Ag^{I} atoms to

Table 1
Crystal data and details of measurements for compounds **1**–**3**

Complex	**1**	**2**	**3**
Formula	$C_9H_{11}AgBF_4N_2S$	$C_{32}H_{39}Ag_3N_8O_9S_4$	$C_{16}H_{20}Ag_2N_4O_6S_2$
Formula weight	373.94	1131.56	644.22
T (K)	293(2)	293(2)	293(2)
System	monoclinic	orthorhombic	monoclinic
Space group	$P2(1)/n$	$Pnma$ $P2(1)/c$	$P2(1)/c$
Unit cell dimensions			
a (Å)	7.378(8)	19.858(7)	7.152(3)
b (Å)	18.86(2)	14.322(5)	15.886(6)
c (Å)	10.22(1)	14.554(5)	9.563(4)
β (°)	107.66(2)		102.966(7)
V (Å^3)	1355(3)	4139(3)	1058.8(7)
D_c (g/cm^3)	1.832	1.816	2.021
Z	4	4	2
Minimum and maximum transmission	0.6344/0.7314	0.7316/0.6807	0.6802/0.5731
μ (Mo Kα) (mm^{-1})	1.669	1.667	2.088
Measured reflections	5417	13 820	4312
Unique reflections	2359	3753	1882
R^a/wR^b	0.0848/0.1893	0.0565/0.1251	0.0287/0.0649

[a] $R = \Sigma(||F_o| - |F_c||)/\Sigma|F_o|$.

[b] $wR = \left[\sum w(|F_o|^2 - |F_c|^2)^2 \Big/ \sum w(F_o^2)^2\right]^{1/2}$.

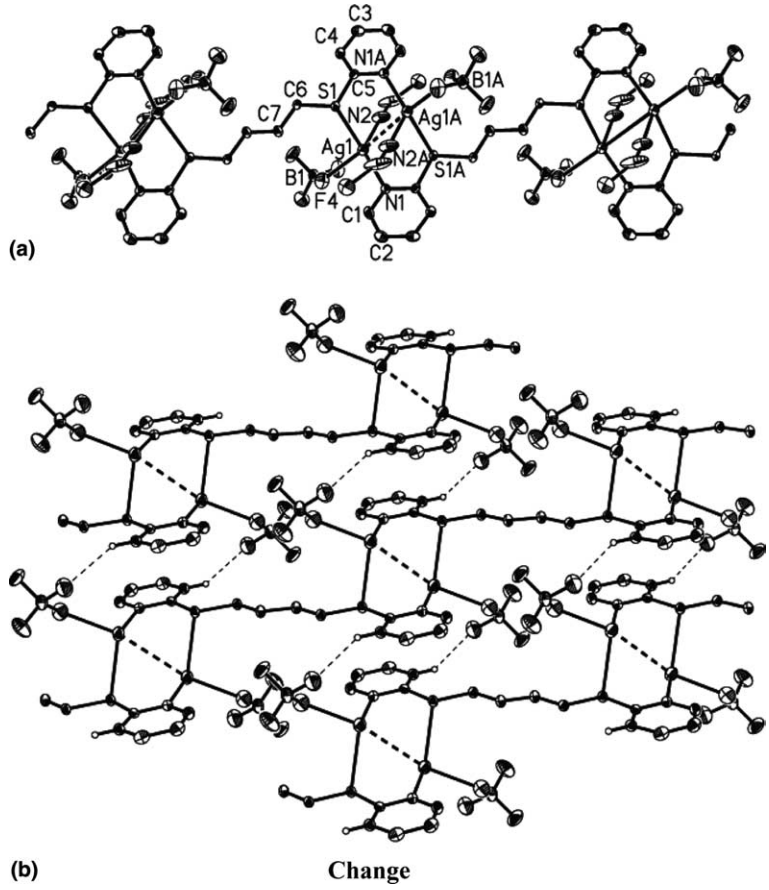


Fig. 1. (a) Perspective view of the 1-D chain of **1** (symmetry code A: $-x + 2$, $-y$, $-z + 2$), and (b) the quasi 2-D network formed by the weak C–H···F hydrogen bonds.

form an 8-membered ring with an inversion center, adopting a chair configuration with two pyridine rings parallel to each other. In the 8-membered ring, the Ag···Ag distance of 3.344(3) Å is slightly shorter than the summed van der Waals radii of two silver atoms (3.44 Å) [22], indicating the existence of some weak

Table 2
Selected bond lengths (Å) and angles (°) for complexes **1**–**3**

1			
Bond lengths			
Ag(1)–N(1)	2.252(4)	Ag(1)–S(1)	2.669(3)
Ag(1)–N(2)	2.334(6)	Ag(1)–Ag(1A)	3.344(3)
Ag(1)–F(4)	2.448(6)		
Bond angles			
N(1)–Ag(1)–N(2)	132.0(1)	N(2)–Ag(1)–F(4)	110.8(2)
N(1)–Ag(1)–F(4)	96.2(1)	N(2)–Ag(1)–S(1)	97.6(1)
N(1)–Ag(1)–S(1)	113.9(1)	F(4)–Ag(1)–S(1)	104.0(1)
2			
Bond lengths			
Ag(1)–N(1)	2.194(6)	Ag(2)–N(2)	2.180(6)
Ag(2)–Ag(3)	3.176(2)	Ag(3)–O(7)	2.516(8)
Ag(3)–O(4)	2.560(8)	Ag(3)–S(2)	2.681(2)
Bond angles			
N(1A)–Ag(1)–N(1)	169.9(3)	N(2A)–Ag(2)–N(2)	175.2(3)
N(2)–Ag(2)–Ag(3)	88.1(2)	O(7A)–Ag(3)–O(7)	47.9(3)
O(7A)–Ag(3)–O(4)	120.8(3)	O(7)–Ag(3)–O(4)	100.2(3)
O(4)–Ag(3)–O(4A)	48.6(3)	O(7)–Ag(3)–S(2)	97.3(2)
O(7)–Ag(3)–S(2A)	132.5(2)	O(4)–Ag(3)–S(2A)	127.1(2)
O(4)–Ag(3)–S(2)	92.7(2)	S(2A)–Ag(3)–S(2)	84.9(1)
O(7)–Ag(3)–Ag(2)	71.5(2)	O(4)–Ag(3)–Ag(2)	155.4(2)
3			
Bond lengths			
Ag(1)–N(1)	2.220(3)	Ag(1)–O(1)	2.474(3)
Ag(1)–O(2)	2.569(3)	Ag(1)–S(1)	2.591(1)
Ag(1)–Ag(1A)	3.123(1)		
Bond angles			
N(1)–Ag(1)–O(1)	139.9(1)	N(1)–Ag(1)–O(2)	119.1(1)
O(1)–Ag(1)–O(2)	49.92(9)	N(1)–Ag(1)–S(1)	132.01(8)
O(1)–Ag(1)–S(1)	87.68(8)	O(2)–Ag(1)–S(1)	94.90(8)
N(1)–Ag(1)–Ag(1A)	85.37(7)	O(1)–Ag(1)–Ag(1A)	120.63(7)
O(2)–Ag(1)–Ag(1A)	77.58(7)	S(1)–Ag(1)–Ag(1A)	69.09(2)

Symmetry codes for **1**, A: $-x+2$, $-y$, $-z+2$, $-z+2$; for **2**, A: x, $-y+1/2$, z; for **3**, A: $-x+1$, $-y+2$, $-z+2$.

Ag···Ag interaction [23–25], and such metal–metal contacts are also found in other d^{10} metal complexes [26].

An interesting point is the stacking pattern of **1** in the solid state. The hydrogen atoms from the pyridine rings of the 8-membered metallomacrocycle have been activated by the positive charge due to the coordination of the nitrogen atoms to the Ag^{I} centers, and two F atoms of the coordinated BF_4^- (here only the larger occupation part of disordered BF_4^- was considered) form the acceptors of two kinds of C–H···F intermolecular hydrogen bonds (Fig. 1(b)), which link the complex to form a 2-D supramolecular framework structure. The C···F separations are 3.352 Å with H···F distances of 2.526 Å, falling into the range of weak C–H···F hydrogen bond interactions [27]. In addition, the H atoms of disordered CH_3CN molecules also form C–H···F weak interactions, which link these 2-D layers into a 3-D framework.

Complex **2** consists of a trinuclear $[Ag_3\mathbf{L}^2_2(NO_3)_2]^+$ cation, an uncoordinated NO_3^- and a CH_3CN solvent molecule. The crystal structure of **2** shows three different Ag^{I} centers lying on a crystallographic plane of symmetry (Fig. 2(a)). Ag(1) is coordinated by two pyridine nitrogens from different $\mathbf{L}^2$ligands showing linear coordination geometry with an N–Ag–N bond angle of 169.9(3)° (Table 2). In addition, NO_3^- shows weak coordination to Ag(1) in the chelated mode with the Ag···O distances of ~2.685 Å. The CH_3CN molecule also weakly coordinates to Ag(1) with an Ag···O distance of 2.716 Å. Ag(2) is coordinated by two pyridine nitrogens from distinct ligands with an N–Ag–N bond angle of 175.2(3)°, but Ag(2) has a different chemical environment from Ag(1). Ag(3) is coordinated to two sulfur atoms of different ligands and four oxygens from two

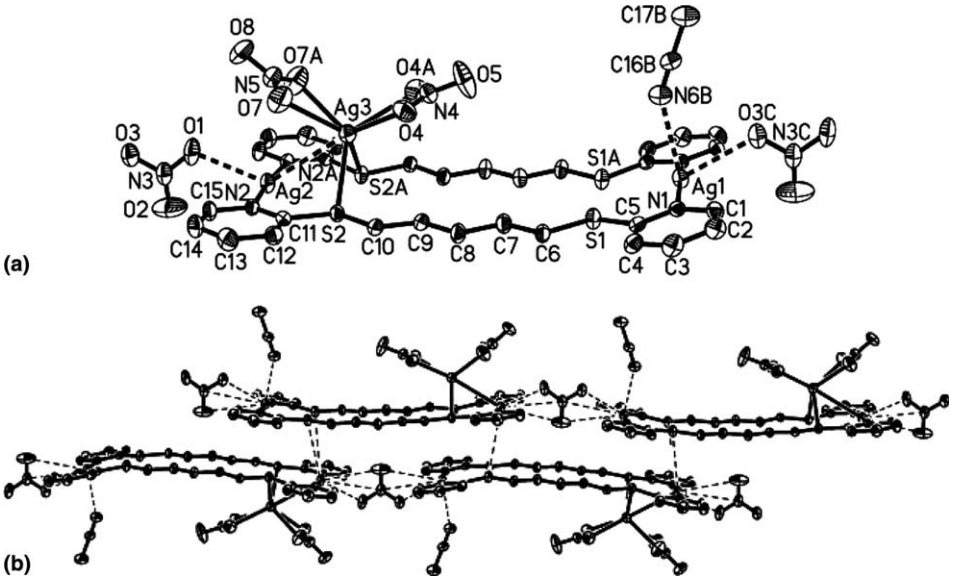


Fig. 2. (a) Perspective view of the trinuclear complex **2** (symmetry codes A: x, $-y+1/2$, z; B: $x-1/2$, y, $-1/2-z$; C: $x-1$, y, z), and (b) the double chain structure formed by weak Ag···S and Ag···O coordination bonds.

chelating nitrate anions to form a rare six-coordination geometry. The Ag–N (average 2.187 Å) and Ag–O [ranging from 2.516(8) to 2.560(8) Å] bond lengths in **2** are in the expected range for such complexes [22], and the Ag–S [2.681(2) Å] distances are close to the values of **1**.

Differing from the reported complexes in which the ligand adopts a bidentate coordination mode [17,19], $\mathbf{L}^2$ in **2** adopts a tridentate coordination mode using its two pyridine nitrogens and a sulfur atom. In the trinuclear structure, the two terminal pyridine rings of each ligand are inclined to each other at an angle of 17.9°, while the two pyridine ring planes around the Ag(1) and Ag(2) centers are basically parallel to each other. A feature of the trinuclear unit is the formation of an Ag···Ag interaction with a distance of 3.176(2) Å which is shorter than that in **1**. Another feature is the stacking pattern of **2** in the solid state. There exist Ag···O weak interactions between Ag(1), Ag(2) and nitrate counter ions with an average distance of 2.650 Å, and the trinuclear units are bridged by nitrate anions using Ag···O weak interactions to form a quasi 1-D chain. In addition, the interchain Ag···S weak interactions link two quasi 1-D chains into a double-chain structure as depicted in Fig. 2(b).

The crystal structure of **3** consists of a 1-D chain in which each Ag^I center is four-coordinated by an N and an S atom from two distinct $\mathbf{L}^3$ ligands as well as two O atoms from chelated nitrate anions (Fig. 3(a)). The coordination geometry of the Ag^I center can be best described as a distorted tetrahedron with bond angles around the Ag^I center ranging from 49.92(9)° to 139.9(1)°. The 8-membered ring formed by two pyridylsulfanyl groups from two $\mathbf{L}^3$ ligands bridging two Ag^I also has an inversion center and adopts a chair configuration with the two pyridine rings parallel to each other. The Ag–N, Ag–S and Ag–O bond lengths are comparable to those in **1**, while the Ag···Ag distance of 3.123(1) Å is significantly shorter than that in **1**, indicating the presence of Ag···Ag interactions. One of the coordinated O atoms from the nitrate ion shows weak coordination to the Ag^I center from another 1-D chain, and these weak interactions link these 1-D chains into a quasi 2-D network (Fig. 3(b)).

In **3**, the ligand adopts an *N*,*N*,*S*,*S*-tetradentate *anti*-bridging mode to coordinate to the Ag^I centers, resulting in an infinite chain, and this kind of coordination mode of $\mathbf{L}^3$ is different from that of the previously reported complexes in which $\mathbf{L}^3$ usually adopts an *N*,*N*-bidentate *anti*-bridging mode [17].

The present study of **1**–**3** further indicates that the coordination modes of the spacer ligands result in different structures [17,19,20]. The ligands $\mathbf{L}^1$, $\mathbf{L}^2$ and $\mathbf{L}^3$ all possess a long flexible segment. Owing to the flexible nature of their spacers, these ligands may be able to adopt various conformations in solution. Depending on their conformation in the self-assembly with metal ions, one may expect the formation of either discrete complexes of the metallomacrocycle type for the *syn* disposition of the coordination sites ($\mathbf{L}^2$) or infinite polymeric structures for the *anti* orientation of the coordination sites ($\mathbf{L}^1$ and $\mathbf{L}^3$). In addition to the strong coordination bonds, there exist other interactions including Ag···Ag contacts, weak coordination bonds

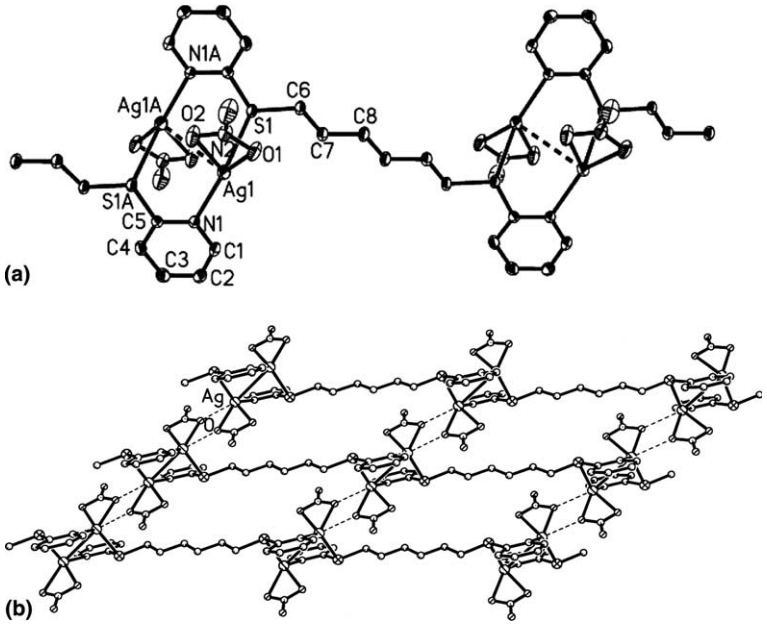


Fig. 3. (a) Perspective view of the 1-D chain of **3** (symmetry code A: $-x+1, -y+2$), and (b) the quasi 2-D network formed by the weak Ag···O coordination bonds.

and weak hydrogen bonds. These weak interactions play a crucial role in the self-organization of supramolecular polymers as well as the stabilization of the complex structures in the solid state.

4. Supplementary materials

Crystallographic data for the structures reported in this paper have been deposited with the Cambridge Crystallographic Data Center (CCDC Nos. 228101, 228102 and 228103). These data can be obtained free of charge via www.ccdc.cam.ac.uk/conts/retrieving.html (or from the CCDC, 12 Union Road, Cambridge CB2 1EZ, UK; fax: +44 1223 336033; e-mail: deposit@ccdc.cam.ac.uk).

Acknowledgements

This work was supported by the National Natural Funds for Distinguished Young Scholars (No. 20225101) and NSFC (No. 20373028).

References

[1] S.R. Batten, R. Robson, Angew. Chem., Int. Ed. 37 (1998) 1460.
[2] M. Fujita, Y.J. Kwon, S. Washizu, K. Ogura, J. Am. Chem. Soc. 116 (1994) 1151.
[3] R. Cao, D.F. Sun, Y.C. Liang, M.C. Hong, K. Tatsumi, Q. Shi, Inorg. Chem. 41 (2002) 2087.
[4] M.L. Tong, Y.M. Wu, J. Ru, X.M. Chen, H.C. Chang, S. Kitagawa, Inorg. Chem. 41 (2002) 4846.
[5] A.J. Blake, G. Baum, N.R. Champness, S.S.M. Chung, P.A. Cooke, D. Fenske, A.N. Khlobystov, D.A. Lemenovskii, W.S. Li, M. Schröder, J. Chem. Soc., Dalton Trans. (2000) 4285.
[6] M. Munakata, L.P. Wu, M. Yamamoto, T. Kuroda-Sowa, M. Maekawa, J. Am. Chem. Soc. 118 (1996) 3117.
[7] A. Matsumoto, T. Tanaka, T. Tsubouchi, K. Tashiro, S. Saragai, S. Nakamoto, J. Am. Chem. Soc. 124 (2002) 8891.
[8] H.F. Lieberman, R.J. Davey, D.M.T. Newsham, Chem. Mater. 12 (2000) 490.
[9] E.S. Alekseyeva, A.S. Batsanov, L.A. Boyd, M.A. Fox, T.G. Hibbert, J.A.K. Howard, J.A.H. MacBride, A. Mackinnon, K. Wade, Dalton Trans. (2003) 475.
[10] G. Barberà, C. Viñas, F. Teixidor, G.M. Rosair, A.J. Welch, J. Chem. Soc., Dalton Trans. (2002) 3647.
[11] L. Carlucci, G. Ciani, P. Macchi, D.M. Proserpio, S. Rizzato, Chem. Eur. J. 5 (1999) 237.
[12] E. Lozano, M. Nieuwenhuyzen, S.L. James, Chem. Eur. J. 7 (2001) 2644.
[13] X.H. Bu, W. Chen, W.F. Hou, M. Du, R.H. Zhang, F. Brisse, Inorg. Chem. 41 (2002) 3477.
[14] Y. Zheng, M. Du, J.R. Li, R.H. Zhang, X.H. Bu, J. Chem. Soc., Dalton Trans. (2003) 1509.
[15] X.H. Bu, W.F. Hou, M. Du, W. Chen, R.H. Zhang, Cryst. Growth Des. 2 (2002) 303.
[16] Y.B. Xie, J.R. Li, Y. Zheng, X.H. Bu, R.H. Zhang, J. Mol. Struct. 645 (2003) 227.
[17] X.H. Bu, Y.B. Xie, J.R. Li, R.H. Zhang, Inorg. Chem. 42 (2003) 7422.
[18] Y.B. Xie, M. Du, J.R. Li, X.H. Bu, R.H. Zhang, Supramol. Chem. 2 (2004) 101.
[19] Y.B. Xie, C. Zhang, J.R. Li, X.H. Bu, J. Chem. Soc., Dalton Trans. (2004) 562.
[20] Y.B. Xie, X.H. Bu, J. Cluster Sci. 14 (2003) 471.
[21] C.M. Hartshorn, P.T. Steel, J. Chem. Soc., Dalton Trans. (1998) 3935.
[22] A.J. Bondi, J. Phys. Chem. 68 (1964) 441.
[23] S.L. Zheng, J.P. Zhang, W.T. Wong, X.M. Chen, J. Am. Chem. Soc. 125 (2003) 6882.
[24] C.M. Hartshorn, P.J. Steel, Inorg. Chem. Commun. 3 (2000) 476.
[25] W.P. Su, R. Cao, M.C. Hong, W.T. Wong, J.X. Lu, Inorg. Chem. Commun. 2 (1999) 241.
[26] C.M. Che, Z. Mao, V.M. Miskowski, M.C. Tse, C.K. Chan, K.K. Cheung, D.L. Phillips, K.H. Leung, Angew. Chem., Int. Ed. 39 (2000) 4084.
[27] D.L. Reger, R.F. Semeniuc, V. Rassolov, M.D. Smith, Inorg. Chem. 43 (2004) 537.

Available online at www.sciencedirect.com
SCIENCE DIRECT®
Polyhedron 24 (2005) 419–426
POLYHEDRON
www.elsevier.com/locate/poly

Reactions of $[ReX_5(NO)]^{2-}$ with triphenylstibine. Spectroscopic investigations of $[ReX_2(NO)(SbPh_3)_3]$, X-ray structures of $[ReCl_2(NO)(SbPh_3)_3]$ and $[ReBr_2Cl(SbPh_3)_3]$ and DFT calculations for $[ReCl_2(NO)(SbPh_3)_3]$

B. Machura [a,*], R. Kruszynski [b,1], M. Jaworska [c]

[a] Department of Inorganic and Radiation Chemistry, Institute of Chemistry, University of Silesia, 9th Szkolna Street, 40006 Katowice, Poland
[b] Department of X-ray Crystallography and Crystal Chemistry, Institute of General and Ecological Chemistry, Lodz University of Technology, 116 Żeromski Street, 90-924 Łódź, Poland
[c] Department of Theoretical Chemistry, Institute of Chemistry, University of Silesia, 9th Szkolna Street, 40006 Katowice, Poland

Received 9 November 2004; accepted 30 November 2004

Abstract

The reactions of $[NBu_4]_2[ReX_5(NO)]$ (X = Cl, Br) with triphenylstibine have been examined and three new rhenium complexes – $[ReCl_2(NO)(SbPh_3)_3]$ (**1**), $[ReBr_2(NO)(SbPh_3)_3]$ (**2**) and $[ReBr_2Cl(SbPh_3)_3]$ (**3**) – have been obtained. The last one has been isolated in a low yield during slow recrystallization of the complex **2** from a mixture of chloroform and ethanol. The stibine rhenium nitrosyls have been characterized by IR and UV–vis spectroscopy. The X-ray structures of **1** and **3** have been determined. The geometric parameters of **1** have been examined using the density functional theory (DFT) method.
© 2005 Elsevier Ltd. All rights reserved.

Keywords: Rrhenium; Stibine; Nitrosyl complexes; X-ray structure; DFT calculations

1. Introduction

The introduction of β^- emitting isotopes ^{188}Re and ^{186}Re in radiotherapy, the similarity with technetium [1–5], and the key role of nitric oxide in human cardiovascular and nervous systems and in immune response to pathogen invasion [6–9] are the main reasons of the still growing interest in rhenium nitrosyl complexes.

Previously, we reported the preparation, spectroscopic and structural characterization of rhenium nitrosyls with triphenylphosphine and triphenylarsine ligands [10–18]. The $[ReOX_3L_2]$ complexes react with NO to give various products, depending on the reaction conditions: $[ReX_3(NO)(OPPh_3)_2]$, $[ReX_3(NO)(PPh_3)_2]$, $[ReX_2(NO)_2(PPh_3)_2]$, $[ReBr_3(NO)(MeCN)(PPh_3)]$, $[ReCl_3(NO)(PPh_3)(OPPh_3)]$, $[ReCl_4(PPh_3)_2]$, $[ReBr_3(NO)(dppe)][ReBr_4(dppe)]$, $[ReX_3(NO)(OAsPh_3)_2]$, $[ReCl_4(OAsPh_3)_2]$ and $[ReCl_3(NO)(AsPh_3)_2]$ $[ReCl_4(AsPh_3)_2]$. The reactions of $[NBu_4]_2[ReX_5(NO)]$ with PPh_3 and $AsPh_3$ lead to $[ReX_3(NO)(PPh_3)_2]$, $[ReBr_3(NO)(AsPh_3)_2]$ and $[ReCl_3(NO)(AsPh_3)_2][ReCl_4(AsPh_3)_2]$.

Now we are extending our studies to the examination of the reactivity of $[NBu_4]_2[ReX_5(NO)]$ (X = Cl, Br) compounds towards triphenylstibine, and here we report the syntheses of the $[ReX_2(NO)(SbPh_3)_3]$ complexes and X-ray structures of $[ReCl_2(NO)(SbPh_3)_3]$ (**1**) and $[ReBr_2Cl(SbPh_3)_3]$ (**3**). The latter has been

* Corresponding author. Tel.: +48 322582441; fax: +48 322599978.
E-mail addresses: bmachura@poczta.onet.pl (B. Machura), kruszyna@p.lodz.pl (R. Kruszynski), mj@tc3.ich.us.edu.pl (M. Jaworska).
[1] A holder of the Foundation for Polish Science (FNP) scholarship.

0277-5387/$ - see front matter © 2005 Elsevier Ltd. All rights reserved.
doi:10.1016/j.poly.2004.11.028

isolated in a low yield during slow recrystallization of the $[ReBr_2(NO)(SbPh_3)_3]$ (**2**) complex from a mixture of chloroform and ethanol. The formation of **3** is particularly interesting since substitution reactions of the nitrosyl ligand are rarely observed [19–21]. This paper also includes the results of the DFT calculations for $[ReCl_2(NO)(SbPh_3)_3]$ based on the B3LYP functional, carried out by using the GAUSSIAN 03 program package.

Gancheff et al. [22] have performed extended tests of the ability of the B3LYP method in the LANL2DZ basis set for rhenium compounds in a geometry optimization and calculation of spectral properties. Although this is not a very extended basis set, its use with DFT has shown it to be sufficient for geometry optimization and calculation of spectral properties. It gives good agreement with the experimental data and its use is especially justified in the case of large molecules.

2. Experimental

2.1. General procedure

All the reagents used for the syntheses were commercially available and were used without further purification. The $[t\text{-}Bu_4N]_2[ReX_5(NO)]$ (X = Cl, Br) complexes were synthesized according to the literature methods [23]. Gaseous NO was generated in the reaction: $2NaNO_2 + 3H_2SO_4 + FeSO_4 \rightarrow 2NO + 2NaHSO_4 + Fe_2(SO_4)_3 + 2H_2O$, and was purified by passing through washers with concentrated KOH solution and a column containing solid NaOH. The reactions were performed under argon atmosphere.

IR spectra were recorded on a Nicolet Magna 560 spectrophotometer in the spectral range 4000–400 cm^{-1} with the samples in the form of KBr pellets. Electronic spectra were measured on a Lab Alliance UV–VIS 8500 spectrophotometer in the range 800–200 nm in deoxygenated dichloromethane solution. Magnetic susceptibilities were measured at 296 K by the Faraday method. Elemental analyses (C, H, N) were performed on a Perkin–Elmer CHN-2400 analyzer.

2.2. Synthesis of $[ReCl_2(NO)(SbPh_3)_3]$ (**1**)

A mixture of $[t\text{-}Bu_4N]_2[ReCl_5(NO)]$ (1 g, 1.15 mmol) and $SbPh_3$ (5.3 g, 15 mmol) in ethanol (50 cm^3) was refluxed for 12 h. The yellow–green precipitate thus formed was filtered and washed with ether. X-ray quality crystals were obtained by recrystallization from a mixture of chloroform and ethanol. Yield 35%.

IR (KBr, cm^{-1}) 3049 (m), 2924 (w), 1683 (vs), 1477 (m), 1430 (s), 1333 (w), 1300 (w), 1261 (w), 1183 (w), 1157 (w), 1066 (m), 1020 (w), 995 (w), 728 (vs), 691 (vs), 449 (m).

Anal. Calc. for $C_{54}H_{45}Sb_3Cl_2NORe$: C, 48.18; H, 3.37; N, 1.04. Found: C, 48.3; H, 3.5; N, 1.1%.

2.3. Synthesis of $[ReBr_2(NO)(SbPh_3)_3]$ (**2**) and $[ReBr_2Cl(SbPh_3)_3]$ (**3**)

A procedure similar to that for **1** was used with $[t\text{-}Bu_4N]_2[ReBr_5(NO)]$ (1.27 g, 1.15 mmol) and $SbPh_3$ (5.3 g, 15 mmol). A yellow–green precipitate of **2** was collected in 38% yield.

IR (KBr, cm^{-1}) 3049 (m), 1681 (vs), 1576 (w), 1479 (m), 1431 (s), 1332 (w), 1302 (w), 1265 (w), 1186 (m), 1157 (w), 1066 (m), 1020 (w), 997 (w), 727 (vs), 692 (vs), 450 (m).

Anal. Calc. for $C_{54}H_{45}Sb_3Br_2NORe$: C, 45.19; H, 3.16; N, 0.98. Found: C, 45.3; H, 3.2; N, 1.1%.

Slow recrystallization of **2** from a mixture of chloroform and ethanol leads to the formation of the $[ReBr_2Cl(SbPh_3)_3]$ complex (**3**) in low yield (~3%).

2.4. Crystal structure determinations and refinement

The X-ray intensity data of **1** and **3** were collected on a KM-4-CCD automatic diffractometer equipped with a CCD detector. 32- and 29-s exposure times were used, respectively, and all the Ewald sphere was collected up to $\theta = 25.11°$. The unit cell parameters were determined from least-squares refinement of the setting angles of 16321 and 7104 strongest reflections, respectively, for **1** and **3**. Details concerning crystal data and refinement are given in Table 1. Lorentz, polarization and numerical absorption corrections [24] were applied. The structures were solved by the Patterson method and subsequently completed by difference Fourier recycling. All the non-hydrogen atoms were refined anisotropically using full-matrix, least-squares techniques. The hydrogen atoms of the phenyl rings were treated as ''riding'' on their parent carbon atoms [d(C–H) = 0.96 Å] and assigned isotropic temperature factors equal to 1.2 times the value of the equivalent temperature factor of the parent carbon atom. SHELXS 97 [25], SHELXL 97 [26] and SHELXTL [27] programs were used for all the calculations. Atomic scattering factors were those incorporated in the computer programs.

2.5. Computational details

The GAUSSIAN 03 program [28] was used in the calculations. The geometry optimization was carried out with the DFT method with the use of the B3LYP functional [29,30].

The LANL2DZ basis set [31] was used on the rhenium and antimony atoms, 6-31G(d) on the nitrogen, chlorine, oxygen and carbon atoms, and 6-31G basis on the hydrogen atoms in the calculations.

Table 1
Crystal data and structure refinement for **1** and **3**

	1	**3**
Empirical formula	$C_{54}H_{45}Sb_3Cl_2NORe$	$C_{54}H_{45}Sb_3Br_2ClRe$
Formula weight	1346.26	1440.62
Temperature (K)	293(2)	293(2)
Wavelength (Å)	0.71073	0.71073
Crystal system	monoclinic	orthorhombic
Space group	$P2_1/n$	$P2_12_12_1$
Unit cell dimensions		
a (Å)	18.8063(5)	13.3916(4)
b (Å)	13.1913(3)	16.2378(5)
c (Å)	19.8266(5)	22.6870(9)
β (°)	91.738(2)	
Volume (Å^3)	4916.3(2)	4933.3(3)
Z	4	4
Density (calculated) (Mg/m^3)	1.819	1.940
Absorption coefficient (mm^{-1})	4.232	5.780
F(000)	2584	2736
Crystal size (mm)	$0.15\times0.15\times0.29$	$0.07\times0.10\times022$
θ range for data collection (°)	2.77–25.11	3.29–25.11
Index ranges	$-22\leqslant h\leqslant 22$ $-15\leqslant k\leqslant 14$ $-23\leqslant l\leqslant 23$	$-15\leqslant h\leqslant 15$ $-19\leqslant k\leqslant 19$ $-27\leqslant l\leqslant 21$
Reflections collected	50963	57700
Independent reflections (R_{int})	8760 (0.0471)	8765 (0.0566)
Completeness to 2θ (%)	95.3	99.6
Data/restraints/parameters	8760/0/587	8765/0/550
Goodness-of-fit on F^2	1.042	1.102
Final R indices [$I>2\sigma(I)$]	$R_1=0.0270$ $wR_2=0.0634$	$R_1=0.0426$ $wR_2=0.0986$
R indices (all data)	$R_1=0.0352$ $wR_2=0.0664$	$R_1=0.0439$ $wR_2=0.0994$
Absolute structure parameter		0.016(8)
Largest difference peak and hole (e/Å^3)	0.751 and −0.677	1.166 and −1.577e

Natural bond orbital (NBO) calculations were performed with the NBO code [32] included in GAUSSIAN 03.

3. Results and discussion

The [t-Bu_4N]$_2$[$ReX_5(NO)$] complexes (X = Cl, Br) react with PPh_3 and $AsPh_3$ to give [$ReX_3(NO)(PPh_3)_2$], [$ReBr_3(NO)(AsPh_3)_2$] and [$ReCl_3(NO)(AsPh_3)_2$][$ReCl_4(AsPh_3)_2$] [18]. The reactions of [t-Bu_4N]$_2$[$ReX_5(NO)$] with triphenylstibine in ethanol lead to the [$ReX_2(NO)(SbPh_3)_3$] complexes. The smaller steric demand of $SbPh_3$ in comparison with PPh_3 and $AsPh_3$ explains the formation of [$ReX_2(NO)(SbPh_3)_3$]. The increase of M–E and E–C (E = P, As or Sb) bond lengths in the order P > As > Sb leads to the decrease of the EPh_3 cone angles [33].

The yield of the [$ReX_2(NO)(SbPh_3)_3$] complexes depends on: (i) the mole ratio of [NBu_4]$_2$[$ReX_5(NO)$] to triphenylstibine (it is the highest when it is ~1:13) and (ii) the reaction time (it drops considerably when the reaction is carried out in less than 12 h). Compounds **1** and **2** were recrystallized from a mixture of $CHCl_3$/EtOH. The crystals of **1** were of good quality, whereas the crystals of **2** were small and badly shaped. Moreover, in the case of the bromine nitrosyl, the formation of a small amount of well-shaped yellow crystals of **3** was observed during the slow recrystallization. The oxidation reactions of rhenium complexes by halogen-containing solvents have been known for years [34]. Substitution reactions of nitrosyl ligands by halogen ligands, however, are very sparse [19–21].

The structure of **1** has been modelled with the Cl and NO ligands disordered over two sites using fractional occupancies equal to 0.45 for Cl(1), N(2), O(2) atoms and 0.55 for Cl(3), N(1) and O(1) atoms. A similar disorder of NO ligands has also been reported for iridium, rhodium and ruthenium complexes [35]. The $SbPh_3$ ligands are arranged in a *meridional* fashion, and the Cl(3) ligand is involved in weak intramolecular hydrogen bonds with the H(36) and H(54) atoms of the phenyl rings [36–38]. Fig. 1 shows a displacement ellipsoid plot of **1** and selected bond lengths and angles of this compound are summarized in Table 2.

Two groups of ligands of **3** (halide ions and stibine molecules) are arranged in a *meridional* fashion, the bromine ligands occupy a *cis* position to each other. Fig. 2 shows the molecular structure of this compound, and selected bond lengths and angles for **3** are summarized in

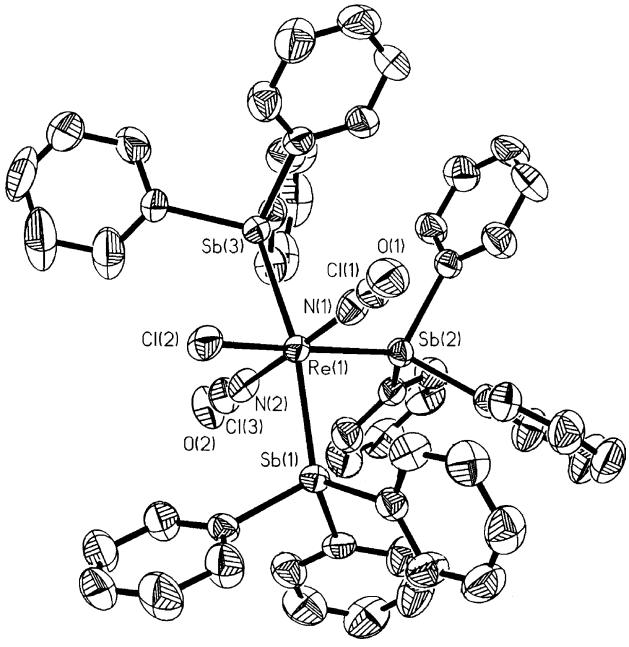


Fig. 1. The molecular structure of **1**.

Table 2
The experimental and optimized bond lengths (Å) and angles (°) for **1**

Bond lengths	Experimental	Optimized	Angles	Experimental	Optimized
Re(1)–Cl(1)	2.353(5)	2.533	N(2)–Re(1)–N(1)	178.2(9)	
Re(1)–Cl(2)	2.4443(10)	2.522	N(2)–Re(1)–Cl(1)	177.0(7)	175.35
Re(1)–Cl(3)	2.362(4)		N(1)–Re(1)–Cl(3)	177.1(7)	
Re(1)–N(1)	1.832(19)		Cl(1)–Re(1)–Cl(3)	176.3(2)	
Re(1)–N(2)	1.753(17)	1.754	N(2)–Re(1)–Cl(2)	92.3(6)	99.99
Re(1)–Sb(1)	2.6945(3)	2.762	N(1)–Re(1)–Cl(2)	86.6(7)	
Re(1)–Sb(2)	2.6640(3)	2.723	Cl(1)–Re(1)–Cl(2)	89.39(19)	84.38
Re(1)–Sb(3)	2.6758(3)	2.752	Cl(3)–Re(1)–Cl(2)	91.85(10)	
N(1)–O(1)	1.13(4)	1.195	N(2)–Re(1)–Sb(1)	84.7(6)	89.77
N(2)–O(2)	1.32(4)		N(1)–Re(1)–Sb(1)	96.5(7)	
			Cl(1)–Re(1)–Sb(1)	97.95(17)	92.46
			Cl(3)–Re(1)–Sb(1)	85.67(10)	
			Cl(2)–Re(1)–Sb(1)	84.29(3)	81.46
			Sb(2)–Re(1)–Sb(1)	94.101(10)	97.23
			Sb(3)–Re(1)–Sb(1)	169.638(10)	165.74
			N(2)–Re(1)–Sb(2)	94.8(6)	97.37
			N(1)–Re(1)–Sb(2)	86.4(7)	
			Cl(1)–Re(1)–Sb(2)	83.60(19)	78.31
			Cl(3)–Re(1)–Sb(2)	95.31(9)	
			Cl(2)–Re(1)–Sb(2)	172.52(3)	162.58
			N(2)–Re(1)–Sb(3)	89.3(6)	90.36
			N(1)–Re(1)–Sb(3)	89.3(7)	
			Cl(1)–Re(1)–Sb(3)	88.30(17)	88.48
			Cl(3)–Re(1)–Sb(3)	88.24(10)	
			Cl(2)–Re(1)–Sb(3)	87.54(3)	84.48
			Sb(2)–Re(1)–Sb(3)	94.809(10)	96.90
			O(1)–N(1)–Re(1)	178(2)	179.1
			O(2)–N(2)–Re(1)	175(2)	

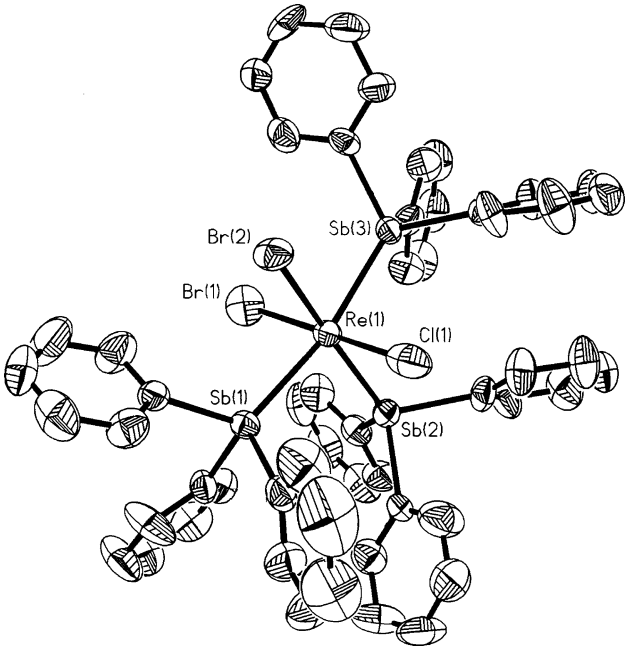


Fig. 2. The molecular structure of **3**.

Table 3
Bond lengths (Å) and angles (°) for **3**

Bond lengths		Angles	
Re(1)–Br(1)	2.5179(16)	Cl(1)–Re(1)–Br(1)	177.56(9)
Re(1)–Br(2)	2.5997(11)	Cl(1)–Re(1)–Br(2)	87.24(8)
Re(1)–Cl(1)	2.436(4)	Br(1)–Re(1)–Br(2)	90.49(5)
Re(1)–Sb(1)	2.6809(7)	Cl(1)–Re(1)–Sb(2)	86.72(8)
Re(1)–Sb(2)	2.6713(7)	Br(1)–Re(1)–Sb(2)	95.54(4)
Re(1)–Sb(3)	2.6873(7)	Br(2)–Re(1)–Sb(2)	173.93(4)
		Cl(1)–Re(1)–Sb(1)	91.23(7)
		Br(1)–Re(1)–Sb(1)	87.72(4)
		Br(2)–Re(1)–Sb(1)	85.80(3)
		Sb(2)–Re(1)–Sb(1)	93.70(2)
		Cl(1)–Re(1)–Sb(3)	93.78(7)
		Br(1)–Re(1)–Sb(3)	86.90(4)
		Br(2)–Re(1)–Sb(3)	85.01(3)
		Sb(2)–Re(1)–Sb(3)	96.02(2)
		Sb(1)–Re(1)–Sb(3)	169.30(2)

Table 3. The conformations of $[ReBr_2Cl(SbPh_3)_3]$ molecules are stabilized by two weak intramolecular hydrogen bonds [35–37]. The Cl(1) ligand is involved in a weak hydrogen bond with the H(20) atom of the phenyl ring, while the Br(1) ion interacts with the H(36) atom.

Due to steric repulsion of the three bulky $SbPh_3$ molecules, the octahedral Re geometries of **1** and **3** show the expected angular distortions. The angles between *cis*-ligands vary between 83.60(19)° and 97.95(17)° for **1**, and 85.01(3)° and 96.02(2)° for **3**; the *trans*-angles are between 169.64(1)° and 178.2(9)° for **1**, and 169.30(2)° and 177.56(9)° for **3**.

There are only a few Re–Sb distances reported in the Cambridge Structural Database, with $[ReCl_2(NO)_2(SbPh_3)_2]$ [39] [Re–Sb: 2.711(8) and 2.710(8) Å] and $[ReCl(CO)_3(SbPh_3)_2]$ [40] [Re–Sb: 2.726(1) and 2.729(2) Å] being the closest chemical examples and showing little longer Re–Sb bond lengths compared to the presented compounds (Tables 2 and 3).

Relative small C–Sb–C tetrahedral angles were found: 94.78(17)°–102.48(17)°, 100.2° (av) for **1** and 95.2(4)°–102.1(4)°, 99.1° (av) for **3**. This is most likely due to the large Sb–C bond lengths making it possible for the phenyl rings to be compressed a little more than that which is encountered for the analogous phosphine and arsine ligands. Table 4 presents the Re–E and E–C bond lengths and C–E–C angles (E = P, As or Sb) for the selected rhenium complexes.

The average Re–NO (1.793 Å) and N–O (1.225 Å) bond lengths and the average value of the Re–N–O angle (176.5°) for **1** confirm a linear coordination of the nitrosyl group, and they are comparable with values found for phosphine and arsine rhenium nitrosyls [13–18].

A notable *trans* influence of the triphenylstibine ligand is observed in both **1** and **3**; the Re–X(2) bond lengths are longer by about 0.08 Å in comparison with the corresponding Re–X distances in *cis* positions to the $SbPh_3$ ligand. A difference between Re–Cl(1) and Re–Cl(3) in **1** is a consequence of the nitrosyl disorder.

The nitrosyl stretching frequency in $[ReX_2(NO)(SbPh_3)_3]$ compounds is independent of the halogen ligand, the strong band corresponding to ν_{NO} appears at ~1680 cm^{-1} in the IR spectrum of the chloro (**1**) and bromo (**2**) nitrosyl. The considerable lowering of the ν_{NO} for $[Re^{I}X_2(NO)(SbPh_3)_3]$ complexes in comparison with the $[Re^{II}X_3(NO)(PPh_3)_2]$ and $[Re^{II}X_3(NO)(AsPh_3)_2]$ nitrosyls [15,17,18] is consistent with the lower oxidation state of the rhenium ion. It results in an increased backdonation of electron density from the filled rhenium d-orbitals into the π* antibonding orbital of the NO group.

The complexes **1** and **2** are diamagnetic, which confirms the low-spin d^6 configuration of the rhenium ion in the O_h field.

Table 5 presents the positions and molar absorption coefficients of the electronic bands for **1** and **2**. The electronic absorption spectra of both rhenium (I) complexes are very similar. They are dominated by three intense bands below 300 nm due to interligand electronic transitions of $SbPh_3$. In addition, two less intense absorption bands appear at ~420 and ~380 nm, and they can be assigned to d–d transitions and metal-to-ligand charge transfer (MLCT) transitions from Re(I) to π* ligand orbitals.

Table 5
Band positions and molar absorption coefficients for **1** and **2**

Band position (nm)	ε
Compound ***1***	
420.0	560
378.5	740
282.5	8440
230.0	14900
215.0	9760
Compound ***2***	
415.0	530
381.0	490
290.5	8200
232.0	12580
223.5	7580

ε is the molar absorption coefficient ($dm^3\ mol^{-1}\ cm^{-1}$).

Considering the magnetic measurements, the geometry of **1** was optimized in the singlet state by the DFT method with the B3LYP functional. The optimized geometry is in quite good agreement with the experimental one, the largest differences are found for the Re–Cl and Re–Sb bond distances. A similar elongation of the rhenium–halogen bond lengths in the B3LYP with different basis sets has been found in other rhenium complexes [41].

Table 6 presents the atomic charges from the natural population analysis (NPA) for **1**. The calculated charge on the nitrogen atom of the nitrosyl group is positive, whereas the oxygen atom is negatively charged. The total charge on the NO group of the title complex is negative: −0.176. The calculated charge on the rhenium atom of **1** is far from the formal charge +1. It results from charge donation from the chloride ions and triphenylstibine ligand, which act as σ-donors. There are large positive charges on the Sb atoms, and the charges on the chloride ions are significantly smaller than −1.

Table 4
The Re–E and E–C bond lengths and C–E–C angles (E = P, As or Sb) for the selected rhenium complexes

Complex	Re–E bond length (average, Å)	E–C bond length (average, Å)	C–E–C angle (average, °)	Reference
$[Re(NO)Cl_3(PPh_3)_2]$	2.530	1.822	104.3	[15]
$[Re(NO)Br_3(PPh_3)_2]$	2.540	1.822	104.3	[17]
$[Re(NO)Cl_3(AsPh_3)_2]$	2.612	1.942	103.4	[18]
$[Re(NO)Br_3(APh_3)_2]$	2.595	1.935	103.7	[18]
$[ReCl_2(NO)_2(SbPh_3)_2]$	2.711	2.114	102.5	[38]
$[ReCl(CO)_3(SbPh_3)]$	2.728	2.137	100.1	[39]
$[ReCl_2(NO)(SbPh_3)_3]$	2.678	2.133	100.2	this work
$[ReBr_2Cl(SbPh_3)_3]$	2.680	2.135	99.1	this work

Table 6
Atomic charges from the natural population analysis (NPA) for **1**

Atom	Atomic charge
Re(1)	−0.271
Cl(1)	−0.515
Cl(2)	−0.498
N(1)	0.148
O(1)	−0.324
Sb(1)	1.650
Sb(2)	1.653
Sb(3)	1.665

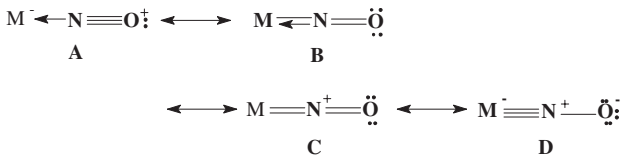
The energies and characters of several highest occupied and lowest unoccupied molecular orbitals of **1** are presented in Table 7. The selected HOMO and LUMO orbitals of **1** are depicted in Fig. 3. The investigated complex is of a large size, the number of basis functions is equal 956. Among the occupied MOs of **1** the largest numbers constitute orbitals of the phenyl rings which are not relevant for the discussion of the bonding. The others have complicated character. The percent participations of the ligand atomic orbitals in the selected HOMO and LUMO orbitals are shown in Table 7.

The bonding of NO to the rhenium center involves a synergic interaction between the nitrosyl ligand orbitals and the metal orbitals. The Re–NO bond consists of two components: (i) a donation of electron density from a σ-type orbital on NO onto the metal orbital and (ii) a donation of electron density from the occupied metal d-orbitals into the π* antibonding orbitals of the NO ligand. The occupied d_{yz} and d_{xz} rhenium orbitals participate in the back-donation from the central ion to the nitrosyl ligand in complex **1**. In the occupied orbitals, the π^*_{NO} are distributed among several highest MOs. A substantial contribution of π_{Re-NO} orbitals are shown in HOMO − 4, HOMO − 2 and HOMO − 1. Percent participations of the d rhenium and π^*_{NO} orbitals in these MOs are very similar. The LUMO + 1, LUMO + 2 and LUMO + 3 orbitals are of π^*_{Re-NO} antibonding character. The LUMO + 1 orbital has prevalent NO character, whereas the LUMO + 2 and LUMO + 3 orbitals are localised almost evenly on the d rhenium and π^*_{NO} orbitals.

Table 7
The energy and character of selected molecular orbitals of **1**

MO	*E* (eV)	Character
HOMO − 14	−6.801	$\pi_{Ph}(80.54)$, $\pi_{Cl}(13.99)$
HOMO − 13	−6.767	π_{Ph}
HOMO − 12	−6.740	π_{Ph}
HOMO − 11	−6.719	π_{Ph}
HOMO − 10	−6.715	π_{Ph}
HOMO − 9	−6.686	π_{Ph}
HOMO − 8	−6.675	π_{Ph}
HOMO − 7	−6.600	π_{Ph}
HOMO − 6	−6.591	π_{Ph}
HOMO − 5	−6.572	π_{Ph}
HOMO − 4	−6.500	$\pi_{Ph}(59.61), \pi_{Cl}(11.93), d_{xz}(7.06) + \pi^*_{NO}(11.59)$
HOMO − 3	−6.410	$\pi_{Cl}(58.88)$, $\pi_{Ph}(28.31)$, $n_{Sb}(5.69)$
HOMO − 2	−6.123	$d_{yz}(23.13) + \pi^*_{NO}(29.37)$, $\pi_{Cl}(37.64)$
HOMO − 1	−5.866	$\pi_{Cl}(28.15), \pi_{Ph}(27.48), n_{Sb}(20.03), d_{xz}(13.0) + \pi^*_{NO}(7.11)$
HOMO	−5.409	$d_{xy}(60.45)$, $\pi_{Cl}(24.02)$
LUMO	−1.006	$d_{x^2-y^2}(28.52) - \sigma_{Sb}(36.07) - \sigma_{Cl}(5.82)$
LUMO + 1	−0.939	$\pi^*_{NO}(40.54) - d_{xz}(22.53), \pi^*_{Ph}(17.56)$
LUMO + 2	−0.852	$\pi^*_{NO}(18.82) - d_{yz}(14.96), \pi^*_{Ph}(38.75), \pi_{Cl}(10.04)$
LUMO + 3	−0.809	$\pi^*_{NO}(15.77) - d_{yz}(17.44), \pi^*_{Ph}(30.76)$
LUMO + 4	−0.795	$\pi^*_{Ph}(30.76), \pi^*_{NO}(7.76) - d_{yz}(7.29)$
LUMO + 5	−0.572	π^*_{Ph}
LUMO + 6	−0.498	π^*_{Ph}
LUMO + 7	−0.442	π^*_{Ph}
LUMO + 8	−0.363	π^*_{Ph}
LUMO + 9	−0.306	π^*_{Ph}
LUMO + 10	−0.294	π^*_{Ph}
LUMO + 11	−0.264	π^*_{Ph}
LUMO + 12	−0.221	π^*_{Ph}

Additional information about the binding in complex **1** was obtained by NBO analysis. Table 8 presents the occupancies and natural atomic orbital compositions (NAO) of the selected NBOs for complex **1**. The occupancies of the bonding and antibonding Re–N bond orbitals (BD_{Re-N} and BD^*_{Re-N} orbitals) confirms a great donation of electron density from the occupied rhenium d-orbitals into the π* antibonding orbitals of the NO ligand. For compound **1**, three natural bond orbitals were detected for the Re–N bond, and one orbital – for the N–O bond. The Re–N bond orbital of σ-character is polarized towards the nitrogen atom (ca. 73% at N) and the s- and d-orbitals of Re take part in the bonding. In the case of the Re–N bond orbitals of π-character, only d-orbitals of Re are included in the bonding. The N–O bond orbital is slightly polarized towards the oxygen end. In the valence-bond treatment a linear bonding mode of the nitrosyl group may be represented by the following resonance forms [42]:



The results of the NBO analysis indicate that the resonance structure D makes a significant contribution to the structure of complex **1**.

It is consistent with the charges on the nitrogen and oxygen atoms of the nitrosyl group and the relatively low nitrosyl stretching frequency.

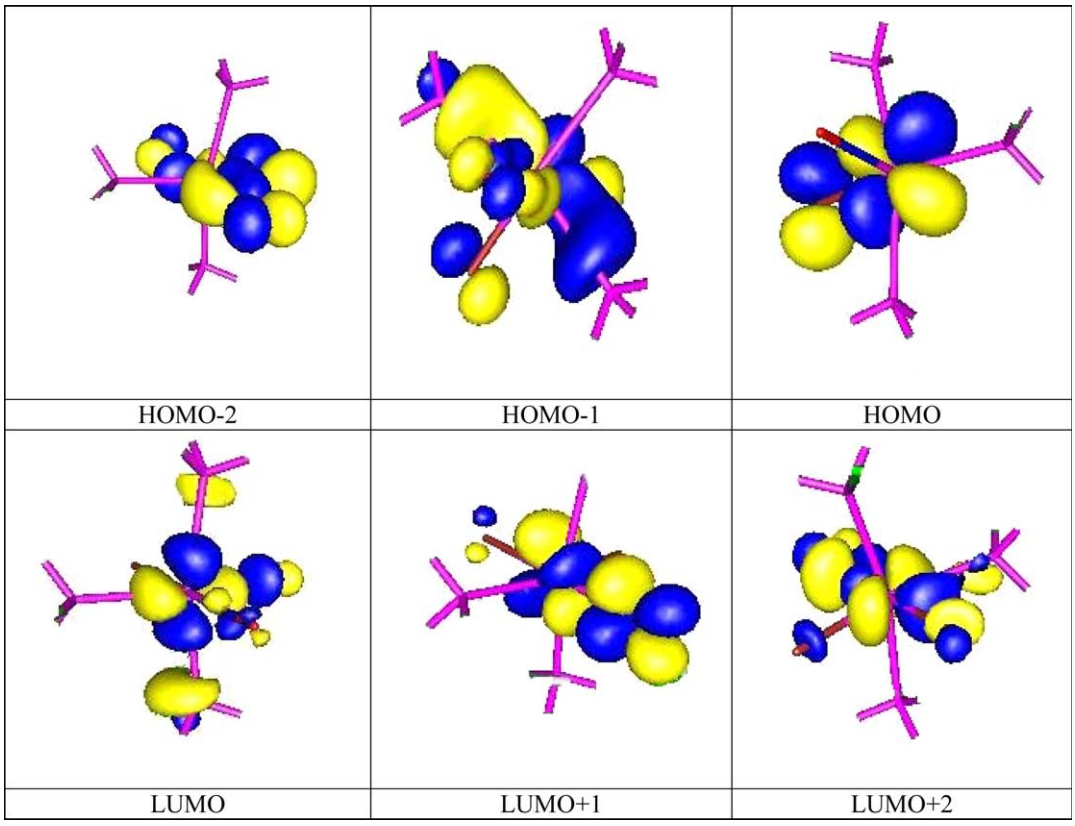


Fig. 3. Selected HOMO and LUMO orbitals for **1**. The phenyl rings are omitted for clarity, they make no contribution to the presented orbitals. Positive values of the orbital contour are represented in blue (0.04 a.u.) and negative values – in yellow (−0.04 a.u.).

Table 8
Selected results of the NBO analysis for **1**

Bond orbital BD	Occupancy		NAO composition		BD*	Occupancy
Re≡N(σ)	1.965	% Re	26.96	s(18.35%) d(81.48%)	Re≡N(σ*)	0.419
		% N	73.04	s(57.54%) p(42.44%)		
Re≡N(π)	1.944	% Re	48.48	d(93.84%)	Re≡N(π*)	0.444
		% N	51.52	p(93.72%)		
Re≡N(π)	1.974	% Re	55.55	d(99.42%)	Re≡N(π*)	0.469
		% N	44.45	p(99.94%)		
N–O	1.996	% N	45.47	s(36.19%) p(63.66%)	N–O(σ*)	0.014
		% O	54.53	s(29.72%) p(70.14%)		

4. Supplementary data

Supplementary data are available from the CCDC, 12 Union Road, Cambridge CB2 1EZ, UK (fax: +44 1223 336033; e-mail: deposit@ccdc.cam.ac.uk or www: http://www.ccdc.cam.ac.uk) on request, quoting the Deposition Nos.: 254986 ($C_{54}H_{45}Sb_3Cl_2NORe$) and 254987 ($C_{54}H_{45}Sb_3Br_2ClRe$).

Acknowledgment

The GAUSSIAN 03 calculations were carried out in the Wrocław Centre for Networking and Supercomputing, WCSS, Wrocław, Poland, under calculational Grant No. 51/96.

References

[1] S.S. Jurisson, J.D. Lydon, Chem. Rev. 99 (1999) 2205.
[2] S. Liu, D.S. Edwards, Chem. Rev. 99 (1999) 2235.
[3] W.A. Volkert, T.J. Hoffmann, Chem. Rev. 99 (1999) 2269.
[4] W. Volkert, W.F. Goeckeler, G.J. Ehrhardt, A.R. Ketring, J. Nucl. Med. 32 (1991) 174.
[5] E.A. Deutsch, K. Libson, J.L. Vanderheyden, in: M. Nicolini, G. Bandoli, U. Mazzi (Eds.), Technetium and Rhenium in Chemistry and Nuclear Medicine 3, Raven Press, New York, 1990, pp. 13–22.

[6] R.M.J. Palmer, A.G. Ferrige, S. Moncada, Nature 327 (1987) 524.
[7] S. Moncada, R.M.J. Palmer, E.A. Higgs, Pharmacol. Rev. 43 (1991) 109.
[8] P.L. Feldman, O.W. Griffith, D.J. Stuehr, Chem. Eng. News 71 (1993) 26.
[9] M. Feeelish, J.S. Stamler (Eds.), Methods in Nitric Oxide Research, Wiley, Chichester, UK, 1996, and references therein.
[10] J.O. Dzięgielewski, B. Machura, J. Marek, Polyhedron 15 (1996) 3713.
[11] J.O. Dzięgielewski, B. Machura, T.J. Bartczak, Polyhedron 15 (1996) 2813.
[12] T.J. Bartczak, W. Czurak, J.O. Dzięgielewski, B. Machura, Polish J. Chem. 72 (1998) 633.
[13] J.O. Dzięgielewski, B. Machura, T. Kupka, T.J. Bartczak, W. Czurak, Polish J. Chem. 72 (1998) 1009.
[14] J.O. Dzięgielewski, B. Machura, T.J. Bartczak, W. Czurak, J. Kusz, J. Warczewski, J. Coord. Chem. 48 (1999) 125.
[15] T.J. Bartczak, W. Czurak, J.O. Dzięgielewski, B. Machura, A. Jankowska, J. Kusz, J. Warczewski, Polyhedron 18 (1999) 2313.
[16] T.J. Bartczak, W. Czurak, J.O. Dzięgielewski, B. Machura, J. Kusz, J. Warczewski, Polish J. Chem. 74 (2000) 265.
[17] T.J. Bartczak, W. Czurak, J.O. Dzięgielewski, B. Machura, A. Jankowska, J. Kusz, J. Warczewski, J. Coord. Chem. 52 (2001) 361.
[18] B. Machura, J.O. Dzięgielewski, S. Michalik, T.J. Bartczak, R. Kruszynski, J. Kusz, Poyhedron 21 (2002) 2617.
[19] G.B. Richter-Addo, P. Legzdins, Chem. Rev. 88 (1988) 991.
[20] M. Kubota, M.K. Chan, Inorg. Chem. 23 (1984) 1636.
[21] P. Diversi, F.F. de Biani, G. Ingrosso, F. Laschi, A. Lucherini, C. Pinzino, P. Zanello, J. Organomet. Chem. 584 (1999) 73.
[22] J. Gancheff, C. Kremer, E. Kremer, O.N. Ventura, J. Mol. Struct. (Theochem) 580 (2002) 107.
[23] D. Giusto, G. Cova, Gazz. Chim. Ital. 102 (1972) 265.
[24] STOE & Cie (1999). X-RED. Version 1.18. STOE & Cie GmbH, Darmstadt, Germany.
[25] G.M. Sheldrick, Acta Crystallogr., Part A 46 (1990) 467.
[26] G.M. Sheldrick, SHELXL97. Program for the solution and refinement of crystal structures, University of Göttingen, Göttingen, Germany, 1997.
[27] G.M. Sheldrick, SHELXTL: release 4.1 for Siemens crystallographic research systems, 1990.
[28] M.J. Frisch, G.W. Trucks, H.B. Schlegel, G.E. Scuseria, M.A. Robb, J.R. Cheeseman, J.A. Montgomery Jr., T. Vreven, K.N. Kudin, J.C. Burant, J.M. Millam, S.S. Iyengar, J. Tomasi, V. Barone, B. Mennucci, M. Cossi, G. Scalmani, N. Rega, G.A. Petersson, H. Nakatsuji, M. Hada, M. Ehara, K. Toyota, R. Fukuda, J. Hasegawa, M. Ishida, T. Nakajima, Y. Honda, O. Kitao, H. Nakai, M. Klene, X. Li, J.E. Knox, H.P. Hratchian, J.B. Cross, C. Adamo, J. Jaramillo, R. Gomperts, R.E. Stratmann, O. Yazyev, A.J. Austin, R. Cammi, C. Pomelli, J.W. Ochterski, P.Y. Ayala, K. Morokuma, G.A. Voth, P. Salvador, J.J. Dannenberg, V.G. Zakrzewski, S. Dapprich, A.D. Daniels, M.C. Strain, O. Farkas, D.K. Malick, A.D. Rabuck, K. Raghavachari, J.B. Foresman, J.V. Ortiz, Q. Cui, A.G. Baboul, S. Clifford, J. Cioslowski, B.B. Stefanov, G. Liu, A. Liashenko, P. Piskorz, I. Komaromi, R.L. Martin, D.J. Fox, T. Keith, M.A. Al-Laham, C.Y. Peng, A. Nanayakkara, M. Challacombe, P.M.W. Gill, B. Johnson, W. Chen, M.W. Wong, C. Gonzalez, J.A. Pople, GAUSSIAN 03, Revision B.03, Gaussian, Inc., Pittsburgh, PA, 2003.
[29] A.D. Becke, J. Chem. Phys. 98 (1993) 5648.
[30] C. Lee, W. Yang, R.G. Parr, Phys. Rev. B 37 (1988) 785.
[31] P.J. Hay, W.R. Wadt, J. Chem. Phys. 82 (1985) 299.
[32] E.D. Glendening, A.E. Reed, J.E. Carpenter, F. Weinhold, NBO (version 3.1).
[33] C.A. Tolman, Chem. Rev. 77 (1977) 313.
[34] G. Rouschias, G. Wilkinson, J. Chem. Soc. A (1968) 993.
[35] S. Chand, R.K. Coll, J.S. McIndoe, Polyhedron 17 (1998) 507, and references therein.
[36] G.A. Jeffrey, W. Saenger, Hydrogen Bonding in Biological Structures, Springer, Berlin, 1994.
[37] G.R. Desiraju, T. Steiner, The Weak Hydrogen Bond in Structural Chemistry and Biology, Oxford University Press, Oxford, 1999.
[38] R Taylor, O. Kennard, J. Am. Chem. Soc. 104 (1982) 5063.
[39] V.D. Fenske, N. Mronga, K. Dehnicke, Z. Anorg. Allg. Chem. 498 (1983) 131.
[40] N.J. Holmes, W. Levason, M. Webster, J. Organomet. Chem. 568 (1998) 213.
[41] N. Psaroudakis, K. Mertis, D.G. Liakos, E.D. Simandiras, Chem. Phys. Lett. 369 (2003) 490.
[42] G.B. Richter-Addo, P. Legzdins, Metal Nitrosyls, Oxford University Press, Oxford, 1992.

Available online at www.sciencedirect.com
SCIENCE DIRECT®
Polyhedron 24 (2005) 427–433
POLYHEDRON
www.elsevier.com/locate/poly

Preparation and structures of polymeric lanthanide nitrate complexes of $CH_3C[CH_2P(O)Ph_2]_3$

Anthony M.J. Lees, Andrew W.G. Platt *

School of Sciences, Staffordshire University, College Road, Stoke-on-Trent ST4 2DE, UK

Received 30 June 2004; accepted 13 December 2004
Available online 12 January 2005

Abstract

The synthesis of complexes between lanthanide nitrates and $MeC(CH_2P(O)Ph_2)_3$ (=L) in ethanol or methanol leads to the formation of polymeric complexes $Ln(NO_3)_3L$ as alcohol solvates. The ligand adopts a chelating–bridging mode. The structures of the complexes $La(NO_3)_3L \cdot EtOH$ and $Pr(NO_3)_3L \cdot MeOH$ are reported and the coordination of L is discussed in terms of that of the related free ligand $EtC(CH_2P(O)Ph_2)_3$. Infrared spectroscopy implies structural differences between the early and later lanthanide complexes.
© 2004 Elsevier Ltd. All rights reserved.

Keywords: Lanthanide nitrate; Complex; Phosphine oxide; Tripdal; Structure

1. Introduction

Phosphine oxide complexes with lanthanides and actinides have been well known for some time [1] and continue to attract interest [2,3]. Polyphosphine oxide complexes have also been much investigated with studies of their structural chemistry and application to the solvent extraction processes in nuclear fuel reprocessing [4–7]. Considerable recent interest in lanthanide complexes has centred on their clinical applications [8]. Complexes with tripodal ligands have been examined as potential relaxivity enhancement agents for magnetic resonance imaging [9,10] and as luminescent probes of biochemical interest [11–13]. The structures adopted by these mainly N, O donor ligands vary from monomeric [11,12,14], oligomeric [9,15] and polymeric [13,16]. Tripodal ligands could effectively block one side of the metal and leave the other face free for the coordination of other substrates. This has been exploited in relaxivity studies where the exposed face of the metal provides sites for water exchange [9].

The structural diversity shown by the complexes prompted us to study the coordination chemistry of relatively simple tripodal ligands, and we have previously investigated the coordination chemistry of the tris-phosphonates $1,3,5[(RO)_2P(O)]_32,4,6Me_3C_6$ (Fig. 1(a)) which formed dimeric structures with bridging ligands $(NO_3)_3LnL_2Ln(NO_3)_3$ [17].

The ligand $MeC(CH_2P(O)Ph_2)_3$ (=L) has potential coordination modes as illustrated in Fig. 1 and from the structural chemistry aspect it is interesting to see which bonding mode is adopted and the reasons for this. Previous studies with transition and p-block metals with similar ligands have identified the tris-chelate by ^{113}Cd NMR measurements with $PhP(O)(C_2H_4P(O)Ph_2)_2$ [18] whilst the complex with $FeCl_3$ with the tetradentate $[Ph_2P(O)C_2H_4]_4C$ give either binuclear or polymeric ionic complexes in which the ligand chelates to two metal centres [19].

* Corresponding author. Tel.: +44 1872 294 784; fax: +44 1782 294 986/745506.
E-mail address: a.platt@staffs.ac.uk (A.W.G. Platt).

0277-5387/$ - see front matter © 2004 Elsevier Ltd. All rights reserved.
doi:10.1016/j.poly.2004.12.003

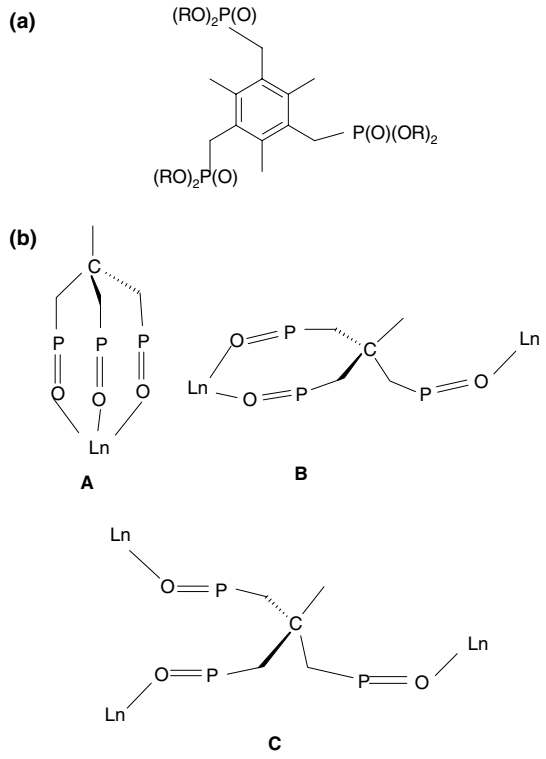


Fig. 1. (a) The tris-phosphonate 1,3,5[$(RO)_2P(O)]_3$2,4,6Me_3C_6. (b) Potential coordination modes of L to metals.

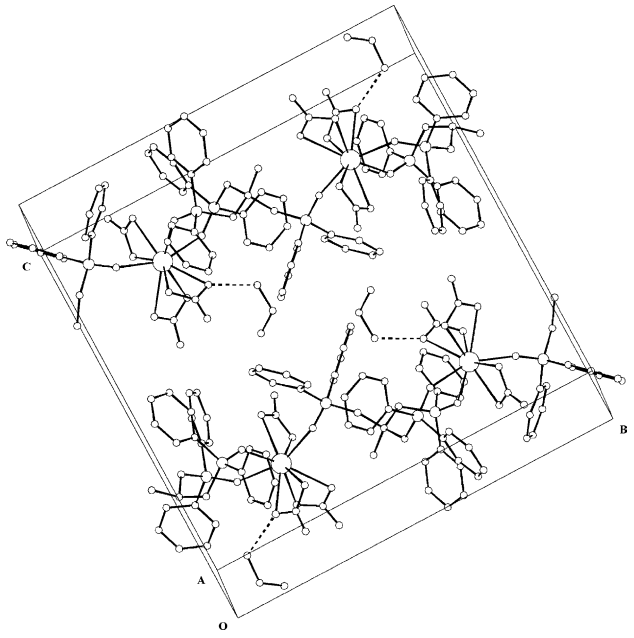


Fig. 3. The unit cell of $LaL(NO_3)_3 \cdot EtOH$ showing polymeric chains running along the crystallographic *b* axis. Hydrogen bonds are indicated by dotted lines.

2. Results and discussion

The complexes were formed by reaction of $MeC(CH_2P(O)Ph_2)_3$ with lanthanide nitrates in hot ethanol, methanol or acetonitrile. The compounds precipitated spontaneously on cooling the alcohol solutions giving $Ln(NO_3)_3L \cdot ROH$ (R = Me, Et) in good yield. The complexes are insoluble in common organic solvents and NMR spectra could not be obtained. Electrospray mass spectra were obtainable for the Yb complex only. Crystals suitable for X-ray diffraction were formed for the lighter lanthanides. Attempts to obtain crystals of the complexes of the heavier lanthanides were not successful. The solid state structures of $La(NO_3)_3L \cdot EtOH$ and $Pr(NO_3)_3L \cdot MeOH$ were determined by single crystal X-ray diffraction and are essentially identical in their coordination geometry around the metal and the ligand structure. The structure of the Pr complex is

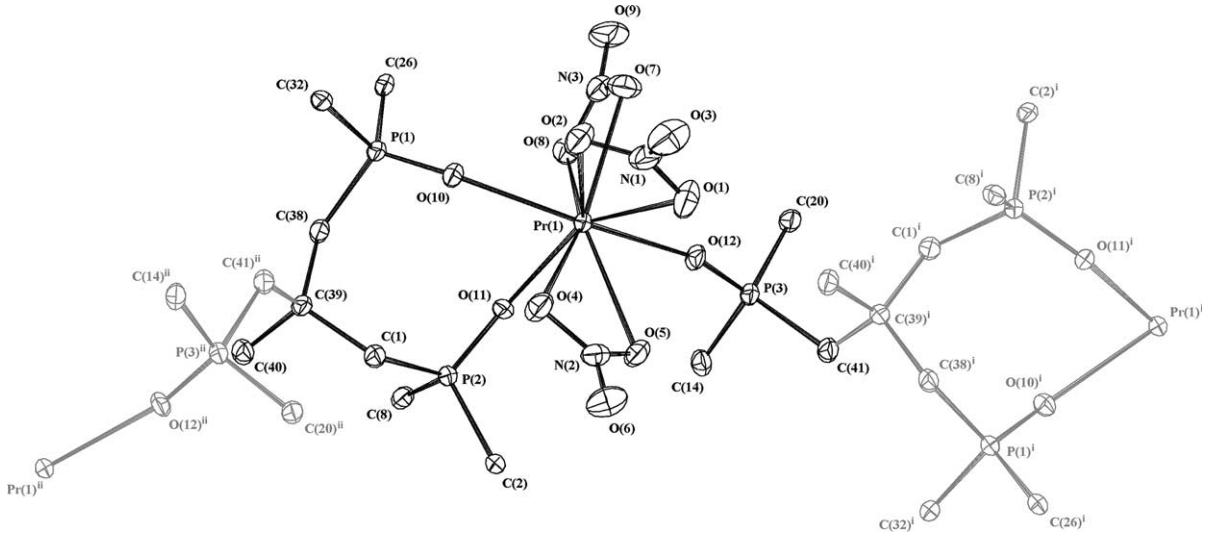


Fig. 2. The coordination of praseodymium in $[PrL(NO_3)_3]_n$. Thermal ellipsoids are drawn at the 50% probability level. Phenyl groups and hydrogen atoms are omitted for clarity. [Symmetry codes: i = $-x + 1.5$, $y - 0.5$, $-z + 1.5$, ii = $-x + 1.5$, $y + 0.5$, $-z + 1.5$].

shown in Fig. 2. The unit cell showing the two polymeric chains of the La complex and the hydrogen bond to ethanol is given in Fig. 3, details of the data collection and refinement for both complexes in Table 1 and selected bond lengths and angles in Table 2. The ligand adopts a bridging–chelating role, Fig. 1(b), B, with two PO groups chelating to give a puckered eight membered ring whilst the third bridges to another lanthanide ion, thus giving a polymeric chain. The P–CH_2–C ring angle ranging between 121.7(3)° and 123.9(3)° is considerably wider than expected for sp^3 hydridised carbon. There is, however, precedent for this in the structure of the

Table 1
Crystal data, data collection and refinement parameters

Crystal data		
Compound	$[LaL(NO_3)_3] \cdot EtOH$	$[PrL(NO_3)_3] \cdot MeOH$
Molecular formula	$C_{41}H_{39}LaN_3O_{12}P_3 + C_2H_6O$	$C_{41}H_{39}PrN_3O_{12}P_3 + CH_4O$
Molecular weight, M_r	1043.64	1031.61
Crystal system	monoclinic	monoclinic
Space group	$P2_1/n$	$P2_1/n$
Unit cell dimensions		
a (Å)	11.2038(3)	11.2812(2)
b (Å)	19.6162(5)	19.5645(4)
c (Å)	20.7538(7)	20.1771(5)
β (°)	99.8350(10)	100.1630(10)
Cell volume, U (Å^3)	4494.2(2)	4383.43(16)
Formula units/unit cell, Z	4	4
Density (calc.), D_x (Mg m^{-3})	1.542	1.563
$F(000)$	2120	2096
Reflections to obtain cell parameters	14304	39400
θ (°)	2.91–27.48	2.91–27.48
λ (Å) (Mo Kα)	0.71073	0.71073
μ (mm^{-1})	1.124	1.289
T (K)	120(2)	120(2)
Crystal description	prism	plate
	colourless	green
Dimensions (mm)	$0.15 \times 0.06 \times 0.05$	$0.1 \times 0.06 \times 0.01$
Data collection and SORTAV *absorption correction [26,27]*		
T_{max}	0.970	0.999
T_{min}	0.950	0.737
Measured reflections	32030	52146
Independent reflections	10129	9735
Observed reflections ($F_o > n\sigma(F_o)$)	5601 ($n = 2$)	7069 ($n = 2$)
R_{int}	0.1114	0.1760
θ_{max} (°)	27.50	27.47
h	$-14 \rightarrow 14$	$-14 \rightarrow 13$
k	$-25 \rightarrow 25$	$-25 \rightarrow 25$
l	$-22 \rightarrow 26$	$-26 \rightarrow 26$
Refinement (on F)^2		
Scattering factors from international tables for crystallography (vol. C)		
Reflections	10129	9735
Parameters/restraints	573/0	560/0
Weighting scheme, w[a]	$[\sigma^2(F_o^2)]^{-1}$	$[\sigma^2(F_o^2) + (0.0403P)^2]^{-1}$
Final R indices[b] ($F_o > n\sigma(F_o)$)	$n = 2$	$n = 2$
$R(F)$	0.0532	0.0463
wR_2 (F^2)	0.0700	0.1017
S	0.854	0.984
R indices[b] *(all data)*		
$R(F)$	0.1350	0.0773
wR_2 (F^2)	0.0813	0.1094
$(\Delta/\sigma)_{max}$	0.001	0.002
$\Delta\rho_{max}$ (e Å^{-3})	0.667	1.136
$\Delta\rho_{min}$ (e Å^{-3})	−0.689	−1.162
Extinction correction	none	none

L = $CH_3C(CH_2Ph_2PO)_3$.

[a] $P = [\mathrm{Max}(F_o^2, 0) + 2F_c^2]/3$.

[b] $R = \sum ||F_o| - |F_c|| / \sum |F_o|$; $wR_2 = \left[\sum w(F_o^2 - F_c^2)^2 \Big/ \sum wF_o^4\right]^{0.5}$.

Table 2
$[Ln((CH_2Ph_2PO)_3CCH_3)(NO_3)_3]$ – selected bond lengths (Å), non-bonding distances (Å) and bond angles (°)

	La	Pr		La	Pr
Ln(1)–O(1)	2.620(3)	2.576(3)	O(10)–Ln(1)–O(11)	74.42(8)	74.97(8)
Ln(1)–O(2)	2.607(3)	2.585(3)	O(10)–Ln(1)–O(12)	156.46(9)	155.47(9)
Ln(1)–O(4)	2.600(3)	2.551(3)	O(11)–Ln(1)–O(12)	91.61(8)	91.94(8)
Ln(1)–O(5)	2.640(3)	2.582(3)			
Ln(1)–O(7)	2.586(3)	2.551(3)	P(1)–C(38)–C(39)	123.9(3)	123.6(3)
Ln(1)–O(8)	2.609(3)	2.572(3)	P(2)–C(1)–C(39)	122.1(3)	121.7(3)
Ln(1)–O(10)	2.441(2)	2.402(2)	P(3)–C(41)–C(39)^{i}	121.2(3)	121.1(2)
Ln(1)–O(11)	2.441(2)	2.399(2)			
Ln(1)–O(12)	2.403(2)	2.374(2)	C(1)–C(38)–C(39)	113.2(3)	113.6(3)
Ln(1)···N(1)	3.043(4)	3.007(4)	N(1)···Ln(1)···N(2)	71.28(10)	73.44(9)
Ln(1)···N(2)	3.043(4)	2.985(4)	N(1)···Ln(1)···N(3)	103.70(11)	102.46(10)
Ln(1)···N(3)	3.036(4)	2.996(4)	N(2)···Ln(1)···N(3)	172.04(10)	170.62(9)
Ln(1)···P(1)	3.8137(11)	3.7766(9)	N(1)···Ln(1)–O(10)	96.66(10)	95.74(9)
Ln(1)···P(2)	3.7220(11)	3.6918(9)	N(1)···Ln(1)–O(11)	154.78(10)	153.16(9)
Ln(1)···P(3)	3.8821(11)	3.8338(9)	N(1)···Ln(1)–O(12)	103.43(10)	104.54(9)
P(1)–O(10)	1.510(3)	1.499(3)	N(2)···Ln(1)–O(10)	102.76(10)	104.47(9)
P(2)–O(11)	1.507(3)	1.507(2)	N(2)···Ln(1)–O(11)	87.47(9)	84.41(9)
P(3)–O(12)	1.506(3)	1.500(2)	N(2)···Ln(1)–O(12)	95.28(10)	94.56(9)
P(1)–C(38)	1.808(4)	1.813(4)	N(3)···Ln(1)–O(10)	83.77(9)	84.19(9)
P(2)–C(1)	1.815(4)	1.821(4)	N(3)···Ln(1)–O(11)	98.78(10)	101.57(10)
P(3)–C(41)	1.813(4)	1.821(4)	N(3)···Ln(1)–O(12)	79.71(9)	78.14(9)
C(1)–C(39)	1.557(5)	1.562(5)	O(10)–Ln(1)–O(11)	74.42(8)	74.97(8)
C(38)–C(39)	1.552(5)	1.554(5)	O(10)–Ln(1)–O(12)	156.46(9)	155.47(9)
C(41)–C(39)^{i}	1.546(5)	1.547(5)	O(11)–Ln(1)–O(12)	91.61(8)	91.94(8)

Symmetry code: i = $-x + 1.5$, $y - 0.5$, $-z + 1.5$.

related free ligand, $EtC(CH_2P(O)Ph_2)_3$ [20] where these angles range from 118.9° to 120.3°. The nitrate groups are bidentate in all cases with one hydrogen bonded to the lattice ethanol. The overall coordination geometry can be considered as a distorted *mer*-LnO_3N_3 octahedron, if the nitrates are taken as pseudo-monodentate ligands. The angles at the lanthanide subtended by the pseudo *trans*-atoms range from 172.04(10)° to 153.16(9)° whilst the *cis*-atoms give angles in the range 104.54(9)–71.28(10)°.

Whilst the atoms of the N(3) nitrate are essentially coplanar with almost linear Ln···N–O vectors, the terminal oxygens of the other two nitrates lie significantly out of the mean NO_2Ln plane. This tilting of the nitrate seems to be linked to the extent of hydrogen bonding or other secondary interactions with the nitrate oxygen atoms. Thus with no short contacts or hydrogen bonds to the oxygens the Ln···N(3)–O(9) angles at 177.9(3)° (La) and 177.4(3)° (Pr) are almost linear. With short contacts between the oxygens and hydrogens of the aromatic rings from adjacent polymer chains the Ln···N(1)–O(3) angle decreases to 172.8(3)° (La) and 173.9(3)° (Pr). Stronger hydrogen bonding interaction with the alcohol leads to a further tilting of the nitrates with Ln···N(2)–O(6) angles of 168.4(3)° (La) and 169.9(3)° (Pr). We have previously observed a this effect [21] when hydrogen bonding between two nitrates and the OH group of $[(MeO)_2P(O)]_2CMe(OH)$ causes tilting of nitrates by a similar amount whilst the third NO_3 ligand which is not involved in any secondary interaction has a linear Ln···N–O arrangement.

The phosphoryl groups fall into two categories; two form the chelate ring and one bridges between two metals. When the coordination of the PO group is unrestricted, as in monodentate phosphine oxides, the angle at the oxygen tends towards 180° [3,21,22]. The adoption of a chelate ring imposes restrictions on this angle, which falls within the range of 140°–150° here, compared with 163°–166° for the less constrained bridging group. This in turn is reflected in the strength of the bonding to the metal ions. The Ln–OP(bridging) distance being around 0.03 Å shorter than Ln–OP(chelating). Comparing the bond lengths observed here with $EtC(CH_2P(O)Ph_2)_3$ [20], it is found that the PO bond lengthens, as expected, on coordination by about 0.15 Å, while the P–C distance shortens by about 0.03 Å.

It is interesting to speculate on the preferred mode of binding of the ligand in these complexes. Examination of the overall geometry of $EtC(CH_2P(O)Ph_2)_3$ shows that two PO groups are relatively close together with an O···O separation of 3.24 Å, with the third PO situated much further away from these with distances of O···O 6.71 and 6.81 Å. This situation is mirrored by the structure of $MeC(CH_2P(O)Ph_2)_3$ in the complexes where the chelating oxygen atoms move slightly closer together (O···O 2.922(3) Å (La), 2.952(3) Å (Pr)) and the bridging oxygen is still considerably removed from these at between 6.509(4) and 6.795(3) Å. Thus on adopting the chelating–bridging bonding mode the ligand has to undergo relatively little reorganisation of its structure. The recently reported complex of Nd with $[CpCo(P(O)(OMe)_2]^-$ shows the ligand bonding

in a tridentate fashion to the metal [23]. Here the secondary structure of the ligands constrains the coordinating PO groups thus favouring coordination mode A. The adoption of the tris-chelating mode of bonding in Cd^{2+} complexes [18] is probably favoured by the lack of competition in the primary coordination sphere (the relatively non coordinating AsF_6^- or SbF_6^- anions were used) and, possibly, by significant covalent metal–ligand interactions. The conformation in the free ligand will mainly reflect the minimised steric repulsions and electrostatic repulsions of the P–O groups, and whilst it obviously has the structural flexibility to adopt other geometries it will only be expected to do so if the overall energy of the complex is minimised as a result. In lanthanide complexes, where electrostatic interactions are expected to dominate, the ligand will adopt a conformation which balances the repulsions between P–O groups with the attraction between oxygen atoms and the lanthanide ion. In our complexes the basic ligand structure appears largely unchanged by the interactions with positively charged lanthanide centres.

3. Infrared spectroscopy

The infrared spectra show the features expected for phosphoryl complexes with bidentate nitrates. The ν_{PO} decreases by about 20 cm^{-1} on coordination and two intense broad envelopes at ~1150 and 1300 cm^{-1} are assigned to the N–O stretches of the coordinated nitrate ligands. A distinction between the spectra of the lighter and heavier lanthanides is apparent in that there is a considerable amount of fine structure evident on the N–O absorptions for $Ln(NO_3)_3L$ (Ln = La–Gd) whilst these bands have a much simplified appearance for the complexes of the heavier metals. This may indicate some changes in the structures but we have been unable to produce crystals suitable for X-ray analysis for these complexes.

4. Electrospray mass spectrometry

Three complexes (La, Nd, Gd and Yb) were investigated in methanol solution. Poor ionisation was apparent for the La, Nd and Gd complexes with $[L + Na]^+$ and $[L + H]^+$ being the main features in the resulting spectra. Better quality spectra were obtained for the Yb complex which showed peaks consistent with dissociation and ligand redistribution. A cluster of peaks of low intensity centred at $m/z = 970.2$ is assigned to $[Yb(NO_3)_2L]^+$ which can be considered as being derived from the solid state structure. The most intense Yb containing ions, however, are multiply charged species such as $[Yb(NO_3)L]^{2+}$, $[YbL_n]^{3+}$ (n = 2–6). Here the compression of the characteristic isotope pattern makes assignment less certain.

5. Experimental

5.1. X-ray data collection, structure determination and refinement

Data were collected by the EPSRC National Crystallography Service at the University of Southampton using previously described procedures [24–27].

The La structure was solved by estimating the position of the metal atom using Patterson methods (SHELXS-97) [28,29], and all remaining non-H atom positions were obtained through consecutive fourier syntheses (SHELXL-97) [30]. Refinement to convergence was by full-matrix least-squares on F^2 data using SHELXL-97 [30] from within the WINGX [31,32] suite of software. The Pr structure was refined by isomorphous replacement into the La structure.

In each of the structures, alcohol molecules were modelled in the interstices between the parallel chains of the lanthanide-triphosphine oxide polymer. In the La structure, peaks in the difference Fourier map indicated ethanol disordered over two positions. A disordered model with complementary site occupation factors was adopted. The site occupation factor refined to a value of 0.524(21). The Pr data were weaker making conclusive assignment of the solvent more difficult. Fewer peaks were evident in the difference Fourier map of the Pr structure in this region, and a plausible solution consisting of a single methanol molecule was adopted.

In both structures, with the exception of the carbon atoms of the alcohol molecules, non-H atoms were refined with anisotropic displacement parameters. All H atoms were refined at idealised geometric positions (phenyl C–H = 0.95 Å, methylene C–H = 0.99 Å, methyl C–H = 0.98 Å, Hydroxyl O–H = 0.84 Å). The H atoms of each functional group of the triphosphine oxide ligand were assigned common, refined isotropic displacement parameters. On convergence, these displacement parameters were: phenyl 0.035(2) $Å^2$ (La), 0.031(2) $Å^2$ (Pr); methylene 0.015(4) $Å^2$ (La), 0.027(5) $Å^2$ (Pr); methyl 0.024(6) $Å^2$ (La), 0.015(5) $Å^2$ (Pr). The H atoms of solvent molecules were given thermal parameters equivalent to 1.2 (non-methyl) or 1.5 (methyl) times those of the carrier atom.

Molecular graphics were generated using SNOOPI [33].

5.2. Electrospray mass spectrometry

Spectra were obtained from the EPSRC National Mass Spectrometry Service at Swansea University as described previously [17].

5.3. Infrared spectroscopy

Infrared spectra were obtained on a Thermo Nicolet Avatar 370 FTIR. The spectra were run without any sample preparation.

5.4. Synthetic work

The ligand was prepared by H_2O_2 oxidation of the phosphine in acetone. The phosphine (5 g) was suspended in 50 ml acetone and hydrogen peroxide (4 g 30% solution) in 20 ml acetone was added over 1 h. The mixture was refluxed for 5 min to give a clear solution, evaporated to 20 ml, cooled in ice and filtered to give 4.40 g white solid. A further crop (1.19 g) was obtained on slow evaporation of the filtrate. Principle infrared bands/cm^{-1}: ν_{PO} 1167 (s) Lit 1185 [34] NMR (MeOD) ^1H 400 MHz, δ 6.4, 6.2 (30H) (m), δ 1.81 d (6H) d $^2J_{PH}$ 11.2 Hz δ 0.84s 3H. ^{31}P 162 MHz, δ 32.1 (s). Mass spectrometry ESMS (MeOH) $[L + H]^+$ $C_{41}H_{40}P_3O_3$ 673.2 (40%), $[L + Na]^+$ $C_{41}H_{39}NaP_3O_3$ 695.5 (100%).

The complexes were prepared by the same general method. Methanol solutions of the lanthanide nitrates and ligand were mixed and warmed to 50 °C for 3 h during which time crystals formed. These were filtered and dried at the pump to give $Ln(NO_3)_3L \cdot EtOH$ in yields of 75–90%.

$La(NO_3)_36H_2O$ (0.63 g, 1.47 mmol) in 50 ml EtOH was added to the ligand (0.49 g, 0.72 mmol) in 20 ml EtOH. On warming colourless crystals formed which were filtered and dried at the pump to give 0.58 g, 81% based on L. *Anal.* expected for $LaC_{43}H_{45}N_3O_{13}P_3$: C, 48.48; H, 3.94; N, 4.21. Found: C, 48.99; H, 4.04; N, 4.28%. Principle infrared bands/cm^{-1}: ν_{PO} 1157(w) 1141(s), ν_{NO} 1482(s), 1458(s), 1308(s), 1271(s).

$Nd(NO_3)_36H_2O$ (0.58 g, 1.25 mmol) in 50 ml EtOH was added to the ligand (0.41 g, 0.61 mmol) in 20 ml EtOH. On warming lilac crystals formed which were filtered and dried at the pump to give 0.50 g, 82% based on L. *Anal*. expected for $NdC_{43}H_{45}N_3O_{13}P_3$: C, 49.22; H, 4.32; N, 4.01. Found: C, 48.89; H, 4.13; N, 3.70%. Principle infrared bands/cm^{-1}: ν_{PO} 1141(s), ν_{NO} 1481(s), 1458(s), 1311(s), 1273(s).

$Gd(NO_3)_36H_2O$ (0.51 g, 1.12 mmol) in 50 ml EtOH was added to the ligand (0.52 g, 0.77 mmol) in 20 ml EtOH. On warming colourless crystals formed which were filtered and dried at the pump to give 0.67 g, 85% based on L. *Anal*. expected for $GdC_{43}H_{45}N_3O_{13}P_3$: C, 48.64; H, 4.27; N, 3.96. Found: C, 47.85; H, 4.15; N, 4.02%. Principle infrared bands/cm^{-1}: ν_{PO} 1141(s), ν_{NO} 1483(s), 1459(s), 1316(s), 1279(s).

$Er(NO_3)_36H_2O$ (0.36 g, 0.80 mmol) in 50 ml EtOH was added to the ligand (0.47 g, 0.69 mmol) in 20 ml EtOH. On warming a pink powder formed which was filtered and dried at the pump to give 0.50 g, 61% based on L. *Anal*. expected for $ErC_{43}H_{45}N_3O_{13}P_3$: C, 48.17; H, 4.23; N, 3.92. Found: C, 47.84; H, 3.98; N, 4.12%. Principle infrared bands/cm^{-1}: ν_{PO} 1145(s), ν_{NO} 1483(s), 1290(s).

6. Supplementary material

Crystallographic data for the structures reported in this paper have been deposited with the Cambridge Crystallographic Data Centre, CCDC 220339 and 220340 for the La and Pr complexes respectively. Copies of this information may be obtained free of charge from The Director, CCDC, 12 Union Road, Cambridge, CB2 1EZ, UK (Fax +44 1223 336033; e-mail deposit@ccdc.cam.ac.uk or www: http://www.ccdc.cam.ac.uk).

Acknowledgements

We thank the Royal Society of Chemistry for support through the research fund and EPSRC for the use of the National Mass Spectrometry Service at Swansea University and the X-ray data collection service at Southampton University. We are also grateful to Stephanie Cornet and Rebeca Alvarez of the Centre for Radiochemistry Research, School of Chemistry, University of Manchester for the NMR spectra of the ligand and for their attempts to obtain spectra from the complexes.

References

[1] D.R. Cousins, F.R. Hart, J. Inorg. Nucl. Chem. 29 (1967) 1745.
[2] J-C. Berthet, M. Nierlich, M. Ephritikhine, Polyhedron 22 (2003) 3475.
[3] L. Deakin, W. Levason, M.C. Popham, G. Reid, M. Webster, J. Chem. Soc., Dalton Trans. (2000) 2439.
[4] A.M.J. Lees, A.W.G. Platt, Inorg. Chem. 42 (2003) 4673.
[5] H.-J. Cristau, D. Virieux, J.-L. Pirat, E. Ansoborlo, M.H. Napoli, F. Paquet, Phosphorus, Sulfur, Silicon 144-146 (1999) 505.
[6] K.L. Nash, C. Lavallette, M. Borkowski, R.T. Paine, X. Gan, Inorg. Chem. 41 (2002) 5849.
[7] E.M. Bond, U. Engelhardt, T.P. Deere, B.M. Rapko, R.T. Paine, J.R. Fitzpatrick, Solvent Extr. Ion Exch. 15 (1997) 381.
[8] D. Parker, J.A.G. Williams, J. Chem. Soc. Dalton Trans. (1996) 3613.
[9] Y. Bretonnière, M. Mazzanti, J. Pécaut, F.A. Dunand, A.E. Merbach, Inorg. Chem. 40 (2001) 6737.
[10] C. Gateau, M. Mazzanti, J. Pécaut, F.A. Dunand, L. Helm, J. Chem. Soc., Dalton Trans. (2003) 2428.
[11] B.P. Murphy, L. Quinti, D.G. Kelly, W.J. Martin, A. Perotti, M.B. Hursthouse, T. Gelbrich, Inorg. Chem. Comm. 5 (2002) 577.
[12] X.-P. Yang, B.-S. Kang, W.-K. Wong, C.-Y. Su, H.-Q. Liu, Inorg. Chem. 42 (2003) 169.
[13] J. Zhang, Y. Tang, M.-Y. Tan, W.-S. Liu, K.-B. Yu, J. Chem. Soc., Dalton Trans. (2002) 832.
[14] J.-P. Costes, A. Dupuis, G. Commenges, S. Lagrave, J.-P. Laurent, Inorg. Chim. Acta 285 (1999) 49.
[15] Y. Bretonnière, M. Mazzanti, R. Wietzke, J. Pécaut, J. Chem. Soc. Chem. Comm. (2000) 1543.

[16] G.S. Conary, D.J. McCabe, R.L. Meline, E.N. Duesler, R.T. Paine, Inorg. Chim. Acta 203 (1993) 11.
[17] J. Fawcett, A.W.G. Platt, S. Vickers, Polyhedron 22 (2003) 1431.
[18] P.A. Dean, Can. J. Chem. 59 (1981) 3221.
[19] J. Ellermann, M. Thierling, Z. Anorg. Allg. Chem. 411 (1975) 15.
[20] A.N. Chekhlov, J. Struct. Chem. 41 (2000) 646.
[21] A.M.J. Lees, J.M. Charnock, R.A. Kresinski, A.W.G. Platt, Inorg. Chim. Acta 312 (2001) 170.
[22] W. Levason, E.H. Newman, M. Webster, Polyhedron 19 (2000) 2697.
[23] H. He, W.-K. Wong, J. Guo, K.-F. Li, W.-Y. Wong, W.-K. Lo, K.-W. Cheah, Inorg. Chim. Acta 357 (2004) 4379.
[24] Collect: Data Collection Software, R. Hooft, Nonius BV, 1998.
[25] Z. Otwinowski, W. Minor, in: C.W. Carter, R.M. Sweet (Eds.), Methods in Enzymology, vol. 276, Macromol. Crystallogr. Part A, Academic Press, London, 1997, p. 307.
[26] SORTAV absorption correction software package R.H. Blessing, Acta Crystallogr. A 51 (1995) 33.
[27] R.H. Blessing, J. Appl. Crystallogr. 30 (1997) 421.
[28] G.M. Sheldrick, SHELXS-97 – A Program for Automatic Solution of Crystal Structures, Release 97-2, University of Goettingen, Germany, 1997.
[29] G.M. Sheldrick, Z. Dauter, K.S. Wilson, H. Hope, L.C. Sieker, Acta Cryst. D 49 (1993) 18.
[30] G.M. Sheldrick, SHELXL-97 – A Program for Crystal Structure Refinement. Release 97-2, University of Goettingen, Germany, 1997.
[31] L.J. Farrugia, WINGX – A Windows Program for Crystal Structure Analysis, University of Glasgow, 1998.
[32] L.J. Farrugia, J. Appl. Crystallogr. 32 (1999) 837–838.
[33] K. Davies, SNOOPI – Molecular Plotting Program, Chemical Crystallography Laboratory, University of Oxford, 1983.
[34] E. Lindner, H. Beer, Chem. Ber. 105 (1972) 3261.

Available online at www.sciencedirect.com
SCIENCE DIRECT®
Polyhedron 24 (2005) 435–441
POLYHEDRON
www.elsevier.com/locate/poly

Synthesis and characterization of the bimetallic polymers $[MS_4Ag_2(Hmimt)_2]_n$ (where M = Mo or W, Hmimt = 1-methylimidazoline-2(3H)-thione): crystal structures of $[WS_4Ag_2(Hmimt)_2]_n$ and $[Ag_2I_2(Hmimt)]_n$

Azizolla Beheshti [a,*], William Clegg [b,*], Neil R. Brooks [b], Fatemeh Sharafi [a]

[a] Department of Chemistry, Faculty of Science, Shahid Chamran University, Ahwaz, Iran
[b] School of Natural Sciences Chemistry, University of Newcastle, Bedson Building, Newcastle upon Tyne NE1 7RU, UK

Received 6 December 2004; accepted 15 December 2004

Abstract

The title compounds were synthesized by the reactions of $[NH_4]_2[MS_4]$ (M = Mo, W), AgI and Hmimt in acetone and characterized by IR, ^{1}H NMR and UV–Vis spectroscopy. The polymeric structure of $[WS_4Ag_2(Hmimt)_2]_n$ was determined by X-ray crystallography. In this compound, there are two distinctly different coordination modes for the silver atoms. One Ag atom has a pseudo-tetrahedral geometry with one terminal monodentate-S Hmimt, two μ_2-S bridging Hmimt and one S atom of a monodentate WS_4 unit. The other is surrounded by four sulfur atoms belonging in pairs to two WS_4 fragments; the coordination geometry is distorted tetrahedral. The $[WS_4Ag_2(Hmimt)_2]_n$ polymer represents the first example of tetrathiometalate anions $[MS_4]^{2-}$ (M = Mo, W, or V) coordinated to another metal atom in a monodentate fashion. In both crystal structures determined the Hmimt ligands are present in the thione form, with coordination taking place via the sulfur atom only.
© 2004 Elsevier Ltd. All rights reserved.

Keywords: Crystal structures; Silver complexes; Thione complexes; Tetrathiometalates; Tungsten complexes; Polymeric network

1. Introduction

Imidazole-type heterocycles represent an important class of ligands in coordination chemistry. The imidazole ring of the amino acid histidine is an essential component of many biological systems, such as proteins, nucleic acids and the vitamin B_{12} coenzyme [1]. Complexes of heterocyclic thiones such as imidazolidine-2-thione (Imt) and diazinane-2-thione (Diaz), and their complexes with transition metals, are of interest in bioinorganic chemistry, because of the search for simple model compounds for metalloproteins. In view of this, Cu(I), Ag(I), Au(I), Hg(II) and Cd(II) complexes with thiones have been widely studied in recent years [2]. The tetrathiometalate anions $[MS_4]^{2-}$ (M = Mo, W) have been shown to be useful and versatile reagents, which play a key role in some biological processes [3,4]. One of their important functions is coordination to other metal ions [5]. They bond to a wide variety of metal centres M′ via the sulfur atoms, thus acting as bi- or tridentate ligands. An important stabilizing factor is the ability of the ligands to delocalize electron density from M′ into low-lying empty d-based orbitals. The present paper details the synthesis and structural

* Corresponding authors. Tel.: +98 611 336 0018; fax: +98 611 333 7009 (A. Beheshti); Tel.: +44 191 222 6649; fax: +44 191 222 6929 (W. Clegg).
E-mail addresses: beheshti_a@hotmail.com (A. Beheshti), w.clegg@ncl.ac.uk (W. Clegg).

0277-5387/$ - see front matter © 2004 Elsevier Ltd. All rights reserved.
doi:10.1016/j.poly.2004.12.002

characterization of a trinuclear complex of the bio-active molecule 1-methyl-imidazoline-2(3H)-thione (Hmimt), commercially known as methimazole, with $[WS_4]^{2-}$ and Ag^+ ions.

2. Experimental

2.1. Materials and physical measurements

Starting materials were purchased from commercial sources and used without further purification. $[NH_4]_2[MoS_4]$, $[NH_4]_2[WS_4]$ and $[NH_4]_2[WOS_3]$ were prepared from them by published methods [6]. The infrared spectra (4000–400 cm^{-1}) were recorded from KBr disks with an FT-IR model BOMEN MB102 spectrometer. UV–Vis spectra of the ligands and complexes were recorded on a JASCO model 7850 spectrophotometer. ^1H NMR spectra were obtained using a Bruker DRX 500 AVANCE spectrometer. Melting points could not be determined, as the complexes decomposed on heating.

2.2. Preparation of $[WS_4Ag_2(Hmimt)_2]_n$ (1)

AgI (0.0585 g, 0.249 mmol) was added to a suspension of $[NH_4]_2[WS_4]$ (0.029 g, 0.0833 mmol) in 30 ml of acetone and the mixture was stirred for ca. 30 min at room temperature. Hmimt (0.045 g, 0.0394 mmol) was added to this solution and the mixture was stirred for another 30 min. The precipitate was centrifuged and filtered off and the filtrate was evaporated to dryness in vacuo. The residue was washed with distilled water (2×2 ml), ethanol (2×2 ml) and diethyl ether (2×5 ml) and dried in vacuo to give a red powder (yield 0.033 g, 75%). Red crystals of this compound were obtained from the freshly made sample in acetone, by slow evaporation of the solvent. The air-stable crystals are insoluble in all usual organic solvents except dimethylformamide (DMF) and dimethylsulfoxide (DMSO).

2.3. Preparation of $[MoS_4Ag_2(Hmimt)_2]_n$ (2)

This compound was prepared in the same way as $[WS_4Ag_2(Hmimt)_2]_n$, using $[NH_4]_2[MoS_4]$ (0.260 g, 1 mmol) instead of $[NH_4]_2[WS_4]$, and an equivalent amount of AgI, and was isolated as a violet powder (yield 0.468 g, 70%).

2.4. Attempted preparation of $[WOS_3Ag_3I(Hmimt)_n]$

The preparative procedure was the same as that used for $[WS_4Ag_2(Hmimt)_2]_n$, with $[NH_4]_2[WOS_3]$ (0.316 g, 1 mmol), AgI (0.704 g, 3 mmol) and Hmimt (0.365 g, 3.2 mmol) in acetone (30 ml). Both IR [ν(W–S) = 448 cm^{-1} and ν(W–O) = 872 cm^{-1}] and UV–Vis (267 nm) spectra confirm the presence of WOS group in the complex, but the complex decomposed when the orange solution was allowed to evaporate slowly, resulting in the formation of micro-crystals of compound **3** with a chemical formula of $C_4H_6Ag_2I_2N_2S$, as confirmed by X-ray analysis. The yield was not determined.

2.5. X-ray crystallography

Crystal data together with other relevant information on the structure determinations for compounds **1** and **3** are listed in Table 1. All measurements were made on a Bruker SMART CCD diffractometer with narrow frames (0.3° in ω). Mo Kα radiation ($\lambda = 0.71073$ Å) was employed for data collection at 150 K. Absorption corrections were based on the high redundancy of symmetry-equivalent and repeated reflections. The structures were solved by direct methods and refined by full-matrix least-squares on all F^2 values. Non-hydrogen atoms were refined with anisotropic displacement parameters. Hydrogen atoms were included in calculated positions and refined with isotropic displacement parameters, riding on their parent atoms. The structure of **1** was found to be twinned. Large residual electron density peaks were found for **3**, as a result of relatively poor diffraction data and the presence of several heavy atoms in the structure, but these have no chemical significance. Programs were standard Bruker AXS control and integration software, SADABS [7] and SHELXTL [8],

Table 1
Crystallographic data

	(1)	(3)
Chemical formula	$C_8H_{12}Ag_2N_4S_6W$	$C_4H_6Ag_2I_2N_2S$
Formula weight	756.2	583.7
Crystal system	monoclinic	triclinic
Space group	$P2_1/c$	$P\bar{1}$
Unit cell dimensions		
a (Å)	17.3551(18)	7.784(3)
b (Å)	13.2762(12)	8.0112(18)
c (Å)	7.9170(4)	10.438(2)
α (°)		76.189(17)
β (°)	93.313(6)	70.27(2)
γ (°)		67.98(2)
V (Å^3)	1821.1(3)	563.3(3)
Z	4	2
D_{calc} (g cm^{-3})	2.751	3.441
μ (mm^{-1})	9.11	9.09
Crystal size (mm)	$0.3 \times 0.2 \times 0.2$	$0.2 \times 0.1 \times 0.1$
θ_{max} (°)	25.2	25.0
Reflections collected	3187	8821
Independent reflections (R_{int})	3187	1986 (0.0842)
Transmission	0.171–0.263	0.442–0.665
Number of parameters	194	101
$R(F, F^2 > 2\sigma)$	0.0448	0.0744
R_w (F^2, all data)	0.1243	0.2112
Goodness-of-Fit on F^2	1.123	1.163
El. density extremes (eÅ^{-3})	2.05 and −2.15	7.94 and −2.24

together with ROTAX [9] and ROTWIN [10] to handle the twinning.

3. Results and discussion

3.1. Infrared spectra

The IR spectra of the complexes (Table 2) exhibit characteristic strong bands at 435 and 455 cm^{-1} for $[WS_4Ag_2(Hmimt)_2]_n$ (**1**) and 441 and 459 cm^{-1} for $[MoS_4Ag_2(Hmimt)_2]_n$ (**2**), assigned to the μ_3-S and μ_2-S stretching vibrations of the WS_4 and MoS_4 groups, respectively. The band at 478 cm^{-1} for $[WS_4Ag_2(Hmimt)_2]_n$ and at 482 cm^{-1} for $[MoS_4Ag_2(Hmimt)_2]_n$ is assigned to ν[W(1)–S(3)] (see Fig. 1 for atom numbering) and the corresponding $\nu(Mo–S_b)$ band. Comparing these values with the corresponding ones for $[NH_4]_2[WS_4]$ (458 cm^{-1}) and $[NH_4]_2[MoS_4]$ (476 cm^{-1}) [11], an increase of π-character of the W(1)–S(3) and $Mo–S_b$ bonds is indicated.

Infrared spectroscopy may also be used to probe the mode of Hmimt ligand coordination. In the IR spectrum of a compound such as Hmimt, where the carbon atom is directly linked to nitrogen, ν(C=S) is strongly coupled and, as a result, there are a number of different bands in the 1570–700 cm^{-1} region, each of which contains some contribution from the C=S stretching mode. This accounts for the difficulty in identification of this band and for the diversity of assignments that have been made [12]. Thus, the thioamide group in Hmimt normally shows four bands in the regions 1570–1395, 1420–1260, 1140–940 and 800–700 cm^{-1} and these bands are known as the thioamide I, II, III and IV bands, respectively. Bands I and II have little C=S content and originate mainly in C=N and NH deformation modes, but III and IV have a significant C=S content [12]. The monodentate sulfur-donating character of ligands of this kind is evident by comparison of the positions of the four thioamide bands in the infrared spectra of the complexes and of the free Hmimt ligand (Table 2). In these complexes, the absence of a ν(SH) band at

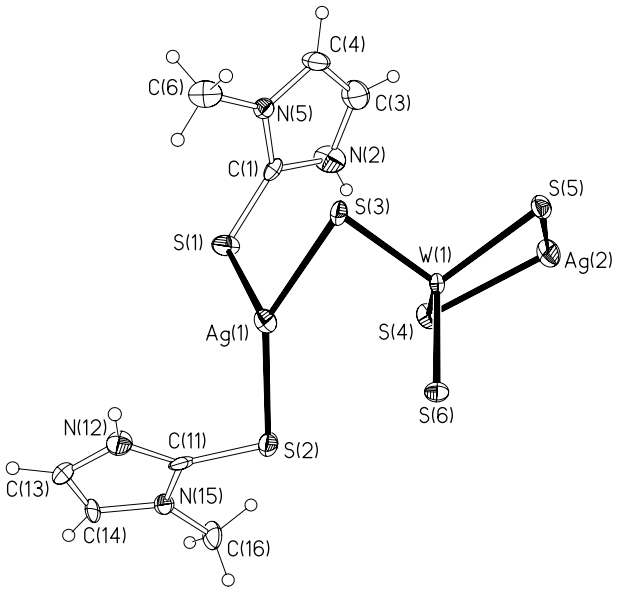


Fig. 1. The asymmetric unit of $[WS_4Ag_2(Hmimt)_2]_n$ (**1**), showing the atom numbering scheme. The two Ag atoms make connections with sulfur atoms in adjacent symmetry-related units to generate the two-dimensional polymeric structure.

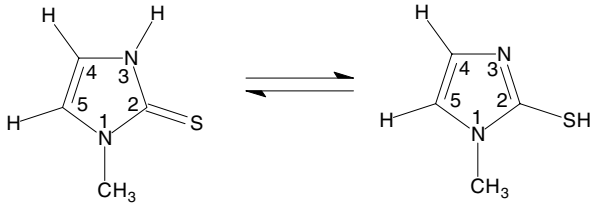
~2500 cm^{-1}, the presence of the ν(NH) band in the range 3193–3227 cm^{-1}, and a low-frequency shift in the ν(C=S) band clearly indicate that the Hmimt ligands are coordinated only via the thione sulfur in the complexes. The NH bands of $[WS_4Ag_2(Hmimt)_2]_n$ are shifted to higher frequency (3227 cm^{-1}) relative to the free ligand (3120 cm^{-1}). These shifts probably result from changes in the electronic state when the ligand coordinates via the thione sulfur and the C=S bond loses some of its double-bond character. This clearly indicates that nitrogen is not involved in coordination. The most significant changes are seen for the thioamide (III) band and especially for the thioamide (IV) band. This has the largest proportion of ν(C=S) activity and the shift to lower frequency of the band [2,13,14] is consistent with ligand thione donation for these complexes. The thioamide (IV) band is particularly affected, with the bands in the free ligand (767 and 740 cm^{-1}) [15]

Table 2
Significant IR bands (cm^{-1}) of the ligand and its complexes

Hmimt	$[WS_4Ag_2(Hmimt)_2]_n$	$[MoS_4Ag_2(Hmimt)_2]_n$	$[WOS_3Ag_3I(Hmimt)_n]$	$[Ag_2I_2(Hmimt)]_n$	Assignment
3120 s	3227 m	3220 m	3193 m	3230 m	ν(N–H)
1571 s	1570 s	1572 s	1570 s	1573 s	ν(C=C + ν(C=N)
1463 s, b	1458 s	1460 s	1463 s	1473 s	Thioamide I
1274 s	1245 w	1255 w	1257 w	1257 m	Thioamide II
1085 s	1095 w	1090 m	1080 w	1095 m	Thioamide III
767 sh	718 s	735 s	720 m	728 s	Thioamide IV
740 m	710 m	717 s			
674 s	664 m	668 m	668 w	668 w	δ(C=S)
529 s	520 w	515 s	513 w	515 w	π(C=S)

b, broad, m, medium, s, strong, vs, very strong, w, weak.

replaced by a sharp but split band at 718 and 710 cm^{-1} in $[WS_4Ag_2(Hmimt)_2]_n$, 735 and 717 cm^{-1} for $[MoS_4Ag_2(Hmimt)_2]_n$. These spectroscopic results are consistent with the structure of $[WS_4Ag_2(Hmimt)_2]_n$ as determined by X-ray crystallography. In the IR spectrum of the complex $[Ag_2I_2(Hmimt)]_n$, the absence of the ν(SH) band and the presence of the ν(NH) band at 3230 cm^{-1}, as well as shifts to lower frequency in the ν(C=S) absorption [ν(C=S) = 515 cm^{-1}], clearly indicate that the Hmimt ligand is coordinated via the thione sulfur.



3.2. Solution spectra

3.2.1. Electronic spectra

The UV–Vis spectra of the compounds **1** and **2** in DMF have effective absorption bands at 261.5 and 492.5 nm for the Mo cluster **2**, and 261.5 and 410 nm for the W cluster **1**. The first strong bands lie in the region for absorption by the free thione and may thus be attributed to thione-based intraligand transitions [16] and the other two absorptions can be assigned as charge-transfer bands of the type (π)S–(d)M (M = Mo, W) arising from the MS_4 moiety; these are red-shifted compared to the free $[MS_4]^{2-}$ anion (397 nm for W and 472 nm for Mo).

3.2.2. ^1H NMR spectra

The ^{1}H NMR spectra of Hmimt and of the complexes in DMSO-d_6 are summarized in Table 3. In the proton spectra of the complexes, the ligand signals are shifted down-field from their positions in the spectrum of the free ligand, suggesting that in DMSO-d_6 the ligand remains coordinated to the metal.

The absence of a weak SH signal of the thiol form of the ligand in the ^{1}H NMR spectra of the complexes confirms that coordination of Hmimt in DMSO-d_6 solution, as in the solid state, takes place only through the sulfur atom. Thus the Hmimt ligands in the complexes are neutral and they are in the thione form.

3.3. Description of the structures

3.3.1. Crystal structure of $[WS_4Ag_2(Hmimt)_2]_n$ (1)

Views of a single repeat unit and the neutral polymeric sheet arrangement of this complex are presented in Figs. 1 and 2, respectively. Important bond lengths and angles are listed in Table 4.

In the complex, there are two distinctly different coordination modes for the silver atoms. Ag(1) has a pseudo-tetrahedral geometry with large compression of the S(3)–Ag(1)–S(1) angle [95.10(13)]° and enlargement of the S(2)–Ag(1)–S(3) angle [147.77(13)]° with respect to ideal tetrahedral. The deviation from ideal tetrahedral geometry is probably due to the large steric hindrance of the Hmimt ligands. Coordination of Ag(1) involves two bridging μ_2-S(thione)-donating Hmimt ligands with average Ag(1)–S(thione) distances of 2.640(4) Å, as well as one terminal monodentate S(thione)-donating Hmimt with Ag(1)–S(2) of 2.488(4) Å and one asymmetrically bridging μ_2-S $[WS_4]^{2-}$ moiety with Ag(1)–S(3) of 2.536(4) Å. The Ag(1)–(μ_2-S)–W bridges between two neighbouring chains join them together to generate the

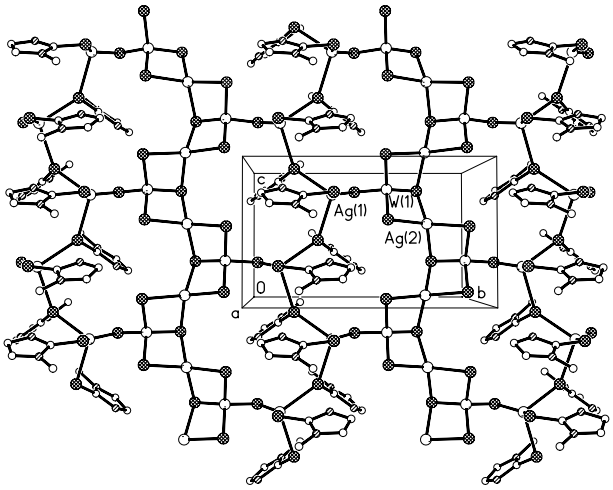


Fig. 2. Polymeric sheet structure of $[WS_4Ag_2(Hmimt)_2]_n$, seen along the unit cell *a* axis. The W and Ag atoms of the 'home' asymmetric unit are labelled. H atoms have been omitted.

Table 3
^{1}H NMR chemical shifts (δ in ppm referred to TMS) of Hmimt and its complexes

Compound	δ(H–N)	δ(H5)	δ(H4)	δ(N–CH_3)
Hmimt	12.03 (s,b)	7.03 (d)	6.85 (d)	3.40 (s)
$[Ag_2WS_4(Hmimt)_2]_n$	12.60 (s)	7.18 (d)	7.04 (d)	3.53 (s)
$[Ag_2MoS_4(Hmimt)_2]_n$	12.25 (s)	7.10 (d)	6.93 (d)	3.47 (s)

b, broad; d, doublet; s, singlet.

Table 4
Selected bond lengths (Å) and angles (°) for compound **1**

Bond lengths			
W(1)–S(3)	2.180(4)	W(1)–S(4)	2.207(4)
W(1)–S(5)	2.269(4)	W(1)–S(6)	2.226(4)
Ag(1)–S(1)	2.649(4)	Ag(1)–S(1A)	2.632(4)
Ag(1)–S(2)	2.488(4)	Ag(1)–S(3)	2.536(4)
Ag(2)–S(4)	2.531(4)	Ag(2)–S(5)	2.537(4)
Ag(2)–S(5B)	2.549(4)	Ag(2)–S(6B)	2.528(4)
S(1)–C(1)	1.715(15)	C(1)–N(2)	1.36(2)
C(1)–N(5)	1.339(19)	N(2)–C(3)	1.35(2)
C(3)–C(4)	1.34(2)	C(4)–N(5)	1.38(2)
N(5)–C(6)	1.46(2)	S(2)–C(11)	1.714(16)
C(11)–N(12)	1.34(2)	C(11)–N(15)	1.357(19)
N(12)–C(13)	1.39(2)	C(13)–C(14)	1.36(2)
C(14)–N(15)	1.377(19)	N(15)–C(16)	1.452(19)
Bond angles			
S(3)–W(1)–S(4)	110.09(15)	S(3)–W(1)–S(5)	104.29(13)
S(3)–W(1)–S(6)	108.46(15)	S(4)–W(1)–S(5)	112.84(14)
S(4)–W(1)–S(6)	108.05(14)	S(5)–W(1)–S(6)	113.00(14)
S(1)–Ag(1)–S(1A)	104.32(8)	S(1)–Ag(1)–S(2)	101.12(14)
S(1A)–Ag(1)–S(2)	104.64(14)	S(1)–Ag(1)–S(3)	95.10(13)
S(1A)–Ag(1)–S(3)	97.95(13)	S(2)–Ag(1)–S(3)	147.77(13)
S(4)–Ag(2)–S(5)	94.75(12)	S(4)–Ag(2)–S(5B)	117.00(13)
S(4)–Ag(2)–S(6B)	123.82(13)	S(5)–Ag(2)–S(5B)	105.26(14)
S(5)–Ag(2)–S(6B)	120.95(13)	S(5B)–Ag(2)–S(6B)	95.18(12)
Ag(1)–S(1)–Ag(1C)	135.45(17)	Ag(1)–S(1)–C(1)	109.1(5)
Ag(1C)–S(1)–C(1)	113.7(5)	Ag(1)–S(2)–C(11)	106.0(5)
W(1)–S(3)–Ag(1)	84.40(12)	W(1)–S(4)–Ag(2)	76.42(12)
W(1)–S(5)–Ag(2)	75.25(11)	W(1)–S(5)–Ag(2D)	74.86(11)
Ag(2)–S(5)–Ag(2D)	102.26(13)	W(1)–S(6)–Ag(2D)	76.01(12)

Symmetry operations for equivalent atoms: (A) $x, -y + 1/2, z + 1/2$; (B) $x, -y + 3/2, z-1/2$; (C) $x, -y + 1/2, z - 1/2$; (D) $x, -y + 3/2, z + 1/2$.

two-dimensional polymeric structure. Narrowing of the Ag(1)–(μ_2-S)–W bridging angle [84.40(12)]° is inevitably accompanied by a reduction in the Ag(1)···W distance (3.178 Å). The $[MXS_3]^{2-}$(X = O, S; M = V, Mo, W) moiety as a bidentate ligand always coordinates to another metal M′ as $M(\mu_2\text{-}S)_2M'$, but here we have the first example of monodentate coordination of this unit to any metal. The observation can be rationalized as $[WS_4]^{2-}$ acting as a strong π-acceptor, while the lone pairs on the sulfur donors of the Hmimt ligands overlap efficiently with the silver orbitals, giving strong π-donation [17]. This situation is reflected in the observed short W–S(3) bond [2.180(4) Å]. This is one of the shortest W–S bridging bonds that have been reported so far, in keeping with the increased π-character of the W–S(3) bond by charge delocalization through the μ_2-S(3) bridging atom. The W–S(3) bond length can be compared with the mean W–S bond lengths in the isolated $[WS_4]^{2-}$ anion [2.165(11) Å] in the ammonium salt [18]. This is consistent with the infrared spectrum of the complex, which exhibits a high-frequency band at 478 cm^{-1} due to the stretching vibration of the W–S(3) bond. In the complex, the independent Hmimt ligands have very similar structure, with localized C=C double bonds. The main difference from the free ligand concerns the C=S (thione) bond length, which shows a partial reduction of π–character and thus a slight lengthening of the C=S(thione) distances [1.715(15) and 1.714(16) Å] relative to the mean free ligand distance (1.685 Å); otherwise, the ligand dimensions are essentially unchanged upon coordination. However, the C=S bond distances in the complex indicate that the C=S bonds are double bonds, as in the free ligand.

Ag(2) is surrounded by four sulfur atoms belonging in pairs to two WS_4 fragments. The $Ag(2)S_4$ tetrahedron shares edges with two WS_4 tetrahedra, generating chains. The tetrahedral environment of Ag(2) is strongly distorted, with S(5)–Ag(2)–S(4) angles of 94.75(12)° within the strained four-membered $Ag(S_b)_2W$ chelate rings. The $Ag(S_b)_2W$ rings are planar and the four Ag(2)–S bonds are chemically equivalent; their distances [av. 2.534(4) Å] can be compared with 2.536(4) Å found for Ag(1)–S(3). The variation in bond angles within the $Ag(S_b)_2W$ plane is striking, in particular, the sharply acute $Ag(2)(S_b)_2W(1)$ angles 75.25°–76.42°, partly due to the requirements of the two lone pairs on S_b, which are accompanied by the expanded S_b–W–S_b [112.84(14)]° and S_b–Ag–S_b [94.75(12)]° angles as shown in Table 4. Owing to the two kinds of bridging modes of the S atoms, the two W–S_b bonds of the $Ag(2)(S_b)_2W$ rings are obviously different in length. The [W–μ_3-S(5)] distance [2.269(4) Å] is longer than the [W–μ_2-S(4)] distance [2.207(4) Å], as is indicated by the vibrational spectrum. More significantly, the observed distortion of the $Ag(S_b)_2W$ plane may imply a direct transnuclear Ag(2)–W bonding interaction. Such an interpretation has been applied in thiometalate systems such as $[Ag(WS_4)_2]^{3-}$ [5]. The Ag(2)···W distances of 2.937 and 2.942 Å of the title compound are 0.297–0.302 Å greater than the sum of the covalent radii, 2.64 Å [19], and can be compared with the 2.971 Å found in the $[Ag(WS_4)_2]^{3-}$ anion.

The overall sheet structure can be regarded as polymeric $Ag(WS_4)^-$ chains (running vertically in Fig. 2) joined together by AgL_2^+ chains (also vertical), in which each Ag^+ ion has one terminal ligand L and shares in two bridging ligands.

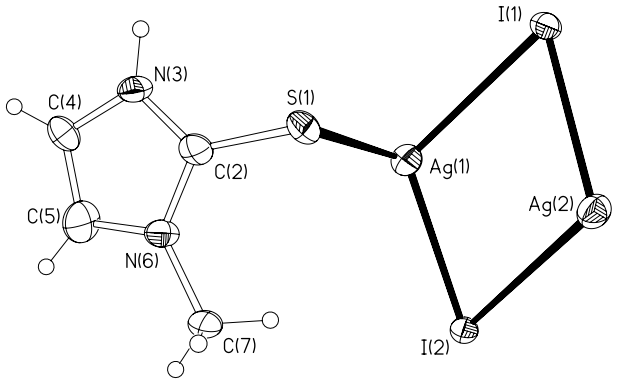


Fig. 3. The asymmetric unit of $[Ag_2I_2(Hmimt)]_n$ (**3**), showing the atom numbering scheme.

3.3.2. Crystal structure of $[Ag_2I_2(Hmimt)]_n$ (3)

The structure of this complex is shown in Figs. 3 (the asymmetric unit) and 4 (the polymeric sheet structure), and selected bond lengths and angles are in Table 5. Each silver atom has an SI_3 donor set and pseduo-tetrahedral geometry, with angles at the metal ranging from 95.85(12)° to 116.48(6)°, and is coordinated by three μ_3-I and one thione μ_2-S. Because of the crystallographic inversion centre, the silver atoms and the bridging μ_3-I atoms from a planar four-membered $Ag_2(\mu_3\text{-}I)_2$ ring. In the $Ag_2(\mu_3\text{-}I)_2$ ring, there are two distinctly different angles Ag–(μ_3-I)–Ag (62.33°) and I–Ag–I (116.15°) and only one type of Ag–(μ_3-I) bond with an average Ag–I distance of 2.871 Å. The Ag–S distance [av. 2.581(5) Å] in this complex is only slightly shorter than the Ag–(μ_2-S) [2.649(4) Å] distance found in $[WS_4Ag_2(Hmimt)_2]_n$. The C–S bond length is 1.706(19) Å in the complex, compared with 1.685 Å in the free ligand [20]. Comparison of these values supports the idea that the C–S distances lengthen upon coordination of the sulfur to the metal. However, the bond distance in the complex indicates that the C=S bond is a double bond, as in the free Hmimt ligand.

The very acute angles about the bridging iodine atoms (ranging from 62.14° to 62.33°), together with short Ag···Ag distances (average length 2.975 Å, slightly longer than 2.89 Å in Ag metal) [21,22] are suggestive of direct Ag–Ag bonding, which is associated with π-stacking interactions between ligands attached to two adjacent metal ions.

The polymeric sheet structure (Fig. 4) is made up of undulating ladders of AgI linked by bridging Hmimt ligands through Ag–S bonds. The ladders extend in the $[1\bar{1}0]$ direction and the sheets are in the (001) plane.

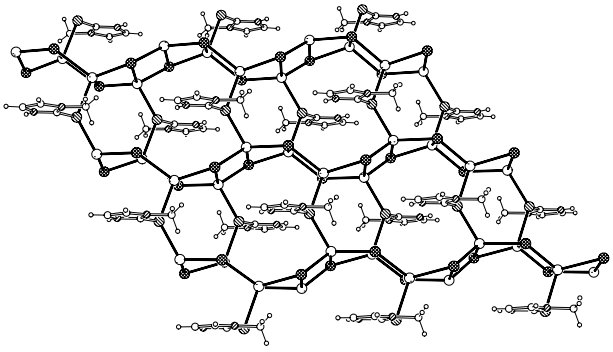


Fig. 4. The polymeric sheet structure of compound (**3**). Ladders of Ag and I atoms run from left to right and are bridged by Hmimt ligands.

Table 5
Selected bond lengths (Å) and angles (°) for compound **3**

Bond lengths			
Ag(1)–I(1)	2.909(2)	Ag(1)–I(1A)	2.855(2)
Ag(1)–I(2)	2.822(2)	Ag(1)–S(1)	2.589(5)
Ag(2)–I(1)	2.827(2)	Ag(2)–I(2)	2.929(2)
Ag(2)–I(2B)	2.895(2)	Ag(2)–S(1C)	2.574(5)
S(1)–C(2)	1.706(19)	C(2)–N(3)	1.33(2)
C(2)–N(6)	1.37(2)	N(3)–C(4)	1.38(2)
C(4)–C(5)	1.35(3)	C(5)–N(6)	1.37(3)
N(6)–C(7)	1.48(3)		
Bond angles			
I(1)–Ag(1)–I(1A)	116.48(6)	I(1)–Ag(1)–I(2)	116.15(6)
I(1A)–Ag(1)–I(2)	108.78(7)	I(1)–Ag(1)–S(1)	95.85(12)
I(1A)–Ag(1)–S(1)	101.85(12)	I(2)–Ag(1)–S(1)	116.57(12)
I(1)–Ag(2)–I(2)	115.35(6)	I(1)–Ag(2)–I(2B)	103.57(6)
I(1)–Ag(2)–S(1C)	119.44(13)	I(2)–Ag(2)–I(2B)	119.80(6)
I(2B)–Ag(2)–S(1C)	99.88(12)	I(2)–Ag(2)–S(1C)	98.69(12)
Ag(1)–I(1)–Ag(1A)	63.52(6)	Ag(1)–I(1)–Ag(2)	62.33(5)
Ag(1A)–I(1)–Ag(2)	117.02(6)	Ag(1)–I(2)–Ag(2)	62.14(5)
Ag(1)–I(2)–Ag(2B)	111.31(6)	Ag(2)–I(2)–Ag(2B)	60.20(6)
Ag(1)–S(1)–Ag(2C)	131.8(2)	Ag(1)–S(1)–C(2)	103.2(6)
Ag(2C)–S(1)–C(2)	103.5(6)		

Symmetry operations for equivalent atoms: (A) $-x+1, -y+2, -z+2$; (B) $-x+2, -y+1, -z+2$; (C) $-x+1, -y+1, -z+2$.

4. Supplementary material

Crystallographic data for the structural analyses have been deposited with the Cambridge Crystallographic Data Centre, CCDC No. 257095 for $[WS_4Ag_2(Hmimt)_2]_n$ and CCDC No. 257096 for $[Ag_2I_2(Hmimt)]_n$. Copies of this information may be obtained free of charge from The Director, CCDC, 12 Union Road, Cambridge CB2 1IZ, UK (fax: +44-1223-336033; e-mail: deposit@ccdc.cam.ac.uk or www: http://www.ccdc. cam.ac.uk).

Acknowledgements

We thank EPSRC (UK) and Shahid Chamran University (Ahwaz, Iran) for financial support.

References

[1] C. Pettinari, M. Pellei, C. Santini, I. Natali, F. Accorroni, A. Lorenzotti, Polyhedron 17 (1998) 4487.
[2] A.A. Isab, S. Ahmad, M. Arab, Polyhedron 21 (2002) 1267, and references therein.
[3] M.P. Coughlan, Molybdenum and Molybdenum Containing Enzymes, Pergamon Press, Oxford, 1980.
[4] C.F. Mills, Chem. Ber. 15 (1979) 512.
[5] A. Müller, E. Diemann, R. Jostes, H. Bögge, Angew. Chem., Int. Ed. Engl. 20 (1981) 934, and references therein.
[6] J.W. McDonald, G.D. Friesen, L.D. Rosenhein, W.E. Newton, Inorg. Chim. Acta 72 (1983) 205.
[7] G.M. Sheldrick, SADABS, Program for Correction of CCD Data, University of Göttingen, Germany, 1997.
[8] G.M. Sheldrick, SHELXTL User Manual, Bruker AXS Inc., Madison, WI, USA, 1997.
[9] R.I. Cooper, R.O. Gould, S. Parsons, D.J. Watkin, J. Appl. Crystallogr. 35 (2002) 168.
[10] M. Pink, V.G. Young Jr., ROTWIN, University of Minnesota, USA, 2000.

[11] G. Alonso, G. Aguirre, I.A. Rivero, S. Fuentes, Inorg. Chim. Acta 274 (1998) 108.
[12] L.J. Bellamy, The Infrared Spectra of Complex Molecules, 3rd ed., Champman and Hall, London, 1975.
[13] E.S. Raper, J.L. Brooks, J. Inorg. Nucl. Chem. 39 (1977) 2163.
[14] E.S. Raper, P.H. Crackett, Inorg. Chim. Acta. 50 (1981) 159.
[15] J. Jolley, W.I. Cross, R.G. Pritchard, C.A. McAuliffe, K.B. Nolan, Inorg. Chim. Acta 315 (2001) 36.
[16] P. Aslanidis, P.J. Cox, S. Divanidis, P. Karagiannidis, Inorg. Chim. Acta 357 (2004) 2677, and references therein.
[17] M. Garner, M.-A. Lehmann, J. Reglinski, M.D. Spicer, Organometallics 20 (2001) 5233.
[18] K. Sasvari, Acta Crystallogr. 16 (1963) 719.
[19] J.K. Stalick, A.R. Siedle, A.D. Mighell, C.R. Hubbard, J. Am. Chem. Soc. 101 (1979) 2903.
[20] E.S. Raper, J.R. Creighton, R.E. Oughtred, I.W. Nowell, Acta Crystallogr. Sect. B 39 (1983) 355.
[21] M.D. Ward, J.A. McCleverty, J.C. Jeffery, Coord. Chem. Rev. 222 (2001) 251.
[22] P.J. Cox, P. Aslanidis, P. Karagiannidis, S. Hadjikakou, Inorg. Chim. Acta 310 (2000) 268.

Available online at www.sciencedirect.com
SCIENCE DIRECT®
Polyhedron 24 (2005) 443–450
POLYHEDRON
www.elsevier.com/locate/poly

Bonding of copper(II) ions by proctolin analogues modified in fifth position of the peptide chain

Teresa Kowalik-Jankowska *, Anna Rajewska, Wioletta Szeszel-Fedorowicz, Danuta Konopińska

Faculty of Chemistry, University of Wrocław, Joliot-Curie 14, 50-383 Wrocław, Poland

Received 28 October 2004; accepted 16 December 2004
Available online 21 January 2005

Abstract

The proctolin (Arg–Tyr–Leu–Pro–Thr, RYLPT) analogues modified in fifth position of the peptide chain (RYLPP, RYLPI, RYLP–Dab, where Dab – 2,4-diamminobutyric acid) have been synthesised and their complexes with H^+ and Cu^{2+} studied by potentiometry and spectroscopy (UV–Vis, CD and EPR) at 25 °C and I = 0.10 mol dm^{-3} (KNO_3). The results obtained support the earlier suggestion on the specific role of a proline residue as a ''break-point'' in copper complex formation with peptides. The presence of a proline residue into the fourth position of the proctolin analogues (RYLPP, RYLPI) leads in wide pH range of the existence the CuL and $CuH_{-1}L$ complexes with expected stabilities. Spectroscopic studies confirm that these are 2N {NH_2, N^-, CO} and 3N {NH_2, $2N^-$, CO} species, respectively. The amine group of the Dab residue of the RYLP–Dab proctolin analogue, in whole pH range (2.5–10.5) is coordinated to the copper(II) ions, and the deprotonation and coordination of the second amide nitrogen atom to the metal ion is prevented. In solution in wide pH range (5–10.5) the 3N {NH_2, N^-, CO, NH_{2Dab}} complex is present. Proctolin and its analogues modified in fifth position contain in the second position of the peptide sequence the Tyr residue and the CD results show that $TyrO^-$–Cu^{2+} bonding is present at pH above 8.
© 2004 Elsevier Ltd. All rights reserved.

Keywords: Proctolin analogues; Copper(II) complexes; Stability constants; Spectroscopic studies

1. Introduction

Proctolin, the first structurally characterized myotropic insect neuromodulator, is a pentapeptide, L-arginyl–L-tyrosyl–L-leucyl–L-prolyl–L-threonine (Arg–Tyr–Leu–Pro–Thr), which was isolated in 1975 by Brown and Starratt [1] from whole-body extracts of the American cockroach *Periplaneta americana.* The peptide has been shown to occur in species of six insect orders and in other invertebrates [2–5]. Proctolin is a neuroactive substance which is found in various neuronal cell types, including motoneurons inervating visceral and skeletal muscles [6,7], neurosecretory [8,9] and sensory neurons [10]. On the basis of myotropic properties manifested in stimulation of contractions of visceral and skeletal muscles [8,9,11,12] of insects and other invertebrates [13], proctolin was classified as an neurotransmitter. Structural modifications by replacement residues in positions 1–5, as well as syntheses of truncated or elongated analogues were made to studies structure–myotropic function relationship [14–16]. Functional significance of the amino acid residues in the peptide chain of the proctolin is described and discussed [17]. Among the proctolin analogues modified in position 5 of the peptide skeleton only C-terminally modified analogues with Ala [14], Val, Ile, Asn, Gln or Ser replacements showed agonistic or weak-agonistic effects [18]. The data suggest that the C-terminal Thr residue plays an important role for myotropic activity in insects.

* Corresponding author. Tel.: +48 71 3757231; fax: +48 71 3282348.
E-mail addresses: terkow@wchuwr.chem.uni.wroc.pl (T. Kowalik-Jankowska), annakow@wcheto.chem.uni.wroc.pl (A. Rajewska).

0277-5387/$ - see front matter © 2004 Elsevier Ltd. All rights reserved.
doi:10.1016/j.poly.2004.12.005

Copper is an essential element widely distributed throughout the body but concentrating particularly in the liver–gall bladder area and the brain. The peptides have been identified as neurotransmitters, many with opiate activity [19]. Many of these peptides contain one or more Pro residues, e.g. substance P (L-Pro in positions 2 and 4 while the antagonist contains D-Pro in position 2), thyrotropin releasing hormone (L-Pro-NH_2 in position 3), and β-casomorphin (L-Pro in positions 2, 4, and 6). In general biologically active forms of such molecules are in the β-conformation, hence a possible role for copper is the biological activation of many neuropeptides [20]. L-Proline does not contain an $–NH_2$ group but the secondary =NH group. Hence when inserted in a peptide chain there is no ionizable hydrogen so that the nitrogen atom is unable to bond to copper [21,22]. As a result proline in the second, third or fourth positions of a short peptide chain acts as a "break-point" to copper coordination allowing the two ends of the chain to behave independently, hence any labile Cu^{2+} present would tend to coordinate neuropeptide molecules and, likely, influence their conformations and so their biological activity [20].

Tyrosine is another interesting component of many neuropeptides, e.g. all enkephalins [23]. The phenolic oxygen of tyrosine can coordinate to Cu(II) but, for steric reasons, cannot bond to a metal ion which is already coordinated to the amide nitrogen of the tyrosine residue. When tyrosine is in an amino acid sequence, however, the phenolic oxygen of the side chain can coordinate to Cu(II) by at least two ways; it can participate in the formation of dimmers or of large ring chelated complexes [24].

The present paper reports the results of combined spectroscopic and potentiometric studies on the copper(II) complexes of proctolin analogues modified in fifth position of the peptide chain. The peptides involved in the study are: Arg–Tyr–Leu–Pro–Pro (RYLPP), Arg–Tyr–Leu–Pro–Ile (RYLPI) and Arg–Tyr–Leu–Pro–Dab (RYLP–Dab, where Dab – 2,4-diamminobutyric acid). This study was performed in order to examine the difference of the binding ability of proctolin analogues modified in position 5, especially the effect of Dab containing the amine group, on the formation of complexes with Cu^{2+}ions.

2. Experimental

2.1. Materials

The proctoline analogues modified in fifth position of the peptide chain were synthesized according to a procedure reported below. As a metal ion source $Cu(NO_3)_2 \cdot 3H_2O$ (Merck) was used. KNO_3, KOH and HNO_3 were Merck products.

2.2. Peptide syntheses, purification and characterization

Peptides were synthesized by the solid-phase method according to the Boc-procedure [25,26]. Dicyclohexylcarbodiimide (DCC, Merck) in the presence of 1-hydroxybenztriazole (OHBt, Aldrich) was used as a coupling reagent. The C-terminal amino acids were bound to the Merrifield resin by a cesium salt procedure to give substitution level of 0.7 mmol/g of Boc–Y–OH, where Y = Ile, Pro, Dab(Z). The protected amino acids were coupled using DCC as a coupling reagent or by the linear anhydride methods. The following amino acid derivatives were used: Boc–Arg(Tos)–OH, Boc–Tyr(OBzl)–OH, Boc–Leu–OH, Boc–Pro–OH (Bachem). The amino acids and DCC were used in 3-fold excess. The N^{α}–Boc-group was subsequently removed with 30% trifluoroacetic acid (TFA) in dichloromethane (DCM) according to standard methods. The neutralization was made with 10% triethylamine (TEA) in DCM. Finally, RYLPP, RYLPI and RYLP–Dab peptides were obtained by deprotection and cleavage from the support resin with trifluoromethanesulfonic acid (CF_3SO_3H) in anisole. All peptides were purified on Sephadex G-25 column by elution with 5% acetic acid and then by preparative HPLC. The peptides after preparative HPLC were dissolved with 5% acetic acid and lyophilizated.

The amino acid composition was confirmed using a Mikrotechna T 339 M analyzer (Czechoslovakia). The optical activity of the chiral compounds was determined with a Polamat polarimeter (Carl Zeiss, Jena, Germany). The molecular wieghts of the peptides were determined using the Finigan Mat TSQ 700 (USA). TLC was performed in three solvent systems on silica gel and visualized using ninhydrin.

The purity of all peptides has been also checked by pH-metric titrations.

2.3. Potentiometric measurements

Stability constants for proton and Cu^{2+} complexes were calculated from pH-metric titrations carried out in argon atmosphere at 298 K using a total volume of 2 cm^3. Alkali was added from a 0.250-cm^3 micrometer syringe which was calibrated by both weight titration and the titration of standard materials.

Experimental details: ligand concentration 2×10^{-3} mol dm^{-3}; metal-to-ligand ratio 1:1.1; ionic strength 0.10 mol dm^{-3} (KNO_3); pH-metric titration on a MOLSPIN pH-meter system using a Russel CMAW 711 semi-mikro combined electrode, calibrated in concentration using HNO_3 [27], number of titrations 2; method of calculation SUPERQUAD [28]. The samples were titrated in the pH region 2.5–10.5. Standard deviations (σ values) quoted were computed by SUPERQUAD and refer to random errors only. They are, however, a good indi-

cation of the importance of the particular species involved in the equilibria.

2.4. Spectroscopic measurements

Solutions were of similar concentrations to those used in potentiometric studies. The solutions for EPR measurements with ethylene glycol (water:glycol, 2:1, v/v) were prepared to ensure good glass formation in frozen solutions. EPR spectra were recorded on a Bruker ESP 300E spectrometer at X-band frequency (9.3 GHz) at 120 K. The EPR parameters were calculated for the spectra obtained at the maximum concentration of the particular species for which well-resolved components were observed. Absorption spectra were recorded on a Beckman DU 650 spectrophotometer in the 850–300 nm range. Circular dichroism (CD) spectra were recorded on a Jasco J-715 spectropolarimeter in the 750–250 nm range. The values of $\Delta\varepsilon$ (i.e. $\varepsilon_l - \varepsilon_r$) and ε were calculated at the maximum concentration of the particular species obtained from potentiometric data.

3. Results and discussion

3.1. Protonation constants

Calculated protonation constants and Cu^{2+} complex formation constants are given in Tables 1 and 2, respectively, together with literature values for related complexes. Calculated species distribution curves for 1:1 Cu^{2+}:L mixtures (0.002 mol dm^{-3}) are shown in

Table 1
Stability constants (log β) and calculated protonation constants for proctolin derivatives modified at fifth position of amino acid sequence and comparable peptides at 298 K and I = 0.10 M (KNO_3)

Peptide log β	HL	H_2L	H_3L	H_4L
RYLPP	9.66 ± 0.01	16.77 ± 0.01	20.61 ± 0.01	
RYLPI	9.54 ± 0.02	16.73 ± 0.02	20.69 ± 0.02	
RYLP–Dab	10.11 ± 0.02	19.43 ± 0.01	26.52 ± 0.02	30.11 ± 0.02
GGGP[a]	8.04	10.95		
GGG–Sar[a]	7.92	10.97		
AAAAA–NH_2[b]	8.04			
Stepwise protonation constants (log K values)	O^-–Tyr	NH_2	COO^-	NH_2
RYLPP	9.66	7.11	3.84	
RYLPI	9.54	7.19	3.96	
RYLP–Dab	9.32 (or 10.11)	7.09	3.59	10.11 (or 9.32)
GGGP[a]		8.04	2.91	
GGG–Sar[a]		7.92	3.04	
AAAAA–NH_2[b]		8.04		

[a] Ref. [37].
[b] Ref. [31].

Table 2
Stability constants (log β) of copper(II) complexes for proctolin derivatives and comparable complexes at 298 K and I = 0.10 M (KNO_3)

Peptide log β	CuHL	CuL	CuH_{-1} L	$CuH_{-2}L$	$CuH_{-3}L$
RYLPP	13.75 ± 0.02	8.67 ± 0.01	1.54 ± 0.01	−7. 92 ± 0.01	−18.49 ± 0.01
RYLPI	13.94 ± 0.01	8.69 ± 0.02	1.31 ± 0.02	−8. 36 ± 0.04	
RYLP–Dab	18.87 ± 0.03	13.07 ± 0.02	3.48 ± 0.03		
GGGP[a]		5.16	−0.48	−7.50	−17.58
GGG–Sar[a]		5.28	−0.22	−7.34	−17.74
AAAAA–NH_2[b]		4.93	−0.66	−8.40	−16.37
log K^*[c] values and deprotonation constants for amide protons (pK) in Cu^{2+} complexes	{NH_2, CO}	{NH_2, N^-, CO}	{NH_2, $2N^-$, CO}	pK_1	pK_2
RYLPP	−3.02	−8.10	−15.23	5.08	7.13
RYLPI	−2.78	−8.05	−15.40	5.27	7.35
RYLP–Dab	+2.46	−3.34		5.80	
GGGP[a]	−2.88	−8.52	−15.54	5.64	7.02
GGG–Sar[a]	−2.64	−8.14	−15.26	5.50	7.12
AAAAA–NH_2[b]	−3.11	−8.70	−16.44	5.59	7.74

[a] Ref. [36].
[b] Ref. [30].
[c] $\log K = \log \beta(CuH_jL) - \log \beta(H_nL)$ (where the index j corresponds to the number of the protons in the coordinated ligand to metal ion and n corresponds to the number of protons coordinated to ligand).

Figs. 1 and 2. Spectroscopic data for the major complexes are given in Table 3.

While values for log K_{HL}, log K_{H2L} for the peptides RYLPP, RYLPI and also log K_{H3L} for the analogue of proctolin RYLP–Dab are precise and reliable, values for the carboxyl protonation are less certain as a result of residual acetate in the peptides that is very difficult to remove. The proctolin analogues were, otherwise, analytically pure. Acetate ions form only very weak complexes with Cu^{2+}; hence, the presence of traces of acetate in the background would not give spurious metal complex formation constants. However the protonation constant of the acetate ion (log $K_a = 4.64$) prevents a precise determination of the protonation constant of the peptide carboxyl group unless the exact acetate concentration is known. In peptides this carboxyl group is normally ionized above pH 3.5; hence the protonation constant would not have any significant influence on the calculation of formation for the Cu^{2+} complexes that form above pH 4. SUPERQUAD gave the same concentration ratios for peptide to acetate over a range of total concentrations of ligand and the calculated formation constants were entirely consistent. Molar ratios found for the peptides studied to acetate were 1:0.785 for RYLPP, 1:0.564 for RYLPI and 1:0.383 for RYLP–Dab.

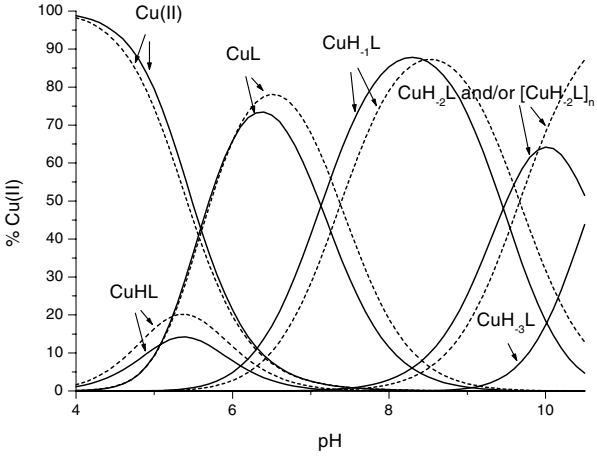


Fig. 1. Species distribution curves for Cu(II) complexes of the RYLPP (solid lines) and RYLPI (dashed lines). Cu(II) to peptide molar ratio 1:1, $[Cu(II)] = 2 \times 10^{-3}$ M.

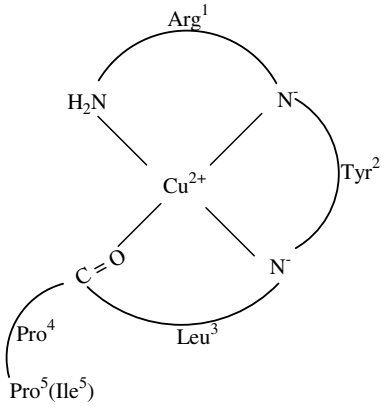


Fig. 2. Proposed structure for the $CuH_{-1}L$ complex of RYLPP and RYLPI peptides.

All peptides studied contain at first position of the peptide chain the arginine. The arginine residue contains a very basic terminal nitrogen atom as a result of resonance stabilization of the protonated guanidine group (log $K \approx 12$) [29]. Under the experimental conditions used, the pH never exceeded 10.5 and, at this value, the degree of deprotonation of the guanidine group is insignificant. Hence the proton was considered as unionisable under the conditions used and its protonation constant ignored.

The neutral forms of the peptides studied can be regarded as H_2L. Both, RYLPP and RYLPI, have three possible protonation centres: the terminal amino nitrogen, the C-terminal carboxylate, and the phenolic oxygen of the Tyr residue. The peptide analogue of proctolin, RYLP–Dab has a additional protonation constant since it has Dab with amine group in side chain of the peptide.

The first protonation constant, log $\beta_{HL} = 9.66$ or 9.54 for the peptides RYLPP or RYLPI (Table 1), respectively, refers to protonation of the phenolate group of the Tyr side chain and this value compares well with literature values [30–32]. The peptide RYLP–Dab has two dissociable protons: the amine group of Dab residue and the phenolic group of the Tyr residue with the values comparable to each other (log $K = 10.11$ and 9.32, Table 1) [30–33]. From a consideration of these log K values, it can be suggested that two sets of deprotonation processes overlap each other. Deprotonation of the amine and tyrosyl groups takes place at around pH 9–10, which means that the log K values cannot be separated and the constants measured are macro-constants. The protonation constant (log $K = 7.09$–7.19) of the N-terminal amine group of the peptides studied is close to those of RKDVG [34] and PACAP 3 [35] peptides containing the same residue in first position (Arg^1).

3.2. Cu(II) complexes with RYLPP and RYLPI

Four and five metal complex species can be fitted to the experimental titration curves obtained for the Cu^{2+}–RYLPI and RYLPP systems: CuHL, CuL, $CuH_{-1}L$, $CuH_{-2}L$ and also $CuH_{-3}L$ (for RYLPP, charges omitted for simplicity, Table 2, Fig. 1). RYLPP and RYLPI contain in amino acid sequence the same donor sets and the potentiometric and spectroscopic results suggest the formation of the complexes with similar coordination modes (Tables 2 and 3, Fig. 1). The coordination of metal ion starts at pH around 4 (Fig. 1). The minor species CuHL with 1N coordination {NH_2, CO}

Table 3
Spectroscopic data for Cu^{2+} complexes of RYLPP, RYLPI and RYLP–Dab

Peptide	Species	Visible		CD		EPR	
	Coordination mode	λ (nm)	ε (M^{-1} cm^{-1})	λ (nm)	$\Delta\varepsilon$ (M^{-1} cm^{-1})	A_{II} (G)	g_{II}
RYLPP	$\{NH_2, CO\}$ [CuHL]					160	2.312
	$\{NH_2, N^-, CO\}$ [CuL]	656[a]	61	657[a]	−0.510	170	2.249
				336[b]	+0.116		
	$\{NH_2, N^-, N^-, CO\}$ $[CuH_{-1}L]$	570[a]	139	584[a]	−1.029	172	2.215
				323[b]	+0.754		
	$\{NH_2, N^-, N^-, O^-_{Tyr}\}$ $[CuH_{-2}L]_n$	570[a]	144	584[a]	−0.795	175	2.214
	and/or $\{NH_2, N^-, N^-, CO\}$ and			370[c]	−0.119		
	$\{NH_2, N^-, N^-, H_2O\}$ $[CuH_{-2}L]$			308[b]	+0.916		
RYLPI	$\{NH_2, N^-, CO\}$ [CuL]	647[a]	101	653[a]	−0.668	172	2.248
				332[b]	+0.134		
				287[d]	−1.661		
	$\{NH_2, N^-, N^-, CO\}$ $[CuH_{-1}L]$	563[a]	176	579[a]	−1.346	174	2.216
				322[b]	+0.646		
	$\{NH_2, N^-, N^-, O^-_{Tyr}\}$ $[CuH_{-2}L]_n$	564[a]	168	577[a]	−1.206	172	2.216
	and/or $\{NH_2, N^-, N^-, CO\}$ and			358[c]	−0.291		
	$\{NH_2, N^-, N^-, H_2O\}$ $[CuH_{-2}L]$			307[b]	+0.684		
				282[d]	−0.066		
RYLP–Dab	$\{NH_2, CO, NH_2\}$ [CuHL]	639[a]	42	659[a]	−0.148		
				278[d]	−0.466		
	$\{NH_2, N^-, CO, NH_2\}$ [CuL]	608[a]	100	628[a]	−0.603	161	2.219
				290[b]	−2.325		
				275sh[d]	−2.015		
	$\{NH_2, N^-, O^-_{Tyr}, NH_2\}$ $[CuH_{-1}L]_n$	595[a]	106	616[a]	−0.593	163	2.220
	and/or $\{NH_2, N^-, CO, NH_2\}$ and			369[c]	−0.356		
	$\{NH_2, N^-, H_2O, NH_2\}$ $[CuH_{-1}L]$			303[c]	+1.493		
				270[d]	−2.506		

[a] d–d transition.
[b] $N^-_{amide} \rightarrow Cu^{2+}$ charge transfer transition.
[c] $O^-_{Tyr} \rightarrow Cu^{2+}$ charge transfer transition.
[d] $NH_2 \rightarrow Cu^{2+}$ charge transfer transition.

is usually found by potentiometric data calculations in metal–peptide systems [36]. This species cannot be supported by spectroscopic data because of its very low concentration, however, for RYLPP, the EPR spectrum for the CuHL species was observed with parameters: A_{II} = 160 G, g_{II} = 2.312 suggesting the $\{NH_2, CO\}$ coordination mode (Table 3) [37]. The CuHL species of both peptides corresponds to the CuL species of penta-alanine amide with the tyrosyl oxygen protonated.

The log K^* values for 1N $\{NH_2, CO\}$ complexes of the peptides studied and the complexes of AAAAA–NH_2, GGGP and GGG–Sar peptides are similar to each other supporting the same coordination mode (Table 2). With increasing pH, the CuHL complex loses the proton to give a species of stoichiometry CuL. The deprotonation constants of the CuHL complexes for RYLPP and RYLPI peptides, $CuHL \leftrightarrow CuL + H^+$ (pK values, 5.08; 5.27; respectively, Table 2) correspond very well to the deprotonation and coordination of the first amide nitrogen to copper(II) ion [38]. The d–d transition energy at 656–647 nm, the presence in CD spectra $N^-_{am} \rightarrow Cu^{2+}$ charge transfer transition at 336–332 nm and the EPR parameters: A_{II} = 172–170 G, g_{II} = 2.249–2.248 support the 2N $\{NH_2, N^-, CO\}$ coordination mode (Table 3) [38–40]. Above pH 6, the CuL complex of both peptides loses the next amide proton to give a $CuH_{-1}L$ species which has three nitrogen donor centres arranged in equatorial plane of the tetragonal geometry around copper(II) ion (Fig. 2). The shift of absorption maximum to 570–563 nm, and the EPR parameters: A_{II} = 174–172 G, g_{II} = 2.216–2.215 suggest coordination of the additional nitrogen donor atom to the copper(II) ion (Table 3) [37,40]. The low value of A_{II} parameter (172–174 G) of the 3N $\{NH_2, 2N^-_{amide}, CO\}$ complex in comparison to those of GGGP (194 G) and GGG–Sar (195 G) [37] may suggest a distortion from the tetragonal geometry around the copper(II) ion.

Increasing the pH above 8 results in the formation of a species of formula $CuH_{-2}L$. The protonations constants of the $CuH_{-2}L$ complex (9.46 and 9.67 for RYLPP and RYLPI, respectively, Table 2) are in good agreement with those for protonations of the

Tyr residues in the free ligands (9.66 and 9.54, respectively, Table 1). It means that in the $CuH_{-2}L$ complex the Tyr residue is deprotonated. The parameters of UV–Vis, CD (d–d transition region) and EPR spectra for the $CuH_{-2}L$ complex are similar to those obtained for $CuH_{-1}L$ complex suggesting similar numbers of N–Cu^{2+} bonds (NH_2 and $2N^-_{amide}$, Table 3). In the CD spectrum for the $CuH_{-2}L$ complex of both peptides the characteristic charge transfer bands the phenolate–$O^- \rightarrow Cu^{2+}$ are observed (Table 3) supporting the coordination of the phenolate oxygen of the Tyr residue to copper(II) ion [24,39,41,42]. At pH about 10 the phenolate oxygen–Cu^{2+} charge transfer transitions were also observed for the Cu^{2+}–Tyr–Tyr and Tyr–Phe systems suggesting the phenolate oxygen coordination in these complexes [43]. For the $CuH_{-2}L$ complex, three coordination positions in equatorial plane are occupied by the nitrogen atoms {NH_2, $2N^-_{amide}$}, and the fourth position may be occupied by the oxygen atoms of the carbonyl group of Leu residue, water molecule or deprotonated phenolate group of the Tyr residue. The Tyr residue in second position of the peptide chain of proctolin analogues cannot be coordinated to Cu^{2+}ions by the phenolate oxygen and the amide nitrogen atoms simultaneously. Therefore, bonding to both atom donors can only occur in polynuclear $(CuH_{-2}L)_n$ complexes (Table 3). For RYLPP pentapeptide by potentiometry at pH above 9 (Fig. 1) the $CuH_{-3}L$ complex was also detected. The presence of the $CuH_{-3}L$ complex may suggest the coordination of the water molecule in the fourth coordination position of the copper(II) ion. The protonation constant of the $CuH_{-3}L$ species equals 10.57 corresponds very well to the deprotonation of the coordinated water molecule [44]. The log K* values for the 1N, 2N and 3N complexes of the both peptides studied are comparable to those of the peptides containing in fourth coordination position the Pro or Sar as ''break-point'' residues in the peptide chain (Table 2).

3.3. Cu(II) complexes with RYLP–Dab peptide analogue

According to potentiometric and spectroscopic results, RYLP–Dab peptide analogue forms with Cu^{2+} ions the CuHL, CuL and $CuH_{-1}L$ species (Table 2, Fig. 3). The coordination of the metal ion starts at pH around 4 with the formation of the 2N {NH_2, CO, NH_2} complex.

The absorption band of the d–d transition at 639 nm and the parameters of CD spectra: the presence of the $NH_2 \rightarrow Cu^{2+}$ charge transfer transition at 278 nm, and d–d transition band at 659 nm clearly indicate to involve 2N coordination with {NH_2, CO, NH_2} bonding mode. The chelate ring forming by the carbonyl oxygen of Arg^1 and amine group of Dab residue is unexpectedly large but the Pro(4) residue is acting as a β-turn in the peptide chain and so forcing the bend required to bring the Dab(5) amine group close to the terminal –NH_2 group [45]. In the CuHL complex the phenolate oxygen of the Tyr residue is protonated. The log K* value for the CuHL complex of RYLP–Dab is about four orders of magnitude higher in comparison to those of RYLPP and RYLPI (Table 2). This increase may be explained by the coordination of the second amine nitrogen atom of the peptide analogue (Dab residue). With increasing pH above 5 the CuL complex is formed with pK value for deprotonation of the CuHL species ($CuHL \leftrightarrow CuL + H^+$) equals 5.80. The formation of the CuL is accompanied by a significant blue shift of the absorption band to 608 nm suggesting coordination of the additional nitrogen atom donor (Table 3, Fig. 4).

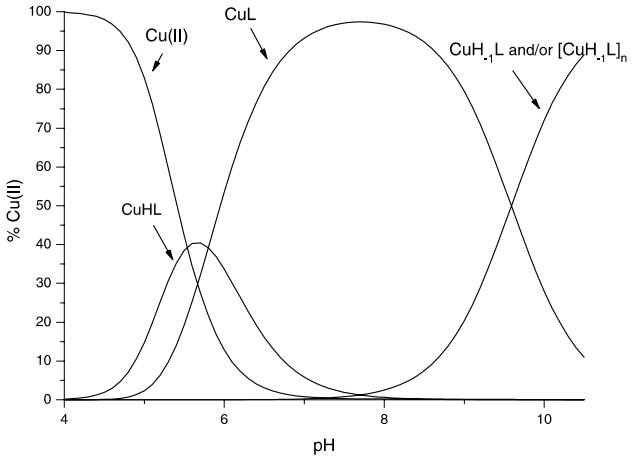


Fig. 3. Species distribution curves for Cu(II) complexes of the RYLP–Dab. Cu(II) to peptide molar ratio 1:1, $[Cu(II)] = 2 \times 10^{-3}$ M.

The EPR parameters for CuL complex: A_{II} = 161 G, and especially g_{II} = 2.219, and the presence in CD spectra the charge transfer transition $N^-_{amide} \rightarrow Cu^{2+}$ at 290 nm, clearly support the 3N {NH_2, N^-_{amide}, CO, NH_2}

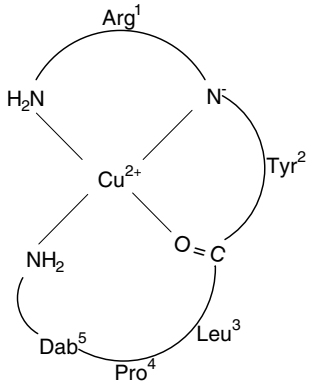


Fig. 4. Proposed structure for the CuL complex of RYLP–Dab peptide.

coordination mode (Table 3). The value for A_{II} is distinctly lower than for the other 3N species which form typical, small, chelate rings [37,46]. Such changes in A_{II} may reflect deformation of the complex plane expected when a macrochelate ring is formed [47]. Moreover, the value of 608 nm for the d–d band energy of the CuL species is a little above that typical of the 3N complexes of simple peptides (ca. 570 nm) but can easily be explained when ligand effects are taken into account since these are in the order $NH_2 < N^-_{amide}$ [48]. As a result a 3N species involving $2NH_2$, N^-_{amide} coordination would be expected to have a higher value for λ_{max} than 3N species involving Cu^{2+}–NH_2 and two $Cu^{2+} - N^-_{amide}$ bonds. The log K^* value for the CuL complex is about 4.6–4.8 orders of magnitude higher in comparison to that of RYLPP and RYLPI (Table 2). This increase of stability may be explained by the coordination of the amine nitrogen atom of Dab residue to the copper(II) ion. In pH range 8–10.5 the $CuH_{-1}L$ species was detected (Fig. 2, Table 2). The deprotonation constant of the CuL complex (pK value, $CuL \leftrightarrow CuH_{-1}L + H^+$) equals 9.59 corresponds very well to that of the phenolate oxygen of the Tyr residue for free ligand (9.32, Tables 1 and 2). The EPR parameters (A_{II}, g_{II}) and the d–d transition energy for the $CuH_{-1}L$ complex are similar to those of the CuL complex suggesting the same 3N bonding mode (Table 3). Moreover, in CD spectrum for the $CuH_{-1}L$ complex the charge transfer transition $O^-_{Tyr} \rightarrow Cu^{2+}$ at 369 nm is observed suggesting the formation of the $(CuH_{-1}L)_n$ polynuclear complexes with 3N $\{NH_2, N^-_{amide}, O^-_{Tyr}, NH_2\}$ coordination mode. RYLP–Dab analogue at high pH may also form the polynuclear complexes as the peptides RYLPP and RYLPI from the same reasons (see above). The presence of the Dab containing the amine nitrogen donor atom in fifth position of the proctolin analogue changes its coordination ability compared to those of RYLPP and RYLPI peptides. The amine nitrogen atom of Dab residue in whole pH range is coordinated to copper(II) ion and its coordination prevents the deprotonation and coordination of the second amide nitrogen atom to the copper(II) ion.

4. Conclusions

L-Proline (Pro, P) residue inserted in a peptide sequence may act as a "break-point" in the coordination of donor centres of the peptide chain to metal ions which are able to deprotonate peptide nitrogens (e.g. Cu^{2+}). Proctolin and its analogues modified in fifth position of the peptide chain contain the proline residue in fourth position, and therefore with Cu^{2+} ions the 1N, 2N and 3N complexes of RYLPP and RYLPI are formed. The presence of L-proline in fourth position of the peptide sequence prevents the deprotonation and coordination of the third amide nitrogen atom and the 4N $\{NH_2, 3N^-\}$ complex is not formed. The insertion of the Dab in fifth position of proctolin peptide sequence changes the coordination ability of the peptide analogue to the copper(II) ions. The amine group of the Dab residue is coordinated to copper(II) in whole (2.5–10.5) pH range and it prevents the deprotonation and coordination of the second amide nitrogen atom. In wide (5–10.5) pH range the CuL complex dominates with the 3N $\{NH_2, N^-, CO, NH_{2Dab}\}$ bonding mode. All proctolin analogues studied in pH above 8 give in CD spectra the charge transfer transition band $O^-_{Tyr} \rightarrow Cu^{2+}$ at 360–370 nm suggesting the formation of phenolate oxygen of Tyr residue–Cu^{2+} bond. The tyrosine residue in second position of the peptide chain is already bonded to the metal ion by the amide nitrogen atom and cannot be coordinated to the same copper(II) ion by the phenolate oxygen for steric reasons. Therefore, the formation of the polynuclear complexes may be suggested.

References

[1] B.E. Brown, A.N. Starratt, J. Insect Physiol. 21 (1975) 1879.
[2] R.E. Sullivan, J. Exp. Zool. 210 (1979) 543.
[3] B.E. Brown, J. Insect Physiol. 23 (1977) 861.
[4] T.L. Swartz, G.M.H. Lee, K.K. Siwicki, D.G. Standaert, E.A. Kravitz, J. Neurosci. 4 (1984) 1300.
[5] I. Orchard, J.H. Balanger, A.B. Lange, J. Neurobiol. 20 (1989) 470.
[6] C.A. Bishop, M. O'Shea, J. Comp. Neurol. 207 (1982) 223.
[7] H. Agricola, M. Eckert, J. Ude, H. Birkenbeil, H. Penzlin, Cell Tiss. Res. 239 (1985) 203.
[8] M. O'Shea, M.E. Adams, Science 213 (1981) 567.
[9] T.A. Miller, Ann. Zoo. 191 (1979) 77.
[10] K.K. Siwicki, B.S. Beltz, T.L. Swartz, E.A. Kravitz, Peptides 6 (1985) 393.
[11] M.E. Adams, M. O'Shea, Science 221 (1983) 286.
[12] G.M. Holman, B.J. Cook, Insect Biochem. 9 (1979) 149.
[13] T.A. Miller, R.E. Sullivan, J. Neurosci. 12 (1981) 629.
[14] A.N. Starrat, B.E. Brown, Biochem. Biophys. Res. Commun. 90 (1979) 1125.
[15] D. Konopińska, G. Rosiński, A. Lesicki, P. Sujak, W. Sobótka, Bull. Pol. Acad. Sci. Chem. 36 (1988) 17.
[16] D. Konopińska, G. Rosiński, W. Sobótka, Pol. J. Chem. 68 (1994) 1437.
[17] D. Konopińska, G. Rosiński, J. Pept. Sci. 5 (1999) 533.
[18] D. Konopińska, M. Kuczer, W. Szeszel-Fedorowicz, G. Rosiński, J. Śliwowska, J. Issberner, R. Osborne, in: S. Bajusz Budapest, F. Hudecz (Eds.), Proc. 25th European Peptide Symposium, Akademiai Kiado, Budapest, 1998, p. 674.
[19] L.L. Iversen, Ann. Rev. Pharmacol. Toxicol. 23 (1983) 1.
[20] L.D. Pettit, G. Formicka-Kozłowska, Neurosci. Lett. 50 (1984) 53.
[21] M. Bataille, H. Kozłowski, G. Formicka-Kozłowska, I. Steel, L.D. Pettit, J. Chem. Soc., Chem. Commun. (1984) 231.
[22] M. Bezer, L.D. Pettit, I. Steel, M. Bataille, S. Djemil, H. Kozłowski, J. Inorg. Biochem. 20 (1984) 13.
[23] F.E. Bloom, Ann. Rev. Pharmacol. Toxicol. 23 (1983) 151.
[24] H. Kozłowski, M. Bezer, L.D. Pettit, M. Bataille, B. Hecquet, J. Inorg. Biochem. 18 (1983) 231.

[25] D. Konopińska, J. Pept. Res. 49 (1997) 457.
[26] M. Kuczer, G. Rosiński, M. Lisowski, B. Picur, D. Konopińska, Int. J. Pept. Prot. Res. 48 (1996) 289.
[27] H. Irving, M.G. Miles, L.D. Pettit, Anal. Chim. Acta 38 (1967) 475.
[28] P. Gans, A. Sabatini, A. Vacca, J. Chem. Soc., Dalton Trans. (1985) 1195.
[29] E.R. Clarke, A.E. Martell, J. Inorg. Nucl. Chem. 32 (1970) 911.
[30] H. Kozłowski, B. Radomska, G. Kupryszewski, B. Lammek, C. Livera, L.D. Petit, S. Pyburn, J. Chem. Soc., Dalton Trans. (1989) 173.
[31] W. Bal, H. Kozłowski, G. Kupryszewski, Z. Maćkiewicz, L.D. Petit, R. Robbins, J. Inorg. Biochem. 52 (1993) 79.
[32] T. Kowalik-Jankowska, W. Leśniak, J. Brasuń, M. Stasiak, M.T. Leplawy, Polyhedron 19 (2000) 241.
[33] R.M. Smith, A.E. Martell, Critical Stability ConstansSecond Supplement, vol. 6, Plenum Press, New York, 1989.
[34] I. Sovago, T. Kiss, A. Gergely, Inorg. Chim. Acta 93 (1984) l53.
[35] T. Kowalik-Jankowska, M. Jasionowski, L. Łankiewicz, J. Inorg. Biochem. 76 (1999) 63.
[36] L.D. Pettit, S. Pyburn, W. Bal, H. Kozłowski, M. Bataille, J. Chem. Soc., Dalton Trans. (1990) 3565.
[37] L.D. Pettit, I. Steel, G. Formicka-Kozłowska, T. Tatarowski, M. Bataille, J. Chem. Soc., Dalton Trans. (1985) 535.
[38] H. Kozłowski, W. Bal, M. Dyba, T. Kowalik-Jankowska, Coord. Chem. Rev. 184 (1999) 319.
[39] C. Livera, L.D. Pettit, M. Bataille, J. Krembel, W. Bal, H. Kozłowski, J. Chem. Soc., Dalton Trans. (1988) 1357.
[40] G. Formicka-Kozłowska, H. Kozłowski, I.Z. Siemion, K. Sobczyk, E. Nawrocka, J. Inorg. Biochem. 15 (1981) 201.
[41] E. Lodyga-Chruścińska, G. Micera, D. Sanna, J. Olczak, J. Zabrocki, H. Kozłowski, L. Chruściński, J. Inorg. Biochem. 76 (1999) 1.
[42] R. Prados, R.K. Boggess, R.B. Martin, R.C. Woodworth, Bioinorg. Chem. 4 (1975) 135.
[43] M. Jeżowska-Bojczuk, J. Baranowski, H. Kozłowski, Pol. J. Chem. 57 (1983) 685.
[44] Ch.O. Onindo, T.Yu. Sliva, T. Kowalik-Jankowska, I.O. Fritsky, P. Buglyo, L.D. Petit, H. Kozłowski, T. Kiss, J. Chem. Soc., Dalton Trans. (1995) 3911.
[45] L.D. Pettit, I. Steel, T. Kowalik, H. Kozłowski, M. Bataille, J. Chem. Soc., Dalton Trans. (1985) 1201.
[46] K. Varnagy, J. Szabo, I. Sovago, G. Malandrinos, N. Hadjiliadis, D. Sanna, G. Micera, J. Chem. Soc., Dalton Trans. (2000) 467.
[47] T. Kowalik-Jankowska, M. Ruta-Dolejsz, K. Wiśniewska, L. Łankiewicz, H. Kozłowski, J. Chem. Soc., Dalton Trans. (2000) 4511.
[48] G.F. Bryce, F.R.N. Gurd, J. Biol. Chem. 241 (1966) 122.

Available online at www.sciencedirect.com
SCIENCE DIRECT®
Polyhedron 24 (2005) 451–461
POLYHEDRON
www.elsevier.com/locate/poly

A *N*,*N*′-diacetate benzodioxotetraazamacrocycle and its transition metal complexes

Sara Lacerda [a], Maria Paula Campello [a], Isabel C. Santos [a], Isabel Santos [a,*], Rita Delgado [b,c,*]

[a] *Departamento de Química, Instituto Tecnológico e Nuclear, Estrada Nacional, 10 Apartado 21, 2685-953 Sacavém, Portugal*
[b] *Instituto de Tecnologia Química e Biológica, UNL, Apartado 127, 2781-901 Oeiras, Portugal*
[c] *Instituto Superior Técnico, Av. Rovisco Pais, 1049-001 Lisboa, Portugal*

Received 8 November 2004; accepted 16 December 2005

Abstract

Reaction of 2,9-dioxo-1,4,7,10-tetraazabicyclo[1.10.1]hexadeca-1(11),13,15-triene-4,7-diacetic acid (**H_2L1**) with $CuCl_2 \cdot 2H_2O$ in ethanol at pH 6 led to the monomeric benzodioxochlorocomplex [Cu(**L′1**)Cl] (**1**) (**HL′1** = monoethylesther of **H_2L1**). X-ray structural analysis has shown that in complex **1** the Cu is five-coordinated by two nitrogen and two oxygen atoms of the macrocycle and by a chloride, displaying a square pyramidal coordination geometry. One of the acetate arms does not coordinate to the Cu and has suffered an in situ ethanolic esterification reaction. The protonation constants of **H_2L1** and the stability constants of its complexes with Cu^{2+}, Ni^{2+}, Zn^{2+}, Cd^{2+} and Pb^{2+} were determined by potentiometric methods and in some cases by ^{1}H NMR spectroscopy. The stability constants of the complexes follow the trend $[Ni(\mathbf{H_{-1}L1})]^- > [Cu(\mathbf{H_{-1}L1})]^- \gg [Pb(\mathbf{H_{-1}L1})]^- > [Zn(\mathbf{H_{-1}L1})]^- > [Cd(\mathbf{H_{-1}L1})]^-$, probably due to steric requirements. Spectroscopic measurements (absorption and EPR) at different pH values have shown the effect of the pH on the coordination sphere of the Cu complexes.
© 2005 Elsevier Ltd. All rights reserved.

Keywords: Macrocycles; Monomeric Cu(II) benzodioxotetraazamacrocycle chloro complex; Stability constants; EPR of copper(II) complexes

1. Introduction

Due to their participation in a great number of important biological processes, all organisms accumulate certain levels of copper, zinc, nickel and iron, in order to survive. However, an excess of these metals is very toxic and macrocyclic polyamine ligands have been explored as possible sequestering chelators. The stability and kinetic inertness of d-transition complexes with macrocyclic polyamines, when compared with those formed with the corresponding linear ligands, make the macrocyclic polyamine complexes interesting for application in a wide variety of areas, such as catalysis, biomimicry, metallotherapy and diagnostic or therapeutic applications in Nuclear Medicine. In this specific field, copper is a very interesting d-transition element due to the large number of radionuclides with physical properties suitable for imaging (^{60}Cu, ^{61}Cu, ^{62}Cu and ^{64}Cu) or therapy (^{64}Cu and ^{67}Cu) [1].

As a part of our ongoing research work on the synthesis and characterisation of complexes with d- and f-transition metals, potentially interesting for radio diagnostic and/or radiotherapy [2–5], we have been exploring the chemistry of the previously described benzodioxotetraazamacrocyclic 2,9-dioxo-1,4,7,10-tetraazabicyclo [1.10.1] hexadeca-1(11),13,15-triene-4,7-diacetic acid (**H_2L1**) (Fig. 1) [6,7].

* Corresponding authors. Tel.: +351 21 9946201; fax: + 351 21 994 1455.
E-mail address: isantos@itn.mces.pt (I. Santos).

0277-5387/$ - see front matter © 2005 Elsevier Ltd. All rights reserved.
doi:10.1016/j.poly.2004.12.008

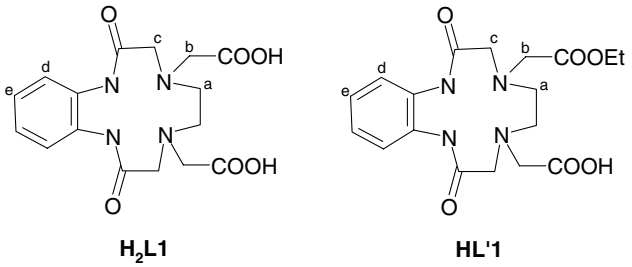


Fig. 1. 2,9-Dioxo-1,4,7,10-tetraazabicyclo[1.10.1]hexadeca-1(11),13, 15-triene-4,7-diacetic acid (**H_2L1**) and its monoethylesther (**HL′1**).

In this work, we describe the new monomeric and neutral chlorocomplex [Cu(**L′1**)Cl] (**1**) (**HL′1** = monoethylesther of **H_2L1**: 4-methylethylesther-2,9-dioxo-1,4,7, 10-tetraazabicyclo[1.10.1]hexadeca-1(11),13,15-triene-7-acetic acid ($C_{18}H_{23}N_4O_6$)). The structural differences between **1** and the dimeric Cu complex, previously described [7], led us to study more deeply the acid–base equilibrium of compound **H_2L1** as well as the stability constants of its complexes with Cu^{2+}, Ni^{2+}, Zn^{2+}, Cd^{2+} and Pb^{2+}, which will be also reported therein.

2. Experimental

2.1. Materials

Reactions were run under nitrogen atmosphere with magnetic stirring. Bulk solvent removal was done by rotary evaporation under reduced pressure and trace solvent removal from solids was done by vacuum pump. Solvents were either used as purchased or dried according to the standard literature procedures. Ethylenediaminetetraacetic dianhydride and *o*-phenylenediamine were obtained from the Aldrich Chemical Co. Copper salts were obtained from Baker's Analyzed. All reagents for synthesis and analyses were of analysis grade.

The benzodioxotetraazamacrocycle-*N*,*N*′-diacetic acid (**H_2L1**) was synthesised as previously described [6]. The purity of the compound was checked by the usual characterisation techniques.

2.1.1. Synthesis of [Cu^{II}(**L′1**)Cl] (**1**)

A solution of $CuCl_2 \cdot 2H_2O$ (0.11 g, 0.651 mmol in 2 cm^3 of ethanol) was added to a solution of **H_2L1** (0.237 g, 0.651 mmol in 8 cm^3 of ethanol). The resulting brown mixture was refluxed for 2 h. After cooling to room temperature, the solution was filtered through diatomaceous earth and washed with methanol. X-ray-quality green single crystals were obtained by slow diffusion of methanol. *Anal.* Calc. for $C_{18}H_{23}ClCuN_4O_6.H_2O$: C, 42.44; H, 5.14; N, 11.00. Found: C, 42.45; H, 4.63; N, 11.02%. UV: 704 nm (54 mol^{-1} dm^3 cm^{-1}), 382 nm (133 mol^{-1} dm^3 cm^{-1}).

2.2. X-ray crystal analyses

Suitable green crystals ($0.25 \times 0.20 \times 0.06$ mm) were mounted in air on a goniometer head. Data were collected at room temperature with the crystal mounted in a glass capillary. An Enraf-Nonius CAD4 diffractometer equipped with graphite monochromatised Mo Kα radiation ($\lambda = 0.71069$ Å) in the ω–2θ scan was used for measurements. Lorentz, polarisation effects and empirical absorption correction based on psi-scans [8] were applied to the collected intensities.

The structure was solved by direct methods using SIR97 [9] and refined by full-matrix least-squares on F^2 methods using the program SHELXL97 [10] and the WINGX software package [11]. All non-hydrogen atoms were refined anisotropically. Hydrogen atoms were placed in calculated positions. Molecular graphics were prepared with Ortep3 [12].

The crystal data and structure refinement details for **1**: Empirical formula, $C_{18}H_{23}N_4O_6ClCu$; $M = 490.39$ g mol^{-1}; Orthorhombic, $P2_12_12_1$, $a = 10.6410(13)$, $b = 13.0690(16)$, $c = 14.505(2)$ Å, $V = 2017.2(4)$ $Å^3$, $Z = 4$, $D_{calc} = 1.615$ g cm^{-3}, $\mu = 1.260$ mm^{-1}, $F(0\,0\,0) = 1012$; 271 parameters, no restraints, 2372 unique reflections measured, of which 2216 observed [$I > 2\sigma(I)$], $R_1 = 0.0624$, $wR_{all} = 0.1130$, Highest peak and deepest hole 0.574 and −0.282 e A^{-3}, θ range: 2.37–25.97°, Limiting indices, $-13 \leqslant h \leqslant 13$, $0 \leqslant k \leqslant 16$, $-17 \leqslant l \leqslant 0$, Goodness-of-fit = 1.061.

2.3. Spectroscopic studies

^1H and ^{13}C NMR spectra were recorded with a Bruker AMX-300 spectrometer at probe temperature in D_2O, using 3-(trimethylsilyl)-propanoic acid-*d*4-sodium salt as internal reference in the ^1H and dioxane in the ^{13}C spectra.

Electronic spectra were measured with a Cary 500 Version 8.01 spectrophotometer using aqueous solutions $\approx 1 \times 10^{-3}$ mol dm^{-3} of the copper complexes and $\approx 2 \times 10^{-3}$ mol dm^{-3} of the nickel complexes, at different pH values: ≈3, ≈6 and 10 for copper and ≈4, ≈8 and ≈11 for nickel complexes. The choice of the pH values was based on the species distribution diagram for each metal, selecting the maximum pH of formation of the species: [ML], $[M(H_{-1}L)]_-$ and $[M(H_{-2}L)]_{2-}$.

EPR spectroscopic measurements of the copper complex were recorded with a Bruker ESP 380 spectrometer equipped with continuous-flow cryostats for liquid nitrogen, operating at X-band. The complexes ($\approx 2 \times 10^{-3}$ mol dm^{-3} in 1:1 DMSO:H_2O solution) were prepared at pH 3.51, 6.37 and 10.26 and were recorded at 96 K. The EPR spectrum of a 1:1 DMSO/H_2O solution of **1** (at pH 3.23) was also recorded.

2.4. Potentiometric measurements

2.4.1. Reagents and solutions

Metal ion solutions were prepared at about 2.5×10^{-3} mol dm^{-3} from the nitrate salts of the metals and were titrated using standard methods [13]. Deionised (Millipore/Milli-Q System) distilled water was used. Carbonate-free solutions of the KOH titrant were obtained, maintained and discarded when the percentage of carbonate was about 0.5% of the total amount of base [14].

2.4.2. Equipment and work conditions

The equipment was used as described before [2–4,15]. The temperature was kept at 25.0 ± 0.1 °C, atmospheric CO_2 was excluded from the cell during the titrations by passing purified nitrogen across the top of the experimental solution in the reaction cell. The ionic strength of the solutions was kept at 0.10 mol dm^{-3} with KNO_3.

2.4.3. Measurements

The $[H^+]$ of the solutions was determined by the measurement of the electromotive force (emf) of the cell, $E = E^{\circ\prime} + Q\log[H^+] + E_j$. $E^{\circ\prime}$, Q, E_j and $K_w = ([H^+][OH^-])$ were obtained as described previously [2–4,15]. The term pH is defined as $-\log[H^+]$. The value of K_w was found equal to $10^{-13.80}$ $(\text{mol dm}^{-3})^2$. The potentiometric equilibrium measurements were made on 20.00 cm^3 of $\approx 2.00 \times 10^{-3}$ mol dm^{-3} ligand solutions diluted to a final volume of 25.00 cm^3, in the absence of metal ions and in the presence of each metal ion for which the C_M:C_L ratio was 1:1. A minimum of two replicate measurements was taken.

The emf data were taken after additions of 0.050 cm^3 increments of standard KOH solution, and after stabilisation in this direction, equilibrium was then approached from the other direction adding standard nitric acid.

In the cases of copper (II) and nickel (II), the degree of complex formation of the metal complexes was too high to prevent the use of the direct potentiometric method. Metal–metal competition titration methods were used. Lead (II) and cadmium (II) were the second metals used, respectively.

2.4.4. Calculation of equilibrium constants

Protonation constants $K_i^H = [H_iL]/[H_{i-1}L][H]$ were calculated by fitting the potentiometric data for the free ligand to the HYPERQUAD program [16]. Stability constants of the various species formed in solution were obtained from the experimental data corresponding to the titration of solutions of different ratios of the ligand and metal ions, also with the aid of the HYPERQUAD program. The initial computations were obtained in the form of overall stability constants or $\beta_{M_mH_hL_l}$ values:

$$\beta_{M_mH_hL_l} = \frac{[M_mH_hL_l]}{[M]^m[L]^l[H]^h}.$$

The hydrolysis constants of the metal ions were taken from the literature and kept constant for the calculations [17].

For ligand **H$_2$L1**, the first protonation constant was determined by ^{1}H NMR titration, due to its high value. For this determination, a solution of **H$_2$L1** (≈0.01 mol dm^{-3}) was prepared in D_2O and the pD was adjusted by addition of DCl or CO_2-free KOD with an Orion 420A instrument fitted with a combined Ingold 405M3 microelectrode. The $-\log[D^+]$ was measured directly in the NMR tube, after the calibration of the microelectrode with buffered aqueous solutions. The final pD was calculated from pD = pH* + (0.40 ± 0.02), where pH* corresponds to the reading of the pH meter [18,19].

3. Results and discussion

The benzodioxotetraazamacrocycle **H$_2$L1** has been synthesised and characterised as previously described [6]. Reaction of **H$_2$L1** with $CuCl_2 \cdot 2H_2O$ in ethanol, at pH 6 in 1:1 (Cu: **H$_2$L1**) molar ratio, resulted in a brown solution, upon refluxing for 2 h. This solution was filtered at room temperature and a small portion of methanol added. Slow diffusion of MeOH led to green monocrystals suitable for X-ray crystallographic analysis. By X-ray diffraction analysis, the complex formed was formulated as [Cu(**L′1**)Cl] (**1**). This is a monomeric Cu^{2+} complex anchored by a modified benzodioxotetraazamacrocycle. In complex **1**, the Cu is five-coordinated by two nitrogen atoms of the macrocyclic backbone, two oxygen atoms, one from one amide group and the other from an acetate arm, and a chloride atom occupies the fifth position. The second acetate arm of the macrocycle does not coordinate to the Cu and it has experienced an in situ ethanolic esterification reaction. The ORTEP drawing of **1** is shown in Fig. 2, and selected bond lengths and angles are listed in Table 1.

The Cu(II) centre displays a five-coordination environment, which can be described as a square pyramidal polyhedron (SP). The basal plane is defined by the N(3), O(2), O(5) and the chloride atoms, while the apical position is occupied by the N(4) atom.

Most of the Cu(II) five-coordinate complexes known display either distorted square pyramidal (SP) or distorted trigonal bipyramidal (TBP) coordination geometries. To evaluate the degree of distortion from the ideal polyhedron mainly two methods have been developed. The simplest method, which can be applied when there is an apical bond distance longer then the others, is based on the ratio of the two basal angles of the square plane, which is given by the expression $\tau = [(\theta - \phi)/$

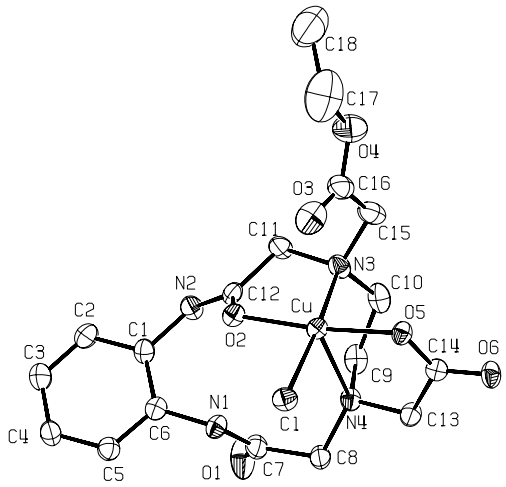


Fig. 2. ORTEP view of the complex **1**; thermal ellipsoids are drawn at 40% probability level.

Table 1
Selected bond lengths (Å) and angles (°) for **1**

Bond lengths			
Cu–O(5)	1.942(4)	O(2)–C(12)	1.265(7)
Cu–O(2)	1.964(4)	O(5)–C(14)	1.264(8)
Cu–N(3)	2.100(6)	O(6)–C(14)	1.225(8)
Cu–N(4)	2.420(5)	O(3)–C(16)	1.246(9)
Cu–Cl	2.2540(19)	O(1)–C(7)	1.220(8)
O(2)–C(12)	1.258(6)	O(4)–C(16)	1.319(10)
Bond angles			
O(5)–Cu–O(2)	172.66(18)	Cl–Cu–N(4)	96.17(14)
O(5)–Cu–N(3)	89.30(17)	C(13)–N(4)–C(9)	111.1(5)
O(2)–Cu–N(3)	83.60(17)	C(13)–N(4)–C(8)	107.4(5)
O(5)–Cu–Cl	96.10(14)	C(9)–N(4)–C(8)	111.9(5)
O(2)–Cu–Cl	91.12(13)	C(13)–N(4)–Cu	99.3(3)
N(3)–Cu–Cl	173.54(17)	C(9)–N(4)–Cu	100.7(4)
O(5)–Cu–N(4)	81.25(18)	C(8)–N(4)–Cu	125.6(4)
O(2)–Cu–N(4)	99.27(17)	C(12)–O(2)–Cu	112.2(4)
N(4)–Cu–N(3)	81.10(18)	C(14)–O(5)–Cu	119.7(4)

60] × 100 (%), being $\tau = 0$ for an ideal SP and $\tau = 100$ for an ideal TBP coordination geometries [20]. For complex **1**, the angles considered were Cl–Cu–N(3) and O(2)–Cu–O(5), and the value calculated for τ was 1.46%. The square plane is folded along the axis defined by Cl, Cu and N(3), yielding a dihedral angle between the planes [Cl, N(3), O(5)] and [O(2), Cl, N(3)] of 5.65(23)°. The angle between basal plane and the apical line Cu–N(4) is 78.91(15)°. The copper is 0.0217(24) Å above the basal plane and the apical N(4) atom is 2.348(6) Å below this plane, yielding a Cu–N(4) apical bond distance of 2.420(4) Å, which is longer than the copper nitrogen bond distance in the basal plane (Cu–N(3), 2.100(6) Å). The dihedral angle between the aromatic ring and the plane defined by the nitrogen atoms of the macrocyclic backbone is 14.45(30)°, being the copper atom 1.6750(31) Å above this plane. The Cu–N(3) bond distance is in the expected range of 1.99–2.08 Å, normally found for five-coordinated Cu(II) complexes stabilised by amines [20a, 21].

In complex **1**, the Cu–O(2) and Cu–O(5) bond lengths are 1.964(4) and 1.942(4) Å, respectively. As in other five-coordinated Cu(II) complexes, the bond Cu–O_{amide} is slightly longer than Cu–$O_{carboxylate}$. The Cu–Cl bond length of 2.254(2) Å in **1** is in the expected range [22].

The formation of the monomeric complex **1**, described herein, is certainly related with the reaction conditions used for the synthesis and recrystallisation of this complex (1:1 **H_2L1**:$CuCl_2 \cdot 2H_2O$, pH 6, ethanol, 2 h reflux, slow diffusion of MeOH), which certainly were also responsible for the in situ sterification of one carboxylic acid arm. In fact, a dimer copper complex, isolated by Fernando and co-workers [7], has been obtained by reacting **H_2L1** with $CuCl_2 \cdot 2H_2O$ in basic aqueous conditions and monocrystals were formed by the slow concentration of this solution. In the dimer, the Cu atom is six-coordinated by two oxygen atoms of the carboxylate arms, an oxygen from an amide group and two nitrogen atoms from the macrocyclic backbone; the sixth coordination position being occupied by an oxygen atom of a carboxylate arm from an adjacent molecule.

Taking into account that different complexes can be formed using different reaction conditions and also the potential interest of copper for biological applications, we decided to study the coordination chemistry of this ligand, including the determination of the stability constants of **H_2L1** with Cu and also with other metals, such as Ni, Zn, Cd and Pb, which also have biological interest, due to their high toxicity. Spectroscopic measurements were also performed in order to understand the structure of some of the complexes in aqueous solution.

3.1. Acid–base behaviour

The acid–base behaviour of compound **H_2L1** has been studied by potentiometry and by ^{1}H NMR spectroscopy. Only four protonation constants were determined. From the remaining two constants, one is very high (corresponding to the amide centre) and the other very low to be determined. Indeed, in our work conditions only one amide centre can be deprotonated, and even this one at very high pH values, then the corresponding constant was determined by ^{1}H NMR spectroscopy. The protonation constants of **H_2L1** are shown in Table 2 as well the values published in literature for other related tetraazamacrocyclic ligands shown in Fig. 3.

Taking into account the structure of **H_2L1**, results published in the literature and our ^{1}H NMR data (see below), the values in Table 2 indicate that the first protonation occurs at one amide nitrogen atom, as already mentioned. The second constant corresponds to the protonation of an amine nitrogen, which in spite of being a low value it is the usual number found for

Table 2
Protonation constants (log units) for **H_2L1** and other similar ligands

Overall protonation constants [stepwise constants]	**H_2L1**[a]	**H_2L1**[b]	**H_2L2**[c,d]	**H_2L3**[c,d]
$\beta_1^H[k_1^H]$	12.81(20) [12.81]			
$\beta_2^H[k_2^H]$	18.84(1) [6.03]	6.07 [6.07]	6.50 [6.50]	6.41 [6.41]
$\beta_3^H[k_3^H]$	22.24(1) [3.40]	9.34 [3.27]	10.04 [3.54]	9.81 [3.40]
$\beta_4^H[k_4^H]$	24.35(3) [2.11]			

[a] This work, 25.0 °C, $I = 0.10$ mol dm^{-3} KNO_3, values in parentheses are standard deviations in the last significant figures.
[b] 25 °C, $I = 0.1$ mol dm^{-3} KCl, [7].
[c] 25 °C, $I = 0.1$ mol dm^{-3} KCl, [23,24].
[d] The β values shown were calculated based on the stepwise stability constants given by the authors.

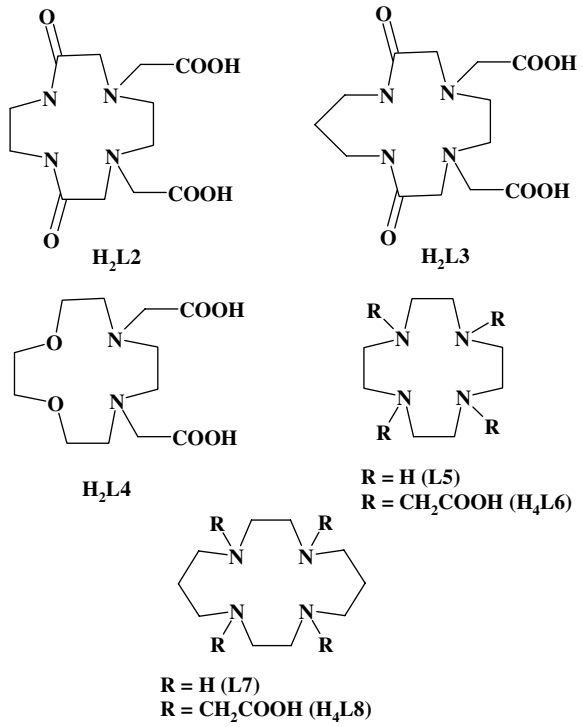


Fig. 3. Tetraazamacrocyclic ligands related with **H_2L1**: **H_2L2** (2,9-dioxo-1,4,7,10-tetraazacyclododecane-4,7-diacetic acid), **H_2L3** (2,9-dioxo-1,4,7,10-tetraaza-cyclotridecane-4,7-diacetic acid), **H_2L4** (1,4-dioxa-7,10-diazacyclododecane-7,10-diacetic acid), **L5** (1,4,7,10-tetraazacyclododecane; cyclen), **H_4L6** (1,4,7,10-tetraazacyclododecane-1,4,7,10-tetraacetic acid; dota), **L7** (1,4,8,11-tetraazacyclotetradecane; cyclam), **H_4L8** (1,4,8,11-tetraazacyclotetradecane-1,4,8,11-tetraacetic acid; teta).

the protonation of amine centres in close proximity of one electron-withdrawing amide group [25,26]. The third constant corresponds to the protonation of the acetate arm bound to the non-protonated amine nitrogen [25] and finally, the fourth constant can be attributed to the protonation of the remaining amine nitrogen or the remaining acetate or both simultaneously.

The first determined protonation constant is so high that only could be determined by ^{1}H NMR titration in the pD range 8–15, Fig. 4.

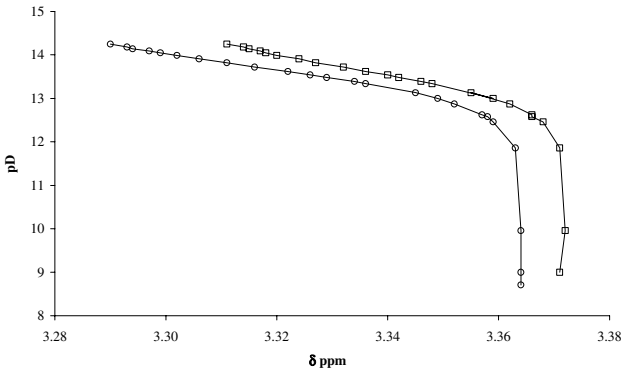


Fig. 4. ^{1}H NMR titration curves of **H_2L1**: proton H_b (○) and proton H_c (□).

The ^{1}H NMR spectra of compound **H_2L1** exhibit four resonances for the entire pD range. At high pD values, the spectra show two multiplets assigned to the aromatic protons (H_d and H_e) and two singlets, integrating for four and two protons, assigned to the H_b, H_c and H_a, respectively. At low pD values, the spectra show only one multiplet resonance for the four aromatic protons (H_d/H_e) and three singlets of equal intensity (2H) for the H_a, H_b and H_c protons.

The variation of chemical shifts (δ) of the H_b and H_c protons in function of pD values were used to determine the first protonation constant. As can be seen in Fig. 4, the δ are downfield shifted when the pD value increases. The shifts are small, because the centre to be protonated is far from H_b or H_c, but significant enough to be used for calculations. Based on these data, two pK_D values were determined independently, converted in pK_H, and the final pK_H given by the average of these. The conversion of the pK_D values in pK_H was made using the correlation pK_D = 0.11 + 1.10pK_H determined for polyaza and polyoxa-polyaza macrocyclic compounds by Delgado et al. [18]. The average pK_H value found was 12.81(4). However if all the experimental errors for the determination of this value were taken into account a standard deviation of about 0.2 should be indicated as more realistic.

The values determined in this work (see Table 2) for the second and the third stepwise protonation constants are comparable to the values previously reported by Cathala et al. [6] and Fernando and co-workers [7]. It was possible to determine the protonation constant of one amide centre for **H_2L1**, and not in the case of **H_2L2** and **H_2L3** and many other similar cyclic amide complexones studied by Fernando and co-workers [23,24,26], due to the presence of the benzene ring in **H_2L1** that turn the adjacent amide more acidic. However, the inclusion of this constant, and also the fourth one, led to an overall basicity for **H_2L1**, which is about 15 log units higher than the previously described value with the consequent repercussions on the stability constant values of its metal complexes.

Potentiometric studies of **H_2L1** with Cu^{2+}, Ni^{2+}, Zn^{2+}, Cd^{2+} and Pb^{2+} were performed also at 25.0 °C and 0.10 M ionic strength in KNO_3, in order to determine the corresponding stability constant. The values found are shown in Table 3, together with those taken from literature for the related **H_2L2** and **H_2L3** macrocycles.

Only mononuclear species were formed with the studied metal ions, namely $[M(\mathbf{H_{-1}L1})]^-$, $[M\mathbf{L1}]$ and $[M(\mathbf{H_{-2}L1})]^{2-}$. The $[M(\mathbf{HL1})]^+$ species only appears with Ni^{2+}, while $[M(\mathbf{H_{-3}L1})]^{3-}$ is formed with Cu^{2+} and Cd^{2+}.

At physiological pH, the $[M(\mathbf{H_{-1}L1})]^-$ complex is formed at about 100% for Cu^{2+} and Ni^{2+}, while for Pb^{2+} and Zn^{2+} this species is the main complex only at pH $\geqslant$ 9, and for Cd^{2+} the amount of $[Cd(\mathbf{H_{-1}L1})]^-$ formed is low at physiological pH, being $[M\mathbf{L1}]$ always present. This information suggests that Ni^{2+} and Cu^{2+} easily deprotonate the first amide centre, while the other studied metal ions only manage to do it at higher pH values. Even though the thermodynamic stability constants do not give structural information, being impossible to ascribe the acid–base reactions that occur at high pH values to amide deprotonation or to the hydrolysis of water molecules directly coordinated to the metal centre. Based in these experiments is also impossible to realize if a structural arrangement occurs upon deprotonation of the amide centre for the nickel and copper complexes. However a slow reaction occurs after the deprotonation of the first amide centre for the case of nickel, because it was found completely different potentiometric curves when the solution containing the metal and ligand in a 1:1 ratio is titrated with base (formation of complexes) or with acid upon the complete formation of complexes which clearly suggests a structural rearrangement (supplementary material).

The Ni(II) complex $[M(\mathbf{H_{-1}L1})]^-$ exhibits the highest thermodynamic stability constant followed by Cu(II) being the corresponding values significantly lower for

Table 3
Stability constants (log units) for complexes of **H_2L1** and other related ligands with several divalent metal ions (charges were ignored)

Ion	Equilibrium quotient	**H_2L1**[a]	**H_2L1**[b]	**H_2L2**[c,d]	**H_2L3**[c,d]
Ni^{2+}	$[ML]/[M]\times[L]$	17.73(8)	9.4	11.27	10.08
	$[M(HL)]/[M]\times[H]\times[L]$	22.81(3)		12.82	11.68
	$[M(H_2L)]/[M]\times[H]^2\times[L]$	27.04(6)			
	$[M(H_{-1}L)]/[M]\times[H]^{-1}\times[L]$	8.76(5)	2.5	1.97	−0.60
	$[M(H_{-2}L)]/[M]\times[H]^{-2}\times[L]$			−11.93	−10.38
Cu^{2+}	$[ML]/[M]\times[L]$	17.13(5)	9.04	11.34	10.46
	$[M(HL)]/[M]\times[H]\times[L]$	21.72(4)		12.63	11.55
	$[M(H_{-1}L)]/[M]\times[H]^{-1}\times[L]$	8.54(6)	4.51	4.04	3.08
	$[M(H_{-2}L)]/[M]\times[H]^{-2}\times[L]$	−2.70(7)	−4.33	−6.37	−2.97
Zn^{2+}	$[ML]/[M]\times[L]$	13.23(4)	7.56	8.98	9.13
	$[M(HL)]/[M]\times[H]\times[L]$	20.40(2)		10.45	11.49
	$[M(H_{-1}L)]/[M]\times[H]^{-1}\times[L]$	2.68(6)	0.42	−0.58	−0.84
	$[M(H_{-2}L)]/[M]\times[H]^{-2}\times[L]$		−10.84	−12.52	−12.08
Cd^{2+}	$[ML]/[M]\times[L]$	12.68(5)		7.3	7.4
	$[M(HL)]/[M]\times[L]\times[H]$	19.84(2)		9.9	9.6
	$[M(H_{-1}L)]/[M]\times[H]^{-1}\times[L]$	2.48(6)		−3.1	−3.2
	$[M(H_{-2}L)]/[M]\times[H]^{-2}\times[L]$	−9.42(4)		−15.4	−15.2
Pb^{2+}	$[ML]/[M]\times[L]$	13.43(2)			
	$[M(HL)]/[M]\times[H]\times[L]$	20.88(1)			
	$[M(H_{-1}L)]/[M]\times[H]^{-1}\times[L]$	3.60(3)			

[a] This work; 25.0 °C, $I = 0.10$ mol dm^{-3} KNO_3, **L** is $\mathbf{H_{-1}L1}^{3-}$, the resulting species upon three successive deprotonation reactions of **H_2L1**, including the deprotonation of one amide group, see text; values in parentheses are standard deviations in the last significant figures.
[b] 25 °C, $I = 0.1$ mol dm^{-3} KCl, [7].
[c] 25 °C, $I = 0.1$ mol dm^{-3} KCl, [23,24].
[d] The β values shown were calculated based on the stepwise stability constants given by the authors.

the other three metal ions, Pb, Zn and Cd. The trend $[Ni(\mathbf{H_{-1}L1})]^- > [Cu(\mathbf{H_{-1}L1})]^- \gg [Pb(\mathbf{H_{-1}L1})]^- > [Zn(\mathbf{H_{-1}L1})]^- > [Cd(\mathbf{H_{-1}L1})]^-$ does not follow the usual Irving–Williams order of stability [27]. However, analogous trends have already been reported. In general, steric requirements of the ligands on complex formation (macrocyclic type or other) or coordination geometry preferences are on the basis of the inversion of stability for the nickel and copper complexes [28].

The stability constant values of **H_2L1** with all the metals studied are higher than the previously reported [7], which is expected on the basis of the different protonation values presented. The direct comparison of values of this work and the previously reported ones can be made by the calculation of pM ($-\log[M^{2+}]$) values. In Table 4 are shown the pM values for the different complexes together with those calculated from the potentiometric data for other related ligands (see Fig. 3), at physiological pH [29]. The pCu and pZn values for **H_2L1** calculated using our stability constants are identical, but the pNi is higher, than the reported ones.

The discrepancy found for Ni probably results from the very high value of its stability constant added to its slow kinetic formation. Indeed this constant, as well as that for the copper complex, was determined by a competition reaction (see Section 2) because the complex is completely formed at the beginning of the titration, this means at very low pH values, see Fig. 5. The ligand **H_2L3** presents lower pM values when compared with those of **H_2L1**, except for zinc. The lower values for **H_2L3** are expected due to the larger cavity size of this macrocycle, although the high value presented for Zn is not expected. The pM values for **H_2L1** and **H_2L2** are very similar suggesting that the introduction of the benzene ring into the framework of **H_2L1** has a minor influence on complex formation, or that the donor atoms involved in the coordination to the metal are not specially affected by the presence of the benzene ring.

Table 4
pM ($-\log[M^{2+}]$)[d] values determined for metal complexes of **H_2L1** at physiological pH

Ion	**H_2L1**[a]	**H_2L1**[b]	**H_2L2**[c]	**H_2L3**[c]
Ni^{2+}	12.32	9.99	11.67	10.04
Cu^{2+}	11.73	11.91	11.64	11.83
Zn^{2+}	8.00	7.99	8.93	9.09
Cd^{2+}	7.45		7.88	7.90
Pb^{2+}	8.33			

[a] This work.
[b] Ref. [7].
[c] Ref. [23,24].
[d] The values were calculated for 100% excess of free ligand, using the program HYSS [29], $C_L = 2C_M = 1 \times 10^{-5}$ mol dm^{-3}, and the stability constants given in Table 2.

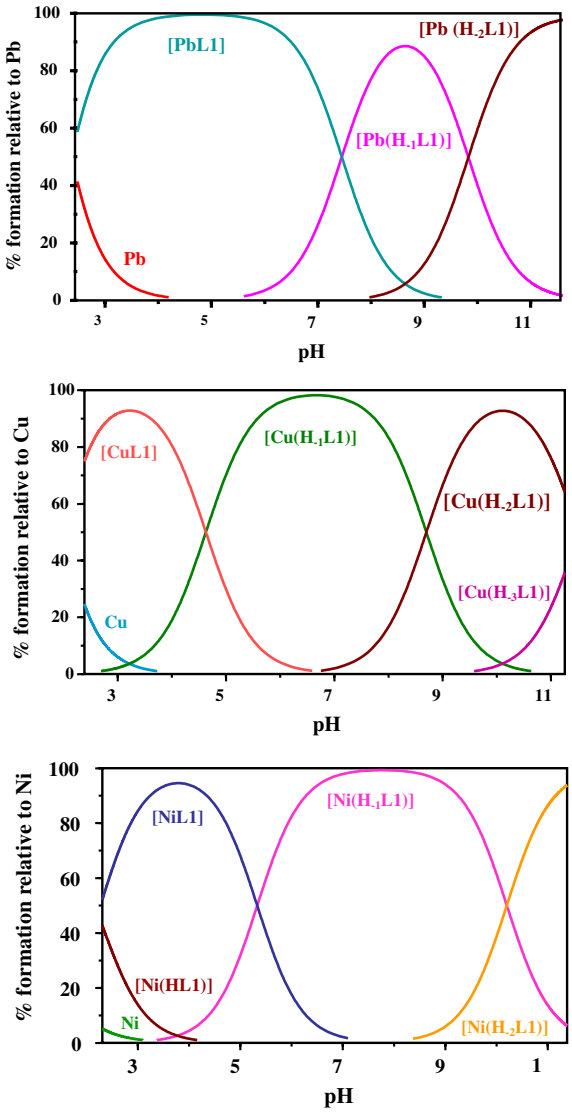


Fig. 5. Species-distribution diagrams for the Pb^{2+}, Cu^{2+} and Ni^{2+} complexes with **H_2L1** in water, $C_L = C_M = 4.201 \times 10^{-5}$ mol dm^{-3}.

3.2. Spectroscopic studies in solution

The UV–Vis-near IR spectra of the Ni(II) and the Cu(II) complexes, and the X-band EPR spectra of the Cu(II) ones were recorded at pH values of about 3, 6.5 and 10 for the copper complexes and about 4, 8 and 11 for the nickel ones. The selected pH values correspond to the maximum percentage of [M**L**], $[M(\mathbf{H_{-1}L})]^-$ and $[M(\mathbf{H_{-2}L})]^{2-}$ species, respectively, with minimum percentage of the other species present, as shown on the species distribution diagrams, see Fig. 5.

3.3. UV–Vis-near IR spectra

The electronic spectra of the Ni/**H_2L1** complexes exhibit at all pH values three main bands typical of distorted octahedral or square pyramidal geometries: one

in the range 1008–952 nm (broadband), the second in the range 597–562 nm and the third at about 380 nm, (Table 5). The spectra were recorded upon full stabilisation (about 18 h) of solutions at each pH. Indeed the slow kinetics, already verified in the potentiometric measurements, was confirmed, the final spectra displaying important differences in number of bands and absorption maxima from those recorded immediately upon preparation.

The visible and especially the near-IR bands shift to higher energies (of about 50 nm for the first and 35 nm for the second one), when the pH increases from 3.76 to 11.39. The observed blue shift indicates an increase of the ligand field, suggesting the coordination of an additional donor atom to the metal centre. The increase of the molar absorptivity accounts to a more distorted geometry of the complex.

The electronic spectra of the copper complexes are not especially informative about the adopted geometry in solution, however the band in the near-IR region points to a distorted geometry, and the blue shifts of the visible band with the increase of the pH were also observed, see Table 5. However, a faster kinetics of formation of the copper complex in comparison with that of nickel was noted, as already mentioned above.

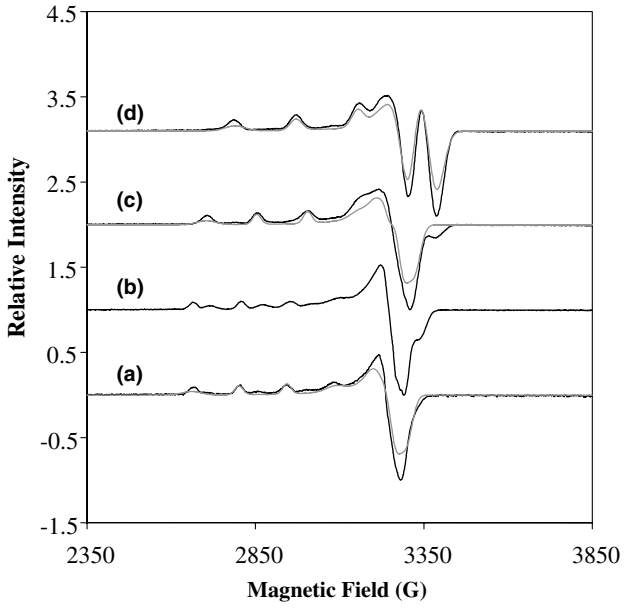


Fig. 6. X-band EPR spectra of copper complexes of **H_2L1** in $\approx 2 \times 10^{-3}$ mol dm^{-3} and 1:1 H_2O/DMSO solutions (black lines) and its simulated spectra (grey lines) at different pH values: (a) pH 3.51; (b) pH 6.37 and (c) pH 10.26. The spectrum of a solution of **1** in 1:1 H_2O/DMSO (pH 3.23) is also shown (d). All the spectra were recorded at 96 K, microwave power of 2.0 mW and modulation amplitude of 1 mT. The frequency was 9.405, 9.407, 9.408 and 9.407 GHz, respectively.

3.4. EPR spectroscopy of copper complexes

The EPR spectra of copper complexes in solution at different pH indicated the presence of only one species, while the EPR spectrum of the solution obtained by dissolving the crystals of **1** in DMSO/H_2O indicated the presence of two species, see Fig. 6. All spectra showed the expected four well-resolved lines at low field, due to the interaction of the unpaired electron spin with the copper nucleus. The hyperfine coupling constants (A) and g values obtained by the simulation of the spectra [30] are shown in Table 6, together with those of other copper (II) complexes taken from literature for comparison. The simulation of the spectra indicates three different g values with $g_z > (g_x + g_y)/2$ and the lowest $g \geqslant 2.04$, which is characteristic of mononuclear copper (II) complexes having rhombic-octahedral with elongation of the axial bonds or distorted square-based pyramidal symmetries, and $d_{x^2-y^2}$ ground state.

At the three pH studied, the complexes have g_z and A_z parameters consistent with different type of donor atoms close lying the metal. At pH 3.51, these parameters are consistent with N_2O_2 equatorial coordination sphere [31]. The differences between them can be visualised in the diagram g_z versus A_z presented in Fig. 7, and rationalised in terms of different axial field for each complex. Indeed, the g_i and A_i values are related to the electronic transitions by the factors derived from the ligand-field theory [32,33]: the g_i values increase

Table 5
Spectroscopic UV–Vis-near IR data for the Ni^{2+} and Cu^{2+} complexes of **H_2L1** at several pH values in aqueous solution and 25 °C

Complex	pH	λ/nm (ε/mol^{-1} dm^3 cm^{-1})
Ni^{2+}/H_2L1	3.76	1008 (27), 597 (8), 375 (19)
	8.02	1151 (28), 1036 (sh., 26), 959 (30), 842 (sh., 20), 595 (20), 363 (sh., 34), 339 (sh., 40)
	11.39	1147 (27), 1017(sh., 31), 952 (39), 850 (sh., 30), 562 (24), 342 (sh., 65)
Cu^{2+}/H_2L1	3.51	752 (65), 487 (sh., 24), 382 (69)
	6.63	1020 (sh., 22), 670 (61), 444 (sh., 60), 375 (450)
	10.10	643 (sh., 160), 560 (186), 384 (197)
1[a]	3.23	704 (54), 382 (133)

[a] Crystals of **1** dissolved in aqueous solution.

Table 6
Spectroscopic EPR parameters for the copper (II) complexes of **H_2L1** and other related ligands taken from literature ($A_i \times 10^4$ cm^{-1})

Ligand/complex (pH)		g_x	g_y	g_z	A_x	A_y	A_z
H_2L1 (3.51)[a]		2.060	2.088	2.338	1.7	7.9	155.1
H_2L1 (6.37)[a]		2.050	2.080	2.293	3.1	12.8	161.4
H_2L1 (10.26)[a]		2.039	2.064	2.194	2.5	13.5	186.8
1 (3.23)[a]	**A**	2.060	2.088	2.336	1.4	6.4	153.6
	B	2.050	2.081	2.293	2.5	11.9	163.8
H_2L1 (6.6)[b]		2.035	2.090	2.290			165.1
H_2L1 (12.0)[b]		2.040		2.195			190.2
H_2L3 (<7)[c]		2.039	2.073	2.336			147.0
H_2L3 (>7)[c]		≈2.0		2.190			188.0
H_2L4 [d]		2.045	2.073	2.251	5.4	16.6	187.8
L5 [e]		2.057		2.198	24.1		184.2
L7[e]		2.049		2.186	38.7		205.0
H_4L6[e]		2.062		2.300			150.3
H_4L8[e]		2.050		2.249			168.0
Cu(H_2O)$_6$[f]		2.08		2.4			134.0

[a] This work.
[b] Ref. [7].
[c] Ref. [23].
[d] Ref. [36a].
[e] Ref. [36b,36c].
[f] Ref. [36d].

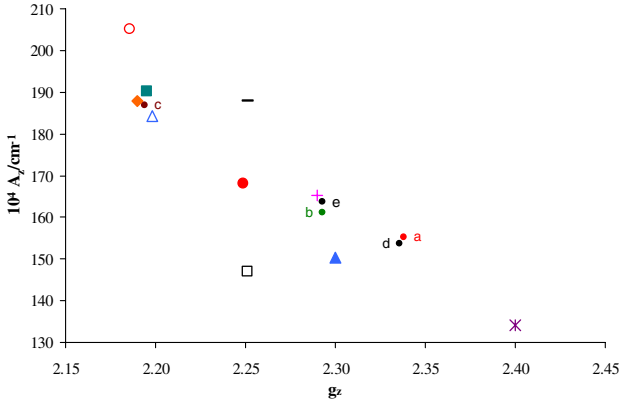


Fig. 7. Diagram A_z vs. g_z EPR parameters for the copper (II) complexes studied (×) and others from literature formed with the following ligands: ● **a** **H_2L1** (pH 3.51), ● **b** **H_2L1** (pH 6.37), ● **c** **H_2L1** (pH 10.26), ● **d** **1** (specie A), ● **e** **1** (specie B), + **H_2L1** (pH 6.6) [7], ■ **H_2L1** (pH 12) [7], ◆ **H_2L3** (pH > 7) [23], □ **H_2L3** (pH < 7) [23], – **H_2L4** [36a], ○ **L7** [36b,36c], △ **L5** [36b,36c], ▲ **H_4L6** [36b,36c], ● **H_4L8** [36b,36c] and ⁎ Cu(H_2O)$_6$ [36d].

and the A_i values decrease as the equatorial ligand field becomes weaker or stronger the axial ligand field and this occurs with the simultaneous red-shift of the d–d absorption bands in the electronic spectra (see Tables 5 and 6) [33–35]. Herein, when the pH increases a blue-shift is observed, and simultaneously the g_z decrease and the A_z values increase, which is consistent with the increase of the equatorial field. These features are also consistent with the potentiometric results, which have shown that the deprotonation of one amide nitrogen atom occurs at pH ~ 6.

The EPR spectrum of crystals of **1** showed that two species are present in different proportions. The g_z and A_z parameters suggest that the crystals of **1** in solution have a different structure than in the solid state, as the chloride atom is probably replaced by an oxygen of a water molecule. The resulting parameters are consistent with a mixture of the spectrum of **H_2L1** at pH 3.51 (specie A) and of **H_2L1** at pH 6.37 (specie B), being the first in a higher proportion (about 75%). This suggests that an equilibrium between the two corresponding structures is responsible by the observed EPR spectrum.

The A_z versus g_z diagram shown in Fig. 7, together with the known geometries of some of the complexes taken from the literature [36], allow the following considerations: (1) the right region of the diagram, having higher g_z and lower A_z values, is occupied by complexes with oxygen atoms in the equatorial plane, such as Cu(H_2O)$_6$ (⁎); (2) in the middle region of the diagram complexes with octahedral geometry are found, having the four nitrogen atoms of the macrocycle forming the equatorial plane and oxygen atoms in the axial positions (● **H_4L8**); (3) the complexes having four nitrogen atoms of the macrocyclic ring at the equatorial plane are located in the left part of the diagram and exhibit square-planar (○ **L7**) or square pyramidal (△ **L5**) geometries. The parameters of the copper complexes of **H_2L1** change considerably with the increase of the pH, with the decrease of g_z, the increase of A_z and a corresponding blue shift, accounting a stronger equatorial ligand field. Indeed, at pH 3.5 these parameters are consistent with a N_2O_2 coordination sphere, while those for the complexes at pH ≈ 6 and ≈10 point to arrangements with stronger equatorial ligand fields, in agreement to the presence of an increased number of nitrogen as donor atoms.

4. Concluding remarks

Although **H_2L1** was reported before, the present study allowed to extend the knowledge of its behaviour and of its metal complexes in solution and in the solid state. Our potentiometric and ^1H NMR studies revealed that the deprotonation of one of the amides occurs at a pH lower than usual due to the presence of the benzene ring into the macrocyclic backbone, allowing its determination. It was also verified that the nickel complex has a thermodynamic stability higher than the copper one, and therefore the usual Irving–Williams trend of stability is not found, probably due to steric strain imposed by the ligand.

By reacting **H_2L1** with $[CuCl_2] \cdot 2H_2O$, in EtOH at pH 6 and using the 1:1 M/L molar ratio, the monomeric complex **1** was obtained. This complex is quite different from the dimeric Cu^{2+} complex isolated previously by Fernando and co-workers [7].

Based on the electronic data, it was possible to predict that at low pH values (pH 3.51) two amine nitrogen atoms and two oxygen atoms from the acetate arms or from the amides of the framework are involved in the coordination sphere of the Cu, as the EPR parameters are consistent with a N_2O_2 donor atoms close lying the metal [31] and the X-ray structure of **1** also suggests. At higher pH values (about 6), the EPR parameters are consistent with a N_3O equatorial coordination sphere for the copper, in agreement also with the blue shift of the band in the visible region. This means that the deprotonation of the amide of the macrocyclic backbone, which occurs in this pH range, leads to a rearrangement of the complex with the repositioning of the Cu atom towards the centre of the macrocycle for the coordination to this amide nitrogen. This probably also happens with the nickel complex, and in this case the rearrangement is kinetically slow, as observed by our potentiometric and UV–Vis results. At high pH values is impossible to predict, based only on our potentiometric experiments, if the deprotonation of the second amide of the macrocycle occurs or if the proton that is titrated in this region derive from the hydrolysis of a water molecule directly coordinated to the metal ion. However, the EPR spectra showed unambiguously that, at least for the copper complex, the increase of the strength of the equatorial ligand field at high pH can only be ascribed to the contribution of the fourth nitrogen of the macrocycle on the metal coordination.

Acknowledgements

The authors acknowledge the financial support from Fundação para a Ciência e a Tecnologia (FCT) and POCTI, with co participation of the European Community fund FEDER (Project No. POCTI/CBO/35859/99). COST D18 is also acknowledged.

Appendix A. Supplementary data

Supplementary data associated with this article can be found, in the online version, at doi:10.1016/j.poly.2004.12.008.

Crystallographic data (excluding structure factors) for the structure of compound **1** have been deposited with the Cambridge Crystallographic Data Centre as supplementary publication no. CCDC-254663. Copies of the data can be obtained free of charge on application to CCDC, 12 Union Road, Cambridge CB2 1EZ, UK [Fax: int. code +44 1223/336 033; E-mail: deposit@ccdc.cam.ac.uk, or www: http://www.ccdc.cam.ac.uk].

References

[1] (a) J. Costamagna, G. Ferraudi, B. Matsuhiro, M. Campos, J. Canales, M. Villagrán, J. Vargas, M.J. Aguirre, Chem. Rev. 196 (2000) 125;
(b) C.J. Anderson, M.A. Green, Y. Fujibayashi, in: M.J. Welch, C.S. Redvanly (Eds.), Handbook of Radiopharmaceuticals: Radiochemistry and Applications, Wiley, New York, 2003, p. 401.
[2] P. Antunes, P.M. Campello, R. Delgado, M.G.B. Drew, V. Félix, I. Santos, J. Chem. Soc., Dalton Trans. (2003) 1852.
[3] K.P. Guerra, R. Delgado, L.M.P. Lima, M.G.B. Drew, V. Félix, J. Chem. Soc., Dalton Trans. (2004) 1812.
[4] F. Marques, K.P. Guerra, L. Gano, J. Costa, M.P. Campello, L.M.P. Lima, R. Delgado, I. Santos, J. Biol. Inorg. Chem. 9 (2004) 859.
[5] I. Santos, A. Paulo, J.D.G. Correia, Topics in Current Chemistry, vol. 252, Springer, Berlin, 2004, p. 45.
[6] B. Cathala, C. Picard, L. Cazaux, P. Tisnès, M. Momtchev, Tetrahedron 51 (1995) 1245.
[7] M.B. Inoue, L. Machi, I.C. Muñoz, S. Rojas-Rivas, M. Inoue, Q. Fernando, Inorg. Chim. Acta 324 (2001) 73.
[8] PSISCANS. A.C.T. North, D.C. Phillips, F.S. Mathews, Acta Crystallogr., Sect. A 24 (1968) 351.
[9] SIR97. A. Altomare, M.C. Burla, M. Camalli, G.L. Cascarano, C. Giacovazzo, A. Guagliardi, A.G.G. Moliterni, G. Polidori, R. Spagna, J. Appl. Crystallogr. 32 (1999) 115.
[10] SHELX97. G.M. Scheldrick, Programs for Crystal Structure Analysis (Release 97-2), Institüt für Anorganische Chemie der Universität, Tammanstrasse 4, D-3400 Göttingen, Germany, 1998.
[11] WINGX. L.J. Farrugia, J. Appl. Crystallogr. 32 (1999) 837.
[12] L.J. Farrugia, J. Appl. Crystallogr. 30 (1997) 565.
[13] G. Shwardzenbach, W. Flaschka, Complexometric Titrations, Methuen & Co, London, 1969.
[14] G. Shwardzenbach, W. Biedermann, Helv. Chim. Acta 31 (1948) 331.
[15] (a) J. Costa, R. Delgado, M.G.B. Drew, V. Félix, A. Saint-Maurice, J. Chem. Soc., Dalton Trans. 12 (2000) 1907;
(b) J. Costa, R. Delgado, M.G.B. Drew, V. Félix, R.T. Henriques, J.C. Waerenborgh, J. Chem. Soc., Dalton Trans. 18 (1999) 3253.
[16] P. Gans, A. Sabatini, A. Vacca, Talanta 43 (1996) 1739.

[17] NIST Standard Reference Database 46. NIST Critically Selected Stability Constants of Metal Complexes Database. Version 5.0. Data collected and selected by R.M. Smith and A.E. Martell, US Department of Commerce, National Institute of Standards and Technology, Washington, DC, 1998.
[18] R. Delgado, J.J.R.F. da Silva, M.T.S. Amorim, M.F. Cabral, S. Chaves, J. Costa, Anal. Chim. Acta 245 (1991) 271.
[19] A.K. Covington, M. Paabo, R.A. Robison, R.G. Bates, Anal. Chem. 40 (1968) 700.
[20] (a) G.A. McLachlan, G.D. Fallon, R.L. Martin, L. Spiccia, Inorg. Chem. 34 (1995) 254;
(b) A.W. Addison, T. Nageswara Rao, J. Reedijk, J. van Rijn, G.C. Verschoor, J. Chem. Soc., Dalton Trans. (1984) 1349.
[21] S.-G. Kang, K. Ryu, J. Kim, Bull. Kor. Chem. Soc. 19 (1998) 1005.
[22] M. Gupta, P. Mathur, R.J. Butcher, Inorg. Chem. 40 (2001) 878.
[23] M.B. Inoue, P. Oram, G. Andreu-de-Riquer, M. Inoue, P. Borbat, A. Raitsimring, Q. Fernando, Inorg. Chem. 34 (1995) 3528.
[24] M.B. Inoue, P. Oram, M. Inoue, Q. Fernando, Inorg. Chim. Acta 246 (1996) 401.
[25] R. Delgado, M.F. Cabral, R. Castanheira, A. Zhang, R. Herrmann, Polyhedron 21 (2002) 2265.
[26] (a) M.B. Inoue, I.C. Muñoz, L. Machi, M. Inoue, Q. Fernando, Inorg. Chim. Acta 311 (2000) 50;
(b) M.B. Inoue, E.F. Velazquez, F. Medrano, K.L. Ochoa, J.C. Galvez, M. Inoue, Q. Fernando, Inorg. Chem. 37 (1998) 4070.
[27] H. Irving, R.J.P.J. Williams, J. Chem. Soc. (1953) 3192.
[28] (a) R. Yang, L.J. Zompa, Inorg. Chem. 15 (1976) 1499;
(b) L.J. Zompa, Inorg. Chem. 17 (1978) 2531;
(c) R.D. Hancock, V.J. Thöm, J. Am. Chem. Soc. 104 (1982) 291;
(d) V.J. Thöm, J.C.A. Boeyens, G.J. McDougall, R.D. Hancock, J. Am. Chem. Soc. 106 (1984) 3198;
(e) D.-Y. Kong, Y.-Y. Xie, Polyhedron 19 (2000) 1527;
(f) M. Sandow, B.L. May, C.J. Easton, S.F. Lincoln, Aust. J. Chem. 53 (2000) 149;
(g) A.V. Bordunov, J.S. Bradshaw, X. Zhang, N.K. Dalley, X. Kou, R.M. Izatt, Inorg. Chem. 35 (1996) 7229;
(h) S.E. Livingstone, E.A. Sullivan, Aust. J. Chem. 22 (1969) 1363;
(i) S. Murakam, J. Inorg. Nucl. Chem. 43 (1981) 335.
[29] L. Alderighi, P. Gans, A. Ienco, D. Peters, A. Sabatini, A. Vacca, Coord. Chem. Rev. 184 (1999) 311.
[30] F. Neese, Diploma Thesis, University of Konstanz, Germany, 1993.
[31] J. Peisach, W.E. Blumberg, Arch. Biochem. Biophys. 165 (1974) 691.
[32] H.R. Gersmann, J.D. Swalen, J. Chem. Phys. 36 (1962) 3221.
[33] P.W. Lau, W.C. Lin, J. Inorg. Nucl. Chem. 37 (1975) 2389.
[34] A.W. Addison, M. Carpenter, L.K.-M. Lau, M. Wicholas, Inorg. Chem. 17 (1978) 1545.
[35] M.J. Maroney, N.J. Rose, Inorg. Chem. 23 (1984) 2252.
[36] (a) S. Chaves, A. Cerva, R. Delgado, Polyhedron 17 (1998) 93;
(b) M.C. Styka, R.C. Smierciak, E.L. Blinn, R.E. DeSimone, J.V. Passariello, Inorg. Chem. 17 (1978) 82;
(c) K. Miyoshi, H. Tanaka, E. Kimura, S. Tsuboyama, S. Murata, H. Shimizu, K. Ishizu, Inorg. Chim. Acta 78 (1983) 23;
(d) E.I. Solomon, K.W. Penfield, D.E. Wilcox, Struct. Bond. 53 (1983) 1.

Available online at www.sciencedirect.com
SCIENCE DIRECT®
Polyhedron 24 (2005) 463–468
POLYHEDRON
www.elsevier.com/locate/poly

Molecular precursors for the CVD of niobium and tantalum nitride

Jenelle E. Bleau [a], Claire J. Carmalt [a,*], Shane A. O'Neill [a], Ivan P. Parkin [a], Andrew J. P. White [b], David J. Williams [b]

[a] Department of Chemistry, Christopher Ingold Laboratories, University College London, 20 Gordon Street, London WC1H 0AJ, UK
[b] Department of Chemistry, Imperial College London, South Kensington, London SW7 2AZ, UK

Received 25 November 2004; accepted 17 December 2004

Abstract

Treatment of $NbCl_5$ with excess $HN(SiMe_2Ph)_2$ in toluene resulted in the formation of crystalline $[NbCl_3(NSiMe_2Ph)(NH_2SiMe_2Ph)]_2$. In the presence of excess 3,5-lutidine (3,5-$Me_2C_5H_3N$), the reaction of $TaCl_5$ with 2 equivalents of $HN(SiMe_3)_2$ resulted in the isolation of the monomeric complex $[TaCl_3(NSiMe_3)(NC_5H_3Me_2\text{-}3,5)_2]$. The X-ray crystal structure of $[TaCl_3(NSiMe_3)(NC_5H_3Me_2\text{-}3,5)_2]$ has been determined. Low pressure chemical vapour deposition of $[NbCl_3(NSiMe_2Ph)(NH_2SiMe_2Ph)]_2$ and $[TaCl_3(NSiMe_3)(NC_5H_3Me_2\text{-}3,5)_2]$ forms thin films of niobium and tantalum nitride, respectively, at 600 °C.
© 2004 Elsevier Ltd. All rights reserved.

Keywords: Tantalum nitride; Niobium nitride; CVD

1. Introduction

Transition metal nitrides constitute a diverse class of materials with many interesting technological applications [1]. For example, the metallic conductivity and refractory stability of transition metal nitrides makes them the materials of choice for diffusion barriers in various metallization structures of advanced microelectronic devices [1]. Of the many nitrides known, titanium nitride (TiN) is the most commonly used of these materials because of its low resistivity, good stability, high resistance to chemical etching and good conformality. However, recent studies involving the interdiffusion of Cu into TiN thin films found that TiN remained stable up to 450 °C for 30 min, after which time Cu started to diffuse into the TiN layer [2]. Therefore, developing an alternative CVD route to a metal nitride capable of withstanding the diffusion of Cu at a high sintering temperature would be advantageous to the microelectronics industry. It has been shown that TaN and Ta_2N act as excellent metallurgical diffusion barriers between Cu and Si and between Al and Si [3]. Tantalum(V) nitride (Ta_3N_5) and tantalum(III) nitride (TaN) are the most common forms of tantalum nitride, however, only TaN thin films are suitable for use as diffusion barriers in integrated circuits. Niobium nitride (NbN) is a hard silver-colored refractory material and has been studied due to its superconducting properties (T_c = 17.3 K) [4].

Attempts to grow niobium and tantalum metal nitride thin films via chemical vapour deposition (CVD) of $[M(NR_2)_n]$ and NH_3 resulted in the formation of nitrides with stoichiometries Nb_3N_4 and Ta_3N_5 [5]. Other CVD processes available for the preparation of metal nitride films include the reaction of $NbCl_5$ or $TaCl_5$ with NH_3, resulting in the formation of NbN or Ta_3N_5, respectively [6]. Preparation of TaN films has also been reported from the CVD reaction of $TaCl_5$, N_2 and H_2 [7]. These reactions release corrosive HCl vapour, which along with the high deposition temperature, makes the

* Corresponding author. Tel.: +44 20 7679 7528; fax: +44 20 7679 7463.
E-mail address: c.j.carmalt@ucl.ac.uk (C.J. Carmalt).

0277-5387/$ - see front matter © 2004 Elsevier Ltd. All rights reserved.
doi:10.1016/j.poly.2004.12.006

process largely unsuitable for microelectronic applications [4].

An alternative approach to transition metal nitride coatings is the use of single-source precursors, which are required to be highly volatile and have a metal–nitrogen bonded fragment at the core of the molecule. There has been heightened interest in metal imido complexes either as single-source metal nitride precursors, or as proposed intermediates in the conversion of metal–nitrogen derivatives to metal nitride [8]. The single-source precursor approach to NbN and TaN is underdeveloped, with only the complexes $[Ta(NR)(NEt_2)_3]$ (R = *t*-Bu, Et) [3,9], $[(t\text{-}BuCH_2)_2TaN]_5$ [10], $[MCl_2(NR)(NHR)(NH_2R)_2]_2$ (M = Nb or Ta, R = NMe_2; M = Nb, R = *t*-Bu) [11] and $[Ta(NEt_2)_5]$ [12] having been investigated to date in any detail.

We have been studying the reactivity of metal halides with silylamines in an attempt to isolate volatile single-source precursors to metal nitrides [13–16]. We have previously found that the trimethylsilyl group is very labile and can lead to materials with no silicon contamination [16]. Herein, we describe the reactivity of MCl_5 with $HN(SiR_2R')_2$ (M = Nb, R = Me, R′ = Ph; M = Ta, R = R′ = Me) under various conditions. The crystal structure of a new complex $[TaCl_3(NSiMe_3)(NC_5H_3Me_2\text{-}3,5)_2]$ is described. Low pressure chemical vapour deposition of the precursors is also discussed.

2. Experimental

2.1. General procedures

All manipulations were performed under a dry, oxygen-free dinitrogen atmosphere using standard Schlenk techniques or in an Mbraun Unilab glove box. All solvents were distilled from appropriate drying agents prior to use (sodium/benzophenone–toluene and hexanes; CaH_2 for CH_2Cl_2). All other reagents were procured commercially from Aldrich and used without further purification. Microanalytical data were obtained at University College London (UCL). BDH microscope slides were used for the CVD experiments.

2.2. Physical measurements

^1H and ^{13}C NMR spectra were recorded on Bruker AMX400 spectrometer at UCL. The NMR spectra are referenced to $CDCl_3$ or C_6D_6, which was degassed and dried over molecular sieves prior to use; ^1H chemical shifts are reported relative to $SiMe_4$ (0.00 ppm). FTIR spectra on a Nicolet 205 instrument. TGA of the compounds were obtained from the Thermal Methods Laboratory at Birkbeck College (ULIRS). X-ray powder diffraction patterns were measured on a Siemens D5000 diffractometer using monochromated Cu $K\alpha_1$ radiation ($\lambda_1 = 1.5406$ Å). The diffractometer used glancing incident radiation (1.5°). Samples were indexed using unit cell and compared to database standards. EDAX was obtained using a JEOL 35-CF instrument and SEM was obtained on a Hitachi S570 instrument using the KEVEX system. X-ray photoelectron spectra were recorded using a VG ESCALAB 220i XL instrument using focused (300 mm spot) monochromatic Al Kα radiation at a pass energy of 20 eV. Scans were acquired with steps of 50 meV. A flood gun was used to control charging and the binding energies were referenced to an adventitious C 1s peak at 284.8 eV. Depth profile measurements were obtained by using argon beam sputtering. UV–Vis spectra were recorded in the range 190–1100 nm using a Helios double beam instrument.

2.3. Preparation of $[NbCl_3(NSiMe_2Ph)\{NH_2(SiMe_2Ph)\}]_2$ (**1**)

$HN(SiMe_2Ph)_2$ (0.8 cm^3, 3.8 mmol) was added to a suspension of $NbCl_5$ (0.4 g, 1.48 mmol) in toluene (20 cm^3) at room temperature. After stirring at room temperature for 3 h, a red solution resulted. The mixture was allowed to stir for a further 12 h resulting in a white crystalline solid and olive-green solution. After filtering using a filter stick a white crystalline solid was obtained, which was washed with hexanes (2×5 cm^3) and dried in vacuo (0.69 g, 93% yield). *Anal.* Calc. for $C_{16}H_{24}Cl_3N_2Si_2Nb$: C, 38.45; H, 4.84; N, 5.61. Found: C, 38.35; H, 4.46; N, 5.48%. ^1H NMR ($CDCl_3$): δ 0.21 (s, 6H, $NSiMe_2Ph$), 0.61 (s, 6H, $NH_2(SiMe_2Ph)$), 3.23 (br, 2H, NH_2), 7.11–7.74 (m, 10H, $NSiMe_2Ph$ and $NH_2(SiMe_2Ph)$). $^{13}C\{^1H\}$NMR ($CDCl_3$): δ 1.7 ($NSiMe_2Ph$), 2.7 ($NH_2(SiMe_2Ph)$), 128.2, 128.8 (*m*-SiC_6H_5), 130.9, 130.2 (*p*-SiC_6H_5), 133.7, 133.9 (*o*-SiC_6H_5), *ipso*-SiC_6H_5 not detected. FT-IR 3258 w, 3202 w, 2957 m, 1428 s, 1258 s, 1180 m, 1116 vs, 1051 m, 998 w, 933 s, 831 vs, 800 vs, 748 m, 699 vs, 594 w, 471 w cm^{-1}.

2.4. Preparation of $[TaCl_3(NSiMe_3)(NC_5H_3Me_2\text{-}3,5)_2]$ (**2**)

$HN(SiMe_3)_2$ (0.95 cm^3, 4.5 mmol) and 3,5-$Me_2C_5H_3N$ (2.30 cm^3, 20.2 mmol) was added to a suspension of $TaCl_5$ (1.50 g, 4.2 mmol) in toluene (20 cm^3) at room temperature. After stirring at room temperature for 20 h, a yellow solution and off-white precipitate resulted. The yellow solution was decanted from the off-white precipitate and filtered through Celite. The solvent was removed in vacuo to give a yellow oil. Triturating this yellow oil with pentane (3×5 cm^3) produced a beige solid, which was washed with pentane (3×5 cm^3) and dried in vacuo (1.33 g, 54% yield). X-ray quality crystals of **2** were obtained at −20 °C over a few

days by dissolving a small amount of the beige solid (~0.3 g) in CH_2Cl_2 (5 cm^3) and overlaying with hexanes (10 cm^3). *Anal*. Calc. for $C_{17}H_{27}Cl_3N_3SiTa$: C, 34.68; H, 4.62; N, 7.14. Found: C, 34.31; H, 4.25; N, 7.12%. ^1H NMR (C_6D_6): δ 0.43 (s, 9H, $Si(CH_3)_3$), 1.53 (s, 6H, $NC_6H_3(CH_3)_2$), 1.70 (s, 6H, $NC_6H_3(CH_3)_2$), 6.40 (s, 1H, *p*-C_6H_3N), 6.59 (s, 1H, *p*-C_6H_3N), 8.60 (s, 2H, *o*-C_6H_3N), 8.94 (s, 2H, *o*-C_6H_3N). $^{13}C\{^1H\}$ NMR(C_6D_6): δ 1.3 ($Si(C H_3)_3$), 17.6 ($NC_6H_3(C H_3)_2$), 17.8 ($NC_6H_3(C H_3)_2$), 133.4 (s, *p*-$NC_6H_3(CH_3)_2$), 133.9 (s, *p*-$NC_6H_3(CH_3)_2$), 139.4 (s, *m*-$NC_6H_3(CH_3)_2$), 140.6 (s, *m*-$NC_6H_3(CH_3)_2$), 150.8 (s, *o*-$NC_6H_3(CH_3)_2$), 151.6 (s, *o*-$NC_6H_3(CH_3)_2$). FT-IR 2348 m, 1632 s, 1604 s, 1534 m, 1482 m, 1403 s, 1254 w, 815 w, 747 m, 677 m, 436 w, 467 w cm^{-1}.

2.5. Low pressure CVD experiments

The same procedure was carried out for all compounds (**1** and **2**) shown here for **2**. A sample of compound **2** (0.3 g) was loaded into the end of a glass ampoule (40 cm length × 16 mm diameter) in the glovebox. Glass substrates (10 cm × 7 mm) were placed carefully inside the ampoule. The ampoule was then placed in a furnace such that 30 cm was inside the furnace and the end containing the sample protruded by 4 cm. The ampoule was heated to a temperature of 600 °C under dynamic vacuum, except for the section of the tube containing the sample. The ampoule was slowly drawn into the furnace over a period of a few minutes until **2** started to melt. Once the compound had decomposed the furnace was allowed to cool to room temperature. A shiny, golden-brown film was deposited on the glass substrates. The film was analyzed by EDAX/SEM, electron probe and reflectance/transmission measurements.

2.6. X-ray crystallography

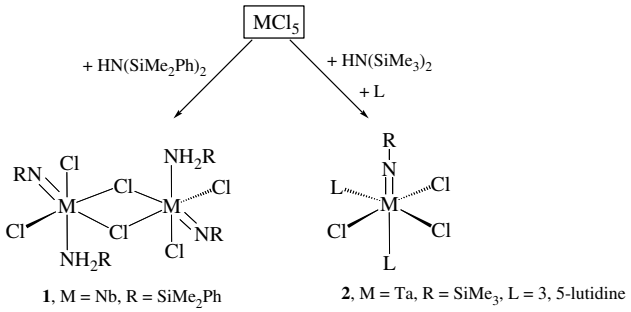
Crystals of **2** were grown from CH_2Cl_2/hexanes layers at −20 °C. Table 2 provides a summary of the crystallographic data for compound **2**, CCDC 249229.

3. Results and discussion

Treatment of $NbCl_5$ with two equivalents of $HN(SiMe_2Ph)_2$, resulted in the formation of white crystalline $[NbCl_3(NSiMe_2Ph)(NH_2SiMe_2Ph)]_2$ (**1**). Analytical data (CHN) for **1** was consistent with the formation of $[NbCl_3(NSiMe_2Ph)(NH_2SiMe_2Ph)]_2$ but unfortunately X-ray quality crystals could not be isolated. The ^1H and ^{13}C NMR of **1** in $CDCl_3$ shows two singlets of equal intensity for two different $SiMe_2Ph$ groups. A broad singlet at 3.23 ppm was observed in the ^1H NMR of **1** corresponding to two equivalent NH_2 protons. The FT-IR of **1** supports the formulation $[NbCl_3(NSiMe_2Ph)(NH_2SiMe_2Ph)]_2$ since two sharp bands above 3100 cm^{-1} corresponding to symmetric and asymmetric N–H stretches of the monosilylated amine, NH_2SiMe_2Ph, were observed [17]. Compound **1** is similar to some related niobium imido complexes, of the type $[NbCl_3(NR)(NH_2R)]_2$ (R = *t*-Bu, *i*-Pr, $SiMe_3$, 2,6-$(CH(CH_3)_2)_2C_6H_3$) [17–21]. The structure of **1** is expected to be similar to the *tert*-butylimido/*tert*-butylamine analogue and related complexes published previously, which are dimeric via chloride bridges [19,21].

The silyamido group in **1** is formed by cleavage of an N–Si bond in $HN(SiMe_2Ph)_2$, to give $Me_2PhSiCl$, and transfer of its proton to a second equivalent of $HN(SiMe_2Ph)_2$. The latter results in the formation of the amine $H_2N(SiMe_2Ph)$, which coordinates to the niobium centre (Scheme 1). Based on related reactions, [17] it is likely that the reaction of $NbCl_5$ with two equivalents of $HN(SiMe_2Ph)_2$ to afford **1**, precedes via the intermediate complex $[Nb(NHSiMe_2Ph)_2Cl_3]$, which then undergoes interligand proton transfer to yield $[NbCl_3(NSiMe_2Ph)(NH_2SiMe_2Ph)]_2$.

The reaction of $TaCl_5$ and $HN(SiMe_3)_2$ in the presence of 3,5-lutidine (3,5-dimethylpyridine, 3,5-$Me_2C_5H_3N$) resulted in the formation of colorless crystalline **2**. Analytical and spectroscopic data for **2** were consistent with the formulation $[TaCl_3(NSiMe_3)(NC_5H_3Me_2\text{-}3,5)_2]$. The monomeric nature of **2** was confirmed by an X-ray crystallographic study (Fig. 1). The geometry at the tantalum centre is distorted octahedral, the metal lying ca. 0.32 Å out of the "equatorial" $\{NCl_3\}$ plane (which is coplanar to within ca. 0.01 Å) in the direction of the imido nitrogen N(1); the *cis* angles involving N(1) [94.6(2)–100.9(2)°] are all noticeably increased from 90°, whilst those involving N(6) are all reduced [81.0(2)°–83.57(13)°] (Table 1). The bond length to the imido nitrogen [1.772(5) Å] is similar to that seen in the related complexes $[TaCl_3(N\text{-}t\text{-}Bu)(py)_2]$ [22] [1.745(5) Å] and $[TaCl_2(NSiMe_3)\{HB(pz)_3\}]$ [23,24] [1.767(6) Å] (where pz = 3,5-dimethylpyrazolyl). The $NSiMe_3$ unit in this latter complex is noticeably more bent than seen here in **2**, the Ta–N–Si angles being 164.8(4)° and 172.2(4)° respectively; the corresponding Si–N distances are 1.742(6) and



Scheme 1.

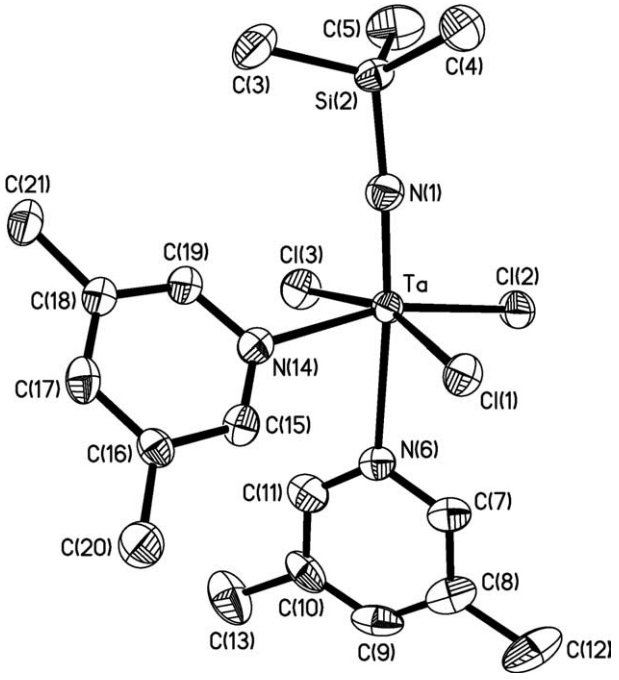


Fig. 1. The molecular structure of **2** (50% probability ellipsoids).

Table 1
Selected bond lengths (Å) and angles (°) for **2**

Bond lengths			
Ta–Cl(1)	2.387(2)	Ta–Cl(2)	2.3588(15)
Ta–Cl(3)	2.389(2)	Ta–N(1)	1.772(5)
Ta–N(6)	2.508(5)	Ta–N(14)	2.271(6)
Bond angles			
Cl(2)–Ta–Cl(1)	91.72(6)	Cl(1)–Ta–Cl(3)	162.12(6)
Cl(1)–Ta–N(1)	99.1(2)	Cl(1)–Ta–N(6)	82.67(13)
Cl(1)–Ta–N(14)	84.22(15)	Cl(2)–Ta–Cl(3)	94.16(6)
Cl(2)–Ta–N(1)	100.9(2)	Cl(2)–Ta–N(6)	83.57(13)
Cl(2)–Ta–N(14)	164.41(14)	Cl(3)–Ta–N(1)	96.4(2)
Cl(3)–Ta–N(6)	81.23(13)	Cl(3)–Ta–N(14)	85.6(2)
N(1)–Ta–N(6)	175.1(2)	N(1)–Ta–N(14)	94.6(2)
N(6)–Ta–N(14)	81.0(2)	Ta–N(1)–Si(2)	172.2(4)

1.736(5) Å respectively. The Ta–N distances to the two 3,5-lutidine ligands are noticeably different, with that to the axial group *trans* to the imido [Ta–N(6) 2.508(5) Å] being more than 0.2 Å longer than that to its equatorial counterpart [Ta–N(14) 2.271(6) Å] (*trans* to chloride), reflecting the strong *trans* influence of the imido ligand. One of these lutidine ligands is involved in an intermolecular π–π stacking interaction with its centrosymmetrically related counterpart, the centroid···centroid and mean interplanar separations being ca. 3.76 and 3.53 Å, respectively. The ^{1}H NMR of **2** indicates that in solution the same structure is adopted with two sets of non-equivalent 3,5-$Me_2C_5H_3N$ signals present. Reaction of $TaCl_5$ and amines has been studied previously [22,25]. A series of related complexes of formula $[TaCl_3(NR)(py)_2]$ have been reported and were prepared via the reaction of $TaCl_5$ and two equivalents of an amine in the presence of sodium silicate and pyridine [26]. No structures of these complexes have been reported.

Table 2
Crystallographic data for compound **2**[a]

Data	**2**
Chemical formula	$C_{17}H_{27}N_3SiCl_3Ta$
Fw	588.81
T (°C)	−90
Space group	$P2_1/n$ (no. 14)
Unit cell dimensions	
a (Å)	10.1945(8)
b (Å)	17.1045(11)
c (Å)	13.6127(8)
β (°)	97.041(5)
V (Å^3)	2355.8(3)
Z	4
ρ_{calc} (g cm^{-3})	1.660
λ (Å)	1.54178
μ (mm^{-1})	12.269
R_1[b]	0.037
wR_2[c]	0.081

[a] Siemens P4 diffractometer, graphite monochromated Cu K radiation, refinement based on F^2.
[b] $R_1 = \Sigma\|F_o|-|F_c\|/\Sigma|F_o|$.
[c] $wR_2 = \left\{\sum[w(F_o^2 - F_c^2)^2]\Big/\sum[w(F_o^2)^2]\right\}^{1/2}$; $w^{-1} = \sigma^2(F_o^2) + (aP)^2 + bP$.

In order to study the decomposition pathway of compounds **1** and **2** thermal analyses were carried out. The TGA (thermal gravimetric analysis) of **1** (10 °C/min from 20 to 500 °C) shows a weight loss of 69.2% (calculated weight loss 78.6% for NbN formation from **1**). This behavior indicates an incomplete decomposition to NbN up to 500 °C, although it is possible that the required weight loss could be attained at higher temperatures (the TGA set-up allows analysis only to 500 °C). The TGA of **2** indicates that this compound may be a suitable single-source precursor for the deposition of TaN thin-films. Thus, the TGA of **2** is clean and shows a total weight loss of 72.9% (calculated weight loss 67% from **2** for the formation of TaN). It is worth noting that TGA at atmospheric pressure only gives an indication of the potential of the precursors to form bulk metal nitrides. Any sublimation of the precursor, a desirable characteristic for low pressure CVD studies, would register as a further mass loss, as observed in the TGA of **2**.

Low pressure CVD of **1** and **2** were investigated, the details of which are described in the Experimental section [16]. Shiny, golden-brown films were deposited on glass substrates from **1** and **2** at 600 °C. The films produced were analyzed by EDAX/SEM, XPS, powder XRD and reflectance/transmission measurements. Both the niobium and tantalum nitride films deposited from **1** and **2**, respectively, were resistant to attack by common solvents (water, acetone, toluene, petroleum ether), concentrated nitric acid and concentrated hydrochloric acid for over 72 h. All the films passed the Scotch tape

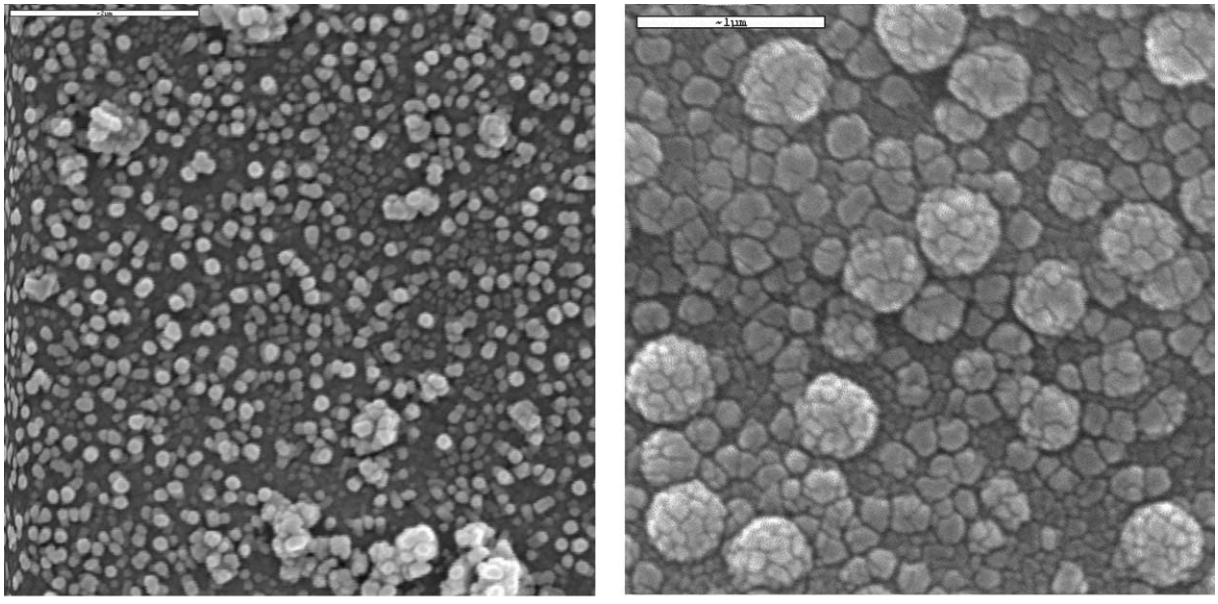
test and could not be abraded with a brass stylus. These results indicate that the films are hard and chemically robust, which are typical properties expected for refractory cubic early transition metal nitrides.

The contact angle of the niobium nitride film was found to be 63° and the tantalum nitride film 70°. Contact angle measurements are valuable in the glass industry in assessing whether films have self cleaning properties. Low contact angles arising from hydrophilic films give rise to the water spreading across the surface and hence washing away any loose dirt. Therefore, the observed contact angles suggest that the nitride films are hydrophobic and not porous, which would significantly decrease the contact angle. The contact angles for both the niobium and tantalum nitride films did not change upon photo-irradiation. This suggests that the surface of the films has minimal oxidation as the corresponding niobium oxides show marked hydrophilicity and photo-induced superhydrophilicity [27]. The tantalum nitride film produced showed a maximum transmission in the visible region (450–700 nm), which is characteristic of tantalum nitride films [28]. The niobium and tantalum nitride films were electrically conducting with typical resistivities of 500 μΩ cm.

X-ray powder diffraction of the film obtained from **1** showed a broad diffraction pattern for NbN consistent with a cubic NaCl structure. Determination of the lattice constant gave a value of $a = 4.34(3)$ Å which compares with a literature value of $a = 4.395$ Å for $NbN_{1.00}$ [29]. Crystallite size determination from line broadening studies of the (200) peak, ignoring strain effects, gave a value of ca. 250 Å. The tantalum nitride films grown from **2** were amorphous to X-rays.

Energy dispersive X-ray analysis showed the presence of niobium and nitrogen in the film grown from **1**; tantalum and nitrogen in the film deposited from **2**. Quantitative analysis by EDAX was not possible as the oxygen signal from the glass substrate (breakthrough to the underlying glass) partially obscured that of the nitrogen from the film. However, EDAX data showed that chlorine contamination was below 0.1%. Wavelength dispersive analysis using an electron probe indicated that the niobium and tantalum to nitrogen ratios were 1:1. By scanning electron microscopy (SEM) the niobium and tantalum nitride films showed the formation of agglomerates of approximately 0.1 μm (Fig. 2). SEM showed that each film grew by a Volmer–Webber type growth mechanism.

The XPS depth profile analysis of the films formed from **1** showed the presence of Nb, N, C and O, those from **2** showed Ta, N, C and O. The carbon concentration dropped dramatically on the first etch, indicating that this was surface bound. Furthermore, no evidence of metal carbide formation was observed. The oxide surface layer was also removed by sputtering to leave the bulk of the film consisting of niobium and nitrogen, or tantalum and nitrogen. No evidence of chloride or silicon contamination (1–2 at.% detection limit) was observed. XPS of films grown from **1** gave Nb 3d and N 1s binding energy shifts of 206.8 and 396.8 eV, respectively. These are in good agreement with previous literature measurements for $NbN_{1.00}$ thin films [5]. The binding energy value for Ta 4f was measured at 18.60 eV and for N 1s was measured at 396.8 eV. The N 1s binding energy is in agreement with published XPS data for $TaN_{1.00}$ [28]. It has been demonstrated that the Ta $4f_{7/2}$ binding



(a) (b)

Fig. 2. SEM of a film grown from: (a) **1**; (b) **2** at by LPCVD at 600 °C.

energy shift in cubic nitrides shifts to lower values with nitrogen content [27].

Thin films of tantalum nitride were also deposited from **2** on aluminum and copper substrates. However, there appeared to be no difference in film composition or morphology with substrate. The advantages of compounds **1** and **2** compared to other single-source precursors to NbN and TaN are: (i) the compounds can be prepared in good yield; (ii) no significant carbon or chlorine contamination is observed in the resulting film; (iii) cubic MN_x films are deposited rather than other stoichiometries, e.g., Nb_3N_4 and Ta_3N_5.

4. Conclusions

The group Vb silylimido complexes, $[NbCl_3(NSiMe_2Ph)(NH_2SiMe_2Ph)]_2$ and $[TaCl_3(NSiMe_3)(NC_5H_3Me_2\text{-}3,5)_2]$ have been synthesized and characterized. X-ray crystallography showed that $[TaCl_3(NSiMe_3)(NC_5H_3Me_2\text{-}3,5)_2]$ is monomeric. Low pressure CVD indicates that $[NbCl_3(NSiMe_2Ph)(NH_2SiMe_2Ph)]_2$ and $[TaCl_3(NSiMe_3)(NC_5H_3Me_2\text{-}3,5)_2]$ are effective niobium nitride and tantalum nitride precursors, respectively. Analysis of these films shows that they are conductive and consist of uniform particles of niobium nitride–NbN or tantalum nitride TaN. Interestingly, despite the presence of silicon and carbon in the silyl subtituent of the imido ligand, these elements were not observed in the film. This indicates that the elimination of R_3SiCl is facile during the LPCVD process.

Acknowledgements

The EPSRC is thanked for Grant GR/R16518. We are also grateful to Dr. M. Odlyha (Birkbeck College) for the TGA.

Appendix A. Supplementary data

Supplementary data associated with this article can be found, in the online version at doi:10.1016/j.poly.2004.12.006.

References

[1] S.T. Oyama (Ed.), The Chemistry of Transition metal Carbides and Nitrides, Blackie Academic and Professional, London, 1996.
[2] J.O. Olowolafe, C.J. Mogab, R.B. Gregory, M. Kottke, J. Appl. Phys. 72 (1992) 4099.
[3] M.H. Tsai, S.C. Sun, H.T. Chiu, C.E. Tsai, S.H. Chuang, Appl. Phys. Lett. 67 (1995) 1128.
[4] G.–L. Oya, Y. Onodera, J. Appl. Phys. 45 (1974) 1389.
[5] R. Fix, R.G. Gordon, D.M. Hoffman, Chem. Mater. 5 (1993) 614.
[6] K. Hieber, Thin Solid Films 24 (1974) 157.
[7] T. Takahashi, H. Itoh, S. Ozeki, J. Less Common Met. 52 (1977) 29.
[8] D.E. Wigley, Prog. Inorg. Chem. 42 (1994) 239.
[9] H.T. Chiu, W.P. Chang, J. Mater. Sci. Lett. 11 (1992) 96.
[10] M.M.B. Holl, P.T. Wolczanski, D. Proserpio, A. Brelecki, D.B. Zax, Chem. Mater. 8 (1996) 2468.
[11] C.H. Winter, K.C. Jayaratne, J.W. Proscia, Mat. Res. Soc. Symp. Proc. 327 (1994) 103.
[12] K. Sugiyama, S. Pac, Y. Takahashi, S. Motojima, J. Electrochem. Soc. 122 (1975) 1545.
[13] C.J. Carmalt, J.D. Mileham, A.J.P. White, D.J. Williams, New J. Chem. 24 (2000) 929.
[14] C.J. Carmalt, J.D. Mileham, A.J.P. White, D.J. Williams, J.W. Steed, Inorg. Chem. 40 (2001) 6035.
[15] C.J. Carmalt, J.D. Mileham, A.J.P. White, D.J. Williams, Dalton Trans. (2003) 4255.
[16] C.J. Carmalt, A.C. Newport, I.P. Parkin, A.J.P. White, D.J. Williams, J. Chem. Soc., Dalton Trans (2002) 4055.
[17] C.M. Jones, M.E. Lerchen, C.J. Church, B.M. Schomber, N.J. Doherty, Inorg. Chem. 29 (1990) 1679.
[18] P.A. Bates, A.J. Nielson, J.M. Waters, Polyhedron 4 (1985) 1391.
[19] T.C. Jones, A.J. Nielson, C.E.F. Rickard, J. Chem. Soc., Chem. Commun. (1984) 205.
[20] A.J. Nielson, Polyhedron 7 (1988) 67.
[21] K.C. Jayaratne, G.P.A. Yap, B.S. Haggerty, A.L. Rheingold, C.H. Winter, Inorg. Chem. 35 (1996) 4910.
[22] H.T. Chiu, S.H. Chuang, C.E. Tsai, G.H. Lee, S.M. Peng, Polyhedron 17 (1998) 2187.
[23] K. Weber, K. Korn, A. Schorm, J. Kipke, M. Lemke, A. Khvorost, K. Harms, J. Sundermeyer, Z. Anorg. Allg. Chem. 629 (2003) 744.
[24] A. Schorm, J. Sundermeyer, Eur. J. Inorg. Chem. (2001) 2947.
[25] M.H. Chisholm, J.C. Huffman, L.-S. Tan, Inorg. Chem. 20 (1981) 1852.
[26] A.V. Korolev, A.L. Rheingold, D.S. Williams, Inorg. Chem. 36 (1997) 2647.
[27] S.A. O'Neill, I.P. Parkin, R.J.H. Clark, A. Mills, N. Elliott, J. Mater. Chem. 13 (2003) 2952.
[28] A.C. Newport, J.E. Bleau, C.J. Carmalt, I.P. Parkin, S.A. O'Neill, J. Mater. Chem. 14 (2004) 3333.
[29] H.J. Goldschmidt, Interstitial Alloys (Nitrides), Butterworths, London, 1967, p. 214.

Available online at www.sciencedirect.com
SCIENCE DIRECT®
Polyhedron 24 (2005) 469–474
POLYHEDRON
www.elsevier.com/locate/poly

The synthesis and lanthanide coordination chemistry of 2,6-bis[(dicyclohexyl)phosphino-methyl]pyridine *N*,*P*,*P*′-trioxide The crystal structure of 2,6-bis[(dicyclohexyl)phosphinomethyl] pyridine *N*,*P*,*P*′-trioxide erbium(III) nitrate

Xinmin Gan [a], Brian M. Rapko [b], Eileen N. Duesler [a], Iris Binyamin [a], Robert T. Paine [a,*], Benjamin P. Hay [b]

[a] *Department of Chemistry, University of New Mexico, Clark Hall, Albuquerque, NM 87131, USA*
[b] *Pacific Northwest National Laboratory, P.O. Box 999, Richland, WA 99352, USA*

Received 26 February 2004; accepted 16 August 2004

Abstract

The title ligand is obtained in two steps with high overall yield, and is soluble in aromatic solvents, making its liquid–liquid extraction performance of potential interest. The ligand forms a stable 1:1 coordination complex with $Er(NO_3)_3$ and the molecular structure was determined by single crystal X-ray diffraction methods. The Er(III) ion is chelated by one tridentate ligand and three bidentate nitrate groups. The structural results are discussed in the context of complexes formed by related ligands.
© 2005 Elsevier Ltd. All rights reserved.

Keywords: Phosphine oxide; Pyridine *N*-oxide; Tridentate chelate; Lanthanide complex; X-ray crystallography

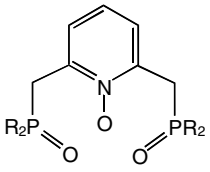
1. Introduction

A number of options are under consideration for the treatment of high level radioactive waste present in spent nuclear fuels. Nuclear incineration is one option that could potentially reduce the hazardous storage period for the transuranic elements and some of their fission products [1]. This process requires that the so-called minor actinides be separated from other elements; therefore, there has been renewed interest in the development of new separations agents that would selectively partition Np, Am and Cm [2,3]. Several families of chelating ligands are under study worldwide with the greatest attention garnered by bifunctional CMP carbamoylmethylphosphonate, $(RO)_2P(O)CH_2C(O)NR'_2$ [4], CMPO carbamoylmethyl phosphine oxide, $RR'P(O)CH_2C(O)NR''_2$ [5–8] and malonamide, $[RR'NC(O)]_2CR''H$ ligands [9–15]. Our group has studied several variants on the CMP/CMPO theme and Hay has reported interesting new variants in the malonamide system [16]. Recently, we have also described the synthesis and coordination chemistry of a series of phosphino pyridine *N*-oxide ligands (**NOPOPO**) [17–23], some of which display favorable extraction performance for trivalent actinide ions in strongly acidic aqueous solutions [24–27]. In order to improve the **NOPOPO** extractant process performance for specific applications, it is necessary to derive additional derivatives that might show modified organic phase solubility, improved aqueous acid stability, improved radiation stability and enhanced metal coordination properties. In this paper, we report the synthesis of

* Corresponding author. Tel.: + 1 505 277 1661; fax: + 1 505 277 2609.
E-mail address: rtpaine@unm.edu (R.T. Paine).

0277-5387/$ - see front matter © 2005 Elsevier Ltd. All rights reserved.
doi:10.1016/j.poly.2004.08.027

an arene soluble **NOPOPO** ligand derivative and its coordination chemistry with $Er(NO_3)_3$. The physical properties and coordination chemistry are compared with data from other recently prepared ligands.



NOPOPO

2. Experimental

2.1. General Information

The organic reagents were purchased from Aldrich Chemical Co. and organic solvents were purchased from VWR. Solvents were dried and distilled using standard procedures. The $Er(NO_3)_3$ was purchased from Ventron. Infrared spectra were recorded on a Mattson 2020 FTIR spectrometer and NMR spectra were recorded on JEOL GSX-400 and Bruker FX-250 spectrometers. Standards employed were Me_4Si (^1H and ^{13}C) and H_3PO_4 (^{31}P) and downfield shifts were assigned as $+\delta$. Mass spectra were obtained from the Midwest Center for Mass Spectrometry, University of Nebraska. Elemental analyses were obtained from Galbraith Laboratories.

2.2. Synthesis of the ligand

Diethyl phosphite (6.08 g, 0.044 mol) in dry diethyl ether (10 ml) and benzene (30 ml) was added dropwise with stirring at 23 °C to cyclohexylmagnesium chloride (66 ml, 2 M solution in Et_2O, 0.13 mol). The temperature of the mixture increased during addition and tetrahydrofuran (THF) (60 ml) was added following completion of the reagent addition. The mixture was then refluxed (oil bath 67 °C, for 2 h) and then 2,6-bis(chloromethyl)pyridine (3.52 g, 0.02 mol) in dry benzene (30 ml) was added with stirring. The resulting mixture was refluxed (5 h) and the solvent removed by vacuum evaporation (23 °C). A saturated aqueous NH_4Cl solution (100 ml) was added to the residue and the mixture extracted with Et_2O/CH_2Cl_2 (5:1) (2×100 ml). The combined organic phases were dried (Na_2SO_4 anhyd.) and vacuum evaporated. The residue was washed with Et_2O (3×40 ml) giving 2,6-bis[(dicyclohexyl)phosphinomethyl]pyridine *P*,*P*′-dioxide (**1**) as a white solid. Yield: 8.7 g, 82%; m.p. 183–184 °C. ^{31}P NMR ($CDCl_3$): δ 50.1. ^1H NMR ($CDCl_3$): δ 1.21–1.37 (m), 1.72–1.97 (m), 3.27 (d, $J = 13.6$ Hz), 7.29 (d, $J = 7.7$ Hz), 7.56 (t, $J = 7.7$ Hz). $^{13}C\{^1H\}$ NMR ($CDCl_3$): δ 25.27, 25.50, 25.81, 26.34, 26.39, 26.54, 26.59, 34.80 (d, $J = 52.6$ Hz), 36.09 (d, $J = 63.9$ Hz), 122.52, 136.84, 153.40, 153.50. IR (KBr, cm^{-1}): 2930, 2850, 1587, 1450, 1275, 1222, 1174, 1118, 893, 835, 745, 594, 563, 493.

To a solution of **1** (7.4 g, 0.014 mol) in $CHCl_3$ (70 ml) was added 3-chloroperoxybenzoic acid (3.8 g, 57–86%, Aldrich). The mixture was stirred (23 °C, 2 h) and then extracted with aqueous saturated $NaHCO_3$–Na_2CO_3 (5:1) solution (80 ml). The aqueous phase (pH 8–9) was washed with CH_2Cl_2 (2×60 ml) and the combined organic phases ($CHCl_3$, CH_2Cl_2) were dried (Na_2SO_4 anhyd.) and then evaporated to dryness at 23 °C leaving 10 g of white solid. This was further purified by column chromatography (silica gel) using $CHCl_3$/MeOH (100:3) as the eluant. White, solid 2,6-bis[(dicyclohexyl)phosphinomethyl]pyridine *N*,*P*,*P*′-trioxide (**2**) was recovered. Yield: 6.5 g, 85.3%; m.p. 197–198 °C. ^{31}P NMR ($CDCl_3$): δ 51.2. ^1H NMR ($CDCl_3$): δ 1.23–1.41 (m), 1.72–1.98 (m), 3.59 (d, $J = 11.8$ Hz), 7.14 (t, $J = 7.8$ Hz), 7.72 (d, $J = 7.8$ Hz). $^{13}C\{^1H\}$ NMR ($CDCl_3$): δ 25.20 (d, $J = 53$ Hz), 25.23, 25.27, 25.53, 25.57, 25.73, 26.30, 26.50, 36.85 (d, $J = 64.6$ Hz), 124.31, 125.86, 144.65, 144.73. IR (KBr, cm^{-1}): 2924, 2850, 1564, 1489, 1444, 1388, 1276, 1242, 1165, 1008, 891, 856, 796, 573, 486. FAB-HRMS: 547.3331 M^+; $C_{31}H_{51}NO_3P_2$ requires M^+ 547.3344. *Anal.* Calc. for $C_{31}H_{51}NO_3P_2$: C, 67.98; H, 9.39; N, 2.56. Found: C, 66.16; H, 9.87; N, 2.50.

2.3. Synthesis of the complex

The complex was prepared by combination of $Er(NO_3)_3 \cdot 5H_2O$ (133 mg, 0.3 mmol) in acetone (6 ml) and **2** (164 mg, 0.3 mmol) in acetone (6 ml). The mixture was stirred (23 °C, 10 min) and filtered. The filtrate was slowly evaporated leaving pink crystals of the complex $Er(\mathbf{2})(NO_3)_3 \cdot (CH_3)_2CO$. IR (KBr, cm^{-1}): 2930, 2858, 1705, 1574, 1481, 1361, 1315, 1222, 1124, 1031, 893, 860, 817, 752, 638, 526, 495. *Anal.* Calc. for $C_{34}H_{57}ErN_4O_{13}P_2$: C, 42.48; H, 5.98; N, 5.83. Found: C, 42.36; H, 5.87; N, 5.87.

2.4. Crystallographic analysis

A pink platelet, $0.46 \times 0.36 \times 0.26$ mm was sealed in a glass capillary and data collected at 20 °C on a Siemens R3m/V diffractometer equipped with a graphite monochromator and using Mo Kα radiation ($\lambda = 0.71073$ Å). Data were collected in the omega scan mode with $\theta = 1.60$–25.00 [28]. A small semi-empirical adsorption correction based on psi scans was applied [29]. The structure was solved by direct methods using SHELX-97 [30]. The refinement was well behaved except that disorder appeared in one cyclohexyl group [C(28), C(31)

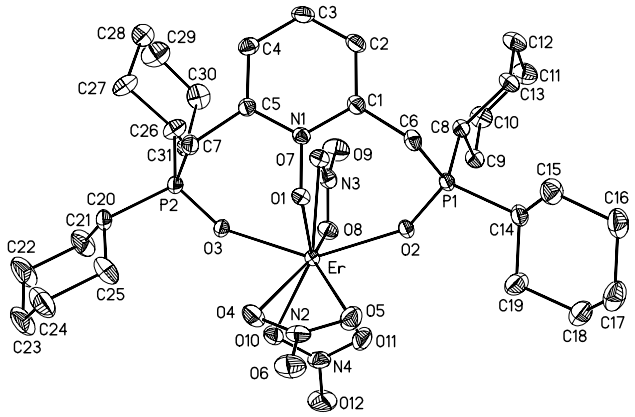


Fig. 1. Molecular structure and atom labelling scheme for Er(**2**)$(NO_3)_3 \cdot (CH_3)_2CO$ (acetone molecule of crystallization and hydrogen atoms omitted for clarity).

76.9%; C(28′), C(31′) 23.1%] on P(2) and in a methyl group in an acetone molecule of crystallization [C(33) 50%, C(33′) 50%]. These atoms were refined with the indicated occupancies and all ordered non-hydrogen atoms were refined anisotropically with H-atoms fixed in idealized positions (riding model) and $U_{iso} = 1.2$–$1.5U_{equiv.}$ of the parent atom. Atom labelling is shown in Fig. 1.

Crystallographic data: empirical formula $C_{34}H_{57}ErN_4O_{13}P_2$, monoclinic space group P_1/c, $a = 13.144(1)$ Å, $b = 17.125(1)$ Å, $c = 19.202(3)$ Å, $\beta = 99.96(1)°$, $V = 4257.1(8)$ Å^3, $Z = 4$, $D_{calc} = 1.496$ g cm^{-3}, $\mu = 2.109$ mm^{-1}, $F(000)$ 1964, 15390 reflections collected, 7509 independent reflections ($R_{int} = 0.0277$), 484 parameters; $R_1(F)[I > 2\sigma(I)] = 0.0278$, $wR_2(F^2) = 0.0642$, where $w^{-1} = [\sigma(F)^2 + gF^2]$, $\Delta\rho_{max} = 0.473$ e Å^{-3}, $\Delta\rho_{min} = -0.777$ e Å^{-3}.

2.5. Molecular modeling

Molecular mechanics calculations were carried out using the MM3 program [31–33], modified to support POS metal atom types [34,35]. Conformational searches of the free ligands, and the complexes $[M(L)(NO_3)_3]$ and $[M(L)_2(NO_3)]^{2+}$ were performed using the Saunders' stochastic search algorithm [36] as implemented in MM3. In all calculations, the dielectric constant was set to 4.0 to approximate the influence of a non-polar organic environment. The input files required to repeat these calculations, including the initial coordinates for all structures and the metal-dependent parameter set, are available as supplementary material.

3. Results and discussion

Our prior ligand design and synthesis work revealed that phosphinomethylpyridine *N*,*P*-oxides act as excellent ligands toward strongly polarizing Ln(III) and Pu(IV) ions [17–23]. In particular, it was found that the specific derivative bis[(diphenylphosphino)methyl] pyridine *N*,*P*,*P*′-trioxide, **NOPOPO** (R = Ph) forms 1:1 and 2:1 L/metal complexes and X-ray crystallographic studies indicate that the ligand binds in a tridentate fashion in both complex classes in the solid state [17–23]. The **NOPOPO** ligand with R = Ph is soluble in $CHCl_3$ and initial solvent extraction analyses showed that these solutions extract Ln(III) and An(III) ions from strongly acidic HNO_3 [24] and HCl [25] solutions. The resulting organic phases undergo facile back-extraction when exposed to weakly acidic aqueous solutions. However, this promising performance for trivalent f-element ion partitioning was negated by the limited solubility of the specific ligand in aromatic or aliphatic organic solvents. As a result, considerable effort has been given to the development of reliable and convenient syntheses of **NOPOPO** derivatives having improved solution properties. Recently, we reported syntheses for several aliphatic derivatives, **NOPOPO** R = *n*-alkyl, and mixed aromatic-aliphatic derivatives, **NOPOPO** R = Ph, *n*-alkyl [22]. These ligands have greatly improved solvation properties in hydrocarbon solvents. Furthermore, the derivative with R = 2-ethylhexyl has good solubility in alkanes. A thorough study of the extraction performance in *n*-dodecane has been completed with $Eu(NO_3)_3$ and $Am(NO_3)_3$ [27]. The results from these studies have stimulated new questions regarding the nature of the chelate interaction with Ln(III) and An(III) ions and in particular the participation of the *N*-oxide group in ligand binding. As a result, it became of interest to obtain a set of ligands with R = Ph, *n*-octyl, 2-EtHx, *n*-hexyl and *c*-hexyl for comparative structural and spectroscopic studies. The *c*-hexyl derivative is particularly interesting since the linear and branched chain aliphatic substituted ligands are oils or waxy solids and none form crystalline complexes that can be structurally compared against the complexes containing aromatic substituents.

The intermediate bis[(dicyclohexyl)phosphinomethyl]pyridine *P*,*P*′-dioxide (**1**) was prepared in good yield by combination of bis(chloromethyl)pyridine and the phosphino Grignard reagent (*c*-hexyl)$_2$P(O)MgCl. The compound shows a single ^{31}P NMR resonance at δ 50.1 which is slightly downfield of the resonances for $[(n\text{-hexyl})_2P(O)CH_2]_2C_5H_3N$ and $[(n\text{-octyl})_2P(O)CH_2]_2C_5H_3N$, δ 47.8 and 47.3, respectively [22]. The compound also shows a doublet in the $^{13}C\{^1H\}$ NMR spectrum, δ 34.80, $J_{PC} = 52.6$ Hz, that is diagnostic of the methylene carbon atoms between the phosphorous atoms and the 2,6-carbon atoms of the pyridine ring. The cyclohexyl ring carbon atoms bonded to the phosphorous atoms display a doublet resonance, δ 36.09, $J_{PC} = 63.9$ Hz, slightly downfield of the exo methylene groups. Compound **1** displays a characteristic strong

absorption in the IR spectrum at 1174 cm^{-1} that is tentatively assigned to the ν_{PO} stretching frequency. Similar IR frequencies are observed for $[(n\text{-hexyl})_2P(O)CH_2]_2C_5H_3N$ and $[(n\text{-octyl})_2P(O)CH_2]_2C_5H_3N$ at 1157 and 1165 cm^{-1}, respectively [22]. No absorption is seen in the region 1260–1240 cm^{-1} typically associated with the ν_{NO} stretching frequency.

Subsequent oxidation of **1** with 3-chloroperoxybenzoic acid gave **2** with greater than 95% yield. Column chromatography was required to remove residual impurities that include **1**. Some loss during separation resulted in isolation of **2** as a white solid in 85% yield. Compound **2** is analytically pure and it displays a parent ion in the FAB-MS. It shows a single resonance in the ^{31}P NMR spectrum, δ 51.2, shifted slightly downfield from the pyridine compound **1**. This downfield shift upon *N*-oxidation is typical [17,18,22]. The $^{13}C\{^1H\}$ NMR spectrum displays a doublet, δ 36.85, $J_{PC} = 64.6$ Hz, that is assigned to the cyclohexyl ring carbon atom bonded to the phosphorous atom. Based on our prior observations, it is expected that upon *N*-oxidation of the pyridine ring, the exo methylene carbon atom resonance would be shifted upfield by 7–10 ppm. For compound **2** only the upfield member of the doublet is clearly resolved with the downfield member being obscured by cyclohexyl ring CH_2 group resonances. The resonance for the exo-CH_2 group is estimated to fall at 25.2 ppm. The IR spectrum of **2** displays a strong absorption at 1165 cm^{-1} which is assigned to ν_{PO} and a second strong absorption at 1242 cm^{-1} that is tentatively assigned to ν_{NO} based upon the assignments made in our earlier reports [17,18,22]. Compound **2** has good solubility in $CHCl_3$ (>0.5 M), useful solubility in benzene (3.3×10^{-2} M), toluene (1.5×10^{-2} M), xylenes (2.2×10^{-2} M) and low solubility in hexane (3.6×10^{-4} M).

From our prior work it is known that $[Ph_2P(O)CH_2]_2C_5H_3NO$ readily forms 1:1 and 2:1 L/M complexes with Ln(III) nitrates [17,18] and chlorides [19] and in each case this **NOPOPO** derivative is bonded to the central Ln(III) ion in a tridentate fashion in the solid state. Tridentate chelate structures were also found for the 1:1 complex $\{[(Ph)(Bz)P(O)CH_2]_2C_5H_3NO\}Er(NO_3)_3$ and the 2:1 complex $\{[Tol_2P(O)CH_2]_2C_5H_3NO\}_2Er(NO_3)_3$ [22]. An interesting variation appeared in the latter case where all three nitrate ions are displaced to the outer coordination sphere and the oxygen atoms of two water molecules appear in the eight coordinate inner sphere. In the case of ligand **2**, it was considered that the large steric volume of the cyclohexyl substituents might inhibit the reorganization of the ligand and therefore lead to bidentate and/or perhaps bridging ligand/metal coordination.

The examination of 1:1 and 2:1 L/M combinations of **2** with $Er(NO_3)_3$ resulted in the isolation of only the 1:1 complex as a crystalline solid. The 2:1 complex may form, but it was not isolated. The 1:1 complex gives strong IR adsorptions at 1222 and 1124 cm^{-1} that are tentatively assigned to coordinated ν_{NO} and ν_{PO} frequencies based upon earlier assignments. The determination of the molecular structure of the complex confirms the 1:1 L/M stoichiometry and the tridentate chelation mode for **2**. A view of the molecule is shown in Fig. 1. The Er(III) is nine coordinate with inner sphere coordination positions occupied by the oxygen atoms from three bidentate nitrate anions and three oxygen donor atoms from ligand **2**. In this regard, the structure is very similar to the structure of $\{[(Ph)(Bz)P(O)CH_2]_2C_5H_3NO\}Er(NO_3)_3$ [22]. However, there are interesting differences. The Er(**2**) complex has two Er–O(P) bond lengths, Er–O(2) 2.249(2) Å and Er–O(3) 2.253(2) Å, that are shorter than the related bond lengths in $\{[(Ph)(Bz)P(O)CH_2C_5H_3NO\}Er(NO_3)_3$ (2.280(7) and 2.281(6) Å), while the Er–O(N) bond length, Er–O(1) 2.318(2) Å, is longer than that in $\{[(Ph)(Bz)P(O)CH_2]_2C_5H_3NO\}Er(NO_3)_3$ (2.278(7) Å). The Er–O bond shortening involving the P=O donor groups in the Er(**2**) fragment may be rationalized by the expected stronger donor strength of the phosphoryl groups, $R_2P(O)$–, containing two alkyl substituents. The resulting stronger, shorter Er–O(P) interactions may result in weakening and concomitant lengthening of the Er–O(N) donor interaction, either through electronic effects or chelate ring strain influences (see Table 1).

In our previous reports on **NOPOPO** ligand/metal complexes, it has proven interesting to evaluate variations in the triangular ligand "footprint" defined by the non-bonded O(P)···O(N)···O(P) distances of the tridentate coordinated **NOPOPO** ligands. Typically, in 1:1 complexes, the footprint approximates an isosceles triangle with nearly equivalent O(P)···O(N) edge distances (~2.86–3.04 Å) and a longer O(P)···O(P) edge distance (~3.1–3.4 Å) with the O(P)···O(P) edge contracting or expanding the most to meet the ionic radius demands of the metal cation. For example, the dimensions of the footprint triangles in $[(Ph)(Bz)P(O)CH_2]_2C_5H_3NO$ $Nd(NO_3)_3$ are O(P)···O(N) 2.991(4) Å, O(P)···O(N) 3.040(4) Å, O(P)···O(P) 3.389(4) Å and those in

Table 1
Selected bond lengths (Å)

Er–O(P)		Er–O(N)	
Er–O(2)	2.249(2)	Er–O(1)	2.318(2)
Er–O(3)	2.253(2)		
$Er–O(N)_{nitrate}$			
Er–O(4)	2.435(3)	Er–O(10)	2.428(2)
Er–O(5)	2.477(3)	Er–O(11)	2.418(3)
Er–O(7)	2.531(2)		
Er–O(8)	2.410(3)		
P=O		N–O	
P(1)–O(2)	1.506(2)	N(1)–O(1)	1.330(3)
P(2)–O(3)	1.503(2)		

$\{[(Ph)(Bz)P(O)CH_2]_2C_5H_3NO\}Er(NO_3)_3$, containing the smaller Er(III) cation, are O(P)···O(N) 2.900(7) Å, O(P)···O(N) 2.961(7) Å, O(P)···O(P) 3.239(8) Å [22]. However, in the complex Er(**2**)$(NO_3)_3$ the footprint triangle is enlarged as indicated by the non-bonded distances O(1)···O(2) 2.993(3) Å, O(1)···O(3) 3.035(3) Å and O(2)···O(3) 4.287(3) Å. The internal bond angle at O(1) is also much more open (90.7°) than has been observed in previous examples (67°–69°). These footprint modifications probably result from the shorter, tighter Er–O(P) coordinate bond interactions in the Er(**2**) fragment, although increased steric demands of the two cyclohexyl groups relative to phenyl and benzyl groups may also contribute. The P=O and N–O bond lengths in Er(**2**)$(NO_3)_3$, P(1)–O(2) 1.506(2) Å, P(2)–O(3) 1.503 Å, N(1)–O(1) 1.330(3) Å are closely comparable with the related distances in $\{[(Ph)(Bz)P(O)CH_2]_2C_5H_3NO\}Er(NO_3)_3$ 1.500(7), 1.498(6) and 1.352(10) Å; therefore, they do not provide additional information about the relative binding strengths of the ligands.

The three inner sphere nitrate anions are each bonded to the Er(III) ion in a bidentate fashion. Those associated with N(1) and N(3) are held in a relatively symmetric fashion with average Er–O (N) distances, 2.456(3) and 2.423(3) Å, while the third nitrate is bonded in a more asymmetric manner, Er–O(7) 2.531(2) Å and Er–O(8) 2.410(3) Å. Such bonding variations for nitrate ions have been observed in related complexes [22]. Lastly, the unit cell contains one slightly disordered acetone molecule per molecular unit and that molecule is not depicted in Fig. 1. It is present as a solvent of crystallization as indicated by the closest approach distances between the carbonyl oxygen atom and near neighbor Er(III) ions, Er···O(13): 6.99, 7.42 and 7.57 Å.

Previous extraction analyses of Ln(III) and An(III) ions from aqueous HNO_3 and HCl solutions by NOPOPO (R = Ph) in $CHCl_3$ solutions and by NOPOPO (R = 2-ethylhexyl) in *n*-dodecane solution indicated that 2:1 ligand/metal complexes form in solution [27]. In studies of the coordination chemistry of NOPOPO ligands with Ln(III) ions it has been possible with some ligands to isolate 2:1 complexes, but in many cases, as observed here with ligand **2**, only the 1:1 complexes are isolated. Whether this is a result of steric, electronic or solvation effects or a combination of factors is not clear.

In the present case, molecular mechanics calculations have been performed to examine the steric differences between the two ligands L = NOPOPO with R = Ph and cyclohexyl (**2**). To quantify the intrinsic steric differences the change in steric energy, ΔU, was calculated for the following reaction:

$$[M(L)(NO_3)_3] + L \rightarrow [M(L)_2(NO_3)]^{2+} + 2NO_3^-$$

where $\Delta U = U(1{:}1)\text{complex} + U(\text{ligand}) - U(2{:}1\ \text{complex}) - 2U(\text{nitrate})$. The computed strain energy differences, $\Delta U = 14.0$ kcal/mol for R = Ph and $\Delta U = 19.4$ kcal/mol for R = cyclohexyl reveal that while significant strain develops with both ligands, the cyclohexyl case is 5.4 kcal/mol less favorable. These ΔU values reflect both conformational reorganization of the ligand and the additional steric crowding present in the 2:1 complexes. The lowest energy resting states of the free ligands have the P = O bond vectors rotated away from the region occupied by the N–O bond vector and reorganization to achieve the observed tridentate metal binding orientations is endoergic and accounts for the bulk of the ΔU values: R = Ph, 8.3 kcal/mol; R = cyclohexyl, 10.1 kcal/mol.

From the foregoing analysis, steric differences alone predict that the 2:1 complex with the cyclohexyl substituents will be 10^4 times less stable than the 2:1 complex with the phenyl substituents at room temperature. However, as mentioned earlier, the unfavorable steric effects may be offset by electronic effects that would tend to favor formation of stronger ligand/metal interactions

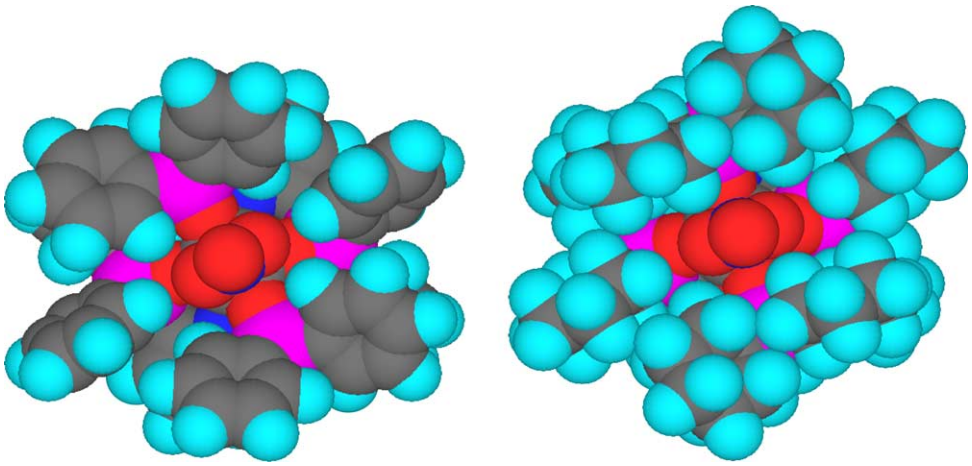


Fig. 2. Computed, energy minimized structures for $Er(NOPOPO)_2(NO_3)^{2+}$ complexes: R = Ph (left); R = cyclohexyl (right).

when cyclohexane substituents are present. In addition, as shown in Fig. 2, in the 2:1 complexes the cyclohexyl substituents more completely engulf the Er(III) cation in a lipophilic environment, which could lead to enhanced solubility in organic phases. Thus, it is possible that NOPOPO with R = cyclohexyl will produce a favorable extraction thermodynamic performance. We plan to explore this point in future solvent extraction studies.

4. Supplementary material

Crystallographic data for the complex have been deposited with the Cambridge Crystallographic Data Centre, CCDC No. 221899. Copies of this material may be obtained free of charge from The Director, CCDC, 12 Union Road, Cambridge, CB2 1EZ, UK (fax: +44 1223 336033; e-mail: deposit@ccdc.cam.ac.uk or www.http://www.ccdc.cam.ac.uk). Structure input files and parameter file used for the MM3 calculations are available on request (ben.hay@pnl.gov).

Acknowledgments

This work was supported by the US Department of Energy by a grant (03ER15419) from Chemical Sciences, Geosciences and Biosciences Office, Office of Basic Energy Sciences, Office of Science and by a grant (73759) from the Environmental Management Science Program, Office of Science.

References

[1] I.G. Draganic, Z.D. Draganic, J.P. Adloff, Radiation and Radioactivity on Earth and beyond, CRC Press, Boca Raton, FL, 1990.
[2] C. Madic, M.J. Hudson, J.O. Liljenzin, J.P. Glatz, R. Nannicini, Z. Kolarik, R. Odoj, New Partitioning Techniques for Minor Actinides. Project Report EUR 19149 En, European Commission, Luxembourg, 2000.
[3] J.N. Mathur, M.S. Murali, K.L. Nash, Solvent Extr. Ion Exch. 19 (2001) 357.
[4] E.P. Horwitz, K.A. Martin, H. Diamond, L. Kaplan, Solvent Extr. Ion Exch. 4 (1986) 449.
[5] E.P. Horwitz, D.G. Kalina, H. Diamond, G.F. Vandegrift, W.W. Schulz, Solvent Extr. Ion Exch. 3 (1985) 75.
[6] M. Ozawa, Y. Koma, K. Nomura, Y. Tanaka, J. Alloys Compds. 271–273 (1988) 538.
[7] J.N. Mathur, M.S. Murali, P.R. Natarajan, L.P. Badheka, A. Bannerji, A. Ramanujam, P.S. Dhami, V. Gopalakrishnan, R.K. Dhumwad, M.K. Rao, Waste Manage. (Oxford) 13 (1993) 317.
[8] B.F. Myasoedov, M.K. Chmutova, I.V. Smirnov, A.U. Shadrin, Global '93: Future Nuclear Systems: Emerging Fuel Cycles and Waste Disposal Options, American Nuclear Society, La Grange Park, IL, 1993.
[9] C. Cuillerdier, C. Musikas, P. Hoel, L. Nigond, X. Vitart, Separ. Sci. Technol. 26 (1991) 1229.
[10] X.F. Tan, Y.S. Wang, T.Z. Tan, G.F. Zhou, B.R. Bao, J. Radioanal. Nucl. Chem. 242 (1999) 123.
[11] B.K. McNamara, G.J. Lumetta, B.M. Rapko, Solvent Extr. Ion Exch. 17 (1999) 1403.
[12] G.J. Lumetta, B.K. McNamara, B.M. Rapko, J.M. Hutchinson, Inorg. Chim Acta 293 (1999) 195.
[13] L. Spjuth, J.O. Liljenzin, M.J. Hudson, M.G.B. Drew, P.B. Iveson, C. Madic, Solvent Extr. Ion Exch. 18 (2000) 1.
[14] A. Facchini, L. Amato, G. Modolo, R. Nannicini, C. Madic, P. Baron, Separ. Sci. Technol. 35 (2000) 1055.
[15] O. Courson, M. Lebrun, R. Malmbeck, G. Pagliosa, K. Römer, B. Sätmark, J.P. Glatz, Radiochim. Acta 88 (2000) 857.
[16] G.J. Lumetta, B.M. Rapko, P.A. Garza, B.P. Hay, R.D. Gilbertson, T.J.R. Weakley, J.E. Hutchinson, J. Am. Chem. Soc. 124 (2002) 5644.
[17] B.M. Rapko, E.N. Duesler, P.H. Smith, R.T. Paine, R.R. Ryan, Inorg. Chem. 32 (1993) 2164.
[18] U. Engelhardt, B.M. Rapko, E.N. Duesler, D. Frutos, R.T. Paine, Polyhedron 14 (1995) 2361.
[19] E.M. Bond, E.N. Duesler, R.T. Paine, H. Nöth, Polyhedron 19 (2000) 2135.
[20] X.M. Gan, S. Parveen, W.L. Smith, E.N. Duesler, R.T. Paine, Inorg. Chem. 39 (2000) 4591.
[21] E.M. Bond, E.N. Duesler, R.T. Paine, M.P. Neu, J.H. Matonic, B.L. Scott, Inorg. Chem. 39 (2000) 4152.
[22] X. Gan, E.N. Duesler, R.T. Paine, Inorg. Chem. 40 (2001) 4420.
[23] X. Gan, R.T. Paine, E.N. Duesler, H. Nöth, J. Chem. Soc., Dalton Trans. (2003) 153.
[24] E.M. Bond, U. Engelhardt, T.P. Deere, B.M. Rapko, R.T. Paine, J.R. FitzPatrick, Solvent Extr. Ion Exch. 15 (1997) 381.
[25] E.M. Bond, U. Engelhardt, T.P. Deere, B.M. Rapko, R.T. Paine, J.R. FitzPatrick, Solvent Extr. Ion Exch. 16 (1998) 967.
[26] E.M. Bond, X. Gan, J.R. FitzPatrick, R.T. Paine, J. Alloys Compds. 271–273 (1998) 1772.
[27] K.L. Nash, C. Lavallette, M. Borkowski, R.T. Paine, X. Gan, Inorg. Chem. 41 (2002) 5849.
[28] G.M. Sheldrick, XSCANS, Version 2.10, Siemens, 1994.
[29] G.M. Sheldrick, XPREP, Version 5.03, Siemens, 1994.
[30] G.M. Sheldrick, SHELXTL-97, Bruker, 1999.
[31] N.L. Allinger, Y.H. Yuh, J.-H. Lii, J. Am. Chem. Soc. 111 (1989) 8551.
[32] J.-H. Lii, N.L. Allinger, J. Am. Chem. Soc. 111 (1989) 8566.
[33] J.-H. Lii, N.L. Allinger, J. Am. Chem. Soc. 111 (1989) 8576.
[34] B.P. Hay, L. Yang, N.L. Allinger, J.-H. Lii, J. Mol. Struct. (THEOCHEM) 428 (1998) 203.
[35] B.P. Hay, O. Clement, G. Sandrone, D.A. Dixon, Inorg. Chem. 37 (1998) 5887.
[36] M. Saunders, J. Am. Chem. Soc. 109 (1987) 3150.

Available online at www.sciencedirect.com
SCIENCE DIRECT®
Polyhedron 24 (2005) 475–480
POLYHEDRON
www.elsevier.com/locate/poly

A new diphosphinite derived from cyclohexane-1,4-diol: oxidation reactions, metal complexes, P–O bond cleavage and X-ray crystal structures of $Ph_2P(E)O(C_6H_{10})OP(E)Ph_2$ (E = S, Se)

Maravanji S. Balakrishna [a,*], P.P. George [a], Shaikh M. Mobin [b]

[a] *Department of Chemistry, Indian Institute of Technology, Bombay, Mumbai 400 076, India*
[b] *National Single-Crystal X-ray Diffraction Facility, Indian Institute of Technology, Bombay, Mumbai 400 076, India*

Received 8 October 2004; accepted 3 December 2004
Available online 1 February 2005

Abstract

The reaction of cyclohexane-1,4-diol with chlorodiphenylphosphine affords bis(phosphinite), $Ph_2PO(C_6H_{10})OPPh_2$ (**1**) in good yield. The bis(phosphinite) (**1**) reacts with H_2O_2, elemental sulfur or selenium to give the corresponding dichalcogenide; the structures of the disulfide (**3**) and diselenide (**4**) derivatives are confirmed by X-ray crystal structure analysis. The reaction of **1** with phosphoryl azide, $N_3P(O)(OPh)_2$ gives the phosphinimine derivative, $(PhO)_2(O)PN{=}PPh_2O(C_6H_{10})OPh_2P{=}NP(O)(OPh)_2$ (**5**) in quantitative yield. Treatment of the ligand **1** with $CpRu(PPh_3)_2Cl$ results in a bis(phosphinite) bridged dinuclear complex, $[CpRuCl(PPh_3)]_2(\mu\text{-}PPh_2O(C_6H_{10})OPPh_2)$ (**7**) whereas the reaction of **1** with Pd(II) and Pt(II) derivatives afford *cis*-chelate complexes, $[MCl_2\{Ph_2PO(C_6H_{10})OPPh_2\}]$ (M = Pd, **8**; Pt, **9**). The reaction of **1** with $Mo(CO)_6$ in the presence of $TMNO \cdot 2H_2O$ does not give the expected *cis*-$[Mo(CO)_4\{Ph_2PO(C_6H_{10})OPPh_2\}]$; instead a cubane-shaped tetranuclear molybdenum(V) complex, $[Mo_4O_4(\mu^3\text{-}O)_4(\mu\text{-}O_2PPh_2)_4]$ (**6**) was obtained due to water assisted cleavage of P–O bonds.
© 2005 Elsevier Ltd. All rights reserved.

Keywords: Bis(phosphinite); Cyclohexane-1,4-diol; Disulfide and diselenide; Crystal structure

1. Introduction

Synthesis of new chelating bis(phosphines) to stabilize transition metals in low valent states is considered to be a most challenging task in view of their potential utility in a variety of metal-mediated organic transformations [1]. To date, a number of such systems with a variety of backbone frameworks have been synthesized and their transition metal chemistry has been explored [2], whereas similar studies on analogous bis(phosphinites) are less extensive, although some of them have proved to be efficient catalysts [3]. Also, the number of bis(phosphinites) having cyclic systems as bridging units are also limited [4]. As a part of our interest [5] in designing new ligand systems with different spacers to control the electronic attributes at the phosphorus centers and to explore their coordination chemistry, we report here the synthesis of a new bis(phosphinite), $Ph_2PO(C_6H_{10})OPPh_2$ (**1**) derived from 1,4-cyclohexanediol, and its chalcogen and imine derivatives and transition metal complexes. The disulfide and diselenide derivatives are structurally characterized.

2. Experimental

All manipulations were performed under an atmosphere of dry nitrogen or argon using standard Schlenk

* Corresponding author. Tel.: +91 22 2576 7181; fax: +91 22 2572 3480/2576 7152.
E-mail address: krishna@iitb.ac.in (M.S. Balakrishna).

0277-5387/$ - see front matter © 2005 Elsevier Ltd. All rights reserved.
doi:10.1016/j.poly.2004.12.009

and vacuum line techniques. Solvents were dried and distilled by standard methods prior to use. The ^{1}H and ^{31}P NMR spectra were recorded on a VXR 300 S spectrometer operating at the appropriate frequencies using tetramethylsilane and 85% H_3PO_4 as internal and external references, respectively. Positive shifts lie downfield of the standard in all cases. Microanalyses were performed on a Carlo Erba Model 1112 elemental analyzer.

2.1. Preparation of $Ph_2PO(C_6H_{10})OPPh_2$ (1)

A solution of PPh_2Cl (1.23 g, 5.57 mmol) in dry toluene (20 ml) was added, with stirring, to a mixture of 1,4-cyclohexanediol (0.32 g, 2.73 mmol) and triethylamine (0.56 g, 5.57 mmol) in toluene (80 ml) at 0 °C. After completion of the addition, the reaction mixture was refluxed under nitrogen with stirring for 24 h. The solution was cooled to 25 °C and Et_3NHCl was filtered off. The filtrate was passed through activated silica gel and then passed through celite and the solvent was evaporated under reduced pressure to give a white residue. An analytically pure sample of **1** was obtained by recrystallizing in a 4:1 mixture of CH_2Cl_2–hexane. Yield: 78% (1.02 g), m.p. 120–122 °C. *Anal*. Calc. for $C_{30}H_{30}O_2P_2$: C, 74.37; H, 6.24. Found: C, 74.21; H, 6.18%. ^{1}H NMR ($CDCl_3$): δ 7.27–8.15 (20H, m, phenyl), 1.62–2.24 (10H, m, cyclohexyl). ^{31}P NMR (300 MHz, $CDCl_3$): δ 106.4 (s).

2.2. Preparation of $Ph_2(O)PO(C_6H_{10})OP(O)Ph_2$ (2)

To a solution of **1** (0.5 g, 1.03 mmol) in acetonitrile was added 1 ml of 10% H_2O_2 and the mixture was stirred for 20 min at 25 °C. On cooling the solution to 0 °C, analytically pure crystalline **2** was obtained in quantitative yield.

A dichloromethane solution **1** on exposure to air also results in the formation of the white crystalline product **2** in quantitative yield. M.p.: 160–162 °C (dec.). *Anal*. Calc. for $C_{30}H_{30}O_4P_2$: C, 69.76; H, 5.85. Found: C, 70.01; H, 5.87%. ^{1}H NMR ($CDCl_3$): δ 7.36–8.16 (20H, m, phenyl), 1.58–2.15 (10H, m, cyclohexyl). ^{31}P NMR (300 MHz, $CDCl_3$): δ 20.9 (s).

2.3. Preparation of $Ph_2(S)PO(C_6H_{10})OP(S)Ph_2$ (3)

A mixture of compound **1** (0.5 g, 1.03 mmol) and sulfur (0.066 g, 2.06 mmol) in toluene (50 ml) was refluxed under nitrogen with stirring for 6 h. The solution was cooled to 25 °C, concentrated to 5 ml under vacuum and 3 ml of hexane was added. Keeping this solution at 0 °C gave the analytically pure sample of **3** in 92% (0.52 g) yield. M.p.: 178–180 °C (dec.). *Anal*. Calc. for $C_{30}H_{30}O_2S_2P_2$: C, 65.67; H, 5.51; S, 11.69. Found: C, 65.47; H, 5.50; S, 11.32%. ^{1}H NMR ($CDCl_3$): δ 7.34–8.16 (20H, m, phenyl), 1.62–2.28 (10H, m, cyclohexyl). ^{31}P NMR (300 MHz, $CDCl_3$): δ 79.4 (s).

2.4. Preparation of $Ph_2(Se)PO(C_6H_{10})OP(Se)Ph_2$ (4)

A mixture of compound **1** (0.5 g, 1.03 mmol) and selenium powder (0.162 g, 2.06 mmol) in toluene (20 ml) was refluxed under nitrogen for 6 h. The solution was then cooled to 25 °C and passed through celite and the solvent was removed under reduced pressure to give a white residue. The analytically pure product of **4** was obtained by recrystallizing in a mixture of CH_2Cl_2–hexane (4:1) at 0 °C. Yield: 80% (0.53 g). M.p.: 254–256 °C. *Anal*. Calc. for $C_{30}H_{30}O_2Se_2P_2$: C, 56.08; H, 4.71. Found: C, 56.07; H, 4.56%. ^{1}H NMR ($CDCl_3$): δ 7.27–8.15 (20H, m, phenyl), 1.62–2.24 (10H, m, cyclohexyl). ^{31}P NMR (300 MHz, $CDCl_3$): δ 82.4 (s); $^{1}J_{PSe}$ = 794.6 Hz.

2.5. Preparation of $(PhO)_2(O)PN{=}PPh_2O(C_6H_{10})OPh_2P{=}NP(O)(OPh)_2$ (5)

A solution of $(PhO)_2(O)PN_3$ (0.18 g, 0.65 mmol) in CH_2Cl_2 (6 ml) was added dropwise to a solution of **1** (0.15 g, 0.31 mmol), also dissolved in CH_2Cl_2 (10 ml) at −78 °C. After the addition was complete the reaction mixture was slowly warmed to room temperature and stirred for 3 h. The solution was then concentrated to 8 ml, 2–3 ml of *n*-hexane was added, and the solution was cooled to 0 °C whereupon **5** precipitated as a analytically pure white crystalline solid. Yield: 93% (0.23 g). M.p.: 148–150 °C (dec.). *Anal*. Calc. for $C_{54}H_{50}N_2O_8P_4 \cdot 0.5CH_2Cl_2$: C, 64.09; H, 5.03; N, 2.74. Found: C, 63.93; H, 4.97; N, 2.63%. ^{1}H NMR (300 MHz, $CDCl_3$): δ 6.78–7.72 (m, 40H, Ph), 1.82 (d, 8H, C_2H_4), 1.51 (m, 2H, CH); $^{31}P\{^{31}H\}$ NMR (300 MHz, $CDCl_3$): δ 20.8 (2P, d, $^{2}J_{PP}$ = 36 Hz), −12.6 (2P, d). MS (FAB): 979 ($M^+ + 1$).

2.6. Preparation of $[Mo_4O_4(\mu^3\text{-}O)_4(\mu\text{-}Ph_2PO_2)_4]$ (6)

To a solution of **1** (0.16 g, 0.34 mmol) and $Mo(CO)_6$ (0.10 g, 0.33 mmol) in CH_2Cl_2 (10 ml) was added a solution of $Me_3NO \cdot 2H_2O$ (0.04 g, 0.36 mmol) in methanol, and the reaction mixture was stirred at room temperature for 18 h, filtered through celite and the solvent was evaporated under reduced pressure. The solid residue obtained was dissolved in a 1:1 diethylether/CH_2Cl_2 mixture. Cooling this solution to 0 °C gave **6** as red crystals. Yield: 85% (0.1 g). M.p.: 168–170 °C. *Anal*. Calc. for $C_{48}H_{40}O_{16}P_4Mo_4 \cdot CH_2Cl_2$: C, 40.16; H, 2.88. Found: C, 40.27; H, 2.79%. ^{1}H NMR (300 MHz, $CDCl_3$): δ 7.26–7.87 (m, 40H, Ph), 5.30 (s, 2H, CH_2Cl_2); $^{31}P\{^{1}H\}$ NMR (300 MHz, $CDCl_3$): δ 44.2 (s).

2.7. Preparation of $[C_5H_5RuCl(PPh_3)]_2(PPh_2O(C_6H_{10})OPPh_2)$ (7)

To a solution of **1** (0.03 g, 0.07 mmol) in CH_2Cl_2 (10 ml) was added, dropwise, a solution of $CpRuCl(PPh_3)_2$ (0.05 g, 0.07 mmol) also in CH_2Cl_2 (10 ml) at room temperature. The mixture was stirred for 8 h before it was concentrated to 5 ml, and 3 ml of petroleum ether was added. Cooling this solution to 0 °C gave **7** as yellow crystals. Yield: 82% (0.08 g). M.p.: 178–182 °C. *Anal.* Calc. for $C_{76}H_{70}O_2P_4Ru_2Cl_2 \cdot CH_2Cl_2$: C, 61.76; H, 4.84. Found: C, 61.51; H, 4.77%. ^{1}H NMR (300 MHz, $CDCl_3$): δ 7.13–8.15 (m, 20H, Ph), 1.91 (d, 8H, C_2H_4), 1.31 (t, 2H, CH); $^{31}P\{^1H\}$ NMR (300 MHz, $CDCl_3$): δ 138.1 (2P, d, $^2J_{PP}$ = 58.6 Hz), 43.3 (2P, d).

2.8. Preparation of $[PdCl_2(Ph_2(O)PO(C_6H_{10})OP(O)Ph_2)]$ (8)

To a solution of $[Pd(NCCH_3)_2Cl_2]$ (0.04 g, 0.23 mmol) (generated in situ by refluxing $PdCl_2$ in CH_3CN for 4 h) in CH_3CN (8 ml) was added, dropwise, a solution of **1** (0.12 g, 0.25 mmol) also in CH_3CN (4 ml), and the reaction mixture was stirred at room temperature for 3 h. The solution was concentrated to 3 ml, and 1 ml of petroleum ether was added. Cooling this solution to 0 °C gave **8** as yellow crystals. Yield: 90.5% (0.25 g). M.p.: 174–176 °C. *Anal.* Calc. for $C_{30}H_{30}Cl_2O_2P_2Pd$: C, 54.4; H, 4.5. Found: C, 54.6; H, 4.5%. ^{1}H NMR (300 MHz, $CDCl_3$): δ 7.24–7.58 (m, 20H, Ph), 1.73 (d, 8H, C_2H_4), 1.33 (m, 2H, CH). $^{31}P\{^1H\}$ NMR (300 MHz, $CDCl_3$): δ 79.4 (s).

2.9. Preparation of $[PtCl_2(Ph_2(O)PO(C_6H_{10})OP(O)Ph_2)]$ (9)

To a solution of [Pt(COD)Cl_2] (0.03 g, 0.08 mmol) in CH_2Cl_2 (5 ml), a solution of **1** (0.02 g, 0.08 mmol) also in CH_2Cl_2 (8 ml) was added dropwise and the reaction mixture was stirred at room temperature for 4 h. The solution was concentrated to 5 ml, and 2 ml of petroleum ether was added. Cooling this solution to 0 °C gave **9** as a white crystalline material. Yield: 98% (0.04 g). M.p.: 158–160 °C. *Anal.* Calc. for $C_{30}H_{30}Cl_2O_2P_2Pt$: C, 48.06; H, 4.03. Found: C, 47.92; H, 3.9%. ^{1}H NMR (300 MHz, $CDCl_3$): δ 7.26–7.64 (m, 20H, Ph), 1.75 (d, 8H, C_2H_4), 1.35 (m, 2H, CH); $^{31}P\{^1H\}$ NMR (300 MHz, $CDCl_3$): δ 76.04 (s), $^1J_{PPt}$ = 4132 Hz.

2.10. Structure determination

Colorless crystals of **3** and **4**, crystallized from CH_2Cl_2 at 0 °C, were mounted on Pyrex filaments with epoxy resin. Unit cell dimensions were determined from 25 well-centered reflections. Intensity data were collected with a Nonium MACH3 diffractometer using graphite-monochromated Mo Kα (0.71073 Å) radiation. Periodic monitoring of check reflections showed stability of the intensity data. The structures were solved by direct methods [6] and refined using SHELXS-97 software [7]. The non-hydrogen atoms were geometrically fixed and allowed to refine using a riding model. Details of the data collections and refinements are summarized in Table 1.

Table 1
Crystallographic data for compounds **3** and **4**

Compound	**3**	**4**
Formula	$C_{30}H_{30}O_2P_2S_2$	$C_{30}H_{30}O_2P_2Se_2$
Molecular weight	548.60	642.40
Crystal size (mm)	$0.4 \times 0.25 \times 0.20$	$0.2 \times 0.17 \times 0.12$
Crystal system	monoclinic	monoclinic
Space group	$P2_1/c$	$P2_1/c$
a (Å)	9.201(7)	12.919(5)
b (Å)	13.141(4)	13.395(1)
c (Å)	12.429(4)	17.661(6)
α (°)	90	90
β (°)	110.51(7)	109.18(8)
γ (°)	90	90
V (Å^3)	1407.5(2)	2886.4(5)
Z	2	4
D_{calc} (g cm^{-3})	1.294	1.478
μ (mm^{-1})	0.329	2.698
T (K)	293(2)	293(2)
Total number of reflections	2124	3076
Number of unique reflections	2124	3076
R_{int}	0.0391	0.0606
R	0.0512	0.1254
R'	0.0984	

3. Results and discussion

The reaction of cyclohexane-1,4-diol with two equivalents of chlorodiphenylphosphine in the presence of triethylamine in toluene affords bis(phosphinite), $Ph_2PO(C_6H_{10})OPPh_2$ (**1**) in good yield. The $^{31}P\{^1H\}$ NMR spectrum of **1** shows a single resonance at 106.4 ppm indicating the symmetric nature of the molecule. Treatment of **1** with 10% H_2O_2 solution in CH_3CN affords the dioxide derivative **2** in quantitative yield. The diethyl ether or acetonitrile solution of **1** on exposure to air also gives the same dioxide after 2–3 days in quantitative yield. The ^{31}P NMR spectrum of **2** shows a singlet at 20.9 ppm, which is considerably deshielded when compared to the parent ligand **1** with a shift of 85.5 ppm. The reaction of **1** with two equivalents of sulfur or selenium in toluene under refluxing conditions affords the corresponding disulfide (**3**) and diselenide (**4**) in 70–80% yield. The disulfide can also be prepared by reacting the chlorodiphenylphosphinesulfide with cyclohexane-1,4-diol. Attempts to synthesize the monochalcogenides have been unsuccessful. The reaction of **1** with one mole

of elemental sulfur or selenium did not give the expected monochalcogenide derivatives, instead dichalcogenides were obtained in low yields and half the original amount of bis(phosphinite) was left unreacted. The physical and analytical data for the compounds are summarized in Section 2 (see Scheme 1).

The ^{31}P NMR spectrum of **3** and **4** show single resonances at 79.4 and 82.4 ppm, respectively. The selenide derivative **4** shows a $^{1}J_{PSe}$ coupling of 795 Hz, characteristic of tetracoordinated pentavalent phosphine selenides [4a,5e,8]. ^{1}H NMR spectra of all the compounds are consistent with the structural compositions. Further, the structures of $Ph_2P(S)OC_6H_{10}OP(S)PPh_2$ (**3**) and $Ph_2P(Se)OC_6H_{10}OP(Se)PPh_2$ (**4**) were confirmed by single crystal X-ray analysis.

The solid-state structures of disulfide, $Ph_2P(S)O(C_6H_{10})OP(S)PPh_2$ (**3**) and diselenide $Ph_2P(Se)O(C_6H_{10})OP(Se)PPh_2$ (**4**) were determined by single-crystal X-ray diffraction studies. The perspective views of the molecular structures of compounds **3** and **4** are shown in Figs. 1 and 2, respectively. Crystal data and details of the structure determinations are given in Table 1 while selected bond lengths and inter-bond angles appear in Table 2.

The phosphorus centers are in typical tetrahedral environments. The P=S bond length of 1.928(1) Å is shorter than those observed in amine derivatives, $Ph_2P(S)N(Ph)C_2H_4N(Ph)P(S)PPh_2$ (1.951(1) Å) [8b] and $Ph_2P(S)N(C_4H_8)NP(S)PPh_2$ [8c] (1.943(1) Å). Interestingly, the P=Se distance in **4** is 2.089(3) Å which is longer than those observed in aminophosphonite, $PhN\{P(Se)(OC_6H_4OMe\text{-}o)_2\}_2$ (2.058(6) Å) or bisphosphinite, $Ph_2P(Se)\{(-OC_{10}H_6)(\mu\text{-}CH_2)(C_{10}H_6O-)\}P(Se)Ph_2$ (2.072(1) Å). However, the P=Se distance in **4** is quite comparable with those found in $Ph_2P(Se)NHP(Se)Ph_2$ (2.085(1) Å). The chalcogen

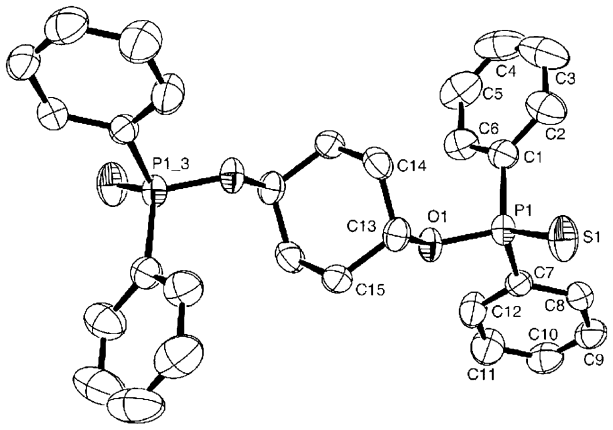


Fig. 1. Perspective view of **3** showing the atom numbering scheme. Hydrogen atoms are omitted for clarity.

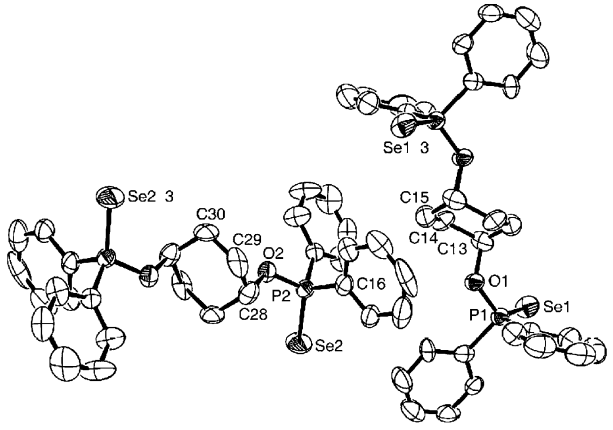
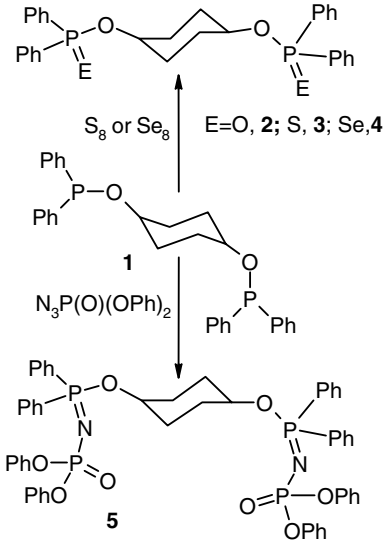


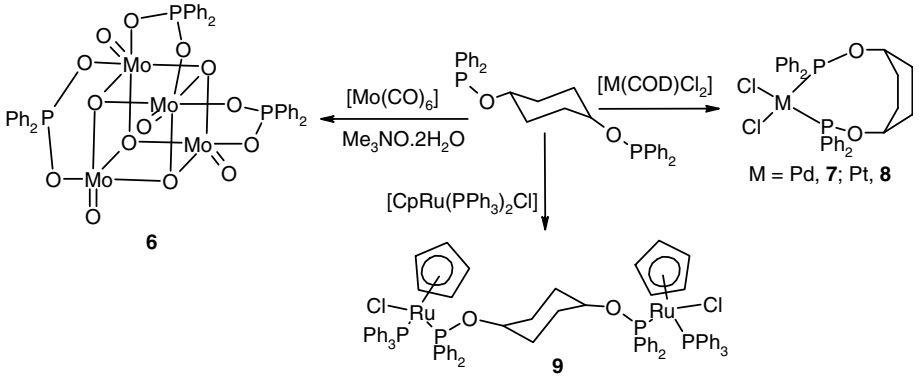
Fig. 2. Perspective view of **4** showing the atom numbering scheme. Hydrogen atoms are omitted for clarity.



Scheme 1.

Table 2
Selected bond distances (Å) and bond angles (°) in **3** and **4**

Compound	**3**	**4**
Bond lengths (Å)		
P(1)–O(1)	1.590(8)	1.596(3)
P(1)–C(7)	1.809(3)	1.809(1)
P(1)–C(1)	1.809(3)	1.799(1)
C(1)–C(2)	1.387(4)	1.371(5)
C(1)–C(6)	1.388(4)	1.387(15)
C(2)–C(3)	1.382(6)	1.382(18)
O(1)–C(13)	1.478(3)	1.504(1)
P(1)–E(1) (E = S or Se)	1.928(2)	2.089(3)
Bond angles (°)		
O(1)–P(1)–C(7)	100.57(14)	100.57(14)
O(1)–P(1)–C(1)	105.02(13)	105.02(13)
C(7)–P(1)–C(1)	105.13(13)	105.13(13)
O(1)–P(1)–S(1)	116.13(9)	116.13(9)
C(7)–P(1)–S(1)	113.39(13)	113.39(13)
C(1)–P(1)–S(1)	115.02(14)	115.02(14)
C(13)–O(1)–P(1)	122.64(17)	122.64(17)



Scheme 2.

atoms in both **3** and **4** are in an approximately *syn*-disposition. The P–O bond distances in **3** and **4** are 1.591(2) and 1.596(3) Å whereas the average P–C bond distances are 1.806(2) Å.

The reaction of **1** with $Mo(CO)_6$ in the presence of $Me_3NO \cdot 2H_2O$ in THF resulted in the formation of a cubane shaped tetramolybdenum(V)oxo complex (**6**), containing four bridging $Ph_2PO_2^-$ units instead of the expected tetracarbonylmolybdenum(0) complex, [$Mo(CO)_4(Ph_2POC_6H_{10}OPPh_2)$] as shown in Scheme 2. It is presumed that during the reaction, the P–O bonds of the ligand **1** undergo hydrolytic cleavage to give Ph_2POH moieties which are readily oxidized to give $Ph_2P(O)OH$. Thus, $Ph_2PO_2^-$ generated in situ readily oxidize Mo to its higher oxidation state and lead to the formation of the unexpected complex **6**. A similar reaction of $Mo(CO)_6$ with *N*,*N*′-bis(diphenylphosphino)-2,6-diaminopyridine, $Ph_2PNH(NC_5H_5)NHPPh_2$ led to the isolation of [$Mo(CO)_3\{Ph_2PNH(NC_5H_5)NHPPh_2$-κP,κP,κN}] which on further aerial oxidation in tetramethylbenzene at 180 °C resulted in P–N bond rupture and formation of $[Mo_4\{(\mu^3\text{-}O)_4(\mu\text{-}Ph_2PO_2)_4\}_4]$. The $^{31}P\{^1H\}$ NMR of **6** shows a single resonance at 42 ppm. The structure of **6** was further confirmed by a single X-ray structure determination. The reaction of ligand **1** with $CpRuCl(PPh_3)_2$ in a 1:1 ratio in dichloromethane at room temperature for 48 h afforded diruthenium complex, $[CpRuCl(PPh_3)]_2(\mu\text{-}PPh_2O(C_6H_{10})OPPh_2)$ (**7**) with the ligand **1** acting as a bridging bidentate ligand as shown in Scheme 2. The $^{31}P\{^1H\}$ NMR spectrum of **7** shows two doublets at 44 and 138.1 ppm which are assigned, respectively, to PPh_3 and phosphinite centers. The $^2J_{PP}$ is 58.6 Hz. Treatment of $M(COD)Cl_2$ (M = Pd, Pt) with 1:1 molar proportions of the ligand **1** in dichloromethane afford the chelate complexes **8** and **9** in good yield. The $^{31}P\{^1H\}$ NMR spectra of **8** and **9** exhibit single resonances at 79.0 and 76.0 ppm ($^1J_{Pt-P} = 4137$ Hz), respectively. The chemical compositions of complexes **6**–**9** are established by element analyses and the proposed structures are consistent with their spectroscopic data.

4. Conclusions

Although, to date, several bisphosphinites are known, the number of bis(phosphinites) having cyclic systems as bridging units are limited. The cyclohexyl group in ligand **1** offers more flexibility for its coordination behavior as demonstrated in the case of Pd(II), Pt(II) and Ru(II) complexes. Interestingly, the reaction of **1** with $Mo(CO)_6$ in the presence of $TMNO \cdot 2H_2O$ gave a cubane-shaped tetramolybdenum(IV) complex containing four bridging $Ph_2PO_2^-$ units, through P–O bond cleavage. This method can be conveniently explored with various other metals to get unexpected but interesting metal oxide clusters which might find application in materials, heterogeneous catalysis and also in heterogenised homogeneous catalysis. The disulfide and diselenide derivatives may also find application in making silver and gold monolayers. Work in this direction is in progress in our laboratory.

Acknowledgements

We thank the Department of Science and Technology (DST), India, for the financial support of the work done at the Indian Institute of Technology, Bombay.

Appendix A. Supplementary data

Crystallographic data for the structural analysis has been deposited with the Cambridge Crystallographic Data Center, CCDC Nos. 201430 (**3**) and 251517 (**4**). Copies of this information may be obtained free of charge from The Director, CCDC, 12 Union Road, Cambridge CB2 1EZ (fax: +44 1223 336 033; deposit@ccdc.cam.ac.uk or www.ccdc.cam.ac.uk). Supplementary data associated with this article can be found, in the online version, at doi:10.1016/j.poly.2004.12.009.

References

[1] (a) L.H. Pignolet, Homogeneous Catalysis with Metal Phosphine Complexes, Plenum Press, New York, 1983;
(b) P.W.N.M. van Leeuwen, Organometallics 16 (1997) 3027;
(c) T.J. Kwok, D.J. Wink, Organometallics 12 (1993) 1954;
(d) H. Bricout, J.F. Carpentier, A. Mortreuz, Tetrahedron Lett. 37 (1996) 6105;
(e) I. Suisse, H. Bricout, A. Mortreux, Tetrahedron Lett. 35 (1994) 413;
(f) D. Gleich, R. Schmid, W.A. Herrmann, Organometallics 17 (1998) 2141;
(g) S. Ganguly, R.M. Roundhill, Organometallics 12 (1993) 4825;
(h) B. Cornils, E.G. Kuntz, J. Organomet. Chem. 502 (1995) 177.

[2] (a) M.S. Balakrishna, V.S.R. Reddy, S.S. Krishnamurthy, J.C.T.R. Burckette St. Laurent, J.F. Nixon, Coord. Chem. Rev. 129 (1994) 1, references cited therein;
(b) J.T. Mague, J. Krinsky, Inorg. Chem. 40 (2001) 1962;
(c) A.M.Z. Slawin, M.B. Smith, J. Woollins, J. Chem. Soc., Dalton Trans. (1998) 1537;
(d) K.V. Katti, V.S.R. Reddy, P.R. Singh, Chem. Soc. Rev. (1995) 97.

[3] (a) G.D. Cuny, S.L. Buchwald, J. Am. Chem. Soc. 115 (1993) 2066;
(b) O. Huttenloch, J. Spieler, H. Waldmann, Chem. Eur. J. 6 (2000) 671;
(c) Z. Csok, G. Szalontai, G. Czira, L. Kollar, J. Organomet. Chem. 475 (1998) 23.

[4] (a) M.S. Balakrishna, R. Panda, J.T. Mague, J. Chem. Soc., Dalton Trans. (2002) 4617;
(b) M.S. Balakrishna, S.S. Krishnamurthy, J. Organomet. Chem. 424 (1992) 243;
(c) K. Yamamoto, S. Momose, M. Funahashi, S. Ebata, H. Ohmura, H. Komatsu, M. Miyawawa, Chem. Lett. 2 (1994) 189.

[5] (a) M.S. Balakrishna, R.M. Abhyankar, J.T. Mague, J. Chem. Soc., Dalton Trans. (1999) 1407;
(b) M.S. Balakrishna, M. Walawalkar, J. Organomet. Chem. 628 (2001) 76;
(c) M.S. Balakrishna, R. Panda, D.C. Smith Jr, A. Klaman, S.P. Nolan, J. Organomet. Chem. 599 (2000) 159;
(d) M.S. Balakrishna, R.M. Abhyankar, M. Walawalkar, Tetrahedron Lett. 42 (2001) 2733;
(e) M.S. Balakrishna, S. Teipel, A.A. Pinkerton, R.G. Cavell, Inorg. Chem. 40 (2001) 1802;
(f) M.S. Balakrishna, R. Panda, J.T. Mague, Inorg. Chem. 40 (2001) 5620;
(g) M.S. Balakrishna, R. McDonald, Inorg. Chem. Commun. 5 (2002) 1786;
(h) S. Priya, M.S. Balakrishna, J.T. Mague, Inorg. Chem. 42 (2003) 1472;
(i) M.S. Balakrishna, R. Panda, J.T. Mague, Polyhedron 22 (2003) 587.

[6] G.M. Sheldrick, SHELXS-93: Program for Crystal Structure Solution, University of Göttingen, Göttingen, Germany, 1993.

[7] G.M. Sheldrick, SHELXL-97: Program for Crystal Structure Refinement, University of Göttingen, Göttingen, Germany, 1997.

[8] (a) M.S. Balakrishna, R. Klein, S. Uhlenbrock, A.A. Pinkerton, R.G. Cavell, Inorg. Chem. 32 (1993) 5676;
(b) M.S. Balakrishna, J.T. Mague, Polyhedron 20 (2001) 2421;
(c) M.S. Balakrishna, P.P. George, J.T. Mague, J. Organomet. Chem. 689 (2004) 3387.

Available online at www.sciencedirect.com
SCIENCE DIRECT®
Polyhedron 24 (2005) 481–485
POLYHEDRON
www.elsevier.com/locate/poly

Syntheses, structures and characterization of heterobimetallic compounds $[Et_4N]_2[(MS_4)Ag_8(SBu^t)_8]$ (M = W, Mo) and $\{[Et_4N][WOS_3Ag_2(S_2COEt)]\}_n$

Jian-Rong Li [a,b], Zhi-Hua Li [a], Shao-Wu Du [a,*], Xin-Tao Wu [a]

[a] State Key Laboratory of Structural Chemistry, Fujian Institute of Research on the Structure of Matter, Chinese Academy of Sciences, Fuzhou, Fujian 350002, PR China
[b] Graduate School of the Chinese Academy of Sciences, Beijing 100039, PR China

Received 23 November 2004; accepted 3 December 2004
Available online 1 February 2005

Abstract

Three new M/Ag/S heterobimetallic compounds $[Et_4N]_2[(MS_4)Ag_8(SBu^t)_8]$ (**1a**, M = W; **1b**, M = Mo) and $\{[Et_4N][WOS_3Ag_2(S_2COEt)]\}_n$ (**2**) have been prepared from the reactions of $[MO_nS_{4-n}]^{2-}$ (M = W, Mo; n = 0–1) with $AgSBu^t$ or AgS_2COEt. Single crystal structural studies show that the compound **1a** contains a $[WS_4]^{2-}$ dianion encapsulated in a neutral octanuclear $(AgSBu^t)_8$ cage via weak Ag···S(WS_4) interactions. In compound **2**, butterfly WOS_3Ag_2 fragments are connected via bidentate bridging $[S_2COEt]^-$ ligands to give a chain polymeric anion. These compounds are fully characterized by IR, UV–vis and microanalyses. Compound **2** is the first W/Ag/S polymer with bidentate thiolato linkages.
© 2005 Elsevier Ltd. All rights reserved.

Keywords: Tetrathiotungstate; Tetrathiomolybdate; Silver (I) compounds; W/Ag/S polymer; Crystal structure; Monocyclic silver alkanethiolates

1. Introduction

The syntheses and characterization of compounds containing thioanions of molybdenum (VI) or tungsten (VI), such as $[W(Mo)O_nS_{4-n}]^{2-}$ (n = 0–2), have been widely studied due to their relevance to biological systems, interesting physicochemical properties and versatile structural types [1–8]. In particular, the study of compounds containing these multidentate chelating ligands with Ag(I) has continued to attract attention because of their high tendency to form Ag–S bonds [9–16]. A common synthetic strategy for the preparation of W(Mo)/Ag/S compounds is to employ neutral species AgX ($X = NO_3^-, Cl^-, Br^-, I^-, CN^-, SCN^-$) to react with $[W(Mo)O_nS_{4-n}]^{2-}$ (n = 0–2), often using transition metal complexes, rare earth metal complexes or alkali metal complexes as cations. These reactions resulted in the formation of a large number of W(Mo)/Ag/S compounds, such as a zigzag chain with unequal steps: $[W_4Ag_4S_{16}\cdot 2Ca(DMSO)_6]_n$ [12], a loose helical chain: $[W_3Ag_3S_{12}\cdot Nd(DMSO)_8]_n$ [13], a single-stranded helical chain: $[W_3Ag_3S_{12}\cdot La(DMAC)(H_2O)_3\cdot(DMAC)_4]_n$ [14], a hanging ladder-like polymer chain: $[W_4Ag_6S_{16}\cdot Ca(DEAC)_6]_n$ [15] and an one-dimensional linear chain: $[WS_4Ag\cdot Li(DMF)_4]_n$ [16]. However, reactions employing AgSR or AgS_2COEt as a silver source to react with thiomolybdates or thiotungstates have not been reported.

Recently we have reported several W(Mo)/Cu/S heterobimetallic clusters prepared from the reactions between $[W(Mo)O_nS_{4-n}]^{2-}$ (n = 0–1) and $CuSBu^t$ or

* Corresponding author. Tel./fax: +86 591 83709470.
E-mail address: swdu@ms.fjirsm.ac.cn (S.-W. Du).

0277-5387/$ - see front matter © 2005 Elsevier Ltd. All rights reserved.
doi:10.1016/j.poly.2004.12.011

Cudtp (dtp = diethyldithiophosphate), such as $[Et_4N]_2[\{MOS_3\}_2Cu_4(\mu\text{-S-Bu}^t)_2]$ (double butterfly), $[Et_4N][\{MOS_3\}_2Cu_6(\mu\text{-S-Bu}^t)_3]$ (double incomplete cubane), $[Bu_4N][\{MOS_3\}_3Cu_9(\mu\text{-S-Bu}^t)_3(\mu_3\text{-S-Bu}^t)]$ (triple incomplete cubane) [17], $[Bu_4N]_2[\{MoOS_3\}_4Cu_{12}(dtp)_6]$ (closed double cubane) and $[Et_4N][\{WS_4Cu_4\}(dtp)_3]$ (1-D polymer) [18]. To expand our studies to the W(Mo)/Ag/S system, we have investigated the reactions of $[W(Mo)O_nS_{4-n}]^{2-}$ (n = 0–1) with $AgSBu^t$ and AgS_2COEt. Herein we report three new compounds prepared from these reactions, namely, $[Et_4N]_2[(MS_4)Ag_8(SBu^t)_8]$ (**1a**, M = W; **1b**, M = Mo) and $[Et_4N][WOS_3Ag_2(S_2COEt)]_n$ (**2**).

2. Experimental

2.1. General procedures

All experiments were carried out in air. Starting materials $[Et_4N]_2[WS_4]$, $[Et_4N]_2[MoS_4]$ and $[Et_4N]_2[WOS_3]$ were prepared by published procedures [19]. Complex $AgSBu^t$ was synthesized by adding $AgNO_3$ to $HSBu^t$ in ethanol. Complex AgS_2COEt was synthesized by the reaction of $AgNO_3$ with potassium ethylxanthate in aqueous solution. Other chemicals were obtained from commercial sources and used without further purification.

2.2. Physical measurements

Infrared spectra were recorded on a Nicolet Magna 750 FT-IR spectrophotometer as KBr pellets in the range 4000–400 cm^{-1}. Electronic spectra were recorded on a Lambda 35 spectrophotometer in MeCN solution between 600 and 200 nm. Elemental analyses were performed in the Elemental Analysis Laboratories at our institute.

2.3. Synthesis of $[Et_4N]_2[(WS_4)Ag_8(SBu^t)_8]$ (**1a**)

Complex $AgSBu^t$ (0.20 g, 1.0 mmol) was added to a DMF solution (5 mL) of $[Et_4N]_2[WS_4]$ (0.29 g, 0.5 mmol). After stirring at room temperature for 30 min, the resulting orange–red solution was filtered. The filtrate was allowed to slowly evaporate in an *i*-PrOH atmosphere to afford **1a** as red crystals. Yield: 54% (based on $AgSBu^t$). IR (KBr pellet, cm^{-1}): ν(W–S) 445 (s). UV–vis (MeCN) λ_{max}/nm (10^{-3} ε_{max}/M^{-1} cm^{-1}): 291(37.3), 407(16.2). *Anal.* Calc. for **1a**: C, 26.83; H, 5.25; N, 1.30. Found: C, 26.70; H, 5.02; N, 1.39%.

2.4. Synthesis of $[Et_4N]_2[(MoS_4)Ag_8(SBu^t)_8]$ (**1b**)

Dark crystals of **1b** were obtained in a 50% yield (based on $AgSBu^t$) by a similar way as for **1a** except $[Et_4N]_2[MoS_4]$ (0.24 g, 0.5 mmol) was used instead of $[Et_4N]_2[WS_4]$. IR (KBr pellet, cm^{-1}): ν(Mo–S) 458 (s). UV–vis (MeCN) λ_{max}/nm ($10^{-3}\varepsilon_{max}/M^{-1}$ cm^{-1}): 243(23.6), 324(22.4), 486(12.4). *Anal.* Calc. for **1b**: C, 27.97; H, 5.48; N, 1.36. Found: C, 27.70; H, 5.28; N, 1.51%.

2.5. Synthesis of $\{[Et_4N][WOS_3Ag_2(S_2COEt)]\}_n$ (**2**)

A solution of $[Et_4N]_2[WOS_3]$ (0.28 g, 0.5 mmol) and AgS_2COEt (0.23 g, 1.0 mmol) in 6 mL of DMF was stirred for 1 h. A small amount of black precipitate was removed by filtration and the filtrate was slowly evaporated in an *i*-PrOH atmosphere to give yellow crystals of **2** (yield 23%). IR (KBr pellet, cm^{-1}): ν(W–S_{br}) 455 (m), 435 (s), 417 (m), ν(W–O) 921 (vs). UV–vis (MeCN) λ_{max}/nm ($10^{-3}\varepsilon_{max}/M^{-1}$ cm^{-1}): 309(8.1), 353(sh)(4.1), 408(sh)(2.6). *Anal.* Calc. for compound **2**: C, 17.30; H, 3.28; N, 1.83. Found: C, 17.32; H, 3.09; N, 1.96%.

2.6. X-ray crystallography

Intensity data for the two compounds were collected at 293(2) K on a Rigaku Mercury CCD area-detector diffractometer with a graphite monochromator utilizing Mo Kα radiation (λ = 0.71073 Å). The structures were solved by direct methods using SHELXS-97 [20]. Anisotropic displacement parameters were refined for all non-hydrogen atoms. The organic hydrogen atoms were generated geometrically (C–H, 0.96 Å). The crystallographic data are summarized in Table 1.

Table 1
Crystallographic data for compounds **1a** and **2**

	1a	**2**
Empirical formula	$C_{48}H_{112}Ag_8N_2S_{12}W$	$C_{11}H_{25}Ag_2NO_2S_5W$
Formula weight	2148.93	763.21
Crystal system	monoclinic	monoclinic
Space group	*C*2/*c*	$P2_1/n$
a (Å)	39.29(5)	11.467(3)
b (Å)	14.83(3)	11.820(3)
c (Å)	27.66(3)	16.564(4)
β (°)	106.434(6)	106.613(1)
V (Å^3)	15,460(4)	2151.4(9)
Z	8	4
F(0 0 0)	8448	1448
ρ_{calc} (g cm^{-3})	1.846	2.356
μ (mm^{-1})	3.815	7.624
θ range (°)	2.02–22.50	3.07–27.48
Data collected	31919	16181
Unique data (R_{int})	9950 (0.0430)	4905 (0.0232)
Observed data [$I > 2\sigma(I)$]	9209	4741
Number of parameters	640	199
Goodness-of-fit on F^2	1.164	1.058
R_1, wR_2 [$I > 2\sigma(I)$][a,b]	0.0721, 0.1722	0.0210, 0.0526

[a] $R_1 = \sum \| F_o \| - | F_c \| / \sum | F_o |$.
[b] $wR_2 = [\sum w(F_o^2 - F_c^2)^2 / \sum w(F_o^2)^2]^{0.5}$.

3. Results and discussion

3.1. Synthesis

The polymeric complex $AgSBu^t$ was not soluble in DMF but it dissolved rapidly in the presence of the tetrathiotungstate anion to form a cyclic octanuclear Ag compound **1a**. The ratio of $AgSBu^t$ to $[Et_4N]_2[WS_4]$ did not change the nature of the product. However, the reaction with 2 equiv. of $AgSBu^t$ gave a better yield of **1a**. The reaction between $[Et_4N]_2[MoS_4]$ and $AgSBu^t$ by the same method afforded $[Et_4N]_2[(MoS_4)Ag_8(SBu^t)_8]$ (**1b**), a Mo analogue of **1a**. The structure of **1b** was confirmed by IR, microanalyses and the X-ray diffraction study. The X-ray crystal data was not good enough and only a raw structure could be obtained. The reactions between $[W(Mo)S_4]^{2-}$ or $[W(Mo)OS_3]^{2-}$ and AgS_2COEt often gave rise to a large amount of Ag_2S precipitation or insoluble solids. However, a polymeric W/Ag/S cluster **2** was successfully isolated from the reaction between $[Et_4N]_2[WOS_3]^{2-}$ and AgS_2COEt in moderate yield under appropriate conditions.

3.2. Infrared and UV–vis spectra

The 400–520 cm^{-1} region of the IR spectra of heterothiometallic cluster compounds containing $[W(Mo)S_4]^{2-}$ moieties has proven to be valuable in studying their structural characteristics [1,21–23]. It has been observed that the ν(M–S) frequency decreases on increasing the number of coordinated hetero-metal atoms (M = W, Mo) [22–24]. The spectra of compounds **1a** and **1b** exhibit a single strong band at 445 and 458 cm^{-1}, which may be contributed to the ν(W = S) and ν(Mo = S) stretching vibrations, respectively. Comparing these values with the corresponding values for $[Et_4N]_2[WS_4]$ (458 cm^{-1}) and $[Et_4N]_2[MoS_4]$ (470 cm^{-1}) reveals some red shift to low frequencies, indicating weakening of the M = S bonds as a result of interactions with Ag atoms. The spectra of compound **2** exhibits a very strong band at 921 cm^{-1}, which is ascribed to the ν(W = O) vibrations, and the bands at 455, 435 and 417 cm^{-1} were due to the vibrations of ν(W-μ_2-S) and ν(W-μ_3-S), respectively [25].

It is apparent that the UV–vis spectra of the clusters are characterized by the three strong absorptions (ν_1, ν_2, ν_3) which are attributable to the S–W(Mo) charge transfer transitions. By comparison with the electronic spectra of $[W(Mo)O_nS_{4-n}]^{2-}$ (n = 0–1), one can see that the addition of Ag(I) to $[W(Mo)O_nS_{4-n}]^{2-}$ (n = 0–1) shifts the spectra of **1a**, **1b** and **2** to lower energies. For example, the ν_1 absorptions for **1a** is at 407 nm, which shifts to lower energies compared to that of $[WS_4]^{2-}$ (398 nm). This low energy shift was different from that observed for another related compound, $[W_2Ag_4S_8(AsPh_3)_4]$, which exhibited a ν_1 absorption at 356 nm [26,27].

3.3. Description of the crystal structure of $[Et_4N]_2[(WS_4)Ag_8(SBu^t)_8]$ (1a)

The complex of compound **1a** consists of an octanuclear monocyclic $[Ag(SBu^t)]_8$ ring, a $[WS_4]^{2-}$ anion and two $[Et_4N]^+$ cations. A view of the anion of compound **1a** is shown in Fig. 1 and selected bond lengths and angles are summarized in Table 2. In the structure of the anion, eight Ag atoms construct a distorted cage with several Ag_4 planes, e.g. atoms Ag2, Ag5, Ag6, Ag9 almost lie in a plane (mean deviation: 0.1668 Å) while the rest are also coplanar (mean deviation: 0.1191 Å). It is noted that this distorted cage structure is different from those reported for the octanuclear monocyclic AgSR ring compounds. For example, the octanuclear cluster $[Ag_8(mba)_{10}]^{12-}$ (H_2mba = 2-mercaptobenzoic acid) is composed of two butterfly type Ag_4S_4 cones [28] and the complexes $(Ag_8SCMeEt_2)_8(PPh_3)_2$ [29,30], $[AgSCH(SiMe)_2]_8$ [31] and $\{[Ag(SC_6H_4\text{-}o\text{-}SiMe_3)]_4\}_2$ [32] all show bis-cyclic structures. In the Ag_8 ring, adjacent Ag atoms are connected through one bridging –SBu^t ligand. The distance between an Ag atom and the bridging –SBu^t ranges from 2.380(5) to 2.453(5) Å, which is similar to the corresponding values in $[Ag_8(mba)_{10}]^{12-}$ [28], $(Ag_8SCMeEt_2)_8(PPh_3)_2$ [29,30], $[AgSCH(SiMe)_2]_8$ [31] and $\{[Ag(SC_6H_4\text{-}o\text{-}SiMe_3)]_4\}_2$ [32]. There are weak secondary metal–metal interactions between the adjacent Ag atoms (Ag3···Ag4: 3.022(6); Ag5···Ag6: 3.184(4) Å), which are intermediate between the Ag–Ag separation found in metallic silver (2.88 Å) [33] and twice the van der Waals radii for silver (3.44 Å) [34,35], and also are comparable to those found in other related compounds [28–32]. A $[WS_4]^{2-}$ fragment

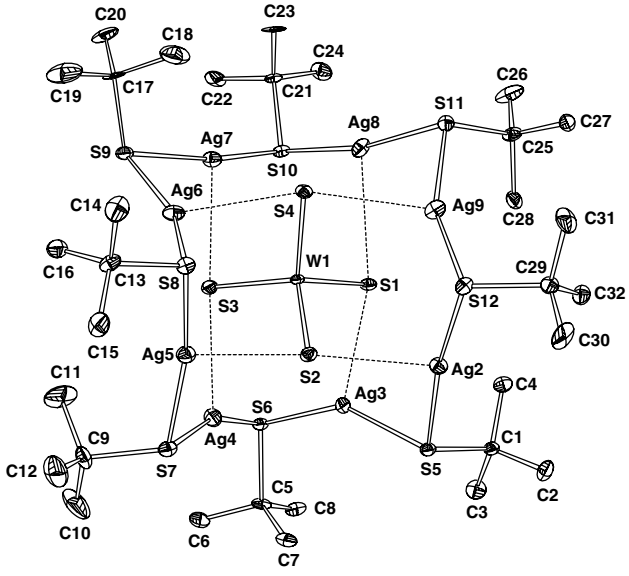


Fig. 1. Structure of the $[(WS_4)Ag_8(SBu^t)_8]^{2-}$ anion of **1a** (20% probability displacement ellipsoids). The hydrogen atoms are omitted for clarity and the weak secondary interactions are drawn as broken lines.

Table 2
Selected bond lengths (Å), distances (Å) and angles (°) for compound **1a**

Bond lengths			
W(1)–S(1)	2.204(5)	Ag(5)–S(7)	2.394(6)
W(1)–S(2)	2.195(5)	Ag(5)–S(8)	2.390(5)
W(1)–S(3)	2.197(5)	Ag(6)–S(8)	2.414(5)
W(1)–S(4)	2.202(5)	Ag(6)–S(9)	2.424(5)
Ag(2)–S(5)	2.390(5)	Ag(7)–S(9)	2.392(6)
Ag(2)–S(12)	2.380(5)	Ag(7)–S(10)	2.392(5)
Ag(3)–S(5)	2.446(5)	Ag(8)–S(10)	2.386(5)
Ag(3)–S(6)	2.453(5)	Ag(8)–S(11)	2.381(5)
Ag(4)–S(6)	2.416(5)	Ag(9)–S(11)	2.390(5)
Ag(4)–S(7)	2.416(6)	Ag(9)–S(12)	2.400(5)
Bond distances			
Ag(2)···S(2)	2.899(7)	Ag(7)–S(3)	2.929(5)
Ag(3)···S(1)	2.796(5)	Ag(8)–S(1)	3.101(5)
Ag(4)···S(3)	2.934(6)	Ag(9)–S(4)	2.933(7)
Ag(5)···S(2)	2.847(7)	Ag(3)–Ag(4)	3.022(6)
Ag(6)···S(4)	2.984(7)	Ag(5)–Ag(6)	3.184(4)
Bond angles			
S(2)–W(1)–S(1)	108.8(2)	S(10)–Ag(7)–S(9)	165.0(2)
S(2)–W(1)–S(3)	108.4(2)	S(11)–Ag(8)–S(10)	167.3(2)
S(2)–W(1)–S(4)	110.9(2)	S(11)–Ag(9)–S(12)	157.3(2)
S(3)–W(1)–S(1)	111.4(2)	Ag(2)–S(5)–Ag(3)	93.0(2)
S(3)–W(1)–S(4)	109.1(2)	Ag(4)–S(6)–Ag(3)	76.7(2)
S(4)–W(1)–S(1)	108.3(2)	Ag(5)–S(7)–Ag(4)	95.3(2)
S(12)–Ag(2)–S(5)	171.5(2)	Ag(5)–S(8)–Ag(6)	83.0(2)
S(5)–Ag(3)–S(6)	145.4(2)	Ag(7)–S(9)–Ag(6)	89.9(2)
S(7)–Ag(4)–S(6)	159.8(2)	Ag(8)–S(10)–Ag(7)	90.5(2)
S(8)–Ag(5)–S(7)	166.9(2)	Ag(8)–S(11)–Ag(9)	93.0(2)
S(8)–Ag(6)–S(9)	157.1(2)	Ag(2)–S(12)–Ag(9)	92.3(2)

is encapsulated in the Ag_8 cage. The coordination geometry about the W atom is tetrahedral with a slight distortion (angles of S–W–S range from 108.3(2)° to 111.4(2)°). The average bond length of W–S is 2.200 Å, which is similar with those reported in the compounds $[H_3NCH_2CH_2NH_3][WS_4]$ [36], $[H_3NCH_2CH_2CH_2NH_3][WS_4]$ [37] and $[PPh_4][WS_3(SH)]$ [38]. The distance between S atoms of the $[WS_4]^{2-}$ fragment and the Ag atoms ranges from 2.796(5) to 3.101(5) Å, revealing weak interactions [29–31], which are also demonstrated by the IR spectrum.

Up until now, there have been only a few crystal structures reported for monocyclic silver alkanethiolates or areneticthiolates AgSR, largely due to difficulties with insolubility and poor crystal habit [30]. One important method around this problem is to react them with small proportions of ligands that are bulky and structure terminating, in order to get the resulting compounds representing monocylic structures. For example, the structures of $Ag_6(SAr)_6(PPh_3)_5$ [39], $(Ag_8SCMeEt_2)_8(PPh_3)_2$, $(Ag_8SBu^t)_{14}(PPh_3)_4$ [30] and $(AgSPh)_7(dppm)_3$ [40] have been determined by employing PPh_3 or dppm as structure-terminating ligands. It is interesting and rare that a $[WS_4]^{2-}$ fragment is encapsulated in a monocyclic $Ag_8(SBu^t)_8$ cage via weak Ag···S interactions, as in compound **1a**, and it is the first example with this kind of structure in the W(Mo)/Ag/S system.

3.4. Description of the crystal structure of $\{[Et_4N][WOS_3Ag_2(S_2COEt)]\}_n$ (2)

The structure of the polymeric anion of **2** is depicted in Fig. 2 and the important bond lengths and angles are listed in Table 3. The cluster skeleton of the repeating unit consists of a butterfly OWS_3Ag_2 cluster, in which the W atom has basically retained the tetrahedral geometry of the free $[WOS_3]^{2-}$ anion. Two such butterfly fragments connected by a pair of ethylxanthato bridges form a double-butterfly dimer. Atom Ag2 is in an approximately trigonal planar environment, coordinated with two S atoms of the oxothiotungstate and one S atom from the bridging ethylxanthato ligand. The coordination environment of Ag1 is almost the same as that of Ag2 except that there is an additional weak Ag···S interaction [2.7917(9) Å] between Ag2 and S of the adjacent OWS_3Ag_2 butterfly unit. These weak Ag–S bonds link the double-butterfly dimers together to form a polymeric chain structure running

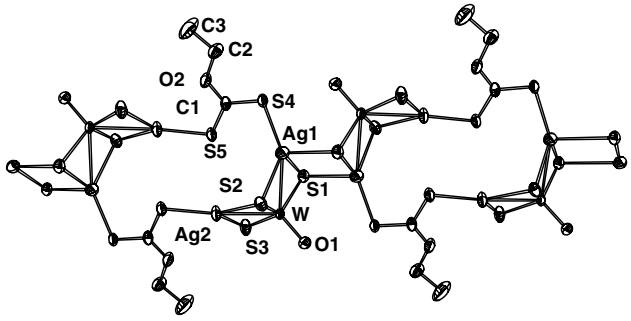


Fig. 2. Structure of the polymeric anion of **2**. The hydrogen atoms are omitted for clarity.

Table 3
Selected bond lengths (Å) and angles (°) for compound **2**

Bond lengths			
W–O(1)	1.726(2)	Ag(1)–S(1)	2.5614(9)
W–S(1)	2.2388(8)	Ag(1)–S(2)	2.5719(9)
W–S(2)	2.2751(9)	Ag(1)–S(1)[1]	2.7917(9)
W–S(3)	2.2210(8)	Ag(2)–S(5)[2]	2.4058(9)
W–Ag(1)	2.9726(6)	Ag(2)–S(2)	2.4884(8)
W–Ag(2)	2.9116(7)	Ag(2)–S(3)	2.5148(9)
Bond angles			
O(1)–W–S(1)	108.19(7)	S(2)–Ag(2)–S(3)	96.45(3)
O(1)–W–S(2)	107.11(7)	S(5)[2]–Ag(2)–S(2)	136.75(3)
O(1)–W–S(3)	107.74(7)	S(5)[2]–Ag(2)–S(3)	126.69(3)
S(1)–W–S(2)	113.34(3)	W–S(1)–Ag(1)	76.20(2)
S(3)–W–S(1)	108.09(3)	W–S(1)–Ag(1)[1]	99.84(3)
S(3)–W–S(2)	112.17(3)	W–S(2)–Ag(1)	75.38(2)
S(1)–Ag(1)–S(2)	94.57(2)	W–S(2)–Ag(2)	75.21(3)
S(4)–Ag(1)–S(1)	133.02(2)	Ag(1)–S(1)–Ag(1)[1]	82.33(3)
S(4)–Ag(1)–S(2)	126.07(3)	Ag(2)–S(2)–Ag(1)	104.91(3)
S(1)–Ag(1)–S(1)[1]	97.67(3)	W–S(3)–Ag(2)	75.59(3)
S(2)–Ag(1)–S(1)[1]	96.43(2)	S(4)–C(1)–S(5)	123.5(2)
S(4)–Ag(1)–S(1)[1]	99.67(3)		

Symmetry transformations used to generate equivalent atoms: [1] $-x+1, -y+2, -z$; [2] $-x+1, -y+1, -z$.

along crystallographic *b* axis. The W–Ag1 distance [2.9726(6) Å] is a little longer than that of W–Ag2 [2.9116(7) Å], but both of them are in the normal range for W/Ag/S clusters [41,42]. As observed in the Cu(I) clusters, the W–S bonds involving triply bonded S (average value 2.257 Å) are slightly longer than that of doubly bonded S [W–S3: 2.210 Å]. W/Ag/S clusters containing butterfly structures are not common, the only example is $WOS_3Ag_2(PPh_3)_3$ [43].

4. Supplementary material

Crystallographic data, excluding structure factors, have been deposited at the Cambridge Crystallographic Data center, CCDC reference numbers 253418 for **1a** and 248288 for **2**. Copies of this information may be obtained free of charge from the Director, CCDC, 12 Union Road, Cambridge, CB2 1EZ, UK (fax: +44-1223-336-033; email: deposit@ccdc.cam.ac.cn or www.ccdc.cam.ac.uk).

Acknowledgements

We thank the State Key Laboratory of Structural Chemistry, Fujian Institute of Research on the Structure of Matter, the Chinese Academy of Sciences (CAS), the Ministry of Science and Technology of China (001CB108906) and the National Science Foundation of China (20333070) for financial support.

References

[1] A. Müller, E. Diemann, R. Jostes, H. Bögge, Angew. Chem., Int. Ed. Engl. 20 (1981) 934.
[2] J. Sola, Y. Do, J.M. Berg, R.H. Holm, J. Am. Chem. Soc. 105 (1983) 105.
[3] S.M. Malinak, D. Coucouvanis, Prog. Inorg. Chem. 49 (2001) 599.
[4] E.D. Simhon, N.C. Baenziger, M. Kanatzidis, M. Draganjic, D. Coucouvanis, J. Am. Chem. Soc. 103 (1981) 1218.
[5] J.P. Lang, Q.F. Xu, R.X. Yuan, B.F. Abrahams, Angew. Chem., Int. Ed. Engl. 43 (2004) 4741.
[6] S. Shi, W. Ji, S.H. Tang, J.P. Lang, X.Q. Xin, J. Am. Chem. Soc. 116 (1994) 3615.
[7] J.P. Lang, H. Kawaguchi, S. Ohnishi, K. Tatsumi, Chem. Commun. (1997) 405.
[8] X.T. Wu, P.C. Chen, S.W. Du, N.Y. Zhu, J.X. Lu, J. Cluster Sci. 5 (1994) 265.
[9] Q. Huang, X.T. Wu, T.L. Sheng, Q.M. Wang, Inorg. Chem. 34 (1995) 4931.
[10] H. Yu, W.J. Zhang, X.T. Wu, T.L. Sheng, Q.M. Wang, P. Lin, Angew. Chem., Int. Ed. Engl. 37 (1998) 2520.
[11] S.F. Gheller, T.W. Hambley, J.R. Rodgers, R.T.C. Brownlee, M.G. O'Connor, M.R. Snow, A.G. Wedd, Inorg. Chem. 23 (1984) 2519.
[12] Q. Huang, X.T. Wu, J.X. Lu, Inorg. Chem. 35 (1996) 7445.
[13] Q. Huang, X.T. Wu, J.X. Lu, Chem. Commun. (1997) 703.
[14] L. Chen, X.T. Wu, X.C. Gao, W.J. Zhang, P. Lin, J. Chem. Soc., Dalton Trans. (1999) 4303.
[15] L. Chen, H. Yu, L.M. Wu, W.X. Du, X.C. Gao, P. Lin, W.J. Zhang, C.P. Cui, X.T. Wu, J. Solid State Chem. 151 (2000) 286.
[16] Y.C. Liang, S.F. Lu, Z.X. Huang, Q.J. Wu, J. Cluster Sci. 13 (2002) 7.
[17] Z.H. Li, S.W. Du, X.T. Wu, J. Chem. Soc., Dalton Trans. (2004) 2438.
[18] Z.H. Li, S.W. Du, X.T. Wu, Inorg. Chem. 43 (2004) 4776.
[19] J.W. McDonald, G.D. Friessen, L.D. Rosenheim, W.E. Newton, Inorg. Chim. Acta 72 (1983) 205.
[20] G.M. Sheldrick, SHELXS-97, Program for X-ray Crystal Structure Solution, University of Göttingen, Göttingen, 1997.
[21] E. Diemann, A. Müller, Coord. Chem. Rev. 10 (1973) 79.
[22] C. Zhang, G.C. Jin, J.X. Chen, X.Q. Xin, K.P. Qian, Coord. Chem. Rev. 213 (2001) 51.
[23] R. Colton, Coord. Chem. Rev. 62 (1985) 145.
[24] A. Müller, W. Jaegermann, W. Hellman, J. Mol. Struct. 100 (1983) 559.
[25] Y.Y. Niu, H.G. Zhang, H.W. Hou, X.Q. Xin, Coord. Chem. Rev. 248 (2004) 169.
[26] G. Sakane, G. Shibahare, H.W. Hou, X.Q. Xin, S. Shi, Inorg. Chem. 34 (1995) 4785.
[27] H.W. Hou, X.Q. Xin, S. Shi, Coord. Chem. Rev. 153 (1996) 25.
[28] K. Nomiya, R. Noguchi, C. Kato, Chem. Lett. (2000) 162.
[29] I. Dance, L. Fitzpatrick, M. Scudder, D. Craig, J. Chem. Soc., Chem. Commun. (1984) 17.
[30] I.G. Dance, L.J. Fitzpatrick, D.C. Craig, M.L. Scudder, Inorg. Chem. 28 (1989) 1853.
[31] K.L. Tang, M. Aslam, E. Block, T. Nicholson, J. Zubieta, Inorg. Chem. 26 (1987) 1488.
[32] E. Block, M. Gernon, H. Kang, G. Ofori-Okai, J. Zubieta, Inorg. Chem. 28 (1989) 1263.
[33] A.F. Wells, Structural Inorganic Chemistry, 4th ed., Oxford University Press, London, 1975, p. 1015.
[34] M. Jansen, Angew. Chem., Int. Ed. Engl. 26 (1987) 1098.
[35] P. Pyykko, Chem. Rev. 97 (1997) 597.
[36] B.R. Srinivasan, S.N. Dhuri, C. Näther, W. Bensch, Acta Cryst. E 58 (2002) m622.
[37] B.R. Srinivasan, S.N. Dhuri, C. Näther, W. Bensch, Acta Cryst. C 59 (2003) m124.
[38] M. Parvez, P.M. Boorman, M.P. Wang, Acta Cryst. C 53 (1997) 413.
[39] I.G. Dance, L.J. Fitzpatrick, M.L. Scudder, Inorg. Chem. 23 (1984) 2276.
[40] X.J. Wang, T. Lange, D. Fenske, B.S. Kang, Z. Anorg. Allg. Chem. 628 (2002) 1158.
[41] A. Müller, H. Bögge, E.K. Ahlborn, Z. Naturforsch B 34 (1979) 1698.
[42] A. Müller, H. Bögge, E.K. Ahlborn, Inorg. Chem. 18 (1979) 2301.
[43] J.H. Wu, Master Thesis, Fujian Institute of Research on the Structure of Matter, Chinese Academy of Sciences, 1993.

Available online at www.sciencedirect.com
SCIENCE DIRECT®
Polyhedron 24 (2005) 487–494
POLYHEDRON
www.elsevier.com/locate/poly

Structure and magnetic properties of one-dimensional metal complexes constructed from alternating dicyanamide linked through binuclear metal tetra-2-pyridylpyrazine subunits

Guang-Yuan Hsu [a], Chin-Wang Chen [a], Sung-Chung Cheng [a], Shin-Huang Lin [a], Ho-Hsiang Wei [a,*], Chin-Jhin Lee [b,*]

[a] *Department of Chemistry, Tamkang University, Ying-Chung Road, Tamsui 25137, Taiwan*
[b] *Ching Kuo Institute of Management and Health, Kee Lung 203, Taiwan*

Received 10 August 2004; accepted 5 December 2004
Available online 2 February 2005

Abstract

The syntheses, structures and magnetic properties of three 1-D complexes with the formulae $[Co_2(tppz)(dca)_4]$ (**1**), $[Ni_2(tppz)(dca)_4]C_2H_5OH$ (**2**) and $[Cu_2(tppz)(dca)(Cl)_2](dca)\cdot H_2O$ (**3**), where tppz = tetra-2-pyridylpyrazine and dca = dicyanamide, are described. Complexes **1**–**3** are one-dimensional metal-complexes. In **1** the dinuclear tppz-chelated Co(II) centers are linked by two double $\mu_{1,5}$-dca ligands. Compound **2** forms a ladder-like structure in which the rungs are formed by bis-chelating tppz bridged dinuclear Ni(II) ions and the uprights by $\mu_{1,5}$-dca units. Compound **3** forms a helical chain structure which consists of alternately single $\mu_{1,5}$-dca linked dinuclear tppz-chelated Cu-centers. The temperature dependence of magnetic measurements show antiferromagnetic couplings between two metal ions with a pathway through tppz and $\mu_{1,5}$-dca in all cases, with $J = -1.10\ cm^{-1}$, $J' = -0.05\ cm^{-1}$ for **1**, $J = -1.28\ cm^{-1}$, $J' = -0.11\ cm^{-1}$ and $D = 9.50\ cm^{-1}$ for **2**, and $J = -10.26\ cm^{-1}$, $J' = -0.06\ cm^{-1}$ for **3**.
© 2005 Elsevier Ltd. All rights reserved.

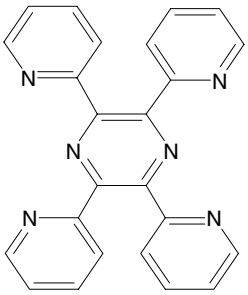
Keywords: Crystal structure; Magnetic properties; Dicyanamide; Tetra-2-pyridylpyrazine; Metal complexes

1. Introduction

The dicyanamide (dca) ligand, $N(CN)_2^-$, possessing three potential donor sites, has been shown to coordinate to metal ions in various modes [1–13]. When it functions as a terminal ligand, usually one of the two nitrile nitrogens coordinates to the metal ion [2,12]. However, in a recent example, preferential coordination of the amide nitrogen has been observed [3]. As a bridging ligand, five types of bridging modes have been structurally characterized so far [1–11,13]; two connecting [2–8], three connecting [1,9,10], four connecting [13] and even five connecting [11]. Furthermore, the introduction of auxiliary ligands with multidentate sites into the metal–dca moiety has led to the design of a series of metal complexes with a wide variety of magneto-structural topologies, e.g., one-dimensional chain [3,4], two-dimensional sheet [5] and several types of three-dimensional networks [4d,6]. Taking into account the above-mentioned aspects, in the present work, three metal complexes with dca and the auxiliary ligand tetra-2-pyridylpyrazine (tppz), $[Co_2(tppz)(dca)_4]$ (**1**), $[Ni_2(tppz)(dca)_4](C_2H_5OH)$ (**2**) and $[Cu_2(tppz)(dca)(Cl)_2](dca)(H_2O)$ (**3**) have been synthesized and magnetostructurally characterized. The ligand tppz (Scheme 1) was first reported by Goodwin and Lyons [14] and there have been reports on the synthesis and characterization of

* Corresponding authors. Tel.: +886 2 26202821; fax: +886 2 26209924 (H.H. Wei), Tel.: +886 2 24373093 (C.-J. Lee).
E-mail addresses: tkwei@mail.tku.edu.tw (H.-H. Wei), cjlee@ems.cku.edu.tw (C.-J. Lee).

0277-5387/$ - see front matter © 2005 Elsevier Ltd. All rights reserved.
doi:10.1016/j.poly.2004.12.010



Tppz

Scheme 1.

some mono-, dinuclear and oligomeric transition metal complexes [15–19], most of which deal with their redox, luminescence and mixed-valence properties. Recently, one-, two- and three-dimensional composite materials constructed from molybdophosphonate and polyoxomolybdate subunits linked through binuclear copper tppz ligands have been reported [20]. To our knowledge there is as yet no investigation on complexes containing both dca and tppz ligands.

2. Experimental

2.1. Synthesis

Nickel(II) perchlorate hexahydrate, cobalt(II) chloride hexahydrate, cupric chloride dihydrate, sodium dicyanamide and tetra-2-pyridylpyrazine were purchased from commercial sources (Aldrich) and used as received.

2.1.1. Synthesis of the complex $[Co_2(tppz)(dca)_4]$ (1)

This compound is obtained as dark red crystalline solid by slow addition of a methanol solution (20 cm^3) containing sodium dicyanamide (190 mg, 2 mmol) to a methanolic solution of $CoCl_2 \cdot 6H_2O$ (0.366 g, 1 mmol) and tetra-2-pyridylpyrazine (tppz) (200 mg, 0.5 mmol). After refluxing for 24 h, the solution was left standing at room temperature. Dark red prismatic crystals suitable for single crystal X-ray analysis appeared after 2 weeks from the resulting solution. Yield: 75%. *Anal.* Calc. for $C_{32}H_{16}Co_2N_{18}$: C, 49.8; H, 2.09; N, 32.7. Found: C, 48.9; H, 2.08; N 31.8%. IR (KBr/cm^{-1}) ν(CN): 2188, 2246, 2343.

2.1.2. Synthesis of the complex $[Ni_2(tppz)(dca)_4]C_2H_5OH$ (2)

To a methanol solution (20 cm^3) of $NiClO_4 \cdot 6H_2O$ (0.366 g, 1 mmol) and tppz (400 mg, 1 mmol) in 20 cm^3 methanol, a solution of $NaN(CN)_2$ (380 mg, 4 mmol) in 20 cm^3 water was added. The solution was stirred at 25 °C for 24 h and then left standing at room temperature for several days. The resulting solution was filtered to remove a green precipitate, which was dissolved in *N,N*-dimethylformamide (dmf)/CH_3OH for crystal growth. After several days dark green crystals of **2** were deposited. Yield: 70%. *Anal.* Calc. for $C_{34}H_{22}Ni_2N_{18}O$: C, 50.04; H, 2.71; N, 30.9. Found: C, 49.68; H, 2.88; N 31.03%. IR (KBr/cm^{-1}) ν(CN): 2190, 2247, 2346.

2.1.3. Synthesis of the complex $[Cu_2(tppz)(dca)(Cl)_2](dca) \cdot H_2O$ (3)

To a methanol solution (10 cm^3) of $CuCl_2 \cdot 2H_2O$ (140 mg, 1 mmol) and tppz (200 mg, 0.5 mmol) in 30 cm^3 methanol, $NaN(CN)_2$ (190 mg, 2 mmol) in 20 cm^3 water was added. The mixture was stirred at 25 °C for 24 h and then left standing at room temperature. After several days dark green block like crystals of **3** were obtained. Yield: 76%. *Anal.* Calc. for $C_{28}H_{20}Cl_2Cu_2N_{12}O_2$: C, 44.6; H, 2.67; N, 22.3. Found: C, 44.8; H, 2.64; N 21.8%. IR (KBr/cm^{-1}) ν(CN): 2182, 2252, 2320.

Table 1
Crystal data and structure refinement for $[Co_2(tppz)(dca)_4]$ (**1**), $[Ni_2(tppz)(dca)_4]C_2H_5OH$ (**2**) and $[Cu_2(tppz)(dca)(Cl)_2](dca) \cdot H_2O$ (**3**)

	1	**2**	**3**
Formula	$C_{32}H_{16}Co_2N_{18}$	$C_{34}H_{22}Ni_2N_{10}$	$C_{28}H_{20}Cl_2Cu_2N_{12}O_2$
Formula weight	770.49	816.12	754.54
Space group	*C2/c*	*C2/c*	*Pcca*
a (Å)	12.7091(5)	18.5179(13)	18.375(6)
b (Å)	12.5614(5)	8.6003(6)	10.674(4)
c (Å)	20.8441(8)	22.2782(15)	15.025(4)
β (°)	100.989(1)	104.188(2)	90
V (Å^3)	3266.6(2)	3440.1(4)	2947(2)
Z	4	4	4
D_{calc} (Mg m^{-3})	1.567	1.576	1.7031
λ (Mo Kα) (Å)	0.71073	0.71073	0.71073
T (K)	295(2)	295(2)	293(2)
Collected reflections	11366	13986	2591
Independent reflections	3332 (R_{int} = 0.0480)	3954 (R_{int} = 0.0291)	2590 (R_{int} = 0.0131)
R_1	0.0370	0.0406	0.0300
R_w	0.0565	0.0963	0.0801

2.2. Physical measurements

IR spectra were recorded on a Bio-Rad FTS-40 FTIR spectrophotometer with samples as KBr disks in the 400–4000 cm^{-1} region. Variable-temperature (2–300 K) magnetic susceptibility measurements under fixed field strength of 1 T were carried out with a Quantum Design MPMS SQUID magnetometer. Diamagnetic corrections were estimated from Pascal's constants [21].

2.3. X-ray crystal structure analysis

Intensity data were collected on a Bruker SMART CCD diffractometer for **1** and **2**, and a Siemens P4 diffractometer for **3** in the ω–2ϑ scan mode at 295 K using graphite monochromated Mo Kα radiation ($\lambda = 0.71073$ Å). The structures were solved by direct and Fourier methods and refined by full-matrix least-squares methods based on F^2 using the programs SHELXS-97 and SHELXL-97 [22]. All non-hydrogen atoms were readily located and refined using anisotropic thermal parameters. Crystallographic details for the structures of **1**–**3** are summarized in Table 1.

3. Results and discussion

3.1. Description of the crystal structures

The selected bonds lengths and angles of complexes **1**, **2** and **3** are listed in Tables 2–4, respectively. The structure of **1** consists of 1-D alternating chains $[Co_2(tppz)(dca)_4]_n$ along the *c*-axis (Figs. 1 and 2), in which the dinuclear tppz-chelated Co(II) units are linked by two double $\mu_{1,5}$-dca groups. As illustrated in Fig. 1, each Co atom is coordinated with a distorted octahedral geometry by six N atoms (three from a tppz bridged ligand, two from $\mu_{1,5}$-dca groups and one from a terminal dca). The $[Co_2(tppz)(dca)_4]$ subunit of **1** is located at a crystallographic center of symmetry. The Co(1)···Co(1b) distance through the tppz ligand is 6.879 Å, whereas the Co(1)···Co(1a) distance through the $\mu_{1,5}$-dca bridge is 7.377 Å. The central pyrazine ring is twisted by 13.2° (defined by the dihedral angle between the planes made up of atoms C(6) N(2) C(7) and C(6B) N(2B) C(7B)), and the planes of coordinated pyridyl rings (N(1)–C(1)–C(2)–C(3)–C(4)–C(5) and N(3)–C(8)–C(9)–C(10)–C(11)–C(12)) are inclined to one another by 7.3°.

The compound $[Ni_2(tppz)(dca)_4]C_2H_5OH$ (**2**) forms a ladder-like 1-D alternating polymer structure along the *b*-axis (Figs. 3 and 4), in which the rungs are formed by centrosymmetric, tridentate bis-chelating tppz bridges and the uprights by two end-to-end bridging $\mu_{1,5}$-dca units (Fig. 3). In addition, the C_2H_5OH molecules are inserted inside the rungs in the ladder-like complex **2** (Fig. 4). The nickel atom is best described as distorted octahedral, the equatorial positions being occupied by four nitrogen atoms: three from tppz

Table 2
Selected bond lengths (Å) and angles (°) for $[Co_2(tppz)(dca)_4]$ (**1**)

Bond lengths			
Co(1)–N(1)	2.140(2)	Co(1)–N(2)	2.114(2)
Co(1)–N(3)	2.156(2)	Co(1)–N(4)	2.044(2)
Co(1)–N(7)	2.125(2)	Co(1)–N(6a)	2.141(2)
Bond angles			
N(4)–Co(1)–N(2)	175.86(9)	N(1)–Co(1)–N(3)	149.48(7)
N(1)–Co(1)–N(4)	108.07(9)	N(7)–Co(1)–N(6a)	175.98(9)
N(4)–Co(1)–N(3)	102.44(9)	C(1)–N(1)–Co(1)	124.7(2)
C(5)–N(1)–Co(1)	117.0(2)	C(7)–N(2)–Co(1)	118.1(2)
C(6)–N(2)–Co(1)	118.1(2)	C(12)–N(3)–Co(1)	125.1(2)
C(8)–N(3)–Co(1)	117.1(2)	C(15)–N(7)–Co(1)	148.4(2)
C(13)–N(4)–Co(1)	168.9(2)	C(16)–N(8)–Co(1a)	152.3(2)
N(4)–Co(1)–N(7)	93.74(8)	N(2)–Co(1)–N(7)	89.28(8)
N(2)–Co(1)–N(1)	74.83(8)	N(7)–Co(1)–N(1)	88.28(8)
N(4)–Co(1)–N(6a)	86.43(8)	N(2)–Co(1)–N(6a)	90.76(8)
N(3)–Co(1)–N(6a)	94.60(8)	N(1)–Co(1)–N(6a)	87.86(8)
N(2)–Co(1)–N(3)	74.72(8)		

Table 3
Selected bond lengths (Å) and angles (°) for $[Ni_2(tppz)(dca)_4]C_2H_5OH$ (**2**)

Bond lengths			
Ni(1)–N(1)	2.102(2)	Ni(1)–N(2)	2.067(2)
Ni(1)–N(3)	2.036(2)	Ni(1)–N(4)	2.018(2)
Ni(1)–N(7)	2.079(2)	Ni(1)–N(9)	2.084(2)
Bond angles			
N(4)–Ni(1)–N(3)	176.54(8)	N(7)–Ni(1)–N(9)	173.58(9)
N(2)–Ni(1)–N(1)	155.34(8)	N(4)–Ni(1)–N(2)	102.65(9)
N(4)–Ni(1)–N(1)	102.01(9)	C(1)–N(1)–Ni(1)	125.4(2)
C(5)–N(1)–Ni(1)	113.7(2)	C(8)–N(2)–Ni(1)	116.2(2)
C(7)–N(3)–Ni(1)	118.0(2)	C(12)–N(2)–Ni(1)	124.1(2)
C(6)–N(3)–Ni(1)	117.8(2)	C(13)–N(4)–Ni(1)	167.3(2)
C(15)–N(7)–Ni(1)	157.9(2)	N(3)–Ni(1)–N(2)	77.67(7)
N(4)–Ni(1)–N(7)	87.71(9)	N(3)–Ni(1)–N(7)	88.82(8)
N(2)–Ni(1)–N(7)	96.15(9)	N(3)–Ni(1)–N(9)	93.12(8)
N(4)–Ni(1)–N(9)	90.33(8)	N(3)–Ni(1)–N(1)	77.74(7)
N(7)–Ni(1)–N(1)	85.23(8)	N(2)–Ni(1)–N(9)	90.25(8)
N(9)–Ni(1)–N(1)	89.20(8)		

Table 4
Selected Bond lengths (Å) and Angles (°) for $[Cu_2(tppz)(dca)(Cl)_2](dca)\cdot H_2O$ (**3**)

Bond lengths			
Cu(1)–N(1)	1.999(2)	Cu(1)–N(2)	1.980(2)
Cu(1)–N(3)	2.016(2)	Cu(1)–N(4)	1.996(2)
Cu(1)–Cl(1)	2.388(2)		
Bond angles			
N(2)–Cu(1)–N(4)	141.14(9)	N(1)–Cu(1)–N(3)	157.98(8)
N(2)–Cu(1)–Cl(1)	109.06(6)	N(4)–Cu(1)–Cl(1)	109.80(7)
C(8)–N(3)–Cu(1)	114.9(2)	C(12)–N(3)–Cu(1)	125.7(2)
C(1)–N(1)–Cu(1)	124.1(2)	C(5)–N(1)–Cu(1)	116.2(2)
C(6)–N(2)–Cu(1)	117.9(2)	C(7)–N(2)–Cu(1)	116.7(2)
N(2)–Cu(1)–N(1)	79.66(9)	N(4)–Cu(1)–N(1)	95.86(9)
N(2)–Cu(1)–N(3)	79.75(8)	N(4)–Cu(1)–N(3)	95.25(9)
N(3)–Cu(1)–Cl(1)	98.15(7)	N(1)–Cu(1)–Cl(1)	95.88(7)

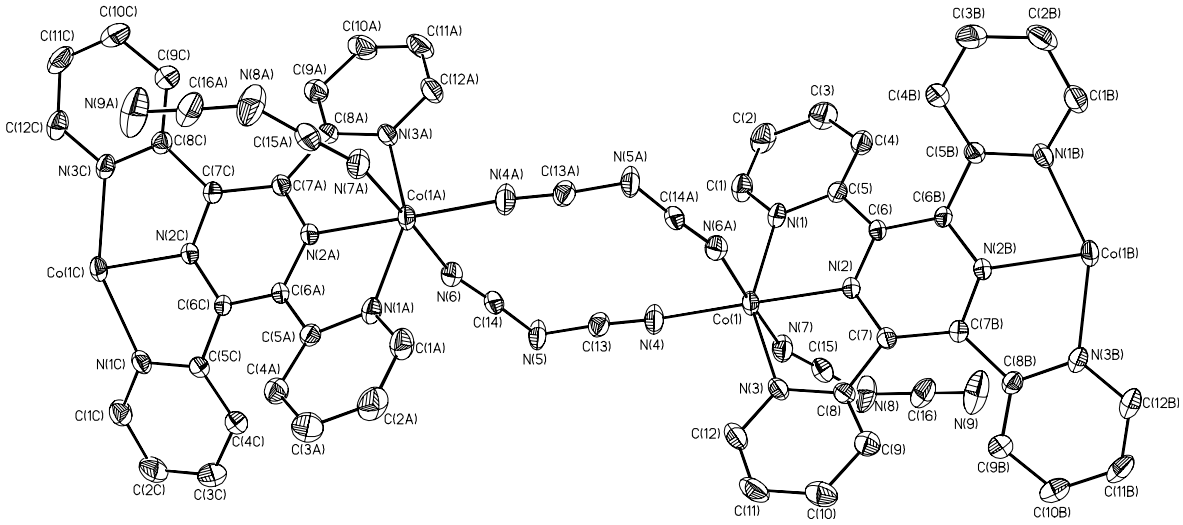


Fig. 1. Perspective drawing of complex **1** with the atom numbering scheme. Thermal ellipsoids are drawn at the 30% probability level.

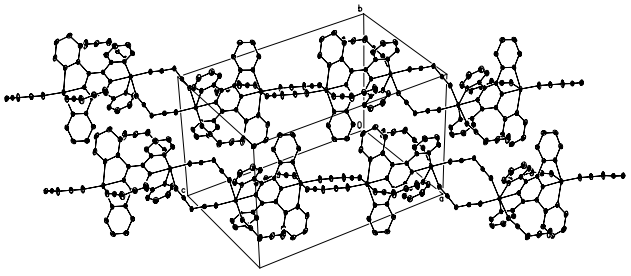


Fig. 2. Unit cell packing view of the formation of the one-dimensional molecular chain in complex **1** along the *c*-axis.

(Ni(1)–N(1) 2.102(2), Ni(1)–N(2) 2.067(2) and Ni(1)–N(3) 2.0358(18) Å), and one from monodentate dca (Ni(1)–N(4) 2.018(2) Å). The apical positions are occupied by two bridging $\mu_{1,5}$-dca (Ni(1)–N(7) 2.079(2) and Ni(1)–N(9) 2.084(2) Å). The Ni(1)···Ni(1a) distance through the tppz ligand is 6.709 Å, whereas the Ni(1)···Ni(1)′ distance through the $\mu_{1,5}$-dca bridge is 8.660 Å. The central pyrazine ring is twisted by 9.9° and the coordinated pyridyl rings are inclined to one another by 12.7°.

The crystal structure of **3** consists of uniform cationic $[Cu_2(tppz)(dca)(Cl)_2]_n^{n+}$ helical chains (Figs. 5 and 6) extending along the *a*-axis, the dca units serving as an asymmetric $\mu_{1,5}$-dca bridging ligand to link the dinuclear Ni–tppz units, such that the convex tppz bow of one chain extends into the concave section of the neighbouring chain (Fig. 6). As seen in Fig. 6, the copper atom has

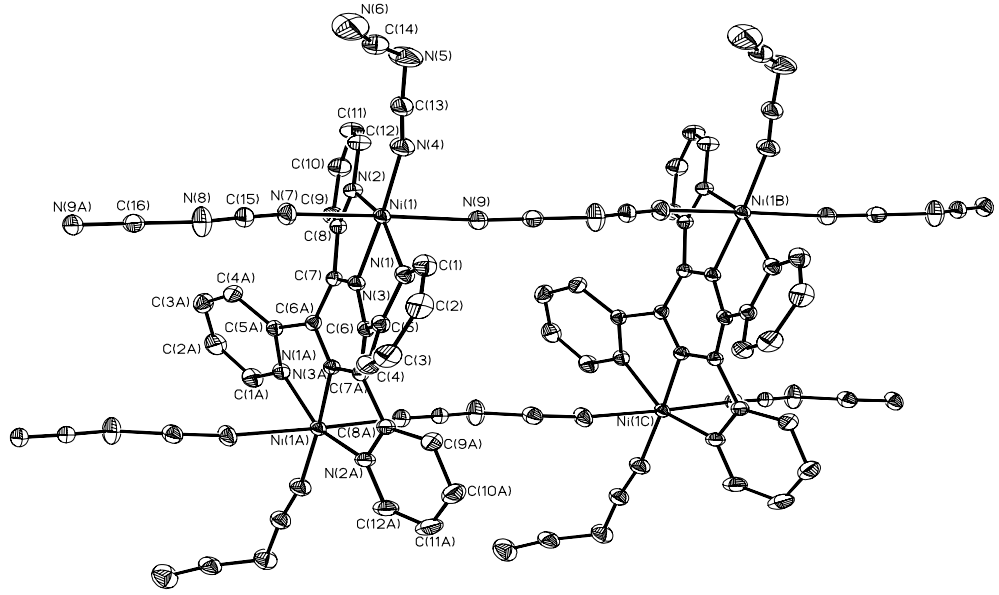


Fig. 3. Perspective drawing of complex **2** with the atom numbering scheme. Thermal ellipsoids are drawn at the 30% probability level. The solvent ethanol molecule was omitted for clarity.

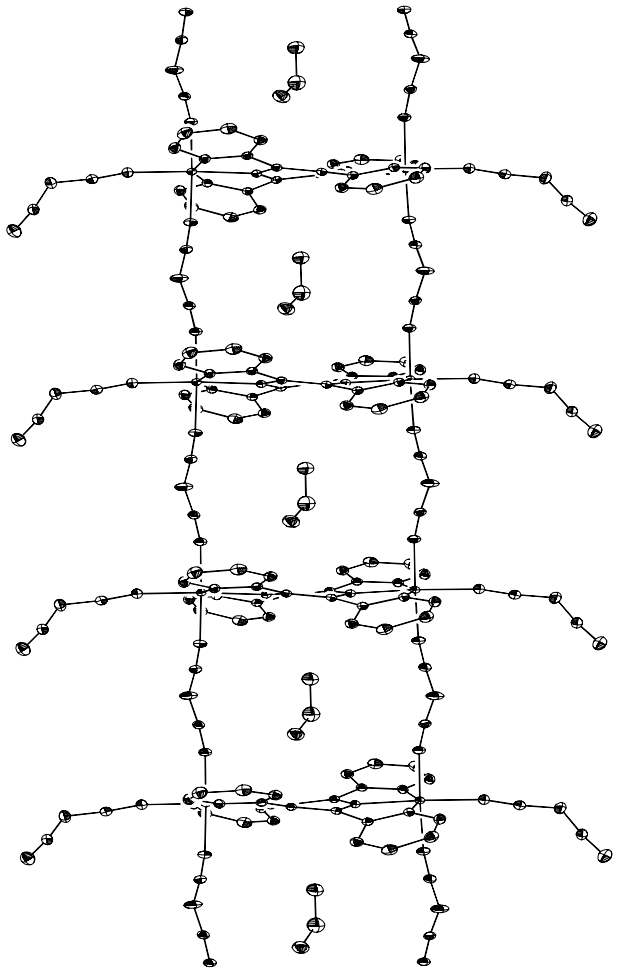


Fig. 4. One-dimensional ladder-like type chain of **2** along the *c*-axis (the solvent ethanol molecules are inserted inside the lattice).

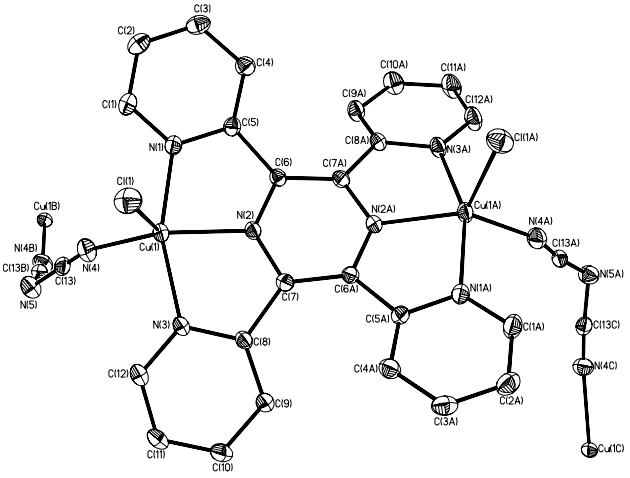


Fig. 5. Perspective view of complex **3** with the atom numbering scheme. Thermal ellipsoids are drawn at the 30% probability level. Anion dca and H_2O molecules are removed for clarity.

a distorted square pyramidal coordination geometry with three tppz nitrogen atoms [Cu(1)–N(1) 1.999(2), Cu(1)–N(2) 1.980(2) and Cu(1)–N(3) 2.016(2) Å] and

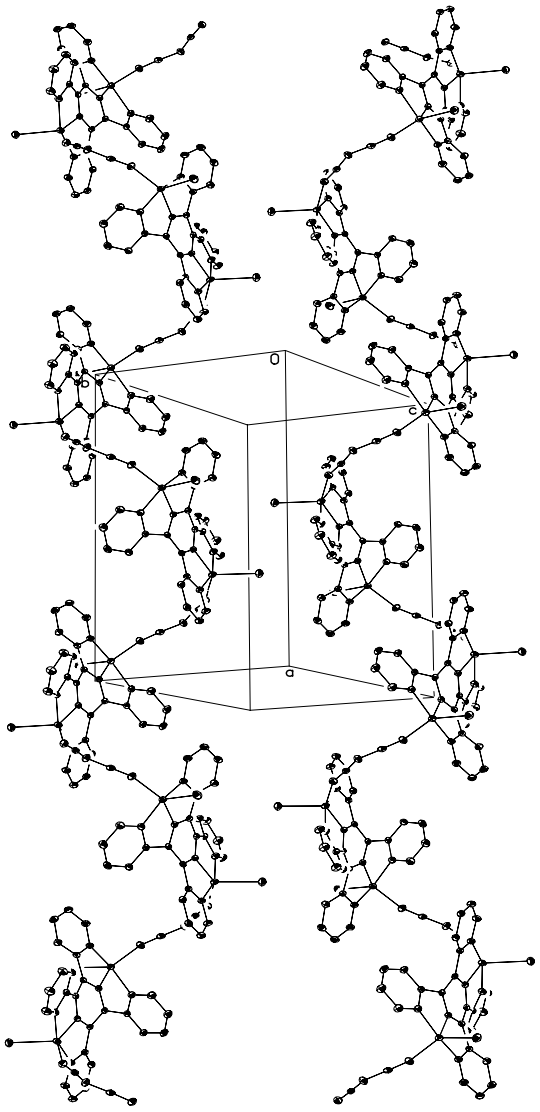


Fig. 6. Perspective view of two helix forms of the one-dimensional chain of **3** with the dca linked Cu–tppz–Cu framework along the *a*-axis.

one $\mu_{1,5}$-dca nitrogen atom [Cu(1)–N(4) 1.996(2) Å] in the equatorial positions and a chloride [Cu(1)–Cl(1) 2.3878(11) Å] in the apical position. The equatorial plane has significant tetrahedral distortion with the copper atom displaced by 0.457 Å from this plane in the direction towards the apical ligand. The Cu(1)···Cu(1a) distance through the tppz ligand is 6.560 Å, whereas the Cu(1)···Cu(1b) distance through the $\mu_{1,5}$-dca bridge is 7.604 Å. The central pyrazine ring is twisted by 10.7° and the coordinated pyridyl rings are inclined to one another by 11.3°.

3.2. Magnetic properties

The magnetic properties of the complexes **1**–**3** in the form of $\chi_m T$ versus T plots (χ_m is the magnetic susceptibility per metal ion) are shown in Fig. 7. For **1**, the value

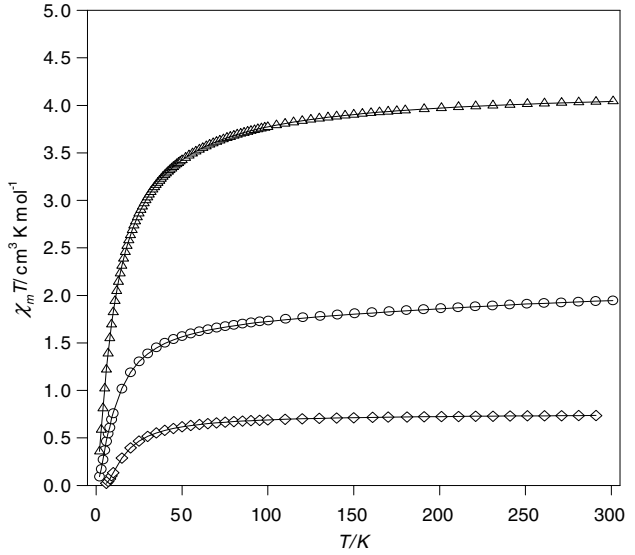


Fig. 7. Temperature dependence of $\chi_m T$ for complexes **1** (-△-), **2** (-○-), and **3** (-◇-) The solid lines are calculated with the fitted parameters reported in the text.

of $\chi_m T$ at 300 K is 4.12 cm^3 mol^{-1} K, as expected for two magnetically isolated spin systems of $S = 3/2$. When the sample is cooled, the $\chi_m T$ values decrease slowly from 300 K, more quickly below 50 K, and drop to 0.20 cm^3 mol^{-1} K down to 2 K. This is in agreement with antiferromagnetic interactions in compound **1**. To fit quantitatively the magnetic data for **1**, we first considered the exchange interaction as the leading term corresponding to the alternating chain with the nearest neighbor exchange interactions described by the spin Hamiltonian:

$$H = -J_1 \sum S_{2i} S_{2i+1} - J_2 \sum S_{2i+1} S_{2i+2} \quad [23]. \tag{1}$$

However, fitting the data with this model gave poor results. Thus, we used the simple model of two spins $S_1 = S_2 = 3/2$ of a Hamiltonian $H = -2JS_1S_2$ with an assumed interdimer exchange interaction (J') pathway through the dca bridges. The final expressions of the temperature dependence of magnetic susceptibility are given as Eqs. (1) and (2):

$$\chi_{\text{dimer}} = \frac{2N\mu_B^2 g^2}{kT}\left[\frac{e^{-10x} + 5e^{-6x} + 14}{e^{-12x} + 3e^{-10x} + 5e^{-6x} + 7}\right], \tag{2}$$

where z is the number of nearest neighbors of the dimers of **1** (2 in this case). An excellent simulation of the experimental magnetic data using Eq. (1) is obtained with $J = -1.10$ cm^{-1}, $J' = -0.05$ cm^{-1}, $g = 2.05$ and the agreement factor $R = 2.0 \times 10^{-5}$ which is defined as

$$\left[\sum\{(\chi_M T)_{obs} - (\chi_M T)_{calc}\}^2 / \sum (\chi_M T)_{obs}^2\right].$$

The results show that the low magnetic coupling constants of J and J' by a pathway through tppz and $\mu_{1,5}$-dca, respectively, are weak antiferromagnetic interactions between cobalt ions.

The $\chi_m T$ versus T plots for **2** are also shown in Fig. 7. The $\chi_m T$ value decreases gradually with decreasing temperature from 1.2 cm^3 mol^{-1} K at 300 K to 0.05 cm^3 mol^{-1} K at 2 K, indicating the presence of antiferromagnetic exchange interactions between the nickel ions in **2**. Considering the structural results, the fitting of the magnetic data of this alternating ladder-like chain of **2** was also attempted using the magnetic susceptibility equation obtained from the alternating form of $H = -J_1\sum S_{2i}S_{2i+1} - J_2\sum S_{2i+1}S_{2i+2}$ [23]. The least-squares fitting of the experimental data to the equation for an alternating chain did not afford reasonable results, especially in the low temperature range. Finally, the experimental magnetic susceptibility data were least-squares fitted to the theoretical expression with zero-field splitting for a magnetic interaction between two $S_1 = S_2 = 1$ ions given by Ginsberg et al. [24], from the Hamiltonian

$$H = -2JS_1S_2 - D(S_{1z}^2 + S_{2z}^2) - g\mu_B H(S_1 + S_2) - zJ'S\langle S\rangle. \tag{3}$$

In which J is the intradimer (Ni–tppz–Ni) exchange parameter, D is the single ion zero-field splitting, zJ' is the effective interdimer exchange pathway through dca bridges (Ni–dca–Ni), z is the number of nearest neighbors of the dimers of **2** (2 in this case) The resulting χ_m expression is

$$\chi_m = (2Ng^2\mu_B^2/3k)[F_1/(T - 4zJ'F_1) + 2F'/(1 - 4zJ')], \tag{4}$$

where F_1 and F' are functions of temperature, zero-field splitting and the intradimer exchange parameter J. The best fitting parameters obtained from minimizing R were $J = -1.28$ cm^{-1}, $J' = -0.11$ cm^{-1} $D = 9.50$ cm^{-1} $g = 2.21$ and $R = 2.0 \times 10^{-4}$. Here, J and J' are the representative magnetic coupling constants for pathways through tppz and $\mu_{1,5}$-dca, respectively.

For complex **3** the $\chi_m T$ versus T plot is shown in Fig. 7, the value of $\chi_m T$ per copper(II) ion decreases gradually on cooling. The $\chi_m T$ values decrease slowly from 0.72 cm^3 mol^{-1} K at 300 K, more quickly below 100 K and tend to 0.08 cm^3 mol^{-1} K down to 2 K. These features are characteristic of a weak antiferromagnetic interaction between a pair of copper(II) ions. We have accordingly analyzed the magnetic data through a numerical expression in a zero field appropriate for an alternating polymeric chain coupling system of $S = 1/2$ given by Hatfield [21a,25]. However, fitting the data with this model gave poor results, consequently, the magnetic data of **3** were analyzed by the use of the Bleaney–Bowers expression (Eqs. (5) and (6)) with interdimer exchange interactions (1) [26] for the exchange coupling in a two spin $S = 1/2$ system.

$$\chi_m = \frac{\chi_{dimer}}{[1 - (2zJ'/N\mu_B^2 g^2)]\chi_{dimer}}, \quad (5)$$

$$\chi_{dimer} = (Ng^2\mu_B^2/kT)[3 + \exp(-2J/kT)]^{-1}. \quad (6)$$

The best-fit parameters obtained through this procedure are $J = -10.26\ cm^{-1}$, $J' = -0.06\ cm^{-1}$, $g = 2.01$ and $R = 2.0 \times 10^{-5}$. Where J and J' also represent magnetic coupling constants of pathways through tppz and $\mu_{1,5}$-dca, respectively.

The results of the present system show that the J values ($J = -1.10\ cm^{-1}$ for **1**, $-1.28\ cm^{-1}$ for **2** and $-10.26\ cm^{-1}$ for **3**) are higher than those of J' ($-0.05\ cm^{-1}$ for **1**, $-0.11\ cm^{-1}$ for **2** and $-0.06\ cm^{-1}$), indicating the tppz bridge should be a better superexchange mediator than the $\mu_{1,5}$-dca bridge. The $\mu_{1,5}$-dca bridge behaves as a poor magnetic mediator, and the magnitude of exchange integrals (J) has been observed in the range -0.05 to $-0.11\ cm^{-1}$, which are in agreement with those in the range -0.06 to $-0.17\ cm^{-1}$ [1–13]. Although no magnetic parameters for polymeric metal complexes with tppz bridging ligands have been reported, we examined the values of J for complexes **1**–**3** in relation to the magnitude of exchange couplings reported for the dinuclear tppz bridged system. According to the literature the J values of magnetic exchange interaction pathways through (i) the pyrazine-bridged metal complexes show negligible or very low values ($J = -3.5$ to $0\ cm^{-1}$) [27], or (ii) the tppz-bridged dinuclear metal complexes show low values ($J \sim 4.0\ cm^{-1}$, $D \sim 10\ cm^{-1}$) for Ni(II) or medium values ($J \sim 15$–$30\ cm^{-1}$) for Cu(II) [19]. In addition, based on the magnetic orbital overlap π- or σ-model, the magnitude of magnetic coupling between two metal ions via a pathway through tppz is dependent on the planarity of the pyrazine ring, dihedral angles between the pyridine ring, or the planarity of the basal coordination plane of the metal ion [19]. The antiferromagnitic exchange parameter J value obtained for the present complexes in the order **1** < **2** < **3** is correlated to their magnetic orbital properties and twisted angles of the central pyrazine ring of the tppz ligand.

4. Conclusions

The combined use of dca and tppz as ligands in generating new transition metal complexes has led to (i) alternating 1-D chains with dca-linked dinuclear tppz-chelated Co(II), Ni(II) and Cu(II) building blocks, and (ii) weak antiferromagnetic exchange interactions between two metal ions via a pathway through dca and tppz bridging ligands.

5. Supplementary material

Crystallographic data have been deposited at the Cambridge Crystallographic Data center, CCDC reference numbers 243241 (**1**), 243240 (**2**) and 243242 (**3**). Copies of this information may be obtained free of charge from the Director, CCDC, 12 Union Road, Cambridge, CB2 1EZ, UK (fax: +44-1223-336-033; email: deposit@ccdc.cam.ac.cn or www.ccdc.cam.ac.uk).

Acknowledgement

This work has been carried out with the financial support of the National Science Council of Taiwan (Grant NSC-92-2113-M-032-008).

References

[1] (a) S.R. Batten, P. Jensen, B. Moubaraki, K.S. Murray, R. Robson, Chem. Commun. (1998) 439;
(b) J.L. Manson, C.R. Kmety, Q.-z. Huang, J.W. Lynn, G.M. Bendele, S. Pagola, P.W. Stephens, L.M. Liable-Sands, A.L. Rheingold, A.J. Epstein, J.S. Miller, Chem. Mater. 10 (1998) 2552;
(c) M. Kurmoo, C.J. Kepert, New J. Chem. (1998) 1515;
(d) H.L. Sun, S. Gao, B.Q. Ma, G. Su, Inorg. Chem. 42 (2003) 5399.
[2] B. Vangdal, J. Carranza, F. Lloret, M. Julve, J. Sletten, J. Chem. Soc., Dalton Trans. (2002) 566.
[3] (a) S.R. Marshall, C.D. Incarvito, W.W. Shum, A.L. Rheingold, J.S. Miller, Chem. Commun. (2002) 3006;
(b) Y.J. Shi, L.H. Li, Y.Z. Li, X.T. Chen, Z. Xue, X.Z. You, Polyhedron 22 (2003) 917;
(c) E. Colacio, I.B. Maimoun, R. Kivekäs, R. Sillanpää, J. Suárez-Varela, Inorg. Chim. Acta 357 (2004) 1465.
[4] (a) G.A. van Albada, M.E. Quiroz-Castro, I. Mutikainen, U. Turpeinen, J. Reedijk, Inorg. Chim. Acta 298 (2000) 221;
(b) A. Escuer, F.A. Mautner, N. Sanz, R. Vicente, Inorg. Chem. 39 (2000) 1668;
(c) A. Claramunt, A. Escuer, F.A. Mautner, N. Sanz, R. Vicente, J. Chem. Soc., Dalton Trans. (2000) 2627;
(d) S. Martin, M.G. Barandika, J.I.R. de Larramendi, R. Cortés, M. Font-Bardia, L. Lezama, Z.E. Serna, S. Solans, T. Rojo, Inorg. Chem. 40 (2001) 3687;
(e) S.R. Batten, P. Jenson, C.J. Kepert, M. Kurmoo, B. Moubaraki, K.S. Murray, D. Price, J. Chem. Soc., Dalton Trans. (1999) 2987;
(f) J.L. Manson, A.M. Arif, J.S. Miller, J. Mater. Chem. 9 (1999) 979.
[5] (a) I. Riggio, G.A. van Albada, D.D. Ellis, A.L. Spek, J. Reedijk, Inorg. Chim. Acta 313 (2001) 120;
(b) S.R. Batten, A.R. Harris, P.; Jensen, K.S. Murray, A. Ziebell, J. Chem. Soc., Dalton Trans. (2000) 3829;
(c) B.-W. Sun, S. Gao, B.-Q. Ma, Z.-M. Wang, New J. Chem. 24 (2000) 953;
(d) A. Claramunt, A. Escuer, F.A. Mautner, N. Sanz, R. Vicente, J. Chem. Soc., Dalton Trans. (2000) 2627;
(e) S.R. Marshall, C.D. Incarvito, J.L. Manson, A.L. Rheingold, J.S. Miller, Inorg. Chem. 39 (2000) 1969;
(f) S.R. Batten, P. Jenson, C.J. Kepert, M. Kurmoo, B. Moubaraki, K.S. Murray, D. Price, J. Chem. Soc., Dalton Trans. (1999) 2987;
(g) J.L. Manson, D.W. Lee, A.L. Rheingold, J.S. Miller, Inorg. Chem. 37 (1998) 5966;
(h) I. Dasna, S. Golhen, L. Ouahab, M. Fettouhi, O. Peña, N. Daro, J.-P. Sutter, Inorg. Chim. Acta 326 (2001) 37.

[6] (a) H.-H. Lin, S. Mohanta, C.-J. Lee, H.-H. Wei, Inorg. Chem. 42 (2003) 1584;
(b) B.-W. Sun, S. Gao, B.-Q. Ma, D.-Z. Niu, Z.-M. Wang, J. Chem. Soc., Dalton Trans. (2000) 4187;
(c) W. Dong, Q.-L. Wang, Z.-Q. Liu, D.-Z. Liao, Z.-H. Jiang, S.-P. Yang, P. Cheng, Polyhedron 22 (2003) 3315.
[7] (a) J.W. Raebiger, J.L. Manson, R.D. Sommer, U. Geiser, A.L. Rheingold, J.S. Miller, Inorg. Chem. 40 (2001) 2578;
(b) P.M. van der Werff, S.R. Batten, P. Jensen, B. Moubaraki, K.S. Murray, Inorg. Chem. 40 (2001) 1718;
(c) S. Triki, F. Thétiot, J.-R. Galán-Mascaros, J. Sala Pala, K. Dunbar, New J. Chem. 25 (2001) 954;
(d) S.R. Marshall, C.D. Incarvito, J.L. Manson, A.L. Rheingold, J.S. Miller, Inorg. Chem. 39 (2000) 1969;
(e) S. Martin, M.G. Barandika, R. Cortès, J.I. Ruiz de Larramendi, M.K. Urtiaga, L. Lezama, M.I. Arriortua, T. Rojo, Eur. J. Inorg. Chem. (2001) 2107.
[8] J.L. Manson, J.A. Schlueter, U. Geiser, M.B. Stone, D.H. Reich, Polyhedron 20 (2001) 1423.
[9] A.M. Kutasi, S.R. Batten, B. Moubaraki, K.S. Murray, J. Chem. Soc., Dalton Trans. (2002) 819.
[10] S.R. Batten, P. Jensen, B. Moubaraki, K.S. Murray, R. Robson, Chem. Commun. (2000) 793.
[11] Y.-J. Shi, X.-T. Chen, Y.-Z. Li, Z. Xue, X.-Z. You, New J. Chem. 26 (2002) 1711.
[12] I. Potocnak, M. Dunaj-Jurco, D. Miklos, J. Jager, Acta Crystallogr., Sect. C 52 (1996) 165.
[13] Y.M. Chow, D. Britton, Acta Crystallogr., Sect. B 31 (1975) 1934.
[14] H.A. Goodwin, F. Lyons, J. Am. Chem. Soc. 81 (1959) 6415.
[15] J.D. Petersen, L.W. Morgan, I. Hsu, M.A. Billadeau, S.E. Ronco, Coord. Chem. Rev. 111 (1991) 319.
[16] (a) R.R. Ruminski, C. Letner, Inorg. Chim. Acta 162 (1989) 175;
(b) R.R. Ruminski, J.L. Kiplinger, Inorg. Chem. 29 (1990) 4581;
(c) R.R. Ruminski, J.L. Kiplinger, T. Cockroft, C. Chase, Inorg. Chem. 29 (1989) 370.
[17] C.R. Arana, H.D. Abrufia, Inorg. Chem. 32 (1993) 194.
[18] (a) R.G. Brewer, G.E. Jensen, K.J. Brewer, Inorg. Chem. 33 (1994) 124;
(b) L.M. Vogler, K.J. Brewer, Inorg. Chem. 35 (1996) 818.
[19] (a) M. Graf, H. Stoeckli-Evans, A. Escuer, R. Vicente, Inorg. Chim. Acta 257 (1997) 89;
(b) C.M. Hartshorn, N. Daire, V. Tondreau, B. Loeb, T.J. Meyer, P. White, Inorg. Chem. 38 (1999) 3200;
(c) A.C. Benniston, V. Grosshenny, A. Harriman, R. Ziessel, J. Chem. Soc., Dalton Trans. (2004) 1227.
[20] (a) Burkholder, V. Golub, C.J. O'Connor, J. Zubieta, Inorg. Chem. 42 (2003) 6729;
(b) D. Hagrman, P. Hagrman, J. Zubieta, Inorg. Chim. Acta 300–302 (2000) 212.
[21] (a) O. Kahn, Molecular Magnetism, VCH, NewYork, 1993;
(b) Miller, M. Drillon (Eds.), Magnetism: Molecules to Materials II, Wiley-VCH, Weinheim, 2001.
[22] (a) G.M. Sheldrick, SHELXL-97, A Program for Crystal Structure Solution, University of Göttingen, Germany, 1990;
(b) G.M. Sheldrick, SHELXL-97, *A* Program for Crystal Structure Refinement, University of Göttingen, Germany, 1997.
[23] R. Cortés, M. Drillon, X. Solans, L. Lezama, T. Rojo, Inorg. Chem. 36 (1997) 677.
[24] A.P. Ginsberg, R.L. Martin, R.W. Brookes, R.C. Sherwood, Inorg. Chem. 11 (1972) 2884.
[25] J.W. Hall, W.E. Marsh, R.R. Weller, W.E. Hatfield, Inorg. Chem. 20 (1981) 1033.
[26] B. Bleaney, K.D. Bowers, Proc. R. Roc. London, Ser. A 214 (1952) 4519.
[27] J. Suarez-Varela, E. Colacio, A. Romerosa, J.C. Avila-Roson, M.A. Hidalgo, J. Romero, Inorg. Chim. Acta 217 (1994) 39.

Available online at www.sciencedirect.com
SCIENCE DIRECT®
Polyhedron 24 (2005) 495–499
POLYHEDRON
www.elsevier.com/locate/poly

Nucleic acid cleavage by a Cu(II) polyaza macrocyclic complex

M.C.B. Oliveira [a], M.S.R. Couto [a], P.C. Severino [a], T. Foppa [a], G.T.S. Martins [b], B. Szpoganicz [b], R.A. Peralta [c], A. Neves [c], H. Terenzi [a,*]

[a] *Laboratório de Expressão Gênica, Departamento de Bioquímica, CCB, UFSC, Florianópolis, SC 88040-900, Brazil*
[b] *Laboratório de Equilíbrio Químico, Departamento de Química, Universidade Federal de Santa Catarina, Brazil*
[c] *Laboratório de Bioinorgânica e Cristalografia, Departamento de Química, Universidade Federal de Santa Catarina, Brazil*

Received 13 April 2004; accepted 8 December 2004

Abstract

The search for efficient artificial nucleases is a consequence of the huge efforts towards DNA sequencing by genome projects around the world. In the present study, we describe the activity of the Cu(II)–BMXD complex (BMXD = 3,6,9,17,20,23-hexaazatricyclo[23.3.1.1^{11,15}]triaconta-1(29),11(30),12,14,25,27-hexaene) as a DNA cleavage agent. The rate constant for the DNA backbone cleavage reaction at room temperature (25 °C) and pH 7.0 was estimated to be 1.1×10^{-6} s^{-1}, which corresponds, approximately, to a half-life ($t_{1/2}$) of one week. We demonstrated that the DNA cleavage reaction promoted by the Cu_2BMXD complex may occur via an oxidative pathway through performing reactions in the presence of free-radical acceptors and comparing the activity under aerobic and anaerobic conditions. The Cu_2BMXD complex reported here is established as a novel artificial nuclease.
© 2005 Elsevier Ltd. All rights reserved.

Keywords: DNA cleavage; Polyaza ligand; Binuclear copper complex; BMXD; Chemical nuclease; DNA–drug interaction

1. Introduction

Drugs or molecules that interact with nucleic acids have been the subject of great interest because they serve as tools in molecular biology and biochemistry, as well as therapeutics [1], especially those capable of nucleic acid cleavage [2]. Chemical nucleases are compounds that mimic the action of enzymatic nucleases [3] and can be alternatively used in biochemical and biotechnological processes. They are smaller than enzymes, which allows them to attack macromolecular regions that are inaccessible to enzymes [4] and also their specificity and efficiency may be modulated [5]. These properties have turned chemical nucleases into useful tools as adjuvants in PCR diagnostics [6], nucleic acid attacking agents [7], nucleic acid structural probes [4], DNA cleaving and marking agents for microarrays [8], controlling agents for fungal diseases [9] and antitumor drugs [10–13]. Chemical nucleases have also been used in studies on the interactions between nucleic acids and proteins [14,15] and on the mode of action of some metalloproteins [16,17]. The polyaza macrocyclic ligand 3,6,9,17,20,23-hexaazatricyclo[23.3.1.1^{11,15}] triaconta-1(29),11(30),12,14,25,27-hexaene (BMXD) (Fig. 1) was first synthesized in 1990 [18].

This ligand consists of a macrocycle formed by two diethylenetriamine moieties separated by two *m*-xylyl bridges, and is capable of coordinating one or two Cu(II) centers via its diethylenetriamine moieties [18]. In aqueous medium, depending on the pH, the metal centers of the dinuclear copper(II) complex (Cu_2BMXD) can, in turn, coordinate hydroxide anions (Fig. 1) as suggested by Martell el al. [18,19], as well as other anions, some of them of biological relevance

* Corresponding author. Tel.: +55 48 331 9589; fax: +55 48 331 9672.
E-mail address: hterenzi@ccb.ufsc.br (H. Terenzi).

0277-5387/$ - see front matter © 2005 Elsevier Ltd. All rights reserved.
doi:10.1016/j.poly.2004.12.016

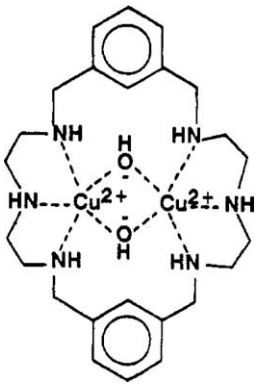


Fig. 1. Chemical structure of the [Cu_2BMXD] complex.

[19–21]. More recently, it has been shown that [Cu_2BMXD] can also form a complex with the dipeptide glycylglycine [22]. It has previously been demonstrated that the BMXD complex shows affinity for ATP and is able to convert it into ADP and orthophosphate through an oxidative process [23]. When coordinating a zinc(II) ion in one or two centers, the BMXD ligand has been shown to bind maleate, pyrophosphate and norleucine [24] and to promote the hydrolytic cleavage of bis(4-nitrophenyl)phosphate (BNP) [25]. In this paper we describe, for the first time, the oxidative cleavage of DNA promoted by the [Cu_2BMXD] complex.

2. Experimental

Abbreviations: BMXD (3,6,9,17,20,23-hexaazatricyclo [23.3.1.1^{11,15}] triaconta-1(29),11(30),12,14,25,27-hexaene), BNP (bis(4-nitrophenyl)phosphate).

The hexabasic macrocycle BMXD ligand has been synthesized according to the literature procedure [18a]. A 10^{-3} M stock solution of [Cu_2BMXD] was prepared by adding $CuCl_2$ to a BMXD solution and neutralizing to pH 7 and the species distribution in aqueous solution has been previously reported [18b]. Plasmid DNA pBSKII (Stratagene) was produced in *Escherichia coli* and extracted following protocols described in the literature [26]. Quality and concentration of the plasmid DNA was assessed by spectrophotometry and the relative amount of supercoiled DNA was evaluated by agarose gel electrophoresis analysis, as previously described [27]. Cleavage experiments were carried out incubating in a 20 μl final volume: 400ng plasmid DNA, corresponding to a final concentration of 30 μM bp (nucleotide base pairs), and 1, 5 or 10 μM [Cu_2BMXD], for 16 h at 50 °C, pH 7.0, in 50 mM PIPES buffer (other conditions are depicted in the figure titles). Reactions were stopped by chilling tubes on ice and adding 4 μl of ice-cold loading-buffer (50% glycerol, 2 M EDTA, 0.05% bromophenol blue). All tests were performed in triplicate. Reaction products observed by agarose gel electrophoresis were digitally recorded and analyzed with the software Scion Image for Windows. Quantified results were subjected to analysis of variance (ANOVA), followed by the Tukey test for honest significant difference (HSD). Electrochemical experiments were performed on a Princeton Applied Research 273 potentiostat/galvanostat. The supporting electrolyte was 0.1 M NaCl in water. Cyclic voltammograms (CV) were obtained with a vitreous carbon working electrode, a platinum wire as an auxiliary electrode, and a Ag/Ag^+ (3 mol l^{-1} NaCl) reference electrode. The scan rate was 100 mV s^{-1}. Potassium hexacyanoferrate(III) was used as an internal standard [28].

3. Results and discussion

In this paper, the activity of the binuclear copper(II) complex [Cu_2BMXD] towards plasmid DNA is described. DNA cleavage activity is achieved at micromolar concentrations of the complex under mild conditions of pH and temperature (Fig. 2).

As shown in Fig. 2, supercoiled plasmid DNA (FI) is converted into nicked circular DNA (FII) when it is incubated with [Cu_2BMXD] for 16 h at 50 °C and at pH 7.0. This conversion is complex-concentration dependent. Plasmid form FI decreased from 79.7% (control) to 56.1%, 29.8% and 21.2%, when the complex concentration is increased from 0 μM (control) to 1, 5 and 10 μM, respectively. DNA cleavage assays were also performed at 20, 30 and 60 °C (Fig. 3) in order to compare our results with the DNA cleavage promoted by metal complexes under conditions similar to those described in previous studies [2,27,29–33].

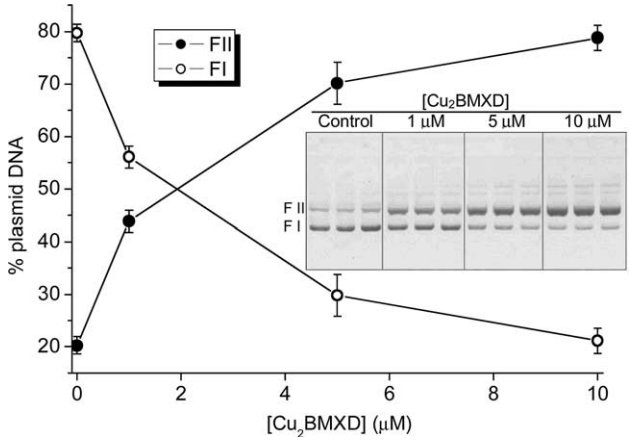


Fig. 2. Plot of % plasmid DNA forms (FI – supercoiled; FII – nicked) after incubation with different concentrations of [Cu_2BMXD] for 16 h at pH 7.0 and 50 °C. Data were obtained from the agarose gel electrophoresis shown in the inset.

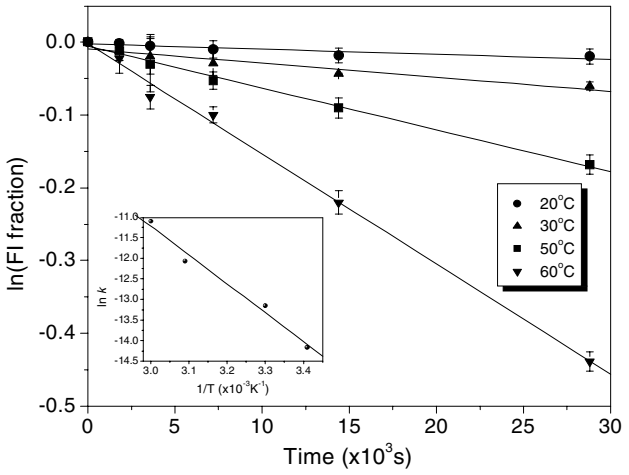


Fig. 3. Effect of temperature on supercoiled plasmid DNA cleavage by [Cu_2BMXD]. All reactions were performed with 20 μM Cu_2BMXD at pH 7.0 (50 mM PIPES buffer). Inset – Arrhenius plot of ln k versus 1/T, obtained from kinetic data.

The rate constant for the DNA cleavage activity promoted by 20 μM [Cu_2BMXD] at 20–60 °C and pH 7.0 was determined by incubating the complex with 10 nM of plasmid DNA for different time periods (Fig. 3, Table 1).

Although there are compounds that are capable of performing remarkable hydrolytic cleavage of DNA [29,32,34], oxidative agents that cleave DNA have been described to be even more efficient. Among these oxidative cleaving DNA agents is bleomycin, capable of promoting double-strand DNA cleavage. This drug complexed with Fe(II) is able to nick plasmid DNA, causing it to pass from the supercoiled to the open circular form with a rate constant of 8.6×10^{-1} h^{-1} in concentrations as little as 0.62 μM [35]. Another iron-complexing agent was reported by Roefles and coworkers to have DNA nicking effects detectable after 20 s of incubation with a catalyst concentration of 1 μM [36]. The [Cu_2BMXD] complex is capable of promoting DNA cleavage with reasonably high efficiency. Most of the chemical compounds described so far to cleave DNA demand a molar concentration many orders of magnitude greater than the concentration of the substrate to perform an activity detectable in a reasonable period of time and under close to physiological conditions [2].

Table 1
Thermodynamic and kinetic parameters of [Cu_2BMXD] DNA cleavage activity

Temperature (°C)	k ($\times 10^{-7}$ s^{-1})
20	7.0 ± 1.6
30	19.3 ± 2.9
50	57.4 ± 2.1
60	151.4 ± 4.8

From data obtained in Fig. 3, and summarized in Table 1, the activation energy for the DNA cleavage reaction was estimated to be 58.6 kJ K^{-1} mol^{-1}, a value that is greater than the diffusion barrier for small molecules. One reason for this barrier could be the DNA structural changes requirement for the complex accommodation, in the slow step of the cleavage mechanism. Another cause for this barrier may be related to the activation of the metal center to produce hydroxyl radicals, given that known hydroxyl radical scavengers (DMSO and glycerol) inhibit plasmid DNA cleavage by [Cu_2BMXD] (Fig. 4). At concentrations of 5 and 10 μM [Cu_2BMXD] a partial inhibition of the cleavage activity in the presence of DMSO was observed. Glycerol was able to partially inhibit the DNA cleavage activity promoted by [Cu_2BMXD] only at the highest complex concentration tested (10 μM).

Complementarily, an aerobic versus anaerobic (argon atmosphere) experiment was performed to investigate the influence of molecular oxygen (O_2) on this DNA cleavage process (Fig. 5). In this experiment, the activity of [Cu_2BMXD] was tested comparatively with that of an Fe-EDTA/DTT system, a known hydroxyl radical producer when in the presence of O_2. It was observed that DNA cleavage promoted by

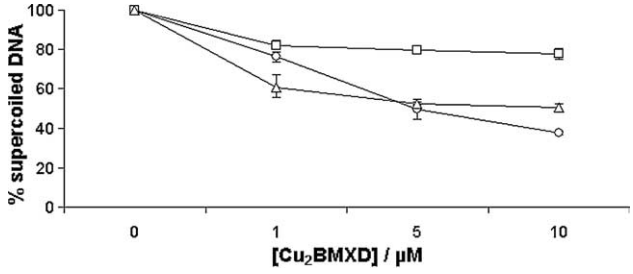


Fig. 4. Percentage of supercoiled DNA in relation to the control after 16 h of incubation at 50 °C. Control (no complex – 0); in the presence of [Cu_2BMXD] 1 μM (1); 5 μM (5) and 10 μM(10), pH 7.0. ○, without free-radical acceptor, △, with glycerol 10%, □, with DMSO 10%. Error bars are indicated.

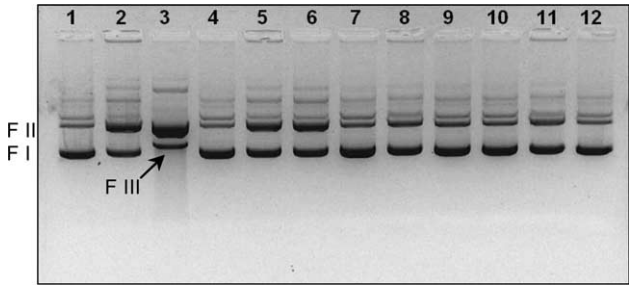


Fig. 5. Incubation of 10 μM (bp) plasmid DNA for 4 h at 50 °C. Lanes 1–6: aerobic atmosphere, lanes 7–12: argon atmosphere. Lanes 1 and 7: Control reactions, lanes 2 and 8: 20 μM Cu_2BMXD, lanes 3 and 9: 100 μM Fe-EDTA + 10 mM DTT, lanes 4 and 10: 400 μM DMSO, lanes 5 and 11: 20 μM [Cu_2BMXD] + 400 μM DMSO, lanes 6 and 12: 100 μM Fe-EDTA + 400 μM DMSO. Plasmid DNA forms: FI – supercoiled; FII – nicked circular; FIII – linear.

Fe-EDTA/DTT, as well as by [Cu_2BMXD] suffered partial inhibition in the presence of the tested free-radical acceptor, DMSO, though this inhibition was less evident for [Cu_2BMXD]. It was also observed that Fe-EDTA/DTT was not able to cleave DNA under an oxygen-free atmosphere while for [Cu_2BMXD] a small residual activity was noted.

These results indicated that the presence of oxygen plays a fundamental role in the process of DNA cleavage by the [Cu_2BMXD] complex. This gives strong evidence of an oxidative process intervening in the DNA cleavage reaction. The initial reduction of the copper centers often requires the participation of a reducing agent [2], some times in great excess, up to 100-fold the concentration of the catalyst [37]. Yet, it has been shown that there are some compounds that do not need external reducing agents to activate the metal centres [35,36,38–41] as has been demonstrated here for [Cu_2BMXD]. However, buffer species such as HEPES, PIPES or MES may fulfil the role of agents to reduce Cu(II) [42].

As shown in Fig. 6 the reaction of [Cu_2BMXD] with DNA is only partially inhibited by changing PIPES for phosphate buffer, thus excluding the amino buffer as a reducing agent in this reaction. It is important to stress that the inhibition caused by phosphate buffer may be due to a competition between the buffer and the DNA for the complex, since it has been previously shown that [Cu_2BMXD] has an affinity for inorganic phosphate [43]. Another important observation is that when 1 ml of experimental solution was prepared with 500 μM of [Cu_2BMXD] under argon atmosphere, a white precipitate formed almost immediately when 250 μM (bp) of DNA was added to the solution. This precipitate was re-dissolved when air was passed

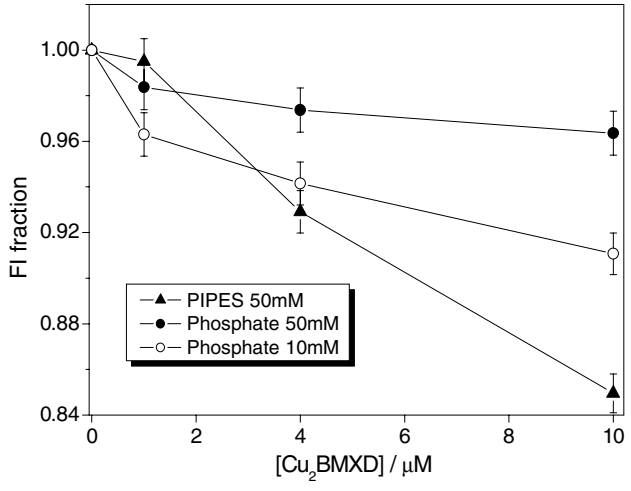


Fig. 6. Effect of buffer on supercoiled plasmid DNA cleavage by [Cu_2BMXD]. All reactions were carried out at pH 7.0 and 50 °C for 8 h.

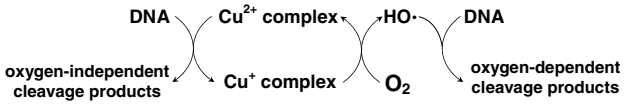


Fig. 7. Scheme of the pathways for oxygen-dependent (and independent) DNA cleavage by Cu_2BMXD.

through the solution, and acquired a blue color. We attribute the production of this precipitate to the reduction of Cu^{2+} to Cu^{+} (less soluble) by DNA, and the dissolution of the white precipitate to a blue solution to the re-oxidation of Cu^{+} to Cu^{2+} in the presence of O_2 (air).

All these results led us to propose, not the mechanisms, but the pathways, or the sequential events, by which the DNA cleavage by [Cu_2BMXD] takes place (Fig. 7).

The electrochemical behaviour of [Cu_2BMXD] was studied using cyclic voltammetry. The cyclic voltammogram of the [Cu_2BMXD] complex measured in H_2O/0.1 M NaCl is shown in Fig. S1 in the potential range −1.0 to 1.0 V versus Ag/Ag^+. The complex shows two irreversible redox processes at −0.46 and −0.59 V versus Ag/Ag^+, regarded as cathodic peak potentials. These irreversible processes are tentatively attributed to the successive one-electron $2Cu^{II} + 1e^- \rightarrow Cu^{II}Cu^{I}$ and $Cu^{II}Cu^{I} + 1e^- \rightarrow 2Cu^{I}$ redox couples. For comparison, two reduction processes at −0.35 and −1.09 V versus Ag/Ag^+ have been reported for a dinuclear copper(II) complex containing dissimilar N_2O_2 coordination environments [44a]. The wave at −0.13 V versus Ag/Ag^+ in the CV (Fig. S1) is attributed to adsorption of the complex onto the electrode surface [44b] while the oxidation wave at +0.22 V is most probably related to the oxidation of the BMXD ligand.

4. Conclusions

We have described a novel chemical nuclease, in the form of a previously identified macrocyclic complex, Cu_2BMXD. The kinetic parameters of the reaction, as well as the temperature and the complex concentration necessary to achieve nucleic acid cleavage, indicate its potential as a gentle footprinting agent and chemical nuclease. Our efforts are now concentrated on the determination of the reaction specificity towards particular DNA sequences or structures and also on the biological activity of the complex.

Acknowledgements

This work was supported by CNPq, Capes, CTPETRO, and PADCTIIISBIO.

Appendix A. Supplementary data

Supplementary data associated with this article can be found, in the online version at doi:10.1016/j.poly.2004.12.016.

References

[1] C. Hennequin, V. Favaudon, Eur. J. Cancer 38 (2002) 223.
[2] J.A. Cowan, Curr. Opin. Chem. Biol. 5 (2001) 634.
[3] G.N. Novodarova, N.Y. Krainova, M.E. Vol'pin, J. Inorg. Biochem. 43 (1991) 693.
[4] W.S. Bowen, W.E. Hill, J.S. Lodmell, Methods 25 (2001) 344.
[5] A.T. Abraham, X. Zhou, S.M. Hecht, J. Am. Chem. Soc. 121 (1999) 1982.
[6] H.A. Avila, D.S. Sigman, L.M. Cohen, R.C. Millikan, L. Simpson, Mol. Biochem. Parasitol. 48 (1991) 211.
[7] M. Wu, D. Stoermer, T.D. Tullius, C.A. Townsend, J. Am. Chem. Soc. 122 (2000) 12884.
[8] J.J. Kelly, B.K. Chernov, I. Tovstanovsky, A.D. Mirzabekov, S.G. Bavykin, Anal. Biochem. 311 (2002) 103.
[9] B. Coyle, P. Kinsella, M. McCann, M. Devereux, R. O'Connor, M. Clynes, K. Kavanagh, Toxicol. In Vitro 18 (2004) 63.
[10] A. Mohindru, J.M. Fisher, M. Rabinovitz, Biochem. Pharmacol. 32 (1983) 3627.
[11] R.W. Byrnes, W.E. Antholine, D.H. Petering, Free Radic. Biol. Med. 13 (1992) 469.
[12] T. Mohammad, Toxicol. In Vitro 18 (2004) 45.
[13] E. Wong, C.M. Giandomenico, Chem. Rev. 99 (1999) 2451.
[14] G.N. Novodarova, N.Y. Krainova, M.E. Vol'pin, V.M. Belkov, N.F. Krynetskaya, Z.A. Shabarova, J. Inorg. Biochem. 51 (1993) 521.
[15] S.M. McLeod, S.E. Aiyar, R.L. Gourse, R.C. Johnson, J. Mol. Biol. 316 (2002) 517.
[16] J. Yang, R.N.S. Wong, M.S. Yang, Chem. Biol. Interact. 125 (2000) 221.
[17] A. Llobet, A.E. Martell, M.A. Martinez, J. Mol. Cat. A 129 (1998) 19.
[18] (a) R. Menif, A.E. Martell, P.J. Squattrito, A. Clearfield, Inorg. Chem. 29 (1990) 4723;
(b) D.A. Nation, J. Reibenspies, A.E. Martell, Inorg. Chem. 35 (1996) 4597.
[19] T.F. Pauwels, W. Lippens, G.G. Herman, A. Goeminne, Polyhedron 17 (1998) 1715.
[20] T.F. Pauwels, W. Lippens, P.W. Smet, G.G. Herman, A.M. Goeminne, Polyhedron 18 (1999) 1029.
[21] E. Ross, R.J. Motekaitis, A.E. Martell, Inorg. Chim. Acta 286 (1999) 55.
[22] G.T. Stein Martins, B. Szpoganicz, V. Tomisic, N. Humbert, M. Elhabiri, A.-M. Albrecht-Gary, L.F. Sala, Inorg. Chim. Acta 357 (2004) 2261.
[23] D.A. Nation, Q. Lu, A.E. Martell, Inorg. Chim. Acta 263 (1997) 209.
[24] T.F. Pauwels, P.W. Smet, A.M. Goeminne, Polyhedron 20 (2001) 2457.
[25] P. Jurek, A.E. Martell, Inorg. Chim. Acta 287 (1999) 47.
[26] F. Ausubel, R. Brent, R. Kingston, D. Moore, J.G. Seidman, J. Smith, K. Struhl, *Escherichia coli*, plasmids and bacteriophages, in: F.M. Ausubel, et al. (Eds.), Short Protocols in Molecular Biology, 3rd ed., Wiley, New York, 1995, p. (1)1.
[27] S.C. Batista, A. Neves, A.J. Bortoluzzi, I. Vencato, R.A. Peralta, B. Szpoganicz, V.V.E. Aires, H. Terenzi, P.C. Severino, Inorg. Chem. Commun. 6 (2003) 1161.
[28] D.R. Lide, Handbook of Chemistry and Physics, 81st ed., CRC Press, Boca Raton, FL, 2000.
[29] B. Zhu, D.-Q. Zhao, J.-Z. Ni, D. Ying, B.-Q. Huang, Z.-L. Wang, J. Mol. Cat. A 135 (1998) 107.
[30] N. Yamashita, M. Murata, S. Inoue, Y. Hiraku, T. Yoshinaga, S. Kawanishi, Mutat. Res. 397 (1998) 191.
[31] M. Sirish, S.J. Franklin, J. Inorg. Biochem. 91 (2002) 253.
[32] G.N. De Iuliis, G.A. Lawrence, S. Fieuw-Makaroff, Inorg. Chem. Commun. 3 (2000) 307.
[33] B. Zhu, D.-Q. Zhao, J.-Z. Ni, Q.-H. Zeng, B.-Q. Huang, Z.-L. Wang, Inorg. Chem. Commun. 2 (1999) 351.
[34] A. Sreedhara, J.D. Freed, J.A. Cowan, J. Am. Chem. Soc. 122 (2000) 8814.
[35] S. Hashimoto, B. Wang, S.M. Hecht, J. Am. Chem. Soc. 123 (2001) 7437.
[36] G. Roelfes, M.E. Branum, L. Wang, L.J. Que, B.L. Feringa, J. Am. Chem. Soc. 122 (2000) 11517.
[37] S.T. Frey, H.H.J. Sun, N.N. Murthy, K.D. Karlin, Inorg. Chim. Acta 242 (1996) 329.
[38] S. Borah, M.S. Melvin, N. Lindquist, R.A. Manderville, J. Am. Chem. Soc. 120 (1998) 4557.
[39] Q. Liang, D.C. Ananias, E.C. Long, J. Am. Chem. Soc. 120 (1998) 248.
[40] B.P. Padmapriya, M.M. Pitie, B., Bioconjug. Chem. 9 (1998) 604.
[41] E. Lamour, S. Routier, J.L. Bernier, J.P. Catteau, C.V. Bailly, H., J. Am. Chem. Soc. 121 (1999) 1862.
[42] F. Wang, L.M. Sayre, Inorg. Chem. 28 (1989) 169.
[43] D.A. Nation, A.E. Martell, R.I. Carroll, A. Clearfield, Inorg. Chem. 35 (1996) 7246.
[44] (a) S.-I. Ohtsuka, M. Kodera, K.-I. Motoda, M. Ohba, H. Okawa, J. Chem. Soc., Dalton Trans. (1995) 2599;
(b) N.N. Murthy, K.D. Karlin, C. Bertini, J. Luchinat, J. Am. Chem. Soc. 119 (1997) 2156.

Available online at www.sciencedirect.com
SCIENCE DIRECT®
Polyhedron 24 (2005) 501–509
POLYHEDRON
www.elsevier.com/locate/poly

Synthesis, structure and antifungal properties of Co(II)–sulfathiazolate complexes

Sebastián Bellú [a], Estela Hure [a], Marcela Trapé [a], Claudia Trossero [a], Gabriel Molina [a], Claudia Drogo [a], Patricia A.M. Williams [b], Ana María Atria [c], Juan Carlos Muñoz Acevedo [c], Susana Zacchino [d], Maximilano Sortino [d], Darío Campagnoli [e], Marcela Rizzotto [a,*]

[a] *Área Química Inorgánica, Suipacha 531, 2000 Rosario, Argentina*
[b] *CEQUINOR, Facultad de Ciencias Exactas, UNLP, cc. 962, La Plata, Argentina*
[c] *Facultad de Ciencias Químicas y Farmacéuticas, Universidad de Chile, Casilla 233, Santiago, Chile*
[d] *Área Farmacognosia, Universidad Nacional de Rosario, Suipacha 531, 2000 Rosario, Argentina*
[e] *Facultad de Ingeniería Química, UNL, Santiago del Estero, 2829-3000 Santa Fe, Argentina*

Received 19 May 2004; accepted 8 December 2004

Abstract

The reaction between sulfathiazole and cobalt(II) leads to a pink solid, $[Co^{II}(ST)_2(H_2O)_4]$ (**1**), which, after 7–10 days in the mother solution, transforms into red crystals of $[Co^{II}(ST)_2(H_2O)_3]_n$ (**2**) (ST = sulfathiazolate). The Co(II) ion exhibits an octahedral environment in both compounds. Differences between them were noted in the IR spectra in the region corresponding to signals of the amine group. Antifungal properties of (**1**) were evaluated, showing activity against both *Aspergillus fumigatus* (the same as the ligand) and *Aspergillus flavus* (better than the ligand).
© 2005 Elsevier Ltd. All rights reserved.

Keywords: Sulfathiazole; Sulfadrugs metal complexes; Cobalt complexes; Antifungal properties

1. Introduction

Among the many and so different families of organic–inorganic chemicals being currently investigated because of their applications, sulfonamides and their N-derivatives are one of the outstanding groups [1].

Sulfonamides were the first effective chemotherapeutic agents employed systematically for the prevention and cure of bacterial infections in humans [2,3]. After the introduction of penicillin and other antibiotics, the popularity of sulfonamides decreased. However, they are still considered useful in certain therapeutic fields, especially in the case of ophthalmic infections as well as infections in the urinary and gastrointestinal tract [4]. Besides, sulfadrugs are still today among the drugs of first election (together with ampicillin and gentamycin) as chemotherapeutic agents in bacterial infections by *Escherichia coli* in humans [5]. The sulfanilamides exert their antibacterial action by the competitive inhibition of the enzyme dihydropterase synthetase towards the substrate *p*-aminobenzoate [6]. Sulfathiazole, (4-amino-*N*-2-thiazolylbencenosulfonamide), HST (Fig. 1), is clinically one of the most used [7].

Neutral sulfonamides are expected to be poor ligands because of the withdrawal of the electron density from

* Corresponding author. Tel.: +543414219910; fax: +543414350214.
E-mail addresses: mrizzott@fbioyf.unr.edu.ar, mrizzot@agatha.unr.edu.ar (M. Rizzotto).

0277-5387/$ - see front matter © 2005 Elsevier Ltd. All rights reserved.
doi:10.1016/j.poly.2004.12.017

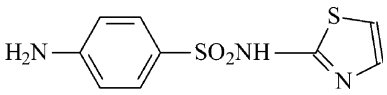


Fig. 1. Sulfathiazole (HST).

the nitrogen atom onto the electronegative oxygen atoms. However, if the sulfonamide N atom bears a dissociable hydrogen atom, this same electron-withdrawing effect increases its acidity and, in the deprotonated form, sulfonamide anions are effective σ-donor ligands [8]. On the other hand, complex formation between metal ions and sulfadrugs, pointing to the combined antibacterial activity of sulfonamides and the antimicrobial activity of heavy metals in some cases, and the activity of the metal complexes themselves, constitute an important field of research [1,2]. Furthermore, sulfadrugs and their metal complexes possess many applications, in addition to antibacterial activity such as diuretic, antiglaucoma or antiepileptic drugs, among others [9–14], like antifungal activity [15,16], and, in many cases, the activity of the metal complex is much better than the ligand alone [1].

Although the synthesis of metal complexes of sulfathiazole has been reported, the structural determination is often incomplete and conflicting [17,18]. Relating to sulfathiazole metal complexes, different compounds were reported in which the sulfathiazole moiety acts with a high versatility in its coordination ability. For example, with Zn(II) the drug acts as a bridging ligand through both the N_{amino} and $N_{thiazole}$ atoms [18]. As a neutral ligand, HST acts as a monodentate ligand, binding the metal ion through the N_{amino} atom [19]. As a deprotonated ligand, ST^- has a variety of coordination behaviors, e.g., besides the Zn(II)–ST complex [18], in Cu(II) complexes coordination through the N-thiazole atom could be seen, and in another case the sulfathiazolato exhibits bidentate behavior linking the metal ion through the $N_{thiazolic}$ and the $N_{sulfonamido}$ atoms [20]. More recently, we have analyzed the interaction of mercury(II) with sulfathiazole: IR and NMR spectral studies suggested a coordination of Hg(II) with the $N_{thiazolic}$ atom, unlike the related Hg-sulfadrugs compounds [21].

Despite its low availability in the earth's crust [22], cobalt plays important roles in biological systems. The most common examples are vitamin B_{12} and coenzyme B_{12}, a cofactor required for a group of enzymatic systems of central importance in biochemistry [23]. Cobalt is vitamin B_{12}'s only apparent biological site. Vitamin B_{12}-deficiency causes the severe disease of pernicious anemia in humans, which indicates the critical role of cobalt. The cobalt in vitamin B_{12} is coordinated to five N atoms, four attributed to a tetrapyrrole (corrin); the sixth ligand is C, provided either by C5 of deoxyadenosine in enzymes such as methylmalonyl-CoA (fatty acid metabolism) or by a methyl group in the enzyme that synthesizes the amino acid methionine in bacteria [24]. Besides, cobalt in organometallic complexes, has been shown to display a wide-ranging reactivity which includes alkyl transfer reactions and insertion reactions of small molecules such as O_2 and SO_2 into metal–alkyl bonds [25]. Because of its high sensitivity to the coordination site geometry and the many experimental techniques that can be used in its characterization, cobalt has been used to replace other metal ions to gather information about changes in metal sites in proteins during protein function [26–29]. Spectroscopic characterization of these systems has revealed that cobalt can be present as Co(II) and Co(III) ions in several types of coordination, which lead to different electronic and magnetic properties. In this context, the use of simple Co-containing systems with low molecular weight ligands is useful for understanding the correlation between spectroscopic and structural properties.

As part of a research program dedicated to the investigation of the structural, physicochemical and biological properties of metal complexes of sulfadrugs, the present paper reports the synthesis, spectral, structure and antifungal studies of compounds of sulfathiazole with Co(II), Co(II)–ST.

2. Experimental

2.1. Materials and methods

Sulfathiazole, as a sodium salt (Sigma, >99%), cobalt (II) chloride hexahydrate (Merck, GR), and all other chemicals of commercially available reagent grade were used as received.

The content of Co was determined by both complexometric back-titration with EDTA (ethylenediaminetetraacetic acid) [30,31] and atomic absorption spectroscopy with a double beam Perkin–Elmer spectrometer, model 3110, at UNL.

Elemental chemical analyses (C, H, N, S) were performed in a microanalyser Carlo Erba EA1108.

IR spectra of powdered samples were measured with a Bruker IFS 66 FTIR-spectrophotometer from 4000 to 400 cm^{-1}, using the KBr pellet technique. The Raman spectrum was measured with a Spex-Ramalog double monochromator spectrometer, using the 514.5 nm line of an Ar ion laser for excitation, over the region 200–2000 cm^{-1}.

Thermogravimetric (TG) and differential thermal analysis (DTA) were performed on a Shimadzu system (models TG-50 and DTA-50, respectively), working in an oxygen flow (50 mL/min) and a heating rate of 10 °C/min. Sample quantities ranged between 10 and 20 mg. Al_2O_3 was used as a DTA standard.

Room temperature magnetic susceptibility was determined with a Cahn-2000 balance, calibrated with $Hg[Co(SCN)_4]$ and at a magnetic field strength of 6 kG.

Electronic spectra were recorded between 200 and 800 nm in a Jasco model 530 double beam spectrophotometer using quartz cells of 1 cm path length at room temperature and in the following solvents: water, methanol (both in order to observe ligand transitions) and DMSO (for d–d transitions). Diffuse reflectance spectra were recorded with a Shimadzu UV-300 instrument, using MgO as an internal standard.

EPR spectroscopy: X-band EPR spectra were recorded as the first derivative of absorption on a Bruker EMX spectrometer operating at 77 K. The microwave frequency was generated with a Bruker 04 ER (9–10 GHz) and measured with a Bruker EMX 048T frequency meter. The magnetic field was measured with a Bruker EMX 035M NMR-probe gaussmeter. Spectral parameters were: 100 kHz field modulation, 10.0 G modulation amplitude, ca. 9.31 GHz microwave frequency, 5.6×10^3 receiver gain, CF = 2000 G, sweep width: 3950 G. Measurements were done on ca. 0.1 mL volume samples of DMSO frozen solution of Co(II)–ST, both pink powder and red crystals, drawn into a plane cell. Typically 1024 points were accumulated per spectrum. Number of scans: 3

Despite Co^{2+} being an excellent paramagnetic shift ion in protein NMR studies [32], it was not possible to take NMR spectra of the complexes because of the paramagnetism observed.

2.2. X-ray crystal structure determination

Highly redundant diffractometer data sets were collected at room temperature ($T = 295$ K) for compound (**2**), up to a 2θ max. of ca. 58°, with a Bruker AXS SMART APEX CCD diffractometer using monochromatic Mo Kα radiation, $\lambda = 0.71069$ Å, and a 0.3° separation between frames. Data integration was performed using SAINT and a semi-empirical absorption correction was applied using SADABS, both programs being included in the diffractometer package. The structure resolution was achieved by Patterson methods and difference Fourier. The structure was refined by least squares on F^2, with anisotropic displacement parameters for non-H atoms. Hydrogen atoms attached to carbon (C–H's) were placed at their calculated positions and allowed to ride onto their host carbons both in coordinates as well as in thermal parameters. Terminal methyl groups were allowed to rotate as well. Hydrogen atoms deemed as potentially active in H-bonding interactions (O–H's and N–H's) were searched in the late Fouriers, and treated in accordance to the data set qualities. In the structure, the amino H atoms [N(6)] were found in the final difference Fourier map and were refined to ensure a reasonable geometry.

All calculations to solve the structures, refine the proposed models and obtain derived results were carried out with the computer programs SHELXS97, SHELXL97 [33a] and SHELXTL/PC [33b]. Relevant parameters of the crystal structure determination are listed in Table 1.

2.3. Biological evaluation

Microorganisms and media: The microorganisms used for the fungistatic evaluation were purchased from the American Type Culture Collection (identified with the initials ATCC) Rockville, MD, USA, or were clinical isolates from CEREMIC, (identified with the capital letter C), Centro de Referencia Micológica, Facultad de Ciencias Bioquímicas y Farmacéuticas, Suipacha 531-(2000)-Rosario, Argentina. *Candida albicans* ATCC 10231, *Saccharomyces cerevisiae* ATCC 9763, *Cryptococcus neoformans* ATCC 32264, *Aspergillus flavus* ATCC 9170, *Aspergillus fumigatus* ATCC 26934, *Aspergillus niger* ATCC 9029, *Trichophyton mentagrophytes* ATCC 9972, *Trichophyton rubrum* C113, *Microsporum gypseum* C115 and *Candida tropicalis* C131 were grown on Sabouraud-chloramphenicol agar slants for 48 h at

Table 1
Crystal data and structure refinement for (**2**)

Identification code	(**2**)
Empirical formula	$C_{18}H_{22}CoN_6O_7S_4$
Formula weight	621.46
Temperature (K)	297(2)
Wavelength (Å)	0.71073
Crystal system	monoclinic
Space group	*Pn*
Unit cell dimensions	
a (Å)	10.2964(13)
b (Å)	10.2680(13)
c (Å)	12.0091(15)
α (°)	90
β (°)	103.067(2)
γ (°)	90
Volume (Å^3)	1236.8(3)
Z	2
Density (calculated) (Mg/m^3)	1.653
Absorption coefficient (mm^{-1})	1.083
F(000)	626
Crystal size (mm)	0.20 × 0.10 × 0.08
Theta range for data collection (°)	1.98 to 27.98
Index ranges	$-12 \leqslant h \leqslant 13$, $-13 \leqslant k \leqslant 12$, $-15 \leqslant l \leqslant 15$
Reflections collected	10009
Independent reflections	5146 [$R_{int} = 0.0446$]
Completeness to theta = 26.00° (%)	99.7
Absorption correction	Φ scans
Maximum and minimum transmission	1.0 and 0.792409
Refinement method	full-matrix least-squares on F^2
Data/restraints/parameters	5146/2/333
Goodness-of-fit on F^2	0.990
Final *R* indices [$I > 2\sigma(I)$]	$R_1 = 0.0563$, $wR_2 = 0.1132$
R indices (all data)	$R_1 = 0.0794$, $wR_2 = 0.1232$
Absolute structure parameter	0.01(2)
Largest difference peak and hole (e/Å^3)	0.472 and −0.304

30 °C. Cell suspensions in sterile distilled water were adjusted to give a final concentration of 10^6 viable yeast cells/mL [34].

The strains were maintained on slopes of Sabouraud-dextrose agar (SDA, Oxoid) and subcultured every 15 days to prevent pleomorphic transformations. Spore suspensions were obtained according to reported procedures [34] and adjusted to 10^6 spores with colony forming ability/mL.

2.4. Antifungal assays

The antifungal activity was evaluated with the agar dilution method by using Sabouraud-chloramphenicol agar for both yeast and dermatophyte species as previously described [35,36]. Stock solutions of compounds (10 mg/mL in DMSO) were diluted to give serial twofold dilutions that were added to each medium resulting in concentrations ranging from 0.10 to 250 mg/mL. MIC for each compound was defined as the lowest concentration that produces no visible fungal growth after the incubation time. Amphotericin B (Janssen Pharmaceutica, Belgium), Ketoconazole (Sigma Chemical Co., St. Louis, MO, USA) and Terbinafine (Novartis, Bs. As., Argentina) were used as positive controls.

2.5. Preparation of the complexes

2.5.1. $[Co(II)(ST)_2(H_2O)_4]$ (1)

10 mL of an aqueous solution of cobalt chloride containing 0.2377 g (1 mmol) of $CoCl_2 \cdot 6H_2O$, was added dropwise to 20 mL aqueous solution of sulfathiazole as the sodium salt, NaST, containing 0.6101 g NaST (2.2 mmol), with stirring at room temperature [2,21]. Immediately, the resulting mixture became blue, because a blue precipitate was formed. Then, the reaction mixture was left to stand at room temperature, away from light. After 4 days the precipitate, which turned into a pink solid, was centrifuged, washed with water several times, filtered off and dried under vacuum, away from light. Yield: 0.567 g, 88.6%.

2.5.2. $[Co(II)(ST)_2(H_2O)_3]_n$ (2)

After several attempts, when the concentrations of both reactive solutions for the obtainment of (**1**) were twice that reported above, the pink precipitate, left in the mother solution between 7 and 10 days, changed into little single red crystals (**2**), suitable for X-ray structural analysis. After 10–12 days, the red crystals were centrifuged, washed with water several times, filtered off and dried under vacuum, away from light. Yield: 0.547 g, 88.0%. Elemental analyses of the red crystals gave satisfactory results for $Co(II)(ST)_2(H_2O)_3$. Found (calc. for $CoC_{18}H_{22}N_6S_4O_7$): C, 34.1 (34.8); H, 3.0 (3.6); N, 13.3 (13.5); S, 21.2 (20.6); Co: 10.2 (9.5). It was not possible to obtain (**2**) from suspensions of (**1**) in water, in the presence and absence of: NaST and NaST plus Co(II), in several concentrations, left about 20 days at room temperature.

3. Results and discussion

3.1. General physicochemical characteristics of (1)

Elemental analyses of the pink powder gave satisfactory results for $Co(II)(ST)_2(H_2O)_4$. Found (calc. for $CoC_{18}H_{24}N_6S_4O_8$): C, 34.2 (33.8); H, 3.2 (3.8); N, 13.0 (13.1); S, 19.8 (20.1); Co: 9.9 (9.2). Compound (**1**) is only slightly soluble in water at room temperature (38 mg/100 mL), but it is soluble in DMSO. In a HCl 1 M solution it suffers hydrolysis, and turns brownish in NaOH 1 M solution, maybe due to oxidation by means of the atmospheric oxygen.

3.2. Crystal description of (2)

The structure of the complex (**2**), $[Co^{II}(ST)_2(H_2O)_3]_n$ as determined by means of X-ray diffraction, resulted in a polymeric chain along the 101 direction. The repeating unit of this chain is a monomeric entity built up of one cobalt atom bonded to three nitrogen atoms from three different ST ligands, N1 of a hanging ST monodentate ligand, N(4) of a bridging ST group and N(6) coming from a neighboring monomeric unit. Completing the coordination sphere three oxygen atoms from water molecules were found (Fig. 2). The cobalt atom exhibits a distorted octahedral coordination sphere. The basal plane of this octahedral sphere is formed by Co(1) N(1) N(4) O(6) N(6A) (with a minimum plane deviation of 0.0174 Å); O(5) and O(7) occupy the apical positions. The Co–O bond distances vary between 2.109 and 2.195 Å and the Co–N distances vary

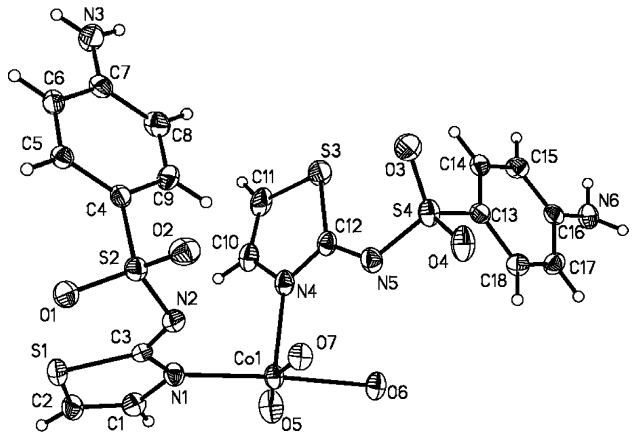


Fig. 2. Structure and atom numbering scheme for (**2**). XP view (Sheldrick, 1994), thermal ellipsoids at 50% probability level.

from 2.114 to 2.220 Å. A selected list of interatomic bond distances and angles are given in Table 2. The bond distances Co–O_{water} and Co–N found are similar to that in other cobalt(II) complexes, e.g., the Co–O_{water} bond distance is 2.090 Å in the complex [Co(L-threonine)$_2$(H_2O)$_2$] [37]. Co–N bond distances vary from 2.039 Å (Co–N_{NCS}) to 2.1951 Å (Co–N_{amino}) in the complex [Co(sulfacetamide)$_2$(NCS)$_2$] [1]. For the complex of cobalt(II) with sulfamethizolate, smtz, and pyridine, py, [Co(smtz)$_2$(py)$_2$(H_2O)], the Co–O_{water} bond distance is shorter (2.0457 Å) than in (**2**) and shorter than the Co–N distances (both $N_{thiadiazole}$ and N_{py}) in the same complex, because its geometry is a distorted octahedral one, with two sulfamethiazolate ligands in the equatorial sites and two water O atoms in the apical positions [38]. In the polymer {[Zn(smtz)$_2$(py)·H_2O]}$_\infty$, the Zn–$N_{thiadiazole}$ bond distances (1.962 and 1.989 Å) are slightly shorter than the Zn–N_{amino} ones (2.070 Å) [39], which is similar to that found in the complex Co(II)–ST (**2**). This fact seems to suggest that the thiazole N atom is able to bind the Co(II) ions much closer compared to the amino N atom, which can be due to the increase of the negative charge on the thiazole ring N atom as a consequence of the charge delocalization through the thiazole ring upon the deprotonation of the sulfonamido group [39].

The chains interact with each other by means of hydrogen bonding, involving the hydrogen atoms of the amino group of the hanging ST monodentate ligand and oxygen atoms of the sulfonamide group belonging to bridging ST group from a nearby chain [H3A···O3 = 2.512 Å, H3A···O4 = 2.680 Å] and also with an oxygen atom from a hanging ST monodentate ligand of the same nearby chain [H3B···O2 = 2.151 Å]. This hydrogen bonding scheme repeats throughout the complete crystal structure (Fig. 3).

Table 2
Selected bond lengths (Å) and angles (°) for (**2**)

Bond lengths (Å)		Angles (°)	
Co(1)–O(7)	2.109(4)	O(7)–Co(1)–N(4)	92.35(18)
Co(1)–N(4)	2.114(5)	O(7)–Co(1)–N(1)	96.47(17)
Co(1)–N(1)	2.128(5)	N(4)–Co(1)–N(1)	96.83(18)
Co(1)–O(5)	2.150(4)	O(7)–Co(1)–O(5)	165.55(17)
Co(1)–O(6)	2.195(4)	N(4)–Co(1)–O(5)	93.0(2)
Co(1)–N(6)#1	2.220(6)	N(1)–Co(1)–O(5)	96.20(18)
C(1)–C(2)	1.334(8)	O(7)–Co(1)–O(6)	80.92(16)
C(16)–N(6)	1.429(8)	N(4)–Co(1)–O(6)	87.88(17)
N(5)–S(4)	1.596(5)	N(1)–Co(1)–O(6)	174.74(18)
N(6)–Co(1)#2	2.220(6)	O(5)–Co(1)–O(6)	85.88(17)
O(1)–S(2)	1.460(4)	O(7)–Co(1)–N(6)#1	85.9(2)
O(2)–S(2)	1.436(5)	N(4)–Co(1)–N(6)#1	171.7(2)
O(3)–S(4)	1.436(4)	N(1)–Co(1)–N(6)#1	91.4(2)
O(4)–S(4)	1.432(4)	O(5)–Co(1)–N(6)#1	86.8(2)
		O(6)–Co(1)–N(6)#1	83.85(19)

Symmetry transformations used to generate equivalent atoms: #1: $x + 1/2, -y + 1, z - 1/2$; #2: $x - 1/2, -y + 1, z + 1/2$.

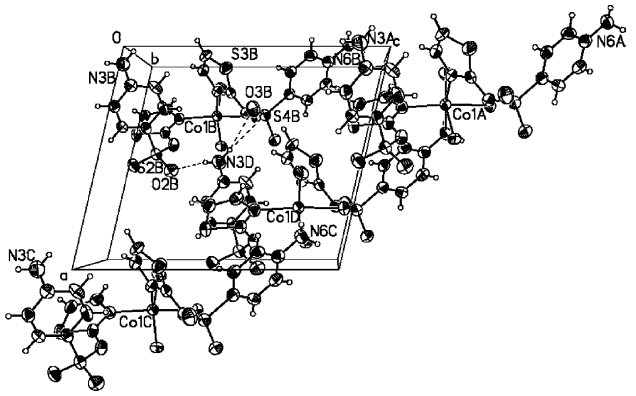


Fig. 3. Crystal packing of (**2**), showing a simplified hydrogen bonding scheme. XP view along *b* axes (Sheldrick, 1994), thermal ellipsoids at 50% probability level.

3.3. Infrared spectra

IR selected spectral data of the Co(II)–ST complexes (pink powder and red crystals) and the ligand (as sulfathiazole and its sodium salt) are presented in Table 3.

In the 3600–3000 cm^{-1} region, broad bands appear for NaST and Co(II)–ST (both pink powder and red crystals) due to the presence of hydration water [40,41]. The strong band at 1536 cm^{-1}, attributed in the sulfadrug to the thiazole ring vibration, was shifted to lower frequencies. This fact is in agreement with the interaction through the $N_{thiazole}$ atom [42]. In the two cobalt compounds the bands attributed to the SO_2 vibrations remain unaltered, suggesting no interaction of the –SO_2-group with the metal ion. This was confirmed for (**1**) by Raman spectroscopy: the symmetric stretching located at 1123 cm^{-1} increased its intensity as expected. According to the observed changes in the IR spectra of (**1**) and (**2**) it is possible to infer that the thiazole nitrogen atoms might be sites of coordination of the cobalt atom with the sulfathiazolato anions in

Table 3
Assignment of the vibrational spectra (frequency: υ, cm^{-1}) of sulfathiazole (HST), its sodium salt (NaST) and its Co(II) complex (Co(II)–ST), as pink powder (**1**) and red crystals (**2**)

HST	NaST	Co(II)–ST (**1**)	Co(II)–ST (**2**)	Assignments
	3589 m	3582 sh	masked	νOH
3346 m	3492 s	3460 s, br	3468 m	$\nu_{as}NH_2$
	3418 s		3443 m	
3320 m	3336 s	3358 s, br	3386 sh	ν_sNH_2
			3358 s	
	1622, m	1629 m	1629 m	δH_2O
1536 vs	1445 vs	1450 s	1445 s	thiazole ring
1324 m	1321 m	1316 m	1318 m	$\nu_{as}SO_2$
1138 s	1131 s	1123 vs	1146 m	ν_sSO_2
920 s	958 s	968 m	962 m	νSN
732 m				ωNH
573 s	569 m	577 m	572 m	ωSO_2
554 m	551 s	553 s	557 m	ωSO_2

both complexes. This conclusion is consistent with related systems containing sulfathiazole and different metal ions [21,43–46]. The differences that are noted in the region between 4000 and 3000 cm^{-1} of the IR spectra of (**1**) and (**2**) are probably due to differences in the coordination of the amino group in both complexes.

3.4. Thermogravimetric behavior

The thermal behavior of compounds HST and Co(II)–ST (**1**), pink powder, are shown in Fig. 4. The thermal degradation of sulfathiazole proceeds in four different stages. The first decomposition process takes place between 10 and 296 °C with about 18.4% weight loss (DTA signals: 175 °C (endo, w) and 207 °C (endo, w)). Upon further heating, the sample loses mass in two steps ($\Delta\omega$ = 8.6% and 6.1%) up to 425 °C, then the decomposition speeds up suddenly with a strong DTA signal at 514 °C (exo, s), giving volatile products.

In the case of Co(II)–ST (**1**), the sample first loses weight corresponding to four water molecules (observed 11.2%, calculated 11.3%) between 15 and 210 °C, DTA: 125 °C (endo, vw). On further heating the decomposition occurs in the range 210–1000 °C, showing that there are at least four chemical processes in progress, associated with three exothermic signals at 287 °C (exo, vw), 466 °C (exo, vw) and 576 °C (exo, vs). The final product, Co_2O_3, could be identified based on its IR spectrum. The final formation of Co_2O_3 entails $\Delta\omega$ = 87% in agreement with the experimental determination. Therefore, the following general decomposition scheme can be formulated:

$$[Co(ST)_2(H_2O)_4] \xrightarrow{\phi,O_2} Co_2O_3 + \text{other volatile products}$$

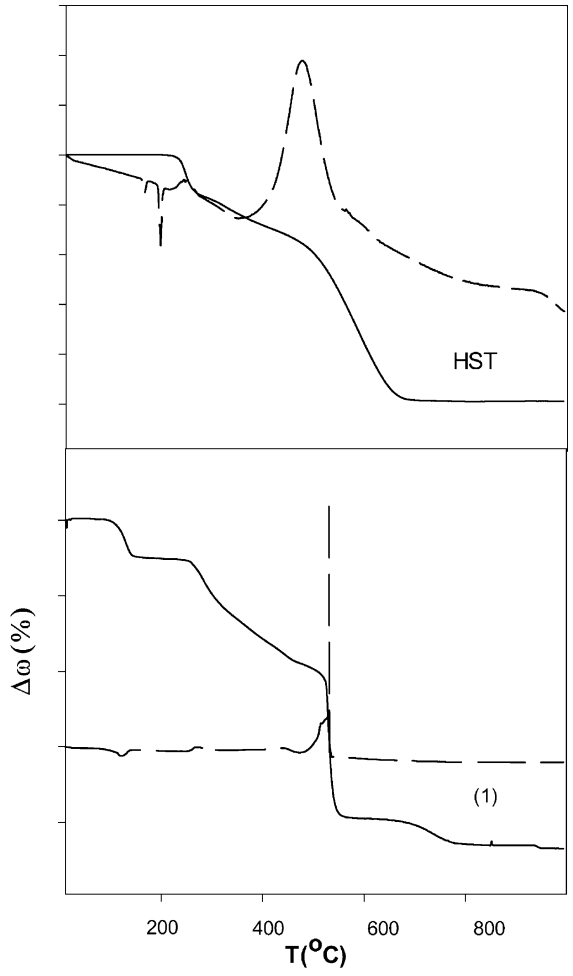


Fig. 4. TG (—) and DTA (- - -) traces for the thermal decomposition of HST and (**1**) system (O_2 flow = 60 cm^3/min, heating rate: 10 °C/min).

3.5. Magnetic behavior

The measured μ_{eff} for Co(II)–ST (1), 4.63 BM, is in the range of 4.1–5.2 BM according to the values expected for a d^7 (s = 3/2) system with spin–orbit coupling [47].

3.6. Electronic spectra

Electronic spectra of complexes can provide valuable information related to bond and structure, since the colors are intimately related to the magnitude of the spacing between d-orbitals (e_g and t_{2g} or e and t_2 orbitals in octahedral and tetrahedral complexes, respectively), which depends on factors such as the geometry of the complex, the nature of the ligands present and the oxidation state of the central metal atom [47].

The diffuse reflectance spectrum was measured in the 400–900 nm range. The spectrum of Co(II)–ST (**1**) suggests an octahedral geometry around the metal ion [48]. There can be observed two of the three possible electronic transitions: $\nu_2[^4T_{1g} \rightarrow {}^4A_{2g}]$ = 610 nm and $\nu_3[^4T_{1g} \rightarrow {}^4T_{1g}(P)]$, multiple structured at 532, 480 (sh) and 435 (sh) nm. The $\nu_1[^4T_{1g} \rightarrow {}^4T_{2g}]$ transition is expected at 1300 nm, outside the measured range.

3.6.1. Electronic spectra in solution

The wavelength of the absorption maxima, in nm, and their respective molar absortivity (ε, in $M^{-1}\,cm^{-1}$) are summarized for both (**1**) and $CoCl_2\cdot 6H_2O$ in methanol and DMSO solutions in Table 4.

The electronic spectrum produced by $CoCl_2\cdot 6H_2O$ in methanol seems very similar to that arising from the octahedral $[Co(H_2O)_6]^{2+}$ complex in water [49]. The major differences between the spectra of (**1**) and $CoCl_2\cdot 6H_2O$ are observed in an aprotic solvent, DMSO, where the two bands observed ($\lambda 1$ and $\lambda 2$) are shifted to lower wavelength for (**1**). The absortion maxima for cobalt chloride in DMSO occur at 615 and 679 nm. The absortion maxima of (**1**) are shifted to lower wavelength respect to the maxima corresponding to $CoCl_2\cdot 6H_2O$,

Table 4
Electronic spectra in solution

Compound	Solvent							
	Methanol				DMSO			
	$\lambda 1$	$\varepsilon 1$	$\lambda 2$	$\varepsilon 2$	$\lambda 1$	$\varepsilon 1$	$\lambda 2$	$\varepsilon 2$
$[Co(II)(ST)_2(H_2O)_4]$ (**1**)	531	33	620 (sh)		539	158	584	213
$CoCl_2 \cdot 6H_2O$	528	8	668	3	615	127	679	185

suggesting an increase in the ligand field strength [50]. Because their ε value in a protic solvent, the two spectra suggest an octahedral environment around the Co(II) ion, while for (**1**) in DMSO there is a tetrahedral arrangement around the Co(II) ion. Comparing both the color of the DMSO solution of (**1**) and the precipitate obtained in the first moment (which turn in a spontaneous way into the pink solid (**1**)), it is possible to suggest that the blue unstable solid obtained as the initial precipitate, could have a tetrahedral geometry around the Co(II) ion.

3.7. EPR measurements

X-band EPR spectra of a frozen DMSO solution of (**1**) and (**2**) were recorded at 77 K. Both spectra were very similar. The isotropic g value is close to 2.9. The hyperfine structure expected for the 100% abundant ^{59}Co isotope ($^{59}I = 7/2$) is not observed in the spectra of both samples (pink solid (**1**) and red crystals (**2**)). This suggests that the magnitude of the exchange interaction between Co(II) ions is larger than the magnitude of the hyperfine coupling parameter A, so the hyperfine structure collapses and gives a single collapsed peak [37]. The collapse of the hyperfine structure produces the observed Lorentzian line shape. A similar line shape EPR spectrum was observed for a complex of Co(II) and citric acid, at pH $\cong$ 5, in the form of its K^+ salt, at 4 K, which would produce mononuclear octahedral Co(II)–citrate species [51]. In the EPR spectrum of Co(II)–ST it is possible to observe a shoulder of the main resonance at a g value of ca. 3.4, which is absent in the Co(II)–citrate one. It might be probably due to the presence of N-atoms coordinated to cobalt in Co(II)–ST, in addition to O-atoms, while in Co(II)–citrate, there are only O-atoms coordinated to Co(II). Another difference with respect to the citrate system is that the resonance of Co(II)–ST is observable at 77 K, which suggests minor intensity of relaxation effects in the sulfathiazole system.

3.8. Antifungal activity

Some metal complexes of sulfadrugs promote rapid healing of skin disorders (e.g., the Ag(I)- and the Zn(II)-sulfadiazine) in preventing bacterial infection in burnt animals [52]. In addition to its well-known antibacterial activity, silver sulfadiazine was recently reported to possess strong antifungal properties [53], which makes it a clinically widely used topical agent for the treatment of wound and burnt infections [54].

Although several classes of antifungal compounds are presently available, resistance to these drugs constantly emerges [55] and it is of crucial importance to investigate new types of antifungal agents in order to prevent this serious medical problem. Metal ions (such as Zn(II)) or metal complexes with putative clinical applications were extensively studied in recent years [56]. Complexes of silver and zinc sulfonamides (and some cerium derivatives) have successfully been used for the last 20 years for the prophylaxis and treatment of microbial and fungal burnt wound infections and they seem to constitute a valuable alternative for resolving the resistance problem [57,58]. Results of the antifungal assay with (**1**) (and NaST in order to compare with the ligand) are showed in Table 5. Only the two species of the *Aspergillus* genus tested were susceptible to both compounds.

When tested against *A. fumigatus*, both compounds, Co(II)–ST (**1**) and NaST, showed the same MIC values suggesting that the activity could be due to the sulfathiazole moiety. In contrast, it is interesting to note that compound (**1**) inhibits *A. flavus* while the ligand NaST does not. This difference in activity could be due to the presence of the metal in the complex which, according with previous reports, might exert its antifungal action by inhibition of enzymes that are involved in the biosynthesis of cell walls of fungi [59].

Table 5
MIC values (μg/mL)[a] of sodium sulfathiazole (NaST) and the Co(II)–sulfathiazolate complex $[Co^{II}(ST)_2(H_2O)_4]$ (**1**) acting against human opportunistic pathogenic fungi

	NaST	(**1**)	Amp	Ket	Terb
C. albicans	>250	>250	0.75	0.50	
C. tropicalis	>250	>250	0.50	0.125	
S. cerevisiae	>250	>250	0.50	0.50	
C. neoformans	>250	>250	0.40	0.25	
A. fumigatus	200	200	3.00	12.50	
A. flavus	>250	100	3.00	2.00	
A. niger	>250	>250	0.90	12.50	
M. gypseum	>250	>250	0.12	0.05	0.01
T. rubrum	>250	>250	0.75	0.25	0.04
T. mentagrophytes	>250	>250	0.10	0.05	0.01

[a] The MIC was confirmed by two replicates. Amp: Amphotericin B; Ket: Ketoconazole; Terb, Terbinafine *Candida albicans* ATCC 10231; *C. tropicalis C Cryptiococccus neofiormans* ATCC 32264; *Saccharomyces cerevisiae* ATCC 9763; *Aspergillus fumigatus* ATCC 26934; *A. flavus* ATCC 9170; *A. niger* ATCC 9029; *Microsporum gypseum* C 115, *Trichophyton rubrum* C 113, *Trichophyton mentagrophytes* ATCC 9972. ATCC: American Type Culture Collection (Rockville, MD, USA); C: CEREMIC, Centro de Referencia Micológica, Facultad de Ciencias Bioquímicas y Farmacéuticas, Suipacha 531-(2000)-Rosario, Argentina.

4. Conclusion

The reaction between sulfathiazole and cobalt(II) leads to two stable compounds, obtained in sequencial steps, whose molecular formulas differ from each other by one water molecule. The IR spectra of both compounds differ in the region of the signals of the amino group. The 6th position around Co(II), which in (**2**) is filled with the amino group of a sulfathiazolate moiety – acting as a bidentated ligand – would be filled with a water molecule in (**1**).

The metal complex Co(II)–ST (**1**) displayed a moderate antifungal activity against both species of *Aspergillus* tested. This activity was showed to be the same as that of the corresponding ligand NaST against *A. fumigatus* but interestingly, it marked an important difference with the antifungal behavior of NaST against *A. flavus*, which was not inhibited by the ligand up to 250 μg/mL.

5. Supporting information available

CCDC 239368 contains the supplementary crystallographic data for this paper. These data can be obtained free of charge via www.ccdc.cam.ac.uk/data_request/cif, by emailing data_request@ccdc.cam.ac.uk, or by contacting the Cambridge Crystallographic Data Centre, 12, Union Road, Cambridge CB2 1EZ, UK; fax: +44 1223 336033.

Acknowledgements

We are grateful for funding from FONDECYT 1020122. J.C.M.A. is a grateful recipient of a Deutscher Akademischer Austauschdienst scholarship. P.A.M.W. is member of the Carrera del Investigador CICPBA. M.R. is member of the Carrera del Investigador CIC-UNR. We also thank Dr. Aviva Levina for the registration of the EPR spectra. S.Z. gives thanks to Agencia de Promociones Científicas y Tecnológicas de Argentina, ANPCyT (PICTR 260) and to Project X.7-PIBEAFUN (Iberian–American Project on Search and Development of Antifungal Agents) of the Iberian-American Program for the Development of Science and Technology (CYTED).

References

[1] F. Blasco, L. Perelló, J. Latorre, J. Borrás, S. Garciá-Granda, J. Inorg. Biochem. 61 (1996) 143.
[2] A. Bult, in: H. Sigel (Ed.), Metal Ions in Biological Systems, 16, Marcel Decker, New York, 1983, p. 261.
[3] Th. Nogrady, Medicinal Chemistry, 2nd ed., Oxford University Press, New York, 1988, p. 383.
[4] E.R. Barnhart (Ed.), Physician's Desk Reference, PDR, 43rd ed., Medical Economics, New York, 1989.
[5] G. Mandell, M. Sande, in: A. Goodman, L. Gilman (Eds.), Las Bases Farmacológicas de la Terapéutica, 6th ed., Ed. Médica Panamericana, Buenos Aires, 1981.
[6] A. García-Raso, J.J. Fiol, S. Rigo, A. López-López, E. Molins, E. Espinosa, E. Borrás, G. Alzuet, J. Borrás, A. Castiñeiras, Polyhedron 19 (2000) 991.
[7] J. Casanova, G. Alzuet, J. Borrás, L. David, D. Gatteschi, Inorg. Chim. Acta 211 (1993) 183.
[8] G. Alzuet, S. Ferrer-Llusar, J. Borrás, J. Server-Carrió, R. Martínez-Máñez, J. Inorg. Biochem. 75 (1999) 189.
[9] A. Bonamartini Corradi, E. Gozzoli, L. Menabue, M. Saladini, L.P. Battaglia, P. Sgarabotto, J. Chem. Soc., Dalton Trans. (1994) 273.
[10] S. Ferrer, J. Borrás, E. Garcia-España, J. Inorg. Biochem. 39 (1990) 297.
[11] C.T. Supuran, F. Mincione, A. Scozzafava, F. Briganti, G. Mincinone, M.A. Ilies, Eur. J. Med. Chem. 33 (1998) 247.
[12] C.T. Supuran, A.J. Scozzafava, Enzyme Inhib. 13 (1997) 37.
[13] A. Jitianu, M.A. Ilies, A. Scozzafava, C.T. Supuran, Main Group Met. Chem. 20 (1997) 14.
[14] A. Scozzafava, L. Menabuoni, F. Mincione, F. Briganti, G. Mincinone, C.T. Supuran, J. Med. Chem. 42 (1999) 2641.
[15] M. Barboiu, M. Cimpoesu, C. Guran, C.T. Supuran, Metal Base Drugs 3 (1996) 227.
[16] F. Briganti, A. Scozzafava, C.T. Supuran, Eur. J. Med. Chem. 32 (1997) 901.
[17] M.H. Torre, G. Facchin, E. Kremer, E. Castellano, O.E. Piro, E.J. Baran, J. Inorg. Biochem. 94 (2003) 200.
[18] J. Casanova, G. Alzuet, S. Ferrer, J. Borrás, S. García-Granda, E. Perez-Carreño, J. Inorg. Biochem. 51 (1993) 689.
[19] J. Casanova, G. Alzuet, J. Borrás, J. Timoneda, S. García-Granda, I. Cándano-García, J. Inorg. Biochem. 56 (1994) 65.
[20] J. Casanova, G. Alzuet, J. Latorre, J. Borrás, Inorg. Chem. 36 (1997) 2052.
[21] S. Bellú, E. Hure, M. Trapé, M. Rizzotto, E. Sutich, M. Sigrist, V. Moreno, Quím. Nova 26 (2003) 188.
[22] S.J. Lippard, J.M. Berg, Principles of Bioinorganic Chemistry, University Science Books, Mill Valley, CA, 1994.
[23] J.J.R. Fraústo da Silva, R.J.P. Williams, The Biological Chemistry of the Elements, Clarendon Press, Oxford, 1997.
[24] I. Bertini, H. Gray, S. Lippard, J. Valentine, Bioinorganic Chemistry, University Science Books, Mill Valley, CA, 1994.
[25] R. Dreos, A. Felluga, G. Nardin, L. Randaccio, P. Siega, G. Tauzher, Inorg. Chem. 40 (2001) 5541.
[26] E. Carvalho, R. Aasa, P. Göthe, J. Inorg. Biochem. 62 (1996) 147.
[27] N. Bonander, T. Vänngard, L. Tsai, V. Langer, H. Nar, L. Sjölin, Proteins 27 (1997) 385.
[28] A. Adrait, L. Jacquamet, L. Pape, A. González de Peredo, D. Aberdam, J.L. Hazemann, J.M. Latour, I. Michaud-Soret, Biochemistry 38 (1999) 6248.
[29] K.R. Strand, S. Karlsen, K.K. Andersson, J. Biol. Chem. 277 (2002) 34229.
[30] G. Schwarzenbach, H. Flaschka, Complexometric Titration, Methuen, London, 1969.
[31] I.M. Kolthoff, E.B. Sandell, E.J. Meehan, Bruckenstein, S. Análisis Químico Cuantitativo, 6th ed. Editorial Nigar S.R.L., Buenos Aires, 1979.
[32] J. Cowan, Inorganic Biochemistry an Introduction, VCH, New York, 1993.
[33] (a) G.M. Sheldrick, SHELXS-97 and SHELXL-97. Programs for structure resolution and refinement, University of Göttingen, Göttingen, Germany, 1997;
(b) G.M. Sheldrick, SHELXTL_PC Version 5.0, Siemens Analytical X-ray Instruments Inc., Madison, WI, USA, 1994.

[34] L.R. Wright, E.M. Scott, S.P. Gorman, J. Antimicrob. Chemother. 12 (1983) 317.
[35] S.A. Zacchino, G.E. Rodríguez, G. Pezzenati, G. Orellana, R.D. Enriz, M. Gonzalez Sierra, J. Nat. Prod. 60 (1997) 659.
[36] S.A. Zacchino, S.N. López, G. Pezzenati, R.L. Furlán, C.B. Santecchia, L. Muñoz, F.A. Giannini, A.M. Rodríguez, R.D. Enriz, J. Nat. Prod. 62 (1999) 1353.
[37] A. Rizzi, C. Brondino, R. Calvo, R. Baggio, M.T. Garland, R. Rapp, Inorg. Chem. 42 (2003) 4409, and references therein.
[38] E. Borrás, G. Alzuet, J. Borrás, J. Server-Carrió, A. Castiñeiras, M. Liu-González, V. Sanz-Ruiz, Polyhedron (2000) 1859.
[39] G. Alzuet, J. Borrás, F. Estevan, M. Liu-González, F. Sanz-Ruiz, Inorg. Chim. Acta 343 (2003) 56.
[40] D. Lin Vien, N.B. Colthup, W.F. Fateley, J.G. Grasselli, Infrared and Raman Characteristic Frequencies of Organic Molecules, Academic Press, Boston, MA, 1991.
[41] B. Smith, Infrared Spectral Interpretation. A Systematic Approach, CRC Press, New York, 1999.
[42] B. Simó, L. Perelló, R. Ortiz, A. Castiñeira, J. Latorre, E. Cantón, J. Inorg. Biochem. 81 (2000) 275.
[43] J. Casanova, G. Alzuet, S. Ferrer, J. Latorre, J.A. Ramírez, J. Borrás, Inorg. Chim. Acta 304 (2000) 170.
[44] M. González-Álvarez, G. Alzuet, J. Borrás, B. Macías, M. Del Olmo, M. Liu-González, F. Sanz, J. Inorg. Biochem. 89 (2002) 29.
[45] R. Yuan, R. Xiong, Z. Chen, P. Zhang, H. Ju, Z. Dai, Z. Guo, H. Fun, X. You, J. Chem. Soc., Dalton Trans. (2001) 774.
[46] E. Chufán, J. Pedregosa, J. Borrás, Vibr. Spectrosc. 15 (1997) 191.
[47] J. Huheey, E. Keiter, R. Keiter, Inorganic Chemistry: Principles of Structure and Reactivity, Harper Collins, New York, 1993.
[48] A.B.P. Lever, Inorganic Electronic Spectroscopy, 2nd ed., Elsevier, The Netherlands, 1984.
[49] F.A. Cotton, G. Wilkinson, Advanced Inorganic Chemistry, 4th ed., Wiley, New York, 1980.
[50] C. Comussi, M. Grespan, P. Polese, R. Portanova, M. Tolazzi, Inorg. Chim. Acta 321 (2001) 49.
[51] N. Kotsakis, C.P. Raptopoulou, A. Terzis, J. Giapintzakis, T. Jakusch, T. Kiss, A. Salifoglou, Inorg. Chem. 42 (2003) 22.
[52] A. García-Raso, J.J. Fiol, G. Martorell, A. López-Zafra, M. Quirós, Polyhedron 16 (1997) 613.
[53] J.B. Wright, K. Lam, D. Hansen, R.E. Burrell, Am. J. Infect. Control 27 (1999) 344.
[54] A.J. Singer, L. Berrutti, S.A. McClain, Wound Repair Regen. 7 (1999) 356.
[55] K. Asai, N. Tsuchimori, K. Okonogi, J.R. Perfect, O. Gotoh, Y. Yoshida, Antimicrob. Agents Chemother. 43 (1999) 1163.
[56] A.Y. Louie, T. Meade, J. Chem. Rev. 99 (1999) 2711.
[57] N. George, J. Faoagali, M. Muller, Burns 23 (1997) 493.
[58] P. Marone, V. Monzillo, L. Perversi, E. Carretto, J. Chemother. 10 (1998) 17.
[59] A. Mastrolorenzo, A. Scozzafava, C. Supuran, Eur. J. Pharm. Sci. 11 (2000) 99.

Available online at www.sciencedirect.com
SCIENCE DIRECT®
Polyhedron 24 (2005) 511–519
POLYHEDRON
www.elsevier.com/locate/poly

Spectroscopic characterization of coordination complexes based on dichlorocopper(II) and poly(4-vinylpyridine): Application in catalysis

Alvaro J. Pardey [a,*], Alcides D. Rojas [a], Jorge E. Yánez [a], Paulino Betancourt [b], Carlos Scott [b], CarlosChinea [c], Caribay Urbina [d], Delfin Moronta [e], Clementina Longo [f]

[a] Centro de Equilibrios en Solución, Escuela de Química, Facultad de Ciencias, Universidad Central de Venezuela, Caracas, Venezuela
[b] Centro de Catálisis Petróleo y Petroquímica, Escuela de Química, Facultad de Ciencias, Universidad Central de Venezuela, Caracas, Venezuela
[c] Centro de Química Organometálica y Macromolecular, Escuela de Química, Facultad de Ciencias, Universidad Central de Venezuela, Caracas, Venezuela
[d] Centro de Microscopía Electrónica, Facultad de Ciencias, Universidad Central de Venezuela, Caracas, Venezuela
[e] Escuela de Física, Facultad de Ciencias, Universidad Central de Venezuela, Caracas, Venezuela
[f] Centro de Investigación y Desarrollo de Radiofármacos, Facultad de Farmacia, Universidad Central de Venezuela, Caracas, Venezuela

Received 15 June 2004; accepted 8 December 2004

Abstract

The formation of transition metal complexes between dichlorocopper(II) and a poly(4-vinylpyridine)/divinylbenzene(2%) polymeric matrix is described in this contribution. The nitrogen atom of the pyridine groups of the organic polymer is coordinatively bonded to the Cu center as suggested by X-ray photoelectron spectroscopy (XPS), UV–vis/diffuse reflectance (UV–vis/DR), electron paramagnetic resonance (EPR), differential scanning calorimetry (DSC) and Fourier transform infrared (FT-IR) techniques. The immobilized catalyst was also characterized by DTA-TGA analysis and the morphology and elemental analysis of this copper/poly(4-vinylpyridine) complex were studied by the scanning electron microscopy/energy dispersive X-ray (SEM/EDX) technique. This material catalyzes the water gas shift reaction as well as the reduction of nitrobenzene to aniline and azobenzene.
© 2005 Elsevier Ltd. All rights reserved.

Keywords: Copper; Poly(4-vinylpyridine); Carbon monoxide; Water gas shift reaction; Spectroscopic characterization

1. Introduction

The characterization of ion-containing polymers has been the subject of numerous investigations. It has been demonstrated that the themophysical properties of polymeric ligands can be modified by coordination to transition metal complexes [1,2].

The $CuCl_2 \cdot 2H_2O$ salt is an attractive candidate to form coordination complexes with the pyridine moieties of poly(4-vinylpyridine). For example, a soluble Cu–pyridine complex of the type $CuCl_2(py)_2$ complex is known [3].

Studies in our laboratories have long been concerned with the use of the rhodium (I) complexes $[Rh(COD)(amine)_2](PF_6)$ (amine = pyridine, 2-picoline, 3-picoline, 4-picoline, 3,5-lutidine or 2,6-lutidine) immobilized on poly(4-vinylpyridine)/divinylbenzene(2%) as catalyst precursors for various chemical reactions (namely, water gas shift reaction (WGSR) [4,5], reduction of nitrobenzene [6,7] and hydroformylation of 1-hexene [8,9]) due to their easy preparation, good stability and high or moderate catalytic activities. The granular nature of this polymer and its insolubility in all organic solvents allows for it isolation by simple filtration [10].

* Corresponding author. Tel.: +58212 605 1225; fax: +58212 481 8723.
E-mail address: apardey@strix.ciens.ucv.ve (A.J. Pardey).

0277-5387/$ - see front matter © 2005 Elsevier Ltd. All rights reserved.
doi:10.1016/j.poly.2004.12.014

We previously reported the homogenous catalysis of the WGSR by copper dichloride dissolved in aqueous substituted pyridine (methyl and dimethyl pyridines) solutions [11]. For example, TF(H_2) of about 6 mol/day for [Cu] = 20 mM (2.0×10^{-4} mol), P(CO) = 1.9 atm at 120 °C was observed for the more active 4-picoline (4-methylpyridine) system. In the course of continuing to explore similar systems in our laboratories it became a matter of interest to study the Cu/P(4-VP) system because it is known that the most commercial active heterogeneous system catalyst for the WGSR contains a mixture of copper and zinc oxide [12].

In the present study, we extend the use of the poly-(4-vinylpyridine)/divinylbenzene(2%) polymeric matrix instead of pyridine as a ligand coordinated to $CuCl_2$ salt. Here, we report the preparation, the characterization by XPS, UV–vis/DR, EPR, DSC, FT-IR, DTA-TGA and SEM/EDX techniques and the catalytic activity of P(4-VP)-immobilized $CuCl_2$ on the water gas shift reaction and the reduction of nitrobenzene.

2. Experimental

2.1. Materials

2-Ethoxyethanol (Aldrich) was distilled from anhydrous stannous chloride. Water was doubly distilled. Poly(4-vinylpyridine)/divinylbenzene(2%) (P(4-VP)), was used as provided by Reilly Industries. Nitrobenzene (Aldrich) was distilled in H_2SO_4 (1 M) and redistilled from $CaCl_2$ prior to use. All gas mixtures He/H_2 (91.4%/8.6%, v/v), CO/CH_4 (95.8%/4.2%, v/v) and CO/CH_4/CO_2/H_2 (84.8%/5.1%/5.3%/4.8%, v/v) were purchased from BOC Gases and were used as received. Dichlorocopper(II) salt (Merck) was used as received.

2.2. Instrumentation

The UV–vis spectra of the solutions (1 cm quartz cell) and of the solids (Labsphere RSA-PE-20 diffuse reflectance cell) were recorded on a Perkin–Elmer Lambda 10 spectrophotometer. Infrared spectra were recorded on a Perkin–Elmer 1760X-FT spectrophotometer using KBr pellets for solid samples. Electron paramagnetic spectroscopy experiments were carried out in a conventional Varian E-line X-band spectrometer, using a rectangular cavity operating in the TE 102 mode. The scanning electron micrographs were recorded on a Hitachi S-500 microscope with an energy dispersive X-ray detector. The thermal behavior studies were carried out using a TA Instruments SDT 2960 Simultaneous DTA-TGA analyzer. Glass transition temperatures were measured on a Perkin–Elmer DSC 7 at a rate of 20 °C/min under a nitrogen purge.

Photoelectron spectra of the solid were recorded with a VG-220i-XL ESCALAB spectrometer using monochromatized X-ray Mg Kα radiation (1235.6 eV). The solid was mounted on a standard sample stud. Nominal resolution was measured as full-width at half-maximum of 1.0 (core-level spectrum) to 1.5 eV (survey spectrum). The analyzed core-level lines were calibrated against the C 1s binding energy set at 285 eV of CH_x neutral carbon. The signals were deconvoluted using mixed Gaussian–Lorentzian curves where the Gaussian character was set at 80%. Since the Cu_{2p} line is rather insensitive to the oxidation state of copper (the Cu $2p_{3/2}$ component is at: 932.6, 932.5, 933.7 and 935.1 eV for Cu, Cu_2O, CuO and $Cu(OH)_2$, respectively), it is important to follow the energy position of the LMM Auger line of Cu.

Gas samples analyses from catalytic runs were performed as described in detail previously [4] on a Hewlett–Packard 5890 Series II programmable (ChemStation) gas chromatograph fitted with a thermal conductivity detector. The column used was Carbosieve-B (80–100) mesh obtained from Hewlett–Packard using a He/H_2 mixture as the carrier gas.

2.3. Complex preparation

A mixture of 0.5 g of P(4-VP) and 0.0341 g (2.0×10^{-4} mol) of $CuCl_2 \cdot 2H_2O$ dissolved in 10 mL of 80% aqueous 2-ethoxyethanol was stirred for 72 h in air until about 99% of the copper was extracted by the polymer from the solution as determined by UV–vis spectrophotometry. The amount of the absorbed copper on P(4-VP) was determined by subtracting the initial amount of copper salt from the unabsorbed one. The resulting blue polymer was filtered, washed with 5 mL of 2-ethoxyethanol/H_2O 8/2, v/v, and dried in vacuum at room temperature. This material will be referred herein as Cu/P(4-VP).

2.4. Catalyst testing

WGSR catalytic runs were conducted in all-glass reactor vessels consisting of a 100 mL round bottomed flask connected to an "O" ring sealed joint to a two-way Rotoflow Teflon stopcock attached to the vacuum line [4]. In a typical run, the loaded polymer beads and 10 mL of 80% aqueous 2-ethoxyethanol were added to the glass reactor vessel, then the solution was degassed by three freeze–pump–thaw cycles. The reaction vessel was charged with a CO/CH_4 mixture at the desired CO partial pressure (1.4 atm at 25 °C, but 1.9 atm at 110 °C), and then suspended in a circulating thermostated glycerol oil bath set at 110 °C for 8–48 h. The specified temperature was maintained at ±0.5 °C by continuously stirring the oil bath as well as the reaction mixture which was provided with a Teflon-coated magnetic stirring bar. Gas samples (1.0 mL) were ana-

lyzed by GC at the end of the reaction time. Methane was used as internal standard to allow calculation of absolute quantities of CO consumed and H_2 and CO_2 produced during a time interval, with calibration curves being prepared periodically for CO, CH_4, H_2, and CO_2, and analyzing known mixtures checked their validities.

Nitrobenzene reduction catalytic runs were conducted in a 150 mL mechanically stirred stainless steel Parr reactor. In a typical run, 0.5 g of the Cu/P(4-VP) solid, 10 mL of 80% aqueous 2-ethoxyethanol and 1.2 mL (8.1×10^{-3} mol) sample of nitrobenzene were added to the reaction vessel. Subsequent to the addition of nitrobenzene, the Parr reactor was charged with the CO/CH_4 mixture (27.2 atm partial CO pressure at 150 °C) and placed in the oil bath at 150 °C for 4–72 h. After a given time, the reaction was stopped, the reactor cooled to room temperature and excess pressure was vented and products analyzed by GC and GC–MS. A response factor method for the GC analyses of the aniline was employed [13]. The GC–MS of the aniline (molecular ion peak at $m/e = 93$ and base peak at $m/e = 65$) and azobenzene (molecular ion peak at $m/e = 182$ and base peak at $m/e = 77$) products is similar to a pure sample of aniline and azobenzene, respectively. Also the organic products were separated by column chromatography and analyzed by ^{13}C and ^{1}H NMR in a Jeol Eclipse 270 NMR spectrometer.

3. Results and discussion

3.1. General aspects

Dissolution of a solid sample of $CuCl_2 \cdot 2H_2O$ (0.0341 g, 2.0×10^{-4} mol) in 10 mL of 80% aq. 2-ethoxyethanol at room temperature leads to the gradual formation of a green–blue solution. This solution in contact with 0.5 g of P(4-VP) under continuous stirring for 72 h in air at room temperature gradually leads to formation of a blue solid material and a colorless solution.

After charging the mixture formed by the Cu/P(4-VP) ([Cu] = 2.5 wt%) blue solid and 10 mL of 80% of aqueous 2-ethoxyethanol with CO (1.9 atm) and heating the reaction vessel and its content at 110 °C in a glycerol bath, the blue solid first changed to a light-blue color, then (over 1–5 min) to a yellow color and to a final light brown–green color, characteristic of the mature catalyst system. The solution above the light brown–green solid remains uncolored.

3.2. Characterization studies

Kirsh et al. [14] reported the characterization by EPR and UV–vis spectroscopies of the water-soluble $CuCl_2$/P(4-VP) system. The P(4-VP) employed in their study was not cross-linked with any copolymer, allowing its solubility in water. They observed the formation of tetrapyridine–Cu(II) complexes, $[CuL_4]^{2+}$ (L = a nitrogen atom of the P(4-VP)). Coordination of the nitrogen atom of the pyridine moiety to the Cu(II) center was proposed. Also, G. Jeschke, provided for this soluble copper (II) complex of poly(4-vinylpyridine) a model for the geometry of the first coordination sphere supported by a combination of EPR, electron-nuclear double resonance methods (ENDOR) and molecular modelling techniques, and found that the structure of this copper complex derives from the propeller structure of $Cu(pyridine)_4$ mainly by rotation of the ligand pyridine rings with a modest tetrahedral distortion [15]. On the other hand, the addition of 2% of divinylbenzene to the poly(4-vinlypyridine) polymer makes the latter insoluble in water and in all organic solvents.

In this section, the results of SEM/EDX, UV–vis/DR, EPR, FT-IR, XPS, DTA-TGA and DSC techniques, which were used to determine the nature of the water insoluble $CuCl_2$/P(4-VP)/divinylbenzene(2%) immobilized species, are discussed.

The SEM with energy dispersive X-ray (EDX) technique was used for studying the morphology of the solid samples. We previously reported a SEM micrograph of a P(4-VP) sample, from which it can be observed that the P(4-VP) is formed by agglomerates of grains with a smooth surface [6]. Fig. 1 corresponds to the micrograph of the solid product of the reaction of P(4-VP) with the $CuCl_2 \cdot 2H_2O$ salt in contact with 80% aqueous



Fig. 1. Scanning electron micrograph of the Cu/P(4-VP) fresh catalyst sample. Magnification 5000×.

2-ethoxyethanol after 72 h of stirring in air. The elemental analysis revealed Cu and Cl in the etched areas. The same type of analysis of the smooth regions, whose morphology had not been modified, did not show the presence of Cu and/or Cl. The observed modifications in some areas on the surface of the polymeric insoluble ligand can be attributed to the anchoring of the Cu(II) center to the P(4-VP).

The UV–vis spectrum of $CuCl_2 \cdot 2H_2O$ dissolved in 80% aqueous 2-ethoxyethanol and the UV–vis/DR spectrum of the Cu/P(4-VP) blue solid sample show the displacement of the d–d transition band from 246 to 384 nm after the immobilization process. The significant difference in the d–d transition bands between the solution and the solid would be a consequence of a different coordination environment around copper (II). Efforts to obtain the UV–vis/DR spectrum of the Cu/P(4-VP) light brown–green solid were unsuccessful inasmuch that this solid undergoes oxidation to produce the blue cupric polymer-complex during the handling procedures. However, the fact that the used catalyst has a light brown–green color suggested that Cu(II) is the predominant oxidation state. It has been stated that Cu(I) complexes would be colorless since d–d electronic transitions are not feasible to take place in a d^{10} system, and metal-to-ligand charge transfer possible for d^{10} complex with aromatic structure also does not occur in the visible region of the spectrum [16].

EPR experiments show signals (Fig. 2(a)) for the Cu/P(4-VP) ([Cu] = 2.5 wt%) fresh catalyst (blue-colored solid) and these indicate the presence of copper(II) d^9 paramagnetic species in this system as expected. Similar EPR behavior was observed on reaction of $CuCl_2 \cdot 2H_2O$ with 4-picoline and 2-picoline [11]. Fig. 2 also shows the EPR spectrum of the used catalyst (light brown–green colored solid) of the same system (b) in the presence of CO. The EPR result is similar to the one observed for the Cu/P(4-VP) (blue-colored solid) system mentioned above. The samples of both did not have the same amounts of Cu/P(4-VP) as a result of handling procedures. In spite of that, the amplitude of both spectra are the same, the amount of the fresh catalyst sample (blue solid) is roughly half that the used catalyst (light brown–green solid). For that reason the intensity of spectrum (a) is smaller than the other spectrum. However, the widening of the spectrum (a) is larger than spectrum (b). The observed strong EPR signal in the used catalyst indicates the presence of copper(II) d^9 species, even though this solid was formed under CO/H_2O mixture at the working temperature. Under these reaction conditions the expected reduction of Cu(II) d^9 paramagnetic species to Cu(I) d^{10} non-paramagnetic species by the CO/H_2O mixture (as reported in the homogeneous $CuCl_2$/aqueous 4-picoline or 2-picoline systems under CO [11]) was not observed. In spite of the presence of the Cu(II) d^9 species at high concentration in the light brown–green solid, both spectra are dissimilar due to different molecular environments that surround the Cu(II) center in both solids. Based on these EPR results it is reasonable to propose the existence of at least two kinds of Cu(II) species in the blue-colored fresh catalyst. Under the CO/H_2O mixture at the working temperature, one of the Cu(II) species is relatively easily reduced to Cu(I) and the other Cu(II) species remains unreduced.

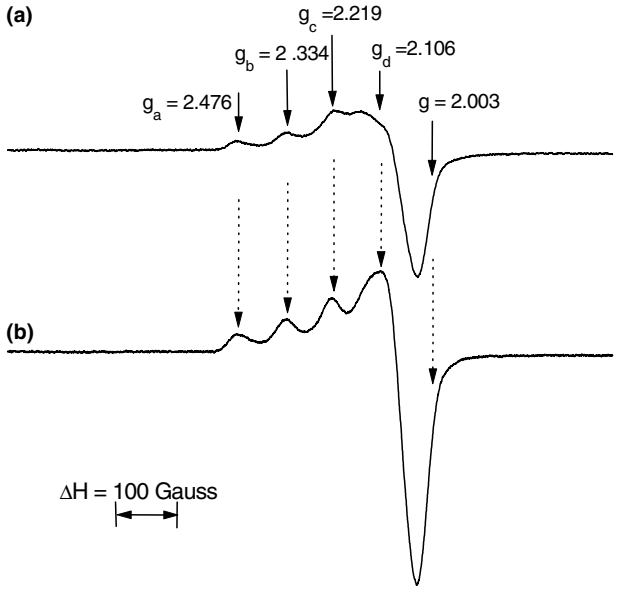


Fig. 2. EPR spectra in the 2500–3500 G region of: (a) Cu/P(4-VP) fresh catalyst; (b) Cu/P(4-VP) used catalyst.

Pomogailo and Golubeva [17] carried out magnetic susceptibility measurements and EPR spectroscopy to study the distribution of cupric ion attached to a polyethylene-grafted poly(acrylic acid) support (PE-gr-PAA). Their EPR studies revealed changes in the form of the EPR spectrum upon increasing the copper concentration in the PE-gr-PAA matrix. For example, a broad asymmetric singlet is observed which increases steadily in intensity as well as in width with increasing copper(II) content. These data indicate the proximity of the structure of Cu(II) polymer-complexes and also suggests the existence of an increase in dipole–dipole interactions between them. The temperature dependence of the magnetic susceptibility as a function of copper content also supports the conclusion of the existence of three types of copper(II) complexes: (1) isolated complexes (type-I) (2) complexes bonded by dipole–dipole interactions (type-II) and (3) clusters with strong exchange interactions (type-III).

The observed narrowing in the width of the hyperfine bands with decreasing Cu(II) content (due to its reduction to Cu(I) by the CO/H_2O couple) seen in the EPR spectrum (b) of our Cu(P-4VP) system is probably due to the existence of the same type of dipole-dipole inter-

action between copper centers described by Pomogailo and Golubeva (type-II complexes). Also our EPR results include the existence of isolated Cu/P(4-VP) complexes (type-I complexes). However, the copper concentration (2.5 wt%) used in our studies is not high enough to form clusters with strong exchange interactions (type-III complexes). The study of the magnetic susceptibility of this Cu/P(4-VP) system, which constitutes an appropriate method for determining the copper valence will be explored in future investigations.

The FT-IR spectrum (KBr pellet) of a P(4-VP) sample shows one C–N ring stretching band (n_{C-N}) at 1596(m, broad) and side group absorption bands (C–C ring stretching vibrations) at 1554(m), 1493(m), 1449(m) and 1415(m, broad) cm^{-1}. On the other hand, the FT-IR spectrum of fresh prepared KBr pellets of $CuCl_2$/P(4-VP) ([Cu] = 2.5 wt%) also shows the same bands, but three of them (1596, 1493 and 1449 cm^{-1}) shifted by ca. +3 cm^{-1}. The slight blue shift observed in the n_{C-N} of Cu/P(4-VP) could indicate N-coordination of the P(4-VP) polymer to the metal [2,16,18]. Unfortunately, a comprehensive molecular explanation is not available.

After charging the Cu/(P4-VP) blue solid with CO atmosphere (1.9 atm) in contact with 10 mL of 80% aqueous solution of 2-ethoxyethanol and heating the reaction vessel in a 110 °C glycerol bath for 6 h, the blue solid changed to a light brown–green color characteristic of the mature catalyst system. The FT-IR spectrum (KBr pellets) of the light brown–green color mature Cu/P(4-VP) catalyst sample shows one band in the v_{CO} region at 2068 cm^{-1} (carbonyl-linear Cu species) suggesting the presence of a single carbonyl copper species [11] anchored to the nitrogen-functionalized polymer. Also, the infrared spectrum of the light brown–green solid shows the v_{C-N} band at 1598 cm^{-1} and the side group absorption bands (C–C ring stretching vibrations) at 1556(m), 1495(m), 1451(m) and 1415(m, broad) cm^{-1}. A slight blue shift of ca. +2 cm^{-1} in the v_{C-N} and the side group absorption bands is observed. However, the presence of the coordinated-CO decreased the blue shift due to the back-bonding donation of dπ atomic orbital of the Cu to the π*-antibonding molecular orbital of the CO, which leads to a competition for electronic density with the π-bonding molecular orbitals of the pyridine ring. Further, a band at 3385 cm^{-1}, characteristic of the coordinated OH group, is observed in both blue and light brown–green solid samples.

Table 1 shows the XPS data for the fresh (blue solid) and used (light brown–green solid) catalysts. The N_{1s} spectrum for free P(4-VP) features a symmetric peak at 399.0 eV. However, the N_{1s} peaks of the fresh and used catalysts are broader and more asymmetric than the one for free P(4-VP), and each peak can be deconvoluted into two peaks, with one at 399.0 eV and the other at 400.3 eV. The peak at 400.3 eV indicates that a fraction of the pyridine nitrogen of the P(4-VP) interacts with the copper cations.

Table 1
XPS data for fresh (blue-colored solid) and used (light brown–green colored solid) catalysts

XPS peak	Binding energy (eV)	
	Fresh catalyst	Used catalyst
N_{1s}	399.0, 400.3	399.0, 400.3
O_{1s}	529.4, 530.4, 531.1	529.4, 530.4, 531.1, 532.0, 533.1
Cl_{2p}	198.0	
C_{1s}	285.0, 285.9	285.0, 284.9
$Cu_{2p3/2}$	933.8	932.5
Cu_{LMM}	569.6	567.8

Two C_{1s} intense peaks are present in the fresh and used catalyst. The first (the main peak) at 285.0 eV, is attributed to the aliphatic carbons of adsorbed contaminants, and the second peak at 285.9 (fresh catalyst) and 284.9 eV (used catalyst) is attributed to carbon linked to the nitrogen atom of the pyridine heterocyclic [19].

The XPS spectrum of the fresh Cu/P(4-VP) catalyst shows $Cu_{2p3/2}$ and Cu_{LMM} peaks at 933.8 and 569.6 eV, respectively, in conjunction with intense shake-up features around 938–945 eV, which are assigned to Cu(II)–OH species [20].

On the other hand, the $Cu_{2p3/2}$ component for the used Cu/P(4-VP) catalyst shows a sharp peak at 932.5 eV and there is no sign of the shake-up features around 938–945 eV, within the detection limits of the XPS technique, and these results suggest the presence of Cu(I) as expected (vide supra). Also, a peak at 567.8 eV was observed, which is typical of metallic copper. It is well known that Cu(I) complexes disproportionate rapidly at ambient temperature to Cu(II) and Cu(0) [21].

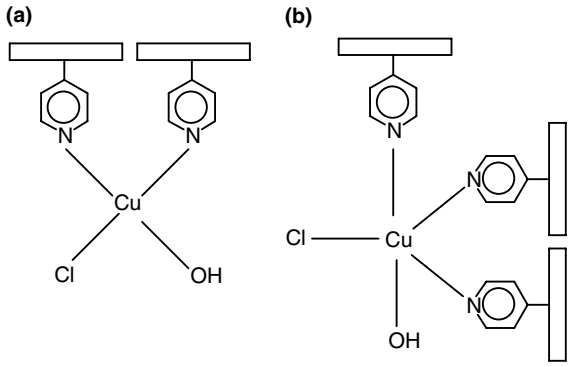
Further, the XPS analysis showed O_{1s} lines, for both fresh and used catalyst. The fresh solid presents peaks at 529.4, 530.4 and 531.1 eV, which could be assigned to Cu(II)–O species (e.g., Cu–OH). The O_{1s} peak of the used catalyst is less intense than in the case of the fresh solid. Two additional signals are observed, at 532.0 and 533.1 eV, which could be due to CO (coordinated to Cu) and to water, respectively. Finally, a XPS peak at 198.0 eV (Cl_{2p}) reveals the presence of chloride that is coordinated to the copper in the fresh catalyst.

The atomic ratios $I_N/I_{Cu} = 2.5$, $I_O/I_{Cu} = 1$ and $I_{Cl}/I_{Cu} = 1$ for the fresh catalyst were calculated from the XPS-peaks intensity ratios using the Scofield cross-section relative to each core level [22]. In such calculations it is assumed that the transmission factor T of the spectrometer and the mean free electron path λ are both functions of the kinetic energy, K.E., of the considered photoelectron [23]. The value of 2.5 for the N/Cu ratio indicates that there are at least two different Cu/P-(4-VP) species; one with two and another with three N atoms bonded to the Cu.

Further, the DTA-TGA data (Fig. 3) show that the Cu/P(4-VP) complex is stable at 250 °C, however a weight loss was observed around 100 °C due to the moisture content coming from the preparative method. The differential scanning calorimetry (DSC) technique was used to determine the glass transition temperatures. The poly(4-vinylpiridine)/2% cross-linked polymer, which exhibits a glass transition temperature (T_g) at 127.1 °C, T_g increases by 23.6 °C after the immobilization of 2.5 wt% of Cu(II) as the $CuCl_2 \cdot 2H_2O$ salt. The produced polymeric coordination complex exhibits a synergistic thermal property and it is related to the coordination of the pyridine moieties of P(4-VP) on the coordination sphere of the Cu(II) center. The pyridine, which is classified as a strong base, can displace one or two water molecules from $CuCl_2 \cdot 2H_2O$ and occupy the vacant coordination site on the Cu. Hence is it possible that the Cu bridges two different polymer chains via coordination to the pyridine lone pair, forming coordination crosslinks as suggested by the XPS results. Therefore, hindered mobility of this nature provides a way for the enhancement in the T_g. It is noteworthy that the enhancing of the glass transition temperature of poly(4-vinylpyridine) after coordination to ruthenium [2] and osmium [24] complexes has been reported.

3.3. Proposed structures for Cu/P(4-VP) complexes

The UV–vis, EPR, FT-IR, XPS and DSC results constitute experimental evidences for the formation of a coordination complex between the nitrogen electron lone pair on the P(4-VP) and the copper center in the $CuCl_2$ salt. Based on these spectroscopic results, we therefore, propose the following structures (Scheme 1). The blue-colored solid contains Cu(II) species. On the other hand, the light brown–green colored solid contains Cu(II) and Cu(I) species. The Cu(I) species present in the used catalyst comes from the reduction of the Cu(II)



Scheme 1. Proposed Cu(II) structures in the fresh catalyst.

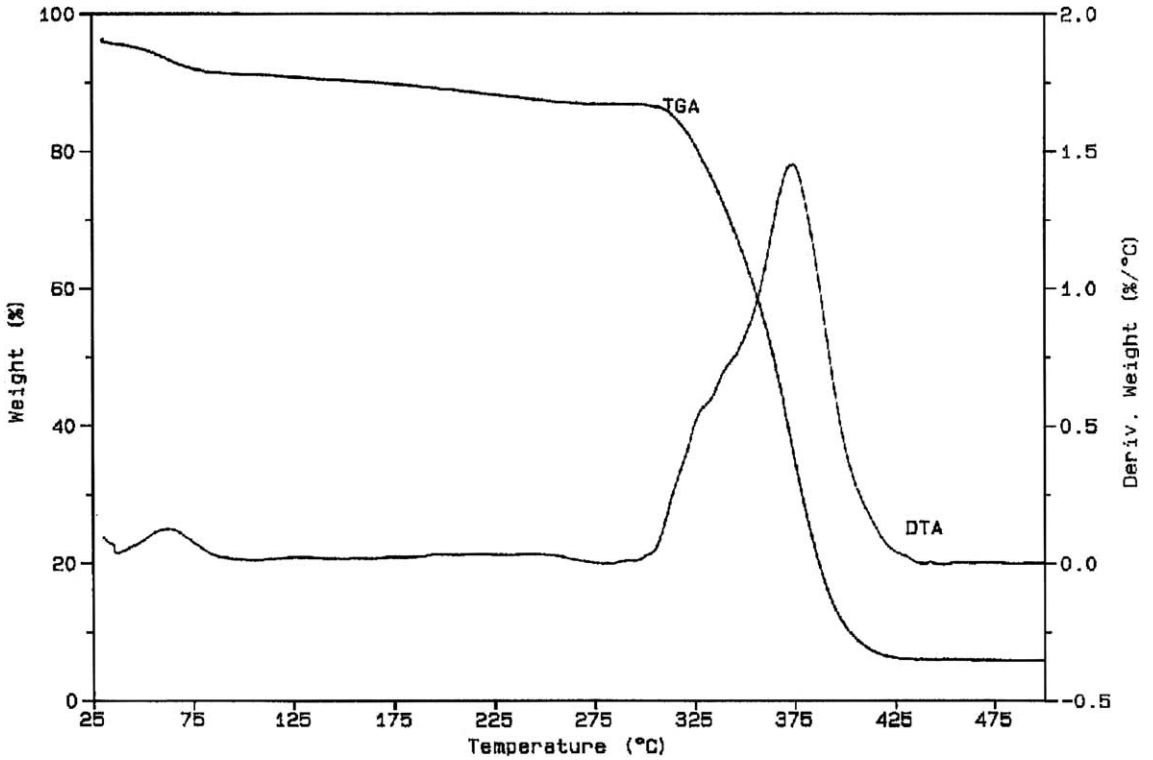


Fig. 3. DTA-TGA curves for the Cu/P(4-VP) fresh catalyst sample.

by the CO/H_2O couple under the catalytic conditions. The ligands coordinated to the Cu(II) d^9 center of the blue-colored solid are Cl^-, vinylpyridine and $(OH)^-$, the last one coming from the hydrolysis of the pyridine residues of P(4-VP). The structures (**a**) and (**b**) correspond to the blue solid. The structure (**a**) has two vinylpyridine groups and the structure (**b**) has three vinylpyridine groups coordinated to the Cu and this assignment is supported by the EPR and XPS results. Also, two and three-coordination of a metal transition ion by coordinating P(4-VP) is well known [2,25]. McCurdie and Belfiore proposed the concept of coordination crosslinks for a metal acting as a bridge between pyridine ligands of two different polymer chains [2]. Based of the DSC results it is likely probable that the Cu(II) species (**a**) and (**b**) are coordinated in a crosslink fashion through the polymeric matrix.

The number of vinylpyridine groups coordinated to Cu(II) and Cu(I) species in the light brown–green colored solid is not known although the Cu(II) and Cu(I) species present in this solid must contain OH^- and CO, and OH^- ligands, respectively. The last assignment is supported by the FT-IR and XPS results.

Although, there is no direct evidence to point which of the two (**a**) and (**b**) copper(II) species of the blue solid is reduced to Cu(I), which further by ligand exchange reaction coordinates a CO molecule. However, Gagné et al. [26] reported the reaction of carbon monoxide with blue $Cu(LBF_2)$ solution at 25 °C (LBF_2 = [difluoro-3,3′-trimethylenedinitrilo-bis(2-butanone oximato)borate]), yielding a yellow solid. The IR and the X ray structure of this yellow solid show a ν_{CO} band at 2068 cm^{-1} and a single monocarbonyl copper(I) with a 20-electron count for the metal atom coordinated to five two-electron donors, $Cu(LBF_2)(CO)$. Accordingly, the similarity in the value of the ν_{CO} band (2068 cm^{-1}) for both Cu(I)–CO/P(4-VP) and $Cu(LBF_2)(CO)$ solids and the absence of an XPS chlorine signal on the Cu(I)–CO/P(4-VP) points to propose that the copper(II) species (**b**) is reduced to Cu(I) by the CO/H_2O couple followed by a substitution of the Cl^- ligand by a CO molecule yielding a five coordinated $[P(4\text{-}VP)_x\text{–}Cu(OH)(CO)]$ ($x = 3$) immobilized species with three vinylpyridine groups (x) bonded to the Cu(I). The structures (**a**) and (**b**) that we proposed for this water insoluble Cu(II)/P(4-VP) system are different from the one proposed for the water soluble copper(II) complex of poly(4-vinypyridine) described at the beginning of Section 3.2. Applications of molecular modelling techniques for our water insoluble system are in progress and their results will be published in a forthcoming paper.

3.4. WGSR catalysis

The copper immobilized complex ([Cu] = 2.5 wt%) in contact with 10 mL of 80% aqueous 2-ethoxyethanol generates a system that shows low catalytic activity for the (WGSR equation (1)) at 110 °C under P(CO) = 1.9 atm. Quantitative analysis of gas samples taken after the reaction solution reached working temperature, indicated that production of H_2 and CO_2 and consumption of CO follow the stoichiometry shown in Eq. (1). The effect of the reaction time on the WGSR catalytic activity was studied. Blank experiments revealed that no WGS reaction occurred in the absence of the catalyst. The activities defined as turnover frequency (turnover frequency (gas) = [(mol of gas)/(mol of Cu) × (rt)] × 24 h, where (rt) is the reaction time in hours) are summarized in Table 2. It is seen that the reaction time variation has no influence on the $TF(H_2)$ and $TF(CO_2)$ values. Also the WGS catalytic activity displayed by this Cu/P(4-VP) system is similar to that showed by the homogeneous $CuCl_2$/amine system described above, under comparable reaction conditions. The catalysis of WGSR by this Cu/P(4-VP) system probably goes through a mechanism similar to that proposed for the $Rh(4\text{-picoline})_2$/P(4-VP)/aqueous 2-ethoxyethanol system [27]. The immobilized carbonyl copper(I), Cu(I)–CO/P(4-VP), species formed under the catalytic conditions plays an important role as a reaction intermediate in the catalytic cycle (namely, it must be subject to nucleophilic attack by water to generate a hydroxycarbonyl copper species, which eventually through successive transformations leads to CO_2 and H_2 WGSR-products).

$$CO + H_2O \rightleftharpoons CO_2 + H_2 \quad (1)$$

3.5. Nitrobenzene reduction catalysis

Immobilized transition metal complexes into polymers combine the good activity, selectivity and reproducibility typical of homogeneous catalysts with the easy product separation and catalyst recovery characteristic of heterogeneous catalysts [28–30].

Table 2
WGSR by $CuCl_2 \cdot 2H_2O$ immobilized on P(4-VP) in contact with 80% aqueous 2-ethoxyethanol[a]

Reaction time (h)	H_2[b] (mol × 10^{-4})	CO_2[b] (mol × 10^{-4})	$TF(H_2)$[c]	$TF(CO_2)$[c]
8	4.5	4.7	6.8	7.1
12	6.6	7.1	6.6	7.0
18	10.2	10.5	6.9	7.0
24	14.6	14.0	7.2	7.1
48	29.2	28.2	7.3	7.0

[a] 0.5 g of P(4-VP), 8 mL of 2-ethoxyethanol, 2 mL of H_2O, [Cu] = 2.0×10^{-4} mol, (2.5 wt%), P(CO) = 1.9 atm at 110 °C.
[b] Based on the gas formed after a given time.
[c] Turnover frequency (gas) = [(mol of gas)/(mol of Cu) × (rt)] × 24 h, where (rt) is the reaction time in hours. Experimental uncertainty ca. 15%.

$CuCl_2 \cdot 2H_2O$ immobilized on P(4-VP) in contact with 80% aqueous 2-ethoxyethanol mainly catalyzes the reduction of nitrobenzene to aniline (98%) (Eq. (2)) and additionally produces a minor amount of azobenzene (2%), under water gas shift reaction conditions. In addition, hydrogen gas from the WGSR was not detected at the end of the reduction process. The turnover frequencies for aniline production were calculated as mol of aniline per mol of $CuCl_2 \cdot 2H_2O$ in 24 h (TF(aniline) = [(mol of aniline)/(mol of Cu) × (rt)] × 24 h). The calculated catalytic activity defined as TF(aniline) was reproducible to ca. 15% for a series of experimental runs. Furthermore, control experiments show that no reaction was detected in the absence of the polymer-immobilized Cu complex. The data obtained from these studies are reported in Table 3. It is seen that the reaction time variation has a slight influence on the TF(aniline) values and that change can be associated with the slight shift to the basic zone on the pH final value of the catalytic mixture due to the increase of the amount of the aniline product (Brønsted base) with time. Reduction of nitrobenzene (1.2 mL) to aniline or other organic products [31] by this Cu/P(4-VP) ([Cu] = 2.5 wt%) system in contact with 10 mL of 80% aqueous 2-ethoxyethanol were not observed under the mild reaction conditions (P(CO) = 1.9 atm at 110 °C) previously employed in the catalysis of the WGSR above described, but under the severe reaction conditions (P(CO) = 27.2 atm at 150 °C) summarized in Table 3.

The nitrobenzene catalytic activities displayed by this Cu/P(4-VP) system are lower than those shown by the immobilized $Rh(amine)_2$/P(4-VP) system [6]. A TF(aniline)/24 h value = 53 (0.65 mmol of aniline formed after 3 h (25% conversion)) was observed under the following reaction conditions: 0.5 g of polymer, 0.26 mL of nitrobenzene, 8 mL of 2-ethoxyethanol, 2 mL of H_2O, [Rh] = 2.0 wt%, P(CO) = 0.9 atm at 100 °C and [nitrobenzene]/[Rh] = 25 for the most active amine (2-picoline) system.

Further, the reduction of nitrobenzene to aniline by this Cu/P(4-VP) catalyst system probably occurs through a mechanism similar to that proposed for the $Rh(2\text{-picoline})_2$/P(4-VP)/aqueous 2-ethoxyethanol system [7]. The immobilized carbonyl copper(I), Cu(I)–CO/P(4-VP), species formed under the catalytic conditions plays an important role as reaction intermediate in the catalytic cycle (namely, a cycloaddition of the nitro group to the Cu–CO bond followed by elimination of CO_2 should lead to the formation of the copper nitrosobenzene $[Cu(\eta^2\text{–ONR})]^+$ species, which eventually through successive transformations leads to aniline and azobenzene production).

Unfortunately, the concentration of Cu(I)–CO/P(4-VP) species formed under the catalytic conditions is small as seen from the EPR studies described above. Perhaps this is the reason for the low catalytic activity observed for both WGSR and nitrobenzene reduction. Finally, analyses of the effects of varying the CO pressure, Cu content and temperature on the activity of this Cu/P(4-VP) catalytic system, which are important parameters for the nitrobenzene reduction, are in progress and they will be reported elsewhere.

$$C_6H_5\text{–}NO_2 + 3CO + H_2O \rightarrow C_6H_5\text{–}NH_2 + 3CO_2 \qquad (2)$$

3.6. Recycling of the anchored catalyst

The recycling efficiency of the $CuCl_2$/P(4-VP) catalyst was studied in the reduction of nitrobenzene. The results are in Table 4. A change of the catalytic activity was observed after a second use. The above results show that the polymer-anchored catalyst does not have high stability. It is recognized that most Cu(I) complexes are air sensitive. Perhaps, during the recycling process the system was contaminated with air even though care was taken to avoid that.

Table 3
Nitrobenzene reduction by $CuCl_2 \cdot 2H_2O$ immobilized on P(4-VP) in aqueous 2-ethoxyethanol[a]

Reaction time (h)	Aniline[b] ($mol \times 10^{-4}$)	pH final	Nitrobenzene conversion (%)	TF (aniline)[c]
4	1.9	7.23	2.3	5.6
8	4.2	7.27	5.1	6.3
12	7.5	7.30	9.3	7.5
18	16.6	6.35	20.4	8.3
24	38.8	6.40	45.3	9.2
72	58.9	6.49	72.1	9.8

[a] 0.5 g of P(4-VP), 8 mL of 2-ethoxyethanol, 2 mL of H_2O, [Cu] = 2.0×10^{-4} mol, (2.5 wt%), 1.2 mL of nitrobenzene (8.1×10^{-3} mol), nitrobenzene/Cu = 44, P(CO) = 27.2 atm at 150 °C.

[b] Based on aniline formed after a given time. Selectivity 98%.

[c] Turnover frequency (aniline) = ([(mol of aniline)/(mol of Cu) × (rt)]) × 24 h, where (rt) is the reaction time in hours. Experimental uncertainty ca. 15%.

Table 4
Recycling efficiency of nitrobenzene reduction catalysis by $CuCl_2 \cdot 2H_2O$ immobilized on P(4-VP) in contact with 80% aqueous 2-ethoxyethanol[a]

Cycle no.	Yield of CO_2[b] (mmol)	Yield of aniline[b] (mmol)	TF (aniline)[c]
1	181.6	58.9	9.8
2	103.1	33.2	5.5
3	19.0	6.1	1.0

[a] 0.5 g of P(4-VP), 8 mL of 2-ethoxyethanol, 2 mL of H_2O, [Cu] = 2.0×10^{-4} mol, (2.5 wt%), 1.2 mL of nitrobenzene (8.1×10^{-3} mol), nitrobenzene/Cu = 44, P(CO) = 27.2 atm at 150 °C.

[b] Based on aniline formed after 72 h. Selectivity 98%.

[c] Turnover frequency (aniline) = ([(mol of aniline)/(mol of Cu) × (rt)]) × 24 h, where (rt) is the reaction time in hours. Experimental uncertainty ca. 15%.

4. Conclusions

The following conclusions can be drawn from the characterization and catalytic studies of the WGSR and nitrobenzene reduction by $CuCl_2 \cdot 2H_2O$ immobilized on the aminated polymer P(4-VP) in contact with aqueous 2-ethoxyethanol under CO.

The characterization study of the immobilized Cu solid by SEM, UV–vis, EPR, FT-IR and XPS techniques shows the variation of the copper environment during the immobilization process. This study suggests that the nitrogen lone pair of the vinylpyridine of the P(4-VP) coordinates to the copper metal center. Coordination crosslinks are also proposed which is consistent with the DSC data. The EPR studies of fresh and used catalyst show that there are two types of immobilized cupric polymer-complex: isolated complex and complexes bonded by dipole–dipole interactions. The presence of terminal carbonyl in the used catalyst, indicated by the IR spectrum under WGSR conditions as well as the EPR and XPS studies, provides strong experimental evidence for the formation of Cu(I)–CO/P(4-VP) complexes as reaction intermediates.

It was found that $CuCl_2 \cdot 2H_2O$ immobilized on P(4-VP) in contact with aqueous 2-ethoxyethanol under CO formed a low active catalyst system for both the WGSR and the reduction of nitrobenzene to aniline and azobenzene.

Acknowledgements

The authors thank CONICIT-VENEZUELA (GC, S1-2435) and CDCH (PI: 03.17.5192.2003). We thank Reilly Industries INC for donating the poly(4-vinylpyridine) cross-linked polymer (lot no. 70515AA). Also, we thank Lic. Luis Vásquez, Facultad de Farmacia, Universidad Central de Venezuela, for the GC–MS measurements and Lic. Juan Alvarez Facultad de Ciencias, Universidad Central de Venezuela, for TGA-DTA measurements.

References

[1] M. Jiang, C. Zhou, Z. Zhang, Polym. Bull. 30 (1993) 445.
[2] M.P. McCurdie, L.A. Belfiore, Polymer 40 (1999) 2889.
[3] C.W. Frank, L.B. Rogers, Inorg. Chem. 5 (1966) 617.
[4] A.J. Pardey, M. Fernández, M. Canestrari, P. Baricelli, E. Lujano, C. Longo, R. Sartori, S.a. Moya, React. Kinet. Catal. Lett. 67 (1999) 325.
[5] A.J. Pardey, M. Fernández, J. Alvarez, C. Urbina, D. Moronta, V. Leon, M. Haukka, T.A. Pakkanen, Appl. Catal. A 199 (2000) 275.
[6] A.J. Pardey, M. Fernández, J. Alvarez, C. Urbina, D. Moronta, V. Leon, C. Longo, P. Baricelli, S.A. Moya, J. Mol. Catal. A 164 (2000) 225.
[7] J. Mayora, M. Fernández, J. Alvarez, M. Ortega, A.J. Pardey, C. Longo, P. Baricelli, E. Lujano, S.A. Moya, Bol. Soc. Chil. Quím. 46 (2001) 121.
[8] A.J. Pardey, J. Brito, M. Fernández, A.B. Rivas, M.C. Ortega, C. Longo, P.J. Baricelli, E. Lujano, S.A. Moya, React. Kinet. Catal. Lett. 74 (2001) 111.
[9] A.J. Pardey, J. Brito, A.B. Rivas, M.C. Ortega, C. Longo, P.J. Baricelli, E. Lujano, M. Yañez, C. Zuñiga, R. López, S.A. Moya, J. Chil. Chem. Soc. 48 (2003) 57.
[10] D. Getman, D. Hagerty, G. Wilson, W.F. Wood, J. Chem. Ed. 61 (1984) 550.
[11] M. Mediavilla, D. Pineda, F. López, D. Moronta, C. Longo, S.a. Moya, P. Baricelli, A.J. Pardey, Polyhedron 17 (1998) 1621.
[12] C.L. Thomas, Catalytic Processes and Proven Catalysts, Academic Press, New York, 1970, p. 104.
[13] H.M. McNair, J.M. Miller, Basic Gas Chromatography, Wiley–Interscience, New York, 1997 (Chapter 8).
[14] Y.E. Kirsh, V.Y. Kovner, A.I. Kokorin, K.I. Zamaraev, V.Y. Chernyak, V.A. Kavanov, Eur. Polym. J. 10 (1974) 671.
[15] G. Jeschke, J. Phys. Chem. B 104 (2000) 8382.
[16] C. Giacomelli, F.C. Giacomelli, A.L. Santana, V. Schmidt, A.T. Nunes-Pires, J.R. Bertolino, A. Spinelli, J. Braz. Chem. Soc. 15 (2004) 818.
[17] A.D. Pomogailo, N.D. Golubeva, J. Inorg. Organometal. Polym. 11 (2001) 67.
[18] K. Nakamoto, Infrared and Raman Spectra of Organic and Coordination Compounds, Wiley, New York, 1997.
[19] D.T. Clark, D.M.J. Lilley, Chem. Phys. Lett. 9 (1971) 234.
[20] Z. Mekhalif, F. Sinapi, F. Laffineur, J. Delhalle, J. Electron, Spectrosc. Relat. Phenom. 121 (2001) 149.
[21] F.A. Cotton, G. Wilkinson, Advanced Inorganic Chemistry, 4th ed., Interscience, New York, 1980, p. 801.
[22] J.H. Scofield, J. Electron, Spectrosc. Relat. Phenom. 8 (1976) 129.
[23] E. Ebel, M.F. Ebel, H. Krocza, Surf. Interface Anal. 12 (1988) 137.
[24] R.J. Forster, J.G. Vos, Macromolecules 23 (1990) 4372.
[25] J.M. Clear, J.M. Kelly, J.G. Vos, Makromol. Chem. 184 (1983) 613.
[26] R.R. Gagné, J.L. Allison, R.S. Gall, C.A. Koval, J. Am. Chem. Soc. 99 (1977) 7170.
[27] A.J. Pardey, M. Fernández, J. Alvarez, M.C. Ortega, M. Canestrari, C. Longo, E. Lujano, P. Aguirre, S.A. Moya, P. Baricelli, Bol. Soc. Chil. Quím. 45 (2000) 347.
[28] F. Ciardelli, in: F. Ciardelli, T. Tsuchida, D. Wöhrle (Eds.), Macromolecular-metal Complexes, Springer, Berlin, 1996, p. 212.
[29] C.D. Frohning, C.W. Kohlpaintner, in: W.A. Herrmann, B. Cornils (Eds.), Applied Homogenous Catalysis with Organometallic Compounds, VCH, Weinheim, NY, 1996 (Chapter 2.1).
[30] A.D. Pomogailo, Catalysis by Polymer-immobilized Metal Complexes, English ed., Gordon and Breach, Singapore, 1998 (Chapter 6).
[31] K. Nomura, J. Mol. Catal. A 130 (1998) 1.

Available online at www.sciencedirect.com
SCIENCE DIRECT®
Polyhedron 24 (2005) 521–531
POLYHEDRON
www.elsevier.com/locate/poly

Gold(III) dithiocarbamate derivatives of *N*-methylglycine: An experimental and theoretical investigation

Luca Ronconi [a], Chiara Maccato [a], Davide Barreca [b], Roberta Saini [a], Mirella Zancato [c], Dolores Fregona [a,*]

[a] *Dipartimento di Scienze Chimiche, Università di Padova, Via Marzolo 1, 35131 Padova, Italy*
[b] *ISTM-CNR and INSTM, Dipartimento di Scienze Chimiche, Università di Padova, Via Marzolo 1, 35131 Padova, Italy*
[c] *Dipartimento di Scienze Farmaceutiche, Università di Padova, Via Marzolo 5, 35131, Padova, Italy*

Received 8 October 2004; accepted 10 December 2004

Abstract

The synthesis and characterization of the gold(III) complexes $[(HSDT)AuX_2]$ and $[(HSDT)_2Au]X$ (X = Cl, Br; HSDT = sarcosinedithiocarbamate (*N*-methylglycinedithiocarbamate)) are reported. In the discussed compounds coordination takes place through the sulfur atoms in a square-planar geometry around the gold(III) metal center. The characterization of the complexes has been carried out by means of elemental analysis, conductance measurements, FT-IR, ^1H and ^{13}C NMR spectroscopy, and thermogravimetric analysis. In addition, the molecular structure of the 1:1 metal-to-ligand complexes has been further investigated by means of density functional calculations, confirming the conclusions reached upon application of the other chemical characterization techniques. The complex $[(HSDT)_3Au]$ has been also synthesized and characterized by mass spectrometry, FT-IR, NMR and X-ray photoelectron spectroscopy, even if a definitive determination of its structure has not been undoubtedly accomplished.
© 2005 Elsevier Ltd. All rights reserved.

Keywords: Gold; S ligands; Chelates; Density functional calculations; X-ray photoelectron spectroscopy; Mass spectrometry

1. Introduction

In the widespread scenario of gold organometallic chemistry [1–3], different aspects are receiving increasing attention, such as the study of gold compounds in unusual oxidation states and stereochemistry [4–7], the bioinorganic chemistry of certain gold complexes for the treatment of rheumatoid arthritis (chrysotherapy) and their antitumor and antimicrobial properties [8]. Other research work has been devoted to the synthesis and properties of gold clusters and other complexes with gold–metal bonds [9,10].

In recent years, much interest has been focused on the synthesis of gold(I) derivatives containing sulfur and/or phosphorous donor ligands [11–13]. Among the former, dithiocarbamate complexes have been extensively studied in view of their applications as vulcanization accelerators, flotation agents and pesticides [14,15]; their antimicrobial activity has been reported [16,17] and they have been used to fight against metal poisoning [18].

In the literature, a large number of gold(I) [19,20], gold(III) [20–22] and gold(II) [4,23] dithiocarbamate syntheses are present. In particular, binuclear gold(I) dithiocarbamate derivatives have drawn considerable recent attention due to their significant medical applications or useful optical properties [19c].

The dithiocarbamate moiety has received much attention in recent years due to its ability to act as a bidentate ligand. Dithiocarbamates may easily undergo many

* Corresponding author. Tel.: +39 0 49 8275159; fax: +39 0 2700500560.
E-mail address: dolores.fregona@unipd.it (D. Fregona).

0277-5387/$ - see front matter © 2005 Elsevier Ltd. All rights reserved.
doi:10.1016/j.poly.2004.12.015

different reactions, thus being useful when studying substitution reactions in cation-bound ligands or between the ligands themselves. The introduction of the dithiocarbamate group in α-amino acids gives rise to molecules with up to three potential bonding residuals: amino (–NH_2, –NHR, –NHRR′), dithiocarbamate (–CSS^-) and carboxylate (–COO^-). Many proteins have cysteine and methionine residuals, which are both characterized by the presence of a sulfur atom in their structure. Consequently, dithiocarbamate derivatives of α-amino acids may be considered as valid models to study the coordination of proteins to metallic cations. Unfortunately, only few literature contributions on the synthesis of such complexes are available up to date [21,24–27].

In this work, compounds formed through reaction of dithiocarbamate derived from *N*-methylglycine (sarcosine) in 1:1, 1:2 and 1:3 metal-to-ligand ratios have been synthesized and characterized by different analytical techniques, in order to gain as much information as possible on their chemico-physical properties. Remarkably, particular attention has been paid to the characterization of 1:3 metal-to-ligand complex, for which a definitive determination of the chemical structure has not been accomplished yet. In the present paper the most relevant experimental and theoretical results are presented and discussed.

2. Experimental

2.1. Apparatus

N-Methylglycine (Aldrich), $KAuCl_4$ and $KAuBr_4$ (Alfa Aesar) were used as received. All other reagents and solvents were used as purchased without any further purification.

Conductivity measurements were carried out with an Amel 134-type conductivity bridge for freshly prepared 1.0×10^{-3} mol L^{-1} solutions in DMSO at (25.0 ± 0.1) °C.

FT-IR spectra were recorded in nujol between two polyethylene tablets on a Nicolet Vacuum Far FT-IR 20F spectrophotometer for the range 50–600 cm^{-1}, and in solid KBr on a Nicolet FT-IR 55XC spectrophotometer for the range 400–4000 cm^{-1}.

^1H NMR spectra were recorded in DMSO-d_6 on a Bruker Avance DRX400 spectrophotometer, equipped with a Silicon Graphics O2 workstation operating in Fourier transform, using tetramethylsilane (TMS) as internal standard. ^{13}C NMR spectra were recorded on the same instrument using TMS as internal standard; proton noise decoupling was normally used to obtain an increase of the observed resonance peaks intensity.

Elemental analyses were performed with a Perkin–Elmer 2400 CHN microanalyser; S, Cl and Br were determined with Schöninger method.

Thermogravimetric and differential scanning calorimetry curves were recorded with a TA Instruments thermobalance equipped with a DSC 2929 calorimeter. Measurements were carried out in the range 25–1400 °C in alumina crucibles under air (flow rate 30 cm^3 min^{-1}) at a heating rate of 10 °C min^{-1}, using alumina as reference.

ESI-MS (electrospray mass spectra) were performed on a Finnegan LCQ ion trap instrument operating in positive ion mode (sheath gas flow N_2: 50 a.u.; source voltage: 4 kV; capillary voltage: 3 V; capillary temperature: 200 °C). 50 μL of the sample (2.9×10^{-3} mol L^{-1} in TFA/H_2O/CH_3CN 1:45:45) were directly injected into the source by a syringe pump with a flow rate of 8.0 μL min^{-1}.

X-ray photoelectron spectra (XPS) were recorded on a ground sample of [$(HSDT)_3Au$] (**6**) by a Perkin–Elmer Φ 5600ci spectrometer at a working pressure of lower than 2.0×10^{-9} mbar with a monochromatized AlKα source (1486.6 eV). The spectrometer was calibrated by assuming the binding energy of the Au($4f_{7/2}$) line at 84.0 eV with respect to the Fermi level. The standard deviation for the binding energy values was ±0.2 eV. Binding energies were corrected for charging effects by assigning to the C(1s) line of adventitious carbon the value of 284.8 eV [28]. After a Shirley-type background subtraction, the spectra were fitted using a non-linear least-square fitting program, adopting Gaussian–Lorentzian peak shapes. The atomic compositions were evaluated using sensitivity factors as provided by Φ V5.4 A software.

All the computational calculations were performed by running ADF 2002.02 code [29], a program package based on density functional theory (DFT). Calculations were run within the generalized gradient approximation (GGA), with the inclusion of Becke–Perdew exchange-correlation formulas [30,31]. A Triple-ξ Slater-type basis set was used for all the atoms in the system and the relativistic effect was also taken into account by employing the ZORA Hamiltonian which included the scalar relativistic coupling. The inner cores of gold (1s–4d), sulfur (1s–2p), oxygen (1s), carbon (1s) and bromine (1s–3d) were treated by the frozen-core approximation. Furthermore, the harmonic frequencies of the system were calculated by the ADF package employing a numerical differentiation of energy gradients in slightly displaced geometries.

2.2. General procedures and methods

N-Methylglycine (Aldrich), $KAuCl_4$ and $KAuBr_4$ (Alfa Aesar) were used as received. All other reagents and solvents were used as purchased without any further purification.

2.2.1. Preparation of the ligand $Ba(SDT) \cdot 3H_2O$ (*1*)

The dithiocarbamate derivative of the α-amino acid *N*-methylglycine (sarcosine) was prepared as the trihy-

drated barium salt, following a method similar to that described by Musil and Irgolic [35]. *N*-methylglycine (22.95 mmol) was reacted with an aqueous solution (70 ml) of $Ba(OH)_2$ (22.96 mmol) and the suspension was magnetically stirred until total dissolution was achieved. In order to prevent the precipitation of barium carbonate, the presence of air was avoided, performing the reaction under a nitrogen atmosphere. Acetone was then added until its content was ~40% of the total volume (25 ml), and subsequently CS_2 (22.95 mmol) was dropwise added. Once CS_2 was dissolved, the solution was kept under stirring at 0 °C under a nitrogen flow for 24 h; formation of the barium salt occurred according to the reaction shown in Fig. 1.

Addition of acetone yielded a white precipitate that was filtered off and washed with acetone. The white solid was finally dried in a desiccator with P_4O_{10}, the final yield being 85%. According to the elemental and thermogravimetric analyses, the compound contains three molecules of water of crystallization.

2.2.2. Synthesis of the complexes [(HSDT)AuX_2] (X = Br (**2**), Cl (**4**))

An aqueous solution (6 ml) of Ba(SDT) · $3H_2O$ (0.98 mmol) was treated with a stoichiometric amount of Na_2CO_3 (0.99 mmol), resulting in the formation of a white precipitate ($BaCO_3$) that was filtered off, and the solution thus obtained was dropwise added to an aqueous solution (2 ml) of $KAuX_4$ (X = Cl, Br; 0.98 mmol) at 0 °C. The solution was subsequently treated with a stoichiometric amount of a 0.2 mol L^{-1} solution of HX (X = Cl, Br; 4.92 ml ≅ 0.98 mmol), yielding a reddish-brown precipitate that was filtered off and washed with water and diethyl ether (Fig. 2).

The reddish-brown solid was finally dried in a desiccator wit P_4O_{10}, the final yield being 80–90%.

2.2.3. Synthesis of the complexes [(HSDT)$_2$Au]X (X = Br (**3**), Cl (**5**))

1:2 metal-to-ligand gold(III) HSDT derivatives were prepared with a method similar to that of the corresponding 1:1 derivatives. These complexes were obtained by reaction of $KAuX_4$ (X = Cl, Br) with Ba(SDT) · $3H_2O$ in a 1:2 molar ratio ($KAuX_4$/Ba(SDT) · $3H_2O$ = 0.52/1.15 mmol), yielding a reddish-brown powder (final yield: 80–85%).

2.2.4. Synthesis of the complex [(HSDT)$_3$Au] (**6**)

An aqueous solution (6 ml) of Ba(SDT) · $3H_2O$ (1.49 mmol) was treated with a stoichiometric amount of Na_2CO_3 (1.50 mmol), resulting in the formation of a white precipitate ($BaCO_3$) that was filtered off. The solution thus obtained was cooled and dropwise treated with an aqueous solution (2 ml) of $KAuCl_4$ or $KAuBr_4$ (0.49 mmol) at 0 °C (and not dropwise added to the gold(III) salt solution, in order to avoid the formation of the 1:2 metal-to-ligand corresponding derivatives). The solution was subsequently treated with a stoichiometric amount of 0.2 mol L^{-1} solution of HCl or HBr, respectively (7.42 ml ≅ 1.49 mmol), yielding a dark brown precipitate that was filtered off and washed with water and diethyl ether. The dark brown solid was finally dried in a desiccator with P_4O_{10}, the final yield being 81%.

3. Results and discussion

N-Methylglycinedithiocarbamate has been synthesized as the barium salt as described elsewhere [24,32]. The gold(III) complexes here reported (Fig. 3) have been prepared by adding the dithiocarbamate ligand to an aqueous solution of $KAuX_4$ (X = Cl, Br) in the appropriate molar ratio.

The analytical data and the conductivity measurements for the ligand and the complexes are reported in Table 1. The compounds are stable at room temperature, insensitive to atmospheric oxygen and moisture and soluble in dimethylsulfoxide (DMSO) only. Conductance measurements are indicative of 1:1 electrolytes for compounds **3** and **5**, while compounds **2**, **4** and **6** are non-conducting in the same solvent [33–35].

3.1. FT-IR spectroscopy

The most significant bands recorded in the FT-IR spectra of the ligand and the complexes have been reported in Table 2.

$$^{-}OOCCH_2N(CH_3)H_2^{+} + CS_{2(l)} + Ba(OH)_2 \xrightarrow[\text{r.t./0 °C}]{H_2O/(CH_3)_2CO} (OOCCH_2N(CH_3)CSS)Ba_{(s)} + 2H_2O$$

Fig. 1. Synthesis of Ba(SDT) · $3H_2O$ (**1**).

$$(OOCCH_2N(CH_3)CSS)Ba + Na_2CO_3 \xrightarrow[\text{r.t.}]{H_2O} (OOCCH_2N(CH_3)CSS)Na_2 + BaCO_{3(s)}$$

$$(OOCCH_2N(CH_3)CSS)Na_2 + KAuX_4 + HX \xrightarrow[0\ ^{\circ}C]{H_2O} [(HOOCCH_2N(CH_3)CSS)AuX_2]_{(s)} + KX + 2NaX$$

Fig. 2. Synthesis of the complexes **2** and **4**.

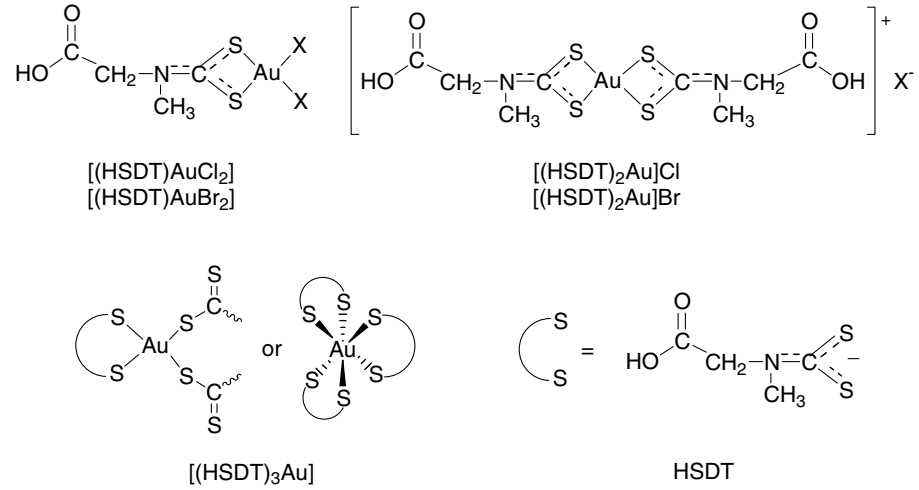


Fig. 3. Chemical drawings of the investigated gold(III) complexes.

Table 1
Analytical data and conductivity measurements [1.0×10^{-3} mol L^{-1} in DMSO, 25.0 °C]

Compound	Found (calculated)					Λ_M (Ω^{-1} cm^2 mol^{-1})
	%C	%H	%N	%S	%X (Cl, Br)	
1	13.46 (13.55)	2.98 (3.13)	4.12 (3.95)	17.89 (18.09)		
2	9.24 (9.22)	1.07 1.16	2.65 (2.67)	12.68 (12.31)	30.97 (30.67)	1.80
3	15.65 (15.87)	1.75 (2.00)	4.34 (4.63)	21.41 (21.19)	13.24 (13.20)	33.67
4	10.96 (11.12)	1.26 (1.40)	3.17 (3.24)	14.64 (14.84)	16.21 (16.41)	2.02
5	17.23 (17.13)	2.34 (2.16)	4.88 (5.00)	22.33 (22.87)	6.38 (6.32)	33.97
6	21.18 (20.90)	2.71 (2.63)	5.92 (6.09)	27.63 (27.90)		2.14

Table 2
Selected IR frequencies (cm^{-1})

Compound	ν(OH)	ν(N–CSS)	ν(C=O)	ν(C–O)	ν(SCS)		ν(SAuS)		(XAuX)	
					Asym.	Sym.	Asym.	Sym.	Asym.	Sym.
1		1484_{st}	1570_{st}[a]	1387_{m}[b]	1010_{w}	622_{w}				
2	$3451_{st,br}$	1571_{st}	1721_{st}	1216_{st}	1007_{w}	608_{m}	384_{st}	353_{w}	248_{st}[c]	227_{m}[c]
3	$3429_{st,br}$	1561_{st}	1718_{st}	1210_{st}	1004_{w}	608_{m}	382_{st}	357_{st}		
4	$3437_{st,br}$	1569_{st}	1719_{m}	1211_{m}	1004_{w}	608_{m}	381_{st}	357_{w}	336_{m}[d] 332_{m}[d]	321_{sh}[d] 316_{m}[d]
5	$3446_{st,br}$	1560_{st}	1718_{m}	1209_{st}	1005_{w}	607_{m}	380_{st}	351_{m}		
6	$3429_{st,br}$	1567_{st}	1716_{m}	1211_{st}	1004_{w}	611_{m}	384_{st}	351_{w}		

w = weak; m = medium; st = strong; sh = shoulder; br = broad.
[a] $\nu_a(COO^-)$.
[b] $\nu_s(COO^-)$.
[c] X = Br.
[d] X = Cl.

The dithiocarbamate compounds exhibit a characteristic band in the range (1450–1580) cm^{-1} assignable to the N–CSS stretching mode [36–38]; this band defines a carbon–nitrogen bond order intermediate between a single bond ($\Delta\tilde{\nu} = (1250–1350)$ cm^{-1}) and a double bond ($\Delta\tilde{\nu} = (1640–1690)$ cm^{-1}) [39]. The presence of a band in the above mentioned range indicates that, of the four possible resonance structures (Fig. 4), in our case we are dealing with a considerable contribution of structure **I**, characterized by a strong delocalization of electrons in the dithiocarbamate moiety.

On passing from the dithiocarbamate barium salt to the complexes, the ν(N–CSS) mode is shifted to higher energies, showing an increase of the carbon–nitrogen double bond character [21,24–26,36]. As regards the halo-derivatives, the ν(N–CSS) band is shifted to higher frequency following the order

$$[(HSDT)_2Au]X < [(HSDT)AuX_2]\ (X = Cl, Br)$$

due to the increase of electron withdrawing effects on increasing the number of halide atoms in the complexes, thus promoting an higher positive charge on the nitrogen atom. Thus we can conclude that the contribution of the structure **IV** (Fig. 4) is greater in the bishalo-derivatives and decreases on passing to the monohalo-derivatives, in which the halide atom is just a counter-ion [20].

The most informative bands due to the carboxylic group are recorded between 1200 and 1730 cm^{-1} both for the ligand and the complexes. For the free dithiocarbamate ligand (**1**) two bands are recorded, one for the antisymmetric mode ($\nu_a(COO^-)$) at 1570 cm^{-1} and another at 1387 cm^{-1} due to the symmetric mode ($\nu_s(COO^-)$), while the spectra of the complexes show two bands at ~1720 and ~1210 cm^{-1} due to ν(C=O) and ν(C–O), respectively. Dithiocarbamates of α-amino acids exhibit bidentate behavior, potentially acting both as *S*,*S*′- and *O*,*O*′-donors; however, the results discussed above undoubtedly demonstrate that the coordination of the ligand does not take place through the carboxylic group, which maintains its acidic form. This is also confirmed by the presence of a strong broad band at around 3400 cm^{-1}, recorded for all the here investigated complexes, assignable to carboxylic O–H stretching vibrations [40].

The bands due to the –CSS moiety are usually coupled to other vibrations and are very sensitive to the environment of this group, allowing us to distinguish between monodentate and bidentate dithiocarbamate coordination. The presence of only one band in the egion (940–1060) cm^{-1} is assumed by Bonati and Ugo [41] to indicate a completely symmetrical bonding of the dithiocarbamate ligand, acting in a bidentate mode (Fig. 5(a)). Conversely, a split band indicates an asymmetrically-bound bidentate ligand ($\Delta\tilde{\nu} < 20$ cm^{-1}, Fig. 5(b)) or a monodentate bound ligand ($\Delta\tilde{\nu} > 20$ cm^{-1}, Fig. 5(c)). In the complexes here reported, the presence of only one band in the investigated region,

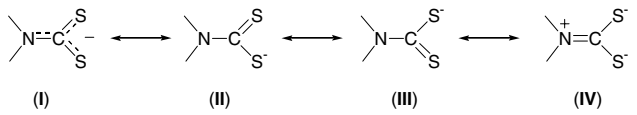


Fig. 4. Resonant forms of the dithiocarbamic –NCSS$^-$ moiety.

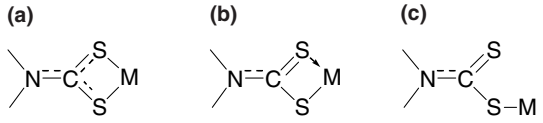


Fig. 5. Different ways of metal–sulfur binding in dithiocarbamate complexes: symmetrical bidentate (a), asymmetrical bidentate (b) and monodentate (c).

commonly attributed to the ν_a(SCS) vibrational mode, suggests a bidentate symmetrical behavior of the dithiocarbamate moiety, ruling out the coordination schemes 5(b) and (c).

For compound [$(HSDT)_3Au$] (**6**) a separate discussion is required. As reported in the literature, gold(III) dithiocarbamate derivatives in a 1:3 metal-to-ligand stoichiometry are generally tetracoordinate in a square-planar geometry with the simultaneous presence of one bidentate and two monodentate dithiocarbamate groups [20]. This case should imply the presence of two well defined N–CSS stretching bands at ~1560 and ~1450 cm^{-1} due to the bidentate and the monodentate ligands, respectively. In addition, as previously discussed, a split band in the range (940–1060) cm^{-1}, assignable to the ν_a(SCS), should be recorded, indicating that dithiocarbamate moieties are linked to the central metal ion in different ways [20]. Surprisingly, for compound **6** only one band was observed for both ν(N–CSS) and ν_a(SCS) at 1567 and 1004 cm^{-1}, respectively, indicating the presence of symmetrically bound dithiocarbamate ligands only, acting in a bidentate mode. This experimental evidence led us to hypothesize the possible existence of an hexacoordinate complex, as previously reported for other gold(III) complexes of tris-dithiocarbamate derivatives of α-amino acids [21].

The two bands recorded in the range (350–380) cm^{-1} are ascribed to $\nu_{a,s}$(SAuS), in agreement with analogous data reported by other authors for similar compounds [37,42].

The bands attributed to the $\nu_{a,s}$(XAuX) (X = Cl, Br) modes are ascribed to the Au–X stretching frequencies for terminal halides [20,42,43]. The above mentioned metal–halide modes have not been found in the spectra of [$(HSDT)_2Au$]X-type complexes, in agreement with the 1:1 electrolyte character of these compounds. It is worth observing that in the far FT-IR spectra of compound **4** the bands assignable to the ν(Au–Cl) vibrations are doubled because of isotopic splitting ν(Au–$^{35/37}$Cl); the existence of only one stable isotope of gold (^{197}Au) helps to make Au–Cl isotopic splitting more easily observable than in the case of chlorides of elements consisting of a mixture of stable isotopes [42].

3.2. ^1H and ^{13}C NMR spectroscopy

The main features of the ^{1}H and ^{13}C NMR spectra of the ligand and the synthesized complexes have been summarized in Table 3.

All the investigated gold(III) complexes have been proved to be stable in DMSO over 48 h. With regards to the alkyl groups bound to the dithiocarbamate moiety, the ^{1}H signals are very close for the free dithiocarbamate ligand (**1**) and the corresponding complexes. A general shift towards larger δ values is observed from the free dithiocarbamate precursor to its gold(III)

Table 3
^{1}H and ^{13}C NMR spectral data [DMSO-d_6, 25.0 °C, ppm]

Compound	^{1}H NMR		^{13}C NMR			
	CH_3	CH_2	CH_3	CH_2	COOH	CSS
1[a]	3.36	4.57	43.98	60.46	176.40[b]	209.73
2	3.38	4.62	35.21	53.11	166.73	193.08
3	3.41	4.63	34.23	52.42	168.15	193.31
4	3.42	4.64	35.87	53.40	166.77	193.42
5	3.42	4.64	34.32	52.60	168.27	193.69
6	3.19	4.49	32.67	46.75	168.17	190.56
	3.48	4.71	34.48	53.64	168.21	195.09

[a] Performed in D_2O.
[b] Due to the $-COO^-$ group.

derivatives, probably due to the lower electron density in the complexes, in which the –NCSS moiety is neutral compared to the free ligand in which such a dithiocarbamic group is anionic [26]. Conversely, for the carbon atoms a significant shielding of the ^{13}C signals, with respect to the free dithiocarbamate ligand, is recorded, in agreement with data reported in the literature for similar compounds [24–26]. The main differences are observable for the ^{13}C signals of the dithiocarbamic carbon atoms. The $\delta(N^{13}CSS)$ values, falling in the range 190–195 ppm, are strongly dependent on both the type of dithiocarbamate–metal bonding and the oxidation state of the metal center [44]. For gold(III) dithiocarbamate derivatives the $\delta(N^{13}CSS)$ values, are usually found in the range 193–201 ppm [45].

There is an appreciable empirical correlation between $\delta(N^{13}CSS)$ values and the carbon–nitrogen stretching vibrations in the infrared spectra: higher ν(N–CSS) values indicate an increased carbon–nitrogen double bond character, which well correlates with lower $\delta(N^{13}CSS)$ values because of a greater electron density on the –NCSS moiety. For the free dithiocarbamate ligand (**1**), there is no charge compensation on the sulfur atoms by coordinated atoms, resulting in extremely low ν(N–CSS) values, correlated with $-N^{13}CSS$ signals located in the upper limit of δ values. All these considerations are fully consistent with data reported in Table 3 for $-N^{13}CSS$ carbon signals.

As concerns compound **6**, it is worth noting that all the $^{1}H/^{13}C$ resonance peaks are doubled; if the hypothesis of an hexacoordinate complex in solid state was correct, these experimental data would suggest that, in solution, a rapid conversion from hexacoordinate to square-planar geometries could exist (Fig. 6) [21].

The downfield $^{1}H/^{13}C$ signals would be then attributed to the bidentate dithiocarbamate ligand, whereas the upfield ones would be ascribed to the monodentate asymmetrically bound HSDT molecules, as coordination through a single sulfur atom would increase the electron density on the –NCSS moiety [44].

Finally, the signals due to the carboxylate/carboxylic carbon atoms are generally shifted by ~9 ppm to lower values with respect to the free ligand (**1**), confirming the complete protonation of the carboxylic group, thus leading to an higher electron density on the carboxylic carbon atom [21].

3.3. Thermal studies

The thermal behavior of the free ligand and the synthesized complexes has been studied by thermogravimetry (TG) and differential scanning calorimetry (DSC) techniques in air flow, in order to establish the different decomposition processes and to confirm the proposed stoichiometries. Experimental data agree to a good extent with the ones obtained by the other spectroscopic techniques, and the results of such analysis, summarized in Table 4, indicate a good correlation between calculated and found weight loss values for all the investigated compounds.

As concerns the free dithiocarbamate ligand (**1**), pyrolysis processes take place in two well-defined steps. The first weight loss at around 100 °C coincides with the endothermic DSC peak and corresponds to the loss of three crystallization water molecules. A second weight loss is recorded at higher temperatures (>200 °C), the pyrolysis process leading to the total conversion to the corresponding metallic sulfate ($BaSO_4$). Several changes in the slope of the TG curve are observed during this second decomposition step, and can be related to the evolution of the hydrocarbon chain as well as to decarboxylation processes [46].

For all the gold(III) dithiocarbamate derivatives **2**–**6**, the thermal degradation occurs in two successive well-defined steps; in Fig. 7 the thermogram of complex **6** is reported as an example. The first TG step corresponds to pyrolysis, decarboxylation and reductive elimination Au(III) → Au(I), thus leading to [Au(SCN)] as a residual, a well known intermediate in the thermal decomposition of metal dithiocarbamates [46,47]. A very intense effect is recorded at higher temperature, that corresponds to removal of the remaining ligand atoms, complete degradation leading to metallic gold [21,25,26]. The formation of metallic gold as the final residual is confirmed by the presence of an endothermic DSC peak at 1066 °C due to the metallic gold melting.

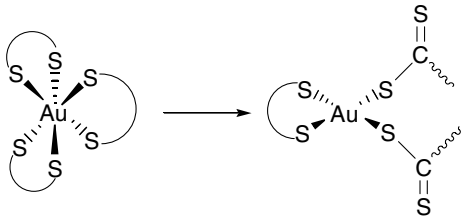


Fig. 6. Hypothesized structural conversion of compound **6** in solution.

Table 4
Thermogravimetric (TG) and differential scanning calorimetry (DSC) data

Compound	Step	Weight loss [%]		DSC
		Found	Calculated	Peak temperature [°C] (process[a])
1	I	15.81	15.24	102.4 (endo)
	II	34.53	34.18	273.4/326.7/345.7/416.2/762.8 (exo)
2	I	51.42	51.05	192.3 (endo)/263.4 (exo)
	II	61.84	62.19	736.3 (exo)
3	I	57.37	57.87	181.5 (endo)/258.9 (exo)
	II	67.90	67.46	731.1 (exo)
4	I	41.00	40.97	181.9 (endo)/258.1 (exo)
	II	53.98	54.41	737.1 (exo)
5	I	54.28	54.53	183.9 (endo)/248.6 (exo)
	II	64.34	64.88	736.2 (exo)
6	I	63.84	63.02	183.9 (endo)/265.8 (exo)
	II	70.89	71.44	735.7 (exo)

[a] Endo/exo = endothermic/exothermic process.

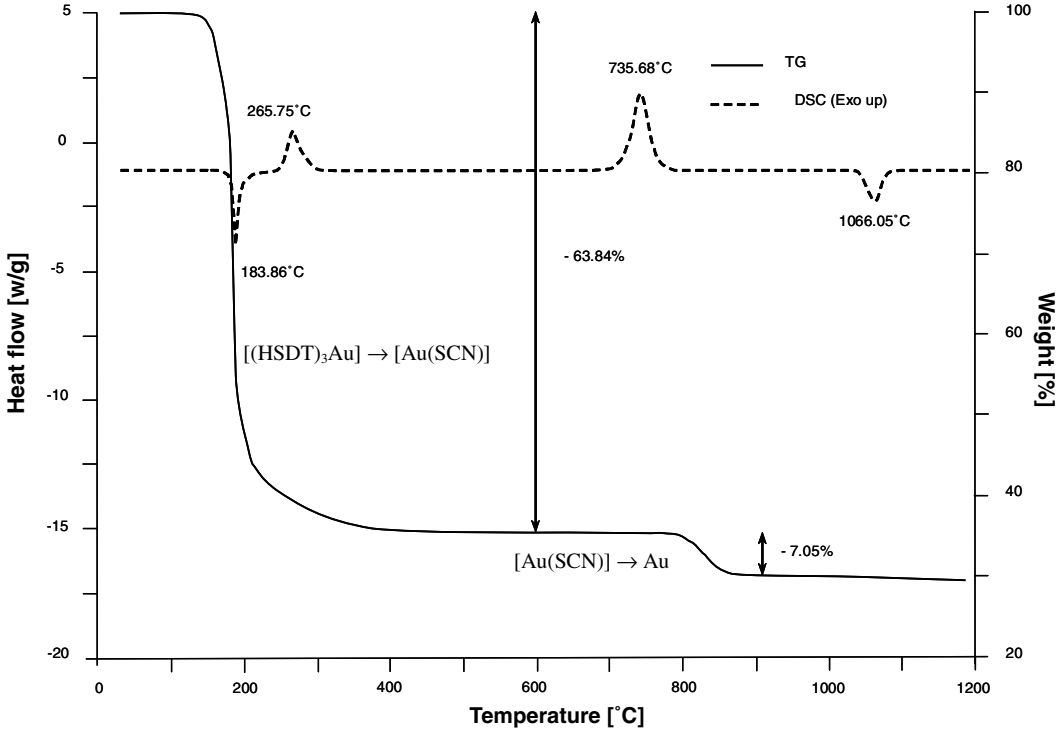


Fig. 7. Thermogram of compound **6**.

3.4. Density functional calculations

Aiming to get useful information about the geometrical structures of the compounds here discussed and their harmonic frequencies, we have chosen as a structural starting point of our theoretical investigation the X-ray study of a palladium(II) analogue compound, [(ESDT)Pd($PrNH_2$)Cl] (ESDT = ethylsarcosinedithiocarbamate), which presents similar ligands and coordination structure around the metallic center [48].

A ball and stick representation of the optimized complex **2** are reported in Fig. 8(a) and (b). The molecular scheme of Fig. 8(b) allows us to observe that almost all the molecule lies on the plane pertaining to the square-planar coordination around the metallic center, with the exception of the –COOH moiety. The optimized geometrical parameters and the corresponding literature experimental values of analogue gold(III) complexes [33] are collected in Table 5. Inspection of this table clearly indicates the good agreement between theoretical and available experimental data.

A further point to take into account is the comparison between the calculated harmonic frequencies pertaining to the optimized system and the IR data collected for

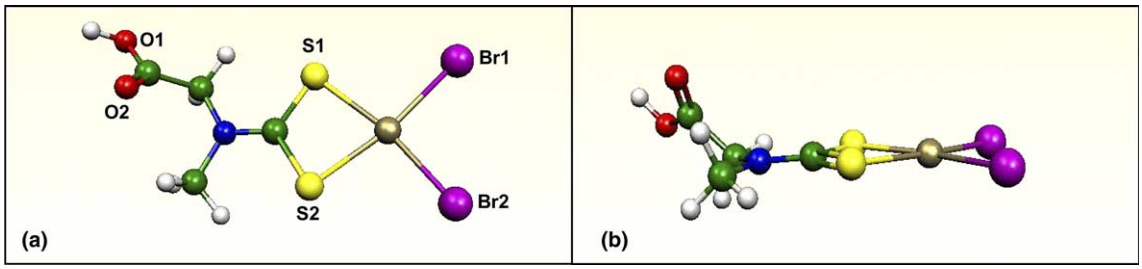


Fig. 8. Ball and stick representation of compound **2** optimized structure: top view (a) and side view (b).

Table 5
Calculated geometrical parameters for compound **2** and literature experimental values

Geometrical parameters	Calculated values	Experimental values [33]
Au–Br1/Br2 (Å)	2.490	2.440
Au–S1 (Å)	2.397	2.373
Au–S2 (Å)	2.392	2.343
C–S1 (Å)	1.737	1.732
C–S2 (Å)	1.732	1.714
N–CSS (Å)	1.341	1.322
N–CH_3 (Å)	1.469	
N–CH_2 (Å)	1.457	
CH_2–COOH (Å)	1.527	
Br–Au–Br (°)	94.4	
S–Au–S (°)	73.9	74.78
C–S1–Au (°)	86.9	86.1
C–S2–Au (°)	87.1	86.7
N–C–S1 (°)	124.5	124.0
N–C–S2 (°)	123.5	123.6

Table 6
Calculated harmonic frequencies and obtained experimental values for compound **2**

Vibrational features	Calculated frequencies (cm^{-1})	Experimental frequencies (cm^{-1})
ν_s(BrAuBr)	222	227
ν_a(BrAuBr)	247	248
ν_s(SAuS)	314	353
ν_a(SAuS)	326	384
ν_s(SCS)	787	608
ν_a(SCS)	1095	1007
ν(C–O)	1213	1216
ν(N–CSS)	1426	1571
ν(C=O)	1746	1721

[(HSDT)$AuBr_2$]; in Table 6 are reported both numerical and experimental vibrational outcomes. The analysis of these data allows us to observe that almost all the calculated frequencies result in good agreement with the experimental ones. We note only one strong discrepancy regarding the values pertaining to –NCSS vibrational modes. This molecular region is probably significantly influenced by the crystal packing in the solid, which was not considered in the theoretical simulation, where we take into account only the full molecular geometry optimization. Consequently, the stretching modes result to be influenced in a different way by the two environments.

Finally, we could get useful information from the values of the Hirshfeld charges collected in Table 7.

The analysis of these data indicates that the gold centre maintains a partial positive charge, while the dithiocarbamic C, N and S atoms result almost neutral; this fact suggests that the π-conjugate electron system on the dithiocarbamate moiety drains charge away from the metallic center.

3.5. Mass spectrometry

The ESI-MS spectrum of complex **6** has been performed in order to clarify its chemical composition. Interpretation of the fragmentation scheme has been a very difficult task. The signal corresponding to the molecular ion was not recorded; the largest *m*/*z* value recorded was 525, corresponding to a 1:2 metal-to-ligand fragment. In Fig. 9, a selection of the recorded fragments is reported. One branch of such a scheme represents a series of fragment, all of them including a gold atom, corresponding to successive loss of parts of the ligands, similarly to data reported in the literature [49,50], the last ion recorded having *m*/*z* = 289, that can tentatively correspond to $[AuS_2CNH_2]^+$. The other branch corresponds to withdrawal of a ligand that loses a sulfur atom and, finally, produces a species with *m*/*z* = 87 that should correspond to $[SCN–C(O)H]^+$.

3.6. X-ray photoelectron spectroscopy

XPS measurements were carried out on complex **6** in order to obtain a better insight into its chemical composition. The obtained data for the sample agree

Table 7
Hirshfeld charges for selected atoms in compound **2**

Atoms	Hirshfeld charges *Q*
Br1	−0.25
Br2	−0.25
S1	−0.02
S2	−0.01
N	−0.01
O1	−0.22
O2	−0.15
C(SS)	0.03
Au	0.27

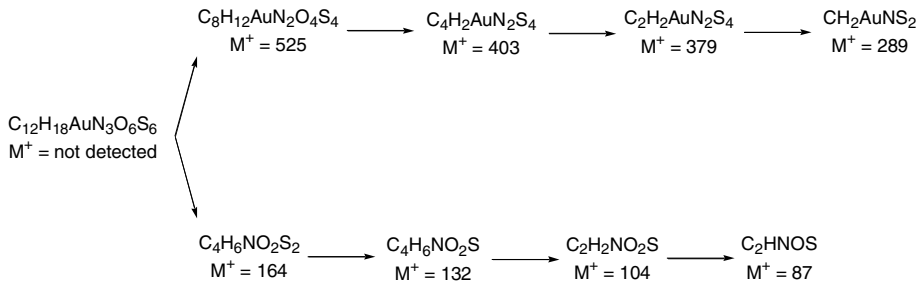


Fig. 9. Selection of the ESI-MS fragments for compound **6**.

to a good extent with those obtained by conventional chemical analysis methods, the atomic ratio being Au:O = 0.12/0.14, Au:N = 0.30/0.30, Au:S = 0.21/0.24 and Au:C = 0.05/0.04 (experimental/calculated). Data for the atomic binding energies (BEs) of **6** have been collected in Table 8 together with the full-width at half-maximum (FWHM); these values agree to a good extent with those reported in the literature for analogous gold(III) complexes of tris-dithiocarbamate derivatives of α-amino acids [21,51,52].

Table 8
Main XPS data recorded for compound **6**

Nucleus	BE (eV)	FWHM
Au $4f_{7/2}$	83.8 (Au(I))	2.0
	86.1 (Au(III))	2.0
S $2p_{3/2}$	162.1	2.8
N 1s	400.0	2.5
O 1s	531.3	3.1

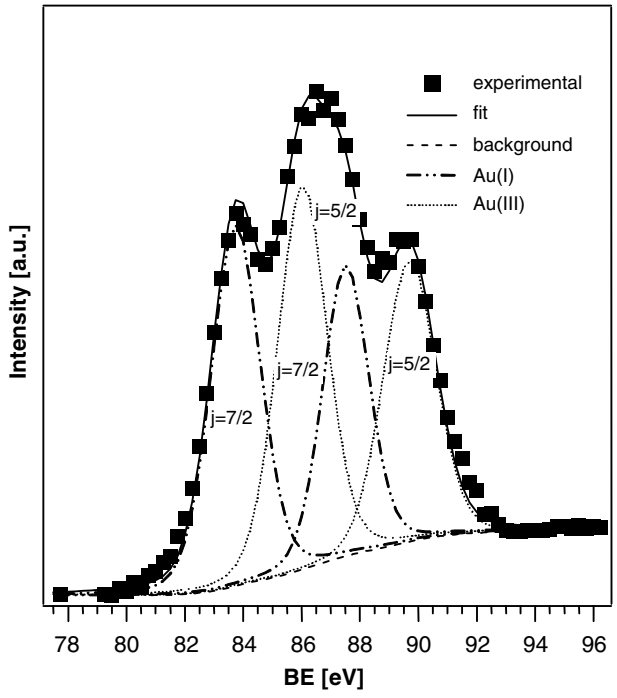


Fig. 10. Deconvolution of the Au(4f) photoelectron peak for compound **6**.

The $Au(4f_{7/2})$ peak analysis required greater attention. The recorder photoelectron signal, together with the bands resulting from the least-squares fitting, is reported in Fig. 10. As a matter of fact, such a signal can be decomposed by means of two distinct doublets, whose $Au(4f_{7/2})$ components are located at BE = 83.8 eV (FWHM = 2.0 eV) and BE = 86.1 eV (FWHM = 2.0 eV). These bands can be ascribed to the presence of gold(I) and gold(III), respectively [53], the former resulting from a partial reduction of gold(III) species in the spectrometer chamber due to the XPS analysis conditions [54–56].

The fact that only one S(2p) signal is recorded could support the hexacoordinate geometry, against a square-planar geometry reported in the literature for some other gold(III) dithiocarbamate derivatives with a 1:3 metal-to-ligand stoichiometry [20]. For square-planar 1:3 complexes, one of the ligands would act as bidentate and the other two as monodentate, coordinating the gold(III) center through one sulfur atom. In such a case, three different signals due to S(2p) orbitals would be expected (that is, one due to sulfur atoms implied in the bidentate coordination, one due to coordinating sulfur atoms belonging to monodentate ligands, and another due to the free sulfur atoms of the monodentate ligand). Indeed, only one single S(2p) signal is recorded in our case. Anyway, at variance with the report by Criado et al. [21], we do not believe that these data alone can support the presence of an hexacoordinate gold(III) geometry in the analyzed complex $[(HSDT)_3Au]$. This claim would be also disproved by the results of density functional calculations.

4. Conclusions

In this paper we report on the synthesis and characterization of five gold(III) dithiocarbamate derivatives of the type $[(HSDT)AuX_2]$, $[(HSDT)_2Au]X$ and $[(HSDT)_3Au]$ (X = Cl, Br; HSDT = *N*-methylglycinedithiocarbamate).

Although none of the complexes here reported has been obtained in the crystalline state, and thus the structure cannot be undoubtedly proposed, the other results suggest that coordination of the 1:1 and 1:2 metal-to-ligand dithiocarbamate derivatives takes place in a near square-planar geometry through the sulfur donating atoms, the –NCSS moiety coordinating the metal atom in a bidentate symmetrical mode and lying in the same plane, as reported in the literature for analogous gold (III) complexes.

A particular case is that of compound $[(HSDT)_3Au]$ whose structure has not been undoubtedly accomplished. Experimental results seem to support the hypothesis of an hexacoordinate tris-dithiocarbamate gold(III) derivative, against a square-planar geometry generally proposed for gold(III) complexes in a 1:3 metal-to-ligand stoichiometry.

Acknowledgements

The authors gratefully acknowledge partial financial support of this work by *Ministero dell'Università e della Ricerca Scientifica e Tecnologica* (Pharmacological and diagnostic properties of metal complexes).

References

[1] R.J. Puddephatt, in: G. Wilkinson, F.G.A. Stone, E.W. Abel (Eds.), Comprehensive Organometallic Chemistry, vol. 2, Pergamon, Oxford, 1982, p. 765.
[2] A. Grahmann, H. Schmidbaur, in: E.W. Abel, F.G.A. Stone, G. Wilkinson (Eds.), Comprehensive Organometallic Chemistry II, vol. 3, Pergamon, Oxford, 1995, p. 1.
[3] M.C. Gimeno, A. Laguna, Gold Bull. 36 (2003) 83.
[4] L.V. Antonova, T.E. Busygina, V.K. Polovnyak, A.E. Usachev, Russ. J. Gen. Chem. 67 (1997) 529.
[5] I.C. Hwang, K. Seppelt, Angew. Chem., Int. Ed. 40 (2001) 3690.
[6] D. Belo, H. Alves, E.B. Lopes, M.T. Duarte, V. Gama, R.T. Henriques, M. Almeida, A. Perez-Benitez, C. Rovira, J. Veciana, Chem. Eur. J. 7 (2001) 511.
[7] V.W.W. Yam, C.K. Li, C.L. Chan, K.K. Cheung, Inorg. Chem. 40 (2001) 7054.
[8] E.R.T. Tiekink, Crit. Rev. Oncol. Hematol. 42 (2002) 225.
[9] H.X. Zhang, C.M. Che, Chem. Eur. J. 7 (2001) 4887.
[10] L. Mezailles, N. Avarvari, N. Maigrot, L. Ricard, F. Mathey, P. LeFloch, L. Cataldo, T. Berclaz, M. Geoffroy, Angew. Chem., Int. Ed. 38 (1999) 3194.
[11] H. Schmidbaur, G. Weidenhiller, O. Steigelmann, Angew. Chem., Int. Ed. 30 (1991) 433.
[12] A. Sladek, K. Angermaier, H. Schmidbaur, Chem. Commun. (1996) 1959.
[13] J.P. Fackler Jr., Inorg. Chem. 41 (2002) 6959.
[14] A. Lopez Garcia, E. Blanco Gonzales, A. Sanz-Medel, Chromatographia 43 (1996) 607.
[15] A.L.J. Rao, N. Verma, A. Kumar, J. Kapoor, Chem. Environ. Res. 4 (1995) 163.
[16] E.M. Walker, H.F. Hardin, G.L. Gale, M.E. Reifsteck, D.J. Connon, M.M. Jones, Res. Common Chem. Pathol. Pharmacol. 63 (1989) 101.
[17] S. Sarac, M. Ertan, A. Balkan, N. Yulua, Arch. Pharm. Weinheim 324 (1991) 449.
[18] F. Caruso, M.L. Chan, M. Rossi, Inorg. Chem. 36 (1997) 3609.
[19] (a) M. Bardají, A. Laguna, M. Laguna, J. Chem. Soc., Dalton Trans. (1995) 1255;
(b) M. Bardají, A. Laguna, M. Laguna, F. Merchán, Inorg. Chim. Acta 215 (1994) 215;
(c) E.J. Fernandez, J.M. Lopez-de-Luzuriaga, M. Monge, E. Olmos, M.C. Gimeno, A. Laguna, P.G. Jones, Inorg. Chem. 37 (1998) 5532.
[20] F. Forghieri, C. Preti, L. Tassi, G. Tosi, Polyhedron 7 (1988) 1231.
[21] J.J. Criado, J.A. Lopez-Aria, B. Macías, L.R. Fernandez-Lago, J.M. Salas, Inorg. Chim. Acta 193 (1992) 229.
[22] R.V. Parish, B.P. Howe, J.P. Wright, J. Mack, R.C. Pritchard, R.G. Buckley, A.M. Elsome, S.P. Fricker, Inorg. Chem. 35 (1996) 1659.
[23] M. Bardají, M.C. Gimeno, P.G. Jones, A. Laguna, M. Laguna, Organometallics 13 (1994) 3415.
[24] M. Castillo, J.J. Criado, B. Macías, M.V. Vaquero, Inorg. Chim. Acta 124 (1986) 127.
[25] J.J. Criado, A. Carrasco, B. Macías, J.M. Salas, M. Medarde, M. Castillo, Inorg. Chim. Acta 160 (1989) 37.
[26] J.J. Criado, I. Fernandez, B. Macías, J.M. Salas, M. Medarde, Inorg. Chim. Acta 174 (1990) 67.
[27] B. Macías, J.J. Criado, M.V. Villa, M.R. Iglesias, M. Castillo, Polyhedron 12 (1993) 501.
[28] D. Briggs, M.P. Seah, Practical Surface Analysis, John Wiley & Sons, Chichester, 1983.
[29] H.H. Murray, G. Garzon, G. Raptus, A.M. Mazany, L.G. Porter, J.P. Fackler, Inorg. Chem. 27 (1988) 836.
[30] A.D. Becke, Phys. Rev. A 38 (1988) 3098.
[31] J.P. Perdew, Phys. Rev. B 33 (1986) 8822.
[32] A. Musil, K. Irgolic, Z. Anal. Chem. 208 (1965) 352.
[33] J.A. Broomhead, L.A.P. Kone-Maguire, J. Chem. Soc. A (1967) 546.
[34] N.N. Greenwood, B.P. Straughon, A.E. Wilson, J. Chem. Soc. A (1968) 2209.
[35] L.A.P. Kone-Maguire, P.S. Sheridan, F. Basolo, R.G. Pearson, J. Am. Chem. Soc. 90 (1968) 5295.
[36] S. Wajda, K. Drabent, Bull. Acad. Polon. Sci., Sci. Chim. 25 (1977) 963.
[37] N. Nakamoto, J. Fujita, R.A. Condrote, Y. Morimoto, J. Chem. Phys. 39 (1963) 42.
[38] G. Durgaprasad, D.N. Sathyanarayana, C.C. Patel, Can. J. Chem. 47 (1969) 631.
[39] A.W. Herlimger, S.N. Wenhold, T.V. Long, J. Am. Chem. Soc. 92 (1970) 6474.
[40] R.M. Silverstein, F.X. Webster, Spectrometric Identification of Organic Compounds, 6th ed., Wiley, New York, 1998.
[41] F. Bonati, R. Ugo, J. Organomet. Chem. 10 (1967) 257.
[42] P.T. Beurskens, H.J.A. Bloaw, J.A. Cras, J.J. Steggerda, Inorg. Chem. 7 (1968) 805.
[43] G.E. Coates, C. Parkin, J. Chem. Soc. (1963) 421.
[44] H.L.M. van Gaal, J.W. Diesveld, F.W. Pijpers, J.G.M. van der Linden, Inorg. Chem. 18 (1979) 3251.
[45] J. Willemse, J.A. Cras, J.J. Steggerda, C.P. Keyzers, Struct. Bond. (Berlin) 28 (1976) 83.
[46] B. Macías, J.J. Criado, M.V. Vaquero, M.V. Villa, Thermochim. Acta 223 (1993) 213.
[47] A. Fernandez-Alba, I.J. Perez-Alvarez, J.L. Martinez-Vidal, E. Gonzalez-Pradas, Thermochim. Acta 211 (1992) 271.
[48] G. Faraglia, D. Fregona, S. Sitran, L. Giovagnini, C. Marzano, F. Baccichetti, U. Casellato, R. Graziani, J. Inorg. Biochem. 83 (2001) 31.
[49] T. Tetsumi, M. Sumi, M. Tanaka, T. Shono, Polyhedron 5 (1986) 706.
[50] A.M. Bond, R. Colton, D.R. Mann, Inorg. Chem. 29 (1990) 4665.

[51] G. Furlani, G. Polzonetti, C. Preti, G. Tosi, Inorg. Chim. Acta 73 (1983) 105.
[52] G. Polzonetti, C. Preti, G. Tosi, Polyhedron 5 (1986) 1969.
[53] J.F. Mulder, W.F. Stickle, P.W. Sobol, K.D. Bomben, Handbook of X-ray Photoelectron Spectroscopy, Perkin–Elmer Corporation, MN, 1992.
[54] P.M.T. van Attekum, J.M. Trooster, J. Chem. Soc., Dalton Trans. (1980) 261.
[55] R.G. Raptis, L.C. Porter, R.J. Emrich, H.H. Murray, J.P. Fackler Jr., Inorg. Chem. 29 (1990) 4408.
[56] R.G. Raptis, J.P. Fackler Jr., Inorg. Chem. 29 (1990) 5003.

Available online at www.sciencedirect.com
SCIENCE DIRECT®
Polyhedron 24 (2005) 533–537
POLYHEDRON
www.elsevier.com/locate/poly

Syntheses and crystal structures of (*E*)/(*Z*)-isomers of 1-ferrocenyl-1-hydroxyimino-3-thiabutane and 1-ferrocenyl-1-hydroxyimino-4-thiapentane

Mirjana D. Vukićević [a], Klaus Wurst [b], Adrian G. Müller [b], Gerhard Laus [c], Rastko D. Vukićević [a,*]

[a] *Department of Chemistry, Faculty of Science, University of Kragujevac, R. Domanovića 12, P.O. Box 60, YU-34000 Kragujevac, Serbia and Montenegro*
[b] *Institute of Inorganic Chemistry, University of Innsbruck, Innrain 52a, A-6020 Innsbruck, Austria*
[c] *Immodal Pharmaka GmbH, Bundesstrasse 44, A-6111 Volders, Austria*

Received 24 August 2004; accepted 14 December 2004

Abstract

Four new potential bidentate ligands – oximes of ferrocenyl ketones containing sulfur in their side chains [(*E*)-, and (*Z*)-(η^5-C_5H_5)Fe(η^5-C_5H_4)–C(=NOH)–$(CH_2)_n$–SCH_3, $n = 1$ or 2] were synthesised and characterized by IR, ^1H and ^{13}C NMR spectral data. Single crystal X-ray structure determinations of these compounds are also reported.
© 2005 Elsevier Ltd. All rights reserved.

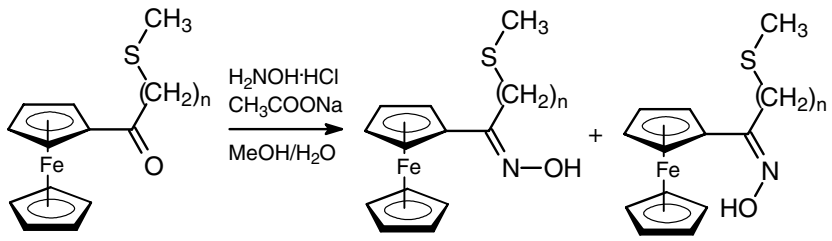
Keywords: Ketones; Oximes; Ferrocene derivatives; Ferrocenyl thialkanones; 1-Ferrocenyl-1-hydroxyiminothialkanes

1. Introduction

Ferrocene derivatives containing one or more heteroatoms have acquired an important position in organic synthesis, since they are suitable ligands capable of coordinating transition metal ions giving complexes with potential applications as catalysts for different synthetic reactions [1]. Recently, selective hydrogenation of multifunctional molecules using homogeneous catalysts which contain bidentate ligands with chiral ferrocene-based backbones has been reviewed [2]. Other reviews have discussed the Ir-catalysed hydroamination and the Pd-catalysed hydrosilylation of alkenes using bidentate ferrocenyl ligands [3]. A number of transition metal complexes with ferrocenylcarbaldehyde acylhydrazones as bidentate ligands have been described [4]. Ligands usually contain nitrogen, oxygen or phosphorus functionalities, but there are only a few sulfur-containing ligands. Bidentate ligands containing nitrogen or sulfur, such as ferrocenylcarbaldehyde thiosemicarbazones [5] or ferrocenoylthioureas [6], are of particular interest considering that these two elements form functionalities known as good electron-donating groups. Such ligands would provide additional possibilities to design complexes of many transition metals. Hence, synthesis of such a type of ferrocene derivatives arouse our interest. Recently, we reported the synthesis of several acylferrocenes including sulfur in their structures [7]. In continuation of these investigations, we synthesised 1-ferrocenyl-1-hydroxyiminothialkanes (isomeric oximes of 1-ferrocenyl-3-thiabutan-1-one, **1a** and 1-ferrocenyl-4-thiapentan-1-one, **1b**; Scheme 1), potential ligands containing

* Corresponding author. Tel.: +381 34 33 50 39; fax: +381 34 33 50 40.
E-mail addresses: vuk@knez.uis.kg.ac.yu, vuk@kg.ac.yu (R.D. Vukićević).

0277-5387/$ - see front matter © 2005 Elsevier Ltd. All rights reserved.
doi:10.1016/j.poly.2004.12.013



1a,b 2a,b 3a,b

1, 2 and 3	n
a	1
b	2

Scheme 1.

nitrogen and sulfur in their side chains in such positions which enable formation of five- and six-membered chelate rings, respectively. Although many oximes containing ferrocene moieties are known [8], commonly derived from formyl and acetylferrocenes, to the best of our knowledge the compounds mentioned above have not been described before. The present paper deals with the details of their synthesis, as well as spectral characterisation including X-ray crystal structures of the (*E*)- and (*Z*)-isomers. It has been previously noted that oxime isomers exhibit different capabilities to form metal complexes [9].

2. Experimental

2.1. Materials and instruments

All chemicals used were commercially available and were used as received. Solvents were purified by distillation. IR spectra were measured with a Perkin–Elmer 457 grating FT instrument. NMR spectra were recorded on a Varian Gemini 200 spectrometer, using $CDCl_3$ as the solvent. Chemical shifts are expressed in ppm using TMS as an internal standard. Melting points were determined by a Kofler hot-plate apparatus. Diffraction intensity data of single crystals were collected by means of a Nonius Kappa CCD with graphite-monochromated Mo Kα radiation via ϕ and ω scans. The structures were solved with direct methods (SHELXS-86) and full-matrix least-squares refined against F^2 (SHELXL-97).

2.2. Preparation of 1-ferrocenyl-1-hydroxyiminothialkanes *2a,2b* and *3a,b*

2.2.1. General procedure

A solution of hydroxylamine hydrochloride (10 mmol) and sodium acetate (10 mmol) in water (6 mL) was added to the respective ketone (**1a**,**b**; 1 mmol). The suspension was stirred vigorously, and methanol was added slowly until the mixture became clear (12–15 mL). This solution was refluxed with stirring overnight. Methanol was distilled off, the remaining suspension was neutralised with saturated sodium bicarbonate and extracted with three 20 mL portions of diethyl ether. The combined organic layers were washed with water and brine, and then dried over anhydrous sodium sulfate. After evaporation of the solvent, the crude product was separated by column chromatography (20 g SiO_2) using toluene as eluent. The first red band was a trace of the corresponding substrate, and the following orange bands were (*E*)-, then (*Z*)-isomeric oximes. Single crystals were obtained by slow evaporation of solutions in dichloromethane.

2.2.2. (*E*)-1-Ferrocenyl-1-hydroxyimino-3-thiabutane (*2a*)

Yield: 66%; m.p. 109–111 °C; IR (KBr): ν_{max} = 3221, 2926, 1641, 1426, 1379, 1299, 1105, 1028, 991, 943, 879, 828, 519, 505, 490 cm^{-1}; ^1H NMR (200 MHz, $CDCl_3$): δ = 2.22 (3H, s), 3.72 (2H, s), 4.20 (5H, s), 4.35 (2H, t, J = 2.0 Hz), 4.64 (2H, t, J = 2.0 Hz), 9.44 (1H, br s); ^{13}C NMR ($CDCl_3$) δ = 16.3, 26.9, 66.9, 69.4, 69.7, 79.2, 155.9.

2.2.3. (*Z*)-1-Ferrocenyl-1-hydroxyimino-3-thiabutane (*3a*)

Yield: 12%; m.p. 85–87 °C; IR (KBr): ν_{max} = 3415, 3210, 3098, 2915, 1637, 1411, 1885, 1106, 1000, 984, 894, 818, 502, 488, 473 cm^{-1}; ^1H NMR (200 MHz, $CDCl_3$): δ = 2.15 (3H, s), 3.53 (2H, s), 4.19 (5H, s), 4.39 (2H, t, J = 2.0 Hz), 4.99 (2H, t, J = 2.0 Hz), 9.71 (1H, br s); ^{13}C NMR ($CDCl_3$) δ = 15.6, 36.7, 69.5, 70.1, 71.0, 72.6, 153.0.

2.2.4. (*E*)-1-Ferrocenyl-1-hydroxyimino-4-thiabutane (*2b*)

Yield: 71%; m.p. 99–101 °C; IR (KBr): ν_{max} = 3552, 3414, 3226, 2916, 1735, 1636, 1618, 1436, 1410, 1379, 1318, 1297, 1151, 1106, 1035, 1025, 1001, 935, 883,

827, 749, 706, 586, 518, 507 cm^{-1}; ^1H NMR (200 MHz, $CDCl_3$): δ = 2.23 (3H, s), 2.89 (4H, m), 4.19 (5H, s), 4.34 (2H, t, J = 2.0 Hz), 4.55 (2H, t, J = 2.0 Hz), 9.64 (1H, br s); ^{13}C NMR ($CDCl_3$) δ = 15.6, 28.2, 31.0, 66.6, 69.3, 69.8, 80.2, 158.0.

2.2.5. (*Z*)-1-Ferrocenyl-1-hydroxyimino-3-thiabutane (**3b**)

Yield: 10%; m.p. 91–93 °C; IR (KBr): ν_{max} = 3414, 2909, 1618, 1412, 1390, 1283, 1260, 1190, 1002, 982, 967, 896, 825, 629, 605, 549, 498, 481 cm^{-1}; ^1H NMR (200 MHz, $CDCl_3$): δ = 2.19 (3H, s), 2.83 (4H, m), 4.19 (5H, s), 4.38 (2H, t, J = 2.0 Hz), 4.90 (2H, t, J = 2.0 Hz), 9.15 (1H, br s); ^{13}C NMR ($CDCl_3$) δ = 15.7, 32.3, 34.2, 69.5, 69.9, 70.1, 70.7, 155.5.

3. Results and discussion

3.1. Synthesis of 1-ferrocenyl-1-(hydroxyimino)thialkanes **2a,b** and **3a,b**

Overnight treatment of ketones **1a** and **1b,** obtained by a previously described procedure [2], with hydroxylamine hydrochloride and sodium acetate in a boiling mixture of methanol and water gave a mixture of the (*E*)/(*Z*)-oxime isomers. After removal of the solvent and extraction, the obtained solid was analyzed by thin layer chromatography on silica, using toluene as eluent and repeating elution three times. In both cases, two products with very close R_f values (accompanied with trace amounts of the starting substrate) were observed. These were separated by careful column chromatography (SiO_2/toluene) giving yellow-orange crystals of (*E*)- and (*Z*)-1-ferrocenyl-1-hydroxyimino-3-thiabutane (**2a** and **3a**) in 78% and (*E*)- and (*Z*)-1-ferrocenyl-1-hydroxyimino-4-thiapentane (**2b** and **3b**) in 81% overall yield, respectively (Scheme 1). The ratio of isomers was estimated on the basis of ^1H NMR data of the unseparated mixture and was found to be **2a/3a** = 85:15 and **2b/3b** = 88:12 in $CDCl_3$, respectively. However, they interconvert on prolonged standing in solution. The (*Z*)-isomers are much less stable, so we were not able to obtain ^1H and ^{13}C NMR spectra of pure compounds **3a** and **3b.**

3.2. Spectral characterisation of 1-ferrocenyl-1-hydroxyiminothialkanes **2a,b** and **3a,b**

IR spectra of the products showed a broad band between 3600 and 2800 (OH) and a strong absorption in the range 1640–1615 cm^{-1} (C=N), characteristic for oximes. This, together with the absence of the C=O absorption, confirmed the transformation of the ketones to the corresponding oximes. In the ^1H NMR spectra of both **2a** and **3a**, three singlets were observed and attributed to the methyl and methylene groups and unsubstituted cyclopentadienide (Cp) rings. The positions of the two expected triplets of the substituted ferrocene rings were significantly different in the (*E*)- and (*Z*)-isomers (δ 4.35 and 4.64 ppm for **2a**, δ 4.40 and 4.99 ppm for **3a**). Similarly, in the ^1H NMR spectra of **2b** and **3b** two singlets and a multiplet were observed as expected, whereas the protons of the substituted Cp rings were positioned at δ 4.34 and 4.56 (for **2b**), and 4.38 and 4.91 ppm (for **3b**). ^{13}C NMR data were also in accordance with the proposed structures. Further proof was provided by X-ray crystal structure determinations of these oximes.

3.3. Crystal structures of 1-ferrocenyl-1-hydroxyiminothialkanes **2a,b** and **3a,b**

In the crystal structures of the title compounds, the Cp rings adopt nearly eclipsed conformations, with average torsion angles of 6° in **3b**, 3° in **2a**, and less than that in **2b** and **3a**. Angles N(1)–C(11)–C(12) are larger in the (*E*)-isomers (124.6° in **2a**, 123.7° in **2b**) than in the (*Z*)-isomers (116.1° and 113.4° in **3a**, and 115.3° in **3b**). The C=N bonds are twisted out of the

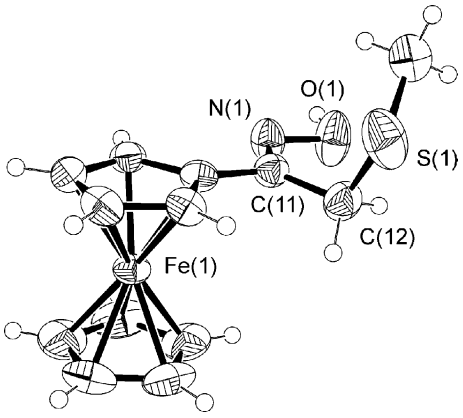


Fig. 1. Molecular structure of **2a** with 50% displacement ellipsoids.

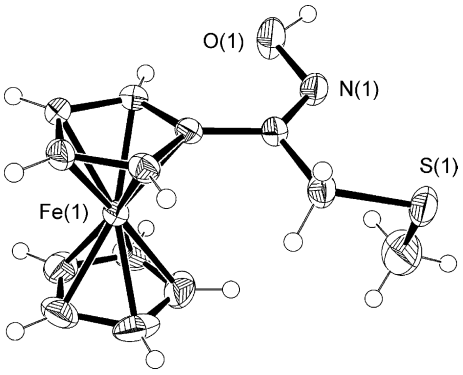


Fig. 2. Molecular structure of **3a** with 50% displacement ellipsoids.

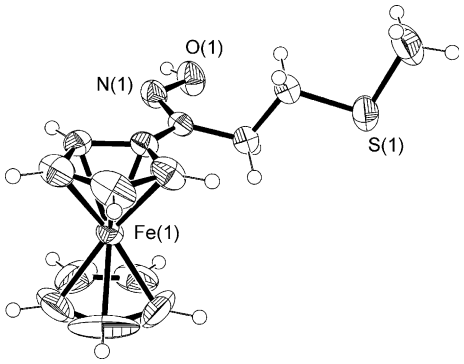


Fig. 3. Molecular structure of **2b** with 50% displacement ellipsoids.

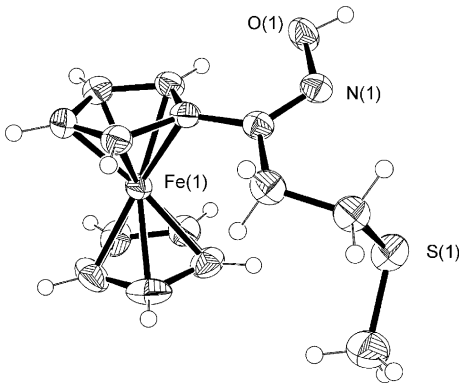


Fig. 4. Molecular structure of **3b** with 50% displacement ellipsoids.

Cp ring plane by dihedral angles of 7.8° in **2a**, 13.0° in **2b**, 16.6° in **3a** and 24.8° in **3b**. In crystals of **3a**, two molecules were found in the asymmetric unit, one of them with the sulfur atom showing a 0.85:0.15 disorder. It is noteworthy that in the latter molecule the C=N bond is rotated inside the Cp ring plane by −9.8°. The oximes form dimers in the crystal by hydrogen bonding between OH and N′, with N′–O distances of 2.775 Å in **2a**, 2.797 Å in **2b**, 2.777, 2.793 Å in **3a** and 2.801 Å in **3b**. There is no evidence for interconversion of the (*E*)/(*Z*)-isomers in the lattice. The molecular structures are shown in Figs. 1–4, and crystal data and structure refinement details are summarised in Table 1.

4. Conclusion

In this work, the synthesis and structural characterisation of (*E*)/(*Z*)-isomeric oximes of 1-ferrocenyl-3-thiabutan-1-one and 1-ferrocenyl-4-thiapentan-1-one are described. These compounds are bidentate ligands containing a thioether group which can be used to design new transition metal complexes. On prolonged standing in solution, an equilibrium is formed between the energetically preferred (*E*)- and less stable (*Z*)-isomers.

Table 1
Summary of crystal data and structure refinement for **2a**,**b** and **3a**,**b**

	2a	**2b**	**3a**	**3b**
Molecular formula	$C_{13}H_{15}FeNOS$	$C_{14}H_{17}FeNOS$	$C_{13}H_{15}FeNOS$	$C_{14}H_{17}FeNOS$
M_r	289.17	303.20	289.17	303.20
Crystal system	monoclinic	monoclinic	triclinic	monoclinic
Space group	*P*2(1)/*n*	*P*2(1)/*c*	$P\bar{1}$	*P*2(1)/*c*
Unit cell dimensions				
a (Å)	7.3680(4)	8.9021(3)	9.7111(3)	15.6584(8)
b (Å)	9.6194(4)	19.9888(5)	10.7874(4)	8.7470(6)
c (Å)	18.7300(9)	7.9338(3)	12.6076	9.6888(4)
α (°)	90	90	77.132(2)	90
β (°)	101.227(3)	103.724(2)	76.932(2)	97.814(3)
γ (°)	90	90	87.439(2)	90
V (Å^3)	1302.10(11)	1371.45(8)	1254.20(8)	1314.70(12)
Z	4	4	4	4
T (K)	233(2)	233(2)	233(2)	233(2)
D_{calc} (g cm^{-3})	1.475	1.468	1.531	1.532
Absorption coefficient (mm^{-1})	1.300	1.238	1.350	1.292
F (0 0 0)	600	632	600	632
Color, habit	yellow plate	orange prism	orange plate	yellow plate
Crystal size (mm)	0.44 × 0.12 × 0.04	0.35 × 0.21 × 0.15	0.35 × 0.31 × 0.09	0.15 × 0.150.03
θ Range for data collection (°)	2.12–25.00	2.04–26.00	1.70–25.97	2.63–14.10
Index ranges	$-8 < h < 8$, $-11 < k < 11$, $-19 < l < 22$	$-10 < h < 0$, $-24 < k < 24$, $-9 < l < 9$	$0 < h < 11$, $-13 < k < 13$, $-14 < l < 15$	$-17 < h < 0$, $-10 < k < 10$, $-11 < l < 11$
Reflections collected	7548	8141	7184	6418
Independent reflections	2363 (R_{int} = 0.0316)	2676 (R_{int} = 0.0244)	4861 (R_{int} = 0.0218)	2066 (R_{int} = 0.0316)
Reflections with $I > 2\sigma(I)$	2179	2392	4236	1758
Data/restraints/parameters	2363/0/161	2676/0/168	4861/0/324	2066/0/169
Goodness-of-fit on F^2	1.052	1.057	1.034	1.052
Final *R* indices [$I > 2\sigma(I)$]	R_1 = 0.0298, wR_2 = 0.0705	R_1 = 0.0323, wR_2 = 0.0749	R_1 = 0.0311, wR_2 = 0.0749	R_1 = 0.0290, wR_2 = 0.0643
wR indices (all data)	R_1 = 0.0343, wR_2 = 0.0729	R_1 = 0.0378, wR_2 = 0.0772	R_1 = 0.0387, wR_2 = 0.0778	R_1 = 0.0394, wR_2 = 0.0683

5. Supplementary data

CCDC Nos. 238572 (**2a**), 238573 (**3a**), 238574 (**2b**) and 238575 (**3b**) contain the supplementary crystallographic data for this paper. These data can be obtained free of charge via www.ccdc.cam.ac.uk/conts/retrieving.html (or from the Cambridge Crystallographic Data Centre, 12, Union Road, Cambridge CB2 1EZ, United Kingdom; fax: +44 1223 336033; or deposit@ccdc.cam.ac.uk).

Acknowledgement

This work was supported by the Ministry of Science and Environmental Protection of the Republic of Serbia (Grant 1245).

References

[1] (a) A. Togni, A. Hayashi, Ferrocenes: Homogenous Catalysts, Organic Synthesis, Material Science, VCH, Weinheim, 1995;
(b) L. Beyer, R. Richter, O. Seidelman, J. Prakt. Chem. 341 (1999) 704.
[2] H.-U. Blaser, C. Malan, B. Pugin, F. Spindler, H. Steiner, M. Studer, Adv. Synth. Catal. 345 (2003) 103.
[3] (a) A. Togni, N. Bieler, U. Burckhardt, C. Kollner, G. Pioda, R. Schneider, A. Schnyder, Pure Appl. Chem. 71 (1999) 1531;
(b) A. Togni, R. Dorta, C. Kollner, G. Pioda, Pure Appl. Chem. 70 (1998) 1477.
[4] (a) Y.-F. Yuan, L.-Y. Zhang, W.-Q. Qian, J.-T. Wang, W.-Y. Liu, T.-Z. Ding, Transit. Metal Chem. 23 (1998) 21;
(b) Q.-S. Li, Y.-J. Sun, X.-M. Li, Y.-X. Ma, J. Coord. Chem. 40 (1996) 319;
(c) Y.-H. Shi, Y.-M. Liang, X.-L. Wu, Q.-B. Song, G.-S. Huang, Y.-X. Ma, J. Coord. Chem. 33 (1994) 295;
(d) P. Gouzerh, Y. Jeannin, V. Marechal, Transit. Metal Chem. 9 (1984) 482.
[5] R. Carballo, J.S. Casas, E. Garcia-Martinez, G. Pereiras-Gabian, A. Sanchez, J. Sordo, E.M. Vazquez-Lopez, J.C. Garcia-Monteagudo, U. Abram, J. Organomet. Chem. 656 (2002) 1.
[6] O. Seidelmann, L. Beyer, G. Zdobinsky, R. Kirmse, F. Dietze, R. Richter, Z. Anorg. Allg. Chem. 622 (1996) 692.
[7] R.D. Vukićević, D. Ilić, Z. Ratković, M. Vukićević, Monatsh. Chem. 132 (2001) 625.
[8] (a) J.K. Lindsay, C.R. Hauser, J. Org. Chem. 22 (1957) 355;
(b) K. Schloegl, H. Mechtler, Monatsh. Chem. 97 (1966) 150;
(c) K. Yamakawa, M. Hisatome, Tetrahedron 26 (1970) 4483;
(d) K. Yamakawa, M. Hisatome, Org. Mass Spectrom. 6 (1972) 167;
(e) D. Astruc, R. Dabard, Tetrahedron 32 (1976) 245;
(f) M. Topolski, J. Rachon, Org. Prep. Proced. Int. 23 (1991) 211;
(g) S.E. Davis, A.C. Church, A.S. Scott, H.L. Throckmorton, S.L. Studer-Marfinez, C.F. Beam, J. Organomet. Chem. 533 (1997) 125;
(h) A.D. Ryabov, G.M. Kazankov, I.M. Panyashkina, V. Oleg, O.V. Grozovsky, O.G. Dyachenko, V.A. Polyakov, L.G. Kuz'mina, J. Chem. Soc., Dalton Trans. (1997) 4385;
(i) F. Ossola, P. Tomasin, F. Benetollo, E. Foresti, P.A. Vigato, Inorg. Chim. Acta 353 (2003) 292;
(j) S. Iyer, G.M. Kulkarni, C. Ramesh, Tetrahedron 60 (2004) 2163.
[9] C. Lopez, R. Bosque, X. Solanas, M. Font-Bardia, J. Organomet. Chem. 539 (1997) 99.

Available online at www.sciencedirect.com
SCIENCE DIRECT®
Polyhedron 24 (2005) 539–548
POLYHEDRON
www.elsevier.com/locate/poly

Synthesis and structural characterization of metal halide complexes containing *N*,*N*′-di(2-methoxyphenyl)formamidine (*o*-HDMophF)

Chun-Wei Yeh [a], Hui-Ling Hu [b], Rung-Hua Liang [a], Kai-Ming Wang [a], Ting-Yi Yen [a], Jhy-Der Chen [a,*], Ju-Chun Wang [c]

[a] *Department of Chemistry, Chung-Yuan Christian University, No. 22 Pu Ren, Chung-Li, Taiwan 320, Taiwan, ROC*
[b] *Department of Chemical Engineering, Nanya Institute of Technology, Chung-Li, Taiwan, ROC*
[c] *Department of Chemistry, Soochow University, Taipei, Taiwan, ROC*

Received 5 June 2004; accepted 14 December 2004

Abstract

The reactions of *N*,*N*′-di(2-methoxyphenyl)formamidine (*o*-HDMophF) with transition metal halide complexes afforded $CuCl_2 \cdot$(*o*-HDMophF), **1**, $[CoX_4][o\text{-}H_2DMophF]_2$ (X = Cl, **2**; Br, **3**) and MCl_2(*o*-HDMophF)$_2$ (M = Cd, **4**; Ni, **5**; Mn, **6**; Pd, **7**). These complexes were characterized by single-crystal X-ray diffraction and elemental analyses. The neutral *o*-HDMophF ligands in complexes **4**–**6** and **7** are coordinated to the metal centers in new bidentate and monodentate fashions, respectively. In the crystal structures of **1**–**7**, C–H···X and/or N–H···X (X = Cl, Br) interactions are found to link the metal units to the *o*-HDMophF ligand or its protonated cation ($o\text{-}H_2DMophF^+$). The neutral *o*-HDMophF compound in **1** adopts the *s-trans-anti-s-trans*-conformation, while those in complexes **4**–**6** and **7** adopt the *s-trans-anti-s-trans*- and *s-cis-anti-s-trans*-conformations, respectively. The $o\text{-}H_2DMophF^+$ cations of complexes **2** and **3** adopt the *s-cis-syn-anti-s-trans* and *s-trans-anti-anti-s-trans* conformations.
© 2005 Elsevier Ltd. All rights reserved.

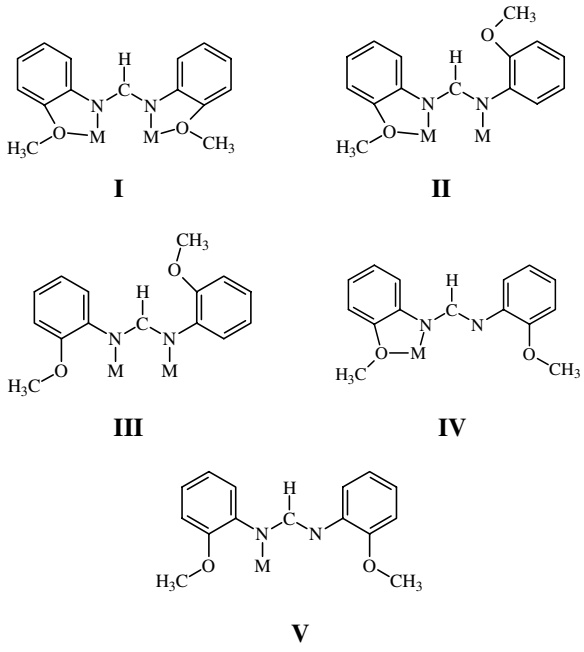
Keywords: Metal halide complexes; Conformation; X-ray structure; Hydrogen bonds; *N*,*N*′-Di(2-methoxyphenyl)formamidine

1. Introduction

The anion of the compound *N*,*N*′-di(2-methoxyphenyl)formamidine, *o*-DMophF$^-$, has been subjected to several studies of its coordination ability to metal centers. Tetradentate, tridentate and bidentate coordination modes **I**–**III** (Scheme 1) have been seen for this anion. In the tetradentate mode of coordination, **I**, two nitrogen atoms and two oxygen atoms are chelating and bridging to the metal centres. Such coordination was found in the dinuclear complex Ag_2(*o*-DMophF)$_2$ [1]. The coordination mode, **II**, which features chelation by one nitrogen atom and one oxygen atom together with the formation of a bridge through the two nitrogen atoms, was found in the dinuclear complex *trans*-$Ru_2(O_2CCH_3)_2$(*o*-DMophF)(*o*-DMophF′) (*o*-DMophF′ = (*o*-methoxyphenyl)(*o*-oxyphenyl)formamidine anion) [2]. The nitrogen atoms of the *o*-DMophF$^-$ ligands in the quadruply bonded complexes, *cis*-$Cr_2(O_2CCH_3)_2$(*o*-DMophF)$_2$ and *trans*-$Mo_2(O_2CCH_3)_2$(*o*-DMophF)$_2$ [3], are bridged to the metal centers, while the oxygen atoms are not coordinated, **III**. No complex containing the neutral *o*-HDMophF ligand or its protonated form $o\text{-}H_2DMophF^+$ has been reported. We report herein several mononuclear complexes of *o*-HDMophF ligands that coordinate to the metal centers in new bidentate and monodentate fashions, **IV** and **V**, respectively. The

* Corresponding author. Tel.: +88632653351; fax: +88632653399.
E-mail address: jdchen@cycu.edu.tw (J.-D. Chen).

0277-5387/$ - see front matter © 2005 Elsevier Ltd. All rights reserved.
doi:10.1016/j.poly.2004.12.012



Scheme 1. Bonding modes *o*-HDMophF ligand and its anion *o*-HDMophF$^-$.

synthesis and structures of $CuCl_2 \cdot$(*o*-HDMophF), $[CoX_4][o\text{-}H_2DMophF]_2$ (X = Cl and Br) and MCl_2 (*o*-HDMophF)$_2$ (M = Cd, Ni, Mn and Pd) and the conformations of the neutral *o*-HDMophF and its protonated cation *o*-H_2DMophF$^+$ form the subject of this report.

2. Experimental

2.1. General procedures

All manipulations were carried out under dry, oxygen-free nitrogen by using Schlenk techniques, unless otherwise noted. Solvents were dried and deoxygenated by refluxing over the appropriate reagents before use. *n*-Hexane and diethyl ether were purified by distillation from sodium/benzophenone, dichloromethane from P_2O_5 and acetonitrile from CaH_2. The visible absorption spectra were recorded on a Hitachi U-2000 spectrophotometer. IR spectra were obtained from a Jasco FT/IR-460 plus spectrometer. Elemental analyses were obtained from a PE 2400 series II CHNS/O analyzer.

2.2. Materials

$CoCl_2 \cdot 6H_2O$, $CoBr_2$, $MnCl_2$, $NiCl_2$ and $PdCl_2$ were purchased from Strem Chemical Co. $CuCl_2 \cdot 2H_2O$ and $CdCl_2 \cdot H_2O$ were purchased from MERCK Co. The ligand *N*,*N*′-di(2-methoxyphenyl)formamidine (*o*-HDMophF) was prepared according to a previously reported procedure [1].

2.3. Preparations

2.3.1. $CuCl_2 \cdot$(*o*-HDMophF)

$CuCl_2 \cdot 2H_2O$ (0.17 g, 0.99 mmol) was added to a solution of *N*,*N*-di(2-methoxy-phenyl)formamidine (*o*-HDMophF) (0.25 g, 0.98 mmol) in 20 ml CH_2Cl_2. The mixture was refluxed for 24 h and then allowed to cool down to room temperature to afford a brown solution and a dark brown solid. The solid was filtered out and *n*-hexane was added to induce precipitation. The precipitate was filtered and washed by ether (3×10 ml) and then dried under reduced pressure to give the dark brown product. Yield: 0.24 g (56%). UV–vis (CH_2Cl_2): 546 nm. *Anal*. Calc. for $C_{15}H_{16}CuCl_2N_2O_2$ (MW = 390.74), C, 46.11; H, 4.13; N, 7.17. Found: C, 46.13; H, 4.16; N, 7.23%. FT-IR (cm^{-1}) (KBr disk): 3197(b), 2963(s), 2345(w), 1685(s), 1638(s), 1594(s), 1524(m), 1508(w), 1459(s), 1340(m), 1286(w), 1259(s), 1175(w), 1113(s), 1021(s), 803(s), 750(s), 457(w), 419(w).

2.3.2. $[CoCl_4][o\text{-}H_2DMophF]_2$

$CoCl_2 \cdot 6H_2O$ (0.24 g, 1.01 mmol) was added to a solution containing *o*-HDMophF (0.51 g, 1.99 mmol) in 20 ml CH_2Cl_2. The mixture was then refluxed for 24 h and allowed to cool down to room temperature to afford a blue solution and a light blue solid. The solid was filtered out and then *n*-hexane was added to induce precipitation. The precipitate was filtered and washed by ether (3×10 ml) and then dried under vacuum to give the light blue product. Yield: 0.44 g (78.4%). UV–vis (CH_2Cl_2): 644 nm. *Anal*. Calc. for $C_{30}H_{34}CoCl_4N_4O_4$ (MW = 715.34), C, 50.37; H, 4.79; N, 7.83. Found: C, 49.93; H, 4.96; N, 7.70%. FT-IR (cm^{-1}) (KBr disk): 3447(b), 1718(w), 1685(s), 1655(s), 1637(w), 1560(m), 1541(s), 1524(w), 1508(m), 1459(s), 1259(s), 1113(m), 1023(s), 799(m), 750(s).

2.3.3. $[CoBr_4][o\text{-}H_2DMophF]_2$

Procedures for **3** were similar to those for **2**. Yield: 0.36 g (40%). UV–vis (THF): 675 nm. *Anal*. Calc. for $C_{30}H_{34}Br_4CoN_4O_4$ (MW = 893.18), C, 40.34; H, 3.84; N, 6.27. Found: C, 40.47; H, 4.04; N, 5.86%. FT-IR (cm^{-1}) (KBr disk): 3448(b), 1716(w), 1685(s), 1654(s), 1633(w), 1562(m), 1541(s), 1520(w), 1509(m), 1458(s), 1257(s), 1116(m), 1025(s), 794(m), 753(s).

2.3.4. $CdCl_2$(*o*-HDMophF)$_2$

Procedures for **4** were similar to those for **2**. Yield: 0.41 g (60%). *Anal*. Calc. for $C_{30}H_{32}CdCl_2N_4O_4$ (MW = 695.92), C, 51.78; H, 4.62; N, 8.05. Found: C, 51.73; H, 4.68; N, 7.88%. UV–vis (CH_2Cl_2): 348 nm. FT-IR (cm^{-1}) (KBr disk): 3189(w), 2938(m), 1735(w), 1685(w), 1649(s), 1591(s), 1514(s), 1459(s), 1433(m), 1396(w), 1333(m), 1288(w), 1258(m), 1245(s), 1183(s), 1157(m), 1118(s), 1048(m), 1026(s), 790(w), 755(s), 669(w), 585(w), 485(w), 418(w).

Table 1
Crystal data for **1**–**7**

Compound	**1**	**2**	**3**	**4**	**5**	**6**	**7**
Formula	$CuC_{15}H_{16}Cl_2O_2N_2$	$CoC_{30}H_{34}Cl_4O_4N_4$	$C_{30}H_{34}Br_4CoN_4O_4$	$CdC_{30}H_{32}Cl_2O_4N_4$	$NiC_{30}H_{32}Cl_2O_4N_4$	$MnC_{30}H_{32}Cl_2O_4N_4$	$PdC_{30}H_{32}Cl_2O_4N_4$
Moleclar weight	390.74	715.34	893.18	695.90	641.21	638.44	689.90
Crystal system	monoclinic	orthorhombic	orthorhombic	monoclinic	monoclinic	monoclinic	monoclinic
Space group	$P2_1/c$	$P2_12_12_1$	$P2_12_12_1$	Cc	$P2_1/c$	$P2_1/c$	$P2_1/c$
a (Å)	7.492(3)	9.6465(13)	9.7008(14)	26.625(5)	15.585(3)	15.8047(12)	7.3195(10)
b (Å)	10.497(4)	13.2075(14)	13.830(2)	38.421(8)	7.6594(16)	7.6909(10)	9.6643(10)
c (Å)	21.293(9)	26.888(2)	26.674(4)	15.974(3)	26.147(5)	26.080(4)	21.185(2)
β (°)	93.10(4)	90	90	108.938(3)	105.996(4)	105.628(10)	97.282(12)
V (Å^3)	1672.2(11)	3425.7(7)	3578.7(9)	15456(5)	3000. 2(10)	3052.9(6)	1486.5(3)
Z	4	4	4	20	4	4	2
D_{calc} (g/cm^3)	1.552	1.387	1.658	1.495	1.422	1.389	1.541
$F(000)$	796	1476	1764	7080	1336	1324	704
μ (Mo Kα) (mm^{-1})	1.632	0.852	0.648	0.920	0.867	0.648	0.846
Data collection instrument	Bruker AXS P4	Bruker AXS P4	Siemens CCD	Siemens CCD	Siemens CCD	Bruker AX4 P4	Bruker AXS P4
λ (Mo Kα) (Å)	0.71073	0.71073	0.71073	0.71073	0.71073	0.71073	0.71073
Range (2θ) for data collection (°)	$3.84 \leqslant 2\theta \leqslant 50.00$	$4.32 \leqslant 2\theta \leqslant 49.98$	$4.24 \leqslant 2\theta \leqslant 50.08$	$4.24 \leqslant 2\theta \leqslant 50.04$	$4.78 \leqslant 2\theta \leqslant 50.12$	$3.60 \leqslant 2\theta \leqslant 50.00$	$3.88 \leqslant 2\theta \leqslant 50.00$
Goodness-of-fit (GOF)[c]	1.083	1.012	1.009	1.200	1.000	1.026	1.010
Final R indices [$I > 2\sigma(I)$][a,b]	$R_1 = 0.0431$, $wR_2 = 0.1217$	$R_1 = 0.0358$, $wR_2 = 0.0794$	$R_1 = 0.0351$, $wR_2 = 0.0576$	$R_1 = 0.0493$, $wR_2 = 0.0950$	$R_1 = 0.0488$, $wR_2 = 0.0464$	$R_1 = 0.0312$, $wR_2 = 0.0794$	$R_1 = 0.0335$, $wR_2 = 0.0686$
R indices (all data)	$R_1 = 0.0556$, $wR_2 = 0.1293$	$R_1 = 0.0537$, $wR_2 = 0.0881$	$R_1 = 0.0680$, $wR_2 = 0.0637$	$R_1 = 0.1050$, $wR_2 = 0.1240$	$R_1 = 0.1199$, $wR_2 = 0.0540$	$R_1 = 0.0429$, $wR_2 = 0.0862$	$R_1 = 0.0611$, $wR_2 = 0.0781$
Largest difference peak and hole (e/Å^3)	0.441 and −0.479	0.240 and −0.181	0.392 and −0.421	0.554 and −0.608	0.326 and −0.267	0.196and −0.238	0.439 and −0.514

[a] $R_1 = \sum\|F_o| - |F_c\|/\sum|F_o|$.

[b] $wR_2 = [\sum w(F_o^2 - F_c^2)^2/\sum w(F_o^2)^2]^{1/2}$, $w = 1/[\sigma^2(F_o^2) + (ap)^2 + (bp)]$, $p = [\max(F_o^2 \text{ or } 0) + 2(F_c^2)]/3$. $a = 0.0656$, $b = 0.9223$, **1**; $a = 0.0461$, $b = 0.2958$, **2**; $a = 0.0334$, $b = 0.0000$, **3**; $a = 0.0278$, $b = 44.6029$, **4**; $a = 0.0234$, $b = 0.0000$, **5**; $a = 0.0422$, $b = 0.7088$, **6**; $a = 0.0306$, $b = 0.7845$, **7**.

[c] GOF $= [\sum w(|F_o^2| - |F_c^2|)^2/(N_{observed} - N_{parameters})]^{1/2}$.

2.3.5. $MnCl_2(o\text{-}HDMophF)_2$

Procedures for **5** were similar to those for **2**. Yield: 0.52 g (82.3%). UV–vis (CH_2Cl_2): 425 nm. *Anal*. Calc. for $C_{30}H_{32}MnCl_2N_4O_4$ (MW = 638.45), C, 56.44; H, 5.05; N, 8.78. Found: C, 56.40; H, 5.07; N, 8.46%. FT-IR (cm^{-1}) (KBr disk): 3177(s), 3033(w), 2939(m), 1648(s), 1591(s), 1513(m), 1496(s), 1463(m), 1432(w), 1378(w), 1333(m), 1299(w), 1256(w), 1239(s), 1181(w), 1157(m), 1116(s), 1048(m), 1024(s), 924(m), 851(w), 831(w), 788(w), 753(s), 721(s), 625(m), 576(w).

2.3.6. $NiCl_2(o\text{-}HDMophF)_2$

Procedures for **6** were similar to those for **2**. Yield: 0.37 g (57.6%). UV–vis (CH_2Cl_2): 362 nm. *Anal*. Calc. for $C_{30}H_{32}NiCl_2N_4O_4$ (MW = 642.20), C, 56.11; H, 5.02; N, 8.72. Found: C, 55.78; H, 4.98; N, 8.55%. FT-IR (cm^{-1}) (KBr disk): 3445(b), 3353(s), 3230(m), 2836(w), 1654(s), 1598(s), 1509(m), 1490(s), 1455(m), 1418(w), 1388(w), 1371(m), 1323(w), 1305(w), 1294(m), 1275(m), 1245(s), 1208(w), 1176(w), 1149(m), 1108(s), 1042(m), 1015(s), 951(m), 843(w), 787(w), 756(s), 598(m), 538(w), 507(w), 490(w), 467(w), 440(w).

2.3.7. $PdCl_2(o\text{-}HDMophF)_2$

Procedures for **7** were similar to those for **2**. Yield: 0.46 g (77%). UV–vis (CH_2Cl_2): 502 nm. *Anal*. Calc. for $C_{30}H_{32}PdCl_2N_4O_4$ (MW = 689.93), C, 52.23; H, 4.67; N, 8.12. Found: C, 52.40; H, 4.66; N, 8.07%. FT-IR (cm^{-1}) (KBr disk): 3448(b), 3357(s), 3233(m), 2838(w), 1655(s), 1598(s), 1514(m), 1494(s), 1458(m), 1420(w), 1389(w), 1371(m), 1328(w), 1309(w), 1297(m), 1277(m), 1246(s), 1208(w), 1185(w), 1157(m), 1115(s), 1048(m), 1023(s), 955(m), 844(w), 789(w), 757(s), 598(m), 538(w), 507(w), 490(w), 467(w), 440(w).

2.4. X-ray crystallography

Single crystal X-ray diffraction data were collected at 22 °C using either a Bruker AXS P4 (complexes **1**, **2** and **6**) or a Siemens CCD diffractometer (complexes **2**, **4** and **5**), which were equipped with graphite-monochromated Mo Kα (0.71073 Å) radiation. Data reduction was carried by standard methods with the use of well-established computational procedures [4].

A light yellow crystal of **1** was mounted on the top of a glass fiber with epoxy cement. Cell constants were derived from least-squares refinement of 40 reflections having $10.1 < 2\theta < 24.8$. The ω-scan data collection method was used to collect the data points at $3.84° < 2\theta < 50.00°$. The structure factors were obtained after Lorentz and polarization correction. An empirical absorption correction based on a series of ψ-scans was applied to the data. The positions of some of the heavier atoms, including the copper atom, were located by direct methods. The remaining atoms were found in a series of alternating difference Fourier maps and least-square refinements [5]. The final residuals of the final refinement were $R_1 = 0.0459$, $wR_2 = 0.1233$. The crystallographic procedures for **2**, **6** and **7** were similar to those for **1**.

A yellow crystal of **3** was mounted on the top of a glass fiber with epoxy cement. The hemisphere data collection method was used to scan the data points at $4.24° < 2\theta < 50.0°$. The structure factors were obtained after Lorentz and polarization correction. An empirical absorption correction based on 'multi-scan' was applied to the data. The positions of some of the heavier atoms, including the Co atom, were located by direct methods. The remaining atoms were found in a series of alternating difference Fourier maps and least-square refinements [5]. The final residuals of the final refinement were $R_1 = 0.0351$, $wR_2 = 0.0673$. The crystallographic procedures for **4** and **5** were similar to those for **3**. For complex **4**, no solution can be obtained if *C*2/*c* was used to solve the structure. The space group *Cc* was then selected to get the final structure.

For complexes **1**, **5**, **6** and **7**, all the hydrogen atoms, except the methyl hydrogen atom, H30A, H30B and H30C in **5**, were located in the difference electron density map and refined isotropically. The hydrogen atoms of complexes **2**, **3** and **4** and H30A, H30B and H30C in **5** were placed in geometrically calculated positions using the HADD program and refined using a riding model. Basic information pertaining to crystal parameters and structure refinement is summarized in Table 1.

3. Results and discussion

3.1. Synthesis

The reactions of *N*,*N*′-di(2-methoxyphenyl)formamidine (*o*-HDMophF) with $CuCl_2 \cdot 2H_2O$, $CoCl_2 \cdot 6H_2O$, $CoBr_2$, $CdCl_2 \cdot H_2O$, $MnCl_2$, $NiCl_2$ and $PdCl_2$ in refluxing CH_2Cl_2 afforded the complexes $CuCl_2 \cdot (o\text{-}HDMophF)$, **1**, $[CoX_4][o\text{-}H_2DMophF]_2$ (X = Cl, **2**; Br, **3**) and $MCl_2(o\text{-}HDMophF)_2$ (M = Cd, **4**; Ni, **5**; Mn, **6**; Pd, **7**), respectively. It is noted that although similar reaction conditions were used to prepare **1**–**7**, different types of products were obtained, presumably due to the different reactivity of the metal centers to *o*-HDMophF.

3.2. Structure of *1*

Yellow complex **1** was solved in the space group $P2_1/c$. Fig. 1 shows the ORTEP drawing of **1**, and the correct formulation for this complex is $CuCl_2 \cdot (o\text{-}HDMophF)$. Selected bond distances and angles are listed in Table 2. The copper atom is bonded to two chlorine atoms to form a linear geometry. The two Cu–Cl distances are 2.1873(15) and 2.1752(15) Å and the Cl–Cu–Cl angle is 178.71(4)°. The packing diagram of complex **1** shows

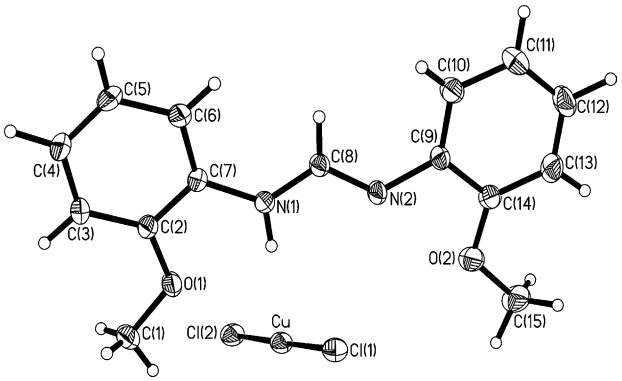


Fig. 1. An ORTEP diagram of complex **1**.

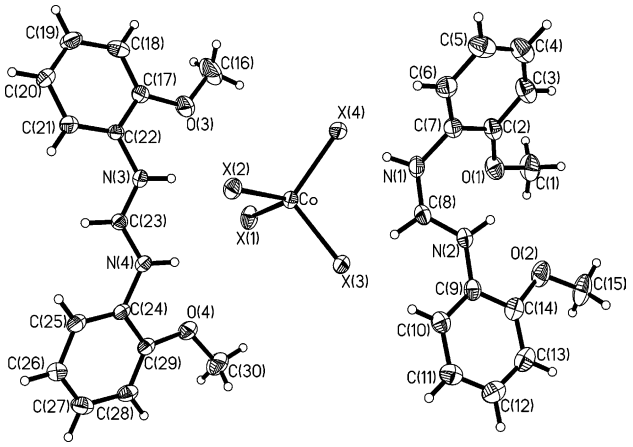


Fig. 2. A representative ORTEP drawing of complexes **2** (X = Cl) and **3** (X = Br).

that the metal units and *o*-HDMophF are interlinked through extensive N–H···Cl and C–H···Cl hydrogen bonds (H···Cl = 2.467–3.204 Å). Some weak Cu···O interactions (3.157 Å) are also found.

3.3. Structures of **2** and **3**

The structures of complexes **2** and **3** were solved in the space group $P2_12_12_1$, and a representative ORTEP drawing is shown in Fig. 2. Selected bond distances and angles are listed in Table 2. The Co atoms in **2** and **3** are bonded to four halide atoms, forming a distorted tetrahedral geometry. The Co–Cl lengths are in the range from 2.2560(12) to 2.2923(12) Å with the Cl–Co–Cl angles varying within the range from 106.34(5)° to 113.23(5)°, while the Co–Br lengths are in the range from 2.3980(9) to 2.4171(9) Å with the Br–Co–Br angles varying within the range from 106.45(3)° to 113.06(4)°. It is noted that two different conformations are observed for the *o*-H_2DMophF$^+$ cations for each complex (vide infra).

The packing diagram of complex **2** and **3** shows that the molecules pack into layers of discrete CoX_4^{2-} (X = Cl, **2** and Br, **3**) anions which are separated by layers of the *o*-H_2DMophF$^+$ cations. The ions interact through extensive N–H···X and C–H···X hydrogen bonds (H···Cl = 2.521–2.903 Å, ∠N–H···Cl and ∠C–H···Cl = 147.5–175.3°; H···Br = 2.527–3.037 Å,

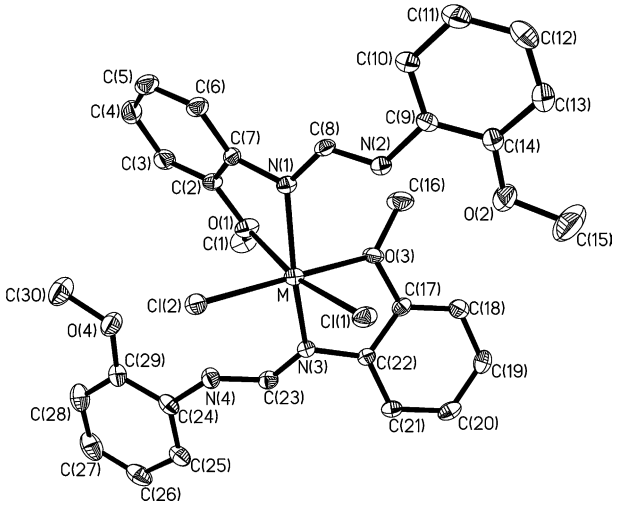


Fig. 3. A representative ORTEP drawing of complexes **4** (M = Cd), **5** (M = Ni) and **6** (M = Mn), showing a Δ configuration.

Table 2
Selected bond distances (Å) and angles (°) for **1**–**3**

1		**2**		**3**	
Bond distances					
Cu(1)–Cl(2)	2.1752(15)	Co–Cl(2)	2.2560(12)	Co–Br(1)	2.3980(9)
Cu(1)–Cl(1)	2.1873(15)	Co–Cl(3)	2.2733(12)	Co–Br(3)	2.4170(10)
		Co–Cl(1)	2.2772(13)	Co–Br(4)	2.4037(9)
		Co–Cl(4)	2.2923(12)	Co–Br(2)	2.4171(9)
Bond angles					
Cl(2)–Cu(1)–Cl(1)	178.71(4)	Cl(2)–Co–Cl(3)	108.49(5)	Br(1)–Co–Br(4)	106.45(3)
		Cl(3)–Co–Cl(1)	111.11(6)	Br(4)–Co–Br(3)	111.07(4)
		Cl(3)–Co–Cl(4)	106.79(4)	Br(4)–Co–Br(2)	113.06(4)
		Cl(2)–Co–Cl(1)	106.34(5)	Br(1)–Co–Br(3)	111.04(4)
		Cl(2)–Co–Cl(4)	110.83(5)	Br(1)–Co–Br(2)	107.60(4)
		Cl(1)–Co–Cl(4)	113.23(5)	Br(3)–Co–Br(2)	107.59(3)

Table 3
Selected bond distances (Å) and angles (°) for **4**

Cd(**1**)		Cd(**2**)		Cd(**3**)		Cd(**4**)		Cd(**5**)	
Bond distances									
Cd(1)–N(3)	2.299(9)	Cd(2)–N(7)	2.319(9)	Cd(3)–N(11)	2.298(10)	Cd(4)–N(13)	2.315(11)	Cd(5)–N(17)	2.324(12)
Cd(1)–N(1)	2.355(9)	Cd(2)–N(5)	2.351(10)	Cd(3)–N(9)	2.344(12)	Cd(4)–N(15)	2.319(11)	Cd(5)–N(19)	2.334(11)
Cd(1)–Cl(1)	2.493(4)	Cd(2)–Cl(4)	2.472(3)	Cd(3)–Cl(6)	2.480(4)	Cd(4)–Cl(7)	2.459(4)	Cd(5)–Cl(10)	2.491(5)
Cd(1)–Cl(2)	2.493(4)	Cd(2)–Cl(3)	2.482(3)	Cd(3)–Cl(5)	2.497(3)	Cd(4)–Cl(8)	2.474(5)	Cd(5)–Cl(9)	2.502(5)
Cd(1)–O(1)	2.551(8)	Cd(2)–O(5)	2.527(9)	Cd(3)–O(11)	2.560(9)	Cd(4)–O(15)	2.562(11)	Cd(5)–O(17)	2.525(10)
Cd(1)–O(3)	2.601(8)	Cd(2)–O(7)	2.620(8)	Cd(3)–O(9)	2.585(9)	Cd(4)–O(13)	2.578(10)	Cd(5)–O(19)	2.574(10)
Bond angles									
N(3)–Cd(1)–N(1)	147.0(3)	N(7)–Cd(2)–N(5)	146.3(3)	N(11)–Cd(3)–N(9)	147.2(4)	N(13)–Cd(4)–N(15)	146.8(4)	N(17)–Cd(5)–N(19)	147.6(4)
N(3)–Cd(1)–Cl(1)	102.0(2)	N(7)–Cd(2)–Cl(4)	98.4(2)	N(11)–Cd(3)–Cl(6)	95.2(3)	N(13)–Cd(4)–Cl(7)	97.4(3)	N(17)–Cd(5)–Cl(10)	99.2(3)
N(1)–Cd(1)–Cl(1)	94.7(2)	N(5)–Cd(2)–Cl(4)	100.1(2)	N(9)–Cd(3)–Cl(6)	100.2(3)	N(15)–Cd(4)–Cl(7)	101.4(3)	N(19)–Cd(5)–Cl(10)	95.4(3)
N(3)–Cd(1)–Cl(2)	97.7(2)	N(7)–Cd(2)–Cl(3)	101.3(2)	N(11)–Cd(3)–Cl(5)	100.0(2)	N(13)–Cd(4)–Cl(8)	100.3(3)	N(17)–Cd(5)–Cl(9)	98.2(3)
N(1)–Cd(1)–Cl(2)	100.0(2)	N(5)–Cd(2)–Cl(3)	96.2(2)	N(9)–Cd(3)–Cl(5)	98.8(3)	N(15)–Cd(4)–Cl(8)	95.8(3)	N(19)–Cd(5)–Cl(9)	100.9(3)
Cl(1)–Cd(1)–Cl(2)	116.3(1)	Cl(4)–Cd(2)–Cl(3)	114.6(1)	Cl(6)–Cd(3)–Cl(5)	116.5(1)	Cl(7)–Cd(4)–Cl(8)	115.7(2)	Cl(10)–Cd(5)–Cl(9)	116.6(2)
N(3)–Cd(1)–O(1)	88.0(3)	N(7)–Cd(2)–O(5)	86.1(3)	N(11)–Cd(3)–O(11)	65.3(3)	N(13)–Cd(4)–O(15)	87.7(3)	N(17)–Cd(5)–O(17)	66.2(4)
N(1)–Cd(1)–O(1)	64.2(3)	N(5)–Cd(2)–O(5)	64.9(3)	N(9)–Cd(3)–O(11)	86.0(3)	N(15)–Cd(4)–O(15)	64.2(4)	N(19)–Cd(5)–O(17)	90.1(4)
Cl(1)–Cd(1)–O(1)	88.1(2)	Cl(4)–Cd(2)–O(5)	152.5(3)	Cl(6)–Cd(3)–O(11)	89.2(2)	Cl(7)–Cd(4)–O(15)	155.0(3)	Cl(10)–Cd(5)–O(17)	157.3(3)
Cl(2)–Cd(1)–O(1)	152.8(2)	Cl(3)–Cd(2)–O(5)	90.7(3)	Cl(5)–Cd(3)–O(11)	152.1(2)	Cl(8)–Cd(4)–O(15)	87.1(2)	Cl(9)–Cd(5)–O(17)	83.7(3)
N(3)–Cd(1)–O(3)	63.9(3)	N(7)–Cd(2)–O(7)	63.7(3)	N(11)–Cd(3)–O(9)	91.0(3)	N(13)–Cd(4)–O(13)	65.2(4)	N(17)–Cd(5)–O(19)	87.4(4)
N(1)–Cd(1)–O(3)	89.8(3)	N(5)–Cd(2)–O(7)	89.8(3)	N(9)–Cd(3)–O(9)	65.0(4)	N(15)–Cd(4)–O(13)	88.8(3)	N(19)–Cd(5)–O(19)	64.3(3)
Cl(1)–Cd(1)–O(3)	156.0(2)	Cl(4)–Cd(2)–O(7)	85.8(2)	Cl(6)–Cd(3)–O(9)	158.0(2)	Cl(7)–Cd(4)–O(13)	86.5(3)	Cl(10)–Cd(5)–O(19)	88.2(2)
Cl(2)–Cd(1)–O(3)	86.0(2)	Cl(3)–Cd(2)–O(7)	157.1(2)	Cl(5)–Cd(3)–O(9)	83.0(2)	Cl(8)–Cd(4)–O(13)	155.7(3)	Cl(9)–Cd(5)–O(19)	153.0(2)
O(1)–Cd(1)–O(3)	72.7(3)	O(5)–Cd(2)–O(7)	71.9(3)	O(11)–Cd(3)–O(9)	74.2(3)	O(15)–Cd(4)–O(13)	73.4(3)	O(17)–Cd(5)–O(19)	74.4(3)

Table 4
Selected bond distances (Å) and angles (°) for **5**–**7**

5		**6**		**7**	
Bond distances					
Ni–N(1)	2.078(3)	Mn–N(3)	2.2492(13)	Pd–N(1)	2.019(3)
Ni–N(3)	2.080(3)	Mn–N(2)	2.2550(13)	Pd–Cl	2.2986(10)
Ni–O(1)	2.211(2)	Mn–O(2)	2.3858(13)		
Ni–O(3)	2.218(2)	Mn–O(3)	2.4097(13)		
Ni–Cl(1)	2.3501(11)	Mn–Cl(1)	2.4157(6)		
Ni–Cl(2)	2.3528(11)	Mn–Cl(2)	2.4089(6)		
Bond angles					
N(1)–Ni–N(3)	160.74(10)	N(3)–Mn–O(2)	89.07(5)	N(1)–Pd–N(1A)	180.00(14)
N(1)–Ni–O(1)	73.57(10)	N(3)–Mn–N(2)	151.65(6)	N(1)–Pd–Cl(A)	90.90(9)
N(3)–Ni–O(1)	91.20(10)	N(3)–Mn–Cl(2)	97.38(4)	Cl(A)–Pd–Cl	180.00(7)
N(1)–Ni–O(3)	92.09(9)	N(2)–Mn–O(2)	67.89(5)	N(1)–Pd–Cl	89.10(9)
N(3)–Ni–O(3)	73.97(10)	O(2)–Mn–Cl(2)	159.76(4)	N(1A)–Pd–Cl	90.90(9)
O(1)–Ni–O(3)	82.78(9)	N(2)–Mn–Cl(2)	99.48(4)		
N(1)–Ni–Cl(1)	99.34(8)	N(2)–Mn–O(3)	89.70(5)		
N(3)–Ni–Cl(1)	93.64(8)	N(3)–Mn–O(3)	68.12(5)		
O(1)–Ni–Cl(1)	168.54(6)	Cl(2)–Mn–O(3)	88.40(4)		
O(3)–Ni–Cl(1)	88.58(7)	O(2)–Mn–O(3)	76.19(5)		
N(1)–Ni–Cl(2)	92.06(8)	N(2)–Mn–Cl(1)	95.71(4)		
N(3)–Ni–Cl(2)	99.79(8)	N(3)–Mn–Cl(1)	100.21(4)		
O(1)–Ni–Cl(2)	89.85(7)	Cl(2)–Mn–Cl(1)	108.80(2)		
O(3)–Ni–Cl(2)	170.17(7)	O(2)–Mn–Cl(1)	88.72(4)		
Cl(1)–Ni–Cl(2)	99.53(4)	O(3)–Mn–Cl(1)	160.74(4)		

∠C–H···Br and ∠N–H···Br = 122.0–171.2°). The distance of the π–π stacking interactions is 4.002 Å.

3.4. Structures of **4**–**6**

Pale crystals of **4** conform to the space group *Cc* with twenty molecules in a unit cell. Five independent $CdCl_2$(*o*-HDMophF)$_2$ molecules were found in each asymmetric unit of **4**. Light yellow crystals of **5** and colorless crystals of **6** all conform to the space group $P2_1/c$ with four molecules in a unit cell. Fig. 3 shows the representative ORTEP drawing for the complexes **4**–**6**. Selected bond lengths and angles for **4**–**6** are listed in Tables 3 and 4, respectively. It is seen from Fig. 3 that the metal atoms are bonded to two *cis* chloride atoms, two *trans* amine nitrogen atoms and two *cis* methoxy oxygen atoms. The *o*-HDMophF ligands chelate the center metal atoms through the amine nitrogen atom and the methoxy oxygen atom to form five-membered rings. The neutral *o*-HDMophF ligands in complexes **4**–**6** are thus coordinated to the metal centers in a new bidentate bonding mode, as shown in **IV**, Scheme 1. The metal centers, which adopt a distorted octahedral coordination geometry, have bond angles that significantly deviate from 90° or 180°, presumably due the chelation of the bidentate *o*-HDMophF ligands. The bis-chelate complexes are all chiral, showing either Δ or Λ configuration, and have approximate C_2 symmetries. As seen in Table 3, the five independent molecules show subtle differences in the bond distances and angles. It is also noted that in complexes **4**–**6** the M-O distances are all significantly longer than the M-N distances. The molecules interact through extensive C–H···Cl hydrogen bonds by means of interactions among the chloride atoms and the C–H hydrogen atoms of the bidentate *o*-HDMophF ligand. The C–H···Cl distances are in the range from 2.705 to 2.879 Å.

3.5. Structure of **7**

Yellow crystals of **7** conform to the space group $P2_1/c$ with two molecules in the unit cell. Fig. 4 shows the

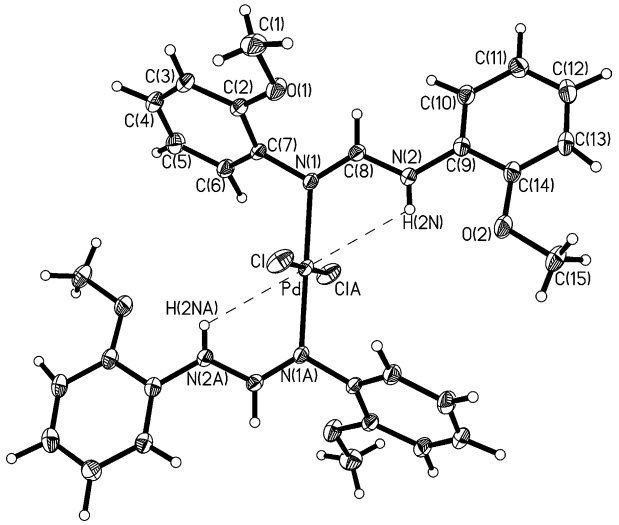


Fig. 4. An ORTEP drawing of complex **7**.

ORTEP drawing for complex **7** and some selected bond distances and angles of interest are given in Table 4. The palladium atom which adopts a distorted square planar coordination geometry is bonded to two *trans* chloride atoms (Pd–Cl = 2.2986(10) Å) and two *trans* amine nitrogen atoms (Pd–N(1) = 2.019(3) Å). In marked contrast to the bonding mode adopted in complexes **4**–**6**, the neutral *o*-HDMophF ligands are coordinated to the Pd atom through only one of the two nitrogen atoms. The oxygen atoms are not coordinated. The neutral *o*-HDMophF ligands in complex **7** are thus coordinated to the metal centers in a new monodentate bonding mode, as shown in **V**, Scheme 1. It is also noted that two short N–H···Pd distances (Pd···H = 2.794 Å, ∠Pd···H–N = 116.0°) which are *trans* to each other are observed.

The molecules interact through extensive C–H···Cl hydrogen bonds by means of interactions among the chloride atoms and the C–H hydrogen atoms of the monodentedate *o*-HDMophF ligand. The C–H···Cl distance is 2.794 Å and the C–H···Cl angle is 160.9°.

3.5.1. Conformation of the neutral *o*-HDMophF and the cation *o*-H_2DMophF$^+$

The neutral *o*-HDMophF or *o*-H_2DMophF$^+$ cation in each complex is not flat, but twisted around the C–N bonds. Table 5 lists the dihedral angles between the two phenyl rings of the neutral *o*-HDMophF or *o*-H_2DMophF$^+$ cation in each complex, as well as the torsional angles used to define their conformations (vide infra, Table 6). It is seen from Table 5 that complex **7** shows the largest dihedral angle. A conformational descriptor for anionic diarylformamidine bearing an *m*-alkoxy substituent has been proposed by Ren and co-authors [6]. Based on their proposition, three stable

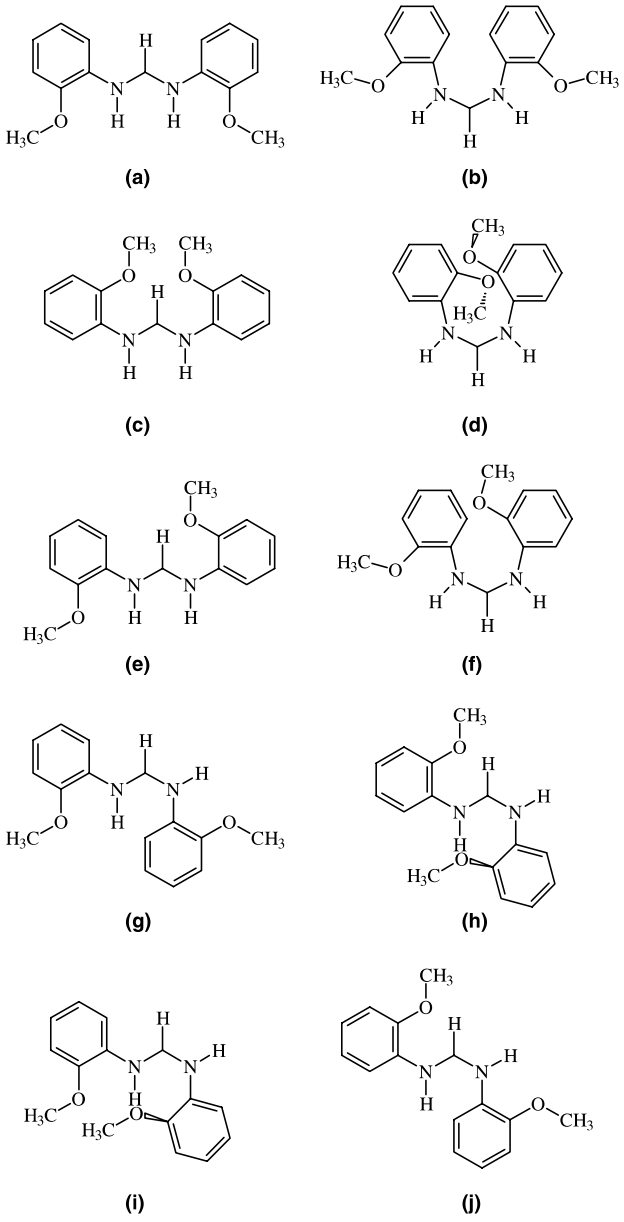
Table 5
Dihedral angles (°) and torsion angles (°) for *o*-HDMophF and *o*-H_2DMophF$^+$ in complexes **1**–**7**

Complex	Dihedral angle (°)		Torsion angle (°)			
1	7.9		169.9		173.6	
2	27.2	43.7	51.2	156.0	152.5	160.2
3	24.5	40.4	48.3	154.3	154.9	162.1
4, Cd(1)	39.5	41.6	141.6	143.7	141.7	139.6
4, Cd(2)	41.7	42.2	141.7	142.7	140.6	139.5
4, Cd(3)	38.4	45.9	145.4	144.0	143.5	145.7
4, Cd(4)	37.1	42.1	144.4	142.3	143.0	139.6
4, Cd(5)	39.5	44.5	144.8	146.1	140.3	145.6
5	30.8	40.2	147.2	155.4	144.8	143.1
6	33.7	40.0	151.7	144.2	143.8	141.9
7	74.2		55.4		163.4	

Table 6
The conformations of *o*-HDMophF, *o*-DMophF$^-$ and *o*-H_2DMophF$^+$ in transition metal complexes

Complex	Bonding modes	Conformation	Reference
Ag_2(*o*-DMophF)$_2$	**I**	*s-trans*, *s-trans*	[1]
trans-$Ru_2(O_2CCH_3)_2$(*o*-DMophF)(*o*-DMophF′)	**II**	*s-cis*, *s-trans*	[2]
cis-$Ru_2(O_2CCH_3)$(*o*-DMophF)$_2$(*o*-DMophF′)	**III**	*s-cis*, *s-trans*	[2]
Cr_2(*o*-DMophF)$_4$	**III**	*s cis*, *s-cis*; *s-cis*, *s-trans*	[9]
cis-$Cr_2(O_2CCH_3)_2$(*o*-DMophF)$_2$	**III**	*s-cis*, *s-trans*	[3a]
$Mo_2(O_2CCH_3)_3$(*o*-DMophF)	**III**	*s-trans*, *s-trans*	[3b]
trans-$Mo_2(O_2CCF_3)_2$(*o*-DMophF)$_2$	**III**	*s-cis*, *s-trans*	[3b]
trans-$Mo_2(O_2CPr^n)_2$(*o*-DMophF)$_2$	**III**	*s-cis*, *s-trans*	[3b]
trans-$Mo_2(O_2CCH_3)_2$(*o*-DMophF)$_2$	**III**	*s-cis*, *s-trans*	[3b]
$Mo_2(O_2CCH_3)$(*o*-DMophF)$Cl_2(PMe_3)_2$	**III**	*s-cis*, *s-trans*	[3b]
trans-$Mo_2(O_2CCH_3)$(DpyF)(*o*-DMophF)$_2$	**III**	*s-cis*, *s-trans*	[10]
trans-$Mo_2(O_2CCH_3)$(DpmF)(*o*-DMophF)$_2$	**III**	*s-cis*, *s-trans*	[10]
trans-$Mo_2(O_2CCH_3)$(DMepyF)$_2$(*o*-DMophF)	**III**	*s-cis*, *s-cis*	[10]
trans-Mo_2(DMepyF)$_2$(*o*-DMophF)$_2$	**III**	*s-cis*, *s-cis*	[10]
1		*s-trans-anti-s-trans*	this work
2		*s-cis-syn-anti-s-trans* *s-trans-anti-anti-s-trans*	this work
3		*s-cis-syn-anti-s-trans* *s-trans-anti-anti-s-trans*	this work
4	**IV**	*s-trans-anti-s-trans*	this work
5	**IV**	*s-trans-anti-s-trans*	this work
6	**IV**	*s-trans-anti-s-trans*	this work
7	**V**	*s-cis-anti-s-trans*	this work

conformations exist for diarylformamidine which are defined as (a) *s-cis*,*s-cis*- (*s-cis*-/*s-trans*- are defined between N–C (methine) bond and the ring C–C bond prioritized by the OR group), (b) *s-cis-s-trans*-, and (c) *s-trans-s-trans*-, respectively. To describe the conformations for the neutral *N*,*N*′-di(2-pyridyl)formamidine (HDpyF) and *N*,*N*′-di(6-methyl-2-pyridyl)formamidine (HDMepyF) ligands, where the amine hydrogen atoms are retained, we have modified this descriptor and show eight possible conformations for the neutral dipyridylformamidine ligands [7]. These eight conformations are: (a) *s-trans-anti-s-trans*, (b) *s-trans-anti-s-cis*, (c) *s-cis-anti-s-trans*, (d) *s-cis-anti-s-cis*, (e) *s-trans-syn-s-trans*, (f) *s-trans-syn-s-cis*, (g) *s-cis-syn-s-trans*, and (h) *s-cis-syn-s-cis*, where *syn* and *anti* indicate the relative positions of the methine and amine hydrogen atoms, respectively. Based on this descriptor, the conformations of the neutral *o*-HDMophF in complexes **1**, **4**, **5** and **6** are assigned as *s-trans-anti-s-trans* while that in complex **7** is *s-cis-anti-s-trans*.



Scheme 2. Possible conformation for the cationic *o*-H_2DMophF$^+$ ligands. (a) *s-trans-anti-anti-s-trans*; (b) *s-trans-syn-syn-s-trans*; (c) *s-cis-anti-anti-s-cis*; (d) *s-cis-syn-syn-s-cis*; (e) *s-trans-anti-anti-s-cis*; (f) *s-trans-syn-syn-s-cis*; (g) *s-trans-trans-syn-s-trans*; (h) *s-cis-anti-syn-s-cis*; (i) *s-trans-anti-syn-s-cis*; and (j) *s-cis-anti-syn-trans*.

To describe the conformation for the *o*-H_2DMophF$^+$ cations in complexes **2** and **3** which contains two amine hydrogen atoms, one more *syn* or *anti* should be added to describe the relative position of the amine hydrogen atoms. As shown in Scheme 2, 10 possible conformations can be drawn for the *o*-H_2DMophF$^+$ cation. Based on this new descriptor, the conformations of the two *o*-H_2DMophF$^+$ cations in complexes **2** and **3** are assigned as *s-cis-syn-anti-s-trans* and *s-trans-anti-anti-s-trans*. Table 6 lists the conformations of the neutral *o*-HDMophF, anionic *o*-DMophF$^-$ and cationic *o*-H_2DMophF$^+$ adopted in the metal complexes reported so far. For comparison, it is noted that the conformation of the cationic H_2DMepyF$^+$ ligands in the complexes *trans*-[$Mo_2(H_2DMepyF)_2(CH_3CN)_4$](ax-$CH_3CN)_2(BF_4)_6 \cdot 2CH_3CN$ and *trans*-[$Mo_2(H_2DMepyF)_2(CH_3CN)_4$](ax-$BF_4)_2(BF_4)_4 \cdot 2CH_3CN$ are similar to those in the anionic diarylformamidine ligands since the amine hydrogen atoms have been removed and these cationic ligands were assigned the *s-cis*, *s-cis* conformation [8].

4. Conclusions

The synthesis and structures of seven complexes containing neutral *o*-HDMophF or its cation *o*-H_2DMophF$^+$ have been successfully accomplished. The *o*-HDMophF ligands in complexes **4**–**6** and **7** are coordinated to the metal centers in new bidentate and monodentate bonding modes, respectively. All of them show supramolecular structures in the solid state by various types of weak interactions, including C–H···X and N–H···X (X = Cl or Br) hydrogen bondings and π–π stacking interactions.

The neutral *o*-HDMophF ligands in complexes **1**, **4**, **5** and **6** adopt the *s-trans-anti-s-trans* conformation while that in complex **7** adopts the *s-cis-anti-s-trans* conformation. The *o*-H_2DMophF$^+$ cations in **2** and **3** adopt the new *s-cis-syn-anti-s-trans*- and *s-trans-anti-anti-s-trans*-conformations.

Acknowledgements

We are grateful to the National Science Council of the Republic of China for support.

Appendix A. Supplementary data

Crystallographic data (CIF files) for the structures **1**–**7** have been deposited with the Cambridge Crystallographic Data Centre, CCDC Nos. 238743–238749. Copies of this information may be obtained free of charge from The Director, CCDC, 12 Union Road, Cambridge CB2 1EZ, UK (fax: +44 1223 336 033; e-mail: deposit@ccdc.cam.ac.uk or www: http://www.ccdc.cam.ac.uk). The packing diagrams for complexes **1**–**7** and the ORTEP diagrams for the five independent molecules of complex **4** are also available (9 pages). Supplementary data associated with this article can be found, in the online version at doi:10.1016/j.poly.2004.12.012.

References

[1] (a) S.J. Archibald, N.W. Alcock, D.H. Busch, D.R. Whitcomb, Inorg. Chem. 38 (1999) 5571;
(b) T. Ren, C. Lin, P. Amalberti, D. Macikenas, J.D. Protasiewicz, J.C. Baum, T.L. Gibson, Inorg. Chem. Commun. 1 (1998) 23.
[2] T. Ren, V. DeSilva, G. Zou, C. Lin, L.M. Daniels, C.F. Campana, J.C. Alvarez, Inorg. Chem. Commun. 2 (1999) 301.
[3] (a) F.A. Cotton, L.M. Daniels, C.A. Murillo, P. Schooler, J. Chem. Soc., Dalton Trans. (2000) 2001;
(b) Y.-Y. Wu, J.-D. Chen, L.-S. Liou, J.-C. Wang, Inorg. Chim. Acta 336 (2002) 71.
[4] (a) SMART/SAINT/ASTRO, Release, 4.03, Siemens Energy and Automation, Inc., Madison, WI, 1995;
(b) XSCANS, Release, 2.1, Siemens Energy and Automation, Inc., Madison, WI, 1995.
[5] SHELXTL-5.10. Bruker Analytical X-ray Instruments Inc., Karlsruhe, Germany, 1997.
[6] S. Radak, Y. Ni, G. Xu, K.L. Shaffer, T. Ren, Inorg. Chim. Acta. 321 (2001) 200.
[7] H.-C. Liang, Y.-Y. Wu, F.-C. Chang, P.-Y. Yang, J.-D. Chen, J.-C. Wang, J. Organomet. Chem. 669 (2003) 182.
[8] H.-Y. Weng, Y.-Y. Wu, C.-P. Wu, J.-D. Chen, Inorg. Chim. Acta 356 (2004) 1369.
[9] F.A. Cotton, L.M. Daniels, C.A. Murillo, P. Schooler, J. Chem. Soc., Dalton Trans. (2000) 2007.
[10] Y.-Y. Wu, T.-C. Kao, J.-D. Chen, C.-H. Hung, Inorg. Chim. Acta 357 (2004) 1002.

Available online at www.sciencedirect.com
SCIENCE DIRECT®
Polyhedron 24 (2005) 549–555
POLYHEDRON
www.elsevier.com/locate/poly

Lanthanide complexes with a chelating methylenediphosphonate

QiongHua Jin [1], Louis Ricard, François Nief *

Laboratoire Hétéroéléments et Coordination, CNRS UMR 7653, DCPH, Ecole Polytechnique, 91128 Palaiseau, France

Received 16 November 2004; accepted 12 January 2005
Available online 29 January 2005

Abstract

The complexation behaviour of the bidentate ligand tetrakis(*O-iso*propyl)methylenediphosphonate (L = $(i\text{PrO})_2\text{P(O)CH}_2\text{-P(O)(O}i\text{Pr)}_2$) with lanthanide ions has been studied by using triflates Ln(OTf)_3 (Ln = La, Pr, Nd) as sources of the Ln^{3+} cations. At the 2:1 L:Ln stoichiometric ratio, adducts of composition $[\text{Ln(OTf)}_3\text{(L)}_2\text{(OH}_2)_2]$ were isolated (Ln = La, Pr, Nd). In the X-ray structure of the cationic $[\text{Nd(OTf)}_2\text{(L)}_2\text{(OH}_2)_2]\text{(OTf)}$, the two coordinated triflates are monodentate. Finally, at higher L/Ln ratios, complexes were difficult to isolate because of a high degree of solvation, but, in one instance, with Ln = La, by using inert atmosphere techniques, the tripositive complex $[\text{La(L)}_4]\text{(OTf)}_3\text{(CH}_3\text{CN)}_3$ has been obtained and characterised by X-ray. By contrast, in the crystal structures of $[\text{Ln(NO}_3)_3\text{(L)}_2]\text{(CH}_3\text{CN)}_2$, (Ln = Ce, Pr, Nd), all three nitrates are bidentate.
© 2005 Elsevier Ltd. All rights reserved.

Keywords: Phosphonates; Lanthanides; Chelates; X-ray crystal structure

1. Introduction

There is currently much interest with respect to the application of lanthanide molecular compounds in organic synthesis, with a particular emphasis in the field of enantioselective catalysis by lanthanide coordination complexes [1]. In this area, complexes with both anionic and neutral ligands have been successfully employed. Since the lanthanide cations are very oxophilic, they are expected to interact strongly with highly polarised oxygen-bearing functional groups: for instance, complexes in which a phosphoryl (P═O) group is coordinated to a lanthanide element are well known [2]. However, structurally characterised complexes in which two phosphoryl moieties have been incorporated in an organic ligand chelated to a lanthanide ion are less common: the additional rigidity conferred to the complex by this type of ligands may have a positive effect for further synthetic and/or catalytic applications. In such complexes, the two phosphoryl groups have been linked to a pyridine N-oxide [3–7], an aromatic residue [8–10], a macrocyclic moiety [11], or to a simple one-carbon unit spacer, like in diphenylphosphinomethane dioxide [12–14] or hydroxydiphosphonates such as $(\text{MeO})_2\text{P(O)-CR(OH)-P(O)(OMe)}_2$ (R = Me, *t*Bu, Ph) [15,16]; in this latter case, the hydroxyl group may induce instability, and an interesting rearrangement can occur in the coordination sphere of the complexed lanthanide.

Some complexes of lanthanide nitrates with tetra-*iso*propyl- [17,18] and tetramethyl methylenediphosphonate [19] have been very recently described and some of them have been structurally characterised [18,19]. This type of ligand is attracting because methylenediphosphonates are very easily accessible in a single step by the Arbuzov reaction of an alkyl phosphite with dibromomethane [20]. Another described route to these compounds involves the reaction of the easily available methylenebis(phosphonic dichloride) with diverse

* Corresponding author. Tel.: +33 0 1 69334794; fax: +33 0 1 69333990.
E-mail address: nief@poly.polytechnique.fr (F. Nief).
[1] Present address: Department of Chemistry, Capital Normal University, Beijing, 100037, PR China.

0277-5387/$ - see front matter © 2005 Elsevier Ltd. All rights reserved.
doi:10.1016/j.poly.2005.01.001

alcohols [21–23]. A great variety of methylenediphosphonate ligands can thus be anticipated, including optically active compounds if the alcohols used derive from the chiral pool.

It therefore seemed to us desirable to structurally characterise lanthanide triflate complexes with the tetra-*iso*propylmethylenediphosphonate: $(i\mathrm{PrO})_2\mathrm{P(O)}\text{-}\mathrm{CH_2P(O)}(\mathrm{O}i\mathrm{Pr})_2$ = L as chelating ligand, because, since the triflates are labile ligands, different complexes than that obtained with the nitrates should be expected with these precursors. We describe hereafter the isolation and crystal structures of complexes of lanthanide triflates with ligand L. We have also obtained crystal structures of cerium, neodymium and praseodymium nitrate complexes with the L ligand that have a slightly different composition and solid-state conformation than that those previously described with lanthanum and praseodymium [18], and we wish to report on them as well.

2. Results and discussion

Lanthanide nitrates have been previously used as precursors in the synthesis of complexes with chelating phosphonates [15–19] and diphosphine oxides [14], whilst the more labile lanthanide triflates have only been engaged in complexation with diphosphine oxides [13]. The reaction of the ligand L and lanthanide nitrates in the 2:1 stoechiometric ratio afforded complexes of which the composition $[\mathrm{Ln(NO_3)_3(L)_2}]$ (Ln = Ce, Pr, Nd, Dy, Y) is consistent with their elemental analysis. They were further characterised by proton NMR (except for Ln = Dy), ^{31}P NMR, and IR spectroscopy. The compounds with Ln = Ce, Nd [17], Pr [17,18] have already been described, but, with Ln = Dy, the compound prepared was assigned the composition $[\mathrm{L_3Dy_2(NO_3)_6}]$ [17]. In our case, we find that with Ln = Dy (and also Y, which is similar in size), the general formula $[\mathrm{Ln(NO_3)_3(L)_2}]$ is better suited. It should be noted that, as previously observed [15,16], acceptable ^{31}P spectra were obtained even with the strongly paramagnetic dysprosium complex, the signal having a linewidth of about 2 kHz. Since the ^{31}P spectrum of $[\mathrm{Y(NO_3)_3(L)_2}]$ was already broad at room temperature ($w1/2$ = ca. 30 Hz), and we suspected this was due to a dynamic process, we undertook a low temperature ^{31}P NMR study. The resulting very complex spectra indicate that several exchange processes with coalescence temperatures between −40 °C and below −100 °C are operative in this compound. This is not too surprising, if one takes into consideration the number of possible isomers in a 10-coordinated complex. For instance, no less than 8 enantiomeric pairs and 3 meso isomers are possible for 5 identical and symmetrical bidentate ligands around a sphenocorona, and many more are to be expected in our case.

A very recent report [18] presented the X-ray structures of $[\mathrm{Ln(NO_3)_3(L)_2}]$ (L = La, Pr) that were obtained by crystallisation of the complexes from dichloromethane–hexane. In this report, Mehring et al. obtained viscous oils obtained by evaporation of their acetonitrile solutions. We found that, on standing, the oils resulting from slow evaporation of acetonitrile solutions of $[\mathrm{Ln(NO_3)_3(L)_2}]$ (Ln = Ce, Pr and Nd) eventually deposited crystals of these complexes containing acetonitrile in the lattice, that we were able to analyse by X-ray. We feel that these structures are of interest because the lanthanide coordination sphere is significantly different in our solvates than in the already described unsolvated complexes [18] (see later for a discussion).

With the triflates, the new isolated products are water solvates of composition $[\mathrm{Ln(OTf)_3(L)_2(OH_2)_2}]$ (Ln = La, Pr, Nd). They were characterised by elemental analysis, ^{1}H and ^{31}P NMR, and X-ray structure with Ln = Nd. When the L:Ln ratio was increased to 4:1, solids were also obtained but they were deliquescent and only in the case of lanthanum could we obtain a few crystals of a compound for which the X-ray analysis revealed that the composition was $[\mathrm{La(OTf)_3(L)_4(CH_3CN)_3}]$. Table 1 presents the X-ray experimental details of all analysed compounds: $[\mathrm{Ln(NO_3)_3(L)_2}](\mathrm{CH_3CN})_2$ (Ln = Ce (**A**), Pr (**B**), Nd (**C**)), $[\mathrm{Nd(OTf)_2(L)_2(OH_2)_2}](\mathrm{OTf})$ (**D**) and $[\mathrm{La(L)_4}]\text{-}\mathrm{OTf})_3(\mathrm{CH_3CN})_3$ (**E**).

2.1. Solid state structures of the nitrates

X-ray quality crystals of **A**, **B** and **C** were obtained from acetonitrile. These three compounds are isomorphous and isostructural.

The structure of **A** is displayed in Fig. 1, and selected bond lengths and distances are presented in Table 2.

We describe in detail the structure of **B**, as a representative example, because its structure can be accurately compared with that of three previously described praseodymium phosphonate complexes: unsolvated $[\mathrm{Pr(NO_3)_2(L)_2}]$ [18]: $\mathbf{B}^0$, $[\mathrm{Pr(NO_3)_2(L^1)_2}]$ [16]: $\mathbf{B}^1$ ($\mathrm{L^1}$ = $[(\mathrm{MeO})_2\mathrm{P(O)}]_2\mathrm{C(OH)Me}$), and $[\mathrm{Pr(NO_3)_2(L^2)_2}]$ [15]: $\mathbf{B}^2$ ($\mathrm{L^2}$ = $[(\mathrm{MeO})_2\mathrm{P(O)}]_2\mathrm{C(OH)Ph}$), The structure of **B** consists of discrete molecules without any apparent intermolecular contacts. Likewise, there are no noticeable short contacts involving the nitrogen atom belonging to the acetonitrile solvent. Like in $\mathbf{B}^0$, $\mathbf{B}^1$ and $\mathbf{B}^2$, the 10-coordinated praseodymium atom in **B** is chelated by the nitrate anions and by the phosphoryl groups of the two phosphonate ligands. In these complexes, one can define an equatorial plane (Pl1) containing the praseodymium atom, one nitrate ligand (nitrogen N1) and the nitrogen atoms (N2 and N1_2) of the other two nitrate ligands. The chelating phosphonates are located on either parts of this plane. The conformation of the two

Table 1
Crystal data and data collection parameters for compounds **A**–**E**

Compound	A	B	C	D	E
Molecular formula	$C_{30}H_{66}CeN_3O_{21}P$	$C_{30}H_{66}N_5O_{21}P_4Pr$	$C_{30}H_{66}N_3NdO_{21}P_4$	$C_{29}H_{64}F_9NdO_{23}P_4S_3$	$C_{61}H_{129}F_9LaN_3O_{33}P_8S_3$
Molecular weight	1096.88	1097.67	1101.00	1316.10	2086.52
Crystal habit	colourless block	colourless block	colourless block	colourless block	colourless block
Crystal dimensions (mm)	$0.28 \times 0.28 \times 0.20$	$0.28 \times 0.20 \times 0.18$	$0.20 \times 0.20 \times 0.18$	$0.20 \times 0.18 \times 0.18$	$0.22 \times 0.22 \times 0.22$
Crystal system	monoclinic	monoclinic	monoclinic	monoclinic	monoclinic
Space group (#)	*C2/c* (#15)	*C2/c* (#15)	*C2/c* (#15)	$P2_1/c$ (#14)	$P2_1/n$ (#14)
a (Å)	28.4000(10)	28.3530(10)	28.3190(10)	18.0820(10)	13.7820(10)
b (Å)	11.3090(10)	11.3130(10)	11.3150(10)	14.4450(10)	28.1060(10)
c (Å)	19.8000(10)	19.7950(10)	19.8070(10)	21.2310(10)	26.3850(10)
β (°)	126.7700(10)	126.8600(10)	126.9600(10)	92.7500(10)	98.6770(10)
V (Å^3)	5094.1(5)	5080.2(5)	5071.4(5)	5539.0(6)	10103.4(9)
Z	4	4	4	4	4
d (g cm^{-3})	1.430	1.435	1.442	1.578	1.372
F(000)	2268	2272	2276	2684	4344
μ (cm^{-1})	1.092	1.158	1.223	1.265	0.699
Maximum θ	30.00	30.03	30.03	30.03	30.03
Reflections measured	13013	12697	13598	28360	38568
Unique data	7354	7388	7378	16099	27854
R_{int}	0.0200	0.0201	0.0239	0.0358	0.0205
Reflections used ($I > 2\sigma(I)$)	6422	6350	6227	10870	19995
wR_2 (all data)	0.0797	0.0996	0.1043	0.0899	0.1837
R_1	0.0320	0.0331	0.0364	0.0371	0.0579
Goodness of fit	1.033	1.099	1.047	0.982	1.069

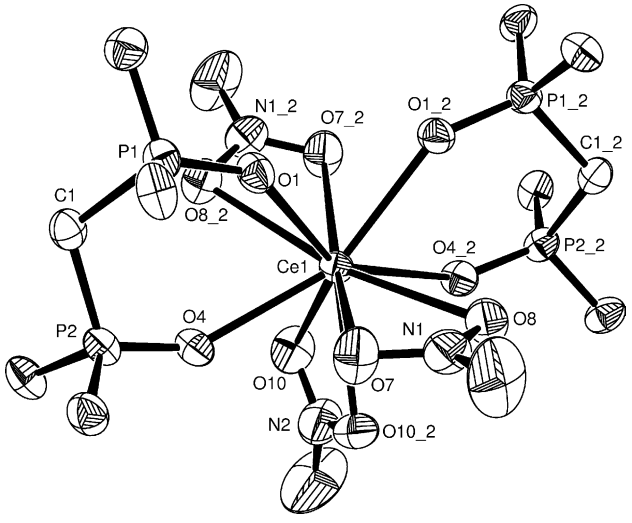


Fig. 1. An ORTEP plot of one molecule of **A** (50% ellipsoids). The *iso*propyl groups, methylene hydrogens, and the acetonitrile solvent molecules have been omitted for clarity.

6-membered rings consisting of the chelated phosphonates and the praseodymium atom is that of a flattened chair, the five heteroatoms (Pr and the two P═O groups) of these two rings being quasi-coplanar (planes Pl2 and Pl3 respectively). Likewise, the ''bite'' angle of the chelating diphosphonate in **B**: 73.26(6)° is similar to that found in $\mathbf{B}^0$: 74.95(6)° and 73.98(6)°, $\mathbf{B}^1$: 72.34(9)°, and $\mathbf{B}^2$: 73.6(3)° and 72.1(3)°. The other praseodymium-centred bonds and distances show no particular or unusual features.

There are, however, noticeable differences between the geometry of **B** and that of $\mathbf{B}^0$, $\mathbf{B}^1$ and $\mathbf{B}^2$, which are very similar to one another. In **B**, two nitrate ligands are almost perpendicular to the equatorial plane Pl1, the dihedral angles being equal to 88°; on the other hand, in $\mathbf{B}^1$ and $\mathbf{B}^2$, the nitrates are more slanted, this angle varyng from 61° to 72°. Even in $\mathbf{B}^0$, which has the same ligands around Pr than **B**, these angles are 57° and 69°. Likewise, the coordination of the diphosphonate ligands is less skewed in **B** than in $\mathbf{B}^0$, $\mathbf{B}^1$ or $\mathbf{B}^2$, as indicated by the value of the dihedral angles Pl2/Pl3 (**B**: 3°, $\mathbf{B}^0$: 24.5°, $\mathbf{B}^1$ and $\mathbf{B}^2$: 25°). Theses differences in geometry have the consequence that the coordination polyhedron around praseodymium in **B**, if one takes into consideration the O…O non bonding distances, is best described as a sphenocorona rather than a bicapped square antiprism in $\mathbf{B}^0$, $\mathbf{B}^1$ and $\mathbf{B}^2$ (Fig. 2). **B** and $\mathbf{B}^0$ can thus be considered as conformational isomers in the solid state.

This type of polyhedron has been observed in other lanthanide complexes [24].

The structures of **A** and **C** do not differ significantly from that of **B** except, of course, for the overall shortening of the Ln–O bonds from **A** to **C** due to the lanthanide contraction.

As a final remark, the configuration of **A**, **B**, $\mathbf{B}^0$, $\mathbf{B}^1$, $\mathbf{B}^2$ and **C** is notably different from that of a related cerium complex with the bis(diphosphino)methane dioxide ligand: $[Ce(NO_3)_3(Ph_2P(O)CH_2P(O)Ph_2)_2]$ [14]. In this latter complex, there is no equatorial plane containing the cerium atom, and the dihedral angle between the ligand planes is 92°.

Table 2
Selected bond lengths (Å) and angles (°) for complexes **A**–**C**

	A (Ln = Ce)	**B** (Ln = Pr)	**C** (Ln = Nd)
Bond lengths			
Ln(1)–O(1)	2.476(1)	2.458(2)	2.446(2)
Ln(1)–O(4)	2.457(1)	2.445(2)	2.430(2)
Ln(1)–O(7)	2.641(2)	2.625(2)	2.602(2)
Ln(1)–O(8)	2.670(2)	2.657(2)	2.642(2)
Ln(1)–O(10)	2.570(2)	2.551(2)	2.531(2)
P(1)–O(1)	1.477(2)	1.477(2)	1.476(2)
P(2)–O(4)	1.477(2)	1.474(2)	1.475(2)
O(7)–N(1)	1.256(3)	1.259(3)	1.260(3)
O(8)–N(1)	1.263(3)	1.260(3)	1.261(3)
O(9)–N(1)	1.222(3)	1.225(3)	1.226(3)
O(10)–N(2)	1.266(2)	1.262(3)	1.266(3)
O(11)–N(2)	1.215(4)	1.216(6)	1.217(6)
Bond angles			
O(1)–Ln(1)–O(1)#2	73.63(6)	73.33(8)	73.02(8)
O(1)–Ln(1)–O(4)	72.90(5)	73.30(6)	73.61(6)
O(1)–Ln(1)–O(4)#2	146.51(5)	146.60(6)	146.57(6)
O(1)–Ln(1)–O(7)	70.45(6)	70.50(7)	70.40(7)
O(1)–Ln(1)–O(7)#2	96.78(6)	96.57(7)	96.18(8)
O(1)–Ln(1)–O(8)	99.09(5)	99.38(6)	99.80(7)
O(1)–Ln(1)–O(8)#2	68.96(5)	68.90(6)	68.86(7)
O(1)–Ln(1)–O(10)	136.59(5)	136.52(6)	136.43(7)
O(1)–Ln(1)–O(10)#2	136.52(6)	136.73(7)	136.80(7)
O(4)–Ln(1)–O(4)#2	140.59(7)	140.1(1)	139.8(1)
O(4)–Ln(1)–O(7)	70.85(5)	70.68(6)	70.68(7)
O(4)–Ln(1)–O(7)#2	114.79(5)	115.10(6)	115.35(7)
O(4)–Ln(1)–O(8)	115.50(5)	115.42(6)	115.50(7)
O(4)–Ln(1)–O(8)#2	69.76(5)	69.80(6)	69.57(7)
O(4)–Ln(1)–O(10)	72.74(6)	72.56(7)	72.53(8)
O(4)–Ln(1)–O(10)#2	71.65(6)	71.40(7)	71.27(7)
O(7)–Ln(1)–O(7)#2	164.4(1)	164.3(1)	163.7(1)
O(7)–Ln(1)–O(8)	47.75(5)	48.02(6)	48.37(7)
O(7)–Ln(1)–O(8)#2	129.68(5)	129.44(6)	129.10(7)
O(7)–Ln(1)–O(10)	120.59(7)	120.72(8)	121.2(1)
O(7)–Ln(1)–O(10)#2	74.72(7)	74.76(8)	74.8(1)
O(8)–Ln(1)–O(8)#2	165.58(8)	165.9(1)	166.4(1)
O(8)–Ln(1)–O(10)	119.34(6)	119.26(7)	119.19(8)
O(8)–Ln(1)–O(10)#2	74.79(6)	74.57(7)	74.12(8)
O(10)–Ln(1)–O(10)#2	49.8(1)	50.0(1)	50.6(1)
O(7)–N(1)–O(8)	117.2(2)	117.1(2)	117.0(2)
O(7)–N(1)–O(9)	121.6(2)	121.5(2)	121.7(3)
O(8)–N(1)–O(9)	121.2(2)	121.3(3)	121.3(3)
O(10)–N(2)–O(10)#2	117.7(3)	117.4(4)	117.4(4)
O(10)–N(2)–O(11)	121.2(2)	121.3(2)	121.3(2)

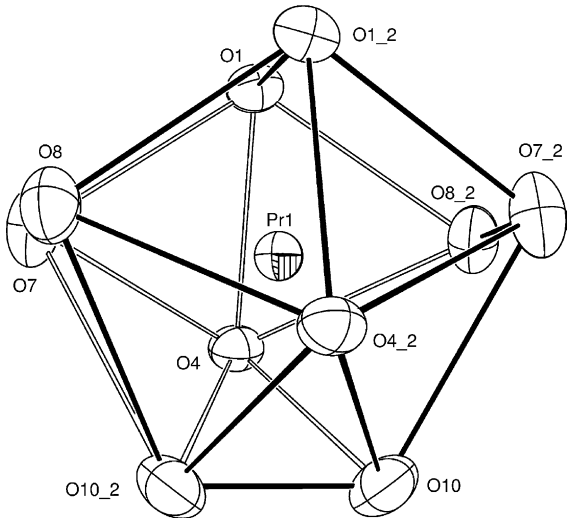


Fig. 2. Coodination polyhedron around praseodymium in **B**.

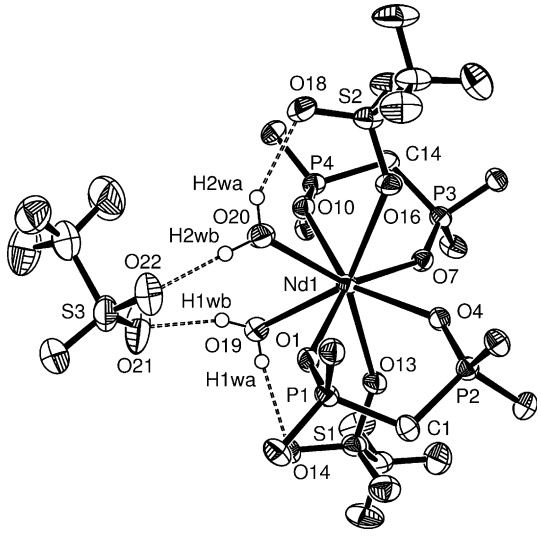


Fig. 3. An ORTEP plot of one molecule of **D** (50% ellipsoids). The *iso* propyl groups and the methylene hydrogens have been omitted for clarity.

2.2. Solid state structures of the triflates

X-ray quality crystals of $[Nd(OTf)_3(L)_2(OH_2)_2]$ (**D**) were also obtained from acetonitrile. The structure of **D** is displayed in Fig. 3, and selected bond lengths and distances are presented in Table 3.

This original structure consists of discrete ion pairs $[Nd(L)_2(OTf)_2(OH_2)_2](OTf)$ without any apparent intermolecular contacts. The 8-coordinated, monocationic neodymium atom is chelated by the phosphoryl groups of the two phosphonate ligands, bonded to two water molecules and to two monodentate triflates; the last triflate is not bonded to neodymium. The data were of sufficient quality that the coordinated water protons could be located and their positions refined. An interesting feature of this structure is that each of these protons interacts via hydrogen bonding with one oxygen atom of either the coordinated or the uncoordinated triflates. The distances span from 1.84 and 1.89 Å (hydrogen bonds to the "loose" triflate) to 2.06 and 2.08 Å (bonds to the coordinated triflates). These type of hydrogen bonds are also present in a few other lanthanide triflate hydrate complexes with chelating ligands [25–27]. The Nd–O (phosphoryl) bonds are quite similar to that found in the analogue of **C**: $[Nd(NO_3)_2(L^1)_2]$ [16], the Nd–O (monodentate triflate) bonds can be compared to that in $[Nd(OTf)_3(OPPh_3)_4]$ [28] and the Nd–O (water) bonds have no noteworthy features. Finally,

Table 3
Selected bond lengths (Å) and angles (°) for complex **D**

Bond lengths			
Nd(1)–O(1)	2.403(2)	Nd(1)–O(4)	2.436(2)
Nd(1)–O(7)	2.428(2)	Nd(1)–O(10)	2.423(2)
Nd(1)–O(13)	2.495(2)	Nd(1)–O(16)	2.496(2)
Nd(1)–O(19)	2.464(2)	Nd(1)–O(20)	2.440(2)
P(1)–O(1)	1.481(2)	P(2)–O(4)	1.486(2)
P(3)–O(7)	1.485(2)	P(4)–O(10)	1.480(2)
O(19)–H(1WA)	0.73(3)	O(19)–H(1WB)	0.82(3)
O(20)–H(2WA)	0.81(3)	O(20)–H(2WB)	0.86(3)
Bond angles			
O(1)–Nd(1)–O(4)	73.50(6)	O(1)–Nd(1)–O(7)	147.37(6)
O(1)–Nd(1)–O(10)	136.35(6)	O(1)–Nd(1)–O(13)	78.42(6)
O(1)–Nd(1)–O(16)	113.93(6)	O(1)–Nd(1)–O(19)	75.46(6)
O(1)–Nd(1)–O(20)	70.69(6)	O(4)–Nd(1)–O(7)	82.97(6)
O(4)–Nd(1)–O(10)	146.71(6)	O(4)–Nd(1)–O(13)	76.76(6)
O(4)–Nd(1)–O(16)	76.24(6)	O(4)–Nd(1)–O(19)	138.48(6)
O(4)–Nd(1)–O(20)	115.74(6)	O(7)–Nd(1)–O(10)	73.72(6)
O(7)–Nd(1)–O(13)	74.36(6)	O(7)–Nd(1)–O(16)	80.89(6)
O(7)–Nd(1)–O(19)	111.06(6)	O(7)–Nd(1)–O(20)	141.40(6)
O(10)–Nd(1)–O(13)	117.76(6)	O(10)–Nd(1)–O(16)	76.86(5)
O(10)–Nd(1)–O(19)	73.43(6)	O(10)–Nd(1)–O(20)	73.50(6)
O(13)–Nd(1)–O(16)	145.19(6)	O(13)–Nd(1)–O(19)	70.52(6)
O(13)–Nd(1)–O(20)	140.39(6)	O(16)–Nd(1)–O(19)	142.75(7)
O(16)–Nd(1)–O(20)	72.31(7)	O(19)–Nd(1)–O(20)	78.06(7)
H(1WA)–O(19)–H(1WB)	115(3)	H(2WA)–O(20)–H(2WB)	109(3)

Fig. 3 shows the square antiprismatic coordination of the neodymium atom.

At the 4:1 ligand to Ln ratio, we were able to isolate a defined product **E** in the case of lanthanum, by working under strict exclusion of air and moisture. The crude crystals that were obtained at low temperature were covered with oil and quickly transferred to the diffractometer: any attempt to dry them resulted in the formation of amorphous product. The composition of **E** was shown by X-ray to be $[La(L)_4](OTf)_3(CH_3CN)_3$ (Fig. 4).

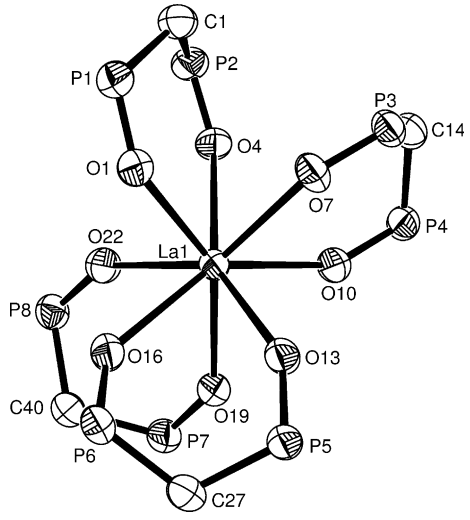


Fig. 4. An ORTEP plot of one molecule of **E** (50% ellipsoids). The *iso*propoxy groups, methylene hydrogens, uncoordinated triflates and acetonitrile solvent molecules have been omitted for clarity.

Selected bond lengths and distances are presented in Table 4.

Here, the 8-coordinated, tricationic lanthanum atom is only chelated by the phosphoryl groups of the four phosphonate ligands and has no interaction with either the lattice acetonitriles or the triflate anions, which have

Table 4
Selected bond lengths (Å) and angles (°) for **E**

Bond lengths			
La(1)–O(1)	2.467(3)	La(1)–O(4)	2.500(2)
La(1)–O(7)	2.529(2)	La(1)–O(10)	2.478(2)
La(1)–O(13)	2.476(2)	La(1)–O(16)	2.535(2)
La(1)–O(19)	2.517(2)	La(1)–O(22)	2.486(2)
P(1)–O(1)	1.473(3)	P(2)–O(4)	1.478(2)
P(3)–O(7)	1.479(2)	P(4)–O(10)	1.477(2)
P(5)–O(13)	1.484(2)	P(6)–O(16)	1.481(3)
P(7)–O(19)	1.478(3)	P(8)–O(22)	1.482(3)
Bond angles			
O(1)–La(1)–O(4)	74.49(8)	O(1)–La(1)–O(7)	71.65(8)
O(1)–La(1)–O(10)	137.48(8)	O(1)–La(1)–O(13)	104.9(1)
O(1)–La(1)–O(16)	76.25(8)	O(1)–La(1)–O(19)	146.34(8)
O(1)–La(1)–O(22)	85.7(1)	O(4)–La(1)–O(7)	74.86(8)
O(4)–La(1)–O(10)	74.65(8)	O(4)–La(1)–O(13)	149.07(8)
O(4)–La(1)–O(16)	135.56(8)	O(4)–La(1)–O(19)	119.88(8)
O(4)–La(1)–O(22)	71.71(8)	O(7)–La(1)–O(10)	72.55(8)
O(7)–La(1)–O(13)	75.72(8)	O(7)–La(1)–O(16)	125.23(8)
O(7)–La(1)–O(19)	139.17(8)	O(7)–La(1)–O(22)	143.56(8)
O(10)–La(1)–O(13)	87.63(8)	O(10)–La(1)–O(16)	145.05(8)
O(10)–La(1)–O(19)	75.51(8)	O(10)–La(1)–O(22)	111.2(1)
O(13)–La(1)–O(16)	71.20(8)	O(13)–La(1)–O(19)	78.21(8)
O(13)–La(1)–O(22)	139.14(8)	O(16)–La(1)–O(19)	73.17(8)
O(16)–La(1)–O(22)	73.4(1)	O(19)–La(1)–O(22)	72.48(8)

thus been expelled from the coordination sphere of lanthanum. Two related complexes with bis(diphosphino)methane dioxide as chelating ligand have been described in the literature: $[Eu(Ph_2P(O)CH_2P(O)Ph_2)_4](H_2O)_2(ClO_4)_3$ [12], and $[La(Ph_2P(O)CH_2P(O)Ph_2)_4](OTf)_3(H_2O)_{1.5}$ [13], in which the coordination of the ligands can be compared to that of **E**. In particular, the La–O and P=O bonds are similar in this latter lanthanum complex and **E**. The coordination geometry of the lanthanum atom in **E** can be described as square antiprismatic.

3. Conclusion and perspectives

We have been able to structurally characterise for the first time methylenediphosphonate complexes of lanthanide triflates, and to extend the range of characterised methylenediphosphonate complexes of lanthanide nitrates. As expected, the triflate ligand is more labile: the lanthanide nitrate bis(methylenediphosphonate) complexes, prepared from the commercial hydrated nitrates, retain all three nitrate ions bonded to the lanthanide metal and no water is coordinated, whilst the lanthanide triflates, bis(methylenediphosphonate) complexes have water in the coordination sphere and one uncoordinated triflate. We have also shown that when used in the 4:1 L:Ln ratio, methylenediphosphonates are able to completely displace the triflates. Our next step will be to use other diphosphonate ligands bearing chiral alcohols at the phosphorus atom. Work in this direction is already in progress.

4. Experimental

4.1. General

All reactions were performed in air with commercially available starting materials and solvents, except for the preparation of **E** which was performed in a Braun Labmaster 130 drybox under argon. ^{1}H NMR spectra were measured at 300.13 MHz, and ^{31}P NMR spectra at 122 MHz (t = 20 °C). Elemental analyses were obtained at the Service de microanalyse du CNRS, Gif-sur-Yvette, France.

4.2. Syntheses

The 2:1 complexes were prepared by mixing together lanthanide nitrates or triflates (0.73 mmol) and $(i\text{PrO})_2P(O)CH_2P(O)(O i\text{Pr})_2$ (0.50 g, 1.45 mmol) in acetonitrile (5 ml). The complexes that precipitated on concentrating the acetonitrile solution were washed in ether and dried in vacuo. The 4:1 complex was prepared as described below.

4.2.1. Bis(methylenediphosphonate) lanthanide nitrate complexes

$[Ce(NO_3)_3\{(i\text{PrO})_2P(O)CH_2P(O)(O i\text{Pr})_2\}_2]$: colourless powder. Yield 0.31 g (77%). *Anal.* Calc. for $C_{26}H_{60}CeN_3O_{21}P_4$: C, 30.77; H, 5.96; N, 4.14. Found: C, 30.65; H, 5.91; N, 3.96%. IR (KBr): $\nu(NO_3^-)$: 1482, 1453, 1315, 1298 cm^{-1}, ν(P=O) 1215 cm^{-1}. ^{1}H NMR (CD_3CN) δ 1.52 (br, $w_{1/2}$ = 15 Hz, 48H, CH_3), 5.63 (br, $w_{1/2}$ = 25 Hz, 8H, CH), 6.68 (br, $w_{1/2}$ = 60 Hz, 4H, CH_2). ^{31}P NMR (CH_3CN): δ 43.2 ($w_{1/2}$ = 25 Hz).

$[Pr(NO_3)_3\{(i\text{PrO})_2P(O)CH_2P(O)(O i\text{Pr})_2\}_2]$: pale yellowish-green powder Yield 0.34 g (84%). *Anal.* Calc. for $C_{26}H_{60}N_3O_{21}P_4Pr$: C, 30.75; H, 5.95; N, 4.14. Found: C, 30.53; H, 5.92; N, 3.87%. NMR and IR data identical to those previously described [18].

$[Nd(NO_3)_3\{(i\text{PrO})_2P(O)CH_2P(O)(O i\text{Pr})_2\}_2]$: pale purple powder. Yield 0.35 g (78%). *Anal.* Calc. for $C_{26}H_{60}N_3NdO_{21}P_4$: C, 30.65; H, 5.94; N, 4.12. Found: C, 30.35; H, 5.88; N, 3.93%. IR (KBr): $\nu(NO_3^-)$: 1483, 1453, 1319, 1301 cm^{-1}, ν(P=O) 1218 cm^{-1}. ^{1}H NMR (CD_3CN) δ 1.45 (br, $w_{1/2}$ = 10 Hz, 24H, CH_3), 1.49 (br, $w_{1/2}$ = 10 Hz, 24H, CH_3), 5.36 (br, $w_{1/2}$ = 30 Hz, 8H, CH), 5.67 (br, $w_{1/2}$ = 80 Hz, 4H, CH_2). ^{31}P NMR (CH_3CN): 82 ($w_{1/2}$ = 180 Hz).

$[Dy(NO_3)_3\{(i\text{PrO})_2P(O)CH_2P(O)(O i\text{Pr})_2\}_2]$: colourless powder. Yield 0.33 g (80%). *Anal.* Calc. for $C_{26}H_{60}DyN_3O_{21}P_4$: C, 30.11; H, 5.83; N, 4.05. Found: C, 29.77; H, 5.71; N, 3.96%. IR (KBr): $\nu(NO_3^-)$: 1504, 1323 cm^{-1}, ν(P=O) 1208 cm^{-1}. ^{31}P NMR (CH_3CN): −64 ($w_{1/2}$ = 2 kHz).

$[Y(NO_3)_3\{(i\text{PrO})_2P(O)CH_2P(O)(O i\text{Pr})_2\}_2]$: colourless powder. Yield 0.31 g (86%). *Anal.* Calc. for $C_{26}H_{60}N_3O_{21}P_4Y$: C, 32.41; H, 6.28; N, 4.36. Found: C, 32.12; H, 6.32; N, 4.01%. IR (KBr): $\nu(NO_3^-)$: 1505, 1326 cm^{-1}, ν(P=O) 1209 cm^{-1}. ^{1}H NMR (CD_3CN): δ 1.35 (d, J_{HH} = 6 Hz, 24H, CH_3), 1.36 (d, J_{HH} = 6 Hz, 24H, CH_3), 2.65 (t, J_{PH} = 21 Hz, 4H, CH_2), 4.78 (m, 8H, CH). ^{31}P NMR (CH_3CN): 17.6.

4.2.2. Bis(methylenediphosphonate) lanthanide triflate complexes

$[La(SO_3CF_3)_3\{(i\text{PrO})_2P(O)CH_2P(O)(O i\text{Pr})_2\}_2(H_2O)_2]$: colourless powder. Yield 0.40 g (86%). *Anal.* Calc. for $C_{29}H_{64}F_9LaO_{23}P_4S_3$: C, 26.57; H, 4.92; N, 0.0. Found: C, 26.08; H, 4.91; N, 0.0%. IR (KBr): ν(O–H) 3278 cm^{-1}, [ν(S–O), ν(C–F)]: 1300, 1234 cm^{-1}, ν(P=O) 1212 cm^{-1}, ν(C–S) 634 cm^{-1}. ^{1}H NMR ($CDCl_3$): δ 1.34 (d, J_{HH} = 6 Hz, 24H, CH_3), 1.35 (d, J_{HH} = 6 Hz, 24H, CH_3), 2.69 (t, J_{PH} = 21 Hz, 4H, CH_2), 3.85 (br, H_2O), 4.94 (m, 8H, CH). ^{31}P NMR ($CDCl_3$): δ 19.7.

$[Pr(SO_3CF_3)_3\{(i\text{PrO})_2P(O)CH_2P(O)(O i\text{Pr})_2\}_2(H_2O)_2]$: pale yellowish-green powder Yield 0.35 g (78%). *Anal.* Calc. for $C_{29}H_{64}F_9O_{23}P_4PrS_3$: C, 26.53; H, 4.90; N, 0.0. Found: C, 26.09; H, 4.86; N, 0.0%. IR (KBr): ν(O–H) 3304 cm^{-1}, [ν(S–O), ν(C–F)]: 1300, 1233 cm^{-1}, ν(P=O) 1199 cm^{-1}, ν(C–S) 635 cm^{-1}. ^{1}H NMR

($CDCl_3$): δ −21.1 (br, $w_{1/2}$ = 60 Hz, 4H, H_2O) 1.12 (br, $w_{1/2}$ = 15 Hz, 24H, CH_3), 3.62 (br, $w_{1/2}$ = 20 Hz, 24H, CH_3), 8.99 (br, $w_{1/2}$ = 35 Hz, 8H, CH), 21.04 (br, $w_{1/2}$ = 60 Hz, 4H, CH_2). ^{31}P NMR ($CDCl_3$): δ 107 ($w_{1/2}$ = 40 Hz).

$[Nd(SO_3CF_3)_3\{(iPrO)_2P(O)CH_2P(O)(OiPr)_2\}_2(H_2O)_2]$: pale purple powder Yield 0.35 g (78%). *Anal*. Calc. for $C_{29}H_{64}F_9NdO_{23}P_4S_3$: C, 26.47; H, 4.90; N, 0.0. Found: C, 26.35; H, 4.82; N, 0.0%. IR (KBr): ν(O–H) 3278 cm^{-1}, [ν(S–O), ν(C–F)]: 1300, 1235 cm^{-1}, ν(P=O) 1214 cm^{-1}, ν(C–S) 635 cm^{-1}. ^{1}H NMR ($CDCl_3$): δ −5.0 (br, $w_{1/2}$ = 100 Hz, 4H, H_2O) 0.90 (br, $w_{1/2}$ = 20 Hz, 24H, CH_3), 2.64 (br, $w_{1/2}$ = 20 Hz, 24H, CH_3), 6.61 (br, $w_{1/2}$ = 35 Hz, 8H, CH), 12.04 (br, $w_{1/2}$ = 60 Hz, 4H, CH_2). ^{31}P NMR ($CDCl_3$): δ 103 ($w_{1/2}$ = 60 Hz).

4.2.3. Tetrakis(methylenediphosphonate) lanthanum triflate complex

Crystals of $[La\{(iPrO)_2P(O)CH_2P(O)(OiPr)_2\}_2(OTf)_3(CH_3CN)_3]$ (**E**) were obtained as follows: Dry lanthanum triflate (0.18 g, 0.36 mmol) and $(iPrO)_2P(O)CH_2P(O)(OiPr)_2$ (0.50 g, 1.45 mmol) were mixed together in acetonitrile (5 ml). The solution volume was reduced to 1 ml and transferred into a glass tube of 5 mm internal diameter. About 2 ml of diethyl ether was carefully layered on top of this solution which was kept at 4 °C. Colourless, transparent crystals appeared after about 48 h. They were immersed in Paratone 8277 oil and quickly mounted on the diffractometer.

4.3. X-ray crystallography

Suitable single crystals of **A**, **B**, **C** and **D** were obtained from concentrated acetonitrile solutions at room temperature, and of **E** as described in Section 4.2.3. X-ray intensities were measured with a Nonius KappaCCD diffractometer at 150(1) K using Mo Kα radiation (λ = 0.71073 Å) and a graphite monochromator. A summary of the crystal structure determinations is presented in Table 1.

5. Supplementary material

CCDC 255823–255827 contains the supplementary crystallographic data for this paper. These data can be obtained free of charge at www.ccdc.cam.ac.uk/conts/retrieving.html [or from the Cambridge Crystallographic Data Centre, 12, Union Road, Cambridge CB2 1EZ, UK; fax: (internat.) +44-1223/336-033; E-mail: deposit@ccdc.cam.ac.uk].

Acknowledgements

Financial support of this work was provided by CNRS and Ecole Polytechnique. QiongHua Jin is grateful for the financial support of a CNRS – K.C. Wang postdoctoral fellowship.

References

[1] H.C. Aspinall, Chem. Rev. 102 (2002) 1807.
[2] F.A. Hart, in: G. Wilkinson (Ed.), Comprehensive Coordination Chemistry, vol. 3, Pergamon Press, Oxford, 1987, pp. 1082–1085.
[3] B.M. Rapko, E.N. Duesler, P.H. Smith, R.T. Paine, R.R. Ryan, Inorg. Chem. 32 (1993) 2164.
[4] X.-M. Gan, E.N. Duesler, R.T. Paine, P.H. Smith, Inorg. Chim. Acta 247 (1996) 27.
[5] E.M. Bond, E.N. Duesler, R.T. Paine, H. Nöth, Polyhedron 19 (2000) 2135.
[6] X.-M. Gan, E.N. Duesler, R.T. Paine, Inorg. Chem. 40 (2001) 4420.
[7] X.-M. Gan, R.T. Paine, E.N. Duesler, H. Nöth, Dalton Trans. (2003) 153.
[8] R.T. Paine, Y.-C. Tan, X.-M. Gan, Inorg. Chem. 40 (2001) 7009.
[9] Y.-C. Tan, X.-M. Gan, J.L. Stanchfield, E.N. Duesler, R.T. Paine, Inorg. Chem. 40 (2001) 2910.
[10] J. Fawcett, A.W.G. Platt, S. Vickers, Polyhedron 22 (2003) 1431.
[11] J. Rohovec, P. Vojtisek, P. Hermann, J. Ludvik, I. Lukes, J. Chem. Soc., Dalton Trans. (2000) 141.
[12] L. Huang, B.-Q. Ma, C.-H. Huang, T.C.W. Mak, G.-Q. Yao, G.-X. Xu, J. Coord. Chem. 54 (2001) 95.
[13] J. Fawcett, A.W.G. Platt, Polyhedron 22 (2003) 967.
[14] A.M.J. Lees, A.W.G. Platt, Inorg. Chem. 42 (2003) 4673.
[15] A.W.G. Platt, D. Simpson, J. Fawcett, D.R. Russell, Inorg. Chim. Acta 223 (1994) 43.
[16] A.M.J. Lees, J.M. Charnock, R.A. Kresinski, A.W.G. Platt, Inorg. Chim. Acta 312 (2001) 170.
[17] W.E. Stewart, T.H. Siddall, J. Inorg. Nucl. Chem. 30 (1968) 1513.
[18] M. Mehring, D. Mansfeld, M. Schürmann, Z. Anorg. Allg. Chem. 630 (2004) 452.
[19] A.M.J. Lees, R.A. Kresinski, A.W.G. Platt, New J. Chem. 28 (2004) 1457.
[20] O.T. Quimby, J.D. Curry, D.A. Nicholson, J.B. Prentice, C.H. Roy, J. Organomet. Chem. 13 (1968) 199.
[21] A.A. Davis, J.J. Rosèn, J.J. Kiddie, Tetrahedron Lett. 39 (1998) 6263.
[22] D.C. Stepinski, D.W. Nelson, P.R. Zalupski, A.W. Herlinger, Tetrahedron 57 (2001) 8637.
[23] P.C.B. Page, M.J. McKenzie, J.A. Gallagher, J. Org. Chem. 66 (2001) 3704.
[24] V.A. Ovchynikov, T.P. Timoshenko, V.M. Amirkhanov, J. Sieler, V.V. Skopenko, Z. Naturforsch. 55b (2000) 262.
[25] J. Chen, Y.-F. Zhang, X. Zheng, A. Vij, D. Wingate, D. Meng, K. White, R.L. Kirchmeier, J.M. Shreeve, Inorg. Chem. 35 (1996) 1590.
[26] C. Husson, P. Delangle, J. Pécaut, P.J.A. Vottéro, Inorg. Chem. 38 (1999) 2012.
[27] A.S. Batsanov, J.I. Bruce, T. Ganesh, P.J. Low, R. Kataky, H. Puschmann, P.G. Steel, J. Chem. Soc., Perkin Trans. 1 (2002) 932.
[28] J. Fawcett, A.W.G. Platt, D.R. Russell, Polyhedron 21 (2002) 287.

Available online at www.sciencedirect.com
SCIENCE DIRECT®
Polyhedron 24 (2005) 557–562
POLYHEDRON
www.elsevier.com/locate/poly

New homogeneous and alternating Mn(II)-azido 1D systems

Morsy A.M. Abu-Youssef [a], Albert Escuer [b,*], Ramon Vicente [b], Franz A. Mautner [c], L. Öhrstrom [d], Mohamed A.S. Goher [a]

[a] Chemistry Department, Faculty of Science, Alexandria University, P.O. Box 426, Ibrahimia, 21321 Alexandria, Egypt
[b] Departament de Química Inorgànica, Universitat de Barcelona, Martí Franqués 1-11, 08028 Barcelona, Spain
[c] Institut für Physikalische und Theoretische Chemie, Technische Universität Graz, A-8010 Graz, Austria
[d] Institutionen för Material ach Ytkem, Chalmers Tekniska Högskola, 41296 Göteborg, Sweden

Received 18 November 2004; accepted 21 January 2005

Abstract

Reaction of sodium azide with manganese(II) and 4-amino-1,2,4-triazol or 3-chloropyridine leads to the 1D systems $[Mn(N_3)_2(4\text{-amtr})_2]_n$ (**1**) or $\{[Mn(N_3)_2(3\text{-Clpy})_2]\cdot 1/2(3\text{-Clpy})\}_n$ (**2**), respectively. Compound **1** crystallises in the *C*2/*m* (monoclinic) group and consists of chains of Mn(II) cations bridged by double $\mu_{1,3}$-azido bridges in trans arrangement. Compound **2** crystallises in the *I*2/*a* (monoclinic) group and in this case the 1D system shows alternating double $\mu_{1,1}$ and $\mu_{1,3}$ bridges. Magnetic properties follow the expected antiferromagnetic (compound **1**) and alternating ferro-antiferromagnetic (compound **2**) behaviour.
© 2005 Published by Elsevier Ltd.

Keywords: Manganese; Magnetochemistry; Crystal structures; 1D systems

1. Introduction

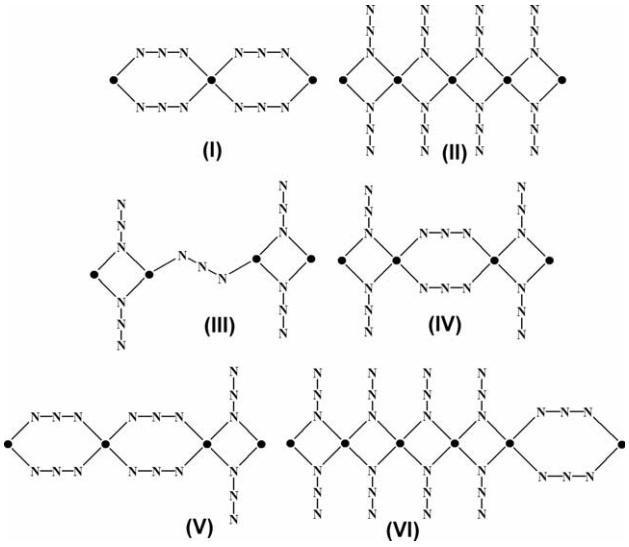
Compounds with general formula $[Mn(N_3)_2(R\text{-py})_2]_n$ in which R-py is a pyridinic ligand with a R group in *meta* or *para*-position, provides a series of 1D derivatives in which the alternance of end-to-end ($\mu_{1,3}$-N_3, EE mode) and end-on ($\mu_{1,1}$-N_3, EO mode) azide bridges results in a complete graduation of magnetic responses [1].

This series of compounds, Scheme 1, goes from compounds containing only EE bridges [2,3a] to compounds containing only EO bridges [3] with antiferromagnetic or ferromagnetic response, respectively (I, II), trough systems in which the ratio of EE:EO bridges is 2:1 (V), [4] 1:1 (III, IV) [1,2a,5] or 1:4 (VI) [4a]. This gradual change of AF/F interactions provides an interesting material to study unusual magnetic properties as the topological ferrimagnetic response of compounds type V, [4] the EPR of chains with a gradual change of the superexchange and dipolar interactions [2a] or to develop theoretical studies to explain the new properties [2a,3b,4b].

As a consequence, study of the coordination chemistry and magnetic properties of azido-bridged systems has deserved the attention of magnetochemists in recent years due to the large number of the well characterised uncommon topologies and magnetic responses. The ability of the azido bridge to give different coordination modes as the EE, generally associated to antiferromagnetic coupling, or EO, generally associated to ferromagnetic coupling, [1] is the key of the versatility of this ligand. Moreover, in some limited cases, more exotic coordination modes as the $\mu_{1,1,1}$, $\mu_{1,1,3}$ or even $\mu_{1,1,1,1}$ and $\mu_{1,1,3,3}$ have been obtained with several cations [6]. In addition to molecular compounds with a wide range

* Corresponding author. Tel.: +93 4021264; fax: +93 4907725.
E-mail addresses: morsy5@link.net (M.A.M. Abu-Youssef), albert.escuer@qi.ub.es (A. Escuer), Mautner@ptc.tu-graz.ac.at (F.A. Mautner), ohrstrom@chem.chalmers.se (L. Öhrstrom).

0277-5387/$ - see front matter © 2005 Published by Elsevier Ltd.
doi:10.1016/j.poly.2005.01.003



Scheme 1. Characterised 1D motifs for Mn(II)-azido chains.

of nuclearity, [1,7] azido ligand easily tends to give extended systems up to 3D dimensionality, containing in the most of the cases EE and EO azido bridges simultaneously, which often gives long range order at moderately low temperatures [1,8].

Following our research on the Mn^{II}/azide/pyridine systems, we have structurally characterized two new systems, using L = 4-amino-1,2,4-triazol (4-amtr) and 3-chloropyridine (3-Clpy) to obtain the 1D systems $[Mn(N_3)_2(4\text{-amtr})_2]_n$ (**1**) and $\{[Mn(N_3)_2(3\text{-Clpy})_2]\cdot 1/2(3\text{-Clpy})\}_n$ (**2**). The two compounds consist of chains in which the manganese atoms are bridged by two azido ligands. For **1** the bridges are exclusively end-to-end, type I, showing the expected antiferromagnetic coupling whereas for **2** there are a regular alternance between the end-to-end and end-on coordination modes, type IV, giving an alternating ferro-antiferromagnetic system. The antiferromagnetic interactions have been correlated with the bond parameters of the bridging fragment on basis on the previously reported coupling model.

2. Experimental

2.1. General and physical measurements

Infrared spectra were recorded on a Bruker IFS-125 model FT-IR spectrophotometer as KBr pellets. Magnetic susceptibility measurements were carried out on polycrystalline samples at the Servei de Magnetoquímica of the University of Barcelona, with a DSM8 pendulum susceptometer working in the range 4–300 K under magnetic fields of approximately 1 T. Diamagnetic corrections were estimated from Pascal Tables.

2.2. Compounds preparation

WARNING! The reported azido complexes are potentially explosive. Only a small amount of material should be prepared and it should be handled with care.

2.2.1. $[Mn(N_3)_2(4\text{-amtr})_2]_n$ (*1*)

Irregular shaped crystals of 1 were separated from a clear aqueous solution (15 mL) containing $Mn(NO_3)_2\cdot 4H_2O$ (0.50 g, 2 mmol), NaN_3 (0.32 g, 5 mmol) and 4-amino-1,2,4-triazol (0.67 g, 8 mmol) after one day at room temperature. Yield: 0.18 g, 60%. $\nu_{as}(N_3)$ 2091 (vs) cm^{-1}. *Anal.* calc. for $C_4H_8MnN_{14}$: C, 15.6; H, 2.6; N, 63.8; Mn, 17.9. Found: C, 15.4; H, 2.5; N, 64.0; Mn, 18.1%.

2.2.2. $\{[Mn(N_3)_2(3\text{-Clpy})_2]\cdot 1/2\ (3\text{-Clpy})\}_n$ (*2*)

An aqueous solution (5 mL) of NaN_3 (0.32 g, 5 mmol) was added drop by drop to a methanolic solution (40 mL) of $Mn(NO_3)_2\cdot 4H_2O$ (0.50 g, 2 mmol) and 3-chloropyridine (0.68 g, 6 mmol). The resulting solution was filtered off and the filtrate was allowed to stand for several days at room temperature to deposit yellow-green crystals. Yield: 0.55 g, 65%. $\nu_{as}(N_3)$ 2135,(vs) and 2064 (vs) cm^{-1}. *Anal.* calc. for $C_{50}H_{40}Cl_{10}Mn_4N_{34}$: C, 35.5; H, 2.4; N, 28.2; Mn, 13.0. Found: C, 35.3; H, 2.2; N, 28.4; Mn, 13.2%.

2.2.3. X-ray data collection for compounds *1* and *2*

The X-ray single-crystal data for **1** [2] were collected on a modified STOE four circle diffractometer at 90(2)[88(2)] K. Crystal size: $0.40\times 0.22\times 0.14$ mm [$0.26\times 0.23\times 0.18$ mm]. The crystallographic data, conditions retained for the intensity data collection, and

Table 1
Crystal data and structure refinement for (**1**) and (**2**)

	1	**2**
Formula	$C_4H_8MnN_{14}$	$C_{50}H_{40}Cl_{10}Mn_4N_{34}$
Fw	307.18	1691.42
Space group	*C*2/*m*	*I*2/*a*
Unit cell dimensions		
a (Å)	15.030(5)	14.118(4)
b (Å)	6.872(3)	14.124(4)
c (Å)	5.362(2)	17.308(7)
α (°)	90	90
β (°)	93.67(3)	108.84(3)
γ (°)	90	90
V (Å^3)	552.7(4)	3266(2)
Z	2	2
T (K)	90	88
λ(Mo Kα) (Å)	0.71069	0.71069
ρ_{calc} (g cm^{-3})	1.846	1.720
μ(Mo Kα) (mm^{-1})	1.211	1.232
$R^a[I>2\sigma(I)]$	0.0421	0.0362
$wR_2{}^b$ (all data)	0.1157	0.0864

[a] $R(F_o)=\sum(F_o-F_c)/\sum F_o$.
[b] $wR(F_o)^2=\{\sum[w((F_o)^2-(F_c)^2)^2]/\sum[w(F_o)^4]\}^{1/2}$.

some features of the structure refinement are listed in Table 1.

Graphite-monochromatized MoKα radiation ($\lambda = 0.71069$ Å) with the ω-scan technique was used to collect the data sets. The accurate unit cell parameters were determined from automatic centring of 28 [35] reflections ($10.2° < \theta < 15.4°$) [$8.8° < \theta < 15.4°$] and refined by least-squares methods. 1262 [4746] reflections, 872 [4053] independent reflections, R_{int} 0.030 [0.021] were collected in the range ($3.3° < \theta < 30.0°$) [$2.9° < \theta < 29.0°$]. Intensity decay of 5% [4%] for control reflections (0 0; 1; 0 −2 0; −1 −1 0) [0 6 0; 3 1 0; 1 1 4], measured after every set of 100 reflections, was observed during data collection. Corrections were applied for Lorentz-polarization effects, intensity decay and for absorption in case of **1**, using the DIFABS [9] computer program. The structures were solved by direct methods using the SHELXS-86 [10] program and refined by full-matrix least-squares methods on F^2, using the SHELXL-93 [11] program incorporated in the SHELXTL/PC V 5.03 [12] program library and the PLATON [13] program. Anisotropic displacement parameters were applied to all non-hydrogen atoms. The hydrogen atoms were assigned with isotropic displacement factors and included in the final refinement cycles by use of geometrical restraints. In case of **2**, split occupancy of 0.5 and geometrical restraints were applied to atoms of disordered 3-Clpy lattice molecule located on the special position with site symmetry 2 (diad). Final $R[I > 2\sigma(I)]$ and wR factor for all observed reflections: 0.0421 and 0.1157 [0.0362 and 0. 0864]; number of refined parameters: 65 [247]. Maximum and minimum peaks in the final difference Fourier synthesis: 0.79 and −1.03 e Å^{-3} [0.48 and −0.37 e Å^{-3}]. Selected bond parameters are given in Tables 2 and 3, respectively.

Table 2
Selected bond lengths [Å] and angles [°] for compound $[Mn(N_3)_2(4\text{-amtr})_2]_n$ (**1**)

Bond lengths			
Mn(1)–N(1)	2.222(3)	N(1)–N(2)	1.386(4)
Mn(1)–N(11)	2.223(2)	N(1)–C(5)	1.301(4)
N(11)–N(12)	1.172(2)	N(2)–C(3)	1.306(4)
		N(4)–N(6)	1.401(3)
Mn(1)···Mn(1B)	5.362(2)	N(4)–C(3)	1.354(4)
		N(4)–C(5)	1.351(3)
Bond angles			
N(1)–Mn(1)–N(1A)	180	Mn(1)–N(11)–N(12)	129.6(2)
N(11)–Mn(1)–N(11A)	180		
N(11C)–Mn(1)–N(11D)	180	N(11)–N(12)–N(11B)	178.3(3)
N(1)–Mn(1)–N(11)	87.52(7)		
N(1)–Mn(1)–N(11A)	92.48(7)		
N(11)–Mn(1)–N(11D)	89.2(1)		
N(11)–Mn(1)–N(11C)	90.8(1)		

Table 3
Selected bond lengths [Å] and angles [°] for compound $\{[Mn(N_3)_2(3\text{-Clpy})_2]\cdot 1/2(3\text{-Clpy})\}_n$ (**2**)

Bond lengths			
Mn(1)–N(1)	2.274(2)	N(11)–N(12)	1.194(2)
Mn(1)–N(2)	2.267(2)	N(12)–N(13)	1.150(3)
Mn(1)–N(11)	2.211(2)	N(21)–N(22)	1.174(2)
Mn(1)–N(11A)	2.222(2)	N(22)–N(23B)	1.170(2)
Mn(1)–N(21)	2.225(2)		
Mn(1)–N(23)	2.193(2)		
Mn(1)···Mn(1B)	5.287(2)		
Mn(1)···Mn(1A)	3.408(2)		
Bond angles			
N(1)–Mn(1)–N(2)	172.43(6)	N(11A)–Mn(1)–N(21)	94.90(7)
N(1)–Mn(1)–N(11)	96.08(6)	N(11A)–Mn(1)–N(23)	170.03(7)
N(1)–Mn(1)–N(11A)	88.73(6)	N(21)–Mn(1)–N(23)	94.84(7)
N(1)–Mn(1)–N(21)	86.81(7)		
N(1)–Mn(1)–N(23)	89.69(7)		
N(2)–Mn(1)–N(11)	90.09(6)	N(11)–N(12)–N(13)	179.8(2)
N(2)–Mn(1)–N(11A)	88.07(6)	N(21)–N(22)–N(23B)	177.6(2)
N(2)–Mn(1)–N(21)	86.62(7)		
N(2)–Mn(1)–N(23)	94.62(7)	Mn(1)–N(11)–Mn(1A)	100.48(7)
N(11)–Mn(1)–N(11A)	79.52(7)	Mn(1)–N21)–N(22)	129.8(2)
N(11)–Mn(1)–N(21)	173.63(6)	Mn(1)–N(23)–N(22B)	131.0(2)
N(11)–Mn(1)–N(23)	90.86(7)	Mn(1)–N(11)–N(12)	127.1(2)

3. Results and discussion

3.1. Crystal structure of $[Mn(N_3)_2(4\text{-amtr})_2]_n$ (1)

The labelled diagram for **1** is shown in Fig. 1. The basic structure consist of octahedrically coordinated manganese atoms in which the coordination sites are occupied by two 4-amino-1,2,4-triazol ligands in *trans* arrangement and four azido ligands. The azido ligands link the manganese atoms in the $\mu_{1,3}$ (EE) coordination mode, giving a 1D system with double azido bridges along the [0 0 1] direction. Bond parameters around Mn^{II} atoms are quite regular with all the bond lengths practically equal, around 2.222 Å and all the Mn–N–N bond angles of 129.6(2)°. Intrachain Mn···Mn distance is 5.362(2) Å.

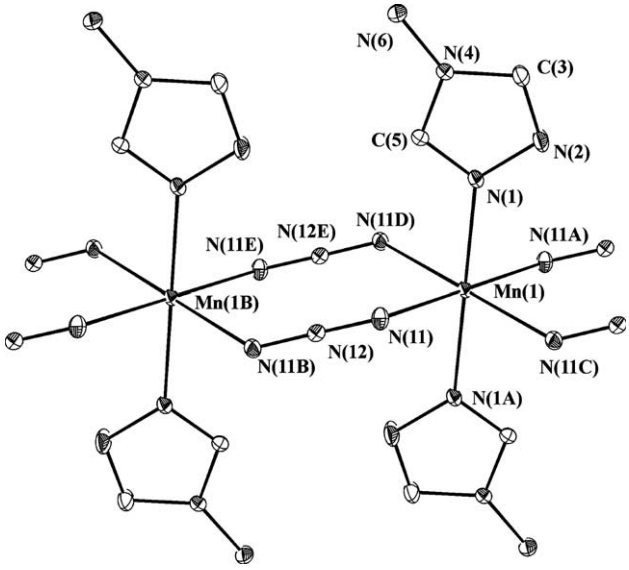


Fig. 1. ORTEP view (50% ellipsoids) of $[Mn(N_3)_2(4\text{-amtr})_2]_n$ (**1**). The chains are oriented along the *c*-axis of the unit cell. *Symmetry codes*: (A) $-x, -y, -z$; (B) $-x, y, -z-1$; (C) $-x, y, -z$; (D) $x, -y, z$.

The Mn–$(\mu_{1,3})_2$–Mn unit shows a chair distortion with a dihedral angle of 22.6(1)° between the azido plane and the plane determined by N(11)–Mn(1)–N(11D), Fig. 2(a).

The H-atoms of the $-NH_2$ group promotes a 3D network on basis of the N(6)–H···N(11) interactions, Fig. 3. N(6)···N(11) distances, 3.098(3) Å corresponds to a strong H-bond.

3.2. Crystal structure of $\{[Mn(N_3)_2(3\text{-}Clpy)_2]\cdot 1/2(3\text{-}Clpy)\}_n$ (2)

The labelled diagram for **2** is shown in Fig. 4. The basic structure consists of manganese atoms in octahedral environment with the coordination sites occupied by two *trans* 3-chloropyridines and four azido ligands. The manganese atoms are linked by double azido bridges, giving a 1D system along [0 0 1] direction, in which the azido ligands show a regular alternance between the $\mu_{1,1}$ and the $\mu_{1,3}$ coordination modes resulting an alternating system.

Mn–N bond lengths to pyridinic ligands (2.267–2.274 Å) are slightly larger than the Mn–N bond lengths to azido ligands (around 2.200 Å). The Mn–$(\mu_{1,1})_2$–Mn unit forms a planar centrosymmetric Mn_2N_2 ring with a Mn(1)–N(11)–Mn(1A) bond angle of 100.48(7)° and a Mn···Mn distance of 3.408(2) Å. The Mn–$(\mu_{1,3})_2$–Mn unit is not fully planar, showing a dihedral angle between the mean azido plane and N(21)–Mn(1)–N(23) plane of 9.77(9)°, with the Mn atoms 0.240(1) Å out the azido plane. In this case, the free 3-Clpy molecule intercalated between the coordinated 3-Clpy ligands forces to increase asymmetrically the interligand distance and produces a very unusual boat-distortion, Fig. 2(b). Mn···Mn distance of 5.287(2) Å. The intercalated 3-Clpy molecule forms mean dihedral angles of 5.5(1)° and 8.2(1)° with the neighbouring coordinated 3-Clpy ligands. The forces that determine the intercalation of neutral ligands in the structure should be attributed to π–π stacking, from the mean distance between the coordinated and intercalated 3-Clpy ligands (around 3.5 Å).

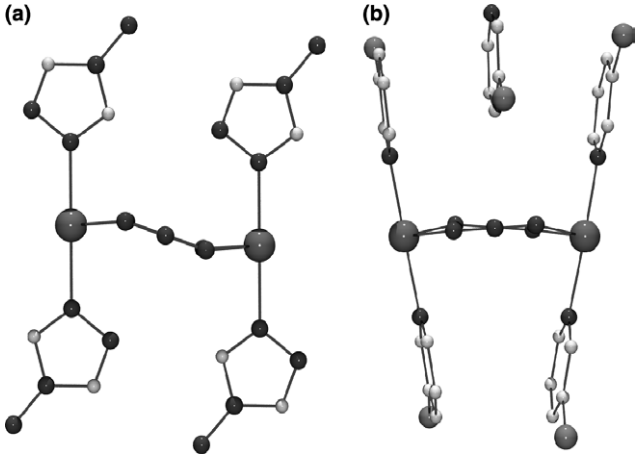


Fig. 2. Chair and boat conformation for the Mn–$(\mu_{1,3})_2$–Mn fragments for compounds **1** (a) and **2** (b).

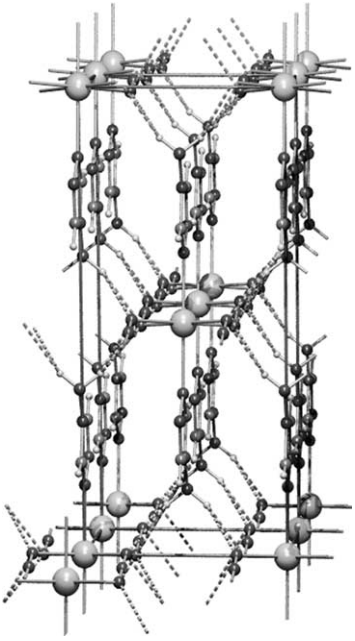


Fig. 3. 3D H-bond network built from the N(6)–H(6)···N(11) contacts for compound **1**.

3.3. Susceptibility measurements and coupling constants evaluation

The $\chi_M T$ product and the molar magnetic susceptibility versus temperature for $[Mn(N_3)_2(4\text{-amtr})_2]_n$ (**1**) and $\{[Mn(N_3)_2(3\text{-Clpy})_2]\cdot 1/2(3\text{-Clpy})\}_n$ (**2**) in the 300–4 K range are plotted in Fig. 5.

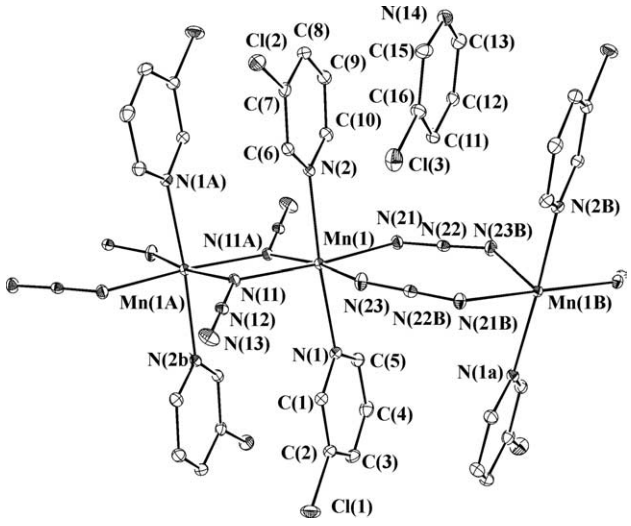


Fig. 4. ORTEP view (50% ellipsoids) with atom labelling scheme of $\{[Mn(N_3)_2(3\text{-}Clpy)_2]\cdot 1/2(3\text{-}Clpy)\}_n$ (**2**). The chains are oriented along the *c*-axis of the unit cell. *Symmetry codes*: (A) $-x+1/2, -y+1/2, -z+1/2$; (B) $-x+1/2, y, -z+1$.

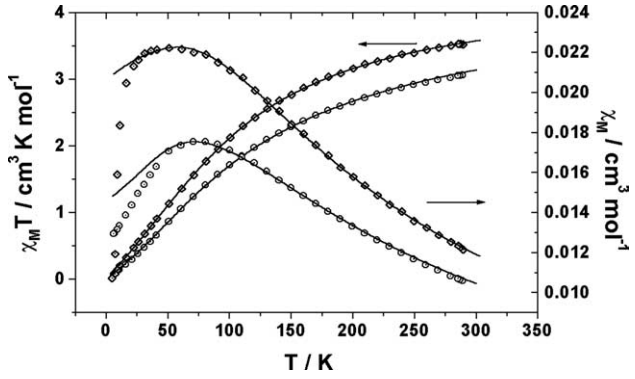


Fig. 5. Plot of χ_M and $\chi_M T$ product for compounds **1** (dot centred circles) and **2** (dot centred squares). Solid lines correspond to the best calculated fit (see text).

As can be expected from the structural data of **1**, this system show antiferromagnetic response: $\chi_M T$ at room temperature takes a 3.06-cm^3 K mol^{-1} value, decreasing continuously on cooling and tends to zero at low temperature, showing a maximum of susceptibility around 75 K. Fit for the experimental data was performed with the analytical expression derived by Fisher [14] for a infinite chain of classical spins, based in the Hamiltonian $H = -J\Sigma S_i \cdot S_{i+1}$ and local spin $S = 5/2$. Best fit parameters for the experimental data in the 50–300 K range were $J = -11.9(6)$ cm^{-1} and $g = 2.00(1)$. Introducing a zJ' parameter in the equation in order to take into account the possible interchain interactions derived from the H-bond network, which involves N(11)-atoms of the azido ligands, the best fit parameters in the 20–300 K range of temperature were $J = -11.1(2)$ cm^{-1}, $zJ' = -3.7(1)$ cm^{-1} and $g = 1.98(1)$. This second fit confirms that main J value is slightly greater than -11 cm^{-1}.

Magnetic response for **2** shows an overall antiferromagnetic behaviour. $\chi_M T$ at room temperature takes a 3.52-cm^3 K mol^{-1} value and decreases continuously on cooling and tends to zero at low temperature, showing a broad maximum of susceptibility at 50 K. Fit for the experimental data was performed with the analytical expression for an alternating system proposed by Drillon and co-workers [15] on basis on the Hamiltonian $H = -J_1\Sigma S_{2i} \cdot S_{2i+1} - J_2\Sigma S_{2i} \cdot S_{2i+2}$. Best fit calculated parameters for the experimental data in the 25–300 K range were $J_1 = -16.7(4)$ cm^{-1}, $J_2 = 6.0(2)$ cm^{-1} and $g = 1.992(4)$.

3.4. Coupling constants correlation

End-to-end coordination mode for the azido ligand has been studied previously from the structure-magnetic behaviour point of view for different electronic configurations [1,3b]. In the Mn^{II} case (d5), was shown that the antiferromagnetic components of the interaction should decrease for larger dihedral angles (δ between the main azido plane and the N–Mn–N plane), indicating that the loss of overlap due to the increase in the torsion angles becomes the driving force that controls the antiferromagnetic coupling. Due to the residual overlap of the t_{2g} orbitals with the non-bonding π MOs of the azido mediator, even for large dihedral δ angles there is always an AF dominant interaction. In the case of double EE azido bridges, the AF coupling was related directly with the degree of chair/boat distortion of the $Mn(\mu_{1,3}\text{-}N_3)_2$–Mn fragment.

In our case, compound **1** is clearly chair distorted with a δ angle of 22.6° whereas **2** exhibits a more planar $Mn(\mu_{1,3}\text{-}N_3)_2$–Mn boat-distorted unit (δ is only 9.77°). These structural parameters are in good qualitative agreement with the lower J_1 value of -11.9 cm^{-1} for **1** in comparison with the J value found of -16.7 cm^{-1} calculated for **2**. On the other hand, the coupling due to the EO bridges for **2**, give the normal ferromagnetic behaviour characteristic of Mn–N–Mn bond angles slightly greater than 100°.

Acknowledgements

A. Escuer and R. Vicente thank the Ministerio de Ciencia y Tecnología (Spain), project BQU2003/0538 for financial support of this research. F.A. Mautner thanks Prof. Belaj and Prof. Kratky (University of Graz) for use of experimental equipment. M.A.M. Abu-Youssef and L. Öhrstrom are grateful to the Swedish International Development Cooperation Agency under the Swedish Research Links program (Grant 348-2002-6879).

Appendix A. Supplementary material

Crystallographic data in CIF format have been deposited with the Cambridge Structural Data Centre as CCDC-252920 and CCDC-252921 for **1** and **2**, respectively. Copies of the data can be obtained free of charge, on application to CCDC, 12 Union Road, Cambridge, CB2 IEZ, UK (fax: +44 1223 336033, e-mail: deposit@ccdc.cam.ac.uk, http://www.ccdc.cam.ac.uk). Supplementary data associated with this article can be found, in the online version, at doi:10.1016/j.poly.2005.01.003.

References

[1] J. Ribas, A. Escuer, M. Monfort, R. Vicente, R. Cortés, L. Lezama, T. Rojo, Coord. Chem. Rev. 193–195 (1999) 1027.
[2] (a) M.L. Hernández, M.G. Barandika, M.K. Urtiaga, R. Cortés, L. Lezama, M.I. Arriortua, J. Chem. Soc., Dalton Trans. (2000) 79;

(b) A. Escuer, R. Vicente, M.A.S. Goher, F.A. Mautner, Inorg. Chem. 37 (1998) 782.
[3] (a) M.A.M. Abu-Youssef, A. Escuer, D. Gatteschi, M.A.S. Goher, F.A. Mautner, R. Vicente, Inorg. Chem. 38 (1999) 5716;
(b) J.L. Manson, A.M. Arif, J.S. Miller, J. Chem. Soc., Chem. Commun. (1999) 1479.
[4] (a) M.A.M. Abu-Youssef, A. Escuer, M.A.S. Goher, F.A. Mautner, G. Reiß, R. Vicente, Angew. Chem., Int. Ed. Engl. 39 (2000) 1624;
(b) M.A.M. Abu-Youssef, M. Drillon, A. Escuer, M.A.S. Goher, F.A. Mautner, R. Vicente, Inorg. Chem. 39 (2000) 5022.
[5] (a) M. Villanueva, J.L. Mesa, M.K. Urtiaga, R. Cortés, L. Lezama, M.I. Arriortua, T. Rojo, Eur. J. Inorg. Chem. (2000) 1581;
(b) L.F. Tang, L. Zhang, L.C. Li, P. Cheng, Z.H. Wang, J.T. Wang, Inorg. Chem. 38 (1999) 6326;
(c) H.Y. Shen, W.M. Bu, E.Q. Gao, D.Z. Liao, Z.H. Jiang, S.P. Yan, G.L. Wang, Inorg. Chem. 39 (2000) 396;
(d) M.A.M. Abu-Youssef, A. Escuer, M.A.S. Goher, F.A. Mautner, R. Vicente, J. Chem. Soc., Dalton Trans. (2000) 413.
[6] M.A.S. Goher, J. Cano, Y. Journaux, M.A.M. Abu-Youssef, F.A. Mautner, A. Escuer, R. Vicente, Chem. Eur. J. 6 (2000) 778, and refs therein.
[7] (a) Z.H. Zhang, X.H. Bu, Z.H. Ma, W.M. Bu, Y. Tang, Q.H. Zhao, Polyhedron 19 (2000) 1559;
(b) Z.E. Serna, L. Lezama, M.K. Urtiaga, M.I. Arriortua, M.G. Barandika, R. Cortés, T. Rojo, Angew. Chem., Int. Ed. Engl. 39 (2000) 344;
(c) G.S. Papaefstathiou, S.P. Perlepes, A. Escuer, R. Vicente, M. Font-Bardia, X. Solans, Angew. Chem., Int. Ed. Engl. 40 (2001) 884;
(d) G.S. Papaefstathiou, A. Escuer, C.P. Raptopoulou, A. Terzis, S.P. Perlepes, R. Vicente, Eur. J. Inorg. Chem. (2001) 1567.
[8] (a) Z.H. Zhang, X.H. Bu, Z.H. Ma, W.M. Bu, Y. Tang, Q.H. Zhao, Polyhedron 19 (2000) 1559;
(b) Z.E. Serna, L. Lezama, M.K. Urtiaga, M.I. Arriortua, M.G. Barandika, R. Cortés, T. Rojo, Angew. Chem., Int. Ed. Engl. 39 (2000) 344;
(c) G.S. Papaefstathiou, S.P. Perlepes, A. Escuer, R. Vicente, M. Font-Bardia, X. Solans, Angew. Chem., Int. Ed. Engl. 40 (2001) 884;
(d) G.S. Papaefstathiou, A. Escuer, C.P. Raptopoulou, A. Terzis, S.P. Perlepes, R. Vicente, Eur. J. Inorg. Chem. (2001) 1567.
[9] N.P.C. Walker, D. Stuart, Acta Crystallogr. Sect. A 39 (1983) 158.
[10] G.M. Sheldrick, SHELXS-86, Program for Solution of Crystal Structures, University of Göttingen, Germany, 1986.
[11] G.M. Sheldrick, SHELXL-93, Program for Refinement of Crystal Structures, University of Göttingen, Germany, 1993.
[12] G.M. Sheldrick, SHELXTL/PC, Release 5.03, Siemens Analytical X-ray Instruments, Madison, WI, 1994.
[13] A.L. Spek, Acta Crystallogr. Sect. A 46 (1990) C34.
[14] M.E. Fisher, Am. J. Phys. 32 (1964) 343.
[15] R. Cortés, M. Drillon, X. Solans, L. Lezama, T. Rojo, Inorg. Chem. 36 (1997) 677.

Available online at www.sciencedirect.com
SCIENCE DIRECT®
Polyhedron 24 (2005) 563–569
POLYHEDRON
www.elsevier.com/locate/poly

Synthesis, characterisation and magnetic properties of cobalt (II) complexes with 3-hydroxypicolinic acid (HpicOH): $[Co(picOH)_2(H_2O)_2]$ and *mer*-$[N(CH_3)_4][Co(picOH)_3] \cdot H_2O$

Penka I. Girginova [a], Filipe A. Almeida Paz [a,b], Helena I.S. Nogueira [a], Nuno J.O. Silva [c], Vítor S. Amaral [c], Jacek Klinowski [b], Tito Trindade [a,*]

[a] *Department of Chemistry, CICECO, University of Aveiro, Campus Santiago, 3810-193 Aveiro, Portugal*
[b] *Department of Chemistry, University of Cambridge, Lensfield Road, CB2 1EW Cambridge, UK*
[c] *Department of Physics, CICECO, University of Aveiro, 3810-193 Aveiro, Portugal*

Received 10 December 2004; accepted 24 January 2005

Abstract

Two complexes with Co^{2+} and 3-hydroxypicolinic acid, $[Co(picOH)_2(H_2O)_2]$ (**I**) and *mer*-$[N(CH_3)_4][Co(picOH)_3] \cdot H_2O$ (**II**), have been synthesised and characterised using single-crystal X-ray diffraction, elemental analysis, infrared spectroscopy, and thermoanalytical measurements. The 3-hydroxypicolinate ligands are coordinated to the Co^{2+} centres via its typical N,O-chelating coordination fashion. While in **I** the presence of two coordinated water molecules leads to the formation of a neutral $[Co(picOH)_2(H_2O)_2]$ complex which is strongly hydrogen bonded to another four neighbouring complexes, in **II** the inclusion of a third $picOH^-$ ligand leads to an anionic octahedral complex, $[Co(picOH)_3]^-$, in which all the N- and O-atoms are occupying *mer* positions. The properties of these two compounds were further investigated by measuring their magnetic behaviour.
© 2005 Elsevier Ltd. All rights reserved.

Keywords: Cobalt complexes; Crystal structures; 3-Hydroxypicolinic acid; Magnetic properties

1. Introduction

3-Hydroxypicolinic acid (HpicOH) is a relatively simple organic molecule, which can act as a versatile ligand with distinct coordination fashions. For example, deprotonation of the carboxylic acid and hydroxyl groups makes O,O-chelation possible with the consequent formation of a typical six-membered chelate ring [1–3]. The mono-deprotonated ligand ($picOH^-$) can also form five-membered chelate rings through the pyridinic nitrogen atom and the carboxylate group (N,O-chelation) with this coordination fashion being the most commonly found in the literature [1–9]. Interestingly, there is only one report for single coordination through the pyridinic nitrogen atom [6], and no examples are known of single coordination via the (de)protonated hydroxyl group.

We have exploited the versatile chelating properties of HpicOH to synthesise a series of lanthanide complexes and investigate the role of this ligand in the photoluminescence of the materials [1]. However, HpicOH is more commonly used with second- and third-row transition metal centres [5–8], and only a handful of structures containing first-row transition cations are found in the literature [2–4,9]. Other derivatives of picolinic acid are also known to form complexes with several metal centres [10,11], particularly those of 2-hydroxynicotinic acid which are of special interest [12,13]. Following our interest in exploring the coordination chemistry of HpicOH, we report on the synthesis, structural characterisation and magnetic behaviour of two novel Co^{2+}

* Corresponding author. Tel.: +351 234 370 726; fax: +351 234 370 084.
E-mail address: ttrindade@dq.ua.pt (T. Trindade).

0277-5387/$ - see front matter © 2005 Elsevier Ltd. All rights reserved.
doi:10.1016/j.poly.2005.01.002

complexes with this ligand: $[Co(picOH)_2(H_2O)_2]$ and *mer*-$[N(CH_3)_4][Co(picOH)_3] \cdot H_2O$.

2. Experimental

2.1. Syntheses

Chemicals were readily available from commercial sources and were used as received without further purification. Syntheses were carried out in PTFE-lined stainless steel reaction vessels (ca. 40 cm^3), under autogeneous pressure and static conditions in a preheated oven at 150 °C. Reactions took place over a period of 48 h after which time the vessels were cooled slowly to ambient temperature before opening.

In a typical synthesis, an aqueous solution of $CoCl_2 \cdot 6H_2O$ (0.5 mmol) was added dropwise to an aqueous solution containing 3-hydroxypicolinic acid (2 mmol) and $[(CH_3)_4N]OH$ (2 mmol) and then the final pH was adjusted to ca. 7 with 1 M CH_3COOH. This mixture was treated under hydrothermal conditions as described above and then transferred into a covered beaker. A pale orange powder of $[Co(picOH)_2(H_2O)_2]$ was obtained (yield: 15.7%) and orange single-crystals of the same compound were grown after 10 days from the supernatant solution (m.p. 160 °C). Red crystals of *mer*-$[N(CH_3)_4][Co(picOH)_3] \cdot H_2O$ could be obtained from the same mother solution after ca. 2 months (m.p. 228 °C).

2.2. Single-crystal X-ray diffraction

Suitable single-crystals of $[Co(picOH)_2(H_2O)_2]$ (**I**) and *mer*-$[N(CH_3)_4][Co(picOH)_3] \cdot H_2O$ (**II**) were mounted on a glass fibre using perfluoropolyether oil [14]. Data for **I** were collected at 180(2) K on a Nonius Kappa charge coupled device (CCD) area-detector diffractometer (Mo Kα graphite-monochromated radiation, $\lambda = 0.7107$ Å), equipped with an Oxford Cryosystems cryostream and controlled by the COLLECT software package [15]. Images were processed using the software packages of Denzo and Scalepack [16] and the data were corrected for absorption by using the empirical method employed in Sortav [17,18]. Data for **II** were collected at ambient temperature (at the Unidade de Raios-X, RIAIDT, University of Santiago de Compostela, Spain) on a Bruker SMART 1000 charge coupled device (CCD) area-detector diffractometer (Mo Kα graphite-monochromated radiation, $\lambda = 0.7107$ Å), controlled by the SMART software package [19]. Images were processed using the SAINTPlus software package [20] and data were corrected for absorption by using the semi-empirical method of SADABS [21]. The two structures were solved by the direct methods of SHELXS-97 [22] and refined by full-matrix least squares on F^2 using SHELXL-97 [23]. Non-hydrogen atoms were directly located from difference Fourier maps and refined with anisotropic displacement parameters. The last difference Fourier map synthesis showed, for **I**, the highest peak (0.354 e $Å^{-3}$) located at 1.14 Å from O(2), and the deepest hole (−0.614 e $Å^{-3}$) located at 0.70 Å from Co(1); for **II**, the highest peak (0.389 e $Å^{-3}$) located at 0.84 Å from O(4), and the deepest hole (−0.490 e $Å^{-3}$) located at 0.67 Å from Co(1).

Hydrogen atoms bound to carbon were placed in calculated positions and refined using a riding model with an isotropic displacement parameter fixed at x times U_{eq} for the atom to which they are attached ($x = 1.5$ for –CH_3 and –OH groups, $x = 1.2$ for the remaining hydrogen atoms). Hydrogen atoms from water molecules were directly located from successive difference Fourier maps and refined with the O–H and H···H distances restrained to 0.95(1) and 1.55(1) Å (for **I**), and 0.85(1) and 1.39(1) Å (for **II**), respectively (in order to ensure a chemically reasonable geometry for these molecules), and using a riding model with an isotropic displacement parameter fixed at 1.5 times U_{eq} of the atom to which they are attached. Hydrogen atoms associated with the –OH groups could also be directly located in successive difference Fourier maps, but their position was instead placed geometrically using HFIX instructions in SHELXL.

Table 1
Crystal and structure refinement data for $[Co(picOH)_2(H_2O)_2]$ (**I**) and *mer*-$[N(CH_3)_4][Co(picOH)_3] \cdot H_2O$ (**II**)

	I	**II**
Formula	$C_{12}H_{12}CoN_2O_8$	$C_{22}H_{24}CoN_4O_9 \cdot H_2O$
Formula weight	371.17	565.40
Temperature (K)	180(2)	180(2)
Crystal system	monoclinic	monoclinic
Space group	$P2_1/c$	$P2_1/n$
a (Å)	11.491(2)	8.2794(20)
b (Å)	9.1413(18)	12.8360(32)
c (Å)	6.8357(14)	23.5421(57)
β (°)	91.84(3)	97.021(4)
Volume ($Å^3$)	717.7(2)	2483.2(11)
Z	2	4
D_c (g cm^{-3})	1.718	1.512
μ (Mo Kα) (mm^{-1})	1.241	0.754
$F(0\,0\,0)$	378	1172
Crystal size (mm)	$0.35 \times 0.23 \times 0.18$	$0.36 \times 0.20 \times 0.15$
Crystal type	brown blocks	orange prisms
θ Range	3.55–27.49	3.57–26.42
Index ranges	$-14 \leqslant h \leqslant 14$, $-11 \leqslant k \leqslant 11$, $-8 \leqslant l \leqslant 8$	$-10 \leqslant h \leqslant 10$, $0 \leqslant k \leqslant 16$, $0 \leqslant l \leqslant 29$
Reflections collected	5621	21 304
Independent reflections	1638 ($R_{int} = 0.0407$)	5075 ($R_{int} = 0.0555$)
Final R indices $[I > 2\sigma(I)]$	$R_1 = 0.0277$, $wR_2 = 0.0711$	$R_1 = 0.0383$, $wR_2 = 0.0905$
Final R indices (all data)	$R_1 = 0.0347$, $wR_2 = 0.0736$	$R_1 = 0.0775$, $wR_2 = 0.1127$
Largest difference peak and hole (e $Å^{-3}$)	0.354 and −0.614	0.389 and −0.490

Information concerning crystallographic data collection and structure refinement details are summarised in Table 1. Selected bond lengths and angles for the two structures are given in Tables 2 and 3. Hydrogen-bonding geometry for the two structures is described in Tables 4 and 5.

Table 2
Bond lengths (in Å) and angles (in °) for $[Co(picOH)_2(H_2O)_2]$ (**I**)[a]

Co(1)–O(1W)	2.0789(13)	O(1W)–Co(1)–O(1)	93.07(5)
Co(1)–O(1)	2.1105(12)	O(1W)–Co(1)–O(1)^{i}	86.93(5)
Co(1)–N(1)	2.1245(15)	O(1W)–Co(1)–N(1)	89.15(6)
		O(1W)–Co(1)–N(1)^{i}	90.85(6)
		O(1)–Co(1)–N(1)	78.23(5)
		O(1)–Co(1)–N(1)^{i}	101.77(5)

[a] Symmetry transformations used to generate equivalent atoms: (i) $-x$, $2-y$, $-z$.

Table 3
Bond lengths (in Å) and angles (in °) for *mer*-$[N(CH_3)_4][Co(picOH)_3]\cdot H_2O$ (**II**)

Bond lengths			
Co(1)–O(1)	2.077(2)	Co(1)–N(1)	2.134(2)
Co(1)–O(4)	2.066(2)	Co(1)–N(2)	2.149(2)
Co(1)–O(7)	2.078(2)	Co(1)–N(3)	2.144(2)
Bond angles			
O(1)–Co(1)–O(7)	97.70(8)	O(4)–Co(1)–N(3)	98.16(9)
O(1)–Co(1)–N(1)	78.45(8)	O(7)–Co(1)–N(1)	87.93(8)
O(1)–Co(1)–N(2)	90.52(9)	O(7)–Co(1)–N(2)	171.45(9)
O(1)–Co(1)–N(3)	93.91(9)	O(7)–Co(1)–N(3)	78.93(8)
O(4)–Co(1)–O(1)	164.80(8)	N(1)–Co(1)–N(2)	96.08(9)
O(4)–Co(1)–O(7)	93.67(8)	N(1)–Co(1)–N(3)	163.84(9)
O(4)–Co(1)–N(1)	91.98(9)	N(3)–Co(1)–N(2)	98.22(9)
O(4)–Co(1)–N(2)	78.68(9)		

Table 4
Hydrogen-bonding geometry (distances in Å and angles in °) for $[Co(picOH)_2(H_2O)_2]$ (**I**)[a]

D–H···A	*d*(D···A)	∠(DHA)
O(1W)–H(1A)···O(2)^{i}	1.799(19)	167(2)
O(1W)–H(1B)···O(1)^{ii}	1.841(10)	168(2)
O(3)–H(3)···O(2)	1.83	146

[a] Symmetry transformations used to generate equivalent atoms: (i) x, $1.5-y$, $1/2+z$; (ii) $-x$, $1/2+y$, $1/2-z$.

Table 5
Hydrogen-bonding geometry (distances in Å and angles in °) for *mer*-$[N(CH_3)_4][Co(picOH)_3]\cdot H_2O$ (**II**)[a]

D–H···A	*d*(D···A)	∠(DHA)
O(3)–H(4A)···O(2)	2.577(3)	145.3
O(6)–H(6A)···O(5)	2.540(3)	147.2
O(9)–H(9)···O(8)	2.547(3)	145.5
O(1W)–H(1A)···O(1)	2.822(3)	172(3)
O(1W)–H(1B)···O(8)^{i}	2.766(3)	169(4)

[a] Symmetry transformations used to generate equivalent atoms: (i) x, $1.5-y$, $1/2+z$.

2.3. Instrumentation

FT-IR spectra were measured from KBr disks (Aldrich, 99%+, FT-IR grade) on a Matson 700 FTIR spectrometer. Elemental analyses for C, H and N were performed in the Microanalysis Laboratory of the University of Aveiro. Thermogravimetric analyses (TGA) were carried out using a Shimadzu TGA-50, with a heating rate of 10 °C/min. Magnetic measurements were performed using a Quantum Design SQUID (Superconducting Quantum Interference Device) magnetometer MPMS at the University of Lisbon (Portugal).

3. Results and discussion

3.1. Crystal structure of $[Co(picOH)_2(H_2O)_2]$ (*I*)

The reaction under aqueous media between Co^{2+} and 3-hydroxypicolinic acid led to the formation of a highly crystalline, air- and light-stable product which was formulated as $[Co(picOH)_2(H_2O)_2]$ (**I**) on the basis of single-crystal X-ray diffraction (Table 1) and elemental analysis. This structure shares striking similarities with those recently reported by Jin and co-workers [4], $[Zn(picOH)_2(H_2O)_2]$ and $[Mn(picOH)_2(H_2O)_2]$, also containing first-row transition metal cations.

Compound **I** is formed by neutral centrosymmetric $[Co(picOH)_2(H_2O)_2]$ complexes (Fig. 1), in which the Co^{2+} centre is located at an inversion centre and six-coordinated to two N,O-chelating $picOH^-$ anionic ligands [bite angle of 78.23(5)°] plus two water molecules, $\{CoN_2O_4\}$, with the coordination geometry resembling a slightly distorted octahedron (Fig. 1 and Table 2). As found in the structures containing Zn^{2+} and Mn^{2+} [4], the water molecules are *trans*-coordinated (Fig. 1) with the O_{water}–Co–O_{water} vector not being exactly perpendicular to the $\{N_2O_2\}$ plane of the octahedron formed by the two $picOH^-$ anionic ligands (Table 2). The vector is indeed tilted by a combination of ca.

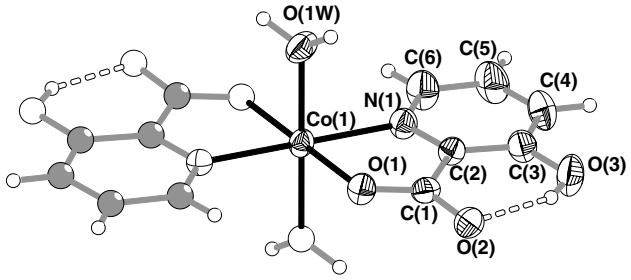


Fig. 1. Schematic representation of the neutral complex $[Co(picOH)_2(H_2O)_2]$ of **I**, emphasising the slightly distorted octahedral coordination environment for the Co^{2+} metal centre. Non-hydrogen atoms belonging to the asymmetric unit are represented with thermal ellipsoids drawn at the 70% probability level. For selected bond lengths (in Å) and angles (in °) see Table 2. For details on the hydrogen-bonding geometry, see Table 4.

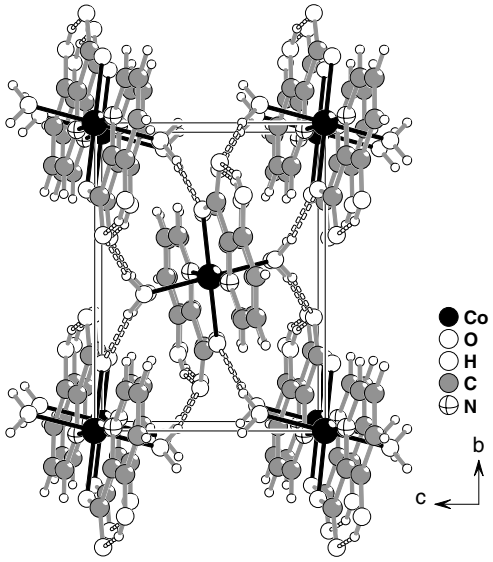


Fig. 2. Crystal packing of **I** viewed in perspective along the *a* direction, showing how the O–H···O hydrogen bond interactions (represented as dashed white-filled bonds) establish physical links between neighbouring $[Co(picOH)_2(H_2O)_2]$ complexes. For details on the hydrogen-bonding geometry, see Table 4.

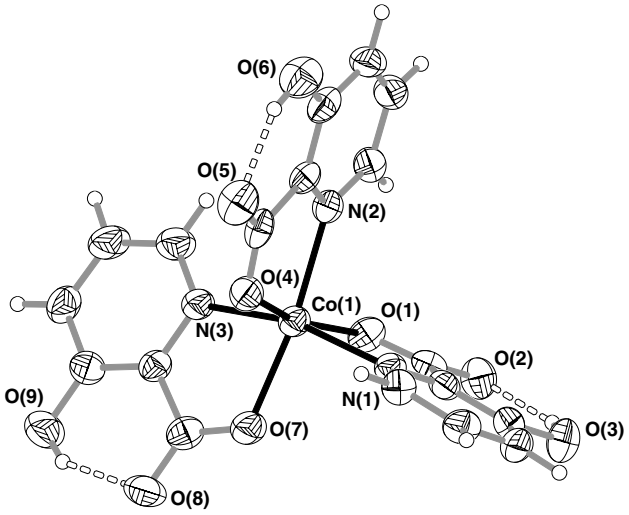


Fig. 3. Schematic representation of the anionic *mer*-$[Co(picOH)_3]^-$ complex in **II**, showing the slightly distorted octahedral coordination environment for the Co^{2+} metal centre and the labelling scheme for selected atoms. Non-hydrogen atoms are represented with thermal ellipsoids drawn at the 70% probability level. For selected bond lengths (in Å) and angles (in °) see Table 3. For details on the hydrogen-bonding geometry, see Table 5.

3.1° and 0.9° in both directions of the $\{N_2O_2\}$ plane, values comparable with those registered for $[Zn(picOH)_2(H_2O)_2]$ and $[Mn(picOH)_2(H_2O)_2]$ (ca. 2.9/0.8 and 2.5/1.2, respectively) [4]. Interestingly, this distortion seems to be driven by the presence of extensive hydrogen-bonding networks in the crystal structures of these structures. In fact, apart from the homonuclear, intra-molecular and strong O–H···O hydrogen bond between the hydroxyl and the carboxylate groups (Fig. 1 and Table 4), each $[Co(picOH)_2(H_2O)_2]$ moiety is further strongly hydrogen-bonded via the coordinated water molecules to another four neighbouring complexes, leading to a recurring $R_2^2(10)$ graph set motif [24] which expands the dimensionality of the structure into the two dimensions (see Fig. 2).

3.2. Crystal structure of *mer*-$[N(CH_3)_4][Co(picOH)_3]\cdot H_2O$ (**II**)

The substitution of the coordinated water molecules from the coordination sphere of **I** by a third 3-hydroxypicolinate ligand leads to the formation of an intriguing *mer*-isomer $[Co(picOH)_3]^-$ complex anion (Fig. 3) which co-exists in the asymmetric unit of **II** with a tetramethylammonium cation plus a water molecule of crystallisation (not shown), corresponding to the empirical formula *mer*-$N(CH_3)_4][Co(picOH)_3]\cdot H_2O$ (**II**).

As in the previous structure, the crystallographically unique Co^{2+} centre appears six-coordinated, $\{CoN_3O_3\}$ (Fig. 3), with a geometry resembling a distorted octahedron due to the geometrical constraints of the $picOH^-$ ligand: on the one hand, the chelating nature of 3-hydroxypicolinate leads to an average bite angle of ca. 78.7° which, although comparable with the analogous value for **I** [78.23(5)°], imposes some strain in the octahedral geometry; on the other, the presence of three large substituent ligands within the first coordination sphere leads to an inherent steric hindrance directly affecting the global geometry of the complex. In fact, these distortions are reflected in the ranges of the *cis* and *trans* angles of the octahedron which can be found within the 78.45(8)°–98.22(9)° and 163.84(9)°–171.45(9)° ranges, respectively (Table 3). The average Co–O and Co–N distances are almost identical (ca. 2.07 and 2.14 Å, respectively) and comparable with those found in related compounds [25,26].

The hydrogen-bonding network present in the crystal structure of **II** is not so extensive as that described for **I**. However, physical bridges via homonuclear and relatively strong O–H···O hydrogen bonds between neighbouring *mer*-$[Co(picOH)_3]^-$ complex anions are assured by the water molecules of crystallisation (Table 5 and Fig. 4) which, along with interactions of the intra-molecular nature, lead to the formation of supramolecular hydrated $\{mer\text{-}[Co(picOH)_3]\cdot H_2O\}^-$ anionic tapes running along the *a* direction (Fig. 4, perpendicular to the plane of the representation). This supramolecular arrangement is constructed from a recurring $C_3^2(7)$ graph set motif [24].

3.3. Magnetic measurements

Magnetisation (M) measurements were performed in the 2–270 K temperature (T) range and in a constant magnetic field of $H = 100$ Oe. No thermal irreversibility

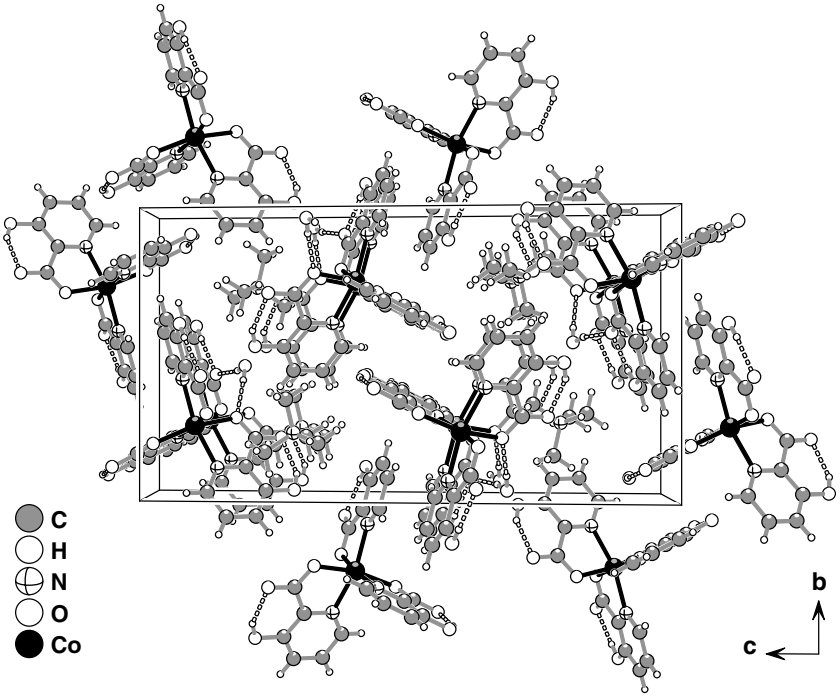


Fig. 4. Crystal packing of **II** viewed in perspective along the *a* direction, with the O–H···O hydrogen-bonding interactions represented as dashed white-filled bonds. The crystallisation water molecule establishes a physical link between neighbouring anionic *mer*-$[Co(picOH)_3]^-$ complexes, leading to the formation of supramolecular hydrated $\{mer\text{-}[Co(picOH)_3]\cdot H_2O\}^-$ anionic tapes running along the *a* direction. For details on the hydrogen-bonding geometry, see Table 5.

was observed since measurements taken with decreasing temperature gave identical results, either after cooling from ambient temperature to 2 K in zero applied magnetic field (zero field cooling), or after cooling under the measurement field.

Fig. 5 represents the magnetic susceptibility multiplied by the temperature (χT, with χ = M/H) for compounds **I** and **II**. The temperature dependence indicates deviation from simple paramagnetic (Curie-like) ion behaviour. Such is ascribed to the influence

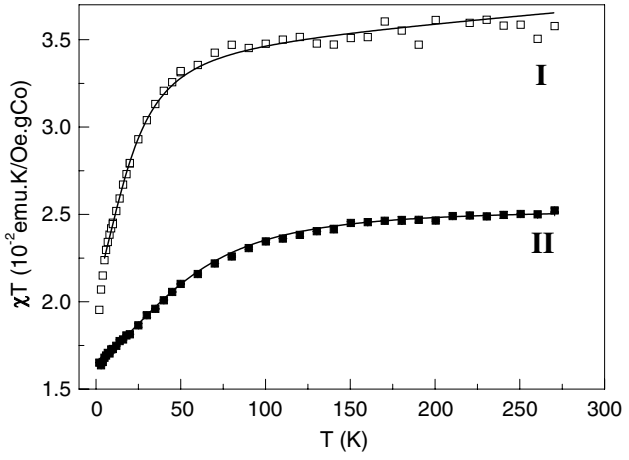


Fig. 5. Temperature dependence of the magnetic susceptibility multiplied by temperature (χT vs. T)for compounds **I** and **II**. Solid lines are fits to Eq. (1) (considering the influence of crystal field).

of crystal field of **I** and **II**, just like it is also observed in several mononuclear systems containing high-spin Co^{2+} ions in an octahedral coordination geometry [27]. The lowest energy levels of the Co^{2+} cations are Γ_6 and Γ_7 doublets, and in a first approximation one can consider that only these two are thermally populated. Hence the total susceptibility, can be described by [27]:

$$\chi = A\frac{g_z^2\chi_z + 8g_x^2\chi_x}{4T} + \chi_0, \quad \text{with}$$
$$\chi_z = \frac{1+9e^{-(2D/T)}}{1+e^{-(2D/T)}} \quad \text{and} \quad \chi_x = \frac{1+\frac{3T}{4D}\left(1-e^{-(2D/T)}\right)}{1+e^{-(2D/T)}}, \tag{1}$$

where $A = N\mu_B^2/3k$, g_z and g_x are the Landé factors associated with z and x directions, respectively, D is the crystal field splitting and χ_0 is the residual temperature independent which accounts for diamagnetic contributions. Within this approximation, D includes the Γ_6 and Γ_7 energy gap and the influence of the orbital momentum [27]. Fitting the data to Eq. (1) (lines in Fig. 5) we obtain $D = 24$ and $65\ cm^{-1}$ for samples **I** and **II**, respectively, in good agreement with the values expected for Co^{2+} cations (Ref. [27] and references therein). From the fitting, it is also feasible to calculate $g_x = 2.1$, $g_z = 2.3$ and $g_x = 1.8$, $g_z = 1.7$. Small variations of these parameters are not critical for the quality of the fit and are subject to absolute errors of the order of 0.1. Although at present we do not have a plausible

Table 6
Analytical and spectroscopic data for 3-hydroxypicolinic acid and compounds **I** and **II**

Compound	Elemental composition (%)[a]			Vibrational data (in cm^{-1})[b]			
	C	N	H	$\nu_{asym}(-CO_2^-)$	ν(C–N)	$\nu_{sym}(-CO_2^-)$	$\nu(C-O)_h$
3 Hydroxypicolinic acid				1701s	1609s	1322s	1282s
I	38.05 (38.83)	7.38 (7.55)	3.55 (3.26)	1644s	1602s	1343s	1268s
II	46.31 (46.73)	9.93 (9.91)	4.83 (4.63)	1631s	1602s	1333s	1248s

[a] Calculated values are in parentheses.
[b] s: strong.

explanation for the difference between these values for the two compounds, the ratio g_z/g_x is ca. 1.1, in good agreement with the values reported for similar compounds (1.06) [27]. The differences registered for the crystal field splitting can be attributed to the influence of the donor atoms present in the Co^{2+} first coordination shell. In fact, compound **II** has one more pyridinic ring bound to the metal, which increases the crystal field splitting, in agreement with the spectrochemical series.

3.4. Vibrational spectroscopy

Selected and diagnostic FT-IR data for compounds **I** and **II** are given in Table 6 (only bands of 3-hydroxypicolinic acid sensitive to metal coordination are reported). Infrared spectroscopy confirms the coordination of $picOH^-$ to the metal centres via the carboxylate group, with the asymmetric stretching $\nu_{asym}(-CO_2^-)$ mode showing shifts up to 70 cm^{-1} to lower wavenumbers when compared with the values registered for the free ligand. Furthermore, the measured values of $\Delta[\nu_{asym}(-CO_2^-) - \nu_{sym}(-CO_2^-)]$ for **I** (301 cm^{-1}) and **II** (298 cm^{-1}) are clear evidence of the presence of carboxylate groups coordinated to the Co^{2+} centres in unidentate fashion [28], in agreement with the N,O-chelation described by the crystal structures (Figs. 1 and 3). The $\nu(C-O)_h$ mode for **I** and **II** shows shifts up to ca. 14 and 34 cm^{-1}, respectively, possibly due to hydrogen-bonding involving the carboxylate groups and the water molecules (Tables 4 and 5). The typical stretching ν(C–N) vibrational mode of substituted pyridines appears for the uncoordinated ligand at 1609 cm^{-1} and shows small shifts (up to 7 cm^{-1}) for the two compounds (Table 6), in good agreement with N,O-chelation involving the nitrogen atom of $picOH^-$.

3.5. Thermal analysis

Thermal decomposition of compound **I** occurs in a multi-step process between ambient temperature and ca. 500 °C leading to the formation of the stoichiometric amount of CoO (total weight loss of 78.1%, calculated 79.8%). The first weight loss (ca. 9.5%) occurs in the 80–180 °C temperature range (DTG peak at 150 °C) and is attributed to the release of the two coordinated water molecules (calculated weight loss of 9.7%). Between 180 and 500 °C, a total weight loss of ca. 68.6% (DTG peaks at 353, 409, 418 and 432 °C) corresponds to the release of the organic component.

The thermal decomposition of **II** between ambient temperature and ca. 550 °C is slightly more complex than that of **I** with more overlapping decomposition steps corresponding to the oxidation of the organic molecules. However, as for **I**, at ca. 550 °C only the stoichiometric CoO residue remains with a total weight loss of ca. 88.6% (calculated 86.7%).

Acknowledgements

We are grateful to the Portuguese Foundation for Science and Technology (FCT) for their general financial POCTI programme supported by FEDER and the Ph.D. scholarships No. SFRH/BD/3024/2000 (to F.A.A.P) and SFRH/BD/10383/2002 (to N.J.O.S.). P.G. thanks CICECO for a research grant. We thank Professor Margarida Godinho for allowing us to perform the magnetic measurements at the Faculty of Sciences, University of Lisbon.

Appendix A. Supplementary data

Crystallographic data (excluding structure factors) for the structures reported in this paper have been deposited with the Cambridge Crystallographic Data Centre as supplementary publication no. CCDC-241918 and -241919. Copies of the data can be obtained free of charge on application to CCDC, 12 Union Road, Cambridge CB2 2EZ, U.K. (fax: (+44) 1223 336033; e-mail: deposit@ccdc.cam.ac.uk, and http://www.ccdc.cam.ac.uk).

Supplementary data associated with this article can be found, in the online version at doi:10.1016/j.poly.2005.01.002.

References

[1] P.C.R. Soares-Santos, H.I.S. Nogueira, V. Felix, M.G.B. Drew, R.A.S. Ferreira, L.D. Carlos, T. Trindade, Chem. Mater. 15 (2003) 100.

[2] E. Kiss, A. Benyei, T. Kiss, Polyhedron 22 (2003) 27.
[3] S. Yano, M. Nakai, F. Sekiguchi, M. Obata, M. Kato, M. Shiro, I. Kinoshita, M. Mikuriya, H. Sakurai, C. Orvig, Chem. Lett. (2002) 916.
[4] C.Y. Sun, X.J. Zheng, L.P. Jin, J. Mol. Struct. 646 (2003) 201.
[5] S.M.O. Quintal, H.I.S. Nogueira, H.M. Carapuca, V. Felix, M.G.B. Drew, J. Chem. Soc., Dalton Trans. (2001) 3196.
[6] S.M.O. Quintal, H.I.S. Nogueira, V. Felix, M.G.B. Drew, New J. Chem. 24 (2000) 511.
[7] A. Dar, K. Moss, S.M. Cottrill, R.V. Parish, C.A. McAuliffe, R.G. Pritchard, B. Beagley, J. Sandbank, J. Chem. Soc., Dalton Trans. (1992) 1907.
[8] S. Gatto, T.I.A. Gerber, G. Bandoli, J. Perils, J.G.H. du Preez, Inorg. Chim. Acta 269 (1998) 235.
[9] A. Shaver, J.B. Ng, D.A. Hall, B.S. Lum, B.I. Posner, Inorg. Chem. 32 (1993) 3109.
[10] R. March, W. Clegg, R.A. Coxall, L. Cucurull-Sanchez, L. Lezama, T. Rojo, P. Gonzalez-Duarte, Inorg. Chim. Acta 353 (2003) 129.
[11] P.C.R. Soares-Santos, H.I.S. Nogueira, V. Felix, M.G.B. Drew, R.A.S. Ferreira, L.D. Carlos, T. Trindade, Inorg. Chem. Commun. 6 (2003) 1234.
[12] P.C.R. Soares-Santos, H.I.S. Nogueira, J. Rocha, V. Felix, M.G.B. Drew, R.A.S. Ferreira, L.D. Carlos, T. Trindade, Polyhedron 22 (2003) 3529.
[13] S.M.O. Quintal, H.I.S. Nogueira, V. Felix, M.G.B. Drew, Polyhedron 21 (2002) 2783.
[14] T. Kottke, D. Stalke, J. Appl. Crystallogr. 26 (1993) 615.
[15] R. Hooft, COLLECT: Data Collection Software, Nonius B.V., Delft, The Netherlands, 1998.
[16] Z. Otwinowski, W. Minor, in: C.W. CarterJr., R.M. Sweet (Eds.), Methods in Enzymology, vol. 276, Academic Press, New York, 1997, p. 307.
[17] R.H. Blessing, Acta Crystallogr., Sect. A 51 (1995) 33.
[18] R.H. Blessing, J. Appl. Crystallogr. 30 (1997) 421.
[19] SMART. Bruker Molecular Analysis Research Tool v. 5.054© Bruker AXS, Madison, WI, USA, 1997–1998.
[20] SAINTPlus. Data Reduction and Correction Program v. 6.01© Bruker AXS, Madison, WI, USA, 1997–98.
[21] G.M. Sheldrick. SADABS v. 2.01, Bruker/Siemens Area Detector Absorption Correction Program Bruker AXS, Madison, WI, USA, 1998.
[22] G.M. Sheldrick, SHELXS-97, Program for Crystal Structure Solution, University of Göttingen, 1997.
[23] G.M. Sheldrick, SHELXL-97, Program for Crystal Structure Refinement, University of Göttingen, 1997.
[24] J. Bernstein, R.E. Davis, L. Shimoni, N.L. Chang, Angew. Chem. Int. Ed. 34 (1995) 1555.
[25] K. Abe, K. Matsufuji, M. Ohba, H. Okawa, Inorg. Chem. 41 (2002) 4461.
[26] Y.C. Liang, M.C. Hong, J.C. Liu, R. Cao, Inorg. Chim. Acta 328 (2002) 152.
[27] O. Kahn, Molecular Magnetism, Wiley-VCH, New York, 1993.
[28] G.B. Deacon, R.J. Phillips, Coord. Chem. Rev. 33 (1980) 227.

Available online at www.sciencedirect.com
SCIENCE DIRECT®
Polyhedron 24 (2005) 571–577
POLYHEDRON
www.elsevier.com/locate/poly

Synthesis and structural characterization of three new manganese(II) diphosphonates with layered and double-chain architectures

Zhong-Ming Sun [a], Jiang-Gao Mao [a,*], Zhen-Chao Dong [b]

[a] State Key Laboratory of Structural Chemistry, Fujian Institute of Research on the Structure of Matter, Chinese Academy of Sciences, Fuzhou 350002, PR China

[b] Hefei National Laboratory for Physical Sciences at Microscale, University of Science and Technology of China, Hefei 230026, PR China

Received 30 September 2004; accepted 7 December 2004

Abstract

Three new Mn(II) diphosphonates have been synthesized by hydrothermal reactions, namely, $Mn(H_2L^1)$ (**1**), $Mn(H_3L^1)_2$ (**2**) ($H_4L^1 = C_6H_5CH_2N(CH_2PO_3H_2)_2$) and $Mn_2(H_2L^2)_2(H_2O)$ (**3**), (H_4L^2 = 4-CH_3–$C_6H_4CH_2N(CH_2PO_3H_2)_2$). The structure of compound **1** features $\langle 0\,0\,1\rangle$ and $\langle 0\,0\,2\rangle$ manganese(II) phosphonate layers, in which the Mn(II) ion is five-coordinated by five oxygens from five diphosphonate ligands in a distorted square pyramidal geometry. The Mn(II) ion in compound **2** is octahedrally coordinated by six phosphonate oxygens from six ligands. Neighboring MnO_6 octahedra are interlinked by bridging diphosphonate ligands into a polymeric double chain along the *c*-axis. Such chains are interlinked by strong hydrogen bonds between non-coordinated phosphonate oxygens into a 2D layer. Compound **3** is composed of $\langle 0\,0\,1\rangle$ and $\langle 0\,0\,2\rangle$ manganese(II) phosphonate layers, in which each metal ion is octahedrally coordinated by five phosphonate oxygens from four ligands and an aqua ligand. In all three compounds, the amine group of the ligand is protonated and the phenyl group is orientated toward the interlayer space.
© 2005 Elsevier Ltd. All rights reserved.

Keywords: Metal diphosphonates; Hydrothermal synthesis; Layered materials; Crystal structure

1. Introduction

During the past two decades, considerable research efforts have been devoted to the synthesis of metal phosphonates with open-framework or microporous structures due to their interesting optical, ion-exchange, catalytic and sensing properties [1]. The strategy of attaching functional groups such as crown ether, amine, hydroxyl and carboxylate groups to the phosphonic acid has proven to be effective for the isolation of a variety of metal phosphonates with open-framework and microporous structures [1–10]. Results of metal compounds with aminodiphosphonic acids, $RN(CH_2PO_3H_2)_2$. have shown that the organic substituent on the amine group plays a subtle role on the structures of the metal phosphonates formed [11]. For instance, $Cd(H_3L)_2$ ($H_4L = C_6H_5CH_2N(CH_2PO_3H_2)_2$) features double chains that are further interlinked by hydrogen bonds. With one more CH_2-group between the phenyl and the amine group, $Cd(H_3L')_2$ ($H_4L' = C_6H_5CH_2CH_2N(CH_2PO_3H_2)_2$) has a layered structure [11a]. Recently, a number of divalent metal compounds of substituted aminodiphosphonic acids, $RN(CH_2PO_3H_2)_2$ have been reported [12]. A copper compound with ethylamine-bis(methylphosphonate) was reported by Makaranets et al. [12a], cobalt(II) and lead(II) complexes with $NH(CH_2PO_3H_2)_2$ were recently reported [12b,12c]. Several layered zirconium fluoride alkylamino-*N*,*N*-bis(methylenephosphonate) complexes have been isolated by Vivani et al. [12d]. To further our studies on metal compounds with substituted aminodiphosphonic

* Corresponding author. Tel.: +865913704836; fax: +865913714946.
E-mail address: mjg@ms.fjirsm.ac.cn (J.-G. Mao).

0277-5387/$ - see front matter © 2005 Elsevier Ltd. All rights reserved.
doi:10.1016/j.poly.2004.12.018

acids, two derivatives of $HN(CH_2PO_3H_2)_2$ were synthesized, namely, $C_6H_5CH_2N(CH_2PO_3H_2)_2$ (H_4L^1) and 4-CH_3-$C_6H_4CH_2N(CH_2PO_3H_2)_2$ (H_4L^2). Hydrothermal reactions of the above two diphosphonic acids and manganese(II) acetate resulted in three new Mn(II) diphosphonates, namely, $Mn(H_2L^1)$ (**1**), $Mn(H_3L^1)_2$ (**2**) and $Mn_2(H_2L^2)_2(H_2O)$ (**3**). Compounds **1** and **3** are layered with different architectures, whereas compound **2** features double chains of the manganese(II) diphosphonate that are hydrogen bonded. Herein, we report their syntheses, crystal structures and characterizations.

2. Experimental

2.1. Materials and methods

The two aminodiphosphonic acids, $C_6H_5CH_2N(CH_2PO_3H_2)_2$ (H_4L^1) and 4-CH_3-$C_6H_4CH_2N(CH_2PO_3H_2)_2$ (H_4L^2), were prepared by a Mannich type reaction according to the procedures previously described [11,13]. All other chemicals were of reagent grade quality from commercial sources and used without further purification. Elemental analyses were performed on a German Elementary Vario EL III instrument. IR spectra were recorded on a Perkin Elmer Spectrum One FT-IR spectrometer on KBr pellets in the range 4000–400 cm^{-1}. TGA analyses were carried out with a TGA/STA449C unit, at a heating rate of 15 °C/min under a nitrogen atmosphere. Magnetic susceptibility measurements on polycrystalline samples of compounds **1** and **3** were performed with a Quantum Design SQUID magnetometer at a field of 1.0 T in the range of 6–300 K. Raw data were corrected for the susceptibility of the container and the diamagnetic contributions of the samples using Pascal's constants. X-ray powder diffraction data were collected on a Rigaku Dmax 2500 diffractometer using Cu Kα radiation (λ = 1.5406 Å) in the 2θ range of 3°–80° with a step size of 0.05° and a counting time of 0.6 s per step.

2.2. Synthesis of $Mn(H_2L^1)$ (*1*)

About 0.5 mmol of $Mn(ac)_2 \cdot 4H_2O$, 0.5 mmol of H_4L^1 and 10 ml of de-ionized water were mixed and the solution's pH value was adjusted to 5.0 by the addition of tetrabutylammonium hydroxide solution (10%). The resultant solution was sealed into a 25-ml Telflon-lined stainless steel autoclave and heated at 160 °C for 5 days (the final pH value is 6.0). Light pink crystals of compound **1** were recovered in 48% yield based on Mn. The measured X-ray powder diffraction pattern matches with the one simulated from its single crystal structure data, thus compound **1** was obtained as a monophase. Elemental *Anal.* for **1**, $C_9H_{13}NO_6P_2Mn$: calc. (found) C 31.06 (31.33), H 3.76 (3.52), N 4.02 (3.88), IR (KBr, cm^{-1}): 3032 m, 2980 m, 2946 br, 2769 w, 2358 w, 1492 m, 1417 m, 1222 m, 1187 s, 1159 s, 998 m, 756 m, 713 m, 561 s, 485 m.

2.3. Synthesis of $Mn(H_3L^1)_2$ (*2*)

A mixture of 0.5 mmol of $Mn(ac)_2 \cdot 4H_2O$, 1.0 mmol of H_4L^1, 10 ml of deionized water and 3.0 ml of tetramethylammonium chloride solution (40%) was sealed into a 25-ml Telflon-lined stainless steel autoclave and heated at 180 °C for 5 days (the initial and final pH values were around 2.0). Small needle-like light pink crystals of compound **2** were collected in a 54% yield based on Mn. Its purity was confirmed by X-ray powder diffraction measurements. Elemental *Anal.* for **2**, $C_{18}H_{28}N_2O_{12}P_4Mn$: calc. (found) C 33.61 (33.38), H 4.39 (4.18), N 4.49 (4.72), IR (KBr, cm^{-1}): 2985 br, 2576 br, 1498 w, 1456 s, 1435 m, 1333 m, 1227 s, 1252 s, 1111 s, 1037 s, 920 s, 891 s, 739 m, 706 m, 552 s, 482 s.

2.4. Synthesis of $Mn_2(H_2L^2)_2(H_2O)$ (*3*)

Compound **3** was synthesized by a similar method used for compound **1**. About 0.5 mmol of $Mn(ac)_2 \cdot 4H_2O$, 0.5 mmol of H_4L^2 and 10 ml of de-ionized water were mixed and the solution's pH value was adjusted to 5.0 by the addition of tetrabutylammonium hydroxide solution (10%). The resultant solution was sealed into a 25-ml Telflon-lined stainless steel autoclave and heated at 160 °C for 5 days (the final pH value is 5.0). Plate-shaped pink crystals of compound **3** were recovered in a 64% yield based on Mn. Its purity was confirmed by X-ray powder diffraction measurements. Elemental *Anal.* for **3**, $C_{20}H_{32}N_2O_{13}P_4Mn_2$: calc. (found) C 32.36 (32.25), H 4.34 (4.52), N 3.77 (3.58), IR (KBr, cm^{-1}): 3280 br, 2978 m, 2940 m, 2834 w, 2310 w, 1616 w, 1459 m, 1419 m, 1295 m, 1193 s, 1122 s, 983 s, 796 m, 761 s, 738 s, 568 s, 489 s, 439 m.

2.5. Crystal structure determinations of compounds *1–3*

Single crystals of compounds **1**–**3** were mounted on a Siemens Smart CCD diffractometer equipped with graphite-monochromated Mo-Kα radiation (λ = 0.71069 Å). Intensity data were collected by the narrow frame method at 293 K. The data sets were corrected for Lorentz and polarization as well as for absorption by the SADABS program [14]. All three structures were solved by direct methods and refined by full-matrix least-squares fitting on F^2 by SHELX-97 [15]. All non-hydrogen atoms were refined with anisotropic thermal parameters and all hydrogen atoms were located at geometrically calculated positions. The hydrogen atoms for the water molecules in compound **3** were not included in the refinement. Crystallographic data and structural refine-

Table 1
Summary of crystal data and details of intensity collection and structural refinements

Compound	1	2	3
Empirical formula	$C_9H_{13}NO_6P_2Mn$	$C_{18}H_{28}N_2O_{12}P_4Mn$	$C_{20}H_{32}N_2O_{13}P_4Mn_2$
Formula weight	348.08	643.24	742.24
Space group	$P2_1/n$	$C2/c$	$I2/a$
a (Å)	5.5708(8)	24.267(2)	10.905(4)
b (Å)	8.481(1)	12.806(1)	7.7762(3)
c (Å)	25.313(4)	7.708	32.554(1)
β (°)	90.496(3)	94.979(5)	95.008(1)
V (Å^3)	1195.9(3)	2386.3(3)	2750.06(2)
Z	4	4	4
D_{calcd} (g cm^{-3})	1.933	1.790	1.793
T (K)	293(2)	293(2)	293(2)
μ (mm^{-1})	1.393	0.891	1.221
Goodness-of-fit	1.090	1.122	1.194
Reflections collected	3321	9624	4141
Independent reflected	2065 (R_{int} = 5.21%)	2967 (R_{int} = 2.48%)	2393 (R_{int} = 3.32%)
R_1, wR_2 [$I > 2\sigma(I)$][a]	0.0556, 0.1167	0.0330, 0.0712	0.0539, 0.1052
R_1, wR_2 (all data)	0.0842, 0.1335	0.0362, 0.0728	0.0735, 0.1187

[a] $R_1 = \sum(F_o - F_c)/\sum F_o$; $wR_2 = (\sum w(F_o^2 - F_c)^2/\sum w(F_o^2)^2)^{1/2}$.

Table 2
Selected bond lengths (Å) and angles (°) for compounds **1**–**3**

Compound **1**			
Mn(1)–O(22)#1	2.062(4)	Mn(1)–O(11)#2	2.094(4)
Mn(1)–O(23)#3	2.120(4)	Mn(1)–O(12)#4	2.158(4)
Mn(1)–O(21)	2.308(4)	Mn(1)–O(13)	2.660(4)
Compound **2**			
Mn(1)–O(11)#1	2.158 (1)	Mn(1)–O(21)#2	2.196(1)
Mn(1)–O(22)#3	2.216(1)		
Hydrogen bonds			
N(1) ··· O(12)#2	2.687(2)	N(1)–H(0a) ··· O(12)#2	151.2
O(13) ··· O(12)#5	2.642(2)	O(13)–H(13a) ··· O(12)#5	167.6
O(23) ··· O(22)#4	2.597(2)	O(23)–H(23a) ··· O(22)#4	162.2
Compound **3**			
Mn(1)–O(11)#1	2.127(3)	Mn(1)–O(23)	2.139(4)
Mn(1)–O(22)#2	2.154(4)	Mn(1)–O(13)#3	2.199(3)
Mn(1)–O(13)	2.275(3)	Mn(1)–O(1W)	2.325(3)
Hydrogen bonds			
N(1) ··· O(23)	2.811(5)	O(21) ··· O(12)#4	2.469(5)

Symmetry transformations used to generate equivalent atoms. For **1**: #1 $-x + 2$, $-y + 1$, $-z$; #2 $-x + 1$, $-y$, $-z$; #3 $-x + 1$, $-y + 1$, $-z$; #4 $x + 1$, y, z. For **2**: #1 $-x$, y, $-z + 1/2$; #2$-x$, y, $-z - 1/2$; #3 $-x$, $-y + 1$, $-z$; #4 x, $1 - y$, $z - 1/2$; #5 $-x$, $-y$, $-z$. For **3**: #1 $-x + 3/2$, y, $-z$; #2 $-x + 2$, $-y + 1$, $-z$; #3 $-x + 2$, $-y$, $-z$; #4 x, $y + 1$, z.

ments for the three compounds are summarized in Table 1. Selected bond lengths and angles are given in Table 2. Further details on the crystallographic studies as well as atomic parameters are given in the Supplementary Material.

3. Results and discussion

The structure of compound **1** features ⟨0 0 1⟩ and ⟨0 0 2⟩ manganese(II) phosphonate layers. The Mn(II) ion is five-coordinated by five phosphonate oxygens of five diphosphonate anions in a distorted square pyramidal geometry. The Mn–O distances range from 2.062(4) to 2.308(4) Å (Table 2), which are comparable to those reported in other Mn(II) phosphonates [2b,9,10]. Each pair of Mn(II) ions are bridged by two diphosphonate groups, forming eight-membered rings (Mn–(O–P–O)$_2$–Mn). The diphosphonate ligand acts as a pentadentate ligand and bridges with five manganese(II) ions. The Mn–O(13) distance of 2.660(4) Å indicates that it is a very weak bond if any. Based on charge balance, the P–O distances as well as its coordination mode, the diphosphonate anion is 2− in charge and the amine group as well as O(13) remain protonated.

The interconnection of Mn(II) by bridging diphosphonate anions lead to ⟨0 0 1⟩ and ⟨0 0 2⟩ layers of Mn(II) phosphonate (Fig. 1). The phenyl groups are orientated

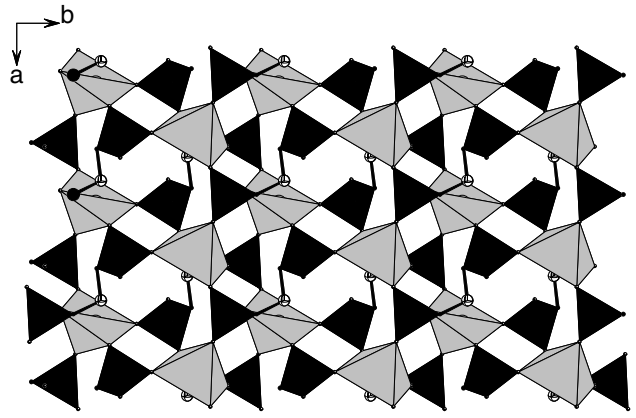


Fig. 1. A ⟨002⟩ manganese(II) phosphonate layer in compound **1**. MnO_5 polyhedra and C–PO_3 tetrahedra are shaded in light and dark grey, respectively. N atoms are drawn as octand circles. The $C_6H_5CH_2$-groups have been omitted for clarity.

toward the interlayer space (Fig. 2). The interlayer distance is about 12.6 Å.

Compound **2** has a *M*/*L* molar ratio of 1:2. It is isostructural with $Cd(H_3L^1)_2$ previously reported [11a]. The Mn(II) ion lies on a position with a twofold symmetry. It is octahedrally coordinated by six oxygens from six phosphonate ligands. The Mn–O distances are in the range of 2.158(1) to 2.216(1) Å (Table 2), which are comparable to those in compound **1** and those reported in other Mn(II) phosphonates [2b,9,10], but are slightly shorter than the Cd–O distances reported in the isomorphous Cd compound [11a]. Unlike that in compound **1**, the diphosphonate ligand in compound **2** is tridentate and bridges with three Mn(II) ions. One phosphonate group (P1) is monodentate, whereas the other phosphonate group (P2) is bidentate. Similar to that in $Cd(H_3L^1)_2$ [11a], the amine group and the two phosphonate groups of the ligand are 1H-protonated. O(13) and O(23) atoms are 1H-protonated based on the P–O distances.

The MnO_6 octahedra are bridged by tridentate diphosphonate ligands to form a one-dimensional double chain along the *c*-axis. These double chains are interlinked via hydrogen bonds formed between non-coordinated phosphonate oxygens into ⟨100⟩ and ⟨200⟩ layers (Figs. 3 and 4). The O(13) ··· O(12) and O(13)–H(13a) ··· O(12) bond length and angle are 2.642(2) Å and 167.6°, respectively. Similarly, the O(23) ··· O(22) and O(23)–H(23a) ··· O(22) bond length and angle are 2.597(2) Å and 162.2°, respectively (Table 2). The protonated nitrogen atom also forms a hydrogen bond with the non-coordinated oxygen (O12). The N(1) ··· O(12) and N(1)–H(0a) ··· O(12) bond length

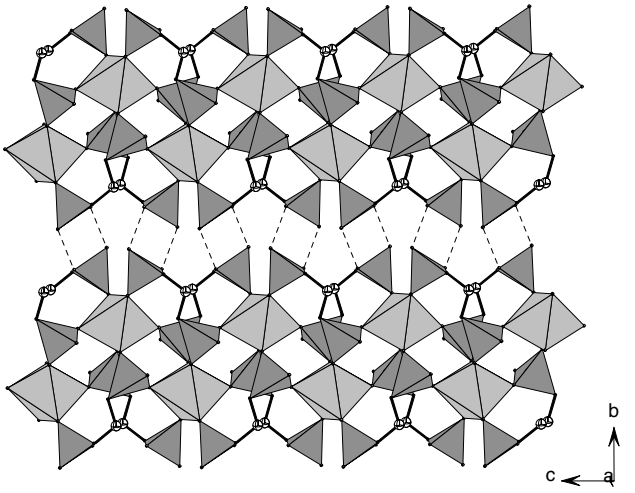


Fig. 3. A ⟨200⟩ manganese(II) phosphonate layer in compound **2**. MnO_6 octahedra and C–PO_3 tetrahedra are shaded in light and dark grey, respectively. N atoms are drawn as octand circles. The $C_6H_5CH_2$-groups have been omitted for clarity. Hydrogen bonds are represented by dotted lines.

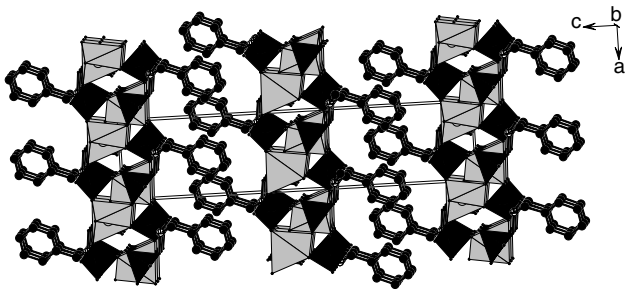


Fig. 2. View of the structure of compound **1** down the *a*-axis. MnO_5 polyhedra and C–PO_3 tetrahedra are shaded in light and dark grey, respectively. N and C atoms are drawn as octand and black circles, respectively.

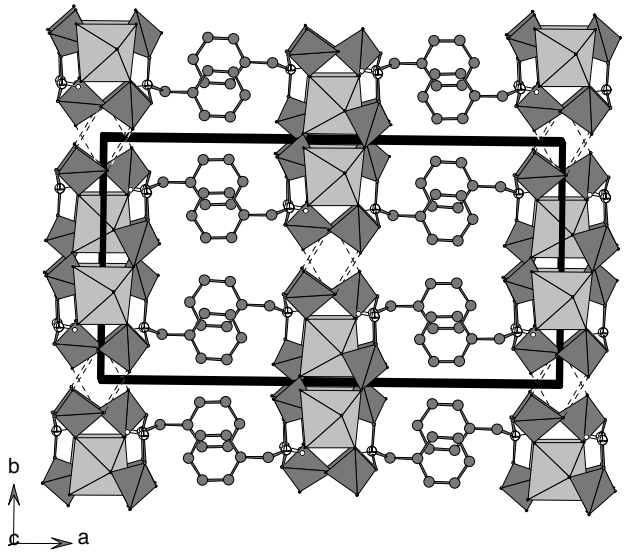


Fig. 4. View of the structure of compound **2** down the *a*-axis. MnO_6 octahedra and C–PO_3 tetrahedra are shaded in light and dark grey, respectively. N and C atoms are drawn as octand and black circles, respectively.

and angle are 2.642(2) Å and 151.2°, respectively (Table 2). The phenyl groups of the diphosphonate ligands are oriented toward the interlayer space (Fig. 6). The interlayer distance of 12.1 Å is slightly smaller than that of the isomorphos Cd compound [11a].

Unlike $Cd(H_3L^2)_2$, with a double chain structure and a *M*/*L* molar ratio of 1:2, $Mn_2(H_2L^2)_2(H_2O)$ (**3**) has a new type of layered structure and a *M*/*L* molar ratio of 1:1. The Mn(II) ion is octahedrally coordinated by five oxygens from four diphosphonate ligands and an aqua ligand. One diphosphonate anion forms an eight-membered chelating ring with Mn(1) (Mn1–O13–P1–C8–N1–C9–P2–O23). The Mn–O distances range from 2.127(3) to 2.325(3) Å (Table 2), which are comparable to those in compounds **1** and **2**. The diphosphonate anion is pentadentate, it chelates with a Mn(II) ion bidentately (O13 and O23) and is also connected to three other Mn(II) ions. O21 and O12 remain non-coordinated and O13 is a bidentate metal linker. This type of coordination mode is different from that of the H_2L^1 anion in compound **1** which is also pentadentate. Two Mn(II) ions are bridged by a pair of O(13) atoms to form a Mn_2O_2 unit. The aqua ligand is also bidentate and bridges with two Mn(II) ions. One oxygen atom (O21) is 1H-protonated, as is the nitrogen atom, based on charge balance, the coordination mode of the ligand as well as P–O distances.

The cross-linkage of Mn(II) ions by bridging aqua and phosphonate ligands results in ⟨001⟩ and ⟨002⟩ manganese(II) phosphonate layers (Fig. 5). Within the 2D layer, each pair of MnO_6 octahedra forms a dimeric unit via edge-sharing (O(13)–O(13)) and such dimeric units are interconnected via corner sharing (the aqua ligand) to form a 1D zigzag chain along the *a*-axis. These 1D chains are further bridged by phosphonate ligands into ⟨001⟩ and ⟨002⟩ layers. This type of layered structure has not been reported in other transition metal aminodiphosphonates. The interlayer distance of 16.28 Å is much larger than those of compounds **1** and **2**, mainly due to the additional methyl group on the phenyl ring (Fig. 6).

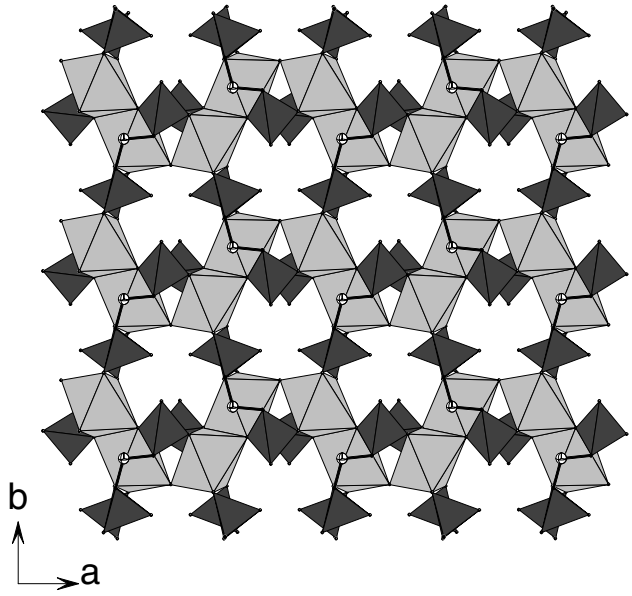


Fig. 5. A ⟨002⟩ manganese(II) phosphonate layer in compound **3**. MnO_6 octahedra and C–PO_3 tetrahedra are shaded in light and dark grey, respectively. N atoms are drawn as octand circles. The 4-Me–$C_6H_4CH_2$-groups have been omitted for clarity.

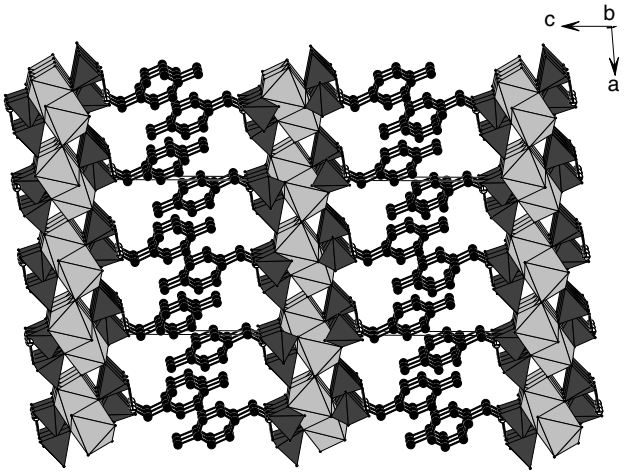


Fig. 6. View of the structure of compound **3** down the *b*-axis. MnO_6 octahedra and C–PO_3 tetrahedra are shaded in light and dark grey, respectively. N and C atoms are drawn as octand and black circles, respectively.

The synthetic conditions for the above three compounds merit further discussions. The neutral aminodiphosphonate ligands occur in zwitterionic forms, that is one proton of one phosphonate group being transferred to the amine group. Upon their complexion with metal ions, the coordination modes adopted and the structures of the metal phosphonates are mainly governed by the pH value of the solution and the *M*/*L* molar ratio used. When the *M*/*L* molar ratio is 1:2 and the reaction media is acidic, metal compounds with a formula of $M(H_3L)_2$ are usually isolated. When a *M*/*L* molar ratio of 1:1 was applied and the reaction was carried out under a weakly acidic condition, an additional proton of the diphosphonate ligand can be deprotoned and $M(H_2L)$ can be obtained. The removal of the remaining two protons requires a higher pH value and higher *M*/*L* molar ratios such as 3:2 and 2:1 [2b]. The different coordination modes of H_2L^1 and H_2L^2 are probably related to the different substituents on the amine group. However more studies are needed to further understand the subtle role which the substituents play.

The broad band centered at 3280 cm^{-1} for compound **3** is due to the H–OH stretching vibration of the water molecule. The sharp bands at 2980 cm^{-1} for **1**, 2985 cm^{-1} for **2**, 2978 cm^{-1} for **3** can be assigned to

the CH_2 stretching vibrations. The broad bands around 2900 cm^{-1} for all three compounds originate from the N–H and O–H stretching vibrations. The bands in the region of 2750 and 2790 cm^{-1} are ν(P–OH), which are characteristic of hydrogen phosphonate groups. The weak band at 1616 cm^{-1} in compound **3** is due to the δ(H–OH) vibration. The set of bands between 1200 and 900 cm^{-1} is due to the stretching vibrations of the tetrahedra C–PO_3 groups.

Compound **1** was stable up to 320 °C. Above this temperature, there was a sharp weight loss continued up to 550 °C, corresponding to the pyrolysis of organic groups. The total weight loss at 1000 °C is 38.4%, which is in good agreement with the calculated one of 38.8% if the final product is assumed to be $Mn(PO_3)_2$. Compound **2** was stable up to 290 °C. Then a continuous weight loss was observed up to 1000 °C, during which two processes occurred: the release of the water molecules formed by the condensation of hydrogen phosphonate groups and the burnt of organic groups. The total weight loss is 54.5%, which is much less than the calculated value of 67%, if the final product is assumed to be $Mn(PO_3)_2$. As a result, the decomposing process was not complete at 1000 °C. The TGA diagrams of compound **3** exhibit two main steps of weight losses. The first step started at 280 °C and ended at 670 °C, during which the aqua ligand was released and the organic groups were burnt. The second weight loss occurred above 820 °C, corresponding to further decomposition of the compound. The final product is $Mn(PO_3)_2$ based on XRD powder studies.

Magnetic properties of compounds **1** and **3** have been measured. At room temperature, the effective magnetic moment (μ_{eff}) for compound **1** is calculated to be 5.83μ_B, which is slightly smaller than the theoretical one (5.93μ_B) for a high spin Mn^{2+} ($S = 5/2$) ion. At low temperatures, the μ_{eff} value decreases with cooling, and reaches 4.22μ_B at 6 K (Fig. 7). Thus. there is an antiferromagnetic interaction between Mn(II) centers at low temperature. Linear fitting of χ^{-1} data with temperature according to Curies–Weiss law in the temperature range of 50–300 K gave the Curie constant of 4.306 emu K mol^{-1} and the Weiss constant (θ) of −2.70 K, indicating a weak antiferromagnetic exchange between the magnetic centers bridged by phosphonate groups (Mn ⋯ Mn 5.027 Å) within the 2D layer. The magnetic interaction between neighboring layers is negligible due to a large interlayer separation. For compound **3**, the μ_{eff} value of 8.22μ_B at 300 K corresponds to two high spin Mn^{2+} ($S = 5/2$) ions. At low temperatures, μ_{eff} decreases with cooling, and reaches 3.31μ_B at 6 K (Fig. 7). Thus there is a significant antiferromagnetic interaction between Mn(II) centers at low temperature. The Curie constant C is 8.86 emu K mol^{-1} and θ is −14.5 K, calculated by fitting of the magnetic data in the temperature range 100–300 K. The stronger antiferromagnetic interaction in compound **3** is due to much shorter Mn ⋯ Mn contacts between two neighboring Mn(II) centers bridged by an aqua ligand (Mn ⋯ Mn 4.014(1) Å) or a pair of phosphonate oxygen atoms (O13) (Mn ⋯ Mn 3.358(1) Å).

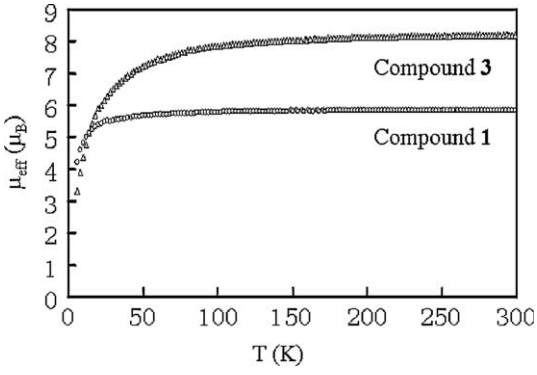


Fig. 7. Plot of effective magnetic moments (μ_{eff}) for compounds **1** and **3** as a function of temperature.

Acknowledgements

This project is supported by the National Natural Science Foundation of China (Grant No. 20371047), Natural Science Foundation of Fujian Province (Grant No. E0420003).

Appendix A. Supplementary material

Crystallographic data for compounds **1**–**3** have been deposited with the Cambridge Crystallographic Center, CCDC Nos. 244374, 244375 and 244376. Copies of this information may be obtained free of charge from The Director, CCDC, 12 Union Road, Cambridge, CB2 1EZ, UK (fax: +44 1233 336 033, email: deposit@ccdc.cam.ac.uk or www:http//www.ccdc.cam.ac.uk). Supplementary data associated with this article can be found, in the online version, at doi:10.1016/j.poly.2004.12.018.

References

[1] (a) A. Clearfield, Metal phosphonate chemistry, in: K.D. Karlin (Ed.), Progress in Inorganic Chemistry, vol. 47, Wiley, New York, 1998, p. 371 (and references therein);
(b) A.K. Cheetham, G. Ferey, T. Loiseau, Angew. Chem. Int. Ed. 38 (1999) 3268;
(c) J. Zhu, X. Bu, P. Feng, G.D. Stucky, J. Am. Chem. Soc. 122 (2000) 11563;
(d) A. Clearfield, Cur. Opin. Solid State. Mater. 6 (2002) 495 (and references therein)..
[2] (a) J.-G. Mao, Z.K. Wang, A. Clearfield, Inorg. Chem. 41 (2002) 3713;
(b) J.-G. Mao, Z. Wang, A. Clearfield, Inorg. Chem. 41 (2002) 2334;

(c) J.-G. Mao, Z. Wang, A. Clearfield, Inorg. Chem. 41 (2002) 6106;
(d) J.-G. Mao, Z. Wang, A. Clearfield, J. Chem. Soc., Dalton Trans. (2002) 4457.
[3] (a) B. Zhang, A. Clearfield, J. Am. Chem. Soc. 119 (1997) 2751;
(b) A. Clearfield, C.V.K. Sharma, B. Zhang, Chem. Mater. 13 (2001) 3099;
(c) C. Sassoye, K. Norton, S.C. Sevov, Inorg. Chem. 42 (2003) 1652;
(d) N. Stock, T. Bein, Angew. Chem. Int. Ed. 43 (2004) 749.
[4] (a) Y.-D. Chang, J. Salta, J. Zubieta, Angew. Chem. Int. Ed. 33 (1994) 325;
(b) E.I. Tolis, M. Helliwell, S. Langley, J. Raftery, R.E.P. Winpenny, Angew. Chem. Int. Ed. 42 (2003) 3804;
(c) S.O.H. Gutschke, D.J. Price, A.K. Powell, P.T. Wood, Angew. Chem. Int. Ed. 40 (2001) 1920;
(d) D.-Y. Kong, Y. Li, J.H. Ross, A. Clearfield, Chem. Commun. (2003) 1720;
(e) V. Chandrasekhar, S. Kingsley, B. Rhatigan, M.K. Lam, A.L. Rheingold, Inorg. Chem. 41 (2002) 1030.
[5] (a) O.R. Evans, H.L. Ngo, W.B. Lin, J. Am. Chem. Soc. 123 (2001) 10395;
(b) C. Serre, N. Stock, T. Bein, G. Férey, Inorg. Chem. 43 (2004) 3159.
[6] (a) N. Stock, S.A. Frey, G.D. Stucky, A.K. Cheetham, J. Chem. Soc., Dalton Trans. (2000) 4292;
(b) N. Stock, T. Bein, J. Solid State Chem. 167 (2002) 330;
(c) N. Stock, M. Rauscher, T. Bein, J. Solid State Chem. 177 (2004) 642.
[7] M.A. Petruska, B.C. Watson, M.W. Meisel, D.R. Talham, Chem. Mater. 14 (2002) 2011.
[8] (a) E.K. Brechin, R.A. Coxall, A. Parkin, S. Parsons, P.A. Tasker, R.E.P. Winpenny, Angew. Chem. Int. Ed. 40 (2001) 2700;
(b) H.-H. Song, P. Yin, L.-M. Zheng, J.D. Korp, A.J. Jacobson, S. Gao, X.-Q. Xin, J. Chem. Soc., Dalton Trans. (2002) 2752.
[9] A. Cabeza, X. Ouyang, C.V.K. Sharma, M.A.G. Aranda, S. Bruque, A. Clearfield, Inorg. Chem. 41 (2002) 2325.
[10] D.M. Poojary, B. Zhang, A. Clearfield, J. Am. Chem. Soc. 119 (1997) 12250.
[11] (a) Z.-M. Sun, B.-P. Yang, Y.-Q. Sun, J.-G. Mao, A. Clearfield, J. Solid State Chem. 176 (2003) 62;
(b) Z.-M. Sun, J.-G. Mao, Y.-Q. Sun, H.-Y. Zeng, A. Clearfield, New J. Chem. 27 (2003) 1326;
(c) Z.-M. Sun, J.-G. Mao, B.-P. Yang, S.-M. Ying, Solid State Sci. 6 (2004) 295.
[12] (a) B.I. Makaranets, T.N. Polynova, N.D. Mitrofanova, M.A. Porai-Koshits, J. Struct. Chem. 32 (1991) 94;
(b) A. Turner, P.A. Jaffres, E.J. MacLean, D. Villemin, V. McKee, G.B. Hix, J. Chem. Soc., Dalton Trans. (2003) 1314;
(c) N. Stock, Solid State Sci. 4 (2002) 1089;
(d) U. Costantino, M. Nocchetti, R. Vivani, J. Am. Chem. Soc. 124 (2002) 8428.
[13] K. Moedritzer, R.R. Irani, J. Org. Chem. 31 (1966) 1603.
[14] SADABS, Bruker Smart and Bruker Shelxtl Package, Bruker AXS GmbH, 1998.
[15] G.M. Sheldrick, SHELXTL, Crystallographic Software Package, SHELXTL, Version 5.1, Bruker-AXS, Madison, WI, 1998.

Available online at www.sciencedirect.com
SCIENCE DIRECT®
Polyhedron 24 (2005) 579–584
POLYHEDRON
www.elsevier.com/locate/poly

First example of atmospheric carbon dioxide uptake by a cyanocomplex: Preparation and structural characterization of $Zn_2(tn)_2(CO_3)Ni(CN)_4 \cdot H_2O$ (*tn* = 1,3-diaminopropane)

Juraj Černák [a,*], Bibiana Ferencová [a], Zdirad Žák [b]

[a] *Department of Inorganic Chemistry, Institute of Chemistry, P. J. Šafárik University, Moyzesova 11, 041 54 Košice, Slovakia*
[b] *Department of Inorganic Chemistry, Masaryk University, Kotlářska 12, 611 37 Brno, Czech Republic*

Received 30 July 2004; accepted 15 December 2004

Abstract

The aqueous system Zn(II)-*tn*-$[Ni(CN)_4]^{2-}$ in contact with air captured carbon dioxide in the form of a carbonato ligand yielded the compound $Zn_2(tn)_2(CO_3)Ni(CN)_4 \cdot H_2O$ by crystallization, which was characterized by elemental analyses, IR spectroscopy and single crystal structure analysis. Its crystal structure is polymeric and is built up of a positively charged framework $[Zn_4(tn)_4(CO_3)_2Ni(CN)_4]_n^{2n+}$, free tetracyanonickellate anions with a nickel atom on the inversion centre and water molecules of crystallization. Two crystallographically different zinc atoms exhibit tetrahedral and penta-coordinations. The zinc atoms are interconnected by two crystallographically independent bridging *tn* ligands, μ_3-CO_3^{2-} carbonato ligand and one centrosymmetric tetracyanonickellate anion acting as *trans*-[-NC-Ni(CN)$_2$-CN-] ligand. The carbonato ligand coordinates three zinc atoms by an unusual mode, two by an unidentate and one by a bidentate fashion with one oxygen donor atom forming two Zn–O coordination bonds.
© 2005 Elsevier Ltd. All rights reserved.

Keywords: Cyanocomplex; Crystal structure; Carbon dioxide uptake; Zinc; Nickel

1. Introduction

Cyanocomplexes exhibit high structural variability due to both terminal and bridging functions of the cyano ligand. This was explored previously in the syntheses of various types of host–guest and mineralominetic systems [1,2]. Recently, coordination oligomers and polymers based on cyanocomplexes have become popular among both chemists and physicists due to their interesting magnetic properties [3–6]. Their synthetic design follows the idea of linking suitable building blocks (''brick and mortar'' method [7]) by bridging cyano ligands. Suitable *N*-donor ligands like *en*, *bipy*, etc. (*en* = 1,2-diaminoethane; *bpy* = 2,2′-bipyridine) coordinated to the cationic central atom act as blocking ligands leaving thus the remaining coordination sites free for the polymerization process and, in such a way, the connectivity of the cationic building block (''brick'') can be tuned. We have used this approach in the preparation of several cyanocomplexes exhibiting mainly low-dimensional character and their magneto-structural correlations were studied [8–10]. The use of 1,3-diaminopropane (*tn*) as blocking ligand and the square $[Ni(CN)_4]^{2-}$ anion as ''mortar'' led to the formation of the complexes $Ni(tn)_2Ni(CN)_4 \cdot H_2O$ [11], $[Cu(tn)_2Ni(CN)_4]_2 \cdot 4H_2O$ [12], two polymorphs of $Cu(tn)Ni(CN)_4$ [13] and $Cd(tn)_2Ni(CN)_4$ [14]. Our initial aim was, for the sake of comparison, to prepare and characterize the zinc analogue of the above mentioned compounds $M(tn)_2Ni(CN)_4 \cdot nH_2O$. From the

* Corresponding author. Tel.: +421 55 62 283 89/+421 55 62 281 14; fax: +421 55 62 221 24.
E-mail address: cernakju@kosice.upjs.sk (J. Černák).

0277-5387/$ - see front matter © 2005 Elsevier Ltd. All rights reserved.
doi:10.1016/j.poly.2004.12.020

aqueous system Zn(II)-*tn*-$[Ni(CN)_4]^{2-}$ large single crystals of the title compound crystallized which unexpectedly contained a μ_3-CO_3^{2-} carbonato ligand. Here, we report its synthesis, characterization and crystal structure.

2. Experimental

2.1. Materials and measurements

1,3-Diaminopropane was purchased commercially from Aldrich and was used as obtained. $K_2[Ni(CN)_4] \cdot H_2O$ was prepared from KCN and $Ni(NO_3)_2 \cdot 6H_2O$ according to the literature [15] and recrystallized from water. KCN, $Ni(NO_3)_2 \cdot 6H_2O$ and $Zn(NO_3)_2$ were of analytical grade (Lachema Brno). Elemental analysis for C, H and N was performed on a Perkin–Elmer 2400 Analyser, contents of metallic elements were determined gravimetrically (Ni) and complexometrically (Zn). IR spectra were taken on a Thermo Nicolet AVATAR FT-IR spectrophotometer in KBr discs (4000–400 cm^{-1}).

2.2. Preparation of $Zn_2(tn)_2(CO_3)Ni(CN)_4 \cdot H_2O$

20 ml of 0.1 M aqueous solution of $K_2[Ni(CN)_4]$ (2 mmol) and 20 ml of 0.1 M aqueous solution of $Zn(NO_3)_2$ (2 mmol) were successively added to 0.67–1.00 ml of *tn* (8–12 mmol) in 10 ml of water. The eventually formed turbidity was removed by filtration. Yellow crystals of the product appeared within two weeks of crystallisation at laboratory temperature. The crystals were filtered off, washed with a small quantity of cold water and ethanol, and dried in air. Yield: 31%.

Anal. Calc. for $C_{11}H_{22}N_8NiO_4Zn_2$ (M_r = 519.81): C, 25.42; H, 4.27; N, 21.56; Ni, 11.29; Zn, 25.16. Found: C, 25.47; H, 4.27; N, 21.23; Ni, 11.85; Zn, 24.78%.

IR spectrum (in cm^{-1}; s = strong, m = medium, w = weak, v = very, sh = shoulder): ν(OH): 3616s, 3424s, $\nu(NH_2)$: 3320vs, 3256vs; $\nu(CH_2)$: 2952s, 2928m, 2904m, 2864m; ν(CN): 2168vs, 2128vs; $\delta(OH_2)$: 1650w; $\delta(NH_2)$: 1612s; $\nu(CO_3)$: 1504vs; $\rho(NH_2)$: 632m, 596w, 560w;ν(Ni–C): 544w δ(Ni–CN): 416m.

2.3. Single crystal X-ray experiment

Cell parameters and data collection were done on a KUMA KM-4κ-axis diffractometer equipped with a CCD area detector (graphite monochromatized Mo Kα radiation, λ = 0.71073 Å) at 150 K on a prismatic single crystal with dimensions 0.15 × 0.15 × 0.10 mm. The relevant crystal data are: monoclinic, a = 10.581(2), b = 17.872(3), c = 9.801(1) Å, β = 95.73(1)°, V = 1844.1(5) $Å^3$, $P2_1/c$, Z = 4, μ = 3.626 mm^{-1}, ρ_c = 1.872 g cm^{-3}.

A total of 928 frames were registered, from these 10478 reflections were collected (the θ range was 3.09°–26.68° and Miller indices limits were $-12 \leqslant h \leqslant 12$, $-21\ k \leqslant 21\ -6 \leqslant l \leqslant 12$). After data reduction and limiting the 2θ range to 50°, 3128 independent reflections were obtained (R_{int} = 0.0330), of these 2806 were observed ($I > 2\sigma(I)$). The completeness of the data was 0.932. An empirical absorption correction based on ψ-scan was used (SHELXTL V5.1 system [16]) with minimum and maximum transmission factors of 0.037 and 0.081. The structure was solved by the heavy atom method using

Table 1
Selected geometric parameters (Å,°) for ZTNC

Zn1–O1	1.9475(14)
Zn1–O3^{i}	1.9499(14)
Zn1–N21^{ii}	2.0257(18)
Zn1–N11^{iii}	2.0614(18)
Zn2–O1	2.3906(15)
Zn2–O2	2.0104(14)
Zn2–N1	2.0150(18)
Zn2–N10	2.0261(17)
Zn2–N20	2.0347(17)
Ni1–C1	1.862(2)
Ni1–C2	1.871(2)
Ni2–C3	1.877(2)
Ni2–C4	1.854(2)
C1–N1	1.150(3)
C2–N2	1.152(3)
C3–N3	1.154(3)
C4–N4	1.153(3)
C5–O3	1.272(3)
C5–O2	1.286(2)
C5–O1	1.288(2)
O1–Zn1–O3^{i}	113.58(6)
O1–Zn1–N21^{ii}	113.20(7)
O3^{i}–Zn1–N21^{ii}	116.86(7)
O1–Zn1–N11^{iii}	102.26(6)
O3^{i}–Zn1–N11^{iii}	103.85(6)
N21^{ii}–Zn1–N11^{iii}	105.01(7)
O2–Zn2–N1	101.44(7)
O2–Zn2–N10	115.82(7)
N1–Zn2–N10	102.18(8)
O2–Zn2–N20	110.04(6)
N1–Zn2–N20	111.71(7)
N10–Zn2–N20	114.56(7)
O2–Zn2–O1	58.73(5)
N1–Zn2–O1	159.52(6)
N10–Zn2–O1	84.12(6)
N20–Zn2–O1	82.33(6)
C1–Ni1–C2	87.83(9)
C4–Ni2–C3	90.69(9)
N1–C1–Ni1	177.3(2)
C1–N1–Zn2	166.92(17)
N2–C2–Ni1	177.7(2)
N3–C3–Ni2	178.5(2)
N4–C4–Ni2	178.0(2)
O3–C5–O2	123.24(18)
O3–C5–O1	120.71(18)
O2–C5–O1	116.05(18)

Symmetry transformations used to generate equivalent atoms: (i) x, 1/2 − y, z − 1/2; (ii) x − 1, y, z; (iii) 2 − x, y − 1/2, 1/2 − z.

Table 2
Possible hydrogen bonds in ZTNC

Donor–H	Donor...acceptor	H...acceptor	Donor–H...acceptor
O4–H41	O4···N4^{i}	H41...N4^{i}	O4–H41...N4^{i}
0.89(3)	3.327(3)	2.45(3)	172(3)
O4–H42	O4...N2^{ii}	H42...N2^{ii}	O4–H42...N2^{ii}
0.81(3)	2.896(3)	2.12(3)	161(3)
N10–H10A	N10....N3^{iii}	H10A...N3^{iii}	N10–H10A...N3^{iii}
0.920	3.030(3)	2.173	155
N10–H10B	N10....O4	H10B...O4	N10–H10B...O4
0.920	2.987(2)	2.087	166
N11–H11A	N11....N4^{iii}	H11A...N4^{iii}	N11–H11A...N4^{iii}
0.920	3.056(3)	2.187	157
N11–H11B	N11....N2^{iv}	H11B...N2^{iv}	N11–H11B...N2^{iv}
0.920	3.287(2)	2.478	147
N20–H20A	N20....N3	H20A...N3	N20–H20A...N3
0.920	3.061(3)	2.205	154
N20–H20B	N20....O2^{iii}	H20B...O2^{iii}	N20–H20B...O2^{iii}
0.920	3.227(2)	2.320	169
N21–H21A	N21....N4^{v}	H21A...N4^{v}	N21–H21A...N4^{v}
0. 920	3.022(3)	2.168	154
N21–H21B	N21....N2	H21B..N2	N21–H21B...N2
0.920	3.388(3)	2.476	171

Equivalent positions: (i) $2-x$, $y+1/2$, $1/2-z$; (ii) $x-1$, y, z; (iii) x, $1/2-y$, $z-1/2$; (iv) $3-x$, $1-y$, $1-z$; (v) $3-x$, $-y$, $1-z$.

the SHELXS 86 program [17]. Refinement based on intensities was performed using the SHELXL 97 program [18]. All but the hydrogen atoms were refined anisotropically. Hydrogen atoms of the water molecule were found in the difference map and their positions were refined using a common isotropic thermal parameter; the remaining hydrogen atoms from the *tn* ligand were placed in calculated positions and their common group isotropic thermal parameters were refined (totally 248 parameters). The final parameters were: $R_1 = 0.0229$, $S = 1.081$, $wR_2 = 0.0472$ (all data), $R_1 = 0.0197$, $wR_2 = 0.0465$ (observed). The final difference map was featureless and the maximum peak and hole were 0.27(7) and $-0.32(7)$ e Å^{-3}. Selected geometric parameters and possible hydrogen bonds are gathered in Tables 1 and 2, respectively. For geometric calculations (hydrogen bond geometry) the program PARST 95 was used [19]. The figures were drawn with the DIAMOND program [20].

3. Results and discussion

3.1. Synthesis

Our initial intention was to prepare a coordination polymer containing as building blocks the $[Zn(tn)_2]^{2+}$ cation and the $[Ni(CN)_4]^{2-}$ anion. An analogous approach when using *en* instead of *tn* led to the formation of $Zn(en)_2Ni(CN)_4$ with a chelate bonded *en* ligand [21] while from the Cd(II)–*tn*–$[Ni(CN)_4]^{2-}$ system the $Cd(tn)_2Ni(CN)_4$ complex was isolated, in which *tn* ligands exhibit bridging character [14]. From the aqueous system Zn(II)–*tn*–$[Ni(CN)_4]^{2-}$, which was in contact with air, crystallized the title compound $Zn_2(tn)_2(CO_3)Ni(CN)_4 \cdot H_2O$ (ZTNC). The fixation of atmospheric CO_2 is not an uncommon phenomenon; it exhibits special interest with regard to the greenhouse effect [22,23]. It has been described that carbon dioxide is captured by amines [24,25]. Several complexes were formed by an insertion of CO_2, either in the form of the carbonato ligand or in another form. Examples that can be mentioned are $[\mu\text{-}CO_3\{Zn(pmap)\}_2](ClO_4)_2$ (*pmap* = bis[2-(2-pyridyl)ethyl]-(2-pyridyl)-methylamine) [26], $[Cu_3(bpy)_6(\mu_3\text{-}CO_3)]_2(ClO_4)_8 \cdot H_2O$ [27] and $\{[tren]Zn(OCO_2Me)\}(BPh_4) \cdot 2MeOH$ (*tren* = tris(2-aminoethyl)amine) [28]. As the initial mother liqueur did not contain a carbonato anion, this presumably was formed by an uptake of carbon dioxide from air. The presence of the diamine *tn* could be helpful for this process. To our knowledge ZTNC is the first example of a cyanocomplex which fixes CO_2. Our attempts to prepare this compound by addition of sodium carbonate to the initial mother liqueur were not successful.

3.2. IR spectra

The IR spectrum of ZTNC is rich and the most important peaks are gathered in the experimental part. Very characteristic are the absorption bands at 2168 and 2128 cm^{-1}, which can be assigned to the stretching vibrations of the cyano groups $\nu(C{\equiv}N)$ [29]; the peak observed at the higher wavenumber can be assigned to bridging cyano groups and the one placed at a lower wavenumber to terminal cyano groups. The presence of the Ni–CN entity is manifested by a strong δ(Ni–CN) vibration observed at 416 cm^{-1}. The *tn* ligands causes many absorption bands; those that are easily identifiable arise from $\nu(NH_2)$ (3320, 3256 cm^{-1}) and $\nu(CH_2)$ (2952s, 2928, 2904, 2864 cm^{-1}) stretching and $\delta(NH_2)$ (1612 cm^{-1}) deformation vibrations. The presence of the water molecule in the structure can be seen from the observation of absorption bands at 3616 and 3424 cm^{-1}, identified as asymmetric and symmetric ν(OH) stretching vibrations. The positions of all these observed absorption bands are very close to those found in the IR spectrum of $Zn(en)_2Ni(CN)_4 \cdot 2H_2O$ [30].

The free carbonato anion has two vibrational modes, E′ and A. Upon coordination the E′ mode is split and the A mode become IR active; the bands corresponding to the E′ mode occur in the 1600–1200 cm^{-1} region [31]. In the IR spectrum of ZTNC in this region several absorption bands at 1612s, 1504vs, 1472vs, 1416vs, 1320m and 1236m cm^{-1} were observed. In $[Cu_3(bpy)_6(\mu_3\text{-}CO_3)]_2(ClO_4)_8 \cdot H_2O$ the absorption bands due to stretching modes arising from the carbonato ligand were observed at 1474 and 1445 cm^{-1} [27]. In the

IR spectrum of the similar $Zn(en)_2Ni(CN)_4$ compound several absorption bands (1608s, 1590vs, 1580vs, 1460w, 1446w, 1384w, 1328m and 1278m cm^{-1}) due to various vibration modes in the amine ligand *en* were observed in this region [30]. Taking into account the intensities and positions of the observed absorption bands in ZTNC and the literature data it is possible to assign the band observed at 1504 cm^{-1} in the spectrum of ZTNC to the C–O stretching mode, but the assignment of the other observed bands to the respective vibration modes is not unambiguous as some overlap may also exist.

3.3. Crystal structure

The crystal structure of ZTNC (Fig. 1) is polymeric. As can be seen from Fig. 2, the zinc atoms which are approximately placed within sheets parallel to the (0 1 0) plane are linked by bridging *tn* and carbonato ligands forming two types of cavities. One type of these cavities is occupied by bridging tetracyanonickellate anions which thus participate in the formation of the positively charged framework $[Zn_4(tn)_4(CO_3)_2Ni(CN)_4]_n^{2n+}$. The second type of cavity contains free tetracyanonickellate anions and water molecules of crystallization. As a consequence, the formed structure can be viewed as a host–guest system in which the host framework accommodates as guests $[Ni(CN)_4]^{2-}$ anions and water molecules. An analogous host–guest system was formed by $[Zn_2(en)_3Ni(CN)_4][Ni(CN)_4] \cdot 3H_2O$ [32].

In the framework, there are two crystallographically and stereochemically different zinc atoms which are catenated by two crystallographically different bridging *tn* molecules. Moreover, two crystallographically equivalent Zn2 atoms are linked by a centrosymmetric bridging tetracyanonickellate anion (Ni1 atom is on the inversion centre) with bridging cyano groups placed in *trans* positions. The Zn1 atom is deformed tetrahedrally coordinated by two oxygen atoms from carbonato anions and two nitrogen atoms from *tn* ligands, the angles being in the range 102.26°–116.86° (Table 1, Fig. 1). At a distance of 2.7750(19) Å from this atom is situated the water molecule O4, the observed distance is too long to be considered as a coordination bond, but there may exist a weak interaction as deduced from the hydrogen bond geometry around the O4 atom (see below).

The Zn2 atom exhibits pentacoordination in the ZnO_2N_2N form; the oxygen atoms arise from the chelate bonded carbonato ligand and the nitrogen atoms from two diamine molecules and one bridging cyano group.

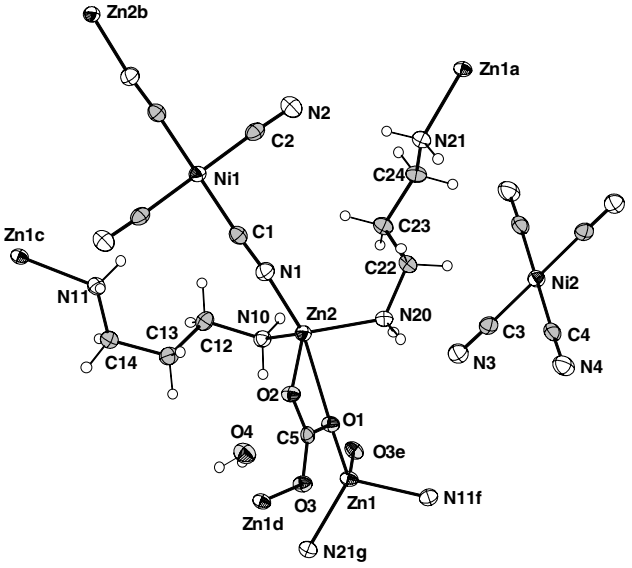


Fig. 1. Thermal ellipsoid drawing of ZTNC along with atom numbering scheme. The symmetry codes are: (a) $1 + x$, y, z; (b) $3 - x$, $1 - y$, $1 - z$; (c) $2 - x$, $0.5 + y$, $0.5 - z$; (d) x, $0.5 - y$, $0.5 + z$; (e) x, $0.5 - y$, $z - 0.5$; (f) $2 - x$, $y - 0.5$, $0.5 - z$; (g) $x - 1$, y, z.

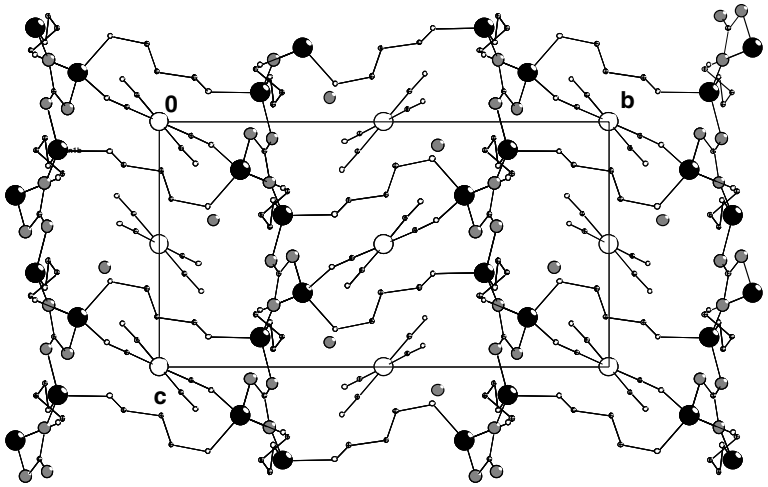


Fig. 2. View of the polymeric character of the structure of ZTNC.

Among the Zn2–X (X is nitrogen or oxygen) bond distances four Zn2–X ones are from the narrow range 2.0104–2.0347 Å and the fifth coordination bond (Zn2–O1) is considerably longer (2.3906(15) Å) (Table 1). The problem of the shape of coordination polyhedra in pentacoordinated complexes was extensively studied, especially for Cu(II) complexes, and various criteria for describing them were derived [33–36]. The calculated τ parameter [33] (0.728) suggests that the shape of the ZnO_2N_2N coordination polyhedron is closer to trigonal bipyramidal, in line with the results of the methods of the sum of angle deviations [34], which give a better *R* factor (0.126) for a trigonal bipyramidal shape than for the square pyramidal (0.152) and tetragonal pyramidal shapes (0.212).

The free tetracyanonickellate anion (Ni2) is placed on the inversion centre. Both Ni1 and Ni2 nickel atoms exhibit square coordination by four cyano ligands. The observed geometric parameters are within the usual values found for such complexes [1].

The μ_3-carbonato ligand forms four coordination bonds to three zinc atoms ($2 \times$ Zn1, Zn2) and thus exhibits bridging as well as chelate character (Fig. 2c). A search in the CCSD [37] has shown that, up until now, this coordination mode (not mentioned in the paper of Huang et al. [27]) was found only in $Cs_2[Pr_2(CO_3)_4]$ [38]. The Zn–O bonds in ZTNC are in the range 1.9475–2.3906 Å which is somewhat more spread than the observed range of 2.028–2.304 Å in $[((benpa)Zn)_2(\mu_2\text{-}CO_3)](ClO_4)_2$ (*benpa* = *N*,*N*-bis-2-(ethylthio)ethyl-*N*-((6-neopentylamino-2-pyridyl)methyl)-amine) with a *bis* (bidentate) binding of the carbonato ligand [39]. The observed C–O bonds are normal [27,39].

Aliphatic diamine ligand *tn* prefers a chelate type of bonding to transition metals ions but in the case of d^{10} elements it is not characteristic; there are only few examples of a chelate bonded *tn* ligand, e.g., in [-Zn(*tn*)-(μ_2-*tn*)-Zn(*tn*)-(μ_2-*tn*)]Cl_4 [40]. More often bridging bonding occurs. As an example one can mention $Cd(tn)_2Ni(CN)_4$ in which the Cd–*tn*–Cd catenation is made up of bridging *tn* ligands with the *tn* skeleton in a *trans–gauche–trans–trans* conformation [14]. In the title compound ZTNC both bridging *tn* ligands are in *gauche–trans–gauche–trans* conformation.

The water molecules are placed in the formed cavities of the structure (Fig. 2). The water molecules form two hydrogen bonds of the O–H···N type with the nitrogen atoms (N2, N4) from the terminal cyano ligands and function as an acceptor for the N10–H10B···O4 hydrogen bond with the amine group from *tn* (Fig. 3). In the direction of the assumed fourth position, corresponding to the tetrahedral orientation of the electron lobes around the O4 oxygen atom, is placed the Zn1 atom at a long distance of 2.7750(19) Å. The observed X···O···Y angles around the O4 atom (X and Y are N2, N4, N10 and Zn1 atoms) exhibit values of 110°, 114°, 103°, 129°, 104° and 90°, and may suggest a weak interaction between O4 and Zn1 atoms. All remaining hydrogen atoms from the *tn* amine groups are involved in weak hydrogen bonds of the N–H···N type with nitrogen atoms of the terminal cyano ligands and N–H···O type with oxygen atom of the carbonato ligand (Fig. 3, Table 2).

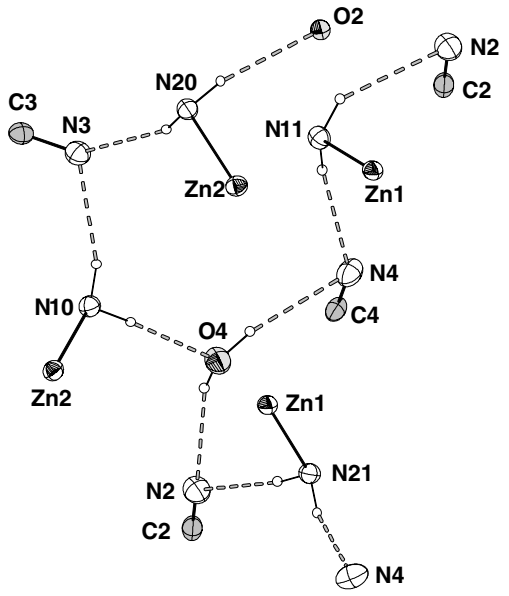


Fig. 3. Possible hydrogen bonds (dashed grey lines) in ZTNC.

4. Supplementary material

Crystallographic data (excluding structure factors) for the structure reported in this paper have been deposited with the Cambridge Crystallographic Data Center as supplementary publication no. CCDC 246271. Copies of the data can be obtained free of charge on application to CCDC, 12 Union Road, Cambridge CB2 1EZ, UK [fax: int. code +44 1223 336 033; E-mail: deposit@ccdc.cam.ac.uk; http://www.ccdc.cam.ac.uk].

Acknowledgement

Financial support on the part of Slovak Grant Agency (VEGA 1/0447/03) is acknowledged.

References

[1] T. Iwamoto, J. Inclus. Phenom. 24 (1–2) (1996) 61.
[2] T. Iwamoto, S. Nishikiori, T. Kitazawa, H. Yuge, J. Chem. Soc., Dalton Trans. (1997) 4127.
[3] M. Verdaguer, A. Bleuzen, V. Marvaud, J. Vaissermann, M. Seuleiman, C. Desplanches, A. Scuiller, C. Train, R. Garde, G. Gelly, C. Lomenech, I. Rosenman, P. Veillet, C. Cartier, F. Villain, Coord. Chem. Rev. 190–192 (1999) 1023.

[4] T. Kitazawa, Y. Gomi, M. Takahashi, M. Takeda, M. Enomoto, A. Miyazaki, T. Enoki, J. Mater. Chem. 6 (1996) 119.
[5] G. Grasa, F. Tuna, R. Gheorghe, D.B. Leznoff, S.J. Rettig, M. Andruh, New J. Chem. 24 (2000) 615.
[6] J. Larionova, M. Gross, M. Pilkington, H. Andres, H. Stoeckli-Evans, H.U. Güdel, S. Decurtins, Angew. Chem. 112 (2000) 1667.
[7] R.D. Willett, Z.M. Wang, S. Molnar, K. Brewer, C.P. Landee, M.M. Turnbull, W.R. Zhang, Mol. Cryst. Liq. Cryst. 232 (1993) 637.
[8] J. Paharová, J. Černák, R. Boča, Z. Žák, Inorg. Chim. Acta 346 (2003) 25.
[9] M. Orendáč, A. Orendáčová, J. Černák, A. Feher, P.J.C. Signore, M.W. Meisel, M. Verdaguer, Phys. Rev. B 52 (1995) 3435.
[10] J. Černák, K.A. Abboud, J. Chomič, M.W. Meisel, M. Orendáč, A. Orendáčová, A. Feher, Inorg. Chim. Acta 311 (2000) 126.
[11] S.Z. Zhan, D. Guo, X.Y. Zhang, C.X. Du, Y. Zhu, R.N. Yang, Inorg. Chim. Acta 298 (2000) 57.
[12] J. Černák, J. Lipkowski, I. Potočňák, A. Hudák, Monatsh. Chem. 132 (2001) 193.
[13] J. Černák, J. Lipkowski, Monatsh. Chem. 130 (1999) 1195.
[14] H. Yuge, A. Mamada, M. Asai, S. Nishikiori, T. Iwamoto, J. Chem. Soc., Dalton Trans. (1995) 3195.
[15] W.C. Fernelius (Ed.), Inorganic Synthesis, vol. II, McGraw-Hill, New York, 1946, p. 227.
[16] Bruker AXS, SHELXTL V5.1 program system.
[17] G.M. Sheldrick, SHELXS 86, in: G.M. Sheldrick, C. Krüger, R. Goddard (Eds.), Crystallographic Computing, 3, Oxford University Press, Oxford, 1985, p. 175.
[18] G.M. Sheldrick, SHELXL 97. Program for the Refinement of Crystal Structures, University of Göttingen, Germany, 1997.
[19] M. Nardelli, PARST 95. J. Appl. Crystallogr. 28 (1995) 659.
[20] Crystal Impact (2000), DIAMOND (Release 2.1.d), Crystal Impact, D-53002 Bonn, Germany.
[21] J. Černák, I. Potočňák, J. Chomič, M. Dunaj-Jurčo, Acta Crystallogr. C 46 (1990) 1098.
[22] J.B. Marston, M. Oppenheimer, R.M. Fujita, S.R. Gaffin, Nature 349 (1991) 573.
[23] D.A. Palmer, R. van Eldik, Chem. Rev. 83 (1983) 651.
[24] S.H. Lin, C.T. Shyu, Environ. Technol. 21 (2000) 1245.
[25] A. Dibenedetto, M. Aresta, R. Girardi, Abstracts of Pap. ACS, 225, 079-Fuel, Part 1 (2003).
[26] J. Dietrich, F.W. Heinemann, A. Schrodt, S. Schindler, Inorg. Chim. Acta 288 (1999) 206.
[27] W. Huang, P.Y. Sun, J.L. Fang, Y.F. Sun, S.H. Gou, Trans. Metal Chem. 28 (2003) 925.
[28] M.M. Ibrahim, K. Ichikawa, M. Shiro, Inorg. Chem. Commun. 6 (2003) 1030.
[29] K. Nakamoto, Infrared and Raman Spectra of Inorganic and Coordination Compounds, Part II, 5th ed., Wiley, New York, 1997.
[30] J. Černák, I. Potočňák, J. Chomič, J. Therm. Anal. 39 (1993) 849.
[31] A.M. Greenaway, T.P. Dasgupta, K.C. Koshy, G.G. Sadler, Spectrochim. Acta 42A (1986) 949.
[32] J. Černák, I. Potočňák, V. Petříček, K. Malý, J. Inclus. Phenom. Mol. Recog. Chem. 14 (1992) 73.
[33] A.W. Addison, T.N. Rao, J. Reedijk, J. van Rijn, G.C. Verschoor, J. Chem. Soc., Dalton Trans. (1984) 1349.
[34] R.R Holmes, J.A. Deiters, J. Am. Chem. Soc. (1977) 3318.
[35] O. Carugo, C.B. Castellani, J. Chem. Soc., Dalton Trans. (1990) 2895.
[36] I. Potočňák, M. Dunaj-Jurčo, D. Mikloš, L. Jäger, Monatsh Chem. 132 (2001) 315.
[37] F.H. Allen, S. Bellard, M.D. Brice, B.A. Cartwright, A. Doubleday, H. Higgs, T. Hummelink, B.G. Hummelink-Peters, O. Kennard, W.D.S. Motherwell, J.R. Rodgers, D.G. Watson, Cambridge Structural Database System (CSDS), Cambridge, UK, Version 5.25, November 2003.
[38] A. Lossin, G. Meyer, Z. Anorg. Allg. Chem. 619 (1993) 2031.
[39] R.A. Allred, L.H. McAlexander, A.M. Arif, L.M. Berreau, Inorg. Chem. 41 (2002) 6790.
[40] G. Ciani, M. Moret, A. Sironi, S. Bruni, F. Cariati, A. Pozzi, T. Manfredini, L. Manabue, G.C. Pellacani, Inorg. Chim. Acta 158 (1989) 9.

Available online at www.sciencedirect.com
SCIENCE DIRECT®
Polyhedron 24 (2005) 585–591
POLYHEDRON
www.elsevier.com/locate/poly

Syntheses and characterizations of Co(II) and Ni(II) complexes of dihydrobis(thioxotetrazolyl)borato with Co[S_4] and Ni[S_4H_2] cores

Yu-Ling Wang, Rong Cao *, Wen-Hua Bi

State Key Laboratory of Structural Chemistry, Fujian Institute of Research on the Structure of Matter, Chinese Academy of Sciences, Graduate School of the Chinese Academy of Sciences, Yangqiao West Road 155, Fuzhou, Fujian 350002, People's Republic of China

Received 23 November 2004; accepted 17 December 2004

Abstract

The sodium salt of the dihydrobis(1-methyl-5-thiotetrazolyl)borato anion $[Btt^{Me}]^-$ has been synthesized by the reaction of $NaBH_4$ with 1-methyl-5-thiotetrazole. Treatment of $Na[Btt^{Me}]$ with anhydrous $CoCl_2$ and $NiCl_2 \cdot 6H_2O$, respectively, gives the complexes $Co(Btt^{Me})_2$ (**1**) and $Ni(Btt^{Me})_2$ (**2**), which have been characterized by IR, ^1H NMR, ESI-MS, UV–Vis spectroscopy as well as X-ray crystallography. Compound **1** contains a central [CoS_4] core and exhibits a slightly distorted trigonal-bipyramidal coordination geometry with a very weak apical Co···H–B interaction, whereas **2** features a central [NiS_4H_2] core in a distorted octahedral coordination geometry and exhibits relatively strong Ni···H–B interactions. These results indicate that the ligand can act in the bidentate (k^2-S,S) or tridentate (k^3-S,S,BH) mode. The electrochemical behavior of **1** and **2** has also been investigated by cyclic voltammetry.
© 2005 Elsevier Ltd. All rights reserved.

Keywords: Dihydrobis(thioxotetrazolyl)borato; Cobalt(II) complex; Nickel(II) complex; Co[S_4] core; Ni[S_4H_2] core; Electrochemistry

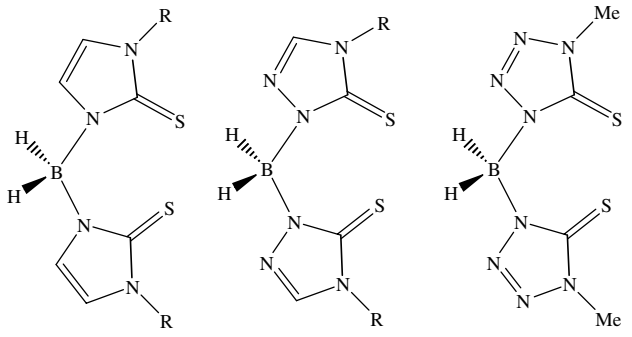
1. Introduction

The soft tripodal ligands Tm and Tt (Tm = hydrotris(thioxoimidazolyl)borato, Tt = hydrotris(thioxotriazolyl)borato) play an important role in coordination chemistry, and their complexes with transition metals have been extensively investigated in recent years as sulfur-rich metalloenzyme models in bioinorganic chemistry [1,2]. Recently, a great deal of attention has focused on the bis-substitution products Bm and Bt (Bm = dihydrobis(thioxoimidazolyl)borato; Bt = dihydrobis(thioxotriazolyl)borato) (Scheme 1) and their metal complexes [3,4]. The soft donor Bm or Bt ligands have also been employed in bioinorganic chemistry to study the structure and reactivity of the active sites of metalloenzymes such as liver alcohol dehydrogenase (LADH) and [NiFe] hydrogenases [3] and in biomedical fields for labelling biomolecules with ^{99m}Tc or $^{186/188}Re$ [4]. To date, the notable examples of this family are $Ni(Bm^{Me})_2$, possessing a central [NiS_4H_2] core, $M(Bm^{Me})_2(CO)_3$ (M = Re or Tc), containing a fac-$[M(CO)_3]^+$ moiety, and $M(Bm^R)_2$ (M = Zn, Cd, Hg), with a central [MS_4] core [3,4]. As previously reported, Bm and Bt can formally act as bidentate ligands through the S atoms. Furthermore, they display agonistic M···H–B interactions toward most transition-metal ions, and this interaction may be influenced by many factors such as the electronic configuration of the metal ions, the substituents of the ligands, the flexibility and conformation of the chelating rings and the nature of the ligating atoms (N or S) [5].

In contrast to the extensively studied Bm and Bt ligands, there is no information on the Btt (Btt = dihydrobis(thioxotetrazolyl)borato) ligand (Scheme 1) and its related metal complexes. In this paper, we report the

* Corresponding author. Tel./fax: +86 591 8379 6710.
E-mail address: rcao@ms.fjirsm.ac.cn (R. Cao).

0277-5387/$ - see front matter © 2005 Elsevier Ltd. All rights reserved.
doi:10.1016/j.poly.2004.12.019



Scheme 1.

syntheses, crystal structures and properties of two complexes, **1** and **2**, of the novel Btt^{Me} (Btt^{Me} = dihydrobis(1-methyl-5-thiotetrazolyl)borato) ligand, which may render models for studying various metalloenzymes derivatives such as Co-LADH [6].

2. Experimental

2.1. Materials and physical measurements

All reagents were commercial reagent grade and used without further purification unless otherwise noted. The solvents CH_3CN and THF were purified and degassed by standard procedures. The synthesis of $Na(Btt^{Me})$ was carried out under N_2 and other reactions were performed in air. The IR spectra were recorded on a Magna750 FT-IR spectrophotometer using KBr pellets from 4000 to 400 cm^{-1}. ^1H NMR spectra were recorded on a Varian UNITY-500 spectrometer (500 MHz). The UV–Vis spectra in CH_3CN solution were measured on a Perkin–Elmer Lambda 900 UV–Vis spectrometer. The electrospray mass spectra (ESI-MS) were run on a Finngan LCQ mass spectrometer using acetonitrile as the mobile phase. Electrochemical experiments were carried out on an Epsilon electrochemical analyzer. Cyclic voltametry (CV) was performed using a conventional three-electrode single compartment cell supplied by BAS Inc. The working electrode was a glassy carbon disc (GCE). The auxiliary electrode was a Pt wire. The reference electrode comprised an Ag wire immersed in acetonitrile solution containing 0.1 M $(Bu_4N)PF_6$ as supporting electrolyte. At the beginning of each experiment a cyclic voltammogram of the solution containing only the supporting electrolyte was measured under nitrogen atmosphere. Then the complexes were added and the resulting complex concentration was ~1 mM. The CV was recorded at a scan rate of 200 mV/s. Formal redox potentials are given vs. the reference system Cp_2Fe/Cp_2Fe^+ in volts.

2.2. Synthesis of the sodium salt of dihydrobis(1-methyl-5-thiotetrazolyl)borato

Under a nitrogen atmosphere 2.32 g of 1-methyl-5-thiotetrazole (20 mmol) and 0.378 g of $NaBH_4$ (10 mmol) were mixed in 30 ml degassed THF solution. The solution was refluxed overnight and the resulting cloudy solution was allowed to cool to room temperature and filtered. The filtrate was concentrated under reduced pressure to 3 ml and the white precipitate formed was washed with CH_2Cl_2 and ether, and then dried in vacuo for 2 h. Yield: 75%. IR data (cm^{-1}): 3070 (w), 2954 (w), 2497 (m), 2480 (m), 1645 (m), 1618 (m), 1510 (m), 1458 (m), 1439 (m), 1392 (s), 1336 (s), 1275 (s), 1196 (s), 1151 (m), 1105 (s), 999 (w), 972 (w), 860 (m), 758 (m), 742 (m), 710 (m), 617 (m), 465 (w). ^1H NMR data: δ 3.72 (s, CH_3). *Anal.* Calc. for $Na(Btt^{Me})$: C, 17.98; H, 3.00; N, 41.95. Found: C, 17.45; H, 2.36; N, 41.69%. UV–Vis (λ/nm ε/$mol^{-1}\,cm^{-1}$): 246 nm (73 900). MS (*m*/*z*, I%): 244, 100 $[Btt^{Me}]^-$.

2.3. Synthesis of $Co(Btt^{Me})_2$ (**1**)

$Na(Btt^{Me})$ 0.11 g (0.4 mmol) and anhydrous $CoCl_2$ 0.026 g (0.2 mmol) were stirred in CH_3OH overnight. The resulting blue precipitate was dissolved in CH_2Cl_2, and hexane was carefully layered over the CH_2Cl_2 solution. After one week blue crystals suitable for X-ray diffraction were obtained. Yield: 53%. IR data (cm^{-1}): 2951 (w), 2472 (m), 2378 (w), 2318 (w), 2291 (w), 1645 (w), 1470 (s), 1425 (s), 1398 (s), 1367 (m), 1364 (s), 1275 (s), 1198 (s), 1147 (m), 1092(m), 1080(m), 1005 (w), 968 (w), 854 (w), 758 (m), 744 (m), 521 (w), 465 (m). *Anal.* Calc. for $C_8H_{16}B_2CoN_{16}S_4$: C, 17.61; H, 2.93; N, 41.09. Found: C, 17.35; H, 2.52; N, 40.71%. ^1H NMR data: δ 3.708 (s, CH_3). UV–Vis (λ/nm ε/$mol^{-1}\,cm^{-1}$): 240 (66 750), 376 (11 120), 565 (750). MS (*m*/*z*, I%): 380, 10, $[Co_2(L)Na]^{4+}$; 545, 12, $[Co(L)_2]^+$; 720, 100, $[Co_3(L)_2(CH_3OH)_2]^{4+}$; 847, 68, $[Co_2(L)_3]^+$.

2.4. Synthesis of $Ni(Bt^{Me})_2$ (**2**)

$Na(Btt^{Me})$ 0.11 g (0.4 mmol) and $NiCl_2 \cdot 6H_2O$ 0.047 g (0.2 mmol) were dissolved in methanol and stirred overnight, and a yellow precipitate was obtained. The product was dissolved in CH_3CN and the resulting solution slowly evaporated in air to give yellow crystals. Yield: 47%. IR data (cm^{-1}): 2951 (w), 2503 (s), 2384 (m), 2276 (s), 2245 (s), 2198 (m), 2017 (w), 1618 (w), 1471 (s), 1419 (s), 1362 (s), 1348 (s), 1277 (s), 1130 (m), 1093 (m), 1068 (m), 1001 (m), 943 (m), 845 (m), 756 (s), 615 (w), 530 (w), 486 (w). *Anal.* Calc. for $C_8H_{16}B_2N_{16}NiS_4$: 17.62; H, 2.94; N, 41.10. Found: C, 17.38; H, 2.63; N, 40.83%. ^1H NMR data: δ 3.715 (s, CH_3). UV–Vis

(λ/nm ε/mol^{-1} cm^{-1}): 246 (60 950); 403 (2490). MS (*m*/*z*, I%): 380, 94, $[Ni_2(L)Na]^{4+}$; 545, 30, $[Ni(L)_2]^{+}$; 567, 58, $[Ni(L)_2Na]^{+}$; 719, 100, $[Ni_3(L)_2(CH_3OH)_2]^{4+}$; 845, 65, $[Ni_2(L)_3]^{+}$.

2.5. X-ray structure determination

X-ray diffraction data were collected on a Bruker P4 diffractometer with a Mercury CCD area detector (Mo Kα; λ = 0.71073 Å) for **1** and on a Siemens Smart CCD area-detector diffractometer (MoKα; λ = 0.71073 Å) for **2**. Empirical absorption correction was applied using the program SADABS [7]. The structures were solved using direct methods and refined by full-matrix least-squares on F^2 with SHELXTL (version 5.10) [8]. Non-hydrogen atoms were refined anisotropically. The hydrogen atoms were placed at their calculated positions except for hydrogen atoms on boron, which were located and refined isotropically for both complexes. The absolute structure of **1** was determined with a Flack parameter of 0.018(10) [9]. Additional information about crystal data collection and refinement parameters for **1** and **2** is presented in Table 1, while selected bond distances and angles are listed in Tables 2 and 3, respectively.

Table 1
Crystallographic data for $Co(Btt^{Me})_2$ and $Ni(Btt^{Me})_2$

	$Co(Btt^{Me})_2$	$Ni(Btt^{Me})_2$
Chemical formula	$C_8H_{16}B_2CoN_{16}S_4$	$C_8H_{16}B_2N_{16}NiS_4$
Formula weight	545.16	544.94
Colour, habit	blue	yellow
Crystal size (mm)	0.28 × 0.25 × 0.20	0.34 × 0.30 × 0.10
Crystal system	orthorhombic	triclinic
Space group	$P2_12_12_1$	$P\bar{1}$
a (Å)	15.451(4)	12.5583(3)
b (Å)	16.422(4)	12.5692(3)
c (Å)	17.474(4)	16.2972(3)
α (°)	90	69.8120(10)
β (°)	90	70.5490(10)
γ (°)	90	89.9820(10)
V (Å^3)	4433.7(18)	2257.47(9)
Z	8	4
F(0 0 0)	2216	1112
D_{calc} (Mg m^{-3})	1.633	1.603
Radiation (λ(Å))	0.71073	0.71073
T (K)	293(2)	293(2)
μ (mm^{-1})	1.185	1.263
Maximum and minimum transmission	0.728 and 0.789	0.644 and 0.881
θ range for data collection (°)	1.000–28.28	0.987–25.02
Measured reflections	36799	11725
Independent reflections	10982	7844
Goodness-of-fit on F^2	1.048	1.037
R_1	0.0385	0.0713
wR_2	0.0799	0.1559
Largest difference peak/hole (e Å^{-3})	0.372 and −0.319	0.472 and −0.536

Table 2
Selected bond lengths (Å) and angles (°) for $Co(Btt^{Me})_2$

Molecule **I**		Molecule **II**	
Bond lengths			
Co1–S1	2.3175(10)	Co2–S5	2.3503(9)
Co1–S2	2.3773(9)	Co2–S6	2.3208(9)
Co1–S3	2.3570(9)	Co2–S7	2.3204(9)
Co1–S4	2.3315(9)	Co2–S8	2.4186(9)
Co1–H1A	2.57(4)	Co2–H3A	2.13(3)
Co1–H2A	2.32(4)	Co2–H4A	2.99(4)
S1–C1	1.697(3)	S5–C9	1.704(3)
S2–C3	1.702(3)	S6–C11	1.703(3)
S3–C5	1.707(3)	S7–C13	1.708(3)
S4–C7	1.699(3)	S8–C15	1.712(3)
B1–H1A	1.12(4)	B3–H3A	1.10(3)
B1–H1B	1.20(4)	B3–H3B	1.09(3)
B2–H2A	1.06(3)	B4–H4A	1.11(4)
B2–H2B	1.16(4)	B4–H4B	1.19(4)
Bond angles			
S1–Co1–S4	140.20(4)	S6–Co2–S7	130.41(4)
S1–Co1–S3	100.94(4)	S6–Co2–S5	115.35(3)
S4–Co1–S3	110.09(3)	S7–Co2–S5	108.03(3)
S1–Co1–S2	107.36(4)	S6–Co2–S8	95.39(3)
S4–Co1–S2	96.22(3)	S7–Co2–S8	106.54(3)
S3–Co1–S2	91.72(3)	S5–Co2–S8	91.58(3)
H1A–B1–H1B	112(2)	H3B–B3–H3A	120(3)
H2B–B2–H2A	112(3)	H4B–B4–H4A	112(3)

Table 3
Selected Bond Lengths (Å) and Angles (°) for $Ni(Btt^{Me})_2$

Molecule **I**		Molecule **II**	
Bond lengths			
Ni1–S1	2.379(3)	Ni2–S5	2.375(3)
Ni1–S2	2.399(3)	Ni2–S6	2.394(3)
Ni1–S3	2.397(3)	Ni2–S7	2.404(3)
Ni1–S4	2.374(3)	Ni2–S8	2.377(3)
Ni1–H1A	1.98(10)	Ni2–H3A	1.87(9)
Ni1–H2A	1.89(10)	Ni2–H4A	1.93(6)
S1–C1	1.707(9)	S5–C9	1.699(9)
S2–C3	1.691(9)	S6–C11	1.677(9)
S3–C5	1.674(9)	S7–C13	1.695(9)
S4–C7	1.705(9)	S8–C15	1.699(9)
B1–H1A	1.09(10)	B3–H3A	1.20(9)
B1–H1B	1.13(10)	B3–H3B	1.22(9)
B2–H2A	1.14(10)	B4–H4A	1.10(10)
B2–H2B	1.11(10)	B4–H4B	1.06(10)
Bond angles			
S4–Ni1–S1	93.19(9)	S5–Ni2–S8	93.28(10)
S4–Ni1–S3	94.80(10)	S5–Ni2–S6	95.51(10)
S1–Ni1–S3	91.62(9)	S8–Ni2–S6	91.72(9)
S4–Ni1–S2	91.62(10)	S5–Ni2–S7	91.77(10)
S1–Ni1–S2	95.41(10)	S8–Ni2–S7	94.69(10)
S3–Ni1–S2	170.20(11)	S6–Ni2–S7	170.00(11)
S4–Ni1–H1A	173(3)	S5–Ni2–H3A	94(3)
S1–Ni1–H1A	94(3)	S8–Ni2–H3A	172(3)
S3–Ni1–H1A	84(3)	S6–Ni2–H3A	89(3)
S2–Ni1–H1A	89(3)	S7–Ni2–H3A	84(3)
S4–Ni1–H2A	93(3)	S5–Ni2–H4A	174(2)
S1–Ni1–H2A	174(3)	S8–Ni2–H4A	92(2)
S3–Ni1–H2A	88(3)	S6–Ni2–H4A	84(3)
S2–Ni1–H2A	84(3)	S7–Ni2–H4A	88(3)
H1A–Ni1–H2A	80(4)	H3A–Ni2–H4A	80(4)
H1A–B1–H1B	113(7)	H3A–B3–H3B	111(6)
H2A–B2–H2B	113(7)	H4A–B4–H4B	117(7)

3. Results and discussion

The procedure of preparing the sodium salt of the dihydrobis(1-methyl-5-thiotetrazolyl)borato anion $[Btt^{Me}]^-$ is similar to that of preparing $Na(Bm^{Me})$ (Bm^{Me} = dihydrobis(thioxoimidazolyl)borato) (Scheme 2) [3a]. Reaction of $Na(Btt^{Me})$ with anhydrous $CoCl_2$ and $Ni(NO_3)_2 \cdot 6H_2O$ (molar ratio 2:1) affords two novel mononuclear complexes $Co(Btt^{Me})_2$ (**1**) and $Ni(Btt^{Me})_2$ (**2**), respectively. Both complexes are soluble in dimethylsulfoxide, acetonitrile and dichloromethane, but insoluble in methanol.

3.1. Crystal structures

X-ray diffraction shows the molecular structures in Figs. 1 and 2. Interestingly, two crystallographically independent molecules are found in the asymmetric unit of **1** and **2**, which are similar in their configuration.

The geometrical parameters of the two independent molecules in the asymmetric unit of **1** are somewhat different from each other (Table 2). The Co–S bond lengths vary from 2.3175(10) to 2.3773(9) Å (Co1) (av. 2.3458 Å) and 2.3204(9) to 2.4186(9) Å (Co2) (av. 2.3525 Å), and the S–Co–S bond angles range from 91.72(3)° to 140.20(4)° (Co1) and 95.39(3)° to 130.41(4)° (Co2). It is noteworthy that **1** has a larger range of S–Co–S bond angles compared with that in previously reported $M(Bm)_2$ complexes (M = Zn, Cd, Hg) (85°–124°), whose coordination geometry around the metal center are slightly distorted tetrahedral [3a]. At a first glance, **1** exhibits a severely distorted tetrahedral geometry in the solid state with a central $[CoS_4]$ core in which the cobalt atom is bound by two Btt^{Me} ligands through four S atoms. The Co1–S2 bond length (2.3773(9) Å) is much longer compared with the other Co–S distances, and the bond angles S2–Co1–S3, S2–Co1–S4 and S2–Co1–S1 are 91.72(3)°, 96.22(3)° and 107.36(4)°, respectively, which are close to 90°. In addition, the S2–Co1–H2A angle

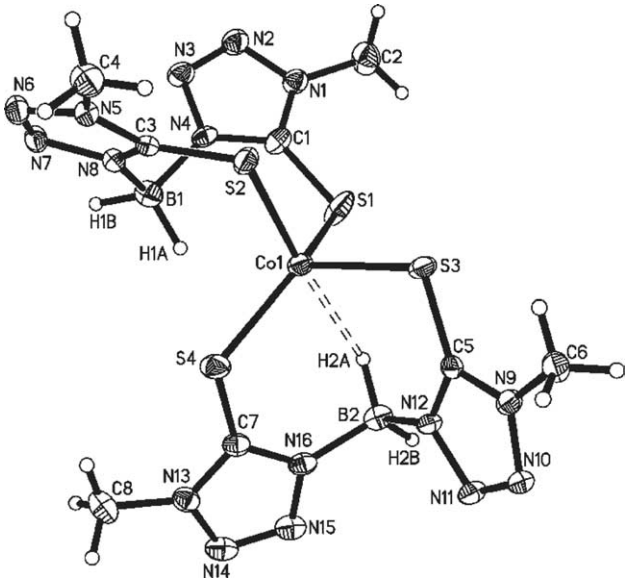


Fig. 1. The ORTEP drawing of molecule I of $Co(Btt^{Me})_2$ with 60% thermal ellipsoids.

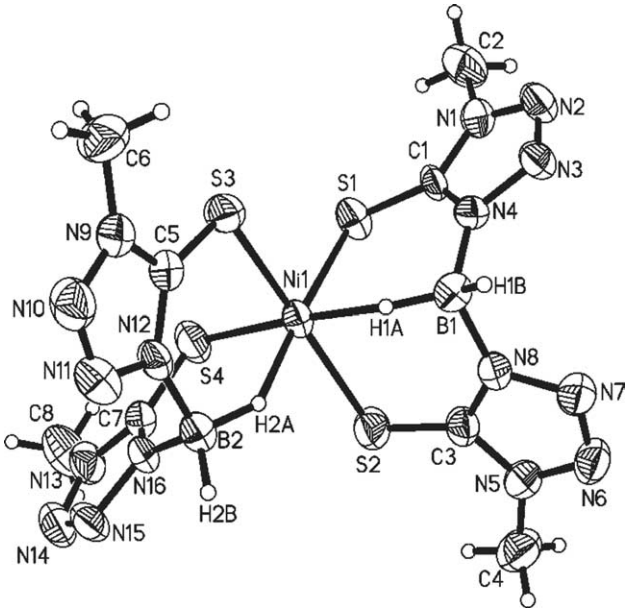
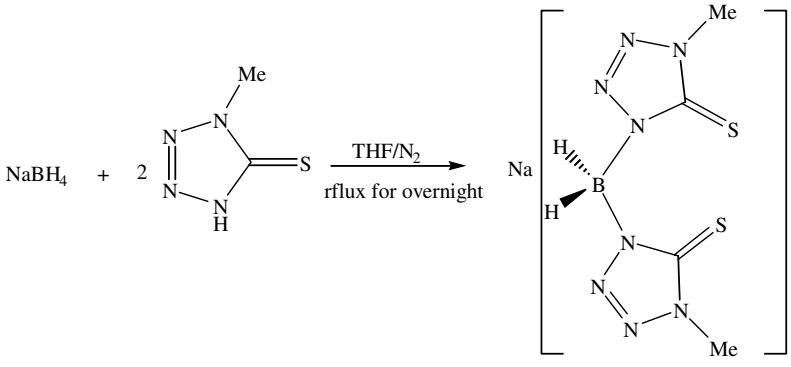


Fig. 2. The ORTEP drawing of molecule I of $Ni(Btt^{Me})_2$ with 50% thermal ellipsoids.



Scheme 2.

(172.0°) is close to the theoretical value of 180° for a trigonal bipyramid. These parameters indicate that the overall geometry around the Co1 atom should be best considered as a distorted trigonal bipyramid, if the very weak Co1···H2A–B2 interaction is taken into account. Interestingly, if the other weaker Co1···H1A–B1 interaction is further considered, the coordination geometry around Co1 can also be described as highly distorted octahedral. The coordination geometry around the Co2 atom is somewhat similar to that around the Co1 atom, however, the long distance of Co2–H4A (2.99(4) Å) indicates no interaction between Co2 and H4A. Hence, only a trigonal-bipyramidal coordination geometry of Co2 should be considered, with the axial bond angle S8–Co2–H3A being 173.6°, and the bond angles S8–Co2–S5, S8–Co2–S6 and S8–Co2–S7 being 91.58(3)°, 95.39(3)° and 106.54(3)°, respectively. The Co–H distances are 2.57(4) (Co1–H1), 2.32(4) (Co1–H2), 2.13(3) (Co2–H3) and 2.99(4) (Co2–H4) Å, respectively, which are much longer than that found in other borohydrido Co derivatives such as $Co(Tm^{Ph})_2$ [Co–H = 2.11(3) Å], $Co(pzBm^{Me})_2$ [(Co–H) = 1.95 Å] and $Co(Bp^{But,Pri})_2$ [(Co–H) = 1.95 Å] (Bp = dihydrobis(pyrazoly)borato) [10–12].

In the crystal structure of complex **2**, the geometrical parameters of the two independent molecules in the asymmetric unit are almost identical within experimental error. The most notable feature of **2** is that it contains a central $[NiS_4H_2]$ core, and the coordination geometry around the Ni atom is described as distorted octahedral, surrounded by four S atoms and two H atoms from two Btt^{Me} ligands with two relatively strong Ni···H–B interactions in which the two borohydrido groups are in a *cis* arrangement. From this viewpoint, the Btt^{Me} ligand acts as an S, S, H tripod. The structure of **2** is similar to that of the closely related nickel complexes $Ni(Bm)_2$ and $Ni(Bt)_2$ [3b,5]. The Ni–H distances are 1.98(10) (Ni1–H1), 1.89(10) (Ni1–H2), 1.87(9) (Ni2–H3) and 1.93(6) (Ni2–H4) Å, which are somewhat longer than that found in $Ni(Bm)_2$ (Ni–H = 1.863 Å) and $Ni(Bt)_2$ (av. Ni–H = 1.86 Å) [3b,5]. The Ni–S bond lengths are slightly different from each other, with those *trans* to the borohydrido groups being slightly shorter than the axial ones.

These different Ni···H and Co···H interactions result that the Btt^{Me} ligands in **1** adopt a 'boat-like' eight-membered ring configuration and in **2** the Btt^{Me} ligands adopt a 'twist' eight-membered ring configuration.

3.2. Infrared spectroscopy

In the IR spectra of the ligand, two medium absorptions at 2497 and 2480 cm^{-1} show the typical B–H stretching vibrations. For complex **1**, the medium absorption at 2472 cm^{-1} can be assigned to a terminal B–H stretching vibration and two weak absorptions at 2378 and 2318 cm^{-1} are indicative of a weak Co···H–B interaction. In the infrared spectrum of **2**, the corresponding bands are at 2550–2350 and 2300–2200 cm^{-1}, respectively. Compared with **1**, the absorption intensity of the B–H bond at low frequency is much greater than that of the corresponding one in **1**, and the result is attributable to the relatively strong Ni···H–B interaction. These are in good agreement with the crystal analytical results.

3.3. Electra spectra

In the UV–Vis spectra of **1** and **2** in CH_3CN solution, the absorptions [λ/nm ε/mol^{-1} cm^{-1}] at 240 (66 750) for **1** and 246 (60 950) for **2** display π–π^* transitions for the coordinated Btt^{Me} ligands, based on the absorption at 246 (73 900) in the spectra of the uncoordinated ligands. The absorption observed at 376 (11 120) in the UV–Vis spectrum of **1** can be assigned to the charge transfer from the ligands to the Co(II) center [6] and the absorption at 565 (750) to a d–d transition [13]. The position of the 376 nm absorption is higher in energy than the band of similar intensity found in $Co(PhTt)_2$ (380 (7400)) (PhTt = phenyltris(methylthio)methylborate) [14]. For **2**, the absorption at 403 (2490) may be associated with the d–d transition [$^3A_{2g}(F) \rightarrow {}^3T_{1g}(P)$] in an octahedral field for a d^8 ion [5], with an energy which is comparable with that observed in the related complex $Ni(Bt)_2$ (417 (1120)) [5].

3.4. Electrochemistry

Electrochemical data of $Na(Btt^{Me})$ and complexes **1** and **2** are summarized in Table 4. The cyclic voltammogram of $Na(Btt^{Me})$ in acetonitrile revealed one irreversible oxidation peak at +0.47 V and one irreversible reduction peak at –1.83 V (vs. Cp_2Fe/Cp_2Fe^+). Figs. 3 and 4 display the cyclic voltammograms of **1** and **2**, respectively. As shown in Fig. 3, a scan initiated in the negative direction reveals an irreversible reduction at

Table 4
Electrochemical data

Complex	E^f (V)	ΔE_p (mV)	$I_{p,ox}/I_{p,red}$	
$Na(Btt^{Me})$	+ 0.47			irrev
	−1.83			irrev
$Co(Btt^{Me})_2$	−1.56			Irrev
	−0.23			irrev
	+0.45			irrev
	0.78	142	1.1	quasi-rev
$Ni(Btt^{Me})_2$	−1.11			irrev
	+0.45			irrev
	+0.75	131	0.73	quasi-rev

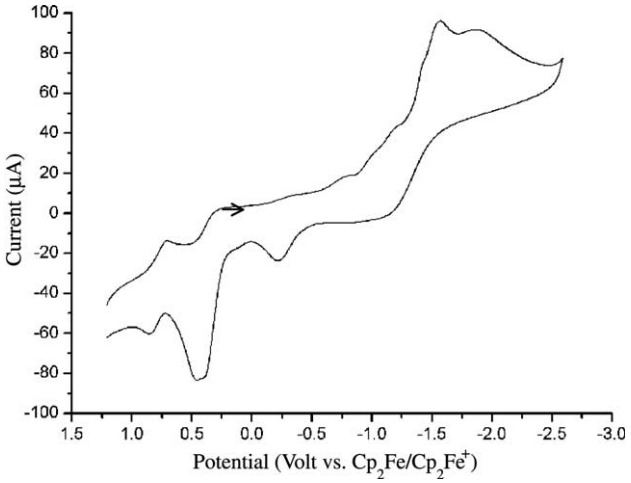


Fig. 3. Cyclic voltammogram of $Co(Btt^{Me})_2$ in 0.1 M TBAP-CH_3CN at a glassy-carbon electrode with a scan rate of 200 mV/s.

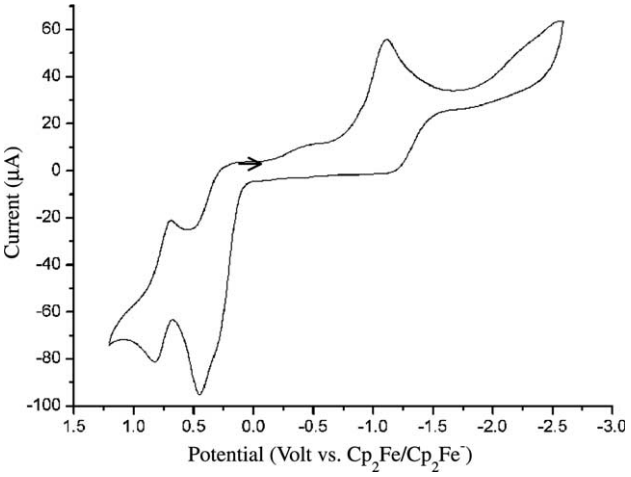


Fig. 4. Cyclic voltammogram of $Ni(Btt^{Me})_2$ in 0.1 M TBAP-CH_3CN at a glassy-carbon electrode with a scan rate of 200 mV/s.

−1.56 V of **1**. Then, an irreversible oxidation at −0.23 V of the reductive product of **1** is observed. It is noted that the irreversible oxidation at 0.45 V should be assigned to the oxidation of the coordinated Btt^{Me} ligands, for the oxidation potentials in **1** and the free ligand are nearly identical. Finally, a quasi-reversible redox process at +0.78 V is observed, which should be contributed to a metal-based quasi-reversible redox process.

Compared with **1**, complex **2** displays similar cyclic electrochemical behavior. An irreversible reduction of **2** at −1.11 V is observed. The irreversible oxidation of the coordinated ligands at +0.48 V is also indicative of the oxidation of the coordinated Btt^{Me} ligands. A metal-based quasi-reversible redox process at +0.75 V is also observed. However, the related complex $Ni(Bm)_2$ exhibits irreversible oxidation [2b].

4. Supplementary materials

Crystallographic data for the structures are available from the Cambridge Crystallographic Data Centre (CCDC Nos. 248456 and 248278 for compounds $Co(Btt^{Me})_2$ and $Ni(Btt^{Me})_2$, respectively). These data can be obtained free of charge via www.ccdc.cam.ac.uk/data_request/cif, by emailing data_request@ccdc.cam.ac.uk, or by contacting The Cambridge Crystallographic Data Centre, 12, Union Road, Cambridge CB2 1EZ, UK; fax: +44 1223 336033.

Acknowledgements

We give thanks for the financial support from the State Key Basic Project (001CB108906) and the National Natural Science Foundation of China (20325106), the Natural Science Foundation of Fujian Province (B982003), and the "one-hundred Talent" Project from CAS.

References

[1] (a) C. Kimblin, B.M. Bridgewater, D.G. Churchill, G. Parkin, Chem. Commun. (1999) 2301;
(b) B.M. Bridgewater, T. Fillebeen, R.A. Friesner, G. Parkin, J. Chem. Soc., Dalton Trans. (2000) 4494;
(c) J. Reglinski, M. Garner, I.D. Cassidy, P.A. Slavin, M.D. Spicer, D.R. Armstrong, J. Chem. Soc., Dalton Trans. (1999) 2119;
(d) C. Kimblin, T. Hascall, G. Parkin, Inorg. Chem. (1997) 2580;
(e) M. Tesmer, M.H. Shu, H. Vahrenkamp, Inorg. Chem. (2001) 4022;
(f) I. Cassidy, M. Garger, A.R. Kennedy, G.B.S. Potts, J. Reglinski, P.A. Slavin, M.D. Spicer, Eur. J. Inorg. Chem. (2002) 1235;
(g) S. Bakbak, C.D. Incarvito, A.L. Rheingold, D. Rabinovich, Inorg. Chem. 41 (2002) 998.
[2] (a) M. Careri, L. Elviri, M. Lanfranchi, L. Marchiò, M.A. Pellinghelli, Inorg. Chem. 42 (2003) 2109;
(b) M. Lanfranchi, L. Marchiò, C. Mora, M.A. Pellinghelli, Inorg. Chimi. Acta 357 (2004) 367.
[3] (a) H.M. Alvarez, T.B. Tran, M.A. Richter, D.M. Alyounes, D. Rabinovich, Inorg. Chem. 42 (2003) 2149;
(b) H.M. Alvarez, M. Krawiec, B.T. Donovan-merkert, M. Fouzi, D. Rabinovich, Inorg. Chem. 40 (2001) 5736.
[4] (a) R. Garcia, A. Paulo, Ñngela Domingos, I. Santos, R. Alberto, J. Am. Chem. Soc. 132 (2000) 11240;
(b) R. Garcia, Ñngela Domingos, A. Paulo, I. Santo, R. Alberto, Inorg. Chem. 41 (2002) 2422;
(c) R. Garcia, A. Paulo, Ñngela Domingos, I. Santos, J. Organomet. Chem. 632 (2001) 41.
[5] R. Cammi, M. Lanfranchi, L. Marchiò, C. Mora, C. Paiola, M.A. Pellinghelli, Inorg. Chem. 42 (2003) 1769.
[6] D. Swenson, N.C. Baenziger, D. Coucouvanis, J. Am. Chem. Soc. 110 (1978) 1932.
[7] Area-Detector Absorption correction; Siemens Industrial Automation, Inc., Madison, WI, 1996.

[8] G.M. Sheldrick, SHELXTL. Version 5.1, Bruker AXS Inc., Madison, WI, USA.
[9] H.D. Flack, Acta Crystallogr., Sect. A 39 (1983) 876.
[10] C. Kimbin, D.G. Churchill, B.M. Bridgewater, J.N. Girard, D.A. Quarless, G. Parkin, Polyhedron 20 (2001) 1891.
[11] C. Kimbin, B.M. Bridgewater, D.G. Churchill, T. Hascall, G. Parkin, Inorg. Chem. 39 (2000) 4240.
[12] P. Ghosh, J.B. Bonanno, G.J. Parkin, J. Chem. Soc., Dalton Trans. (1998) 2779.
[13] A. Bernalte-García, F.J. García-Barros, F.J. Higes-Rolando, F. Luna-Giles, Polyhedron 24 (2001) 3315.
[14] C. Ohrenberg, P. Ge, P. Schebler, C.G. Riordan, G.P.A. Yap, A.L. Rheingold, Inorg. Chem. 35 (1996) 749.

Available online at www.sciencedirect.com
SCIENCE DIRECT®
Polyhedron 24 (2005) 593–599
POLYHEDRON
www.elsevier.com/locate/poly

Polymethylene spacer regulated structural divergence in cadmium complexes: Unusual trigonal prismatic and severely distorted octahedral coordination

Suparna Banerjee [a], Ashutosh Ghosh [a,*], Biao Wu [b], Paul-Gerhard Lassahn [b], Christoph Janiak [b,*]

[a] Department of Chemistry, University College of Science and Technology, University of Calcutta, 92, A.P.C. Road, Kolkata 700 009, India
[b] Institut für Anorganische und Analytische Chemie, Universität Freiburg, Albertstr. 21, 79104 Freiburg, Germany

Received 5 September 2004; accepted 3 January 2005

Abstract

Chelation of the tetradentate pyridyl di-Schiff-base ligands, *N*,*N*′-bis-(1-pyridin-2-yl-ethylidene)-propane-1,3-diamine (L^1) or *N*,*N*′-bis-(1-pyridin-2-yl-ethylidene)-ethane-1,2-diamine (L^2) to a cadmium(II) centre reveals interesting structural deviations from regular octahedral geometry in the resulting hexacoordinated complexes $[Cd(L^1)(NCS)_2]$ (**1**) and $[Cd(L^2)(NCS)_2]$ (**2**), respectively. The two tetradentate ligands L^1 and L^2 differ only in the polymethylene chain – $(CH_2)_3$ and $(CH_2)_2$, respectively, which connects the two halves of the symmetric ligands. Complex **1** assumes a trigonal prismatic (TP) geometry. The structure of **2** reveals a severely distorted octahedral geometry. The structural differences between $[Cd(L^1)(NCS)_2]$ (**1**) and $[Cd(L^2)(NCS)_2]$ (**2**) can be traced to the length of the polymethylene spacers and the formation of a six- versus a five-membered metal-chelate ring together with the pyramidal $Cd(L^1)$ and planar $Cd(L^2)$ arrangement.
© 2005 Elsevier Ltd. All rights reserved.

Keywords: Di-Schiff-bases; Cadmium complexes; Trigonal prism; Distortion; Chelate effect

1. Introduction

Octahedral coordination geometries are ubiquitous as the fundamental geometries of transition metal hexacoordinated complexes. Non-octahedral structures can be realized by considering a trigonal twist about the threefold axis of the octahedron (twist angle $\phi = 60°$) with a trigonal prismatic (TP) stereochemistry at $\phi = 0°$ (cf. Scheme 1). TP coordination was first observed [1] for the layer lattices of heavy metal sulphides (MoS_2 and WS_2) but could only be rationalized as peculiarities of the solid state. Structural authentication of a TP geometry in a discrete molecule was first available in the year 1965 and the concerned work of Eisenberg and Ibers [2] merits paramount importance from a chemical point of view. The breakthrough was then followed by a good number of structurally characterized TP complexes in cases of various 3d, 4d and 5d transition metals under differing ligand environments. Scrutiny of the underlying aspects in favour of TP coordination with much regard to electronic and steric influences of metals and ligands had started earlier [3–12]. Later on, theoretical analyses, i.e., ab initio calculations at the DFT level [13–17], ligand field-based models [18] and continuous symmetry measures [19] efficiently correlated the experimental findings and, of course, provided a sophisticated perspective of optimized structure–energy relationships.

* Corresponding authors. Tel.: +91 33 23599298; fax: +91 33 3519755 (A. Ghosh).
E-mail addresses: ghosh_59@yahoo.com (A. Ghosh), janiak@unifreiburg.de (C. Janiak).

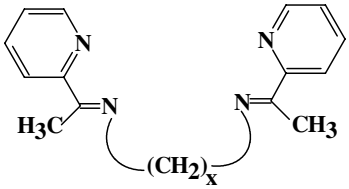
0277-5387/$ - see front matter © 2005 Elsevier Ltd. All rights reserved.
doi:10.1016/j.poly.2005.01.005

The trigonal prismatic geometry for a metal ion with a d^{10} electronic configuration is not unexpected as there is no crystal field stabilization energy. In Zn(II) complexes, the TP geometry has been previously established [20,21]. A perfectly prismatic structure of Cd(II) was found in the potassium salt of the tris(acetylacetonato) complex [22], and distorted trigonal prisms were observed with other ligands such as nitrates, carboxylates, triamines, oxalato and a derivative of triazacyclononane [23,24]. However, to the best of our knowledge no TP geometry with a neutral, tetradentate Schiff-base ligand has been reported up to date. Herein we describe a neutral trigonal prismatic cadmium complex of the formula $[Cd(L^1)(NCS)_2]$ incorporating the tetradentate ligand *N*,*N*′-bis-(1-pyridin-2-yl-ethylidene)-*propane*-1,3-diamine (L^1). Use of the closely related ligand *N*,*N*′-bis-(1-pyridin-2-yl-ethylidene)-*ethane*-1,2-diamine (L^2) in the complex $[Cd(L^2)(NCS)_2]$ resulted in a severely distorted octahedral geometry. The structural differences are investigated in terms of conformational requirements of the ligands.

2. Results and discussion

2.1. Synthesis of the ligands and complexes

Facile condensation of 2-acetylpyridine with 1,3-diaminopropane or 1,2-diaminoethane in a 2:1 molar ratio furnished the two neutral tetradentate ligands *N*,*N*′-bis-(1-pyridin-2-yl-ethylidene)-propane-1,3-diamine (L^1) and *N*,*N*′-bis-(1-pyridin-2-yl-ethylidene)-ethane-1,2-diamine (L^2), respectively.



x = 3, L = L^1
x = 2, L = L^2

$$Cd(OAc)_2\cdot 2H_2O + L + 2NH_4SCN \xrightarrow[\text{magnetic stirring}]{\text{dry methanol}} [Cd(L)(NCS_2)]\downarrow + 2NH_4OAc + 2H_2O \quad (1)$$

L=L^1, **1**
L=L^2, **2**

At ambient temperature, reaction of L with $Cd(OAc)_2\cdot 2H_2O$ in dry methanol in the presence of NH_4SCN yielded two neutral cadmium complexes, **1** and **2** (Eq. (1)). The products were insoluble in the reaction medium and were isolated in the pure form via filtration.

2.2. Bonding and geometrical features

Compound **1** is a molecular complex with the tetradentate chelating *N*,*N*′-bis-(1-pyridin-2-yl-ethylidene)-propane-1,3-diamine ligand and two terminal (N-bound) isothiocyanato groups around the cadmium centre. Thus each cadmium atom is coordinated by six nitrogen donors, two from the *cis*-arranged NCS groups and four from the organic ligand. A molecular view and selected bond parameters of **1** are displayed in Fig. 1 and Table 1, respectively. A mirror plane passes through the molecule which contains Cd1, C9 and the two NCS groups and relates the two halves of the organic ligand. Significant distortion from classical octahedral towards TP geometry is clearly revealed in the molecular structure. An idealized octahedron is made up with two exactly parallel, staggered equilateral triangles of side *s* with an inter-triangular distance *h* (Scheme 1). Evaluation

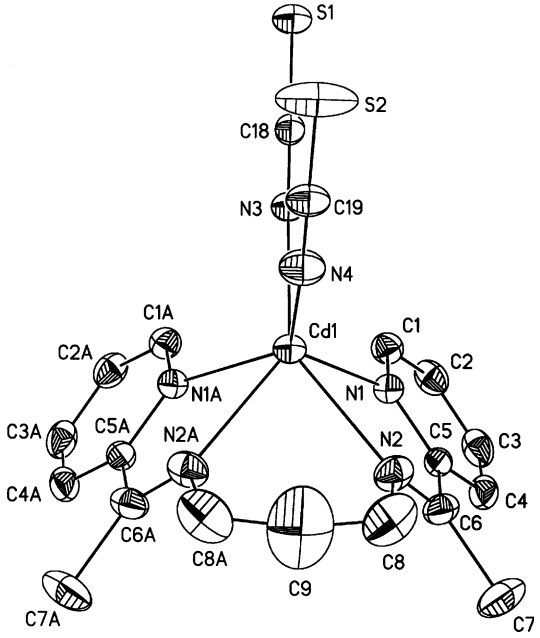
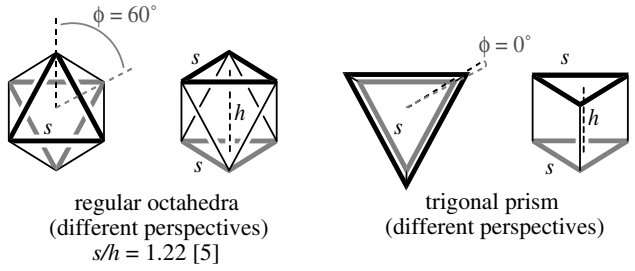


Fig. 1. Perspective view and atom labelling scheme of **1**. All the non-hydrogen atoms are represented by 20% thermal probability ellipsoids.

Table 1
Selected bond distances (Å) and angles (°) for compound $[Cd(L^1)(NCS)_2]$ (**1**)

Distances			
Cd(1)–N(1)	2.358(2)	Cd(1)–N(4)	2.255(4)
Cd(1)–N(2)	2.393(2)	Cd(1)–N(1A)	2.358(2)
Cd(1)–N(3)	2.316(3)	Cd(1)–N(2A)	2.393(2)
Angles			
N(4)–Cd(1)–N(3)	84.97(13)	N(3)–Cd(1)–N(1)	86.63(8)
N(1)–Cd(1)–N(2)	68.45(8)	N(3)–Cd(1)–N(2)	142.46(7)
N(4)–Cd(1)–N(2)	93.11(9)	N(2)–Cd(1)–N(2A)	75.05(13)
N(4)–Cd(1)–N(1)	134.92(5)	N(1)–Cd(1)–N(1A)	88.47(10)

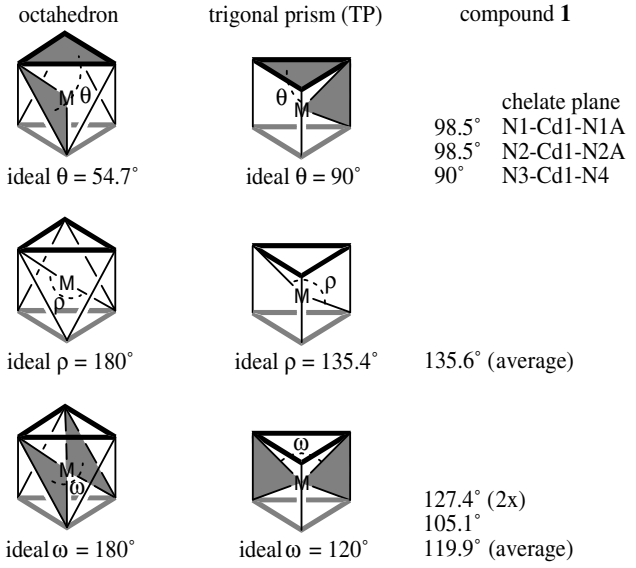


Scheme 1. Octahedron and trigonal prism with enhanced triangular faces and relevant parameters for the assessment of their relationship and distortion. ϕ is the twist angle between the enhanced triangles around the C_3 axis.

of the *s*/*h* ratio and twist angle (ϕ) value for the hexacoordinated complexes provides a measure of trigonal distortion [5].

The CdN_6 coordination sphere in **1** can be described as being constituted of two triangles (N3, N1, N1A and N4, N2, N2A) with an average side (*s*) of 3.228 Å. These two N_3 triangles are slightly tilted with a dihedral angle of 8.8° and an inter-triangular separation between the centroids of 2.802 Å (*h*). A view of the $Cd1N_6$ motif showing the twist angles ϕ is represented in Fig. 2. The torsion angles N–C_n–C_n'–N′ (C_n, C_n' = centroids of the two N_3 triangles; N, N′ = near eclipsed pair of donor atoms) of 0°, 6° and 6° are fairly close to the twist angle of a regular TP geometry (ϕ = 0°). The average twist angle of 4° in **1** is similar to the trigonal prismatic complex Zn[(py)$_3$tach] [20]. The *s*/*h* ratio in **1** is 1.15 indicating an elongation relative to an ideal trigonal prism with square faces (*s* = *h*, *s*/*h* = 1.00). Consideration of the angular parameters θ, ρ and ω (Scheme 2) in the comparison between octahedral and trigonal prismatic limiting structures clearly indicates that compound **1** can be regarded as a trigonal prism (see parameters for **1** in Scheme 2).

A molecular view of [Cd(L^2)(NCS)$_2$] (**2**) with the tetradentate ligand *N*,*N*′-bis-(1-pyridin-2-yl-ethylidene)-ethane-1,2-diamine (L^2) (with a shorter dimethylene spacer in place of L^1) is depicted in Fig. 3 and selected



Scheme 2. Angular parameters involved in the comparison between the octahedral and trigonal prismatic limiting structures. θ = angle between the mean plane of the two N_3 triangles and the chelate planes defined by the metal and each pair of near eclipsed N vertices. ρ = angle between the metal and *trans* N-donor sites. ω = angle between the triangular faces defined by the metal and near eclipsed N atoms.

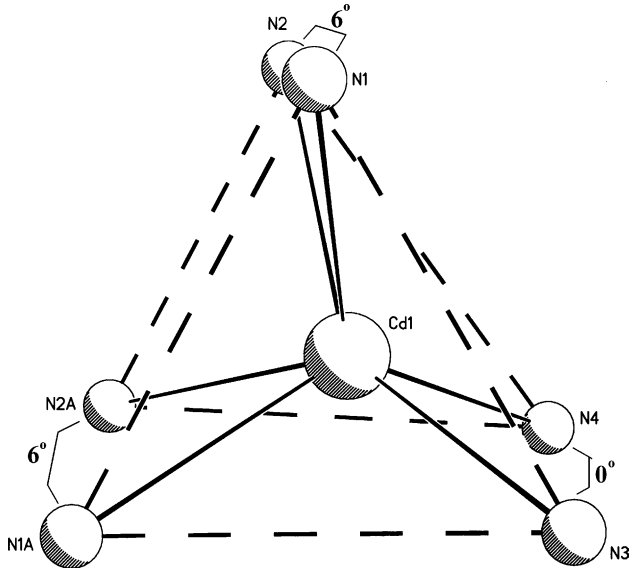


Fig. 2. ORTEP view of the CdN6 coordination sphere of **1** showing all the individual twist angles. Non-bonded N···N distances (Å): N1···N1A···N3 triangle N1/N1A···N3 3.206, N1···N1A 3.290; N2···N2A···N4 triangle N2/N2A···N4 3.376, N1···N1A 2.915.

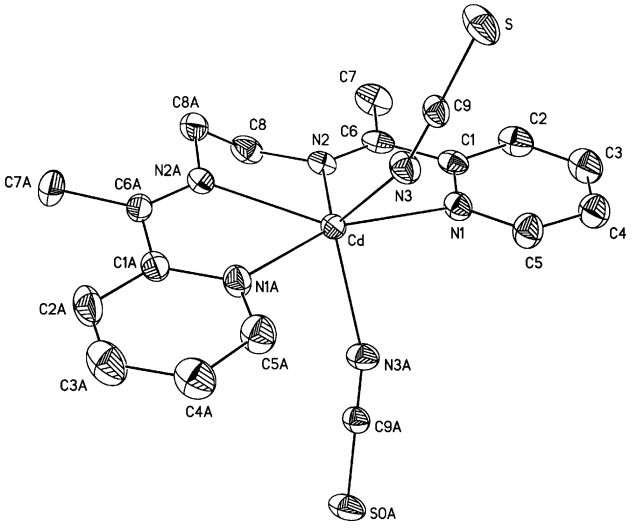


Fig. 3. Perspective view and atom labelling scheme of **2**. All the non-hydrogen atoms are represented by 20% thermal probability ellipsoids.

bond parameters are listed in Table 2. The CdN_6 coordination sphere is strongly distorted from an octahedron with a crystallographic twofold symmetry axis passing through the metal atom and the midpoint of the C8–C8A bond of L^2. The six nitrogen atoms in **2** at an average distance of 2.356 Å define a polyhedron that is neither close to the octahedral nor the TP geometry. The structure may be imagined to consist of two symmetry related N_3 triangles (N1, N2, N3 and N1A, N2A, N3A) with an average side (s) of 3.246 Å and separated by a distance (h) of 2.786 Å. Then the s/h ratio of ~1.17 (<1.22) indicates an elongated octahedral structure. The triangular twist angle ϕ measured at the donor atoms N1, N3A or N1A, N3 is only 8.3° with the imaginary C_3 axis passing through the centroids of the imagined triangles. Such a small angle would be close to the prismatic limit ($\phi = 0°$, Scheme 1). Yet, the third donor set N2, N2A is twisted by 41.3° about the threefold axis towards the octahedral extreme (60°). The average *trans* angles ∠N1–Cd–N1A and ∠N3–Cd–N3A at ~133° are also close to the prismatic limit ($\rho = 135.4°$, Scheme 2). The deviation in **2** mimics the benzenedithiolato-chelated d^0–Ta(V) ion [25] where an average twist angle ϕ of 19.3° also indicated a significant departure from a regular octahedral coordination. In **2** the average dihedral angle θ of 59.8° is closer to an octahedral than to a TP geometry. Dihedral angles ω between the individual CdN_2 planes are averaged at only 60.3°, consistent with severe distortion.

2.3. Comparison of ligand binding in *1* and *2*

In the following the structural divergence in the cadmium complexes **1** and **2** will be comparatively discussed on the basis of the geometrical selectivity and bonding aspects of the concerned ligands.

(i) The Cd(L^1) moiety in **1** defines a square pyramidal geometry. The metal atom is displaced upward by ~1.2 Å from the plane comprised of the L^1 donor atoms N1, N2, N2A and N1A. This does not allow the coordination polyhedron to be completed to an octahedron via the $(NCS)_2$ coordination. In **2** the metal atom along with the L^2 donor atoms N1, N2, N2A and N1A constitutes a planar arrangement (mean deviation = 0.09 Å) and would welcome the two NCS groups to complete a close to octahedral geometry. The two Cd(L) situations are portrayed by space-filling models represented in Fig. 4. It is well known that chelate ligands giving rise to a five-membered chelate ring (e.g. an N–C–C–N ligand moiety) are better suited for larger metal ions whereas a chelate ligand yielding a six-membered chelate ring (e.g. an N–C–C–C–N ligand moiety) is better for smaller metal ions [26]. This assumes the metal ion at the intersection of the N lone-pairs and the chelate ring near its energy minimum. Thus, the N–C–C–C–N ligand moiety simply cannot accommodate the large Cd ion within its plane. The N lone-pairs and with it the pyridylimine moieties are tilted out of the N–C–C–C–N plane, so that the TP structure results (Fig. 4). On the other hand, the N–CH_2–CH_2–N ligand moiety in compound **2** is much better suited for accommodating the large Cd ion in the plane of a five-membered chelate ring. Therefore, the tetradentate ligand in compound **2**, with its five-membered chelate rings could span the equatorial plane in a distorted octahedral geometry.

(ii) The ratio of the ligand bite (b = distance between the donor atoms) to the average Cd1–N distance (a) in **1** is not compatible with the chelate being able to span the edge of the octahedron ($b/a = 1.41$ for the ideal octahedron). In **1** the bite

Table 2
Selected bond distances (Å) and angles (°) for compound $[Cd(L^2)(NCS)_2]$ (**2**)

Distances			
Cd–N(1)	2.460(3)	Cd–N(2)	2.372(3)
Cd–N(3)	2.236(3)		
Angles			
N(3)–Cd–N(3A)	109.83(18)	N(1)–Cd–N(1A)	156.01(17)
N(3)–Cd–N(2)	120.99(12)	N(2)–Cd–N(2A)	70.99(16)
N(3)–Cd–N(2A)	114.90(11)	N(3)–Cd–N(1A)	85.02(11)
N(3)–Cd–N(1)	81.25(11)	N(2)–Cd–N(1A)	137.03(12)
N(2)–Cd–N(1)	66.84(12)		

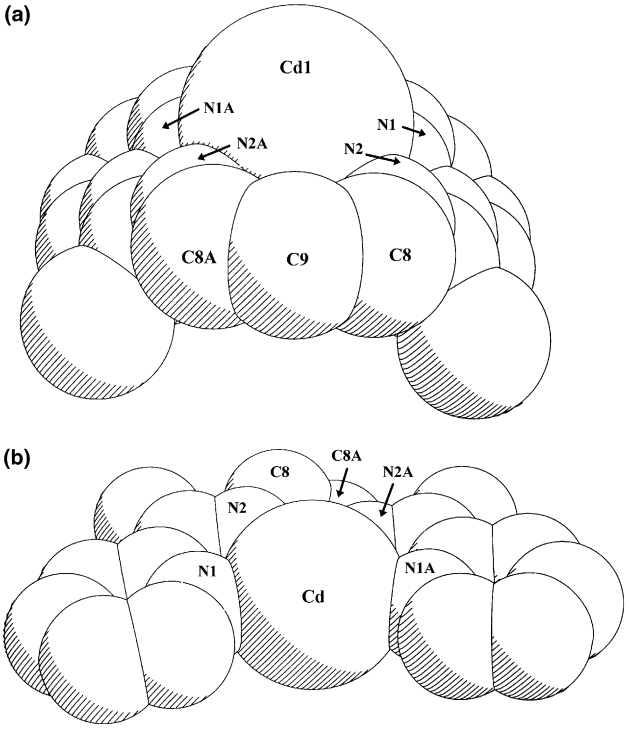


Fig. 4. Space-filling model of metal–L moiety for **1** (a) and **2** (b).

is quite short (b/a = 1.24) and L^1 encapsulates the metal atom in a TP fashion (b/a = 1.31 for ideal TP). In **2** the ratio (b/a = 1.37) is much closer to the octahedral limit.

(iii) In complex **1** the intermolecular packing along the crystallographic *b*-direction is controlled by π-stacking interactions [27] between the pyridyl planes (Figs. 5(a) and (b)). The overlapping ring planes are related by a center of inversion, thus, are exactly parallel. The ring slippage has a slip angle of 24.6° and a vertical displacement between the ring centroids of 1.58 Å (centroid separation 3.796 Å, interplanar distance 3.45 Å). [27,28]. The shortest overlapping carbon contact C5-C1[3] is 3.45 Å. Therefore, the π-stacking in **1** corresponds closely to strong π-interactions which are classified by centroid–centroid contacts <3.8 Å, slip angles <25° and vertical displacements <1.5 Å [27]. On the other hand, the intermolecular packing in **2** exhibits only very weak π-stacking interactions between the pyridyl planes deduced by rather long centroid–centroid distances (>4.2 Å), large interplanar distances (>3.65 Å) together with large slip angles (=30°) and vertical displacements (>2.1 Å) between the ring centroids [27].

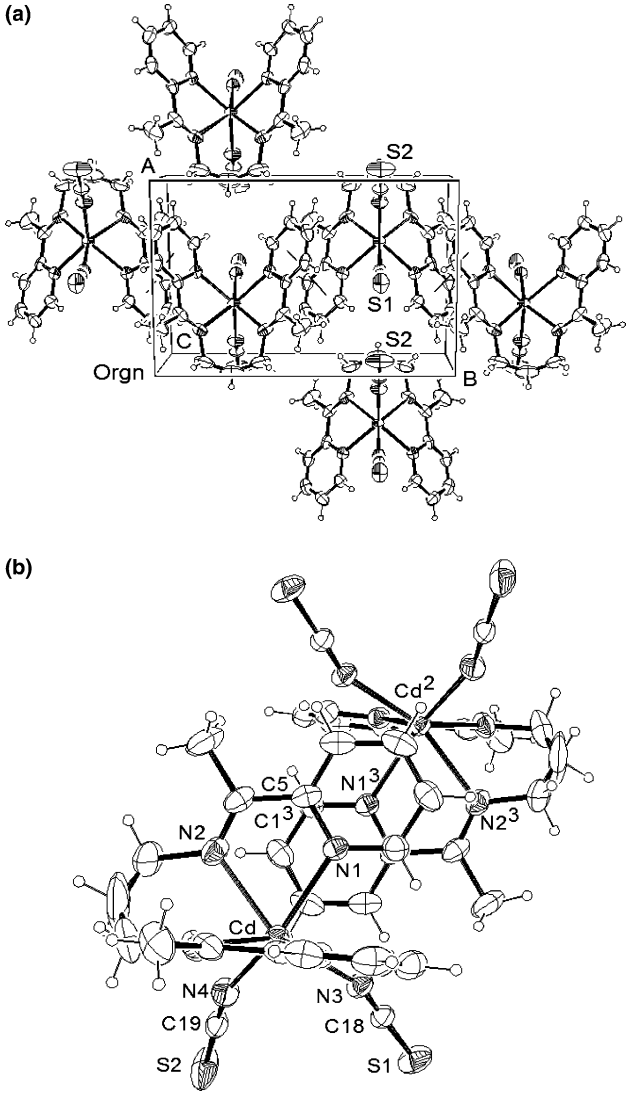


Fig. 5. (a) Intermolecular π-stacking (thin lines) along *b* in **1**. (b) Perpendicular view of the π-overlap between two molecules to show the typical ring slippage; symmetry transformation [2] = 1 − *x*, y − 1/2, 1 − *z*; [3] = 1 − *x*, 1 − *y*, 1 − *z*.

2.4. ^1H NMR spectra

The ^1H NMR spectrum of diamagnetic $[Cd(L^1)(NCS)_2]$ (**1**), in DMSO–d_6 at room temperature exhibits sharp singlets at δ = 3.92 and 2.36 ppm due to six methylene protons which is fully consistent with the crystallographically imposed mirror symmetry. The eight pyridyl proton signals do not exhibit spin structure and appear as broad singlets at 8.95, 8.29 and 7.83 ppm with the relative intensities 1:2:1. The methyl resonance is observed at 2.46 ppm as a sharp singlet as expected.

The ^1H NMR spectrum of $[Cd(L^2)(NCS)_2]$ (**2**), in DMSO–d_6 at room temperature revealed well resolved spin-spin structures for the pyridyl protons in the domain of 8.82–7.43 ppm. The methylene proton resonance appeared as a singlet at 3.84 ppm, in agreement with the presence of a twofold axis bisecting the C–C bond of the dimethylene moiety of the ligand. Like **1**, the methyl resonance was observed as a sharp singlet at 2.42 ppm.

3. Experimental

3.1. Materials and measurements

$Cd(OAc)_2 \cdot 2H_2O$, 2-acetylpyridine and 1,3-diaminopropane were purchased from Fluka AG (Switzerland). Ammonium thiocyanate and 1,2-diaminoethane were obtained from S.D. Fine Chemicals (India). Reagent grade solvents were distilled and dried by standard methods and were used for all reactions. Spectral measurements were carried out using the following equipment: IR (KBr disc), Perkin–Elmer RXI FT-IR spectrometer; ^1H NMR (DMSO–d_6, s = singlet, d = doublet, t = triplet), Bruker 300 MHz FT NMR, FAB Mass spectra JEOL JMS 600 spectrometer. A Perkin–Elmer 2400 Series II elemental analyzer was used for microanalysis (C, H, N).

3.2. Preparations

3.2.1. Ligands

L^1: 1,3-Diaminopropane (1.11 g, 15 mmol) and 2-acetylpyridine (3.63 g, 30 mmol) were refluxed in 30 mL of dry methanol for 8 h. The resulting solution

was evaporated under reduced pressure to obtain a yellowish-brown semi-solid mass. The mass was then extracted thrice (3 × 10 mL) with *n*-hexane, which on slow evaporation afforded deep yellow needles. The product was finally dried under vacuum over fused $CaCl_2$. Yield: 2.77 g (65%). *Anal.* Calc. (%) for $C_{17}N_4H_{20}$: C, 72.83; H, 7.19; N, 19.98. Found: C, 72.91; H, 7.13; N, 19.93. IR (ν/cm^{-1}): 1680 ($\nu_{C=N}$). FAB Mass spectrum: *m*/*z* 281 $(L^1 + 1)^+$. ^{1}H NMR {δ(*J*/Hz), DMSO–d_6}: Pyridyl protons, 8.52 (d, *J* = 7.0, 2H), 7.96 (d, *J* = 7.8, 2H), 7.80 (t, *J* = 7.4, 2H), 7.37 (t, *J* = 6.8, 2H); methylene protons, 3.82 (s, 4H), 3.48 (s, 2H); methyl protons, 2.34 (s, 6H).

L^2: The ligand was prepared by a procedure similar as that for L^1, by starting with 1,2-diaminoethane (0.9 g, 15 mmol) and 2-acetylpyridine (3.63 g, 30 mmol) to obtain a yellow semi-solid mass, which on recrystallization from *n*-hexane gave pale yellow product. Yield: 2.44 g (61%). *Anal.* Calc. (%) for $C_{16}N_4H_{18}$: C, 72.22; H, 6.75; N, 21.09. Found: C, 72.15; H, 6.81; N, 21.04. IR (ν/cm^{-1}): 1681 ($\nu_{C=N}$). FAB Mass spectrum: *m*/*z* 267 $(L^2 + 1)^+$. ^{1}H NMR {δ(*J*/Hz), DMSO–d_6}: Pyridyl protons, 8.56 (d, *J* = 7.0, 2H), 7.98 (d, *J* = 8.2, 2H), 7.79 (t, *J* = 7.8, 2H), 7.32 (d, *J* = 7.8, 2H); methylene protons, 3.75 (s, 4H); methyl protons, 2.32 (s, 6H).

3.2.2. Complexes

*[Cd(L^1)(NCS)$_2$] (**1**)*. To a solution of $Cd(OAc)_2 \cdot 2H_2O$ (0.133 g, 0.5 mmol) in 15 mL dry methanol was added (0.006 g, 1 mmol) of NH_4SCN. To the resulting solution (0.140 g, 0.5 mmol) of L^1 dissolved in 10 mL dry methanol was added in one go. The solution gradually became turbid and to ensure complete reaction magnetic stirring was continued for 3 h, and the reaction was left overnight at room temperature for complete precipitation. The solid was then collected by filtration, thoroughly washed with cold methanol and finally dried under vacuum over fused $CaCl_2$. Yield: 234 mg (92% with respect to L^1). *Anal.* Calc. (%) for $C_{19}N_6H_{20}S_2Cd$: C, 44.84; H, 3.96; N, 16.51. Found: C, 44.88; H, 3.89; N, 16.57. IR (ν/cm^{-1}): 2072 (ν_{NCS}). FAB Mass spectrum: *m*/*z* 510 $(\mathbf{1} + 1)^+$. ^{1}H NMR {δ(*J*/Hz), DMSO–d_6}: Pyridyl protons, 8.95 (s, 2H) 8.29 (s, 4H), 7.83 (s, 2H); methylene protons, 3.92 (s, 4H of C8 and C8A atoms); 2.36 (s, 2H of C9 atom); methyl protons, 2.46 (s, 6H).

[Cd(L^2)(NCS)$_2$] (**2**). The complex was prepared by a similar procedure. Yield: 222 mg (90% with respect to L^2). *Anal.* Calc. (%) for $C_{18}N_6H_{18}S_2Cd$: C, 43.68; H, 3.67; N, 16.98. Found: C, 43.73; H, 3.61; N, 17.04. IR (ν/cm^{-1}): 2070 (ν_{NCS}). FAB Mass spectrum: *m*/*z* 496 $(\mathbf{2} + 1)^+$. ^{1}H NMR {δ(*J*/Hz), DMSO–d_6}: Pyridyl protons, 8.82 (d, *J* = 6.8, 2H), 8.12 (t, *J* = 7.5, 2H), 7.87 (t, *J* = 7.2, 2H), 7.43 (d, *J* = 8.0, 2H); methylene protons, 3.84 (s, 4H); methyl protons, 2.42 (s, 6H).

Table 3
Crystal data for complexes **1** and **2**

	1	**2**
Formula	$C_{19}H_{20}CdN_6S_2$	$C_{18}H_{18}CdN_6S_2$
M	508.93	494.93
System	monoclinic	orthorhombic
Space group	*P*2(1)/*m*	*Pccn*
Unit cell dimensions		
a (Å)	8.7047(16)	10.1510(19)
b (Å)	13.090(2)	12.370(2)
c (Å)	9.4678(17)	16.058(3)
α (°)	90.00	90.00
β (°)	101.313(3)	90.00
γ (°)	90.00	90.00
V (Å^3)	1057.9(3)	2016.4(6)
Z	2	4
D (Mg m^{-3})	1.598	1.630
T (K)	233(2)	243(2)
μ (mm^{-1})	1.246	1.305
Collected reflections	9494	16895
Independent reflections	2658	2526
R_{int}	0.0165	0.0399
Observed reflections [$I > 2\sigma(I)$]	2281	1505
Parameters	139	123
R_1, wR_2 [$I > 2\sigma(I)$]	0.0293, 0.0818	0.0367, 0.0727
R_1, wR_2 [all data]	0.0343, 0.0838	0.0697, 0.0818
Goodness-of-fit	1.068	1.065

3.3. Crystal structure determination

Crystals of **1** and **2** were grown by slow evaporation of solvent from DMSO solution. Data collection were performed by the ω-scan method within the limits $2.19° \leqslant \theta \leqslant 28.66°$ and $2.54° \leqslant \theta \leqslant 28.87°$ for **1** and **2**, respectively, on a Bruker AXS CCD diffactometer with graphite monochromated Mo Kα radiation (λ = 0.71073 Å) radiation. Data collection and cell refinement were carried out with SMART [29], data reduction with SAINT [29], and experimental absorption correction with SADABS [30].

Structure analysis and refinement. The structure was solved by direct methods (SHELXS-97) [31]; refinement was done by full-matrix least squares on F^2 using the SHELXL-97 program suite [31]. All non-hydrogen positions were found and refined with anisotropic temperature factors. The hydrogen atoms were calculated with appropriate riding models (AFIX 43 for aromatic hydrogens on pyridine, AFIX 23 for CH_2 and AFIX 33 for CH_3) and U_{eq}(H) = 1.2 U_{eq}(C) for CH and CH_2 and U_{eq}(H) = 1.5 U_{eq}(C) for CH_3. Significant crystal data are listed in Table 3. Graphics were obtained with ORTEP 3 for Windows [32–34]. Supramolecular interactions (π-contacts) were calculated with PLATON for Windows [35–37].

4. Conclusion

The effect of variation of the polymethylene spacer length in the pyridyl Schiff-base ligands L^1 (spacer

–$(CH_2)_3$–) and L^2 (spacer –$(CH_2)_2$–) was studied in the case of neutral hexacoordinated structures with the $Cd(NCS)_2$ fragment. The molecular structures of the resulting complexes strongly deviate from the classical octahedron, with $[Cd(L^1)(NCS)_2]$ showing a trigonal prismatic coordination polyhedron around cadmium. This and the structural differences between $[Cd(L^1)(NCS)_2]$ (**1**) and $[Cd(L^2)(NCS)_2]$ (**2**) can be traced to the length of the methylene spacers and the formation of a six- versus a five-membered metal-chelate ring together with the pyramidal $Cd(L^1)$ and planar $Cd(L^2)$ arrangement.

Acknowledgements

One of the authors (S. Banerjee) is thankful to the University Grant Commission (UGC), India for awarding a Junior Research Fellowship (Sanction No. UGC/548/jr. Fellow Sc. 2001/2002). The work of C. Janiak was supported by DFG grant JA 466/10-2.

Appendix A. Supplementary data

CCDC reference numbers are 216947 and 228070 for **1** and **2**, respectively. Copies of the data can be obtained free of charge on application to CCDC, 12 Union Road, Cambridge CB2 1EZ, UK (fax: +44 1223 336033; email: deposit@ccdc.cam.ac.uk or www: http://www.ccdc.cam.ac.uk). Supplementary data associated with this article can be found, in the online version at doi:10.1016/j.poly.2005.01.005.

References

[1] R.G. Dickinson, L. Pauling, J. Am. Chem. Soc. 45 (1923) 1466.
[2] (a) R. Eisenberg, J.A. Ibers, J. Am. Chem. Soc. 87 (1965) 3776;
(b) R. Eisenberg, J.A. Ibers, Inorg. Chem. 5 (1966) 411.
[3] E.I. Stiefel, R. Eisenberg, R.C. Rosenberg, H.B. Gray, J. Am. Chem. Soc. 88 (1966) 2956.
[4] R. Eisenberg, H.B. Gray, Inorg. Chem. 6 (1967) 1844.
[5] E.I. Stiefel, G.F. Brown, Inorg. Chem. 11 (1972) 434.
[6] R.A.D. Wentworth, Coord. Chem. Rev. 9 (1972) 171.
[7] R. Eisenberg, Progr. Inorg. Chem. 12 (1970) 295.
[8] J.M. Howell, A.R. Rossi, R. Hoffmann, J. Am. Chem. Soc. 98 (1976) 2484.
[9] G.N. Schrauzer, V.P. Mayweg, J. Am. Chem. Soc. 88 (1966) 3235.
[10] K.R. Dymock, G.J. Palenik, Inorg. Chem. 14 (1975) 1220.
[11] (a) C.H. Langford, E. Billig, S.I. Shupack, H.B. Gray, J. Am. Chem. Soc. 86 (1964) 2958;
(b) A. Davison, N. Edelstein, R.H. Holm, A.H. Mani, Inorg. Chem. 4 (1965) 55;
(c) A. Davison, N. Edelstein, R.H. Holm, A.H. Mani, J. Am. Chem. Soc. 86 (1964) 2799.
[12] (a) D.G. Blight, D.L. Kepert, Inorg. Chem. 11 (1972) 1556;
(b) D.L. Kepert, Inorg. Chem. 11 (1972) 1561.
[13] S.K. Wang, T.A. Albright, O. Eisenstein, Inorg. Chem. 28 (1989) 1611.
[14] P. Rosa, L. Ricard, P.L. Floch, F. Mathey, G. Sini, O. Eisenstein, Inorg. Chem. 37 (1998) 3154.
[15] M. Kaupp, Angew. Chem., Int. Ed. 40 (2001) 3534.
[16] M. Kaupp, Chem. Eur. J. 4 (1998) 1678, and references therein.
[17] (a) B. Roessler, V. Pfennig, K. Seppelt, Chem. Eur. J. 7 (2001) 3652;
(b) K. Seppelt, Acc. Chem. Res. 36 (2003) 147.
[18] P. Comba, A.M. Sargeson, L.M. Engelhardt, J.M.B. Harrowfield, A.H. White, E. Horn, M.R. Snow, Inorg. Chem. 24 (1985) 2325, and references therein.
[19] S. Alvarez, D. Avnir, M. Llunell, M. Pinsky, New. J. Chem. (2002) 996.
[20] W.O. Gillum, J.C. Huffman, W.E. Streib, R.A.D. Wentworth, J. Chem. Soc., Chem. Commun. (1969) 843.
[21] C.L. Onnerud, H.C. Zur Loye, Inorg. Chem. 35 (1996) 2155.
[22] T.M. Greaney, C.L. Raston, A.H. White, E.L. Maslen, J. Chem. Soc., Dalton Trans. (1975) 876.
[23] (a) S.-L. Li, T.C.W. Mak, J. Chem. Soc., Dalton Trans. (1995) 1519;
(b) E.B. Adamska, R.B. Jarzebowska, L. Lomozik, Polyhedron 21 (2002) 739;
(c) O. Schlager, K. Weighardt, H. Grondey, A. Rufinska, B. Nuber, Inorg. Chem. 34 (1995) 6440;
(d) P.V. Bernhardt, P. Comba, T.W. Hambley, G.A. Lawrence, K. Varnagy, J. Chem. Soc., Dalton Trans. (1992) 355.
[24] (a) R. Vaidhyanathan, S. Natarajan, C.N.R. Rao, Chem. Mater. 13 (2001) 3524;
(b) R. Vaidhyanathan, S. Neeraj, P.A. Prasad, S. Natarajan, C.N.R. Rao, Angew. Chem., Int. Ed. Engl. 39 (2000) 3470.
[25] J.L. Martin, J. Takats, Inorg. Chem. 14 (1975) 1358.
[26] (a) C. Janiak, in: E. Riedel (Ed.), Moderne Anorganische Chemie, 2nd ed., de Gruyter, Berlin, 2003, p. 187;
(b) R.D. Hancock, Crown Compounds: Toward Future Applications, in: S.R. Cooper (Ed.), VCH, Weinheim, 1992, pp. 167–190;
(c) P.-G. Lassahn, V. Lozan, B. Wu, A.S. Weller, C. Janiak, J. Chem. Soc., Dalton Trans. (2003) 4437, and references therein.
[27] C. Janiak, J. Chem. Soc., Dalton Trans. (2000) 3885.
[28] (a) C. Janiak, S. Deblon, H.-P. Wu, M.J. Kolm, P. Klüfers, H. Piotrowski, P. Mayer, Eur. J. Inorg. Chem. (1999) 1507;
(b) H.-P. Wu, C. Janiak, G. Rheinwald, H. Lang, J. Chem. Soc., Dalton Trans. (1999) 183;
(c) C. Janiak, L. Uehlin, H.-P. Wu, P. Klüfers, H. Piotrowski, T.G. Scharmann, J. Chem. Soc., Dalton Trans. (1999) 3121;
(d) H.-P. Wu, C. Janiak, L. Uehlin, P. Klüfers, P. Mayer, Chem. Commun. (1998) 2637.
[29] SAINT, Data Reduction and Frame Integration Program for the CCD Area-detector System. Bruker Analytical X-ray Systems, Madison, WI, USA, 1997.
[30] G.M. Sheldrick, Program SADABS: Area-detector Absorption Correction, University of Göttingen, Germany, 1996.
[31] G.M. Sheldrick, SHELXS-97, SHELXL-97, Programs for Crystal Structure Analysis, University of Göttingen, Germany, 1997.
[32] M.N. Burnett, C.K. Johnson, ORTEP-III: Oak Ridge Thermal Ellipsoid Plot Program for Crystal Structure Illustrations, Oak Ridge National Laboratory Report ORNL-6895, 1996.
[33] L.J. Farrugia, ORTEP 3 for Windows, Version 1.076, University of Glasgow, 1997–2002.
[34] L.J. Farrugia, J. Appl. Crystallogr. 30 (1997) 565.
[35] A.L. Spek, Acta Crystallogr., Sect. A 46 (1990) C34.
[36] A.L. Spek, PLATON Version 29–11–98.
[37] L.J. Farrugia, Windows Implementation, University of Glasgow, 1998.

Available online at www.sciencedirect.com
SCIENCE DIRECT®
Polyhedron 24 (2005) 601–610
POLYHEDRON
www.elsevier.com/locate/poly

Chelating behavior of 2-hydroxyacetophenone *N*(4)-disubstituted thiosemicarbazones: Facile formation of Mn(IV) complexes – X-ray structure, EPR and cyclic voltammetric studies

Rohith P. John [a,1], Anandram Sreekanth [a,2], Maliyeckal R. Prathapachandra Kurup [a,*], Hoong-Kun Fun [b]

[a] *Department of Applied Chemistry, Cochin University of Science and Technology, Kochi 682022, India*
[b] *X-ray Crystallography Unit, School of Physics, Universiti Sains Malaysia, 11800 USM, Penang, Malaysia*

Received 22 September 2004; accepted 3 January 2005

Abstract

Reaction of tridentate ONS donor ligands H_2L^1, H_2L^2 and H_2L^3 (H_2L^1 = 2-hydroxyacetophenone hexamethyleneimine-3-thiosemicarbazone; H_2L^2 = 2-hydroxyacetophenone morpholine-3-thiosemicarbazone; H_2L^3 = 2-hydroxyacetophenone *N*(4)-methyl, phenyl thiosemicarbazone) with $Mn(OAc)_2 \cdot 4H_2O$ afforded manganese(IV) complexes of the type $[MnL_2]$ in an ethanol–methanol mixture under air. The crystal structure of $Mn(L^2)_2 \cdot 0.25H_2O$ reveals an octahedral geometry with the ligand coordinated in a meridional fashion. The molecule is packed in the crystal lattice with extended hydrogen bonding networks. EPR spectra of the complexes in frozen solution at 77 K show a weak signal at $g \approx 4$ and a strong sextet at $g \approx 2$ consistent with manganese(IV) in an octahedral environment. Cyclic voltammetry in DMSO/ dichloromethane show quasi-reversible peaks corresponding to the Mn(IV)/ Mn(III) redox couple.
© 2005 Elsevier Ltd. All rights reserved.

Keywords: Manganese(IV); Thiosemicarbazone; X-rays; ESR; Cyclic voltammetry

1. Introduction

The coordination chemistry of manganese has continued to attract attention in recent years due to its presence in several biological systems [1]. A mononuclear Mn(III) centre was found in the active site of some enzymes that display superoxide dismutase activity [2]. In addition, manganese plays an important role in the oxygen-evolving complex (OEC) of photosystem-II [3]. Detailed investigations indicate that the photosystem II (PS II) has an oxo-bridged tetramanganese cluster (Mn_4) as its key structural feature [4]. However the possibility of a mononuclear manganese(IV) center in the S_2 state of PS II cannot be ruled out [5]. Since the manganese is believed to be in its +2 to +4 oxidation state a number of different OEC model complexes were synthesized and their properties investigated [6]. Besides, the use of mononuclear manganese(IV) complexes in catalytic oxidation of organic compounds [7] makes the investigation of mononuclear manganese(IV) complexes more important. Synthetic monomanganese(IV) species in

* Corresponding author. Tel.: +91 484 2575804; fax: +91 484 2577595.
E-mail addresses: rohitjohn@yahoo.com (R.P. John), sran@esr.phys.chem.ethz.ch (A. Sreekanth), mrp@cusat.ac.in, mrp_k@yahoo.com (M.R.P. Kurup).
[1] Present address: Inorganic Synthesis Laboratory, College of Science and Technology, Hanyang University (Ansan), 1271 Sa 1 dong, Ansan, South Korea, 426 791.
[2] Present address: Laboratorium fur Physikalische Chemie, Eidgenössische Technische Hochschule, Honggerberg, CH-8093 Zurich, Switzerland.

0277-5387/$ - see front matter © 2005 Elsevier Ltd. All rights reserved.
doi:10.1016/j.poly.2005.01.004

biomimetic O, N coordination are also of vital importance in the above perspective. Over the past two decades quite a few manganese(IV) complexes have been isolated and characterised [8,9].

Manganese(IV) is considered as an enigmatic oxidation state; it is usually attained in oxidizing conditions or in the presence of strong bases, except in cases where the presence of phenolato or alcoholato groups in the ligands may bring about the oxidation of Mn(II) into the Mn(III) or even the Mn(IV) oxidation state in aerobic conditions [10]. However the reaction conditions, nature of the ligands or the ligand donor set that yield a stable manganese complex in its +2, +3 or +4 state are yet not clear [11,12]. While a monoprotic ligand with an NNS donor set is likely to give a manganese(II) complex [13], a diprotic ligand with an ONS donor set is most likely to give a manganese(III) or (IV) complex under aerobic condition. It has been reported previously that manganese(II) compounds react with primary hydroxamic acids in aerobic condition, producing Mn(IV) hydroximato complexes with a conjugated metal–ligand ring [14]. In contrast, secondary hydroxamic acids that cannot form conjugated ring systems yield only Mn(II) complexes, while bidentate thiohydroxamic acids yield Mn(IV) complexes from Mn(III) precursors in the presence of oxidizing species [15]. It has also been observed that diprotic ONS donor ligands derived from salicylaldehyde derivatives – (*o*-OH)$RC_6H_3CH{=}N{-}NHC(=S)$-R′ – that can form conjugated metal–ligand ring systems yield manganese(IV) complexes when R′ is NH_2 or NHPh [16]. As part of our efforts to optimise the factors that determine the spontaneous oxidation of manganese(II) to manganese(IV) in the presence of air, we prepared three manganese complexes of 2-hydroxyacetophenone *N*(4) disubstituted thiosemicarbazones (H_2L) (Fig. 1). While Mukhopadhyay et al. [12] have reported formation and characterization of manganese(IV) complexes of *N*(4)-monosubstituted salicylaldehyde thiosemicarbazones, it was not supported by X-ray crystal structure data. Very recently, an optically active manganese(IV) complex was reported whose structure was confirmed by X-ray crystallography [17]. Herein, we report the serendipitous formation of three Mn(IV) complexes of 2-hydroxyacetophenone *N*(4)-disubstituted thiosemicarbazones, discuss their spectral properties, redox behavior and the X-ray crystal structure of one of them (compound **2**).

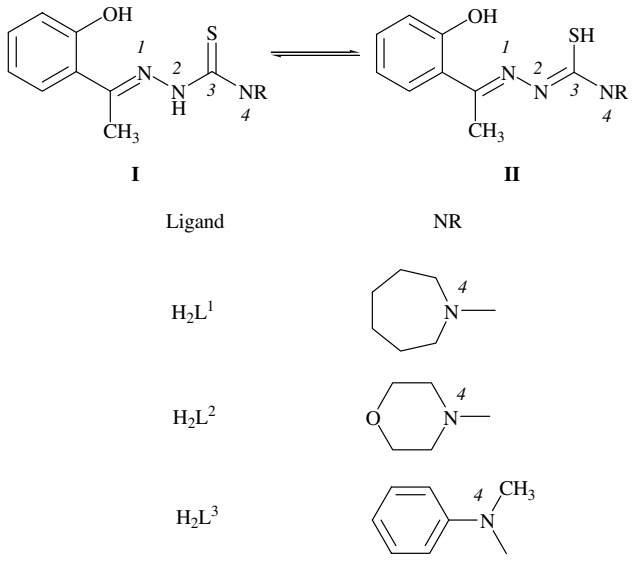


Fig. 1. Schematic diagram of the ligands used for preparation of the complexes.

2. Experimental

2.1. Materials and methods

The thiosemicarbazones H_2L^1, H_2L^2 and H_2L^3 were prepared as reported previously [18]. All the ligands were purified by recrystallisation, manganese(II) acetate tetrahydrate (Reagent grade, E. Merck) was purified by standard methods and solvents were purified by standard procedures before use.

2.2. Preparation of the complexes

2.2.1. $[Mn(L^1)_2]$ (**1**)

To a hot ethanol solution (25 mL) of the thiosemicarbazone, H_2L^1 (0.291 g, 1.0 mmol), was added 10 mL of a methanolic solution of manganese(II) acetate tetrahydrate (0.122 g, 0.5 mmol) with stirring. The yellow solution changed slowly into a coffee brown color on continued stirring. A deep brown residue appeared within 10 min. Stirring was continued for another 20 min. The deep brown precipitate was washed with ethanol followed by ether. It was then dried over P_4O_{10} in vacuo: Yield 0.21 g (67%). *Anal.* Calc. for $C_{30}H_{38}MnN_6O_2S_2$ (633.73): C, 56.77; H, 6.19; N, 13.24; Mn, 8.66. Found: C, 57.26; H, 6.09; N, 13.42; Mn, 8.82%.

2.2.2. $[Mn(L^2)_2]\cdot H_2O$ (**2**)

To a hot ethanol solution (20 mL) of the thiosemicarbazone, H_2L^2 (0.28 g, 1.0 mmol), was added 10 mL of a methanolic solution of manganese(II) acetate tetrahydrate (0.122 g, 0.5 mmol) with stirring. The yellow solution changed into a deep greenish black color in barely a minute. Black powdery material began to form within 3 min. Stirring was continued for an hour, the product formed was allowed to settle, it was filtered, washed with ethanol and ether in succession and then dried over

P_4O_{10} in vacuo. Yield 0.26 g (83%). MS (FAB): m/z = 627 $[Mn(L^2)_2 \cdot H_2O]^+$ (15), 609 $[Mn(L^2)_2]^+$ (100). *Anal*. Calc. for $C_{26}H_{30}MnN_6O_4S_2.H_2O$ (627.63): C, 49.76; H, 5.14; N, 13.39; Mn, 8.75. Found: C, 50.05; H, 5.22; N, 12.94; Mn, 8.83%. X-ray quality crystals were obtained over a period of 13 days by diffusion of ethanol into a dichloromethane solution.

2.2.3. $[Mn(L^3)_2]$ (**3**)

To a hot ethanol solution (20 mL) of the thiosemicarbazone, H_2L^3 (0.30 g, 1.0 mmol), was added 10 mL of methanolic solution of manganese(II) acetate tetrahydrate (0.122 g, 0.5 mmol) with stirring. The yellow solution changed into a deep brown color in a few minutes. Brownish black microcrystals settled within 5 min. The solution was set aside undisturbed for complete crystallization, which was then filtered after 2 h, the product was washed with ethanol and ether. It was then dried over P_4O_{10} in vacuo. Yield 0.25 g, (76%). *Anal*. Calc. for $C_{32}H_{30}MnN_6O_2S_2$ (649.69): C, 59.16; H, 4.65; N, 12.94; Mn, 8.46. Found: C, 59.32; H, 4.74; N, 13.05; Mn, 8.47%.

2.3. Physical measurements

Elemental analyses were performed on a Heraeus Elemental Analyzer at CDRI, Lucknow. The metal contents were determined in a Perkin–Elmer AAnalyst 700 Atomic Absorption Spectrometer, after decomposing the compounds by standard methods. Magnetic measurements were performed in the polycrystalline state on a Gouy magnetic balance using $Hg[Co(SCN)_4]$ as a calibrant. Diamagnetic corrections for various atoms and structural units were computed from Pascal's constants. The effective magnetic moments were calculated from the corrected molar susceptibilities of the complexes using Curie's relation. The FT-IR spectra were recorded on a Shimadzu DR 8001 series FTIR spectrometer as KBr pellets and the electronic spectra were recorded on a Shimadzu 160A UV–Vis spectrophotometer in dichloromethane solvent. Diffuse reflectance spectra were recorded on Ocean Optics, Inc. SD200 Fiber Optic Spectrometer in a magnesium oxide matrix. The EPR spectra were recorded on a Varian E-112 Spectrometer using TCNE as the standard marker, with 100 kHz modulation frequency and 0.2 mT modulation amplitude. The cyclic voltammetric measurements were performed on a BAS CW-50 electrochemical measurement unit. The cyclic voltammetric (CV) measurements were done after degassing (N_2 bubbling for 15 min.) dichloromethane (DCM)/dimethylsulfoxide (DMSO) solutions (10^{-3} M) containing 0.1 M tetrabutylammoniumperchlorate (TBAP) as the supporting electrolyte. The three-electrode system consisted of platinum foil (counter), glassy carbon (working) and silver–silver chloride (reference) electrodes.

2.4. X-ray crystallography

Data for complex **2** was collected at 213(2) K on a Siemens SMART PLATFORM diffractometer equipped with a CCD area detector and a graphite monochromator utilizing MoKα radiation (λ = 0.71073 Å). Data collection parameters are listed in Table 1. Cell refinement and data reduction for the compound were performed using the SAINT program [19]. A total of 16 741 reflections were collected resulting in 6818 unique reflections. The intensities were corrected for Lorentz and polarization effects. The structure was solved by a direct method procedure, as implemented in the SHELXTL program [20]. The positions of all the non-hydrogen atoms were included in the full-matrix least-squares refinement, using the SHELXTL program. The positions of all the H-atoms were geometrically fixed at calculated positions, and they were allowed to ride on the corresponding non-hydrogen atoms. The final R-factor converged to 0.054 (wR_2 = 0.1083); the maximum and minimum values of electron densities in the final electron density maps were 0.785 and −0.971 e Å^{-3}, respectively.

Table 1
Crystal data and structure refinement for $Mn(L^2)_2 \cdot 0.25H_2O$

Empirical formula	$C_{26}H_{30.50}N_6O_{4.25}S_2Mn$
Formula weight (M)	614.12
Temperature (T, K)	213(2)
Wavelength (λ, Å)	0.71073
Crystal system,	monoclinic
Space group	$P2_1/c$
Unit cell dimensions	
a (Å)	10.0456(2)
b (Å)	9.2579(3)
c (Å)	14.5613(2)
β (°)	96.764(1)
Volume (Å^3)	2797.38(8)
Z	4
Calculated density (ρ, Mg/m^3)	1.458
Absorption coefficient (μ, mm^{-1})	0.666
F(000)	1278
Crystal size (mm)	0.44 × 0.26 × 0.16
θ Range for data collection (°)	2.54–28.29
Reflections collected	16 741
Independent reflections	6818 [R_{int} = 0.1229]
Completeness to θ	28.29 (97.9%)
Absorption correction	semi-empirical from equivalents
Maximum and minimum transmission	0.9009 and 0.7582
Refinement method	full-matrix least-squares on F^2
Data/restraints/parameters	6818/0/367
Goodness-of-fit on F^2	0.857
Final R indices [$I > 2\sigma(I)$]	R_1 = 0.0540, wR_2 = 0.1083
R indices (all data)	R_1 = 0.1038, wR_2 = 0.1228
Extinction coefficient	0.0016(4)
Largest differential peak and hole (e Å)	0.792 and −0.983

3. Results and discussion

3.1. Preparation of the compounds

The thiosemicarbazones act as dibasic tridentate ONS donor ligands and deep brown colored manganese complexes were formed from the reaction mixture. Elemental analysis and the FAB mass spectra of the prepared complexes indicated that the complexes have a stoichiometry $M^{IV}L_2$. The magnetic moment values of the compounds were in the range 3.9–4.1 BM, which indicate that the manganese could be in a d^3 high spin electronic configuration. While formation of Mn^{4+} complexes occur under oxidizing conditions [21], we were able to obtain manganese(IV) complexes in a simple and straightforward reaction using 2-hydroxyacetphenone *N*(4)-disubstituted thiosemicarbazone. Although we were not able to pursue the reaction kinetics leading to the formation of such a system, we could assign a notable difference in the behavior of different thiosemicarbazone ligands towards stabilizing the different oxidation states of manganese.

3.2. X-ray structural properties

An X-ray quality single crystal of compound **2** $[Mn(L^2)_2 \cdot 0.25H_2O]$ of $0.44 \times 0.26 \times 0.16$ mm dimension was grown by slow diffusion of ethanol into a dichloromethane solution of the compound over period of 13 days. The ORTEP diagram of compound **2** is shown in Fig. 2. Each thiosemicarbazone acts as a dibasic tridentate chelating agent. Bond lengths and bond angles are presented in Table 2. The ligands with their donor atoms are arranged around the manganese ion in a meridional fashion. However unlike in many other complexes where the thiosemicarbazone moiety is planar

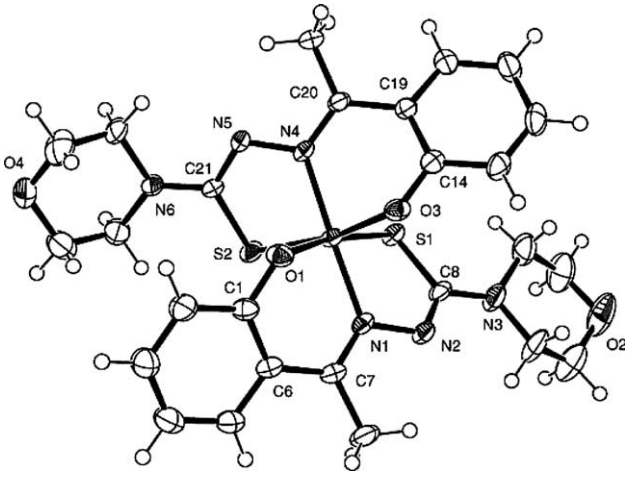


Fig. 2. ORTEP diagram of compound **2** showing 50% probability ellipsoids. Hydrogen atoms are shown as small spheres of arbitrary radii. The water molecule is omitted for clarity.

Table 2
Selected bond distances (Å) and angles (°) for $Mn(L^2)_2 \cdot 0.25H_2O$

Bond distances			
Mn–O(3)	1.870(2)	O(1)–C(1)	1.336(3)
Mn–O(1)	1.878(2)	O(3)–C(14)	1.337(3)
Mn–N(1)	1.983(2)	N(1)–C(7)	1.319(3)
Mn–N(4)	1.993(2)	N(1)–N(2)	1.399(3)
Mn–S(1)	2.3131(9)	N(2)–C(8)	1.311(4)
Mn–S(2)	2.3217(9)	N(4)–C(20)	1.313(3)
S(1)–C(8)	1.758(3)	N(4)–N(5)	1.398(3)
S(2)–C(21)	1.764(3)	N(5)–C(21)	1.316(4)
Bond angles			
O(3)–Mn(1)–O(1)	90.95(9)	O(3)–Mn(1)–S(2)	169.43(6)
O(3)–Mn(1)–N(1)	91.33(9)	O(1)–Mn(1)–S(2)	90.52(7)
O(1)–Mn(1)–N(1)	88.75(9)	N(1)–Mn(1)–S(2)	99.16(8)
O(3)–Mn(1)–N(4)	87.98(9)	N(4)–Mn(1)–S(2)	81.48(7)
O(1)–Mn(1)–N(4)	93.62(9)	S(1)–Mn(1)–S(2)	88.95(3)
N(1)–Mn(1)–N(4)	177.54(10)	C(8)–S(1)–Mn(1)	91.66(10)
O(3)–Mn(1)–S(1)	91.36(7)	C(21)–S(2)–Mn(1)	91.22(11)
O(1)–Mn(1)–S(1)	170.18(6)	C(1)–O(1)–Mn(1)	122.10(19)
N(1)–Mn(1)–S(1)	81.66(7)	C(14)–O(3)–Mn(1)	119.96(18)
N(4)–Mn(1)–S(1)	95.99(7)		

[17,22], in compound **2** it has undergone considerable distortion from planarity. The distortion of the thiosemicarbazone moiety deprives itself of the electron delocalization possible in its conjugated backbone. While O1, O3, S1 and S2 lie in the equatorial plane, N1 and N4 occupy the axial positions of the distorted octahedron. The length of Mn–N and Mn–O bonds are in good agreement with the corresponding bonds in the complex bis(salicylato)(bipyridine) manganese(IV) [23]. There is a marked decrease in metal ligand bond lengths when Mn(II) complexes of Schiff bases are compared to those of Mn(IV): {Mn(IV)–O(phenolate) = 1.906 Mn(II)–O(phenolate) = 2.054 Mn(IV)–N(imine) 2.005 Mn(II)–N(imine) 2.258 [21]. Manganese(II) and manganese(IV) complexes (high spin d^5 and d^3, respectively) adopt octahedral coordination geometries [24] compared to manganese(III) complexes (high spin d^4) that undergo Jahn–Teller distortion. The coordination geometry around manganese resembles that of an $Mn^{IV}N_4O_2$ manganese(IV) amide species [9c] having an acyclic amine function. The *cis* and *trans* angles are in the ranges 81°.48–99.16° and 169°.43–177.54°. The MnO_2S_2 fragment is distorted from the mean plane by 0.18 Å. Each thiosemicarbazone fragment is subtending an angle of 170.18° and 169.43° at the Mn center, which is smaller than 180° that is expected for an ideal octahedron. The planes containing Mn, O1, N1, S1, N4 and Mn, O3, N1, S2, N4 are deviated from the mean plane by 0.02 Å and 0.01 Å (Mn), respectively. The inter-planar angles lie in the interval of 85–89°. The Mn–N distance is longer than the average Mn–O distance by more than 0.1 Å and is longer than other $Mn–N_{(azomethine)}$ bond lengths reported previously, which indicate a marginal axial distortion along the N–Mn–N axis. A similar

structure is suggested for the other complexes, **1** and **3**, based on other spectral measurements.

The Mn ion is displaced from the plane of the hydroxyacetophenone-imine fragment O1, C1, C6, C7, N1 by 0.73 Å. Therefore, the phenol-imine chelate ring can be considered as folded along the O1, N1 line, which is referred to as a ''step-forming distortion'' observed in chelates of salicylaldehydes [25]. The manganese ion is displaced by 0.88 Å from the plane formed by N1, N2, C8 and S1. This leads to an envelop like conformation for the chelate ring consisting of Mn, N1, N2, C8 and S1, whose folding occurs along the N1, S1 line. This distortion causes a skewed arrangement of the ligand moiety around the metal, leading to a ''butterfly'' type structure for the molecule about the metal centre. Compound **2** is associated with a molecule of water with partial occupancy in its crystal lattice. There is extensive hydrogen bonding and C–H...π interactions in the crystal lattice as a consequence of packing. The C–H...π and classical and non-classical hydrogen bonding interactions are listed in Table 3.

3.3. IR and electronic properties

The infrared spectral data are given in Table 4. A new band at ca. 1591 cm^{-1} is due to the newly formed C=N bond as a result of the enolisation. It is further supported by the absence of a band due to the NH group in the 3100–3300 cm^{-1} region in all the complexes that was present in the thiosemicarbazone ligands. Coordination of the azomethine nitrogen with manganese is evidenced by a shift of the band at ca. 1600 to ca. 1560 cm^{-1}. The details of the electronic spectra recorded in dichloromethane solution are given in Table 5. All the compounds are found to be stable in dichloromethane and chloroform. The spectra in the visible region is typical of $Mn^{IV}O_2N_2S_2$ complexes reported previously [11,12]. While bands at ca. 450 and 620 nm are broad and intense as CT bands, others are shoulders or buried under these high intensity bands. The unusually intense peaks in the visible region ($\log\varepsilon \approx 3$) are attributed to the ''intensity stealing'' influence of the sulfur/oxygen containing ligands, whereby the intensity of the bands in the visible region are enhanced. The bands at ca. 720, 620 and 510 nm (Table 5) of compounds **1**–**3** can be attributed to $^4A_{2g} \rightarrow {}^4T_{2g}$, $^4A_{2g} \rightarrow {}^4T_{1g}$, $^4A_{2g} \rightarrow {}^4T_{1g}$ (P) transitions [9b,21,26] and the intense band at ca. 450 nm to the $S(p_\pi) \rightarrow Mn(d_\pi)$ LMCT transition, [12,15] while the broad high intensity peak at ca. 360 nm can be assigned to the phenolate → Mn charge transfer band which is identical to octahedral Mn^{4+} complexes of Schiff base ligands containing phenolate/hydroxylate donor groups [9a,27]. The solution in DMF also gives a similar spectrum. However, bands in the visible region appear at lower wavelength with lower intensity when a solution in DMF is allowed to

Table 3
H-bonding, and C–H...π interactions in compound **2**

D–H...A	*d*(D–H) (Å)	*d*(H...A) (Å)	*d*(D...A) (Å)	∠(DHA) (°)
C(5)–H(5A)...O(4)[a]	0.94	2.47	3.385(4)	163.4
C(15)–H(15A)...S(2)[b]	0.94	2.77	3.671(3)	162
C(25)–H(25A)...O(1W)[b]	0.98	2.42	3.214(10)	137.6
C(11)–H(11B)...O(1W)[c]	0.98	2.35	3.276(10)	156.3

X–H(I)...Cg(J)	H...Cg (Å)	X...Cg (Å)	∠H–X...Cg (°)
C–H...π interactions			
C(11)–H(11A) [1]...Cg(7)[d]	2.9236	3.667	133.49
C(13)–H(13B)[1] Cg(8)[e]	2.9678	3.821	147.51
O(1w)–H(1w) [2]...Cg(7)[f]	3.2419	3.303	86.63

Equivalent position code: (a) $-x$, $y + 1/2$, $-z + 1/2$; (b) x, $-y + 1/2$, $z - 1/2$; (c) $x + 1$, y, $z - 1$; (d) $1 + x$, y, z; (e) x, $1/2 - y$, $1/2 + z$; (f) x, $1/2 - y$, $-1/2 + z$.
Cg(7)=C(1), C(2), C(3), C(4), C(5), C(6); Cg(8)=C(14), C(15), C(16), C(17), C(18), C(19).
D, donor; A, acceptor; Cg, centroid.

Table 4
IR spectral bands/cm^{-1} for the manganese complexes **1**–**3**

Compound	$\nu_{(C=^1N)}$	$\nu_{(^2N=C)}$	$\nu_{(^1N-^2N)}$	$\nu_{(Mn-N)}$	$\nu_{(C=S)}$	$\delta_{(C=S)}$	$\nu_{(C-O)}$
H_2L^1	1603s		997m		1383s	839m	1252s
$Mn(L^1)_2$ (**1**)	1559m	1591	1017m	442w	1367s	810m	1132s
H_2L^2	1605s		1017m		1374s	835m	1219s
$Mn(L^2)_2 \cdot H_2O$ (**2**)	1566m	1591s	1030m	439w	1300s	808m	1113s
H_2L^3	1601s		995m		1375s	791m	1222s
$Mn(L^3)_2$ (**3**)	1558m	1592s	1024m	444w	1307s	764m	1124s

s, strong; m, medium; w, weak; sh, sharp.

Table 5
Magnetic moments (298 K), EPR data and electronic spectral data for compounds **1**–**3**

Compound	μ_{eff}, μ_B	EPR parameters			UV–Vis data[d], λ_{max}/nm (log ε)
		g (298 K)[a]	g (77 K)[b]	A (77 K)[c]	
$Mn(L^1)_2$ (**1**)	4.04	4.47, 1.98	3.82, 1.998	271	722 (3.35), 616 (3.41), 513 (3.71), 453 (3.84), 361 (4.34), 306 (4.53), 235 (4.52)
$Mn(L^2)_2 \cdot H_2O$ (**2**)	4.07	2.66	1.999	254	768 (3.16), 629 (3.46), 505 (3.71), 445 (3.84), 363 (4.42), 301 (4.66), 235 (4.61)
$Mn((L^3)_2$ (**3**)	3.94	3.44, 1.97	4.14, 1.999	254	720 (3.28), 620 (3.37), 509 (3.67), 454 (3.78), 362 (4.36), 309 (4.54), 240 (4.53)

[a] Measured in the polycrystalline form.
[b] Measured in DMF.
[c] Expressed in MHz.
[d] In dichloromethane.

stand for a day. This could be due to the coordination of DMF with the manganese metal center and a probable change in oxidation state. The solid-state diffuse reflectance spectra of the complexes show a broad band extending from 480 to 800 nm with peak ca. 550 nm corresponding to octahedral manganese d^3 systems.

3.4. EPR spectra

The EPR spectra of compounds **1**–**3** in the polycrystalline state at 298 K and in DMF solution at 77 K (Fig. 3) are comparable to the spectral features of previously reported Mn(IV) complexes. The EPR spectral parameters are presented in Table 5. The Mn(IV) ion is a d^3 system and hence can be treated theoretically similar to Cr(III) compounds. In a crystal field of strict octahedral symmetry a d^3 ion has a $^4A_{2g}$ ground state leading to an isotropic $g \approx 2$ resonance [28]. Distortion and spin orbit coupling split the quartet ground state into two Kramer's doublets separated by $2(D^2 + 3E^2)^{1/2}$, where D and E are, respectively, axial and rhombic zero-field-splitting parameters. The nature of the polycrystalline or glassy state EPR spectra varies widely depending on values of D, E and microwave quantum value hv [29]. The spectrum becomes simple under limiting conditions. The two limiting cases are when the zero-field splitting parameter $2D$, is either much larger or much smaller than hv. In the first case the feature at low field ($g \approx 4$) is predicted to be strong while the $g \approx 2$ component is weak as reported previously [11,30]. When D is small the $g \approx 2$ signal should dominate with a weaker signal in the low-field region as observed for tris(thiohydroxamato) manganese(IV) [15], tris(dithiocarbamato) manganese(IV) [31], manganese(IV) amide [9c] and salicylaldehyde thiosemicarbazone and dithiocarbazate manganese(IV) complexes [12,14]. In the case of the present complexes $g_{eff} \approx 4$ varies between 4.5 and 3.4 in the solid state at 298 K and between 4.1 and 3.8 in DMF at 77 K. This might be due to marginal changes in the geometry of the molecule upon dissolution. In compounds **1** and **3** the $g \approx 4$ signal is asymmetric, broad and weak without any resolved ^{55}Mn hyperfine splitting, while the $g \approx 2$ signal is moderately strong with well-resolved ^{55}Mn hyperfine splitting ($I = 5/2$). All the three compounds have an A value ranging from 250 to 270 MHz (91–97 G), this is comparable with values reported for $Mn^{IV}O_3S_3$ ($A \approx 100$ G) [15] and $Mn^{IV}S_6$ ($A \approx 95$ G) [32] systems having $2D \ll hv$. In all the three cases, weak signals corresponding to forbidden transitions ($\Delta M_S = \pm 1$, $\Delta M_I = \pm 1$) were observed between the hyperfine sextet lines in the $g \approx 2$ signal. The spectrum in DMF at 77 K is devoid of any significant feature at $g \approx 4$. This is an extreme case when the value of D is negligible compared to hv, i.e., the complex is nearly an ideal octahedron. However, none of the manganese complexes in DMF solution at room temperature give any spectra. In distorted manganese(IV) complexes, i.e., one lacking cubic symmetry, the zero-field splitting may be quite significant. Its magnitude depends on the relative orientation of the molecular axis and the magnetic field direction, molecular tumbling will modulate this interaction and the line broadening will be so large as to cause the EPR signal often to go undetected [32].

3.5. Cyclic voltammetry

The redox properties of the complexes were investigated by cyclic voltammetry at a glassy carbon working electrode in DMSO and dichloromethane solvents using a silver–silver chloride reference electrode. The cyclic voltammograms are shown in Fig. 4 and redox potentials are listed in Table 6. Both the cyclic responses are single electron redox processes. The response at more positive potential can be due to the $Mn^{IV}L_2$–$Mn^{III}L_2^-$ redox couple, while the one at more negative potential can be assigned to the $Mn^{III}L_2^-$–$Mn^{II}L_2^{2-}$ couple [33]. The $Mn^{IV}L_2$–$Mn^{III}L_2^-$ redox couple of compound **2** is observed at ~0.1 V more positive a value than those of the other two.

The electrode reactions occur at different potentials in DMSO and dichloromethane solvents. Both Mn^{IV}/Mn^{III} and Mn^{III}/Mn^{II} potentials lie at more positive values (~0.2 V) in DMSO compared to those in dichloromethane, indicating that the Mn(IV) compounds are

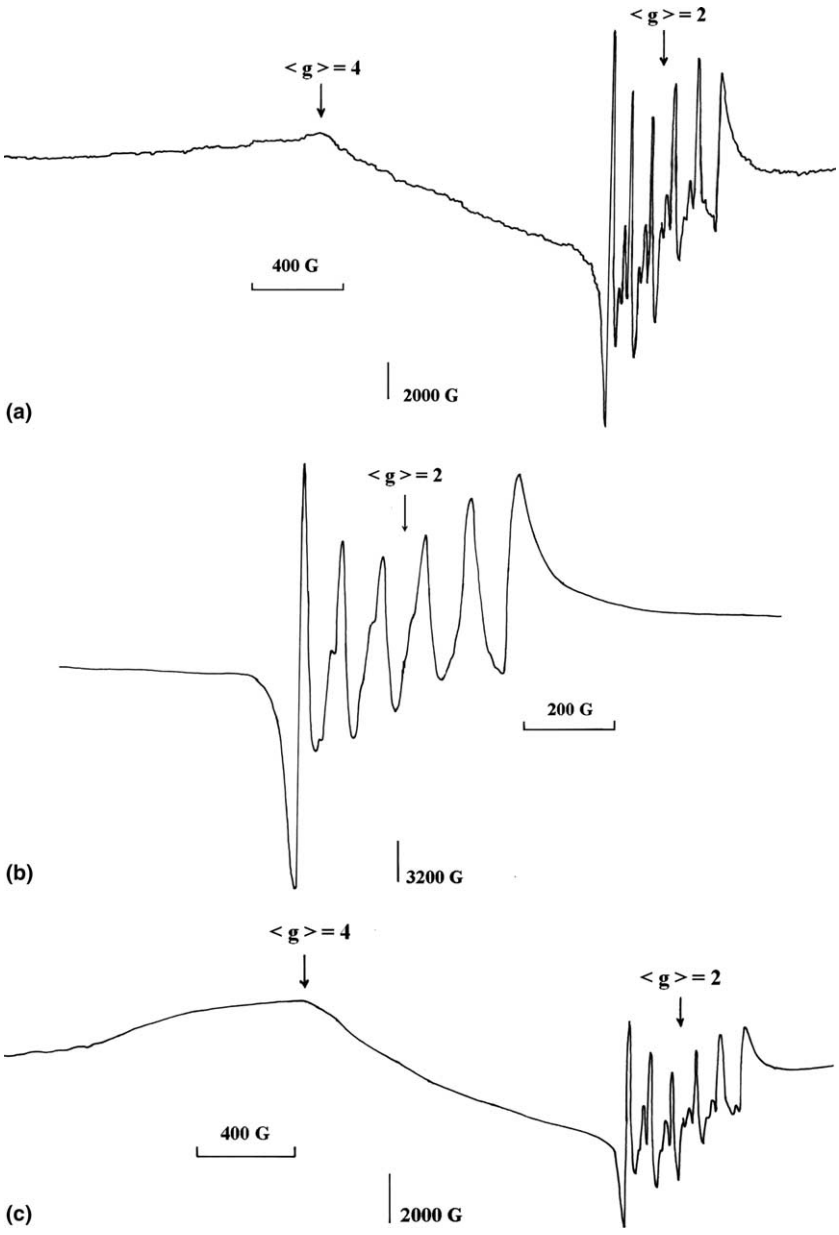


Fig. 3. EPR spectra of (a) $Mn(L^1)_2$ (**1**), (b) $Mn(L^2)_2 \cdot H_2O$ (**2**) and (c) $Mn(L^3)_2$ (**3**) at 77 K in DMF.

relatively stable in the latter solvent. The lower reduction potential (∼−0.1 V) may be the reason why complexes tend to fade color on standing in DMSO. The ligands in complexes **1**–**3** differ only in the nature of *N*(4) substituents. In complex **1** the *N*(4) substituent can be considered as an aliphatic group, in compound **2** the oxygen containing six membered ring is more electron withdrawing, while in compound **3** the presence of a electron releasing methyl group and electron withdrawing phenyl group compensate for each other and overall have an effect similar to that of the hexamethylene imine group in complex **1**. As a consequence the potentials of complexes **1** and **3** are very close in either solvent while that of complex **2** is more positive. This indicates that the ease of formation of the Mn(IV) complex is less spontaneous for compound **2** than for compounds **1** and **3**.

The Mn^{IV}/Mn^{III} redox couple is quasi-reversible (ΔE_p = 90–190 mV) in both DMSO and dichloromethane, while Mn^{III}/Mn^{II} is irreversible in all cases except for compound **2** in dichloromethane where the couple shows quasi-reversible nature. Absence of an anodic peak in both solvents (irreversible) corresponding to a Mn^{III}/Mn^{II} couple suggests MnL_2^{2-} is unstable in either solvent. A comparison of Mn^{IV}/Mn^{III} reduction potentials reported previously versus SCE, for a salicylate-pyridine complex lie well on the positive side (+0.44 V versus SCE) [23] while the trend is similar for MnO_4N_2

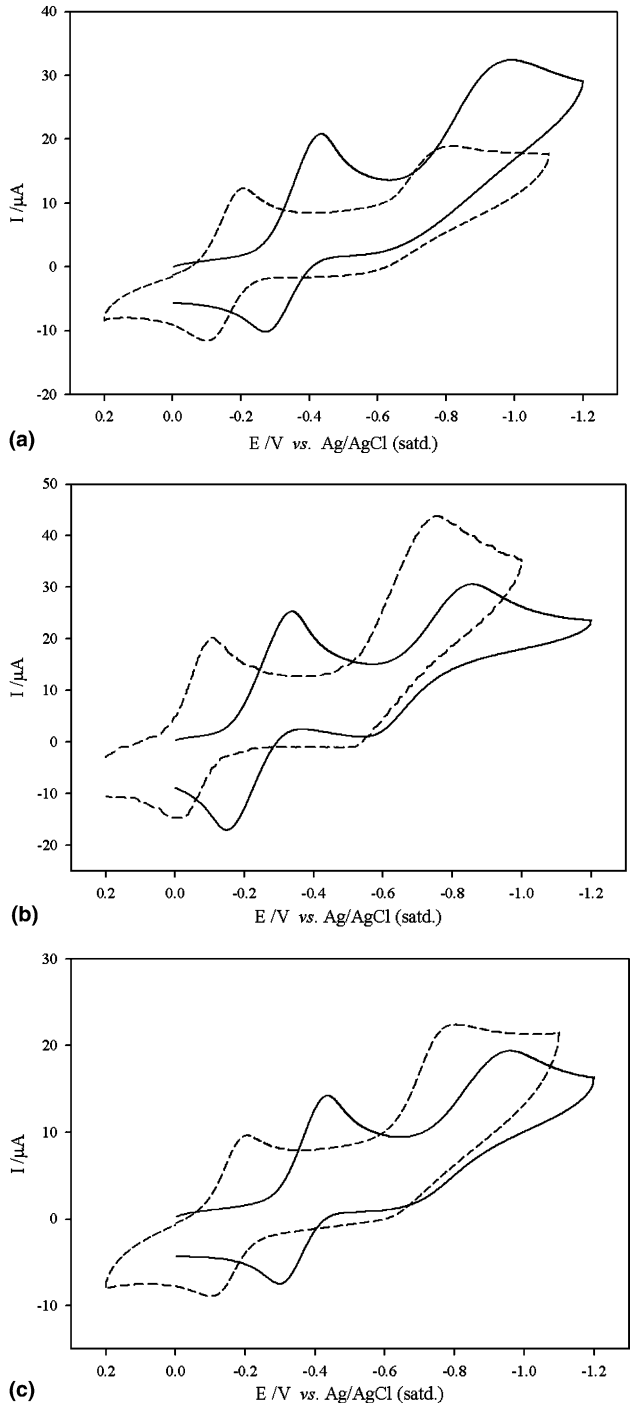


Fig. 4. Cyclic voltammogram of (a) $Mn(L^1)_2$ (**1**), (b) $Mn(L^2)_2 \cdot H_2O$ (**2**), (c) $Mn(L^3)_2$ (**3**) at a scan rate of 100 mV/s in dichloromethane (solid line) and DMSO (dashed line) solvents.

complexes for carboxylato coordinated MnL_2 than those in salicylaldimine complexes involving alkoxide coordination [21]. In the case of 2-hydroxy-2′-carboxy-5-methylazobenzene manganese complex, $Mn(azc)_2$, the Mn^{IV}/Mn^{III} couple lies more positive than the corresponding phenolate derivative – 2,2′-dihydroxyazobenzene manganese complex – $Mn(azp)_2$ [10]. The more positive Mn^{IV}/Mn^{III} cathodic reduction potential is due to the lower pK value of the carboxylic donor atoms compared to phenolate donor atoms [10,11,21]. Compounds **1**–**3** in this work show comparatively lower potentials in either solvent than the corresponding phenolate donor set ligands. The borderline nature of the thiolate group of the thiosemicarbazone could explain the spontaneous formation from the Mn(II) precursor and stabilization of the manganese(IV) complexes in the present case.

Table 6
Electrochemical data[a] of compounds **1**–**3**

Compound	Solvent	Mn(IV)–Mn(III) E^0_{298}, V (ΔE_p, mV)[b]	Mn(III)–Mn(II) E^0_{298}, V (ΔE_p, mV)
$Mn(L^1)_2$ (**1**)	CH_2Cl_2	−0.35 (162)	−0.99[c]
	DMSO	−0.15 (108)	−0.82[c]
$Mn(L^2)_2 \cdot H_2O$ (**2**)	CH_2Cl_2	−0.24 (188)	−0.70 (318)
	DMSO	−0.06 (93)	−0.65 (210)
$Mn(L^3)_2$ (**3**)	CH_2Cl_2	−0.37 (136)	−0.96[c]
	DMSO	−0.16 (98)	−0.80[c]

[a] Supporting electrolyte is TBAP (0.1 M); working electrode glassy carbon; reference electrode is Ag/AgCl (satd.).
[b] E^0_{298} is calculated as the average of anodic (E_{pa}) and cathodic (E_{pc}) peak potentials; $\Delta E_p = E_{pa} - E_{pc}$.
[c] Cathodic peak potential.

4. Conclusion

Based on our observation in this study, we contradict the suggestion that electron delocalisation along the ligand moiety can be one factor that may promote ambient oxidation of manganese(II) to manganese(IV). However it may be true that electron releasing groups in the ligand moiety or in the ring structure can facilitate the formation of manganese(IV) complexes. In a previous report salicylaldehyde thiosemicarbazone having methyl or Br substituents on the aromatic ring system has yielded Mn(IV) complexes [12], while the presence of a methyl group on the thiosemicarbazone moiety, as observed in our case, has facilitated its formation rather easily. Besides, substitution at the N(4) position can be said to have negligible influence on Mn(II)–Mn(IV) oxidation as thiosemicarbazones that have mono, di or no substituent(s) were found to give manganese(IV) complexes. Semicarbazones of hydroxyaldehydes/ketones were found to give only Mn(II) complexes despite the fact that they differ in having an oxygen donor atom instead of sulfur [34]. This indicates that a soft donor atom, such as sulfur, plays an important role in accomplishing the Mn(II) to Mn(IV) conversion and stabilizing the later. However further efforts are needed to optimise the factors that determine the facile conversion of Mn(II) to Mn(IV) by proper variation of the substituents on the thiosemi-

carbazone moiety to control the electronic factors. In short, we have accomplished the facile synthesis of three manganese(IV) complexes of *N*(4)-disubstituted thiosemicarbazones of 2-hydroxyacetophenone and characterized them by IR, UV–Vis and EPR spectroscopic methods. The structure of one of them, compound **2**, was established by X-ray crystallography and was found to have an octahedral geometry with the ligands coordinated in a meridional fashion. The reduction potential of the manganese(IV)–manganese(III) couple was found to be low and is predicted to be due to a higher p*K* value of the donor atoms.

5. Supplementary information

Crystallographic data for the structural analysis has been deposited with the Cambridge Crystallographic Data center, CCDC 229814 for compound $Mn(L^2)_2 \cdot H_2O$ reported in this paper. Copies of this information may be obtained free of charge from the Director, The Cambridge Crystallographic Data Centre, 12 Union Road, Cambridge CB2 1EZ, UK (fax: +44 1223 336033; e-mail: deposit@ccdc.cam.ac.uk or http://www.ccdc.cam.ac.uk/data_request/cif).

Acknowledgements

Authors R.P.J. thanks CSIR, New Delhi, Government of India and A.S. thanks Cochin University of Science and Technology, India, for the financial assistance. H.K.F. thank the Malaysian Government and Universiti Sains Malaysia for the research Grant R&D No. 305/PFIZIK/610961. Special thanks to Professor Pyo-Myung Ho, Sunchon National University for help in cyclic voltammetric studies. The help of RSIC, CDRI, Lucknow and RSIC, IIT Bombay for various other analyses is also greatly acknowledged.

References

[1] (a) V.L. Pecoraro, Manganese Redox Enzymes, VCH, New York, 1992;
(b) W.F. Beyer, I. Fridovich, Biochemistry 24 (1985) 6460;
(c) A. Willing, H. Follman, G. Auling, Eur. J. Biochem. 170 (1988) 603;
(d) M.L. Ludwig, K.A. Pattridge, W.C. Stallings, Manganese in Metabolism and Enzyme Function, Academic Press, New York, 1986, p. 405 (Chapter 21).
[2] W.C. Stallings, K.A. Pattridge, R.K. Strong, M.L. Ludwig, J. Biol. Chem. 55 (1984) 10664.
[3] (a) C.E. Holloway, M. Melnik, Rev. Inorg. Chem. 16 (1996) 101;
(b) C.W. Hoganson, G.T. Babcock, Science 277 (1997) 1953;
(c) C. Tommos, G.T. Babcock, Acc. Chem. Res. 31 (1998) 18;
(d) N.A. Law, M.T. Caudle, V.L. Pecoraro, Adv. Inorg. Chem. 46 (1999) 305.
[4] (a) N. Tamura, M. Ikeuchi, Y. Inoue, Biochim. Biophys. Acta 973 (1989) 281;
(b) V.K. Yachandra, K. Sauer, M.P. Klein, Chem. Rev. 96 (1996) 2927.
[5] O. Hannson, A. Aasa, T. Vanngard, Biophys. J. 51 (1987) 825.
[6] (a) K. Wieghardt, Angew. Chem., Int. Ed. Engl. 33 (1994) 725;
(b) R. Manchanda, G.W. Brudvig, R.H. Crabtree, Coord. Chem. Rev. 144 (1995) 1.
[7] (a) B. Frank, G. Dunkelmann, H.J. Lubs, Angew. Chem., Int. Ed. Engl. 6 (1967) 1075;
(b) P.A. Chaloner, Handbook of Coordination Catalysis in Organic Chemistry, Butterworths, London, 1986.
[8] (a) M. Mikuria, D. Jie, Y. Kakuta, T. Tokii, Bull. Chem. Soc. Jpn. 66 (1993) 1132;
(b) M.K. Chan, W.H. Armstrong, Inorg. Chem. 28 (1989) 3777;
(c) A.V. Lakshmi, N.R. Sangeetha, S. Pal, Ind. J. Chem., Sect. A 36 (1997) 844;
(d) M.T. Caudle, J.W. Kampf, M.L. Kirk, P.G. Rasmussen, V.L. Pecoraro, J. Am. Chem. Soc. 119 (1997) 9297;
(e) D. Gopal, P.K. Bharadwaj, D. Gosh, B. Chaudhari, R. Banerjee, Chem. Commun. (2001) 323.
[9] (a) S.K. Chandra, P. Basu, D. Ray, S. Pal, A. Chakravorty, Inorg. Chem. 29 (1990) 2423;
(b) S. Dutta, P. Basu, V.L. Pecoraro, Inorg. Chem. 30 (1991) 4031;
(c) S.K. Chandra, A. Chakravorty, Inorg. Chem. 31 (1992) 760.
[10] S. Dutta, P. Basu, R. Chakravorty, Inorg. Chem. 30 (1991) 4031.
[11] R. Mukhopadhyay, S. Bhattacharjee, C.K. Pal, S. Karmakar, R. Bhattacharyya, J. Chem. Soc., Dalton Trans. (1997) 2267.
[12] R. Mukhopadhyay, S. Bhattacharjee, R. Bhattacharyya, J. Chem. Soc., Dalton Trans. (1994) 2799.
[13] (a) A. Usman, I.A. Razak, S. Chantrapromma, H.-K. Fun, A. Sreekanth, S. Sivakumar, M.R.P. Kurup, Acta Crystallogr., Sect. C 58 (2002) 461;
(b) B.S. Garg, M.R.P. Kurup, S.K. Jain, Y.K. Bhoon, Transition Met. Chem. 18 (1988) 92.
[14] R. Mukhopadhyay, A.B. Chatterjee, R. Bhattacharyya, Polyhedron 11 (1992) 1353.
[15] S. Pal, P. Ghosh, A. Chakravorty, Inorg. Chem. 24 (1985) 3704.
[16] B.-K. Koo, U.K. Lee, Bull. Korean Chem. Soc. 23 (2002) 613.
[17] C.P. Pradeep, T. Htwe, P.S. Zacharias, S.K. Das, New J. Chem. 28 (2004) 735.
[18] (a) R.P. John, A. Sreekanth, M.R.P. Kurup, S.M. Mobin, Polyhedron 21 (2002) 2515;
(b) R.P. John, A. Sreekanth, V. Rajakannan, T.A. Ajith, M.R.P. Kurup, Polyhedron 23 (2004) 2549.
[19] Siemens, SMART and SAINT, Area Detector Control and Integration Software, Siemens Analytical X-ray Instruments Inc., Madison, WI, USA, 1996.
[20] G.M. Sheldrick, SHELXTL, Version 5.1, Bruker AXS Inc., Madison, WI, 1997.
[21] D.P. Kessissoglou, X. Li, W.M. Butler, V.L. Pecoraro, Inorg. Chem. 26 (1987) 2487.
[22] (a) R.P. John, A. Sreekanth, M.R.P. Kurup, A. Usman, A.R. Ibrahim, H.-K. Fun, Spectrochim. Acta 59A (2003) 1359;
(b) A. Sreekanth, U.L. Kala, C.R. Nayar, M.R.P. Kurup, Polyhedron 23 (2004) 41;
(c) M. Joseph, V. Suni, M.R.P. Kurup, M. Nethaji, Polyhedron 23 (2004) 3069.
[23] P.S. Pavacik, J.C. Huffman, G. Christou, J. Chem. Soc., Chem Commun. (1986) 43.
[24] (a) M.W. Lynch, D.N. Hendrickson, B.J. Fitzgerald, C.G. Pierpont, J. Am. Chem. Soc. 106 (1984) 2041;
(b) J.R. Hartmann, B.M. Foxman, S.R. Cooper, Inorg. Chem. 23 (1984) 1381;
(c) K. Weighart, U. Bossek, D. Ventur, J. Weiss, J. Chem. Soc., Chem Commun. (1985) 346;

(d) D.P. Kessissoglou, X. Li, W.M. Butler, V.L. Pecoraro, Prog. Photosyth. Res. (1987) 725.
[25] N. Bag, G.K. Lahiri, S. Bhattacharya, L.R. Flavello, A. Chakravorty, Inorg. Chem. 27 (1988) 4396.
[26] M. Koikawa, H. Okawa, S. Kida, J. Chem. Soc., Dalton Trans. (1988) 641.
[27] U. Auerbach, T. Weyhermüller, K. Wieghardt, B. Nuber, E. Bill, C. Butzlaff, A.X. Trautwein, Inorg. Chem. 32 (1993) 508.
[28] (a) P. Moews, Inorg. Chem. 5 (1966) 5;
(b) B.R. McGarvey, in: R.L. Karlin (Ed.), Transition Metal Chemistry, vol. 3, Marcel Dekker, New York, 1966, p. 89.
[29] (a) E. Pederson, H. Toftlund, Inorg. Chem. 13 (1974) 1603;
(b) D.C. Bradley, R.G. Copperthwaite, S.A. Cotton, K.D. Sales, J.F. Gibson, J. Chem. Soc., Dalton Trans. (1973) 191.
[30] (a) K.D. Magers, C.G. Smith, D.T. Sawyer, Inorg. Chem. 19 (1980) 492;
(b) D.T. Richens, D.T. Sawyer, J. Am. Chem. Soc. 101 (1979) 3681.
[31] K.L. Brown, R.M. Golding, P.C. Healy, K.J. Jessop, W.C. Tennant, Aus. J. Chem. 27 (1974) 2075.
[32] (a) B. Bleaney, R.S. Rubins, Proc. Phys. Soc. (Lond.) 77 (1961) 103;
(b) R.M. Golding, R.H. Newman, A.D. Rae, W.C. Tennant, J. Chem. Phys. 57 (1972) 1912.
[33] M. Koikawa, H. Okawa, J. Chem. Soc., Dalton Trans. (1988) 641.
[34] (a) W. Liufang, P. Zhouren, W. Xin, Y. Shuyan, L. Qinhui, W. Qi, Polyhedron 12 (1993) 1505;
(b) A. Kumar, Usha, S. Chandra, Synth. React. Inorg. Met.-Org. Chem. 22 (1992) 971.

Available online at www.sciencedirect.com
SCIENCE DIRECT®
Polyhedron 24 (2005) 611–618
POLYHEDRON
www.elsevier.com/locate/poly

Silver(I) interaction and complexation with sterically hindered sulfur-containing diphenol derivatives

N.V. Loginova [a,*], A.A. Chernyavskaya [a,b], G.I. Polozov [a], T.V. Koval'chuk [a], E.V.Bondarenko [b], N.P. Osipovich [c], A.A. Sheryakov [b], O.I. Shadyro [a]

[a] Department of Inorganic Chemistry, Belarusian State University, Leningradskaya str. 14, Minsk 220050, Belarus
[b] Center for Examinations and Tests in Health Service Republican Unitary Enterprise, Tovarishchesky lane 2a, Minsk 220037, Belarus
[c] Research Institute for Physical Chemical Problems of the Belarusian State University, Leningradskaya str. 14, Minsk 220050, Belarus

Received 15 December 2004; accepted 3 January 2005

Abstract

The interaction between silver(I) ions with 3,5-di(*tert*-butyl)-1,2-benzenediol (**I**) and sulfur-containing derivatives of sterically hindered diphenols: 4,6-di(*tert*-butyl)-3-(2-hydroxyethylsulfanyl)-1,2-benzenediol (**II**), 2-(2,5-dihydroxyphenylsulfanyl)acetic acid (**III**), 2-(2,5-dihydroxy-3,4,6-trimethylphenylsulfanyl)acetic acid (**IV**), 2-[4,6-di(*tert*-butyl)-2,3-dihydroxyphenylsulfanyl]acetic acid (**V**), 5,7-di(*tert*-butyl)-8-hydroxy-2,3-dihydro-1,4-benzoxathiin-2-one (**VI**), 3-[4,6-di(*tert*-butyl)-2,3-dihydroxyphenylsulfanyl]-2-methyl-carboxyamidopropanoic acid (**VII**) was studied. A competition of redox process and complexation is possible when these organic compounds interact with silver(I) ions. **I**–**IV**, **VI** and **VII** were found to reduce Ag(I) to Ag(0), silver sol formation being possible under certain conditions. The sols were examined by TEM and optical spectroscopy methods. The interaction of **V** with silver(I) ions is not accompanied by a redox reaction, the latter being hindered by complexation. The complexation was studied by potentiometric titration, and the complex of **V** with Ag(I) was characterized by the means of X-ray powder diffraction, elemental analysis, TG/DTA and IR spectroscopy. The antimicrobial activities of **V** and its Ag(I) complex, evaluated by minimum inhibitory concentration (MIC), were also tested.
© 2005 Elsevier Ltd. All rights reserved.

Keywords: Silver(I) complex; Sterically hindered diphenols; Silver sol; Antimicrobial activities; Electronic spectra

1. Introduction

Silver and its compounds are widely known as effective catalysts, elements of optical and electronic devices, pharmaceuticals and medical materials [1–8]. Ag(I) complexes have shown a variety of noteworthy antimicrobial activities, although the mechanisms of action are not yet entirely clarified. Of particular note is the fact that essentially all types of Ag(I) pharmaceuticals do not give rise to microorganisms' resistance, in contrast to many antibiotics. Other biological effects have also been observed, such as antifungal and antitubercular activities [9]. At the same time a few Ag(I) complexes have been investigated in this connection. The main aims of that research were the synthesis of pharmacologically active Ag(I) complexes with Ag(I)–O, Ag(I)–N, Ag(I)–S and Ag(I)–P bond, and the establishment of structural relationships of such complexes with bioactivities [10–26]. However, in some cases the elucidation of this problem is complicated by the fact that many Ag(I) complexes are hard to crystallize

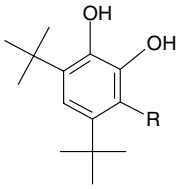
* Corresponding author. Tel.: +375 172 095516; fax: +375 172 264696/265567.
E-mail address: loginonv@bsu.by (N.V. Loginova).

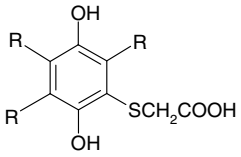
0277-5387/$ - see front matter © 2005 Elsevier Ltd. All rights reserved.
doi:10.1016/j.poly.2005.01.007

and some are believed to be polymeric [10–12,27,28]. One of the key factors determining the antimicrobial effects of Ag(I) complexes is reported to be the nature of the atom coordinated to Ag(I) and its bonding properties, rather than the solubility, charge, chirality or degree of polymerization of the complexes [12,15,17–19,21,22,24]. Moreover, it has been found that most Ag(I) complexes with the same or similar core structures consisting of the same coordinating donor atoms have shown very similar spectra of the antimicrobial activities, in particular Ag(I) complexes with the dimeric Ag_2O_4-core molecular structure [14,16,18,19,21]. The broader spectrum of the antimicrobial activities exhibited by these Ag(I)–oxygen bonding complexes is attributed to a direct interaction or complexation of the silver(I) ion with biological ligands [24]. These ligands contain the potential target sites for the inhibition of bacterial and yeast growth by these Ag(I) complexes that reportedly might be the sulfur-containing residues of proteins. It has been presumed that one of the key factors leading to a broad spectrum of antimicrobial activities is the ease of ligand-exchange between Ag–O cores and Ag–S (biological ligand) bonds, caused by the weak Ag(I)–O bond strengths [24,29].

In this connection it is of interest to study various aspects of silver chemistry, specifically the peculiarities of silver(I) ion interactions with organic compounds incorporating the O-donor atoms coordinated to the Ag(I) center. The structure–activity correlation in the antimicrobial and antifungal activities by Ag(I)–oxygen bonded complexes with organic ligands of that kind is also of interest. It should be noted that many of these organic compounds are biologically active themselves. Studying the interaction and complexation of bioactive organic ligands with metal ions is a topical line of investigation on the chemistry of complexes, because metal ions can change the magnitude and directionality of the pharmacological effects of organic ligands as pharmaceuticals [9], while coordinated metals are often more active and less toxic as opposed to the respective metal ions [30,31]. In addition, the coordinated ligands are supposed to play the role of a carrier of the metal ions to the biological systems.

In the present work we have studied the interactions of silver(I) ions with 3,5-di(*tert*-butyl)-1,2-benzenediol (**I**) and sulfur-containing derivatives of sterically hindered diphenols (SHD): 4,6-di(*tert*-butyl)-3-(2-hydroxyethylsulfanyl)-1,2-benzenediol (**II**), 2-(2,5-dihydroxy- phenylsulfanyl)acetic acid (**III**), 2-(2,5-dihydroxy-3,4,6-trimethylphenyl-sulfanyl)acetic acid (**IV**), 2-[4,6-di(*tert*-butyl)-2,3-dihydroxyphenylsulfanyl]acetic acid (**V**), 5,7-di(*tert*-butyl)-8-hydroxy-2,3-dihydro-1,4-benzoxathiin-2-one (**VI**), 3-[4,6-di(*tert*-butyl)-2,3-dihydroxyphenyl-sulfanyl]-2-methyl-carboxyamidopropanoic acid (**VII**).





I – R=H
II – R=SCH_2CH_2OH
V – R=SCH_2COOH
VII – R=$SCH_2CH(NHCOCH_3)COOH$

III –R= H
IV –R= CH_3

Many of the derivatives of SHD were found to be universal inhibitors of free-radical processes, effectively retarding both oxidation processes and free-radical reactions of fragmentation of biomolecules (lipids, peptides, carbohydrates, vitamins, etc.) [32,33]. Activation of that sort of processes may cause a wide variety of diseases in man, including cardiovascular, neurodegenerative, oncological, hemorragic and other diseases [34]. Studying bioactivities of synthesized multipurpose inhibitors of free-radical reactions in experiments with animals and with model systems lends support to their use in medicine being promising. Thus, an effective bioantioxidant has been found among them, which is distinguished by pronounced antihypoxic and anti-inflammatory properties [35]. A sulfur-containing derivative thereof exhibits high antiviral, neurotropic and nootropic activity, and is superior to piracetam [36–38].

Derivatives of SDH can participate in complexation as ligands due to electron-donor atoms of their functional groups and to peculiarities of their structure, but some of them are known to be active as reductants (especially in alkali medium) [39]. That is why both their complexation with Ag(I) ions and redox interaction were studied here.

Among the derivatives of SHD investigated in our work it was only 2-[4,6-di(*tert*-butyl)-2,3-dihydroxyphenylsulfanyl]acetic acid that did not reduce Ag(I) ions in solution, but formed a complex therewith. The complexation in solution was studied by potentiometric titration. The solid complex that we have first obtained was tolerant of heat and light, and it was characterized by means of elemental analysis, thermogravimetric and differential thermal analysis (TG/DTA), FT-IR and X-ray diffraction. However, a full structural analysis could not be performed because no crystals suitable for single-crystal X-ray analysis were obtained. A special investigation showed that most of the metal complexes formed with the SHD derivatives containing one or two *tert*-butyl groups were hard to crystallize. A similarly hindered crystallization was found also for many metal complexes with hinokitiol ligand that is the 4-isopropyl-substituted compound of tropolone [24]. Their structure can be revealed by Rietveld analysis using X-ray powder diffraction data. Unfortunately, X-ray diffraction analysis of

the Ag(I) complex powder sample we had synthesized showed that it had decomposed while the X-ray diffraction pattern was registered, and that lack of tolerance to X-rays became the "fatal" circumstance which prevented us from using the above mentioned method to elucidate the structure of the complex either with a powder or with a monocrystalline sample. Therefore our notion of the coordination core of the Ag(I) complex was formed on the basis of findings provided by other physico-chemical methods and reported here.

We also estimated the antimicrobial and antifungal activities of the Ag(I) complex as compared with those of the free ligand.

If the interaction of SHD derivatives with silver(I) ions resulted in the latter being reduced, those systems were used to produce stable silver sols without any special stabilizers added. The sols were examined by transmission electron microscopy (TEM) and UV spectroscopy methods.

2. Experimental

2.1. Materials and methods

Chemicals were purchased from commercial sources and were used without further purification. The SHD derivatives were prepared according to [36,40,41]. The purity of these compounds was checked by thin-layer chromatography, and their structures were characterized by ^{1}H and ^{13}C NMR measurements and IR spectra. The preparation of the Ag(I) complex is described later.

Potentiometric titration was carried out in water–ethanol (1/1, v/v) solution as the SHD derivatives are generally hardly soluble in water. These solutions were prepared with twice-distilled water before every experiment and used immediately. A digital pH/mV-meter I-130 was used to monitor the e.m.f. variations of electrochemical cells opposing a silver-wire electrode to a silver chloride reference electrode. The silver chloride electrode was connected to the solution to be titrated by a salt bridge filled with KNO_3 solution (0.1 mol dm^{-3}). All measurements were carried out at 25 ± 0.1 °C and at a constant ionic strength of 0.1 mol dm^{-3} KNO_3. The titrations were carried out with continuous magnetic stirring by adding portions of $AgNO_3$ solution to that of the ligand. Argon was bubbled through the solutions during the titrations to ensure the absence of oxygen. To determine the composition and stability constants of the Ag(I) complexes formed on Ag(I) interaction with **V**, $AgNO_3$ solutions (2×10^{-5} and 4×10^{-5} mol dm^{-3}) were titrated with 10^{-2} mol dm^{-3} ligand solution. The set of ln β_n values were obtained by mathematical analysis of the ln ($[Ag(I)]_{total}/[Ag(I)]_{free}$) versus [L] relationships [42]. To determine the conditions of Ag(I) interaction with the ligand **V**, which favor the production of only one complex with Ag(I):ligand = 1:2, ligand solutions (2×10^{-3} and 4×10^{-3} mol dm^{-3}) were titrated with 0.1 mol dm^{-3} $AgNO_3$ solution.

Infrared spectra of the solids (the ligand **V** and the synthesized Ag(I) complex) were recorded by a Spectrum 1000 spectrophotometer in the wavelength range 4000–400 cm^{-1} at room temperature, using nujol mulls of the ligand and its complex and polyethylene windows.

Thermogravimetric (TG) and differential thermal analyses (DTA) were performed with an OD103 instrument. TG/DTA measurements were run under air between 20 and 900 °C (10 °C min^{-1}).

CHN elemental analyses were carried out according to the standard methods by the Microanalytical Laboratory, Bioorganic Chemistry Institute, National Academy of Sciences, Belarus. Silver and sulfur determinations were carried out using an atomic emission spectrometer with an inductively coupled plasma excitation source (Spectroflame Modula). A sample of the Ag(I) complex was decomposed under treatment with $HNO_3 + H_2O_2$ using a Milestone mls 1200 mega microwave digestion system. After the complex had been decomposed, the contents of silver and sulfur in the resulting solution was determined.

X-ray powder diffraction patterns of the free ligand **V** and its Ag(I) complex sample were measured at room temperature with an X-ray diffractometer DRON–3.0 (Co Kα radiation, MnO_2-filter, 1°/min, in the range of 2θ from 5° to 70°). As the complex tended to decompose while the X-ray diffraction pattern was registered, for each successive angle range of 10° a new portion of the sample was used.

Optical absorbance spectra of sols were registered in the wavelength range from 300 to 700 nm using the two-beam spectrophotometer "SPECORD M40 UV-VIS". The spectra were interpreted with regard to the spectral characteristics of the water–ethanol solutions of the SHD derivatives at pH 6 or 9. To determine the size and shape of the particles by TEM method, an EM-125 K instrument was used.

2.2. Synthesis of the Ag(I) complex with 2-[4,6-di-(tert-butyl)-2,3-dihydroxyphenylsulfanyl]acetic acid (V)

1.6 ml of $AgNO_3$ solution in water (0.1 mol dm^{-3}) was added dropwise to a clear solution of 0.32 mmol of ligand **V** in water–ethanol (1/1, v/v) mixture, the reaction vessel being shielded from light. A white precipitate formed instantaneously. After 1 h stirring, it was collected on a membrane filter (JG 0.2 μm), washed with ethanol (100 ml) and water (100 ml), and dried in vacuo (yield >98%). The relatively photostable compound was soluble in dimethylformamide (DMF), dimethylsulfoxide (DMSO), acetonitrile, sparingly soluble in ethanol, *i*-propanol, *n*-butanol, but insoluble in water, diethyl

ether and chloroform. When the complex was dissolved in the media with high donor numbers, it decomposed with time to yield silver particles [43]. *Anal*. Calc. for $C_{32}H_{47}O_8S_2Ag$: C, 52.53; H, 6.43; O, 17.51; S, 8.76; Ag, 14.77. Found: C, 52.37; H, 6.40; O, 17.90; S, 8.67; Ag, 14.63%.

2.3. Synthesis of the silver sols

Silver sols were produced by slowly (drop by drop) adding a solution of the organic reductant (compounds **I**–**VII**) to a water–ethanol $AgNO_3$ solution under permanent stirring, at pH 6 or 9. Silver(I) stock solutions were standardized by means of potentiometric titrations. Sodium tetraborate buffer was used to provide the basic medium. The silver concentration in the sols was 1×10^{-4} mol dm^{-3}. The sols were stored in closed, light-tight vessels.

2.4. Antimicrobial activities

Antimicrobial activities of free ligand **V** and its silver(I) complex were estimated by a minimum inhibitory concentration (MIC, μg/ml) as usual. The evaluation of their inhibitory effect on the bacterial and fungal growth was carried out by the twofold serial dilution method [44]. The following test microorganisms were used: *Escherichia coli* (ATCC 25922), *Pseudomonas aeruginosa* (ATCC 9027), *Candida albicans* (ATCC 855-653), *Bacillus subtilis* (ATCC 6633), *Staphylococcus aureus* (209–P), *Proteus vulgaris* (collection of Medical Postgraduate Education Academy of Belarus). The compounds were dissolved in DMSO and tested at concentrations ranging from 62.5 to 10^3 μg ml^{-1} (for the ligand) and from 31.2 to 500 μg ml^{-1} (for the complex). Test inoculum of 25×10^4 bacteria ml^{-1} and 25×10^4 yeasts ml^{-1} were applied. The absence of microbial growth after an incubation period of 24 h at 37 °C for bacteria or of 48 h at 30 °C for fungi was taken to be a criterion of effectiveness. In every case MIC was determined as the lowest concentration of the compound under study, which inhibits the bacterial and fungal growth, compared with the control system in which the bacteria and fungi were grown in the absence of any test compound. The amount of DMSO in the medium was 1% and did not affect the growth of the tested microorganisms. There were three replicates for each dilution. Results were always verified in three separate experiments.

3. Results and discussion

It has been found that silver(I) ions are reduced to give the metal when they interact with compounds **I**–**VII** at pH 6 or 9, except for compound **V** which does not reduce silver(I) ions at pH 6.

When **I** was used to produce Ag sols at different pH, the absorbance maxima characteristic of colloidal silver appeared in the UV–Visible spectra of the sols: at 412 nm (pH 9) and at 405 nm (pH 6) (Fig. 1(a), 1).

No sol was produced when $AgNO_3$ reacted with **II**, but a silver mirror was formed on the bottom and walls of the reaction vessel at pH 6 and 9, suggesting the autocatalytic nature of the reaction [45]. No absorbance maxima of colloidal silver were observed in the UV–Visible spectra in that case.

The sol produced by Ag(I) reduction with **III** at pH 9 was orange–brown, with a maximum at 410 nm present in its absorbance spectrum (Fig. 1(a), 2). A yellow–orange sol was formed at pH 6, which became light-green upon aging. The absorbance spectrum is characterized by a maximum at 309 nm, which, according to [46], can be evidence for large aggregates of silver particles present in the sol, which is shown to be the case by TEM (Fig. 2).

A pink sol was formed when Ag(I) was reduced with **IV** in alkali medium. The as-prepared sol had an absorbance maximum at 430 nm (Fig. 1(a), 3). The sol produced at pH 6 was yellow, with an absorbance maximum at 420 nm.

No colloidal silver was formed by reacting Ag(I) with **V** at pH 6, as evidenced by the characteristic absorbance maximum being absent in that case. Yet **V** does reduce Ag(I) in alkali medium. An absorbance maximum is observed at 360 nm, which, according to [47], may be assigned to subcolloidal silver (Fig. 1(b), 1). The system is unstable: a grey coarse-dispersion precipitate of metallic silver is formed overnight.

An absorbance maximum at 420 nm characteristic of Ag colloids over 2 nm in size was observed in the as-prepared sol when Ag(I) was reduced with **VI** at pH 9 (Fig. 1(b), 2). The reduction of Ag(I) at pH 6 yields a brown–grey sol, with a rather broad absorbance maximum about 512 nm, characteristic of silver colloids 25–60 nm in size (the aforesaid refers to the as-prepared sol).

The absorbance spectrum for the system produced by Ag(I) interacting with **VII** demonstrates a strong narrow maximum at 430 nm (Fig. 1(b), 3). According to [48], it is evidence of silver colloids 5–10 nm in size. A pale-pink sol was produced at pH 6, which demonstrated a very broad (from 404 to 700 nm) maximum in the absorbance spectrum, with a small shoulder at 309 nm, disappearing on aging.

Thus, according to the spectral data, silver sols are formed most effectively when silver(I) ions are reduced with the compound **III**, its structure lacking *tert*-butyl substituents in the benzene ring. The methyl substituents appearing in the structure of **IV** markedly decrease the capacity of this compound for reduction of silver(I) ions, esulting in the sol production. The diphenol with just *tert*-butyl substitutors in the benzene ring (**I**) proved

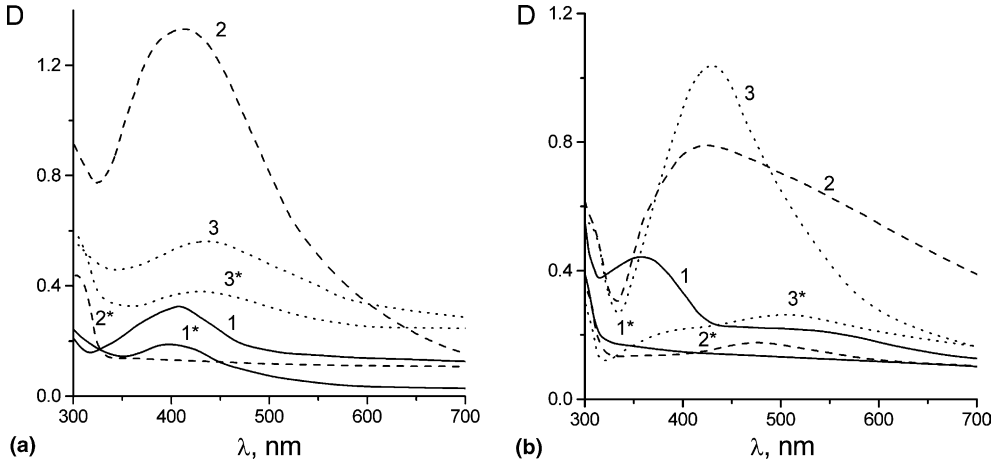


Fig. 1. Absorbance spectra of as-prepared silver sols produced using the compounds: (a) 1 – **I**, 2 – **III**, 3 – **IV**; (b) 1 – **V**, 2 – **VI**, 3 – **VII** (* is for the spectra of the silver sols produced at pH 6).

to be even less efficient at producing the silver sol. But the introduction of sulfur-containing substituents, as in the structures of **II**, **VI**, **VII**, results in the sol forming somewhat more actively.

TEM investigation showed that silver colloids and their aggregates in the sols are surrounded by a layer presumably formed by organic reductant compounds and their oxidation products (Fig. 2). That layer may make the sols stable. Particle sizes of silver colloids vary from 10 to 35 nm.

Ag(I) reduction with **V** at pH 6 was found to be hindered by a competing process yielding an insoluble compound. As the most likely product here is a complex, the direct potentiometric titration method was chosen to characterize it. When $AgNO_3$ interacts with **V**, complexation occurs according to: $Ag(I) + L \leftrightarrow AgL$ and $Ag(I) + 2L \leftrightarrow AgL_2$. Using the potentiometric study results the constants $\beta_1 = 2.5 \times 10^3$ и $\beta_2 = 2.5 \times 10^6$ were calculated. Based on that data, synthetic conditions were created to purposefully provide the preferential formation of the complex with $Ag(I):L = 1:2:AgNO_3$ solution was added in small portions to the ligand solution under continuous stirring, so that the complexation always took place with an excess of ligand present. The fact that it was only one, AgL_2, complex thus was formed under those conditions was confirmed by the results of titration of the ligand solution with that of $AgNO_3$. The titration curve was S-shaped and had only one inflection. The results of the titration allowed us to determine the molar ratio of Ag(I) to the ligand, which was found to be 1:2. The complex is characterized by an X-ray pattern of its own, differing significantly from that of **V**.

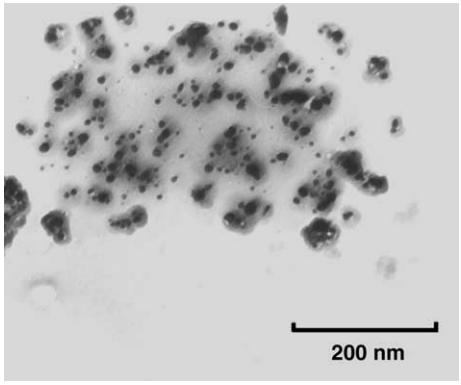


Fig. 2. TEM image of silver nanoparticles and their aggregates surrounded by a layer presumably formed by organic reductant compounds and their oxidation products.

Thermal analyses in flowing air with identification of the end products by X-ray powder diffraction has shown the complex to be anhydrous and unsolvated, because the DTA curve lacks any endothermic peaks over a wide range from 60 to 150 °C. The Ag(I) complex decomposes over the thermal range 180–540 °C to give silver metal. The agreement between the experimental (85.10%) and theoretical (85.24%) weight losses for the above process confirms the formula of the Ag(I) complex. The DTA curve shows a complicated process with exothermic peaks at 150, 260, 380, 420 °C. The first exothermic peak observed at 150 °C may be due to the thermal polymerization of the complex without any noticeable weight loss [49]. The second exothermic peak observed at 260 °C corresponds to the maximal weight loss due to the thermal destruction of an organic ligand [50]. The third peak observed at 380 °C corresponds to a small weight loss and, according to [51], is most likely due to decarboxylation of coordinated (deprotonated) carboxylic groups. Above 400 °C pyrolitic decomposition of the ligand takes place, as usual.

In the IR spectrum of the ligand **V** there is a strong band at 1695 cm^{-1} and a weaker one at 1775 cm^{-1} which can be assigned to the stretching C=O vibrations of the COOH group (Fig. 3(a)). The former band

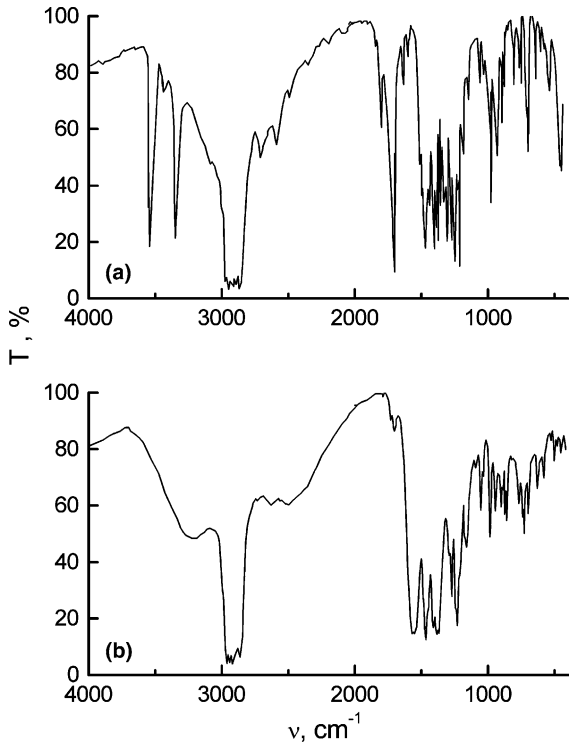


Fig. 3. Solid FT-IR spectra of **V** (a) and its Ag(I) complex (b).

becomes quite weak, and the latter virtually disappears in the spectrum of the complex (Fig. 3(b)), while a new band at 1556 cm^{-1} appears, which can be assigned to a COO^- antisymmetric stretching vibration.

Thus, we may suggest that the ligand molecules are coordinated via the carboxylic group. The simultaneous presence of a band corresponding to the stretching vibrations of C=O in a COOH group at 1697 cm^{-1} and the band at 1556 cm^{-1}, corresponding to COO^-, allows us to suggest that Ag(I) substitutes the hydrogen atom of COOH only in one of the coordinated ligand molecules. Narrow bands at 3550–3350 cm^{-1} are present in the ligand spectrum, which are assigned to stretching O–H vibrations. According to [52], bulky substituents in a ligand molecule may hinder intermolecular association. In the spectrum of the Ag(I) complex, instead, the respective bands are broadened and virtually merged into one band at 3300 cm^{-1}, suggesting that OH groups are coordinated to the metal ion or form hydrogen bonds. A polymeric Ag(I) complex also can be formed with **V**, as that type of structure, according to [16,18,19], is not uncommon with Ag(I) complexes.

Antimicrobial activities of the Ag(I) complex, which is (according to IR data) an Ag(I)–O bonding compound, together with those of the ligand **V** are listed in Table 1, as estimated by the MIC (μg ml^{-1}). It should be emphasized that antimicrobial tests of these compounds were first performed here. The metal-free ligand **V**, 2-[4,6-di-(*tert*-butyl)-2,3-dihydroxyphenylsulfanyl]acetic acid, has shown moderate activities (125 and 62.5 μg ml^{-1}) against Gram-positive bacteria (*B. subtilis*, *St. aureus*) and no activity (>1000 μg ml^{-1}) against Gram-negative bacteria (*E. coli*, *Ps. aeruginosa*, *Pr. vulgaris*) and yeast (*C. albicans*). The Ag(I) complex, on the contrary, was found to be considerably more active against a wide spectrum of Gram-negative and -positive bacteria and much better at inhibiting the growth of *C. albicans* than the free ligand **V** (Table 1).

Table 1
Antimicrobial activities of the free 2-[4,6-di(*tert*-butyl)-2,3-dihydroxyphenylsulfanyl]acetic acid (ligand **V**) and its Ag(I) complex evaluated by minimum inhibitory concentration (MIC, μg ml^{-1})

Microbe	Ligand **V**	Ag(ligand **V**)$_2$
Escherichia coli	>1000	62.5
Proteus vulgaris	>1000	62.5
Pseudomonas aeruginosa	1000	<31.2
Staphylococcus aureus	125	62.5
Bacillus subtilis	62.5	<31.2
Candida albicans	>1000	31.2

Hence, the complexation of Ag(I) with the ligand **V** leads to appreciably enhancing the activities, a substantial effect being found with some of the cultures. Of particular note is the activity against *C. albicans* in connection with the currently central investigations into the synthesis and in vitro testing of new metal-based anti-fungal drugs [22–26]. Similar broad spectra were also obtained in the case of previously investigated Ag(I) complexes with other organic ligands formed by Ag(I)–N and/or Ag(I)–O bonding [12,24], and literature findings are mostly consistent with those presented here. Yet another important experimental fact is that for the above mentioned complexes the antimicrobial activity spectra were broader than those observed in the Ag(I)–S and Ag(I)–P bonding compounds [11,13–15,20], allowing us to argue for the previous suggestion about the same or similar antimicrobial mechanism and mode of action for the complexes of that type, in which the crucial factors are the kind of atom (O, N) coordinated to Ag(I) and its moderate bonding strength as well as the ease of ligand-exchange reactions with some biological ligands, such as proteins, which comprise a donor S-atom [24]. It must be also emphasized that our findings concerning the Ag(I) complex activity cannot be interpreted unambiguously, because the Ag(I) complex under study is unlikely to remain intact throughout the screening protocol, with the result that the MIC values reflect the combined effect of the action of the Ag(I) complex, Ag(I) ions and, probably, silver colloids, which might be generated in the test media.

4. Conclusion

When SPH derivatives under study interact with silver(I) ions, two competitive processes are possible: redox process and complexation. The compounds **I**–**IV**,

VI and **VII** are found to reduce silver(I) to silver(0), silver sol formation being possible under certain conditions. Raising the pH up to 9 favors the sol formation, while the effectiveness of this process is lower at the lower pH value of 6, and sometimes the silver reduction arrests itself. The properties of the sols (dispersion, coloration, stability) largely depend on the nature of the organic reductant used.

Thus, among the sulfur-containing SPH derivatives studied we have found **V** to stand out as the compound which is distinguished by its interaction with Ag(I) being unaccompanied by a redox reaction, the latter being hindered by a competitive complexation. The data of the spectral investigation are evidence for the formation of a coordination core of the complex where two ligands are bound to Ag(I) by oxygen atoms of COOH and OH functional groups. However, if just a carboxylic group and a hydroxyl in the ortho-position are present in the organic compound, it is not enough for a stable complex to be formed, as conformed by the lack of a complex with **I**. In contrast to the free ligand **V**, the Ag(I) complex shows a broad spectra of antimicrobial activities. These facts may be of interest in the design of new effective metal-based drugs. In this paper we did not set ourselves the task of testing the antimicrobial activity of the sols synthesized, because the high lability and difficulties of preparation of liophobic sols is known to drastically decrease the possibilities of their use as medicines.

References

[1] T. Hayakawa, S. Tamil Selvan, M.J. Nogam, Non-Cryst. Solids 259 (1999) 16.
[2] W.-L. Dai, J.-L. Li, Y. Cao, Q. Liu, J.-F. Deng, Catal. Lett. 64 (2000) 37.
[3] A.A. Scalisi, G. Compagnini, L. D'Urso, O. Puglisi, Appl. Surf. Sci. 226 (2004) 237.
[4] B.S. Bal'zhinimaev, Kinetika i Kataliz 40 (1999) 879, in Russian.
[5] Yu. I. Petrov, Fizika Malykh Chastits, Nauka, Mscow, 1986 (in Russian).
[6] R.B. Thurman, C.P. Gerba, CRC Crit. Rev. Environ. Control 18 (1989) 295.
[7] R. Lopez-Garzon, J.M. Lopez-Gonzalez, G. Alvarez-Cienfuegos, M.A. Romero-Molina, A. Navarrete-Guijosa, M.M. Herrador-Pino, J. Inorg. Biochem. 38 (1990) 139.
[8] K.M. Davies, G.E. Hobson, D. Grierson, Plant Cell Environ. 11 (1988) 729.
[9] E.E. Kriss, I.I. Volchenskova, A.S. Grigor'eva, K.B. Yatsimirskii, L.I. Budarin, Koordinatsionnye Soedineniya Metallov v Meditsine, Nauk. Dumka, Kiev, 1986 (in Russian).
[10] K. Nomiya, Y. Kondoh, K. Onoue, N.C. Kasuga, H. Nagano, M. Oda, T. Sudoh, S. Sakuma, J. Inorg. Biochem. 58 (1995) 255.
[11] K. Nomiya, K. Onoue, Y. Kondoh, N.C. Kasuga, H. Nagano, M. Oda, S. Sakuma, Polyhedron 14 (1995) 1359.
[12] K. Nomiya, K. Tsuda, T. Sudoh, M. Oda, J. Inorg. Biochem. 68 (1997) 39.
[13] K. Nomiya, K. Tsuda, N.C. Kasuga, J. Chem. Soc., Dalton Trans. (1998) 1653.
[14] K. Nomiya, K. Tsuda, Y. Tanabe, H. Nagano, J. Inorg. Biochem. 69 (1998) 9.
[15] K. Nomiya, R. Noguchi, M. Oda, Inorg. Chim. Acta 298 (2000) 24.
[16] K. Nomiya, S. Takahashi, R. Noguchi, J. Chem. Soc., Dalton Trans. (2000) 1343.
[17] K. Nomiya, S. Takahashi, R. Noguchi, J. Chem. Soc., Dalton Trans. (2000) 2091.
[18] K. Nomiya, S. Takahashi, R. Noguchi, J. Chem. Soc., Dalton Trans. (2000) 4369.
[19] K. Nomiya, S. Takahashi, R. Noguchi, S. Nemoto, T. Takayama, M. Oda, Inorg. Chem. 39 (2000) 3301.
[20] K. Nomiya, R. Noguchi, T. Shigeta, Y. Kondoh, K. Tsuda, K. Ohsawa, N.C. Kasuga, M. Oda, Bull. Chem. Soc. Jpn. 73 (2000) 1143.
[21] K. Nomiya, H. Yokoyama, J. Chem. Soc., Dalton Trans. (2002) 2483.
[22] I. Tsyba, B.B. Mui, R. Bau, R. Noguchi, K. Nomiya, Inorg. Chem. 42 (2003) 8028.
[23] M. McCann, B. Coyle, J. Briody, F. Bass, N. O'Gorman, M. Devereux, K. Kavanagh, V. McKee, Polyhedron 22 (2003) 1595.
[24] K. Nomiya, A. Yoshizawa, K. Tsukagoshi, N.C. Kasuga, S. Hirakawa, J. Watanabe, J. Inorg. Biochem. 98 (2004) 46.
[25] S. Abuskhuna, J. Briody, M. McCann, M. Devereux, K. Kavanagh, J.B. Fontecha, V. McKee, Polyhedron 23 (2004) 1249.
[26] B. Coyle, M. McCann, K. Kavanagh, M. Devereux, V. McKee, N. Kayal, D. Egan, C. Deegan, G.J. Finn, J. Inorg. Biochem. 98 (2004) 1361.
[27] R.C. Elder, M.K. Eidsness, Chem. Rev. 87 (1987) 1027.
[28] R. Bau, J. Am. Chem. Soc. 120 (1998) 9380.
[29] K. Nomiya, S. Yamamoto, R. Noguchi, H. Yokoyama N.C. Kasuga, K. Ohyama, C. Kato, J. Inorg. Biochem. 95 (2003) 208.
[30] Z. Guo, P. Sadler, Angew. Chem. Int. Ed. 38 (1999) 1512.
[31] N.P. Farrell (Ed.), Uses of Inorganic Chemistry in Medicine, Royal Society of Chemistry, Cambridge, 1999.
[32] O.I. Shadyro, G.K. Glushonok, T.G. Glushonok, I.P. Edimecheva, A.G. Moroz, A.A. Sosnovskaya, I.L. Yurkova, G.I. Polozov, Free Radical Res. 36 (2002) 859.
[33] O.I. Shadyro, I.P. Edimecheva, G.K. Glushonok, N.I. Ostrovskaya, G.I. Polozov, H. Murase, T. Kagiya, Free Radical Res. 37 (2003) 1087.
[34] B. Halliwell, Drugs 42 (1991) 569.
[35] G.N. Shilov, A.I. Balakleevskii, O.I. Shadyro, V.A. Timoshchuk, Russ. 182759, Ofits. Bull. Rossiiskogo Agentstva po Patentam I Tovarnym Znakam, 26, 1993 (in Russian).
[36] D.K. Petrikevch, V.A. Timoshchuk, O.I. Shadyro, O.T. Andreeva, V.I. Votyakov, V.E. Zhelobkovich, Khim.-Farm. Zhurn. 12 (1995) 32 (in Russian).
[37] T.A. Mikhas'ko, B.V. Dubovik, O.I. Shadyro, G.I. Polozov, Meditsinskie Novosti 4 (2002) 81 (in Russian).
[38] O.I. Shadyro, V.A. Timoshchuk, G.I. Polozov, V.N. Povalishev, O.T. Andreeva, V.E. Zhelobkovich, Khim.-Farm. Zhurn. 7 (1999) 25 (in Russian).
[39] T.H. James, The Theory of The Photographic Process, Macmillan, New York, 1977.
[40] L.A. Maslovskaya, D.K. Petrikevch, V.A. Timoshchuk, O.I. Shadyro, Zhurn. Obshchei Khimii 66 (1996) 1893 (in Russian).
[41] L.A. Maslovskaya, D.K. Petrikevch, V.A. Timoshchuk, O.I. Shadyro, Zhurn. Obshchei Khimii 66 (1996) 1899 (in Russian).
[42] D. De Marco, G. Zona, Thermochim. Acta 386 (2002) 173.
[43] M.C. Parfenova, A.A. Chernyavskaya, N.V. Loginova, G.I. Polozov, V.E. Agabekov, in: V.E. Borisenko, S.V. Gaponenko, V.S. Gurin (Eds.), Physics, Chemistry and Application of Nanostructures, World Scientific, Singapore, 2003, p. 381.

[44] G.N. Pershin (Ed.), Metody Experimental'noi Khimioterapii, Meditsina, Moscow, 1971, p. 103 (in Russian).
[45] V.V. Sviridov (Ed.), Khimicheskoe Vosstanovlenie Metallov iz Vodnykh Rastvorov, Universitetskoe, Minsk, 1987 (in Russian).
[46] A.N. Pestryakov, A.A. Davydov, L.N. Kurina, Zhurn. Fiz. Khimii 60 (1986) 2081 (in Russian).
[47] B.G. Ershov, D.A. Troitskii, N.L. Suchov, Khimia Vysokikh Energii 25 (1991) 213 (in Russian).
[48] S.F. Chernov, Zhurn. Nauchn. Prikl. Fotogr. Kinematogr. 32 (1987) 203 (in Russian).
[49] Termoliz Koordinatsionnykh Soedinenii, Fan, Tashkent, 1986 (in Russian).
[50] Y.N. Kukushkin, V.F. Budakova, G.N. Sedova, Termicheskie Prevrashcheniya Koordinatsionnykh Soedinenii v Tverdoi Faze, Izd. Leningradskogo universiteta, Leningrad, 1981 (in Russian).
[51] V.A. Logvinenko, Termicheskii Analiz Koordinatsionnykh Soedinenii i Klatratov, Nauka, Novosibirsk, 1982 (in Russian).
[52] K. Nakamoto, IR Spektry i Spektry KR Neorganicheskikh i Koordinatsionnykh Soedinenii, Mir, Moscow, 1991, p. 505 (in Russian).

Available online at www.sciencedirect.com
SCIENCE DIRECT®
Polyhedron 24 (2005) 619–625
POLYHEDRON
www.elsevier.com/locate/poly

Raman spectra and structure of $PbCl_2$–ACl (A = K, Cs) melts

V. Dracopoulos, D.Th. Kastrissios, G.N. Papatheodorou *

Foundation for Research and Technology, Hellas, Institute of Chemical Engineering and High Temperature Chemical Processes – FORTH-ICE/HT, P.O. Box 1414, GR-26504, Patras, Greece
Department of Chemical Engineering, University of Patras, GR-26504, Patras, Greece

Received 12 July 2004; accepted 4 January 2005

Abstract

Quantitative Raman spectra of molten $PbCl_2$–ACl (A = K, Cs) mixtures have been measured at different compositions and at temperatures up to 680 °C. Spectral changes upon melting the Cs_4PbCl_6, $CsPbCl_3$, KPb_2Cl_5 and $PbCl_2$ solids have been also measured. All spectra of melts are mainly characterized by an isotropic (polarized) ν_P and an anisotropic (depolarized) ν_D band. The intensity and position of the ν_P ($\sim 237 \pm 2\ cm^{-1}$) and ν_D ($\sim 113 \pm 3\ cm^{-1}$) bands remain practically constant at $X_{PbCl_2} \leqslant 0.5$ indicating that the structure is predominated by coordination polyhedra of the type $Pb_nCl_{3n}^{n-}$ ($n \leqslant 4$). With increasing $PbCl_2$ mole fraction the ν_P and ν_D bands shift to the "red" and the "blue", respectively, reaching the corresponding values of 215 and 132 cm^{-1} in pure molten $PbCl_2$. Furthermore, the intensity ratio of the anisotropic to isotropic spectra increases indicating contributions to the scattering intensity arising from dipole–induced-dipole interactions in these melts.
© 2005 Elsevier Ltd. All rights reserved.

Keywords: Pb(II) chloride melts; Raman spectroscopy; Coordination in melts; Dipole–induced-dipole interactions; Molten salts

1. Introduction

Molten lead (II) chloride and its mixtures with alkali metal halides have been the subject of a series of physicochemical investigations in the early days of molten salt research [1]. The structure of these melts has been also studied by Raman [2] and X-ray diffraction [3] spectroscopies. Solid $PbCl_2$ and the solid binary compounds with alkali metal chlorides exhibit solid phase transformations and have been extensively studied [4]. Furthermore, a series of glasses involving $PbCl_2$ have been prepared and appear to have rather interesting optical properties [5].

The present work concerns the Raman spectra of molten $PbCl_2$–KCl and $PbCl_2$–CsCl systems. Composition dependent measurements are correlated to the melt structure. The changes of vibrational modes on melting the compounds $PbCl_2$, KPb_2Cl_5, $CsPbCl_3$ and Cs_4PbCl_6 have been also measured. The purpose of this work is to contribute to the understanding of the melt structure as well as of the structure of the amorphous materials involving lead (II) chloride.

2. Experimental

The source of all chemicals used was Alfa Chemical Co. (99% purity). The $PbCl_2$ was further purified by sublimation in sealed fused silica containers. The KCl and CsCl were recrystallized from the melt in special vacuum of argon filled furnaces. Details for the purification of different metal chlorides can be found elsewhere [6]. The congruently melting binary compounds ($A_nPb_mCl_{n+2m}$; A = K, Cs) were prepared by mixing and melting the appropriate amounts of the $PbCl_2$ and ACl salts in fused silica containers and then rapid cooling to room temperature. All operations were carried out in either

* Corresponding author. Tel.: +302610 993 586; fax: +302610 990 987.
E-mail address: gpap@iceht.forth.gr (G.N. Papatheodorou).

0277-5387/$ - see front matter © 2005 Elsevier Ltd. All rights reserved.
doi:10.1016/j.poly.2005.01.013

sealed fused silica containers and/or in a nitrogen filled glove box with less than 1 ppm H_2O.

Details for the Raman systems and techniques used for measuring spectra at elevated temperatures can be found elsewhere [6]. The molten binary mixtures $PbCl_2$–KCl and $PbCl_2$–CsCl have a yellowish coloration which becomes deeper with increasing $PbCl_2$ mole fraction and/or temperature. So, the melts partially absorb the Ar-ion laser lines and thus no semi-quantitative intensity measurements are possible. At temperatures up to 700 °C, there is no significant absorption of the 647.1 nm Kr-ion laser line and thus spectra excited with this line permitted relative intensity measurements and a comparison of intensities from cells containing different $PbCl_2$ compositions. For these quantitative measurements the optical geometry, the scattering volume and the spectral conditions were kept the same [6b] and thus the relative per mole of $PbCl_2$ intensities could be calculated. The measured Raman bands were rather broad and their frequencies were determined within 1–2 cm^{-1}. The reduced isotropic and anisotropic spectra were calculated by methods described elsewhere [7].

3. Results and discussion

3.1. Melting the binary compounds

The Raman spectra of the four solids listed in Table 1 have been measured from LN_2 temperature up to a few degrees above their melting points. Apart from band broadening and slight frequency shifts the spectra of the solids remained unchanged at all temperatures and no solid phase transitions were detected. The spectra of the solids at room temperature and of the melts are shown in Fig. 1. The crystal structures of these compounds show that the coordination of lead (II) can vary from 9 to 6 (Table 1). In the case of Cs_4PbCl_6 independent octahedral $PbCl_6^{4-}$ species with D_{3d} distortions are formed. The $\nu_t = 201$ cm^{-1} frequency, measured in the solid, corresponds to the terminal Pb–Cl stretching frequency (A_{1g}) of the "octahedra". For the same compound, the pair of the bands above 50 cm^{-1} are assigned to two modes arising from the splitting of the

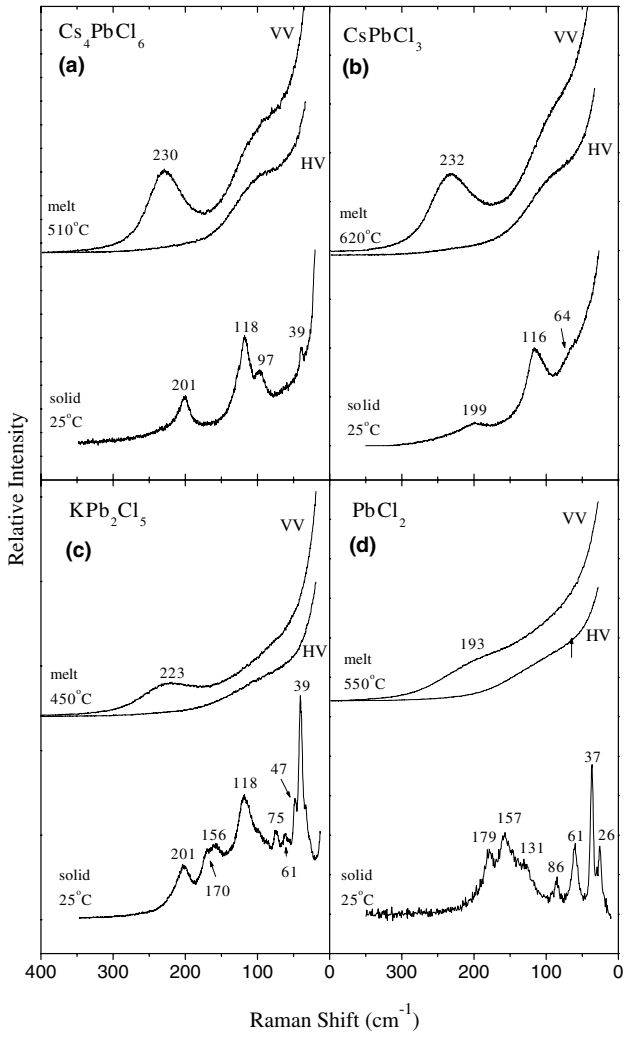


Fig. 1. Changes of vibrational modes upon melting the polycrystalline compounds Cs_4PbCl_6, $CsPbCl_3$, KPb_2Cl_5 and $PbCl_2$. Spectral conditions: $\lambda_0 = 647.1$ nm, laser power 150 mw, spectral slit width 2.5 cm^{-1}, scan rate 1 cm^{-1} s^{-1}.

Table 1
Binary compounds of $PbCl_2$ with KCl and CsCl

Compound	Crystal structure[a]	Coordination No of Pb[a]	Raman spectra of solid	Melting points[a] (°C)	Highest Raman frequency of solid[e] (cm^{-1})	Highest Raman frequency of melt[e,f] (cm^{-1})
$PbCl_2$	orthorhombic $Pnma/D_{2h}^{16}$	9	single crystal[b]	495	179	193 (215)
KPb_2Cl_5	monoclinic $P2_1/C_{2h}^5$	7; 9	polycrystalline[c]	434	201	216 (232)
$CsPbCl_3$	orthorhombic $Pmmm/D_{2h}^{13}$	6	single crystal[d]	605	199	232 (237)
Cs_4PbCl_6	hexagonal $R-3c/D_{3d}^6$	6	polycrystalline[c]	496	201	230 (235)

[a] Ref. [4a].
[b] Ref. [8].
[c] This work.
[d] Ref. [4b].
[e] From data in Fig. 1.
[f] Number in parenthesis are frequencies calculated from the reduced isotropic spectra.

T_{2g} octahedral mode in the D_{3h} symmetry of the $PbCl_6^{4-}$ (i.e., $T_{2g} \rightarrow A_{1g} + E_g$). In all other compounds the lead (II) polyhedra share their chlorides with neighboring lead (II) cations and thus the anticipated Pb–Cl frequencies are expected to be near but lower relative to the terminal ν_t frequencies. As noted in Table 1 some of these compounds have been studied as single crystals by Raman spectroscopy and certain assignments of the measured bands have been made.

Upon melting $PbCl_2$ (Fig. 1) the spectra are dominated by a weak polarized and a weak depolarized band over a relatively intense and extended liquid wing. The melt spectra of all other compounds have more defined bands, but all of them are mainly characterized by one polarized and one depolarized band. All measured bands are "blue" shifted relative to the "octahedral" ν_t frequency. As shown in Table 1, the polarized frequency of the melt, for all these compounds, do not differ much, especially if the temperature/liquid wing correction is applied by using the reduced [7] representation of the spectra (see also Figs. 2 and 3). Thus, the polarized band in these melts lays in the range ~215 to ~237 cm^{-1} and shows no obvious correlation to the solid frequencies. It is also noteworthy that these frequencies are above the octahedral Pb–Cl stretching frequency ($\nu_t \approx 201$ cm^{-1}), which implies that the Pb(II) coordination polyhedra in the melt are more likely to have a coordination number less than six.

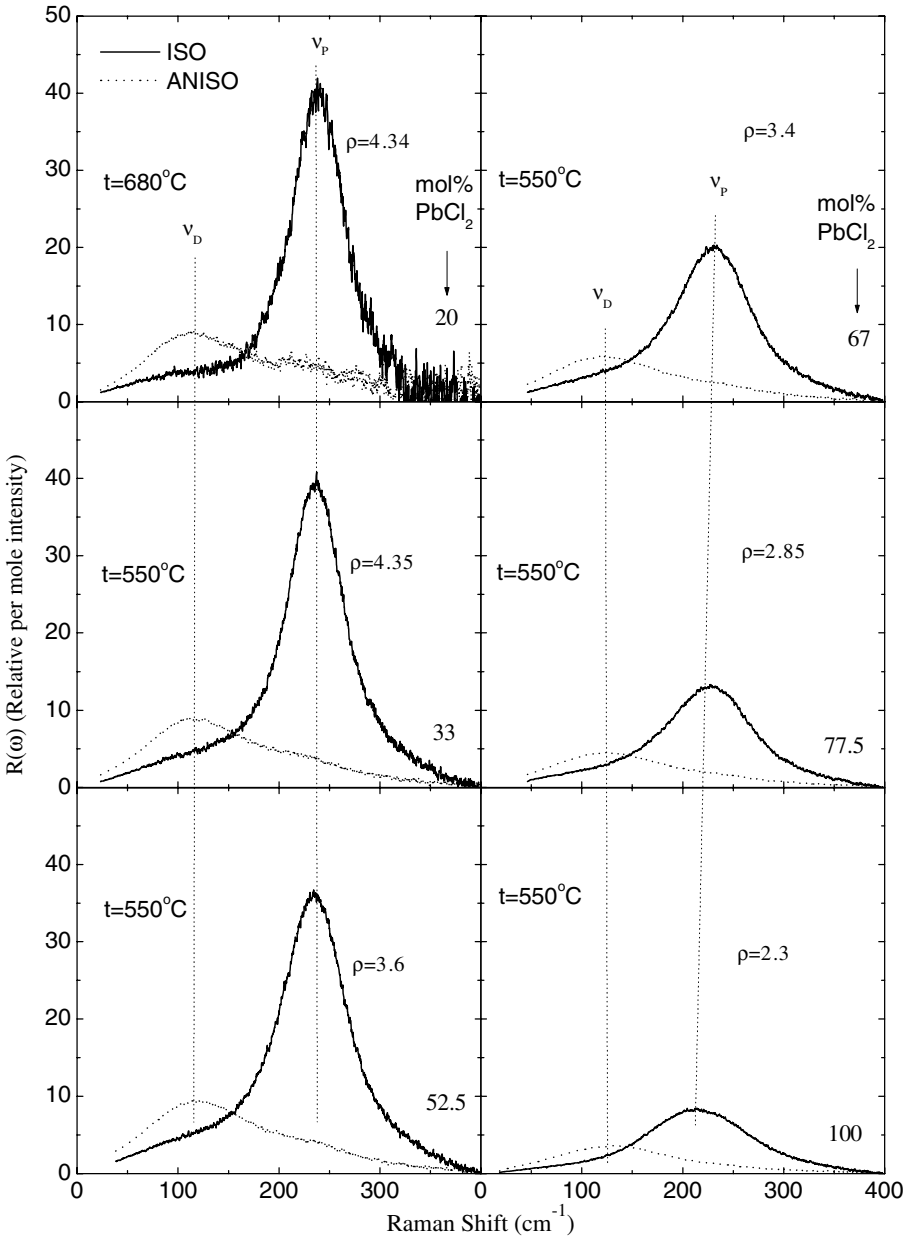


Fig. 2. Relative reduced per mole isotropic and anisotropic spectra of $PbCl_2$–KCl melt mixtures at different compositions. Spectral conditions as in Fig. 1 ρ gives the intensity ratio of the ν_D to ν_P peak intensities in the reduced ISO and ANISO spectra.

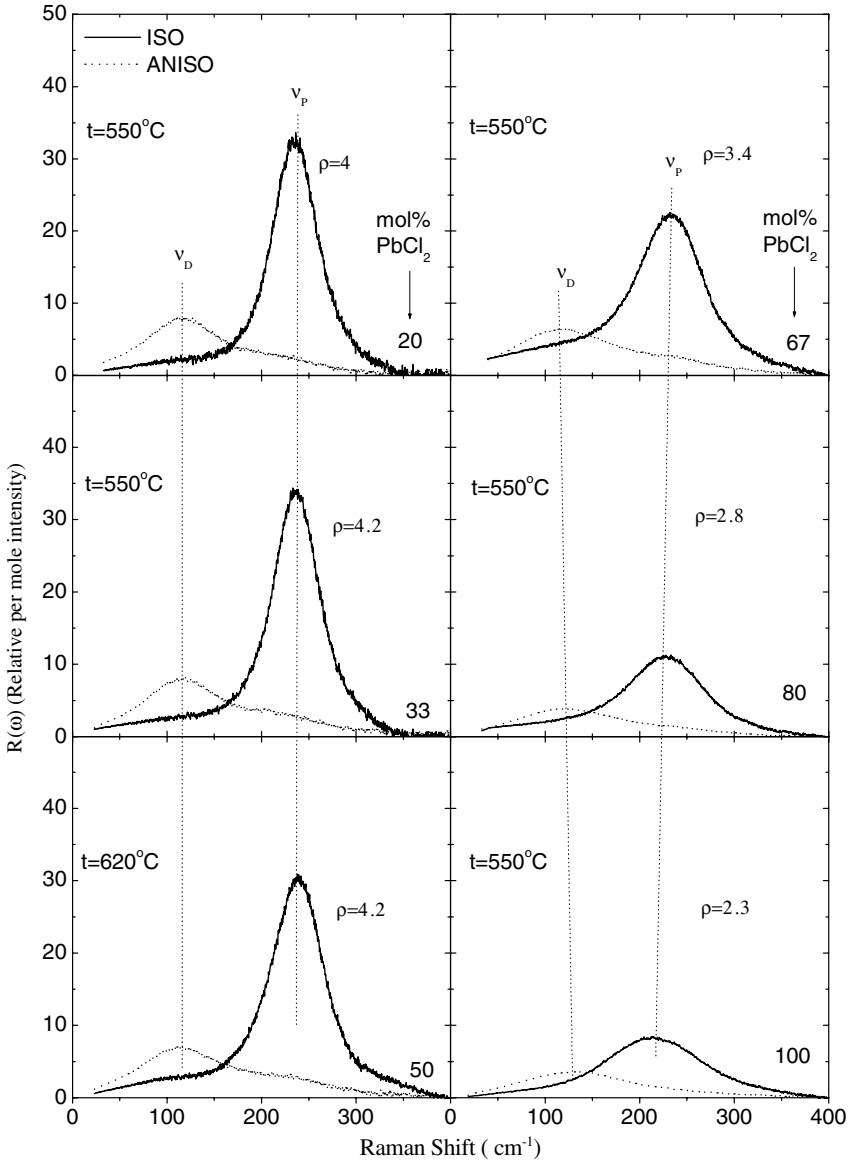


Fig. 3. Relative reduced per mole isotropic and anisotropic spectra of $PbCl_2$–CsCl mixtures at different compositions. Spectral conditions as in Fig. 1, ρ as in Fig. 2.

3.2. Isotropic and anisotropic spectra of mixtures and predominant vibrational modes

For both the $PbCl_2$–KCl and $PbCl_2$–CsCl molten systems, Raman spectra were measured at different compositions and in most cases at 550 °C. For two compositions (90 mol% KCl and 50 mol% CsCl) the spectra were measured at a temperature a few degrees above the liquidus. Following the procedures of our earlier work [7], we have calculated the reduced isotropic and anisotropic contributions to the Raman scattering and the results are shown in Figs. 2 and 3. The units on the $R(\omega)$ abscissa represent the relative per mole of $PbCl_2$ intensity. Two main bands marked as ν_P and ν_D predominate the isotropic and anisotropic spectra, respectively.

It should be noted here that for an isotropic ionic medium, the mechanism for light scattering is related to the fluctuations of the polarizability tensor $\Delta\Pi$ which is expressed [9] in terms of the anisotropic (ANISO) and isotropic (ISO) contributions:

$$\Delta\Pi_{\mathrm{ISO}} = \Pi^{\mathrm{Sr}}_{\mathrm{ISO}} + \Pi^{\gamma}_{\mathrm{ISO}} \tag{1}$$

$$\Delta\Pi_{\mathrm{ANISO}} = \Pi^{\mathrm{DID}}_{\mathrm{ANISO}} + \Pi^{\mathrm{B}}_{\mathrm{ANISO}} + \Pi^{\mathrm{SR}}_{\mathrm{ANISO}} + \Pi^{\gamma}_{\mathrm{ANISO}} \tag{2}$$

The different terms are: Π^{SR} refers to a short range term which describes the effect of near neighbor interactions of the ionic charge clouds; Π^{DID} is the dipole–induced-dipole (DID) interactions of an ion with the neighboring ions (including first and second coordination shears); Π^{B} and Π^{γ} give the change in polarizability induced on a given ion by the Coulomb field gradient

and the Coulomb field, respectively. All four terms contribute to the light scattering spectra but in certain cases due to cross correlation a degree of mutual cancellation may occur [9].

Simulations of light scattering intensities [9c] have shown that the isotropic SR term (Eq. (1)) arises mainly from the stretching frequencies of the coordination polyhedra involved in the melt structure. Thus, the main isotropic band (ν_P) in the region ~215–237 cm^{-1} (Figs. 2 and 3) is attributed to Pb–Cl stretching frequencies of the lead (II) coordination polyhedra predominating the structure. As pointed out before, the frequency region of the isotropic band imposed indirectly an average coordination of less than six. The quantitative Raman measurements permitted the evaluation of the relative per mole intensities on going from pure $PbCl_2$ to the dilute solutions; it appears that the dilute solutions have a much higher per mole scattering intensity than the mixtures rich in $PbCl_2$. Furthermore, the ratios $\rho = D_P/D_D$ of the peak intensity of the reduced ν_P band relative to the ν_D band are also calculated and marked in the figures. It appears that:

obs.: (1a) in dilute solutions and up to 50 mol% $PbCl_2$ the frequency of the isotropic (ν_p) band and the ratio ρ do not change much.
obs.: (1b) in the same mole fraction region the anisotropic band (ν_D) also shows the same characteristics, i.e., about constant frequency and constant per mole intensity.

These observations are best interpreted to indicate that the same coordination polyhedra predominate the melt structure and contribute to the average stretching frequency in the region $X_{PbCl_2} \leqslant 0.5$. The maximum mole fraction of 0.5 implies a molar stoichiometry for these species with an average of 1 $PbCl_2$:1 ACl or in other words a general species of the type $Pb_nCl_{3n}{}^{n-}$. Examples of structures with such a stoichiometry are given in Fig. 4. With the exception of the trigonal (or pyramidal) $PbCl_3{}^-$ species, the other structures are dominated by lead (II) tetrahedra bridged by edges or corners. For $PbCl_3{}^-$ in aqueous solution a stretching frequency of ~249 cm^{-1} has been reported [10], while by comparing the terminal frequency of $CdCl_6{}^{4-}$ and $CdCl_4{}^{2-}$ [11] to that of $PbCl_6{}^{4-}$ a terminal tetrahedral frequency of $PbCl_4{}^{2-}$ can be scaled to be 232 cm^{-1}. In other words, the observed value ν_P = 230 cm^{-1} ($X_{PbCl_2} \leqslant 0.5$) is compatible with all these structures (n = 2,3,4) with the Pb–Cl stretching frequency arising from the tetrahedra participating in the structures. Furthermore, the $PbCl_3{}^-$ species in C_{3v} symmetry cannot be definitely excluded since a proper pyramidal angle may shift the Pb–Cl frequency close to the 230 cm^{-1} value. On the other hand, structures with $n \geqslant 5$ are unlikely to be present since they correspond to highly charged species which are not commonly found in melts.

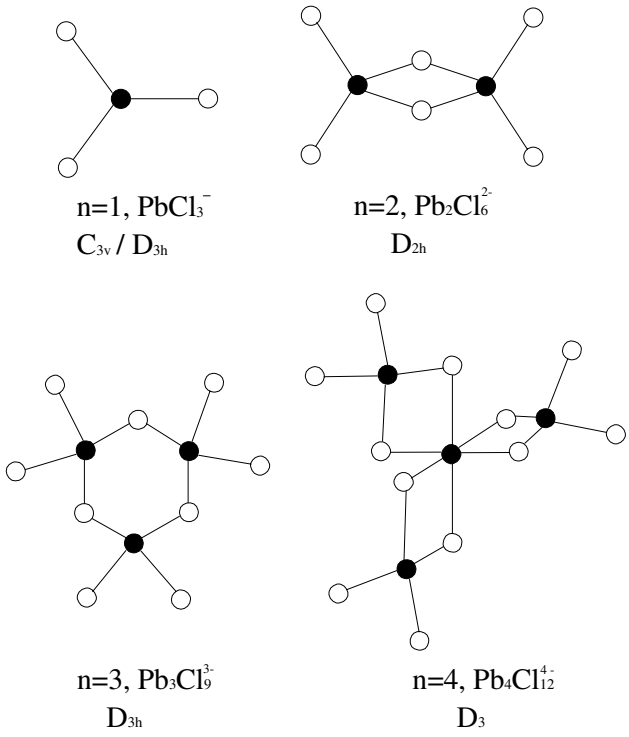


Fig. 4. Molecular models of $Pb_nCl_{3n}{}^{n-}$ anionic species. n = 1 corresponds to a trigonal planar (D_{3h} point symmetry) or a pyramidal (C_{3v}) molecule. n = 2 and n = 3 are the dimer-four atom ring molecule (D_{2h}) and the trimer-six atom ring molecule (D_{3h}), respectively, composed of bridged tetrahedra. n = 4 corresponds to two possible structures, one is an extension of the trimer structure, the tetramer with four bridged tetrahedra forming an eight atom ring (D_{4h}), the other shown here is a tetramer composed by an octahedra edge bridged with three tetrahedra (D_3).

The enthalpy of mixing data for the $PbCl_2$–CsCl system [12] show that the enthalpy interaction parameter exhibits a shallow minimum between 25 and 35 mol% $PbCl_2$. This points out towards the existence of species that stabilize thermodynamically the mixture with $PbCl_2$–CsCl stoichiometries of 1:2, 1:3 and 1:4 while species with 1:1 ratios are difficult to reconcile. Thus, the interpretation of the thermodynamic and spectroscopic data appear to be at odds. This discrepancy may be bridged if it is assumed that at $X_{PbCl_2} \leqslant 0.5$ a continuous multi-species equilibrium takes place involving all the 1:1 species (Fig. 4) as well as species with different stoichiometries (e.g., $PbCl_4{}^{2-}$, $PbCl_6{}^{4-}$). The average stretching frequency of all the species involved is centered at ~230 cm^{-1} which is close to the Pb–Cl tetrahedral frequency. In conclusion the Raman data support the formation of anionic coordination polyhedra in melts with $X_{PbCl_2} \leqslant 0.5$ but do not point out a definite predominant lead (II) species in these melts.

3.3. Anisotropic spectra and DID interactions

As the $PbCl_2$ mole fraction increases from above 0.5 to 1.0 the following spectral changes are observed:

obs.: (2a) the frequency of the isotropic ν_P band shifts progressively from $\sim$235 cm^{-1} in the 50/50 mixture to $\sim$215 in pure molten $PbCl_2$.
obs.: (2b) a similar shift occurs for the anisotropic ν_D band.
obs.: (2c) in the same composition range the per mole ($PbCl_2$) isotropic intensity decreases by a factor of four
obs.: (2d) the anisotropic band ν_D gains intensity relative to the isotropic ν_D band, reaching a ratio $\rho = 2.3$ in molten $PbCl_2$.

The ν_P red shift (obs.: 2a) presumably implies that the average coordination increases with increasing $PbCl_2$ content. X-ray diffraction data of molten $PbCl_2$ suggest a coordination number of either 8 [3a], 7 [3b] or 6 [3c]. The latest value of six [3c] arises from corrections of previous data [3b] and appears to be more accurate. For the same melt $\nu_P = 215\ cm^{-1}$ is below the average tetrahedral frequency ($\sim$235 cm^{-1}) and is closer to an octahedral frequency ($\sim$205 cm^{-1}). Thus, the suggested value of six, by the recent X-ray data, is somehow compatible with the observed Raman frequency. However, the decreasing per mole intensity (obs.: 2c) implies that the contribution of the SR term (Eq. (1)) is diminishing and that the cation–anion nearest neighbor interactions are weakened. An account of this could be given by examining the competition between cations for a common anion. In melts rich in ACl the second nearest neighbors to the Pb^{2+} are the A^+ cations. With increasing $PbCl_2$ the A^+ cations are replaced by the doubly charged, highly polarizable Pb^{2+} cations which attract more efficiently the chlorides of the lead (II) polyhedra. This in turn weakens the Pb–Cl interactions within the polyhedra and red shifts the corresponding frequency.

The increasing anisotropic intensity (obs.: 2d) is a phenomenon observed previously in the spectra of other molten salt systems involving large and highly polarizable cations and is related to the DID interactions between neighboring cations [7,13]. The studies of alkali metal chlorides and fluorides show that for highly polarizable cations (e.g., Cs^+) the anisotropic intensity is even higher than that of the isotropic intensity [7]. The DID term (Eq. (2)) becomes rather important for such systems overcoming the other interactions. In a similar way the spectra of rare earth fluoride (LnF_3) systems with alkali fluorides show that with increasing LnF_3 mole fraction and/or Ln^{+3} ionic size the anisotropic intensity of the bending modes increases and in certain cases (e.g., LaF_3–KF) approaches the isotropic intensity. This effect was attributed to the diminishing shielding of the Ln^{3+} cations by the coordinating fluorides which enhanced the DID interaction between nearest neighbor cations (Ln–Ln) [13].

The ionic radius of Pb^{2+} is $\sim$1.19 Å and thus the shielding by the chloride anions in the coordination polyhedra is not very effective. Even in pure molten $PbCl_2$, with an anticipated (see above) coordination number of six, the shielding of the Pb^{2+} by the chloride is not complete and this allows the neighboring Pb^{2+} cations to interact. Due to Pb^{2+} high polarizability ($\alpha \approx 2.65$ $Å^3$) [14] the "pure" DID interactions between lead (II) ions are enhanced and give rise to strong anisotropic scattering (like in the cases of CsCl [7c] and CsF [7b] melts) which is superimposed on the bending modes of the coordination polyhedra. The result in the reduced spectra is a rather strong anisotropic band with a maximum arising from a superposition of the bending modes band(s) and the reduced anisotropic band of the "pure" DID scattering. When molten $PbCl_2$ is diluted with alkali chlorides, the neighboring cations change gradually and the Pb–Pb, DID interactions diminish; this alters the relative contributions of the DID and bending modes to the ν_D band and thus its maximum may shift with composition (obs.: 2b). Finally, it should be noted that the shielding of the central Pb^{2+} cation by the chlorides changes during the vibrational motion of the coordination polyhedra. For a breathing symmetric vibration (i.e., isotropic) the chlorides move towards and against the neighboring cations and a rather symmetric average shielding is imposed. On the other hand, the bending modes change locally the shielding in certain directions which in turn influences the cation–cation DID interactions asymmetrically along the same direction. In other words, the enhanced anisotropic scattering indicates that there should be coupling between the polyhedra bending modes and the DID interaction between neighboring cations.

References

[1] G.J. Janz, Molten Salt Handbook, Academic Press, New York, 1967.
[2] (a) V.A. Maroni, J. Chem. Phys. 54 (1971) 4126;
(b) R. Oyamada, J. Phys. Soc. Jpn 36 (1973) 903.
[3] (a) H. Ohno, M. Yoroki, K. Furukawa, Y. Takagi, T. Nakamura, J. Chem. Soc., Faraday Trans. 74 (1978) 1861;
(b) H. Morikawa, M. Miyake, Y. Takagi, F. Marumo, J. Chem. Soc., Faraday Trans. 77 (1981) 1967;
(c) M. Ablanov, H. Matsuura, R. Takagi, Electrochemistry 67 (1999) 839.
[4] (a) K. Nitsch, M. Dušek, M. Niki, K. Polák, M. Rodová, Prog. Cryst. Growth Charact. 33 (1995) 11, and references therein;
(b) C. Carabatos-Nédelec, M. Qussaid, K. Nitsch, J. Raman Spectrosc. 34 (2003) 388, and references therein.
[5] (a) I.V. Kityk, J. Phys. Chem. B 107 (2003) 10083;
(b) J.H. Yang, N.L. Dai, S.Y. Dai, L. Wen, L.L. Hu, Z.H. Jiang, Chem. Phys. Lett. 376 (2003) 671;
(c) R. Balda, J. Fernandez, A. Mendioroz, M. Voda, M. Al-Salem, Phys. Rev. B 68 (2003) 165101, and references therein.

[6] (a) G.N. Papatheodorou, S.N. Yannopoulos, in: M. Gaune-Escard (Ed.), Molten Salts: from Fundamentals to Applications, Kluwer Academic, Dordrecht, 2002, pp. 47–106, and references therein;
(b) S. Boghosian, G.N. Papatheodorou, J. Phys. Chem. 93 (1989) 415.
[7] (a) S.N. Yannopoulos, A.G. Kalampounias, A. Chrissanthopoulos, G.N. Papatheodorou, J. Chem. Phys. 118 (2003) 3197;
(b) V. Dracopoulos, G.N. Papatheodorou, Phys. Chem. Chem. Phys. 2 (2000) 2021;
(c) G.N. Papatheodorou, S.G. Kalogrianitis, T.G. Mihopoulos, E.A. Pavlatou, J. Chem. Phys. 105 (1996) 2262.
[8] (a) G.A. Ozin, Can. J. Chem. 48 (1970) 2931;
(b) B. Willemsen, J. Inorg. Nucl. Chem. 33 (1971) 3963.
[9] (a) P.A. Madden, K.F. O'Sullivan, J.A.B. Board, P.W. Fowler, J. Chem. Phys. 94 (1991) 918;
(b) P.A. Madden, K.F. O'Sullivan, J. Chem. Phys. 95 (1991) 1980;
(c) P.A. Madden, M. Wilson, F. Hutchinson, J. Chem. Phys. 120 (2004) 6609.
[10] K. Nakamoto, Infrared and Raman Spectra of Inorganic and Coordination Compounds (Part A), 5th ed., Wiley, New York, 1997.
[11] J.H.R. Clarke, P.J. Hartley, Y. Kuroda, J. Phys. Chem. 76 (1972) 1831.
[12] F.G. McCarty, O.J. Kleppa, J. Phys. Chem. 68 (1964) 3846.
[13] (a) V. Dracopoulos, B. Gilbert, B. Borrensen, G.N. Photiadis, G.N. Papatheodorou, J. Chem. Soc., Faraday Trans. 93 (1997) 3081;
(b) V. Dracopoulos, B. Gilbert, G.N. Papatheodorou, J. Chem. Soc., Faraday Trans. 94 (1998) 2601.
[14] P.W. Fowler, N.C. Pyper, Proc. Royal Soc. Lond. A 398 (1985) 377.

Available online at www.sciencedirect.com
SCIENCE DIRECT®
Polyhedron 24 (2005) 627–637
POLYHEDRON
www.elsevier.com/locate/poly

A comparison of the coordination geometries of some 4-methylimidazole-5-carbaldehyde complexes with Zn(II), Cd(II) and Co(II) ions in the solid state and aqueous solution

Barbara Barszcz [a,*], Stanisław A. Hodorowicz [b], Katarzyna Stadnicka [b], Agnieszka Jabłońska-Wawrzycka [b]

[a] *Institute of Chemistry, Pedagogical University, 5 Chęcińska Str., 25-020 Kielce, Poland*
[b] *Faculty of Chemistry, Jagiellonian University, 30-060 Kraków, Poland*

Received 2 December 2004; accepted 4 January 2005

Abstract

Reactions of Zn(II), Cd(II) and Co(II) ions with 4-methylimidazole-5-carbaldehyde (4-Me-5-CHOIm) afforded four novel complexes $[Zn(4\text{-Me-5-CHOIm})_4](NO_3)_2$ (**1**), $[Cd(4\text{-Me-5-CHOIm})_4](NO_3)_2(H_2O)$ (**2**), $[Co(4\text{-Me-5-CHOIm})_2(H_2O)_2](NO_3)_2$ (**3**) and $[Co(4\text{-Me-5-CHOIm})_2(NO_3)_2]$ (**4**). Compounds **1**–**3** were characterized by X-ray diffraction, establishing tetrahedral ($I\bar{4}$), distorted dodecahedral ($C2/c$) and octahedral ($P\bar{1}$) coordinating geometries of the metal ions, respectively. The crystal structure of **3** includes in the unit cell two symmetry-independent cations: $[Co(1)L_2(H_2O)_2]^{2+}$ and $[Co(2)L_2(H_2O)_2]^{2+}$which differ slightly in bond lengths and valence angles. In solution, NMR and potentiometric methods have confirmed the preference of the central ions not only to adopt a specific coordination number and geometry of coordination polyhedra, but also the function of the ligands which can be either monodentate (ZnN_4) or bidentate (CdN_4O_4 and CoN_2O_4).
© 2005 Elsevier Ltd. All rights reserved.

Keywords: N,O ligand; Cadmium; Zinc; Cobalt; Coordination geometries; Crystal structures; Stability constants

1. Introduction

Zinc is the second most prominent trace metal in the human body and is involved in a large number of enzymatic functions, fulfilling both structural (Zn-finger family protein) [1–6] and catalytic roles [1,7–9]. There are a number of zinc enzymes in the cytoplasm in which the metal ion coordinates only N, O donor ligands [10,11]. For example: superoxide dismutase with the ZnN_4 chromophore at the active center, carbonic anhydrase (ZnN_3, H_2O) or leucine, amine-peptidase (ZnO_4). The role of metal ions in such active centers is fundamental and the structural characterization of the local metal coordination sites is essential in understanding their function. Removal of the zinc from the holoenzyme or the replacement of Zn(II) by the chemically similar Cd(II) ion, generally results in apoprotein having no catalytic activity [12,13]. Additionally, cadmium has been designated as a human carcinogen by the International Agency for Research on Cancer and the US National Toxicology Program [14,15]. Therefore, an especially important question in current coordination chemistry is how a protein selects a specific metal, e.g., Zn^{II} but not Cd^{II}, from the mixture of ions present in a cell or in another environment [16]. All of the above mentioned zinc metalloproteins contain one or more imidazole ligands of the amino acid residue histidine. For this reason, simple imidazole heterocycles [17] are generally used in model studies of local metal coordination sites.

* Corresponding author. Tel./fax: +48413614942.
E-mail address: basiab@pu.kielce.pl (B. Barszcz).

0277-5387/$ - see front matter © 2005 Elsevier Ltd. All rights reserved.
doi:10.1016/j.poly.2005.01.016

Basically, this study had the following four main goals: (1) the synthesis, crystal structure and spectroscopic studies of some low molecular weight complexes of zinc(II) and cadmium(II) with 4-methylimidazole-5-carbaldehyde (4-Me-5-CHOIm), (2) to present the coordination chemistry of Co(II)-4-Me-5-CHOIm complexes taking into account that Co(II)-compounds have been shown to be important tools in the study of the zinc(II) chromophore in the active centre of metalloenzymes [18], (3) to compare the stability constants of some imidazole complexes with a number of alkyl substituted imidazoles with Co(II), Zn(II) and Cd(II) in aqueous solution based on results obtained from potentiometric measurements, (4) to determine how well conventional structural data for examining complexes correlate with NMR and potentiometric studies in aqueous solution.

2. Experimental

2.1. Investigation in the solid state

2.1.1. Reagents and physical measurement

$Cd(NO_3)_2 \cdot 4H_2O$, $Zn(NO_3)_2 \cdot 6H_2O$ and $Co(NO_3)_2 \cdot 6H_2O$ were purchased from Merck Chemical Company and 4-Me-5-CHOIm (Aldrich 99%) were used as received. Elemental analyses were run on a Model 240 Perkin–Elmer CHN Analyzer. Infrared spectra (Perkin–Elmer 180 spectrophotometer; 4000–400 cm^{-1}) were recorded in KBr and FIR spectra (400–30 cm^{-1}) in Nujol with specimens applied as a suspension of the complexes in Nujol onto a polyethylene window. Raman spectra were performed at room temperature with a Bio-Rad spectrometer, resolution 4 cm^{-1}. The incident radiation (λ = 1064 nm) was provided by a Neodymium laser YAG (Spectra-Physics). The electronic spectra (Cary 5 UV–Vis–NIR spectrophotometer; 5000–30 000 cm^{-1}) were recorded in Nujol mulls. Magnetic measurements were carried out on a magnetic susceptibility balance (Sherwood Scientific) at room temperature by Guoy's method using $Hg[Co(NCS)_4]$ as the calibrant.

2.1.2. Preparation of the complexes

*2.1.2.1. $[ZnL_4](NO_3)_2$ (**1**).* A sample of 4-Me-5-CHOIm (3 mmol, 0.330 g) dissolved in mixture of analytically pure MeOH (12 mL) and redistilled water (12 mL) was added to the same solvents (24 mL) containing 0.5 mmol (0.149 g) of $Zn(NO_3)_2 \cdot 6H_2O$. The molar ratio M:L was 1:6. The solution was stirred for 7 h and left to crystallize at room temperature. After two weeks colourless crystals of the complex suitable for X-ray investigation were obtained. The product was filtered and dried under vacuum. The colourless crystals were collected in 39% yield. *Anal.* Calc. for $C_{24}H_{20}N_{10}O_{10}Zn$: C, 45.8; H, 3.2; N, 22.2. Found: C, 45.4; H, 3.0; N, 22.1%.

Selected vibrations (FT-IR and FT-Raman in italics; cm^{-1}): ν(NH) 3164vb *(3164)*; ν(C=O) 1669vs *(1668)*; interaction between ν(C=C) and ν(C–N) 1524vs *(1528)*; $\nu(NO_3)$ 1381vb *(1382)*.

*2.1.2.2. $[CdL_4](NO_3)_2(H_2O)$ (**2**).* 4-Me-5-CHOIm (2.0 mmol, 0.220 g) dissolved in 20 mL of analytically pure EtOH was stirred with 0.5 mmol (0.154 g) of $Cd(NO_3)_2 \cdot 4H_2O$ dissolved in 20 mL of the same solvent. The molar ratio M:L was 1:4. The solution was left to crystallize at room temperature. After three weeks colourless crystals of a compound suitable for X-ray investigation were obtained. The precipitate was separated by filtration and washed with 30 mL of 2-propanol, before being dried under vacuum. The colourless crystals were collected in 74% yield. *Anal.* Calc. for $C_{20}H_{26}N_{10}O_{11}Cd$: C, 34.6; H, 3.8; N, 20.2. Found: C, 34.5; H, 3.5; N, 20.0%.

Selected vibrations (FT-IR and FT-Raman in italics; cm^{-1}): ν(OH, lattice water) 3608s; ν(NH) 3144vb *(3133)*; ν(C=O) 1656vs *(1656)*; interaction between ν(C=C) and ν(C–N) 1512vs *(1512)*; $\nu(NO_3)$ 1360vb *(1364)*.

*2.1.2.3. $[CoL_2(H_2O)_2](NO_3)_2$ (**3**).* A mixture of $Co(NO_3)_2 \cdot 6H_2O$ (0.073 g, 0.25 mmol) in propan-2-ol (20 mL) and 4-Me-5-CHOIm (0.111 g, 1.0 mmol) in propan-2-ol (20 mL) was stirred at room temperature for 1 h. The molar ratio Co:L was 1:4. After evaporation of half the solution (5 days), orange-pink crystals of $[CoL_2(H_2O)_2](NO_3)_2$, suitable for X-ray analysis, were collected by vacuum filtration and dried in a vacuum box. In addition, a small amount of a violet precipitate of $[CoL_2](NO_3)_2$ was obtained from the residual filtrate. The crystals were collected in 33% yield. *Anal.* Calc. for $C_{10}H_{16}N_6O_{10}Co$: C, 27.3; N, 19.1; H, 3.7. Found: C, 27.6; N, 18.9; H, 3.7%.

Selected vibrational bands (FT-IR and FT-Raman in italics; cm^{-1}): ν(OH, coordinated water) 3407vb; ν(C=O) 1614vs *(1613)*; interaction between ν(C=C) and ν(C–N) 1525vs *(1528)*; $\nu(NO_3)$ 1481s.

*2.1.2.4. $[CoL_2](NO_3)_2$ (**4**).* A solution of $Co(NO_3)_2 \cdot 6H_2O$ (0.145 g, 0.5 mmol) in a mixture of propan-2-ol (15 mL) and trimethyl orthoformate (5 mL) was slowly added to a solution of 4-Me-5-CHOIm (0.111 g, 1.0 mmol) in propan-2-ol (20 mL). The molar ratio Co:L was 1:2. The mixture was stirred for 30 min, and then left standing at room temperature. Passive evaporation of ca. half the volume resulted in a violet precipitate. The precipitate was collected by vacuum filtration and dried in a vacuum box. Unfortunately, the violet crystals of definite stoichiometry were not suitable for X-ray investigation. The crystals were collected in 43% yield. *Anal.* Calc. for $C_{10}H_{12}N_6O_8Co$: C, 29.8; N, 20.8; H, 3.0. Found: C, 30.0; N, 20.6; H, 2.9%.

Selected vibrational bands (FT-IR and FT-Raman in italics; cm^{-1}): ν(NH) 3140vb *(3138)*; ν(C=O) 15620vs *(1620)*; interaction between ν(C=C) and ν(C–N) 1524vs *(1528)*; $\nu(NO_3)$ 1360vb *(1358)*.

2.1.3. X-ray crystal structure analysis

Diffraction intensity data for single crystals of the Cd(II), Zn(II) and Co(II) complexes were collected at room temperature on a KappaCCD (Nonius) diffractometer with graphite-monochromated Mo Kα radiation ($\lambda = 0.71073$ Å). Corrections for Lorentz, polarization and absorption effects [19] were applied. The structures were solved by direct methods using the program package SIR-92 [20] and refined using a full-matrix least square procedure on F^2 using SHELXL-97 [21]. Anisotropic displacement parameters for all non-hydrogen atoms and isotropic temperature factors for hydrogen atoms were introduced. Further details of the structures analysis are given in Table 1 and in the supplementary material.

2.2. Solution studies

2.2.1. Potentiometric measurements

The stability constants of the proton and metal(II) complexes were determined by pH-metric titration of 5 cm^3 samples in aqueous solutions. The ligand concentration was 1.0×10^{-1} or 5×10^{-2} mol dm^{-3} and the metal ion:HL^+ ratios were 1:4, 1:6, 1:8. The ionic strength was adjusted to $I = 0.5$ mol dm^{-3} with KNO_3 in each case. The titration was performed over the range pH 2.5–8.7 or 2.5–5.6 for aldehydes. All titration solutions were thermostated at 25 ± 0.1 °C using the constant-temperature water-bath. The pH was measured using PHM-84 pH-meter (Radiometer) and a GK 2400C combination electrode. The electrode system was calibrated by periodic titration of HCl of known titre with a NaOH solution according to [23]. The dissociation constants of the conjugate acid and the stability constants, β_n of the complexes were refined by the SUPERQUAD program [24].

Table 1
Crystal data and structure refinement parameters for **1**, **2** and **3**

	1	**2**	**3**
Empirical formula	$C_{24}H_{20}N_{10}O_{10}Zn$	$C_{20}H_{26}N_{10}O_{11}Cd$	$C_{10}H_{16}N_6O_{10}Co$
Formula weight	629.86	694.91	439.22
Temperature (K)	293(2)	293(2)	293(2)
Wavelength (Å)	0.71073	0.71073	0.71073
Crystal system	tetragonal	monoclinic	triclinic
Space group	$I\bar{4}$	$C2/c$	$P\bar{1}$
Unit cell dimensions			
a (Å)	14.3440(2)	19.1850(3)	6.8057(2)
b (Å)	14.3440(3)	7.7430(1)	11.2325(2)
c (Å)	7.4601(3)	19.1040(4)	13.0605(3)
α (°)	90	90	64.9390(10)
β (°)	90	97.7650(7)	83.7780(10)
γ (°)	90	90	73.5960(10)
Volume ($Å^3$)	1534.92(7)	2811.87(8)	867.53(4)
Z	2	4	2
Calculated density (Mg/m^3)	1.363	1.642	1.681
Absorption coefficient (mm^{-1})	0.863	0.851	1.055
$F(000)$	648	1408	450
Crystal size (mm)	$0.32 \times 0.22 \times 0.17$	$0.27 \times 0.22 \times 0.15$	$0.25 \times 0.22 \times 0.04$
Theta range for data collection (°)	2.84–27.49	2.84–29.14	3.12–27.49
Index ranges	$0 \leqslant h \leqslant 18$, $-12 \leqslant k \leqslant 13$, $-9 \leqslant l \leqslant 9$	$0 \leqslant h \leqslant 26$, $-8 \leqslant k \leqslant 10$, $-26 \leqslant l \leqslant 25$	$-8 \leqslant h \leqslant 8$, $-14 \leqslant k \leqslant 14$, $-16 \leqslant l \leqslant 16$
Reflections collected/unique	3466/1753 [$R_{(int)} = 0.039$]	6931/3769 [$R_{(int)} = 0.0151$]	7002/3941 [$R_{(int)} = 0.0257$]
Completeness to 2θ (%)	98.8	99.2	99.1
Refinement method	full-matrix least-squares on F^2	full-matrix least-squares on F^2	full-matrix least-squares on F^2
Data/restraints/parameters	1753/0/112	3769/0/227	3941/0/288
Goodness-of-fit on F^2	1.082	1.098	1.071
Final R indices [$I > 2$sigma(I)]			
R_1	0.0482	0.0270	0.0398
wR_2	0.1288	0.0697	0.1079
R indices (all data)			
R_1	0.0496	0.0302	0.0540
wR_2	0.1332	0.0716	0.1168
Largest diff. peak and hole (e $Å^3$)	0.514 and −0.260	0.356 and −0.541	0.430 and −0.312

2.2.2. NMR measurements

NMR spectra of the D_2O solutions (294 K) of the Cd(II) and Zn(II) complexes were taken on a Mercury-400BB spectrometer and were recorded at 400.09 MHz. The chemical shifts were referenced to the proton signals of 1,4-dioxane (3.75 ppm) as an internal standard. An aqueous solution (D_2O) of cadmium(II) or zinc(II)-4-Me-5-CHOIm in 1:4 molar ratio was prepared using 1 cm^3 solution of $Cd(NO_3)_2 \cdot 4H_2O$ (0.925 g, 0.3 mmol) or $Zn(NO_3)_2 \cdot 6H_2O$ (0.0892 g, 0.3 mmol) dissolved in 2 cm^3 D_2O and 2 cm^3 of the stock solution of the ligand (0.16517 g, 1.5 mmol 4-Me-5-CHOIm dissolved in 5 cm^3 D_2O).

4-Me-5-CHOIm: ^{1}H NMR (D_2O) δ: 9.63 (s, 1H, C*H*O), 7.74 (s, 1H, C*H*), 4.85 (s, N*H*, H_2 (residual water from D_2O)), 2.47 (s, 3H, CH_3) ppm.

Cd(II)-4-Me-5-CHOIm: ^{1}H NMR (D_2O) δ: 9.78 (s, 1H, C*H*O), 7.89 (s, 1H, C*H*), 4.82 (s, N*H*, H_2 ($Cd(NO_3)_2 \cdot 4H_2O$), H_2 (residual water from D_2O)), 2.60 (s, 3H, CH_3) ppm.

Zn(II)-4-Me-5-CHOIm: ^{1}H NMR (D_2O) δ: 9.71 (s, 1H, C*H*O), 8.00 (s, 1H, C*H*), 4.84 (s, N*H*, H_2 ($Zn(NO_3)_2 \cdot 6H_2O$), H_2 (residual water from D_2O)), 2.59 (s, 3H, CH_3) ppm.

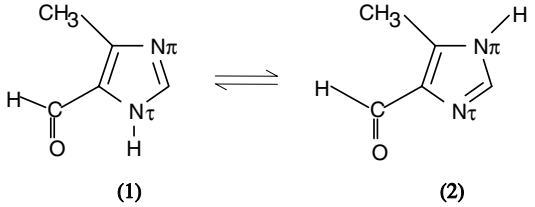
2.2.3. Spectroscopic measurements

The visible-range absorption spectra of the Co(II) complexes in aqueous solution were recorded on a Specord M-500 (Carl Zeiss, Jena) spectrophotometer. Solutions for these measurements were prepared using the initial metal concentration 2×10^{-2} mol dm^{-3} and the concentration ratio of metal–ligand was 1:6. The highest concentration of the protonated ligand was 0.12 mmol dm^{-3}. The absorption spectra were recorded after pH adjustment by NaOH or HNO_3 at constant ionic strength (I = 0.5 M).

3. Results and discussion

3.1. Single crystal X-ray diffraction studies

The two nitrogen atoms present at positions 4 and 5 in the unsaturated imidazole ring induce the tautomerism shown in Scheme 1.



Scheme 1. The tautomeric equilibrium between 4-Me-5-CHOIm (**1**) and 4-CHO-5-MeIm (**2**).

Our previous investigation of Cu(II) complexes [25] revealed stabilization of tautomer (2) as the only one able to form a chelate ring with the central atom. Hence it was interesting to investigate the preference of the central ion to adopt a specific coordination number and the geometry of coordination polyhedra. An important second goal was to understand the influence of the nature of the donor atoms and the function of the optionally monodentate or bidentate ligands. The X-ray diffraction method proved to be indispensable in this part of the investigations.

*3.1.1. Molecular structure of the Zn(II) complex **1***

The molecular structure of the $[Zn(4\text{-CHO-}5\text{-MeIm})_4]^{2+}$ ion is presented in Fig. 1. Selected geometrical data are given in Table 2. Compound (**1**) crystallizes in a tetragonal system. The central zinc atom occupies the special position ($2\,c\,\bar{4}$) and the other atoms are in the general position (8 g 1) of the space group $I\bar{4}$ (ITC No. 82). In the coordination sphere of the central ion there are four 4-CHO-5-MeIm (tautomer 2) moieties. Each molecule acts as a monodentate ligand [26] coordinated to the zinc ion through the unprotonated nitrogen atom (Nτ) of the heterocyclic ring (chromophore ZnN_4). The four identical zinc–nitrogen bond lengths [2.022(3) Å] as well as the values of the nitrogen–zinc–nitrogen angles [111.8(1)° and 105.0(1)°] indicate that tetrahedral coordination is a good approximation for the zinc(II) central ion. The

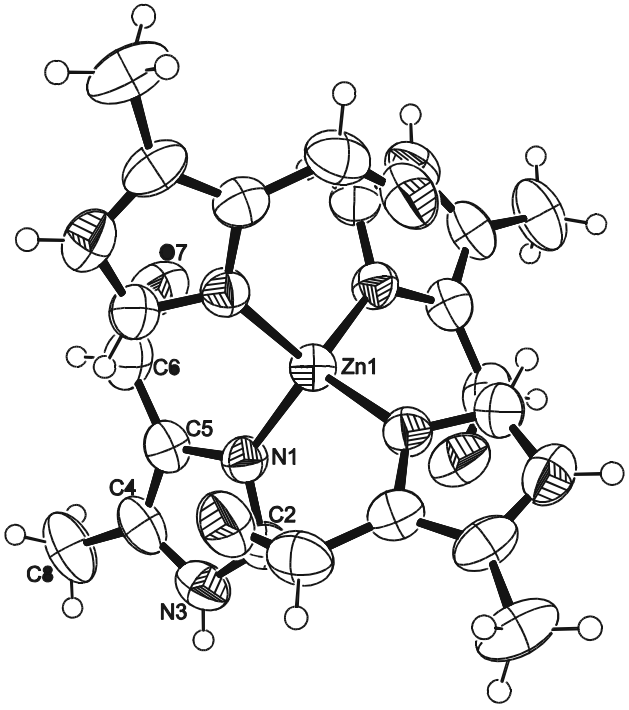


Fig. 1. Molecular structure of $[Zn(4\text{-CHO-}5\text{-MeIm})_4](NO_3)_2$ (**1**) with the atom numbering scheme. Atomic displacement ellipsoids are shown at the 50% probability level (ORTEP-32 [22]).

Table 2
Selected bond lengths (Å) and valence angles (°) for **1** and references complexes

Compound	Zn–N	Zn···O Zn–O	N–Zn–N	O–Zn–N
1	2.022(3)	3.065(3)	111.8(1)	
			105.0(1)	
$[(Mima)_2Zn(SC_6F_5)_2]$ [27a]	2.048(3)	3.061	97.2(1)	
	2.055(3)			
$[ZnBr_2(MPA)]$ [27b]	2.05(2)	2.10(1)		80.3(6)
	2.06(1)	2.11(1)		80.2(6)
$[(PicA)Zn(SC_6F_5)_2]$ [27a]	2.07(1)	2.24(1)		73.4(7)
$[(OpyA)Zn(SC_6F_5)_2]$ [27a]	2.059(2)	2.165(2)		77.85(6)

Mima, *N*-methylimidazole-2-carbaldehyde; MPA, 6-methylpyridine-2-carbaldehyde; PicA, picoline-6-carbaldehyde; OpyA, 2-methoxypyridine-6-carbaldehyde.

aldehyde groups of the azole molecules are oriented in such a way that their O atoms do not interact directly with the zinc atom [the Zn–O distance of 3.065 Å is rather long]. Similar phenomena were observed by Vahrenkamp and co-workers [27] who examined Zn(II) complexes with *N*-methylimidazole-2-carbaldehyde and thiolate donors. However, aldehydes derived from pyridine act as bidentate ligands and form five membered N,O chelate rings with the zinc cation. The geometric parameters for some representative Zn(II) complexes are compared in Table 2. The charge of the cationic complexes is balanced by two nitrate anions which are involved in hydrogen bonds of the N–H···O type with the imidazole ligands. The geometry of these hydrogen bonds is presented in Table 5. Oxygen atoms of the nitrate groups are disordered equally between two sites [site occupancy factor 0.5]. The packing in the crystal structure of (**1**) is shown in Fig. 2.

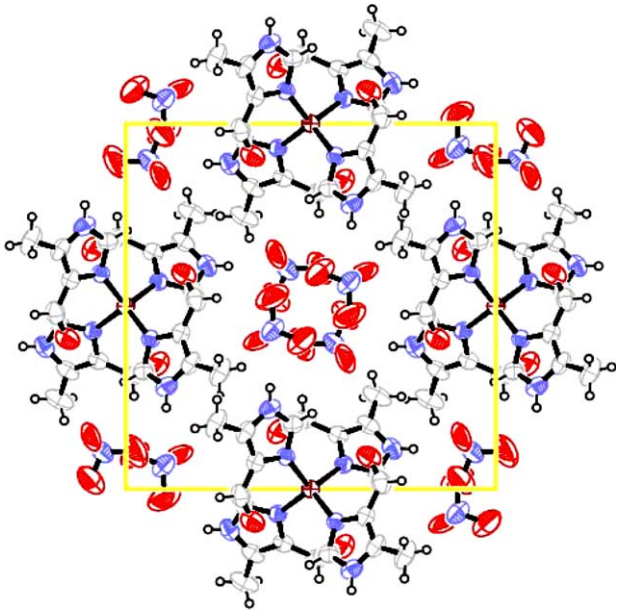


Fig. 2. Packing in the crystal structure of $[Zn(4\text{-CHO-5-MeIm})_4](NO_3)_2$ (**1**) viewed along *c*-axis of the unit cell.

3.1.2. Molecular structure of the Cd(II) complex 2

The cadmium complex crystallizes in the monoclinic system (space group *C*2/*c*, ITC No. 15). The $[Cd(4\text{-CHO-5-MeIm})_4]^{2+}$ cation has C_2 symmetry coinciding with the crystallographic symmetry. The four 4-CHO-5-MeIm (tautomer 2) molecules act as N,O bidentate ligands. The Cd atom is eight-coordinated with four 'pyridinic' nitrogen atoms of the imidazole rings and four oxygen atoms of the aldehyde groups (Fig. 3(a)). Selected geometrical data for (**2**) are given in Table 3. The shape of the coordination polyhedron can be described as a distorted dodecahedron of C_2 symmetry (Fig. 3(b)). The most interesting feature of the dodecahedron is that the oxygen atoms occupy the vertices with four neighbours and the nitrogen atoms are in the vertices with five neighbours. Cadmium–nitrogen bond distances of 2.292(1) and 2.298(1) Å are similar to those observed for other eight-coordinated N,O Cd(II) complexes and cadmium–oxygen distances of 2.745(1) and 2.700(1) Å are, in general, slightly longer than those found in the literature [28]. It is noteworthy that the complex cation $[Zn(4\text{-CHO-5-MeIm})_4]^{2+}$ obtained by us is a rare example of a dodecahedron composed of N,O donors present in small-molecule ligands. In the crystal structure, N–H groups of the ligands form bifurcated hydrogen bonds to the oxygen atoms of the nitrate groups. The geometry of the hydrogen bonds is given in Table 5.

3.1.3. Molecular structure of the Co(II) complex 3

The crystal structure of (**3**) includes in the unit cell two symmetry-independent cations: $[Co(1)L_2(H_2O)_2]^{2+}$ and $[Co(2)L_2(H_2O)_2]^{2+}$ which differ slightly in bond lengths and valence angles, (a phenomenon which is reflected in the IR spectra-vide infra). The coordination spheres of Co(1) and Co(2) are presented in Fig. 4(a),(b) together with the atom numbering scheme. Selected bond distances and valence angles are listed in Table 4. In both six-coordinate cobalt(II) complexes two molecules of 4-CHO-5-MeIm (L-tautomer 2) and two water molecules are coordinated to the central ion forming a chromophore of the CoN_2O_4 type. The

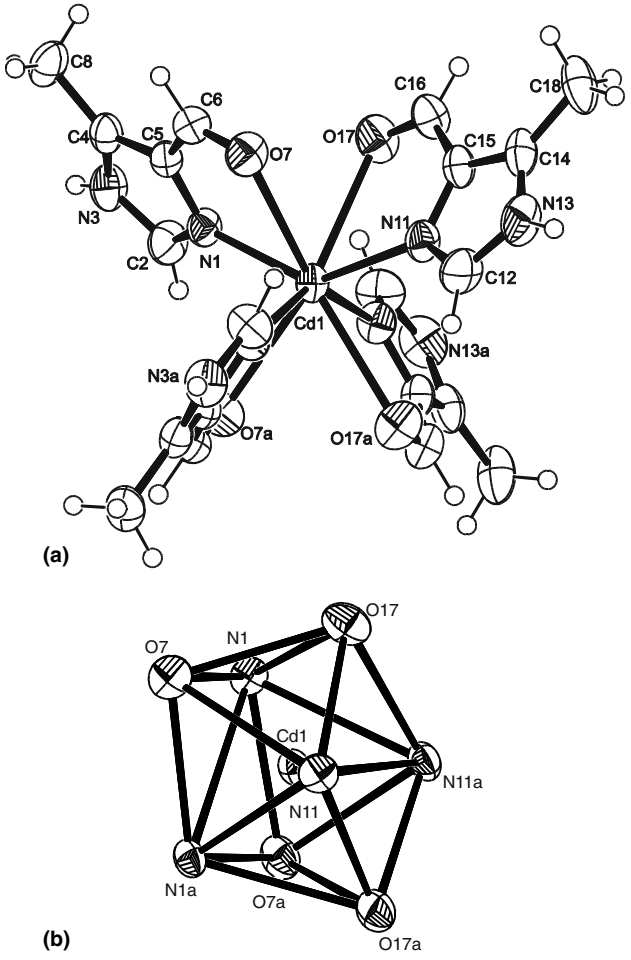


Fig. 3. (a) Molecular structure with the atom numbering scheme for eight-coordinated $[Cd(4\text{-Me-5-CHOIm})_4](H_2O)(NO_3)_2$ (**2**), (b) coordination polyhedron of (**2**). Details as for Fig. 1.

Table 3
Selected bond lengths (Å) and valence angles (°) for **2**

Bond lengths			
Cd(1)–N(1)	2.298(1)	Cd(1)–N(11)	2.292(1)
Cd(1)–O(7)	2.700(1)	Cd(1)–O(17)	2.745(1)
Bond angles			
N(1)–Cd(1)–N(1)a	103.05(7)	N(11)–Cd(1)–N(11)a	100.00(8)
N(1)–Cd(1)–N(11)	138.96(5)	N(11)–Cd(1)–N(1)a	92.61(5)
N(1)–Cd(1)–O(7)	67.60(4)	N(11)–Cd(1)–O(17)	66.66(5)
N(1)–Cd(1)–O(7)a	76.87(5)	N(11)–Cd(1)–O(17)a	78.39(5)
N(1)–Cd(1)–O(17)	78.15(5)	N(11)–Cd(1)–O(7)	79.80(5)
N(1)–Cd(1)–O(17)a	141.60(5)	N(11)–Cd(1)–O(7)a	143.65(5)
O(7)–Cd(1)–O(7)a	121.47(6)	O(17)a–Cd(1)–O(17)	124.61(6)
O(7)–Cd(1)–O(17)a	145.80(4)	O(17)–Cd(1)–O(7)	68.11(5)
C(2)–N(1)–Cd(1)	135.2 (1)	C(12)–N(11)–Cd(1)	133.6(1)
C(5)–N(1)–Cd(1)	119.2 (1)	C(15)–N(11)–Cd(1)	120.6(1)
C(6)–O(7)–Cd(1)	109.9(1)	C(16)-O(17)–Cd(1)	109.6(1)

Symmetry transformations used to generate equivalent atoms: (a) $-x+1, y, -z+1/2$.

4-CHO-5-MeIm molecules act as bidentate N,O ligands, coordinating through the 'pyridinic' nitrogen atom of the imidazole ring (Nτ) and the oxygen atom of the aldehyde group. The shape of Co(1) and Co(2) coordination polyhedra is that of a distorted octahedron of symmetry $\bar{1}$, with the equatorial plane defined by the 4-CHO-5-MeIm bidentate ligands and two water molecules occupying axial positions (i.e. in a *trans* position to each other). This example of a Co(II) complex could be considered as a geometric *trans*-isomer of an analogous Co(II) complex with imidazole-4-acetate, the crystal structure of which has been recently reported [29]. In the imidazole-4-acetate Co(II) complex there are two

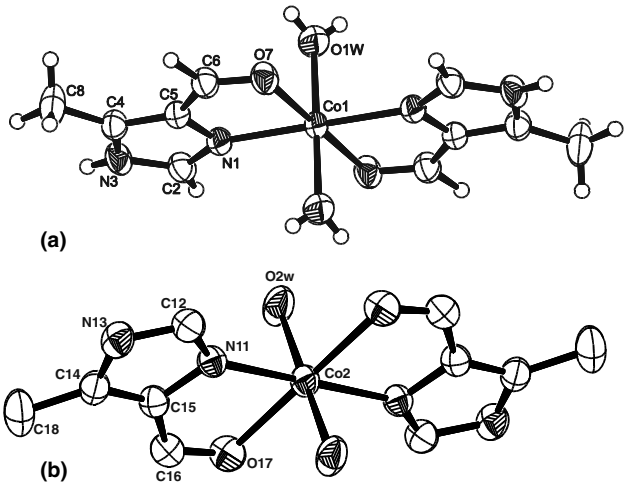


Fig. 4. Structure of two symmetry independent cations of (**3**): (a) $[Co(1)L_2(H_2O)_2]^{2+}$, (b) $[Co(2)L_2(H_2O)_2]^{2+}$ with the atom numbering scheme. Details as for Fig. 1.

Table 4
Selected bond lengths (Å) and valence angles (°) for **3**

Bond lengths			
Co(1)–O(1W)	2.047(2)	Co(2)–O(2W)	2.066(2)
Co(1)–O(1W)a	2.047(2)	Co(2)–O(2W)b	2.066(2)
Co(1)–N(1)a	2.103(2)	Co(2)–N(11)b	2.085(2)
Co(1)–N(1)	2.103(2)	Co(2)–N(11)	2.085(2)
Co(1)–O(7)	2.186(2)	Co(2)–O(17)b	2.189(2)
Co(1)–O(7)a	2.186(2)	Co(2)–O(17)	2.189(2)
Bond angles			
O(1W)–Co(1)–O(1W)a	180.0(1)	O(2W)–Co(2)–O(2W)b	180.0(1)
O(1W)–Co(1)–N(1)a	91.5(1)	O(2W)–Co(2)–N(11)b	86.9(1)
O(1W)a–Co(1)–N(1)a	88.5(1)	O(2W)–Co(2)–N(11)	93.1(1)
O(1W)a–Co(1)–N(1)	91.5(1)	O(2W)b–Co(2)–N(11)	86.9(1)
N(1)a–Co(1)–N(1)	180.0(1)	N(11)b–Co(2)–N(11)	180.0(1)
O(1W)–Co(1)–O(7)	90.6(1)	O(2W)–Co(2)–O(17)b	92.3(1)
O(1W)a–Co(1)–O(7)	89.4(1)	O(2W)b–Co(2)–O(17)b	87.7(1)
N(1)a–Co(1)–O(7)	101.5(1)	N(11)b–Co(2)–O(17)b	77.9(1)
N(1)–Co(1)–O(7)	78.5(1)	N(11)–Co(2)–O(17)b	102.1(1)
O(1W)a–Co(1)–O(7)a	90.6(11)	O(2W)b–Co(2)–O(17)	92.3(1)
N(1)a–Co(1)–O(7)a	78.5(1)	N(11)b–Co(2)–O(17)	102.1(1)
N(1)–Co(1)–O(7)a	101.5(1)	N(11)–Co(2)–O(17)	77.9(1)
O(7)–Co(1)–O(7)a	180.0(1)	O(17)b–Co(2)–O(17)	180.0(1)

Symmetry transformations used to generate equivalent atoms: (a) $-x, -y+1, -z$; (b) $-x+1, -y+1, -z+1$.

Table 5
The geometry of hydrogen bonds for **1**, **2** and **3**

	Donor-H···Acceptor$_{(\text{acceptor position})}$	D–H (Å)	H···A (Å)	D···A (Å)	∠D–H···A (°)
1	N(3)–H(3)···O(21)$_{(-y, x-1, -z+1)}$	0.86	1.95	2.793(7)	164.8
2	N(3)–H(3)···O(21)$_{(-x+1/2, y-1/2, -z+1/2)}$	0.90(3)	2.15(3)	3.034(3)	168(2)
	N(3)–H(3)···O(22)$_{(-x+1/2, y-1/2, -z+1/2)}$	0.90(3)	2.58(3)	3.281(3)	135(2)
	N(13)–H(13)···O(21)$_{(-x+1, -y+1, -z+1)}$	0.91(3)	2.20(3)	3.075(3)	160(3)
	N(13)–H(13)···O(23)$_{(-x+1, -y+1, -z+1)}$	0.91(3)	2.37(3)	3.130(3)	140(3)
3	O(1W)–H(1A)···O(21)	0.77(5)	2.22(5)	2.966(3)	163(5)
	O(1W)–H(1A)···O(23)	0.77(5)	2.35(5)	2.953(3)	135(4)
	O(1W)–H(1B)···O(43)$_{(x, y-1, z)}$	0.65(4)	2.09(5)	2.736(4)	177(5)
	N(3)–H(3)···O(41)	0.83(4)	2.09(4)	2.879(3)	159(4)
	O(2W)–H(2A)···O(21)$_{(-x, -y+1, -z+1)}$	0.67(4)	2.09(4)	2.756(3)	175(4)
	O(2W)–H(2B)···O(22)	0.76(4)	2.08(5)	2.839(3)	174(4)
	N(13)–H(13)···O(23)$_{(x, y+1, z)}$	0.82(3)	1.98(3)	2.782(3)	166(3)

bidentate azole molecules as N,O ligands and two water molecules (in *cis* positions to each other). The bond lengths [Co–N = 2.071(1), 2.092(1) and Co–O = 2.128(1), 2.135(1) Å] are slightly shorter than those observed by us for (**3**). The crystal structure of the *cis*-Co(II) isomer is stabilized by hydrogen bonds of the O–H···O type to the coordinated oxygen atom of a water molecule and to the third molecule of water, which is outside the coordination sphere. Similar features were also observed for *cis*-Co(II) complexes with 1-benzyl-2-hydroxymethylimidazole [30]. The charge of the cationic complexes of (**3**) is balanced by two nitrate anions which interact as acceptors with water molecules and N–H groups of imidazole ligands via hydrogen bonds, the geometry of which is given in Table 5.

3.2. The IR and Raman spectra

The Zn(II) and Cd(II) complexes are insoluble in most common solvents except DMSO. The NMR spectra – almost identical to that of the free parent aldehyde – gave no further information. This observation however, does not exclude the possibility that donor solvent replaces 4-Me-5-CHOIm in the zinc and cadmium complexes upon dissolution. Therefore, we only use in solution NMR as a tool for examining the coordination affinity of 4-Me-5-CHOIm towards Cd^{II} and Zn^{II} (vide infra). The characteristic IR (Raman) bands and relevant crystallographic data are listed in Table 6. Upon coordination of 4-CHO-5-MeIm with transition metals, the aldehyde ν(C=O) band, except for the Zn-complex, is shifted to lower wavenumber compared to the free ligand, thus proving the expected M–O coordination. There is some correlation between this shift and the lengths of the M–O bond. The longer the metal–oxygen distance, the smaller the value of $\Delta\nu$. The position and appearance of a prominent doublet at 1614 and 1586 cm^{-1} in the ν(CO) region of the spectrum of **3** correlate with the X-ray data and indicate the presence two independent cations in the unit (Fig. 5). Additionally, the structure of the Co(II)-complex shows that the two molecules of 4-CHO-5-MeIm are in the *xy* plane and the ν(C=O) band is shifted by about 50 cm^{-1}. These are typical for the values of transition metal complexes with planar aldehydes [27,31]. Therefore, the similar value of the ν(C=O) shift ($\Delta\nu$ = 47 cm^{-1}) probably indicates the same arrangement of the aldehyde ligands in complex **4**. Interestingly, only the IR spectra of this complex show an additional strong band at 1481 cm^{-1} indicating a bidentate coordination of one nitrate group to Co(II) ion [32,33] which give as a final result, the CoN_2O_4 chromophore.

3.3. The d–d electronic spectra and magnetic properties

Ligand-field spectra of the $[CoL_2(H_2O)_2](NO_3)_2$ (**3**) complex were recorded in the solid state as well as in solution (methanol). The spectrum of complex **3** in the

Table 6
Relevant crystallographic and IR(Raman) data for complexes with 4-CHO-5-MeIm (L)

Complex	Shape of polyhedron	M–N (Å)	M–O (Å)	ν(C=O) (cm^1)	$\Delta\nu$	ν(M–O) (cm^{-1})	ν(M–N) (cm^1)
$[ZnL_4](NO_3)_2$	tetrahedral ($I\bar{4}$)	2.022(3)	3.065[a]	1669(1668)	+2(+5)		274(270)
$[CuL_4H_2O)_2(NO_3)_2$ [19]	dodecahedral ($P\bar{1}$)	1.995(3)–2.028(3)	2.816(3)–3.002(3)	1663	−4	363	300
$[CdL_4](H_2O)(NO_3)_2$	dodecahedral ($C2/c$)	2.292(1)–2.298(1)	2.700(1)–2.745(1)	1656(1656)	−11(−7)	338, 352(375)	119(115)
$[CoL_2(H_2O)_2](NO_3)_2$	octahedral ($P\bar{1}$)	2.103(2)(Co1) 2.085(2)(Co2)	2.047(2)–2.86(2)(Co1) 2.066(2)–2.189(2)(Co2)	1614/1586 (1613)	−53/−81 (−50)	386, 377(371)	280(285)

[a] M···O interactions.

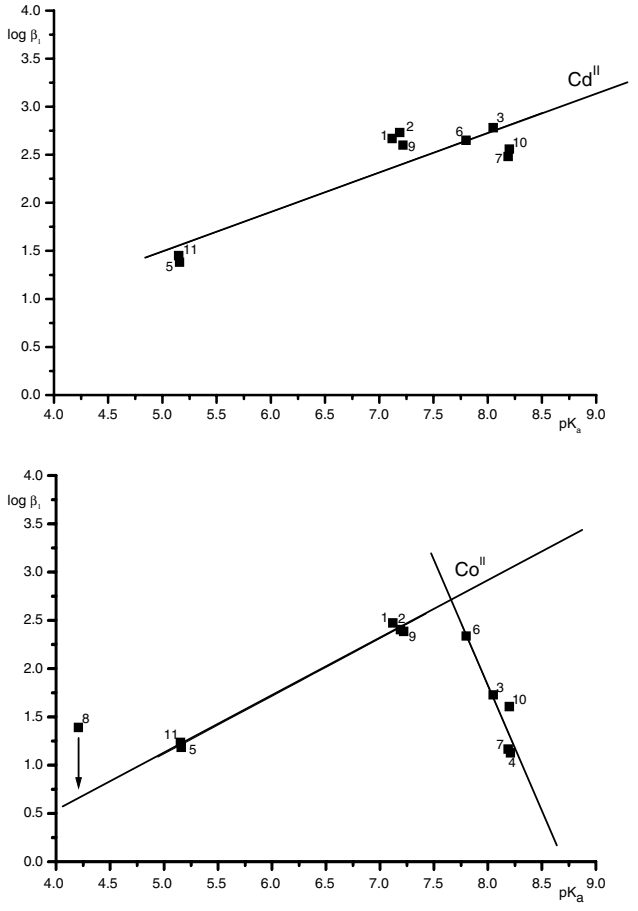


Fig. 5. The dependence of $\log\beta_1 = f(pK_a)$ for the complexes of Cd^{II} and Co^{II} with imidazole derivatives **1**–**11** (Table 7).

solid state (diffuse reflectance) is characterized by two d–d strong bands and one band of weaker intensity, which are consistent with an octahedral geometry [34]. The first band (ν_1 = 1103 nm) is assigned to the transition $^4T_{2g} \rightarrow {}^4T_{1g}(F)$, while the second ($\nu_2$ = 593 nm), a weak band, is assigned to the transition $^4A_{2g} \rightarrow {}^4T_{1g}(F)$. The third band ($\nu_3$ = 492 nm) assigned to the transition $^4T_{1g}(P) \rightarrow {}^4T_{1g}(F)$ is diffuse and asymmetric, indicating overlap of several bands. The positions of individual bands for the complexes, assuming a Gauss distribution, are: 433 and 518 nm. However, the calculated Racah parameter (B) value is not reliable considering the mixture of two complexes and distortion of the coordinate polyhedron due to the unsymmetrical Co–N and Co–O bonds forming the chelate ring. When the spectrum of complex **3** in methanol solution is recorded, the position of the d–d transition band shifts only slightly to 513 nm 'red shift' (ε = 17.6 M^{-1} cm^{-1}). These results suggest that the coordination sphere around the cobalt(II) ions in solution is the same as in the solid state.

The electronic spectrum of the solid complex **4** shows two strong d–d bands at 1234 and 530 nm (523, 474-Gauss distribution) and a very weak one at 589 nm. The presence of the three chelate rings strongly suggests an even greater distortion from regular octahedral geometry to that observed in complex **3**. The position of the d–d band in the spectrum of complex **4** in methanol solution (ε = 17.7 M^{-1} cm^{-1}) is the same as the position of the analogous one in complex **3**. We regard this as additional evidence for the presence of a species similar in structure to complex **3**. However, when the spectrum of complex **4** is taken in methanol solution, the position of the d–d bands shifts towards the UV region (from 530 to 513 nm) (a partial exchange of the nitrate anion with the methanol molecules).

The effective magnetic moments of the cobalt(II) complexes at room temperature are 4.53 and 4.55 μ_B for (**3**) and (**4**), respectively. These values are consistent with high-spin six-coordinate complexes.

3.4. Investigation in aqueous solution

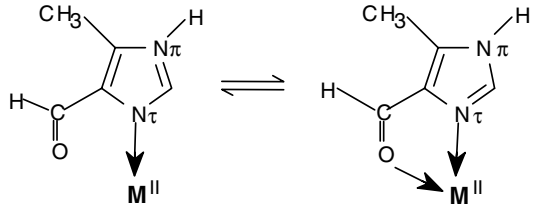
In order to understand why different elements are found in association with some different organic groups, we have compared the data obtained for the model complexes in the solid state to those in aqueous solution. The acid dissociation constants of protonated imidazolecarbaldehydes and some imidazole derivatives as reference compounds, as well as the equilibrium stability constants of their complexes with Co(II), Zn(II) and Cd(II) determined by the pH potentiometric technique at 298 K are given in Table 7. The data show that the basicity of ligands depends on the side group of the imidazole ring. The basicities of carbaldehyde derivatives are about three orders of magnitude smaller, due to the withdrawing effect of the CHO group, which changes the electron density of the pyridine type nitrogen atom. In order to generalize the conclusion following from the potentiometric investigation of the imidazole complexes, Fig. 5 presents an exemplary correlation between the values of the logarithms of the stability complex of the first complexes of Co(II) and Cd(II) and the ligand basicity. The result indicates that the stability of cadmium(II) complexes, contrary to those of zinc(II) [44] and cobalt(II) do not depend on the steric hindrance to complexation presented by some ligands. All of the experimental points for Cd(II) complexes are found on one line. For Co(II) (Fig. 5(b)) complexes the points corresponding to $\log\beta_1 = f(pK_a)$ for the chosen imidazole derivatives lie about two intersecting lines which were plotted according to linear approximation coefficients, calculated by the least-squares method. The points corresponding to derivatives containing an alkyl substituent situated in position 2 or 4, which present steric hindrance to complexation, are found on the line with negative slope. From our earlier studies [37,38,40,41,43,44] it follows that such ligands, in reaction with the Co(II) and Zn(II) ions, decrease the coordination number of the central ion from six to four. This results in a configuration equilibrium of the octahe-

Table 7
Stability constants of imidazole and some imidazole derivatives with Co^{II}, Zn^{II} and Cd^{II} ions in aqueous solution at 298 K and $I = 0.5$ mol dm^{-3}(KNO_3)

Ligand	Central ion	$\log\beta_1$	$\log\beta_2$	$\log\beta_3$	$\log\beta_4$	$\log\beta_5$	Ref.
Imidazole[1] $pK_a = 7.12$	Co^{II}	2.47	4.40	5.85	6.85		[35]
	Zn^{II}	2.56	4.89	7.16	9.19		[35]
	Cd^{II}	2.67	4.87	6.01	7.14		[35]
1-Methylimidazole[2] $pK_a = 7.19$	Co^{II}	2.40	4.40	5.85	6.95		[36]
	Zn^{II}	2.70	4.80				[36]
	Cd^{II}	2.73(2)	4.64(2)	6.30(2)	6.80(4)		this work
2-Methylimidazole[3] $pK_a = 8.05$	Co^{II}	1.73	3.05	3.84	6.16		[37]
	Zn^{II}	1.88	3.99	7.49	9.32		[37]
	Cd^{II}	2.78(3)	4.74(3)	5.84(4)			this work
1,2-Dimethylimidazole[4] $pK_a = 8.21$	Co^{II}	1.13	2.39	3.81	4.32		[38]
	Zn^{II}	1.92	4.32	7.11	9.00	9.62	[38]
1-Methylimidazole-2-carbaldehyde[5] $pK_a = 5.16$	Co^{II}	1.18	1.68	3.22			[39]
	Zn^{II}	1.41	2.24	3.88			[39]
	Cd^{II}	1.38(2)	2.20(4)	3.85(4)			this work
4(5)-Methylimidazole[6] $pK_a = 7.80$	Co^{II}	2.34	4.09	5.33	6.67		[40]
	Zn^{II}	2.48	5.06	4.74	10.52	12.62	[40]
	Cd^{II}	2.65	4.65	6.30	6.70		[40]
4,5-Dimethylimidazole[7] $pK_a = 8.19$	Co^{II}	1.17					[41]
	Zn^{II}	2.48					[41]
	Cd^{II}	2.48	4.30				[41]
4-Methylimidazole-5-carbaldehyde[8] $pK_a = 4.20$	Co^{II}	1.38(2)	2.45(5)				this work
	Zn^{II}	1.59(3)	3.18(3)	3.96(7)			this work
1-Propylimidazole[9] $pK_a = 7.22$	Co^{II}	2.38	4.20	5.44	6.90	7.88	[42]
	Zn^{II}	2.62	4.68	7.25	9.19	9.99	[42]
	Cd^{II}	2.60(2)	4.92(3)	6.96(3)	8.74(3)	10.20(4)	this work
1-Propyl-2-Methylimidazole[10] $pK_a = 8.24$	Co^{II}	1.61	2.00	3.08	5.40		[43]
	Zn^{II}	1.35	4.40	7.45	9.41	10.45	[43]
	Cd^{II}	2.56(3)	4.06(2)	5.57(4)			this work
1-Propylimidazole-2-carbaldehyde[11] $pK_a = 5.15$	Co^{II}	1.23	1.59	3.03			[43]
	Zn^{II}	1.65	2.11	4.19			[43]
	Cd^{II}	1.45(3)	2.45(2)	3.76(2)			this work

dron ↔ tetrahedron type. For cobalt(II) complexes this is supported by the position of the absorption maximum and by a high value of the mean molar absorption (ε) coefficient [37,38,40,41,43,44]. The points corresponding to the other Co(II) complexes are found on the line with positive slope. A CHO group situated at position 2 or 4, contrary to CH_3, does not present a steric hindrance to complexation and suggests that an additional interaction of the oxygen atom with the metal ion exists which results in the formation of a weak, five membered chelate. It leads to the establishment a new configurational equilibrium for Co(II) and Cd(II) complexes (Scheme 2).

For example: $[M(H_2O)_5L]^{2+} \leftrightarrow [M(H_2O)_4L]^{2+} + H_2O$ ($M = Co^{II}$, Cd^{II}). Such additional interaction of Co(II) with an O donor atom from the CHO group of 4-Me-5-CHOIm is reflected in an increased complex stability (Fig. 5(b)). According to Siegel [45] a positive value of the differences ($\log\Delta_{M/L} = \log\beta_{1\,exp} - \log\beta_{1\,calc} = 0.64$) between the experimentally measured stability constants ($\log\beta_{1\,exp} = 1.38$) and those expected on the basis of the



Scheme 2. The intramolecular configurational equilibrium for Co(II) and Cd(II) complexes with 4-CHO-5-MeIm.

acid–base properties of the ligand ($\log\beta_{1\,calc} = 0.66$) reflects the extent of the formation of the chelate complex in equilibrium.

The possibility of equilibrium (1) for Cd(II) complexes in aqueous solution (D_2O) is supported by NMR data. The NMR spectra allow coordinated and uncoordinated CHO groups in Cd(II) and Zn(II) complexes to be distinguished. The extent of Zn–O and Cd–O interaction with the aldehyde oxygen can be

estimated by taking into account the $\Delta\delta$ values. These are twofold higher for Cd-4-Me-5-CHOIm compounds ($\Delta\delta = 0.15$ ppm). Than for zinc(II) complexes ($\Delta\delta = 0.08$ ppm.). The role 4-Me-5-CHOIm plays towards the Cd(II) ion (bidentate N,O donor ligand) or as a *N*-monodentate when coordinated to Zn(II), still remains to be elucidated. Both possibilities agree well with the X-ray data (Figs. 1, 3(a)) of Zn(II) and Cd(II) complexes in the solid state (vide supra).

The visible-range absorption spectra of the Co(II) complexes with 4-Me-5-CHOIm in aqueous solutions suggests that complexation in this system involves replacing water molecules in the hydration sphere of the central ion by the ligand molecules with retention of the pseudo-octahedral structure (pH 4.4, $\lambda = 514$ nm, $\varepsilon = 18\ M^{-1}cm^{-1}$).

3.5. Conclusion

In the present study, new complexes of Zn^{II}, Cd^{II} and Co^{II} with 4-Me-5-CHOIm have been prepared and structurally characterized. The structures of all the compounds are very different from each other. In Zn(II) complexes the most common structural motif is one in which a tetrahedral zinc center is attached to four molecules of the ligand. The cobalt derivatives exhibit an octahedral structure in which two imidazoles coordinate to cobalt in a bidentate fashion, while the cadmium complex exhibits an unusual eight-coordinate structure (CdN_4O_4). This comparison clearly emphasizes that zinc has a greater preference for tetrahedral ZnN_4 coordination than do either cobalt or cadmium, an observation that is in accord with the prevalent role of zinc in the structural sites of enzymes. Moreover, the fact that the zinc complexes exhibit different structures to those of cobalt and cadmium should be taken into consideration while using these metals as spectroscopic probes for studying zinc enzymes. The structural data obtained correlate well with studies of these complexes in aqueous solution. The NMR and potentiometric studies have confirmed different modes of coordination of 4-CHO-5-MeIm in the zinc(II) ions (monodentate) in comparison to cobalt(II) and cadmium(II) ions in which the pyridine-like nitrogen atom of the imidazole ring and the oxygen atom of CHO group participate in formation of the coordination bonds. This results in the formulation of a five-membered chelate ring. Furthermore, we have observed some differences in the strength of donor capacity between the Nτ and Nπ nitrogen atoms of the imidazole ring. Coordination by Nτ atoms gives shorter bonds (Table 2.) and more stable complexes in solution (higher value of β_n). Both structural and potentiometric data suggest 4-Me-5-CHOIm as a potentially good chelator for the removal of toxic cadmium from the body.

4. Supplementary material

Crystallographic data (excluding structure factors) for the structures reported in this paper have been deposited with the Cambridge Crystallographic Data Centre as supplementary publication numbers: CCDC 247515–247517 (for **1**–**3**). Copies of the data can be obtained free of charge on application to CCDC, 12 Union Road, Cambridge CB2 1EZ, UK; (fax: +44 1223 336 033, e-mail: deposit@ccdc.cam.ac.uk or http://www.ccdc.com.ac.uk).

References

[1] J.E. Coleman, Annu. Rev. Biochem. 61 (1992) 897.
[2] J.M. Berg, H.A. Godwin, Annu. Rev. Biophys. Biomol. Struct. 26 (1997) 357.
[3] J.S. Hanas, D.J. Hazuda, D.F. Bogenhagen, F.Y.-H. Wu, C.-W. Wu, J. Biol. Chem. 258 (1983) 14120.
[4] M.F. Summers, T.L. South, B. Kim, D. Hare, Biochemistry 29 (1990) 329.
[5] M. Petkovich, N.J. Brand, A. Krust, P. Chambon, Nature 330 (1987) 444.
[6] (a) B.L. Vallee, D.S. Auld, Acc. Chem. Res. 26 (1993) 543;
(b) D.W. Christianson, Adv. Protein Chem. 42 (1991) 281;
(c) P. Gockel, R. Vogler, M. Gelinsky, A. Meißner, H. Albrich, H. Vahrenkamp, Inorg. Chim. Acta 323 (2001) 16.
[7] B.L. Vallee, D.S. Auld, Biochemistry 29 (1990) 5647.
[8] D.W. Christianson, J.D. Cox, Annu. Rev. Biochem. 68 (1999) 33.
[9] J.L. Alberts, K. Nadassy, S.J. Wodak, Protein Sci. 7 (1998) 1700.
[10] J.J.R. Fraústo da Silva, R.J.P. Williams, The Biological Chemistry of the Elements, Oxford University Press, Oxford, 1991.
[11] R.J.P. Williams, J.J.R. Fraústo da Silva, The Natural Selection of the Chemical Elements, Oxford University Press, Oxford, 1996.
[12] I.M. Armitage, A.J.M. Schoot Viterkamp, J.R. Chlebowski, J.E. Coleman, J. Magn. Reson. 29 (1978) 375.
[13] H. Beinert, Coord. Chem. Rev. 33 (1980) 55.
[14] International Agency for Research on Cancer Monographs, Cadmium, IARC Press, Lyon vol. 58, 1993, p. 119.
[15] M.P. Waalkes, J. Inorg. Biochem. 79 (2000) 241.
[16] T. Dudey, C. Lim, Chem. Rev. 103 (2003) 773.
[17] L. Rulíšek, J. Vondrášek, J. Inorg. Biochem. 71 (1998) 115.
[18] J.J. Legg, Coord. Chem. Rev. 25 (1978) 103.
[19] (a) B.V. Nonius, Nonius COLLECT, Delft, The Netherlands 1997–2000;
(b) Z. Otwinowski, W. Minor, Methods Enzymol. 276 (1997) 307.
[20] A. Altomare, G. Cascarano, C. Giacovazzo, C. Guagliardi, M.C. Burla, G. Palidori, M. Camalli, J. Appl. Cryst. 27 (1994) 4350.
[21] G.M. Scheldrick, SHELXL-97: Program for Crystal Structure Refinement, University of Göttingen, Germany, 1997.
[22] L. Faruggia, J. Appl. Cryst. 32 (1999) 837.
[23] A. Braibanti, G. Ostacoli, P. Paoletti, L.D. Pettit, S. Sammartanto, Pure Appl. Chem 59 (1987) 1721.
[24] P. Gans, A. Sabatini, A. Vacca, J. Chem. Soc., Dalton Trans. (1985) 1195.
[25] B. Barszcz, T. Głowiak, J. Jezierska, Polyhedron 18 (1999) 3713.
[26] L.S. Long, L.S. Zheng, X.M. Chen, S.W. Ng, Main Group Metal Chem. 24 (2001) 461.
[27] (a) B. Müller, A. Schneider, M. Tesmer, H. Vahrenkamp, Inorg. Chem. 38 (1999) 1900;
(b) B. Müller, H. Vahrenkamp, Eur. J. Inorg. Chem. (1999) 137.

[28] (a) F. Hueso-Ureña, S.B. Jiménez-Pulido, M.N. Moreno-Carretero, M. Quirós-Olozábal, J.M. Salas-Peregrín, Inorg. Chim. Acta 277 (1998) 103;
(b) M.A. Romero, M.N. Moreno, J. Ruiz, M.P. Sánchez, F. Nieto, Inorg. Chem. 25 (1986) 1498;
(c) E.R. Acuña-Cueva, R. Faure, N.A. Illán-Cabeza, S.B. Jiménez-Pulido, M.N. Moreno-Carretero, M. Quirós-Olozábal, Inorg. Chim. Acta 342 (2003) 209;
(d) A.A. Naiini, V. Young, J.G. Verkade, Polyhedron 14 (1995) 393;
(e) J.M. Grevy, F. Tellez, S. Bernés, H. Nöth, R. Contreras, N. Barba-Behrens, Inorg. Chim. Acta 339 (2002) 532;
(f) N. Niklas, F. Hampel, G. Liehr, A. Zahl, R. Alsfasser, Chem. Eur. J. 7 (2001) 5135.
[29] K. Kurdziel, T. Głowiak, S. Materazzi, J. Jezierska, Polyhedron 22 (2003) 3123.
[30] B. Barszcz, T. Głowiak, K. Detka, Polyhedron 22 (2003) 1329.
[31] (a) B. Müller, H. Vahrenkamp, Eur. J. Inorg. Chem. (1999) 117;
(b) B. Müller, H. Vahrenkamp, Eur. J. Inorg. Chem. (1999) 129.
[32] K. Kurdziel, T. Głowiak, J. Jezierska, J. Chem. Soc., Dalton Trans. (2000) 1095.
[33] K. Nakamoto, Infrared and Raman Spectra of Inorganic and Coordination Compounds, Wiley, New York, 1986.
[34] A.B.P. Lever, J. Chem. Educ. (1968) 711.
[35] G. Berthon, C. Luca, Anal. Chim. Acta 51 (1970) 239.
[36] B. Lenarcik, B. Barszcz, Roczniki Chemii, Ann. Soc. Chim. Polonorum 51 (1977) 1849.
[37] B. Lenarcik, J. Kulig, P. Laidler, Roczniki Chemii, Ann. Soc. Chim. Polonorum 48 (1974) 1151.
[38] B. Lenarcik, B. Barszcz, J. Chem. Soc., Dalton Trans. (1980) 24.
[39] J. Kulig, Unpublished data.
[40] B. Lenarcik, K. Obłak, Roczniki Chemii, Ann. Soc. Chim. Polonorum 51 (1977) 2079.
[41] B. Lenarcik, K. Kurdziel, Pol. J. Chem. 55 (1981) 737.
[42] B. Lenarcik, B. Barszcz, Pol. J. Chem. 53 (1979) 963.
[43] B. Barszcz, J. Kulig, J. Jezierska, J. Lisowski, Pol. J. Chem. 73 (1999) 447.
[44] B. Barszcz, J. Kulig, J. Chem. Soc., Dalton Trans. (1993) 1559.
[45] (a) Z. Sigel, Chem. Soc. Rev. 33 (2004) 191;
(b) M.J. Sánchez-Moreno, A. Fernández-Botello, R.B. Gómez-Coca, R. Griesser, J. Ochocki, A. Kotynski, J. Niclós-Gutiérrez, V. Moreno, H. Siegel, Inorg. Chem. 43 (2004) 1311.

Available online at www.sciencedirect.com
SCIENCE DIRECT®
Polyhedron 24 (2005) 639–644
POLYHEDRON
www.elsevier.com/locate/poly

Laser ablation synthesis of new binary chalcogen molecules from the selenium–sulfur system

Ondrej Šedo [a], Milan Alberti [b,*], Josef Havel [a]

[a] Department of Analytical Chemistry, Faculty of Science, Masaryk University, Kotlářská 2, 611 37 Brno, Czech Republic
[b] Research Department for the Structural Study of Molecular Ensembles, Faculty of Science, Masaryk University, Kotlářská 2, 611 37 Brno, Czech Republic

Received 24 November 2004; accepted 5 January 2005

Abstract

Laser ablation synthesis of heteroatomic Se_mS_n molecules from selenium, selenium–sulfur mixtures and selenium disulfide alone or mixed with selenium and sulfur was studied using common MALDI–TOF (matrix assisted laser desorption-ionization–time of flight) mass spectrometric instrumentation. From elemental gray and red selenium, the formation of Se_m^+ ($m = 2$–9) and Se_m^- ($m = 1$–7) was achieved. Composite Se_mS_n species were obtained when laser pulses were applied onto a selenium–sulfur mixture or to solid selenium disulfide (SeS_2). For the first time, nine-membered Se_mS_n compounds are observed. Likewise, it was observed that positively charged mixed substances formed were of higher molecular weight than the negatively charged ones. Ions $Se_mS_n^-$ with $m + n = 3$ or 4 and $Se_mS_n^+$ with $m + n = 5$ or 8 dominate in the mass spectra of SeS_2. At least 12 new selenium sulfides not described in the literature were identified from the mass spectra, while most of them were generated from selenium disulfide and detected in the positive mode. Their stoichiometry was confirmed using isotopic pattern modelling.
© 2005 Elsevier Ltd. All rights reserved.

Keywords: Selenium; Sulfur; Selenium disulfide; Laser ablation synthesis; TOF mass spectrometry

1. Introduction

Interaction of laser radiation with solid materials results in several processes. Laser pulses in some cases initialize formation of various species. Mass spectrometry was found to be a powerful tool for studying species formed during laser ablation processes [1].

For preparation of semiconductive nanocrystalline selenium films, beside sublimation of selenium grains and annealing of the amorphous selenium film [2], pulsed laser ablation is becoming the most prospective method. The TOF mass spectrometric identification of charged homopolyatomic species after laser ablation of selenium powder has firstly been reported by Giardini Guidoni et al. [3]. This process has also been studied by Hearley et al. [4], who observed formation of Se_m^+ ($m = 1$–5) and Se_m^- ($m = 1$–6) ions. The cyclic structure of the Se_m ($m = 3$–8) species has been calculated ab initio using the Hartree–Fock method [5]. First-principles local-density-functional calculations of Se_m ($m = 3$–8) have revealed the fact that Se_6 and Se_8 are the most stable species, which is in agreement with two selenium forms identified in crystalline structures [6]. The nature of selenium films created by pulsed laser deposition strongly depends on experimental conditions, such as laser energy density, the number of laser pulses and the nature of the substrate [7].

Sulfur and selenium atoms can be connected together in many ways, often forming heterocyclic compounds

* Corresponding author. Tel.: +420 5 41 129 344; fax: +420 5 41 21 12 14.
E-mail addresses: sedo@post.cz (O. Šedo), alberti@chemi.muni.cz (M. Alberti).

0277-5387/$ - see front matter © 2005 Elsevier Ltd. All rights reserved.
doi:10.1016/j.poly.2005.01.012

that usually possess from six to eight atoms. The procedures for their preparation can be found elsewhere [8, 9 and references therein] . Twelve-membered rings 1,2-Se_2S_{10}, 1,7-Se_2S_{10} and 1,2,3,4,5-Se_5S_7 have also been prepared [10]. According to ab initio MO calculations possible stability of 10-membered Se_5S_5 rings has also been proposed [11]. Smaller Se_mS_n compounds with $n + m \leqslant 6$, Se_4S_4, Se_5S_2, Se_5S_3 and Se_6S positively charged and with $n + m \leqslant 4$ negatively charged were identified from mass spectra produced via laser ablation synthesis from selenium–sulfur melt [4].

The most powerful method for the determination of the structure of Se_mS_n compounds is evidently ^{77}Se NMR [12,13]. Enrichment of the samples by ^{77}Se increases the quality of NMR spectra [14,15]. The ^{77}Se NMR chemical shifts of Se_mS_n were found to be in good agreement with the theoretical values calculated from ab initio molecular orbital and density functional techniques involving Stuttgart relativistic large core effective core potential approximation [16]. Complex mixtures of selenium sulfides can effectively be separated by HPLC [17]. Selenium sulfides undergo interconversion reactions with unknown mechanisms, where formation of intermediates containing hypervalent sulfur atoms is estimated [18], however, unambiguous experimental elucidation of this process is still missing.

Mixed SeS_n ($n = 1$–7) species have been identified by mass spectrometry in sulfur–quartz ores from the Southern Urals [19]. Composite Se_mS_n ($m + n \leqslant 8$) species were identified in mass spectra after electron impact ionization of a selenium–sulfur mixture previously heated and extracted from CCl_4 [20]. Selenium monosulfide was found to be carcinogenic to livers of male and female rats and livers and lungs of female mice [21]. Selenium disulfide has been patented as an antidandruff agent for shampoos [22,23]. Toxicological studies of selenium disulfide have, for example, determined its LD 50 orally for rats as 138 mg/kg [24].

Chalcogen-based thin solid films of composition, s, $SrS_{1-x}Se_x$ or $ZnS_{1-x}Se_x$ possess interesting opto-electronic properties with highly perspective technological applications [25]. Also selenium–sulfur film doped by paraffins and prepared via pulsed laser deposition performs optical memory properties [26].

Laser ablation synthesis from sulfur, selenium and sulfur–selenium mixture was described by Hearley et al. [4]. However, in that work the resolution of the mass spectrometer was too low to allow monitoring of isotopic patterns of the peaks. Therefore, the charge of the observed species could not be determined from the spectra, as, e.g., signals of Se_3^- and Se_6^{2-} were not distinguishable. Moreover, in the case of mixed selenium–sulfur species, the signals of Se_mS_n were equal to $Se_{m+2}S_{n-5}$, because the mass of two atoms of the isotope ^{80}Se (159.83304 Da) is close to five atoms of the isotope ^{32}S (159.86035). Because such pairs of compounds have significantly different isotopic patterns, mass spectrometer with resolution over 500 is needed to distinguish them. In this work, we have therefore re-examined the selenium–sulfur system.

2. Experimental

2.1. Chemicals and reagents

Elemental gray selenium, selenium disulfide, guanosine-5′-monophosphate bradykinin, α-cyano-4-hydroxycinnamic acid and harmane were obtained from Sigma–Aldrich (Steinheim, Germany), red selenium from Charles Druce Ltd. (London, United Kingdom) and elemental sulfur from Spolek pro chemickou a hutní výrobu (Ústí nad Labem, Czech Republic). Benzene was purchased from Lachema a.s. (Brno, Czech Republic). The purity of bradykinin and selenium disulfide was 98%, all other chemicals were of analytical or higher grade purity.

2.2. Apparatus

Mass spectra measurements were performed on an AXIMA CFR (Kratos Analytical, Manchester, United Kingdom) mass spectrometer with nitrogen laser (337 nm) from Laser Science Inc. (Franklin, MA, USA). Molecular ions $[M + H]^+$ of α-cyano-4-hydroxycinnamic acid and bradykinin were applied for external calibration in the positive mode. For the negative mode, molecular $[M - H]^-$ ions of harmane and guanosine-5′-monophosphate were used. Each mass spectrum was accumulated from at least 100 laser shots. The ultrasound bath UC 006 DM1 was obtained from Tesla (Rožnov pod Radhoštěm, Czech Republic).

2.3. Procedure of synthesis

The approach used for laser ablation synthesis in this work is the same as that described in our previous works [27,28]. A suspension containing 1 mg ml^{-1} of fine powdered elements, selenium disulfide or their mixtures in benzene in volume of 1 μl was pipetted onto a sample plate and dried in an air stream at room temperature. Laser pulses initiated the synthesis and products formed were analyzed with pulsed extraction in negative and positive modes, and in linear or reflectron arrangements.

3. Results and discussion

3.1. Se_m and S_n homopolyatomics

In the first stage, powdered elements were applied on the sample probe using a simple procedure described in

the experimental part. When a laser power of 2.0 mW is exceeded, formation of homopolyatomic selenium species is seen both in the positive and negative modes. Positively charged Se_m^+ ($m = 2$–9) and negatively charged Se_m^- ($m = 1$–7) species are detected from powdered red or gray selenium and no different results were observed between these allotropic modifications of selenium. An example of mass spectra obtained from gray selenium in the linear negative mode is shown in Fig. 1. In contrast to previous observations [4], the resolution of Axima-CFR allows us to monitor isotopic patterns of the ions. The detailed view on the Se_5^- anion in Fig. 2 shows an excellent agreement with the model calculated from natural abundance of selenium isotopes. Moreover, the presence of multiply charged selenium species can unambiguously be excluded. The stability of all observed selenium species was examined with the Post-source Decay (PSD) technique. Even with the highest laser power that is possible to be applied with the instrumentation (6 mW), no fragments of Se_m parent ions were observed. It is therefore possible to conclude that the species are relatively stable, more than similar sulfur compounds, which yield intense S_{n-1} and S_{n-2} fragments [27]. Detailed information about formation and behavior of S_n species produced by laser ablation synthesis from the powdered element can be found elsewhere [27,28].

3.2. Mixture of the elements

Several ways of generating mixed Se_mS_n compounds have been examined. Similarly to the phosphorus–sulfur system described before [27], laser ablation synthesis from a simple elemental mixture has been done and the results were compared with those when the selenium–sulfur mixture was previously treated with ultrasound. Moreover, laser ablation of selenium disulfide and also mixtures with elements eventually sonicated have also been studied.

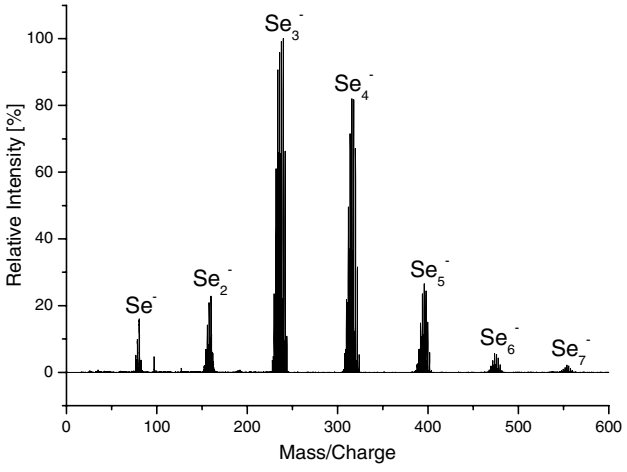


Fig. 1. Mass spectra of negatively charged selenium species produced during laser ablation of gray selenium powder. Linear negative mode with pulsed extraction, laser power of 2.67 mW.

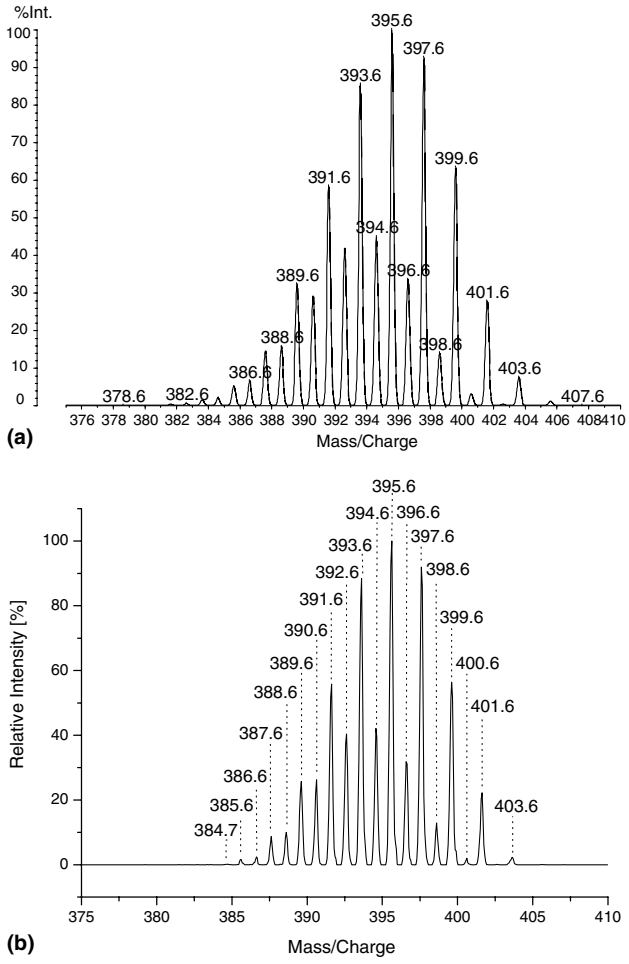


Fig. 2. Theoretical isotopic distribution of the Se_5 ion (a) in comparison with the detailed view on the experimental Se_5^- mass spectra (b).

When laser pulses are aimed at the area where selenium and sulfur are in contact, generation of singly charged heteroatomic ions is achieved. The stoichiometry of the species identified in the mass spectra both in the positive and negative modes is shown in Tables 1 and 2. A difference between theoretical and experimental peak intensities exceeding 5% was considered as an indication of two isotopic patterns overlapping. Compounds with nearly all possible atom combinations for $n + m \leqslant 5$ are formed. Moreover, some additional signals corresponding to a higher number of selenium atoms in these compounds were detected in the negative mode. On the other hand, positively charged species with relatively high selenium–sulfur ratio are also generated. We suggest that the predominance of selenium atoms in the mixed species allows them to be charged negatively and, on the other hand, more sulfur atoms in the species facilitate the possession of the positive

Table 1
Review of the stoichiometry of $Se_mS_n^-$ species identified from the mass spectra of a mixture of selenium and sulfur

Se_mS_n	n = 0	1	2	3	4	5	6	7	8	9	10
m = 0		■	■	■	■	■					
1	■	■	■	■	■	■	■				
2	■	■	■	■							
3	■	■	■								
4	■	■	■								
5	■	■									
6	■	■									
7	■										
8											

Table 2
Review of the stoichiometry of $Se_mS_n^+$ species identified from the mass spectra of the mixture of selenium and sulfur

Se_mS_n	n = 0	1	2	3	4	5	6	7	8	9	10
m = 0			■	■	■	■	■	■	■	■	■
1		■	■	■	■	■	■	■	■	■	
2	■	■	■	■	■		■	■			
3	■		■		■	■					
4	■	■	■								
5	■										
6											
7											
8											

charge. Applying ultrasound for homogenization of the mixture and consecutive laser ablation did not bring any increase in the number of mixed compounds and no sono-synthesis was observed. It is interesting to note that ultrasound had significant influence on the number of species ionized after treatment of the phosphorus–sulfur mixture [28].

These results are only in partial agreement with the findings of Hearley et al. [4]. Our results suggest in addition to previously identified ions, negatively charged Se_mS_n compounds with $n + m = 5$. The authors also observed different peaks that correspond to positively charged eight-membered molecules. However, this difference may be a result of the sample preparation where the mixture of selenium and sulfur was prepared by co-melting of the elements.

3.3. Selenium disulfide

Mass spectra resulting from laser ablation of selenium disulfide are shown in Figs. 3 and 4. The stoichiometry of the selenium sulfides is summarized in Tables 3 and 4. A significant difference between abundance of ions obtained in positive and negative modes was observed. In the negative mode, mixed compounds Se_mS_n with $n + m = 3$ or 4 dominate in the spectra. Population of heavier species is lower and does not exceed the molecular weight of 500 Da. On the contrary, in the positive mode, the species with $n + m = 5$ or 8 dominate in mass spectra and species with low molecular weight almost cannot be observed.

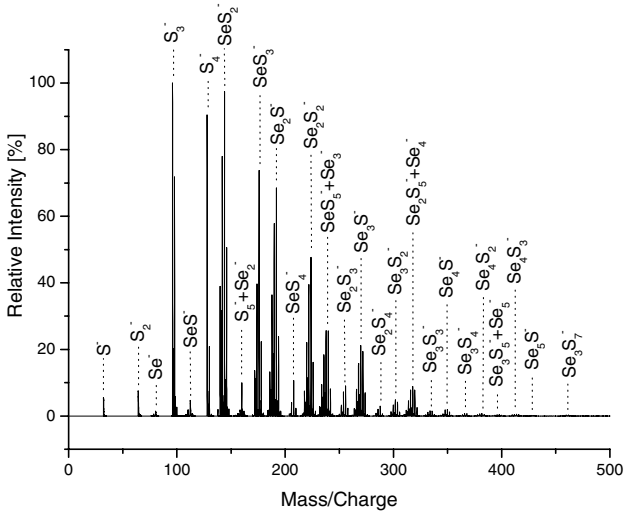


Fig. 3. Mass spectra obtained from laser ablation of selenium disulfide. Linear negative mode with pulsed extraction, laser power of 2.83 mW.

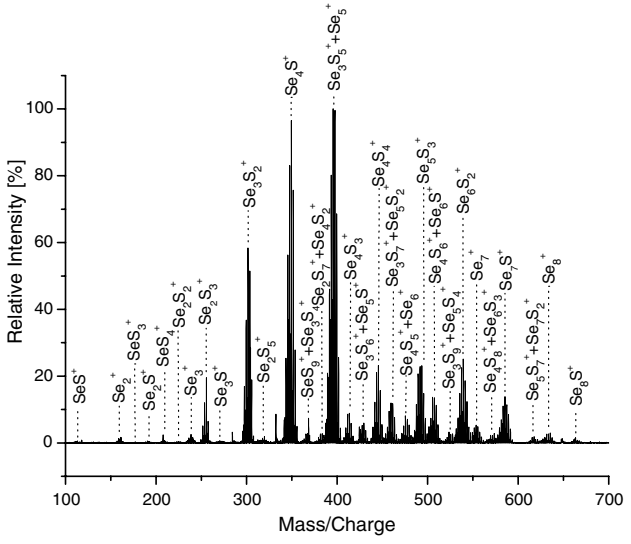


Fig. 4. Mass spectra obtained from laser ablation of selenium disulfide. Linear positive mode with pulsed extraction, laser power of 2.67 mW.

Table 3
Review of the stoichiometry of $Se_mS_n^-$ species identified from the mass spectra of SeS_2 (displayed in Fig. 3)

Se_mS_n	n = 0	1	2	3	4	5	6	7	8	9	10
m = 0		■	■	■	■	■					
1	■	■	■	■	■	■					
2	■	■	■	■	■	■					
3	■	■	■	■	■	■		■			
4	■	■	■	■							
5	■	■									
6											
7											
8											

Table 4
Review of the stoichiometry of $Se_mS_n^+$ species identified from the mass spectra of SeS_2 (displayed in Fig. 4)

Se_mS_n	n = 0	1	2	3	4	5	6	7	8	9	10
m = 0											
1		■		■	■					■	
2	■	■	■	■		■		■			
3	■	■	■		■	■	■	■		■	
4		■	■	■	■	■	■		■		
5	■	■	■	■	■			■			
6	■	■	■	■							
7	■	■	■								
8	■	■									

Twenty-five either positively or negatively charged highly abundant species generated from selenium–sulfur mixture or selenium disulfide were studied using the Post-source Decay technique. Besides examining the stability of the ions, the aim of the experiments was to find out whether the species with the same stoichiometry but different origin yield equal fragments under the same conditions. In this way, we wanted to estimate whether their structure is the same or not (isomers).

The experiments revealed that most of the selenium sulfides generated have behavior similar to sulfur homopolyatomics, losing one sulfur atom when laser power of 4.0 mW is exceeded [27]. The behavior of species with the same stoichiometry and different source (e.g., negatively charged ions with $m/z = 269$ Da) was found to be the same, as they lose equally one sulfur atom after exceeding the same threshold laser power. That means that no difference in the properties of these species was observed. Therefore, it is possible to suggest that they possess the same structure. The only exception in the behavior was found in the case of positively charged eight-membered species generated from SeS_2. These compounds undergo interesting fragmentation paths, including the loss of polyatomic neutral species. The compounds $Se_4S_4^+$ and $Se_5S_3^+$ yield a S_3 fragment, $Se_6S_2^+$ loses particles S_2 and SeS_2. In addition, Se_7S^+ ionization with high laser power results in the loss of neutral atoms S, Se and the particle SeS.

It was found that mixing selenium disulfide with selenium or sulfur does not increase the number of species formed. Conversely, in the equimolar mixture of selenium and selenium disulfide, formation of compounds with higher numbers of sulfur atoms, such as SeS_9^+, $Se_2S_n^+$ ($n = 5, 7$), $Se_3S_9^+$ and $Se_mS_5^-$ ($m = 1$–2), is suppressed. Also here, all mixtures were homogenized by ultrasound without any increase in the number of Se_mS_n molecules observed.

An overview of all known compounds together with new compounds synthesized in this work is given in Table 5. In total, 12 new heteroatomic species were identified. However, atoms in all these compounds can be arranged into numerous isomeric forms and therefore, the total number of new species formed can be much higher.

It follows from a comparison of the results summarized in Tables 1 and 3 or in Tables 2 and 4 that the number and the nature of the species formed from laser ablation of the elemental mixture and from selenium disulfide is significantly different. It seems that some of the Se–S bonds in selenium disulfide are not broken during the LA process and therefore, species with higher

Table 5
Review of all observed Se_mS_n compounds (black cells) together with already known compounds (crosses)

Se_mS_n	n = 0	1	2	3	4	5	6	7	8	9	10
m = 0		X	X	X	X	X	X	X	X	X	X
1	X	X	X	X	X	X	X	X			
2	X	X	X	X	X	X	X				X
3	X	X	X	X	X	X				■	
4	X	X	X	X	X				■		
5	X	X	X	X	■			X			
6	X	X	X	■							
7	X	X	■								
8	X										

molecular weight can be formed. Most of the newly observed species correspond to Se_mS_n compounds with $n + m = 9$. Nine-membered heteroatomic selenium–sulfur species have not yet been reported. Hypervalence of some of the atoms previously supposed in relation to interconversion reactions of selenium sulfides [18] is possible. Eventually, during the LA process some interconversion reactions between Se_mS_n molecules take place and the fast analytical procedure applied in this work allows them to be detected.

4. Conclusions

Twelve compounds of stoichiometry SeS_n ($n = 8$, 9), Se_2S_7, Se_3S_n ($n = 6$, 7, 9), Se_4S_n ($n = 5$, 6, 8), Se_5S_4, Se_6S_3 and Se_7S_2 have been newly identified. Most of them were obtained via laser ablation synthesis of selenium disulfide powder in the positive mode. Laser ablation of selenium, sulfur and their mixtures has also been examined and the mass spectra were interpreted including isotopic pattern modelling. Compounds with the same stoichiometry but different origin (SeS_2 or Se–S mixture) were found to perform identical Post-source Decay behavior, losing one sulfur atom when high laser power is applied for their generation. Selenium species Se_m^- ($m = 1$–7) and Se_m^+ ($m = 2$–9) have unambiguously been identified. The effect of ultrasound homogenization was found to have no influence on the ionization process when selenium–sulfur mixtures were subsequently ablated. The same was observed for mixtures arising from selenium disulfide. The advantage of laser ablation synthesis as a tool for generation and TOF mass spectrometric identification of new compounds in Se–S systems has been proved in this work.

Acknowledgements

This work was supported by the Ministry of Education, Youth and Sports of the Czech Republic, Project No. MSM 143 1000 11.

References

[1] A. Mele, D. Consalvo, D. Stranges, A. Giardini-Guidoni, R. Teghil, Int. J. Mass Spectrom. Ion Process. 95 (1990) 359.
[2] A. Umehara, S. Nitta, H. Furukawa, S. Nonomura, Appl. Surf. Sci. 119 (1997) 176.
[3] A. Giardini Guidoni, A. Mele, S. Piccirillo, G. Pizzella, R. Teghil, NATO ASI Series, Series C: Mathematical and Physical Sciences, 1992, p. 374 (Phys. Chem. Finite Syst.: Cluster Cryst., vol. 2).
[4] A.K. Hearley, B.F.G. Johnson, J.S. McIndoe, D.G. Tuck, Inorg. Chim. Acta 334 (2002) 105.
[5] S. Kohara, A. Goldbach, N. Koura, M.L. Sabounhi, L.A. Curtiss, Chem. Phys. Lett. 287 (1998) 282.
[6] Z.Q. Li, J.Z. Yu, K. Ohno, Phys. Rev. B 52 (1995) 1524.
[7] M. Quintana, E. Haro-Poniatowski, J. Morales, N. Batina, Appl. Surf. Sci. 195 (2002) 175.
[8] R.S. Laitinen, Acta Chem. Scand. A 41 (1987) 361.
[9] R.S. Laitinen, P. Pekonen, R.J. Suontamo, Coord. Chem. Rev. 130 (1994) 1.
[10] R. Steudel, D. Jensen, Polyhedron 9 (1990) 1199.
[11] R.S. Laitinen, J. Taavitsinen, H. Tiainen, P. Pekonen, Phosphorus Sulfur Silicon 125 (1997) 253.
[12] R.S. Laitinen, P. Pekonen, Y. Hiltunen, T.A. Pekkanen, Acta. Chem. Scand. 43 (1989) 436.
[13] R. Steudel, B. Plinke, D. Jensen, Polyhedron 10 (1991) 1037.
[14] P. Pekonen, Y. Hiltunen, R.S. Laitinen, T.A. Pekkanen, Inorg. Chem. 29 (1990) 2770.
[15] P. Pekonen, Y. Hiltunen, R.S. Laitinen, T.A. Pekkanen, Inorg. Chem. 30 (1991) 2679.
[16] J. Komulainen, R.S. Laitinen, R.J. Suontamo, Can. J. Chem. 80 (2002) 1435.
[17] R. Steudel, E.M. Strauss, D. Jensen, Z. Naturforsch. 45b (1990) 1282.
[18] J. Taavitsainen, H. Lange, R.S. Laitinen, J. Mol. Struct. (Theochem.) 453 (1998) 197.
[19] E.Y. Buslaeva, G.A. Bulakhov, Dokl. Akad. Nauk. 342 (1995) 665.
[20] R. Cooper, J.V. Culka, J. Inorg. Nucl. Chem. 29 (1967) 1217.
[21] F.R. Moore, G.A. Urda, G. Krishna, J.C. Theiss, Mutation Res. 367 (1996) 33.
[22] M.M. Baldwin, A.P. Young Jr., US pat 2,694,669 (1954 to Abbott).
[23] E.J. Matson, J. Soc. Cosmet. Chem. 7 (1956) 459.
[24] L.M. Cummins, E.T. Kimura, Toxicol. Appl. Pharmacol. 20 (1971) 89.
[25] J. Ihanus, E. Lambers, P.H. Holloway, M. Ritala, M. Leskelä, J. Cryst. Growth 260 (2004) 440.
[26] A. Lörinczi, J. Optoelectron. Adv. Mater. 5 (2003) 1081.
[27] M. Alberti, O. Šedo, J. Havel, Polyhedron 22 (2003) 2601.
[28] O. Šedo, Z. Voráč, M. Alberti, J. Havel, Polyhedron 23 (2004) 1199.

Available online at www.sciencedirect.com
SCIENCE DIRECT®
Polyhedron 24 (2005) 645–653
POLYHEDRON
www.elsevier.com/locate/poly

Synthesis, structure and properties of monomeric strontium and barium complexes containing terminal η^2-3,5-di-*tert*-butylpyrazolato ligands

Hani M. El-Kaderi, Mary Jane Heeg, Charles H. Winter *

Department of Chemistry, Wayne State University, 5101 Cass Avenue, Detroit, MI 48202, USA

Received 30 July 2004; accepted 7 January 2005

Abstract

Treatment of $Ba(N(SiMe_3)_2)_2(THF)_2$ with tetraglyme or triglyme (1 equiv) followed by 3,5-di-*tert*-butylpyrazole (2 equiv) in toluene afforded bis(3,5-di-*tert*-butylpyrazolato)(tetraglyme)barium (68%) and bis(3,5-di-*tert*-butylpyrazolato)(triglyme)barium (32%) as colorless solids after crystallization from hexane. Similar treatment of $Sr(N(SiMe_3)_2)_2(THF)_2$ with tetraglyme, triglyme or *N*,*N*,*N*′,*N*″,*N*″-pentamethyldiethylenetriamine (PMDETA) (1 equiv) followed by 3,5-di-*tert*-butylpyrazole (2 equiv) in toluene afforded bis(3,5-di-*tert*-butylpyrazolato)(tetraglyme)strontium (50%), bis(3,5-di-*tert*-butylpyrazolato)(triglyme)strontium (73%) and bis(3,5-di-*tert*-butylpyrazolato)(PMDETA)strontium(II) (64%), respectively, as colorless solids. The X-ray crystal structures of these complexes revealed monomeric molecules in which each metal coordination sphere is capped by one neutral polydentate ligand and two terminal η^2-pyrazolato ligands. Volatility studies showed that these complexes fail to sublime, and rather decompose under sublimation conditions with neutral ligand loss for the barium complexes and loss of the neutral ligands and 3,5-di-*tert*-butylpyrazole for the strontium complexes.
© 2005 Elsevier Ltd. All rights reserved.

Keywords: N ligands; Strontium; Barium; Pyrazolato ligands; CVD precursors

1. Introduction

There is considerable interest in organometallic complexes of the heavier group 2 elements (Ca, Sr, Ba) that can serve efficiently as precursors in chemical vapor deposition (CVD) film growth processes [1–3]. Desirable properties of CVD precursors include high thermal stability, acceptable volatility below the decomposition temperature, lack of elements that might contaminate the thin film material, as well as efficient film growth chemistry. These restrictions are particularly challenging in the heavier alkaline earth metals because of the large ion sizes and low charge/radius ratios, which lead to polymeric complexes, weak ligand–metal interactions and generally low thermal stability [4]. Therefore, careful selection of ligands is a central issue in the design of CVD precursors for the heavier group 2 elements. To date, cyclopentadienyl, β-diketonato and β-ketoiminato ligands have been the most widely employed in group 2 CVD precursors, since these ligands can provide monomeric structures with sufficient thermal stability to allow vapor transport [1–3]. However, many problems have been encountered in film growth with these existing precursors, including low vapor pressure, erratic vapor transport, unacceptably high carbon incorporation in the thin film materials and premature precursor decomposition by loss of neutral ligands. To overcome some of these problems, fluorinated β-diketonato ligands have been employed to increase the Lewis acidity of the group

* Corresponding author. Tel.: +1 313 577 5224; fax: +1 313 577 8289.
E-mail address: chw@chem.wayne.edu (C.H. Winter).

0277-5387/$ - see front matter © 2005 Elsevier Ltd. All rights reserved.
doi:10.1016/j.poly.2005.01.011

2 metal centers and thus enhance thermal stability, and polydentate donor ligands have been used to saturate the coordination spheres of the metal ions [1,3d,3e]. In addition, alternative film growth procedures have been employed to minimize problems with thermal precursor decomposition. These have included aerosol-assisted CVD [5], spray pyrolysis [6], spray MOCVD [7], supercritical fluid transport CVD [8], atomic layer deposition [9] and liquid delivery MOCVD [10].

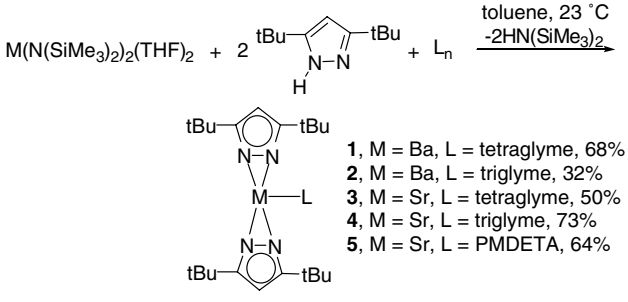
Recently, we have reported the synthesis and characterization of several magnesium [11] and calcium [12] complexes that contain various nitrogen donor ligands. The majority of our efforts in this area have been aimed at preparing volatile pyrazolato complexes that might be used as CVD precursors, since the pyrazolato ligand bears some similarity to the widely used cyclopentadienyl and β-diketiminato ligands. The pyrazolato ligand is a versatile nitrogen donor ligand, and has been employed with metals across the periodic table [13]. Very few pyrazolato complexes of strontium and barium have been reported [14]. In related work, neutral 3,5-dimethylpyrazole was used as a capping ligand in several volatile barium and strontium β-diketonato complexes [15]. While heavier group 2 CVD precursors with nitrogen donor ligands remain poorly developed, $Ba(tmhd)_2(hmtt)$ (tmhd = tetramethylheptanedionate; hmtt = 1,1,4,7,10,10-hexamethyltriethylenetetramine) binds hmtt selectively over tetraglyme and exhibits enhanced vapor transport relative to $Ba(tmhd)_2$(tetraglyme) [16]. $Ba(tmhd)_2(tetraen)_2$ (tetraen = triethylenetetramine) has been evaluated as a precursor to YBCO films, and is claimed to be substantially more volatile and thermally stable than related $Ba(tmhd)_2$ sources [17]. Marks and colleagues [3e] have reported a series of thermally stable precursors of the formula $Ba(hfac)_2$(polyether) (hfac = 1,1,1,5,5,5-hexafluoro-2,4-pentanedionato), and a key to their thermal stability is the electron-withdrawing character of the hfac ligand. Based upon these precedents, exploration of group 2 compounds containing electron-withdrawing nitrogen donor ligands such as pyrazolato might provide new leads for group 2 CVD source compounds.

Within the above context, we report the synthesis and structural characterization of several monomeric strontium and barium complexes that contain pyrazolato ligands along with neutral polydentate nitrogen and oxygen donor ligands. Solid state structural determinations reveal monomeric complexes with terminal η^2-pyrazolato ligands. The polydentate donor ligands saturate the remaining coordination sites and thus ensure the formation of monomeric complexes. The complexes described herein are not volatile, and instead decompose upon heating with loss of the neutral donor ligands. Thus, the bis(pyrazolato)metal fragment does not possess sufficient Lewis acidity to impart the thermal stability that is required for use in a CVD precursor.

2. Results and discussion

2.1. Synthesis and properties of new complexes

Even though we have employed salt metathesis routes to prepare many magnesium [11i] and calcium [12] pyrazolato complexes, this method was not successful for the synthesis of the strontium and barium pyrazolato complexes described herein. Instead, salt methathesis routes afforded complex reaction mixtures from which pure products could not be isolated. Previous workers with barium and strontium have emphasized that the larger ionic size and the reduced electronegativity of strontium and barium tend to lead to polymeric insoluble species, which are often charged "ate" complexes [18]. An alternative route to complexes of the heavier alkaline earth metals is through protonation reactions involving silylamido precursors [14c,19]. Thus, we examined the reactions of 3,5-di-*tert*-butylpyrazole (tBu$_2$pzH) with silylamido complexes of strontium and barium. Treatment of $Ba(N(SiMe_3)_2)_2(THF)_2$ [20] with 2 equivalents of tBu$_2$pzH in the presence of tetraglyme or triglyme (1 equiv) afforded Ba(tBu$_2$pz)$_2$(tetraglyme) (**1**, 68%) and Ba(tBu$_2$pz)$_2$(triglyme) (**2**, 32%) as colorless crystals after workup (Eq. (1)). Analogous treatment of $Sr(N(SiMe_3)_2)_2(THF)_2$ [21] with tBu$_2$pzH in the presence of tetraglyme, triglyme or *N*,*N*,*N*′,*N*″,*N*″-pentamethyldiethylenetriamine (PMDETA) afforded Sr(tBu$_2$pz)$_2$(tetraglyme) (**3**, 50%), Sr(tBu$_2$pz)$_2$(triglyme) (**4**, 73%) and Sr(tBu$_2$pz)$_2$(PMDETA) (**5**, 64%) as colorless crystalline solids.



(1)

The formulations and structures of **1**–**5** were established by spectral and analytical methods and by X-ray crystallography. As described below, the solid state structures of **1**–**5** consist of monomeric complexes containing terminal η^2-tBu$_2$pz ligands and the neutral donor ligand L with its maximum number of Lewis basic sites coordinated to the metal centers. The NMR spectra of **1**–**5** are simple and consist of well-resolved, sharp signals for both the proton and the carbon atoms. In the ^{1}H NMR spectra of **1**–**4**, the signals for the *tert*-butyl groups and the pyrazolato ligand core methine fragment appear in a narrow range of δ = 1.61–1.64 and δ = 6.41–6.29 ppm, respectively. A small difference was observed

for the *tert*-butyl group ^{1}H NMR resonance in **5**, which appears slightly upfield at $\delta = 1.55$ ppm. In the $^{13}C\{^1H\}$ NMR of **1–5**, the signals for the carbon atoms of the pyrazolato ligand core methine fragment appear between $\delta = 96.05$ and 97.67 ppm.

To assess the potential use of **1–5** as precursors in CVD applications, preparative sublimation experiments were carried out in a horizontal sublimation apparatus. Samples of **1–5** (~0.5 g) were loaded in the sublimation apparatus under argon and then were heated gradually at 0.05 torr. Complexes **1** and **2** did not sublime, but decomposed at about 130–150 °C to afford the neutral ligands at the cold end of the sublimation tube and nonvolatile white residues at the hot end of the sublimation tube. The nonvolatile residues were insoluble in toluene and were not analyzed further. Presumably, these complexes are of the formula $[Ba(tBu_2pz)_2]_n$. Thermal decomposition was also observed for **3–5**, however, both the neutral ligands and some of the tBu_2pzH sublimed between 130 and 150 °C. Again, the nonvolatile residues were insoluble in toluene, and were not analyzed further.

2.2. X-ray crystal structures of *1–3*

The X-ray crystal structures of **1–5** were determined in order to establish the molecular geometry about the metal center and the binding modes of the pyrazolato ligands. The diffraction experiments for **4** and **5** yielded poor results and are not discussed herein. However, the molecular structures of **4** and **5** were unambiguously established from these analyses. Experimental crystallographic data for **1–3** are summarized in Table 1, selected bond lengths and angles are given in Tables 2–4 and perspective views are presented in Figs. 1–3.

Table 1
Crystal data and data collection parameters for **1–3**

	Complex **1**	Complex **2**	Complex **3**
Empirical formula	$C_{32}H_{60}BaN_4O_5$	$C_{30}H_{56}BaN_4O_4$	$C_{32}H_{60}SrN_4O_5$
Formula weight	718.18	674.13	668.46
Space group	*C2/c*	*P2(1)/c*	*Fdd2*
a (Å)	24.327(11)	12.4674(9)	24.162(3)
b (Å)	19.554(9)	19.4923(14)	31.066(3)
c (Å)	18.093(8)	15.3582(12)	10.1115(10)
β (°)	114.549(11)	108.7570(10)	90
V (Å^3)	7829(6)	3534.1(5)	7589.9(14)
Z	8	4	8
Temperature (K)	295(2)	193(2)	295(2)
λ (Å)	0.71073	0.71073	0.71073
Density calculated (g cm^{-3})	1.219	1.267	1.170
μ (mm^{-1})	1.052	1.159	1.459
$R(F)$ (%)	5.80	2.85	3.31
$R_w(F)$ (%)	12.55	6.26	8.27

$R(F) = \sum(\|F_o| - |F_c\|)/\sum|F_o|$.
$R_w(F) = \left[\sum w(F_o^2 - F_c^2)^2 / \sum w(F_o^2)^2\right]^{1/2}$.

Table 2
Selected bond lengths (Å) and angles (°) for **1**

Bond lengths			
Ba–N(1)	2.726(5)	Ba–N(2)	2.763(5)
Ba–N(3)	2.756(5)	Ba–N(4)	2.702(5)
Ba–O(1)	2.848(5)	Ba–O(2)	2.852(6)
Ba–O(3)	2.797(7)	Ba–O(4)	2.899(8)
Ba–O(5)	2.865(9)		
Bond angles			
N(1)–Ba–N(2)	29.17(14)		
N(1)–Ba–N(3)	151.25(16)		
N(1)–Ba–N(4)	131.51(15)		
N(3)–Ba–N(4)	29.25(13)		
N(3)–Ba–N(2)	179.12(14)		
N(4)–Ba–N(2)	151.62(14)		

Table 3
Selected bond lengths (Å) and angles (°) for **2**

Bond lengths			
Ba–N(1)	2.709(2)	Ba–N(2)	2.678(2)
Ba–N(3)	2.723(2)	Ba–N(4)	2.692(2)
Ba–O(1)	2.861(2)	Ba–O(2)	2.8522(18)
Ba–O(3)	2.8138(18)	Ba–O(4)	2.8115(18)
Bond angles			
N(1)–Ba–N(2)	29.76(6)		
N(1)–Ba–N(3)	120.88(6)		
N(1)–Ba–N(4)	107.96(6)		
N(3)–Ba–N(4)	29.76(6)		
N(3)–Ba–N(2)	126.12(6)		
N(2)–Ba–N(4)	100.77(6)		

Table 4
Selected bond lengths (Å) and angles (°) for **3**[a]

Bond lengths	
Sr–N(1)	2.5629(19)
Sr–N(2)	2.578(2)
Sr–O(1)	2.631(3)
Sr–O(2)	2.752(2)
Sr–O(3)	2.707(2)
Bond angles	
N(1)–Sr–N(2)	31.36(7)
N(1)#1–Sr–N(1)	173.58(10)
N(1)–Sr–N(2)#1	153.69(7)
N(2)#1–Sr–N(2)	135.42(10)

[a] The designator #1 indicates a symmetry related position $1/2 - x$, $1/2 - y$, z.

Complex **1** crystallizes from hexane as nine-coordinate, monomeric molecules (Fig. 1). Each barium center is bonded to two η^2-tBu_2pz ligands and one η^5-tetraglyme ligand. The overall geometry about the barium ions is distorted pentagonal bipyramidal if the centers of the nitrogen–nitrogen bonds of the pyrazolato ligands are considered to be monodentate donors. The tetraglyme ligand is situated in the equatorial plane, with the barium atom and five tetraglyme oxygen atoms being approximately coplanar. The η^2-tBu_2pz ligands occupy the axial sites. The barium–nitrogen bond distances range between 2.702(5) and 2.763(5) Å. The longer barium–nitrogen bond lengths are associated with the

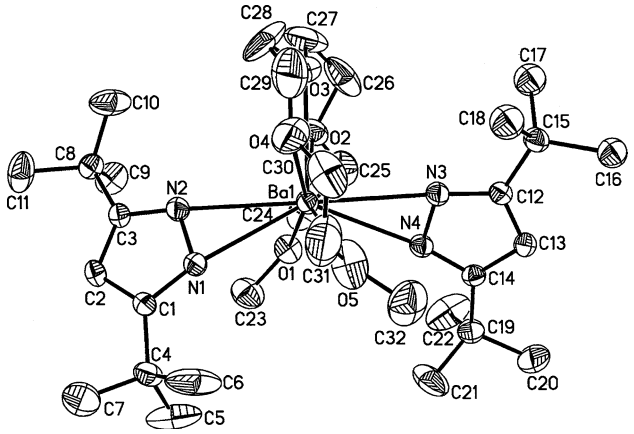


Fig. 1. Perspective view of **1** with probability ellipsoids at the 20% level.

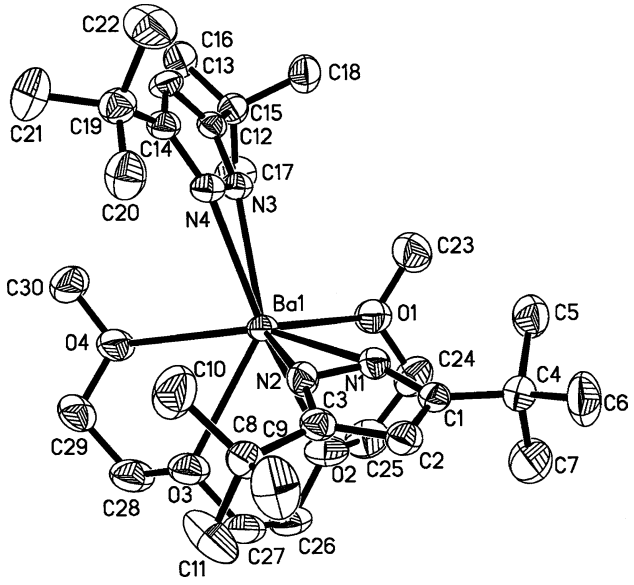


Fig. 2. Perspective view of **2** with probability ellipsoids at the 50% level.

nitrogen atoms (N(2), N(3)) that are farther from the open mouth of the tetraglyme ligand, and it is highly likely that this slight lengthening is due to steric interactions between the tetraglyme carbon atom backbone and the *tert*-butyl groups containing C(8) and C(15). However, the differences between the short and long barium–nitrogen bonds are small ($\Delta_{Ba-N} = 0.047$, 0.054 Å), and are consistent with η^2-bonding of the tBu$_2$pz ligand. The nitrogen–barium–nitrogen bite angles are 29.17(14)° and 29.25(13)°. The planes of the C_3N_2 cores of the tBu$_2$pz ligands are twisted from each other by 57.3(3)°. The tetraglyme ligand wraps around the barium center with barium–oxygen bond lengths of 2.797(7)–2.899(8) Å.

Complex **2** exists as an eight-coordinate monomeric molecule in which the barium center is bonded to two η^2-pyrazolato ligands and one η^4-triglyme ligand (Fig. 2). The triglyme ligand oxygen atoms are approximately

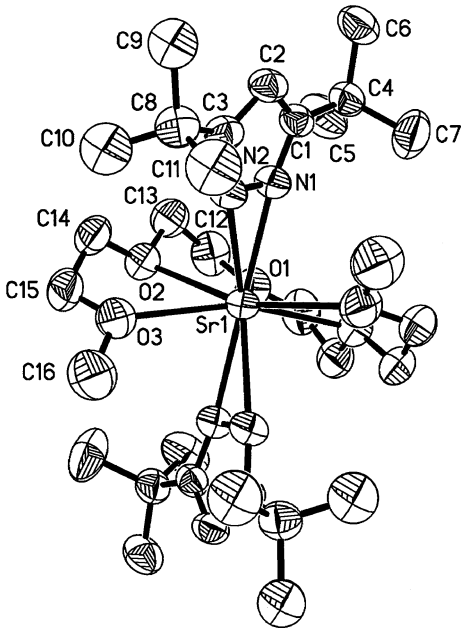


Fig. 3. Perspective view of **3** with probability ellipsoids at the 50% level.

coplanar with the barium center, while the pyrazolato ligands are *trans* to each other with a bent arrangement towards the open side of the triglyme ligand. Therefore, the geometry about the barium center is distorted octahedral if the centers of the nitrogen–nitrogen bonds of the pyrazolato ligands are considered to be monodentate donors. The barium–nitrogen bond distances range between 2.678(2) and 2.723(2) Å. This range is slightly shorter than that of **1**, which is most likely due to the lower coordination number of the barium atom of **2**, compared to that of **1**. Within each tBu$_2$pz ligand, the differences in the barium–nitrogen bond lengths ($\Delta_{Ba-N} = 0.031$ Å) are at the edge of experimental uncertainty. Thus, the tBu$_2$pz ligand exhibits idealized η^2-bonding. The bite angles of the pyrazolato ligands about the barium atom are 29.76(6)°. The C_3N_2 cores of the tBu$_2$pz ligands are twisted from each other by 49.16(8)°. The twisting of the pyrazolato ligand cores may result from steric interactions between the *tert*-butyl groups containing C(8) and C(19). The triglyme ligand is bonded to the barium center through four approximately coplanar oxygen atoms with barium–oxygen bond lengths of 2.812(2)–2.861(2) Å.

Complex **3** crystallizes from hexane as a 9-coordinate monomer (Fig. 3). The molecule is located on a twofold rotation axis that passes through both the strontium center and O(1). The strontium ion is coordinated to two η^2-pyrazolato ligands and one η^5-tetraglyme ligand, with an overall geometry that is similar to that of **1**. The strontium–nitrogen bond lengths are 2.563(2) and 2.578(2) Å, and are consistent with idealized η^2-bonding of the tBu$_2$pz ligand. The bite angle of the pyrazolato

ligand is 31.36(7)°, which is slightly larger than the related values in **1** and **2** due to the shorter strontium–nitrogen bond lengths in **3**. The C_3N_2 cores of the tBu$_2$pz ligands are twisted from each other by 66.43(8)°. The twisting of the pyrazolato ligand cores may result from steric interactions between the *tert*-butyl groups containing C(8) and C(8′). The strontium–oxygen bond distances range between 2.631(3) and 2.752(2) Å.

2.3. Comments on the synthetic route to *1*–*5*

As noted above, protonation reactions between M(N(SiMe$_3$)$_2$)$_2$(THF)$_2$ (M = Sr, Ba) and tBu$_2$pzH in the presence of the neutral polydentate ligand L provide **1**–**5** in moderate to good crystallized yields. A recent report on pyrazolato complexes of calcium, strontium and barium has summarized the synthetic approaches reported to date [14c]. Treatment of M(N(SiMe$_3$)$_2$)$_2$(THF)$_2$ (M = Ca, Sr, Ba) with 3,5-dimethylpyrazole (Me$_2$pzH) afforded low and variable yields of M(Me$_2$pz)$_2$(Me$_2$pzH)$_4$. With the correct stoichiometry of 1:6, free Me$_2$pzH was obtained in the product mixture and M(Me$_2$pz)$_2$(Me$_2$pzH)$_4$ could not be isolated as pure materials. This result contrasts with the efficient preparations of **1**–**5** described herein. It is possible that the liberated HN(SiMe$_3$)$_2$ competes with Me$_2$pzH for coordination to the metal centers, which could result in a mixture of products. In the preparation of **1**–**5**, the neutral donor ligands L should bind with higher formation constants than monodentate ligands such as HN(SiMe$_3$)$_2$ or tBu$_2$pzH. Thus, the success or failure of protonation reactions involving M(N(SiMe$_3$)$_2$)$_2$(THF)$_2$ may be dependent upon the relative donor properties of the new ligands versus the parent pyrazoles and HN(SiMe$_3$)$_2$. Other side reactions of group 2 amido complexes have been reported during protonation reactions [22].

2.4. Comparison of the solid state structures of *1*–*3* with those of previously reported group 2 pyrazolato complexes

Until recently, structurally characterized pyrazolato complexes of strontium and barium were limited to [Ba{(Me$_2$pz)$_3$Ge}$_2$] · (dioxane)$_{0.5}$ [14a] and [Ba$_6$(Me$_2$pz)$_8$(THF)$_6${(OSiMe$_2$)$_2$O}$_2$] [14b]. [Ba{(Me$_2$pz)$_3$Ge}$_2$] · (dioxane)$_{0.5}$ has barium–nitrogen distances of 2.779(4)–2.967(4) Å, which are longer than those in **1** and **2** because the pyrazolato ligands in [Ba{(Me$_2$pz)$_3$Ge}$_2$] · (dioxane)$_{0.5}$ are bridging while those in **1** and **2** are terminal. [Ba$_6$(Me$_2$pz)$_8$(THF)$_6${(OSiMe$_2$)$_2$O}$_2$] has barium–nitrogen distances of 2.665(9)–2.694(8) Å for the terminal η^2-Me$_2$pz ligands and 2.792(7)–3.007(8) Å for the bridging $\mu,\eta^2{:}\eta^5$-Me$_2$pz ligands. The barium–nitrogen distances in the terminal η^2-Me$_2$pz ligands are similar to the values found in **1** (2.702(5)–2.763(5) Å) and **2** (2.678(2)–2.723(2) Å). [Ba$_6$(Me$_2$pz)$_8$(THF)$_6${(OSiMe$_2$)$_2$O}$_2$] contains terminal η^2-pyrazolato ligands, like **1** and **2**, but it also contains $\mu,\eta^2{:}\eta^5$-pyrazolato ligands.

A recent report by Deacon and Ruhlandt-Senge described the synthesis and structural characterization of a series of group 2 pyrazolato complexes that included M(Ph$_2$pz)$_2$(THF)$_4$ (M = Ca, Sr, Ba), M(Ph$_2$pz)$_2$(DME)$_n$ (M = Ca, Sr, n = 2; M = Ba, n = 3) and M(Me$_2$pz)$_2$(Me$_2$pzH)$_4$ (M = Ca, Sr) [14c]. This study provides the first examples of strontium pyrazolato complexes, and greatly increases the amount of structural data that is available for complexes of the heavier group 2 metal containing pyrazolato ligands. In eight-coordinate M(Ph$_2$pz)$_2$(THF)$_4$, the strontium–nitrogen and barium–nitrogen distances range between 2.539(3)–2.639(3) and 2.736(5)–2.813(5) Å, respectively. For nine-coordinate **3**, the strontium–nitrogen distances (2.563(2), 2.578(2) Å) are similar to those in Sr(Ph$_2$pz)$_2$(THF)$_4$, in spite of the difference in coordination numbers at the metal center. For nine-coordinate **1** and eight-coordinate **2**, the barium–nitrogen distances (**1**, 2.702(5)–2.763(5) Å; **2**, 2.678(2)–2.723(2) Å) are similar to slightly shorter than the analogous values in Ba(Ph$_2$pz)$_2$(THF)$_4$. It is possible that the polydentate ether ligands in **1**–**3** are less bulky than four monodentate tetrahydrofuran ligands, which allows closer approach of the tBu$_2$pz ligands. In eight-coordinate Sr(Ph$_2$pz)$_2$(DME)$_2$, the strontium–nitrogen bond lengths range between 2.539(3) and 2.566(3) Å, whereas the barium–nitrogen distances in ten-coordinate Ba(Ph$_2$pz)$_2$(DME)$_3$ lie between 2.735(4) and 2.796(4) Å. Again, these values overlap with those of **1**–**3**. The strontium–nitrogen bond length for the pyrazolato ligands in six-coordinate Sr(Me$_2$pz)$_2$(Me$_2$pzH)$_4$ is 2.622(2) Å, which is within the same range as those observed in **3**. Thus, the metal–nitrogen bond lengths in **1**–**3**, M(Ph$_2$pz)$_2$(THF)$_4$, M(Ph$_2$pz)$_2$(DME)$_n$ and M(Me$_2$pz)$_2$(Me$_2$pzH)$_4$ are not particularly sensitive to the coordination number at the metal center. Instead, variations in the metal–nitrogen distances may originate from intramolecular and intermolecular steric interactions between the pyrazolato ligand carbon atom substituents and the carbon backbones of the neutral donor ligands. Since the bonding in complexes of the heavier group 2 elements is predominantly ionic [1a,1d], small variations in the metal–nitrogen bond lengths are unlikely to be high in energy and can be balanced by crystal packing interactions.

The results described herein, coupled with previous reports of group 2 pyrazolato complexes [11i,12,14], demonstrate that η^2-pyrazolato ligand bonding is strongly preferred. Until recently, the η^2-pyrazolato ligand coordination mode was rare and was limited to a few lanthanide and actinide complexes [13]. However, work in the past few years has greatly expanded the number of crystallographically characterized complexes with η^2-pyrazolato ligands [23], and there is a good

precedent for this coordination mode. Since the bonding in group 2 complexes is predominantly ionic, it is very likely that η^2-pyrazolato ligand bonding is preferred because it entails maximum charge contact between the filled nitrogen-based orbitals and the positively charged metal ions.

2.5. Comments on CVD precursor design for the group 2 elements

Marks and coworkers have described the synthesis of barium CVD precursors of the formula $Ba(hfac)_2$(polyether) [3e], and have demonstrated that these precursors are thermally stable and can be delivered steadily in the gas phase using thermal evaporation. However, the presence of fluorine in these precursors is a liability, since fluorine can degrade the properties of many thin film materials. It was our original thought that replacement of the hfac ligand by a pyrazolato ligand might lead to complexes that retain high thermal stability, since the electronegative nitrogen atoms might impart electron withdrawing properties similar to those of the hfac ligand. In our previous report on calcium pyrazolato complexes of the formula $Ca(t\text{Bu}_2\text{pz})_2(L)$ [12], we noted that only $Ca(t\text{Bu}_2\text{pz})_2$(triglyme) was volatile and proposed that the volatility in these complexes was related to the steric fit of the neutral polydentate ligand about the calcium center. Thus, it was possible that analogous complexes of the larger ions strontium and barium would be thermally stable and volatile due to decreased intramolecular steric interactions between the pyrazolato and L ligands. This prediction was the motivation for the present study. However, the results of this study have demonstrated that **1**–**5** lack sufficient thermal stability to serve as CVD precursors, and instead decompose upon heating in the solid state to afford the neutral ligand and $t\text{Bu}_2\text{pzH}$. The lower charge/radius ratios of strontium and barium ions make them weaker Lewis acids than the calcium ion. Thus, the metal centers in **1**–**5** are not sufficiently strong Lewis acids to retain the neutral Lewis bases at temperatures required for vapor transport. Potential approaches to increase the Lewis acidity of strontium and barium complexes include the use of more electron-withdrawing fluorinated pyrazolato ligands or to use more nitrogen-rich electron withdrawing heterocyclic ligands such as 1,2,4-triazolate or tetrazolate. These and other objectives are being currently pursued in our laboratory.

2.6. Conclusions

We have prepared and structurally characterized a series of monomeric strontium and barium complexes that contain $t\text{Bu}_2\text{pz}$ ligands and neutral polyether or polyamine donor ligands. The $t\text{Bu}_2\text{pz}$ ligands bond to the metal centers with the terminal η^2-coordination mode, and the neutral polydentate ligands then saturate the remaining coordination sites. These complexes fail to sublime and are therefore not of potential utility in CVD applications that employ thermal precursor delivery. However, the results described herein complexes provide further insight into the coordination of pyrazolato ligands to group 2 metal centers, and offer new directions in the design of volatile precursors for film growth.

3. Experimental

3.1. General considerations

All reactions were performed under an inert atmosphere of argon using either glovebox or Schlenk line techniques. Toluene and hexane were distilled from sodium. PMDETA, triglyme and tetraglyme were purchased from Aldrich Chemical Company and were dried by distillation from sodium prior to use. $Ba(N(SiMe_3)_2)_2(THF)_2$ [20] and $Sr(N(SiMe_3)_2)_2(THF)_2$ [21] were prepared according to literature methods. 3,5-Di-*tert*-butylpyrazole was synthesized according to a literature method [24]. ^1H and $^{13}C\{^1H\}$ NMR spectra were obtained at 300 or 75 MHz in benzene-d_6. Infrared spectra were obtained using Nujol as the medium. Elemental analyses were performed by Midwest Microlab, Indianapolis, IN. Melting points were obtained on a Haake-Buchler HBI digital melting point apparatus and are uncorrected.

3.2. Preparation of bis(3,5-di-tert-butylpyrazolato)(tetraglyme)barium (*1*)

A 100 ml Schlenk flask was charged with $Ba(N(SiMe_3)_2)_2(THF)_2$ (0.251 g, 0.416 mmol), tetraglyme (0.092 ml, 0.416 mmol) and toluene (30 ml). The resultant mixture was stirred at ambient temperature for 0.25 h. To this solution was added $t\text{Bu}_2\text{pzH}$ (0.150 g, 0.832 mmol) and the resultant mixture was stirred for an additional 3 h. The volatile components were removed under reduced pressure to afford a colorless crystalline solid. This solid was redissolved in hexane (40 ml) and was stored at −25 °C for 24 h to afford **1** as colorless crystals (0.200 g, 67%): m.p. 250–260 °C (dec, loses tetraglyme); IR (Nujol, cm^{-1}) 3096 (m), 1504 (s), 1353 (s), 1313 (m), 1218 (m), 1097 (s), 1022 (m), 1006 (s), 994 (s), 948 (s), 869 (w), 851 (s), 831 (w), 764 (s); ^1H NMR (benzene-d_6, 23 °C, δ) 6.36 (s, 2H, pyrazolato ring C–***H***), 3.18 (m, 4H, CH_3–O–CH_2CH_2–O–$CH_2C\boldsymbol{H}_2$), 3.15 (m, 4H, CH_3–O–CH_2CH_2–O–$C\boldsymbol{H}_2CH_2$), 2.97 (m, 4H, CH_3–O–$CH_2C\boldsymbol{H}_2$–O–CH_2CH_2), 2.92 (m, 4H, CH_3–O–$C\boldsymbol{H}_2CH_2$O–CH_2CH_2), 2.71 (s, 6H, O–$C\boldsymbol{H}_3$), 1.64 (s, 32H, $C(C\boldsymbol{H}_3)_3$); $^{13}C\{^1H\}$ NMR (benzene-d_6, 23 °C, ppm) 158.26 (s, pyrazolato ring ***C***–$C(CH_3)_3$),

96.09 (s, pyrazolato ring ***C***–H), 70.51 (s, CH_3–O–***C***H_2CH_2–O–CH_2CH_2), 70.32 (s, CH_3–O–CH_2***C***H_2–O–CH_2CH_2), 68.99 (s, CH_3–O–CH_2CH_2–O–***C***H_2CH_2), 68.82 (s, CH_3–O–CH_2CH_2O–CH_2***C***H_2), 58.29 (s, O–***C***H_3), 32.54 (s, pyrazolato ***C***$(CH_3)_3$), 32.32 (s, pyrazolato C(***C***$H_3)_3$).

Anal. Calc. for $C_{32}H_{60}BaN_4O_5$: C, 53.52; H, 8.42; N, 7.80. Found: C, 53.24; H, 8.35; N, 7.93%.

3.3. Preparation of bis(3,5-di-tert-butylpyrazolato)(triglyme)barium (2)

In a fashion similar to the preparation of **1**, treatment of $Ba(N(SiMe_3)_2)_2(THF)_2$ (0.251 g, 0.416 mmol) with triglyme (0.800 ml, 0.416 mmol) and *t*Bu_2pzH (0.150 g, 0.832 mmol) in toluene (30 ml) afforded **2** as colorless crystals (0.090 g, 32%): m.p. 210 °C (dec); IR (Nujol, cm^{-1}) 1507 (s), 1402 (m), 1355 (s), 1314 (m), 1247 (s), 1220 (m), 1202 (s), 1091 (s), 1069 (s), 1020 (w), 1008 (s), 994 (s), 943 (s), 864 (m), 842 (s), 825 (w), 766 (s); ^{1}H NMR (benzene-d_6, 23 °C, δ) 6.41 (s, 2H, pyrazolato ring C–***H***), 3.03 (s, 4H, C***H***$_2$–O–CH_2CH_2), 2.96 (s, 8H, CH_2–O–C***H***$_2$C***H***$_2$), 2.78 (s, 6H, O–C***H***$_3$), 1.63 (s, 32H, C(C***H***$_3)_3$); ^{13}C{^{1}H} NMR (benzene-d_6, 23 °C, ppm) 158.59 (s, pyrazolato ring ***C***–C$(CH_3)_3$), 96.95 (s, pyrazolato ring ***C***–H), 70.69 (s, ***C***H_2–O–CH_2CH_2), 69.86 (s, CH_2–O–***C***H_2CH_2), 69.76 (s, CH_2–O–CH_2***C***H_2), 58.29 (s, O–***C***H_3), 32.25 (s, pyrazolato ***C***$(CH_3)_3$), 32.32 (s, pyrazolato C(***C***$H_3)_3$).

Anal. Calc. for $C_{30}H_{56}BaN_4O_4$: C, 53.45; H, 8.37; N, 8.31. Found: C, 53.36; H, 8.03; N, 8.06%.

3.4. Preparation of bis(3,5-di-tert-butylpyrazolato)(tetraglyme)strontium (3)

In a fashion similar to the preparation of **1**, treatment of $Sr(N(SiMe_3)_2)_2(THF)_2$ (0.230 g, 0.416 mmol) with tetraglyme (0.092 ml, 0.416 mmol) and *t*Bu_2pzH (0.150 g, 0.832 mmol) in toluene (30 ml) afforded **3** as colorless crystals (0.140 g, 50%): m.p. 180–185 °C; IR (Nujol, cm^{-1}) 3096 (m), 1504 (s), 1423 (s), 1400 (s), 1377 (vs), 1317 (s), 1283 (w), 1266 (w), 1245 (vs), 1202 (s), 1117 (vs), 1096 (vs), 1067 (vs), 1025 (vs), 1006 (s), 997 (m), 951 (s), 875 (w), 854 (vs), 834 (w), 801 (w), 766 (vs); ^{1}H NMR (benzene-d_6, 23 °C, δ) 6.29 (s, 2H, pyrazolato ring C–***H***), 3.23 (m, 8H, CH_3–O–CH_2CH_2–O–C***H***$_2$C***H***$_2$), 3.04 (m, 4H, CH_3–O–CH_2C***H***$_2$–O), 2.98 (m, 4H, CH_3–O–C***H***$_2CH_2$–O), 2.66 (s, 6H, O–C***H***$_3$), 1.61 (s, 32H, C(C***H***$_3)_3$); ^{13}C{^{1}H} NMR (benzene-d_6, 23 °C, ppm) 158.50 (s, pyrazolato ring ***C***–C$(CH_3)_3$), 96.05 (s, pyrazolato ring ***C***–H), 70.83 (s, CH_3–O–***C***H_2CH_2–O–CH_2CH_2), 69.86 (s, CH_3–O–CH_2***C***H_2–O–CH_2CH_2), 68.99 (s, CH_3–O–CH_2CH_2–O–***C***H_2CH_2), 68.61 (s, CH_3–O–CH_2CH_2O–CH_2***C***H_2), 58.42 (s, O–***C***H_3), 32.46 (s, pyrazolato ***C***$(CH_3)_3$), 32.28 (s, pyrazolato C(***C***$H_3)_3$).

Anal. Calc. for $C_{32}H_{60}N_4O_5Sr$: C, 57.50; H, 9.05; N, 8.38. Found: C, 57.42; H, 8.86; N, 8.35%.

3.5. Preparation of bis(3,5-di-tert-butylpyrazolato)(triglyme)strontium (4)

In a fashion similar to the preparation of **1**, treatment of $Sr(N(SiMe_3)_2)_2(THF)_2$ (0.230 g, 0.416 mmol) with triglyme (0.080 ml, 0.416 mmol) and *t*Bu_2pzH (0.150 g, 0.832 mmol) in toluene (30 ml) afforded **4** as colorless crystals (0.190 g, 73%): m.p. 173–175 °C; IR (Nujol, cm^{-1}) 1508 (s), 1318 (w), 1248 (s), 1221 (w), 1203 (m), 1118 (w), 1093 (m), 1069 (m), 1022 (s), 1000 (s), 995 (s), 937 (s), 868 (s), 844 (s), 828 (w), 765 (s), 668 (w); ^{1}H NMR (benzene-d_6, 23 °C, δ) 6.35 (s, 2H, pyrazolato ring C–***H***), 3.15 (s, 4H, C***H***$_2$–O–CH_2CH_2), 2.97–2.91 (m, 8H, CH_2–O–CH_2C***H***$_2$), 2.79 (s, 6H, O–C***H***$_3$), 1.64 (s, 32H, C(C***H***$_3)_3$); ^{13}C{^{1}H} NMR (benzene-d_6, 23 °C, ppm) 158.71 (s, ***C***–C$(CH_3)_3$), 96.62 (s, pyrazolato ring ***C***–H), 70.34 (s, ***C***H_2–O–CH_2CH_2), 69.53 (s, CH_2–O–***C***H_2CH_2), 68.75 (s, CH_2–O–CH_2***C***H_2), 58.89 (s, O–***C***H_3), 32.46 (s, pyrazolato ***C***$(CH_3)_3$), 32.38 (s, pyrazolato C(***C***$H_3)_3$).

Anal. Calc. for $C_{30}H_{56}N_4O_4Sr$: C, 57.71; H, 9.04; N, 8.97. Found: C, 56.65; H, 8.88; N, 9.01%.

3.6. Preparation of bis(3,5-di-tert-butylpyrazolato)-(PMDETA)strontium (5)

In a fashion similar to the preparation of **1**, treatment of $Sr(N(SiMe_3)_2)_2(THF)_2$ (0.230 g, 0.416 mmol) with PMDETA (0.087 ml, 0.416 mmol) and *t*Bu_2pzH (0.150 g, 0.832 mmol) in toluene (30 ml) afforded **5** as colorless crystals (0.165 g, 64%): m.p. 138–140 °C; IR (Nujol, cm^{-1}) 1511 (w), 1305 (w), 1247 (s), 1220 (w), 1150 (w), 1105 (w), 1012 (s), 993 (w), 774 (s); ^{1}H NMR (benzene-d_6, 23 °C, δ) 6.34 (s, 2H, pyrazolato ring C–***H***), 2.19 (m, 8H, C***H***$_2$C***H***$_2$), 2.08 (s, 12H, NC***H***$_3$), 1.77 (s, 3H, CH_2N(C***H***$_3$)CH_2), 1.55 (s, 32H, C(C***H***$_3)_3$); ^{13}C{^{1}H} NMR (benzene-d_6, 23 °C, ppm) 159.12 (s, pyrazolato ring ***C***–C$(CH_3)_3$), 96.62 (s, pyrazolato ring ***C***–H), 57.02 (s, N–***C***H_2CH_2), 55.51 (s, N–CH_2***C***H_2), 45.25 (s, N–(***C***$H_3)_2$), 42.13 (s, N–***C***H_3), 32.33 (s, overlapped pyrazolato ***C***$(CH_3)_3$) and pyrazolato C(***C***$H_3)_3$.

Anal. Calc. for $C_{31}H_{61}N_7Sr$: C, 60.10; H, 9.93; N, 14.14. Found: C, 59.72; H, 9.31; N, 15.41%.

3.7. X-ray structure determinations of 1–5

Crystalline samples of **1**–**5** were mounted in sealed thin wall capillaries under nitrogen atmosphere for X-ray data collection. All crystal structures were collected on a Bruker P4/CCD diffractometer equipped with Mo radiation. For each collection, a full sphere of data was collected at 10 s/frame with 0.2° between each frame. The frame data were indexed and integrated with

the manufacturer's SMART and SAINT software. Absorption corrections were applied with Sheldrick's SADABS program and the structure was solved and refined using the programs of SHELX-97. All reported crystal structures consist of monomeric neutral complexes with no associated solvent or ions. The crystal structures of **4** and **5** had considerable disorder and were solved only to the point of positive structural identifications. Data for **1**–**3** are contained in Tables 1–4 and Figs. 1–3.

Complex **1** crystallized as colorless rhomboids. Data collection proceeded at room temperature. Hydrogen atoms were placed in calculated positions. Substantial disorder is evident in both the *tert*-butyl substituents and in the tetraglyme ethylene linkages, and is reflected in large thermal ellipsoids. Alternate and partial occupancy positions were defined for one disordered *tert*-butyl group (C(16)–C(18)) and the partial atoms were kept isotropic.

Complex **2** crystallized as colorless rods. Diffraction data were collected at −80 °C. Hydrogen atoms were placed in calculated positions for the *tert*-butyl groups, and in observed refined positions for all others.

Complex **3** crystallized as colorless mounds that were cut for data collection at room temperature. Hydrogen atoms were placed in calculated positions and were held riding. Alternate and partial occupancy positions were defined for one disordered *tert*-butyl group (C(9)–C(11)) and the partial atoms were kept isotropic. All other nonhydrogen atoms were refined anisotropically. The strontium atom is located on a crystallographic twofold axis.

4. Supplementary material

Crystallographic data for the structural analyses have been deposited with the Cambridge Crystallographic Data Centre, quoting No. 246332 for **1**, No. 246333 for **2** and No. 246334 for **3**. Copies of this information may be obtained free of charge from The Director, CCDC, 12 Union Road, Cambridge CB2 1EZ, UK (fax: +44-1233-336-033; e-mail: deposit@ccdc.cam.ac.uk or www: http://www.ccdc.cam.ac.uk).

Acknowledgements

We thank the Army Research Office (Grants Nos. DAAD19-01-1-0575 and W911NF-04-1-0332) for generous support of this research.

References

[1] For reviews, see: (a) T.P. Hanusa, Organometallics 21 (2002) 2559;
(b) J.S. Matthews, W.S. Rees Jr., Adv. Inorg. Chem. 50 (2000) 173;
(c) D.J. Otway, W.S. Rees Jr., Coord. Chem. Rev. 210 (2000) 279;
(d) P. Jutzi, N. Burford, Chem. Rev. 99 (1999) 969;
(e) W.A. Wojtczak, P.F. Fleig, M.J. Hampden-Smith, Adv. Organomet. Chem. 40 (1996) 215;
(f) D. Schulz, T.J. Marks, Adv. Mater. 6 (1994) 719;
(g) A.R. Barron, W.S. Rees Jr., Adv. Mater. Opt. Electron. 2 (1993) 271.

[2] Leading references to cyclopentadienyl precursors: (a) T. Hatanpää, M. Vehkamäki, I. Mutikainen, J. Kansikas, M. Ritala, M. Leskelä, J. Chem. Soc., Dalton Trans. (2004) 1181;
(b) M. Vehkamäki, T. Hänninen, M. Ritala, M. Leskelä, T. Sajavaara, E. Rauhala, J. Keinonen, Chem. Vap. Deposition 7 (2001) 75;
(c) M. Vehkamäki, T. Hänninen, M. Ritala, M. Leskelä, Electrochem. Solid-State Lett. 2 (1999) 504.

[3] Leading references to β-diketonato and β-ketoiminato precursors: (a) A. Kosola, M. Putkonen, L.-S. Johansson, L. Niinistö, Appl. Surf. Sci. 211 (2003) 102;
(b) V. Sannila, J. Ihanus, M. Ritala, M. Leskelä, Chem. Vap. Deposition 4 (1998) 227;
(c) A.R. Teren, J.A. Belot, N.L. Edleman, T.J. Marks, B.W. Wessels, Chem. Vap. Deposition 6 (2000) 175;
(d) D.B. Studebaker, D.A. Neumayer, B.J. Hinds, C.L. Stern, T.J. Marks, Inorg. Chem. 39 (2000) 3148;
(e) J.A. Belot, D.A. Neumayer, C.J. Reedy, D.B. Studebaker, B.J. Hinds, C.L. Stern, T.J. Marks, Chem. Mater. 9 (1997) 1638;
(f) Y.-S. Min, Y.J. Cho, D. Kim, J.-H. Lee, B.M. Kim, I.M. Lee, I. Lee, Chem. Vap. Deposition 7 (2001) 146;
(g) W.-C. Shin, K.-J. Choi, N.-K. Seong, E.-S. Choi, B.-H.D. Kim, S.-G. Yoon, Chem. Vap. Deposition 8 (2002) 221;
(h) C. Isobe, K. Hironaka, S. Hishikawa, Adv. Mater. Opt. Electron. 10 (2000) 183;
(i) R.G. Gordon, S. Barry, R.R. Broomhall-Dillard, D.J. Teff, Adv. Mater. Opt. Electron. 10 (2000) 201;
(j) J.S. Lee, S.H. Hong, K. Woo, W. Lee, Chem. Vap. Deposition 10 (2004) 67;
(k) Y.-S. Min, Y.J. Cho, D. Kim, J.-H. Lee, I. Yoon, K.-M. Park, S.S. Lee, B.R. Cho, Chem. Vap. Deposition 9 (2003) 241.

[4] (a) T.P. Hanusa, Chem. Rev. 93 (1993) 1023;
(b) R.D. Shannon, Acta Cryst. A 32 (1976) 751.

[5] (a) C. Roger, T.S. Corbitt, M.J. Hampden-Smith, T.T. Kodas, Appl. Phys. Lett. 65 (1994) 1021;
(b) C.Y. Xu, M.J. Hampden-Smith, T.T. Kodas, Adv. Mater. 6 (1994) 746.

[6] D.S. Albin, S.H. Risbud, Adv. Ceram. Mater. 2 (1987) 243.

[7] H.J. Gysling, A.A. Weinberg, T.N. Blanton, Chem. Mater. 4 (1992) 900.

[8] (a) B.N. Hansen, M.H. Brooks, R.M. Barkley, R.E. Sievers, Chem. Mater. 4 (1992) 749;
(b) E.N. Antonov, V.N. Bagratashvili, G.V. Mishakov, V.K. Popov, S.M. Howdle, in: Proceedings of the III International Symposium on Supercritical Fluids, Strasbourg, vol. 3, 1994, p. 369.

[9] (a) S. Yamamoto, A. Kawaguchi, S. Oda, Mater. Sci. Eng. B 41 (1996) 87;
(b) Z. Wang, S. Oda, M. Karlsteen, U. Sodervall, M. Willander, Jpn. J. Appl. Phys., Part 1 39 (2000) 4164;
(c) H.-J. Song, W. Koh, S.-W. Kang, Mater. Res. Soc. Symp. Proc. 567 (1999) 469;
(d) T. Hatanpää, J. Ihanus, J. Kansikas, I. Mutikainen, M. Ritala, M. Leskelä, Chem. Mater. 11 (1999) 1846.

[10] (a) F. Weiss, J. Lindner, J.P. Senateur, C. Dubourdieu, V. Galindo, M. Audier, A. Abrutis, M. Rosina, K. Fröhlich, W. Haessler, S. Oswald, A. Figueras, J. Santiso, Surf. Coat. Technol. 133 (2000) 191;

(b) T. Kawahara, M. Yamamauka, A. Yuuki, K. Ono, Jpn. J. Appl. Phys. 34 (1995) 5077;
(c) P.C. van Buskirk, S.M. Bilodeau, J.F. Roeder, P.S. Kirlin, Jpn. J. Appl. Phys. 35 (1996) 2500.

[11] (a) H.M. El-Kaderi, A. Xia, M.J. Heeg, C.H. Winter, Organometallics 23 (2004) 2652;
(b) A. Xia, H.M. El-Kaderi, M.J. Heeg, C.H. Winter, J. Organomet. Chem. 682 (2003) 224;
(c) A. Xia, M.J. Heeg, C.H. Winter, Organometallics 22 (2003) 1793;
(d) A. Xia, J.E. Knox, H.B. Schlegel, M.J. Heeg, C.H. Winter, Organometallics 22 (2003) 4060;
(e) A. Xia, M.J. Heeg, C.H. Winter, J. Organomet. Chem. 682 (2003) 224;
(f) A. Xia, M.J. Heeg, C.H. Winter, J. Am. Chem. Soc. 124 (2002) 11264;
(g) A. Xia, M.J. Heeg, C.H. Winter, Organometallics 21 (2002) 4718;
(h) A.R. Sadique, M.J. Heeg, C.H. Winter, Inorg. Chem. 40 (2001) 6349;
(i) D. Pfeiffer, M.J. Heeg, C.H. Winter, Angew. Chem., Int. Ed. 37 (1998) 2517;
(j) J.L. Sebestl, T.T. Nadasdi, M.J. Heeg, C.H. Winter, Inorg. Chem. 37 (1998) 1289.

[12] D. Pfeiffer, M.J. Heeg, C.H. Winter, Inorg. Chem. 39 (2000) 2377.

[13] For reviews, see: (a) J.E. Cosgriff, G.B. Deacon, Angew. Chem. Int. Ed. 37 (1998) 286;
(b) G. La Monica, G.A. Ardizzoia, Progr. Inorg. Chem. 46 (1997) 151;
(c) A.P. Sadimenko, S.S. Basson, Coord. Chem. Rev. 147 (1996) 247;
(d) S. Trofimenko, Progr. Inorg. Chem. 34 (1986) 115;
(e) S. Trofimenko, Chem. Rev. 72 (1972) 497.

[14] (a) A. Steiner, G.T. Lawson, B. Walfort, D. Leusser, D. Stalke, J. Chem. Soc., Dalton Trans. (2001) 219;
(b) A. Steiner, D. Stalke, Inorg. Chem. 34 (1995) 4846;
(c) J. Hitzbleck, A.Y. O'Brien, C.M. Forsyth, G.B. Deacon, K. Ruhlandt-Senge, Chem. Eur. J. 10 (2004) 3315.

[15] C. Pettinari, F. Marchetti, R. Pettinari, V. Vertlib, A. Drozdov, I. Timokhin, S. Troyanov, Y.-S. Min, D. Kim, Inorg. Chem. Acta 355 (2003) 157.

[16] R.A. Gardiner, D.C. Gordon, G.T. Stauf, B.A. Vaartstra, R.L. Ostrander, A.L. Rheingold, Chem. Mater. 6 (1994) 1967.

[17] H. Zama, T. Morishita, Jpn. J. Appl. Phys. 35 (1996) L770 (Part 2).

[18] K.G. Caulton, L.G. Hubert-Pfalzgraf, Chem. Rev. 90 (1990) 969.

[19] M. Westerhausen, Coord. Chem. Rev. 176 (1998) 157.

[20] B.A. Vaartstra, J.C. Huffman, W.E. Streib, K.G. Caulton, Inorg. Chem. 30 (1991) 121.

[21] M. Westerhausen, Inorg. Chem. 30 (1991) 96.

[22] For examples, see: (a) S. Chadwick, U. Englich, K. Ruhlandt-Senge, Angew. Chem. Int. Ed. 37 (1998) 3007;
(b) W. Vargas, U. Englich, K. Ruhlandt-Senge, Inorg. Chem. 41 (2002) 5602.

[23] For selected recent examples, see: (a) I.A. Guzei, A.G. Baboul, G.P.A. Yap, A.L. Rheingold, H.B. Schlegel, C.H. Winter, J. Am. Chem. Soc. 119 (1997) 3387;
(b) C. Yélamos, M.J. Heeg, C.H. Winter, Inorg. Chem. 38 (1999) 1871;
(c) G.B. Deacon, E.E. Delbridge, C.M. Forsyth, P.C. Junk, B.W. Skelton, A.H. White, Aust. J. Chem. 52 (1999) 733;
(d) N.C. Mösch-Zanetti, R. Krätzner, C. Lehmann, T.R. Schneider, I. Usón, Eur. J. Inorg. Chem. (2000) 13;
(e) K.R. Gust, J.E. Knox, M.J. Heeg, H.B. Schlegel, C.H. Winter, Angew. Chem. Int. Ed. 41 (2002) 1591;
(f) K. Most, S. Kopke, F.D. Antonia, N.C. Mösch-Zanetti, Chem. Commun. (2002) 1676;
(g) W. Zheng, N.C. Mösch-Zanetti, T. Blunck, H.W. Roesky, M. Noltemeyer, H.-G. Schmidt, Organometallics 20 (2001) 3299;
(h) G.B. Deacon, C.M. Forsyth, A. Gitlits, B.W. Skelton, A.H. White, J. Chem. Soc., Dalton Trans. (2004) 1239.

[24] J. Elguéro, E. Gonzalez, R. Jacquier, Bull. Soc. Chim. Fr. (1968) 707.

Available online at www.sciencedirect.com
SCIENCE DIRECT®
Polyhedron 24 (2005) 655–662
POLYHEDRON
www.elsevier.com/locate/poly

The effect of various substituents on the structural parameters of the $P(O)[N(CH_3)(CH_2C_6H_5)]_2$ moiety. Syntheses and spectroscopic characterization of some new phosphoramidates, crystal structures of $P(O)(X)[N(CH_3)(CH_2C_6H_5)]_2$, $X = C_6H_5C(O)NH$, Cl and $CCl_3C(O)NH$

Khodayar Gholivand *, Mehrdad Pourayoubi, Zahra Shariatinia, Hossein Mostaanzadeh

Department of Chemistry, Tarbiat Modares University, P.O. Box 14115-175, Tehran, Iran

Received 27 July 2004; accepted 18 January 2005

Abstract

Some new phosphoramidates with the general formula $P(O)(X)[N(CH_3)(CH_2C_6H_5)]_2$, $X = C_6H_5C(O)NH$ (**1**), Cl (**2**), $CCl_3C(O)NH$ (**3**), $N(CH_3)_2$ (**4**) and 4-NO_2–C_6H_4NH (**5**) were prepared and characterized by IR, ^1H, ^{13}C, ^{31}P NMR spectroscopy and elemental analysis. The structures have been determined for compounds **1**–**3**. Compounds **1** and **3** were obtained in the form of centrosymmetric dimers which were produced by intermolecular –P=O···H–N– hydrogen bonds. In molecules **1**–**5**, containing carbon atoms with two bond distances from the phosphorus atoms, $^2J(P,CH_2) > {}^2J(P,CH_3)$.
© 2005 Elsevier Ltd. All rights reserved.

Keywords: X-ray crystallography; NMR spectra; Phosphoramidate; Hydrogen bond

1. Introduction

Phosphoramidates are attractive to study owing to their extensive applications in biochemistry [1,2]. Although many compounds of this series have been reported [3–6], only a few crystal structures, of the formula $P(O)[N(H)R]X_2$ [7], $P(O)[N(H)R]_3$ [8,9], $RC(O)N(H)P(O)X_2$ [10] and $RC(O)N(H)P(O)[NR^1R^2]_2$ [11–13], are currently known. These compounds were used as O-donor ligands in the reaction with small and hard metal ions [14] and the lithiations of them were discussed [8]. The P–N bond characteristics and its influence on ^{31}P NMR chemical shifts were considered [15] and also P–C and P–H coupling constants were discussed in order to obtain assignments, conformational and configurational analysis [16,17].

In this study, we report the structures of three new phosphoramidates: *N*-benzoyl, *N*′,*N*″-bis(*N*-benzylmethyl)phosphoric triamide **1**, *N*,*N*′-bis(*N*-benzylmethyl), phosphoramidic chloride **2**, and *N*-trichloroacetyl, *N*′,*N*″-bis(*N*-benzylmethyl)phosphoric triamide **3**. We also considered the structural parameters of several previous reported structures [18–23]. Furthermore, we synthesized two other phosphoramidates: *N*,*N*-dimethyl, *N*′,*N*″-bis(*N*-benzylmethyl)phosphoric triamide **4** and *N*-4-nitrophenyl, *N*′,*N*″-bis(*N*-benzylmethyl)phosphoric triamide **5**. Two bond distance coupling constants, $^2J(P,C)_{benzylic}$ of these molecules were compared to $^2J(P,C)_{methyl}$.

* Corresponding author. Tel.: +98 21 8011001x3443; fax: +98 21 8006544.
E-mail address: gholi_kh@modares.ac.ir (K. Gholivand).

0277-5387/$ - see front matter © 2005 Elsevier Ltd. All rights reserved.
doi:10.1016/j.poly.2005.01.010

2. Experimental

2.1. Materials

Dimethylamine solution (40% in water), 4-nitroaniline (⩾99%), phosphorus pentachloride (⩾98%), formic acid (98%), phosphorus oxychloride (⩾98%) (Fluka) and *N*-benzylmethylamine (⩾98%), benzamide (>98%), 2,2,2-trichloroacetamide (>98%) (Merck) were used as supplied. In all reactions, low temperature conditions were used.

2.2. X-ray measurements

X-ray data were collected on an Enraf Nonius CAD4 for compound **1** and a Bruker SMART 1000 CCD single crystal diffractometer for compounds **2** and **3** with graphite monochromated Mo Kα radiation (λ = 0.71073 Å). The structures were refined with SHELXL-97 [24] by full matrix least squares on F^2. The positions of hydrogen atoms were obtained from the difference Fourier map. Routine Lorentz and polarization corrections were applied and an absorption correction was performed for compounds **2** and **3** using the SADABS program [25].

2.3. Spectroscopic measurements

^{1}H, ^{13}C and ^{31}P NMR spectra were recorded on a Bruker Avance DRS 500 spectrometer. ^{1}H and ^{13}C chemical shifts were determined relative to internal TMS, ^{31}P chemical shifts relative to 85% H_3PO_4 as external standard. Infrared (IR) spectra were recorded on a Shimadzu model IR-60 spectrometer. Elemental analysis was performed using a Heraeus CHN-O-RAPID apparatus.

2.4. Syntheses

$C_6H_5C(O)NHP(O)Cl_2$ and $CCl_3C(O)NHP(O)Cl_2$ were prepared similar to the procedure by Kirsanov et al. [26,27] and $Me_2NP(O)Cl_2$ and 4-NO_2–$C_6H_4NHP(O)Cl_2$ were prepared similar to the procedure by Keat and Shaw [28] and Johnson et al. [29], respectively.

2.4.1. *N*-benzoyl, *N*′,*N*″-bis(*N*-benzylmethyl)phosphoric triamide (**1**)

N-benzylmethyl amine (1.21 g, 10 mmol) was added to a solution of *N*-benzoyl phosphoramidic dichloride (0.595 g, 2.5 mmol) in chloroform (40 ml) and stirred at −5 °C. After 4 h, the solvent was removed and the residue that formed was stirred in H_2O. The product was filtered and washed with H_2O and recrystallized from chloroform/*n*-heptane; m.p. 141 °C. *Anal.* Calc. for $C_{23}H_{26}N_3O_2P$: C, 67.80; H, 6.43; N, 10.31. Found: C, 67.83; H, 6.40; N, 10.30%. ^{31}P NMR ($CDCl_3$): δ 16.65 (m). ^{13}C NMR ($CDCl_3$): δ 168.95 (s, C═O), 138.04 (d, ^3J(P,C) = 4.2 Hz), 133.49 (d, ^3J(P,C) = 8.7 Hz), 132.38 (s), 128.64 (s), 128.46 (s), 128.27 (s), 128.12 (s), 127.23 (s), 53.10 (d, ^2J(P,C) = 5.3 Hz), 33.82 (d, ^2J(P,C) = 5.0 Hz). ^{1}H NMR ($CDCl_3$): δ 2.72 (d, ^3J(PNCH) = 10.3 Hz, 6H, $2CH_3$), 4.22 (dd, ^3J-(PNCH) = 9.3 Hz, ^2J(H,H) = 15.0 Hz, 2H, $2CH_{benzylic}$), 4.37 (dd, ^3J(PNCH) = 9.3 Hz, ^2J(H,H) = 15.0 Hz, 2H, $2CH_{benzylic}$), 7.22–7.44 (m, 12 Ar–H), 7.50 (t, ^3J(H,H) = 7.2 Hz, 1Ar–H), 8.16 (d, ^3J(H,H) = 7.7 Hz, 2Ar–H), 9.64 (s, NH, 1H). ^{1}H{^{31}P} NMR ($CDCl_3$): δ 2.72 (s), 4.22 (d, ^2J(H,H) = 15.0 Hz), 4.37 (d, ^2J(H,H) = 15.0 Hz), 7.21–7.53 (m), 9.64 (s). IR (KBr, cm^{-1}): 3050 (νNH), 1885, 1666 (νC═O), 1446, 1179 (νP═O), 1001, 937, 869 (νP–N), 700 (νP–N).

2.4.2. *N*,*N*′-bis(*N*-benzylmethyl)phosphoramidic chloride (**2**)

N-benzylmethyl amine (2.41 g, 20 mmol) was added to a solution of phosphoryl chloride (0.76 g, 5 mmol) in acetonitrile (25 ml) and stirred at −5 °C. After 8 h, the precipitate was filtered and the product was obtained from solution by column chromatography [silica gel; hexane:ethyl acetate (4:1)]; m.p. 120 °C. *Anal.* Calc. for $C_{16}H_{20}ClN_2OP$: C, 59.54; H, 6.25; N, 8.68. Found: C, 59.51; H, 6.21; N, 8.66%. ^{31}P NMR ($CDCl_3$): δ 34.18 (m). ^{13}C NMR ($CDCl_3$): δ 138.11 (d, ^3J(P,C) = 5.5 Hz), 129.34 (s), 129.14 (s), 128.34 (s), 53.54 (d, ^2J(P,C) = 4.0 Hz), 34.11 (d, ^2J(P,C) = 3.5 Hz). ^{1}H NMR ($CDCl_3$): δ 2.63 (d, ^3J(PNCH) = 12.6 Hz, 6H, $2CH_3$), 4.33 (m, 4H, $2CH_2$), 7.29–7.44 (m, 10Ar–H). ^{1}H{^{31}P}NMR ($CDCl_3$): δ 2.63 (s), 4.33 (m), 7.29–7.44 (m). IR (KBr, cm^{-1}): 3015, 1484, 1442, 1334, 1219, 1190 (νP═O), 1126, 1064, 949, 910, 786 (νPN), 699, 631, 530 (νPCl), 446.

2.4.3. *N*-trichloroacetyl, *N*′,*N*″-bis(*N*-benzylmethyl)-phosphoric triamide (**3**)

N-benzylmethyl amine (0.97 g, 8 mmol) was added to a solution of trichloroacetyl phosphoramidic dichloride (0.56 g, 2 mmol) in acetonitrile (40 ml) and stirred at −5 °C. After 4 h, the solvent was removed and the residue that formed was stirred in H_2O. The product was filtered and washed with H_2O and recrystallized from chloroform/*n*-heptane; m.p. 153 °C. *Anal.* Calc. for $C_{18}H_{21}Cl_3N_3O_2P$: C, 48.18; H, 4.72; N, 9.36. Found: C, 48.16; H, 4.70; N, 9.37%. ^{31}P NMR (d_6-DMSO): δ 13.86 (m). ^{13}C NMR (d_6-DMSO): δ 163.50 (s, C═O), 139.27 (d, ^3J(P,C) = 4.8 Hz), 129.81 (s), 129.48 (s), 128.63 (s), 93.08 (d, ^3J(P,C) = 9.6 Hz, CCl_3), 59.63 (s), 51.82 (d, ^2J(P,C) = 4.9 Hz), 33.23 (d, ^2J(P,C) = 4.6 Hz). ^{1}H NMR (d_6-DMSO): δ = 2.49 (d, ^3J(PNCH) = 10.2 Hz, 6H, $2CH_3$), 4.16 (d, ^3J(PNCH) = 9.1 Hz, 4H, $2CH_2$), 7.26–7.39 (m, 10Ar–H), 10.34 (b, 1H, NH). ^{1}H{^{31}P}NMR (d_6-DMSO):

δ 2.49 (s), 4.16 (s), 7.26–7.39 (m), 10.34 (b). IR (KBr, cm^{-1}): 3405 (νNH), 3020, 2915, 2760, 1712 (νC=O), 1452, 1348, 1230, 1198 (νP=O), 1145, 1008, 948, 876 (νPN), 834, 794 (νPN), 695, 669 (νCCl), 588, 491, 453.

2.4.4. N,N-dimethyl, N′,N″-bis(N-benzylmethyl)-phosphoric triamide (4)

N-benzylmethyl amine (0.81 g, 5 mmol) was added to a solution of *N*,*N*-dimethylphosphoramidic dichloride (2.42 g, 20 mmol) in acetonitrile (30 ml) and stirred at −5 °C. After 8 h, the precipitate was filtered and the product was obtained from solution by column chromatography [silica gel; hexane:ethyl acetate (8:1)]. *Anal.* Calc. for $C_{18}H_{26}N_3OP$: C, 65.24; H, 7.91; N, 12.61. Found: C, 65.23; H, 7.89; N, 12.63%. ^{31}P NMR ($CDCl_3$): δ 25.48 (m). ^{13}C NMR ($CDCl_3$): δ 138.44 (d, ^3J(P,C) = 4.5 Hz), 130.24 (s), 128.23 (s), 127.13 (s), 53.18 (d, ^2J(P,C) = 4.6 Hz), 37.03 (d, ^2J(P,C) = 4.0 Hz), 33.92(d, ^2J(P,C) = 3.7 Hz). ^1H NMR ($CDCl_3$): δ 2.54 (d, ^3J(PNCH) = 9.1 Hz, 6 H, $N(CH_3)_2$), 2.69 (d, ^3J(PNCH) = 9.6 Hz, 6H, $2CH_3$), 4.10 (dd, ^3J-(PNCH) = 8.3 Hz, ^2J(H,H) = 14.8 Hz, 2H, $2CH_{benzylic}$), 4.20 (dd, ^3J(PNCH) = 8.3 Hz, ^2J(H,H) = 14.8 Hz, 2H, $2CH_{benzylic}$), 7.23–7.36 (m, 10Ar–H). $^1H\{^{31}P\}$NMR ($CDCl_3$): δ 2.54 (s), 2.69 (s), 4.10 (d, ^2J(H,H) = 14.8 Hz), 4.20 (d, ^2J(H,H) = 14.8 Hz), 7.23–7.36 (m). IR (KBr, cm^{-1}): 3415, 2920, 2765, 2420, 1724, 1443, 1296, 1204 (νP=O), 998, 946, 778 (νPN), 731 (νPN), 694, 592, 472.

2.4.5. N-4-nitrophenyl, N′,N″-bis(N-benzylmethyl)-phosphoric triamide (5)

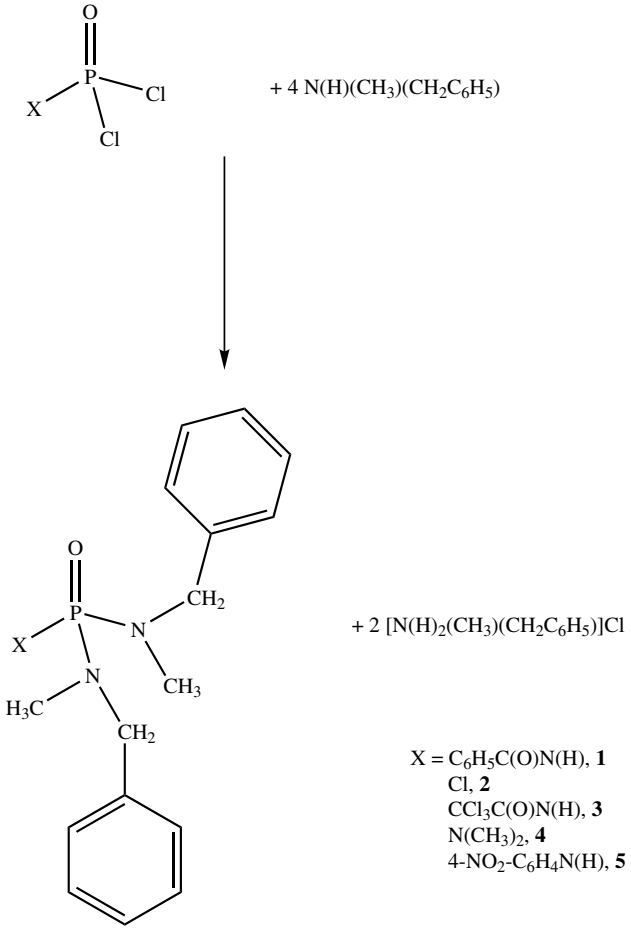
N-benzylmethyl amine (0.97 g, 8 mmol) was added to a mixture of *N*-4-nitrophenyl phosphoramidic dichloride (0.51 g, 2 mmol) in carbon tetrachloride (30 ml) and stirred at −5 °C. After 6 h, the solvent was removed and the residue that formed was stirred in H_2O. The product was filtered and washed with H_2O; m.p. 115 °C. *Anal.* Calc. for $C_{22}H_{25}N_4O_3P$: C, 62.26; H, 5.94; N, 13.20. Found: C, 62.24; H, 5.95; N, 13.18%. ^{31}P NMR (d_6-DMSO): δ 14.79 (m). ^{13}C NMR (d_6-DMSO): δ 141.73 (s), 137.17 (d, ^3J(P,C) = 4.0 Hz), 128.71 (s), 128.34 (s), 128.27 (s), 127.74 (s), 125.55 (s), 117.15 (d, ^2J(P,C) = 6.5 Hz), 53.13 (d, ^2J(P,C) = 4.8 Hz), 34.04 (d, ^2J(P,C) = 4.4 Hz). ^1H NMR (d_6-DMSO): 2.63 (d, ^3J(PNCH) = 10.0 Hz, 6H, $2CH_3$), 4.25 (dd, ^3J-(PNCH) = 7.1 Hz, ^2J(H,H) = 14.8 Hz, 2H, $2CH_{benzylic}$), 4.27 (dd, ^3J(PNCH) = 7.1 Hz, ^2J(H,H) = 14.8 Hz, 2H, $2CH_{benzylic}$), 7.16 (d, ^3J(H,H) = 9.1 Hz, 2Ar–H), 7.33 (m, 10Ar–H), 8.07 (d, ^3J(H,H) = 9.1 Hz, 2Ar–H), 8.30 (d, ^2J(PNH) = 9.2 Hz, 1H, NH). $^1H\{^{31}P\}$NMR (d_6-DMSO): δ 2.63 (s), 4.25 (d, ^2J(H,H) = 14.8 Hz), 4.27 (d, ^2J(H,H) = 14.8 Hz), 7.16 (d, ^3J(H,H) = 9.1 Hz), 7.33 (s), 8.07 (d, ^3J(H,H) = 9.1 Hz), 8.30 (s, 1 H, NH). IR (KBr, cm^{-1}): 3145 (νNH), 2905, 1587 (νNO_2), 1490, 1470, 1327 (νNO_2), 1291, 1247 (νP=O), 1198, 1164, 1103, 969, 902 (νPN), 840, 769, 720 (νPN), 690, 531.

3. Results and discussion

The reaction of *N*-benzylmethylamine with *N*-benzoyl phosphoramidic dichloride, trichloroacetyl phosphoramidic dichloride, phosphoryl chloride, *N*,*N*-dimethyl phosphoramidic dichloride and *N*-4-nitrophenyl phosphoramidic dichloride leads to the corresponding phosphoramidates, Scheme 1. The general synthetic methods involve the reactions between the halogen–phosphorus compounds with an amine either alone (in excess) or in the presence of another HCl scavenger (such as triethylamine). The main challenge in these reactions is the separation of the phosphoramidate from the alkylammonium chloride byproduct.

3.1. NMR Study

The molecules **1**–**5** indicate two various ^2J(P,C) coupling constants for the CH_3 and CH_2 groups in the



Scheme 1. Preparation of compounds **1**–**5**.

Table 1
$^2J(P,C)_{aliphatic}$ and $^2J(P,C)_{benzylic}$, Hz in some phosphoramidates

No.	Compound	$^2J(P,C)_{aliphatic}$	$^2J(P,C)_{benzylic}$	Reference
1	$P(O)(C_6H_5C(O)NH)[N(CH_3)(CH_2C_6H_5)]_2$	5.0	5.3	[a]
2	$P(O)(Cl)[N(CH_3)(CH_2C_6H_5)]_2$	3.5	4.0	[a]
3	$P(O)(CCl_3C(O)NH)[N(CH_3)(CH_2C_6H_5)]_2$	4.6	4.9	[a]
4	$P(O)[N(CH_3)_2][N(CH_3)(CH_2C_6H_5)]_2$	3.7, 4.0 $[N(CH_3)_2]$	4.6	[a]
5	$P(O)(p\text{-}NHC_6H_4NO_2)[N(CH_3)(CH_2C_6H_5)]_2$	4.4	4.8	[a]
6	$(4\text{-}CH_3\text{–}C_6H_4\text{–}O)_2P(O)[N(C_2H_5)(CH_2C_6H_5)]$	3.5	4.9	[21]
7	$(4\text{-}CH_3\text{–}C_6H_4\text{–}O)P(O)(Cl)[N(C_2H_5)(CH_2C_6H_5)]$	3.6	4.6	[21]

[a] This work.

benzylmethylamine moiety, furthermore, compound **4** shows a $^2J(P,C)$ coupling constant for the CH_3 in the $N(CH_3)_2$ group. $^2J(P,C)$ coupling constants in these compounds are in the range of 3.5–5.3 Hz and for each compound $^2J(P,CH_2) > {}^2J(P,CH_3)$, Table 1. The presence of phenyl groups linked to CH_2 causes the deshielding of the CH_2 carbon atoms relative to the CH_3 carbon atoms. Methylene and methyl carbon atoms in compounds **1**–**5** appear in the range of 51.82–53.54 and 33.23–34.11 ppm in ^{13}C NMR spectra, respectively. The deshielding of the methylene groups leads to a greater interaction with the corresponding phosphorus atoms. Also, in compounds with the $P(O)[N(CH_2CH_3)(CH_2C_6H_5)]$ moiety [21], Table 1, $^2J[P,(CH_2)_{benzylic}] > {}^2J[P,(CH_2)_{aliphatic}]$.

The *ipso*-carbon atoms of the phenyl rings related to the amine groups are split into doublet signals by their phosphorus atoms, $^3J(P,C)$ coupling constant, also molecules **1** and **3** show a $^3J(P,C)$ coupling constant for the benzoyl and trichloroacetyl groups of 8.7 and 9.6 Hz, respectively. NH signals of compounds **1** and **3** do not show two bond distance couplings with the P atom, $^2J(PNH)$, but in molecule **5**, a doublet signal is obtained for NH with $^2J(PNH) = 9.2$ Hz. The protons of methyl and methylene groups in these compounds indicate $^3J(PNCH)$ coupling constants. Fig. 1 indicates the multiplet structure in the ^{31}P NMR spectrum of compound **5** which is produced by the couplings with H atoms of two $N(CH_3)(CH_2C_6H_5)$ groups, the measured $^3J(PNCH)$ from the ^1H NMR spectrum for this compound are 10 and 7.1 Hz (for the methyl and methylene protons of the $P\text{–}N(CH_3)(CH_2C_6H_5)$ moiety). The two benzylic protons are diastereotopic and usually appear with different chemical shifts, but when the rotational energy barrier around the P–N bond is low, these appear with equal chemical shifts on the NMR timescale. Each of

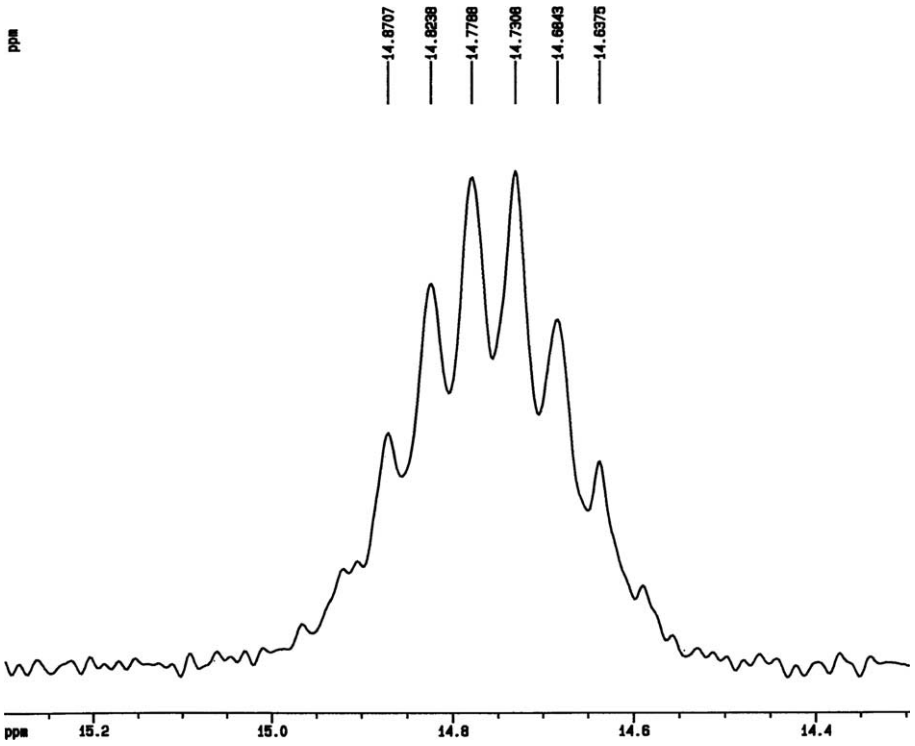


Fig. 1. ^{31}P NMR spectrum of compound **5**.

the benzylic protons (of compounds **1**, **2**, **4** and **5**) represents the splitting by the phosphorus atom, ^3J(PNCH), followed by ^2J(H,H) splitting. Compound **3** shows only a doublet signal produced by a ^3J(PNCH) coupling constant (the benzylic protons do not have different chemical shifts at 298 K). A similar result was obtained for the benzylic protons of $(CH_3)(C_6H_5CH_2)$ NP(O)(Cl)(4-$OC_6H_4CH_3$) [30] (a doublet peak at 4.26 ppm) which on lowering the temperature, the protons appear with different chemical shifts.

3.2. X-ray crystallography investigation

Single crystals of compounds **1**–**3** were obtained from a solution of chloroform and 1-heptane after slow evaporation at room temperature. The crystal data and the details of the X-ray analysis are given in Table 2, selected bond lengths and angles are given in Table 3. Molecular structures of compounds **1**–**3** are shown in Figs. 2–4.

Both compounds **1** and **3** contain one amidic hydrogen atom and form centrosymmetric dimers, see Fig. 5 for compound **3**, that are produced by two equivalent intermolecular –P═O···H–N– hydrogen bonds (Table 4). The earlier studied *N*-benzoyl, phosphoric triamides exist either in the form of dimeric aggregates [31] or as polymeric chains [32].

In molecules **1** and **3**, the phosphoryl and the carbonyl groups are anti, Figs. 2 and 4. The phosphorus atoms in the structures **1**–**3** have a slightly distorted tetrahedral configuration. The bond angles around the P(1) atoms in these compounds are in the range of 118.9°–102.53°, for the angles O(1)–P(1)–N(2) and N(2)–P(1)–Cl(1) in structure **2**. For both compounds **1** and **3**, the highest values of the bond angles around phosphorus atoms were obtained for the angles O(1)–P(1)–N(2) and N(2)–P(1)–N(1). The angles O(1)–P(1)–N(1) in compounds **1** and **3**, 105.55(12)° and 104.81(8)°, are lower than the angles O(1)–P(1)–N(2) and O(1)–P(1)–N(3) (118.26(13)°, 109.80(13)° for **1** and 117.53(9)°, 112.05(9)° for **3**).

P(1)–N(2) and P(1)–N(3) bond lengths are 1.630(3) and 1.629(2) Å in compound **1** and 1.6312(17) and 1.6271(17) Å in compound **3**. Also, in compound **2** P(1)–N(1) and P(1)–N(2) are 1.610(4) and 1.634(4) Å, respectively. They are significantly shorter than the typical P–N single bond length (1.77 Å) [33]. The shortening of PN bond lengths is likely related to an electrostatic effect (polar bond) which overlaps with P–N σ bond [34]. In compounds **1** and **3**, the P(1)–N(1)

Table 2
Crystallographic data for **1**, **2** and **3**

	1	**2**	**3**
Empirical formula	$C_{23}H_{26}N_3O_2P$	$C_{16}H_{20}ClN_2OP$	$C_{18}H_{21}Cl_3N_3O_2P$
Formula weight	407.44	322.76	448.70
Temperature (K)	293(2)	116(2)	120(2)
Wavelength (Å)	0.71073	0.71073	0.71073
Crystal system	triclinic	orthorhombic	triclinic
Space group	$P\bar{1}$	$P2_12_12_1$	$P\bar{1}$
Unit cell dimensions			
a (Å)	9.832(4)	6.939(2)	10.363(2)
b (Å)	10.949(4)	7.176(2)	10.862(2)
c (Å)	11.631(5)	32.447(10)	11.023(2)
α(°)	91.99(3)	90	71.81(3)
β (°)	100.51(3)	90	67.44(3)
γ (°)	115.35(3)	90	63.29(3)
V (Å^3)	1103.5(8)	1615.8(9)	1008.7(4)
Z, calculated density (Mg m^{-3})	2, 1.226	4, 1.327	2, 1.477
Absorption coefficient (mm^{-1})	0.148	0.336	0.553
F(0 0 0)	432	680	464
Crystal size (mm)	0.6 × 0.2 × 0.2	0.8 × 0.6 × 0.2	0.6 × 0.3 × 0.2
θ Range for data collection (°)	1.80–26.97	2.51–24.00	2.03–30.06
Limiting indices	$0 \leqslant h \leqslant 12$; $-13 \leqslant k \leqslant 12$; $-14 \leqslant l \leqslant 14$	$-7 \leqslant h \leqslant 7$; $-8 \leqslant k \leqslant 8$; $-36 \leqslant l \leqslant 37$	$-14 \leqslant h \leqslant 14$; $-14 \leqslant k \leqslant 15$; $-15 \leqslant l \leqslant 15$
Reflections collected/unique (R_{int})	5063/4774 (0.0255)	10 637/2381 (0.0642)	12 120/5854 (0.0165)
Completeness to θ (%)	99.4	94.5	98.7
Absorption correction	none	semi-empirical from equivalents	semi-empirical from equivalents
Refinement method	full-matrix least-squares on F^2	full-matrix least-squares on F^2	full-matrix least-squares on F^2
Data/restraints/parameters	4774/0/262	2381/0/190	5854/0/244
Goodness-of-fit on F^2	1.009	0.992	0.990
Final R indices	$R_1 = 0.0612$; $wR_2 = 0.1243$	$R_1 = 0.0647$; $wR_2 = 0.1219$	$R_1 = 0.0445$; $wR_2 = 0.0917$
R indices (all data)	$R_1 = 0.0854$; $wR_2 = 0.1340$	$R_1 = 0.0671$; $wR_2 = 0.1229$	$R_1 = 0.0498$; $wR_2 = 0.0937$
Absolute structure parameter		−0.06(17)	
Largest differential peak and hole (e Å^{-3})	0.369 and −0.405	0.657 and −0.342	0.709 and −0.778

Table 3
Selected bond lengths (Å) and angles (°) for compounds **1**–**3**

1		**2**		**3**	
Bond lengths					
P(1)–N(1)	1.676(2)	P(1)–O(1)	1.459(4)	P(1)–O(1)	1.4785(15)
P(1)–N(2)	1.630(3)	P(1)–N(1)	1.610(4)	P(1)–N(3)	1.6271(17)
P(1)–N(3)	1.629(2)	N(1)–C(7)	1.463(6)	P(1)–N(2)	1.6312(17)
O(2)–C(1)	1.216(3)	N(1)–C(8)	1.461(6)	P(1)–N(1)	1.7037(16)
N(1)–C(1)	1.372(3)	P(1)–N(2)	1.634(4)	O(2)–C(2)	1.212(2)
P(1)–O(1)	1.476(2)	P(1)–Cl(1)	2.0554(19)	C(1)–C(2)	1.562(3)
N(2)–C(8)	1.452(4)	N(2)–C(9)	1.468(6)	Cl(2)–C(1)	1.763(2)
N(3)–C(16)	1.451(3)	N(2)–C(10)	1.451(6)	Cl(3)–C(1)	1.756(2)
N(2)–C(9)	1.460(4)	C(1)–C(2)	1.390(8)	Cl(1)–C(1)	1.780(2)
N(3)–C(17)	1.466(4)	C(1)–C(6)	1.388(8)	N(1)–C(2)	1.357(2)
C(1)–C(2)	1.491(4)	C(2)–C(3)	1.386(9)	N(2)–C(3)	1.457(2)
C(22)–C(23)	1.371(5)	C(15)–C(16)	1.364(8)	N(2)–C(4)	1.467(2)
Bond angles					
O(1)–P(1)–N(1)	105.55(12)	O(1)–P(1)–N(1)	114.2(2)	O(1)–P(1)–N(3)	112.05(9)
O(1)–P(1)–N(2)	118.26(13)	O(1)–P(1)–N(2)	118.9(2)	O(1)–P(1)–N(2)	117.53(9)
O(1)–P(1)–N(3)	109.80(13)	N(1)–P(1)–N(2)	105.4(2)	N(3)–P(1)–N(2)	106.79(9)
N(2)–P(1)–N(3)	104.49(13)	O(1)–P(1)–Cl(1)	107.70(19)	O(1)–P(1)–N(1)	104.81(8)
N(2)–P(1)–N(1)	106.08(13)	N(1)–P(1)–Cl(1)	106.94(18)	C(3)–N(2)–P(1)	124.81(14)
N(3)–P(1)–N(1)	112.81(13)	N(2)–P(1)–Cl(1)	102.53(16)	C(4)–N(2)–P(1)	120.09(13)
O(2)–C(1)–N(1)	121.4(3)	C(8)–N(1)–C(7)	115.5(4)	C(11)–N(3)–C(12)	115.75(16)
C(1)–N(1)–P(1)	127.6(2)	C(8)–N(1)–P(1)	122.6(3)	C(11)–N(3)–P(1)	122.60(13)
C(8)–N(2)–C(9)	113.6(3)	C(7)–N(1)–P(1)	120.9(4)	N(1)–C(2)–C(1)	113.86(16)
C(8)–N(2)–P(1)	118.2(2)	C(10)–N(2)–C(9)	114.4(4)	N(3)–P(1)–N(1)	110.94(9)
C(16)–N(3)–C(17)	114.8(2)	C(10)–N(2)–P(1)	122.7(3)	N(2)–P(1)–N(1)	104.43(8)
C(16)–N(3)–P(1)	125.8(2)	C(9)–N(2)–P(1)	121.8(3)	C(2)–N(1)–P(1)	127.13(13)
C(9)–N(2)–P(1)	125.5(2)	C(2)–C(1)–C(6)	120.5(5)	C(3)–N(2)–C(4)	114.76(16)
C(17)–N(3)–P(1)	119.41(19)	C(3)–C(2)–C(1)	119.6(6)	C(12)–N(3)–P(1)	121.54(14)
N(1)–C(1)–C(2)	116.6(2)	C(2)–C(3)–C(4)	119.6(5)	N(3)–C(12)–C(13)	113.37(16)
N(3)–C(17)–C(18)	114.1(3)	C(11)–C(16)–C(15)	119.6(5)	O(2)–C(2)–N(1)	126.63(18)
C(3)–C(2)–C(1)	123.6(3)	C(11)–C(16)–C(10)	120.9(5)	O(2)–C(2)–C(1)	119.48(16)
C(23)–C(18)–C(17)	120.4(3)	C(15)–C(16)–C(10)	119.5(5)	N(2)–C(4)–C(5)	114.25(16)

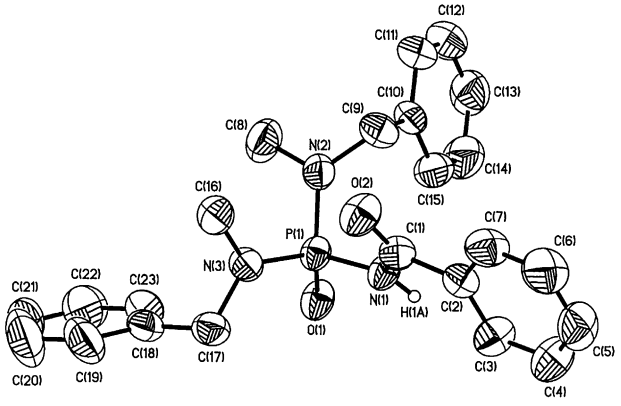


Fig. 2. Molecular structure and atom-labelling scheme for $P(O)(C_6H_5\text{-}C(O)NH)[N(CH_3)(CH_2C_6H_5)]_2$, compound **1** (50% probability ellipsoids).

bond lengths (1.676(2) and 1.7037(16) Å, respectively) are longer than the P(1)–N(2) and P(1)–N(3) bond lengths due to the resonance interaction with the C=O system that causes a partial multiple-bond character in N(1)–C(1) (compare N(1)–C(1) in compound **1** and

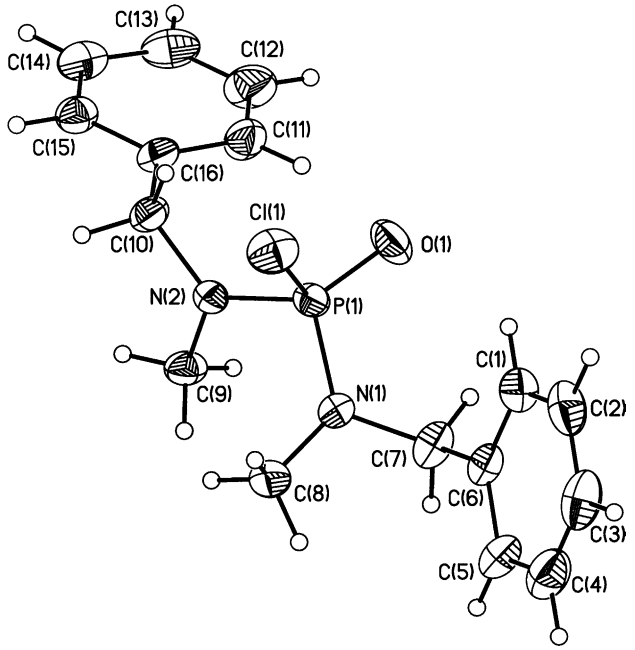


Fig. 3. Molecular structure and atom-labelling scheme for $P(O)(Cl)[N(CH_3)(CH_2C_6H_5)]_2$, compound **2** (50% probability ellipsoids).

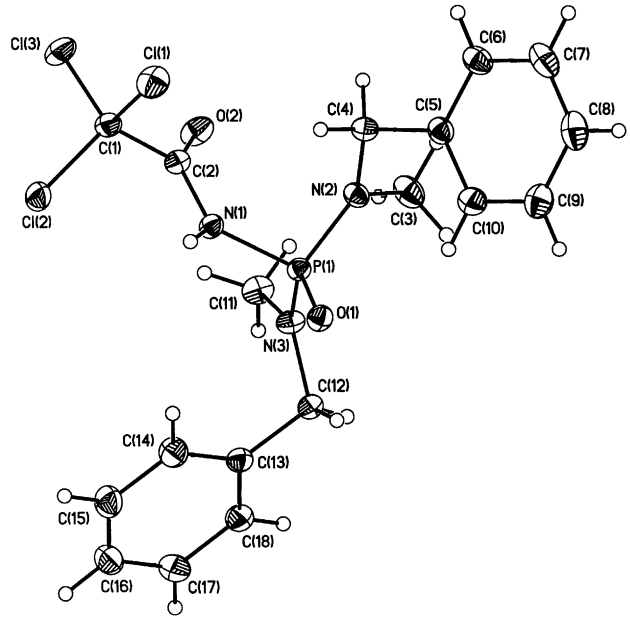


Fig. 4. Molecular structure and atom-labelling scheme for $P(O)(CCl_3C(O)NH)[N(CH_3)(CH_2C_6H_5)]_2$, compound **3** (50% probability ellipsoids).

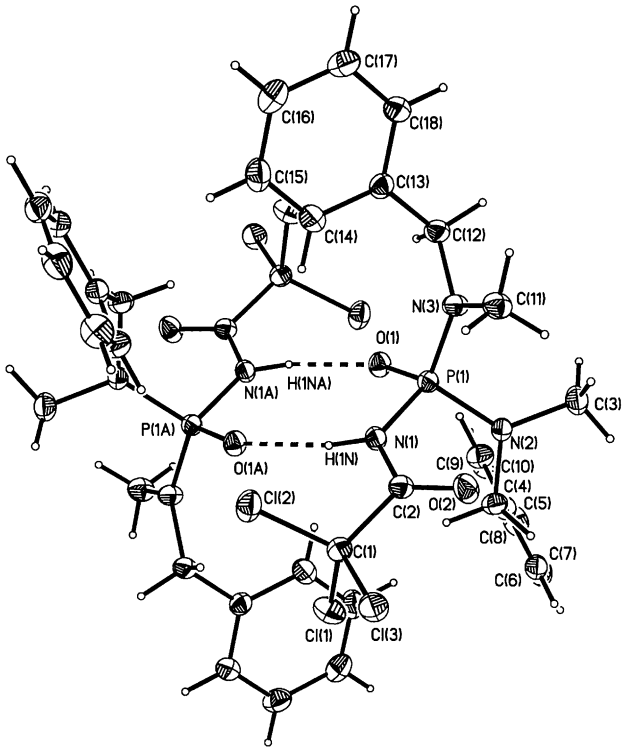


Fig. 5. Centrosymmetric dimer of compound **3**, produced by hydrogen bonds.

N(1)–C(2) in compound **3** with other N–C bond lengths, Table 3). In the previous reported structures, we obtained the P–N bond lengths of (O)P–N(H)–C(O) and $P–NR^1R^2$ moieties in the range of 1.678(2)–1.718(3) Å and 1.6032(17)–1.642(2) Å, respectively (Table 5).

The environment of the nitrogen atoms is practically planar. In compound **1**, the angles C(8)–N(2)–C(9), C(8)–N(2)–P(1) and C(9)–N(2)–P(1) are 113.6(3)°, 118.2(2)° and 125.5(2)°, respectively, with average 119.1°. Similar results were obtained for the bond angles around N(3) atom (average 120°). Also, the sum of the surrounding angles for N(1), N(2) in compound **2** and N(2), N(3) in compound **3** are 359°, 358.9° and 359.7°, 359.9°, respectively. Furthermore, the angles C(1)–N(1)–P(1) in compound **1** and C(2)–N(1)–P(1) in compound **3** are 127.6(2)° and 127.13(13)°. These results confirm the sp^2 hybridization for the nitrogen atoms,

Table 4
Hydrogen bonds D–H···A for compounds **1** and **3**

Compound	D–H···A	*d*(D–H)	*d*(H···A)	∠DHA	*d*(D···A)
1	N1–H1A···O1′ [$-x$, $-y+1$, $-z$]	0.860	1.967	165.87	2.809(3)
3	N1–H1N···O1 [$1-x$, $-y$, $-z$]	0.891	1.915	168.13	2.794(2)

Table 5
P=O and P–N bond lengths (Å) in some phosphorus compounds

Compound	P=O	P–N	P–N	P–N	Reference
$P(O)(C_6H_5C(O)NH)[N(CH_3)(CH_2C_6H_5)]_2$	1.476(2)	1.631(3)	1.631(2)	1.678(2)[c]	[a]
$P(O)(Cl)[N(CH_3)(CH_2C_6H_5)]_2$	1.471(2)	1.615(2)	1.635(3)		[a]
$P(O)(CCl_3C(O)NH)[N(CH_3)(CH_2C_6H_5)]_2$	1.4785(15)	1.6271(17)	1.6312(17)	1.7037(16)[c]	[a]
$P(O)(CCl_3C(O)NH)[NH(tert\text{-}C_4H_9)]_2$	1.466(2)	1.608(3)	1.611(4)	1.718(3)[c]	[18]
$P(O)(C_6H_5C(O)NH)[NH(tert\text{-}C_4H_9)]_2$[b]	1.473(2), 1.476(2)	1.629(2), 1.619(3)	1.629(2), 1.629(2)	1.711(2)[c], 1.704(2)	[18]
$P(O)(C_6H_5C(O)NH)(C_4H_8N)_2$	1.487(3)	1.615(4)	1.618(4)	1.679(4)[c]	[19]
$P(O)[N(CH_3)_2](p\text{-}NHC_6H_4CH_3)_2$	1.478(3)	1.626(3), $N(CH_3)_2$	1.642(2)		[22]
$P(O)[N(CH_3)_2](p\text{-}OC_6H_4NO_2)_2$	1.4547(14)	1.6032(17)			[23]
$P(O)(p\text{-}OC_6H_4CH_3)_2[(C_6H_5)(CH_3)CH\text{-}NH]$[b]	1.462(3), 1.469(3)	1.610(5), 1.614(5)			[21]

[a] This work.
[b] These compounds appear as two crystallographically independent molecules.
[c] The data are related to P–N of the (O)P–N(H)–C(O) moiety.

although due to repulsion and steric interactions, some angles are greater and others are smaller than 120°.

The P=O bond lengths in molecules **1**–**3** are 1.476(2), 1.459(4) and 1.478(2) Å, which are larger than the normal P=O bond length (1.45 Å) [33]. The P=O bond lengths in our previously reported structures are in the range of 1.455(1)–1.487(3) Å (Table 5).

4. Supplementary data

Crystallographic data for the structures in this paper have been deposited with Cambridge Crystallographic Data Center as Supplementary Publication Nos. CCDC 240844 ($C_{23}H_{26}N_3O_2P$), 240845 ($C_{16}H_{20}Cl_1N_2OP$) and 240846 ($C_{18}H_{21}Cl_3N_3O_2P$). Copies of the data may be obtained, free of charge, on application to CCDC, 12 Union Road, Cambridge CB2 1EZ, UK (fax: +44 1223 336033; E-mail: deposit@ccdc.cam.ac.uk or http://www.ccdc.cam.ac.uk).

References

[1] D. Barak, A. Ordentlich, D. Kaplan, R. Barak, D. Mizrahi C. Kronman, Y. Segall, B. Velan, A. Shafferman, Biochemistry 39 (2000) 1156.
[2] W.D. Mallender, T. Szegletes, T.L. Rosenberry, Biochemistry 39 (2000) 7753.
[3] A.B. Ouryupin, M.I. Kadyko, P.V. Petrovskii, E.I. Fedin, Tetrahedron Asymm. 6 (1995) 1813.
[4] G. Zon, S.M. Ludeman, W. Egan, J. Am. Chem. Soc. 99 (1977) 5785.
[5] H. Wan, T.A. Modro, Synthesis (1996) 1227.
[6] S. Bauermister, A.M. Modro, T.A. Modro, A. Zwierzak, Can. J. Chem. 69 (1991) 811.
[7] M.P. Du Plessis, T.A. Modro, L.R. Nassimbeni, Acta Crystallogr. B 38 (1982) 1504.
[8] T. Chivers, M. Krahn, G. Schatte, M. Parvez, Inorg. Chem. 42 (2003) 3994.
[9] G.J. Bullen, F.S. Stephens, R.J. Wade, J. Chem. Soc. A (1969) 1804.
[10] P.M. Narula, C.S. Day, B.A. Powers, M.A. Odian, A. Lachgar, W.T. Pennington, R.E. Noftle, Polyhedron 18 (1999) 1751.
[11] K.E. Gubina, V.A. Ovchynnikov, V.M. Amirkhanov, V.V. Skopenko, O.V. Shishkin, Z. Naturforsch. 55b (2000) 495.
[12] K.E. Gubina, V.M. Amirkhanov, Z. Naturforsch. 55b (2000) 1015.
[13] K.E. Gubina, V.A. Ovchynnikov, V.M. Amirkhanov, T.Y.u. Silva, V.V. Skopenko, T. Glowiak, H. Kozowski, Z. Naturforsch. 54b (1999) 1357.
[14] K.E. Gubina, J.A. Shatrava, V.A. Ovchynnikov, V.M. Amirkhanov, Polyhedron 19 (2000) 2203.
[15] S.A. Bourne, X.Y. Mbianda, T.A. Modro, L.R. Nassimbeni H. Wan, J. Chem. Soc., Perkin Trans. 2 (1998) 83.
[16] J.M.A. Al-Rawi, G.Q. Behnam, N. Ayed, R. Kraemer, Magn. Reson. Chem. 23 (1985) 728.
[17] Z. Zalán, T.A. Martinek, L. Lázár, F. Fülöp, Tetrahedron 59 (2003) 9117.
[18] K. Gholivand, M. Pourayoubi, Z. Anorg. Allg. Chem. 630 (2004) 1330.
[19] K. Gholivand, M. Pourayoubi, H. Mostaanzadeh, Anal. Sci. 20 (2004) x-51.
[20] K. Gholivand, M.D. Alavi, M. Pourayoubi, Z. Kristallogr. NCS 219 (2004) 124.
[21] K. Gholivand, Z. Shariatinia, M. Pourayoubi, Z. Naturforsch. 60b (2005) 67.
[22] K. Gholivand, A. Tadjarodi, S.W. Ng, Acta Crystallogr. E57 (2001) 472.
[23] K. Gholivand, A. Tadjarodi, S.W. Ng, Acta Crystallogr. E58 (2002) 200.
[24] G.M. Sheldrick, SHELEX V. 5.10, Structure Determination Software Suit, Bruker AXS, Madison, WI, USA, 1998.
[25] G.M. Sheldrick, in: SADABS V. 2.01, Bruker/Siemens Area Detector Absorption Correction Program, Bruker AXS, Madison, WI, USA, 1998.
[26] A.V. Kirsanov, R. Makitra, J. Gen. Chem. 26 (1956) 907.
[27] A.V. Kirsanov, G.I. Derkach, Zhur. Obshchei Khim. 26 (1956) 2082.
[28] R. Keat, R. Shaw, J. Chem. Soc. A (1968) 703.
[29] O. Johnson, M. Murray, G. Woodward, J. Chem. Soc., Dalton Trans. (1989) 821.
[30] K. Gholivand, S. Dehghanpour, G. Gerivani, H.R. Bijanzadeh, Phosphorus Sulfur Silicon 157 (2000) 11.
[31] V. Mizrahi, T.A. Modro, Crystallogr. Struct. Commun. 11 (1982) 627.
[32] O.N. Rebrova, V.N. Biyushkin, T.I. Malinovski, V.M. Ovrutskii, L.D. Protsenko, T.N. Dneprova, M.D. Mazus, Dokl. AN. SSSR (Russia) 324 (1992) 103.
[33] D.E.C. Corbridge, Phosphorus, an Outline of Its Chemistry, Biochemistry and Technology, 5th ed., Elsevier, The Netherlands, 1995.
[34] D.G. Gilheany, Chem. Rev. 94 (1994) 1339.

Available online at www.sciencedirect.com
SCIENCE DIRECT®
Polyhedron 24 (2005) 663–670
POLYHEDRON
www.elsevier.com/locate/poly

Synthesis, crystal structures and spectroscopic characterization of $[Ti_8O_8(OOCR)_{16}]$ (where R = Bu^t, CH_2Bu^t, $C(CH_3)_2Et$)

P. Piszczek [a,*], M. Richert [a], A. Grodzicki [a], T. Głowiak [*,b], A. Wojtczak [a]

[a] *Faculty of Chemistry, Nicolaus Copernicus University, ul. Gagarina 7, 87-100 Toruń, Poland*
[b] *Faculty of Chemistry, University of Wrocław, ul. F. Joliot-Curie 14, 50-383 Wrocław, Poland*

Received 3 December 2004; accepted 18 January 2005

Abstract

Multinuclear titanium(IV) oxo carboxylates of the general formula $[Ti_8O_8(OOCR)_{16}]$ (where R = Bu^t (**1**), CH_2Bu^t (**2**), $C(CH_3)_2Et$ (**3**)) have been synthesized in a reaction of titanium isopropoxide with the appropriate organic acids in a molar ratio of 1:2. The composition and structure of these compounds were identified by elemental analysis, IR, NMR and X-ray single-crystal diffraction. The crystal structure of **1** was solved in the orthorhombic space group *Pbca*. Titanium atoms form oligomeric $[Ti_8(\mu_2\text{-}O)_8]$ rings, where each Ti cation is surrounded by six oxygen atoms (two μ_2-oxo and four μ-carboxylato bridges). Within the ring the Ti–Ti distances between neighboring titanium ions range from 3.333(1) to 3.366(1) Å and the mean value of the Ti–Ti–Ti angle is 134.2(1.3)°. Results of IR, NMR and MS studies proved that in the structures of **2** and **3**, multinuclear $[Ti_8(\mu_2\text{-}O)_8]$ clusters stabilized by carboxylate bridges are also formed. TGA/DTG, MS and variable temperature IR + (VT-IR) studies have been carried out in order to determine the thermal stability and thermal decomposition mechanism of the Ti(IV) carboxylates mentioned above.
© 2005 Elsevier Ltd. All rights reserved.

Keywords: Titanium(IV); Multinuclear carboxylates; X-ray structure; IR; NMR; TGA; MS

1. Introduction

The study of the synthesis of titanium(IV) oxo carboxylates, structural characteristics and pyrolysis pathway are motivated by their potential applications as sol–gel or chemical vapor deposition (CVD) precursors. According to the literature reports, two methods are used in preparation of Ti(IV) oxo carboxylate derivatives. Complexes of the general formula $O[Ti(OOCR)_3]_2$ were the main products of a multistage reaction of titanium tetrachlorine with organic acids [1,2]. During the process mentioned above, $[TiCl_{4-x}(OOCR)_x]$ (x = 1–4) derivatives have also been isolated [3–5]. Barrow et al. [6,7] showed that titanium(IV) oxo chloro-carboxylates $O[TiCl_2(OOCBu^t)(Bu^tCOOH)]_2$ and $O[TiCl(OOCBu^t)_2]_2$ were the main products of the reaction between $TiCl_4$ and trimethylacetic acid in a 1:2.5 molar ratio. The crystal structure of $[\{TiCl_2(OOCBu^t)(Bu^t\text{-}COOH)\}_2O]$ is formed of dimers, composed of Ti atoms octahedrally surrounded by oxygen atoms of one oxygen bridge (μ_2-O) and two bifurcated carboxylates (μ-O) of the *syn–syn* type. The Ti–O distances were 1.77 Å for Ti-(μ_2-O) and 1.99–2.09 Å for Ti-(μ-O) [7].

The stoichiometric reaction of titanium alkoxides ($Ti(OR')_4$; R′ = Et, Pr^i) with carboxylic acids is the next method of synthesizing titanium oxo carboxylates [8,9]. Titanium oxo carboxylato alkoxides were crystallized from 1:1–4 molar ratio mixtures of $Ti(OR')_4$/HOOCR. X-ray diffraction studies exhibited that the following four types of complexes may be formed: (a) $[Ti_6O_4(OR)_{12}(O_2CR')_4]$, (b) $[Ti_6O_4(OR)_8(O_2CR')_8]$, (c) $[Ti_4O_4(OR)_4(O_2CR')_4]$ and (d) $[Ti_6O_6(OR)_6(O_2CR')_6]$ (R = Et, Pr^i, R′ = Me, Np (neopentyl), Bu^t, Ph) [10–16].

* Corresponding author. Tel.: +48 56 6114 316; fax: +48 56 652 477.
E-mail address: piszczek@chem.uni.torun.pl (P. Piszczek).

0277-5387/$ - see front matter © 2005 Elsevier Ltd. All rights reserved.
doi:10.1016/j.poly.2005.01.014

The main factor influencing the formation of these types of multinuclear Ti(IV) clusters is the nature of the alkoxide and carboxylate ligands [13]. Ammala et al. [17] report that $[Ti_6O_6(OCH_2Bu^t)_6(O_2CPh)_6]$ and $[Ti_6O_4(OPr^n)_8(O_2CPh)_8]$ were also synthesized in the reaction of $[Fe_4(\mu_3\text{-}O)_2(O_2CPh)_8(py)_2]$ with $Ti(OPr^n)_4$ in toluene. The application of the large excess of organic acid leads to the formation of Ti(IV) oxo carboxylato derivatives (e.g., polymeric chains of $[TiO(OAc)_2]_n$ were obtained for the ratio 1:10) [8,9].

In the reported work we have focused on structural studies and spectral characteristics of multinuclear Ti(IV) carboxylato derivatives, synthesized from titanium isopropoxide and HOOCR, R = Bu^t, CH_2Bu^t, $C(CH_3)_2Et$. Analysis of the thermogravimetric (TGA), MS-EI, and variable temperature IR spectroscopy have been used in order to study the thermal stability of the synthesized compounds and their thermal decomposition pathway.

2. Experimental

The studied compounds were synthesized under argon atmosphere, using standard Schlenk line and glovebox techniques. $Ti(OPr^i)_4$ (prepared from $TiCl_4$ (Aldrich) and 2-propanol (Aldrich) in the presence of trimethylamine) was freshly vacuum distilled prior to use, whereas Bu^tCOOH, Bu^tCH_2COOH and $Et(Me)_2CCOOH$, (Aldrich) were used as received.

Infrared (IR) spectra were recorded on a Perkin–Elmer Spectrum 2000 spectrometer within the range 160–4000 cm^{-1} with a medium slit width and a peak resolution of 2.0 cm^{-1}. The crystals were studied as a powder dispersed in a KBr pellet (400–4000 cm^{-1}) and as a Nujol suspension between CsI plates (160–700 cm^{-1}). The low temperature IR spectra (liquid nitrogen temperature (LNT)) have been recorded using a SPECAC variable temperature cell. Solution ^1H and ^{13}C NMR spectra ([D_8]toluene) were recorded using a 5-mm solution probe on a Varian Gemini 200. Solid state ^{13}C NMR spectra were registered on a Bruker AMX 300. Thermogravimetric analysis (TGA) was carried out using the SDT 2960 TA Instrument, in nitrogen atmosphere from 25 to 500 °C at a ramp rate of 3° min^{-1}. Mass spectra were recorded with a MS AMD-604 spectrometer, using the EI method, at 70 eV, in the range 150–350 °C.

2.1. Preparation of $[Ti_8O_8(OOCR)_{16}]$

$Ti(OPr^i)_4$ (1.00 g, 3.52 mmol) was added dropwise to a solution of organic acid (7.04 mmol, 0.72 g of Bu^tCOOH, 6.90 mmol, 0.80 g of Bu^tCH_2COOH or 0.80 g of $Et(CH_3)_2CCOOH$) in toluene (3.00 cm^3), and stirred for 12 h. Crystals were grown by slow evaporation of the reaction mixture under argon atmosphere (glovebox). The colorless crystals were obtained after 2–3 days.

2.1.1. $Ti_8O_8(OOCBu^t)_{16}$ (1)

Yield: 0.56 g (55.0%). The % Ti was gravimetrically determined as TiO_2, according to the Meth-Cohn et al. method [13]. *Anal.* Calc. for $C_{80}H_{144}O_{40}Ti_8 \times C_7H_8$: C, 47.03; H, 6.85; Ti, 17.30. Found: C, 47.33; H, 7.03; Ti, 17.46%. IR (KBr, cm^{-1}) 1545 (s, COO), 1512 (m, COO), 1429 (s, COO), 1417 (m, COO), 1229 (m, C–Me_3), 750 (m, Ti–O), 611 (m, Ti–O), 504 (m, Ti–O). ^{13}C NMR (solid, δ, ppm) 26.5 (CH_3), 38.7 (C–(CH_3)$_3$), 188.2, 186.7 (COO).

2.1.2. $Ti_8O_8(OOCCH_2Bu^t)_{16}$ (2)

Yield: 0.25 g (24.2%). *Anal.* Calc. for $C_{81}H_{146}O_{40}Ti_8$: C, 48.99; H, 7.47; Ti, 16.30. Found: C, 47.66; H, 7.45; Ti, 16.80%. IR (KBr, cm^{-1}) 1540 (s, COO), 1507 (m, COO), 1421 (s, COO), 1410 (s, COO), 1209 (m, C–Me_3), 754 (m, Ti–O), 601 (m, Ti–O), 507 (m, Ti–O).^{13}C NMR (solid, δ, ppm) 49.5 (CH_3), 29.8 (C–(CH_3)$_3$), 181.5 (COO).

Table 1
Crystal data and structure refinement for $[Ti_8O_8(OOCBu^t)_{16}]$

Empirical formula (chemical unit)	$C_{80}H_{144}O_{40}Ti_8$
Formula weight	2129.18
Temperature (K)	293(2)
Wavelength (Å)	0.71073
Crystal system	orthorhombic
Space group	*Pbca* (no. 61)
Unit cell dimensions	
a (Å)	30.464(4)
b (Å)	27.361(4)
c (Å)	32.549(4)
Volume (Å^3)	27130.42(629)
Z	8
D_{calc} (Mg/m^3)	1.222
Absorption coefficient (mm^{-1})	0.52
F(0 0 0)	10 552
Crystal size (mm)	0.30 × 0.25 × 0.20
Theta range for data collection (deg)	3.30–28.56
Index ranges	
h	−40 to 29
k	−36 to 34
l	−42 to 43
Reflections collected	181 753
Independent reflections [R_{int}]	32 502 [0.0857]
Refinement method	full-matrix least-squares on F^2
Data/parameters/restraints	32 502/1627/90
Goodness-of-fit on F^2	1.086
Final *R* indices [$I > 2\text{sigma}(I)$]	$R_1 = 0.0999$; $wR_2 = 0.2523$
R indices (all data)	$R_1 = 0.1587$; $wR_2 = 0.3132$
Largest difference between peak and hole	3.341; −0.754

$R_1 = \sum(||F_o| - |F_c||)/\sum|F_o|$.

$wR_2 = [\sum w(F_o^2 - F_c^2)^2/\sum(w|F_o|^2)^2]^{1/2}$.

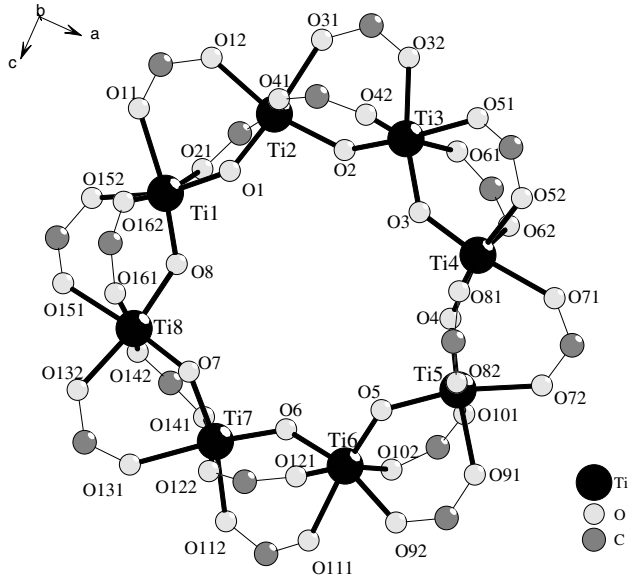


Fig. 1. Crystal structure of **1** with the atom numbering scheme, Bu^t groups have been omitted for clarity.

2.1.3. $Ti_8O_8(OOCC(CH_3)_2Et)_{16}$ (**3**)

Yield: 0.30 g (29.0%). *Anal*. Calc. for $C_{81}H_{146}O_{40}Ti_8$: C, 48.99; H, 7.47; Ti, 16.30. Found: C, 48.77; H, 7.70; Ti, 16.06%. IR (KBr, cm^{-1}) 1552 (s, COO), 1411 (s, COO), 1417 (m, COO), 1203 (m, C–Me$_3$), 756 (m, Ti–O), 641 (m, Ti–O), 552 (m, Ti–O). ^{13}C NMR (solid, δ, ppm) 9.1, 33.9 (Et), 24.5 (CH_3), 43.3, 43.1 (C–$(CH_3)_2$Et), 188.0, 186.5 (COO).

Table 2
Atomic coordinates of the $[Ti_8(\mu_2\text{-}O)_8(O_2C)_{16}]$ cluster ($\times 10^4$) and equivalent isotropic displacement parameters (Å$^2 \times 10^3$) for glow

	x	*y*	*z*	U_{eq}
Ti1	1596(1)	5768(1)	5804(1)	31(1)
Ti2	2119(1)	6119(1)	4945(1)	30(1)
Ti3	3142(1)	6493(1)	4716(1)	28(1)
Ti4	4033(1)	6734(1)	5285(1)	31(1)
Ti5	4329(1)	6473(1)	6246(1)	29(1)
Ti6	3768(1)	6206(1)	7098(1)	29(1)
Ti7	2757(1)	5809(1)	7321(1)	28(1)
Ti8	1807(1)	5865(1)	6810(1)	29(1)
O1	1981(1)	6137(1)	5463(1)	30(1)
O2	2742(1)	6159(1)	4977(1)	29(1)
O3	3475(1)	6708(1)	5171(1)	29(1)
O4	4047(1)	6387(1)	5789(1)	28(1)
O5	3844(1)	6451(1)	6612(1)	30(1)
O6	3228(1)	5863(1)	7024(1)	29(1)
O7	2339(1)	6042(1)	6937(1)	28(1)
O8	1910(1)	5716(1)	6244(1)	30(1)
O11	1128(1)	5828(1)	5314(1)	38(1)
O12	1483(1)	6091(1)	4758(1)	38(1)
O21	1793(1)	5158(1)	5519(1)	35(1)
O22	2116(1)	5383(1)	4928(1)	32(1)
O31	2222(1)	6057(1)	4298(1)	40(1)
O32	2904(1)	6318(1)	4160(1)	36(1)
O41	2094(1)	6840(1)	4844(1)	38(1)
O42	2767(1)	7105(1)	4687(1)	31(1)
O51	3586(1)	6948(1)	4369(1)	35(1)
O52	4158(1)	7116(1)	4775(1)	41(1)
O61	3561(1)	5930(1)	4638(1)	36(1)
O62	4174(1)	6108(1)	4984(1)	38(1)
O71	4725(1)	6792(1)	5340(1)	38(1)
O72	4920(1)	6518(1)	5960(1)	38(1)
O81	4005(1)	7373(1)	5595(1)	37(1)
O82	4284(1)	7204(1)	6214(1)	38(1)
O91	4721(1)	6653(1)	6765(1)	38(1)
O92	4313(1)	6512(1)	7326(1)	40(1)
O101	4464(1)	5773(1)	6378(1)	36(1)
O102	4123(1)	5602(1)	6970(1)	35(1)
O111	3750(1)	5931(1)	7704(1)	41(1)
O112	3095(1)	5584(1)	7821(1)	36(1)
O121	3441(1)	6783(1)	7327(1)	36(1)
O122	2796(1)	6493(1)	7549(1)	36(1)
O131	2216(1)	5761(1)	7735(1)	33(1)
O132	1595(1)	5954(1)	7393(1)	35(1)
O141	2609(1)	5112(1)	7181(1)	34(1)
O142	1917(1)	5161(1)	6944(1)	34(1)
O151	1153(1)	5592(1)	6717(1)	35(1)
O152	1088(1)	5393(1)	6052(1)	40(1)
O161	1549(1)	6512(1)	6644(1)	33(1)
O162	1313(1)	6391(1)	5998(1)	36(1)
C11	1143(2)	5979(2)	4959(2)	36(1)
C21	1951(2)	5067(2)	5163(2)	34(1)
C31	2531(2)	6133(2)	4061(2)	37(1)
C41	2354(2)	7162(2)	4716(2)	32(1)
C51	3914(2)	7192(2)	4464(2)	34(1)
C61	3930(2)	5820(2)	4782(2)	37(1)
C71	5005(2)	6670(2)	5607(2)	34(1)
C81	4129(2)	7496(2)	5950(2)	36(1)
C91	4658(2)	6687(2)	7146(2)	37(1)
C101	4386(2)	5497(2)	6677(2)	33(1)
C111	3491(2)	5688(2)	7919(1)	33(1)
C121	3084(2)	6827(2)	7517(2)	35(1)
C131	1819(2)	5890(2)	7727(2)	31(1)
C141	2258(2)	4919(2)	7050(1)	31(1)
C151	963(1)	5381(2)	6426(1)	31(1)
C161	1344(2)	6644(2)	6322(2)	35(1)

U_{eq} is defined as one third of the trace of the orthogonalized *U*ij tensor.

2.2. X-ray crystallography

The diffraction data were collected at 100(2) K for a $0.30 \times 0.25 \times 0.20$ mm single crystal using Kuma CCD diffractometer, Mo Kα radiation $\lambda = 0.71073$ Å. The 181753 reflections were measured with the $\omega - 2\theta$ method. A shape-based absorption correction was applied for **1** (RED167 package of programs, Oxford Diffraction, 2000) with the maximum and minimum transmissions of 0.9037 and 0.8603. The structure was solved by direct methods and refined with a full-matrix least-squares procedure on F^2 using the SHELX-97 program package [18]. Details of the data collection and structure refinement are presented in Table 1.

Table 3
Selected bond distances [Å] and angles [°] for **1**

Distances [Å]	
Ti-(μ-O)	
Ti1–O1	1.904(3)
Ti1–O8	1.727(3)
Ti2–O1	1.738(3)
Ti2–O2	1.904(3)
Ti3–O2	1.746(3)
Ti3–O3	1.892(3)
Ti4–O3	1.741(3)
Ti4–O4	1.896(3)
Ti5–O4	1.733(3)
Ti5–O5	1.900(3)
Ti6–O5	1.731(3)
Ti6–O6	1.910(3)
Ti7–O6	1.734(3)
Ti7–O7	1.894(3)
Ti8–O8	1.915(3)
Ti8–O7	1.739(3)
Ti-(OOCBu^t)	
Ti1–O11	2.146(3)
Ti1–O21	2.001(3)
Ti1–O152	2.025(3)
Ti1–O162	2.013(3)
Ti2–O22	2.015(3)
Ti2–O12	2.030(3)
Ti2–O41	2.002(3)
Ti2–O31	2.138(4)
Ti3–O51	2.156(3)
Ti3–O42	2.031(3)
Ti3–O32	2.006(3)
Ti3–O61	2.014(3)
Ti4–O62	2.020(3)
Ti4–O52	1.996(3)
Ti4–O71	2.120(3)
Ti4–O81	2.021(4)
Ti5–O72	2.031(3)
Ti5–O82	2.006(3)
Ti5–O101	2.007(3)
Ti5–O91	2.128(3)
Ti6–O111	2.112(3)
Ti6–O121	2.010(3)
Ti6–O102	2.019(3)
Ti6–O92	2.003(3)
Ti7–O122	2.016(3)
Ti7–O112	2.024(3)
Ti7–O141	2.013(3)
Ti7–O131	2.134(3)
Ti8–O142	2.003(3)
Ti8–O132	2.018(3)
Ti8–O151	2.152(3)
Ti8–O161	2.010(3)
Ti–Ti	
Ti1–Ti2	3.358(12)
Ti2–Ti3	3.366(12)
Ti3–Ti4	3.352(12)
Ti4–Ti5	3.333(12)
Ti5–Ti6	3.338(12)
Ti6–Ti7	3.344(12)
Ti7–Ti8	3.341(12)
Ti8–Ti1	3.348(13)
Ti-(μ-O)-Ti	
Ti1–O1–Ti2	134.34(18)
Ti2–O2–Ti3	134.45(17)

Table 3 (*continued*)

Angles [°]	
Ti3–O3–Ti4	134.67(18)
Ti4–O4–Ti5	133.32(17)
Ti5–O5–Ti6	133.59(18)
Ti6–O6–Ti7	133.14(18)
Ti7–O7–Ti8	133.63(18)
Ti8–O8–Ti1	133.60(18)

3. Results and discussion

3.1. Synthesis

$Ti(OPr^i)_4$ was added to a stirred solution of HOOCR (R = Bu^t, CH_2Bu^t, $C(CH_3)_2Et$) in toluene, (molar ratio alkoxide/acid = 1:2, Ar atmosphere, room temperature (RT)). At the beginning, the reaction mixture became turbid but after 2 h, a clear solution was formed. Colorless crystals were grown by slow evaporation (glovebox) of the solvent over 2–3 days. Based on the results of elemental analysis, the general formula of the synthesized complexes was determined as $[Ti_8O_8(OOCR)_{16}]$, where R = Bu^t (**1**), CH_2Bu^t (**2**), $C(CH_3)_2Et$ (**3**). However microanalysis data suggest the presence of solvent molecules (toluene) in the crystal lattice of **1**. Single crystals, suitable for crystallographic studies were obtained only for compound **1**, but their stability was very low, and they were destroyed in air (RT), with the formation of a white crystalline powder. During the crystallization of **2** and **3** only crystalline powder was formed. Compounds **1**–**3** were insoluble in aliphatic and sparingly soluble in aromatic solvents.

3.2. Crystal structure

Due to the low stability of **1** in the air at RT, the X-ray measurements were carried out at low temperature (~100 K). The poor quality of crystals obtained for **2** and **3** made their crystallographic studies impossible. The chemical unit of **1**, with the atom-numbering scheme, is shown in Fig. 1. Crystal data and atomic coordinates are listed in Tables 1 and 2. The selected bond distances and angles are presented in Table 3.

The ring molecule of the reported complex is composed of eight distorted $[TiO_6]$ octahedra linked by two μ_2-O (*cis*) and four μ-O (carboxylate) bridges (Fig. 1, Table 3). The $[Ti_8(\mu_2\text{-}O)_8]$ ring is not planar. The Ti_8 ring conformation with alternating positive and negative values of Ti–Ti–Ti–Ti torsion angles resembles the cyclohexane chair conformation, but their absolute values vary from 5.11(7)° for Ti1–Ti2–Ti3–Ti4 to 37.14(7)°

for Ti6–Ti7–Ti8–Ti1. The *rms* deviation of Ti ions from the Ti_8 best plane is 0.2073 Å.

Eight of the bridging carboxylates are positioned approximately in the ring plane (Fig. 1), the dihedral angles between the Ti_2COO planes and the best plane of the Ti_8 ring range from 8.88(5)° to 21.85(3)°, with the mean value being 16.5(4)°. The remaining eight carboxylates form the bridges between the Ti ions alternating between the two sides of the ring plane and are approximately perpendicular to that plane. The dihedral angles between the Ti_8 best plane and the Ti_2COO planes vary from 72.81(7)° to 81.29(6)°, with a mean value of 77.8(3)°.

The bridging oxygen atoms in the $[Ti_8(\mu_2\text{-}O)_8]$ rings form alternating longer and shorter Ti–O bonds, the average Ti–O distances and *esd* in the series being 1.904(8) and 1.735(7) Å for the longer and shorter bonds, respectively. The angles in that ring vary from 133.15(1)°–134.67(1)° to 132.42(1)°–136.28(1)° for Ti–O–Ti and Ti–Ti–Ti, respectively (Table 3). Also the oxo bridges form alternating shorter 1.997(3)–2.031(3) Å and longer 2.114(3)–2.156(3) Å Ti–O bonds. In the octahedral environment of each Ti ion, they occupy the *trans* positions relative to the shorter and longer carboxylate Ti–O bonds mentioned above. The other two *trans* trimethyl acetate bridges are positioned outside the $[Ti_8(\mu_2\text{-}O)_8]$ rings, and the corresponding Ti–O(carboxylate) distances vary in the range 2.002(3)–2.013(3) and 2.013(3)–2.031(3) Å.

Kickelbick and Scubert [16] reported an oligomeric ring structure of the general formula $[Ti_9O_8(OPr^i)_4(OOCC(Me){=}CH_2)_{16}]$ (monoclinic, space group *Ia*). That complex consisted of a ring of nine $[TiO_6]$ octahedra linked by six μ_2-O, two μ_3-O and 16 μ_2-O(OOC) bridges. Also in that case, the non-equivalent Ti–O bonds of μ_2-oxo bridges (1.90–1.93 and 1.72–1.74 Å) were compensated by asymmetric Ti–O distances of *trans* carboxylate groups (1.97–2.11 and 2.09–2.16 Å). Analysis of the literature reports exhibited that in another type of $[Ti_x(\mu_n\text{-}O)_y]$ (n = 2, 3) cluster the Ti–O distances were shorter, e.g., in the structure of $([Ti_6O_6(OPr^i)_6(O_2CBu^t)_6]$, Ti-($\mu_3$-O) = 1.878(4), 1.890(2) and 2.142(3) Å [14], and in $[Ti_6O_4(Opr^n)_8(O_2CR)_8]$ (R = CH_3, Ph), Ti-($_2$-O) = 1.724(6)–1.768(2) and 1.900(6)–1.942(2) Å, and Ti-(μ_3-O) = 1.911(2), 1.941(2) and 2.082(2) Å [9,16].

The low temperature experiment for the reported complex **1** allowed building a satisfactory model for the majority of the $OOCBu^t$ moieties. Only for two Bu^t groups the rotational disorder was accounted for in the final model. Both these groups do not participate in intermolecular interactions between the adjacent rings. The complex molecules of **1** form some hydrophobic interactions with the adjacent molecules via their Bu^t groups on the side surfaces and around the ring. However, the important component of the packing interactions is due to the toluene molecules found in the structure. Two of them are positioned near the ring center, between the $OOCBu^t$ moieties perpendicular to the molecule ring plane. Another two toluene molecules participate in the packing interactions involving the carboxylate ligands positioned in the ring plane.

3.3. Analysis of NMR data

The ^{13}C NMR spectroscopy in the solid state have been used to study the structural similarities between **1**, **2** and **3**. Also, ^1H and ^{13}C NMR spectra of $[D_8]$toluene solutions of these compounds were registered in

Table 4
The solid-state and solution NMR studies of $[Ti_8O_8(OOCR)_{16}]$ (R = Bu^t (**1**), CH_2Bu^t (**2**), $C(CH_3)_2Et$ (**3**))

Compound	Method	δ [ppm]							
		CH_3 (Et)	CH_2 (Et)	CH_2	CH_3 (CMe_2)	CH_3 (Bu^t)	C (CMe_2)	C (Bu^t)	C (COO)
(**1**)	^{13}C – s. st.					26.5		38.7	186.7
									188.2
	^{13}C – C_7D_8					27.2		39.3	187.4
						27.4		39.5	188.6
	^1H – C_7D_8					1.2 (s)			
						1.1 (s)			
(**2**)	^{13}C – s. st.			49.5		29.8			181.5
	^{13}C – C_7D_8			48.9		30.1		30.9	183.6
				50.1				31.1	182.7
	^1H – C_7D_8			2.3 (s)		1.2 (s)			
(**3**)	^{13}C – s. st.	9.1	33.9		24.5		43.3		186.5
							43.1		188.0
	^{13}C – C_7 D_8	9.7	34.3		25.0		43.6		187.4
		10.3	34.6		25.6		43.7		189.0
	^1H – C_7D_8	1.1 (t)	1.7 (q)		1.3 (s)				
		J_{H-H} = 4.0 Hz	J_{H-H} = 4.0 Hz						

The solid-state ^{13}C NMR spectra were registered on a Bruker AMX 300, solution ^1H, ^{13}C NMR spectra ($[D_8]$ toluene) were recorded using a 5-mm solution probe on a Varian Gemini 200 spectrometer.

order to determine the structural changes of the investigated compounds after their solubilization. The observed chemical shifts are listed in Table 4.

The signals due to the carbon atoms of coordinated carboxylate groups are located between 180.3 and 188.2 ppm in the solid-state ^{13}C NMR spectra of **1**–**3**. In spectra of **1** and **3**, the carbon atoms show two lines of equal intensity at 186.6 and 188.1 ppm, whereas a wide single signal at 180.5 ppm is found in the spectrum of **2** (Table 4). However, a detailed analysis of the C(COO) peak in the spectrum of this compound revealed that it also consists of two components, with $\delta = 180.3$ and 180.7 ppm. Considering crystallographic data, the above phenomenon can be explained by the presence of two different types of carboxylate groups in the structures of **1**–**3**. Crystallographic data showed that the COO groups formed the bridges in the plane of the $[Ti_8(\mu_2\text{-}O)_8]$ ring, exhibiting asymmetry of the C–O bond lengths, 1.237(6)–1.250(5) (shorter) and 1.263(6)–1.299(6) Å (longer). Differences in the length of bonds formed by the carboxylate group bridges outside of the ring plane were smaller (1.258(6)–1.276(5) and 1.261(5)–1.275(6) Å). The ^{13}C NMR studies suggest that **1** and **3** form a similar type of carboxylate group interaction in $[Ti_8O_8(OOCR)_{16}]$ molecules. Undetected splitting of the C(COO) signal, observed in the ^{13}C NMR spectrum of **2**, can be interpreted as a result of the smaller differences between the length of the C–O bonds formed by COO groups outside compared to within the $[Ti_8(\mu_2\text{-}O)_8]$ ring plane.

Analysis of ^{13}C NMR spectra of **1**–**3** $[D_8]$toluene solutions shows clear similarities in the chemical shift and splitting of the resonance signals with their analogs in the solid state spectra (Table 4). The NMR data reveal the presence of two types of carboxylate groups in the structure of the studied compounds, which is consistent with the X-ray structure of **1**. In ^1H NMR spectra of **1**–**3** $[D_8]$toluene solutions, only the signals attributed to appropriate hydrocarbon groups were detected.

3.4. Infrared spectra studies

IR spectra of the studied carboxylates were registered at liquid nitrogen temperature (LNT), in conditions analogous to the single crystal X-ray measurements. In order to study similarities between the structures of **1**–**3**, a detailed analysis of IR spectra in the following ranges (a) 1350–1600 cm^{-1} and (b) 400–900 cm^{-1} have been carried out. The wavenumbers of absorption bands registered in the above regions are listed in Table 5.

3.4.1. Stretching frequencies of carboxylate ligands

The split bands attributed to $\nu_{as}(COO)$ and $\nu_s(COO)$ vibrations were found in the ranges 1500–1575 and 1400–1440 cm^{-1} (Table 5). Values of the $\Delta[\nu_{as}(COO) - \nu_s(COO)]$ parameter, calculated for the suitable band components were 116 and 94 cm^{-1}, 116 and 107 cm^{-1} for **1** and **3**, as well as 131 and 103 cm^{-1} for **2**. Comparison of the above results with the literature data [19–22] indicate that the detected $\nu_{as}(COO)$ frequencies and Δ parameter values correspond to bidendate carboxylate groups, participating in *syn–syn* bridges. The different interactions of COO ligands in the structure of the studied compounds are the main factor that causes splitting of the stretching band. That conclusion is consistent with the structural and NMR data presented in this paper.

Table 5
Wavenumbers [cm^{-1}] for the vibrations of acetate ions and oxo bridges (M–O–M) in LNT spectra of $[Ti_8O_8(OOCR)_{16}]$ (where R = Bu^t (**1**), CH_2Bu^t (**2**), $C(CH_3)_2Et$ (**3**))

Modes	**1** [cm^{-1}]	**2** [cm^{-1}]	**3** [cm^{-1}]
			1574 (m)
$\nu_{as}(COO)$	1546 (s)	1552 (s)	1552 (s)
		1540 (s)	
	1512 (m)	1507 (m)	1519 (m)
$\delta_{as}(CH_3)$, $\delta_{as}(CH_2)$	1486 (m)	1478 (m)	1477 (m)
	1458 (w)	1463 (m)	1455 (m)
$\nu_s(COO)$, $\delta_{as}(CH_3)$	1429 (s)	1421 (s)	1436 (m)
	1419 (m)	1405 (m)	1413 (m)
$\delta(CH_3)$	1378 (m)	1376 (m)	1388 (m)
$\delta(CH_3)$			1371 (m)
$\delta(CH_3)$	1361 (m)	1357 (m)	1367 (m)
$\nu_{as}(Ti\text{–}O\text{–}Ti)(\mu_3\text{-}O)$	750 (s)	754 (m)	758 (m)
		714 (m)	722 (m)
$\delta(OCO)$	611 (s)		641 (m)
$\delta(OCO)$	583 (m)	601 (s)	552 (w)
$\rho(OCO)$; out of plane	504 (m)	507 (w)	502 (m)
$\rho(OCO)$; out of plane	481 (m)	480 (w)	478 (m)
$\nu(CCC)$		460 (w)	450 (w)
$\rho(OCO)$; in plane	443 (m)	435 (w)	435 (vw)
$\rho(OCO)$; in plane	431 (w)	429 (w)	420 (w)

3.4.2. Absorption bands between 400 and 900 cm^{-1}

The bands due to vibrations of carboxylate ligands and M–O–M titanium-oxide bridges of $[Ti_8(\mu_2\text{-}O)_8]$ rings have been found in the range 400–900 cm^{-1} (Table 5). According to the literature data [19,22], their frequencies can be assigned to COO bending ($\delta_s(O\text{-}CO)$ = 551–641 cm^{-1}) and rocking ($\rho(COO)$ = 419–507 cm^{-1}) modes.

The band for Ti–O–Ti stretching modes ($\nu_a(Ti\text{–}O\text{–}Ti)$) was found in the range 714–758 cm^{-1} (Table 5). According to Nakamoto's report on vibrational spectra of complexes containing M-(μ_2-O) bridges in their structure [19], the bands assigned to M–O–M asymmetric vibrations appear in the IR spectrum, while symmetric ones appear in the Raman spectrum. The frequency for the bands mentioned above depends on the type of oxygen bridge and the number of concomitant carboxylate bridges. For the linear M-(μ_2-O) monobridges $\nu_a(M\text{–}O\text{–}M) \cong 843\text{–}885\ cm^{-1}$, and for non-linear one,

ν_a(M–O–M) ≅ 827 cm^{-1}. Presence of the oxygen bridge in the vicinity of carboxylate bridges causes the frequency shift of the ν_a(M–O–M) vibrations towards 749–772 cm^{-1} [19]. In IR spectra of **2** and **3**, the appearance of ν_a(TiOTi) bands at 714, 754 cm^{-1} (**2**), and at 722, 758 cm^{-1} (**3**) was observed. That confirms the formation of non-linear Ti–O–Ti bridges near the Ti-carboxylate ones in the structure of these compounds, similar to those found in the structure of **1**.

The possible low temperature phase transition and thermal stability of Ti–O bonds in [Ti$_8$(μ_2-O)$_8$] clusters have been investigated by means of variable temperature IR spectroscopy (VT-IR). Analysis of the dependence between the frequency of Ti–O–Ti motions (ν_a(TiOTi)) and the temperature exhibited only insignificant shifts (6–7 cm^{-1}) of this band towards higher wavenumbers in the spectra of **2** and **3**. These results suggest that the stability of [Ti$_8$(μ_2-O)$_8$] rings is very high and a temperature phase transition does not occur. The temperature evolution of the ν_a(TiOTi) frequency, observed in VT-IR spectra of **1**, was significantly higher (15–16 cm^{-1}). Moreover only for this compound, clear changes in the diagram slopes between 0 and 60 °C were observed (Fig. 2). Considering crystallographic and TGA data, the latter effect can be explained by the loss of solvent molecules from the crystal lattice of **1**.

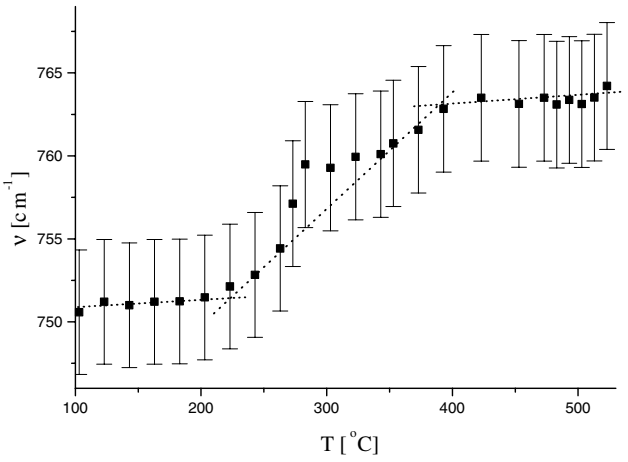


Fig. 2. Temperature evolution of the ν_a(TiOTi) band in the VT-IR spectra of [Ti$_8$O$_8$(O$_2$CBu^t)$_{16}$] (SPECTRUM 2000, KBr, −175 to 250 °C).

3.5. Thermal characterization

The thermal decomposition mechanism of Ti(IV) ring carboxylates was studied using thermogravimetric and differential thermal analysis (TG/DTA) methods over the temperature range 25–550 °C with a heating rate of 3 °C min^{-1} under a nitrogen atmosphere. The TGA/DTA data of **1** show that the decomposition proceeded in four endothermic stages, with maxima at 63, 260, 370 and 421 °C, with a weight loss of 73.4%. A multistep thermal decomposition was also observed for **2** and **3**; the maxima of endothermic stages were found at 108, 311, 381, 417 °C (weight loss: 70.1%) for **2**, and 300, 340, 393, 410 °C (weight loss: 71.2%) for **3**. Thermogravimetric analysis exhibited that the pyrolysis of **1**–**3** proceed with their complete conversion to TiO$_2$. Moreover, one endothermic peak near 63 °C is observed for **1**, which can be explained by the loss of solvent molecules from the crystal lattice of this compound.

Table 6
The mass spectra of [Ti$_8$O$_8$(OOCR)$_{16}$], where R = Bu^t (**1**), CH$_2$Bu^t (**2**), C(Me)$_2$Et (**3**), registered between 150 and 350 °C (MS-EI 70 eV)

	Fragmentation Ion	*m/z*	*T* [°C]							
			150	200	240	260	280	300	320	350
(**1**)	[Ti$_4$O$_4$(O$_2$CBu^t)(O$_2$CH)$_2$]$^+$	448	53.3	85.7						
	[Ti$_3$O(O$_2$CBu^t)$_2$(O$_2$CCH$_3$)$_2$]$^+$	480	**100**	**100**						
	[Ti$_8$O$_8$(O$_2$CBu^t)$_7$(O$_2$CC$_2$H$_2$)]$^+$	1286	15.3	30.4						
	[Ti$_8$O$_{10}$(O$_2$CBu^t)$_{10}$]$^+$	1554				5.7	43.9	38.1	32.2	28.9
	[Ti$_8$O$_{10}$(O$_2$CBu^t)$_{11}$]$^+$	1655						49.7	**100**	**100**
	[Ti$_8$O$_8$(O$_2$CBu^t)$_{14}$]$^+$	1926				11.0	10.6			
	[Ti$_8$O$_8$(O$_2$CBu^t)$_{15}$]$^+$	2027	5.5	29.4	**100**	**100**	63.2	14.6		
(**2**)	[Ti$_2$O$_2$(O$_2$CCH$_2$Bu^t)$_2$]$^+$	356	68.8	62.8				6.6		
	[Ti$_8$O$_8$(O$_2$CCH$_2$Bu^t)(O$_2$CCH$_3$)$_3$(O$_2$CH)]$^+$	849			41.1	41.8	35.0	35.2	22.1	1.7
	[Ti$_8$O$_8$(O$_2$CCH$_2$Bu^t)$_3$(O$_2$CC$_4$H$_8$)]$^+$	956		3.9	36.5	43.5	6.2	14.2	8.2	
	[Ti$_8$O$_8$(O$_2$CCH$_2$Bu^t)$_4$(O$_2$CCH$_3$)$_4$(O$_2$CC$_3$H$_6$)]$^+$	1064			19.5	14.5	4.3	5.8	6.7	
	[Ti$_8$O$_8$(O$_2$CCH$_2$Bu^t)$_9$(O$_2$CCH$_3$)(O$_2$CCH)$_2$]$^+$	1696		5.6	21.0	20.3	17.6	16.7	18.8	1.1
	[Ti$_8$O$_8$(O$_2$CCH$_2$Bu^t)$_{10}$(O$_2$CH)$_2$(O$_2$CCH$_3$)]$^+$	1811		29.6	**100**	**100**	**100**	70.7	90.4	4.6
	[Ti$_8$O$_8$(O$_2$CCH$_2$Bu^t)$_{14}$(O$_2$CCH$_3$)$_2$]$^+$	2241		6.6	75.6	58.4	28.2	20.3	11.4	
(**3**)	[Ti$_2$O(O$_2$CCMe$_2$Et)(O$_2$CCH)(O$_2$CC$_2$H$_4$)]$^+$	356	**100**	**100**						
	[Ti$_8$O$_8$(O$_2$CCMe$_2$Et)(O$_2$CCH$_3$)$_3$(O$_2$CH)]$^+$	849			37.9	15.4	10.2	3.1	6.2	7.1
	[Ti$_8$O$_8$(O$_2$CCMe$_2$Et)$_2$(O$_2$CCH$_3$)$_4$(O$_2$CC$_3$H$_6$)]$^+$	1064			56.3	54.4	45.0	13.2	13.7	1.5
	[Ti$_8$O$_8$(O$_2$CCMe$_2$Et)$_8$(O$_2$CBu^t)]$^+$	1534			22.4	13.3	10.5	6.4	7.7	8.2
	[Ti$_8$O$_8$(O$_2$CCMe$_2$Et)$_9$(O$_2$CCH$_3$)(O$_2$CH)$_2$]$^+$	1696			15.8	10.6	6.8	3.6	9.8	13.6
	[Ti$_8$O$_8$(O$_2$CCMe$_2$Et)$_9$(O$_2$CCH$_3$)$_3$(O$_2$CH)$_2$]$^+$	1814		2.8	41.7	20.4	11.4	7.4	33.0	41.1
	[Ti$_8$O$_8$(O$_2$CCMe$_2$Et)$_{14}$(O$_2$CCH$_3$)$_2$]$^+$	2240		4.7	**100**	**100**	**100**	**100**	**100**	**100**

Analysis of MS-EI spectra, registered in the temperature range 150–350 °C confirms the formation of the [Ti-(μ_2-O)]$_8$ rings stabilized by carboxylate bridges in the structures of all the studied compounds. Results of MS-EI experiments are presented in Table 6. Multinuclear titanium species were detected below 200 °C, which indicates partial decomposition of these compounds at lower temperatures. The characteristic peaks at $m/z = 2027$ ($[Ti_8O_8(OOCBu^t)_{15}]^+$), $m/z = 1811$ ($[Ti_8O_8(OOCCH_2Bu^t)_{10}(OOCCH_3)(OOCH)_2]^+$) and $m/z = 2240$ ($[Ti_8O_8(OOCC(Me)_2Et)_{14}(OOCCH_3)_2]^+$) with 100% intensity appear above 240 °C. Also TG/DTA data show the beginning of the mass detachment of samples **1**–**3** at this temperature. Simultaneously, the presence of multinuclear fragmentation ions above 240 °C indicates their thermal stability, which may be useful for their transport in the gas phase. That factor may be important for application of these compounds as precursors in the chemical vapor deposition methods. Comparison of **1**–**3** MS data showed that the thermal stability of multinuclear Ti(IV) fragmentation ions increases in the row $Bu^t < CH_2Bu^t < C(Me)_2Et$.

4. Conclusions

New titanium multinuclear Ti(IV) oxo carboxylates, with the general formula $[Ti_8O_8(OOCR)_{16}]$, where R = Bu^t (**1**), CH_2Bu^t (**2**), $C(CH_3)_2Et$ (**3**), have been synthesized in a reaction of titanium isopropoxide ($Ti(OPr^i)_4$) with suitable organic acids, in the molar ratio 1:2. X-ray studies of **1** revealed that the structure of this compound is formed by rings, composed of eight distorted [TiO_6] octahedra connected by two μ_2-O and four μ_2-O (carboxylate) bridges. Structural data exhibited the presence of solvent molecules (toluene) in the crystal lattice of **1**. The thermogravimetric and IR studies proved that solvent molecules are removed from the structure of this compound between 0 and 60 °C. The obtained results prove that the low stability of the crystals of **1** is caused by the presence of solvent molecules in the crystal lattice and their loss at room temperature. Spectral analysis of **1**–**3** powders showed that these compounds form a ring structure of the general formula $[Ti_8O_8(OOCR)_{16}]$. Variable temperature IR studies indicate the high thermal stability of the studied multinuclear Ti(IV) oxo carboxylates. Analysis of MS-EI data suggests that during the thermal decomposition of **1**–**3**, volatile multinuclear Ti-oxide species are formed above 240 °C. The stability of these species changes in the row $Bu^t < CH_2Bu^t < C(Me)_2Et$.

5. Supplementary data

Crystallographic data for the structural analysis have been deposited with the Cambridge Crystallographic Data Centre, CCDC No. 256553. Copies of this information may be obtained free of charge from The Director, CCDC, 12 Union Road, Cambridge CB2 1EZ, UK (fax: +44-1233-336-033; e-mail: deposit@ccdc.cam.ac.uk or www: http://www.ccdc.cam.ac.uk).

Acknowledgements

The authors acknowledge the Polish Committee for Science Research for financial support Grant No. 4T09A 152 23.

References

[1] R.N. Kapoor, K.C. Pande, R.C. Mehrotra, J. Indian Chem. Soc. 35 (1958) 157.
[2] R.Ch. Paul, R.Ch. Kumar, O.B. Baidya, R. Kapoor, Aust. J. Chem. 31 (1978) 425.
[3] K.L. Jaura, H.S. Banga, R.L. Kaushik, J. Indian Chem. Soc. 39 (1962) 531.
[4] D. Schwartz, C. Johnson, J. Ludwig, M.L. Morris, J. Inorg. Nucl. Chem. 26 (1964) 2025.
[5] N.W. Alcock, D.A. Brown, T.F. Illson, S.M. Roe, M.G.H. Wallbridge, J. Chem. Soc., Dalton Trans. (1991) 873.
[6] N.W. Alcock, P.N. Bartlett, D. Gordon, T.F. Illson, M.G.H. Wallbridge, J. Chem. Soc., Chem. Commun. (1986) 614.
[7] M. Barrow, D.A. Brown, N.W. Alcock, H.J. Clase, M.G.H. Wallbridge, J. Chem. Soc., Dalton Trans. (1994) 195.
[8] I.D. Varma, R.C. Mehrotra, J. Prakt. Chemie 4 (1959) 235.
[9] S. Doeuff, M. Henry, C. Sanchez, Mater. Res. Bull. 25 (1990) 1519.
[10] S. Doeuff, Y. Dromzee, F. Taulelle, C. Sanchez, Inorg. Chem. 28 (1989) 4439.
[11] I. Laaziz, A. Larboot, C. Guizard, J. Durand, L. Cot, Acta Crystallogr. C46 (1990) 2332.
[12] T.J. Boyle, T.M. Alam, C.J. Tafoya, Inorg. Chem. 37 (1998) 5588.
[13] X. Lei, M. Shang, T.P. Fehlner, Organometallics 15 (1996) 3779.
[14] R. Papiernik, L.G. Hubert-Pfalzgraf, J. Vaissermann, M.C. Henriques Baptista Goncalves, J. Chem. Soc., Dalton Trans. (1998) 2285.
[15] P. Piszczek, A. Grodzicki, M. Richert, A. Wojtczak, Inorg. Chim. Acta 357 (2004) 2769.
[16] G. Kickelbick, U. Schubert, Eur. J. Inorg. Chem. (1998) 159.
[17] P.S. Ammala, S.R. Batten, C.M. Kepert, L. Spiccia, A.M. van der Bergen, B.O. West, Inorg. Chim. Acta 353 (2003) 75.
[18] G.M. Sheldrick, SHELXS97 and SHELXL97, University of Göttingen, Germany, 1997.
[19] K. Nakamoto, Infrared and Raman Spectra of Inorganic and Coordination Compounds, part B/V ed., Wiley, New York, 1997, p. 58, 172.
[20] G.B. Deacon, R.J. Phillips, Coord. Chem. Rev. 33 (1980) 227.
[21] N.W. Alcock, V.M. Tracy, J. Chem. Soc., Dalton Trans. (1976) 2243.
[22] V. Koleva, D. Stoilova, J. Mol. Struct. 61 (2002) 1.

Available online at www.sciencedirect.com
SCIENCE DIRECT®
Polyhedron 24 (2005) 671–677
POLYHEDRON
www.elsevier.com/locate/poly

Synthesis, structure and properties of mercury complexes with a new extended tetrathiafulvalene 4,5-dithiolate ligand

He-Rui Wen [a], Jing-Lin Zuo [a,*], Thomas A. Scott [b], Hong-Cai Zhou [b], Xiao-Zeng You [a]

[a] *Coordination Chemistry Institute, State Key Laboratory of Coordination Chemistry, Nanjing University, Nanjing 210093, China*
[b] *Department of Chemistry and Biochemistry, Miami University, Oxford, OH 45056-1465, USA*

Received 21 October 2004; accepted 21 January 2005

Abstract

A new extended tetrathiafulvalene (TTF) dithiolate ligand, benzotetrathiafulvalenedithiolate ($btdt^{2-}$), together with mercury complexes based on it, have been synthesized and characterized by cyclic voltammetry, ESR, IR and magnetic susceptibility measurements. The crystal structure of $(Me_4N)_2[Hg(btdt)_2] \cdot 4/3H_2O \cdot 2/3C_4H_9O$ (**4**) is determined, in which the central Hg atom is in an approximately tetrahedral coordination environment. Both ESR and cyclic voltammetry studies show that there is very little conjugating interaction between the two extended TTF dithiolate ligands. The neutral complex $Hg(btdt)_2$ (**5**) is prepared from **4** by oxidation with iodine. The electrical conductivity of **5** was measured as compressed pellets and the room temperature conductivity is 0.0015 S cm^{-1}. Magnetic susceptibility measurements reveal that complex **5** is a radical antiferromagnet.
© 2005 Elsevier Ltd. All rights reserved.

Keywords: Benzotetrathiafulvalenedithiolate; Mercury complexes; Crystal structure; Conductivity; Magnetic susceptibility

1. Introduction

Metal complexes of 1,2-dithiolene ligands have been intensively studied as materials for molecular conductors and superconductors [1]. The crystal structure of these complexes reveal that intermolecular interaction through the sulfur–sulfur interatomic contact is the basic requirement for high conductivity. The incorporation of more heteroatoms, such as S or Se, into the periphery of the structure stabilizes the interactions via direct S···S or Se···Se overlap on the adjacent inter- and intra-stack ions. Recently metal complexes with extended tetrathiafulvalenedithiolene ligands have been of great interest because of their possible extended π-conjugation system and their better electrical conduction properties [2–14]. A few highly conducting molecule crystals of nickel, copper and gold complexes with extended TTF ligands have been reported [4–6]. Since the basic idea on the design of a molecular conductor is to reduce the HOMO–LUMO energy gap in the molecule by extending the π conjugated system and improving the planarity [12], the synthesis of highly conjugated and planar ligands becomes the main target. However, in these metal complexes with extended TTF dithiolate ligands, the side groups on the TTF framework all are alkyl groups. As we know, the length and type of the side alkyl group on the TTF framework have great effect on the conducting properties of the resulted complexes [3,10]. Bulky alkyl groups on the TTF framework will lead to molecules with non-compact packing, which decrease the intermolecular reaction. In order to eliminate the alkyl group effect on the TTF framework and increase the planarity and π-conjugation of the extended TTF dithiolate, we report herein the synthesis of a new extended TTF dithiolate ligand, benzotetrathiafulvalenedithiolate, together with mercury complexes based on this ligand.

* Corresponding author. Tel.: +86 25 8359 3893; fax: +86 25 8331 7761.
E-mail address: zuojl@nju.edu.cn (J.-L. Zuo).

0277-5387/$ - see front matter © 2005 Elsevier Ltd. All rights reserved.
doi:10.1016/j.poly.2005.01.015

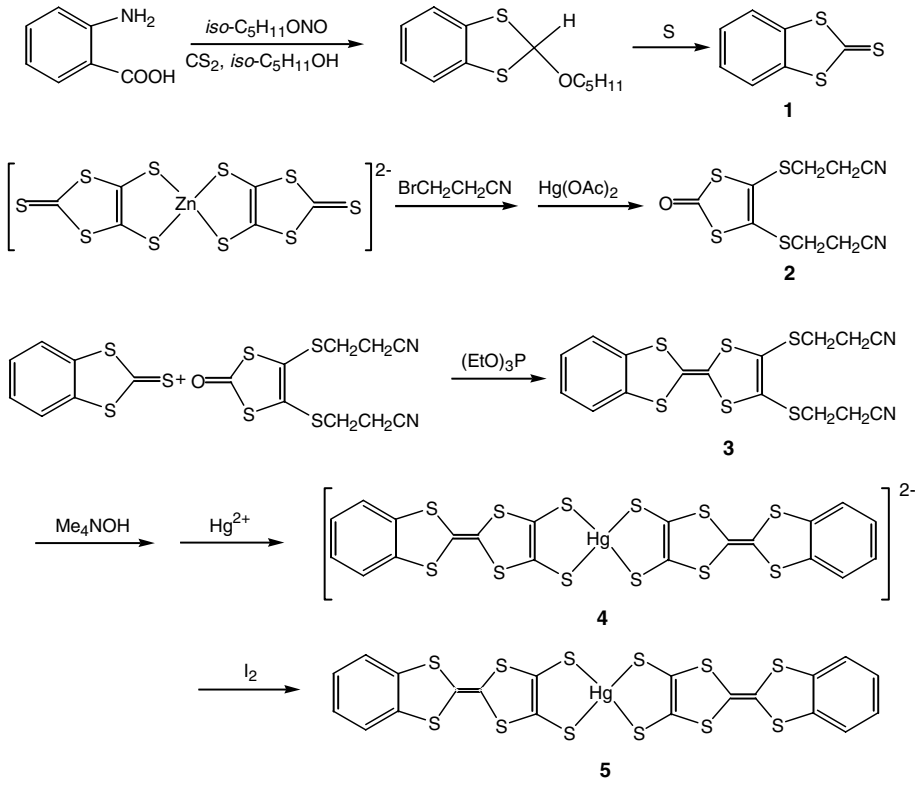
2. Experimental

2.1. General procedures

Reagent-grade tetrahydrofuran (THF) was purified and distilled with standard methods. Other solvents and chemicals were purchased from commercial sources and used as received. Schlenk techniques were used in carrying out manipulation under nitrogen atmosphere. Elemental analyses for C, H and N were performed on a Perkin–Elmer 240C analyzer. The ESR spectra were measured using a Bruker ER 200-D-SRC spectrometer. The IR spectra were taken on a Vector22 Bruker Spectrophotometer (400–4000 cm^{-1}) with KBr pellets. NMR spectra were measured on a Bruker AM 500 spectrometer. Cyclic voltammetry data were recorded by an EG&G PAR Model 273 electrochemical analytical instrument. The magnetic susceptibility was measured using a Quantum Design MPMS-XL7 SQUID magnetometer at temperatures ranging from 1.8 to 300 K. The temperature dependence of the resistivity was measured by the conventional four-probe method using a copper wire attached with indium in the temperature range of 80–293 K. The $btdt^{2-}$ ligand and the related complexes were synthesized as shown in Scheme 1.

2.2. Preparation of 2,3-bis(2-cyanoethylthio)-benzotetrathiafulvalene (3)

2-Thioxo-1,3-benzodithiol (**1**) [15,16] and 5-bis-(2-cyanoethylthio)-1,3-dithiole-2-one (**2**) [9] were synthesized as described in the literature. Under a nitrogen atmosphere, to the mixture of **1** (0.92 g, 5 mmol) and **2** (0.86 g, 3 mmol) was added 25 ml of freshly distilled $P(OC_2H_5)_3$. The reaction mixture was heated at 110 °C for 1 h and then allowed to cool to room temperature. After 25 ml of methanol was added to the above suspension, on filtering an orange-red precipitate was collected and washed with methanol, which was then chromatographed on a silica gel column using dichloromethane as the eluent. Orange-yellow powder **3** was obtained. Yield: 0.72 g (56%, based on **2**). *Anal.* Calc. for $C_{16}H_{12}N_2S_6$: C, 45.28; H, 2.83; N, 6.60; S, 45.28. Found: C, 45.21; H, 2.65; N, 6.88; S, 45.35%. IR (KBr cm^{-1}): *v* 3446(w), 1567(w), 1441(m), 1426(s), 1408(s), 1320(w), 1281(m), 1118(m), 892(s), 770(m), 736(s), 675(w), 415(m). ^1H NMR ($CDCl_3$): $\delta = 2.77$ (t, 4H, CH_2), 3.12 (t, 4H, CH_2), 7.16 (m, 2H, Ph), 7.28 (d, 2H, Ph). ^{13}C NMR ($CDCl_3$): = 19.32, 31.72, 117.87, 122.43, 126.61, 128.39, 136.50. EI–MS: 424 (M^+, 25.6), 370 (13), 286 (15), 196 (50), 152 (70), 108 (73), 54 (100).



Scheme 1.

2.3. Preparation of $(Me_4N)_2[Hg(btdt)_2] \cdot 4/3H_2O \cdot 2/3C_4H_9O$ (4)

Under a nitrogen atmosphere, a methanol solution of Me_4NOH (0.45 ml, 25% (w/w), 1 mmol) was added to **3** (212 mg, 0.5 mmol) in 20 ml of THF at −5 °C. A red-orange precipitate was observed immediately and the reaction mixture was left stirring at the same temperature for 30 min. THF was removed in vacuo at 10 °C and the resulting pink solid was dissolved in 20 ml of methanol. Then $Hg(OAc)_2$ (80 mg, 0.25 mmol) in 10 ml of methanol was added and a gold-yellow precipitate was observed immediately, the reaction mixture was left to stir at 0 °C for 12 h. The gold-yellow precipitate was filtered off, washed with methanol and ether, and dried in vacuo. Yield: 210 mg (86%). *Anal.* Calc. for $C_{28}H_{32}N_2S_{12}Hg$: C, 34.26; H, 3.26; N, 2.86; S, 39.16. Found: C, 34.16; H, 3.28; N, 3.02; S, 39.42%. IR (KBr cm^{-1}): *v* 3442(w), 3018(w), 1598(m), 1566(m), 1479(s), 1445(s), 1433(m), 1118(w), 1022(w), 947(s), 864(m), 746(m), 674(w), 467(w). Air-stable gold-yellow plate-shaped crystals of $(Me_4N)_2[Hg(btdt)_2] \cdot 4/3H_2O \cdot 2/3C_4H_9O$ were obtained by slow diffusion of diethyl ether into a solution of the product in acetonitrile.

2.4. Preparation of $[Hg(btdt)_2]$ (5)

Microcrystalline complex **5** was obtained by slow diffusion of iodine vapor into a DMF solution of complex **4** under nitrogen. The microcrystalline precipitate was filtered off, washed with DMF, acetonitrile, methanol and ether, and then dried in vacuo. *Anal.* Calc. for $C_{20}H_8S_{12}Hg$: C, 28.83; H, 0.96; S, 46.12; N, 0. Found: C, 29.10; H, 0.91; S, 46.23; N, 0%. IR (KBr cm^{-1}): *v* 1564(m), 1467(s), 1444(s), 1431(s), 1282(s), 1257(m), 1197(s), 1117(s), 1026(m), 959(m), 886(w), 770(m), 733(s), 674(m), 469(w).

3. X-ray crystallography

The structure of complex **4**, $(Me_4N)_2[Hg(btdt)_2] \cdot 4/3H_2O \cdot 2/3C_4H_9O$, was determined. The crystal was mounted in Infineum oil and placed in a dinitrogen cold stream on a Siemens (Bruker) SMART CCD-based diffractometer. Cell parameters were retrieved using SMART software and refined using SAINT on all observed reflections. Data were collected using the following strategy: 606 frames of 0.3° in with $\phi = 0°$, 435 frames of 0.3° in ω with $\phi = 90°$, and 235 frames of 0.3° in ω with $\phi = 180°$. An additional 50 frames of 0.3° in ω with $\phi = 0°$ were collected to allow for decay correction. The highly redundant data sets were reduced using SAINT and corrected for Lorentz and polarization effects. Absorption corrections were applied using SADABS supplied by Bruker. Structures were solved by direct methods using the program SHELXL-97. The positions of the metal atoms and their first coordination spheres were located from direct-methods *E*-maps; other non-hydrogen atoms were found in alternating difference Fourier syntheses and least-squares refinement cycles and, during the final cycles, refined anisotropically. Hydrogen atoms were placed in calculated positions and refined as riding atoms with a uniform value of U_{iso}. Crystallographic parameters and agreement factors are contained in Table 1.

Table 1
Summary of crystal and experimental data for complex **4**

Formula	$C_{92}H_{124}N_6O_6S_{36}Hg_3$
Formula weight	3165.90
Crystal system	orthorhombic
Space group	*Pbcn* (no.60)
Unit cell dimensions	
a (Å)	25.253(1)
b (Å)	16.910(1)
c (Å)	29.893(1)
α (°)	90
β (°)	90
γ (°)	90
Z	4
V (Å^3)	12765.3(9)
D_{calc} (g cm^{-3})	1.647
T (K)	213
λ (Å)	0.71073
μ (mm^{-1})	4.236
F (000)	6328
2max(°)	52.0
hkl Range	$-31 \leqslant h \leqslant 25$, $-20 \leqslant k \leqslant 20$, $-36 \leqslant l \leqslant 35$
Collected	78278
Unique	12563
Parameters	645
Goodness-of-fit	0.911
R_1 [$I > 2\sigma(I)$]	0.0526
wR_2 [$I > 2\sigma(I)$]	0.0921
(*D* map) maximum/minimum (e Å^{-3})	−1.866/1.745

4. Result and discussion

4.1. Synthesis

The benzotetrathiafulvalenedithiolene was prepared similar to the literature method [9]. The synthetic procedure is shown in Scheme 1. Cyanoethyl was used as the protecting group in the cross-coupling reaction to synthesize the unsymmetrical TTF derivative. By silica gel column chromatography, using CH_2Cl_2 as eluent, 2, 3-bis(2-cyanoethylthio)-5,6-benzotetrathiafulvalene was obtained in high yield (56%). Under nitrogen atmosphere, the cyanoethyl group was removed by using Me_4NOH as the base in THF at −5 °C, which generated the dithiolate. Then the dithiolate ligand reacted further

with mercury(II) ions and resulted the isolation of the metal complex. The analytically pure neutral complex **5** was obtained by slow diffusion of iodine vapor into a DMF solution of complex **4** under nitrogen. The yielded microcrystalline powder sample of complex **5** is insoluble in common solvents.

4.2. Crystal structure of *4*

There are one and half molecules of complex **4** in each asymmetric unit. The atom labeling scheme of one anion part of the solvated complex, $(Me_4N)_2[Hg(btdt)_2]\cdot 4/3H_2O\cdot 2/3C_4H_9O$, is shown in Fig. 1. The selected bond lengths and angles are listed in Table 2. The mercury atom is in an approximately tetrahedral geometry. The dihedral angle between the planes [S1, S2, S3, S4, C10, C11] and [S7, S8, S9, S10, C20 C21] is 90.3°. In the five-membered ring containing the mercury atom, the average Hg–S and C=C bond lengths are 2.532(2) and 1.352(9) Å, respectively. The S–C bond distance of the dithiolate are 1.732(6)–1.755(6) Å, which are somewhat shorter than the S–C bond distance of the two TTF units (1.745(7)–1.780(7) Å). The bond angles of S(1)–Hg–S(2) and S(7)–Hg–S(8) are 89.02(5)° and 88.74(5)°, respectively, which are smaller than the idealized tetrahedral value. The dihedral angle between the planes [S7, S8, S9, S10, C20. C21, C22] and [S11, S12, C23–C29] is 132.1°, and the angle between the planes [S1, S2, S3, S4, C10, C11, C12] and [S5, S6, C13–C19] is 132.8°. The two TTF units in complex deviate from planarity due to the non-planar coordination of the central atom Hg and the packing effects of intermolecular adjacent TTF units. The packing diagram for complex **4** is shown in Fig. 2, the short intermolecular S···S distances in crystal are 3.868 Å ($S(5)\cdots S(12)^a$, symmetry operations: $x, 1-y, 1.5+z$), 3.949 Å ($S(3)\cdots S(12)^a$) and 3.956 Å ($S(5)\cdots S(10)^a$), which are somewhat shorter than that of the similar mercury complex with an extended TTF ligand [3].

Table 2
Selected bond lengths (Å) and angles (°) for complex **4**

Bond lengths			
Hg(1)–S(1)	2.497(2)	Hg(1)–S(2)	2.563(2)
Hg(1)–S(7)	2.553(1)	Hg(1)–S(8)	2.517(1)
S(1)–C(10)	1.755(6)	S(2)–C(11)	1.732(6)
S(3)–C(10)	1.767(6)	S(3)–C(12)	1.745(7)
S(4)–C(12)	1.748(7)	S(4)–C(11)	1.749(6)
S(5)–C(14)	1.780(7)	S(5)–C(13)	1.752(7)
S(6)–C(15)	1.754(8)	S(6)–C(13)	1.750(7)
S(7)–C(21)	1.745(7)	S(8)–C(20)	1.733(7)
S(9)–C(21)	1.750(6)	S(9)–C(22)	1.757(7)
S(10)–C(20)	1.774(6)	S(10)–C(22)	1.747(7)
S(11)–C(25)	1.730(7)	S(11)–C(23)	1.745(7)
S(12)–C(23)	1.770(7)	S(12)–C(24)	1.740(8)
C(10)–C(11)	1.353(9)	C(20)–C(21)	1.352(9)
C(12)–C(13)	1.352(8)	C(22)–C(23)	1.338(9)
C(14)–C(15)	1.377(10)	C(24)–C(25)	1.405(10)
C(15)–C(16)	1.387(10)	C(14)–C(19)	1.387(10)
C(25)–C(26)	1.438(10)	C(24)–C(29)	1.380(10)
Bond angles			
S(1)–Hg(1)–S(2)	88.98(5)	S(7)–Hg(1)–S(8)	88.71(5)
S(1)–Hg(1)–S(8)	130.64(5)	S(2)–Hg(1)–S(7)	113.01(5)
S(2)–Hg(1)–S(8)	117.68(6)	S(1)–Hg(1)–S(7)	119.81(6)
Hg(1)–S(1)–C(10)	97.2(2)	Hg(1)–S(8)–C(20)	96.9(2)
Hg(1)–S(7)–C(21)	96.3(2)	Hg(1)–S(2)–C(11)	95.9(2)
S(1)–C(10)–C(11)	128.4(5)	S(2)–C(11)–C(10)	129.5(5)
S(1)–C(10)–S(3)	114.1(4)	S(2)–C(11)–S(4)	114.7(4)
S(8)–C(20)–C(21)	129.7(5)	S(7)–C(21)–C(20)	128.4(5)
S(7)–C(21)–S(9)	114.0(4)	S(8)–C(20)–S(10)	114.6(4)
S(3)–C(12)–S(4)	113.3(3)	S(9)–C(22)–S(10)	113.3(3)
$S(5)\cdots S(10)^a$	3.956(3)	$S(3)\cdots S(12)^a$	3.949(3)
$S(5)\cdots S(12)^a$	3.868(3)		

Symmetry operations a: $x, 1-y, 1.5+z$.

4.3. Cyclic voltammetry

Cyclic voltammetry of the ligand **3** and complex **4** were carried out on a Macroscopic platinum-disc electrode in DMF solution, and the reference electrode was Ag/AgCl (using 0.1 mol dm^{-3} $(Bu_4N)ClO_4$ as supporting electrolyte, 100 mV S^{-1}). The ligand **3** shows a single electron oxidation peak at 0.8 V. Similar to the mercury complex with TTF ligand [3], a single oxidation peak at 0.48 V was observed for complex **4**, indicating that the two TTF units in complex **4** were completely absent of interaction and independently oxidized to remove one electron with equal potential in DMF solvent. This is the reason that the monoanionic species of **4** is difficult to isolate.

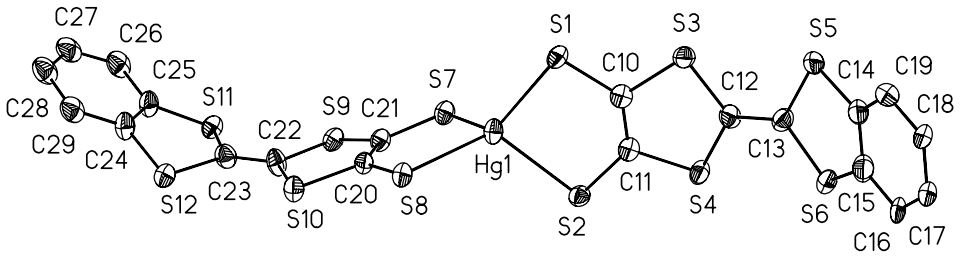


Fig. 1. An ORTEP drawing of the dianion $[Hg(btdt)_2]^{2-}$ showing the atom labelling. The counter ions and hydrogen atoms have been omitted for clarity.

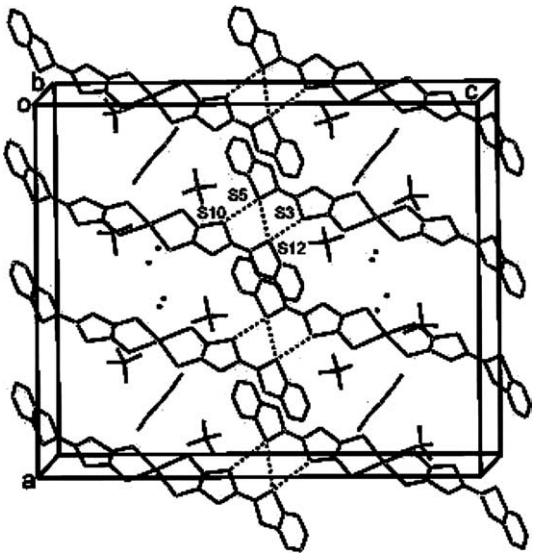


Fig. 2. Packing diagram for complex $[Hg(btdt)_2]^{2-}$ showing the arrangement of the anion and the short intermolecular S···S contacts.

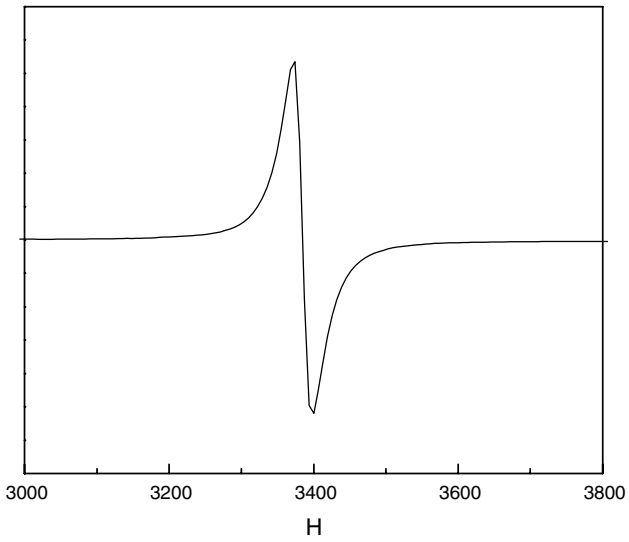


Fig. 3. ESR spectrum of complex $Hg(btdt)_2$ (**5**) at 110 K.

4.4. ESR spectra

The ESR spectrum of the neutral complex **5** was measured in the solid state at 110 K. Complex **5** contained a singlet with a g value of 2.003 (Fig. 3). There is little conjugation interaction between the two linked TTF dithiolate units in this molecule since complex **5** has approximately tetrahedral coordination around the Hg atom, as shown in structural analyses. Each extended TTF dithiolate unit has an independent single electron radical, which accounts for the singlet observed in the ESR spectrum. The result is in accord with other neutral mercury complexes with a TTF-based ligand [3].

4.5. Magnetic properties

Magnetic susceptibility measurements for complex **5** were performed on a Quantum Design MPMS-XL7 SQUID magnetometer at temperatures ranging from 1.8 to 300 K. For complex **5**, at the room temperature, $\chi_M T$ is 0.042 emu K mol^{-1}, much smaller than the value (0.75) of two electrons radicals in a molecule sheet. As the temperature is lowered, the $\chi_M T$ value decreases al-

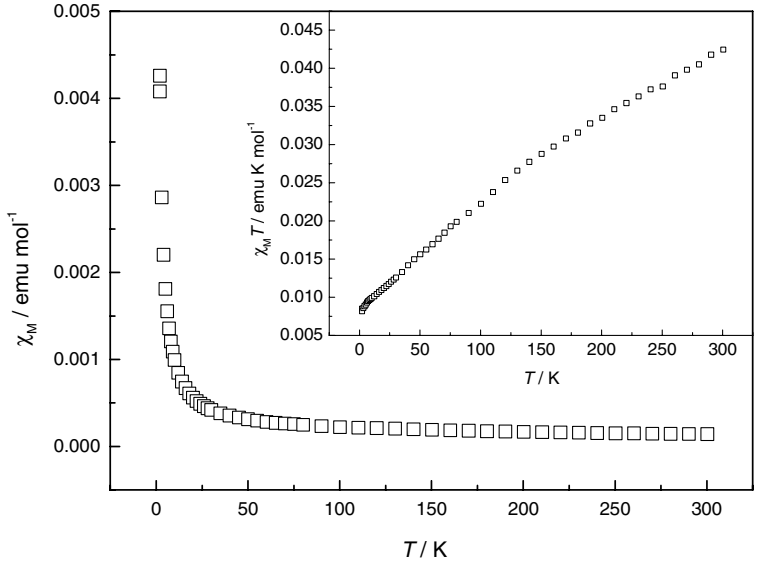


Fig. 4. Temperature dependence of the χ_M and $\chi_M T$ (inset) for complex $Hg(btdt)_2$ (**5**).

most linearly to reach 0.008 emu K mol^{-1} at 2 K (Fig. 4), implying that an antiferromagnetic interaction dominates the magnetic properties of this complex over the whole temperature range. Since the absence of a conjugation interaction between the two TTF dithiolate groups of the intramolecule, due to the tetrahedral coordination around the central Hg atom, each TTF dithiolate group is viewed as an independent radical cation. This was confirmed by the ESR spectrum of complex **5** which contained a singlet with a g value of 2.003. Thus, the intramolecular spin coupling between the radicals is not the source leading to the strong antiferromagnetic properties of complex **5**. It is suggested that the strong antiferromagnetic coupling results from intermolecular exchange, since the spin widely delocalizes in the individual TTF-dithiolate group and further leads to the effective intermolecular interaction. It is consistent with the ESR result exhibiting no coupling radical cation in the molecule. Using the mean-field expression of the Curie–Weiss temperature $\theta = 2zj'S(S+1)/3k_B$ [17], the magnetic interaction $zj'k_B$ between the radicals can be estimated to be ca. -465.3 K (-322.9 cm^{-1}) with $S = 1/2$, which supports the results mentioned above.

4.6. Electrical conductivities

The electrical conductivities of neutral complex **5** were measured as compressed pellets over the range 80–293 K (Fig. 5), the room temperature conductivity is 0.0015 S cm^{-1} and the activation energy is 0.24 eV. Since the Hg atom is in an approximately tetrahedral environment, with two non-planar coordinating dithiolate ligands, only a very weak conjugation interaction between the two extended TTF dithiolate units exists in complex which together with the molecule's non-compact packing lead to lower conductivity. From room temperature to 125 K, the change in the value of resistivity (ρ) is very small. Below 125 K the value of ρ increases rapidly on lowering the temperature, indicating that complex **5** is a semiconductor.

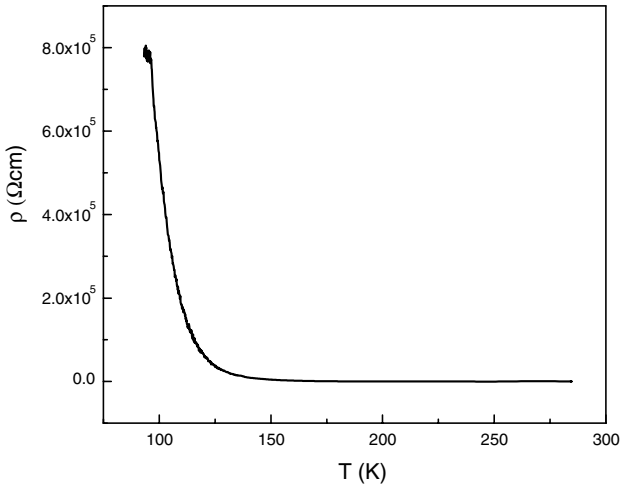


Fig. 5. Temperature dependence of the electrical resistivity of $Hg(btdt)_2$ (**5**).

The work on the nickel analogs of this new tetrathiafulvalene 4,5-dithiolate ligand, and experiments aimed at highly conducting metal complexes and multi-functional materials are current under way in our laboratory.

Acknowledgments

This work was supported by The Major State Basic Research Development Program (G2000077500), the National Natural Science Foundation of China (NSF20201006 and 90101028), the Petroleum Research Fund of the American Chemical Society (PRF 38794-G3). The X-ray diffractometer is supported by NSF Grant EAR-0003201.

Appendix A. Supplementary data

CCDC- 244536 contains the supplementary crystallographic data for this paper. These data can be obtained free of charge at www.ccdc.cam.ac.uk/conts/retrieving.html or from the Cambridge Crystallographic Data Centre, 12 Union Road, Cambridge CB2 1EZ, UK [Fax: (internat.) +44-1223/336-033; e-mail: deposit @ccdc.cam.ac.uk]. Supplementary data associated with this article can be found, in the online version at doi:10.1016/j.poly.2005.01.015.

References

[1] N. Robertson, L. Cronin, Coord. Chem. Rev. 227 (2002) 93.
[2] N.L. Narvor, N. Robertson, T. Weyland, J.D. Kilburn, A.E. Underhill, M. Webster, N. Svenstrup, J. Becher, Chem. Commun. (1996) 1363.
[3] N.L. Narvor, N. Robertson, E. Wallace, J.D. Kilburn, A.E. Underhill, P.N. Bartlett, M. Webster, J. Chem. Soc., Dalton Trans. (1996) 823.
[4] H. Tanaka, Y. Okano, H. Kobayashi, W. Suzuki, A. Kobayashi, Science 291 (2001) 285.
[5] H. Tanaka, H. Kobayashi, A. Kobayashi, J. Am. Chem. Soc. 124 (2002) 10002.
[6] W. Suzuki, E. Fujiwara, A. Kobayashi, Y. Fujishiro, E. Nishibori, M. Takata, M. Sakata, H. Fujiwara, H. Kobayashi, J. Am. Chem. Soc. 125 (2003) 1486.
[7] M. Sasa, E. Fujiwara, A. Kobayashi, S. Ishibashi, K. Terakura, Y. Okano, H. Fujiwara, H. Kobayashi, J. Mater. Chem. 15 (2005) 155.
[8] A. Kobayashi, H. Tanaka, M. Kumasaki, H. Torii, B. Narymbetov, T. Adachi, J. Am. Chem. Soc. 121 (1999) 10763.
[9] M. Kumasaki, H. Tanaka, A. Kobayashi, J. Mater. Chem. 8 (1998) 301.

[10] T. Nakazono, M. Nakano, H. Tamura, G. Matsubayashi, J. Mater. Chem. 9 (1999) 2413.
[11] K. Ueda, Y. Kamata, M. Iwamatsu, T. Sugimoto, H. Fujita, J. Mater. Chem. 9 (1999) 2979.
[12] A. Kobayashi, H. Tanaka, H. Kobayashi, J. Mater. Chem. 11 (2001) 2078.
[13] K. Ueda, M. Goto, M. Iwamatsu, T. Sugimoto, S. Endo, N. Toyota, K. Yamamoto, H. Fujita, J. Mater. Chem. 8 (1998) 2195.
[14] M. Nakano, A. Kuroda, G.. Matsubayashi, Inorg. Chim. Acta 254 (1997) 189.
[15] J. Nakayama, E. Seki, M. Hoshino, J. Chem. Soc. Perkin Trans. (1978) 468.
[16] J. Nakayama, H. Sugiura, M. Hoshino, Tetrahed. Lett. 24 (1983) 2585.
[17] M. Ebangelisti, J. Bartolome, L.J. de Jongf, G. Filoti, Phys. Rev. B 66 (2002) 144410.

Available online at www.sciencedirect.com
SCIENCE DIRECT®
Polyhedron 24 (2005) 679–684
POLYHEDRON
www.elsevier.com/locate/poly

Studies on cobalt(II), nickel(II) and copper(II) derivatives of some new *meso*-aryl substituted octabromoporphyrins

Regimol G. George, M. Padmanabhan *

School of Chemical Sciences, Mahatma Gandhi University, Priyadarshini Hills, Kottayam 686560, Kerala, India

Received 13 November 2003; accepted 24 January 2005

Abstract

A series of Co(II), Ni(II) and Cu(II) derivatives of a variety of porphyrins with tolyl (H_2TxTP) and naphthyl (H_2NxTP) moieties as *meso*-substituents are synthesised and characterised. H_2TxTP has the tolyl functions bonded to *meso*-carbons at the *o*-, *m*- or *p*-positions of the tolyl moieties while H_2NxTP has naphthyl groups bonded through their α- or β-positions. Their octabromo derivatives (MTxOBP and MNxOBP) were also synthesised by electrophilic substitution at the β-pyrrole positions. Optical spectra showed that the Q bands remain almost unaltered for both tolyl and naphthyl derivatives of the nonbrominated porphyrins while the B bands of their naphthyl derivatives are seen to be more red-shifted than their tolyl analogues. Even though a similar trend based on the *meso*-substituents is observed among all MTxOBP and MNxOBP derivatives, a substantial red-shift is seen for all the bromoderivatives compared to their nonbrominated species MTxTP and MNxTP. The energy difference $\Delta\bar{\nu}$ associated with this red-shift of the Soret band is seen to be in the range 1700–2050 cm^{-1} for Co(II) and Ni(II) derivatives, the naphthyl derivatives always having higher values. Energy level reordering due to electron-withdrawing Br-substituents, distortion bringing about non-planarity in the π-framework resulting in HOMO–LUMO level changes and the mesomeric effect due to *meso*-aryl moieties can be considered to be the reasons for the observed spectral changes. The EPR spectra of the Cu(II) derivatives of bromoporphyrins have lower $A_{\parallel}^{Cu}$ and $A_{\perp}^{Cu}$ hyperfine values compared to their nonbrominated analogues, indicating enhanced delocalisation of electron spin to the octabromoporphyrinato moiety. An enhanced Cu–N σ-covalency is seen in the Cu(II)–bromoporphyrins, as evident from their lower α^2 values.
© 2005 Elsevier Ltd. All rights reserved.

Keywords: Cu(II) porphyrins; Co(II) porphyrins; Ni(II) porphyrins; Octabromoporphyrins; Electronic properties; EPR studies; Tetratolylporphyrins; Tetranaphthylporphyrins

1. Introduction

Synthesis of varyingly substituted porphyrins and their metalloderivatives continues to be an active area of research owing to their wide applications as versatile catalysts, enzyme mimics, nonlinear optical materials and as candidates for photodynamic therapy [1–6]. The fact that there are twelve substitutional sites on the periphery and a highly tunable π framework which can act as an electron sink makes electronic and redox modulation of the porphyrin macrocycle an interesting and fruitful exercise leading to products of varying chemical, optical and photophysical properties [7–12]. We have been interested in developing electronically and structurally modified porphyrins, especially on solid polymer matrices, and have demonstrated their ability to carry out a few enzyme mimetic reactions efficiently [13–18]. Knowing the ability of Br substitution to bring

* Corresponding author. Tel.: +91 481 273 1036; fax: +91 481 273 1009.
E-mail address: padman_mgu@yahoo.co.in (M. Padmanabhan).

0277-5387/$ - see front matter © 2005 Elsevier Ltd. All rights reserved.
doi:10.1016/j.poly.2005.01.008

about interesting electronic, redox and structural modification of aryl porphyrins, we have synthesised and studied some of the interesting properties of a series of octabromoporphyrins and also their Fe(III) and Mn(III) derivatives [19–21]. The studies on such perbrominated porphyrins are of great relevance in the context of growing interest on nonplanar porphyrins which are generated either by substitution of the β-pyrrole positions by bulky/electron withdrawing substituents or by incorporating bulky groups at the *meso*-positions. Realising the biological significance of such distorted porphyrins is one of the major concerns of experimental and theoretical chemists alike with regard to tracing the origin of their red-shifts [22–25]. In this work we report the synthesis and characterisation of Co(II), Ni(II) and Cu(II) derivatives of some *meso*-tolyl and *meso*-naphthyl porphyrins and also their octabromo derivatives and discuss salient features of their spectral properties.

2. Experimental

Pyrrole (Fluka) was distilled over KOH pellets, under reduced pressure before use. The α-naphthaldehyde and β-naphthaldehyde (E. Merck) were used as such. All the solvents employed in the present study were of spectral grade and were distilled before use. Liquid bromine procured from Ranbaxy and basic alumina obtained from Acmes were used as received. The metal salts (E. Merck) were also used without further purification. The UV–Vis spectral measurements were carried out with a Shimadzu 160A UV–Vis spectrophotometer. Elemental analyses were done using a Perkin–Elmer CHN analyzer. The EPR Spectra were measured on a Varian E-109 X-band spectrometer with the micropower set at 5 mW and with a modulation frequency of 100 K. The solution of copper(II) porphyrins was made in a toluene–methanol mixture with a concentration ca. 10^{-4} M. The 'g' marker employed was TCNE radical.

2.1. Preparation

2.1.1. Free-base porphyrins H_2TxTP, H_2NxTP, H_2TxOBP and H_2NxOBP

The free-bases of tetratolyl (H_2TxTP) and tetranaphthyl porphyrins (H_2NxTP) including those reported earlier [19] were synthesised by Adler's method involving the condensation between pyrrole and the respective aldehydes in propionic acid medium [26]. Their brominated free-bases, tolyl (H_2TxOBP) and naphthyl porphyrins (H_2NxOBP), were prepared by brominating the Cu(II) derivatives of the respective porphyrins H_2TxTP and H_2NxTP, based on the reported procedure [19,27]. The yields of the bromoderivatives were in the range 75–80%.

2.1.2. Cobalt(II), nickel(II) and copper(II) complexes of H_2TxTP and H_2NxTP

The metallation of the nonbrominated porphyrins H_2TxTP and H_2NxTP was carried out by a known procedure. The free-base tolylporphyrins H_2TxTP (0.5 g, 0.74 mmol) or free-base naphthylporphyrins H_2NxTP (0.5 g, 0.61 mmol) were dissolved in a suitable solvent mixture ($CHCl_3$:CH_3OH, 40 mL, 1:1, v/v). To this, the metal carrier $CoCl_2 \cdot 6H_2O$ (1.6 g, 7 mmol), $Cu(CH_3COO)_2 \cdot 4H_2O$ (1.4 g, 7 mmol) or $NiCl_2 \cdot 6H_2O$ (1.7 g, 7 mmol) dissolved in glacial CH_3COOH (1.5 mL) was added for the synthesis of the respective metalloderivatives. NaOAc was employed as a base. On refluxing the reaction mixture on a water bath, the metallation gets initiated as evident from the UV–Vis spectral measurements. The metallation usually gets completed within 4 h for Co(II) derivatives, 6–8 h for Ni(II) derivatives and 2 h for Cu(II) derivatives. The reaction mixture was washed repeatedly with water to remove the unreacted metal salts and the metalloporphyrins formed were purified by column chromatography on basic alumina using $CHCl_3$ as eluent and were further purified by recrystallisation using hexane/$CHCl_3$ mixture. Metallation was confirmed by UV–Vis spectroscopy. Yields were in the range of 80–85% for Co(II), 70–75% for Ni(II) and 85–90% for Cu(II) complexes.

2.1.3. Cobalt(II), nickel(II) and copper(II) complexes of H_2TxOBP and H_2NxOBP

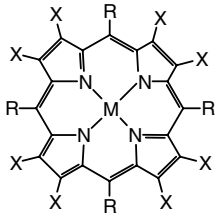
The metallation of all the bromoporphyrins could be carried out at room temperature. To a solution of the metal carrier of $CoCl_2 \cdot 6H_2O$ (2 g, 8.75 mmol), $NiCl_2 \cdot 6H_2O$ (2.12 g, 8.75 mmol) or $Cu(CH_3COO)_2 \cdot 4H_2O$ (1.75 g, 8.75 mmol) in $CHCl_3$:MeOH mixture (60 mL, 2:1, v/v) was added H_2TxOBP (0.60 g, 0.46 mmol) or H_2NxOBP (0.66 g, 0.46 mmol), 2 mL of glacial $MeCO_2H$ and 1 g of powdered NaOAc. The reaction mixture was stirred either at room temperature or on a water bath for about 1–2 h. The completion of the metallation reaction was monitored by electronic spectroscopy. The mixture was then taken in a separating funnel, washed repeatedly with water after which the organic phase was separated and dried over anhydrous Na_2SO_4. The compound was purified by column chromatography (basic Al_2O_3, $CHCl_3$ eluent) to obtain the metalloderivative and then by recrystallisation using hexane/$CHCl_3$ mixture (yield 95%).

3. Results and discussion

The free-base porphyrins, which are purified by careful column chromatography, are characterised by chemical analysis, electronic and ^1H NMR studies [19–21]. All the free-base porphyrins gave reasonably good ^1H NMR signals as reported by us earlier [19]. The effect

due to various aryl groups at the *meso*-positions and also due to the Br substitution at the eight β-pyrrole positions on the optical absorption, fluorescence emission and redox potential of the free-base porphyrins has been reported by us recently [19,20].

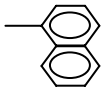
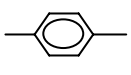
As mentioned in the preparatory section all the metalloporphyrins were purified by column chromatography. The compounds were characterised by electronic and EPR studies. The various Co(II), Ni(II) and Cu(II) derivatives of both the nonbrominated and brominated porphyrins prepared are summarised in Table 1, wherein the substituents indicated in (*1*) are specified.



(*1*)

It is seen that among the nonbrominated porphyrins, the naphthyl derivatives undergo easier metallation than the tolyl derivatives. This could be attributed to the possible distortional change brought about on the porphyrin ring in H_2NxTP by the bulkier *meso*-naphthyl groups as compared to the tolyl porphyrins. The metallation of all the bromoporphyrins are also found to be very facile as it could be carried out at room temperature. It is known that all perbrominated porphyrins tend to exist in a highly distorted form because of the presence of bulky Br atoms at the eight β-pyrrole positions [27,28]. Since the mechanism of metallation involved has been proposed to be following a "sitting atop mechanism," such a distortion also can be expected to facilitate metallation processes. Further, the electron withdrawing effect due to the eight Br-atoms at the β-pyrrole positions can be expected to help substantially the deprotonation step of the –NH protons, augmenting the metallation. Compared to cobalt(II) and nickel(II) derivatives, the copper(II) metalloporphyrins are seen to be easily formed.

Table 1
The Co(II), Ni(II) and Cu(II) derivatives of porphyrins developed in the study

R	X	M	Porphyrin	Analysis (%)[a]		
				C	H	N
	H	Co	CoNαTP	83.10(82.50)	4.19(4.12)	6.49(6.40)
	Br	Co	CoNαOBP	47.20(47.90)	1.90(1.86)	3.40(3.70)
	H	Ni	NiNαTP	82.76(82.60)	4.02(4.13)	6.32(6.42)
	Br	Ni	NiNαOBP	48.20(47.90)	1.74(1.86)	3.60(3.72)
	H	Cu	CuNαTP	82.18(82.14)	4.06(4.10)	6.36(6.38)
	Br	Cu	CuNαOBP	47.77(47.75)	1.82(1.85)	3.78(3.70)
	H	Co	CoNβTP	82.62(82.50)	4.24(4.12)	6.50(6.40)
	Br	Co	CoNβOBP	47.45(47.90)	1.84(1.86)	3.68(3.70)
	H	Ni	NiNβTP	82.71(82.60)	4.18(4.13)	6.38(6.42)
	Br	Ni	NiNβOBP	47.50(47.90)	1.99(1.86)	3.84(3.72)
	H	Cu	CuNβTP	82.20(82.14)	4.11(4.10)	6.30(6.38)
	Br	Cu	CuNβOBP	47.92(47.75)	1.77(1.85)	3.74(3.70)
	H	Co	CoToTP	79.32(79.20)	4.87(4.95)	7.63(7.70)
	Br	Co	CoToOBP	41.50(42.38)	2.12(2.06)	4.42(4.12)
	H	Ni	NiToTP	79.10(79.22)	5.06(4.95)	7.76(7.70)
	Br	Ni	NiToOBP	42.48(42.39)	2.01(2.06)	4.24(4.12)
	H	Cu	CuToTP	78.75(78.70)	4.86(4.91)	7.60(7.65)
	Br	Cu	CuToOBP	42.19(42.24)	2.10(2.05)	4.14(4.10)
	H	Co	CoTmTP	79.14(79.20)	4.92(4.95)	7.80(7.70)
	Br	Co	CoTmOBP	41.85(42.38)	2.18(2.06)	4.24(4.12)
	H	Ni	NiTmTP	79.26(79.22)	4.98(4.95)	7.74(7.70)
	Br	Ni	NiTmOBP	42.40(42.39)	2.03(2.06)	4.04(4.12)
	H	Cu	CuTmTP	78.62(78.70)	4.96(4.91)	7.64(7.65)
	Br	Cu	CuTmOBP	42.31(42.24)	2.08(2.05)	4.13(4.10)
	H	Co	CoTpTP	79.32(79.20)	4.87(4.95)	7.63(7.70)
	Br	Co	CoTpOBP	42.01(42.38)	2.36(2.06)	4.10(4.12)
	H	Ni	NiTpTP	79.07(79.22)	5.05(4.95)	7.78(7.70)
	Br	Ni	NiTpOBP	42.33(42.39)	2.12(2.06)	4.26(4.12)
	H	Cu	CuTpTP	78.79(78.70)	4.76(4.91)	7.69(7.65)
	Br	Cu	CuTpOBP	42.04(42.24)	2.17(2.05)	4.13(4.10)

[a] Calculated values are given in parentheses.

3.1. Electronic spectra

The electronic spectra of the metal complexes were recorded in $CHCl_3$ at 298 K. The data are presented in Table 2. Some of the salient features associated with the electronic spectra are given below.

The Co(II), Ni(II) and Cu(II) porphyrins of the nonbrominated forms of the tetratolyl and tetranaphthyl porphyrins show characteristic absorption peaks of typical *meso*-aryl derivatives. We see that the B band of the naphthyl derivatives in all their metalloderivatives have absorptions at higher wavelength compared to their tolyl derivatives. However, we do not observe any perceptible difference in the absorption maxima for both B and Q bands among the various tolyl derivatives and also within the naphthyl species.

The cobalt(II) complexes of the brominated porphyrins manifest significant changes compared to their nonbrominated species. Both B and Q bands for the complexes are seen to be red-shifted compared to their nonbrominated derivatives. The red-shift $\Delta\bar{\nu}$ was calculated as the energy difference of the Soret band in wavenumbers between the complexes of brominated and nonbrominated porphyrins. The energy difference $\Delta\bar{\nu}$ for them is seen to be in the range 1915–2130 cm^{-1}, the naphthyl species having larger differences than the tolyl derivatives. As in the case of cobalt(II) derivatives, the nickel(II) species of all the brominated porphyrins also show red-shifted B and Q bands, which is evident from Table 2. The $\Delta\bar{\nu}$ for the B band for these complexes was found to be between 1770 and 1940 cm^{-1} which is comparatively lower than that for their Co(II) derivatives.

In the case of Cu(II) bromoporphyrins, the expected red-shifts are also seen for both B and Q bands, but the significant feature, however, is the appearance of two overlapping peaks centered ca. 445 and 470 nm for the B band of the Cu(II) complexes of brominated porphyrins compared to their nonbrominated species. This phenomenon is not manifested by their analogous Ni(II) and Co(II) derivatives. In all the three metal derivatives, $\Delta\bar{\nu}$ is seen to be the lowest for the *ortho*-tolyl porphyrins and the highest for their naphthyl derivatives. The underlying factors involved in the above spectral features could be summarised as below.

The fact that the naphthyl porphyrins have a greater red-shifted Soret band as compared to the tolyl derivatives in all their Co(II), Cu(II) and Ni(II) complexes

Table 2
Electronic spectral data of Co(II), Ni(II) and Cu(II) derivatives of brominated and nonbrominated porphyrins in $CHCl_3$ at 298 K

Porphyrin	B band (nm) ($\varepsilon \times 10^{-4}$)[a]	Q band (nm) ($\varepsilon \times 10^{-4}$)[a]	$\Delta\bar{\nu}$ (cm^{-1})[b]
CoToTP	409(19.95)	528(2.69)	
CoTmTP	412(21.38)	530(2.81)	
CoTpTP	412(20.89)	530(2.81)	
CoNαTP	414(20.42)	530(2.63)	
CoNβTP	416(20.89)	531(2.75)	
CuToTP	414(23.99)	537(2.39)	
CuTmTP	415(24.55)	538(2.51)	
CuTpTP	414(25.12)	540(2.51)	
CuNαTP	419(23.44)	541(2.39)	
CuNβTP	420(24.55)	542(2.34)	
NiToTP	415(16.22)	527(1.99)	
NiTmTP	416(16.98)	528(2.04)	
NiTpTP	417(17.38)	530(2.08)	
NiNαTP	419(16.60)	528(2.06)	
NiNβTP	420(16.98)	531(2.08)	
CoToOBP	445(16.60)	560(1.28)	1918
CoTmOBP	448(16.98)	562(1.35)	1950
CoTpOBP	450(17.38)	564(1.35)	2050
CoNαOBP	454(16.98)	565(1.31)	2128
CoNβOBP	454(16.98)	566(1.35)	2012
CuToOBP	446(13.18), 462(sh)	579(1.73) 624(sh)	1620, 2510
CuTmOBP	445(sh), 468(13.49)	581(1.77) 625(sh)	1725, 2729
CuTpOBP	448(sh), 469(13.80)	582(1.86) 628(sh)	1833, 2833
CuNαOBP	458(sh), 473(13.49)	583(1.82) 627(sh)	2032, 2725
CuNβOBP	467(13.50) (broad)	580(1.77) 627(sh)	2340
NiToOBP	448(24.55)	560(1.90)	1770
NiTmOBP	451(25.70)	561(1.95)	1920
NiTpOBP	451(26.30)	561(1.95)	1810
NiNαOBP	456(25.12)	563(1.99)	1940
NiNβOBP	455(26.30)	563(1.95)	1800

[a] Molar extinction coefficient ε in $10^{-4}/dm^3\ mol^{-1}\ cm^{-1}$.
[b] $\Delta\bar{\nu} = \bar{\nu}_2 - \bar{\nu}_1$, where $\bar{\nu}_1$ is the energy of the B band for brominated porphyrin and $\bar{\nu}_2$ that for the corresponding nonbrominated porphyrin.

for both brominated and nonbrominated forms could be attributed to the higher mesomeric participation of the naphthyl moieties with the macrocyclic π-framework by adjusting the porphyrin-aryl dihedral angle. Because of a less extended π-system, the tolyl groups will have lesser conjugative participation with the porphyrin π-framework than their naphthyl analogues. The fact that all the metalloderivatives of *o*-tolyl porphyrins in their brominated and nonbrominated forms have their B and Q bands absorbing at lower wavelength could be attributed to the inability of the *o*-tolyl groups to tilt in order to reduce the dihedral angle for better conjugative interaction because of higher steric strain caused by $-CH_3$ groups at the *ortho*-position of the *meso*-tolyl moieties.

The pronounced red-shift observed for the Co(II), Ni(II) and Cu(II) derivatives of all the brominated porphyrins compared to their nonbrominated derivatives can be explained in terms of the electronic change caused by the electron-withdrawing Br-groups coupled with distortion of the porphyrin framework brought about by the bulky Br-atoms at the eight pyrrole β-positions [19,27,28]. The trend in the red-shift of B band observed for tolyl and naphthyl derivatives of the Br-substituted porphyrins is similar for their Co(II), Ni(II) and Cu(II) complexes and could be explained by considering the various factors which influence the energies of both the HOMO and LUMOs of the metalloporphyrins. It is evident that the eight Br substituents at the β-pyrrole positions would drain out electron density from the porphyrin – framework making the macrocycle more susceptible to reduction [19,27]. The concerted action by the electronegative Br atoms would also make the system resistant to oxidation. These would result in lowering of both LUMOs and the HOMO levels. One of the major factors for the red-shift of the porphyrins (in both B and Q) is essentially this electronic effect. Coupled with this electronic modulation there is also a significant effect due to a steric factor. The bulky Br-atoms at the eight pyrrole β-positions would bring about major structural distortion within the porphyrin framework to ease steric strain. Such a distortion would cause a significant perturbation in conjugation, the effect of which would be significant alteration of π-energy levels including destabilisation of the HOMO and some lowering of the LUMOs. INDO level calculation has testified such a reordering in the energy levels of the frontier orbitals on distortion [29]. Because of the lowered symmetry the degenerate e_g^* orbitals (LUMOs) can be expected to be split, lowering the energy of one component. A substantial reduction in the HOMO–LUMO gap is, therefore, expected because of such a geometry variation. The major red-shift observed on bromination can be attributed essentially to these factors.

It is known that while Co(II) and Ni(II) porphyrins show affinity to Lewis-bases and ligating solvents and coordinate them at the axial positions of the metal centre, while Cu(II) porphyrins exhibit no such tendency and remain unligated. We have verified this with Lewis-bases like pyridine and imidazole for all the MTxTP and MNxTP of nonbrominated porphyrins. We were, however, interested in knowing whether Cu(II) derivatives of bromoporphyrins would have any affinity towards Lewis-bases because of the strong electron accepting ability of the bromoporphyrinato framework (compared to the nonbrominated porphyrins). While Co(II) and Ni(II) derivatives of the bromoporphyrins were found to show enhanced affinity towards Lewis-bases, their Cu(II) derivatives were still resistant to any adduct formation, as evident from practically no change seen in the electronic spectra even in an excess of base.

3.2. EPR spectra

The EPR spectra of all the Cu(II) porphyrins were measured at the X-band frequency to understand both the electronic and bonding features between the paramagnetic Cu(II) and the porphyrinato moiety. The spectra were recorded in a toluene–methanol mixture at liquid nitrogen temperature. While two hyperfine peaks of the parallel components of the anisotropic spectra are clearly discernible in the low field, the other two are seen overlapped in the perpendicular component. The spin

Table 3
EPR spin-Hamiltonian parameters of copper(II) derivatives of brominated and nonbrominated porphyrins

Porphyrin	$g_\parallel$	$g_\perp$	$A_\parallel^{Cu}$ (mT)	$A_\parallel^{N}$ (mT)	$A_\perp^{Cu}$ (mT)	$A_\perp^{N}$ (mT)	α^2
CuToTP	2.21	2.07	20.3	1.5	3.3	1.47	0.564
CuTmTP	2.21	2.07	20.0	1.5	3.3	1.48	0.555
CuTpTP	2.20	2.07	19.8	1.5	3.0	1.48	0.550
CuNαTP	2.20	2.07	20.0	1.5	3.5	1.47	0.555
CuNβTP	2.21	2.07	20.0	1.5	3.3	1.48	0.555
CuToOBP	2.21	2.05	19.1	n.r[a]	3.1	1.50	0.532
CuTmOBP	2.22	2.06	19.0	n.r[a]	3.0	1.51	0.528
CuTpOBP	2.20	2.07	19.3	n.r[a]	3.0	1.52	0.535
CuNαOBP	2.22	2.05	19.1	n.r[a]	3.1	1.51	0.535
CuNβOBP	2.21	2.05	19.1	n.r[a]	3.1	1.51	0.532

[a] Not resolvable.

Hamiltonian parameters for the copper(II) compounds were extracted from the spectra by a known procedure [30], by considering the axial symmetry of the metalloporphyrins. The value of α^2 (σ-covalency factor) was also evaluated from the EPR parameters using the Kivelson and Neiman equation [31], $\alpha^2 = (A^{\parallel}/P + (g_{\parallel} - 2.0023) + 3/7(g_{\perp} - 2.0023) + 0.04)$, where P is the spin–orbit coupling factor. It is known that metalloporphyrins are sensitive to the molecular environment around them. This has been well demonstrated by the difference in electronic spectra observed for these complexes. The EPR data also yield similar results, as exemplified by the variations in the spin Hamiltonian parameters for Cu(II) in different molecular environments. The various parameters evaluated for the Cu(II)-porphyrins are presented in Table 3.

The $g_{\parallel}$ and $g_{\perp}$ values, along with other parameters, are in conformity with a square planar geometry for all the brominated and nonbrominated copper(II) porphyrins studied [32,33]. The nature of the *meso*-aryl substituents is not seen to be affecting these parameters significantly. However, the hyperfine constants $A_{\parallel}^{Cu}$ and $A_{\perp}^{Cu}$ are found to be altered considerably in copper(II) bromoporphyrins compared to their nonbrominated porphyrins. All the brominated porphyrins have $A_{\parallel}^{Cu}$ around 19 mT which is less than their nonbrominated porphyrins ($A_{\parallel}^{Cu}$ ca. 20 mT). Similarly the $A_{\perp}^{Cu}$ are found to be lowered from ca. 3.5 mT to ca. 3 mT on bromination. The lower Cu-hyperfine values seen for the copper(II) bromoporphyrins can be understood from the fact that the porphyrinato moiety, being depleted in electron density by the eight peripheral Br atoms, would withdraw electron density from the metal $d_{x^2-y^2}$ orbital thus delocalising the free electron significantly onto the ligand moiety compared to the Cu(II)-nonbrominated porphyrins. The higher Cu-hyperfine constants found for the metal derivatives of nonbrominated porphyrins implies more delocalisation of the unpaired Cu electron.

The α^2 value evaluated from the spin Hamiltonian parameters represents the bonding coefficient of the b_1 molecular orbital (which is a linear combination of metal $d_{x^2-y^2}$ and four in plane sp^2 hybridised orbitals of the porphyrinato moiety, one on each of the N atoms) and gives a qualitative idea about the measure of σ-covalency of the Cu–N bond. The stronger the in-plane σ-bond interaction between Cu^{2+} and N's, the higher is the energy of the b_1 molecular orbital because of its antibonding character. The α^2 values evaluated for all the Cu(II)-nonbrominated porphyrins are in the range 0.555–0.564, showing that the *meso*-substituents have little influence on the nature of the M–N covalent bonding. However, in the case of the brominated species, the α^2 values are lowered to 0.528 indicating more σ-covalency between copper and nitrogen facilitated by the electron-withdrawing Br substituents, which are in direct interaction with the porphyrin π-system.

References

[1] R.E. White, M.J. Coon, Annu. Rev. Biochem. 49 (1980) 315.
[2] T.G. Traylor, S. Tsuchiya, Inorg. Chem. 26 (1987) 1338.
[3] P.E. Ellis, J.E. Lyons, Coord. Chem. Rev. 105 (1990) 181.
[4] G.B. James, F.S. Molinaro, J.A. Ibers, J.P. Collman, J.I. Brauman, E. Rose, K.S. Suslick, J. Am. Chem. Soc. 102 (1980) 3224.
[5] H.L. Anderson, Chem. Commun. (1999) 2323.
[6] T.J. Dougherty, Photochem. Photobiol. 45 (1987) 879.
[7] J.B. Kim, J.J. Leonard, F.R. Longo, J. Am. Chem. Soc. 94 (1972) 3986.
[8] P.S. Traylor, D. Dolphin, T.G. Traylor, J. Chem. Soc., Chem. Commun. (1984) 279.
[9] M. Gouterman, R.J. Hall, G.–E. Khalil, P.C. Martin, E.G. Shankland, R.L. Cerny, J. Am. Chem. Soc. 111 (1972) 3702.
[10] H.J. Callot, Tetrahedron Lett. (1973) 4987.
[11] R. Bonnett, G.F. Stephenson, J. Org. Chem. 30 (1965) 2791.
[12] L. Gong, D. Dolphin, Can. J. Chem. 63 (1985) 401.
[13] M.V. Vinodu, M. Padmanabhan, J. Porphy. Phthalo. 5 (2001) 763.
[14] M.V. Vinodu, M. Padmanabhan Sci, J. Polym. Part A, Polym. Chem. 39 (2001) 326.
[15] T. Mathew, S. Kuriakose, M. Padmanabhan, J. Appl. Polym. Sci. 59 (1996) 23.
[16] M.V. Vinodu, M. Padmanabhan, J. Appl. Polym. Sci. 89 (2003) 3925.
[17] M.V. Vinodu, M. Padmanabhan, Proc. Indian Acad. Sci. (Chem. Sci.) 113 (2001) 1.
[18] M.V. Vinodu, M. Padmanabhan, Proc. Indian Acad. Sci. (Chem. Sci.) 110 (1998) 461.
[19] R.G. George, M. Padmanabhan, Polyhedron 22 (2003) 3145.
[20] R.G. George, M. Padmanabhan, Proc. Indian Acad. Sci. (Chem. Sci.) 115 (2003) 263.
[21] R.G. George, M. Padmanabhan, Trans. Metal Chem. 28 (2003) 858.
[22] A.K. Wertsching, A.S. Koch, S.G. Dimagno, J. Am. Chem. Soc. 123 (2001) 3932.
[23] E.K. Woller, S.G. DiMagno, J. Org. Chem. 62 (1997) 1588.
[24] H. Ryeng, A. Ghosh, J. Am. Chem. Soc. 124 (2002) 8099.
[25] C.J. Medforth, M.O. Senge, K.M. Smith, L.D. Sparks, J.A. Shelnutt, J. Am. Chem. Soc. 114 (1992) 9859.
[26] A.D. Adler, F.R. Longo, J.D. Finarelli, J. Goldmacher, J. Assour, L. Korsakoff, J. Org. Chem. 32 (1967) 476.
[27] P. Bhyrappa, V. Krishnan, Inorg. Chem. 30 (1991) 239.
[28] D. Mandon, P. Ochsenbein, J. Fischer, R. Weiss, K. Jayaraj, R.N. Austin, A. Gold, P.S. White, O. Briguad, P. Battioni, D. Mansuy, Inorg. Chem. 31 (1992) 2044.
[29] K.M. Barkigia, M.D. Berber, J. Fajer, C.J. Medforth, M.W. Renner, K.M. Smith, J. Am. Chem. Soc. 112 (1990) 8851.
[30] P.W. Lau, W.C. Lin, J. Inorg. Nucl. Chem. 37 (1975) 2389.
[31] D. Kivelson, R. Neiman, J. Chem. Phys. 35 (1961) 149.
[32] J. Fajer, M.S. Davis, in: D. Dolphin (Ed.), The Porphyrins, vol. 4, Academic Press, New York, 1979, p. 197.
[33] P.T. Manoharan, M.T. Rogers, in: T.F. Yen (Ed.), ESR of Transition Metal Chelates, Plenum Press, New York, 1969, p. 143.

Available online at www.sciencedirect.com
SCIENCE DIRECT®
Polyhedron 24 (2005) 685–691
POLYHEDRON
www.elsevier.com/locate/poly

In situ infrared and EXAFS studies of an Ag cluster in zeolite X

Yushi Suzuki *,[a], Naoyuki Matsumoto [a], Takeshi Ainai [b], Takafumi Miyanaga [a,*], Hideoki Hoshino [b]

[a] *Department of Materials Science and Technology, Faculty of Science and Technology, Hirosaki University, 3 Bunkyo-cho, Hirosaki 036-8561, Japan*
[b] *Faculty of Education, Hirosaki University, 1 Bunkyo-cho, Hirosaki 036-8560, Japan*

Received 12 November 2004; accepted 25 January 2005

Abstract

The in situ measurements of infrared spectra and the Ag K-edge EXAFS spectra of the fully Ag^+ exchanged zeolite X (Ag_{86}–X) were carried out from room temperature to 300 °C under vacuum. By evacuation at room temperature the O–H stretch vibration (ν(O–H)) mode around 3 μm disappears and the coordination number of oxygen around Ag, N_{Ag-O}, decreases due to removal of water molecules. The T–O asymmetric stretch (ν_{as}(T–O)) mode associated with zeolite framework oxygen appears around 10 μm. These infrared spectra are fitted by summing up Gaussian peaks. The positions of the main two peaks are 1000 and 1100 cm^{-1} at room temperature. At 100 °C, a third infrared peak appears at around 955 cm^{-1}, the total N_{Ag-O} becomes small and the coordination number of Ag around Ag, N_{Ag-Ag}, is 0.5. These results suggest that Ag atoms change sites in the zeolite and play an important role as a precursor of the Ag clusters. At 300 °C, the peaks around 1000 and 1100 cm^{-1} shift to 1050 and 1140 cm^{-1}, respectively, and N_{Ag-Ag} becomes 2.9, which indicates that the Ag clusters attached to the zeolite framework are stabilized at high temperature. When the zeolite with Ag clusters is exposed to atmosphere, it is found that: (1) the ν(O–H) mode around 3 μm appears again, (2) there are two main peaks (1000 and 1100 cm^{-1}) and a small peak around 856 cm^{-1} and (3) the local structure of the Ag clusters formed at 300 °C never reverses.
© 2005 Elsevier Ltd. All rights reserved.

Keywords: IR; EXAFS; Ag cluster; Zeolite; In situ

1. Introduction

Zeolites are crystalline aluminosilicates showing unique properties due to the presence of channels and cages in the structure. There are a number of applications as molecular sieves and catalysts [1]. Zeolite frameworks are made of SiO_4 and AlO_4 tetrahedra connected by corners. The negatively charged Al sites are neutralized by the charge-balancing framework cations, such as the Na^+ ion. There are 86 Na^+ ions in a unit cell of zeolite X. The Na^+ ions are exchanged by Ag^+ ions when the zeolites are put in a solution containing Ag^+ ions. In the fully Ag^+-exchanged zeolite X (Ag_{86}–X), 86 Ag^+ ions are located: (i) at site I (the center of the hexagonal prism), (ii) at site II (single six-ring in the large cage) and at site III (sequence of four-rings in the large cavity) [2]. When the hydrated Ag_{86}–X, with a white color, is heated under vacuum, the color changes into yellow and the silver ions are reduced to Ag atoms which form silver clusters consisting of the reduced Ag atoms and Ag^+ ions [3,4]. The silver clusters are stabilized by the silicate matrix, that is, the zeolite framework.

Measurements of the infrared vibrational spectra [5–8] give information on the dynamics of the zeolite framework and the cations. Extended X-ray absorption fine structure (EXAFS) measurements are suitable for observations of the local structure around Ag^+ ions or Ag atoms which are attached to the framework in the

* Corresponding author. Tel.: +81 1 7239 3551; fax: +81 1 7239 3551.
E-mail addresses: uc@cc.hirosaki-u.ac.jp (Y. Suzuki), takaf@cc.hirosaki-u.ac.jp (T. Miyanaga).

0277-5387/$ - see front matter © 2005 Elsevier Ltd. All rights reserved.
doi:10.1016/j.poly.2005.01.009

zeolite. For example, silver-almina catalysis are investigated by in situ infrared spectroscopy and EXAFS [9]. It is interesting to study the effect of the formation of Ag clusters on the zeolite framework of Ag_{86}–X by means of infrared and EXAFS measurements which enable us to prepare complementary information.

In this paper, we report the results obtained by the in situ infrared and XAFS measurements for Ag_{86}–X heated from room temperature (RT) to 300 °C under vacuum. The effect of the formation of Ag clusters on the zeolite framework is discussed.

2. Experimental

Ag_{86}–X powder samples were prepared by immersing Na_{86}–X ($Na_{86}[(AlO_2)_{86}(SiO_2)_{106}]_{46} \cdot 2H_2O$) zeolite in 0.1 M $AgNO_3$ solution for 12 h at 25 °C. The solution was stirred every hour. After careful filtration the Ag^+-exchanged X zeolite powder was dried at room temperature in the darkroom. The amounts of the exchanged Ag^+ ions in the X zeolite were determined by means of electron probe microanalyzer (EPMA, JX A-8800L, JEOL) [10,11]. The Ag_{86}–X zeolite was set into the in situ infrared and EXAFS measurement vacuum cell (RVX-I) in which the sample can be heated up to 300 °C and cooled down to liquid nitrogen temperature under vacuum. Ag_{86}–X and Na_{86}–X samples were used for infrared measurements and Ag_{86}–X was used for the EXAFS measurements. NaCl single crystal windows were used for infrared measurements and Kapton® films were used for EXAFS measurements. A high-purity Si single-crystal wafer was used as the substrate for the infrared measurements. Zeolite powder was deposited on the wafer, then blown off an excessive specimen with a hand blower. A small quantity of zeolite was stuck electrostatically. For EXAFS measurement, the sample was filled in the space of a glass filter sandwiched by two cover glasses. The glass filter was suitable for removing H_2O vapor from the zeolite. These glass parts were set in the copper holder. The sample thickness was about 3 mm for obtaining a reasonable edge jump (more than 1.0) of the Ag K-absorption edge.

The infrared light absorption spectra were obtained at normal incidence of radiation. The infrared measurements were performed on a BOMEN MB-100 spectrometer equipped with a liquid nitrogen-cooled HgCdTe detector at 4 cm^{-1} resolution with 128 interferometric scans. The sample was held at one temperature for more than 2 h in the heating operation and then cooled down to room temperature where the infrared spectra were obtained. Ag K-edge (25.5 keV) EXAFS spectra were measured at BL-10B of Photon Factory in KEK using the Si (3 1 1) channel-cut monochrometer. The energy and current of the storage ring were 3.0 GeV and 250–300 mA, respectively. The EXAFS spectra for the sample heated in a vacuum were obtained at liquid nitrogen temperatures in order to reduce the Debye–Waller effect. The EXAFS measurement for the sample under atmospheric pressure was carried out at 300 K. The analyses of the EXAFS data were performed by XANADU code [12] and FEFF6.01 code [13].

3. Results

3.1. Infrared absorption spectra

Fig. 1 shows the infrared spectra of hydrated Na_{86}–X and Ag_{86}–X under air at room temperature. In the hydrated state Na_{86}–X and Ag_{86}–X give very similar spectra. There are some absorption bands at the 3 and 10 μm regions. The strongest vibration bands at 10 μm region are assigned to a T–O asymmetric stretch (ν_{as}(T–O)) involving a motion primarily associated with oxygen atoms [14].

3.1.1. Ag_{86}–X

Fig. 2(A) shows the change of infrared spectra for Ag_{86}-(ν_{as}(T–O)) at room temperature as a function of evacuation time. The absorption bands around 3 μm vanish after ca. 5 min evacuation. These bands are assigned to the O–H stretching vibration (ν(O–H)) of water and/or OH group adsorbed in zeolite. Since water molecules confined in the zeolite framework are present up to 350 °C [4], it is difficult to understand why the IR spectra of the O–H stretches due to the water molecules vanish in ca. 5 min evacuation at room temperature. A further IR study on the O–H stretches is now planned.

The ν_{as}(T–O) bands at 10 μm region change drastically on evacuation. The intensity of the shoulder near 1100 cm^{-1} increases and the shoulder grows into peak

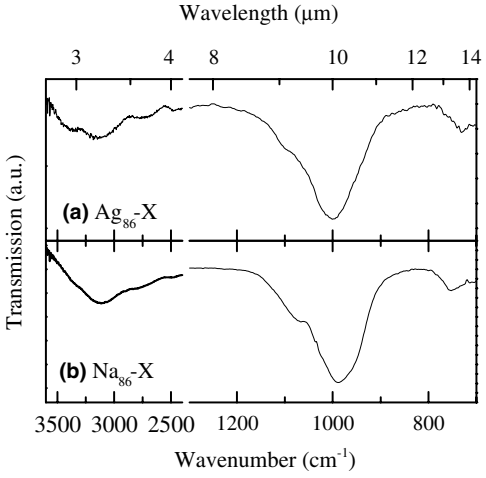


Fig. 1. Infrared absorption spectra of zeolite-X in air at RT. (a) Ag_{86}–X, (b) Na_{86}–X.

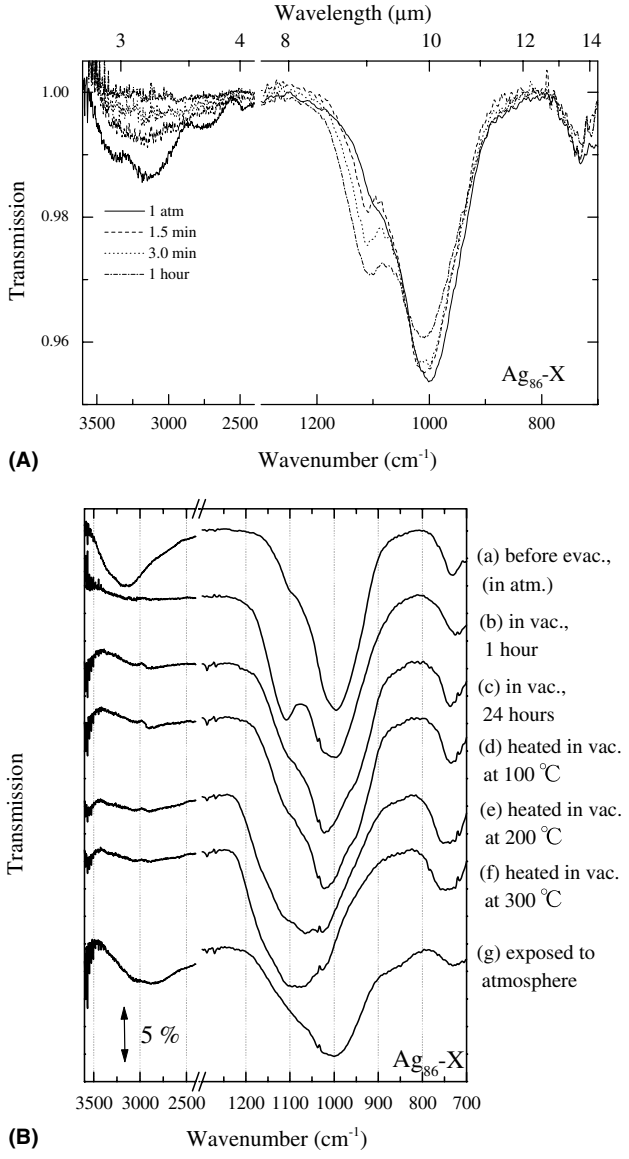


Fig. 2. Infrared absorption spectra of zeolite Ag_{86}–X. (A) Time-variations of infrared spectra under evacuation. (B) Infrared absorption spectra under different conditions. (a) Before evacuation (in atm), (b) in vacuum, 1 h, (c) in vacuum, 24 h, (d) heated in vacuum at 100 °C, (e) heated in vacuum at 200 °C, (f) heated in vacuum at 300 °C, (g) sample was exposed to air after heating and evacuating. All spectra are measured at room temperature.

after 1 h evacuation. These spectral changes on evacuation are considered to arise from the field balance in the zeolite framework due to a change in the position of Ag^+ ions caused by desorption of water from the zeolite cage.

The infrared spectral changes in the process of the formation of silver clusters in Ag_{86}–X heated at various temperatures under vacuum are shown in Fig. 2(B). After evacuating for 24 h (c) at RT, the bands around 10 μm change considerably. The intensity of the band near 1100 cm^{-1} slightly decreases and a new shoulder is observed around 950 cm^{-1}. It is noted that there is little difference between the spectrum heated at 100 °C (d) after evacuation for 1 h and the spectrum evacuated for 24 h at RT (c). After the sample was heated at 200 °C (e), the absorption spectrum changes drastically. A lower wavenumber shoulder of the main peak at 1000 cm^{-1}, which was observed in 24 h (c) and 100 °C (d), vanishes and the higher wavenumber shoulder becomes ambiguous. From (c) stage to (e) stage, some Ag^+ ions are reduced to Ag atoms which play as a precursor for the formation of silver clusters. At 300 °C (f), the absorption spectrum is almost similar to (e) in shape, but the peak shifts to higher wavenumber. These spectral changes arise from the changes of ν_{as}(T–O) in the zeolite framework by growth of the silver clusters.

When the sample was cooled down to RT from 300 °C and exposed to air, the absorption band around 3 μm appears again ((g) in Fig. 2(B)) as seen in stage (a) in Fig. 2(B). This suggests that the framework structure of the hydrated zeolite does reverse. On the other hand, the IR bands assigned to ν_{as}(T–O) do not return by absorbing moisture. A trailing edge around 850 cm^{-1} grows in addition to the 10 μm region band.

On the other hand, for the samples that were exposed to air after 24 h evacuation at RT and/or heated at 100 °C, the IR spectra do completely return to the spectra before evacuation.

3.1.2. Na_{86}–X

Fig. 3(A) shows the change of infrared spectra for Na_{86}–X at RT as a function of evacuation time. As shown for Ag_{86}–X, the absorption bands in the 3 μm region vanish after evacuation (b). At the absorption bands around 10 μm, there appear shoulders at the low wavenumber side. These spectral changes finish after ca. 5 min. After the 24 h evacuation at RT ((c) in Fig. 3(B)), the intensity of the shoulder at lower wavenumber decreases. The spectrum at 100 °C ((d) in Fig. 3(B)) is the same as that for the 24 h evacuation. It is noted that the spectra for Na_{86}–X do not change further as the temperature rises to 200 (e) and 300 °C (f) under evacuation, which is totally different behavior from Ag_{86}–X. When Na_{86}–X is exposed to air after heating up to 300 °C ((f) in Fig. 3(B)), the spectrum (g) is found to be the same as that before evacuation.

From these results, it is pointed out that the zeolite framework in Na_{86}–X has not changed on heating up to 300 °C. Moreover, it is quite apparent that the Ag atoms give influence to the framework by heating and the effect of Ag on the framework is entirely different from that of Na.

3.2. EXAFS

Figs. 4 and 5 show the EXAFS $k\chi(k)$ spectra and their Fourier transforms for Ag_{86}–X measured at 100 K after heating to various temperatures, respectively. There are two peaks in Fourier transform ((b) in Fig. 5): peak A

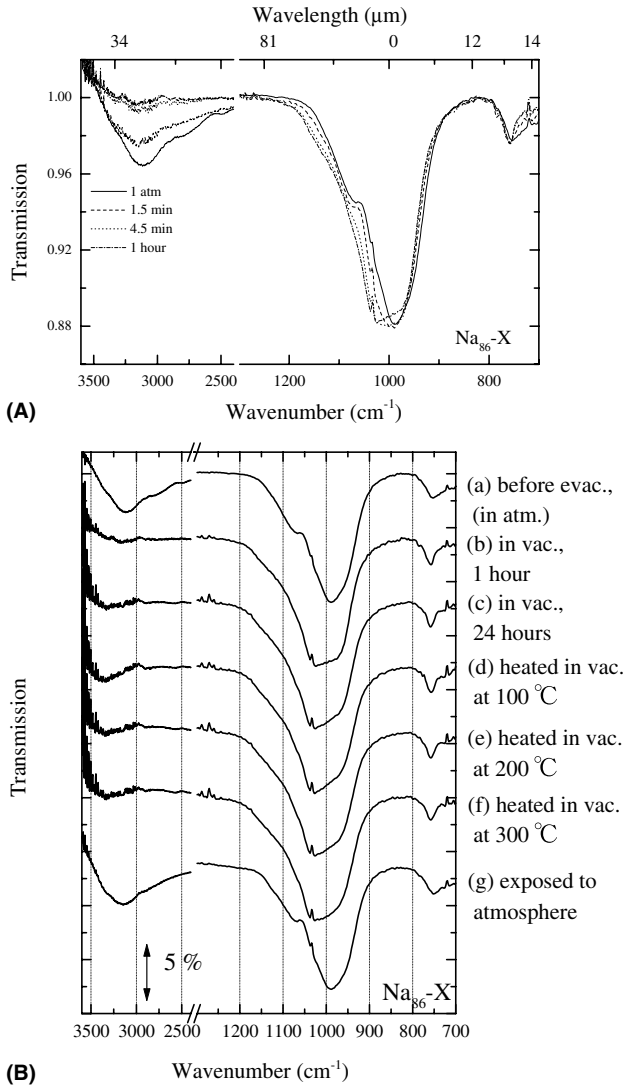


Fig. 3. Infrared absorption spectra of zeolite Na_{86}–X. (A) Time-variations of infrared spectra under evacuation. (B) Infrared absorption spectra at different conditions. (a) Before evacuation (in atm), (b) in vacuum, 1 h, (c) in vacuum, 24 h, (d) heated in vacuum at 100 °C, (e) heated in vacuum at 200 °C, (f) heated in vacuum at 300 °C, (g) sample was exposed to atmosphere after heating and evacuating. All spectra are measured at room temperature.

around 2 Å and peak B around 3 Å. Peak A is considered to come from Ag–O contributions (H_2O and oxygens in the framework) and peak B is from longer Ag–O and Ag–Ag contributions, as reported for the silver clusters in Ag–A zeolite [10]. A similar double peak was obtained in the Fourier transform for the Ag/Al_2O_3 (Ag; 0.6 wt%) system [9]. The behavior of peak B is interesting: the intensity of peak B slightly decreases after the sample was heated to 100 °C and increases again after being heated to 200 °C, though the changes are small. On the other hand, the intensity of peak B increases outstandingly after heating to 300 °C. This large change can be found clearly in the $k\chi(k)$ spectra ((e) in Fig. 4).

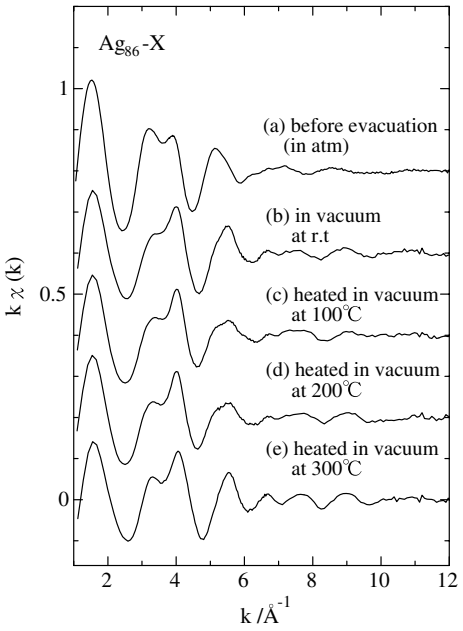


Fig. 4. EXAFS $k\chi(k)$ spectra of the Ag K-edge for Ag_{86}–X under different conditions. (a) Before evacuation (in atm), (b) in vacuum at RT, (c) heated in vacuum at 100 °C, (d) heated in vacuum at 200 °C, (e) heated in vacuum at 300 °C. The spectrum of (a) was measured at RT, and the spectra from (b) to (e) were measured at 100 K.

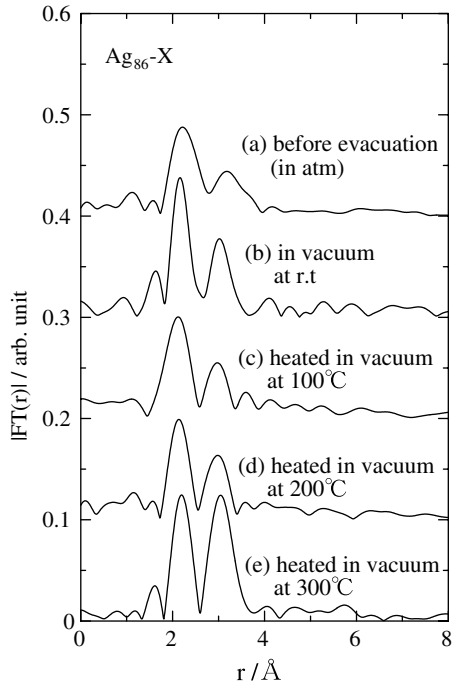


Fig. 5. Fourier transforms for the corresponding EXAFS spectra shown in Fig. 4.

In order to discuss quantitatively the change of local structure around Ag in the Ag_{86}–X zeolite, we perform non-linear least-square fitting (curve-fitting) to the EXAFS spectra using the following equation:

$$\chi(k) = \sum_j \frac{S_0^2 N_j}{kr_j^2} f_j(k, r_j) \exp(-2\sigma_j^2 k^2) \times \exp(-2r_j/\lambda(k)) \sin[2kr_j + \varphi_j(k)], \quad (1)$$

where r_j is the interatomic distance between X-ray absorbing and photoelectron scattering atoms in jth shell, N_j is the coordination number of the jth shell. $f_j(k, r_j)$ and $\phi_j(k)$ are the backscattering amplitude and phase shift functions, which were calculated by FEFF 6.01 code [12]. The k-range used in a curve-fitting method is from about 3.0–11.5 $Å^{-1}$ for the Ag K-edge. $\lambda(k)$ is the photoelectron mean free path obtained by the FEFF 6.01 calculation [12]. As in the case for Ag–A zeolite [9], we applied the three-shell fitting method to Ag_{86}–X. The three-shell model consists of two Ag–O (short and long contact distances) and one Ag–Ag contact. The Ag–O contact with a short distance is represented by Ag–O(1) and the contact with long distance by Ag–O(2).

The structural parameters obtained from the curve-fitting are compiled in Table 1. An example of the curve-fitting for Ag_{86}–X heated up to 300 °C is shown in Fig. 6. The quality of the fitting is fairly good. During the evacuation at RT, the contact distance of Ag–O(1) decreases from 2.38 ± 0.02 to 2.29 ± 0.02 Å and $N_{Ag–O(1)}$ decreases from 4.1 ± 0.2 to 2.1 ± 0.2, which indicates that some H_2O molecules attached to Ag^+ ions and the zeolite framework are removed. By removal of water, the contact distances of Ag–O(2) and Ag–Ag decrease, while the coordination numbers of $N_{Ag–O(2)}$ increase but those of $N_{Ag–Ag}$ decrease.

By heating Ag_{86}–X from RT to 100 °C under vacuum it is found for the Ag–O(1) contact, the distance decreases from 2.29 to 2.27 Å and $N_{Ag–O(1)}$ remains at 2.1. For Ag–O(2), the contact distance increases from 2.96 to 3.01 Å but $N_{Ag–O(2)}$ decreases from 3.8 to 2.9. It is noted that $N_{Ag–Ag}$ decreases from 1.2 to 0.6 and the Ag–Ag contact distance decreases from 2.88 to 2.78 Å. These changes suggest that Ag^+ ions are reduced to Ag atoms by further removal of water. Between 100 and 200 °C, the coordination number of Ag–Ag is found to be small; that is, 0.6 at 100 °C and 0.5 at 200 °C. This small coordination number suggests that the Ag atoms change sites in the zeolite. By heating from 200 to 300 °C, the Ag–O(1) and Ag–O(2) contacts show little changes in the contact distances and in the coordination number, respectively. On the other hand, $N_{Ag–Ag}$ increases dominantly from 0.5 to 2.9, which is much larger than $N_{Ag–Ag}$ at RT. This increase of $N_{Ag–Ag}$ at 300 °C suggests the formation of an Ag cluster consisting of Ag atoms and Ag^+ ions in Ag_{86}–X.

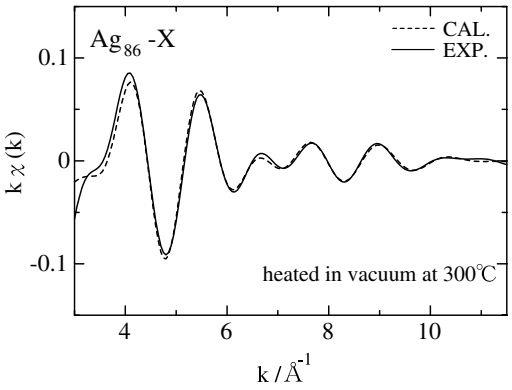


Fig. 6. Comparison between experimental $k\chi(k)$ spectra and the corresponding calculated curve for Ag_{86}–X measured after the sample was heated at 300 °C.

When air was introduced into the sample chamber after the clusters had been formed in Ag_{86}–X at 300 °C, it is found the local structure around Ag does not reverse to the state before evacuation. This indicates that the Ag clusters in Ag_{86}–X are stable due to presence of moisture.

4. Discussion

Now we discuss the effect of the formation of Ag clusters on the zeolite framework in the Ag_{86}–X zeolite during heating under vacuum. As shown in Fig. 2(A), the changes in ν_{as}(T–O) due to the contribution from the zeolite framework are observed by the infrared measurements in the wavenumber region between 800 and 1200 cm^{-1}. Such changes are shown in Fig. 7. The curves in Fig. 7 are derived from the data shown in Fig. 2(B). These spectra are fitted by summing up two or three

Table 1
Structural parameters (r, contact distance; N, coordination number; and σ, root mean square displacement) obtained from the EXAFS curve-fitting method measured at 100 K for Ag_{86}–X

	Ag–O(1)			Ag–O(2)			Ag–Ag		
	r (Å)	N	σ (Å)	r (Å)	N	σ (Å)	r (Å)	N	σ (Å)
(a) RT (atm)[a]	2.38	4.1	0.14	3.05	2.3	0.13	2.99	2.0	0.14
(b) After RT (vacuum)	2.29	2.1	0.08	2.96	3.8	0.12	2.88	1.2	0.13
(c) After 100 °C	2.27	2.1	0.10	3.01	2.9	0.12	2.78	0.6	0.13
(d) After 200 °C	2.27	1.6	0.09	2.99	3.7	0.12	2.80	0.5	0.13
(e) After 300 °C	2.28	1.9	0.09	2.94	3.6	0.13	2.84	2.9	0.13

Error in r is ±0.02 Å, in N is ±0.2 and in σ is ±0.03 Å.
[a] Measured at room temperature in atmosphere.

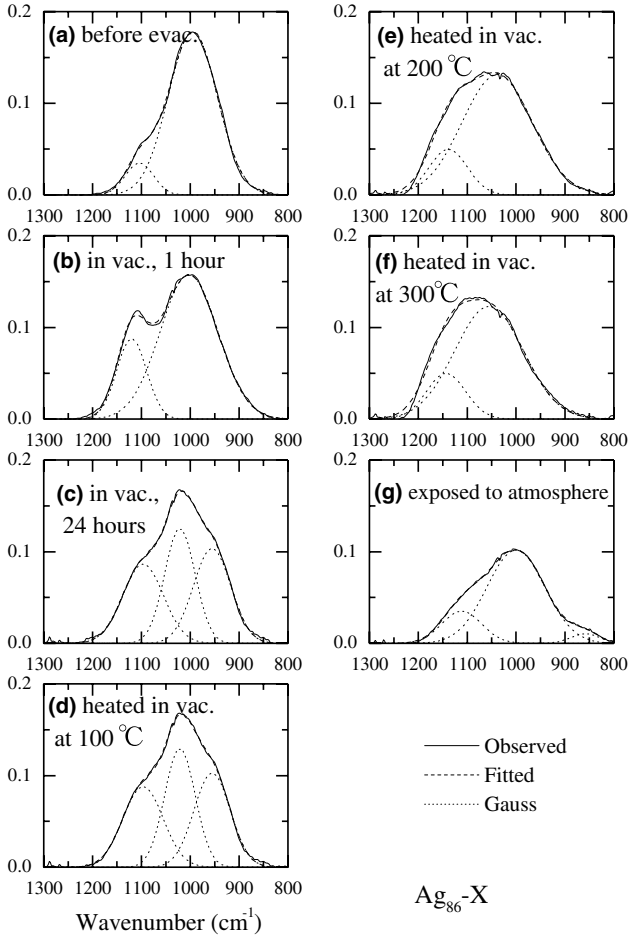


Fig. 7. Gaussian peak fitting of the infrared absorption spectra for Ag_{86}–X. (a) Before evacuation (in atm), (b) in vacuum, 1 h, (c) in vacuum, 24 h, (d) heated in vacuum at 100 °C, (e) heated in vacuum at 200 °C, (f) heated in vacuum at 300 °C, (g) sample was exposed to air after heating up to 300 °C in vacuum.

Gaussian peaks represented as dotted curves in Fig. 7. The quality of the fitting is fairly good.

In the change from (a) to (b), the disappearance of the ν(O–H) mode around 3 μm is observed. As shown in Fig. 7, the position of the main peak remains around 1000 cm^{-1}, but the intensity of a side peak around 1100 cm^{-1} increases and shifts to higher wavenumber (from 1104 to 1120 cm^{-1}). In this stage the infrared spectra are fitted by two Gaussian peaks. The information on the coordination numbers and the contact distances of Ag–O(1) and Ag–O(2), respectively, derived from the EXAFS analysis are related to the interaction between Ag^+ ions (or Ag atoms) and the zeolite framework. The coordination number $N_{Ag–O(1)}$ decreases from 4.1 to 2.1 and the distances of the Ag–O and Ag–Ag contacts decrease in this stage. Before evacuation (that is, in the hydrated state), Ag^+ ions exist on the basis of the balance of fields by the zeolite framework and water molecules. As the vacuum-dehydration of Ag_{86}–X proceeds, the water molecules are removed. This results in the decrease of the contribution to the zeolite framework from water molecules and the increase in the attraction between Ag^+ ion and the zeolite framework.

A drastic change is observed in the cases of (c) and (d). In these stages the infrared spectra are fitted by three Gaussian peaks, which is completely different from the stages (a) and (b) at RT and the stages (e) and (f) at high temperatures. The intensity of the main peak around 1000 cm^{-1} decreases remarkably and shifts slightly to a larger wavenumber (from 1002 to 1020 cm^{-1}). Additionally, a new peak appears at a lower wavenumber around 955 cm^{-1}. As seen from Table 1, the total coordination number of oxygen (the sum of $N_{Ag–O(1)}$ and $N_{Ag–O(2)}$) decreases from 5.9 at RT to 5.0 at 100 °C. In the same temperature range, the Ag–Ag contact distance decreases from 2.88 to 2.78 Å and $N_{Ag–Ag}$ from 1.2 to 0.6. As the dehydration proceeds, the repulsion between Ag^+ ions becomes weak because Ag atoms are produced by the removal of water and the potential barriers related to the Ag^+ ions and zeolite framework become comparatively low. The mobility of Ag atoms is expected to increase by raising temperature. The appearance of the peak around 955 cm^{-1} may relate to the alteration of the positions of Ag atoms in the zeolite.

As the temperature is raised to 200 °C (e), the peak in the low wavenumber (around 955 cm^{-1}) disappears and the infrared spectrum is fitted by two peaks. The broad main peak appears at 1039 cm^{-1} and a small peak at 1150 cm^{-1}. As seen from Table 1, the distance for the Ag–Ag contact increases from 2.78 Å at 100 °C to 2.84 Å at 200 °C. The total coordination number of oxygens around Ag at 200 °C is 5.3 and larger than that at 100 °C is 5.0. From these results, it is expected that at 200 °C some Ag atoms move into sites I and I′ in the zeolite [2] and may play as a precursor of Ag clusters. In the spectrum at 300 °C (f) the IR spectrum is fitted by two peaks. The main peak appears at 1055 cm^{-1} and a small peak at 1150 cm^{-1}. It is important to point that there is little change in the spectra between 200 and 300 °C. With increasing temperature from 200 to 300 °C, $N_{Ag–Ag}$ changes from 0.5 to 2.9. This indicates that Ag clusters are formed at sites I and I′ where a great portion of Ag contributes to cluster formation with the total coordination number of oxygens around Ag being 5.5.

When the zeolite, heated up to 300 °C, is cooled down to room temperature and exposed to atmosphere, the ν(O–H) mode around 3 μm appears again. Around the 10 μm region there appear two peaks whose positions are the same as those observed before evacuation (a) and a small peak at low wavenumber (856 cm^{-1}) (g). This suggests that the framework structure of the zeolite does reverse to the state before evacuation. From the EXAFS results it is found that the local structure of the Ag clusters formed at 300 °C does not reverse when the zeolite is cooled down to room temperature and

exposed to atmosphere. From these results it is concluded that the Ag clusters are stable and the framework structure of the zeolite does reverse considerably on exposure to atmosphere after heating up to 300 °C.

From the EXAFS parameters compiled in Table 1, it is expected that the framework O(1) interacts with Ag^+ ions, since the contact distance remains to be around 2.27 Å in the temperature range between 100 and 300 °C. The framework O(2) may interact with Ag atoms above 100 °C, judging from the decrease in the contact distances, due to the reduced amount of positive charges of the Ag^+ ions, from 3.01 Å at 100 °C to 2.94 Å at 300 °C.

5. Summary

The in situ infrared and EXAFS measurements were carried out for Ag_{86}–X heated up to 300 °C under vacuum. By evacuation at room temperature, the ν(O–H) mode around 3 μm disappears and the coordination number of oxygen around Ag decreases due to removal of water molecules. The T–O asymmetric stretch, (ν_{as} (T–O)) mode associated with zeolite framework oxygen, appears around the 10 μm region. These IR spectra are fitted by two or three Gaussian peaks. The positions of the main peaks are 1000 and 1100 cm^{-1} at room temperature. At 100 °C a new peak appears around 955 cm^{-1}, the total $N_{Ag–O}$ becomes small and $N_{Ag–Ag}$ is 0.5, which suggests that the Ag atoms change sites in the zeolite and play an important role as a precursor of the Ag clusters. At 300 °C, the corresponding peak positions shift to 1050 and 1140cm^{-1} and $N_{Ag–Ag}$ becomes 2.9, which indicates that the size of the Ag clusters attached to the zeolite framework becomes large at high temperature. It is suggested that there is a transition region from the state consisting mainly of Ag^+ ions to the state containing Ag clusters formed by Ag atoms and Ag^+ ions in the temperature range between 100 and 200 °C. When the zeolite with Ag clusters is exposed to atmosphere, it is found that: (1) the ν(O–H) mode around 3 μm appears again, (2) there appear two peaks (1000 and 1100 cm^{-1}) and a small peak around 856 cm^{-1} and (3) the local structure of the Ag clusters formed at 300 °C does not reverse.

Acknowledgements

We thank Mr. S. Matsuda for his support on the EXAFS measurements and Mr. R. Kakizaki for his support on the Infrared measurements. This work was performed under the approval of Proposal Nos. 2000G272 and 2002G279 of Photon Factory (KEK). This work was partially supported by the Research Grants of Hirosaki University.

References

[1] J.A. Rabo (Ed.), Zeolite Chemistry and Catalysis ASC Monograph No. 171, American Chemical Society, Washington, DC, 1976.
[2] L.R. Gellens, W.J. Mortier, J.B. Uytterhoeven, Zeolite 1 (1981) 11.
[3] T. Sun, K. Seff, Chem. Rev. 94 (4) (1994) 857.
[4] Y. Kim, K. Seff, J. Phys. Chem. 91 (3) (1987) 668.
[5] E.M. Flaningen, H. Khatami, H.A. SzymanskiMolecular Sieve Zeolites. Advances in Chemical Series, vol. 101, American Chemical Society, Washington, DC, 1971.
[6] J. Godber, G.A. Ozin, J. Phys. Chem. 92 (1988) 354.
[7] A. Boumiz, J. Cartigny, E. Cohen de Lara, J. Phys. Chem. 96 (1992) 5419.
[8] K.S. Smirnov, M. Le Maire, C. Bremard, D. Bougeard, Chem. Phys. 179 (1994) 445.
[9] K. Shinizu, J. Shibata, H. Yoshida, A. Satsuma, T. Hattori, Appl. Catal. B 2 (30) (2001) 151.
[10] T. Miyanaga, H. Hoshino, H. Endo, J. Syncrotron Rad. 8 (2001) 557.
[11] H. HoshinoBulletin of the Faculty of Education, vol. 75, Hirosaki University, 1996, p. 29.
[12] H. Sakane, T. Miyanaga, I. Watanabe, N. Matsubayashi, S. Ikeda, Y. Yokoyama, Jpn. J. Appl. Phys. 32 (1993) 4641.
[13] J.J. Rehr, J. Mustre de Leon, S.I. Zabinsky, R.C. Albers, J. Am. Chem. Soc. 113 (1991) 5135.
[14] S.A. Rodriguez, Vib. Spectrosc. 9 (1995) 225.

Available online at www.sciencedirect.com
SCIENCE DIRECT®
Polyhedron 24 (2005) 693–699
POLYHEDRON
www.elsevier.com/locate/poly

Di- and tetranuclear silver (I)-saccharinate complexes with 2-pyridineethanol and 2-pyridinepropanol: Syntheses, crystal structures, spectroscopic and thermal analyses of $[Ag_2(sac)_2(pyet)_2]$ and $[Ag_4(sac)_4(pypr)_2]$

Veysel T. Yilmaz [a,*], Sevim Hamamci [a], William T.A. Harrison [b], Carsten Thöne [c]

[a] Department of Chemistry, Faculty of Arts and Sciences, Ondokuz Mayis University, 55139 Kurupelit, Samsun, Turkey
[b] Department of Chemistry, University of Aberdeen, Meston Walk, Aberdeen AB24 3UE, Scotland, UK
[c] Institut für Anorganische und Analytische Chemie, Technische Universitat Braunschweig, Postfach 3329, 38023 Braunschweig, Germany

Received 20 December 2004; accepted 31 January 2005

Abstract

Two new (saccharinato)silver (I) complexes, $[Ag_2(sac)_2(pyet)_2]$ and $[Ag_4(sac)_4(pypr)_2]$ (sac = saccharinate, pyet = 2-pyridineethanol and pypr = 2-pyridinepropanol), have been prepared and characterized by elemental analyses, IR, thermal analysis and single crystal X-ray diffraction. Both complexes crystallize in triclinic space group of $P\bar{1}$. In $[Ag_2(sac)_2(pyet)_2]$, two monomeric $[Ag(sac)_2(pyet)]$ units are doubly bridged by the sulfonyl oxygen atoms of the sac ligands, forming an $[Ag_2(sac)_2(pyet)_2]$ dimer, in which each silver (I) centre is three coordinate with a T-shaped coordination and the Ag···Ag separation is 5.205 Å. The dimeric units are connected by strong O–H···$O_{sulfonyl}$ intermolecular hydrogen bonds into a one-dimensional chain running parallel to *b*. The one-dimensional hydrogen bonded chains are further linked by π(sac)–π(pyet) stacking interactions. The tetranuclear complex, $[Ag_4(sac)_4(pypr)_2]$, is achieved by bridging of $[Ag_2(sac)_2]$ with two [Ag(sac)(pypr)] units through the sulfonyl oxygen atoms of the sac ligands. The two silver (I) ions in the centre with a short Ag–Ag bond distance of 2.8480(13) Å exhibit a T-shaped geometry with three sac ligands, while the two terminal silver (I) ions are coordinated by a sac ligand and a pypr ligand in a near linear geometry. The tetranuclear units are held together by O–H···O and C–H···O hydrogen bonds.
© 2005 Elsevier Ltd. All rights reserved.

Keywords: Saccharinate; 2-Pyridineethanol; 2-Pyridinepropanol; Dinuclear and tetranuclear silver (I)

1. Introduction

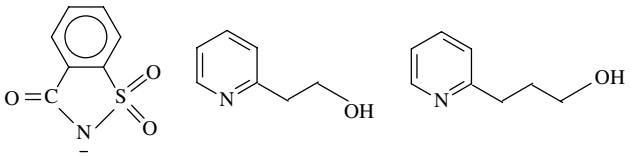
Saccharin, alternatively named 1,2-benzisothiazoline-3-(*2H*)one 1,1-dioxide or *o*-sulphobenzimide in the form of its water soluble sodium salt, is widely used as a non-caloric sweetener and food additive [1]. The coordination chemistry of saccharin is interesting. Although no metal complexes of neutral saccharin are known, the corresponding, deprotonated, saccharinate anion (sac) acts as a polyfunctional ligand due to the presence of the negatively charged imino nitrogen, carbonyl oxygen and sulfonyl oxygen atoms. The most common coordination mode of sac is ligation through the nitrogen atom, usually observed in the aquabis(saccharinato) complexes of divalent transition metals [2–6] and coordination via the carbonyl or sulfonyl oxygen is less common.

In recent years, we have investigated the synthesis, spectroscopic, thermal and structural properties of transition metal complexes of sac with substituted pyridine

* Corresponding author. Tel.: +90 362 457 6020; fax: +90 362 457 6081.
E-mail address: vtyilmaz@omu.edu.tr (V.T. Yilmaz).

0277-5387/$ - see front matter © 2005 Elsevier Ltd. All rights reserved.
doi:10.1016/j.poly.2005.01.006

ligands, especially those containing additional donor groups such as alkylhydroxyl and alkylamine. We have recently focused our investigations into the complexation of sac with silver (I), since these species are very rare and only two silver (I) complex of sac, [Ag(sac)] [7] and $[Ag(sac)(PPh_3)_2]$ [8] have appeared previously in the literature. Recently, we reported the two new silver (I)-saccharinato complexes Na[Ag(sac)] [9] and $[Ag_2(\mu\text{-sac})_2(\mu\text{- hep})_2]_n$, where hep is *N*-(2-hydroxyethyl)piperazine [10]. In this study, we report the synthesis, spectroscopic and thermal characterizations and crystal structures of two new (saccharinato)silver (I) complexes with 2-pyridineethanol (pyet) and 2-pyridinepropanol (pypr), namely $[Ag_2(sac)_2(pyet)_2]$ and $[Ag_4(sac)_4(pypr)_2]$.



sac *pyet* *pypr*

2. Experimental

2.1. Materials

$AgNO_3$, $Na(sac)\cdot 2H_2O$, pyet and pypr were purchased commercially and used as received.

2.2. Preparation of the silver (I) complexes

Pyet (0.12 g, 1 mmol) was added to an aqueous solution (20 ml) of $AgNO_3$ (0.17 g, 1 mmol) and the resulting solution was mixed with an aqueous solution (20 ml) of $Na(sac)\cdot 2H_2O$ (0.24 g, 1 mmol) at room temperature. The resulting solution was kept in darkness at room temperature and colorless single crystals of $[Ag_2(sac)_2(pyet)_2]$ were obtained after two days. Yield: 82%. d.p. 127 °C. *Anal.* Calc. for $C_{28}H_{26}N_4O_8S_2Ag_2$: C, 40.7; H, 3.2; N, 6.8; S, 7.8. Found: C, 40.5; H, 3.3; N, 6.10; S, 7.5%.

The following method was used for the preparation of $[Ag_4(sac)_4(pypr)_2]$. Solid $Na(sac)\cdot 2H_2O$ (0.24 g, 1 mmol) was added to a solution (40 ml) of $AgNO_3$ (0.17 g, 1 mmol) in a water and isopropanol mixture (1:1, v:v) and this resulted in the formation of a white precipitate, which was dissolved by the addition of pypr (0.14g, 1 mmol) to the reaction medium. After a week at room temperature, colourless crystals of $[Ag_4(sac)_4(pypr)_2]$ were formed. Yield: 25%. d.p. 132 °C. *Anal.* Calc. for $C_{44}H_{38}N_6O_{14}S_4Ag_4$: C, 36.8; H, 2.7; N, 5.9; S, 8.9. Found: C, 36.5; H, 2.8; N, 5.8; S, 9.0%.

2.3. Physical measurements

IR spectra were recorded a Jasco FT-IR-430 spectrophotometer as KBr pellets in the frequency range 4000–300 cm^{-1}. The elemental analyses (C, H, N and S contents) were determined on a Vario EL Elemental Analyser. Thermal analysis curves (TG and DTA) were obtained using a Rigaku TG8110 thermal analyzer in a static air atmosphere. A sample of 5–10 mg was used.

2.4. X-ray structure determination

Intensity data for $[Ag_2(sac)_2(pyet)_2]$ and $[Ag_4(sac)_4(pypr)_2]$ were collected using Bruker SMART1000 CCD and Enraf Nonius KappaCCD area diffractometers with graphite monochromated Mo Kα radiation ($\lambda = 0.71073$ Å) at 133(2) and 120(2) K, respectively. The structures were solved with SHELXS 97 and refined using SHELX 97 [11]. All the non-hydrogen atoms were refined anisotropically. All the hydrogen atoms, except the hydroxyl H atoms in $[Ag_2(sac)_2(pyet)_2]$, were placed in idealised locations and refined by riding on their carrier atoms, whereas the hydroxyl hydrogen atoms of

Table 1
Crystallographic data for $[Ag_2(sac)_2(pyet)_2]$ and $[Ag_4(sac)_4(pypr)_2]$

Compounds	$[Ag_2(sac)_2(pyet)_2]$	$[Ag_4(sac)_4(pypr)_2]$
Empirical formula	$C_{28}H_{26}N_4O_8S_2Ag_2$	$C_{44}H_{38}N_6O_{14}S_4Ag_4$
Formula weight	826.38	1434.52
T (K)	133(2)	120(2)
Radiation, λ (Å)	0.71073	0.71073
Crystal system	triclinic	triclinic
Space group	$P\bar{1}$	$P\bar{1}$
Unit cell dimensions		
a (Å)	8.1254(6)	7.9499(2)
b (Å)	8.9300(6)	9.7924(3)
c (Å)	10.1782(6)	30.5148(8)
α (°)	87.327(3)	86.1339(8)
β (°)	74.734(3)	88.4027(10)
γ (°)	89.735(3)	78.4552(10)
V (Å^3)	711.67(8)	2321.93(11)
Z	1	2
D_c (g/cm^3)	1.928	2.052
μ (mm^{-1})	1.582	1.918
$F(0\,0\,0)$ 412	1416	
θ range (°)	2.08–30.03	2.92–27.50
Index range (h, k, l)	−11/11, −12/12, −14/14	−10/10, −12/12, −39/39
Reflections collected	14 105	40 039
Independent reflections	4145	10 637
Maximum and minimum transmission	0.801 and 0.684	0.831 and 0.678
Data/restraints/parameters	4145/0/203	10 637/6/649
Goodness-of-fit on F^2	1.073	1.210
R_1 [$I > 2\sigma(I)$]	0.0189	0.0894
R_2 and wR_2 indices (all data)	0.0203 and 0.0500	0.0999 and 0.2394
Largest difference peak and hole (e Å^{-3})	0.623 and −0.499	3.138 and −1.512

$[Ag_2(sac)_2(pyet)_2]$ were refined freely. The molecular plots were prepared by using ORTEPIII [12]. The details of data collection, refinement and crystallographic parameters are summarized in Table 1.

3. Results and discussion

3.1. Synthesis

The mixed-ligand silver (I) complexes of sac with pyet and pypr were prepared by the direct reaction of silver (I), sac and pyet or pypr in solution. The composition of the complexes was determined by elemental and TG analyses. The binuclear complex was obtained in a high yield over 80%, whereas the yield of the tetranuclear complex was relatively low (25%). Although no other complex was isolated from the same reaction solution of the tetranuclear complex, the low yield of the complex may be due to the presence of other species with very high solubility. The elemental analyses were consistent with their proposed formulae. Both complexes are insoluble in warm H_2O and common alcohols such as methanol or ethanol, but soluble in warm H_2O–alcohol mixtures. Both complexes are non-hygroscopic and light-stable at room temperature. $[Ag_2(sac)_2(pyet)_2]$ does not melt, but decomposes at 127 °C, whereas $[Ag_4(sac)_4(pypr)_2]$ melts with decomposition at 132 °C.

3.2. IR spectra

The most significant absorption bands in the IR spectra of the title complexes together with their assignments are given in Table 2. The position of the bands in the spectra of both complexes is similar. The strong and broad bands in the 3330–3350 cm^{-1} range are attributed to the ν(OH) vibrations of the pyet and pypr ligands. The relatively weak bands at 2900–3070 cm^{-1} are due to the ν(CH) vibrations. The absorption band of the carbonyl group of sac in $[Ag_2(sac)_2(pyet)_2]$ appears at ca. 1649 cm^{-1} as a very strong, single band. The frequency of the carbonyl group is characteristic of *N*-coordinated sac ligands as reported for Na[Ag(sac)] [9] and Na(sac) · $2H_2O$ [13]. However, the C=O bands in $[Ag_4(sac)_4(pypr)_2]$ are observed at 1651 and 1626 cm^{-1} as two distinct and strong bands, indicating the different interactions of the sac ligands. The higher absorption band is due to an *N*-bonded sac in which its carbonyl group remains uncoordinated, whereas the band at lower frequency shows the coordination of the sac ligand through the carbonyl group, shifting by ca. 25 cm^{-1} compared to the higher band. This shift is in agreement with the participation of the carbonyl oxygen in metal bonding as also observed in the IR spectrum of [Ag(sac)] [14]. The absorption bands at ca. 1580 and 1460 cm^{-1} correspond to the ring ν(CC) vibrations. The stretching vibrations of $\nu_{asym.}(SO_2)$ and $\nu_{sym.}(SO_2)$ occur characteristically at ca. 1290 and 1150 cm^{-1}, respectively. In both complexes, the asymmetric stretching band at around 1280 cm^{-1} are found to split into two or three bands, although the S–O distances in both complexes are almost identical. Additional peaks at ca. 1330 and 970 cm^{-1} are attributed to the symmetric and asymmetric stretching modes of the CNS moiety of the sac ligands, respectively. The *N*-coordination of the py ligands is confirmed by the absorption bands at around 675 cm^{-1} due to γ(py) [15].

Table 2
Selected IR spectroscopic data[a] for $[Ag_2(sac)_2(pyet)_2]$ and $[Ag_4(sac)_4(pypr)_2]$

Assignment	$[Ag_2(sac)_2(pyet)_2]$	$[Ag_4(sac)_4(pypr)_2]$
ν(OH)	3327s, b	3347s, b
ν(CH)	3066w, 2931vw	3040w, 2920vw
ν(CO)	1649vs, 1622sh	1651vs, 1626sh
ν(CC)	1587vs	1583vs
ν(CC)	1458m	1458vs
ν_{sym}(CNS)	1331s	1336s
$\nu_{asym}(SO_2)$	1288vs, 1257s	1288vs, 1271vs, 1250vs
$\nu_{sym}(SO_2)$	1151vs	1155vs
ν_{asym}(CNS)	966vs	970vs, 953vs
ν(CCC)	773m, 748s	773m, 744s
γ(CH) (py)	676m	675s

b, broad; vw, very weak; w, weak; vs, very strong; s, strong; m, medium and sh, shoulder.
[a] Frequencies in cm^{-1}.

3.3. Thermal behaviour

The thermal decomposition pathways of the title complexes were followed up to 600 °C in a static atmosphere of air. $[Ag_2(sac)_2(pyet)_2]$ is stable up to 127 °C and then begins to decompose in three stages. Elimination of the pyet ligand occurs in the first stage of decomposition between 127 and 240 °C with three endothermic effects at 150, 189 and 213 °C. The experimental mass loss of 29.5% agrees well with the calculated mass loss of 29.8%. The decomposition of the sac moiety occurs in the second and third stages in the temperature range 250–517 °C with two violently exothermic DTA peaks at 370 and 464 °C (mass loss: found 44.5%, calcd. 44.1%). As well as microanalyses, the mass loss calculations suggest that the residue left as a final decomposition product is metallic silver. Total mass loss is 74.0% and the final residue consisting mainly of silver forms 26.0% of the total mass (calcd. 26.1%).

$[Ag_4(sac)_4(pypr)_2]$ follows a different decomposition path compared to that of the dimeric complex. It begins to decompose with melting at 132 °C. The first decomposition stage between 132 and 231 °C corresponds to the endothermic removal of two pypr ligands with a mass loss of 19.4% (calcd. 19.1%). In the next stages, the exothermic degradation of four sac ligands occurs

in the 235–528 °C range with a small and two sharp exothermic DTA peaks at 256, 435 and 489 °C, and results in the formation of silver metal as the end product. The experimental total mass loss value of 70.5% is consistent with the calculated value 69.9%.

3.4. Description of the crystal structure of $[Ag_2(sac)_2(pyet)_2]$

A molecular view of $[Ag_2(sac)_2(pyet)_2]$ with the atom numbering scheme is shown in Fig. 1. The selected bond lengths and angles together with the hydrogen bonding geometry are given in Table 3. The complex crystallizes in the triclinic space group $P\bar{1}$. The structure consists of individual molecules of dinuclear $[Ag_2(sac)_2(pyet)_2]$ units formed from doubly bridged monomeric [Ag-$(sac)_2$(pyet)] units joined through the sulfonyl oxygen atoms of the sac ligands (Fig. 1). Each silver (I) centre is three coordinated by an *N*-bonded sac ligand, an *N*-bonded pyet ligand and the bridging sulfonyl oxygen atom of sac in the adjacent $[Ag(sac)_2(pyet)]$ unit, exhibiting a distorted T-shaped AgN_2O coordination environment. In the dimeric unit, there is an eight-membered chelate ring with an Ag···Ag separation of 5.205 Å, indicating the absence of any interaction between two silver centres. We have previously observed that the pyet ligand behaves as a bidentate donor via the N and hydroxyl O atoms to other divalent transition metals [16–18]. Here, it acts a monodentate ligand through the N atom and the hydroxyl O atom remains uncoordinated.

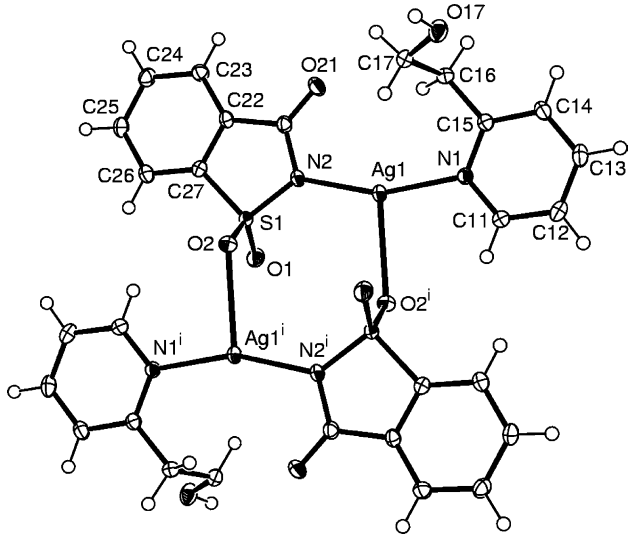


Fig. 1. Dimeric molecular unit in $[Ag_2(sac)_2(pyet)_2]$ with the atom labelling scheme and 50% thermal ellipsoids (arbitrary spheres for the H atoms). Symmetry code: (i) = $-x$, $2-y$, $-z$.

Table 3
Selected geometrical data for $[Ag_2(sac)_2(pyet)_2]$[a]

Bond lengths (Å) and angles (°)			
Ag1–N1	2.1753(11)	N1–Ag1–N2	159.14(4)
Ag1–N2	2.1444(12)	N1–Ag1–$O2^i$	96.11(4)
Ag1–$O2^i$	2.6454(10)	N2–Ag1–$O2^i$	104.75(4)

D–H···A	*d*(D–H)	*d*(H···A)	*d*(D···A)	∠(DHA)
Hydrogen bonds				
O17–H17···$O1^{ii}$	0.82(2)	2.02(3)	2.8083(17)	163(2)
C12–H12···$O17^{ii}$	0.95	2.55	3.4133(19)	150
C16– H16B···$O21^{iii}$	0.99	2.43	3.4124(16)	172

[a] Symmetry operations: (i) $-x$, $2-y$, $-z$; (ii) x, $y-1$, z; (ii) $1-x$,

The Ag–N_{sac} and Ag–N_{pyet} bond distances are similar, being 2.1753(11) and 2.1444(12) Å, respectively. The Ag–N_{sac} bond distance is similar to the corresponding values found in [Ag(sac)] [2.16 Å] [7], Na[Ag(sac)] [2.1405(11)] and 2.1570(11) Å] [9], but differs from the bond values reported for $[Ag(sac)(PPh_3)_2]$ [2.285(8) Å] [8] and $[Ag_2(\mu\text{-sac})_2(\mu\text{-hep})_2]_n$ [2.084(2) Å] [10]. The bridging Ag–$O_{sulfonyl}$ bond distance of 2.6454(10) Å is comparable to that of Na[Ag(sac)] [2.6390(10) Å] [9], but significantly longer than the corresponding bond in [Ag(sac)] (2.45 Å) [7].

The sac ligand is essentially planar with a root-mean-square (rms) deviation of the non-hydrogen atoms (excluding the sulfonyl O atoms) from the best least-squares plane of 0.03 Å and the pyet ligand is also planar with an rms deviation of 0.004 Å, but C17 and O17 atoms deviate by 1.375(2) and 2.241(2) Å, respectively, from the best pyet plane. The sac and pyet ligands coordinate to silver (I) in an approximately linear fashion with an N–Ag–N angle of 159.14(5)°. The dihedral angle between the planes of sac and pyet is 5.65(6)°, showing the approximately coplanar arrangement of their ring systems.

The individual $[Ag_2(sac)_2(pyet)_2]$ molecules are linked by strong hydrogen bonds between the hydrogen of the hydroxyl group and the uncoordinated sulfonyl O atom of the sac ligands in the neighbouring units, forming a one-dimensional chain running parallel to the *b*-axis (see Fig. 2(a)). The one-dimensional hydrogen bonded chains are further linked by non-conventional intermolecular C–H···O hydrogen bonds and π(sac)–π(pyet) stacking interactions [Cg···Cg = 3.75(7) Å] as shown in Fig. 2(b).

3.5. Description of the crystal structure of $[Ag_4(sac)_4(pypr)_2]$

The molecular structure of the tetranuclear silver (I) complex $[Ag_4(sac)_4(pypr)_2]$ with the atom labelling is shown in Fig. 3. The selected bond lengths and angles are given in Table 4. The compound crystallizes in the triclinic space group $P\bar{1}$ and has two tetrameric molecules in its asymmetric unit with a similar conformation. The structure consists of isolated molecules of [Ag_4 $(sac)_4(pypr)_2$], which are built up from the bridging of

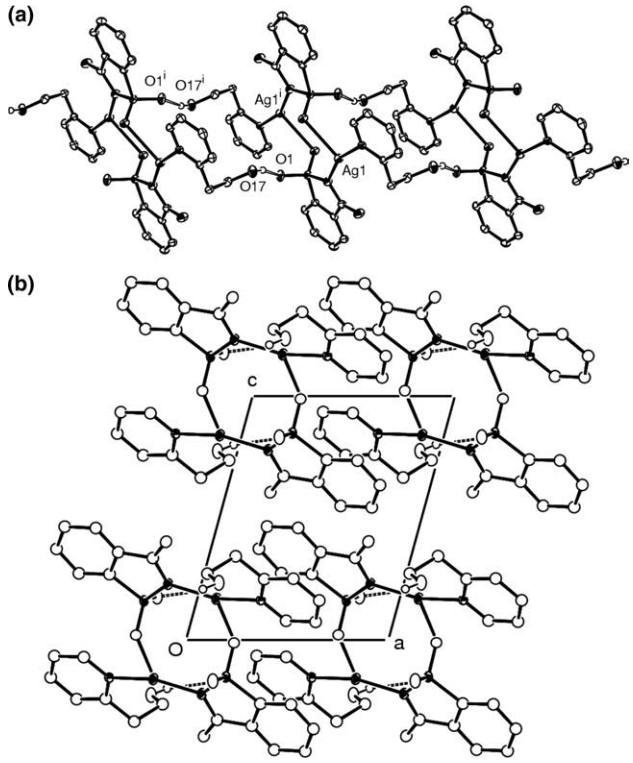


Fig. 2. (a) A fragment of the hydrogen bonded one-dimensional chain of $[Ag_2(sac)_2(pyet)_2]$. Symmetry code: i = –*x*, –*y*, –*z*. (b) Projection of the structure of $[Ag_2(sac)_2(pyet)_2]$ on the *ac* plane, showing π(sac)–π (pyet) interactions. The phenyl and ethylene H atoms are removed for clarity.

the central $[Ag_2(sac)_2]$ unit with two [Ag(sac)(pypr)] units through the sulfonyl oxygen atoms of the sac ligands. $[Ag_4(sac)_4(pypr)_2]$ exhibits two different silver centres. The two silver (I) ions (Ag1 and its symmetry-equivalent partner $Ag1^i$) in the centre exhibit a T-shaped planar $AgNO_2$ geometry with three sac ligands, while the two outer silver (I) ions (Ag2 and $Ag2^i$) are coordinated by a sac ligand and a pypr ligand in a near linear AgN_2 geometry [N2–Ag2–N3 = 168.6(4)°]. The sac ligands in the central $[Ag_2(sac)_2]$ unit act as a bidentate chelating ligands via the N and carbonyl O atoms forming an roughly planar eight-membered chelate ring. The central Ag1 pair of silver atoms appear to be interacting based on the Ag–Ag^i (i = 1 – *x*, 1 – *y*, –z) distance of 2.8480(13) Å, while Ag2 has no metal neighbours within 5 Å. The separation of the two central Ag3 atoms in the second asymmetric molecule of $[Ag_4(sac)_4(pypr)_2]$ is 2.8590(13) Å. These silver–silver contacts are some 0.60 Å shorter than twice the van der Waals radius of silver (3.44 Å) and clearly indicate a strong bonding interaction between the Ag1 and the Ag3 centres in the tetranuclear complex. The Ag–Ag distances found in $[Ag_4(sac)_4(pypr)_2]$ are also much shorter than those reported for other tetranuclear silver units $[Ag_4(SPh)_4(PPh_3)_4]$ [3.1300(3) Å] [19] and $[Ag_4(tren(mim)_3)_2]^{4+}$ [2.929(1) and 3.1313(9) Å] [20], where SPh and tren(mim)$_3$ are thiolate and tris {2-2(1-methyl)imidazolyl]methyliminoethyl} amine, respectively. The significance of short silver–silver distances has been debated: Jansen reported a value of 3.30 Å as the upper limit for an Ag···Ag contact in coordination compounds [21], whereas Dance et al. [22] stated that since the linear geometry at silver (I) indicates the fulfilment of its coordination requirements, there is no bonding interaction between silver (I) centres as close to each other as 2.886 Å in $[Ag(SCMeEt)_2]_n$. However, we argue that there is a significant bonding interaction between the silver centres at the short distances in the present $[Ag_4(sac)_4(pypr)_2]$ complex.

The Ag–N_{sac} bond distances in $[Ag_4(sac)_4(pypr)_2]$ are similar to those reported for the related silver (I)-saccharinato complexes [7,9–11], but the terminal Ag–N_{sac}

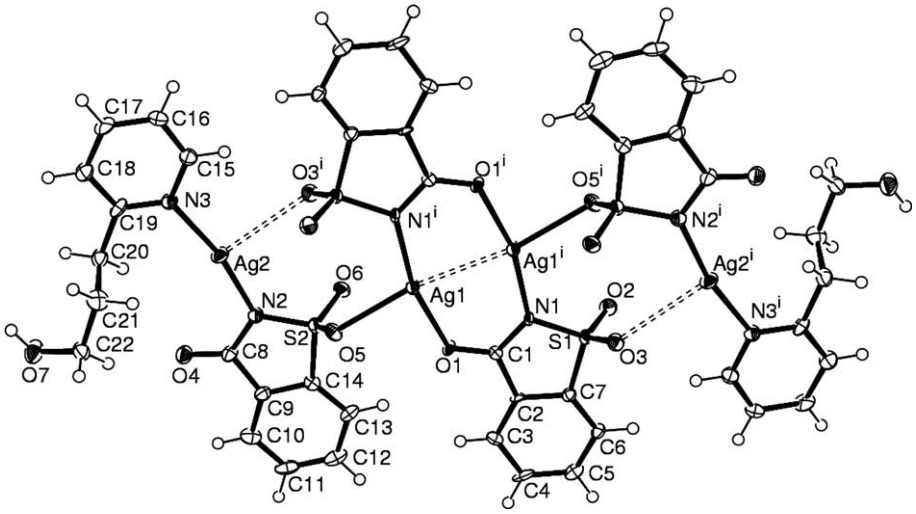


Fig. 3. View of tetrameric unit in $[Ag_4(sac)_4(pypr)_2]$ with the atom labelling scheme and 50% thermal ellipsoids (arbitrary spheres for the H atoms). Symmetry code (i) = 1 – *x*, 1 – *y*, –*z*. The asymmetric unit of the complex contains two molecules and one of them was removed for clarity.

Table 4
Selected geometrical data for $[Ag_4(sac)_4(pypr)_2]$[a]

Bond lengths (Å) and angles (°)			
Ag1–N1^{i}	2.184(10)	N1–Ag1–O1^{i}	165.5(3)
Ag1–O1	2.230(8)	N1–Ag1–O5^{i}	106.2(3)
Ag1–O5	2.431(9)	O1–Ag1–O5	88.2(3)
Ag2–N2	2.102(10)	N2–Ag2–N3	168.6(4)
Ag2–N3	2.140(10)	N2–Ag2– O3^{i}	99.0(3)
Ag2–O3^{i}	2.960(9)	N3–Ag2– O3^{i}	92.2(3)
Ag1–Ag1^{i}	2.8480(13)		

D–H···A	*d*(D–H)	*d*(H···A)	*d*(D···A)	∠(DHA)
Hydrogen bonds[b]				
O7–H1···O10^{ii}	0.90	1.89	2.793(14)	180
O14–H2···O2^{i}	0.90	1.89	2.788(14)	180
C16–H16···O14^{iii}	0.95	2.48	3.360(17)	154
C38–H38···O7^{iv}	0.95	2.20	3.127(17)	165
C40–H40···O2^{i}	0.95	2.38	3.289(17)	161

[a] Symmetry operations: (i) $1-x, 1-y, -z$; (ii) $1-x, 1-y, 1-z$; (iii) $1+x, y, z$; and (iv) $1+x, y-1, z$.
[b] O10, O17 and C38 and C40 atoms belongs to the second molecule in the asymmetric unit of the compound.

bond distances are noticeably longer than the corresponding bonds and the Ag–O_{sac} bonds in the central unit. The Ag–$O_{carbonyl}$ bond distance of 2.230(8) Å is almost identical to that observed in [Ag(sac)] [2.22 Å] [7], but slightly shorter than those found in $[Ag_2(\mu\text{-sac})_2(\mu\text{-hep})_2]_n$ [2.2535(11) and 2.3010(14) Å] [10]. The bridging Ag–$O_{sulfonyl}$ bond distance of 2.431(9) Å is similar to the equivalent value observed in [Ag(sac)] (2.45 Å) [7], but is significantly shorter than the 2.6390(10) Å found in Na[Ag(sac)] [9]. Furthermore, there is a weaker interaction between the sulfonyl O atoms of the sac ligands in the central unit and the silver (I) centres at the terminal units, yielding a Ag–$O_{sulfonyl}$ bond distance of 2.960(9) Å and probably suggesting the "semi-coordination" of the sulfonyl group of sac to silver (I). The Ag–N_{pypr} bond distance is 2.140(10) Å. Similarly, the hydroxyl group of pypr is uncoordinated in $[Ag_4(sac)_4(pypr)_2]$ in contrast to the bidentate coordination behaviour in the presence of divalent transition metals [23–25]. This may be explained in terms of hard and soft acids and bases. As a soft acid, silver (I) will not prefer a hard base OH for coordination.

The ring systems of sac and pypr are planar. The rms deviations from the best planes of the sac1 with N1, sac2 with N2 and pypr species are 0.010, 0.016 and 0.012 Å, respectively. The displacement of the silver (I) ions from the corresponding planes is as follows: Ag1 from sac1 = 0.356(11) Å, Ag2 from sac2 = 0.212(9) Å and Ag2 from pypr = 0.0429(19) Å. The planes of sac and pypr coordinated the terminal Ag2 atoms are roughly coplanar with a dihedral angle of 10.7(6)°.

The unit-cell packing of the molecules of $[Ag_4(sac)_4(pypr)_2]$ is shown in Fig. 4. Relevant hydrogen bonds are listed in Table 4. The packing of the tetramers forms

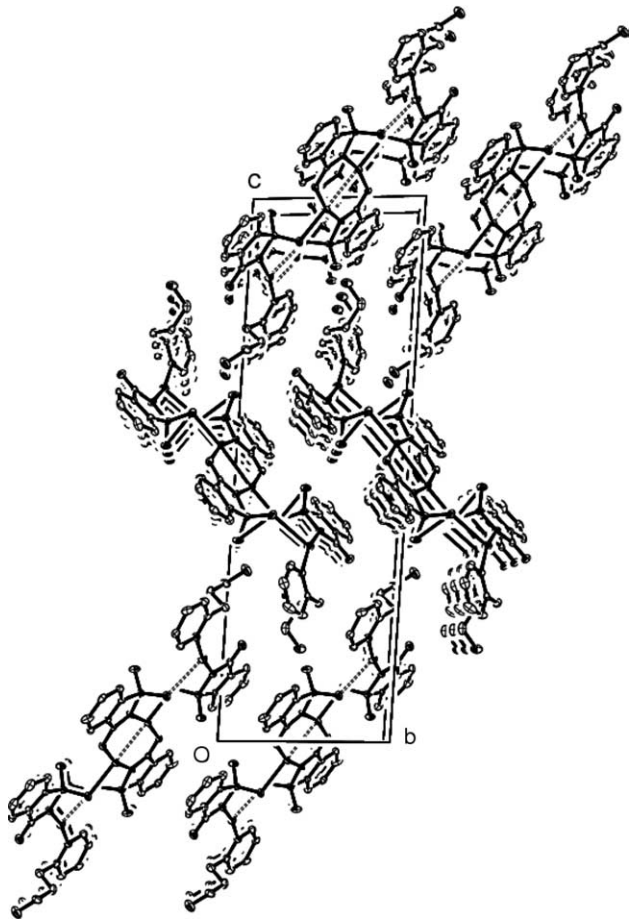


Fig. 4. A view of the unit cell of $[Ag_4(sac)_4(pypr)_2]$ viewed along the *a* axis. It shows the packing of the tetramers to form a herringbone motif. The phenyl and ethylene H atoms are removed for clarity.

a herring-bone motif. The two molecules in the asymmetric unit of the structure are connected by strong intermolecular O–H···O bonds (H···O = 1.89 Å), involving the hydroxyl H of pypr and sulfonyl O of sac. The O10, O17 and C38 and C40 atoms belongs to the second molecule in the asymmetric unit of the compound. The strong hydrogen bonds form hydrogen bonded dimers, which are further linked by C–H···O interactions, resulting in a layered structure. The C38–H38···O7^{iv} bond has an exceptionally short H···O contact of 2.20 Å, but this may arise from unmodelled disorder of some of the carbon atoms in the py ring containing C38.

4. Supplementary material

Crystallographic data for the structures reported in the paper have been deposited at the CCDC as supplementary data, CCDC Nos. 253479 and 253480 for $[Ag_2(sac)_2(pyet)_2]$ and $[Ag_4(sac)_4(pypr)_2]$, respectively. Copies of the data can be obtained on application to CCDC, 12 Union Road, Cambridge CB2 1EZ, UK

(Fax: +44 1223 336033; E-mail: deposit@ccdc.cam.ac.uk; http://www.ccdc.cam.ac.uk).

Acknowledgement

This work was supported financially by Ondokuz Mayis University.

References

[1] D.J. Ager, D.P. Pantaleone, S.A. Henderson, A.L. Katritzky, I. Prakash, D.E. Walters, Angew. Chem. Int. Ed. 37 (1998) 1802.
[2] E.W. Ainscough, E.N. Baker, A.M. Brodie, Inorg. Chim. Acta 172 (1990) 185.
[3] B. Kamenar, G. Jovanovski, Cryst. Struct. Commun. 11 (1982) 257.
[4] Z. Haider, K.M.A. Malik, K.J. Ahmed, H. Hess, H. Riffel, M.B. Hursthouse, Inorg. Chim. Acta 72 (1983) 21.
[5] F.A. Cotton, G.E. Lewis, C.A. Murillo, W. Schwotzer, G. Valle, Inorg. Chem. 23 (1984) 4038.
[6] S.Z. Haider, K.M.A. Malik, K.J. Ahmed, Inorg. Synth. 72 (1985) 47.
[7] R. Weber, M. Gilles, G. Bergerhoff, Z. Kristallogr. 206 (1993) 273.
[8] S.W. Ng, Z. Kristallogr. 210 (1995) 206.
[9] V.T. Yilmaz, S. Hamamci, C. Thone, Z. Anorg. Allg. Chem. 630 (2004) 1641.
[10] S. Hamamci, V.T. Yilmaz, W.T.A. Harrison, J. Mol. Struct. 734 (2005) 191.
[11] G.M. Sheldrick, SHELX-97, Programs for Crystal Structure Analysis, University of Göttingen, Germany, 1997.
[12] L.J. Farrugia, J. Appl. Crystallogr. 30 (1997) 565.
[13] O.V. Quinzani, S. Tarulli, O.E. Piro, E.J. Baran, E.E. Castellano, Z. Naturforsch. B52 (1997) 183.
[14] E.J. Baran, C.C. Wagner, J. Raman Spectrosc. 32 (2001) 1064.
[15] K. Nakamoto, Infrared and Raman Spectra of Inorganic and Coordination Compounds, Part B, 5th ed., Wiley, New York, 1997.
[16] V.T. Yilmaz, S. Hamamci, C. Thone, Cryst. Res. Technol. 37 (2002) 1143.
[17] V.T. Yilmaz, S. Hamamci, C. Thone, Z. Anorg. Allg. Chem. 629 (2003) 711.
[18] V.T. Yilmaz, S. Hamamci, C. Thone, J. Coord. Chem. 56 (2003) 787.
[19] L.S. Ahmed, J.R. Dilworth, J.R. Miller, N. Wheatley, Inorg. Chim. Acta 278 (1998) 229.
[20] S.-P. Yang, H.-L. Zhu, X.-H. Yin, X.-M. Chen, L.-N. Ji, Polyhedron 19 (2000) 2237.
[21] M. Jansen, Angew. Chem. Int., Ed. Engl. 26 (1987) 1098.
[22] I.G. Dance, L.J. Fitzpatrick, A.D. Rae, M.L. Scudder, Inorg. Chem. 22 (1983) 3785.
[23] V.T. Yilmaz, S. Hamamci, O. Andac, C. Thone, W.T.A. Harrison, Transition Met. Chem. 28 (2003) 676.
[24] V.T. Yilmaz, S. Hamamci, C. Thone, Cryst. Res. Technol. 38 (2003) 992.
[25] S. Hamamci, V.T. Yilmaz, W.T.A. Harrison, J. Coord. Chem. 56 (2003) 1033.

Available online at www.sciencedirect.com
SCIENCE DIRECT®
Polyhedron 24 (2005) 701–709
POLYHEDRON
www.elsevier.com/locate/poly

Crystal, molecular and electronic structure of the $[ReCl_3(bipy)(PPh_3)]$ complex

B. Machura [a,*], R. Kruszynski [b], M. Jaworska [c], Piotr Lodowski [c]

[a] Department of Inorganic and Radiation Chemistry, Institute of Chemistry, University of Silesia, 9th Szkolna St., 40-006 Katowice, Poland
[b] Department of X-ray Crystallography and Crystal Chemistry, Institute of General and Ecological Chemistry, Lodz University of Technology, 116 Żeromski St., 90-924 Łódź, Poland
[c] Department of Theoretical Chemistry, Institute of Chemistry, University of Silesia, 9th Szkolna St., 40-006 Katowice, Poland

Received 17 August 2004; accepted 2 February 2005

Abstract

X-ray structure of the $[ReCl_3(bipy)(PPh_3)]$ complex has been determined and its geometric parameters have been examined using the density-functional theory method. The UV–Vis spectrum of the complex has been discussed on the basis of the electronic transitions of $[ReCl_3(bipy)(PPh_3)]$ calculated with the time-dependent DFT method.
© 2005 Elsevier Ltd. All rights reserved.

Keywords: Rhenium(III) complexes; Bipyridine ligand; X-ray structure; DFT calculations

1. Introduction

Design of biological labels for various therapeutic, diagnostic and mechanistic applications is currently in the centre of scientific research. Transition metal complexes can be covalently linked to different biomolecules in electron-transfer studies and other analytical applications [1–3]. In this context, rhenium polypyridine complexes show a great potential to be developed in bioanalytical applications in view of their photophysical and photochemical properties. A wide of diimine rhenium complexes have been recently synthesized and studied in detail [4–12].

The $[ReCl_3(MeCN)(PPh_3)]$ complex has proven to be useful precursor in the synthesis of other Re(III) compounds [13,14]. Rouschias and Wilkinson [15] reported the synthesis of $[ReCl_3(MeCN)(PPh_3)]$ in 1967, along with its reactions with pyridyl ligands that led to the formation of $[ReCl_3(py)_3]$, $[ReCl_3(py)_2(PPh_3)]$ and $[ReCl_3(bipy)(PPh_3)]$. However, the crystal and molecular structure of the $[ReCl_3(bipy)(PPh_3)]$ complex has not been determined, and reports of rhenium (III) complexes with 2,2′-bipirydyl ligand are sparse. The only structurally characterised rhenium (III) bipirydyl complexes appear to be $[ReBr_3(CO)_2(bipy)]$ [16], $[ReCl_2(bipy)_2][PF_6]$ [17] $[Re(p\text{-}CH_3C_6H_4S)\{SCH_2CH(NHCOCH_3)COO\}(bipy)]$ [18] and $[ReCl(bipy)(Tp)][OTf]$ (Tp = hydridotris(pyrazolyl)borate) [19].

Here, we present X-ray and electronic structure of the $[ReCl_3(bipy)(PPh_3)]$ complex. The electronic structure of $[ReCl_3(bipy)(PPh_3)]$ has been determined basing on the results of the density-functional theory (DFT) calculations. The spin-allowed triplet–triplet electronic transitions of $[ReCl_3(bipy)(PPh_3)]$ have been calculated with the time-dependent DFT method (TDDFT) and the UV–Vis spectrum of the title complex has been discussed on this basis.

The recent calculations with the TDDFT method for open- and closed-shell of 5d-metal complexes (including rhenium complexes) have supported the TDDFT

* Corresponding author. Tel.: +48322582441; fax: +48322599978.
E-mail addresses: bmachura@poczta.onet.pl (B. Machura), kruszyna@p.lodz.pl (R. Kruszynski), mj@tc3.ich.us.edu.pl (M. Jaworska).

0277-5387/$ - see front matter © 2005 Elsevier Ltd. All rights reserved.
doi:10.1016/j.poly.2005.02.001

method to be applicable for such systems giving good assignment of experimental spectra [20–26].

2. Experimental

2.1. General procedure

All solvents were of reagent grade and were used as received. Ammonium perrhenate, Ph_3P and bipyridine (bipy) were purchased from Aldrich and used as received. The $[ReCl_3(bipy)(PPh_3)]$ complex was prepared according to the literature method [15].

IR spectra were recorded on a Nicolet Magna 560 spectrophotometer in the spectral range 4000–400 cm^{-1} with the samples in the form of KBr pellets. Electronic spectra were measured on a spectrophotometer Lab Alliance UV–VIS 8500 in the range 800–220 nm in deoxygenated dichloromethane solution. Magnetic susceptibilities were measured at 296 K by the Faraday method. Elemental analyses (C, H, N) were performed on a Perkin–Elmer CHN-2400 analyzer.

2.2. Crystal structures determination and refinement

The X-ray intensity data of $[ReCl_3(bipy)(PPh_3)]$ were collected on a KM-4-CCD automatic diffractometer equipped with CCD detector with 44 s exposure time was used and a quarter of Ewald sphere was collected. The unit cell parameters were determined from least-squares refinement of the setting angles of 3697 strongest reflections. Details concerning crystal data and refinement are given in Table 1. Lorentz, polarization and numerical absorption corrections [27] were applied. The structure was solved by means of the Patterson method and subsequently completed by the difference Fourier recycling. All the non-hydrogen atoms were refined anisotropically using full-matrix, least-squares technique. The hydrogen atoms of the phenyl rings were treated as ''riding'' on their parent carbon atoms [*d*(C–H) = 0.96 Å] and assigned isotropic temperature factors equal 1.2 times the value of equivalent temperature factor of the parent carbon atom. SHELXS97 [28], SHELXL97 [29] and SHELXTL [30] programs were used for all the calculations. Atomic scattering factors were those incorporated in the computer programs.

2.3. Computational details

GAUSSIAN 03 program [31] was used in the calculations. The geometry optimization was carried out with the DFT method with the use of B3LYP functional [32,33] and different basis set on the rhenium atom: LANL2DZ, LANL2DZ with additional d ($\alpha = 1.0$) and f ($\alpha = 1.0$) functions [34] and SDD with effective core potential [35]. 6-31G(d) basis set was used for the chlorine, nitrogen, phosphorous and carbon atoms and 6-31G on the hydrogen atoms The electronic spectrum was calculated with the TDDFT method [36]. The nature of the intramolecular hydrogen bonds was studied by means of the Bader theory of atoms in molecules (AIM) [37]. The AIM method was extended and implemented within GAUSSIAN program and Ahlrichs DFT Coulomb Fitting Basis Set was used on the rhenium atom in the AIM calculations [38,39].

Table 1
Crystal data and structure refinement for $[ReCl_3(bipy)(PPh_3)]$

Empirical formula	$C_{28}H_{23}Cl_3N_2PRe$
Formula weight	711.00
Temperature (K)	291(2)
Wavelength (Å)	0.71073
Crystal system	monoclinic
Space group	$P2_1/n$
Unit cell dimensions	
a (Å)	10.204(2)
b (Å)	24.381(5)
c (Å)	11.005(2)
β (°)	106.77(3)
Volume (Å^3)	2621.4(9)
Z	4
Density (calculated) (Mg/m^3)	1.802
Absorption coefficient (mm^{-1})	5.023
$F(0\,0\,0)$	1384
Crystal size (mm)	$0.14 \times 0.14 \times 0.03$
θ Range for data collection (°)	3.47–25.11
Index ranges	$-12 \leqslant h \leqslant 11$, $0 \leqslant k \leqslant 29$, $0 \leqslant l \leqslant 13$
Reflections collected/independent	4654/4654
Completeness to $2\theta = 50.2°$ (%)	97.2
Maximum and minimum transmission	0.8721 and 0.5419
Data/restraints/parameters	4654/0/316
Goodness-of-fit on F^2	1.090
Final R indices [$I > 2\sigma(I)$]	$R_1 = 0.0586$
	$wR_2 = 0.1512$
R indices (all data)	$R_1 = 0.0725$
	$wR_2 = 0.1633$
Largest difference peak and hole (e/Å^3)	2.850 and −2.088

3. Results and discussion

The $[ReCl_3(bipy)(PPh_3)]$ complex was obtained in the reaction of $[ReCl_3(MeCN)(PPh_3)_2]$ with bipyridine according to the literature method [15]. The elemental analysis of the complex is in good agreement with its formulation. The characteristic band corresponding to the ν(CN), ν(C=C) modes of the bipy ligand appears at 1604 cm^{-1} in the IR spectrum of $[ReCl_3(bipy)(PPh_3)]$. The $[ReCl_3(bipy)(PPh_3)]$ complex shows room temperature magnetic moment of 1.7 BM. This value is typical of mononuclear complexes with low-spin rhenium (III) (d^4) ions in O_h field [40], and arises because of the large spin–orbit coupling ($\xi = 2500$ cm^{-1}) [41]. A similar deviation from the expected value (2.8 BM) has been found for $[ReX_2(pymS)(PPh_3)]$ (X = Cl, Br, I) [42,43],

$[ReCl_3(NCR)(PPh_3)_2]$ (R = Me, Et, Ph), $[ReCl_3$ (NCR)-$(P(p\text{-tol})_3)]$ (R = Me, Et) [44] and $[ReCl_3(\eta^3\text{-}N,N,P\text{-}N\{CH_2CH_2PPh_2\}CH_2CH_2P(O)Ph_2\})]$ [45].

3.1. Crystal structure

The $[ReCl_3(bipy)(PPh_3)]$ complex crystallises in the monoclinic space group $P2_1/n$ and its crystal structure is composed of the molecules located in general positions linked via weak intermolecular C(19)–H(19)···Cl(3)(1#: $-x$, $-y$, $-z+1$) hydrogen bonds [46–48] (D···A distance 3.442(11) Å and D–H···A angle 135.9°).

Fig. 1 depicts the perspective drawing of $[ReCl_3(bipy)(PPh_3)]$ with atomic numbering. The structure shows a distorted octahedral geometry about Re with the three bromine ligands arranged in a facial fashion. The N–Re–N bond angle of 75.9(3)° is less than 90°, as required by the bite distance exerted by the steric demand of the chelating bipyridine ligand. The intramolecular hydrogen bond [42–44] linking C(6)–H(6)···Cl(3) (D···A distance 3.520(14) Å and D–H···A angle 154.0°), C(19)–H(19)···Cl(3) (D···A distance 3.304(11) Å and D–H···A angle 124.8°), C(18)–H(18)···Cl(3) (D···A distance 3.765(11) Å and D–H···A angle 152.3°), C(6)–H(6)···Cl(2) (D···A distance 3.604(12) Å and D–H···A angle 102.8°) and C(28)–H(28)···Cl(2) (D···A distance 3.342(11) Å and D–H···A angle 125.4°) provide additional stabilisation of the $[ReCl_3(bipy)(PPh_3)]$ complex. The presence of the intramolecular hydrogen bonds in the structure of $[ReCl_3(bipy)(PPh_3)]$ was confirmed by the AIM calculations. The selected geometrical and topological parameters of the hydrogen bonds are summarised in Table 2. If H-bonds exist, the ranges of ρ_{BCP} and $\nabla^2\rho_{BCPv}$ (BCP = bond critical point) are 0.002–0.035e/a_0^3 and 0.024–0.139e/a_0^5, respectively [49]. The calculated ρ and $\nabla^2\rho$ values for $[ReCl_3(bipy)(PPh_3)]$ are in good agreement with the criteria of the charge density and the Laplacian of the charge density at the bond critical points.

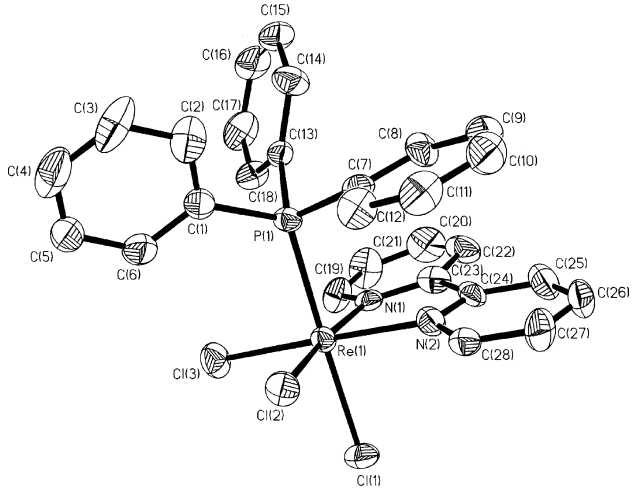


Fig. 1. Thermal ellipsoid plot of $[ReCl_3(bipy)(PPh_3)]$ showing the atom numbering scheme (50% probability ellipsoids). The hydrogen atoms are omitted for clarity.

Table 2
The selected geometrical (C···Cl distance) and topological parameters (electronic densities – $\rho_{H\cdots Cl}$ (in e/a_3^0)) and Laplacians of electronic densities – $\nabla^2\rho_{H\cdots Cl}$ (in e/a_5^0) for the bond critical points of H···Cl bonds for $[ReCl_3(bipy)(PPh_3)]$

Hydrogen bond	C···Cl (Å)	$\rho_{H\cdots Cl}$	$\nabla^2\rho_{H\cdots Cl}$
C(6)–H(6)···Cl(2)	2.667	0.011	0.041
C(28)–H(28)···Cl(2)	2.498	0.016	0.056
C(18)–H(18)···Cl(3)	2.716	0.010	0.034
C(19)–H(19)···Cl(3)	2.519	0.015	0.054

Table 3
The experimental and optimized bond lengths (Å) and angles (°) for $[ReCl_3(bipy)(PPh_3)]$

Bond lengths	Exp.	Optimized			Bond angles	Exp.	Optimized		
		LANL2DZ	LANL2DZ*	SDD			LANL2DZ	LANL2DZ*	SDD
Re(1)–Cl(1)	2.434(2)	2.453	2.453	2.423	N(2)–Re(1)–N(1)	75.9(3)	76.33	76.34	75.78
Re(1)–Cl(2)	2.372(3)	2.435	2.433	2.413	N(2)–Re(1)–Cl(3)	169.7(2)	170.02	170.10	169.70
Re(1)–Cl(3)	2.364(3)	2.436	2.434	2.416	N(1)–Re(1)–Cl(3)	94.8(2)	93.93	94.02	94.24
Re(1)–N(1)	2.099(8)	2.102	2.102	2.120	N(2)–Re(1)–Cl(2)	95.8(2)	93.53	93.50	93.41
Re(1)–N(2)	2.094(8)	2.100	2.099	2.119	N(1)–Re(1)–Cl(2)	171.7(2)	169.72	169.71	169.03
Re(1)–P(1)	2.450(2)	2.513	2.515	2.521	Cl(3)–Re(1)–Cl(2)	93.47(9)	96.13	96.07	96.47
					N(2)–Re(1)–Cl(1)	86.4(2)	86.58	86.54	86.60
					N(1)–Re(1)–Cl(1)	89.2(2)	86.76	86.74	86.81
					Cl(3)–Re(1)–Cl(1)	89.24(10)	90.75	90.72	90.35
					Cl(2)–Re(1)–Cl(1)	89.76(10)	91.03	91.10	90.73
					N(2)–Re(1)–P(1)	90.6(2)	95.42	95.47	95.89
					N(1)–Re(1)–P(1)	94.0(2)	97.00	96.96	96.09
					Cl(3)–Re(1)–P(1)	94.42(10)	87.85	87.85	87.60
					Cl(2)–Re(1)–P(1)	86.50(9)	85.48	85.47	86.75
					Cl(1)–Re(1)–P(1)	174.91(8)	176.07	176.12	176.55

Exp. stands for experimental; LANL2DZ* – LANL2DZ basis set with additional d ($\alpha = 1.0$) and f ($\alpha = 1.0$) functions.

The most important experimental bond lengths and angles of $[ReCl_3(bipy)(PPh_3)]$ are reported in Table 3. The Re–N bond lengths (2.099(8) and 2.094(8) Å) of the title complex are similar to those found for the other rhenium (III) polypyridyl compounds: in $[ReCl_2(bipy)_2]PF_6$ – 2.094(5) and 2.096(5) Å [17] and in the $[ReL(terpy)_2]^{2+}$ (L = Cl, OH, NCS) complexes – about 2.10 Å [50]. These values are significantly shorter than comparable distances for saturated amine complexes, where metal-to-ligand π-back bonding is not possible, for instance, the Re–NH_2 distance in the $[Re(N_2)(ampy)(tbpy)(PPh_3)]PF_6$ compound is 2.197(7) [51]. A lengthening of the Re–N_{bipy} distances in Re(V) complexes [52–56], consistent with the notion of the greatest M–L back bonding occurring when the metal is most electron-rich, also confirms a significant π-back bonding between the rhenium and bipy ligand of $[ReCl_3(bipy)(PPh_3)]$. The Re–Cl(1) distance (2.434(2) Å) is affected by *trans* influence of the triphenylphosphine and is therefore longer than the Re–Cl(2) (2.372(3) Å) and Re–Cl(3) (2.364(3) Å) bond lengths located in *trans* positions to the bipy ligand.

The bond valences (v_{ij}) were computed as $v_{ij} = \exp[(R_{ij} - d_{ij})/B]$ [57–59], where d_{ij} is the observed bond length and R_{ij} is the bond-valence parameter (in the formal sense R_{ij} is the single-bond length between i and j atoms [60]). The R_{Re-N}, R_{Re-P}, R_{Re-Cl}, were taken as 2.06, 2.46 and 2.23 [57], respectively, and the value of B was taken as 0.37 [53]. The computed bond valences of the rhenium are $v_{Re-N} = 0.90$, 0.91 $v_{Re-P} = 1.03$ and $v_{Re(1)-Cl} = 0.58$, 0.68, 0.70 v.u. [valence units], thus PPh_3 moiety is strongest bonded to the rhenium and chloride substituents are bonded weakest.

Table 4
The Mulliken atomic charges and spin densities of $[ReCl_3(bipy)(PPh_3)]$

Atom	Atomic charge	Spin density
Re(1)	0.277	1.910
Cl(1)	−0.359	0.055
Cl(2)	−0.353	0.093
Cl(3)	−0.358	0.090
P(1)	1.214	−0.054
N(1)	−0.613	−0.034
N(2)	−0.610	−0.032

3.2. The optimized geometry, charge distribution, spin densities and molecular orbitals

The geometry of $[ReCl_3(bipy)(PPh_3)]$ was optimized in triplet and singlet states using the DFT method with

Table 5
The energy and character of the selected molecular orbitals with α and β spins for $[ReCl_3(bipy)(PPh_3)]$

	MOs with α spin		MOs with β spin	
	E (eV)	Character	*E* (eV)	Character
HOMO − 17	−8.535	σ(Cl), σ(N)	−8.795	π(bipy)
HOMO − 16	−8.469	π(Cl), σ(Cl)	−8.596	σ(Cl), (N)
HOMO − 15	−8.387	π(Cl), σ(Cl)	−8.463	σ(Cl), (N)
HOMO − 14	−8.163	π(Cl), π(bipy)	−8.261	π(Cl), σ(Cl)
HOMO − 13	−7.565	π(Cl), σ(Cl), π(Ph), n(P)	−7.884	π(Cl)
HOMO − 12	−7.461	π(Ph), π(Cl),	−7.782	π(Cl)
HOMO − 11	−7.351	π(bipy), π(Cl)	−7.482	π(Ph), π(Cl)
HOMO − 10	−7.324	π(Cl), π(bipy)	−7.438	π(Ph)
HOMO − 9	−7.254	π(Ph)	−7.351	π(bipy)
HOMO − 8	−7.124	π(Ph), π(bipy)	−7.258	π(Ph)
HOMO − 7	−6.953	π(Ph), π(Cl)	−7.124	π(Ph), π(Cl), π(bipy)
HOMO − 6	−6.786	π(Cl), π(Ph)	−7.103	π(Cl), π(Ph)
HOMO − 5	−6.738	π(Ph)	−6.868	π(Ph), π(Cl)
HOMO − 4	−6.578	π(Cl), π(Ph)	−6.736	π(Ph), π(Cl)
HOMO − 3	−6.470	π(Cl), π(Ph), n(P)	−6.710	π(Ph), π(Cl)
HOMO − 2	−5.840	d_{xy}(Re), π(Cl)	−6.390	π(Cl), π(Ph), n(P)
HOMO − 1	−5.746	d_{xz}(Re), π(Cl)	−6.380	π(Cl), π(Ph)
HOMO	−5.492	d_{yz}(Re), π(Cl)	−4.876	d_{xz}(Re), π(Cl)
LUMO	−2.466	π*(bipy)	−2.852	d_{yz}(Re), π(bipy), π(Cl)
LUMO + 1	−1.483	π*(bipy)	−2.576	d_{xy}(Re), π(bipy), π(Cl)
LUMO + 2	−1.391	π*(bipy)	−2.378	π*(bipy), d_{xy}(Re)
LUMO + 3	−1.085	d_{z2}(Re)–σ(Cl)–σ(P), π(P) + π*(Ph)	−1.444	π*(bipy)
LUMO + 4	−0.884	π(P) + π*(Ph)	−1.326	π*(pzH), d_{xy}(Re)
LUMO + 5	−0.688	π(P) + π*(Ph)	−0.932	d_{z2}(Re)–σ(Cl)–σ(P), π(P) + π*(Ph)
LUMO + 6	−0.501	π*(Ph)	−0.876	π(P) + π*(Ph)
LUMO + 7	−0.392	π*(Ph)	−0.652	π(P) + π*(Ph)
LUMO + 8	−0.053	d_{x2-y2}–σ(N)–σ(Cl)	−0.495	π*(Ph)
LUMO + 9	0.039	d_{z2}(Re)–σ(Cl)–σ(P), π*(Ph)	−0.328	π*(Ph)
LUMO + 10	0.076	π*(Ph)	0.078	π*(Ph)
LUMO + 11	0.104	π*(bipy)	0.097	π*(bipy)

the B3LYP functional. The energy of the singlet state is of 15.8 kcal higher. The optimized geometric parameters (with different basis sets on the rhenium atom) of the triplet state are gathered in Table 3. The optimised geometries are in good agreement with the experimental one, the largest differences are found for the Re–Cl and Re–P bond distances. The similar elongation of rhenium–halogene and rhenium–phosphorous bond lengths in the B3LYP has been found in other rhenium complexes [14,61]. The differences of the calculated and experimental Re–Cl(2,3) bonds lengths can be explained by strong hydrogen bond involving Cl(2) and Cl(3) atoms. The formation of the hydrogen bond causes local deficiency of electron density on the chloride ions and consequently the Cl(2) and Cl(3) ligands are closer to the rhenium atom in the experimental structure.

Table 4 presents the Mulliken atomic charges and spin densities for $[ReCl_3(bipy)(PPh_3)]$. The calculated charge on the rhenium atom is considerable lower than the formal charge +3. It results from a charge donation from the chloride ions and triphenylphosphine ligand, which act as σ-donors. There is large positive charge on the P atom and the charges on the chloride ligands are significantly smaller than −1. The bipy ligand of $[ReCl_3(bipy)(PPh_3)]$ acts as an electron acceptor, the charges on the bipyridine nitrogen atoms bonded with the rhenium atom are negative.

In the title complex, there is positive spin density of about 2 on the rhenium atom and small negative or positive spin densities on the donor atoms of the other ligands (Table 4). It confirms the presence of two unpaired electrons on the rhenium atom.

3.3. Molecular orbitals

The energies and characters of several highest occupied and lowest unoccupied molecular orbitals of $[ReCl_3(bipy)(PPh_3)]$ are presented in Table 5. The selected HOMO and LUMO orbitals of $[ReCl_3(bipy)(PPh_3)]$ with α spin are depicted in Fig. 2. Most of the MOs of the title complex has complicated character. The percent participation of atomic orbitals in the selected HOMO

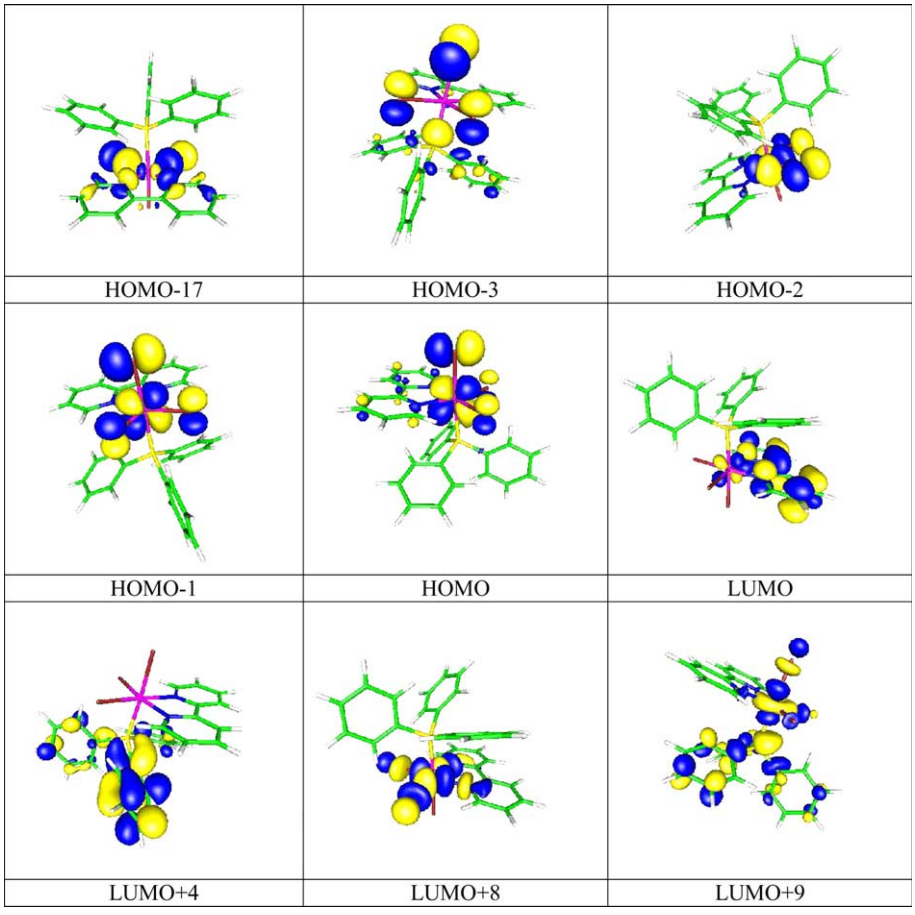


Fig. 2. The selected HOMO and LUMO orbitals with α spin for $[ReCl_3(bipy)(PPh_3)]$. Positive values of the orbital contour are represented in blue (0.04 au) and negative values – in yellow (−0.04 au). (For interpretation of the references to color in this figure legend, the reader is referred to the web version of this article.)

Table 6
The percent participation of the ligand atomic orbitals in the highest occupied and lowest unoccupied molecular orbitals for [$ReCl_3$(bipy)(PPh_3)]

MO with α spin	Re (d)	Cl	bipy	P	Ph	MO with β spin	Re (d)	Cl	bipy	P	Ph
HOMO − 17	6.32	46.89	36.08	0.92	2.19	HOMO − 17	0.39	1.09	93.29	0.30	4.52
HOMO − 16	13.84	58.61	10.85	1.97	8.81	HOMO − 16	6.29	59.92	22.77	1.09	3.20
HOMO − 15	16.51	56.62	9.14	2.86	8.92	HOMO − 15	6.65	51.87	32.02	0.80	1.88
HOMO − 14	17.84	42.22	32.21	0.47	7.06	HOMO − 14	11.04	66.05	1.35	5.73	9.07
HOMO − 13	7.36	26.32	9.95	11.95	40.45	HOMO − 13	10.84	74.60	5.56	0.18	7.87
HOMO − 12	0.87	23.70	5.13	1.03	68.57	HOMO − 12	7.10	69.65	10.13	0.78	12.09
HOMO − 11	0.85	32.57	41.47	0.19	24.88	HOMO − 11	5.50	30.32	7.25	9.43	44.00
HOMO − 10	0.67	40.79	36.61	0.34	21.41	HOMO − 10	1.03	8.84	2.96	1.29	85.04
HOMO − 9	0.44	4.48	2.41	0.15	92.33	HOMO − 9	0.09	1.53	80.72	0.11	17.49
HOMO − 8	0.86	3.09	19.89	0.33	75.79	HOMO − 8	0.05	2.70	2.81	0.22	94.01
HOMO − 7	5.37	29.02	7.28	3.32	53.98	HOMO − 7	0.90	25.70	14.01	0.34	58.74
HOMO − 6	5.55	42.56	7.46	3.71	37.57	HOMO − 6	0.58	61.72	10.95	0.20	26.23
HOMO − 5	1.32	10.99	1.57	0.71	84.79	HOMO − 5	2.26	23.67	3.88	4.65	64.48
HOMO − 4	1.22	69.90	2.84	0.14	25.77	HOMO − 4	0.51	14.53	1.80	1.54	81.08
HOMO − 3	1.02	62.84	0.56	12.23	21.39	HOMO − 3	3.12	35.93	5.55	4.16	48.43
HOMO − 2	56.96	35.50	5.70	0.07	0.86	HOMO − 2	0.50	71.32	1.11	11.31	14.47
HOMO − 1	54.11	37.42	4.39	0.35	3.07	HOMO − 1	0.74	84.48	3.15	0.96	10.30
HOMO	53.34	31.16	10.61	0.61	2.68	HOMO	50.32	21.22	21.76	1.17	3.82
LUMO	6.97	1.77	86.55	1.30	1.81	LUMO	57.97	16.45	14.62	2.39	7.96
LUMO + 1	2.90	0.80	90.69	0.73	3.77	LUMO + 1	58.45	13.93	24.08	0.96	1.40
LUMO + 2	1.71	0.31	93.72	0.59	3.20	LUMO + 2	25.09	5.50	64.69	1.07	2.63
LUMO + 3	13.86	6.83	3.88	15.16	49.80	LUMO + 3	4.81	0.81	89.66	0.61	3.04
LUMO + 4	0.80	0.29	3.22	6.96	87.15	LUMO + 4	6.18	1.55	78.95	2.74	9.74
LUMO + 5	3.19	1.70	1.54	16.03	76.88	LUMO + 5	10.66	3.68	5.67	11.56	57.80
LUMO + 6	0.15	0.27	1.93	1.75	94.30	LUMO + 6	0.91	0.25	2.07	7.01	88.48
LUMO + 7	6.83	5.37	7.09	3.79	74.77	LUMO + 7	2.41	0.81	2.28	13.00	80.41
LUMO + 8	42.24	24.40	31.44	0.13	0.43	LUMO + 8	0.37	0.22	1.99	1.46	94.63
LUMO + 9	21.63	17.16	5.48	14.21	38.81	LUMO + 9	3.76	2.07	5.58	2.09	84.82
LUMO + 10	0.62	1.11	9.75	1.98	85.23	LUMO + 10	0.42	0.45	11.53	1.63	85.01
LUMO + 11	0.31	0.31	85.15	0.16	13.82	LUMO + 11	0.39	0.09	84.30	0.15	14.94

and LUMO orbitals for [$ReCl_3$(bipy)(PPh_3) are shown in Table 6. The MO compositions was determined on the basis of Mulliken analysis.

Among the highest occupied MOs of [$ReCl_3$(bipy)(PPh_3)], the largest numbers constitute π orbitals of the bipyridine and phenyl rings with a contribution from the Cl atoms. The rhenium d_π atomic orbital (d_{xz}, d_{yz} and d_{xy}) and π orbitals of the chlorine ligands, but in anti-bonding arrangement, make main contributions into the HOMO − 2, HOMO − 1 and HOMO with α-spin and HOMO, LUMO and LUMO + 1 with β-spin. The d_z^2 rhenium orbital with an antibonding admixture of the chlorine and phosphorus lone pairs orbitals constitute the LUMO + 9 with α-spin and LUMO + 5 with β-spin orbitals. The largest participation of the $d_{x^2-y^2}$ rhenium orbital is visible in the LUMO + 8 with α-spin and the LUMO + 13 with β-spin. The LUMO, LUMO + 1 and LUMO + 2 with α-spin and LUMO + 1 and LUMO + 2 with α-spin have predominantly π*(bipy) character. The triphenylphosphine ligand participates in the higher LUMO orbitals. The HOMO − 3 with α-spin and HOMO − 2 with β-spin are π orbitals of the chloride ligands and phenyl groups with a substantial contribution from the free electron pairs on the phosphorus atom. The LUMO + 3, LUMO + 4, LUMO + 5 with α-spin and the LUMO + 5, LUMO + 6, LUMO + 7 with β-spin present π interaction of the phosphorous orbitals with π* orbitals of the phenyl groups.

3.4. Electronic spectrum

The experimental and calculated electronic spectra of [$ReCl_3$(bipy)(PPh_3)] are presented in Fig. 3. Each calculated transition in Fig. 3(b) was represented by a Gaussian function with the height equal to the oscillator strength and width equal to 0.04.

Table 7 shows the spin-allowed triplet–triplet electronic transitions calculated with the TDDFT method and the assignments of the calculated transitions to the experimental absorption bands for [$ReCl_3$(bipy)(PPh_3)].

The investigated complex is of large size, the number of basis functions is equal 560. Eighty electron transitions calculated by the TDDFT method do not comprise all the experimental absorption bands. The UV–Vis spectrum of [$ReCl_3$(bipy)(PPh_3)] was calculated only to 290 nm, so the shortest wavelength

experimental band (at 228.8 nm) cannot be assigned to the calculated transitions, and the assignments of the band at 301.0 nm may be incomplete. Considering that the solution spectra of PPh_3 and bipy exhibit intense absorption bands in 260–200 nm region, some additional intraligand and interligand transitions are expected to be found at higher energies in the calculation.

The calculations result in many transitions. Some of them have very small oscillator strengths. Except for the electronic transitions of d → d character and the low energy part of the spectrum, only transitions with oscillator strengths larger than 0.0050 are listed in Table 7.

The assignment of the calculated transitions to the experimental bands is based on the criterion of the energy and oscillator strength of the calculated transitions. In the description of the electronic transitions the main components of the molecular orbital are used. The HOMO − 2, HOMO − 1, HOMO and LUMO + 8 with α-spin and HOMO, LUMO and LUMO + 1 with β-spin. orbitals are treated as d orbitals.

The broad and intense (Fig. 3) longest wavelength experimental band of $[ReCl_3(bipy)(PPh_3)]$ with maximum at 636.8 nm is mainly attributed to two transition of $d \rightarrow \pi^*_{bipy}$ character with large oscillator strength calculated at 834.6 nm.

The experimental band at 436.6 nm is assigned to the transitions of MLCT ($d \rightarrow \pi^*_{bipy}$) and LMCT ($\pi_{Cl} \rightarrow d$ and $\pi_{Ph} \rightarrow d$) type, calculated in the range 540–433 nm.

The transitions calculated between 400 and 350 nm are ascribed to the experimental band at 401 nm. These transitions are of MLCT ($d \rightarrow \pi^*_{bipy}$) and LLCT ($\pi_{Cl} \rightarrow \pi^*_{bipy}$ and $\pi_{Ph} \rightarrow \pi^*_{bipy}$) character.

The experimental absorption band at 301 nm is assigned to the transition calculated in the range 340–290 nm. Among these electronic transitions are transitions of d → d, LMCT ($\pi_{Cl} \rightarrow d$, and $\pi_{Ph} \rightarrow d$ and $\pi_{bipy} \rightarrow d$), MLLCT ($d \rightarrow \pi^*_{bipy}$, $d \rightarrow \pi^*_{Ph}$) and LLCT ($\pi_{Cl} \rightarrow \pi^*_{bipy}$, $\pi_{Ph} \rightarrow \pi^*_{bipy}$ and $\pi_{Ph} \rightarrow \pi^*_{Ph}$) origin. The transitions of d → d have small oscillator strengths and they do not contribute significantly to the overall shape of the spectrum. They are hidden under the more intense transitions of CT type.

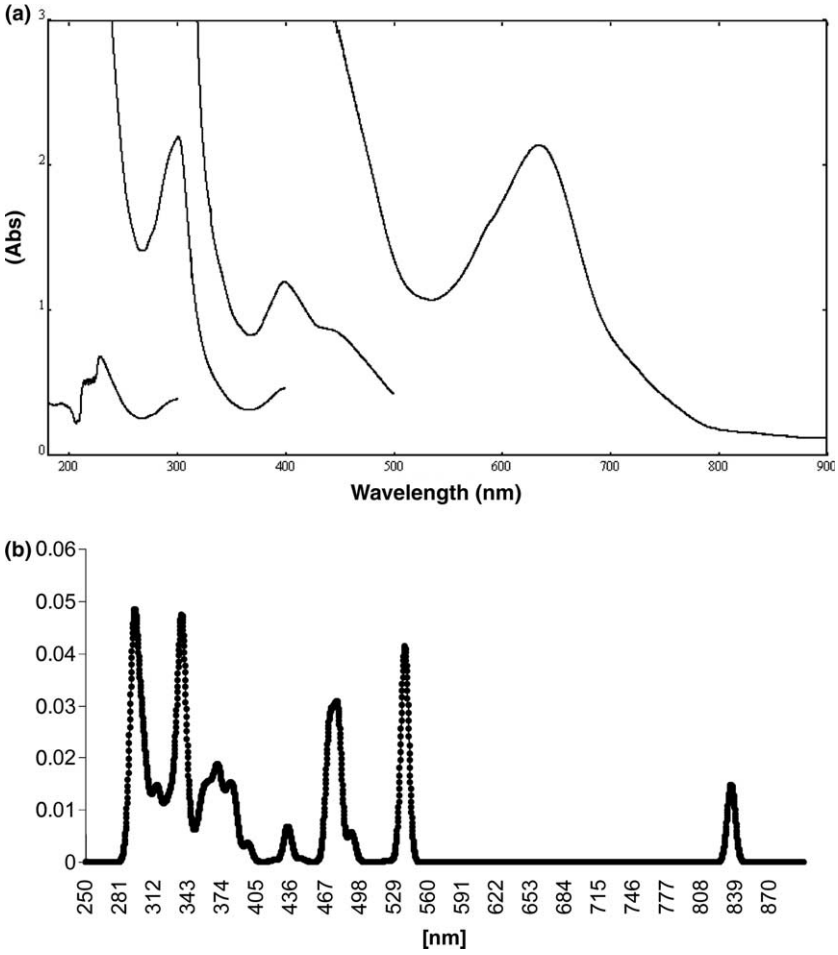


Fig. 3. The experimental (a) and calculated (b) electronic absorption spectrum of $[ReCl_3(bipy)(PPh_3)]$.

Table 7
The spin-allowed triplet-triplet electronic transitions calculated with the TDDFT method and the assignments of the calculated transitions to the experimental absorption bands for $[ReCl_3(bipy)(PPh_3)]$

The most important orbital excitations	Character	λ (nm)	E (eV)	f	Experimental Λ (nm) (E [eV]) ε
H(β) → L + 2(β)	d → π*(bipy)	834.6	1.49	*0.0149*	
H(α) → L(α)	d → π*(bipy)	539.0	2.30	*0.0413*	
H-2(β) → L(β)	π(Cl)/n(P) → d	490.8	2.53	*0.0056*	
H(β) → L + 3(β)	d → π*(bipy)	478.5	2.59	*0.0273*	636.8 (1.95) 2175
H-1(β) → L(β)	π(Cl) → d	471.1	2.63	*0.0121*	
H(β) → L + 3(β)	D → π*(bipy)	470.9	2.63	*0.0131*	
H-3(β) → L(β)	π(Ph)/π(Cl) → d	433.0	2.86	*0.0069*	
H(α) → L + 1(α)	d → π*(bipy)	384.5	3.22	*0.0091*	
H(α) → L + 1(α)	d → π*(bipy)	377.5	3.28	*0.0089*	
H(α) → L + 2(α)	d → π*(bipy)	370.5	3.35	*0.0098*	
H-3(α) → L(α)	π(Cl)/n(P) → π*(bipy)	369.6	3.35	*0.0051*	436.6 (2.84) 2950
H-4(α) → L(α)	π(Cl)/π(Ph) → π*(bipy)	361.4	3.43	*0.0081*	
H-4(α) → L(α)	π(Cl)/π(Ph) → π*(bipy)	356.5	3.48	*0.0087*	
H(α) → L + 8(α)	d → d	352.5	3.52	*0.0002*	
H(β) → L + 13(β)	d → d				401.0 (3.09) 3600
H-5(α) → L + 5(α)	π(Ph) → π*(Ph)	339.4	3.65	*0.0058*	
H-4(β) → L + 10(β)	π(Ph) → π*(Ph)				
H-2(α) → L + 3(α)	d/π(Cl) → d/π*(Ph)	337.1	3.68	*0.0109*	
H-2(α) → L + 3(α)	d/π(Cl) → d/π*(Ph)	336.4	3.69	*0.0254*	
H-3(β) → L + 2(β)	π(Cl)/π(Ph)/n(P) → π*(bipy)				
H-9(β) → L(β)	π(bipy) → d	330.8	3.75	*0.0097*	
H-2(α) → L + 8(α)	d → d	322.4	3.85	*0.0023*	
H-12(β) → L(β)	π(Cl) → d	315.6	3.93	*0.0069*	
H-1(α) → L + 8(α)	d → d	308.5	4.02	*0.0018*	
H(α) → L + 8(α)	d → d	306.1	4.05	*0.0008*	301.0 (4.12) 19 950
H-8(α) → L(α)	π(Ph) → d	301.4	4.11	*0.0056*	
H(β) → L + 11(β)	d → π*(bipy)				
H-8(α) → L(α)	π(Ph) → d	300.5	4.13	*0.0053*	
H-7(β) → L + 2(β)	π(Ph)/π(Cl) → π*(bipy)	294.6	4.21	*0.0100*	
H-13(β) → L + 1(β)	π(Cl) → d	294.6	4.21	*0.0174*	
H-13(α) → L(α)	π(Ph)/(Cl) → π*(bipy)	293.1	4.23	*0.0051*	
H-9(α) → L(α)	π(Ph) → π*(bipy)				
H-9(α) → L(α)	π(Ph) → π*(bipy)	292.5	4.24	*0.0062*	
H-14(β) → L(β)	π(Cl) → d				228.8 (5.42) 56 475

4. Supplementary data

Supplementary data for $C_{28}H_{23}Cl_3N_2PRe$ are available from the CCDC, 12 Union Road, Cambridge CB2 1EZ, UK (fax: +44-1223-336033; e-mail: deposit@ccdc.cam.ac.uk or www: http://ccdc.cam.ac.uk) on request, quoting the deposition number 247591.

Acknowledgement

The Gaussian 03 calculations were carried out in the Wrocław Centre for Networking and Supercomputing, WCSS, Wrocław, Poland under calculational Grant No. 51/96.

Crystallographic study was financed by funds allocated by the Ministry of Scientific Research and Information Technology to the Institute of General and Ecological Chemistry, Technical University of Łódź.

References

[1] J.R. Winkler, H.B. Gray, Chem. Rev. 92 (1922) 369.
[2] K.E. Erkkila, D.T. Odom, J.K. Barton, Chem. Rev. 99 (1999) 2777.
[3] K.K.W. Lo, D.Ch.M. Ng, W.K. Hui, K.K. Cheung, J. Chem. Soc., Dalton Trans. (2001) 2634.
[4] Y.B. Dong, L. Yang, K.K. Cheung, A. Mayr, J. Organomet. Chem. 598 (2000) 55.
[5] E. Hevia, J. Perez, V. Riera, D. Miguel, Organometallics 21 (2002) 5312.
[6] E. Hevia, J. Perez, V. Riera, D. Miguel, P. Campomanes, M.I. Menendez, T.L. Sordo, S. Garcia-Granda, J. Am. Chem. Soc. 125 (2003) 3706.
[7] D.C. Gerbino, E. Hevia, D. Morales, M.E. Navarro-Clemente, J. Perez, L. Riera, D. Miguel, Chem. Commun. (2003) 328.
[8] A.J. Blake, M.W. George, E.L. Little, J.J. Turner, Acta Crystallogr., Sect. E 57 (2001) m378.
[9] E. Hevia, J. Perez, V. Riera, D. Miguel, Chem. Commun. (2002) 1814.
[10] J. Guerrero, O.E. Piro, E. Wolcan, M.R. Feliz, G. Ferraudi, S.A. Moya, Organometallics 20 (2001) 2842.
[11] P. Ferreira, W.M. Xue, E. Bencze, E. Herdtweck, F.E. Kuhn, Inorg. Chem. 40 (2001) 5834.

[12] J.H. Jung, D.M. Hoffman, T.R. Lee, J. Organomet. Chem. 599 (2000) 112.
[13] P. Ghosh, A. pramanik, N. Bag, A. Chakravorty, J. Chem. Soc., Dalton Trans. (1992) 1883.
[14] B. Machura, M. Jaworska, R. Kruszynski, Polyhedron 23 (2004) 1819.
[15] G. Rouschias, G. Wilkinson, J. Chem. Soc. A (1967) 993.
[16] M.G.B. Drew, K.M. Davis, D.A. Edwards, J. Marshalsea, J. Chem. Soc., Dalton Trans. (1978) 1098.
[17] L.E. Helberg, S.D. Orth, M. Sabat, W.D. Harman, Inorg. Chem. 35 (1996) 5584.
[18] D. Papagiannopoulou, I.C. Pirmettis, M. Pelecanou, Ch. Tsoukalas, C.P. Raptopoulou, A. Terzis, E. Chiotellis, M. Papadopoulos, Inorg. Chim. Acta 346 (2002) 270.
[19] T.B. Gunnoe, S.H. Meiere, M. Sabat, W.D. Harman, Inorg. Chem. 39 (2000) 6127.
[20] M.C. Aragoni, M. Arca, T. Cassano, C. Denotti, F.A. Devillanova, F. Isaia, V. Lippolis, D. Natali, L. Niti, M. Sampietro, R. Tommasi, G. Verani, Inorg. Chem. Commun. 5 (2002) 869.
[21] P. Romaniello, F. Lelj, Chem. Phys. Lett. 372 (2003) 51.
[22] P. Norman, P. Cronstrand, J. Ericsson, Chem. Phys. 285 (2002) 207.
[23] J. Bossert, N.B. Amor, A. Strich, C. Daniel, Chem. Phys. Lett. 342 (2001) 617.
[24] C.E. Powell, M.P. Cifuentes, A.M. McDonagh, S.K. Hurst, N.T. Lucas, C.D. Delfs, R. Stranger, M.G. Humphrey, S. Houbrechts, I. Asselberghs, A. Persoons, D.C.R. Hockless, Inorg. Chim. Acta 352 (2003) 9.
[25] J.P. Morral, C.E. Powell, R. Stranger, M.P. Cifuentes, M.G. Humphrey, G.A. Heath, J. Organomet. Chem. 670 (2003) 248.
[26] P. Romaniello, F. Lelj, J. Mol. Struct. Theochem. 636 (2003) 23.
[27] STOE & Cie (1999). X-RED. Version 1.18. STOE & Cie GmbH, Darmstadt, Germany.
[28] G.M. Sheldrick, Acta Crystallogr., Sect. A 46 (1990) 467.
[29] G.M. Sheldrick, SHELXL97. Program for the Solution and Refinement of Crystal Structures, University of Göttingen, Germany, 1997.
[30] G.M. Sheldrick, SHELXTL: release 4.1 for Siemens Crystallographic Research Systems, 1990.
[31] M.J. Frisch, G.W. Trucks, H.B. Schlegel, G.E. Scuseria, M.A. Robb, J.R. Cheeseman, J.A. Montgomery Jr, T. Vreven, K.N. Kudin, J.C. Burant, J.M. Millam, S.S. Iyengar, J. Tomasi, V. Barone, B. Mennucci, M. Cossi, G. Scalmani, N. Rega, G.A. Petersson, H. Nakatsuji, M. Hada, M. Ehara, K. Toyota, R. Fukuda, J. Hasegawa, M. Ishida, T. Nakajima, Y. Honda, O. Kitao, H. Nakai, M. Klene, X. Li, J.E. Knox, H.P. Hratchian, J.B. Cross, C. Adamo, J. Jaramillo, R. Gomperts, R.E. Stratmann, O. Yazyev, A.J. Austin, R. Cammi, C. Pomelli, J.W. Ochterski, P.Y. Ayala, K. Morokuma, G.A. Voth, P. Salvador, J.J. Dannenberg, V.G. Zakrzewski, S. Dapprich, A.D. Daniels, M.C. Strain, O. Farkas, D.K. Malick, A.D. Rabuck, K. Raghavachari, J.B. Foresman, J.V. Ortiz, Q. Cui, A.G. Baboul, S. Clifford, J. Cioslowski, B.B. Stefanov, G. Liu, A. Liashenko, P. Piskorz, I. Komaromi, R.L. Martin, D.J. Fox, T. Keith, M.A. Al-Laham, C.Y. Peng, A. Nanayakkara, M. Challacombe, P.M.W. Gill, B. Johnson, W. Chen, M.W. Wong, C. Gonzalez, J.A. Pople, GAUSSIAN 03, Revision B.03, Gaussian Inc., 2003.
[32] A.D. Becke, J. Chem. Phys. 98 (1993) 5648.
[33] C. Lee, W. Yang, R.G. Parr, Phys. Rev. B 37 (1988) 785.
[34] P.J. Hay, W.R. Wadt, J. Chem. Phys. 82 (1985) 299.
[35] T. Leiniger, A. Nicklass, H. Stoll, M. Dolg, P. Schwerdtfeger, J. Chem. Phys. 105 (1996) 1052.
[36] M.E. Casida, in: J.M. Seminario (Ed.), Recent Developments and Applications in Modern Density Functional Theory, Theoretical and Computational Chemistry, vol. 4, Elsevier, Amsterdam, 1996.
[37] R.F.W. Bader, Atoms in Molecules. A Quantum Theory, Oxford University Press, New York, 1990.
[38] K. Eichkorn, O. Treutler, H. Ohm, M. Haser, R. Ahlrichs, Chem. Phys. Lett. 240 (1995) 298.
[39] K. Eichkorn, F. Weigend, O. Treutler, R. Ahlrichs, Theor. Chim. Acc. 97 (1997) 119.
[40] J.E. Fergusson, Coord. Chem. Rev. 1 (1966) 459.
[41] A. Earnshaw, B.N. Figgis, J. Lewis, R.D. Peacock, J. Chem. Soc. (1961) 3132.
[42] G. Battistuzzi, M. Cannio, R. Battistuzzi, Polyhedron 19 (2000) 2163.
[43] G. Battistuzzi, M. Borsari, R. Battistuzzi, Polyhedron 16 (1997) 2093.
[44] C. Pearson, A.L. Beauchamp, Inorg. Chim. Acta 237 (1995) 13.
[45] V. Bertolasi, A. Marchi, L. Marvelli, R. Rossi, C. Bianchini, I. De los Rios, M. Peruzzini, Inorg. Chim. Acta 327 (2002) 140.
[46] G.R. Desiraju, T. Steiner, The Weak Hydrogen Bond in Structural Chemistry and Biology, Oxford University Press, Oxford, 1999.
[47] G.A. Jeffrey, W. Saenger, Hydrogen Bonding in Biological Structures, Springer, 1994.
[48] U. Koch, P. Popelier, J. Phys. Chem. 99 (1995) 9747.
[49] R. Taylor, O. Kennard, J. Am. Chem. Soc. 104 (1982) 5063.
[50] J. Rall, F. Weingart, D.M. Ho, M.J. Heeg, F. Tisato, E. Deutsch, Inorg. Chem. 33 (1994) 3442.
[51] S.D. Orth, J. Barrerra, M. Sabat, W.D. Harman, Inorg. Chem. 33 (1994) 3026.
[52] W.-M. Xue, Y. Wang, M.Ch.-W. Chan, Z.-M. Su, K.-K. Cheung, Ch.-M. Che, Organometallics 17 (1998) 1946.
[53] M.A. Masood, B.P. Sullivan, D.J. Hodgson, Inorg. Chem. 38 (1999) 5425.
[54] M. Bakir, B.P. Sullivan, J. Chem. Soc., Dalton Trans. (1995) 1733.
[55] R. Chiozzone, R. Gonzalez, C. Kremer, G. De Munno, J. Faus, Inorg. Chim. Acta 325 (2001) 203.
[56] E. Hevia, J. Perez, V. Riera, D. Miguel, Organometallics 22 (2003) 257.
[57] M. O'Keeffe, N.E. Brese, Acta Crystallogr., Sect. B 47 (1997) 192.
[58] M. O'Keeffe, N.E. Brese, J. Am. Chem. Soc. 113 (1991) 3226.
[59] i.d. brown, Bond-length–bond-valence relationship in inorganic solids, in: H.B. Burgi, J.D. Dunitz (Eds.), Structure Correlation, Part III, VCH Publishers, Weinheim/New York, 1994, pp. 405–429.
[60] L. Sieron, M. Bukowska-Strzyzewska, Acta Crystalllogr., Sect. C 55 (1999) 1230.
[61] N. Psaroudakis, K. Mertis, D.G. Liakos, E.D. Simandiras, Chem. Phys. Lett. 369 (2003) 490.

Available online at www.sciencedirect.com
SCIENCE DIRECT®
Polyhedron 24 (2005) 711–721
POLYHEDRON
www.elsevier.com/locate/poly

Salicylaldoxime (H_2salox) in iron(III) carboxylate chemistry: Synthesis, X-ray crystal structure, spectroscopic characterization and magnetic behavior of trinuclear oxo-centered complexes

Catherine P. Raptopoulou *, Yiannis Sanakis, Athanassios K. Boudalis, Vassilis Psycharis

Institute of Materials Science, N.C.S.R. "Demokritos", 15310 Aghia Paraskevi, Athens, Greece

Received 20 January 2005; accepted 11 February 2005

Abstract

Two new neutral trinuclear oxo-centered complexes, $[Fe_3(\mu_3\text{-}O)(O_2CPh)_5(salox)L_1L_2]$ [$L_1 = L_2 = MeOH$ (**1**), $L_1 = EtOH$, $L_2 = H_2O$ (**2**)] are reported. In both complexes, the central oxygen atom is bridging the three iron(III) ions, which form a triangle with an average edge of ~3.3 Å. The central $[Fe_3(\mu_3\text{-}O)]^{7+}$ core is planar. The benzoato ligands are coordinated through the usual *syn*,*syn* μ_2:η^1:η^1 mode and the salicylaldoximato ligand shows the common μ_2:η^1:η^1:η^1 coordination mode. Two of the iron(III) ions have an O_6 coordination environment while the third has an O_5N one. The two crystallographically independent trimers in the structure of **1** (**a** and **b**, respectively) through intermolecular interactions form polymeric chains of the . . .a–a–b–b. . . type, along the *ac* diagonal of the unit cell. In **2**, again through intermolecular interactions, the trimers form layers lying parallel to the [1 0 1] plane. Mössbauer spectra at room temperature from polycrystalline samples of **1** and **2** give rise to two well-resolved doublets with an average isomer shift consistent with high spin iron(III) ions. The two doublets, at 2:1 ratio, are characterized by different quadrupole splitting and are assigned to the nonequivalent iron(III) ions of the clusters. Magnetic measurements of **1** and **2** in the 2–z300 K temperature range show antiferromagnetic interactions between the iron(III) ions in the trimers stabilizing a $S = 1/2$ ground state. The derived values for the exchange interaction constants fall in the range usually found in $[Fe_3(\mu_3\text{-}O)]^{7+}$ clusters. Solid state X-band EPR spectra of **1** and **2** at liquid helium temperatures give rise to broad lines extending several hundred Gauss, indicating weak intermolecular interactions. EPR spectra from **1** and **2** in an acetone glass at 4.2 K exhibit a strong symmetric signal at $g \sim 2.0$ which is attributed to the $S = 1/2$ ground state of the clusters.
© 2005 Elsevier Ltd. All rights reserved.

Keywords: Trinuclear oxo-centered Fe(III) complexes; Salicylaldehyde oxime; Magnetochemistry; Crystal structures; EPR spectroscopy; Mössbauer spectroscopy

1. Introduction

Our interest in the coordination chemistry of phenolic oximes is related to our continuing effort to synthesize polynuclear 3d metal clusters in a quest for new molecule-based magnetic materials. 'Metal-oximates' have been attracting the interest of inorganic chemists, since they can be used as 'building blocks' for the designed synthesis of polynuclear clusters [1]. According to this synthetic route, the ligands already bound to one metal have free coordination sites and can bind to a second metal of the same or different kind. The major advantages of this method are, the better control of the reaction and of the products formed, factors that cannot be controlled by following the self-assembly route. By using the strategy of 'metal oximates' as building blocks, various homo- and hetero-metal complexes have been synthesized [2–8]. The propensity of phenolic oximes to form polynuclear complexes by using both the oxime

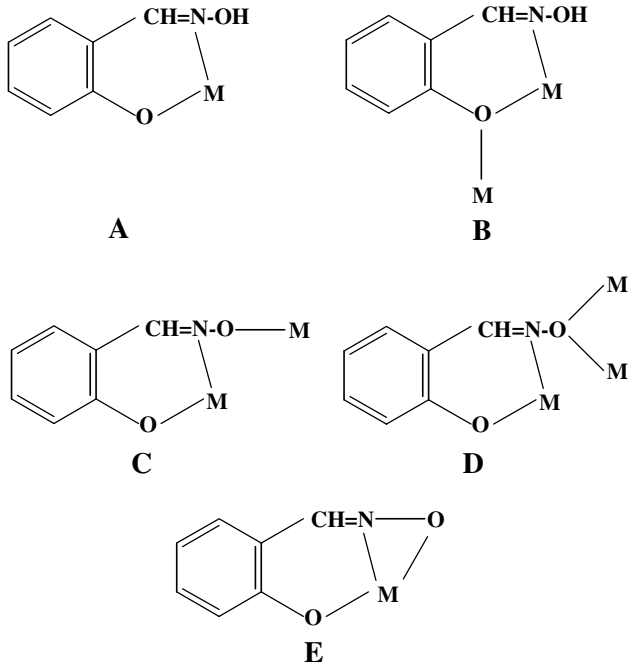
* Corresponding author. Tel.: +3210 6503365; fax: +3210 6519430.
E-mail address: craptop@ims.demokritos.gr (C.P. Raptopoulou).

0277-5387/$ - see front matter © 2005 Elsevier Ltd. All rights reserved.
doi:10.1016/j.poly.2005.02.002

and phenolate groups as chelating and/or bridging units, along with their ability to act in their mono- or di-anionic form, make them interesting candidates for the exploration of their metal coordination chemistry [9].

In their mono-anionic form, phenolic oximes usually act as chelating agents through their oximate nitrogen and phenolate oxygen atoms (mode A in the following scheme) in a variety of mono- and poly-nuclear metal complexes [10–14]. A more interesting coordination mode, includes the use of the phenolate oxygen atom as both chelating and bridging agent (mode B) [10,15].

In their di-anionic form, phenolic oximes usually use their phenolate oxygen and oximate nitrogen atoms to chelate to one metal ion and their oximate oxygen as bridging unit to bind a second metal (mode C). A variety of di- [16–18], tri- [14,19] and tetranuclear [20–22] metal complexes presenting the μ_2:η^1:η^1:η^1 coordination mode have been reported. The oximate oxygen atom can also bind two metal ions, presenting the μ_3:η^1:η^2:η^1 coordination mode (mode D) giving rise to higher nuclearity complexes, such as hexanuclear [23,24], although this coordination mode is also observed in trinuclear [25] and tetranuclear [11] complexes. There is also one example [10] where the dianion of phenolic oximes can act as chelating tridentate ligand according to mode E.



Further restricting our discussion to polynuclear iron(III) complexes with the simplest member of the phenolic oximes, 2-hydroxy-benzaldehyde (salicylaldoxime, H_2salox), only a few examples have been reported. As far as we know, the only example of iron(III) salicylaldoximato complex is the tetranuclear [11] cluster [{Fe(Hsalox)(salox)}$_4$], in which the four Hsalox$^-$ act as chelating agents through their phenolate oxygen and oximate nitrogen atoms (mode A), whilst the four salox^{2-} further use their oximate oxygen atom to bind to two additional metal centers (mode D). In the remaining examples, coligands have been used to complete the coordination spheres of iron(III) centers in polynuclear complexes. In the dinuclear compound [(Me_3tacn)Fe(III)(salox)$_3$Fe(III)] [16], as well as in the tetranuclear compound [(Me_3tacn)$_2$Fe$_4$(salox)$_2$(μ_3-O)$_2$(μ_2-CH_3CO_2)$_3$](ClO_4) [20] (where Me_3tacn = 1,4,7-trimethyl-1,4,7-triazacyclononane) the dianion of salicylaldoxime adopts the μ_2:η^1:η^1:η^1 coordination mode. The only trinuclear iron(III) salicylaldoximato complex known so far is [(C_2H_5)$_3$NH][Fe_3O(Hsalox)(salox)$_2$ (salmp)] [19] (salmp = 2-(bis(salicylideneamino)-methyl) phenol, a new ligand formed during the reaction process), where the Hsalox$^-$ ligands act as chelating units and the salox^{2-} ligands adopt the μ_2:η^1:η^1:η^1 coordination mode.

The aim of our project is to explore the use of salicylaldoxime in iron(III) carboxylate chemistry, encouraged by our previous results on manganese(III) [24]. Herein, we report the first results of our project, in particular the synthesis, X-ray crystal structure, spectroscopic (solid state and frozen solutions EPR, Mössbauer) characterization and magnetic behavior of two neutral trinuclear oxo-centered iron(III) complexes, [Fe_3 (μ_3-O)-(O_2CPh)$_5$(salox)L_1L_2] (L_1 = L_2 = MeOH (**1**), L_1 = EtOH, L_2 = H_2O (**2**)). The reported complexes are the first examples of trinuclear carboxylato iron(III) complexes with salicylaldoxime, and can be considered as precursors for the synthesis of higher nuclearity complexes, based on the principle of using 'metal oximates' as 'building blocks' for polynuclear clusters. In both compounds, the salox^{2-} ligands adopt the μ_2:η^1:η^1:η^1 coordination mode (mode C) thus, the possibility of further using the oximate oxygen atom, under certain reaction conditions, to bind to a second metal is left open.

2. Experimental

2.1. Compound preparations

All manipulations were performed under aerobic conditions using materials as received (Aldrich Co). All chemicals and solvents were of reagent grade.

2.1.1. [Fe_3(μ_3-O)(O_2CPh)$_5$(salox)(MeOH)$_2$] · 1.25MeOH · 1.05H_2O (**1**)

A methanolic solution of H_2salox (0.069 g, 0.50 mmol) was stirred under reflux, until sodium benzoate (0.216 g, 1.50 mmol) was added. The reflux continued for 30 min and then $Fe(NO_3)_3 \cdot 9H_2O$

(0.202 g, 0.50 mmol) was added. The color of the solution immediately turned to deep brown. After 24 h of reflux, small amounts of a brown-red solid were filtered, washed with MeOH and identified as compound **1** by FT-IR spectroscopy. The brown filtrate was sealed and after a period of one week X-ray quality brownish-red crystals of **1** were formed (Yield: 0.34 g, ~70%). The crystals of **1** were collected by filtration, washed with cold MeOH and dried in vacuo. The resulting powder analyzed as solvent-free. *Anal.* Calc. for (**1**) ($C_{44}H_{38}NO_{15}Fe_3$): C, 53.47; H, 3.88; N, 1.42. Found: C, 53.45; H, 3.86; N, 1.40%.

2.1.2. $[Fe_3(\mu_3\text{-}O)(O_2CPh)_5(salox)(EtOH)(H_2O)]\cdot EtOH$ (**2**)

The procedure followed was the same as described above, but $FeCl_3\cdot 6(H_2O)$ and ethanol were used instead (Yield: 0.35 g, ~70%). The powder of **2** analyzed as solvent-free. *Anal.* Calc. for (**2**) ($C_{44}H_{38}NO_{15}Fe_3$): C, 53.47; H, 3.88; N, 1.42. Found: C, 53.45; H, 3.87; N, 1.39%.

2.2. General and physical measurements

Elemental analysis for carbon, hydrogen, and nitrogen was performed on a Perkin Elmer 2400/*II* automatic analyzer. Infrared spectra were recorded as KBr pellets in the range 4000–500 cm^{-1} on a Bruker Equinox 55/S FT-IR spectrophotometer. EPR spectra were recorded on a Bruker ER 200D-SRC X-band spectrometer equipped with an Oxford ESR 9 cryostat in 4.2–300 K temperature range. Variable temperature magnetic susceptibility measurements were carried out on polycrystalline samples of **1** and **2** in the 2.0–300 K temperature range using a Quantum Design MPMS SQUID susceptometer under a magnetic field of 1000 G. Magnetization measurements were carried out at 2.5 K over the 0–5 T magnetic field range. Diamagnetic corrections for the complexes were estimated from Pascal's constants. Mössbauer spectra were taken with a constant acceleration spectrometer using a ^{57}Co (Rh) source at RT and a variable temperature Oxford cryostat.

2.2.1. X-ray crystallography and solution of structures

Brownish-red prismatic crystals of **1** ($0.05\times0.25\times0.75$ mm) and **2** ($0.05\times0.15\times0.25$ mm) were mounted in capillary with drops of mother liquid. Diffraction measurements were made on a Crystal Logic Dual Goniometer diffractometer using graphite monochromated Mo radiation. Important crystal data and parameters for data collection for **1** are reported in Table 1. Unit cell dimensions were determined and refined by using the angular settings of 25 automatically centered reflections in the range $11° < 2\theta < 23°$. Intensity data were recorded using a θ–2θ scan. Three standard reflections, monitored every 97 reflections showed less than 3% intensity fluctuation and no decay. Lorentz, polarization and ψ-scan absorption corrections were applied using Crystal Logic software. The structures were solved by direct methods using SHELXS-86 [26] and refined by full matrix least-squares techniques on F^2 with SHELXL-97 [27]. Further experimental crystallographic details for **1**: $2\theta_{max} = 40°$, scan speed 1.2°/min; scan range 1.7 + $\alpha_1\alpha_2$ separation; reflections collected/unique/used, 7740/7452 [R_{int} = 0.0332]/7452; 779 parameters refined; $(\Delta/\sigma)_{max} = 0.014$; $(\Delta\rho)_{max}/(\Delta\rho)_{min} = 0.725/-0.579$ e/Å^3; R/R_w (for all data), 0.1223/0.2282. The crystals of **1** were of poor diffraction ability, despite their sufficient size, so the data collection stopped at $2\theta = 40°$ because over half of the reflections collected were unobserved. Nevertheless, the quality of the data is adequate to establish the structure. Due to the lack of sufficient number of data only the metal ions and the coordinated atoms as well as the $salox^{2-}$ ligands were refined anisotropically. The phenyl rings of the benzoates were refined isotropically and fixed to the geometry of a regular hexagon. Hydrogen atoms on the phenyl rings and on the methyl groups of the coordinated methanols were introduced at calculated positions as riding on bonded atoms. Further experimental crystallographic details for **2**: $C_{46}H_{44}NO_{16}Fe_3$, fw = 1033.93, a = 15.12(2) Å, b = 15.61(2) Å, c = 20.15(2) Å, β = 95.26(3)°, V = 4736(2) Å^3, $Z = 4$, space group $P2_1/n$, $2\theta_{max} = 35°$ (data collected between 35° and 40° was more than 70% unobserved and it was not used), scan speed 1.2°/min; scan range 1.7 + $\alpha_1\alpha_2$ separation; reflections collected/unique/used, 3125/2971 [R_{int} = 0.0401]/2971; 208 parameters refined; $(\Delta/\sigma)_{max} = 0.013$; $(\Delta\rho)_{max}/(\Delta\rho)_{min} = 0.96/-0.91$ e/Å^3; R/R_w (for 1797 refs with $I > 2\sigma(I)$), 0.2486/0.5077; R/R_w (for all data), 0.3458/0.5897. The crystals of **2** were very small in size

Table 1
Crystallographic data for complex $\mathbf{1}\cdot 1.25MeOH\cdot 1.05H_2O$

Formula	$C_{45.25}H_{46.1}Fe_3NO_{17.3}$
Formula weight	1048.30
Space group	$P2_1/c$
Unit cell dimensions	
a (Å)	19.67(2)
b (Å)	26.96(2)
c (Å)	19.70(2)
β (°)	98.84(3)
V (Å^3)	10323(2)
Z	8
T (°C)	298
Radiation	Mo Kα
ρ_{calcd} (g/cm^3)	1.348
μ (mm^{-1})	0.899
R_1[a]	0.0775
wR_2[a]	0.1994

$R_1 = \sum(|F_o| - |F_c|)/\sum(|F_o|)$ and $wR_2 = \{\sum[w(F_o^2 - F_o^2)^2]/\sum[w(F_o^2)^2]\}^{1/2}$ for 5082 reflections with $I > 2\sigma(I)$.

[a] $w = 1/[\sigma^2(F_o^2) + (aP)^2 + bP]$ and $P = ((\max F_o^2, 0) + 2F_c^2)/3$; a = 0.1046, b = 86.0886.

and of very poor diffraction quality. Repeated efforts to grow larger crystals proved unsuccessful. We continued with data collection in order to establish the gross structure of the complex. Since the structure of **2** proved quite similar to that of **1**, we felt that complete structural characterization was not crucial. Thus, the refinement was done with anisotropic thermal parameters for the iron(III) ions only, whilst all the rest atoms were refined isotropically. No H-atoms were included in the refinement. The phenyl rings of the salox^{2-} and benzoate ligands were fitted to the geometry of a regular hexagon. The crystallographic analysis revealed the presence of one ethanol of crystallization per trimeric complex.

3. Results and discussion

3.1. Syntheses

As mentioned earlier, our aim was to investigate the use of salicylaldehyde oxime (H_2salox) to the iron(III) carboxylate chemistry, extending our previous experience on manganese [24]. The 1:1 molar ratio reaction of $Mn(O_2CR)_2$ (R = Me, Ph) and H_2salox in EtOH led to the hexanuclear complexes $[Mn_6O_2(O_2CR)_2(salox)_6(EtOH)_4]$ (R = Me, Ph). These complexes contain the novel $[Mn_6^{III}(\mu_3\text{-}O)_2\ (\mu_2\text{-}OR)_2]^{12+}$ core, whose topology consists of six Mn ions arranged as two $\{Mn_3(\mu_3\text{-}O)\}$ subunits bridged by two oximato oxygen atoms. Both compounds proved to behave as single molecule magnets (SMM) and are the first members of a new class of manganese-based SMMs containing exclusively Mn^{III} ions with blocking temperature greater than 2 K. In order to investigate the possibility of synthesizing the corresponding polynuclear iron(III) complexes and to study their magnetic properties, we have designed the 1:3:1 molar ratio reaction of $Fe^{3+}/PhCO_2^-/H_2$salox in alcoholic media. The 1:3:1 molar ratio has been chosen so that the M/carboxylate/H_2salox ratio remains the same in going from manganese(II) to iron(III) ions. But it turned out that in the iron(III) case, the amount of the carboxylate ions was very high, and the trinuclear oxo-centered complexes **1** and **2** were formed. The salox^{2-} ions are coordinated through the usual μ_2:η^1:η^1:η^1 mode while the possibility of further use of the oximato oxygen atom to bridge a second metal and to increase the nuclearity of the derived complex has failed. Nevertheless, we still consider compounds **1** and **2** as useful staring materials for polynuclear iron(III) complexes, under different reaction conditions.

The synthesis of **1** and **2** can be summarized in Eqs. (1) and (2), respectively, based on the reasonable assumption that H_2O from the starting materials and/or the solvent is the source of the O^{2-} ion.

$$3Fe(NO_3)_3\cdot 9H_2O + 5PhCO_2Na + H_2salox + 2MeOH \xrightarrow{MeOH} [Fe_3O(O_2CPh)_5(salox)(MeOH)_2] + 5NaNO_3 + 4HNO_3 + 26H_2O \quad (1)$$

$$3FeCl_3\cdot 6H_2O + 5PhCO_2Na + H_2salox + EtOH \xrightarrow{EtOH} [Fe_3O(O_2CPh)_5(salox)(EtOH)(H_2O)] + 5NaCl + 4HCl + 16H_2O \quad (2)$$

3.2. IR spectroscopy

In the IR spectrum of both **1** and **2**, medium-intensity bands at 3451, 3063, 2924 cm^{-1} (for **1**) and 3414, 3063, 2980 cm^{-1} (for **2**), are assigned to the $\nu(OH)_{H_2O}$, $\nu(CH)_{aromatic}$, $\nu(CH_3)$, respectively. Strong intensity bands at 1598 cm^{-1} and medium intensity bands at 1286 cm^{-1} observed in the spectrum of both complexes are assigned to the ν(C=N) and ν(N–Oox) of the salicylaldoximato ligand [28]. The frequencies of the $\nu_s(CO_2)$ bands of $PhCO_2^-$ coincide in the spectra of **1** (1406 cm^{-1}), and **2** (1405 cm^{-1}). The bands at 1557 cm^{-1} in **1** and **2**, respectively, are assigned to the $\nu_{as}(CO_2)$ of the benzoato ligands. The difference Δ ($\Delta = \nu_{as}(CO_2) - \nu_s(CO_2)$) for **1** is 151 cm^{-1} and for **2** is 152 cm^{-1}, less than that for NaO_2CPh (184 cm^{-1}), as expected for the bridging modes of benzoate ligation [29]. A strong intensity band at 480 cm^{-1} in the spectra of **1** and at 478 cm^{-1} in the spectra of **2** is characteristic of the presence of the $[Fe_3O]$ moiety in the structures of **1** and **2**.

3.3. Structural description of $[Fe_3(\mu_3\text{-}O)(O_2CPh)_5(salox)(MeOH)_2]\cdot 1.25MeOH\cdot 1.05H_2O$ (1)

Compound **1** crystallizes in the monoclinic space group $P2_1/c$ with two crystallographically independent trinuclear complexes in the asymmetric unit (further reported as molecules **1a** and **1b**). The structure of the molecule **1a** is given in Fig. 1. Selected bond distances and angles for both **1a** and **1b** are listed in Table 2. The structure of **1** consists of a trinuclear iron(III) oxo-centered complex. The three Fe^{III} ions in **1a** form an isosceles triangle whilst in **1b** the triangle is best described as scalene (see Table 2). The Fe–O_{oxo} bond distances are in the range 1.86–1.94 Å in both molecules **1a** and **1b**, and the central $[Fe_3(\mu_3\text{-}O)]^{7+}$ moiety is planar. Ions Fe(2) and Fe(3) in molecule **1a** and the corresponding ions Fe(5) and Fe(6) in molecule **1b** have an octahedral oxygen rich coordination environment, while ions Fe(1) and Fe(4) in molecules **1a** and **1b**, respectively, have a distorted octahedral O_5N coordination geometry. The angles within the tetragonal plane of the octahedron range from 82.2° to 97.5° for **1a** and from 78.5° to 99.1° for **1b**. The angles involving the axial positions of the

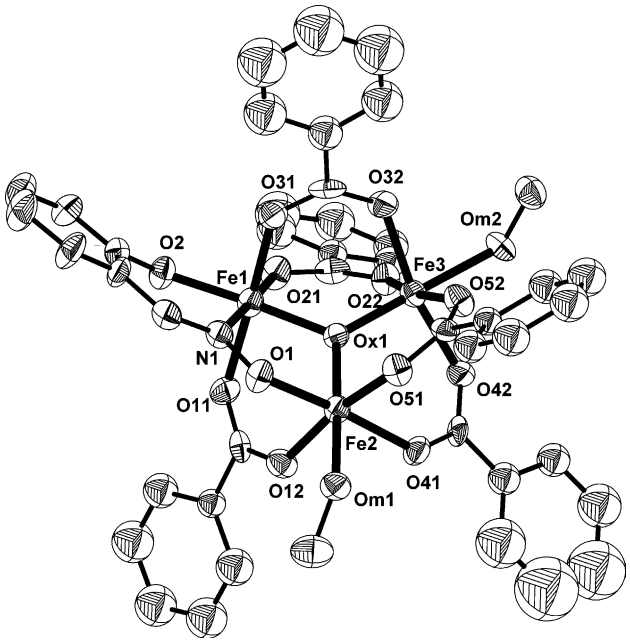


Fig. 1. The molecular structure of the molecule **1a** with the atomic labelling (40% thermal probability ellipsoids).

octahedron range from 168.5° to 178.5° and from 163.9° to 178.1° in **1a** and **1b**, respectively.

The salicylaldoximato ligand shows the common μ_2:η^1:η^1:η^1 coordination mode with the N–O oximato group and the phenolate oxygen atom lying above and below the $[Fe_3(\mu_3\text{-}O)]^{7+}$ plane, respectively. The Fe–$O_{oximato}$ bond distances are 1.982 Å in both molecules **1a** and **1b**, the Fe–$O_{phenoxy}$ are 1.914 and 1.930 Å in molecules **1a** and **1b**, respectively. The Fe–$N_{oximato}$ bond lengths are 2.133 and 2.145 Å in molecules **1a** and **1b**, respectively. The whole salicylaldoximato ligand is planar and makes an angle of 51.1° and 65.3° with the $[Fe_3(\mu_3\text{-}O)]^{7+}$ plane in molecules **1a** and **1b**, respectively.

The benzoato ligands are coordinated in the common *syn*,*syn* μ_2:η^1:η^1 mode. The Fe–$O_{carboxylato}$ bond distances are in the range 1.977–2.029 and 1.990–2.052 Å in molecules **1a** and **1b**, respectively.

The polymeric lattice structure of **1**, shown in Fig. 2, arises from the strong intermolecular interactions between the isolated trimers. More specifically, the oximato oxygen atom O(1) in molecule **1a** is strongly interacting (most likely through hydrogen bonding interactions) to a coordinated methanolic oxygen atom Om(1) belonging to a centrosymmetrically related molecule **1a** [O(1)...Om(1′) = 2.574 Å (1 − *x*, −*y*, 1 − *z*)]. Thus, a dimer of trimers of the a–a type, is formed though two intermolecular interactions across a center of symmetry. The closest Fe···Fe interatomic distance in the a–a dimer is Fe(2)···Fe(2′) = 5.067 Å. The same feature is observed in the case of molecule **1b**, where the oximato oxygen atom O(61) is strongly interacting (most likely through H-bonding interactions) to a coordinated methanol Om(3) from a centrosymmetrically related molecule **1b** [O(61)...Om(3″) = 2.666 Å (2 − *x*, −*y*, 2 − *z*)]. Thus, a dimer of trimers of the b–b type, is formed due to the double interactions described above. The closest Fe···Fe interatomic distance in the b–b dimer is Fe(5)···Fe(5″) = 5.207 Å. Apart from the formation of dimers, another feature is also observed in the lattice structure of **1**. The phenoxy oxygen atom O(62) of molecule **1b** is

Table 2
Selected bond distances (Å) and angles (°) for **1** · 1.25MeOH · 1.05H_2O

*Molecule **1a***					
Bond distances					
Fe(1)–Ox(1)	1.944(8)	Fe(2)–Ox(1)	1.882(9)	Fe(3)–Ox(1)	1.855(8)
Fe(1)–O(2)	1.914(10)	Fe(2)–O(1)	1.982(9)	Fe(3)–O(42)	1.977(11)
Fe(1)–O(21)	1.999(10)	Fe(2)–O(12)	2.004(11)	Fe(3)–O(22)	1.983(11)
Fe(1)–O(31)	2.013(12)	Fe(2)–O(41)	2.012(10)	Fe(3)–O(32)	2.006(10)
Fe(1)–O(11)	2.020(12)	Fe(2)–O(51)	2.017(11)	Fe(3)–O(52)	2.029(10)
Fe(1)–N(1)	2.133(11)	Fe(2)–Om(1)	2.070(10)	Fe(3)–Om(2)	2.110(9)
Fe(1)...Fe(2)	3.254(2)	Fe(1)...Fe(3)	3.327(2)	Fe(2)...Fe(3)	3.251(2)
Bond angles					
Fe(1)–Ox(1)–Fe(2)	116.5(4)	Fe(2)–Ox(1)–Fe(3)	120.9(2)	Fe(3)–Ox(1)–Fe(1)	122.3(4)
*Molecule **1b***					
Bond distances					
Fe(4)–Ox(2)	1.932(9)	Fe(5)–Ox(2)	1.877(9)	Fe(6)–Ox(2)	1.868(9)
Fe(4)–O(62)	1.930(10)	Fe(5)–O(61)	1.982(10)	Fe(6)–O(82)	1.998(10)
Fe(4)–O(81)	1.990(11)	Fe(5)–O(111)	2.008(10)	Fe(6)–O(92)	2.006(12)
Fe(4)–O(71)	2.012(11)	Fe(5)–O(72)	2.009(9)	Fe(6)–O(102)	2.011(12)
Fe(4)–O(91)	2.052(11)	Fe(5)–O(101)	2.045(12)	Fe(6)–O(112)	2.028(11)
Fe(4)–N(61)	2.145(13)	Fe(5)–Om(3)	2.099(10)	Fe(6)–Om(4)	2.103(10)
Fe(4)...Fe(5)	3.222(2)	Fe(4)...Fe(6)	3.317(2)	Fe(5)...Fe(6)	3.284(2)
Bond angles					
Fe(4)–Ox(2)–Fe(5)	115.5(4)	Fe(5)–Ox(2)–Fe(6)	122.5(4)	Fe(6)–Ox(2)–Fe(4)	121.5(5)

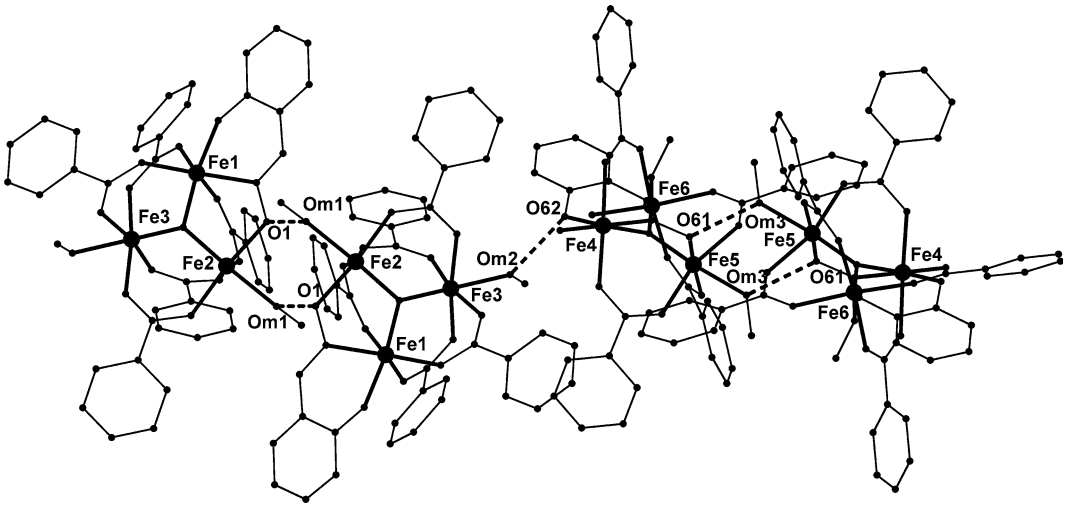


Fig. 2. Plot of the polymeric chains of **1** along the *ac* diagonal. The intermolecular interactions between the trimers are shown as dashed lines.

strongly interacting (most likely through H-bond) to the second coordinated methanolic oxygen Om(2) of molecule **1a** [O(62)···Om(2″) = 2.693 Å (2 − *x*, −*y*, 2 − *z*)]. Thus, polymeric chains of alternative dimers of the …a–a–b–b… are formed along the *ac* diagonal of the unit cell. The closest Fe···Fe interatomic distance in the a–b part of the chain is Fe(3)···Fe(4″) = 5.518 Å.

3.4. Structural description of $[Fe_3(\mu_3\text{-}O)(O_2CPh)_5(salox)(EtOH)(H_2O)]\cdot EtOH$ (2)

The structure of **2** (Figure S1) is analogous to that of compound **1**, the only difference being in the monodendate ligands completing the octahedral coordination around the iron(III) ions (one ethanol and one water molecules instead of two methanols in **1**). The three Fe^{III} ions form a scalene triangle with edges 3.207, 3.277 and 3.306 Å. The Fe–O_{oxo} bond distances are in the range 1.835–1.923 Å and the central $[Fe_3(\mu_3\text{-}O)]^{7+}$ moiety is planar. Ions Fe(2) and Fe(3) have an octahedral oxygen rich coordination environment, while Fe(1) has a distorted octahedral O_5N coordination geometry.

Despite its similarities in the molecular structure with that of **1**, compound **2** presents a different lattice structure originated by the existence of intermolecular interactions between the isolated trimers. Strong intermolecular interactions (possibly through H-bonds) between the oximato oxygen atom O(1) and the coordinated ethanolic oxygen atom Oe(1) of a centrosymmetrically related trimer [O(1)…Oe(1′) = 2.674 Å (−*x*, −*y*, 1 − *z*)], and between the phenolate oxygen atom O(2) and the coordinated water molecule Ow(1) of a neighboring trimer [O(2)…Ow(1″) = 2.967 Å (0.5 − *x*, −0.5 + *y*, 0.5 − *z*)], are responsible for the 2D polymeric network (parallel to the [1 0 1] crystallographic plane) in **2** (Figure S2). The closest Fe…Fe interatomic distances due to the H-bonding interactions are Fe(2)…Fe(2′) = 5.075 Å, and Fe(1)…Fe(3″) = 5.913 Å.

Compounds **1** and **2** can be considered as part of the large 'basic carboxylates' family of trivalent oxo-centered trinuclear compounds with the general formula $[M_3(\mu_3\text{-}O)(O_2CR)_6L_3]$ (L = terminal monodentate ligand). The only difference between the 'basic carboxylates' and compounds **1** and **2** is that, one of the carboxylates and one of the terminal ligands have been replaced by the oximato and phenoxy group of the salicylaldoxime, respectively. In that sense, bond distances and angles in the coordination sphere are in the ranges found for several iron(III) 'basic carboxylates' [30–37].

3.5. Mössbauer spectra

Fig. 3 shows Mössbauer spectra from powder samples of **1** and **2** recorded at room temperature in the absence of an external magnetic field. The spectra for both compounds consist of two well resolved doublets. Solid lines above the spectra are theoretical simulations assuming two iron sites at 2:1 ratio with the parameters quoted in Table 3. For both compounds the isomer shifts for sites I and II are typical for high spin Fe^{III} in an octahedral environment comprising O/N atoms.

From the crystal structure of complex **1**, site I which represents the majority species is readily assigned to the iron sites with O_6 environment whereas site II, the minority species, is assigned to the iron site with O_5N coordination. Site II is characterized by a significantly larger ΔE_Q relatively to site I. The ΔE_Q parameter reflects the degree of asymmetry around the Fe ion. This can be asymmetry of Fe–L bond lengths and coordination geometry, or asymmetry in the nature of donor atoms (N or O). In terms of coordination geometry, significant *trans* effects are experienced by Fe(2), Fe(3) in

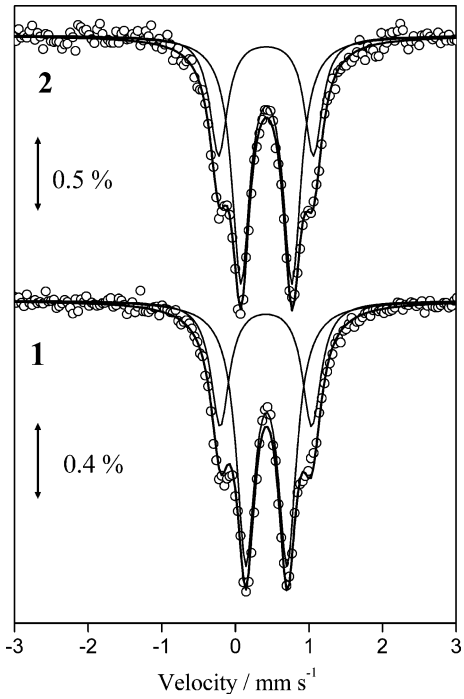


Fig. 3. Room temperature Mössbauer spectra from solid powder samples of **1** and **2**. Solid lines are theoretical spectra assuming two different iron sites with the parameters quoted in Table 3.

Table 3
Mössbauer parameters for **1** and **2**

Complex	Site	Temperature (K)	δ[a,b,c]	ΔE_Q[a,c]	$\Gamma/2$[a,d]	Area (%)[d]
1	I	300	0.42(1)	0.56(1)	0.15	67
		4.2	0.54(1)	0.61(1)	0.19	
	II	300	0.41(1)	1.24(1)	0.15	33
		4.2	0.53(1)	1.15(1)	0.19	
2	I	300	0.42(1)	0.70(1)	0.14	67
		4.2	0.55(1)	0.79(1)	0.19	
	II	300	0.41(1)	1.29(1)	0.14	33
		4.2	0.54(1)	1.31(1)	0.19	

[a] In mm s^{-1}.
[b] Isomer shifts are reported relative to iron metal at room temperature.
[c] Number in parentheses represent errors in the last digit.
[d] Fixed.

molecule **1a**, and by Fe(5), Fe(6) in molecule **1b**, with the shortest bond being the Fe–(μ_3-O^{2-}) in each case. The corresponding *trans* effect experienced by atoms Fe(1) and Fe(4) is insignificant (see Table 2). In terms of donor atoms, there are two iron atoms with asymmetric O_5N chromophores [Fe(1) and Fe(4)] and four atoms with more symmetric O_6 chromophores [Fe(2), Fe(3), Fe(5) and Fe(6)]. The Mössbauer spectra, therefore, indicate that the O_5N coordination should be considered responsible for the larger ΔE_Q value of site II.

The resolution of the spectrum of complex **1** does not allow us to distinguish the two crystallographically different molecules **1a** and **1b**. We observe however that the spectrum exhibits fairly narrow lines suggesting that the iron sites in molecules **1a** and **1b** are characterized by similar Mössbauer parameters and especially ΔE_Q. The situation for complex **2** is similar and the O_5N coordinated iron atom [Fe(1)] with a larger ΔE_Q is assigned to site II, despite its more symmetric octahedral coordination geometry.

At 4.2 K and in the absence of external magnetic fields a slight broadening of the doublets for both complexes is observed (Fig. S3). No magnetic ordering is evidenced at 4.2 K. The broadening can be attributed to the onset of magnetic relaxation effects. Alternatively, structural changes may occur leading to three distinct sites. Although the deconvolution of the spectra is not unique both can be simulated assuming two sites at 2:1 ratio as in the room temperature case with the parameters quoted in Table 3 (Fig. S3). The average isomer shift for both compounds at 4.2 K is 0.54 mm s^{-1} and the difference in the isomer shifts with the room temperature spectra is due to the second order Doppler effect [38].

3.6. Magnetic behaviour

For complex **1**, the $\chi_M T$ product at 300 K is 3.94 cm^3 mol^{-1} K (Fig. 4), significantly lower than the theoretically expected value for three non-interacting $S = 5/2$ spins (13.14 cm^3 mol^{-1} K), suggesting antiferromagnetic interactions. Upon cooling, the $\chi_M T$ product decreases to 0.31 cm^3 mol^{-1} K at 2 K, without extrapolating to zero as the temperatures tends to zero, which agrees with the interplay of antiferromagnetic interactions, and a magnetic ground state.

As analyzed in the description of the structures, complex **1** actually consists of two independent molecules (**1a** and **1b**), with two rather different geometries; isosceles (for **1a**) and scalene (for **1b**, see description of structures). Due to the different geometries it is expected that

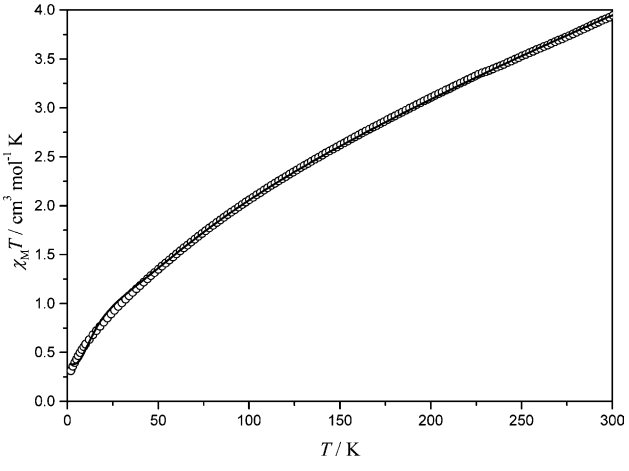


Fig. 4. $\chi_M T$ vs. T experimental data for complex **1**, and theoretical curves based on the Hamiltonian of Eq. (3), using the parameters of solution **A**.

1a and **1b** have different magnetic properties. However, consideration of two different magnetic entities for the analysis of the bulk magnetic susceptibility data would lead to a large number of parameters with a small degree of reliability. Therefore, we have analyzed the data assuming one single trinuclear species.

Initial attempts to simulate the magnetic properties of the complex by considering a single exchange constant, J did not yield satisfactory results. It was, therefore, concluded that a model taking into account a second exchange constant, J', should be considered. The Hamiltonian used was

$$\hat{H} = -2J(\hat{S}_1\hat{S}_3 + \hat{S}_2\hat{S}_3) - 2J'\hat{S}_1\hat{S}_2. \quad (3)$$

The fitting process yielded two solutions of comparable quality (with g fixed to 2.0), as is usually the case for complexes containing the $[Fe_3O]^{7+}$ core, with a $S = 1/2$ ground state [39,40]. The best-fit parameters were, **A**: $J = -27.3\ cm^{-1}$, $J' = -42.7\ cm^{-1}$, $g = 2.0$ ($R = 1.2 \times 10^{-3}$) and **B**: $J = -34.7\ cm^{-1}$, $J' = -24.6\ cm^{-1}$, $g = 2.0$ ($R = 1.7 \times 10^{-3}$). This is better depicted by an error surface plot of J versus J', which reveals the existence of two minima (Figure S4). Both these solutions imply a $S = 1/2$ ground state.

In order to verify the validity of these results, a simulation of the M versus H curve at 2.5 K was carried out with the MAGPACK program package [41,42], using the best-fit parameters of solutions **A** and **B**. These reproduced the experimental curves very nicely, producing practically superimposable curves, without the use of a paramagnetic impurity fraction (Fig. 5).

The situation is similar in the case of complex **2**, with the $\chi_M T$ product decreasing smoothly from 3.65 $cm^3\ mol^{-1}\ K$ at 300 K down to 0.28 $cm^3\ mol^{-1}\ K$ at 2 K, without extrapolating to zero (Fig. 6). For the analysis of the data we assumed the same model as above. The fit shown in Fig. 6 was carried out over the 8–300 K temperature region. Two solutions of comparable quality were determined, their parameters being, **A**: $J = -35.9\ cm^{-1}$, $J' = -29.8\ cm^{-1}$, $g = 2.0$ ($R = 3.7 \times 10^{-4}$) and **B**: $J = -31.3\ cm^{-1}$, $J' = -41.2\ cm^{-1}$, $g = 2.0$ ($R = 4.3 \times 10^{-4}$). Fitting over the 2–300 K temperature range yielded small discrepancies at low temperatures. These discrepancies are attributed to the presence of weak intermolecular interactions.

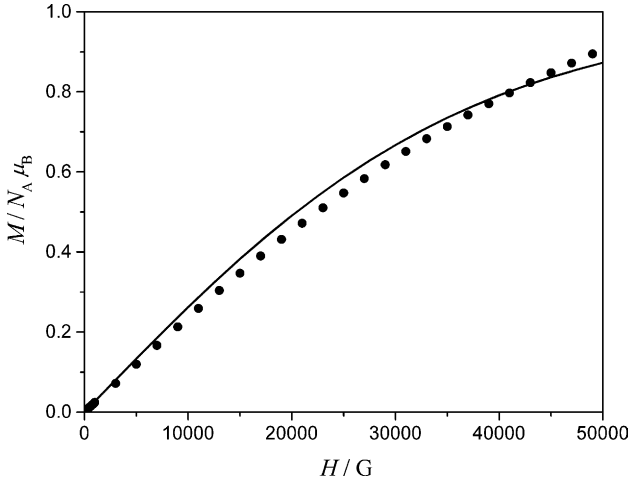


Fig. 5. Variation of the magnetization M vs. the applied field H at 2.5 K for complex **1**. The curves calculated according to the parameters of solutions **A** or **B** are superimposable.

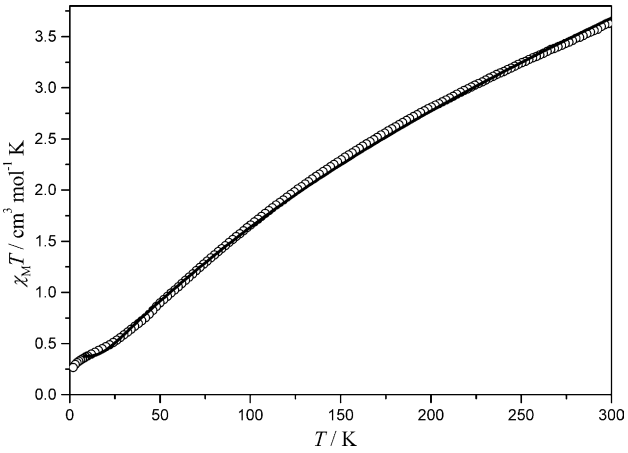


Fig. 6. $\chi_M T$ vs. T experimental data for complex **2**, and the theoretical curve based on the Hamiltonian of Eq. (3) (solution **B**).

The existence of two minima in the fitting procedure of the magnetic susceptibility data is an inherent property of trinuclear complexes [40]. It would be reasonable to correlate the value of the exchange coupling constants with the metric characteristics of the complexes. This approach however may not be realistic in the present case. First, complex **1** consists of two different molecules and the unambiguous determination of the individual magnetic properties is not feasible from the present bulk magnetic susceptibility measurements. Second, even in the simpler case of equilateral complexes the necessity of at least two different exchange coupling constants for the reproduction of the magnetic susceptibility measurements indicate that magnetostructural correlations are not straightforward and other factors have to be taken into account. We observe however that on average, the derived values for the exchange constants for solutions **A** and **B** for both complexes fall well within the range of values usually found in trinuclear complexes [43–47].

3.7. EPR spectroscopy

EPR spectra from powder samples for both complexes at 4.2 K are shown in Fig. 7. For compound **1** the spectra reveal a feature at $g \sim 2.0$ accompanied by broad features at lower magnetic fields. For compound **2** an additional broad feature is observed at higher magnetic fields. The magnetic susceptibility data indicate that the clusters are characterized by a $S = 1/2$ ground state, however the EPR signals cannot be attributed to

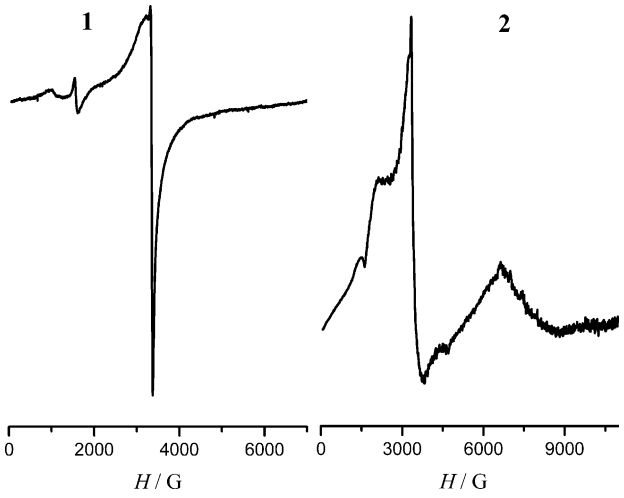


Fig. 7. EPR spectrum from a solid powder sample of **1** and **2** at 4.2 K. EPR conditions: microwave frequency, 9.41 GHz; microwave power, 50 mW; modulation amplitude 10 G_{pp}.

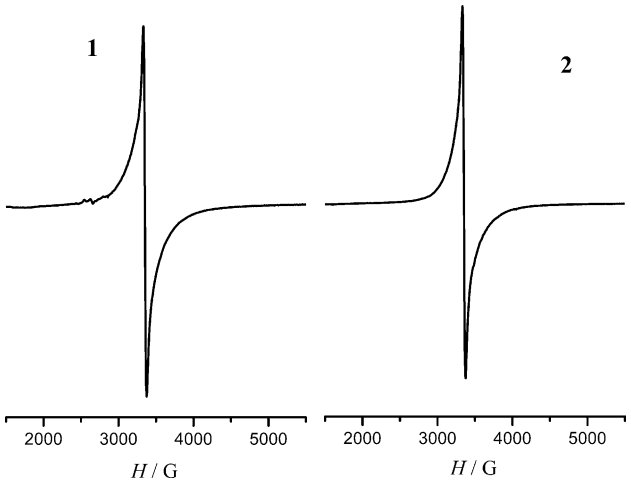


Fig. 8. EPR spectrum from **1** and **2** in acetone glass at 4.2 K. EPR conditions: microwave frequency, 9.41 GHz; microwave power, 2 mW; modulation amplitude 10 G_{pp}.

isolated $S = 1/2$ systems. We attribute this behaviour to intermolecular interactions present in the solid state. This is supported by the crystal structure revealing intermolecular interactions between neighbouring trimers. We note that the low temperature magnetic susceptibility data for complex **2** cannot be reproduced with isolated trimers and the EPR spectra support weak intermolecular interactions. For compound **1** the intermolecular interactions appear to be weak enough, so they do not affect the magnetic susceptibility data. However, weak dipolar interactions may substantially affect the EPR spectra. For instance a weak dipolar interaction between two $S = 1/2$ systems of the order of $\sim 0.05\ cm^{-1}$ can be hardly discernible in bulk magnetic susceptibility measurements, but it will critically affect the EPR measurements leading to spectra extending in a large magnetic field region.

In order to eliminate the solid-state effects, we studied by EPR both compounds in an acetone glass, a weakly coordinating solvent. The 4.2 K spectra are shown in Fig. 8. A strong signal is observed at $g \sim 2.0$ for both compounds. The signal is characterized by a symmetric derivative feature with a line-shape which is better described by a Lorenztian curve. The temperature dependence of this signal indicates that it arises from a ground state. The dependence of the signal on microwave power and the line-shape argues against a free radical species. Further, it is improbable that this signal arises from monomeric Fe^{III} ($S = 5/2$) species resulting from decomposition of the compound upon solvation in acetone. Usually such species gives rise to signals at higher g-values (for instance at $g \sim 4.3$) as a result of zero-field splitting effects. No such signals are observed in the present case. A monomeric Fe^{III} ($S = 1/2$) low spin species can be also excluded because in this case fairly anisotropic signals are expected.

On the other hand, it is reasonable to assume that the EPR signals of Fig. 8 arise from the $S = 1/2$ ground state of isolated trimers in both compounds. The symmetric line-shape of the signals suggests an isotropic system. This is indeed expected from a trimer comprising Fe^{III} ($S = 5/2$) sites antiferromagnetically coupled with the isotropic Heisenberg–Dirac–van Vleck Hamiltonian as the main interaction. Although symmetric EPR lines are expected this is rarely met in trinuclear complexes of Fe^{III} ($S = 5/2$) or Cr^{III} ($S = 3/2$) [39,48–53]. Usually, in such systems, non-Heisenberg interactions such as antisymmetric exchange and/or single-ion zero-field splitting terms result in an anisotropic $S = 1/2$ ground state. Due to the anisotropy, broad EPR signals are observed extending to high field values with $g \ll 2.0$. In the present case the signal is symmetric and confined at the $g \sim 2.0$ region indicating that the contribution of these terms is negligible. From this point of view compounds **1** and **2** are rare cases of triferric complexes where the anticipated $S = 1/2$ EPR signals are indeed observed.

4. Conclusions

As part of our continuing efforts to synthesize polynuclear iron(III) complexes with novel magnetic properties, we have reacted H_2salox with iron(III) in the presence of carboxylates. The two new neutral iron(III) complexes, $[Fe_3(\mu_3\text{-}O)(O_2CPh)_5(salox)L_1L_2]$ ($L_1 = L_2 =$ MeOH (**1**), $L_1 =$ EtOH, $L_2 = H_2O$ (**2**)) derived, contain the $[Fe_3O]^{7+}$ core found in 'basic iron carboxylates'. In complexes **1** and **2** however two iron atoms are in an O_6 coordination environment whereas the third is found in an O_5N one. A detailed characterization of complexes **1** and **2** including spectroscopic and magnetic studies has been carried out. The nonequivalence of the

iron(III) ions is depicted in the Mössbauer spectra. The magnetic properties are interpreted within the context of a trimer with exchange constants typical for complexes with the $[Fe_3(\mu_3\text{-}O)]^{7+}$ core and a $S = 1/2$ ground state. The crystal structure analysis of **1** reveals intermolecular interactions between the trimers forming 1D polymeric chains. In **2** the intermolecular interactions lead to the formation of a 2D network. These interactions give rise to broad EPR spectra in the solid state. The $salox^{2-}$ ligand adopts the usual $\mu_2{:}\eta^1{:}\eta^1{:}\eta^1$ coordination mode, while the possibility of further use of the oximate oxygen atom to bridge to a second metal is left open. In that sense, compounds **1** and **2** can be considered as important starting materials for the synthesis of higher nuclearity clusters under certain reaction conditions.

Acknowledgements

The Greek General Secretariat of Research and Technology is acknowledged for supporting the present work within the frame of the Competitiveness EPAN 2000–2006, Centers of Excellence # 25. We also thank Dr. D. Stamopoulos for the magnetic measurements.

Appendix A. Supplementary data

Full crystallographic details have been deposited in CIF format with the Cambridge Crystallographic Data Centre. Copies of the data can be obtained free of charge on request from the CCDC, 12 Union Road, Cambridge CB2 1EZ, UK (fax: +44 1223 336408, e-mail: deposit@ccdc.cam.ac.uk or www. at http://www.ccdc.cam.ac.uk) quoting the deposition numbers CCDC 261079 (**1**), and CCDC 261080 (**2**). Four figures showing the molecular and lattice structure of **2**, the Mössbauer spectra from powder samples of **1** and **2** at 4.2 K, and the surface error plot of J versus J' (with $g = 2.00$), as well as a table of the bond distances and angles around the coordination sphere of the three iron(III) ions in **1**, are also given as supplementary material. Supplementary data associated with this article can be found, in the online version, at doi:10.1016/j.poly.2005.02.002.

References

[1] O. Kahn, Molecular Magnetism, VCH-Verlagsgesellschaft, Weinhein, 1991.
[2] D. Luneau, H. Oshio, H. Okawa, S. Kida, J. Chem. Soc., Dalton Trans. (1990) 2283.
[3] P. Chaudhuri, M. Winter, P. Fleischhauer, W. Haase, U. Florke, H.-J. Haupt, J. Chem. Soc., Chem. Commun. (1990) 1728.
[4] P. Chaudhuri, M. Winter, B.P.C. Della Vedova, E. Bill, A. Trautwein, S. Gehring, P. Fleischhuer, B. Nuber, J. Weiss, Inorg. Chem. 30 (1991) 2148.
[5] D. Luneau, H. Oshio, H. Okawa, S. Kida, Chem. Lett. (1989) 443.
[6] H. Okawa, M. Koikawa, S. Kida, D. Luneau, H. Oshio, J. Chem. Soc., Dalton Trans. (1990) 469.
[7] R. Ruiz, F. Lloret, M. Julve, M.C. Munoz, C. Bois, Inorg. Chim. Acta 219 (1994) 179.
[8] E. Colacio, J.M. Dominguez-Vera, A. Escuer, M. Klinga, R. Kivekas, A. Romerosa, J. Chem. Soc., Dalton Trans. (1995) 343.
[9] P. Chaudhuri, Coord. Chem. Rev. 243 (2003) 143.
[10] A.G. Smith, P.A. Tasker, D.J. White, Coord. Chem. Rev. 241 (2003) 61.
[11] J.M. Thorpe, R.L. Beddoes, D. Collison, C.D. Garner, M. Helliwell, J.M. Holmes, P.A. Tasker, Angew. Chem. Int. Ed. 38 (1999) 1119.
[12] L.F. Larkworthy, D.C. Povey, J. Crystallogr. Spectrosc. Res. 13 (1983) 413.
[13] M. Gallagher, M.F.C. Ladd, L.F. Larkworthy, D.C. Povey, K.A.R. Salib, J. Crystallogr. Spectrosc. Res. 16 (1986) 967.
[14] P. Chaudhuri, M. Hess, T. Weyhermüller, E. Bill, H.-J. Haupt, U. Flörke, Inorg. Chem. Commun. 1 (1998) 39.
[15] R. Willem, A. Bouhdid, A. Meddour, C. Camacho-Camacho F. Mercier, M. Gielen, M. Biesemans, F. Ribot, C. Sanchez, E.R.T. Tieknik, Organometallics 16 (1997) 4377.
[16] P. Chaudhuri, M. Winter, P. Fleischhauer, W. Haase, U. Flörke, H.-J. Haupt, Inorg. Chim. Acta 212 (1993) 241.
[17] C.N. Verani, E. Bothe, D. Burdinski, T. Weyhermüller, U. Flörke, P. Chaudhuri, Eur. J. Inorg. Chem. (2001) 2161.
[18] S. Liu, H. Zhu, J. Zubieta, Polyhedron 8 (1989) 2473.
[19] E. Bill, G. Krebs, M. Winter, M. Gerdan, A.X. Trautwein, U. Flörke, H.-J. Haupt, P. Chaudhuri, Chem. Eur. J. 3 (1997) 193.
[20] P. Chaudhuri, E. Rentschler, F. Birkelbach, C. Krebs, E. Bill T. Weyhermüller, U. Flörke, Eur. J. Inorg. Chem. (2003) 541.
[21] P. Chaudhuri, M. Winter, P. Fleischhauer, W. Haase, U. Flörke, H.-J. Haupt, J. Chem. Soc., Chem. Commun. (1993) 566.
[22] P. Chaudhuri, F. Birkelbach, M. Winter, V. Staemmlar, P. Fleischhauer, W. Haase, U. Flörke, H.-J. Haupt, J. Chem. Soc., Dalton Trans. (1994) 2313.
[23] P. Chaudhuri, M. Hess, E. Rentschler, T. Weyhermüller, U. Flörke, New J. Chem. (1998) 553.
[24] C.J. Milios, C.P. Raptopoulou, A. Terzis, F. Lloret, R. Vicente, S.P. Perlepes, A. Escuer, Angew. Chem. Int. Ed. 43 (2004) 210.
[25] V. Zerbib, F. Robert, P. Gouzerh, J. Chem. Soc., Chem. Commun. (1994) 2179.
[26] G.M. Sheldrick, SHELXS-86: Structure Solving Program, University of Göttingen, Germany, 1986.
[27] G.M. Sheldrick, SHELXL-97: Crystal Structure Refinement, University of Göttingen, Germany, 1997.
[28] M. Alexiou, C. Dendrinou-Samara, C.P. Raptopoulou, A. Terzis, D.P. Kessissoglou, Inorg. Chem. 41 (2002) 4732.
[29] G.B. Deacon, R.J. Phillips, Coord. Chem. Rev. 33 (1980) 227.
[30] F. Degang, W. Guoxiong, T. Wenxia, Y. Kaibei, Polyhedron 20 (1993) 2459.
[31] E.M. Holt, S.L. Holt, W.F. Tucker, R.O. Asplund, K.J. Watson, J. Am. Chem. Soc. 96 (1974) 2621.
[32] V.M. Lynch, J.W. Sibert, J.L. Sessler, B.E. Davis, Acta Crystallogr. C 47 (1991) 866.
[33] A.B. Blake, L.R. Fraser, J. Chem. Soc., Dalton Trans. (1975) 193.
[34] R.V. Thundathil, E.M. Holt, S.L. Holt, K.J. Watson, J. Am. Chem. Soc. 99 (1977) 1818.
[35] K. Anzenhofer, J. De Boer, J. Rec. Tav. Chim. 88 (1969) 286.
[36] A.M. Bond, R.J.H. Clark, D.G. Humphrey, P. Panagiotopoulos, B.W. Skelton, A.H. White, J. Chem. Soc., Dalton Trans. (1998) 1845.
[37] C.E. Anson, J.P. Bourke, R.D. Cannon, U.A. Jayasooriya, M. Molinier, A.K. Powell, Inorg. Chem. 36 (1997) 1265, and refs therein.
[38] N.N. Greenwood, T.C. Gibb, Mössbauer Spectroscopy, Chapman and Hall, London, 1971.

[39] A.K. Boudalis, Y. Sanakis, F. Dahan, J.-P. Tuchagues, Inorg. Chem., submitted for publication.
[40] D.H. Jones, J.R. Sams, R.C. Thompson, J. Chem. Phys. 81 (1984) 440.
[41] J.J. Borrás-Almenar, J.M. Clemente-Juan, E. Coronado, B.S. Tsukerblat, Inorg. Chem. 38 (1999) 6081.
[42] J.J. Borrás-Almenar, J.M. Clemente-Juan, E. Coronado, B.S. Tsukerblat, J. Comput. Chem. 22 (2001) 985.
[43] R.D. Cannon, R.P. White, Prog. Inorg. Chem. 36 (1988) 195.
[44] R.D. Cannon, U.A. Jayasooriya, R. Wu, S.K. arapKoske, J.A. Stride, O.F. Nielsen, R.P. White, G.J. Kearley, D. Summerfield, J. Am. Chem. Soc. 116 (1994) 11869.
[45] F.E. Sowrey, C. Tilford, S. Wocadlo, C.E. Anson, A.K. Powell, S.M. Bennington, W. Montfrooij, U.A. Jayasooriya, R.D. Cannon, J. Chem. Soc., Dalton Trans. (2001) 862.
[46] G.J. Long, W.T. Robinson, W.P. Tappmeyer, D.L.J. Bridges, J. Chem. Soc., Dalton Trans. (1973) 573.
[47] J.F. Duncan, C.R. Kanekar, K.F. Mok, J. Chem. Soc. A (1969) 480.
[48] Y.V. Rakitin, Y.V. Yablokov, V.V. Zelentzov, J. Magn. Reson. 43 (1981) 288.
[49] A. Caneschi, A. Cornia, A.C. Fabretti, D. Gatteschi, W. Malavasi, Inorg. Chem. 34 (1995) 4660.
[50] Y.V. Yablokov, V.A. Gaponenko, A.V. Ablov, T.N. Zhkhareva, Sov. Phys. Solid. State 15 (1973) 251.
[51] H. Nishimura, M. Date, J. Phys. Soc. Jpn. 54 (1985) 395.
[52] M. Honda, M. Morita, M. Date, J. Phys. Soc. Jpn. 61 (1992) 3773.
[53] A. Vlachos, V. Psycharis, C.P. Raptopoulou, N. Lalioti, Y. Sanakis, M. Fardis, M. Karayanni, G. Papavassiliou, A. Terzis, Inorg. Chim. Acta 357 (2004) 3162.

Available online at www.sciencedirect.com
SCIENCE DIRECT®
Polyhedron 24 (2005) 723–729
POLYHEDRON
www.elsevier.com/locate/poly

Synthesis, crystal structure and thermal behaviour of $[La(hfa)_3(Phen)_2]$ (hfa = hexafluoroacetylacetonate, Phen = *o*-phenanthroline)

A.Yu. Rogachev [a,*], L.Kh. Minacheva [b], V.S. Sergienko [b], I.P. Malkerova [b], A.S. Alikhanyan [b], V.V. Stryapan [a], N.P. Kuzmina [a]

[a] *Department of Chemistry, Moscow State University, Moscow 119992, Russia*
[b] *Kurnakov Institute of General and Inorganic Chemistry, Moscow 119991, Russia*

Received 28 April 2004; accepted 4 June 2004
Available online 20 July 2004

Abstract

The mixed ligand complex $[La(hfa)_3(Phen)_2]$ (**I**) was obtained by the interaction of $La(hfa)_3$ and Phen; its composition does not depend on the stoichiometry of the reagents. According to the X-ray single crystal analysis data, complex **I** crystallizes in the monoclinic space group $P2_1/n$, with $a = 13.583(3)$ Å, $b = 16.959(3)$ Å, $c = 18.860(4)$ Å, $\beta = 94.71(3)°$ and $Z = 4$. The structure of **I** consists of isolated mononuclear molecules, the coordination number of La being 10. Thermal behaviour and composition of the vapor phase have been studied for **I** by thermal analysis and mass-spectrometry using a Knudsen cell. The mixed ligand complex **I** was found to sublime congruently in the temperature range 370–460 K: $[La(hfa)_3(Phen)_2]_{(s)} = [La(hfa)_3(Phen)]_{(g)} + Phen_{(g)}$, $\Delta_r H^0(T) = 316.2 \pm 1.8$ kJ/mol.
© 2004 Elsevier Ltd. All rights reserved.

Keywords: Mixed ligand complexes; Ten-coordinated lanthanum complexes; Crystal structures; Thermal behaviors; Mass-spectrometry studies

1. Introduction

The interest in coordination chemistry of lanthanide β-diketonates, $Ln(dik)_3$, is based on the possibility of their use as NMR shift reagents [1], luminescent materials [2,3] and as volatile precursors in the chemical vapor deposition of thin films with electrical and magnetic properties [4,5]. One of the most important features of lanthanide β-diketonates is the possibility to coordinate additional neutral donor ligands (Q) and to form mixed ligand complexes $[Ln(dik)_3(Q)_n]$. The formation of such complexes is based on coordinative unsaturation of the metal in $Ln(dik)_3$ and depends on the Lewis acidity–basicity of both $Ln(dik)_3$ and Q, and on sterical hindrances [6]. The combination of $Ln(dik)_3$ with Q into one molecule of $[Ln(dik)_3(Q)_n]$ offers wide possibilities for modifying the functional properties of lanthanide β-diketonates.

Over the last four decades an extensive literature, dedicated to the synthesis, structure and properties of mixed ligand lanthanide β-diketonates, has evolved. The mixed ligand complexes of $Ln(dik)_3$ with N-donor ligands Phen and Bipy are of a special interest since the insertion of these ligands into the coordination sphere of $Ln(dik)_3$ has significantly influences on the luminescent properties and volatility of lanthanide β-diketonates [7,8]. Mixed ligand complexes of the common composition $[Ln(dik)_3(Q)]$ (Q = Phen, Bipy) were prepared for practically all the lanthanides, and for many β-diketonate ligands – acetylacetonate (acac), dipivaloylmethanate (thd), dibenzoylmethanate (dbm),

* Corresponding author. Tel.: +7-095-939-38-36; fax: +7-095-939-09-98.
E-mail address: rogachev@inorg.chem.msu.ru (A.Yu. Rogachev).

0277-5387/$ - see front matter © 2004 Elsevier Ltd. All rights reserved.
doi:10.1016/j.poly.2004.06.006

pivaloylacetonate (pta) [9–11]. The analysis of the X-ray structure data shows the central lanthanide ion in these mixed ligand complexes to be eight coordinated and to form four chelate rings – three with β-diketonate ligands and one with Phen or Bipy. However, among the $[Ln(dik)_3(Q)]$ (Q = Phen, Bipy) complexes published to date, there is no data about hfa complexes, where hfa – hexafluoroacetylacetonate. Meanwhile, the synthesis, structure and properties of such mixed ligand complexes are indubitably of especial interest because the hfa ligand contains two electron-withdrawing CF_3 groups that increase the Lewis acidity of $Ln(hfa)_3$, contrary to other non-fluorinated lanthanide β-diketonates. One would expect $Ln(hfa)_3$ to be the most active for the addition of neutral ligands. In reality, in 2001 [12] it was found that the early lanthanide elements, which have larger ionic radii, form 10-coordinated complexes of the type $[Ln(hfa)_3(Q)_2]$ (Q = Phen, Bipy, Ln = La, Ce, Pr, Nd, Sm), whereas the elements at the end of the lanthanide series form eight coordinated complexes $[Ln(hfa)_3(Q)]$ (Q = Phen, Bipy, Ln = Dy, Tb, Ho, Yb). The X-ray crystal structure of $[Ln(hfa)_3(Bipy)_2]$ was determined and coordination of two Bipy ligands was confirmed. In our opinion, the complexes $[Ln(hfa)_3(Q)_2]$ (Q = Phen, Bipy) are very interesting objects not only in respect of their structural features, but due to their volatility and thermal dissociation stability:

$$[Ln(dik)_3(Q)_n] \rightarrow Ln(dik)_3 + nQ$$

So, in [11] it was found that $[Ce(pta)_3(Phen)]$ sublimes congruently. The thermal stability of $[Ln(hfa)_3(Q)_2]$ was not studied in [12]. Here we report the synthesis of $[La(hfa)_3(Phen)_2]$ by a different method from that published in [12], the crystal structure of this complex, the results of thermal analysis and mass-spectrometry data as well as the sublimation of $La(hfa)_3$.

2. Experimental

2.1. General

Analytically pure reagents $La_2(CO_3)_3 \cdot 8H_2O$, Hhfa, KOH and $Phen \cdot H_2O$ from Merck were used. Dry Phen was obtained by dehydration of $Phen \cdot H_2O$ at 140 °C (0.01 Torr).

The C, H and N contents were determined by conventional elemental analysis. The lanthanum content was determined titrimetrically.

IR spectra were recorded on a Perkin–Elmer 1600 FTIR spectrometer as Nujol and hexachlorobutadiene mulls between KBr plates in the region 4000–400 cm^{-1}.

^1H NMR spectra were recorded on a Bruker AC-600P spectrometer in $CDCl_3$/TMS.

Thermogravimetric analysis was carried out under argon on a Perkin–Elmer Pyris Diamond thermal analyzer at a heating rate of 10 °C min^{-1}. Isothermal vacuum sublimation experiments were done with 100 mg samples in a glass test tube for 30 min at 0.01 Torr. Weight losses were determined gravimetrically and controlled by titrimetric analyses of the sublimates.

2.2. Synthesis

The starting complex $La(hfa)_3$ was prepared according to the procedure described in [13].

A solution of 0.18 mg (1 mmol) Phen in 25 ml of EtOH was mixed with a hot solution of 0.56 mg (0.5 mmol) $La(hfa)_3$ in 25 ml of EtOH. The mixture was refluxed under stirring for 2 h, resulting in a clear colorless solution. The volume of the solution was reduced to a half under slow evaporation of the solvent at room temperature, and yielded a microcrystalline precipitate after one day. Yield: ~80%. *Anal.* Calc.: C, 41.79; H, 1.69; N, 5.00; La, 12.4. Found: C, 41.67; H, 1.87; N, 4.99; La, 12.4%. IR (cm^{-1}): 1652 (C–O), 1525 (C–C), 1254, 1204, 1146 (C–F), 1592, 1580, 880, 730 (Phen). ^1H NMR (δ, ppm): 9.13 (d, 4H, $^3J = 6$ Hz), 7.95 (d, 4H, $^3J = 8$ Hz), 7.85 (t, 4H, $^3J = 8$ Hz), 7.38 (t, 4H, $^3J = 6$ Hz), 5.65 (s, 3H).

By using $Phen \cdot H_2O$ instead of anhydrous Phen and by changing the molar ratio of $[La(hfa)_3]$:[Phen] from 1:2 to 1:1, the same product $[La(hfa)_3(Phen)_2]$ was obtained with a yield of about 80–85%, calculated with respect to Phen.

2.3. Crystal structure determination

Suitable single crystals of $[La(hfa)_3Phen_2]$ (**I**) were grown by recrystallization of the crude product from EtOH solution.

The diffraction data were collected on an Enraf-Nonius CAD-4 automatic diffractometer (Mo Kα radiation, $\lambda = 0.71073\,E$, $2\theta/\omega$-scanning, θ-max = 28.0°, graphite monochromator). The crystallographic data along with some details of data collection and structure refinement are given in Table 1. On data processing, Lorenz and polarization factors were introduced.

The structure was determined by direct methods (SHELXS-86 [14]) and refined using the full-matrix least-squares method (SHELXL-97 [15]). The structure refinements were carried out anisotropically for all non-hydrogen atoms. Hydrogen atoms were placed in their calculated positions (C–H $0.93\,E$) and refined isotropically in the riding mode. Some of the CF_3 groups were disordered with occupancies in the range of 0.47–0.53. The most important bond distances are given in Table 2.

2.4. Mass-spectrometry and study of the vapor phase

The mass spectra of $[La(hfa)_3]$ and $[La(hfa)_3(Phen)_2]$ were recorded on a MS 1301 spectrometer having a

Table 1
Crystal data and structure refinement for $[La(hfa)_3Phen_2]$

Empirical formula	$LaC_{39}H_{19}F_{18}N_4O_6$
Formula weight	1120.49
Temperature (K)	298(2)
Crystal system	monoclinic
Space group	$P2_1/n$
a (Å)	13.583(3)
b (Å)	16.959(3)
c (Å)	18.860(4)
α (°)	90.00
β (°)	94.71(3)
γ (°)	90.00
V (Å^3)	4330(1)
Z	4
$D_{calc.}$ (g/cm^3)	1.719
Absorption coefficient (mm^{-1})	1.114
$F(000)$	2192
Crystal size (mm)	0.280.180.28
h, k, l ranges for data collection	$-1<h<17$, $0<k<22$, $-24<l<24$
Reflections collected	11 653
Independent reflections	10 362
Refinement method	full-matrix least-squares on F^2
Goodness-of-fit on F^2	0.941
$R_1[I<2\sigma(I)]$	0.0521
ωR_2	0.1331
Largest difference peak and hole (eÅ^{-3})	0.670 and −1.068

Table 2
Selected bond lengths for $[La(hfa)_3Phen_2]$ (**I**) and $[La(hfa)_3Bipy_2]$ (**II**) [12]

I		**II**	
Bond	d (Å)	Bond	d (Å)
La–O(1)	2.501 (6)	La–O(1)	2.524 (3)
La–O(2)	2.554 (7)	La–O(2)	2.541 (2)
La–O(3)	2.568 (6)	La–O(3)	2.524 (3)
La–O(4)	2.519 (7)	La–O(4)	2.541 (2)
La–O(5)	2.587 (7)	La–O(5)	2.557 (2)
La–O(6)	2.561 (7)	La–O(6)	2.557 (2)
La–N(1)	2.765 (7)	La–N(1)	2.773 (3)
La–N(2)	2.781 (7)	La–N(2)	2.771 (3)
La–N(3)	2.748 (9)	La–N(3)	2.773 (3)
La–N(4)	2.799 (9)	La–N(4)	2.771 (3)

50–1500 amu mass range, and using 80, 60 and 14 eV ionizing electrons. The complexes were vaporized from a Knudsen effusion cell. The ratio of surface of evaporation to surface of the effusion hole was about 600. The cell temperature was measured with a Pt/Pt(Rh) thermocouple (±1°). The experiments were carried out in the range of 339–393 K for $[La(hfa)_3]$ and 370–460 K for $[La(hfa)_3(Phen)_2]$. The main ion peaks in mass spectra of $[La(hfa)_3]$ at 364 K and $[La(hfa)_3(Phen)_2]$ at 440 K are given in Table 3.

Vapor pressure versus temperature was determined by means of isothermal vaporization experiments and the use of the Herz-Knudsen equation. The enthalpy of sublimation was calculated from the temperature dependences of ion current intensities by using the Clausius–Clapeyron equation and a least-squares method.

Table 3
Intensities of the main ion currents (relative units) in the mass spectra of $[La(hfa)_3]$ ($U=80$ eV) and $[La(hfa)_3(Phen)_2]$ ($U=60$eV)

$La(hfa)_3$ (364 K)		$[La(hfa)_3(Phen)_2]$ (440 K)	
Ion	I (%)	Ion	I (%)
$[La(hfa)\text{-}2CF_3]^+$	24	$[Phen]^+$	61
$[La(hfa)]^+$	45	$[(hfa)]^+$	8
$[La(hfa)_2]^+$	100	$[La(hfa)\text{-}OCCH_2CF_3]^+$	29
$[La_2(hfa)_3\text{-}2CF_3]^+$	89	$[La(hfa)\text{-}F]^+$	9
$[La_2(hfa)_3]^+$	3	$[La(hfa)\text{-}5F]^+$	10
$[La_2(hfa)_3\ F]^+$	49	$[La(hfa)]^+$	100
$[La_2(hfa)_5]^+$	5	$[La(hfa)_2(Phen)]^+$	94
$[La_2(hfa)_5\text{-}2CF_3]^+$	15	$[La(hfa)_2\text{-}F]^+$	55
		$[La(hfa)_3(Phen)\text{-}3F]^+$	4

3. Results and discussions

3.1. Synthesis and structure description

$[La(hfa)_3(Phen)_2]$ was obtained by the interaction of the lanthanide β-diketonate with the neutral donor ligand in ethanol. It was found that a change of the reagents molar ratio $[La(hfa)_3]$:[Phen] = 1:1, 1:2 and the use of hydrated reagents instead anhydrous ones does not result in a change of the complex composition, giving the same product with the stoichiometry $[La(hfa)_3(Phen)_2]$. A similar situation was described in [12], where for the synthesis of $[La(hfa)_3(Q)_2]$ (Q = Bipy, Phen), the single-step reaction between $La(CF_3SO_3)_3$, Hhfa, CsOH and either Bipy or Phen in a molar ratio 1:3:3:1 in MeOH was used. In [12] the yield of $[La(hfa)_3(Phen)_2]$, calculated with respect to Phen, was about 10%. In our method of synthesis, the yield achieved was 80%. The IR and ^{1}H NMR spectroscopy data confirm the formation of $[La(hfa)_3(Phen)_2]$.

The structure of $[La(hfa)_3(Phen)_2]$ (**I**) consists of isolated mononuclear molecules, with the coordination number of the central lanthanum atom being ten (Fig. 1). The ten donor atoms (four nitrogen atoms from Phen and six oxygen atoms from hfa ligands) are situated in a coordination sphere of the central lanthanum atom, forming a sphenocrown as the coordination polyhedron (Fig. 2).

After $[La(hfa)_3(Bipy)_2]$ (**II**) [12], the structure of **I** is the second example of a structurally characterized ten-coordinated tris-β-diketonate lanthanide complex. The structures of **I** and **II** are similar – three hfa ligands and two neutral ligands (Phen or Bipy) are coordinated by the La atom. It should be noted that some differences are caused by the replacement of Bipy ligands by Phen ligands. So, the structure **II** possesses a C_2 rotation axis through the γ-carbon atom of one hfa ligand and the La

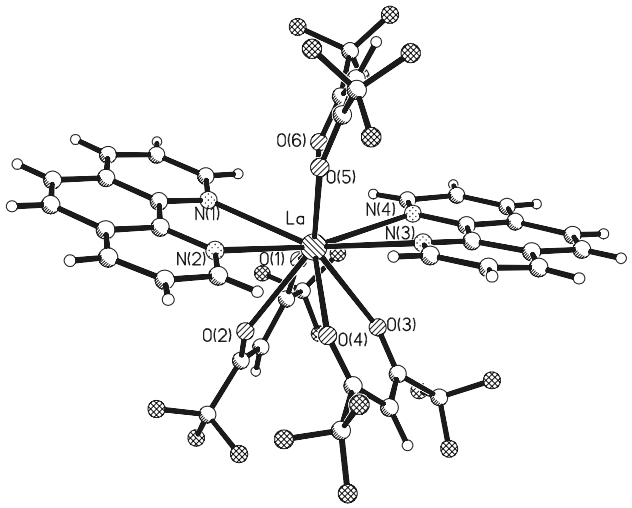


Fig. 1. Molecular structure of $[La(hfa)_3Phen_2]$. For statistical disordered atoms of F, one position is shown.

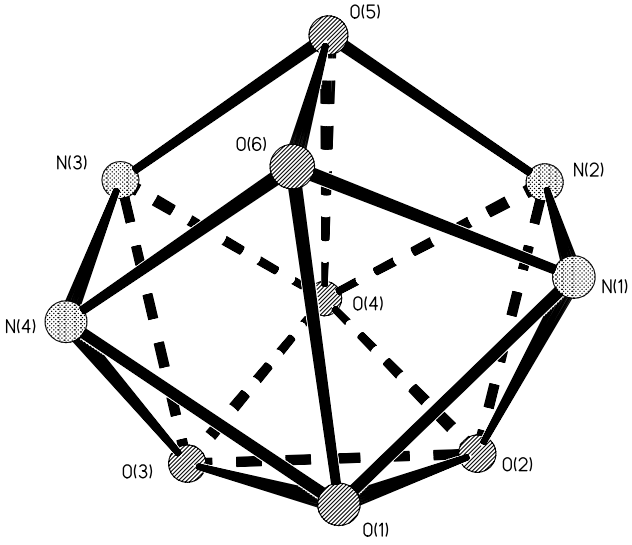


Fig. 2. Coordination polyhedron of La in the structure of $[La(hfa)_3Phen_2]$ – distorted sphenocrown.

atom. In a molecule of **I**, the symmetry axis is absent and the La–O distances vary with a wider range than in **II** (Table 2). However, the average value of La–O bond lengths is the same in **I** and **II** and is equal to 2.548(7) Å. A similar picture is observed with the La–N distances: in **I** the values of La–N bonds vary in the range 2.748(9)–2.799(9) Å and in **II** two the La–N distances are 2.773(3) and 2.771(3) Å, so in **I** the average distance La–N is practically the same (2.773 Å) as in the case of **II**. The similarity of structures **I** and **II** to one another would be expected as both ligands Bipy and Phen have a very similar donor and geometrical characteristics.

The analysis of the packing mode of **I** is of especial interest because in some structures of β-diketonate complexes with Phen ligands an intermolecular π–π stacking interaction between Phen ligands of neighboring molecules occurs. For example, in the crystal structure of barium β-diketonates with two Phen ligands $[Ba(dik)_2(Phen)_2]$ (Hdik = Hthd [16], Hpta [17] and Hhfa [18]), $[Ba(dik)_2(Phen)_2]$ molecules are stacked in the crystal structure forming infinite chains. In the crystal structure of $[La(thd)_3(Phen)]$ [19], the intermolecular π–π stacking interaction results in the formation of dimers. In the case of **I**, the crystal structure consists of centro-symmetrical pairs of $[La(hfa)_3(Phen)_2]$ molecules too (Fig. 3). The phenanthroline ligands from two centrosymmetrically situated neighboring molecules are parallel and the distance between their planes is equal to 3.35 Å. However, π–π interactions between these Phen ligands do not occur because their planes are not overlapped (Fig. 3).

3.2. Thermal behavior of *I*

Upon heating under argon, complex **I** melts at 223 °C and then undergoes two major stages of weight loss (Fig. 4). The first weight loss occurs over 210–310 °C. The DTA and DTG curves show only one narrow endothermic peak in this temperature range at 294 °C. The value of the weight loss at this stage (68%) significantly exceeds the value calculated for the removal of two Phen molecules (32%). On the basis of these facts, it is believed that partial sublimation of $[La(hfa)_3(Phen)_2]$ can take place in this temperature range. The second, smooth stage follows in the temperature range of 310–580 °C, corresponding to about 11% of the total weight loss (79%). This stage corresponds to the thermal decomposition of **I** under argon.

Upon heating in a glass reactor under low pressure (0.01 Torr), the total sublimation of **I** occurs over the temperature range of 200–220 °C, and only one fraction of sublimate was collected in the colder part of the reactor. The elemental analysis and ^1H NMR spectroscopy data showed that the solid sublimate was identical to the starting material.

In order to determine whether $[La(hfa)_3(Phen)_2]$ exists in the vapor phase, or if the solid dissociates into gaseous $La(hfa)_3$ and Phen which recombine in the cold part of the reactor, mass-spectrometry experiments were carried out, not only for the mixed ligand complex but also for the parent complex $La(hfa)_3$.

3.3. Mass-spectrometry study

La(hfa)$_3$. The mass spectrum of $La(hfa)_3$ shows that the major species correspond to mono- and di-lanthanum-containing ions with *m/z* of 553 ($[La(hfa)_2]^+$), 761 ($[La_2(hfa)_3\text{-}2CF_3]^+$), 918 ($[La_2(hfa)_3F]^+$) and 346 amu ($[La(hfa)]^+$). Therefore, the saturated vapor over anhydrous $La(hfa)_3$ consists mainly of monomeric and

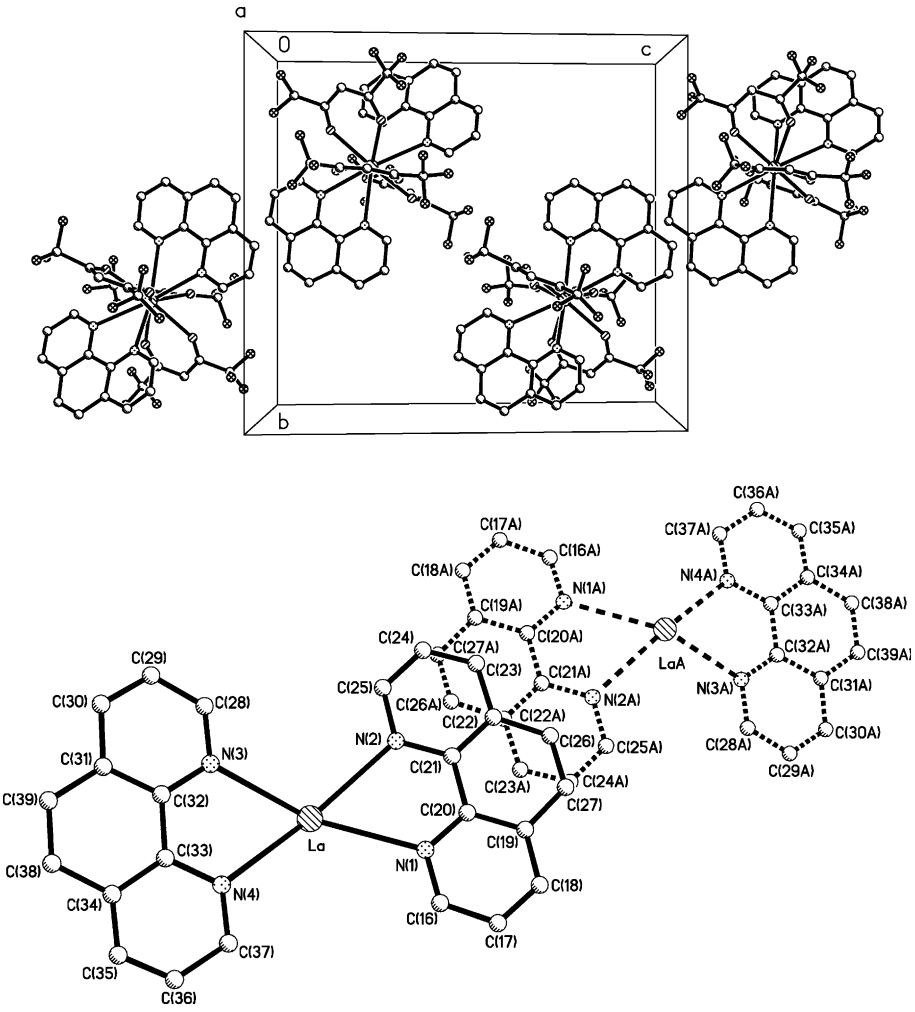


Fig. 3. The crystal packing of $[La(hfa)_3Phen_2]$ (along the *a* axes) and overlap scheme of centrosymmetrically related Phen entities.

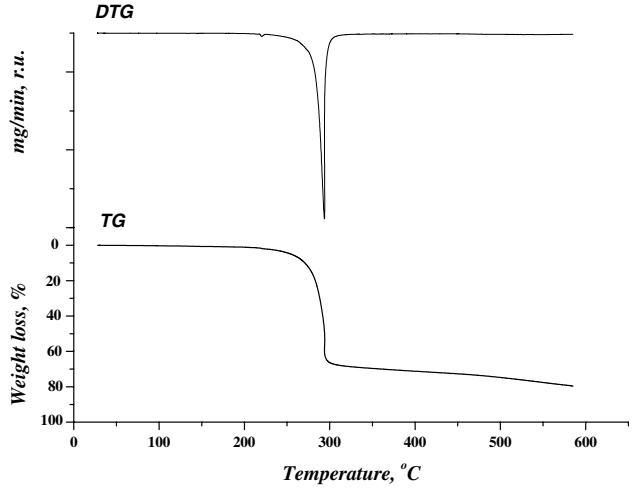


Fig. 4. TG and DTG curves for $[La(hfa)_3Phen_2]$.

dimeric molecules. The sublimation of $La(hfa)_3$ can be described by two parallel processes:

$$[La(hfa)_3]_{(s)} = [La(hfa)_3]_{(g)}$$

$$2[La(hfa)_3]_{(s)} = [La(hfa)_3]_{2(g)}$$

At 364 K, the respective saturated vapor pressures are 6.5×10^{-6} atm for $La(hfa)_3$, and 1.6×10^{-5} atm for $[La(hfa)_3]_2$. The enthalpies of sublimation of the monomeric and dimeric molecules were calculated in the temperature 339–393 K:

$$\Delta_s H^0([La(hfa)_3], k, T) = 102 \pm 7 \text{ kJ/mol}$$

$$\Delta_s H^0([La(hfa)_3]_2, k, T) = 117 \pm 8 \text{ kJ/mol}$$

Most probably, the complicated composition of the saturated vapor over $[La(hfa)_3]$ is the result of the oligomeric structure of this anhydrous complex. The crystal structure of anhydrous $[La(hfa)_3]$ is unknown (and for other anhydrous lanthanide hexafluoroacetylacetonates too), because these complexes, formed by vacuum sublimation, are glassy and only form crystalline products by coordination of additional ligands – H_2O or other neutral organic molecules. A similar vapor composition (monomeric and dimeric species) was found for $[Y(hfa)_3]$ [20], however, in the case of $[Y(hfa)_3]$ the vapor

phase consisted mainly of monomeric molecules $Y(hfa)_3$. The complex $[Y(hfa)_3]$ is more volatile than $[La(hfa)_3]$, which is in good agreement with the tendency to increase lanthanide β-diketonate volatility with a decrease of the ionic radii of these elements [21].

[La(hfa)$_3$(Phen)$_2$]. In contrast to $[La(hfa)_3]$, ions including two lanthanum atoms were not found in the mass spectra of **I**. Peaks assigned to the undissociated form of the mixed ligand complex do not appear (Table 3) even when the ionizing electron energy is lowered to 14 eV. The major species are $[La(hfa)]^+$, $[La(hfa)_2(Phen)]^+$, $[Phen]^+$, $[La(hfa)_2\text{-}F]^+$ (Table 3).

To determine a mechanism of $[La(hfa)_3(Phen)_2]$ sublimation and vapor phase composition, the curves of ionization efficiency for the main species were studied and experiments of full isothermal evaporation of samples were carried out. The analysis of the curves of ionization efficiency, obtained for the main species, show that the vapor phase over $[La(hfa)_3(Phen)_2]$ consisted of $[La(hfa)_3(Phen)]$ and Phen. From the results of full isothermal evaporation experiments it was found that the intensities of the main ion currents were constant during evaporation and the mixed ligand complex $[La(hfa)_3(Phen)_2]$ sublimed quantitatively (without formation of a nonvolatile residue in the Knudsen cell). On the basis of these data, there are grounds for believing that the mixed ligand complex $[La(hfa)_3(Phen)_2]$ sublimes congruently in the selected temperature range:

$$[La(hfa)_3(Phen)_2]_{(s)} = [La(hfa)_3(Phen)]_{(g)} + Phen_{(g)} \quad (1)$$

At 381 K in the vapor over $[La(hfa)_3(Phen)_2]$, the vapor pressure of $[La(hfa)_3(Phen)]$ is equal to 2.3×10^{-7}atm. The temperature dependencies of $[Phen]^+$, $[La(hfa)_2(Phen)]^+$, $[La(hfa)_3(Phen)\text{-}3F]^+$ and $[La(hfa)]^+$ ion current intensities were studied in the temperature range of 370–460 K, and the values of coefficient a in these linear dependencies ($I=aT+b$) were calculated (Table 4). For these four main ions the values of the coefficient a obtained are in close agreement, confirming that the vapor phase over **I** consists of two species – Phen and $[La(hfa)_3(Phen)]$ only and that this complex sublimed congruently according to Eq. 1. Using these data, the standard enthalpy of reaction 1 was calculated:

$$\Delta_r H^0(T) = 316.2 \pm 1.8 \text{ kJ/mol}.$$

So, the conversion of $[La(hfa)_3]$ into the mixed ligand complex $[La(hfa)_3(Phen)_2]$ leads to a decrease of volatility in spite of the mononuclear structure of the latter and the absence of strong intermolecular interactions in the structure of **I**. It can be explained taking into consideration the increase of the molecular mass during formation of the mixed ligand complex. The molecules $[La(hfa)_3(Phen)_2]$ do not exist in the vapor phase, although in the crystal structure both the Phen ligands are equal to each other (Table 2). The stability of $[La(hfa)_3(Phen)]$ in the vapor was expected as similar species were found in the mass spectrum of $[Ce(pta)_3(Phen)]$ [11]. However, for mixed ligand complexes $[Ln(dik)_3(Phen)]$, where Hdik represents the non-fluorinated β-diketones Hacac or Hthd, the molecular ions were not fixed in the vapor phase by mass-spectrometry [8]: under heating these complexes dissociate into $[Ln(dik)_3]$ and Phen. The difference in the sublimation schemes of these mixed ligand complexes depends on the Lewis acidity of the lanthanide β-diketonates, which is the strongest in the case of complexes with hfa ligands. The thermal behavior of $[La(hfa)_3(Phen)_2]$ can be compared to the data obtained for the barium complex, containing two Phen molecules too [19]. According to the mass-spectrometry data, $[Ba(hfa)_2(Phen)_2]$ sublimes incongruently in two stages – evolution of one Phen molecule followed by sublimation of $[Ba(hfa)_2(Phen)]$. The fact that the sublimation schemes are different for **I** and $[Ba(hfa)_2(Phen)_2]$, demonstrate the same influence of the Lewis acidity of metal β-diketonates on the stability of their mixed ligand complexes in respect to evolution of Phen under heating.

Table 4
The values of coefficients a, calculated from the temperature dependence ($I=aT+b$) of $[Phen]^+$, $[La(hfa)_2(Phen)]^+$, $[La(hfa)_3(Phen)\text{-}3F]^+$ and $[La(hfa)]^+$ ion current intensities (370–460 K)

$[Phen]^+$	$[La(hfa)_2(Phen)]^+$	$[La(hfa)_3(Phen)\text{-}3F]^+$	$[La(hfa)]^+$
7.54 ± 0.08	8.17 ± 0.04	8.19 ± 0.12	7.93 ± 0.06
8.49 ± 0.03	8.42 ± 0.06	8.47 ± 0.04	8.32 ± 0.03
8.50 ± 0.06	8.49 ± 0.04	8.67 ± 0.09	8.32 ± 0.07
	7.95 ± 0.05	8.27 ± 0.09	8.48 ± 0.04
			8.01 ± 0.09
8.18 ± 0.07	8.26 ± 0.05	8.40 ± 0.09	8.21 ± 0.06

4. Supplementary data

Supplementary material has been sent to the Cambridge Data Centre, 12 Union Road, Cambridge CB2 1EZ, UK as supplementary material No. 228858 and can be obtained by contacting the CCDC and quoting the article details and the corresponding SUP number.

Acknowledgement

This work was supported by Russian Foundation of Basic Research (Grant 02-03-33204).

References

[1] J.-C.G. Bunzli, N. Andre, M. Elhabiri, G. Muller, C. Piguet, J. Alloys Comp. 303–304 (2000) 66.
[2] G.J. Blasse, Alloys Comp. 192 (1993) 17.

[3] J. Kido, Y. Okamoto, Chem. Rev. 102 (2002) 2357.
[4] T.T. Kodas, M.J. Hampden-Smith (Eds.), The Chemistry of Metal CVD, VCH, Weinheim, 1994 432 p.
[5] O.Yu. Gorbenko, I.E. Graboy, M.A. Novozhilov, A.R. Kaul, G. Wahl, V.L. Svetchnikov, J. Phys. IV Fr. 11 (2001) Pr3.
[6] R.C. Mehrotra, R. Bohra, D.P. Gaur, Metal β-Diketonates and Allied Derivatives, Academic Press, London, 1978 427 p.
[7] G.F. de Sa, O.L. Malta, C. de Mello Donega, et al., Coord. Chem. Rev. 196 (2000) 165.
[8] H.G. Dzyubenko, L.I. Martynenko, Russ. J. Inorg. Chem. 31 (1986) 1699.
[9] W.H. Watsow, R.J. Williams, N.R. Stemple, J. Inorg. Nucl. Chem. 34 (1972) 501.
[10] Gmelin, Hand Book of Inorganic Chemistry, Syst No. 39, V. D3, Berlin/Heidelberg/NY/Tokyo, 1984, p. 65.
[11] M. Becht, K.-H. Dahmen, V. Gramlich, A. Marteletti, Inorg. Chim. Acta 248 (1996) 27.
[12] D.R. van Staveren, G.A. van Albada, J.G. Haasnoot, H. Kooijman, A.M.M. Lanfredi, P.J. Nieuwenhuizen, A.L. Spek, Ugozzoli, T. Weyhermuller, J. Reedijk, Inorg. Chim. Acta 315 (2001) 163.
[13] N.P. Kuzmina, G.N. Kupriyanova, S.I. Troyanov, Russ. J. Coord. Chem. 26 (2000) 390.
[14] G.M. Sheldrick, Acta Crystallogr. A 46 (1990) 467.
[15] G.M. Sheldrick, SHELXL-97. Program for the Refinement of Crystal Structures, University Göttingen, Germany, 1997.
[16] N. Kuzmina, V. Ivanov, S. Troyanov, L. Martynenko, A. Alikhanyan, I. Malkerova, J. Chem. Vap. Deposition 1 (1995) 72.
[17] N. Kuzmina, M. Ryazanov, S. Troyanov, V. Kezko, Russ. J. Inorg. Chem. 45 (2000) 38.
[18] N. Kuzmina, M. Ryazanov, S. Troyanov, Polyhedron 18 (1999) 2177.
[19] L.Kh. Minacheva, A.Yu. Rogachev, N.P. Kuzmina, V.S. Sergienko, Russ. J. Inorg. Chem. 48 (2003) 1822.
[20] A. Gleizes, M. Julve, N. Kuzmina, A. Alikhanyan, I. Malkerova, Eur. J. Inorg. Chem. 4 (1998) 1169.
[21] E.W. Berg, J.J.C. Acosta, Analyt. Chim. Acta 40 (1968) 101.

Available online at www.sciencedirect.com
SCIENCE DIRECT®
Polyhedron 24 (2005) 731–738
POLYHEDRON
www.elsevier.com/locate/poly

Synthesis, properties and gas phase collision-induced dissociation of the heptanuclear doubly bridged complex $[Ru(bpy)_2(BPE)_2\{Ru_3O(CH_3COO)_6(py)_2\}_2](PF_6)_4$

Henrique E. Toma [a,*], Sofia Nikolaou [b], Marcos N. Eberlin [c], Daniela M. Tomazela [c]

[a] *Instituto de Química, Universidade de São Paulo, CaixaPostal 26077, CEP 05513-970, São Paulo, Brazil*
[b] *Departamento de Química, Faculdade de Filosofia, Ciências e Letras de Ribeirão Preto, Universidade de São Paulo, FFCLRP – USP, Ribeirão Preto, Brazil*
[c] *Instituto de Química, Laboratório Thomson de Espectrometria de Massas, Universidade Estadual de Campinas UNICAMP, Campinas, Brazil*

Received 30 June 2004; accepted 27 January 2005
Available online 25 March 2005

Abstract

The $[Ru(bpy)_2(BPE)_2\{Ru_3O(CH_3COO)_6(py)_2\}_2](PF_6)_4$ complex, in which bpy = 2,2′-bipyridine, BPE = *trans*-1,2-*bis*(4-pyridyl)ethylene and py = pyridine, provides an interesting case of a heptanuclear mixed compound containing two triangular $[Ru_3O]$ clusters attached to a ruthenium polypyridine center. The composition and structural properties of this doubly bridged complex were investigated by means of electrospray mass (ESI-MS) and tandem mass (ESI-MS/MS) spectrometric experiments and NMR spectroscopy (^1H and ^{13}C). The characteristic multi-isotopic distribution, 1/4 *m*/*z* peak separation and dissociation chemistry of the isotopologue $[Ru(bpy)_2(BPE)_2\{Ru_3O(CH_3COO)_6(py)_2\}_2]^{4+}$ cation provided detailed and unequivocal MS characterization of the complex. In the electronic spectra of the heptanuclear complex broad bands were observed at 427 and 696 nm, and ascribed, respectively, to $[Ru(bpy)_2(BPE)_2]$ metal-to-ligand charge-transfer and to $[Ru_3O]$ internal cluster transitions. The characteristic waves associated with the $[Ru_3O]^{1-/0/1+/2+/3+}$ redox couples were found at −1.02, 0.16, 1.20, 2.11 V (versus SHE) in the cyclic voltammograms. Another broad wave was observed at −1.22 V, involving superimposed $bpy^{0/-}$ and $BPE^{0/1-}$ redox processes, and a peculiar wave at 1.48 V, exhibiting only a half of the relative intensity, was assigned to the central $Ru^{3+/2+}$ redox pair. Despite the two conjugated BPE bridges, the electrochemical and spectroelectrochemical data indicated only a weak coupling through the π-system in the heptanuclear complex.
© 2005 Elsevier Ltd. All rights reserved.

Keywords: Ruthenium clusters; Ruthenium polypyridines; Polynuclear complexes; ESI-MS

1. Introduction

Trinuclear complexes of the general formula $[M_3O(CH_3COO)_6(L)_3]^n$ (M = transition metal, L = solvent or *N*-heterocyclic ligands) feature a triangular structure in which the metal ions are held together by μ-oxo and carboxylate bridges [1–3]. In the particular case of triruthenium compounds, the electronic interaction among the ruthenium ions is usually so strong that the central core $[Ru_3O]^+$ is totally delocalized, behaving as a single metal center [1–4]. From an electrochemical viewpoint, it constitutes an appealing electroactive moiety, since the $[Ru_3O]$ unit displays up to five reversible redox processes in the −1.5 to 2.5 V (versus SHE) range and the choice of terminal and bridging ligand modulates its electrochemical behavior [5,6]. Moreover, each monoelectronic process is accompanied by drastic

* Corresponding author. Tel.: +55 11 30913887; fax: +55 11 38155579.
E-mail address: henetoma@iq.usp.br (H.E. Toma).

0277-5387/$ - see front matter © 2005 Elsevier Ltd. All rights reserved.
doi:10.1016/j.poly.2005.01.020

chromatic changes [7,8] providing a suitable combination of electronic stimuli and spectroscopic response.

More recently, these trinuclear ruthenium complexes have been increasingly used in the assembly of supramolecular structures [9–11] and to study intramolecular electron transfer reactions in symmetric dimers [12]. The binding of these species to ruthenium polypyridines complexes, simulating $[Ru(bpy)_3]^{2+}$ [13–16], would provide interesting prototypes to study photoinduced energy or electron transfer reactions.

The *trans*-1,2-*bis*(4-pyridyl)ethylene bridge (BPE) is also of interest as such a species belongs to a class of organic ligands bearing C=C double bonds capable of undergoing reversible *trans* → *cis* photoisomerization [17–19]. This type of functionality is being currently exploited for storage and processing information at the molecular level. The isomerization driven by light can actually lead to selective changes in the molecular conformation, modifying the spectroscopic behavior of the system in a controllable fashion [20,21] and promoting, in some cases, molecular motion [22].

This work deals with the chemistry of the BPE doubly bridged heptanuclear complex $[Ru(bpy)_2(BPE)_2\{Ru_3O(CH_3COO)_6(py)_2\}_2](PF_6)_4$ (Fig. 1). We report herein a unique assembly of polymetallic species that combines the rich redox characteristics of the cluster species and the remarkable chemical and photophysical properties of ruthenium(II) polypyridine complexes. Special emphasis is given to its structural characterization by means of NMR spectroscopy (^1H and ^{13}C), and electrospray mass (ESI-MS) and tandem mass (ESI-MS/MS) spectrometric experiments. The MS experiments, in particular, confirms the characteristic multi-isotopic distribution and dissociation chemistry expected for a $[Ru(bpy)_2(BPE)_2\{Ru_3O(CH_3COO)_6(py)_2\}_2]^{4+}$ quadruply charged gaseous cation providing detailed and unequivocal MS characterization of this heptanuclear doubly bridged ruthenium complex.

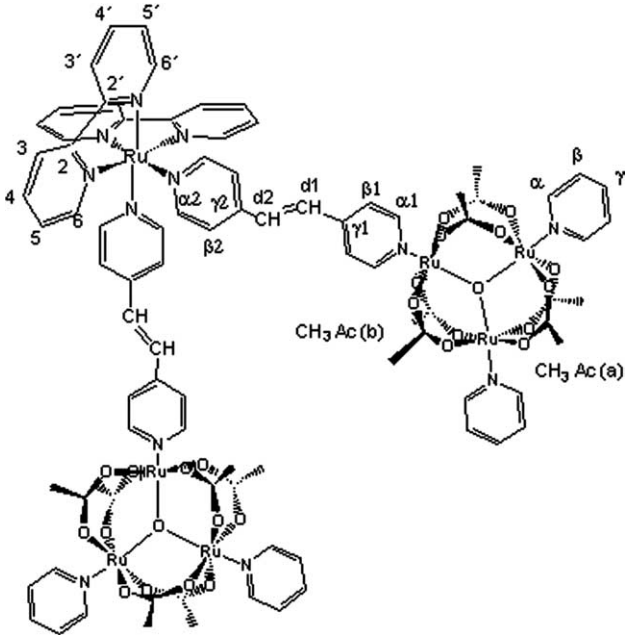


Fig. 1. Structural representation of the heptanuclear complex $[Ru(bpy)_2(BPE)_2\{Ru_3O(CH_3COO)_6(py)_2\}_2]^{4+}$ in which the numbering scheme for the assignment of the corresponding NMR spectra is also indicated.

2. Experimental

2.1. Synthesis

The $[Ru(bpy)(BPE)_2](PF_6)_2$ and $[Ru_3O(CH_3COO)_6(py)_2(CH_3OH)]PF_6$ complexes were synthesized according to reported procedures [10,23].

2.1.1. $[Ru(bpy)_2(BPE)_2\{Ru_3O(CH_3COO)_6(py)_2\}_2](PF_6)_4$

$[Ru(bpy)_2(BPE)_2](PF_6)_2 \cdot 2H_2O$ (60 mg, 0.056 mmol) was dissolved in CH_2Cl_2 (20 ml) and allowed to react with $[Ru_3O(CH_3COO)_6(py)_2(CH_3OH)]PF_6$ (113 mg, 0.112 mmol) for 72 h, at room temperature, in the dark. The solution was filtered and the liquid was treated with diethyl ether, giving a greenish brown solid. This material was collected on a filter, dissolved in CH_2Cl_2 and purified by chromatography using a neutral alumina column. The product was eluted with a mixture of 50% CH_3CN:CH_2Cl_2 (v/v) and the corresponding solution was evaporated to dryness. After dissolving in a minimum volume of CH_2Cl_2, the solution was filtered onto stirring diethyl ether, giving a dark solid, which was collected on a filter and washed with diethyl ether (50 mg, 30%). Required for $C_{88}H_{92}N_{12}O_{26}Ru_7P_4F_{24} \cdot 3(C_4H_{10}O)$: C, 37.0; H, 3.8; N, 5.2. Found: C, 37.4; H, 4.1; N, 5.6%.

2.2. Physical measurements

Electrospray ionization mass and tandem mass spectra were recorded on a Q-Tof (Micromass) mass spectrometer with quadrupole (Qq) and high resolution orthogonal time of flight (o-TOF) hybrid configuration operated under conditions described in detail elsewhere [24]. The sample introduction was performed using a syringe pump (Harvard Apparatus, Pump 11) set to 10 μl/min pumped through an uncoated fused-silica capillary. All samples were dissolved in pure methanol. The ESI mass spectrum was acquired using an ESI capillary voltage of 3 kV and a cone voltage of 10 V. For the ESI tandem mass spectrum, the mass-selected ions were dissociated using 20 eV collisions with argon.

One dimensional ^1H NMR spectra and two dimensional COSY and HETCOR spectra were recorded on a Varian 300 MHz, model INOVA 1 spectrometer, employing 2×10^{-2} mol l CD_3CN solutions, at room

temperature. UV–Vis spectra were recorded on a Hewlett-Packard model 8453 diode array spectrophotometer, using 10^{-5} mol l solutions.

Cyclic voltammetry was carried out with a Princeton Applied Research model 283 potentiostat. A platinum disk electrode was employed for the measurements, using the conventional Luggin capillary arrangement with an $Ag/AgNO_3$ (0.010 mol l) reference electrode in CH_3CN containing 0.100 mol l tetraethylammonium perchlorate (TEAP). A platinum wire was used as the auxiliary electrode. All the $E_{1/2}$ values presented here were converted to SHE by adding 0.503 V to the observed values. A three electrode system was used for the spectroelectrochemical measurements, arranged in a rectangular quartz cell of 0.025 cm internal optical path length. A gold minigrid was used as transprecursor working electrode, in the presence of the above mentioned auxiliary and reference electrodes.

Steady-state emission spectra were recorded on a LS-100 Photon Technology International Inc. spectrophotometer, at room temperature and 77 K. Photoisomerization measurements were carried out with a 150 W Xenon Arc Lamp and a f/3.4 Monochromator (Applied Photophysics), by irradiating 10% CH_3CN:H_2O samples of the BPE ligand at 313 nm and of the heptanuclear species at 297 nm.

3. Results and discussion

3.1. ^1H and ^{13}C NMR spectra

The ^1H and ^{13}C NMR spectra of the $[Ru(bpy)_2(BPE)_2\{Ru_3O(CH_3COO)_6(py)_2\}_2](PF_6)_4$ complex are complicated by the large number of signals. Preliminary analysis indicated five non-magnetically equivalent types of aromatic rings: the pyridine rings, two peripheral bpy rings (labelled as **2**, **3**, **4**, **5**, **6** and **2′**, **3′**, **4′**, **5′**, **6′**) and two different rings corresponding to the bridging ligand, one bound to the $[Ru_3O]$ core and the other bound to the $[Ru(bpy)_2]$ center. The assignment was made based on careful evaluation of the 2D correlation NMR spectra, guided by a comparison with data for the complex $[Ru_3O(CH_3COO)_6(py)_2(BPE)]PF_6$ and with the literature data [25,26].

As one can see in Table 1, the δ values of the $[Ru(bpy)_2]$ protons follow the same trends observed for the $[Ru(bpy)_3]^{2+}$ complex [25,27]; the same behavior is observed for the ^{13}C signals in comparison with the free bpy ligand. Owing to coordination to the ruthenium ion, free rotation of the bpy rings is not possible; hence protons **3** and **3′** are sterically strained in such a way that the Van der Waals interaction between them causes a deshielding effect, shifting their signals to lower field in relation to other protons of that ligand. As expected, protons **4**, **5** and **5′** appear as triplets with values of δ varying between 7.2 and 8.1 ppm due to the non-equivalence of the bpy rings. Protons **4′** are superimposed with protons **6′**.

Table 1
^1H and ^{13}C chemical shifts (δ/ppm) for the heptanuclear complex $[Ru(bpy)_2(BPE)_2\{Ru_3O(CH_3COO)_6(py)_2\}_2](PF_6)_4$ in CD_3CN solution (see labels in Fig. 1)

Position	(^1H) δ/ppm		(^{13}C) δ/ppm	
	Complex	Free ligand[a]	Complex	Free ligand[a]
Pyridine				
α	0.17	8.6	126.61	149.9
β	5.80	7.2	115.13	123.7
γ	6.56	7.6	138.64	135.7
Acetate				
CH_3 (a)	4.88	2.1	−4.10	20.7
CH_3 (b)	4.78	2.1	−4.10	20.7
C═O (a), (b)			200.16	177.7
BPE				
α_1	0.47	8.65	126.47	150.7
β_1	6.06	7.45	112.75	121.4
γ_1, γ_2			145.35	145.5
d_1	6.71	7.29	129.60	130.5
d_2	~7.14[b]	7.29	131.32	130.5
β_2	~7.14[b]	7.45	124.20	121.4
α_2	8.14	8.65	158.48	150.7
2,2′-Bipyridine				
2,2′			154.76	156.2
3′	8.24	8.42	124.74	123.5
3	8.31	8.42	125.04	123.5
4′	7.83	7.77	138.93	136.7
4	8.02	7.77	139.03	136.7
5′	7.28	7.25	128.58	121.0
5	7.66	7.25	128.95	121.0
6′	7.79	8.67	153.42	149.1
6	8.79	8.67	153.60	149.1

[a] Data from Ref. [30].
[b] H signals d_2 and β_2 are superimposed.

Protons **6′** are subjected to the so called *ring current* effects. These protons are located in the shielding region of the pyridinic aromatic rings and, therefore, have their signals shifted to higher field in relation to the free ligand. However, protons **6** appear downfield shifted; this shift could be addressed assuming that the BPE rings are not co-planar to each other, being otherwise inclined in such a way that subjects protons **6** to the deshielding region.

For the $[Ru_3O(CH_3COO)_6(py)_2]$ moiety, the δ values (Table 1) follow the pattern dictated by the paramagnetic anisotropy of the $[Ru_3O]$ core [1].

In the heptanuclear complex, two signals assigned to the acetate protons are observed (consistent with the presence of two magnetically non-equivalent acetate sites; i.e., four *vicinal* and two in opposite positions with respect to the bridging ligand). For the BPE bridging ligand, a splitting in the proton (and carbon) signals (Table 1) is observed, attributed to the double bond, which constitute a singlet in the free ligand. This split-

ting reflects a decrease in the symmetry of the ligand owing to the bridging coordination mode between two different metallic units. Note that the J coupling constant of the d_1 proton is equal to 16.5 Hz, a value that is typical for the *trans*-isomer [28]. This signal is shifted to higher field, showing that it is sensitive to the paramagnetic anisotropy of the [Ru_3O] unit. This effect is also expressed in the δ values observed for the α_1 and β_1 protons attached to the BPE ring directly bound to the paramagnetic center and for the pyridinic rings, whose corresponding protons appear shifted to higher fields in relation to free pyridine. The magnitude of this effect diminishes with the distance from the [Ru_3O] core and this pattern can be explained considering both dipolar and contact mechanisms for the paramagnetic interactions in the molecule [29]. These interactions are also responsible for the fact that the signals for the acetate methyl protons are shifted in the opposite direction as those of pyridine, whereas inverse trends for protons and carbon shifts are observed for the acetate signals.

3.2. Mass spectrometric structural characterization

ESI-MS and ESI-MS/MS experiments are being increasingly used in the structural characterization of organometallic and metallorganic species, as well as of loosely bonded cationic and ionic coordination species participating as key reaction intermediates [31,32]. In our case, ESI provided an efficient technique for "fishing" directly from solution to the gas phase, both ionic components of the supramolecular complex [Ru(bpy)$_2$(BPE)$_2${Ru$_3$O(CH$_3$COO)$_6$(py)$_2$}$_2$](PF$_6$)$_4$, i.e., either the quadruply charged cationic species [Ru(bpy)$_2$(BPE)$_2${Ru$_3$O(CH$_3$COO)$_6$(py)$_2$}$_2$]$^{4+}$ or the singly charged anionic species PF_6^-, allowing their corresponding mass detection, and isotopic and structural characterization.

The ESI mass spectrum in the positive ion mode of a methanolic solution of the complex detected a prominent cluster of isotopologue cations (*m*/*z* 610 for the most abundant) separated by 1/4 *m*/*z* units, which matched perfectly the features expected for Ru(bpy)$_2$(BPE)$_2${Ru$_3$O(CH$_3$COO)$_6$(py)$_2$}$_2$]$^{4+}$. The characteristic, multi-component isotopic pattern resulting from the presence of seven multi-isotope ruthenium atoms also matched perfectly that calculated for this cation. The ESI mass spectrum in the negative ion mode detected a prominent single and monoisotopic anion of *m*/*z* 145 (144.96) corresponding to PF_6^-.

For structural characterization, the entire cluster of the many quadruply charged isotopologue ions [Ru(bpy)$_2$(BPE)$_2${Ru$_3$O(CH$_3$COO)$_6$(py)$_2$}$_2$]$^{4+}$ (*m*/*z* 610) were mass-selected and subjected to 15 eV collision-induced dissociation (Fig. 2). Dissociation was observed to occur mainly by successive breaking of the BPE–ruthenium bonds, showing this bond to be the weakest for the complex. As summarized in Fig. 3, the quadruply

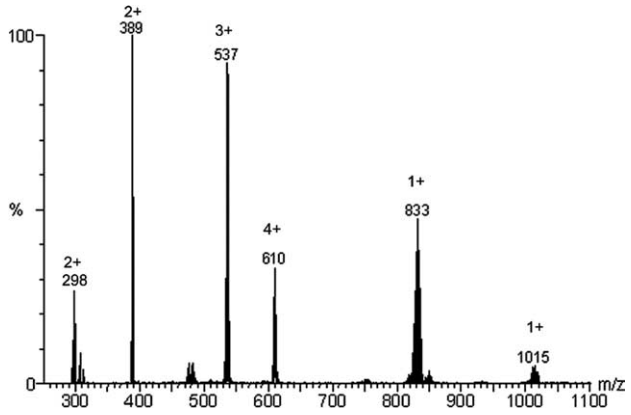


Fig. 2. ESI tandem mass spectrum for 15 eV collision-induced dissociation of [Ru(bpy)$_2$(BPE)$_2${Ru$_3$O(CH$_3$COO)$_6$(py)$_2$}$_2$]$^{4+}$ ions (*m*/*z* 610). The charge states for the ions are indicated.

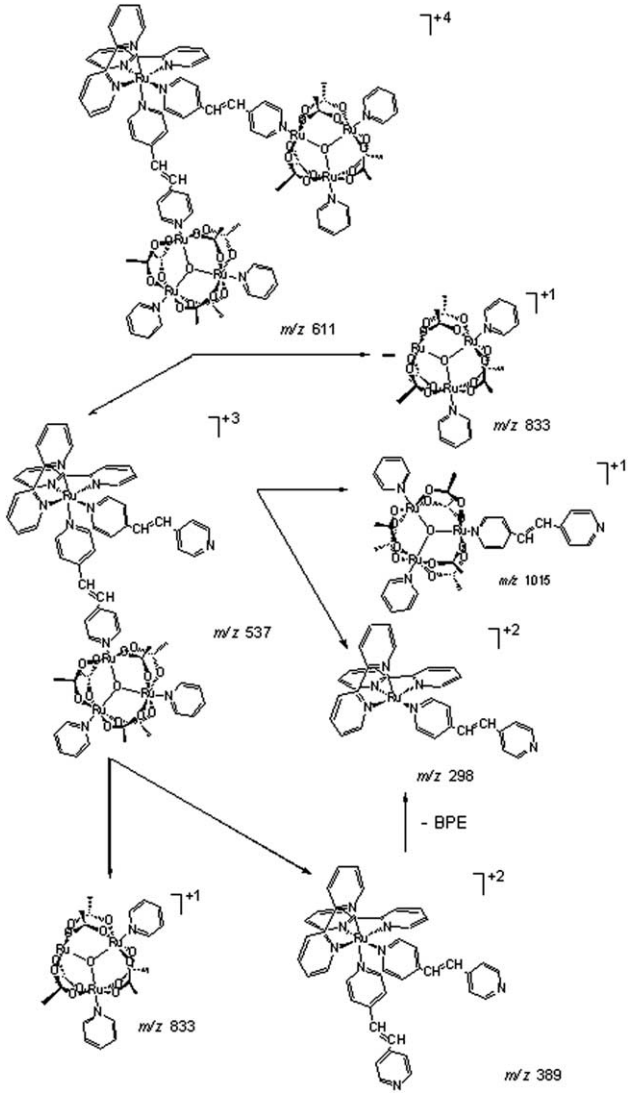


Fig. 3. Dissociation routes for the 15 eV collision-induced dissociation of gaseous [Ru(bpy)$_2$(BPE)$_2${Ru$_3$O(CH$_3$COO)$_6$(py)$_2$}$_2$]$^{4+}$ ions.

charged Ru_7-precursor ions (*m*/*z* 610) dissociate by charge partitioning, with BPE–Ru bond breaking, to form both a triply charged cluster of Ru_4-isotopologue fragment ions (*m*/*z* 537) separated by 1/3 *m*/*z* units and a singly charged cluster of Ru_3-isotopologue ions (*m*/*z* 833) separated by one *m*/*z* unit. The triply charged Ru_4-isotopologue ions (*m*/*z* 537) dissociate in turn via two competitive pathways that give either (i) a doubly charged cluster of Ru_1-isotopologue fragment ions (*m*/*z* 389) separated by 1/2 *m*/*z* units and a singly charged cluster of Ru_3-isotopologue fragment ions (*m*/*z* 833) or (ii) a singly charged cluster of Ru_3-isotopologue fragment ions (*m*/*z* 1015) and doubly charged cluster of Ru_1-isotopologue fragment ions (*m*/*z* 298) separated by 1/2 *m*/*z* units. These ions can also be formed from the doubly charged Ru_1-isotopologue fragment ions (*m*/*z* 389) via the loss of a neutral molecule of BPE. Note in Fig. 3, the characteristic isotopic distribution of both the Ru_7-precursor ion and of all of its Ru_n-fragment ions as well as the charge-diagnostic *m*/*z* separation within each cluster, matching perfectly those expected for the proposed structures.

3.3. Absorption spectra

In Fig. 4 one can see the absorption spectra of the $[Ru(bpy)_2(BPE)_2\{Ru_3O(CH_3COO)_6(py)_2\}_2](PF_6)_4$ complex. The spectra can be readily interpreted by comparing with the reported data for the model compounds $[Ru(bpy)_2(BPE)_2](PF_6)_2$ and $[Ru_3O(CH_3COO)_6(py)_2(BPE)]PF_6$ [33–35]. The intense bands in the ultra-violet region, i.e., 291 nm ($\varepsilon = 11.7 \times 10^4\ mol^{-1}\ l\ cm^{-1}$) can be assigned to the pyridinic ligand $\pi \rightarrow \pi^*$ transitions; in the visible region one can observe the MLCT bands of the $[Ru(bpy)_2]$ unit at 427 nm ($3.89 \times 10^4\ mol^{-1}\ l\ cm^{-1}$), as confirmed by spectroelectrochemical measurements. Finally, the near infra-red broad band at 696 nm ($1.29 \times 10^4\ mol^{-1}\ l\ cm^{-1}$) is consistent with the typical IC (intra-cluster) transitions, which occurs within an energy level manifold, generated by the combination of the ruthenium and central oxygen orbitals in the $[Ru_3O(CH_3COO)_6]$ fragment [35].

It is worth noting that the bridging coordination of the $[Ru_3O]$ cores does not affect significantly the energy of the MLCT bands, in comparison to the mononuclear precursors $[Ru(bpy)_2(BPE)_2]^{2+}$ ($\lambda_{max} = 430$ nm); the same is valid for the IC transition, in comparison with the $[Ru_3O(CH_3COO)_6(py)_2(BPE)]PF_6$ complex ($\lambda_{max} = 693$ nm) [33–35].

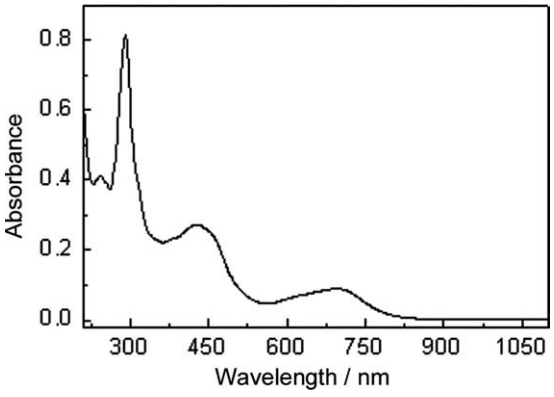


Fig. 4. Absorption spectrum of the $[Ru(bpy)_2(BPE)_2\{Ru_3O(CH_3COO)_6(py)_2\}_2](PF_6)_4$ complex, in acetonitrile solution.

3.4. Electrochemical measurements

The profile of the voltammograms shown in Fig. 5 consists of four reversible, two electron waves at −1.02, 0.16, 1.20, 2.11 V (versus SHE), ascribed to the $[Ru_3O]^{1-/0/1+/2+/3+}$ redox processes, one mono-electronic wave at 1.48 V, ascribed to the $Ru^{2+/3+}$ pair and finally a wave corresponding to the reduction of the pyridinic ligands. The peak current relation observed for the $[Ru_3O]^{1+/2+}$ and $Ru^{2+/3+}$ pairs have an approximated value of 2:1, being consistent with the proposed coordination of one $[Ru(bpy)_2]$ moiety to two $[Ru_3O]$ cores. The occurrence of only one wave associated with the redox processes in the two $[Ru_3O]$ units demonstrates that electronic coupling between them is not enough to promote detectable splittings in the cyclic voltammograms.

In Fig. 6 one can see the results of the spectroelectrochemical measurements. The observed behavior is consistent with that of monomeric trinuclear complexes [1], as well as with that of analogous polynuclear systems [36,37]. The first reduction process (Fig. 6(a)) implies in a destabilization of the $[Ru_3O]$ energy levels, owing to the increase of electron population, causing bathochromic shifts of both IC (696–915 nm) and

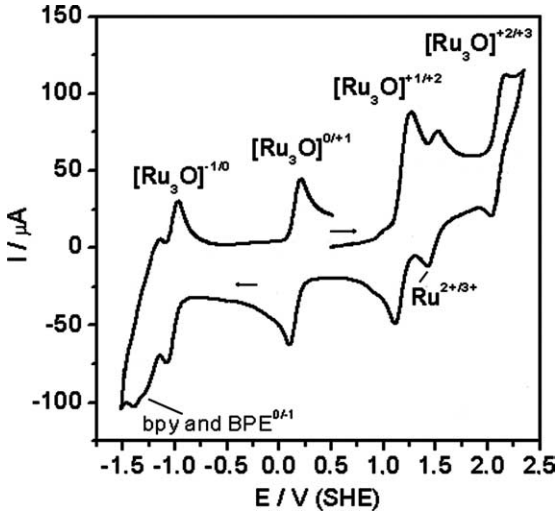


Fig. 5. Cyclic voltammogram of the $[Ru(bpy)_2(BPE)_2\{Ru_3O(CH_3COO)_6(py)_2\}_2](PF_6)_4$ complex in 3×10^{-3} mol l acetonitrile solutions, 0.1 mol l TEAP, room temperature, scan rate = 200 mV s^{-1}.

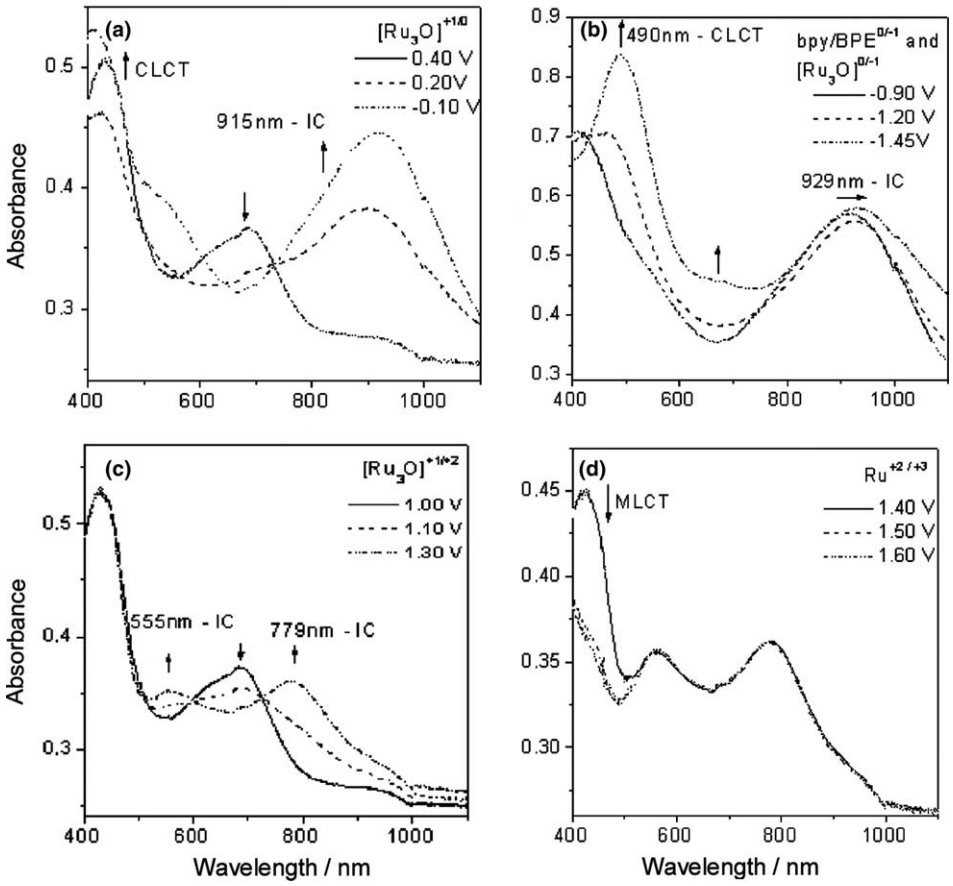


Fig. 6. Spectroelectrochemical behavior of $[Ru(bpy)_2(BPE)_2\{Ru_3O(CH_3COO)_6(py)_2\}_2](PF_6)_4$ in 3×10^{-3} mol l acetonitrile solutions, 0.1 mol l TEAP, as a function of the applied potentials.

CLCT bands (intensification of the shoulder observed between 400 and 500 nm). In the second reduction process (Fig. 6(b)), besides an additional destabilization of the $[Ru_3O]$ levels due to the addition of a second electron to each unit, an increase in intensity around 680 nm is observed, ascribed to a CLCT transition to the BPE bridge; this behavior is in agreement with that observed earlier for trinuclear complexes bridged by π-conjugated ligands [10,36,38].

The oxidation of the $[Ru_3O]$ center (Fig. 6(c)) is accompanied by the splitting of the IC band at 696 nm into two components at 555 and 779 nm. Finally, the oxidation of the $[Ru(bpy)_2]$ moiety, centered in the metal, leads to the decay of the MLCT band (Fig. 6(d)), once the electron involved in this transition is removed.

Under the experimental conditions of the spectroelectrochemical measurements, it was not possible to reach the positive potential corresponding to the last oxidation wave observed in the cyclic voltammetry.

3.5. Photophysical assays

Many attempts to detect luminescence emission for the complex were made in this work. In general, degassed solutions of the compound, in acetonitrile, ethanol (room temperature), and in ethanol glasses (77 K), were excited at the MLCT wavelength, but in no case the typical MLCT[3] luminescence of the $[Ru(bpy)_n]$ chromophore [13] could be detected. Also, the expected photoisomerization of the coordinated BPE ligand was not observed, in contrast to the free BPE ligand, which exhibited a *cis–trans* isomerization quantum yield of $\phi = 0.24$ in 10% acetonitrile:water solution, in agreement with the literature data [39].

For a series of $[Ru(bpy)_2(Cl)B]^{2+}$ compounds, in which B = pyrazine, 4-4′-bipyridine, 1,2-*bis*(4-pyridyl)ethane or *trans*-1,2-*bis*(4-pyridyl)ethylene (BPE), it has been observed that the emission quantum yield (ϕ_{em}) is extremely low, owing to d–d states [40]. Nevertheless, for the compound containing the bridging BPE ligand, the value of ϕ_{em} is even lower, indicating an additional pathway for energy loss, such as an energy transfer from the ^{3}MLCT to the BPE triplet state involved in photoisomerization. For the $[Ru(bpy)_2(BPE)_2\{Ru_3O(CH_3COO)_6(py)_2\}_2](PF_6)_4$ complex, this particular BPE excited state can undergo further energy (or electron) transfer to the $[Ru_3O]$ low lying IC states, which would finally decay by a non-radiative mechanism, thus, explaining the quenching of the *trans* → *cis*

photoisomerization. Actually, it has been shown that both energy and electron transfer can provide possible quenching pathways of ^{3}MCLT states (and probably of the bridge low lying triplet state), depending on the oxidation state of the $[Ru_3O]$ core [37].

4. Final remarks

A novel heptanuclear doubly bridged complex $[Ru(bpy)_2(BPE)_2\{Ru_3O(CH_3COO)_6(py)_2\}_2](PF_6)_4$ has been described. Detailed structural characterization of this supramolecular complex by ESI-MS(/MS) and NMR spectroscopy is fully consistent with the binding of two $[Ru_3O]$ units to the $[Ru(bpy)_2]$ center. The observed absorption profile, as well as its electrochemical behavior, are in agreement with a doubly bridged structure involving weakly interacting metallic units. Such weak electronic interaction, however, is strong enough to quench its photophysical properties, so that the emission from the $[Ru(bpy)_2]$ center has not been observed, either at room temperature or at 77 K, also preventing the characteristic *trans* → *cis* photoisomerization of the BPE bridging ligand.

Acknowledgments

We acknowledge the Brazilian agencies CNPq, CAPES and FAPESP and the Millennium Institute of Complex Materials.

References

[1] H.E. Toma, K. Araki, A.D.P. Alexiou, S. Nikolaou, S. Dovidauskas, Coord. Chem. Rev. 219 (2001) 187.
[2] A.D.P. Alexiou, S. Dovidauskas, H.E. Toma, Quim. Nova 23 (2000) 785.
[3] T.M. Busleva, S.N. Red'kina, O.V. Rudnitskaya, Russ. J. Coord. Chem. 25 (1999) 3.
[4] R.C. Rocha, H.E. Toma, Quim. Nova 25 (2002) 624.
[5] H.E. Toma, C.J. Cunha, C. Cipriano, Inorg. Chim. Acta 154 (1988) 63.
[6] A.D.P. Alexiou, H.E. Toma, J. Chem. Res. (S) (1993) 464.
[7] H.E. Toma, C. Cipriano, J. Electroanal. Chem. 263 (1989) 313.
[8] H.E. Toma, F. Matsumoto, C. Cipriano, J. Electroanal. Chem. 346 (1993) 261.
[9] S. Nikolaou, H.E. Toma, J. Chem. Res. (S) (2000) 326.
[10] (a) H.E. Toma, A.D.P. Alexiou, J. Braz. Chem. Soc. 6 (1995) 267; (b) H.E. Toma, A.D.P. Alexiou, J. Chem. Res. (S) (1995) 134.
[11] (a) K. Araki, S. Dovidauskas, H. Winnischofer, A.D.P. Alexiou, H.E. Toma, J. Electroanal. Chem. 498 (2001) 152; (b) S. Dovidauskas, K. Araki, H.E. Toma, J. Porphyr. Phthaloc. 4 (2000) 727; (c) S. Dovidauskas, H.E. Toma, K. Araki, H.C. Sacco, Y. Iamamoto, Inorg. Chim. Acta 305 (2000) 206; (d) H.E. Toma, K. Araki, E.O. Silva, Monatsh. Chem. 129 (1998) 975.
[12] T. Ito, T. Hamaguchi, H. Nagino, T. Yamaguchi, J. Washington, C.P. Kubbiak, Science 227 (1997) 660.
[13] A. Juris, V. Balzani, F. Barigelletti, S. Campagna, P. Belser, A. von Zelewsky, Coord. Chem. Rev. 84 (1988) 85.
[14] (a) V. Balzani, A. Juris, M. Venturi, S. Campagna, S. Serroni, Chem. Rev. 96 (1996) 759; (b) L. de Cola, P. Belser, Coord. Chem. Rev. 177 (1998) 301.
[15] (a) M. Venturi, A. Credi, V. Balzani, Coord. Chem. Rev. 185 (1999) 233; (b) F. Scandola, R. Argazzi, C.A. Bignozzi, M.T. Indelli, J. Photochem. Photobiol. A 82 (1994) 191; (c) F. Scandola, R. Argazzi, C.A. Bignozzi, C. Chiorboli, M.T. Indelli, M.A. Rampi, Coord. Chem. Rev. 125 (1993) 283.
[16] (a) V. Balzani, F. Scandola, in: Supramolecular Photochemistry, Ellis Horwood Chichester, UK, 1991; (b) R. Bergonzi, L. Fabbrizzi, M. Licchelli, C. Mangano, Coord. Chem. Rev. 170 (1998) 31; (c) S. Campagna, C. Di Pietro, F. Loiseau, B. Maubert, N. McClenaghan, R. Passalacqua, F. Puntoriero, V. Ricevuto, S. Serroni, Coord. Chem. Rev. 229 (2002) 67; (d) S. Serroni, S. Campagna, F. Puntoriero, C. Di Pietro, N.D. McClenaghan, F. Loiseau, Chem. Soc. Rev. 30 (2001) 367.
[17] H. Meier, Angew. Chem., Int. Ed. Engl. 31 (1992) 1399.
[18] H. Görner, F. Elisei, U. Mazzucato, J. Phys. Chem. 95 (1991) 4000.
[19] V.W. Yam, V.C. Lau, L. Wu, J. Chem. Soc., Dalton Trans. (1998) 1461.
[20] P. Gütlich, Y. Garcia, T. Woike, Coord. Chem. Rev. 219 (2001) 839.
[21] R. Ziessel, M. Hissler, A. El-ghayoury, A. Harriman, Coord. Chem. Rev. 178 (1998) 1251.
[22] V. Balzani, A. Credi, F.M. Raymo, J.F. Stoddart, Angew. Chem. Int. Ed. 39 (2000) 3348.
[23] (a) B.P. Sullivan, D.J. Salmon, T.J. Meyer, Inorg. Chem. 17 (1978) 3334; (b) S.A. Adeyemi, E.C. Johnson, F.J. Miller, T.J. Meyer, Inorg. Chem. 12 (1973) 2371; (c) M.J. Powers, T.J. Meyer, J. Am. Chem. Soc. 102 (1980) 1289.
[24] J.B. Domingos, E. Longhinotti, T.A.S. Brandão, L.S. Santos, M.N. Eberlin, C.A. Bunton, F. Nome, J. Org. Chem. 69 (2004) 7898.
[25] E.C. Constable, J. Lewis, Inorg. Chim. Acta 70 (1983) 251.
[26] S. Nikolaou, M. Uemi, H.E. Toma, Spectrosc. Lett. 34 (2001) 267.
[27] E.C. Constable, K.R.A. Seddon, J. Chem. Soc., Chem. Commun. (1982) 34.
[28] (a) S. Sun, E. Robson, N. Dunwoody, A.S. Silva, I.M. Brinn, A.J. Lees, Chem. Commun. (2000) 201; (b) V.W. Yam, V.C. Lau, L. Wu, J. Chem. Soc., Dalton Trans. (1998) 1461.
[29] I. Bertini, C. Luchinat, Coord. Chem. Rev. 150 (1996) 1.
[30] Standard Spectra Collection, Sadtler Research Lab., Bio-Rad Inc., Philadelphia, PA.
[31] (a) R. Colton, A. D'Agostinho, J.C. Traeger, Mass Spectrom. Rev. 14 (1995) 79; (b) D.A. Plattner, Int. J. Mass Spectrom. 207 (2001) 125; (c) J. Griep-Raming, S. Meyer, T. Bruhn, J.O. Metzger, Angew. Chem. Ind. Ed. 41 (2002) 2738; (d) R. Arakawa, S. Tachiyashiki, T. Matsuo, Anal. Chem. 67 (1995) 4133.
[32] (a) D.M. Tomazela, I. Mayer, F.M. Engelmann, K. Araki, H.E. Toma, M.N. Eberlin, J. Mass Spectrom. 39 (2004) 1161; (b) S.H. Toma, M. Uemi, S. Nikolaou, D.M. Tomazela, M.N. Eberlin, H.E. Toma, Inorg. Chem. 43 (2004) 3521; (c) D.M. Tomazela, F.C. Gozzo, G. Eberling, J. Dupont, M.N. Eberlin, Inorg. Chim. Acta 357 (2004) 2349; (d) R.M.S Pereira, V.I. Paula, R. Buffon, D.M. Tomazela, M.N. Eberlin, Inorg. Chim. Acta 357 (2004) 2100; (e) G. Cerchiaro, P.L. Saboya, A.M. da Costa Ferreira, D.M. Tomazela, M.N. Eberlin, Trans. Metal Chem. 29 (2004) 495;

(f) S.H. Toma, S. Nikolaou, D.M. Tomazela, M.N. Eberlin, H.E. Toma, Inorg. Chim. Acta 357 (2004) 2253;
(g) A.A. Sabino, A.H.L. Machado, C.R.D. Correia, M.N. Eberlin, Angew. Chem. Int. Ed. 43 (2004) 2514.
[33] R.W. Callahan, G.M. Brown, T.J. Meyer, Inorg. Chem. 14 (1975) 1443.
[34] M.J. Powers, R.W. Callahan, D.J. Salmon, T.J. Meyer, Inorg. Chem. 15 (1976) 894.
[35] J.A. Baumann, D.J. Salmon, S.T. Wilson, T.J. Meyer, W.E. Hatfield, Inorg. Chem. 17 (1978) 3342.
[36] S. Nikolaou, H.E. Toma, Polyhedron 20 (2001) 253.
[37] S. Nikolaou, H.E. Toma, J. Chem. Soc., Dalton Trans. (2002) 352.
[38] (a) J.A. Baumann, D.J. Salmon, S.T. Wilson, T.J. Meyer, Inorg. Chem. 18 (1979) 2472;
(b) J.A. Baumann, S.T. Wilson, D.J. Salmon, P.L. Hood, T.J. Meyer, J. Am. Chem. Soc. 101 (1979) 2916;
(c) S.T. Wilson, R.F. Bondurant, T.J. Meyer, D.J. Salmon, J. Am. Chem. Soc. 97 (1975) 2285.
[39] (a) D.G. Whitten, M.T. McCall, Tetrahedron Lett. 23 (1968) 2755;
(b) D.G. Whitten, M.T. McCall, J. Am. Chem. Soc. 91 (1969) 5097;
(c) D.G. Whitten, Y.J. Lee, J. Am. Chem. Soc. 92 (1970) 415;
(d) Y.J. Lee, D.G. Whitten, L. Pedersen, J. Am. Chem. Soc. 93 (1971) 6330;
(e) D.G. Whitten, Y.J. Lee, J. Am. Chem. Soc. 94 (1972) 9142;
(f) A.R. Gutierrez, D.G. Whitten, J. Am. Chem. Soc. 98 (1976) 6233.
[40] J.C. Curtis, J.S. Berstein, T.J. Meyer, Inorg. Chem. 24 (1985) 385.

Available online at www.sciencedirect.com
SCIENCE DIRECT®
Polyhedron 24 (2005) 739–746
POLYHEDRON
www.elsevier.com/locate/poly

Manganese(II) complexes of pyridyl-azo-imidazoles. Single crystal X-ray structures of 3′-PyaiH and $[Mn(3'\text{- PyaiEt})_4](ClO_4)_2$ (3′-PyaiH = 2-(3′-pyridylazo)imidazole; 3′-PyaiEt = 1-ethyl-2-(3′-pyridylazo)imidazole)

T. Mathur [a], U.S. Ray [a], J.-C. Liou [b], J.S. Wu [b], T.-H. Lu [b], C. Sinha [c,*]

[a] Department of Chemistry, The University of Burdwan, Burdwan 713104, India
[b] Department of Physics, National Tsing Hua University, Hsinchu, Taiwan 300, ROC
[c] Department of Chemistry, Jadavpur University, Kolkata 700 032, India

Received 24 September 2004; accepted 31 January 2005
Available online 25 March 2005

Abstract

Pyridine and imidazole are connected by an azo group (—N=N—) to synthesize 2-[(3′-pyridyl)azo]imidazole (3′-PyaiH) and this has been confirmed by X-ray structure determination. The N(1)-alkylation gives 1-alkyl-2-[(3′-pyridyl)azo]imidazole (3′-PyaiR′) (R′ = Me (**2a**), Et (**2b**), Bz (**2c**)). The reaction between $Mn(ClO_4)_2 \cdot 6H_2O$ and 3′-PyaiR′ in methanol has synthesized $[Mn(3'\text{-PyaiR}')_4](ClO_4)_2$ (**3**). The structure has been confirmed by single crystal X-ray diffraction study in one case, in addition to other spectral characterization. The structure reveals a tetrahedral orientation of four ligands coordinating through imidazole-N only. Cyclic voltammetry exhibits a Mn(III)/Mn(II) couple at >1.1 V along with azo reductions. However, the reaction of $MnCl_2 \cdot 4H_2O$ + 3′-PyaiR′ in the presence of NaN_3 or NH_4CNS (1:2:2 mole proportion) has synthesized $Mn(3'\text{-PyaiR}')_2(X)_2$ (X = N_3 (**4**), NCS (**5**)).
© 2005 Elsevier Ltd. All rights reserved.

Keywords: Pyridyl-azo-imidazoles; Manganese(II) tetrahedral; X-ray; Electrochemistry

1. Introduction

For the last decade we have been engaged in the design of several types of heterocyclic azo compounds and studies on their complexes [1–3]. This type of molecule has several advantages. To quote a few, the azo group is photochromic, redox responsive, pH-sensitive; stabilizes low valent metal oxidation states due to the presence of a low-lying azo-centred π*-molecular orbital, serves as a molecular switch, is used as a metal ion indicator in complexometric titration, dyes and pigments in textile industry [4–8]. Bi-heterocyclic azo ligands are of current interest [5,7,9] because of their photoswitching property, non-linear optical property, etc. The majority of biheterocyclic azo compounds are symmetric systems in which two identical heterocyclic units are linked by the —N=N— group. Unsymmetric biheterocyclic azo compounds are scarce. A report of thiazole —N=N— imidazole has been appeared in the literature [10]. We have reported a second example of unsymmetric bi-hetetero-cyclic azo compounds, pyridyl-azo-imidazoles (**1**) and their Cd(II) and Ag(I) complexes [11]. The ligands belong to a special case of multimodal systems [12].

In this work, we report on the manganese(II) complexes of 1-alkyl-2-[(3′-pyridyl)azo]imidazoles (3′-PyaiR′, **2**) and their derivatives. Manganese is chosen

* Corresponding author. Tel.: +91 098 3063 2450; fax: +91 033 2414 6584.
E-mail address: c_r_sinha@yahoo.com (C. Sinha).

0277-5387/$ - see front matter © 2005 Elsevier Ltd. All rights reserved.
doi:10.1016/j.poly.2005.01.017

because of its essential structural and catalytic role in many proteins [13]. The active site involves the binding of imidazoles-N from histidine residues to Mn(II). Besides, the high local spin value of Mn(II) (d^5) enable this metal ion in the exploration of magnetic materials [14,15]. The pseudohalides, especially azide (N_3^-) and thiocyanate (SCN^-) are versatile bridging ligands [14–16] in the synthesis of transition metal complexes for improving the magnetic exchange phenomenon. This work also characterizes manganese(II)-azido/thiocyanato complexes of the pyridyl-azo-imidazole system. The X-ray structures of the free ligand, 2-(3′-pyridylazo)imidazole and tetrakis-{1-ethyl-2-(3′-pyridylazo)imidazole} manganese(II) perchlorate (**3**) are also reported herein. However, reaction of $MnCl_2$, 3′-PyaiR′ and NaN_3/NH_4CNS give $Mn(3'\text{-PyaiR}')_2(X)_2$ (X = N_3(**4**), NCS (**5**)) which have been characterized by spectroscopic techniques.

2. Experimental

2.1. Materials

Published methods [11] were used to prepare 1-alkyl-2-(3′-pyridylazo)imidazoles (3′-PyaiR′ where R′ = Me (**2a**), Et (**2b**), Bz (**2c**)) (Scheme 1). $Mn(ClO_4)_2.6H_2O$ was prepared by adding $MnCO_3$ to a warm $HClO_4$ solution (1:1, v/v) and then recrystallizing from water in the presence of a few drops of $HClO_4$. All other chemicals and organic solvents used for the preparation work were of reagent grade, received from SRL, India. Purification of MeCN and preparation of [*n*-Bu_4N][ClO_4] were done following the literature method [3].

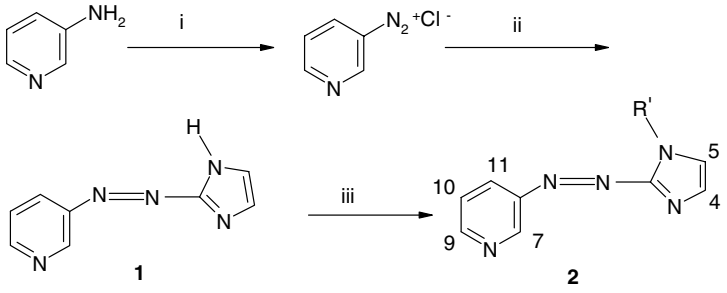
2.2. Physical measurements

Microanalyses (C, H, N) were performed using a Perkin–Elmer 2400 CHNO/S elemental analyzer. Spectroscopic measurements were carried out using the following instruments: UV–Vis spectra, reflectance spectra, JASCO UV–Vis/NIR model V-570; IR spectra (KBr disk, 4000–200 cm^{-1}), JASCO FT-IR model 420. Molar conductances were measured by a Systronics conductivity meter, solute concentration ($\sim10^{-3}$ M) in MeCN. Estimation of manganese was carried out by microwave digestion followed by potassium periodate oxidation to pink permanganate, which was determined by a spectrophotometric process [17]. Electrochemistry was carried out with a PAR electrochemistry system 250 potentiostat/versastat and 270 software package. In the cyclic voltametry the following conditions were used: solvent, dry MeCN; supporting electrolyte, [*n*Bu_4N][ClO_4] ($\sim$0.1 M); solute concentration ($\sim10^{-3}$ M); working electrode, Pt-disk mili electrode; reference electrode, SCE; auxiliary electrode, Pt-wire; scan rate, 50 mV s^{-1}; formal potential, $E^0 = 0.5(Ep_a + Ep_c)$, where Ep_a and Ep_c are anodic and cathodic peak potentials, respectively; ΔEp ($|Ep_a - Ep_c|$) is the peak-to-peak separation. All experiments were done under a dry N_2 atmosphere at 295(2) K. EPR spectra were measured in MeCN solution at room temperature (298 K) and liquid nitrogen temperature (77 K) using a Bruker ESR spectrometer model EMX 10/12, X-band ER 4119 HS cylindrical resonator.

2.2.1. Preparation of tetrakis 1-methyl-2-[(3′-pyridyl)azo]imidazole manganese(II) percholate, $[Mn(3'\text{-PyaiMe})_4](ClO_4)_2$ (**3a**)

A methanolic solution (15 ml) of 1-methyl-2-[(3′-pyridyl)azo]imidazole (3′-PyaiMe, 0.3 g, 1.60 mmol) was added dropwise to $Mn(ClO_4)_2 \cdot 6H_2O$ (0.2 g, 0.56 mmol) in the same solvent (20 ml) at room temperature (298 K). The mixture was stirred for 15 min and a small portion of yellow mass was filtered and rejected. The filtrate was kept undisturbed for a few days. A bright orange-red crystalline compound was filtered and washed with cold water and methanol. Finally it was dried in vacuo. The isolated yield was 0.25 g (61%).

All other complexes were prepared by the same procedure and yields varied from 60% to 70%. Microanalytical data of the complexes are as follows: $[Mn(3'\text{-PyaiMe})_4](ClO_4)_2$ (**3a**): *Anal.* Calc. for $C_{36}H_{36}N_{20}O_8Cl_2Mn$: C, 43.11; H, 3.59; N, 27.94; Mn, 5.49. Found: C, 43.25; H, 3.65; N, 27.80; Mn, 5.65%. IR (KBr disk)



R′ = Me (**2a**), Et (**2b**), CH_2Ph (**2c**)

Scheme 1.

(cm^{-1}); $\nu(ClO_4)$, 1090 (s), 625(w); ν(C=N), 1580 (m); ν(N=N), 1440 (m). UV–Vis spectral data (in MeCN) (λ_{max}/nm) ($10^{-3}\,\varepsilon\,M^{-1}\,cm^{-1}$): 424 (10.44), 376 (59.16). Magnetic data: μ, 5.8 BM. EPR data (77 K) $g = 2.02$, $A = 88$ G. $[Mn(3'\text{-PyaiEt})_4](ClO_4)_2$ (**3b**): *Anal.* Calc. for $C_{40}H_{44}N_{20}O_8Cl_2Mn$: C, 45.37; H, 4.16; N, 26.47; Mn, 5.20. Found: C, 45.26; H, 4.06; N, 26.35; Mn, 5.08%. IR (KBr disk) (cm^{-1}); $\nu(ClO_4)$, 1093 (s), 624(w); ν(C=N), 1583 (m); ν(N=N), 1442 (m). $[Mn(3'\text{-PyaiBz})_4](ClO_4)_2$. UV–Vis spectral data (in MeCN) (λ_{max}/nm) ($10^{-3}\,\varepsilon\,M^{-1}\,cm^{-1}$): 422 (9.11), 378 (53.36). Magnetic data: μ, 5.7 BM. EPR data (77 K) $g = 2.02$, $A = 90$ G. $[Mn(3'\text{-PyaiBz})_4](ClO_4)_2$ (**3c**): *Anal*. Calc. for $C_{60}H_{52}N_{20}O_8Cl_2Mn$: C, 55.13; H, 3.98; N, 21.44; Mn, 4.21. Found: C, 55.00; H, 3.90; N, 21.55; Mn, 4.05%. IR (KBr disk) (cm^{-1}); $\nu(ClO_4)$, 1090 (s), 627(w); ν(C=N), 1600 (m); ν(N=N), 1440 (m). UV–Vis spectral data (in MeCN) (λ_{max}/nm) ($10^{-3}\,\varepsilon\,M^{-1}\,cm^{-1}$): 422 (7.21), 376 (33.75). Magnetic data: μ, 5.7 BM. EPR data (77 K) $g = 2.00$, $A = 85$ G.

2.2.2. Preparation of bis-{1-methyl-2-[(3′-pyridyl)azo] imidazole}-bis-azido-manganese(II), $Mn(3'\text{-PyaiMe})_2(N_3)_2$ (**4a**)

To an aqueous solution (10 ml) of $MnCl_2 \cdot 4H_2O$ (0.2 g, 0.77 mmol), NaN_3 (0.1 g, 1.54 mmol) was added and stirred for 15 min. 3′-PyaiMe (0.29 g, 1.55 mmol) in MeOH (15 ml) was added in dropwise and stirred for another 15 min. A brown precipitate appeared, which was then filtered. The filtrate was kept undisturbed and allowed to evaporate slowly for a week. A brown crystalline product was isolated by filtration, washed with water and cold methanol. It was then dried over a $CaCl_2$ dessicator. Yield: 0.186 g (47%). $[Mn(3'\text{-PyaiEt})_2(N_3)_2]$ (**4b**) was prepared by the same procedure. Microanalytical data are as follows: $[Mn(3'\text{-PyaiMe})_2(N_3)_2]$ (**4a**): *Anal.* Calc. for $C_{18}H_{18}N_{16}Mn$: C, 42.11; H, 3.51; N, 43.66; Mn, 10.72. Found: C, 42.04; H, 3.43; N, 43.75; Mn, 10.91%. IR (KBr disk) (cm^{-1}); $\nu(N_3)$, 2069 (s); ν(C=N), 1587 (m); ν(N=N), 1403 (m). UV–Vis spectral data (in MeOH) (λ_{max}/nm) ($10^{-3}\,\varepsilon\,M^{-1}\,cm^{-1}$): 448 (7.53), 374 (21.54). Magnetic data: μ, 5.0 BM. EPR data (77 K) $g = 2.01$, $A = 128$ G. $[Mn(3'\text{-PyaiEt})_2(N_3)_2]$ (**4b**): *Anal*. Calc. for $C_{20}H_{22}N_{16}Mn$: C, 44.36; H, 4.07; N, 41.40; Mn, 10.17. Found: C, 44.27; H, 4.00; N, 41.48; Mn, 10.30%. IR (KBr disk) (cm^{-1}); $\nu(N_3)$, 2077 (s); ν(C=N), 1622 (m); ν(N=N), 1405 (m). UV–Vis spectral data (in MeOH) (λ_{max}/nm) ($10^{-3}\,\varepsilon\,M^{-1}\,cm^{-1}$): 450 (8.13), 376 (19.15). Magnetic data: μ, 5.2 BM. EPR data (77 K) $g = 2.03$, $A = 130$ G.

2.2.3. Preparation of bis-{1-methyl-2-[(3′-pyridyl)azo] imidazole}-bis-(thiocyanato)-manganese(II), $Mn(3'\text{-PyaiMe})_2(NCS)_2$ (**5a**)

To an aqueous solution (10 ml) of $MnCl_2.4H_2O$ (0.2 g, 0.77 mmol), NH_4NCS (0.12 g, 1.58 mmol) was added and stirred for 15 min. 3′-PyaiMe (0.31 g, 1.54 mmol) in MeOH (15 ml) was added in dropwise and stirred for another 15 min. A brown red precipitate was separated and then filtered. The filtrate was evaporated slowly in air and crystals were separated, washed with water and cold methanol. These were then dried over $CaCl_2$. Yield: 0.2 g (48%). $Mn(3'\text{-PyaiEt})_2(NCS)_2$ (**5b**) was prepared by the same procedure. Microanalytical data are as follows: $Mn(3'\text{-PyaiMe})_2(NCS)_2$, (**5a**). *Anal.* Calc. for $C_{20}H_{18}N_{12}S_2Mn$: C, 44.04; H, 3.30; N, 30.83; Mn, 10.09. Found: C, 44.16; H, 3.22; N, 30.92; Mn, 9.75%. IR (KBr disk) (cm^{-1}); ν(NCS), 2095 (s); ν(C=N), 1600 (m); ν(N=N), 1400 (m); ν(C=S), 770 (m). UV–Vis spectral data (in MeOH) (λ_{max}/nm) ($10^{-3}\,\varepsilon\,M^{-1}\,cm^{-1}$): 448 (3.26), 372 (12.79). Magnetic data: μ, 5.2 BM. EPR data (77 K) $g = 2.00$, $A = 110$ G. $Mn(3'\text{-PyaiEt})_2(NCS)_2$ (**5b**): *Anal*. Calc. for, $C_{22}H_{22}N_{12}S_2Mn$: C, 46.07; H, 3.84; N, 29.32; Mn, 9.60. Found: C, 46.00; H, 3.90; N, 28.94; Mn, 9.48%. IR (KBr disk) (cm^{-1}); ν(NCS), 2098 (s); ν(C=N), 1597 (m); ν(N=N), 1402 (m); ν(C=S), 773 (m). UV–Vis spectral data (in MeOH) (λ_{max}/nm) ($10^{-3}\,\varepsilon\,M^{-1}\,cm^{-1}$): 450 (5.42), 374 (16.18). Magnetic data: μ, 5.1 BM. EPR data (77 K) $g = 2.01$, $A = 118$ G.

2.3. X-ray crystal structure analysis of 3′-PyaiH (**1**) and $[Mn(3'\text{-PyaiEt})_4](ClO_4)_2$ (**3b**)

Suitable X-ray quality crystals of the compounds were obtained by slow evaporation of ethanolic solutions of the compounds. Data were collected with a Siemens SMART CCD diffractometer using graphite-monochromatized Mo Kα radiation ($\lambda = 0.71073$ Å). The data are set out in Table 1. Unit cell parameters were determined from least-squares refinement of setting angles with 2θ in the range $4.16° \leqslant 2\theta \leqslant 56.48°$ for **1** and $2.1° \leqslant 2\theta \leqslant 56.74°$ for **3b**. The total data collected are 1952 and 26073 out of which unique data are 1090 and 4262 for **1** and **3b**, respectively. The hkl range are $-13 \leqslant h \leqslant 6$, $-12 \leqslant k \leqslant 11$, $-10 \leqslant l \leqslant 11$ for **1** and $-25 \leqslant h \leqslant 26$, $-16 \leqslant k \leqslant 16$, $-26 \leqslant l \leqslant 25$ for **3b**. Reflection data were recorded using the ω scan technique. Data were corrected for Lorentz polarization effects and for linear decay. Semi-empirical absorption corrections based on ψ-scans were applied. The structures were solved by heavy atom methods using SHELXS-97 and successive difference Fourier syntheses. All non-hydrogen atoms were refined anisotropically. The hydrogen atoms were fixed geometrically and refined using the riding model. In the final difference Fourier map the residual minima and maxima were [−0.259, 0.182 (e/Å^3) for **1** and −0.318, 0.297 (e/Å^3) for **3b**] carried out using SHELXL-97.

Table 1
Summarized crystallographic data for 3′-PyaiH (**1**) and [Mn(3′-PyaiEt)$_4$](ClO$_4$)$_2$ (**3b**)

	3′-PyaiH (**1**)	[Mn(3′-PyaiEt)$_4$](ClO$_4$)$_2$ (**3b**)
Empirical formula	$C_8H_7N_5$	$C_{44}H_{48}N_{16}O_8Cl_2Mn$
Formula weight	173.19	1054.82
Temperature (K)	295(2)	294
Crystal system	monoclinic	monoclinic
Space group	$P2_1/c$	$C2/c$
Crystal size (mm)	$0.20\times0.20\times0.10$	$0.15\times0.15\times0.20$
Unit cell dimensions		
a (Å)	9.889(3)	19.8396(16)
b (Å)	9.758(3)	12.4341(16)
c (Å)	8.964(3)	19.4646(19)
β (°)	97.166(7)	90.506(2)
V (Å)^3	858.3(4)	4801.5(9)
Z	4	4
λ(Å)	0.71073	0.71073
μ(Mo Kα) (mm^{-1})	0.091	0.457
D_{calc} (g cm^{-3})	1.340	1.459
Refine parameters	119	641
Reflection collected	1952	26 073
Unique data[a]	1090	4262
R_1[b]	0.0499	0.0382
wR_2[c]	0.1027	0.0542
Goodness-of-fit[d]	1.019	0.960

[a] $I > 2\sigma(I)$.
[b] $R_1 = \sum||F_o|-|F_c||/\sum|F_o|$.
[c] $wR_2=[\sum w(F_o^2-F_c^2)^2/\sum w(F_o^2)^2]^{1/2}$, $w=1/[\sigma^2(F_o^2)+(0.0445P)^2+0.0000P]$ for 3′-PyaiH (**1**), and $w=1/[\sigma^2(F_o^2)+(0.0100P)^2+0.0000P]$ for **3b**, where $P=(F_o^2+2F_c^2)/3$.
[d] Goodness-of-fit is defined as $[\sum w(F_o^2-F_c^2)^2/(n_o-n_v)]^{1/2}$, where n_o and n_v denote the number of data and variables.

3. Results and discussion

3.1. Ligands

1-Alkyl-2-[(3′-pyridyl)azo]imidazoles (3′-PyaiMe, **2a**; 3′-PyaiEt, **2b**; 3′-PyaiBz, **2c**) were synthesized by alkylation of 3′-PyaiH using alkyl halide (R′X) in dry THF in the presence of NaH. Spectral characterization of ligands have been reported elsewhere [11]. X-ray quality crystals of 3′-PyaiH have been isolated from an ethanolic solution of the compound.

3.2. Molecular structure

A view of 3′-PyaiH with the atom numbering scheme is shown in Fig. 1 and selected bond parameters are listed in Table 2. Both imidazole and pyridyl fragments are planar and the azo group is virtually coplanar with these groups. The dihedral angle between the two least squares planes is only 6.9(2)°. The N=N bond length is 1.268(2) Å. The distance is close to the reported data (1.267(3) Å) for 1-ethyl-2-(naphthyl-α-azo)imidazolium hexafluorophosphate but longer than the N–N distance of [HaaiMeH$^+$](ClO$_4$). The bonding strength between azo-N(1) and 3-pyridyl-[C(1)–N(1), 1.422(9) Å] is weaker than that of azo-N(2) and imidazole-C(6) [C(6)–N(2), 1.395(6) Å]. This suggests that the intramolecular interaction between azo and imidazole wave functions is stronger than that of pyridyl orbitals. The imidazole N(5)–H is intermolecularly hydrogen bonded with a second imidazole N(4) [N(5)–H$\cdots$N(4); distances: N(5)–H, 0.86; N(4)$\cdots$H, 2.020(6); N(5)$\cdots$N(4), 2.840(2) Å; angle, ∠N(5)–H$\cdots$N(4), 158.8(9)°] and forms a 1D-chain. The 3′-pyridyl group of the molecule is arranged alternately about the 1D-chain (Fig. 2).

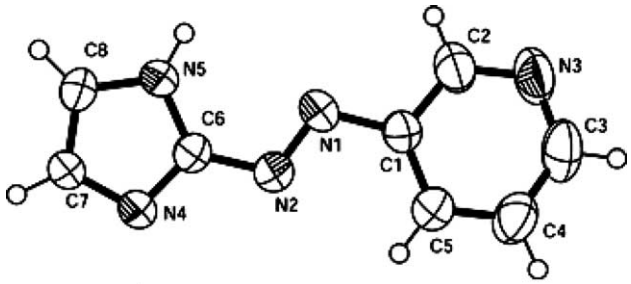


Fig. 1. A view of 3′-PyaiH with the atom numbering scheme.

Table 2
Selected bond lengths (Å) and bond angles (°) for 3′-PyaiH

Bond length (Å)		Bond angle (°)	
N(1)–N(2)	1.2682(19)	N(2)–N(1)–C(1)	112.76(14)
N(1)–C(1)	1.423(2)	N(1)–N(2)–C(6)	113.48(14)
N(2)–C(6)	1.396(2)	N(2)–C(6)–N(5)	127.10(14)
N(4)–C(6)	1.317(2)	N(2)–C(6)–N(4)	121.16(14)
N(5)–C(6)	1.348(2)	N(4)–C(6)–N(5)	111.74(14)
N(3)–C(2)	1.333(2)		
N(3)–C(3)	1.322(3)		

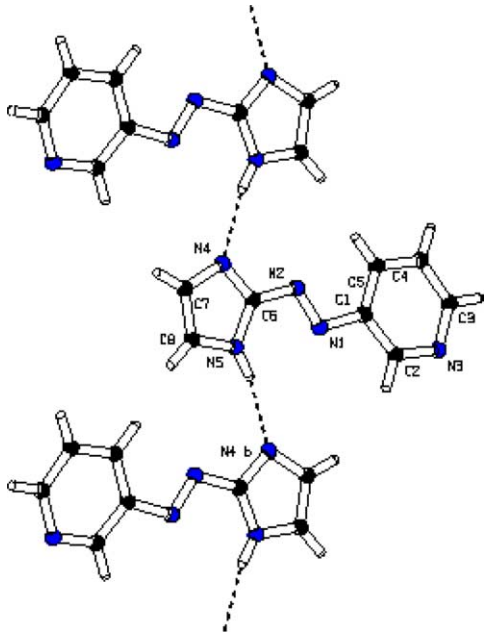


Fig. 2. A 1D chain of 3′-PyaiH.

3.3. The complexes

The reaction of a methanolic solution of 3′-PyaiR′ with $Mn(ClO_4)_2 \cdot 6H_2O$ in a 3:1 stoichiometry of ligand:-metal, aiming to prepare trischelated manganese(II) complexes, has isolated tetrahedral $[Mn(3'\text{-PyaiR}')_4](ClO_4)_2$ (**3**). The composition of the complexes has been determined by microanalytical and spectroscopic data. The molar conductances in MeCN suggest they are 1:2 electrolytic in nature. A single crystal X-ray structure determination confirms the structure of the complexes.

3.4. Spectral and magnetic studies

Infrared spectra show a very strong unstructured transmission centered at 1090–1093 cm^{-1} with a weak stretch at 625 cm^{-1}, which is referred to $\nu(ClO_4)$. Moderately intense stretching at 1580–1590 and 1440–1445 cm^{-1} are due to ν(C=N) and ν(N=N), respectively. A significant observation is the blue shifting of the N=N stretch by 20–25 cm^{-1} in the complexes relative to the free ligand values [11]. In the complexes of the chelated azoimine function $\overline{\text{Mn-N=N-C-N-}}$ π-back donation (dπ(M) → π*(azo)) usually reduces ν(N=N) [1–4]. An increase in ν(N=N) has concluded a no-bond impression between azo-N and Mn(II). The coordination of imidazole-N with Mn(II) may reduce the probability of charge population at π*(azo). This may be the reason for the blue shift of the azo stretch in the complexes.

Solution electronic spectra of the complexes show an intense transition <400 nm which are assigned to ligand centered transitions. Two weak ($\varepsilon \sim 10^3$ dm^3 mol^{-1} cm^{-1}) transitions observed at >440 nm may be referred to the combination of MLCT and d–d transitions. The spectral profile nature is in support of a Td–Mn(II) stereochemistry [17].

The magnetic moment, μ_{eff}, is av. 5.7 BM at 300 K (Table 2) as expected for an isolated $S = 5/2$ Mn(II) monomer. The EPR spectra of a solution in MeCN at 77 K display $g \approx 2$, $m_s = +1/2$ to $-1/2$ fine structure transition split into six hyperfine lines, as expected for a ^{55}Mn(II) complex ($I = 5/2$). A notable feature of the spectra is the relatively low value of the hyperfine coupling constant A, 80–90 G. A low hyperfine coupling constant (A) and high spin magnetic moment data are secondary evidences for tetrahedral Mn(II) stereochemistry [18]. However, the EPR profile cannot distinguish imidazole-N/azo-N coordination. IR spectral data and X-ray structural characterization of one of the complexes (vide infra) suggest imidazole-N coordination to Mn(II).

3.5. Molecular structure

3.5.1. $[Mn(3'\text{-PyaiEt})_4](ClO_4)_2$ (**3b**)

Fig. 3 shows the molecular structure of the complex $[Mn(3'\text{-PyaiEt})_4](ClO_4)_2$ (**3b**) along with the atomic numbering scheme used. Selected bond distances and angles are listed in Table 3. The cationic complex consists of a central manganese atom surrounded by four 3′-PyaiEt ligands. The Mn atom is sitting at the center of inversion of a tetrahedron and one half of the molecule is symmetry generated. Imidazole, azo and phenyl groups are coplanar with a small mean deviation (<0.04 Å). 3′-PyaiEt acts as a monodentate ligand and binds through imidazole-N. The coordination environment about Mn is compressed along the crystallographic c axis in such a way that two of the N–Mn–N angles are greater than the tetrahedral angle, with values N(1)–Mn(1)–N(1*), 132.2(2)° and N(5)–Mn(1)–N(5*), 136.1(2)°. The remaining N–Mn–N angles are less than 109.5° (Table 3). Bond length and bond angles data support a distorted tetrahedral geometry. The Mn–N bond lengths are 2.215(6) and 2.157(6) Å. The N=N bond distance is av. 1.273(7) Å

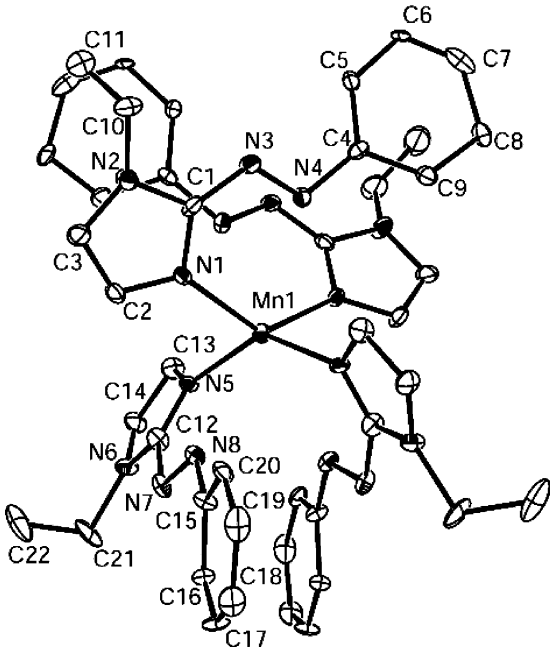


Fig. 3. ORTEP plot of the $[Mn(3'\text{-PyaiEt})_4]^{2+}$ unit.

Table 3
Selected bond distances and bond angles of $[Mn(3'\text{-PyaiEt})_4](ClO_4)_2$ (**3b**)

Bond length (Å)		Bond angle (°)	
Mn(1)–N(1)	2.215(6)	N(1)– Mn(1)–N(5)	96.4(2)
Mn(1)–N(5)	2.157(6)	N(1)–Mn(1)–N(1*)	132.2(2)
N(3)–N(4)	1.247(7)	N(1)–Mn(1)–N(5*)	101.0(2)
N(7)–N(8)	1.299(8)	N(5)–Mn(1)–N(5*)	136.1(2)
Cl(1)–O(1)	1.392(5)	O(3)–Cl(1)–O(1)	114.1(5)
Cl(1)–O(2)	1.362(6)	O(1)–Cl(1)–O(2)	104.7(4)
Cl(1)–O(3)	1.335(6)	O(1)–Cl(1)–O(4)	107.7(4)
Cl(1)–O(4)	1.358(5)	O(3)–Cl(1)–O(2)	116.3(6)
		O(3)–Cl(1)–O(4)	106.5(5)
		O(2)–Cl(1)–O(4)	107.2(5)

(the free ligand value is 1.268(2) Å (vide supra)). The pendant azopyridyl group is oriented in such a way to reduce steric and electronic repulsions. Two ClO_4^- anions balance the charge of the complex and they do not show any non-covalent interactions with the rest of the molecule (see Table 4).

3.6. *Mn(3′-PyaiR′)$_2$(X)$_2$ (X = N$_3$ (**4**), NCS (**5**))*

Upon reaction of a methanolic solution of $Mn(OAc)_2 \cdot 4H_2O$, 3′-PyaiR′ and NaN_3 or NH_4SCN in a 1:2:2 mole proportion, brown red crystalline products of composition Mn(3′-PyaiR′)$_2$(X)$_2$ (X = N_3 (**4**), NCS (**5**)) have been isolated. Microanalytical data support the composition (vide experimental section). The complexes are non-electrolytes. We have failed to grow X-ray quality crystals of the complexes. The structural identification has been carried out by spectroscopic data.

The IR spectra of Mn(3′-PyaiR′)$_2$(N$_3$)$_2$ (**4**) exhibit a strong sharp stretch corresponding to $\nu_{as}(N_3)$ at 2065–2080 cm^{-1}. A similar observation for Mn(3′-PyaiR′)$_2$-(NCS)$_2$ (**5**) at 2090–2100 cm^{-1} along with a medium strong band at 770–775 cm^{-1} refers to ν(CN) and ν(CS) of a coordinated NCS group [16]. We have not attempted to assign all the bands appearing in the IR spectra. However, on comparing with free ligand spectra, the medium strong stretches at 1585–1605 and 1430–1440 cm^{-1} have been assigned to ν(C=N) and ν(N=N), respectively.

The complexes are sparingly soluble in common organic solvents ($CHCl_3$, CH_2Cl_2, CH_3CN, CH_3OH, etc.), but they are soluble in DMF and DMSO. The solution electronic spectra of the complexes in DMF show weak spin forbidden d–d bands at 510–530 (sh) and 450–470 nm, corresponding to an octahedral symmetry, [17] along with a high intense intraligand charge-transfer transition <400 nm. The diffused reflectance spectra of the complexes in the solid state also exhibit similar transitions and this supports structural stability of the complexes in solution.

The magnetic moment μ_{eff} is av. 5.1 BM at 300 K which is as expected for d^5 (S = 5/2) Mn(II) monomeric complexes. The EPR spectra of the polycrystalline powders and solutions (DMF) of the complexes have been recorded at room temperature (298 K) and at liquid N_2 temperature (77 K). The low resolution of the polycrystalline spectra is usual where the metal centres are relatively close together, the hyperfine splittings are poor due to paramagnetic exchange narrowing. The solution spectra show better resolution, therefore these spectra (77 K) were used to determine the EPR parameters. The spectra show the usual six line (I = 5/2) hyperfine splitting, centred at $g \approx 2.0$ which is usual for Mn(II) complexes. Each hyperfine line in the spectra splits into three super-hyperfine lines. The peak-to-peak band width is larger (110–130 G) than the separation observed in case of tetrahedral $Mn(RaaiR')_4^{2+}$ (80–90 G). This supports the interaction of imidazole-N/azo-N with Mn(II).

3.7. Cyclic voltammetry

Redox properties of the manganese complexes have been studied by cyclic voltammetry (CV) using a platinum working electrode. Voltammogram data are collected in Table 2 and a representative voltammogram is shown in Fig. 4. A couple appearing at >1.0 V versus SCE is referred to the Mn(III)/Mn(II) redox process [19]. The quasireversibility of the process is examined from the peak-to-peak separation, ΔEp > 100 mV. The one electron nature of the redox process has been compared with the current height data of $Fe(CN)_6^{3-}$/$Fe(CN)_6^{4-}$. Ligand reductions are irreversible in nature and the Ep_c values are near to the free ligand values. The reduction corresponds to electron accommodation in the azo dominated orbitals. Electrochemical data reveal that tetrahedral Mn(II), $Mn(3'\text{-PyaiR}')_4^{2+}$ and Mn(3′-PyaiR′)$_2$(N$_3$)$_2$ compounds have similar redox efficiency. Mn(3′-PyaiR′)$_2$(NCS)$_2$ show a relatively low Mn(III)/Mn(II) potential. In terms of stabilization of the Mn(II)

Table 4
Cyclic voltammetric data of the complexes in MeCN[a]

Compound	Mn(III)/Mn(II)	Ligand reductions[b]		
Mn(3′-PyaiMe)$_4$(ClO$_4$)$_2$ (**3a**)	1.34 (120)	−0.40 (150)	−0.75 (160)	−1.46[c]
Mn(3′-PyaiEt)$_4$(ClO$_4$)$_2$ (**3b**)	1.38 (140)	−0.41 (160)	−0.76 (140)	−1.41[c]
Mn(3′-PyaiBz)$_4$(ClO$_4$)$_2$ (**3c**)	1.40 (130)	−0.36 (140)	−0.70 (130)	−1.30[c]
Mn(3′-PyaiMe)$_2$(N$_3$)$_2$ (**4a**)	1.26 (125)	−0.44 (140)	−0.68 (130)	−1.27[c]
Mn(3′-PyaiEt)$_2$(N$_3$)$_2$ (**4b**)	1.33 (130)	−0.40 (140)	−0.62 (130)	−1.35[c]
Mn(3′-PyaiBz)$_2$(N$_3$)$_2$ (**4c**)	1.30 (120)	−0.33 (130)	−0.57 (130)	−1.28[c]
Mn(3′-PyaiMe)$_2$(NCS)$_2$ (**5a**)	1.18 (140)	−0.55 (130)	−0.86 (120)	−1.45[c]
Mn(3′-PyaiEt)$_2$(NCS)$_2$ (**5b**)	1.24 (130)	−0.50 (120)	−0.76 (130)	−1.41[c]
Mn(3′-PyaiBz)$_2$(NCS)$_2$ (**5c**)	1. 28 (130)	−0.48 (130)	−0.80 (130)	−1.38[c]

[a] Pt-disk working electrode, Pt-wire auxiliary and SCE, scan rate 50 mV s^{-1}, supporting electrolyte, [nBu$_4$N][ClO$_4$]; potential $E_{1/2}$ = (Ep_a+ Ep_c)/2, V, $\Delta Ep = |Ep_a - Ep_c|$ mV.

[b] Ligand reductions refer to [—N=N—]/[–N–N–]$^-$ and [–N–N–]$^-$/[–N–N–]$^{-2}$.

[c] Epc, V.

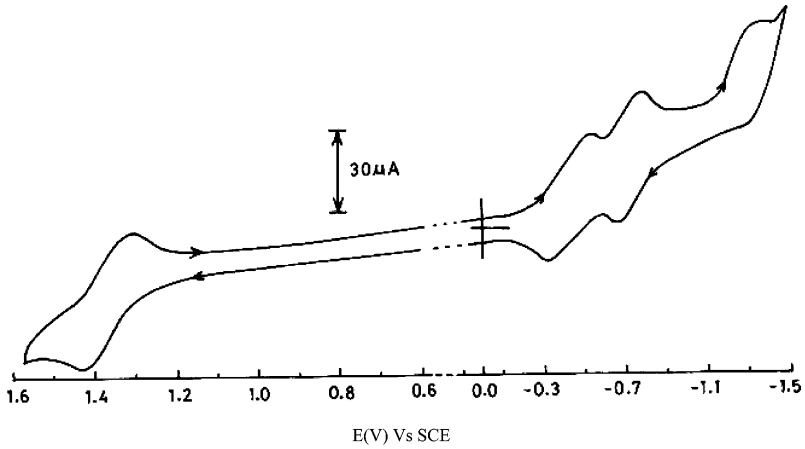


Fig. 4. Cyclic voltammogram of $[Mn(3'\text{- PyaiEt})_4](ClO_4)_2$ in MeCN using a Pt-disk electrode.

state, the potential data suggest that imidazole-N and azido-N have almost the same efficiency, and the structural change from Td (in $Mn(3'\text{-PyaiR}')_4^{2+}$) to Oh (in $Mn(3'\text{-PyaiR}')_2(N_3)_2$) has insignificant effect on the energy of the redox levels. It may be due to weak the interaction between Mn(II) and N(azo) (3′-PyaiR′).

3.8. EHMO calculation

To account for the spectral and electrochemical properties of the compounds a theoretical calculation has been carried out with the framework of Huckel formalism (EHMO) using X-ray crystallographic coordinates. Orbital composition of 3′-PyaiH determines that the HOMO is dominated by the azo group (88%) and the LUMO is composed of the azoimidazole function (azo, 60%; imidazole, 25%). Thus, the intraligand charge transfer may be ascribed to $\pi(\text{azo}) \rightarrow \pi^*(\text{azoimidazole})$. In the complex both HOMO and LUMO are constituted by Mn and azo-N wave functions. It is interesting to note that the two coordinated ligands in the asymmetric unit (which upon growing gives four tetrahedrally oriented ligands) have different contributions to the MOs. The two coordinated ligands contribute separately to the constitute HOMO and LUMO. Imidazole contributes only a little amount (4%) to the MOs. The LUMO has a share of 55% azo from one ligand while the HOMO contains 43% azo-N from the other ligand. Mn contributes to both the molecular orbitals: HOMO, 32% and LUMO, 26%. Thus, the electronic transition HOMO → LUMO may be ascribed as a combination of d–d, MLCT and interligand charge transfer transitions.

The no bond situation between Mn(II) and azo-N has prevented the π-back bonding from dπ [Mn(II)] to π* (azo), however, the charge delocalization is associated with the imidazole group and is transmitted to the azo group by extended conjugation, —N=N—imidazole—N—Mn—N—imidazole—N=N—. The process does not reduce the effective π-charge density on the azo function. This in turn has little influence on the bond length and IR frequency of the —N=N— group.

4. Conclusion

We have synthesized tetrahedral Mn(II) complexes of 1-alkyl-2-(3′-pyridylazo)imidazoles. The ligands serve as monodentate imidazole-N donors to synthesize high spin $[Mn(3'\text{-PyaiR}')_4](ClO_4)_2$ complexes. Redox properties show a high potential Mn(III)/Mn(II) couple. The pendant pyridylazo group with N(py) and N(azo) donor centres remain free in the molecule and may serve as a metal seeking agent. The metallo-ligand property of the molecules is under investigation. $Mn(3'\text{-PyaiR}')_2(X)_2$ (X = N_3, NCS) are also reported.

5. Supplementary material

Crystallographic data for the structures have been deposited with the Cambridge Crystallographic data center, CCDC No. 250732 for 3′-PyaiH (**1**) and 250733 for $[Mn(3'\text{-PyaiEt})_4](ClO_4)_2$ (**3b**). Copies of this information may be obtained free of charge from the Director, CCDC, 12 Union Road, Cambridge CB2 1EZ, UK (Fax: +44 1223 336033, e-mail: deposit@ccdc.cam.ac.uk or www: http://www.ccdc.cam.ac.uk).

Acknowledgments

Financial support was received from the Council of Scientific and Industrial Research (CSIR), New Delhi. One of us (U.S.R.) is thankful to the University Grants Commission New Delhi, for a fellowship. Our sincere thanks to Dr. G. Mostafa, Department of Physics, Jadavpur University for his help with the crystallography.

References

[1] G.K. Rauth, S. Pal, D. Das, C. Sinha, A.M.Z. Slawin, J.D. Woollins, Polyhedron 20 (2001) 363, and references therein.
[2] P.K. Santra, P. Byabartta, S. Chattopadhyay, L.R. Falvello, Eur. J. Inorg. Chem. (2002) 1124, and references therein.
[3] Sk. Jasimuddin, P. Byabartta, C. Sinha, G. Mostafa, T.H. Lu, Inorg. Chim. Acta 357 (2004) 2015.
[4] T.K. Misra, D. Das, C. Sinha, Polyhedron 16 (1997) 4163.
[5] J. Otsuki, N. Omokawa, K. Yoshiba, I. Yoshiba, I. Yoshikawa, T. Akasaka, T. Suenobu, T. Takido, K. Araki, S. Fukuzumi, Inorg. Chem. 42 (2003) 3057.
[6] A. Ueno, T. Kuwabara, A. Nakamura, F. Toda, Nature 356 (1992) 136.
[7] T. Akasaka, J. Otsuki, K. Araki, Chem. Eur. J. (2002) 130.
[8] A.I. Vogel, A Text Book of Quantitative Inorganic Analysis, 3rd ed., ELBS & Longman, London, 1975, p. 429.
[9] W. Kaim, Coord. Chem. Rev. 219 (2001) 463.
[10] P.-O. Astrand, K.L. Bak, S.P.A. Sauer, Chem. Phys. Lett. 343 (2001) 171.
[11] T. Mathur, S.k. Jasimuddin, H. Milton, J.D. Woollins, C. Sinha, Inorg. Chim. Acta 357 (2004) 3503.
[12] P.K. Santra, U.S. Ray, S. Pal, C. Sinha, Inorg. Chim. Commun. 4 (2001) 269.
[13] V.L. Pecoraro (Ed.), Manganese Redox Enzymes, VCH Publishers, New York, 1992.
[14] J. Ribas, A. Escure, M. Monfort, R. Vicente, R. Cortes, L. Lezama, T. Rojo, Coord. Chem. Rev. 193-195 (1999) 1027.
[15] U.S. Ray, S.k. Jasimuddin, B.K. Ghosh, M. Monfort, J. Ribas, G. Mostafa, T.-H. Lu, C. Sinha, Eur. J. Inorg. Chem. (2004) 250.
[16] B.G. Chand, U.S. Ray, G. Mostafa, T.-H. Lu, C. Sinha, Polyhedron 23 (2004) 1669.
[17] A.B.P. Lever, Inorganic Electronic Spectroscopy, Elsevier Science, Amsterdam, 1984.
[18] R.L. Dutta, A. Syamal, Elements of Magnetochemistry, second ed., Affiliated East-west Press, New Delhi, 1993.
[19] A. Saha, P. Majumder, S. Goswami, J. Chem. Soc., Dalton Trans. (2000) 1703.

Available online at www.sciencedirect.com
SCIENCE DIRECT®
Polyhedron 24 (2005) 747–758
POLYHEDRON
www.elsevier.com/locate/poly

The Mn(II)-2,2′-dipyridylamine-pseudohalide system: Synthesis, crystal structure and luminescence behaviour of $[Mn(dpa)_2(X)_2]\cdot H_2O$ and $[Mn(dpa)_2(X)(OH_2)]ClO_4$ (dpa = 2,2′-dipyridylamine; $X = N_3^-$, NCO^-)

Doyel Bose [a], Golam Mostafa [b], Hoong-Kun Fun [c], Barindra K. Ghosh [a,*]

[a] *Department of Chemistry, The University of Burdwan, Golapbag, Burdwan 713 104, India*
[b] *Department of Physics, Jadavpur University, Kolkata 700 032, India*
[c] *X-ray Crystallography Unit, School of Physics, Universiti Sains Malaysia, 11800 USM, Penang, Malaysia*

Received 7 December 2004; accepted 31 January 2005
Available online 25 March 2005

Abstract

Four complexes of the type $[Mn(dpa)_2(X)_2]\cdot H_2O$ (dpa = 2,2′-dipyridylamine; $X = N_3^-$, **1**; $X = NCO^-$, **2**) and $[Mn(dpa)_2(X)(OH_2)]ClO_4$ ($X = N_3^-$, **3**; $X = NCO^-$, **4**) have been synthesized using single-pot reactions of manganese(II) salt, dpa and X in 1:2:2 and 1:2:1 molar ratios, respectively. The compounds have been characterized by microanalytical, physicochemical, spectroscopic and magnetic results. Room temperature magnetic moments (μ_{eff}) are in the range 5.88–5.97 BM and are typical of high-spin manganese(II) complexes (t_{2g}^5 idealized, $S = 5/2$). The complexes display a Mn(III)–Mn(II) couple at ~0.6 V versus SCE in DMF solutions. X-ray structure determinations show that in **1**–**4** the manganese(II) centres are in a distorted octahedral environment. Compounds **1** and **2** contain the MnN_6 chromophore, completed by two bidentate dpa units and two terminal azido groups in **1** or *N*-coordinated cyanato ligands in **2**, along with a water of crystallization. In **3** and **4**, one water molecule acts as a coordinating ligand replacing one of the terminal pseudohalides in **1** and **2**, respectively, resulting in a MnN_5O chromophore. The amine H, terminal azido N or cyanato O, O and H's of the water molecule are engaged in extensive hydrogen bonding of the type N–H···N, O–H···N and N–H···O in **1** and **2**. Additionally O–H···O bonding is observed in **3** and **4**. Supramolecular 2D sheet structures are obtained arising from such weak intermolecular forces. All the complexes display high-energy intraligand $^1(\pi–\pi^*)$ fluroscence and intraligand $^3(\pi–\pi^*)$ phosphorescence in glassy solutions (DMF at 77 K).
© 2005 Elsevier Ltd. All rights reserved.

Keywords: Manganese(II)-pseudohalides; 2,2′-Dipyridylamine; X-ray structure; Luminescence

1. Introduction

The designed construction [1,2] of metallosupramolecular assemblies [3,4] derived from appropriate combinations of metal ions and organic ligands is a rapidly developing area of current research towards the preparation of functional materials [5–8]. The controlled reactions in appropriate ratios of donor and acceptor building blocks held together by covalent [9] as well as non-covalent forces [10] results in variable molecular and crystalline architectures [11]. Recently, we have established the composition of tailored superstructures of zinc(II)azides containing 2,2′-dipyridylamine (dpa) with active amine (–NH–) hydrogen [12]. In continuation, we aim to investigate the binding of this tailored diimine to paramagnetic manganese(II). Dpa may

* Corresponding author. Tel.: +91 342 2558545; fax: +91 342 2530452.
E-mail address: barin_1@yahoo.co.uk (B.K. Ghosh).

0277-5387/$ - see front matter © 2005 Elsevier Ltd. All rights reserved.
doi:10.1016/j.poly.2005.01.021

behave as a versatile ligand ranging from monodentate, chelating bi-dentate to bridging tri-dentate [12–17]. However, harnessing hydrogen bonded networks through its active amine (–NH–) hydrogen as a proton donor that may lead to supramolecular architectures is very scarce [16]. Manganese is widespread in biology [18,19] because of its availability in different oxidation states controlling the active site of structures, physico-chemical properties and functions of enzymes. Weak interactions via non-covalent forces are found in several metalloenzymes and metalloproteins affecting a number of biologically important processes [20–22].

In search of a metallosupramolecule based on manganese(II) centres we have successfully synthesized and X-ray crystallographically characterized four mononuclear complexes of types $[Mn(dpa)_2(X)_2]\cdot H_2O$ (in **1** and **2**) and $[Mn(dpa)_2(X)(OH_2)]ClO_4$ (in **3** and **4**) ($X = N_3^-$, NCO^-) through the one-pot reactions of manganese(II) chloride (**1** and **2**) and manganese(II) perchlorate (**3** and **4**) with dpa and X in the molar ratios 1:2:2 and 1:2:1, respectively. The presence of N–H···O, O–H···N, O–H···O and N–H···N types of intermolecular forces are responsible for the formation of supramolecular two-dimensional (2D) sheet structures from the individual zero-dimensional (0D) units. It is of note that a cursory report on the Mn(II)–dpa polymer in combination with azide is reported [17] but such weak interactions among the polymers are not cited. The details of synthesis, structure and physico-chemical characterization of these supramers are cited below.

2. Experimental

2.1. Materials

High-purity 2,2′-dipyridylamine (Fluka, Germany), manganese(II) chloride tetrahydrate (E. Merck, India), sodium azide (E. Merck, India) and sodium cyanate (E. Merck, India) were purchased from the respective concerns and used as received. Manganese(II) perchlorate hexahydrate was prepared by treatment of manganese(II) carbonate (E. Merck, India) with perchloric acid (E. Merck, India) followed by slow evaporation on a steam-bath, filtration through a fine glass frit and preservation in a desiccator containing concentrated sulfuric acid for subsequent use. All other chemicals and solvents were AR grade and were used as received. Purification of solvent (DMF) and preparation of supporting electrolyte ($[Et_4N][ClO_4]$) for electrochemical work were executed following published procedures [23].

Caution! Azido compounds and perchlorate salts of metal ions are potentially explosive. Only a small amount of material should be prepared and handled with care.

2.2. Physical measurements

Elemental analyses (carbon, hydrogen and nitrogen) were performed on a Perkin–Elmer 2400 CHNS/O elemental analyzer. IR spectra (KBr discs, 4000–300 cm^{-1}) were recorded using a Jasco FT-IR Model 420 spectrometer. Molar conductances were measured using a Systronics conductivity meter where the cell constant was calibrated with 0.01 M KCl solution and dry DMF was used as solvent. Ground state absorption and steady state fluorescence measurements were made with a Jasco Model V-530 UV–vis spectrophotometer and Hitachi Model F-4010 spectrofluorometer, respectively. Time resolved fluorescence measurements were carried out using a time correlated single photon counting (TCSPC) spectrometer from Edinburgh Instruments, Model 199; a hydrogen filled coaxial flash lamp with a pulse width of 1.2 ns at FWHM and a Philips XP-2020Q photomultiplier tube were, respectively, used as the excitation source and the fluorescence detector. Magnetic susceptibilities were measured with a PAR 155 vibrating sample magnetometer with $Hg[Co(SCN)_4]$ as the reference. Electrochemical measurements were carried out with the use of computer controlled EG&G PARC Verastat Model 270 electrochemical instrument using a platinum disk working electrode as described elsewhere [23]. The solutions were IR compensated and the results were collected at 298 K. The following parameters and relations were used: scan rate (v), 50 mV s^{-1}; formal potential $E^\circ = 0.5(E_{pa} + E_{pc})$ where E_{pa} and E_{pc} are anodic and cathodic peak potentials, respectively; ΔE_p is the peak-to-peak separation. The potentials are referenced to a saturated calomel electrode (SCE) and are uncorrected for the junction contributions.

2.3. Preparation of complexes

Mononuclear **1** and **2** were prepared from chloride and perchlorate salts of manganese(II) using the same (1:2:2) mole ratio of the metal ion, dpa and azide/cyanate. Compounds **3** and **4** were prepared using a 1:2:1 ratio of manganese(II) perchlorate, dpa and azide/cyanate; the corresponding ratio with chloride resulted in **1** and **2**, but with very low yield. The typical syntheses are described below.

2.3.1. $[Mn(dpa)_2(N_3)_2]\cdot H_2O$ (**1**)

Dpa (0.11 g, 0.648 mmol) in acetonitrile (5 cm^3) was added slowly to a $MnCl_2\cdot 4H_2O$ (0.641 g, 0.324 mmol) solution (10 cm^3) in the same solvent. NaN_3 (0.042 g, 0.648 mmol) in water (5 cm^3) was added dropwise to it. After filtration through a fine glass frit, the supernatant colourless solution was kept in a dark place at room temperature (298 K) for slow evaporation. Light yellow crystals of **1** were deposited within a week, which were

separated by filtration, washed several times with ether and dried in vacuo over silica gel indicator. The yield was 0.030 g (75%). *Anal*. Calc. for $C_{20}H_{20}N_{12}OMn$ (**1**): C, 48.10; H, 4.04; N, 33.66. Found: C, 48.20; H, 4.09; N, 32.98%. IR (KBr, cm^{-1}): $\nu(N_3)$ 2070, 2048; ν(N–H) 3343. Λ_M (DMF, $\Omega^{-1}\,cm^2\,mol^{-1}$): 5. UV–vis ($\lambda$, nm): 315.

2.3.2. $[Mn(dpa)_2(NCO)_2]\cdot H_2O$ (2)

Complex **2** was synthesized similarly as in **1** except that NaNCO (0.042 g, 0.648 mmol) was added instead of NaN_3. The reaction solution was processed as above. The yield of the colourless crystals was found to be 0.029 g (72%). *Anal*. Calc. for $C_{22}H_{20}N_8O_3Mn$ (**2**): C, 52.91; H, 4.04; N, 22.44. Found: C, 52.26; H, 4.07; N, 22.39%. IR (KBr, cm^{-1}): ν(NCO) 2200, 2181; ν(N–H) 3347. Λ_M (DMF, $\Omega^{-1}\,cm^2\,mol^{-1}$): 8. UV–vis ($\lambda$, nm): 312.

2.3.3. $[Mn(dpa)_2(N_3)(OH_2)]ClO4$ (3)

The synthesis of **3** was carried out by slowly adding NaN_3 (0.021 g, 0.324 mmol) in H_2O (5 cm^3) to a mixture containing dpa (0.11 g, 0.648 mmol) and manganese(II) perchlorate (0.362 g, 0.324 mmol) in acetonitrile (15 cm^3). The colourless solution was filtered through a fine glass frit and kept in a dark place for slow evaporation. Square shaped colourless crystals of **3** suitable for X-ray crystallography were obtained within 10 days. The product was collected by filtration, washed with ether and dried in vacuo over silica gel indicator; yield, 0.046 g (70%). *Anal*. Calc. for $C_{20}H_{20}N_9O_5ClMn$ (**3**): C, 43.14; H, 3.62; N, 22.64. Found: C, 43.24; H, 3.74; N, 22.59%. IR (KBr, cm^{-1}): $\nu(N_3)$ 2053; ν(N–H) 3352; ν(OH), 3419; $\nu(ClO_4)$ 1084, 623. Λ_M (DMF, Ω^{-1} cm^2 mol^{-1}): 120. UV–vis (λ, nm): 317.

2.3.4. $[Mn(dpa)_2(NCO)(OH_2)]ClO_4$ (4)

A similar procedure as in **3** was followed for complex **4** except that NaNCO (0.021 g, 0.324 mmol) was added instead of NaN_3. Yield, 0.047 g (72%). *Anal*. Calc. for $C_{21}H_{20}N_7O_6ClMn$ (**4**): C, 45.30; H, 3.62; N, 17.61. Found: C, 45.39; H, 3.68; N, 17.70%. IR (KBr, cm^{-1}): ν(NCO) 2196; ν(N–H) 3341; ν(OH), 3421; $\nu(ClO_4)$ 1083, 634. Λ_M (DMF, Ω^{-1} cm^2 mol^{-1}): 130. UV–vis (λ, nm): 315.

2.4. X-ray crystallography

A summary of the key crystallographic information of complexes **1**–**4** is given in Tables 1 and 2. Data were

Table 1
Crystal data and structure refinement parameters for **1** and **2**

Compound	**1**	**2**
Emperical formula	$C_{20}H_{20}N_{12}OMn$	$C_{22}H_{20}N_8O_3Mn$
Formula weight	499.42	499.40
T (K)	293(2)	293(2)
Crystal system	triclinic	orthorhombic
Space group	$P\bar{1}$	$P2_12_12_1$
a (Å)	7.8292(2)	8.5313(1)
b (Å)	9.4557(2)	15.862
c (Å)	16.4145(5)	16.8025(2)
β (°)	84.2660(10)	90
V (Å^3)	1117.08(5)	2273.72(4)
Z	2	4
D_{calc} (Mg m^{-3})	1.485	1.459
μ (mm^{-1})	0.632	0.623
F(000)	514	1028
Crystal size (mm)	0.40 × 0.340.28	0.40 × 0.34 × 0.16
θ Ranges (°)	2.47–25.00	2.68–25.00
$h/k/l$	−9/9, −11/9, −19/15	−10/10, −18/14, −17/19
Number of reflections collected	5407	11 057
Number of independent reflections	3794	3967
Completeness to θ (%)	96.3	99.19
T_{max} and T_{min}	0.8429 and 0.7861	0.9069 and 0.7888
Goodness-of-fit on F^2	0.997	0.972
Final R indices [$I > 2\sigma(I)$]	R_1 = 0.0687, wR_2 = 0.1762	R_1 = 0.0393, wR_2 = 0.825
R indices (all data)	R_1 = 0.0793, wR_2 = 0.1827	R_1 = 0.0514, wR_2 = 0.0858
Largest peak and hole (e Å^{-3})	0.974 and −0.799	0.297 and −0.530

Table 2
Crystal data and structure refinement parameters for **3** and **4**

Compound	**3**	**4**
Emperical formula	$C_{20}H_{20}N_9O_5ClMn$	$C_{21}H_{20}N_7O_6ClMn$
Formula weight	556.84	556.83
T (K)	293(2)	293(2)
Crystal system	triclinic	triclinic
Space group	$P\bar{1}$	$P\bar{1}$
a (Å)	9.1454(5)	9.1522(2)
b (Å)	10.3517(6)	10.3087(2)
c (Å)	13.3313(8)	13.3138(2)
β (°)	105.4730(10)	104.9530(10)
V (Å^3)	1202.19(12)	1198.40
Z	2	2
D_{calc} (Mg m^{-3})	1.533	1.538
μ (mm^{-1})	0.710	0.713
F(000)	568	568
Crystal size (mm)	0.30 × 0.30 × 0.24	0.16 × 0.34 × 0.54
θ Ranges (°)	2.85–24.99	2.44–25.00
$h/k/l$	−10/10, −11/12, −11/15	−10/7, −12/11, −14/17
Number of reflections collected	5903	5737
Number of independent reflections	4144	4046
Completeness to θ (%)	97.8	95.8
T_{max} and T_{min}	0.8481 and 0.8153	0.8945 and 0.6995
Goodness-of-fit on F^2	0.975	0.979
Final R indices [$I > 2\sigma(I)$]	R_1 = 0.0754, wR_2 = 0.1934	R_1 = 0.0951, wR_2 = 0.2277
R indices (all data)	R_1 = 0.0927, wR_2 = 0.2180	R_1 = 0.1162, wR_2 = 0.2479
Largest peak and hole (e Å^{-3})	0.886 and −0.819	1.207 and −1.508

collected on a SMART CCD diffractometer using graphite monochromated Mo Kα radiation ($\lambda = 0.71073$ Å) with a detector distance of 4 cm and swing angle of −35°. A hemisphere of the reciprocal space was covered by a combination of three sets of exposures; each set had a different ϕ angle (0°, 88°, 180°) and each exposure of 30 s covered 0.30 in ω. The data collected were reduced using the program SAINT [24] and an empirical absorption correction was carried out using the SADABS [25] program. Reflections with $2\theta \leqslant 55°$ were used for further processing. The structures of all the complexes were solved using direct methods and refined using the full-matrix least-squares method on F^2_{abs} using the SHELXTL [26] software package. All non-hydrogen atoms were anisotropically refined. The water hydrogens were first located from the difference maps and then were constrained to ride on the carrier oxygen atom with U_{iso} values also constrained to 1.5 U_{eq} of the carrier atom for refinement. The molecular graphics were created using SHELXTL. Atomic scattering factors and anomalous dispersion corrections were taken from the International Tables for X-ray Crystallography [27].

3. Results and discussion

3.1. Synthesis and formulation

Dipseudohalide complexes $[Mn(dpa)_2(N_3)_2] \cdot H_2O$ (**1**) and $[Mn(dpa)_2(NCO)_2] \cdot H_2O$ (**2**) were prepared as crystalline products through the one-pot reactions of 1:2:2 mole ratios of manganese(II) chloride, dpa and the pseudohalides (N_3^-/NCO^-), respectively, in aqueous acetonitrile solutions (1:3). Attempts to prepare compounds of the type polynuclear $[Mn(dpa)_2(X)]_nY_n$ or dinuclear $[Mn(dpa)_2(X)]_2Y_2$ [$X = N_3^-$ or NCO^-; $Y = ClO_4$] with a 1:2:1 ratio of $Mn(ClO_4)_2 \cdot 6H_2O$, dpa and N_3^-/NCO^- produced $[Mn(dpa)_2(N_3)(OH_2)]ClO_4$ (**3**) and $[Mn(dpa)_2(NCO)(OH_2)]ClO_4$ (**4**). With the metal chloride, a 1:2:1 ratio resulted in the formation of **1** and **2** with very low yields. However, addition of perchlorate ions in the reaction medium leads to **3** and **4**. This shows the presence of perchlorate ions are needed to isolate **3** and **4**, but its absence, leads to formation of compounds **1** and **2**.

Microanalytical (C, H and N) results and spectroscopic data are useful in this regard to formulate the products. The air-stable moisture-insensitive complexes **1**–**4** are insoluble in common solvents like methanol, ethanol, dichloromethane and acetonitrile, but are soluble in warm dimethylformamide and dimethylsulfoxide. Room temperature solid phase magnetic susceptibility measurements show that the manganese(II) complexes have moments close to their spin only value ($S = 5/2$): 5.88 BM (**1**); 5.89 BM (**2**); 5.93 BM (**3**) and 5.97 BM (**4**). In dimethylformamide **1** and **2** behave as non-electrolytes but a 1:1 electrolytic nature is realized in **3** and **4** [28] as evident from their conductivity values. A point of interest in the IR spectra are the bands [29] due to azide in **1** and **3** and cyanate in **2** and **4**. The asymmetric stretch ν_{asym} (N_3) appears as strong bands at 2070 and 2048 cm^{-1} in **1** and a single band at 2053 cm^{-1} in **3**. Stretches due to the cyanato group are seen at 2200 and 2181 cm^{-1} in **2**, and at 2196 cm^{-1} in **4**. Observation of the two such stretches in **1** and **2** are in line with the *cis* orientation of the pseudohalides. A distinguishable band could be expected for the azide symmetric (ν_{sym}) stretching mode in **1** and **3**, but only a weak signal at about ∼1324 cm^{-1} is observed. A signal corresponding to the azide and cyanate bending vibration, δ, can also be observed at about 638 cm^{-1} (**1** and **3**) and 640 cm^{-1} (**2** and **4**). In the region 420 and 366 cm^{-1}, two medium-to-weak bands are assignable to the ν(M–NCO) stretch, similar to other metal cyanato complexes with M–NCO bonds [30]. The ν(M–O)(H_2O) absorption bands [30] appear in the range 560–480 cm^{-1} for complexes **3** and **4**. Presence of $\nu(ClO_4)$ bands at ∼1080 and ∼620 cm^{-1} in **3** and **4** are noticed. The mild splitting in the perchlorate stretch indicates its involvement in some kind of secondary interactions. Furthermore, the IR spectra of **1**–**4** feature [17] the bands characteristic of the dpa molecule, seen in the stretching and bending modes of C–C and C–N bonds in the ranges between 1645–1390 and 1270–750 cm^{-1}. The –NH– and the –OH– bonds are noticeable at ∼3350 and ∼3430 cm^{-1}, respectively, and are in the higher wavelength region than the ideal value.

Complexes **1**–**4** show intense absorption bands at [31] around 315 nm, which are assigned to intraligand π–π* transitions, as these are similar to that of the free ligand (315 nm) [12]. The six-coordinated high-spin manganese(II) belongs to the $3d^5$ system. There is no excited state with the spin multiplicity six and all the electronic transitions in these complexes are doubly forbidden, (Laporte as well as spin). No bands in the visible region are detected, as expected for an octahedral manganese(II) complex. Reflectance spectra and electronic spectra in DMF solutions are akin in all complexes, reflecting gross structure and electronic structure in the solid state and solution.

3.2. Structure

The structural analyses show that complexes **1** and **2** consist of mononuclear units which are further engaged in hydrogen bonding among themselves and with water of crystallization or counter ions to give supramolecular 2D sheet structures. The ORTEP diagram of the individual unit, the perspective view of the hydrogen bonded sheets and the three dimensional orientation of the

sheets of these complexes are shown in Figs. 1–6 for **1** and **2** and Figs. 7–9 for **3** and **4**.

3.2.1. $[Mn(dpa)_2(N_3)_2]\cdot H_2O$ (**1**) and $[Mn(dpa)_2(NCO)_2]\cdot H_2O$ (**2**)

ORTEP diagrams with the atom labelling scheme of the mononuclear units of **1** and **2** are shown in Figs. 1 and 2. The coordination polyhedron around manganese(II) in both the complexes are best described as distorted octahedron with a MnN_6 chromophore. The coordination includes two chelated tailored diimines (—N=C–NH–C=N–) ligated by four pyridine N atoms [N(1), N(3), N(4), N(6)] and two terminal azide/cyanate N atoms. Three pyridine nitrogens of two different dpa units and one nitrogen of the pendant azido/cyanato group define the equatorial plane around the manganese(II) centres. The deviation of each nitrogen atom from the basal plane in **1** are −0.087, 0.075, 0.091, and −0.079 Å for N(3), N(10), N(1), N(4), and in **2** are 0.004, 0.004, −0.004, and −0.004 Å for N(8), N(4), N(1), N(6), respectively. In **1**, the deviation of manganese(II) from the mean plane is 0.177 Å while that in **2** is −0.195 Å.

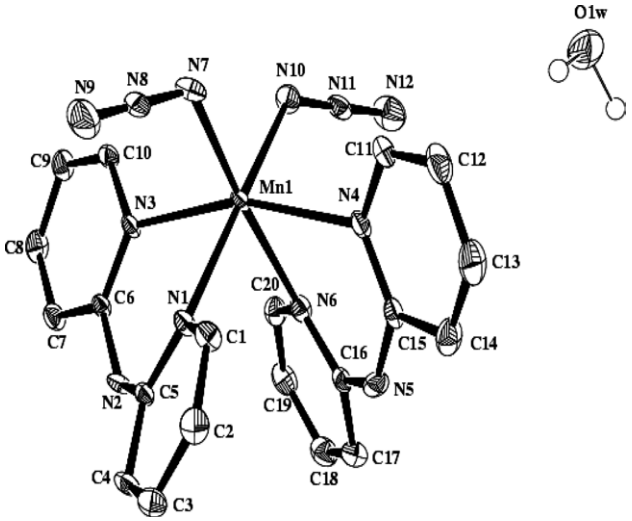


Fig. 1. ORTEP representation of the monomeric $[Mn(dpa)_2(N_3)_2]\cdot H_2O$ (**1**) with the atom numbering scheme and 40% probability ellipsoids for all non-hydrogen atoms.

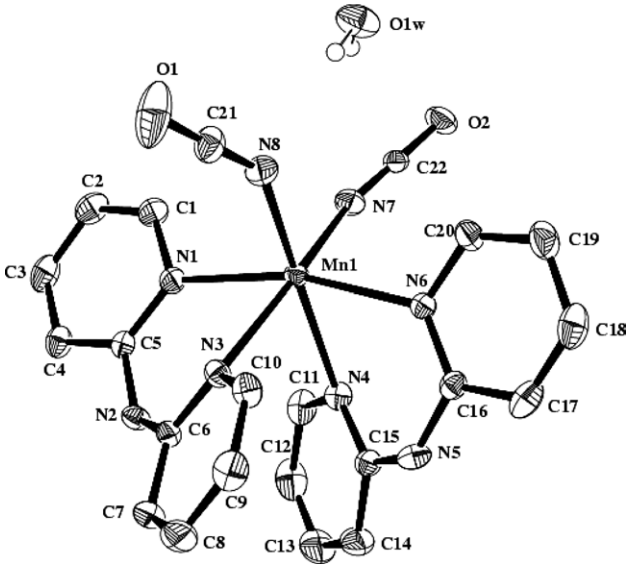


Fig. 2. ORTEP diagram of the monomeric $[Mn(dpa)_2(NCO)_2]\cdot H_2O$ (**2**) with the atom numbering scheme and 40% probability ellipsoids for all non+hydrogen atoms.

The Mn(1)–N distances are significantly greater than the sum of the covalent radii (1.96 Å) but show sufficient coherency with complexes containing pyridine nitrogens bonded to manganese(II) [32,33]. The two dpa ligands chelate the manganese atom with Mn(1)–N distances within a similar range: 2.234(3)–2.318(3) Å in **1** and 2.267(2)–2.324(2) Å in **2**. These distances are greater than Mn(1)–N(N_3/NCO) distances which are in the range, 2.139(2)–2.190(3) Å. Distortion from ideal octahedral coordination is very significant from the ranges of *cisoid* and the *transoid* angles which show sufficient deviation from ideality (Tables 3 and 4). The angles subtended by the dpa units in **2** [76.74(8)°–76.88(8)°] are close to those in compound **1** [77.70(10)°–78.81(10)°]. The angle between the two chelate planes in **1** is 55.39(12)° and in **2** is 47.93(10)°. The dpa ligands are not planar as the dihedral angles between planar pyridine rings (N1, C1 → C5 and N3, C6 → C10; N4, C11 → C15 and N6, C16 → C20) are 21.84(13)° and 14.01(14)° for **1**, and 26.23(12)° and 19.67(12)° for **2**, respectively. Two azides/cyanates are in a *cis* orientation with an angle of 92.24(12)°/97.21(10)°. The N(7)–N(8) [1.176(4) Å] and N(10)–N(11) [1.178(4) Å] distances are greater than N(8)–N(9) [1.155(5) Å] and N(11)–N(12) [1.169(5) Å] distances, respectively, as expected, and the values are very similar to different transition metal azido complexes [32]. Both the azide as well as the cyanate ligands have the expected linear geometry, with N–N–N angles of 178.3(4)°, 178.6(4)°, respectively, for N(9), N(12) and N–C–O angles of 178.4(4)°, 177.7(3)°, respectively, for O(1), O(2). The N(8)–N(7)–Mn(1) and N(11)–N(10)–Mn(1) angles are 122.7(2)° and 128.3(3)°, respectively, which reflects the bending coordination nature of the azides. Similar bending coordination is also observed in the cyanato ligands in **2** with C(21)–N(8)–Mn(1) and C(22)–N(7)–Mn(1) angles of 144.8(2)° and 158.1(2)°. The Mn···Mn separation between the nearest neighbours in each 1D chain in **1** is 7.829 Å, and that within the sheets in **2** is 8.439 Å.

The packing diagram of **1** in the *bc* plane exhibits a hydrogen bonded 1D supramolecular chain. The water of crystallization, unbound nitrogen of the terminal azide and the amine (–NH–) hydrogen play a vital role in the formation of this type of architecture (Table 5). The end nitrogen atom [N(12)] of one terminal azide

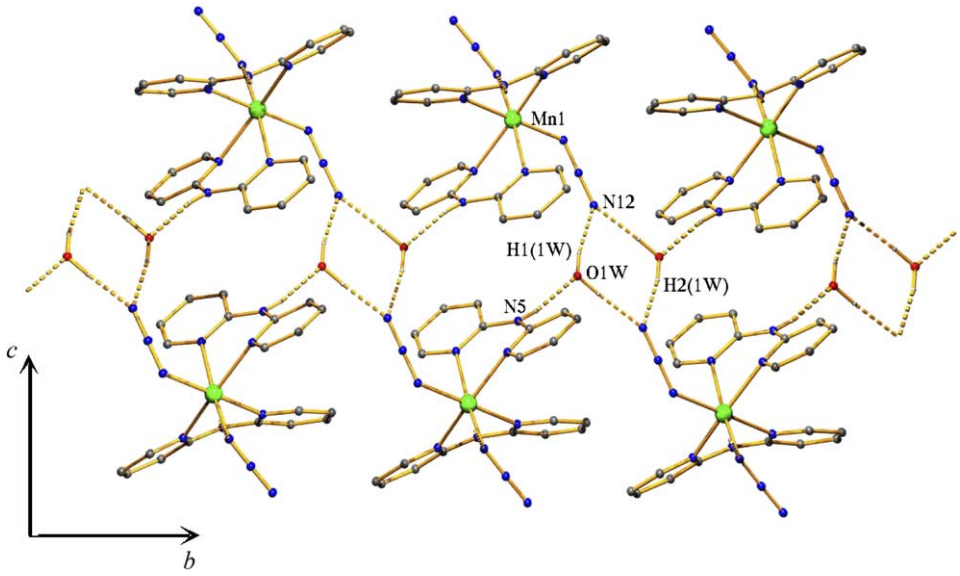


Fig. 3. Hydrogen bonded 1D chains formed by the lattice water in **1**.

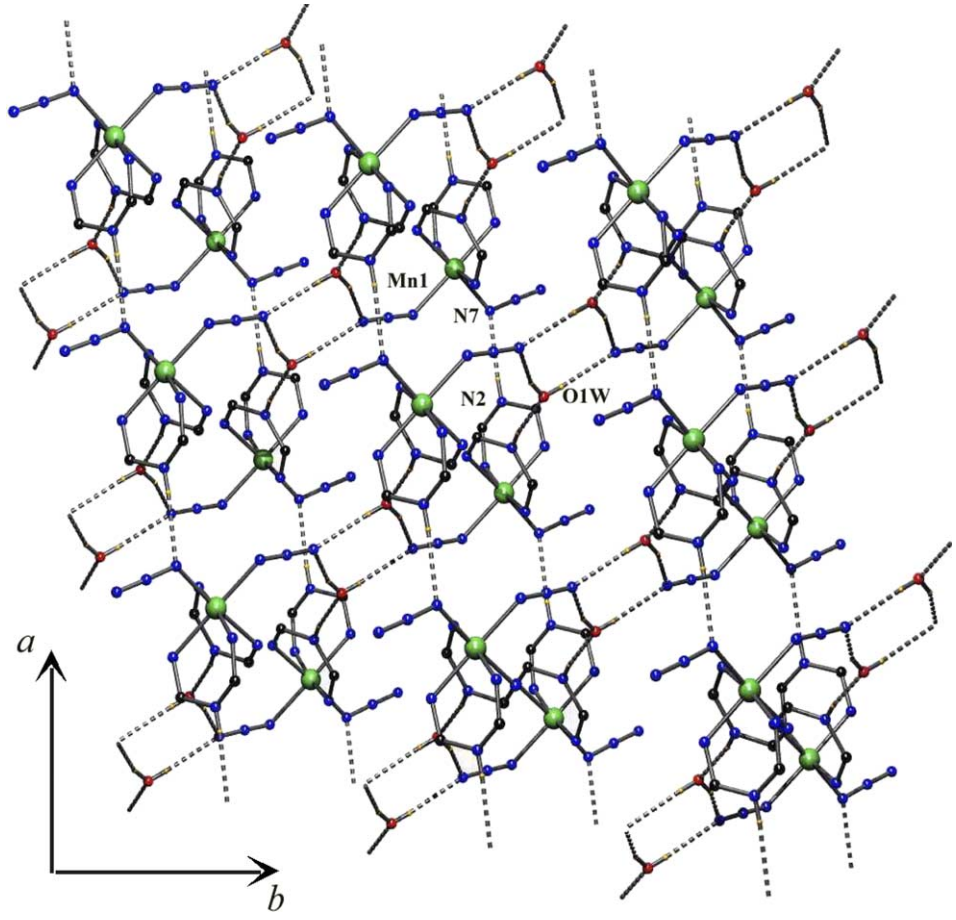


Fig. 4. A perspective view of the supramolecular 2D sheet formed by the N–H···N H-bonding in **1**.

of a mononuclear unit is hydrogen bonded to two hydrogens [H(1W1) and H(2W1)] of two different water molecules by bifurcated hydrogen bonding [H(1W1)···N(12) 1.9571 Å; ∠O(1W)–H(1W1)···N(12), 176.07°]. Another unit placed diagonally is similarly hydrogen bonded to a second water molecule. The oxygen atoms

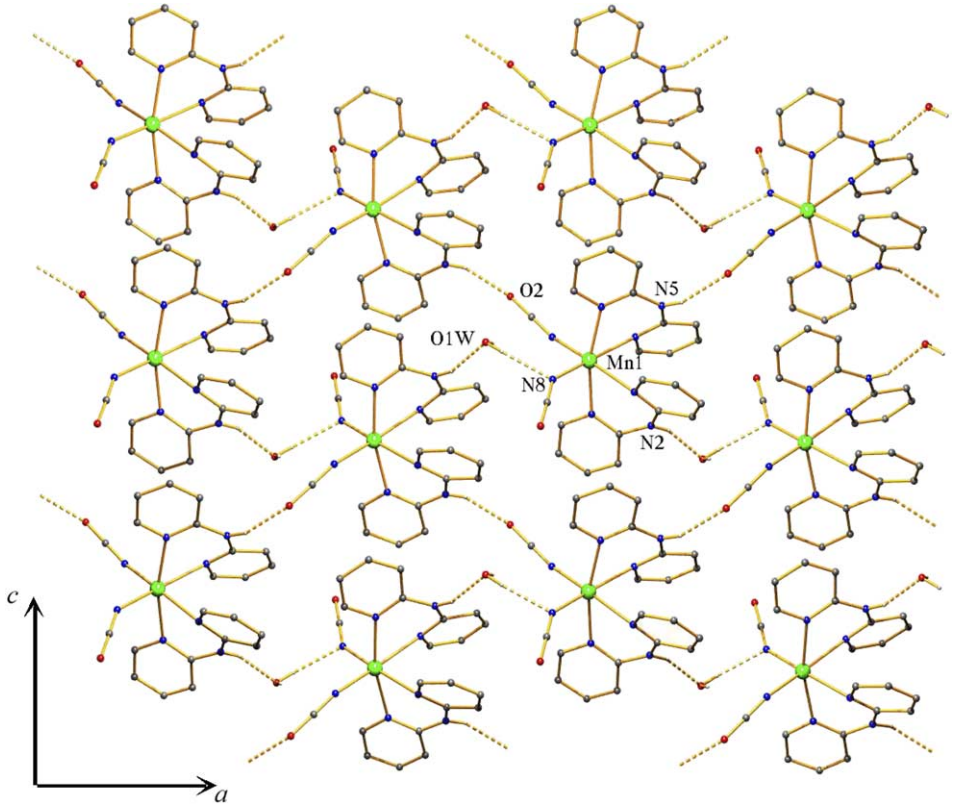


Fig. 5. Hydrogen bonded 2D supramolecular sheets formed by the lattice water in **2**.

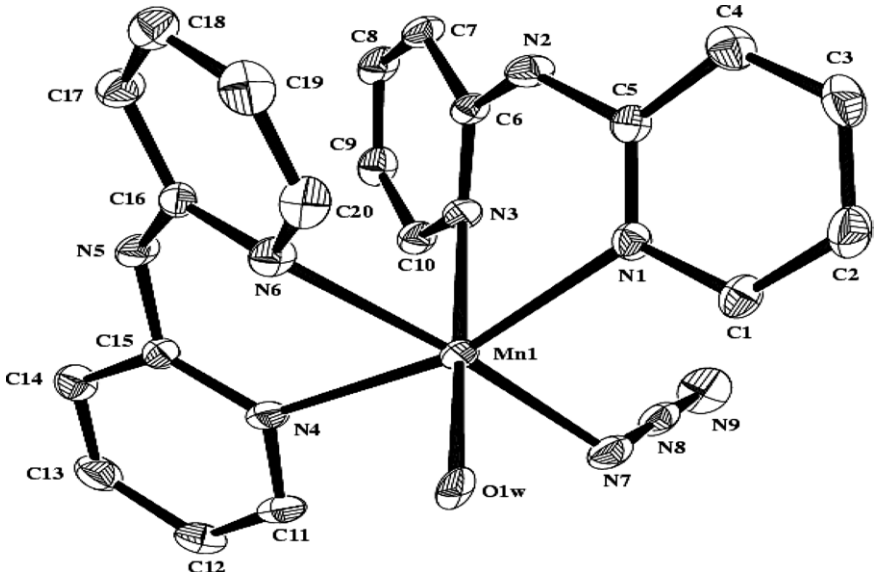


Fig. 6. ORTEP diagram of $[Mn(dpa)_2(N_3)(OH_2)]^+$ (**3**) with the atom numbering scheme and 40% probability ellipsoids for all non-hydrogen atoms.

[O(1W) and O(2W)] of these water of crystallizations are further hydrogen bonded to the amine hydrogens [N(5)] of two other mononuclear units [H(5A)···O(1W), 2.0068 Å; ∠N(5)–H(5A)···O(1W), 165.37°]. Thus four neighbouring mononuclear units are held together through such bifurcated H-bonding interactions to two donor water molecules (Table 5) to form a cyclic motif, $R_2^4(8)$ in Etter's graph notation [34]. These motifs in turn result in one dimensional chains (Fig. 3). These 1D chains are further connected through N–H···N hydrogen bonding between amine nitrogen [N(2)] donors and [N(7)] of bound azido nitrogen acceptors.

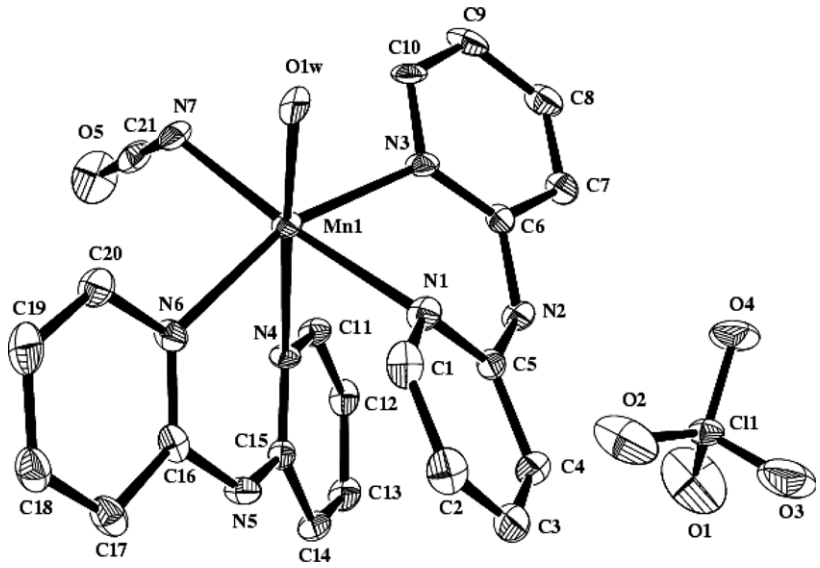


Fig. 7. ORTEP representation of $[Mn(dpa)_2(NCO)(OH_2)]ClO_4$ (**4**) with the atom numbering scheme and 40% probability ellipsoids for all non-hydrogen atoms.

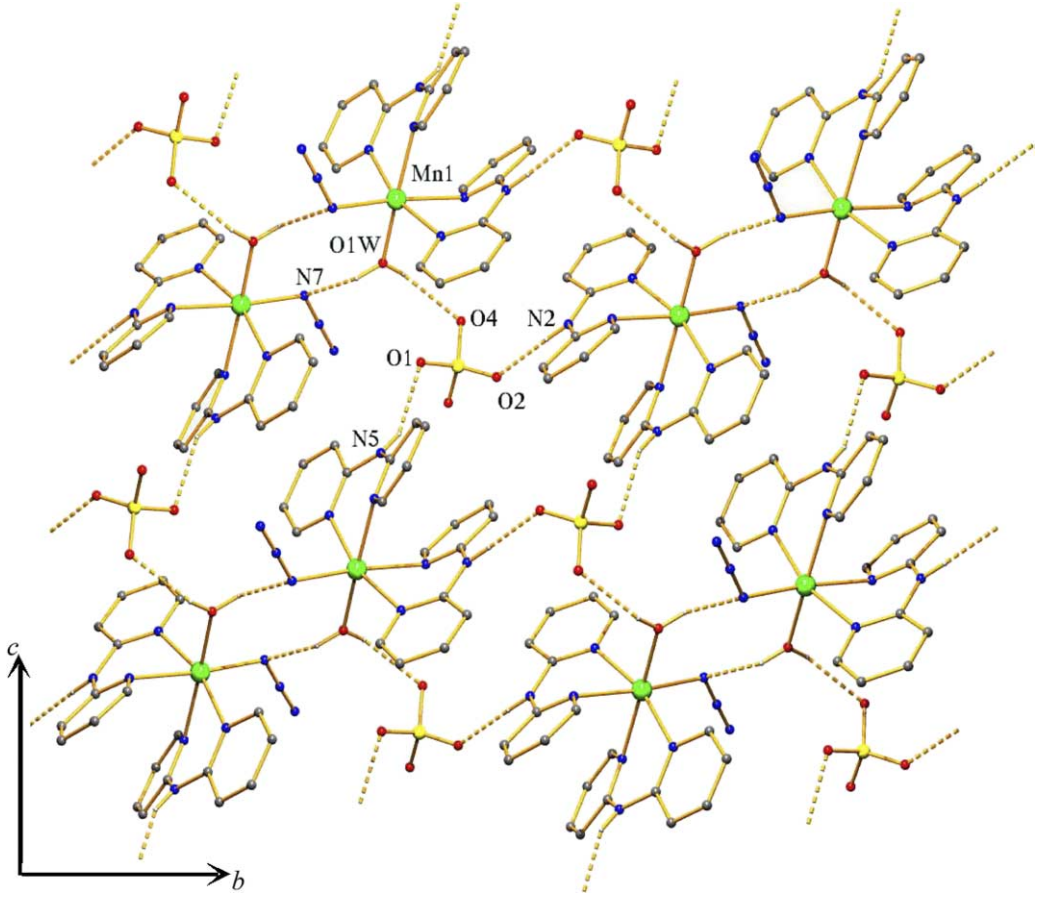


Fig. 8. A Perspective view of 2D supramolecular sheets formed by H-bonding in **3** and **4**.

These two hydrogen bonding systems are interwoven and facilitates a 2D supramolecular sheet in the *ab* plane (Fig. 4).

In **2** the packing diagram is very different from that seen in **1**. Fig. 5 shows the hydrogen bonded 2D sheet structure of the complex in the *ac* plane. Each unit is

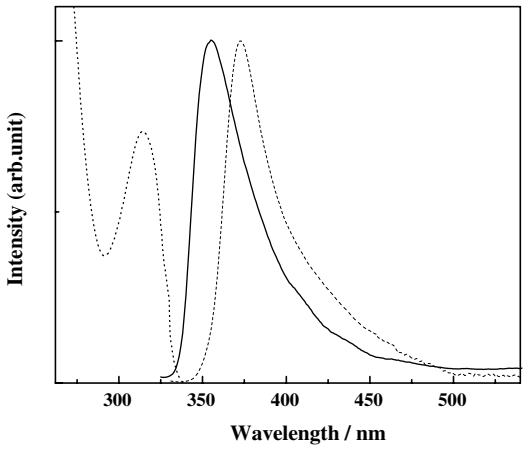


Fig. 9. Emission spectra of **1**: UV in DMF solution at 298 K (·····), fluorescence (——), phosphorescence in DMF glassy solution (------).

Table 3
Selected bond distances (Å) and angles for (°) **1**

Bond distances (Å)			
Mn(1)–N(1)	2.277(3)	Mn(1)–N(7)	2.190(3)
Mn(1)–N(3)	2.234(3)	Mn(1)–N(10)	2.183(3)
Mn(1)–N(4)	2.265(3)	N(7)–N(8)	1.176(4)
Mn(1)–N(6)	2.318(3)	N(8)–N(9)	1.155(5)
N(10)–N(11)	1.178(4)	N(11)–N(12)	1.169(5)
Bond angles (°)			
N(1)–Mn(1)–N(3)	78.81(10)	N(4)–Mn(1)–N(7)	96.36(11)
N(1)–Mn(1)–N(4)	87.86(10)	N(4)–Mn(1)–N(10)	95.05(11)
N(1)–Mn(1)–N(6)	87.54(10)	N(6)–Mn(1)–N(7)	174.06(11)
N(1)–Mn(1)–N(7)	92.53(10)	N(6)–Mn(1)–N(10)	88.07(11)
N(1)–Mn(1)–N(10)	174.11(10)	N(7)–Mn(1)–N(10)	92.24(12)
N(3)–Mn(1)–N(4)	161.51(11)	Mn(1)–N(7)–N(8)	122.7(2)
N(3)–Mn(1)–N(6)	88.87(10)	Mn(1)–N(10)–N(11)	128.3(3)
N(3)–Mn(1)–N(7)	96.97(11)	N(7)–N(8)–N(9)	178.3(4)
N(3)–Mn(1)–N(10)	97.18(11)	N(10)–N(11)–N(12)	178.6(4)
N(4)–Mn(1)–N(6)	77.70(10)		

Table 4
Selected bond distances (Å) and angles for (°) **2**

Bond distances (Å)			
Mn(1)–N(1)	2.267(2)	Mn(1)–N(8)	2.159(3)
Mn(1)–N(3)	2.324(2)	N(7)–C(22)	1.168(3)
Mn(1)–N(4)	2.309(2)	N(8)–C(21)	1.166(4)
Mn(1)–N(6)	2.272(2)	O(1)–C(21)	1.202(4)
Mn(1)–N(7)	2.139(2)	O(2)–C(22)	1.216(3)
Bond angles (°)			
N(1)–Mn(1)–N(3)	76.74(8)	N(4)–Mn(1)–N(7)	93.13(8)
N(1)–Mn(1)–N(4)	92.07(8)	N(4)–Mn(1)–N(8)	166.77(8)
N(1)–Mn(1)–N(6)	165.91(8)	N(6)–Mn(1)–N(7)	95.66(8)
N(1)–Mn(1)–N(7)	93.63(9)	N(6)–Mn(1)–N(8)	93.86(9)
N(1)–Mn(1)–N(8)	95.46(9)	N(7)–Mn(1)–N(10)	97.21(10)
N(3)–Mn(1)–N(4)	80.81(8)	Mn(1)–N(7)–C(22)	158.1(2)
N(3)–Mn(1)–N(6)	92.67(8)	Mn(1)–N(8)–C(21)	144.8(2)
N(3)–Mn(1)–N(7)	168.34(9)	N(7)–C(22)–O(2)	177.7(3)
N(3)–Mn(1)–N(8)	90.34(9)	N(8)–C(21)–O(1)	178.4(4)
N(4)–Mn(1)–N(6)	76.88(8)		

Table 5
Hydrogen bond distances (Å) and angles (°) for**1** and **2**

D–H···A	D–H	H···A	D···.A	D–H···A
*Compound **1***				
O(1W)–H(1W1)···N(12)[a]	0.9365	1.9571	2.892(5)	176.07
O(1W)–H(2W1)···N(12)[b]	0.9431	1.9580	2.888(5)	168.31
N(2)–H(2A)···N(7)[c]	0.8603	2.3003	3.073(5)	149.50
N(5)–H(5A)···O(1W)[c]	0.8601	2.0068	2.847(4)	165.37
*Compound **2***				
N(2)–H(2A)···O(1W)[d]	0.8600	2.1033	2.930(3)	160.90
O(1W)–H(2W)···N(8)	0.9029	2.0590	2.955(3)	171.72
N(5)–H(5A)···O(2)[e]	0.8601	2.1282	2.942(3)	157.73

Symmetry codes: a x, $1+y$, z; b $1-x$, $-y$, $1-z$; c $-1+x$, y, z; d $1/2-x$, $1-y$, $1/2+z$; e $3/2-x$, $1-y$, $1/2+z$.

hydrogen bonded to four neighbouring units; directly to two units and to two other units via a water molecule each (Table 5). The bound nitrogen [N(8)] of a terminal cyanate of each unit participates in an O–H···N type of bonding with a nearby water molecule, having a H(2W)···N(8) distance of 2.0590 Å and ∠O(1W)–H(2W)···N(8), 171.72°. The pendant oxygen atom [O(2)] of another cyanate of the same unit hydrogen bonds to an amine hydrogen of another unit with H(5A)···O(2), 0.8601 Å and ∠N(5)–H(5A)···O(2), 157.73°. Two amine hydrogens from the two dpa ligands of this same unit further hydrogen bond to a water molecule [N–H···O(W)] and an oxygen atom of a cyanate [N–H···O] of a different unit. Thus each water molecule is hydrogen bonded to two mononuclear units.

3.2.2. $[Mn(dpa)_2(N_3)(OH_2)]ClO_4$ (**3**) and $[Mn(dpa)_2(NCO)(OH_2)]ClO_4$ (**4**)

Both the complexes consist of mononuclear units containing a $[Mn(dpa)_2(X)(OH_2)]^+$ cation and a ClO_4^- anion each, which are further engaged in hydrogen bonding among themselves to give a supramolecular 2D sheet structure. No coordination of the anions is observed.

Figs. 7 and 8 depict the ORTEP drawing with the atom numbering scheme of the mononuclear units of **3** and **4**, respectively. The complex cations possess a six-coordinated environment with a $Mn^{II}N_5O$ chromophore, namely each of the manganese atoms is coordinated by four nitrogen atoms [N(1), N(3), N(4), N(6)] from two bidentate dpa ligands, one nitrogen from the terminal azide/cyanate [N(7)] and an oxygen atom [O(1W)] of the coordinated aquo ligand. The equatorial plane in **3** is made up of N1, N3, N4 and O1W, from two dpa ligands and an aquo moiety, where the corresponding deviations are −0.064, 0.065, −0.086 and 0.057 Å, respectively. The manganese atom deviates 0.16 Å from the plane. In **4**, the deviations are −0.055, 0.062, −0.060 and 0.054 Å, for N3, N4, N6 and O1W, with a deviation of 0.206 Å of the manganese(II) centre out of the equatorial N_3O plane.

The manganese(II)–N distances are characteristic of typical high-spin manganese(II) complexes. The Mn(1)–N bond lengths and the N–Mn(1)–N bite angles are comparable to those in dpa–manganese(II) structures. The shortest distance (Tables 6 and 7) within the cation is the bond between Mn(II) and oxygen atom of the aqua ligand, followed by Mn(II)–$N_{azide/cyanate}$ and Mn(II)–N_{dpa} distances. Mn–O (H_2O) distances of both complexes are within the ranges found for other Mn(II)-aquo complxes. In **3** and **4** the angle between the two chelate planes is 51.44(16)° and 51.50(2)°. The dpa ligands are not planar as the dihedral angles between the planar pyridine rings (N1, C1 → C5 and N3, C6 → C10; N4, C11 → C15 and N6, C16 → C20) are 21.61(19)°, 17.0(2)° in **3** and 18.0(3)°, 20.7(2)° in **4**. The azide ligand in **3** has the expected linear geometry, with N–N–N angles of 178.6(5)° for N(9). The N(8)–N(7)–Mn(1) angle is 123.0(3)° which reflects the highly bending coordination nature of the azide. In **4** the cyanate ligand also has the expected linear geometry, with the N–C–O angle of 178.9(7)° for O(5). The C(21)–N(7)–Mn(1) angle is 129.1(5)° which reflects the highly bent nature of the cyanate.

Table 6
Selected bond distances (Å) and angles for (°) **3**

Bond distance (Å)			
Mn(1)–N(1)	2.233(4)	Mn(1)–O(1W)	2.152(3)
Mn(1)–N(3)	2.277(4)	N(7)–N(8)	1.208(6)
Mn(1)–N(4)	2.241(4)	N(8)–N(9)	1.155(6)
Mn(1)–N(6)	2.298(4)	O(1W)–H(1W)	0.9000
Mn(1)–N(7)	2.168(4)	O(1W)–H(2W)	0.9000
Bond angles (°)			
O(1W)–Mn(1)–N(1)	94.69(16)	N(1)–Mn(1)–N(7)	94.33(15)
O(1W)–Mn(1)–N(3)	172.76(15)	N(3)–Mn(1)–N(4)	88.64(14)
O(1W)–Mn(1)–N(4)	95.41(15)	N(3)–Mn(1)–N(7)	95.62(14)
O(1W)–Mn(1)–N(6)	87.13(14)	N(3)–Mn(1)–N(6)	87.82(13)
O(1W)–Mn(1)–N(7)	89.77(15)	N(4)–Mn(1)–N(6)	78.31(14)
N(1)–Mn(1)–N(3)	80.12(14)	N(4)–Mn(1)–N(7)	97.95(15)
N(1)–Mn(1)–N(4)	164.10(14)	N(6)–Mn(1)–N(7)	174.90(15)
N(1)–Mn(1)–N(6)	89.97(14)		

Table 7
Selected bond distances (Å) and angles for (°) **4**

Bond distances (Å)			
Mn(1)–N(1)	2.304(5)	Mn(1)–N(7)	2.140(5)
Mn(1)–N(3)	2.240(5)	Mn(1)–O(1W)	2.170(5)
Mn(1)–N(4)	2.288(5)	N(7)–C(21)	1.175(9)
Mn(1)–N(6)	2.236(5)	C(21)–O(5)	1.200(9)
Bond angles (°)			
O(1W)–Mn(1)–N(1)	85.44(19)	N(1)–Mn(1)–N(7)	175.22(19)
O(1W)–Mn(1)–N(3)	95.17(19)	N(3)–Mn(1)–N(4)	88.24(17)
O(1W)–Mn(1)–N(4)	171.22(19)	N(3)–Mn(1)–N(6)	162.74(18)
O(1W)–Mn(1)–N(6)	94.6(2)	N(3)–Mn(1)–N(7)	98.26(19)
O(1W)–Mn(1)–N(7)	92.0(2)	N(4)–Mn(1)–N(6)	80.22(17)
N(1)–Mn(1)–N(3)	77.97(18)	N(4)–Mn(1)–N(7)	95.50(19)
N(1)–Mn(1)–N(4)	87.37(17)	N(6)–Mn(1)–N(7)	95.60(19)
N(1)–Mn(1)–N(6)	88.65(18)	N(1)–C(21)–O(5)	178.9(7)

The packing diagrams of **3** and **4** are exactly the same and are represented by Fig. 9. The most interesting feature in **3** and **4** is that the interionic hydrogen bonds play an important role in the crystal packing and the stability of the complexes. Adjacent units are cross-linked by three types (N–H···O, O–H···O and O–H···N) of intermolecular hydrogen bonds, which stabilize the conformation. Through the interionic hydrogen bonds, the cations are linked into supramolecular 2D layers. The coordinated water molecules and the perchlorate anions are involved in the hydrogen bonded network. The hydrogen bonding parameters are shown in Table 8 for **3** and **4**. The sheets in **3** and **4** propagate in the *bc* plane as shown in Fig. 9.

A cyclic motif $R_2^2(8)$ in Etter's graphs notation [34] between the two mononuclear cationic units is formed by hydrogen bonding involving a hydrogen of the aquo ligand of one unit and a bound nitrogen of the terminal pseudohalide of the second unit and vice versa. This results in the formation of supramolecular dinuclear species held together solely by hydrogen bonds [O(1W)–H(2W)···N(7); H(2W)···N(7), 2.0800 Å (**3**) and 2.1265 Å (**4**), ∠O(1W)–H(2W)···N(7), 136.13° (**3**), 135.74° (**4**)]. The Mn···Mn separation forming the loop within the sheet is 5.669 Å (**3**) and 5.642 Å (**4**). Each such dimers are further hydrogen bonded separately to six perchlorate anions. Thus each perchlorate anion is hydrogen bonded to three different mononuclear cationic units. Two of the three hydrogen bonded oxygens are involved in a N–H···O type of interaction with the active amine (N2 and N5) hydrogens of dpa ligands of two different units [N–H···O: H(2B)···O(2), 2.1963 Å; ∠N(2)–H(2B)···O(2), 151.30°; H(5A)···O(1), 2.0765 Å; ∠N(5)–H(5A)···O(1), 177.15° (**3**) and H(2B)···O(2), 2.0757 Å; ∠N(2)–H(2B)···O(2), 178.07°; H(5A)···O(3), 2.1973 Å; ∠N(5)–H(5A)···O(3) 151.76°; (**4**)]. The third oxygen hydrogen bonds to hydrogen [H(1W)] of the bound aquo ligand [O(1W)–H(1W)···O(4); H(1W)···O(4), 2.2551 Å (**3**), 2.2483 Å (**4**); ∠O(1W)–H(1W)···O(4), 151.44° (**3**), 152.79° (**4**)]. From Fig. 9 it is clearly

Table 8
Hydrogen bond distances (Å) and angles (°) for **3** and **4**

D–H···A	D–H	H···A	D···A	D–H···A
*Compound **3***				
O(1W)–H1(1W)···O(4)	0.9001	2.2551	3.076(7)	151.44
O(1W)–H(2W)···N(7)[a]	0.9005	2.0800	2.800(6)	136.13
N(2)–H(2B)···O(2)[b]	0.8603	2.1963	2.980(7)	151.30
N(5)–H(5A)···O(1)[c]	0.8607	2.0765	2.936(8)	177.15
*Compound **4***				
O(1W)–H(1W)···O(4)[c]	0.8996	2.2483	3.076(8)	152.79
N(2)–H(2B)···O(2)	0.8607	2.0757	2.936(11)	178.07
O(1W)–H(2W)···N(7)[a]	0.9005	2.1265	2.842(7)	135.74
N(5)–H(5A)···O(3)[d]	0.8611	2.1973	2.984(9)	151.76

Symmetry codes: a $1-x, 1-y, 1-z$; b $x, 1+y, z$; c $1-x, 1-y, -z$; d $1-x, 2-y, -z$.

seen that the pendant atoms of the terminal pseudohalides are oriented in such a manner that they lie very close to one of the pyridine rings. This orientation thus facilitates the C–H···O(5)/N(9) type of hydrogen bonding. Also due to the close disposition of the fourth oxygen of the perchlorate ions to a pyridine ring of dpa, a weak C–H···O type of hydrogen bonding is also possible in both complexes. These weak bondings add to the stability of the crystal lattice.

3.3. Electrochemical studies

Cyclic voltammetry of the complexes was recorded in DMF solutions using platinum as the working electrode. A quasi-reversible oxidation response is observed at 0.60 V (**1**), 0.62 V (**2**), 0.65 V (**3**), 0.68 V (**4**), presumably due to the electrode reactions as shown in the following equations:

$$[Mn^{III}(dpa)_2(X)_2]^{1+} \underset{-e}{\overset{+e}{\rightleftharpoons}} [Mn^{II}(dpa)_2(X)_2] \quad (1)$$

$$[Mn^{III}(dpa)_2(X)(OH_2)]^{2+} \underset{-e}{\overset{+e}{\rightleftharpoons}} [Mn^{II}(dpa)_2(X)(OH_2)]^{1+} \quad (2)$$

Presence of a neutral water molecule in **3** and **4** in place of an anionic pseudohalide in **1** and **2** leads to an increase of the potential. The one-electron stoichiometry of couple 1 and 2 was confirmed by comparison of the current height with that of the manganese(II)–manganese(III) couple of other complexes [35].

3.4. Luminescence spectra

The spectroscopic data of all four complexes are listed in Table 9. Complexes with dpa, feature two intense absorptions at 315 nm, which is assignable to the intraligand π–π* transitions. The emission energy of complexes **1**–**4** in DMF solutions at 298 K are almost of similar value ($\lambda_{max} \sim 350$ nm) and are assignable to the intraligand fluorescence. The lifetimes of the fluorescence are within the range of 2.83–2.87 ns. In glassy solution (DMF at 77 K), $^3(\pi–\pi^*)$ phosphorescence has been observed at ~425 nm (Fig. 9) in all the complexes.

Table 9
Photophysical data for **1** to **4**

Sample	Absorption (λ/nm)	Emission (λ/nm)		Lifetime (ns)
		Fluorescence[a]	Phosphorescence[b]	
1	315	355	425	2.87
2	312	353	422	2.83
3	317	354	425	2.83
4	315	354	425	2.85

[a] DMF at room temperature (298 K).
[b] DMF at 77 K.

4. Conclusion

We have reported a homologous series based on manganese complexes of dpa ligand that contains aqua molecules either as a coordinating ligand or as water of crystallization, displaying strong hydrogen bonded networks. This study also shows the use of the N–H group of dpa as a strategy to harness hydrogen bonding with adjacent metal centres with potential proton acceptor site(s), resulting in different crystalline architectures. Difference in the disposition of the aqua ligand (within the coordination sphere or outside it) leads to different supramolecular networks [36]. The metal ions play a vital role in strengthening the hydrogen bonds by influencing the hydrogen bonding properties of donors and acceptors. So this work based on a $3d^5$ metal provokes us to further study new systems with different metal ions, dpa or dpa-like ligands and pseudohalides or other related units.

5. Supplementary data

Crystallographic data for the structural analysis have been deposited with the Cambridge Crystallographic Data Centre, CCDC Nos. 209024 (**1**), 209026 (**2**), 209023 (**3**) and 209025 (**4**). Copies of this information can be obtained free of charge from the Director, CCDC, 12 Union Road, Cambridge CB2 IEZ, UK (fax: +44 1223 336033; e-mail: deposit@ccdc.cam.ac.uk or www.ccdc.cam.ac.uk).

Acknowledgements

Financial support from the Department of Science and Technology (DST) and Council of Scientific and Industrial Research (CSIR), New Delhi, India is gratefully acknowledged.

References

[1] P. Comba, T.W. Hambley, Molecular Modelling of Inorganic and Coordination Compounds, 2nd ed., VCH, Weinheim, 2001.
[2] (a) G.R. DesirajuCrystal Design: Structure and Function. Perspectives in Supramolecular Chemistry, vol. 7, Wiley, Chichester, 2003;
(b) C.J. Elsevier, J. Reedijk, P.H. Walton, M.D. Ward, J. Chem. Soc., Dalton Trans. (2003) 1869.
[3] (a) J.-M. Lehn, Supramolecular chemistry: concepts and perspectives, VCH, Weinheim, 1995;
(b) J.W. Steed, J.L. Atwood, Supramolecular Chemistry, Wiley, New York, 2000.
[4] O. Almarsson, M.J. Zawarotko, Chem. Commun. (2004) 1889.
[5] (a) J.S. Miller, M. Drillon (Eds.), Magnetism: Molecules to Materials IV, Wiley–VCH, Weinheim, 2003;

(b) E.C. Sanudo, W. Wernsdorfer, K.A. Abboud, G. Christou, Inorg. Chem. 43 (2004) 4137.
[6] B. Cornils, W.A. Herrmann, R. Schlogl (Eds.), Catalysis from A to Z: A Concise Encyclopedia, Wiley, New York, 2000.
[7] (a) T. Yamaguchi, T. Inagawa, H. Nakazumi, S. Irie, M. Irie, Chem. Mater. 12 (2000) 869;
(b) K. Uchida, Y. Kawai, Y. Shimizu, V. Vill, M. Irie, Chem. Lett. (2000) 654.
[8] O. Margeat, P.G. Lacroix, J.P. Costes, B. Donnadieu, C. Lepetit, K. Nakatani, Inorg. Chem. 43 (2004) 4743.
[9] S. Leininger, B. Olenyuk, P.J. Stang, Chem. Rev. 100 (2000) 853.
[10] (a) T. Steiner, Angew. Chem. Int. Ed. 41 (2002) 48;
(b) G.R. Desiraju, Acc. Chem. Res. 35 (2002) 565.
[11] (a) J.M. Lehn, Chem. Eur. J. 6 (2000) 2097;
(b) O.M. Yaghi, M. O'Keeffe (Eds.), Design of Solids From Molecular Building Blocks: Golden Opportunity for Solid State Chemist, special issue of J. Solid State Chem. (2000) 152;
(c) M. Schweiger, S.R. Seidel, A.M. Arif, P.J. Stang, Inorg. Chem. 41 (2002) 2556.
[12] D. Bose, Sk.H. Rahaman, G. Mostafa, R.D. Bailey Walsh, M.J. Zaworotko, B.K. Ghosh, Polyhedron 23 (2004) 545.
[13] (a) K.-Y. Ho, W.-Y. Yu, K.-K. Cheung, C.-M. Che, Chem. Commun. (1998) 2101;
(b) S. Youngme, P. Phuengphai, S. Booncoon, N. Chaichit, Polyhedron 23 (2004) 1685.
[14] H. Zhu, M. Strobele, Z. Yu, Z. Wang, H.-J. Meyer, X. You, Inorg. Chem. Commun. 4 (2001) 577.
[15] (a) G.J. Pyrka, M. El-Mekki, A.A. Pinkerton, J. Chem. Soc., Chem. Commun. (1991) 84;
(b) J.F. Berry, F.A. Cotton, P. Lei, C.A. Murillo, X. Wang, Inorg. Chem. 42 (2003) 377;
(c) J.F. Berry, F.A. Cotton, L.M. Daniels, C.A. Murillo, X. Wang, Inorg. Chem. 42 (2003) 2418.
[16] K.-Y. Ho, W.-Y. Yu, K.-K. Cheung, C.-M. Che, J. Chem. Soc., Dalton Trans. (1999) 1581.
[17] M. Villanueva, J.L. Mesa, M.K. Urtiaga, R. Cortés, L. Lezama, M.I. Arriortua, T. Rojo, Eur. J. Inorg. Chem. (2001) 1581.
[18] (a) J.W. Whittmaker (Ed.), Mn and Its Role in Biological Processes, vol. 37, Marcel Dekker, New York, 2000, p. 587;
(b) J.-Y. Xu, H.-D. Bian, Q.-L. Wang, W. Gu, S.-P. Yan, D.-Z. Liao, P. Cheng, Z.-H. Jiang, P.-W. Shen, Z. Anorg. Allg. Chem. 629 (2003) 1063.
[19] M. Lundberg, M.R.A. Blomberg, P.E.M. Siegbahn, Inorg. Chem. 43 (2004) 264.
[20] G.C. Dismukes, Chem. Rev. 96 (1996) 2909.
[21] W. Ruttinger, G.C. Dismukes, Chem. Rev. 97 (1997) 1.
[22] N.A. Law, M.T. Caudle, V.L. Pecoraro, in: A.G. Sykes (Ed.), Advances in Inorganic Chemistry, vol. 46, Academic Press, London, 1998, p. 305.
[23] H. Chowdhury, D. Bose, S.H. Rahaman, B.K. Ghosh, Indian J. Chem. A 42 (2003) 2772.
[24] G.M. Sheldrick, SAINT V4: Software Reference Manual, Siemens Analytical X-ray Systems, Madison, WI, USA, 1996.
[25] G.M. Sheldrick, SADABS: Program for Empirical Absorption Correction of Area Detector Data, University of Göttingen, Göttingen, Germany, 1996.
[26] G.M. Sheldrick, SHELXTL V5.1: Software Reference Manual, Bruker AXS, Inc., Madison, WI, USA, 1997.
[27] A.L. Spek, Acta Crystallogr., Sect. A 46 (1996) C34.
[28] W.J. Geary, Coord. Chem. Rev. 7 (1971) 81.
[29] K. Nakamoto, Infrared and Raman Spectra of Inorganic and Coordination Compounds: Part B, 5th ed., Wiley, New York, 1997.
[30] F.A. Mautner, M.A.S. Goher, N.A. Al-Salem, Polyhedron 16 (1997) 2877.
[31] A.B.P. Lever, Inorganic Electronic Spectroscopy, 2nd ed., Elsevier, New York, 1984.
[32] (a) S. Dalai, P.S. Mukherjee, T. Mallah, M.G.B. Drew, N.R. Chaudhuri, Inorg. Chem. Commun. 5 (2002) 472;
(b) U. Ray, S.K. Jasimuddin, B.K. Ghosh, M. Monfort, J. Ribas, G. Mostafa, T.-H. Lu, C. Sinha, Eur. J. Inorg. Chem. (2004) 250.
[33] M.L. Hernandez, M.K. Urtiaga, M.G. Barandika, R. Cortes, L. Lezama, N. Pinta, M.I. Arriortua, T. Rojo, J. Chem. Soc., Dalton Trans. (2001) 3010.
[34] M.C. Etter, J. Phys. Chem. (1991) 4601.
[35] C. Hureau, S. Blanchard, M. Nierlich, G. Blain, E. Riviere, J.-J. Girerd, E.A. -Mallart, G. Blondin, Inorg. Chem. 43 (2004) 4415.
[36] (a) S.K. Ghosh, P.K. Bharadwaj, Inorg. Chem. 43 (2004) 5180;
(b) D.R. Turner, M.B. Hursthouse, M.E. Light, J.W. Steed, Chem. Commun. (2004) 1354.

Available online at www.sciencedirect.com
SCIENCE DIRECT®
Polyhedron 24 (2005) 759–764
POLYHEDRON
www.elsevier.com/locate/poly

Ligand substitution reaction in the parent cluster (μ_3-FcCHC)$FeCo_2(CO)_9$ and structural characterization of its CO substituted derivatives

Li-Min Han [a], Quan-Ling Suo [a,*], Yi-Bing Wang [a], Jie-Hui Ye [a], Ning Zhu [a], Xue-Bing Leng [b], Jie Sun [c]

[a] *Chemical Engineering College, Inner Mongolia University of Technology, Hohhot 010062, PR China*
[b] *Institute of Elemento-organic Chemistry, Nankai University, Tianjin 300071, PR China*
[c] *Shanghai Institute of Organic Chemistry, the Chinese Academy of Sciences, Shanghai 200032, PR China*

Received 27 November 2004; accepted 31 January 2005
Available online 23 March 2005

Abstract

The new mixed metal carbonyl clusters (μ_3-FcCHC)$FeCo_2(CO)_7$dppm (Fc = $C_5H_5FeC_5H_4$, ferrocenyl; dppm = $Ph_2PCH_2PPh_2$) (**1**), (μ_3-FcCHC)$FeCo_2(CO)_8$L [L = PPh_3 (**2**); $AsPh_3$ (**3**)] and (μ-FcC≡CH)$Co_2(CO)_5PPh_3$ (**4**) have been synthesized by facile substituted reactions. The crystal and molecular structures of **1**, **2** and **3** have been determined by single crystal X-ray analysis; the ligand dppm replaces two equatorial carbonyls from two $Co(CO)_3$ groups in the $FeCo_2$ core, and the ligands PPh_3 and $AsPh_3$ replace one equatorial carbonyl from a $Co(CO)_3$ group. The new compounds were characterized by IR, ^1H, ^{13}C, ^{31}P (for **1**, **2**) NMR and MS. The electrochemical properties for **1**, **2**, **3** and **5** were investigated and the results show that the replacement of CO alters the electron density on the cluster core $FeCo_2$ leading to a variety of interactions between $FeCo_2$ and the apical FcCHC, and making the Fe of the ligand FcCHC in clusters **1**, **2** and **3** turn into a redox center.
© 2005 Elsevier Ltd. All rights reserved.

Keywords: Mixed metal cluster; Substituted reaction; Molecular structure; Ferrocenylacetylide

1. Introduction

The site-selective substitution reactions of mixed-metal carbonyl clusters have attracted a great deal of interest since the 1970s [1–3]. Previous studies have shown that the carbonyls bound to cobalt centers are more prone to nucleophilic substitution by two electron donor ligands than the carbonyls bound to the metals Fe and Ru [4,5]. Alkyne and alkynyl species bearing a C≡C functional group belong to a class of surface species which may play a pivotal role in various catalytic reactions such as CO hydrogenation [6,7]. Metal carbonyl clusters bearing ferrocenylacetylide have been demonstrated to possess interesting redox properties [8] and electrocommunication [9]. The incorporation of the ferrocenyl group into clusters through an organic conjugated bridge would lead to some interesting electrochemical properties because both the ferrocenyl group and the transition-metal clusters can function as redox centers of electron transfer entities [10]. The parent cluster (μ_3-FcCHC)$FeCo_2(CO)_9$ (**5**) was obtained by the reaction of (μ-FcC≡CH)$Co_2(CO)_6$ with $Fe_2(CO)_9$ [11]. Although the syntheses and structures of ferrocenylacetylenic cluster compounds have been studied in some detail [12–14], there is as yet no report on the substitution reactions of the parent cluster **5**.

* Corresponding author. Tel./fax: +86 471 657 5796.
E-mail address: szj@imut.edu.cn (Q.-L. Suo).

0277-5387/$ - see front matter © 2005 Elsevier Ltd. All rights reserved.
doi:10.1016/j.poly.2005.01.018

We describe here the preparation and structural characterizations of four new substituted derivatives of **5**. The crystal and molecular structures of **1**, **2** and **3** were determined by X-ray diffraction, and their electrochemical properties investigated by cyclic voltammetry.

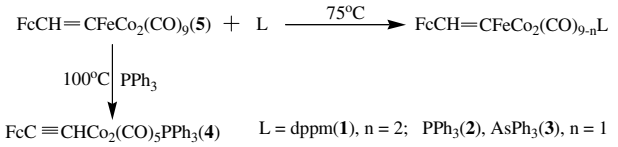
2. Experimental

All reactions and manipulations were carried out using standard Schlenk techniques under an atmosphere of pure nitrogen. Solvents were purified, dried and distilled under a nitrogen atmosphere prior to use. Reactions were monitored by TLC. Chromatographic separations and purification were performed on 200–300 mesh silica gel. Dppm, PPh_3 and $AsPh_3$ were purchased from Fluka. The starting material (μ_3-FcCHC)$FeCo_2(CO)_9$ (**5**) was prepared according to the literature method [11]. The new mixed metal carbonyl clusters **1**, **2**, **3** and **4** have been synthesized by facile substituted reactions (see Scheme 1).

IR spectra were recorded on a Nicolet FT-IR spectrometer with KBr discs. Elemental analyses were carried out on an Elementar var III-type analyzer. $^1H(^{13}C)$ NMR spectra in $CDCl_3$ were recorded on a Jeol-Jnm-Al 300FT-MHz spectrometer. ^{31}P NMR spectra in CH_2Cl_2 were recorded on a Bruker AC-500 NMR spectrometer. The mass spectra were determined using a Micromass LCT instrument. The electrochemical properties were determined using a BAS 100A-type analyzer. Melting points were determined with a XT-4 melting point apparatus.

2.1. Synthesis of (μ_3-FcCHC)$FeCo_2(CO)_7$dppm (**1**)

A toluene solution of (μ_3-FcCHC)$FeCo_2(CO)_9$ (100 mg, 0.156 mmol), dppm (60 mg, 0.156 mmol) and 11 mg Me_3NO was stirred for 24 h at 75 °C. The solvent of the resulting dark-green mixture was removed under vacuum. The residue was dissolved in a minimal amount of chloroform and was subjected to chromatographic separation on a silica gel column (2.0 × 40 cm). Elution with a mixture of hexane–benzene (1:1, v/v) afforded a dark-green brand (**1**). Crystals of **1** were obtained by recrystallization from hexane–CH_2Cl_2 at −20 °C. Yield: 31%, m.p.: 225 °C (decomposed). *Anal.* Calc. for $C_{44}H_{32}Co_2Fe_2O_7P_2 \cdot CH_2Cl_2$: C, 51.47; H, 3.24. Found: C, 51.35; H, 3.07%. IR (KBr disk): *ν*(CO) 2040s, 1995s, 1979vs, 1961s, 1929s cm^{-1}. ^1H NMR ($DCCl_3$, *δ*): 7.18–7.40 (m, 20H, C_6H_5), 6.68 (s, 1H, ≡CH), 3.83–4.24 (m, 9H, C_5H_5, C_5H_4), 2.17 (s, 2H, CH_2). ^{13}C NMR ($DCCl_3$, *δ*): 189.0, 176.6 (CO); 129.0, 130.1, 131.7 (C_6H_5); 104.3 (–C≡C–); 69.0 (C_5H_5, C_5H_4); 44.4 (–CH_2–). ^{31}P NMR (CH_2Cl_2, *δ*): 52.45, 45.90 (br, dppm). MS (ESI) 937 (M^+–CO).



Scheme 1.

2.2. Synthesis of (μ_3-FcCHC)$FeCo_2(CO)_8PPh_3$ (**2**)

A toluene solution of (μ_3-FcCHC)$FeCo_2(CO)_9$ (100 mg, 0.156 mmol), PPh_3 (41 mg, 0.156 mmol) and 11 mg Me_3NO was stirred for 12 h at 75 °C. The solvent of the resulting dark-green mixture was removed under vacuum. The residue was dissolved in a minimal amount of chloroform and was subjected to chromatographic separation on a silica gel column (2.0 × 40 cm). Elution with a mixture of hexane–benzene (1:1, v/v) afforded a dark-green brand. The crystals of **2** were obtained by recrystallization from hexane–CH_2Cl_2 at −20 °C. Yield: 38%, m.p.: 155 °C. *Anal.* Calc. for $C_{38}H_{25}Co_2Fe_2O_8P$: C, 52.41; H, 2.87. Found: C, 52.67; H, 2.96%. IR (KBr disk): *ν*(CO) 2041s, 1996vs, 1985s, 1977vs, 1946s, 1911w cm^{-1}. ^1H NMR ($DCCl_3$, *δ*): 7.15–7.48 (m, 15H, C_6H_5), 6.77 (s, 1H, ≡CH), 4.03–4.28 (m, 9H, C_5H_5, C_5H_4). ^{13}C NMR ($DCCl_3$, *δ*): 128.7, 130.0, 130.5, 133.2 (C_6H_5); 101.9 (–C≡C–), 69.2, 69.5 (C_5H_5, C_5H_4). ^{31}P NMR (CH_2Cl_2, *δ*): 49.78 (br, PPh_3). MS (ESI) 870 (M^+).

2.3. Synthesis of (μ_3-FcCHC)$FeCo_2(CO)_8AsPh_3$ (**3**)

A toluene solution of (μ_3-FcCHC)$FeCo_2(CO)_9$ (100 mg, 0.156 mmol), $AsPh_3$ (48 mg, 0.156 mmol) and 11 mg Me_3NO was stirred for 16 h at 75 °C. The solvent of the resulting dark-green mixture was removed under vacuum. The residue was dissolved in a minimal amount of chloroform and was subjected to chromatographic separation on a silica gel column (2.0 × 40 cm). Elution with a mixture of hexane–benzene (1:1, v/v) afforded a dark-green brand (**3**). Crystals of **3** were obtained by recrystallization in hexane–CH_2Cl_2 at −20 °C. Yield: 38%, m.p.: 154 °C. *Anal.* Calc. for $C_{38}H_{25}Co_2Fe_2O_8As$: C, 49.91; H, 2.74. Found: C, 50.26; H, 2.98%. IR (KBr disk): *ν*(CO) 2065s, 2020vs, 2003s, 1985s, 1972s, 1959s cm^{-1}. ^1H NMR ($DCCl_3$, *δ*): 7.26–7.48 (m, 15H, C_6H_5), 6.84 (s, 1H, ≡CH), 4.19–4.26 (m, 9H, C_5H_5, C_5H_4). ^{13}C NMR ($DCCl_3$, *δ*): 209.5 (CO); 129.0, 130.3, 132.8 (C_6H_5); 101.7 (–C≡C–); 69.3 (C_5H_5, C_5H_4). MS (ESI) 914 (M^+).

2.4. Synthesis of (μ-FcCCH)$Co_2(CO)_5PPh_3$ (**4**)

Synthesis of **4** follows the procedure described for **2**, with the exception of at 100 °C for 6 h instead of 75 °C for 12 h.Compound **4**: Yield: 14%, m.p.: 131 °C. *Anal.*

Calc. for $C_{35}H_{25}Co_2FeO_5P$: C, 57.55; H, 3.42. Found: C, 57.24; H, 3.91%. IR (KBr disk): ν(CO) 2057m, 2001vs, 1963s cm^{-1}. ^1H NMR ($DCCl_3$, δ): 7.14–7.29 (m, 15H, C_6H_5), 5.40 (s, 1H, ≡CH), 3.33–4.48 (m, 9H, C_5H_5, C_5H_4). ^{13}C NMR ($DCCl_3$, δ): 128.5, 128.7, 132.1, 133.7 (C_6H_5); 101.6 (–C≡C–), 69.2, 69.9 (C_5H_5, C_5H_4). MS (ESI) 730 (M^+).

2.5. X-ray crystallography of the new clusters 1, 2 and 3

Crystal data were measured at 20 °C on a Bruker SMART 1000 CCD for **1** and on a Bruker SMART APEX CCD for **2** and **3** with graphite monochromated Mo Kα ($\lambda = 0.71073$ Å) radiation. The cell refinement, data collection and reduction were done by Bruker SAINT and SMART [15]. An absorption correction based on SADABS was applied [16]. All structures were solved by direct methods [17]. All non-hydrogen atoms were refined by full matrix least-squares on F^2. Hydrogen atoms were located and refined by the geometry method. The structure solution and refinement were performed by SHELXSL97 [18]. The crystal data and details of measurements are summarized in Table 1.

3. Results and discussion

3.1. Synthesis and characterization of the new clusters

The reactions of the parent cluster **5** with dppm, PPh_3 and $AsPh_3$ ligands in toluene at 75 °C in the presence of trimethylamine oxide (Me_3NO) give the substituted derivatives (μ_3-FcCHC)$FeCo_2(CO)_7$dppm (**1**) and (μ_3-FcCHC)$FeCo_2(CO)_8L$ [L = PPh_3 (**2**); $AsPh_3$ (**3**)], respectively. The cluster (μ-FcC≡CH)$Co_2(CO)_5PPh_3$ (**4**) was obtained when the reaction temperature was accidentally increased up to 100 °C, and the same compound had been obtained by the replacement reaction of (μ-FcC≡CH)$Co_2(CO)_6$ with PPh_3 [19]. Trimethylamine oxide plays the role of an oxygen transfer agent and

Table 1
Crystal data and structure refinement for **1**, **2** and **3**

Identification code	**1**	**2**	**3**
Empirical formula	$C_{44}H_{32}O_7P_2Co_2Fe_2CH_2Cl_2$	$C_{38}H_{25}O_8PCo_2Fe_2$	$C_{38}H_{25}O_8AsCo_2Fe_2$
Formula weight	1049.12	870.11	914.06
Crystal system	monoclinic	monoclinic	monoclinic
Space group	$P2_1/n$	$P2_1/n$	$P2_1/n$
Unit cell dimensions			
a (Å)	21.077(8)	13.635(1)	13.744(1)
b (Å)	11.333(5)	10.450(7)	10.425 (1)
c (Å)	20.365(8)	25.297(2)	25.290(3)
α (°)	90	90	90
β (°)	111.513(1)	91.996(1)	91.942(2)
γ (°)	90	90	90
Volume (Å^3)	4525(3)	3602.1(4)	3621.6(6)
Z	4	4	4
Density (calculated) (Mg/m^3)	1.540	1.604	1.676
Absorption coefficient (mm^{-1})	1.586	1.790	2.643
F(000)	2120	1752	1824
Crystal size (mm)	0.400.20 × 0.10	0.67 × 0.29 × 0.26	0.68 × 0.51 × 0.37
θ Range for data collection (°)	2.38–25.00	1.67–28.35	2.11–28.41
Limiting indices	$-25 \leqslant h \leqslant 23$, $-13 \leqslant k \leqslant 9$, $-24 \leqslant l \leqslant 16$	$-17 \leqslant h \leqslant 14$, $-13 \leqslant k \leqslant 10$, $-32 \leqslant l \leqslant 33$	$-17 \leqslant h \leqslant 16$, $-13 \leqslant k \leqslant 13$, $-32 \leqslant l \leqslant 18$
Reflections collected	17454	21715	21739
Independent reflections	7642 (R_{int} = 0.1284)	8428 (R_{int} = 0.0600)	8499 (R_{int} = 0.1304)
Completeness to θ (%)	95.8	93.8	93.5
Maximum and minimum transmission	1.00000 and 0.520539	1.00000 and 0.71235	1.00000 and 0.40234
Data/restraints/parameters	7642/201/571	8428/0/560	8499/0/464
Goodness-of-fit on F^2	1.081	0.815	0.892
Final R indices [$I > 2\sigma(I)$]	R_1 = 0.0844, wR_2 = 0.1045	R_1 = 0.0365, wR_2 = 0.0628	R_1 = 0.0501, wR_2 = 0.1037
R indices (all data)	R_1 = 0.2254, wR_2 = 0.1467	R_1 = 0.0604, wR_2 = 0.0670	R_1 = 0.0709, wR_2 = 0.1096
Largest difference peak and hole (e Å^{-3})	0.731 and −0.943	0.449 and −0.316	1.034 and −1.545
Weighing scheme	$w = 1/[\sigma^2(F_o^2) + (0.0340P)^2 + 0.0000P]$, where $P = (F_o^2 + 2F_c^2)/3$	$w = 1/[\sigma^2(F_o^2) + (0.0187P)^2 + 0.0000P]$, where $P = (F_o^2 + 2F_c^2)/3$	$w = 1/[\sigma^2(F_o^2) + (0.0418P)^2 + 0.0000P]$, where $P = (F_o^2 + 2F_c^2)/3$

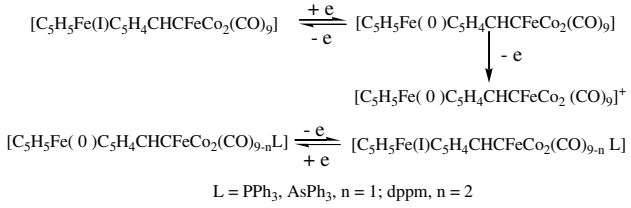
accelerates the substitution reaction [20]. The IR spectra of **1–4** indicate characteristic absorption of the terminal carbonyl ligand in the region 2065–1929 cm^{-1}. In comparison with the IR spectrum of the parent cluster **5** (2095, 2056, 2042, 2023, 2001, 1973 cm^{-1}), the CO absorption of the new clusters shift to lower frequencies and this is consistent with the fact that dppm and L ligands are stronger σ-electron donors and weaker π-electron acceptors than CO. The ^{1}H, ^{13}C, ^{31}P NMR reflect there are FcC≡CH, PPh_3, $AsPh_3$ and dppm ligands in new clusters, respectively. The clusters **1**, **2** and **3** more easily dissolve in polar solvents such as THF, chloroform and toluene than in non-polar solvents, and the cluster **4** is soluble in both non-polar solvents such as hexane and in polar solvents.

3.2. Electrochemical properties of the clusters *1, 2, 3 and 5*

The electrochemical properties of the clusters **1**, **2**, **3** and **5** have been studied by cyclic voltammetry at 298 K in a standard three-electrode system with NEt_4ClO_4 in CHCN solution as the supporting electrolyte. The results are given in Table 2.

The i_{pa}/i_{pc} and ΔE data of Table 2 show the clusters **1**, **2** and **3** undergo a quasi-reversible one-electron oxidation at 0.66, 0.63 and 0.65 V, respectively, which is slightly less than that of their parent cluster **5**. The smaller $E_{1/2}$ values for **1**, **2** and **3** relative to that of their parent cluster **5** suggests that the ligands dppm, PPh_3 and $AsPh_3$ are stronger σ-electron donors than CO. The ΔE and $E_{1/2}$ data for the parent cluster **5** and ligand FcC≡CH indicate that in **5** the first peak at 0.52 V corresponds to an irreversible one-electron oxidation on the cluster core $FeCo_2$ [3] and the second peak at 0.69 V to a quasi-reversible one-electron oxidation on Fe of the ligand FcCHC (see Scheme 2).

The electrochemical data show that the reduction–oxidation on Fe of the ligand FcCHC becomes easier with the replacement of CO by PPh_3, $AsPh_3$ or dppm. The replacement of CO alters the electron density on the $FeCo_2$ cluster core, leading to an interaction between $FeCo_2$ and FcCHC, turning Fe of the latter into a reduction–oxidation center.



Scheme 2.

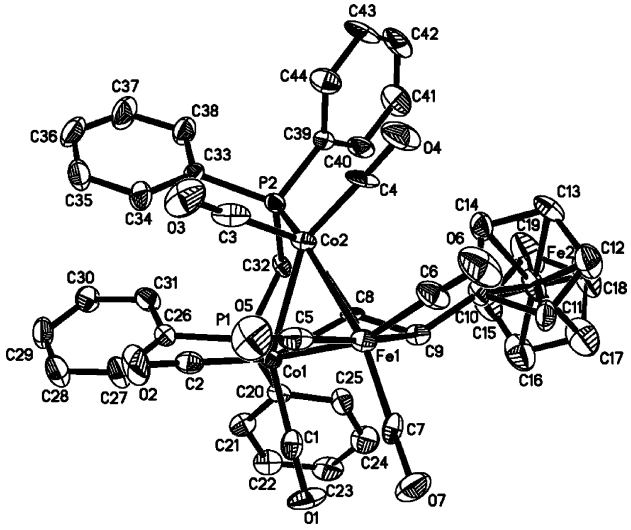


Fig. 1. Molecular structure of **1**.

3.3. Molecular structures of the clusters *1, 2 and 3*

Compounds **2** and **3** are isomorphous. The molecular structures of **1**, **2** and **3** were determined by X-ray single crystal analysis. Crystal data and relevant structural parameters are enumerated in Table 1. The structures, with the atom numbering scheme, of **1** and **3** are shown in Figs. 1 and 2, and selected bond lengths and angles are listed in Tables 3 and 4.

The molecular structures of **1** and **3** are similar to that of the parent cluster **5** [11], that is based on a ferrocenylacetylenic unit $FcC_BH{=}C_A$ and a $FeCo_2$ cluster core. The replacement of CO leads to a variety of interactions between the $FeCo_2$ cluster core and the ferrocenylacety-

Table 2
Voltammetric data[a]

Cluster	Reduction–first oxidation							Second oxidation	
	E_{pc}	E_{pa}	ΔE	$E_{1/2}$	$i_{pc}\times10^6$	$i_{pa}\times10^6$	i_{pa}/i_{pc}	E_{pa}	$i_{pa}\times10^6$
1	0.36	0.66	0.30	0.51	1.06	1.13	1.07		
2	0.32	0.63	0.31	0.48	1.62	2.25	1.39		
3	0.39	0.65	0.26	0.52	1.10	1.51	1.37		
5	0.49	0.69	0.20	0.59	1.67	1.91	1.14	0.52	3.05
R	0.53	0.83	0.30	0.68	3.85	5.01	1.30		

[a] Platinum electrode (Ag/Ag^+ standard) with 0.001 M TEAP at 20 °C in 100 mV scan rate. E_{pc} = cathodic peak potential (V); E_{pa} = anodic peak potential (V); $\Delta E = E_{pa} - E_{pc}$; $E_{1/2}$ = half-wave potential (V); i_{pc} = cathodic peak current (A); i_{pa} = anodic peak current (A). R: FcC≡CH.

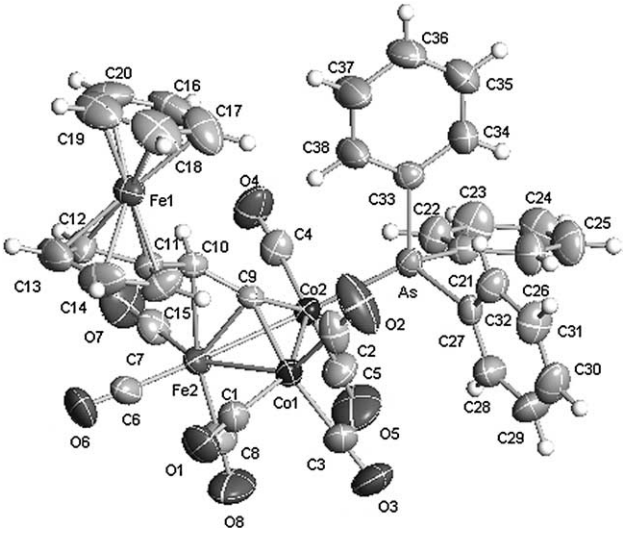


Fig. 2. Molecular structure of **3**.

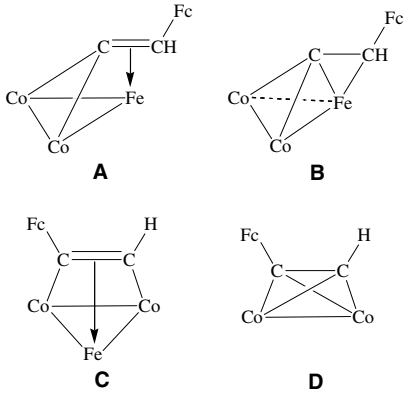
Table 3
Selected bond lengths [Å] and angles [°] for **1**

Bond lengths			
Co(1)–Co(2)	2.491(2)	Co(2)–C(8)	1.880(8)
Co(1)–Fe(1)	2.550(2)	Fe(1)–C(8)	1.975(8)
Co(1)–P(1)	2.211(3)	Fe(1)–C(9)	2.274(8)
Co(1)–C(8)	1.871(9)	P(1)–C(32)	1.828(8)
Co(2)–Fe(1)	2.550(2)	C(8)–C(9)	1.37(1)
Co(2)–P(2)	2.211(3)	C(9)–C(10)	1.49(1)
Bond angles			
Co(1)–Co(2)–Fe(1)	60.8(5)	C(32)–P(1)–Co(1)	109.1(3)
Co(1)–Fe(1)–Co(2)	58.5(5)	C(8)–Co(1)–Co(2)	48.5(2)
Co(2)–Co(1)–Fe(1)	60.8(5)	C(8)–Co(2)–Co(1)	48.2(3)
P(1)–Co(1)–Co(2)	97.7(8)	Co(1)–C(8)–Co(2)	83.2(1)
P(1)–Co(1)–Fe(1)	144.5(9)	Fe(1)–C(8)–C(9)	83.5(5)
P(2)–Co(2)–Co(1)	95.5(8)	Fe(1)–C(9)–C(8)	59.6(5)
P(2)–Co(2)–Fe(1)	146.4(9)	Fe(1)–C(9)–C(10)	117.5(6)
P(1)–C(32)–P(2)	110.9(4)	C(8)–C(9)–C(10)	128.4(8)

Table 4
Selected bond lengths [Å] and angles [°] for **3**

Bond lengths			
Co(1)–Co(2)	2.499(7)	Co(2)–C(9)	1.867(3)
Co(1)–Fe(2)	2.528(7)	Fe(2)–C(9)	1.966(3)
Co(1)–C(9)	1.878(3)	Fe(2)–C(10)	2.251(3)
Co(2)–Fe(2)	2.520(7)	C(9)–C(10)	1.362(5)
Co(2)–As	2.332(6)	C(10)–C(11)	1.460(5)
Bond angles			
Co(1)–Co(2)–Fe(2)	60.49(2)	C(9)–Co(2)–Co(1)	48.3(1)
Co(1)–Fe(2)–Co(2)	59.35(2)	Co(1)–C(9)–Co(2)	83.7(1)
Co(2)–Co(1)–Fe(2)	60.16(2)	Fe(2)–C(9)–C(10)	83.0(2)
As–Co(2)–Co(1)	101.70(2)	Fe(2)–C(10)–C(9)	60.1(2)
As–Co(2)–Fe(2)	159.63(3)	Fe(2)–C(10)–C(11)	114.4(2)
C(9)–Co(1)–Co(2)	47.9(1)	C(9)–C(10)–C(11)	127.8(3)

lenic unit in which the C_A–Co bond and C_B–Fe bond are slightly shorter than that of the parent cluster **5**. The pair of Co–Fe bonds and a Co–Co bond constitute an isosceles triangle. The C_A–Co(1) and C_A–Co(2) bond lengths (1.871 and 1.880 Å for **1**; 1.873 and 1.869 Å for **2**; 1.878 and 1.867 Å for **3**) are nearly equal, which is different from those of the parent cluster **5** (1.86 and 1.91 Å). The triangle C_ACo(1)Co(2) is also an isosceles triangle. The Fe–C_A and Fe–C_B (1.975 and 2.274 Å for **1**; 1.969 and 2.260 Å for **2**; 1.966 and 2.251 Å for **3**) bond lengths show that the apical $FcC_BH{=}C_A$ group is attached to the $FeCo_2$ core in coordination mode **A** rather than **B** or **C** (see Scheme 3). In **4** the coordination of the ferrocenylacetylenic unit $FcC_B{\equiv}C_AH$ with Co-Co adopts the **D** mode [19]. The C_A–C_B bond lengths of the apical $FcC_BH{=}C_A$ group in **1** (1.373 Å), **2** (1.376 Å) and **3** (1.362 Å), that is close to a C=C double bond, are longer than that in the parent cluster **5** (1.35 Å), which indicates the reinforcing interaction between Fe and the $C_A{=}C_B$ group. The Co(2)–As bond length (2.3324 Å) in **3** is longer than the average Co–P bond length (2.2208 Å) in **1** and **2** as expected from the different covalent radii of arsenic (1.21 Å) and phosphorus (1.10 Å). The new clusters **1**, **2** and **3** each have 48 cluster valence electrons in accordance with Lauher's rule.



Scheme 3.

4. Supplementary material

Crystallographic data for the structural analysis have been deposited at the Cambridge Crystallographic Data Center, CCDC Nos. 221861, 221864 and 221862 for complexes **1**, **2** and **3**, respectively. Copies of this information may be obtained free of charge from the Director, CCDC, 12 Union Road, Cambridge CB2 1EZ, UK (fax: +44 1223 336033; e-mail: deposit@ccdc.cam.ac.uk or on the web: http://www.ccdc.cam.ac.uk).

Acknowledgments

We are grateful to the Startup Foundation of China Scholar Abroad, the Inner Mongolia Talent Foundation and the Inner Mongolia Science Foundation for financial support of this work.

References

[1] R. Rossetti, G. Gervasio, P.L. Stanghellini, J. Chem. Soc., Dalton Trans. (1978) 222.
[2] P. Braunstein, J. Rose, D. Toussaint, Organometallics 13 (1994) 2472.
[3] Q.L. Suo, H. Zhang, Y.B. Wang, L. Wang, L.H. Weng, X.B. Leng, J. Organomet. Chem. 631 (2001) 87.
[4] P. Braunstein, J. Rose, P. Granger, J. Raya, S.E. Bouaoud, D. Grandjean, Organometallics 10 (1991) 3686.
[5] P. Braunstein, L. Mourey, J. Rose, P. Granger, T. Richert, F. Balegroune, D. Grandjean, Organometallics 11 (1992) 2628.
[6] E. Sappa, A. Tiripicchio, P. Braunstein, Coord. Chem. Rev. 65 (1985) 219.
[7] M.C. Chung, A. Sakural, M. Akita, Y. Moro-oka, Organometallics 18 (1999) 4684.
[8] A. Tarraga, P. Molina, D. Curiel, V.M. Desamparados, Organometallics 20 (2001) 2145.
[9] R.D. Adams, B. Qu, M.D. Smith, T.A. Albright, Organometallics 21 (2002) 2970.
[10] J.H.K. Yip, J.G. Wu, K.Y. Wong, K.W. Yeung, J.J. Vittal, Organometallics 21 (2002) 1612.
[11] S.L. Wu, E.R. Ding, Y.Q. Yin, J. Sun, J. Organomet. Chem. 570 (1998) 71.
[12] C.U. Pittman, L.R. Smith, J. Organomet. Chem. 90 (1975) 203.
[13] K.I. Hardeastle, A.J. Deeming, D. Nuel, N.I. Powell, J. Organomet. Chem. 375 (1989) 217.
[14] A.J. Deeming, M.S.B. Felis, D. Nuel, N.I. Powell, D.A. Tocher, K.I. Hardeastle, J. Organomet. Chem. 384 (1990) 181.
[15] Bruker, SMART and SAINT, Area Detector Control and Integration Software. Bruker Analytical X-ray Instruments Inc., Madison, WI, USA, 1998.
[16] G.M. Sheldrick, SADABS, Siemens Area Detector Absorption, Correction Software, University of Göttingen, Germany, 1997.
[17] G.M. Sheldrick, Acta Crystallogr., Sect. A 46 (1990) 467.
[18] Bruker, SHELXTL97, Bruker Analytical X-ray Instruments Inc., Madison, WI, USA, 1997.
[19] J.H. Ye, Q.L. Suo, Y.B. Wang, L.M. Han, X.B. Leng, Chin. J. Inorg. Chem. 20 (2004) 559.
[20] P. Braunstein, J. Rose, D. Toussaint, Organometallics 13 (1994) 2472.

Available online at www.sciencedirect.com
SCIENCE DIRECT®
Polyhedron 24 (2005) 765
POLYHEDRON
www.elsevier.com/locate/poly

Corrigendum

Corrigendum to: "Coordination geometries in bis(di-2-pyridylamine)copper(II) complexes. Crystal structures and spectroscopic properties of $[CuL_2(H_2O)_2](S_4O_6)$, $[CuL_2(CF_3SO_3)_2]$ and $[CuL_2(SO_4)]_2[CuL_2(H_2O)_2](PF_6)_2 \cdot 2H_2O$ (L = di-2-pyridylamine)" [Polyhedron 21 (2002) 247–253]

Sujittra Youngme [a,*], Narongsak Chaichit [b]

[a] *Department of Chemistry, Faculty of Science, Khon Kaen University, Khon Kaen 40002, Thailand*
[b] *Department of Physics, Faculty of Science and Technology, Thammasart University Rangsit, Pathumthani 12121, Thailand*

Received 22 February 2005
Available online 25 March 2005

The structure of the compound $[Cu(dpyam)_2(OH_2)_2](S_4O_6)$ (**1**) was refined in the non-centrosymmetric space group *Cc* (No. 9) (original CIF number CCDC-168976), $Z = 4$, but it better described in *C*2/*c* (No. 15), $Z = 4$ by adding the centre of symmetry. The coordinate translations are: $x' = x - 1/3$; $y' = y - 1/4$; $z' = z - 0.269$. Thus the original CIF file has been replaced by the correct CIF file with space group $P\bar{1}$ and the same CIF number (CCDC-168976).

The structure of the compound $[Cu(dpyam)_2(CF_3SO_3)_2]$ (**2**) was refined in the non-centrosymmetric space group *P*1 (No. 1) (original CIF number CCDC-168977), $Z = 1$ which is incorrect as omission of a centre of symmetry. The correct space group is $P\bar{1}$ (No. 2), $Z = 1$ and the coordinate transformations are: $x' = x - 0.328$; $y' = y - 0.465$; $z' = z - 0.364$. Thus, the original CIF file has been replaced by the correct CIF file with space group $P\bar{1}$ and the same CIF number (CCDC-168977).

DOI of original article: 10.1016/S0277-5387(01)00993-7.
* Corresponding author. Fax: +66 43 243 338.
E-mail address: sujittra@kku.ac.th (S. Youngme).

0277-5387/$ - see front matter © 2005 Elsevier Ltd. All rights reserved.
doi:10.1016/j.poly.2005.03.003

Available online at www.sciencedirect.com
SCIENCE DIRECT®
Polyhedron 24 (2005) 767
POLYHEDRON
www.elsevier.com/locate/poly

Corrigendum

Corrigendum to: "The coordination chemistry of dinitrato-di-2-pyridylamine copper(II). Crystal structures of catena-poly[[(di-2-pyridylamine)(nitrato-*O*,*O*′)copper(II)]-μ-nitrato-*O*:*O*′] and bis(nitrato-*O*,*O*′)(di-2-pyridylamine)copper(II) dihydrate" [Polyhedron 21 (2002) 943–950]

Sujittra Youngme [a,*], Narongsak Chaichit [b], Kannikar Damnatara [a]

[a] *Department of Chemistry, Faculty of Science, Khon Kaen University, Khon Kaen 40002, Thailand*
[b] *Department of Physics, Faculty of Science and Technology, Thammasart University Rangsit, Pathumthani 12121, Thailand*

Received 22 February 2005
Available online 25 March 2005

The structure of the compound [Cu(dpyam)-$(O_2NO)_2$] · $2H_2O$ (**2**) was refined in the non-centrosymmetric space group $P1$ (No. 1) (original CIF number CCDC-168989), $Z = 1$ which is incorrect as omission of a centre of symmetry. The correct space group is $P\bar{1}$ (No. 2), $Z = 1$ and the coordinate transformations are: $x' = x - 0.023$, $y' = y - 0.499$, $z' = z - 0.239$. Thus, the original CIF file has been replaced by the correct CIF file with space group $P\bar{1}$ and the same CIF number (CCDC-168989).

DOI of original article: 10.1016/S0277-5387(02)00857-4.
* Corresponding author. Fax: +66 43 243 338.
E-mail address: sujittra@kku.ac.th (S. Youngme).

0277-5387/$ - see front matter © 2005 Elsevier Ltd. All rights reserved.
doi:10.1016/j.poly.2005.03.002

Available online at www.sciencedirect.com
SCIENCE DIRECT®
Polyhedron 24 (2005) 769
POLYHEDRON
www.elsevier.com/locate/poly

Corrigendum

Corrigendum to: "The crystal structure and electronic properties of a *cis*-distorted octahedral CuN_4O_2 chromophore: $[Cu(dpyam)_2(OXO)]^+$, OXO = ONO^-, O_2CH^- and ONO^-" [Polyhedron 23 (2004) 1685–1694]

Sujittra Youngme [a,*], Pongthipun Phuengphai [a], Saksit Booncoon [a], Narongsak Chaichit [b]

[a] *Department of Chemistry, Faculty of Science, Khon Kaen University, Khon Kaen 40002, Thailand*
[b] *Department of Physics, Faculty of Science and Technology, Thammasat University Rangsit, Pathumthani 12121, Thailand*

Received 22 February 2005
Available online 25 March 2005

In Table 5 on page 1691 M–O(2) of the complex **6** should read 2.876 and not 2.076 as listed.
The figure (i) $[Cu(dpyam)_2(O_2CH)](BF_4)$ (**6**) in Fig. 4 on page 1690 is incorrect. The correct figure is:

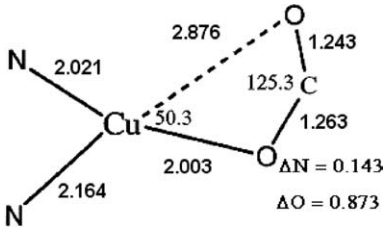


Fig. 4.

DOI of original article: 10.1016/j.poly.2004.03.020.
* Corresponding author. Fax: +66 43 243 338.
E-mail address: sujittra@kku.ac.th (S. Youngme).

0277-5387/$ - see front matter © 2005 Elsevier Ltd. All rights reserved.
doi:10.1016/j.poly.2005.03.004

Available online at www.sciencedirect.com
SCIENCE DIRECT®
Polyhedron 24 (2005) 771–776
POLYHEDRON
www.elsevier.com/locate/poly

Self-assembly of [M(Hida)$_2$] (Hida$^-$ = iminodiacetate; M = Pd and Pt) in a 2D supramolecular network via extensive hydrogen bonded interactions: Synthesis, X-ray crystal structure, spectroscopic and thermal studies

Jishnunil Chakraborty [a], Heike Mayer-Figge [b], William S. Sheldrick [b], Pradyot Banerjee [a,*]

[a] *Department of Inorganic Chemistry, Indian Association for the Cultivation of Science, 2A–2B Raja S. C. Mullick Road, Kolkata 700 032, India*
[b] *Lehrstuhl für Analytische Chemie, Ruhr-Universität Bochum, Universitätsstrasse 150, D-44780 Bochum, Germany*

Received 6 May 2004; accepted 20 September 2004
Available online 12 April 2005

Abstract

Two hydrogen-bonded palladium(II) and platinum(II) complexes, [Pd(Hida)$_2$] (**1**) and [Pt(Hida)$_2$] (**2**) (Hida$^-$ = iminodiacetate), have been synthesized and characterized by single crystal X-ray diffraction analyses. Hida$^-$ serves as a bidentate ligand coordinating to both Pd(II) and Pt(II) through its nitrogen and oxygen atom, exhibiting a square planar geometry with a *trans* configuration. The uncoordinated carboxylic group and the imino group of the ligand are involved in strong intermolecular hydrogen bonding to form a two dimensional layered network in both the complexes. The network is propagated along the *ac*-plane and stacks orthogonally to the *b*-axis. The thermogravimetric analyses for complexes **1** and **2** reveal stepwise decomposition processes indicating the probable decarboxylation of the free and bonded carboxylates. As there are two types of hydrogen bonding (N–H···O, O–H···O) present in both the complexes, two endothermic peaks regarding heat change are evident from their DSC diagrams.
© 2005 Elsevier Ltd. All rights reserved.

Keywords: Palladium(II) and platinum(II); Iminodiacetate; Crystal structures; Hydrogen bonded 2D network; Thermal studies; FAB mass spectra

1. Introduction

In the context of supramolecular assembly and crystal engineering, various types of interaction are being exploited to build up multi-dimensional networks [1–3]. Such compounds attain a special place due to their potential applications in the field of catalysis [4], non-linear optics [5,6], electrical conductivity [7], biological recognition [8] and molecular sieves [9]. A wide variety of extended networks can, however, be obtained by connecting metal complexes via non-covalent forces, e.g., strong (O–H···O, N–H···O) and weak (C–H···O) conventional H-bonds [10]. Infinite complexes involving acyclic and macrocyclic frameworks are often assembled through metal coordination of suitable bridging ligands [11]. The assembly process of these frameworks is highly influenced by a number of factors, e.g., the coordination nature of metal ions, the structural and functional characterization of organic ligands, the nature of the solvent, temperature and pH of the medium, the metal–ligand ratio, template and counter ions [12–14]. A subtle alteration in any of these factors might result in new complexes with different structural topologies and functions.

* Corresponding author. Tel.: +91 33 2473 4971; fax: +91 33 2473 2805.
E-mail address: icpb@mahendra.iacs.res.in (P. Banerjee).

0277-5387/$ - see front matter © 2005 Elsevier Ltd. All rights reserved.
doi:10.1016/j.poly.2004.09.033

Smith and Sawyer [15,16] have reported several 1:1 and 1:2 complexes of iminodiacetic acid (H_2ida) with Pd(II) and Pt(II). In the 1:1 complexes, H_2ida functions as a tridentate (N,O,O′) ligand with a chloride ion occupying the remaining site of the square-planar Pd(II) and Pt(II) centers. The 1:2 complexes are assigned the *trans* configuration, with each ligand forming one acetate ring. The results of a detailed study of their proton NMR spectra in D_2O as a function of pH and temperature have been summarized. Infrared spectra of the complexes have been measured to characterize their structures further. These complexes have not, however, been crystallographically characterized. Considering that carboxylic group ligands might adopt various coordination modes, and the proton in the carboxylic acid might be controlled by minor variation in reaction conditions, we have extended the study of complex formation of Pd(II) and Pt(II) with iminodiacetic acid which might assume supramolecular structures via both coordinate covalent bonds and hydrogen bonds as the building blocks. The successful synthesis and crystal structure elucidation of the complexes [Pd(Hida)$_2$] (**1**) and [Pt(Hida)$_2$] (**2**) have been achieved by us following a different route. The thermal behavior of the complexes has been studied by TG–DSC techniques that further support the extended layer structures formed through intermolecular hydrogen bonding interactions in the complexes.

2. Experimental

2.1. Materials

Palladium chloride ($PdCl_2$) and potassium tetrachloroplatinate(II) used in the palladium and platinum complexes were obtained from Arora-Matthey Limited (India). Potassium chloride and sodium hydroxide were purchased from Merck. Potassium tetrachloropalladate(II) was prepared by the reaction of $PdCl_2$ and KCl. Iminodiacetic acid was a Sigma product. Double distilled water was used throughout.

2.2. Physical measurements

Elemental analyses were carried out in a 2400 Series-II CHN analyzer, Perkin–Elmer, USA. IR spectra were recorded in a Nicolate Magna IR 750 Series-II IR spectrophotometer. The ^{1}H NMR spectra were recorded on a 300 MHz Bruker Avance DPX 300 machine, Switzerland in D_2O solvent with TMS as the internal standard. The TGA was done by a Mettler Toledo TGA/SDTA 851^e system. DSC was recorded on a Perkin–Elmer DSC 7 instrument. FAB mass spectra were recorded on a Fisons VG Autospec mass spectrometer with 3-nitrobenzyl alcohol as the matrix.

2.3. Synthesis of the compounds

2.3.1. Preparation of the monosodium salt of iminodiacetic acid, NaHida

Iminodiacetic acid (0.9 g, 7 mmol) was suspended in a minimum volume of water. To this mixture, NaOH (0.3 g, 7 mmol) was added and dissolved in 10 cm^3 water. The mixture was stirred magnetically for 30 min at 50 °C. The solution was then filtered to remove any suspended material. To the filtrate dehydrated ethanol was added slowly, thereby yielding the white crystalline monosodium salt of iminodiacetic acid, NaHida. It was filtered off and dried in air. Yield 80% (0.87 g). *Anal.* Calc. for $C_4H_6NO_4Na$: C, 30.9; H, 4.0; N, 9.0. Found: C, 30.8; H, 4.1; N, 9.2%.

2.3.2. Synthesis of trans-[Pd(Hida)$_2$] (*1*)

K_2PdCl_4 (0.1 g, 0.3 mmol) was dissolved in 15 cm^3 double distilled water to give a brown solution. To this solution, NaHida (0.05 g, 0.3 mmol) was added and dissolved in 10 cm^3 of double distilled water. The color changed from deep brown to yellow. The solution was stirred for 30 min, filtered to remove any suspended material and kept at room temperature for 5 days to produce pale yellow crystals of complex **1**. The crystals were filtered off, washed with water and then dried in air. The yield was 40% (0.013 g) based on Pd. *Anal.* Calc. for $C_8H_{12}N_2O_8Pd$: C, 25.9; H, 3.2; N, 7.6. Found: C, 25.8; H, 3.3; N, 7.3%.

2.3.3. Synthesis of trans-[Pt(Hida)$_2$] (*2*)

K_2PtCl_4 (0.1 g, 0.25 mmol) was dissolved in 15 cm^3 double distilled water to give a red solution. To this solution, NaHida (0.04 g, 0.25 mmol) was added and dissolved in 10 cm^3 of double distilled water. The color changed from red to light yellow. The solution was stirred for 30 min, filtered to remove any suspended material and kept at room temperature for 3 days to produce yellowish white crystals of complex **2**. The crystals were filtered off, washed with water and then dried in air. The yield was 50% (0.024 g) based on Pt. *Anal.* Calc. for $C_8H_{12}N_2O_8Pt$: C, 20.9; H, 2.6; N, 6.0. Found: C, 20.8; H, 2.7; N, 6.1%.

2.4. Crystal structure determination and structural refinement of complexes *1* and *2*

Single crystals of both **1** and **2** were grown from water. These were then mounted on, respectively, a Siemens P4 4-circle-diffractometer and an Oxford Diffraction Sapphire 2-CCD, both of which were equipped with graphite monochromated Mo Kα radiation ($\lambda = 0.71073$ Å). Unit cell dimensions and intensity data were measured at 293 K for both **1** and **2**. The structures were solved by direct methods and refined by full-matrix least-squares based on F^2 with anisotropic

Table 1
Crystal data and structure refinement for the complexes

Formula	$C_8H_{12}N_2O_8Pd$	$C_8H_{12}N_2O_8Pt$
Formula weight	370.62	459.28
Crystal system	monoclinic	monoclinic
Space group	$P2_1/c$	$P2_1/c$
a (Å)	6.1704(12)	6.1382(12)
b (Å)	9.805(2)	9.820(2)
c (Å)	9.4030(19)	9.4542(19)
β (°)	91.98(3)	91.38(3)
V (Å^3)	568.5(2)	569.7(2)
Z	2	2
D_{calc} (g/cm^3)	2.165	2.677
μ (mm^{-1})	1.674	12.357
$F(000)$	368	432
T (K)	293	293
λ (Å)	0.71073 (Mo Kα)	0.71073 (Mo Kα)
$\theta_{Min-Max}$ (°)	3.30–30.00	3.0–25.0
Number of unique data	1437	984
Observed data [$I > 2\sigma(I)$]	1108	766
Data/restraints/parameters	1437/1/89	984/1/92
Goodness-of-fit on F^2	1.046	1.125
Final R indices [$I > 2\sigma(I)$]	$R_1 = 0.0449$, $wR_2 = 0.1033$	$R_1 = 0.0544$, $wR_2 = 0.1299$
R indices (all data)	$R_1 = 0.0617$, $wR_2 = 0.1105$	$R_1 = 0.0670$, $wR_2 = 0.1406$

thermal parameters for non-hydrogen atoms using SHELXS-97 [17] (structure solution) and SHELXL-97 [18] (structure refinement). The hydrogen atoms were included in structure factor calculations at their idealized positions. Information concerning crystallographic data collection and refinement of the structures is summarized in Table 1.

3. Results and discussion

3.1. Synthesis and spectroscopic characterization of the complexes

It is worthy to note that the present methods of synthesis for both complexes are significantly different from those adopted by Smith and Sawyer [15,16] for the 1:2 complexes of palladium(II) and platinum(II) with iminodiacetate. The starting material for the palladium complex was palladium(II) nitrate, which was reacted with a twofold excess of iminodiacetic acid by warming briefly on a steam bath. The preparation of the corresponding platinum(II) complex involves heating an aqueous solution of K_2PtCl_4 with a fourfold excess of the ligand for several hours (>5).

Significant IR bands (KBr): 1586 sb (ν_{COO^-}) and 1734 sb (ν_{COOH}) cm^{-1} for **1**; 1598 sb and (ν_{COO^-}) 1734 sb (ν_{COOH}) cm^{-1} for **2**.

The ^{1}H NMR spectrum of NaHida in D_2O exhibits two singlets at 2.14 and 3.56 ppm. These correspond to N–H and the four protons of two $-CH_2$ groups, respectively. The ^{1}H NMR spectra of **1** and **2** were recorded in D_2O with TMS as an internal standard at 24 °C. The spectrum of **1** consists of two equally intense peaks with an AB pattern at 3.52 and 3.58 ppm (J_{AB} = 18.0 Hz) and a singlet at 3.22 ppm. The AB pattern, for the two types of acetate proton, and the singlet are assigned to the ring and free acetate protons, respectively, of the *trans* isomer.

The proton NMR spectrum of **2** also exhibits an AB pattern (δ_A = 3.99 ppm, δ_B = 3.97 ppm, J_{AB} = 6.8 Hz) for the ring acetate protons (J_{Pt-HA} = 7.05 Hz, J_{Pt-HB} = 6.78 Hz) and a singlet at 3.22 ppm for the free acetate protons. It may be noted that in neither of the spectra for **1** and **2**, could a N–H resonance or H–N–C–H coupling be noted owing to rapid N–H proton exchange.

The FAB mass spectra show single peak for each of the compounds. The one for the palladium(II) complex exhibits a mass peak centerd at *m*/*z* 371 (100%) $[M + H]^+$; this corresponds to a monomeric formulation based on ^{106}Pd. In the same way, the platinum(II) complex displays a peak at *m*/*z* 460 (100%) $[M + H]^+$ corresponding to a monomer based on the ^{195}Pt isotope.

3.2. Description of the structures of trans-[Pd(Hida)$_2$] and trans-[Pt(Hida)$_2$]

The crystal structure and atomic numbering scheme of *trans*-[Pd(Hida)$_2$] are shown in Fig. 1. Selected bond lengths and angles are given in the tables. As the data show, these molecules are mononuclear complexes with

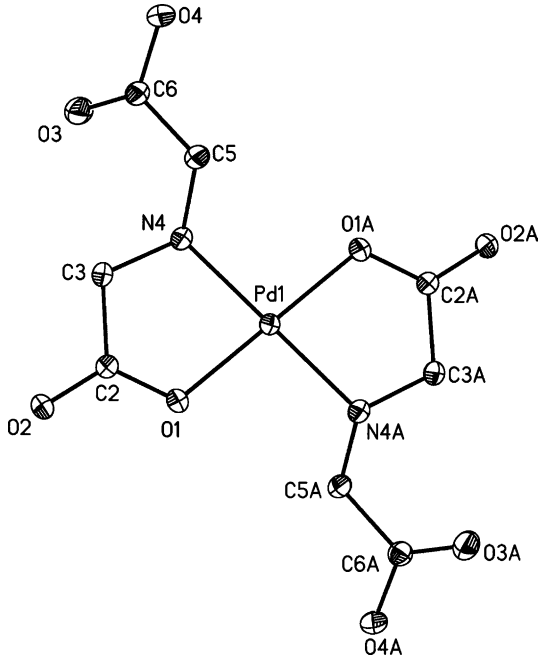


Fig. 1. ORTEP view of *trans*-[Pd(Hida)$_2$] (**1**), showing 30% probability thermal ellipsoids and the numbering scheme. H atoms are omitted for clarity.

a square planar coordination geometry around the Pd/Pt atom. The metal atom is located in the plane of two nitrogen (*trans*-N,N) and two oxygen atoms (*trans*-O,O) of the ligand molecules. The average Pd–N bond length in **1** is 2.061(4) Å, which is considerably larger than the value usually noted [19–21]. A comparable value of 2.059 Å is reported for the Pd(II) macrocycle having the 2-imino-4-thiobiuret [22] ligand, and the deviation might be attributed to the fact that the imino function is involved in hydrogen bonding. On the other hand, normal Pt–NH_2R bonds are in the range 2.03–2.06 Å [23–25] and match well with that observed here. The Pd–O and Pt–O distances (1.988(4) and 2.014(9) Å) are close to the literature values [21,26,27]. The O1–Pd1–O1a (a = $1-x$, $-y$, $-z$) and N4–Pd1–N4a bond angles are strictly 180°. The O1–Pd1–N4 bond angles of 84.1(2)° (83.6(3)° for **2**) within the chelate rings are normal compared to reported values [26,27]. It may be noted that in either of the complexes, the metal–nitrogen bond length is longer than that of the metal–oxygen, reflecting the greater *trans* influence of the N-atom compared to the O-atom of the ligand.

Fig. 2 shows the molecular packing for complex **1**, comprising of an infinite 2D chain in which the molecules in the crystal are held together by a system of hydrogen bonding. This packing is clearly affected by the intermolecular hydrogen bonding occurring between O4–H4···O2k (k = $1+x$, $1/2-y$, $-1/2+z$) and N4–H41···O2c (c = $1-x$, $-1/2+y$, $-1/2-z$) which is responsible for the conformation and stability of the layered network. This network lies in the *ac*-plane and stacks orthogonally to the *b*-axis. To achieve internal charge balance, the non-coordinated oxygen atoms O4 of each carboxylate group must be protonated (hydrogen atoms H4). The O2 atoms of the iminodiacetate groups of both **1** and **2** provide a hydrogen bond acceptor site for the hydrogen atoms H4 and H41 (from N4) from a neighboring formula unit. Other weak intermolecular hydrogen bonds C3–H31···O1h (h = x, $1/2-y$, $-1/2+z$), C3–H32···O3e (e = x, $1/2-y$, $1/2+z$) and C5–H51···O1a occur in complexes **1** and **2**. These are listed in Tables 2 and 3, with the widely accepted criteria that hydrogen bonds should be less than the sum of van der Waals radii of H and the acceptor atom. The values are comparable with those in other palladium and platinum complexes [20]. The shortest distance between two

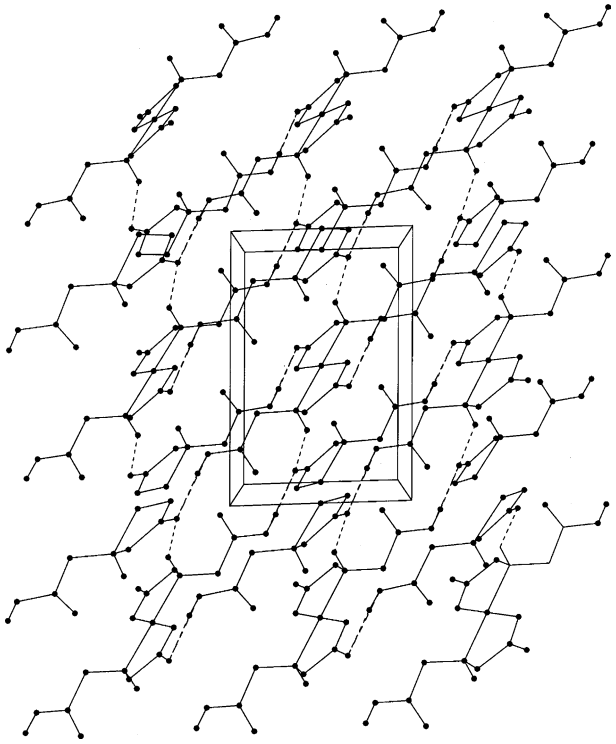


Fig. 2. Molecular packing of **1** showin the hydrogen bonded two-dimensional layer structure.

Table 2
Selected bond lengths (Å) and angles (°) in complex **1** with esds in parentheses[a]

Bond lengths (Å)			
Pd1–O1	1.988(4)	C2–O1	1.282(6)
Pd1–N4	2.061(4)	C6–O4	1.319(6)
Bond angles (°)			
O1–Pd1–N4	84.1(2)	O1–Pd1–O1a	180.0
O1a–Pd1–N4a	84.1(2)	N4–Pd1–N4a	180.0
Hydrogen bonds (Å, °)			
D–H···A	D···A	H···A	∠D–H···A
O4–H4···O2k	2.645(5)	1.84	168.2
N4–H41···O2c	3.041(6)	2.29	139.0
C3–H31···O1h	3.399(7)	2.45	165.9
C3–H32···O3e	3.200(7)	2.52	127.1
C5–H51···O1a	3.168(7)	2.58	119.1

[a] Symmetry transformations used to generate equivalent atoms: a = $1-x$, $-y$, $-z$; c = $1-x$, $-1/2+y$, $-1/2-z$; e = x, $1/2-y$, $1/2+z$; h = x, $1/2-y$, $-1/2+z$; k = $1+x$, $1/2-y$, $-1/2+z$.

Table 3
Selected bond lengths (Å) and angles (°) in complex **2** with esds in parentheses[a]

Bond lengths (Å)			
Pt1–O1	2.014(9)	C2–O1	1.272(16)
Pt1–N4	2.066(10)	C6–O4	1.305(15)
Bond angles (°)			
O1–Pt1–N4	83.6(4)	O1–Pt1–O1a	180.0
O1a–Pt1–N4a	83.6(4)	N4–Pt1–N4a	180.0
Hydrogen bonds (Å, °)			
D–H···A	D···A	H···A	∠D–H···A
O4–H4···O2k	2.637(13)	1.85	162.0
N4–H41···O2c	3.053(13)	2.31	139.0
C3–H31···O3	3.211(16)	2.52	128.0
C3–H32···O1h	3.428(15)	2.48	164.0
C5–H51···O1a	3.151(15)	2.57	119.0

[a] Symmetry transformations used to generate equivalent atoms: a = $1-x$, $-y$, $-z$; c = $1-x$, $-1/2+y$, $-1/2-z$; e = x, $1/2-y$, $1/2+z$; h = x, $1/2-y$, $-1/2+z$; k = $1+x$, $1/2-y$, $-1/2+z$.

Pd(II) centers lying in two adjacent sheets is 6.82 Å while that for the Pt(II) analogue is similar. The double layers of the complexes are held together by weak van der Waals' forces.

3.3. Thermal studies

The TGA diagram (Fig. 3) of complex **1** clearly shows three weight loss steps. The first mass loss in the region 220–260 °C corresponds to the loss of two CO_2 molecules from the free carboxylic acid groups of the complex. The observed weight loss of 23.76% is in agreement with the calculated one (23.74%). The second step (260–325 °C) is a composite one corresponding to the decarboxylation of the bound carboxylate and the –NH– groups. The third step (325–380 °C) involves complete decomposition of the complex. The final product is PdO. The total weight loss of 68.2% matches fairly with the calculated one (67.0%). The TGA curve of complex **2** indicates two main weight losses. The first one from 180 to 310 °C corresponds to the decarboxylation of the complex along with some organic decomposition indicating an observed weight loss of 29.4%. The second weight loss from 310 to 340 °C corresponds to the burning of the organic groups with a weight loss of 30.9%. The total weight loss of 60.4% matches with the calculated one (60.0%) if the final product is assumed to be undecomposed *trans*-[Pt(Hida)$_2$]. It is evident from this fact that the decomposition process is not complete.

The DSC thermogram of **1** at ambient pressure has been shown in Fig. 4. The thermogram clearly shows two endothermic peaks, which may indicate the presence of two types of intermolecular hydrogen bond in the complex. In the temperature range 83–116 °C, the peak temperature is 95.5 °C with $\Delta H = -0.56$ J g^{-1}. The other peak shows a heat change ($\Delta H = -0.58$ J g^{-1}) at the peak temperature 156.1 °C in the range 133–182 °C. It is obvious that the first heat change at the lower temperature corresponds to the dislodging of hydrogen bonds of the N4–H41···O2c linkage (H41···O2c = 2.29/2.30 Å) and the second one of the O4–H4···O2k linkage (H4···O2k = 1.84/1.85 Å). In the DSC diagram of complex **2** there are also two endothermic peaks, one with $\Delta H = -0.54$ J g^{-1} at the peak temperature 87.4 °C, and the other having $\Delta H = -0.87$ J g^{-1} at 160.5 °C. Due to the decrease of cell volume, the high-temperature molecular framework of both crystals is more compact, making the transition irreversible. This implies that the non-covalent (H-bonding) interaction plays a significant role in the formation of the 2D infinite sheet-like structure of the complexes.

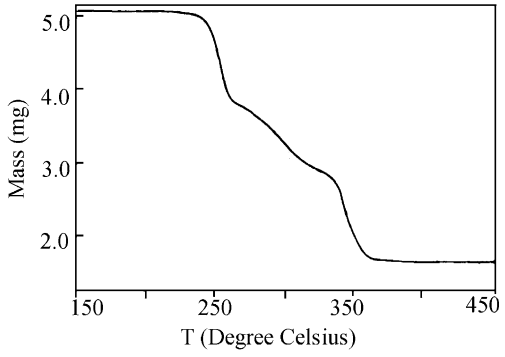


Fig. 3. Thermogram of **1** showing the three-step decomposition process.

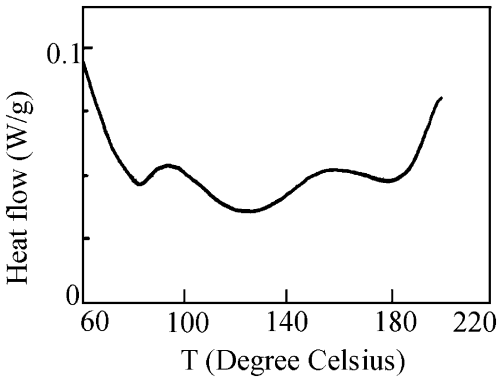


Fig. 4. DSC profile indicating two endothermic peaks showing the presence of hydrogen bonding in **1**.

4. Supplementary data

Full details of the crystal structure analyses of **1** and **2** have been deposited with the Cambridge Crystallographic Data Centre (CCDC Nos. 237476 and 237477). Copies may be obtained free of charge on application to the Director, CCDC, 12 Union Road, Cambridge CB2 1EZ, UK (fax (int. code): +44 1223 336 033, e-mail: deposit@ccdc.cam.ac.uk).

Acknowledgements

We thank Dr. A. Ghosh (Department of Chemistry, University of Calcutta) and Prof. A.K. Nandi (Polymer Science Unit, IACS, Kolkata) for assistance in getting the measurements of thermal studies.

References

[1] J.-M. Lehn, Supramolecular Chemistry: Concepts and Perspectives, VCH, Weinheim, 1995, p. 5.
[2] D. Braga, L. Maini, F. Grepioni, Angew. Chem., Int. Ed. Engl. 37 (1998) 2240.
[3] G.R. Desiraju, Acc. Chem. Res. 29 (1996) 441.

[4] K. Marioka, N. Murase, H. Yamamoto, J. Org. Chem. 58 (1993) 2938.
[5] S.M. LeCours, H.-W. Guan, S.G. DiMagno, C.H. Wang, M.J. Therien, J. Am. Chem. Soc. 118 (1996) 1497.
[6] S.L. Darling, E. Stulz, N. Feeder, N. Bampos, J.K.M. Sanders, New J. Chem. 24 (2000) 261.
[7] B.F. Hoskins, R. Robson, J. Am. Chem. Soc. 112 (1990) 1546.
[8] (a) M. Edgar, R. Mitchell, A.M.Z. Slawin, P. Lightfoot, P.A. Wright, Chem. Eur. J. 7 (2001) 5168;
(b) C.B. Aakeröy, A.M. Beatty, D.S. Leinen, K.R. Lorimer, Chem. Commun. (2000) 935.
[9] A. Yuan, J. Zou, B. Li, Z. Zha, C. Duan, Y. Liu, Z. Xu, S. Keizer, Chem. Commun. (2000) 1279.
[10] T. Steiner, Angew. Chem., Int. Ed. 41 (2002) 48.
[11] P.N.W. Baxter, in: J.-M. Lehn (Ed.), Comprehensive Supramolecular Chemistry, vol. 9, Pergamon Press, Oxford, 1996 (Chapter 5).
[12] (a) A.N. Khlobystov, A.J. Blake, N.R. Champness, D.A. Lemenovskii, A.G. Majouga, N.V. Zyk, M. Schröder, Coord. Chem. Rev. 222 (2001) 155;
(b) O.S. Jung, Y.J. Kim, Y.A. Lee, J.K. Park, H.K. Chae, J. Am. Chem. Soc. 122 (2000) 9921;
(c) M. Maekawa, H. Konaka, Y. Suenaga, T. Kuroda-Sowa, M. Munakata, J. Chem. Soc., Dalton Trans. (2000) 4160;
(d) R.H. Wang, M.C. Hong, W.P. Su, Y.C. Liang, R. Cao, Y.J. Zhao, J.B. Weng, Inorg. Chim. Acta 323 (2001) 139.
[13] (a) M. Scherer, D.L. Caulder, D.W. Johnson, K.N. Raymond, Angew. Chem., Int. Ed. 38 (1999) 1587;
(b) B.J.S. Johnson, R.C. Schroden, C. Zhu, A. Stein, Inorg. Chem. 40 (2001) 5972;
(c) A.J. Blake, N.R. Champness, P.A. Cooke, J.E.B. Nicolson, Chem. Commun. (2000) 665;
(d) J. Makarević, M. Jokić, B. Perić, V. Tomišić, B. Kojić-Prodić, M. Žinić, Chem. Eur. J. 7 (2001) 3328.
[14] (a) L. Pan, E.B. Woodlock, X. Wang, K.C. Lam, A.L. Rheingold, Chem. Commun. (2001) 1762;
(b) K.S. Min, M.P. Suh, J. Am. Chem. Soc. 122 (2000) 6834;
(c) O.S. Jung, S.H. Park, K.M. Kim, H.G. Jang, Inorg. Chem. 37 (1998) 5781.
[15] B.B. Smith, D.T. Sawyer, Inorg. Chem. 7 (1968) 1526.
[16] B.B. Smith, D.T. Sawyer, Inorg. Chem. 8 (1969) 379.
[17] G.M. Sheldrick, Acta Crystallogr., Sect. A 46 (1990) 467.
[18] G.M. Sheldrick, SHELXL-97: Program for Crystal Structure Refinement, University of Göttingen, Göttingen, Germany, 1997.
[19] S.O. Sommerer, A.J. Jircitano, B.L. Westcott, K.A. Abboud, J.A.K. Bauer, Acta Crystallogr., Sect. C 53 (1997) 707.
[20] M.A. Makhyoun, N.A. Al-Salem, M.S. El-Ezaby, Inorg. Chim. Acta 123 (1986) 117.
[21] S. Dey, P. Banerjee, S. Gangopadhyay, P. Vojtíšek, Transition Met. Chem. 28 (2003) 765.
[22] E. Doxiadi, R. Vilar, A.J.P. White, D.J. Williams, Polyhedron 22 (2003) 2991.
[23] C.J.L. Lock, P. Pilon, Acta Crystallogr., Sect. B 37 (1981) 45.
[24] F.D. Rochon, R. Melanson, M. Doyon, Inorg. Chem. 26 (1987) 3065.
[25] F.D. Rochon, R. Melanson, M. Doyon, Can. J. Chem. 67 (1989) 2209.
[26] N. Nagao, T. Kobayashi, T. Takayama, Y. Koike, Y. Ono, T. Watanabe, T. Mikami, M. Suzuki, T. Matumoto, M. Watabe, Inorg. Chem. 36 (1997) 4195.
[27] D.M.L. Goodgame, T.E. Müller, D.J. Williams, Polyhedron 14 (1995) 2557.

Available online at www.sciencedirect.com
SCIENCE DIRECT®
Polyhedron 24 (2005) 777–783
POLYHEDRON
www.elsevier.com/locate/poly

Solid-state ^{111}Cd NMR studies on cadmium(II)-2,*x*-pyridinedicarboxylates. Crystal structure of 2,4-pyridinedicarboxylato triaqua cadmium(II) hemihydrate: $[Cd(II)(2,4\text{-pydc})(H_2O)_3]\cdot 1/2H_2O$

Guillermo Mendoza-Díaz [a,*], Graciela Rigotti [b], Oscar E. Piro [b], Elsa E. Sileo [c]

[a] *Universidad de Guanajuato, Facultad de Química, Noria Alta s/n, Guanajuato, Gto. 36050, Mexico*
[b] *Departamento de Física, Facultad de Ciencias Exactas, Universidad Nacional de La Plata and and Instituto de Física de La Plata (CONICET), C. C. 67, 1900 La Plata, Argentina*
[c] *Departamento de Química Inorgánica, Analítica y Química Física, Facultad de Ciencias Exactas y Naturales, Universidad de Buenos Aires, Pabellón II, Ciudad Universitaria, C1428EHA, Buenos Aires, Argentina*

Received 30 September 2004; accepted 2 February 2005
Available online 13 April 2005

Abstract

The synthesis and characterisation by solid-state ^{111}Cd NMR of Cd(2,3-), Cd(2,4-), Cd(2,5-) and Cd(2,6-pyridinedicarboxylato)$\cdot x H_2O$ is reported. Results indicate that the ^{111}Cd NMR signal is very sensitive to the relative position of both carboxylates. Similar shifts (at 54.0 and 55.4 ppm) are found for the 2,4- and the 2,6-isomers where the carboxylates groups are *meta* to each other. For the 2,3- and 2,5-derivatives (carboxylates in *ortho* and *para* positions), the signals are detected at 119.6 and 84.2 ppm. The crystal and molecular structure of the seven-coordinated cadmium complex, $[Cd(2,4\text{-pyridinedicarboxylato})(H_2O)_3]\cdot 1/2H_2O$ is also reported. This data allows a correlation between Cd–O and Cd–N coordination and geometry with ^{111}Cd chemical shifts. Additional coupling between ^{111}Cd and ^{14}N in 2,3- (also found in 2,4-pydc) suggests only one N is coordinated to Cd. The anisotropy magnitude, $\Delta\sigma$, and the asymmetry parameter, η, are also analysed.
© 2005 Elsevier Ltd. All rights reserved.

Keywords: Solid-state ^{111}Cd NMR; Pyridinedicarboxylate; Lutidinate; Crystal structure

1. Introduction

Metal pyridinedicarboxylates have interesting properties in biological systems [1–4], and their presence seems to be related with metal-transport and cell membrane protection in some microorganisms [5,6]. These compounds are derived from pyridinedicarboxylic acids (H_2pydc) that form a series that includes the 2,3-, 2,4-, 2,5- and 2,6-pyridinedicarboxylic isomers. Cadmium forms 1:1 complexes with all four isomers and it may exhibit various coordination modes, depending on the relative position of the donor sites: the oxygen atoms from the two carboxylic groups and the nitrogen atom from the pyridinic ring. Because of the donor sites and the variety in relative positions, metal pyridinedicarboxylates may provide excellent models for less characterised samples of biological interest.

^{111}Cd NMR (more commonly ^{113}Cd NMR) spectroscopy is a sensitive probe of the Cd environment as the number and type of coordinating groups and the geometry around the metal ion can be correlated with the ^{111}Cd chemical shift. This signal is highly sensitive to oxygen

* Corresponding author. Tel.: +52 473 7320006; fax: +52 473 7330177.
E-mail address: mendozag@quijote.ugto.mx (G. Mendoza-Díaz).

0277-5387/$ - see front matter © 2005 Elsevier Ltd. All rights reserved.
doi:10.1016/j.poly.2005.02.007

and nitrogen atom coordination, and the technique is particularly useful in the study of biological compounds of different complexity. Furthermore, Cd(II) may be exchanged for other divalent metals, such as Zn(II), Ca(II), Cu(II) or Mg(II) in several biological compounds and thus this spectroscopic method provides a route for the study of a large variety of ligand–metal environments [7]. Also, some groups have been using ^{113}Cd NMR as a ''spin spy'' in Zn containing proteins, where the strategy is to replace Zn with Cd and use NMR to explore the metal environment in the protein [7,8].

When NMR spectroscopy data is collected in solution, the correlation between cadmium chemical shifts and the coordination number is pH and concentration dependent. On the contrary, solid-state NMR data overcomes the problems associated with the dynamics of fluid systems [9] and adds the advantage of providing the three principal components of the shielding tensor [10,11], rather than the average value normally obtained in solution. Thus, the chemical shift tensor obtained in the solid state is highly sensitive to the local environment of Cd atoms. The technique may be applied to insoluble compounds and the measured data may be correlated with crystallographic information, and structural predictions can be made for compounds of unknown structural characteristics.

In the present work, as a part of a general study of metal(II) pyridinedicarboxylates, we present the synthesis and the determination of the ^{111}Cd chemical shift by CP-MAS NMR under isotropic conditions of the insoluble 1:1 cadmium derivatives of the 2,3-; 2,4-; 2,5 and 2,6-pyridinedicarboxylic acids. We also report the main components of the ^{111}Cd chemical shift tensors using ^{111}Cd CP NMR under static rotor conditions. The crystal structure of [Cd(2,4-pyridinecarboxylato)-$(H_2O)_3$]·1/2H_2O is also presented, thus providing a good example for correlating Cd–O and Cd–N distances and geometry with ^{111}Cd chemical shift.

2. Experimental

2.1. Materials and characterisation of the solids

The ligands 2,3-; 2,4-; 2,5- and 2,6-pyridinedicarboxylic acid (Fluka Products) as well as all the other reagents (analytical-grade purity) were used as provided. Water was purified by a Millipore Milli-Q system yielding 18 MΩ cm. Elemental analyses (C, H, N) was performed on a Carlo Erba EA 1108 microanalyser. Water content in the samples was obtained from thermogravimetric analyses obtained using Shimadzu TGA-51H equipment with powdered samples of about 25 mg under an inert (N_2) atmosphere (temperature range 25–650 °C). Powder XRD data were collected on a Siemens D5000 diffractometer using graphite monochromated Cu Kα radiation.

All the compounds were prepared by adding 4 mL of a NaOH solution (1 M) and 2 mL of a $CdCl_2$ solution (1 M) to a suspension of each pyridinedicarboxylic acid (2.0×10^{-3} mol) in 100 mL of bidistilled water. The solids were obtained by slow evaporation of the solutions at 298 K; the colourless crystals formed were collected by filtration and washed with bidistilled water. Only crystals of the 2,4-pydc derivative were suitable for crystal structure determination.

Compound **1** *(Cd(2,3-pydc)·3H_2O)*. Calc. for $Cd(C_7H_3NO_4)\cdot 3H_2O$: C, 25.34; H, 2.71, N, 4.22; H_2O, 16.29. Found: C, 25.42; H, 2.85; N, 4.29; H_2O, 16.53%.

Compound **2** *(Cd(2,4-pydc)·3.5H_2O)*. Calc. for $Cd(C_7H_3NO_4)\cdot 3.5H_2O$: C, 24.67; H, 2.94, N, 4.11; H_2O, 18.51. Found: C, 24.84; H, 3.07; N, 4.30; H_2O, 19.30%.

Compound **3** *(Cd(2,5-pydc)·2H_2O)*. Calc. for $Cd(C_7H_3NO_4)\cdot 2H_2O$: C, 26.80; H, 2.23, N, 4.46; H_2O, 11.48. Found: C, 27.23; H, 2.36; N, 4.73; H_2O, 11.76%.

Compound **4** *(Cd(2,6-pydc)·1.5H_2O)*. Calc. for $Cd(C_7H_3NO_4)\cdot 1.5H_2O$: C, 27.59; H, 1.97, N, 4.59; H_2O, 8.86. Found: C, 27.66; H, 2.15; N, 4.73; H_2O, 8.81%.

3. Crystallography

X-ray measurements were made at 293(2) K on an Enraf-Nonius CAD-4 diffractometer with graphite-monochromated Mo Kα radiation (λ: 0.71073 Å) operating in a ω–2θ scanning mode, 3107 reflections were collected. Accurate unit cell parameters were determined from least-squares refinement of the $[(\sin\theta/\lambda)]^2$ values of 25 reflections in the 2θ range 22.08–35.38° (scan width $0.8 + 0.35\tan\theta$). Corrections for Lorentz-polarisation factors were applied to the intensity values. Absorption corrections were applied (maximum and minimum transmission factors of 0.867 and 0.708) [12]. The structure was solved by Patterson and Fourier methods and the final molecular model obtained by anisotropic full-matrix least-squares refinement of non-hydrogen atoms. Data reduction and correction structure solution and refinement programs used were SDP [13], SHELX-76 [14], SHELX-86 [15] and SHELX-93 [16]. The refinement method was full-matrix least-squares on F^2. The samples were colourless thin crystal plates, of about $0.08 \times 0.16 \times 0.20$ mm^3 that diffracted poorly. Only about 48% of the X-ray intensity data up to 0.76 Å resolution were above two standard deviations of measurement errors. All the H-atoms in the aromatic ring and four H-atoms of the bonded-to-Cd water hydrogen atoms were located in a difference Fourier map. However, only the pyridinic hydrogen atoms were included in the final model positioned on a stereochemical basis. They were refined with the riding model employing a common iso-

Table 1
Crystal data and structure refinement for $[Cd(2,4\text{-pydc})(H_2O)_3]\cdot 0.5H_2O$

Empirical formula	$C_7H_{10}NO_{7.5}Cd$
M	340.40
Crystal system	orthorhombic
Space group (number)	*Pbna* (60)
a (Å)	8.6744(9)
b (Å)	14.129(5)
c (Å)	17.265(5)
U (Å^3)	2116.0(9)
Z	8
D_c (g cm^{-3})	2.194
μ (mm^{-1})	2.097
F(000)	1376
θ Range (°)	2.36–27.99
hkl Ranges	0–1, 1–8, −1–22
Reflections: independent, observed	2172 [R_{int} = 0.035]; 1477
Data/restraints/parameters	2172/0/151
Final R indices [$I > 2\sigma(I)$]	R_1 = 0.042, wR_2 = 0.098
R_1 and wR_2 (all data)	0.079, 0.118
Goodness-on-fit on F^2	1.057
Largest differential peak and hole (e Å^{-3})	0.82[a] and −0.90

R indices defined as: $R_1 = \sum||F_o| - |F_c||/\sum|F_o|$, $wR_2 = [\sum w(F_o^2 - F_c^2)^2/\sum w(F_o^2)^2]^{1/2}$.
[a] Close to the cadmium atom position.

tropic displacement parameter that in the final run converged to $U = 0.03(1)$ Å^2.

Supplementary material available: table of atomic coordinates, anisotropic thermal parameters, bond lengths and angles, hydrogen atom positions and H-bond distances and calculated and observed structure factor amplitude. Crystallographic data and processing parameters are summarised in Table 1.

4. Cadmium-111 NMR spectroscopy

The ^{111}Cd solid-state NMR spectra of compounds **1**–**4** were recorded on a VARIAN Unity-plus 300 MHz spectrometer using cross-polarisation (CP), magic-angle spinning (MAS) and high power dipolar decoupling. $Cd(CO_3)$, (−30 ppm) was used as a reference [17]. The sample was inserted into a 7 mm silicon nitride rotor. In a typical collection of the isotropic spectra, the relevant parameters employed were: spin rate 5000 Hz, contact time of 2.0 ms, delay time of 4 s, between 258 and 1032 scans were recorded. 7.8 μS of pulse width (90° pulse). For static measurements, the number of scans were increased to a minimum of 6000. All other parameters were kept as previously described.

5. Results and discussion

5.1. Crystallographic structural results

The solid is polymeric and crystallises in the centrosymmetric space group *Pbna*. Selected bond lengths and angles are grouped in Table 2. Fig. 1 is an ORTEP [18] drawing of the complex showing the labelling of the non-hydrogen atoms and their displacement ellipsoids. To complete the environment around Cd(II) and to show the connectivity of the polymeric structure in the unit cell, a symmetry related $[Cd(II)(2,4\text{-pydc})(H_2O)_3]$ molecule through the glide plane operation $x - 1/2$, y, $1/2 - z$ has been included in the plot.

The Cd(II) ion is seven-coordinated by two 2,4-pyridinedicarboxylate groups and three water molecules; an interstitial H_2O molecule, O(4W) is not bounded to Cd. The coordination polyhedron exhibits a geometry that can be described as a distorted pentagonal bipyramid. The equatorial plane is formed by a nitrogen atom and one oxygen (O(4)) from the 2-carboxylate group of the aromatic ring, two oxygen atoms (O(3)′ and O (4)′) both from a neighbouring 2-carboxylate group and an oxygen (O(3W)) from a water molecule. Two H_2O li-

Table 2
Selected bond distances (Å) and angles (°) for $[Cd(2,4\text{-pydc})(H_2O)_3]\cdot 0.5H_2O$

Cd–O(1W)	2.259(5)	O(1W)–Cd–O(2W)	177.1(2)
Cd–O(2W)	2.310(5)	O(1W)–Cd–N	92.5(2)
Cd–O(3W)	2.305(5)	O(1W)–Cd–O(4)	93.7(2)
Cd–N	2.366(6)	O(1W)–Cd–O(4)#1	83.3(2)
Cd–O(4)	2.347(5)	O(4)–Cd–N	69.9(2)
Cd–O(3)#1	2.364(5)	O(3W)–Cd–N	83.2(2)
Cd–O(4)#1	2.567(5)	O(3W)–Cd–O(4)#1	75.3(2)
C(1)–C(6)	1.523(8)	O(3)#1–Cd–O(4)#1	52.4(2)
C(6)–O(3)	1.235(8)	O(4)–Cd–O(3)#1	80.5(2)
C(6)–O(4)	1.240(8)	O(3)–C(6)–O(4)	123.9(6)
C(3)–C(7)	1.540(9)	O(1)–C(7)–O(2)	126.8(7)
C(7)–O(1)	1.243(9)	C(7)–O(2)	1.254(8)

Symmetry transformations used to generate equivalent atoms: (#1) $x - 1/2$, y, $-z + 1/2$; (#2) $x + 1/2$, y, $-z + 1/2$.

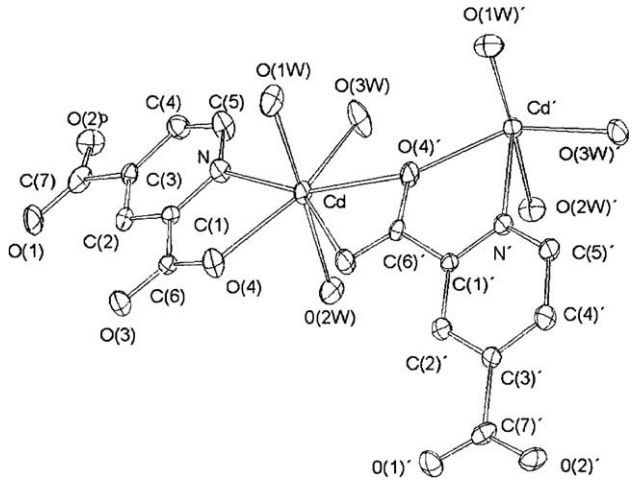


Fig. 1. ORTEP drawing of $[Cd(2,4\text{-pydc})(H_2O)_3]\cdot 0.5H_2O$ showing the non-H atoms labelling and their displacement ellipsoids at 30% probability. The crystallisation water molecule is not included in the plot.

gands, O(1W) and O(2W), are found in the axial positions. The equatorial plane around Cd presents an elongation in the Cd–O(4) direction as shown by the distances Cd–O(3W) = 2.305(5) Å, Cd–N = 2.366(6) Å, Cd–O(3′) = 2.364(5) Å and Cd–O(4) = 2.567(5) Å.

Although several other polymeric hepta-coordinated cadmium(II) carboxylate complexes have been reported, the more striking feature of this compound is that neither of the two oxygen atoms from the 4-carboxylate group are bonded to the metal ion, forming a pendant $-RCOO^-$ group. This fact is perhaps responsible for the formation of zigzag chains of –Cd(II)–O(4)–Cd(II)– in which the Cd(II) ions are bonded through its equatorial planes (see Fig. 2), thus determining a polymeric structure where the chains run approximately in the crystallographic *a*-direction (angle Cd–O(4)–Cd#2 = 151.1(2)°). Similar Cd–O–Cd links have been found in some parts of the structures of the three-dimensional polymeric compounds cadmium(II) malonate monohydrate [19], cadmium diacetate [20] and cadmium maleate [21,22].

The pyridinic ring and the carboxylate groups in the 2- and 4-positions are almost coplanar (angle O(2)–C(7)–C(3)–C(4) = 6.7° and angle O(4)–C(6)–C(1)–N = 6.4°), the organic moieties are arranged in layers, which are parallel to the (*ac*)-crystallographic plane. The C–O bond lengths in the 2-carboxylate are shorter than in the pendant 4-carboxylate, compare distances C(6)–O(3) = 1.235(8) Å and C(6)–O(4) = 1.240(8) Å with distances C(7)–O(1) = 1.243(7) Å and C(7)–O(2) = 1.254(8) Å, respectively; angles are also smaller, angle in 2-carboxylate O(3)–C(6)–O(4) = 123.9(6)° and angle in 4-carboxylate O(1)–C(7)–O(2) = 126.8(7)°, this may be attributable to the fact that the carboxylate in the 4-position is not coordinated to Cd thus it is supporting a larger electronic density.

Interaction between layers is mainly through hydrogen bonds provided by the interstitial O(4W) water molecule that bridges the O(1) from one layer to the O(3W) from a layer below. The O(4W) is on a two fold rotation axis, distances and angle in the bridge are, O(4W)–O(3W) = 2.826(6) Å, O(4W)–O(1) = 2.735(7) Å and O(3W)–O(4W)–O(1) = 105.7(2)°. Hydrogen bonding among layers is completed through O(3W) interaction with O(3) and O(4W) and O(1) and O(2) with axial groups O(W1) and O(W2).

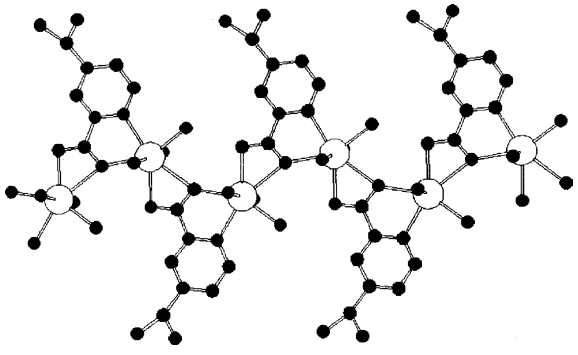


Fig. 2. Plot of the [Cd(2,4-pydc)(H_2O)$_3$] complex showing the zigzag arrangement of the Cd ions in the crystal.

5.2. Cadmium-111 NMR spectroscopy

The CP MAS ^{111}Cd NMR spectra of the powdered samples are shown in Fig. 3. The resonance signals for the compounds Cd(2,3-), Cd(2,4-), Cd(2,5-) and Cd(2,6-pydc)·$x$$H_2O$, are detected at 119.6, 54.0, 84.2 and 55.4 ppm, respectively. Similar shifts at lower frequencies, 54.0 and 55.4 ppm, are measured for the 2,4- and the 2,6-isomers (the carboxylates groups are *meta* to each other); whereas shifts measured at 119.6 and 84.2 ppm, differ considerably for the 2,3- and 2,5-derivatives (the carboxylates groups are *ortho*- and *para*-, respectively). Also, a splitting of the signal is detected for the 2,3- and 2,4-pydc derivatives. This fact is due to a quadrupolar interaction and scalar coupling between ^{111}Cd and ^{14}N (I(^{111}Cd) = 1/2 and I(^{14}N) = 1) that are not completely removed by magic-angle spinning.

According to Olivieri et al. [23], the signal resulting from ^{111}Cd quadrupolar coupled to ^{14}N with MAS is a doublet with a splitting of

$$S_1 = \frac{9\chi D}{20Z}\left(3\cos^2\beta_{CdN} - 1 + \eta\sin^2\beta_{CdN}\cos 2\alpha_{CdN}\right),$$

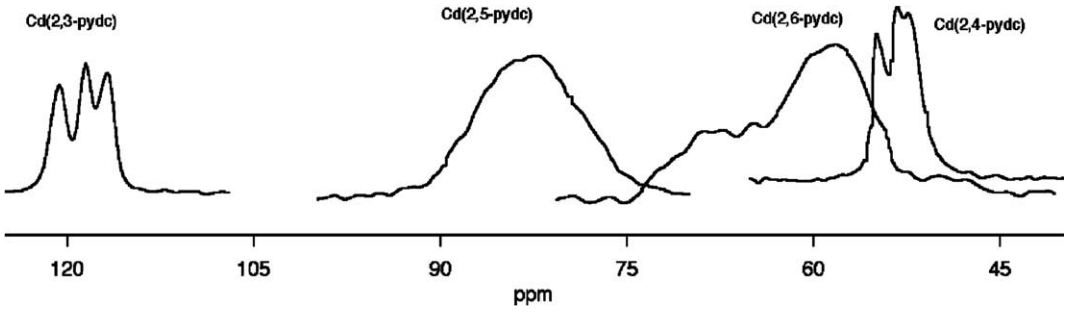


Fig. 3. CP-MAS ^{111}Cd NMR spectra of the cadmium complexes with the different 2,*x*-pyridinedicarboxylates. The splitting due to residual dipolar and the J coupling between ^{111}Cd and ^{14}N is observed in the 2,3-pydc and 2,4-pydc complexes.

where $D = \gamma_{Cd}\gamma_N h/4\pi^2 r^3$ is the dipolar coupling between ^{111}Cd and ^{14}N, Z is the Zeeman energy of ^{14}N, χ is the quadrupole coupling constant, η is the asymmetry in the quadruple coupling tensor, and α and β are the polar and azimuthal angles that define the orientation of the Cd–N bond with respect to the principal axis of the electric field gradient tensor. The magnitude of the splitting is strongly dependent on the internuclear Cd–N distance.

When, in addition to the dipolar (and quadrupolar) interaction, the z-direction of the J tensor and the internuclear direction of Cd–N are coincident, a new contribution from the anisotropy of the J tensor (called J-coupling) is also detected, and an additional ΔJ term must be included in the previous equation [24]:

$$S = \frac{9\chi(D - \Delta J/3)}{20Z}\left(3\cos^2\beta_{CdN} - 1 + \eta\sin^2\beta_{CdN}\cos 2\alpha_{CdN}\right).$$

Thus, if a nitrogen atom is coordinated to only one cadmium atom, a splitting into three signals with separations of $J + S$ and $J - S$ may be observed. The observation of this splitting of the signal gives an immediate determination of the number of bonded nitrogen atoms.

The triplets detected in the 2,4-pydc and 2,3-pydc derivatives confirm that both compounds present the Cd atom coordinated to only one N. This result agrees with the crystal structure resolution of [Cd(2,4-pydc)-$(H_2O)_3$]·1/2H_2O (this paper), where the Cd atom is hepta-coordinated (vide supra) and with preliminary structural studies on Cd(2,3-pydc)·3H_2O [25] that show the Cd ion is hexa-coordinated in a trigonal antiprismatic geometry, surrounded by one N, two O (from different carboxylate groups) and three water molecules.

The measured J-coupling between ^{111}Cd and ^{14}N are J_{Cd-N} = 87.8 Hz, S = 22.8 Hz and J_{Cd-N} = 123.5 Hz, S = 19.5 Hz for the 2,4-pydc and 2,3-pydc, respectively. These data indicate a stronger coupling in the 2,3-derivative and consequently a shorter Cd–N distance (calculated Cd–N distances in 2,3- and 2,4- are 2.311 and 2.366(6) Å respectively).

The static CP NMR spectra present only a broad signal for all the compounds. The detected broadening of the signals is mainly due to the anisotropy of the chemical shift. All the broadening that normally comes from the proton-cadmium dipolar coupling is almost completely removed in CP-experiments (by the high power decoupling). Considering that the broadening effect is mainly due to the anisotropy in the chemical shift, the measured signals can be decomposed into three Lorentzians curves from which the diagonal components of the anisotropy tensor, σ_{11}, σ_{22} and σ_{33}, can be obtained. Fig. 4 shows the spectrum and the deconvoluted signals for Cd(2,5-pydc). The anisotropy magnitude, $\Delta\sigma$, and the asymmetry parameter, η, were also calculated for all compounds.

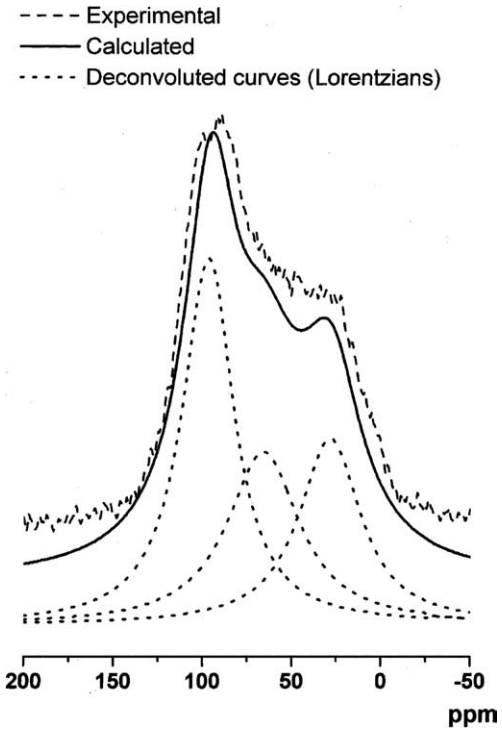


Fig. 4. Experimental and calculated spectrum of Cd(2,5-pydc) obtained from the sum of three deconvoluted Lorentzian components. Each of those components is assigned to the components of the chemical shift anisotropy tensor (see Table 3).

Summarised in Table 3 are the isotropic chemical shifts obtained by CP-MAS as well as those obtained from the equation $\delta_{iso(calc)} = \sigma_{11} + \sigma_{22} + \sigma_{33}$, the principal components of the shielding tensors, the chemical shift anisotropy ($\Delta\sigma$) and the asymmetry parameters, η, of the four 2,x-pydc derivatives studied here. A nice agreement between the experimental δ_{iso} and the calculated value is observed. The absolute differences are Cd(2,3-pydc): 1.98 ppm, Cd(2,4-pydc): 1.11 ppm, Cd(2,5-pydc): 7.8 ppm and Cd(2,6-pydc): 1.98 ppm, but even for the biggest difference the simulated spectrum is in good agreement with the experimental spectrum as can be seen in Fig. 4. These line shape analyses of the powder patterns, indicate differences in the shielding anisotropy of these pyridine-dicarboxylates, however information about the orientation of the tensor in a molecule fixed axis system cannot be determined. This can be done using single crystal NMR, which has also the advantage of having about 5 times more sensitivity than the powder technique [26]. Unfortunately, in this study, the size of the crystals was good for X-ray studies but still too small for a good NMR study.

The anisotropy magnitude $\Delta\sigma$ follow the order: Cd(2,3-pydc) (antiprism) > Cd(2,6-pydc) > Cd(2,5-pydc) > Cd(2,4-pydc) (hepta-coordinated), indicating that the 2,3-derivative shows the larger distortion around the

Table 3
Diagonal components of the shift tensors, chemical shift anisotropies ($\Delta\sigma$) and asymmetry parameters, η, for the Cd(2,*x*-pydc) compounds

Compound[a]	σ_{11} (ppm)	σ_{22} (ppm)	σ_{33} (ppm)	$\delta_{iso(exp)}$ (ppm)	$\delta_{iso(calc)}$ (ppm)	$\Delta\sigma$[b]	η[c,*]	η_{csa}[#]
Cd(2,4-pydc)	90.38	47.64	27.39	54.03	55.14	41.62	0.64	1.54
Cd(2,6-pydc)	136.30	46.39	−10.54	55.40	57.38	101.89	0.78	1.32
Cd(2,5-pydc)	104.94	78.26	46.00	84.20	76.40	45.60	0.91	0.88
Cd(2,3-pydc)	181.13		2.7	119.67	121.65	178.43	1	0

[a] Values for compounds reported previously are referred to $Cd(ClO_4)_2$ 0.1 M. Values for compounds reported in this study are referred to $Cd(CO_3)$, (−30.0 ppm).
[b] $\Delta\sigma$ is the anisotropy magnitude: $\Delta\sigma = -\delta_{33} + 0.5(\delta_{11} + \delta_{22})$.
[c] η or η_{csa} is the asymmetry parameter.
[*] Calculated [26] as $\eta = 1 - |(\delta_{33} - 2\delta_{22} + \delta_{11})/(\delta_{33} - \delta_{11})|$.
[#] Calculated [25] as $\eta_{csa} = (\delta_{11} - \delta_{22})/((\delta_{11} + \delta_{22} + \delta_{33})/3 - \delta_{33})$.

cadmium ion. The same compound shows $\sigma_{11} = \sigma_{22}$ and therefore $\eta = 1$, which means that the tensor, and consequently Cd(2,3-pydc), present an axial symmetry [27]. Other authors employ different expressions where $\eta = 0$ has the same meaning (see footnote on Table 3) [28]. The magnitude of $\Delta\sigma$ (178 ppm) also indicates a very elongated complex as found in the structural resolution. On the contrary, Cd(2,4-pydc) shows a smaller η value (0.64), this fact also agrees with the structures of both compounds.

The ^{111}Cd chemical shifts differ for the various Cd(2,*x*-pydc) compounds. The δ_{iso} values encountered for the 2,6-pydc and the seven-coordinated 2,4-pydc derivatives suggest that the derivatives with carboxylates groups *meta* to each other cause similar chemical shifts. The η value of the former complex indicates that the complex has a higher symmetry than the 2,4-pydc derivative, which is a more rhombic distorted. The magnitude of the anisotropy, on the other hand, is bigger for the 2,6-pydc compound and predicts that some of the bonds in the complex should be very elongated. The 2,3-pydc isomer (two carboxylates in an *ortho*-position) show the highest δ_{iso} values (119.6 ppm). Although published data [7] indicate that δ_{iso} is shifted to higher fields when the coordination number is increased, the crystal structure of Cd(2,3-pydc) rules out this trend and the increase in δ_{iso} can only be explained by the relative position of the two carboxylate groups.

Also, the intermediate value of δ_{iso} encountered for 2,5-pydc (84.20 ppm) cannot be ascribed to a difference in coordination number, and it may be only related to the *para*-position of the carboxylate groups. The η value (0.9) of 2,5-pydc indicates axial symmetry.

6. Conclusions

Solid-state ^{111}Cd is a sensitive probe in insoluble cadmium pyridinedicarboxylates and the signals are related to the position of the second carboxylate group. The technique provides information on the chemical shifts anisotropy and ^{14}N coupling that may reveal the cadmium environment. The smallest values for δ_{iso} are found for the 2,4- and 2,6-isomers (carboxylates in *meta*-positions to each other), and highest value is found in the 2,3-isomer (carboxylates in the *ortho*-position). The calculated $\Delta\sigma$ values follow the trend Cd(2,3-pydc) > Cd(2,6-pydc) > Cd(2,5-pydc) > Cd(2,4-pydc), indicating that the 2,3-derivative shows the larger distortion around the cadmium ion. However, a study of single crystals of this family could help to better understand the relationship between magnetic and geometric anisotropy.

7. Supplementary material

Crystallographic data have been deposited with the CCDC. Copies of this information may be obtained free of charge from The Director, CCDC, 12 Union Road, Cambridge CB2 1EZ, UK (fax: +44 1223 336033, e-mail: deposit@ccdc.cam.ac.uk or www: http://www.ccdc.cam.ac.uk) quoting the deposition number CCDC JV/CCDC 176923.

Acknowledgements

This work was partially supported by the Universidad de Buenos Aires (Grant TX80) and the Consejo Nacional de Investigaciones Científicas y Técnicas (CONICET) of Argentina. The X-ray diffraction experiments were carried out at the National Diffraction Laboratory (LANADI), La Plata, Argentina. G.R. is member of the Carrera del Investigador Científico de la Comisión de Investigaciones Científicas de la Pcia. de Buenos Aires.

References

[1] C. Dette, H. Waertzig, H. Uhl, Pharmazie 48 (1994) 276.
[2] H. Taguchi, Vitamin (1997) 71.
[3] H. Taguchi, M. Maeda, H. Nishitani, K. Okumura, Y. Shimabayashi, K. Iwai, Biosci. Biotechnol. Biochem. (1992) 56.

[4] M. Hiroshi, N. Maki, O. Hiroshi, S. Kotsumi, S. Yoshide, I. Kazno, Biotechnol. Biochem. 56 (1992) 1921.
[5] B. Setlow, P. Setlow, Appl. Envir. Microbiol. 59 (1993) 640.
[6] P. Gerhardt, R.E. Marquis, in: I. Smith, R.A. Slepecky, P. Setlow (Eds.), Regulation of Procaryotic Development, American Society for Microbiology, Washington DC, 1989 (Chapter 2).
[7] M.F. Summers, Coord. Chem. Rev. 86 (1988) 43.
[8] J.E. Coleman, Metallobiochemistry, Part D, in: J.F. Riordan, B.L. Valee (Eds.), Methods in Enzymology, vol. 227, Academic Press, San Diego, CA, 1993, pp. 16–43.
[9] P.S. Marchetti, P.D. Ellis, R.G. Bryant, J. Am. Chem. Soc. 107 (1985) 8191.
[10] M. Merhring, High Resolution NMR Spectroscopy in Solids, Springer-Verlag, Berlin, 1983.
[11] C.A. Fyfe, Solid State NMR for Chemists, CFC Press, Ontario, 1983.
[12] W.R. Busing, H.A. Levy, Acta Crystallogr. 10 (1957) 180.
[13] B.A. Frenz, Enraf-Nonius Structure Determination Package, Enraf-Nonius, Delft, The Netherlands, 1983.
[14] G.M. Sheldrick, SHELX a Program for Crystal Structure Determination, University of Cambridge, Cambridge, England, 1976.
[15] G.M. Sheldrick, Acta Crystallogr. A 46 (1990) 467.
[16] G.M. Sheldrick, SHELXL-93, a Program for Crystal Structure Refinement, University of Göttingen, Germany, 1993.
[17] M.F. Summers, Coord. Chem. Rev. 86 (1988) 43.
[18] C.K. Johnson, ORTEP, Report ORNL-3794, Oak Ridge National Laboratory, TN, 1965.
[19] K.H. Chung, E. Hong, Y. Do, C.H. Moon, J. Chem. Soc., Dalton Trans (1996) 3363.
[20] M.L. Post, J. Trotter, J. Chem. Soc., Dalton Trans. (1974) 1922.
[21] W. Harrison, J. Trotter, J. Chem. Soc., Dalton Trans. (1972) 956.
[22] M.L. Post, J. Trotter, J. Chem. Soc., Dalton Trans. (1974) 674.
[23] A.C. Olivieri, L. Frydman, L.E. Diaz, J. Magn. Reson. 75 (1987) 50.
[24] A.C. Olivieri, J. Magn. Reson. 81 (1989) 201.
[25] E.E. Sileo, D. Vega, unpublished results.
[26] S. Ganapathy, V.P. Chacko, G. Bryant, J. Chem. Phys. 81 (1984).
[27] P.J. Barrie, A. Gyani, M. Motevalli, P. O'Brien, Inorg. Chem. 32 (1993) 3862.
[28] G.S.H. Lee, K.J. Fisher, A.M. Vassallo, J.V. Hanna, I.G. Dance, Inorg. Chem. 32 (1993) 66.

Available online at www.sciencedirect.com
SCIENCE DIRECT®
Polyhedron 24 (2005) 785–790
POLYHEDRON
www.elsevier.com/locate/poly

Synthesis and characterization of a versatile bis(pyridylether) ligand and its complexes with Ag(I), Cu(II) and Co(II)

Christiana Siaw-Lattey, Hongming Zhang, David Y. Son *

Department of Chemistry, Southern Methodist University, P.O. Box 750314, Dallas, TX 75275-0314, USA

Received 1 October 2004; accepted 2 February 2005
Available online 13 April 2005

Abstract

A new bis(pyridylether) ligand **L** was synthesized in 46% yield from the reaction of two equivalents of 2-pyridylethanol with α,α′-dibromo-*o*-xylene in the presence of sodium hydroxide. Ligand **L** possesses structural features that allow it to react either intermolecularly or in a chelating fashion with transition metal ions. With $AgNO_3$, ligand **L** forms a helical metallopolymer. Ligand **L**, in combination with 2-pyridylethanol, reacts with $Cu(ClO_4)_2$ to form a bridged dinuclear complex. With $Co(NCS)_2$, ligand **L** behaves as a chelating ligand to give a monomeric octahedral complex.
© 2005 Elsevier Ltd. All rights reserved.

Keywords: Nitrogen ligands; Helical structures; Self-assembly; Supramolecular chemistry; N,O ligands

1. Introduction

The interaction of organic multidentate ligands with transition metal ions can lead to a variety of molecular architectures, including macrocycles, polyhedra and linear and helical polymers [1–3]. As might be expected, ligand structure plays a critical role in the type of structure formed. Flexible ligands favor the formation of chelates or macrocycles, while stiff ligands often result in polymeric complexes. In recent research, we have focused on the synthesis of new bis(pyridyl) ligands in which the pyridyl groups are separated by spacer groups of varying flexibility. Depending on the spacer group, we found these ligands interact with silver(I) salts to form either chelated complexes [4] or helical polymers [5].

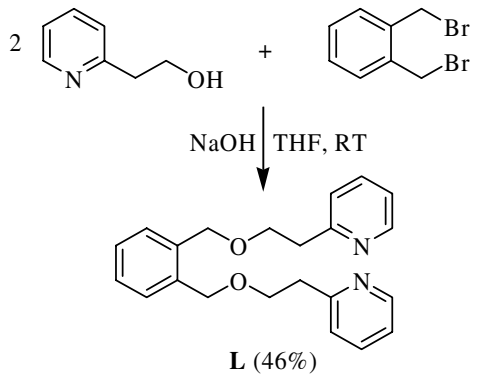
Supramolecular structure is also affected by the choice of metal ion. For a given ligand, the resulting complex structure is governed by the geometric preferences of the ion. As a part of our fundamental investigations in the synthesis of new multidentate heterocyclic ligands [4–6], we have sought to synthesize ligands that are flexible enough to accommodate a variety of geometric configurations, depending on the coordinated metal ion. In this report, we describe the synthesis of one such bis(pyridyl) ligand and its coordination preferences with Ag(I), Cu(II) and Co(II), metal ions that are known to exhibit a variety of coordination geometries with pyridyl ligands. This ligand reacts with Ag(I) to give a polymeric structure but reacts with Cu(II) and Co(II) to give monomeric complexes in which it is either a bridging or chelating ligand.

2. Results and discussion

The new bis(pyridylether) ligand **L** was synthesized in 46% yield from the reaction of 2-pyridylethanol with α,α′-dibromo-*o*-xylene in THF, in the presence of sodium hydroxide (Scheme 1). This reaction was not as straightforward as it may seem, as other common bases

* Corresponding author. Tel.: +1 214 768 8813; fax: +1 214 768 4089.
E-mail address: dson@smu.edu (D.Y. Son).

0277-5387/$ - see front matter © 2005 Elsevier Ltd. All rights reserved.
doi:10.1016/j.poly.2005.02.008



Scheme 1.

such as triethylamine, diisopropylethylamine, potassium carbonate, potassium hydroxide and lithium hydroxide were ineffective as proton acceptors. Furthermore, this reaction was unsuccessful with α,α′-dichloro-*o*-xylene as the starting material. Ligand **L**, isolated as a yellow oil, is stable under normal room conditions but hygroscopic. As can be seen from the structure of **L**, the ortho substitution pattern and the position of the pyridine nitrogen atoms suggest that this ligand can be chelating. However, the length and flexibility of the arms also allows the possibility of intermolecular complexation. Furthermore, the oxygen atoms present in the pyridyl arms may serve as additional donor atoms [7].

When an aqueous solution of silver nitrate was added to an acetone solution of **L** (1:1 ratio), a cloudy solution resulted which cleared within seconds. The solution was stored in the refrigerator and fine needle-like crystals formed in approximately 3 days.[1] After redissolving the crystals in methanol and adding water, orange block crystals (**Ag**–**L**) formed in 58% yield from the refrigerated solution after approximately one week. The ^{1}H NMR spectrum of **Ag**–**L**, which itself dissolved slowly into acetone-D_6, showed the pyridine proton signals to be spread out and shifted downfield compared to the spectrum of ligand **L**, suggesting Ag–L complexation in solution (Fig. 1). X-Ray crystal analysis of **Ag**–**L** revealed that **L** reacted intermolecularly with Ag(I) to give a one-dimensional helical polymer (Fig. 2). Structurally related bis(pyridylether) ligands such as 1,4-bis(2-pyridyloxymethyl)benzene and 1,4-bis(2-pyridylmethoxy)benzene have been reported to give π–π stabilized zigzag metallopolymers on interaction with $AgNO_3$ [8]. Each helical repeat unit of **Ag**–**L** consists of two ligands and two silver ions. The N–Ag–N bond angle of 160.49(14)° is distorted from linearity due to additional coordination of a nitrate ion oxygen atom (Ag–O(1) 2.591(4) Å), and weaker coordinations from two oxygen atoms of two separate ligands (Ag–O(12) 3.343(3) Å; Ag–O(22A) 2.748(3) Å). We observed no evidence for π–π interactions within each helical strand, as the stacked aryl rings are separated by 8.508(1) Å.

[1] We did not obtain X-ray quality crystals from reactions of **L** with silver triflate or silver tetrafluoroborate.

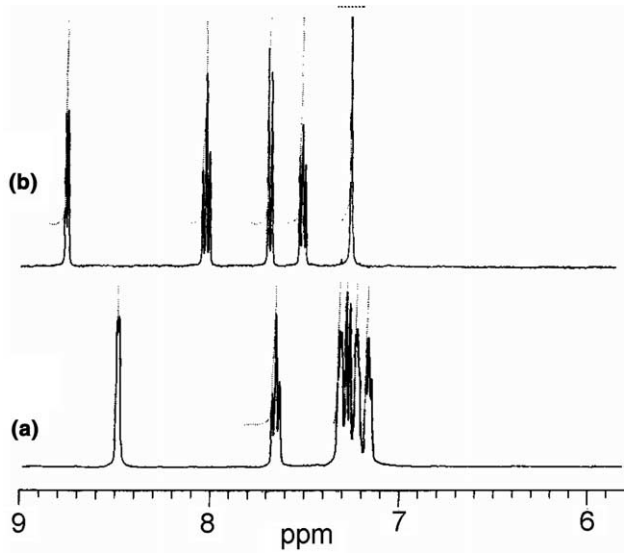


Fig. 1. ^{1}H NMR spectra (aromatic region) in [D_6]acetone of (a) **L**, and (b) **Ag**–**L**.

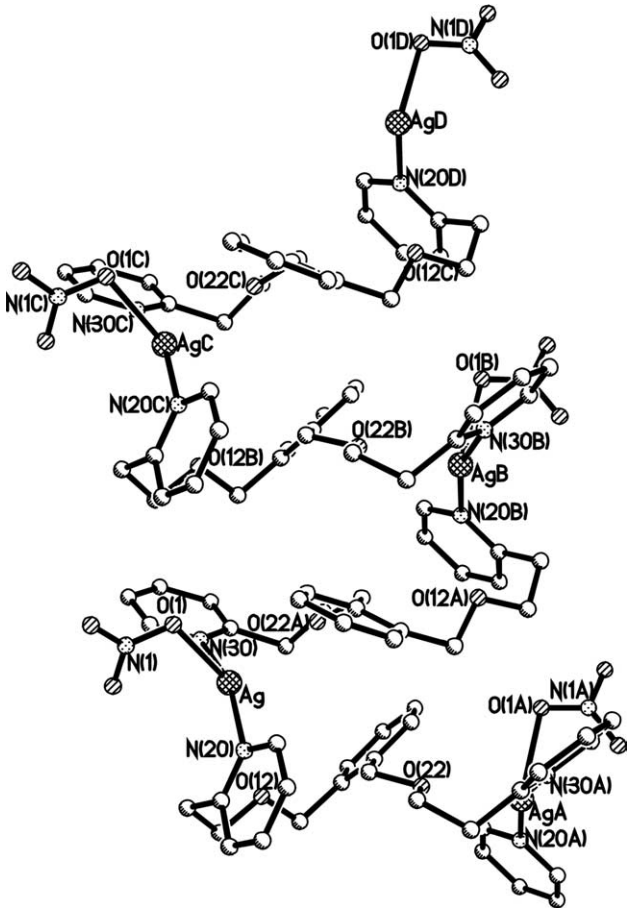


Fig. 2. Subsection of **Ag**–**L** (hydrogen atoms omitted for clarity).

Additionally, there is very little overlap between pyridine rings on adjacent strands. The asymmetric unit of **Ag–L** also included a noncoordinating molecule of water and disordered acetone. Elemental analysis data reflected the loss of the acetone on removal of the crystals from solution.

In various experiments involving the reaction of ligand **L** with copper(II) perchlorate, ($Cu(ClO_4)_2$), we isolated green powders from which X-ray quality crystals could not be grown. In a subsequent experiment, we accidentally utilized a sample of **L** that also contained 2-pyridylethanol in an approximate 5.6/1 mole ratio (**L**/2-pyridylethanol). Reaction of this impure sample with $Cu(ClO_4)_2$ in methanol/dichloromethane resulted in the formation of dark green crystals intermixed with a green powder after several days in a refrigerator. Careful examination revealed the crystals to be blue plates (**Cu–L**) of X-ray quality. Crystallographic analysis revealed a dinuclear structure in which the two Cu ions are pentacoordinate (Fig. 3). The asymmetric unit consists of one molecule of **L**, two deprotonated molecules of 2-pyridylethanol, two noncoordinating perchlorate anions and two molecules of dichloromethane. Elemental analysis data indicated that the dichloromethane molecules were lost on removal of the crystals from solution. Ligand **L** bridges the two copper ions through the pyridine nitrogen atoms (Cu(1)–N(20) 2.006(3) Å; Cu(2)–N(30) 2.007(2) Å) and in a weaker fashion through the oxygen atoms in the arms (Cu(1)–O(12) 2.341(2) Å; Cu(2)–O(22) 2.362(2) Å). Each of the two deprotonated 2-pyridylethanol molecules coordinates to separate copper ions through the pyridine nitrogens (Cu(1)–N(31) 1.997(3) Å; Cu(2)–N(41) 2.009(2) Å). Furthermore, the oxygen atoms of the 2-pyridylethanol molecules form bridges [9–12] between the two copper ions to give a distorted square (Cu(1)–O(1)–Cu(2) 100.31(9)°; Cu(1)–O(2)–Cu(2) 100.92(9)°) with a slight pucker (Cu(1)–O(1)–Cu(2)–O(2) torsion angle −6.2°).

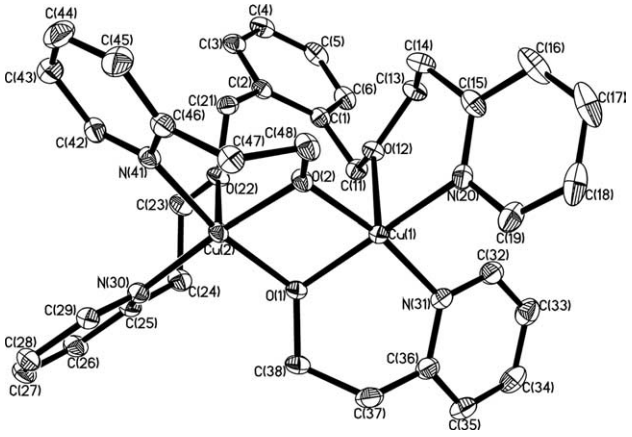


Fig. 3. ORTEP plot of **Cu–L** (50% probability, hydrogen atoms omitted for clarity).

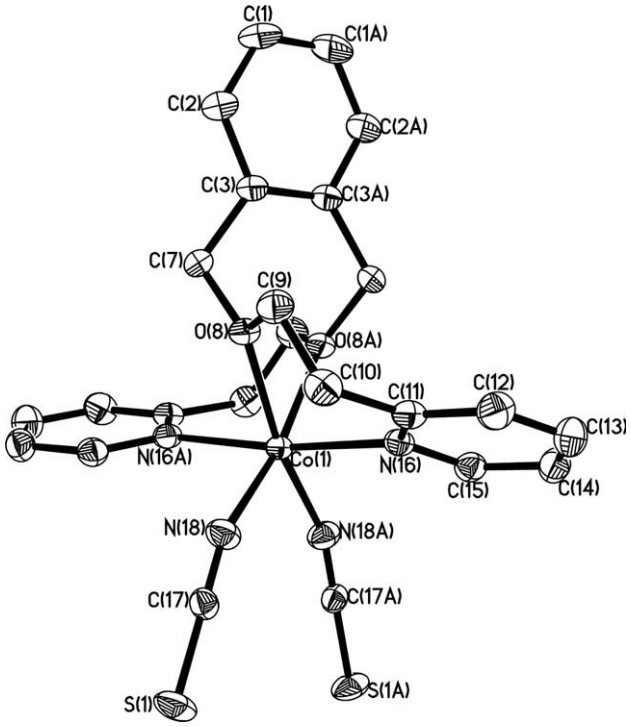


Fig. 4. ORTEP plot of **Co–L** (50% probability, hydrogen atoms omitted for clarity).

A Cu–Cu interatomic distance of 2.9752(5) Å in **Cu–L** is similar to that found in certain bridged Cu_2 complexes such as $(PPh_3)_2Cu_2(\mu\text{-}Cl)_2(\mu\text{-}4,4'\text{-bipy})$ (2.997(1) Å) [13] and the oxygen-bridged $[Cu_2(bis(1\text{-methyl-2-benzimidazolyl})ethane)_2(CH_3O)_2](ClO_4)_2$ complex (2.9872(16) Å) [9]. As might be expected from the stoichiometry of **Cu–L**, we found that the yield of the complex could be increased by increasing the amount of 2-pyridylethanol in the ligand mixture. However, we have still been unable to isolate X-ray quality crystals from the reaction of $Cu(ClO_4)_2$ with pure **L**.[2]

When **L** was mixed with $Co(NCS)_2$ in methanol, an intense blue-green colored solution formed in addition to some blue precipitate. A layer of hexane was added and the mixture was kept in a refrigerator for several weeks, resulting in the formation of purple solid clumps. The purple clumps were redissolved in acetone and layered with hexane, resulting in the formation of purple rodlike crystals in 64% yield (**Co–L**) after several days.[3] No crystals could be grown from the original blue precipitate. X-Ray crystallographic analysis revealed **Co–L** to be a monomeric octahedral complex, with **L** as a chelating ligand (Fig. 4). In **Co–L**, the two arms of **L**

[2] We were unsuccessful in obtaining crystalline products from the reaction of pure **L** with copper(II) chloride, copper(II) nitrate, copper(II) tetrafluoroborate or copper(II) iodide.

[3] Other cobalt(II) salts we examined included cobalt chloride, cobalt bromide and cobalt nitrate.

twist over each other resulting in the two pyridine rings being *trans*, with Co–N bond lengths of 2.1646(16) Å. The N(16)–Co–N(16A) bond angle is slightly deviated from linearity (172.95(8)°). As in the cases of **Ag–L** and **Cu–L**, we observe interactions between the oxygen atoms in the arms of **L** and the metal. In **Co–L**, the two oxygen atoms occupy *cis* positions with Co–O bond distances of 2.2136(13) Å. The coordination sphere is completed with two $(NCS)^-$ anions. The asymmetric unit also includes a molecule of disordered acetone, which elemental analysis data indicate is lost on removal of the crystals from solution.

3. Conclusion

We have synthesized a versatile bis(pyridylether) ligand **L** by a process involving readily available starting materials. By virtue of its structure, **L** can accommodate a variety of geometric conformations in metal complexes, depending on the preference of the transition metal ion. With silver(I), a helical metallopolymer is formed while reactions with Cu(II) and Co(II) result in the formation of a dinuclear and mononuclear complex, respectively. These results suggest that **L** is a good candidate for the formation of well-defined complexes with other transition metal ions. Continued investigations in our laboratory will focus on these studies and the design of other new multidentate ligands.

4. Experimental

General remarks: All reactions were performed under an atmosphere of nitrogen unless stated otherwise. Tetrahydrofuran (THF) was dried over activated 4 Å molecular sieves before use. The following chemicals were obtained from Fisher Scientific, Acros, or Sigma-Aldrich: tetrahydrofuran (THF), dichloromethane (CH_2Cl_2), sodium hydroxide powder (NaOH), anhydrous magnesium sulfate ($MgSO_4$), 2-pyridylethanol and α,α′-dibromo-*o*-xylene. NMR spectra were obtained using a 400 MHz Bruker Avance DRX multinuclear NMR spectrometer. IR spectra were recorded on a Nicolet Magna-IR 560 Spectrometer ESP.

4.1. Ligand *L*

A 100-mL round-bottomed flask equipped with a magnetic stir bar and rubber septum was charged with NaOH (3.03 g, 75.6 mmol) and 2-pyridylethanol (4.3 mL, 37.8 mmol). THF (50 mL) was added and after stirring at room temperature for 30 min, α,α′-dibromo-*o*-xylene (5.0 g, 18.9 mmol) was added. The resulting tan suspension was stirred overnight at room temperature. The suspension was filtered to remove salts and excess NaOH. CH_2Cl_2 (70 mL) was added to the dark yellow filtrate and the organic layer was washed twice with saturated aqueous NH_4Cl, twice with deionized H_2O and dried over anhydrous $MgSO_4$. Solvent removal via rotary evaporation yielded a dark yellow oil that was purified by filtration through a 5-cm silica gel column, using 1:1 ethyl acetate/hexane to remove any unreacted xylene reagent. The product was flushed out using 100% acetone as eluent. The clear light yellow oil obtained after solvent removal was redissolved in CH_2Cl_2 (20 mL) and washed with deionized H_2O to remove all traces of the pyridine starting material. Drying the organic layer over $MgSO_4$ and concentration afforded **L** as a yellow oil in 46% yield (3.04 g). *Anal*. Calc. for $C_{22}H_{24}N_2O_2$: C, 75.83; H, 6.94; N, 8.04. Found: C, 75.59; H, 7.20; N, 7.97%. ^{1}H NMR (400 MHz, [D$_6$]acetone): δ 3.0 (t, $^3J = 6.6$ Hz, –CH_2CH_2Pyr, 4H), 3.8 (t, $^3J = 6.6$ Hz, –OCH_2CH_2, 4H), 4.50 (s, –OCH_2Ph, 4H), 7.23–8.5 (m, aromatic H, 12H). ^{13}C NMR (100.62 MHz, [D$_6$]acetone): δ 38.8 (–CH_2CH_2Pyr), 69.9 (–CH_2CH_2Pyr), 70.4 (–OCH_2Ph), 121.0, 123.7, 127.5, 128.5, 136.3, 137.3, 147.5, 159.8. IR (neat): ν(cm^{-1}) 3065–3009 (aromatic C–H, m), 2861 (alkyl C–H, m), 1592–1568 (aromatic C=C, s), 1476 (alkyl C–C, s).

4.2. Complex *Ag–L*

To a 10-mL screw-capped vial was added pure **L** (0.10 g, 0.29 mmol). Approximately 3 mL of acetone was added to dissolve the ligand. In a separate vial, $AgNO_3$ (0.049 g, 0.30 mmol) was dissolved in 1 mL of deionized H_2O. The solution of $AgNO_3$ was added to the solution of **L** with a pipette by gently dripping off the side of the vial, without agitation. The resulting cloudiness dissipated within seconds, and the vial was stored in a refrigerator. Fine needle-like crystals formed in about 3 days. The supernatant was decanted and approximately 3 mL of methanol was added to dissolve the crystals. An additional 1 mL of water was also added. The solution was placed in the refrigerator and yellow-orange crystals formed in about one week. Yield: 0.089 g (58%); m.p.: 75–80 °C. *Anal*. Calc. for $C_{22}H_{24}N_3O_5Ag \cdot H_2O$: C, 49.27; H, 4.89; N, 7.83. Found: C, 49.27; H, 4.61; N, 7.93%. ^{1}H NMR (400 MHz, [D$_6$]acetone): δ 3.3 (t, $^3J = 6.6$ Hz, –CH_2CH_2Pyr, 4H), 3.8 (t, $^3J = 6.6$ Hz, –OCH_2CH_2, 4H), 4.5 (s, –OCH_2Ph, 4H), 7.2 (S, Ph, 4H), 7.4 (td, Pyr, 2H), 7.6 (d, Pyr, 2H), 7.9 (td, Pyr, 2H), 8.7 (d, Pyr, 2H). IR (KBr): ν(cm^{-1}) 1436–1384 (N=O, s).

4.3. Complex *Cu–L*

To a 10-mL screw-capped vial was added **L** (0.10 g, 0.29 mmol), consisting of 0.0941 g **L** and 0.0059 g 2-pyridylethanol. About 3 mL of methanol was added. $Cu(ClO_4)_2 \cdot 6H_2O$ (0.11 g, 0.29 mmol) was added and

Table 1
Crystal data for **Ag–L**, **Cu–L**, and **Co–L**

	Ag–L	**Cu–L**	**Co–L**
Empirical formula	$[C_{22}H_{24}AgN_3O_5] \cdot 1/2[C_3H_6O] \cdot 1/2[H_2O]$	$[C_{36}H_{40}Cl_2Cu_2N_4O_{12}] \cdot 2[CH_2Cl_2]$	$[C_{24}H_{24}CoN_4O_2S_2] \cdot [C_3H_6O]$
Formula weight	556.36	1088.55	581.60
Temperature (K)	100(2)	100(2)	200(2)
Wavelength (Å)	0.71073	0.71073	0.71073
Crystal system	monoclinic	monoclinic	monoclinic
Space group	*P*2(1)/*c*	*P*2(1)/*c*	*C*2/*c*
Unit cell dimensions			
a (Å)	12.4417(18)	10.9408(6)	16.7232(10)
b (Å)	8.5081(12)	23.7999(12)	13.9394(8)
c (Å)	22.708(3)	17.3657(9)	13.9360(8)
α (°)	90	90	90
β (°)	90.995(2)	102.694(1)	120.701(1)
γ (°)	90	90	90
Volume ($Å^3$)	2403.4(6)	4411.3(4)	2793.3(3)
Z	4	4	4
Density (calculated) (Mg/m^3)	1.538	1.639	1.383
Absorption coefficient (mm^{-1})	0.882	1.393	0.799
F(000)	1140	2224	1212
Crystal size (mm)	$0.39 \times 0.33 \times 0.29$	$0.41 \times 0.30 \times 0.15$	$0.32 \times 0.11 \times 0.10$
Theta range for data collection (°)	1.79–28.30	1.91–28.30	2.03–28.26
Reflections collected	27844	53575	16836
Independent reflections [$R_{(int)}$]	5826 [0.047]	10669 [0.030]	3407 [0.031]
Maximum and minimum transmission	0.781 and 0.724	0.8204 and 0.5963	0.924 and 0.785
Data/restraints/parameters	5826/0/316	10669/0/559	3407/7/187
Goodness-of-fit on F^2	1.165	1.014	1.096
Final *R* indices [$I > 2\sigma(I)$]	$R_1 = 0.071$, $wR_2 = 0.181$	$R_1 = 0.052$, $wR_2 = 0.141$	$R_1 = 0.044$, $wR_2 = 0.104$
Largest difference peak and hole	$R_1 = 0.079$, $wR_2 = 0.187$	$R_1 = 0.058$, $wR_2 = 0.146$	$R_1 = 0.050$, $wR_2 = 0.108$
R Indices (all data) (e $Å^{-3}$)	3.025 and −1.357	2.297 and −1.980	0.618 and −0.261

the reactants mixed, resulting in the formation of an intense green solution. A 1 mL layer of dichloromethane was added to the resulting green solution after which the reaction was stored in a refrigerator. Dark green crystals and some green powder formed in about 4 days. Because the crystalline solid could not be quantitatively separated from the powdery precipitate, a yield could not be determined. M.p.: 167–168 °C. *Anal*. Calc. for $C_{36}H_{40}N_4O_4Cu_2(ClO_4)_2$: C, 47.06; H, 4.39; N, 6.10. Found: C, 47.09; H, 4.37; N, 6.00%. IR (KBr): $\nu(cm^{-1})$ 1086 (Cl–O, s).

4.4. Complex *Co–L*

To a 10-mL screw-capped vial was added pure **L** (0.10 g, 0.29 mmol). Methanol (approximately 3 mL) and $Co(NCS)_2$ (0.50 g, 0.29 mmol) was added and the vial swirled to dissolve and mix the reactants, resulting in the formation of an intense blue-green color and some blue precipitate. A purple color was observed when light was shone through the solution. After layering with 1 mL of hexane, the vial was stored in a refrigerator (in a subsequent experiment we found that the hexane layer was unnecessary). Clumps of purple solid formed in a few weeks. These were manually isolated and redissolved in acetone (3 mL) to form a clear blue solution. A layer of hexane was added and the mixture placed in a refrigerator. The blue precipitate was dissolved in methanol and layered with hexane and cooled in the freezer but no crystals formed. Crystals from the purple solid formed in about 3 days. Yield: 64% (0.10 g); m.p.: 94–96 °C. *Anal*. Calc. for $C_{22}H_{24}N_2O_2Co(SCN)_2 \cdot H_2O$: C, 53.23; H, 4.84; N, 10.35. Found: C, 53.11; H, 4.79; N, 9.83%. IR (KBr): $\nu(cm^{-1})$ 2071 (C═N, s).

5. X-Ray crystallographic study

All data were collected on a Bruker APEX diffractometer equipped with a CCD detector. The structures were solved by direct-methods and subsequent difference Fourier syntheses using the SHELXTL program package (G.M. Sheldrick, SHELXTL, Bruker Analytical X-Ray Systems, Inc., 1990). Crystal data and refinement

Table 2
Selected bond lengths (Å) and angles (°) for **Ag–L**

Bond lengths		Bond angles	
Ag–N(20)	2.185(4)	N(20)–Ag–N(30)	160.49(14)
Ag–N(30)	2.206(3)	N(20)–Ag–O(1)	93.62(12)
Ag–O(1)	2.591(4)	N(30)–Ag–O(1)	95.04(13)
Ag–O(12)	3.343(3)		
Ag–O(22A)	2.748(3)		

Table 3
Selected bond lengths (Å) and angles (°) for **Cu–L**

Bond lengths		Bond angles	
Cu(1)–O(2)	1.929(2)	O(2)–Cu(1)–O(1)	79.16(8)
Cu(1)–O(1)	1.932(2)	O(2)–Cu(1)–N(31)	170.50(10)
Cu(1)–N(31)	1.997(3)	O(1)–Cu(1)–N(31)	91.63(10)
Cu(1)–N(20)	2.006(3)	O(2)–Cu(1)–N(20)	94.38(9)
Cu(1)–O(12)	2.341(2)	O(1)–Cu(1)–N(20)	168.77(10)
Cu(1)–Cu(2)	2.9752(5)	N(31)–Cu(1)–N(20)	94.33(10)
Cu(2)–O(2)	1.928(2)	O(2)–Cu(1)–O(12)	88.66(8)
Cu(2)–O(1)	1.942(2)	O(1)–Cu(1)–O(12)	100.07(8)
Cu(2)–N(30)	2.007(2)	N(31)–Cu(1)–O(12)	95.31(9)
Cu(2)–N(41)	2.009(2)	N(20)–Cu(1)–O(12)	88.85(9)
Cu(2)–O(22)	2.362(2)	O(2)–Cu(2)–O(1)	78.94(9)
		O(2)–Cu(2)–N(30)	173.64(10)
		O(1)–Cu(2)–N(30)	97.87(9)
		O(2)–Cu(2)–N(41)	89.66(9)
		O(1)–Cu(2)–N(41)	168.59(9)
		N(30)–Cu(2)–N(41)	93.44(10)
		O(2)–Cu(2)–O(22)	97.54(8)
		O(1)–Cu(2)–O(22)	88.00(8)
		N(30)–Cu(2)–O(22)	87.79(9)
		N(41)–Cu(2)–O(22)	93.95(9)
		O(2)–Cu(2)–Cu(1)	39.55(6)
		O(1)–Cu(2)–Cu(1)	39.72(6)
		N(30)–Cu(2)–Cu(1)	137.59(7)
		N(41)–Cu(2)–Cu(1)	128.97(7)
		O(22)–Cu(2)–Cu(1)	89.65(5)

Table 4
Selected bond lengths (Å) and angles (°) for **Co–L**

Bond lengths		Bond angles	
Co(1)–N(18)	2.0407(17)	N(18)–Co(1)–N(18A)	94.81(10)
Co(1)–N(16)	2.1646(16)	N(18)–Co(1)–N(16A)	92.64(6)
Co(1)–O(8)	2.2136(14)	N(18)–Co(1)–N(16)	92.13(6)
		N(16A)–Co(1)–N(16)	172.95(8)
		N(18)–Co(1)–O(8)	94.07(6)
		N(18A)–Co(1)–O(8)	170.40(6)
		N(16A)–Co(1)–O(8)	91.09(5)
		N(16)–Co(1)–O(8)	83.39(6)
		O(8)–Co(1)–O(8A)	77.33(7)

parameters are listed in Table 1. Selected bond lengths and bond angles for **Ag–L**, **Cu–L**, and **Co–L** are listed in Tables 2–4.

6. Supplementary data

CCDC Nos. 242392–242394 contains the supplementary crystallographic data for this paper. These data can be obtained free of charge at www.ccdc.cam.ac.uk/conts/retrieving.html [or from the Cambridge Crystallographic Data Centre, 12 Union Road, Cambridge CB2 1EZ, UK; fax: (internat.) +44 1223/336 033; e-mail: deposit@ccdc.cam.ac.uk].

Acknowledgments

The authors thank the National Science Foundation (Grant No. 0092495) and the Welch Foundation (Grant No. 1375) for support of this work.

References

[1] G.F. Swiegers, T.J. Malefetse, Chem. Rev. 100 (2000) 3483.
[2] S. Leininger, B. Olenyuk, P.J. Stang, Chem. Rev. 100 (2000) 853.
[3] A.N. Khlobystov, A.J. Blake, N.R. Champness, D.A. Lemenovskii, A.G. Majouga, N.V. Zyk, M. Schröder, Coord. Chem. Rev. 221 (2001) 155.
[4] P. Sengupta, H. Zhang, D.Y. Son, Inorg. Chem. 43 (2004) 1828.
[5] M.K. Kalra, H. Zhang, D.Y. Son, Inorg. Chem. Commun. 7 (2004) 1019.
[6] S.R. Gondi, D.Y. Son, Synth. Commun. 34 (2004) 3061.
[7] C.M. Hartshorn, P.J. Steel, Inorg. Chem. 35 (1996) 6902.
[8] C.M. Hartshorn, P.J. Steel, J. Chem. Soc., Dalton Trans. (1998) 3927.
[9] G.A.v. Albada, W.J.I. Smeets, A.L. Spek, J. Reedijk, Inorg. Chim. Acta 260 (1997) 151.
[10] D.A. McMorran, P.J. Steel, J. Chem. Soc., Dalton Trans. (2002) 3321.
[11] S. Youngme, C. Chailuecha, G.A. van Albada, C. Pakawatchai, N. Chaichit, J. Reedijk, Inorg. Chim. Acta 357 (2004) 2532.
[12] S.P. Foxon, D. Utz, J. Astner, S. Schindler, F. Thaler, F.W. Heinemann, G. Liehr, J. Mukherjee, V. Balamurugan, D. Ghosh, R. Mukherjee, J. Chem. Soc., Dalton Trans. (2004) 2321.
[13] J. Lu, G. Crisci, T. Niu, A.J. Jacobson, Inorg. Chem. 36 (1997) 5140.

Available online at www.sciencedirect.com
SCIENCE DIRECT®
Polyhedron 24 (2005) 791–798
POLYHEDRON
www.elsevier.com/locate/poly

Synthesis, electrochemical, and spectroelectrochemical properties of tetrakis(13,17-dioxa nonacosane-15-sulphanyl) phthalocyaninato zinc(II)

Ismail Yilmaz [a,*], Ayşegül Gürek [b], Vefa Ahsen [b]

[a] Department of Chemistry, Technical University of Istanbul, Maslak, Istanbul 34469, Turkey
[b] Gebze Institue of Technology, Department of Chemistry, PO Box 141, Gebze, 41400, Turkey

Received 29 December 2004; accepted 3 February 2005
Available online 14 April 2005

Abstract

Tetrakis(13,17-dioxa nonacosane-15-sulphanyl) phthalocyaninato zinc(II), ZnPc(SCH($CH_2OR)_2)_4$, where R = $C_{12}H_{25}$, was synthesised and its electrochemical and spectroelectrochemical properties were investigated in dichloromethane. The neutral complex undergoes two quasi-reversible one-electron oxidations and two quasi-reversible one-electron reductions in CH_2Cl_2 containing 0.1 M tetra-*n*-butylammonium perchlorate (TBAP). The half-wave potentials for oxidation of the complex are located at $E_{1/2}$ = 0.61 and 1.38 V, while the two reductions are located at $E_{1/2} = -0.87$ and -1.11 V versus SCE. These potentials show little or no difference compared to those of unsubstituted ZnPc and other SR substituted phthalocyanines under the same experimental conditions, thus suggesting weak electron-donating effects of the peripheral alkylthio substituents on the phthalocyanine rings. The well-defined UV–Vis spectra of electro-reduced and electro-oxidised species, $[ZnPc(-3)(SCH(CH_2OR)_2)_4]^-$, $[ZnPc(-4)(SCH(CH_2OR)_2)_4]^{2-}$ and $[ZnPc(-1)(SCH(CH_2OR)_2)_4]^+$, were obtained by applied potentials ($E_{app} = -1.04$ V, $E_{app} = -1.62$ V, and $E_{app} = 1.20$ V, respectively) in a thin-layer cell. The first and second reduction products showed characteristic spectral changes corresponding to mono- and di-anionic species of zinc phthalocyanines, and the first oxidation showed spectral changes corresponding to the formation of a mono-cationic dimer.
© 2005 Elsevier Ltd. All rights reserved.

Keywords: Phthalocyanines; Electrochemistry; Spectroelectrochemistry; Zinc

1. Introduction

The importance of phthalocyanines in many fields, such as molecular electronics [1–3], non-linear optics [4–6], liquid crystals [7–10], gas sensors [11–13], photosensitisers [14–16], catalysts [17–20], semiconductive materials [21,22], photovoltaic cells [23–25], and electrochromic displays [26–29], is increasing rapidly as a result of novel compounds with functional groups on the phthalocyanine core or different types of metal in the centre. An important shortcoming of phthalocyanines is their low solubility in common organic solvents, which hinders their wider application. The introduction of alkoxy [30,31] or alkylthio [32–34] substituents to the phthalocyanine cores provides the desired solubility and has turned out to be powerful means of modifying the chemical and physical properties of phthalocyanines. Electron-donating or electron-withdrawing groups on phthalocyanine macrocycle strongly affect not only the position of the longwave absorption bands in the electronic spectra but also the electrode potentials of their

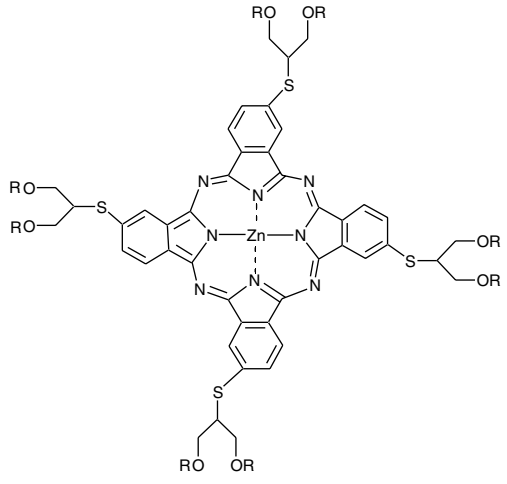
* Corresponding author. Tel.: +90 212 285 6831; fax: +90 212 285 6386.
E-mail address: iyilmaz@itu.edu.tr (I. Yilmaz).

0277-5387/$ - see front matter © 2005 Elsevier Ltd. All rights reserved.
doi:10.1016/j.poly.2005.02.018

reduced or oxidised species in electrochemical reactions [30,35–37]. Phthalocyanines with alkylthio substituents tend to shift the absorption bands to longer wavelengths in the near-IR compared with unsubstituted ones, thereby making an important contribution in semiconductor laser applications [38].

In most applications of phthalocyanine complexes, a good understanding of the redox properties of these complexes is important. Spectroelectrochemical studies of phthalocyanines facilitate understanding of the nature of the redox processes that may take place at either the central metal atom or the phthalocyanine ring, and usually cannot be distinguished by electrochemistry only. Spectroelectrochemical studies of phthalocyanines are also important with regard to their possible use as electrochromic materials, where several colours are displayed depending on the potential applied to the electrode surface [39–42].

Our laboratories have recently reported the synthesis, and electrochemical and spectroelectrochemical properties of double-decker lutetium(III) phthalocyanines and tetrathia macrocycle-bridged metal phthalocyanines substituted with long-alkylthio chains in aqueous and non-aqueous media [39–42]. In this work, the synthesis, and electrochemical and spectroelectrochemical characterisation of tetrakis(13,17-dioxa nonacosane-15-sulphanyl) phthalocyaninato zinc(II), $ZnPc(SCH(CH_2OR)_2)_4$, where $R = C_{12}H_{25}$ (Fig. 1), are reported. Long-alkyl chains introduced into the peripheral position of the phthalocyanine unit provide high solubility in non-coordinating solvents (e.g., dichloromethane, chloroform, diethylether, *n*-hexane), which has been observed for long-alkyl chains or bulky-groups introduced into mono, unsymmetrical, double-decker phthalocyanines, and quinoxaline or some oxime complexes [43–48].



$ZnPc[SCH(CH_2OR)_2]_4$

where $R = C_{12}H_{25}$

Fig. 1. Tetrakis(13,17-dioxa nonacosane-15-sulphanyl) phthalocyaninato zinc(II).

The electrochemistry and spectroelectrochemistry of $ZnPc(SCH(CH_2OR)_2)_4$ were determined in CH_2Cl_2 containing 0.1 M TBAP. Thus, detailed information is provided on several electrochemically generated redox species, such as $[ZnPc(-3)(SCH(CH_2OR)_2)_4]^-$, $[ZnPc(-4)(SCH(CH_2OR)_2)_4]^{2-}$ and $[ZnPc(-1)(SCH(CH_2OR)_2)_4]^+$, which remain stable and keep their colour changes throughout the thin-layer spectroelectrochemical timescale. The first and second reduction products formed with the applied potentials ($E_{app} = -1.04$ V and $E_{app} = -1.62$ V) in a thin-layer cell showed characteristic spectral changes corresponding to mono- and dianionic species of zinc phthalocyanines. On the other hand, the appearance of the first oxidation product with the applied potential ($E_{app} = 1.20$ V) in the thin-layer cell showed characteristic spectral changes corresponding to dimeric formation of mono-cationic species in CH_2Cl_2.

2. Experimental

2.1. Chemicals and reagents

Dichloromethane (CH_2Cl_2) was treated with H_2SO_4 three times and distilled over P_2O_5 and CaH_2 prior to use. Dimethylsulfoxide (DMSO) was freshly distilled after drying over alumina. Tetra-*n*-butylammonium perchlorate (TBAP, Fluka Chemical Co.) was recrystallised from ethyl alcohol and dried in a vacuum oven at 40 °C for at least 1 week prior to use. Ferrocene was recrystallised from ethyl alcohol before using. 4-(13,17-Dioxa nonacosane-15-sulphanyl) phthalonitrile was prepared according to the procedure available in the literature [49].

2.2. Instrumention

^1H and ^{13}C NMR spectra were recorded on a Bruker 200 MHz spectrometer. Infrared (IR) spectra were recorded as KBr pellets on a Perkin–Elmer 983 spectrophtometer. Fast atom bombardment (FAB) mass spectrum was obtained on a VG-ZAB-SPEC spectrometer using *m*-nitrobenzyl alcohol as matrix. Elemental analyses were carried out in Marmara Research Center. Cyclic voltammograms (CV) were carried out using CV measurements with Princeton Applied Research Model 273 potentiostat controlled by an external PC. A three electrode system was used for CV measurements in CH_2Cl_2 and consisted of a glassy carbon working electrode, a platinum wire counter electrode, and a saturated calomel reference electrode (SCE). The reference electrode was separated from the bulk solution by a fritted-glass bridge filled with the

solvent/supporting electrolyte mixture. The ferrocene/ferrocenium couple (Fc/Fc^+) was used as an internal standard but all potentials in the paper are referenced to the SCE. Solutions containing ZnPc(SCH-$(CH_2OR)_2)_4$ were deoxygenated by a stream of high purity nitrogen for at least 5 min. before running the experiment and the solution was protected from air by a blanket of nitrogen during the experiment. Controlled potential electrolysis (CPE) was performed with Princeton Applied Research Model 273 potentiostat/Galvanostat. An ''H'' type cell with a fritted glass to separate the cathodic and anodic portions of the cell was used for bulk electrolysis. The working and counter electrodes were platinum and the reference electrode was a SCE. The sample and solvent were transferred into the electrolysis cell under nitrogen. UV–Vis spectroelectrochemical experiments were performed with a home-built thin-layer cell that utilised a light transparent platinum gauze working electrode. Potentials were applied and monitored with an Princeton Applied Research Model 273 potentiostat. Time-resolved UV–Vis spectra and spectrophotometric titration experiment were recorded Hewlett–Packart Model 8453 diode array spectrophotometer.

2.3. Synthesis of tetrakis(13,17-dioxa nonacosane-15-sulfanyl) phthalocyaninato zinc(II)

A mixture of 4-(13,17-dioxa nonacosane-15-sulfanyl) phthalonitrile (0.717 g, 1.26 mmol), anhydrous zinc acetate (0.059 g, 0.32 mmol) and quinoline (1 ml) was heated and stirred at 195–200 °C for 24 h under argon. After cooling to room temperature, the mixture was treated with ethanol (10 ml) and the waxy precipitate was separated. The dark green metallo-phthalocyanine was isolated by column chromatography (Silica gel, CH_2Cl_2:*n*-hexane/1:1). This compound was soluble in common organic solvents. Yield: 0.220 g (30%). *Anal*. Calc. for $C_{140}H_{232}N_8O_8S_4Zn$: C, 70.95; H, 10.30; N, 4.48. Found: C, 71.58; H, 9.95; N, 4.77%. IR [(KBr)ν_{max}/cm^{-1}]: 2920–2855 (CH_2), 1600, 1465, 1380, 1305, 1260, 1105 (C–O–C), 910, 815, 740. ^1H NMR ($CDCl_3$): δ ppm = 0.83 (t, 24H, CH_3), 1.15 (m, 144H, CH_2), 1.71 (m, 16H, OC–CH_2), 3.65 (t, 16H, OCH_2), 4.02 (br, 20H, CH and OCH_2), 7.85–8.05 (m, 4H, ArH), 8.45–8.87 (m, 8H, ArH). ^{13}C NMR (APT) ($CDCl_3$): δ ppm = 14.1 (CH_3), 22.7 (CH_2), 26.4 (CH_2), 29.3–29.8 (CH_2), 31.9 (CH_2), 48.6 (CH), 70.5 (OCH_2), 71.8 (OCH_2–CHS), 122.0 (Ar CH), 122.5 (Ar CH), 123.6 (Ar CH), 131.3 (Ar CH), 133. 9 (Ar C), 136.5 (Ar C), 138.1 (Ar C), 144. 2 (Ar C). MS (FAB): *m*/*z* (%): 2348.1 (66) $[M]^+$, 1936.0 (25) $[M - CH(CH_2OC_{12}H_{25})_2]^+$, 1792.9 (9), 1524.5 (10) $[M - 2(CH(CH_2OC_{12}H_{25})_2)]^+$, 1296.5 (6), 1178.6 (8), 705.3 (29) $[M - 4(CH(CH_2OC_{12}H_{25})_2)]^+$, 588.3 (100).

3. Results and discussion

3.1. Synthesis and spectral characterisation

Formation of tetrakis(13,17-dioxa nonacosane-15-sulphanyl) phthalocyaninato zinc(II), ZnPc(SCH $(CH_2OR)_2)_4$ was achieved in a good yield by cyclotetramerisation reaction of 4-(13,17-dioxa nonacosane-15-sulphanyl) phthalonitrile [49] with anhydrous zinc acetate in a high-boiling solvent such as quinoline. Column chromatography with silica gel was employed to obtain pure product.

The desired compound, which had four long-alkylthio ($SCH(CH_2OR)_2$) groups on the periphery of phthalocyanine macrocycle, was isolated as a mixture of isomers, electrochemical properties of which appear to be the same. This is not a surprise. Similar electrochemical behaviour of the isomers were reported earlier for some tetra-substituted phthalocyanine complexes [39,50]. The dark green waxy product was readily soluble in common organic solvents such as chloroform, tetrahydrofuran, benzene, and toluene. This is clearly due to the introduction of long-alkylthio chains on the peripheral position of phthalocyanine core. Thus, $ZnPc(SCH(CH_2OR)_2)_4$ could be thoroughly characterised by ^1H and ^{13}C NMR and UV–Vis spectroscopy, in addition to elemental analysis. Mass spectrum of $ZnPc(SCH(CH_2OR)_2)_4$ by the FAB technique also showed relatively intense molecular ion peak with the clear apperance of the fragmentation peaks corresponding to the stepwise loss of alkoxy ($OC_{12}H_{25}$) groups (Fig. 2).

In the IR spectrum, characteristic vibration peaks corresponding to the ether groups (C–O–C) at 1105 cm^{-1} and CH_2 stretching at 2920–2855 cm^{-1} are common for such groups on the phthalocyanine cores. The sharp peak belong to the C≡N vibrations in phthalonitrile derivative disappeared after phthalocyanine formation. In the ^1H NMR analysis of the compound in deuteriated chloroform, $ZnPc(SCH(CH_2OR)_2)_4$ showed characteristic chemical shift at 7.85–8.05 and 8.45–8.87 ppm belong to deshielded aromatic protons, along with the peaks from CH, CH_2, and CH_3 protons between 0.83 and 4.02 ppm for the peripherally substituted groups on the phthalocyanine cores.

The high solubility of $ZnPc(SCH(CH_2OR)_2)_4$ has enabled us to obtain the ^{13}C NMR spectrum. The attached proton test (APT) indicates the presence of three tertiary carbons of phthalocyanine core in the aromatic region, 122.0, 122.5, and 131.3 and the signals for aliphatic carbon atoms appeared between 14.1 and 71.8 ppm, as expected.

A close investigation of the mass spectrum of $ZnPc(SCH(CH_2OR)_2)_4$ confirmed the proposed structure. The mass spectrum of $ZnPc(SCH(CH_2OR)_2)_4$ was obtained by the FAB technique using a *m*-nitro

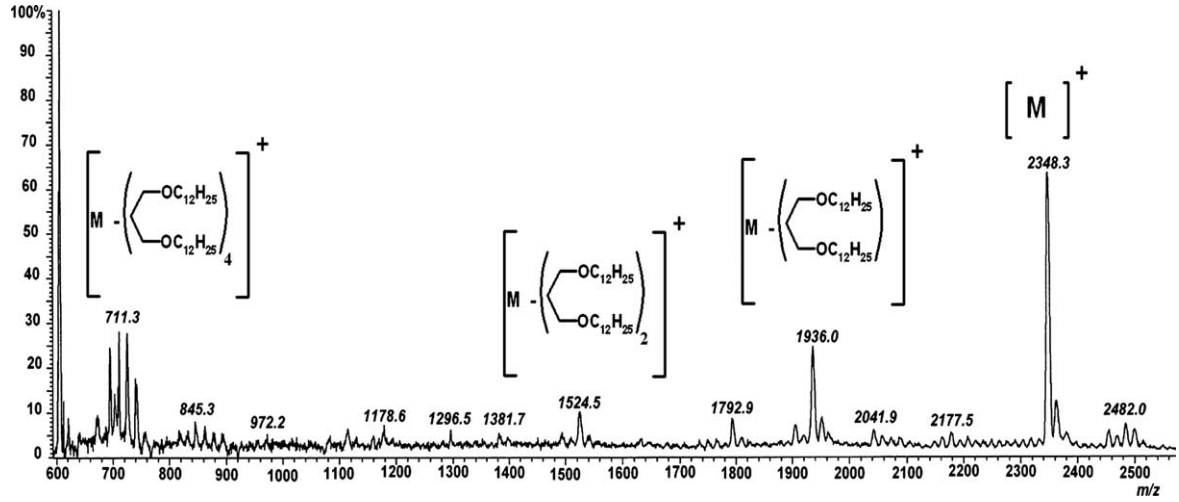


Fig. 2. The mass spectrum of $ZnPc(SCH(CH_2OR)_2)_4$.

benzyl alcohol (MNBA) as matrix. In addition to the $[M]^+$ peak, fragments were observed at 1936.0 (25) $[M - CH(CH_2OC_{12}H_{25})_2]^+$, 1792.9 (9), 1524.5 (10) $[M - 2(CH(CH_2OC_{12}H_{25})_2)]^+$, 1296.5 (6), 1178.6 (8), 705.3 (29) $[M - 4(CH(CH_2OC_{12}H_{25})_2)]^+$, 588.3 (100).

3.2. Electrochemistry

Oxidation and reduction reactions of ZnPc in solution or film states are expected to occur at the phthalocyanine ring only, since Zn metal is electroinactive [50]. Fig. 3 shows a typical cyclic voltammogram of

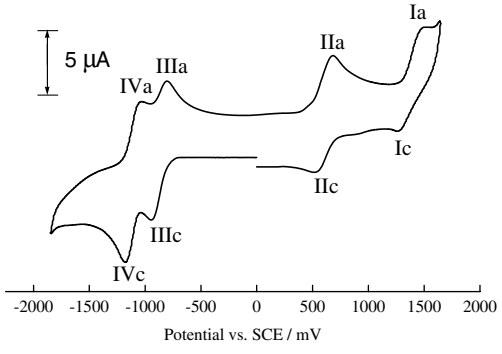


Fig. 3. Cyclic voltammograms of $ZnPc(SCH(CH_2OR)_2)_4$ in CH_2Cl_2 solution containing 0.1 M TBAP. Scan rate = 0.1 V/s.

$ZnPc(SCH(CH_2OR)_2)_4$, which undergoes two quasi-reversible one-electron oxidations and two quasi-reversible one-electron reductions with the corresponding cathodic and anodic peaks in CH_2Cl_2 containing 0.1 M TBAP. The half-wave potentials for reduction of $ZnPc(SCH(CH_2OR)_2)_4$ in CH_2Cl_2, 0.1 M TBAP are located at $E_{1/2} = -0.87$ and -1.11 V, while the two oxidations are located at $E_{1/2} = 0.61$ and 1.38V versus SCE. The half-wave potentials of $ZnPc(SCH(CH_2OR)_2)_4$ and some unsubstituted and alkylthio substituted zinc phthalocyanines from the literature are given in Table 1. The difference between the half-wave potentials of the first reduction and first oxidation processes for $ZnPc(SCH(CH_2OR)_2)_4$, which resembles the energy difference between highest occupied and lowest unoccupied molecular orbitals (HOMO and LUMO), is 1.48 V. This value is in accord with those of unsubstituted and substituted zinc phthalocyanines in Table 1. The potential difference between the first and second reduction processes of the $ZnPc(SCH(CH_2OR)_2)_4$ is 0.24 V, which compares to an average separation for the first and second reduction processes of alkylthio-substituted zinc phthalocyanines at the Pc ring system. Thus, these two couples are assigned to successive ring reduction processes, namely $[ZnPc(-2)(SCH(CH_2OR)_2)_4]/[ZnPc(-3)(SCH(CH_2OR)_2)_4]^-$ and $[ZnPc(-3)(SCH(CH_2OR)_2)_4]^-/[ZnPc(-4)(SCH(CH_2OR)_2)_4]^{2-}$, respectively. Only a few re-

Table 1
Half-wave potentials of $(SCH(CH_2OR)_2)_4$ ZnPc and selected zinc phthalocyanines

Solvent/condition	Compound	Supporting electrolyte	Ox2 (I)	Ox1 (II)	Red1 (III)	Red2 (IV)	Reference
CH2Cl2	$ZnPc(SCH(CH_2OR)_2)_4$	TBAP	1.38 (0.19)	0.61 (0.11)	−0.87 (0.10)	−1.11 (0.11)	tw
DMF	ZnPc	TBAP		0.67	−0.86	−1.30	[30,35]
DMSO	$ZnPc(SC_2H_4OH)_8$	TBAP		0.60	−0.74	−1.11	[51]
CH2Cl2	$ZnPc(SC_6H13)_8$	TBAP		0.64	−0.79	−1.10	[52]

Values of ΔE_p ($=E_{pa} - E_{pc}$) for $ZnPc(SCH(CH_2OR)_2)4$ are given in parenthesis; tw: this work.

ports have given a potential value for the second-step ring oxidation of zinc phthalocyanines, where the potential difference between first oxidation and second oxidation reactions was reported to be about 0.7 V, which is consistent with what was observed for ZnPc(SCH $(CH_2OR)_2)_4$ in this work. Thus, the first and second oxidation processes are based on ring-centred oxidation reactions, namely [ZnPc(-2)$(SCH(CH_2OR)_2)_4$]/[ZnPc(-1) $(SCH(CH_2OR)_2)_4]^+$ and [ZnPc(-1)$(SCH(CH_2OR)_2)_4]^+$/ [ZnPc(0)$(SCH(CH_2OR)_2)_4]^{2+}$, respectively.

The introduction of electron-donating groups to the phthalocyanine cores is expected to lead to an increase in the electron density of the central metal atom, thereby making the MPc complex easier to oxidise and harder to reduce [30,35]. This effect was clearly demonstrated by the fact that the half-wave potentials of $ZnPc(OC_4H_9)_8$ are negatively shifted compared to those of ZnPc [30,35]. Similar behaviour for alkylthio-substituted phthalocyanines could be expected. However, the compound synthesised here and reports on alkylthio-substituted zinc phthalocyanines show little or no difference in their first reduction potentials compared to those of unsubstituted ZnPc [30,35]. For example, the first reduction potential ($E_{1/2}$) for the ZnPc in dimethylformamide is −0.86 V versus SCE, while they are −0.87, −0.74 and −0.79 V versus SCE for ZnPc(SCH(CH_2- $OR)_2)_4$, $ZnPc(SC_2H_4OH)_8$ [51] and $ZnPc(SC_6H_{13})_8$ [52] in CH_2Cl_2 and DMSO, respectively. These data indicate the weak electron-donating influence of the alkylthio-groups on the average electron density of the metal phthalocyanines. A similar weak electron-donating influence of the alkylthio-groups was observed for the complexes investigated before under the same experimental conditions, $[(C_6H_{13}S)_8Pc]_2Lu$ [40,41], $[(C_{12}H_{25}$- $S)_4Pc]_2Lu$ [39] and $[(RS)_6CoPc]_2CR$ [42]. The behaviour of the substituent effect for the oxidation potential of ZnPc(SCH$(CH_2OR)_2)_4$ has been observed to be similar to that of ZnPc. The redox processes of ZnPc(SCH $(CH_2OR)_2)_4$ were examined as a function of potential scan rate in order to ascertain the mode of mass transport. The cathodic and anodic currents for the oxidation and reduction couples in CH_2Cl_2 each increased in direct proportion to the square root of scan rate between 0.02 and 0.25 V/s, thus suggesting that the redox reactions in solution are controlled by diffusion [53]. The peak cathodic and peak anodic current ratio, i_{pc}/i_{pa} for wave I, II, III and IV approached unity, which indicated that these electrochemical reactions were not accompanied by any other physical or chemical processes. The reversibility and stability of the electrogenerated oxidised and reduced species were examined spectroelectrochemically. The controlled potential coulometric (CPC) study indicated that the number of electrons transferred for electrochemical reactions of the complex is one for each oxidation and reduction process.

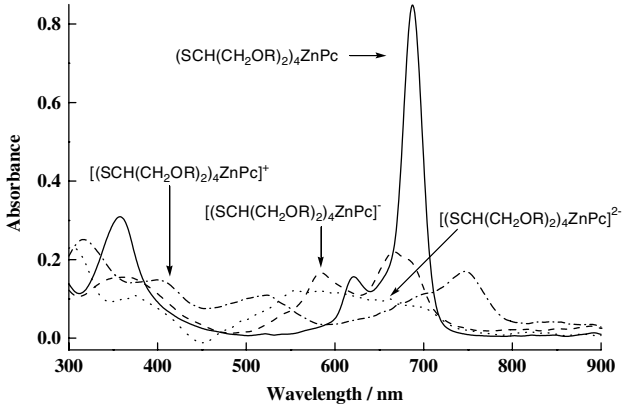


Fig. 4. UV–Vis spectra of $ZnPc(SCH(CH_2OR)_2)_4$ (solid line), $[ZnPc(-3)(SCH(CH_2OR)_2)_4]^-$ (dashed line), $[ZnPc(-4)(SCH(CH_2OR)_2)_4]^{2-}$ (dot line), and $[ZnPc(-1)(SCH(CH_2OR)_2)_4]^+$ (dashed dot line) in CH_2Cl_2 containing 0.2 M TBAP.

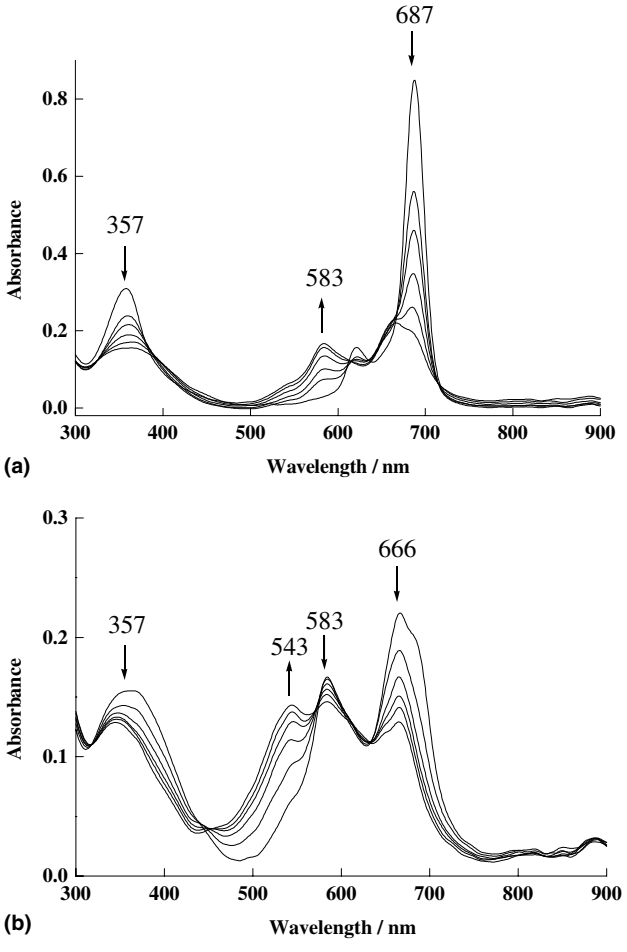


Fig. 5. Time-resolved UV–Vis spectral changes of ZnPc(SCH-$(CH_2OR)_2)_4$ (a) during the first reduction at E_{app} = −1.04V (b) during the second reduction at E_{app} = −1.62 V.

3.3. UV–Vis spectra of electro-oxidised and electro-reduced complexes

Typical absorption spectra for the neutral ZnPc (SCH $(CH_2OR)_2)_4$ and its electrochemically generated

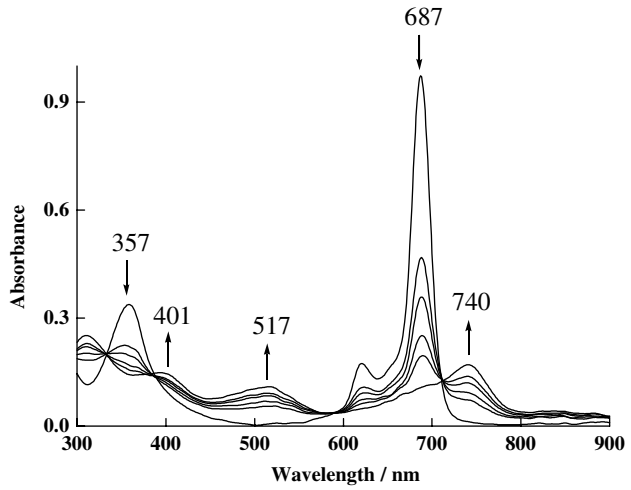


Fig. 6. Time-resolved UV–Vis spectral changes of $ZnPc(SCH(CH_2OR)_2)_4$ during the first oxidation at $E_{app} = 1.20$ V in CH_2Cl_2 solution containing 0.2 M TBAP.

species, $[ZnPc(-3)(SCH(CH_2OR)_2)_4]^-$, $[ZnPc(-4)(SCH(CH_2OR)_2)_4]^{2-}$, $[ZnPc(1)(SCH(CH_2OR)_2)_4]^+$ and $ZnPc(0)(SCH(CH_2OR)_2)_4]^{2+}$, are shown in Fig. 4, Fig. 5(a) and (b), and Fig. 6. The spectroscopic data for neutral and electrochemically generated species are also given in Table 2. The typical UV–Vis spectra of neutral $ZnPc(SCH(CH_2\ OR)_2)_4$ exhibited characteristic Q and B bands. The Q-band observed at 687 nm in the visible region could be attributed to the $\pi \rightarrow \pi^*$ transition from the highest occupied molecular orbital (HOMO) to the lowest unoccupied molecular orbital (LUMO) of the Pc(-2) ring, while the B-band observed at 357 nm in the UV region could be ascribed to deeper π-levels $\rightarrow$ LUMO transition. Both B and Q bands of $ZnPc(SCH(CH_2OR)_2)_4$ are slightly shifted to longer wavelengths compared to unsubstituted ZnPc, but are centred at higher energy compared to hexylthio-substituted zinc phthalocyanines. Such a red shift is an indication that the energy gap between the highest occupied molecular orbital (HOMO) and lowest unoccupied molecular orbital (LUMO) of the complex are narrower than those of the ZnPc, thereby increasing the electroconductivity of the molecule [40].

Spectroelectrochemical studies of metal phthalocyanines provide detailed information on the electron-transfer reaction, the colour changes and the number of electrons for each redox process on the electrode surface [39–41]. However, some spectroelectrochemical characterisations of phthalocyanines could be difficult because of the aggregation behaviour of phthalocyanine molecules in solution. The spectroelectrochemical measurements in this work provide well-defined UV–Vis spectra of electrogenerated species of $ZnPc(SCH(CH_2OR)_2)_4$ due to the lack of aggregation properties of the complex, thereby allowing a good evaluation of spectral changes corresponding to the reduced and oxidised species of $ZnPc(SCH(CH_2OR)_2)_4$ in solution. $ZnPc(SCH(CH_2OR)_2)_4$ was stepwise oxidised or reduced in a thin-layer cell with the applied potentials and the resulting UV–Vis spectra were measured as a function of time. Examples of the time-resolved spectra are shown in Fig. 5(a) and (b) and Fig. 6 and a summary of the spectroscopic data is given in Table 2.

The UV–Vis spectral changes upon the first reduction of $ZnPc(SCH(CH_2OR)_2)_4]$ with applied potential ($E_{app} = -1.04$ V) in a thin-layer cell containing 0.2 M TBAP in $CH_2\ Cl_2$ are shown in Fig. 5(a) and Fig. 4 (dashed line) for the final spectrum of $[ZnPc(-3)(SCH(CH_2OR)_2)_4]^-$. This reduction is accompanied with a change of colour from green to blue-green. Isosbestic points are observed at 385, 614, 665, and 717 nm. The spectrum is typical of a ZnPc(-3) species, characterised by the appearance of new bands at 583 and 666 nm with a blue shift and a decrease in intensity of the Q-band centred at 687 nm [54,55]. The spectrum also shows a broadness and a decrease in the intensity of the B-band. The spectroscopic changes that appeared with the formation of the new bands for the first reduced product are similar to those for the previously observed ZnPc [54,55]. The electron-transfer reaction was reversible on the spectroelectrochemical timescale and the original spectrum (and colour) of the neutral compound was obtained upon re-oxidation. It could be concluded that the reduced phthalocyanine remained fully stable throughout the experiment. The well-defined UV–Vis spectral changes during the second reduction of $ZnPc(SCH(CH_2OR)_2)_4$ with applied potential ($E_{app} = -1.62$ V) in the thin-layer cell are shown in Fig. 5(b) and Fig. 4 (dot line) for the final spectrum of $[ZnPc(-4)(SCH(CH_2OR)_2)_4]^{2-}$. The reduction product results in a colour change from blue-green to purple. Isosbestic points are observed at 318, 445, 572, and 631 nm. A decrease in intensity of the Q and B bands and the appearance of a new band at 543 nm are observed. Re-oxidation at a positive potential of ring-reduced species

Table 2
UV–Vis spectral data of $[ZnPc(SCH(CH_2OR)_2)_4]^n$ in CH_2Cl_2 containing 0.2 M TBAP

Charge, n	species	λ, nm (log ε)			
0	$ZnPc(SCH(CH_2OR)_2)_4$	357 (4.01)		620 (4.01)	687 (4.80)
+1	$[ZnPc(-1)(SCH(CH_2OR)_2)_4]^+$	322 (4.21)	401 (3.99)	517 (3.85)	740 (4.05)
−1	$[ZnPc(-3)(SCH(CH_2OR)_2)_4]^-$	357 (4.00)		583 (4.04)	666 (4.15)
−2	$[ZnPc(-4)(SCH(CH_2OR)_2)_4]^{2-}$	345 (3.89)	543 (3.97)	583 (3.98)	666(3.92)

generates the starting material with the same Q-band intensity.

UV–Vis spectral changes upon the first oxidation of $ZnPc(SCH(CH_2OR)_2)_4]$ with applied potential (E_{app} = 1.20 V) CH_2Cl_2 are shown in Fig. 6 and Fig. 4 (dashed dot line) for the final spectrum of $[ZnPc(-1)(SCH(CH_2OR)_2)_4]^+$. Isosbestic points are observed at 332, 338, 590, and 711 nm. The Q band shifts to high energy due to differential spin-pairing energy, which is centred at 517 nm as a broad band. The new band at low intensity also appears at 740 nm. It could be attributed to the presence of a hole in $1a_{1u}$ which permits transition from eg(π) levels lying below the $1a_{1u}$. B bands with a small blue shift are also observed. The broad and low-intensity spectrum is very similar to those reported for the ring oxidations of phthalocyanines [56–58] and metalloporphyrins [59], which form phthalocyanine and porphyrin cation radical species. The characteristic band centred at 822 nm describes the monomeric form of mono-cationic species of unsubstituted zinc phthalocyanines. The new band centred at 740 nm and the lack of a new band in the range 800 and 1000 nm for $[ZnPc(-1)(SCH(CH_2OR)_2)_4]^+$ could be assigned to the dimeric formation of the mono-cationic species. This behaviour is similar to what was observed for the dimeric formation of the mono-cationic species of ZnPc in solution. Re-reduction at a negative potential of ring-oxidised species generates the starting material with the same Q-band intensity, which means the oxidised product remains stable during the spectroelectrochemical process.

Acknowledgements

The support of Research Fund of Technical University of Istanbul and State Planning Organization (DPT) is gratefully acknowledged. This work was also supported, in part, by a Grant-inAid from Turkish Academy of Science.

References

[1] J. Simon, P. Bassoul (Eds.), Design of Molecular Materials: Supramolecular Engineering, John Wiley & Sons, Chichester, 2000, p. 197.
[2] X. Lu, K.W. Hipps, J. Phys. Chem. B 101 (1997) 5391.
[3] W. Göpel, Synth. Met. 41 (1991) 1087.
[4] M.A. Diaz Garcia, I. Ledoux, J.A. Duro, T. Torres, F. Agullo-Lopez, J. Zyss, J. Phys. Chem. 98 (1994) 8761.
[5] G.Y. Yang, M. Hanack, Y.W. Lee, Y. Chen, M.K.Y. Lee, D. Dini, Chem. Eur. J. 9 (2003) 2758.
[6] A. Gonzalez-Cabello, C.G. Claessens, G. Martin-Fuch, I. Ledoux-Rack, P. Vazquez, J. Zyss, F. Agullo-Lopez, T. Torres, Synth. Met. 137 (2003) 1487.
[7] H. Eichhorn, D. Wöhrle, D. Pressner, Liq. Cryst. 22 (1997) 643.
[8] D. Lelievre, M.A. Petit, J. Simon, Liq. Cryst. 4 (1989) 707.
[9] K. Hatsusaka, K. Ohta, J. Porhyrins, Phthalocyanines (2003) 105.
[10] J.A. Duro, G. DelaTorre, J. Barbera, J.L. Serrano, T. Torres, Chem. Mater. 8 (1996) 1061.
[11] G.E. Collins, N.R. Amstrong, J.W. Pankow, C. Oden, R. Brina, C. Anbour, J.P. Dodelet, J. Vac. Sci. Technol. A 11 (1993) 1383.
[12] J.D. Wright, P. Roisin, G.P. Rigby, R.J.M. Nolte, M.J. Cook, S.C. Thorpe, Sensor. Actuat. B: Chem. 13 (1993) 276.
[13] P. Roisin, J.D. Wright, R.J.M. Nolte, O.E. Sielcken, S.C. Thorpe, J. Mater. Chem. 2 (1992) 131.
[14] I. Rosenthal, in: C.C. Leznoff, A.B.P. Lever (Eds.), The Phthalocyanines Properties and Applications, vol. 4, VCH Publishers, New York, 1996, p. 485.
[15] P. Zimcik, M. Miletin, J. Ponec, M. Kostka, Z. Fiedler, J. Photochem. Photobiol. A 155 (2003) 127.
[16] C.M. Allen, W.M. Sharman, J.E. Van Lier, J. Porhyr. Phthalocya. 5 (2001) 161.
[17] J.H. Zagal, Coord. Chem. Rev. 119 (1992) 89.
[18] N. Kobayashi, W.A. Nevin, Appl. Organomet. Chem. 10 (1996) 579.
[19] W.J. Todd, F. Bailly, J. Pavez, P.W. Faguy, R.P. Baldwin, R.M. Buchanan, J. Am. Chem. Soc. 120 (1998) 4887.
[20] A.L. Bouwkamp-Wijnoltz, W. Visscher, J.A.R. van Veen, E. Boellaard, A.M. van der Kraan, S.C. Tang, J. Phys. Chem. B 106 (2002) 12993.
[21] G. Guillaud, J. Simon, J.P. Germain, Coord. Chem. Rev. 178 (1998) 1433.
[22] R. Zhou, F. Josse, W. Göpel, Z.Z. Özturk, O. Bekaroğlu, Appl. Organomet. Chem. 10 (1996) 557.
[23] D. Wöhrle, D. Meissner, Adv. Mater. 3 (1991) 129.
[24] T.A. Yourre, L.I. Rudaya, N.V. Klimova, V.V. Shamanin, Semiconductors 37 (2003) 807.
[25] D. Wöhrle, L. Kreienhoop, G. Schnurpfeil, J. Elbe, B. Tennigkeit, S. Hiller, D. Schlettwein, J. Mater. Chem. 5 (1995) 1819.
[26] C.L. Lin, C.C. Lee, K.C. Ho, J. Electroanal. Chem. 524 (2002) 81.
[27] R. Jones, A. Krier, K. Davidson, Thin Solid Films 298 (1997) 228.
[28] M. Bakkush, M.M. Salleh, M. Yahaya, I. AbuTalib, Solid State Ionics 86 (1996) 983.
[29] N. Toshima, T. Tominaga, S. Kawamura, Bull. Chem. Soc. Jpn. 69 (1996) 245.
[30] D. Wöhrle, V. Schmidt, J. Chem. Soc., Dalton Trans. (1998) 549.
[31] W. Eberhardt, M. Hanack, Synthesis 1 (1997) 95.
[32] A.G. Gürek, O. Bekaroğlu, J. Chem. Soc., Dalton. Trans. (1994) 1419.
[33] İ. Gürol, V. Ahsen, O. Bekaroğlu, J. Chem. Soc., Dalton Trans. (1994) 497.
[34] A.G. Gürek, Ö. Bekaroğlu, J. Porhyr. Phthalocya. 1 (1997) 67.
[35] A. Louati, M. Elmeray, J.J. Andre, J. Simon, K.M. Kadish, M. Gross, A. Giraudeau, Inorg. Chem. 24 (1985) 1175.
[36] M. Kandaz, I. Yılmaz, O. Bekaroğlu, Polyhedron 19 (2000) 115.
[37] I. Yılmaz, O. Bekaroğlu, Chem. Ber. 129 (1996) 967.
[38] S. Hayashida, N. Hayashi, Chem. Lett. (1990) 2137.
[39] K.M. Kadish, T. Nakanishi, A.G. Gürek, V. Ahsen, I. Yılmaz, J. Phys. Chem. B 105 (2001) 9817.
[40] I. Yılmaz, T. Nakanishi, A. Gürek, K.M. Kadish, J. Porhyr. Phthalocya. 7 (2003) 227.
[41] T. Nakanishi, I. Yılmaz, N. Nakashima, K.M. Kadish, J. Phys. Chem. B 107 (2003) 12789.
[42] I. Yılmaz, M. Kocak, Polyhedron 23 (2004) 1279.
[43] S. Dabak, A.G. Gürek, E. Musluoğlu, V. Ahsen, O. Bekaroğlu, New J. Chem. 25 (2001) 1583.
[44] G. Gümüs, V. Ahsen, J. Porhyr. Phthalocya. 6 (2002) 489.
[45] M. Kandaz, I. Yilmaz, S. Keskin, A. Koca, Polyhedron 21 (2002) 825.
[46] S. Dabak, A. Gül, O. Bekaroğlu, Chem. Ber. 127 (1994) 2009.
[47] M. Kandaz, S.Z. Coruhlu, I. Yılmaz, A.R. Ozkaya, Transition Metal. Chem. 27 (2002) 877.

[48] I. Yilmaz, O. Bekaroğlu, J. Chem. Res. S (1998) 374.
[49] A.G. Gürek, V. Ahsen, F. Heinemann, P. Zegenmaier, Mol. Cryst. Liq. Cryst. 338 (2000) 75.
[50] A.B.P. Lever, E.L. Milaeva, E. Speier, in: C.C. Leznoff, A.B.P. Lever (Eds.), The Phthalocyanines Properties and Applications, vol. 3, VCH Publishers, New York, 1993, p. 42.
[51] A.R. Özkaya, E. Hamuryudan, Z.A. Bayır, O. Bekaroğlu, J. Porhyr. Phthalocya. 4 (2000) 689.
[52] A.R. Özkaya, A.G. Gurek, A. Gül, Ö. Bekaroğlu, Polyhedron 11 (1997) 1877.
[53] A.J. Bard, L.R. Faulkner (Eds.), Electrochemical Methods: Fundamentals and Applications, second ed., John Wiley & Sons, New York, 2001, p. 228.
[54] A.B.P. Lever, E.L. Milaeva, E. Speier, in: C.C. Leznoff, A.B.P. Lever (Eds.), The Phthalocyanines Properties and Applications, vol. 3, VCH Publishers, New York, 1993, p. 231.
[55] J. Mack, M.J. Stillman, J. Am. Chem. Soc. 116 (1994) 1292.
[56] T. Nyokong, Z. Gasyna, M.J. Stillman, Inorg. Chem. 26 (1987) 548.
[57] T. Nyokong, Z. Gasyna, M.J. Stillman, Inorg. Chim. Acta 112 (1986) 11.
[58] G. Ferraudi, S. Oishi, S. Muraldiharan, J. Phys. Chem. 88 (1984) 5261.
[59] J. Fajer, D.C. Borg, A. Forman, D. Dolphin, R.H. Felton, J. Am. Chem. Soc. 92 (1970) 3451.

Available online at www.sciencedirect.com
SCIENCE DIRECT®
Polyhedron 24 (2005) 799–806
POLYHEDRON
www.elsevier.com/locate/poly

Potentiometric and spectroscopic studies on copper(II) complexes of non-proteinogenic histidine analogues

K. Várnagy [a,*], E. Garribba [b], D. Sanna [c], I. Sóvágó [a], G. Micera [b]

[a] Department of Inorganic and Analytical Chemistry, University of Debrecen, P.O. Box 21, H-4010 Debrecen, Hungary
[b] Department of Chemistry, University of Sassari, Via Vienna 2, I-07100 Sassari, Italy
[c] Istituto C.N.R. di Chimica Biomolecolare, Sezione di Sassari, Trav. La Crucca 3 Reg. Baldinca, I-07040 Sassari, Italy

Received 3 November 2004; accepted 10 February 2005
Available online 18 April 2005

Abstract

Copper(II) complexes of the histidine analogues: β-(2-pyridyl)-DL-alanine, β-(2-thienyl)-DL-alanine, β-(1,2,4-triazol-1-yl)-DL-alanine, β-(2-thiazolyl)-DL-alanine ligands, and for comparison α-(2-thienyl)glycine and 2-(2-aminoethyl)pyridine, were studied by potentiometric, UV–VIS, EPR and thermogravimetric techniques. The amino acid residues of the ligands were described as the main binding sites forming mono- and bis-(ligand) complexes, but the interaction between aromatic triazolyl and pyridyl nitrogen atoms and the copper(II) ion also was detected in the case of β-(1,2,4-triazol-1-yl)-DL-alanine and β-(2-pyridyl)-DL-alanine. The presence of heteroaromatic rings in the amino acid analogues influences the amino acid like coordination mode in the order imidazole > pyridyl ∼ triazolyl > thiazolyl ∼ thienyl rings.
© 2005 Elsevier Ltd. All rights reserved.

Keywords: Copper(II) complexes; Histidine analogue; pH-Potentiometry; EPR spectroscopy

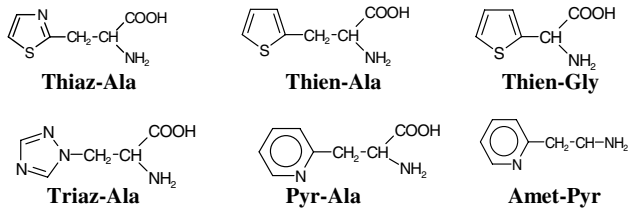
1. Introduction

The growing interest in the synthesis and studies of non-proteinogenic α-amino acids is due to their biological and toxicological properties. The substitution of naturally occurring amino acids in peptides with their structural analogues can produce dramatic changes in biological activity of peptides. For example, the presence of pyridyl-α-alanine or ring substituted derivatives instead of histidine in angiotensin II significantly decreases its substantial pressor acitivity [1]. The histidine decarboxylase enzyme is highly specific for L-histidine, but its structural analogues – β-pyridyl-2-alanine, β-thiazole-2-alanine and β-(1,2,4-triazole-3-alanine) – serve as poor substrates or enzyme inhibitors [2,3]. Moreover, as free α-amino acids they have been found to possess anti-inflammatory [4] and antitumor-antibiotic activities [2,3]. In recent years numerous non-proteinogenic α-amino acids analogues to histidine, phenylalanine, tyrosine have been synthesised and studied [5], but these studies were performed mainly from biological aspects. The imidazole group of histidine is, however, essential for metal binding activity of metalloenzymes. Its substitution with structural analogues in the enzyme could significantly change the metal binding ability too. The interactions between metal ions and different histidine analogue compounds have not been widely investigated yet. There are some literature data about the stereoselectivity of copper(II), nickel(II), cobalt(II) and zinc(II) complexes of the β-pyridyl-2-alanine ligand [6]; proton and 3d metal complexes of compounds containing heterocyclic rings (pyridyl, thiazolyl, pyrazol, thienyl) and amino [7–9] or carboxylate groups [10].

We report the results of the solution equilibrium studies of copper(II) complexes of histidine analogues:

* Corresponding author. Tel.: +36 525 12900; fax: +36 524 89667.
E-mail address: varnagy@tigris.klte.hu (K. Várnagy).

0277-5387/$ - see front matter © 2005 Elsevier Ltd. All rights reserved.
doi:10.1016/j.poly.2005.02.010



Scheme 1.

β-(2-pyridyl)-DL-alanine (Pyr-Ala), β-(2-thienyl)-DL-alanine (Thien-Ala), β-(1,2,4-triazol-1-yl)-DL-alanine (Triaz-Ala) and β-(2-thiazolyl)-DL-alanine (Thiaz-Ala) ligands, and for comparison α-(2-thienyl)glycine (Thien-Gly) and 2-(2-aminoethyl)pyridine (Amet-Pyr) (see Scheme 1).

2. Experimental

2.1. Materials

The amino acid analogues : β-(2-pyridyl)-DL-alanine, β-(2-thienyl)-DL-alanine, β-(1,2,4-triazol-1-yl)-DL-alanine, β-(2-thiazolyl)-DL-alanine, α-(2-thienyl)glycine and 2-(2-aminoethyl)pyridine were purchased from Bachem and their purities were checked by TLC and HPLC methods. Concentrations of the ligand stock solutions were determined by potentiometric titrations. A stock solution of copper(II) was prepared from analytical grade reagents and the concentration was checked gravimetrically via the precipitation of oximates.

2.2. Potentiometric measurements

The pH-potentiometric titrations in the pH range 2.0–11.0 were performed on 3–4 cm^3 samples in the concentration range 2×10^{-3}–8×10^{-3} mol dm^{-3} at metal ion to ligand ratios ranging between 1:5 and 1:1. Argon was bubbled through the samples to ensure the absence of oxygen and to stir the solutions. Measurements were carried out at 298 K and at a constant ionic strength of 0.2 mol dm^{-3} KCl with a Radiometer pHM84 pH-meter equipped with a 6.0234.100 combined glass electrode (Metrohm) and a Dosimat 715 automatic burette (Metrohm) containing carbonate-free potassium hydroxide in known concentration. The number of experimental points reached around 50–70 data (cm^3 – pH) for each titration curve. The pH readings were converted into hydrogen ion concentration as described earlier [11].

Protonation constants of the ligands and the overall stability constants (log β_{pqr}) of the systems were calculated by means of general computational programs, PSEQUAD [12] and SUPERQUAD [13] using Eqs. (1) and (2).

$$pM + qH + rL \rightleftharpoons M_pH_qL_r, \tag{1}$$

$$\beta_{pqr} = \frac{[M_pH_qL_r]}{[M]^p\cdot[H]^q\cdot[L]^r}. \tag{2}$$

2.3. Spectroscopic measurements

UV–VIS spectra of the copper(II) complexes were recorded on a Hewlett Packard HP 8453 or JASCO UVI-DEC-610 spectrophotometer in the same concentration range as used for the potentiometry. Anisotropic X-band EPR spectra (9.15 GHz) of frozen solutions were recorded at 120 K, using a Varian E-9 spectrometer after addition of 10% ethylene glycol to ensure good glass formation in frozen solutions. The copper(II) stock solutions for EPR measurements were prepared from $CuSO_4\cdot5H_2O$ enriched with ^{63}Cu to get better resolution of the EPR spectra. For this purposes metallic copper (99.3% ^{63}Cu and 0.7% ^{65}Cu) was purchased from JV Isoflex, Moscow, Russia and converted to the sulfate.

2.4. Synthesis of the solid complex of β-(2-thienyl)-DL-alanine

The solid complex was obtained by dissolving in 50 ml of water, 0.5 mmol of Thien-Ala (85.6 mg) and 0.25 mmol of natural $CuSO_4\cdot5H_2O$ (^{63}Cu plus ^{65}Cu) (62.4 mg). NaOH was added to the solution under stirring until pH ~5. The reaction was performed at room temperature. A sky-blue polycrystalline precipitate was separated off after ca. 1 h. It was filtered off, washed with cool water and Et_2O dried at room temperature. Thermogravimetric data were obtained with a Perkin–Elmer TGS-2 apparatus under a nitrogen flow. Elemental analysis (C, H, N) was carried out with a Perkin–Elmer 240 B elemental analyser. IR spectra were recorded with a FT Bruker IFS-66 interferometer using KBr disks in the range 4000–500 cm^{-1}.

Anal. Calc. for $C_{14}H_{16}N_2O_4S_2Cu$ (403.96 g/mol): C, 41.63; H, 3.99; N, 6.93; CuO, 19.7. Found: C, 41.51; H, 3.77; N, 6.87%; CuO, 19.0%.

IR (KBr, cm^{-1}): 3265(s), 3147(s), 2952(w), 1633(vs), 1439(m), 1374(s), 1355(s), 1296(m), 1136(m), 1106(s), 973(w), 870(w), 845(m), 812(w), 710(s), 699(s).

3. Results and discussion

3.1. Protonation constants

The amino acid analogues (Thien-Gly, Thien-Ala, Thiaz-Ala, Triaz-Ala and Pyr-Ala) have principally three dissociable protons: the carboxyl group, the protonated amino group and the protonated aromatic group, which may take part in proton equilibrium pro-

Table 1
Protonation constants of the ligands ($T = 298$ K, $I = 0.2$ mol dm^{-3}; standard deviations are in parentheses)

	HL	H_2L	pK (COOH)	pK (Ar)	pK (NH_2)
Thien-Gly	8.38(1)	10.02(3)	1.64		8.38
Thien-Ala	8.82(1)	10.81(2)	1.99		8.82
Thiaz-Ala	8.38(1)	10.49(1)	2.11		8.38
Triaz-Ala	7.63(1)	9.42(1)	1.79		7.63
Pyr-Ala	8.86(1)	12.82(2)	<1	3.96	8.86
Amet-Pyr	9.63(2)	13.64(2)		4.01	9.63
2-Picolyl-amine [9]	8.69	10.83		2.04	8.79
His [18]	9.09	15.11	1.7	6.02	9.09
Histamine [19]	9.89	16.06		6.17	9.89
Phe [20]	9.11	11.33	2.22		9.11
Ala [14]	9.68	12.03	2.35		9.68

cesses. In the case of aliphatic amino acids the deprotonation of carboxylic and ammonium groups occur around pH 2 and 9, respectively (Gly:pK(COOH) = 2.36, p$K(NH_3^+) = 9.55$ [14] and see Table 1). The heteroaromatic compounds connected as side chains in our ligands themselves are also weak bases (pK values for pyridine: 5.26 [15], 1,2,4-triazole: 2.50 [16], thiazole: 2.68 [17]).

The protonation constants of the studied ligands and some others for comparison are collected in Table 1.

It is clear from these data that the highest pK values belong to the deprotonation of the ammonium group. However, only one more protonation process can be detected by potentiometric titration. For Pyr-Ala it can correspond to the pK value of the pyridine ring, and this is in good agreement with that detected for Amet-Pyr. In the case of the other four amino acid analogues (Triaz-Ala, Thiaz-Ala, Thien-Ala, Thien-Gly) the carboxylate group is a stronger base than the aromatic nitrogen donor atoms and this means that the pK values are characteristic for the proton equilibrium of the carboxylate group.

It can be concluded from an examination of Table 1 that the presence of an aromatic ring, due to its electron withdrawing effect, similarly decreases the pK values of both the ammonium and carboxylic group to Phe [20] and His [18]. Because of the decreasing basicity of the carboxylate group of Pyr-Ala, it was not possible to determine its pK value by potentiometry. On the other hand, the amino acid moiety decreases significantly the proton acceptor ability of the aromatic rings too. These processes take place only below pH 1.5, in agreement with literature data and similar effects were observed earlier for β-(2-pyridyl)-L-alanine, β-(2-pyridyl)-DL-alanine (pK(Ar) = 3.89, $pK(NH_3^+) = 8.95$) [6] and for 4,2′-aminoethylthiazole (pK(Ar) = 1.68, $pK(NH_3^+) = 9.53$) [7].

3.2. Copper(II) complexes of Thien-Gly, Thien-Ala and Thiaz-Ala

The stability constants of the copper(II) complexes are collected in Table 2.

It seems from the stoichiometry of the complexes that three amino acid analogues, Thien-Gly, Thien-Ala and Thiaz-Ala, form mono- and bis(ligand) complexes, $[CuL]^+$ and $[CuL_2]$. The ligands are coordinated to the metal centre in these complexes via (COO^-, NH_2) donor groups, similarly to the simple amino acids. This coordination mode is supported by the VIS and EPR parameters of the $[CuL]^+$ and $[CuL_2]$ complexes (see Table 3) which are in good agreement with those of Ala [22]. The log(K_1/K_2) values, which characterise the binding of the second ligand to the copper(II) ion, are similar to each other and to that of Phe [20].

These values, however, are lower than that of Ala [14] suggesting a favourable stacking interaction between the aromatic side chains in the bis(ligand) complexes [18,23]. The stability constants and spectroscopic parameters of the copper(II) complexes of Thien-Gly and Thien-Ala are similar. The fact that the aromatic thienyl ring, independently from the distance between the aromatic ring and amino acid moiety in the molecule, does not influence the complex formation processes also establishes the amino acid like coordination in both cases.

Table 2
Stability constants (logβ) of copper(II) complexes ($T = 298$ K, $I = 0.2$ mol dm^{-3}; standard deviations are in parentheses)

	Thien-Gly	Thien-Ala	Thiaz-Ala	Triaz-Ala	Pyr-Ala	Amet-Pyr	2-Picolyl-amine [9]	Phe [20]	Ala [14]	His [21]	Histamine [19]
CuHL				10.28(6)	11.91(3)					14.07	
CuL	7.00(1)	7.68(1)	8.20(1)		8.24(3)	7.44(1)	9.40	7.86	8.07	10.04	9.58
CuH_2L_2										27.13	
$CuHL_2$					19.72(9)					23.63	21.79
CuL_2	12.75(2)	14.37(3)	15.20(3)	12.81(6)	15.43(3)	12.62(2)	17.20	14.77	14.79	17.82	16.06
Cu_2L_2				17.39(3)							
$CuH_{-1}L$						0.00(2)				1.5	1.2
$CuH_{-2}L$						–11.54(2)					
$Cu_2H_{-2}L_2$										8.0	7.00
pK(MHL/ML)					3.67					4.03	
pK(MHL_2/ML_2)					4.29					5.81	5.73
log(K_1/K_2)	1.25	0.99	1.20		1.05	2.26	1.60	0.95	1.35	2.26	3.10

Table 3
UV-VIS and EPR spectral parameters of the copper(II) complexes

		Thien-Gly	Thien-Ala	Thiaz-Ala	Ala [22]
ML	Coordination mode	(COO^-, NH_2)	(COO^-, NH_2)	(COO^-, NH_2)	(COO^-, NH_2)
	λ_{max} [nm] (ε [dm^3 mol^{-1} cm^{-1}])	700 (34)	690 (35)	709 (45)	
	$A_\parallel$ [10^{-4} cm^{-1}]; $g_\parallel$		164.0; 2.312	164.2; 2.296	165.2; 2.308
ML_2	Coordination mode	$2\times$(COO^-, NH_2)	$2\times$(COO^-, NH_2)	$2\times$(COO^-, NH_2)	$2\times$(COO^-, NH_2)
	λ_{max} [nm] (ε [dm^3 mol^{-1} cm^{-1}])	628 (68)	620 (61)	639 (94)	620 (60)
	$A_\parallel$ [10^{-4} cm^{-1}]; $g_\parallel$		179.7; 2.253	180.5; 2.239	179.6; 2.251
	$g_\parallel/A_\parallel$		125	124	125

In the case of Thien-Ala, the complex formation process was investigated in the solid state too. The stoichiometry of the complex isolated from a solution containing copper(II) and ligand in a 1:2 ratio was determined by means of elemental and thermogravimetric analysis and the results confirm the Cu:L = 1:2 stoichiometry and the lack of water in the solid complex. The electronic spectra of the powder show two neighbouring absorptions centred at 540 and 580 nm, which is consistent with the literature data on the electronic spectrum of the [Cu(L-Ala)$_2$] solid complex [24]. A definitive indication of the coordination mode of the ligand in this complex has been obtained by dissolving the solid compound in a non-coordinating solvent. It is slightly or not soluble in methanol, ethylene glycol, DMSO and CH_3CN, but it is partially soluble in DMF. The EPR parameters obtained from the spectrum of the filtrate are $g_\parallel = 2.244$, $A_\parallel = 184\times10^{-4}$ cm^{-1}. These data are similar to those of the bis chelated complex formed by natural Cu(II) with L-Ala in aqueous solution ($g_\parallel = 2.250$, $A\|\ = 185\times10^{-4}$ cm^{-1}) [25] indicating the $2\times$(COO^-, NH_2) coordination mode in the solid complex.

3.3. Copper(II) complexes of Triaz-Ala, Pyr-Ala and Amet-Pyr

The speciation of Cu(II)–Triaz-Ala and –Pyr-Ala systems are different from that of the other ligands. The complex formation processes start in more acidic pH values than in the case of simple amino acids (Fig. 1) and the formation of protonated complexes can be supposed.

It was not possible to calculate the stability constants of the protonated bis(ligand) complexes probably because of the low amount of the species, but the EPR spectra indicate its formation in low concentration (Fig. 2(c)). The $[CuHL]^{2+}$ complex, however, predominates around pH 2 both in equimolar solution and with an excess of ligand (Fig. 2(b)).

In both complexes, the copper(II) ions are bound to one or two ligands via the aromatic nitrogen and the amino group is protonated. The EPR parameters of $[CuHL]^{2+}$ and $[CuH_2L_2]^{2+}$ (see Table 4) are comparable with those, recorded with natural $CuSO_4\cdot5H_2O$, of [Cu(imidazole)]$^{2+}$ ($g_\parallel = 2.359$, $A_\parallel = 145\times10^{-4}$ cm^{-1}) and [Cu(imidazole)$_2$]$^{2+}$ ($g_\parallel = 2.314$, $A_\parallel = 160\times10^{-4}$ cm^{-1}) [22], respectively. The difference can be attributed to the presence of ^{65}Cu in the imidazole complexes, which increases the $A_\parallel$ and decreases the $g_\parallel$ values.

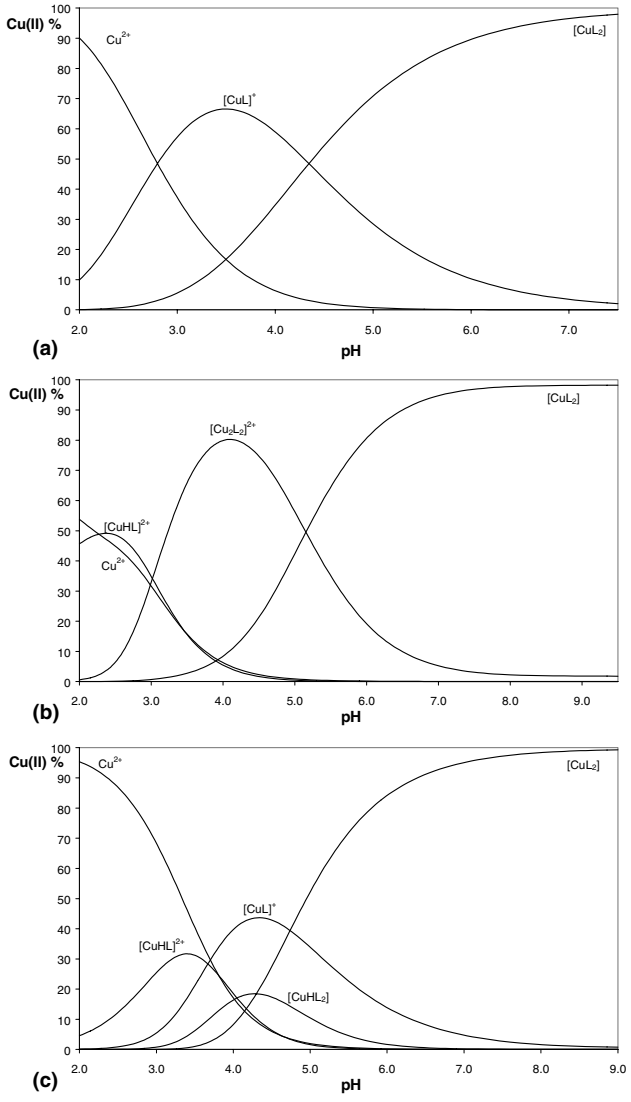


Fig. 1. Species distribution of the complexes formed in the copper(II)-ligand systems ($c_L = 4\times10^{-3}$ mol dm^{-3}, $c_{Cu(II)} = 2\times10^{-3}$ mol dm^{-3}) (a) L = Thiaz-Ala, (b) L = Triaz-Ala, (c) L = Pyr-Ala.

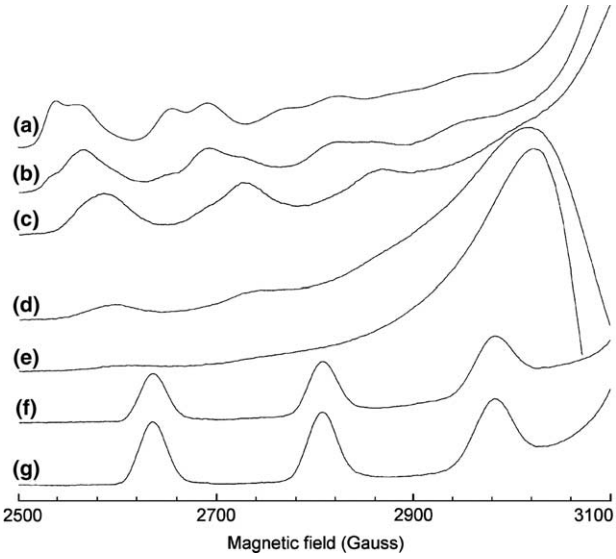


Fig. 2. Low-field parallel region of the X-band anisotropic EPR spectra recorded on the ^{63}Cu(II)–Triaz-Ala system at 140 K at different copper(II)-to-ligand molar ratios and pH values. Copper(II) concentration was 5×10^{-3} mol dm^{-3}. (a) Cu(II):L = 1:1, pH 1.42; (b) Cu(II):L = 1:2, pH 2.24; (c) Cu(II):L = 1:2, pH 3.03; (d) Cu(II):L = 1:2, pH 3.25; (e) Cu(II):L = 1:2, pH 4.00; (f) Cu(II):L = 1:2, pH 6.40; (g) Cu(II):L = 1:2, pH 10.27.

The deprotonation of the amino group is accompanied by a significant change of EPR spectra (Fig. 2). The spectra detected in the equimolar solution ($c_{Cu(II)} = 5 \times 10^{-3}$ mol dm^{-3}, pH of 3–8; $c_{Cu(II)} = 5 \times 10^{-2}$ mol dm^{-3}, pH of 2–8) and at excess of ligand (Cu:L = 1:2, pH of 3–6) show a broad, unresolved and isotropic band centred at $g \sim 2.130$ (Figs. 2(d) and (e)). A weak resonance can be simultaneously observed at 1560 G in the $\Delta M = \pm 2$ region. It reveals that di- or polynuclear species with dipolar coupling of the copper(II) ions are formed (the fitting of potentiometric data was made by the assumption of the formation of a dinuclear $[Cu_2L_2]^{2+}$ complex). In these species the ligands are bound both via amino acid like coordination and via an aromatic nitrogen donor, resulting in a ligand bridged structure. A water molecule completes the equatorial plane of the metal ion. The presence of di- or polynuclear species confirms that in the case of Triaz-Ala, the nitrogen donor atom of the aromatic ring in position 4 is not in a chelatable position with the terminal amino group and the involvement of all three donor groups of the molecule in the binding of the metal ions can take place only in a polynuclear structure. It means, however, that the tridentate coordination of Triaz-Ala can neither be supposed in $[CuL_2]$ species. The spectroscopic data obtained for $[CuL_2]$ are similar to those of bis(ligand) complexes of Thien-Ala and Ala and different from those of Pyr-Ala or His, supporting the amino acid like coordination in the $[CuL_2]$ species.

The complex formation processes of Pyr-Ala are also different from Thien-Gly, Thien-Ala and Thiaz-Ala. Similarly to Triaz-Ala, protonated mono- and bis-(ligand) complexes are present in a small amount around pH 3.5 (Fig. 1(c)). The coexistence of $[CuHL]^+$ species with the aqua ion is indicated by the shoulder high-field of the parallel hyperfine resonance of the spectrum detected in equimolar solution at pH 3.09 and at excess of ligand (1:2 ratio) at pH 3.52 (Fig. 3(a)).

Only approximated EPR parameters can be extracted (Table 4), because the formation of carboxylate complexes does not affect the EPR parameters very significantly in comparison to the aqua ion ($g_\parallel = 2.406$, $A_\parallel = 134 \times 10^{-4}$ cm^{-1}) [22]. In the $[CuHL]^{2+}$ species the ligand may bind monodentately via the pyridine nitrogen donor or carboxylate group or bidentately via amino acid like coordination. The spectroscopic parameters are, however, significantly different from those of amino acid like coordinated copper(II) complexes. It means that in the $[CuHL]^{2+}$ complex the amino group is protonated.

Table 4
UV–VIS and EPR spectral parameters of the copper(II) complexes

		Triaz-Ala	Pyr-Ala	Amet-Pyr	His	Histamine [22]
CuHL	Coordination mode	1 × Triaz N	Pyr N/COO$^-$		(COO$^-$, NH$_2$)	
	λ_{max} [nm] (ε [dm^3 mol^{-1} cm^{-1}])	782 (18)	743 (27)		750 [26]	
	$A_\parallel$ [10^{-4} cm^{-1}]; $g_\parallel$	143.0; 2.367	~137; ~2.38		176.6; 2.305 [22]	
CuL	Coordination mode		(NH$_2$, Pyr N) + ax COO$^-$	(NH$_2$, Pyr N)	(NH$_2$, Im N) + ax COO$^-$	(NH$_2$, Im N)
	λ_{max} [nm] (ε [dm^3 mol^{-1} cm^{-1}])		662 (45)	637 (66)	670 [26]	669
	$A_\parallel$ [10^{-4} cm^{-1}]; $g_\parallel$		170.2; 2.304	169.2; 2.290		179.2; 2.292
CuH_2L_2	Coordination mode	2 × Triaz N				
	$A_\parallel$ [10^{-4} cm^{-1}]; $g_\parallel$	148.9; 2.330				
CuL_2	Coordination mode	2 × (COO$^-$, NH$_2$)	(NH$_2$, Pyr N); COO$^-$, NH$_2$)	2 × (NH$_2$, pyr N)	(NH$_2$, Im N); COO$^-$, NH$_2$)	2 × (NH$_2$, Im N)
	λ_{max} [nm] (ε [dm^3 mol^{-1} cm^{-1}])	630 (65)	612 (89)	597 (93)	640 [26]	594
	$A_\parallel$ [10^{-4} cm^{-1}]; $g_\parallel$	183.8; 2.254	188.9; 2.235	189.6; 2.215	190.9; 2.230 [22]	199.9; 2.223
	$g_\parallel/A_\parallel$	123	118	117	117	111

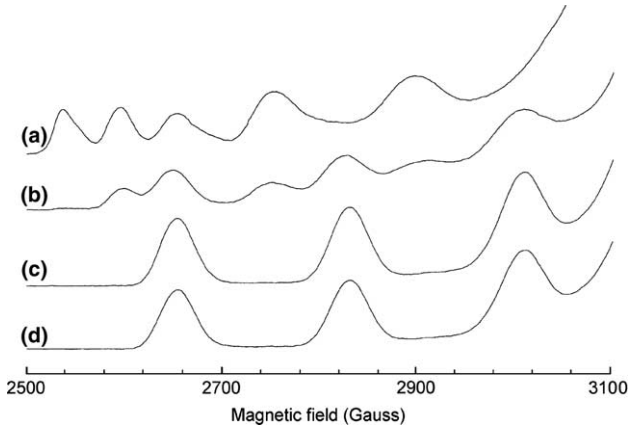


Fig. 3. Low-field parallel region of the X-band anisotropic EPR spectra recorded on the ^{63}Cu(II)–Pyr-Ala system at 140 K at different pH values. Copper(II)-to-ligand molar ratio was 1:2 and copper(II) concentration was 5×10^{-3} mol dm^{-3}, pH: (a) 3.52; (b) 3.97; (c) 7.84; (d) 10.12.

Information about the interaction between the copper(II) ion and the monodentately coordinated ligand can be obtained from value log $\beta([CuHL]^{2+})$ – log $\beta([HL]) = 11.91 - 8.86 = 3.05$. From the comparison of this data with stability constants of $[CuL]^{2+}$ formed in copper(II)–pyridine (log $\beta_1 = 2.49$ [15]) and copper(II)–acetic acid (log $\beta_1 = 1.81$ [15]) systems, the coordination of the aromatic pyridine nitrogen of the ligand can be concluded. This coordination mode is supported by UV–VIS parameters (Table 4), which corresponds to one nitrogen donor coordinated copper(II) complex. (The calculated λ_{max} for coordination of one aromatic nitrogen on the basis of Billo's empirical formulae [27] is 760 nm). On the other hand, the EPR parameters are close to those reported for the Cu(II)–COO^- interaction that exists in the copper(II)–lactobionic acid system ($g_\parallel = 2.369$, $A_\parallel = 138 \times 10^{-4}$ cm^{-1}) [28], so the protonated complex with carboxylate coordination cannot be excluded. $[CuHL]^{2+}$ is followed by the formation of a minor species, $[CuHL_2]^+$, not detectable by EPR spectroscopy.

The deprotonation processes of $[CuHL]^{2+}$ and $[CuHL_2]^+$ belong to the deprotonation of the amino group. The pK values of these processes (Table 2) are much lower than p$K(NH_3^+)$ values, due to the coordination of the amino group and formation of chelates in $[CuL]^+$ and $[CuL_2]$ complexes. The comparison of EPR parameters with those of the monochelated complex of L-Ala [22] (Table 3) and Amet-Pyr (Table 4) reveals the coordination of the (NH_2, Pyr N) donor set with the possible weak interaction of a carboxylate group in the axial position. The EPR parameters of $[CuL_2]$ are different with respect to those of the bis(ligand) complex of L-Ala (Table 3) and Amet-Pyr (Table 4). Particularly, the $g_\parallel$ value is intermediate between the two species: the $g_\parallel$ value of the bis(ligand) complex formed by Amet-Pyr is sensibly lower and substantiates coordination of four nitrogen donor atoms, whilst the $[CuL_2]$ complex of L-Ala is bound only by two nitrogen donor atoms. These data, however, are in good agreement with the parameters measured for the mixed complex formed by Amet-Pyr and Gly ($g_\parallel = 2.236$ and $A_\parallel = 187 \times 10^{-4}$ cm^{-1}), with coordination of the (NH_2, Pyr N; COO^-, NH_2) set, [22] revealing the same type of donor set in $[CuL_2]$ species of Pyr-Ala. The EPR parameters are comparable also with those reported by Micera et al. for the mixed complex [Cu(His)(Ala)], ($g_\parallel = 2.239$ and $A_\parallel = 192 \times 10^{-4}$ cm^{-1}) and for [Cu(His)-(Val)], ($g_\parallel = 2.239$ and $A_\parallel = 190 \times 10^{-4}$ cm^{-1}) [29]. In these cases a mixed CuN_3O coordination mode has been proposed with a (COO^-, NH_2) donor set of the aliphatic amino acid and with the (NH_2, Im N) set of histidine. This conclusion is supported by the electronic absorption data for CuL_2 (612 nm), which are very similar to those of complex $[Cu(Amet\text{-}Pyr))(Gly)]^+$ ($\lambda_{max} = 614$ nm and $\varepsilon_{max} = 71$ M^{-1} cm^{-1}) [22] and [Cu(His)(Ala)] (610 nm) and [Cu(His)(Val)] (610 nm) [29]. The weak coordination of a carboxylate group of one ligand and of an aromatic nitrogen atom of the second one in the two axial positions cannot be excluded on the basis of our measurement.

The $g_\parallel/A_\parallel$ values (see the last rows of Tables 3 and 4) of Pyr-Ala and Amet-Pyr are similar to each other (118 and 117, respectively) and are different from that of Ala (125), indicating a marked planarity of the $[CuL_2]$ complexes, greater than that of L-Ala. In the case of Amet-Pyr, however, the log(K_1/K_2) value is much higher than that of Pyr-Ala. In the bis(ligand) complex of Amet-Pyr, two amino and two aromatic nitrogen donors are bound in the equatorial plane of the copper(II) centre. As it was published earlier [21], the coordination of mixed aromatic N, amino N and O donor atoms are much more preferable than the binding of $2 \times (NH_2$, Ar N) donor groups. For Pyr-Ala, EPR measurements were performed in a more concentrated equimolar solution ($c_{Cu(II)} = c_L = 5 \times 10^{-2}$ mol dm^{-3}) too. In this case a polynuclear $[(CuL)_n]$ species is the major complex in the pH range 4–6. In this species each Cu(II) ion should be surrounded by amino- and pyridine nitrogens and an oxygen atom of a carboxylate group in the equatorial region, and each ligand acts as a bridge between two Cu(II) ions. The arrangement is comparable to that of the analogous species formed by Triaz-Ala. In the spectrum recorded at pH 4.62 the presence in the $\Delta M = \pm 1$ region of an unresolved broad and isotropic resonance centred at $g = 2.098$ can be observed, by which the resonances of the monomers are superimposed (Fig. 4). This indicates a magnetic interaction of two or more $S = 1/2$ ions, even if the lack of fine and hyperfine resolution hinders the advance of a hypothesis about the particular structure of the complex. The presence of a signal in $\Delta M = \pm 2$ region at $H = 1540$ G substantiates our

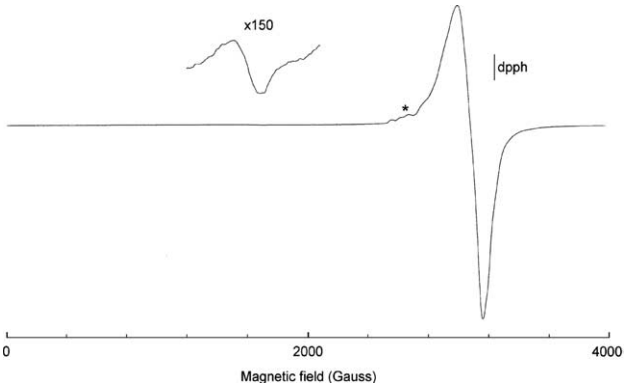


Fig. 4. X-band anisotropic EPR spectrum recorded at 140 K on the ^{63}Cu(II)–Pyr-Ala system at pH 4.62 and metal concentration 5×10^{-2} M. The signals attributable to monomeric species are denoted with an asterisk. The $\Delta M = \pm 2$ transition has been amplified 150-fold.

hypothesis. The approximated λ_{max} value is 672 nm ($\varepsilon_{max} = 33\ M^{-1}\ cm^{-1}$), which corresponds a polynuclear species with the set (NH_2, Pyr N, COO^-, H_2O) coordinated to the copper(II) ions. This value is slightly higher than that of the mixed species [Cu(2-(2-aminoethyl)pyridine)(oxalato)], characterised by a (NH_2, Pyr N, COO^-, COO^-) donor set ($\lambda_{max} = 647$ nm) [22]. The presence of a water molecule instead of a carboxylate ion in the coordination sphere of copper(II) would increase the λ_{max} value by about 20 nm [27].

4. Conclusion

The complex forming properties of five non-proteinogenic histidine analogues were studied and the results of their copper(II) complexes are summarised in this paper. The main binding sites of all five amino acid ligands are the amino acid moiety and in all cases amino acid like coordinated complexes are present in almost the whole pH range studied. Depending on the type of aromatic ring, however, the complex formation processes and/or stability of complexes are affected more or less compared to those of simple amino acids.

For three ligands, Thien-Gly, Thien-Ala and Thiaz-Ala, the coordination of aromatic donor groups was not detected in any species, but similarly to Phe the stability of bis(ligand) complexes is enhanced due to the stacking effect of aromatic rings.

The interaction between aromatic triazolyl or pyridyl nitrogen atoms and copper(II) ion was assumed in the case of Triaz-Ala and Pyr-Ala. It results in the formation of protonated mono- and bis-(ligand) complexes in strong acidic media with monodentate binding of the ligands. Following the deprotonation of the amino group, the binding of all donor groups (amino, carboxylate and aromatic nitrogen) can be supposed. In the case of Triaz-Ala, because of the steric effect, it could exist only as a polynuclear structure with ligand bridging, while tridentate coordination of Pyr-Ala was detected in the mononuclear complexes formed in diluted solution ($c_L = 5 \times 10^{-3}$ mol dm^{-3}). The polynuclear structure, however, also can be formed in the copper(II)–Pyr-Ala system, but with a more concentrated solution ($c_L = 5 \times 10^{-2}$ mol dm^{-3}) than in the case of Triaz-Ala.

As a conclusion, we can state that the presence of heteroaromatic rings in an amino acid analogue can influence the amino acid like coordination mode. Their effects decrease in order imidazole > pyridyl ~ triazolyl > thiazolyl ~ thienyl rings.

Acknowledgements

This work was supported by the Hungarian Scientific Research Fund (Hungary, OTKA T042722) and by the Ministry of Education (István Széchenyi Research Grant). The authors thank Mrs. Á. Gönczy for her valuable experimental work.

References

[1] K. Hsieh, E.C. Jorgensen, J. Med. Chem. 22 (1979) 1199.
[2] G.W. Chang, E. Snell, Biochemistry 7 (1968) 2005.
[3] S. Tanase, B.M. Guirard, E. Snell, J. Biol. Chem. 260 (1985) 6738.
[4] D.C. Roberts, F. Vellaccio, The Peptides, Academic, New York, 1983.
[5] A. Dondoni, A. Massi, E. Minghini, V. Berolasi, Tetrahedron 60 (2004) 2311.
[6] P.R. Rechani, R. Nakon, R.J. Angelici, Bioinorg. Chem. 5 (1976) 329.
[7] F. Holmes, F. Jones, J. Chem. Soc.(A) (1960) 2398.
[8] F. Holmes, J. Chem. Soc.(A) (1967) 1702.
[9] G. Anderegg, Helv. Chim. Acta 54 (1971) 509.
[10] G. Arena, R. Cali, E. Maccarone, A. Passerini, J. Chem. Perkin Trans. Soc. 2 (1993) 1941.
[11] H. Irving, G. Miles, L.D. Pettit, Anal. Chim. Acta 38 (1967) 475.
[12] L. Zékány, I. Nagypál, in: D.J. Leggett (Ed.), Computational Methods for the Determination of Formation Constants, Plenum Press, New York, 1985, pp. 291–299.
[13] P. Gans, A. Sabatini, A. Vacca, J. Chem. Soc., Dalton Trans. (1985) 1196.
[14] A. Gergely, I. Sóvágó, J. Inorg. Nucl. Chem. 35 (1973) 4355.
[15] D. Banerjea, T. Kaden, H. Sigel, Inorg. Chem. 20 (1981) 2586.
[16] B. Lenarcik, K. Kurdziel, M. Gabryszewski, J. Inorg. Nucl. Chem. 42 (1980) 587.
[17] B. Barszcz, M. Gabryszewski, J. Kulig, B. Lenarcik, J. Chem. Soc., Dalton Trans. (1986) 2025.
[18] T. Kiss, Complexes of amino acids, in: K. Burger (Ed.), Biocoordination Chemistry, Ellis Horwood, New York, 1990, pp. 57–134.
[19] I. Sóvágó, A. Gergely, Inorg. Chim. Acta 20 (1976) 27.
[20] A. Gergely, I. Sóvágó, I. Nagypál, R. Király, Inorg. Chim. Acta 6 (1972) 435.
[21] I. Sóvágó, T. Kiss, A. Gergely, J. Chem. Soc., Dalton Trans. (1978) 964.
[22] E. Garribba, G. Micera, D. Sanna, unpublished results.
[23] R.B. Martin, Met. Ions Biol. Syst. 9 (1979) 1.

[24] M.A. Hitchman, L. Kwan, L.M. Engelhardt, A.H. White, J. Chem. Soc., Dalton Trans. (1987) 457.
[25] E. Chruscinska, E. Garribba, G. Micera, A. Panzanelli, J. Inorg. Biochem. 75 (1999) 225.
[26] T.P. Kruck, B. Sarkar, Can. J. Chem. 54 (1971) 509.
[27] E.J. Billo, J. Inorg. Nucl. Chem. Lett. 10 (1974) 613.
[28] S. Bouhsina, P. Decock, H. Kozlowski, G. Micera, J. Swiatek, J. Inorg. Biochem. 42 (1991) 57.
[29] P. Cocetta, S. Deiana, L. Erre, G. Micera, P. Piu, J. Coord. Chem. 12 (1983) 213.

Available online at www.sciencedirect.com
SCIENCE DIRECT®
Polyhedron 24 (2005) 807–821
POLYHEDRON
www.elsevier.com/locate/poly

Complexes derived from hydrolytically 'unstable' hydrazone ligands – Some unexpected products

Timothy L. Kelly [a], Victoria A. Milway [a], Hilde Grove [a], Virginie Niel [a], Tareque S.M. Abedin [a], Laurence K. Thompson [a,*], Liang Zhao [a], Rosemary G. Harvey [a], David O. Miller [a], Michael Leech [b], Andrés E. Goeta [b], Judith A.K. Howard [b]

[a] *Department of Chemistry, Memorial University, Elizabeth Avenue, St. John's, Nfld, Canada A1B 3X7*
[b] *Department of Chemistry, University of Durham, Durham DH1 3LE, UK*

Received 15 October 2004; accepted 11 February 2005
Available online 13 April 2005

Abstract

Polyfunctional ligands derived from condensation reactions in which small molecules, e.g., water, an alcohol, etc., are eliminated can suffer the ravages of hydrolytic attack on reaction with transition metal ions in aqueous based solvents, or solvents containing small amounts of water. A series of such reactions is described involving hydrazone based ligands, in which hydrolyzed ligand fragments, and their resulting coordination complexes, are produced. Structures are reported to identify these products, which reveal some unexpected ligand rearrangements. Variable temperature magnetic data are discussed for some dinuclear complexes, and a DFT study is presented to rationalize an unusual ligand transformation.
© 2005 Elsevier Ltd. All rights reserved.

Keywords: Hydrazone ligands; Complexes; Copper; Nickel; Iron; Cobalt; Hydrolysis; Structure; Magnetism

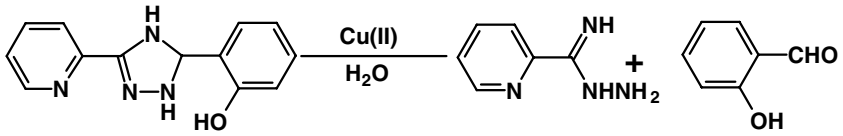
1. Introduction

Ligands derived from condensation reactions, which involve elimination of small molecules, e.g., water, or an alcohol, are at risk of hydrolytic attack in solvents that contain water, when reacted with transition metal salts. Such reactions can be promoted or catalyzed by the presence of the transition metal ion, whose high ionic potential can in many cases exert a significant polarizing effect on the hydrolytically vulnerable bonds. In some cases the complexes which are formed contain 'expected' hydrolysis products, but in other cases some surprising results can occur.

In a recent report the ligand L1 was shown to be hydrolytically unstable in the presence of $CuBr_2$ in aqueous acetonitrile, and a mixed oxidation state $Cu(II)_4Cu(I)_2$ complex of the ligand picolinamide hydrazone (PAH) was produced (Scheme 1) [1]. The reduction of copper(II) was associated with the presence of acetonitrile and the reducing capacity of salicylaldehyde, detected during the reaction. The symmetrical open chain diazine ligands PAHAP and PZHPZ (Chart 1) react with Fe(III) nitrate in aqueous solution to spontaneously form the reduced dinuclear $[Fe(II)_2(L)_3]^{4+}$ (L = PAHAP, PZHPZ) complex ions in low yield, suggesting the formation of hydrazine based fragments, presumably resulting from hydrolysis of an imine group, which act as metal ion reductants. In the case of PAHAP, reaction with Fe(III) nitrate also produces the complex ion $[Fe(III)(POAP-H)(H_2O)_2(NO_3)]^{2+}$ (POAP, Chart 1) as a minor product, indicating the imine group as an initial point of hydrolytic

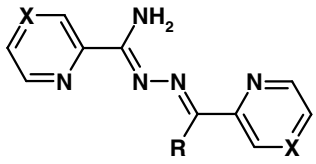
* Corresponding author. Tel.: +1 709 737 8750; fax: +1 709 737 3702.
E-mail address: lthomp@mun.ca (L.K. Thompson).

0277-5387/$ - see front matter © 2005 Elsevier Ltd. All rights reserved.
doi:10.1016/j.poly.2005.02.016

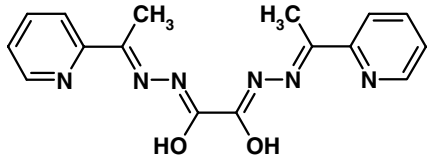


L1 PAH

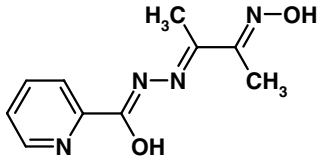
Scheme 1.



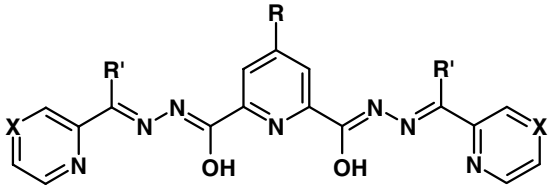
PAHAP (X=CH, R=NH_2), PZHPZ (X=N, R=NH_2), POAP (X=CH, R=OH)



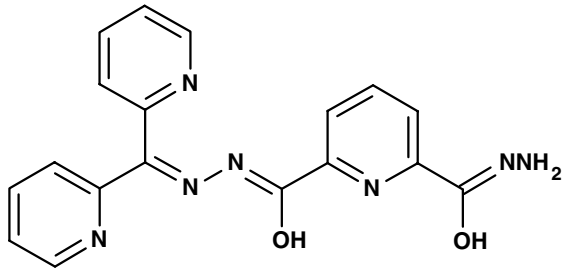
L2



L3



L4 (R=Cl, R'=Phenyl, X=CH)
L5 (R=Cl, R'=NH_2, X=N)



L6

Chart 1.

attack in the formation of the analogous acyl ligand, presumably promoted by the coordination of the highly polarizing Fe(III) center [2].

The present report discusses transition metal complexes derived from a group of extended polyfunctional diazine ligands L2–L6 (Chart 1), in which metal ion based ligand hydrolysis has occurred at a 'vulnerable' ligand C=N site, with the formation of complexes containing rearranged ligands and ligand fragments. The ligand L3 has been reported elsewhere, along with a number of coordination complexes, but there is no evidence for ligand hydrolysis [3]. The ligand L4 undergoes hydrolysis in the presence of Co(II) in air, and with Cu(II) salts, but remains intact on reaction with Ni(II) carbonate. Structures are reported for some iron, nickel and copper complexes, and the magnetic properties of some polynuclear copper and iron products are discussed. DFT studies are highlighted in one nickel case where an unusual ligand transformation takes place.

2. Experimental

2.1. Physical measurements

Infrared spectra were recorded as Nujol mulls using a Mattson Polaris FTIR instrument. Mass spectra were obtained using a VG Micromass 7070HS spectrometer and an Agilent 1100 series LC/MSD spectrometer. C, H, N analyses on dried samples were carried out by the Canadian Microanalytical Service, Delta, B.C., Canada. Variable temperature magnetic data (2–300 K) were obtained with a Quantum Design MPMS5S Squid magnetometer operating at 0.1–5.0 T. Calibrations were carried out with a palladium standard cylinder, and the normal diamagnetic corrections were applied.

2.2. Syntheses

2.2.1. L2

2-Acetyl pyridine (3.70 g, 0.0300 mol) was dissolved in methanol (100 mL). Oxalic acid dihydrazide (1.77 g, 0.0150 mol) was added and the mixture refluxed for 12 h. A white precipitate formed, which was separated by filtration, washed with methanol and ether and dried under vacuum (Yield 4.4 g, 91%); m.p. dec. >260 °C. Mass spectrum (*m*/*z*) 189, 162, 134, 106, 78 (molecular ion not observed). IR (ν cm^{-1}) 1681 (C=O), 1012 (pyr). *Anal*. Calc. for $C_{16}H_{16}N_6O_2$: C, 59.25; H, 4.97; N, 25.91. Found: C, 58.67; H, 4.94; N, 25.72%.

2.2.2. L3

Butanedione monoxime (5.04 g, 0.0498 mol) was dissolved in absolute ethanol (40 mL). Picolinic acid hydrazide (3.32 g, 0.0242 mol) was added and the mixture refluxed for several hours with the formation of a white suspended solid. The fine white precipitate was filtered off and washed with methanol (Yield 4.86 g, 91%). Recrystallization from acetonitrile produced colorless crystals, but crystals suitable for structural determination were obtained from the reaction of $Gd(NO_3)_3$ and L3 in a MeCN, MeOH, H_2O mixture, in which there appeared to be no Gd complex formation. Mass spectrum (*m*/*z*) 221 (MH^+), 203, 182, 124, 108, 79. IR (ν cm^{-1}) 3343 (OH), 1677 (C=O), 995 (pyr). *Anal*. Calc. for $C_{10}H_{12}N_4O_2$: C, 54.55; H, 5.45; N, 25.45. Found: C, 54.55; H, 5.58; N, 25.41%.

2.2.3. L4

2-Benzoylpyridine (7.44 g, 41 mmol) was dissolved in $CHCl_3$ (220 mL). 4-Chloro-2,6-pyridine carboxylic acid hydrazide (2.30 g, 10 mmol) was added, along with dry methanol (30 mL), and the mixture was refluxed for 72 h. The volume of the resulting solution was reduced by about 50%, and methanol (30 mL) was added and heating continued until a white precipitate formed. The precipitate was collected by suction filtration, and washed with methanol and diethyl ether (Yield 3.6 g, 65%); m.p. 288–294 °C. Mass spectrum (*m*/*z*) 560 (M), 542 ($M - H_2O$). IR (ν, cm^{-1}) 1697 (C=O), 1574 (C=N), 997 (py). *Anal*. Calc. for $C_{31}H_{22}N_7O_2Cl\cdot 0.5H_2O$: C, 65.49; H, 4.05; N, 17.25. Found: C, 65.25; H, 3.95; N, 17.33%.

2.2.4. L6

2,6-Pyridine carboxylic acid hydrazide (0.93 g, 5.0 mmol) was added to a solution of dipyridyl ketone (1.84 g, 10 mmol) in absolute ethanol (50 mL), and the mixture was refluxed for 10 h. The product formed as a white solid during the reaction, and was filtered off, washed with ethanol and dried in air (Yield 1.7 g, 90%). *Anal*. Calc. for $C_{18}H_{15}N_7O_2(C_{29}H_{21}N_9O_2)_{0.22}$; C, 61.34; H, 4.14; N, 26.35. Found: C, 61.31; H, 4.09; N, 26.19%. The reaction appears to have produced a mixture of mono and disubstituted ligands, with about 20% disubstituted. Separation could not be effected cleanly, and so the mixture was used in the reaction with $Cu(NO_3)_2$ (vide infra).

*2.2.5. $[Cu_2(L7)_2(C_2O_4)(H_2O)_2(NO_3)_2]$ (**1**), $[Cu_2(L7)_2(C_2O_4)](ClO_4)_2$ (**2**)*

L2 (0.324 g, 1.00 mmol) was added to a warm solution of $Cu(NO_3)_2\cdot 3H_2O$ (0.483 g, 2.00 mmol) in $MeOH/H_2O$ (10/5 mL), forming a green solution. Dark green crystals, suitable for a structural analysis, were obtained on standing the solution at room temperature over several days (Yield 0.37 g, 45%). *Anal*. Calc. for $[(C_7H_9N_3)_2Cu_2(C_2O_4)(H_2O)_2(NO_3)_2]$: C, 29.78; H, 3.44; N, 17.36. Found: C, 29.79; H, 3.33; N, 17.67%. **2** was produced under similar conditions using copper(II) perchlorate (Yield 50%). *Anal*. Calc. for $[(C_7H_9N_3)_2Cu_2(C_2O_4)](ClO_4)_2$: C, 28.08; H, 2.65; N, 12.28. Found: C, 28.37; H, 2.63; N, 12.24%.

*2.2.6. $[Ni(L8)]Br\cdot CHCl_3$ (**3**)*

$NiBr_2$ (0.24 g, 1.0 mmol) was suspended in 50/50 $CH_3CN/MeOH$ (20 mL). L3 (0.20 g, 0.90 mmol) was added and the mixture was heated with stirring. A clear orange solution formed, which was filtered and allowed to stand, forming a red orange powder (Yield 55%). Recrystallization from $CHCl_3$ gave red block shaped crystals suitable for structural determination. A similar reaction with $Ni(ClO_4)_2\cdot 6H_2O$ and $Ni(NO_3)_2\cdot 6H_2O$ gave $[Ni(L8)](ClO_4)\cdot H_2O$ and $[Ni(L8)](NO_3)\cdot 2H_2O$, respectively, as red powders (Yield 60–70%). *Anal*. Calc. for $[(C_{16}H_{15}N_6O_2)Ni](ClO_4)\cdot H_2O$: C, 38.55; H, 3.41; N, 16.86. Found: C, 38.27; H, 3.30; N, 16.73%. *Anal*. Calc. for $[(C_{16}H_{15}N_6O_2)Ni](NO_3)\cdot 2H_2O$: C, 40.08; H, 3.97; N, 20.46. Found: C, 39.56; H, 3.29; N, 20.37%. Similar infrared spectral bands associated with the ligand L8 are observed in all three compounds.

*2.2.7. $[Cu_2(L9)(L10)]\cdot 2H_2O\cdot CH_3OH\cdot L11$ (**4**)*

L4 (0.10 g, 0.18 mmol) was added to a solution of copper acetate (0.18 g, 0.45 mmol) in methanol (20 mL), forming a clear brown solution. Red brown crystals of **4**, suitable for a structural determination, were obtained in low yield (35 mg) after allowing the solution to evaporate to a small volume. *Anal*. Calc. for $[(C_{19}H_{11}N_4O_3Cl)(C_7H_2NO_4Cl)Cu_2](C_{12}H_9N_3)\cdot 7H_2O$: C, 44.53; H, 3.52; N, 10.94. Found: C, 44.47; H, 2.67; N, 11.08%. The dried analytical sample contains no methanol.

*2.2.8. $[Fe_2(PZHPZ)_3](ClO_4)_4\cdot 2CH_3CN$ (**5**)*

L5 [4] (0.070 g, 0.16 mmol) was added to a degassed solution of $Fe(ClO_4)_2\cdot 6H_2O$ (0.122 g, 0.48 mmol) in CH_3CN (10 mL) under an Ar atmosphere. The mixture was heated to reflux for 10 min., and then left at room temperature. Purple crystals formed after several days in the Ar atmosphere (Yield 50 mg), which were kept under the mother liquor prior to structural analysis. Solvent loss occurred on exposure of the bulk sample to air. *Anal*. Calc. for $[(C_{10}H_{10}N_8)_3Fe_2](ClO_4)_4\cdot 7H_2O$: C, 26.45; H, 3.26; N, 24.68. Found: C, 26.40; H, 2.69; N, 24.93% (air dried sample).

*2.2.9. $[Cu_2(L12\text{-}2H)](NO_3)_2\cdot 1.5H_2O$ (**6**)*

L6 (0.25 g, 0.50 mmol) was added to a solution of $Cu(NO_3)_2\cdot 3H_2O$ (0.72 g, 3.0 mmol) in $MeOH/H_2O$ (20/10 mL) and the mixture was warmed. Green crystals were obtained from the resulting green solution on standing at room temperature (Yield 0.21 g, 68%). *Anal*.

Calc. for $(C_{18}H_{11}N_5O_3)Cu_2(NO_3)_2\cdot 1.5H_2O$. C, 34.68; H, 2.26; N, 15.73. Found: C, 34.50; H, 2.12; N, 16.10%.

2.2.10. [Ni(L4-2H)] (7)

$NiCO_3$ (0.18 g, 1.5 mmol) was suspended in 1:1 MeCN/EtOH (20 mL). L4 (0.10 g, 018 mmol) was added and the mixture was heated. Water (5 mL) was added and heating continued for 15 min. with the formation of a red solution. The solution was filtered to remove excess nickel carbonate, and allowed to stand at room temperature. Red crystals suitable for structural analysis formed after two days (Yield 60 mg, 55%).

2.3. X-ray crystallography

The diffraction intensities of a green prismatic crystal of **1** were collected with graphite-monochromatized Mo Kα X-radiation (rotating anode generator) using a Bruker P4/CCD diffractometer at 193(1) K to a maximum 2θ value of 52.8°. The data were corrected for Lorentz and polarization effects. The structure was solved by direct methods [5,6]. All atoms except hydrogen atoms were refined anisotropically. Hydrogen atoms were placed in calculated positions with isotropic thermal parameters set to 20% greater than their bonded partners, and were not refined. Neutral atom scattering factors [7] and anomalous-dispersion terms [8,9] were taken from the usual sources. All other calculations were performed with the teXsan [10] crystallographic software package.

Diffraction data were collected for **3**–**5** in a similar manner. Abbreviated structural data for **1**, **3**–**5** are reported in Table 1.

The diffraction intensities of a colourless single crystal of L3 were collected with graphite-monochromated Cu Kα X-radiation using a Rigaku AFC6S diffractometer at 299(1) K and the ω–2θ scan technique to a 2θ value of 120.1°. The data were corrected for Lorentz and polarization effects. The structure was solved by direct methods [5,6]. All atoms except hydrogen atoms were refined anisotropically. Hydrogen atoms were introduced with isotropic thermal parameters set 20% greater than those of their bonded partners at the time of their inclusion. They were optimized by positional refinement. Neutral atom scattering factors [7] and anomalous-dispersion terms [8,9] were taken from the usual sources. All calculations were performed with the teXsan [10] crystallographic software package. Diffraction data for **7** (red prism) were collected in a similar manner. Abbreviated structural details for L3 and **7** are listed in Table 1.

Diffraction data for a single crystal of **6** (green prism, $0.30\times0.40\times0.20$ mm) were collected using a Bruker SMART CCD diffractometer, equipped with an Oxford Cryostream N_2 cooling device [11], with graphite monochromatized Mo Kα radiation. Cell parameters were determined and refined using the SMART software [12a], raw frame data were integrated using the SAINT program [12b] and the structure was solved using direct methods and refined by full-matrix least squares on F^2 using SHELXTL [13]. Non-hydrogen atoms were refined with anisotropic atomic displacement parameters (adps). Hydrogen atoms bound to carbon atoms were placed in geometrically calculated positions with isotropic adps 1.2 times that of the parent atom.

Table 1
Summary of crystallographic data for **1**, L3, **3**–**7**

Compound	**1**	L3	**3**	**4**	**5**	**6**	**7**
Empirical formula	$C_{32}H_{44}N_{16}Cu_4O_{24}$	$C_{10}H_{12}O_2N_4$	$C_{34}H_{32}Br_2Cl_6N_{12}Ni_2O_4$	$C_{39}H_{30}N_8O_{10}Cl_2Cu_2$	$C_{34}H_{36}N_{26}O_{16}Cl_4Fe_2$	$C_{18}H_{19}N_7O_{13}Cu_2$	$C_{31}H_{20}N_7O_2NiCl$
Formula weight	1286.96	220.23	1162.66	968.69	1318.39	668.48	616.7
Wavelength (Å)	0.71073	1.54178	0.71073	0.71073	0.71073	0.71073	0.71703
Crystal system	triclinic	monoclinic	triclinic	monoclinic	monoclinic	monoclinic	monoclinic
Space group	$P\bar{1}$	$P2_1/c$ (#14)	$P\bar{1}$ (#2)	$C2/c$	$C2/c$ (#15)	Cc	Cc
a (Å)	10.1578(8)	5.706(4)	7.3323(11)	29.927(3)	17.4322(13)	25.513(2)	14.405(3)
b (Å)	13.4753(11)	25.812(4)	11.5251(16)	8.8728(8)	15.6919(12)	7.1249(6)	17.663(5)
c (Å)	17.8890(14)	7.337(3)	13.7813(19)	30.906(3)	20.7481(15)	16.8915(14)	10.689(4)
α (°)	103.473(1)	90	71.791(3)	90	90	90	90
β (°)	90.963(1)	100.19(4)	75.089(3)	109.832(2)	99.335(2)	129.9970(10)	103.73(3)
γ (°)	105.493(2)	90	79.892(3)	90	90	90	90
V (Å^3)	2286.5(3)	1063.6(7)	1063.3(2)	7720.1(12)	5600.4(6)	2352.2(3)	2642(1)
$D_{calc.}$ (g cm^{-3})	1.869	1.375	30821.816	1.667	1.563	1.888	1.550
Temperature (K)	193(2)	299(1)	193(2)	193(2)	193(2)	100(2)	299(1)
Z	2	4	1	8	4	4	4
μ (cm^{-1})	19.42	8.31	32.01	13.12	7.94	1.894	8.81
Reflections/parameters	8631/704	977/182	3698/280	7878/550	5733/404	5371/437	2206/376
Final R_1, wR_2	0.0645, 0.200	0.056, 0.057 (R,R_w)	0.0562, 0.1385	0.0443, 0.1114	0.064, 0.2049	0.0171, 0.0465	0.043, 0.040 (R,R_w)

$R_1 = \sum[||F_o| - |F_c||]/\sum|F_o|$, $wR_2 = [\sum[w(|F_o|^2 - |F_c|^2)^2]/\sum[w(|F_o|^2)^2]]^{1/2}$.
$R = \sum||F_o| - |F_c||/\sum|F_o|$, $R_w = [\sum w(|F_o| - |F_c|)^2/\sum wF_o^2]^{1/2}$.

2.4. Computational details

All calculations were carried out using GAUSSIAN-03 [14]. Ligand and complex structures were optimized using Becke's hybrid B3LYP functional [15]. The split-valence with polarization (SVP) basis set of Ahlrichs and coworkers [16] was felt to provide a good compromise between computational accuracy and efficiency, and was used for all calculations, except where noted. For all geometry optimizations, frequencies were also calculated to ensure that the structures were genuine minima on the potential energy hypersurface (no imaginary frequencies were found).

3. Results and discussion

3.1. Structures

3.1.1. $[Cu_2(L7)_2(C_2O_4)(H_2O)_2(NO_3)_2]$ (1)

The molecular structure of **1** is comprised of three similar dinuclear fragments, all involving the bidentate ligand 2-acetylpyridine hydrazone (L7), and a bridging oxalate. In combination they are represented by the averaged formula above. Relevant bond distances and angles are listed in Table 2. Two fragments are shown in Fig. 1(a). The Cu(3) fragment has four distant nitrates bound to a 'flat' dinuclear center, with long Cu–O contacts (Cu(3)–O(12) 2.524(4) Å, Cu(3)–O(14) 2.468(4) Å). Cu–L in plane distances fall in the range 1.973–1.985 Å, and the Cu–Cu distance is 5.149(3) Å. The bridging oxalate has a typical geometry. The Cu(3) dinuclear subunit is hydrogen bonded to the Cu(4) subunit (Fig. 1(a); O(15)–O(9) 2.795(5) Å, O(9)–O(13) 2.786(6) Å). Subunit Cu(4) has a similar geometry with five-coordinate square pyramidal copper centers, and with each metal having an axially bound water molecule (Cu(4)–O(9) 2.273(4) Å). The third dinuclear subunit (Fig. 1(b)) has a similar structure with square pyramidal copper centers, and axial contacts to oxygen atoms from a disordered combination of a water molecule and a nitrate (Cu(1)–O(21) 2.345(5) Å, Cu(2)–O(20) 2.365(5) Å). Other dimensions within this dinuclear subunit are similar to those involving Cu(3) and Cu(4).

3.1.2. L3

The structure of the ligand (L3) is shown in Fig. 2, and relevant bond distances and angles are listed in Table 3. The good refinement shows that a proton resides on N(2) and that the C–O bond has predominantly double bond character (C(6)–O(1) 1.230(5) Å). The N(2)–N(3) distance (1.389(5) Å) indicates this bond to have mostly single bond character. One interesting structural feature that bears on the reactivity of this ligand surrounds the *anti* (*trans*) conformation of the ligand as a whole, and in particular with respect to the two methyl groups, as indicated by the torsional angles C(10)–C(8)–C(7)–C(9) and C(7)–N(3)–N(2)–C(6) (177.4°, 178.1°, respectively), which are both very large. DFT calculations on L3, which utilize the B3LYP functional and 6-31G(d) basis set, indicate that the *anti* form

Table 2
Distances (Å) and angles (°) for $[Cu_2(L7)_2(C_2O_4)(H_2O)_2(NO_3)_2]$ (**1**)

Cu1–N1	1.965(5)
Cu1–N2	1.971(5)
Cu1–O2	1.974(4)
Cu1–O1	1.974(4)
Cu1–O21	2.346(5)
Cu2–N5	1.943(5)
Cu2–N4	1.975(5)
Cu2–O4	1.983(4)
Cu2–O3	1.983(4)
Cu2–O20	2.367(5)
Cu3–N7	1.968(5)
Cu3–O5	1.972(4)
Cu3–O6	1.973(4)
Cu3–N8	1.984(5)
Cu4–N10	1.970(5)
Cu4–O8	1.973(4)
Cu4–O7	1.985(5)
Cu4–N11	1.987(5)
Cu4–O9	2.273(4)
N1–Cu1–N2	82.0(2)
N1–Cu1–O2	173.75(19)
N2–Cu1–O2	95.80(19)
O6–Cu3–N8	95.0(2)
N10–Cu4–O8	97.6(2)
N10–Cu4–O7	168.6(2)
O8–Cu4–O7	84.91(18)
N10–Cu4–N11	81.2(2)
O8–Cu4–N11	170.21(19)
N1–Cu1–O1	96.87(19)
N2–Cu1–O1	175.23(18)
O2–Cu1–O1	84.84(16)
N1–Cu1–O21	91.3(2)
N2–Cu1–O21	94.28(19)
O2–Cu1–O21	94.72(17)
O1–Cu1–O21	90.38(18)
N5–Cu2–N4	81.7(2)
N5–Cu2–O4	175.2(2)
N4–Cu2–O4	99.62(19)
N5–Cu2–O3	93.5(2)
N4–Cu2–O3	172.54(19)
O4–Cu2–O3	84.75(16)
N5–Cu2–O20	90.7(2)
N4–Cu2–O20	95.0(2)
O4–Cu2–O20	93.82(18)
O3–Cu2–O20	90.71(18)
N7–Cu3–O5	98.4(2)
N7–Cu3–O6	176.7(2)
O5–Cu3–O6	84.74(18)
N7–Cu3–N8	81.8(2)
O5–Cu3–N8	179.3(2)
O7–Cu4–N11	94.4(2)
N10–Cu4–O9	99.26(18)
O8–Cu4–O9	91.20(16)
O7–Cu4–O9	91.82(16)
N11–Cu4–O9	98.58(17)

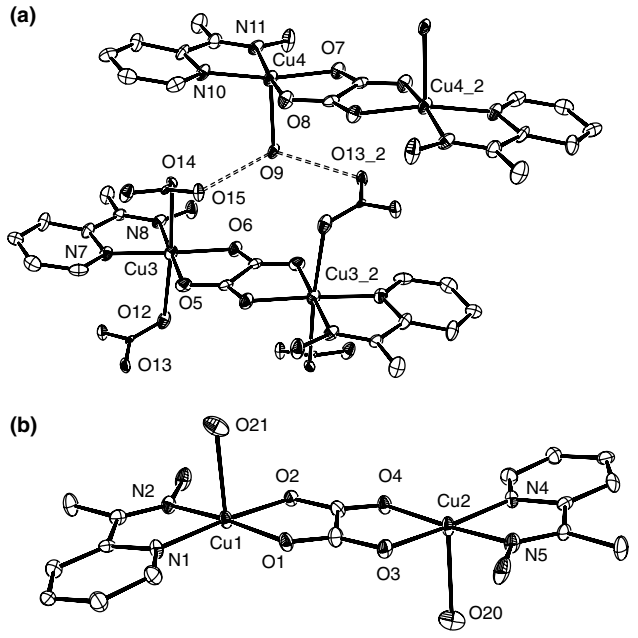


Fig. 1. (a) Structural representation of two dinuclear fragments in **1** (40% probability thermal ellipsoids). (b) Structural representation of a third dinuclear fragment in **1** (40% probability thermal ellipsoids).

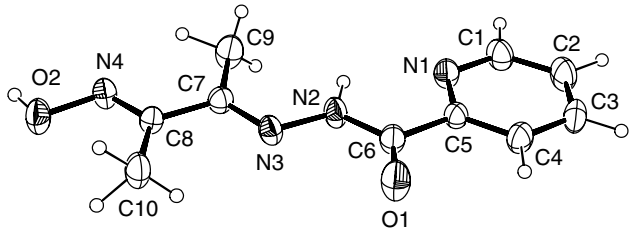


Fig. 2. Structural representation of L3 (40% probability thermal ellipsoids).

Table 3
Distances (Å) and angles (°) for L3

O1–C6	1.230(5)
O2–N4	1.408(5)
N1–C1	1.336(6)
N1–C5	1.342(5)
N2–N3	1.389(5)
N2–C6	1.332(6)
N3–C7	1.297(5)
N4–C8	1.291(6)
C1–C2	1.380(7)
C2–C3	1.372(8)
C4–C5	1.372(6)
C5–C6	1.501(6)
C7–C8	1.459(6)
C7–C9	1.490(7)
C8–C10	1.507(7)
C1–N1–C5	116.7(5)
N3–N2–C6	120.8(4)
N2–N3–C7	115.4(4)
O2–N4–C8	111.3(4)
N1–C1–C2	123.4(5)
C1–C2–C3	118.7(5)
C2–C3–C4	118.7(5)
C3–C4–C5	119.3(5)
N1–C5–C4	123.2(5)
N1–C5–C6	116.5(4)
C4–C5–C6	120.3(4)
O1–C6–N2	125.6(5)
O1–C6–C5	120.5(5)
N2–C6–C5	113.9(4)
N3–C7–C8	114.9(4)
N3–C7–C9	125.3(5)
C8–C7–C9	119.9(5)
N4–C8–C7	113.9(4)
N4–C8–C10	124.7(4)
C7–C8–C10	121.4(4)

is more stable than the *eclipsed* form, with an energy difference of ~25 kJ/mol.

3.1.3. [Ni(L8)]Br·CHCl$_3$ (3)

The molecular structure of **3** is shown in Fig. 3(a), and relevant bond distances and angles are given in Table 4. The obvious first point of discussion is the fact that the starting ligand (L3) is not present, but a new Schiff base ligand L8 is formed, based on a central butane-dione fragment. L8 acts in a tetradentate fashion coordinating to the nickel ion via two diazine nitrogen atoms, a pyridine nitrogen and an oxygen atom, creating quite a strong in plane crystal field. This is strong enough to cause the Ni(II) ion to be low spin (vide infra). The NiN_3O subunit is essentially planar (O(1)–Ni–N(5) 179.8(2)°, N(3)–Ni–N(6) 178.9(2)°), with very short Ni-ligand contacts (1.828–1.887 Å). Both C–O bonds have predominantly double bond character (C(6)–O(1) 1.285(6) Å, C(11)–O(2) 1.222(6) Å), and since the ligand has lost one proton, nitrogen atoms N(3) and N(5) bear a formal negative charge, consistent with the short Ni–N distances. The second proton (H(1)) resides on pyridine nitrogen N(1) (difference map), thus giving the complex ion a formal charge of 1+. The bromide ion (Br(1)) balances the charge, and is hydrogen bonded to H(1) and also to a chloroform molecule (Br(1)–H(16) 2.692(6) Å, Br(1)–H(1) 2.467(6) Å).

The flat nature of the Ni(II) ion, generated by the strong in plane crystal field, predisposes the whole ligand to adopt a fairly flat overall conformation, with the methyl groups in an unexpected *cis*-conformation (see structure of L3). The molecules are arranged in a stacked, alternating, *trans*-conformation in the lattice, with pairs of molecules related by an inversion centre. There are many relatively short (<4 Å) intermolecular contacts between individual molecules, e.g., N(4) and O(1) (3.304 Å) (highlighted in Fig. 3(b)), with the Ni–Ni distances between molecules in the stack alternating as 3.663(3), and 4.743(4) Å. Any axial contacts to the nickel centres between molecules are considered too weak to be of bonding significance. However, the intermolecular contacts are clearly instrumental in the parallel arrangement of the molecules of **3**. The complexes

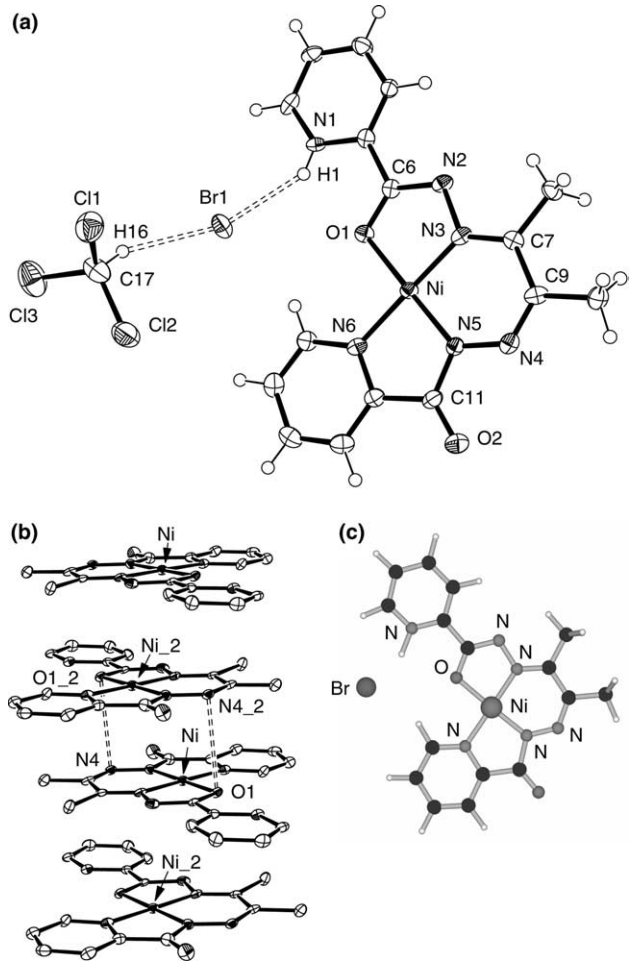


Fig. 3. (a) Structural representation of **3** (40% probability thermal ellipsoids). (b) Extended structural representation of **3** (40% probability thermal ellipsoids). (c) Optimized geometry for **3** (B3LYP/SVP).

Table 4
Distances (Å) and angles (°) for [Ni(L8)]Br·$CHCl_3$ (**3**)

Ni–N5	1.828(5)
Ni–N3	1.831(5)
Ni–O1	1.865(4)
Ni–N6	1.887(5)
N2–N3	1.397(7)
N4–N5	1.350(7)
N1–H1	0.80(9)
N5–Ni–N3	93.9(2)
N5–Ni–O1	178.8(2)
N3–Ni–O1	85.05(19)
N5–Ni–N6	85.4(2)
N3–Ni–N6	178.9(2)
O1–Ni–N6	95.61(19)
C6–O1–Ni	108.1(4)
C1–N1–C5	122.3(5)
C1–N1–H1	120(7)
C5–N1–H1	117(7)

$[Ni(L8)](ClO_4)\cdot H_2O$ and $[Ni(L8)](NO_3)\cdot 2H_2O$ are assumed to have similar overall structures.

Of note is the fact that the DFT structure (Fig. 3(c)) and X-ray structure (Fig. 3(a)) of [Ni(L8)]Br are in excellent agreement. For the square-planar nickel coordination sphere, the average deviation in bond lengths between the two structures was 0.02 Å. The average deviation in bond angles was 0.6°. This is comparable to results reported by Jang et al. [17] for the structures of iron carbonyls, where differences between B3LYP (double-ζ plus polarization basis set) and X-ray crystal structures were on the order of 0.02 Å and 0.5° for bond lengths and angles, respectively. For a medium-sized transition metal complex such as **3** (41 atoms, with 467 basis functions), such agreement is quite reasonable. This indicates the theory and basis set used are likely sufficient for the obtainment of good quality results.

3.1.4. $[Cu_2(L9)(L10)]\cdot 2H_2O\cdot CH_3OH\cdot L11$ (**4**)

The structure of the asymmetric unit in **4** is shown in Fig. 4, and relevant bond distances and angles are listed in Table 5. The original ligand L4 is clearly absent, and instead the complex contains three different ligand fragments derived from L4; the mono-acid ligand (L9), 4-chloro-2,6-pyridinedicarboxylate (L10) and 3-phenyltriazolo[1,5-a]pyridine (L11). Cu(1) and Cu(2) are bridged by the N–N diazine group in L9. A pyridine nitrogen (N(4)) and a carboxylate oxygen (O(2)) and the other pyridine nitrogen (N(1)) complete coordination to Cu(1). Cu(2) is bonded to the hydrazone oxygen O(1) from L9, and three donors (N(5), O(4), O(7)) from the dicarboxylate ligand L10. Cu(1) has four short in plane contacts (1.903–2.006 Å), but in the extended structure a fifth axial contact (Cu(1)–O(3) 2.632(3) Å) indicates that the geometry is axially elongated square-pyramidal (vide infra) (N(3)–Cu(1)–O(2) 162.2°, N(4)–Cu(1)–N(1) 173.4°). Cu(2) has a distorted square pyramidal coordination geometry within the asymmetric unit, with short in plane distances (1.903–2.033 Å), and a longer axial contact (N(2)–Cu(2) 2.368(3) Å). However, in the extended structure (vide infra) a sixth contact (Cu(2)–O(6) 2.375(2) Å) shows that the geometry is actually axially elongated octahedral. There are no anions in the structure indicating that both ligands have

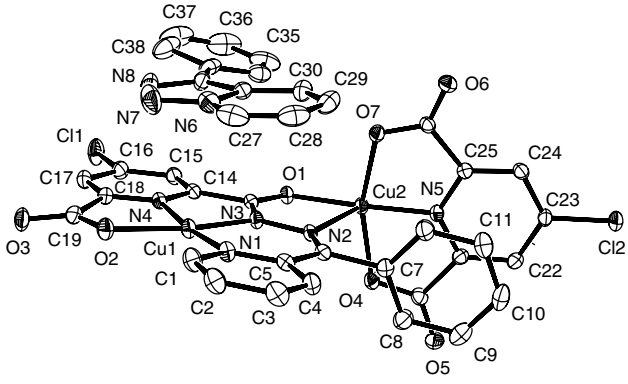


Fig. 4. Structural representation of the asymmetric unit in **4** (30% probability thermal ellipsoids).

Table 5
Distances (Å) and angles (°) for $[Cu_2(L9)(L10)]\cdot 2H_2O\cdot CH_3OH\cdot L11$ (**4**)

Cu1–N4	1.903(3)
Cu1–N1	1.922(3)
Cu1–N3	1.926(3)
Cu1–O2	2.005(2)
Cu2–N5	1.903(2)
Cu2–O1	1.971(2)
Cu2–O7	2.031(2)
Cu2–O4	2.033(2)
Cu2–N2	2.368(3)
Cu2–O6	2.375(2)
N2–N3	1.377(3)
N6–N7	1.359(5)
N7–N8	1.315(5)
N4–Cu1–N1	173.41(11)
N4–Cu1–N3	81.24(11)
N1–Cu1–N3	94.16(11)
N4–Cu1–O2	81.01(10)
N1–Cu1–O2	103.56(10)
N3–Cu1–O2	162.24(10)
N5–Cu2–O1	173.00(10)
N5–Cu2–O7	80.65(10)
O1–Cu2–O7	99.77(9)
N5–Cu2–O4	80.07(10)
O1–Cu2–O4	99.81(9)
O7–Cu2–O4	160.38(9)
N5–Cu2–N2	111.93(9)
O1–Cu2–N2	75.06(8)
O7–Cu2–N2	88.88(9)
O4–Cu2–N2	94.98(9)
N5–Cu2–O6	83.71(9)
O1–Cu2–O6	89.33(8)
O7–Cu2–O6	87.60(9)
O4–Cu2–O6	93.84(9)
N2–Cu2–O6	163.17(8)

lost two protons. This is consistent with the in plane Cu–O and Cu–N distances. The torsional angle Cu(1)–N(3)–N(2)–Cu(2) (178°) indicates an almost *trans* disposition of the copper atoms about the N–N single bond; however, this is an orthogonal magnetic connection (vide infra). The copper equatorial planes are also connected by a longer N–C–O pathway through N(3) and O(1).

A remarkable feature of the structure is the presence of the 'uncoordinated', fused triazole molecule L11. Fig. 4 shows that the phenyl triazole is held in place above three rings associated with the coordinated ligand L9. The pyridine ring is positioned above the N(1) pyridine ring in L9, the phenyl ring above the chloro-pyridine ring in L9 and the triazole ring above the chelate ring involving O(2) in L9. Distances between these rings subunits are relatively short (e.g., 3.3–4.0 Å) indicating that there are significant π-stacking interactions at play, which help to stabilize the location of the triazole molecule. The shortest distance (3.386 Å) is between N(7) and O(2). This is quite remarkable, possibly unprecedented in normal coordination chemistry, and highlights the importance of π stacking forces as a means of 'holding' a molecule in close proximity to a metal ion site. One is reminded of the unusual stabilization of a tryptophan moiety close to the active site in galactose oxidase, with a possibly similar interaction with a tyrosine ligand [18]. Also the phenyl ring of L9 is positioned above the pyridine ring (N(5)) in L11, with short contacts between ring atoms (3.45–3.77 Å) highlighting the nice fit of the aromatic rings in this complex.

The overall structure of **4** reveals some further surprises. The dinuclear subunit shown in Fig. 4 actually forms a dimer through a carboxylate bridge (O(6)) linking Cu(2) with its symmetry related counterpart. Also, the tetranuclear subunits are cross-linked to form a zig-zag chain, via symmetry related O(6) atoms (Fig. 5), and finally the zig-zag chains are cross-linked into a 2D grid by long axial O(3)–Cu(1) contacts (2.632(3) Å) shown in Fig. 6. The global direct connectivity between the copper atoms in all cases links the metal ions orthogonally, thus predisposing the system

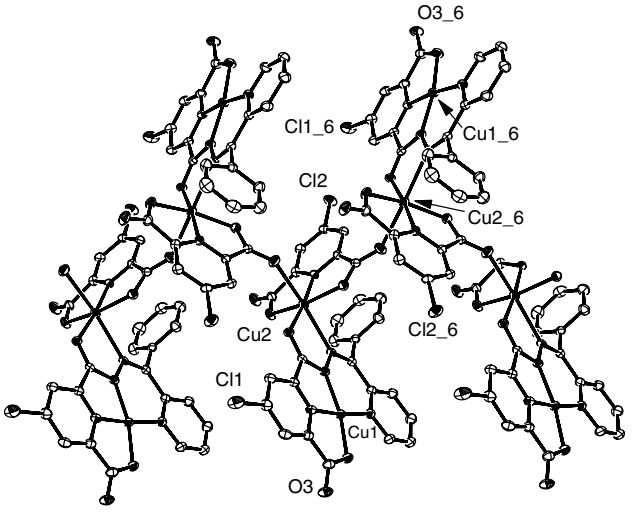


Fig. 5. Structural representation of the chain motif in **4** (30% probability thermal ellipsoids).

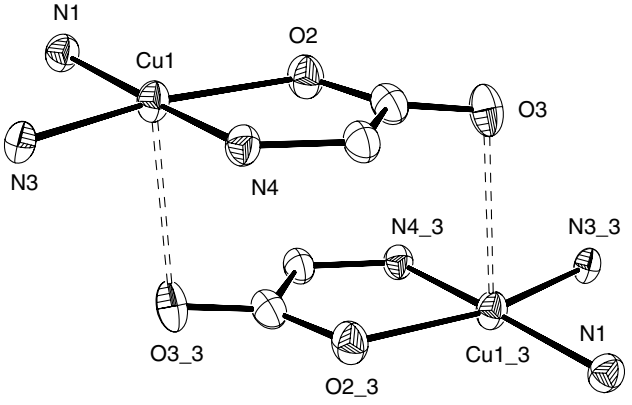


Fig. 6. Extended cross linked structural representation of the chains in **4** (40% probability thermal ellipsoids).

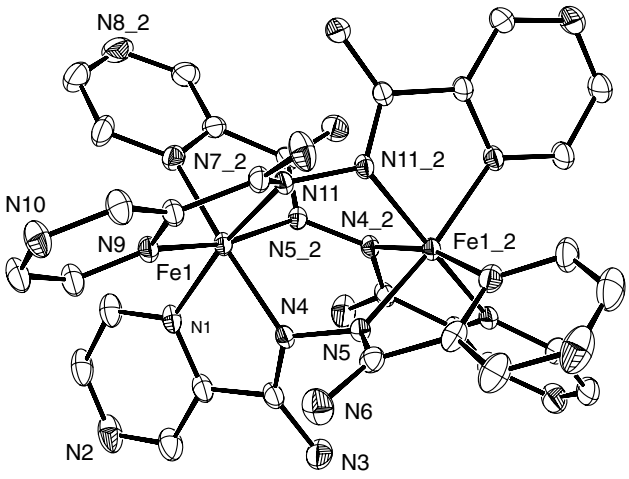


Fig. 7. Structural representation of **5** (40% probability thermal ellipsoids).

to the absence of significant antiferromagnetic exchange (vide infra).

3.1.5. $[Fe_2(PZHPZ)_3](ClO_4)_4\cdot 2CH_3CN$ (**5**)

The molecular structure of **5** is shown in Fig. 7, and relevant bond distances and angles are listed in Table 6. L5 is clearly absent and the simple pyrazine amidrazone ligand is involved in coordination to Fe(II). Three ligands are wrapped around the two iron(II) centers in a spiral fashion, with three single N–N bonds connecting the metal ions. The dinuclear complex cation is essentially identical to that reported previously for the complex $[Fe_2(PZHPZ)_3](NO_3)_4\cdot 5H_2O$ [2], obtained from the reaction of $Fe(NO_3)_3$ with PZHPZ (Chart 1), with slight differences in internal dimensions. Fe–N distances

Table 6
Distances (Å) and angles (°) for $[Fe_2(PZHPZ)_3](ClO_4)_4\cdot 2CH_3CN$ (**5**)

Fe1–N9	1.958(3)
Fe1–N1	1.963(3)
Fe1–N11	1.964(3)
Fe1–N5	1.964(3)
Fe1–N4	1.968(3)
Fe1–N7	1.971(3)
N4–N5	1.412(4)
N11–N11	1.409(5)
N9–Fe1–N1	95.86(12)
N9–Fe1–N11	79.92(12)
N1–Fe1–N11	167.86(13)
N9–Fe1–N5	167.53(12)
N1–Fe1–N5	95.87(12)
N11–Fe1–N5	89.38(11)
N9–Fe1–N4	97.49(12)
N1–Fe1–N4	79.65(12)
N11–Fe1–N4	89.56(12)
N5–Fe1–N4	88.76(11)
N9–Fe1–N7	95.19(13)
N1–Fe1–N7	94.84(13)
N11–Fe1–N7	96.87(12)
N5–Fe1–N7	79.62(12)
N4–Fe1–N7	166.62(13)

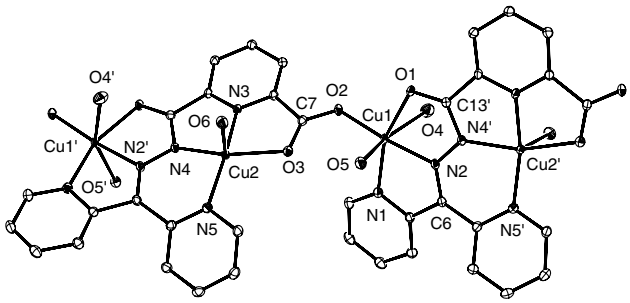


Fig. 8. Structural representation of **6** (40% probability thermal ellipsoids).

in **5** are slightly longer (1.961–1.970 Å) in keeping with a slightly larger Fe–Fe separation (3.621(3) Å). Torsional angles (Fe–N–N–Fe) are very small (43.8°) indicating an acute arrangement of Fe–N bonds about the N–N single bonds (N–N 1.411–1.413 Å). The generally short Fe–N distances are indicative of a strong ligand field for Fe(II), consistent with the low spin nature of this compound (vide infra).

3.1.6. $[Cu_2(L12\text{-}2\,H)](NO_3)_2\cdot 1.5H_2O$ (**6**)

The structure of **6** is shown in Fig. 8, and relevant bond distances and angles are listed in Table 7. The structure reveals that the starting ligand (L6) has been hydrolysed at the hydrazide function during the reaction

Table 7
Distances (Å) and angles (°) for $[Cu_2(L12\text{-}2H)](NO_3)_2\cdot 1.5H_2O$ (**6**)

Cu1–O2	1.9168(13)
Cu1–N2	1.9410(15)
Cu1–N1	2.0213(14)
Cu1–O1	2.0935(12)
Cu1–O4	2.4079(14)
N2–N4	1.346(2)
Cu2–N3	1.9419(14)
Cu2–N4	1.9427(14)
Cu2–N5	1.9822(14)
Cu2–O3	2.1002(12)
Cu2–O6	2.1771(13)
O2–Cu1–N2	174.14(6)
O2–Cu1–N1	103.86(5)
N2–Cu1–N1	79.41(6)
O2–Cu1–O1	96.49(5)
N2–Cu1–O1	80.18(5)
N1–Cu1–O1	159.59(5)
O2–Cu1–O4	94.34(5)
N2–Cu1–O4	80.35(6)
N1–Cu1–O4	97.29(6)
O1–Cu1–O4	79.47(5)
N3–Cu2–N4	79.52(6)
N3–Cu2–N5	165.47(6)
N4–Cu2–N5	90.72(6)
N3–Cu2–O3	78.96(5)
N4–Cu2–O3	155.74(5)
N5–Cu2–O3	108.03(5)
N3–Cu2–O6	97.21(5)
N4–Cu2–O6	107.92(6)
N5–Cu2–O6	96.02(5)
O3–Cu2–O6	85.81(5)

with copper nitrate in aqueous methanol to form the corresponding acid. The individual carboxylate ligands result in the formation of a 1D chain, with dinuclear subunits. Each ligand coordinates in a heptadentate fashion binding to Cu(1) via two pyridine nitrogen atoms, one diazine nitrogen atom and a carboxylate oxygen, and to Cu(2) via pyridine and diazine nitrogen atoms, and a terminal hydrazone oxygen. The square-pyramidal Cu(2) coordination sphere is completed by an axial water molecule (Cu(2)–O(6) 2.177(2) Å), and two axial water molecules complete the Jahn–Teller distorted six-coordinate Cu(1) (Cu(1)–O(4) 2.408(1) Å; Cu(1)–O(5) 2.480(1) Å). The chain is propagated by *syn–anti* carboxylate bridging between the dinuclear subunits through oxygen O(2), which binds equatorially to both Cu(1) and Cu(2). The Cu(1)′–N(2)′–N(4)–Cu(2) torsional angle (164.7°) indicates an almost *trans* disposition of the copper basal planes relative to the N–N bridge (Cu(1)–Cu(2)′ 4.683(2) Å). The *syn–anti* carboxylate bridge leads to a much larger metal ion separation (Cu(1)–Cu(2) 5.336(2) Å).

The presence of two nitrate anions per dinuclear subunit indicates that the ligand has lost two protons. The carboxylate is clearly one site of deprotonation. Establishing the other site of deprotonation depends on a clear identification of the bond order within the C(6)–N(2)–N(4)′–C(13)′–O(1) framework (bond distances 1.301, 1.346, 1.354, 1.249 Å, respectively). This is difficult, and is complicated by very short Cu(1)–N(2) and Cu(2)′–N(4)′ distances (1.941(2), 1.943(1) Å, respectively). One could safely conclude that the charge is delocalized within this bridging ligand framework.

3.1.7. [Ni(L4-2H)] (7)

The molecular structure of **7** is shown in Fig. 9, and important distances and angles are listed in Table 8. The complex consists of one full ligand (L4) bonded to a single four coordinate Ni(II) center, via pyridine nitrogen atoms N(1) and N(4), and diazine nitrogen atoms N(3) and N(5). The Ni–N distances are very short (1.82–1.91 Å), typical of square planar Ni(II), but the nickel geometry has a slight tetrahedral distortion (N(3)–Ni(1)–N(5) 164°, N(1)–Ni(1)–N(4) 159°). No anions are present and so the ligand bears a 2− charge. C–O distances are very short (C(13)–O(1) 1.232(7) Å, C(19)–O(2) 1.222(7) Å), indicating them to have double bond character. The sites of deprotonation are, therefore, reasonably assigned to N(3) and N(5). There are no close contacts of significance between individual molecules in the lattice.

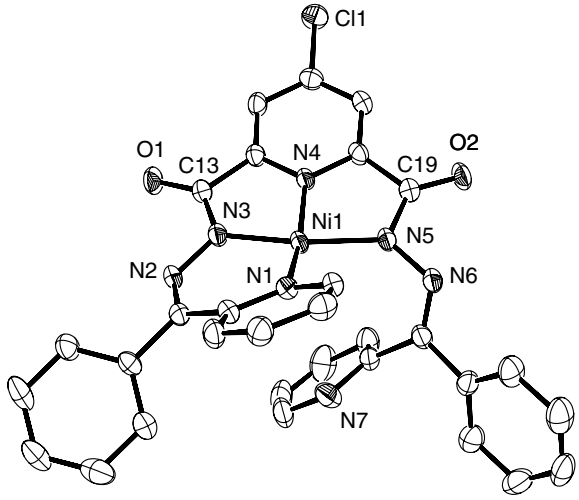


Fig. 9. Structural representation of **7** (40% probability thermal ellipsoids).

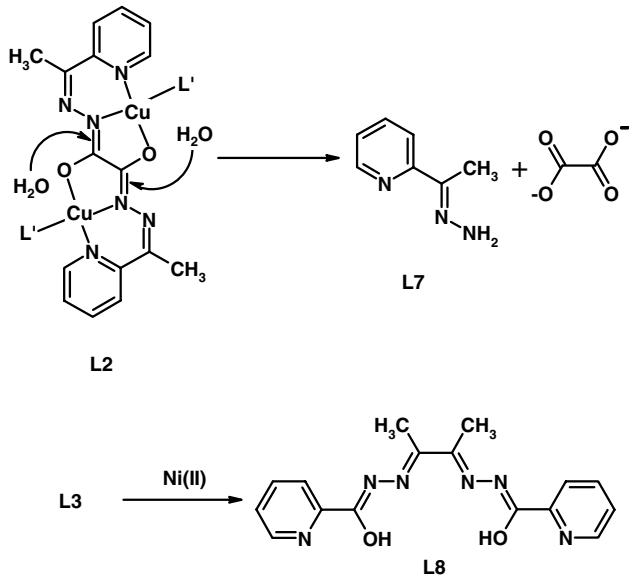
Table 8
Distances (Å) and angles (°) for [Ni(L4-2H)] (**7**)

Ni1–N1	1.906(5)
Ni1–N3	1.843(5)
Ni1–N4	1.822(5)
Ni1–N5	1.930(5)
N2–N3	1.378(7)
N5–N6	1.411(7)
N1–Ni1–N3	94.0(2)
N1–Ni1–N4	159.4(2)
N1–Ni1–N5	102.1(2)
N3–Ni1–N4	83.7(3)
N3–Ni1–N5	163.7(2)
N4–Ni1–N5	81.8(3)

3.2. Ligand decomposition reactions

L2 was prepared by the reaction of diethyl oxalate with hydrazine, followed by the reaction of the dihydrazide with 2-acetylpyridine. The production of 2-acetylpyridine hydrazone (L7) and oxalate on reaction with $Cu(NO_3)_2$ in aqueous methanol indicates ligand hydrolysis at the oxalate imine sites rather than the acetyl imine sites. Pre-coordination of two copper(II) ions to the ligand (e.g., as in Scheme 2) would lead to Lewis acid promoted nucleophilic attack by water at the oxalate C=N sites, thus producing oxalate, which could then simply bridge the two copper centers. The 2-acetylpyridine hydrazone could then pivot about the pyridine–copper bond to assume its coordination role as indicated in the structure of **1**. A similar hydrolytic decomposition appears to have occurred for **2**. It is of interest to note that this ligand forms a stable tetranuclear Ni(II) complex $[Ni_4(L2)_4](BF_4)_4 \cdot 6H_2O$, with no evidence of ligand decomposition [19].

The ligand in **3** (L8), produced from the reaction of L3 with $NiBr_2$, would be expected as the product from the direct reaction of butane-2,3-dione and 2-picolinic acid hydrazide. However, ligand L3 was derived from butanedione monoxime, and was characterized by



Scheme 2.

X-ray crystallography so leaving little doubt as to its identity (Scheme 2). In our hands L3 was found to be fairly unreactive to transition metal salts in general, and this was attributed in part to the *anti* conformation of the ligand itself (Fig. 2), which would probably impede the simultaneous coordination of the pyridine and oxime ends of the ligand.

In order for L3 to bind to a metal ion in a chelating fashion a significant energy expenditure (vide supra) would be required to bring suitable donor groups into an appropriate chelating conformation. Two reasonable chelation isomers are possible on reaction with nickel bromide (Fig. 10(a) and (b); Br is proposed as a co-ligand), of which the oxime N-bonded example (a) is the more stable than (b) by 86 kJ mol^{-1}. With this isomer, polarization of both C=N bonds in L3 would occur, and so would provide a hydrolytic mechanism by which both picolinic hydrazide and the methyl ketone shown in Fig. 10 (c) could be released prior to reaction to form L8. It is of interest to note that reaction of L3 with other Ni(II) salts also produced red diamagnetic complexes of L8 (e.g., $[Ni(L8)](ClO_4)\cdot H_2O$ and $[Ni(L8)](NO_3)\cdot 2H_2O$), and it is reasonable to assume that they are all produced by the same hydrolytic process. The square planar Ni(II) complex (**3**) was calculated to be 30 kJ mol^{-1} more stable than the initially proposed [Ni(L3)Br] chelate (Fig. 10(a)). Since the same ligand rearrangement was observed with several nickel salts, it suggests that this might be the overall driving force for the hydrolytic process.

A recent report indicates that complexes of L3 with Cr(III), Fe(III), Co(II), Ni(II), Cu(II), Zn(II), Cd(II) and UO_2^{2+} can be produced by refluxing the ligand with the appropriate metal salt in ethanol. No evidence for ligand decomposition was presented, and no structures were reported. It is of interest to note that a diamagnetic orange nickel(II) complex, [Ni(L3-H)Cl], was discussed [3].

L4 is part of a growing group of tritopic ligands based on a central 2,6-picolinic dihydrazide framework, which form predominantly $[M_9(\mu\text{-}O)_{12}]$ $[3\times3]$ grid structures [20–26]. A similar ligand (L4′) (Chart 1, L4; R = H) appears to be quite stable in its reaction with Mn(II) salts, and the complex $[Mn_9(L4')_6](NO_3)_6\cdot 12H_2O$ has been produced in a reasonable yield, and shown to have a $[Mn_9(\mu\text{-}O)_{12}]$ $[3\times3]$ grid structure by single crystal X-ray diffraction [26]. However, reaction of L4 with copper acetate in methanol in the presence of air produces as the main product complex **4**. The formation of the mono-carboxylate ligand L9, and the dicarboxylate ligand L10 clearly results from a 'reverse hydrolysis' reaction in which the full hydrazone ligand L4 has undergone nucleophilic attack by water at the 2,6-pyridine dicarboxylic acid sites, rather than at the Schiff base imine positions (Scheme 3). This is presumably encouraged by the pre-coordination of L4 to Cu(II), at least in the central pyridine cavity, although it is highly likely that the pre-coordination involves a trinuclear copper(II) complex, similar to other linear $Cu(II)_3$ complexes observed with this class of ligand [25,27].

Perhaps the most surprising result is the formation of the triazole derivative 3-phenyl-triazolo[1,5-a]pyridine (L11). It is of interest to note that the 2-pyridyl analogue 3-(2-pyridyl)-triazolo[1,5-a]pyridine is produced by the reaction of di-2-pyridyl ketone and hydrazine hydrate in methanol–water (1:1) in the presence of air [28], or by the oxidation of di-2-pyridyl ketone hydrazone with nickel(II) peroxide in benzene [29]. It also appears to have resulted from a reaction between a di-2-pyridyl

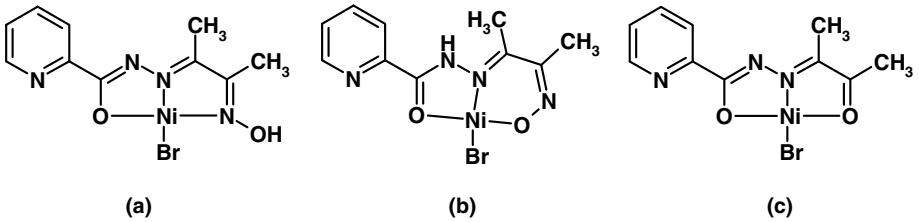
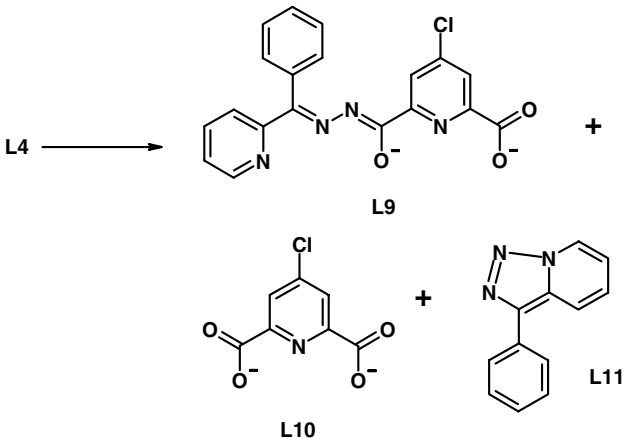


Fig. 10. Chelation isomers for L3 (a,b) and proposed hydrolysis product (c).



Scheme 3.

ketone hydrazone and copper nitrate in air via an oxidative cyclization, producing the copper(II) complex of the triazole [28]. The hydrazone of 2-benzoyl pyridine can also be oxidatively cyclized to the corresponding triazole 3-phenyl-triazolo[1,5-a]pyridine, by reaction with silver oxide [30]. The simultaneous formation of the mono- and di-acid ligands (L9, L10) suggests that phenyl-2-pyridyl ketone hydrazone is formed first, which then oxidatively cyclizes under mild conditions in the presence of air to produce L11. This process may be catalyzed by the presence of Cu(II) ions.

L4 reacts with cobalt(II) nitrate in CH_3CN/CH_3OH in air to form the complex $[(L4)_3(L9)_6Co(III)_6Co(II)_6(H_2O)_6(NO_3)_6]$ $[Co(H_2O)_6](NO_3)_8(CH_3CN)_3(H_2O)_6$ (**8**), which contains both L4 and L9, and has been reported previously [31]. Two views are shown in Figs. 11(a) and (b) looking down the trigonal axis of the molecule, and from a side view, respectively. The mono-carboxylate ligand L9 binds six metal ions on each trigonal face, with three Co(2) (Co(II)) atoms bridged by *syn–anti* carboxylates in an inner triangular array, with hydrazone oxygen atoms bridging each of them to the outer Co(1) (Co(III)) centers. The Co(1) centers are linked by the two end N_2O pockets of the tritopic ligands L4 to form the dodecanuclear array. The thirteenth cobalt(II) ion appears in the lattice in part to balance the overall charge. There is no evidence to suggest the formation of the di-acid (L10) or the triazole (L11), but again this reaction serves to illustrate the hydrolytic instability of the hydrazone function in this class of ligand.

The formation of the carboxylate ligand L9 from L4 on reaction with $Co(NO_3)_2$ underlines the hydrolytic instability of the hydrazone linkages and the fact that Co(II) is capable of mediating nucleophilic attack at the imine site. The presence of Co(II) at the carboxylate site is a surprise since Co(III) would be expected to be more highly polarizing and to prefer the oxygen rich environment generated in the internal trigonal core. In

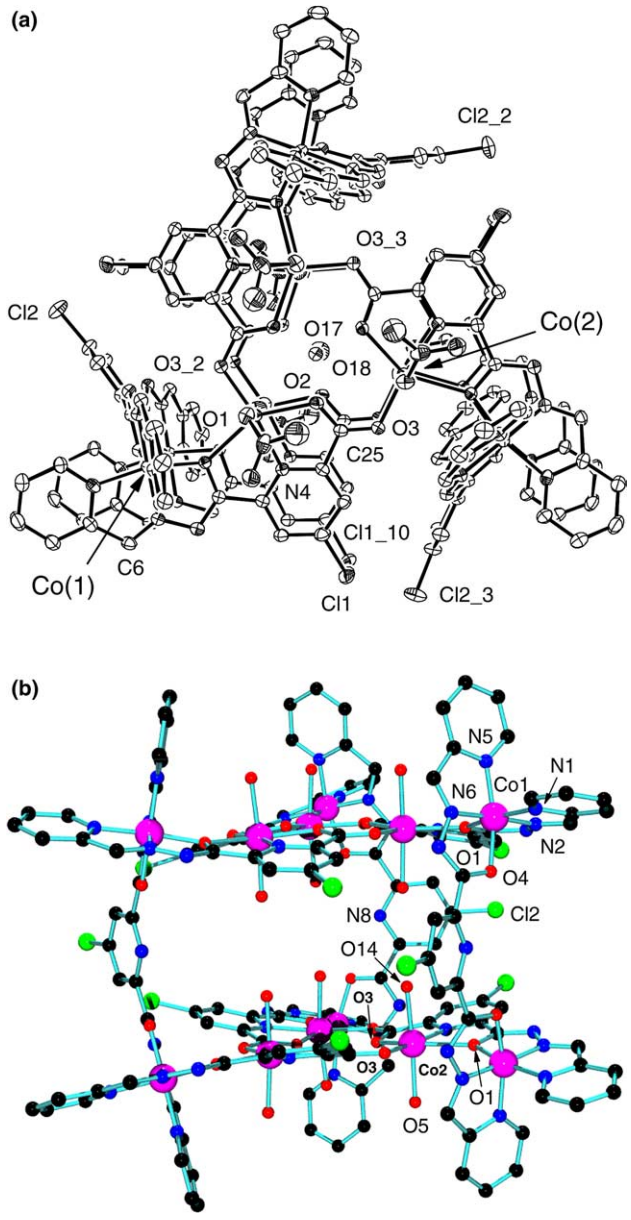
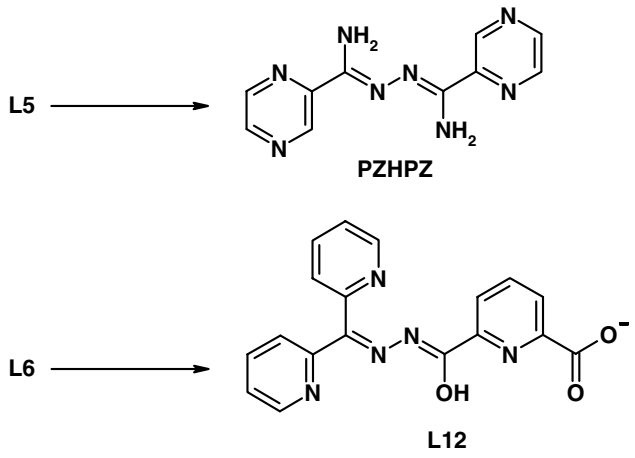


Fig. 11. (a) Structural representation of **8** viewed down the threefold symmetry axis (4% probability thermal ellipsoids), with phenyl rings removed for clarity. (b) Structural representation of **8** viewed at 90° to the threefold symmetry axis (POVRAY ©image).

view of the fact that no ligand decomposition occurs in the reaction between $NiCO_3$ and L4, this suggests that Co(III) is instrumental in the formation of L9.

The formation of the Fe(II) complex **5** containing the bis-bidentate ligand PZHPZ (Chart 1) from L5 (Scheme 4) is somewhat surprising, and indicates a different ligand decomposition mechanism. In this case any water involved in the hydrolysis must have arisen mostly from the hydrated metal salt itself, since CH_3CN was used as the solvent. This type of ligand contains amidrazone fragments at the ends, which are produced by reaction of, e.g., a picolinic-dihydrazide with the



Scheme 4.

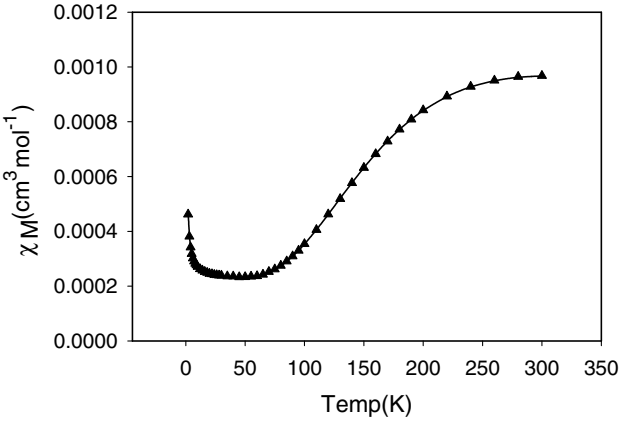


Fig. 12. Variable temperature magnetic data for **1**. The solid line represents the best fit result to Eq. (1) (see text for fitted parameters).

methylimidate ester derived from 2-cyanopyridine or 2-cyanopyrazine. Direct synthesis of PZHPZ can be achieved in high yield by the reaction of 2-pyrazinamide hydrazone with 2-pyrazine methylimidate [2]. It seems reasonable to assume that a reverse hydrolytic step has occurred in the reaction of L5 with a metal ion, in which the appropriate amidrazone is produced as one product by hydrolysis of the imine linkage adjacent to the central pyridine ring. It seems highly unlikely that the appropriate imidate would be produced as well, raising the question as to how PZHPZ is produced. The elimination of a hydrazine molecule between two condensing amidrazone moieties seems unlikely, but perhaps the formation of an amide by metal ion promoted hydrolysis at the peripheral imine C=N group could lead to a more simple metal ion facilitated condensation to produce PZHPZ.

L6 undergoes a simple hydrolysis reaction at the hydrazide carbonyl group on reaction with Cu(II) in aqueous methanol to produce the corresponding carboxylic acid (Scheme 4). This presumably is effected by pre-coordination of the Cu(II) ion to the hydrazide group first, which would polarize the carbonyl group and enhance electrophilic attack by water at the carbon atom.

3.3. Magnetic properties

The variable temperature magnetic properties of **1** show a rise in susceptibility with increasing temperature to a maximum around 300 K (Fig. 12), indicating significant intramolecular antiferromagnetic exchange. The low temperature increase corresponds to the presence of paramagnetic impurity. Given the structure of **1**, with essentially isolated oxalate bridged dinuclear copper(II) species, the data were fitted to a simple exchange expression for two interacting $S = 1/2$ centres ($H_{ex} = -2J\{S_1 \cdot S_2\}$) adapted for a paramagnetic impurity fraction (ρ), Weiss-like temperature correction (θ) and temperature independent paramagnetism ($N\alpha$) (Eq. (1)). A good fit gave $g = 2.21(1)$, $J = -171.5(4)$ cm^{-1}, $\rho = 0.0011$, $\theta = 0$ K, $N\alpha = 200 \times 10^{-6}$ cm^3 mol^{-1}

$$\chi_M = \frac{2Ng^2\beta^2}{k(T-\theta)}\left[\frac{1}{(3+\exp(-2J/kT))}\right](1-\rho) + \left(\frac{Ng^2\beta^2}{4kT}\right)\rho + N\alpha \quad (1)$$

($10^2R = 0.41$; $R = [\sum(\chi_{obs.} - \chi_{calc.})^2 / \sum \chi^2_{obs.}]^{1/2}$). The solid line in Fig. 12 was calculated with these parameters. The large singlet–triplet splitting (343 cm^{-1}) in this case is typical for oxalate bridged di-copper(II) complexes [32]. Compound **2** gave an essentially identical profile of susceptibility as a function of temperature, and fitting of the data to Eq. (1) gave $g = 2.24(4)$, $J = -172(8)$ cm^{-1}, $\rho = 0.0075$, $\theta = -0.2$ K, $N\alpha = 134 \times 10^{-6}$ cm^3 mol^{-1} ($10^2R = 1.7$). This clearly indicates the structural similarity between **1** and **2**, and oxalate bridging.

Complex **3** is diamagnetic, consistent with the square planar structure and the strong in plane ligand field. The corresponding nitrate and perchlorate complexes are also diamagnetic. Complex **7** is also diamagnetic, consistent with its square-planar structure. The variable temperature magnetic properties of **4** show that the magnetic moment is essentially constant between 2 and 300 K (2.9–3.2 μ_B/mol), indicative of essentially isolated spin centers. This is consistent with the structure, which shows a strictly orthogonal connection between Cu(1) and Cu(2) through the diazine (N–N) bridge. The long equatorial, non-orthogonal connection between Cu(1) and Cu(2) via N(3) and O(1) clearly does not lead to any significant spin exchange.

Complex **5** is essentially diamagnetic from 2 to 300 K, indicative of a low spin Fe(II) system, and identical to the behaviour of the iso-structural complex $[Fe_2(PZHPZ)_3](NO_3)_4$ [2]. The chain structure of **6** creates an alternating bridging arrangement between

the copper ions with N–N and *syn–anti* carboxylates connecting the copper magnetic orbitals directly. The presence of a direct *trans* diazine bridge with a large Cu–N–N–Cu torsional angle (164.7°) would suggest quite strong antiferromagnetic exchange [33], while the *syn–anti* carboxylate bridge would not be expected to generate significant exchange [34,35]. Variable temperature magnetic data (Fig. 13) show molar susceptibility reaching a maximum at ~200 K, indicating quite strong antiferromagnetic exchange coupling between the copper centres. Given the likely dominance of the diazine bridge in the exchange process, the data were fitted to Eq. (1), giving $g = 2.20(3)$, $2J = -234(2)\ \mathrm{cm}^{-1}$, $\theta = 1.4\ \mathrm{K}$, $\rho = 0.027$, $N\alpha = 120 \times 10^{-6}\ \mathrm{cm}^3\ \mathrm{mol}^{-1}$ ($10^2R = 3.3$; $R = [\sum(\chi_{\mathrm{obs.}} - \chi_{\mathrm{calc.}})^2/\sum\chi_{\mathrm{obs.}}{}^2]^{1/2}$). The solid line in Fig. 13 is calculated with these fitted parameters. This result is entirely consistent with *trans* N–N bridge connecting Cu(1) and Cu(2) [33]. The small positive θ correction might be considered to arise from the *syn–anti* carboxylate bridge, since the chains are well separated in the extended structure.

The dodecanuclear cobalt complex **8** actually contains thirteen cobalt ions ($Co(III)_6Co(II)_7$), with the $[Co(II)(H_2O)_6]^{2+}$ ion residing in the lattice. The variable temperature magnetic data show a slight variation in moment from 11.0 μ_B at 300 K to 10.2 μ_B at 100 K, followed by a smooth decrease to 8.5 μ_B at 2 K. The gradual drop in moment is indicative of possible weak intra-molecular antiferromagnetic exchange, but because of the complexities involved with fitting magnetic data for Co(II) systems in general no attempt has been made to evaluate an exchange integral. The *syn–anti* carboxylate triangular bridging arrangement of the Co(II) centres would not be expected to lead to significant coupling, which is consistent with the observed data [34,35]. This arises from a mismatch of the metal orbitals in the case of copper, which would be expected to have a similar effect in the present situation, in addition to the long distances of separation of the Co(II) centres (5.180 Å).

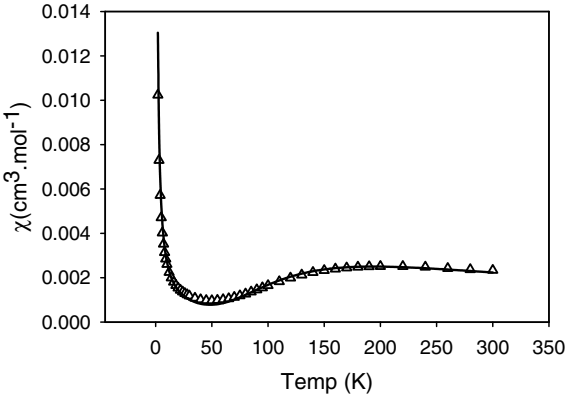


Fig. 13. Variable temperature magnetic data for **6**. The solid line represents the best fit result to Eq. (1) (see text for fitted parameters).

4. Conclusions

Seemingly innocent ligands, based on condensed hydrazone derivatives, have been shown to undergo some unexpected hydrolytic decomposition reactions in the presence of transition metal ions, with some fragments re-arranging to new ligands and some being incorporated into novel complex structures. In one most unusual case oxidatively cyclized 3-phenyl-triazolo [1,5a]-pyridine (L11) is trapped in a complex structure via extensive aromatic π interactions only, but is not coordinated. In another case a novel dodecanuclear Co(II)/Co(III) cluster is produced by the fortuitous combination of a hydrolyzed mono-carboxylate ligand with a complete dihydrazone ligand. In most cases the products can only be successfully characterized by an X-ray structural determination.

5. Supplementary data

Crystallographic data for the structural analyses have been deposited with the Cambridge Crystallographic Data Centre, CCDC reference numbers 237242–237247, 254194 for **1**, **3**–**7**, L3, respectively. Copies of this information may be obtained free of charge from the Director, CCDC, 12 Union Road, Cambridge, CB2 1EZ, UK (fax: +44 1223 336033; e-mail: deposit@ccdc.cam.ac.uk or www: http://www.ccdc.cam.ac.uk).

Acknowledgements

We thank NSERC (Natural Sciences and Engineering Research Council of Canada), the Research Council of Norway (HG), and EPSRC (JAKH) for financial support, and Dr. R. McDonald, University of Alberta, for structural data.

References

[1] Z. Xu, L.K. Thompson, D.O. Miller, E. Ruiz, S. Alvarez, Inorg. Chem. 42 (2003) 1107.
[2] Z. Xu, L.K. Thompson, D.O. Miller, H.J. Clase, J.A.K. Howard, A.E. Goeta, Inorg. Chem. 37 (1998) 3620.
[3] T.H. Rakha, Trans. Met. Chem. 24 (1999) 659.
[4] L.K. Thompson, L. Zhao, Z. Xu, D.O. Miller, W.M. Reiff, Inorg. Chem. 24 (2003) 128.
[5] (a) G.M. Sheldrick, SHELX-97, 1997;
(b) SIR-97: A. Altomare, M. Cascarano, C. Giacovazzo, A. Guagliardi, J. Appl. Crystallogr. 26 (1993) 343.
[6] P.T. Beurskens, G. Admiraal, G. Beurskens, W.P. Bosman, R. de Gelder, R. Israel, J.M.M. Smits, The DIRDIF-94 program system,

Technical Report of the Crystallography Laboratory, University of Nijmegen, The Netherlands, 1994.
[7] D.T. Cromer, J.T. WaberInternational Tables for X-ray Crystallography IV, vol. IV, The Kynoch Press, Birmingham, England, 1974, Table 2.2 A.
[8] J.A. Ibers, W.C. Hamilton, Acta Crystallogr. 17 (1964) 781.
[9] D.C. Creagh, W.J. McAuley, in: A.J.C. Wilson (Ed.), International Tables for Crystallography, vol. C, Kluwer Academic Publishers, Boston, 1992, pp. 219–222, Table 4.2.6.8.
[10] teXsan for Windows: Crystal Structure Analysis Package, Molecular Structure Corporation, 1997.
[11] J. Cosier, A.M. Glazer, J. Appl. Crystallogr. 19 (1986) 105.
[12] (a) Siemens. SMART Data Collection Software, Ver. 4.050; Siemens Analytical X-ray Instruments Inc., Madison, WI, 1996;
(b) Siemens. SAINT Data Reduction Software, Version 4.050; Siemens Analytical X-ray Instruments Inc., Madison, WI, 1996.
[13] Sheldrick, G.M., SHELXTL 5.04/VMS, An integrated system for solving, refining and displaying crystal structures from diffraction data. Siemens Analytical X-ray Instruments Inc., Madison, WI, 1995.
[14] M.J. Frisch, G.W. Trucks, H.B. Schlegel, G.E. Scuseria, M.A. Robb, J.R. Cheeseman, J.A. Montgomery Jr., T. Vreven, K.N. Kudin, J.C. Burant, J.M. Millam, S.S. Iyengar, J. Tomasi, V. Barone, B. Mennucci, M. Cossi, G. Scalmani, N. Rega, G.A. Petersson, H. Nakatsuji, M. Hada, M. Ehara, K. Toyota, R. Fukuda, J. Hasegawa, M. Ishida, T. Nakajima, Y. Honda, O. Kitao, H. Nakai, M. Klene, X. Li, J.E. Knox, H.P. Hratchian, J.B. Cross, C. Adamo, J. Jaramillo, R. Gomperts, R.E. Stratmann, O. Yazyev, A.J. Austin, R. Cammi, C. Pomelli, J.W. Ochterski, P.Y. Ayala, K. Morokuma, G.A. Voth, P. Salvador, J.J. Dannenberg, V.G. Zakrzewski, S. Dapprich, A.D. Daniels, M.C. Strain, O. Farkas, D.K. Malick, A.D. Rabuck, K. Raghavachari, J.B. Foresman, J.V. Ortiz, Q. Cui, A.G. Baboul, S. Clifford, J. Cioslowski, B.B. Stefanov, G. Liu, A. Liashenko, P. Piskorz, I. Komaromi, R.L. Martin, D.J. Fox, T. Keith, M.A. Al-Laham, C.Y. Peng, A. Nanayakkara, M. Challacombe, P.M.W. Gill, B. Johnson, W. Chen, M.W. Wong, C. Gonzalez, J.A. Pople, GAUSSIAN-03, Revision B.05, Gaussian, Inc., Pittsburgh PA, 2003.
[15] A.D. Becke, J. Chem. Phys. 98 (1993) 5648.
[16] A. Schaefer, H. Horn, R. Ahlrichs, J. Chem. Phys. 97 (1992) 2571.
[17] J.H. Jang, J.G. Lee, H. Lee, Y. Xie, H.F. Schaefer, J. Phys. Chem. A 102 (1998) 5298.
[18] N. Ito, S.E.V. Phillips, C. Stevens, Z.B. Ogel, M.J. McPherson, J.N. Keen, K.D.S. Yadav, P.F. Knowles, Nature 350 (1991) 87.
[19] L. Zhao, V. Niel, L.K. Thompson, Z. Xu, V.A. Milway, R.G. Harvey, D.O. Miller, C. Wilson, M. Leech, J.A.K. Howard, S.L. Heath, J. Chem. Soc., Dalton Trans. (2004) 1446.
[20] L. Zhao, C.J. Matthews, L.K. Thompson, S.L. Heath, Chem. Commun. (2000) 265.
[21] L. Zhao, Z. Xu, L.K. Thompson, S.L. Heath, D.O. Miller, M. Ohba, Angew. Chem. Int. Ed. 39 (2000) 3114.
[22] O. Waldmann, R. Koch, S. Schromm, P. Müller, L. Zhao, L.K. Thompson, Chem. Phys. Lett. 332 (2000) 73.
[23] O. Waldmann, L. Zhao, L.K. Thompson, Phys. Rev. Lett. 88 (2002) 066401-1-4.
[24] L. Zhao, Z. Xu, L.K. Thompson, D.O. Miller, Polyhedron 20 (2001) 1359.
[25] Z. Xu, L.K. Thompson, D.O. Miller, Polyhedron 21 (2002) 1715.
[26] L. Zhao, Z. Xu, H. Grove, V.A. Milway, L.N. Dawe, T.S.M. Abedin, L.K. Thompson, T.L. Kelly, R.G. Hynes, D.O. Miller, L. Weeks, J.G. Shapter, K.J. Pope, Inorg. Chem. 43 (2004) 3812.
[27] L. Zhao, L.K. Thompson, Z. Xu, D.O. Miller, D.R. Stirling, J. Chem. Soc., Dalton Trans. (2001) 1706.
[28] L.P. Battaglia, M. Carcelli, F. Ferraro, L. Mavilla, C. Pelizzi, G. Pelizzi, J. Chem. Soc., Dalton Trans. (1994) 2651.
[29] H. Ogura, S. Mineo, K. Nakagawa, S. Shiba, Yakugaka Zasshi 101 (1981) 329.
[30] J.H. Boyer, R. Borgers, L.T. Wolford, J. Am. Chem. Soc. 79 (1957) 678.
[31] V.A. Milway, L.K. Thompson, D.O. Miller, Chem. Commun. (2004) 1790.
[32] M. Julve, M. Verdaguer, A. Gleizes, M. Philoche-Levisalles, Inorg. Chem. 23 (1984) 3808.
[33] L.K. Thompson, Z. Xu, A.E. Goeta, J.A.K. Howard, H.J. Clase, D.O. Miller, Inorg. Chem. 37 (1998) 3217.
[34] E. Colacio, J.M. Domínguez-Vera, M. Ghazi, R. Kivekäs, M. Klinga, J.M. Moreno, Eur. J. Inorg. Chem. (1999) 441.
[35] E. Colacio, M. Ghazi, R. Kivekäs, J.M. Moreno, Inorg. Chem. 39 (2000) 2882.

Available online at www.sciencedirect.com
SCIENCE DIRECT®
Polyhedron 24 (2005) 823–830
POLYHEDRON
www.elsevier.com/locate/poly

Synthesis and characterization of new polynuclear lanthanide coordination polymers with 4,4′-oxybis(benzoic acid)

Yi-Bo Wang [a], Chang-Yan Sun [a], Xiang-Jun Zheng [a], Song Gao [b], Shao-Zhe Lu [c], Lin-Pei Jin [a,*]

[a] *Department of Chemistry, Beijing Normal University, Xinjiekou Road, Beijing 100875, PR China*
[b] *State Key Laboratory of Rare Earth Materials Chemistry and Applications, College of Chemistry and molecular Engineering, Peking University, Beijing, 100871, PR China*
[c] *Laboratory of Excited States Processes, Chinese Academy of Sciences; Changchun Institute of Optics, Fine Mechanics and Physics, Chinese Academy of Sciences, Changchun 130021, PR China*

Received 8 December 2004; accepted 22 February 2005
Available online 14 April 2005

Abstract

Three new polynuclear lanthanide coordination polymers $[Ln_5(\mu_3\text{-}OH)(oba)_7(H_2O)_2]_n \cdot 0.5nH_2O$ (Ln = Eu (**1**), Ho (**2**)) and $[Yb_6(oba)_9(H_2O)]_n$ (**3**) (H_2oba = 4,4′-oxybis(benzoic acid)), were prepared by hydrothermal reactions. **1** and **2** are isomorphous and exhibit complicated three-dimensional structures based on $[Ln_5(\mu_3\text{-}OH)(oba)_7(H_2O)_2]$ building blocks. In the asymmetric unit, there are five different coordination environments of Ln(III) ions, including a trinuclear hydroxo core. Complex **3** is a three-dimensional coordination polymer built up from a hexanuclear building block. In **3**, Yb(III) ions have six different chemical environments and are in a regular arrangement, resulting in pseudohexagonal prisms along the *a*-axis. The luminescent property of **1** and magnetic behaviors of **2** and **3** have also been studied.
© 2005 Elsevier Ltd. All rights reserved.

Keywords: Polynuclear; Coordination polymer; Lanthanide; Magnetic susceptibility; Photophysical property

1. Introduction

Coordination polymers have been extensively studied recently due to their interesting structures coupled with their promising applications in ion and solvent molecule exchanges [1–5], gas sorption [6–10], luminescence [11,12], magnetism [13,14] and catalytic behavior [15–17]. While much current research has focused on transition metal coordination polymers [18–27], lanthanide coordination polymers, particularly polynuclear systems, have received less attention owing to the high coordination number and the variable coordination environments of the lanthanides. However, the introduction of polynuclear lanthanide species into the skeleton may create unusual architectures, and polynuclear lanthanide complexes may also exhibit promising magnetic and luminescence properties as a consequence of the unique spectroscopic and electronic characteristics associated with their $4f^n$ electronic configuration. Only a few examples of polynuclear lanthanide coordination polymers have been prepared by lanthanide hydrolysis controlled by different supporting ligands [28–31]. The cubane-like tetranuclear $[Ln_4(\mu_3\text{-}OH)_4]^{8+}$ unit is a common structural motif in these complexes [29–31]. Here, we report pentanuclear lanthanide coordination polymers $[Ln_5(\mu_3\text{-}OH)(oba)_7(H_2O)_2]_n \cdot 0.5nH_2O$ (Ln = Eu (**1**), Ho (**2**)), in which both hydroxyl and carboxyl groups link the lanthanide (III) ions into building

* Corresponding author. Tel.: +01058805522/861062205522; fax: +8601058802075/861062202075.
E-mail address: lpjin@bnu.edu.cn (L.-P. Jin).

0277-5387/$ - see front matter © 2005 Elsevier Ltd. All rights reserved.
doi:10.1016/j.poly.2005.02.022

blocks, and a hexanuclear ytterbium coordination polymer $[Yb_6(oba)_9(H_2O)]_n$ (**3**).

2. Experimental

2.1. Chemicals and measurements

$EuCl_3 \cdot 6H_2O$, $HoCl_3 \cdot 6H_2O$ and $YbCl_3 \cdot 6H_2O$ were prepared by dissolving their oxides in concentrated hydrochloric acid, respectively, and the solvents were evaporated to dryness. The lanthanide and water contents of the lanthanide chloride hydrates were determined by EDTA titration. All the other reagents were commercially available and used without further purification. Elemental analyses were performed on an Elementar Vario EL analyzer. The IR spectra were recorded with a Nicolet Avatar 360 FT-IR spectrometer using the KBr pellet technique. The luminescence spectra were recorded at 77 K using a YAG:Nd laser with an excitation wavelength of 355 nm and a SPEX 1403 double grating monochromator. The temperature dependence of magnetic susceptibility for crystalline samples was recorded on an Oxford MagLab 2000 magnetometer in the temperature range of 2–300 K.

2.2. Synthesis

*$[Eu_5(oba)_7(OH)(H_2O)_2]_n \cdot 0.5n(H_2O)$ (**1**)*. A mixture of $EuCl_3 \cdot 6H_2O$ (0.037 g, 0.1 mmol), H_2oba (0.039 g, 0.15 mmol), H_2O (10 ml) and 0.65 M NaOH aqueous solution (0.31 ml, 0.20 mmol) was sealed in a 23-ml stainless-steel reactor with a Teflon liner and heated at 200 °C for 72 h, then slowly cooled to room temperature. Colorless crystals of **1** were obtained. Yield: 0.02 g (38.4%). *Anal*. Calc. for $C_{98}H_{62}Eu_5O_{38.50}$: C, 45.00; H, 2.37; Found: C, 44.89; H, 2.32%. IR (KBr, cm^{-1}): 3447m, 1598s, 1524s, 1400s, 1253s, 1233s, 1160s, 1012w, 881m, 784s, 656w.

*$[Ho_5(oba)_7(OH)(H_2O)_2]_n \cdot 0.5nH_2O$ (**2**)*. Light yellow crystals of **2** were prepared in the same manner as above. Yield: 0.017 g (31.9%). *Anal*. Calc. for $C_{98}H_{62}Ho_5O_{38.50}$: C, 43.91; H, 2.11; Found: C, 44.05; H, 2.30%. IR (KBr, cm^{-1}): 3459m, 1599s, 1526s, 1414s, 1254s, 1235s, 1161s, 1012w, 882m, 784s, 658m.

*$[Yb_6(oba)_9(H_2O)]_n$ (**3**)*. Colorless crystals of **3** were obtained in the same manner. Yield: 0.048 g (43.5%). *Anal*. Calc. for $C_{126}H_{74}O_{46}Yb_6$: C, 45.01; H, 2.16; Found: C, 44.99; H, 2.24%. IR (KBr, cm^{-1}): 3439m, 1599s, 1533s, 1417s, 1305m, 1252s, 1161s, 1097m, 1012w, 881m, 783s, 656w.

2.3. X-ray diffraction determination

The X-ray single crystal data collections for complexes **1**–**3** were performed on a Bruker Smart 1000 CCD diffractometer, using graphite-monochromated Mo Kα radiation ($\lambda = 0.71073$ Å). Semi-empirical absorption corrections were applied using the SADABS program. The structures were solved by direct methods and refined by full-matrix least square on F^2 using the SHELXTL-97 program [32]. All non-hydrogen atoms were refined anisotropically. The hydrogen atoms were generated geometrically and treated by a mixture of independent and constrained refinement. The crystallographic data for complexes **1**–**3** are listed in Table 1, and selected bond lengths (Å) in Table 2.

Table 1
Crystal data for **1**–**3**

Compound	**1**	**2**	**3**
Empirical formula	$C_{98}H_{62}Eu_5O_{38.50}$	$C_{98}H_{62}Ho_5O_{38.50}$	$C_{126}H_{74}O_{46}Yb_6$
Formula weight	2615.28	2680.13	3360.08
Crystal system	monoclinic	monoclinic	monoclinic
Space group	*P*2(1)/*c*	*P*2(1)/*c*	*Pc*
a (Å)	27.983(7)	27.947(9)	14.657(4)
b (Å)	20.538(5)	20.367(6)	23.113(7)
c (Å)	15.833(4)	15.730(5)	20.187(5)
α (°)	90	90	90
β (°)	90.736(5)	90.572(5)	115.408(16)
γ (°)	90	90	90
Z	4	4	2
V (Å^3)	9099(4)	8953(5)	6177(3)
ρ_{calcd} (g cm^{-3})	1.909	1.988	1.806
Temperature (K)	293(2)	293(2)	293(2)
μ (mm^{-1})	3.491	4.464	4.584
Reflections collected	26254, 12718	48535, 18197	31616, 19620
Total, independent, R_{int}	0.1724	0.0651	0.0536
λ (Mo Kα), (Å)	0.71073	0.71073	0.71073
R_1, wR_2 [$I > 2\sigma(I)$]	0.0560, 0.0742	0.0504, 0.1105	0.0611, 0.1343

Table 2
Selected bond lengths (Å) for **1**–**3**

1					
Eu(1)–O(1)	2.68(1)	Eu(2)–O(35)#1	2.28(2)	Eu(4)–O(20)	2.71(1)
Eu(1)–O(2)	2.42(1)	Eu(2)–O(37)	2.43(1)	Eu(4)–O(24)	2.33(1)
Eu(1)–O(6)#3	2.45(1)	Eu(2)–O(38)	2.48(1)	Eu(4)–O(26)#7	2.41(1)
Eu(1)–O(11)	2.48(2)	Eu(3)–O(7)	2.53(1)	Eu(4)–O(29)#3	2.49(1)
Eu(1)–O(15)#2	2.43(1)	Eu(3)–O(12)	2.33(2)	Eu(4)–O(31)#3	2.42(1)
Eu(1)–O(17)#1	2.36(2)	Eu(3)–O(14)#2	2.29(1)	Eu(5)–O(5)	2.39(1)
Eu(1)–O(34)#1	2.47(2)	Eu(3)–O(21)#4	2.26(1)	Eu(5)–O(9)	2.27(1)
Eu(1)–O(38)	2.36(1)	Eu(3)–O(27)#6	2.33(1)	Eu(5)–O(20)	2.36(1)
Eu(2)–O(1)	2.39(1)	Eu(3)–O(36)	2.42(1)	Eu(5)–O(25)	2.32(1)
Eu(2)–O(6)	2.58(1)	Eu(3)–O(38)	2.36(1)	Eu(5)–O(29)	2.53(1)
Eu(2)–O(7)	2.49(1)	Eu(4)–O(4)	2.30(1)	Eu(5)–O(30)	2.44(1)
Eu(2)–O(16)#4	2.40(1)	Eu(4)–O(10)#3	2.37(1)	Eu(5)–O(31)	2.61(1)
Eu(2)–O(22)#4	2.35(1)	Eu(4)–O(19)	2.43(1)	Eu(5)–O(32)	2.43(1)

Symmetry operation: #1 $x + 1$, $-y + 1/2$, $z - 1/2$; #2 $-x$, $-y + 1$, $-z - 1$; #3 x, $-y + 1/2$, $z - 1/2$; #4 $x + 1$, y, z; #5 x, $-y + 1/2$, $z + 1/2$; #6 $-x$, $y + 1/2$, $-z + 1/2$; #7 x, y, $z - 1$.

2					
Ho(1)–O(1)	2.76(1)	Ho(2)–O(35)#1	2.20(1)	Ho(4)–O(20)	2.71(1)
Ho(1)–O(2)	2.35(1)	Ho(2)–O(37)	2.39(1)	Ho(4)–O(24)	2.28(1)
Ho(1)–O(6)#3	2.40(1)	Ho(2)–O(38)	2.42(1)	Ho(4)–O(26)#6	2.36(1)
Ho(1)–O(11)	2.40(1)	Ho(3)–O(7)	2.55(1)	Ho(4)–O(29)#3	2.46(1)
Ho(1)–O(15)#2	2.33(1)	Ho(3)–O(12)	2.28(1)	Ho(4)–O(31)#3	2.36(1)
Ho(1)–O(17)#1	2.31(1)	Ho(3)–O(14)#2	2.26(1)	Ho(5)–O(5)	2.33(1)
Ho(1)–O(34)#1	2.37(1)	Ho(3)–O(21)#4	2.24(1)	Ho(5)–O(9)	2.26(1)
Ho(1)–O(38)	2.33(1)	Ho(3)–O(27)#5	2.27(1)	Ho(5)–O(20)	2.32(1)
Ho(2)–O(1)	2.32(1)	Ho(3)–O(36)	2.35(1)	Ho(5)–O(25)	2.25(1)
Ho(2)–O(6)	2.54(1)	Ho(3)–O(38)	2.32(1)	Ho(5)–O(29)	2.48(1)
Ho(2)–O(7)	2.43(1)	Ho(4)–O(4)	2.25(1)	Ho(5)–O(30)	2.37(1)
Ho(2)–O(16)#4	2.32(1)	Ho(4)–O(10)#3	2.30(1)	Ho(5)–O(31)	2.62(1)
Ho(2)–O(22)#4	2.31(1)	Ho(4)–O(19)	2.37(1)	Ho(5)–O(32)	2.37(1)

Symmetry operation: #1 $x + 1$, $-y + 1/2$, $z - 1/2$; #2 $-x + 2$, $-y + 1$, $-z + 1$; #3 x, $-y + 1/2$, $z - 1/2$; #4 $x + 1$, y, z; #5 $-x + 2$, $y + 1/2$, $-z + 5/2$; #6 x, y, $z - 1$.

3					
Yb(1)–O(2)	2.23(3)	Yb(3)–O(15)	2.31(2)	Yb(5)–O(12)	2.23(2)
Yb(1)–O(7)	2.24(2)	Yb(3)–O(21)	2.47(2)	Yb(5)–O(35)#4	2.23(2)
Yb(1)–O(10)#1	2.25(2)	Yb(3)–O(22)	2.34(2)	Yb(5)–O(37)#5	2.20(2)
Yb(1)–O(11)	2.22(2)	Yb(3)–O(25)#2	2.15(2)	Yb(5)–O(39)	2.51(4)
Yb(1)–O(42)#1	2.26(2)	Yb(3)–O(26)	2.23(2)	Yb(5)–O(40)	2.27(3)
Yb(1)–O(45)	2.30(4)	Yb(3)–O(30)#4	2.25(2)	Yb(5)–O(41)#1	2.33(2)
Yb(2)–O(4)#3	2.59(2)	Yb(3)–O(31)	2.20(2)	Yb(5)–O(42)#1	2.60(2)
Yb(2)–O(5)#3	2.33(2)	Yb(4)–O(1)#6	2.29(4)	Yb(5)–O(44)	2.26(4)
Yb(2)–O(14)	2.30(2)	Yb(4)–O(6)#6	2.25(2)	Yb(6)–O(4)#6	2.31(2)
Yb(2)–O(15)	2.58(2)	Yb(4)–O(7)#6	2.60(2)	Yb(6)–O(17)#7	2.22(2)
Yb(2)–O(16)	2.25(2)	Yb(4)–O(9)#5	2.20(1)	Yb(6)–O(19)#8	2.22(2)
Yb(2)–O(20)#2	2.20(2)	Yb(4)–O(27)	2.26(2)	Yb(6)–O(34)#4	2.21(2)
Yb(2)–O(21)	2.32(2)	Yb(4)–O(29)#4	2.15(2)	Yb(6)–O(36)#5	2.20(2)
Yb(2)–O(24)#2	2.29(2)	Yb(4)–O(32)	2.28(2)	Yb(6)–O(47)	2.22(2)

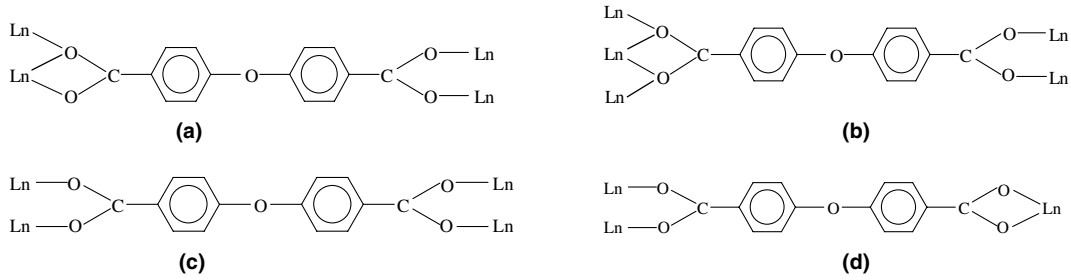
Symmetry operation: #1 $x - 1$, $-y + 1$, $z - 1/2$; #2 $x - 1$, $-y$, $z - 1/2$; #3 x, $y - 1$, $z + 1$; #4 $x + 1$, y, z; #5 $x - 1$, y, z; #6 x, $-y + 1$, $z + 1/2$; #7 x, $-y$, $z - 1/2$; #8 $x - 1$, y, $z - 1$.

3. Results and discussion

3.1. Description of the structures

In complexes **1**–**3**, the carboxyl groups of the H_2oba ligands are all deprotonated and adopt four kinds of coordination modes (see Scheme 1). **1** and **2** are isomorphous and thus only the structures of **1** and **3** will be discussed here.

*$[Eu_5(oba)_7(OH)(H_2O)_2]_n \cdot 0.5nH_2O$ (**1**)*. Complex **1** is a three-dimensional polymer containing rugby-like channels. Three types of coordination modes of oba^{2-} ligands are present in the structure: (a) one carboxylate group of the oba^{2-} ligand adopts a bridging bidentate



Scheme 1. The coordination modes of oba^{2-} ligands in **1**–**3**.

mode, while the other adopts a chelating-bridging tridentate mode, connecting four Eu(III) ions ($^{a}oba^{2-}$, Scheme 1(a)); (b) one carboxylate group of the oba^{2-} ligand adopts a bridging bidentate mode, while the other adopts a chelating-bridging tetradentate mode, connecting five Eu(III) ions ($^{b}oba^{2-}$, Scheme 1(b)); (c) each carboxylate group of the oba^{2-} ligand adopts a bridging bidentate mode, connecting four Eu(III) ions ($^{c}oba^{2-}$, Scheme 1(c)). The asymmetric unit of **1** consists of five Eu(III) ions, seven oba^{2-} ligands, one hydroxyl group, two coordinated water molecules and half a lattice water molecule. The coordination environments of five Eu(III) ions are shown in Fig. 1(a) and the details are listed in Table 3. For clarity, we may divide the coordination environments into two parts (Fig. 1(b) and (c)), which are connected by one $^{a}oba^{2-}$ and two $^{b}oba^{2-}$ ligands. In Fig. 1(b), Eu1, Eu2 and Eu3 are linked together by one μ_3-OH, and therefore a distorted tetrahedron is formed by three Eu^{3+} ions and one oxygen atom of μ_3-OH, where the distance of the oxygen atom of

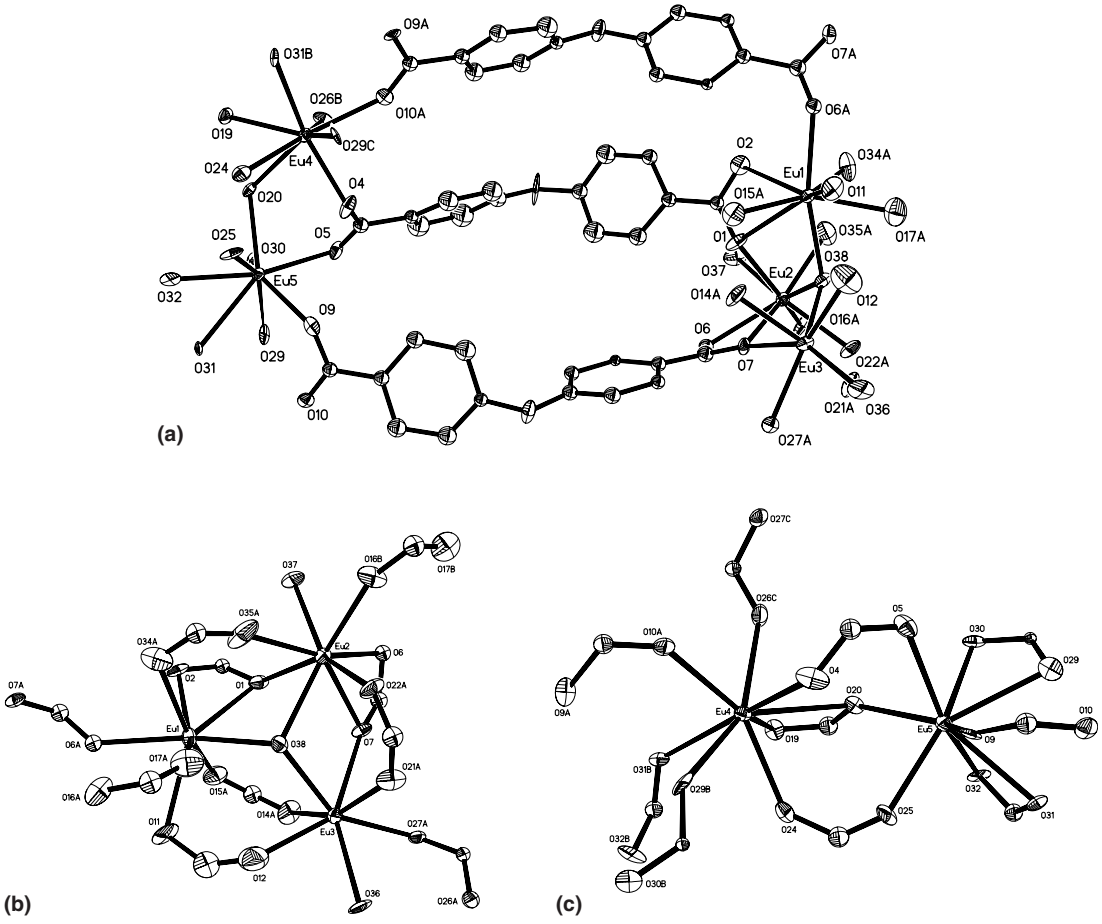


Fig. 1. (a) The coordination environment of Eu^{3+} ions in **1**; (b) The coordination environment of Eu^{3+} ions of the trinuclear core; (c) The coordination environment of the other two Eu^{3+} ions in **1** with thermal ellipsoids at 20% probability. All hydrogen atoms and partial carbon atoms are omitted for clarity.

Table 3
The coordination environment of Eu^{3+} in **1**

Metal atom	CN	No. of Coordinated μ_3-OH	No. of coordinated carboxyl oxygen atoms			No. of coordinated H_2O
			$^{a}oba^{2-}$	$^{b}oba^{2-}$	$^{c}oba^{2-}$	
Eu1	8	1	4	1	2	
Eu2	8	1	3	2	1	1
Eu3	7	1	1	1	3	1
Eu4	8		6	1	1	
Eu5	8		6	1	1	

CN, coordination number; No, number.

μ_3-OH to the triangular metal face is 0.639Å. In the europium hydroxo core, the separations of Eu1···Eu2, Eu2···Eu3 and Eu1···Eu3 are 3.898, 3.977 and 4.119 Å, respectively, and a pair of adjacent Eu^{3+} ions are bridged by two carboxylate groups of two oba^{2-} ligands through bridging bidentate and chelating-bridging tridentate fashion. Thus the europium hydroxo core is surrounded by the six carboxyl groups and a cage-like structure is produced. In the trinuclear core, the average distances of Eu1–O(COO^-), Eu2–O(COO^-), Eu3–O(COO^-) and Eu–O(OH^-) are 2.470, 2.416, 2.347 and 2.400 Å, respectively, which are in accord with the values in $[Eu_{15}(\mu_3\text{-}OH)_{20}(\mu_5\text{-}X)]^{24+}$ [33]. The other two Eu^{3+} ions (Fig. 1(c)), Eu4 and Eu5, are bridged by three carboxyl groups of three oba^{2-} ligands through bridging bidentate and chelating-bridging tridentate coordination modes. The average distances of Eu4–O(COO^-) and Eu5–O(COO^-) are 2.430 and 2.418 Å, which are in agreement with the common distances of Eu–O(COO^-), and the distance of Eu4···Eu5 is 4.281 Å. The Eu(III) ions along the *a*-axis are bridged by $^{a}oba^{2-}$ and $^{b}oba^{2-}$ ligands into one-dimensional double-chains with rugby-like micropores. These chains are further cross-linked by oba^{2-} ligands, resulting in the formation of a three-dimensional network, as shown in Fig. 2. There are small rugby-like channels along the *c*-axis.

*$[Yb_6(oba)_9(H_2O)]_n$ (**3**)*. Complex **3** is a three-dimensional polymer. The hexanuclear species $[Yb_6(oba)_9(H_2O)]$ may be viewed as the building block. There are three types of coordination modes of oba^{2-} ligands in **3**: (a) one carboxylate group of the oba^{2-} ligand adopts a bridging bidentate mode, while the other adopts a chelating-bridging tridentate mode, connecting four Yb(III) ions ($^{a}oba^{2-}$, Scheme 1(a)); (b) each carboxylate group of the oba^{2-} ligand adopts a bridging bidentate mode, connecting four Yb(III) ions ($^{c}oba^{2-}$, Scheme 1(c)); (c) one carboxylate group of the oba^{2-} ligand adopts a bridging bidentate mode, while the other adopts a chelating bidentate mode, connecting three Yb(III) ions ($^{d}oba^{2-}$, Scheme 1(d)). In the asymmetrical unit of **3**, there are six Yb(III) ions, nine oba^{2-} ligands and one aqua ligand. The coordination environment of Yb(III) ions is shown in Fig. 3 and the details are listed in Table 4. For clarity we can also divide the Yb(III) ions into two parts: part 1 consists of Yb1, Yb5 and Yb6; while part 2 consists of Yb2, Yb3 and Yb4. The two parts are linked by two $^{a}oba^{2-}$ ligands. In part 1, Yb5 and Yb6 are connected by two bridging bidentate carboxyl groups of two oba^{2-} ligands; while Yb5 and Yb1 are connected by two bridging bidentate carboxylate groups and one chelating-bridging tridentate carboxyl group of three oba^{2-} ligands. In part 2, Yb3 is connected to Yb4 by three bridging bidentate carboxyl groups of three oba^{2-} ligands, and connected to Yb2 by two chelating-bridging tridentate carboxyl groups and one bridging bidentate carboxylate group of three oba^{2-} ligands. The average distances of Yb–O(COO^-)

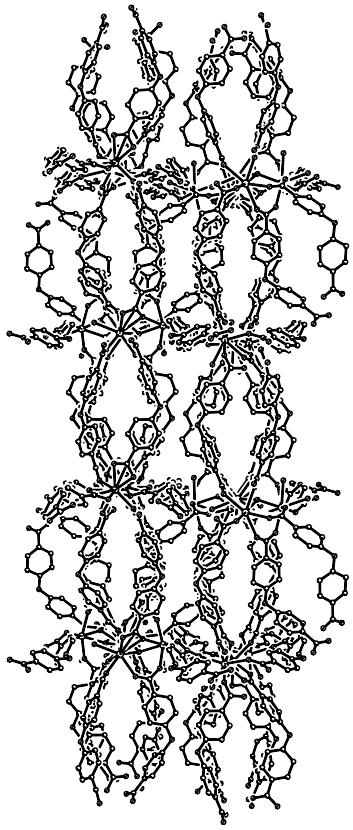


Fig. 2. The three-dimensional network of **1** viewed along the *c*-axis.

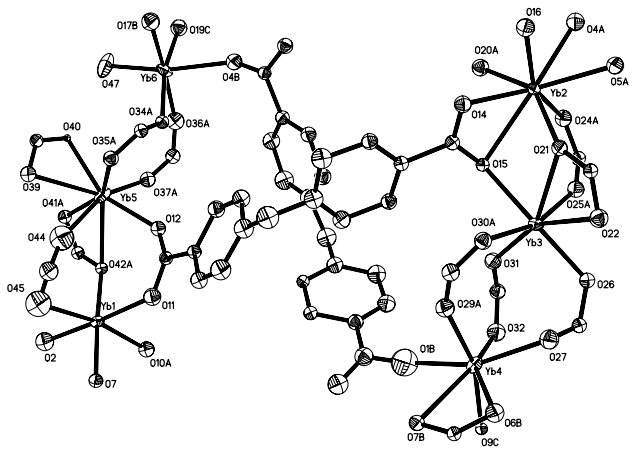


Fig. 3. The coordination environment of Yb^{3+} ions in **3** with thermal ellipsoids at 20% probability. All hydrogen atoms are omitted for clarity.

Table 4
The coordination environment of Yb^{3+} in **3**

	CN	No. of carboxyl oxygen atoms			No. of coordinated H_2O
		$^{a}oba^{2-}$	$^{c}oba^{2-}$	$^{d}oba^{2-}$	
Yb1	6	6			
Yb2	8	6	2		
Yb3	7	4	3		
Yb4	7	4	3		
Yb5	8	4	1	3	
Yb6	6	1	3	1	1

CN, coordination number; No, number.

(from Yb1 to Yb6) are 2.249, 2.356, 2.280, 2.290, 2.330 and 2.231 Å, respectively, and the separations of Yb1···Yb5, Yb5···Yb6, Yb2···Yb3 and Yb3···Yb4 are 4.002, 4.510, 3.823 and 4.330 Å, respectively.

In each asymmetrical unit of **3**, six Yb(III) ions are arranged in the form of a non-planar six-member ring. And along the *a*-axis, two adjacent six-member rings are parallel to each other. As shown in Fig. 4, for instance, a six-member ring constructed by Yb2J, Yb3J, Yb4J, Yb1J, Yb5J and Yb6J is parallel to an adjacent six-member ring formed by Yb2M, Yb3M, Yb4M, Yb1M Yb5M and Yb6M. These two rings are pillared by oba^{2-} ligands along the *a*-axis to yield a pseudohexagonal prism, which is the first example of such an array of lanthanide (III) ions. These pseudoprisms are cross-linked by oba^{2-} ligands, resulting in the formation of a three-dimensional network.

Comparing the structures of **1**–**3**, it can be seen that oba^{2-} ligands display different coordination modes. In **1** and **2**, there are three kinds of oba^{2-} ligands: $^{a}oba^{2-}$, $^{b}oba^{2-}$ and $^{c}oba^{2-}$; while in **3**, the three kinds of oba^{2-} ligands are $^{a}oba^{2-}$, $^{c}oba^{2-}$ and $^{d}oba^{2-}$. The different coordination modes of oba^{2-} ligands lead to the different structures.

Although the "O" atoms between two benzene rings in each oba^{2-} ligand do not participate in the coordination to Ln(III) ions, however, they are important in the structure. With the presence of these "O" atoms, oba^{2-} ligands act as V-shaped, not linear ligands. It is the V-shaped configuration of oba^{2-} ligands, which facilitates the benzene rings and carboxylate groups to adjust their steric configurations more freely and allow the oba^{2-} ligands to display a variety of coordination modes.

3.2. Photophysical properties of complex *1*

The room temperature spectra of powders for **1** are less developed, we comment about low temperature spectra only. The high-resolution emission spectrum of **1** corresponding to $^{5}D_0 \rightarrow {}^{7}F_J$ ($J = 0$–4) transitions excited by 355 nm at 77 K is shown in Fig. 5. The most intensive transition is $^{5}D_0 \rightarrow {}^{7}F_2$, which implies red emission light of **1**. The number of components of the $^{5}D_0 \rightarrow {}^{7}F_1$ transition indicates the presence of more than one chemically different Eu(III) ions site [34]. The intensity of the $^{5}D_0 \rightarrow {}^{7}F_0$ transition is relatively weak and the emission band is broad (see the inserted spectrum in Fig. 5). The inhomogeneous broadening of the $^{5}D_0 \rightarrow {}^{7}F_0$ emission band arises from the site to site variation of the local field acting on the ions, and has consequently been studied by selective excitation techniques.

Setting the analyzing wavenumber to 16233 cm^{-1} and scanning in the range of 578.72–580.4 nm ($^{7}F_0 \rightarrow {}^{5}D_0$), the excitation spectrum (Fig. 6) was obtained. There are two obvious groups of peaks located at about 579.4 and 580.0 nm. The negative charges on the ligands around Eu1, Eu2, Eu3, Eu4 and Eu5 are approximately 3.4, 2.5, 2.6, 3.3 and 3.2, respectively. They can be divided into two groups. One group (3.4, 3.3 and 3.2) contains Eu1, Eu4 and Eu5. The other group (2.5 and 2.6) contains Eu2 and Eu3. As is known, the peak position of $^{7}F_0 \rightarrow {}^{5}D_0$ will shift to lower energy with increasing negative charge on the ligands [35]. So the left peak denoted as A in Fig. 6 can be ascribed to the contribution of $^{5}D_0$ levels of Eu2 and Eu3, and the right peak denoted as B in Fig. 6 can be ascribed to the contribution of $^{5}D_0$ levels of Eu1, Eu4 and Eu5.

3.3. Magnetic properties

The temperature dependence of the magnetic susceptibility of **2** was measured in the temperature range 2–300 K (Fig. 7). The magnetic susceptibility above 50 K obeys the Curie–Weiss law [$\chi = C/(T - \theta)$] with $C = 71.43$ cm^3 mol^{-1} K and $\theta = -10.79$ K. The C value is close to the expected value of 70.35 cm^3 mol^{-1} K for five non-interacting Ho^{3+} free ions. The continuous

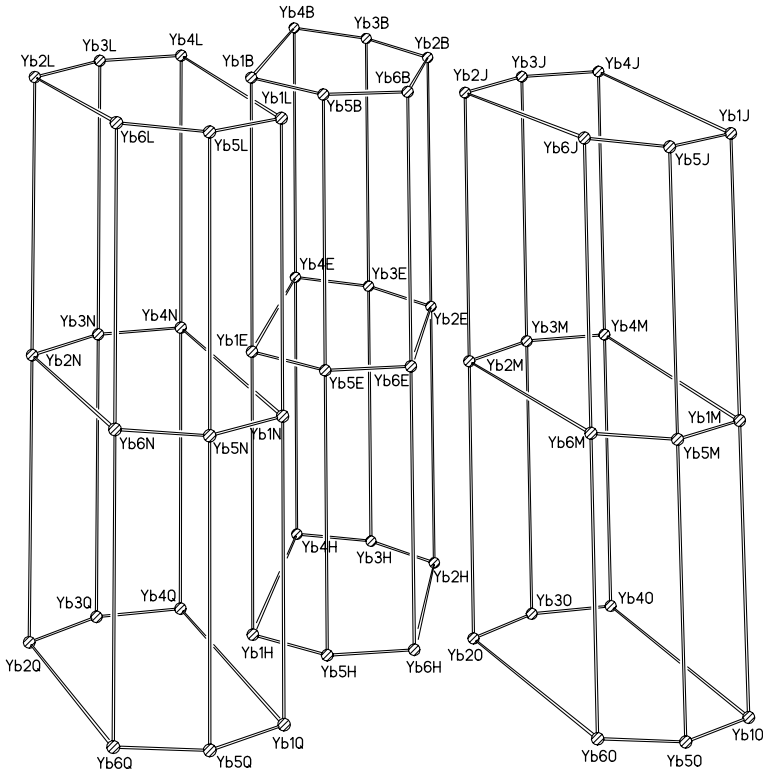


Fig. 4. The hexagonal pseudoprism distribution of Yb(III) ions in **3**.

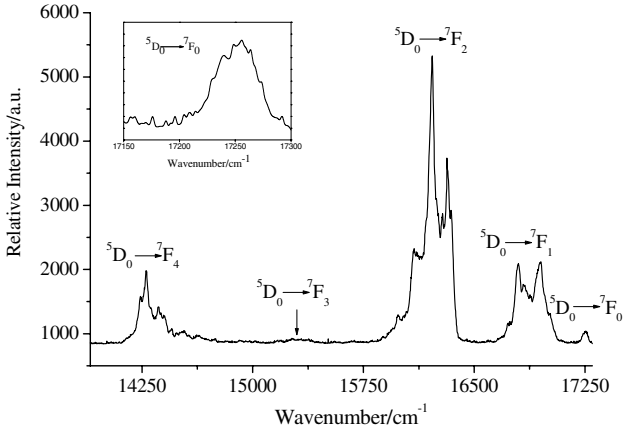


Fig. 5. Emission spectrum of **1** corresponding to $^5D_0 \rightarrow {}^7F_J$ (J = 0–4) transitions at 77 K, λ_{exc} = 355 nm.

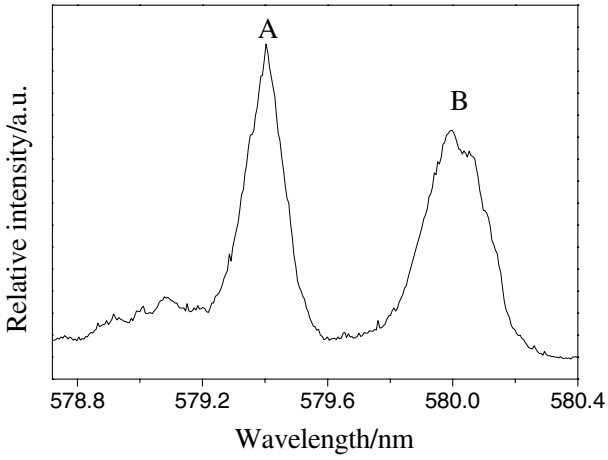


Fig. 6. $^7F_0 \rightarrow {}^5D_0$ excitatation spectrum of powders for **1** recorded at 77 K, λ_m = 616 nm.

decrease in $\chi_M T$ upon cooling should be mainly attributed to the crystal field splitting of a single Ho^{3+} ion together with the possible contribution of the weak interaction through oxygen atoms of hydroxyl and carboxylate bridge with 3.910–4.043 Å Ho···Ho distances.

The variable-temperature magnetic susceptibility of **3** is displayed in Fig. 8, where χ_M is the corrected molar magnetic susceptibility per [Yb_6] unit. At room temperature, the value of $\chi_M T$ is 13.41 $cm^3\,mol^{-1}\,K$, which is approximately close to the calculated value for six Yb free ions (15.42 $cm^3\,mol^{-1}\,K$). Upon cooling, $\chi_M T$ decreases steadily and fast at low temperatures. These results primarily arise from the splitting of the ligand field of the Yb(III) ion together with the possible contribution of the weak antiferromagnetic coupling between Yb(III) ions, considering a possible interaction through two carboxylate bridges with 3.823–4.510 Å Yb···Yb distances. The magnetic susceptibility above 100 K obeys the Curie–Weiss law with the Weiss constant $\theta = -42.61$ K and the Curie constant $C = 15.43$ $cm^3\,mol^{-1}\,K$.

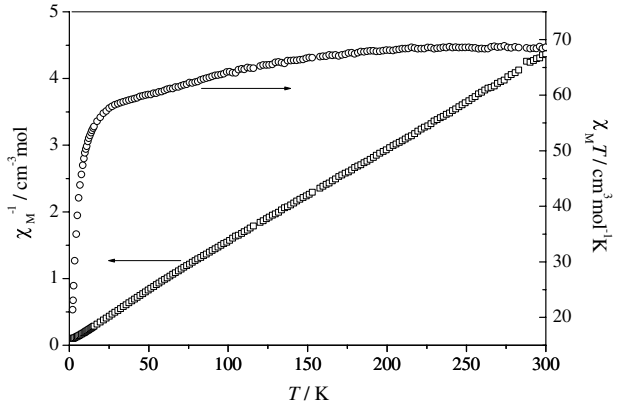


Fig. 7. Plot of the temperature dependence of $\chi_M T$ (○) and χ_M^{-1} (□) for **2** (per $[Ho]_5$ unit).

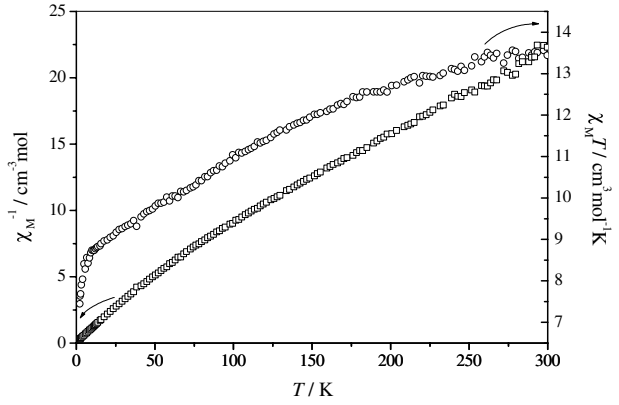


Fig. 8. Plot of the temperature dependence of $\chi_M T$ (○) and χ_M^{-1} (□) for **3** (per $[Yb]_6$ unit).

4. Supplementary material

Crystallographic data for the structural analysis have been deposited with the Cambridge Crystallographic Data Centre, CCDC Nos. 250474, 250475 and 250476 for **1**–**3**, respectively. Copies of this information may be obtained free of charge from the CCDC, 12 Union Road, Cambridge, CB2 1EZ, UK (fax: +44-1223-336-033; e-mail: deposit@ccdc.cam.ac.uk or www: http://www.ccdc.cam.ac.uk).

Acknowledgements

This work was supported by National Natural Science Foundation of China (20331010).

References

[1] B.F. Hoskins, R. Robson, J. Am. Chem. Soc 111 (1989) 5962.
[2] B.F. Hoskins, R. Robson, J. Am. Chem. Soc. 112 (1990) 1546.
[3] O.M. Yaghi, H. Li, J. Am. Chem. Soc. 117 (1995) 10401.
[4] G.B. Gardner, D. Venkataraman, J.S. Moore, S. Lee, Nature 374 (1995) 792.
[5] B.F. Abrahams, P.A. Jackson, R. Robson, Angew. Chem. Int. Ed. 37 (1998) 2656.
[6] O.M. Yaghi, G. Li, H. Li, Nature 378 (1995) 703.
[7] D. Venhataraman, G.B. Gardner, S. Lee, J.S. Moore, J. Am. Chem. Soc. 117 (1995) 11600.
[8] M. Kondo, T. Yoshitomi, K. Seki, H. Matsazaka, S. Kitagawa, Angew. Chem. Int. Ed. 36 (1997) 1725.
[9] O.M. Yaghi, M. O'Keeffe, N.W. Ockwig, H.K. Chae, M. Eddaoudi, J. Kim, Nature 423 (2003) 705.
[10] M. Eddaoudi, J. Kim, N. Rosi, D. Vodak, J. Wachter, M. O'Keeffe, O.M. Yaghi, Science 300 (2003) 1127.
[11] T.M. Reineke, M. Eddaoudi, M. Fehr, D. Kelley, O.M. Yaghi, J. Am. Chem. Soc. 121 (1999) 1651.
[12] B.D. Chandler, A.P. Côtó, D.T. Cramb, J.M. Hill, G.K.H. Shimizu, Chem. Commun. (2002) 1900.
[13] G.J. Halder, C.J. Kepert, B. Moubaraki, K.S. Murray, J.D. Cashion, Science 298 (2002) 1762.
[14] D. Maspoch, D. Ruiz-Molina, K. Wurst, N. Domingo, M. Cavallini, F. Biscarini, J. Tejada, C. Rovira, J. Veciana, Nature Mater. 2 (2003) 190.
[15] M. Fujita, Y.J. Kwon, S. Washizu, K. Ogura, J. Am. Chem. Soc. 116 (1994) 1151.
[16] J.S. Seo, D. Wang, H. Lee, S.I. Jun, J. Oh, Y.J. Jeon, K. Kim, Nature 404 (2000) 982.
[17] O.R. Evans, H.L. Ngo, W. Lin, J. Am. Chem. Soc. 123 (2001) 10395.
[18] S. Kitagawa, M. Munakata, Trends Inorg. Chem. 3 (1993) 437.
[19] M.J. Zaworotko, Chem. Soc. Rev. 23 (1994) 283.
[20] M. Munakata, Adv. Inorg. Chem. 46 (1998) 173.
[21] A.J. Blake, N.R. Champness, P. Hubberstey, W.S. Li, M.A. Withersby, M. Schröder, Coord. Chem. Rev. 183 (1999) 117.
[22] M. Eddaoudi, D.B. Moler, H. Li, B. Chen, T.M. Reineike, M. O'Keeffe, O.M. Yaghi, Acc. Chem. Res. 34 (2001) 319.
[23] A.N. Khlobystov, A.J. Blake, N.R. Champness, D.A. Lemenovskii, A.G. Majouga, N.V. Zyk, M. Schröder, Coord. Chem. Rev. 222 (2001) 155.
[24] B. Moulton, M.J. Zaworotko, Chem. Rev. 101 (2001) 1629.
[25] O.R. Evans, W. Li, Acc. Chem. Res. 35 (2002) 511.
[26] K. Kim, Chem. Soc. Rev. 31 (2002) 96.
[27] S. Kitagawa, S. Kawata, Coord. Chem. Rev. 224 (2002) 11.
[28] C. Serre, N. Stock, T. Bein, G. Férey, Inorg. Chem. 43 (2004) 3159.
[29] R. Wang, H. Liu, M.D. Carducci, T. Jin, C. Zheng, Z. Zheng, Inorg. Chem. 40 (2001) 2743.
[30] B.Q. Ma, D.S. Zhang, S. Gao, T.Z. Jin, C.H. Yan, G.X. Xu, Angew. Chem. Int. Ed. 39 (2000) 3644.
[31] X.J. Zheng, L.P. Jin, S. Gao, Inorg. Chem. 43 (2004) 1600.
[32] G.M. Sheldrick, SHELX-97, PC-version, University of Göttingen, Germany, 1997.
[33] R. Wang, H.D. Selby, H. Liu, M.D. Carducci, T. Jin, Z. Zheng, J.W. Anthis, R.J. Staples, Inorg. Chem. 41 (2002) 278.
[34] J.-C.G. Bünzli, G.R. Choppin, Lanthanide Probes in Life, Chemical and Earth Sciences, Elsevier, Amsterdam, 1989.
[35] M. Albin, W.DeW. Horrocks Jr., Inorg. Chem. 24 (1985) 895.

Available online at www.sciencedirect.com
SCIENCE DIRECT®
Polyhedron 24 (2005) 831–836
POLYHEDRON
www.elsevier.com/locate/poly

Syntheses, crystal structures and characterization of a series of heterothiometallic gold(I) complexes containing bridging diphosphine ligands

Li Song [a,b], Sheng-Qing Xia [a], Sheng-Min Hu [a], Shao-Wu Du [a,*], Xin-Tao Wu [a]

[a] *State Key Laboratory of Structural Chemistry, Fujian Institute of Research on the Structure of Matter, Chinese Academy of Sciences, Fuzhou, Fujian 350002, PR China*

[b] *Graduate School of the Chinese Academy of Sciences, Beijing 100039, PR China*

Received 25 January 2005; accepted 25 February 2005
Available online 13 April 2005

Abstract

A series of tetranuclear heterothiometallic clusters $[Et_4N]_2[(MS_4)_2Au_2(dppe)]$ (**1**: M = Mo; **2**: M = W), $[PPh_4]_2[(MoOS_3)_2Au_2(dppe)]$ (**3**), $[Et_4N]_2[(WOS_3)_2Au_2(dppe)]$ (**4**) (dppe = 1,2-bis(diphenylphosphino)ethane), $[Et_4N]_2[(MS_4)_2Au_2(dppf)]$ (**5**: M = Mo; **6**: M = W) and $[Et_4N]_2[(MOS_3)_2Au_2(dppf)]$ (**7**: M = Mo; **8**: M = W) (dppf = 1,1′-bis(diphenylphosphino)ferrocene) have been synthesized from the reactions of thiometalates $[MXS_3]^{2-}$ (M = Mo or W, X = O or S), $AuCl(SC_4H_8)$ and dppe or dppf. The crystal structures of the complexes **2**, **4** and **6** have been determined by single-crystal X-ray diffraction studies. In the molecular structures of these complexes, the two linear M/Au/S units are linked via bidentate phosphines dppe or dppf. The complexes have been fully characterized by IR, UV–vis as well as elemental analyses. These clusters all exhibit room-temperature luminescence in the solid state.
© 2005 Elsevier Ltd. All rights reserved.

Keywords: Heterothiometalates; Gold; Luminescence; Diphosphine; Crystal structure

1. Introduction

The synthetic and structural chemistry of heterothiometallic clusters, especially the Mo(W)/Cu(Ag)/S cluster compounds, has developed rapidly in recent years due to their fascinating biochemical interests [1–3] and potential applications such as catalysis [4] and optical limiting materials [5]. In contrast with the almost well-established Mo(W)/Cu(Ag)/S system [6], the study of Mo(W)/Au/S cluster compounds is still young. To our knowledge, only a few cluster complexes of this system have been synthesized till now [7–11]. Examples include cluster complexes with unidentate ligands PPh_3 or $AsPh_3$, etc., such as $[MS_4Au_2(PPh_3)_2]$ [12,13], $[MS_4Au_2(AsPh_3)_2]$ [14,15] (M = Mo or W), $[WS_4Au_2(Ph_2PCH_3)_2]$ [16] and $[MoS_4Au_2(PCy_3)_2]$ [17]. However, the complexes with bidentate phosphines have not been seen before. In this paper, we succeeded in co-opting the bidentate dppe and dppf as bridging ligands into the Mo(W)/Au/S system leading to the formation of eight new cluster compounds, namely, $[Et_4N]_2[(MS_4)_2Au_2(dppe)]$ (**1**: M = Mo; **2**: M = W), $[PPh_4]_2[(MoOS_3)_2Au_2(dppe)]$ (**3**), $[Et_4N]_2[(WOS_3)_2Au_2(dppe)]$ (**4**), $[Et_4N]_2[(MS_4)_2Au_2(dppf)]$ (**5**: M = Mo; **6**: M = W) and $[Et_4N]_2[(MOS_3)_2Au_2(dppf)]$ (**7**: M = Mo; **8**: M = W).

In contrast to many Au(I) compounds whose photoluminescent properties have been extensively studied [18–20], the photoluminescent properties of heterometallic Mo(W)/Au(I)/S complexes remain essentially

* Corresponding author. Tel./fax: +86 591 83709470.
E-mail address: swdu@ms.fjirsm.ac.cn (S.-W. Du).

0277-5387/$ - see front matter © 2005 Elsevier Ltd. All rights reserved.
doi:10.1016/j.poly.2005.02.021

unexplored. Recently, clusters $[Cu_3(dppm)_3(WS_4)]ClO_4$ [21] and $[Cu_4(dcpm)_4(MS_4)](ClO_4)_2$ (M = Mo or W) [17] have been observed to be photoluminescent. In our study, we found that the title complexes also showed photoluminescent properties.

2. Experimental

2.1. General procedures

Experiments were carried out in air. $[Et_4N]_2[MS_4]$ (M = Mo or W), $[Et_4N]_2[WOS_3]$ and K_2MoOS_3 were prepared according to the literature methods [22]. Other chemicals were obtained from commercial sources and were used as received.

2.2. Physical measurements

FT-IR spectra in the 400–4000 cm^{-1} range were recorded on a Perkin–Elmer FT-IR spectrometer using KBr pellets. UV–vis spectra were measured on a Perkin–Elmer instrument Lambda 35 UV/VIS spectrometer. The C, H and N analyses were carried out on an Elemental Vario EL III analyzer. Room-temperature fluorescence spectra were measured on a FLS920P spectrometer with a laser at 397 nm as the excitation light.

2.3. Preparation of the Mo(W)/Au/S compounds

In a typical reaction, a mixture of $[AuCl(SC_4H_8)]$ (0.125 mmol, 0.0800 g) and dppe (0.125 mmol, 0.0498 g) in CH_2Cl_2 (5 mL) was stirred for 20 min and then added to a solution of $[Et_4N]_2[MoS_4]$ (0.25 mmol, 0.1212 g) in CH_2Cl_2 (5 mL). The mixture was stirred for 1 h and filtered. The red precipitate was dissolved in DMF (3 mL). Slow diffusion of *i*PrOH into the solution gave air stable red crystals of **1**. Other compounds were prepared in a similar way as described above. A summary of the characterization data for compounds **1**–**8** is listed in Table 1.

2.4. X-ray crystallography

The data for **2** was collected at 293.15 K on a Siemens SMART CCD diffractometer and the data for **4** and **6**

Table 1
Characterization data for complexes **1**–**8**

Compound	IR (KBr disk, cm^{-1})	UV–vis (CH_3CN) (λ_{max}/nm(ε/M^{-1} cm^{-1} × 10^{-4}))	Elemental analyses		Yield (%)
			Calculated	Found	
1	519s, 505s, 489vs, 463m, 439m, 421w	241(5.82), 313(5.13), 445(1.05), 468(1.14)	C: 33.60 H: 4.30 N: 1.87	33.93 4.01 1.86	42
2	519s, 492s, 481s, 463m, 432m, 422m	211(4.56), 274(2.69), 293(1.49), 315(0.47), 392(0.92)	C: 30.08 H: 3.85 N: 1.67	30.30 3.63 1.71	63
3[a]	894vs, 519s,494vs, 466m, 439s, 424w	227(6.73), 260(1.78), 268(1.74), 275(1.56), 308(0.62), 377(0.22), 430(0.13)	C: 47.17 H: 3.65 N: 0.71	47.26 3.26 0.72	31
4[b]	910vs, 520s, 486vs, 467m, 426s	233(6.55), 264(3.45), 329(1.59), 360(1.02)	C: 31.42 H: 4.13 N: 1.67	31.10 3.83 1.71	50
5[c]	525m, 500s, 486vs, 436m	241(6.23), 315(4.51), 443(0.94), 467(1.02)	C: 37.30 H: 4.58 N: 3.11	37.09 4.48 3.11	39
6	524m, 501w, 479vs, 441w, 426s	228(6.66), 273(4.83), 320(0.97), 391(1.31)	C: 32.76 H: 3.74 N: 1.53	32.95 3.86 1.57	48
7	894vs, 526s, 493vs, 437m, 426w	237(3.70), 264(2.19), 311(1.16), 379(0.41), 438(0.29)	C: 36.96 H: 4.22 N: 1.72	36.57 3.90 1.71	31
8[d]	908vs, 525s, 505m, 483vs, 471m, 427s	235(6.39), 263(3.93), 329(1.27), 361(0.81)	C: 33.97 H: 4.03 N: 2.24	33.65 3.87 2.19	36

[a] Containing one solvent molecule of DMF.
[b] Containing a half solvent molecule of EtOH.
[c] Containing two solvent molecules of DMF.
[d] Containing one solvent molecule of DMF.

Table 2
Crystallographic data for compounds **2**, **4** and **6**

	2	**4**	**6**
Empirical formula	$C_{42}H_{64}Au_2N_2P_2S_8W_2$	$C_{44}H_{69}Au_2N_2O_{2.5}P_2S_6W_2$	$C_{50}H_{68}Au_2FeN_2P_2S_8W_2$
Formula mass	1677.01	1681.94	1832.97
Crystal system	monoclinic	monoclinic	monoclinic
Space group	*C*2/*c*	*P*2(1)/*n*	*P*2(1)/*n*
Unit cell dimensions			
a (Å)	17.000(1)	9.508(1)	14.623(1)
b (Å)	21.619(2)	13.575(1)	12.161(1)
c (Å)	14.884(1)	22.233(1)	16.832(1)
α	90.00	90.00	90.00
β	94.110(2)	100.050(3)	91.410(3)
γ	90.00	90.00	90.00
V (Å^3)	5456.1(8)	2825.6(2)	2992.3(3)
Z	4	2	2
$D_{calc.}$ (g cm^{-3})	2.041	1.986	2.034
μ(Mo Kα) (mm^{-1})	9.959	9.548	9.319
R_1[a] [$I > 2\sigma(I)$]	0.0610	0.0391	0.0395
wR_2[b] [$I > 2\sigma(I)$]	0.1230	0.1078	0.1034

[a] $R_1 = \sum ||F_o| - |F_c|| / \sum |F_o|$.

[b] $wR_2 = \left[\sum w(F_o^2 - F_c^2)^2 \Big/ \sum w(F_o^2)^2\right]^{1/2}$.

were collected at 130.15 K on a RIGAKU MERCURY CCD diffractometer with graphite-monochromated Mo Kα radiation ($\lambda = 0.71073$ Å). The structures were solved by direct methods and refined on F^2 by full-matrix least-squares procedures using the SHELXTL software suite [23]. All non-hydrogen atoms were refined anisotropically except for those with disordered positions. All H atoms were located theoretically and not refined, except that H atoms belonging to the disordered atoms were not located. The occupancies of these disordered components were assumed to be 0.50 for each disordered atom. For cluster **2** and **6**, due to the disordered C atoms of $[Et_4N]^+$, some non-bond C···C distance were abnormal at these positions. Nevertheless, the C–C bond lengths involving the disordered C atoms were all reasonable. For cluster **4**, a solvent molecule EtOH is disordered. EtOH was used during the preparation of the starting materials and some may have been left behind. So it is comprehensible that a EtOH molecule is in the structure. A summary of the crystallographic data of **2**, **4** and **6** is presented in Table 2.

3. Results and discussion

3.1. Syntheses

Treatment of $[AuCl(SC_4H_8)]$ with dppe or dppf in CH_2Cl_2 followed by the addition of one equiv. of $[Et_4N]_2[MXS_3]$ (M = Mo or W, X = O or S) resulted in the precipitation of complexes **1**, **2**, **4**, **5**, **6** and **8**. Crystals of **2**, **4** and **6** could be obtained via slowly diffusion of *i*PrOH to their DMF solutions. Similar reactions with half equiv. of $[Et_4N]_2[MXS_3]$ gave polymeric compounds which would not dissolve in any solvent and were not further identified. Complexes **3** and **7** were synthesized by reacting K_2MoOS_3 with [AuCl(dppe)] or [AuCl(dppf)] in DMF and were isolated as the PPh_4^+ and Et_4N^+ salts, respectively.

3.2. Infrared and UV–vis spectroscopic studies

As shown in Table 1, the IR spectra of these complexes show typical absorptions around 520 cm^{-1} due to the Au–P bonds. Other bands at ca. 500 cm^{-1} can be assigned to the vibrations *v*(M═S) according to the literature data and those at lower frequencies are attributed to bridging sulfur atoms [6]. As expected, the vibrations *v*(M═O) are observed at ca. 900 cm^{-1}. The electronic spectra of the compounds derived from MS_4^{2-} (M = Mo or W) have similar patterns to those of the starting materials except that several new bands appear. In addition, for the compounds derived from MOS_3^{2-} (M = Mo or W), the UV–vis spectra are shifted in the direction of shorter wavelengths owing to the coordination of Au atoms to the central MOS_3^{2-} cores [6].

3.3. Crystal structures of 2, 4 and 6

The molecular structure of compound **2** was confirmed by a single-crystal X-ray diffraction study. The structure of the anion of **2** is shown in Fig. 1 and selected bond lengths and angles are listed in Table 3. The skeleton of the cluster core contains one W, two bridging S, two terminal S and one Au atom. Two cluster cores, orientated in opposite directions, are linked via a dppe bridging ligand to form a Z-like

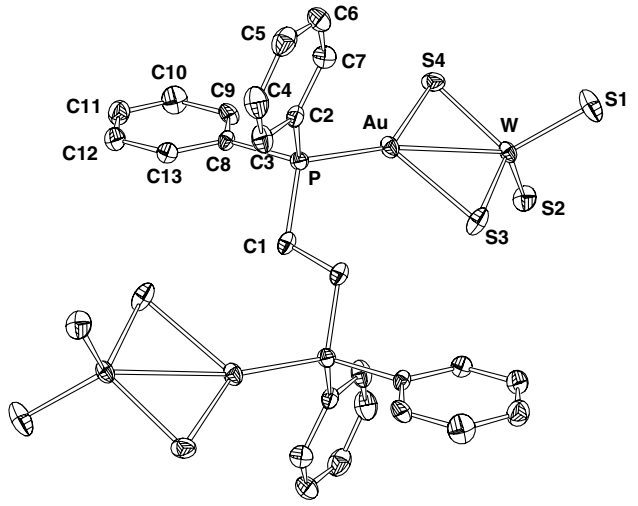


Fig. 1. Structure and labelling of the $[(WS_4)_2Au_2(dppe)]^{2-}$ anion of **2**. Thermal ellipsoids are drawn at the 20% probability level. All H atoms are omitted for clarity.

Table 3
Selected bond lengths (Å) and angles (°) for complexes **2**, **4** and **6**

Complex **2**[a]			
W–S(1)	2.139(2)	S(1)–W–S(4)	109.2(1)
W–S(2)	2.157(2)	S(2)–W–S(3)	109.9(1)
W–S(3)	2.260(2)	S(2)–W–S(4)	107.9(1)
W–S(4)	2.259(2)	S(3)–W–S(4)	110.4(1)
Au–S(3)	2.473(2)	S(3)–Au–S(4)	99.6(1)
Au–S(4)	2.388(2)	P–Au–S(3)	119.9(1)
Au–P	2.254(2)	P–Au–S(4)	140.5(1)
Au–W	2.859(1)	P–Au–W	169.3(1)
S(1)–W–S(2)	109.3(1)	W–S(3)–Au	74.1(1)
S(1)–W–S(3)	110.1(1)	W–S(4)–Au	75.9(1)
Complex **4**[b]			
W–O(1)	1.733(7)	O(1)–W–S(3)	108.3(3)
W–S(1)	2.174(3)	S(1)–W–S(2)	110.5(1)
W–S(2)	2.266(2)	S(1)–W–S(3)	110.3(1)
W–S(3)	2.262(2)	S(2)–W–S(3)	110.6(1)
Au–S(2)	2.437(2)	S(2)–Au–S(3)	100.5(1)
Au–S(3)	2.407(2)	P–Au–S(2)	126.6(1)
Au–P	2.262(2)	P–Au–S(3)	132.9(1)
Au–W	2.827(1)	P–Au–W	173.1(1)
O(1)–W–S(1)	108.1(2)	W–S(2)–Au	73.8(1)
O(1)–W–S(2)	109.0(3)	W–S(3)–Au	74.5(1)
Complex **6**[c]			
W–S(1)	2.249(2)	S(1)–W–S(4)	109.4(1)
W–S(2)	2.243(3)	S(2)–W–S(3)	108.3(1)
W–S(3)	2.151(2)	S(2)–W–S(4)	108.0(1)
W–S(4)	2.149(3)	S(3)–W–S(4)	110.5(1)
W–Au	2.837(1)	S(1)–Au–S(2)	99.5(1)
Au–P	2.264(2)	P–Au–S(1)	133.4(1)
Au–S(1)	2.398(2)	P–Au–S(2)	126.9(1)
Au–S(2)	2.447(2)	P–Au–W	173.9(1)
S(1)–W–S(2)	110.9(1)	W–S(1)–Au	75.2(1)
S(1)–W–S(3)	109.8(1)	W–S(2)–Au	74.3(1)

Symmetry transformations used to generate equivalent atoms: [a]For **2**: #1: $-x+1$, y, $-z+1/2$; #2: $-x+1/2$, $-y+1/2$, $-z$. [b]For **4**: #1: $-x+2$, $-y$, $-z$; #2: $-x+1$, $-y$, $-z$. [c]For **6**: #1: $-x+1$, $-y+1$, $-z+1$.

structure. A crystallographic inversion center overlaps the symmetry of the molecule. In each S_2WS_2Au fragment, the WS_4^{2-} dianion acts as a bidentate ligand coordinating one Au atom through two bridging S atoms leaving the other two S atoms uncoordinated. The tungsten atom has a distorted tetrahedral coordination geometry with S–W–S angles in the range of 107.9(1)–110.4(1)°. The mean bond length of W=S_t is 2.148(2) Å, which is characteristic of a pure double bond and consistent with the values reported for the starting material $(NH_4)_2WS_4$ [24]. The two W–S_{br} bond lengths, 2.259(2)–2.260(2) Å, are within the normal range for the W–μ-S bonds observed for other W/Au/S clusters and are considered to be single bonds. The gold center shows a trigonal planar geometry with the total of the angles around the gold being about 360.0°. The gold–tungsten distance is 2.859(1) Å, which is slightly greater than those in the complexes $[WS_4Au_2(PPh_3)_2]$ [13] at 2.823(1) Å, $[WS_4Au_2(AsPh_3)_2]$ [15] at 2.803(1) Å and $[WS_4Au_2(Ph_2PCH_3)_2]$ [16] at 2.839(1) Å. The narrow W–S–Au angles [74.1(1)° and 75.9(1)°], which are comparable to other related terminal phosphine ligand derivatives, also reflect the existence of a relatively strong metal–metal bond. Finally, the Au–P bond length is 2.254(2) Å which is a little greater than that found in $[WS_4Au_2(PPh_3)_2]$ [13].

The molecular structure of **4** is shown in Fig. 2 and important bond lengths and angles are given in Table 3. The structure resembles that of **2** except that a W=S bond in **2** is replaced by a W=O bond in **4**. The compound shows crystallographic inversion symmetry as in complex **2**. The tungsten atom also shows a tetrahedral geometry with the angles ranging from 108.1(2)°

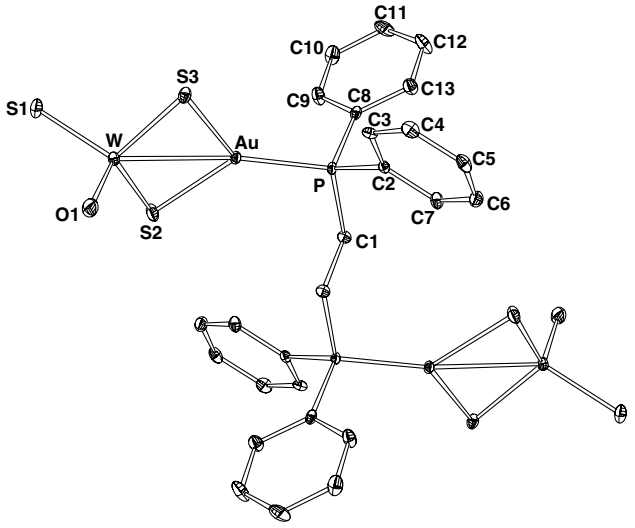


Fig. 2. Structure and labelling of the $[(WOS_3)_2Au_2(dppe)]^{2-}$ anion of **4**. Thermal ellipsoids are drawn at the 20% probability level. All H atoms are omitted for clarity.

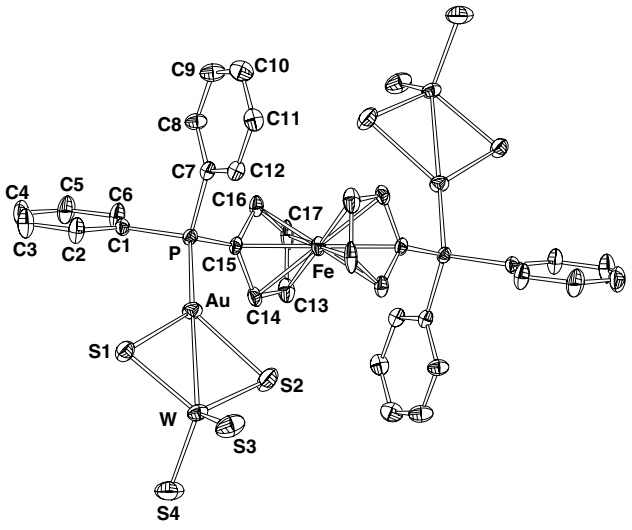


Fig. 3. Structure and labelling of the $[(WS_4)_2Au_2(dppf)]^{2-}$ anion of **6**. Thermal ellipsoids are drawn at the 20% probability level. All H atoms are omitted for clarity.

to 110.6(1)°, while the Au atom has a trigonal planar geometry with the sum of the angles being about 360.0°. The W–Au distance is 2.827(1) Å, which is comparable to that of $[WS_4Au_2(PPh_3)_2]$ [13] [2.823(1) Å] but significantly smaller than that of **2** [2.859(1) Å]. As expected, the mean W–S–Au angle [74.2(1)°] of **4** is smaller than that of **2** [75.0(1)°].

The crystal structure of **6** was determined by a single-crystal X-ray diffraction study. An ORTEP diagram of the anion is shown in Fig. 3 and selected bond lengths and angles are given in Table 3. As found in the structures of **2** and **4**, a crystallographic center of symmetry is located at the center of the anion of **6**. The structure of the anion of **6** is closely related to that of **2** except that the two linear W/Au/S fragments are interconnected through a dppf ligand rather than a dppe ligand. The W–Au distance is 2.837(1) Å, an intermediate value between those for **2** and **4**. The bond lengths and angles within the W/Au/S fragment are typical and those for the dppf ligand are all normal.

3.4. Luminescent properties

The luminescent data for clusters **1**–**8** are listed in Table 4. Fig. 4 depicts the emission spectra of clusters **1**–**4** in the solid state at 298 K.

The emission observed for clusters **1**–**4** range from 564 to 662 nm, which are much higher than that of the free ligand dppe (434 nm). Therefore, we tentatively assign the origin of the emission as the ligand-to-metal charge transfer (LMCT) transition. For the series of clusters **5**–**8** with dppf as the ligand, it is likely that the emissions at 570–664 nm are due to the intraligand (IL) transition ($\pi \rightarrow \pi^*$) localized on the dppf moieties.

Table 4
Luminescent data for **1**–**8**

Compound	Emission λ_{max} (nm)
$[Et_4N]_2[(MoS_4)_2Au_2(dppe)]$ (**1**)	622
$[Et_4N]_2[(WS_4)_2Au_2(dppe)]$ (**2**)	564
$[PPh_4]_2[(MoOS_3)_2Au_2(dppe)]$ (**3**)	662
$[Et_4N]_2[(WOS_3)_2Au_2(dppe)]$ (**4**)	656
$[Et_4N]_2[(MoS_4)_2Au_2(dppf)]$ (**5**)	658
$[Et_4N]_2[(WS_4)_2Au_2(dppf)]$ (**6**)	664
$[Et_4N]_2[(MoOS_3)_2Au_2(dppf)]$ (**7**)	596
$[Et_4N]_2[(WOS_3)_2Au_2(dppf)]$ (**8**)	570

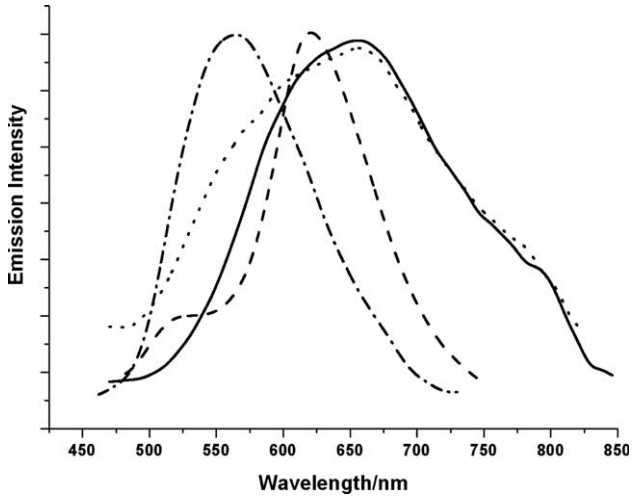


Fig. 4. Solid-state emission spectra of **1** (---), **2** (-·-), **3** (—) and **4** (···) at 298 K.

4. Supplementary material

CCDC-252791 (**2**), 252792 (**4**) and 252793 (**6**) contain the supplementary crystallographic data for this paper. These data can be obtained free of charge at www.ccdc.cam.ac.uk/conts/retrieving.html [or from the Cambridge Crystallographic Data Centre, 12 Union Road, Cambridge CB2 1EZ, UK; fax: (internat.) +44 1223/336 033; E-mail: deposit@ccdc.cam.ac.uk].

Acknowledgments

We express our gratitude to Prof. Xue-Qi Ye, Li-Ming Wu and Mr. En Ma for helpful advice and discussions. This research was supported by grants from the State Key Laboratory of Structural Chemistry, Fujian Institute of Research on the Structure of Matter, Chinese Academy of Sciences (CAS), the Ministry of Science and Technology of China (001CB108906) and the National Science Foundation of China (20333070).

References

[1] R.H. Holm, Chem. Soc. Rev. 10 (1981) 455.
[2] R.H. Holm, Adv. Inorg. Chem. 38 (1992) 1.
[3] L.J. Laughlin, D. Coucouvanis, J. Am. Chem. Soc. 117 (1995) 3118.
[4] S.H. Laurie, Eur. J. Inorg. Chem. (2000) 2443.
[5] S. Shi, W. Ji, S.H. Tang, J.P. Lang, X.Q. Xin, J. Am. Chem. Soc. 116 (1994) 3615.
[6] H.W. Hou, X.Q. Xin, S. Shi, Coord. Chem. Rev. 153 (1996) 25.
[7] A. Müller, H. Dornfeld, G. Henkel, B. Krebs, M.P.A. Viegers, Angew. Chem., Int. Ed. Engl. 17 (1978) 52.
[8] H.P. Kim, S. Kim, R.A. Jacobson, R.J. Angelici, J. Am. Chem. Soc. 108 (1986) 5154.
[9] M. Wang, D. Miguel, E.M. López, J. Pérez, V. Riera, C. Bois, Y. Jeannin, J. Chem. Soc., Dalton Trans. (2003) 961.
[10] J.P. Lang, H. Kawaguchi, K. Tatsumi, J. Organomet. Chem. 569 (1998) 109.
[11] J.P. Lang, H. Yu, S.J. Ji, Z.R. Sun, Phys. Chem. Chem. Phys. 5 (2003) 5127.
[12] J.M. Charnock, S. Bristow, J.R. Nicholson, C.D. Garner, W. Clegg, J. Chem. Soc., Dalton Trans. (1987) 303.
[13] R.G. Pritchard, L.S. Moore, R.V. Parish, C.A. Mcauliffe, B. Beagley, Acta Cryst. C44 (1988) 2022.
[14] F. Canales, M.C. Gimeno, P.G. Jones, A. Laguna, J. Chem. Soc., Dalton Trans. (1997) 439.
[15] H.G. Zheng, W. Ji, M.L.K. Low, G. Sakane, T. Shibahara, X.Q. Xin, J. Chem. Soc., Dalton Trans. (1997) 2357.
[16] J.C. Huffman, R.S. Roth, A.R. Siedle, J. Am. Chem. Soc. (1976) 4340.
[17] C.M. Che, B.H. Xia, J.S. Huang, C.K. Chan, Z.Y. Zhou, K.K. Cheung, Chem. Eur. J. 7 (2001) 3998.
[18] J.M. Forward, Z. Assefa, J.P. Fackler Jr., J. Am. Chem. Soc. 117 (1995) 9103.
[19] S.D. Hanna, S.I. Kha, J.I. Zink, Inorg. Chem. 35 (1996) 5813.
[20] V.W.W. Yam, E.C.C. Cheng, K.K. Cheung, Angew. Chem., Int. Ed. Engl. 38 (1999) 197.
[21] C.K. Chan, C.X. Guo, R.J. Wang, T.C.W. Mak, C.M. Che, J. Chem. Soc., Dalton Trans. (1995) 753.
[22] J.W. McDonald, G.D. Friesen, L.D. Rosenhein, W. Newton, Inorg. Chim. Acta 72 (1983) 205.
[23] G.M. Sheldrick, Bruker SHELSTL-PC, University of Göttingen, Germany, 1997.
[24] A. Müller, H. Bogge, E. Koniger-Ahlborn, W. Hellmann, Inorg. Chem. 18 (1979) 2301.

Available online at www.sciencedirect.com
SCIENCE DIRECT®
Polyhedron 24 (2005) 837–845
POLYHEDRON
www.elsevier.com/locate/poly

Study of the interaction between oxovanadium(IV) and hydroxamic acids

Péter Buglyó *, Norbert Pótári

University of Debrecen, Department of Inorganic and Analytical Chemistry, P.O. Box 21, H-4010 Debrecen, Hungary

Received 7 February 2005; accepted 9 March 2005
Available online 14 April 2005

Abstract

The interaction between oxovanadium(IV) and primary hydroxamic acids (aceto- (HAha), benzohydroxamic acid (HBha) or *N*-hydroxy-*N*′-[3-(*N*-hydroxy-carbamoyl)-propyl]-heptane-1,7-dicarboxamide (H_2Diha)) as well as the corresponding *N*-methyl substituted hydroxamic acids (HMeAha, HMeBha, H_2MeDiha) was studied by pH-potentiometric and pH-stat methods in aqueous solution. Stoichiometry and stability constants of the VO(IV) complexes formed in the pH range 2.0–5.0 were determined and the effect of the substituents on the C or N atoms of the hydroxamic group is discussed. The dihydroxamic acids are more effective oxovanadium(IV) binders than the monohydroxamic ones. Above pH = 4.5–5.0 (depending upon ligand excess), slow redox reaction was found in all the systems studied. During this process, beside the oxidation of VO(IV) to the appropriate V(V)–hydroxamate complex, formation of amides as reduction products was detected under anaerobic conditions. The same reaction can also take place when stirring sparingly soluble VOA_2 type complexes (A: Bha or MeBha) in water in the absence of oxygen. The exact stoichiometry of the redox reaction was determined by pH-stat measurements and found to be $2VO(R_1CON(R_2)O)_2 + R_1CON(R_2)OH + H_2O = 2[VO_2(R_1CON(R_2)O)_2]^- + 2H^+ + R_1CON(R_2)H$ (R_1: CH_3, C_6H_5; R_2: H, CH_3) for the monohydroxamates. The *N*-methyl hydroxamic acids tend to oxidise VO^{2+} significantly slower than the corresponding primary ones.
© 2005 Elsevier Ltd. All rights reserved.

Keywords: Hydroxamic acids; Oxovanadium(IV) complexes; Stability constants; pH-potentiometry; Amide formation; Vanadium(V)

1. Introduction

Hydroxamic acids form stable, five-membered [O,O] chelates with many metal ions [1]. Based on this interaction numerous microorganisms developed hydroxamate type metal sequestering siderophores for the uptake, storage and transport of metal ions with biological relevance [2]. Especially hard metals and their higher oxidation states are capable to form the most stable hydroxamate complexes. Although the interaction of vanadium(V) with numerous monohydroxamic acids is well documented in the literature [3–6], it is much less known about the corresponding oxovanadium(IV) complexes. Furthermore, the effect of the substituents at the C or N atoms of the hydroxamic group on the stability of the oxovanadium(IV) hydroxamate chelates has not been investigated yet.

Some of the results in the literature obtained for VO(IV)–hydroxamate systems are contradictory. Dessì et al. [7] have studied the interaction between VO(IV) and aceto-, benzo- or *N*-phenyl-benzohydroxamic acids by EPR. It was found that primary monohydroxamic acids can undergo two deprotonation processes and thus act as either hydroxamato(1-) or hydroximato(2-) ligands forming 1:1 or 1:2 complexes with different protonation degrees. Recently, the VO(IV)–acetohydroxamate system was investigated at high excess of ligand

* Corresponding author. Tel.: +36 52 512900; fax: +36 52 489667.
E-mail address: buglyo@delfin.unideb.hu (P. Buglyó).

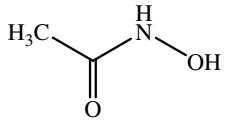
0277-5387/$ - see front matter © 2005 Elsevier Ltd. All rights reserved.
doi:10.1016/j.poly.2005.03.007

(1:6 or higher) by da Silva Santos et al. [8] using pH-potentiometry and spectrophotometry. The same complexation pattern was found as by Dessì et al.

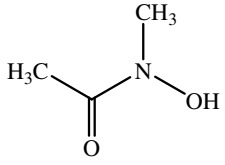
On the contrary, a study by Brown et al. [9] on the interaction of VO(IV) with *N*-substituted mono- or dihydroxamic acids at anaerobic conditions revealed that the ligands undergo oxygen abstraction on reaction with the metal ion to form V(V) hydroxamates and the corresponding amides. During the redox reaction the metal ion is oxidized directly by the hydroxamic acid. Slow irreversible reaction was also found when studying the complex formation reactions between oxovanadium(IV) and aceto-, propio- or alaninehydroxamic acids by pH-potentiometry [10]. It was found that in the pH-range 4.0–5.0 the usual waiting time was not enough to reach pH equilibrium. Re-acidification of the titrated samples indicated the formation of V(V) by change in colour from the initial pale blue to yellow [10].

Similar irreversible reaction was also found between U(IV) and *N*-phenyl-benzohydroxamic acid, where beside U(VI), the formation of the reduction product of the ligand, *N*-phenyl-benzamide, was detected [11]. Other studies on the interaction of Fe(II) with natural tris hydroxamic acids, desferrioxamine B (H_4DFB^+) or desferricoprogen (DFC), also revealed that these ligands are capable to oxidize the metal ion directly under anaerobic conditions with the formation of the corresponding highly stable Fe(III) complexes and DFB- or DFC-monoamide [12,13].

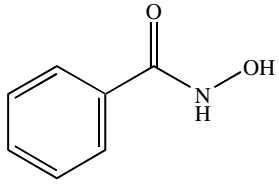
The goal of this work was to study the interaction between oxovanadium(IV) and a set of mono- and dihydroxamic acids (see Scheme 1) in aqueous solution using pH-potentiometry and, to compare the effect of the substituents at the C or N atoms of the hydroxamic group on the stability of the metal chelates. We also present our results on the slow redox reaction observed above



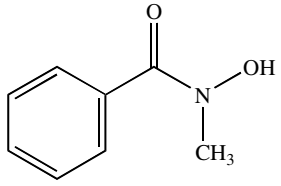
Acetohydroxamic acid (**HAha)**



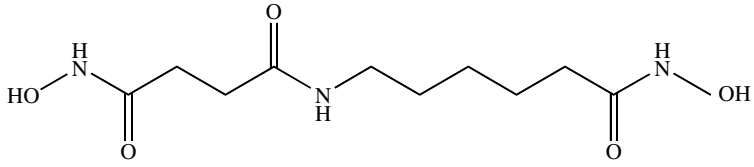
N-Me-Acetohydroxamic acid (**HMeAha**)



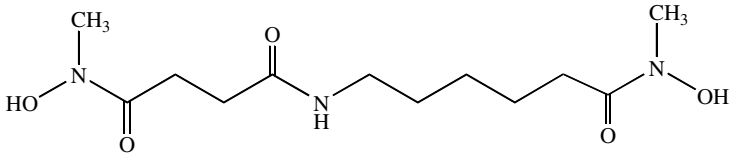
Benzohydroxamic acid (**HBha)**



N-Me-Benzohydroxamic acid (**HMeBha**)



N-hydroxy-N'-[3-(N-hydroxycarbamoyl)-propyl]-heptane-1,7-dicarboxamide (**H_2Diha**)



N-Me-N-hydroxy-N'-[3-(N-Me-N-hydroxycarbamoyl)-propyl]-heptane-1,7-dicarboxamide (**H_2MeDiha**)

Scheme 1.

pH = 5.0 in these systems yielding V(V) and the appropriate amide under anaerobic conditions.

2. Experimental

2.1. Reagents

Acetohydroxamic acid (HAha), benzohydroxamic acid (HBha), vanadyl sulphate hydrate and sodium vanadate were Aldrich or BDH products of puriss. quality and were used as received. Syntheses of the dihydroxamic acids was published previously [14]. *N*-methyl-acetohydroxamic (HMeAha) and *N*-methylbenzohydroxamic (HMeBha) acids were prepared according to the literature methods [15] by reacting *N*-methylhydroxylamine with acetylchloride or benzoylchloride in basic methanol at 0 °C. The crude products were purified with vacuum distillation to afford colourless oils. HMeAha: ^{1}H NMR (360 MHz, D_2O) δ = 2.11 (3H, s, CH_3–CO), 3.22 (3H, s, N–CH_3); ESI-MS *m*/*z*: 90 (M + 1). HMeBha: ^{1}H NMR (300 MHz, D_2O) δ = 3.33 (3H, s, N–CH_3), 7.49 (5H, br, Ar); ESI-MS *m*/*z*: 152 (M + 1).

For all the ligands the purities were also checked from the prepared stock solutions by pH-potentiometric titrations and the equivalent weights were determined by the Gran method [16]. A VO(IV) stock solution was prepared according to Nagypál and Fábián [17] and standardised for metal ion concentration by permanganate titration, VIS spectrophotometry or ICP-AES and for hydrogen ion concentration by pH-potentiometry, using the appropriate Gran function [16].

2.2. Potentiometric measurements

The stability constants of the proton and VO(IV) complexes of the ligands were determined by pH-potentiometric titration of 10.0 ml samples. The ionic strength was adjusted to 0.20 M KCl in each solution studied. In all cases, the temperature was 25.0 ± 0.1 °C. The ligand concentration was in the range 2–10 mM and the molar ratios in the VO(IV)–ligand systems were in the range 1:1 to 1:20. All the titrations were performed over the range pH 2–11 or until precipitation occurred with a carbonate- and oxygen free KOH solution of known concentration (~0.2 mol dm^{-3}), under a purified argon atmosphere. After adding VO(IV) to the ligand solution at pH ~ 2.0, the sample to be titrated was completely deoxygenated by bubbling argon through it. The titrations were carried out in a special glass vessel with an NS joint for the electrode and for adding the KOH solution to ensure strictly anaerobic conditions. As usual, a maximum change in pH of 0.002 within 30 s was allowed in each titration point to reach pH equilibrium, however, more than 10 min was never allowed to wait after adding an aliquot of base. At least two parallel titrations were carried out. The reproducibility of the titration points included in the evaluation was within 0.005 pH unit throughout the whole pH range. Titration points with 10 min waiting time were omitted from the calculations. The average number of points per system used in the calculations was 60.

pH was measured with a Radiometer pHM 84 instrument equipped with a Metrohm combined electrode with NS joint (type 6.0233.100), calibrated for hydrogen ion concentration according to Irving et al. [18]. A pK_w value of 13.76 ± 0.01 was determined and used for the calculations. Protonation constants of the ligands (K_i = [H$_i$A]/[H][H$_{i-1}$A]) were determined using Superquad computer program [19]. The concentration stability constants β_{pqr} = [M$_p$H$_q$A$_r$]/[M]^p[H]^q[A]^r for the metal complexes were calculated with the aid of the PSEQUAD program [20]. The uncertainties (σ values) in the stability constants are given in parenthesis in the Table 1.

During the calculations the following VO(IV)–hydroxo complexes were assumed: [VO(OH)]$^+$ (log β_{1-10} = −5.94) and [{VO(OH)}$_2$]$^{2+}$ (log β_{2-20} = −6.95) calculated from the data published by Henry et al. [21], the Davies equation being used to take into consideration the different ionic strengths, [VO(OH)$_3$]$^-$ (log β_{1-30} =

Table 1
Stepwise protonation constants (log K_i) of the ligands and stability constants (log β_{pqr}) of their oxovanadium(IV) complexes at 25.0 °C and at I = 0.20 M (KCl); standard deviations are given in parenthesis

	HAha	HMeAha	HBha	HMeBha	H_2Diha	H_2MeDiha
log K_1 (HA)	9.25(1)	8.69(1)	8.65(1)	8.30(1)	9.68(1)	9.28(1)
log K_2 (H_2A)					8.82(1)	8.47(1)
pH-range	2.0–5.0	2.0–5.0	2.0–5.0	2.0–4.0	2.0–5.0	2.0–5.0
VOHA					18.56(1)	18.66(6)
VOA	8.69(1)	8.85(1)	8.43(1)	8.89(4)	16.54(1)	17.30(3)
VOH$_{-1}$A	3.69(2)		3.16(7)	4.43(5)		
VOA_2	15.90(1)	16.45(1)	15.58(4)	16.51(2)		
Fitting[a]	0.0035	0.0017	0.0028	0.0027	0.0015	0.0020
Log K[b]	−0.56	0.16	−0.22	0.59	−1.96	−0.45

[a] The average difference between the calculated and experimental titration curves expressed in cm^3 of the titrant.
[b] K refers to the equilibria VO^{2+} + HA = VOA^+ + H^+ (monohydroxamic acids) or VO^{2+} + H_2A = VOA + 2H^+ (dihydroxamic acids).

−18.0) and $[(VO)_2(OH)_5]^-$ (log β_{2-50} = −22.5) with data taken from [22].

2.3. pH-stat measurements

In order to measure the amount of the protons liberated during the redox process at anaerobic conditions and thus to determine the stoichiometry of the redox reaction between the metal ion and the ligands, pH-stat measurements were carried out in the VO(IV)–HAha, VO(IV)–HMeAha, VO(IV)–H_2Diha or VO(IV)–H_2MeDiha systems using a Radiometer TTT 60 titrator. At 1:7–1:8 or 1:4 (H_2Diha, H_2MeDiha) metal-to-ligand ratio where the ligand concentration was 2.0–4.0 mM, the added amount of base was monitored in the function of time to keep constant the initial pH of 5.5 in the samples during the measurements.

2.4. Study of the oxidation of VO(IV) in the solid complexes

IR spectra were measured as a KBr disk on a Perkin Elmer FTIR spectrometer. ESI mass spectra were recorded on a Bruker BIOTOF II ESI-TOF instrument equipped with a Cole Palmer 74900 Series pump. Microanalyses were performed at the University of Szeged, Hungary.

$V^{IV}O(Bha)_2$, and for comparative purposes $K[V^{V}O_2(Bha)_2]$ were prepared under argon from aqueous solutions with the reaction of two equivalents of the respective ligand and one equivalent of metal ion at pH = 3 according to the literature procedures [3,23] and the poorly soluble microcrystalline solids obtained were characterised by IR, ESI-MS or micro analytical methods giving satisfactory results. Elemental analysis: *Anal*. Calc. for $V^{IV}O(Bha)_2$: C, 49.57; N, 8.26. Found C, 49.20; N, 8.04%. *Anal.* Calc. for $K[V^{V}O_2(Bha)_2]$: C, 42.64; N, 7.10. Found: C, 42.68; N, 6.81%. IR (cm^{-1}) for $VO(Bha)_2$ 993 (V=O); for $K[VO_2(Bha)_2]$ 946 (V=O).

In order to monitor the redox reaction in the VO(IV)–HBha system, in a few experiments the non-isolated solid, $VO(Bha)_2$, was further stirred in aqueous solution under an argon atmosphere. After 24 h the complex was filtered off, washed with water, dried and checked for composition by IR (993 and 932 cm^{-1} (V=O)) and microanalysis (Found: C, 45.67; N, 7.45%). The untreated mother liquors were also analysed for benzamide by ESI-MS.

3. Results and discussion

3.1. Protonation processes of the ligands

Protonation processes of the hydroxamic acids were re-examined and the protonation constants (log K_i) calculated are summarised in Table 1. The log K_i values are in good agreement (less than 0.04 log units) with published data obtained at the same experimental conditions [14,24]. The protonation constant determined in this work for HMeBha (8.30) fits also in the general trend of log K_i values for monohydroxamates with different substituents. The differences in acidity of the ligands have already been discussed [24].

3.2. VO^{2+} complexes of the hydroxamic acids

With HBha and HMeBha purple microcrystalline precipitation occurred in the presence of the metal ion at 4 mM concentration (vide infra) therefore the titrations were carried out at a ligand concentration of 2 mM. In all systems, slow base consumption processes were observed in solution starting at pH 4.2–5.0 and 10 min was not enough to reach pH equilibrium at these titration points. Repeated titration of the samples after decreasing the pH down to 2.0 revealed that irreversible, redox processes took place even in the absence of oxygen. This is illustrated in the Fig. 1, where, as a representative example, the different shape of the titration curves of the VO(IV)–H_2Diha system is shown at 1:2 ratio. The yellow colour of the re-acidified samples at pH = 2.0 also indicated the formation of VO_2^+(V) during the titration. This result, which has already been found in VO^{2+}–monohydroxamate systems [10,25], is in contradiction with recently published solution equilibrium study, where no indication for any redox reaction was found at higher ligand excess [8].

Due to the irreversible process outlined above the titration curves were evaluated in the pH range 2.0–5.0 only. For all the monohydroxamic acid systems the formation of $[VOA]^+$ and $[VOA_2]$ as major species was detected with the involvement of one or two (O,O) hydroxamate chelates, respectively. The same binding mode was found previously by EPR [7]. The assumption of $[VOH_{-1}A]$ improved the fit significantly. The calculated stability constants are summarised in Table 1, while a representative speciation of the VO(IV)–HBha system is shown in Fig. 2. The log β values obtained for the complexes in the VO(IV)–HAha system (Table 1) are in reasonable agreement with published data ($[VOA]^+$: 8.58, $[VOA_2]$: 16.21) [8].

In order to compare the effect of the substituents at the C (Me versus Ar) or N (H versus Me) atoms of the hydroxamic group of the ligands (see Scheme 1) on VO^{2+} binding, the proton displacement equilibrium constants were calculated (last row in Table 1). These derived constants (monohydroxamic acids: log K = log K_{VOA} − log K_1; dihydroxamic acids: log K = log K_{VOA} − log K_1 − log K_2) refer to the following equilibria: $VO^{2+} + HA \rightleftharpoons [VOA]^+ + H^+$ or $VO^{2+} + H_2A \rightleftharpoons [VOA] + 2H^+$, respectively. Higher value of log K indicates stronger metal–ligand interaction. Comparison between

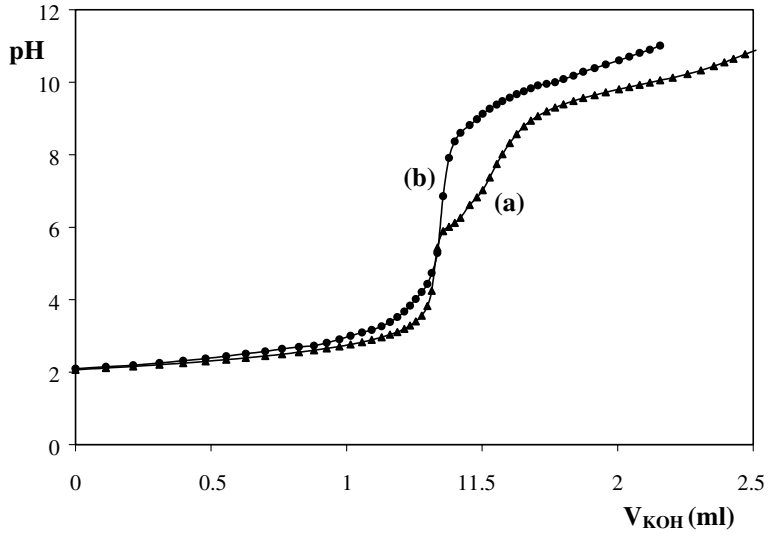


Fig. 1. Titration curve of the oxovanadium(IV)–H_2Diha system at 1:2 ratio (a) and repeated titration after acidifying (b), $c_{VO(IV)}$ = 2 mM, I = 0.2 M (KCl), T = 25.0 °C.

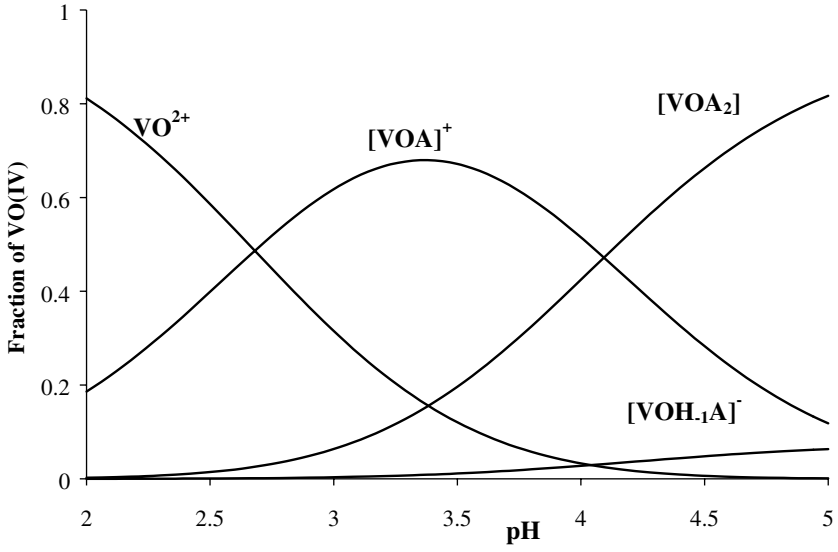


Fig. 2. Speciation curves of the complexes formed in the VO(IV)–HBha system at 1:4 ratio, c_{HBha} = 4 mM, I = 0.2 M (KCl), T = 25.0 °C.

the corresponding derived constants (last row in Table 1) reveals that the N–Me ligands form 0.7–0.8 log unit more stable [VOA] complexes than the corresponding primary hydroxamates. The stability difference between the metal chelates of the C substituted (Me versus Ar) pairs is only 0.3–0.4 log unit in favour of the aromatic ligands. Similar trends were previously also found for Fe(III) or Cu(II) systems [26,12] and originate from the more pronounced effect of N substitution compared to C substitution on the delocalisation of the lone pair of N into the C–N bond. Delocalisation increases the electron density on the carbonyl oxygen thus yielding higher stability for the metal chelate. On the other hand, due to the lower effect of C substitution and favoured charge distribution in the presence of π-electrons, the electron withdrawing effect of the phenyl group does not appear in the stability of the complexes [24].

For the dihydroxamic systems (VO(IV)–H_2Diha or VO(IV)–H_2MeDiha) the useful parts of the titration curves (below pH 5.0) could be fitted well with the assumption of the formation of $[VOHA]^+$ and [VOA]. $[VOHA]^+$ may contain one (O,O) chelate while the other functional group is protonated. On increasing pH deprotonation and coordination of the second hydroxamic group to the metal ion takes place. This binding mode is supported by previous results on the VO^{2+}-desferrioxamine B (H_4DFB^+) system [25], in which the species $[VOH_2DFB]^+$ was found to have two (O,O) chelates around the metal ion. The H_4DFB^+ model compound, H_2MeDiha, with the same length and structure

of the connecting chain of H_4DFB^+, is therefore co-ordinated most probably in the same manner. Comparison of the proton displacement equilibrium constants calculated for $[VOH_2DFB]^+$ ($\log\beta_{VOH_2DFB} - \log\beta_{H_4DFB} = 37.09–37.59 = -0.50$) [25] with that of [VOA] formed in the H_2MeDiha system ($\log\beta_{VOA} - \log\beta_{H_2A} = 17.30–17.75 = -0.45$) (Table 1) also indicates identical binding modes.

Direct comparison of the metal binding strength of HAha (a monohydroxamate) with that of H_2Diha (a dihydroxamate) via derived equilibrium constants is difficult due to the different stoichiometry of the complexes with the same donor atom environment around the metal ion. Therefore pVO ($-\log[VO^{2+}]_{free}$) values were calculated at pH = 4.0 where bis chelated complexes are the major species in both systems but neither slow redox processes nor hydrolysis of the free VO^{2+} took place. pVO values at pH = 4.0 (c_{VO} = 2 mM; c_{HAha} = 4 mM or c_{H_2Diha} = 2 mM) for the HAha (3.50) and for the H_2Diha (4.67) systems indicate that H_2Diha is stronger metal binder. This difference suggests the effect of polychelate formation with the dihydroxamic acid.

3.3. Monitoring the redox reaction in solution

The slow base consumption processes observed above pH 4.2–5.0 were studied in detail in the VO(IV)–HAha, VO(IV)–HMeAha, VO(IV)–H_2Diha and VO(IV)–H_2MeDiha systems. It was found that to the 1:1 ratio corresponded the widest pH range where 10 min waiting time was not enough to reach pH equilibrium. With increasing ligand excess the oxidation of VO^{2+} started at higher pH and the non-equilibrium pH range became narrower. The irreversible process took place, however, to a certain degree even at twenty fold ligand excess. The hindrance of this slow reaction applying increasing ligand excess may suggest the involvement of a 1:1 species rather than bis chelated complex in the redox process.

Our finding is in contradiction with earlier results, in which the speciation of the VO(IV)–HAha system is determined in the range pH = 2–11 without any indication for the redox process [7,8]. The formation of the EPR silent side product, VO_2^+(V), on one hand [7], and the large ligand excess used in the solution equilibrium work [8], which is found in this study to suppress the redox reaction, on the other hand, may explain the contradictory results. Due to the disturbing redox reaction the stability constants published by da Silva Santos et al. [8] can only be considered as tentative values. Nevertheless, the speciation model provided by them is supported by EPR [7] which confirms the presence of the hydroximato type complexes, $[VOH_{-1}(Aha)_2]^-$ and $[VOH_{-2}(Aha)_2]^{2-}$, above pH = 7.

A brief comparison of the rate of the oxidation of VO(IV) at anaerobic conditions in the presence of primary or secondary hydroxamic acids revealed that with any of the *N*-methyl derivatives, this process is significantly slower than with the corresponding primary ligands. This is illustrated in Fig. 3, where beside the titration curves of the VO(IV)–H_2Diha or VO(IV)–H_2MeDiha systems at 1:1 ratio the pH-ranges are also depicted where 10 min waiting time was not enough to reach pH equilibrium. As it is seen in Fig. 3, at identical titration parameters, with Diha (a) the base consumption is significantly larger and the non-equilibrium pH-range during the titration is wider than with MeDiha (b) indicating faster process (liberation of protons) in the former system.

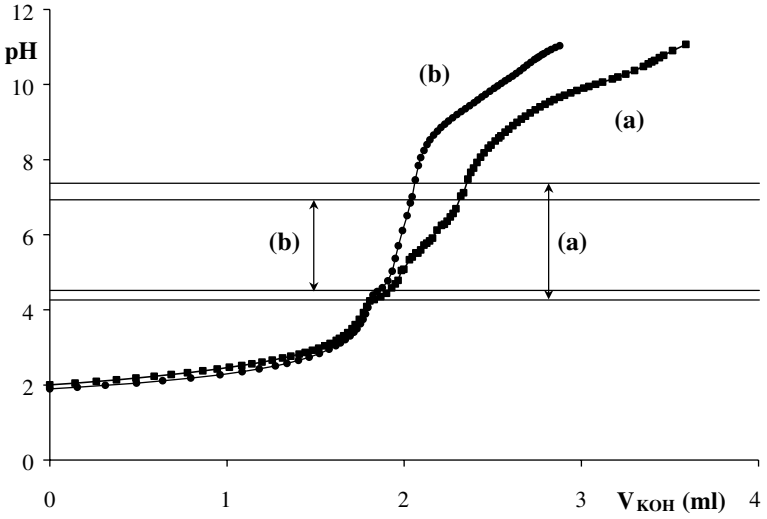


Fig. 3. Titration curves and pH-ranges where 10 min waiting time was not enough to reach pH equilibrium in the VO(IV)–H_2Diha (a) or VO(IV)–H_2MeDiha (b) system at 1:1 ratio, $c_{VO(IV)}$ = 4 mM, I = 0.2 M (KCl), T = 25.0 °C.

3.4. Study of the redox process in heterogeneous system

Previous work has already demonstrated that different *N*-substituted mono- and dihydroxamic acids are capable to oxidize VO(IV) to V(V) in solvent mixture with the parallel formation of the corresponding amides [9]. In this study freshly prepared, sparingly soluble complex obtained from VO(IV)–HBha solution was characterised as $VO(Bha)_2$. For comparison, the corresponding V(V) complex was also synthesized and characterised by microanalysis and IR (see Section 2). In another experiment, VO(IV) was again reacted with HBha and the purple microcrystalline solid obtained was further stirred in solution under argon for 24 h. An almost black solid was isolated, dried and analyzed for composition. Decrease in the carbon and nitrogen content (see Section 2) compared to that of $VO(Bha)_2$ is consistent with the partial oxidation of VO(IV) to V(V) in the solid complex. The practically unchanged C/N ratio in the VO(IV)-(6.12), V(V)-(6.27) complex and in the solid (6.13) isolated after 24 h also supports the sole oxidation of the metal ion, if it is still partial, and the lack of any decomposition of the coordinated ligand. After 24 h and after filtering the solid, analysis of the mother liquor by ESI-MS also proved the presence of the reduction product of benzohydroxamic acid, benzamide (m/z = 122 (M + 1)), in solution (Fig. 4).

3.5. Determination of the stoichiometry of the redox reaction

Due to the difficult separation and extensive purification of the products, earlier study with secondary hydroxamic acids was not successful in determining the accurate stoichiometry of the reaction between the hydroxamic acids and VO(IV) [9]. In this work therefore, pH-stat measurements were carried out in solution in order to determine the amount of the protons liberated during the process. Using high ligand excess, at pH = 5.5, where the bis complex is exclusively formed, the deprotonation of the uncomplexed ligand does not occur and the redox process is found to proceed, the base consumption of samples was monitored as a function of time under anaerobic conditions. Typical time dependence curves in the VO(IV)–HAha and VO(IV)–HMeAha systems are shown in Fig. 5. It should be mentioned that due to the slightly different analytical concentrations of the components in the two samples the volume of the base solution which was necessary to keep the pH at 5.5 is also different. As it is shown in Fig. 5 secondary ligands were found to react much more slowly than the primary ones in agreement with the potentiometric studies. While more than 10 h in the VO(IV)–HAha system, about 30 h in the VO(IV)–HMeAha system was necessary for the reaction to be completed. Further stirring showed no proton liberation

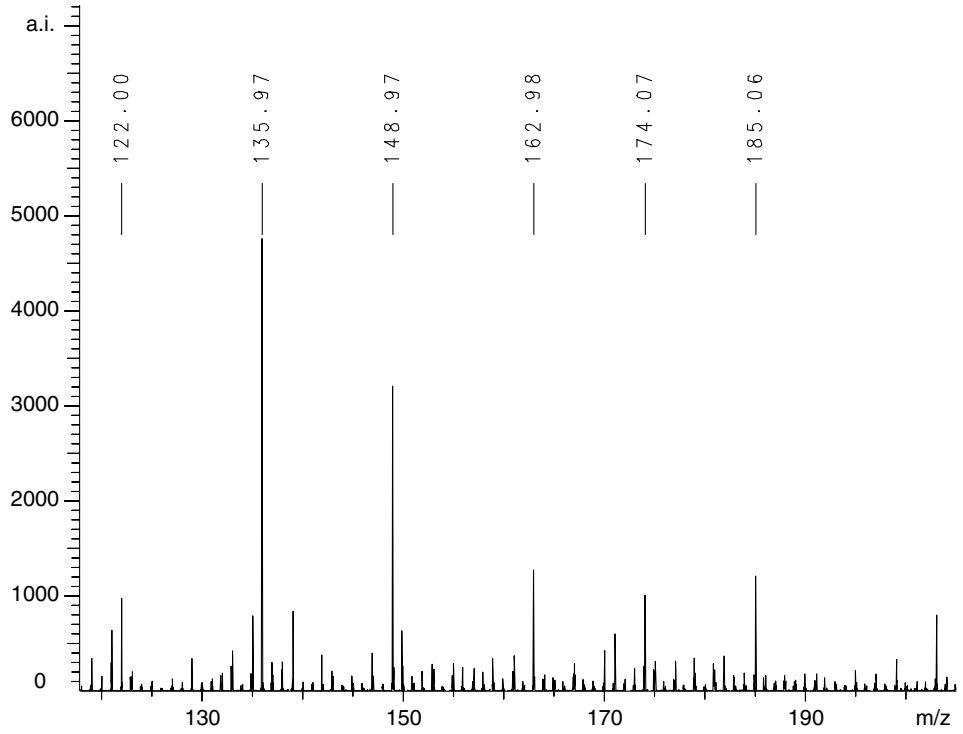


Fig. 4. ESI-MS spectrum of the mother liquor after filtering the solid complex formed in the VO(IV)–HBha system after 24 h stirring under argon. M/z = 122.0 indicates the formation of benzamide.

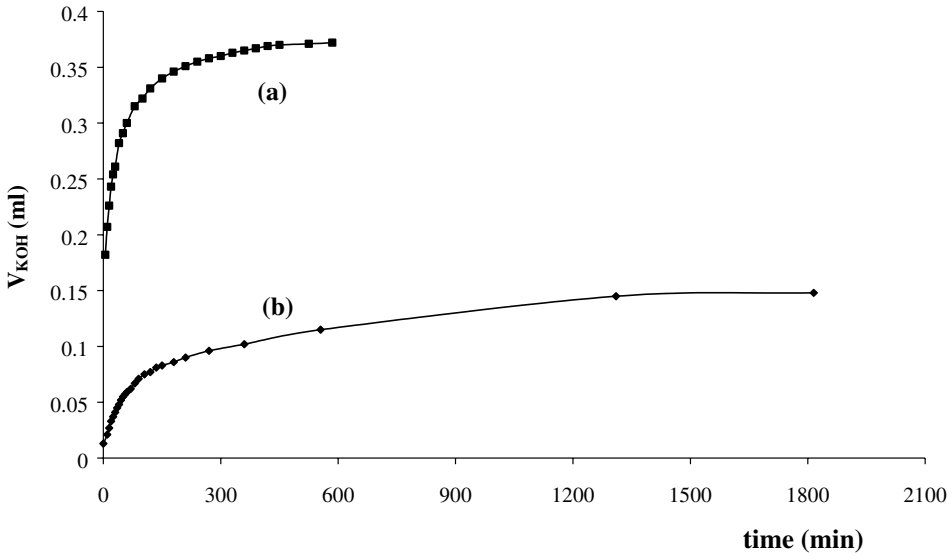


Fig. 5. pH-stat curves recorded at pH = 5.5 in the VO(IV)–HAha (a) or VO(IV)–HMeAha (b) system at 1:8 ratio, $c_{VO(IV)}$ = 2.56 mM (a) or 2.10 mM (b), I = 0.2 M (KCl), T = 25.0 °C.

or any other change in the samples. Preliminary experiments indicated the liberation of one equivalent of proton pro metal ion in the HAha system, according to Eq. (1).

$$2VO(Aha)_2 + HAha + H_2O = 2[VO_2(Aha)_2]^- + 2H^+ + CH_3CONH_2 \quad (1)$$

pH-stat measurements carried out with HAha, HMeAha, H_2Diha or H_2MeDiha proved the stoichiometry given by Eq. (1), where one mole of hydroxamic group oxidises two moles of VO(IV) with the formation of two protons and one mole of amide. With all the four ligands the difference in the amounts of the consumed and calculated base necessary for neutralising the protons was found to be less than 4%.

4. Conclusion

Both mono- and dihydroxamic acids form stable VO(IV) complexes in the pH range 2.0–5.0. The effect of the substituents at the nitrogen of the hydroxamic group on stability of the VO(IV) chelate was found higher than that at carbon in agreement with earlier results for Fe(III) or Cu(II) systems [12] due to the more pronounced effect of N substitution compared to C substitution on the delocalisation of the lone pair of N into the C–N bond. H_2Diha or H_2MeDiha showed increased VO(IV) binding capability in the complexes where the denticity of the ligands was higher than that of monohydroxamates.

Depending upon ligand excess, above pH = 4.5–5.0 slow redox reaction was found in all the aqueous systems studied under anaerobic conditions. During this reaction the ligands were capable to oxidise VO(IV) to the V(V)–hydroxamate complex with the parallel formation of the corresponding amide. pH-stat measurements were used to determine the exact stoichiometry of this process. Both primary and *N*-methyl monohydroxamic acids react with two equivalents of VO^{2+} in aqueous solution. For the secondary hydroxamic acids the rate of redox reaction with VO^{2+} is significantly slower than for the corresponding primary ones.

Further studies are in progress to characterise the active species involved in the redox process and to explore the differences in rate of the reaction for the primary and secondary ligands.

Acknowledgement

This work was supported by the Hungarian Science Research Fund (OTKA T 46366, TS 040685). P.B. gratefully acknowledges the Hungarian Academy of Sciences for a János Bolyai Research Fellowship.

References

[1] B. Kurzak, H. Kozlowski, E. Farkas, Coord. Chem. Rev. 114 (1992) 169.
[2] A.-M. Albrecht-Gary, A.L. Crumbliss, in: A. Sigel, H. Sigel (Eds.), Metal Ions in Biological Systems, vol. 35, Marcel Dekker, New York, 1998.
[3] R.L. Dutta, S. Lahiry, J. Indian, Chem. Soc. 39 (1962) 860.
[4] R.R. Nanewar, U. Tandon, Talanta 25 (1978) 352.
[5] D.C. Fisher, S.J. Barclay-Peet, C.A. Balfe, K.N. Raymond, Inorg. Chem. 28 (1989) 4399.
[6] R.T. Yamaki, E.B. Paniago, S. Carvalho, O.W. Horwarth, W. Kam, J. Chem. Soc., Dalton Trans. (1997) 4817.

[7] A. Dessì, G. Micera, D. Sanna, L.S. Erre, J. Inorg. Biochem. 48 (1992) 279.
[8] J.M. da Silva Santos, S. Carvalho, E.B. Paniago, H.A. Duarte, J. Inorg. Biochem. 95 (2003) 14.
[9] D.A. Brown, H. Bögge, R. Coogan, D. Doocey, T.J. Kemp, A. Müller, B. Neumann, Inorg. Chem. 35 (1996) 1674.
[10] P. Buglyó, Ph.D. Thesis, Lajos Kossuth University, Debrecen, Hungary, 1993.
[11] W.L. Smith, K.N. Raymond, J. Inorg. Nucl. Chem. 41 (1979) 1431.
[12] E. Farkas, É.A. Enyedy, H. Csóka, J. Inorg. Biochem. 79 (2000) 205.
[13] E. Farkas, É.A. Enyedy, I. Pócsi, J. Inorg. Biochem. 98 (2004) 1957.
[14] E. Farkas, P. Buglyó, É.A. Enyedy, V.A. Gerlei, M.A. Santos, Inorg. Chim. Acta 339 (2002) 215.
[15] V.K. Gupta, S.G. Tandon, J. Indian, Chem. Soc. 46 (1969) 831.
[16] G. Gran, Acta Chem. Scand. 4 (1950) 559.
[17] I. Nagypál, I. Fábián, Inorg. Chim. Acta 61 (1982) 109.
[18] H.M. Irving, M.G. Miles, L.D. Pettit, Anal. Chim. Acta 38 (1967) 475.
[19] P. Gans, A. Sabatini, A. Vacca, J. Chem. Soc., Dalton Trans. (1985) 1195.
[20] L. Zékány, I. Nagypál, in: D. Leggett (Ed.), Computational Methods for the Determination of Stability Constants, Plenum, New York, 1985.
[21] R.P. Henry, P.C.H. Mitchell, J.E. Prue, J. Chem. Soc., Dalton Trans. (1973) 1156.
[22] H. Komura, M. Hayashi, H. Imanaga, Bull. Chem. Soc., Japan (1977) 2927.
[23] R.L. Dutta, S. Ghosh, J. Indian, Chem. Soc. 44 (1967) 369.
[24] E. Farkas, E. Kozma, M. Pethö, K.M. Herlihy, G. Micera, Polyhedron 19 (1998) 3331.
[25] P. Buglyó, N. Culeddu, T. Kiss, G. Micera, D. Sanna, J. Inorg. Biochem. 60 (1995) 45.
[26] A.L. Crumbliss, in: G. Winkelman (Ed.), CRC Handbook of Microbial Iron Chelates, CRC Press, New York, 1991.

Available online at www.sciencedirect.com
SCIENCE DIRECT®
Polyhedron 24 (2005) 847–852
POLYHEDRON
www.elsevier.com/locate/poly

Structure and solution properties of the cadmium(II)-substituted tungstoarsenate $[Cd_4Cl_2(B\text{-}\alpha\text{-}AsW_9O_{34})_2]^{12-}$

Firasat Hussain, Li-Hua Bi, Urs Rauwald, Markus Reicke, Ulrich Kortz *

International University Bremen, School of Engineering and Science, P.O. Box 750 561, 28725 Bremen, Germany

Received 17 January 2005; revised 15 March 2005; accepted 16 March 2005
Available online 18 April 2005

Abstract

The cadmium(II)-substituted tungstoarsenate $[Cd_4Cl_2(B\text{-}\alpha\text{-}AsW_9O_{34})_2]^{12-}$ (**1**) has been synthesized and characterized in the solid state by XRD, IR, elemental analysis and in solution by ^{183}W and ^{111}Cd NMR. Single crystal X-ray analysis was carried out on $Cs_4K_3Na_5[Cd_4Cl_2(B\text{-}\alpha\text{-}AsW_9O_{34})_2]\cdot 20H_2O$. Polyanion **1** consists of two lacunary $[B\text{-}\alpha\text{-}AsW_9O_{34}]^{9-}$ Keggin moieties linked via a rhomblike ($Cd_4O_{14}Cl_2$) group leading to a sandwich-type structure. Interestingly, the two external Cd atoms have a terminal Cl ligand, but the derivative with terminal water ligands, $[Cd_4(H_2O)_2(B\text{-}\alpha\text{-}AsW_9O_{34})_2]^{10-}$ (**2**), can also be prepared as shown by ^{183}W and ^{111}Cd solution NMR.
© 2005 Elsevier Ltd. All rights reserved.

Keywords: Polyoxometalate; Tungstoarsenate; Cadmium; Sandwich-type structure; Single crystal XRD; ^{183}W and ^{111}Cd NMR

1. Introduction

Polyoxometalates (POMs) have been known for almost 200 years and a century later the first structural details were revealed [1]. POMs constitute a rapidly growing class of molecular metal–oxygen clusters with an enormous diversity of structures [2–8]. The significant interest in POM chemistry is driven by potential applications in many areas including catalysis, medicine, material science, and nano/biotechnology [4–8].

Amongst all known transition metal substituted polyoxometalates (TMSPs), the sandwich-type species are probably the largest subfamily [9]. In 1973 Weakley et al. [10a] described the first sandwich-type polyoxoanion, $[Co_4(H_2O)_2(B\text{-}\alpha\text{-}PW_9O_{34})_2]^{10-}$. Since then, several other derivatives of this structural type have been reported. To date, the class of Weakley-type sandwich species consists of the Keggin derivatives $[M_4(H_2O)_2(B\text{-}\alpha\text{-}XW_9O_{34})_2]^{n-}$ ($n = 12$, X = Ge^{IV}, Si^{IV}, M = Mn^{2+}, Cu^{2+}, Zn^{2+}, Cd^{2+}; $n = 10$, X = P^V, As^V, M = Mn^{2+}, Co^{2+}, Ni^{2+}, Cu^{2+}, Zn^{2+}, Cd^{2+}; $n = 6$, X = P^V, As^V, M = Fe^{3+}; $n = 16$, X = M = Cu^{2+}; $n = 10$, X = M = Fe^{3+}) and the Wells-Dawson derivatives $[M_4(X_2W_{15}O_{56})_2]^{n-}$ (X = P^V, As^V, $n = 16$, M = Mn^{2+}, Co^{2+}, Ni^{2+}, Cu^{2+}, Zn^{2+}, Cd^{2+}, $n = 12$, M = Fe^{3+}) [10].

Other types of sandwich-type POMs are also known and include species based on two lone-pair containing α-Keggin fragments, e.g., $[\alpha\text{-}As^{III}W_9O_{33}]^{9-}$. The first member of this class ($[Cu_3(H_2O)_2(\alpha\text{-}AsW_9O_{33})_2]^{12-}$) was reported by Hervé and coworkers in 1982 [11a]. Since then several isostructural derivatives have been characterized [11b–h,12f]. Another class of sandwich-type POMs is based on two lone-pair containing, β-Keggin fragments, e.g., $[\beta\text{-}Sb^{III}W_9O_{33}]^{9-}$. The first members of this class, $[M_2(H_2O)_6(WO_2)_2(\beta\text{-}SbW_9O_{33})_2]^{(14-2n)-}$

* Corresponding author. Tel.: +49 421 200 3235; fax: +49 421 200 3229.
E-mail address: u.kortz@iu-bremen.de (U. Kortz).

0277-5387/$ - see front matter © 2005 Elsevier Ltd. All rights reserved.
doi:10.1016/j.poly.2005.03.010

(M^{n+} = Fe^{3+}, Co^{2+}, Mn^{2+}, Ni^{2+}), were reported by Krebs and coworkers in 1997 [12a]. Since then many more isostructural derivatives have been reported [12b–f]. The last class of sandwich-type POMs is based on two *A*-α-Keggin fragments, e.g., $[A\text{-}\alpha\text{-}PW_9O_{34}]^{9-}$. The first member of this class, $[Co_3(H_2O)_3(A\text{-}\alpha\text{-}PW_9O_{34})_2]^{12-}$, was reported by Knoth et al. in 1985 [13a]. Since then some isostructural derivatives have been identified [13b–f].

Surprisingly little work on cadmium-substituted polyoxotungstates has been reported to date, especially regarding structurally characterized species. Nevertheless, the diamagnetic nature of Cd-containing POMs has prompted some NMR studies. Twenty years ago Contant [14] reported for the first time on cadmium-containing Keggin and Wells-Dawson species. In 1995 Kirby and Baker [15] reported on a NMR study of the first sandwich-type polyoxometalate including Cd^{2+} ions. More recently, Bi et al. [10p,q] prepared Cd-substituted, sandwich type polyanions based on the tungstoarsenate fragments $[As_2W_{15}O_{56}]^{12-}$ and $[AsW_9O_{34}]^{9-}$, respectively. Very recently, Alizadeh et al. [16] synthesized and structurally characterized the tetra-cadmium containing $[Cd_4(H_2O)_2(PW_9O_{34})_2]^{10-}$.

Here we report on interaction of Cd^{2+} ions with the trilacunary Keggin derivative $[A\text{-}HAsW_9O_{34}]^{8-}$ in aqueous solution.

2. Experimental

2.1. Materials and methods

All chemicals were of reagent grade and used as purchased. The IR spectra were recorded on a Nicolet Avatar FTIR spectrophotometer as KBr pellets. Elemental analysis was performed by Kanti Labs Ltd. in Mississauga, Canada.

2.2. Synthesis of lacunary polyanion precursor $Na_8[A\text{-}HAsW_9O_{34}] \cdot 11H_2O$

A 30 g (91 mmol) sample of $Na_2WO_4 \cdot 2H_2O$ and 1.18 g (5.1 mmol) As_2O_5 were dissolved in 40 mL of water. Subsequently, the pH was adjusted to 8.4 using glacial acetic acid. After a few seconds the solution became cloudy and after about 2 min a white precipitate started to form. The solution was stirred for another 30 min and then the solid was isolated on a sintered funnel. The product was washed three times with ethanol and air-dried with aspiration. IR: 937(m), 884(m), 851(m), 765(s), 672(m), 518(w), 472(w), 444(w) cm^{-1}. This procedure is different from that reported previously by one of us, which involves using H_3AsO_4 instead of As_2O_5 [10q].

2.3. Synthesis of $Cs_4K_3Na_5[Cd_4Cl_2(B\text{-}\alpha\text{-}AsW_9O_{34})_2] \cdot 20H_2O$ (**1a**)

A 0.33 g (1.66 mmol) sample of $CdCl_2 \cdot H_2O$ was dissolved with stirring in 20 mL of 0.5 M NaAc buffer (pH 4.8). Then 2.00 g (0.75 mmol) of $Na_8[A\text{-}HAsW_9O_{34}] \cdot 11H_2O$ was added. The solution was heated to 80 °C for about 1 h and filtered after it had cooled. Then 0.5 mL of 1.0 M CsCl and 0.5 mL of 1.0 M KCl solutions were added to the filtrate. Slow evaporation at room temperature led to 1.8 g (yield 78%) of a white crystalline product after about one week. IR: 951(s), 882(s), 835(s), 784(s), 746(sh), 724(s), 480(w), 442(w) cm^{-1}. *Anal.* Calc. for **1a**: Cs, 8.6; K, 1.9; Na, 1.9; W, 53.4; Cd, 7.3; As, 2.4; Cl, 1.2. Found: Cs, 8.3; K, 2.1; Na, 1.9; W, 53.9; Cd, 7.1; As, 2.4; Cl, 1.3%.

2.4. ^{183}W and ^{111}Cd NMR spectroscopy

All NMR spectra were recorded on a 400 MHz JEOL ECX instrument at room temperature using D_2O as a solvent. The ^{183}W NMR measurements were performed at 16.656 MHz in 10 mm tubes and the ^{111}Cd measurements were performed at 84.757 MHz in 5 mm tubes. As references (external standards) we used aqueous solutions of 1 M Na_2WO_4 and 0.1 M $Cd(ClO_4)_2$, respectively.

2.5. X-ray diffraction analysis

A colorless crystal with dimensions $0.26 \times 0.12 \times 0.08$ mm was selected and mounted on a glass fiber for indexing and intensity data collection at 167 K on a Bruker D8 SMART APEX CCD single-crystal diffractometer using Mo Kα radiation (λ = 0.71073 Å). Direct methods were used to solve the structure and to locate the heavy

Table 1
Crystal data and structure refinement for $Cs_4K_3Na_5[Cd_4Cl_2(B\text{-}\alpha\text{-}AsW_9O_{34})_2] \cdot 20H_2O$ (**1a**)

Empirical formula	$As_2Cd_4Cl_2Cs_4H_{40}K_3Na_5O_{88}W_{18}$
Formula weight	6192.0
Space group (No.)	$P2_1/n$ (14)
Unit cell dimensions	
a (Å)	13.1402(12)
b (Å)	19.0642(17)
c (Å)	17.5666(15)
β (°)	90.274(2)
Volume (Å^3)	4400.5(7)
Z	2
Temperature (°C)	−106
Wavelength (Å)	0.71073
D_{calc} (Mg m^{-3})	4.608
Absorption coefficient (mm^{-1})	27.069
R [$I > 2\sigma(I)$][a]	0.046
R_w (all data)[b]	0.107

[a] $R = \sum ||F_o| - |F_c|| / \sum |F_o|$.
[b] $R_w = [\sum w(F_o^2 - F_c^2)^2 / \sum w(F_o^2)^2]^{1/2}$.

atoms (SHELXS97). Then the remaining atoms were found from successive difference maps (SHELXL97). Routine Lorentz and polarization corrections were applied and an absorption correction was performed using the SADABS program [17]. Crystallographic data are summarized in Table 1.

3. Results and discussion

3.1. Synthesis and structure

We have synthesized the dimeric tungstoarsenate(V) $[Cd_4Cl_2(B\text{-}\alpha\text{-}AsW_9O_{34})_2]^{12-}$ (**1**) as a mixed cesium–potassium–sodium salt. The title polyanion consists of two trilacunary $[B\text{-}\alpha\text{-}AsW_9O_{34}]^{9-}$ Keggin units linked via a rhomblike $Cd_4O_{14}Cl_2$ group resulting in a sandwich-type structure with idealized C_{2h} symmetry (see Fig. 1). Polyanion **1** was synthesized by interaction of Cd^{2+} ions with the trilacunary precursor $[A\text{-}HAsW_9O_{34}]^{8-}$ in aqueous acidic medium upon heating to 80 °C. This indicates that the Keggin precursor has undergone isomerization from $A\text{-}AsW_9 \rightarrow B\text{-}AsW_9$ during the course of the reaction. However, this transformation is well known and has been observed in solution and in the solid state [10q].

Bond valence sum (BVS) calculations confirm that there are no protonation sites on **1**, indicating that the charge of the title polyanion must be −12 [18]. Crystallographically we could identify only 4 Cs^+, 3 K^+ and 3 Na^+ counterions, but elemental analysis indicated that indeed 5 Na^+ ions were present in **1a**. Therefore the charge of −12 for **1** is fully balanced in the solid state by an appropriate number of counterions. Disorder of some alkali ions (in particular sodium) is a common problem in polyanion chemistry.

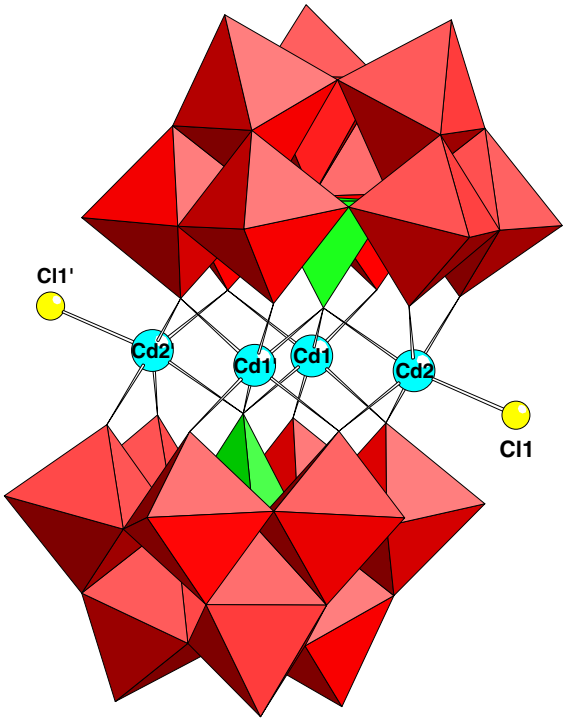


Fig. 1. Combined polyhedral/ball and stick representation of $[Cd_4Cl_2(B\text{-}\alpha\text{-}AsW_9O_{34})_2]^{12-}$ (**1**).

The structural type of **1** had first been described in 1973 by Weakley et al. [10a] for $[Co_4(H_2O)_2(PW_9O_{34})_2]^{10-}$. To date this Keggin-based structure is known for most first-row transition metals (including mixed-metal derivatives) and it has also been possible to substitute the tetrahedral phosphorus(V) heteroatom by arsenic(V), silicon(IV), germanium(IV), iron(III), and copper(II) [10]. Therefore, this structural type represents one of the largest TMSP families.

The Weakley-type structures have in common that the two external transition metal ions in the central rhombus have one terminal ligand each, whereas the two internal metal ions do not have any terminal ligands. In all of the above known derivatives with the Weakley structure, the terminal ligand on the external transition metal ions is a water molecule. However, in **1** the two external cadmium ions have a chloro ligand instead of a water molecule. Clearly, the chloride ions originate from the cadmium source ($CdCl_2 \cdot H_2O$) which we used for the synthesis of **1**. Nevertheless, it must be remembered that synthesis of **1** is carried out in aqueous solution, so that the number of water molecules dominates by far the chloride ions. Therefore, the external cadmium ions incorporated in **1** have a strong preference for chloro rather than aqua ligands.

Recently one of us reported on the aqua derivative of **1** which was formulated as $[Cd_4(H_2O)_2(B\text{-}\alpha\text{-}AsW_9O_{34})_2]^{10-}$ based on IR [10q]. Very recently Alizadeh et al. [16] reported on $[Cd_4(H_2O)_2(B\text{-}\alpha\text{-}PW_9O_{34})_2]^{10-}$ which represents the phosphorus derivative of **1**. They prepared this polyanion by reaction of $Cd(NO_3)_2 \cdot 4H_2O$ with $Na_8[A\text{-}\beta\text{-}HPW_9O_{34}] \cdot 24\text{-}H_2O$ in aqueous acidic medium (pH 6). These authors characterized their product in solution by ^{31}P and ^{113}Cd NMR. Very recently our group has synthesized the germanium(IV) derivative $[Cd_4(H_2O)_2(B\text{-}\alpha\text{-}GeW_9O_{34})_2]^{12-}$ by reaction of $CdCl_2$, GeO_2, and $Na_2WO_4 \cdot 2H_2O$ in 0.5 M sodium acetate buffer (pH 4.8) [10u]. Interestingly, the external cadmium ions in the product polyanion contain aqua rather than chloro ligands. It is possible that the higher affinity of Cd^{2+} for chloro ions is overcompensated by charge density considerations of the germanium(IV) based polyanion. Specifically, the hypothetical dichloro derivative $[Cd_4Cl_2(B\text{-}\alpha\text{-}GeW_9O_{34})_2]^{14-}$ would have a charge of 14−, which is apparently less stable than the diaqua derivative $[Cd_4(H_2O)_2(B\text{-}\alpha\text{-}GeW_9O_{34})_2]^{12-}$ with a charge of 12−. Interestingly, our $[Cd_4(H_2O)_2(B\text{-}\alpha\text{-}GeW_9O_{34})_2]^{12-}$ and

the $[Cd_4Cl_2(B\text{-}\alpha\text{-}AsW_9O_{34})_2]^{12-}$ reported here have both the same charge of −12.

It is of interest to evaluate in detail the bond lengths and angles of the cadmium centers in **1** and to compare these with the isostructural derivatives $[Cd_4(H_2O)_2(B\text{-}\alpha\text{-}PW_9O_{34})_2]^{10-}$ and $[Cd_4(H_2O)_2(B\text{-}\alpha\text{-}GeW_9O_{34})_2]^{12-}$. In general, as Cd^{2+} is a d^{10} ion no Jahn–Teller distortion is expected. In fact, the two inner Cd centers of **1** exhibit a fairly regular coordination sphere and the Cd(1)-O distances range from 2.19 to 2.34(1) Å. On the other hand, the coordination sphere of the external Cd(2) shows a Jahn–Teller distortion, which is most likely due to the presence of the terminal chloro ligand. The equatorial Cd(2)–O distances range from 2.24 to 2.29(1) Å, whereas the axial Cd(2)–O and Cd(2)–Cl distances are 2.47(1) and 2.475(4) Å, respectively. The bond angles in the central $Cd_4Cl_2O_{14}$ fragment can be classified according to the type of bridging ligand. The Cd–O–Cd angles involving the μ_4-oxo ligand O1As are: Cd1–O1As–Cd1′ 101.2(4)°, Cd1–O1As–Cd2 93.3(3)° and Cd1–O1As–Cd2 94.6(3)°, respectively. On the other hand, the angles around the μ_3-oxo ligands O8C2 and O9Cd are: Cd1–O8C2–Cd2 98.9(4)° and Cd1–O9Cd–Cd2 100.4(4)°. The Cd···Cd separations in **1** are as follows: Cd1···Cd2 3.533(2) Å, Cd1···Cd2′ 3.494(2) Å and Cd1···Cd1′ 3.614(2) Å, respectively.

Comparison of these parameters for **1** with those of the structurally closely related $[Cd_4(H_2O)_2(B\text{-}\alpha\text{-}GeW_9O_{34})_2]^{12-}$ [10u] and $[Cd_4(H_2O)_2(B\text{-}\alpha\text{-}PW_9O_{34})_2]^{10-}$ [16] allows to draw the following conclusions: the terminal chloro ligands in **1** result in a significantly longer terminal cadmium bond (Cd–Cl 2.475(5) Å) compared to those in the two aqua compounds (2.260(14) and 2.309(8) Å). This is the reason for the more pronounced Jahn–Teller distortion of the external Cd centers in **1**, which in turn results in larger Cd1···Cd2 distances (e.g., 3.494(2) Å, 3.533(2) Å in **1** versus 3.357(2) Å, 3.404(2) Å in $[Cd_4(H_2O)_2(B\text{-}\alpha\text{-}GeW_9O_{34})_2]^{12-}$).

We were also able to synthesize the aqua derivative of **1** with the proposed formula $[Cd_4(H_2O)_2(B\text{-}\alpha\text{-}AsW_9O_{34})_2]^{10-}$ (**2**) as based on IR and multinuclear NMR (see below). Polyanion **2** was prepared by an analogous procedure as **1**, but $Cd(NO_3)_2 \cdot 4H_2O$ was used instead of $CdCl_2 \cdot H_2O$ to ascertain the absence of chloride ions.

3.2. NMR Studies

Tungsten-183 NMR is a very powerful solution technique in polyanion chemistry to obtain structural information. The fact that polyanions **1** and **2** are diamagnetic makes them ideal candidates for NMR studies. In addition both species contain cadmium ions and therefore we decided to perform a detailed ^{183}W and ^{111}Cd NMR study on **1** and **2**. If the dimeric, sandwich-type polyanion structure with C_{2h} symmetry is preserved in solution, then five peaks (intensity ratio 2:2:2:2:1) are expected in ^{183}W NMR and two peaks (1:1) are expected for ^{111}Cd NMR. In fact, this is exactly what we observed. The room-temperature ^{183}W NMR spectrum of **1** exhibits five peaks at −75.9, −92.0, −94.2, −109.8, −121.8 ppm with intensity ratios 1:2:2:2:2 (see Fig. 2, top). For **2** we obtained an almost identical spectrum with five peaks at −75.9, −92.6, −94.3, −107.9, −119.9 ppm and the anticipated intensity ratios (see Fig. 2, bottom). As expected, a change of the terminal ligand on the external cadmium centers in **1** and **2** does not affect the chemical shifts of the tungsten centers significantly. In fact, only four of the six belt tungsten atoms in each Keggin unit should be affected, as they are only 3 bonds from the terminal chloro ligands in **1** or aqua ligands in **2** (see Fig. 1). Therefore we suggest that the two upfield signals in the ^{183}W NMR spectra of **1** and **2** (see Fig. 2) correspond most likely to those tungsten atoms in question. All other tungsten centers are further away from the terminal cadmium ligands in **1** and **2**. Of course, the unique cap tungsten atom corresponds to the smallest, most downfield signal. The ^{183}W NMR spectra of **1** and **2** correspond also very nicely to our results on the isostructural germanium derivatives $[Cd_4(H_2O)_2(B\text{-}\alpha\text{-}GeW_9O_{34})_2]^{12-}$ and $[Zn_4(H_2O)_2(B\text{-}\alpha\text{-}GeW_9O_{34})_2]^{12-}$ [10u].

The ^{111}Cd NMR spectrum of **1** shows two singlet peaks at 55.3 and 14.7 ppm, respectively (see Fig. 3, top). The upfield signal is very broad which is probably due to the quadrupolar moment of the chloro ligand. Therefore, we can assign this signal to the external cadmium ions in **1** whereas the other, sharp signal corre-

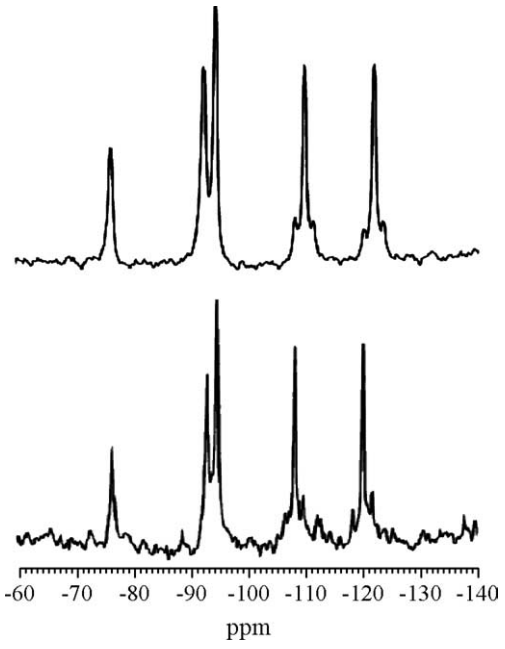


Fig. 2. Tungsten-183 NMR spectra of $[Cd_4Cl_2(B\text{-}\alpha\text{-}AsW_9O_{34})_2]^{12-}$ (**1**), top, and $[Cd_4(H_2O)_2(B\text{-}\alpha\text{-}AsW_9O_{34})_2]^{10-}$ (**2**), bottom.

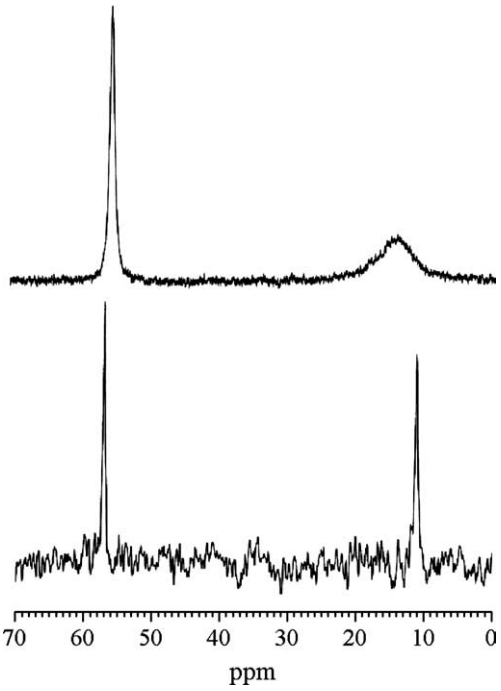


Fig. 3. Cadmium-111 NMR spectra of $[Cd_4Cl_2(B\text{-}\alpha\text{-}AsW_9O_{34})_2]^{12-}$ (**1**), top, and $[Cd_4(H_2O)_2(B\text{-}\alpha\text{-}AsW_9O_{34})_2]^{10-}$ (**2**), bottom.

sponds to the internal cadmium centers. The ^{111}Cd NMR spectrum of **2** exhibits two sharp peaks at 57.0 and 11.1 ppm, respectively, with equal intensities (see Fig. 3, bottom). This is fully consistent with water molecules as terminal ligands on the external cadmium ions. In analogy to **1** we assign the upfield signal at 11.1 ppm to the external cadmium ions and the downfield signal at 57.0 ppm to the internal cadmium ions of **2**. These results are also in good agreement with Alizadeh et al. [16], who performed ^{113}Cd NMR studies on $[Cd_4(H_2O)_2(B\text{-}\alpha\text{-}PW_9O_{34})_2]^{10-}$. They observed a very similar chemical shift for the internal cadmium ions (52.76 ppm), but the signal for the outer cadmium centers is significantly more downfield (26.25 ppm). This difference in ^{111}Cd NMR behavior must be due to the different hetero atoms X (X = As, P), as all other parameters are the same for both polyanions (e.g., structure, charge). Our work shows that this 'hetero atom effect' is more pronounced for the external than the internal cadmium ions. The nuclear shielding of the outer cadmium centers is a much better sensor for the type of hetero atom present than that of the internal cadmiums, in spite of the fact that the Cd–O bond lengths and Cd–O–X angles are very similar in both cases.

4. Conclusion

The dimeric, cadmium-substituted tungstoarsenate $[Cd_4Cl_2(B\text{-}\alpha\text{-}AsW_9O_{34})_2]^{12-}$ (**1**) has been synthesized by reaction of Cd^{2+} ions with $[A\text{-}HAsW_9O_{34}]^{8-}$ in aqueous, acidic medium. Polyanion **1** has a sandwich-type structure based on two $[B\text{-}\alpha\text{-}AsW_9O_{34}]^{9-}$ Keggin moieties encapsulating four cadmium centers in a rhomblike ($Cd_4O_{14}Cl_2$) group. Therefore, **1** represents only the second structurally characterized, Cd-containing polyanion and it is the first structurally characterized, Cd-containing tungstoarsenate(V). An interesting aspect of **1** is the fact that the external cadmium centers have terminal chloro ligands. Nevertheless we were also able to synthesize the aqua derivative $[Cd_4(H_2O)_2(B\text{-}\alpha\text{-}AsW_9O_{34})_2]^{10-}$ (**2**). Both species were investigated by ^{183}W and ^{111}Cd NMR in solution and we have shown that the former is an ideal method to establish the purity and to confirm the overall polyanion structure of **1** and **2**. On the other hand, the latter is an ideal technique to study the local coordination environment of the cadmium ions and it also allows to clearly distinguish **1** and **2** due to peak broadening caused by the quadrupolar chloride ions. Furthermore, this effect allows to assign the two Cd NMR peaks to the two types of cadmium ions in **1** and **2** and it also allows to indirectly assign some of the ^{183}W NMR peaks of the title polyanions.

In conclusion, synthesis of diamagnetic derivatives (e.g., Cd^{2+}, Zn^{2+}) of TMSPs is very attractive, as it allows to perform multinuclear NMR studies in solution involving addenda atoms (e.g., ^{183}W, ^{111}Cd). Although single crystal X-ray analysis is the most powerful technique to establish novel polyanion structures, multinuclear NMR is a very important, complementary tool to establish the structural integrity of polyanions in solution. Considering that polyanions have a multitude of potential applications in solution (e.g., medicine, catalysis) such diamagnetic complexes can be considered as model compounds to help understand structure-activity relationships of entire families of polyanions.

5. Supplementary material

One X-ray crystallographic file in CIF format. This material can be obtained from the Fachinformationszentrum Karlsruhe, Abt. PROKA, 76344 Eggenstein-Leopoldshafen, Germany (fax: +49 7247 808 666; e-mail: crysdata@fiz-karlsruhe.de) on quoting the depository number CSD – 415053.

Acknowledgments

U.K. thanks the International University Bremen for research support. X-ray measurements were made during a visit of U.K. in the laboratory of Prof. M.T. Pope at Georgetown University, USA. U.K. thanks the Georgetown University Chemistry Department for allowing use of the X-ray diffractometer. Fig. 1 was gen-

erated by DIAMOND Version 3.0a (copyright Crystal Impact GbR).

References

[1] (a) J. Berzelius, Pogg. Ann. 6 (1826) 369;
(b) J.F. Keggin, Nature 131 (1933) 908;
(c) J.F. Keggin, Proc. Roy. Soc. A 144 (1934) 75.

[2] M.T. Pope, Heteropoly and Isopoly Oxometalates, Springer Verlag, Berlin, 1983.

[3] M.T. Pope, A. Müller, Angew. Chem., Int. Ed. 30 (1991) 34.

[4] M.T. Pope, A. Müller (Eds.), Polyoxometalates: From Platonic Solids to Anti-retroviral Activity, Kluwer, Dordrecht, The Netherlands, 1994.

[5] C. Hill (Ed)., Chemical Reviews, Polyoxometalates, 1998.

[6] M.T. Pope, A. Müller (Eds.), Polyoxometalate Chemistry: From Topology via Self-assembly to Applications, Kluwer, Dordrecht, The Netherlands, 2001.

[7] T. Yamase, M.T. Pope (Eds.), Polyoxometalate Chemistry for Nanocomposite Design, Kluwer, Dordrecht, The Netherlands, 2002.

[8] J.J. Borrás-Almenar, E. Coronado, A. Müller, M.T. Pope (Eds.), Polyoxometalate Molecular Science, Kluwer, Dordrecht, The Netherlands, 2004.

[9] M.T. Pope, Comp. Coord. Chem. II 4 (2003) 635.

[10] (a) T.J.R. Weakley, Howard T. Evans Jr., J.S. Showell, G.F. Tourné, C.M. Tourné, J. Chem. Soc., Chem. Commun. (1973) 139;
(b) R.G. Finke, M. Droege, J.R. Hutchinson, O. Gansow, J. Am. Chem. Soc. 103 (1981) 1587;
(c) R.G. Finke, M.W. Droege, Inorg. Chem. 22 (1983) 1006;
(d) Howard T. Evans Jr., C.M. Tourné, G.F. Tourné, T.J.R. Weakley, J. Chem. Soc., Dalton Trans. (1986) 2699;
(e) R.G. Finke, M.W. Droege, P.J. Domaille, Inorg. Chem. 26 (1987) 3886;
(f) S.H. Wasfi, A.L. Rheingold, G.F. Kokoszka, A.S. Goldstein, Inorg. Chem. 26 (1987) 2934;
(g) T.J.R. Weakley, R.G. Finke, Inorg. Chem. 29 (1990) 1235;
(h) C.J. Gómez-García, E. Coronado, J.J. Borrás-Almenar, Inorg. Chem. 31 (1992) 1667;
(i) N. Casañ-Pastor, J. Bas-Serra, E. Coronado, G. Pourroy, L.C.W. Baker, J. Am. Chem. Soc. 114 (1992) 10380;
(j) C.J. Gómez-García, E. Coronado, P. Gómez-Romero, N. Casañ-Pastor, Inorg. Chem. 32 (1993) 3378;
(k) C.J. Gómez-García, J.J. Borrás-Almenar, E. Coronado, L. Ouahab, Inorg. Chem. 33 (1994) 4016;
(l) X.-Y. Zhang, G.B. Jameson, C.J. O'Connor, M.T. Pope, Polyhedron 15 (1996) 917;
(m) X. Zhang, Q. Chen, D.C. Duncan, C. Campana, C.L. Hill, Inorg. Chem. 36 (1997) 4208;
(n) X. Zhang, Q. Chen, D.C. Duncan, R.J. Lachicotte, C.L. Hill, Inorg. Chem. 36 (1997) 4381;
(o) J.M. Clemente-Juan, E. Coronado, J.R. Galán-Mascarós, C.J. Gómez-García, Inorg. Chem. 38 (1999) 55;
(p) L.-H. Bi, E.-B. Wang, J. Peng, R.-D. Huang, L. Xu, C.-W. Hu, Inorg. Chem. 39 (2000) 671;
(q) L.-H. Bi, R.-D. Huang, J. Peng, E.-B. Wang, Y.-H. Wang, C.-W. Hu, J. Chem. Soc., Dalton Trans. (2001) 121;
(r) U. Kortz, S. Isber, M.H. Dickman, D. Ravot, Inorg. Chem. 39 (2000) 2915;
(s) E.M. Limanski, M. Piepenbrink, E. Droste, K. Burgemeister, B. Krebs, J. Clust. Sci. 13 (2002) 369;
(t) C. Rosu, D.C. Crans, T.J.R. Weakley, Polyhedron 21 (2002) 959;
(u) U. Kortz, S. Nellutla, A.C. Stowe, N.S. Dalal, U. Rauwald, W. Danquah, D. Ravot, Inorg. Chem. 43 (2004) 2308.

[11] (a) F. Robert, M. Leyrie, G. Hervé, Acta. Crystallogr., Sect. B 38 (1982) 358;
(b) M. Bösing, A. Nöh, I. Loose, B. Krebs, J. Am. Chem. Soc. 120 (1998) 7252;
(c) U. Kortz, N.K. Al-Kassem, M.G. Savelieff, N.A. Al Kadi, M. Sadakane, Inorg. Chem. 40 (2001) 4742;
(d) B. Botar, T. Yamase, E. Ishikawa, Inorg. Chem. Commun. 4 (2001) 551;
(e) T. Yamase, B. Botar, E. Ishikawa, K. Fukaya, Chem. Lett. (2001) 56;
(f) P. Mialane, J. Marrot, E. Rivière, J. Nebout, G. Hervé, Inorg. Chem. 40 (2001) 44;
(g) U. Kortz, S. Nellutla, A.C. Stowe, N.S. Dalal, J. van Tol, B.S. Bassil, Inorg. Chem. 43 (2004) 144;
(h) L.-H. Bi, M. Reicke, U. Kortz, B. Keita, L. Nadjo, R.J. Clark, Inorg. Chem. 43 (2004) 3915.

[12] (a) M. Bösing, I. Loose, H. Pohlmann, B. Krebs, Chem. Eur. J. 3 (1997) 1232;
(b) I. Loose, E. Droste, M. Bösing, H. Pohlmann, M.H. Dickman, C. Roşu, M.T. Pope, B. Krebs, Inorg. Chem. 38 (1999) 2688;
(c) B. Krebs, E. Droste, M. Piepenbrink, G. Vollmer, C.R. Acad. Sci. Paris, Ser. IIc 3 (2000) 205;
(d) U. Kortz, M.G. Savelieff, B.S. Bassil, B. Keita, L. Nadjo, Inorg. Chem. 41 (2002) 783;
(e) E.M. Limanski, D. Drewes, E. Droste, R. Bohner, B. Krebs, J. Mol. Struct. 656 (2003) 17;
(f) D. Drewes, E.M. Limanski, M. Piepenbrink, B. Krebs, Z. Anorg. Allg. Chem. 630 (2004) 58.

[13] (a) W.H. Knoth, P.J. Domaille, R.D. Farlee, Organometallics 4 (1985) 62;
(b) W.H. Knoth, P.J. Domaille, R.L. Harlow, Inorg. Chem. 25 (1986) 1577;
(c) R.G. Finke, B. Rapko, T.J.R. Weakley, Inorg. Chem. 28 (1989) 1573;
(d) F. Xin, M.T. Pope, J. Am. Chem. Soc. 118 (1996) 7731;
(e) N. Laronze, J. Marrot, G. Hervé, Inorg. Chem. 42 (2003) 5857;
(f) L.-H. Bi, U. Kortz, B. Keita, L. Nadjo, H. Borrmann, Inorg. Chem. 43 (2004) 8367.

[14] (a) R. Contant, J. Chem. Res. (S) (1984) 120;
(b) R. Contant, J. Chem. Res. (M) (1984) 1063;
(c) G.M. Maksimov, G.N. Kustova, K.I. Matveev, T.P. Lazarenko, Koord. Khim. 15 (1989) 788.

[15] J.F. Kirby, L.C.W. Baker, J. Am. Chem. Soc. 117 (1995) 10010.

[16] M.H. Alizadeh, H. Razavi, F.M. Zonoz, M.R. Mohammadi, Polyhedron 22 (2003) 933.

[17] G.M. Sheldrick, SADABS, University of Göttingen, Göttingen, 1996.

[18] I.D. Brown, D. Altermatt, Acta Crystallogr., Sect. B 41 (1985) 244.

Available online at www.sciencedirect.com
SCIENCE DIRECT®
Polyhedron 24 (2005) 853–863
POLYHEDRON
www.elsevier.com/locate/poly

Polymer and cage-type structures in silver(I) complexes with heterocyclic thiones and bridging diphosphine ligands. Crystal structures of $[Ag(\mu\text{-dpppent})(tHpymtH)(ONO_2)]_n$ and $[Ag_2(\mu\text{-}trans\text{-dppen})_3(pymtH)_2](NO_3)_2 \cdot CH_3CN$

P. Aslanidis [a,*], S. Divanidis [a], P.J. Cox [*,b], P. Karagiannidis [a]

[a] Aristotle University of Thessaloniki, Faculty of Chemistry, Inorganic Chemistry Laboratory, P.O. Box 135, GR- 541 24 Thessaloniki, Greece
[b] School of Pharmacy, The Robert Gordon University, Schoolhill, Aberdeen AB 10 1FR, Scotland, United Kingdom

Received 22 February 2005; accepted 16 March 2005
Available online 14 April 2005

Abstract

Reaction of silver(I) nitrate with equimolar amounts of the rigid diphos ligand *trans*-1,2-bis(diphenylphosphino)ethene (*trans*-dppen) and some heterocyclic thiones (L) in acetonitrile/methanol solvent gave rise to triply-bridged coordination cages $[Ag_2(\mu_2\text{-}trans\text{-dppen})_3L_2](NO_3)_2$. On the other hand, the complexes produced when using the flexible 1,5-bis(diphenylphosphino)pentane (dpppent) turned out to be diphosphine-bridged polymers of the type $[Ag(\mu_2\text{-dpppent})(L)(ONO_2)]_n$ with the diphosphine ligand acting as bridge between two pseudo-tetrahedraly coordinated metal centres. The structures of one representative for each of the two aforementioned series of complex compounds, namely, $[Ag_2(\mu_2\text{-}trans\text{-dppen})_3(pymtH)_2](NO_3)_2$ (pymtH = pyrimidine-2-thione) and $[Ag(\mu_2\text{-dpppent})(tHpymtH)\ (ONO_2)]_n$ (tHpymtH = tetrahydropyrimidine-2-thione) have been established by single-crystal X-ray diffraction.
© 2005 Elsevier Ltd. All rights reserved.

Keywords: Silver(I) complexes; Heterocyclic thiones; 1,5-Bis(diphenylphosphino)pentane; *trans*-1,2-Bis(diphenylphosphino)ethene; Crystal structures

1. Introduction

Sulfur donors are known to be good ligands for monovalent group-11 cations [1], and the research field concerning silver(I) in sulfur-dominated coordination spheres is vast and ever expanding. Among the frequently used S-donors, the extended family of heterocyclic thioamides, are of particular interest since their metal complexes are known to have relevance to biological systems [2–4]. The coordination mode of the neutral thioamides, also known as ''thiones'', towards soft acids is virtually limited to the thione-S monodentate and bidentate (μ_2-S) types, thus the majority of the Ag(I) complexes bearing simple neutral ligands such as pyridine-2-thione or pyrimidine-2-thione are monomeric or dimeric exhibiting the common trigonal planar or tetrahedral coordination around the metal centre [5]. Our previous approach to this area involved the employment of neutral thioamide ligands in heteroleptic phosphane derivatives of Ag(I) halides or Ag(I) nitrate, whereby some examples of monomers [6,7] or symmetric dimers [8], with pseudo-tetrahedraly coordinated silver(I) have been structurally characterized. On the other hand, oligomeric or polymeric Ag(I) species can be obtained [9–11] for thioamide ligands in their thionate anionic form, generated by deprotonation. It

* Corresponding author. Tel.: +32310997694; fax: +32310997738.
E-mail addresses: p.j.cox@rgu.ac.uk (P.J. Cox), aslanidi@chem.auth.gr (P. Aslanidis).

0277-5387/$ - see front matter © 2005 Elsevier Ltd. All rights reserved.
doi:10.1016/j.poly.2005.03.009

should be noted, however, that a few silver-thione polymers of neutral pyridine-2-thione constructed on the basis of μ_2-S or μ_3-bridges, are also known [12,13].

Bidentate phosphines exhibit excellent ligating properties towards almost all transition metals [14–16] and diphosphine containing silver(I) complexes have attracted widespread attention [17]. Taking into account that the double bridging coordination mode of both diphosphines and heterocyclic thiones is quite common for univalent group-11 metal complexes, we recently introduced a series of oligomethylene-backboned diphosphines $Ph_2P(CH_2)_nPPh_2$ as a second soft donor with the aim of provoking some variability in the nuclearity of silver-thione complexes. The role of the flexibility of the bridging phosphine in controlling product selectivity in the formation of a multisilver complex is already recognized. Thus, while with long-chained flexible diphosphines, silver(I) salts with oxo-anions selectively form dinuclear (2:2) macrocycles, the rigid bis(diphenylphosphino) acetylene (dppa) gives stable cationic disilver complexes with triply-bridging diphosphine units [18,19]. On the other hand, by proper selection of thiolato ligands, novel oligonuclear structures can be constructed for Ag(I) complexes containing short bite diphosphines like bis(diphenylphosphino)methane [20]. In this context, our related work was initially devoted to silver(I) nitrate derivatives of some heterocyclic thiones containing bridging 1,2-bis(diphenylphosphino) ethane (dppe) and 1,4-bis(diphenylphosphino)butane (dppb). Interestingly, the only common feature of the two types of structures was the presence of pseudo-tetrahedraly coordinated metal centres exhibiting the same P_2S_2 donor set, since the complexes bearing the longer chained diphosphine (dppb) were found to be quadroubly bridged dimers build by a perfect combination of two kinds of bridges, whereas polymerization occurred in the case of dppe [21]. To prove the role of chain length, bulkines and flexibility of the bidentate phosphine and to gain more information concerning the effect of polymerization, we decided to include further potentially bidentate/bridging diphosphines in our studies. In this paper, we present our results on the use of the long chained 1,5-bis(diphenylphosphino)pentane (dppp) and the rigid *trans*-1,2-bis(diphenylphosphino)ethene (*trans*-dppen).

2. Experimental

2.1. Materials and instruments

Commercially available silver nitrate, *trans*-1,2-bis(diphenylphosphino)ethene (*trans*-dppen) and 1,5-bis(diphenylphosphino)pentane (dpppent) were used as received while the thiones (Merck or Aldrich) were recrystallized from hot ethanol prior to their use. All the solvents were purified by respective suitable methods and allowed to stand over molecular sieves. Infra-red spectra, molar conductivities in 10^{-3} M solutions in acetonitrile, magnetic susceptibility measurements and elemental analyses for carbon, nitrogen and hydrogen were performed as described previously [22]. Thermogravimetric analyses were performed on a SETSYS-1200 machine with DTG facility in dry nitrogen atmosphere. Sample sizes were in the range 8–10 mg and open Pt crucibles were used. The heating rate was 10°/min.

2.2. X-ray crystallographic study

Single crystals of **3** and **10** suitable for X-ray crystallographic study were grown by slow concentration of acentonitrile/methanol solutions of the compounds over several days at ambient temperature. X-ray diffraction data were collected on an Enraf-Nonius Kappa CCD area-detector diffractometer. The programs DENZO [23] and COLLECT [24] were used in data collection and cell refinement. Details of crystal and structure refinement are shown in Table 1. The structures were solved using program SIR97 [25] and refined with program SHELX-97 [26]. Molecular plots were obtained with program ORTEP-3 [27].

2.3. Synthesis of complexes *1–14*

The complexes were prepared according to the following general procedure. A suspension of silver nitrate (0.5 mmol) and 1,5-bis(diphenylphosphino)pentane or *trans*-1,2-bis(diphenylphosphino)ethene (0.5 mmol) in 20 cm^3 acetonitrile was stirred at 50 °C until a white precipitation was formed. A solution of the appropriate thione (0.5 mmol) in methanol was then added and the new suspension was stirred to clearness. The resulting solution was filtered off and the clear solution was kept at room temperature. Slow evaporation of the solvent at room temperature gave the microcrystalline solid, which was filtered off and dried in vacuo.

2.4. $[Ag(\mu\text{-dpppent})(py2SH)(NO_3)]_n$ (*1*)

Pale yellow crystals. Yield: 263 mg (73%), m.p. 177 °C; *Anal*. Calc. for $C_{34}H_{35}AgN_2O_3P_2S$: C, 56.59; H, 4.89; N, 3.88. Found: C, 56.49; H, 4.79; N, 3.76%; Λ_m (mho cm^2 mol^{-1}): 93; IR (cm^{-1}): 3452m, 3049w, 2920w, 1707s, 1601s, 1584vs, 1434vs, 1384vs, 1302vs, 1222s, 1139vs, 1098s, 1025vs, 997s, 741vs, 693vs, 617s, 512vs, 486s, 445s; UV–Vis (λ_{max}, $\log\varepsilon$): ($CHCl_3$); 260 (4.37), 289 (4.29), 361 (3.91).

2.5. $[Ag(\mu\text{-dpppent})(pymtH)(NO_3)]_n$ (*2*)

Yellow crystals. Yield: 220 mg (61%), m.p.155 °C; *Anal*. Calc. for $C_{33}H_{34}AgN_3O_3P_2S$: C, 54.86; H, 4.74;

Table 1
Crystal data and structure refinement for $[Ag(dpppent)(tHpymtH)(NO_3)]_n$ (**3**) and $[Ag_2(trans\text{-}dppen)_3(pymtH)]_2](NO_3)_2 \cdot CH_3CN$ (**10**)

	3	**10**
Chemical formula	$[C_{33}H_{38}AgN_3O_3P_2S]_n$	$C_{86}H_{76}Ag_2N_4P_6S_2.2NO_3 \cdot CH_3CN$
Formula weight	726.53 (monomer unit)	1796.26
Temperature (K)	120(2)	120(2)
Wavelength (Å)	0.71073	0.71073
Crystal system	monoclinic	orthorhombic
Space group	*C*2/*c*	*Pna*2$_1$
Unit cell dimensions		
a (Å)	36.7814(10)	31.0485(5)
b (Å)	9.5500(5)	20.5143(3)
c (Å)	18.8438(8)	13.2654(3)
α (°)	90	90
β (°)	99.209(3)	90
γ (°)	90	90
Volume (Å^3)	3529.7(7)	8449.2(3)
Z	8	4
D_{calc} (Mg/m^3)	1.477	1.412
Absorption coefficient (mm^{-1})	0.817	0.683
F (000)	2992	3680
Crystal size (mm)	0.30 × 0.28 × 0.04	0.43 × 0.30 × 0.20
θ Range for data collection (°)	3.03–27.41	3.05–27.48
Index ranges	$-46 \leqslant h \leqslant 47$, $-12 \leqslant k \leqslant 12$, $-24 \leqslant l \leqslant 24$	$-39 \leqslant h \leqslant 40$, $-20 \leqslant k \leqslant 26$, $-17 \leqslant l \leqslant 17$
Reflections collected	34188	62951
Independent reflections [R_{int}]	7393 [0.0822]	18864 [0.0461]
Completeness to θ = 27.47°	99.1%	99.6%
Maximum and minimum transmission	0.9681 and 0.7917	0.8754 and 0.7576
Refinement method	full-matrix least-square on F^2	full-matrix least-squares on F^2
Data/restrains/parameters	7393/11/478	18864/6/1038
Goodness-of-fit on F^2 (S)	1.009	1.045
Final *R* indices [(*I*) > 2σ (*I*)]	$R_1 = 0.0571$, $wR_2 = 0.1160$	$R_1 = 0.0436$, $wR_2 = 0.0911$
R indices (all data)	$R_1 = 0.1215$, $wR_2 = 0.1365$	$R_1 = 0.0655$, $wR_2 = 0.0982$
Final weighting scheme	Calc. $w = 1/[\sigma_2(F_o^2) + (0.0491P)^2 + (21.1062P)]$ where $P = (F_o^2 + 2F_c^2)/3$	Calc. $w = 1/[\sigma_2(F_o^2) + (0.0433P)^2 + (2.2006P)]$ where $P = (F_o^2 + 2F_c^2)/3$
Largest difference peak and hole (e Å^3)	0.903 and −0.953	0.926 and −0.627 (close to solvent)

N, 5.82. Found: C, 54.68; H, 4.81; N, 5.69%; Λ_m (mho cm^2 mol^{-1}): 79; IR (cm^{-1}): 3452w, 3048w, 2920m, 1707s, 1603s, 1584vs, 1482s, 1434vs, 1384vs, 1302vs, 1222s, 1178vs, 1098s, 1026s, 997s, 741vs, 693vs, 512s, 486s, 445m; UV–Vis (λ_{max}, log ε): ($CHCl_3$); 256 (4.33), 291 (3.95), 350 (3.10).

2.6. *[Ag(μ-dpppent)(tHpymtH)(NO$_3$)]$_n$ (**3**)*

Colorless crystals. Yield: 207 mg (57%), m.p. 230 °C; *Anal*. Calc. for $C_{33}H_{38}AgN_3O_3P_2S$: C, 54.55; H, 5.27; N, 5.78. Found: C, 54.27; H, 5.24; N, 5.81%; Λ_m (mho cm^2 mol^{-1}): 96; IR (cm^{-1}): 3286m, 3049w, 2939w, 1707m, 1608m, 1547vs, 1481s, 1435vs, 1384vs, 1306vs, 1207s, 1098vs, 1025s, 816s, 741vs, 695vs, 511vs, 478s, 418s; UV–Vis (λ_{max}, log ε): ($CHCl_3$); 253 (4.32), 297 (3.94).

2.7. *[Ag(μ-dpppent)(mtdztH)(NO$_3$)]$_n$ (**4**)*

Colorless crystals. Yield: 226 mg (61%), m.p. 145 °C; *Anal*. Calc. for $C_{32}H_{34}AgN_3O_3P_2S_2$: C, 51.76; H, 4.61; N, 5.66. Found: C, 52.05; H, 4.78; N, 5.76%; Λ_m (mho cm^2 mol^{-1}): 93; IR (cm^{-1}): 3453w, 3050w, 2924m, 1586s, 1482vs, 1435vs, 1385vs, 1284vs, 1197s, 1098s, 1049s, 998s, 740vs, 694vs, 511vs, 480s, 432s; UV–Vis (λ_{max}, log ε): ($CHCl_3$); 254 (4.36), 307 (4.29).

2.8. *[Ag(μ-dpppent)(mftztH)(NO$_3$)]$_n$ (**5**)*

Colorless crystals. Yield: 266 mg (67%), m.p. 249 °C; *Anal*. Calc. for $C_{33}H_{34}AgF_3N_4O_3P_2S$: C, 49.95; H, 4.32; N, 7.06. Found: C, 49.10; H, 3.99; N, 6.90%; Λ_m (mho cm^2 mol^{-1}): 104; IR (cm^{-1}): 3456w, 3051m, 2924m, 1707m, 1616m, 1483vs, 1435vs, 1384vs, 1283s, 1203s, 1149s, 1090s, 741vs, 693vs, 511s, 479m; UV–Vis (λ_{max}, log ε): ($CHCl_3$); 257 (4.38), 355 (4.09).

2.9. *[Ag(μ-dpppent)(bzoxtH)(NO$_3$)]$_n$ (**6**)*

Brownish crystals. Yield: 291 mg (75%), m.p. 135 °C; *Anal*. Calc. for $C_{36}H_{35}AgN_3O_4P_2S$: C, 56.77; H, 4.63; N, 3.68. Found: C, 57.26; H, 4.83; N, 3.71%; Λ_m (mho cm^2 mol^{-1}): 103; IR (cm^{-1}): 3440m, 3051m,

2924w, 1616m, 1515vs, 1435vs, 1385vs, 1306vs, 1255s, 1198s, 1136vs, 1096vs, 923s, 740vs, 694vs, 605s, 512vs, 482s, 424s; UV–Vis (λ_{max}, $\log\varepsilon$): ($CHCl_3$); 257 (4.21), 305 (4.22), 335 (3.16).

2.10. [Ag(μ-dpppent)(mbzimtH$_2$)(NO$_3$)]$_n$ (7)

Colorless crystals. Yield: 225 mg (58%), m.p. 152 °C; *Anal*. Calc. for $C_{37}H_{38}AgN_3O_3P_2S$: C, 57.37; H, 4.94; N, 5.42. Found: C, 56.97; H, 4.99; N, 5.34%; Λ_m (mho cm^2 mol^{-1}): 89; IR (cm^{-1}): 3435w, 3051m, 2923w, 1617s, 1520s, 1484vs, 1456vs, 1435vs, 1384vs, 1307vs, 1185s, 1098s, 1026s, 804s, 740vs, 694vs, 628s, 512vs, 479s, 430m; UV–Vis (λ_{max}, $\log\varepsilon$): ($CHCl_3$); 255 (4.37), 303 (4.37).

2.11. [Ag(μ-dpppent)(pur6SH)(NO$_3$)]$_n$ (8)

Pale yellow crystals. Yield: 263 mg (69%), m.p. 170 °C; *Anal*. Calc. for $C_{34}H_{34}AgN_5O_3P_2S$: C, 53.55; H, 4.42; N, 9.18. Found: C, 52.98; H, 4.60; N, 8.96%; Λ_m (mho cm^2 mol^{-1}): 86; IR (cm^{-1}): 3435w, 3050w, 2922w, 1709m, 1594vs, 1570vs, 1482vs, 1435vs, 1384vs, 1207vs, 1158s, 1099vs, 1025s, 999vs, 932vs, 856vs, 741vs, 694vs, 590s, 511vs, 481s, 431s; UV–Vis (λ_{max}, $\log\varepsilon$): ($CHCl_3$); 255 (4.31), 335 (4.25).

2.12. [Ag$_2$(μ-trans-dppen)$_3$(py2SH)$_2$](NO$_3$)$_2$ (9)

Pale yellow crystals. Yield: 206 mg (47%), m.p. 224 °C; *Anal*. Calc. for $C_{88}H_{76}Ag_2N_4O_6P_6S_2$: C, 60.35; H, 4.37; N, 3.20. Found: C, 59.89; H, 4.19; N, 3.16%; Λ_m (mho cm^2 mol^{-1}): 137; IR (cm^{-1}): 3446w, 3048w, 2980w, 1583vs, 1481s, 1435vs, 1384vs, 1308vs, 1186s, 1098vs, 1024s, 997vs, 741vs, 693vs, 539vs, 519vs, 493s; UV–Vis (λ_{max}, $\log\varepsilon$): ($CHCl_3$); 258 (4.34), 282 (4.22), 360 (3.20).

2.13. [Ag$_2$(μ-trans-dppen)$_3$(pymtH)$_2$](NO$_3$)$_2$ (10)

Yellow crystals. Yield: 197 mg (45%), m.p. 198 °C; *Anal*. Calc. for $C_{86}H_{74}N_6Ag_2O_6P_6S_2$: C, 58.91; H, 4.25; N, 4.79. Found: C, 58.69; H, 4.57; N, 4.58%; Λ_m (mho cm^2 mol^{-1}): 124; IR (cm^{-1}): 3445w, 3050w, 2861w, 1600s, 1574vs, 1479vs, 1434vs, 1384vs, 1327vs, 1214s, 1177vs, 1096s, 1026s, 975s, 794m, 743vs, 694vs, 506vs, 488vs, 463s, 335m; UV–Vis (λ_{max}, $\log\varepsilon$): ($CHCl_3$); 262 (4.30), 286 (4.27), 370 (3.18).

2.14. [Ag$_2$(μ-trans-dppen)$_3$(tHpymtH)$_2$](NO$_3$)$_2$ (11)

White crystals. Yield: 247 mg (56%), m.p. 256 °C; *Anal*. Calc. for $C_{86}H_{82}N_6Ag_2O_6P_6S_2$: C, 58.64; H, 4.69; N, 4.77. Found: C, 58.01; H, 4.49; N, 4.54%; Λ_m (mho cm^2 mol^{-1}): 121; IR (cm^{-1}): 3060w, 1564vs, 1480vs, 1435vs, 1384vs, 1296vs, 1220vs, 1157vs, 1096vs, 1025vs, 998s, 918s, 812s, 742vs, 692vs, 508vs, 465vs, 416s, 350m; UV–Vis (λ_{max}, $\log\varepsilon$): ($CHCl_3$); 254 (4.32), 279 (3.97), 351 (2.17).

2.15. [Ag$_2$(μ-trans-dppen)$_3$(bzoxtH)$_2$](NO$_3$)$_2$ (12)

Braunish crystals. Yield: 256 mg (56%), m.p. 210 °C; *Anal*. Calc. for $C_{92}H_{76}N_4Ag_2O_8P_6S_2$: C, 60.33; H, 4.18; N, 3.06. Found: C, 59.87; H, 4.18; N, 2.99%; Λ_m (mho cm^2 mol^{-1}): 126; IR (cm^{-1}): 3438w, 3051w, 1615m, 1515s, 1479s, 1435vs, 1384vs, 1308s, 1257vs, 1182s, 1138vs, 1097vs, 1026s, 925s, 742vs, 694vs, 507s, 491s, 423s; UV–Vis (λ_{max}, $\log\varepsilon$): ($CHCl_3$); 252 (4.32), 272 (3.15), 355 (2.98).

2.16. [Ag$_2$(μ-trans-dppen)$_3$(mtdztH)$_2$](NO$_3$)$_2$ (13)

White crystals. Yield: 233 mg (52%), m.p. 221 °C; *Anal*. Calc. for $C_{84}H_{74}N_6Ag_2O_6P_6S_4$: C, 56.25; H, 4.16; N, 4.68. Found: C, 56.01; H, 4.10; N, 4.67%; Λ_m (mho cm^2 mol^{-1}): 122; IR (cm^{-1}): 3445w, 3050w, 1640s, 1552s, 1480vs, 1435vs, 1384vs, 1308vs, 1197s, 1097vs, 1058vs, 998s, 812m, 741vs, 693vs, 509vs, 476s, 432s, 344m; UV–Vis (λ_{max}, $\log\varepsilon$): ($CHCl_3$); 251 (4.11), 307 (4.02), 341 (2.87).

2.17. [Ag$_2$(μ-trans-dppen)$_3$(mftztH)$_2$](NO$_3$)$_2$ (14)

White crystals. Yield: 270 mg (57%), m.p. 249 °C; *Anal*. Calc. for $C_{86}H_{74}N_8Ag_2F_6O_6P_6S_2$: C, 54.50; H, 3.93; N, 5.91. Found: C, 53.91; H, 4.08; N, 5.75%; Λ_m (mho cm^2 mol^{-1}): 115; IR (cm^{-1}): 3.362 w, 3174w, 2965w, 1560vs, 1435vs, 1384vs, 1310vs, 1221vs, 1096s, 997s, 811m, 752s, 742vs, 694vs, 509vs, 479s, 416s; UV–Vis (λ_{max}, $\log\varepsilon$): ($CHCl_3$); 250 (4.40), 298 (4.19).

3. Results and discussion

3.1. Preparative considerations

Before discussing the experimental results, we should point out that both, 1,5-bis(diphenylphosphino)pentane (dpppent) and *trans*-1,2-bis(diphenylphosphino)ethene (*trans*-dppen) showed a marked preference for the formation of macrocycles in their reactions with Cu(I), in the presence of heterocyclic thione ligands [28–30], whereas *cis*-1,2-bis(diphenylphosphino)ethene yielded predominantly chelated monomeric species [31].

The reaction between equimolar quantities of silver(I) nitrate and 1,5-bis(diphenylphosphino) pentane (dpppent) followed by the addition of one equivalent of the apropriate thione (L) [L = pyridine-2-thione (py2SH), pyrimidine-2-thione (pymtH), tetrahydropyrimidine–thione (tHpytH), 5-methyl-1,3,4-thiadiazole-2-thione

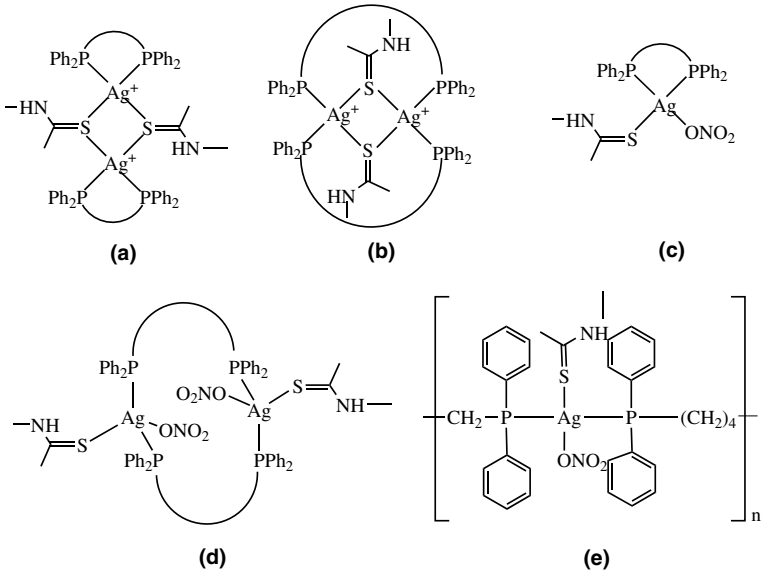
(mtdztH), benz-1,3-oxazoline-2-thione (bzoxtH), 5-methyl-benz-1,3-imidazole-2-thione (mbzimtH_2), 4-methyl-5-trifluoromethyl-4H-1,2,4-triazoline-3(2H)-thione (mftztH), and 6-mercaptopurine (pur6SH) in dry acetonitrile/methanol solution at 30 °C afforded microcrystalline solids which, on analysis were found to be of composition [$AgNO_3$(dpppent)L] (compounds **1**–**8**).

According to our previous experience with thione/phosphine complexes of Ag(I) nitrate, Ag^+ tends to adopt a tetrahedral coordination whith the counterion kept outside the coordination sphere, despide its strong coordination ability. Within the meaning of this criterion, two structures (structures **a** and **b**, Scheme 1) come into question that reproduce the above given stoichiometry.

On the other hand, if the coordination of the nitrate anion is weak, the formation of a monomeric, dimeric or polymeric complex (structures **c**–**e**, respectively), could be possible, but formation of **c** is unlikely as it is less compatible with the stereochemical characteristics of the long-chained diphosphine applied. Indeed, the structure determination of the tetrahydropyrimidine-2-thione complex (compound **3**) by X-ray diffraction confirmed compounds **1**–**8** to be coordination polymers of type [Ag(μ-dpppent)(L)(ONO_2)]$_n$.

In general, diphosphines bearing a long-chained flexible backbone, are expected to bridge metal centres forming dimeric macrocycles of type [M(diphos)$_2$M] rather than polymeric adducts, the later being continuously favoured upon decreasing the diphosphine chain length. Indeed, the ability of 1,5-bis(diphenylphosphino)pentane to serve as a bridge between two metal centres in monovalent coinage metal complexes is well documented, among others in a recent publication of Pettinari and co-workers [32], where the flexible diphosphine was shown to predominantly form dimers of type [M(μ-dpppent)(μ-X)]$_2$ (M = Cu, Ag and X = Br, I). Likewise, treating an acetonitrile solution of Cu(I) chloride with stoichiometric amounts of dpppent and a heterocyclic thione ligand, the complexes formed were of the formula [CuCl(dpppent)L], whereby the thione-free dimer [Cu(μ-dpppent)(μ-Br)]$_2$ was found to be the only product of the analogous reactions when copper(I) bromide was used [30]. Consequently, the formation of the polymers under investigation was considered as unpredictable with respect to the geometrical features of the diphos ligand applied. Moreover, it contrasted, regarding the stoichiometric composition of the products formed, with the findings of our recent work on analogous $AgNO_3$ compounds, where the use of 1,2-bis(diphenylphosphino)ethane (dppe) afforded polymers of general formula [Ag(dppe)(L)$_2$]$_n$(NO_3)$_n$ [21], with the latter containing ionic outer-sphere nitrate groups. Thus, following the same procedure, we repeated the reactions using the apropriate thione in a twofold excess, aiming to attain cationic complexes, but we obtained once more compounds **1**–**8**. Likewise, we treated compounds **1**–**8** with two equivalents of an apropriate thione per formula unit, however the products isolated in all the cases turned out to be once more the polymeric complexes initially used as starting materials.

The second series of mixed ligand complexes obtained on treating silver(I) nitrate with equimolar quantities of *trans*-1,2-bis(diphenylphosphino)ethene (*trans*-dppen) and the same set of heterocyclic thiones was of the composition [($AgNO_3$)$_2$(*trans*-dppen)$_3$(L)$_2$]. On the basis of the above composition it was presumed that these compounds could be phosphine-bridged dinuclear cages. This was indeed found for six of the thiones applied (compounds **9**–**14**), but not for mbzimtH_2 or



Scheme 1.

pur6SH, where the reaction, carried out under the same experimental conditions as usual, gave in both cases a powder of uncertain stoichiometry.

Complexes **1**–**14** are diamagnetic, air stable, microcrystalline solids, only slightly soluble in common organic solvents. In accordance with their polymeric nature, the molar conductivities of complexes containing dpppent (compounds **1**–**8)** in dry acetonitrile solutions are somewhat lower than those of the dinuclear compounds **9**–**14**, but still fairly high to suggest complete ionization in solution.

3.2. Spectroscopic characterization

The solid state FT-IR spectra of complexes **1**–**14**, recorded in the range 4000–250 cm^{-1} provide useful information regarding the mode of thione ligand coordination. They show the disappearance of the S–H stretching band around 2560 cm^{-1} due to the "free" ligands and the presence of the ν(NH) band in the 3190–3230 cm^{-1} region, suggesting M–S bond formation. Moreover, they contain all of the bands required by the presence of heterocyclic thioamides occurring in their thione form, with shifts indicating the exclusive S-coordination mode of these ligands. Further, they show all the expected strong phosphine bands, which remain practically unshifted upon coordination. The asymmetric N–O stretching mode (ν_1) of the NO_3 anion appears as a band of medium intensity in the 1375–1285 cm^{-1} range, in some cases not recognizable because of overlapping with strong absorptions due to the thione and phosphine ligands. Unfortunately, nothing certain can be stated about the coordination mode of the nitrate ion since the thione ligands strongly absorb in the regions where the bands associated with coordinated nitrate occur.

The electronic absorption spectra of the complexes in chloroform solutions appear to be mainly of intraligand character, consisting of two intense sharp bands in the 250–260 and 282–307 nm regions, as well as an additional rather broad band with maximum at 335–370 nm. The first two bands can be attributed to intraligand $\pi^* \leftarrow \pi$ transitions on the phenyl group of the phosphine ligands, since the uncoordinated 1,5-bis(diphenylphosphino)pentane and *trans*-1,2-bis(diphenylphosphino) ethene both reveal two strong absorptions at 259 and 287.5 nm and 258.5 and 296 nm, respectively, which are known to undergo small shifts upon coordination to Ag(I). The lower energy band lies in the region where the free thiones absorb, expressing a small red shift as a consequence of the coordination to Ag(I) and should be, therefore, considered as a thione-originating intraligand transition which possess some MLCT character [33,34] (Fig. 1).

3.3. Thermal decomposition

Thermal analysis in nitrogen atmosphere shows the complexes **1**–**8** decompose in three or four stages. Fig. 2 illustrates TG and DTA data curves for the polymeric $[Ag(NO_3)(dpppent)(tHpymtH)]_n$ (compound **3**). The three low temperature initial stages involve a weak endothermic and a very strong exothermic effect in the temperature range 240–360 °C and are connected with an overall weight loss of ~16% which is consistent with gradually thermal breakdown of the tetrahydropyrimidine-2-thione ligand. Note that the very strong exothermic effect is an attribute of the decomposition of complexes bearing non-aromatic thione ligands, whereby the corresponding DTA courve in the case of aromatic thione compounds allways show endothermic events instead.

The observed mass loss (~67%) in the final, slightly endothermic stage, show excellent agreement for simultaneous loss of the diphosphine molecule and conversion of the resultant silver nitrate to Ag_2O under NO_2 evolution. However no clear distinction between these

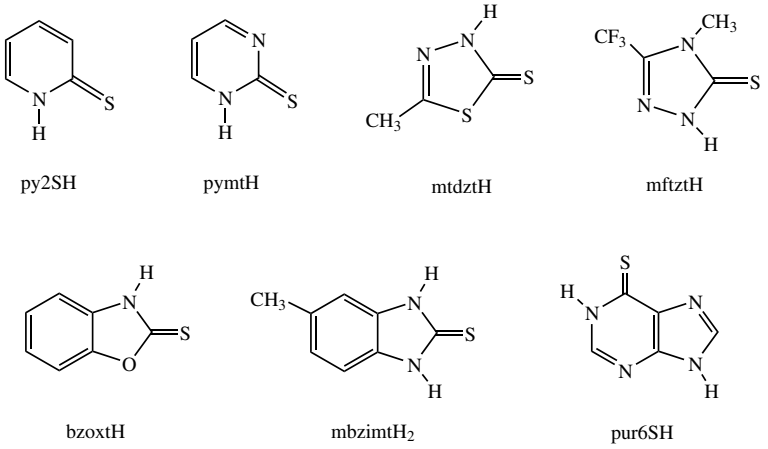


Fig. 1. The heterocyclic thione ligands used with their abbreviations.

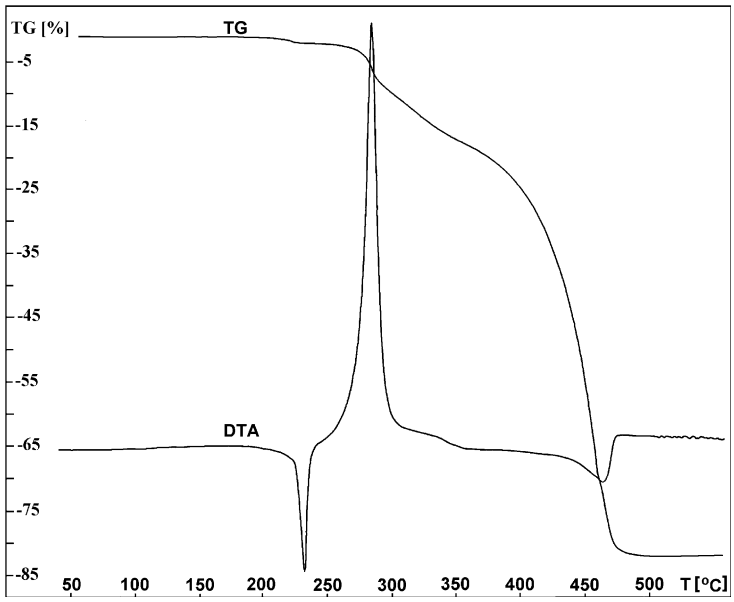


Fig. 2. TG and DTG curves for compound **3**.

two processes can be made, thus this stage must be somewhat complicated in character.

Complexes **9**–**14** show an analogous decomposition patern but they are in general thermally less stable, decomposition being usually completed at 450 °C. Noticeable is the particular short final stage, that extends over a temperature range of only 60 °C. In the majority of the cases solvent retention occurs at the temperature of 190 °C indicated by a strong exothermic effect connected with a weight loss corresponding to one molecule of CH_3CN per formula unit.

3.4. Crystal structures

Colorless crystals of **3** suitable for X-ray were obtained by slow evaporation of a CH_3CN/CH_3OH solution of the compound. The complex crystallizes in the monoclinic space group *C*2/*c*, with eight monomer units in the unit cell. Details regarding the crystal data collection and refinement for the complex are reported in Table 1. Bond lengths and angles around the Ag(I) are listed in Table 2. Fig. 3 shows the monomeric unit of the complex with the labelling of the atoms, and Fig. 4 the resultant polymer. The structure is substantially disordered, with each of the individual components of the monomeric entity being affected in some degree. Four of the five carbon atoms (C5–C8) in the pentane chain are disordered over two sites, whereas disorder in the thione ligand involves three carbons (C3–C5). Similarly the three oxygen atoms in the NO_3 ion are highly disordered. Moreover, there are high displacement parameters associated with an aryl group attached to P2, which had to be restricted to a hexagon with ideal bond lengths and angles.

Complex **3** is a coordination polymer consisting of Ag(I) cations linked through the phosphorous atoms of the 1,5-bis(diphenylphosphino)pentane ligand. Each silver nucleus completes the familiar tetrahedral coordination environment considering the S-atom from the tetrahydropyrimidine-2-thione ligand, one O-atom from the weakly coordinated nitrate anion and the two bridging P-atoms belonging to two different diphosphine units. The repeating unit extends into an infinite one-dimensional chain formed by linking Ag and P1 atoms by unit cell translations along the *b* axis, in which the tetrahydropyrimidine-thione units are ordered in a *syn* configuration.

Table 2
Selected bond lengths (Å) and angles (°) for **3**

Bond lengths (Å)			
Ag–P(2)	2.4541(14)	P(1)–C(9)	1.837(5)
Ag–P(1)[a]	2.4666(14)	P(2)–C(5B)	1.70(3)
Ag–S(1)	2.5623(15)	N(3)–O(1A)	1.232(9)
Ag–O(1A)	2.535(8)	N(3)–O(2A)	1.148(8)
S(1)–C(1)	1.712(6)	N(3)–O(3A)	1.227(9)
Bond angles (°)			
P(2)–Ag–P(1)[a]	132.75(5)	P(1)[a]–Ag–O(1A)	99.7(2)
P(2)–Ag–S(1)	110.07(6)	Ag–S(1)–C(1)	113.92(19)
P(1)[a]–Ag–S(1)	108.25(6)	O(2A)–N(3)–O(1A)	120.7(9)
P(2)–Ag–O(1A)	103.6(3)	O(2A)–N(3)–O(3A)	125.2(9)
S(1)–Ag–O(1A)	94.64(18)	O(3A)–N(3)–O(1A)	113.9(8)
Hydrogen bridges			
O(1A)···N(1)	2.721(9)	N(1)–H(1)	0.88
O(1A)···H(1)	1.90	O(1A)···H(1)–N(1)	155°
O(2A)[b]···N(2)	3.034(11)	N(2)–H(2)	0.88
O(2A)[b]···H(2)	2.23	O(2A)[b]···H(2)–N(2)	153°

[a] Atom coordinates transposed by $x, y-1, z$.
[b] Atom coordinates transposed by $x, -2-y, 0.5+z$.

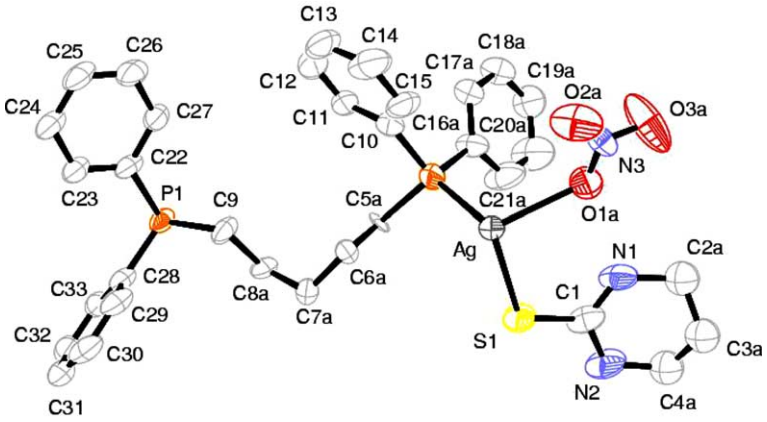


Fig. 3. The monomeric unit [Ag(μ-dpppent)(tHpymtH)(ONO_2)] of **3** with atom labels (disorder removed). Displacement ellipsoids are shown in the 50% probability level.

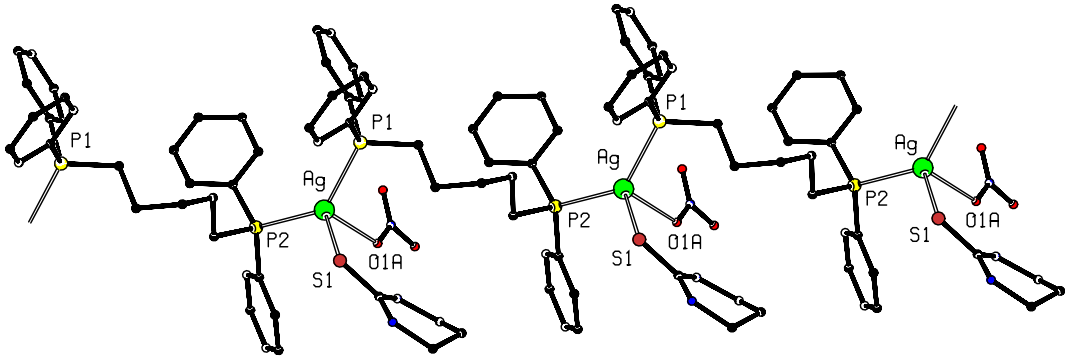


Fig. 4. A view of the polymeric chain [Ag(dpppent)(tHpymtH)(NO_3)]$_n$ with hydrogen atoms removed for clarity. Displacement ellipsoids are shown at the 50% probability level.

Considering the angles involving the central metal atom, there are considerable distortions from the ideal tetrahedral geometry, the most remarkable being the P(1)#−Ag–P(2) angle, with a large value of 132.75(5)° which can be partly accounted for the steric hindrance induced by the bulky phenyl-rings of the two phosphine units, but probably also for the presence of the weakly coordinated nitrate. Namely, the weak anion-cation interaction, indicated by the large Ag–O distance of 2.535(8) Å, is associated with angles involving the coordinated nitrate oxygen-atom that are less than the ideal tetrahedral value of 109.4°, thus allowing an appropriate opening up of the angle between the sterically demanding groups. Another remarkable feature in the structure of **3** is the quite large Ag–S–C angle of 113.92(19)°, which may be attributed to the presence of a strong hydrogen N–H···O bridge (Table 2).

The Ag–S bond distance of 2.5623(15) Å, coincident with the sum of the corresponding atomic radii, is typical for this bonding arrangement. Likewise, the two Ag–P distances lie within the limits of 2.426–2.504 Å found for a number of complexes containing tetracoordinated silver atoms bonded to two phosphorus atoms [35,36] and vary little [Ag(1)–P(1) = 2.4501(5), [Ag(1)– P(2) = 2.4658(5) Å]. Finally, the geometrical characteristics of the tetrahydropyrimidine-thione ligand, where the sex-membered ring adopts an envelope conformation, are not altered noticeable upon coordination.

Compound **10** crystallizes in the orthorhombic space group *Pna2*$_1$, with 4 discrete molecules in the unit cell as well as four lattice CH_3CN molecules. Main bond lengths and angles are given in Table 3 and a perspective drawing showing the atom numbering is shown in Fig. 5.

The crystal structure of **10** is built by dinuclear units in which the two tetrahedral silver centres are linked by three bridging diphosphine units, whereby the fourth position of each tetrahedron is occupied by the S-atom of a thione unit. Interestingly, the two thione rings are almost parallel to each other adopting a relative *cis* orientation. Each of the two nitrate anions is placed near to a thione unit and is adjusted to its nitrogen-bound hydrogen atom via hydrogen bonding interactions (see Table 3). Furthermore, each of these counterions is close

Table 3
Selected bond lengths (Å) and angles (°) for **10**

Bond lengths (Å)			
Ag(1)–P(1)	2.4979(14)	P(2)–C(13)	1.804(4)
Ag(1)–P(2)	2.5131(11)	P(3)–C(11)	1.813(4)
Ag(1)–P(3)	2.5211(13)	P(4)–C(10)	1.808(4)
Ag(1)–S(1)	2.5660(10)	P(5)–C(12)	1.808(4)
Ag(2)–P(5)	2.5123(12)	P(6)–C(14)	1.810(4)
Ag(2)–P(4)	2.5370(12)	O(1)–N(5)	1.264(7)
Ag(2)–P(6)	2.5379(11)	O(2)–N(5)	1.236(6)
Ag(2)–S(2)	2.5923(10)	O(3)–N(5)	1.253(5)
S(1)–C(1)	1.693(4)	O(4)–N(6)	1.191(6)
S(2)–C(5)	1.689(4)	O(5)–N(6)	1.247(8)
P(1)–C(9)	1.825(4)	O(6)–N(6)	1.332(7)
Bond angles (°)			
P(1)–Ag(1)–P(2)	111.56(4)	P(4)–Ag(2)–S(2)	110.82(4)
P(1)–Ag(1)–P(3)	113.12(4)	P(6)–Ag(2)–S(2)	101.48(3)
P(2)–Ag(1)–P(3)	100.39(4)	C(1)–S(1)–Ag(1)	102.78(13)
P(1)–Ag(1)–S(1)	109.69(4)	C(5)–S(2)–Ag(2)	103.60(14)
P(2)–Ag(1)–S(1)	104.65(3)	O(2)–N(5)–O(3)	123.1(5)
P(3)–Ag(1)–S(1)	116.71(4)	O(2)–N(5)–O(1)	119.9(4)
P(5)–Ag(2)–P(4)	111.00(4)	O(3)–N(5)–O(1)	117.1(5)
P(5)–Ag(2)–P(6)	114.65(4)	O(4)–N(6)–O(5)	124.0(7)
P(4)–Ag(2)–P(6)	108.78(4)	O(4)–N(6)–O(6)	119.3(7)
P(5)–Ag(2)–S(2)	109.75(5)	O(5)–N(6)–O(6)	116.6(5)
Hydrogen bridges			
O(2)[a]···N(2)	2.831	N(2)–H(2)	0.88
O(2[a])···H(2)	1.956	O(2)[a]···H(2)–N(2)	173°
O(1)[a]···N(2)	3.063		
O(1)[a]···H(2)	2.539	O(1)[a]···H(2)–N(1)	119
O(3)[b]···N(4)	2.871	N(4)–H(4)	0.88
O(3)[b]···H(4)	2.018	O(3)···H(4)–N(4)	163°
O(1)[b]···N(4)	3.102		
O(1)[b]···H(4)	2.532	O(1)[b]···H(4)–N(4)	123

[a] Atom coordinates transposed by $-x+1, -y+1, z+0.5$.
[b] Atom coordinates transposed by $-x+1, -y, z+0.5$.

to a lattice CH_3CN molecule, which will not be further discussed as there is no evidence of any specific interaction involving this latter solvent molecule. One of the nitrate ions is hydrogen bonded to both thione units (Fig. 6). As well as the N–H···O bonds (Fig. 6, Table 3) there is also evidence of N–H···N interactions.

trans-1,2-Bis(diphenylphosphino)ethene (*trans*-dppen) is well known to serve as a phosphorus(σ) donor bridge between metal centres in coordination compounds [28,29,37,38]. However, in view of the rigidity of the diphosphine backbone, the formation of the three-fold bridging motif realized in the complex under discussion should be considered as quite strained, the more so as this rigidity is accompanied with a remarkable accumulation of stericaly demanding Ph_2PCH_2-units around the metal centres. Nevertheless, some related triply bridged $[M_2L_3]$ complexes with rigid bridging diphosphines such as $Ph_2P{-}C{\equiv}C{-}PPh_2$ [39] and $Ph_2P{-}C{\equiv}C{-}C{\equiv}C{-}PPh_2$ [40] have been characterised in the solid state. Among the Ag(I) complexes, this cage structure is known to exist, with no terminal ligands and thus with trigonal coordination of the two metal atoms, in the triply-bridged disilver helical complexes $[Ag_2(\mu_2\text{-dppa})_3]^{2+}$

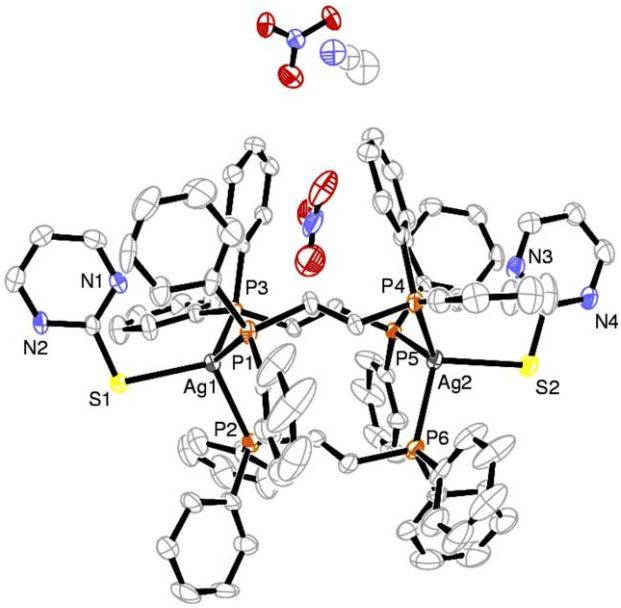


Fig. 5. A view of $[Ag_2(\textit{trans}\text{-dppen})_3(tHpymtH)_2](NO_3)_2 \cdot CH_3CN$ (**10**) with hydrogen atoms and disorder removed for clarity. Displacement ellipsoids are shown at the 50% probability level.

bearing the rigid bis-(diphenylphosphino)acetylene (dppa) [19]. Some examples of such cages with more or less strong anion–cation interactions, thus exhibiting tetrahedrally coordinated Ag(I) centres have been also reported recently [41]. Further related $[Ag_2L_3]$ complexes involve 2,6-bis(diphenylphosphino)pyridine [42], 3,6-bis(diphenylphosphino)pyridazine [42] and 2,9-bis(diphenylphosphino)-1,8-naphthyridine [43]. With *trans*-dppen, evidence for the formation of discrete $[Ag_2L_3]$ cages was found in solution, although, on crystallization, only the corresponding ring-opened polymeric structures could be obtained [41].

The geometrical characteristics of the structure under investigation generally refer to those of other silver(I) complexes tetrahedrally coordinated by phosphine and thione ligands. There are six different Ag–P bond distances around the two Ag(I) centres, each of them within the limits expected for a complex containing a tetracoordinated silver atom bearing phosphorus and sulfur donor ligands [44]. Likewise the two Ag–S distances [2.5660(10) and 2.5923(10) Å] are typical for this type of ligation. Interestingtly, the formation of the $Ag(PP)_3Ag$ cage does not require significant conformational rearrangements on the part of the diphosphine ligands; upon coordination the two P atoms of each diphosphine unit twist about the ethene bridge altering the dihedral angle through the four atoms by about 8°, taken as the average of the torsion angles P(1)–C(9)–C(10)–P(4), P(3)–C(11)–C(12)–P(5) and P(2)–C(13)–C(14)–P(6), with respect to the corresponding value (176.6°) in the free *trans*-dppen [45], thus only moderately modifying the bite size of the diphosphine.

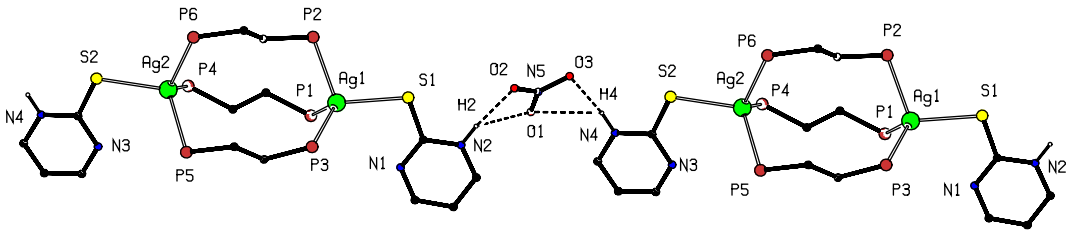


Fig. 6. Plot showing the N–H···O hydrogen bonds linking a nitrate ion to two thione units. Phenyl rings and hydrogen atoms are removed for clarity.

4. Conclusion

Two series of heterocyclic thione ligated silver(I) nitrate complexes in which Ag(I) centres are bridged either by 1,5-bis(diphenylphosphino)pentane or *trans*-1,2-bis(diphenylphosphino)ethene have been prepared and spectroscopically characterised. The complexes bearing the former long chained dpppent contain weakly coordinated nitrate groups and are polymeric. This contrast with the hitherto observed coordination behaviour of this flexible diphos ligand, since the majority of its univalent group I_B metal complexes are dinuclear macrocycles. Likewise as non-predictable should be considered the behaviour of the rigid bridging ligand *trans*-dppen, which is known to preferably form dinuclear macrocycles, as it favours in the present case the selective formation of triply bridged disilver derivatives, indepentend from the metal-to-ligand ratio applied. These results clearly demonstrate that factors other than the chain length, flexibility or stereochemical constrains between bulky groups on the part of the bridging ligand additionally play an important role in determining the structure being formed in each case. In this context, at least the effect of polymerization observed seems to be of particular interest and will be, therefore, object of more extensive studies.

5. Supplementary material

CCDC- 263254 (**3**) and CCDC-263255 (**10**) contain the supplementary crystallographic data for this paper. These data can be obtained free of charge at www.ccdc.cam.ac.uk/conts/retrieving.html [or from the Cambridge Crystallographic Data Centre, 12, Union Road, Cambridge CB2 1EZ, UK; fax: (internat.) +44-1223/336-033; e-mail: deposit@ccdc.cam.ac.uk].

Acknowledgements

We thank the EPSRC X-ray crystallography service at the University of Southampton for collecting the X-ray data.

References

[1] H. Sigel, V.M. Rheinberger, B.E. Fischer, Inorg. Chem. 18 (1979) 3334.
[2] R.H. Holm, E.I. Solomon, Chem. Rev. (1996) 96.
[3] J.A. Garcia-Vazquez, J. Romero, A. Sousa, Coord. Chem. Rev. 193–195 (1999) 691, and references therein.
[4] P.D. Akrivos, Coord. Chem. Rev. 181–210 (2001) 213.
[5] (a) E.S. Raper, Coord. Chem. Rev. 61 (1985) 115;
(b) G. Giusti, G. Geier, A. Currao, R. Nesper, Acta Cryst. C 52 (1996) 1914.
[6] P. Karagiannidis, P. Aslanidis, S. Kokkou, C.J. Cheer, Inorg. Chim. Acta 172 (1990) 247.
[7] W. McFarlane, P.D. Akrivos, P. Aslanidis, P. Karagiannidis, C. Hatzisymeon, M. Numan, S. Kokkou, Inorg. Chim. Acta 281 (1998) 121.
[8] P.J. Cox, P. Aslanidis, P. Karagiannidis, S. Hadjikakou, Inorg. Chim. Acta 310 (2000) 268.
[9] P.A. Perez-Jourido, J.A. Garcia-Vazquez, J. Romero, M.S. Louro, A. Sousa, Q. Chen, Y. Chang, J. Zubieta, J. Chem. Soc., Dalton Trans. (1996) 2047.
[10] L. Zhang, H.-X. Zhang, C.-L. Chen, L.-R. Deng, B.-S. Kang, Inorg. Chim. Acta 355 (2003) 49.
[11] I.C. Dance, L.J. Fitzpatrick, A.D. Rae, M.L. Scudder, Inorg. Chem. 22 (1983) 3785.
[12] W. Su, M. Hong, J. Weng, Y. Liang, Y. Zhao, R. Cao, Z. Zhou, A.S.S. Chan, Inorg. Chim. Acta 331 (2002) 8.
[13] W. Su, R. Cao, M. Hong, W.-T. Wong, J. Lu, Inorg. Chem. Commun. 2 (1999) 241.
[14] C.A. McAuliffe, W. Levason, Phosphine, Arsine and Stibine Complexes of the Transition Elements, Elsevier, Amsterdam, 1979.
[15] R.J. Puddephatt, Chem. Soc. Rev. (1983) 99.
[16] B. Chaudret, B. Delavaux, R. Poilblanc, Coord. Chem. Rev. 86 (1988) 191.
[17] Effendy, C. di Nicola, M. Fianchini, C. Pettinari, B.W. Skelton, N. Somers, A.H. White, Inorg. Chim. Acta 358 (2005) 748.
[18] S.L. James, E. Lozano, M. Nieuwenhuyzen, Chem. Commun. (2000) 617.
[19] E. Lozano, M. Nieuwenhuyzen, S.L. James, Chem. Eur. J. (2001) 2644.
[20] L. Zhang, H.-X. Zhang, C.-L. Chen, L.-R. Deng, B.-S. Kang, Inorg. Chim. Acta 355 (2003) 49.
[21] P. Aslanidis, P.J. Cox, S. Divanidis, P. Karagiannidis, Inorg. Chim. Acta 357 (2004) 2677.
[22] P. Karagiannidis, S.K. Hadjikakou, P. Aslanidis, A. Hountas, Inorg. Chim. Acta 178 (1990) 27.
[23] Z. Otwinowski, W. Minor, Methods in enzymology, in: C.W. Carter Jr., R.M. Sweet (Eds.), Macromolecular Crystallography, vol. 276, Academic Press, 1997, Part A, p. 307.
[24] R. Hooft, COLLECT Data Collection Software, Nonius B.V., 1998.
[25] A. Altomare, M.C. Burla, M. Camalli, G.L. Cascarano, C. Giacovazzo, A. Guagliardi, A.G.G. Moliterni, G. Polidori, R. Spagna, J. Appl. Cryst. 27 (1994) 434.

[26] G.M. Sheldrick, SHELXL-97. Program for Crystal Structure Analysis (Release 97-2), University of Goettingen, Germany, 1997.
[27] L.J. Farrugia, J. Appl. Crystallogr. 30 (1977) 565.
[28] P. Aslanidis, P.J. Cox, S. Divanidis, P. Karagiannidis, Inorg. Chim. Acta 357 (2004) 4231.
[29] S. Divanidis, P.J. Cox, P. Karagiannidis, P. Aslanidis, Polyhedron 24 (2004) 351.
[30] S. Divanidis, PhD Thesis, University of Thessaloniki, 2004.
[31] P. Aslanidis, P.J. Cox, S. Divanidis, P. Karagiannidis, Inorg. Chim. Acta 357 (2004) 1063.
[32] Effendy, C.D. Nicola, M. Fianchini, C. Pettinari, B.W. Skelton, N. Somers, A.H. White, Inorg. Chim. Acta 358 (2005) 763.
[33] A.A. Del Paggio, D.R. McMillin, Inorg. Chem. 22 (1983) 691.
[34] C. Kutal, Coord. Chem.Rev. 99 (1990) 213.
[35] D. Coucouvanis, N.C. Benzinger, S.M. Johnson, Inorg. Chem. 13 (1974) 1191.
[36] D.D. Heinrich, J.P. Fackler Jr., P. Lahuerta, Inorg. Chim. Acta 116 (1986) 15.
[37] W. Oberhauser, T. Stampfl, C. Bachmann, R. Haid, C. Langes, H. Kopacka, K.-H. Ongania, P. Brüggeller, Polyhedron 19 (2000) 913.
[38] G.B. Jacobsen, B.L. Shaw, M. Thornton-Pett, J. Organomet. Chem. 323 (1987) 313.
[39] G. Hogarth, T. Norman, Polyhedron 15 (1996) 2859.
[40] M. Semmelmann, D. Fenske, J.F. Corrigan, J. Chem. Soc. Dalton Trans. (1998) 2541.
[41] E. Lozano, M. Nieuwenhuyzen, S.L. James, Chem. Eur. J. 7 (2001) 2644.
[42] S.-M. Kuang, L.-M. Zhang, Z.Z. Zhang, B.-M. Wu, C.W. Mak, Inorg. Chim. Acta 284 (1999) 278.
[43] V.J. Catalano, H.M. Kar, B.L. Bennett, Inorg. Chem. 39 (2000) 121.
[44] W. McFerlane, P.D. Akrivos, P. Aslanidis, P. Karagiannidis, C. Hatzisymeon, M. Numan, S. Kokkou, Inorg. Chim. Acta 281 (1998) 121.
[45] H. Schmidbaur, G. Reber, A. Schier, F.E. Wagner, G. Müller, Inorg. Chim. Acta 147 (1988) 143.

Available online at www.sciencedirect.com
SCIENCE DIRECT®
Polyhedron 24 (2005) 865–871
POLYHEDRON
www.elsevier.com/locate/poly

Synthesis and X-ray crystal structures of dinuclear hydrogen-bonded cadmium and lead 2-aminoethanethiolates

Mohan S. Bharara [1], Chong H. Kim, Sean Parkin, David A. Atwood *

Department of Chemistry, University of Kentucky, Lexington, KY 40506, USA

Received 31 August 2004; accepted 27 January 2005
Available online 25 April 2005

Abstract

Under varying conditions the reaction of cysteamine hydrochloride ($SHCH_2CH_2NH_3$)Cl with stoichiometric amounts of Cd and Pb salts in water gave $[Cd_{2.5}Cl_5(SCH_2CH_2NH_3)]$ (**1**), $[Cd(SCH_2CH_2NH_2)_2]$ (**2**), $[Pb_2Cl(SCH_2CH_2NH_2)_3]$ (**3**) and $[Pb_2(SCH_2CH_2NH_2)_3](NO_3)_{0.67}(Cl)_{0.33}$ (**4**). Compound **1** is a molecular solid, one that contains a solid state-like core, but is nevertheless soluble in common organic solvents. The geometry around the Cd atoms in **1** are octahedral with varying numbers of sulfur and chlorine atoms. In contrast the pentacoordinate Cd atoms in **2** possess distorted square pyramidal geometry comprised of cysteamine sulfur and nitrogen atoms. Compounds **3** and **4** are structurally similar despite the presence and involvement of the anion in **4**. The Pb atoms in **3** possess both distorted square pyramidal and octahedral geometry, while in **4** the geometry around the Pb atoms is distorted square pyramidal. The NO_3 and Cl anions in **4** participate in more extensive hydrogen bonding by comparison to **3**, which has a Cl anion only. The hydrogen bonding in these compounds is not confined to the presence or absence of anions, as it is also observed between the amine of cysteamine with adjacent sulfur and nitrogen atoms. Full characterization of the compounds was achieved using IR, ^{1}H NMR, ^{13}C NMR, EA, Mass Spectrometry and X-ray crystallography.
© 2005 Elsevier Ltd. All rights reserved.

Keywords: Cadmium; Lead; 2-Aminoethanethiolate; Intermolecular hydrogen-bonding

1. Introduction

Cysteamine (2-aminoethanethiol, $SHCH_2CH_2NH_2$) may be considered a derivative of either cysteine ($HSCH_2CH(NH_2)COOH$) or Penicillamine ($SH(CH_3)_2CCH(NH_2)COOH$) and its chemistry with transition metals has been studied extensively. The compounds may be used as alkylating agents and as a radiation protectant [1]. Mononuclear and polynuclear complexes of Ni(II) with cysteamine were the first reported examples [2]. Since then a wide range of metal complexes with various stoichiometries have been reported [3,4]. These are of the formula: M_xL_y ($x = 3$–6, $y = 4$–12, L = cysteamine and M = Au^+, $Cu^{1+/2+}$, Cd^{2+}, Co^{3+}, Fe^{3+}, Hg^{2+}, Ir^{3+}, $Mo^{3+/4+}$, Ni^{2+}, Os^{3+}, Pb^{2+}, Pd^{2+}, Pt^{2+}, Re^{3+}, Rh^{3+}, Ru^{3+}, Zn^{2+}) [1,3–7] and ML_2 for the alkaline earth metals and Bi^{3+}, $Ag^{1+/2+}$, Pd^{2+}, Zn^{2+}, ReO^{5+} and Ni^{2+} [8–10]. The study of mercaptide ions as donors, especially 2-aminoethanethiol, of mL_2 stoichiometry have not been subjected to detailed study as the complexes obtained are extremely insoluble, bridged and/or even polymeric in nature, making structural studies prohibitively difficult [3]. Recently, Bi^{3+} and ReO^{5+} cysteamine complexes of ML_2 stoichiometry have been characterized by X-ray structures [10,11]. In recently reported Pb-cysteamine complexes ($PbCl_2 \cdot (SCH_2CH_2NH_3)$, $Pb(SCH_2CH_2NH_2)_2 \cdot 2PbCl(SCH_2CH_2NH_2)$ and $Pb(SCH_2CH_2NH_2)_2$), the molecules are held together through intermolecular Pb–S bonds, unlike **3**

* Corresponding author. Tel.: +859 2577304; fax: +859 3231069.
E-mail addresses: mohan8sk@hotmail.com (M.S. Bharara), datwood@uky.edu (D.A. Atwood).
[1] Tel.: +859 3232225; fax: +606 3231069

0277-5387/$ - see front matter © 2005 Elsevier Ltd. All rights reserved.
doi:10.1016/j.poly.2005.01.019

and **4** reported here [12]. This clearly implies that the reaction conditions affect the structural chemistry.

Our continued interest in aqueous chemistry of heavy metal-thiolates led us to study Cd and Pb-aminoethanethiolates [13,14]. In a previous study with cysteamine [15], we have shown that binding to Hg in water results in a linear S–Hg–S linkage (bond angle 168.53°). This follows the precedent found in other monodentate thiolate ligands such as cysteine [16,17]. There were also some S–H hydrogen bonding, something that has not been observed for Hg containing metalloproteins such as MerR and MerP [18,19]. Here, we describe the cysteamine complexes of Cd(II) and Pb(II) which, in addition to forming unique structures, also possess extensive hydrogen-bonding involving something that has not been reported previously for similar dinuclear complexes.

2. Experimental

All the reactions were carried out at room temperature in deionized water. The reagents $CdCl_2$, $CdCO_3$, $Pb(Ac)_2 \cdot 3H_2O$ and $PbNO_3$ (J.T. Baker) and cysteamine hydrochloride (TCI America) were used as received. NMR (^1H and ^{13}C) data were obtained with JEOL-GSX-400 and 270 instruments operating at 199.17 and 399.78 MHz using d^6-DMSO and D_2O as solvents, with tetramethylsilane as the reference. IR data were recorded as KBr pellets on a Matheson Instrument 2020 Galaxy Series spectrometer and are reported in cm^{-1}. X-ray data for **1**–**4** were collected on a Nonius Kappa-CCD unit using Mo Kα radiation and crystallographic data are summarized in Table 1. For bond lengths and bond angles see Tables 3–6. A summary of the IR spectra for compounds **1**–**4** in tabular form is included in the supplementary information.

2.1. Preparation of $[Cd_{2.5}Cl_5(SCH_2CH_2NH_3)]$ (**1**)

Cadmium (II) chloride (0.94 g, 5 mmol) was added to a stirring solution of cysteamine hydrochloride (1.14 g, 10 mmol) in deionized water (20 mL) and the resulting mixture was stirred over 3 days. The solution was then filtered to remove a white precipitate and the filtrate was allowed to stand for 4 weeks in the refrigerator (4 °C), during which colorless crystals were formed. Crystalline yield: 0.29 g (10%), m.p. 222–224 °C (dec). ^1H NMR (d^6-DMSO, 200 MHz, ppm): δ 2.69 (t, 4H, CH_2N), 3.14 (t, 4H, CH_2S), 7.75 (s, 6H, NH_3). ^{13}C NMR (d^6-DMSO, 200 MHz, ppm): δ 33.9 (CH_2S), 43.1 (CH_2N). IR (KBr, ν/cm^{-1}): 657 (C–S), 1230 (C–N, stretching), 1258, 1320, 1376, 1427 (S–CH_2), 1491, 1561, 1583 (–NH_2 and N–H, bending), 2361, 2938, 3130 (NH_3^+), 3450 (R–NH_2, stretching). MS (EI, positive): m/z 247 $(M + 2)^+$, 171 $(M - SCH_2CH_2NH_2)^+$, 92 $(M - 2(SCH_2CH_2NH_2))^+$, 76 $(SCH_2CH_2NH_2)^+$. *Anal.* Calc. for $C_4H_{14}N_2S_2Cl_5Cd_{2.5}$: C, 7.84; H, 2.30; N, 4.57; S, 10.47. Found: C, 7.65; H, 2.20; N, 4.55; S, 10.43%.

Table 1
Crystallographic data for compounds **1**–**4**

Data/compound	**1**	**2**	**3**	**4**
Empirical formula	$C_4H_{14}N_2S_2Cd_{2.5}Cl_5$	$C_4H_{12}N_2S_2Cd$	$C_6H_{18}N_3S_3Pb_2Cl$	$C_6H_{18}N_{3.67}O_{2.02}S_3Pb_2Cl_{0.33}$
Molecular weight	612.54	264.68	678.24	696.15
Temperature (K)	173 (1)	145(2)	145 (2)	206 (2)
Wavelength (Å)	0.71073	0.71073	0.71073	0.71073
Crystal system	monoclinic	triclinic	monoclinic	monoclinic
Space group	$P21/n$	$P\bar{1}$	$P21/n$	$P21/n$
Unit cell dimensions				
a (Å)	10.4530 (6)	6.2800 (10)	9.1680 (10)	9.3600 (10)
b (Å)	8.1430 (5)	8.2360 (10)	9.5880 (10)	9.5300 (10)
c (Å)	17.5180 (8)	8.5420 (10)	16.707 (2)	17.057 (10)
α (°)	90	92.270 (10)	90	90
β (°)	90.426 (3)	99.566 (10)	95.410 (10)	95.860 (10)
γ (°)	90	102.563 (10)	90	90
V (Å^3)	1491.07 (14)	423.92 (10)	1462.1 (3)	1513.5 (3)
Z	4	2	4	4
Absorption coefficient (mm^{-1})	4.694	2.990	23.587	22.685
$F(000)$	1156	260	1216	1254
Crystal size	$0.11 \times 0.10 \times 0.06$	$0.08 \times 0.08 \times 0.08$	$0.16 \times 0.10 \times 0.10$	$0.15 \times 0.14 \times 0.05$
Goodness-of-fit on F^2	1.050	1.081	0.492	1.049
R_1 (on F, $I > 2\sigma(I)$)	0.0354	0.0154	0.0249	0.0327
R_1 (all data)	0.0513	0.0176	0.0359	0.0453
wR_2 (on F^2, $I > 2\sigma(I)$)	0.0737	0.0350	0.0625	0.0582
wR_2 (all data)	0.0787	0.0355	0.0686	0.0619

2.2. Preparation of $[Cd(SCH_2CH_2NH_2)_2]$ (2)

To a stirring solution of cysteamine hydrochloride (1.14 g, 10 mmol) in deionized water (20 mL) sodium hydroxide (0.80 g, 20 mmol) was added followed by addition of cadmium carbonate (0.86 g, 5 mmol). The mixture was stirred over one day and then solution was filtered to isolate a white precipitate. The filtrate was allowed to stand for 3 days in the refrigerator (4 °C), during which colorless crystals formed in near quantitative yield. Crystalline yield: 0.62 g (47%), m.p. 172–174 °C. ^{1}H NMR (D_2O, 200 MHz, ppm): δ 2.73 (t, 4H, CH_2N), 3.01 (t, 4H, CH_2S). ^{13}C NMR (D_2O, 200 MHz, ppm): δ 28.29 (CH_2S), 44.02 (CH_2N). IR (KBr, ν/cm^{-1}): 622–661 (C–S), 1051, 1064, 1120, 1214, 1228 (C–N, stretching), 1423 (S–CH_2), 1580 (–NH_2 and N–H, bending), 3551 (R–NH_2, stretching). MS (EI, positive): m/z 266 $(M + 2)^+$, 190 $(M - SCH_2CH_2NH_2)^+$, 114 $(M - 2(SCH_2CH_2NH_2))^+$, 76 $(SCH_2CH_2NH_2)^+$. *Anal.* Calc. for $C_4H_{12}N_2S_2Cd$: C, 18.15; H, 4.57; N, 10.58; S, 24.23. Found: C, 18.00; H, 4.62; N, 10.51; S, 24.05%.

2.3. Preparation of $[Pb_2Cl(SCH_2CH_2NH_2)_3]$ (3)

To a stirring solution of cysteamine hydrochloride (1.14 g, 10 mmol) in deionized water (20 mL) sodium hydroxide (0.80 g, 20 mmol) was added followed by addition of lead acetate trihydrate (1.90 g, 5 mmol) and the mixture was stirred over one day. The solution was then filtered to remove a yellow precipitate and the filtrate was allowed to stand for 3 days in the refrigerator (4 °C), during which pale yellow crystals formed. Crystalline yield: 0.64 g (19%), m.p.: 120–122 °C. ^{1}H NMR (D_2O, 200 MHz, ppm): δ 2.852 (t, 6H, CH_2N), 3.028 (t, 6H, CH_2S). ^{13}C NMR (D_2O, 200 MHz, ppm): δ 29.1 (CH_2S), 48.5 (CH_2N). IR (KBr, ν/cm^{-1}): 668–657 (C–S), 1032, 1065, 1105, 1219 (C–N, stretching), 1417 (S–CH_2), 1596 (–NH_2 and N–H, bending), 3463 (R–NH_2, stretching). MS (EI, positive): 359 $(Pb(SCH_2CH_2NH_2)_2)^+$, 282 $(Pb(SCH_2CH_2NH_2))^+$, 76 $(SCH_2CH_2NH_2)^+$. *Anal.* Calc. for $C_6H_{18}N_3S_3ClPb_2$: C, 10.63; H, 2.67; N, 6.20; S, 14.18. Found: C, 10.24; H, 2.48; N, 5.87; S, 13.37%.

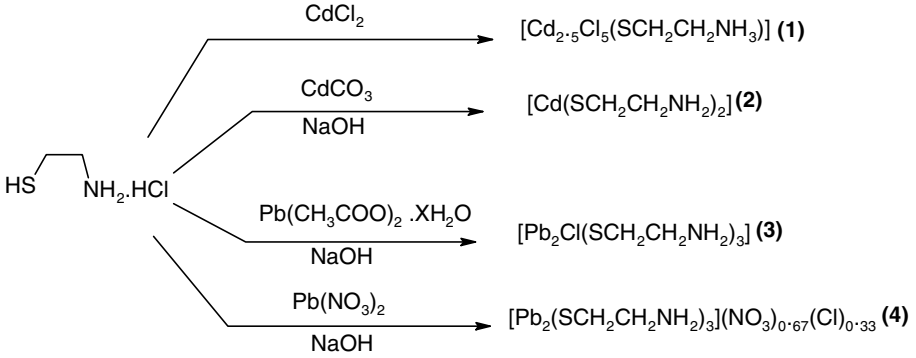
2.4. Preparation of $[Pb_2(SCH_2CH_2NH_2)_3](NO_3)_{0.67}(Cl)_{0.33}$ (4)

Sodium hydroxide (0.80 g, 20 mmol) was added to a stirring solution of cysteamine hydrochloride (1.14 g, 10 mmol) in deionized water (20 mL) followed by addition lead nitrate (1.66 g, 5 mmol) and the mixture was stirred over a day. The solution was then filtered to remove a white precipitate, and the filtrate was allowed to stand for 10 days in the refrigerator (4 °C), during which colorless crystals formed. Crystalline yield: 0.41 g (24%), m.p. 132–134 °C. ^{1}H NMR (d^6-DMSO, 200 MHz, ppm): δ 2.746 (m, 4H, CH_2N), 3.204 (t, 4H CH_2S). ^{13}C NMR (d^6-DMSO, 200 MHz, ppm): δ 30.0 (CH_2S), 49.3 (CH_2N). IR (KBr, ν/cm^{-1}): 628–706 (C–S), 1046-1221 (C–N, stretching), 1430 (S–CH_2), 1593 (–NH_2 and N–H, bending), 3448 (R–NH_2, stretching). MS (EI, positive): 359 $(Pb(SCH_2CH_2NH_2)_2)^+$, 282 $(Pb(SCH_2CH_2NH_2))^+$, 76 $(SCH_2CH_2NH_2)^+$. *Anal.* Calc. for $C_6H_{18}N_{3.67}S_3O_{2.02}Cl_{0.33}Pb_2$: C, 10.35; H, 2.61; N, 7.38; S, 13.82. Found: C, 10.36; H, 2.57; N, 7.36; S, 13.55%.

3. Result and discussion

3.1. Synthesis and characterization

Cysteamine hydrochloride and various metal salts were combined in a 1:1 ratio in deionized water to produce compounds **1**–**4** (Scheme 1). Compounds **1**, **2** and **4** gave white precipitates, while **3** was isolated as a yellow precipitate. The compounds were isolated by filtration in high yields (60–90%) and the supernatants were used to grow X-ray quality crystals at 4 °C. The characterization data (IR, NMR, EA, Mass Spectrometry) were matched for both the precipitates and the crystals. The



Scheme 1. Synthesis of compounds **1**–**4**.

Table 2
NMR data for cysteamine hydrochloride and compounds **1**–**4**

^{1}H and ^{13}C NMR/ compounds (in ppm)	Cysteamine hydrochloride	**1**	**2**	**3**	**4**
^{1}H NCH_2	2.69	2.69	2.73	2.85	2.74
^{1}H SCH_2	2.99	3.14	3.01	3.02	3.20
^{13}C NCH_2	42.8	43.1	44.0	48.5	49.3
^{13}C SCH_2	22.2	33.9	28.2	29.1	30.0

compounds are soluble in hot water but not in common organic solvents.

In the ^{1}H NMR for **1**–**4** (Table 2), single peaks were observed for the CH_2N and CH_2S groups, which is consistent with symmetrical structures in solution. When bound to the metal ion the ligand hydrogen atoms become more deshielded compared to the free ligand, cysteamine hydrochloride. However, in **1** no change in the chemical shift for CH_2N confirms the presence of a free amine. The significant shifts in CH_2S peaks in the ^{1}H and ^{13}C spectra for compounds **1**–**4** indicate a strong metal–sulfur interaction.

In the IR spectra for **1**–**4** the C–S and S–CH_2 stretches are shifted to lower frequencies when compared to free cysteamine hydrochloride. This implies coordination of the metal to the thiols. The ammonium bands at 2938–3130, 1561–1583 cm^{-1} and no change in the C–N stretching in **1** indicate free amine. For **2**–**4** the NH_2 stretching and bending modes are observed at higher frequencies compared to the free ligand, indicating the presence of a metal–nitrogen contact. In the mass spectrum for **2** the parent peak is observed at 266 (*m*/*z*) while the successive loss of two cysteamine units is observed for all the complexes.

4. Description of structures

Compound $[Cd_{2.5}Cl_5(SCH_2CH_2NH_3)]$ (**1**) has three-dimensional connectivity indicative of a solid-state material but it is nevertheless soluble in common solvents. This qualifies **1** as a "molecular solid" [20]. The structure contains layers of $(Cd(Cl)SR)_x$ perpendicular to one another (Fig. 1). The structure is comprised of alternate opposite open cores of hexacoordinate Cd with Cl and S present at the corners. Similar polymeric chains with hexacoordinate Cd atoms are also observed in $[Cd_2(5\text{-}CF_3\text{–}pyS)_4(DMF)]_n$, where the coordination is completed by S, N of the ligand and solvent, DMF [21]. This is not observed for **1**, where the coordination is completed by S and Cl to achieve octahedral geometry. The repeating pattern observed in the unit is Cd1(2S,4Cl)–Cd2(S,5Cl)–Cd1(2S,4Cl) and so on. Cd1 and Cd3 are coordinated to two sulfurs and four chlorines with two chlorides involved in bridging with another unit, whereas Cd2 is bonded to one sulfur, one terminal chlorine and four core bonded chlorine atoms.

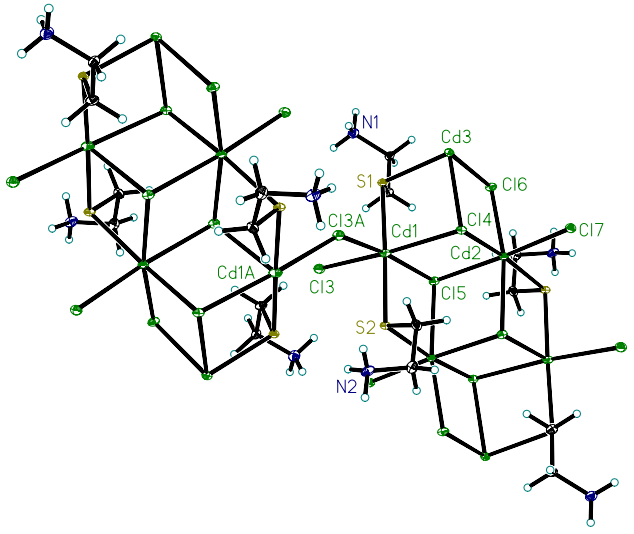


Fig. 1. View of the unique repeating unit of compound **1** at 50% thermal ellipsoids value.

Selected bond lengths and angles are given in Table 3. The Cd–S bond length varies in different cores. For Cd1 and Cd3, the distances are nearly the same (average 2.498 Å) while for Cd2, the bond distance is comparatively higher (2.601 Å). By comparison, $[CdBr_2(C_5H_{13}NS)]$, which also contains polymeric Cd–S chains has Cd–S distances ranging from 2.515 to 2.520 Å [22].

Variation in the Cd–Cl bond lengths is also observed for different chlorides (terminal, core bonded and bridging) as well as for different Cd atoms. For Cd(1), the distance between Cd and the core bonded chlorine is shorter (average 2.808 Å), compared to the bridging chlorine (2.920 Å). The bond lengths of chloride present in the core are nearly the same with an average distance of 2.790 Å. For Cd(2), Cd–Cl bond distances for core bonded and terminal chloride are nearly the same.

Table 3
Selected bond lengths (Å) and bond angles (°) for **1**

Cd(1)–S(1)	2.4825 (14)	Cd(2)–S(2)′	2.6018 (14)
Cd(1)–S(2)	2.4995 (14)	Cd(2)–Cl(2)	2.6679 (14)
Cd(1)–Cl(1)	2.8875 (15)	Cd(2)–Cl(3)	2.6968 (14)
Cd(1)–Cl(2)	2.8276 (14)	Cd(2)–Cl(4)	2.6372 (13)
Cd(1)–Cl(3)	2.7895 (14)	Cd(2)–Cl(5)	2.6060 (14)
Cd(3)–S(1)	2.5417 (14)	Cd(3)–Cl(2)	2.8159 (13)
Cd(3)–Cl(4)	2.7306 (13)		
S(2)–Cd(1)–S(1)	178.22 (5)	S(2)–Cd(1)–Cl(3)	84.70 (4)
S(1)–Cd(1)–Cl(3)	95.85 (4)	S(2)–Cd(1)–Cl(2)	96.23 (5)
S(1)–Cd(1)–Cl(2)	85.52 (5)	Cl(3)–Cd(1)–Cl(2)	82.67 (4)
S(2)–Cd(1)–Cl(1)	91.66 (5)	S(1)–Cd(1)–Cl(1)	86.68 (5)
Cl(3)–Cd(1)–Cl(1)	87.82 (4)	Cl(2)–Cd(1)–Cl(1)	167.01 (4)
S(2)–Cd(1)–Cl(1)′	84.86 (4)	S(1)–Cd(1)–Cl(1)′	94.80 (4)
Cl(3)–Cd(1)–Cl(1)′	167.25 (4)	Cl(2)–Cd(1)–Cl(1)′	91.20 (4)
Cl(1)–Cd(1)–Cl(1)′	99.79 (2)	S(2)′–Cd(2)–Cl(5)	90.65 (4)
Cl(5)–Cd(2)–Cl(4)	90.22 (4)	Cl(5)–Cd(2)–Cl(2)	88.05 (4)
Cd(1)–Cl(1)–Cd(1)′	142.52 (5)	Cd(2)–Cl(2)–Cd(1)	94.74 (4)
Cd(2)′–Cl(3)–Cd(1)	90.50 (4)	Cd(1)–S(2)–Cd(2)′	101.90 (5)

However a shorter Cd–Cl distance with a terminal chlorine, compared to bridged is observed in the complex $[Cd_2Cl_4(C_{14}H_{23}N_4OPS)_2]$ [23], where the bridging Cd–Cl distance is 2.644 Å, compared to terminal Cd–Cl, 2.387 Å. The S–Cd–S angle in **1** is almost linear (178.2° and 180.0°) due to the presence of a regular structure, when compared to the similar complex $[CdBr_2(C_5H_{13}NS)]$ (126.9°) [22]. The linear Cl–Cd–Cl angle (range 167–180°) and average angle of 90° signify octahedral geometry around the metal ion, whereas in $[Cd_2Cl_4(C_{14}H_{23}N_4OPS)_2]$ [23] a distorted tetrahedral geometry around Cd is indicated by Cl–Cd–Cl angles, ranging from 89° to 112°. The terminal amine is oriented away from the core with a N1–C2–C1 angle of 111.9° to reduce steric interactions. There are no signs of intramolecular hydrogen-bonding observed within a unit. However, intermolecular hydrogen-bonding involving chlorine with amines on adjacent units is observed. Similar hydrogen-bonding has been observed in $[CdBr_2(C_5H_{13}NS)]$ [22], where bromine is involved in inter-chain hydrogen-bonding with adjacent ammonium groups.

Compound (**2**) consists of discrete $[Cd(SCH_2CH_2NH_2)_2]$ molecules (Fig. 2) that are linked through intermolecular hydrogen bonds (Fig. 3). Selected bond lengths and angles are shown in Table 4. Cd is pentacoordinate, bonded to three sulfur and two nitrogen atoms in a distorted square pyramidal geometry. In the dimeric structure the two cadmium atoms are related by a center of inversion situated at the mid-point of the line between the two metal centers. One of the ligands acts as a terminal chelating unit (S, N) while the other behaves as both a chelate and a bridge through the sulfur. The Cd_2S_2 core is nearly planar with average internal angles close to 90°, with two different fused five-membered cysteamine rings (axial, terminal cysteamine unit and equatorial, cysteamine unit attached to the core). The Cd–S

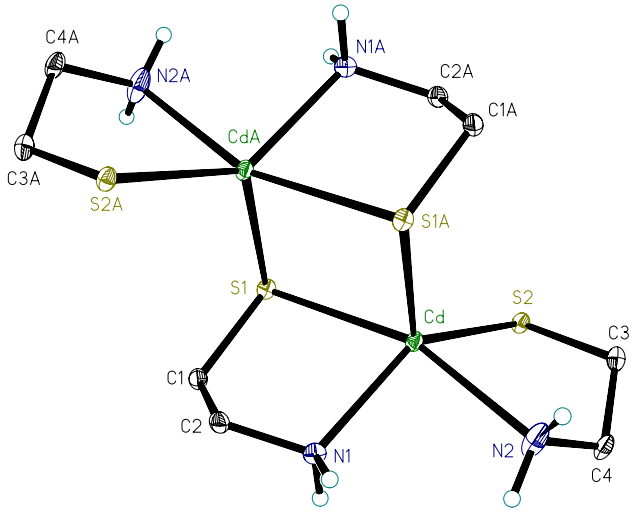


Fig. 2. Molecular structure of compound **2**.

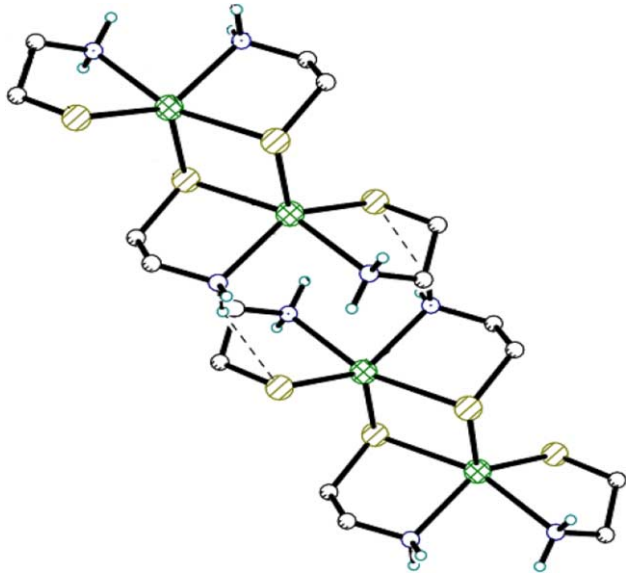


Fig. 3. View of the unit cell of compound **2** emphasizing the intermolecular hydrogen bonding.

Table 4
Selected bond lengths (Å) and bond angles (°) for **2**

Cd–N(1)	2.3087 (18)	Cd–N(2)	2.436 (2)
Cd–S(1)	2.7359 (7)	Cd–S(1)′	2.5813 (7)
Cd–S(2)	2.4920 (7)	S(1)–Cd′	2.5843 (7)
N(1)–Cd–N(2)	85.54 (7)	N(1)–Cd–S(2)	137.38 (5)
N(2)–Cd–S(2)	81.66 (5)	N(1)–Cd–S(1)	78.22 (5)
N(2)–Cd–S(1)	161.82 (6)	S(2)–Cd–S(1)	104.85 (2)
S(1)′–Cd–S(1)	93.54 (2)	Cd′–S(1)–Cd	86.46 (2)
N(1)–Cd–S(1)′	101.85 (5)	N(2)–Cd–S(1)′	97.79 (6)

bond distances vary from 2.492 to 2.735 Å in axial, equatorial and the central core but are comparable to related sulfur-bridged compounds (2.537–2.713 Å) as well as those containing S/N ligands (2.466–2.673 Å) [22–24]. The Cd–N bond distances are also different in both four- (2.308 Å) and five-membered fused rings (2.436 Å) but comparable to Cd–N bond distances in similar complexes [23–27].

The Cd–S1 distance is larger than Cd–S2 and Cd–N1 is smaller than Cd–N2 implying a stronger Cd–S bond in the axial position. The Cd–S and Cd–N bond distances show an opposite trend, similarly observed for distorted octahedral $[Cd(3\text{-}CF_3\text{–}pyS)_2(DMF)_2]$ [21]. The cysteamine units in axial and equatorial positions are neither perpendicular nor parallel to each other (N(1)–Cd–S(1)′, 101.8° and C(1)–S(1)–Cd(1)′, 102.9°). The deformity is due to the interaction of the sulfur and nitrogen with the amine hydrogen of the equatorial cysteamine molecule of another unit. The presence of the M_2S_2 core and intermolecular hydrogen-bonding (N–H–S, N–H 0.92 Å and H–S 2.95 Å) results in the distortion of planarity of the axial cysteamine ring. The equatorial and the axial cysteamine have torsion angles

Cd–S(2)–C(3)–C(4) 48.9° and Cd–S(1)–C(1)–C(2) 28.6°, that minimize strain energy.

In the structure of $[Pb_2Cl(SCH_2CH_2NH_2)_3]$ (**3**), four- and five-coordinate Pb, are observed (Fig. 4). The Pb atoms possess stereochemically active lone pairs giving four-coordinate Pb a distorted square pyramidal geometry and five-coordinate Pb an octahedral geometry. The five-coordinate Pb atoms form a planar four-membered M_2S_2 ring with average internal angles of nearly 90°.

The Pb–S distance in the pentacoordinate Pb is larger than the Pb–S distance of tetracoordinate Pb (Table 5). The bridging Pb–S distance (2.897 Å) between tetra and pentacoordinate Pb is in agreement with other related lead–thiolate complexes (2.671–2.960 Å) [28,29]. The Pb–N distance in pentacoordinate Pb is smaller compared to Pb–N in tetracoordinate Pb. These distances are comparable to [Pbc[15]crown-5](SCN)$_2$ [30], where the Pb–N distances range from 2.436 to 2.532 Å. The Pb–S and Pb–N bond distances in different units are opposite with a stronger Pb–S bond in the axial position. This trend is also observed in **2**. When compared to a similar complex $Pb(SCH_2CH_2NH_2)_2$ the Pb–S and Pb–N distances are in agreement [12].

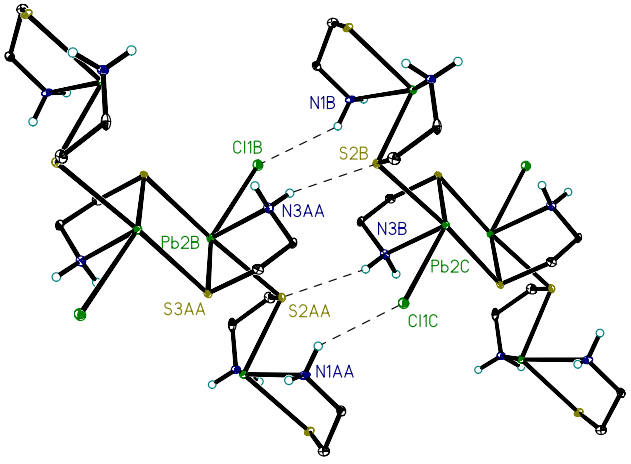


Fig. 4. A view of the repeating units of **3** showing inter-molecular hydrogen-bonding.

Table 5
Selected bond lengths (Å) and bond angles (°) for **3**

Pb(1)–N(1)	2.629 (6)	Pb(1)–N(2)	2.613 (7)
Pb(1)–S(1)	2.713 (2)	Pb(1)–S(2)	2.673 (2)
Pb(2)–S(2)	2.897 (2)	Pb(2)–N(3)	2.394 (7)
Pb(2)–S(3)	2.7377 (19)	Pb(2)–S(3)′	3.053 (2)
Pb(2)–Cl(1)	3.082 (2)		
N(1)–Pb(1)–S(1)	73.17 (15)	N(1)–Pb(1)–S(2)	86.41 (16)
N(2)–Pb(1)–S(1)	81.08 (16)	N(2)–Pb(1)–S(2)	73.51 (16)
N(3)–Pb(2)–S(2)	83.89 (18)	N(3)–Pb(2)–S(3)	73.61 (17)
S(2)–Pb(1)–S(1)	99.56 (6)	S(3)–Pb(2)–S(2)	83.81 (6)
S(2)–Pb(2)–S(3)′	165.09 (5)	S(3)–Pb(2)–S(3)′	84.35 (6)

The tetra-coordinate Pb unit is linked to the M_2S_2 core Pb through one of its sulfur atoms, which is nearly linear (165.0°), very much comparable to the polymer sheet $Pb(SCH_2CH_2OH)(NO_3)$ (162.7°) [31] and $Pb(SPh)_2$ (158.9°) [29]. The bond angles around the tetracoordinate Pb are nearly equal within the ring (73°) and between two cysteamine units (83° and 86°). The chloride bonded to the central Pb forms a hydrogen-bond with the $-NH_2$ group of the tetracoordinate Pb of another unit (Fig. 4). The NH of the cysteamine attached to the core form a hydrogen-bond with the sulfur of the tetracoordinate Pb of a second unit. Hence the intermolecular hydrogen-bonding is responsible for the stacking of the molecules and making the Pb_2S_2 cores parallel to each other. Such stacking is also observed in $Pb(SPh)_2$ [29]. The whole molecule is symmetrical with an axis going through the plane of the four membered Pb_2S_2 ring.

The crystal structure of $[Pb_2(SCH_2CH_2NH_2)_3](NO_3)_{0.67}(Cl)_{0.33}$ (**4**) reveals two types of Pb, both in a four coordinate geometry (Fig. 5). The M_2S_2 core, fused five membered cysteamine above and below the core plane and four coordinate metal linked to the core with sulfur as in **4**, is also observed in **3**. The axial Pb–S bond lengths (average 2.697 Å) are shorter than the Pb–S bond lengths of the core (average 2.989 Å). The bridging Pb–S distance (2.893 Å) connecting the core and the axial unit is nearly the same as the bridging Pb–S bond of **3** (2.987 Å). Like compounds **2** and **3**, Pb–S and Pb–N distances also show opposite trends in axial and the core units. Except for the presence of chloride attached to central Pb in **3**, compounds **3** and **4** are nearly identical and have similar lattice parameters (Table 1). Bond lengths and bond angles for **4** are given in Table 6. The presence of extensive hydrogen-bonding in **4** might explain the higher thermal stability compared to **3**. This

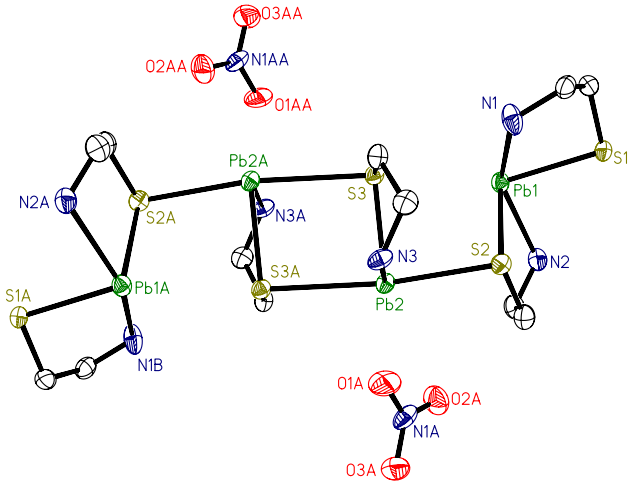


Fig. 5. Molecular structure of compound **4.** The counter anions are 2/3rd NO_3^- and 1/3rd Cl^- (sitting at the same position). For the sake of clarity, only NO_3^- are shown.

Table 6
Selected bond lengths (Å) and bond angles (°) for **4**

Pb(1)–N(1)	2.604 (7)	Pb(1)–N(2)	2.575 (7)
Pb(1)–S(1)	2.7138 (19)	Pb(1)–S(2)	2.6806 (19)
Pb(2)–S(2)	2.893 (2)	Pb(2)–N(3)	2.411 (7)
Pb(2)–S(3)	2.704 (2)	Pb(2)–S(3)′	3.0857 (19)
N(1)–Pb(1)–S(1)	72.39 (14)	N(1)–Pb(1)–S(2)	84.28 (16)
N(2)–Pb(1)–S(1)	83.32 (14)	N(2)–Pb(1)–S(2)	73.54 (15)
N(3)–Pb(2)–S(2)	84.43 (16)	N(3)–Pb(2)–S(3)	74.15 (17)
S(2)–Pb(1)–S(1)	100.78 (6)	S(2)–Pb(2)–S(3)′	168.83 (6)
S(3)–Pb(2)–S(2)	86.00 (6)	S(3)–Pb(2)–S(3)′	87.00 (6)
Pb(1)–S(2)–Pb(2)	96.11 (6)	Pb(2)–S(3)–Pb(2)′	95.65 (6)

is due to the presence of NO_3^- anions, which supplies more hydrogen bonding contacts than single chloride anions. The amine hydrogens are also weakly hydrogen bonded to sulfur and chlorine atoms as observed in **2** and **3**.

5. Conclusion

In the present manuscript we have described the Cd(II) and Pb(II) compounds of 2-aminoethanethiol with the help of crystal structures. As the reactions were carried out following the same general procedure the products were similar. Compounds **2**, **3** and **4** show structural similarities involving bridging sulfurs to form a four-membered M_2S_2 core. Beside the central core, fused five-membered axial (with tetracoordinate metal) and equatorial (with pentacoordinate metal) cysteamine units are also observed in in **2**, **3** and **4**. It is important to note that the reaction conditions affect the structural chemistry as in **3** and **4** there is no Pb–Pb interaction observed, compared to a similar $Pb(SCH_2CH_2NH_2)_2$ complex [12]. A common feature of all the four compounds is intermolecular hydrogen-bonding involving nitrogen/sulfur and the counter anions.

Acknowledgments

This work was supported by the University of Kentucky Tracy's Farmer Center for the Environment and the State of Kentucky Research Challenge Trust Fund. NMR instruments used in this research were obtained with funds from the CRIF program of the National Science Foundation (Grant CHE 997841) and from the Research Challenge Trust Fund of the University of Kentucky.

Appendix A. Supplementary data

Crystallographic data for the structures analysis for compounds **1**–**4** have been deposited with the Cambridge Crystallographic Data Center, CCDC Nos. 210040–210043, respectively. Copies of the information may be obtained free from The Director, CCDC, 12 Union Road, Cambridge CB2 1EZ, UK (Tel.: +44 1223 336408; fax: +44 1223 336033). Supplementary data associated with this article can be found, in the online version, at doi:10.1016/j.poly.2005.01.019.

References

[1] G.B. Brubaker, M.G. Henk, D.W. Johnson, Inorg. Chim. Acta 100 (1985) 201.
[2] K.A. Jensen, Anorg. Allgem. Chem. 265 (1936) 229.
[3] D.H. Busch, D.C. Jicha, Inorg. Chem. 1 (1962) 872.
[4] R.E. DeSimone, T. Ontko, L. Wardman, E.L. Blinn, Inorg. Chem. 14 (1975) 1313.
[5] D.H. Busch, J.W. Wrathall, Inorg. Chem. 2 (1963) 1182.
[6] C.H. Wei, L.F. Dahl, Inorg. Chem. 9 (1970) 1878.
[7] Y. Yamada, Y. Miyashita, K. Fujisawa, K. Okamoto, Bull. Chem. Soc. Jpn. 75 (2002) 1151.
[8] Y. Tsuchitani, T. Ando, K. Ueno, Bull. Chem. Soc. Jpn. 36 (1963) 1534.
[9] C.W. Schalpfer, K. Nakamoto, Inorg. Chim. Acta 6 (1972) 177.
[10] T. Konno, Y. Shimazaki, M. Kawai, M. Hirotsu, Inorg. Chem. 40 (2001) 4250.
[11] G.G. Briand, N. Burford, T.S. Cameron, W. Kwiatkowski, J. Am. Chem. Soc. 120 (1998) 11374.
[12] H. Fleischer, D. Schollmeyer, Inorg. Chem. 43 (2004) 5529.
[13] M.M. Matlock, K.R. Henke, D.A. Atwood, Water Res. 35 (2001) 3649.
[14] M.M. Matlock, B.S. Howerton, M. Van Aelstyn, K.R. Henke, D.A. Atwood, Water Res. 37 (2003) 579.
[15] C. Kim, S. Parkin, M. Bharara, D.A. Atwood, Polyhedron 21 (2002) 225.
[16] S. Hideyo, L.B. Theodore, J. Am. Chem. Soc. 87 (1965) 1904.
[17] Y.K. Sze, A.R. Davis, G.A. Neville, Inorg. Chem. 14 (1975) 1969.
[18] P.S. Watton, J.G. Wright, F.M. MacDonnell, J.W.S. Bryson, T.V. O'Halloran, J. Am. Chem. Soc. 112 (1990) 2824.
[19] G. Fleissner, M.D. Reigle, T.V. O'Halloran, T.G. Spiro, J. Am. Chem. Soc. 120 (1998) 12690.
[20] H.W. Roesky, Solid. State. Sci. 3 (2001) 777.
[21] A. Sousa-Pedrares, J. Romero, J.A. Garcia-Vazquez, M.L. Duran, I. Casanova, A. Sousa, Dalton Trans. 7 (2003) 1379.
[22] W. Clegg, I. Casals, P. Gonzalez-Duarte, Acta Cryst. C 49 (1993) 129.
[23] V.C. Renz-Kreikebhom, B. Stromburg, U. Engelhardt, Acta Cryst. C 47 (1991) 1403.
[24] M.T.F. Tarafdar, J. Khoo-Teng, K.A. Crouse, A.M. Ali, B.M. Yamin, H.K. Fun, Polyhedron (2002) 1.
[25] A. Castineiras, E. Bermejo, D.X. West, L.J. Ackerman, J. Valdes-Martinez, S. Hernandez-Ortega, Polyhedron 18 (1999) 1463.
[26] V.U. Engelhardt, B. Renz-Kreikebohm, Acta Cryst. C 45 (1989) 1679.
[27] E. Lopez-Torres, M.A. Mendiola, J. Rodriguez-Procopio, M.T. Sevilla, E. Colacio, J.M. Moreno, I. Sobrados, Inorg. Chim. Acta 323 (2001) 130.
[28] P.K. Bharadwaj, B.W. Arbuckle, W.K. Musker, Inorg. Chim. Acta 142 (1988) 243.
[29] D.A. Rae, D.C. Craig, I.G. Dance, M.L. Scudder, P.A. Dean, M.A. Kmetic, N.C. Payne, J.J. Vittal, Acta Cryst. B 53 (1997) 457.
[30] H.J. Brugge, R. Folsing, A. Knochel, Polyhedron 4 (1985) 1493.
[31] W. Clegg, I.L. Abrahams, C.D. Garner, Acta Cryst. C 40 (1984) 1367.

Available online at www.sciencedirect.com
SCIENCE DIRECT®
Polyhedron 24 (2005) 872–880
POLYHEDRON
www.elsevier.com/locate/poly

Triruthenium clusters bearing bridging dppm and capping sulfido ligands: X-ray structures of $[Ru_3(CO)_6(\mu_3\text{-}CO)(\mu_3\text{-}S)(PPh_3)(\mu\text{-}dppm)]$ and $[Ru_3(CO)_6(\mu_3\text{-}S)_2(PPh_3)(\mu\text{-}dppm)]$

Md. Iqbal Hyder [a], G.M. Golzar Hossain [b], Shariff E. Kabir [a,*], Md. Arzu Miah [a]

[a] Department of Chemistry, Jahangirnagar University, Savar, Dhaka 1342, Bangladesh
[b] Department of Chemistry, Cardiff University, P.O. Box 912, Park Place, Cardiff CF10 3TB, UK

Received 9 November 2004; accepted 2 February 2005
Available online 29 April 2005

Abstract

Treatment of $[Ru_3(CO)_{10}(\mu\text{-}dppm)]$ (**1**) with $PPh_3{=}S$ at ambient temperature in THF gave the known compound $[Ru_3(CO)_7(\mu_3\text{-}CO)(\mu_3\text{-}S)(\mu\text{-}dppm)]$ (**2**) and the new compound $[Ru_3(CO)_6(\mu_3\text{-}CO)(\mu_3\text{-}S)(PPh_3)(\mu\text{-}dppm)]$ (**3**). Compound **3** can also be prepared by the room temperature reaction of **2** with PPh_3 in the presence of Me_3NO. A similar reaction of $[Ru_3(CO)_7(\mu_3\text{-}S)_2(\mu\text{-}dppm)]$ (**4**) with PPh_3 afforded (**3**), $[Ru_3(CO)_6(\mu_3\text{-}S)_2(PPh_3)(\mu\text{-}dppm)]$ (**5**) together with the previously reported compound $[(\mu\text{-}H)_2Ru_3(CO)_7(\mu_3\text{-}S)(\mu\text{-}dppm)]$ (**6**). In contrast, a similar treatment of the sulfur-selenium compound $[Ru_3(CO)_7(\mu_3\text{-}S)(\mu_3\text{-}Se)(\mu\text{-}dppm)]$ (**7**) with PPh_3 afforded only $[Ru_3(CO)_6(\mu_3\text{-}S)(\mu_3\text{-}Se)(PPh_3)(\mu\text{-}dppm)]$ (**8**). Both compounds **5** and **8** exist as two isomers in solution, arising from the reversible migration of a metal–metal bond, induced by the dppm ligand. The reaction of **6** with PPh_3 under the same conditions gave $[(\mu\text{-}H)_2Ru_3(CO)_6(\mu_3\text{-}S)(PPh_3)(\mu\text{-}dppm)]$ (**9**). Protonation of **4** and **7** by trifluoroacetic acid gave the mono-protonated species $[(\mu\text{-}H)Ru_3(CO)_7(\mu_3\text{-}S)_2(\mu\text{-}dppm)]^+$ (**10**) and $[(\mu\text{-}H)Ru_3(CO)_7(\mu_3\text{-}Se)(\mu_3\text{-}S)(\mu\text{-}dppm)]^+$ (**11**), respectively, isolated as their PF_6 salts. All the compounds have been characterized by spectroscopic data together with single crystal X-ray diffraction studies for **3** and **5**.
© 2005 Elsevier Ltd. All rights reserved.

Keywords: Triruthenium clusters; Sulfido ligands; Bis(diphenylphosphino)methane, Triphenylphosphine; X-ray structures

1. Introduction

Transition metal carbonyl clusters containing sulfido ligands have received considerable attention due to their application in cluster aggregation reactions and in generating new coordination modes and geometries [1–3]. Sulfido ligands are valuable agents for the synthesis and stabilization of metal cluster complexes [4]. Several synthetic routes are available for the preparation of sulfido or selenido transition-metal clusters, among these, those that involve the oxidative addition of $Ph_3P{=}E$ (E = S or Se) to zero-valent metal centers appear to be the most effective [5]. This method, takes advantage of the frailty of the $Ph_3P{=}E$ bond and has been successfully used by the Tiripicchio group to synthesize tertiary phosphine substituted iron and ruthenium clusters containing capping chalcogenido ligands [6,7]. This method is effective in producing monophosphine as well as diphosphine-substituted sulfido and selenido clusters, but the monophosphine derivatives of iron and ruthenium clusters containing capping sulfido ligands are

* Corresponding author. Present address: Department of Chemistry, University of Montana, Missoula, MT 59812, USA. Tel.: +406 243 2592; fax: +406 243 4227.
E-mail address: skabir_ju@yahoo.com (S.E. Kabir).

0277-5387/$ - see front matter © 2005 Elsevier Ltd. All rights reserved.
doi:10.1016/j.poly.2005.02.006

generally large in numbers in compare to the diphosphine derivatives [2,6]. Recently, we became interested in the synthesis of capping chalcogenido trimetallic clusters from the oxidative addition reactions of dppm=E or PPh_3=E (E = S or Se) with osmium and ruthenium carbonyl clusters [2,8,9]. We have very recently reported the synthesis of the capping sulfido triruthenium clusters $[Ru_3(CO)_7(\mu_3\text{-}S)_2(\mu\text{-dppm})]$, $[(\mu\text{-}H)_2Ru_3(CO)_7(\mu_3\text{-}S)(\mu\text{-dppm})]$, $[Ru_3(CO)_7(\mu_3\text{-}CO)(\mu_3\text{-}S)(\mu\text{-dppm})]$ and $[Ru_3(CO)_6(\mu_3\text{-}CO)(\mu_3\text{-}S)\{\eta^1\text{-}C(NMe_2)_2\}(\mu\text{-dppm})]$ from the reaction of $[Ru_3(CO)_{10}(\mu\text{-dppm})]$ with tetramethylthiourea [10]. The reaction of the corresponding osmium analog $[Os_3(CO)_{10}(\mu\text{-dppm})]$ with tetramethylthiou rea afforded the capping sulfido cluster $[Os_3(CO)_7(\mu_3\text{-}S)_2(\mu\text{-dppm})]$ [11]. Furthermore, we have also reported [8] that the reaction of $[Ru_3(CO)_{10}(\mu\text{-dppm})]$ with dppmS provides a number of sulfido complexes $[Ru_3(CO)_7(\mu_3\text{-}S)_2(\mu\text{-dppm})]$, $[Ru_3(CO)_7(\mu_3\text{-}CO)(\mu_3\text{-}S)(\mu\text{-dppm})]$, $[Ru_3(CO)_5(\mu_3\text{-}CO)(\mu_3\text{-}S)(\mu\text{-dppm})]$ and $[Ru_3(CO)_6(\mu_3\text{-}CO)(\mu_3\text{-}S)(\mu\text{-dppm})(\eta^1\text{-}Ph_2PCH_2P(=O)Ph_2)]$. As a continuation of our previous work, we have now investigated the reaction of $[Ru_3(CO)_{10}(\mu\text{-dppm})]$ (**1**) with Ph_3P=S. We have also investigated the reactions of $[Ru_3(CO)_7(\mu_3\text{-}S)_2(\mu\text{-dppm})]$ (**4**), $[Ru_3(CO)_7(\mu_3\text{-}S)(\mu_3\text{-}Se)(\mu\text{-dppm})]$ (**7**) and some related compounds with PPh_3 in the presence of Me_3NO and the results are described in the present paper.

2. Experimental

All the reactions were performed under a nitrogen atmosphere using standard Schlenk techniques. Solvents were dried and distilled prior to use by standard methods (CH_2Cl_2 over CaH_2 and THF from sodium benzophenone). The starting clusters $[Ru_3(CO)_{10}(\mu\text{-dppm})]$ (**1**) [12], $[Ru_3(CO)_7(\mu_3\text{-}S)_2(\mu\text{-dppm})]$ (**4**) [10] and $[Ru_3(CO)_7(\mu_3\text{-}S)(\mu_3\text{-}Se)(\mu\text{-dppm})]$ (**7**) [10] were prepared according to the known procedures. Infrared spectra were recorded on a Shimadzu FT-IR 8101 spectrophotometer. ^1H and $^{31}P\{^1H\}$ NMR spectra were recorded on a Bruker DPX 400 spectrometer. Mass spectra were recorded on a Varian Mat 312 mass spectrometer.

2.1. Reaction of 1 with PPh_3S

A THF solution (30 mL) of **1** (0.100 g, 0.103 mmol) and PPh_3S (0.033 g, 0.112 mmol) was stirred at room temperature for 1.5 h. The solvent was removed under reduced pressure and the residue was chromatographed by TLC on silica gel. Elution with cyclohexane/CH_2Cl_2 (3:2, v/v) developed three bands. The first band was too small for complete characterization. The second band gave the known compound $[Ru_3(CO)_7(\mu_3\text{-}CO)(\mu_3\text{-}S)(\mu\text{-dppm})]$ (**2**) (0.028 g, 29%) while the third band gave $[Ru_3(CO)_6(\mu_3\text{-}CO)(\mu_3\text{-}S)(PPh_3)(\mu\text{-dppm})]$ (**3**) (0.026 g, 24%) as orange crystals from hexane/CH_2Cl_2 at −4 °C. *Anal.* Calc. for $C_{50}H_{37}O_7P_3Ru_3S$: C, 50.97; H, 3.17. Found: C, 51.25; H, 3.33%. IR (νCO, CH_2Cl_2): 2029sh, 2008vs, 1992s, 1960s cm^{-1}; IR(νCO, KBr): 1744w cm^{-1}; ^1H NMR (CD_2Cl_2): δ 7.34 (m, 35H), 3.92 (m, 1H), 3.49 (m, 1H); $^{31}P\{^1H\}$ NMR(CD_2Cl_2): δ 50.4 (s, 1P), 28.3 (s, 2P); Mass spectrum: *m/z* 1177 (M^+).

2.2. Reaction of 4 with PPh_3

A methanolic solution (1 mL) of Me_3NO (0.010 g, 0.112 mmol) was added dropwise to a dichloromethane solution (35 mL) of **4** (0.100 g, 0.105 mmol) and triphenylphosphine (0.035 g, 0.120 mmol) over about 10 min. The resulting reaction mixture was stirred at room temperature for 45 min. The solvent was removed under reduced pressure and the residue chromatographed by TLC on silica gel. Elution with cyclohexane/CH_2Cl_2(7:3, v/v) developed four bands. The first band afforded $[(\mu\text{-}H)_2Ru_3(CO)_7(\mu_3\text{-}S)(\mu\text{-dppm})]$ (**6**) (0.007 g, 8%) while the second band was unreacted **4** (0.005 g). The third band yielded $[Ru_3(CO)_6(\mu_3\text{-}S)_2(PPh_3)(\mu\text{-dppm})]$ (**5**) (0.033 g, 35%) as red crystals from heptane/CH_2Cl_2 at −4 °C. *Anal.* Calc. for $C_{49}H_{37}O_6P_3Ru_3S_2$: C, 49.78; H, 3.16. Found: C, 49.98; H, 3.35%. IR (νCO, CH_2Cl_2): 2019s, 2000vs, 1964m, 1944m cm^{-1}; ^1H NMR (CD_2Cl_2): δ 7.33 (m, 35H), 4.10 (m, 1H), 3.94 (m, 1H), 3.07 (t, 2H, J = 11.8 Hz); $^{31}P\{^1H\}$ NMR (CD_2Cl_2): δ 69.7 (s, 2P), 56.4 (s, 1P), 47.3 (s, 1P), 26.4 (d, 1P, J = 29.0 Hz), 16.8 (d, 1P, J = 29.0 Hz); Mass spectrum: *m/z* 1181 (M^+). The fourth band gave **3** (0.010 g, 11%) as orange crystals from heptane/CH_2Cl_2 at −4 °C.

2.3. Reaction of 7 with PPh_3

A similar reaction of **7** (0.030 g, 0.032 mmol) with PPh_3 (0.010 g, 0.120 mmol) in the presence of Me_3NO (0.006 g, 0.067 mmol) at room temperature afforded $[Ru_3(CO)_6(\mu_3\text{-}S)(\mu_3\text{-}Se)(PPh_3)(\mu\text{-dppm})]$ (**8**) (0.018 g, 55%) as red crystals from hexane/CH_2Cl_2 at −4 °C. *Anal.* Calc. for $C_{49}H_{37}O_6P_3Ru_3SSe$: C, 49.64; H, 3.12. Found: C, 50.12; H, 3.27%. IR (νCO, CH_2Cl_2): 2019s, 1998vs, 1964s, 1944m cm^{-1}; ^1H NMR (CD_2Cl_2): δ 7.38 (m, 35H), 4.20 (m, 1H), 3.98 (m, 1H), 3.19 (t, 2H, J = 10.8 Hz); $^{31}P\{^1H\}$ NMR (CD_2Cl_2): δ 59.7 (s, 2P), 54.5 (s, 1P), 48.0 (s, 1P), 22.9 (d, 1P, J = 25.8 Hz), 13.5 (d, 1P, J = 25.8 Hz); Mass spectrum: *m/z* 1228 (M^+).

2.4. Reaction of 6 with PPh_3

A similar reaction of **6** (0.030 g, 0.032 mmol) with PPh_3 (0.010 g, 0.120 mmol) and Me_3NO (0.005 g, 0.056 mmol) followed by similar chromatographic separation gave $[(\mu\text{-}H)_2Ru_3(CO)_6(\mu_3\text{-}S)(PPh_3)(\mu\text{-dppm})]$ (**9**) (0.018 g, 55%) as orange crystals from hexane/CH_2Cl_2 at −4 °C. *Anal.* Calc. for $C_{49}H_{39}O_6P_3Ru_3S$: C, 51.08;

H, 3.41. Found: C, 51.62; H, 3.52%. IR (νCO, CH_2Cl_2): 2047vs, 1991s, 1973s cm^{-1}; ^1H NMR (CD_2Cl_2): δ 7.25 (m, 35H), 3.90 (m, 1H), 3.66 (m, 1H), −18.08 (dt, 1H, J = 12.8, 39.2 Hz), −18.85 (dd, 1H, J = 12.0, 30.0 Hz); $^{31}P\{^1H\}$ NMR (CD_2Cl_2): δ 38.1 (s, 1P), 25.0 (d, 1P, J = 45.5 Hz), 24.3 (d, 1P J = 45.5 Hz); Mass spectrum: m/z 1151 (M^+).

2.5. Reaction of **2** with PPh_3

A similar reaction to that above of **2** (0.040 g, 0.042 mmol), PPh_3 (0.015 g, 0.057 mmol) and Me_3NO (0.007 g, 0.078 mmol) followed by a similar chromatographic separation gave **3** (0.017 g, 40%).

2.6. Protonation of **4**

An excess of CF_3COOH (one drop from a Pasteur pipette) was added to a CD_2Cl_2 solution (0.5 mL) of **4** (0.025 g, 0.011 mmol) in an NMR tube. After recording ^1H and $^{31}P\{^1H\}$ NMR spectra, the volatiles were removed under vacuum, and the residue was dissolved in methanol (5 mL). Addition of a methanolic solution of ammonium hexafluorophosphate (0.022 g) followed by a few drops of water gave a yellow precipitate which was recrystallized from CH_2Cl_2/Et_2O to give [(μ-H)-$Ru_3(CO)_7(\mu_3\text{-}S)_2(\mu\text{-dppm})$][$PF_6$] (**10**) (0.016 g, 64%) as yellow crystals. IR (νCO, CH_2Cl_2): 2105s, 2054vs, 2014vs, 1985m cm^{-1}; ^1H NMR (CD_2Cl_2): δ 7.35 (m, 20H), 3.85 (t, 2H, J = 10.0 Hz), −10.25 (dd, J = 8.0, J = 18.4 Hz); $^{31}P\{^1H\}$ NMR (CD_2Cl_2): δ 68.2 (d, 1P, J = 87.0 Hz), 41.8 (d, 1P, J = 87.0 Hz).

2.7. Protonation of **7**

A similar protonation of **7** followed by similar work-up gave [$Ru_3(CO)_7(\mu_3\text{-}S)(\mu_3\text{-}Se)(\mu\text{-dppm})$][$PF_6$] **(11)**. IR ($\nu$CO, CH_2Cl_2): 2106s, 2052vs, 2014vs, 1985m cm^{-1}; ^1H NMR ($CDCl_3$): δ 7.39 (m, 20H), 3.91 (m, 2H), −10.17 (dd, J = 8 Hz, J = 18.4 Hz); $^{31}P\{^1H\}$ NMR ($CDCl_3$): 67.9 (t, J = 24.9 Hz), 41.2 (t, J = 19.9 Hz).

2.8. X-ray crystallography

Crystals of **3** and **5** suitable for X-ray diffraction studies were grown by an interlayer diffusion technique from CH_2Cl_2/heptane at −4 °C. Crystallographic data were collected using a FAST area detector diffractometer

Table 1
Crystal data and structure refinement for **3** and **4**

	3	**5**
Formula weight	1177.98	1182.03
Crystal system	orthorhombic	triclinic
Empirical formula	$C_{50}H_{37}O_7P_3Ru_3S$	$C_{49}H_{37}O_6P_3Ru_3S_2$
Space group	*Pbca*	$P\bar{1}$
Unit cell dimensions		
a (Å)	14.8318(2)	12.9655(2)
b (Å)	16.3063(3)	17.0742(3)
c (Å)	38.1778(9)	21.6190(4)
α (°)	90	90.1815(7)
β (°)	90	105.7751(8)
γ (°)	90	99.0433(6)
Volume (Å^3)	9233.4(3)	4543.10(14)
Z	8	4
D_{calc} (Mg m^{-3})	1.695	1.728
Absorption coefficient (mm^{-1})	1.170	1.232
F(000)	4688	2352
Crystal size (mm)	0.20 × 0.10 × 0.08	0.16 × 0.08 × 0.06
θ Range for data collection (°)	2.95–25.33	2.94–27.45
Limiting indices	$-17 \leqslant h \leqslant 17$	$-16 \leqslant h \leqslant 16$
	$-19 \leqslant k \leqslant 19$	$-21 \leqslant k \leqslant 22$
	$-45 \leqslant l \leqslant 45$	$-28 \leqslant l \leqslant 28$
Reflections collected	26774	78760
Independent reflections [R_{int}]	7946 [0.0748]	20589 [0.1077]
Maximum and minimum transmission	0.9122 and 0.7996	0.9297 and 0.8272
Data/restraints/parameters	7946/0/577	20589/0/1135
Goodness-of-fit on F^2	0.962	1.003
Final R indices [$I > 2\sigma(I)$]	R_1 = 0.0423	R_1 = 0.0514
	wR_2 = 0.0693	wR_2 = 0.1032
R indices (all data)	R_1 = 0.0780	R_1 = 0.1055
	wR_2 = 0.0758	wR_2 = 0.1221
Largest difference in peak and hole (e Å^{-3})	0.772 and −0.691	0.787 and −1.112

Details in common: X-ray radiation, Mo Kα (λ = 0.71073 Å), temperature (K) 150(2), refinement method: full-matrix least-squares on F^2.

and Mo Kα radiation ($\lambda = 0.71073$ Å) by following a previously described procedure [13]. The unit cell parameters were determined by the least-square refinement of the diffractometer angles for 250 reflections and the data were corrected for absorption using DIFABS [14]. The structures were solved by direct methods (SHELXS-97) [15] and refined on F^2 by full-matrix least-squares (SHELXL-97) [16] using all unique data. All non-hydrogen atoms were anisotropic. The hydrogen atoms were included in calculated positions (riding model). The crystal data and refinement details are summarized in Table 1.

3. Results and discussion

The reaction of $[Ru_3(CO)_{10}(\mu\text{-dppm})]$ (**1**) with $PPh_3{=}S$ at ambient temperature gave the previously reported compound $[Ru_3(CO)_7(\mu_3\text{-CO})(\mu_3\text{-S})(\mu\text{-dppm})]$ (**2**) and the new compound $[Ru_3(CO)_6(\mu_3\text{-CO})(\mu_3\text{-S})(PPh_3)(\mu\text{-dppm})]$ (**3**) in 29% and 24% yields, respectively (Scheme 1). Compound **3** can also be prepared in 40% yield by the room temperature reaction of **2** with PPh_3 in the presence of Me_3NO. We have recently synthesized **2** from the reaction between **1** and tetramethylthiourea, and it has been characterized by a solid-state structure determination [10]. Compound **3** has been characterized by a combination of spectroscopic data and single crystal X-ray diffraction studies.

The molecular structure of **3** is depicted in Fig. 1, crystal data are collected in Table 1 and selected bond distances and angles are given in Table 2. This molecule has a well-known bicapped triangular structure, composed of three ruthenium atoms, one triply bridging sulfido, one triply bridging carbonyl ligand, a bridging dppm, a PPh_3 and six terminal carbonyl groups. The three Ru–Ru bond distances {Ru(1)–Ru(3) = 2.8008(5), Ru(1)–Ru(2) = 2.8318(5) and Ru(2)–Ru(3) = 2.8206(5) Å} are almost equal in magnitude. The three acute angles [Ru(1)–Ru(3)–Ru(2) = 60.496(14), Ru(2)–Ru(1)–Ru(3) = 60.098(14), and Ru(1)–Ru(2)–Ru(3) = 59.405(13)°] are also almost equal thus providing an equilateral triangle, which is nearly symmetrically capped by the sulfur atom {Ru(1)–S(1) = 2.3585(12), Ru(3)–S(1) = 2.3826(12) and Ru(2)–S(1) = 2.3686(11) Å}, but asymmetrically capped by the carbonyl group with three different Ru–C distances {Ru(2)–C(1) = 2.163(4), Ru(1)–C(1) = 2.201(4) and Ru(3)–C(1) = 2.151(4) Å}. It has also a mirror

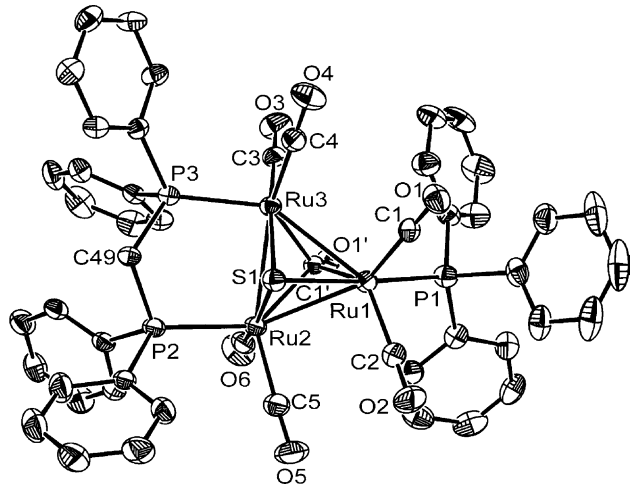
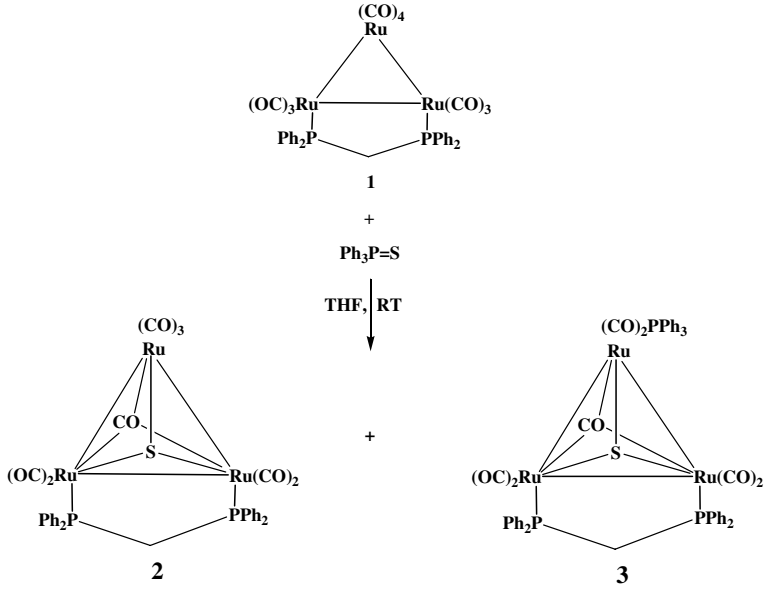


Fig. 1. ORTEP drawing of $[Ru_3(CO)_6(\mu_3\text{-CO})(\mu_3\text{-S})(PPh_3)(\mu\text{-dppm})]$ (**3**). Thermal ellipsoids are drawn at the 50% probability level.



Scheme 1.

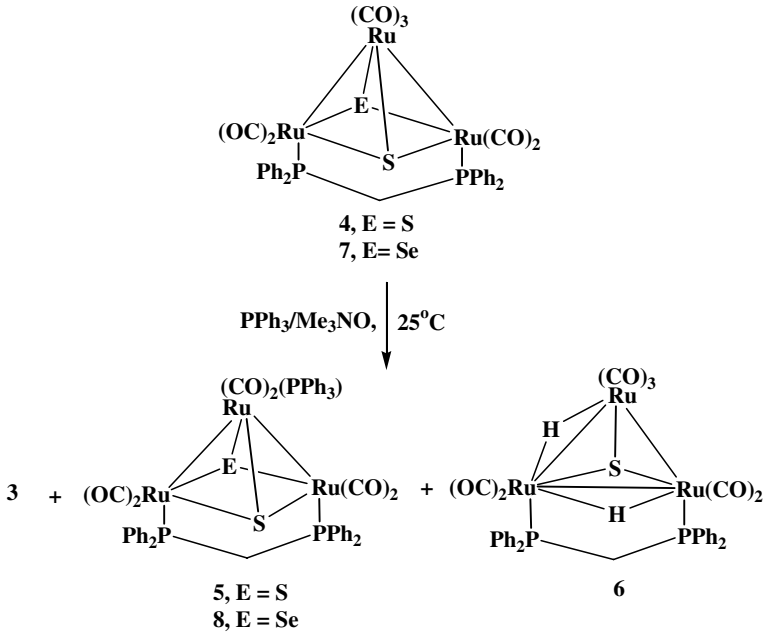
Table 2
Selected bond distances (Å) and angles (°) for $[Ru_3(CO)_6(\mu_3\text{-}CO)(\mu_3\text{-}S)(PPh_3)(\mu\text{-}dppm)]$ (**3**)

Ru(1)–Ru(2)	2.8318(5)	Ru(2)–P(2)	2.3491(13)
Ru(1)–Ru(3)	2.8008(5)	Ru(3)–P(3)	2.3050(13)
Ru(2)–Ru(3)	2.8206(5)	Ru(2)–C(1′)	2.163(4)
Ru(1)–S(1)	2.3585(12)	Ru(3)–C(1′)	2.151(4)
Ru(2)–S(1)	2.3686(11)	Ru(1)–P(1)	2.3530(13)
Ru(3)–S(1)	2.3826(12)		
Ru(1)–Ru (3)–Ru(2)	60.496(14)	Ru(3)–C(1′)–Ru(1)	80.10(13)
Ru(2)–Ru(1)–Ru(3)	60.099(14)	Ru(2)–C(1′)–Ru(1)	80.91(14)
Ru(1)–Ru (2)–Ru(3)	59.405(13)	Ru(2)–C(1′)–Ru(3)	81.66(14)
Ru(1)–S(1)–Ru(3)	72.42(3)	C(1′)–Ru(3)–Ru(1)	50.74(11)
Ru(3)–S(1)–Ru(2)	72.83(3)	C(1′)–Ru(3)–Ru(2)	49.35(11)
Ru(1)–S(1)–Ru(2)	73.60(3)	S(1)–Ru(1)–Ru(2)	53.36(3)
P(2)–Ru(2)–Ru(3)	87.17(4)	S(1)–Ru(2)–Ru(3)	53.81(3)
P(1)–Ru(1)–Ru(3)	118.23(4)	P(2)–C(20)–P(1)	112.1(2)

plane passing through the Ru(1) atom and bisecting the Ru(2)–Ru(3) bond and the methylene carbon, C(49), of the dppm ligand. Each of the Ru atoms is ligated by the two terminal carbonyl groups. The PPh_3 ligand is coordinated to the Ru(1) atom in an axial position and lies on the mirror plane. The structure of **3** may be deduced from **2** [10] by the replacement of one axially positioned CO by a PPh_3 ligand. The Ru(1)–P(1) bond distance of 2.3530(13) Å, involving the terminal PPh_3 ligand, is comparable to those found in $[Ru_4(CO)_{12}(\mu\text{-}CO)(\mu_4\text{-}Se)_2(PPh_3)_2]$ {average 2.351(4) Å} [17]. The Ru–P bond distances involving the bridging dppm ligand {Ru(2)–P(2) = 2.3491(13) and Ru(3)–P(3) = 2.3054(13) Å} are comparable to the corresponding distances in **1** {2.322(2) and 2.334(2) Å} [12] and **2** {2.334(2) and 2.366(2) Å} [10]. The dppm ligand is coplanar with three Ru atoms. The compound contains 48 valence electrons, as expected for an electron precise trinuclear cluster containing three metal–metal bonds and each metal atom can achieve an 18-electron configuration.

The spectroscopic data of **3** are in accord with the solid-state structure. The mass spectrum shows the molecular ion peak at *m*/*z* 1177 and ion multiplets corresponding to the successive loss of six carbonyl groups. In addition to the *ν*(CO) stretching vibration bands due to the terminal carbonyl ligands between 2029s and 1960m cm^{-1}, the infrared spectrum of **3** exhibits a low energy absorption band at 1744 cm^{-1} due to the triply bridging carbonyl ligand. The $^{31}P\{^1H\}$ NMR spectrum exhibited two singlets at δ 50.4 and 28.3 with a relative intensity of 1:2. The singlet at δ 28.3 is due to the equivalent phosphorus atoms of the dppm ligand and that at δ 50.4 is assigned to the PPh_3 ligand. In addition to the usual resonances for the phenyl protons of dppm and PPh_3 ligands, the ^1H NMR spectrum shows two multiplets at δ 3.92 and 3.49 for the two diastereotopic methylene protons of the dppm ligand.

The reaction of $[Ru_3(CO)_7(\mu_3\text{-}S)_2(\mu\text{-}dppm)]$ (**4**) with PPh_3 in the presence of Me_3NO at room temperature gave **3** and $[Ru_3(CO)_6(\mu_3\text{-}S)_2(PPh_3)(\mu\text{-}dppm)]$ (**5**) in addition to the known compound $[(\mu\text{-}H)_2Ru_3(CO)_7(\mu_3\text{-}S)(\mu\text{-}dppm)]$ (**6**) in 11%, 35% and 8% yields, respectively (Scheme 2). A similar reaction of $[Ru_3(CO)_7(\mu_3\text{-}S)(\mu_3\text{-}Se)(\mu\text{-}dppm)]$ (**7**) with PPh_3 afforded only $[Ru_3(CO)_6(\mu_3\text{-}S)(\mu_3\text{-}Se)(PPh_3)(\mu\text{-}dppm)]$ (**8**). The dihydrido compound **6** is supposed to be formed by the displacement of a triply bridging sulfido ligand in **4** by two bridging hydride ligands. We have previously



Scheme 2.

reported **6** as a by product derived from the reaction of **1** with tetramethylthiourea [10]. Compounds **5** and **8** have been characterized by a combination of elemental analysis, infrared, ^{1}H NMR, $^{31}P\{^{1}H\}$ NMR and mass spectroscopic data together with single crystal X-ray diffraction studies for **5**.

The crystal of **5** contains two crystallographically independent molecules in its asymmetric unit. Both molecules are structurally similar, and an ORTEP diagram of the molecular structure of one of these molecules is shown in Fig. 2. The crystal data are given in Table 1 and the selected bond distances and angles are collected in Table 3. The molecule consists of an open cluster of three ruthenium atoms with two metal–metal bonds {Ru(1)–Ru(2) = 2.8106(6), Ru(1)–Ru(3) = 2.8280(5) Å} and a non-bonded separation of 3.569(5) Å, along the Ru(2)–Ru(3) edges, six terminal carbonyl ligands, a triphenylphosphine, two triply bridging sulfido ligands and a bridging dppm ligand. Both the metal–metal bonds are nearly equal in magnitude and the average value {2.8196 (5) Å} is comparable to the average Ru–Ru bond distances in $[Ru_3(CO)_7(\mu_3\text{-}Se)_2(\mu\text{-}dppe)]$ {2.806(2) Å} [18]. The dppm ligand spans the non-bonded metal–metal edge through the two phosphorus atoms occupying axial sites of the two basal metal atoms. The Ru–P distances involving the dppm ligand {Ru(2)–P(2) = 2.3031(13) and Ru(3)–P(3) = 2.2889(13) (Å)} are slightly shorter than those found in **1** [12]. The two P atoms of the dppm ligand are essentially coplanar with the three Ru atoms and the methylene carbon atom (C49) is seen to lie on the off-plane. The P(2)–C(49)–P(3) angle of 120.7(3)° is significantly larger than the theoretical one (113°) [6a], an indication of the strain for the dppm molecule. Each of Ru(1), Ru(2) and Ru(3) are ligated by the two equatorially bound carbonyl ligands. The PPh_3 ligand is axially coordinated to the apical Ru(1) atom. The Ru–S distances to the central seven-coordinate ruthenium atom Ru(1), {Ru(1)–S(1) = 2.3931(12) and Ru(1)–S(2) = 2.4131(13) Å} are slightly longer than those found to the external six-coordinate ruthenium atoms {2.3596(12)–2.4024(13) Å}. The structure is similar to that of **4** with the exception of the presence of a PPh_3 ligand coordinated to the apical Ru(1) and it occupies an axial site. The Ru(1)–P(1) bond distance of 2.3262(13) Å involving the terminal PPh_3 ligand is comparable to that found in **3**. The PPh_3 ligand is lying in the mirror plane of the molecule passing through the Ru(1), S(1), S(2) and C(49) atoms. The Ru–P bond distances involving the bridging dppm ligand {Ru(2)–P(2) = 2.3031(13) and Ru(3)–P(3) = 2.2889(13) Å} are comparable to the corresponding distances in **1** [12], **2** [10] and **3**. As usual, the triply bridging sulfido ligand acts as a four-electron donor and the dppm donates four electrons to the cluster which results in a total of 50 valence electrons and the observation of two formal Ru–Ru bonds present

Table 3
Selected bond distances (Å) and angles (°) for $[Ru_3(CO)_6(\mu_3\text{-}S)_2(PPh_3)(\mu\text{-}dppm)]$ (**5**)

	Molecule 1	Molecule 2
Ru(1)–Ru(2)	2.8106(6)	2.8202(5)
Ru(1)–Ru(3)	2.8280(5)	2.8309(6)
Ru(1)–S(1)	2.3931(12)	2.3937(12)
Ru(2)–S(1)	2.4024(13)	2.3873(12)
Ru(3)–S(1)	2.3921(12)	2.3905(13)
Ru(1)–S(2)	2.4131(13)	2.4158(13)
Ru(2)–S(2)	2.3596(12)	2.3615(13)
Ru(3)–S(2)	2.3602(13)	2.3637(12)
Ru(1)–P(1)	2.3262(13)	2.3439(13)
Ru(2)–P(2)	2.3031(13)	2.3013(13)
Ru(3)–P(3)	2.2889(13)	2.2990(13)
P(2)–C(49)	1.846(4)	1.84091(5)
P(3)–C(49)	1.840(5)	1.852(4)
Ru(2)–Ru(1)–Ru(3)	78.544(15)	78.335(15)
S(1)–Ru(1)–Ru(3)	53.76(3)	53.67(3)
S(1)–Ru(2)–Ru(1)	53.97(3)	53.96(3)
S(1)–Ru(1)–Ru(2)	54.27(3)	53.75(3)
S(2)–Ru(1)–Ru(3)	52.81(3)	52.83(3)
S(2)–Ru(2)–Ru(1)	54.81(3)	54.71(6)
S(2)–Ru(1)–Ru(2)	53.04(3)	52.93(3)
P(1)–Ru(1)–Ru(2)	119.91(4)	124.45(3)
P(1)–Ru(1)–Ru(3)	121.40(4)	120.79(4)
P(2)–Ru(2)–Ru(1)	136.69(4)	135.15(4)
P(3)–Ru(3)–Ru(1)	134.44(4)	136.98(4)
S(1)–Ru(2)–S(2)	80.36(4)	80.34(4)
S(1)–Ru(1)–S(2)	79.48(4)	79.12(4)
S(1)–Ru(3)–S(2)	80.56(4)	80.23(4)
P(3)–Ru(2)–S(1)	88.69(4)	94.39(4)
P(3)–Ru(3)–S(2)	99.25(5)	96.30(4)
Ru(3)–S(1)–Ru(2)	96.23(5)	96.67(5)
Ru(2)–S(2)–Ru(3)	98.27(4)	98.11(4)
Ru(3)–S(2)–Ru(1)	72.65(4)	72.63(4)
Ru(3)–S(1)–Ru(1)	72.46(4)	72.56(4)
Ru(1)–S(1)–Ru(2)	71.76(4)	72.30(3)
Ru(2)–S(2)–Ru(1)	72.15(4)	72.35(4)
P(3)–C(49)–P(2)	120.7(3)	121.2(3)

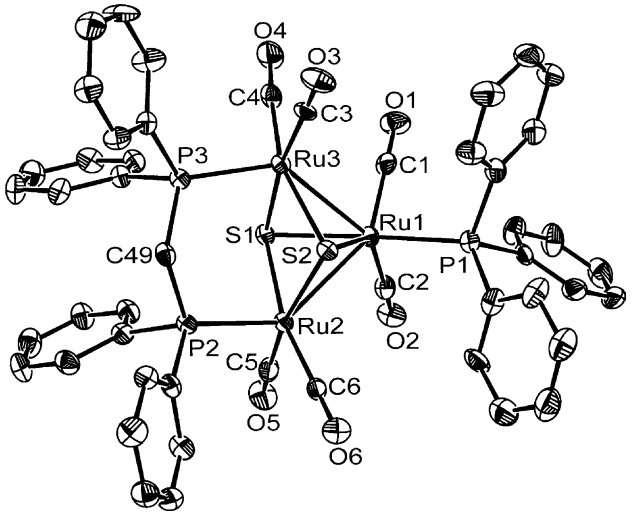


Fig. 2. ORTEP drawing of $[Ru_3(CO)_6(\mu_3\text{-}S)_2(PPh_3)(\mu\text{-}dppm)]$ (**5**). Thermal ellipsoids are drawn at the 50% probability level.

in the trinuclear framework is consistent with the electron count.

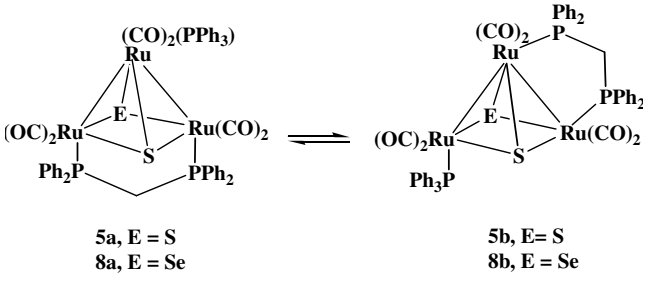
The infrared spectra of **5** and **8** are very similar indicating that they are structurally similar. The ^{1}H and $^{31}P\{^{1}H\}$ NMR data of both **5** and **8** indicate that they exist as a mixture of two isomers in solution. In addition to the usual phenyl resonances in the aromatic region, the aliphatic region of the ^{1}H NMR spectra contains two multiplets and a triplet. For **5**, the multiplets at δ 4.10 and 3.94 are due to the methylene protons of the minor isomer **5b** while the triplet at δ 3.07 is due to the major isomer **5a**. Similarly for **8,** the multiplets at δ 4.20 and 3.98 are due to the methylene protons of the minor isomer **8b** and the triplet at 3.19 is assigned to the major isomer **8a**. Consistent with this, the $^{31}P\{^{1}H\}$ NMR spectrum of each of **5** and **8** exhibits three singlets and two doublets. For **5**, the singlets at δ 69.7 and 47.3 are due to the ^{31}P nuclei of the dppm and triphenylphosphine ligands, respectively, of the major isomer **5a** whereas the doublets at δ 26.4 and 16.8 (J = 29.0 Hz) are due to the ^{31}P nuclei of the dppm and the singlet at δ 56.4 is due to PPh_3 ligand of the minor isomer **5b**. Similarly for **8**, the doublets at δ 22.9 and 13.5 (J = 25.8 Hz) and the singlet at δ 48.0 have been assigned to the ^{31}P nuclei of the minor isomer **8b** whereas the singlets at δ 59.7 and 54.5 are due to the major isomer **8a**. The $^{31}P\{^{1}H\}$ NMR spectrum thus indicates that the phosphorus nuclei of dppm ligand are equivalent in the major isomer, but they are non-equivalent in the minor isomer. In the major isomer, the dppm ligand bridges the two non-bonded ruthenium atoms whereas in the minor isomer, it spans one of the metal–metal edges. The short-bite dppm ligand pushes the basal Ru atoms to approach in such a way that a fluxional motion takes place in solution consisting of the reversible migration of a metal–metal bond from a side of the open triangle to the basal plane as shown in Scheme 3. This fluxional behavior of **5** and **8** is similar to that exhibited by $[Ru_3(CO)_7(\mu_3\text{-}Se)_2(\mu\text{-dppm})]$ in which the reversible migration of a Ru–Ru bond from a side of the open triangle to the basal plane induced by the dppm ligand has been reported [6b]. Thus compound **8** is structurally similar to **5**, but it contains a triply bridging Se atom in place of one of the triply bridging S atoms.

Treatment of **6** with PPh_3 in the presence of Me_3NO at room temperature afforded the PPh_3 substituted compound $[(\mu\text{-H})_2Ru_3(CO)_6(\mu_3\text{-S})(PPh_3)(\mu\text{-dppm})]$ (**9**) (Scheme 4) in 55% yield. Unfortunately, we were unable to grow crystals for X-ray quality of **9,** therefore, the characterization is made on the spectroscopic data.

The IR spectrum of **9** indicates that all the carbonyl groups are of a terminal type. In addition to the usual phenyl resonances, the ^{1}H NMR spectrum in the aliphatic region exhibits two multiplets at δ 3.90 and 3.66 due to methylene protons of the dppm ligand. The hydride region of the ^{1}H NMR spectrum contains a doublet of triplets at δ −18.08 (J = 12.8, J = 32.0 Hz) and a doublet of doublets at δ −18.85 (J = 12.0, J = 39.2 Hz), indicating the presence of two bridging hydride ligands. The $^{31}P\{^{1}H\}$ NMR spectrum shows three equal intensity signals, two doublets at δ 25.0 and 24.3 due to the nonequivalent ^{31}P nuclei of the dppm ligand and a singlet at δ 38.1 due to the PPh_3 ligand. The FAB mass spectrum shows the molecular ion peak at m/z 1151, consistent with the formulation of $[(\mu\text{-H})_2Ru_3(CO)_6(\mu_3\text{-S})(PPh_3)(\mu\text{-dppm})]$, and fragmentation peaks due to the sequential loss of six carbonyl ligands. Thus the spectroscopic data of **9** are quite consistent with a structure where the PPh_3 ligand is coordinated to the rear ruthenium atom and one hydride ligand bridges the same Ru–Ru edge as the dppm and the other hydride bridges one of the remaining Ru–Ru edges as seen in the precursor **6**. It is interesting to note that compound **6** is dynamic at room temperature owing to the edge hopping of the hydride ligands [19], but the displacement of a CO by a PPh_3 suppresses such a dynamic behavior in **9**.

In order to compare the protonation of **4** and **7** with that of **1** we have reacted these compounds with CF_3COOH. As expected treatment of **4** and **7** with an excess of trifluoroacetic acid afforded the cationic hydrido derivatives $[(\mu\text{-H})Ru_3(CO)_7(\mu_3\text{-S})_2(\mu\text{-dppm})]^+$ (**10**) and $[(\mu\text{-H})Ru_3(CO)_7(\mu_3\text{-Se})(\mu_3\text{-S})(\mu\text{-dppm})]^+$ (**11**), respectively (Scheme 5), isolated as their PF_6 salts.

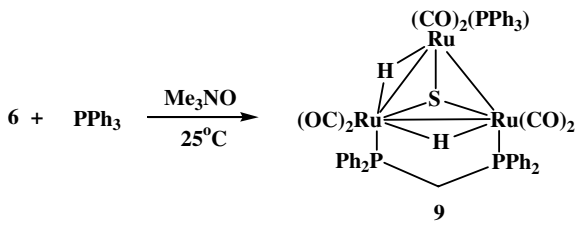
Unfortunately, suitable single crystals could not be grown for any of the protonated species for X-ray analysis. So, their characterization was done on the basis of spectroscopic data. The ν(CO) stretching frequencies of **10** and **11** are shifted to higher wave numbers than those



5a, E = S
8a, E = Se

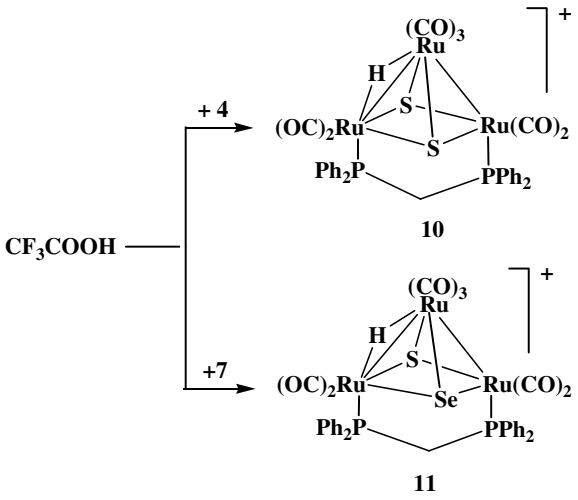
5b, E= S
8b, E = Se

Scheme 3.



9

Scheme 4.



Scheme 5.

of their respective parent compounds. This increase in CO stretching frequencies for the protonated species is due to the decrease in electron density at the metal centers. The π back donation to π* CO orbitals is decreased, which in turn, increases the CO bond order and, concomitantly, the CO stretching frequencies [20]. The ^{1}H NMR spectra of the protonated species in the hydride region contain a doublet of doublets {δ −10.25 (J = 8.0, J = 18.4 Hz) for **10** and −10.25 (J = 8.0 Hz, J = 18.4 Hz) for **11**} in agreement with the assumption that the hydride is bridging one of the bonded ruthenium–ruthenium edges not bridged by the dppm ligand. The $^{31}P\{^{1}H\}$ NMR spectra of **10** and **11** exhibit two doublets {δ 67.9 and 41.2 (J = 19.92 Hz) for **10**; δ 68.2 and 41.8 (J = 87.0 Hz) for **11**} indicating that the ^{31}P nuclei of the dppm ligand are non-equivalent.

4. Conclusions

We have found that the reaction of **1** with PPh_3=S at ambient temperature afforded the known compound **2** and the new compound **3** (Scheme 1). The reaction of **4** with PPh_3 in the presence of Me_3NO at ambient temperature furnished two new compounds **3** and **5**, in addition to the previously reported compound **6** (Scheme 2). In contrast, a similar reaction of **7** with PPh_3 afforded exclusively **8**. The X-ray crystallographic analysis unambiguously reveals that **3** contain a Ru_3S core with a triply bridging carbonyl ligand on one face of the ruthenium triangle and the triply bridging sulfido ligand on the opposite face. On the other hand, **5** is a bi-capped "open" cluster having the basic Ru_3S_2 skeleton to which the dppm ligand bridges the open Ru–Ru edge. The PPh_3 ligand in both complexes **3** and **5** occupies the axial position of the apical ruthenium atom. Both compounds **5** and **8** exist as two isomers in solution arising from the reversible migration of a metal–metal bond induced by the dppm ligand.

Acknowledgment

The support of this research by the Ministry of Science and Technology, Government of the Peoples Republic of Bangladesh is gratefully acknowledged.

Appendix A. Supplementary data

Crystallographic data for the compounds have been deposited with the Cambridge Crystallographic Data Centre, CCDC Nos. 254506 (**3**) and 254507 (**5**). Copies of this information may be obtained free of charge from The Director, CCDC, 12 Union Road, Cambridge, CB2 1EZ, UK (fax: +44-1223-3360333 or e-mail: deposit@ccdc.cam.ac.uk or www: http://www.ccdc.cam.ac.uk). Supplementary data associated with this article can be found, in the online version at doi:10.1016/j.poly.2005.02.006.

References

[1] (a) R.D. Adams, I.T. Horvath, S. Wang, Inorg. Chem. 24 (1985) 172;
(b) R.D. Adams, I.T. Horvath, J. Am. Chem. Soc. 106 (1984) 1869;
(c) R.D. Adams, I.T. Horvath, L.W. Yang, J. Am. Chem. Soc. 105 (1983) 1533.
[2] S.E. Kabir, S. Pervin, N.C. Sarker, A. Yesmin, T.A. Siddiquee, D.T. Haworth, D.W. Bennett, K.M.A. Malik, J. Organomet. Chem. 681 (2003) 23.
[3] T. Akhter, N. Begum, D.T. Haworth, D.W. Bennett, S.E. Kabir, M.A. Miah, N.C. Sarker, T.A. Siddiquee, E. Rosenberg, J. Organomet. Chem. 689 (2004) 2571.
[4] (a) M. Hidai, S. Kuwata, Y. Mizobe, Acc. Chem. Res. 33 (2000) 46;
(b) K.H. Whitmire, J. Coord. Chem. 17 (1988) 95;
(c) R.D. Adams, Polyhedron 4 (1985) 2003;
(d) T. Shibihara, Coord. Chem. Rev. 123 (1993) 73;
(e) K.H. Whitmire, J. Coord. Chem. 17 (1998) 95;
(f) R.D. Adams, J. Cluster Sci. 1 (1990) 249;
(g) S.W.A. Fong, T.S.A. Hor, J. Chem. Soc., Dalton Trans. (1999) 639.
[5] D. Cauzzi, C. Graiff, G. Predieri, A. Tiripicchio, in: P. Braunstein, L.A. Oro, P.R. Raithby (Eds.), Metal Clusters in Chemistry, 3, VCH, Weinheim, 1999, p. 193.
[6] (a) D. Cauzzi, C. Graiff, M. lanfranchi, G. Predieri, A. Tiripichio, J. Organomet. Chem. 536–537 (1997) 497;
(b) D. Cauzzi, C. Graiff, G. Predieri, A. Tiripichio, C. Vignali, J. Chem. Soc., Dalton Trans. (1999) 237.
[7] (a) P. Baistrocchi, D. Cauzzi, M. Lanfranchi, G. Predieri, A. Tiripicchio, M.T. Camellini, Inorg. Chim. Acta 235 (1995) 173;
(b) P. Baistrocchi, M. Careri, D. Cauzzi, C. Graiff, M. Lanfranchi, P. Manini, G. Predieri, A. Tiripicchio, Inorg. Chim. Acta 252 (1996) 367;

(c) D. Cauzzi, C. Graiff, C. Massera, G. Predieri, A. Tiripicchio, J. Cluster Sci. 12 (2001) 259;
(d) D. Cauzzi, C. Graiff, C. Massera, G. Predieri, A. Tiripicchio, Inorg. Chim. Acta 300–302 (2000) 471.
[8] S.E. Kabir, S.J. Ahmed, M.I. Hyder, M.A. Miah, D.W. Bennett, D.T. Haworth, T.A. Siddique, E. Rosenberg, J. Organomet. Chem. 689 (2004) 3412.
[9] H. Akter, A.J. Deeming, S.E. Kabir, G.M.G. Hossain, D.N. Mondol, A. Sharmin, D.A. Tocher, J. Organomet. Chem. (communicated).
[10] S.J. Ahmed, A.J. Deeming, M.I. Hyder, S.E. Kabir, M.A. Miah, E. Nordlander J. Organomet. Chem. (communicated).
[11] K.A. Azam, G.M.G. Hossain, K.M.A. Malik, M.A. Mottalib, S. Pervin, N.C. Sarker, Polyhedron 21 (2002) 381.
[12] M.I. Bruce, B.K. Nicholson, M.L. Williams, Inorg. Synth. 28 (1990) 225.
[13] J.A. Darr, S.R. Drake, M.B. Hursthouse, K.M.A. Malik, Inorg. Chem. 32 (1993) 5704.
[14] N.P.C. Walker, D. Stuart, Acta Crystallogr. Sect. A 39 (1983) 158.
[15] G.M. Sheldrick, Acta Crystallogr. Sect. A 46 (1990) 467.
[16] G.M. Sheldrick, SHELXL-97 Program for Crystal Structure Refinement, University of Göttingen, Germany, 1997.
[17] P. Baistrocchi, D. Cauzzi, M. Lanfranchi, G. Predieri, A. Tiripicchio, M.T. Camellini, Inorg. Chim. Acta 235 (1995) 173.
[18] D. Cauzzi, C. Graiff, M. Chiara, G. Predieri, A. Tiripicchio, D. Acquotti, J. Chem. Soc., Dalton Trans. (1999) 3515.
[19] A.W. Coleman, D.F. Jones, P.H. Dixneuf, C. Brisson, J.-J. Bonnet, G. Lavigne, Inorg. Chem. 23 (1984) 952.
[20] G.M.G. Hossain, M.I. Hyder, S.E. Kabir, K.M.A. Malik, M.A. Miah, T.A. Siddiquee, Polyhedron 22 (2003) 633.

Available online at www.sciencedirect.com
SCIENCE DIRECT®
Polyhedron 24 (2005) 881–888
POLYHEDRON
www.elsevier.com/locate/poly

Highly efficient orange-emitting OLEDs based on phosphorescent platinum(II) complexes

Inamur R. Laskar, Shih-Feng Hsu, Teng-Ming Chen *

Department of Applied Chemistry, National Chiao Tung University, Hsinchu, Taiwan

Received 9 November 2004; accepted 4 February 2005
Available online 25 April 2005

Abstract

The syntheses, characterisations, photophysical properties and their applications in organic light emitting devices of a series of 2-phenylbenzothiazolato (bt)/substituted 2-phenylbenzothiazolato (X-bt) platinum(II) based square-planar complexes [(X-bt)Pt(acac); acac = acetylacetonate; X = unsubstituted (**1**), F (**2**), OMe (**3**) and CF_3 (**4**)] are discussed. Reaction of K_2PtCl_4 with btH/X-btH in glacial acetic acid for a few days results in the dinuclear chloro-bridged Pt(II) complex, (bt/X-bt)Pt(μ-Cl)Pt(bt/X-bt) which is cleaved with acetylacetone to give the corresponding mononuclear (bt/X-bt)Pt(acac) complex. The (MeO-bt)Pt(acac) complex has been characterized by X-ray single crystal structure analysis. The packing diagram shows the Pt–Pt distances and the intermolecular spacings are 3.369 and 3.360 Å, respectively, which is consistent with excimer formation. It has also been supported by time-resolved photoluminescence (PL) measurements. The nature of the lowest emitting states are the triplet MLCT as well as triplet π–π* states and it has been tuned according to the electronic properties of the substituents. The electroluminescent (EL) devices were fabricated by doping platinum complexes **1** and **2** (the corresponding devices denoted as D-1 and D-2, respectively) into the host CBP (4,4′-(*N*,*N*′-dicarbazole)biphenyl), in the emitting zone with a doping content of 5%, 7% and 9%. The EL performances for these devices are exceptionally high (14.3 and 16.0 cd A^{-1} @2 mA cm^{-2} and luminances 10 550 and 11 320 cd m^{-2} @100 mA cm^{-2} for D-1 and D-2, respectively).
© 2005 Elsevier Ltd. All rights reserved.

Keywords: 2-Phenylbenzothiazole; Platinum(II)-complex; Photoluminescence; Eximer; Electroluminescence; Dopant

1. Introduction

The development of organometallic based optoelectronics, such as light-emitting devices, chemosensors and photovoltaic dye-sensitized devices [1] is one of the exciting applications of transition metal complexes. Extensive work on cyclometallating or oligopyridine complexes of Ru(II) [2], Os(II) [3], Re(I) [4] and Ir(III) [5] have been studied for their long triplet excited-state lifetimes, high emission quantum yields and tunable emission wavelengths in the above mentioned areas. Recently, significant research has been focused on the syntheses of cyclometallated complexes of iridium(III) and particularly in light emitting diodes [5]. Platinum(II) complexes have also been used as luminescent centres in organic light-emitting diodes (OLEDs) [6]. Only few of the reported platinum(II) complexes are emissive at room temperature in solution. Pt(II) species chelated with aromatic ligands, such as bipyridine, phenanthroline, 2-phenylpyridine or similar derivatives, emit in solution from excited states localized on the aromatic systems. These Pt(II) complexes benefit from having relatively high metal-centred (MC) states when compared to their palladium analogues [7]. If the emitting states (MLCT or intraligand) and MC states lie too close in energy, they can thermally equilibrate, thereby quenching

* Corresponding author. Tel.: +88635712121x56526; fax: +88635723764.
E-mail address: tmchen@mail.nctu.edu.tw (T.-M. Chen).

0277-5387/$ - see front matter © 2005 Elsevier Ltd. All rights reserved.
doi:10.1016/j.poly.2005.02.009

the emission through fast radiationless decay through the MC states [8]. Moreover, the open coordination centres of the square planar platinum(II) complex can allow for other deactivating pathways to occur through metal interactions with the environment [9]. These facts are responsible for not so encouraging photoluminescence (PL) and electroluminescence (EL) performances of platinum based complexes. Recently, Che et al. reported new orange-yellow emitting schiff-base complexes of platinum(II) [10] showing modest results. The present work reports the syntheses and characterization of some strong orange-emitting cyclometallated platinum(II) complexes, (bt)Pt(acac) (**1**)/(X-bt)Pt(acac) (X = F (**2**), OMe (**3**), CF_3 (**4**); bt = 2-phenylbenzothiazolato; acac = acetylacetonate), study of their photophysical properties, X-ray single crystal structure analysis of (MeO-bt)Pt-(acac) and their applications in OLEDs.

2. Experimental

2.1. Materials

Potassium tetrachloroplatinate(II) was purchased from Alfa Aesar, USA, 2,4-pentanedione from Lanscaster, 2-ethoxyethanol and glacial acetic acid from Tedia Company, Ins. and the rest of the chemicals and solvents (AR grade) from Tokyo Kasei Kogyo Co. Ltd., Japan, and they were used as received.

2.2. Instrumentation

The ultraviolet–visible (UV–Vis) spectra of the phosphorescent Ir(III) complexes were measured on an UV–Vis spectrophotometer (Agilent model 8453) and corrected for background due to solvent absorption. Photoluminescence (PL) spectra were carried out with a spectrofluorometer (Jobin-Yvon Spex, model Fluorolog-3). The photo-physical measurements of these complexes have been carried out in aerated dichloromethane. NMR spectra were recorded on a Varian 300 MHz. MS spectrometer (EI and FAB) were taken by micromass TRIO–2000. Elemental analyses have been carried out by using a Heraeus CHN-O-RAPID analyzer. TG–DTA analysis was carried out by using a thermal analyzer (SEIKO 1TG/DTA 200). Emission lifetimes were obtained by exponential fitting of emission decay curves recorded on a Continuum NY61 spectrofluorometer.

2.3. Crystallography

Single crystal diffraction data for Pt(MeO-bt)(acac) were collected on a Bruker Smart-CCD diffractometer equipped with a normal focus, 3kW sealed-tube X-ray source (λ = 0.71073 Å). The intensity data were collected in the ω scan mode (width of 0.3/° frame) and corrected for *Lp* and absorption effects using the SAINT [11] program. Cell refinement and data reduction were carried out using the program Bruker SHELXTL [12]. The structure was solved by direct methods using the SHELXTL [12] version 5.1 software packages. The structure was further refined by full-matrix least-squares methods based on F^2 using SHELXTL version 5.1 [12]. Non-hydrogen atom positions were refined anisotropically, whereas the hydrogen positions were not refined.

2.4. Syntheses

bt/X-bt (X = –F, –OMe, $–CF_3$): The detailed synthetic procedure of these ligands has been described in the literature [13].

(bt/X-bt)Pt(μ-Cl)$_2$Pt(bt/X-bt) [14]: The ligands (2 mmol) were added to a suspension of potassium tetrachloroplatinate (1 mmol) in glacial acetic acid (300 ml) and the reaction mixture was stirred for several days (3–5 days) whilst maintaining the temperature at ~80 °C, which resulted in a yellow coloured product that was distinctly discernable from the red platinum(II) salt. The product was isolated through filtration and washed with water, acetone and ether 5–6 times to remove almost all the excess starting materials.

(bt)Pt(μ-Cl)$_2$Pt(bt). Yield: 45%. *Anal*. Calc. for $C_{26}H_{16}N_2Cl_2S_2Pt_2$: C, 35.4; H, 1.8; N, 3.2. Found: C, 35.2; H, 1.8; N, 3.1%.

(F-bt)Pt(μ-Cl)$_2$Pt(F-bt). Yield: 48%. *Anal*. Calc. for $C_{26}H_{14}N_2F_2Cl_2S_2Pt_2$: C, 34.0; H, 1.5; N, 3.1. Found: C, 33.7; H, 1.7; N, 3.1%.

(MeO-bt)Pt(μ-Cl)$_2$Pt(MeO-bt). Yield: 50%. ^{1}H NMR (300 MHz, $CDCl_3$): 9.92 (d, 1H, J = 8.7 Hz), 9.93 (d, 1H, J = 7.5 Hz), 8.40 (d, 2H, J = 8.6 Hz), 7.92 (d, 1H, J = 6.3 Hz), 7.78 (d, 1H, J = 6.7 Hz), 7.52 (m, 2H), 7.35 (m, 2H), 6.96 (d, 2H, J = 8.2 Hz), 6.53 (d, 1H, J = 7.2 Hz), 5.56 (s, 1H), 3.81 (s, 3H), 3.51 (s, 3H). *Anal*. Calc. for $C_{28}H_{20}N_2O_2Cl_2S_2Pt_2$: C, 35.4; H, 1.8; N, 3.2. Found: C, 35.2; H, 1.8; N, 3.1%.

(CF_3-bt)Pt(μ-Cl)$_2$Pt(CF_3-bt). Yield: 44%. *Anal*. Calc. for $C_{28}H_{14}N_2F_6Cl_2S_2Pt_2$: C, 33.0; H, 1.4; N, 2.8. Found: C, 32.9; H, 1.4; N, 3.0%.

(bt/X-bt)Pt(acac) [15]: The dinuclear complexes (1 mmol) were dissociated into the mononuclear platinum(II) complexes by reacting with acetylacetone (2.5 mmol) in the presence of sodium carbonate (8 mmol) and 2-ethoxyethanol (10 ml) as solvent under refluxing conditions for 12 h. These complexes show better solubility in common organic solvents with respect to their corresponding dinuclear complexes. These complexes were recrystallised from a mixture of dichloromethane and methanol (1:1).

(bt)Pt(acac): ^{1}H NMR (300 MHz, $CDCl_3$): 9.20 (d, 1H, J = 8.1 Hz), 7.80 (d, 1H, J = 8.1 Hz), 7.69 (d, 1H,

J = 7.5 Hz), 7.47 (m, 3H), 7.19 (d, 1H, J = 7.5 Hz), 7.10 (t, 1H, J = 7.2 Hz), 5.56 (s, 1H), 2.09 (s, 3H), 2.03 (s, 3H). FABMS: *m/z*: 504, Calc. 504.1. *Anal*. Calc. for $C_{18}H_{15}NO_2SPt$: C, 42.8; H, 3.0; N, 2.8. Found: C, 42.5; H, 3.0; N, 2.7%.

(F-bt)Pt(acac): ^{1}H NMR (300 MHz, $CDCl_3$): 9.17 (d, 1H, J = 8.1 Hz), 7.79 (d, 1H, J = 12 Hz), 7.44 (m, 4H), 6.81 (d, 1H, J = 6.0 Hz), 5.78 (s, 1H), 2.10 (s, 3H), 2.04 (s, 3H). FABMS: *m/z*: 522, Calc. 522.1. *Anal*. Calc. for $C_{18}H_{14}NO_2SPt$: C, 41.4; H, 2.7; N, 2.7. Found: C, 42.5; H, 2.6; N, 2.7%.

(MeO-bt)Pt(acac): ^{1}H NMR (300 MHz, $CDCl_3$): 9.11 (d, 1H, J = 8.4 Hz), 7.75 (d, 1H, J = 8.4 Hz), 7.51 (t, 1H, J = 6.7 Hz), 7.39 (m, 2H), 7.19 (d, 1H, J = 2.4 Hz), 6.67 (dd, 1H, J = 2.4, 8.7 Hz), 5.56 (s, 1H), 3.89 (s, 1H), 2.08 (s, 3H), 2.02 (s, 3H). FABMS: *m/z*: 534, Calc. 534.1. *Anal*. Calc. for $C_{19}H_{17}NO_3SPt$: C, 41.4; H, 3.2; N, 2.6. Found: C, 41.2; H, 3.2; N, 2.5%.

(CF_3-bt)Pt(acac): ^{1}H NMR (300 MHz, $CDCl_3$): 9.24 (d, 1H, J = 8.7 Hz), 7.93 (s, 1H), 7.85 (d, 1H, J = 7.2 Hz), 7.52 (m, 3H), 7.34 (d, 1H, J = 7.5 Hz), 5.59 (s, 1H), 2.35 (s, 3H), 2.26 (s, 3H). FABMS: *m/z*: 572, Calc. 572.1. *Anal*. Calc. for $C_{19}H_{14}NO_2F_3SPt$: C, 39.9; H, 2.4; N, 2.4. Found: C, 39.8; H, 2.4; N, 2.4%.

2.5. OLED fabrication and testing

Organic layers were fabricated by high-vacuum thermal evaporation onto a glass substrate precoated with an indium–tin-oxide (ITO) layer with a sheet resistance of 20 Ω. Prior to use, the ITO surface was ultrasonicated in a detergent solution followed by rinsing with deionized (DI) water, dipped into acetone, trichloroethylene and 2-propanol, and then degreased with a vapor of 2-propanol. After degreasing, the substrate was oxidized and cleaned in a UV-ozone chamber before it was loaded into an evaporator. In a vacuum chamber at a pressure of 10^{-6} torr, 500 Å of NPB (*N*,*N*′-di-1-napthyl-*N*,*N*′-diphenylbenzidine) as the hole transporting layer; 200 Å the complex doped (7%) CBP as the emitting layer; 100 Å of BCP (2,9-dimethyl-4,7-diphenyl-1,10-phenanthroline) as a hole and exciton blocking layer (HBL); 650 Å of Alq_3 (*tris*(8-quinolinato)aluminium) as electron transport layer; and a cathode composed of 10 Å lithium fluoride and 2000 Å aluminum were sequentially deposited onto the substrate to give the device structure. Fig. 1(a) and (b) show the multilayer structure of the device and the chemical structures of the molecules used in fabricating the EL device, respectively. The current–voltage (*I–V*) profiles and light intensity characteristics for the above-fabricated devices were measured in a vacuum chamber of 10^{-6} torr at ambient temperature using a Keithley 2400 Source Meter/2000 Multimeter coupled to a PR 650 Optical Meter.

3. Results and discussion

3.1. Syntheses and characterizations

The synthetic routes for the platinum(II) complexes described here involves two steps. In the first step, K_2PtCl_4 is reacted with an excess of bt/substituted bt to produce a chloride-bridged dinuclear complex (Fig. 2, inset), i.e. (bt/X-bt)Pt(μ-Cl)$_2$Pt(bt/X-bt). All these complexes, except (MeO-bt)Pt(μ-Cl)$_2$Pt(MeO-bt), are almost insoluble in common organic solvents which makes them impossible for solution phase characterization. The polar methoxy substituent is assumed to be responsible for making the corresponding dinuclear platinum(II) complex have a better solubility in more or less polar organic solvents. The ^{1}H NMR spectrum

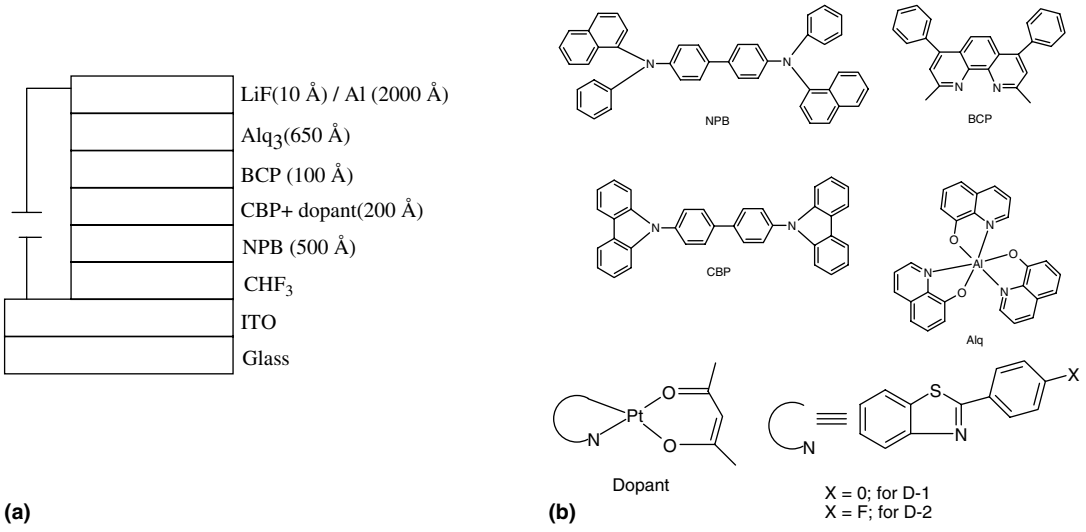


Fig. 1. (a) Multilayer device structure. (b) The chemical structures of the molecules used in this device.

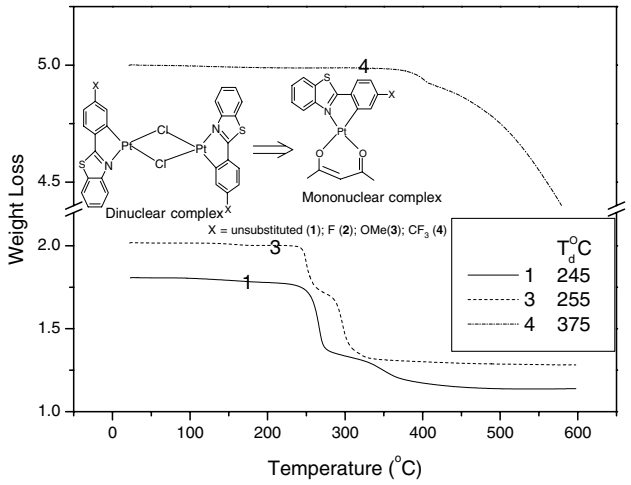


Fig. 2. TGA thermograms of the platinum(II) complexes **1**, **3** and **4**, T_d represents decomposition temperature (inset: the chemical structures of the complexes investigated).

of (MeO-bt)Pt(μ-Cl)$_2$Pt(MeO-bt) (deposited) shows the splitting of the methyl proton in the methoxy substituent of the dinuclear complex, suggesting that the two non-equivalent methoxy protons exist in the two separate ligands of that complex. It is the result from different interactions with the solvent molecules. The chloride-bridged dinuclear complexes can be readily dissociated to emissive, mononuclear complexes by replacing the bridging chlorides with monoanionic 2,4-pentanedionate (Fig. 2, inset). These mononuclear complexes were characterised by ^{1}H NMR spectra and elemental analyses, but ^{13}C NMR spectra were not recorded due to not having the required level of solubility in deuterated solvents. Thermogravitometric analysis (TGA) shows the stability of these complexes in the range of 245–375 °C (Fig. 2) and they can be easily sublimed at low pressure (10^{-3} mmHg).

3.2. Crystal structures

X-ray single crystal structure analysis was carried out for one of the platinum complexes **3**, which authenticates the square planar geometry (discrepancy factor ~5%; Fig. 3(a)). X-ray quality single crystals of the complex were grown by slow diffusion of methanol into a dichloromethane solution of **3**. The bond length of Pt1–N1 (2.02 Å) is slightly larger compared to that of common Pt–N bonds, as this N is opposite to the acetylacetonate oxygen atom, having a weak *trans* influence. The bond length of Pt1–O2 (2.085 Å) is higher compared to that of Pt1–O1 (1.994 Å), as O2 is *trans* to carbon which has a strong *trans*-influence. The bond length of Pt1–C9 (1.967 Å) is consistent with other reported cyclometallated complexes [6d,16]. The Pt(1)–O(1) (1.994 Å) and Pt(1)–O(2) (2.085 Å) bond lengths are also consistent with other reported cyclometallated–diketonato derivatives [17]. The C(9)–Pt(1)–O(1), 90.65(16)°; C(9)–Pt(1)–N(1), 80.48(17)°; O(1)–Pt(1)–N(1), 171.11(15)°; C(9)–Pt(1)–O(2), 176.82(15)°; O(1)–Pt(1)–O(2), 91.23(13)°; N(1)–Pt(1)–O(2), 97.62(14)° bond angles are typical for cyclometallates and –diketonate derivatives of Pt [16,17]. There is very little distortion away from the square plane. The molecular packing diagram of Pt(MeObt)(acac) (Fig. 3(b)) shows the molecules pack as head-to-tail dimers; each molecule of the dimer is related to the other by a center of inversion. The short inter plane and metal–metal distances (Pt1···Pt1 = 3.369; Pt2···Pt2 = 3.369; Plane–Plane = 3.360 Å;

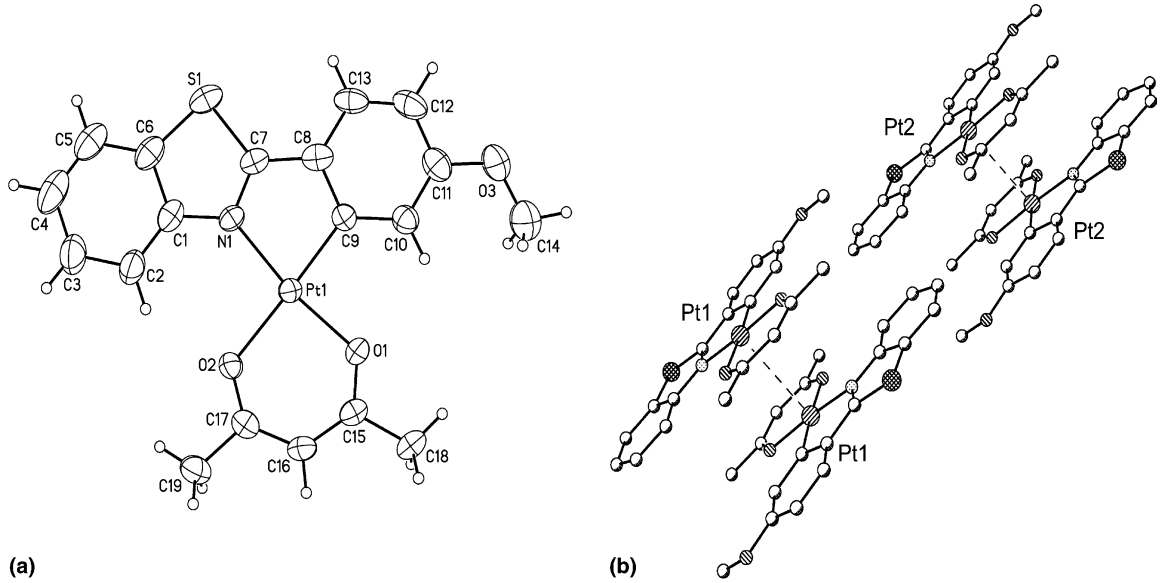


Fig. 3. (a) Molecular structure of complex **3** (shows 50% thermal probability); (b) molecular packing diagram showing the π stacking of complex **3**.

centre of symmetry is formed between the acac and the five membered ring) suggest that there exist extensive π–π and metal–metal interactions [6d] which support the excimer formation.

3.3. Photophysical behavior

The absorption spectra of all the complexes in dichloromethane were recorded at room temperature, and show intense higher energy transitions $^1\pi$–π^* (280–350 nm; $\varepsilon \sim 5 \times 10^3$ dm^3 mol^{-1} cm^{-1}) as well as comparatively lower energy, broad triplet state transitions (350–475 nm; $\varepsilon \sim 2 \times 10^3$ dm^3 mol^{-1} cm^{-1}), as shown in Fig. 4. These broad MLCT states exhibit solvatochromic effects. The complexes emit orange light in the solid state as well as in solution. Highly structured PL emission and sharp vibronic progressions of ~2185 cm^{-1} were observed (Fig. 5). These observations helped us to identify the nature of the lowest-emitting states of both triplet π–π* and MLCT character. In general, the electron-donating substituent raises the highest occupied molecular orbitals (HOMO) and the lowest unoccupied molecular orbitals (LUMO) and the reverse is truth for an electron-withdrawing substituent [18,19]. The complex **4** which contains electron-withdrawing substituted (–CF_3) benzothiazolate shows a bathochromic shifted emission, while those contain electron-releasing substituted (–F (**2**), –MeO (**3**)) benzothiazolates undergo *ipso*-chromic shifted emission with respect to the unsubstituted complex, **1**, as shown in Fig. 5. Hence it can be inferred that the position occupied by the substituents in (2-phenyl)-benzothiazolate of the iridium(III) complexes are dominated by LUMO character. The maximum absorbance and emission of all the complexes are listed in Table 1. The excimer formation was evidenced through the time resolved photoluminescence measurements [20]. The emission kinetic trace for one of the complexes **4** produced by excitation at 378 nm and monitored near the lower energy shoulder emission (e.g., 656 nm; Fig. 5) shows monoexponential decay behavior. The reciprocal of the lifetimes (known as emission decay rate constant, k_{obs}) obtained are shown in Fig. 6 as a function of concentration. The lifetime was found to decrease steadily with increasing concentration, indicative of excimer formation. The emission lifetime of the monomer of complex **4** at infinite dilution, τ_0 (0.58 μs), and the apparent rate constant of self-quenching, k_Q, were determined by using Eq. (1) (0.58 μs; 7×10^8 M^{-1} s^{-1}) from the linear variation of the observed emission decay constant, k_{obs}, as a function of the concentration of the complex, [Pt]. The high value of k_Q indicates extensive excimer formation. It should also be true for the other platinum(II) complexes.

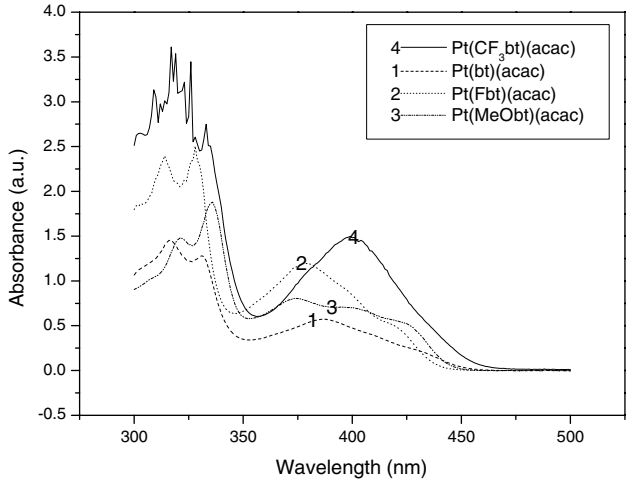


Fig. 4. UV–Vis absorption spectra of the complexes **1**, **2**, **3** and **4** measured at 298 K showing the tuning of the lowest excited state.

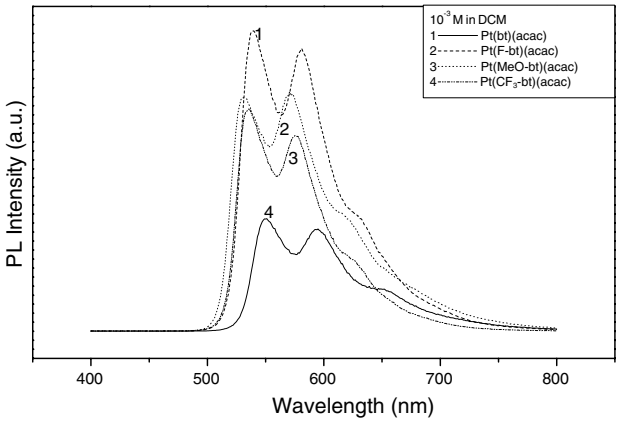


Fig. 5. PL spectra showing tuning of emission wavelength with respect to the electronic properties of the substituents.

$$k_{obs} = 1/\tau_0 + k_Q[Pt]\ [20] \quad (1)$$

Table 1
Absorption and emission properties of the platinum(II) complexes **1**–**4**

Complexes	abs, λ_{max}, nm (logε)[a]	Emission at 298 K, λ_{max}, nm[a]
1	228 (6.0); 254 (5.9); 262 (5.7); 316 (5.8); 330 (5.7); 387 (5.4); 431 (5.0)	539; 580
2	228 (5.8); 252 (5.7); 313 (5.6)sh; 327 (5.6); 377 (5.3)sh; 416 (5.0)	531; 571
3	228 (6.2); 242 (6.1)sh; 279 (5.9); 320 (6.1); 334 (6.1); 373 (5.7); 402 (5.6)sh; 423 (5.5)sh	534; 575
4	228 (6.2); 259 (6.2); 318 (6.1); 333 (6.0)sh; 398 (5.7)b	551; 594

[a] In dichloromethane; sh, shoulder; b, broad.

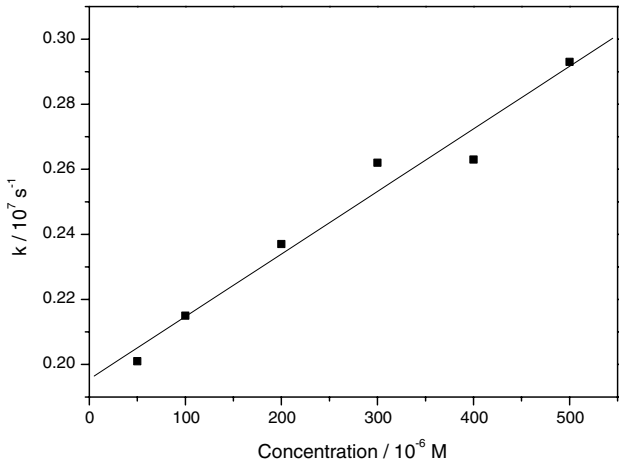


Fig. 6. Plot of the measured luminescence decay constants versus concentration of platinum complex **4**.

3.4. Electroluminescence

All these complexes are thermally stable up to 245–375 °C and they can be easily sublimed at low pressure (10^{-3} mmHg) and emit tunable bright yellow-orange light at room temperature. All these features make them good emitters in highly efficient EL devices. The platinum complexes, **1** and **2** (the corresponding devices denoted as D-1 and D-2, respectively) were doped into the host material, CBP (4,4′-(*N*,*N*′-dicarbazole)biphenyl), in the emitting zone with doping contents of 5%, 7% and 9%. The observed device performances were found to vary marginally throughout the doping concentration range (Table 2). Current-density, voltage and luminance characteristics (*I*–*V*–*L*) for devices D-1 and D-2 with 5% doping level are shown in Fig. 7(a) and (b), respectively. Comparison of device performances for the devices D-1 and D-2 at 5% doping level are also summarized in Table 3, which show the maximum luminance yields of 14.3 and 16.0 cd A^{-1} @2 mA cm^{-2} for D-1 and D-2, respectively. The maximum emission wavelength (λ_{em}^{max}) for D-2 shows apparent *ipso*-chromic shift with respect to that of device D-1 (Fig. 8), as observed in PL emission spectra. The maximum emission wavelengths in the EL spectra are found to be independent of the applied voltage (for current density up to 100 mA cm^{-2}), but show bathochromically shifted emission with increasing doping concentration. The EL intensity of the shoulder peak

Table 2
EL performance of D-1 and D-2 at different dopant concentrations [at 20 mA cm^{-2} current density in parentheses]

Device	wt%	V_d (V)	L_{max} (cd m^{-2})	CIE		$\eta_{ext.\ max}$ (%)	$\eta_{L,\ max}$ (cd A^{-1})	$\eta_{P,\ max}$ (lm W^{-1})
				x	*y*			
D-1	5	10.7	2573	0.48	0.50	4.9	12.9	3.8
	7	11.2	2638	0.49	0.48	5.6	13.2	3.7
	9	10.6	2197	0.52	0.47	5.3	11.0	3.3
D-2	5	11.2	2820	0.47	0.50	5.7	14.1	4.0
	7	11.5	2769	0.48	0.58	6.9	13.8	3.8
	9	11.7	2442	0.47	0.58	6.7	12.2	3.3

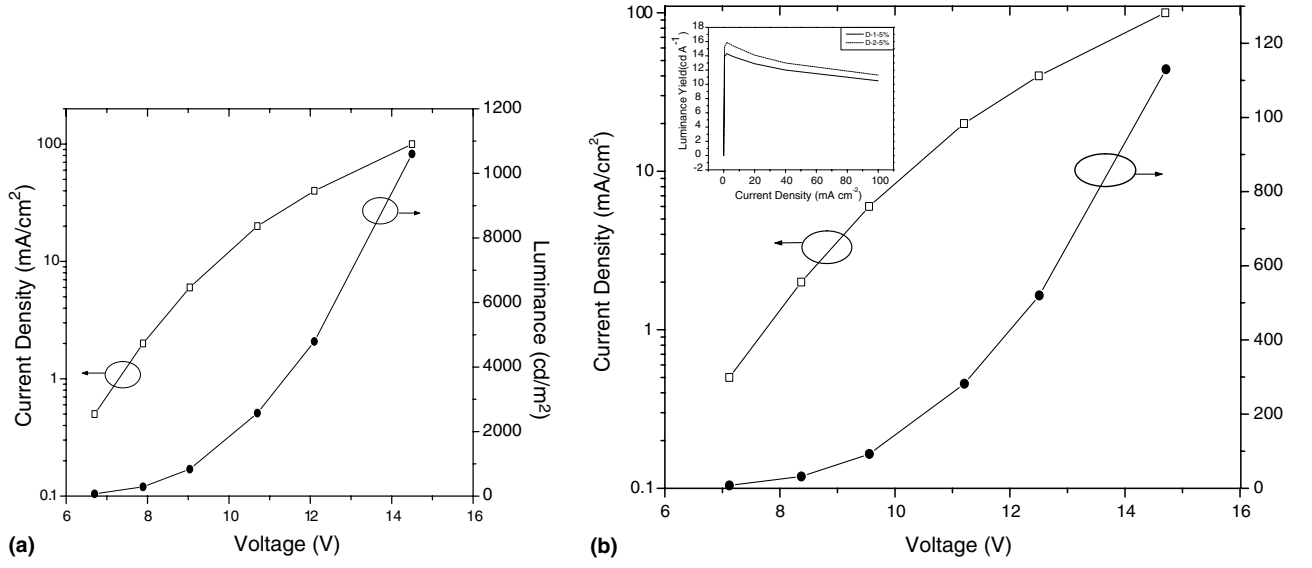


Fig. 7. Current density, voltage and luminance characteristics for OLED using complexes **1** (a) and **2** (b) with 5% doping level (b: inset: plot of luminescence efficiency vs. current density).

Table 3
Comparison of EL performances for D-1 and D-2 with 5% doping level operated at different current densities

Current density (mA cm^{-2})	V (V)		L (cd m^{-2})		CIE				η_{ext} (%)		η_L (cd A^{-1})		η_P (lm W^{-1})	
					x	y	x	y						
	D-1	D-2	D-1	D-2	D-1		D-2		D-1	D-2	D-1	D-2	D-1	D-2
0.5	6.7	7.1	70	77	0.40	0.50	0.49	0.50	5.4	6.5	13.9	15.3	6.5	6.5
2.0	7.9	8.4	286	319	0.49	0.50	0.48	0.51	5.5	6.6	14.3	16.0	5.7	6.6
6.0	9.0	9.6	834	924	0.49	0.50	0.48	0.51	5.3	6.3	13.9	14.8	4.8	6.3
20.0	10.7	11.2	2573	2820	0.48	0.50	0.48	0.51	4.9	5.7	12.9	14.1	3.8	5.7
40.0	12.1	12.5	4787	5197	0.48	0.50	0.48	0.51	4.6	5.3	12.0	13.0	3.1	5.3
100.0	14.5	14.7	10550	11320	0.48	0.50	0.47	0.51	4.0	4.6	10.6	11.3	2.3	4.6

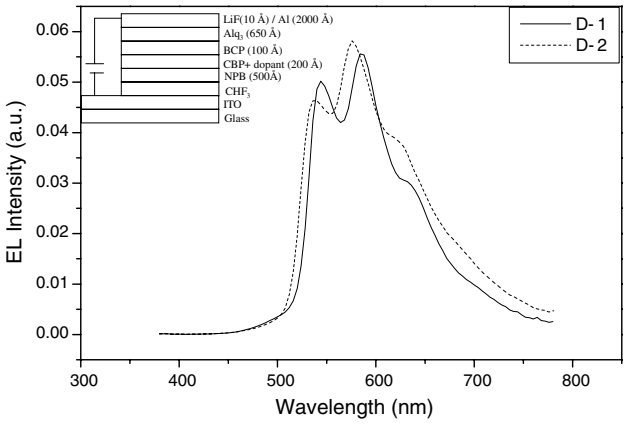


Fig. 8. EL spectra for the platinum(II) complexes **1** and **2** (inset: multilayer EL device configuration).

(~625–630 nm) has been observed to increase with increasing doping concentration, whereas that of the other two major peaks was found to decrease (~540 and ~584 nm). These observations support that the emission from the shoulder peak is generated from the excimer and it is also consistent with the results obtained from the molecular packing diagram (Fig. 3(b)) and concentration dependent luminescence decay measurements discussed before. It is to be noted that at 100 mA cm^{-2} current density, the luminances are found to be 10550 and 11320 cd m^{-2}, obtained for D-1 and D-2, respectively, and under similar conditions there have not been significant changes of luminance yields (i.e., 10.6 and 11.3 cd A^{-1}, for D-1 and D-2, respectively).

4. Conclusion

The syntheses and characterizations of a series of platinum(II) complex dopants have been performed. The EL performances of OLEDs employing these platinum(II) dopants are found to be substantially superior to those previously reported for OLEDs based on cyclometallated platinum(II) complexes [6]. These EL results were even far better than those previously reported [21] where a similar type of cyclometallated iridium(III) dopants were used in the same device structure. It should be mentioned that the device containing fluoro-substituted dopant shows relatively better EL performances with respect to that using the unsubstituted benzothiazolato Pt(II) complex.

Acknowledgements

The work has been supported in part by the Program for Promoting University Academic Excellence from Ministry of Education, Taiwan, ROC under the Contract No. 91-E-FA04-2-4 (B).

Appendix A. Supplementary data

Crystallographic data for the structural analysis have been deposited with the Cambridge Crystallographic Data Centre, CCDC No. 247375 for compound Pt(MeO-bt)(acac). Copies of this information may be obtained free of charge from the Director, CCDC, 12 Union Road, Cambridge, CB2 1EZ, UK (fax: +44 1223 336033; email: deposit@ccdc.cam.ac.uk or http://www.ccdc.cam.ac.uk). Supplementary data associated with this article can be found, in the online version at doi:10.1016/j.poly.2005.02.009.

References

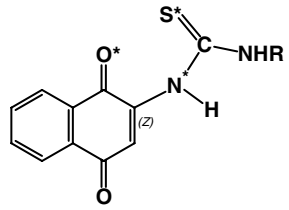
[1] (a) V. Balzani, A. Credi, F. Scandola, L. Fabbrizzi, A. Poggi (Eds.), Transition Metals in Supramolecular Chemistry, Kluwer, Dordrecht, The Netherlands, 1994;
(b) J.M. Lehn, Supramolecular chemistry-concepts and perpectives, VCH, Weinheim, Germany, 1995;
(c) C.A. Bignozzi, J.R. Schoonover, F. Scandola, Prog. Inorg. Chem. 44 (1997) 1.
[2] (a) F.G. Gao, A.J. Bard, J. Am. Chem. Soc. 122 (2000) 7426;
(b) M. Grätzel, Nature 414 (2001) 338;
(c) C.F. Chow, B.K.W. Chiu, M.H.W. Lam, W.Y. Wong, J. Am. Chem. Soc. 125 (2003) 7802.
[3] (a) J. Breu, C. Kratzer, H. Yersin, J. Am. Chem. Soc. 122 (2000) 2548;
(b) B. Carlson, G.D. Phelan, W. Kaminsky, L. Dalton, X. Jiang, S. Liu, A.K.Y. Jen, J. Am. Chem. Soc. 124 (2002) 14162.

[4] (a) V.W.W. Yam, Chem. Commun. (2001) 789;
(b) K.K.W. Lo, W.K. Hui, D.C.M. Ng, J. Am. Chem. Soc. 124 (2002) 9344.
[5] (a) I.M. Dixon, J.P. Collin, J.P. Sauvage, L. Flamigni, S. Encinas, F. Barigelletti, Chem. Soc. Rev. (2000) 385;
(b) S. Lamansky, P. Djurovich, D. Murphy, F. Abdel-Razzaq, H.E. Lee, C. Adachi, P.E. Burrow, S.R. Forrest, M.E. Thompson, J. Am. Chem. Soc. 123 (2001) 4304;
(c) Md.K. Nazeeruddin, R. Humphry-Baker, D. Berner, S. Rivier, L. Zuppiroli, M. Graetzel, J. Am. Chem. Soc. 125 (2003) 8790;
(d) W.J. Finkenzeller, H. Yersin, Chem. Phys. Lett. 377 (2003) 299;
(e) P. Coppo, E.A. Plummer, L. De Cola, Chem. Commun. (2004) 1774.
[6] (a) M.A. Baldo, d.F. O'Brien, Y. You, A. Shoustikov, S. Sibley, M.E. Thompson, S.R. Forrest, Nature 395 (1998) 151;
(b) R.C. Kwong, S. sibley, T. Dubovoy, M.A. Baldo, S.R. Forrest, M.E. Thompson, Chem. Mater. 11 (1999) 3709;
(c) V. Cleave, G. Yahioglu, P.L. Barny, R.H. Friend, N. Tessler, Adv. Mater. 11 (1999) 285;
(d) J. Brooks, Y. Babayan, S. Lamansky, P.I. Djurovich, I. Tsyba, R. Bau, M.E. Thompson, Inorg. Chem. 41 (2002) 3055.
[7] F. Barigelletti, D. Sandrini, M. Maestri, V. Balzani, A. von Zelewsky, L. Chassot, P. Jolliet, U. Maeder, Inorg. Chem. 27 (1988) 3644.
[8] T.K. Aldridge, E.M. Stacy, D.R. Mcmillin, Inorg. Chem. 33 (1994) 722.
[9] J.M. Bevilacqua, R. Eisenberg, Inorg. Chem. 33 (1994) 2913.
[10] C. Che, S. Chan, H. Xiang, M.C.W. Chan, Y. Liu, Y. Wang, Chem. Commun. (2004) 1484.
[11] G.M. Sheldrick, SAINT; Bruker Analytical X-ray Instrument Division; Madison, WI, 1998.
[12] G.M. Sheldrick, SHELXTL, version 5.1; Bruker AXS GmbH, Karlsruhe, Germany, 1998.
[13] A. Brembilla, D. Roizard, P. Lochon, Synth. Commun. 20 (1990) 3379.
[14] G.W.V. Cave, F.P. Fanizzi, R.J. Deeth, W. Errington, J.P. Rourke, Organometallics 19 (2000) 1355.
[15] S. Lamansky, M.E. Thompson, V. Adamovich, P.I. Djurovich, C. Adachi, M.A. Baldo, S.R. Forrest, R. Kwong, US patent, 0182441 A1, 2002.
[16] J. Breu, K.J. Range, A. von Zelewsky, H. Yersin, Acta Crystallogr. C 53 (1997) 562.
[17] M. Ghedini, D. Pucci, A. Crispini, G. Barberio, G. Barberio, Organometallics 18 (1999) 2116.
[18] R. Pohl, J. Pavel Anzenbacher, Org. Lett. 5 (2002) 2769.
[19] R. Pohl, V.A. Montes, J. Shinar, J. Pavel Anzenbacher, J. Org. Chem. 69 (2004) 1723.
[20] J.A. Williams, A. Beeby, E. Stephen Davies, J.A. Weinstein, C. Wilson, Inorg. Chem. 42 (2003) 8609.
[21] I.R. Laskar, T.-M. Chen, Chem. Mater. 16 (2004) 111.

at 600 nm, an axially elongated electronic environment ($g_{\parallel} \gg g_{\perp} > 2.0$) appropriate for a $d_{x^2-y^2}$ ground state [5] and positive redox potentials of the Cu(II)/Cu(I) couple [6], ranging from +0.150 to +0.80 V. However, it has been suggested that copper(II)–thiolato/thionato complexes are usually unstable with respect to intramolecular redox reorganizations thus forming Cu(I), disulfide and other thiolato derived oxidation products [7]. The thermodynamics of these reactions could be disfavored if the reduction potential of the Cu(II)/Cu(I) couple is suppressed by (a) imposing the appropriate stereochemistry [8] that favors copper(II); (b) introducing multiple bond character at the sulfur donor site [9]; (c) use of bulky substituents on ligands [10] or (d) the sulfur center should be electronically constrained by the adjacent redox active part of the ligating systems [2].

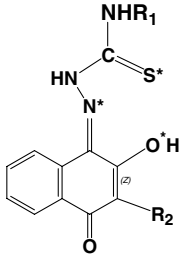
One such attempt is explored in the present work by incorporating the redox active quinone/semiquinone redox couple [11] in close proximity of thione or thiol sulfur center which probably could control the electronic as well as electrochemical behavior of their copper(II) complexes. The tridentate ONS ligating system of thiosemicarbazones can provide a thione/thiolato sulfur center while the naphthoquinone segment may complement the other aspect of constraining this center necessary for the stability of Cu(II) species.

Thiosemicarbazones are unique amongst the sulfur family of ligating systems not only because they possess a wide range of biological properties [12] but also due to the fact that their complexes exhibit various structural, electronic as well as biological potentialities [13]. The coupled chromophore of quinone–thiosemicarbazones probably may increase the covalent character in copper–ligand bonding thus disfavoring thiol oxidation and may enhance the stability of copper(II)–thiolato/thionato complexes. This work is an extension of our recent efforts in understanding the structural, electrochemical and biological properties of transition metal thiosemicarbazones complexes [14]. The present communication describes the detailed EPR analysis and redox behavior of pseudo-square-planar copper(II)–quinone thiosemicarbazones complexes possessing either thione or thiol sulfur centers. The copper(II) complexes described herein have been synthesized using ligands as presented in Fig. 1.



R= H; L_5 =2 -thiosemicarbazido-1,4-naphthoquinone

R= CH_3;L_6 =2 -(N^4-methyl)-thiosemicarbazido-1,4-naphthoquinone



$R_1 = R_2 = H$; L_1 = 2-hydroxy-1,4-naphthoquinone-1-thiosemicarbazone

$R_1 = H$, $R_2 = CH_3$; L_2 = 3-methyl-2-hydroxy-1,4-naphthoquinone-1-thiosemicarbazone

$R_1 = H$, $R_2 = Cl$; L_3 = 3-chloro-2-hydroxy-1,4-naphthoquinone-1-thiosemicarbazone

$R_1 = CH_3 = R_2 = H$; L_4 =

2-hydroxy-1,4-naphthoquinone-1-(N^4-methyl)thiosemicarbazone

Fig. 1. The naphthoquinone thiosemicarbazone ligating system with atoms marked as * denoting binding sites for the ligands.

2. Experimental

2.1. Materials

Copper chloride dihydrate, 2-hydroxy-1,4-naphthoquinone, thiosemicarbazide and N^4-methyl-thiosemicarbazide were purchased from Fluka A.G. and were used without further purification. Solvents were purified by the literature methods [15] prior to their use. Ligands are synthesized according to the procedures described earlier by Miller and co-workers [16].

2.2. Preparation of the ligands

2.2.1. Preparation of L_1–L_3

To a suspension of 0.01 mol of quinone (2-hydroxy-1,4-naphthoquinone; 3-methyl-2-hydroxy-1,4-naphthoquinone and 3-chloro-2-hydroxy-1,4-naphthoquinone) in water, 10 ml of 0.1 N NaOH was added so as to obtain a dark red solution. An aqueous-methanolic (50%) solution of thiosemicarbazide (0.01 mol) was then added dropwise to the above solution with constant stirring. The mixture was further stirred for about 3 h at the end of which the solution was neutralized with 10% HCl, until precipitation. The crude product was recrystallized from aqueous methanol and dried under vacuum over $CaCl_2$ yielding a reddish yellow crystalline product (L_1–L_3, respectively). The analyses (%) for the ligands are as follows:

L_1: Calc. for $C_{11}H_9N_3O_2S$: C, 53.48; H; 3.67; N; 16.99; S, 12.97. Observed: C, 53.81; H, 3.51; N, 17.38; S, 12.68. L_2: Calc. for $C_{12}H_{11}N_3O_2S$: C, 55.17; H, 4.21; N, 16.08; S, 12.32. Observed: C, 54.93; H, 4.07; N, 16.64; S, 12.68. L_3: Calc. for $C_{11}H_9N_3O_2SCl$: C,

46.90; H, 2.68; N, 14.91; S, 12.32. Observed: C, 46.17; H, 2.91; N, 15.47; S, 12.03. IR (KBr, cm^{-1}): 3410 ν(–OH); 3350, 3270 ν(–NH); 1620 ν(C=N); 1160, 820 ν(C=S).

2.2.2. Preparation of L_4

This was synthesized according to a similar procedure outlined earlier except instead of thiosemicarbazide, its N^4-methyl derivative was reacted with 2-hydroxy-1,4-naphthoquinone. L_4: Calc. for $C_{12}H_{11}N_3O_2S$: C, 55.17; H, 4.21; N, 16.08; S, 12.32. Observed: C, 55.02; H, 4.18; N, 16.83; S, 12.65.

IR (KBr, cm^{-1}): 3410 ν(–OH); 3370, 3280 ν(–NH); 1620 ν(C=N); 1160, 820 ν(C=S).

2.2.3. Preparation of L_5 and L_6

To a methanolic suspension of 2-hydroxy-1,4-naphthoquinone (0.01 mol), 10 mL of glacial acetic acid was added so as to adjust the pH to ca. 4.5 and the mixture was warmed to get a clear solution. An aqueous-methanolic (50%) solution of thiosemicarbazide or N^4-methyl thiosemicarbazide (0.01 mol) was then added dropwise to the above solution with constant stirring. The mixture was further stirred for about 3 h at the end of which a dark red colored solid started precipitating after 30 min. The crude product thus obtained was recrystallized from aqueous methanol and dried under vacuum over $CaCl_2$ yielding reddish yellow crystalline products (L_5 and L_6, respectively). The analyses (%) are as follows:

L_5: Calc. for $C_{11}H_9N_3O_2S$: C, 53.48; H, 3.67; N, 16.99; S, 12.97. Observed: C, 53.40; H, 3.24; N, 17.22; S, 12.60. L_6: Calc. for $C_{12}H_{11}N_3O_2S$: C, 55.17; H, 4.24; N, 16.08; S, 12.26. Observed: C, 54.79; H, 4.00; N, 16.48; S, 12.43.

IR (KBr, cm^{-1}): 3390, 3270 ν(–NH); 1680 ν (^{4}C=O); 1610 ν(^{1}C=O); 1162, 820 ν(C=S).

2.3. Preparation of copper(II)–thiosemicarbazone complexes

A general procedure adopted for the synthesis of the copper(II) complexes of L_1–L_6 was as follows:

Equimolar quantities (0.002 M) of the ligands (L_1–L_6) and copper(II) chloride dihydrate were dissolved in 20 mL of methanol separately and these solutions were degassed with N_2 for 5 min. The copper solution was added dropwise to ligand solution under N_2 atmosphere in a Schlenk assembly with constant stirring. After the complete addition of the copper solution, the pH of the reaction mixture was adjusted to 6–7 using alcoholic ammonia solution (6% v/v). The precipitated complexes were filtered, washed with acetone, recrystallized from methanol and dried under vacuum over $CaCl_2$. These complexes hereafter are referred as Cu_1–Cu_6, corresponding to ligands L_1–L_6.

2.4. Physical measurements

Elemental analyses were carried out using a Hosli-Holland C, H, and N analyzer. The magnetic susceptibility was measured at room temperature on a Faraday type magnetic balance with a permanent magnetic field of 7000 G and the instrument was calibrated with $Hg[Co(SCN)_4]$. The IR spectra were recorded on a Perkin–Elmer FTIR spectrometer using KBr discs while UV–Vis spectral measurements of DMSO solutions were made on a Shimadzu UV-300 spectrophotometer. The X-band ESR spectra at 298 and 77 K were recorded on a Varian ESR spectrometer with 100 kHz field modulation frequency and the instrument was calibrated with DPPH as the standard. Cyclic voltammetric experiments were performed on a BAS CV-27 assembly equipped with an X–Y recorder. Measurements were made on degassed 10 mM DMSO solutions of the complexes (N_2 bubbled for 15 min prior to measurements) containing 0.1 M tetraethyl ammonium perchlorate as a supporting electrolyte. The working system consisted of Pt-inlay (working), Pt-disc (auxiliary) and Ag/AgCl (reference) electrodes. The Ag/AgCl reference electrode was calibrated with the ferricinium/ferrocene redox couple, located at $E_{1/2}$ = +0.40 V (ΔE_p = 0.06 V).

3. Results and discussion

The interaction of L_1–L_6 with copper(II) chloride yields mono-ligand complexes with [CuLCl] composition (Table 1). All the complexes are non-electrolytic in nature indicating the coordination of the chloride ion to the metal center. The room temperature magnetic moments for these complexes (1.74–1.95 BM) correspond to the values normally observed for square-planar copper(II) compounds [17]. Slight deviation from the 'spin-only' value probably originates from mixing-in effects due to effective low symmetry.

3.1. Infrared spectra

The significant IR bands with their assignments of the copper(II) complexes in the region 4000–200 cm^{-1} are presented in Table 2. The IR spectra of L_1–L_4 exhibit an intermolecularly hydrogen bonded ν(–OH) vibration at ~3400 cm^{-1} [18], which disappears after complexation with the copper ions. It is further corroborated with the downfield shift of 50–80 cm^{-1} for ν(C–O) as well as an appearance of a band at 500 cm^{-1} due to a ν(Cu–O) stretch in the spectra of the copper complexes [19]. An azomethine nitrogen ν(C=N) band around 1620 cm^{-1} in the uncomplexed thiosemicarbazones undergoes a shift towards the lower energy side by ~40 cm^{-1} in the spectra of Cu_1–Cu_4. The bonding of the imine nitrogen as one of the coordinating sites is

Table 1
Analytical and room temperature magnetic moment data for Cu_1–Cu_6

Complex	% Yield	Analytical data					μ_{eff} (BM)
		% C	% H	% S	% Cl	% Cu	
Cu_1	84	37.74	2.17	9.01	9.52	18.32	1.78
$[CuC_{11}H_8N_3O_2SCl]$		(38.26)	(2.31)	(9.27)	(10.28)	(18.42)	
Cu_2	76	39.83	2.86	9.76	10.17	16.84	1.74
$[CuC_{12}H_{10}N_3O_2SCl]$		(40.11)	(2.78)	(8.91)	(9.87)	(17.70)	
Cu_3	72	34.06	1.95	8.25	19.01	15.58	1.90
$[CuC_{11}H_9N_3O_2SCl_2]$		(34.69)	(2.10)	(8.41)	(18.63)	(16.70)	
Cu_4	80	39.90	2.64	9.24	10.06	17.33	1.95
$[CuC_{12}H_{10}N_3O_2SCl]$		(40.11)	(2.78)	(8.91)	(9.87)	(17.70)	
Cu_5	75	37.95	2.18	9.11	9.88	18.07	1.76
$[CuC_{11}H_8N_3O_2SCl]$		(38.26)	(2.31)	(9.27)	(10.28)	(18.42)	
Cu_6	79	39.74	2.52	9.26	9.95	17.52	1.92
$[CuC_{12}H_{10}N_3O_2SCl]$		(40.11)	(2.78)	(8.91)	(9.87)	(17.70)	

Table 2
Significant IR spectral data (cm^{-1}) for Cu_1–Cu_6

Assignment	Cu_1	Cu_2	Cu_3	Cu_4	Cu_5	Cu_6
γ(N–H)	3280	3300	3295	3280	3290	3260
$\gamma(C{=}O)_{free}$	1650	1660	1645	1660	1650	1660
$\gamma(C{=}O)_{chelated}$					1610	1600
γ (C=N)	1580	1570	1580	1575	1590	1585
γ(C–S)	770	780	765	780	1335w, 785m	1327w, 780m
γ(Cu–O)	515	520	510	520	510	515
γ(Cu–N)	440	445	435	445	470	480
γ(Cu–S)	380	385	365	380	370	375
γ(Cu–Cl)	320	325	310	330	320	325

further confirmed with the presence of a band in the range 435–480 cm^{-1} assigned to a ν(Cu–N) vibration for these complexes [14f]. The increase for the ν(N–N) frequency in the spectra of the complexes is probably due to enhanced double bond character through chelation, thus offsetting the loss of electron density via donation to the metal ion, and is supportive of azomethine nitrogen coordination. The thiocarbonyl absorption around 820 cm^{-1} is found to be shifted towards lower wavenumbers by ~40–60 cm^{-1} and is indicative of thionato sulfur coordination [20]. The ν(Cu–S) vibration in the range 340–365 cm^{-1} further corroborates the sulfur bonding.

Copper complexes of $\mathbf{L}_5$ and $\mathbf{L}_6$ exhibit different absorption characteristics as compared to complexes of $\mathbf{L}_1$–$\mathbf{L}_4$. The quinone carbonyl stretch is observed at two different frequencies. The free $\nu(^4C{=}O)$ band at 1650 cm^{-1} for the free ligands does not exhibit any change after complexation while the chelated carbonyl $\nu(^1C{=}O)$ absorption undergoes a substantial decrease by ~50 cm^{-1} in the spectra of Cu_5 and Cu_6 [18]. It implies that the ^{1}C-quinone carbonyl is one of the coordinating centers, which is further confirmed by a new band at 510 cm^{-1} due to ν(Cu–O) vibration. A downward shift of 50 cm^{-1} for the $\nu(C{-}N^1)$ spectral band of the thiosemicarbazide linkage along with a characteristic ν(Cu–N) stretch at 480 cm^{-1} is indicative of hydrazinic nitrogen coordination [21]. On the other hand, the $\nu(^2N{-}H)$ vibration from the same linkage disappears in the complexes, suggesting the deprotonation of the ^{2}N–H proton thus forming a thiolato sulfur center. It means that this center is involved in coordination as evidenced from the decrease in the frequency (by ~60 cm^{-1}) of the thioamide band, which is partly ν(C=S) and found at 820 cm^{-1} in the uncomplexed thiosemicarbazone ligands. In addition, a new band appears at 1590 cm^{-1} due to the formation of the —C=N chromophore as a consequence of thiol formation, along with the emergence of a ν(Cu–S) band at 370 cm^{-1}, thus corroborating the thiol formation [22].

Although ligands $\mathbf{L}_1$–$\mathbf{L}_6$ possess identical donor sets (ONS), there exists a slight difference in the type of donor atom bonded to the copper(II) ion. Thus, $\mathbf{L}_1$–$\mathbf{L}_4$ have imine nitrogen, phenolic oxygen and thione sulfur as potential bonding sites while $\mathbf{L}_5$ and $\mathbf{L}_6$ coordinates through hydrazinic nitrogen, quinone carbonyl and thiol sulfur (atoms marked as * in Fig. 1 represent the point of attachments for $\mathbf{L}_1$–$\mathbf{L}_6$).

All the complexes exhibit a sharp band at 340 cm^{-1} originating from a ν(Cu–Cl) vibration indicating the presence of chloride coordination thus completing the

square-planar geometry for the present series of complexes [23].

3.2. Electronic spectra

The significant absorption peaks for all the complexes in DMSO are depicted in Table 3. The ligands exhibit two broad signals in the region 39400 and 30240 cm^{-1}, presumably arising from $n \rightarrow \pi^*$ and $\pi \rightarrow \pi^*$ transitions [24] which remain unaffected in the spectra of Cu_1–Cu_4. However, for Cu_5 and Cu_6, the later absorption shows a slight shift (~5 nm) to the higher energy side indicating the enolization of the thiocarbonyl group. Such an effect is observed for thiosemicarbazone complexes containing thiolato binding [13].

The electronic spectra of the complexes in DMSO solution exhibit characteristic absorption curves corresponding to the square-planar geometry. For square-planar complexes with a $d_{x^2-y^2}$ ground state, three spin-allowed transitions are expected [25], viz., $^2B_{1g} \rightarrow {}^2A_{2g}$ ($d_{x^2-y^2} \rightarrow d_{z^2}$), $^2B_{1g} \rightarrow {}^2B_{2g}$ ($d_{x^2-y^2} \rightarrow d_{xy}$) and $^2B_{1g} \rightarrow {}^2E_g$ ($d_{x^2-y^2} \rightarrow d_{xz,yz}$). It is rather difficult to resolve these bands because they are very close in energy and individual transfers cannot be distinguished. In our case, the first transition appears as a shoulder ($\Delta_\parallel$) in the region 14000–16000 cm^{-1} (Table 3) while the broad absorption around 21000 cm^{-1} is assigned to the second ($\Delta_\perp$) transition. The third peak, however, may have been obscured by an intense LMCT charge transfer band, a characteristic feature usually found to be associated with metal–thiosemicarbazone complexes [13]. These bands are utilized for evaluating the covalency parameters from ESR studies.

3.3. ESR studies

All the magnetically non-diluted polycrystalline powdered complexes (Cu_1–Cu_6) exhibit asymmetrical EPR spectra from which the approximate $g_\parallel$ and $g_\perp$ values were determined. However, these spectra are not self-explanatory with regard to the hyperfine structure, which indicate the existence of a strong dipolar interaction between the central metal ion and the bound strong field ligands as a consequence of enhanced spin lattice relaxation. EPR spectra of DMSO solutions at 298 K (Fig. 2) exhibit four fairly resolved components originating from −3/2, −1/2, 1/2 and 3/2 transitions ($\Delta M_s = \pm 1$). The signal corresponding to $M_I = -3/2$ splits clearly into three peaks because of super-hyperfine structure (shf) due to an imine or hydrazinic nitrogen atom of the bound ligand molecules. The analysis of this hyperfine structure results in three components with a splitting of about 15 G and an intensity ratio very close to 1:2:1. From this spectrum, the isotropic spectrochemical splitting factor (g_0), isotropic hyperfine splitting constant ($^{Cu}A_0$) and isotropic ligand super-hyperfine constant ($^{N}A_0$) are calculated and those are subsequently used in the evaluation of other spectral parameters.

The effective spin-Hamiltonian describing the EPR spectra of copper(II) complexes in a tetragonal (D_{4h}) crystal field [26] can be written as:

$$H = \beta[g_\parallel H_z S_z + g_\perp (H_x S_x + H_y S_y)] + {}^{Cu}A_\parallel S_z I_z(\mathrm{Cu}) + {}^{Cu}A_\perp [S_x I_x(\mathrm{Cu}) + S_y I_y(\mathrm{Cu})] + [{}^{N}A_\parallel S_z I_z(\mathrm{N}) + {}^{N}A_\perp \{S_x I_x(\mathrm{N}) + S_y I_y(\mathrm{N})\}],$$

where the terms involved have their usual meanings.

The low temperature (77 K) DMSO frozen glass EPR spectra (Fig. 3) of these complexes display four line copper hyperfine lines, characteristic of monomeric copper(II) complexes with $g_\perp$ component having super-hyperfine interactions. Since the super-hyperfine structure is well resolved, it seems that the quinone–thiosemicarbazone ligating system (ONS) appears to be coplanar with the two chelate rings, thus corroborating the nearly planar geometry ($g_\parallel > g_\perp$). Kivelson and Nieman [27] have pointed out that compounds having $g_\parallel \geqslant 2.3$ are ionic in nature while those with $g < 2.3$ are covalent in character. The $g_\parallel$ values for the present series of complexes (Table 3) reveal the appreciable covalency with $d_{x^2-y^2}$ as the ground state.

Table 3
UV–Vis and EPR spectral data for Cu_1–Cu_6

Parameter	Cu_1	Cu_2	Cu_3	Cu_4	Cu_5	Cu_6
$\Delta_\parallel(^2B_{1g} \rightarrow {}^2B_{1g})$[a]	15550	14815	15985	14620	16393	16416
$\Delta_\perp(^2B_{1g} \rightarrow {}^2B_{1g})$[a]	21275	21625	21410	21815	22095	22630
g_0	2.101	2.109	2.109	2.107	2.101	2.104
$g_\parallel$	2.213	2.223	2.218	2.227	2.205	2.209
$g_\perp$	2.046	2.053	2.055	2.048	2.049	2.052
$^{Cu}A_0$[b]	76.0	73.7	72.6	71.0	74.0	70.0
$^{Cu}A_\parallel$[b]	170	162	166	158	178	174
$^{Cu}A_\perp$[b]	29.0	27.5	25.0	27.0	25.0	23.7
$^{N}A_0$[b]	15.8	15.5	15.2	14.9	14.9	15.2

[a] cm^{-1}.
[b] $\times 10^{-4}$ cm^{-1}.

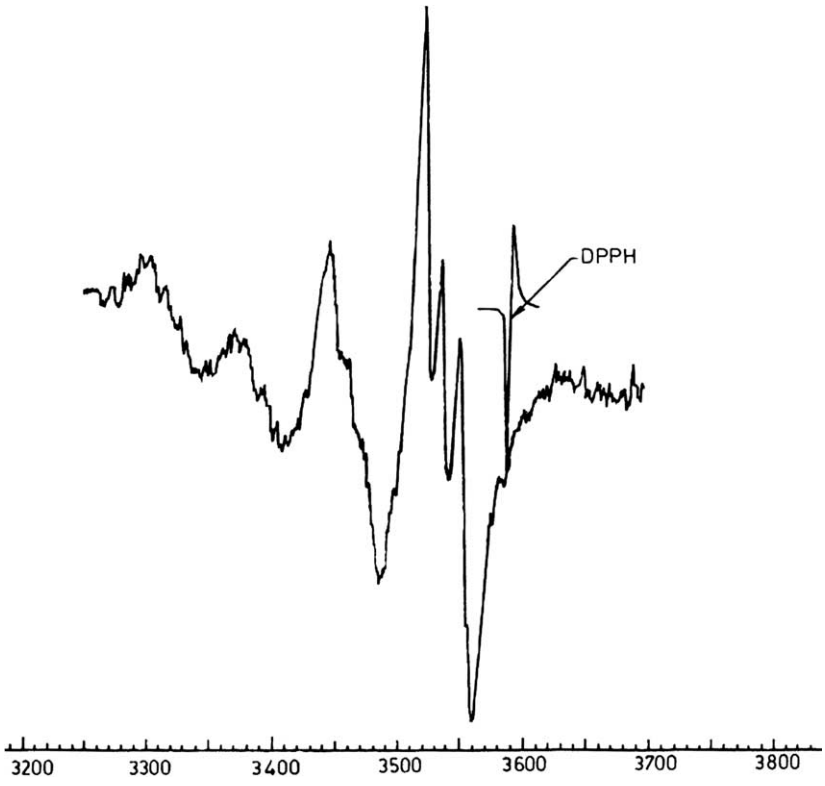


Fig. 2. EPR spectrum of Cu_2 in DMSO at 298 K.

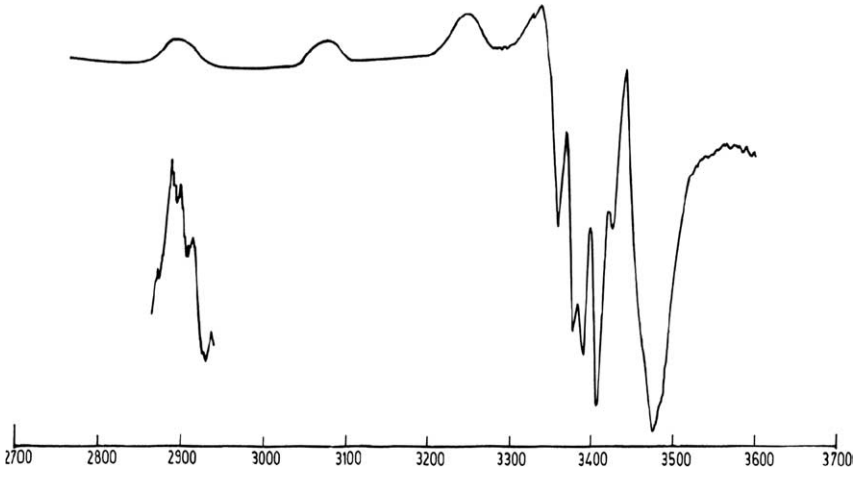


Fig. 3. EPR spectrum of Cu_2 in DMSO at 77 K.

Considering the pattern of the EPR spectra and the square-planar geometry from the electronic absorption spectra, it is quite logical to assume a tetragonal environment for the present series of copper(II) complexes. The unpaired spin is placed in an antibonding B_{1g} orbital. The ground state wave functions for this as well as for other antibonding orbitals in the LCAO-MO model are [26]:

$$\Psi A_{1g} = \gamma(d_z^2) - 1/2(1-\gamma'^2)^{1/2}[\sigma_x^{(1)} + \sigma_y^{(2)} - \sigma_x^{(3)} - \sigma_y^{(4)}],$$

$$\Psi B_{1g} = \alpha(d_{x^2-y^2}) - \alpha'\{[-\sigma_x^{(1)} + \sigma_y^{(2)} + \sigma_x^{(3)} - \sigma_y^{(4)}]/2\},$$

$$\Psi B_{2g} = \beta d_{xy} - \beta'\{[P_y^{(1)} + P_x^{(2)} - P_y^{(3)} - P_x^{(4)}]/2\},$$

$$\Psi E_{1g} = \gamma d_{xy} - \gamma'\{[P_z^{(1)} - P_z^{(3)}]/2^{1/2}\},$$

where α, α', β, β', γ and γ' represent in plane σ-bonding, in plane π-bonding and out of plane π-bonding

coefficients from metal and ligand orbitals, respectively. The ligand orbital involved in the in plane σ-bonding are considered to have sp^2 hybrid orbitals [29]. Overlap is included for the function describing in plane σ-bonding as $\alpha^2 - 2\alpha' S + \alpha'^2 = 1$, where $S = 0.093$ is the overlap integral between the copper $d_{x^2-y^2}$ orbital and the ligand orbital. These coefficients are evaluated from the following expressions [28] as:

$$g_{\parallel} - 2.0023 = (-8\lambda_0\alpha^2\beta^2/\Delta_{\parallel})[1 - (2\alpha'/\alpha)S - (\alpha'/2\alpha\beta)(1-\beta^2)^{1/2}\tau(n)],$$

$$g_{\perp} - 2.0023 = (-2\lambda_0\alpha^2\gamma^2/\Delta_{\perp})[1 - (2'/\alpha)\mathrm{S} - (\alpha'/2\alpha)(1-\gamma^2)^{1/2}\tau(n)],$$

$$^{\mathrm{Cu}}A_{\parallel} = P[\{-\alpha^2(4/7 + K_0) - 2\lambda\alpha^2\{(4\beta^2/\Delta_{\parallel}) + (3\gamma^2/7\Delta_{\perp})\},$$

$$^{\mathrm{Cu}}A_{\perp} = P[\alpha^2(2/7 - K_0) + 22/14(\lambda\alpha^2\gamma^2/\Delta_{\perp})],$$

$$^{\mathrm{N}}A_{\parallel} = (\alpha'^2/4)g_{\mathrm{N}}\beta_{\mathrm{N}}[(8\pi/9)|\Psi_0^2|_{2\mathrm{s}} + (8/15)\langle r^{-3}\rangle_{2\mathrm{p}}],$$

$$^{\mathrm{N}}A_{\perp} = (\alpha'^2/4)g_{\mathrm{N}}\beta_{\mathrm{N}}[(8\pi/9)|\Psi_0^2|_{2\mathrm{s}} - (8/15)\langle r^{-3}\rangle_{2\mathrm{p}}]\},$$

where λ_0 is the spin–orbit coupling constant for the copper(II) ion ($-828\ \mathrm{cm}^{-1}$), K_0 is the Fermi contact term (0.43), P is the free ion dipole term ($-0.036\ \mathrm{cm}^{-1}$), $\tau(n)$ is the integral over the ligand function (0.333), S is the overlap integral between $d_{x^2-y^2}$ and normalized nitrogen orbitals (0.093), $|\Psi_0^2|_{2\mathrm{s}}$ measures the 2s electron density at the ^{14}N nucleus ($32.4 \times 10^{24}\ \mathrm{cm}^{-3}$) and $\langle r^{-3}\rangle_{2\mathrm{p}}$ is the average value of r^{-3} for nitrogen 2p orbitals ($20.9 \times 10^{24}\ \mathrm{cm}^{-3}$).

For copper(II) complexes with a $^2B_{1g}$ ground state in D_{4h} symmetry ($g_{\parallel} > g_{\perp}$), the '$g$' values may be expressed [30] as:

$$K_{\parallel}^2 = (g_{\parallel} - 2.0023)\Delta_{\parallel}/8\lambda_0,$$

$$K_{\perp}^2 = (g_{\perp} - 2.0023)\Delta_{\perp}/2\lambda_0,$$

where $K_{\parallel}$ and $K_{\perp}$ are the parallel and perpendicular components of the orbital reduction factor (K). According to Hathaway [31], for pure σ-bonding $K_{\parallel} \approx K_{\perp} \approx 0.77$, for in plane π-bonding $K_{\parallel} < K_{\perp}$ whereas $K_{\parallel} > K_{\perp}$ implies strong out of plane π-bonding. The lower K values and $K_{\parallel} < K_{\perp}$ for copper(II)–thiosemicarbazones are indicative of covalent nature and strong in plane π-bonding. For these complexes, the G values are greater than or equal to 4 suggesting that there is negligible interaction between two copper(II) centers [32] as well as appreciable ligand field strength of quinone–thiosemicarbazones.

The in plane σ-covalency parameter (α^2) was calculated following the simplified equation suggested by Kivelson and Nieman [27] as:

$$\alpha^2 = -A_{\parallel}/ - 0.036 + (g_{\parallel} - 2.0023) + (3/7)(g_{\perp} - 2.0023) + 0.04.$$

The α^2 values (0.67–0.69) accounts for the fraction of the unpaired electron density located on the copper(II) ion (Table 4). These values are comparable to the one obtained for copper complexes of thiosemicarbazones [21,32–35] indicating the presence of appreciable covalency in the σ-bond. The other parameter α'^2 was obtained from the normalization condition of the B_{1g} orbital, $\alpha^2 - 2\alpha\alpha' S + \alpha'^2 = 1$. It represents the fraction of electron density donated from the nitrogen for σ-bond formation.

In-plane and out-of plane π-bonding parameters are evaluated from the following relations as:

$$\alpha^2\beta^2 = [(g_{\parallel} - 2.0023)\Delta_{\parallel}]/8\lambda_0,$$

$$\alpha^2\gamma^2 = [(g_{\perp} - 2.0023)\Delta_{\perp}]/2\lambda_0,$$

$$\beta^2 = 2\beta'^2 - 1,$$

$$\gamma^2 = 2\gamma'^2 - 1.$$

The β'^2 value (0.42–0.45) accounts for electron density on the ligand through the nitrogen atom, which indicates that the unpaired electron is largely delocalized along the quinone–thiosemicarbazone linkage. Such a pronounced feature may be attributed to the synergistic effect of the sulfur center having a vacant π-orbital as well as the charge accumulating property of the quinone moiety [11]. β'^2 values also approximately represent the % of electron delocalization on the nitrogen site and consequently reveal that it spends ≈42–44% of its time

Table 4
Simulated LCAO−MO coefficients and bonding parameters from EPR data for Cu_1–Cu_6

Parameter	Cu_1	Cu_2	Cu_3	Cu_4	Cu_5	Cu_6
G	4.1	4.2	3.9	4.2	4.1	4.0
$K_{\parallel}$	0.6042	0.6025	0.6077	0.6042	0.6082	0.6156
$K_{\perp}$	0.6817	0.6946	0.6759	0.6579	0.6893	0.6640
K_0	0.3224	0.3651	0.3746	0.3404	0.3633	0.3896
$f(\alpha)$	130.17	137.22	133.61	140.95	123.87	126.95
α^2	0.6814	0.6845	0.6753	0.6781	0.6917	0.6824
α'^2	0.8178	0.8041	0.8460	0.8452	0.8116	0.8449
β^2	0.7923	0.8013	0.8262	0.8134	0.7986	0.8237
β'^2	0.4341	0.4251	0.4355	0.4218	0.4589	0.4561
γ^2	0.8178	0.8015	0.8246	0.8059	0.8163	0.8307
γ'^2	0.6428	0.6937	0.6216	0.6265	0.6406	0.6273

on quinone thiosemicarbazone ligands. Similarly, the other π-bonding parameter γ'^2, also significantly contribute for substantial delocalization of electron density within the sulfur-nitrogen-quinone ligating centers. Such a pronounced effect results in the formation of stable chelate rings of copper–thiosemicarbazone bonds, thus conferring nearly planar geometry around the copper center.

EPR parameters also reflect the degree of tetrahedral distortion of square-planar copper(II) complexes. From structurally well-characterized copper complexes of thiosemicarbazones [13], it has been observed that increase in $g_{\|}$ values with concomitant decrease in $^{Cu}A_{\|}$ components lead to an increase in the tetrahedral distortion. The degree of distortion $f(\alpha)$ $(=g_{\|}/A_{\|})$ is regarded as an index of deviation from idealized geometry. Values of 110–120 are typical for planar complexes, while the range of 130–150 is characteristic of slight to moderate distortion and 180–250 cm^{-1} indicate considerable distortion [36,37]. Values from 127 to 141 cm^{-1} for the present series of complexes suggest a small to moderately distorted geometry. Fig. 4 depicts the correlationship between $g_{\|}$, $A_{\|}$ and $f(\alpha)$ for Cu_1–Cu_6. Inspection of this diagram [38] suggests that the '$g_{\|}$' values linearly varies with $f(\alpha)$, as a consequence of the destabilization of the square planar geometry. Moreover, this tetrahedral distortion influences the copper hyperfine structure, suggesting that the unpaired electron is asymmetrically delocalized along the chelate rings. Thione sulfur binding for Cu_1–Cu_4 probably induces more structural deformations leading to substantial departure from the planar geometry. On the other hand, the thiol sulfur present in Cu_5 and Cu_6 enforces the structure to remain in a nearly square-planar geometry. Such a difference may originate from the fact that thiolato sulfur binding incorporates greater covalency in the metal–ligand bonding through delocalized dπ–pπ in-plane π–bonding as evidenced from the higher β'^2 values.

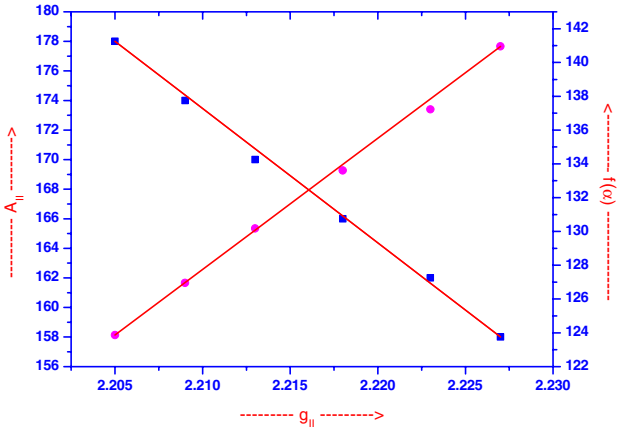


Fig. 4. Variation of $g_{\|}$ with $A_{\|}$ (■) and degree of tetrahedral distortion (●). The straight lines represents the best-fit curve.

4. Electrochemistry

The redox behavior of the copper(II) complexes have been investigated by cyclic voltammetry at a platinum electrode in the range from +1.0 to −2.0 V. In the positive range, the oxidation process Cu(II)/Cu(III) can be observed while scanning between 0 and −2.0 V is found to be associated with copper and quinone reduction steps.

Fig. 5 depicts the cyclic voltammetric response exhibited by Cu_2 in DMSO. In the scan between 0 and −2.0 V, the reduction process occurring at A is directly associated with reoxidation peak at E in the reverse scan, suggesting one electron redox change (Table 5) originating from the chemically reversible [Cu($\mathbf{L}_2$)Cl] → [Cu($\mathbf{L}_2$)Cl]$^-$ but electrochemically quasi-reversible Cu(II)/Cu(I) redox couple [39]. The other subsequent reduction peak B is ill shaped with its counterpart D at a more −ve potential ($E_c > -1.4$ V) and this possibly proceeds via two e^- transfer changes for quinone to catechol [11].

Analysis of the cyclic voltammetric response of peak A/E (Fig. 5) for these complexes indicates that the ratio of i_{pa}/i_{pc} is approximately equal to unity and the peak-to-peak separation (ΔE_p) is in the range of 0.70–0.110 V. In the absence of either uncompensated solution resistance or anomalous electrode surface effects, the marked departure of ΔE_p from 0.059 V can be qualitatively assumed as an index of occurrence of significant geometrical reorganizations accompanying the redox changes [40]. It is expected that the Cu(II)/Cu(I) couple experiences some structural reorganization

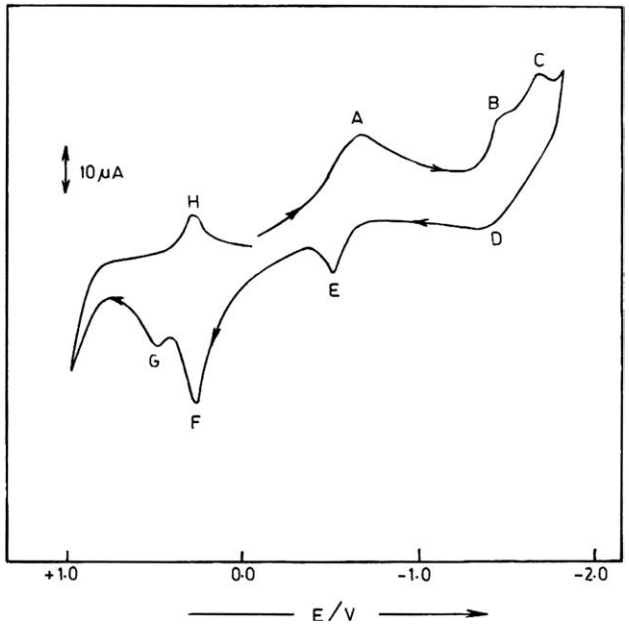


Fig. 5. Cyclic voltammetric response of Cu_2 in DMSO at a scan rate of 100 mV s^{-1}.

Table 5
Cyclic voltammetric data for Cu_1–Cu_6

Parameter	Cu_1	Cu_2	Cu_3	Cu_4	Cu_5	Cu_6
E_{pc} (V)	−0.56	−0.63	−0.59	−0.68	−0.475	−0.530
E_{pa} (V)	−0.48	−0.53	−0.50	−0.57	−0.405	−0.445
$E_{1/2}$ (V)	−0.52	−0.58	−0.545	−0.625	−0.45	−0.49
ΔE_p (V)	0.080	0.100	0.090	0.110	0.070	0.085
% i_{pc}/i_{pa}	97	94	92	95	98	97
E_{pc} (V)	+0.30	+0.37	+0.315	+0.405	+0.26	+0.275
E_{pa} (V)	+0.47	+0.51	+0.495	+0.535	+0.37	+0.385
$E_{1/2}$ (V)	+0.385	+0.44	+0.405	+0.47	+0.315	+0.330
ΔE_p (V)	0.170	0.140	0.180	0.130	0.110	0.110
% i_{pc}/i_{pa}	83	88	87	88	87	87

barrier in view of the likely rearrangement from square planar Cu(II) to pseudo-tetrahedral Cu(I). However, cyclic voltammetric tests performed either on any copper(II) complex in the presence of a saturated DMSO solution of TEAP exhibited no variations in the diagnostic electrochemical features. It, therefore, could be originating from the chemical equilibrium between square-planar to tetrahedral (or pseudo-tetrahedral) geometries with concomitant departure from pure electrochemical reversibility for the Cu(II)/Cu(I) couple as measured by mean ΔE_p values of ~0.090 V at 0.01 V s^{-1} for the present series of complexes.

The often interrelated factors which raises the $E_{1/2}$ value of the Cu(II)/Cu(I) couple may be considered to be: (i) those which stabilize Cu(II) species by reducing its crystal field stabilization energy (CFSE) either by decreasing the ligand σ-donor ability or by constraining the geometry of the copper center favoring Cu(I) and (ii) the presence of π-acceptor ligands which favors the formation of Cu(I) species [41]. Patterson and Holm [42] have shown that softer ligands tend to favor more positive $E_{1/2}$ values while hard acids give rise to more negative values. As mentioned earlier, the effects of stereo-chemical changes on redox potentials are directly correlated to conversion of square-planar copper(II) species to tetrahedral Cu(I) products, the redox potentials observed for the present series of complexes indicate a moderate strength for quinone–thiosemicarbazones. It implies that greater deformation in the chelate rings of a coordinated thiosemicarbazone ligand induces substantial departure from square planar geometry with more difficulty in stabilizing the Cu(I) state, an observation in concurrence with the earlier speculation from EPR spectral studies. The influence of geometrical distortions on the redox properties can be asserted by the plot (Fig. 6) of $f(\alpha)$ versus $E_{1/2}$ wherein it is observed that the increase in tetrahedral distortion leads to more negative values of Cu(II)/Cu(I) reduction potentials [42]. The linear relationship observed for these complexes may originate from thione/thiol sulfur coordination, position of methyl substitution as well as charge accumulation tendency of the quinonoidal structure. As expected,

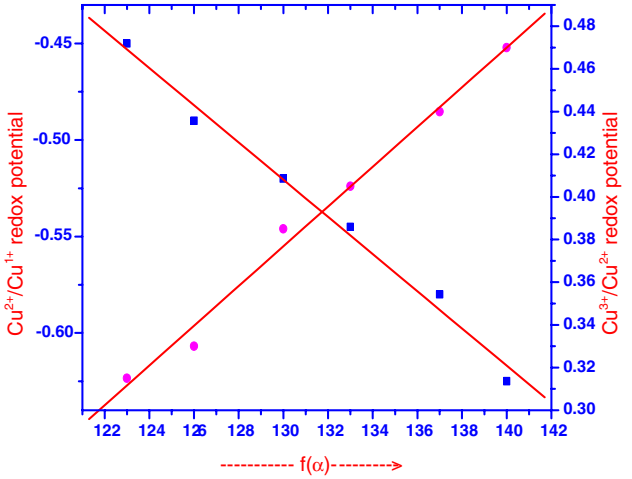


Fig. 6. Correlation of degree of tetrahedral distortion $f(\alpha)$ against Cu^{2+}/Cu^{1+} (■) and Cu^{3+}/Cu^{2+} (●) redox potentials. The straight lines represent the best-fit curve.

methyl substitution on the thiosemicarbazone side chain ($\mathbf{L_4}$) exerts more distortion in the structure of the Cu_4 complex. A similar correlation has also emerged from ESR studies. Finally, it should be mentioned here that the potentials of the Cu(II)/Cu(I) couple of the present series of complexes are notably more positive than those reported for thiosemicarbazone complexes [21,33,43]. Beyond any doubt, the negative shift is obviously due to the difference in the chemical environment and the chromophore around the Cu(II) ions. Nevertheless, it is likely attributable not only to inductive electronic factors but also because of columbic effects such as formation of charged or neutral sulfur donor sites.

The cyclic voltammetric behavior of Cu_1–Cu_6 between +1.0 and 0 V exhibit cathodic response (peak H) in the range 0.275–0.405 V with its counterpart (peak G) in the range 0.370–0.535 V. This feature corresponds to a quasi-reversible Cu(III)/Cu(II) redox process as indicated by ΔE_p values as well as non-equivalent current intensities of cathodic and anodic peaks (% i_{pc}/i_{pa}). The redox process associated with oxidation of Cu(II) to Cu(III) for all the complexes [43] may probably

originate due to the presence of a thione/thiol sulfur center and redox active quinone moiety. Since the quinone ring is planar and the thiosemicarbazide side chain is flexible, the ligand can adopt different conformations so as to fit the smaller sized Cu(III) ion, thus favoring the oxidation process. Moreover, this oxidation step results in the formation of a low-spin d^8 Cu(III) state with a preference for a square-planar geometry [44]. It is quite likely that this process does not proceed via a change in the geometry of the complex in DMSO solution. This fact is clearly reflected in Table 5, indicating that the Cu(III) state can be stabilized at relatively lower oxidation potential. Interestingly enough, the observed redox potentials for the present series are significantly lower than those reported earlier for thiosemicarbazone complexes [33,45,46], thus reflecting the influence of the electronic features of the redox active quinone moiety. The extent of electrochemical stability may be assessed from the correlation (Fig. 6) between the $E_{1/2}$ values for the Cu(III)/Cu(II) redox process with that of the degree of tetrahedral distortion $f(\alpha)$. Inspection of this figure indicates a linear relationship, revealing that departure from a square-planar structure of the complex leads to destabilization of the copper(III) species formed in the solution. Also, the type of bound sulfur center and quinone segment of the ligand seems to modulate the redox behavior of these complexes.

The other peaks (C and F) are related either to quinone redox forms or coupled chemical reactions at the electrode surface. Some of them loose intensity on repetitive and reverse scanning.

5. Conclusions

EPR spectral properties of the copper(II)–quinone thiosemicarbazones revealed appreciable covalency in the metal–ligand bonding, presumably arising out of copper(II)–thione/thiol coordination. The fraction of electron density (~42–45%) from the copper center is distributed over the entire chelate rings of the ligand molecules suggesting that there is extensive delocalization through in-plane π-bonding as well as σ-bonding interactions. Moreover, these complexes possess a significant amount of tetrahedral distortion as a consequence of deviation from square-planar to tetrahedral geometry leading to increased $g_{\|}$ values with a concomitant decrease in the $A_{\|}$ parameter. It implies that the planarity of the [CuONSCl] chromophore is disturbed due to the presence of the π-acceptor sulfur center along with the substituents on the ligands. Redox properties of these complexes indicate that the Cu(II)/Cu(I) redox couple is associated with structural reorganizations from square-planar to tetrahedral geometry. The linear relationship between degree of tetrahedral distortion and $E_{1/2}$ values suggest that the thiol complexes (Cu_5 and Cu_6) are electrochemically more versatile for electron transfer reactions as compared to the thione complexes (Cu_1–Cu_4). Such a difference stems from the fact that the thiolato complexes contain the redox active quinone form, which may be controlling the electronic structure of the complex through intramolecular reorganizations leading to enhanced thermodynamic stability. Moreover, Cu(III)/Cu(II) redox changes are also found to be present at fairly higher potentials for the thione complexes, implying that the thiol complexes are both structurally and electrochemically more stable. Thus, Cu_5 and Cu_6 complexes represent better structural mimics of blue copper proteins. The present study highlights that the spectroscopic parameters together with the redox behavior may be regarded as an index for constructing potentially feasible structural models of copper containing metallo-enzymes. Also, it is possible to modulate the copper–sulfur interactions by incorporating an appropriate ligating system which may modulate the electronic and stereochemical features that are necessary for stabilizing the copper(II) center.

References

[1] D.R. McMillian, H.R. Engeseth, in: K.D. Karlin, J. Zubieta (Eds.), Biological and Inorganic Copper Chemistry, Adenine Press, Guilderland, NY, 1986.
[2] E. Bouwman, W.L. Driessen, J. Reedjik, Coord. Chem. Rev. 104 (1990) 143.
[3] (a) J.M. Guss, H.C. Freeman, J. Biol. Chem. 169 (1983) 521;
(b) J.M. Guss, H.D. Bartuniak, H.C. Freeman, Acta Crystallogr. B 48 (1992) 790.
[4] (a) B.G. Malstrom, P. Wittung-Stafshede, Coord. Chem. Rev. 185–186 (1999) 127;
(b) H.B. Gray, B.G. Malstrom, R.J.P. Williams, J. Biol. Inorg. Chem. 5 (2000) 551.
[5] E.I. Solomon, K.W. Penfield, D.E. Wilcox, Struct. Bond. 53 (1981) 1.
[6] (a) R.H. Holm, P. Kennepohl, E.I. Solomon, Chem. Rev. 96 (1996) 2239;
(b) E.I. Solomon, L.B. LaCroix, D.W. Randall, Pure Appl. Chem. 70 (1998) 799.
[7] (a) E. John, P.K. Bharadwaj, J.A. Potenza, H.J. Suchager, Inorg. Chem. 25 (1986) 3065;
(b) J. Whelan, B. Bosnich, Inorg. Chem. 25 (1986) 3671.
[8] A.R. Amundsen, J. Whelar, B. Bosnich, J. Am. Chem. Soc. 99 (1977) 6730.
[9] J. Becher, D.J. Brockway, K.S. Murray, P.J. Newman, H. Toftlund, Inorg. Chem. 21 (1982) 1791.
[10] A.W. Addison, E. Sinn, Inorg. Chem. 22 (1983) 1225.
[11] (a) C.G. Pierpont, Coord. Chem. Rev. 219–221 (2001) 415;
(b) C.G. Pierpont, Coord. Chem. Rev. 216–217 (2001) 99.
[12] (a) J. Li, L.M. Zheng, I. King, T.W. Doyle, S.H. Chen, Curr. Med. Chem. 8 (2001) 121;
(b) K.C. Lee, J. Noveroske, B. Almassian, Int. J. Toxicol. 19 (2000) 85;
(c) R.A. Finch, M. Liu, S.P. Grill, W.C. Rose, R. Loomis, K.M. Vasquez, Y. Cheng, A.C. Sartorelli, Biochem. Pharmacol. 59 (2000) 983;
(d) M. Hooper, Chem. Soc. Rev. 16 (1987) 43;
(e) M. Hooper, M.G. Purohit, Prog. Med. Chem. 20 (1983) 1.

[13] (a) S.B. Padhye, G.B. Kauffman, Coord. Chem. Rev. 63 (1985) 127;
(b) D.X. West, S.B. Padhye, P.B. Sonawane, Struct. Bond. 76 (1991) 1;
(c) D.X. West, A.E. Liberta, S.B. Padhye, R.C. Chikate, P.B. Sonawane, A.S. Kumbhar, R.G. Yerande, Coord. Chem. Rev. 123 (1993) 49.
[14] (a) S.B. Padhye, R.C. Chikate, A.S. Kumbhar, J.M. Shallom, M.P. Chitnis, Biol. Met. 5 (1992) 67;
(b) R.C. Chikate, P.B. Sonawane, A.S. Kumbhar, S.B. Padhye, R.J. Butcher, Inorg. Chim. Acta 205 (1993) 59;
(c) P.B. Sonawane, R.C. Chikate, A.S. Kumbhar, S.B. Padhye, R.J. Doedens, Polyhedron 13 (1994) 195;
(d) A. Murugkar, S. Padhye, S. Guha-Roy, U. Wagh, Inorg. Chem. Commun. 2 (1999) 545;
(e) Z. Afrasiabi, E. Sinn, S. Padhye, S. Dutta, S. Padhye, C. Newton, C.E. Anson, A.K. Powell, J. Inorg. Biochem. 95 (2003) 306;
(f) Z. Afrasiabi, E. Sinn, J. Chen, Y. Ma, A.L. Rheingold, L.N. Zakharov, N. Rath, S. Padhye, Inorg. Chim. Acta 357 (2004) 271;
(g) J. Chen, Y. Huang, G. Liu, Z. Afrasiabi, E. Sinn, S. Padhye, Y. Ma, Toxicol. Appl. Pharmacol. 197 (2004) 40.
[15] D.D. Perrin, W.L.F. Armasego, D.R. Perrin, Purification of Laboratory Chemicals, Pergamon Press, London, 1966.
[16] (a) K.H. Dudley, H.W. Miller, P.W. McKee, J. Org. Chem. 34 (1969) 2759;
(b) F.I. Carrol, H.W. Miller, R. Meck, J. Chem. Soc. C (1970) 1993.
[17] B.N. Figgis, J. Lewis, Prog. Inorg. Chem. 6 (1970) 37.
[18] P.L. Garge, R.C. Chikate, S.B. Padhye, J.M. Savariault, P. deLoth, J.P. Tuchagues, Inorg. Chem. 29 (1990) 3315.
[19] K. Nakamoto, Infrared and Raman Spectra of Inorganic and Coordination Compounds, Part B, fifth ed., Wiley, New York, 1977.
[20] E. Labisbal, K.D. Haslow, A.S. Pedrares, J.V. Martines, S.H. Ortega, D.X. West, Polyhedron 22 (2003) 2831.
[21] P. Bindu, M.R.P. Kurup, T.R. Satyakeerty, Polyhedron 18 (1999) 321.
[22] K.A. Ketcham, J.K. Swearingrn, A. Castineiras, I. Garcia, E. Bermejo, D.X. West, Polyhedron 20 (2001) 3265.
[23] D.X. West, N.M. Kozub, G.A. Bain, Transition Met. Chem. 21 (1996) 52.
[24] A.B.P. Lever, Inorganic Electronic Spectroscopy, second ed., Elsevier, Amsterdam, 1984.
[25] (a) B. Harikumar, M.R.P. Kurup, T.N. Jayaprakash, Transition Met. Chem. 22 (1997) 507;
(b) P. Bindu, M.R.P. Kurup, Transition Met. Chem. 22 (1997) 578.
[26] A.H. Maki, B.R. McGarvey, J. Chem. Phys. 29 (1961) 35.
[27] D. Kivelson, R. Niemen, J. Chem. Phys. 35 (1961) 149.
[28] B.J. Hathaway, D.E. Billing, Coord. Chem. Rev. 5 (1970) 143.
[29] M.J.M. Campbell, A.J. Collis, R. Grzeskowiak, Bioinorg. Chem. 6 (1976) 305.
[30] B.J. Hathaway, G. Wilkinson, R.D. Gillard, J.A. McCleverty (Eds.), Comprehensive Coordination Chemistry II, vol. 5, Pregamon, Oxford, 1987.
[31] B.J. Hathaway, Struct. Bond. 14 (1973) 60.
[32] M. Joseph, V. Suni, M.R.P. Kurup, M. Nethaji, A. Kishore, S.G. Bhat, Polyhedron 23 (2004) 2069.
[33] R.P. John, A. Sreekanth, V. Rajakannan, T.A. Ajith, M.R.P. Kurup, Polyhedron 23 (2004) 2549.
[34] A. Sreekanth, M.R.P. Kurup, Polyhedron 22 (2003) 3321.
[35] R.P. John, A. Sreekanth, M.R.P. Kurup, A. Usman, A.R. Ibrahim, H.K. Fun, Spectrochim. Acta 59A (2003) 1349.
[36] A.W. Addison, Spectroscopic and redox trends from model copper complexes, in: K.D. Karlin, J. Zubieta (Eds.), Copper Coordination Chemistry: Biological and Inorganic Perspectives, Adenine Press, New York, 1983.
[37] V.V. Pavlischuk, Theor. Exp. Chem. 31 (1995) 1.
[38] J. Peisach, W.E. Blumberg, Arch. Biochem. Biophys. 165 (1974) 691.
[39] A.M. Bond, R.L. Martin, Coord. Chem. Rev. 54 (1984) 23.
[40] A.R. Hendrickson, R.L. Martin, N.M. Rhode, Inorg. Chem. 15 (1976) 2115.
[41] E.V.R. Askimova, A.Y. Nazarenko, L. Chen, P.W. Krieger, A.M. Herrera, V.V. Tarasov, P.D. Robinson, Inorg. Chim. Acta 324 (2001) 1.
[42] G.S. Patterson, R.H. Holm, J. Bioinorg. Chem. 4 (1975) 1257.
[43] E. Franco, E. Lopez-Torres, M.A. Mendiola, M.T. Sevilla, Polyhedron 19 (2000) 441.
[44] X.H. Bu, X.Ch. Cao, D.L. An, R.H. Zhang, C. Thomas, E. Kimura, J. Chem. Soc., Dalton Trans. (1998) 433.
[45] A. Arquero, M.A. Mendiola, P. Souza, M.T. Sevilla, Polyhedron 15 (1996) 165.
[46] Z. Durackova, M.A. Mendiola, M.T. Sevilla, A. Valent, Bioelectrochem. Bioenerg. 48 (1999) 109.

2. Experimental

2.1. Materials

4-Methylphenol, 4-chlorophenol, *N*,*N*-diethylamino-1,3-propandiamine, morpholine, cyclohexylamine and DMF were obtained commercially and used without purification. Tetrabutylammoniumperchlorate (TBAP) was recrystallised from methanol (*Caution*: Although no problems were encountered, suitable care and precautions should be taken when handling the perchlorate salts, as these are potentially explosive). Analytical grade copper perchlorate, copper acetate, copper chloride and other reagents were used as such without further purification.

2.2. Physical measurements

Elemental analysis was carried out with a Heraeus-CHN-Rapid Analyzer. ^{1}H NMR spectra were recorded using a 90 MHz spectrometer, (model EM 390) and IR spectra were recorded on a Shimadzu IR-408 spectrometer using KBr discs. Electronic spectra were recorded on a Hitachi-320 spectrophotometer. The FAB mass spectra were recorded on a Jeol SX 102/DA-6000 Mass spectrometer. Variable temperature (77–300 K) magnetic susceptibility measurements were performed on the Princeton Applied Research Model-155 vibrating sample Magnetometer operating at 5000 G and calibrated with metallic nickel supplied with the instrument. The cyclic voltammograms were obtained in an apparatus comprising a PAR model-175 universal programmer, Model-173 Potentiostat/Galvanostat, Model-176 current follower and Model-179 coulomb/ampere hour meter (EG&G Ltd.) and Hitachi (057) Perkin–Elmer X–Y recorder. Platinum foils (1 cm^2) were used as the working electrode, as well as counter electrodes, and Ag/AgCl as the reference electrode. The ferrocenium/ferrocene (1+) couple was used as an internal standard. The potentials reported are relative to the Ag/AgCl electrode and $E_{1/2}$ of the ferrocenium/ferrocene (Fe^+/Fe) couple, which under the experimental conditions is 470 mV in DMF and ΔE_p for Fe^+/Fe is 70 mV. Electrochemical measurements were carried out under a N_2 atmosphere. TBAP was used as the supporting electrolyte (0.1 M) and all the complex solutions were around 10^{-3} M concentration.

2.3. Synthesis of the precursor compounds

2.3.1. N,N-Bis(2-hydroxy-5-methylbenzyl)-N′,N′-diethyl-1,3-propane diamine P.C.-1

N,*N*-Diethyl-1,3-propanediamine (6.5 g, 0.05 mol) was added with cooling to a solution prepared by dissolving paraformaldehyde (3 g, 0.1 mol) in methanol (60 ml) containing KOH (0.05 g). To this, 4-methylphenol (10.8 g, 0.1 mol) in methanol (60 ml) was added. The solution was then heated to reflux for 6 h and the solvent was removed under vacuo. The product obtained as yellow oil was recrystallised from cold methanol.

Yield: 12 g (65%). *Anal*. Calc. for $C_{23}H_{34}N_2O_2$: C, 74.55; H, 9.25; N, 7.56. Found: C, 74.51; H, 9.21; N, 7.60%. ^{1}H NMR ($CDCl_3$, δ ppm): 6.7–6.8 (m, aromatic CH), 3.65 (d, 4H, benzyl CH_2), 2.6–2.7 (m, 8H, NCH_2), 2.25 (s, 6H, aromatic CH_3), 1.8 (s, 2H, alkyl CH_2), 1.1 (m, 6H, alkyl CH_3). Selected IR data (KBr, υ cm^{-1}): 3400, 1470.

2.3.2. N,N-Bis(2-hydroxy-5-chlorobenzyl)-N′,N′-diethyl-1,3-propane diamine P.C.-2

Synthesis of this precursor compound, using 4-chlorophenol in the place of 4-methylphenol, was carried out following the same procedure as above. The yellow oil P.C.-2 was recrystallised from cold methanol.

Yield: 15 g (73%). *Anal*. Calc. for $C_{21}H_{28}O_2N_2Cl_2$: C, 61.31; H, 6.86; N, 6.81. Found: C, 61.30; H, 6.86; N, 6.83%. Selected IR data (KBr, υ cm^{-1}): 3350, 1470.

2.3.3. N,N-Bis(2-hydroxy-5-methylbenzyl)-cyclohexylamine P.C.-3

Cyclohexylamine (5 g, 0.05 mol) was added to a cold methanolic solution (60 ml) containing paraformaldehyde (3 g, 0.1 mol) and 0.025 g of KOH. To this solution, 4-methylphenol (10.8 g, 0.1 mol) in methanol (60 ml) was added. After gently refluxing the reaction mixture for 6 h, the solvent was removed by slow evaporation at room temperature. The white solid was washed with cold methanol, filtered and recrystallised from hot methanol.

Yield: 11.6 g (57%), m.p: 180 °C. *Anal*. Calc. for $C_{22}H_{29}NO_2$: C, 77.84; H, 8.61; N, 4.13. Found: C, 77.83; H, 8.63; N, 4.15%. ^{1}H NMR ($CDCl_3$, δ ppm): 6.7–6.9 (m, aromatic CH), 3.5–3.8 (d, 4H, benzyl CH_2), 2.4–2.7 (m, 2H, cyclohexyl N–CH), 2.25 (s, 6H, aromatic CH_3), 1.2–1.8 (m, 11H, ring CH_3). Selected IR data (KBr, υ cm^{-1}): 3450, 1475.

2.4. Synthesis of ligands

2.4.1. N,N-Bis{2-hydroxy-5-methyl-3-(morpholin-1-ylmethyl)benzyl}-N′,N′-diethyl-1,3-propanediamine (L^1H_2)

The precursor compound P.C.-1 (3.7 g, 0.01 mol) in ethanol (100 ml) was mixed with an excess of morpholine (2 g, 0.023 mol), and formaldehyde (35%, 2.5 ml, 0.025 mol) was added slowly with stirring. The solution was then heated to reflux for 24 h with the addition of 2 ml formalin at approximately 8 h intervals. The resulting mixture was evaporated under vacuo. The yellow oil obtained was washed with saturated sodium carbonate solution (20 ml) and then extracted with chloroform. The product L^1H_2 was obtained as yellow oil on

evaporation of the chloroform layer. The crude L^1H_2 was then recrystallised from ethanol.

Yield: 3.1 g (55%). *Anal*. Calc. for $C_{33}H_{52}N_4O_4$: C, 69.68; H, 9.21; N, 9.85. Found: C, 69.69; H; 9.20; N, 9.82%. ^{1}H NMR ($CDCl_3$, δ, ppm): 6.8 (d, 4H, aromatic CH); 3.5–3.8 (t, 16 H, benzyl CH_2, morpholine OCH_2), 2.5 (d, 12H, NCH_2), 2.3 (s, 6H, aromatic CH_3), 1–1.8 (m, 2H, alkyl CH_2), 0.8–1 (m, 6H, alkyl CH_3). Selected IR data (KBr, υ cm^{-1}): 3450, 1470.

2.4.2. N,N-Bis{2-hydroxy-5-chloro-3-(morpholin-1-ylmethyl)benzyl}N′,N′-diethyl-1,3-propanediamine (L^2H_2)

Synthesis of the ligand L^2H_2 was carried out following the above procedure using P.C.-2 (4.11 g, 0.01 mol) in the place of the P.C.-1. The ligand was recrystallised from ethanol.

Yield: 4.5 g (74%). *Anal*. Calc. for $C_{31}H_{46}N_4O_4Cl_2$: C, 61.08; H, 7.61; N, 9.19. Found: C, 61.10; H, 7.61; N, 9.21%. ^{1}H NMR ($CDCl_3$, δ, ppm): 6.68–7.06 (d, 4H, aromatic CH), 3.68 (s, 8H, benzyl CH_2, 4H, morpholine OCH_2), 2.25 (s, NCH_2), 1.6 (m, 2H, alkyl CH_2), 1.2–1.4 (m, 6H, alkyl CH_3). Selected IR data (KBr, υ cm^{-1}): 3450, 1480.

2.4.3. N,N-Bis{2-hydroxy-5-methyl-(3-piperidin-1-ylmethyl)benzyl} cyclohexylamine (L^3H_2)

P.C.-3 (6.76 g, 0.02 mol) in methanol was mixed with piperidine (1.87 g, 0.22 mol). Then formaldehyde (35%, 2 ml, 0.02 mol) was added dropwise with stirring under cooling. This mixture was stirred for 24 h at room temperature and then heated gently under reflux for 8 h. The alcohol was removed under vacuo and a yellow oil was extracted with dichloromethane and recrystallised from ethanol.

Yield: Yellow oil, 6 g (69%). *Anal*. Calc. for $C_{34}H_{51}N_3O_2$: C, 76.50; H, 9.63; N, 7.87. Found: C,76.54; H, 9.65; N, 7.84%. ^{1}H NMR ($CDCl_3$, δ, ppm): 7.18–6.76 (m, 5H, aromatic CH), 3.56 (s, 6H, benzyl CH_2), 2.5 (d, 1H, cyclohexyl NCH_2), 2.2 (s, aromatic CH_3), 1.2–1.5 (m, 16H, ring CH_2). Selected IR data (KBr, υ cm^{-1}): 3450, 1470. Mass spectrum: *m*/*z* 436.

2.5. Synthesis of the copper complexes

2.5.1. Synthesis of $[Cu_2L^1(ClO_4)_2]\cdot 2CH_3OH\cdot 2H_2O$ (**1a**)

The ligand L^1H_2 (1.86 g, 3.3 mmol) and lithium hydroxide (0.28 g, 6.6 mmol) in methanol were boiled and copper(II) perchlorate (2.44 g, 6.6 mmol) in hot methanol was added and heated to reflux for several hours. The solution was filtered when hot and the volume was reduced to one third and kept at room temperature. A dark green coloured compound was filtered and dried in vacuo. The complex was recrystallised from methanol.

Yield: 2 g (61%). *Anal*. Calc. for $C_{35}H_{62}Cu_2N_4O_{16}Cl_2$: C, 42.36; H, 6.30; N, 5.65; Cu, 12.81. Found: C, 42.40; H, 6.31; N, 5.66; Cu, 12.84%. Selected IR data (KBr, υ cm^{-1}): 3320, 1460,1100, 625 (perchlorate) [27] 480, 280. UV–Vis: λ_{max} (nm) (ε, M^{-1} cm^{-1}) (DMF): 690(232), 410(sh), 340(sh), 287(14626). μ_{eff}: 1.51 BM.

The following complexes were also prepared by carrying out the same procedure but varying the ligand (L^1H_2 and L^2H_2) and/or copper(II) salt, and the products were recrystallised from methanol.

2.5.2. $[Cu_2L^1Cl_2]\cdot 2CH_3OH$ (**1b**)

The complex $[Cu_2L^1Cl_2]\cdot 2CH_3OH$ was synthesized by following the previously described procedure for complex **1a**, using copper(II) chloride salt instead of copper(II) perchlorate. Colour: Green. Yield: 2.2 g (81%). *Anal*. Calc. for $C_{35}H_{58}Cu_2N_4O_6Cl_2$: C, 50.72; H, 7.05; N, 6.76; Cu, 15.33. Found: C, 50.71; H, 7.02; N, 6.80; Cu, 15.37%. Selected IR data (KBr, υ cm^{-1}): 3300, 1480, 480, 310–325, 280. UV–Vis: λ_{max} (nm) (ε, M^{-1} cm^{-1}) (DMF): 720(259), 405(sh), 325(sh), 290(11419). μ_{eff}: 1.63 BM.

2.5.3. $[Cu_2L^1Br_2]\cdot 2CH_3OH$ (**1c**)

The complex $[Cu_2L^1Br_2]\cdot 2CH_3OH$ was synthesized by following the previously described procedure for the complex **1a**, using copper(II) bromide salt instead of copper(II) perchlorate. Colour: Green. Yield: 2.25 g (75%). *Anal*. Calc. for $C_{35}H_{58}Cu_2N_4O_6Br_2$: C, 45.80; H, 6.37; N, 6.10; Cu, 13.85. Found: C, 45.79; H, 6.35; N, 6.15; Cu, 13.90%. Selected IR data (KBr, υ cm^{-1}): 3250, 1480, 480, 280, 270. UV–Vis: λ_{max} (nm) (ε, M^{-1} cm^{-1}) (DMF): 730(278), 410(sh), 320(sh), 287(12208). μ_{eff}: 1.64 BM.

2.5.4. $[Cu_2L^2(ClO_4)_2]\cdot 2CH_3OH\cdot 2H_2O$ (**2a**)

The complex $[Cu_2L^2(ClO_4)_2]\cdot 2CH_3OH\cdot 2H_2O$ was synthesized by following the previously described procedure for the complex **1a**, using L^2H_2 instead of L^1H_2. Colour: Dark green. Yield: 2.5 g (73%). *Anal*. Calc. for $C_{33}H_{56}Cu_2N_4O_{16}Cl_4$: C, 38.34; H, 5.46; N, 5.42; Cu, 12.29. Found: C, 38.30; H, 5.48; N, 5.46; Cu, 12.30%. Selected IR data (KBr, υ cm^{-1}): 3300, 1460, 1100,625, 480, 280. UV–Vis: λ_{max} (nm) (ε, M^{-1} cm^{-1}) (DMF): 680(281), 400(sh), 320(sh), 290(12850). FAB-MS *m*/*z* (% intensity): $[Cu_2L^2]^{2+}\cdot 2H_2O$, 770(5). μ_{eff}: 1.68 BM.

2.5.5. $[Cu_2L^2Cl_2]\cdot 2CH_3OH$ (**2b**)

The complex $[Cu_2L^2Cl_2]\cdot 2CH_3OH$ was synthesized by following the previously described procedure for the complex **1a**, using L^2H_2 instead of L^1H_2 and copper chloride in place of copper perchlorate. Colour: Green. Yield: 2.3 g (78%). *Anal*. Calc. for $C_{33}H_{52}Cu_2N_4O_6Cl_4$: C, 45.57; H, 6.03; N, 6.44; Cu, 14.61. Found: C, 45.55; H, 6.01; N, 6.40; Cu, 14.59%. Selected IR data (KBr, υ cm^{-1}): 3250, 1460, 470, 320, 285. UV–Vis: λ_{max} (nm)

(ε, $M^{-1}\,cm^{-1}$) (DMF): 720(236), 390(sh), 360(sh), 290(13222). μ_{eff}: 1.69 BM.

2.5.6. $[Cu_2L^2Br_2]\cdot 2CH_3OH$ (**2c**)

The complex $[Cu_2L^2Br_2]\cdot 2CH_3OH$ was synthesized by following the previously described procedure for the complex **1a**, using L^2H_2 instead of L^1H_2 and copper bromide in place of copper perchlorate. Colour: Green. Yield: 2.6 g (79%). *Anal.* Calc. for $C_{33}H_{52}Cu_2N_4O_6Cl_2Br_2$: C, 41.35; H, 5.47; N, 5.84; Cu, 13.26. Found: C, 41.31; H, 5.43; N, 5.85; Cu, 13.22%. Selected IR data (KBr, υ cm^{-1}): 3250 1470, 470 (Cu–N); 310 (Cu–Br); 285 (Cu–O). UV–Vis: λ_{max} (nm) (ε, $M^{-1}\,cm^{-1}$) (DMF): 730(259), 390(sh), 340(sh), 290(14192). μ_{eff}: 1.68 BM.

2.5.7. $[Cu_2L^3(OAc)_2]\cdot 2H_2O$ (**3a**)

The ligand L^3H_2 (1.44 g, 3.3 mmol) and lithium hydroxide (0.16 g, 6.6 mmol) in methanol were boiled and copper(II) acetate (1.43 g, 6.6 mmol) in hot methanol was mixed and refluxed for several hours. The solution was filtered when hot and the volume was reduced to one third and kept at room temperature. The dark green colour compound was filtered and dried in vacuo. The complex was recrystallised from methanol. The other complexes were also prepared by carrying out the same procedure but varying the copper(II) salt.

Yield: 1.9 g (77%). *Anal.* Calc. for $C_{38}H_{59}Cu_2N_3O_8$: C, 56.14; H, 7.31; N, 5.17; Cu, 15.63. Found: C, 56.10; H, 7.27; N, 5.16; Cu, 15.60%. Selected IR data (KBr, υ cm^{-1}): 3350, 1600 (terminal acetate), 1590 (bridged acetate) [28,29], 485 (Cu–N), 280 (Cu–O). UV–Vis: λ_{max} (nm) (ε, $M^{-1}\,cm^{-1}$) (DMF): 690(277), 430(sh), 340(sh), 285(11142). μ_{eff}: 1.61 BM.

The other complexes derived from this ligand (L^3H_2) are given below.

2.5.8. $[Cu_2L^3Cl_2].CH_3OH\cdot 2H_2O$ (**3b**)

The complex $[Cu_2L^3Cl_2]\cdot CH_3OH\cdot 2H_2O$ was synthesized by following the previously described procedure for the complex **3a**, using copper chloride in the place of copper acetate. Colour: Green. Yield: 1.5 g (65%). *Anal.* Calc. for $C_{35}H_{57}Cu_2N_3O_5Cl_2$: C, 52.69; H, 7.20; N, 5.27; Cu, 15.93. Found: C, 52.70; H, 7.17; N, 5.28; Cu, 15.91%. Selected IR data (KBr, υ cm^{-1}): 3350, 1470, 470 (Cu–N), 325 (Cu–Cl), 280 (Cu–O). UV–Vis λ_{max} (nm) (ε, $M^{-1}\,cm^{-1}$) (DMF): 700(230), 433(sh), 330(sh), 292(13714). μ_{eff}: 1.63 BM.

2.5.9. $[Cu_2L^3Br_2]\cdot CH_3OH\cdot 2H_2O$ (**3c**)

The complex $[Cu_2L^3Br_2]\cdot CH_3OH\cdot 2H_2O$ was synthesized by following the previously described procedure for the complex **3a**, using copper bromide in the place of copper acetate. Colour: Green. Yield: 1.75 g (67%). *Anal.* Calc. for $C_{35}H_{57}Cu_2N_3O_5Br_2$: C, 47.41; H, 6.48; N, 4.74; Cu, 14.33. Found: C, 47.38; H, 6.47; N, 4.72; Cu, 14.31%. Selected IR data (KBr, υ cm^{-1}) 3250, 1480, 480 (Cu–N), 300 (Cu–Br), 285 (Cu–O). UV–Vis: λ_{max} (nm) (ε, $M^{-1}\,cm^{-1}$) (DMF): 720(194), 390(sh), 330(sh), 290(10110). FAB-MS. *m/z* (% intensity): $[Cu_2L^3Br]^+$, 641(10). μ_{eff}: 1.65 BM.

3. Results and discussion

The precursor compounds were synthesised using the literature method [30]. The yield of the precursor compounds was as follows. P.C.-1: 65%, P.C.-2: 73% and P.C.-3: 57%. All the precursor compounds were recrystallised using cold methanol. Binucleating hexadentate (L^1H_2 and L^2H_2) and pentadentate (L^3H_2) ligands were prepared by the mannich base reaction of the respective precursor compound, substituted amine and formaldehyde in a 1:1:1 molar ratio. The yield of the ligands was found to be in the range 55–74%. The ligands were recrystallised from ethanol and used for the complex syntheses. Schemes 1 and 2 show the syntheses of the ligands and their complexes. The yields of the complexes fall in the range 61–81%. The recrystallised samples of the complexes were used for the analyses. Attempts to recrystallise the complexes with different solvents using various methods, like slow evaporation, diffusion etc, resulted in microcrystalline compounds not suitable for X-ray diffraction study.

The electronic spectra of the complexes are recorded in DMF solvent. All the complexes exhibit a band around 680–730 nm due to a d–d transition [31,32]. The peak in the region 320–360 nm is due to a ligand to metal charge transfer (LMCT) transition [26,33,34]. In addition to the above said two bands, all the complexes show considerably greater intensity around 245–290 nm. This is due to an intraligand transition [34–36]. The higher λ_{max} value for all these complexes (d–d transition) are characteristic for a trigonal bipyramid geometry of the Cu(II) ion [24,31,36–40].

3.1. Magnetic properties of the complexes

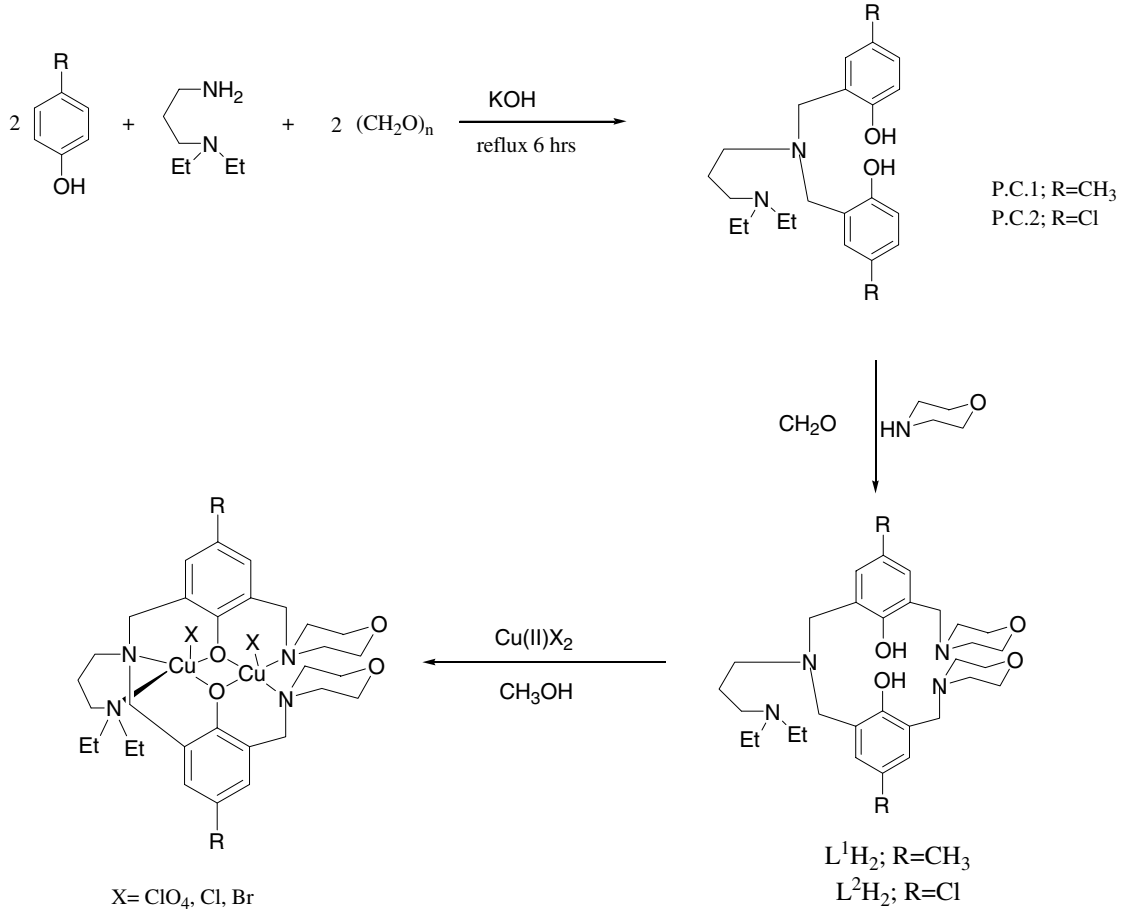
The values of the magnetic moments observed at room temperature for the binuclear copper(II) complexes were found to be 1.51–1.69 BM, smaller than the spin only value. This clearly indicates the occurrence of an antiferromagnetic exchange interaction within the molecule. Variable temperature magnetic susceptibility measurements were performed on a powdered sample in the temperature range 77–300 K. The results are displayed in Fig. 1. The best fit values of $-2J$, g and P are given in the Table 1. The data for the various complexes are fitted to a modified Bleaney–Bowers equation [41] to evaluate the singlet–triplet energy separation ($-2J$):

$$\chi_m = Ng^2(\beta^2/3kT)[3 + \exp(-2J/kT)]^{-1}(1 - P) + (0.45P/T) + N_\alpha,$$

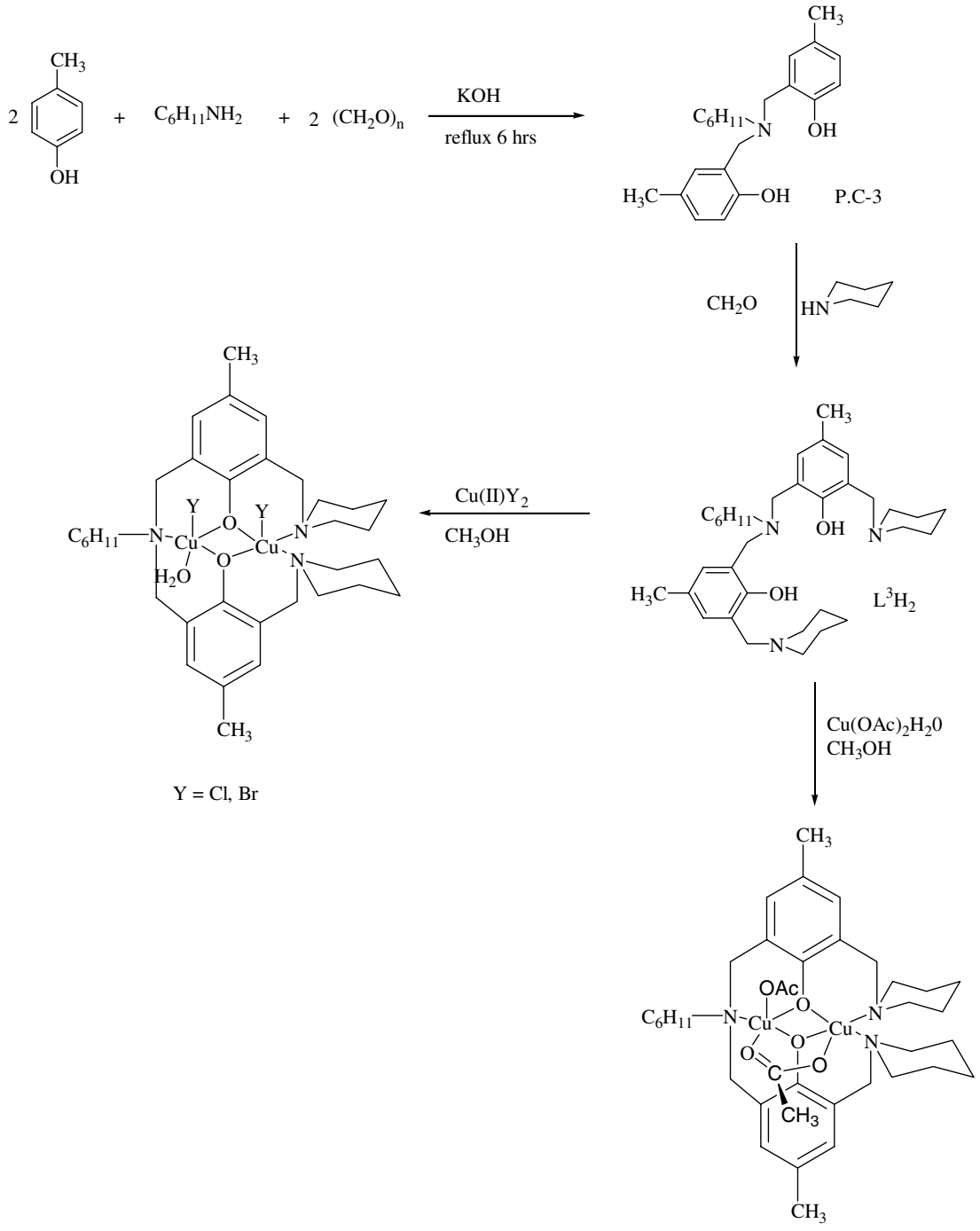
where χ_m is the paramagnetic susceptibility per metal atom after the correction for diamagnetism. N is Avagadro's number, β is the Boltzman constant, g is the average gyromagnetic ratio and P is the fraction of monomeric copper(II) impurities. $-2J$ is the singlet–triplet energy separation. N_α is the temperature independent, usually assumed to be 120×10^{-6} cgs units for copper(II) compounds. The value of the exchange integral $-2J$ for the complexes varies from 45 to 178 cm^{-1}, indicative of weak antiferromagnetic coupling between the copper(II) ions. The observed singlet–triplet energy separation ($-2J$) of complexes **1a** and **1c** are 112 and 116 cm^{-1}, respectively, and for the complexes **2a** and **2c** the observed $-2J$ values are 45 and 52 cm^{-1}, respectively. The observed low value may be due to more flexible nature of the propylene linkage [42]. The complex **3a**, exhibits a higher $-2J$ value of 178 cm^{-1}. This higher value shows that one of the acetate anions may form an additional bridge between the copper(II) ions [42–44], apart from the phenolate bridge. The exchange integral value for **3c** is 106 cm^{-1}. The very close $-2J$ values observed for complexes **1a**, **1c** and **3c** indicate the presence of only only phenolate bridge between the copper(II) ions.

Copper complexes with distorted square planar geometry generally show higher exchange integral values [20] and they exhibit λ_{max} values between 520 and 630 nm. The observed λ_{max} value (680–730 nm) indicates a deviation from planar geometry to trigonal bipyramidal geometry around the Cu(II) ions [42]. This deviation in the geometry leads to a smaller exchange integral value.

A higher $-2J$ value is observed for complexes of L^1H_2 when compared to complexes of L^2H_2.This higher $-2J$ value may be due to the geometry around Cu(II) ions and also due to the substitution effect in the ligand. Complexes **1a** (L^1Cu_2) and **2a** (L^2Cu_2) show λ_{max} around 680 and 690 nm, respectively. This 10 nm difference does not have much influence on the structure of the complexes which may have more or less the same geometry. So the change in the magnetic exchange interaction is more influenced by substitution in the ring than the geometry. Presence of an electron withdrawing group at the para position of the bridging phenoxide ion in L^2H_2 will decreases the electron density around the Cu(II) centers [42,45–51] when compared to the methyl group



Scheme 1. Synthesis of ligand L^1H_2 and L^2H_2 and their complexes.



Scheme 2. Synthesis of ligand L^3H_2 and its complexes.

Table 1
Magnetic exchange parameters for the complexes

Complexes	$-2J$ (cm^{-1})	g	P
1a	112	1.839	0.001
1c	116	1.896	0.015
2a	45	1.940	0.015
2b	52	1.830	0.001
3a	178	2.016	0.001
3c	106	2.06	0.001

present in L^1H_2. Reduction in the electron density weakens the Cu–O bond and reduces the spin exchange interaction.

3.2. ESR spectral analysis

ESR spectra of the complexes were recorded in DME solvent at liquid nitrogen temperature (77 K). The absorption signal for both complexes **2c** and **3a** consists

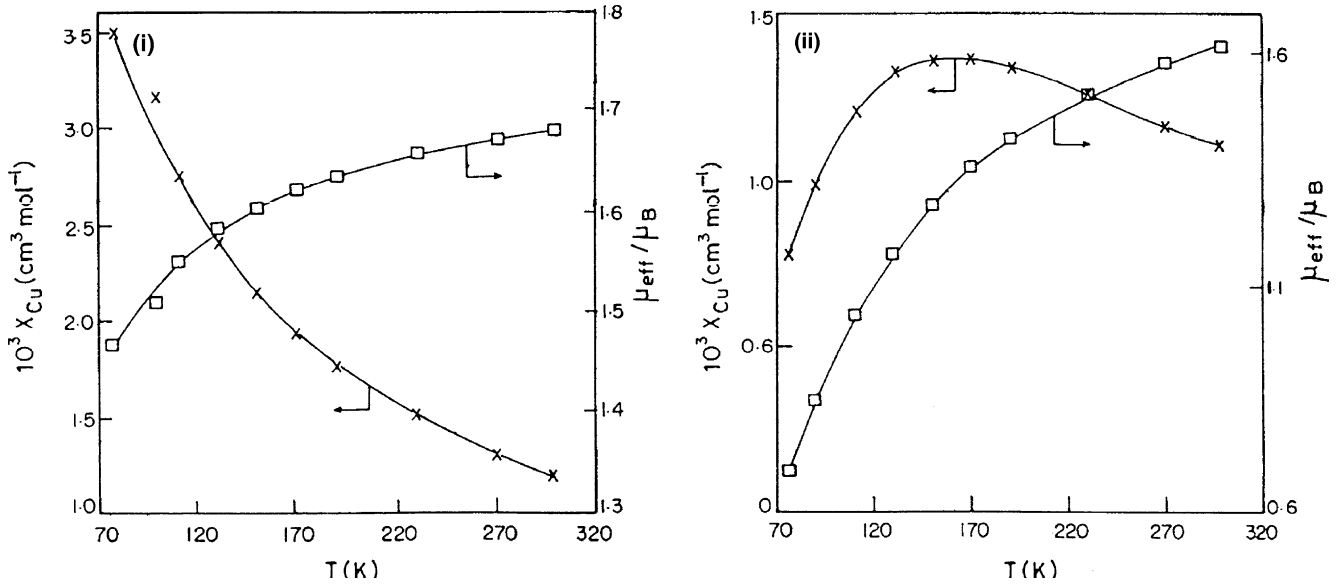


Fig. 1. Temperature variations of magnetic susceptibility (×) and effective magnetic moment (□) for the complexes (i) $[Cu_2L^2(ClO_4)_2]\cdot 2CH_3OH\cdot 2H_2O$ **2a**, (ii) $[Cu_2L^3(OAc)_2]\cdot 2H_2O$ **3a**.

of a broad band centered at about $g = 2$. Hyperfine splitting due to the spin of the copper nucleus was not detected because of the broadness of signal. These observations confirm the occurrence of super exchange coupling between the copper(II) ions in the binuclear complexes.

3.3. Electrochemistry

Conductivity measurements [52] of binuclear copper(II) complexes in DMF solvent resulted in Λ_m values in the range 10–15 Λ_m/S/cm^2/M^{-1}, indicating the complexes are neutral. The cyclic voltammograms of the complexes are recorded in DMF solvent and are reproduced in Fig. 2 (scan rate 50 mV/s). The electrochemical data of the complexes are presented in Table 2. It has been observed for all the complexes (i) the E_{pc} and E_{pa} values change with scan rate (ii) ΔE_p values increase with increasing scan rate, and were found to be more than 60 mV and (iii) the cathodic peak currents (I_c) are greater than the anodic (I_a) peak currents. These observations indicate that the nature of the electron transfer processes is quasi-reversible.

The first reduction potential for all the complexes was observed in the potential range −0.48 to −0.8 V (E^1_{pc}) and the second reduction potential was observed in the potential range −0.76 to −1.4 V (E^2_{pc}). Coulometric experiments conducted at 100 mV higher than the first reduction potential show the consumption of one electron per molecule ($n = 0.95$). The same experiments conducted at 100 mV slightly higher than the second reduction potential confirms the consumption of two electrons per molecule ($n = 1.92$). The redox process may involve the following steps.

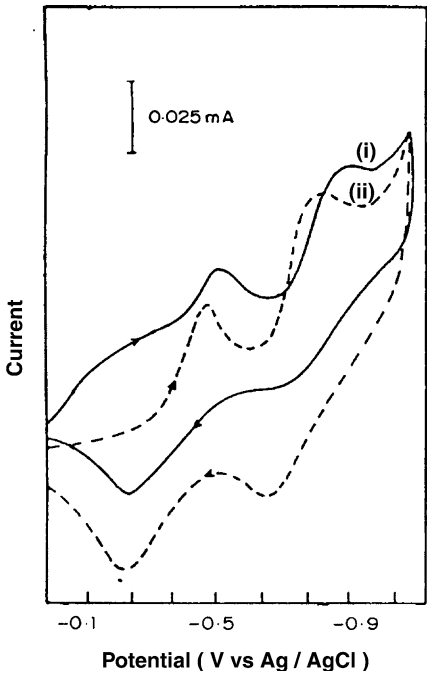


Fig. 2. Cyclic voltammogram of (i) $[Cu_2L^1Br_2]\cdot 2CH_3OH$ **1c** (——). (ii) $[Cu_2L^2Br_2]\cdot 2CH_3OH$ **2c** (-----) in DMF solvent at 25 °C (scan rate 50 mV/s).

$$Cu^{II}Cu^{II} \overset{E^1_{pc}}{\rightleftharpoons} Cu^{II}Cu^{I} \overset{E^2_{pc}}{\rightleftharpoons} Cu^{I}Cu^{I}$$

The first reduction potential for the perchlorate complex **1a** was observed at −0.62 V which is a more negative potential than the corresponding halo complexes **1b** and **1c**. Upon halide ion coordination the geometry around the copper may be distorted from planarity. The distortion in the geometry is observed from the red shift in the

Table 2
Electrochemical data for the complexes

Complexes	E^1_{pc} (V)	E^1_{pa} (V)	ΔE_p (mV)	$E^1_{1/2}$ (V)	E^2_{pc} (V)	E^2_{pa} (V)	ΔE_p (mV)	$E^2_{1/2}$ (V)
1a	−0.62	−0.42	200	−0.52	−1.38	−1.08	300	−1.23
1b	−0.56	−0.28	280	−0.42	−1.30	−0.92	380	−1.11
1c	−0.50	−0.30	200	−0.40	−0.80	−0.66	140	−0.73
2a	−0.60	−0.36	240	−0.48	−1.32	−1.10	220	−1.21
2b	−0.53	−0.26	270	−0.40	−1.24	−0.92	320	−1.08
2c	−0.48	−0.28	200	−0.38	−0.76	−0.62	140	−0.69
3a	−0.80	−0.64	160	−0.72	−1.30	−1.10	200	−1.20
3b	−0.60	−0.34	260	−0.47	−1.04	−0.98	60	−1.01
3c	−0.52	−0.36	160	−0.44	−0.80	−0.70	100	−0.75

λ_{max} values of the halo complexes. It is known that more distortion in the coordination geometry around the metal will favour electrochemical reduction and hence the anodic shift in the first reduction potential occurs [31,38]. A similar trend had been observed among other series of complexes.

The first reduction potential of complex **3a** was observed at −0.8 V, which is more negative than other complexes **3b** and **3c**. In addition to a phenolate bridge, the presence of an acetate bridge enhances the complex to show a greater negative potential as evidenced from a higher exchange integral value (178 cm^{-1}).

The reduction potential is also affected by the substituents at the para position of the phenoxide of the phenyl rings. Replacement of a methyl group with a relatively electron withdrawing chloride shifts the first as well as the second reduction to more anodic potentials. The electron withdrawing substituent decreases the electron density around the metal ion and favours easy reduction [47,48].

The higher $E^1_{1/2}$ and $E^2_{1/2}$ values for the chloro complexes compared to the bromo complexes indicate that the addition of an electron to the chloro complex is more difficult than the bromo complex. This may be due to higher basicity of the chloride ion when compared to the bromide ion.

4. Conclusion

This paper describes binuclear copper(II) complexes of two ligand systems. In the first system (L^1H_2 and L^2H_2) only substitution in the ligand is varied. In the second system (L^3H_2), the external bridging system is varied. The magnetic exchange interaction and electrochemical properties of binuclear copper(II) complexes within the first system does not vary when compared to second system. The substitution in the ligand has much less influence than the bridging ligands between the metal centers in the complexes. This may be due to a change in the geometry around the copper ions in the complexes.

Acknowledgement

We thank the University Grant Commission, New Delhi, Government of India, for financial support to one of the authors, P. Kamatchi.

References

[1] K.D. Karlin, Z. Tyeklar (Eds.), Bioinorganic Chemistry of Copper, Chapman and Hill, New York, 1993.
[2] Bidyut K. Santra, Pattubala A.N. Reddy, Munirathinam Nethaji, Akhil R. Chakravarthy, Inorg. Chem. 41 (2002) 1328.
[3] K.D. Karlin, A.D. Zuberbuhler, in: J. Reedijk, E. Bouwman (Eds.), Bioinorganic Catalysis, Marcel Dekker, New York, 1999, p. 469.
[4] S.B. Harkins, J.C. Peters, J. Am. Chem. Soc. 126 (2004) 2885.
[5] Carsten Gerdemann, Christoph Eicken, Bernt Krebs, Acc. Chem. Res. 35 (2002) 183.
[6] Shu-An Li, Jiang Xia, De-Xi Yang, Yan Xu, Dong-Feng Li, Mei-Fang Wu, Wen-Xia Tang, Inorg. Chem. 41 (2002) 1807.
[7] R. Kannappan, R. Mahalakshmy, T.M. Rajedran, R. Venkatesan, P. Sambasiva Rao, Proc. Indian Acad. Sci. 115 (2003) 1.
[8] Ademir Neves, Liane M. Rossi, Adailton J. Bortoluzzi, Bruno Szpoganicz, Clayton Wiezbicki, Erineu Schwingel, Inorg. Chem. 41 (2002) 1788.
[9] Hong-Chang Liang, Christiana Xin Zhang, Mark J. Henson, Roger D. Sommer, Karen R. Hatwell, Susan Kaderli, Andreas D. Zuberbuhler, Arnold L. Rheingold, Edward I. Solomon, Kenneth D. Karlin, J. Am. Chem. Soc. 124 (2002) 4170.
[10] W.H. Lang, K.E. Van Holde, Proc. Natl. Acad. Sci. USA 88 (1991) 244.
[11] F. Zippel, F. Ahlers, R. Werner, W. Haase, H.F. Nolting, B. Krebs, Inorg. Chem. 35 (1996) 3409.
[12] M.J. Ettinger, in: R. Lontine (Ed.), Copper Proteins and Copper Enzymes, vol. 3, CRC Press, Boca Raton, FL, 1984, p. 175.
[13] H. Furutachi, A. Ishida, H. Miyasaka, N. Fukita, M. Ohba, H. Okawa, M. Koikawa, J. Chem. Soc., Dalton Trans. (1999) 367.
[14] H. Okawa, H. Furutachi, D.E. Fenton, Coord. Chem. Rev. 174 (1998) 51.
[15] D.G. McCollum, B. Bosnich, Inorg. Chim. Acta 270 (1998) 13.
[16] D.G. McCollum, G.P.A. Yap, A.L. Rheingold, B. Bosnich, J. Am. Chem. Soc. 118 (1996) 1365.
[17] D. Saravanakumar, N. Sengottuvelan, V. Narayanan, M. Kandaswamy, K. Chinnakali, G. Senthilkumar, H.K. Fun, Eur. J. Inorg. Chem. (2004) 872.
[18] M. Thirumavalavan, P. Akilan, M. Kandaswamy, Inorg. Chem. 42 (2003) 3308.
[19] Anna L. Gavrilova, Brice Bosnich, Chem. Rev. 104 (2004) 349.

[20] P. Zanello, S. Tamburini, P.A. Vigato, G.A. Mazzocchin, Coord. Chem. Rev. 77 (1987) 165.
[21] P.A. Vigato, S. Tamburini, D.E. Fenton, Coord. Chem. Rev. 106 (1990) 25.
[22] A.J. Atkins, D. Black, A.J. Blake, A. Marin-Becerra, S. Parsons, L. Ruiz-Ramirez, M. Schroder, Chem. Commun. (1996) 457.
[23] M. Lubben, B.L. Feringa, J. Org. Chem. 59 (1994) 2227.
[24] M. Thirumavalavan, P. Akilan, M. Kandaswamy, Supramolecular Chem. 16 (2004) 137.
[25] Marcel Lubben, Ronald Hage, Auke Meetsma, Koos Byma, Ben L. Feringa, Inorg. Chem. 34 (1995) 2217.
[26] Elena V. Rybak-Akimova, Daryle H. Bush, Pawan K. Kahol, Nicholas Pinto, Nathaniel W. Alcock, Howard J. Clase, Inorg. Chem. 36 (1997) 510.
[27] Xian-He Bu, Miao Du, Zhi-Liang Shang, Ruo-Hua Zhang, Dai-Zheng Liao, Inorg. Chem. 39 (2000) 4190.
[28] D.V. Bautista, J.C. Dewan, L.K. Thompson, Can. J. Chem. 60 (1982) 2583.
[29] G. Bullock, F.W. Hartstock, L.K. Thompson, Can. J. Chem. 61 (1983) 57.
[30] W.J. Burke, R.P. Smith, C. Weatherbee, J. Org. Chem. 71 (1952) 510.
[31] C. Belle, C. Beguin, I. Gautier-Luneau, S. Hamman, C. Philouze, J.L. Pierre, F. Thomas, S. Torelli, Inorg. Chem. 41 (2002) 479.
[32] B.J. Hathaway, D.E Billing, Coord. Chem. Rev. 5 (1970) 143.
[33] K.J. Obserhausen, J.F. Richardson, R.M. Buchanan, J.K. McCusker, D.N. Hendrickson, Jean-MareLatour, Inorg. Chem. 30 (1991) 1357.
[34] Ty Garber, S.V. Wallendael, D.P. Rillema, M. Kirk, W.E. Hatfield, J.H. Welch, P. Singh, Inorg. Chem. 29 (1990) 1863.
[35] P.B. Murch, F.C. Bradley, P.D. Boyle, V. Papaefthymiou, L. Que Jr., J. Am. Chem. Soc. 109 (1987) 7993.
[36] L.F. Taylor, W.M. Coleman, Inorg. Chim. Acta 63 (1982) 183.
[37] J.P. Costes, F. Dahan, J.P. Laurent, J. Chem. Soc., Dalton Trans. (1989) 1017.
[38] S.K. Mandal, L.K. Thompson, M.J. Newlands, A.K. Biswas, B. Adhikary, K. Nag, E.J. Gabe, F. Lee, Can. J. Chem. 67 (1989) 662.
[39] C. Fraser, B. Bosnich, Inorg. Chem. 33 (1994) 338.
[40] Hiromasa Kurosaki, Hiroyuki Koike, Sachiko Omori, Yukiko Ogata, Yoshihiro Yamaguchi, Masafumi Goto, Inorg. Chem. Commun. 7 (2004) 1229.
[41] B. Bleaney, K.D. Bowers, Proc. R. Soc., London. Ser. A 214 (1952) 451.
[42] Elena V. Rybak-Akimova, Daryle H. Busch, Pawan K. Kahol, Nicholas Pinto, Nathaniel W. Alcock, Howard J. Clase, Inorg. Chem. 36 (1997) 510.
[43] G.D. Fallon, S.K. Murray, W. Mazurek, M.J. O'Connor, Inorg. Chim. Acta 96 (1985) 153.
[44] Y. Nishida, M. Takeuchi, K. Takahashi, S. Kida, Chem. Lett. (1985) 631.
[45] L.K. Thompson, S.K. Mandal, S.S. Tandon, J.N. Bridson, M.K. Park, Inorg. Chem. 35 (1996) 3117.
[46] P. Amudha, M. Kandaswamy, L. Govindaswamy, D. Velmurugan, Inorg. Chem. 37 (1998) 4486.
[47] M.J. MaeLachlan, M.K. Park, L.K. Thompson, Inorg. Chem. 35 (1996) 5492.
[48] M. Thirumavalavan, P. Akilan, M. Kandaswamy, K. Chinnakali, G. Senthilkumar, H.K. Fun, Inorg. Chem. 42 (2003) 3308.
[49] N. Sengottuvelan, D. Saravanakumar, S. Sridevi, V. Narayanan, M. Kandaswamy, Supramolecular Chem. 16 (2004) 129.
[50] A.W. Addison, L.L. Borer, E. Sinn, Models of Cu(II) proteins, in: M.J. Stillman, C.F. Shaw, K.T. Suzuki (Eds.), Metallothioneins – Synthesis, Structure and Properties of Metallothioneins, Pytochelatins and Metal–thiolate Complexes, VCH Publishers, USA, 1992, p. 387 (Chapter 15), and refs cited.
[51] R.J. Butcher, J.W. Overman, E. Sinn, J. Am. Chem. Soc. 102 (1980) 3276, and refs cited.
[52] W.J. Geary, Coord. Chem. Rev. 7 (1971) 81.

In continuation of such studies, our investigations on dichloro-mono (1-phenylamidino-*O*-alkylurea)copper (II) (alkyl = methyl, ethyl, *n*-propyl, *n*-butyl, *n*-amyl) have shown that in these complexes, copper(II) ions exist as monomers having square planar geometry. Evidence was also obtained for the magnetic field induced "molecular alignment" in some of these complexes cooled in a magnetic field (10 KG) to 77 K [2]. Recently, we have synthesized and reported two types of copper complexes, viz., [Cu(II)(1-phenylamidino-*O*-*n*-butylurea)en$(H_2O)]_2^{2+}$ and [Cu(II) sulfato-mono(1-phenylamidino-*O*-methylurea)]$_2$ [3]. Fine structure characteristics of the $S = 1$ system, were obtained in both complexes with zero field splitting (ZFS) of 0.0525 and 0.0225 cm^{-1}, respectively, suggesting the formation of binuclear complexes in the solid state. The presence of a half-field signal ($\Delta M_s = \pm 2$) in the complex [Cu(II)(1-phenylamidino-*O*-*n*-butylurea)en$(H_2O)]_2^{2+}$ further confirmed the formation of a binuclear complex. On dissolution in dimethyl formamide (DMF) and methanol (MeOH), breaking of the binuclear complex into a mononuclear complex takes place, in addition to change in ligation to an axial position. This is reflected in the electronic spectra of the complex in solution. An important finding of our previous study is that among the different alcohols used in forming mixed complexes with en, only [Cu(II)(1-phenylamidino-*O*-*n*-butylurea)en$(H_2O)]_2^{2+}$, prepared from dichloro 1-phenylamidino-*O*-*n*-butylurea copper(II), is ferromagnetic in nature. It is our interest to synthesize a number of copper(II) complexes with *n*-butyl substituted dicyandiamide in different alcohols and to study their spectroscopic properties in order to investigate the nature of the complexes in the solid and solution states. In the EPR spectra of frozen complexes in DMF, the interaction of Cu^{2+}–Cu^{2+} pairs ($S = 1$) were detected. The formation of the binuclear complex was confirmed by the presence of a half-field transition ($\Delta M_s = \pm 2$) at ca. 1600 G.

It has been reported that coordinated amidino-*O*-alkylurea acts as a versatile hydrogen-bonding ligand [4–7] and hydrogen-bonding interactions are of great importance in biological systems [8–11]. Recently, Suksangpanya et al. [12] studied the interaction of transition metal complexes containing this type of ligand having versatile hydrogen-bonding capacity with DNA bases. In view of the above points, we have also extended our investigations to biological activities in terms of the antibacterial and antifungal properties of bis(1-*n*-butylamidino-*O*-alkylurea) copper(II) complexes. The complexes show growth inhibitory activity against pathogenic fungi, viz., *Ceratocystis paradoxa*, *Aspergillus niger*, *Trichoderma koningii*, and pathogenic bacteria, viz., *Bacillus* sps(1), *Bacillus* sps(3). Investigations on these complexes are presented in this paper.

2. Experiment

2.1. Materials and instrumentation

All the chemicals used were of reagent grade. Sodium dicyanoamide was purchased from Fluka and *n*-butyldicyandiamide was prepared by an earlier reported method [13].

2.2. Preparation of bis(1-n-butylamidino-O-alkylurea)copper(II)chloride complexes

The complexes were prepared by refluxing cupric chloride dihydrate (0.01 mol) and *n*-butyldicyandiamide (0.02 mol) on a water bath for 1–3 h in the appropriate alcohols. The pink or purple complexes so obtained were washed repeatedly with the appropriate alcohols and acetone. They were dried in air. The analytical, magnetic susceptibility and electronic data are presented in Table 1.

2.3. Physical measurements

Infrared (IR) spectra of pellets were recorded on a Bruker IFS-66V spectrometer and far IR spectra using polyethylene pellets in the range 500–50 cm^{-1}. Photoacoustic spectra (PAS) on solid samples were recorded using a home-made spectrophotometer in the 350–800 nm range using a tungsten halogen lamp as the source [14], whereas absorption spectra in solution were recorded on a Beckman DU640 spectrophotometer. A Philips PR-9500 bridge was used for conductivity measurements. Magnetic susceptibility measurements were carried out with a PAR 155 Vibrating Sample Magnetometer. EPR spectra were recorded using a Bruker ESP 300 spectrometer operating at X-band (9.5 GHz) with 100 KHz field modulation. The g values were calculated relative to a 2,2 diphenyl-1 picrylhydrazil (DPPH) standard with $g = 2.0036$. Temperature was varied in the range 100–350 K using a Bruker Variable temperature accessory B VT-2000. Elemental analysis was carried out on a Perkin–Elmer 240C and the amount of copper was determined by decomposing the complexes with a mixture of HNO_3 and H_2SO_4 and finally by performing an iodometric titration.

3. Results and discussions

3.1. IR spectra

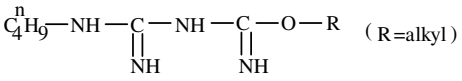
n-Butyldicyandiamide(Bu^{n}dcda) has a strong nitrile(C$\equiv$N) band at 2176 cm^{-1}. In the IR spectra of bis(ligand)copper(II) complexes, there is the absence of a band around 2176 cm^{-1} and also there is no C=O stretching band around 1740 cm^{-1} indicating that the

Table 1
Analytical data, magnetic moment, molar conductivities and electronic spectral data of solid bis(1-*n*-butylamidino-*O*-alkylurea)copper(II) complexes

Compound	Complex	Color	MP (°C)	Analytical found/(calc)(%)				Conductance in MeOH at 25 °C		λ_{max} (cm^{-1}) in methanol	μ_{eff} (BM)	Yield (%)
				C	H	N	Cu	Conc. (mm)	ΛM (Ω^{-1} cm^2mol^{-1})			
Bundcda			92	51.43 (51.42)	8.60 (8.57)	40.03 (40.00)						
$[Cu(Bu^nAMeUH)_2]Cl_2 \cdot 3H_2O$	**1**	light pink	84	31.60 (31.54)	7.20 (7.13)	21.10 (21.03)	12.16 (11.93)	2	126	17 936	1.92	75
$[Cu(Bu^nAEtUH)_2]Cl_2 \cdot 2H_2O$	**2**	light pink	82	35.40 (35.38)	7.36 (7.37)	18.97 (20.64)	11.71 (11.71)	2	158	18 240	2.00	80
$[Cu(Bu^nAPr^nUH)_2]Cl_2 \cdot 2H_2O$	**3**	violet	83	37.84 (37.85)	7.75 (7.71)	19.76 (19.62)	11.15 (11.13)	2	150	18 250	1.88	80
$[Cu(Bu^nAPr^iUH)_2]Cl_2$	**4**	light pink	170	40.42 (40.40)	7.50 (7.48)	20.90 (20.95)	12.00 (11.88)	2	127	17 954	1.82	79
$[Cu(Bu^nABu^nUH)_2]Cl_2$	**5**	light pink	156	42.64 (42.66)	7.85 (7.80)	19.95 (19.90)	11.30 (11.29)	2	131	18 310	1.89	83
$[Cu(Bu^nABu^iUH)_2]Cl_2$	**6**	light pink	140	42.65 (42.66)	7.90 (7.80)	19.95 (19.90)	11.37 (11.29)	2	131	18 036	1.95	81

Bu^nAMeUH = 1-*n*-butylamidino-*O*-methylurea; Bu^nAEtUH = 1-*n*-butylamidino-*O*-ethylurea; Bu^nAPr^nUH = 1-*n*-butylamidino-*O*-*n*-propylurea; Bu^nAPr^iUH = 1-*n*-butylamidino-*O*-*i*-propylurea; Bu^nABu^nUH = 1-*n*-butylamidino-*O*-*n*-butylurea; Bu^nABu^iUH = 1-*n*-butylamidino-*O*-*i*-butylurea.

complexing ligand is not *n*-butyl substituted guanylurea. Instead all bis(ligand) complexes have a very strong ν_a (C–O–C) stretch at ca. 1190–1220 cm^{-1} and ν_s(C–O–C) at ca. 960 cm^{-1} [15] to support 1-*n*-butylamidino-*O*-alkylurea(I). Further the IR spectra of Bu^ndcda showed a band at ca. 1615 cm^{-1} for the butylamidine (azomethine) C=N stretching, this had a downward shift (ν 20–34 cm^{-1}) in all the bis(ligand) complexes showing that the azomethine nitrogen is coordinated to the metal ion. This downward shift is further supported by the lowering of ν(C–N) [16,3]. The increase in value of ν (C=N) to ca. 1656 cm^{-1} in all the complexes is presumably due to a change in the C=N bond order, on coordination through the nitrogen atom, facilitated by the transfer of electron density from the C–O–C moiety. The electron density on the N=C–O–C fragment of 1-*n*-butylamidino-*O*-alkylurea is delocalized in the complexes and the =C–O– bond order is raised [2,3,17]. The presence of new bands at ca. 475 cm^{-1} is due to (Cu–N) in all the complexes.



(I)

3.2. Electronic spectra

The electronic spectra of $Cu(1\text{-}Bu^nAAUH)_2]Cl_2$ complexes in MeOH showed a typical broad absorption band in the range 17 936–18 310 cm^{-1} (Table 1). The photoacoustic signals of bis(1-*n*-butylamidino-*O*-methyl urea)copper(II) chloride in the solid state showed a broad band ca. 18 980 cm^{-1}. The observed spectra are consistent with a distorted octahedral geometry around copper(II), having 1-*n*-butylamidino-*O*-alkylurea as ligands. Compared to the solid state spectra, the solution spectra were shifted to lower energy, probably as a result of axial ligation. Also the shift in the absorption band was strongly dependent on the nature of the solvent. For $[Cu(Bu^nAEtUH)]_2Cl_2 \cdot 2H_2O$, the following bands were observed (Absorption bands in cm^{-1}): 15 873 (Py), 16 520 (DMSO), 17 093 (DMF) and 18 240 (MeOH). The room temperature magnetic susceptibility of the complexes was found to be in the range 1.82–2.00 BM. These values are close to the spin-only value of 1.73 BM for a d^9 configuration. The conductivity measurements of the complexes in MeOH suggest that the complexes are 1:2 electrolytes [18].

3.3. EPR studies

EPR spectra of polycrystalline samples of $Cu(1\text{-}Bu^nAAUH)_2]Cl_2$ (1-Bu^nAAUH = 1-*n*-butylamidino-

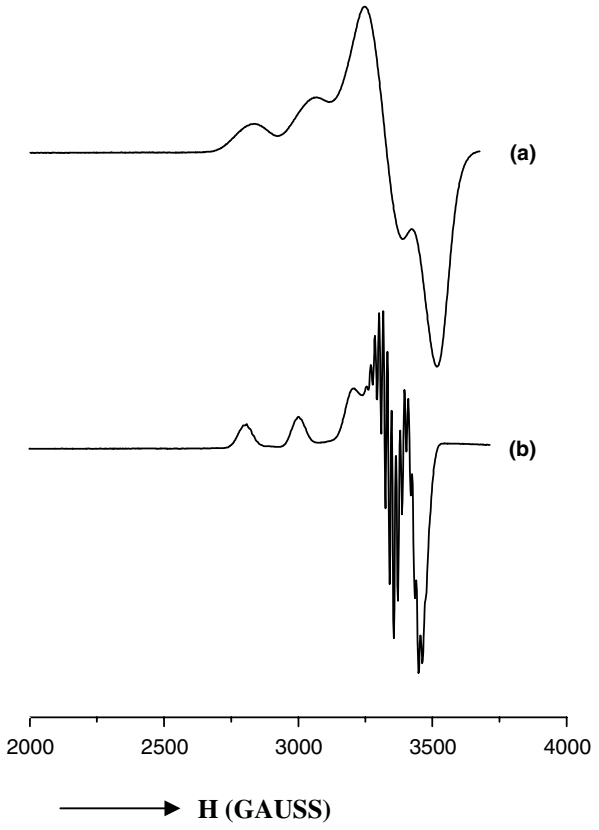


Fig. 1. EPR spectra of complex **3** (a) in solid at 300 K and (b) in methanol at 100 K.

O-alkylurea and alkyl = methyl, ethyl, *n*-propyl, *i*-propyl, *n*-butyl and *i*-butyl) showed the copper(II) signal having axial symmetry. In addition, a relatively weak $\Delta M_s = \pm 2$ transition was observed at 1550 G (g ca. 4.00). A typical room temperature spectrum for the complex bis(1-*n*-butylamidino-*O*-*n*-propylurea)copper (II) chloride is shown in Fig. 1(a). In order to establish the extent of covalency in the metal-ligand interaction and to reduce the broadening due to spin–spin interactions in solids, the EPR spectra of the copper(II) complexes in MeOH and DMF were recorded at 300 and 100 K.

3.4. Solution studies

In MeOH, a quartet hyperfine structure with m_I dependent linewidths was seen at 100 K. The EPR parameters $g_\parallel$, $g_\perp$, $A_\parallel{}^{Cu}$ and $A_\perp{}^{Cu}$ were measured from the anisotropic spectra (Fig. 1(b)) of magnetically diluted copper complexes in frozen MeOH solutions at 100 K (Table 2(a)), which showed that the complexes exist as mononuclear species in MeOH.

The EPR parameters and d–d transition energies were used to evaluate the bonding parameters α^2, β^2 and γ^2, which may be regarded as measures of the covalency of the in-plane σ-bonds and the in-plane and out-of-plane π-bonds, respectively. The in-plane σ-bonding parameter α^2 was calculated using the expression of Kivelson and Neiman [19]

$$\alpha^2 = -\left(\frac{A_\parallel}{0.036}\right) + \left(g_\parallel - 2.0023\right) + \frac{3}{7}(g_\perp - 2.0023) + 0.04.$$

The orbital reduction factors $K_\parallel$ and $K_\perp$ were estimated from the expressions [20,21].

$$K_\parallel^2 = (g_\parallel - 2.0023)E_{d\text{–}d}/8\lambda_0,$$
$$K_\perp^2 = (g_\perp - 2.0023)E_{d\text{–}d}/2\lambda_0,$$

Table 2
(a) EPR and bonding parameters of bis(1-*n*-butylamidino-*O*-alkylurea)copper(II) complexes in MeOH

Complex	Temp (K)	$A_\parallel$ (G)	$A_\perp$ (G)[a]	A_{iso} (G)	$g_\parallel$	$g_\perp$	g_{iso}	α^2	β^2	γ^2	K	$K_\parallel$	$K_\perp$	G
1	300			80										
	77	200	30	87	2.1990	2.0580	2.1050	0.8156	0.9248	0.8527	0.3669	0.7298	0.7767	4.6799
2	300			78.5										
	77	195	26	82	2.1990	2.0520	2.1010	0.8235	0.9083	0.8452	0.3605	0.7360	0.7399	4.5525
3	300			80										
	77	196	27	83	2.2035	2.0550	2.1045	0.7706	0.9148	0.9388	0.3432	0.7445	0.7621	3.7033
4	300			76.5										
	77	200	27	85	2.2100	2.0550	2.1067	0.8272	0.9199	0.8367	0.3731	0.7503	0.7559	4.8080
5	300			80.5										
	77	195	29	84	2.2000	2.0521	2.1014	0.8255	0.9244	0.8543	0.3517	0.7392	0.7420	4.6573
6	300			82										
	77	195	25	83	2.2140	2.0590	2.1107	0.8272	0.9199	0.8667	0.3655	0.7592	0.7858	4.8080

(b) EPR parameters of copper binuclear (B) and mononuclear (M) complexes with different ligands

Matrix	$g_\parallel$	$g_\perp$	g_{iso}	$A_\parallel$ (G)	$A_\perp$ (G)	A_{iso} (G)	D (G)
$(Cu^{2+})_2$ in $[Cu(Bu^nABu^nUH)_2]Cl_2$(B)	2.1600	2.0530	2.0887	90			180
$(Cu^{2+})_2$ in $[Cu(Bu^nABu^iUH)_2]Cl_2$ (B)	2.1602	2.0527	2.0885	96			179
Cu^{2+} in $[Cu(1\text{-}AAUH)_2]Cl_2$[1] (M)	2.1760	2.0580	2.0973	218	25	~89	
Cu^{2+} in $[Cu(NH_3)_4]^{2+}$[24] (M)	2.2160	2.0340	2.0947	160			
Cu^{2+} in $[Cu(NH_3)_4][PtCl_4]$ [25](M)	2.2170	2.0510	2.1063	211	28	~89	

[a] $A_\perp$ for monomers is estimated by using equation $A_{iso} = (A_\parallel + 2A_\perp)/3$ from RT spectra, $A^N \approx 15$–17 G.

where $K_{\|} = \alpha^2\beta^2$, $K_{\perp} = \alpha^2\gamma^2$, and λ_0 represents the one electron spin–orbit coupling constant for the free ion, equal to $-828\ \mathrm{cm}^{-1}$. Significant information about the nature of bonding in the copper(II) complex can be derived from the magnitude of $K_{\|}$ and $K_{\perp}$. In case of a pure σ-bonding $K_{\|} \approx K_{\perp}$ ca. 0.77, whereas $K_{\|} < K_{\perp}$ implies considerable in-plane π-bonding, while for out of plane π-bonding $K_{\|} > K_{\perp}$. Furthermore, α^2, β^2 and γ^2 have values much less than 1 (the value for 100% ionic bonding, this value decreasing with increasing covalent bonding). In all the complexes it is observed that $K_{\|} < K_{\perp}$, indicating the presence of significant in plane π-bonding.

The effect of different alkyl groups on the ligand in the formation of binuclear complexes was studied by recording the EPR spectra of these complexes in frozen solutions of DMF at 100 K. This is shown in Fig. 2. At lower temperatures, the EPR spectrum of bis(1-*n*-butylamidino-*O*-methylurea)copper(II)chloride consisted of an axially symmetric spectrum ($g_{\|} = 2.1990$, $g_{\perp} = 2.0580$) having a weak quartet hyperfine structure on the parallel components arising from the interaction of an unpaired electron with a single copper nucleus ($I = 3/2$) (Fig. 2(a)). This signal is typical of a copper mononuclear complex ($S = 1/2$). Apart from this, a weak signal at half the resonance field ($\Delta M_s = \pm 2$) was observed. The origin of this signal is discussed in the next section. It may be mentioned that Wasson and Trapp [1] investigated copper(II) complexes with *O*-alkyl-1 amidinourea (alkyl = methyl, ethyl, *n*-propyl) using EPR spectroscopy. However, all the complexes were reported to be mononuclear complexes ($S = 1/2$) having a square planar structure CuN_4^{2-}.

The higher analogs of bis(1-*n*-butylamidino-*O*-alkylurea)copper(II) chloride (alkyl = *n*-butyl and *i*-butyl) (Fig. 2(e) and (f)) showed well resolved spectra showing several features associated with the triplet state ($S = 1$) of the binuclear complex. The half-field resonance ($\Delta M_s = \pm 2$) exhibited a well resolved seven line hyperfine structure with an average hyperfine splitting of $A = 95$ G. This was in agreement with reported exchange coupled copper(II) binuclear complexes [3]. With regard to the allowed $\Delta M_s = \pm 1$ transitions, the lowest field resonance (parallel components) observed at 2975 G showed a seven line hyperfine structure similar to that of the $\Delta M_s = \pm 2$ transition, whereas, at higher fields only a few lines could be seen. In addition to this, an intense pair of bands at ca. 3270 and 3435 G, due to the perpendicular component of the triplet state, were observed in the EPR spectra. The hyperfine coupling constant observed on the parallel components of the binuclear complex ($A_{\|} = 95$ G) is nearly half of that observed for the corresponding mononuclear complexes ($A_{\|} = 200$ G) which further confirms the formation of binuclear complex from its monomers. Within the series, the formation of binuclear species went on increasing from bis(1-*n*-butylamidino-*O*-methylurea)copper(II)-chloride to bis(1-*n*-butylamidino-*O*-*n*-butyl/*i*-butylurea) copper(II) chloride. The most accurate values of $g_{\|}$, $g_{\perp}$, $A_{\perp}^{Cu}$ and D for the binuclear complexes were deduced by computer simulation assuming axial symmetry. Fig. 3(a) and (b) show the EPR spectra of the bis(1-*n*-butylamidino-*O*-*n*-butylurea)copper(II)chloride complex in second harmonic and first harmonic presentation respectively. The simulated spectrum (Fig. 3(c)) was obtained by adjusting the relative amounts of the binuclear and mononuclear complexes. The best fit of the simulated spectrum with the experimental one was obtained by using a binuclear to mononuclear complex weight ratio of 0.85:0.15. The spin Hamiltonian parameters used

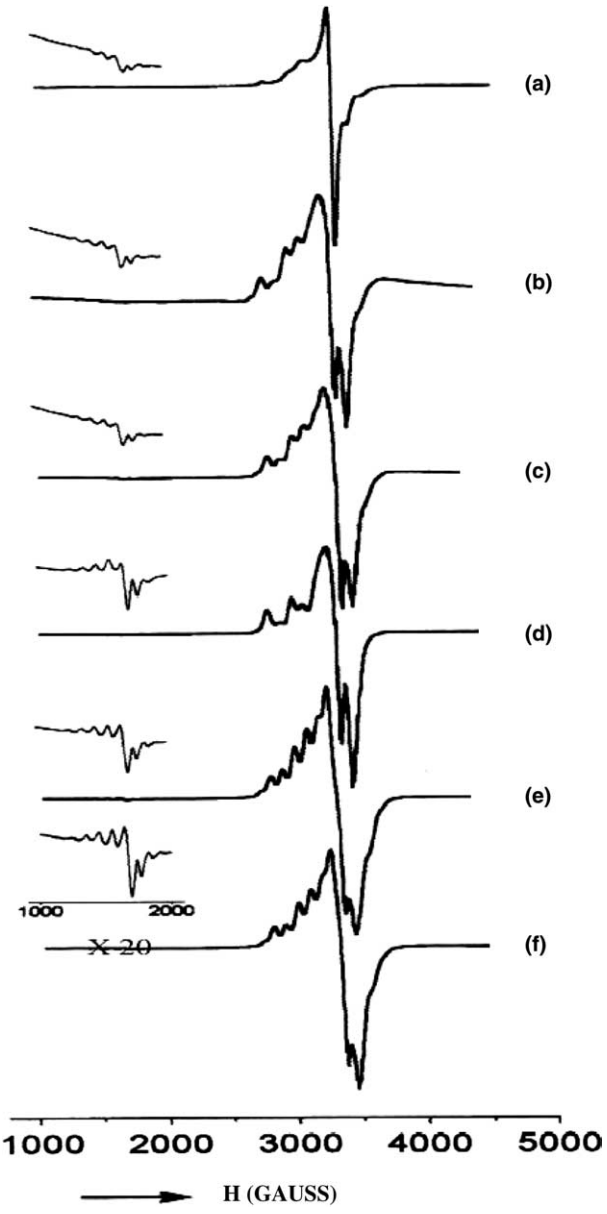


Fig. 2. EPR spectra of different copper complexes in DMF at 100 K: (a) for complex **1**, (b) for complex **2**, (c) for complex **3**, (d) for complex **4**, (e) for complex **5**, (f) for complex **6**.

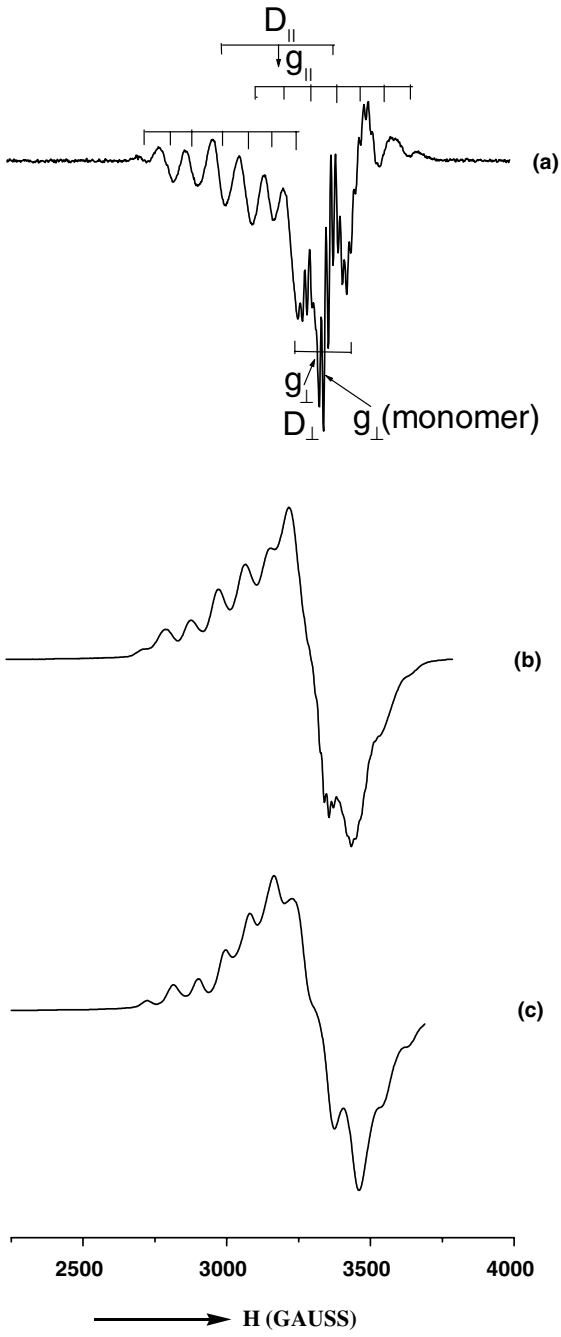


Fig. 3. EPR spectra of complex **5** in DMF at 100 K (a) second harmonic spectrum, (b) first harmonic spectrum and (c) simulated spectrum for complex generated by adjusting the relative amounts of binuclear to mononuclear complex in the weight ratio 0.85:0.15.

for the simulation of binuclear and mononuclear complexes are given in Table 2(a) and (b). The observed g values for the copper complexes were close to those reported for copper complexes having a nearly square planar geometry. The trend in g value ($g_{\|} > g_{\perp} > 2.00$) suggested that the unpaired electron in the copper(II) ion is in the $d_{x_2-y_2}$ orbital. The average distance between two interacting copper ions in the binuclear complexes was calculated from the zero field splitting (D term) by using the equation $D = 3g^2\beta^2/2r^3 = 1.39 \times 10^4\ (g/r^3)$ and was estimated to be nearly 5.5 Å.

Similar triplet state spectra have been reported in a μ-oxalato binuclear copper(II) complex, [(mpym)$(H_2O)(NO_3)Cu(C_2O_4)Cu$ $(NO_3)(H_2O)$ (mpym)] · $2H_2O$ [mpym = 4-methoxy-2-(5-methoxy-3-methyl-1H-pyrazole-1-yl)-6-methylpyrimidine] [22]. The discrete binuclear species consists of a copper ion in a strongly elongated octahedral environment coordinated by two nitrogen atoms and two oxygen atoms of the bridging oxalato group in the equatorial plane, and the water molecule and nitrate ion in axial positions. The presence of nine line super hyperfine structure ($^{14}A^{N} \sim 15$ G) on the lowest field parallel component of the bis(1-*n*-butylamidino-

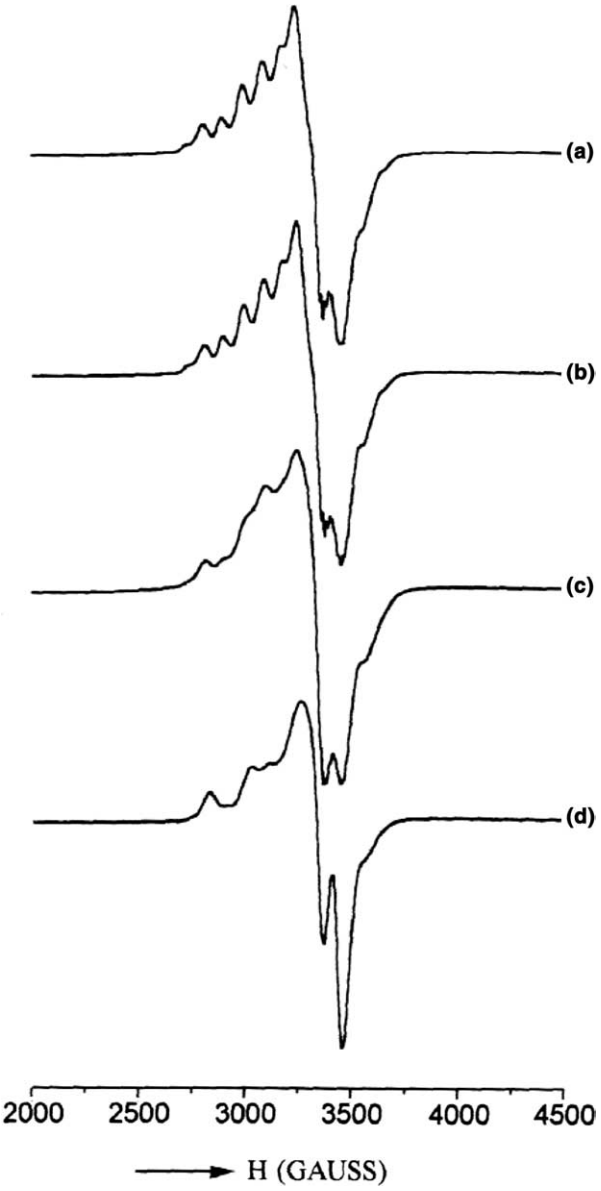


Fig. 4. EPR spectra of complex **5** at different temperatures: (a) 100 K; (b) 145 K; (c) 175 K; (d) 200 K.

Table 3
The antibacterial and antifungal properties of bis(1-*n*-butylamidino-*O*-alkylurea)copper(II) complexes in DMF

Test organism	Sterile DW	DMF	Complex **1**	Complex **2**	Complex **4**	Complex **5**	Complex **6**
Fungal culture							
Ceratocystis paradoxa		+(1.4)	+(2.7)	+(1.5)	+(1.9)	+(2.3)	+(2.4)
Aspergillus niger		+(1.4)	+(1.8)	+(1.4)	+(1.6)	+(1.5)	+(1.4)
Trichoderma koningii		+(0.19)	+(1.2)	+(1.8)	+(1.5)	+(0.9)	+(1.3)
Rhizopus sps.							
Bacterial culture							
Bacillus sps(1)		+(0.9)	+(1.4)	+(1.4)	+(0.9)	+(1.3)	+(1.6)
Bacillus sps(2)							
Bacillus sps(3)			+(0.9)	+(1.4)	+(0.8)		+(1.0)
Total number of culture sensitive			5	4	4	3	4

Parentheses show the diameter of the inhibition zone in cm.

O-methylurea)copper(II)chloride complex in the frozen state and in solution at room temperature clearly suggests that, in all the complexes, the copper ion is bound to four nitrogens in the equatorial plane.

The temperature dependence of the EPR spectra of the bis(1-*n*-butylamidino-*O*-*n*-butylurea)copper(II)chloride complex in DMF is shown in Fig. 4. The EPR spectrum changed drastically as the sample was heated from 100 to 200 K. The low temperature spectrum consists of predominantly binuclear species. The relative intensity of the binuclear species decreased while the signal due to mononuclear species grew in intensity as the complex was heated between 100 and 175 K. On further heating above this temperature the EPR spectra only showed the presence of mononuclear species. Similar changes were observed for the other complexes. The nature of the changes detected in the EPR spectra at different temperatures suggests that in bis(1-*n*-butylamidino-*O*-alkylurea)copper(II)chloride complexes, there is a monomer-binuclear complex equilibrium in DMF.

3.5. Biological activities

Biological activities in terms of the antibacterial and antifungal properties of bis(1-*n*-butylamidino-*O*-alkylurea)copper(II) complexes were determined by the standard 'disc diffusion' method [23]. The bacteria and fungi were grown in nutrient agar and potato dextrose agar (PDA) plates respectively. The compounds to be tested were dissolved in DMF to a final concentration of 1% and soaked in filter paper discs of 5 mm diameter and 1 mm thickness. These filter papers were found to hold a quantity of 0.01 cm^3 solution. These discs were placed on the already seeded plates (of 0.1 ml of test organisms with an approximate density of 1×10^6 CFU/ml) and incubated at 28 ± 1 °C for 24 to 48 h. A clearing zone around the disc indicated the inhibitory activity of the compound on the organism.

The results of antibacterial and antifungal studies are given in Table 3. The majority of the complexes were found to be active against test organisms. Bis(1-*n*-butylamidino-*O*-methylurea)copper(II)chloride was found to have the highest activity against bacteria and fungi whereas the other complexes were moderate and less active. The studied complexes were found to be inactive against some organisms.

4. Conclusions

We have synthesized copper(II) complexes of the type $[Cu\ (1\text{-}Bu^nAAUH)_2]Cl_2$ ($1\text{-}Bu^nAAUH$ = 1-*n*-butylamidino-*O*-alkylurea and alkyl = methyl, ethyl, *n*-propyl, *i*-propyl, *n*-butyl, *i*-butyl). These complexes were characterized by elemental analyses, magnetic moments, conductivity measurements, electronic, IR and EPR studies. The important conclusion of the present investigations is the formation of binuclear species from its monomers in frozen DMF solutions as the complexes were cooled below 200 K. The presence of half-field signals $\Delta M_s = \pm 2$ with seven line hyperfine structure in the frozen solutions confirms the existence of the binuclear complex. Within the series, the formation of binuclear species increased from bis(1-*n*-butylamidino-*O*-methylurea)copper(II)chloride to bis(1-*n*-butylamidino-*O*-*n*-butyl/*i*-butylurea)copper(II)chloride. However, all the complexes were present as mononuclear species in MeOH. The trend in *g* value ($g_\parallel > g_\perp > 2.00$) suggested that the unpaired electron in the copper(II) ion is in the $d_{x^2-y^2}$ orbital. The optical and EPR studies indicated a nearly square planar geometry around the copper ion. The interionic distance r was estimated to be nearly 5.5 Å. Most of the complexes exhibited antibacterial and antifungal activity, however, bis(1-*n*-butylamidino-*O*-methyl urea)copper(II)chloride was found to be highly active.

Acknowledgments

The authors express their gratitude to Dr. V.K. Manchanda, Head, Radiochemistry Division for his

keen interest in this work. The authors thank Dr. A.R. Dhobale for recording photoacoustic spectra in the solid state. One of the authors (R.K. Hemakumar Singh) is grateful to Manipur University, Imphal for a leave grant.

References

[1] J.R. Wasson, C. Trapp, J. Phys. Chem. 73 (1969) 3763.
[2] L.S. Ajitkumar, O.S. Ibopishak, A.S. Manihar, R.S. Hemakumar, R.M. Kadam, M.K. Bhide, M.D. Sastry, Trans. Met. Chem. 26 (2001) 532.
[3] L.S. Ajitkumar, O.S. Ibopishak, A.S. Manihar, R.S. Hemakumar, R.M. Kadam, M.K. Bhide, A.R. Dhobale, M.D. Sastry, Spectrochim. Acta A 60 (2004) 1593.
[4] M.J. Begley, P. Hubberstey, C.H.M. Moore, J. Chem. Res. Synop. (1991) 334.
[5] M.J. Begley, P. Hubberstey, C.H.M. Moore, J. Chem. Res. Synop. (1986) 172.
[6] A.J. Black, P. Hubberstey, U. Suksangpanya, C. Wilson, J. Chem. Soc., Dalton Trans. (2000) 3873.
[7] U. Suksangpanya, A.J. Blake, P. Hubberstey, D.J. Parker, S.J. Teat, C. Wilson, Cryst. Eng. Comm. 5 (2003) 23.
[8] G.A. Jeffrey, An Introduction to Hydrogen Bonding, Oxford University Press, Oxford, 1997.
[9] G.A. Jeffrey, Crystallogr. Rev. 3 (1995) 213.
[10] T.E. Creighton, Protein, Structure and Molecular Properties, second ed., W.H. Freeman, New York, 1996.
[11] G.A. Jeffrey, W. Saenger, Hydrogen Bonding in Biological Structure, Springer-Verlag, Heidelberg, 1991.
[12] U. Suksangpanya, A.J. Black, P. Hubberstey, C. Wilson, Cryst. Eng. Comm. 6 (15) (2004) 70.
[13] F.H.S. Curd, F.L. Rose, J. Chem. Soc. (1946) 729.
[14] A.R. Dhobale, T.P. Chaturvedy, S. Venkiteswaran, M.D. Sastry, Bhabha Atomic Research Centre, External Report No. E/019, 1996.
[15] M. Jamnicky, P. Segla, M. Koman, Polyhedron 14 (1995) 1837.
[16] A. Das, A. Bagchi, S.R. Saha, Ind. J. Chem. A 29 (1990) 361.
[17] P.F.B. Barnard, J. Chem. Soc. A (1969) 2140.
[18] W.J. Geary, Coord. Chem. Rev. 7 (1971) 81.
[19] D. Kivelson, R. Neiman, J. Chem. Soc., Dalton Trans. 35 (1961) 149.
[20] B.N. Figgis, Introduction to Ligand Fields, Interscience, New York, 1966, p. 295.
[21] D.X. West, J. Inorg. Nucl. Chem 43 (1984) 3169.
[22] L. Soto, J. Garcia, E. Escriva, M. Beneto, F. Dahan, J.-P. Tuchagues, J.-P. Legros, J. Chem. Soc., Dalton Trans. (1991) 2619.
[23] C.H. Collins, P.M. Lyne, Microbiological Methods, University Park Press, Baltimore, 1970, p. 422.
[24] W.B. Williamson, J.H. Lunsford, J. Phys. Chem. 80 (1976) 2664.
[25] B.J. Hathaway, in: G. Wilkinson, R.D. Gillard, J.A. McCleverty (Eds.), Comprehensive Coordination Chemistry, Pergamon Press, 1987, p. 533 (Chapter 53, ref-903).

Fe(III) [12] metal ions by means of acetylacetonate chelation leading to neutral linear (BeL^1_2, CuL^1_2) or triangular (AlL^1_3, FeL^1_3) molecular complexes. The pyridyl termini of the building blocks could be easily involved in the formation of extended coordination frameworks with a variety of metal ions, such as Cu(I,II), Co(II) and Cd(II) [11,12]. Further modification of the tecton functionality is feasible by extension of the organic portion as well as varying the position of the pyridyl pendant on the diketonate frame, which may afford either linear or angular M–N binding directions (Scheme 1). In this paper, we report on the synthesis and structures of pyridyl functionalized beryllium diketonates and cadmium (zinc) heterometallic coordination polymers thereafter.

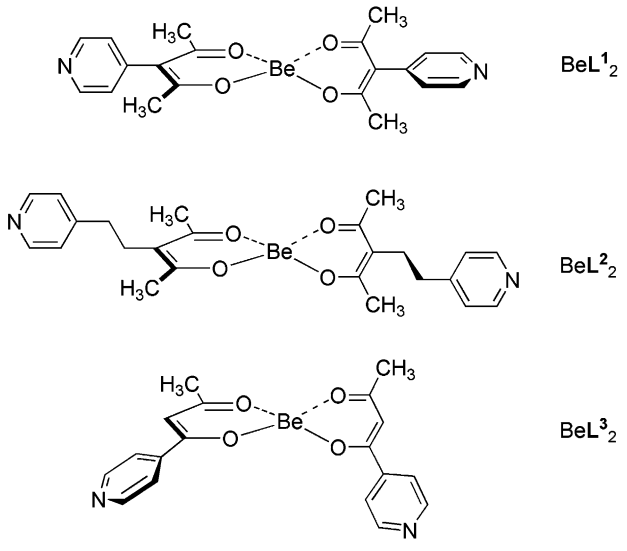
2. Results and discussion

Pyridyl functionalized beryllium diketonates exist as molecular complexes. Crystal structures $[BeL^1_2]_2 \cdot H_2O \cdot CH_3OH$ (**1**), BeL^2_2 (**2**) and BeL^3_2 (**3**) reveal the expected tetrahedral [BeO_4] environment of the central atom, with typical coordination geometry: the Be–O separations and ∠O–Be–O angles are uniform and lie within the ranges of 1.60–1.62 Å and 105–113°, respectively (Fig. 1). The solvated structure $[BeL^1_2]_2 \cdot H_2O \cdot CH_3OH$ (**1**) comprises of a finite supramolecular ensemble, in which association of two molecular [BeL^1_2] moieties occurs via hydrogen bonding, N···HOH···N between pyridyl–N sites and a water molecule (N(4)···O(9) 2.87, N(1)···O(9) 2.92 Å, Fig. 1(a)). The latter forms additional a relatively strong hydrogen bond with the methanol molecule (O(9)···O(10) 2.79 Å). All the molecular beryllium species retain the pyridyl–N donor functions that were not employed in the coordination and thus these compounds may be considered as potential "metalloligands" for the preparation of mixed-metal complexes. Actually linear molecules BeL^1_2 and BeL^2_2 involve side nitrogen atoms situated at 14 and 18 Å, respectively, and hence in combination with transition metal ions the pyridyl N-donors BeL^1_2 and BeL^2_2 could serve as monodentate or exobidentate ligands, bridging pairs of metal atoms at distances of ca. 18 and 23 Å, respectively. In view of the metalloligand geometry, tecton BeL^1_2 is relatively rigid rod-like linker, while evident geometric flexibility of the BeL^2_2 tecton is imposed by two ethylene "spacers" connecting the diketonate and pyridyl fragments. In the structure of BeL^2_2 (**2**), the latter both prefer to adopt an *anti*- conformation to each other (looking straight down the C–C bond of the aliphatic ethylene spacer), with a corresponding torsion angle C(3)–C(6)–C(7)–C(10) of −175° (Fig. 1(b)). Unlike these cases, the BeL^3_2 tecton adopts a geometrically rigid structure and orthogonal orientation of the two chelates at the tetrahedral Be^{2+} matrix dictates a nearly angular situation of the pyridyl groups, with a bite angle of ca. 110° (Fig. 1(c)). This angular configuration of the side pyridyl functions within the metalloligand BeL^3_2 is especially well suited for designing heterometallic squares or rhomboids, in combination with octahedral metal ions.

In the structure $[Cd\{BeL^1_2\}_2Cl_2] \cdot H_2O$ (**4**), the cadmium atom adopts a nearly tetrahedral coordination geometry with two chlorides and two N-coordinated beryllium tectons in the coordination sphere (Fig. 2, Table 1). The terminal uncoordinated pyridyl groups are involved in hydrogen bonding with the water molecule, N···HOH···N (N(2)···O(5) 2.92 Å, ∠O–H---N 158°), that provides a bridge between two molecular complexes, and the overall structure exists as a coordination/hydrogen bonded zig-zag polymer. The hydrogen bonding association is quite similar to that observed in the structure $[BeL^1_2]_2 \cdot H_2O \cdot CH_3OH$ (**1**).

The crystal structures of compounds **5**–**8** have several common features, presumably associated with a complementary shape form of BeL^1_2 tectons and their ability to afford tight antiparallel packing. The closest alignment of the extended organic molecules predetermines the simplicity of the resulting coordination patterns that exist in the form of linear chains and hence the cadmium (zinc) ion coordinates only two pyridyl nitrogen atoms, in *trans*-positions. Recently, we have discussed other examples of the intrinsic role of ligand–ligand packings for coordination geometries [11,13,14].

Thus, in structure $[Cd\{BeL^1_2\}(MeOH)(NO_3)_2] \cdot CHCl_3 0.5MeOH$ (**5**) the heptacoordinated Cd(II) ions are bridged axially by the bidentate linear BeL^1_2 tectons, leading to infinite 1D $[Cd\{BeL^1_2\}]_\infty$ chains. The other coordination sites of the cadmium are filled by oxygen



Scheme 1.

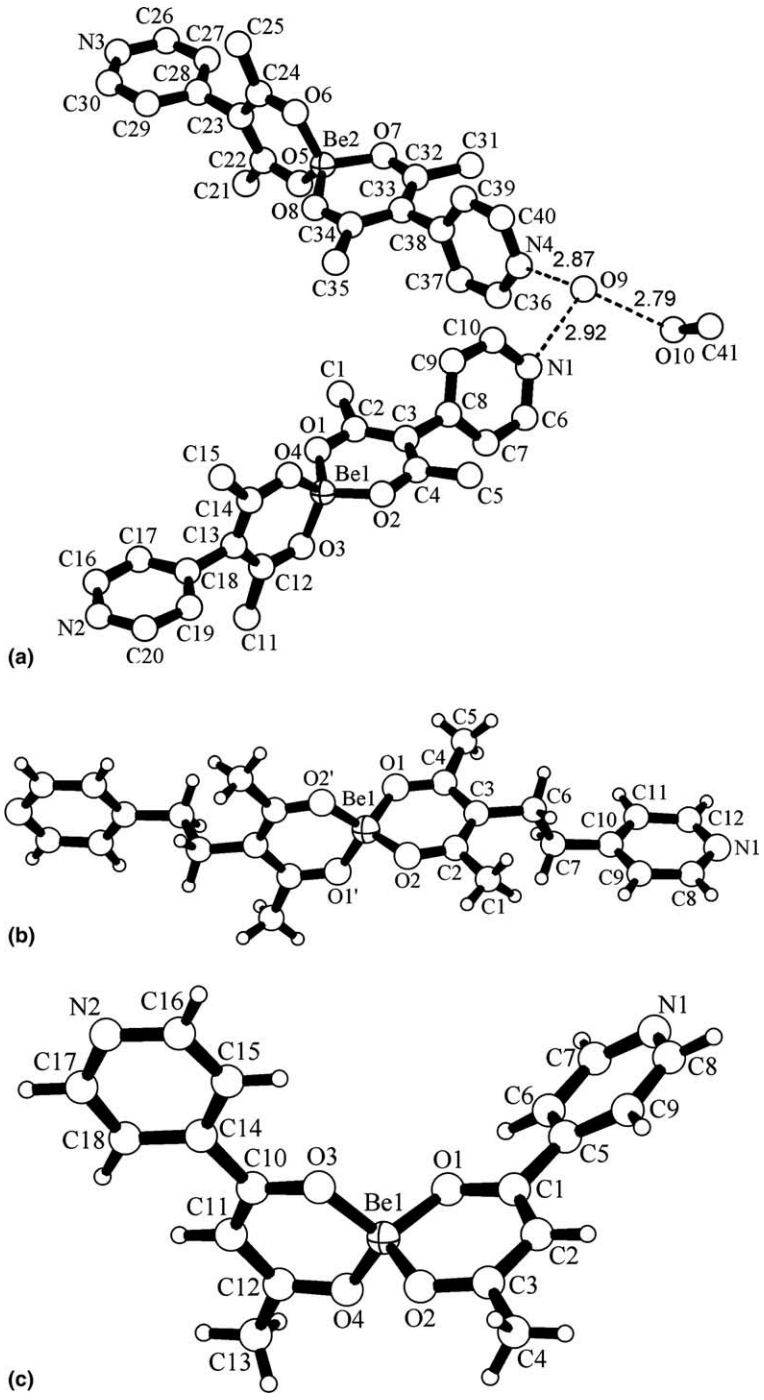


Fig. 1. Molecular structures of berillium diketonates: (a) three-component hydrogen bonded associate $[Be\mathbf{L}^{1}{}_{2}]_2 \cdot H_2O \cdot CH_3OH$ (**1**) (hydrogens are omitted for clarity); (b) $Be\mathbf{L}^{2}{}_{2}$ complex **2**; (c) $Be\mathbf{L}^{3}{}_{2}$ complex **3**.

atoms of two bidentate nitrates, bound in an almost symmetrical fashion, and a coordinated methanol molecule. Two neighbouring $[Cd\{Be\mathbf{L}^{1}{}_{2}\}]_\infty$ chains are held together, as double-chains, by means of hydrogen bondings between the coordinated methanol molecule and nitrate OH---O 1.93 Å; ∠OH---O 160°, Fig. 3(a). The two components consisting of the double-chain are packed tightly and the shortest separation between cadmium atoms of neighbouring chains is 6.07 Å. Such a close situation of the metal ions in the space effects the ease of their further interconnection by a suitable bridging anion, instead of the terminal nitrate in **5**.

This possibility for increasing the dimensionality of the structure was demonstrated by a cadmium thiocyanate complex $[Cd\{Be\mathbf{L}^{1}{}_{2}\}(NCS)_2] \cdot 0.5MeOH$ (**6**), a 2D layered structure which is supported by the bridging

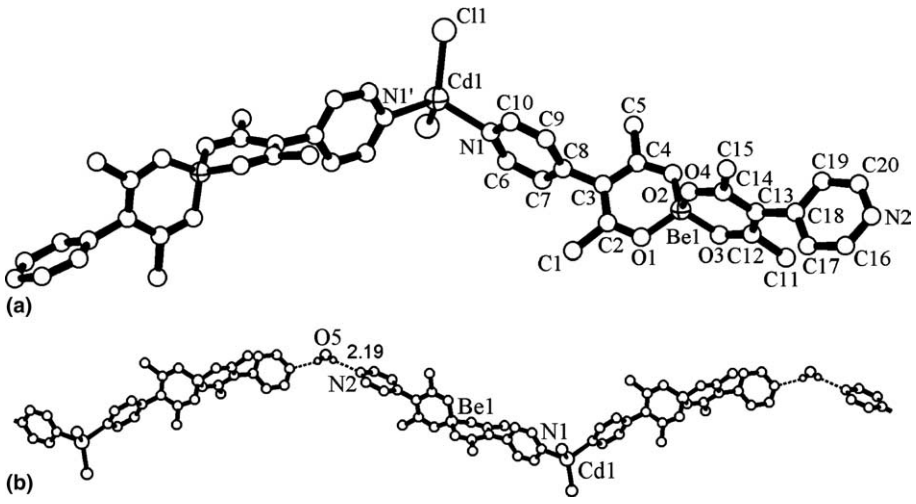


Fig. 2. (a) Tetrahedral coordination environment of the cadmium(II) ion involving two pyridyl–N donors of $Be\mathbf{L}^{1}_{2}$ tectons and chlorides in the structure $[Cd\{BeL_2\}_2Cl_2]\cdot H_2O$ (**4**); (b) Fragment of 1D coordination/H-bonded chains $[Cd\{BeL_2\}_2Cl_2]$---HOH---$[Cd\{BeL_2\}_2Cl_2]$ showing intermolecular hydrogen bonding.

Table 1
Selected bond distances (Å) and angles (°) for heterobimetallic complexes **4**–**8**

$[Cd\{Be\mathbf{L}^{1}_{2}\}_2Cl_2]\cdot H_2O$ (**4**) (a: $1-x, y, 1.5-z$)			
Cd(1)–N(1)	$2\times 2.257(2)$	N(1)–Cd(1)–Cl(1)	101.81(7)
Cd(1)–Cl(1)	$2\times 2.4042(8)$	N(1)–Cd–N(1a)	108.7(1)
Be(1)–O	1.603(4)–1.623(5)	Cl(1)–Cd(1)–Cl(1a)	127.68(5)
$[Cd\{Be\mathbf{L}^{1}_{2}\}(MeOH)(NO_3)_2]\cdot CHCl_3\cdot 0.5MeOH$ (**5**) (a: $x, y-1, z+1$)			
Cd(1)–N(1)	2.280(1)	Cd(1)–O(6)	2.479(2)
Cd(1)–N(2a)	2.294(2)	Be(1)–O	1.606(3)–1.611(3)
Cd(1)–O(11)	2.300(2)	N(1)–Cd(1)–N(2a)	174.35(6)
Cd(1)–O(8)	2.387(2)	O(8)–Cd(1)–O(5)	84.20(6)
Cd(1)–O(5)	2.443(2)	O(11)–Cd(1)–O(9)	83.49(6)
Cd(1)–O(9)	2.449(2)	O(11)–Cd(1)–O(8)	136.19(6)
$[Cd\{Be\mathbf{L}^{1}_{2}\}(NCS)_2]\cdot 0.5MeOH$ (**6**) (a: $1-x, 1-y, 2-z$; b: $1-x, -y, 2-z$; c: $x+2, y, z-1$)			
Cd(1)–N(4a)	2.303(1)	Cd(1)–S(1)	2.7630(4)
Cd(1)–N(3b)	2.316(1)	Be(1)–O	1.602(2)–1.613(2)
Cd(1)–N(2c)	2.342(1)	N(2)–Cd(1)–N(1)	179.50(4)
Cd(1)–N(1)	2.354(1)	N(4a)–Cd(1)–N(3)	178.75(5)
Cd(1)–S(2)	2.7624(4)	S(2)–Cd(1)–S(1)	172.13(1)
$[Zn\{Be\mathbf{L}^{1}_{2}\}(H_2O)_4](ClO_4)_2$ (**7**) (a: $y-0.25, 1.25-x, 0.25-z$)			
Zn(1)–N(1)	$2\times 2.079(2)$	Be(1)–O	1.612(2)–1.615(2)
Zn(1)–O(1)	$4\times 2.160(2)$		
Zn(2)–N(2)	$2\times 2.133(2)$	N(1)–Zn(1)–O(1)	89.19(3)
Zn(2)–O(2)	$4\times 2.141(2)$	N(2a)–Zn(2)–O(2)	88.11(3)
$[Cd\{Be\mathbf{L}^{1}_{2}\}(H_2O)_4](ClO_4)_2$ (**8**)			
Cd(1)–N(1)	$2\times 2.26(5)$	Be(1)–O	1.58(5)–1.68(7)
Cd(1)–O(3)	$4\times 2.338(7)$		
Cd(2)–N(2)	$2\times 2.32(4)$	N(1)–Cd(1)–O(3)	92.6(2)
Cd(2)–O(4)	$4\times 2.326(7)$	N(2)–Cd(2)–O(4)	89.6(2)

function of the $Be\mathbf{L}^{1}_{2}$ tecton and typical *N*,*S*-thiocyanate bridges (Fig. 3(b)). Packing of successive $[Cd\{Be\mathbf{L}^{1}_{2}\}]_\infty$ chains is antiparallel with perfect complementary shape, while a pair of thiocyanate ions bridge the cadmium atoms of neigbouring chains. The octahedral environment of the cadmium atoms consists of two sulfur (2.76 Å) and four nitrogen atoms, the pyridyl–N donors are in *trans*-positions.

For two isostructural compounds $[M(H_2O)_4\{Be\mathbf{L}^{1}_{2}\}](ClO_4)_2$ (M = Zn **7**, Cd **8**) the higher dimensionality (3D) has been realized by means of hydrogen bonding involving coordinated water molecules of the linear $[M(H_2O)_4\{Be\mathbf{L}^{1}_{2}\}]_\infty$ chains and uncoordinated ClO_4^- anions (for **7**, OH---O 2.78 and 2.98 Å, ∠OH---O 155° and 172°, respectively, Fig. 4). The cadmium (zinc) ions coordinate two pyridyl–N donors in *trans*-positions and

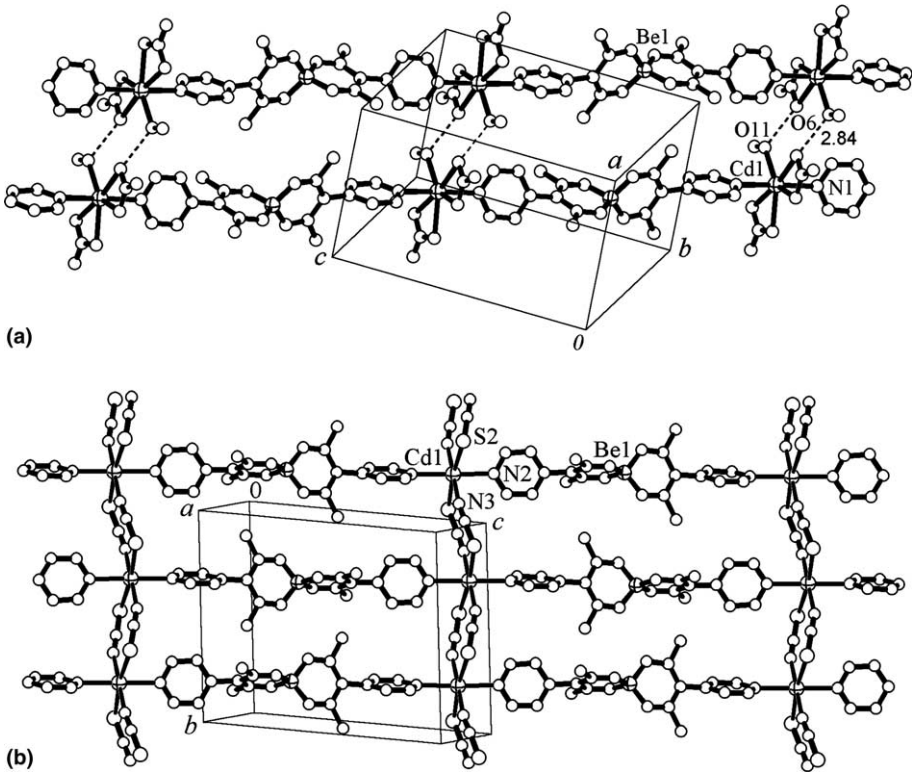


Fig. 3. (a) 1D coordination/H-bonded double-chain polymer $[Cd\{BeL^1_2\}(MeOH)(NO_3)_2]\cdot CHCl_3\cdot 0.5MeOH$ (**5**) involving heptacoordinated Cd(II) ions bridged axially by the bidentate linear BeL^1_2 tectons; two neighbouring chains are linked together by means of hydrogen bonding between a coordinated methanol molecule and nitrate; (b) View of the 2D layered structure $[Cd\{BeL^1_2\}(NCS)_2]\cdot 0.5MeOH$ (**6**) supported by the bridging function of the BeL^1_2 tecton and *N*,*S*-thiocyanate bridges.

four equatorial coordination sites are occupied by water molecules. Each perchlorate anion provides hydrogen bond bridging of two closely situated coordination chains (Fig. 4(b)). The result of this bonding is a simple 3D octahedral six-connected framework, in which a third of the links are BeL^1_2 coordination bridges and two thirds of the links are hydrogen bonded ClO_4^- ions. Two identical frameworks interpenetrate [15] without significant bonding interactions.

The structure of the heterobimetallic complex $[Cd_2\{BeL^2_2\}_3(MeOH)(NO_3)_3](NO_3)\cdot 4.5MeOH$ (**9**) is even more complicated (Table 2). Each cadmium ion coordinates three pyridyl–N groups adopting a typical T-shape CdN_3 geometry. Within the $Cd/\{BeL^2_2\}$ portion, total interconnection of these T-shape blocks results in the generation of a 2D "bilayer" architecture (Fig. 5). The latter is one of seven known supramolecular isomers of $[M_2L_3]$ polymers involving bitopic bridging ligands [16–20] and has also been reported for related systems with 1,2-bis(4-pyridyl)ethane [21]. One of the two unique cadmium atoms shows characteristic seven-fold coordination completed with two bidentate nitrate ligands [16,22,23] while coordination of Cd(1) is slightly unusual and involves the methanol molecule and two bridging nitrate groups (Fig. 5(a) and (b)). This situation is remarkable: extended BeL^2_2 tectons bridge pairs of cadmium atoms at large distances of 23 Å and alignment of the Cd–$\{BeL^1_2\}$–Cd fragments is dominated by the demands of the shape-complementary packing of the organic portion, similarly to the above systems. Thus, the close situation of the Cd(1) centers, at 5.12 Å, is a prerequisite effecting unusual double nitrate bridging. These bridges connect the $[Cd_2\{BeL^2_2\}_3]$ bilayers pairwise in a fashion shown in Fig. 5, yielding a double bilayer supporting large interval voids. The overall 3D supramolecular structure is generated by interpenetration of successive double bilayers in the crystal.

The metalloligand BeL^3_2 has a rigid molecular structure supporting angular binding directions of pyridyl–N donors and offers a synthetic strategy for construction of supramolecular squares in combination either with octahedral or tetrahedral metal centers. The cadmium ion in $[Cd\{BeL^3_2\}_2I_2]\cdot 2CHCl_3$ (**10**) adopts a nearly octahedral coordination polyhedron including four pyridyl nitrogen atoms in the equatorial plane and two iodides in axial positions. This affords formation of 1D chains of heterometallic sharing Cd-vertices. Each square provides an internal cage of about 3.6×3.0 Å size, well suited for housing a guest chloroform molecule. The latter is situated exactly inside the square and disordered over two overlapping positions related by inversion (Fig. 6).

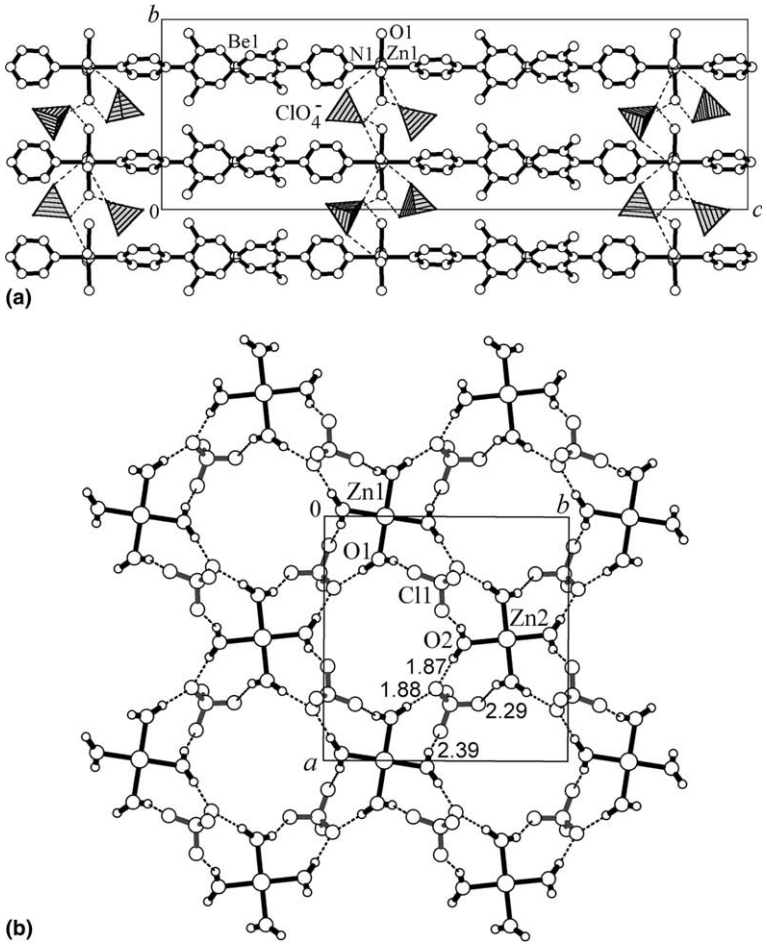


Fig. 4. Projections of the structure of $[Zn(H_2O)_4\{BeL^1{}_2\}](ClO_4)_2$ (**7**) showing (a) linear Zn/Be coordination chains, (b) OH---O hydrogen bonding between ClO_4^- anions and coordinated water molecules that unite chains into a 3D coordination/H-bonded octahedral network.

Table 2
Selected bond distances (Å) and angles (°) for heterobimetallic complexes **9** and **10**

$[Cd_2\{BeL^2{}_2\}_3(MeOH)(NO_3)_3](NO_3)\cdot 4.5MeOH$ (**9**) (a: $x+1, y+1, z$; b: $-1-x, 1-y, 2-z$)			
Cd(1)–N	2.288(3)–2.324(4)	Cd(2)–O(17)	2.485(3)
Cd(2)–N	2.306(3)–2.331(3)	Be–O	1.589(6)–1.623(9)
Cd(1)–O(16)	2.305(4)	N(1)–Cd(1)–N(2a)	176.1(1)
Cd(1)–O(13)	2.373(4)	O(16)–Cd(1)–O(13)	163.2(1)
Cd(1)–O(14b)	2.415(3)	N(3)–Cd(1)–O(14b)	174.0(1)
Cd(2)–O(21)	2.400(3)	O(18)–Cd(2)–O(20)	85.5(1)
Cd(2)–O(18)	2.412(3)	N(4)–Cd(2)–O(17)	83.5(1)
Cd(2)–O(20)	2.483(4)	O(20)–Cd(2)–O(17)	137.7(1)
$[Cd\{BeL^3{}_2\}_2I_2]\cdot 2CHCl_3$ (**10**) (a: $-x, 1-y, -1-z$)			
Cd(1)–N(1)	$2\times 2.380(3)$	Be(1)–O	1.605(6)–1.620(6)
Cd(1)–N(2)	$2\times 2.500(3)$	N(1)–Cd(1)–N(2a)	86.9(1)
Cd(1)–I(1)	$2\times 2.9084(3)$	N(2a)–Cd(1)–I(1)	90.40(8)

An additional set of guest molecules is located between the coordination chains.

3. Conclusion

The work demonstrates the potential of pyridyl functionalized diketonate ligands for construction of heterobimetallic coordination polymers. Molecular beryllium diketonate species provide an easy access to the family of extended N-donor bridges with tuneable effective length and geometry. Increasing the structure's dimensionality could be provided by bridging counteranions (SCN^-) or by partial hydrogen bonding. The crystal packing patterns observed for the complexes are essentially influenced by shape complementarity of the molec-

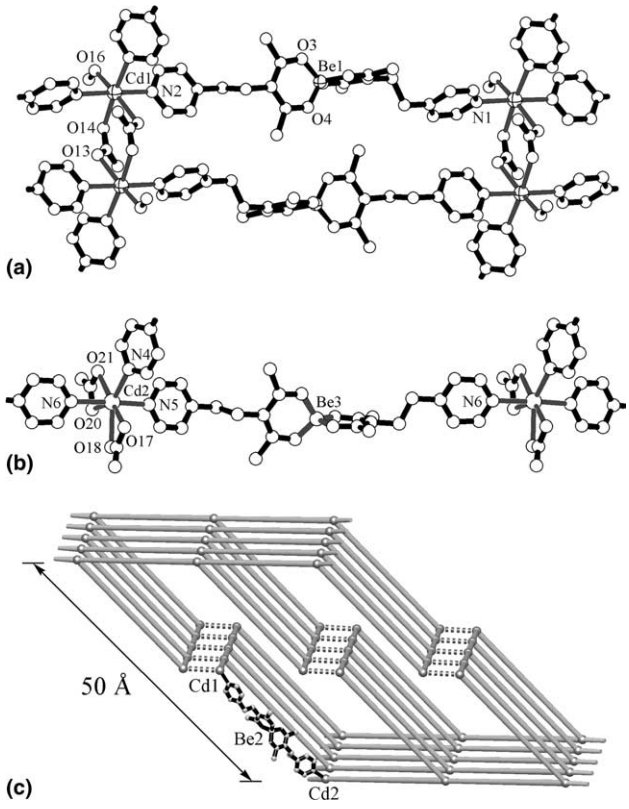


Fig. 5. Two types of coordination environment of cadmium atoms in structure $[Cd_2\{BeL^2_2\}_3(MeOH)(NO_3)_3](NO_3)\cdot 4.5MeOH$ (**9**) involving the characteristic T-shape CdN_3 motif: (a) pairs of bridging nitrate groups connect Cd/Be coordination topologies. Note the closest situation of shape-complementary BeL^2_2 tectons; (b) heptacoordination of Cd(2) ions completed with two bidentate nitrate groups; (c) overall 2D "double bilayer" topology of the coordination network in **9**; broken lines represent double nitrate bridging that connects two separate Cd/Be bilayers.

ular beryllium diketonate blocks. Beryllium diketonate supporting angular orientation of pyridyl–N functions offers a potential for the generation of metal-organic squares and their integration into polymeric superstructures.

4. Experimental

4.1. Reagents and general procedures

Compounds HL^1 [24], HL^3 [25] and BeL^1_2 [11] were prepared according to the literature procedures. All chemicals used were of reagent grade. Absolute ethanol was freshly distilled from Mg ethoxide.

The IR spectra were recorded on a UR-10 (Carl Zeiss, Jena) spectrometer in the range 4000–400 cm^{-1}. Samples were prepared as KBr pellets. ^1H NMR (400 MHz) spectra were recorded in $CDCl_3$.

4.2. Synthesis of β-diketones, beryllium and heterobimetallic complexes

The synthetic methods for the preparation of pyridyl functionalized β-diketones HL^1, HL^2 and HL^3 are diverse. HL^1 has been prepared by acylation of 4-picoline [24], while HL^3 has been synthesized by means of the Claisen condensation [25]. Compound HL^2 has been described in a patent [26]. Insertion of the 4-pyridylethylene group into an acetylacetone fragment was achieved by the Michael addition. Treatment of Hacac, 4-vinylpyridine (taken in excess) in the presence of NaOEt at reflux for 2 h followed by a work-up procedure afforded the product HL^2 in 33% yield (Scheme 2).

The target molecular beryllium diketonates were readily prepared in moderate yields of up to 62% according to Scheme 3. The compounds are colorless crystalline solids, which are well soluble in common organic solvents such as methanol, $CHCl_3$, CH_2Cl_2 and poorly soluble in water. Single crystals of $[BeL^1_2]_2\cdot H_2O\cdot CH_3OH$, BeL^2_2 and BeL^3_2 suitable for

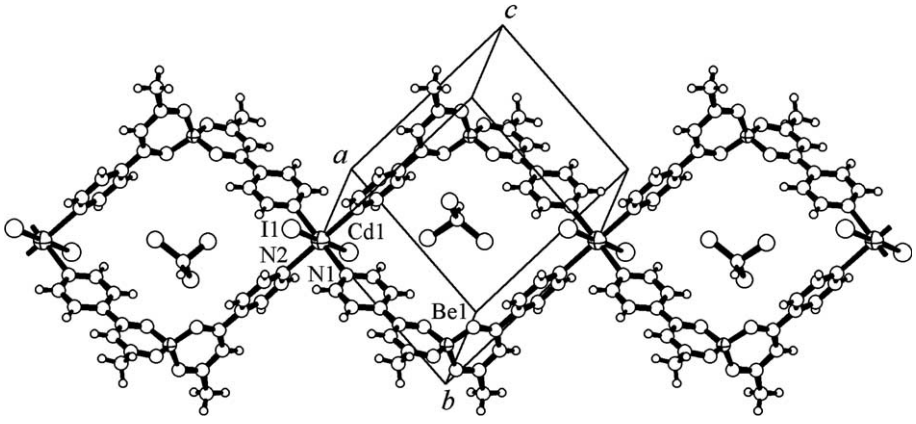
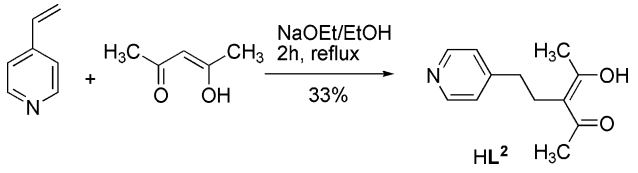
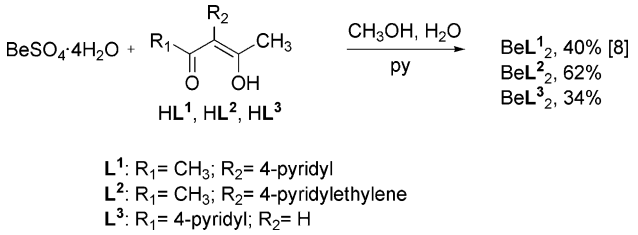


Fig. 6. 1D chain of supramolecular squares sharing Cd-vertices in the structure of $[Cd\{BeL^3_2\}_2I_2]\cdot 2CHCl_3$ (**10**), supported by octahedral cadmium centers and angular N-donor BeL^3_2 bridges. Each rectangular cavity has inner dimensions of 3.6×3.0 Å and is populated with a guest chloroform molecule.



Scheme 2.



Scheme 3.

X-ray analysis were obtained by slow evaporation of methanolic solutions.

4.2.1. 3-(4-Pyridylethylene)-2,4-pentanedione, HL^2

Following a general procedure [27], acetylacetone (28.5 g, 0.285 mol) was added to a solution of NaOEt (1.09 g [0.047 mol] Na in 19 mL of absolute ethanol) leading to the formation of a white precipitate. The mixture was heated to reflux (oil bath temperature ~115 °C). To the boiling solution freshly distilled 4-vinylpyridine (15.0 g, 0.142 mol) in 5 mL of absolute ethanol was added over 15 min. The slightly yellow solution was stirred under reflux for 2 h. Ethanol was removed in vacuum and the residue was acidified with diluted HCl to pH 7–8, leading to precipitation. The resultant mixture was kept in a refrigerator overnight (−10 °C) and then water (300 mL) was added. The aqueous solution was extracted with $CHCl_3$ (3 × 100 mL). The organic layer was dried over Na_2SO_4 and the solvent was removed. The residue was distilled in a vacuum, yielding 9.63 g (33%) of a yellowish oil, which was solidified in a refrigerator (b.p. 153–168 °C/1 mm). ^1H NMR ($CDCl_3$) is complicated due to keto-enol tautomerism of the compound: δ, 2.07 (s), 2.18–2.20 (bs), 2.40–2.75 (bm), 3.61–3.65 (m), 7.12–7.16 (m), 7.19–7.22 (m), 8.48–8.52 (m), 16.81 (s).

4.2.2. Bis-[3-(4-pyridylethylene)-2,4-pentanedione]-beryllium, BeL^2_2

A solution of $BeSO_4 \cdot 4H_2O$ (0.886 g, 5.00 mmol) in 6.5 mL H_2O was slowly added to a solution of HL^2 (2.28 g, 11.1 mmol) and pyridine (810 μL) in CH_3OH/H_2O (11.5 mL, 10.5:1) over 5 min. The resultant solution was stirred at r.t. for 10 min and then 15 mL water was added dropwise. A colorless precipitate of the complex was formed spontaneously after 10–15 min stirring. The solid was filtered off, washed with cold CH_3OH/H_2O (5 mL, 1:3) and dried. The yield was 1.30 g (62%). IR (cm^{-1}) 3080w, 3000w, 2980w, 2935w, 1585s, 1480s, 1430m, 1380s, 1315m, 1290w, 1280w, 1230w, 1190m, 1160w, 1025m, 990m, 915w, 870s, 850s, 805m, 775w, 750w, 720w, 665w, 570w, 520m, 465w; ^1H NMR ($CDCl_3$) δ 2.19 (s, 12H), 2.57–2.63 (m, 4H), 2.73–2.79 (m, 4H), 7.21 (d, J = 6.0 Hz, 4H), 8.55 (d, J = 6.0 Hz, 4H).

4.2.3. Bis-[1-(4-pyridyl)-1,3-butanedione]beryllium, BeL^3_2

A solution of $BeSO_4 \cdot 4H_2O$ (3.30 g, 18.6 mmol) in 10 mL H_2O was slowly added to a solution of HL^3 (6.10 g, 37.4 mmol) and pyridine (1.5 mL) in CH_3OH (20 mL) over 30 min. The precipitate was filtered off and washed with water (3 × 30 mL). The solid was recrystallized with 2-propanol/$CHCl_3$, affording the crystalline product (2.10 g, 34%). IR (cm^{-1}) 3050w, 2920w, 1590s, 1555s, 1540s, 1520s, 1495s, 1420s, 1395s, 1370s, 1325s, 1230w, 1215m, 1120m, 1030s, 995w, 980m, 870w, 850m, 825s, 795m, 780m, 760m, 710w, 690w, 670w, 615w, 585w, 545m, 525w, 515w, 465w, 445w; ^1H NMR ($CDCl_3$) δ 2.32 (s, 6H), 6.40 (s, 2H), 7.83 (d, J = 6.0 Hz, 4H), 8.75 (d, J = 6.0 Hz, 4H).

Coordination compounds $[Cd\{BeL^1_2\}_2Cl_2] \cdot H_2O$ (**4**), $[Cd\{BeL^1_2\}(NCS)_2] \cdot 0.5MeOH$ (**6**) and $[Cd\{BeL^3_2\}_2I_2] \cdot 2CHCl_3$ (**10**) were obtained by using a layering technique, in yields up to 20%, 73% and 68%, respectively. In a typical synthesis, a solution of the metal salt (0.10 mmol) in MeOH (or MeOH/H_2O for **4**) was layered over a solution of BeL^1_2(BeL^3_2) (0.10 mmol) in $CHCl_3$/MeOH. Slow interdiffusion of the layers within ca. two weeks afforded crystallization of the heterobimetallic complex.

Crystals of **5**, **7**–**10** suitable for single crystal X-ray structural analysis were grown by the partial evaporation of the solvent from a solution of the compounds in a mixture of chloroform and methanol at r.t. over a 5–7 day period.

4.2.4. $[Cd\{BeL^1_2\}(MeOH)(NO_3)_2] \cdot CHCl_3 \cdot 0.5MeOH$ (5)

Solutions of BeL^1_2 (36 mg, 0.10 mmol) in $CHCl_3$/MeOH (1 mL, 4:1) and $Cd(NO_3)_2 \cdot 4H_2O$ (30 mg, 0.097 mmol) in 1 mL MeOH were combined. The resulting mixture was filtered off and the filtrate was left for 2 days to afford colorless crystals of the compound (49 mg, 66%). $[Cd_2\{BeL^2_2\}_3(MeOH)(NO_3)_3](NO_3) \cdot 4.5MeOH$ (**9**) was obtained similarly in 44% yield.

4.2.5. $[Zn\{BeL^1_2\}(H_2O)_4](ClO_4)_2$ (7)

Solutions of BeL^1_2 (36 mg, 0.10 mmol) in $CHCl_3$/MeOH (2 mL, 4:1) and $Zn(ClO_4)_2 \cdot 6H_2O$ (37 mg, 0.099 mmol) in 2 mL MeOH were combined and the mixture was left for 7 days to afford colorless platelets of the complex (28 mg, 40%). $[Cd\{BeL^1_2\}(H_2O)_4](ClO_4)_2$ (**8**) was prepared in a similar fashion in 50% yield.

Table 3
Crystal data for $[BeL^1_2]_2 \cdot H_2O \cdot MeOH$ (**1**); BeL^2_2 (**2**); BeL^3_2 (**3**); $[Cd\{BeL^1_2\}_2Cl_2] \cdot H_2O$ (**4**); $[Cd\{BeL^1_2\}(MeOH)(NO_3)_2] \cdot CHCl_3 \cdot 0.5MeOH$ (**5**); $[Cd\{BeL^1_2\}(NCS)_2] \cdot 0.5MeOH$ (**6**); $[Zn\{BeL^1_2\}(H_2O)_4](ClO_4)_2$ (**7**); $[Cd\{BeL^1_2\}(H_2O)_4](ClO_4)_2$ (**8**); $[Cd_2\{BeL^2_2\}_3(MeOH)(NO_3)](NO_3) \cdot 4.5MeOH$ (**9**); $[Cd\{BeL^3_2\}_2I_2] \cdot 2CHCl_3$ (**10**)

	1	2	3	4	5	6	7	8	9	10
Formula	$C_{40}H_{40}Be_2N_4O_8 \cdot H_2O \cdot CH_3OH$	$C_{24}H_{28}BeN_2O_4$	$C_{18}H_{16}BeN_2O_4$	$C_{40}H_{40}Be_2$ $CdCl_2N_4O_8 \cdot H_2O$	$C_{21}H_{24}BeCdN_4O_{11} \cdot CHCl_3 \cdot 0.5CH_3OH$	$C_{12}H_{20}BeCdN_4$ $O_4S_2 \cdot 0.5CH_3OH$	$C_{20}H_{28}BeCl_2$ $N_2O_{16}Zn$	$C_{20}H_{28}BeCdCl_2$ N_2O_{16}	$C_{73}H_{88}Be_3Cd_2N_{10}$ $O_{25} \cdot 4.5CH_3OH$	$C_{36}H_{32}Be_2CdI_2N_4O_8 \cdot 2CHCl_3$
M	772.84	417.5	333.34	924.10	765.24	485.87	697.72	744.75	1901.55	1271.61
T (K)	123	123	223	123	123	123	123	123	223	123
Crystal system	monoclinic	monoclinic	orthorhombic	monoclinic	triclinic	triclinic	tetragonal	tetragonal	triclinic	triclinic
Space group	$P2_1/n$	$C2/c$	$Pbca$	$C2/c$	$P\bar{1}$	$P\bar{1}$	$I4_1/a$	$I4_1/a$	$P\bar{1}$	$P\bar{1}$
Unit cell dimensions										
a (Å)	18.2882(4)	10.8837(4)	10.677(1)	27.8507(9)	10.8669(3)	7.1626(1)	12.1635(5)	12.2079(3)	15.378(2)	9.6800(3)
b (Å)	11.4567(3)	9.8385(4)	15.575(1)	11.0825(4)	11.2217(3)	11.8788(2)			17.940(2)	9.8966(3)
c (Å)	19.6958(5)	20.8808(8)	19.557(2)	13.9571(5)	13.4627(3)	16.0524(3)	37.414(2)	38.3284(6)	18.821(2)	13.3469(4)
α (°)					100.277(1)	78.804(1)			101.116(2)	75.116(2)
β (°)	99.326(1)	96.431(2)		103.319(1)	90.815(1)	77.726(1)			114.079(2)	71.281(1)
γ (°)					107.702(1)	76.924(1)			91.376(2)	80.634(1)
U (Å^3)	4072.2(2)	2221.8(2)	3252.2(6)	4192.1(3)	1534.77(7)	1284.57(4)	5535.4(4)	5712.2(2)	4621.1(10)	1165.84(6)
Z	2	4	8	4	2	2	8	8	2	1
μ(Mo Kα) (cm^{-1})	0.90	0.84	0.96	7.06	10.35	10.32	11.60	10.29	5.40	21.88
$2\theta_{max}$ (°)	52.7	55.7	54.6	57.4	57.4	60.1	59.1	60.0	54.2	57.4
Measurement/unique reflections	39968/8249	7784/2632	17614/3644	22248/5334	17966/7752	19472/7345	24761/3756	28951/3873	27479/19369	10499/5786
R_{int}	0.083	0.045	0.021	0.084	0.018	0.015	0.062	0.094	0.023	0.023
Parameters refined	514	197	290	346	394	405	295	193	1112	313
R_1, wR_2 ($I > 2\sigma$ (I))	0.067, 0.185	0.052, 0.118	0.037, 0.099	0.049, 0.101	0.030, 0.081	0.023, 0.060	0.037, 0.096	0.056, 0.115	0.059, 0.137	0.039, 0.102

Most of the heterobimetallic coordination polymers readily lose the incorporated guest molecules of the solvents (MeOH, $CHCl_3$) in air within minutes, with loss of crystallinity and disintegration of the structure. Pyridylacetylacetone coordination polymers **4**–**8** also slowly decompose under mother solutions.

4.3. Crystal structure determination

Crystallographic measurements for compounds **1**–**10** were made using a Siemens SMART CCD area-detector three-circle diffractometer (Graphite monochromated Mo Kα radiation, $\lambda = 0.71073$ Å, exposure time was 30–40 s per frame). The data frames were integrated using SAINT and empirical absorption corrections (SADABS) were employed. The structures were solved by direct methods and refined by full-matrix least-squares techniques in anisotropic approximations using SHELXS-86 and SHELXL-97 [28,29]. In structures **2**–**4** and **7**, the hydrogen atoms were located from the difference-Fourier syntheses and refined isotropically. In the other cases the positions of the hydrogen atoms were idealized and included in the calculations with their isotropic U values set invariant at 0.08 Å^2 (**1**, **8**) or at 1.2 times the level with respect to the U_{eq} values of the corresponding carbon atom. Hydrogen atoms of non-coordinated solvate methanol molecules were not added. In **7**, the perchlorate anions are disordered over two closely situated positions with partial contributions of 0.82 and 0.18; structures **5** and **6** shows equal disordering of solvate methanol molecules and in structure **10** both unique chloroform molecules are equally disordered over two overlapping positions related by inversion. The refinement proceeded smoothly and therefore it was possible to refine the atoms of disordered groups anisotropically. In structure **9** one of the solvate methanol molecules lies at a center of inversion and thus both carbon and oxygen atoms, which are related by symmetry, were refined as carbon atoms. Crystal data are given in Table 3.

Acknowledgments

The research was supported by a grant from the Deutsche Forschungsgemeinschaft (J.S. and K.V.D.) and Royal Society Fellowship (A.N.Ch.).

Appendix A. Supplementary data

Full crystallographic data for **1-10** (CCDC 255510-255519) have been deposited at the Cambridge Crystallographic Database Centre and are available on request from the Director CCDC, 12 Union Road, Cambridge, CB2 1EZ, UK (fax: +44-1223-336-033; e-mail: deposit @ccdc.cam.ac.uk or www.ccdc.cam.ac.uk). Supplemen-

tary data associated with this article can be found, in the online version at doi:10.1016/j.poly.2005.02.023.

References

[1] R. Lescouëzec, J. Vaissermann, C. Ruiz-Pérez, F. Lloret, R. Carrasco, M. Julve, M. Verdaguer, Y. Dromzee, D. Gatteschi, W. Wernsdorfer, Angew. Chem., Int. Ed. Engl. 42 (2003) 1483.
[2] I.V. Kozhevnikov, Chem. Rev. 98 (1998) 171.
[3] H. Weiner, Y. Hayashi, R.G. Finke, Inorg. Chem. 38 (1999) 2579.
[4] C. Janiak, J. Chem. Soc., Dalton Trans. (2003) 2781.
[5] C.N.R. Rao, S. Natarajan, R. Vaidhyanathan, Angew. Chem., Int. Ed. Engl. 43 (2004) 1466.
[6] A. Kamiyama, T. Noguchi, T. Kajawara, T. Ito, Angew. Chem., Int. Ed. Engl. 39 (2000) 3130.
[7] S. Noro, S. Kitagawa, M. Yamashita, T. Wada, Chem. Commun. (2002) 222.
[8] (a) S.S. Turner, D. Collinson, F.E. Mabbs, M. Halliwell, J. Chem. Soc., Dalton Trans. (1997) 1117;
(b) B. Chen, F.R. Fronczek, A.W. Maverick, Chem. Commun. (2003) 2166;
(c) I. Boldog, E.B. Rusanov, A.N. Chernega, J. Sieler, K.V. Domasevitch, Angew. Chem., Int. Ed. Engl. 40 (2001) 3435.
[9] S.R. Halper, M.R. Malachowski, H.M. Delaney, S.M. Cohen, Inorg. Chem. 43 (2004) 1242.
[10] L. Carlucci, G. Ciani, D.M. Proserpio, F. Porta, Angew. Chem., Int. Ed. Engl. 42 (2003) 317.
[11] V.D. Vreshch, A.N. Chernega, J.A.K. Howard, J. Sieler, K.V. Domasevitch, J. Chem. Soc., Dalton Trans. (2003) 1707.
[12] V.D. Vreshch, A.B. Lysenko, A.N. Chernega, J.A.K. Howard, H. Krautscheid, J. Sieler, K.V. Domasevitch, J. Chem. Soc., Dalton Trans. (2004) 2899.
[13] K.V. Domasevitch, J. Sieler, E.B. Rusanov, A.N. Chernega, Z. Anorg. Allg. Chem. 628 (2002) 51.
[14] P.V. Solntsev, J. Sieler, A.N. Chernega, J.A.K. Howard, T. Gelbrich, K.V. Domasevitch, J. Chem. Soc., Dalton Trans. (2004) 695.
[15] S.R. Batten, R. Robson, Angew. Chem. Int. Ed. Engl. 37 (1998) 1460.
[16] B. Moulton, M.J. Zaworotko, Chem. Rev. 101 (2001) 1629.
[17] K.N. Power, T.L. Hennigar, M.J. Zaworotko, New J. Chem. 22 (1998) 177.
[18] A. Rujiwatra, C.J. Kepert, M.J. Rosseinsky, Chem. Commun. (1999) 2307.
[19] S. Kitagawa, M. Kondo, Bull. Chem. Soc. Jpn. 71 (1998) 1739.
[20] C.J. Kepert, M.J. Rosseinsky, Chem. Commun. (1999) 375.
[21] R. Atencio, K. Biradha, T.L. Hennigar, K.M. Poirier, K.N. Power, C.M. Seward, N.S. White, M.J. Zaworotko, Cryst. Eng. 1 (1998) 203.
[22] M.A. Withersby, A.J. Blake, N.R. Champness, P.A. Cooke, P. Hubberstey, M. Schroder, New J. Chem. 23 (1999) 573.
[23] Y.B. Dong, M.D. Smith, R.C. Layland, H.C. Zur Loye, Chem. Mater. 12 (2000) 1156.
[24] L.G. Mackay, H.L. Anderson, J.K.M. Sanders, J. Chem. Soc., Perkin Trans. 1 (1995) 2269.
[25] B. Singh, G.Y. Lesher, K.C. Pluncket, E.D. Pagani, D.C. Bode, R.G. Bentley, M.J. Connell, L.T. Hamel, P.J. Silver, J. Med. Chem. 35 (1992) 4858.
[26] N. Fukazawa, H. Iizuka, T. Ito, M. Maruyama, M. Hirayama, T. Kitano, Jpn. Kokai Tokkyo Koho (1986) 4, JP 61180770, Patent written in Japanese.
[27] B.V. Boekelheide, S. Rothchild, J. Am. Chem. Soc. (1949) 879.
[28] G.M. Sheldrick, SHELXL-97, A System of Computer Programs for X-ray Structure Determination, University of Göttingen, Göttingen, Germany, 1997.
[29] G.M. Sheldrick, Acta Crystallogr. A46 (1990) 467.

Available online at www.sciencedirect.com
SCIENCE DIRECT®
Polyhedron 24 (2005) 927–939
POLYHEDRON
www.elsevier.com/locate/poly

Synthesis and structural characterization of some arylamidinium diphenylphosphinates: Formation of one-, two- and three-dimensional networks by charge-assisted hydrogen bonds

Jianping Guo, Wai-Kwok Wong *, Wai-Yeung Wong

Department of Chemistry, Hong Kong Baptist University, 224 Waterloo Road, Kowloon Tong, Hong Kong, PR China

Received 17 January 2005; accepted 22 February 2005
Available online 29 April 2005

Abstract

In the presence of air, the interaction of $AgSO_3CF_3$ with phosphorus–nitrogen π-electron-rich compounds $ArC(=NPPh_2)[N(SiMe_3)_2]$ (Ar = phenyl, *p*-tolyl, 4-pyridyl, 3-pyridyl and 2-pyridyl) and $1,4\text{-}C_6H_4\{C(=NPPh_2)[N(SiMe_3)_2]\}_2$ in acetonitrile led to the formation of metallic silver and the oxidative cleavage product $\{[ArC(NH_2)_2](Ph_2PO_2)\}_n$ (Ar = phenyl, **1**; *p*-tolyl, **2**; 4-pyridyl, **3**; 3-pyridyl, **4**; 2-pyridyl, **5**) and $[\{1,4\text{-}C_6H_4[C(NH_2)_2]_2\}(Ph_2PO_2)_2]_n$ (**6**), respectively. Structural analyses of compounds **1**–**6** revealed that these ionic salts are held together by charge-assisted hydrogen bonds forming 1D, 2D and 3D polymeric networks.
© 2005 Elsevier Ltd. All rights reserved.

Keywords: Amidinium diphenylphosphinate; Charge-assisted hydrogen bond; Crystal structures; Electrostatic force; Oxidative cleavage

1. Introduction

The construction of polymeric networks is an intensive research area within the realm of supramolecular chemistry because of their potential uses in materials science [1]. The molecular design, synthesis and structure of supramolecular polymeric networks depend strongly on the properties of the building blocks and the strength and directional characteristics of the interactions among these components. The proper disposition of connections leads to the formation of infinite assemblies in the solid state. Generally, the types of construction blocks for supramolecular polymers can be divided into three main groups, the first one involving their components being held together by hydrogen bonds, the second by coordination bonds, and the third by electrostatic forces. Hydrogen bonds that are cooperative with electrostatic forces are known as charge-assisted hydrogen bonds. Many examples of self-assembled coordination polymers which contain a nanotube [2], cage [3], core [4], cyclic ring [5] or helix [3,6,7] in their networks and of multiple hydrogen-bonded complexes [7–9] have been reported.

There are fewer examples in which the components are held together by charge-assisted hydrogen bonds. The use of the diprotonated 4,4′-bipyridine as a hydrogen bond donor unit and $[MCl_n]^{m-}$ (M = Pd, Pt, Zn, Mn, Os, Fe) as an acceptor to form several polymeric molecular networks has been designed and reported by Orpen [10]. A similar strategy has also been applied to the formation of infinite networks using $PtCl_4^{2-}$ and 4,4′-bis(piperidinium) derivatives [11]. Brammer reported a similar design to produce polymeric supramolecular networks by various platinum chloride and 1,4-diazabicyclooctane [12]. Burrows used guanidinium and sulfonated phosphane to form a charge-assisted hydrogen-bonded layer structure [13]. Hosseini and coworkers have successfully employed the bis(amidinium) dication in the construction of 1D charge-assisted

* Corresponding author. Tel.: +852 3411 7011; fax: +852 3411 5862.
E-mail address: wkwong@hkbu.edu.hk (W.-K. Wong).

0277-5387/$ - see front matter © 2005 Elsevier Ltd. All rights reserved.
doi:10.1016/j.poly.2005.02.020

polymeric chains and some of them are connected by hydrogen bonds to form 2D networks [14]. They also used a dication and a metal-containing anion to build 1D, 2D and 3D metal-containing electrostatic supramolecular polymers [15].

We are interested in the preparation and structure of organic supramolecular polymers in which the components are linked together strongly by charge-assisted hydrogen bonds. The strategy to the design of these organic crystals was based on the iterative assembly processes between complementary units that are held together simultaneously by strong but less directional electrostatic forces along with weak but directional hydrogen bonds. Much research work by Hosseini's group [14] has shown that the diprotonated bis(amidinium) dication provides four acidic N–H protons pointing outwards and the dicarbonylate dianion provides four oxygens for the hydrogen bonding. Since every two protons are fixed on the same side of the skeleton, the cation is capable of forming a di-hapto mode of interaction, which results in a 1D arrangement with the anions.

In order to develop 2D and 3D organic molecular networks, tri- or multi-hapto modes of hydrogen bonding interaction is the key factor. Arylamidinium cations of compounds **1**–**5** that can provide four acidic N–H protons pointing outwards and are thus capable of producing four hydrogen bonds in a tetra-hapto mode of interaction seemed to be an appropriate candidate of choice. Moreover, the diprotonated dication of compound **6** contributes eight N–H hydrogen bonds in an octa-hapto mode of interaction (Chart 1). The anion of compounds **1**–**6**, diphenylphosphinate, can offer oxygen atoms as acceptors to form hydrogen bonds with three cations among **1**–**6**.

2. Experimental

2.1. General procedures

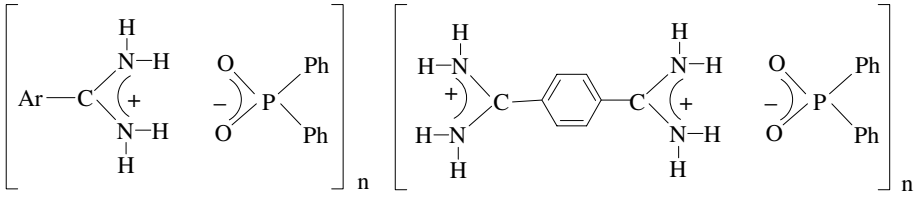
Unless otherwise stated, the reactions were carried out under nitrogen atmosphere in flamed Schlenk-type glassware on a dual manifold Schlenk line. Solvents were pre-dried. All chemicals used were of reagent grade, obtained from Aldrich or Fisher Scientific Chemical Company. NMR spectra were measured in appropriate solvents on a Varian INOVA 400 MHz FT-NMR spectrometer. Fast atom bombardment (FAB) mass spectra were recorded on a Finnigan MAT SSQ710 mass spectrometer and electrospray ionization high-resolution mass spectra (ESI-HRMS) were performed on a quadrupole-time of flight (Q-TOF) mass spectrometer equipped with a turbo ionspray source (PE SCIEX API QSTAR Pulsar i, Applied Biosystem). The IR spectra were recorded using KBr pellets on Perkin–Elmer Paragon 1000PC or Nicolet Nagan-IR 550 Series II FTIR spectrometers, and excitation and fluorescence spectra on a Photon Technology International (PTI) Alphascan spectrofluorimeter. Elemental analyses were performed by the Shanghai Organic Institute of the Chinese Academy of Sciences and Shanxi University.

2.2. Preparation of phenylamidinium diphenylphosphinate (*1*)

$AgSO_3CF_3$ (0.26 g, 1.00 mmol) in acetonitrile (30 ml) was added to a solution of $PhC(=NPPh_2)[N(SiMe_3)_2]$ (0.45 g, 1.00 mmol) in THF (10 ml). Upon stirring the solution in air at room temperature for 2 h, black metallic silver was observed. The reaction mixture was then filtered. The filtrate was allowed to evaporate slowly in air at room temperature to give colorless crystals of **1**. Yield: 0.23 g, 69%, m.p. 266–267 °C. ESI-HRMS (in methanol, positive mode): *m/z* positive mode, 121.0768 ($[PhC(NH_2)_2]^+$, $C_7H_9N_2$ requires 121.0765); negative mode, 217.0422 ($[Ph_2PO_2]^-$, $C_{12}H_{10}O_2P$ requires 217.0418). ^{31}P-{^1H} NMR (DMSO-d_6): δ 16.8 (s). ^1H NMR (DMSO-d_6): δ 7.30 (m, 6H, Ph), 7.56–7.78 (m, 9H, Ph), 9.01 (br m, 2H, NH_2), 11.12 (br m, 2H, NH_2).

2.3. Preparation of p-tolylamidinium diphenylphosphinate (*2*)

Compound **2** was produced using the same reaction conditions and procedures as for **1**. $AgSO_3CF_3$ (0.21 g, 0.82 mmol) and $(4\text{-}MeC_6H_4)C(=NPPh_2)[N(SiMe_3)_2]$ (0.38 g, 0.82 mmol) were used. Yield: 0.24 g, 83%, m.p. 284–285 °C. ^1H NMR (DMSO-d_6): δ 2.38 (s, 3H, CH_3), 7.29–7.31 (m, 6H, Ar), 7.38 (d, J = 8.0 Hz, 2H, Ar),



1–5 **6**

Chart 1.

7.64–7.69 (m, 6H, Ar), 8.96 (br m, 2H, NH_2), 11.06 (br m, 2H, NH_2). ^{13}C NMR (DMSO-d_6): δ 21.7, 127.0, 128.1, 128.2, 128.3, 129.7, 130.1, 131.5, 131.6, 142.0, 143.3, 144.4, 166.1. ^{31}P-{^1H} NMR (DMSO-d_6): δ 16.9 (s). ESI-HRMS (in methanol): *m/z* positive mode, 135.0913 ($[(4\text{-}MeC_6H_4)C(NH_2)_2]^+$, $C_8H_{11}N_2$ requires 135.0922); negative mode, 217.0399 ($[Ph_2PO_2]^-$, $C_{12}H_{10}O_2P$ requires 217.0418). IR (cm^{-1}, in KBr): 3147bs, 2921bs, 1705m, 1614m, 1593m, 1559m, 1488m, 1437m, 1131s, 1070w, 1038s, 1018s, 999m, 822m, 720s, 698m, 555s.

2.4. Preparation of 4-pyridylamidinium diphenylphosphinate (3)

The synthesis of compound **3** followed the same procedures as for **1**. $AgSO_3CF_3$ (0.26 g, 1.00 mmol) and $(4\text{-}NC_5H_4)C(=NPPh_2)[N(SiMe_3)_2]$ (0.45 g, 1.00 mmol) were used. Yield: 0.25 g, 75%, m.p. 241–242 °C. *Anal.* Calc. for $C_{18}H_{18}N_3O_2P \cdot 0.25H_2O$: C, 62.88; H, 5.38; N, 12.23. Found: C, 62.83; H, 5.50; N, 8.55%. ESI-HRMS (in methanol): *m/z* positive mode, 122.0714 ($[4\text{-}NC_5H_4C(NH_2)_2]^+$, $C_6H_8N_3$ requires 122.0718); negative mode, 217.0422 ($[Ph_2PO_2]^-$, $C_{12}H_{10}O_2P$ requires 217.0418). ^{31}P-{^1H} NMR (DMSO-d_6): δ 17.2 (s). ^1H NMR (DMSO-d_6): δ 7.35 (m, 5H, Ar), 7.66–7.73 (m, 7H, Ar), 8.84 (m, 2H, Ar), 9.38 (br m, 2H, NH_2), 10.34 (br m, 2H, NH_2). IR (cm^{-1}, in KBr): 3369bw, 3053w, 1662w, 1486w, 1433s, 1251m, 1100m, 951s, 740m, 700s, 529m.

2.5. Preparation of 3-pyridylamidinium diphenylphosphinate (4)

Compound **4** was prepared similarly. $AgSO_3CF_3$ (0.26 g, 1.00 mmol) and $(3\text{-}NC_5H_4)C(=NPPh_2)[N(SiMe_3)_2]$ (0.45 g, 1.00 mmol) were used. Yield: 0.26 g, 76.7%, m.p. 249–250 °C. ESI-HRMS (in methanol): *m/z* positive mode, 122.0725 ($[3\text{-}NC_5H_4C(NH_2)_2]^+$, $C_6H_8N_3$ requires 122.0718); negative mode, 217.0427 ($[Ph_2PO_2]^-$, $C_{12}H_{10}O_2P$ requires 217.0418). ^{31}P-{^1H} NMR (DMSO-d_6): δ 17.0 (s). ^1H NMR (DMSO-d_6): δ 7.31 (d, $J = 1.2$ Hz, 6H, Ar), 7.59–7.63 (m, 1H, Ar), 7.65–7.69 (m, 4H, Ar), 8.16 (d, $J = 8$ Hz, 1H, Ar), 8.82–8.84 (m, 1H, Ar), 8.93 (d, $J = 1.2$ Hz, 1H, Ar), 9.16 (br, m, NH_2), 11.22 (br, m, NH_2). ^{13}C NMR (DMSO-d_6): δ 123.8, 125.8, 127.6, 127.7 129.2, 131.0, 131.1, 136.0, 141.2, 142.5, 148.5, 153.7, 164.3. IR (cm^{-1}, in KBr): 3140bs, 2923bs, 1711m, 1597m, 1529w, 1472m, 1436m, 1420m, 1130vs, 1037s, 1016s, 866m, 825m, 757m, 721s, 700s, 561s.

2.6. Preparation of 2-pyridylamidinium diphenylphosphinate (5)

Compound **5** was also prepared in a similar manner. $AgSO_3CF_3$ (0.23 g, 0.89 mmol) and $(2\text{-}NC_5H_4)C(=NPPh_2)[N(SiMe_3)_2]$ (0.40 g, 0.89 mmol) were used. Yield: 0.22 g, 73%, m.p. 246–247 °C. ESI-HRMS (in methanol): *m/z* positive mode, 122.0712 ($[2\text{-}NC_5H_4C(NH_2)_2]^+$, $C_6H_8N_3$ requires 122.0718); negative mode, 217.0410 ($[Ph_2PO_2]^-$, $C_{12}H_{10}O_2P$ requires 217.0418). ^{31}P-{^1H} NMR (DMSO-d_6): δ 17.0 (s). ^1H NMR (DMSO-d_6): δ 7.29–7.31 (m, 6H, Ar), 7.66–7.71 (m, 4H, Ar), 7.73–7.77 (m, 1H, Ar), 8.09–8.13 (m, 1H, Ar), 8.20–8.22 (m, 1H, Ar), 8.79–8.81 (m, 1H, Ar), 9.30 (br m, NH_2), 11.10 (br m, NH_2). ^{13}C NMR (DMSO-d_6): δ 123.0, 127.6, 127.8, 128.3, 129.3, 129.3, 131.0 131.1, 138.4, 141.1, 142.3, 144.8, 149.9, 162.2. IR (cm^{-1}, in KBr): 3182bs, 2948bs, 1711m, 1591w, 1571w, 1529w, 1462m, 1436m, 1177s, 1130vs, 1042s, 1022s, 1001s, 861w, 809w, 721s, 706m, 555s.

2.7. Preparation of 1,4-phenylenediamidinium diphenylphosphinate (6)

Compound **6** was similarly prepared. $AgSO_3CF_3$ (0.26 g, 1.00 mmol) and $1,4\text{-}C_6H_4\{C(=NPPh_2)[N(SiMe_3)_2]\}_2$ (0.41 g, 0.50 mmol) were used. Yield: 0.23 g, 77%, m.p. 289–290 °C. ESI-HRMS (in methanol): *m/z* positive mode, 82.0522 ($\{1,4\text{-}C_6H_4[C(NH_2)_2]_2\}^{2+}$, half of $C_8H_{12}N_4$ requires 82.0525); negative mode, 217.0422 ($[Ph_2PO_2]^-$, $C_{12}H_{10}O_2P$ requires 217.0418). ^{31}P-{^1H} NMR (DMSO-d_6): δ 16.8 (s). ^1H NMR (DMSO-d_6): δ 7.31 (m, 11H, Ar), 7.65–7.70 (m, 9H, Ar), 7.93 (m, 4H, Ar), 9.18 (br m, 2H, NH_2), 11.46 (br m, 2H, NH_2). IR (cm^{-1}, in KBr): 3347bs, 3171bs, 2964m, 1674s, 1550s, 1441s, 1405m, 1265s, 1089bs, 845s, 700s, 545s.

2.8. X-ray crystallography

Crystals of **1**, **2**, $\mathbf{3} \cdot CH_3CN$, $\mathbf{4} \cdot 0.5THF$, **5** and $\mathbf{6} \cdot 2H_2O$ suitable for X-ray diffraction were grown by slow evaporation of each respective solution of these compounds in air. The intensity data were collected with a Bruker AXS SMART 1000 CCD area-detector diffractometer with graphite-monochromated Mo Kα radiation ($\lambda = 0.71073$ Å) at 293 K. The collected frames were processed with the proprietary software SAINT [16] and an absorption correction was applied (SADABS [17]) to the collected reflections. The structures of these molecules were solved by direct methods and expanded by standard difference Fourier syntheses using the software SHELXTL [18]. Structure refinements were made on F^2 using the full-matrix least-squares technique. All non-hydrogen atoms were refined with anisotropic displacement parameters. Hydrogen atoms were placed in their idealized positions and allowed to ride on the respective carbon atoms. Pertinent crystallographic data and other experimental details are summarized in Table 1.

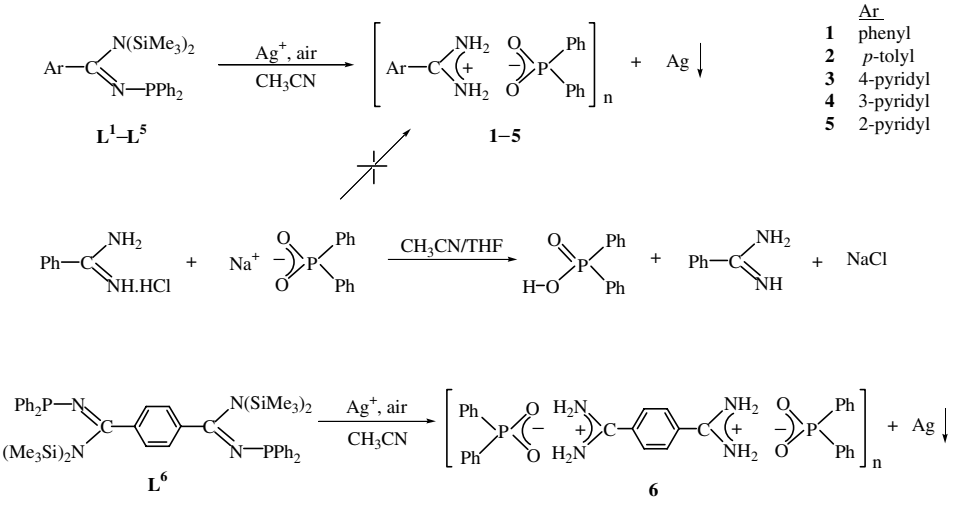
Table 1
Crystal data and refinement for compounds **1**–**6**

Compound	**1**	**2**	**3** · CH_3CN	**4** · 0.5THF	**5**	**6** · $2H_2O$
Empirical formula	$C_{19}H_{19}N_2O_2P$	$C_{20}H_{21}N_2O_2P$	$C_{20}H_{21}N_4O_2P$	$C_{20}H_{22}N_3O_{2.5}P$	$C_{18}H_{18}N_3O_2P$	$C_{64}H_{68}N_8O_{10}P_4$
M	338.33	352.36	380.38	375.38	339.32	1233.14
Crystal system	monoclinic	monoclinic	monoclinic	monoclinic	orthorhombic	monoclinic
Space group	$P2_1/c$	$C2/c$	$P2_1/n$	$P2_1/n$	$Pmn2_1$	$P2_1/c$
a (Å)	10.1996(9)	24.313(3)	13.002(2)	13.2545(8)	29.742(3)	18.790(1)
b (Å)	9.8534(8)	9.890(1)	8.780(1)	8.5690(6)	10.307(1)	12.5749(8)
c (Å)	18.111(2)	16.511(2)	18.262(2)	17.998(1)	8.5605(9)	27.299(2)
α (°)	90	90	90	90	90	90
β (°)	94.261(2)	102.287(2)	107.369(3)	106.213(1)	90	101.204(1)
γ (°)	90	90	90	90	90	90
V (Å^3)	1815.2(3)	3879.1(8)	1989.7(5)	1962.8(5)	2624.3(5)	6327.3(7)
Z	4	8	4	4	6	4
F(0 0 0)	712	1488	788	792	1068	2576
$D_{calc.}$ (g cm^{-3})	1.238	1.207	1.260	1.270	1.288	1.290
μ (Mo Kα) (mm^{-1})	0.164	0.156	0.160	0.162	0.172	0.183
Reflections collected	10339	11268	11570	11040	15468	36792
Unique reflections	4071	4382	4526	4367	6023	14274
Observed reflections	2240	1868	2063	2796	4580	6960
Goodness-of-fit on F^2	0.909	0.834	0.857	0.936	1.007	0.909
R_1, wR_2 [$I > 2\sigma(I)$]	0.0447, 0.1121	0.0521, 0.1140	0.0569, 0.1303	0.0462, 0.1141	0.0412, 0.0821	0.0486, 0.1242
R_1, wR_2 (all data)	0.0897, 0.1282	0.1381, 0.1396	0.1302, 0.1541	0.0756, 0.1253	0.0662, 0.0939	0.1162, 0.1467

3. Results and discussion

3.1. Synthesis and structural characterization

Phosphorus–nitrogen compounds are π-electron-rich compounds and potential precursors for inorganic polymers with unusual properties. This led to considerable interest in the syntheses of phosphorus–nitrogen compounds and their coordination chemistry towards transition metals. We have synthesized a series of phosphorus–nitrogen ligands (**L**^{1}–**L**^{6} in Scheme 1) and studied their coordination chemistry towards transition metals of Group VI, VII, VIII and X. We also intended to further explore their coordination chemistry towards Group XI metals. However, in the presence of air, the interaction of $AgSO_3CF_3$ with phosphorus–nitrogen π-electron-rich compounds [19] $ArC(=NPPh_2)[N(SiMe_3)_2]$ (Ar = phenyl, *p*-tolyl, 4-pyridyl, 3-pyridyl and 2-pyridyl) and 1,4-$C_6H_4\{C(=NPPh_2)[N(SiMe_3)_2]\}_2$ in acetonitrile led to the formation of metallic silver and the oxidative cleavage product $\{[ArC(NH_2)_2](Ph_2PO_2)\}_n$ (Ar = phenyl, **1**; *p*-tolyl, **2**; 4-pyridyl, **3**; 3-pyridyl, **4**; 2-pyridyl, **5**) and $[\{1,4\text{-}C_6H_4[C(NH_2)_2]_2\}(Ph_2PO_2)_2]_n$ **6**, respectively (Scheme 1). To elucidate the mechanism of the oxidative cleavage process, the reaction of Ag(I) with ligand **L**^{3} was monitored by ^{31}P NMR spectroscopy. Under oxygen free conditions, upon the addition of excess $AgSO_3CF_3$ to a solution of **L**^{3} in CH_2Cl_2, the ^{31}P NMR



Scheme 1.

Table 2
Selected bond lengths and bond angles of compounds **1**–**6**

Compound	1	2	3	4	5	6
C(1)–N(1)	1.304(2)	1.303(3)	1.304(3)	1.304(2)	1.304(3)	1.303(3)
C(1)–N(2)	1.304(2)	1.305(3)	1.297(3)	1.308(2)	1.315(3)	1.313(3)
C(19)–N(4)					1.303(2)	
C(8)–N(3)						1.303(3)
C(8)–N(4)						1.317(3)
P(1)–O(1)	1.507(1)	1.507(2)	1.504(2)	1.501(1)	1.507(2)	1.487(2)
P(1)–O(2)	1.508(1)	1.510(2)	1.499(2)	1.507(1)	1.502(2)	1.521(2)
P(2)–O(3)					1.501(2)	1.504(2)
P(2)–O(4)						1.489(2)
N(1)–C(1)–N(2)	121.41(17)	121.5(2)	123.1(3)	122.77(18)	122.2(2)	119.8(2)
N(3)–C(8)–N(4)						122.3(2)
N(5)–C(9)–N(6)						121.4(2)
N(7)–C(16)–N(8)						119.6(2)

resonance of $\mathbf{L^3}$ at δ 36.5 disappeared completely within 10 min and a new broad singlet appeared at δ 46.1, which was the only ^{31}P signal observable in the reaction mixture. This downfield shift of the ^{31}P resonance of the ligand indicated the formation of a Ag(I) phosphine complex. The new resonance at δ 46.1 persisted in solution and no new resonance was observed even after 5 h. However, as soon as a solution of the Ag(I) phosphine complex was exposed to air, metallic silver was precipitated out from the solution, and a resonance at δ 16.8 corresponding to $(Ph_2PO_2)^-$ anion appeared in the resultant ^{31}P NMR spectrum. Oxidative cleavage of the N–P bond of $ArC(=NPPh_2)[N(SiMe_3)_2]$ to $(Ph_2PO_2)^-$ by a transition metal complex has been observed previously [20]. In fact, the P–N ligands, when dissolved in solution, would slowly be oxidized by air to give the corresponding ionic salt via oxidative cleavage. For instance, when a solution of $\mathbf{L^1}$ in CH_2Cl_2 was exposed to air, the ^{31}P NMR spectrum showed that

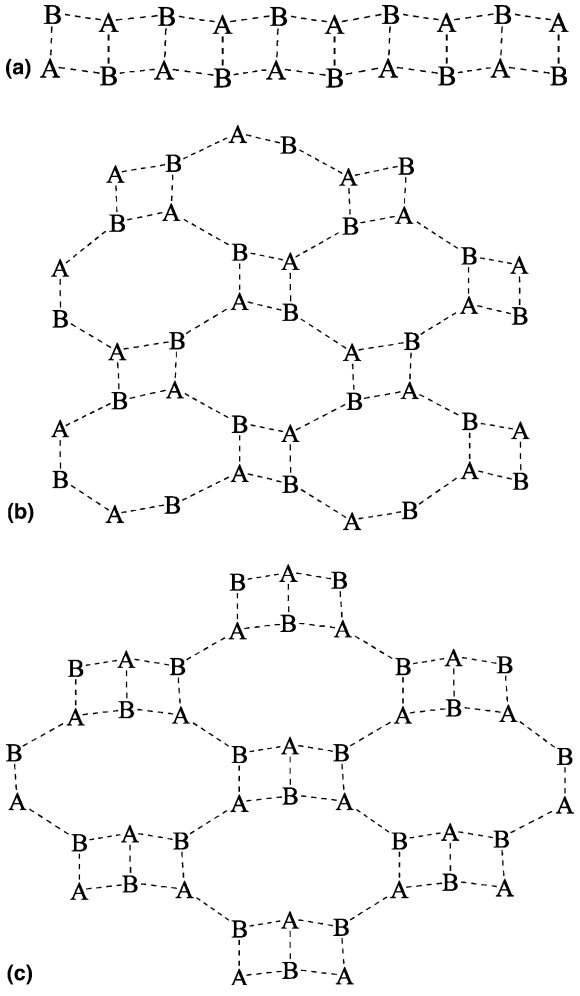


Fig. 1. Schematic diagrams showing the arrangements of cations and anions for (a) **1** and **2**, (b) **3** and **4**, and (c) **5**, where **A** is the cation and **B** the anion.

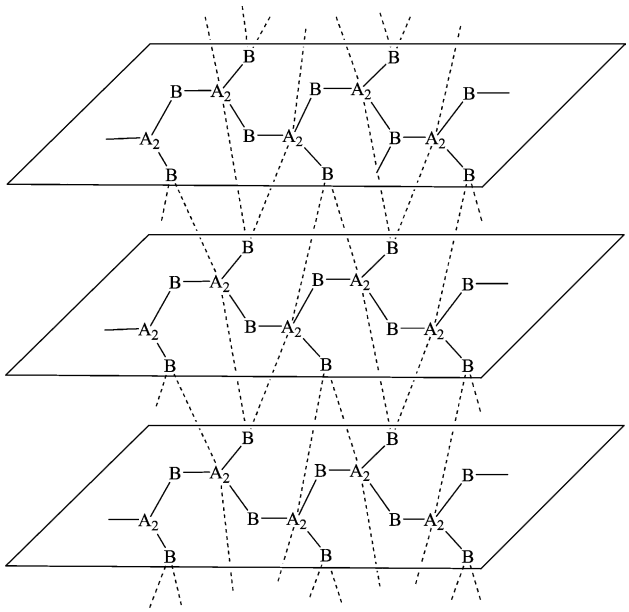


Fig. 2. Schematic diagram showing the arrangement of cations and anions for **6**, where $\mathbf{A_2}$ is the dication and **B** the anion.

a peak corresponding to the $(Ph_2PO_2)^-$ anion slowly appeared in about 24 h with the formation of a white precipitate, which was confirmed to be compound **1** by NMR (^1H and ^{31}P), MS (FAB, both positive and negative modes) and X-ray crystallography. The oxidative cleavage of $\mathbf{L^1}$ to **1** by air was very slow and took more than a week to complete. This suggested that Ag(I) assisted and accelerated the oxidative cleavage process and a Ag(I) phosphine complex intermediate was involved in the process. Attempts to isolate and characterize the Ag(I) intermediate are as yet unsuccessful. Furthermore, we found that the metathesis of benzamidine hydrochloride monohydrate (BHC) with sodium diphenylphosphinate (SDPP) did not give **1**. When the two salts were dissolved in a solvent mixture of 1:1 tetrahydrofuran and acetonitrile at room temperature

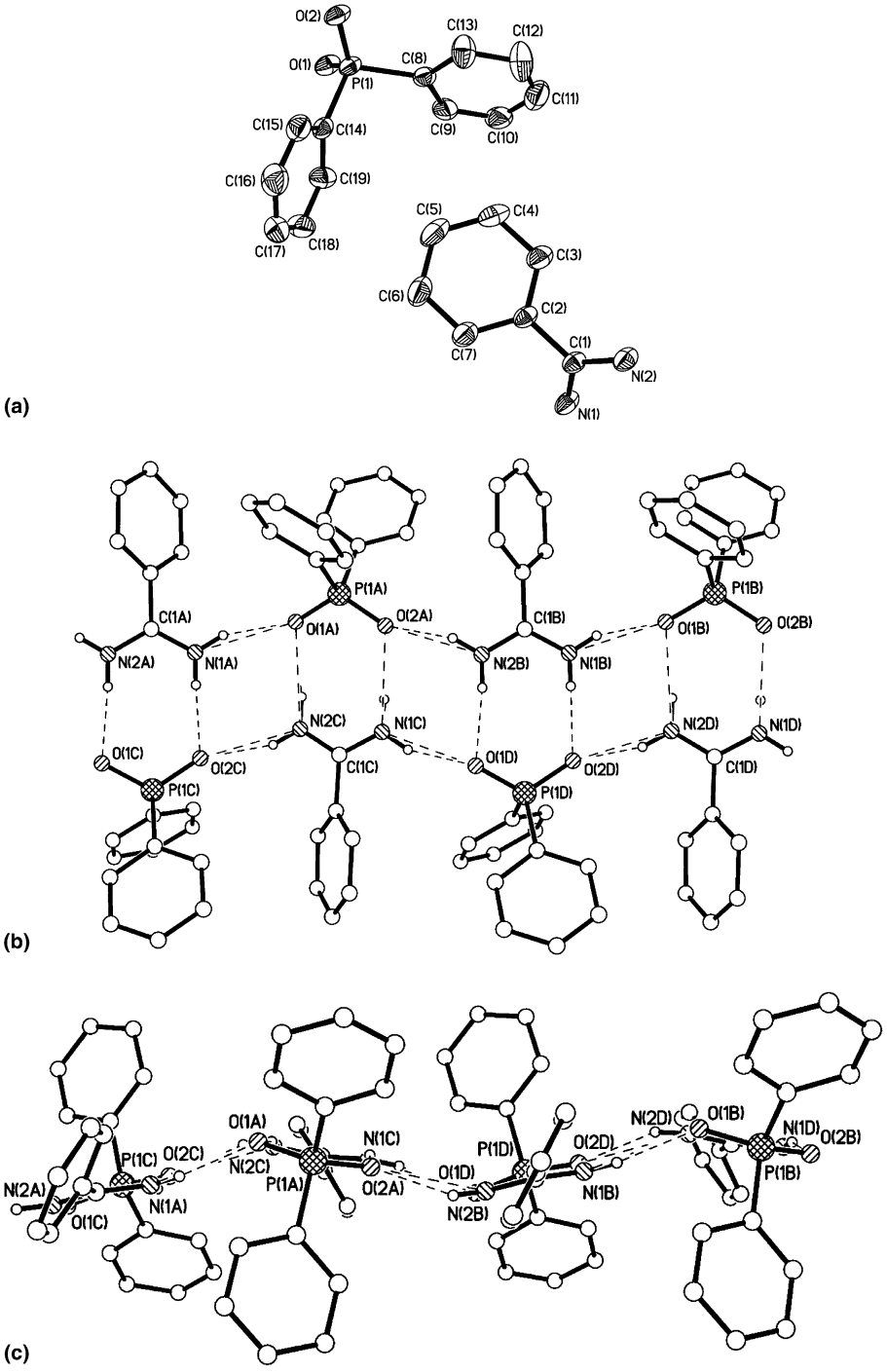


Fig. 3. (a) ORTEP drawing of **1**. (b) Crystal packing diagram for **1** with the hydrogen bonds between cations and anions indicated by the dashed lines. (c) Side-view of the molecular packing showing the 1D polymeric skeleton.

and stirred for 24 h, colorless crystals of benzamidine and diphenylphosphinic acid were isolated by slow evaporation of the solvents at room temperature.

The structures of compounds **1**–**6** were ascertained by X-ray crystallography. Selected bond lengths and bond angles are given in Table 2. Structural analyses revealed that these ionic salts are held together by the electrostatic forces between the cation and the anion, and strengthened by hydrogen bonds to form, depending on the nature of the aryl groups, a 1D, 2D or 3D polymeric network (Figs. 1 and 2). The C–N and P–O distances of **1**–**6** are very similar and the major difference among **1**–**6** lies in their spatial arrangements. Within the NCN fragment of the arylamidinium cations of **1**–**6**, the C–N distances are in the range of 1.297(3)–1.315(3) Å, and the NCN angles in the range of 119.6(2)–123.1(3)°. These values are comparable to those of the cyclic bis(amidinium) dication (C–N distances, 1.29–1.32 Å ; NCN angle, 112.5°) [15e]. Within the OPO fragment of the diphenylphosphinate anion, the P–O distances fall in the range of 1.4873(17)–1.5213(16) Å. The C–N and P–O distances indicate that the charge of the amidinium cation $[ArC(NH_2)_2]^+$ (**A**) or dication $[(NH_2)_2CC_6H_4C(NH_2)_2]^{2+}$ ($\mathbf{A_2}$) and the diphenylphosphinate anion $[Ph_2PO_2]^-$ (**B**) is delocalized over the N–C–N and O–P–O frameworks, respectively.

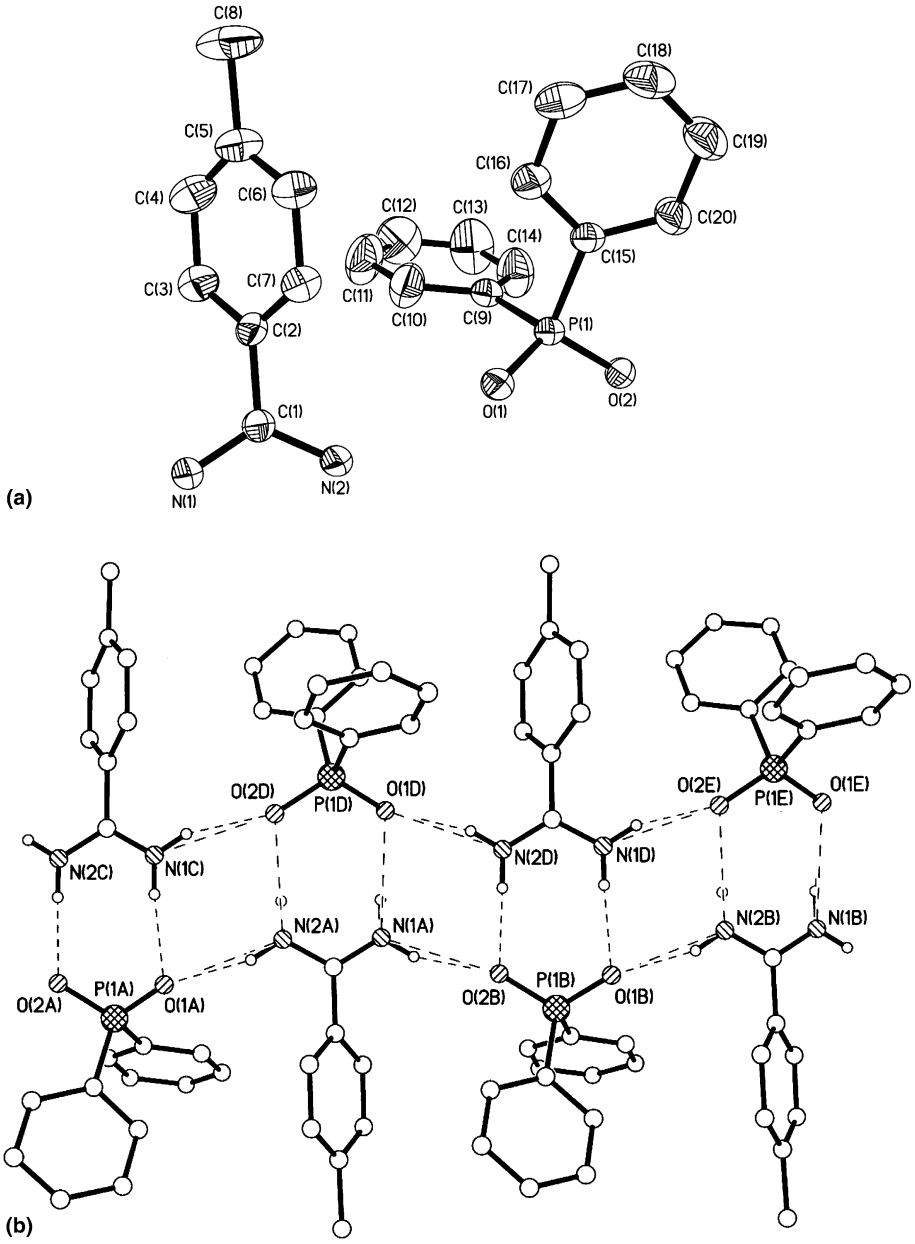


Fig. 4. (a) ORTEP drawing of **2**. (b) Crystal packing diagram for **2** with the hydrogen bonds between cations and anions indicated by the dashed lines.

Fig. 3(a) shows a perspective drawing of **1**. For the amidinium cation, the dihedral angle formed between the NCN plane and the phenyl ring plane is 51.1°. Fig. 3(b) shows four subunits in the crystal lattice. The distance between N(1A) and O(2C) is 2.791 Å, N(2A) and O(1C) is 2.855 Å, and that between O(2C) and N(2C) is 2.762 Å, N(1A) and O(1A) is 2.812 Å. It means that the electrostatic force between **A** and its neighboring unit **B** is approximately the same in all directions. Moreover, the distance between the oxygen atoms of **B** and the hydrogen atoms of the NH_2 groups is around 1.98 (±0.03) Å, indicating the presence of N–H···O hydrogen bonds. By the association of electrostatic forces and hydrogen bonds, **A** and **B** are gathered rationally and regularly to form a 1D polymeric network. The molecular packing for **1** can be best represented

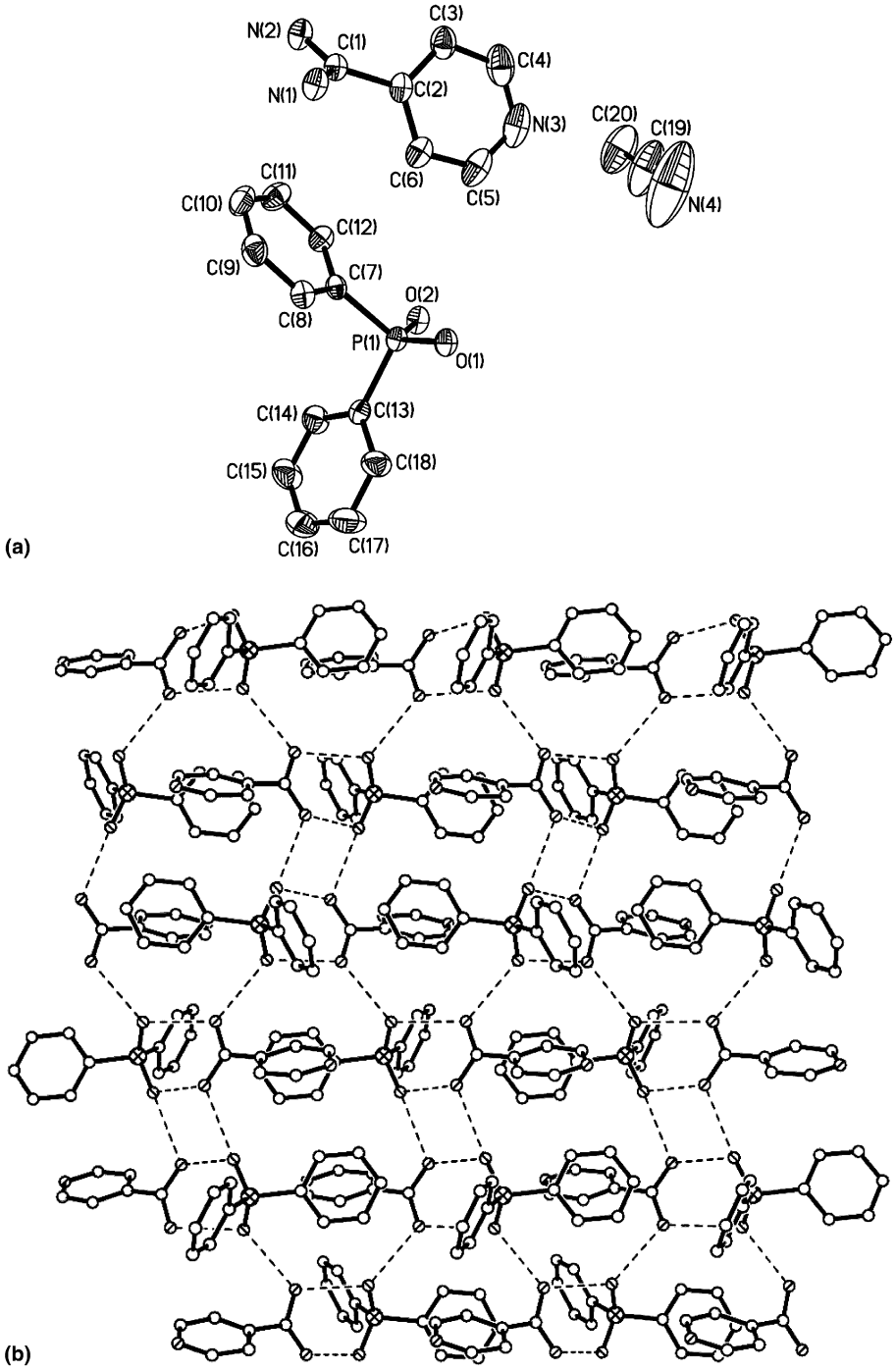


Fig. 5. (a) ORTEP drawing of **3**. (b) Crystal packing diagram for **3** with the hydrogen bonds between cations and anions indicated by the dashed lines.

by Fig. 1(a). The crystal structure of **2** is very similar to that of **1** where cations and anions are gathered rationally and regularly to form a 1D zig-zag polymeric structure (Fig. 4). Within the conjugated cation $[(p\text{-}CH_3C_6H_4)C(NH_2)_2]^+$ (**A**), the tolyl plane forms a dihedral angle of 46.6° with the [N(1)C(1)N(2)] plane.

The molecular structure of **3** is shown in Fig. 5(a) and bears a close resemblance to that of **1** and **2**. The dihedral angle formed between the conjugated NCN plane and the pyridyl ring plane is 56.1°. Likewise, every cation interacts with three anions and vice versa. The distance between every nitrogen atom and the nearest oxygen atom is ca. 2.86 (±0.08) Å. The distance between oxygen atoms and hydrogen atoms in N–H···O bonds is ca. 2.04 (±0.04) Å. However, the network structure of **3** is very different from that of **1** and **2**. Fig. 5(b) shows the molecular packing diagram of **3**. The cations and anions gathered to form a 2D planar polymeric motif. A simplified diagram of the lattice of **3** is shown in Fig. 1(b).

The molecular structure (Fig. 6(a)) of **4** is very similar to that of **3**. The dihedral angle formed between the conjugated NCN plane and the pyridyl ring plane is 50.7°. As in **3**, every cation interacts with three anions and vice versa. The distance between every nitrogen atom and the nearest oxygen atom is ca. 2.87 (±0.07) Å. The distance between oxygen atoms and hydrogen atoms in N–H···O bonds is ca. 2.04 (±0.04) Å. Fig. 6(b) shows the packing diagram of **4** in which the cations and

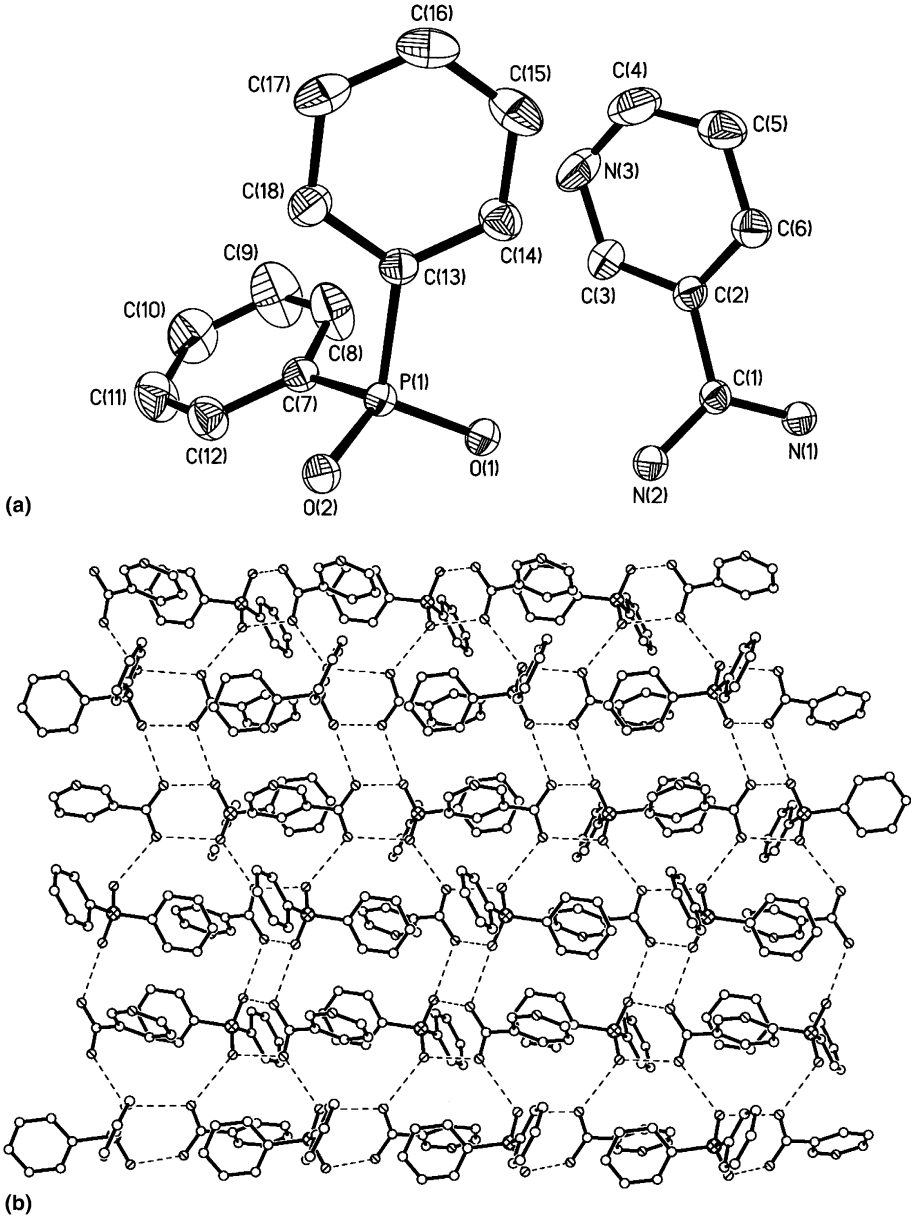


Fig. 6. (a) ORTEP drawing of **4**. (b) Crystal packing diagram for **4** with the hydrogen bonds between cations and anions indicated by the dashed lines.

anions are arranged in a 2D planar polymeric structure (Fig. 1(b)).

The molecular structure of **5** is shown in Fig. 7(a). The dihedral angle formed between the conjugated NCN [N(1)C(1)N(2)] plane and the pyridyl ring is 43.2°. There is another half of the molecule in the same unit cell. A whole molecule can be organized by combining half of the molecule in one unit cell with the other half of the molecule of another unit cell. The dihedral angle formed between the conjugated NCN [N(4)C(19)N(4A)] and the pyridyl ring is 2.7° and is very different from that of the other molecule. Every cation interacts with three anions and vice versa in the crystal packing. The distance between every nitrogen atom and the nearest oxygen atom is ca. 2.80 (±0.04) Å. The distance between oxygen and hydrogen atoms in N–H···O bonds is ca. 2.01 (±0.05) Å. Similar to **3** and **4**, cations and anions tend to form a 2D planar polymer

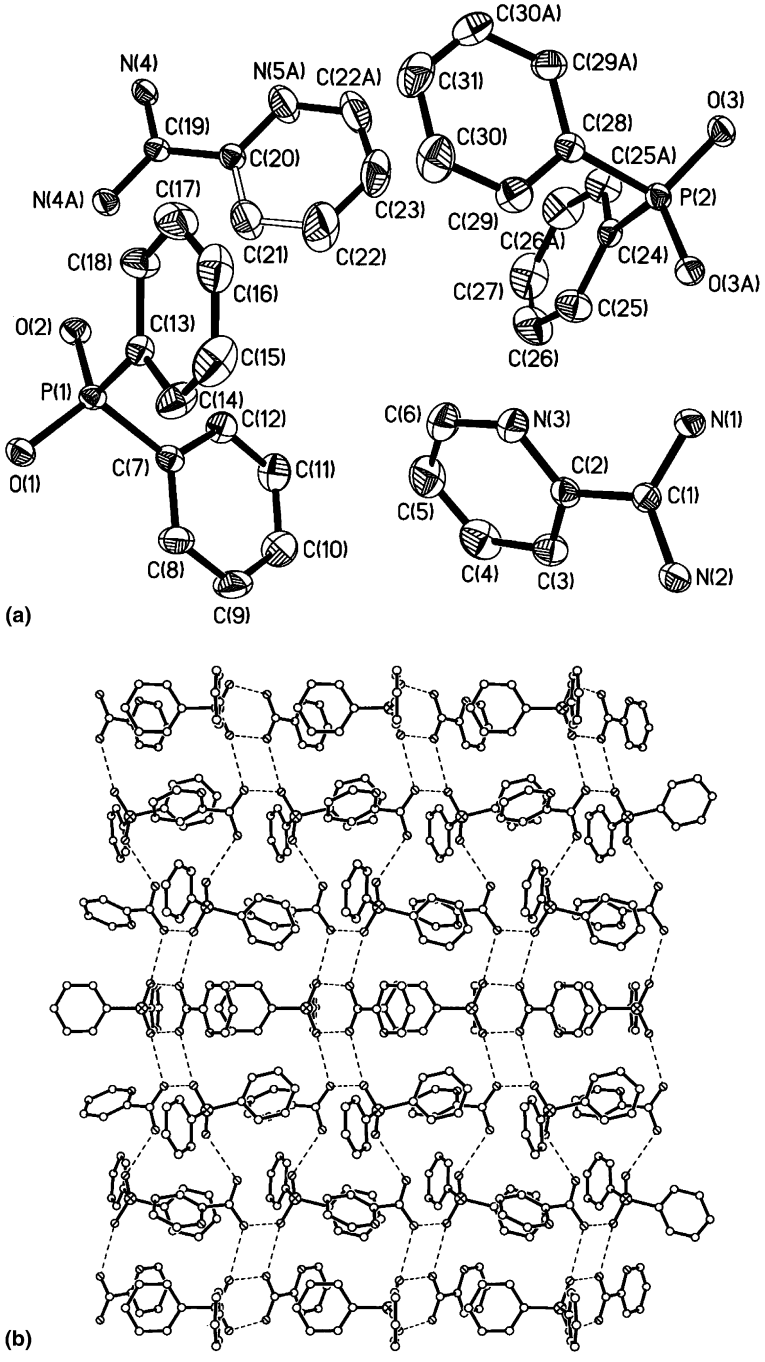


Fig. 7. (a) ORTEP drawing of **5**. (b) Crystal packing diagram for **5** with the hydrogen bonds between cations and anions indicated by the dashed lines.

(Fig. 7(b)). However, three molecules, instead of two as in **3**, are connected together in the lattice of **5** and Fig. 1(c) gives a good representation of this lattice arrangement.

Single-crystal X-ray analysis of **6** revealed that other than having a bis(amidinium) dication, its molecular structure (Fig. 8(a)) is similar to those of **1**–**5**. There are two independent molecules in the unit cell. The C–N and P–O distances are comparable to those of **1**–**5**. For **6**, the dihedral angles formed between the plane of the phenylene ring and the NCN planes are 12.8 [N(1)C(1)N(2)] and 42.8° [N(3)C(8)N(4)], and between the two NCN planes is 30.4°. For the other independent molecule, the corresponding dihedral angles are 35.4°, 3.4° and 33.5°. With the use of a dication, the molecular arrangement in the crystal structure of **6** is more complex than those observed in **1**–**5** and Fig. 8(b) shows a portion of the crystal packing. It is clear from the simple schematic diagram shown in Fig. 2 that compound **6** forms a three-dimensional polymeric network. It looks like a stair, in which every plane is a step. There are two association types of anions in **6**. One is associated with two cations located in the same plane, having O ··· N distances of 2.764 and 2.867 Å. Another is associated with three cations, in which one is located on the same plane and two located on another plane above or below, having O ··· N distances of 2.750, 2.756 and 2.896 Å (or 2.882, 2.788 and 2.832 Å), respectively. The two different sets of distances are due to the two NCN planes of

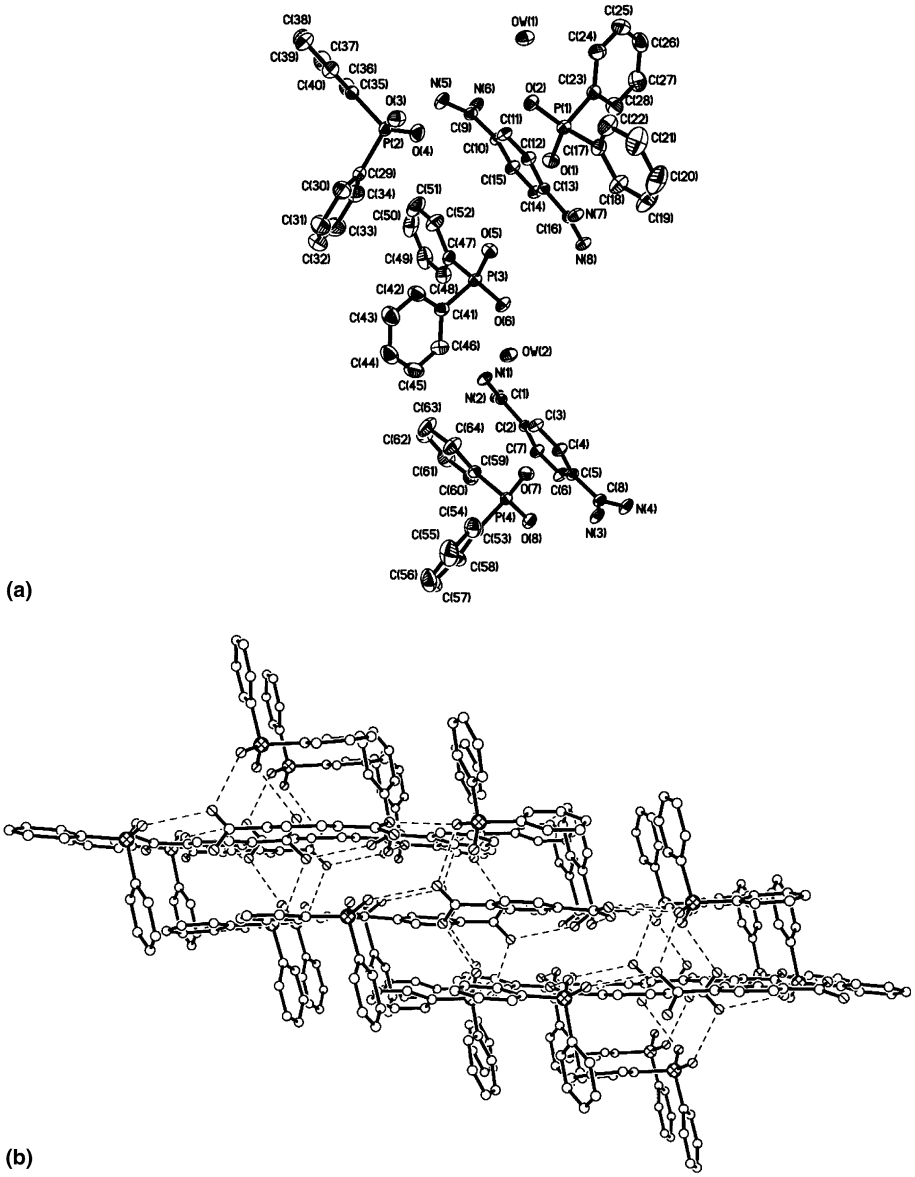


Fig. 8. (a) ORTEP drawing of **6**. (b) Crystal packing diagram for **6** with the hydrogen bonds between cations and anions indicated by the dashed lines.

one dication having different dihedral angles with the phenylene ring.

3.2. Optical and spectroscopic properties

To examine the significance and extent of hydrogen bonding interactions in our compounds, the solid-state fluorescence properties of **1** and **3** have been studied and compared with that of BHC and SDPP. The excitation and emission spectra of **1** and **3** should be similar to that of BHC and SDPP if hydrogen bonding is insignificant. Fig. 9 showed the solid-state fluorescence excitation spectra and emission spectra of compound **1**, BHC and SDPP. Relative to that of BHC and SDPP, the positions of the maximum excitation and emission wavelengths of **1** are remarkably bathochromically shifted. The excitation and emission peaks of **1** appear at 373 and 466 nm, respectively, whereas those of BHC are at 308 and 350 nm, and SDPP at 300 and 324 nm, respectively. The excitation and emission peaks of **3** (Fig. 10) are at 345 and 475 nm, respectively. The substantial red shift in the excitation and emission maxima for **1** and **3** as compared with those of BHC and SDPP suggests that hydrogen bonding interactions in their solid-state structures is significant and extensive. We believe that such hydrogen bonding should be present in all cases.

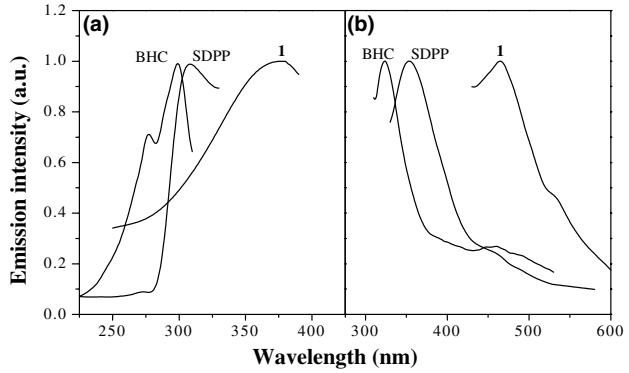


Fig. 9. (a) Excitation and (b) emission spectra of benzamidine hydrochloride (BHC), sodium diphenylphosphinate (SDPP), and **1**.

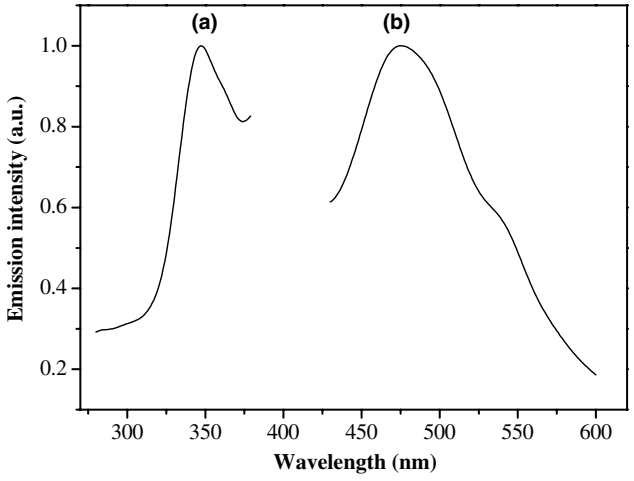


Fig. 10. (a) Excitation and (b) emission spectra of **3**.

Because of the special solid-state structures of **1**–**6**, some typical absorption peaks appeared in their infrared spectra. For the secondary amine salt, vibrations involving anti-symmetric and symmetric NH_2^+ stretchings are characterized by strong multiple IR absorptions located in the 3000–2700 cm^{-1} region [21]. The double strong broad peaks ranging from 3400 to 2700 cm^{-1} indicate the N–H vibration of $[ArC(NH_2)(NH_2)]^+$ group. The characteristic stretching frequencies of the C = N group are in the range from 1605 to 1674 cm^{-1} [21]. The strong peaks around 1710 cm^{-1} are due to the C–N stretching absorption of the $[ArC(NH_2)(NH_2)]^+$ group. Acid salts containing the PO_2^- group have two strong IR bands in the region 1323–1092 cm^{-1} (out-of-phase stretch) and 1164–995 cm^{-1} (in-phase stretch). Acid salts of the type $R_2PO_2^-$ absorb in the lower part of the region. The two peaks around 1130 and 1035 cm^{-1} should be the P–O stretches of $[Ph_2PO_2]^-$. The three typical absorption bands of **1**–**6** are listed in Table 2.

The ^1H, ^{31}P and ^{13}C NMR spectra have been investigated in DMSO-d_6 for **1**–**6**. Since compounds **3** and **6** have very low solubility in DMSO, satisfactory ^{13}C NMR spectra could not be obtained in these two cases. The chemical shift data are listed in Table 3. The ^{31}P chemical shifts of all six compounds are very similar and appear in the range from δ 16–18 ppm. The ^1H

Table 3
IR and NMR data of compounds **1**–**6**

Compound	IR absorption in cm^{-1} (KBr)			NMR data (DMSO-d_6)		
	N–H	C–N	P–O of $Ph_2PO_2^-$	^{31}P	^1H of NH_2	^{13}C of $[-C(NH_2)_2]^+$
1	3140, 2933	1711	1130, 1037	16.8	11.12, 9.01	166.5
2	3147, 2921	1705	1131, 1038	16.9	11.31, 8.88	166.1
3	3369, 3053	1662	1251, 1172	17.2	10.34, 9.38	
4	3140, 2923	1711	1130, 1037	17.0	11.22, 9.16	164.3
5	3182, 2948	1711	1130, 1042	17.0	11.10, 9.30	162.2
6	3347, 3171	1674	1260, 1171	16.8	11.48, 9.18	

chemical shifts of the NH_2 protons are similar too, and appear around δ 11.0 and 9.0 ppm. This indicates that there are two kinds of NH protons in the solution state. The characteristic ^{13}C chemical shifts of $[-C(NH_2)(NH_2)]^+$ appear in the range from δ 162 to 167 ppm.

4. Supplementary material

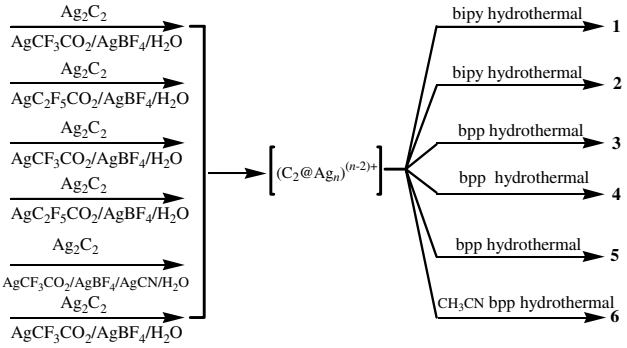
Crystallographic data for the structural analysis have been deposited with the Cambridge Crystallographic Data Center, CCDC Nos. 257438–257443 for compounds **1**–**6**, respectively. Copies of this information may be obtained free of charge from the Director, CCDC, 12 Union Road, Cambridge CB2 1EW, UK (fax: +44 1223 336 033; E-mail: deposit@ccdc.cam.ac.uk or www: http://www.ccdc.cam.ac.uk).

Acknowledgments

We thank the Hong Kong Baptist University and the Hong Kong Research Grants Council (HKBU 2021/99P) for financial support.

References

[1] J.-M. Lehn, in: A. Ciferri (Ed.), Supramolecular Polymers, Marcel Dekker, New York, 2000, pp. 615–641.
[2] (a) M. Hong, Y. Zhao, W. Su, R. Cao, M. Fujita, Z. Zhou, S.C. Chan, Angew. Chem. Int. Ed. 39 (2000) 2468;
(b) X.M. Zhang, M.L. Tong, M.L. Gong, X.M. Chen, Eur. J. Inorg. Chem. (2003) 138.
[3] (a) M. Fujita, Chem. Soc. Rev. 27 (1998) 417;
(b) M. Scherer, D.L. Caulder, D.W. Johnson, K.N. Raymond, Angew. Chem. Int. Ed. 38 (1999) 1587;
(c) R.-D. Schnebeck, E. Freisinger, B. Lippert, Chem. Commun. (1999) 675;
(d) M. Oh, G.B. Carpenter, D.A. Sweigart, Organometallics 22 (2003) 2364.
[4] (a) M.D. Levin, P.J. Stang, J. Am. Chem. Soc. 122 (2000) 7428;
(b) P.D. Beer, P.A. Gale, Angew. Chem. Int. Ed. 40 (2001) 486;
(c) C. Bucher, R.S. Zimmerman, V. Lynch, V. Král, J.L. Sessler, J. Am. Chem. Soc. 123 (2001) 2099.
[5] (a) F. Würthner, A. Sautter, Chem. Commun. (2000) 445;
(b) T.K. Maji, S. Konar, G. Mostafa, E. Zangrando, T.H. Lu, N.R. Chaudhuri, J. Chem. Soc., Dalton Trans. (2003) 171;
(c) D. Sun, R. Cao, Y. Sun, W. Bi, X. Li, Y. Wang, Q. Shi, X. Li, Inorg. Chem. 42 (2003) 7512;
(d) H.W. Roeskey, M. Andruh, Coord. Chem. Rev. 236 (2003) 91.
[6] (a) F.M. Tabellion, S.R. Seidel, A.M. Arif, P.J. Stang, Angew Chem. Int. Ed. 40 (2001) 1529;
(b) A.J. Blake, N.R. Champness, P.A. Cooke, J.E.B. Nicolson, Chem. Commun. (2000) 665.
[7] B. Moulton, M.J. Zaworotko, Chem. Rev. 101 (2001) 1629.
[8] (a) M.J. Zaworotko, Chem. Commun. (2001) 1;
(b) F.H. Beijer, H. Kooijman, A.L. Spek, R.P. Sijbesma, E.W. Meijer, Angew. Chem. Int. Ed. 37 (1998) 75;
(c) P.S. Corbin, S.C. Zimmerman, J. Am. Chem. Soc. 120 (1998) 9710;
(d) J.L. Sessler, R. Wang, Angew. Chem. Int. Ed. 37 (1998) 1726.
[9] (a) W.E. Allen, C.J. Fowler, V.M. Lynch, J.L. Sessler, Chem. Eur. J. 7 (2001) 721;
(b) I. Huc, Eur. J. Org. Chem. (2004) 17;
(c) D.M.P. Mingos (Ed.), Supramolecular Assembly via Hydrogen Bonds in Structure and Bonding, vols. 108 and 111, Springer, Berlin, 2004.
[10] (a) G.R. Lewis, A.G. Orpen, Chem. Commun. (1998) 1873;
(b) A.L. Gillon, A.G. Orpen, J. Starbuck, X.-M. Wang, Y. Rodriguez-Martin, C. Ruiz-Pérez, Chem. Commun. (1999) 2287;
(c) B. Dolling, A.L. Gillon, A.G. Orpen, J. Starbuck, X.-M. Wang, Chem. Commun. (2001) 567.
[11] A. Angeloni, A.G. Orpen, Chem. Commun. (2001) 343.
[12] J.C. MarequeRivas, L. Brammer, Inorg. Chem. 37 (1998) 4756.
[13] A.D. Burrows, R.W. Harrington, M.F. Mahon, S.J. Teat, Eur. J. Inorg. Chem. (2003) 1433.
[14] (a) M.W. Hosseine, R. Ruppert, P. Schaeffer, A. De Cian, N. Kyritsakas, J. Fischer, Chem. Commun. (1994) 2135;
(b) M.W. Hosseine, G. Brand, P. Schaeffer, R. Ruppert, A. De Cian, J. Fischer, Tetrahedron Lett. 37 (1996) 1405;
(c) O. Félix, M.W. Hosseine, A. De Cian, N. Kyritsakas, J. Fischer, Angew. Chem. Int. Ed. 36 (1997) 102;
(d) O. Félix, M.W. Hosseine, A. De Cian, J. Fischer, Tetrahedron Lett. 38 (1997) 1755;
(e) O. Félix, M.W. Hosseine, A. De Cian, J. Fischer, Tetrahedron Lett. 38 (1997) 1933;
(f) O. Félix, M.W. Hosseine, A. De Cian, N. Kyritsakas, J. Fischer, Chem. Commun. (2000) 281;
(g) M.W. Hosseini, Coord. Chem. Rev. 240 (2003) 157.
[15] (a) C. Kleina, E. Graf, M.W. Hosseini, A.D. Cian, J. Fisher, Chem. Commun. (2000) 239;
(b) D. Braga, L. Maini, F. Grepioni, A. De Cian, O. Félix, J. Fischer, M.W. Hosseine, New J. Chem. 24 (2000) 547;
(c) S. Ferlay, S. Koenig, M.W. Hosseine, J. Pansanel, A.D. Cian, N. Kyritsakas, Chem. Commun. (2002) 218;
(d) S. Ferlay, O. Félix, M.W. Hosseine, J.-M. Planeix, N. Kyritsakas, Chem. Commun. (2002) 702;
(e) C. Paraschiv, S. Ferlay, M.W. Hosseine, V. Bulach, J.-M. Planeix, Chem. Commun. (2004) 2270.
[16] SAINT, Reference manual, Siemens Energy and Automation, Madison, WI, 1994–1996.
[17] G.M. Sheldrick, SADABS, Empirical Absorption Correction Program, University of Göttingen, Germany, 1997.
[18] G.M. Sheldrick, SHELXTL™, Reference Manual, version 5.1, Siemens, Madison, WI, 1997.
[19] (a) W.K. Wong, T. Jiang, W.T. Wong, J. Chem. Soc., Dalton Trans. (1995) 3087;
(b) W.K. Wong, T. Jiang, D.W.J. Kwong, W.T. Wong, Polyhedron 14 (1995) 1109;
(c) W.K. Wong, C. Sun, W.T. Wong, J. Chem. Soc., Dalton Trans. (1997) 3387.
[20] W.Y. Wong, W.K. Wong, C.-D. Sun, W.T. Wong, J. Organomet. Chem. 612 (2000) 160.
[21] D. Lin-Vien, N.B. Colthup, W.G. Fateley, J.G. Grasselli, The Handbook of Infrared and Raman Characteristic Frequencies of Organic Molecules, Academic Press, New York, 1991.



Scheme 1.

the rigid linear bipy and conformationally flexible bpp ligands for the linkage of labile $C_2@Ag_n$ cages, which are presumed to be formed in situ, in the construction of solid-state architectures. The synthetic procedure shown in Scheme 1 yielded the following six complexes: $[Ag_{13}(C_2)_2(CF_3CO_2)_9(bipy)_4(H_2O)_3]$ (**1**), $[Ag_{18}(C_2)_2(C_2F_5CO_2)_{18}(bipyH)_4]\cdot 3H_2O$ (**2**), $[Ag_6(C_2)(CF_3CO_2)_4(bpp)]$ (**3**), $[Ag_6(C_2)(C_2F_5CO_2)_5(bppH)]_n$ (**4**), $[Ag_6(C_2)(CF_3CO_2)_5(bppH)]_n$ (**5**) and $[Ag_{23}(C_2)_4(CF_3CO_2)_{15}(bpp)_6]\cdot H_2O$ (**6**).

2. Experimental

2.1. Synthesis

All chemicals were purchased from ACROS and Aldrich and used without further purification. Ag_2C_2 was prepared as described previously [4]. *Caution!* Thoroughly dried Ag_2C_2 detonates easily upon mechanical shock, and only a small quantity should be used in any chemical reaction. Excess amount can be disposed of via slow decomposition in an alkaline solution [8]. To ensure safety, we used moist Ag_2C_2 in all preparations.

2.1.1. $[Ag_{13}(C_2)_2(CF_3CO_2)_9(bipy)_4(H_2O)_3]$ (*1*)

Excess moistened Ag_2C_2 (~0.5 g, 2 mmol) was added to 1 mL of a concentrated aqueous solution of $AgCF_3CO_2$ (0.885 g, 4 mmol) and $AgBF_4$ (0.244 g, 1.3 mmol) in a plastic beaker with stirring. The undissolved amount of Ag_2C_2 was filtered off, and then 30 mg bipy was added to the filtrate. The resulted suspension was placed in a 25 mL Teflon-lined stainless steel reaction vessel and subjected to hydrothermal conditions at 108 °C for 40 h, and then cooled to room temperature at 6 °C/h. Colorless rhombus-like crystals of **1** were isolated in ~65% yield. *Anal.* Calc. for $C_{62}H_{38}Ag_{13}F_{27}N_8O_{21}$: C, 23.67; H, 1.22; N, 3.56. Found: C, 23.59; H, 1.16; N, 3.50%.

2.1.2. $[Ag_{18}(C_2)_2(C_2F_5CO_2)_{18}(bipyH)_4]\cdot 3H_2O$ (*2*)

Complex **2** was synthesized in a similar manner to complex **1** using $AgC_2F_5CO_2$ instead of $AgCF_3CO_2$. Colorless block-like crystals were isolated in ~40% yield. *Anal.* Calc. for $C_{98}H_{42}Ag_{18}F_{90}N_8O_{39}$: C, 23.91; H, 0.86; N, 2.28. Found: C, 23.85; H, 0.82; N, 2.31%.

2.1.3. $[Ag_6(C_2)(CF_3CO_2)_4(bpp)]$ (*3*)

Excess moistened Ag_2C_2 (~0.5 g, 2 mmol) was added to 1 mL of a concentrated aqueous solution of $AgCF_3CO_2$ (0.455 g, 2 mmol) and $AgBF_4$ (0.248 g, 1.3 mmol) in a plastic beaker with stirring. The undissolved amount of Ag_2C_2 was filtered off, and then 52 mg (0.26 mmol) of bpp was added to the filtrate. The resulted suspension was placed in a 25 mL Teflon-lined stainless steel reaction vessel and subjected to hydrothermal conditions at 110 °C for 36 h, and then cooled to room temperature at 6 °C/h. Colorless block-like crystals of **3** were isolated in ~57% yield. *Anal.* Calc. for $C_{23}H_{14}Ag_6F_{12}N_2O_8$: C, 20.90; H, 1.07; N, 2.12. Found: C, 20.73; H, 1.01; N, 2.15%.

2.1.4. $[Ag_6(C_2)(C_2F_5CO_2)_5(bppH)]_n$ (*4*)

Complex **4** was synthesized in a similar manner to complex **3** using $AgC_2F_5CO_2$ instead of $AgCF_3CO_2$. Colorless block-like crystals were isolated in ~45% yield. *Anal.* Calc. for $C_{30}H_{15}Ag_6F_{25}N_2O_{10}$: C, 20.09; H, 0.84; N, 1.56. Found: C, 19.93; H, 0.91; N, 1.61%.

2.1.5. $[Ag_6(C_2)(CF_3CO_2)_5(bppH)]_n$ (*5*)

This complex was obtained serendipitously from an attempt to trap CN^- inside the silver cage by introducing AgCN into the reaction system. Excess Ag_2C_2 (~0.5 g, 2 mmol) and AgCN (~0.06 g, ~0.5 mmol) were added to 1 mL of a concentrated aqueous solution of $AgCF_3CO_2$ (0.455 g, 2 mmol) and $AgBF_4$ (0.245 g, 1.26 mmol) in a plastic beaker with stirring until saturated. The undissolved amount of Ag_2C_2 and AgCN was filtered off, and 52 mg (0.26 mmol) bpp was added to the filtrate. The resulted suspension was treated with the hydrothermal method as described above. Colorless block-like crystals were isolated in ~40% yield. *Anal.* Calc. for $C_{25}H_{15}Ag_6F_{15}N_2O_{10}$: C, 19.45; H, 0.98; N, 1.81. Found: C, 19.37; H, 1.02; N, 1.78%.

2.1.6. $[Ag_{23}(C_2)_4(CF_3CO_2)_{15}(bpp)_6]\cdot H_2O$ (*6*)

When the procedure for **1** was repeated with addition of several drops of CH_3CN under hydrothermal reaction condition, colorless block-like crystals of complex **6** were harvested in ~60% yield. *Anal.* Calc. for $C_{116}H_{86}Ag_{23}F_{45}N_{12}O_{31}$: C, 25.43; H, 1.58; N, 3.07. Found: C, 25.50; H, 1.62; N, 2.98%.

2.2. X-ray crystallography

X-ray measurements on single crystals of complexes **1**–**6** were performed on a Bruker SMART 1000 CCD diffractometer using Mo Kα radiation ($\lambda = 0.71073$Å) at 293 K. Data collection and reduction were performed

Table 1
Crystallographic data for complexes **1**–**6**

Complex	**1**	**2**	**3**	**4**	**5**	**6**
Formula	$C_{62}H_{38}Ag_{13}F_{27}N_8O_{21}$	$C_{98}H_{42}Ag_{18}F_{90}N_8O_{39}$	$C_{23}H_{14}Ag_6F_{12}N_2O_8$	$C_{30}H_{15}Ag_6F_{25}N_2O_{10}$	$C_{25}H_{15}Ag_6F_{15}N_2O_{10}$	$C_{116}H_{86}Ag_{23}F_{45}N_{12}O_{31}$
Formula weight	3146.27	5606.93	1321.58	1685.66	1435.61	5479.92
Space group	$P\bar{1}$ (No. 2)	$P2_1/n$ (No. 14)	$C2/c$ (No. 15)	$C2/c$ (No. 15)	$P2_1/c$ (No. 14)	$P2_1/n$ (No. 14)
a (Å)	16.004(3)	31.029(2)	31.996(3)	28.215(1)	14.4311(7)	18.490(1)
b (Å)	16.064(3)	18.145(1)	14.620(1)	16.839(1)	29.933(1)	28.467(2)
c (Å)	19.532(4)	31.591(2)	15.374(1)	18.6152(8)	8.4926(4)	28.755(2)
α (°)	103.728(4)	90	90	90	90	90
β (°)	100.696(4)	118.374(1)	113.717(1)	92.441(1)	99.035(1)	92.462(1)
γ (°)	117.940(4)	90	90	90	90	90
V (Å^3)	4044(1)	15650.0(2)	6584.3(9)	8836.3(7)	3623.0(3)	15121.0(1)
Z	2	4	8	8	4	4
μ (mm^{-1})	3.207	2.374	3.615	2.767	3.311	3.027
Total reflections	21953	83592	22149	23482	19501	89713
Unique reflections	14130	27555	7968	7775	6371	29707
R_{int}	0.0407	0.0769	0.0373	0.0441	0.0550	0.1101
Data [$I > 2\sigma(I)$]	9663	13606	5506	5136	4816	11489
Goodness-of-fit on F^2	0.962	0.985	0.972	1.048	1.167	0.860
Number of parameters	1315	2279	488	649	605	2016
$\delta\rho_{max}$ and $\delta\rho_{min}$ (e Å^{-3})	2.029 and −0.926	1.088 and −1.273	1.359 and −0.928	2.290 and −1.315	1.924 and −1.470	2.666 and −1.317
Final R indices[a] [$I > 2\sigma(I)$]	$R_1 = 0.0510$, $wR_2 = 0.1206$	$R_1 = 0.0602$, $wR_2 = 0.1433$	$R_1 = 0.0370$, $wR_2 = 0.0907$	$R_1 = 0.0767$, $wR_2 = 0.2249$	$R_1 = 0.0667$, $wR_2 = 0.1364$	$R_1 = 0.0652$, $wR_2 = 0.1587$
R indices (all data)	$R_1 = 0.0785$, $wR_2 = 0.1374$	$R_1 = 0.1370$, $wR_2 = 0.1854$	$R_1 = 0.0606$, $wR_2 = 0.1022$	$R_1 = 0.1069$, $wR_2 = 0.2585$	$R_1 = 0.0891$, $wR_2 = 0.148$	$R_1 = 0.1643$, $wR_2 = 0.1989$
Parameters (p, q) in weighting scheme[b]	(0.0772, 0)	(0.0914, 0)	(0.0563, 0)	(0.1627, 0)	(0.0463, 41.2046)	(0.0988, 0)

[a] $R_1 = \sum\|F_o| - |F_c\|/\sum|F_o|$; $wR_2 = \{\sum[w(F_o^2 - F_c^2)^2]/\sum[w(F_o^2)^2]\}^{1/2}$.
[b] $w = 1/[\sigma^2(F_o^2) + (pP)^2 + qP]$, where $P = [\max(F_o^2, 0) + 2F_c^2]/3$.

using SMART and SAINT software [9], with frames of 0.3° oscillation in the θ range $2° < \theta < 28°$. An empirical absorption correction was applied using the SADABS program [10]. The structures were solved by direct method and all non-hydrogen atoms were refined anisotropically by full-matrix least squares on F^2 using the SHELXTL program package [11]. In complex **5**, atom Ag5 is disordered over two positions. The crystal data and details of refinement are summarized in Table 1, and selected bond distances and angles are listed in the legends for figures.

3. Results and discussion

The group 11 (Cu, Ag, Au) acetylenediides exhibit properties that are characteristic of covalent polymeric solids, but their proneness to detonation upon mechanical shock and insolubility in common solvents present serious difficulties in structural characterization. As a working hypothesis, it is presumed that depolymerization of silver acetylenediide occurs upon dissolving in a concentrated aqueous solution of soluble silver salts to afford labile polyhderal $C_2@Ag_n$ cage species. The assembly of such $C_2@Ag_n$ aggregates to form a crystalline solid is a complex process that is influenced by the presence of ancillary ligands, co-existing anions, and solvate molecules.

3.1. $[Ag_{13}(C_2)_2(CF_3CO_2)_9(bipy)_4(H_2O)_3]$ (1)

X-ray structure determination has revealed that complex **1** has a three-dimensional architecture, in which the basic building block is a double cage comprising 13 silver atoms with each single cage encapsulating an acetylenediide dianion. As shown in Fig. 1, the double cage is generated from edge sharing of a distorted pentagonal bipyramid (Ag1 to Ag7 cage **A**) and an irregular bicapped trigonal prism (cage **B**). For cage **A**, the equatorial silver atoms lie with 0.26 Å of their least-squares plane. The enclosed C_2^{2-} dianion is π-coordinated to the two apices (Ag6 and Ag7) with Ag–C bond distances in the range of 2.432(9)–2.627(8) Å. The C_2^{2-} binds to the equatorial silver atoms via four σ- and one π-Ag–C interactions in the range 2.100(9)–2.525(8) Å. As to cage **B**, atom sets Ag5Ag8Ag10a and Ag4Ag9Ag10 constitute two triangular faces making a dihedral angle of 23.9°. Atoms Ag11 and Ag12 cap the faces Ag5Ag8Ag10a and Ag4Ag9Ag10, respectively. The enclosed C_2^{2-} dianion coordinates to its neighboring silver atoms via σ-type Ag–C interactions in the range of 2.098(9)–2.59(1) Å [12]. Two such double cages share an edge Ag10Ag10a to form a centrosymmetric Ag_{24} quadruple cage, whose remaining coordination sits are filled by the trifluoroacetate and aqua ligands.

The $[Ag_{24}(C_2)_4(CF_3CO_2)_{16}(H_2O)_6]$ unit are further connected by independent bipy ligands I and II to form a chain along the $[\bar{1}\,1\,0]$ direction, and such chains are further interlinked by bipy ligands III and IV to span a layer orientated parallel to the $(1\,1\,\bar{1})$ plane. Argentophilic interactions between atoms of the type Ag2–Ag2a (3.244(2) Å) further connects the layers into a three-dimensional architecture [13] (Figs. 2 and 3).

Of the nine independent trifluoroacetate groups in the asymmetric unit, one simply acts as a space-filling anion without coordination to a silver(I) atom. The others adopt monodentate or μ_2-*O*,*O*′ modes around the silver(I) cage.

3.2. $[Ag_{18}(C_2)_2(C_2F_5CO_2)_{18}(bipyH)_4]\cdot 3H_2O$ (2)

In the crystal structure of **2**, the building unit is a quasi-centrosymmetric double cage composed of 16 silver(I) atoms, with each single cage encapsulating an acetylenediide dianion, as shown in Fig. 4. Each single cage takes the shape of a distorted monocapped square antiprism. For the lower cage, atom sets Ag1Ag2Ag3Ag4 and Ag5Ag6Ag7Ag8 are each coplanar within 0.01 and 0.14 Å, respectively, making a dihedral angle of 6.5°. Atom Ag9 caps the Ag5Ag6Ag7Ag8 face. As to the upper cage, atom sets Ag9Ag10Ag11Ag12 and Ag13Ag14Ag15Ag16 are each coplanar within 0.18 and 0.03 Å, respectively, making a dihedral angle of 5.1°. Atom Ag7 caps the Ag9Ag10Ag11Ag12 face. These two single cages share an edge Ag7Ag9 to form the double cage. A C_2^{2-} species is entrapped in each silver polyhedron and stabilized mainly by σ-type interactions. The Ag–C bond lengths range from 2.20(1) to 2.69(1) Å (Fig. 4).

Eighteen independent pentafluoropropionate ligands exhibit three kinds of coordination modes around the $(C_2)_2@Ag_{16}$ double cage, namely one monodentate, one μ_3-*O*,*O*,*O*′ and 16 μ_2-*O*,*O*′.

The four bipy ligands in the asymmetric unit are each protonated at one terminal to satisfy the charge balance. They are pairwise coordinated to the remaining silver(I) atoms, giving rise to two $[Ag(bipyH)_2]^{3+}$ cations with bond lengths Ag17–N2 2.147(9), Ag17–N3 2.14(1), Ag18–N6 2.138(9), Ag18–N7 2.116(9) Å.

Three solvated water molecules in the asymmetric unit serve as acceptors in hydrogen bonding, with the C and N atoms of the bipy ligands acting as donors as shown in Table 2.

Presumably, the existence of the $[Ag(bipyH)_2]^{3+}$ cations promotes the formation of the anionic cluster $[Ag_{16}(C_2)_2(C_2F_5CO_2)_{18}]^{6-}$. The hydrophobic tails of the pentafluoropropionate ligands prevent further linkage between adjacent silver polyhdera, yielding a discrete supermolecule. This is analogous to the case of $[(Ag_2C_2)(AgC_2F_5CO_2)_6(L)_3(H_2O)]\cdot H_2O$ (L = 4-hydroxyquinoline), in which the presence of pentafluoropropionate, 4-hydroxyquinoline and aqua ligands obstruct further linkage between silver polyhedra [14]. Another

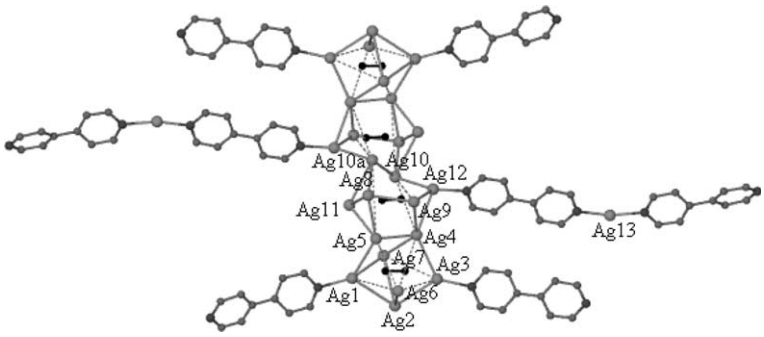


Fig. 1. Arrangement of bipy ligands around the quadruple silver(I) cage in **1**. Trifluoroacetate ligands have been omitted for clarity. Symmetry code: (a) $-x+1, -y+1, -z$. Selected bond distances (Å): C1–C2 1.23(1), C3–C4 1.20(1), C1–Ag2 2.458(8), C1–Ag7 2.627(8), C1–Ag3 2.105(8), C1–Ag6 2.589(9), C1–Ag4 2.356(8), C2–Ag2 2.525(8), C2–Ag7 2.432(9), C2–Ag6 2.530(9), C2–Ag1 2.100(9), C2–Ag5 2.366(8), C3–Ag4 2.415(9), C3–Ag10 2.438(9), C3–Ag12 2.109(8), C3–Ag9 2.363(9), C4–Ag5 2.59(1), C4–Ag8 2.321(9), C4–Ag10 2.547(9), C4–Ag11 2.098(9).

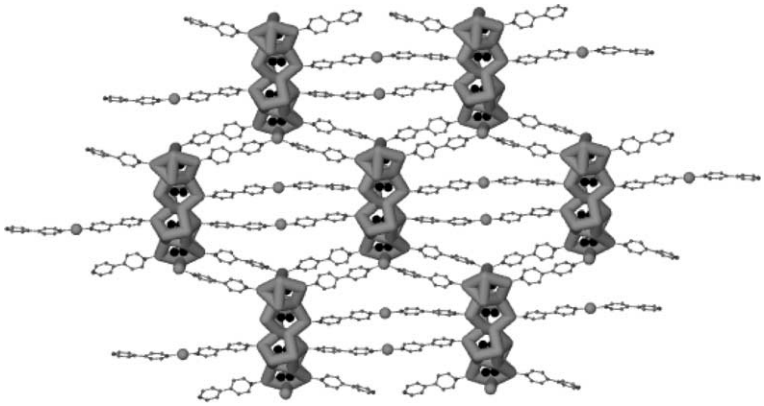


Fig. 2. Layer structure in **1** parallel to the $(1\,1\,\bar{1})$ plane constructed from $[Ag_{24}(C_2)_4(CF_3CO_2)_{16}(H_2O)_6]$ moieties that are interconnected by bipy ligands, as viewed from the [1 1 0] direction. All the aqua ligands have been omitted for clarity.

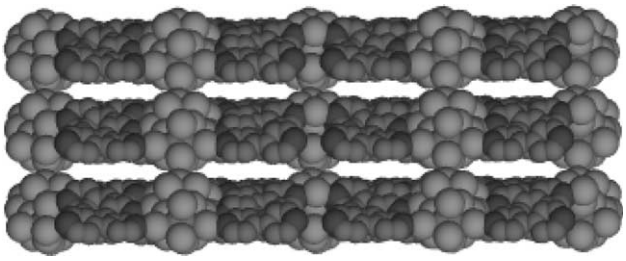


Fig. 3. Three-dimensional architecture of **1** generated from linkage of layers by argentophilic Ag(I)···Ag(I) interactions viewed from [1 1 2] direction.

feature common to **2** and $[(Ag_2C_2)(AgC_2F_5CO_2)_6(L)_3(H_2O)]\cdot H_2O$ is the existence of the $(C_2)_2@Ag_{16}$ double cage of similar geometry.

Judging from the results obtained here and in our previous reports, it can be inferred that whenever ancillary ligands participate in the formation of a higher-dimensional architecture, the $C_2@Ag_n$ cages tend to be highly distorted, whereas the cages in the discrete clusters are much more regular in shape [14,15]. A plausible explanation is that the competition of the ancillary

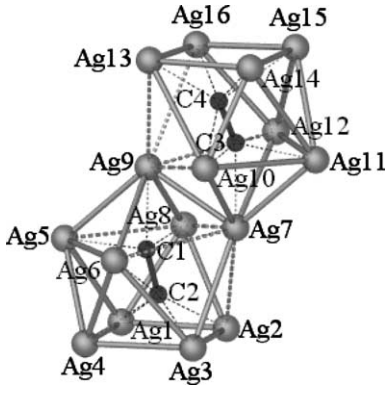


Fig. 4. Double cage unit $(C_2)_2@Ag_{16}$ in **2** generated from two monocapped square antiprisms sharing an edge. The Ag···Ag distances longer than 3.4 Å (twice the van der Waals radius of silver atom) are represented by thick broken lines. The Ag–C bonds are represented by thin broken lines. Selected bond distances (Å): C1–C2 1.22(1), C3–C4 1.18(1), C2–Ag1 2.50(1), C2–Ag2 2.30(1), C2–Ag3 2.24(1), C2–Ag4 2.34(1), C1–Ag5 2.24(1), C–1Ag6 2.42(1), C2–Ag6 2.69(1), C3–Ag7 2.26(1), C1–Ag7 2.67(1), C1–Ag8 2.32(1), C1–Ag9 2.20(1), C3–Ag9 2.63(1), C3–Ag10 2.40(1), C4–Ag10 2.67(1), C3–Ag11 2.36(1), C3–Ag12 2.23(1), C4–Ag13 2.23(1), C4–Ag14 2.46(1), C4–Ag15 2.31(1), C4–Ag16 2.45(1).

Table 2
Bond lengths and bond angles of hydrogen bonds in complex **2**

D–H···A	D···A (Å)	H···A (Å)	D–H···A (°)	Symmetry operator
N5–H5a···O1w	2.742	1.986	146.1	$x, y+1, z$
N1–H1a···O2w	2.752	1.972	150.2	x, y, z
C89–H89a···O3w	3.371	2.783	122.1	x, y, z

ligands with the acetylenediide and perfluorocarboxylate anions for coordination sites around the silver(I) atoms may lead to the distortion of the $C_2@Ag_n$ cages.

3.3. $[Ag_6(C_2)(CF_3CO_2)_4(bpp)]$ (**3**)

X-ray structure determination revealed that complex **3** has a bpp-bridged layer structure. The basic building block is a $C_2@Ag_8$ single cage in the form of a distorted triangulated dodecahedron (Fig. 5). Atom sets Ag1-Ag2Ag6bAg3 and Ag4Ag5Ag6Ag1a are each coplanar within 0.06 and 0.19 Å, respectively, making a dihedral angle of 97.1°. The enclosed C_2^{2-} dianion retains its triple bond character and bonds to the neighboring silver(I) atoms with both σ- and π-type interactions in the range 2.122(5)–2.640(5) Å.

Two single cages share edge Ag1Ag1a to form a centrosymmetric double cage, and such cages are further fused together to form an infinite column via sharing of the edge Ag6Ag6b, together with further connection of the type Ag3Ag3b, as shown in Fig. 5.

Two kinds of coordination modes of the trifluoroacetate ligands are found in **3**, namely μ_3-*O*,*O*,*O*′ and μ_2-*O*,*O*′. The flexible bpp ligands, each with its $-CH_2CH_2CH_2-$ spacer adopting a TG conformation [16], further interlink the infinite silver(I) columns to generate a two-dimensional network in the *bc* plane with Ag5–N1 2.306(5), Ag3–N2 2.208(4) Å (Fig. 6).

3.4. $[Ag_6(C_2)(C_2F_5CO_2)_5(bppH)]_n$ (**4**)

Complex **4** has a branched-tree architecture, in which the basic building block is a $C_2@Ag_7$ single cage in the shape of a distorted monocapped trigonal prism. Triangular faces Ag1Ag2Ag3 and Ag4Ag5Ag6 make a dihedral angle of 14.4°, and atom Ag7 caps the latter face.

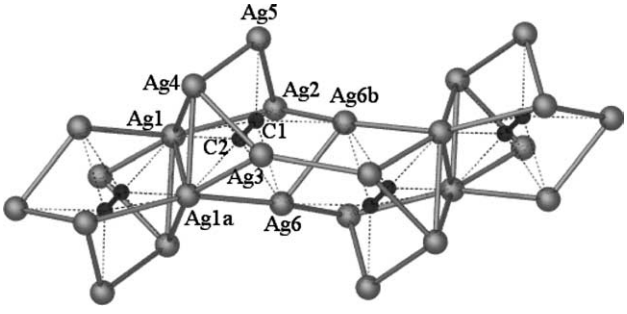


Fig. 5. Portion of an infinite column in **3** generated from edge-sharing of $C_2@Ag_8$ single cages. Symmetry code: (a) $-x+1, -y, -z+1$ (b) $-x+1, y, 0.5-z$. Selected bond lengths (Å): C1–C2 1.217(7), C2–Ag1a 2.268(5), C1–Ag1 2.571(5), C2–Ag1 2.640(5), C1–Ag2 2.122(5), C2–Ag3 2.187(5), C2–Ag4 2.243(5), C1–Ag5 2.368(5), C2–Ag6 2.441(5), C1–Ag6 2.500(5), C1–Ag6b 2.566(5).

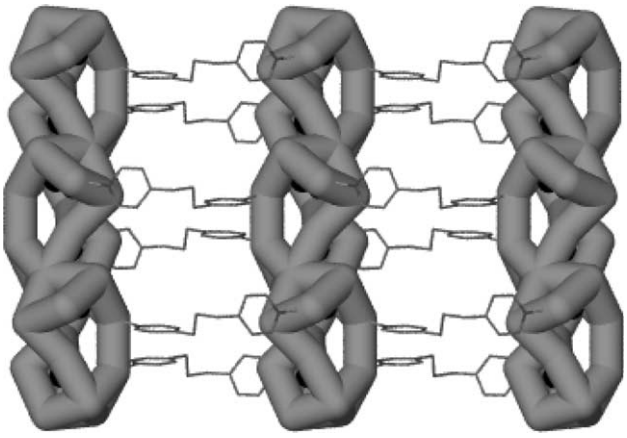


Fig. 6. Two-dimensional network of **3** constructed from bpp bridging of silver(I) columns. Trifluoroacetate ligands have been omitted for clarity.

Two single cages are fused together via sharing of the vertex Ag1, together with further connections of the types Ag3–Ag7a and Ag3a–Ag7, to form a centrosymmetric double cage AA′. An infinite silver column is generated in the sequence AA′AA′··· parallel to the *c* direction via vertex-sharing at Ag5 (Fig. 7).

One terminal of the bpp ligand is protonated and the other coordinated to a silver atom of type Ag7, and such ligation results in the attachment of cationic branches to the silver backbone. As in the case of **3**, the flexible bpp ligands adopt the TG conformation (Fig. 8).

3.5. $[Ag_6(C_2)(CF_3CO_2)_5(bppH)]_n$ (**5**)

Complex **5** is virtually iso-structural to **4**, featuring the same $C_2@Ag_7$ cage and branched-tree architecture. In **5**, atom sets Ag1Ag2Ag3 and Ag4Ag5Ag3a constitute the two trigonal faces of a distorted monocapped trigonal prism, making a dihedral angle of 6.6°, with Ag6 caps the Ag4Ag5Ag3a face. The trapped C_2^{2-} dianion coordinated to the silver(I) vertices with mixed σ/π interaction in the range 2.13(1)–2.64(1) Å.

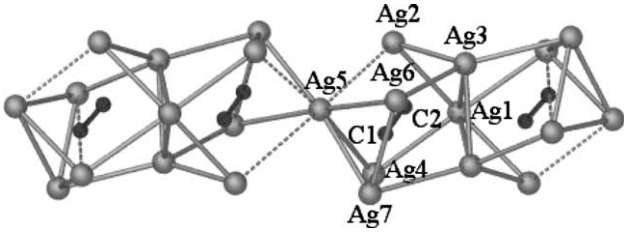


Fig. 7. Portion of an infinite column in **4** generated from vertex- and face-sharing of $C_2@Ag_7$ cages in the shape of a distorted monocapped trigonal prism.

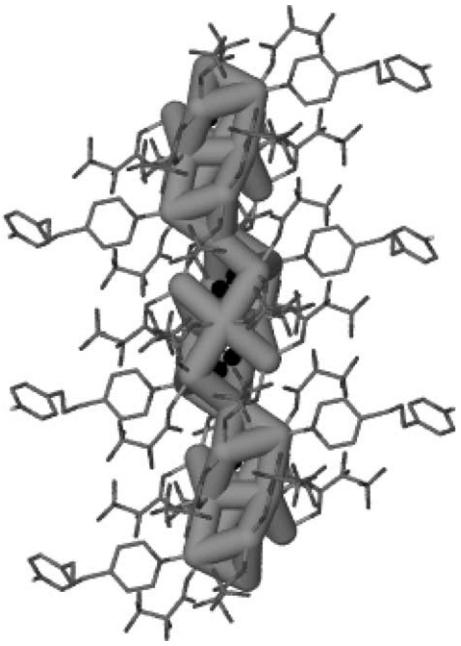


Fig. 8. Infinite branched-tree architecture in **4** generated from the attachment of protonated bpp ligands to the silver(I) backbone.

The silver(I) cages are fused together via sharing of vertex Ag3a, with further connections of Ag1–Ag5a, Ag4–Ag5a and Ag4–Ag6a, to form an infinite column, as shown in Fig. 9.

One terminal of the bpp ligand is protonated and the other is coordinated to a silver atom of type Ag2 (N2–Ag2 2.14(1) Å), and such ligation results in the attachment of cationic branches to the silver backbone, which resembles that found in **4**.

3.6. $[Ag_{23}(C_2)_4(CF_3CO_2)_{15}(bpp)_6]\cdot H_2O$ (**6**)

The basic building block in **6** is an unusual example of a silver(I) column composed of four consecutive

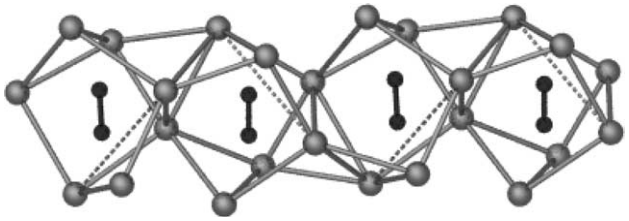


Fig. 9. Portion of an infinite column in **5** generated from edge-sharing of $C_2@Ag_7$ single cages in the shape of a distorted monocapped trigonal prism. Symmetry code: (a) $x, -y + 1/2, z + 1/2$ (b) $x, y, z + 1$.

$C_2@Ag_n$ cages fused in a row. The specific geometries of each polyhedron are shown in Fig. 10. Cage **A** takes the shape of a distorted monocapped trigonal prism, with atom sets Ag3Ag4Ag5 and Ag1Ag2Ag21b constituting the triangular face, making a dihedral angle of 9.2°. The rectangular face Ag3Ag4Ag21bAg1 (mean atomic deviation 0.06 Å) is capped by Ag6 lying about 2.3 Å above it. Cage **D** is best described as an irregular monocapped trigonal antiprism, in which Ag21Ag22Ag23 and Ag17Ag19Ag20 constitute two trigonal faces at a dihedral angle of 14.7°. Atom Ag2a caps the irregular face Ag19Ag20Ag21Ag23. Cages **B** and **C** are essentially distorted triangular dodecahedra. For **B**, atom sets Ag11Ag12Ag13Ag3 and Ag7Ag8Ag9Ag10 are each coplanar within 0.26 and 0.21 Å, respectively, making a dihedral angle of 87.5°. For **C**, atom sets Ag7Ag16Ag17Ag18 and Ag12Ag13Ag14Ag15 are each coplanar within 0.23 and 0.09 Å, respectively, making a dihedral angle of 89.3°. This sequence of four fused polyhedra is repeated by the *c* translation to form an infinite column with embedded C_2^{2-} along its stem. The bpp ligands, which take the TG configuration, all function as μ_2-bridges to connect the silver(I) columns into a two-dimensional architecture, as shown in Fig. 11.

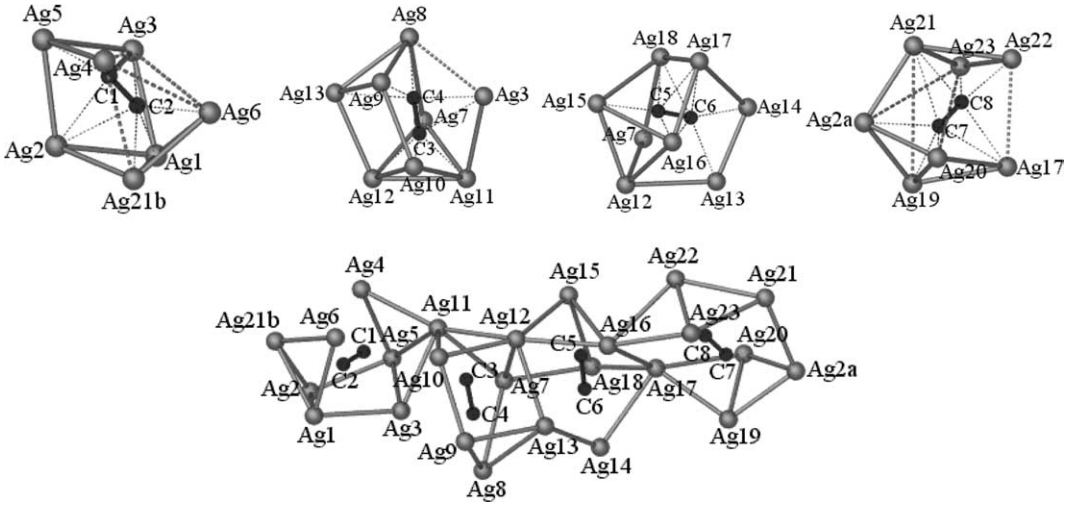


Fig. 10. Cages **A** and **D** (distorted monocapped trigonal prisms), **B** and **C** (distorted triangular dodecaheda), fused to form the building block in **6**.



Fig. 11. Two-dimensional architecture of **6** generated from bpp-bridged silver(I) columns.

4. Conclusion

We have shown that a variety of discrete and higher-dimensional supramolecular structures can be constructed by linking $C_2@Ag_n$ polyhedra with 4,4′-bipyridine or bis(4-pyridyl)propane. The present findings, together with our previous reports [4,5,14,15], provide some insight into the expected geometry of cage motifs in silver(I) double/multiple salts. In general, the generation of a higher-dimensional architecture tends to favor the appearance of distorted polyhedral cages, as exemplified by complexes **1** and **2**. In the presence of ancillary ligands that have significantly lower affinity than the acetylenediide and perfluorocarboxylate anions for coordination to silver(I) atoms, regular cage motifs can often be harvested. This work opens the gate to further investigations of the influence of diverse types of bridging ligands on the assembly of $C_2@Ag_n$ cages.

Acknowledgement

This work is supported by the Hong Kong Research Grants Council (CERG Ref. No. CUHK 401704).

Appendix A. Supplementary materials

Crystallographic data for the crystal structures reported in this paper have been deposited with the Cambridge Crystallographic Data Centre (CCDC Nos. 258256–258261). This material can be obtained free of charge from the Director, CCDC, 12 Union Road, Cambridge CB2 1EZ, UK (fax: +44 1223 336 033; e-mail: deposit@ccdc.cam.ac.uk or http://www.ccdc.cam.ac.uk). Supplementary data associated with this article can be found, in the online version at doi:10.1016/j.poly.2005.03.005.

References

[1] (a) R. Murugavel, M.G. Walawalkar, M. Dan, H.W. Roesky, C.N.R. Rao, Acc. Chem. Res. 37 (2004) 763;
(b) R. Ruiz, J. Faus, F. Lloret, M. Julve, Y. Journaux, Coord. Chem. Rev. 193–195 (1999) 1069;
(c) A.J. Blake, N.R. Champness, P. Hubberstey, W.-S. Li, M.A. Withersby, M. Schroder, Coord. Chem. Rev. 183 (1999) 117;
(d) P.J. Stang, B. Olenyuk, Acc. Chem. Res. 30 (1997) 502.
[2] C. Benelli, A.J. Blake, E.K. Brechin, S.J. Coles, A. Graham, S.G. Harris, S. Meier, A. Parkin, S. Parsons, A.M. Seddon, R.E.P. Winpenny, Chem. Eur. J. 6 (2000) 883.
[3] (a) M.P. Berthelot, Ann. (1866) 245;
(b) N.R. Thompson, in: J.C. BailarJr., H.J. Emeléus, T. Nyholm, A.F. Trotman-Dickenson (Eds.), Comprehensive Inorganic Chemistry, vol. 3, Pergamon Press, Oxford, 1973, p. 102;
(c) J.A. Shaw, E. Fisher, J. Am. Chem. Soc. 68 (1946) 2745;
(d) R. Vestin, E. Ralf, Acta Chem. Scand. 3 (1949) 101;
(e) A.D. Redhouse, P. Woodward, Acta Crystallogr. 17 (1964) 616.
[4] (a) G.-C. Guo, G.-D. Zhou, T.C.W. Mak, J. Am. Chem. Soc. 121 (1999) 3136;
(b) G.-C. Guo, G.-D. Zhou, Q.-G. Wang, T.C.W. Mak, Angew. Chem., Int. Ed. 37 (1998) 630;
(c) G.-C. Guo, Q.-G. Wang, G.-D. Zhou, T.C.W. Mak, Chem. Commun. (1998) 339.
[5] M.I. Bruce, P.J. Low, Adv. Organomet. Chem. 50 (2004) 399, 443.
[6] (a) H.W Roesky, M. Andruh, Coord. Chem. Rev. 236 (2003) 91;
(b) T.J.J. Kinnunen, M. Haukka, E. Pesonen, T.A. Pakkanen, J. Organomet. Chem. 655 (2002) 31;
(c) O.M. Yaghi, H. Li, C. Davis, D. Richardson, T.L. Groy, Acc. Chem. Res. 31 (1998) 474;
(d) D. Maspoch, R.-M. Daniel, K. Wurst, C. Rovira, J. Veciana, Chem. Commun. (2004) 1164;
(e) W.S. Han, S.W. Lee, Dalton Trans. (2004) 1656;
(f) S. Mukhopadhyay, P.B. Chatterjee, D. Mandal, G. Mostafa, A. Caneschi, S.J. Van, T.J.R. Weakley, M. Chaudhury, Inorg. Chem. 43 (2004) 413;
(g) L. Carlucci, G. Ciani, D.M. Proserpio, S. Rizzato, CrystEngComm. 4 (2002) 121;
(h) L. Pan, E.B. Woodlock, X.-T. Wang, K.-C. Lam, A.L. Rheingold, Chem. Commun. (2001) 1762;
(i) F.M. Tabellion, S.R. Seidel, A.M. Arif, P.J. Stang, J. Am. Chem. Soc. 123 (2001) 11982;
(j) C. Janiak, Dalton Trans. (2003) 2781;
(k) S.-L. Zhang, M.-L. Tong, X.-M. Chen, Coord. Chem. Rev. 246 (2003) 185;
(l) M. Munakata, L.P. Wu, T. Kuroda-Sowa, Adv. Inorg. Chem. 46 (1999) 173.
[7] (a) Z.-M. Sun, J.-G. Mao, Y.-Q. Sun, H.-Y. Zeng, A. Clearfield, Inorg. Chem. 43 (2004) 336;
(b) L.-H. Huang, H.-M. Kao, K.-H. Lii, Inorg. Chem. 41 (2002) 2936;
(c) C.-H. Huang, L.-H. Huang, K.-H. Lii, Inorg. Chem. 40 (2001) 2625;
(d) C.-Y. Chen, F.-R. Lo, H.-M. Kao, K.-H. Lii, Chem. Commun. (2000) 1061;
(e) C.V.K. Sharma, R.D. Rogers, Chem. Commun. (1999) 83.

[8] D.K. Breitinger, W.A. Herrmann (Eds.), Synthetic Methods of Organometallic and Inorganic Chemistry, vol. 5, Thieme, Stuttgart, 1999, pp. 38–39.
[9] Bruker, SMART-5.0 and SAINT-4.0 for Windows NT: Area Detector Control and Integration Software, Burker Analytical X-ray Systems Inc., Madison, WI, 1998.
[10] G.M. Sheldrick, SADABS: Program for Empirical Absorption Correction of Area Detector Data, University of Göttingen, Göttingen, Germany, 1996.
[11] G.M. Sheldrick, SHELXTL-5.1 for Windows NT: Structure Determination Software Programs, Bruker Analytical X-ray Systems, Inc., Madison, WI, 1997.
[12] (a) M. Munakata, L.P. Wu, G.L. Ning, Coord. Chem. Rev. 198 (2000) 171;
(b) M. Munakata, L.P. Wu, T. Kuroda-Sowa, M. Maekawa, Y. Suenaga, G.L. Ning, T. Kojima, J. Am. Chem. Soc. 120 (1998) 8610;
(c) M. Wen, M. Maekawa, M. Munakata, Y. Suenaga, T. Kuroda-Sowa, Inorg. Chim. Acta 338 (2002) 111;
(d) M. Wen, M. Munakata, Y. Suenaga, T. Kuroda-Sowa, M. Maekawa, Inorg. Chim. Acta 332 (2002) 18;
(e) M. Munakata, S.Q. Liu, H. Konaka, T. Kuroda-Sowa, Y. Suenaga, M. Maekawa, H. Nakagawa, Y. Yamazaki, Inorg. Chem. 43 (2004) 633.
[13] S. Sailaja, M.V. Rajasekharan, Inorg. chem. 42 (2003) 5675.
[14] X.-L. Zhao, Q.-M. Wang, T.C.W. Mak, Inorg. Chem. 42 (2003) 7872.
[15] (a) X.-L. Zhao, T.C.W. Mak, Dalton Trans. (2004) 3212;
(b) Q.-M. Wang, T.C.W. Mak, Inorg. Chem. 42 (2003) 1637.
[16] (a) E.-Q. Gao, Z.-M. Wang, C.-S. Liao, C.-H. Yan, New J. Chem. 26 (2002) 1096;
(b) L. Carlucci, G. Ciani, D.W.V. Gudenberg, D.M. Proserpio, Inorg. Chem. 36 (1997) 3812;
(c) B. Rather, M.J. Zaworotko, Chem. Commun. (2003) 830.

bioactivity. In this context, a broad array of medicinal applications of metal complexes has been investigated and several recent reviews summarize advances in this field [7–12]. Previous studies have been carried out on the chemotherapeutic and anti-microbial activity of a limited number of metal-coumarin complexes. Kumar et al. [13,14] synthesised a number of hydroxy-substituted coumarin transition metal complexes, which included a series of complexes of hydroxynitrocoumarins, hydroxyaminocoumarins, 4-hydroxy-3-phenylazocoumarin and 8-acetyl-4-methylumbelliferone. The complexes were tested for their antifungal ability using *Rhizoctonia solani* (causative organism for sheath blight in rice plants) and also against the bacterial strain *Escherichia coli*. Their results demonstrated that metal complexes displayed greater inhibition of microbial growth than free ligands and, furthermore, activity was comparable to that of the commercial bactericide, Agrimycin-100. Kostova et al. [15–20] have carried out a series of studies on the cytotoxicity of lanthanide and zirconium complexes of hydroxylated coumarins and reported IC_{50} values of 50–300 μM for the neodymium complexes of bis-coumarins when screened using HL-60, Hl-60/Dox and SKW-3 cell lines. A recent study by Nath et al. [21] has shown that triorganotin(IV) derivatives of 7-hydroxycoumarin, and their adducts with 1,10-phenanthroline (phen), have potent anti-inflammatory activity.

We have previously studied the chemotherapeutic potential of a series of metal-free hydroxynitrocoumarins [22–27]. These compounds were tested against both normal human and neoplastic skin cell lines and were found to be selectively cytotoxic to human skin malignant melanocytes and renal cell carcinoma. An earlier study had found that 7-hydroxy-8-nitrocoumarin was cytotoxic to a panel of cell lines including K562 (human erythroleukemic), HL-60 (human promyelocytic) and CHrC5 (Chinese hamster ovary) [28]. It was thought that the biological activity exhibited by the compounds could be increased by their coordination to a metal centre and a study to investigate this proposal is currently underway. However, a tandem study on the antimicrobial activity of a series of these metal complexes was carried out given the results obtained by Kumar et al. [13,14] on related coumarin complexes.

The present paper details the synthesis of a Cu(II) and a number of Ag(I) hydroxynitrocoumarin complexes and their subsequent in vitro screening against a range of Gram positive and Gram negative bacterial strains and also against a clinical isolate of *Candida albicans*. In addition, a silver(I) complex containing hydroxynitrocoumarin and phen ligands also isolated and its anti-microbial activity was investigated.

2. Experimental

2.1. Chemistry

Chemicals and solvents were purchased from Sigma–Aldrich Co. (Dorset, UK), with the exception of 4-methyl-7-hydroxy-8-nitro-chomen-*2*-one (hmncH) which was obtained from Lancaster (Lancashire, UK) and used without further purification. Infrared spectra of solids (in a KBr matrix) were recorded in the region 4000–400 cm^{-1} on a Nicolet Impact 410 Fourier-Transform Infrared spectrophotometer. A JEOL JNM-LA300 FT-NMR spectrometer was used to record ^1H NMR spectra (−5 to 15 ppm from TMS) and ^{13}C NMR spectra (−33 to 233 ppm from TMS) as solutions in d^6-DMSO. Microanalytical data were provided by the Microanalytical Laboratory, National University of Ireland, Belfield, Dublin 4. Solid state magnetic susceptibility measurements were carried out at room temperature in the Dublin Institute of Technology, Cathal Brugha Street, Dublin 1, using a Johnson Matthey Magnetic Susceptibility Balance with $[HgCo(SCN)_4]$ being used as a reference standard.

2.1.1. $[Cu(hnc)_2(H_2O)_2]\cdot 2H_2O$ (*1*)

A solution of $CuCl_2\cdot 2H_2O$ (0.082 g, 0.48 mmol) in water (10 cm^3) was added to a solution of NaOH (0.04 g, 0.97 mmol) and 4-hydroxy-3-nitro-*2H*-chromen-2-one (hncH) (0.20 g, 0.97 mmol) in water (10 cm^3) and the mixture left to stir for 2 h. After standing for 2 days, a green product precipitated which was filtered off, washed with cold water and methanol and then dried in a vacuum oven at 40 °C. The solid was recrystallised from water. Yield: 0.20 g (81%). The complex was soluble in DMSO, and sparingly soluble in ethanol, methanol and water. *Anal.* Calc. C, 42.24; H, 2.32; N, 5.47; Cu, 12.77. Found: C, 43.04; H, 2.08; N, 5.27; Cu, 12.46%. IR (KBr): 3471, 3447, 2950, 1686, 1671, 1613, 1552, 1467, 1376, 1343, 1281, 1261, 1212 cm^{-1}. μ_{eff} = 2.01 BM.

2.1.2. $[Ag(hnc)]$ (*2*)

A solution of $AgNO_3$ (0.164 g, 0.96 mmol) in water (10 cm^3) was added to a solution of NaOH (0.04 g, 0.97 mmol) and hncH (0.20 g, 0.97 mmol) in water (10 cm^3) and the mixture left to stir for 2 h. Upon standing a yellow precipitate formed, which was filtered off, washed with methanol and cold water and then dried under vacuum at 40 °C. The solid was recrystallised from water. Yield: 0.14 g (46%). The complex was soluble in DMSO, and sparingly soluble in methanol, ethanol and water. *Anal.* Calc. C, 34.42; H, 1.28; N, 4.46%. Found: C, 34.33; H, 1.16; N, 4.28%. ^1H NMR: Ar–H5 (7.88 ppm, 1H, ddd, J = 7.88, 1.83, 0.36 Hz), Ar–H6 (7.22 ppm, 1H, brd, J = 7.53 Hz), Ar–H7 (7.51 ppm,

1H, dt, $J = 8.61$, 7.5, 1.83 Hz) Ar–H8 (7.17 ppm, 1H, ddd, $J = 8.82$, 1.11, 0.36 Hz); ^{13}C NMR: C2, 167.6; C3, 120.47; C4, 152.44; C4a, 122.29; C5, 125.59; C6, 122.89; C7, 132.08; C8, 116.02; C8a, 157.58 ppm. IR (KBr): 1687, 1610, 1584, 1462, 1434, 1347, 1308, 1286 cm^{-1}.

*2.1.3. [Ag(hmnc)] (**3**)*

A solution of $AgNO_3$ (0.169 g, 0.995 mmol) in water (10 cm^3) was added over a period of 10 min to a solution of NaOH (0.04 g, 0.97 mmol) and hmncH (0.20 g, 0.90 mmol) in water (10 cm^3) at room temperature. A brown/red solid immediately precipitated and the resulting suspension was left to stir for 1 h. The solid was filtered off, washed with cold water and dried under vacuum at 40°C. Yield: 0.180 g (61%). The complex was soluble in DMSO and insoluble in all other common solvents. *Anal.* Calc. C, 36.16; H, 1.84; N, 4.27. Found: C, 37.08; H, 1.80; N, 4.15%. ^1H NMR: CH_3 (2.3 ppm, 3H, d, $J = 0.7$ Hz), Vinyl–H, (5.7 ppm, 1H, d, $J = 0.7$ Hz), Ar–H5 (6.3-7.3 ppm, 1H, d, $J = 9.3$ Hz), Ar–H6 (6.33 ppm, 1H, d, $J = 9.3$ Hz) ^{13}C NMR: C2, 166.44; C3, 103.0; C4, 159.81; C4a, 102.38; C5, 125.9; C6, 120.3; C7, 154.48; C8, 130; C8a, 148.21; CH_3, 18 ppm. IR (KBr): 3412, 1719, 1617, 1588, 1541, 1506, 1420, 1369, 1329, 1276 cm^{-1}.

*2.1.4. [Ag(phen)$_2$hnc] (**4**)*

A solution of $AgNO_3$ (0.123 g, 0.72 mmol) in water (10 cm^3) was added to a solution of phen (0.131 g, 0.72 mmol) in ethanol (10 cm^3) giving an immediate yellow precipitate. This suspension was then added to a solution comprising hncH (0.15 g, 0.72 mmol) and NaOH (0.029 g, 0.72 mmol) in water (10 cm^3) over a 10 min period at room temperature. The mixture was then refluxed for 1 h and the resulting yellow solid was filtered off, washed with cold water and dried under vacuum at 40 °C. Yield: 0.180 g (74%). The complex was soluble in DMSO, methanol and ethanol and sparingly soluble in water. *Anal.* Calc. C, 58.7; H, 2.98; N, 10.38. Found: C, 57.7; H, 2.94; N, 9.96%. ^1H NMR: Phen–H H2, (9.17 ppm, 4H, dd, $J = 4.6$, 1.6 Hz), H3, (8.01 ppm, 4H, dd, $J = 4.6$, 8.2 Hz), H4, (8.78 ppm, 4H, dd, $J = 1.6$, 8.3 Hz) H5 (8.22 ppm, 4H, s) hnc protons Ar–H5 (7.86 ppm, 1H, ddd, $J = 7.7$, 1.8, 0.4 Hz) Ar–H6 (7.20 ppm, 1H, dt, $J = 7.7$, 1.11 Hz) Ar–H7 (7.49 ppm, 1H, dt, $J = 8.61$, 1.7 Hz), Ar–H8 (7.47 ppm, 1H, dd, $J = 8.6$, 1.1 Hz) IR (KBr): 3442, 1685, 1619, 1570, 1509, 1462, 1421, 1297, 1208 cm^{-1}.

2.2. Antifungal susceptibility testing

A clinical isolate of *C. albicans* ATCC 10231 was obtained from American Type Culture Collection (Maryland, USA). Antifungal susceptibility testing was performed using broth microdilution assays according to the National Committee for Clinical Laboratory standards (Document M27-A2) protocol with slight modifications. M27-A2 method was altered by substituting Antibiotic Medium 3 (Oxoid Ltd.) for RPMI 1640 medium. Using this method minimum inhibitory concentrations (MICs) were determined by UV spectrophotometer at 405 nm by comparing the turbidity of growth in each well. MIC_{80} is defined as the lowest concentration of drug that inhibits growth by 80%.

2.3. Anti-microbial testing

All bacterial isolates were obtained from clinical samples: *Staphylococcus aureus* (urinary track infection), methicillin-resistant *S. aureus* (wound infection), *Staphylococcus simulans* (facial skin), *Micrococcus luteus* (facial skin) *E. coli* (gastro-intestinal tract), *Bacillus oleronius* (facial skin), *Pantoea agglumerans* (facial skin). The Gram-positive strains used were *S. aureus* (SA), *methycillin-resistant S. aureus* (MRSA), *S. simulans* (S.Sim.) and *M. luteus* (Ml) and the Gram negative strains were *E. coli* (E.Coli), *B. oleronius* (BO) and *P. agglumerans* (PA).

The coumarin complexes were tested against four Gram positive and three Gram negative strains to determine their antibacterial activity. Bacterial strains were grown overnight in nutrient broth medium at 30 °C and 200 rpm in an orbital incubator. The absorbance of these cultures was measured at 660 nm and cultures were diluted to an optical density of 0.1. The cell suspension (100 μl) was added to the wells of a 96 well plate containing novel coumarin derivative dissolved in nutrient broth medium in serial dilutions from 100 to 0.25 μg/ml. Plates were incubated at 30 °C for 24 h and the optical density was measured spectrophotometrically (Dynex Technology) at 660 nm.

3. Results and discussion

3.1. Complex synthesis and spectral characterisation

$[Cu(hnc)_2(H_2O)_2] \cdot 2H_2O$ (**1**) and [Ag(hnc)] (**2**) were prepared in aqueous solution by deprotonating the hydroxy group of hncH with NaOH and then adding copper(II) chloride dihydrate and silver(I) nitrate, respectively. [Ag(hmnc)] (**3**) was synthesised in a similar manner. The mixed-ligand Ag(I) complex [Ag(phen)$_2$hnc] (**4**) was prepared by treating silver(I) nitrate with phen (1:1) and subsequent reaction with a solution containing hncH and NaOH.

The infrared spectra of the complexes and free ligands were recorded in KBr matrix. The most significant changes in absorption frequencies between the

free and coordinated ligands are the $\nu_{asym}(NO_2)$ stretch of the nitro group, the ν(C=O) and ν(C–O) stretches of the lactone (in hncH), and the phenoxy alcohol ν(O–H) stretch (in hmncH). The values for the ν_{asym} nitro for all of the complexes (ca. 1580 cm^{-1}), when compared with that of the free ligand (ca. 1535 cm^{-1}), have all increased, but the effect on ν_{sym} nitro is more difficult to determine as there are many overlapping bands in this region. The ν_{C-O} stretch of the alcohol on both the lactone (in hncH) and the phenoxy (in hmncH) rings also decreased by 80–100 cm^{-1} upon formation of the complexes. Both of these shifts would be consistent with bonding to the metal being through the nitro and hydroxyl/phenoxy oxygen groups, to form a 6-membered chelate ring. There was also a significant shift in the $\nu_{C=O}$ bond, which lowers by ca. 60 cm^{-1} upon complexation for the hncH complexes but hardly at all for the hmncH complex. This is not too surprising,as in the hncH complexes the carbonyl is located on the same lactone ring as the ligand binding site. Such a large shift in $\nu_{C=O}$ in similar complexes has been taken as evidence that complexation occurs through the carbonyl oxygen atom [15–20]. It has recently been shown that, in the case of 7-hydroxy-4-methylcoumarin complexes of Na^+, Cu^+ and H^+, where bonding is through the phenolate anion, coordination to the cation induced polarisation on the lactone ring and resulted in significant shifts in the carbonyl stretching frequency [31]. In the mixed-ligand species **4** distinctive bands for the phen ligand were evident at 1421, 853 and 738 cm^{-1}.

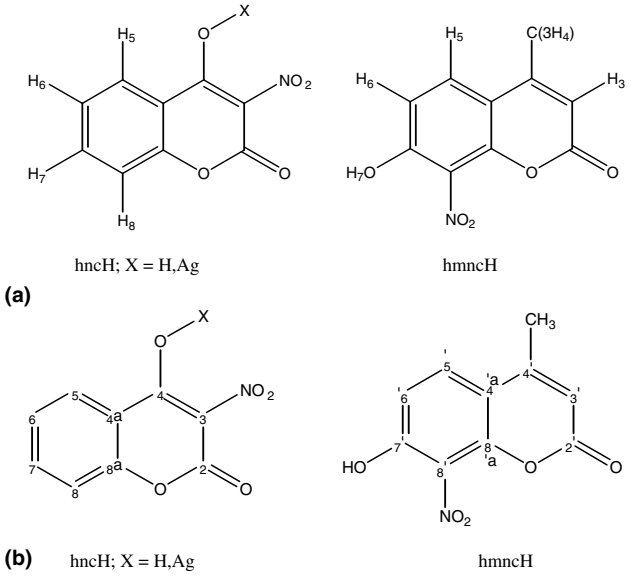


Fig. 1. Structures of the hncH and hmncH ligands used in this study showing atom numbering used in (a) ^{1}H NMR spectral assignments and (b) ^{13}C NMR spectral assignments.

The ^{1}H NMR solution spectra of the Ag(I) complexes show resonance shifts for all of the complexes relative to the uncoordinated ligand (see Fig. 1 for atom numbering). For the hncH complexes, coordination through the nitro and phenoxy oxygen atoms of the lactone ring results in upfield shifts of between 0.03 and 0.06 ppm for the protons on the fused aromatic ring, particularly so for the mixed hncH–phen complex **4**. Also of note is the disappearance of the exchangeable hydrogen peak for the now deprotonated and coordinated hydroxy oxygen atom of the complexed ligands. The ^{13}C NMR spectra show that the carbon atoms on the lactone ring which is attached to the nitro groups experience the most significant downfield shift (ca. 40 ppm) upon coordination of the Ag(I) cation.

The ^{1}H NMR spectrum of the Ag(I) hmncH complex **3** shows significant downfield shifts (ca. 0.15–0.7 ppm) for all protons, particularly those on the aromatic ring, when compared to the metal-free ligand. Similar shifts were noted in the ^{13}C NMR spectrum, with the largest being for the carbon atoms attached to the hydroxy and nitro groups (−15 and +40 ppm, respectively). There was no significant shift observed for the carbonyl carbon atom upon coordination to the metal. The ^{1}H NMR spectrum of the hncH–phen complex **4** has additional signals at 9.18, 8.80, 8.05 and 8.00 ppm corresponding to the presence of the two phen ligands and the integrals confirm the 2:1 phen:coumarin ratio.

3.2. X-ray crystal structure of $[Cu(hnc)_2(H_2O)_2] \cdot 2H_2O$ (1)

The X-ray crystal structure of **1** is shown in Fig. 2. Selected bond lengths and angles are given in Table 2. Although Kumar et al. [14] had previously isolated a Cu(II) complex of hncH, their assignment of the structure isolated is quite different to that reported herein. The metal center in **1** exhibits octahedral geometry, comprising two bidentate hnc^- ligands and two monodentate water ligands. The water molecules are *trans* to one another with Cu–O (water) bond lengths of 1.9557(14) and 1.9957(13) Å to O11 and O12, respectively, and an O12–Cu–O11 bond angle of 177.76(6)°. The hnc^- ligands are coordinated to the metal via the deprotonated hydroxy group and one oxygen of the nitro group. The geometry of the ligands relative to one another is *trans*, as is the geometry of the individual binding sites relative to one another [O5–Cu–O10 179.37(5), O1–Cu–O6 176.96(5)°]. The Cu–O (hnc) bond lengths are unremarkable as they lie in a similar range to previously reported distances [32,33]. The packing structure diagram for **1** (Fig. 3), illustrates the extent of hydrogen-bonding in the gross array, with the lactone

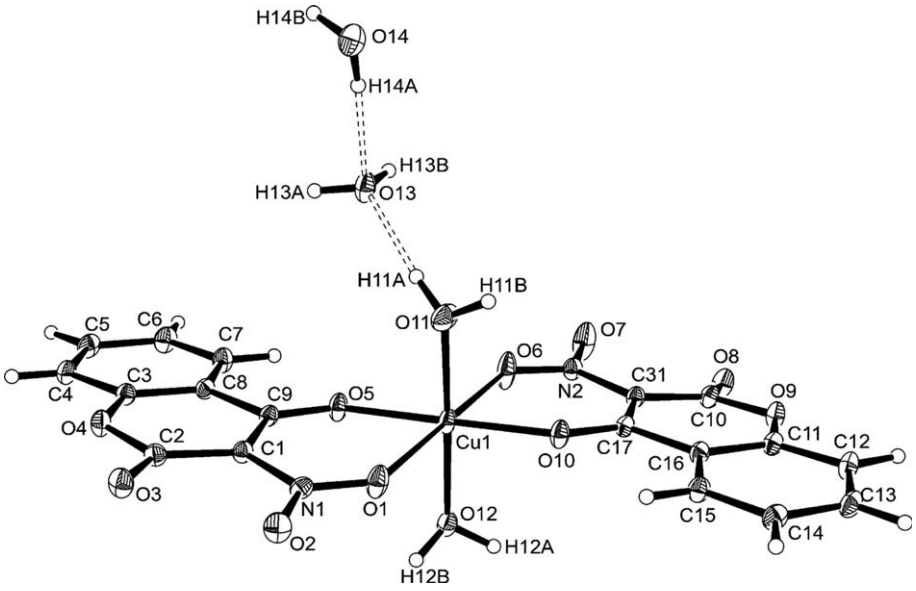


Fig. 2. Crystal structure of $[Cu(hnc)_2(H_2O)_2] \cdot 2H_2O$. Ellipsoids are represented at the 30% probability level.

Table 1
Crystal data and structure refinement for **1** and **2**

Compound	**1**	**2**
Empirical formula	$C_{18}H_{16}CuN_2O_{14}$	$C_9H_4AgNO_5$
Formula weight	547.87	314.00
Crystal system	monoclinic	monoclinic
Space group	P_1/c	P_1/c
Unit cell dimensions		
a (Å)	8.7610(1)	8.8770(1)
b (Å)	15.1230(2)	6.7120(1)
c (Å)	15.8230(2)	14.4640(2)
β (°)	103.489(1)	101.899(1)
U (Å^3)	2038.60(4)	843.28(2)
Z	4	4
D_c (g cm^{-3})	1.785	2.473
μ (mm^{-1})	1.156	2.394
F (000)	1116	608
Crystal size (mm)	$0.30 \times 0.13 \times 0.13$	$0.35 \times 0.30 \times 0.10$
θ Range for data collection (°)	3.78–30.01	4.18–30.03
Index ranges	$-12 \leqslant h \leqslant 12$; $-21 \leqslant k \leqslant 21$; $-22 \leqslant l \leqslant 22$	$-12 \leqslant h \leqslant 12$; $-9 \leqslant k \leqslant 9$; $-20 \leqslant l \leqslant 20$
Reflections collected	39853	17349
Independent reflections [R_{int}]	5916 [0.0388]	2460 [0.0477]
Reflections observed ($I > 2\sigma(I)$)	5168	2351
Absorption correction	semi-empirical from equivalents	semi-empirical from equivalents
Maximum and minimum transmission	0.90, 0.83	0.79, 0.65
Data/restraints/parameters	5916/8/349	2460/0/146
Goodness-of-fit on F^2	1.054	1.127
R_1, wR_2 [$I > 2\sigma(I)$]	0.0329, 0.0853	0.0271, 0.0708
R indices (all data)	0.0409, 0.0894	0.0299, 0.0719
Largest difference in peak and hole (e Å^{-3})	0.661, −0.560	1.071, −1.686

carbonyl and the nitro group interacting with the lattice water molecules which are, in turn, involved in hydrogen-bonding to the two ligated waters. This extensive H-bonding within the crystal could account for the observed shift in the IR carbonyl stretching frequency.

3.3. X-ray crystal structure of [Ag(4-OH-3-NO$_2$-C)] (**2**)

The X-ray crystal structure of **2** is shown in Fig. 4 and selected geometric data are given in Table 3. The complex is polymeric, with each silver having seven contacts within its coordination sphere and being bonded to four separate coumarin molecules. In particular, within the asymmetric unit there is one axial Ag–O(O1) and one equatorial Ag–O(O5) bond, at 2.5102(17) and 2.3531(16) Å, respectively. Axial metal coordination is completed by an Ag–C6 interaction (2.527(2) Å) to the coumarin moiety generated by the $1 - x$, $1/2 + y$, $1/2 - z$ symmetry operation. While this Ag–C bond is interesting, comparable interactions have been

Table 2
Selected bond lengths (Å) and angles (°) for $[Cu(hnc)_2(H_2O)_2] \cdot 2H_2O$ (**1**)

Cu(1)–O(10)	1.9300(11)	Cu(1)–O(5)	1.9304(11)
Cu(1)–O(11)	1.9557(14)	Cu(1)–O(12)	1.9957(13)
Cu(1)–O(6)	2.2764(13)	Cu(1)–O(1)	2.3254(12)
O(10)–Cu(1)–O(5)	179.37(5)	O(10)–Cu(1)–O(11)	89.42(5)
O(5)–Cu(1)–O(11)	90.23(6)	O(10)–Cu(1)–O(12)	91.51(5)
O(5)–Cu(1)–O(12)	88.86(5)	O(11)–Cu(1)–O(12)	177.76(6)
O(10)–Cu(1)–O(6)	79.51(5)	O(5)–Cu(1)–O(6)	100.00(5)
O(11)–Cu(1)–O(6)	94.54(7)	O(12)–Cu(1)–O(6)	87.63(6)
O(10)–Cu(1)–O(1)	102.40(4)	O(5)–Cu(1)–O(1)	78.11(5)
O(11)–Cu(1)–O(1)	87.86(6)	O(12)–Cu(1)–O(1)	89.95(5)
O(6)–Cu(1)–O(1)	176.96(5)		

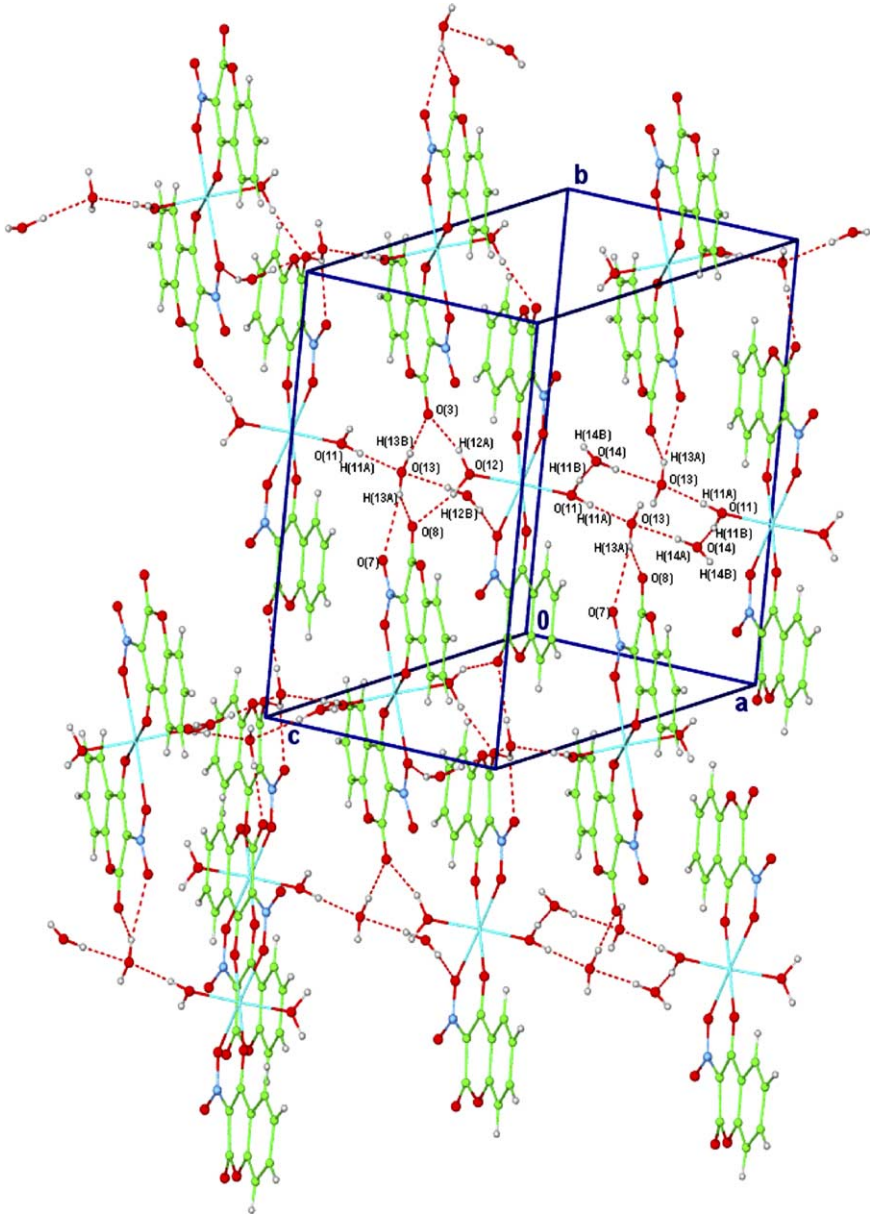


Fig. 3. Crystal packing structure of $[Cu(4\text{-hnc})_2(H_2O)_2] \cdot 2H_2O$.

previously reported for Ag(I) polycyclic aromatic complexes [39]. In the equatorial plane, each silver is also coordinated to two lactone oxygens (O3) from neighbouring molecules in the lattice. [Ag–O3[a] 2.4733(15), Ag–O3[b] 2.4970(16) Å; [a]symmetry operator $-x$, $1/2 + y$, $1/2 - z$, [b]symmetry operator x, $-1/2 - y$, $z - 1/2$]. There are also two potential longer contacts to the metal in the equatorial plane. [Ag–O2[b] 2.6784(17), Ag–O4[c], 2.7841(13) Å; [b]symmetry operator $-x$, $1/2 + y$, $z - 1/2$, [c]symmetry operator x, $-1/2 - y$, $1/2 - z$]. Bond distances for Ag–O_{OH}, Ag–$O_{C=O}$, Ag–O_{NO} and Ag–C are similar to others previously reported [34–36]. The axial bond angles of the C6‴(aryl)–Ag–O1 (nitro) (172.5°), the O5(hydroxy)-Ag–O3′(carbonyl) (72°) and O5(hydroxy)–Ag–O1(nitro) (66.8°), as well as others given in Table 3, suggests that the geometry at the metal centre is best described as a distorted pentagonal bipyramid.

3.4. Antimicrobial results

The metal-free ligands and complexes were screened for their in vitro antimicrobial activities against selected Gram positive bacteria {*S. aureus* (SA), *methicillin-resistant S. aureus* (MRSA), *S. simeoleus* (S.Sim.), *M. luteus* (Ml)} and Gram negative bacteria {*E. coli* (E.Coli), *B. olenius* (BO), *P. agglumerans* (PA)} and also against the pathogenic fungus *C. albicans* (Can). The results are presented in Table 4 as MIC_{80} values (in μM) which is the minimum concentration required to inhibit 80% of the growth of the microbe at 30 °C.

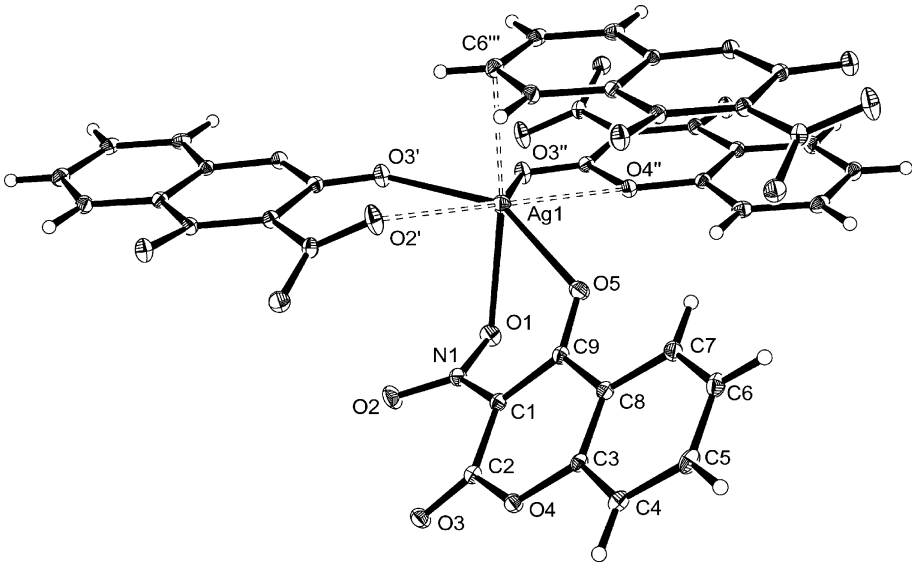


Fig. 4. Crystal structure of [Ag(4hnc)]. Ellipsoids are represented at the 30% probability level. Atoms in asymmetric unit denoted by unprimed labels. Singly, doubly and triply primed atom labels denote atoms generated via the $1 - x$, $1/2 + y$, $1/2 - z$, $-x$, $1/2 + y$, $1/2 - z$ and x, $-1/2 - y$, $-1/2 + z$ symmetry operations.

Table 3
Selected bond lengths (Å) and angles (°) for [Ag(hnc)] (**2**)

Ag(1)–O(5)	2.3531(16)	Ag(1)–O(3)#1	2.4733(15)
Ag(1)–O(3)#2	2.4970(16)	Ag(1)–O(1)	2.5102(17)
Ag(1)–C(6)#3	2.527(2)	C(6)–Ag(1)#6	2.527(2)
O(3)–Ag(1)#4	2.4733(15)	O(3)–Ag(1)#5	2.4970(16)
O(5)–Ag(1)–O(3)#1	148.98(5)	O(5)–Ag(1)–O(3)#2	123.85(6)
O(3)#1–Ag(1)–O(3)#2	71.79(6)	O(5)–Ag(1)–O(1)	66.80(5)
O(3)#1–Ag(1)–O(1)	89.93(5)	O(3)#2–Ag(1)–O(1)	86.43(5)
O(5)–Ag(1)–C(6)#3	117.14(6)	O(3)#1–Ag(1)–C(6)#3	83.99(6)
O(3)#2–Ag(1)–C(6)#3	95.79(7)	O(1)–Ag(1)–C(6)#3	172.50(6)
		Ag(1)#4–O(3)–Ag(1)#5	108.21(6)

Table 4
Antimicrobial activity given as the concentration of compound required to inhibit cell growth by 80% [MIC_{80} (μM)]

Compound	SA	MRSA	S.Sim	Ml	E.Coli	BO	PA	*C. albicans* 10231
HncH	>500	>500	>500	>500	>500	>500	>500	>500
HmnH	>500	>500	>500	>500	>500	>500	>500	>500
1,10-Phen	23.9	14.7	20	29.8	>500	>500	41.4	15
$Cu(ClO_4)_2 \cdot 6H_2O$	>500	>500	>500	>500	>500	>500	>500	>500
$AgNO_3$	69.4	124.1	16.9	64.6	69.5	31.4	67.7	66.8
1	>500	>500	>500	>500	>500	>500	>500	>500
2	143.3	114.6	124.2	70.1	41.1	82.8	117.8	219.6
3	129.3	32.6	141.1	59.4	151.6	136.9	157.4	246.6
4	32.1	2.2	16.9	16.0	44.7	16.9	15.3	4.5

The metal-free ligands, $[Cu(hnc)_2(H_2O)_2] \cdot 2H_2O$ (**1**) and the simple Cu(II) salt showed no significant antibacterial or antifungal activity. For the silver-containing samples the antimicrobial activity of the simple salt $AgNO_3$ was, almost without exception, superior to that of [Ag(hnc)] (**2**) and [Ag(hmnc)] (**3**) across all of the bacterial and the fungal species studied. However, one interesting exception to that trend was in the activity of complexes **2** and **3** against the clinically important bacterium MRSA. [Ag(hmnc)] (**3**) was approximately four times more active that $AgNO_3$ against MRSA. In general however, the phen-containing complex $[Ag(phen)_2hnc]$ (**4**) displayed the greatest inhibitory effects against all of the microbes studied, with its performances against the bacterium MRSA and the fungal isolate *C. albicans* being the most emphatic. The phen ligand itself also showed considerable activity against test strains, but complex **4** was still six times more active against MRSA and three times more active against *C. albicans*, than phen and was compara-

ble in activity to the commercially available fungicides clortrimazole and ketoconazole (MIC_{80} = 5.5 and 25 μM, respectively). We and others have reported the anti-*Candida* activity of several other phen complexes [37–39]. The activity of phen complexes is believed to be related to the abstraction by the phen ligands of metal ions present in trace amounts in the growth media, and that it is the resulting metal-phen complexes that are responsible for the high anti-*Candida* activity. The present work has shown that while the presence of phen in a complex does indeed increase the anti-*Candida* activity of the resulting complex, it is likely that the coumarin-metal moieties have a role to play as well.

4. Conclusions

The results presented here demonstrate that a number of potent anti-bacterial and antifungal agents have been synthesised. In particular, $[Ag(phen)_2hnc]$ (**4**) shows good activity against methicillin-resistant *S. aureus* (MRSA) but not against the drug susceptible variant *S. aureus*. Complex **4** is also active against *C. albicans* and is more potent than metal-free phen. Since MRSA is frequently associated with superficial infections of wounds and ulcers the ability of **4** to inhibit the growth of MRSA might indicate a possible clinical use for the complex. It is possible that the complex compound could be incorporated into an ointment or cream for topical application to the affected area to retard the development and dissemination of infection. **4** is active against *C. albicans* and compares favourably with some of the conventional anti-fungal agents, such as clortrimazole and ketoconazole. With drug-resistant strains of microbes increasing in importance in the clinical setting, these new compounds may offer alternative candidates to those compounds presently in clinical use. A study is currently under way to elucidate the mechanism of action of the most active compounds.

5. X-ray crystallography

Single crystals of **1** and **2** were analysed at 150 K using a Nonius Kappa CCD diffractometer equipped with graphite monochromated Mo Kα radiation. Details of the data collections, solutions and refinements are given in Table 1. Both structures were solved using SHELXS-97 [29] and refined using full-matrix least-squares in SHELXL-97 [30]. Convergence was uneventful, with the following points of note.

The asymmetric unit in **1** was seen to contain two molecules of water in addition to one full molecule of the copper complex. The water hydrogen atoms were all located and refined at distances of 0.89 Å from the relevant parent atoms. In **2** the asymmetric unit is comprised of one full ligand moiety, bonded in bidentate fashion to a silver atom. Both refinements were implemented using full-matrix least-squares.

Crystallographic data for **1** and **2** have been deposited with the Cambridge Crystallographic Data Centre as supplementary publications CCDC 253929 and 253930, respectively. Copies of the data can be obtained free of charge on application to CCDC, 12 Union Road, Cambridge CB2 1EZ, UK [fax: (+44) 1223 336033, e-mail: deposit@ccdc.cam.ac.uk].

References

[1] J.W. Suttie, Clin. Cardiol. 13 (VI) (1990) 16.
[2] A.H. Bedair, N.A. El-Hady, M.S. Abd El-Latif, A.H. Fakery, A.M. El-Agrody, Il Farmaco 55 (2000) 708.
[3] T. Patonay, G. Litkei, R. Bognar, J. Eredi, C. Miszti, Pharmazie 39 (1984) 86.
[4] C. Gnerre, M. Catto, F. Leonetti, P. Weber, P.A. Carrupt, C. Altomare, A. Carotti, B.J. Testa, Med. Chem. 43 (2000) 4747.
[5] D.A. Egan, P. James, D. Cooke, R. O'Kennedy, Cancer Lett. 118 (1997) 201.
[6] M. Jiménez, J.J. Mateo, R. Mateo, J. Chrom. A 870 (2000) 473.
[7] C. Xin Zhang, S. Lippard, Curr. Opin. Chem. Biol. 7 (2003) 481.
[8] H. Sakurai, Y. Kojima, Y. Yoshikawa, K. Kawabe, H. Yasui, Coord. Chem. Rev. 226 (2002) 187.
[9] P.J. Sadler, H. Li, H. Sun, Coord. Chem. Rev. 185–186 (1999) 689.
[10] H. Ali, J.E. van Lier, Chem. Rev. 99 (1999) 2379.
[11] A.Y. Louie, T.J. Meade, Chem. Rev. 99 (1999) 2711.
[12] W.A. Volkert, T.J. Hoffman, Chem. Rev. 99 (1999) 2269.
[13] B.B. Kumar, V.J. Raju, V. Ranabaore, M.C. Ganorkar, Oriental J. Chem. 3 (1987) 34.
[14] B.B. Kumar, V.J. Raju, V. Ranabaore, J. Arch. Chem. 4 (1986) 35.
[15] I. Manolov, I. Kostova, T. Netzeva, S. Konstantinov, M. Karaivanova, Arch. Pharm. Pharm. Med. Chem. 333 (2000) 93.
[16] I. Kostova, I. Manolov, I. Nicolova, N. Danchev, Il Farmaco 56 (2001) 707.
[17] I. Pencheva, I. Kostova, S. Konstantinov, E. Naidenova, M. Karaivanova, I. Manolov, Acta Pharm. 48 (1998) 127.
[18] I. Kostova, I. Manolov, G. Momekov, Eur. J. Med. Chem. 39 (2004) 765.
[19] I. Kostova, I. Manolov, I. Nicolova, S. Konstantinov, M. Karaivanova, Eur. J. Med. Chem. 36 (2001) 339.
[20] I. Kostova, I. Manolov, M. Karaivanova, Arch. Pharm.Pharm. Med. Chem. 334 (2001) 157.
[21] M. Nath, R. Jairath, G. Eng, X. Song, A. Kumar, J. Organomet. Chem. 690 (2005) 134–144.
[22] G.J. Finn, B.S. Creaven, D.A. Egan, Melan. Res. 11 (2001) 461.
[23] G.J. Finn, E. Kenealy, B.S. Creaven, D.A. Egan, Cancer Lett. 183 (2002) 61.
[24] G. Finn, B.S. Creaven, D.A. Egan, Cancer Lett. 205 (2003) 69.
[25] G. Finn, B.S. Creaven, D.A. Egan, Cancer Lett. 214 (2004) 43.
[26] G. Finn, B.S. Creaven, D.A. Egan, Biochem. Pharm. 67 (2004) 1779.
[27] G. Finn, B.S. Creaven, D.A. Egan, Eur. J. Pharm 481 (2003) 159.
[28] D. Egan, P. James, D. Cooke, R. O'Kennedy, Cancer Lett. 118 (1997) 201.
[29] G.M. Sheldrick, SHELX-86. Program for the Solution of Crystal Structures, University of Göttingen, Germany, 1986.

[30] G.M. Sheldrick, SHELX-97. Program for Crystal Structure Refinement, University of Göttingen, Germany, 1997.
[31] I. Georgieva, T. Mihaylov, G. Bauer, N. Trefafilova, Chem. Phys. 300 (2004) 119.
[32] F. Tuna, G.I. Pascu, J.P. Sutter, M. Andruh, S. Golhen, J. Guillevic, H. Pritzkow, Inorg. Chim. Acta 342 (2003) 131.
[33] A.F. Stassen, W. Driessen, J.G. Hassnoot, J. Reedijk, Inorg. Chim. Acta 350 (2003) 57.
[34] K.M. Chi, K.H. Chen, H.C. Lin, K.J. Lin, Polyhedron 16 (1997) 2147.
[35] M. Munakata, L.P. Wu, G.L. Ning, Coord. Chem. Rev. 198 (2000) 171.
[36] M. Munakata, M. Wen, Y. Suenga, T. Kuroda-Sowa, M. Maekawa, M. Anahata, Polyhedron 20 (2001) 2321.
[37] M. McCann, M. Devereux, M. Geraghty, D. O'Shea, J. Mason, L. O'Sullivan, Metal-Based Drugs 7 (2000) 185.
[38] M. McCann, B. Coyle, S. McKay, P. McCormack, K. Kavanagh, M. Devereux, V. McKee, R. O'Gorman, M. Clynes, Biometals 16 (2003) 321.
[39] I. Druta, R. Dannac, M. Ungureanu, G. Grosu, G. Drochioiu, Ann. Pharm. Fr. 60 (2003) 321.

2. Experimental

2.1. Reagents and general procedures

All manipulations were carried out under argon, using standard Schlenk techniques. Solvents were distilled from drying agents and degassed. The NMR spectra were recorded in C_6D_6 or C_7D_8 at ambient probe temperature using the following Bruker instruments: DRX 400 (^{1}H, 400.32 MHz) or Avance 300 (^{1}H, 300.13; ^{13}C, 75.5 MHz) and referenced internally to residual solvent resonances (chemical shift data in δ). ^{13}C NMR spectra were all proton-decoupled. Elemental analyses were determined by the Institute for Soil, Climate and Water, Pretoria, South Africa. The mass spectrum was recorded on a VG 70 SEQ Micromass. The following abbreviations are used throughout the experimental section: bs = broad singlet, d = doublet, dd = doublet of doublet, m = multiplet, s = singlet, t = triplet. Coupling constants (J) are given in Hz.

2.2. Synthetic procedures

2.2.1. Reaction of $LiCHR_2$ with $C_6H_3(Pr^i{}_2\text{-}2,6)NC$ in hexane

A solution of $C_6H_3(Pr^i{}_2\text{-}2,6)NC$ (0.75 g, 4.03 mmol) in hexane (25 ml) was added dropwise to a suspension of $LiCHR_2$ (0.67 g, 4.03 mmol) in hexane (30 ml) at −80 °C. The reaction mixture was allowed to warm up to room temperature and stirred for 15 h to give an orange reaction mixture. Filtration of the reaction mixture and concentration of the filtrate gave upon cooling to −60 °C orange crystals of compound **2** (0.30 g, 27%). Melting point 135 °C. Elemental *Anal.* Calc. for $C_{34}H_{24}N_2Si_2$ requires: C, 74.64; H, 9.97; N, 5.12. Found: C, 74.41; H, 9.80; N, 5.10%. Mass spectrum [*m*/*z* (%)]: 546 (11 $[M]^+$), 503 (5, $[M - Pr^i]^+$), 473 (60, $[M - SiMe_3]^+$), 385 (22, $[M - C_6H_3Pr^i{}_2]^+$). ^{1}H NMR (C_6D_6): δ 0.18 (s, $SiMe_3$, 18 H), 1.53 [d, $CHMe_2$, $^3J(^1H–^1H)$ = 6.86 Hz, 24H], 2.79 (septet, $CHMe_2$, 4H), 6.72 (s, CH, 2H), 6.94 (s, *p*-H, 2H), 7.34 (s, *m*/*o*-H, 4H). ^{13}C NMR (C_6D_6): δ −1.1 (s, $SiMe_3$), 22.6, 22.8 (s, $CHMe_2$), 28.4, 28.7 (s, $CHMe_2$), 123.2, 124.1 (Ar–C), 133.1 (s, *C*H), 134.9, 149.7 (*ipso* C), 184.9 (s, CN).

2.2.2. Reaction of [LiN(Ar)C(R)CHR] and $SnCl_2$ [Ar = $C_6H_3(Pr^i{}_2\text{-}2,6)$; R = $SiMe_3$]

Solid $SnCl_2$ (0.18 g, 0.95 mmol) was added to a solution of [LiN(Ar)C(R)CHR] (**1a**) (see Section 2.2.3) (0.69 g, 1.96 mmol) in diethyl ether (30 ml) at −30 C. The reaction mixture was allowed to warm to room temperature and stirred for 15 h. Removal of volatiles in vacuo and extraction of the residue with hexane gave orange crystals of **2** (0.30 g, 56%).

2.2.3. Synthesis of [LiN(Ar)C(R)CHR] (**1a**)

$LiCHR_2$ (0.51 g, 3.07 mmol) was dissolved in diethyl ether (30 ml). The solution was cooled to −90 °C and a solution of $C_6H_3(Pr^i{}_2\text{-}2,6)NC$ (0.57 g, 3.07 mmol) in diethyl ether (20 ml) was added drop-wise. The reaction mixture was allowed to warm to room temperature during a period of 3 h, then stirred for further 12 h to give a deep orange solution. After removing the diethyl ether in vacuo and extracting the residue with hexane, the orange solution was concentrated. After cooling the solution for a period of 2 weeks without obtaining crystals, the solvent was removed in vacuo leaving a viscous red oil (0.86 g, 79%). ^{1}H NMR spectroscopic characterisation (all lines very broad) of the oil was consistent with the formation of compound **1a**. ^{1}H NMR (C_6D_6): δ 0.37 and 0.50 (bs, $SiMe_3$, 9H), 1.36 [bs, $CHMe_2$, 12H], 3.53 (bs, $CHMe_2$, 2H), 3.85 (bs, CH, 1H) 7.14 and 7.30 (bs, Ar–H, 3H).

2.2.4. Synthesis of [LiN(Ar)C(R)CHR(thf)$_2$] (**1b**) [Ar = $C_6H_3(Pr^i{}_2\text{-}2,6)$; R = $SiMe_3$]

A solution of $C_6H_3(Pr^i{}_2\text{-}2,6)NC$ (1.07 g, 5.71 mmol) in hexane (15 ml) was added to a solution of $LiCHR_2$ (0.95 g, 5.71 mmol) in thf (20 ml) at −80 °C. The reaction mixture was allowed to warm to room temperature and was stirred for 15 h to give a deep red solution. After removing all the volatiles in vacuo and extracting the residue in hexane (25 ml) the deep red solution was filtered. Concentration and cooling of the filtrate gave red crystals of compound **1b** (1.52 g, 38%). ^{1}H NMR (C_6D_6): δ 0.10 (s, $SiMe_3$, 9H), 0.40 (s, $SiMe_3$, 9H), 1.25 [bs, CH_2(thf) and $CHMe_2$, 14H], 1.39 [d, $CHMe_2$, 6H], 3.41 (bs, OCH_2, 8H), 3.55 (bs, $CHMe_2$, 2H) 4.25 (s, CH, 1H), 7.15 [bs, Ar–H and C_6D_5H]; ^{1}H NMR (C_7D_8, 203 K, 2 isomers): δ 0.42, 0.66, 0.69, 0.75 (s, $SiMe_3$) 1.32 [bs, CH_2(thf)], 1.40 [bs, $CHMe_2$], 1.48 [d, $CHMe_2$], 1.65 [bs, $CHMe_2$], 1.82 [d, $CHMe_2$], 3.41 (bs, OCH_2), 3.76 (bs, $CHMe_2$) 3.92, 3.98 (s, CH), 7.33–7.44 [Ar–H].

2.2.5. Synthesis of [LiN(Ar)C(R)CHPh(tmen)] (**1c**) [Ar = $C_6H_3(Pr^i{}_2\text{-}2,6)$; R = $SiMe_3$]

A solution of $C_6H_3(Pr^i{}_2\text{-}2,6)NC$ (0.40 g, 2.26 mmol) in diethyl ether (15 ml) was added to a solution of LiCH(R)Ph(tmen) (0.60 g, 2.26 mmol) in diethyl ether (20 ml) at −60 °C. The reaction mixture was stirred over night in an acetone cool bath allowing it to warm up to room temperature over a period of 15 h. The solvent was then completely removed in vacuo to give a yellow solid. The product was extracted into hexane, the solution was concentrated and cooled to −20 °C yielding yellow crystals of **1c** (0.50 g, 50%). ^{1}H NMR (C_6D_6): δ 0.19 (s, $SiMe_3$, 9H), 1.28 [d, $CHMe_2$, $^3J(^1H–^1H)$ = 6.83 Hz, 6H], 1.42 [d, $CHMe_2$, $^3J(^1H–^1H)$ = 6.82 Hz, 6H], 1.51 (bs, NCH_2, 4H), 1.65, (bs, NMe_2, 12H), 3.51 (m, $CHMe_2$, 2H) 5.21 (s, CH, 1H), 7.05 [t,

$^3J(^1H–^1H)$ = 7.77 Hz, 1H], Ph hidden under solvent peak, 7.83 [d, $^3J(^1H–^1H)$ = 7.77 Hz, 2H].

2.2.6. Synthesis of [LiN(Ar)C(R)CHPh(tmen)] (1d) [Ar = $C_6H_3(Bu^t_2$-2,5); R = $SiMe_3$]

Compound **1d** was synthesised as described for **1c** from $C_6H_3(Bu^t_2$-2,5)NC (0.41 g, 1.95 mmol) and LiCH(R)Ph(tmen) (0.56 g, 1.95 mmol) in diethyl ether (30 ml) at −70 °C. Red crystals of **1d** (0.46 g, 47%) were obtained after recrystallisation from hexane at −60 °C. ^{1}H NMR (C_6D_6): δ 0.23 (s, $SiMe_3$, 9H), 1.38 (s, Bu^t, 9H), 1.58 (s, very broad, tmen, 16H), 1.76 (s, Bu^t, 9H), 5.29 (s, CH, 1H), 6.68 (s, Ph, 2H), 6.85 (dd, Ph, J = 8.23 Hz, J = 2.21 Hz, 1H), 2H hidden under solvent peak, 7.39 (d, Ph, ^3J = 8.23 Hz, 1H), 8.03 (d, Ph, ^3J = 7.70 Hz, 2H); ^{13}C NMR (C_6D_6): 2.6 (s, $SiMe_3$), 31.9, 32.0 (s, Bu^t), 34.4, 35.8 [s, CMe_3], 44.0 (bs, NMe_2), 56.0 (s, NCH_2), 98.4 (CH), 118.5, 123.0, 126.5, 129.8, 140.9, 144.6, 146.9, 153.3, 158.9, 165.7 (Ar–C), 197.6 (CN).

2.3. Crystal structure determination

Intensity data were collected on a Bruker SMART 1K CCD area detector diffractometer with graphite monochromated Mo Kα radiation (50 kV, 30 mA). The collection method involved ω-scans of width 0.3°. Data reduction was carried out using the program SAINT+ [7].

The crystal structures were solved by direct methods using SHELXTL [8]. Non-hydrogen atoms were first refined isotropically followed by anisotropic refinement by full matrix least-squares calculation based on F^2 using SHELXTL. Hydrogen atoms were located from the difference map and then positioned geometrically and allowed to ride on their respective parent atoms. Further crystallographic data are summarised in Table 1. Diagrams and publication materials were generated using SHELXTL [8], PLATON [9] and ORTEP3 [10].

3. Results and discussion

3.1. Synthesis

The lithium-1-azaallyl complexes **1** were obtained in moderate yields from the reaction of $LiCHR_2$ or LiCH(R)Ph(tmen) (R = $SiMe_3$, tmen = *N*,*N*,*N*′,*N*′-tetramethylethylendiamine) with ArNC [Ar = $C_6H_3(Pr^i_2$-2,6) or $C_6H_3(Bu^t_2$-2,5)] in the presence of polar solvents (Et_2O or thf) at low temperatures [(i) in Scheme 1]. In analogy to previous studies it is believed that the formation of the lithium-1-azaallyls involves the insertion of the lithium alkyl into the aryl isocyanide to give a lithioaldimine [ArN=C(Li)CHRR′] intermediate followed by a 1,2 trimethylsilyl shift from C → C [3a]. A variation of the reaction conditions by replacing Et_2O or thf with hexane led in the case of the reaction of $LiCHR_2$ and $C_6H_3(Pr^i_2$-2,6)NC unexpectedly to a mixture of compounds from which the diazahexatriene **2** was isolated in low yield as the only product [(ii) in Scheme 1]. The related compound, ArN=C(R)CH=CHC(R)=NAr, was recently obtained as a side-product of the synthesis of $\overline{[LiN(Ar)C(R)CHC(R)NAr]}$[R = $SiMe_3$, Ar = $C_6H_3(Bu^t_2$-2,5)] from the reaction of $LiCHR_2$ with $C_6H_3(Bu^t_2$-2,5)NC [5]. The formation of diazahexatrienes as a new class of product in the $LiCHR_2$/ArNC system is not fully understood but oxidative coupling of two 1-azaallyl anions $[ArNC(R)CHR]^-$ and the consecutive loss of two trimethylsilyl groups may be implicated. The related coupling of $[LiN(R)C(Bu^t)CHR]_2$ with iodine yielding RN=C(Bu^t) CHR–CHRC(Bu^t)=NR has been described previously [11]. Attempts to use **1a** as a ligand transfer reagent to synthesise a tin derivative of **1a** were not successful and led to the formation of **2** [(iii) in Scheme 1].

The lithium-1-azaallyls are yellow (**1c**) or red solids (**1b**, **1d**) that are highly air sensitive and very soluble in hydrocarbons. The orange diazahexatriene **2** is moderately soluble in hexane and stable in moist air.

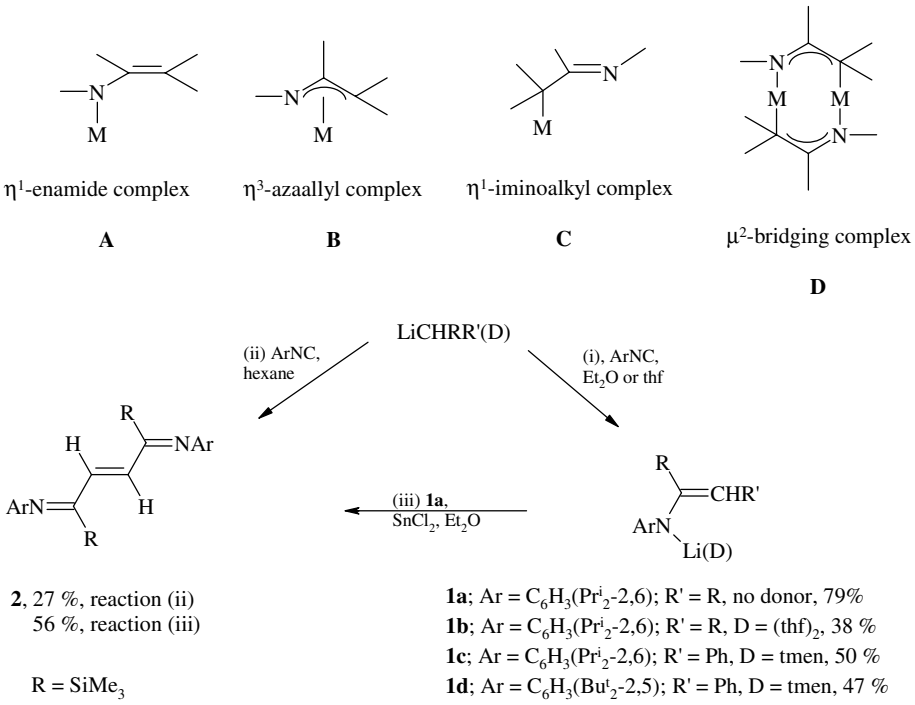
The room temperature ^{1}H NMR spectra of **1a** and to a lesser degree **1b** showed broad lines indicating the presence of a mixture of possible isomers (**A**–**C**) and/or rotamers [hindered rotation around the N–C(azaallyl) bond of the ligand]. Variable temperature ^{1}H NMR studies of a solution of **1b** in C_7D_8 demonstrated the existence of two isomers at −70 °C. The room temperature ^{1}H NMR spectra of **1c** and **1d** were in contrast well resolved showing the existence of a single isomer in solution. The characteristic signal for the 1-azaallyl proton (C*H* R) was found at δ 4.3 (**1b**) and δ 5.2 (**1c**, **1d**) indicating solution structures with considerable double bond character in the 1-azaallyl backbone best represented by **A**. Metal-1-azaallyls with solution structures similar to **B** or **C** were found to show C*H*R signals at higher field strength (δ 2.5–3.5) [3e]. The corresponding signal in **2** was found at δ 6.72 as expected for an olefinic proton and close to the previously reported value of δ 6.52 for $C_6H_3(Bu^t_2$-2,5)-N=C(R)CH=CHC(R)=N$C_6H_3(Bu^t_2$ -2,5) [5].

3.2. Structural studies

The lithium-1-azaallyls that have been crystallographically characterised in the last two decades suggest that their structures may be classified in three structural types (I–III) depending on the aggregation state and the presence or absence of additional neutral donors in the form of coordinating solvents or internal donor groups. Type I (e.g., **E**) [12] is found in the absence of donor groups leading invariably to dimeric or in the case of $[LiN(R)C(Bu^t)CH_2]_3$ [13] trimeric structures featuring a central $(LiN)_2$ or $(LiN)_3$ core that is stabilised by

Table 1
Crystal data and refinement for compounds **1**–**2**

Compound	**1b**	**1c**	**1d**	**2**
Empirical formula	$C_{28}H_{52}LiNO_2Si_2$	$C_{29}H_{48}LiN_3Si$	$C_{31}H_{52}LiN_3Si$	$C_{34}H_{54}N_2Si_2$
M	497.83	473.73	501.79	546.97
T (K)	173(2)	173(2)	173(2)	173(2)
Wavelength (Å)	0.71073	0.71073	0.71073	0.71073
Crystal system	monoclinic	orthorhombic	monoclinic	triclinic
Space group	$P2_1/c$	$Pbca$	$P2_1/n$	$P\bar{1}$
Unit cell dimensions				
a (Å)	16.1483(18)	17.745(4)	11.2209(17)	9.8746(12)
b (Å)	11.4012(12)	16.581(3)	20.612(3)	10.1468(13)
c (Å)	17.8476(19)	20.138(4)	14.974(2)	10.2891(13)
α (°)	90	90	90	65.046(2)
β (°)	103.566(2)	90	109.245(3)	86.066(2)
γ (°)	90	90	90	73.271(2)
U (Å^3)	3194.2(6)	5925(2)	3269.8(8)	856.56(19)
Z	4	8	4	1
$D_{calc.}$ (Mg/m^3)	1.035	1.062	1.019	1.060
μ (mm^{-1})	0.133	0.099	0.093	0.127
$F(000)$	1096	2080	1104	300
Crystal size (mm)	$0.40 \times 0.28 \times 0.22$	$0.40 \times 0.10 \times 0.10$	$0.46 \times 0.24 \times 0.22$	$0.40 \times 0.32 \times 0.22$
θ-Range for data collection (°)	1.30–28.30	1.96–26.00	1.75–26.00	2.24–28.30
Index ranges	$-21 \leqslant h \leqslant 20$, $-15 \leqslant k \leqslant 15$, $-12 \leqslant l \leqslant 23$	$-21 \leqslant h \leqslant 16$, $-20 \leqslant k \leqslant 20$, $-24 \leqslant l \leqslant 24$	$-13 \leqslant h \leqslant 12$, $-24 \leqslant k \leqslant 25$, $-13 \leqslant l \leqslant 18$	$-13 \leqslant h \leqslant 13$, $-13 \leqslant k \leqslant 7$, $-13 \leqslant l \leqslant 12$
Reflections collected	21995	33417	19228	6019
Independent reflections	7903 [$R_{(int)} = 0.0357$]	5814 [$R_{(int)} = 0.0629$]	6421 [$R_{(int)} = 0.0379$]	4122 [$R_{(int)} = 0.0136$]
Completeness to θ_{max} (%)	99.5	100.0	99.9	96.9
Absorption correction	none	none	none	none
Maximum and minimum transmission	0.9713 and 0.9488	0.9902 and 0.9614	0.9798 and 0.9585	0.9727 and 0.9511
Data/restraints/parameters	7903/0/317	5814/0/318	6421/0/338	4122/0/183
Goodness-of-fit on F^2	1.109	1.011	1.030	1.039
Final R indices [$I > 2\sigma(I)$]	$R_1 = 0.0522$, $wR_2 = 0.1466$	$R_1 = 0.0443$, $wR_2 = 0.1021$	$R_1 = 0.0491$, $wR_2 = 0.1193$	$R_1 = 0.0401$, $wR_2 = 0.1036$
R indices (all data)	$R_1 = 0.0962$, $wR_2 = 0.1664$	$R_1 = 0.0842$, $wR_2 = 0.1206$	$R_1 = 0.0824$, $wR_2 = 0.1342$	$R_1 = 0.0524$, $wR_2 = 0.1104$
Largest difference peak and hole (e Å^{-3})	0.774 and −0.315	0.234 and −0.237	0.639 and −0.299	0.319 and −0.215



Scheme 1. Reactions of LiCHRR′(D) with isocyanides.

additional interactions between the Li atom and the delocalised π electrons of the 1-azaallyl ligand (η^3-azaallyl, **B**). In the case of the α-picoline derivative $[C_5H_4N(CR_2Li\text{-}2)]_2$ such an arrangement would destroy the aromaticity of the pyridine ring and a bridging iminoalkyl structure (**D**) is consequently favoured [14]. Type II (e.g., **F**) [3a] is observed in the presence of a single monodentate solvent molecule (or internal donor group) giving rise to dimeric or less frequently trimeric structures. The $(LiN)_2$ or $(LiN)_3$ is typically retained but the Li···C interaction between the Li atom and the 1-azaallyl backbone is increasingly supplemented or replaced by coordination of the Li atom to the donor solvent or an internal donor group (η^1-enamide, **A**). In the case of $[LiN(R)C(Bu^t)CHR'(thf)]_2$ [R = SiMe(OMe)$_2$, R′ = SiMe$_3$ or R = R′ = SiMe$_2$OMe] [15] the $(LiN)_2$ ring is replaced by an eight-membered $\overline{LiNSiOLiNSiO}$ macrocycle. A few complexes with bidentate co-ligands also fall into this category. More frequently, however, the presence of a bidentate or two monodentate ligand results in monomeric structures of type IIIa (e.g., **G**) [4e] with strong coordination of the Lewis base (frequently N, O) to the trigonal planar Li atom that may be supplemented by further Li···C interactions to the 1-azaallyl depending on the steric and electronic properties of the substituents and the presence or absence of other groups such as Ph that can compete with the azaallyl for coordination to the Li atom. **H** [16] may serve as an example were additional coordination of the phenyl ring to the Li atom is favoured over coordination to the 1-azaallyl backbone. The unexpected type IIIa structure of $[LiN(R)C(C_6H_4Br\text{-}4)CR_2(thf)]$ (R = SiMe$_3$) [17] having only a single thf ligand is likely to be the result of steric crowding of the complex due to the presence of three bulky trimethylsilyl groups that prevent dimerisation to a type II structure. Type IIIb structures are typically found in compounds with three or more additional donor atoms leading to monomeric structures (η^1-enamide, **A**) with approximately tetrahedral coordination of the lithium atom and little interaction between lithium and the 1-azaallyl backbone. Structurally characterised lithium-1-azaallyl complexes reported in the literature are found in Table 2.

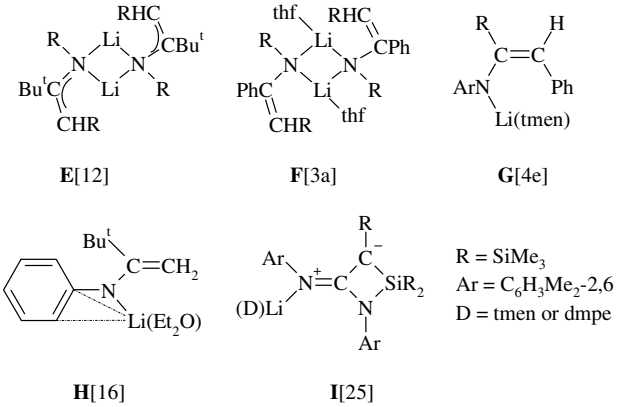


Table 2
Crystallograpically characterised lithium-1-azaallyl complexes

Compound	Type	Aggr.[a]	Donor[b]	No.[c]	Reference
$[LiN(R)C(Bu^t)CHR]_2$ (**E**)	I	2			[12]
$[LiN(R)C(Bu^t)CHCH(R)Bu^n]_2$	I	2			[3a]
$[LiN(R)C(Bu^t)CH_2]_3$	I	3			[13]
$[C_5H_4N(CR_2Li\text{-}2)]_2$	I	2			[14]
$[LiC_8H_4N(Me_2\text{-}3)(CH_2\text{-}2)(Et_2O)]$	II	2	Et_2O	1	[1b]
$[LiN(R)C(Ph)CH(R)(thf)]_2$ (**F**)	II	2	thf	1	[3a]
$[LiN(Ph)(c\text{–}C_6H_9)(NHPr^i_2)]_2$	II	2	$NHPr^i_2$	1	[3f]
$[C_5H_4N\{C(H)RLi\text{-}2\}(Et_2O)]_2$	II	2	Et_2O	1	[14]
$[C_5H_4N\{CH(R)Li\text{-}2\}(tmen)]_2$	II	2	tmen	1	[14]
$[LiN(SiMe_2OMe)C(Ph)CHR]_3$	II	3	OMe	1	[15]
$[LiN(SiMe_2OMe)C(Bu^t)CHR]_2$	II	2	OMe	1	[15]
$[LiN(Ph)C(Bu^t)CH_2(Et_2O)]_2$ (**H**)	II	2	Et_2O	1	[16]
$[LiN(SiMe_2OMe)C(Ad)CHR]_2$	II	2	OMe	1	[18]
$[LiN(H)C(Bu^t)CHPr^n$ (HMPA)$]_2$	II	2	$OP(NMe_2)_3$	1	[19]
$[C_5H_4N\{CH(SiMe_2Bu^t)Li\text{-}2\}(tmen)]_2$	II	2	tmen	2	[20]
$[C_5H_4N\{CH(Ph)Li\text{-}2\}(tmen)]_2$	II	2	tmen	2	[20]
$[C_5H_3N(CHR_2\text{-}2)\{C(R)C(Bu^t)N(R)Li\text{-}6\}]_2$	II	2	Pyr	1	[23]
$[C_5H_4N\{CHC(Bu^t)N(R)Li\text{-}2\}]_2$	II	2	Pyr	1	[28]
$[C_5H_4N\{C(R)C(Ph)N(R)Li\text{-}2\}]_2$	II	2	Pyr	1	[28]
[LiN(R)C(Ph)CH(Ph)(tmen)]	IIIa	1	tmen	2	[3a]
$[C_6H_4\{\{CHC(Bu^t)N(R)Li\}_2\text{-}1,2\}(tmen)_2]$	IIIa	1	tmen	2	[4b]
$[C_6H_4\{\{CHC(R)N(Bu^t)Li\}_2\text{-}1,3\}(tmen)_2]$	IIIa	1	tmen	2	[4b]
$[C_6H_4\{\{CHC(R)N(Bu^t)Li\}_2\text{-}1,2\}(tmen)_2]$	IIIa	1	tmen	2	[4b]
$[C_5H_4N\{CHC(Ph)N(R)\text{-}2,6\}_2Li][Li(tmen)_2]$	IIIa	1	NR, Pyr	2	[4c]
$[C_5H_4N\{\{CHC(R)N(Bu^t)Li\}_2\text{-}2,6\}(tmen)]$	IIIa	1	NBu^t, Pyr	2	[4c]
$[C_5H_4N\{\{CHC(Bu^t)N(R)Li\}_2\text{-}2,6\}(thf)_2]$	IIIa	1	NR, Pyr	2	[4c]
$[LiN(C_6H_3Me_2\text{-}2,6)C(R)CH(Ph)(tmen)]$ (**G**)	IIIa	1	tmen	2	[4e]
$[C_5H_4N(CR_2Li\text{-}2)(tmen)]$	IIIa	1	tmen	2	[14]
$[C_5H_4N(CR_2Li\text{-}2)C_5H_4N(CHR_2\text{-}2)]$	IIIa	1	$C_5H_4N(CHR_2)$	1	[14]
$[C_5H_4NCH(R)Li\text{-}2(sp)]$	IIIa	1	sparteine	2	[14]
$[LiN(R)C(C_6H_4Br\text{-}4)CR_2(thf)]$	IIIa	1	thf	1	[17]
$[LiC_6H_4NC(Ph)R\text{-}2(tmen)]$	IIIa	1	tmen	2	[20]
$[C_6H_3\{\{NCH(R)Li\}_2\text{-}2,6\}(tmen)_2]$	IIIa	1	tmen	2	[24]
Compound **I**	IIIa	1	tmen (dmpe)	2	[25]
$[(Et_2O)LiN(Pr^i)CHC(Me)CH(Ph)C\text{–}]_2$	IIIa	1	Et_2O	2	[26]
$[LiN(R)C(Bu^t)C_6H_7$ (R-3)(tmen)]	IIIa	1	tmen	2	[27]
$LiN(R)C(Bu^t)CHCHCHR(tmen)$	IIIa	1	tmen	2	[27]
$[C_5H_3N\{\{C(Me)N(Ar)Li_2\text{-}2\}_2\ \{C(CH_2)N(Ar)Li\text{-}6\}(thf)_4]$	IIIa	1	thf	2	[33]
$[LiN(SiMe_2NMe_2)C(Bu^t)CHPh(tmen)]$	IIIb	1	NMe_2, tmen	3	[21]
$[C_5H_3N\{C(CH_2)N(Ar)Li\text{-}2\}\{C(Me)NAr\text{-}6\}(thf)]$	IIIb	1	thf, NAr, Pyr	3	[22]
$[C_5H_4NC(R)C(Ph)N(R)Li\text{-}2(Et_2O)(PhCN)]$	IIIb	1	Et_2O, PhCN	3	[28]
$[LiN(H)C_5H_4N\{CH(R)\text{-}2\}(pmdeta)]$	IIIb	1	pmdeta	3	[29]
$[LiN(H)C(Me)CH(CN)(Pyr)_2]_2$	IIIb	2	CN, Pyr	3	[30]
$[C_6H_3(Bu^n\text{-}1)(C(Me)NAr\text{-}2)C(Me)N(Ar)Li\text{-}3(tmen)]$	IIIb	1	tmen, NAr	3	[31]
$[LiN\{C_6H_2(Bu^t_3\text{-}2,4,6)\}CH{=}CHPr^n(thf)_3]$	IIIb	1	thf	3	[32]

[a] Degree of aggregation.
[b] Neutral donor (solvent or internal group).
[c] Number of additional donor atoms per Li (excluding N of azaallyl).

The preference for *syn*- or *anti*-conformation in lithium-1-azaallyls is of interest. The lithium-1-azaallyls that have been crystallographically characterised so far adopt with few exceptions a *syn*-conformation of the Li atom with respect to the double bond. This is in agreement with theoretical calculations by Armstrong et al. [19] who found that the *syn*-conformation of $[LiN(H)C(Bu^t)CH_2]$ is stabilised by 9.4 kcal/mol compared to the *anti*-conformation. The lithium complex **I** is so far the only example of a lithium-1-azaallyl with a trigonal planar Li atom adopting an *anti*-conformation possibly as a result of **I** being a zwitterion in which the azaallyl backbone is part of a strained four-membered ring [25].

The molecular structures of compounds **1b**–**1d** with the atom numbering scheme are illustrated in Figs. 1–3, selected bond distances and angles are summarised in Table 3. All three complexes are monomeric with

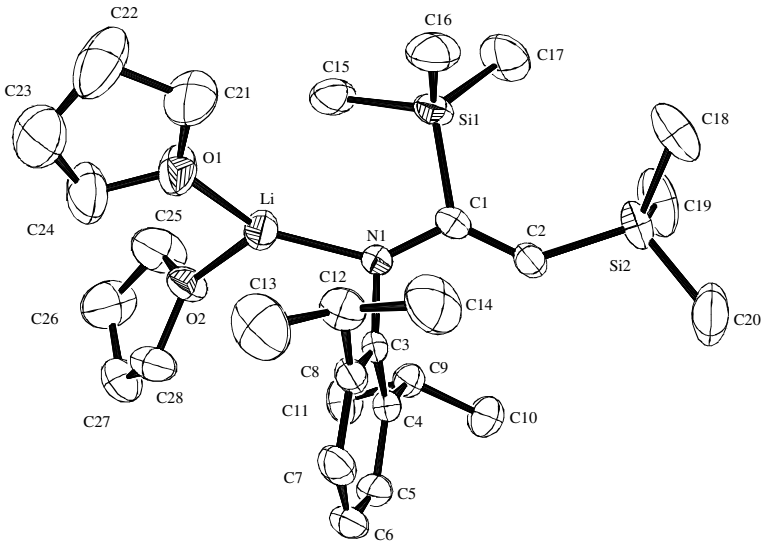


Fig. 1. Molecular structure of **1b**. Thermal ellipsoids are drawn on the 50% probability level. H atoms have been omitted for clarity.

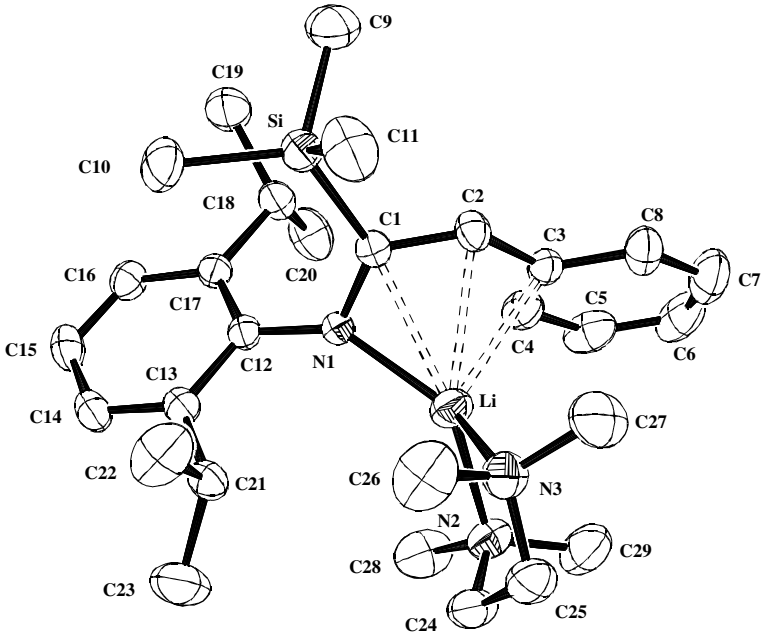


Fig. 2. Molecular structure of **1c**. Thermal ellipsoids are drawn on the 50% probability level. H atoms have been omitted for clarity.

two additional donor atoms and therefore belong to type IIIa with the shortest distance (Li–N1, Table 3) between the Li atom and the negatively charged N atom of the 1-azaallyl ligand and considerably longer contacts to the neutral donor atoms (except O2) of the solvent molecules. The coordination around the Li atom is approximately trigonal planar (Σ°Li, Table 3) in all three complexes with the largest deviation from planarity for complex **1d**. Complexes **1c** and **1d** show additional Li···C contacts to C1–C3 and C4(C8), respectively, in the range of 2.45 to 2.52 Å. The contact distances and geometries are similar to related complexes in category III and may be best compared to [LiN($C_6H_3Me_2$-2,6)C(R)CHR(tmen)] [4e] or [LiN(R)C(Ph)CHPh(tmen)] [3a].

Possibly as a result of steric crowding that is evident from the large angles around the sp^2 hybridised carbons C1 and C2 in the backbone [C2–C1–Si1 126.1(1)°, N1–C1–C2 126.1(2)°, C1–C2–Si2 134.5(2)°], **1b** is exceptional in being the first example of a lithium-1-azaallyl being a *Z* isomer (with regard to the two $SiMe_3$ groups) and adopting an *anti*-conformation

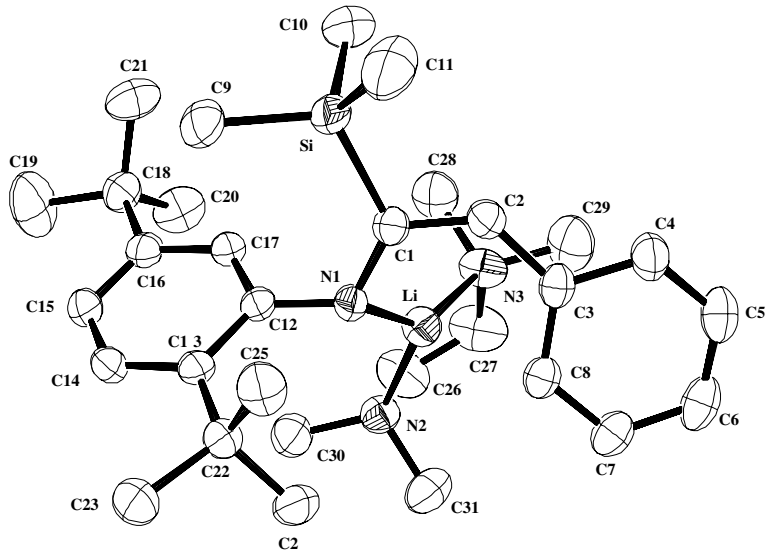


Fig. 3. Molecular structure of **1d**. Thermal ellipsoids are drawn on the 50% probability level. H atoms have been omitted for clarity.

Table 3
Selected bond distances (Å) and angles (°) for compounds **1b**, **1c**, and **1d**

Compound	**1b**	**1c**	**1d**
Li–N1	1.9234(4)	2.016(3)	1.988(4)
Li–D1[a]	1.971(4)	2.114(4)	2.109(4)
Li–D2[b]	1.901(4)	2.147(4)	2.069(4)
Li···C1		2.446(4)	[2.614(4)]
Li···C2		2.459(4)	
Li···C(Ar)[c]	[2.636(4)]	2.530(4)	
Li···C8			2.506(4)
N1–C1	1.378(2)	1.362(2)	1.356(2)
C1–C2	1.379(3)	1.393(2)	1.392(2)
C1–Si1/Si	1.883(2)	1.912(2)	1.918(2)
C2–Si2	1.827(2)		
Σ°Li[d]	357.3(2)	357.0(2)	350.7(2)
N1–C1–C2	126.1(2)	120.6(2)	121.7(2)
N1–C1–Si1	107.4(1)	127.8(1)	126.9(1)
C2–C1–Si1	126.1(1)	111.4(1)	111.3(1)

[a] D1 = O1 for **1b**; N1 for **1c** and **1d**.
[b] D2 = O2 **1b**; N2 for **1c** and **1d**.
[c] C(Ar) = C3 (**1b**, *ipso*-C of N-bound Ar ring); C3 (**1c**, *ipso*-C of Ph ring).
[d] Sum of bond angles around Li.

(with regard to lithium). The four atoms Li, N1, C1 and C2 are essentially planar [largest deviation from planarity for N1 0.024(1) Å] with the aryl ring (C3–C8) being approximately perpendicular (74.1°) to this plane. It is also noteworthy that further contacts between Li and one methyl group of Si1 [Li···C15 2.808(4) Å] and the *ipso*-C of the aryl ring [Li···C3 2.636(4) Å] increase the coordination sphere around Li in **1b** from trigonal planar to distorted trigonal bipyramidal. The significantly shorter C2–Si2 bond distance of 1.827(2) Å in **1b** as compared to the C1–Si1 bond distances in **1b**–**1d** may be an indication of a possible stabilisation (Si–C δ*–π interaction) of the partial negative charge on C2 by the adjacent trimethylsilyl group. The ability of Si to stabilise carbanions has previously been well established [34].

In all three complexes there is only limited delocalisation in the backbone of the azaallyl ligand (η^1-enamide, **A**) as evident from the N1–C1 and C1–C2 bond distances (Table 3) that correspond to N–C single and C=C double bonds, respectively.

The molecular structure of compound **2** with the atom numbering scheme is illustrated in Fig. 4, selected bond distances are found in Table 4.

Compound **2** crystallises as a monomer with half a molecule of **2** in the asymmetric unit, the other half being generated by a centre of inversion. Compound **2** is a rare example of a structurally characterised diazahexatriene and has a structural precedence in $C_6H_3(Bu^t_2\text{-}2,5)N{=}C(R)CH{=}CHC(R){=}NC_6H_3(Bu^t_2\text{-}2,5)$ [5] and the related hydrazine and hydroxylamine derivatives R′N=CHC(COPh)=C(COPh)CH=NR′ [R′ = $NHC_6H_3[(NO_2)_2$-2,4]] [35] or HON=C(NH_2)-CH=CHC(NH_2)=NOH [36]. The atoms N1, C13, C14 and their symmetry related equivalents in the backbone of the molecule show little deviation from planarity as evident from their torsion angles [C14′–C14–C13–N1 −175.5(2)°; C14′–C14–C13–Si1 −3.2(2)°; C1–N1–C13–C14 4.5(2)°]. The N=C, C–C and C=C bond distances (Table 4) are similar to those in $C_6H_3(Bu^t_2\text{-}2,5)N{=}C(R)CH{=}CHC(R){=}NC_6H_3$ (Bu^t_2- 2,5) and alternate between single and double bonds with only a limited degree of delocalisation not uncommon in related linear conjugated C=C double bond systems [37].

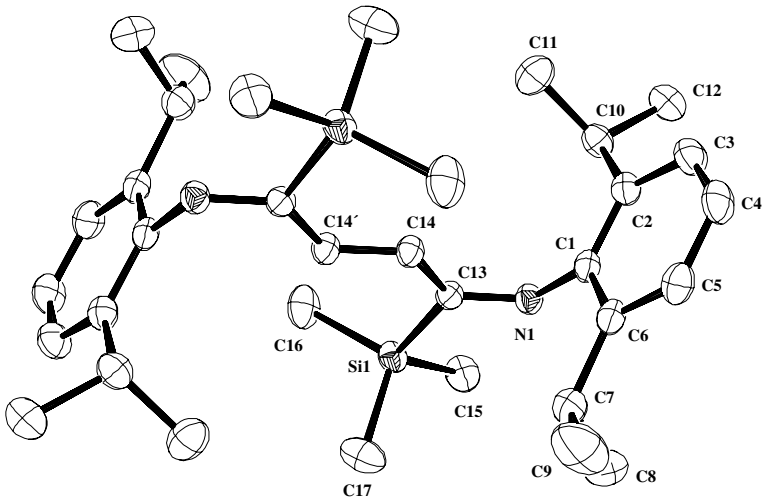


Fig. 4. Molecular structure of **2**. Thermal ellipsoids are drawn on the 50% probability level. H atoms have been omitted for clarity.

Table 4
Selected bond distances (Å) for compounds **2**

N1–C1	1.432(2)	N1–C13	1.295(2)
C13–C14	1.472(2)	C14–C14′	1.339(2)

′ $-x+1, -y, -z+1$.

4. Supplementary data

Full crystallographic data (CCDC 257844 for compound **1b**, 257845 for compound **1c**, 25786 for compound **1d** and 257847 for compound **2**) have been deposited at the Cambridge Crystallographic Database Centre and are available on request from the Director, CCDC, 12 Union Road, Cambridge, CB2 1EZ, UK (fax: +44 1223 336 033; e-mail: deposit@ccdc.cam.ac.uk or http://www.ccdc.cam.ac.uk).

Acknowledgements

The authors thank the IUCr (bursary for BO) and the University of the Witwatersrand for financial support.

References

[1] (a) J.K. Whitesell, M.A. Whitesell, Synthesis (1983) 527;
(b) L.M. Jackman, L.M. Scarmoutzos, B.D. Smith, P.G. Willard, J. Am. Chem. Soc. 110 (1988) 6058.
[2] C.F. Caro, M.F. Lappert, P.G. Merle, Coord. Chem. Rev. 219–221 (2001) 605.
[3] (a) P.B. Hitchcock, M.F. Lappert, M. Layh, D.-S. Liu, R. Sablong, T. Shun, J. Chem. Soc., Dalton Trans. (2000) 2301;
(b) P.B. Hitchcock, M.F. Lappert, M. Layh, J. Chem. Soc., Dalton Trans. (1998) 1619;
(c) P.B. Hitchcock, M.F. Lappert, M. Layh, A. Klein, J. Chem. Soc., Dalton Trans. (1999) 1455;
(d) P.B. Hitchcock, J. Hu, M.F. Lappert, M. Layh, J. Severn, J. Chem. Soc., Chem. Commun. (1997) 1189;
(e) R.J. Bowen, J. Caddy, M.A. Fernandes, M. Layh, M.A. Mamo, Polyhedron 23 (2004) 2273;
(f) R.A. Wanat, D.B. Collum, G. van Duyne, J. Clardy, R.T. DePue, J. Am. Chem. Soc. 108 (1986) 3415.
[4] (a) P.B. Hitchcock, M.F. Lappert, M. Layh, Chem. Commun. (1998) 201;
(b) W.-P. Leung, H. Cheng, D.-S. Liu, Q.-G. Wang, T.C.W. Mak, Organometallics 19 (2000) 3001;
(c) W.-P. Leung, H. Cheng, H.L. Hou, Q.-C. Yang, Q.-G. Wang, T.C.W. Mak, Organometallics 19 (2000) 5431;
(d) W.-P. Leung, H. Cheng, R.-B. Huang, Q.-C. Yang, T.C.W. Mak, Chem. Commun. (2000) 451;
(e) P.B. Hitchcock, M.F. Lappert, M. Layh, J. Chem. Soc., Dalton Trans. (2001) 2409.
[5] M.A. Fernandes, M. Layh, B. Omondi, Progr. Organomet. Chem. Res. (accepted).
[6] M.A. Fernandes, M.F. Lappert, M. Layh, B. Omondi, Chem. Commun. (2003) 656.
[7] Bruker, SAINT+, Version 6.02 (includes XPREP and SADABS), Bruker AXS INC., Madison, WI, USA, 1999.
[8] Bruker, SHELXTL, Version 5.1 (includes XS, XL, XP, XSHELL), Bruker AXS INC., Madison, WI, USA, 1999.
[9] A.L. Spek, J. Appl. Crystallogr. 36 (2003) 7.
[10] L.J. Farrugia, J. Appl. Crystallogr. 30 (1997) 565.
[11] P.B. Hitchcock, M.F. Lappert, S. Tian, J. Organomet. Chem. 549 (1997) 1.
[12] P.B. Hitchcock, M.F. Lappert, D.-S. Liu, J. Chem. Soc., Chem. Commun. (1994) 2637.
[13] A. Antiñolo, C. Huertas, I. Del Hierro, M.F. Lappert, A. Otero, S. Prahsar, A.M. Rodriguez, E. Villaseñor, Organometallics 17 (1998) 5874.
[14] (a) R.I. Papasergio, C.L. Raston, A.H. White, J. Chem. Soc., Chem. Commun. (1983) 1419;
(b) R.I. Papasergio, B.W. Skelton, P. Twiss, A.H. White, C.L. Raston, J. Chem. Soc., Dalton Trans. (1990) 1161.
[15] P.B. Hitchcock, M.F. Lappert, X.-H. Wei, J. Organomet. Chem. 683 (2003) 83.
[16] R. Knorr, H. Dietrich, W. Mahdi, Chem. Ber. 124 (1991) 2057.
[17] M.F. Lappert, M. Layh, Tetrahedron Lett. 39 (1998) 4745.
[18] F. Antolini, B. Gehrhus, P.B. Hitchcock, M.F. Lappert, Angew. Chem. Int. Ed. 41 (2002) 2568.
[19] D.R. Armstrong, W. Clegg, L. Dunbar, S.T. Liddle, M. MacGregor, R.E. Mulvey, D. Reed, S.A. Quinn, J. Chem. Soc., Dalton Trans. (1998) 3431.

[20] W.P. Leung, L.-H. Weng, R.-J. Wang, T.C.W. Mak, Organometallics 14 (1995) 4832.
[21] H.P. Shi, D.-S. Liu, S.-P. Huang, Acta Crystallogr., Sect. E 59 (2003) m339.
[22] I. Khorobkov, S. Gambarotta, G.P.A. Yap, P.H.M. Budzelaar, Organometallics 21 (2002) 3088.
[23] R.J. Bowen, M.A. Fernandes, M. Layh, J. Organomet. Chem. 689 (2004) 1230.
[24] R. Hacker, P. von Rague Schleyer, G. Reber, G. Müller, L. Brandsma, J. Organomet. Chem. 316 (1986) C4.
[25] (a) P.B. Hitchcock, M.F. Lappert, M. Layh, Angew. Chem., Int. Ed. 38 (1999) 501;
(b) R.J. Bowen, M.A. Fernandes, P.B. Hitchcock, M.F. Lappert, M. Layh, J. Chem. Soc., Dalton Trans. (2002) 3253.
[26] V. Lorenz, H. Görls, J. Scholz, Angew. Chem. Int. Ed. 42 (2003) 2253.
[27] P.B. Hitchcock, M.F. Lappert, W.-P. Leung, D.-S. Liu, T.C.W. Mak, Z.-X. Wang, J. Chem. Soc., Dalton Trans. (1999) 1263.
[28] B.-J. Deelman, M.F. Lappert, H.-K. Lee, T.C.W. Mak, W.-P. Leung, P.-R. Wei, Organometallics 16 (1997) 1247.
[29] P.C. Andrews, D.R. Armstrong, C.L. Raston, B.A. Roberts, B.W. Skelton, A.H. White, J. Chem. Soc., Dalton Trans. (2001) 996.
[30] A.G. Avent, A.D. Frankland, P.B. Hitchcock, M.F. Lappert, Chem. Commun. (1996) 2433.
[31] S. Nückel, P. Burger, Organometallics 19 (2000) 3311.
[32] F. Bosold, M. Marsch, K. Harms, G. Boche, Z. Kristallogr. – New Cryst. Struct. 216 (2001) 427.
[33] D. Enright, S. Gambarotta, G.P.A. Yap, P.H.M. Budzelaar, Angew. Chem. Int. Ed. 41 (2002) 3873.
[34] A.C. Hopkinson, M.H. Lien, J. Org. Chem. 46 (1981) 998, and references therein.
[35] F.I. Guseinov, G.Y. Klumentova, V.M. Ismailov, V.V. Moskva, A.T. Gubaidullin, I.A. Litvinov, N.S. Zefirov, Dokl. Akad. Nauk SSSR 358 (1998) 492.
[36] E.A. Bruton, L. Brammer, F.C. Pigge, C.B. Aakeroy, D.S. Leinen, New. J. Chem. 27 (2003) 1084.
[37] Cambridge Crystallographic Data Centre, VISTA, Cambridge Crystallographic Data Centre, 12 Union Road, Cambridge, England, 1995.

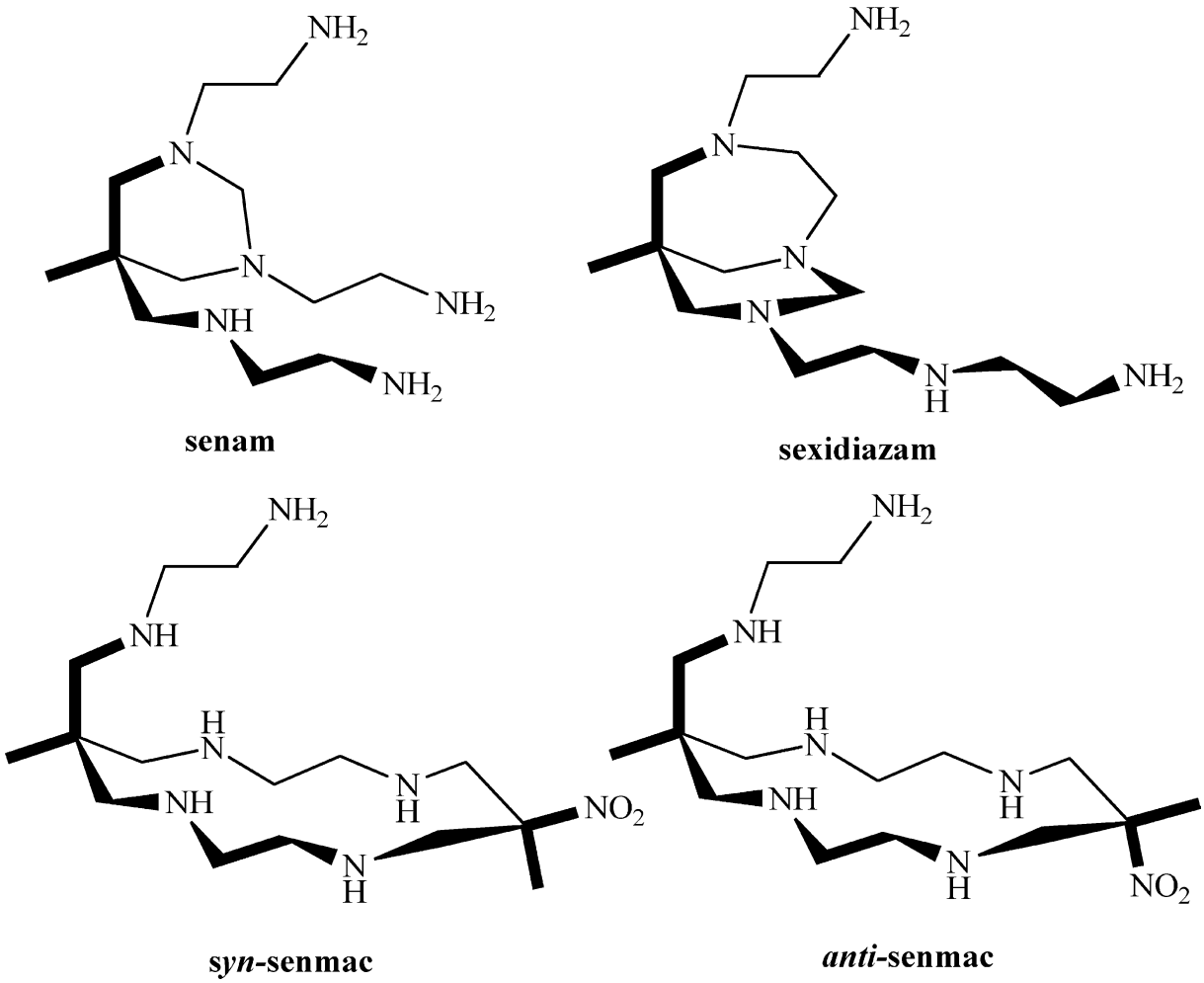


Fig. 1. Some of the possible macrocyclic ligand species derived from "sen".

its definition resulted in characterisation of an aminal derivative of the ligand. The aminal formation may be a consequence of solvent methanol oxidation catalysed by Cu(II), as an aminal is also formed in a synthesis under similar conditions of the Cu(II) complex of another podand hexamine.

2. Experimental

2.1. Synthesis

3,7-diaza-5-(4′-amino-2′-azabutyl)-5-methylnonane-1,9-diamine (sen), as its hexahydrochloride, was prepared from the benzenesulfonate of 2-hydroxymethyl-2-methyl-propane-1,3-diol (1,1,1-tris(benzenesulfonyloxymethyl) ethane) via its reaction with 1,2-ethanediamine following literature procedures [6].

Cu(II) complex of a mono-aminal derivative of sen ("senam"). Methanolic NaOH (1.0 g in 50 mL) was added to a slurry of sen·6HCl (1.9 g) in methanol (50 mL) and the mixture stirred vigorously for 30 min before precipitated NaCl was filtered out. $CuCl_2\cdot 2H_2O$ (1.1 g) in methanol (600 mL) was added to give a violet solution, which was was evaporated to dryness. The violet residue was dissolved in water, excess $NaClO_4$ added and the solution allowed to slowly evaporate at room temperature. A structure determination (see below) on the crystals obtained showed them to be the triperchlorate of the complex of the monoprotonated ligand, $[Cu(senamH)(OClO_3)_2]ClO_4$ (**1**). *Anal.* Calc. for $C_{12}H_{31}Cl_3CuN_6O_{12}$: C, 23.20; H, 5.03; N, 13.53. Found: C, 23.1; H, 4.7; N, 13.2%. Use of $[NH_4][PF_6]$ in place of $NaClO_4$ as the precipitant provided crystals once again of the complex of the monoprotonated ligand, here as its chloride-di-(hexafluorophosphate), $[Cu(senamH)Cl(FPF_5)](PF_6)\cdot 2H_2O$ (**2**), the composition also being deduced from a structure solution. Yield, 2.0 g (75%). *Anal.* Calc. for $C_{12}H_{35}ClCuF_{12}N_6O_2P_2$: C, 21.06; H, 5.15; N, 12.28. Found: C, 21.4; H, 5.3; N, 12.0%.

1-(2″-aminoethyl)-3-(7′amino-2′,4′-diazaheptyl)-3-methyl-cyclo-1,5-diazaheptane, isolated in the form of its

monoaminal derivative, *''sexidiazam''*, *as its Cu(II) complex*. 1,1,1-Tris(benzenesulfonyloxymethyl)ethane (22 g) was dissolved in diethylentriamine (dien, 25 g) and the solution was heated at 120 °C for three days under a nitrogen atmosphere. NaOH (4.9 g) in methanol (200 mL) was added to the cooled mixture, followed by $CuCl_2 \cdot 2H_2O$ (55 g). The methanol was then evaporated off under reduced pressure. The blue-violet residue was dissolved in water (2 L) and subjected (in portions) to chromatography on Na^+-form SP Sephadex using 0.30 mol L^{-1} sodium chloride as eluant. Two major components were separated, the first proving to be simply the Cu(II) complex of dien. The second component eluate was evaporated to dryness and the residue extracted with ethanol to leave the bulk of the NaCl undissolved. The extract was then taken to dryness and the blue residue (8.9 g) redissolved in water. Addition of $NaClO_4$ and slow evaporation of the solution at ambient temperature provided crystals of $[Cu(sexidiazamH)Cl(OClO_3)]ClO_4$ (**3**) suitable for a structure determination. *Anal*. Calc. for $C_{14}H_{33}Cl_3CuN_6O_8$: C, 28.82; H, 5.70; N, 14.41. Found: C, 29.0; H, 5.9; N, 14.3%.

Cu(II) complexes of 6(aminoethylaminomethyl)-6, 13-dimethyl-13-nitro-1,4,8,11-tetra-azacyclotetradec-ane (''senmac''). A methanolic solution containing Cu(II) and sen in the ratio 3:2 was prepared exactly as described above for the synthesis of **1** and **2**, then mixed with nitroethane (1.0 g), aqueous formaldehyde (37%, 4 g), triethylamine (2.0 g) and water (100 mL), filtered to remove some greenish material, and heated at 60 °C for 12 h. After being cooled to room temperature, the solution was acidified with acetic acid (2 mL) and then evaporated to dryness under vacuum. The red-violet residue was dissolved in water and subjected to chromatography on Na^+-form SP Sephadex using 0.15 mol L^{-1} trisodium citrate as eluant. Five components, F1–F5, were thereby separated (as distinct from six, with the ryongamine complex as the leading species, in earlier work [5]), the third being present in too small a quantity to be adequately characterised. After recovery of each complex as its chloride (F1 0.12 g; F2 0.15 g; F4 0.38 g; F5 0.42 g) using Dowex 50W × 2/HCl, attempts were made to obtain crystalline derivatives suitable for structure determinations. In the cases of F2 and F5, these were successful using pyridine-2,6-dicarboxylate (dipicolinate = $dipic^{2-}$, actually found to be present in its monoprotonated form, $Hdipic^-$) plus perchlorate as the counter-anions, giving what proved to be identical species $[Cu(senmacH)(Hdipic\text{-}O)](ClO_4)_2 \cdot 1.5H_2O$ (**4**), whereas for F4, perchlorate alone ultimately proved to be the most useful additional counter-anion, giving $[Cu(senmacH)Cl(OClO_3)](ClO_4)_2 \cdot 3H_2O$ (**5**). No means of satisfactorily crystallising F1 was found. *Anal*. Calc. for $C_{22}H_{43}Cl_2CuN_8O_{15.50} = [Cu(senmacH)(Hdipic\text{-}O)](ClO_4)_2 \cdot 1.5H_2O$: C, 32.94; H, 5.40; N, 13.97. Found:

Table 1
Crystal data and structure refinement details

Complex	**1**	**2**	**3**	**4**	**5**
Chemical formula	$C_{12}H_{31}Cl_3CuN_6O_{12}$	$C_{12}H_{35}ClCuF_{12}N_6O_2P_2$	$C_{14}H_{33}Cl_3CuN_6O_8$	$C_{22}H_{43}Cl_2CuN_8O_{15.5}$	$C_{15}H_{43}Cl_4CuN_7O_{17}$
M (g mol^{-1})	621.32	684.39	583.35	802.08	798.90
Crystal system	orthorhombic	monoclinic	triclinic	monoclinic	monoclinic
Space group	$P2_12_12_1$	$C2/c$	$P\bar{1}$	$C2/c$	$C2/c$
a (Å)	11.6198(4)	12.5916(8)	8.5417(8)	28.4482(14)	40.576(3)
b (Å)	13.1020(3)	29.515(2)	12.1037(14)	22.4011(12)	9.1561(6)
c (Å)	15.8703(6)	14.1334(8)	12.3134(14)	11.5307(6)	17.2926(14)
α (°)	90	90	76.154(5)	90	90
β (°)	90	96.219(4)	71.826(6)	109.008(5)	107.325(4)
γ (°)	90	90	72.622(6)	90	90
V (Å^3)	2416.14(14)	5221.6(6)	1139.2(2)	6947.5(7)	6133.0(8)
Z	4	8	2	8	8
D_{calc} (g cm^{-3})	1.708	1.741	1.701	1.534	1.730
μ(Mo Kα) (mm^{-1})	1.304	1.170	1.365	0.861	1.145
F(000)	1284	2792	606	3344	3320
Reflections collected	16713	17338	7880	22677	20211
Independent reflections	4508	4792	4003	6345	5792
Observed reflections [$I > 2\sigma(I)$]	4096	3301	2731	3354	3596
R_{int}	0.053	0.089	0.065	0.069	0.108
Parameters refined	308	327	290	451	455
R_1	0.030	0.079	0.049	0.087	0.056
wR_2	0.069	0.226	0.111	0.258	0.133
S	1.029	1.055	1.030	0.989	1.038
$\Delta\rho_{min}$ (e Å^{-3})	−0.22	−0.89	−0.35	−0.62	−0.48
$\Delta\rho_{max}$ (e Å^{-3})	0.27	1.57	0.48	0.89	0.62

Table 2
Environment of the Cu(II) atom: selected bond lengths (Å) and angles (°)

Complex ***1***	
Cu–N1	2.009(3)
Cu–N2	2.069(3)
Cu–N3	2.014(3)
Cu–N4	2.019(3)
N1–Cu–N2	86.25(10)
N2–Cu–N3	92.74(10)
N3–Cu–N4	84.97(11)
N4–Cu–N1	96.04(11)
Complex ***2***	
Cu–N1	2.015(6)
Cu–N2	2.017(6)
Cu–N3	2.061(5)
Cu–N4	2.031(6)
Cu–Cl	2.5732(19)
N1–Cu–N2	84.6(2)
N2–Cu–N3	92.5(2)
N3–Cu–N4	85.5(2)
N4–Cu–N1	95.4(3)
N1–Cu–Cl	90.3(2)
N2–Cu–Cl	101.43(17)
N3–Cu–Cl	96.10(16)
N4–Cu–Cl	96.14(18)
Complex ***3***	
Cu–N1	2.052(4)
Cu–N2	2.074(4)
Cu–N4	2.014(4)
Cu–N5	2.085(4)
Cu–Cl1	2.5627(13)
N1–Cu–N2	92.45(15)
N2–Cu–N4	85.75(15)
N4–Cu–N5	94.46(14)
N5–Cu–N1	85.30(14)
N1–Cu–Cl1	98.82(10)
N2–Cu–Cl1	109.90(11)
N4–Cu–Cl1	88.44(12)
N5–Cu–Cl1	86.20(11)
Complex ***4***	
Cu–N1	2.022(6)
Cu–N2	2.025(6)
Cu–N3	2.017(6)
Cu–N4	2.023(6)
Cu–O3	2.287(5)
N1–Cu–N2	93.8(2)
N2–Cu–N3	86.2(2)
N3–Cu–N4	93.7(2)
N4–Cu–N1	86.0(2)
N1–Cu–O3	88.7(2)
N2–Cu–O3	99.6(2)
N3–Cu–O3	94.0(2)
N4–Cu–O3	84.8(2)
Complex ***5***	
Cu–N1	2.019(4)
Cu–N2	2.007(4)
Cu–N3	2.016(4)
Cu–N4	2.014(4)
Cu–Cl1	2.7002(14)
N1–Cu–N2	91.65(16)
N2–Cu–N3	86.61(16)
N3–Cu–N4	94.31(16)
N4–Cu–N1	87.13(16)
N1–Cu–Cl1	97.61(13)
N2–Cu–Cl1	93.50(13)
N3–Cu–Cl1	86.85(12)
N4–Cu–Cl1	90.37(12)

C, 32.8; H, 5.7; N, 14.2%. *Anal*. Calc. for $C_{15}H_{43}Cl_4CuN_7O_{17}$ = [Cu(senmacH)Cl(OClO$_3$)](ClO$_4$)$_2$·3H$_2$O: C, 22.55; H, 5.43; N, 12.27. Found: C, 23.0; H, 5.8; N, 12.1%.

2.2. Crystallography

The data for the five compounds were collected at 100(2) K on a Nonius Kappa-CCD area detector diffractometer [8] using graphite-monochromated Mo Kα radiation (λ 0.71073 Å). The crystals were introduced in glass capillaries with a protecting "Paratone-N" oil (Hampton Research) coating. The unit cell parameters were determined from ten frames, then refined on all data. A 180° φ-range was scanned with 2° steps during data collection, with a crystal-to-detector distance fixed to 28 mm. The data were processed with DENZO-SMN [9]. The structures were solved by direct methods or Patterson map interpretation with SHELXS-97 and subsequent Fourier-difference synthesis and refined by full-matrix least-squares on F^2 with SHELXL-97 [10]. Absorption effects were corrected empirically with the program DELABS from PLATON [11]. The terminal atom N6 in **4** and the nitro group and one perchlorate anion in **5** were found disordered over two positions each, which were refined with occupancy parameters constrained to sum to unity. All non-hydrogen atoms were refined with anisotropic displacement parameters, with some restraints for some fluorine and water oxygen atoms in **2** and some perchlorate and water oxygen atoms in **4**. The hydrogen atoms bound to nitrogen and oxygen atoms were found on Fourier-difference maps (except those of one water molecule in **2** and those of N6 and the water molecules in **4**). The carbon-bound hydrogen atoms were introduced at calculated positions. All hydrogen atoms were treated as riding atoms with a displacement parameter equal to 1.2 (NH, OH, CH, CH$_2$) or 1.5 (CH$_3$) times that of the parent atom. The absolute configuration in **1** was determined from the value of the Flack parameter [−0.009(11)] [12]. Crystal data and structure refinement parameters are given in Table 1 and selected bond lengths and angles in Table 2. The molecular plots were drawn with SHELXTL [13].

3. Results and discussion

While six-coordination for Cu(II) with N-donor ligands is far from exceptional [14], numerous tetramine complexes in which the metal is essentially square planar, with weak axial ligation, are well known [4,5,15–18]. Thus, there is a basis for expecting that a sexidentate amine like sen could form complexes with Cu(II) having a 3:2 M:L stoichiometry. For a homologue of sen, such a complex has been characterised by elemental analysis [6c] and, for a sen derivative where CH_2OH replaces CH_3, a tetranuclear complex in which four of the N-donors of one ligand molecule are bound to one metal and the remaining two to another, has been structurally characterised [19]. Aqueous reaction mixtures containing CuX_2, with X a variety of different anions, and sen in a 3:2 ratio readily provide solid complexes but, despite numerous efforts, we were unable to obtain any of these in a crystalline form suitable for a structure determination. However, on using a methanolic medium to prepare the complex prior to its crystallisation from water, suitable crystals were obtained by both the addition of $NaClO_4$ or $[NH_4][PF_6]$ to a solution of the chloride. The structure solutions for both crystals show the presence of a very similar complex of the Cu(II) cation with a monoprotonated form of an aminal derivative of sen, ''senam'', (Fig. 2) and it is presumed that the molecule of formaldehyde incorporated to form the aminal must arise from a Cu-catalysed oxidation of methanol during the synthesis. A similar aminal structure is found in a ryongamine though, in this case, the reaction mixture contained deliberately added formaldehyde [5]. Another similarity with the ryongamine structure is that the ligand is present in a form where the pendent arm is monoprotonated (not unexpectedly for the ryongamine, since it was isolated from an acidic solution). This may simply be a consequence of the lack of deliberate pH control during the crystallisation processes but does indicate that binding of Cu(II) (present, initially, in sufficient quantities) to the pendent arm must be relatively weak, at least when one of the donors is an aminal-N.

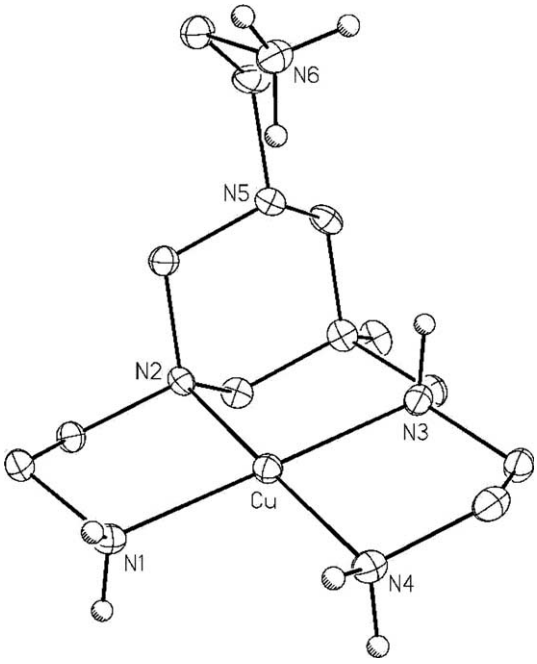


Fig. 2. View of complex **1**. The counter-ions and the carbon-bound hydrogen atoms are omitted for clarity. Displacement ellipsoids are drawn at the 30% probability level.

In $[Cu(senamH)(OClO_3)_2]ClO_4$ (**1**), the Cu atom has close to a square planar environment (Fig. 1, Table 2), but two longer contacts with perchlorate ions complete the coordination sphere to give an axially elongated octahedron, with unequal Cu–O(ClO_3) distances, 2.551(3) and 2.615(3) Å, reflecting the asymmetry of the ligand structure with respect to the CuN_4 plane. The formation of the aminal unit restricts the movement of the pendent arm such that it is turned back over the CuN_4 plane, with the third (uncoordinated) perchlorate anion being involved in H-bonding to the terminal NH_3^+ group of the pendent arm and to both coordinated NH_2 units on an adjacent complex cation. The pendent-arm NH_3^+ group is also H-bonded to the bound oxygen of coordinated perchlorate. The two five-membered chelate rings on Cu are of opposite conformation (δ,λ), the usual situation for a ''232tet'' derivative [17,18] when the central, six-membered ring has a chair form, though the presence of the pendent arm and the aminal unit renders the whole complex chiral and, in accord with the space group $P2_12_12_1$, only one configuration of the complex appears in the lattice, viz., it must crystallise as a ''racemic mixture''. In $[Cu(senamH)Cl(FPF_5)](PF_6)\cdot 2H_2O$ (**2**), distortions of the coordination environment (Fig. 3) due to the aminal bridge and the markedly asymmetric axial contacts (Cu–Cl 2.573(2) Å, Cu–FPF_5 2.937(6) Å) are associated with the five-membered rings being of identical, chiral conformations, despite the retention of an essentially chair conformation for the six-membered link. Paradoxically, this is associated with crystallisation in a centrosymmetric lattice where the complex cations can be regarded as lying in sheets parallel to the *ac* plane, with their chirality alternating from one sheet to the next. The sheets form pairs in that the Cu–Cl vectors of adjacent sheets are oriented either towards or away from one another into the region between the layers. As part of a complicated network of H-bonds, here involving the anions (coordinated and ''free'') as well as water molecules, hexafluorophosphate anions appear to bridge complex cations in a given sheet by quite short contacts (F···N 2.873(10) Å, although N–H···F is only 123.3°) to the pendent-arm NH_3^+ group, The two structures illustrate the subtlety of the factors that may determine the solid state array in a crystalline complex.

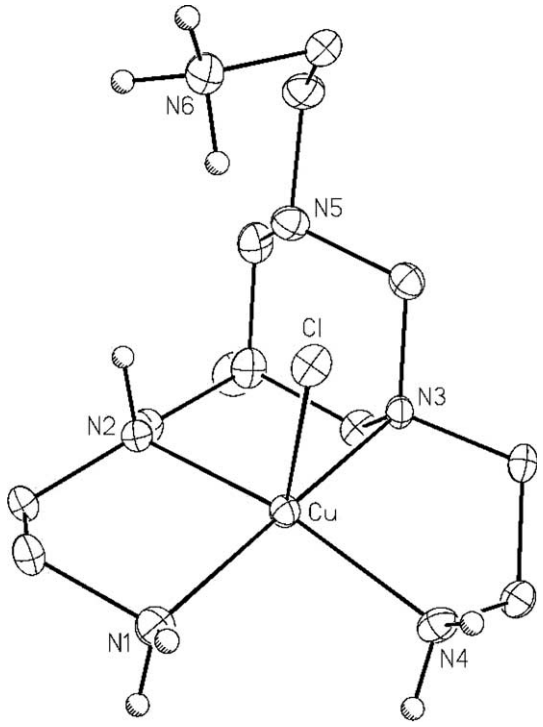


Fig. 3. View of complex **2**. The counter-ions, the solvent molecules and the carbon-bound hydrogen atoms are omitted for clarity. Displacement ellipsoids are drawn at the 20% probability level.

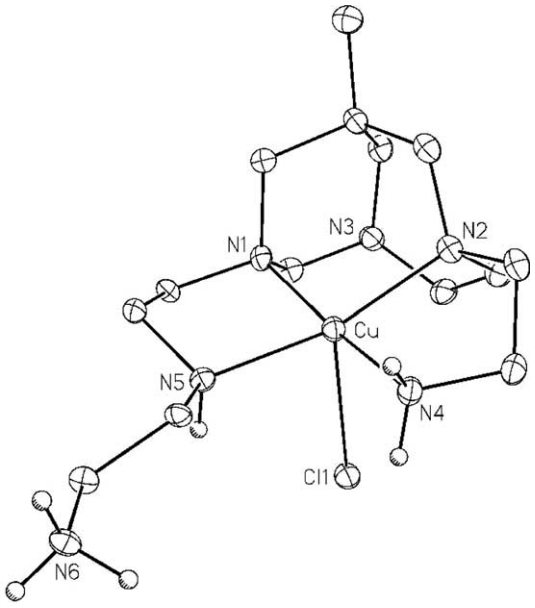


Fig. 4. View of complex **3**. The counter-ions and the carbon-bound hydrogen atoms are omitted for clarity. Displacement ellipsoids are drawn at the 30% probability level.

Confirming the ready formation of aminals in complex ion systems of this and many similar [2] types, and the stability of the six-membered-ring aminal, a closely related complex was isolated during efforts to characterise the Cu(II) complex of the product of the reaction between 1,1,1-tris(benzenesulfonyloxymethyl)ethane and diethylentriamine. The nature of the polyamine ligand (a sexidentate diazepan derivative, hence ''sexidiaz'', being ''sexidiazam'' as its aminal), as is apparent from the structure of the complex, [Cu(sexidiazamH)Cl($OClO_3$)]ClO_4 (**3**) (Fig. 4), shows that what is a minor pathway in the reaction between 1,1,1-tris(benzenesulfonyloxymethyl)ethane and ethane-1,2-diamine [20] has become the major one with 3-azapentane-1,5-diamine (diethylenetriamine), leading to a ligand which is not a simple podand. Once again, the Cu(II) environment is essentially a tetragonally distorted octahedral one (Table 2), with unsymmetrical axial interactions (Cu–Cl 2.563(1) Å, Cu–$OClO_3$ 2.897(4) Å). As in [Cu(senamH)Cl(FPF_5)](PF_6)·$2H_2O$, this unsymmetrical axial coordination is associated with the five-membered chelate rings in a given complex cation having the same conformation and the lattice being centrosymmetric, with cations of one configuration lying in alternating planes. The six-membered ring containing the aminal unit is dimensionally very similar to those in [Cu(senamH)($OClO_3$)$_2$]ClO_4 and [Cu(senamH)Cl(FPF_5)](PF_6)·$2H_2O$, except that the substituent on the uncoordinated aminal-N has an axial, rather than an equatorial orientation, presumably as a consequence of this nitrogen atom now being part also of a seven-membered chelate ring.

It is possible that relatively unstable aminal species are formed in the macrocyclisation reactions of the Cu(II)/sen system, since, despite clear chromatographic separations of five species, after recovery of the complex ions under strongly acidic conditions, crystal structure determinations showed the second and fifth species to be identical. Difficulties encountered in attempting to crystallise the residue from the first fraction may also reflect decomposition resulting in the formation of a mixture, and it may be that the first and fourth components are related in the same way as the second and fifth. In any case, in neither of the two macrocyclic complexes for which the structures were determined was an aminal unit present and, presumably partly in consequence of this, the pendent arms extend directly out from the macrocycles. In [Cu(senmacH)(dipic-O)(OH_2)](ClO_4)$_2$·1.5H_2O (**4**), the species isolated from the second and fifth components, the expected macrocycle is present and in the very commonly encountered ''cyclam *trans*-III'' conformation [15,21], with the methyl substituents on the opposed six-membered chelate rings being *syn*, so that the methyl group at the C–NO_2 centre is equatorial and that at the C(pendent arm) centre is axial (Fig. 5). The pendent arm is therefore an equatorial substituent and extends maximally from the macrocycle periphery, though with the terminal NH_3^+ group being disordered over two orientations. The Cu(II) centre has an axial carboxylate-O ligand [Cu–O(dipic) 2.287(5) Å] and a more remote axial interaction with a water molecule

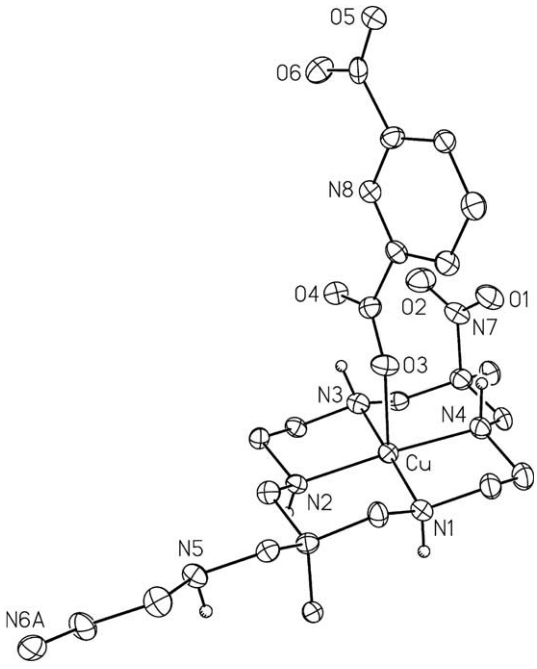


Fig. 5. View of complex **4**. The counter-ions, the solvent molecules and the carbon-bound hydrogen atoms are omitted for clarity. Only one position of the disordered atom N6 is represented. Displacement ellipsoids are drawn at the 30% probability level.

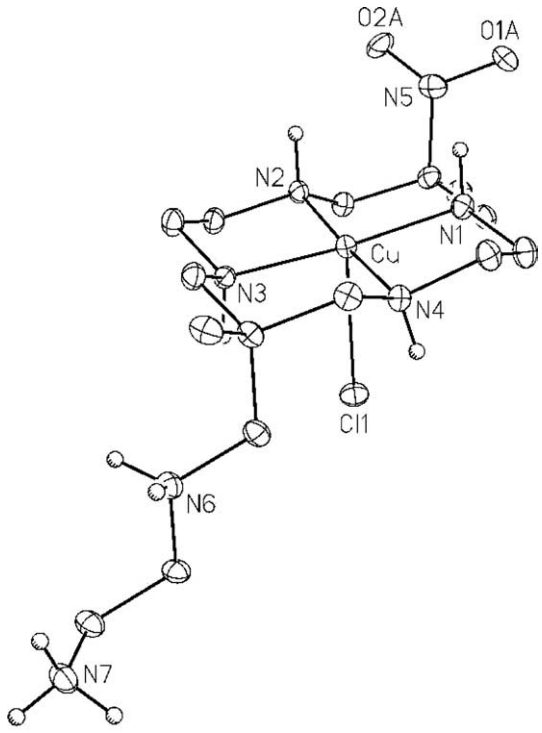


Fig. 6. View of complex **5**. The counter-ions, the solvent molecules and the carbon-bound hydrogen atoms are omitted for clarity. Only one position of the disordered nitro group is represented. Displacement ellipsoids are drawn at the 30% probability level.

[Cu–OH_2 2.585(6) Å], with the former being to the same side of the mean macrocyclic plane as the nitro group and pendent arm substituents. Charge balance requires that the uncoordinated carboxylate group retains its proton, although its exact location was not found in the crystal structure. There are numerous H-bonding interactions throughout the lattice and one of the consequences is that the complex cations form pairs in which there is symmetrical bonding of the uncoordinated dipicolinate carboxylate to NH units of the pendent arm of the adjacent complex. (Extensive H-bonding involving unidentate dipicolinate is also seen in a Mn(III) cyclam complex [22].) The planes of the dipicolinate rings lie parallel throughout the lattice but this does not seem to signify any stacking interactions [23], since little overlap in projection of the rings is apparent and no C···C contact is <3.6 Å. The nitro group planes lie essentially parallel to those of the dipicolinate groups and in fact the only contact which might be regarded as of a stacking kind is that between a nitro-O and the uncoordinated oxygen of the carboxylate group bound to Cu, where O···O = 3.254(6) Å.

In [Cu(senmacH)Cl($OClO_3$)](ClO_4)$_2\cdot 3H_2O$ (**5**), again the expected macrocycle is present and is in the *trans*-III conformation, though here the substituents are *anti*, with both methyl groups being equatorial, so that the pendent arm, being axial, is less extended laterally from the macrocycle (Fig. 6). The Cu(II) is bound axially to a chloride ion [Cu–Cl 2.700(1) Å] and a slightly closer perchlorate-O [Cu–O(ClO_3) 2.603(4) Å]. The extension of the Cu–Cl bond with respect to that found in comlex **3** is associated with a lattice which has an obvious layer structure, in various ways reminescent of that of [Cu(senamH)Cl(FPF_5)](PF_6)$\cdot 2H_2O$. The cations lie in sheets parallel to *ac*, with separations alternating between ~14 and ~8 Å. All Cu–Cl vectors are oriented into the larger space, which is also occupied by perchlorate anions and water molecules, giving an extended H-bonding array in which each chloride interacts with 3 water molecules [Cl1···O 3.133(4), 3.168(4) and 3.181(4) Å]. The pendent arms form part of the same array, each $-NH_2^+CH_2CH_2NH_3^+$ unit chelating a water molecule. Only nitro groups and perchlorate anions occupy the smaller space and, although there is disorder of both entities, it is appears possible that there may be some attractive O···O interactions [24] between them.

4. Conclusions

The present work demonstrates that it is possible to conduct a very simple and efficient synthesis of quite sophisticated pendent arm macrocycles, providing both *syn* and *anti* isomers of functionalised cyclam-like ligands in comparable yields. The simplicity and rapidity of the method, coupled to the ease with which Cu(II) can be removed from such macrocycles [16], suggest it should be advantageous over methods known for

syntheses of some similar ligands [25]. The aminal formation processes further characterised here and observed in the original work on "ryongamines" [5] are an obvious means of controlling the orientation of pendent arms with respect to the macrocyclic centre which can be added to the employment of a ligand in different isomeric forms to the same end. Note that the detection of comparable amounts of both *syn* and *anti* isomers of unfunctionalised ryongamines under the conditions of synthesis used herein suggest that the *syn* isomer of the functionalised ryongamine could well have been present in the products of the earlier synthesis.

5. Supplementary material

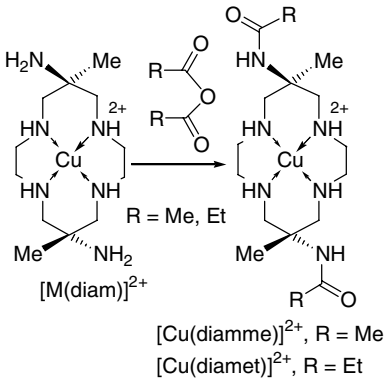
Crystallographic data for the structural analysis have been deposited with the Cambridge Crystallographic Data Centre, CCDC Nos. 264310–264314. Copies of this information may be obtained free of charge from The Director, CCDC, 12 Union Road, Cambridge CB2 1EZ, UK (fax: +44 1223 336033; e-mail: deposit@ccdc.cam.ac.uk or www: http://www.ccdc.cam.ac.uk).

Acknowledgement

This work was supported by the Brain Busan Project 2004 and Kosin University.

References

[1] L.F. Lindoy, The Chemistry of Macrocyclic Ligand Complexes, University Press, Cambridge, 1989.
[2] M.P. Suh, Adv. Inorg. Chem. 44 (1997) 93.
[3] P.V. Bernhardt, G.A. Lawrance, Coord. Chem. Rev. 104 (1990) 297.
[4] (a) For some recent examples, see P.V. Bernhardt, E.J. Hayes, Inorg. Chem. 42 (2003) 1371;
(b) P.V. Bernhardt, E.J. Hayes, Inorg. Chem. 41 (2002) 2892;
(c) P.V. Bernhardt, E.G. Moore, M.J. Riley, Inorg. Chem. 41 (2002) 3025;
(d) P. Comba, Y.D. Lampeka, A.Y. Nazarenko, A.I. Prikhod'ko, H. Pritzkow, Eur. J. Inorg. Chem. (2002) 1464.
[5] J.M. Harrowfield, Y. Kim, Y.H. Lee, P. Thuéry, Eur. J. Inorg. Chem. (2003) 2913.
[6] (a) R.J. Geue, G.H. Searle, Aust. J. Chem. 36 (1986) 927;
(b) J.L. Sarneski, F.L. Urbach, J. Am. Chem. Soc. 93 (1971) 884;
(c) R.W. Green, K.W. Catchpole, A.T. Philip, F. Lions, Inorg. Chem. 2 (1963) 597, and references therein.
[7] J.M. Harrowfield, G. Jang, Y. Kim, P. Thuéry, J. Vicens, J. Chem. Soc., Dalton Trans (2002) 1241.
[8] Kappa-CCD Software, Nonius B.V., Delft, The Netherlands, 1998.
[9] Z. Otwinowski, W. Minor, Methods Enzymol. 276 (1997) 307.
[10] G.M. Sheldrick, SHELXS-97 and SHELXL-97, University of Göttingen, Germany, 1997.
[11] A.L. Spek, PLATON, University of Utrecht, The Netherlands, 2000.
[12] H.D. Flack, Acta Crystallogr., Sect. A 39A (1983) 876.
[13] G.M. Sheldrick, SHELXTL, Version 5.1, Bruker AXS Inc., Madison, WI, 1999.
[14] P.V. Bernhardt, R. Bramley, L.M. Engelhardt, J.M. Harrowfield, D.C.R. Hockless, B.R. Korybut-Daszkiewicz, E.R. Krausz, T. Morgan, A.M. Sargeson, B.W. Skelton, A.H. White, Inorg. Chem. 34 (1995) 3589, and references therein.
[15] N.F. Curtis, in: G.A. Melson (Ed.), Coordination Chemistry of Macrocyclic Compounds, Plenum Press, New York, 1979, p. 219 (Chapter 4).
[16] P.S. Donnelly, J.M. Harrowfield, B.W. Skelton, A.H. White, Inorg. Chem. 40 (2001) 5645.
[17] P.V. Bernhardt, J.M. Harrowfield, Y. Kim, G.A. Koutsantonis, Y.H. Lee, P. Thuéry, Inorg. Chem. 43 (2004) 1681, 1689.
[18] P.V. Bernhardt, T.E. Dyahningtyas, S.C. Han, J.M. Harrowfield, I.-C. Kim, Y. Kim, G.A. Koutsantonis, E. Rukmini, P. Thuéry, Polyhedron 23 (2004) 869.
[19] P.V. Bernhardt, Y. Kim, unpublished.
[20] K. Tomioka, U. Sakaguchi, H. Yoneda, Inorg. Chem. 23 (1984) 2863.
[21] (a) B. Bosnich, C.K. Poon, M.L. Tobe, Inorg. Chem. 4 (1965) 1102;
(b) M.A. Donnelly, M. Zimmer, Inorg. Chem. 38 (1999) 1650.
[22] N. Shaikh, A. Panja, P. Banerjee, M. Kubiak, Z. Ciumik, M. Puchalska, J. Legendziewicz, P. Vojtsek, Inorg. Chim. Acta 357 (2004) 25.
[23] C. Janiak Soc., J. Chem. Dalton Trans. (2000) 3885.
[24] P.M. Zorky, O.V. Grineva, J. Incl. Phenom. Macrocyclic Chem. 48 (2004) 81.
[25] P.M. Angus, R.J. Geue, N.K.B. Jensen, F.K. Larsen, C.J. Qin, A.M. Sargeson, J. Chem. Soc., Dalton Trans. (2002) 4260.



Scheme 1.

3. Structural study

The structure of *di*(perchlorato-κ^1O)-($R^1R^4S^8S^{11}$-*trans*-6,13-bisethylamido-6,13-dimethyl-1,4,8,11-tetraazacyclotetradecane-$\kappa^4N^1N^4N^8N^{11}$)copper(II), [Cu(diamet)$(OClO_3)_2$] was determined by X-ray diffractometry, see Section 4.2 for details. The structure is centrosymmetrical and molecular, with copper in square-planar coordination by the four endocyclic secondary amine nitrogen atoms of the macrocycle and with weaker axial interactions with perchlorate oxygen atoms O2 and O2 ($1-x$, $1-y$, $1-z$), see Fig. 1 and Table 1 for significant dimensions. The macrocycle has a conformation with near symmetrical chair and gauche conformations of the chelate rings, see Table 2 for displacements from CuN_2 planes for the chelate rings. The perchlorate ions are also linked to the cation by hydrogen bonds N1–H1···O2 ($1-x$, $1-y$, $1-z$). The amide groups do not interact with the copper, but form N–H···N and N–H···O intramolecular hydrogen bonds and also N–H···O intermolecular hydrogen bonds between amide groups which link the "molecules" into a chain; see Table 3 for hydrogen bond parameters.

The structure of the cation is similar to that for the nickel(II) compound [1], which has the $[Ni(diamet)]^{2+}$ cation in the same configuration and closely similar conformation, with *trans*-coordinated oxygen atoms of water or hydrogen carbonate, except that the M–N distances are shorter and the M–O distances longer for copper(II). Structures have been reported for *trans*-*RRSS*-[Cu(diam)$(OClO_3)_2$] [2], *trans*-*RRSS*-[Cu(diam)$(H_2O)_2$]$(ClO_4)_2$ [3] and *trans*-*RRSS*-[Cu(diam-H_2)$(OClO_3)_2$]$(ClO_4)_2$ [4], all with similar coordination geometry and macrocycle conformations.

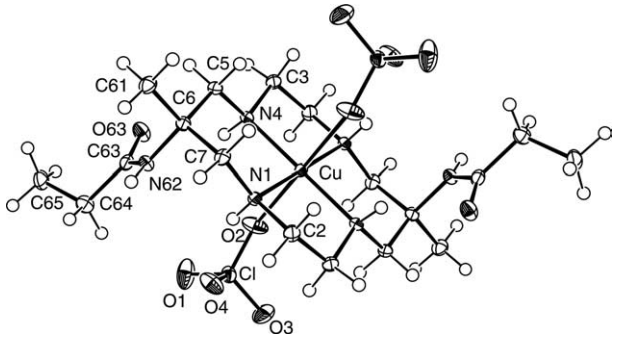


Fig. 1. The "molecule" of *trans*-[Cu(diamet)$(OClO_3)_2$] drawn [6] with displacement ellipsoids at the 50% confidence level, with H-atoms shown as circles of arbitrary radius.

Table 1
Selected dimensions (Å, °) for *trans*-[Cu(diamet)$(OClO_3)_2$]

Atoms	Distance	Atoms	Angle
Cu–N1	2.012(2)	N1–Cu–N4	86.62(8)
Cu–N4	1.996(2)	N1–Cu–N4^i	93.38(8)
Cu–O2	2.528(2)	N1–Cu–O2	93.20(8)
		N4–Cu–O2	81.75(8)

Symmetry codes: $i = 1-x, 1-y, 1-z$.

Table 2
Displacement of atoms (Å) from the CuN_4 plane for *trans*-[Cu(diamet)$(OClO_3)_2$]

Atom	Displacement	Atoms	Displacement
C2	0.337(4)	C3	0.360(4)
C5	0.811(4)	C6	0.494(5)
C7	0.853(5)	C61	1.368(6)
N62	−0.916(5)	C63	−1.873(6)
O63	−1.763(5)	C64	−3.151(6)
C65	−3.671(8)	O2	−2.499(2)

Table 3
Hydrogen-bond parameters(Å, °) for *trans*-[Cu(diamet)$(OClO_3)_2$]

Atoms	D–H	H···A	D···A	D–H···A
N1–H1···O4	0.82(3)	2.22(3)	2.970(3)	153(2)
N1–H1···O2	0.82(3)	2.93(3)	3.318(3)	111(2)
N1–H1···N62	0.82(3)	2.55(3)	2.896(3)	107(2)
N4–H4···O63	0.84(3)	2.15(3)	2.836(3)	138(3)
N4–H4···O2	0.84(3)	2.57(3)	2.988(3)	112(2)
N62–H6D···O63^i	0.80(3)	2.16(3)	2.917(3)	160(3)

Symmetry codes: $i = x + 1/2, -y, -z + 1/2$.

4. Experimental

The compound [Cu(diam)]$(ClO_4)_2$ [4] was prepared from diam [5] and dried by heating at 100 °C. DMSO can be substituted for DMF in the preparations; commercial anhydrous DMF and DMSO were used; these solvents need not be rigorously dried.

The perchlorate salts described were not observed to be shock sensitive and decomposed non-violently if strongly heated. They should still be treated with the caution due to any perchlorate compound.

4.1. Synthesis of compounds

4.1.1. (trans-6,13-Bis-ethylamido-6,13-dimethyl-1,4,8,11-tetraazacyclotetradecane)copper(II) perchlorate, [Cu(diamet)](ClO$_4$)$_2$

[Cu(diam)](ClO$_4$)$_2$ (1 g) was dissolved in DMF (1 g) by warming. Propionic anhydride (1 g) was added and the solution heated at c. 100 °C for 30 min. Propan-2-ol (20 cm^3) was added and after 1 h. the red crystals were filtered off, yield 90+%. The reaction was faster than the analogous reaction for nickel(II). The *product* crystallizes in two forms, as with the nickel(II) analogue, (a) from DMF/propan-2-ol or rapidly from water and (b) slowly from water as large crystals. *Anal.* Calc. for $C_{18}H_{38}Cl_2N_6NiO_{10}$: C, 34.2; H, 6.1; N, 13.3. Found (a): C, 34.2; H, 6.2; N, 13.3%. (b): C, 34.3; H, 6.1; N, 13.3%. Spectra; infrared {ν_{max} (cm^{-1})} (a): ν(NH) 3342sp, 3234sp, 3069w,br; amide bands 1674, 1547; (b): ν(NH) 3279, 3219, 3093w; amide bands 1649, 1555); visible spectrum in water (same for both forms): {λ_{max} (nm) (ε) (mol dm^{-3} cm^{-1})} 504 (76); in 1 mol dm^{-3} NaOH; 514 (82).

4.1.2. (trans-6,13-Bis-methylamido-6,13-dimethyl-1,4,8,11-tetraazacyclotetradecane)copper(II) perchlorate hemihydrate, [Cu(diamme)](ClO$_4$)$_2$·1/2H$_2$O

The red compound was prepared as for the propionyl homologue by using acetic anhydride. *Anal.* Calc. for $C_{16}H_{35}Cl_2CuN_6O_{10.5}$: C, 31.3; H, 5.7; N, 13.7. Found: C, 31.1; H, 5.7; N, 13.6%. Infrared spectrum {ν_{max} (cm^{-1})}: ν(NH) 3398sp, 3242sp; amide bands 1668, 1527; visible spectrum {λ_{max} (nm) (ε) (mol dm^{-3} cm^{-1})}; in water 512 (43); in 1 mol dm^{-3} NaOH; 512 (88).

4.2. Structural study

4.2.1. Crystal data [7]

$C_{18}H_{42}Cl_2CuN_6O_{10}$, M_r = 632.98, red block grown from water, 0.75 × 0.38 × 0.24 mm, orthorhombic, space group *Pbca*, a = 9.513(1), b = 14.731(2), c = 18.659(3) Å, Z = 4, cell parameters from 4511 reflections.

4.2.2. Data collection

Bruker SMART 1K CCD area detector diffractomer, ω scans, Mo Kα radiation, T = 118(2) K, multi-scan absorption correction (based on symmetry-related measurements [8]), T_{min} = 0.495, T_{max} = 0.992, 8428 measured reflections. (average R equivalents 0.0450), $h - 9 \rightarrow 11$, $k - 13 \rightarrow 17$, $l - 23 \rightarrow 23$, θ_{min} 2.77°, θ_{max} 26.35°, 2444 independent reflections, 1793 reflections with $I > 2\sigma(I)$.

4.2.3. Refinement [9]

Refinement on F^2, $R[F^2 > 2\sigma(F^2)] = 0.038$, $wR(F^2) = 0.099$ $(w = 1/[\sigma^2(F_o^2) + (0.0553P)^2 + 0.7095P]$ where $P = (F_o^2 + 2F_c^2)/3)$, 183 parameters.

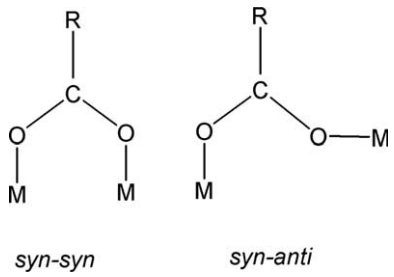
H(N) atoms were located from difference syntheses and their positions refined, H(C) atoms are riding in calculated positions.

Appendix A. Supplementary Data

Crystallographic data has been deposited with the Cambridge Crystallographic Data Centre; CCDC 261006. Copies may be obtained free of charge from the Director, CDCC, 12 Union Road, Cambridge, CBZ 1EZ, UK (fax: +44-1223-336-033; e-mail: deposit@ccdc.cam.ac.uk or http://www.ccdc.cam.uk). Supplementary data associated with this article can be found in the online version, at doi:10.1016/j.poly.2005.03.013.

References

[1] N.F. Curtis, H. Puschmann, Polyhedron 24 (2005) 281.
[2] G.A. Lawrance, B.W. Skelton, A.H. White, P. Comba, Aust. J. Chem. 39 (1986) 1101.
[3] P.V. Bernhardt, L.A. Jones, P.C. Sharpe, J. Chem. Soc., Dalton Trans. (1997) 1169.
[4] P. Comba, N.F. Curtis, G.A. Lawrance, A.M. Sargeson, B.W. Skelton, A.H. White, Inorg. Chem. 25 (1986) 4260.
[5] N.F. Curtis, G.J. Gainsford, A. Siriwardena, D.C. Weatherburn, Aust. J. Chem. 46 (1993) 755.
[6] L.J. Farrugia, J. Appl. Cryst. 30 (1997) 565, OadsRTEP-32.
[7] Bruker SMART (version 5.054), SADABS (version 2.03) and SAINT (version 6.02A), Bruker AXS Inc., Madison, Wisconsin, USA, 1997.
[8] R.H. Blessing, Acta Crystallogr., Sect. A 51 (1995) 33.
[9] G.M. Sheldrick, SHELXTL (version 5.10). Programs for the Solution and Refinement of Crystal Structures, 1997.



Scheme 1.

Scheme 1). Specially, the *syn–anti* mode confirmation is very rare and only a limited number of X-ray structures have been reported with this *syn–anti* acetate bridging mode [9,10,12,14–20].

However, to the best of our knowledge, so far only one polymeric Cu(II) structure with an N-containing ligand has been published with acetate as the bridging molecule in a $[–\mu\text{-OAc–Cu–}\mu\text{-OAc–Cu}]_n$ fashion [9].

In this study, we report the synthesis, spectroscopic characterization and magnetic properties of $\{[Cu(dpa)(CH_3COO)](ClO_4)\cdot 0.5THF\}_n$, a new polymeric copper(II) compound with an infinite zig-zag chain structure, having the acetate ligand in a *syn–anti* bridging mode.

2. Experimental

2.1. General remarks and physical measurements

All starting reagents and solvents were purchased from commercial sources and were used as received. C, H, N analyses were performed on a Perkin–Elmer 2400 Series II analyzer. Infrared spectra (4000–300 cm^{-1}) were recorded on a Perkin–Elmer Paragon 1000 FT-IR spectrometer equipped with a Golden Gate ATR device, using the reflectance technique. Ligand field spectra were obtained on a Perkin–Elmer Lambda 900 spectrophotometer using the diffuse reflectance technique, with MgO as a reference. Magnetic susceptibility measurements (5–300 K) were carried out using a Quantum Design MPMS-5 5T SQUID magnetometer. Data were corrected for the magnetization of the sample holder and for diamagnetic contributions, which were estimated from the Pascal constants.

2.2. Synthesis of the compound

To an acetonitrile solution (10 ml) containing $Cu(ClO_4)_2\cdot 6H_2O$ (0.37 g, 1 mmol) and dpa (0.2 g, 1 mmol) was added slowly an acetonitrile (5 ml) solution containing CH_3COOH (0.02 g, 0.33 mmol) and Et_3N (0.03 g, 0.33 mmol). The reaction mixture was stirred for 10 min and was then filtered to remove the impurities. The resulted blue filtrate was diluted with 10 ml of THF and it was allowed to stand at room temperature. After 2 days dark blue crystals were obtained. Yield: 0.31 g (ca. 66%). *Anal.* Calc. for $C_{16}H_{19}ClCuN_3O_{6.5}$: C, 42.1; H, 4.2; N, 9.2. Found: C, 42.7; H, 4.5; N, 8.9%. UV–Vis (λ_{max}/nm): 632, 380, 314, 279.

The positive ion mass spectrum of a fresh solution of the compound in acetonitrile exhibits a prominent signal at $m/z = 320$ (relative intensity $I = 100\%$ in the range $m/z = 100$–500). This signal matches very well with the calculated isotopic distribution for $[Cu(dpa)(CH_3COO)]^+$.

2.3. X-ray crystallography and data collection

Intensity data for a single crystal were collected using Mo Kα radiation ($\lambda = 0.71073$ Å) on a Nonius KappaCCD diffractometer. The structure was solved by automated Patterson methods using DIRDIF-99 [21] and was refined on F^2 by least-squares procedures using SHELXL-97 [22]. A SADABS multiscan correction [23] was applied. The hydrogen atoms of the methyl group were refined as rigid rotors to match maximum electron density in a difference Fourier map. All other hydrogens were placed at calculated positions and were refined riding on the parent atoms. The THF molecule is disordered around a centre of symmetry. A suitable disorder model could be defined in which the THF molecule partly occupies one of the two possible positions and orientations, each having a site occupation factor of 0.5. Geometric calculations and molecular graphics were performed with the PLATON package [24]. Crystallographic data are listed in Table 1.

Table 1
Crystallographic data for the $\{[Cu(dpa)(CH_3COO)](ClO_4)\cdot 0.5THF\}_n$

Chemical formula	$C_{16}H_{19}ClCuN_3O_{6.5}$
Molecular weight	456.34
Crystal system	monoclinic
Space group	$P2_1/n$ (No. 14)
a (Å)	10.6956(6)
b (Å)	7.7949(3)
c (Å)	23.3892(13)
β (°)	99.064(5)
V (Å^3)	1925.63(17)
Z	4
D_{calc} (Mg m^{-3})	1.574
μ (Mo Kα) (mm^{-1})	1.314
Crystal size (mm)	$0.26\times0.20\times0.07$
T (K)	208
Data collected	39 520
Unique data	4417
R_{int}	0.045
$R(F)$ [$I > 2\sigma(I)$]	0.0570
R_w (F^2)	0.1475
S	1.06
$\Delta\rho_{min}$ and $\Delta\rho_{max}$ (e Å^{-3})	−0.65 and 1.33

3. Results and discussions

3.1. Description of the crystal structure of $\{[Cu(dpa)(CH_3COO)](ClO_4)\cdot 0.5THF\}_n$

A plot of the title compound with the atomic labelling scheme is shown in Fig. 1, with selected bond lengths and angles listed in Table 2. The molecular structure of the title compound consists of one-dimensional ladder-like chains in which the CH_3COO^- acts as an asymmetric didentate bridging ligand, ClO_4^- anions and disordered THF molecules. Each copper(II) atom is five-coordinated and adopts a square-pyramidal geometry with a N_3O_2 donor set. The coordination geometry is slightly distorted from square pyramidal, as ascertained by the observed τ value of 0.06 (the structure index is defined as $\tau = (\beta - \alpha)/60$, where β and α are the largest coordination angles, $\tau = 0$ for square pyramidal (SP) and $\tau = 1$ for trigonal bipyramidal (TBP) geometry [25]). One oxygen atom of an acetate bridge and the three nitrogen atoms of the dpa ligand constitute the basal plane of the square pyramid, and the oxygen of a symmetry-related acetate bridge occupies the apical position of the square pyramid. The copper(II) atom lies 0.015(3) Å above the basal plane toward the acetate oxygen atom O(32)b. The largest distortions from the square pyramidal geometry are indicated by the O(31)–Cu(1)–N(3) = 168.98(12)° and N(1)–Cu(1)–N(2) = 165.14(13)° angles. The Cu(II) atoms are connected through single *syn–anti* acetate bridges with a Cu···Cu separation of 4.039 Å, forming is this way a 1D zig-zag polymeric compound (Fig. 2).

Table 2
Selected bond lengths (Å) and bond angles (°) for $\{[Cu(dpa)(CH_3COO)](ClO_4)\cdot 0.5THF\}_n$

Bond lengths (Å)	
Cu(1)–O(31)	1.950(2)
Cu(1)–O(32)b	2.388(3)
Cu(1)–N(1)	1.984(3)
Cu(1)–N(2)	1.998(3)
Cu(1)–N(3)	1.985(3)
Cu(1)–Cu(1)a	4.0399
Bond angles (°)	
O(31)–Cu(1)–N(1)	97.86(12)
O(31)–Cu(1)–N(2)	96.92(12)
O(31)–Cu(1)–N(3)	168.98(12)
O(31)–Cu(1)–O(32)b	102.27(10)
N(1)–Cu(1)–N(2)	165.14(13)
N(1)–Cu(1)–N(3)	83.00(14)
N(1)–Cu(1)–O(32)b	87.12(12)
N(2)–Cu(1)–N(3)	82.20(14)
N(2)–Cu(1)–O(32)b	91.25(12)
N(3)–Cu(1)–O(32)b	88.74(12)

Symmetry codes: a = 1/2 − *x*, −1/2 + *y*, 1/2 − *z*; b = 1/2 − *x*, 1/2 + *y*, 1/2 − *z*.

3.2. Infrared and ligand-field characterisation

The infrared spectra of the title compound exhibits the bands expected for the organic ligands and

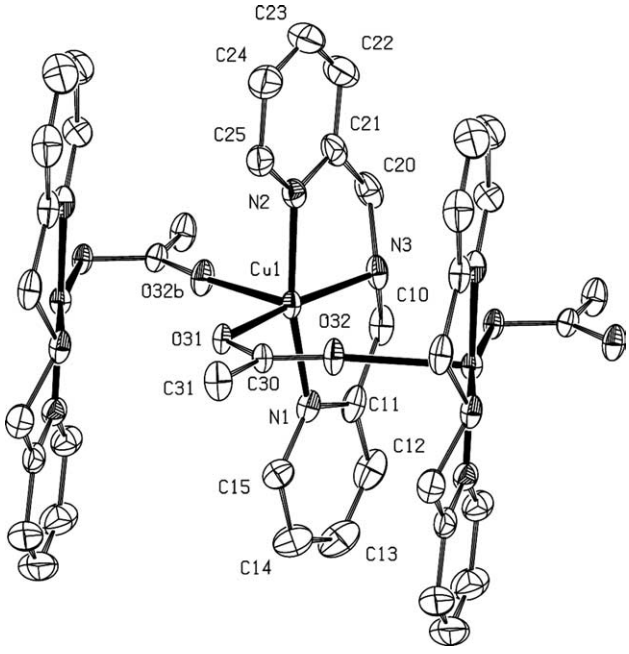


Fig. 1. Thermal ellipsoid plot at 50% probability of $\{[Cu(dpa)(CH_3COO)](ClO_4)\cdot 0.5THF\}_n$ with atom-labelling scheme. Hydrogen atoms, the uncoordinating perchlorate anion and the disordered THF molecule are omitted for clarity. Atoms marked with a "b" are generated by a twofold screw axis.

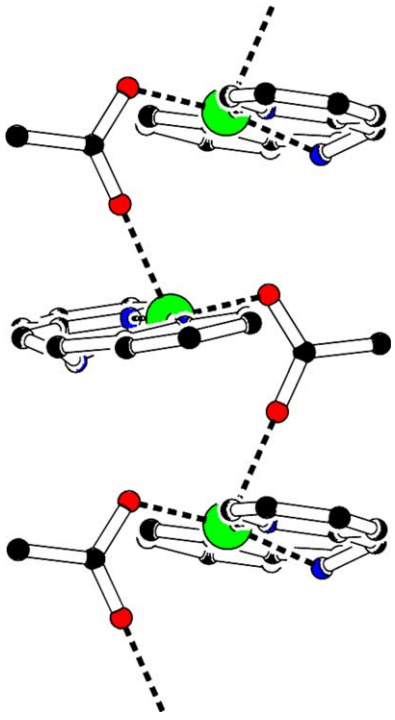


Fig. 2. The zig-zag chain of Cu–OAc units.

counterion. Particularly, the asymmetric stretching vibration ν_{asym}(COO) is observed at 1613 cm^{-1}, while the symmetric stretching vibration ν_{sym}(COO) appears at 1449 cm^{-1}. The difference between ν_{asym}(COO) and ν_{sym}(COO) of about 164 cm^{-1} agrees with a bridging coordination mode for the acetate molecule [9,12,26]. The ligand field spectrum of the compound shows a broad band with a maximum at 15.7×10^{-3} cm^{-1} characteristic of a copper(II) $d_{zx}, d_{yz} \rightarrow d_{x^2-y^2}$ ($^2B_1 \rightarrow {}^2E$) transition [27] in a tetragonal ligand field, in which the copper(II) has a distorted square-pyramidal coordination environment.

3.3. EPR and magnetic properties

The EPR spectrum measured as a powdered solid at RT and 77 K shows an unresolved axial $S = 1/2$ signal with $g_\perp$ of 2.06 and a $g_\parallel$ of 2.24. The EPR spectrum recorded in frozen solution (DMF/MeOH 1:1 mixture) at 77 K shows a resolved spectrum with $g_\perp$ of 2.04, a $g_\parallel$ of 2.26 and an $A_\parallel$ of 17.9 mT, consistent with the planar geometry and the $CuN_3O(O)$ chromophore [28].

The magnetisation of a powdered sample of $\{[Cu(dpa)(CH_3COO)](ClO_4) \cdot 0.5THF\}_n$ was measured from 5 to 300 K in an applied field of 0.1 T. The resulting molar magnetic susceptibility, χ_M, is plotted in Fig. 3. On lowering the temperature from 300 to 5 K, the χ_M value stays almost constant (μ_{eff} around 1.60–1.65 BM, which is slightly below the theoretical value expected for one non-coupled Cu(II) centre with $S = 1/2$). At around 50 K the χ_M value start to increase until it reaches a value of about 0.10 cm^3 mol^{-1} K at 5 K (μ_{eff} around 1.78 BM), a behaviour indicative of a very weak ferromagnetic coupling between Cu centres.

The temperature dependence of χ_m has been fitted using the equation [29] derived from the Heisenberg exchange Hamiltonian for an uniformly spaced chain of spins with $S = 1/2$: $H = -J\sum_{i=1}^{n-1} S_{A_i} \cdot S_{A_i+1}$ (in which A_i are the nearest neighbour Cu(II) ions and the exchange parameter J is positive for ferromagnetic and negative for an antiferromagnetic interaction). A Temperature Independent Paramagnetism (TIP) of 60×10^{-6} cm^3 mol^{-1} per Cu(II) ion has been used. The best fit of the experimental magnetic susceptibility data for a chain (solid line in Fig. 3) was obtained using the magnetic parameters $g = 2.0$, $J = 0.21$ cm^{-1}, p (which is the paramagnetic impurity which is present in the bulk sample) 0.41%, with a final $R = 1.09 \times 10^{-6}$. As the Cu···Cu distance is fairly large (4.039 Å) this very weak ferromagnetic interaction most likely occurs via the Cu–O–C–O–Cu pathway. This is consistent with a few other formato and acetato bridged polymeric compounds, $\{[Cu(di\text{-}2\text{-}pyridylamine)(\mu\text{-}O_2CH)(OH_2)]_n(NO_3)_n\}$ and $\{[Cu(diethylenetriamine)(\mu\text{-}O_2C\text{-}H_3)]_n(ClO_4)_n\}$, which also exhibit a weak ferromagnetic interaction with J values of 0.75 and 0.52 cm^{-1}, respectively [10,30].

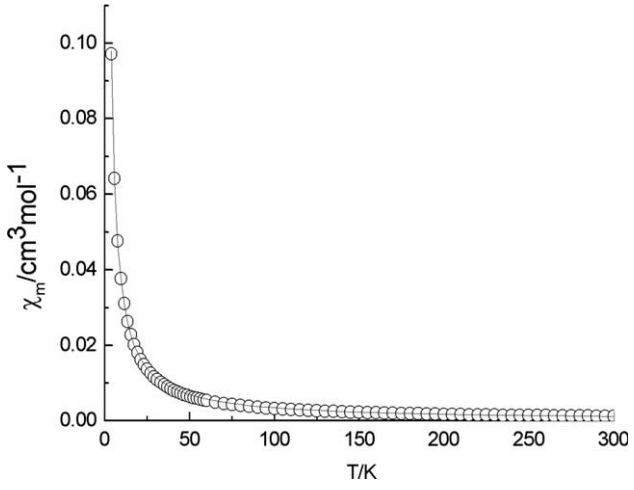


Fig. 3. Temperature dependence of χ_M vs. T per Cu atom. The solid lines is the best fit with $J = 0.21$ cm^{-1} (see text).

4. Conclusions

In this paper, an unusual *syn–anti* acetato-bridged Cu(II) compound is presented, which adopts a 1D zigzag polymeric array. The magnetic interaction is very weak ($J = 0.21$ cm^{-1}), which is not surprising as the Cu–Cu distance is fairly large, and the magnetic orbitals are orthogonal.

5. Supplementary material

Crystallographic data (excluding structure factors) have been deposited with the Cambridge Crystallographic Data Centre as supplementary publication No. CCDC 262052. Copies of the data can be obtained free of charge on application to The Director, CCDC, 12 Union Road, Cambridge CB2 1EZ, UK (fax: +44 1223 336 033; e-mail: deposit@ccdc.cam.ac.uk or www: http//www.ccdc.cam.ac.uk).

Acknowledgements

This work was in part financially supported by the Dutch Economy, Ecology, Technology (EET) programme, a joint programme of the Ministry of Economic Affairs, the Ministry of Education, Culture and Science, and the Ministry of Housing, Spatial Planning and the Environment. The work described in the present paper has been supported by the Leiden University Study group WFMO (Werkgroep Fundamenteel Materialen Onderzoek).

References

[1] D. Gatteschi, O. Kahn, J.S. Miller, F. Pallacio, Adv. Mater. 3 (1991) 161.
[2] C.N.R. Rao, S. Natarajan, R. Vaidhyanathan, Angew. Chem., Int. Ed. 43 (2004) 1466.
[3] H. Müller-Buschbaum, Angew. Chem., Int. Ed. Engl. 30 (1991) 723.
[4] M. Palaniandavar, S. Mahadevan, M. Köckerling, G. Henkel, J. Chem. Soc., Dalton Trans. (2000) 1151.
[5] M. Palaniandavar, R.J. Butcher, A.W. Addison, Inorg. Chem. 35 (1996) 467.
[6] K.-Y. Choi, H. Ryu, N.-D. Sung, M. Suh, J. Chem. Crystallogr. 33 (2003) 947.
[7] G.-S. Huang, J.-K. Lai, C.-H. Ueng, C.-C. Su, Transition Met. Chem. 25 (2000) 84.
[8] N. Niklas, F. Hampel, G. Liehr, A. Zahl, R. Alsfasser, Chem. Eur. J. 7 (2001) 5135.
[9] B.-H. Ye, L.-N. Ji, F. Xue, T.C.W. Mak, Polyhedron 17 (1998) 2687.
[10] D.K. Towle, S.K. Hoffmann, W.E. Hatfield, P. Singh, P. Chaudhuri, Inorg. Chem. 27 (1988) 394.
[11] P. Gentschev, M. Lüken, N. Möller, A. Rompel, B. Krebs, Inorg. Chem. Commun. 4 (2001) 753.
[12] I.A. Koval, P. Gamez, O. Roubeau, W.L. Driessen, M. Lutz, A.L. Spek, J. Reedijk, Inorg. Chem. 42 (2003) 868.
[13] C.T. Zeyrek, A. Elmali, Y. Elerman, J. Mol. Struc. (Theochem) 680 (2004) 159, and references cited therein.
[14] L.-G. Zhu, S. Kitagawa, Inorg. Chem. Commun. 5 (2002) 358.
[15] B. Chiari, O. Piovesana, T. Tarantelli, P.F. Zanazzi, Inorg. Chem. 32 (1999) 4834.
[16] C.A. Crawford, E.F. Day, W.E. Streib, J.C. Huffman, G. Christou, Polyhedron 13 (1994) 2933.
[17] S.P. Perlepes, E. Libby, W.E. Streib, K. Folting, G. Christou, Polyhedron 11 (1992) 923.
[18] S. Warzeska, R. Krämer, Chem. Ber. 128 (1995) 115.
[19] V. Tangoulis, C.P. Raptopoulou, A. Terzis, S. Paschalidou, S.P. Perlepes, E.G. Bakalbassis, Inorg. Chem. 36 (1997) 3996.
[20] J. Valo, M. Näsäkkälä, Acta Chem. Scan. 48 (1994) 20.
[21] P.T. Beurskens, G. Admiraal, G. Beurskens, W.P. Bosman, S. Garcica-Granda, R.O. Gould, J.M.M. Smits, C. Smykalla, The DIRDIF Program System: Technical Report of the Crystallography Laboratory, University of Nijmegen, Nijmegen, 1992.
[22] G.M. Sheldrick, SHELXL-97: Program for the Refinement of Crystal Structures, University of Göttingen, Göttingen, Germany, 1997.
[23] G.M. Sheldrick, SADABS: Program for Emperical Absorption Correction, University of Göttingen, Göttingen, Germany, 1996.
[24] A.L. Spek, J. Appl. Crystallogr. 36 (2003) 7.
[25] A.W. Addison, T.N. Rao, J. Reedijk, J. van Rijn, G.C. Verschoor, J. Chem. Soc., Dalton Trans. (1984) 1349.
[26] K. Nakamoto, Infrared and Raman Spectra of Inorganic and Coordination Compounds, fourth ed., Wiley, New York, 1986.
[27] B.J. Hathaway, Struct. Bond. (Berlin) 57 (1991) 2801.
[28] B.J. Hathaway, in: G. Wilkinson, R.D. Gill, J.A. McCleverty (Eds.), Comprehensive Coordination Chemistry, vol. 5, Pergamon Press, Oxford, 1987.
[29] O. Kahn, Molecular Magnetism, VCH, New York, 1993, p. 253.
[30] S. Youngme, P. Phuengphai, N. Chaichit, G.A. van Albada, S. Tanase, J. Reedijk, Inorg. Chim. Acta (2005) in press.

environment mainly from industrial sources, especially oil refineries and power plants using vanadium-rich fuel oil and coal. Such sources can mobilize appreciable amounts of vanadium and increase the natural background level [16,17]. It is highly useful to examine the recovery and removal of vanadium from the viewpoint of exploitation of undeveloped resources and environmental control.

Anion-exchange resins and chelating resins have been used for separation and concentration procedures [18,19], however, there are very few reports about the adsorption mechanism of vanadium. Chitosan which is an amino-polysaccharide extracted from crustacean shells is effective for removing vanadate anions from dilute solutions under acidic conditions. Guzmán et al. [20] had shown, on the basis of the speciation of vanadate in an external acidic solution, that the high adsorbability of chitosan was attributed to the strong ion exchange interaction between the protonated amine sites of chitosan and anionic isopolyvanadate species such as decamer. Considering the optimum pH for the adsorption, however, chitosan would be inadequate for the practical application to separate and concentrate of vanadium in natural water, such as sea water, without pretreatment. The ion exchange adsorption of such highly charged anionic species would also be greatly suppressed by the coexisting high concentration of background electrolytes. Furthermore, isopolyvanadates in the environment are negligible at the quite low concentration of vanadium (μg dm^{-3} levels or less in sea water [21,22]).

ECTEOLA–Cellulose, which has generally been used for separation of biopolymers [23–25], is a reaction product of epichlorohydrin, triethanolamine and cellulose. The concrete chemical structure is not clear, however, it does contain diethanolamine groups as anchor groups (Fig. 1). Because vanadate can react with tri- or tetradentate ethanolamine derivatives to form a pentacoordinated vanadium(V) complex at neutral to weakly basic pH [26–29], it is expected that ECTEOLA–Cellulose can be used as a chelating adsorbent for the separation and concentration of vanadium from a matrix. In the present work, therefore, the interaction of vanadium(V) oxoanions with ECTEOLA–Cellulose was examined by using distribution and ^{51}V NMR measurements. The NMR method for gel suspension samples is an excellent technique for the speciation of adsorbed species in the gel phase [7–10,30,31] and the characterization of the nature of the gel internal solution [32,33]. The complexation of vanadate with ethanolamine derivatives, such as ethanolamine (EA), diethanolamine (DEA), methyldiethanolamine (MDEA) and triethanolamine (TEA), which would be analogues of the functional group of ECTEOLA–Cellulose, was also investigated by ^{51}V NMR spectroscopy. A comparison between the complexation of vanadate with the functional groups of the gel and with the ethanolamine derivatives gave important information about the adsorption of vanadium(V) onto ECTEOLA–Cellulose.

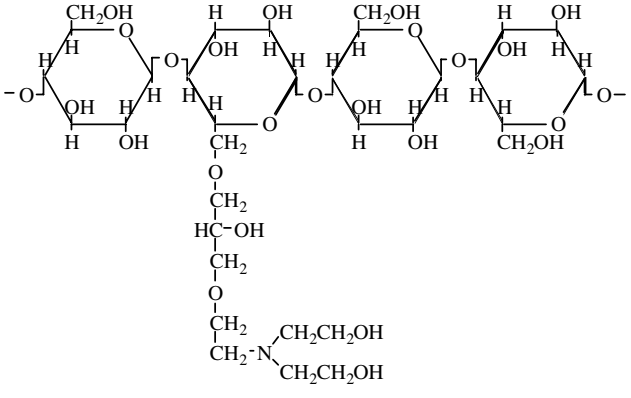


Fig. 1. Expected functional group of ECTEOLA–Cellulose.

2. Experimental

2.1. Materials

All chemicals were of analytical grade and used without further purification. ECTEOLA–Cellulose was obtained from SERVA Electrophoresis (Germany). The nitrogen content of the gel, which corresponds to the amount of functional groups introduced, was 0.40 mmol g^{-1} by an elemental analysis. Stock solutions of sodium vanadate were prepared as described in [34].

2.2. Distribution measurements

The effect of pH in the equilibrated solution on the adsorption of vanadate onto ECTEOLA–Cellulose was examined under acidic conditions as follows: to 20 cm^3 of a 4.0×10^{-6} mol dm^{-3} vanadate solution ($I = 0.01$, CH_3COONa–HCl), in which the pH was adjusted with a little amount of HCl or NaOH solution, 0.1 g of ECTEOLA–Cellulose was added. The mixture was stirred mechanically for 90 min at room temperature and then the pH of the equilibrated solution was measured. The vanadium(V) concentration in the equilibrated solution was determined by ion-exchange phase visible light absorptiometry [22].

We also examined the adsorption behavior under weakly basic conditions as follows: to 20 cm^3 of a 4.0×10^{-4} mol dm^{-3} vanadate solution ($I = 0.1$, NaCl), in which the pH was adjusted with a little amount of HCl or NaOH solution, 0.5 g of ECTEOLA–Cellulose was added. The mixture was stirred mechanically and then the pH of the equilibrated solution was measured in the same way as that for the acidic conditions. The vanadium(V) concentration in the equilibrated

solution was determined spectrophotometrically with 4-(2-pyridylazo)resorcinol (PAR, Dojin, Japan) as a coloring reagent [21]. The gels in equilibrium with the vanadate solutions were also used for ^{51}V NMR measurements.

To evaluate the formation constant of vanadate with ECTEOLA–Cellulose, the variation of the adsorbability for ECTEOLA–Cellulose with the concentration of vanadate in the equilibrated solution ($I = 0.1$) at pH 8.7 was investigated in the same way as mentioned above.

The distribution coefficient K_d is expressed as $K_d = (C_V^{int} - C_V^{eq})v/C_V^{eq}m$, where v is the volume of the solution (20 cm^3), m is the mass of the gel, C_V^{int} is the initial concentration of vanadium(V), and C_V^{eq} is the concentration of vanadium(V) in the equilibrated solution.

2.3. NMR measurements

^{51}V NMR measurements were performed on a JEOL JNM-GSX 500 spectrometer with a 10 mm multinuclear probe at 25 ± 1 °C. The standard NMR parameters were as follows: an observed frequency of 131.5 MHz, the flip angle was approximately 90° (32 μs), the pulse repetition time was 0.5 s and the spectral width was 151.5 kHz. The field frequency lock was achieved with a ^{2}H resonance of D_2O solution in a 2 mm concentric tube. Chemical shifts are reported relative to an external reference of $VOCl_3$ via a second reference of 0.5 mol dm^{-3} vanadate in a 2 mol dm^{-3} NaOH solution which gives the high-field resonance at −541.2 ppm relative to that of $VOCl_3$ [35]. Complexation of vanadate with various ethanolamine derivatives was examined at 1.0×10^{-3} mol dm^{-3} total vanadate concentration and at varying pH. The concentrations of various vanadium(V) species in solutions were determined from the fractions of the total integrated areas observed in ^{51}V NMR spectra. The NMR spectra for ECTEOLA–Cellulose in equilibrium with vanadate solutions were measured in the same way as those for ordinary solution samples.

3. Results and discussion

Vanadate undergoes condensation reactions to form a variety of isopolyvanadates including a dimer, *cyclo*-tetramer, *cyclo*-pentamer and decamer in aqueous solutions [36,37]. The concentrations of monomeric vanadates are dependent on both pH and the total vanadate concentration. In the presence of a ligand, further reactions will occur to give complexes of which characteristics can be deduced from ^{51}V NMR spectroscopy. Because the complexation is observed only in alkaline solution, equilibria examined in this paper are basicaly written with the components, diprotonated vanadate $H_2VO_4^-$ ($pK_{aV} = 8.17$ [38]), non-protonated free ethanolamine derivative and H^+. Protonation constants of ethanolamine derivatives were taken from [26,39].

3.1. EA system

A reversible complexation of vanadate occurs to provide tetrahedrally coordinated esters in the presence of a large amount of ethanol in aqueous media [40]. Despite EA being a simple ligand, such as ethanol, the nature of the complexation with vanadate has not been clarified yet. The concentrations of various vanadate species are dependent on pH, and it is, therefore, expected that the reaction between vanadate and EA is dependent on pH. First, the complexation was examined at a constant concentration ratio of EA to total vanadate as a function of pH. Fig. 2 shows ^{51}V NMR spectra of solutions containing 1.0×10^{-3} mol dm^{-3} vanadate and 0.4 mol dm^{-3} EA at various pH. The large signal, whose chemical shift is dependent on pH, is due to free $H_2VO_4^-/HVO_4^{2-}$ (V_1). The other signals at −570 ∼−576, −579 and −587 ppm are dimer (V_2), *cyclo*-tetramer (V_{4c}) and *cyclo*-pentamer (V_{5c}), respectively. The small and broad signal is ascribed to complexes.

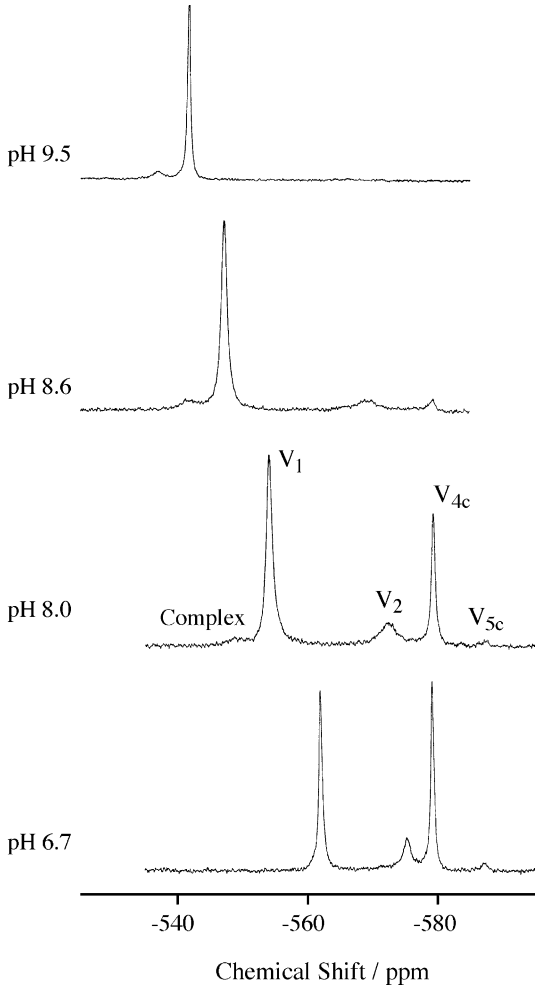


Fig. 2. ^{51}V NMR spectra of solutions containing 1.0×10^{-3} mol dm^{-3} vanadate and 0.4 mol dm^{-3} EA at different pH. V_1: $H_2VO_4^-/HVO_4^{2-}$; V_2: dimer; V_{4c}: *cyclo*-tetramer; V_{5c}: *cyclo*-pentamer.

Since the chemical shift of the signal is dependent on the pH of the solution, protonated and deprotonated complexes should be added to the speciation scheme.

When complexes with low stability and with 1:n stoichiometry are formed, the concentration ratio of the complexes to vanadate ($[\text{complexes}]/([H_2VO_4^-]+[HVO_4^{2-}])$) is proportional to C_{EA}^n under a condition of $C_{EN} \gg C_V$ at a constant pH, where C_{EA} and C_V are the total concentrations of EA and vanadium(V). In order to estimate the stoichiometry of the complexes the quotient $([\text{complexes}]/([H_2VO_4^-]+[HVO_4^{2-}]))$ which is calculated from ^{51}V NMR intensities is plotted against C_{EA} at a constant pH of 10 (where $C_{EA} \gg C_V$). The plot can be fitted on a straight line passing through the origin (Fig. 3), which shows that the stoichiometry of the complexes is 1:1. Possible binding structures for the 1:1 complexes of vanadate with EA are shown in Scheme 1. The following equilibria should be taken into consideration in this system:

$$H_2VO_4^- + H_2NCH_2CH_2OH \rightleftharpoons VL(N,O) + H_2O$$

$$\beta_{VL(N,O)} = \frac{[VL(N,O)]}{[H_2VO_4^-][EA]}. \quad (1)$$

$$H_2VO_4^- + H_2NCH_2CH_2OH \rightleftharpoons VL(O) + H_2O$$

$$\beta_{VL(O)} = \frac{[VL(O)]}{[H_2VO_4^-][EA]}. \quad (2)$$

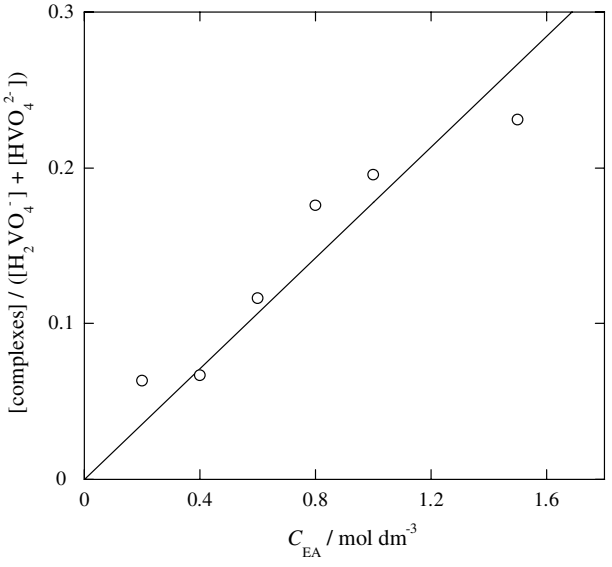
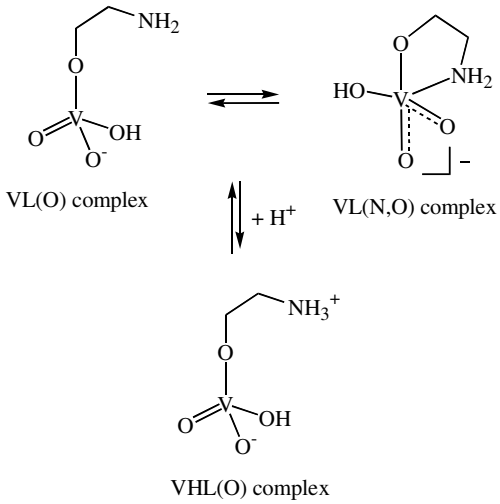


Fig. 3. Determination of the stoichiometry of vanadate complexes with EA at pH 10. The quotient of $[\text{complexes}]/([H_2VO_4^-]+[HVO_4^{2-}])$, which is estimated from ^{51}V NMR intensities, is expressed as a function of total concentration of EA, C_{EA}.



Scheme 1.

$$H_2VO_4^- + H_2NCH_2CH_2OH + H^+ \rightleftharpoons VHL(O) + H_2O$$

$$\beta_{VHL(O)} = \frac{[VHL(O)]}{[H_2VO_4^-][EA][H^+]}. \quad (3)$$

$$VHL(O) \rightleftharpoons VL(N,O) + H^+$$
$$VHL(O) \rightleftharpoons VL(O) + H^+$$

$$K_{aVL} = \frac{([VL(N,O)] + [VL(O)])[H^+]}{[VHL(O)]}. \quad (4)$$

Since only one resonance, whose chemical shift is dependent on pH, is observed for these expected complexes, the observed chemical shift would be expressed by the following equation:

$$\delta_{obs} = \frac{[VL(N,O)]\delta_{(N,O)} + [VL(O)]\delta_{(O)} + [VHL(O)]\delta_{H(O)}}{[VL(N,O)] + [VL(O)] + [VHL(O)]}$$
$$= \frac{\delta_{(N,O),(O)}K_{aVL}/[H^+] + \delta_{H(O)}}{K_{aVL}/[H^+] + 1}, \quad (5)$$

where $\delta_{(N,O)}$, $\delta_{(O)}$ and $\delta_{H(O)}$ represent the individual chemical shifts of VL(N,O), VL(O) and VHL(O), respectively, and $\delta_{(N,O),(O)}$ is an apparent characteristic chemical shift for non-protonated species as follows:

$$\delta_{(N,O),(O)} = \frac{[VL(N,O)]\delta_{(N,O)} + [VL(O)]\delta_{(O)}}{[VL(N,O)] + [VL(O)]}. \quad (6)$$

The acid dissociation constant of the vanadate complexes K_{aVL} and the characteristic chemical shifts $\delta_{(N,O),(O)}$ and $\delta_{H(O)}$ were estimated by a least-square-fitting of the experimental points in Fig. 4 to Eq. (5) and were found to be $pK_{aVL} = 7.8$, $\delta_{(N,O),(O)} = -536$ ppm and $\delta_{H(O)} = -563$ ppm.

One can easily estimate a value of $([VL(N,O)]+[VL(O)]+[VHL(O)])/([H_2VO_4^-][EA])$ from the NMR signal intensity ratio of the complexes to free vanadate, and pK_a values of $H_2VO_4^-$ ($pK_{aV} = 8.17$ [38]) and HEA^+

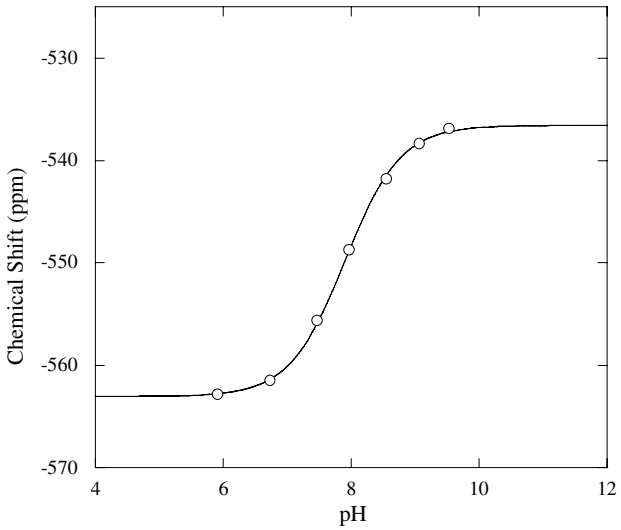


Fig. 4. Change in chemical shift of the V–EA complexes against pH. Solid line is a theoretical curve using the values obtained.

(protonated ethanolamine, $pK_{aL} = 9.5$ [39]). The quotient is expressed as follows:

$$\frac{[VL(N,O)] + [VL(O)] + [VHL(O)]}{[H_2VO_4^-][EA]} = \beta_{VL(N,O)} + \beta_{VL(O)} + \beta_{VHL(O)}[H^+]. \quad (7)$$

As shown in Fig. 5, the plot of the values $([VL(N,O)] + [VL(O)] + [VHL(O)])/([H_2VO_4^-][EA])$ estimated versus the hydrogen ion concentration gave a straight line, and the values of $\log(\beta_{VL(N,O)} + \beta_{VL(O)}) = 1.0$ and $\log\beta_{VHL(O)} = 8.5$ were obtained from the intercept and slope, respectively.

At pH 10, Eq. (7) can be simplified as

$$\frac{[VL(N,O)] + [VL(O)]}{[H_2VO_4^-]} = \left(\beta_{VL(N,O)} + \beta_{VL(O)}\right)[EA]. \quad (8)$$

The plot of the ratio on the left versus the free ligand concentration [EA] can be fitted on a straight line passing through the origin (Fig. 6). From the slope of the line, the value of $\log(\beta_{VL(N,O)} + \beta_{VL(O)}) = 1.2$ was obtained. This value is almost the same as the $\log(\beta_{VL(N,O)} + \beta_{VL(O)})$ value determined by the analysis with Eq. (7) in Fig. 5, and therefore we employed the average value of 1.1.

The combination of Eqs. (1)–(3) with Eq. (4) gives the following equation:

$$K_{aVL} = \frac{\beta_{VL(N,O)} + \beta_{VL(O)}}{\beta_{VHL(O)}}, \quad (9)$$

where $\beta_{VL(N,O)} + \beta_{VL(O)}$ and $\beta_{VHL(O)}$ values evaluated using Figs. 5 and 6 also give $pK_{aVL} = 7.4$, which is almost identical with the value determined from the pH dependence of the chemical shift as shown in Fig. 4. These show that the data are internally consistent. The pK_{aVL} value evaluated is much lower than the pK_a value of HEA^+ ($pK_{aL} = 9.50$ [39]), which means that coordination of the amine nitrogen to pentacoordinated vanadium(V) promotes the deprotonation. That is, the predominant binding structure of the non-protonated 1:1 complex is the (N,O)-bidentate complex VL(N,O), not VL(O).

3.2. DEA, MDEA and TEA systems

DEA, MDEA and TEA can be analogues of the functional group of ECTEOLA–Cellulose. Knowledge on the complexation of vanadate with such ethanolamine

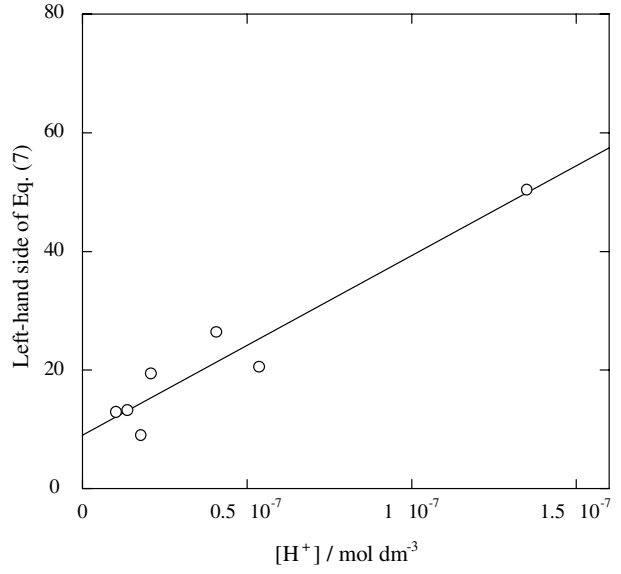


Fig. 5. Determination of formation constants of the 1:1 complexes of vanadate with EA. The quotient on the left of Eq. (7) is plotted as a function of hydrogen ion concentration, $[H^+]$.

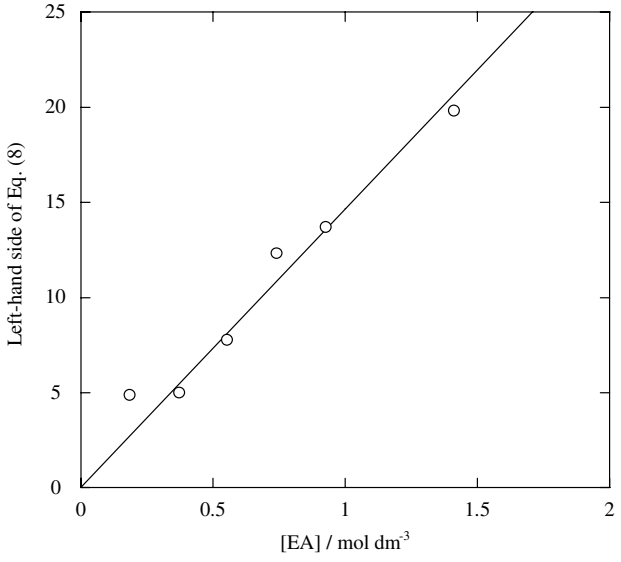


Fig. 6. Determination of formation constants of the 1:1 complexes of vanadate with EA at pH 10. The quotient on the left of Eq. (8) is plotted as a function of free EA concentration, [EA].

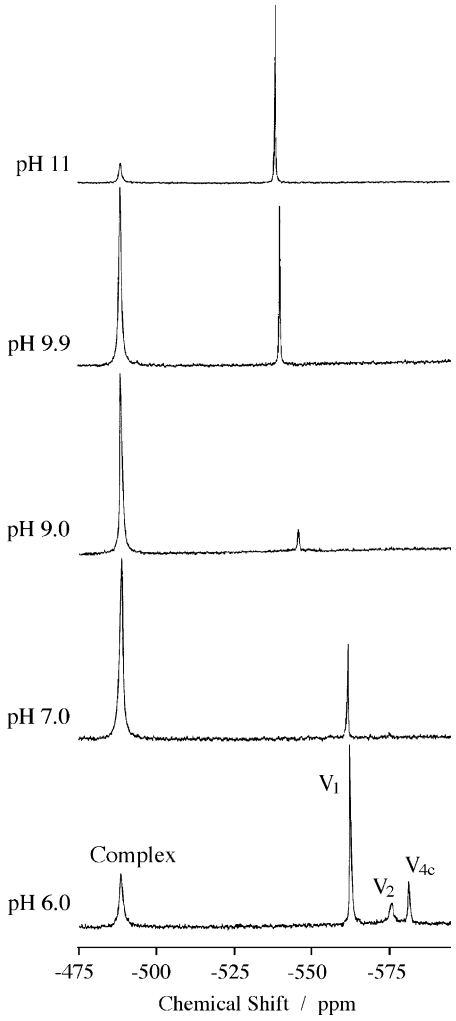
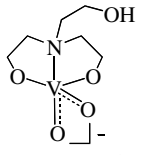


Fig. 7. ^{51}V NMR spectra of solutions containing 1.0×10^{-3} mol dm^{-3} vanadate and 0.1 mol dm^{-3} TEA at different pH. V_1: $H_2VO_4^-/HVO_4^{2-}$; V_2: dimer; V_{4c}: *cyclo*-tetramer.

derivatives should provide important information about the interaction with ECTEOLA–Cellulose. Binding of vanadate with these ethanolamine derivatives occurs spontaneously in aqueous solution to produce a limited number of products. Fig. 7 shows the ^{51}V NMR spectra for solutions containing vanadium(V) and TEA at different pH values. The new signal at −489 ppm, the chemical shift being independent of the pH of the solution, is assigned to a complex. Crans et al. [26,28] concluded by ^{51}V and ^{17}O NMR studies that the stoichiometry of the complex was 1:1, the overall charge of the complex was −1 and the binding structure was as follows:



(N,O,O) complex

The formation constant of the (N,O,O) complex can be written as follows:

$$H_2VO_4^- + TEA \rightleftharpoons VL(N,O,O) + 2H_2O$$

$$\beta_{(N,O,O)} = \frac{[VL(N,O,O)]}{[H_2VO_4^-][TEA]}. \quad (10)$$

We estimated the concentration ratio $[VL(N,O,O)]/[H_2VO_4^-]$ from the corresponding NMR signal intensities and pK_a of $H_2VO_4^-$, and then plotted this ratio against free ligand concentration [TEA] (Fig. 8). We obtained a good straight line passing through the origin and estimated the formation constant from the slope (Table 1). We also got signals due to the same type of (N,O,O) complex for DEA and MDEA systems. The formation constants of $H_2VO_4^-$ with DEA and MDEA were evaluated in the same way as that for TEA and are listed in Table 1 together with their chemical shift values. The formation constants evaluated agree well with the values reported by Crans et al. ($\log\beta_{(N,O,O)} = 3.0$ for DEA [27], 3.0 for MDEA [41] and 3.3 for TEA [26]). EA undergoes a comparatively weak interaction with vanadate compared with DEA, MDEA and TEA. The formation of monodentate and monochelate complexes such as VL(N,O), VL(O) and VHL(O) complexes was ignored in the tridentate and tetradentate ligand systems, since the presence of these less stable complexes would have a minimal effect on any conclusions obtained.

To illustrate the equilibrium conditions, a distribution diagram for the V–TEA system was calculated and plotted using the formation constant determined and oligomerization constants reported in [38]. Fig. 9 shows the distribution diagram for solutions containing 1.0×10^{-3} mol dm^{-3} vanadate and 0.1 mol dm^{-3} TEA (the same conditions as in Fig. 7). The experimental

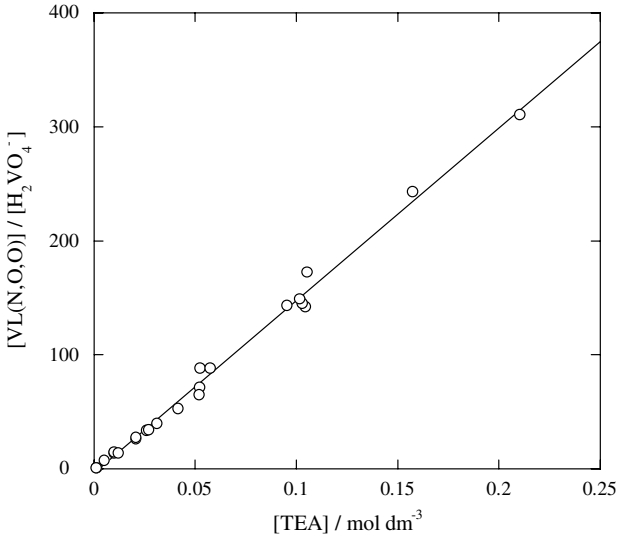


Fig. 8. Determination of the formation constant of the (N,O,O) complex for the V–TEA system.

Table 1
Formation constants and chemical shifts of vanadate complexes with ethanolamine derivatives and ECTEOLA–Cellulose

Ligand		$\log\beta_{(N,O,O)}$	Chemical shift
$HN(CH_2CH_2OH)_2$	DEA	3.3	−495
$H_3CN(CH_2CH_2OH)_2$	MDEA	3.6	−488
$N(CH_2CH_2OH)_3$	TEA	3.2	−489
ECTEOLA–Cellulose		3.6	−490

^{51}V NMR data are indicated by symbols for the respective species. The experimental points could be plotted well on the lines calculated.

3.3. ECTEOLA–Cellulose system

Tracey and Gresser [42] have demonstrated that sugars interact with vanadate to form a variety of complexes. However, the complexibility is quite low compared with the diethanolamine derivatives. In the case of cellulose gels, furthermore, cellulose forms hydrogen bonds to cross-link each other, which would prevent the complexation with vanadate species. In the ECTEOLA–Cellulose system, therefore, the interaction of vanadates with the glucopyranoside residues has been ignored, and the following two mechanisms can participate in the vanadium(V) adosorption: anion exchange under acidic conditions and complex formation under alkaline conditions. Fig. 10 shows the pH dependence of vanadium(V) adsorption onto ECTEOLA–Cellulose under acidic conditions (pH 3.0–6.5). The adsorbability is quite high and the maximum is around pH 5.5. Considering the pK_a values of ethanolamine derivatives (pK_{aL} = 7.8 for $HTEA^+$ [39]), at least a part of the functional groups of ECTEOLA–Cellulose would be protonated at a pH lower than 8, then the gel would function as a weakly basic anion exchanger. The feature of the pH-dependence of K_d values almost agrees well with the distribution of dimer and *cyclo*-tetramer as a function of pH. Although the presence of isopolymer species in the bulk solution can be ignored under the conditions examined, the high adsorbability in the acidic solutions should mainly be ascribed to the strong interaction between the protonated functional groups of ECTEOLA–Cellulose and the anionic isopolyvanadates. This topic will be discussed elsewhere. Anyway, on the contrary to the result for the chitosan system reported by Guzmán et al., the decamer could not be a predominant active species for the adsorption at a quite low initial concentration of vanadium(V) ($C_V = 4.0\times10^{-6}$ mol dm^{-3}).

Taking the practical use of ECTEOLA–Cellulose for the removal and recovery of vanadium from sea water into account, we examined the adsorption mechanism at a pH higher than 6 in detail. ECTEOLA–Cellulose would contain diethanolamine groups as an anchor group, so that vanadate should react with the functional group to form the (N,O,O) complex as in the case of TEA, DEA and MDEA. The combination of distribution and NMR measurements makes it possible to clarify the nature of vanadium(V) adsorption. Fig. 11 shows the pH dependence of vanadium(V) adsorption onto ECTEOLA–Cellulose at higher pH values. Below pH about 9, the vanadium(V) adsorbability of this gel increases with the decrease in pH. In comparison with the result in Fig. 10, the adsorbability at the same pH was greatly reduced due to the higher concentration of the supporting electrolyte. Fig. 12 shows ^{51}V NMR spectra for ECTEOLA–Cellulose in equilibrium with

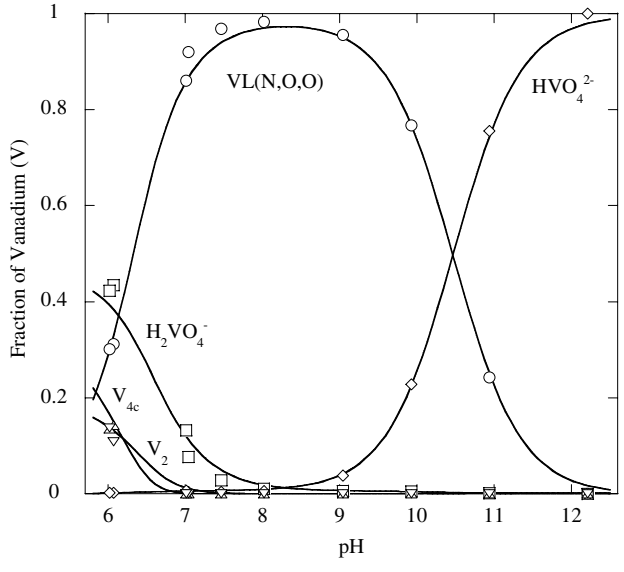


Fig. 9. Distribution diagram for solutions containing 1.0×10^{-3} mol dm^{-3} vanadate and 0.1 mol dm^{-3} TEA. The experimental NMR data points are indicated by symbols, ○: VL(N,O,O) complex; □: $H_2VO_4^-$; ◇: HVO_4^{2-}; △: dimer; ▽: *cyclo*-tetramer.

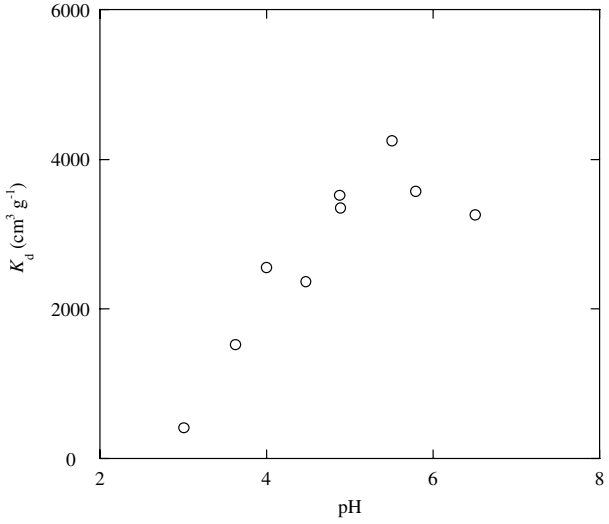


Fig. 10. pH dependence of vanadium(V) adsorption onto ECTEOLA–Cellulose at lower pH. ECTEOLA–Cellulose: 0.1 g; 4.0×10^{-6} mol dm^{-3} vanadate solution (I = 0.01, CH_3COONa–HCl): 20 cm^3.

vanadate solutions, in which the initial concentration of vanadium(V) ($C_V = 4.0 \times 10^{-4}$ mol dm^{-3}) is the same as that of the adsorption experiments in Fig. 11. These NMR spectra for gel suspensions contain signals of vanadium(V) species which exist in both gel and equilibrated solution. At pH 10 the signal at −540 ppm is ascribed to free vanadate in the equilibrated solution and in ECTEOLA–Cellulose. At this pH no adsorption occurs (Fig. 11). At pH lower than 8.7, we can get signals of the dimer and *cyclo*-tetramer for the gel samples. These signals were not observed for the equilibrated solution under the present experimental conditions. This clearly shows that the adsorption is due to the interaction of the dimer and *cyclo*-tetramer with the protonated functional groups, as well as in the case of the acidic conditions. At pH 8.7 a new ^{51}V NMR signal was observed in the gel phase (Fig. 12). This signal could not be observed for the equilibrated solution alone. The chemical shift is around −490 ppm, which is the same as that of the (N,O,O) complex of vanadate with DEA, MDEA or TEA. That is, this is the signal due to the −1 charged (N,O,O)-tridentate complex of pentacoordinate vanadium(V) with the functional group of ECTEOLA–Cellulose. The complexation, which means the fixation of vanadium(V) onto the gel matrix, causes a line broadening. The maximum signal intensity of the (N,O,O) complex is around pH 8 (Fig. 12), and the fraction change agrees well with that of the 1:1 complex with TEA (Fig. 9). These NMR spectra unambiguously show that the adsorption is the consequence of the complexation in addition to the interaction of the isopolyvanadates with the protonated functional groups under weakly basic conditions. The change in the concentration of supporting electrolytes has a small effect on the complexation. It is expected, therefore, that ECTEOLA–Cellulose can be used as a chelating adsorbent for the separation and concentration of a quite low concentration of vanadium from a matrix containing a high concentration of electrolytes under weakly basic conditions.

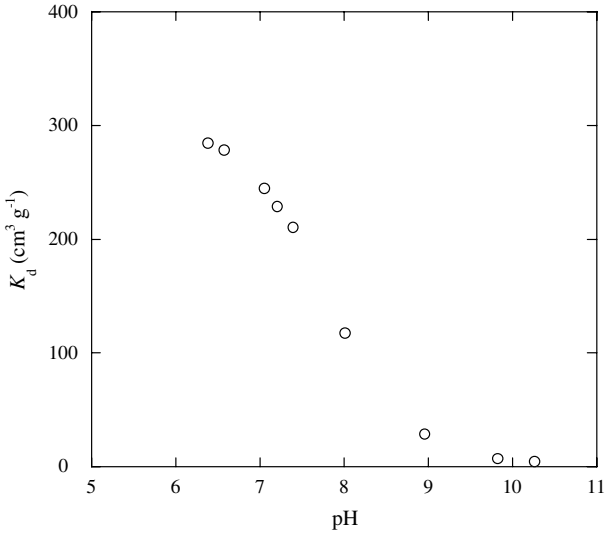


Fig. 11. pH dependence of vanadium(V) adsorption onto ECTEOLA–Cellulose at higher pH. ECTEOLA–Cellulose: 0.5 g; 4.0×10^{-4} mol dm^{-3} vanadate solution ($I = 0.1$, NaCl): 20 cm^3.

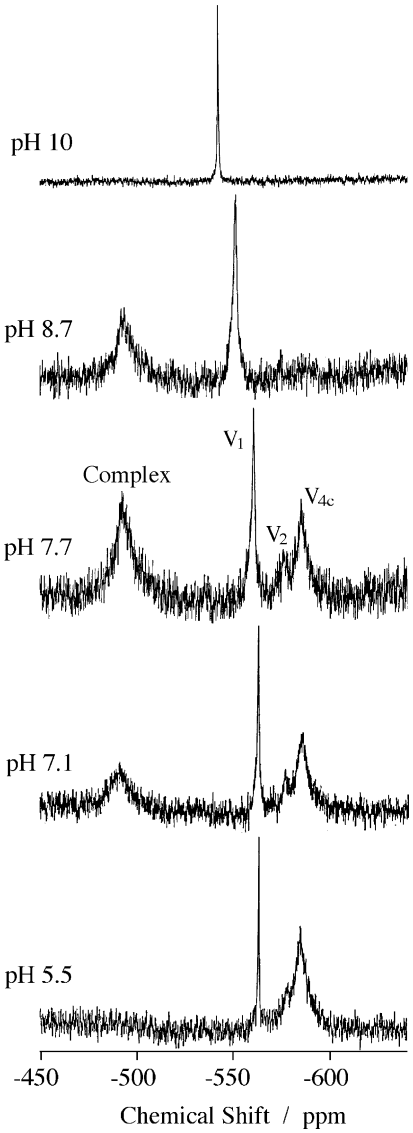


Fig. 12. ^{51}V NMR spectra for ECTEOLA–Cellulose in equilibrium with a solution ($I = 0.1$) containing 4.0×10^{-4} mol dm^{-3} vanadate at various pH. V_1: $H_2VO_4^-/HVO_4^{2-}$; V_2: dimer; V_{4c}: *cyclo*-tetramer.

In order to estimate the formation constant of the (N,O,O) complex of vanadate with the functional group of ECTEOLA–Cellulose, we have carried out a Langmuir analysis. As can be seen from the NMR spectra in Fig. 12, there is no isopolyvanadate in the gel phase at pH 8.7. The adsorption takes place at this pH mainly due to the complexation of vanadate with the functional group inside the gel. This is one piece of important information we can get from ^{51}V NMR spectroscopy. Therefore, the Langmuir analysis was done for the adsorption of vanadate onto ECTEOLA–Cellulose at

pH 8.7. The quotient, $\overline{C}_V/([H_2VO_4^-]\overline{C}_L)$, is given by the following equation:

$$\frac{\overline{C}_V}{[H_2VO_4^-]\overline{C}_L} = \frac{[\overline{H_2VO_4^-}] + [\overline{HVO_4^{2-}}] + [\overline{VL(N,O,O)}]}{[H_2VO_4^-]([\overline{L}] + [\overline{HL}] + [\overline{VL(N,O,O)}])}, \quad (11)$$

where upper bar refers to the gel phase, and C_V and C_L are the total concentrations of vanadium(V) species and the functional group of ECTEOLA–Cellulose, respectively. The adsorbability of vanadium(V) is strong enough to assume $[\overline{H_2VO_4^-}] + [\overline{HVO_4^{2-}}] \ll [\overline{VL(N,O,O)}]$. Considering the p$K_a$ of $HTEA^+$, most of the functional groups might be in the deprotonated form at pH 8.7, that is, $[\overline{L}] \gg [\overline{HL}]$. Since the gel reveals no ion-exchange ability, $[H_2VO_4^-] = [\overline{H_2VO_4^-}]$ can be assumed. Then, we can get the following equation:

$$\frac{[H_2VO_4^-]}{\overline{C}_V} = \frac{1}{\bar{\beta}_{(N,O,O)}\overline{C}_L} + \frac{[H_2VO_4^-]}{\overline{C}_L}, \quad (12)$$

where $\bar{\beta}_{(N,O,O)}$ is the formation constant of the (N,O,O) complex of vanadate with the functional group of ECTEOLA–Cellulose

$$\bar{\beta}_{(N,O,O)} = \frac{[\overline{VL(N,O,O)}]}{[\overline{H_2VO_4^-}][\overline{L}]}. \quad (13)$$

According to Eq. (12), the value on the left was plotted against $[H_2VO_4^-]$. As shown in Fig. 13, a good linear relationship was obtained. From the slope and intercept, we estimated the formation constant of the 1:1 complex with ECTEOLA–Cellulose as $\log \bar{\beta}_{(N,O,O)} = 3.6$, which is almost the same as those with DEA, MDEA and TEA (Table 1).

From the slope of the plot in Fig. 13, we also evaluated the total concentration of functional groups which are available for the complexation as $\overline{C}_L = 0.08$ mmol/g. The $\overline{C}_L$ value evaluated is much smaller than the nitrogen content 0.40 mmol/g in the gel determined by the elemental analysis. This means that only 20% of the functional groups introduced exist as the expected structure shown in Fig. 1. The rest of the functional groups are not suitable for complexation, because of further reactions among cellulose, epichlorophydrin and the functional groups introduced in the course of the sysnthesis of ECTEOLA–Cellulose.

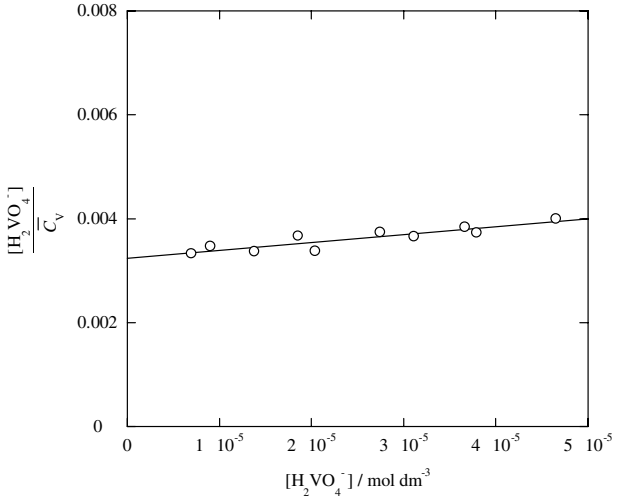


Fig. 13. Langmuir plot for the adsorption of vanadium(V) onto ECTEOLA–Cellulose at pH 8.7.

4. Conclusion

Although anion-exchange resins and chelating resins have been used for separation and concentration procedures, there are very few reports about the adsorption mechanism of vanadium. In the present work, the interaction of vanadium(V) oxoanions with ECTEOLA–Cellulose was examined by using distribution and ^{51}V NMR measurements. The strong adsorbability of vanadium(V) onto ECTEOLA–Cellulose under acidic conditions is ascribed to anion exchange of isopolyvanadate species formed only in the ion exchanger. On the contrary, the vanadium(V) adsorbability in the alkaline region is the consequence of the complexation of vanadate with the functional group to form the −1 charged 1:1 (N,O,O)-tridentate complex. The formation constant of the (N,O,O) complex with ECTEOLA–Cellulose was estimated to be $\log \bar{\beta}_{(N,O,O)} = 3.6$, which was almost the same as those with analogues of the functional group. Since the change in the concentration of supporting electrolytes has a small effect on the complexation, it is expected that ECTEOLA–Cellulose can be used as a chelating adsorbent for the separation and concentration of a quite low concentration of vanadium from a matrix containing a high concentration of electrolytes under weakly basic conditions.

Above all, the present study gave us a guiding principle for the recovery and removal of vanadium, and opened up opportunities to develop an advanced functional gel for further practical application.

Acknowledgements

This work was partially supported by the Salt Science Research Foundation (No. 0413), and the Steel Industry Foundation for the Advancement of Environmental Protection Technology.

References

[1] C. Kantipuly, S. Katragadda, A. Chow, H.D. Gesser, Talanta 37 (1990) 491.
[2] S. Kaneko, W. Takahashi, Colloid Surface 47 (1990) 69.
[3] A. Nakajima, Talanta 57 (2002) 537.

[4] T.M. Suzuki, D.A.P. Tanaka, M.A.L. Tanco, M. Kanesato, T. Yokoyama, J. Environ. Monitor. 2 (2000) 550.
[5] B.F. Senkal, N. Bicak, React. Funct. Polym. 55 (2003) 27.
[6] Y. Miyazaki, K. Yoshimura, S. Matsuoka, Y. Miura, H. Sakashita, K. Ishimaru, Polyhedron 22 (2003) 909.
[7] K. Yoshimura, Y. Miyazaki, S. Sawada, H. Waki, J. Chem. Soc., Faraday Trans. 92 (1996) 651.
[8] Y. Miyazaki, C. Shao, S. Matsuoka, K. Yoshimura, J. Ion Exchange 14 (Suppl.) (2003) 33.
[9] C. Shao, Y. Miyazaki, S. Matsuoka, K. Yoshimura, H. Sakashita, Macromolecules 33 (2000) 19.
[10] K. Yoshimura, Y. Miyazaki, F. Ota, S. Matsuoka, H. Sakashita, J. Chem. Soc., Faraday Trans. 94 (1998) 683.
[11] C. Shao, S. Matsuoka, Y. Miyazaki, K. Yoshimura, Analyst 127 (2002) 1614.
[12] T.M. Suzuki, D.A.P. Tanaka, T. Yokoyama, Y. Miyazaki, K. Yoshimura, J. Chem. Soc., Dalton Trans. (1999) 1639.
[13] C. Shao, S. Matsuoka, Y. Miyazaki, K. Yoshimura, T.M. Suzuki, D.A.P. Tanaka, J. Chem. Soc. Dalton Trans. (2000) 3136.
[14] C. Shao, S. Matsuoka, Y. Miyazaki, K. Yoshimura, Anal. Sci. 17 (Suppl.) (2001) i1475.
[15] H. Matsuo, Y. Miyazaki, H. Takemura, S. Matsuoka, H. Sakashita, K. Yoshimura, Polyhedron 23 (2004) 955.
[16] K.K. Bertine, E.D. Goldberg, Science 173 (1971) 233.
[17] W.H. Zoller, Science 183 (1971) 198.
[18] T. Soldi, M. Peasavento, G. Alberti, Anal. Chim. Acta 323 (1996) 27.
[19] L. Minelli, E. Veschetti, S. Giammanco, G. Mancini, M. Ottaviani, Microchem. J. 67 (2000) 83.
[20] J. Guzmán, I. Saucedo, R. Navarro, J. Revilla, E. Guibal, Langmuir 18 (2002) 1567.
[21] K. Yoshimura, H. Kaji, E. Yamaguchi, T. Tarutani, Anal. Chim. Acta 130 (1981) 345.
[22] S. Matsuoka, K. Yoshimura, A. Tateda, Anal. Chim. Acta 317 (1995) 207.
[23] R.M. Kothari, M.W. Taylor, J. Chromatogr. A 73 (1972) 449.
[24] M.J. Harber, J.L. Maddocks, J. Chromatogr. A 101 (1974) 231.
[25] G.M. Campo, S. Campo, A.M. Ferlazzo, R. Vinci, A. Calatroni, J. Chromatogr. B 765 (2001) 151.
[26] D.C. Crans, P.K. Shin, Inorg. Chem. 27 (1988) 1797.
[27] D.C. Crans, P.M. Ehde, P.K. Shin, L. Pettersson, J. Am. Chem. Soc. 113 (1991) 3728.
[28] D.C. Crans, H. Chen, O.P. Anderson, M.M. Miller, J. Am. Chem. Soc. 115 (1993) 6769.
[29] D.C. Crans, P.K. Shin, J. Am. Chem. Soc. 116 (1994) 1305.
[30] Y. Miyazaki, H. Waki, J. Chem. Soc., Faraday Trans. 89 (1993) 3925.
[31] Y. Miyazaki, G. Kura, H. Tsuzuki, H. Sakashita, J. Chem. Soc., Faraday Trans. 92 (1996) 3587.
[32] A. Marton, Y. Miyazaki, Progr. Colloid Polym. Sci. 117 (2001) 153.
[33] A. Marton, H. Sakashita, Y. Miura, E. Hiramatsu, Y. Miyazaki, Talanta 59 (2003) 217.
[34] A.S. Tracey, M.J. Gresser, S. Liu, J. Am. Chem. Soc. 110 (1988) 5869.
[35] W.J. Ray Jr., D.C. Crans, J. Zheng, J.W. Burgner II, H. Deng, M. Mahroof-Tahir, J. Am. Chem. Soc. 117 (1995) 6015.
[36] L. Pettersson, B. Hedman, I. Andersson, N. Ingri, Chem. Scripta 22 (1983) 254.
[37] L. Pettersson, I. Andersson, B. Hedman, Chem. Scripta 25 (1985) 309.
[38] K. Elvingson, A.G. Baró, L. Pettersson, Inorg. Chem. 35 (1996) 3388.
[39] R.M. Smith, A.E. Martell, Critical Stability Constants, vol. 6, Plenum Press, New York, 1989, Second Supplement, p. 173.
[40] M.J. Gresser, A.S. Tracey, J. Am. Chem. Soc. 107 (1985) 4215.
[41] D.C. Crans, I. Boukhobza, J. Am. Chem. Soc. 120 (1998) 8069.
[42] A.S. Tracey, M.J. Gresser, Inorg. Chem. 27 (1988) 2695.

polyurethane foams [12], for room temperature vulcanisation of silicon rubbers [13], for transesterifications [14], for acetylations of alcohols [15] and for dehydrations of alcohols to ethers [16]. The diverse structural motifs known in this family of compounds are primarily attributed to the ambidentate character of the carboxylate ligands and also the tendency of the tin atom to expand its coordination sphere from four to seven. Steric and electronic attributes of organic substituents on tin and/or the carboxylate moiety impart significant influence on the structural characteristics of tin carboxylates. Recently, a number of carboxylate ligands bearing additional strategically placed functional group(s)/donor atom(s) capable of multidentate coordination have been used to derive a structurally interesting class of tin compounds [17].

In recent years a number of authors [18] have synthesized *S*,*N*-ligands of the type $(CH_2)_n(SAz)_2$ (Scheme 1) based on a nitrogenated aromatic ring system such as benzimidazole (Scheme 1(a)) or pyridine (Scheme 1(b)). These ligands are able to coordinate by both S and the neighbouring N atom, and hence to form stable chelate rings of five or more atoms [19–22].

Bearing in mind the above, we have developed a strategy for producing a new class of monoanionic and polyfunctional *N*,*O*,*S*-ligands of considerable co-ordinative flexibility. Toward this end, we report now the synthesis and characterization of some new complexes obtained from the interaction of a number of triorganotin(IV) halides with the novel sodium bis(2-pyridylthio)acetate ligand (Scheme 1(d)).

Crystallisation of the compound $\{[(pyS)_2CHCO_2]Sn(CH_3)_3\}_n$ (**2**), from chloroform/diethyl ether solution, yields the complex $\{[(pyS)_2CHCO_2]Sn(CH_3)_3\}_n \cdot CHCl_3$, which has been characterized by X-ray crystallography.

2. Experimental

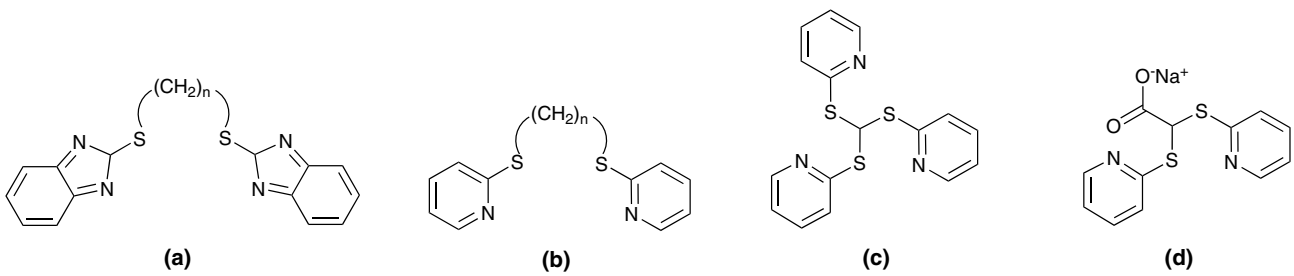
2.1. General

All reagents were purchased from Aldrich (Milwaukee) and used as received. All syntheses were carried out under a nitrogen atmosphere. All solvents were distilled and degassed with dry nitrogen prior to use. The samples for microanalysis were dried in vacuo to constant weight (20 °C, ca. 0.1 Torr). Elemental analyses (C, H, N, S) were performed with a Fisons Instruments 1108 CHNS-O Elemental analyser. IR spectra were recorded from 4000 to 100 cm^{-1} with a Perkin–Elmer System 2000 FT-IR instrument. ^1H and ^{119}Sn NMR spectra were recorded on a VXR-300 Varian instrument operating at room temperature (respectively at 300 MHz for ^1H, 75 MHz for ^{13}C and 111.9 MHz for ^{119}Sn). Melting points were taken on an SMP3 Stuart Scientific Instrument. The electrical conductivity measurements (Λ_m, reported as Ω^{-1} cm^2 mol^{-1}) of acetone or dichloromethane solutions were taken with a Crison CDTM 522 conductimeter at room temperature. Electrospray mass spectra (ESIMS) were obtained in positive- or negative-ion mode on a Series 1100 MSD detector HP spectrometer, using an acetone mobile phase. The compounds were added to the reagent grade acetone to give solutions of approximate concentration 0.1 mM. These solutions were injected (1 μl) into the spectrometer via a HPLC HP 1090 Series II fitted with an autosampler. The pump delivered the solutions to the mass spectrometer source at a flow rate of 300 μl min^{-1}, and nitrogen was employed both as a drying and nebulizing gas. Capillary voltages were typically 4000 and 3500 V for the positive- and negative-ion mode, respectively. Confirmation of all major species in this ESIMS study was aided by comparison of the observed and predicted isotope distribution patterns, the latter calculated using the IsoPro computer program [23].

2.2. Synthesis

2.2.1. Synthesis of $[(pyS)_2CHCO_2]Na$ (*1*)

2-Mercaptopyridine (5.508 g, 50.0 mmol) was added to a solution of NaOH (3.600 g, 90.0 mmol) in 40 ml of absolute ethanol. After 1 day stirring, a solution of dichloroacetic acid (3.198 g, 25.0 mmol) in 40 ml of absolute ethanol was added drop wise to the sodium salt so obtained, and this mixture was stirred for 4 days and then heated at gentle reflux for 12 h to give a pale yellow emulsion. The mixture was allowed to cool to r.t. and concentrated and then filtered



Scheme 1.

affording a pale yellow solid. The crude product was recrystallized in ethanol/acetone (1:1) yielding Na-[(pyS)$_2$CHCO$_2$] (**1**) as pale yellow microcrystalline needles. Yield: 76%, m.p. 213–215 °C. ^{1}H NMR (D$_2$O, 293 K): δ 5.78 (s, 1H, C*H*CO$_2$), 7.20 (m, 2H, 5-C*H*), 7.44 (m, 2H, 3-C*H*), 7.67 (m, 2H, 4-C*H*), 8.30 (m, 2H, 6-C*H*). ^{1}H NMR (CD$_3$OD, 293 K): δ 6.08 (s, 1H, C*H*CO$_2$), 7.08 (m, 2H, 5-C*H*), 7.45 (m, 2H, 3-C*H*), 7.62 (m, 2H, 4-C*H*), 8.33 (m, 2H, 6-C*H*). ^{1}H NMR (CDCl$_3$, 293 K): δ 5.60 (s, 1H, C*H*CO$_2$), 7.10 (m, 2H, 5-C*H*), 7.50 (m, 2H, 3-C*H*), 7.65 (m, 2H, 4-C*H*), 8.36 (m, 2H, 6-C*H*). ^{13}C NMR (CD$_3$OD, 293 K): δ 5.44 (*C*HCO$_2$), 121.48 (5-*C*H), 123.93 (3-*C*H), 138.18 (4-*C*H), 150.28 (6-*C*H), 160.40 (2-*C*H). IR (nujol, cm^{-1}): 3046w (CH), 1615s (ν_{asym} C=O), 1581m, 1555m (C=C + C=N), 1411m (ν_{sym} C=O), 1376m, 1132m, 745m. ESIMS (major positive-ions, CH$_3$OH), *m/z* (%): 301 (100) [{(pyS)$_2$-CHCO$_2$H} + Na$^+$]$^+$, 579 (80) [{(pyS)$_2$CHCO$_2$H}$_2$ + Na$^+$]$^+$. ESIMS (major negative-ions, CH$_3$OH), *m/z* (%): 110 (100) [(pyS)]$^-$, 233 (30) [{(pyS)$_2$CHCO$_2$} − CO$_2$]$^-$, 577 (30) [{(pyS)$_2$CH-CO$_2$}$_2$ + Na$^+$]$^-$. *Anal.* Calc. for C$_{12}$H$_9$N$_2$NaO$_2$S$_2$: C, 47.99; H, 3.02; N, 9.33; S, 21.35. Found: C, 48.02; H, 3.08; N, 9.03, S, 21.40%.

2.2.2. {[(pyS)$_2$CHCO$_2$]Sn(CH$_3$)$_3$}$_n$ (2)

To a CH$_2$Cl$_2$ solution (50 ml) of Me$_3$SnCl (0.199 g, 1.0 mmol), Na[(pyS)$_2$CHCO$_2$] (0.300 g, 1.0 mmol) was added. The mixture reaction was stirred for 12 h at room temperature, then solvent was removed on a rotary evaporator and chloroform was added (20 ml). The NaCl was removed by filtration and the filtrate reduced to half volume. Then diethyl ether was added (40 ml) and a yellow precipitate afforded, which was filtered off, washed with *n*-hexane (10 ml) and dried to constant weight under reduced pressure. Yield: 58%, m.p. 138–140 °C. ^{1}H NMR (CDCl$_3$, 293 K): δ 0.53 (s, 9H, Sn–C*H*$_3$, ^2J(Sn–^{1}H) = 57.3 Hz), 6.55 (s, 1H, C*H*CO$_2$), 7.00 (m, 2H, 5-C*H*), 7.24 (m, 2H, 3-C*H*), 7.51 (m, 2H, 4-C*H*), 8.43 (m, 2H, 6-C*H*). ^{119}Sn NMR (CDCl$_3$, 293 K): δ 149.2 (s). ^{13}C NMR (CDCl$_3$, 293 K): δ −1.98 (s, Sn-*C*H$_3$, ^1J(^{119}Sn, ^{13}C) = 410 Hz), 48.89 (*C*HCO$_2$), 120.20 (5-*C*H), 122.50 (3-*C*H), 136.34 (4-*C*H), 149.55 (6-*C*H), 157.42 (2-*C*H). IR (nujol, cm^{-1}): 3190w, 3058w (CH), 1616s (ν_{asym} C=O), 1574s, 1558s (C=C + C=N), 1413m (ν_{sym} C=O), 550sbr (Sn–C), 509s, 485sh (Sn–O). ESIMS (major positive-ions, CH$_3$OH), *m/z* (%): 164 (20) [(CH$_3$)$_3$Sn]$^+$, 442 (100) [(CH$_3$)$_3$Sn{(pyS)$_2$CHCO$_2$H}]$^+$, 905 (70) [{(CH$_3$)$_3$-Sn}$_2${(pyS)$_2$CHCO$_2$}$_2$ + Na$^+$]$^+$. ESIMS (major negative-ions, CH$_3$OH), *m/z* (%): 110 (100) [(pyS)]$^-$, 233 (40) [{(pyS)$_2$CHCO$_2$} − CO$_2$]$^-$, 718 (20) [(CH$_3$)$_3$Sn-{(pyS)$_2$CHCO$_2$}$_2$]$^-$. *Anal.* Calc. for C$_{15}$H$_{18}$N$_2$O$_2$S$_2$Sn: C, 40.73; H, 4.10; N, 6.34; S, 14.47. Found: C, 40.35; H, 4.20; N, 6.08; S, 14.08%.

2.2.3. {[(pyS)$_2$CHCO$_2$]Sn(C$_4$H$_9$)$_3$} (3)

Compound **3** was prepared similarly to compound **2**, stirring (C$_4$H$_9$)$_3$SnCl (0.326 g, 1.0 mmol) and Na[(pyS)$_2$-CHCO$_2$] (0.300 g, 1.0 mmol) in dichloromethane solution (30 ml). Re-crystallization from petroleum ether gave complex **3** as a micro-crystalline solid (55% yield), m.p. 66–68 °C. ^{1}H NMR (CDCl$_3$, 293 K): δ 0.83 (t, 9H, C*H*$_3$ of Sn–Bu^n), 1.15–1.35 (m, 12H, C*H*$_2$ of Sn–Bu^n), 1.45–1.65 (m, 6H, C*H*$_2$ of Sn–Bu^n), 6.50 (s, 1H, C*H*CO$_2$), 6.97 (m, 2H, 5-C*H*), 7.23 (m, 2H, 3-C*H*), 7.46 (m, 2H, 4-C*H*), 8.40 (m, 2H, 6-C*H*). ^{119}Sn NMR (CDCl$_3$, 293 K): δ 130.3 (s). IR (nujol, cm^{-1}): 3176w, 3095w (CH), 1614m (ν_{asym} C=O), 1577m, 1557m (C=C + C=N), 1415m (ν_{sym} C=O), 619br, 603sbr (Sn–C), 506sbr, 481sh (Sn–O). ESIMS (major positive-ions, CH$_3$OH), *m/z* (%): 290 (60) [(C$_4$H$_9$)$_3$Sn]$^+$, 323 (30) [{(pyS)$_2$CHCO$_2$} + 2Na$^+$]$^+$, 568 (80) [(C$_4$H$_9$)$_3$Sn{(pyS)$_2$-CHCO$_2$H}]$^+$, 590 (60) [{(C$_4$H$_9$)$_3$Sn}{(pyS)$_2$CHCO$_2$} + Na$^+$]$^+$, 1158 (100) [{(C$_4$H$_9$)$_3$Sn}$_2${(pyS)$_2$CHCO$_2$}$_2$ + Na$^+$]$^+$. ESIMS (major negative-ions, CH$_3$OH), *m/z* (%): 110 (40) [(pyS)]$^-$, 233 (20) [{(pyS)$_2$CHCO$_2$} − CO$_2$]$^-$, 845 (100) [(C$_4$H$_9$)$_3$Sn{(pyS)$_2$CHCO$_2$}$_2$]$^-$. *Anal.* Calc. for C$_{24}$H$_{36}$N$_2$O$_2$S$_2$Sn: C, 50.81; H, 6.40; N, 4.94; S, 11.30. Found: C, 50.75; H, 6.72; N, 4.83; S, 11.22%.

2.2.4. {[(pyS)$_2$CHCO$_2$]Sn(C$_6$H$_{11}$)$_3$} (4)

Compound **4** was prepared similarly to compound **2**, by using (C$_6$H$_{11}$)$_3$SnCl (0.404 g, 1.0 mmol) and Na-[(pyS)$_2$CHCO$_2$] (0.300 g, 1.0 mmol) in dichloromethane solution (30 ml). Re-crystallization from petroleum ether gave complex **4** as a micro-crystalline solid (60% yield), m.p. 104–106 °C. ^{1}H NMR (CDCl$_3$, 293 K): δ 1.06–1.94 (m, 33H, C$_6$*H*$_{11}$), 6.47 (s, 1H, C*H*CO$_2$), 6.97 (m, 2H, 5-C*H*), 7.26 (m, 2H, 3-C*H*), 7.47 (m, 2H, 4-C*H*), 8.40 (m, 2H, 6-C*H*). ^{119}Sn NMR (CDCl$_3$, 293 K): δ 73.2 (s). IR (nujol, cm^{-1}): 3137w, 3038w (CH), 1651m (ν_{asym} C=O), 1574m, 1557m (C=C + C=N), 1414m (ν_{sym} C=O), 552sbr (Sn–C), 491sbr, 483sh (Sn–O). ESIMS (major positive-ions, CH$_3$OH), *m/z* (%): 279 (100) [{(pyS)$_2$CHCO$_2$H} + H$^+$]$^+$, 647 (40) [{(C$_6$H$_{11}$)$_3$Sn}{(pyS)$_2$CHCO$_2$H}]$^+$. ESIMS (major negative-ions, CH$_3$OH), *m/z* (%): 110 (100) [(pyS)]$^-$, 233 (20) [{(pyS)$_2$CHCO$_2$} − CO$_2$]$^-$, 923 (30) [(C$_6$H$_{11}$)$_3$Sn{(pyS)$_2$-CHCO$_2$}$_2$]$^-$. *Anal.* Calc. for C$_{30}$H$_{42}$N$_2$O$_2$S$_2$Sn: C, 55.82; H, 6.56; N, 4.34; S, 9.93. Found: C, 55.35; H, 6.92; N, 4.03; S, 9.30%.

2.2.5. {[(pyS)$_2$CHCO$_2$]Sn(C$_6$H$_5$)$_3$} (5)

Compound **5** was prepared similarly to compound **2**, by using (C$_6$H$_5$)$_3$SnCl (0.386 g, 1.0 mmol) and Na [(pyS)$_2$ CHCO$_2$] (0.300 g, 1.0 mmol) in dichloromethane solution (30 ml). Re-crystallization from petroleum ether gave complex **5** as a micro-crystalline solid (72% yield), m.p. 108–110 °C. ^{1}H NMR (CDCl$_3$, 293 K): δ 6.55 (s, 1H, C*H*CO$_2$), 6.89 (m, 2H, 5-C*H*), 7.17 (m, 2H, 3-C*H*), 7.38–7.85 (m, 17H, C$_6$*H*$_5$ and 4-C*H*),

8.15 (m, 2H, 6-C*H*). ^{119}Sn NMR ($CDCl_3$, 293 K): δ −100.2 (s). IR (nujol, cm^{-1}): 3150w (CH), 1656s (ν_{asym} C=O), 1580m, 1557m (C=C + C=N), 1414m (ν_{sym} C=O), 482mb (Sn–O), 274s (Sn–C). ESIMS (major positive-ions, CH_3OH), *m/z* (%): 383 (80) $[(C_6H_5)_2Sn(pyS)]^+$, 628 (80) $[(C_6H_5)_3Sn\{(pyS)_2CHCO_2H\}]^+$, 717 (100) $[\{(C_6H_5)_3Sn\}O\{(C_6H_5)_3Sn\} + H^+]^+$, 977 (30) $[\{(C_6H_5)_3Sn\}_2\{(pyS)_2CHCO_2\}]^+$, 1278 (60) $[\{(C_6H_5)_3Sn\}_2\{(pyS)_2CHCO_2\}_2 + Na^+]^+$. ESIMS (major negative-ions, CH_3OH), *m/z* (%): 110 (100) $[(pyS)]^-$, 233 (40) $[\{(pyS)_2CHCO_2\} - CO_2]^-$, 627 (10) $[\{(C_6H_5)_3Sn\}\{(pyS)_2CHCO_2\} - H^+]^-$, 905 (60) $[\{(C_6H_5)_3Sn\}\{(pyS)_2CHCO_2\}_2]^-$. *Anal.* Calc. for $C_{30}H_{24}N_2O_2S_2Sn$: C, 57.44; H, 3.86; N, 4.47; S, 10.22. Found: C, 57.13; H, 4.00; N, 4.07; S, 10.08%.

2.3. X-ray crystallography

The crude complex **2** was dissolved in chloroform/diethyl ether solution; a single crystal of $\{[(pyS)_2CHCO_2]Sn(CH_3)_3\}_n \cdot CHCl_3$ suitable for X-ray diffraction analysis was obtained and mounted on a Rigaku AFC5R diffractometer using graphite-monochromatized Cu Kα radiation (1.54178 Å) and a rotating anode generator. The crystals are triclinic, a = 10.132(5) Å, b = 13.845(3) Å, c = 14.783(3) Å, α = 84.39(2)°, β = 77.90(2)°, γ = 88.15(3)°, V = 2018(1) A^3, T = 293 K, space group $P\bar{1}$ (no. 2), Z = 2, μ(Cu Kα) = 14.2 mm^{-1}, 6676 reflections measured, 6375 unique (R_{int} = 0:053), 3489 observed ($I > 3\sigma(I)$) were used in all calculations. The cell parameters were refined by least squares from the angular positions of 14 reflections in the range 68.77° < 2θ < 63.98°. The data were measured at room temperature for 6.1° < 2θ < 124.5° using a θ/2θ scan technique. The data were processed to yield values of I and $\sigma(I)$ corrected for Lorentz, polarisation and absorption effects. The psi scans used for the last correction present severe values (about 15%) of the transmission coefficients. The observed reflections were processed by the direct methods program SIR2004 [24], which provided the complete structure. The successive fourier maps showed the presence of a molecule of chloroform. All non-hydrogen atoms were refined by full-matrix least squares method with anisotropic thermal parameters. The hydrogen atoms were idealised (C–H = 0.96 Å). Each H atom was assigned the equivalent isotropic temperature factor of the parent atom multiplied for 1.3 and allowed to ride on it. At the end of the refinement, a further semi empirical absorption correction was made on the basis of the method of Walker and Stuart [25], using the program written by Ugozzoli [26] and then the structure converged at the final $R(F)$ and $wR(F^2)$ of 0.056 and 0.074, respectively. The final difference Fourier map with a root-mean-square deviation of electron density of 0.2 e $Å^{-3}$ showed no significant features. Calculations were performed using the SIR2004 structure determination package Crystallographic data have been deposited at the CCDC and allocated the deposition number CCDC 264907.

3. Results and discussion

Complexes **2**–**5** have been synthesized by methathetic reaction of $Na[(pyS)_2CHCO_2]$ (**1**) (Scheme 1(d)) with SnR_3Cl acceptors in CH_2Cl_2 solution (Eq. (1)).

$$Na[(pyS)_2CHCO_2] + SnR_3Cl \rightarrow \underset{\mathbf{2\text{–}5}}{[(pyS)_2CHCO_2]SnR_3} + NaCl$$

2 R = CH_3 **3** R = ^{n}Bu
4 R = Cy **5** R = Ph (1)

The derivatives **2**–**5** are stable in air. The complexes are stable in alcohols, acetone, acetonitrile and chlorinated solvents, and they are non-electrolytes in CH_2Cl_2 solution. The identity of these compounds has been established by ESI-MS, IR and multinuclear (^{1}H and ^{119}Sn) NMR spectral studies.

The infrared spectra carried out on the solid samples (nujol mull) showed all the expected bands for the ligand and the tin moieties: weak absorptions near 3100 cm^{-1} are due to the pyridine rings C–H stretching and medium to strong absorptions in the range 1550–1580 cm^{-1} are related to ring "breathing" vibrations.

The presence of the COO moiety is detected by intense absorptions in the range 1614–1656 cm^{-1} and 1413–1415 cm^{-1} due to the asymmetric and symmetric CO_2^- stretching mode, respectively, not significantly shifted with respect to the free ligand (ν_{asym} CO_2^- = 1615 cm^{-1}, ν_{sym} CO_2^- = 1411 cm^{-1}).

In the far-IR region medium to strong absorptions appear upon coordination, due to the stretching modes of Sn–N and Sn–R [27]. The absence of Sn–Cl stretching vibrations in the spectra of **2**–**5** confirms the substitution of the chloride in the complexes formation. In the far-IR spectra the Sn–C stretching frequencies fall as strong or medium broad bands in the range 550–619 cm^{-1} for alkyl derivatives **2**–**4**, and at 274 cm^{-1} for tri(phenyl) complex **5**; these absorptions well agree with the trends previously observed in similar N-donor complexes [28]. In the far-IR spectra of **2**–**5** absorptions assigned to Sn–O have been always detected between 481 and 509 cm^{-1}.

The room temperature ^{1}H NMR spectra of derivatives **2**–**5**, in $CDCl_3$ solution (see Section 2), exhibit only one set of signals for the protons of the pyridyl rings of the $[(pyS)_2CHCO_2]^-$ ligand.

Upon interaction of ligand **1** with organotin(IV) acceptors, for all complexes studied, no significantly large shifts were evident for the proton atoms of pyridyl rings: this implies a lack of direct bond involvement of these rings with the metal. In contrast, in the ^{1}H

NMR spectra of complexes **2**–**5** the signals due to the C*H*COO group exhibit significant downfield shift (from 6.08 ppm in the free ligand to 6.47–6.55 ppm in the complexes): this is suggestive of a strong bonding of the tin atom to the carboxylate group of complexes.

The tin-hydrogen, $^{2}J(^{119}Sn,^{1}H)$, and tin-carbon, $^{1}J(^{119}Sn,^{13}C)$, coupling constants in various cases can be correlated with the percentage of s-character which the Sn atom presents in the Sn–C bond and hence $^{2}J(^{119}Sn,^{1}H)$ and $^{1}J(^{119}Sn,^{13}C)$ may give information about the coordination number of tin [29,30]. In the tri(methyl)tin(IV) derivative **2** the tin-proton coupling constant $^{2}J(^{119}Sn,^{1}H)$ is 57.3 Hz, falling in the range of four-coordinated trimethyltin(IV) species [30]. The tin-carbon coupling constant of compound **2**, $^{1}J(^{119}Sn,^{13}C)$, is 410 Hz; on the basis of Lockarts's equation [29], the Me–Sn–Me angle is estimated to 111°, suggesting a distorted tetrahedral disposition of Me groups.

The ^{119}Sn chemical shifts of triorganotin(IV) derivatives **2**–**5**, at 149.2, 130.3, 73.2 and −100.2 ppm, respectively, are in accordance with those of four-coordinated triorganotin(IV) complexes involving S-, O- or N-donors [31–33].

Electrospray ionization is considered a 'soft' ionization technique and is particularly suitable for study of labile organotin systems in solution. ESI mass spectra, dissolved in methanol solution and detected at fragmentation voltage of 30 V, show molecular ion peaks and structurally important fragment ions. For the ligand **1** significant fragments at *m*/*z* 301 and 579 in the positive- and at *m*/*z* 577 in the negative-ion spectra have been attributable to aggregates of the ligand with Na^{+}; peaks at *m*/*z* 110 and 233, respectively, due to the fragments $[(pyS)]^{-}$ and $[\{(pyS)_2CHCO_2\} - CO_2]^{-}$, are present in the negative-ion spectrum of **1**. Peaks at *m*/*z* 110, 233, 279 and 323, due to the free O-donor ligand or its decomposition fragments, are also present in the spectra of all derivatives **2**–**5**.

Peaks due to the free organotin(IV) acceptors $[R_3Sn]^{+}$ are present in the cationic spectra of derivatives **2** and **3**, due to the instability of these triorganotin derivatives. The instability of triorganotin(IV) derivatives in methanol solutions is also demonstrated by the presence in the positive-ion spectrum of the triphenyl derivative **5** of a fragment at *m*/*z* 383, due to the aggregate $[(C_6H_5)_2Sn(pyS)]^{+}$. In the electrospray spectra of all the triorganotin derivatives **2**–**5**, peaks due to species containing the triorganotin fragments associated to one or two molecules of the ligand have been detected.

Crystallisation of the compound $\{[(pyS)_2CHCO_2]Sn(CH_3)_3\}_n$ (**2**), from chloroform/diethyl ether solution, yields the chloroform complex $\{[(pyS)_2CHCO_2]Sn(CH_3)_3\}_n \cdot CHCl_3$. The identity of **2** has been established by elemental analysis, IR, NMR spectroscopy, and X-ray crystallography. The structure consists of polymeric chains and the molecular structure of two units of the polymer $\{[(pyS)_2CHCO_2]Sn(CH_3)_3\}_n \cdot CHCl_3$ with labelling for the main atoms is shown in Fig. 1. The geometry of $[(pyS)_2CHCO_2]Sn(CH_3)_3$ is similar in the two independent unit and bond lengths and angles are given in Table 1. The tin atom is five-coordinated, being bonded to two oxygen atoms and three methyl groups, respectively. The coordination sphere is essentially distorted trigonal bi-pyramidal with the three equatorial positions being taken up by the methyl substituents and the two axial positions being occupied by oxygens (O–Sn–O = 169.9(3)°, averaged angle). In this mode the tin atom has the least electronegative groups in the equatorial position and the electronegative

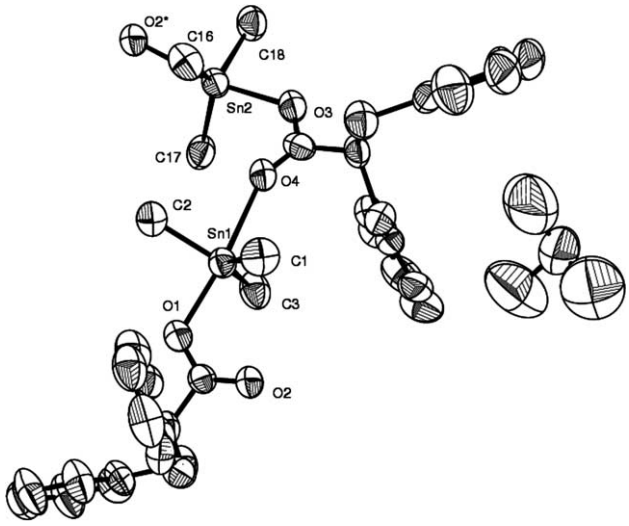


Fig. 1. Molecular structure of two units of the polymer $\{[(pyS)_2CHCO_2]Sn(CH_3)_3\}_n \cdot CHCl_3$, (including the equivalent O2*, $1 + x, y, z$) with 50% displacement ellipsoids and labelling of atoms around the tin atoms.

Table 1
Selected tin environmental parameters

Distances (Å)			
Sn1–O1	2.179(7)	Sn2–O3	2.184(9)
Sn1–O4	2.534(7)	Sn2–O2(*)	2.489(9)
Sn1–C1	2.12(1)	Sn2–C16	2.11(1)
Sn1–C2	2.10(2)	Sn2–C17	2.08(1)
Sn1–C3	2.13(1)	Sn2–C18	2.13(1)
Angles (°)			
C2–Sn1–O1	90.7(5)	C18–Sn2–O3	90.9(4)
O4–Sn1–O1	169.7(3)	O2(*)–Sn2–O3	170.0(3)
O4–Sn1–C2	83.0(4)	O2(*)–Sn2–C18	81.2(5)
C3–Sn1–O1	92.3(4)	C16–Sn2–O3	92.7(5)
C3–Sn1–C2	119.3(6)	C16–Sn2–C18	118.7(5)
C3–Sn1–O4	83.7(3)	C16–Sn2–O2(*)	85.8(5)
C1–Sn1–O1	99.6(4)	C17–Sn2–O3	96.8(5)
C1–Sn1–C2	110.7(6)	C17–Sn2–C18	112.3(5)
C1–Sn1–O4	90.2(4)	C17–Sn2–O2(*)	91.9(5)
C1–Sn1–C3	128.3(6)	C17–Sn2–C16	127.8(5)

*Equivalent position: $1 + x, y, z$.

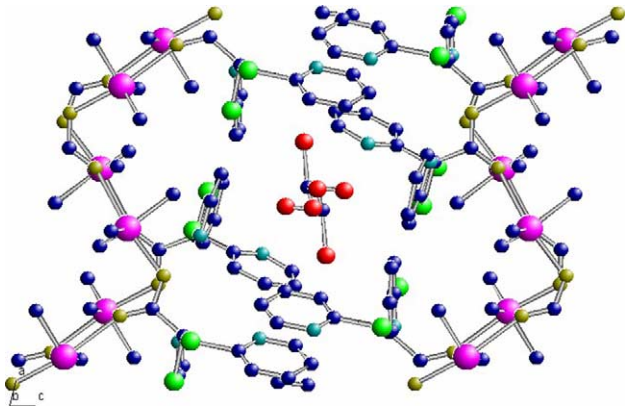


Fig. 2. Projection on the *ac* plane of the polymeric complex $\{[(pyS)_2CHCO_2]Sn(CH_3)_3\}_n \cdot CHCl_3$.

oxygens in the axial position. The Sn–O distances are non-equivalent with the Sn–O (carboxyl) being slightly longer (2.512(8) Å, averaged bond length) than the other (2.182(8) Å, averaged bond length). Thus the R–CO_2 does not function as symmetric bridging ligand. Because of the variation of the bond distances the tin is displaced from the equatorial plane of the three methyl groups towards the covalently bond oxygen by about 0.15(1) Å. The C–Sn–C angles ranging from 110.7(6)° to 128.3(6)°.

In the chain structure the carboxylate unit functions as a bridging ligand and connects two different tin centers in a intermolecular manner. The preference for the chain structure seems to be the natural consequence of the principles of five-coordination. In this mode the tin atom is in a trigonal-bipyramidal geometry and has the least electronegative groups in the equatorial position and the electronegative oxygens in the axial position. In solution the polymeric structure breaks down to monomeric structure (even in a non-coordinating solvent such as $CDCl_3$), as evidenced by ^{119}Sn NMR.

The polymeric chains are along the *a* axis and form channels occupied by the solvent molecules, as illustrated in Fig. 2, where the projection on the *ac* plane of the unit cell is shown. The two pyridine rings of the two independent $[(pyS)_2CHCO_2]$ moieties make a dihedral angle of 96.1(5)° and 80.4(5)°, respectively, and form the walls of the channels. Short contact is present between nitrogen atom of a pyridine ring and the carbon atom of the chloroform (N1–C31($x, y, z-1$) = 3.39(3) Å).

Acknowledgements

We are grateful to the University of Camerino (FAR and Progetto Strategico di Ricerca di Ateneo) for financial help.

References

[1] (a) M. Gielen, Appl. Organometal. Chem. 16 (2002) 481;
(b) M. Gielen, Coord. Chem. Rev. 151 (1996) 41.
[2] (a) R.R. Holmes, Acc. Chem. Res. 22 (1989) 190;
(b) J. Beckmann, K. Jurkschat, Coord. Chem. Rev. 215 (2001) 267;
(c) V.K. Jain, Coord. Chem. Rev. 135/136 (1994) 809;
(d) V. Chandrasekhar, S. Nagendran, V. Baskar, Coord. Chem. Rev. 235 (2002) 1.
[3] (a) G. Gioia Lobbia, G. Valle, S. Calogero, P. Cecchi, C. Santini, F. Marchetti, J. Chem. Soc., Dalton Trans. (1996) 2475;
(b) S. Calogero, G. Valle, G. Gioia Lobbia, C. Santini, P. Cecchi, L. Stivano, J. Organomet. Chem. 526 (1996) 269.
[4] (a) M. Pellei, C. Pettinari, G. Gioia Lobbia, C. Santini, A. Drozdov, S. Troyanov, Inorg. Chem. Commun. 4 (2001) 708;
(b) M. Pellei, G. Gioia Lobbia, M. Ricciutelli, C. Santini, Polyhedron 22 (2003) 499;
(c) M. Pellei, C. Santini, G. Gioia Lobbia, F. Cantalamessa, C. Nasuti, M. Di Prinzio, R. Gabbianelli, G. Falcioni, Appl. Organometal. Chem. 19 (2005) 583.
[5] C. Pettinari, C. Santini, Polypyrazolylborate and scorpionate ligands, in: J.A. McClaverty, T.J. Meyer (Eds.), Comprehensive Coordination Chemistry II – from Biology to Nanotechnology, vol. 1, Elsevier Ltd, Oxford, UK, 2004, p. 159.
[6] (a) E.R.T. Tiekink, Appl. Organomet. Chem. 1 (1991) 1;
(b) E.R.T. Tiekink, Trends Organomet. Chem. 1 (1994) 71.
[7] (a) R. Garcia-Zarracino, J. Ramos-Quinones, H. Hopfl, Inorg. Chem. 42 (2003) 3835;
(b) J.H. Wengrovius, M.F. Garbauskas, Organometallics 11 (1992) 1334;
(c) T.M. Andrews, F.A. Bower, B.R. LaLiberte, J.C. Montermoso, J. Am. Chem. Soc. 80 (1958) 4102.
[8] R.C. Poller, The Chemistry of Organotin Compounds, Logos Press, London, 1970.
[9] H.V. Smith, Organotin Stabilizers, The Tin Research Institute, Greenford, 1959.
[10] (a) L. Pellerito, L. Nagy, Coord. Chem. Rev. 224 (2002) 111;
(b) M. Nath, S. Pokharia, R. Yadav, Coord. Chem. Rev. 215 (2001) 99;
(c) M.J. Clarke, F. Zhu, D.R. Frasca, Chem. Rev. 99 (1999) 2511.
[11] J.K. Tsagatakis, N.A. Chaniotakis, R. Altmann, K. Jurkschat, R. Willem, J.C. Martins, E. Bakker, Y. Qin, Helv. Chim. Acta 84 (2001) 1952.
[12] S. Karpel, Tin and its Uses 125 (1980) 1.
[13] W. Knoll, Chemistry and Technology of Silicones, Academic Press, New York, 1968.
[14] J. Otera, Chem. Rev. 93 (1993) 1449.
[15] S. Durand, K. Sakamoto, A. Orita, J. Otera, A. Duthie, D. Dakternieks, M. Schulte, K. Jurkschat, Organometallics 19 (2000) 3220.
[16] D. Marton, D. Slaviero, G. Tagliavini, Tetrahedron 45 (1989) 7099.
[17] (a) C. Ma, Q. Jiang, R. Zhang, J. Organomet. Chem. 678 (2003) 148;
(b) C. Pettinari, F. Marchetti, R. Pettinari, D. Martini, A. Drozdov, S. Troyanov, J. Chem. Soc., Dalton Trans. (2001) 1790;
(c) M. Gielen, H. Dalil, L. Ghys, B. Boduszek, E.R.T. Tiekink, J.C. Martins, M. Biesemans, R. Willem, Organometallics 17 (1998) 4259;
(d) J.S. Casas, A. Castiñeiras, M.D. Couce, N. Playa, R. Russo, A. Sánchez, J. Sordo, J.M. Varela, J. Chem. Soc., Dalton Trans. (1998) 1513;
(e) D. Dakternieks, T.S.B. Baul, S. Dutta, E.R.T. Tiekink, Organometallics 17 (1998) 3058;
(f) T.P. Lockhart, Organometallics 7 (1988) 1438.

[18] (a) E.B. Bouwman, W.L. Driessen, J. Reedijk, Coord. Chem. Rev. 104 (1990) 143;
(b) B. Adhikary, S. Liu, C.R. Lucas, Inorg. Chem. 32 (1993) 5957;
(c) B. Adhikary, C.R. Lucas, Inorg. Chem. 33 (1994) 1376;
(d) S.S. Tandon, L.K. Thompson, M.E. Manuel, J.N. Bridson, Inorg. Chem. 33 (1994) 5555;
(e) S.C. Davies, M.C. Durrant, D.L. Hughes, K. Leidenberger, C. Stapper, R.L. Richards, J. Chem. Soc., Dalton Trans. (1997) 2409;
(f) J.E. Barclay, S.C. Davies, D.J. Evans, S.A. Fairhurst, C. Fowler, R.A. Henderson, D.L. Hughes, K.E. Oglieve, Transition Met. Chem. 23 (1998) 701;
(g) L.R. Hanton, K. Lee, Inorg. Chem. 38 (1999) 1634;
(h) J.L. Chou, D.N. Horng, J.P. Chyn, K.M. Lee, F.L. Urbach, G.H. Lee, H.L. Tsai, Inorg. Chem. Comm. 2 (1999) 392;
(i) C.J. Matthews, W. Clegg, S.L. Heath, N.C. Martin, M.N.S. Hill, J.C. Lockhart, Inorg. Chem. 37 (1998) 199;
(j) C.J. Matthews, W. Clegg, M.R.J. Elsegood, T.A. Leese, D. Thorp, P. Thornton, J.C. Lockhart, J. Chem. Soc., Dalton Trans. (1996) 1531.

[19] (a) A. Yuchi, M. Shiro, H. Wada, G. Nakagawa, Bull. Chem. Soc. Jpn. 65 (1992) 2275;
(b) C.Y. Su, B.S. Kang, J. Sun, Y.X. Tong, Z.N. Chen, J. Chem. Res. (S) (1997) 454;
(c) A.W. Addison, T.N. Rao, J. Reedijk, J. van Rijn, G.C. Verschoor, J. Chem. Soc., Dalton Trans. (1984) 1349;
(d) A. Castiñeiras, W. Hiller, J. Strähle, M.V. Paredes, J. Sordo, Acta Crystallogr. C 41 (1985) 41;
(e) J.L. Chou, J.P. Chyn, F.L. Urbach, D.F. Gervasio, Polyhedron 19 (2000) 2215.

[20] (a) A. Castiñeiras, W. Hiller, J. Strähle, J. Bravo, J.S. Casas, M. Gayoso, J. Sordo, J. Chem. Soc., Dalton Trans. (1986) 1945;
(b) M.V. Castaño, A. Macías, A. Castiñeiras, A. Sánchez-González, E. García-Martínez, J.S. Casas, J. Sordo, W. Hiller, E.E. Castellano, J. Chem. Soc., Dalton Trans. (1990) 1001.

[21] J.S. Casas, A. Castiñeiras, E. García-Martínez, A. Sánchez-González, J. Sordo, E.M. Vázquez-López, U. Russo, Polyhedron 15 (1996) 891.

[22] J.S. Casas, A. Castiñeiras, E. García-Martínez, P. Rodríguez-Rodríguez, U. Russo, A. Sánchez, A. Sánchez-González, J. Sordo, Appl. Organomet. Chem. 13 (1999) 69.

[23] Mike Senko, IsoPro 3.0 MS/MS software, Isotipic abundance simulator version 3.0. National High Magnetic Field Laboratory, 243 Buena Vista Ave, #502, Sunnyvale, CA 94086.

[24] M.C. Burla, R. Calandro, M. Camalli, B. Carrozzini, G.L. Cascarano, L. De Caro, C. Giacovazzo, G. Polidori, R. Spagna, J. Appl. Cryst. 38 (2005) 381.

[25] N. Walker, D. Stuart, Acta Cryst. A 39 (1983) 158.

[26] F. Ugozzoli, Comput. & Chem. 11 (1987) 109.

[27] K. Nakamoto, Infrared and Raman Spectra of Inorganic and Coordination Compounds; Part A: Theory and Applications in Inorganic Chemistry, fifth ed., John Wiley & Sons, New York, 1997.

[28] C. Pettinari, M. Pellei, M. Miliani, A. Cingolani, A. Cassetta, L. Barba, A. Pifferi, E. Rivarola, J. Organomet. Chem. 553 (1998) 345.

[29] T.P. Lockart, W.F. Manders, J. Am. Chem. Soc. 109 (1987) 7015.

[30] T.P. Lockart, W.F. Manders, Inorg. Chem. 25 (1986) 892.

[31] W.D. Honnick, M.C. Hughes, C.D. Schaeffer, J.J. Zuckerman, Inorg. Chem. 15 (1976) 1391.

[32] K. Handlíř, A. Lyčka, J. Holeček, M. Nádvorník, V. Pejchal, A. Sebald, Collect. Czech. Chem. Commun. 59 (1994) 885.

[33] C. Pettinari, F. Marchetti, A. Gregori, A. Cingolani, J. Tanski, M. Rossi, F. Caruso, Inorg. Chim. Acta 257 (1997) 37.

and fructose residues, and the torsional angles, ϕ and ψ, O-5(g)–C-1(g)–O-1(g)–C-2(f) and C-1(g)–O-1(g)–C-2(f)–O-5(f), respectively (Fig. 1(a)), and our expectation was that these angles would not change markedly on formation of the complex, as was indicated by the earlier PM3(tm) optimization and is consistent with the higher level computations as shown later.

The geometry of the complex, initially optimized by using semi-empirical PM3(tm) parameters [5a], is similar to that shown in Fig. 1(b), which was obtained by a higher level DFT optimization. The optimized structure of sucrose is shown in Fig. 1(a) for comparison with that of the complex.

The initial PM3(tm) optimization had indicated that the Δ-complex should be strongly preferred over the Λ-complex, but it incorrectly predicted deprotonation of OH-1(f) rather than OH-2(g), as had been shown by ^{1}H NMR spectroscopy [5a]. An additional problem was that the predicted CH-3(g)–OH-3(g) torsional angle in the complex did not fit the evidence of a very low ^{1}H NMR coupling constant in DMSO. There was predicted distortion of both phenanthroline rings from planarity, which appeared to be due to competing interactions between a glucose or fructose residue with the front face of a phenanthroline, and a hydrogen of the other phenanthroline with the other (rear) face [5b]. In the structure shown in Fig. 1(b) the front face of the phenanthroline, designated A, is towards the hydroxyl group, OH-1(f), of the fructose residue and the rear face is towards H-9(B) of the second phenanthroline, designated B. The front face of phenanthroline B is towards the glucose residue, and the rear face is towards H-9(A) of phenanthroline A. The phenanthroline positions are numbered 1-10, and N1-(A) and N-1(B) are trans at Co(III). As in earlier work, phenanthroline A is shown in Fig. 1(b) as being attached to the upper coordination site of Co(III) with the sucrose residue on the left, and ligated glucose to the front, and B is attached to the lower site of Co(III) [5].

The PM3(tm) semi-empirical model has been parameterized to reproduce geometries of transition metal compounds, rather than energies [6–8], which may account for its inability to predict the correct position of deprotonation of sucrose in the dicationic complex. We have therefore carried out ab initio geometrical optimizations, using the following basis sets: HF 3-21(G*) and 6-31(G*), and DFT BP/6-31(G*), and at the higher levels we used LACVP* pseudopotentials at Co(III) [6,7].

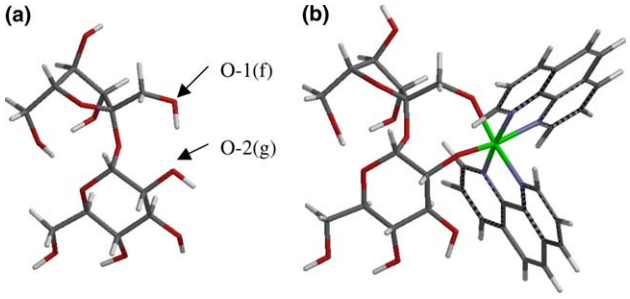


Fig. 1. Structures of sucrose (a) and the complex (b) from DFT optimizations. Phenanthroline ring A is attached to the upper coordination site of Co(III), and B is attached to the lower coordination site and is adjacent to the glucose residue.

2. Methods

Structures were optimized by using Spartan 04 (Wavefunction) starting from the geometrically optimized structures given earlier by using PM3(tm), and heats of formation were initially calculated by using the 3-21(G*) basis set, which provides adequate information under some conditions. Further information was obtained by using HF 6-31(G*) or DFT BP/6-31(G*) basis sets with LACVP* pseudopotentials [6,7]. Heats of formation are given to the nearest kcal mol^{-1}, as in the earlier work [5]. Assignments of all the ^{1}H NMR signals in D_2O and DMSO-d_6 had been made earlier [5], including those of the phenanthrolines, which were based on connectivities and the rules of Ito et al. [9].

3. Results and discussion

An initial comparison of conclusions from the semi-empirical, PM3(tm) and the HF treatments was based on the HF 3-21(G*) basis set which gave the Δ-complex energetically preferred over the Λ-complex by 18 kcal mol^{-1}; the corresponding difference from the PM3(tm) optimization had been 9 kcal mol^{-1} [5a]. There is no physical evidence for the existence of the Λ-complex of sucrose(phen)$_2$, either method of calculation fits this observation, and we did not examine the preference for the Δ-complex over the Λ-complex at higher levels. As noted, the PM3(tm) calculation had incorrectly indicated that deprotonation of OH-1(f) would be preferred over that of OH-2(g) by 3 kcal mol^{-1}, however, calculations at the HF 3-21(G*) and LACVP*/6-31(G*) levels indicate that deprotonation of OH-2(g) is preferred by ca. 5 kcal mol^{-1}, in agreement with experiment [5a]. The inability of the semi-empirical PM3(tm) treatment to predict relative energies for deprotonation is probably due to the reliance on geometrical criteria for parameterization for transition metals [6,7].

To this extent, calculation of energies for the HF optimized structures removes an anomaly in the PM3(tm) treatment [5a], but it introduces an error in the geometry of OH-1(f), which from the ^{1}H NMR spectral evidence in DMSO is pyramidal, in agreement with

the PM3(tm) optimized structure shown as Fig. 2 in [5a]. The ^{1}H signals at OH-1(f) and CH-2(f) had been assigned, and the coupling constants of OH-1(f) with H-1′(f) and H-1(f) in DMSO are 9.5 and 4.0 Hz, respectively, consistent with the predicted torsional angles of 170° and −75°, respectively, at the PM3(tm) level [5a]. The HF optimizations give a near planar OH-1(f), inconsistent with the NMR data [5a], and structures with torsional angles constrained to the values which fit the coupling constants are disfavored by 3 and 2 kcal mol^{-1} in 3-21 (G*) and 6-31 (G*) calculations, respectively. These constrained HF structures relax to the incorrect planar structure on removal of the constraint. Limitations of HF treatments of some pyramidal structures have been noted [6]. The structure re-optimized with the BP/6-31 (G*) basis set and LACVP* pseudopotentials for Co(III) had torsional angles of 176° and −68° between OH-1(f) and H-1′(f) and H-1(f), respectively, in reasonable agreement with the NMR coupling constants in DMSO and the earlier semi-empirical optimization [5a]. This structure from the DFT optimization with the estimated torsional angles is shown in Figs. 1(b) and 2 with H-1′(f) towards and H-1(f) away from the viewer and illustrates the pyramidal geometry at OH-1(f). Except as noted, the HF and DFT structures of the complex are in other respects similar, although only geometries from the latter and PM3(tm) are in Table 1 or the figures.

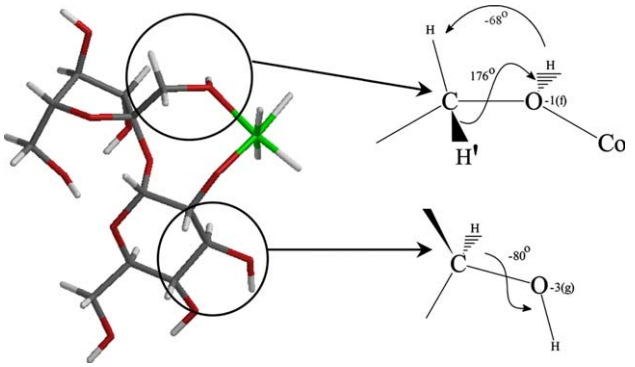


Fig. 2. Structure of the complex with the phenanthroline groups removed for clarity. The insets show the DFT computed torsional angles at CH–OH-1(f) and CH–OH-3(g).

Predicted geometries at Co(III) from the DFT optimization are shown in Table 1, and include comparison with values obtained earlier from the PM3(tm) treatment [5].

As for the parent sugar, the conformation of the sucrose moiety in the complex is defined by the bond angle, C-1(g)–O–C-2(f), between the glucose and fructose residues, and the torsional angles, ϕ and ψ [4], which are shown in Table 1 for the complex. We used DFT to optimize the geometry of sucrose to be consistent with the treatment of the geometry of the Co(III) complex. The structure at the BP/6-31(G*) level shown in Fig. 1(a) is similar to those in the crystal and from other treatments [4,10]. Computed values of the torsional angles ϕ and ψ are 108.6° (107.8°) and −35.6° (−44.8°), respectively, and the C-1(g)–O–C-2(f) bond angle is 117.8° (114.3°), and these are similar to values in the crystal [4], which are in parentheses. These values are similar to those calculated earlier [5,10] and are consistent with the original assumption that complexation does not significantly perturb the sucrose moiety. We note that our computation is for an isolated molecule and does not cover crystal packing or interactions with the environment [10]. However, ^{1}H NMR spectroscopy had shown that the conformation did not change significantly in going from D_2O to DMSO-d_6 [5a].

3.1. Semi-empirical and ab initio geometries

Computed geometries of the Δ-sucrose complex illustrated in Figs. 1 and 2, and Table 1, and given earlier [5],

Table 1
Geometry of Δ-sucrose $Co(phen)_2^{2+}$ [a]

Bonding to sucrose moiety			
Bond/torsional angle (°)			
O-2(g)–Co–O-1(f)	C-1(g)–O–C-2(f)	ϕ	ψ
95.1 (92.8)	117.7 (117.8)	112.0 (114.5)	−36.5 (−51.2)
Bond length/distance (Å)			
Co–O-2(g)	Co–O-1(f)	O-2(g)–O-1(f)	
1.88 (1.89)	2.03 (2.03)	2.89 (2.84)	
Bonding to phenanthroline nitrogens			
Bond angle (°)			
N-10(A)–Co–N-1(A)	N-10(B)–Co–N-1(B)		
81.6 (89.9)	84.6 (89.7)		
Bond length (Å)			
Co–N-1(A)	Co–N-10(A)	Co–N-1(B)	Co–N-10(B)
1.97 (1.93)	2.03 (1.96)	1.97 (1.93)	1.92 (1.92)

[a] Values in parentheses are from the PM3(tm) optimization [5a,5b].

show that PM3(tm) and DFT methods generate similar results, so far as the positions of bonding between sucrose and Co(III)$(phen)_2$ are concerned. However, the PM3(tm) incorrectly predicts the site of protonation in forming the dicationic complex, and indicates that there should be considerable bowing of both phenanthroline groups.

Each phenanthroline is sandwiched between H-9 of the other phenanthroline and either the glucose or fructose moiety. In terms of either semi-empirical (PM3(tm)), or ab initio optimizations using HF or DFT treatments H-9 of one phenanthroline is ca. 2.7 Å from the rear of the other phenanthroline, cf. [9]. The fructose ring is not very close to phenanthroline A, but the glucose ring is close to phenanthroline B, and O-3(g) is ca. 3.1 Å from the center of this ring, from the DFT optimization. Some of these predicted interatomic distances are therefore within the sum of the van der Waals radii and the half-thickness of an arene [11].

Bowing of a phenanthroline depends on the forms of the non-bonding interactions with either the sugar residue or the other phenanthroline, being repulsive or attractive. There is extensive evidence for non-classical –HO hydrogen bonding [12], and Nishio et al. [13] concluded that π-H–C interactions may be modestly attractive. The PM3(tm) optimization had indicated extensive bowing of both phenanthrolines, with phenanthroline A presenting a convex face and a modest tilt towards the sugar residue, and B presenting a concave face towards the sugar and a tilt away from it [5b]. The extent of bowing was given by the dihedrals between the outer rings of the phenanthrolines and the tilt was with respect to the N–Co–N plane, as illustrated in Fig. 2(a) and (b) in [5b] and discussed in detail in that reference. It appeared from this earlier optimization that repulsion from the rear between H-9(B) and phenanthroline A is greater than repulsion of the latter from the front by the fructose residue, but that for phenanthroline B repulsion by the glucose residue is dominant.

Predicted distortions of the phenanthrolines in the DFT optimization are significantly less than from the earlier PM3(tm) optimization [5b]. This is also the situation for the HF optimizations, although these geometries are not shown, because in this respect they are very similar to those in Figs. 1 and 3. The predicted bowing of phenanthroline A is almost zero rather than 15°, and the tilt is <1° rather than 6°, as given earlier, and the new DFT results are illustrated in Fig. 3, where (a) shows phenanthroline ring A viewed in profile with H1 and H2 projecting forward from the plane of the paper. Fig. 3(b) shows phenanthroline ring B viewed in profile with H5 and H6 projecting forward of the plane of the paper. The predicted bowing of phenanthroline B, as given by the sum of the dihedrals, is 16° rather than 19° and the tilt is 3° rather than 6°, estimated as outlined in [5b].

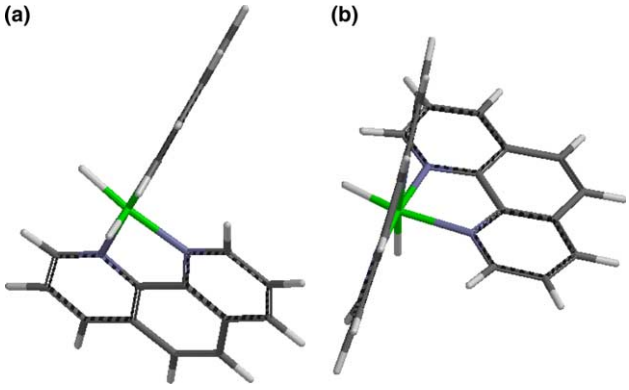


Fig. 3. Bowing of phenanthroline rings, shown in profile, with the sugar residue removed for clarity, and illustrating the predicted near planarity of ring A (a) and bowing of ring B (b).

It appears that in the PM3(tm) optimization the π-HO and π-H–C interactions are treated as repulsive, with consequent distortion of both phenanthrolines, whereas repulsion is less evident in the ab initio optimizations. There is limited direct physical evidence regarding geometries of phenanthroline groups in mixed Co(III) complexes and possible distortions due to interactions with adjacent groups [9]. There is only modest bowing in the mixed carbonato complex, but this third ligand is small and should not interfere with the two phenanthroline groups [18], and Hennig et al. [19] note distortions in some bis-phenanthroline complexes. However, variations in the NMR chemical shifts of the phenanthroline hydrogens [5b] provide evidence on distortions of these groups and indicate that it is less for phenanthroline A than B. The ^{1}H NMR chemical shifts of each phenanthroline group decrease in going from H-2 to H-9 [5b], which, for other Co(III)bis-phenanthroline complexes, was ascribed by Ito et al. [9] to π-shielding by the other phenanthroline group. For phenanthroline A, which is predicted to be near planar (Fig. 3(a)), the approximate decrease is 2.2 ppm, but for B, which is predicted to be bowed (Fig. 3(b)), it is approximately 2.7 ppm [5b], and larger than expected if π-shielding were the only factor controlling the chemical shifts [9]. A deviation from planarity of phenanthroline B should decrease its aromatic character and be reflected in the decrease in the relevant ^{1}H chemical shifts being larger for phenanthroline B than A. Chemical shifts of H-8 and 9 are lower for phenanthroline B than for phenanthroline A, but differences are small for the other positions, excepting H-2, A and B, which are close to the ligating nitrogens and the sucrose residue [5b]. These decreases in chemical shift are in addition to those due to π-shielding by the other phenanthroline as discussed by Ito et al. [9].

As shown in Fig. 1(b), little congestion is predicted between the fructose ring and phenanthroline A, which means that the conformation of the fructose hydroxymethyl group (C-1(f)–OH-1(f)) is not perturbed

and is consistent with the computed torsional angles between OH-1(f) and the hydrogens on C-1(f), as shown in Fig. 2(a), and the ^{1}H coupling constants [5a]. However, congestion between the glucose ring and phenanthroline B should influence the interaction between the latter and OH-3(g). The difference between predicted torsional angles from the semi-empirical and DFT optimizations is consistent with the H-3(g)–OH-3(g) spin–spin coupling constant in DMSO [5a], which depends on the torsional angle between the axial CH-3(g) and OH-3(g), and should be sensitive to the interaction between this OH group and phenanthroline B. The coupling constant must be very low, <2 Hz [5a], much lower than that for a freely rotating CH_2OH group, ca. 6.5 Hz [14], or that expected from the computed torsional angle of −149° from the PM3(tm) optimization which would indicate a significant coupling constant, and was originally ascribed to an apparent π-HO repulsion [5a]. However, the predicted torsional angle of −80° from the DFT optimization (Fig. 2) corresponds to a low coupling constant in accord with experiment and less repulsion between this OH group and phenanthroline B than that predicted earlier from the PM3(tm) optimization [5].

The Co(III)–oxygen bond lengths from the DFT and PM3(tm) optimizations are similar, but DFT generally gives longer Co–N bonds, and therefore lower predicted bond angles (Table 1). Both treatments predict modest deviations from a strictly octahedral symmetry at Co(III), which, as noted earlier [5b], is consistent with assignments of the CD spectra in the d–d region of mixed complexes [3b,5a] and structural evidence on other Co(III) complexes [15,16].

4. Conclusions

Except for differences in bowing of the phenanthroline rings, the predicted deprotonation of OH-2(g), rather than of OH-1(f), and the CH-3(g)–OH-3(g) torsional angle, predicted geometries from the earlier PM3(tm) optimization are not very different to those from the present ab initio treatments, and are better than the HF optimizations as regards the pyramidal geometry of OH-1(f), although DFT does not have this problem. These treatments neglect interactions with solvents, but examination of absorption, circular dichroism and NMR spectroscopy had shown that the structure does not change significantly in going from water to DMSO, despite marked differences between these solvents, especially as regards hydrogen bonding [5a,5b]. The ab initio treatments predict deprotonation of OH-2(g), consistent with the NMR evidence on the structure of the dicationic complex.

Semi-empirical methods and molecular modeling, where appropriate force fields are available [6,7,17,18], are much more economical in time than ab initio methods. This advantage is important in treating geometries, although not necessarily energies, of complex molecules [19]. Computational methods appear to be useful in predicting structures of transition metal complexes with polyol ligands where X-ray crystallography cannot be used, provided that the conclusions are supported by experimental evidence, for example from electronic and NMR spectroscopy.

Acknowledgments

J.P. acknowledges support from FONDECYT Project 2970036 and the University of Chile, DI I2-O3/12-2.

References

[1] (a) M. Zimmer, Chem. Rev. 95 (1995) 2629;
(b) K. Hegetschweiler, Chem. Soc. Rev. 28 (1999) 239;
(c) B. Gyuresic, L. Nagy, Coord. Chem. Rev. 203 (2000) 81.
[2] D.W. Whitfield, S. Skojkovski, B. Sarkar, Coord. Chem. Rev. 122 (1993) 171.
[3] (a) S. Bunel, C. Ibarra, E. Moraga, J. Parada, A. Blasko, C.A. Bunton, Carbohydr. Res. 312 (1998) 191;
(b) J. Parada, S. Bunel, E. Moraga, C. Ibarra, N.D. Gillitt, C.A. Bunton, Polyhedron 20 (2001) 2223.
[4] (a) S.M. Brown, H.A. Levy, Acta Crystallogr., Sect. B 29 (1973) 790;
(b) J.C. Hanson, L.C. Sieker, L.H. Jensen, Acta Crystallogr., Sect. B 29 (1973) 797.
[5] (a) J. Parada, S. Bunel, C. Ibarra, G. Larrazabal, E. Moraga, N.D. Gillitt, C.A. Bunton, Carbohydr. Res. 333 (2001) 185;
(b) J. Parada, S. Bunel, C. Ibarra, G. Larrazabal, N.D. Gillitt, C.A. Bunton, Polyhedron 21 (2002) 2215.
[6] C.J. Cramer, Computational Chemistry, Wiley, New York, 2002 (Chapters 5–8).
[7] W.J. Hehre, A Guide to Molecular Mechanics and Quantum Chemical Calculations, Wavefunction, Irvine, 2003 (Chapter 2).
[8] J.J.P. Stewart, J. Comput. Chem. 111 (1990) 543.
[9] H. Ito, J. Fujita, T. Ito, Bull. Chem. Soc. Jpn. 44 (1971) 723.
[10] (a) S. Bagley, M. Odelius, A. Laaksonen, G. Widmalm, Acta Chem. Scand. 48 (1994) 792;
(b) A.D. French, A.M. Kelterer, C.J. Cramer, G.P. Johnson, M.K. Dowd, Carbohydr. Res. 326 (2000) 305.
[11] F.A. Cotton, G. Wilkinson, Advanced Inorganic Chemistry, 3rd ed., Wiley, New York, 1972, p. 120.
[12] I. Alcorta, I. Rozas, J. Elquero, Chem. Soc. Rev. 27 (1998) 163.
[13] M. Nishio, Y. Umezawa, M. Hirota, Y. Takeuchi, Tetrahedron 51 (1995) 8665.
[14] (a) B. Adams, L. Lerner, J. Am. Chem. Soc. 114 (1992) 4824;
(b) L. Poppe, H. van Halbeek, J. Am. Chem. Soc. 114 (1992) 1092.
[15] E.C. Niederhoffer, A.E. Martell, R. Rudolf, A. Clearfield, Inorg. Chem. 27 (1982) 3734.
[16] H. Hennig, J. Sieler, R. Benedix, J. Kaiser, L. Sjoelin, O. Linquist, Z. Anorg. Allg. Chem. 464 (1980) 151.
[17] (a) J.C.A. Boeyens, P. Comba, Coord. Chem. Rev. 212 (2001) 3;
(b) R.J. Deeth, Coord. Chem. Rev. 212 (2001) 11;
(c) P.O. Noorby, P. Brandt, Coord. Chem. Rev. 212 (2001) 79.
[18] C.J. Cramer, Computational Chemistry, Wiley, New York, 2002 (Chapter 2).
[19] S.-K. Goh, D.S. Marynick, J. Comput. Chem. 22 (2001) 1881.

prepared by reacting phosphorus pentachloride with trichloroacetamide, followed by addition of methanol in accordance with the literature method [8].

Metal salts Na[L] (**1**), Rb[L] (**2**), Tl[L] (**3**) were synthesized in aqueous-alcoholic media.

2.1.1. Na[L] (*1*)

Sodium carbonate (0.106 g, 1 mmol) was added in several portions to a solution of H[L] (0.541 g, 2 mmol) in 10 ml of aqueous 2-propanol (1:3). The solution was stirred with heating until total dissolution of Na_2CO_3 was observed. The solvent was removed in vacuo and the colorless product recrystallized from isopropanol. Yield: 0.573 g, 98%. *Anal*. Calc. for $C_4H_6Cl_3NNaO_4P$: C, 16.43; H, 2.07; N, 4.79. Found: C, 16.47; H, 2.1; N, 4.67%. ^{1}H NMR (D_2O): 3.55 d [6H, $^3J_{PH}$ 11.2 Hz, $PO(OCH_3)_2$]; ^{31}P NMR (D_2O): 16.09 h [$^3J_{PH}$ 11.3 Hz, $PO(OCH_3)_2$]. Na[L-d_6] (**1a**). The compound was obtained as **1**. $NaHCO_3$ and D[L-d_6] were used as starting materials. Yield: 0.585 g, 98%.

2.1.2. Rb[L] (*2*)

Rubidium carbonate (0.231 g, 1 mmol) was added in parts to 10 ml of an aqueous-alcoholic (1:3) solution of [HL] (0.541 g, 2 mmol). A solution of the product was allowed to stand at room temperature in a vacuum desiccator over $CaCl_2$ for 20 days, after which the colorless well-faceted crystals that were deposited were filtered out, washed with few drops of isopropanol and dried over $CaCl_2$. Yield: 0.653 g, 92%. *Anal*. Calc. for $C_4H_6Cl_3NRbO_4P$: C, 13.54; H, 1.70; N, 3.95. Found: C, 13.2; H, 1.76; N, 3.64%. ^{1}H NMR (D_2O): 3.57 d [6H, $^3J_{PH}$ 11.2 Hz, $PO(OCH_3)_2$]; ^{31}P NMR: (D_2O) 16.11 h $^3J_{PH}$ 11.3 Hz, $PO(OCH_3)_2$].

The thallium compound Tl[L] (**3**) was synthesized in a similar fashion by reacting HL (0.584 g, 2 mmol) and Tl_2CO_3 (0.4688 g, 1 mmol) in aqueous 2-propanol. Yield: 0.824 g, 87%. *Anal*. Calc. for $C_4H_6Cl_3NTlO_4P$: C, 10.14; H, 1.28; N, 2.96. Found: C, 10.14; H, 1.42; N, 2.93%. ^{1}H NMR (D_2O): 3.57 d [6H, $^3J_{PH}$ 11.2 Hz, $PO(OCH_3)_2$]; ^{31}P NMR: (D_2O) 16.09 h $^3J_{PH}$ 11.3 Hz, $PO(OCH_3)_2$].

2.1.3. PPh_4[L] (*4*)

To a solution of **1** (0.584 g, 2 mmol) in 10 ml acetonitrile, a solution of 0.838 g PPh_4Br (2 mmol) in 15 ml CH_3CN was added under stirring. Then, the reaction mixture was cooled to room temperature. The white precipitate of NaBr was filtered off, and the solvent was removed in vacuo and the yellow product was recrystallized from isopropanol and hexane. Yield: 1.132 g, 93%. *Anal*. Calc. for $C_{28}H2_6Cl_3NO_4P_2$: C, 55.24; H, 4.30; N, 2.3. Found: C, 55.0; H, 4.15; N, 2.16%. ^{1}H NMR (D_2O): 7.74 m [8H $(PPh_4)^+$ – *ortho*, 7.56 m [12H $(PPh_4)^+$ – *meta* + *para*], 3.55 d [6H, $^3J_{PH}$ = 11.2 Hz, L^-]; ^{31}P NMR: (D_2O) 23.48 m $(PPh_4)^+$, 16.03 [$^3J_{PH}$ 11.3 Hz, $PO(OCH_3)_2$].

2.1.4. $(PPh_4)_2$[L]Br · H_2O (*5*)

To a solution of Na[L], that was prepared as above, PPh_4Br (0.838 g, 2 mmol in 15 ml CH_3CN) was added in the ratio 1:2. The white precipitate of NaBr was filtered off, the solvent was removed in vacuo and the off-white product was recrystallized from an isopropanol–hexane mixture. Yield: 0.941 g, 90%. *Anal*. Calc. for $C_{52}H_{48}BrCl_3NO_5P_3$: C, 59.7; H, 4.63; N, 1.34. Found: C, 60.0; H, 4.63; N, 1.30%. ^{1}H NMR $(CD_3)_2CO$: 7.93 m [20H, $(PPh_4)^+$], 3.25 d [3H, $^3J_{PH}$ = 11.2 Hz, L^-]; ^{31}P NMR: ($(CD_3)_2CO$) 24.05 m $(PPh_4)^+$, 13.05 [$^3J_{PH}$ 11.3 Hz, $PO(OCH_3)_2$].

2.1.5. $(PPh_4)_2$[Na_4L_6] (*6*)

To a solution of 0.8772 g (3 mmol) Na[L], 0.419 g PPh_4Br (1 mmol in 10 ml CH_3CN) was added. The white precipitate of NaBr was filtered off, the solvent was removed in vacuum and the colourless product was recrystallized from isopropanol and hexane. Yield: 1.015 g, 85%. *Anal*. Calc. for $C_{72}H_{76}Cl_{18}N_6Na_4O_{24}P_8$: C, 36.22; H, 3.21; N, 3.52. Found: C, 36.54; H, 3.32; N, 3.41%. ^{1}H NMR ($(CD_3)_2CO$): 7.9 m [10H, $(PPh_4)^+$], 3.53 d [9H, $^3J_{PH}$ 11.2 Hz, $PO(OCH_3)_2$]; ^{31}P NMR ($(CD_3)_2CO$): 22.35 m $(PPh_4)^+$, 12.64 h ($^3J_{PH}$ = 11.2 Hz, $PO(OCH_3)_2$).

All the compounds are soluble in water, DMFA, DMSO, acetone, sparingly soluble in isopropanol, 1,4-dioxane and insoluble in non-polar aprotic solvents.

2.1.6. [$SbPh_4$L] (*7*)

To a solution of Na[L] (0.293 g 1 mmol) in 10 ml acetonitrile was added $SbPh_4Br$ (0.511 g, 1 mmol) in 15 ml acetonitrile. After 15 min, a white precipitate of NaBr was filtered off and the solution was allowed to stand in a vacuum desiccator over $CaCl_2$. After a while colorless crystals of **7** precipitated from the solution, that were recrystallized from isopropanol. The compound is soluble in polar protic solvents, insoluble in water, ethers, benzene and alkanes. Yield: 0.569 g, 85%. *Anal*. Calc. for $C_4H_6Cl_3NTlO_4P$: C, 47.73; H, 4.43; N, 1.99. Found: C, 47.70; H, 4.65; N, 1.74%. ^{1}H NMR ($(CD_3)_2CO$): 7.88 dd [8H, $^3J_{HH}$ = 8.4 Hz, $^4J_{HH}$ = 1.6 Hz, $(SbPh_4)^+$ – *ortho*], 7.61 m [12H, $(SbPh_4)^+$ – *meta* + *para*], 3.25 d [6H, $^3J_{PH}$ = 11.2 Hz, L^-]; ^{31}P NMR ($(CD_3)_2CO$): 12.08 h ($^3J_{PH}$ = 11.2 Hz, L^-).

2.2. Methods

2.2.1. NMR, IR-spectroscopy

IR spectra of the compounds were recorded on an UR-10 spectrometer in the range 400–4000 cm^{-1} (samples as KBr pellets or nujol mulls). ^{1}H and ^{31}P NMR spectra were recorded on a Varian AMX 400 spec-

Table 1
Crystal data and structure refinement for **1**–**7**

	1	**2**	**3**	**4**	**5**	**6**	**7**
Empirical formula	$C_4H_6Cl_3NO_4PNa$	$C_4H_6Cl_3NO_4PRb$	$C_4H_6Cl_3NO_4PTl$	$C_{28}H_{26}Cl_3NO_4P_2$	$C_{52}H_{48}BrCl_3NO_5P_3$	$C_{72}H_{76}Cl_{18}N_6O_{24}P_8Na_4$	$C_{28}H_{31}Cl_3NO_4PSb$
Crystal system	triclinic	triclinic	monoclinic	monoclinic	monoclinic	monoclinic	monoclinic
Temperature (K)	293	223	293	293	293	293	293
Space group	$P\bar{1}$	$P\bar{1}$	$P2_1/c$	$P2_1/c$	$P\bar{1}$	$P2_1/c$	$P2_1/c$
Unit cell dimensions							
a (Å)	6.010(1)	11.7400(6)	7.033(1)	7.4396(4)	9.5054(8)	14.3848(6)	13.088(3)
b (Å)	9.581(2)	12.0180(6)	9.570(1)	24.852(1)	13.5877(1)	24.8616(9)	13.999(3)
c (Å)	9.774(2)	19.1636(9)	16.748(3)	15.6860(7)	20.033(2)	14.0177(6)	17.049(3)
α (°)	87.22(3)	74.676(1)	90.00	90.00	105.256(1)	90.00	90.00
β (°)	84.14(3)	84.039(1)	98.42(1)	100.046(1)	98.171(2)	97.488(4)	108.24(3)
γ (°)	86.47(3)	63.485(1)	90.00	90.00	94.030(2)	90.00	90.00
V (Å^3)	558.3(2)	2333.1(2)	1115.1(2)	2855.8(2)	2455.1(4)	4970.4(3)	2967(1)
Z	2	8	4	4	2	2	4
D_{calc} (g cm^{-3})	1.739	2.021	2.828	1.416	1.415	1.595	1.578
μ (mm^{-1})	9.13	5.055	1.549	0.468	1.147	0.713	1.288
$2\theta_{max}$ (°)	79.92	26.04	52.0	26.02	27.09	28.76	27.54
Reflections collected	2271	13560	2192	16419	15092	34240	15754
Independent reflections (R_{int})	2271(0.0000)	9037 (0.0173)	1740 (0.02)	5595(0.0409)	10498(0.0215)	11930(0.0291)	6065(0.0318)
Data/parameters	1733/164	8213/533	1740/127	5222/371	10418/594	11925/595	5015/408
GOF^2	1.113	1.079	1.78	0.846	1.040	1.107	1.071
R_1, wR_2 (obs.)	0.0478, 0.1300	0.0402, 0.0993	0.036, 0.048	0.0592, 0.1376	0.0497, 0.1215	0.0391, 0.1088	0.0323, 0.0710
R_1, wR_2 (all data)	0.0600, 0.1871	0.0592, 0.1173		0.1084, 0.1851	0.0817, 0.1470	0.0571, 0.1159	0.0510, 0.0906
Largest difference in peak and hole (e Å^{-3})	0.516, −0.435	1.834, −0.894	0.92,	0.965, −0.300	0.593, −0.570	0.837, −0.715	0.578, −1.024

trometer at room temperature in deuterated water (D_2O) or acetone (acetone d_6) solutions (TMS internal standard).

2.2.2. Crystallography

Details of the data collections and refinements are given in Table 1. Data were collected at room temperature (except **2**, $T = 223$ K) using an Enraf-Nonius CAD-4 for **3**, KUMA KM-4 and Mo-radiation for **6** and Cu-radiation for **1** or with a SMART CCD system for **2**, **4**, **5**, **7**, using Mo-radiation. The structures were solved by the heavy atom method. All non-hydrogen atoms were refined anisotropically. The positions of the hydrogen atoms were idealized. Refinements were by full-matrix least squares based on F^2 and using SHELX-86 and SHELXL-93 [9,10].

3. Results and Discussion

3.1. NMR and IR spectroscopy

The difference in ^{31}P NMR chemical shifts between P═O (12–16 ppm.) is typical and can readily be compared to the related compounds with the formula $CCl_3C(O)NHP(O)R$. The ^1H NMR spectra and CHN analyses were satisfactory for all compounds.

The IR spectra of the compounds have a number of common features (Table 2), that coincide with the literature data [11]. The IR bands in the region 3080 cm^{-1} observed in the spectrum of the neutral ligand, may be ascribed to ν(NH) vibrations of the amide protons. These bands are absent in the spectra of all compounds **1**–**7**, which is evidence for the deprotonated form of the ligand. The spectra for compounds **1**–**7** reveal significantly lower frequencies of ν(PO) compared with HL ($\Delta\nu$(PO) = 40–85 cm^{-1}), reflecting the binding via the phosphoryl oxygen atom [12]. In the case of compound **6** the splitting of the ν(PO) band is caused by the μ^3-dentate function of the phosphoryl oxygen of the "axial" ligand. The ν(CO) values in the spectra of the compounds are shifted to lower frequencies ($\Delta\nu$(CO) = 58–107 cm^{-1}) due to delocalization of π-electron density in the chelate frame under deprotonation or coordination. These facts were observed for a wide range of phosphoramide chelate systems [13,14].

3.2. Description of the structures

The covalence degree of the metal–ligand interaction (in the six-membered chelate metal cycles, e.g., β-diketonates, diphosphinates) directly depends on the nature of the central ion, donor atoms and planarity of the chelate moiety. For the carbacylamidophosphates, the criterion of planarity may be considered to be the value of the torsion angle OPNC ($\angle$PNCO = 0°) [7], which reflects the delocalization degree of π-electron density in the chelate frame as a whole. Thereupon the above-mentioned structures will be studied.

The structures of compounds **1** and **3** are composed of centrosymmetric dimers (Fig. 1(a) and (b)) that are formed by the bridging function of the phosphoryl oxygen atom. The result is a tricyclic system with a central planar four-membered M_2O_2 ring and an overall ladder structure: parameters Na(1) ··· Na(1a) = 3.506(3) Å; $\angle$Na(1)O(1)Na(1a) = 94.28(1)°, $\angle$O(1)Na(1)O(1a) = 85.74(1)° in **1** and parameters Tl(1)–Tl(1a) = 4.111(1) Å, $\angle$Tl(1)O(1)Tl(1a) = 96.2(4)°, $\angle$O(1)Tl(1)O(1a) = 83.8(3)° for **3** (Table 3). A similar type of bonding was observed earlier in $[Na\{(OPPh_2)(SPPh_2)N\}\cdot 2THF]_2$ [15]. The nitrogen atom N(1) and oxygen atoms of methoxy groups of the neighboring dimer moieties are also involved in coordination to each sodium and thallium atom. Thus, polymeric ladder structures for **1** and **3** are realized (Fig. 1(c)).

The unique part of **2** consists of four structurally independent Rb^+ ions (Fig. 2): the closest contact Rb-L exceeds 2.8 Å, so it might be considered as mainly an ionic type of bond. Thus, each L has bridging oxygen atoms of phosphoryl and carbonyl groups. The bridging function of the carbonyl oxygen atom of the amidophosphate ligands was observed for the first time.

The coordination pattern of the amidophosphate ligands (codified here as $\mathbf{L^1}$, $\mathbf{L^2}$, $\mathbf{L^3}$ and $\mathbf{L^4}$ corresponding

Table 2
Main IR absorption bands and their assignments, for the compounds (cm^{-1})

Compound	ν(N–H)	ν(C═O)	ν(C–N)	ν(P═O)	ν(C–Cl)
H[L]	3080	1732	1450	1270	675
Na[L]		1625	1350	1200	685
Rb[L]		1630	1345	1210	680
Tl[L]		1625	1325	1175	670
PPh_4[L]		1670	1350	1230	680
$(PPh_4)_2$[L]Br · H_2O		1640	1350	1195	680
$(PPh_4)_2[Na_4L_6]$		1675–1635	1350	1180–1115	690
$[SbPh_4L]$		1645	1325	1140	680
K[PhC(O)NP(O)Ph_2][a]		1523	1591	1141	

[a] Published data [13].

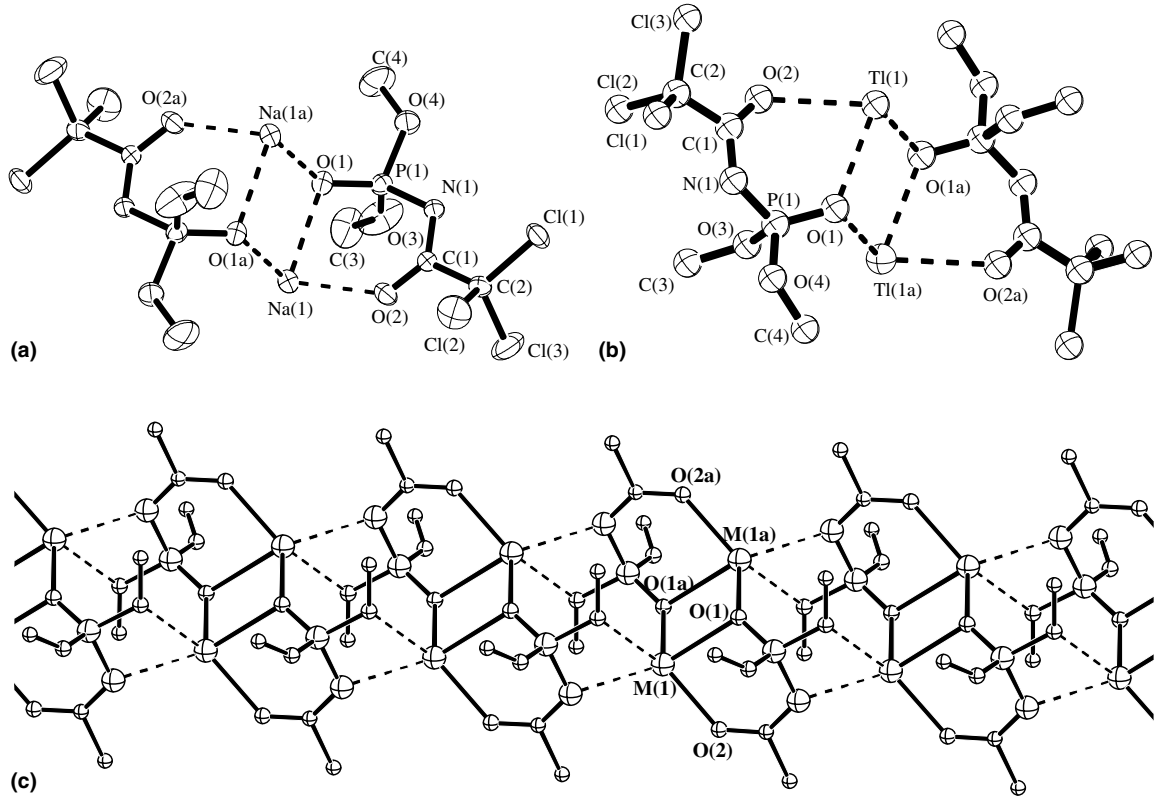


Fig. 1. Molecular dimeric structures of NaL (**a**), TlL (**b**) and the polymeric arrangement for the above-mentioned compounds (**c**) (where M = Na, Tl; chlorine atoms of the CCl_3 group are omitted).

Table 3
Structural peculiarities of some carbacylamidophosphates compounds

Compound	Parameters							
	d(CO) (Å)	*d*(CN) (Å)	*d*(PO) (Å)	*d*(CO–M) (Å)	*d*(PO–M(1)) (Å)	*d*(PO–M(1a)) (Å)	∠CNPO (°)	Mean deviation from OCNPO (Å)
H[L][a]	1.202(2)	1.347(2)	1.459(2)		1.964(3)[b]		180°	0.0801
Na[L]	1.225(4)	1.306(4)	1.466(2)	2.273(3)	2.499(3)	2.280(4)	52.5°	0.212
Rb[L]								
L^1	1.239(1)	1.292(1)	1.437(1)	2.846(2)	3.001(2)	2.847(2)	54.46(1)	0.217
L^2	1.231(1)	1.323(1)	1.468(0)	2.938(1)	2.848(1)	2.836(1)	63.71(1)	0.248
L^3	1.236(1)	1.310(1)	1.468(0)	2.859(1)	2.857(1)	2.887(1)	58.05(1)	0.251
L^4	1.224(1)	1.299(0)	1.458(1)	3.218(2)	3.064(1)	2.834(1)	23.82(1)	0.071
Tl[L]	1.245(1)	1.309(8)	1.470(5)	2.736(6)	2.610(5)	2.905(1)	42.5°	0.162
PPh_4[L]	1.215(5)	1.303(6)	1.419(3)				80.1°	0.264
$(PPh_4)_2$[L]Br · H_2O	1.228(4)	1.319(4)	1.466(3)		2.017(6)[b]		62.3°	0.245
$(PPh_4)_2[Na_4L_6]$								
L^1	1.235(1)	1.39(1)	1.488(9)	2.38(1)	2.31(2)	2.302(5)	10.15°,	0.02
L^2	1.234(2)	1.33(1)	1.483(1)	2.255(9)	2.46(2)	2.60(4)	40.37°,	0.137
L^2						2.415(2)		
L^3	1.212(5)	1.31(2)	1.49(1)	2.202(2)	2.39(4)	2.30(2)	43.311°	0.188
$SbPh_4$[L]	1.559(3)	1.109(9)	1.432(3)		2.446(3)		79.4°	0.309

[a] Published data in [12].
[b] P(O) ··· H distance.

to the oxygen atoms of methoxy groups) is different (schematic representations are depicted in **a** and **b**). The distortion of the chelate frame in the rubidium compound (**a**, **b**) can be explained in terms of the availability of a weak contact Rb–O(CH_3) and has been reflected in the values of the torsion angles (Table 3).

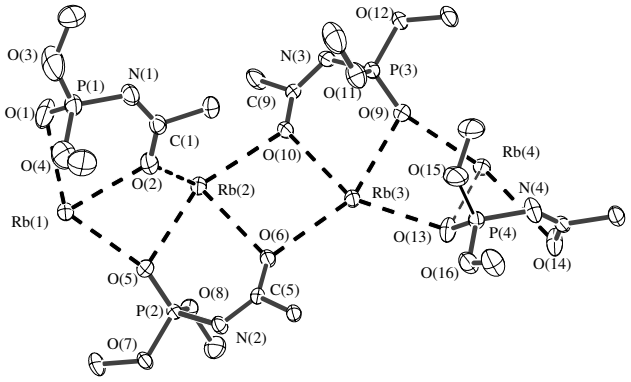
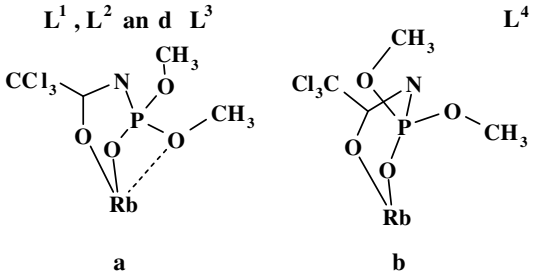


Fig. 2. Structure of RbL. The protons of methyl groups and chlorine atoms are omitted for clarity.



The molecular structures of **1**, **2** and **3** show the ligand's coordination to the metal ion via the oxygen atoms of phosphorylic and carbonylic groups, forming a six-membered chelate ring arrangement in which the ring can be viewed as a heterocycle containing five different atoms. Each chelate cycle is not planar. Table 3 lists the maximum deviation from the mean plane for all compounds. The corresponding bond lengths M–O(P) and M–O(C) in each chelate frame are 2.499(3) and 2.273(3) Å for **1**, 2.94 and 2.96 Å (average) for **2**, 2.610(5) and 2.736(6) Å for **3**; c.f. the sum of ionic radii are $\Sigma_{M^+ + O^{2-}}(Na, O) = 2.36$ Å, $\Sigma_{M^+ + O^{2-}}(Rb, O) = 2.92$ Å, $\Sigma_{M^+ + O^{2-}}(Tl, O) = 2.86$ Å, [16]. There are few previous crystallographic determinations to make comparisons. The most appropriate are $[TlPh_2\{(SPPh_2)_2N\}]$ [11] and $K[(SPPh_2)_2N]$ [17].

In the Na, Rb and Tl salts the C–N–P system is angular (values of the angle C–N–P are shown in Table 3) as it is in the free ligand, but the (O)CNP(O) skeleton has the *syn*-conformation for all compounds. Within the ligand moiety the phosphorous–oxygen and carbon–oxygen distances are significantly longer (Table 3) compared with the free ligand [4]. In contrast, the phosphorous–nitrogen bonds in HL are significantly shorter (0.055 Å (**1**), 0.063 Å (**2**), 0.062 Å (**3**)), suggesting an increase in double bond character as a result of π-delocalization [15]. Taking into consideration that alkali metals are hard Lewis acids, the covalence contribution in the interaction $M^+ - L^-$ is realized. This is also reflected in the values of the torsion angle PNCO (Table 3). The coordination geometry around the sodium, rubidium and thallium atoms in their compounds are irregular (Fig. 3(a) and (b)): C.N. for Na, Rb and Tl atoms in their compounds are 5, 7 and 6, respectively.

The X-ray structures of **4** and **5** reveals that there are no contacts shorter than 2.72 Å between the cation and anion. The tetraphenylphosphonium salt (**4**) contains a non-solvated and deprotonated phosphorylic ligand (Fig. 4(a)). In compound **5** (Fig. 4(b)), two anions L^-(O=P) and Br^- are associated into an ensemble by means of hydrogen bonding with a solvate water molecule [H(2) ··· O(1) 2.017(6) Å, O(5) ··· O(1) 2.840(5) Å, O(5)–H(2) ··· O(1) 167.2(2)°, H(1) ··· Br(1) 2.656(6) Å, O(5) ··· Br(1) 3.365(5) Å, O(5)–H(1) ··· Br(1) 175.3(6)°]. Geometrical parameters of the chelate frame in these structures have some differences from those for the alkali metals and thallium compounds. The mean C=O and P=O distances in **4** are decreased by 0.01 and 0.04 Å, respectively, in contrast with the sodium salt, while the bond CN lengths are almost the same. Such variations in the bond lengths testify that there are no bonding contacts for the carbacylamidophosphate anion in compound **4**. Otherwise there are no significant differences in bond lengths in chelate **5** (deprotonated anionic ligand) compared to that in **1** (Table 3). The presence of the above H-bond evidently stabilizes the structure **5**. These data all agree well with the results of the IR-spectroscopic study (Table 2).

The chelate (O)PNC(O) frame in **4** and **5** are non-planar with maximum deviations of atoms from the mean PNCO plane of 1.241 and 1.162 Å, respectively. This implies an increase in the CNPO torsion angles for both compounds in contrast with those in **1**–**3** (Table 3). Thus, the ionic type of binding realized in compounds **4** and **5** causes the decrease of π-conjugation in the chelate moiety.

The X-ray structure of **6** reveals an unexpected type of coordination moiety $[Na_4L_6]^{2-}$ (Fig. 5); there are no shortened contacts between the cations and anion. Such a type of self-assembly in coordination compounds is realized due to the influence of the PPh_4^+ anion and μ-dentate function of the phosphoryl oxygen atoms.

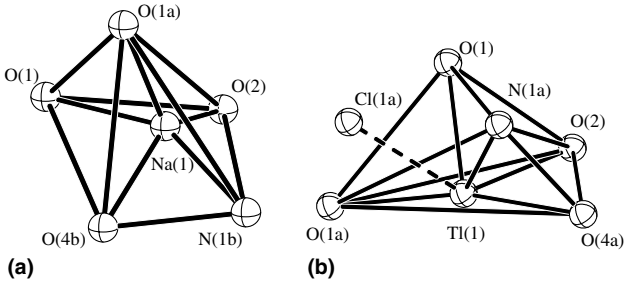


Fig. 3. Coordination polyhedra of NaL (**a**) and TlL (**b**).

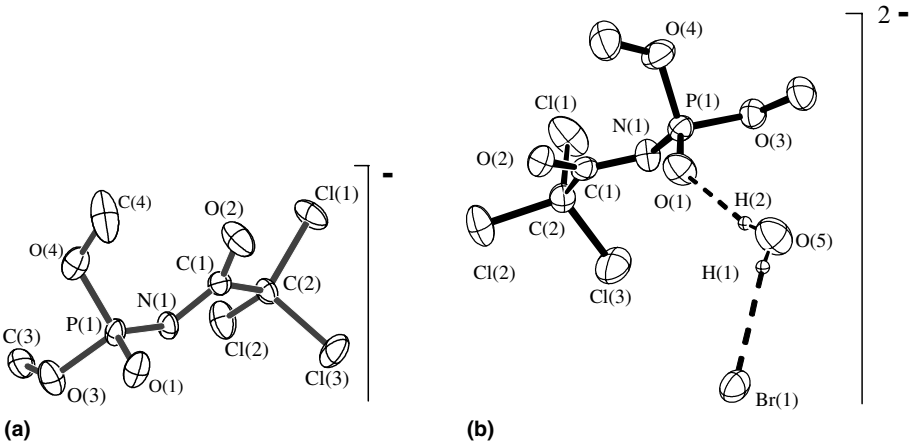


Fig. 4. The anionic moieties in the structure of $PPh_4[L]$ (**a**), $(PPh_4)_2[L]Br \cdot H_2O$ (**b**).

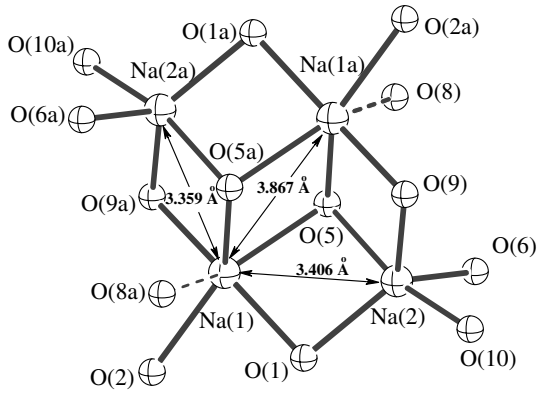


Fig. 5. Na_4-frame geometry and coordination arrangement of Na-atoms.

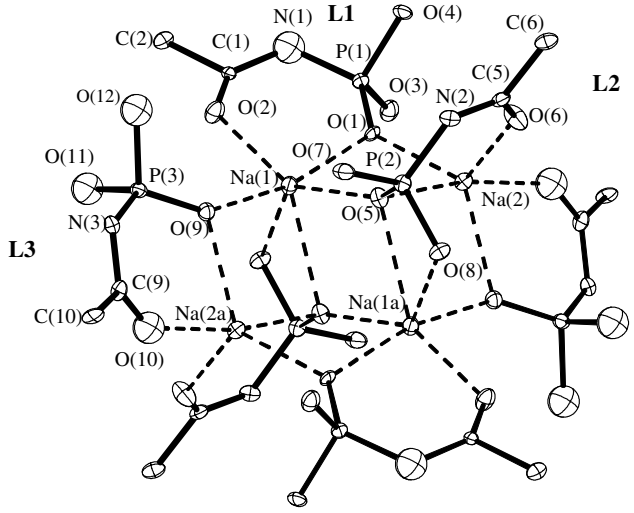


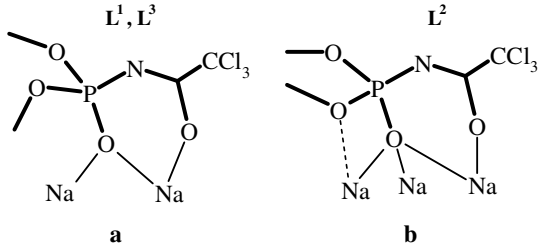
Fig. 6. Structure of the anion $(PPh_4)_2[Na_4L_6]$ (CH_3^-, Cl^- atoms are omitted).

Similarly to the sodium and thallium salts described above, the central ion is coordinated to the ligands in a bidentate-chelate manner. A four-membered planar Na_4 unit has formed (Fig. 5) because of the μ-function of the phosphoryl oxygens, as will be shown later. The corresponding angles Na(1)–Na(2)–Na(1a) and Na(2a)–Na(1)–Na(2) are 69.73(1)° and 110.27(1)°, respectively.

The dihedral angles between the Na_4 plane and the mean planes of the corresponding chelate frames are $\mathbf{L^1}$ – 19.7° – an "equatorial" position, $\mathbf{L^2}$ – 83° – an "axial" position and $\mathbf{L^3}$ – 45.8 – a "meridian" position (the coordination pattern of the carbacylamidophosphate ligands codified here as $\mathbf{L^1}$, $\mathbf{L^2}$ and $\mathbf{L^3}$) (Fig. 6).

Na atoms in the structure of **6** have different environments: C.N. Na(1) = 6 (distorted octahedron with axial axis O(1)–Na(1)–O(9) (∠165.56°)); C.N. Na(2) = 5 (distorted trigonal bipyramid with axial O(10a)–Na(2)–O(5) (∠169.96°)) (Fig. 7).

In contrast to **1**, the phosphoryl oxygen atoms of ligands $\mathbf{L^1}$ (O(1)) and $\mathbf{L^3}$ (O(9)) have a μ^2-bridging function and in $\mathbf{L^2}$ (O(5)) a μ^3-bridging function (schematic representations are depicted in **a** and **b**), as a consequence the acido-ligands in the complex anion are not equivalent. These data all agree well with the results of the IR-spectroscopic study (Table 2). Such dentate differences have an effect on the corresponding NaO(P) contacts: the μ^3-dentate oxygen atom, consisting of an "axial" ligand, forms longer contacts with the three sodium atoms than the μ^2-phosphoryl oxygen (Δ = 0.1–0.3 Å). All these parameters are comparable with those in **1** (Table 3).



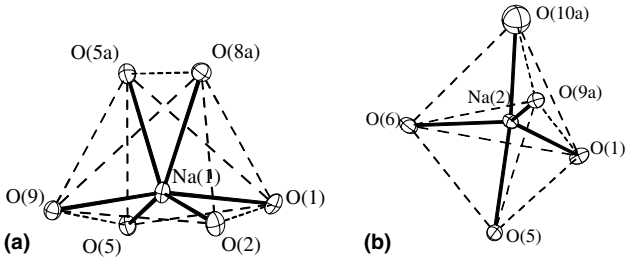


Fig. 7. Coordination polyhedra of sodium atoms in $(PPh_4)_2[Na_4L_6]$: (**a**) Na(1), (**b**) Na(2).

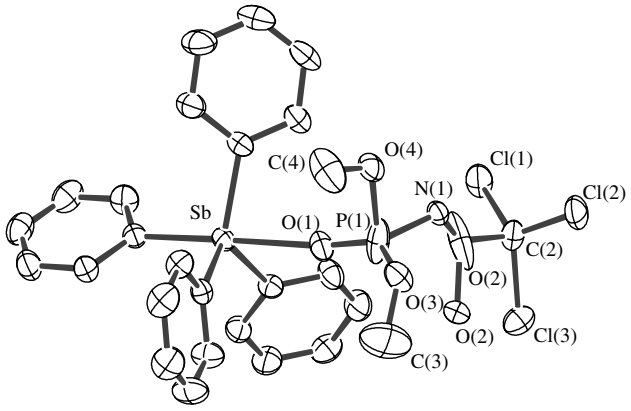


Fig. 8. Molecular structure of $[SbPh_4L]$.

The PNCO torsion angles values for $\mathbf{L^2}$ and $\mathbf{L^3}$ are similar and for $\mathbf{L^1}$ – significantly less than that in NaL (Table 3).

The molecular structure of the antimony complex **7** shows a monodentate coordination of the phosphorylic ligand via the phosphoryl oxygen atom (Fig. 8). The central Sb(1) atom adopts a fivefold coordination with a slightly distorted trigonal bipyramid. One of the phenyl cycles and the O(1) oxygen atom occupy the axial positions (∠[C(40)–Sb(1)–O(1)] = 176.5°). Three equatorial phenyls are non-planar and shifted to the side of $\{L^-\}$, on average by 8°.

The Sb–O bond length is 2.44 Å. The value of the SbOP angle slightly deviates from linearity (172.0°) and is significantly bigger then SbOC in $SbPh_4OCH_3$ (∠SbOC = 126° [18]). The P═O bond length is 1.432(3) Å, which is somewhat less than those in all the above structures, except in **4**. A discussion of all the another parameters in the chelate frame is complicated due to disordering of the trichloroacetamidic part.

The value of the torsion angle OPNC is 79.4° and takes an intermediate position between the same value for **4** (80.1°) and **5** (62.3°), which exhibits a minimum of π-conjugation.

4. Conclusions

The coordination behavior of dimethyl-*N*-trichloracetylamidophosphate towards singly charged cations reveals principal differences from complexes with d- and f-metals studied earlier. The main feature of this ligand is the disposition to form bi- and polymeric structures and associates. It was shown that creation of especial steric conditions (the application of cations with one vacant place for coordination – $SbPh_4^+$) was necessary for the formation of simple systems. Using non-coordinating ions (PPh_4^+) permits the synthesis and to characterize structurally of the ''free'' non-solvated anion. These data could be used for the molecular design of coordination systems based on carbacylamidophosphates.

5. Supplementary data

Crystallographic data have been deposited at the Cambridge Crystallographic Data Center, CCDC Nos: **1** – 237495; **2** – 237497; **3** – 237496; **4** – 237498; **5** – 237499; **6** – 237500; **7** – 237501. Copies of this information may be obtained free of charge from the Director CCDC, 12 Union Road, Cambridge, CB2 1EZ, UK (fax: +44 1223 336033; e-mail: deposit@ccdc.cam.ac.uk or http://www.ccdc.ac.uk).

References

[1] P. Bhattacharyya, A.M.Z. Slawin, M.B. Smith, D. Woollins, Inorg. Chem. 35 (1996) 3675.
[2] P. Bhattacharyya, A.M.Z. Slawin, D.J. Williams, J.D. Woollins, J. Chem. Soc., Dalton Trans. (1995) 3189.
[3] A.M.Z. Slawin, M. Wainwright, D. Woollins, New J. Chem. 24 (2000) 69.
[4] R. Richter, J. Sieler, H. Borrmann, A. Simon, N.T.T. Chau, et al., Phosphorous, Sulfur, Silicon 60 (1991) 107.
[5] E.A. Bundya, V.M. Amirkhanov, V.A. Ovchynnikov, V.A. Trush, K.V. Domasevitch, J. Sieler, V.V. Skopenko, Z. Naturforsch. 54b (1999) 1033.
[6] M. Borzechowska, V. Trush, I. Turowska-Tyrk, W. Amirkhanov, J. Legendziewicz, J. Alloy Compd. 341 (2002) 98.
[7] G. Oczko, J. Legendziewicz, V. Trush, V. Amirkhanov, New J. Chem. 27 (2003) 948.
[8] A.V. Kirsanov, G.I. Derkach, Zh. Obsch. Khim. 26 (1956) 2631.
[9] G.M. Sheldrick, SHELXS-86, Acta Crystallogr., Sect. A 46 (1990) 467.
[10] G.M. Sheldrick, SHELXL-93, Program for the Refinement of Crystal Structures, University of Gottingen, Gottingen, Germany, 1993.
[11] D.J. Birdsall, J. Green, T.Q. Ly, Eur J. Inorg. Chem. (1999) 1445.
[12] V.M. Amirkhanov, V.A. Trush, Zh. Obshchei Khimii 65 (1995) 1120.
[13] Tuan Q. Ly, J.D. Woollins, Coord. Chem. Rev. 176 (1998) 469.
[14] K.E. Gubina, V.A. Ovchynnikov, J. Swiatek-Kozlowska, V.M. Amirkhanov, T.Yu. Sliva, K.V. Domasevitch, Polyhedron 21 (2002) 963.
[15] J. Yang, J.E. Drake, S. Hernandez-Ortega, R. Rosler, et al., Polyhedron 16 (1997) 4066.
[16] R.D. Shannon, Acta Crystallogr., Sect. A 32 (5) (1976) 751.
[17] A.M.Z. Slawin, J. Ward, D.J. Williams, J.D. Woollins, J. Chem. Soc., Chem. Commun. (1994) 421.
[18] Shen Kei-Wei, W.E. McEwen, S.J. La Placa, J. Am. Chem. Soc. 90 (1969) 1718.

metal ion materials containing bio-relevant pyrazolyl thiosemicarbazones and related ligands, the present paper reports the syntheses and spectroscopic identification of new Ni(II) complexes with 5-methyl-3-formylpyrazole-3-piperidinylthiosemicarbazone (HMP_z3Pi), with novel findings from X-ray crystallography of $[Ni(HMP_z3Pi)_2]Cl_2 \cdot 2H_2O$.

2. Experimental

All reagents were of AR/GR grade and were obtained from commercial sources and used without further purification. Spectral and conductance measurements were performed using spectrograde solvents.

2.1. Preparation of 5-methyl-3-formylpyrazole-3-piperidinylthiosemicarbazone (HMP_z3Pi)

The title ligand, HMP_z3Pi (Fig. 1), has been synthesised and thoroughly characterised by physical methods for the first time, as reported in an earlier communication [8g].

2.2. General method of preparation of nickel (II) complexes: $[Ni(HMP_z3Pi)_2]X_2 \cdot 2H_2O$ (X = Cl, Br, ClO_4, BF_4 and NO_3)

The reported Ni(II) complexes have been prepared by refluxing ethanolic solutions of the ligand (1.05 mmol) and the corresponding hydrated Ni(II) salt (0.525 mmol) in a water bath for about 30 min. On slow evaporation of the green solutions, each of the desired Ni(II) complexes crystallised out, was filtered off, washed with cold ethanol and was dried over anhydrous $CaCl_2$; the yield has been recorded to be 75–80%. Diffractable quality dark green crystals of $[Ni(HMP_z3Pi)_2]Cl_2 \cdot 2H_2O$ were obtained on slow crystallisation.

Caution! Extreme care has been taken while treating organic compounds with nickel (II) perchlorate, as potentially explosive mixtures might be formed.

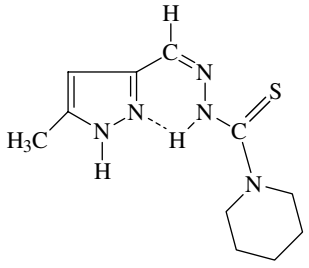


Fig. 1. Structural formulation of 5-methyl-3-formylpyrazole-3-piperidinylthiosemicarbazone (HMP_z3Pi).

2.3. Physical measurements

All physical measurements and analytical procedures adopted for characterisation of the Ni(II) complexes are similar to those described earlier [8e,8h].

2.4. Structure determination

X-ray diffraction data of the ligand (HMP_z3Pi) were collected on a Bruker–Nonius MACH3 diffractometer, while those of the complex $[Ni(HMP_z3Pi)_2]Cl_2 \cdot 2H_2O$ were collected on a CCD diffractometer. The radiation used in either case was Mo Kα and the data were corrected for Lorentz and polarisation effects. The structures were solved by direct methods and refined using the full matrix least squares method based on $|F_{obs}|^2$ [9]. The non-hydrogen atoms were refined anisotropically, while the hydrogen atoms, either located from difference electron density maps or generated using idealised geometry, were used in the structure factor calculations with isotropic thermal parameters using the "riding" model. Neutral atom scattering factors [10] were used and anomalous dispersion effects were included in F_{calc} [11]. The crystallographic data are summarised in Table 3. The final positional and thermal parameters are available as supplementary material.

3. Results and discussion

3.1. Characterisation of 5-methyl-3-formylpyrazole-3-piperidinylthiosemicarbazone (HMP_z3Pi)

The title ligand, HMP_z3Pi, has been characterised by elemental analyses (C, H and N), IR, ^1H NMR and mass spectrum and the results have been reported earlier

Table 1
Analytical data and other pertinent physico-chemical properties of nickel (II) complexes of 5-methyl-3-formylpyrazole-3-piperidinylthiosemicarbazone (HMP_z3Pi)

Complex (colour)	Elemental analyses found (calc.)				Conductivity at 30 °C in MeOH (Ω^{-1} cm^2 mol^{-1})	μ_{eff} (BM) at 300 K
	% C	% H	% N	% Ni		
$[Ni(HMP_z3Pi)_2]Cl_2 \cdot 2H_2O$ (dark green)	39.2 (39.5)	5.6 (5.7)	20.8 (21.0)	8.6 (8.8)	211	3.12
$[Ni(HMP_z3Pi)_2]Br_2 \cdot 2H_2O$ (grey green)	34.8 (34.9)	4.9 (5.0)	18.8 (18.5)	7.7 (7.8)	207	3.09
$[Ni(HMP_z3Pi)_2](ClO_4)_2 \cdot 2H_2O$ (dark green)	33.0 (33.2)	4.8 (4.8)	17.9 (17.6)	7.4 (7.4)	210	3.07
$[Ni(HMP_z3Pi)_2](BF_4)_2 \cdot 2H_2O$ (yellowish green)	34.2 (34.3)	5.0 (4.9)	18.5 (18.2)	7.8 (7.6)	196	3.26
$[Ni(HMP_z3Pi)_2](NO_3)_2 \cdot 2H_2O$ (dirty green)	36.2 (36.6)	5.0 (5.3)	23.7 (23.3)	8.0 (8.1)	192	3.22

[8g]. The proposed structural formulation (Fig. 1) of the ligand, HMP_z3Pi has been established by X-ray crystallography in the present communication.

3.2. Characterisation of the Ni(II) complexes

The reported Ni(II) complexes gave satisfactory C, H, N and metal analyses and conform to the general composition: $[Ni(HMP_z3Pi)_2]X_2 \cdot 2H_2O$ (X = Cl, Br, ClO_4, BF_4 and NO_3). The molar conductance values in MeOH (30 °C) classify them as 1:2 electrolytes [12] (Table 1). All the reported complexes are paramagnetic (μ_{eff} = 3.07–3.26 BM), as expected for a normal spin free d^8 system.

3.2.1. Spectral studies

The solid state electronic spectra (DRS) of all the reported nickel (II) complexes are similar in nature and exhibit three bands in the regions 11 723–11 919 cm^{-1} [$^3A_{2g}$ (F) → $^3T_{2g}$ (F)(ν_1)], 17 241–17 574 cm^{-1} [$^3A_{2g}$ (F) → $^3T_{1g}$ (F)(ν_2)] and 27 248–27 624 cm^{-1} [$^3A_{2g}$ (F) → $^3T_{1g}$ (P)(ν_3)], which correspond to an overall octahedral symmetry.

The MeOH solution spectra of the nickel (II) complexes show two bands in the regions 11 751–11 834 cm^{-1} (ν_1) and 17 212–17 544 cm^{-1} (ν_2), which are very much similar to those in the solid state, thereby suggesting no gross electronic or geometric change of the species on dissolution in the said solvent. The absence of the ν_3 band corresponding to $^3A_{2g}$ (F) → $^3T_{1g}$ (P) transition, in all cases, might lie in the UV region, where it may be obscured by intense internal π → π* transition of the ligand or intense CT absorption bands [8h,13,14]. The characteristic IR bands (4000–200 cm^{-1}) for the free ligand, HMP_z3Pi, when compared with those of its Ni(II) complexes, offer significant indications regarding the bonding sites of the primary ligand molecule (Table 2). A negative shift in the $\nu_{(CH=N)}$ band (1610 cm^{-1}) in the free ligand spectrum to the lower value (1580–1590 cm^{-1}) in its complexes indicate coordination of the azomethine nitrogen to the central metal ion; the IR bands at 470–485 cm^{-1} in the complexes are then assignable to $\nu_{(Ni–N)}$ [8,13–15]. IR bands at 1525 and 630 cm^{-1} in the free ligand spectrum, assignable to $\nu_{(C=N)}$ (pyrazole ring) and the in-plane deformation of the pyrazole ring, respectively, have been found to shift to the higher frequency region, pointing to the participation of the tertiary ring nitrogen atom (^2N) as a potential bonding site [8h,13–16]. The appearance of bands at 280–292 cm^{-1} in the complexes are then assignable to $\nu_{(Ni–N)}$ (pyrazole ring) [8,13–15]. An intense band at 860 cm^{-1} in the spectrum of the free ligand, corresponding to $\nu_{(C=S)}$, has been found to shift to lower frequency regions (785–795 cm^{-1}) in the complexes,

Table 3
Crystal data for HMP_z3Pi (I) and $[Ni(HMP_z3Pi)_2]Cl_2 \cdot 2H_2O$ (**II**)

Compound	Ligand **I**	Complex **II**
Empirical formula	$C_{11}H_{17}N_5S$	$C_{22}H_{38}N_{10}S_2O_2Cl_2Ni$
Formula weight	251.36	668.35
T (K)	293(2)	293(2)
Crystal system	orthorhombic	triclinic
Crystal colour	colourless	dark green
Space group	*Pbca*	$P\bar{1}$
a (Å)	13.836(1)	9.273(1)
b (Å)	11.169(1)	11.698(1)
c (Å)	17.415(1)	15.385(1)
α (°)	90	104.411(2)
β (°)	90	105.728(2)
γ (°)	90	95.951(2)
Unit cell volume (Å^3)	2691.1(3)	1529.3(3)
Z	8	2
λ (Mo Kα) (Å)	0.71073	0.71073
$d_{calc.}$ (g cm^{-3})	1.241	1.451
μ (mm^{-1})	0.228	0.984
F(000)	1072	700
θ Range for data collection (°)	2.3–24.9	1.8–29.0
Index ranges	$0 \leqslant h \leqslant 16$; $0 \leqslant k \leqslant 13$; $0 \leqslant l \leqslant 20$	$-12 \leqslant h \leqslant 10$; $-14 \leqslant k \leqslant 15$; $-20 \leqslant l \leqslant 20$
Reflections collected	2371	12121
Independent reflections	2371 (R_{int} = 0.000)	7504 (R_{int} = 0.041)
Refinement method	full-matrix least-squares on F^2	full-matrix least-squares on F^2
Observed reflections [$I > 2\sigma(I)$]	1260	5381
Number of parameters	154	367
Number of restraints	0	6
Goodness-of-fit on F^2	1.166	1.030
$R_1[I > 2\ \sigma(I)]$	0.0629	0.0435
wR_2	0.2106	0.1049
Largest difference in peak and hole (e Å^{-3})	0.26 and −0.32	0.40 and −0.45

$R_1 = \sum\|F_o\| - |F_c\|/\sum|F_o|$. $wR_2 = \{\sum[(F_o^2 - F_c^2)^2]/\sum[w(F_o^2)^2]\}^{1/2}$; $w = 1/[\sigma^2(F_o^2) + (aP)^2 + bP]$, where a = 0.1064 and b = 0.0000 for (**I**), and a = 0.0552 and b = 0.5971 for (**II**). $P = (F_o^2 + 2F_c^2)/3$ for both structures.

Table 2
Selected IR bands (in cm^{-1}) for the ligand (HMP_z3Pi) and its nickel (II) complexes

Compound	$\nu_{(CH=N)}$ (azomethine)	$\nu_{(C=N)}$ (pyrazole)	$\nu_{(C=S)}$	$\nu_{(Ni–N)}$ (azomethine)	$\nu_{(Ni–N)}$ (pyrazole)	$\nu_{(Ni–S)}$
HMP_z3Pi	1610	1525	860	–	–	–
$[Ni(HMP_z3Pi)_2]Cl_2 \cdot 2H_2O$	1580	1545	795	470	290	380
$[Ni(HMP_z3Pi)_2]Br_2 \cdot 2H_2O$	1587	1548	785	480	282	373
$[Ni(HMP_z3Pi)_2](ClO_4)_2 \cdot 2H_2O$	1585	1555	792	476	285	365
$[Ni(HMP_z3Pi)_2](BF_4)_2 \cdot 2H_2O$	1590	1550	787	485	292	380
$[Ni(HMP_z3Pi)_2](NO_3)_2 \cdot 2H_2O$	1587	1545	785	476	280	373

indicating the coordination of the thione sulfur to nickel (II); moreover, the appearance of a new band in the region (365–380 cm^{-1}) in the complexes is assignable to $\nu_{(Ni-S)}$ [8,17,18].

3.3. Crystal structures of HMP_z3Pi (*I*) and $[Ni(HMP_z3Pi)_2]Cl_2 \cdot 2H_2O$ (*II*)

Figs. 2 and 3 show the ORTEP-3 [19] diagrams of the ligand, HMP_z3Pi, and the complex, $[Ni(HMP_z3Pi)_2]Cl_2 \cdot 2H_2O$, respectively, together with the atom numbering schemes. The crystallographic asymmetric unit in the ligand comprises of a single HMP_z3Pi molecular moiety, while that in the complex comprises of a $[Ni(HMP_z3Pi)_2]^{2+}$ cation, two Cl^- counter ions and two molecules of water of crystallisation. Some selected bond distances, bond angles and torsion angles in the two structures are compiled and compared in Table 4.

The nickel (II) ion has a distorted octahedral coordination in the complex. Two molecules (A and B) of the

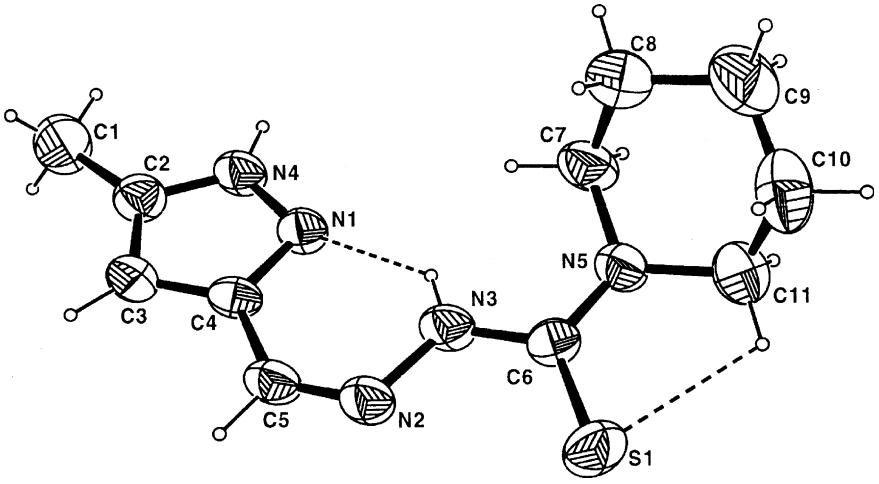


Fig. 2. ORTEP plot of HMP_z3Pi showing the atom numbering scheme.

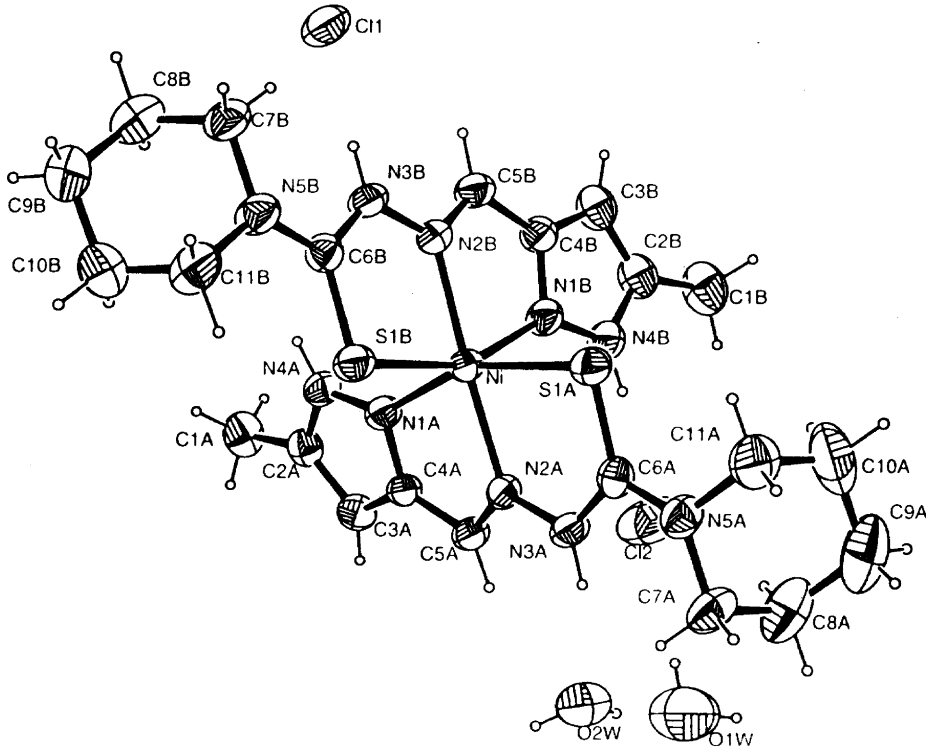


Fig. 3. ORTEP plot of $[Ni(HMP_z3Pi)_2]Cl_2 \cdot 2H_2O$ showing the atom numbering scheme.

Table 4
Characteristic bond lengths (Å), bond angles (°) and torsion angles (°) of HMP_z3Pi (**I**) and $[Ni(HMP_z3Pi)_2]Cl_2 \cdot 2H_2O$ (**II**)

	Free ligand (**I**)	Complex (**II**)	
		Ligand A	Ligand B
Bond distances			
Ni–S1		2.3971(9)	2.3895(8)
Ni–N1		2.085(2)	2.099(2)
Ni–N2		2.023(2)	2.027(2)
S1–C6	1.668(4)	1.689(3)	1.691(3)
C5–N2	1.273(7)	1.275(3)	1.279(3)
N2–N3	1.378(6)	1.364(3)	1.362(3)
N3–C6	1.362(6)	1.346(3)	1.348(4)
C6–N5	1.347(6)	1.332(4)	1.326(3)
N1–C4	1.350(6)	1.331(3)	1.329(3)
C4–C5	1.456(6)	1.443(4)	1.442(4)
Bond angles			
N1–C4–C5	121.6(4)	116.4(2)	116.2(2)
C4–C5–N2	130.9(5)	114.8(2)	115.2(2)
C5–N2–N3	116.3(4)	119.3(2)	119.6(2)
N2–N3–C6	119.8(4)	117.5(2)	118.1(2)
N3–C6–S1	121.8(3)	121.0(2)	120.8(2)
N3–C6–N5	113.7(4)	117.2(2)	116.9(2)
S–C6–N5	124.5(4)	121.7(2)	122.3(2)
Torsion angles			
N2–N3–C6–S1	−1.4(6)	−0.7(3)	−0.2(4)
N2–N3–C6–N5	179.6(4)	177.8(2)	178.3(2)
S1–C6–N5–C7	−158.4(4)	−174.2(2)	−179.4(3)
C5–N2–N3–C6	−178.7(4)	169.6(2)	−179.0(3)
C4–C5–N2–N3	−1.8(8)	178.5(2)	−178.5(2)
N1–C4–C5–N2	9.8(9)	−0.8(3)	5.4(4)
Bond angles around the Ni(II) ion			
S1A–Ni–N1A	157.52(7)	S1B–Ni– N1B	157.62(7)
S1A–Ni–N2A	80.15(6)	S1B–Ni–N2B	80.44(6)
S1A–Ni–N1B	90.83(8)	S1B–Ni–N1A	93.74(6)
S1A–Ni–N2B	101.88(6)	S1B–Ni–N2A	105.73(6)
N1A–Ni–N2A	77.47(8)	N1B–Ni–N2B	77.19(9)
N1A–Ni–N2B	100.15(8)	N1B–Ni–N2A	96.60(9)
N1A–Ni–N1B	89.67(9)	N2A–Ni–N2B	173.43(8)
S1A–Ni–S1B	94.30(3)		

neutral tridentate ligand, 5-methyl-3-formylpyrazole-3-piperidinylthiosemicarbazone (HMP_z3Pi), coordinate to the Ni(II) ion via the pyrazolyl (tertiary) nitrogens [N(1A), N(1B)], the azomethine nitrogens [N(2A), N(2B)] and the thio-keto sulfurs [S(1A), S(1B)], to form four five-membered chelate rings [Ni–S(1A)–C(6A)–N(3A)–N(2A), Ni–S(1B)–C(6B)–N(3B)–N(2B), Ni–N(1A)–C(4A)–C(5A)–N(2A) and Ni–N(1B)–C(4B)–C(5B)–N(2B)]. The two azomethine nitrogen atoms [N(2A) and N(2B)] coordinate to the Ni(II) ion in a *trans* orientation, while the pyrazolyl ring nitrogen [N(1A) and N(1B)] and the thione sulfur atoms [S(1A) and S(1B)] are in a cis-coordination. This coordination is analogous to that observed in the crystal structures of similar Ni(II) complexes [15,8h].

The slight shortening of the Ni–N(azomethine) [Ni–N(2)] distances compared to the Ni–N(pyrazolyl) [Ni–N(1)] distances (Table 4) may be attributed to the fact that the azomethine nitrogen is a harder base compared to the pyrazolyl nitrogen. A similar effect has also been observed in the structure of $[Ni(HMP_zNBu_2)_2](ClO_4)_2$ [Ni–N(azomethine) 2.037(3), Ni–N(pyrazolyl) 2.112(3)] [8h].

As expected, the S(1)–C(6) double bond distance of 1.668(4) Å in the free ligand is lengthened to 1.689(3) and 1.691(3) Å in ligands A and B, respectively, with a shortening of the N(3)–C(6) bonds, from 1.362(6) Å in the free ligand to 1.346(3) Å [ligand A] and 1.348(4) Å [ligand B] in the complex (Table 4). The significant closing of the C(4)–C(5)–N(2) and N(1)–C(4)–C(5) angles by about 16° and 5°, respectively, as indicated in Table 4, may be attributed to geometrical necessity for coordination.

The two coordinating ligands are more or less planar, with C(3A) and N(3A) in ligand A, and C(2B) and N(3B) in ligand B, having the largest deviations in opposite directions [C(3A): +0.225(3) Å, N(3A): −0.171(2) Å, C(2B): +0.176(4) Å and C(4B): −0.079(3) Å] from the least-squares mean planes through Ni–S(1)–C(6)–N(3)–N(2)–C(5)–C(4)–C(3)–C(2)–N(4)–N(1). The ligands A and B coordinate orthogonally to the metal ion, the dihedral angle between them being 89.69(2)°. The three individual rings in either ligand, namely, the pyrazole and the two five-membered chelate rings, are individually almost planar with small dihedral angles between them. The maximum dihedral angle of 11.31(7)° is between the pyrazole ring N(1A)–N(4A)–C(2A)–C(3A)–C(4A) and the chelate ring Ni–S(1A)–C(6A)–N(3A)–N(2A).

The piperidine rings, both in the free ligand and in the complex, are in chair conformations [20]: in the free ligand, $q_2 = 0.044(6)$ Å, $q_3 = 0.562(6)$ Å, $Q = 0.564(6)$ Å, $\theta = 4.5(6)°$; in the complex, the corresponding parameters are $q_2 = 0.063(4)$ Å, $q_3 = 0.587(4)$ Å, $Q = 0.591(4)$ Å, $\theta = 6.1(4)°$ in ligand A, and $q_2 = 0.050(4)$ Å, $q_3 = 0.569(4)$ Å, $Q = 0.571(4)$ Å, $\theta = 5.0(5)°$ in ligand B [20].

It is known [21] that many thiosemicarbazone ligands exist in solution as two conformers, E and Z. In the present crystallographic study, the Z-form, as indicated by the C(4)–C(5)–N(2)–N(3) torsion angle of −1.8(8)°, was obtained in the solid state for the free ligand. In the complex, $[Ni(HMP_z3Pi)_2]Cl_2 \cdot 2H_2O$, the coordinating ligands exist as E conformers [C(4)–C(5)–N(2)–N(3) torsion angle is 178.5(2)° in ligand A and −178.5(2)° in ligand B], as necessitated by the requirements of coordination. Therefore, Z conformers of the ligand which could be present in solution must be transformed to the E-form before complexation. A possible mechanism for this transformation, leading to an unusual rotation about the azomethine (C=N) double bond, is shown in Fig. 6. The feasibility of this mechanism is due to the electropositive character of the azomethine carbon, C(5), as reported earlier [8b,22].

The intermediate conversion from a double bond to a single bond allows the rotation of the thiosemicarbazone moiety to bring the sulfur atom, S(1), to the *cis*-position with respect to the pyrazolyl nitrogen, N(1), in order to permit complex formation. The C(5)–N(2) bond [1.273(7) Å in the free ligand] resumes its double bond character in the complex [1.275(3) Å in ligand A and 1.279(3) Å in ligand B], once the complexation with Ni(II) is completed.

Table 5 gives the details of the hydrogen bonding and C–H···X contacts. In the free ligand (**I**), an intramolecular hydrogen bond [N(3)–H(3)···N(1)], and two C–H···X contacts [C(11)–H(11B)···S(1) and C(7)–H(7A)···N(3)] stabilise the conformation of the molecule about the C(4)–C(5), N(2)–N(3), N(3)–C(6) and C(6)–N(5) single bonds [Fig. 4]. Each ligand molecule is doubly hydrogen bonded to a symmetry related molecule *via* N(4)–H(4)···S(1) and N(4)–H(4)···N(2) bonds,

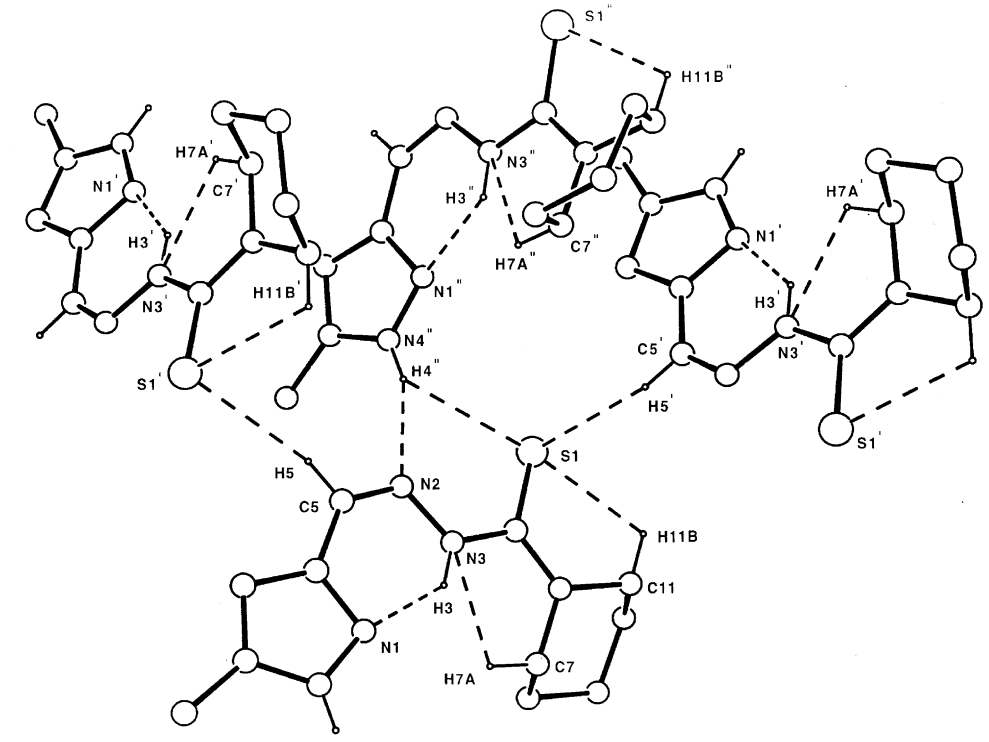


Fig. 4. Hydrogen bonding and CH···X contacts in the crystal structure of HMP_z3Pi.

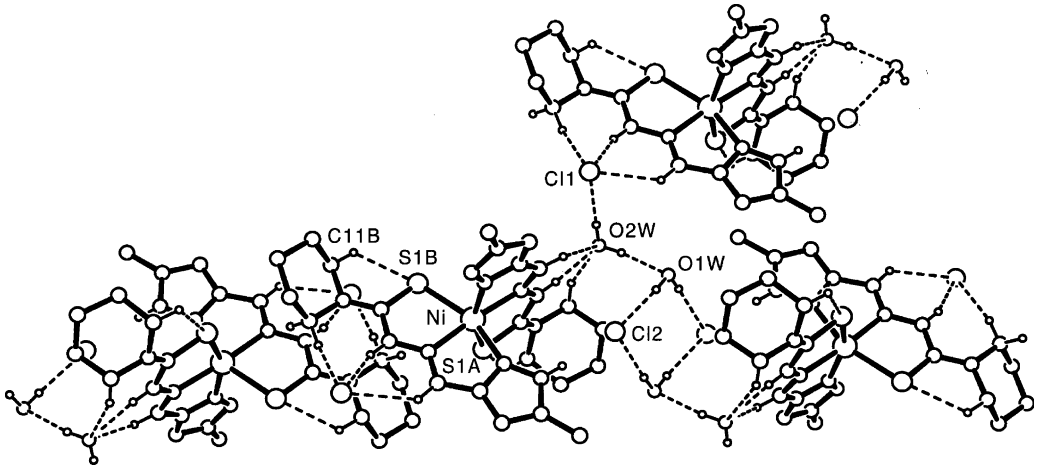


Fig. 5. Hydrogen bonding pattern in the crystal structure of $[Ni(HMP_z3Pi)_2]Cl_2 \cdot 2H_2O$. A few of the representative atoms have been labelled.

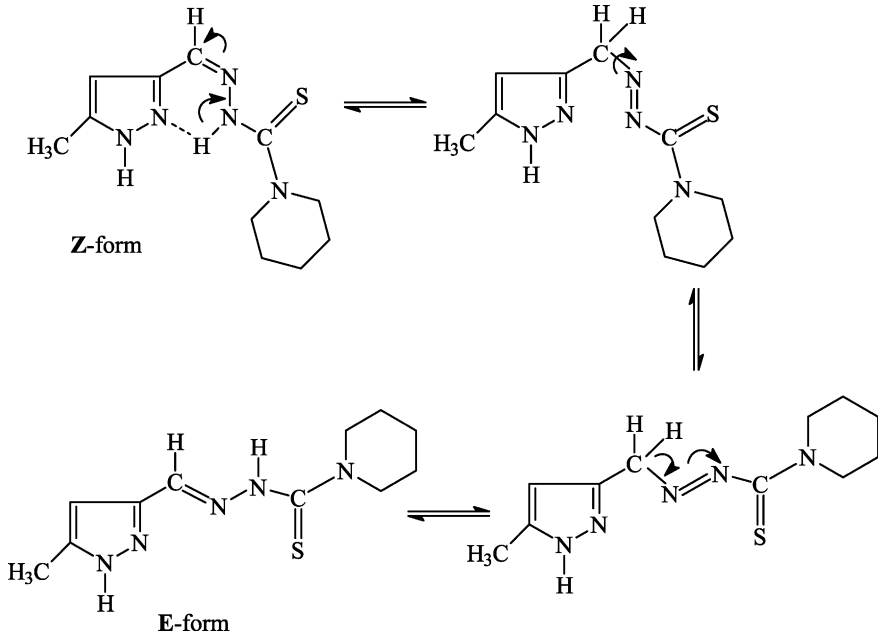


Fig. 6. Reaction mechanism showing the rotation about the azomethine double bond.

Table 5
Hydrogen bonding distances (Å) and angles (°), including C–H···X contacts

D–H···A	D–H	H···A	D···A	∠D–H···A
*Free ligand (**I**)*				
N(3)–H(3)···N(1)	0.86	2.02	2.703(5)	135
N(4)–H(4)···S(1)^{i}	0.86	2.83	3.402(4)	125
N(4)–H(4)···N(2)^{i}	0.86	2.15	2.972(6)	161
C(5)–H(5)···S(1)^{ii}	0.93	2.77	3.660(5)	161
C(7)–H(7A)···N(3)	0.97	2.36	2.776(6)	105
C(11)–H(11B)···S(1)	0.97	2.56	3.054(6)	112
*Complex (**II**)*				
O(1W)–H(11W) ···Cl(2)	0.84(5)	2.35(4)	3.188(4)	173(5)
O(1W)–H(12W) ···Cl(2)^{iii}	0.84(5)	2.38(5)	3.216(5)	173(6)
O(2W)–H(21W) ···O(1W)	0.84(4)	1.93(3)	2.758(5)	171(4)
O(2W)–H(22W)···Cl(1)^{iv}	0.84(4)	2.34(4)	3.179(3)	172(4)
N(3A)–H(3AB)···O(2W)	0.86	1.98	2.808(3)	162
N(3B)–H(3BB)···Cl(1)	0.86	2.35	3.145(3)	153
N(4B)–H(4BA)···Cl(2)	0.86	2.18	3.038(3)	174
C(5A)–H(5AA)···O(2W)	0.93	2.59	3.295(4)	133
C(5B)–H(5BA)···Cl(1)	0.93	2.71	3.453(3)	137
C(7A)–H(7AA)···O(2W)	0.97	2.34	3.223(5)	152
C(7A)–H(7AA)···N(3A)	0.97	2.41	2.763(4)	101
C(7B)–H(7BA)···Cl(1)	0.97	2.69	3.581(3)	153
C(7B)–H(7BA)···N(3B)	0.97	2.38	2.786(4)	105
C(7B)–H(7BB)···S(1A)^{v}	0.97	2.86	3.673(4)	142
C(11A)–H(11B)···S(1A)	0.97	2.51	3.003(4)	112
C(11B)–H(11D)···S(1B)	0.97	2.49	3.017(3)	114

Symmetry equivalents: (i) $-1/2 + x$, y, $3/2-z$; (ii) $-x$, $1/2 + y$, $3/2-z$; (iii) $4-x$, $-y$, $1-z$; (iv) x, $1 + y$, z; (v) $4-x$, $-1 - y$, $2-z$.

and also has a C(5)–H(5)···S(1) contact with yet another symmetry related moiety.

The two water molecules play important roles in the crystal structure of the complex (**II**). The water oxygen, O(1W), is the donor in two O–H···Cl bonds with two different chloride ions related by symmetry, and is the acceptor in an O–H···O bond with the second water molecule. The second water oxygen, besides being the donor in the aforesaid O–H···O bond, donates its second hydrogen to a chloride ion, Cl(1), to form a O–H···Cl hydrogen bond. This water oxygen, in its turn, accepts a hydrogen from a hydrazinic nitrogen, N(3A), to form a N–H···O bond; in addition, it is the acceptor of two C–H···O contacts, one from a piperidinyl carbon, C(7A), and the other from a azomethine carbon, C(5A). The chloride ion, Cl(1), accepts two regular hydrogen bonds, one, as mentioned above, from the water oxygen, O(2W), and the other from a hydrazinic nitrogen, N(3B). The two C–H···Cl contacts with this chloride ion are with the azomethine carbon, C(5B), and the piperidinyl carbon, C(7B). The second chloride ion, Cl(2), besides accepting two hydrogen bonds from two different symmetry related water oxygens, O(1W), is also involved in a N–H···Cl hydrogen bond with a pyrazolyl secondary nitrogen atom, N(4B). Both the hydrazinic nitrogen atoms, N(3A) and N(3B), take part in intramolecular C–H···N contacts with neighbouring piperidinyl carbon atoms, C(7A) and C(7B), thereby arresting free rotation of the piperidinyl ring about the C(6)–N(5) single bond. The C(7)–N(5)–C(6)–N(3) torsion angles are 7.3(4)° in ligand A and 2.1(5)° in ligand B. The usual C–H···S contacts reported in similar complexes are also observed in the present structure: C(11A)–H(11B)···S(1A) and C(11B)–H(11D)···S(1B) [8h,15]. There is an additional C(7B)–H(7BB)···S(1A) contact between two symmetry related moieties. Fig. 5 shows the hydrogen bonding and C–H···X contacts observed in the structure of the complex species.

4. Conclusion

The present study shows that the title ligand of the pyrazolyl thiosemicarbazone series, HMP_z3Pi, undergoes complexation with nickel (II) and furnishes bischelates, with two ligands coordinating with nickel (II) orthogonally in a distorted octahedral environment; the azomethine nitrogens are *trans* to each other, while the pyrazolyl tertiary ring nitrogens and the thione sulfurs are in *cis*-positions. X-ray crystallography of both the uncomplexed ligand and its nickel (II) complexes reveals an interesting feature that the thiosemicarbazone moiety of the ligand undergoes an unexpected rotation about the azomethine double bond during complex formation with nickel (II).

Acknowledgement

One of us (N.C.S.) is thankful to the University of Calcutta for providing the state-funded research fellowship during the tenure of this work.

Appendix A. Supplementary data

Crystallographic data for the structures reported herein have been deposited with the Cambridge Crystallographic Data Centre, CCDC Nos. being 213951 and 213952. Copies of this information may be obtained free of charge from the Director, CCDC, Data Centre, 12 Union Road, Cambridge, CB2 1EZ, UK (fax: +44-1223-336033; e-mail: deposit@ccdc.cam.ac.uk or www: http://www.ccdc.cam.ac.uk). Supplementary data associated with this article can be found, in the online version, at doi:10.1016/j.poly.2005.01.024.

References

[1] M.J.M. Campbell, Coord. Chem. Rev. 15 (1975) 279.
[2] A. Mohsen, M.E. Omar, I.M. Labouta, M.G. Kasem, J. Bourdais, J. Pharm. Sci. 72 (1983) 1226.
[3] D.L. Klayman, J.F. Bartosevich, T.S. Griffin, C.J. Mason, J.P. Scovill, J. Med. Chem. 22 (1979) 855.
[4] E.J. Blanz, F.A. French, Cancer Res. 28 (1968) 2419.
[5] M.C. Miller, C.N. Stineman, J.R. Vance, D.X. West, I.M. Hall, Anticancer Res. 18 (1998) 4131.
[6] M.C. Miller, C.N. Stineman, J.R. Vance, D.X. West, I.M. Hall, Appl. Organomet. Chem. 13 (1999) 9.
[7] J.P. Scovill, D.L. Klayman, C. Lambros, G.E. Childs, W. Antholing, D.H. Petering, J. Med. Chem. 27 (1984) 87.
[8] (a) A. Mitra, T. Banerjee, P. Roychowdhury, S. Chaudhuri, P. Bera, N. Saha, Polyhedron 16 (1997) 3735;
(b) P. Bera, R.J. Butcher, N. Saha, Chem. Lett. (1998) 559;
(c) N.C. Saha, A. Seal, R.J. Butcher, N. Saha, J. Ind. Chem. Soc. 78 (10–12) (2002) 601;
(d) P. Bera, R.J. Butcher, S. Chaudhuri, N. Saha, Polyhedron 21 (2002) 1;
(e) N.C. Saha, R.J. Butcher, S. Chaudhuri, N. Saha, Polyhedron 21 (2002) 779;
(f) N.C. Saha, A. Saha, R.J. Butcher, S. Chaudhuri, N. Saha, Inorg. Chim. Acta 339 (2002) 348;
(g) N.C. Saha, R.J. Butcher, S. Chaudhuri, N. Saha, Polyhedron 22 (2003) 375;
(h) N.C. Saha, R.J. Butcher, S. Chaudhuri, N. Saha, Polyhedron 22 (2003) 383;
(i) D.K. Sau, N. Saha, R.J. Butcher, S. Chaudhuri, Trans. Met. Chem. 28 (2003) 229.
[9] G.M. Sheldrick, SHELX97, Program for Refinement of Crystal Structure, University of Göttingen, Göttingen, Germany, 1997.
[10] D.T. Cromer, J.T. Weber, International Tables for X-ray Crystallography, Table 2.2A, vol. IV, The Kynoch Press, 1994.
[11] J.A. Ibers, W.C. Hamilton, Acta Crystallogr. 17 (1964) 781.
[12] W.J. Geary, Coord. Chem. Rev. 7 (1971) 81.
[13] N. Saha, N. Mukherjee, Polyhedron 3 (1984) 1135.
[14] A.K. Barik, S. Paul, S.K. Kar, R.J. Butcher, J.C. Bryan, Polyhedron 18 (1998) 571.
[15] (a) M. Mathew, G.J. Palenik, J. Am. Chem. Soc. 91 (1969) 6310;
(b) K.A. Ketchem, I. Garcia, J.K. Swearingen, A.K. El-Sawaf, E. Bermejo, A. Castiñeiras, D.X. West, Polyhedron 21 (2002) 859, and references therein.
[16] (a) R.C. Agarwal, T.R. Rao, J. Inorg. Nucl. Chem. 40 (1978) 1177;
(b) J.R. Ferraro, Appl. Spectrosc. 23 (1969) 60.
[17] K. Chattopadhyay, D. Chattopadhyay, J. Banerjee, R. Kuroda, S. Ghosh, Polyhedron 16 (1997) 1925.
[18] G. Devoto, M. Massacesi, R. Pinna, G. Ponticelli, Spectrochim. Acta, Part A 38 (1982) 725.
[19] L.J. Farrugia, J. Appl. Crystallogr. 30 (1997) 565.
[20] D. Cromer, J.A. Pople, J. Am. Chem. Soc. 97 (1975) 1334.
[21] (a) I. Antonini, F. Claudi, P. Franchetti, M. Grifantini, S. Martelli, J. Med. Chem. 20 (1977) 447;
(b) D.X. West, S.B. Padhye, P.B. Sonawane, Struct. Bond. 76 (1991) 1;
(c) D.X. West, C.S. Carlson, C.P. Galloway, A.E. Liberta, C.R. Daniel, Trans. Met. Chem. 15 (1990) 91;
(d) D.X. West, B.L. Mokijewski, H. Gebremedhin, T.J. Romack, Trans. Met. Chem. 17 (1992) 384;
(e) D.X. West, M.A. Lockwood, A.E. Liberta, X. Chen, R.D. Willett, Trans. Met. Chem. 18 (1993) 221;
(f) E. Bermejo, R. Carballo, A. Castiñeiras, R.R. Domínguez, C. Maichle-Mössmer, J. Strähle, D.X. West, Polyhedron 18 (1999) 3695;
(g) G.F. de Sousa, D.X. West, C.A. Brown, J.K. Swearingen, J. Valdés-Martínez, R.A. Toscano, S. Herñandez-Ortega, M. Hörner, A.J. Bortoluzzi, Polyhedron 19 (2000) 841.
[22] N.R. Sangeetha, S. Pal, Samudranil Pal, Polyhedron 19 (2000) 2713.

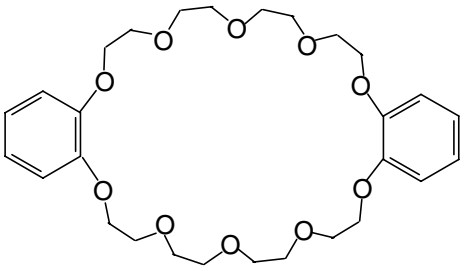


Fig. 1. Structural drawing of dibenzo-30-crown-10 (DB30C10).

pair with the metal complex cation (MCE^+) and a strong ion pair promotes efficient extraction from aqueous solution into a less polar organic phase ($CHCl_3/CH_2Cl_2$) [7]. Recently, competitive binding studies using large crown ethers (crown-18 to crown-24) with picrate, iodide anions and monovalent alkali metal cations (Li^+, Na^+, K^+, Rb^+ and Cs^+) have been reported by Talanova et al. [8]. The picrate anion formed a strong ion pair, which significantly enhanced the extraction process compared to that found with the iodide anion.

The aim of the present study is to investigate the selectivity of large crown ligands towards alkali and alkaline earth metal ions that are present together in solution at high concentrations, e.g., salt bitterns. Bittern, which is a by-product of salt manufacture, is comprised mainly of Na^+, K^+, Mg^{2+}, Ca^{2+}, SO_4^{2-}, and Cl^-, the concentration of Na^+, K^+, Mg^{2+} and Ca^{2+} being 0.5–1.5, 0.5–1.0, 3.0–5.0 and 0.1–0.2 M, respectively. In a previous study we have reported results of K^+/Na^+ selectivity with dibenzo-21-crown-7 and dibenzo-24-crown-8 [9]. Since the K^+ ion has a relatively larger diameter than Na^+, Ca^{2+} and Mg^{2+} cations, we reasoned that the K^+ ion would bind to DB30C10 (Fig. 1) more strongly than the other cations, which could lead to higher selectivity for potash extraction. In fact, we found that the selectivity towards K^+ is higher with DB30C10 compared to DB21C7 and DB24C8. Herein we report the extraction equilibrium constant for K^+ with DB30C10 and the relative selectivities towards Na^+, K^+, Ca^{2+} and Mg^{2+} present either as an equimolar mixture or in a bittern. The crystal structure of [K-DB30C10][picrate] and molecular mechanics calculations to rationalize the observations are also reported.

2. Experimental

2.1. Materials

The compound dibenzo-30-crown-10 (DB30C10) was purchased from Aldrich. KCl, NaCl, $CaCl_2$, $MgCl_2$, KOH and NaOH were of analytical grade and purchased from S.d.Fine Chemicals. Picric acid was procured from Sara fine chemicals. Potassium picrate and sodium picrate were prepared by reacting picric acid with aqueous KOH and NaOH, respectively. Analytical grade dichloromethane was purchased from Ranbaxy and Milli-Q (Millipore Corporation) water was used throughout.

2.2. Physical measurements

The UV–Vis spectra were recorded on a model 8452A Hewlett–Packard diode array spectrophotometer. NMR spectra were recorded on a model DPX 200 Bruker FT-NMR instrument. The cation concentration was measured on a Dionex 500 ion chromatograph.

2.3. Extraction equilibrium constant for potassium (K_e)

2.3.1. Determination of the concentration of picrate (A, Eq. (9)) in the extract (organic phase)

Into 5 cm^3 aqueous solution of KOH (1×10^{-4} M) and picric acid (1×10^{-4} M) was added 5 cm^3 of dichloromethane solution containing 2×10^{-5} M DB30C10. The contents were shaken vigorously in a vortex mixer for 10 min and the dichloromethane layer was separated and passed through anhydrous $MgSO_4$ bed to remove traces of water. The concentration of picrate in this solution – which is expected to be equivalent to the concentration of metal ion extracted since it is present as the counter ion of the complexed ligand – was determined spectrophotometrically (λ_{max}, 376 nm, $\varepsilon = 1.8 \times 10^4$ in dichloromethane). This experiment was carried out at room temperature (25 °C) with different concentrations (0.2×10^{-4}–2.0×10^{-4} M) of crown ether, keeping the metal ion concentration fixed ($c = 1 \times 10^{-4}$ M, ionic strength $I = 1 \times 10^{-4}$). This methodology was followed for four different concentrations of the metal ion (c = 0.0001, 0.001, 0.01 and 0.1 M; I = 0.001, 0.001, 0.01 and 0.1, respectively). Thus 40 different values of A were obtained corresponding to four different concentrations of the metal ion.

2.3.2. Determination of the partition coefficient (P_e, Eq. (9))

The partition coefficient of the crown ether in the biphasic system comprising of dichloromethane and water was determined (25 °C) by equilibration of the two phases, followed by indirect estimation of the ligand in the aqueous layer. In a typical experiment 5 cm^3 water was added to an equal volume of 5×10^{-4} M dichloromethane solution of DB30C10, the two phases were vigorously shaken (10 min) and the aqueous layer was separated. To the aqueous layer were added solid KOH (to make 0.1 M solution), picric acid (to make 5×10^{-3} M solution) and an equal volume of dichloromethane. The ionic strength (I) of the aqueous layer was 0.1. The contents were vigorously shaken to re-extract the crown ether in the K^+-complexed form into the organic layer, with picrate as the counter ion.

Spectrophotometric analysis of picrate in this solution yielded the concentration of DB30C10 in the original aqueous phase. The concentration of the DB30C10 in the original organic layer was also estimated spectrophotometrically, and mass balance was satisfactory. The partition coefficient (P_e) was calculated using the equation: $P_e = [CE]_{aq}/[CE]_{org}$. This experiment was repeated with various concentrations of crown ether in dichloromethane and the average value of P_e was estimated.

2.3.3. Determination of the stability constant of the K^+-complex in the aqueous phase (K_s, Eq. (9))

The stability constant for complex formation in the aqueous phase (K_s) was determined spectrophotometrically following a recently published procedure by Buschmann, which is well suited to ligands with low solubility such as DB30C10 [10]. In a typical experiment, into 5 cm^3 aqueous solutions of KOH of various concentrations ($c = 1\times10^{-3}$, 5×10^{-3}, 1×10^{-2}, 5×10^{-2} and 1×10^{-1} M; $I = 0.001$, 0.005, 0.01, 0.05 and 0.1, respectively) was added 2.7 mg (amount required to make 5 cm^3 1×10^{-3} M solution) of DB30C10 and the reaction mixture was stirred for 24 h at 25 °C. The solutions were then filtered on a 0.2 μm pore size filter paper and the absorbance of the filtrate at 274 nm (λ_{max}) was measured, it gave the combined concentrations (A) of the uncomplexed ligand and metal-complex formed. Likewise, the absorbance due to the ligand under saturated condition (A_0) was estimated as follows: solid DB30C10 (5.4 mg) was suspended in 50 cm^3 of water and stirred. Every 2 h interval about a 5 cm^3 aliquot was taken, filtered through 0.2 μm pore size filter paper, and the concentration of the ligand in the filtrate was determined spectrophotometrically. This was continued until the solution became saturated (14 h), when there was no significant change in the absorbance of the 274 nm band. The average of the three limiting values was considered as the concentration of the ligand in saturated solution. A straight line was obtained by plotting $A/A_0 - 1$ as a function of the initial concentration of the metal ion, the slope of which gave K_s (6.80 ± 0.1).

2.4. Selectivity determination

In a typical experiment, 2.3 mg picric acid (0.01 mmol) was added into 5 cm^3 of an aqueous solution of the equimolar mixture of ions/bittern. Dichloromethane solution (5 cm^3) containing 2×10^{-3} M DB30C10 was added next. The two-phase mixture was vigorously shaken in a vortex mixer for 10 min and the solution was transferred to a separating funnel and allowed to stand for 30 min. The dichloromethane layer was then separated and passed through a bed of anhydrous $MgSO_4$ to remove traces of water, transferred to a crucible, stripped of solvent by gentle heating on a water bath, and then heated in a furnace at 550 °C for 4 h. The residue was dissolved in deionized water (~5 cm^3) and filtered on 0.2 μm filter paper. The relative concentrations of the cations in the filtrate were determined by ion chromatography using Ion Pac CS12 (2 mm) analytical column and 20 mM methylsulfonic acid as eluant with a flow rate of 0.25 cm^3/min. Quantification was made using a standard solution containing a mixture of NaCl, KCl, $MgCl_2$ and $CaCl_2$ (~15 ppm each).

2.5. Preparation of [K-DB30C10][picrate]

A methanolic solution (10 cm^3) of potassium picrate (66.7 mg, 0.25 mmol) was added to DB30C10 (134.2 mg) dissolved in 10 cm^3 of chloroform and the resulting mixture was stirred at room temperature for 6 h. The solution was then evaporated to dryness at room temperature. The yellow solid thus obtained was recrystallized from chloroform–toluene (1:1), which gave needle shaped crystals suitable for single crystal X-ray diffraction studies; ^{1}H NMR ($CDCl_3$): δ 3.67 (s, 16H), 3.74 (d, 8H), 4.01(d, 8H), 6.75 (m, 4H), 6.89 (m, 4H), 8.79 (s, 2H).

2.6. X-ray crystallography

Cell parameters and diffraction intensities for the compound were measured at room temperature on an Enraf-Nonius CAD-4 X-ray diffractometer using graphite monochromatized Mo Kα radiation (0.7107 Å) in the range $\theta = 2$–25° and 25 reflections with θ in the range 9–12° were used for getting accurate cell dimensions. The crystal orientation, refinement of the cell parameters and intensity measurements were carried out using the program CAD-4 PC [11]. The Lorentz polarization corrections and data reduction were carried out using the NRCVAX programme [12]. The structure was solved by direct methods and after the complete convergence of non-hydrogen atoms anisotropically, H-atoms were either fixed stereochemically by the riding model using SHELX-97 or located from the difference Fourier map [13]. The final cycles of least-squares refinements yielded the R-value [$R_1 = 0.0791$ ($wR_2 = 0.2395$)] for the complex.

3. Results and discussion

3.1. Extraction equilibrium of the potassium ion

Two-phase extraction using the picrate anion has been reported earlier for quantitative determination of relative complexing abilities of ligands [14–16]. The picrate anion has an absorption band at 378 nm in dichloromethane, whereas crown ethers do not absorb in this

region. Blank experiments without DB30C10, but otherwise under similar experimental conditions, indicated the absence of picrate in the organic phase, i.e., the picrate independently is unable to extract the metal ion into the organic layer. Therefore, the concentration of the complex can be determined by estimating the concentration of the extracted picrate, as described in the experimental section. Typical UV–Vis spectral changes of the organic phase with increasing concentration of DB30C10 are shown in Fig. 2. When KOH is replaced with NaOH, the concentration of picrate in the organic phase is much lower (Fig. S1, supplementary material).

The extraction equilibrium constant was calculated following the method published by Frensdorff [15]. The two-phase equilibrium for the system containing metal ion (M^+), picrate anion (A^-) and crown ether (CE) can be defined as

$$M^+_{aq} + A^-_{aq} + CE_{org} \overset{K_e}{\rightleftharpoons} MCEA_{org} \quad (1)$$

where $MCEA_{org}$ designates the ion pair. To evaluate K_e, the distributions of all species in both phases have to be considered, which can be accounted by the following equilibria:

$$MCEA_{org} \overset{K_d}{\rightleftharpoons} MCE^+_{org} + A^-_{org} \quad (2)$$

$$CE_{org} \overset{P_e}{\rightleftharpoons} CE_{aq} \quad (3)$$

$$M^+_{aq} + CE_{aq} \overset{K_s}{\rightleftharpoons} MCE^+_{aq} \quad (4)$$

The extraction constant (K_e), dissociation constant of MCEA in the organic phase (K_d), partition coefficient of DB30C10 in water–dichloromethane (P_e) and the stability constant of MCE^+ in the aqueous phase (K_s) can be expressed as

$$K_e = [MCEA]_{org}/[M^+]_{aq}[A^-]_{aq}[CE]_{org}, \quad (5)$$

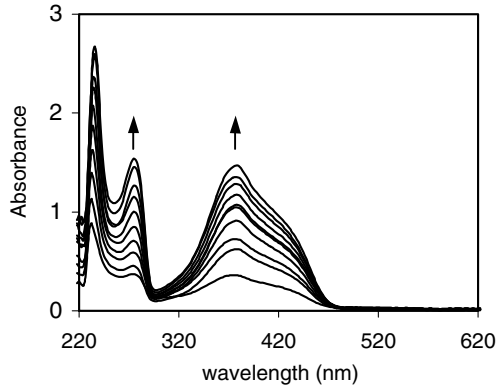


Fig. 2. UV–Vis spectral changes of the extracted organic phase containing [K-DB30C10][picrate] with increasing concentration of the ligand (2×10^{-5} to 2×10^{-4} M); $[K^+] = 0.01$ M and [picrate] = 1×10^{-4} M.

$$K_d = [MCE^+]_{org}[A^-]_{org}/[MCEA]_{org}, \quad (6)$$

$$P_e = [CE]_{aq}/[CE]_{org}, \quad (7)$$

$$K_s = [MCE^+]_{aq}/[M^+]_{aq}[CE]_{aq}. \quad (8)$$

From Eqs. (5)–(8) we can get [15,16],

$$K_e = \frac{[1 + P_e + P_e K_s f(M_0\text{–}A)][2A + K_d - (K_d^2 - 4K_d A)^{1/2}]}{2f[M_0\text{–}A][A_0\text{–}A][CE_0\text{–}A]}, \quad (9)$$

where f is the single ion activity coefficient of the aqueous cation and A is the concentration of the picrate anion in the organic phase; M_0, A_0 and CE_0 are the initial concentrations of the metal ion, picrate and crown, respectively. M_0, A_0 and CE_0 are known for a given system. After incorporating values of P_e, K_s and A obtained experimentally, the two unknowns left in Eq. (9) are K_e and K_d. The value of K_d was optimized by calculating values of K_e from Eq. (9) for a given value of K_d followed by regression analysis.

The partition coefficient P_e was determined by equilibration of DB30C10 in water–dichloromethane phases, followed by its indirect spectrophotometric estimation as described in Section 2. P_e was determined over a range of concentrations of CE and the average value estimated was 1.9×10^{-2}.

The stability constant for complex formation in the aqueous phase (K_s) was estimated using Eq. (10),

$$A/A_0 - 1 = \frac{(\varepsilon_2/\varepsilon_1)K_s}{1 + K_s[CE]_{sat}} C_{salt}, \quad (10)$$

where A is the absorbance due to the ligand and the complex formed (the ligand and the associated complex absorb at the same wavelength), A_0 is the absorbance due to the ligand under saturated condition, ε_1 and ε_2 are molar absorptivities of DB30C10 and its K^+-complex, respectively, $[CE]_{sat}$ is the concentration of the ligand under saturated conditions, and C_{salt} is the initial concentration of the metal ion. A and A_0 were determined experimentally, as described in the Section 2. When $(A/A_0 - 1)$ is plotted against C_{salt}, the slope b can be expressed as

$$b = \frac{(\varepsilon_2/\varepsilon_1)K_s}{1 + K_s[CE]_{sat}}. \quad (11)$$

From Eq. (11) K_s can be written as

$$K_s = \frac{b}{(\varepsilon_2/\varepsilon_1) - b[CE]_{sat}}. \quad (12)$$

Using the value of b and applying the assumptions: (i) $\varepsilon_2/\varepsilon_1 \sim 1$; (ii) $b[CE]_{sat} \ll 1$ (as the solubility of the ligand in water is very low), the value of K_s obtained from Eq. (12) was 6.80 ± 0.1 at 25 °C.

By replacing the experimentally determined values of P_e, K_s and A in Eq. (9) the best fit to the data was

obtained with $K_d = 1.1 \pm 0.6 \times 10^{-6}$, for which the corresponding value of K_e was $2.9 \pm 0.2 \times 10^6$. The accuracy of the regression analysis has been tested by plotting (A/A_0) as a function of [crown]:[picrate] ratio with experimental and calculated data for various metal ion concentrations (Fig. 3). Excellent matching of the experimental and calculated curves indicates good regression analysis for the determination of K_e. The K_e value we obtained for DB30C10 is comparable to that obtained for the A-isomer of dicyclohexyl-18-crown-6 (4×10^6), but significantly higher than that of dibenzo-18-crown-6 (7×10^5) [15]. K_e provides a quantitative idea of the efficiency of extraction of the crown–picrate complex from the aqueous to organic phase. The efficiency of the process reflects not only the strength of the complex formed but also the ability to make an effective ion pair between the cationic and anionic species, as evident from the crystal structure of the complex (vide infra).

It has been reported that Na^+ forms complexes with DB30C10 having 1:1, 2:1 and 3:2 metal:ligand ratios [17]. Similar inconsistent compositions for the Na^+ complex of DB30C10 was also noted by us from ^1H NMR spectral data of the isolated complexes. Because of its low ionic diameter, there is also the possibility for Mg^{2+} and Ca^{2+} to form complexes of inconsistent compositions. Formation of mixed metal complexes comprising these ions (Na^+, Mg^{2+} and Ca^{2+}) also cannot be ruled out. This complicates the determination of K_e for Na^+, Mg^{2+} and Ca^{2+} extraction and such determination was, therefore, not attempted. However, we carried out experimentally the picrate extraction with Na^+ under similar experimental conditions as for K^+ and Fig. 4 shows comparative results for the two metal ions. It can be seen that extraction efficiency of Na^+ is comparatively much poorer.

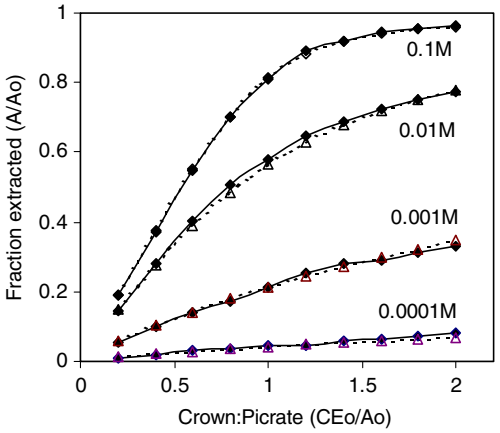


Fig. 3. The fraction of picrate/metal ion extracted is shown as a function of [crown]:[picrate] ratio with different metal ion concentrations. Full curves are from experimental absorbance values and dotted curves are from the calculated absorbance values obtained using the evaluated $K_e = 2.9 \times 10^6\ M^{-2}$ and $K_d = 1.1 \times 10^{-6}$ M.

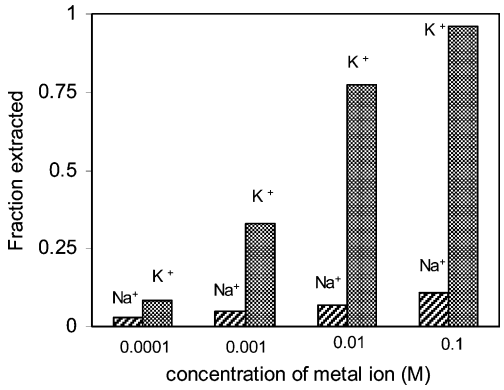


Fig. 4. Bar diagram showing the fraction of Na^+/K^+ extracted with increasing the concentration of metal ions.

3.2. Selectivity

The high extraction equilibrium observed for K^+ in the studies reported above with DB30C10 encouraged us to explore the application of this ligand for selective extraction of the potassium ion from mixtures of ions. Selectivities of the metal ions (Na^+, K^+, Mg^{2+} and Ca^{2+}) were determined by ion chromatographic assay (Fig. S2 shows a typical chromatogram, supplementary material) of the initial aqueous phase and the organic phase following extraction. Experiments were carried out with (i) aqueous solution containing equimolar amounts of Na^+, K^+, Mg^{2+} and Ca^{2+} as chloride salts, and (ii) bittern. Distributions of the metal ions in the original solutions and in the organic extracts, together with values of the observed selectivity ratios, are shown in Table 1. As can be seen from the data for the synthetic mixture, DB30C10 shows high selectivity towards K^+ and the order of selectivity is: $K^+ \gg Na^+ \sim Mg^{2+} > Ca^{2+}$. In the case of bittern, where the absolute concentrations of the ions are higher and their relative concentrations also differ, there are discernible differences in the selectivity ratios. Nevertheless, even in this case, the high selectivity towards K^+ is evident. The results can be rationalized in terms of the crystal structure of the potassium salt of DB30C10 discussed below and the theoretical calculations of conformational geometry and selectivity.

3.3. Crystal structure

The molecular structure of the cation $[K\text{-DB30C10}]^+$ with I^- and SCN^- anions have been established previously by single crystal X-ray studies [18a,18b]. The crystal structure of $[K\text{-DB30C10}]^+$ with the picrate anion was determined in view of the importance of the latter in the extraction process [8]. Crystallographic data for [K-DB30C10](picrate) is given in Table 2. Structures with the picrate counter ion have been reported previously for other crowns, e.g.,15C5, 18C6 with Na^+ and K^+; 21C7, 24C8 with Rb^+ and Cs^+ [8,19].

Table 1
Concentrations of metal ions in the original solutions and potassium selectivity (K^+/M^{n+}) in the extract

Solution	Concentration, M/(%)								Selectivity ratio[a]		
	Original solution				Extract						
	$[Na^+]$	$[K^+]$	$[Mg^{2+}]$	$[Ca^{2+}]$	Na^+	K^+	Mg^{2+}	Ca^{2+}	K^+/Na^+	K^+/Mg^{2+}	K^+/Ca^{2+}
Bittern	0.5(8.2)[b]	0.7(19.2)	4.0(68.9)	0.1(3.7)	(4.9)	(83.4)	(11.1)	(0.6)	7.3	27.0	26.8
Mixture[c]	0.1(18.2)	0.1(30.9)	0.1(19.1)	0.1(31.7)	(4.9)	(88.3)	(5.2)	(1.6)	10.6	10.5	56.6

[a] The ratio is calculated by [% of K^+ in the extract][% of M^{n+} in the original solution]/[% of M^{n+} in the extract][% of K^+ in the original solution].
[b] Distribution in % is given in the parenthesis.
[c] An artificial solution containing equimolar (0.1 M) amount of the cations.

Table 2
Summary of crystallographic data for the potassium complex of DB30C10

Chemical formula	$C_{34}H_{42}KN_3O_{17}$
Formula weight	830.81
a (Å)	19.590(10)
b (Å)	18.057(4)
c (Å)	12.524(4)
β (°)	120.38(3)
Z	4
V (Å^3)	3822(2)
Crystal system	monoclinic
Space group	C_2/c
Radiation used λ (Å)	0.71073
$\rho_{calc.}$ (g cm^{-3})	1.397
Absorption coefficient, μ (cm^{-1})	2.18
Temperature (°C)	23
Final $R(F_o^2)$[a]	0.0791
Weighted $R(F_o^2)$ [b]	0.2395

[a] $R = \sum ||F_o| - F_c|| / \sum |F_o|$.
[b] $R_w = [\sum w(F_o^2 - F_c^2)^2] / \sum [w(F_o^2)^2]^{1/2}$; $w = 1/\sigma(F_o)^2$.

A PLUTO view of [K-DB30C10][picrate] showing the atom-numbering scheme is depicted in Fig. 5. Both cation and anion possess a twofold symmetry. The potassium ion occupies a special position, with the twofold symmetry passing through the C(11)–C(12) atoms of the crown moiety, whereas in the picrate anion the twofold axis bisects the molecule through the N(2), C(18), C(15) and O(6) atoms. The potassium ion is completely covered by the folded ligand, the oxygen atoms of which interact strongly with the cation. The K–O distances vary from 2.867 to 3.056 Å. The C(7)–C(10) carbon atoms of the crown moiety show a high temperature factor, indicating flipping of these atoms leading to a dynamic disorder.

The packing diagram (Fig. S3) shows that two pairs of cations and anions orient in such a way that they are in close proximity to each other. This pairing, which is on account of the π…π, C–H…π and C–H…O interactions, has been well documented in the literature for various supramolecular systems [20]. The terminal phenyl rings of the associated molecular pairs exhibit strong π…π stacking interactions with the picrate anions [Cg(1)…Cg(2) = 3.99 Å, symmetry codes: $1 - x$, $-y$, $1 - z$ and x, $-y$, $-1/2 + z$, where Cg(2) is the centroid

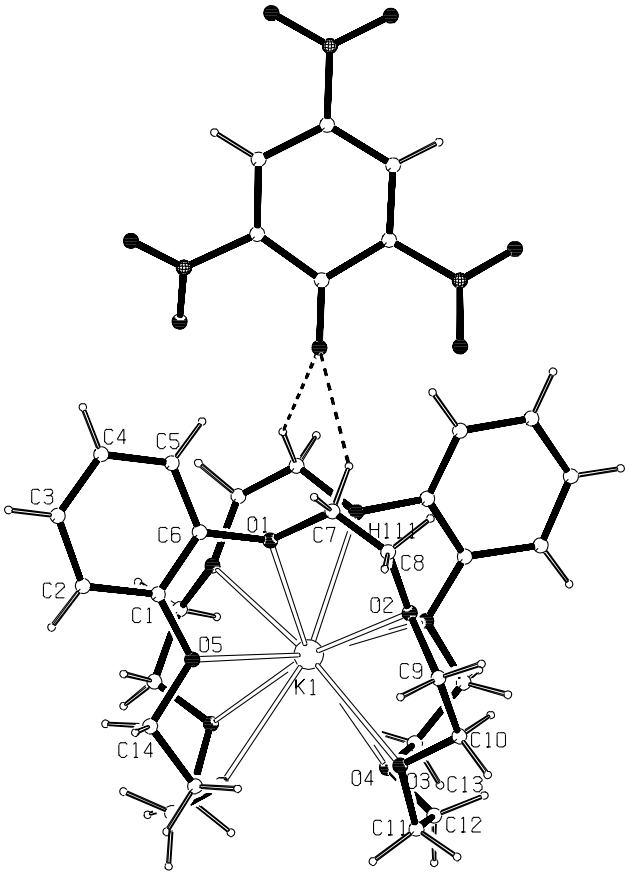


Fig. 5. PLUTO view of the complex [K-DB30C10][picrate] showing the numbering scheme and C–H…O interactions between deprotonated hydroxyl oxygen of picrate and CH_2 of the crown.

of the picrate phenyl ring]. The symmetry related oxygen [O(8)] of the nitro group of the picrate anion from either end is involved in a C–H…O interaction with the CH_2 moiety [H(141)] of the crown ether [H(141)…O(8) = 2.47 Å, C(14)…O(8) = 3.36 Å, ∠C(14)–H(141)…O(8) = 144.0°, symmetry code: $1/2 + x$, $1/2 + y$, z]. The protons associated with C(7) and C(9) also exhibit C–H…π and C–H…O interactions. H(92), attached to the C(9) atom of the crown ring, exhibits a C–H…π interaction with the centroid [Cg(1)] of the phenyl ring consisting of C(1)–C(6) atoms of the associated molecule [H(92)–Cg(1) = 3.14 Å; C9…Cg(1) = 3.824 Å; ∠C(9)–H(92)…

Cg(1) = 128.4°; symmetry = 1/2 + x, 1/2 − y, 1/2 + z]. The deprotonated hydroxyl oxygen [O(6)] of the picrate anion shows a C–H...O interaction with H(72), attached to the C(7) carbon atom of the adjacent cationic moiety [H(72)...O(6) = 2.47 Å, C(7)...O(6) = 3.340 Å, ∠C(7)–H(72)...O(6) = 146.7° symmetry code: −x, y, 1/2 − z]. Since there is evidence of dynamic disorder in C(7) and C(9), there is some uncertainty in the C–H...π and C–H...O interaction parameters involving these two carbon atoms. However, the short distances observed provide evidence of strong ion pair interactions. Similar interactions – albeit weaker than in the solid state – may also exist in solution, leading to effective ion pairing that would facilitate the extraction process.

4. Molecular mechanics study

A number of theoretical studies including molecular mechanics, molecular dynamics, Monte Carlo simulations and quantum chemical calculations have been performed on macrocyclic receptor molecules such as crown ethers, cryptands and hemispherands [21–23]. Among the many crown ethers, 18-crown-6, its complexation with alkali metal ions, and the effect of solvation have been studied in great detail at all levels of theory [21a,21b,21f,21h,21i,21l,21m]. Grootenhuis and Kollman [21b] have performed an elegant MM/MD study of the complexation of DB30C10 with alkali metal ions. Their studies were performed with available solid-state structures and hence no extensive search was performed in the conformational space of the structures of DB30C10 studied using molecular mechanics.

We have employed molecular mechanics (MMFF94) force field using a Monte Carlo conformation search, as implemented in TITAN [24], to examine the conformations of DB30C10 and its complexation with Na^+, K^+, Mg^{2+} and Ca^{2+}. We have not performed any search using solid-state structures since these are not available for the complexes of DB30C10-Mg^{2+}, DB30C10-Ca^{2+} and monomolecular DB30C10-Na^+.

Although many studies have been performed using MMFF94 [25], we undertook some initial force field calculations on 18-crown-6 to assess the reliability of the MM calculations. This ligand has been well studied in the past by other computational methods. MM calculations on *Ci* and *D3d* forms of the crown ether, which are the two lowest energy conformations, suggest that the *Ci* form is 8.3 kcal/mol lower in energy compared to the *D3d* form. This is in fair agreement with earlier molecular mechanics and quantum chemical results [21a,21m]. Having verified the reliability of the technique, a search of uncomplexed DB30C10 conformers was performed next and 4356 trial conformations were generated, of which 100 were retained based on structural dissimilarity and energetic considerations. Finally, nine unique low energy conformations (within a 5 kcal/mol window) were identified (Fig. S4, supplementary material). The ethylene –oxy– units on each side of the benzene ring can rotate and generate the major structural changes found in this set of conformers. These sampled conformers of DB30C10 are found in folded conformations (I, Fig. S4), half-folded conformations (IV, Fig. S4) and unfolded forms (VII, Fig. S4), indicating that there is no significant energetic preference for a particular conformation. The lowest energy conformation identified through the calculations is the folded form, whereas the conformation is unfolded in the crystal structure study carried out by Bush and Truter [18]. The difference may be on account of additional stabilization of the unfolded conformation in the crystal structure as a result of strong intermolecular CH...π and CH...O interactions evident from the structure [18]. We examined the complexation of the K^+ cation with the lowest energy forms of both folded and unfolded conformations of DB30C10. In each calculation, around 5000 structures were sampled and 100 conformers retained. Irrespective of whether one starts with the folded or unfolded ligand conformation, the calculated low energy conformations of the complex indicate that DB30C10 completely wraps around the cation. Fig. 6 shows the lowest energy conformation (I) and also the low energy conformation (II) that is in best agreement with the conformation in the crystal structure observed by others and us. All the eight low energy conformations within the 5 kcal/mol energy window are given in Fig. S5. The calculated distances between the complexed K^+ cation and donor oxygen atoms in Fig. 6(II) range from 2.82 to 3.07 Å in a symmetrical fashion, in close agreement with the distances of 2.87–3.05 Å found experimentally.

In view of the good match of one of the predicted low energy conformations of K^+–DB30C10 with the experimental data, we undertook similar calculations for 1:1 complexes with Na^+, Ca^{2+} and Mg^{2+} (Figs. S6–S9). Some of the sampled low energy complexed conformations of Na^+–DB30C10 [e.g., Fig. S6 (VII)] show an empty pocket where a second Na^+ can be accommodated. Indeed, incorporation of a second Na^+ has been demonstrated from the crystal structure [17c]. We have performed calculations for two sodium ions in DB30C10 crown ether (Fig. S7) and the lowest energy conformation shows that the two sodium ions are 4.4 Å apart, in good agreement with the crystal structure wherein the sodium ions are separated by 4.0 Å [17c]. Even though the diameter of Ca^{2+} (1.98 Å) is close to that of Na^+ (1.90 Å), its complexation behavior is different, with no evidence of the two pockets found with Na^+. The low energy conformations obtained through calculations are shown in Fig. S8. The folded conformation of the ligand is visible, as in the case of K^+. The conformation adopted by Mg^{2+}–DB30C10 is quite different; DB30C10 adopts a twisted conformation around

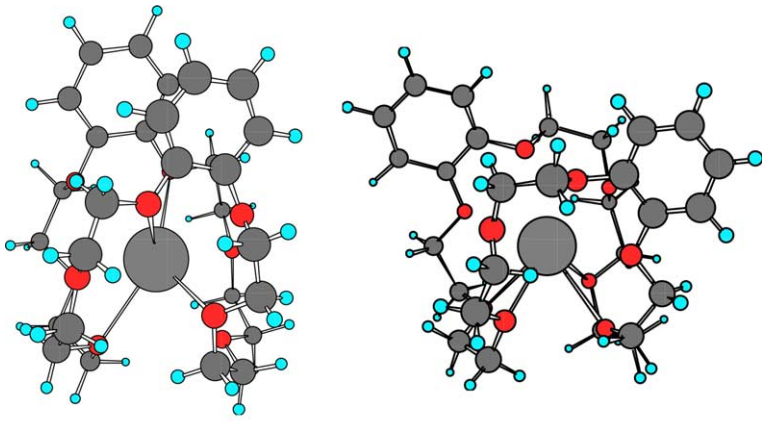


Fig. 6. Two of the eight low energy conformations (energy differences within a 5 kcal/mol window) of [K^+–DB30C10] obtained using MMFF94. (I) is the lowest in energy while (II) is in best agreement with the crystal structure of [K^+–DB30C10].

the Mg^{2+} cation (Fig. S9). The interacting distances between the Mg^{2+} cation and ligand oxygens vary between 2.12 and 3.60 Å: the oxygen atoms on the benzene rings interact weakly as they are located at the larger distance of 3.60 Å while the remaining eight oxygen atoms interact strongly (2.12–2.3 Å) with the Mg^{2+} cation (Fig. S9). Based on higher-level quantum chemical calculations [21o], Glendening and Feller have found a similar conformation with even smaller crowns, such as 18-crown-6, complexed to the Mg^{2+} ion.

To investigate theoretically the hierarchy of selectivity of DB30C10 towards the various cations, we have examined the ionic exchange reaction in Eq. (13),

$$K^+\text{–DB30C10} + M^{+/2+}{}_{(hyd)} \rightarrow K^+{}_{(hyd)} + M^{+/2+}\text{–DB30C10} \quad (13)$$

The exothermicity of this reaction can be considered a measure of the selectivity towards the various cations ($M^{+/2+} = Na^+$, K^+, Mg^{2+}, Ca^{2+}). Wipff et al. [21a,21b] previously reported the selectivity of alkali metal ions for Eq. (13) using a molecular mechanics approach for calculating exothermicity for a hydration sphere of six water molecules around the naked cation. High level quantum chemical calculations have also been performed and the results could qualitatively reproduce the experimental trend [21f,21l,21m,21o]. In the present work we have utilized experimental enthalpies of hydration [26],[1] and have assumed that the water molecules in the free cation are replaced with oxygen atoms of the crown ligand in the complexed state. Table 3 shows the selectivity of DB30C10 crown ether towards the various cations. The calculations suggest the trend: $K^+ > Na^+ > Ca^{2+} > Mg^{2+}$. The calculated results are in agreement with the high selectivity and K_e value for K^+ found experimentally. However, the trends predicted for the other ions are not entirely in agreement with the experimental data. Clearly, other factors such as competitive kinetics of complexation must also be important.

Table 3
Calculated ionic exchange reaction energies with experimental enthalpies of hydration using Eq. (11) (kcal/mol) at MMFF94[a]

	$M^{+/+2}$	$\Delta E^{a,b}$
K^+	Na^+	−10.7
K^+	Ca^{2+}	−157.6
K^+	Mg^{2+}	−205.5

[a] Calculated with use of the lowest energy conformations in each case.
[b] Negative enthalpy differences represent the preference for the K^+ ion.

5. Conclusions

K^+ interacts strongly with DB30C10 in the presence of picrate as a counter ion, leading to a high value ($2.9 \pm 0.2 \times 10^6$) of the extraction equilibrium constant. The crystal structure of [K-DB30C10][picrate] reported herein provides evidence of strong ion pair interactions. Such interactions presumably also exist in the solution state of the complex and facilitate its transport from the aqueous to organic phase. This combination of ligand and counter ion was employed to successfully extract K^+ from bittern and also from an equimolar mixture containing Na^+, K^+, Mg^{2+} and Ca^{2+} ions, with ca. 83% and 88% selectivity, respectively. High selectivity towards K^+ is predicted by molecular mechanics calculations, following the trend: $K^+ > Na^+ > Ca^{2+} > Mg^{2+}$, in reasonable agreement with the observed

[1] A more precise hydration energy for the cations has been used, considering experimental enthalpies of hydration of the cations instead of the cation–water cluster model with four to six water molecules.

results. The trend emanates from a balance between the energetics of crown–cation interaction and cation solvation.

Acknowledgments

We are grateful to the Department of Science and Technology (DST), Government of India, for financial support. The assistance of Dr. A.K. Bilakhiya during the initial stage of this project is gratefully acknowledged.

Appendix A. Supplementary data

Crystallographic files, in CIF format, CCDC 203945 can be obtained free of charge at www.ccdc.cam.ac.uk/conts/retrievel.html or from The Cambridge Crystallographic Data Center, 12 Union Road, Cambridge CB2 1EZ, UK; fax (internat.). +44-1223/336-033. email: deposit@ccdc.ac.uk. UV–Vis spectral changes of the extracted organic phase containing the Na^+ complex (Fig. S1), the ion chromatogram of the extracted organic phase (Fig. S2), the packing diagram of the complex showing the C–H···O interaction (Fig. S3), the low energy conformations of uncomplexed DB30C10 (Fig. S4) and its complexes with Na^+, K^+, Ca^{2+} and Mg^{2+} (Figs. S5–S9), respectively, are available. Supplementary data associated with this article can be found, in the online version at doi:10.1016/j.poly.2005.01.022.

References

[1] (a) C.J. Pedersen, J. Am. Chem. Soc. 89 (1967) 7017;
(b) C.J. Pedersen, J. Am. Chem. Soc. 92 (1970) 391;
(c) C.J. Pedersen, H.K. Frensdorff, Angew. Chem. Int. Ed. Engl. 11 (1972) 16;
(d) C.J. Pedersen, Angew. Chem. Int. Ed. Engl. 27 (1988) 1021.
[2] (a) R.M. Izatt, J.S. Bradshaw, S.A. Nielsen, J.D. Lamb, J.J. Christensen, Chem. Rev. 85 (1985) 271;
(b) R.M. Izatt, K. Pawlak, J.S. Bradshaw, Chem. Rev. 91 (1991) 1721;
(c) D.M. Dishong, C.J. Diamond, M.I. Cinoman, G.W. Gokel, J. Am. Chem. Soc. 105 (1983) 586;
(d) B. Zhang, A. Clearfield, J. Am. Chem. Soc. 119 (1997) 2751;
(e) X.X. Zhang, R.M. Izatt, J.S. Bradshaw, K.E. Krakowiak, Coord. Chem. Rev. 174 (1998) 179;
(f) P. Buhlmann, E. Pretsch, E. Bakker, Chem. Rev. 98 (1998) 1593;
(g) A. Yamauchi, T. Hayashita, S. Nishizawa, M. Watanabe, N. Teramae, J. Am. Chem. Soc. 121 (1999) 2319;
(h) Y. Habata, T. Saeki, S. Akabori, X.X. Zhang, J.S. Bradshaw, Chem. Commun. (2000) 1469;
(i) S. Mochizuki, R.L. Smith Jr., H. Inomata, Chem. Commun. (2000) 1381;
(j) A.V. Bajaj, N.S. Poonia, Coord. Chem. Rev. 87 (1988) 55.
[3] (a) J.-M. Lehn, Science 227 (1985) 849;
(b) R.M. Izatt, K. Pawlak, J.S. Bradshaw, R.L. Bruening, Chem. Rev. 95 (1995) 2529;
(c) Y.A. Zolotov (Ed.), Macrocyclic Compounds in Analytical Chemistry, Wiley, New York, 1997;
(d) B Moyer, in: G.W. Gokel (Ed.), Comprehensive Supramolecular Chemistry, vol. I, Pergamon, New York, 1996, p. 377.
[4] R.M. Izatt, J.J. Christensen, Synthesis of Macrocyles. The Designing of Selective Complexing Agents, Wiley Interscience, New York, 1987.
[5] (a) F. Vogtle, E. Weber, in: S. Patai, Z. Rappoport (Eds.), Crown Ethers and Analogs, Wiley, New York, 1989, p. 207;
(b) P.D.J. Gootenhuis, P.D.V. Wal, D.N. Reinhoudt, Tetrahedron 43 (1987) 397.
[6] (a) K.H. Wong, G. Konizer, J. Smid, J. Am. Chem. Soc. 92 (1970) 666;
(b) S. Zdenek, P. Paolo, Anal. Chem. 62 (1990) 1010.
[7] (a) U. Olsher, M.G. Hankins, D.Y. Kim, R.A. Bartsch, J. Am. Chem. Soc. 115 (1993) 3370;
(b) J.D. Lamb, J.J. Christensen, S.R. Izatt, K. Bedke, M.S. Astin, R.M. Izatt, J. Am. Chem. Soc. 102 (1980) 3399;
(c) R. Inglesias, S.A. Dassie, L.M. Yudi, A.M. Baruzzi, Anal. Sci. 14 (1998) 231.
[8] G.G. Talanova, N.S.A. Elkarim, V.S. Talanov, R.E. Hanes Jr., H.-S. Hwang, R.A. Bartsch, R.D. Rogers, J. Am. Chem. Soc. 121 (1999) 11281.
[9] P. Agnihotri, B. Ganguly, E. Suresh, P. Paul, P.K. Ghosh, Ind. J. Chem. Sec. A. 42A (2003) 2283 (invited paper, Diamond Jubilee year of CSIR).
[10] (a) H.-J. Buschmann, E. Cleve, U. Denter, E. Schollmeyer, J. Phys. Org. Chem. 10 (1997) 781;
(b) H.-J. Buschmann, G. Weng, E. Cleve, E. Schollmeyer, Acta Chim Slov. 47 (2000) 55.
[11] CAD4-PC Software, Version 5, Enraf-Nonius, Delft, 1989.
[12] E.I. Gabe, Y. Le Page, I.P. Charland, F.L. Lee, P.S. White, J. Appl. Cryst. 22 (1989) 384.
[13] G.M. Sheldrick, SHELXL-97. Program for Crystal Structure Determination, University of Göttingen, Germany, 1997.
[14] J.S. Kim, O.J. Shon, J.W. Ko, M.H. Cho, I.Y. Yu, J. Vicens, J. Org. Chem. 65 (2000) 2392.
[15] H.K. Frensdorff, J. Am. Chem. Soc. 93 (1971) 4684.
[16] G.-X. He, A. Abe, T. Ikeda, F. Wada, K. Kikukawa, T. Matsuda, Bull Chem. Soc. Jpn. 59 (1986) 674.
[17] (a) M. Shamsipur, A.I. Popov, J. Am. Chem. Soc. 101 (1979) 4051;
(b) H.D.H. Stover, L.J. Maurice, A. Delville, C. Detellier, Polyhedron 4 (1985) 1091;
(c) J.D. Owen, M.R. Truter, J. Chem. Soc. (1979) 1831.
[18] (a) M.A. Bush, M.R. Truter, J. Chem. Soc., Perkin Trans. (1972) 345;
(b) J.D. Owen, M.R. Truter, J.N. Wingfield, Acta Crystallogr., Sect. C 40 (1984) 1515.
[19] (a) V.W. Bhagwat, H. Manohar, N.S. Poonia, Inorg. Nucl. Chem. Lett. (1981) 207;
(b) N.S. Poonia, Proc. Indian Natn. Sci. Acad. 52A (1986) 931.
[20] (a) G.R. Desiraju, Angew. Chem. Int. Ed. Engl. 34 (1995) 2328;
(b) G.R. Desiraju, T. Steiner, The Weak Hydrogen Bond in Structural Chemistry and Biology, Oxford University Press, Oxford, 1999;
(c) T. Steiner, Angew. Chem. Int. Ed. Engl. 41 (2002) 48.
[21] (a) G. Wipff, P. Weiner, V. Kollman, J. Am. Chem. Soc. 104 (1982) 3249;
(b) P.D.J. Grootenhius, P. Kollman, J. Am. Chem. Soc. 111 (1989) 2152;
(c) M.G.B. Drew, D.G. Nicholson, J. Chem. Soc., Dalton Trans. (1986) 1543;
(d) P.D.J. Grootenhius, J. van Eerden, E.J.R. Sudholter, D.N. Reinhoudt, A. Roos, S. Harkema, D. Feil, J. Am. Chem. Soc. 109 (1987) 4792;
(e) P.K. Weiner, S. Profeta Jr., G. Wipff, T. Havel, I.D.

Kuntz, R. Langride, P.A. Kollman, Tetrahedron 39 (1983) 1113;
(f) D. Feller, M.A. Thompson, R.A. Kendall, J. Phys. Chem. A 101 (1997) 7292;
(g) W.P. Anderson, P. Behm Jr., T.M. Glennon, J. Phys. Chem. 101 (1997) 1920;
(h) L.X. Dang, P.A. Kollman, J. Phys. Chem. 99 (1995) 55;
(i) J. van Eerden, S. Harkema, D. Feil, J. Phys. Chem. 92 (1988) 5076;
(j) G. Ranghino, S. Romano, J.M. Lehn, G. Wipff, J. Am. Chem. Soc. 107 (1985) 7873;
(k) W.F.van Gunsteren, H.J.C. Berendsen, in: J. Hermans (Ed.), Molecular Dynamics and Protein Structure, Polycrystal Book Service, Western Springs, 1985, p. 5;
(l) D. Feller, J. Phys. Chem. A 101 (1997) 2723;
(m) E.D. Glendening, D. Feller, M. Thompson, J. Am. Chem. Soc. 116 (1994) 10657;
(n) P.A. Kollman, P.D.J. Grootenhuis, M.A. Lopez, Pure Appl. Chem. 61 (1989) 593;
(o) E.D. Glendening, D. Feller, J. Am. Chem. Soc. 118 (1996) 6052;
(p) T.P. Straatsma, J.A. McCammon, J. Chem. Phys. 91 (1989) 3631.

[22] (a) R. Geue, S.H. Jacobson, R. Pizer, J. Am. Chem. Soc. 108 (1986) 1150;
(b) G. Wipff, P.A. Kollman, Novu. J. Chim 9 (1985) 457.

[23] (a) P.D. Grootenhuis, J. van Eerden, P.J. Dijkstra, S. Hakema, D.N. Reinhoudt, J. Am. Chem. Soc. 109 (1987) 8044;
(b) P.A. Kollman, G. Wipff, U.C. Singh, J. Am. Chem. Soc. 107 (1985) 2212.

[24] (a) T.A. Halgren, J. Comput. Chem. 17 (1996) 490;
(b) TITAN, Wavefunction, Inc, 18401 Von Karman Avenue, Suite 370, Irvine CA 92612, USA, Schrodinger, Inc., 1500 SW First Avenue, Suite 1180, Portland, OR 97201, USA.

[25] (a) K.J. Koch, F.C. Gozzo, D. Zhang, M.N. Eberlin, R.G. Cooks, Chem. Commun. (2001) 1854;
(b) M.S. Ward, F.-T. Lin, R.E. Shepherd, Inorg. Chim. Acta 343 (2003) 231;
(c) R. van de Coevering, M. Kuil, R.J.M.K. Gebbink, G. van Koten, Chem. Commun. (2002) 1636;
(d) J. Fawcett, G.A. Griffiths, J.M. Percy, S. Pintat, C.A. Smith, N.S. Spencer, E. Uneyama, Chem. Commun. (2004) 302;
(e) M. Arca, A.J. Blake, J. Casabò, F. Demartin, F.A. Devillanova, A. Garau, F. Isaia, V. Lippolis, R. Kivekas, V. Muns, M. Schröder, G. Verani, J. Chem. Soc., Dalton Trans. (2001) 1180;
(f) J.S. Lomas, A. Adenier, J. Chem. Soc., Perkin Trans. 2 (2002) 1264;
(g) D. Duran, V. Aviyente, C. Baysal, J. Chem. Soc., Perkin Trans. 2 (2002) 670;
(h) U. Kuhl, M. von Korff, K. Baumann, C. Burschka, U. Holzgrabe, J. Chem. Soc., Perkin Trans. 2 (2001) 2037;
(i) P. Boman, B. Eliasson, R.A. Grimm, S.W. Staley, J. Chem. Soc., Perkin Trans. 2 (2001) 1130;
(j) E. Butkus, J. Malinauskienė, S. Stončius, Org. Biomol. Chem 1 (2003) 391.

[26] (a) F.A. Cotton, G. Wilkinson, Advanced Inorganic Chemistry, third ed., 1972, p. 645;
(b) More precise hydration energy for cations have been used-considering experimental enthalpies of hydration of the cations instead of cation–water cluster model with four to six water molecules.

formation of chiral three-dimensional architectures [3d]; the intercalation of $MePh_3P^+$ in the dicyanamide-bridged system leads to a three-dimensional network containing this cation in cavities [4a]. Although there are several examples in the literature illustrating the modification of network topology through simple cation templation, systematic studies concerning the role of the size and the nature of counter ions on the structural organization of coordination polymers have never been investigated.

Numerous bimetallic assemblies based on hexa- [5], hepta- [6] and octa-cyanometallate [7] building blocks form an important family of molecule-based magnets presenting a variety of structures and interesting magnetic and photo-magnetic properties. Among these, coordination polymers based on the $Mn^{2+}/[Mo(CN)_7]^{4-}$ system have recently attracted considerable interest [6,8]. A self-organization of this system leads to formation of two thermodynamically stable pseudo-dimorphic three-dimensional frameworks $Mn_2(H_2O)_5[Mo(CN)_7]\cdot nH_2O$ ($n = 4.00$, 4.75), which order ferrimagnetically below 51 K [9]. The presence of a counter cation in this system changes the topology of supramolecular networks and, as a consequence, their magnetic properties. Firstly, the intercalation of the large flexible counter cation $N(CH_3)_4^+$ leads to the formation of $[N(CH_3)_4]_2[Mn(H_2O)]_3[Mo(CN)_7]_2\cdot 2H_2O$ presenting anisotropic three-dimensional structure which orders ferrimagnetically below 86 K [10]. In this case, the three-dimensional network adopts $N(CH_3)_4^+$ in its cavities. Secondly, the use of the cation K^+ affords the formation of a two-dimensional coordination polymer $K_2[Mn(H_2O)_2]_3[Mo(CN)_7]_2\cdot 6H_2O$ (**1**) having an ordering temperature at 39 K [11]. Its structural organization consists in anionic cyano-bridged {MnMo} double sheets alternated with the counter cation. Thirdly, in a preliminary communication, we showed that the intercalation of NH_4^+ into $Mn^{2+}/[Mo(CN)_7]^{4-}$ leads to the formation of $(NH_4)_2Mn_3(H_2O)_4[Mo(CN)_7]_2\cdot 4H_2O$ (**2**) presenting a structure similar to **1**, but a three-dimensional [12]. It orders ferrimagnetically below 53 K. Such preliminary results encouraged us to further investigate the role of a counter cation and analyse the different factors which can influence the structural organization of $Mn^{2+}/[Mo(CN)_7]^{4-}$.

In this article, we present two pseudo-dimorphic phases $(NH_4)_2Mn_3(H_2O)_4[Mo(CN)_7]_2\cdot nH_2O$ ($n = 4$ for **2** and $n = 5$ for **3**) obtained by intercalation of NH_4^+ in the $Mn^{2+}/[Mo(CN)_7]^{4-}$ system and compare their structures with **1**. We analyse the size, the geometry, the polarizability and other characteristics of the counter cations NH_4^+ and K^+ in order to understand their role as structuring agents. In particular, the influence of previously unknown unconventional ionic interactions cation$\cdots\pi(C{\equiv}N)$ (cation = NH_4^+, K^+) on the structural organization of $Mn^{2+}/[Mo(CN)_7]^{4-}$ was established and confirmed by theoretical investigations using binuclear Mn–Mo cyano-bridged models.

2. Experimental

2.1. Synthesis

Unless otherwise noted, all manipulations were performed at ambient temperature using reagents and solvents as received. The precursor $K_4[Mo(CN)_7]\cdot 2H_2O$ was prepared as already described [13].

2.1.1. $(NH_4)_2Mn_3(H_2O)_4[Mo(CN)_7]_2\cdot nH_2O$ ($n = 4$ for **2** and 5 for **3**)

Compound **2** was obtained by slow diffusion in an H-shaped tube under argon atmosphere of two deoxygenated aqueous solutions containing (0.150 g, 3.1×10^{-4} mol) $K_4[Mo(CN)_7]\cdot 2H_2O$ and (0.183 g, 7.2×10^{-4} mol) $[Mn(H_2O)_6](NO_3)_2$, respectively, in the presence of NH_4NO_3 (0.2 g, 1.88×10^{-3} mol). After a few months, dark green crystals with a parallelepiped shape were formed (Fig. 1S, Supplementary materials). The crystals of compound **3** were detected in the same H-shaped tube beside **2**. Both compounds are stable in air and no any changes were observed in the structures during few weeks. Yield: 0.06 g, 18%.

Anal. Calc. for $C_{14}H_{24}Mn_3Mo_2N_{16}O_8$ (**2**): C, 18.65; H, 2.66; Mn, 18.29; Mo, 21.31; N, 24.87%. *Anal.* Calc. for $C_{14}H_{26}Mn_3Mo_2N_{16}O_9$ (**3**): C, 18.29; H, 2.83; Mn, 17.94; Mo, 20.89; N, 24.38%. Found: C, 18.78; H, 2.89; Mn, 18.35; Mo, 21.26; N, 24.97%.

IR (KBr, cm^{-1}): 3613, 3587(m), 3518(m), 3285(s), 2112(s), 2091(s), 2012(m), 1625(m), 1414(m), 1262(w), 1099(w), 681(m), 579(m), 418(m).

The first dehydrated form $(NH_4)_2Mn_3(H_2O)_4[Mo(CN)_7]_2$ was obtained by heating of the mixture of **2** and **3** at 80 °C under argon. *Anal.* Calc. for $C_{14}H_{16}Mn_3Mo_2N_{16}O_4$: C, 20.27; H, 1.93; Mn, 19.89; Mo, 23.16; N, 27.03. Found: C, 20.42; H, 2.09; Mn, 20.05; Mo, 23.56; N, 27.57%.

The second dehydrated form $(NH_4)_2Mn_3[Mo(CN)_7]_2$ was obtained by heating of the mixture of **2** and **3** at 160 °C under argon. *Anal.* Calc. for $C_{14}H_8Mn_3Mo_2N_{16}$: C, 22.20; H, 1.05; Mn, 21.78; Mo, 25.36; N, 29.60. Found: C, 22.05; H, 0.05; Mn, 21.45; Mo, 25.56; N, 29.97%.

2.2. X-ray crystallography and structure solution

The crystallographic structure of **1** initially solved in the non-centrosymmetrical space group *C*2/1 (No. 5) [11a] was corrected and re-solved in the centrosymmetrical space group *C*2/*c* (No. 15) [6c,11c]. The crystal structure of **2** was published in a preliminary communication [12]. The crystallographic data for complexes **2** and **3** are listed in Table 1. For both structures data collection were

performed at low temperature ($T = 180$ K) on a IPDS STOEII diffractometer using a graphite-monochromatic Mo Kα radiation ($\lambda = 0.71073$ Å) and equipped with an Oxford Cryosystems Cryostream Cooler Device. The final unit cell parameters have been obtained by means of a least-squares refinement performed on a set of 8000 well-measured reflections, and a crystal decay has been monitored. No significant fluctuations of intensities were observed during the data collection. Structures have been solved by Direct Methods using SHELXS-97 [14], and refined by means of least-squares procedures on a F^2 with the aid of the program SHELXL-97 includes in WinGX version 1.63 [15]. The Atomic Scattering Factors were taken from International tables for X-ray Crystallography. Due to the symmetry operators on which have been located the molecules of H_2O hydrogen atoms have to be disordered, consequently could not be located. Semi-empirical corrections absorption were applied [16] and all non-hydrogen atoms were anisotropically refined, in the last cycles of refinement weighting schemes were used, where weights are calculated from the following formula: $w = 1/[\sigma^2(F_o^2) + (aP)^2 + bP]$, where $P = (F_o^2 + 2F_c^2)/3$.

2.3. Physical measurements

Infrared spectra were recorded as KBr disks or Nujol mulls between NaCl plates on a Nicolet Model 510P spectrophotometer. Thermogravimetry analysis (TGA) were performed using a Netzsch STA 409 instrument under argon atmosphere from 25 to 700 °C at a heating rate of 1 °C min^{-1}; volatiles were determined using a Balzers QMG 421 quadruple mass spectrometer coupled with the ATG equipment. Magnetic susceptibility data were collected with a Quantum Design MPMS-XL SQUID magnetometer on polycrystalline samples. The data were corrected for the sample holder and the diamagnetism contributions calculated from the Pascal's constants [17].

2.4. Computational details

The calculations have been performed with the energy-consistent relativistic effective core potentials (RECPs) derived by the Stuttgart group (called SDD) [18]. For the Mo atom, the core consists of the 1s–3s, 2p–3p, 3d atomic orbitals and the basis set is [8s7p6d]/(6s5p3d). For the Mn atom, the core consists of the 1s–2s and 2p atomic orbitals and the basis set is [8s7p6d1f]/(6s5p3d1f). For the K atom, the core consists of the 1s–2s and 2p atomic orbitals and the basis set is [7s6p]/(5s4p) and for C and N atoms, the 1s orbital is in the core, and the basis set is [4s4p]/(2s2p). H atoms are described by the 6-31G basis set. This basis set will be referred to as BAS1. A more extended basis set, referred to BAS2, has been deduced from BAS1 by augmenting some atomic basis with one diffuse s, one

Table 1
Crystal data and structure refinement for **2** and **3**

Compound	**2**	**3**
Empirical formula	$C_7N_8O_4Mn_{1.5}Mo$	$C_{3.5}N_4O_{2.25}Mn_{0.75}Mo_{0.5}$
Formula weight	438.50	223.25
T (K)	180(2)	180(2)
λ (Å)	0.71073	0.71073
Crystal system	monoclinic	monoclinic
Space group	*C*2/*c* (No. 15)	*C*2/*c* (No. 15)
Unit cell dimensions		
a (Å)	28.978(6)	28.666(6)
b (Å)	7.1790(10)	7.2250(10)
c (Å)	15.765(3)	7.776(2)
β (°)	105.99(3)	105.41(3)
V (Å^3)	3152.8(10)	1552.6(6)
Z	8	8
D_{calc} (Mg m^{-3})	1.848	1.910
Absorption coefficient (mm^{-1})	2.004	2.039
$F(000)$	1676	854
2θ Range for data collection (°)	3.3–52.1	2.9–48.4
Reflections collected/unique (R_{int})	11908/3057 (0.0329)	6241/1335 (0.0311)
Completeness to 2θ°	26.01 98.4%	48.22 99.1%
Refinement method	full-matrix least-squares on F^2	full-matrix least-squares on F^2
Data/restraints/parameters	3057/0/196	1335/0/118
Absorption corrections	semi-empiricals^{DIFABS} [16]	semi-empiricals^{DIFABS} [16]
T_{min}–T_{max}	0.510–0.848	0.573–0.870
Goodness-of-fit on F^2	1.021	1.089
Scheme of ponderation	weight $= 1/[\sigma^2(F_o^2) + (0.0394P)^2 + 0.4551P]$ where $P = (F_o^2 + 2F_c^2)/3$	weight $= 1/[\sigma^2(F_o^2) + (0.0515P)^2 + 0.4551P]$ where $P = (F_o^2 + 2F_c^2)/3$
Final R indices [$I > 2\sigma(I)$]	$R_1 = 0.0263$, $wR_2 = 0.0614$	$R_1 = 0.0255$, $wR_2 = 0.0699$
R indices (all data)	$R_1 = 0.0376$, $wR_2 = 0.065$	$R_1 = 0.0307$, $wR_2 = 0.0721$

diffuse p and one polarization d functions. The following exponents have been used: for K, $\zeta_s = \zeta_p = 0.0047$ and $\zeta_d = 0.2$, for N, $\zeta_s = \zeta_p = 0.0639$ and $\zeta_d = 0.8$, for C, $\zeta_s = \zeta_p = 0.0438$ and $\zeta_d = 0.8$. All calculations have been performed with the GAUSSIAN-98 program [19].

In order to calibrate the basis set, a preliminary study has been carried out. The system $NH_4^+ + CN^-$ has been studied with different basis sets (see Table 4) assuming a fixed geometry: a NH bond lies in the medium plane of CN, H pointing towards CN and N being at 3.6 Å from C and N. The CN distance is 1.8 Å. In this table, SDD+sp+d is BAS2. Basis set superposition error (BSSE) corrections are carried out using the counterpoise method of Boys and Bernardi [20]. The addition of diffuse s and p functions to the SDD basis set is crucial as well as the use of augmented basis sets because of the negatively charged ion CN^-. The results obtained with BAS2 agree with those obtained with the much larger basis set aug-cc-pVTZ. In order to mimic the interaction, we are interested in this article, two potassium atoms have been added. In this case, the dependency to the quality of the basis set is not as crucial and the agreement between the basis sets is excellent as long as they have diffuse functions and the effect of the BSSE correction is negligible. Similar conclusions are obtained for the interaction between K^+ and CN^-, where K^+ is constrained to lie at a distance of 3 Å of both C and N: there is a weak dependency to the basis set. The difference between NH_4^+ and K^+ must be due to the higher polarizability of the former, more available to take the electrons from the cyano group when the basis is too small. Finally, both for geometry optimization and interaction energy calculations, the basis set BAS2 has been used to describe K^+, NH_4^+ and the five neighbouring cyano groups in all calculations. The rest of the cluster has been described with BAS1 since it is less involved in the intermolecular interaction. In these three systems, the effect of the method has been checked as well: MP2 and B3LYP give the same interaction energies and the discrepancy with HF is quite small because the main effect of the interaction energies are of electrostatic, exchange and induction nature.

The molybdenum site geometry analysis was performed using Continuous Shape Measures calculation [25].

3. Results and discussion

3.1. Pseudo-dimorphic phases $(NH_4)_2Mn_3(H_2O)_4[Mo(CN)_7]_2 \cdot nH_2O$ ($n = 4$ for **2** and $n = 5$ for **3**).

3.1.1. Synthesis

The slow diffusion of two aqueous solutions containing $K_4[Mo(CN)_7] \cdot 2H_2O$ [13] and $[Mn(H_2O)_6](NO_3)_2$, respectively, in the presence of NH_4NO_3 in an H-shape tube under argon atmosphere provided dark green crystalline plates of $(NH_4)_2Mn_3(H_2O)_4[Mo(CN)_7]_2 \cdot 4H_2O$ (**2**) (Fig. 1S, Supplementary materials). Crystals of $(NH_4)_2Mn_3(H_2O)_4[Mo(CN)_7]_2 \cdot 5H_2O$ (**3**) were also detected in an H-shaped tube beside **2**. Both types of crystals have the same shape and colour and their separation is possible only by crystallographic tests. The examination of numerous randomly chosen crystals of different H-tubes gave around 80% of **2** and 20% of **3** in the mixture.

The infrared stretches (Fig. 2S, Supplementary materials) ν(CN) 2012(m), 2091(s), 2112(s) cm^{-1} for **2** and **3** are shifted toward higher frequencies from those of $K_4[Mo(CN)_7] \cdot 2H_2O$ (2035(w), 2067(s), 2080(m), 2100(w) cm^{-1}) clearly showing the coordination of all the CN^- groups to manganese [26]. In addition, the presence of several sharp peaks indicates crystallographically non-equivalent CN groups in the complexes and the distortion of the Mo site from D_{5h} symmetry. The presence of N–H absorptions (1414(m), 3285(s), 3318(m), 3587(m) cm^{-1}) clearly indicates the presence of NH_4^+ in the network. The X-ray structures (vide infra) are in agreement with these results.

3.1.2. Crystal structures

The crystal structure of **2** has been published in a preliminary communication [12]. The X-ray crystallographic study performed for **2** and **3** at 180 K reveals that both of them crystallize in the monoclinic system with *C*2/*c* (No. 15) space group (Table 1). Both structures possess one Mo site and two Mn sites, namely Mn1 and Mn2. The Mo atoms are surrounded by five –C–N–Mn1 linkages and two –C–N–Mn2 linkages, as can be seen in Fig. 1(a) and (b). The Mo–C bond lengths range from 2.112(3) to 2.166(9) Å (with a mean value of 2.138 Å) for both compounds. All of the Mo–C–N bond angles are close to 180°, ranging from 175.51(26)° to 179.00(27)° for **2** and from 176.26(29)° to 179.87(44)° for **3**. Geometries of the molybdenum sites of **2** and **3** were analysed by using Continuous Shape Measures calculations. Five models were considered: heptagon (D_{7h}), hexagonal pyramid (C_{6v}), pentagonal bipyramid (D_{5h}), capped octahedron (C_{3v}) and capped trigonal prism (C_{2v}). The obtained results clearly show that the molybdenum site geometry in **2** corresponds to the perfect-capped trigonal prism (C_{2v}) while the site geometry in **3** is compatible with the intermediate polyhedron between the trigonal prism and the capped octahedron (Table 1S, Supplementary materials). In both cases, the geometry of $[Mo(CN)_7]^{4-}$ unit is changed from a pentagonal bipyramid (D_{5h}) in the starting compound $K_4[Mo(CN)_7] \cdot 2H_2O$ [13]. Such flexibility of the building block geometry was commonly observed with the compounds presenting phenomena of pseudo-polymorphism [27].

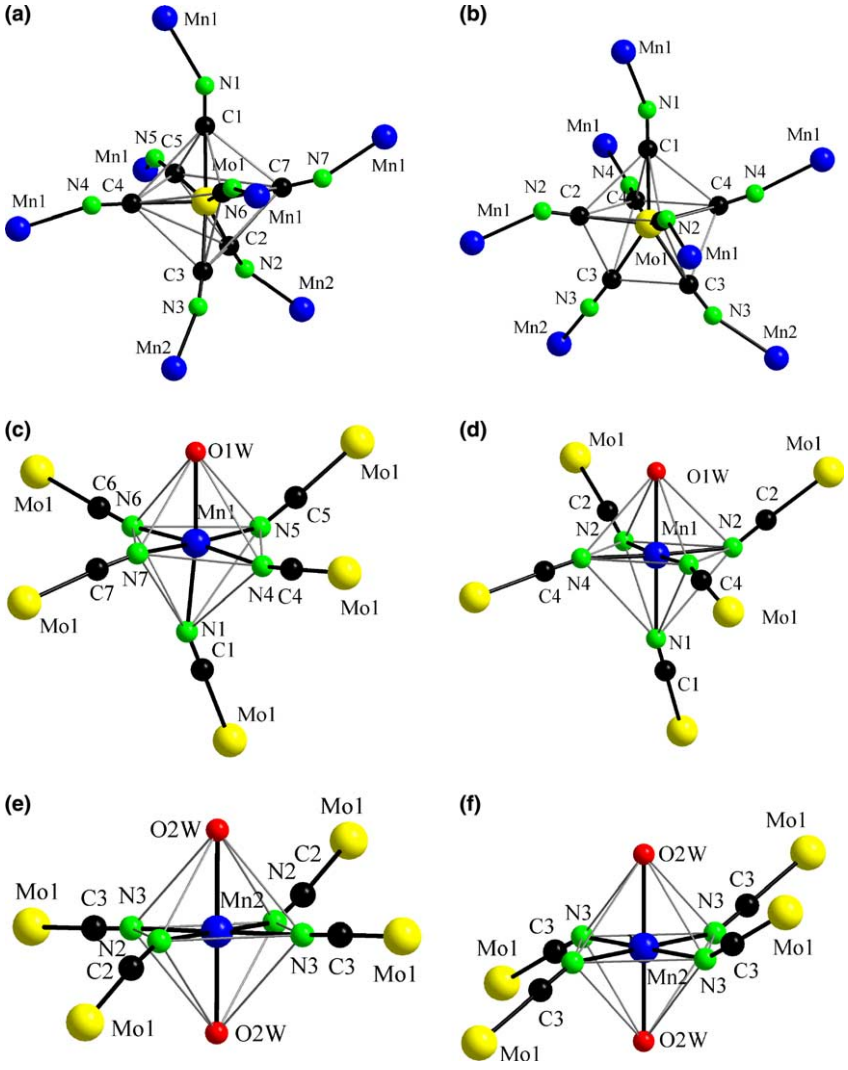


Fig. 1. Local coordination environments of: (a) Mo site for compound **2**; (b) Mo site for compound **3**; (c) Mn 1 site for compound **2**; (d) Mn1 sites for compound **3**; (e) Mn2 site for compound **2**; (f) Mn2 site for compound **3**.

Both structures show six-coordinate Mn1 and Mn2 sites. The Mn1 sites are surrounded by five N–C–Mo linkages and one water molecule forming a distorted octahedral environment (Fig. 1(c) and (d)). The Mn2 ions are surrounded by four N–C–Mo linkages and two water molecules in the *trans* positions leading also to a distorted octahedral environment (Fig. 1(e) and (f)). The Mn–N–C bond angles deviate significantly from 180°, ranging from 142.26(24)° to 167.08(27)° for **2** and from 145.27(43)° to 164.36(29)° for **3**.

Although **3** is not strictly isostructural to **2**, the organization of the three-dimensional structure is similar. The cyano-bridged networks may be described as a corrugated grid-like sheets parallel to the *bc* plane, which are formed by cyano-bridged rhombus motifs, $\{MoC4N4Mn1N2C2\}_2$ in the case of **3** (Fig. 2, Fig. 3S, Supplementary materials). In this plane, the Mo–Mn1 separations across a cyano-bridge range from 5.29 to 5.40 Å. Each two parallel sheets are connected by $Mn2(C3N3)_4$ rhombus running along the *b* axis to form a double sheet parallel to the *bc* plane. These double sheets are also connected to each other by the C1N1 bridge to form the three-dimensional structure (Fig. 3, Fig. 4S, Supplementary materials). The Mo–Mn1 distance through the C1N1 is equal to 5.372 Å for **2** and 5.311 Å for **3**. The NH_4^+ counter cations (N11) are intercalated between the double sheets running along the *bc* plane and are situated in the centres of cubic cavities formed by the anionic networks (Figs. 3 and 4(a)).

It should be noted that a similar structural arrangement was observed for **1** but in this case the double sheets are separated by K^+ and not connected to each other forming a two-dimensional structure (Fig. 4(b)). The shorter inter-double sheet distance for **1** (Mo–Mo) is equal to 7.253 Å.

The three-dimensional arrangement of the crystal structures of **2** and **3** results in channels running along

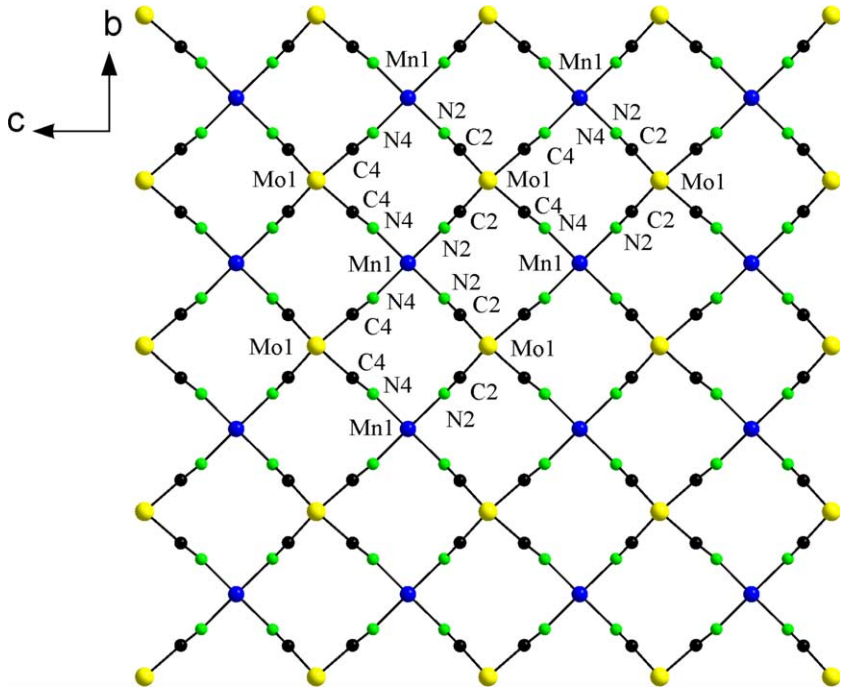


Fig. 2. A view of the structure of **3** in the *bc* plane, showing a corrugated grid-like plan. Mn2 atoms, hydrogen atoms and solvents molecules have been omitted for clarity.

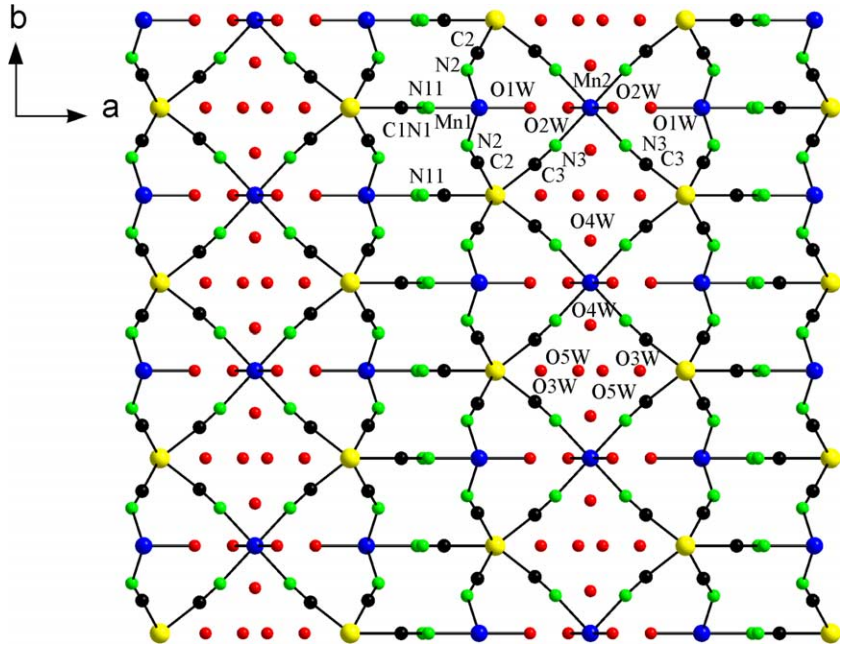


Fig. 3. A view of the structure of **3** in the *ab* plane. Hydrogen atoms have been omitted for clarity.

the *b* axis occupied by coordinated and water of crystallization molecules as shown in a whole view of the structure of **2** viewed in the *ac* plane (Fig. 4(a), Fig. 5S, Supplementary materials). Fig. 5(a)–(d) shows the hydrogen-bonding pathway between water molecules, which are coordinated to manganese atoms and crystallized in the cell for **2** and **3**. In both structures, the four coordinated water molecules situated in the *ac* plane are linked together by means of hydrogen bonds forming a non-centrosymmetrical lozenge $\{O1WO2W\}_2$ in the centre of the channel (Fig. 5(a) and (b)). Four water molecules of crystallization situated in the *ac* plane are also linked by hydrogen bonds and form lozenges {O3WO4W} for **2** and {O3WO5W} for **3**. On the other

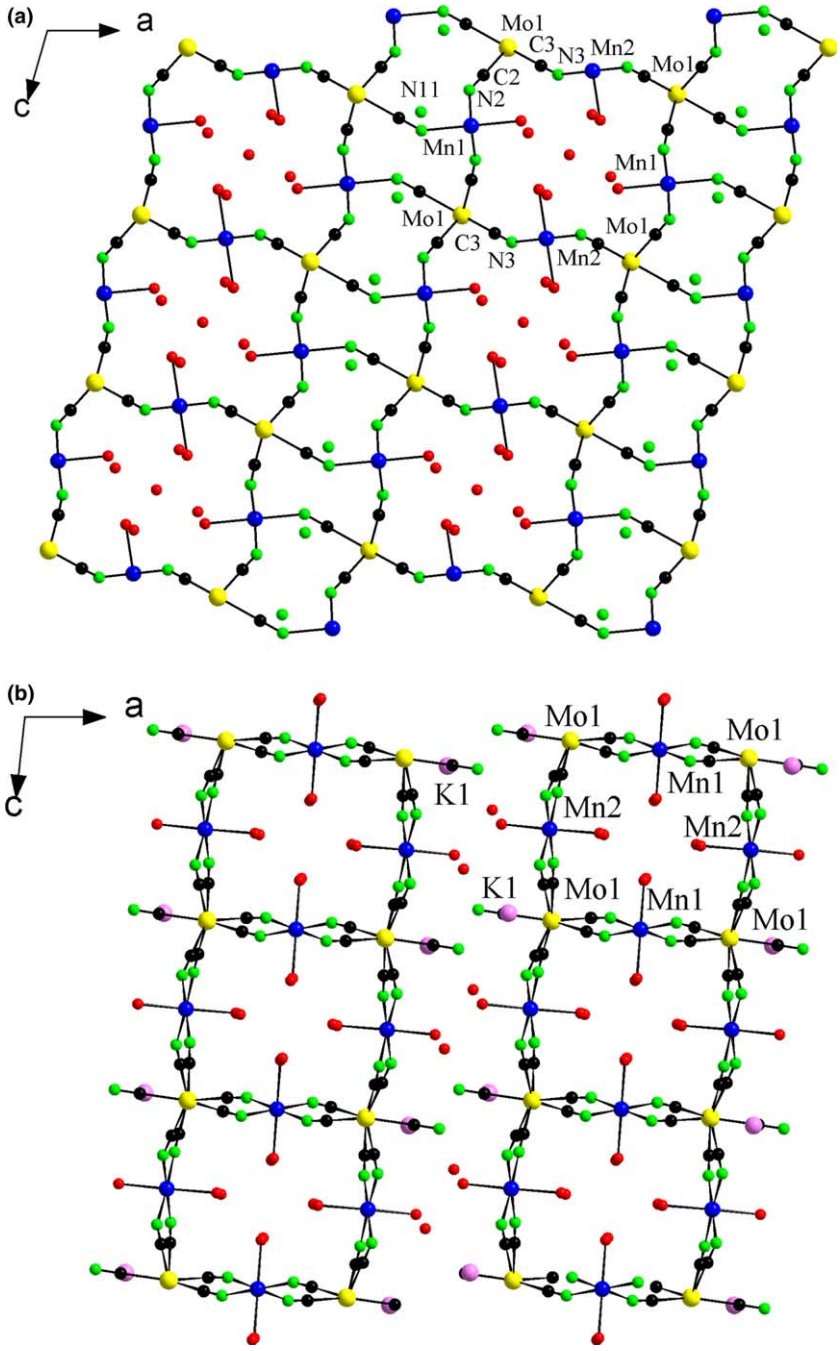


Fig. 4. Global view of the crystal structures in the *ac* plane of (a) **3** and (b) **1**. Hydrogen atoms have been omitted for clarity.

hand, the O2W atoms are linked by hydrogen bonds to the O4W atoms of the water molecules of crystallization and the later are linked to the O3W in **2** or O5W in **3** resulting in columns of water clusters inserted in the channels delimited by the cavities running along the *b* direction (Fig. 5(c) and (d)). The distances implied in hydrogen-bonding pathway (Table 2) are in agreement with the previously reported hydrogen bonds [28]. The cavity size without water molecules may be estimated as (9.123×7.883) Å^2 (or as a cavity volume of 195 Å^3) for **2** and as (9.175×7.776) Å^2 (a cavity volume of 190 Å^3) for **3**. It should be noted that analogous cavities containing hydrogen bonded water clusters were observed in the case of the two-dimensional compound **1** with a cavity size of (9.072×8.104) Å^2 (a cavity volume of 206 Å^3). The cavities found in these three compounds may be used for intercalation of guest molecules having appropriate size and nature.

3.1.3. Thermogravimetric analysis

The thermogravimetric analysis of the mixture of **2** and **3** was performed under argon atmosphere from

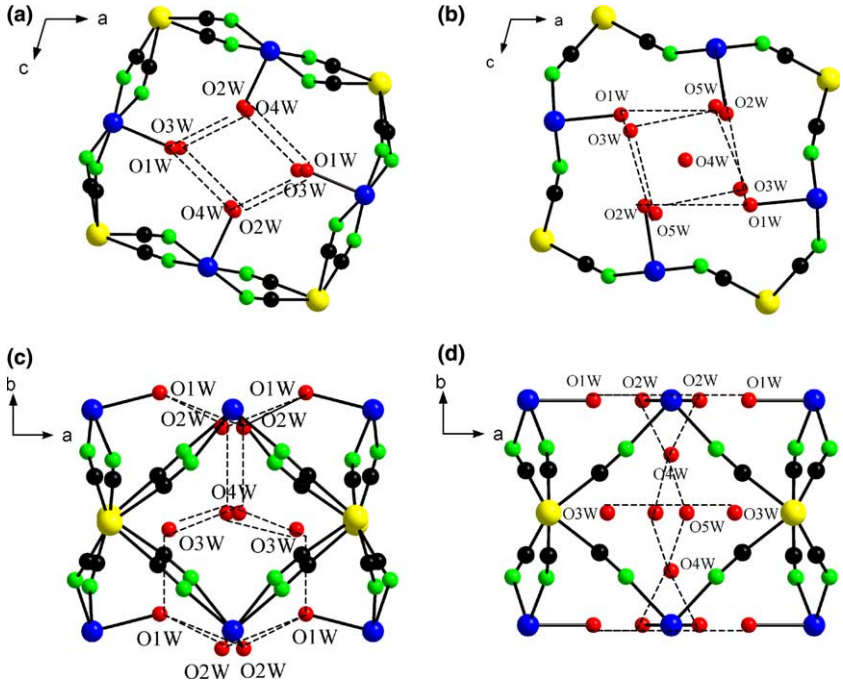


Fig. 5. Fragments of crystal structures showing hydrogen-bonding pathway (dashed line) between coordinated to Mn and crystallized water molecules: (a) for the structure of **2** along the *b* axis; (b) for the structure of **3** along the *b* axis; (c) for the structure of **2** along the *c* axis; (d) for the structure of **3** along the *c* axis.

Table 2
Distances in hydrogen bonding water networks in **2** and **3**

D···A	Distances for **2** (Å)	D···A	Distances for **3** (Å)
O1W···O2W	3.104	O1W···O3W	3.168
	3.329		3.536
O3W···O4W	2.716	O3W···O5W	2.974
	2.784		2.899
O2W···O4W	2.785	O2W···O4W	2.706
O1W···O3W	2.758	O1W···O4W	3.166
		O4W···O5W	2.785
		O4W···O3W	2.803

room temperature up to 700 °C. The curve exhibits four well-pronounced weight losses as the temperature was increased at a heating rate of 1 °C min^{-1}, as shown in Fig. 6(a). The weight loss steps can be determined by the inflection points at 70, 125, 370 and 632 °C, respectively. The first weight loss of 8.4% is in agreement with the loss of the four water molecules of crystallization. This value is slightly higher than the calculated one (8.0%) due to the presence in the mixture of around 20% of the compound **3** containing five water molecules of crystallization. The second weight loss of 8% is consistent with the loss of four coordinated water molecules. The TGA/MASS analysis of the gas evolved during these weight loss steps indicates the presence of water with the ionic current $m/z = 18$ (for H_2O^+). The probable formation of $(NH_4)_2Mn_3(H_2O)_4[Mo(CN)_7]_2$ at the first step and $(NH_4)_2Mn_3[Mo(CN)_7]_2$ at the second step of dehydration was confirmed by elemental analyses of the samples obtained by heating of the mixture at 80 and 160 °C, respectively. However, the determination of the crystal structures of these dehydrated forms was not successful. The third and fourth weight loss steps of 13.0% and 14.7% correspond to the loss of cyano ligands and ammoniac that induces the decomposition of the compound.

The TGA of compound **1**, having a two-dimensional structure was performed in order to compare the results. The curve shows four weight losses with the inflexion points at 93, 170, 400 and 627 °C (Fig. 6(b)). The first weight loss of 10.7% corresponds to the loss of the six water molecules of crystallization and the formation of $K_2[Mn(H_2O)_2]_3[Mo(CN)_7]_2$. The second loss of 10.6% is in accord with the loss of the six water molecules coordinated to the manganese ion. As in the case of **2** and **3**, the TGA/MASS analysis of the gas evolved during these two weight loss steps indicates the presence of water (ionic current $m/z = 18$ for H_2O^+). Unfortunately, several attempts to determine the crystal structure of **1** after heating of a single crystal at 115 and 215 °C were not successful. The third and fourth weight losses of 8.4% and 14.4%, respectively, correspond to the decomposition of the compound.

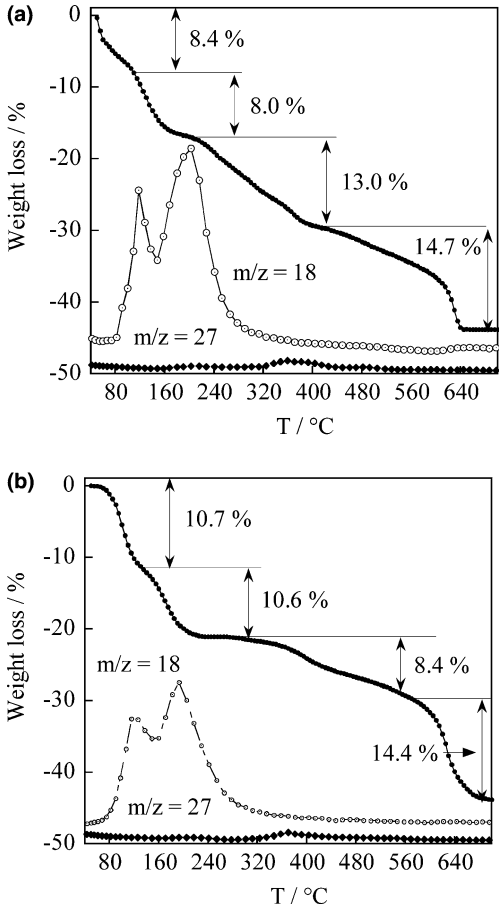


Fig. 6. TGA (•) and TGA/MASS (–○– ionic current $m/z = 18$ for H_2O^+, –♦– ionic current $m/z = 27$ for HCN^+) curves for: (a) a polycrystalline sample containing **2** and **3**; (b) a polycrystalline sample of **1**. Heating rate is 1 °C min^{-1}.

3.2. Role of cations in the structural organization of the $Mn^{2+}/[Mo(CN)_7]^{4-}$ system

3.2.1. K^+ and as templates in $Mn^{2+}/[Mo(CN)_7]^{4-}$

In order to establish the role of the counter cations in the structural organization of the $Mn^{2+}/[Mo(CN)_7]^{4-}$ system, we analyse characteristics of K^+ and NH_4^+ and their behaviour as templates. From the structural point of view, both of them modify the structural organization of $Mn^{2+}/[Mo(CN)_7]^{4-}$ and their intercalation in this system provides the formation of a similar network but with a different dimensionality: in the case of NH_4^+, the structure is three-dimensional and in the case of K^+, the structure is two dimensional. The fragments of the structures of **1**–**3** showing the cavities incorporated counter cations are shown in Fig. 7. In the case of **2** and **3**, NH_4^+ is situated in the centre of the cubic cavity $\{Mn1(CN)_3Mo\}_4$ formed by anionic network, as shown in Fig. 7(a) and (b). The distances between NH_4^+ (N11) and cyano bridges are listed in Table 3. In both cases, three distances N11···N were found shorter than all others indicating the possibility of weak interactions between NH_4^+ and π system of cyano bridges. In the case of the compound **1**, K^+ is situated in the centre of one of the two half-cavities $\{Mn2(O2W)(CN)_3Mo\}_2$ and the opposite side is occupied by a water molecule of crystallization, O6W. Short distances between K^+ and cyano bridges on the one hand and K^+ and the water molecule of crystallization (O6W) on the other hand were found (Table 3) that is indicative of the presence of weak interactions $K^+\cdots\pi(C{\equiv}N)$ and $K^+\cdots$water (Fig. 7(c)).

The factors determined the behaviour of K^+ and NH_4^+ as template as follows: (i) the relative ionic radii of these cations which correspond to 1.51 Å for NH_4^+ and 1.52 Å (CN = 6) or 1.65 Å (CN = 8) for K^+ [29]; (ii) the polarisability which equal to 8.83 a.u. for NH_4^+ and 5.52 a.u. for K^+ [29]; (iii) the geometry of cations: NH_4^+ adopts a tetrahedral geometry while K^+ is a spherical cation; (iv) the hydration energy which equal to 71 kcal mol^{-1} for NH_4^+ and 77 kcal mol^{-1} for K^+ [30]; (v) capacity to create weak interactions with an anionic network: both of them can establish ionic interactions but NH_4^+ is also known as a good donor in hydrogen bonding. It should be noted that the unconventional ionic or hydrogen bonds between the cations such as NH_4^+ and K^+ with the π-system of C_2H_4,

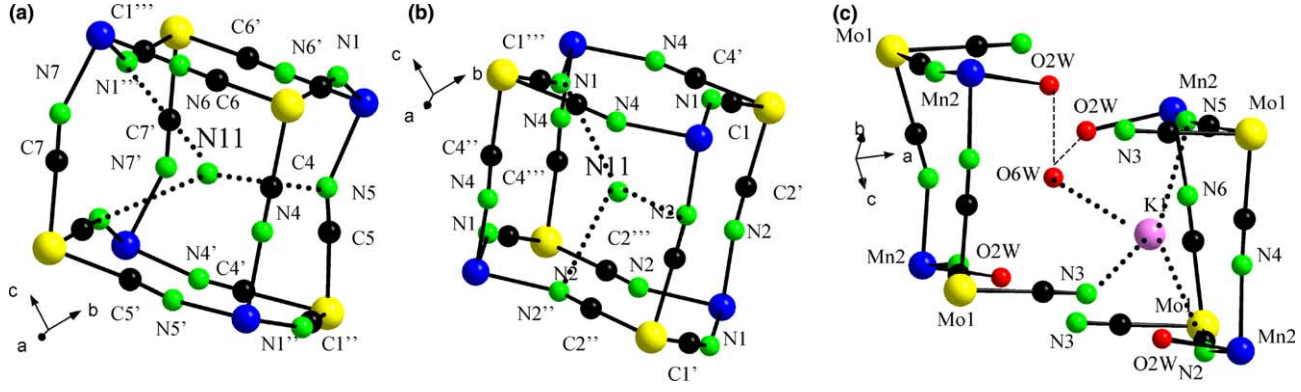


Fig. 7. Fragment of the structures showing the cavity containing cation in the centre: (a) for **2**; (b) for **3**; (c) for **1**. Dashed lines indicate the shorter distances.

Table 3
Distances K···A for **1** and N11···A for **2** and **3**

A	N11···A for **2**	A	N11···A for **3**	A	K ···A for **1**
C6	3.580	C4	4.028	C5	3.129
N6	3.469	N4	3.856	N5	3.050
C6′	3.826	C4′	4.064	C6	3.174
N6′	3.581	N4′	4.160	N6	3.320
C4	3.592	C1	3.754	C4	3.299
N4	3.473	N1	3.708	N4	3.316
C5	3.556	C2	3.520	C2	3.131
N5	3.072	N2	3.149	N2	3.278
C4′	3.839	C2′	3.508	C3	3.307
N4′	3.650	N2′	3.311	N3	3.488
C5′	3.579	C1′	4.416	N3′	2.762
N5′	3.561	N1′	4.604	O6W	2.835
C1	3.991	C2″	3.520		
N1	4.065	N2″	3.149		
C1′	3.383	C2‴	3.508		
N1′	3.206	N2‴	3.311		
C7	4.112	C1″	3.754		
N7	4.297	N1″	3.708		
C7′	4.066	C4″	4.028		
N7′	3.914	N4″	3.856		
C1″	4.408	C4‴	4.064		
N″	4.539	N4‴	4.160		
C1‴	3.722	C1‴	3.563		
N1‴	3.409	N1‴	3.186		

acetylenic groups or an aromatic π-system of benzene and its derivatives are well-known in the literature [31]. However, to the best of our knowledge, this type of interactions where the electron donor is a π-bond of a bridged C≡N ligand have never been investigated.

3.2.2. *Theoretical investigations on cation···π(C≡N) interactions (cation = NH_4^+, K^+)*

In order to inspect the possibility of the formation of unconventional ionic or hydrogen bonds between cations···π-system of cyano ligands (cation = NH_4^+, K^+) and to evaluate their contribution in the structural organization of the $Mn^{2+}/[Mo(CN)_7]^{4-}$ system, we performed a theoretical study using the model consisting in a binuclear cyano-bridged Mo–Mn framework surrounded by its coordination sphere. To model a three-dimensional structure of a molecular cluster, the structure has to be simplified: it appeared that the most satisfying model was to keep the bridging structure of all the cyano groups and to replace the terminal metal atoms by potassium atoms: although a potassium is a crude model for a metal centre, it adequately plays the role of an acceptor with respect to the cyano ligand and consequently accounts for the ligand field on the metal atom opposite with respect to the cyano group. The considered complex is thus $[(KCN)_4\ H_2O\ Mn\ NC\ Mo\ (CNK)_6]^{4+} + K^+$ or NH_4^+. We have only considered the ferromagnetic state although the complex is antiferromagnetic for practical reason and because we were not interested in the magnetic modeling of the molecule. The magnetic state has no influence on the intermolecular distances. Geometry optimization is done assuming the C_s symmetry: no negative frequency was found.

The geometries of the two complexes $[(KCN)_4H_2O\ Mn\ NC\ Mo\ (CNK)_6]^{4+} + NH_4^+$ or K^+ have been optimized; the most important geometrical parameters are summarized in Table 5 and compared to the crystallographic values; the two optimized structures found are plotted in Fig. 8(a) and (b). Almost all the optimized distances match well to the experimental ones, the most important discrepancy arises in the metal–ligand bonds: they tend to be overestimated and a large difference is obtained between the bond with the bridging cyano and the terminal ones. In the case of molybdenum, the bond with the terminal cyano is shorter than the one with the bridging one and vice versa for the manganese. This should be due to the different interaction of the carbon and nitrogen atoms forming the cyano group with the cation: the nitrogen atom is more nucleophilic than the carbon one and tends to be as close as possible to the cation. In the case of Mo, the carbon atom is linked to the metal and in order to approach closer to the cation, the nitrogen atom pushes the cyano group towards the metal. In the Mn coordination sphere, the nitrogen is linked to the metal and tends to move away to be close to the cation. One may consider that this cluster is a satisfactory model of the crystal when noticing that we completely neglect the strain of the three-dimensional structure and the electrostatic interaction with the rest of the crystal. This geometry optimization suggests that there is a cation–π interaction between K^+ or NH_4^+ and the cyano groups. These cations play an active role in determining the geometry of the complex: indeed both

Table 4
Interaction energies calculated with B3LYP and different basis sets at fixed geometry (see text), without and with BSSE correction

Basis set			$NH_4^+ + CN^-$		$NH_4^+ + KCNK^+$		$K^+ + CN^-$	
C, N	K	H	ΔE	ΔE BSSE	ΔE	ΔE BSSE	ΔE	ΔE BSSE
SDD	SDD	6-31G [21]	−114	−111	−42	−43	−105	−105
SDD+sp		6-31G	−106	−106	−44	−44		
SDD+d		6-31G	−116	−114	−40	−41		
SDD+sp+d	SDD+sp+d	6-31++G** [21]	−108	−108	−42	−42	−107	−107
6-311+G* [22]		6-31++G**	−108	−108	−42	−42		
aug-cc-VTZ [23]	ANO [24]	aug-cc-VTZ [23]	−110	−110	−42	−42	−107	−107

All energies in kcal mol^{-1}. K in $KCNK^+$ is described by SDD.

Table 5
Geometrical parameters issued from the geometry optimization of $[(KCN)_4\ H_2O\ Mn\ NC\ Mo\ (CNK)_6]^{4+} + X^+$ (calc.) and from crystallographic data (exp.)

X	K		NH_4	
	Calculated	Expermental	Calculated	Experimental
$X–N_b$	2.95	3.05–3.49	3.03	3.07–4.60
$X–N_a$	3.07		3.02	
$X–N_c$	2.93		3.06	
$X–C_b$	3.11	3.13–3.31	3.25	3.38–4.42
$X–C_a$	3.18		3.22	
$X–C_c$	3.61		3.75	
$C_b–N_b$	1.17	1.13–1.24	1.17	1.15–1.16
$C_a–N_a$	1.18		1.18	
$C_c–N_c$	1.17		1.17	
$Mo–C_b$	2.27	2.11–2.18	2.29	2.11–2.18
$Mo–C_a$	2.18		2.17	
$Mn–N_b$	2.27	2.16–2.34	2.27	2.11–2.26
$Mn–N_c$	2.34		2.55	
$Mo–C_b–N_b$	172	177–178	170	178–180
$Mo–C_a–N_a$	174		175	
$Mn–N_b–C_b$	173	160–175	180	145–164
$Mn–N_c–C_c$	155		156	

C_b, N_b belong to the bridge, C_a, N_a form the two equivalent cyano groups linked to Mo and the cation, C_c, N_c the cyano linked to Mn and the cation. Distances are in Å and angles in °. The experimental data are the two extreme ones. The distance to NH_4^+ means the distance to the N atom.

crystals are very distorted, M–CN is far from linearity and there is a large dispersion of the metal–ligand bond distances.

The geometries do not point out a large difference of behaviour between K^+ and NH_4^+: K^+ is slightly closer to the cyano groups by a tenth of angstrom. The calculated interaction energies corrected from the BSSE are -43 kcal mol^{-1} for NH_4^+ and -41 kcal mol^{-1} for K^+ (-41 and -40 kcal mol^{-1} before correction): this difference between the two cations appears negligible. These interactions are repulsive and to analyse the possible existence of a minimum, we have studied the interaction of the two cations with the very simple molecular system $[QCNQ]^{0/2+}$, a cyano group with a CN distance of 1.17 Å, sandwiched by two positive charges: either potassium atoms or punctual charges $Q = 1$ or $Q = 0.5$. The geometry of this system is linear and is kept fixed. Results are summarized in Table 6. The interaction between two positive ions is dissociative but in most of the cases, there is a well corresponding to a cation$-\pi$ interaction. The well is favoured by an atom of K compared to a punctual charge and by more distant charges because the interaction of the cation with the two positive charges is thus reduced. Furthermore, the interaction of K^+ or NH_4^+ with the neutral QCNQ is strongly attractive: in the case of a distance of 2.2 Å, which is a realistic distance for a coordination complex, the cation distance to the nitrogen of the cyano group is 2.9 and 3.0 Å for

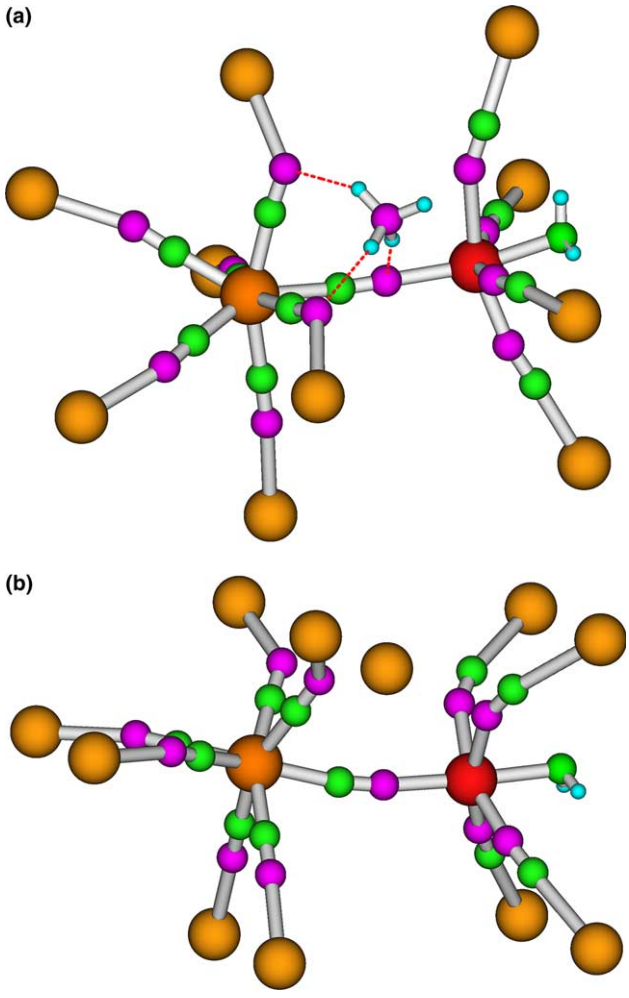


Fig. 8. (a) Optimized geometry for $(KNC)_6$ Mo CN Mn $(NCK)_4$ $OH_2 + NH_4^+$; (b) optimized geometry of $(KNC)_6$ Mo CN Mn $(NCK)_4OH_2 + K^+$.

K^+ and NH_4^+, respectively, and the dissociation energies are 22 and 25 kcal mol^{-1}, respectively. The equilibrium distances match well the distances obtained in the large complex and confirms that there is cation–π interaction in the complex and not only a cation embedded in a cage. The value of the interaction with the QCNQ system is much larger than in the NH_4^+–ethene system: 10 kcal mol^{-1} [32]. This must be due to the higher electron density on the cyano group compared to the ethene because of its negative charge. Furthermore, Kim et al. [32] have compared the interaction of K^+ and NH_4^+ with ethene and have analysed the different contributions to the interaction energy using the SAPT method [33]: as in this study, K^+ lies closer to ethene than ammonium while the interaction is stronger for the latter by 2 kcal mol^{-1}. The contribution of induction is larger than the electrostatic one, which is opposite to the case of cation–water interaction. Because the cation–π distance is slightly larger for ammonium, the induction and

Table 6
Interaction between K^+ or NH_4^+ with QCNQ where Q is either a K atom or a punctual charge

Cation	Q	Distances			Energies	
		N–Q fixed	N–cat_{min} optimized	N–cat_{bar} optimized	ΔE_{bar}	ΔE_{diss}
K^+	K	2.2	no			
		2.5	3.3	3.8	0.2	−50.0
		2.8	3.1	3.3	2.0	−43.0
	$Q = 1.0$	2.2	no			
		2.5	no			
		2.8	3.2	4.1	1.0	−48.0
	$Q = 0.5$	2.2	2.9	no		22.0
		2.5	2.9	no		27.0
		2.8	2.8	no		32.0
NH_4^+	K	2.2	3.5	3.9	0.5	−53.0
		2.5	2.9	4.2	3.0	−47.0
		2.8	3.1	4.6	7.0	−40.0
	$Q = 1.0$	2.2	no			
		2.5	3.5	3.9	1.0	−51.0
		2.8	3.2	4.4	4.0	−43.0
	$Q = 0.5$	2.2	2.9	no		25.0
		2.5	2.9	no		30.0
		2.8	2.8	no		35.0

$N–cat_{min}$ and $N–cat_{bar}$ are the N–cation distances at the minimum (no means a dissociative interaction) and at the top of the barrier (if any), ΔE_{bar} is the height of the barrier compared to the minimum energy, ΔE_{diss} is the dissociation energy. Distances are in Å and energies in kcal mol^{-1}.

exchange terms are slightly smaller compared to potassium but this difference is overcompensated with the electrostatic contribution. The conformation of the complex with NH_4^+ allows three N–H bonds out of four to point toward a cyano bridge and to give rise to a hydrogen bond. The three bonds pointing towards a cyano are longer by 0.01 Å, which shows a very small hydrogen bond effect.

4. Conclusion

In summary, pseudo-dimorphic phases $(NH_4)_2Mn_3(H_2O)_4[Mo(CN)_7]_2 \cdot nH_2O$ where $n = 4$ for **2** and $n = 5$ for **3** have been obtained by the introduction of NH_4^+ in the system $Mn^{2+}/[Mo(CN)_7]^{4-}$. The compounds present similar three-dimensional networks of low symmetry and order ferrimagnetically below 53 K. From a structural point of view, we have outlined the difference of behaviours between the guest counter ions NH_4^+ and K^+, which have close size but different nature. The intercalation of both of them modifies the structural organization of the system $Mn^{2+}/[Mo(CN)_7]^{4-}$, however, K^+ motivates the formation of a two-dimensional structure while the introduction of NH_4^+ leads to the formation of a three-dimensional network.

The comparison of the structural organizations of compounds **1**, **2** and **3** shows that in the case of **1**, a water molecule is present together with K^+ in the cavity, which is not the case in **2** and **3**. The hydration energy of K^+ is larger compared to NH_4^+ and K^+ is able to establish ion–dipole interactions with water molecules stronger that NH_4^+. The overall size of $K\cdots H_2O$ is much larger that the size of NH_4^+ which provides the formation of a two-dimensional network in the case of **1**.

Theoretical investigations were performed in order to establish the presence of unconventional ionic or hydrogen bonds between cations and π-system of cyano bridges, which may explain the role of these cations as structural agents. The study shows that: (i) in both cases, there is an important ionic cation–π interaction between K^+ or NH_4^+ and a bridging cyano group between two metals whose effective charge is about 0.5. The distortions showed by the crystallographic structures originate in the interaction between the complex and these cations; (ii) the interactions with the two cations are very similar: the distance $K\cdots CN$ is eventually smaller as anticipated when comparing the ionic radii, but the interaction is slightly larger with ammonium because of the electrostatic contribution being higher due to the larger polarizability of ammonium (8.83 a.u.) compared to K^+ (5.52 a.u.); (iii) NH_4^+ establishes negligible hydrogen bonding with $\pi(C{\equiv}N)$. Consequently, while the ionic bonds cation$\cdots\pi$ play an important role in the structural organization of $Mn^{2+}/[Mo(CN)_7]^{4-}$, but no difference in K^+ and NH_4^+ behaviour was established by theoretical study.

Acknowledgements

The authors thank Mr. Alain Mari for magnetic measurements. The authors thank the CNRS and the Université Montpellier II for financial support and the Norwegian High Performance Computing Consortium (NOTUR) for grants of computing time.

Appendix A. Supplementary materials

Crystallographic data for the structural analysis of **3** have been deposited with the Cambridge Crystallographic Data Centre, CCDC 247302. The crystallographic data of **2** are given in a preliminary communication (CCDC 235836) [12]. Copies of this information may be obtained free of charge from The Director, CCDC, 12 Union Road, Cambridge CB2 1EZ, UK (fax: +44 1223 336033, e-mail: deposit@ccdc.cam.ac.uk, http://www.ccdc.cam.ac.uk). Supplementary

data associated with this article can be found, in the online version at doi:10.1016/j.poly.2005.02.003.

References

[1] (a) O. Kahn, Molecular magnetism, VCH, New York, 1993;
(b) J.-M. Lehn, Supramolecular Chemistry, VCH Verlagsgesellschaft mbH, Germany, 1995.

[2] J.S. Miller, M. Drillon (Eds.), Magnetism: from Molecules to Materials, vols. 1 and 2, Wiley–VCH, Weinheim, 2001.

[3] (a) H. Tamaki, Z.J. Zhong, N. Matsumoto, S. Kida, M. Koikowa, N. Achiwa, Y. Hashimoto, J. Am. Chem. Soc. 114 (1992) 6974;
(b) L.O. Atovmyran, G.V. Shilov, R.N. Lyubovskaya, E.I. Zhilyaceva, N.S. Ovanesvan, S.I. Pirumova, I.G. Gusakovskaya, JETP Lett. 58 (1993) 766;
(c) C. Mathonière, S.G. Carling, D. Yusheng, P. Day, Chem. Commun. (1994) 1551;
(d) S. Decurtins, H.W. Schmalle, P. Schneuwly, J. Ensling, P. Gütlich, J. Am. Chem. Soc. 116 (1994) 9521;
(e) S. Decurtins, H.W. Schmalle, P. Schneuwly, H.R. Oswald, Inorg. Chem. 32 (1993) 1888.

[4] (a) P.M. Van der Werff, S.R. Batten, P. Jensen, B. Moubaraki, K.S. Murray, Inorg. Chem. 40 (2001) 1718;
(b) E. Colacio, F. Lloret, I.B. Maimoun, R. Kivekas, R. Sillanpaa, J. Suârez-Varela, Inorg. Chem. 42 (2003) 2720.

[5] (a) O. Hatlevik, W.E. Buschmann, J. Zhang, J.L. Manson, J.S. Miller, Adv. Mater. 11 (1999) 914;
(b) S.M. Holmes, G.S. Girolami, J. Am. Chem. Soc. 121 (1999) 5593;
(c) B.G. Morin, C. Hahm, A.J. Epstein, J.S. Miller, J. Appl. Phys. 75 (1994) 5782;
(d) J.S. Miller, Adv. Mater. 6 (1994) 322;
(e) S. Ferlay, T. Mallah, R. Ouahès, P. Veillet, M. Verdaguer, Inorg. Chem. 38 (1999) 229;
(f) W.E. Buschmann, S.C. Paulson, C.M. Wynn, M. Girtu, A.J. Epstein, H.S. White, J.S. Miller, Adv. Mater. 9 (1997) 645;
(g) W.R. Entley, G.S. Girolami, Science 268 (1995) 397;
(h) S. Ferlay, T. Mallah, R. Ouahès, P. Veillet, M. Verdaguer, Nature 378 (1995) 701;
(i) V. Gadet, T. Mallah, I. Castro, M. Verdaguer, J. Am. Chem. Soc. 114 (1992) 9213;
(j) T. Mallah, S. Thiébaut, M. Verdaguer, P. Veillet, Science 262 (1993) 1554.

[6] (a) J. Long, Chem. Commun. (1999) 945;
(b) O. Kahn, J. Larionova, L. Ouahab, Chem. Commun. (1999) 945;
(c) J. Larionova, S. Willemin, B. Donnadieu, B. Henner, Ch. Guérin, B. Gillon, A. Goujon, J. Phys. Chem. Sol. 65 (2004) 677.

[7] (a) G. Rombaut, M. Verelst, S. Golhen, L. Ouahab, C. Mathonière, O. Kahn, Inorg. Chem. 40 (2001) 1151;
(b) A.K. Sra, M. Andruh, O. Kahn, S. Golhen, L. Ouahab, J.V. Yakhmi, Angew. Chem. Int. Ed. 38 (1999) 2606;
(c) S.-I. Ohkoshi, N. Machida, Z.J. Zhong, K. Hashimoto, Synth. Met. 122 (2001) 523;
(d) B. Sieklucka, J. Szklarzewicz, T.J. Kemp, W. Errington, Inorg. Chem. 39 (2000) 5156;
(e) Z.J. Zhong, H. Seino, Y. Mizobe, M. Hidai, M. Verdaguer, S.-I. Ohkoshi, K. Hashimoto, Inorg. Chem. 39 (2000) 5095;
(f) Z.J. Zhong, H. Seino, Y. Mizobe, M. Hidai, A. Fujishima, S.-I. Ohkoshi, K. Hashimoto, J. Am. Chem. Soc. 122 (2000) 2952;
(g) R. Garde, C. Desplanches, A. Bleuzen, P. Veillet, M. Verdaguer, Mol. Cryst. Liq. Cryst. 334 (1999) 587;
(h) Y. Song, S. Ohkoshi, Y. Arimoto, H. Seino, Y. Mizobe, K. Hashimoto, Inorg. Chem. 42 (2003) 1848;
(i) P. Franz, L. Keller, M. Pilkington, J. Ensling, S. Decurtins, in: Mid-term Conference on the ESF Programme Molecular Magnets Davos, 2001, p. H4.

[8] S. Tanase, F. Tuna, Ph. Guionneau, T. Maris, G. Rombaut, C. Mathonière, M. Andruh, O. Kahn, J.-P. Sutter, Inorg. Chem. 42 (2003) 1625.

[9] (a) J. Larionova, R. Clérac, J. Sanchiz, O. Kahn, S. Golhen, L. Ouahab, J. Am. Chem. Soc. 120 (1998) 13088;
(b) J. Larionova, O. Kahn, J. Bartolome, R. Burriel, M. Castro, V. Ksenofontov, Ph. Gütlich, Chem. Mater. 11 (1999) 3400;
(c) J. Larionova, O. Kahn, S. Golhen, L. Quahab, R. Clérac, Inorg. Chem. 38 (1998) 3621.

[10] J. Larionova, R. Clérac, B. Donnadieu, Ch. Guérin, Chem. Eur. J. 8 (2002) 2712.

[11] (a) J. Larionova, O. Kahn, S. Gohlen, L. Ouahab, R. Clérac, J. Am. Chem. Soc. 121 (1999) 3349;
(b) J.A. Stride, B. Gillon, A. Goukassov, J. Larionova, R. Clérac, O. Kahn, C. R. Acad. Sci. 4 (2001) 1;
(c) X.F. Le Goff, C. Coulon, B. Donnadieu, R. Clerac, Phys. IV 114 (2004) 633.

[12] X.F. Le Goff, S. Willemin, C. Coulon, J. Larionova, B. Donnadieu, R. Clerac, Inorg. Chem. 43 (2004) 4784.

[13] (a) R.C. Young, J. Am. Chem. Soc. 54 (1932) 1402;
(b) G.R. Rossman, F.D. Tsay, H.B. Gray, Inorg. Chem. 12 (1973) 824;
(c) M.B. Hursthouse, K.M. Malik, A.M. Soares, J.F. Gibson, W.P. Griffith, Inorg. Chim. Acta 45 (1980) L81.

[14] G.M. Sheldrick, SHELX-97 [Includes SHELXS-97, SHELXL-97, CIFTAB]: Programs for Crystal Structure Analysis (Release 97-2), Institüt für Anorganische Chemie der Universität, Tammanstrasse 4, D-3400 Göttingen, Germany, 1998.

[15] L. Farrugia, J. Appl. Crystallogr. 32 (1999) 837.

[16] N. Walker, D. Stuart, Acta Crystallogr. Sect. A 39 (1983) 158.

[17] E.A. Boudreaux, L.N. Mulay (Eds.), Theory and Applications of Molecular Paramagnetism, Wiley, New York, 1976.

[18] W. Küchle, M. Dolg, H. Stoll, H. Preuss, J. Chem. Phys. A 100 (1994) 7535.

[19] M.J. Frisch, G.W. Trucks, H.B. Schlegel, G.E. Scuseria, M.A. Robb, J.R. Cheeseman, V.G. Zakrzewski, J.A. Montgomery, R.E. Stratmann, J.C. Burant, S. Dapprich, J.M. Millam, A.D.K. Daniels, K.N. Kudin, M.C. Strain, O. Farkas, J. Tomasi, V. Barone, M. Cossi, R. Cammi, B. Mennucci, C. Pomelli, C. Adamo, S. Clifford, J. Ochterski, G.A. Petersson, P.Y. Ayala, Q. Cui, K. Morokuma, D.K. Malick, A.D. Rabuck, K. Raghavachari, J.B. Foresman, J. Cioslowski, J.V. Ortiz, B.B. Stefanov, G. Liu, A. Liashenko, P. Piskorz, I. Komaromi, R. Gomperts, R.L. Martin, D.J. Fox, T. Keith, M.A. Al-Laham, C.Y. Peng, A. Nanayakkara, C. Gonzalez, M. Challacombe, P.M.W. Gill, B.G. Johnson, W. Chen, M.W. Wong, J.L. Andres, M. Head-Gordon, E.S. Replogle, J.A. Pople, GAUSSIAN-98 (Revision A.11), Gaussian, Inc., Pittsburgh, PA, 1998, at the DFT level using the hybrid functional B3LYP;
(a) A.D. Becke, Phys. Rev. A 38 (1988) 3098;
(b) C. Lee, W. Yang, R.G. Parr, Phys. Rev. B 37 (1988) 785;
(c) P.J. Stevens, J.F. Devlin, C.F. Chabalowski, M.J. Frisch, J. Phys. Chem. 98 (1994) 11623.

[20] S. Boys, F. Bernardi, Mol. Phys. 19 (1970) 553.

[21] W.J. Hehre, R. Ditchfield, J.A. Pople, J. Chem. Phys. 56 (1972) 2257.

[22] R. Krishnan, J.S. Binkley, R. Seeger, J.A. Pople, J. Chem. Phys. 72 (1980) 650.

[23] T.H. Dunning, J. Chem. Phys. 90 (1989) 1007.

[24] P.-O. Widmark, B.J. Persson, B. Roos, Theor. Chim. Acta 79 (1991) 419.

[25] M. Llunell, D. Casanova, J. Cirera, J.M. Bofill, P. Alemany, S. Alvarez, M. Pinsky, D. Avnir, Shape (1.1), Universitat de Barcelona, Barcelona, Spain, 2003.

[26] K. Nakamoto, Infrared and Raman Spectra of Inorganic and Coordination Compounds, second ed., Wiley–Interscience, New York, 1970.
[27] (a) T.L. Hanningar, D.C. MacQuarrie, P. Losier, R.D. Rogers, M.J. Zaworotko, Angew. Chem. Int. Ed. 36 (1997) 972;
(b) B. Moulton, M.J. Zaworotko, Chem. Rev. 101 (2001) 1629;
(c) A. Nangia, G.R. Desiraju, Chem. Commun. (1999) 605;
(d) J.A. Swift, A.M. Reynolds, M.D. Ward, J. Am. Chem. Soc. 120 (1998) 5887.
[28] (a) G.A. Jeffrey, An introduction to hydrogen bonding, Oxford University Press, New York, 1997;
(b) J.P. Glusker, in: E. Weber (Ed.), Design of Organic Solids: Topic in Current Chemistry, vol. 198, Springer, Berlin, 1998, p. 1.
[29] J.M. Martin, R.F. Hess, P.D. Boyl, Inorg. Chem. 43 (2004) 3242.
[30] D.R. Lide, CRC Handbook of Chemistry and Physics, 84th ed., CRC Press, Boca Raton, FL, 2003–2004.
[31] (a) C.A. Deakyn, M. Meot-Ner, J. Am. Chem. Soc. 107 (1985) 474;
(b) J. Sunner, K. Nishizava, P. Kebarle, J. Phys. Chem. 85 (1981) 1814;
(c) P. Kollman, J. McKelvey, A. Johansson, S. Rothenberg, J. Am. Chem. Soc. 97 (1975) 955.
[32] (a) D. Kim, S. Hu, P. Tarakeshwar, K.S. Kim, J. Phys. Chem. A 107 (2003) 1228;
(b) J.C. Ma, D.A. Dougherty, Chem. Rev. 97 (1997) 1303.
[33] G. Chalasiński, M.M. Szczęśniak, Chem. Rev. 94 (1994) 1723.

Elemental analyses of C, H and N were performed by the MEDAC LTD Vrunel Science Center, United Kingdom. IR spectra were recorded with a Nicolet Impact 420 FT-IR spectrometer using KBr pellets. Magnetic susceptibilities were measured with a Quantum Design SQUID susceptometer.

2.2. Synthesis

2.2.1. Synthesis of $[Fe_3(L1)_2(\mu\text{-}OCH_3)_2Cl_2](FeCl_4)\cdot H_2O$ (2)

About 58 mg of **1** in 2 ml CH_3OH was added slowly into a hot solution of 35 mg $FeCl_3$ in 3 ml CH_3OH at 50 °C. The solution was stirred at 50 °C for another 2 min prior to filtration, and then allowed to stand overnight to give orange-yellow prismatic crystals of **2**. Yield: 29%. *Anal*. Calc. for $Fe_4Cl_6C_{40}H_{42}N_6O_{11}$: C, 39.42; H, 3.47; N, 6.89. Found: C, 39.69; H, 3.47; N, 6.77%. IR (KBr): 3440w, 2935w, 1602m, 1575w, 1439m, 1265m, 1225m, 1163w, 1113m, 1057s, 1024s, 978m, 816m, 769m, 688m, 648w cm^{-1}.

2.2.2. Synthesis of $Fe(L2)Cl_2\cdot H_2O$ (3a)

This complex was obtained as orange-red crystals by the procedure used for complex **2**, except that CH_3OH was substituted by a mixed solvent of CH_3CN and H_2O in 10:1 volume ratio. Yield: 47%. *Anal*. Calc. for $FeCl_2C_{17}H_{12}N_3O_3$: C, 47.15; H, 2.79; N, 9.70. Found: C, 46.93; H, 2.89; N, 9.65%. IR (KBr): 3417m, 3099m, 1685m, 1597m, 1440w, 1325w, 1296w, 1227m, 1169w, 1074w, 1018m, 984w, 839w, 792w, 760m, 663m cm^{-1}.

2.2.3. Synthesis of $Fe(L2)Cl_2\cdot THF$ (3b)

About 35 mg $FeCl_3$ was dissolved in 1 ml CH_3CN and 0.1 ml H_2O at 50 °C, to which 58 mg of **1** in 1 ml CH_3CN was added slowly. After stirring for 5 min, the orange solution was filtered and THF was allowed to diffuse into it. Orange-red crystals of **3b** were obtained after several weeks. Yield: 38%. *Anal*. Calc. for $FeCl_2C_{17}H_{12}N_3O_3$ (THF removed in vacuum): C, 47.15; H, 2.79; N, 9.70. Found: C, 46.74; H, 2.73; N, 9.45. IR (KBr): 3581s, 3513s, 3407brs, 3136brs, 3080s, 2802w, 1685m, 1591s, 1462m, 1321m, 1294m, 1226s, 1180m, 1040s, 1014s, 982w, 930w, 843m, 764s, 713m, 675s cm^{-1}.

2.2.4. Synthesis of $Fe(L3)Cl_2\cdot THF$ (3c)

About 35 mg $FeCl_3$ was dissolved in 1 ml anhydrous CH_3CN and 0.2 ml CH_3OH at 50 °C. To this solution 58 mg of **1** in 1 ml anhydrous CH_3CN was added slowly. After stirring for 5 min, the orange solution was filtered, and anhydrous THF was allowed to diffuse into the solution. Orange-red crystals of **3c** were obtained after several weeks. Yield: 33%. *Anal*. Calc. for $FeCl_2C_{18}H_{14}N_3O_3$ (THF been removed by heating): C, 48.36; H, 3.16; N, 9.40. Found: C, 48.32; H, 3.34; N, 10.90. IR

Table 1
Crystallographic data of ligand **1** and complexes **2**, **3a**, **3b** and **3c**

Complex	1a	1b	2	3a	3b	3c
Empirical formula	$C_{17}H_{11}N_3O_2$	$C_{17}H_{11}N_3O_2$	$C_{40}H_{42}Cl_6N_6O_{11}Fe_4$	$C_{17}H_{14}Cl_2N_3O_4Fe$	$C_{19}H_{16}Cl_2N_3O_{3.5}Fe$	$C_{20}H_{18}Cl_2N_3O_{3.5}Fe$
Formula weight	289.29	289.29	1218.9	451.07	469.10	483.12
Crystal size	$0.24\times0.17\times0.16$	$0.26\times0.17\times0.16$	$0.28\times0.26\times0.23$	$0.43\times0.24\times0.17$	$0.67\times0.24\times0.15$	$0.61\times0.47\times0.35$
Crystal system	monoclinic	monoclinic	monoclinic	orthorhombic	triclinic	triclinic
Space group	*C*2/*c*	*C*2/*c*	*Cc*	*Pbcn*	$P\bar{1}$	$P\bar{1}$
Unit cell dimensions						
a (Å)	14.187(2)	13.142(2)	17.9347(9)	18.349(3)	7.931(2)	7.972(1)
b (Å)	6.3616(8)	9.134(1)	13.2564(7)	14.692(2)	11.954(2)	12.005(2)
c (Å)	16.703(2)	12.235(1)	21.384(1)	15.265(2)	12.115(3)	12.600(2)
α (°)	90	90	90	90	101.670(4)	104.533(3)
β (°)	110.923(3)	109.814(3)	97.520(1)	90	107.290(4)	99.975(3)
γ (°)	90	90	90	90	92.786(4)	93.694(3)
V (Å^3)	1408.0(3)	1381.9(3)	5040.5(4)	4115.(1)	1066.8(4)	1142.4(3)
Z	4	4	4	8	2	2
D_{calc} (g/cm^3)	1.365	1.390	1.604	1.449	1.460	1.405
μ (Mo Kα) (mm^{-1})	0.093	0.094	1.507	1.018	0.984	0.921
F(000)	600	600	2464	1816	478	494
Reflections collected	4765	3643	16698	17148	5766	6234
Independent reflections (R_{int})	1696 (0.0506)	1217 (0.0378)	8419 (0.0529)	3630 (0.1197)	3748 (0.0406)	4004 (0.0403)
Observed reflections [$I > 2\sigma(I)$]	763	925	6304	1932	2457	2553
Parameters	102	101	613	263	325	334
Goodness-of-fit	0.966	1.162	1.000	1.051	1.017	1.034
R_1 [$I > 2\sigma(I)$][a]	0.0522	0.0689	0.0486	0.0697	0.0665	0.0898
wR_2 (all data)[b]	0.1746	0.1619	0.1207	0.2386	0.1840	0.2642

[a] $R_1 = \Sigma\||F_o| - |F_c|\|/\Sigma|F_o|$.
[b] $wR_2 = [\Sigma w(F_o^2 - F_c^2)^2/\Sigma w(F_o^2)^2]^{1/2}$.

(KBr): 3101s, 2927m, 1682s, 1639s, 1603s, 1531w, 1442m, 1381m, 1325w, 1296m, 1227m, 1167m, 1070m, 1020s, 837w, 787m, 760m, 665m, 532w cm^{-1}.

2.3. X-ray crystallography

Crystals mounted inside Lindemann glass capillaries were used for data collection on a Bruker SMART 1000 CCD diffractometer operating at 50 kV and 30 mA using Mo Kα radiation ($\lambda = 0.71073$ Å) at 293 K. Data collection and reduction were performed using the SMART and SAINT software [24]. An empirical absorption correction was applied using the SADABS program [25]. The structures were solved by direct methods and refined by full-matrix least squares on F^2 using the SHELXTL program package [26]. The THF molecules in **3b** and **3c** were treated using a disordered model, which was refined isotropically in the case of **3b**. In the structures of **2** and **3a**, the water hydrogen atoms could not be located. Crystallographic data of complexes **1a**, **1b**, **2**, **3a**, **3b** and **3c** are listed in Table 1.

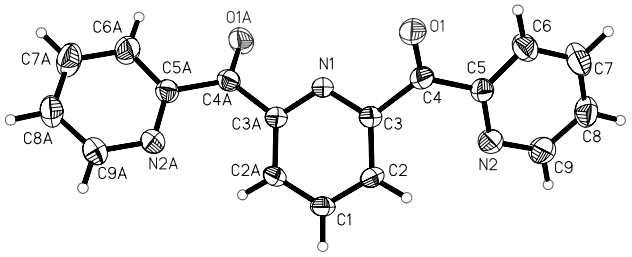


Fig. 1. Molecular structure of compound **1**. Non-hydrogen atoms are shown as 30% probability ellipsoids.

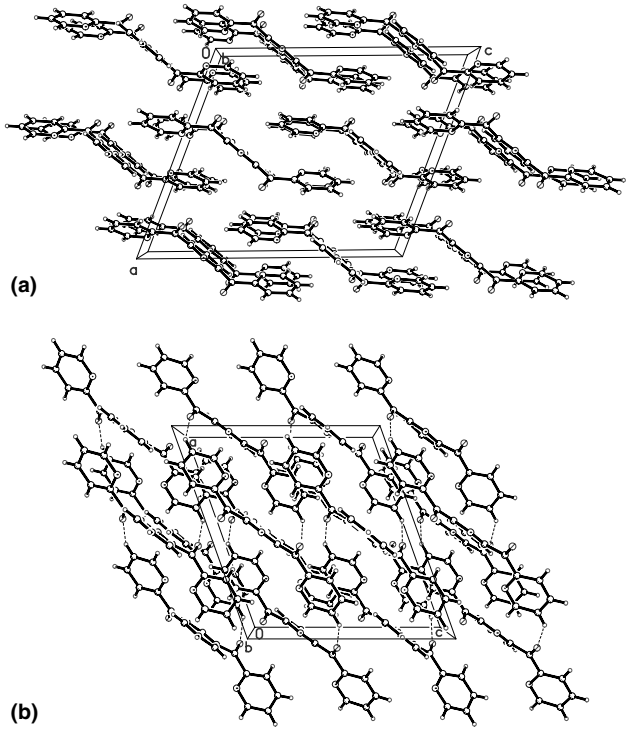


Fig. 2. (a) Packing diagram of **1a** viewed along the *b*-axis. The center-to-center separation between a pair of parallel pyridine rings from adjacent ligands is ca. 3.95 Å. (b) Packing diagram of **1b** viewed along the *b*-axis. The hydrogen-bonded layers (C8–H8A···O1 136°; C8···O1 3.237 Å) match the (0 0 2) planes, and very weak π–π interactions connect them into a three-dimensional network. The center-to-center separation between two parallel pyridine rings from adjacent layers is ca. 4.09 Å.

3. Results and discussion

3.1. Crystal structure of ligand *1*

Two polymorphs of **1** can be crystallized using different solvents: form **1a** from ethyl acetate has a packing featuring very weak π–π interactions (Fig. 1), and form **1b** from water is consolidated by both π–π interactions and intermolecular C–H···O=C hydrogen bonds (Fig. 2). Molecule **1** has site symmetry 2 in both crystalline forms **1a** and **1b**, but the pair of torsion angles along the atom chain N–C–C(carbonylic)–C–N are (−136.3°, −12.5°) and (155.6°, −22.5°), respectively, indicating that different conformations are adopted by **1** in these

Table 2
Comparison of the bond lengths (Å) and angles (°) of two polymorphs of compound **1**

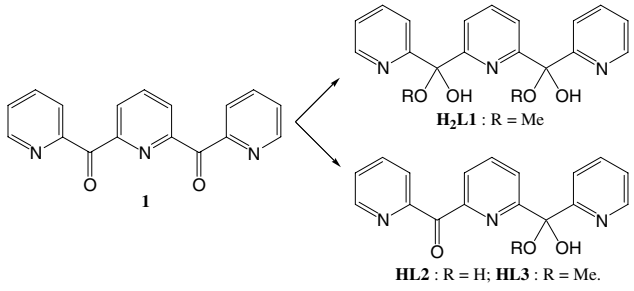
	1a	**1b**
O(1)–C(4)	1.224(3)	1.213(4)
N(1)–C(3)	1.344(2)	1.332(3)
N(2)–C(9)	1.331(3)	1.333(4)
N(2)–C(5)	1.337(3)	1.341(4)
C(1)–C(2)	1.376(3)	1.379(4)
C(2)–C(3)	1.391(3)	1.389(4)
C(3)–C(4)	1.506(3)	1.511(4)
C(4)–C(5)	1.494(3)	1.500(4)
C(5)–C(6)	1.374(3)	1.385(4)
C(6)–C(7)	1.374(4)	1.376(4)
C(7)–C(8)	1.364(4)	1.371(5)
C(8)–C(9)	1.369(4)	1.383(5)
C(3)–N(1)–C(3)#1	117.7(2)	118.3(4)
C(9)–N(2)–C(5)	117.0(2)	116.3(3)
C(2)#1–C(1)–C(2)	119.6(3)	118.9(4)
C(1)–C(2)–C(3)	118.6(2)	118.7(3)
N(1)–C(3)–C(2)	122.7(2)	122.7(3)
N(1)–C(3)–C(4)	112.8(2)	114.2(3)
C(2)–C(3)–C(4)	124.5(2)	122.9(3)
O(1)–C(4)–C(5)	120.0(2)	119.4(3)
O(1)–C(4)–C(3)	118.5(2)	118.9(3)
C(5)–C(4)–C(3)	121.5(2)	121.7(3)
N(2)–C(5)–C(6)	122.6(2)	123.5(3)
N(2)–C(5)–C(4)	117.9(2)	117.8(3)
C(6)–C(5)–C(4)	119.4(2)	118.7(3)
C(7)–C(6)–C(5)	119.0(3)	118.8(3)
C(8)–C(7)–C(6)	119.1(3)	118.5(3)
C(7)–C(8)–C(9)	118.3(3)	118.9(3)
N(2)–C(9)–C(8)	124.0(3)	123.9(3)

Symmetry code: #1: $-x$, y, $-z + 1/2$.

two polymorphs. Comparison of the bond lengths and angles of **1a** and **1b** are listed in Table 2. Almost all of the bond lengths in **1b** are a little longer than the corresponding ones in **1a**, except for the similar distances of C2–C3 and the significant longer C=O bond length in **1a** than that in **1b**.

3.2. Hydrolysis/solvolysis of ligand *1* and solvent controlled formation of complexes

As **1** contains two carbonyl groups each flanked by a pair of pyridyl rings, it readily undergoes metal-assisted hydration or alkanol addition under different conditions to give the di-hemiketal $\mathbf{H_2L1}$, the *gem*-diol **HL2** and the hemiketal **HL3** (Scheme 1), the deprotonated forms of which are potential polydentate ligands that can adopt a variety of coordination modes.



Scheme 1. Hydrolysis and solvolysis of ligand **1**.

The reaction of **1** with $FeCl_3$ in hot methanol yielded crystalline complex $[Fe_3(\mathbf{L1})_2(\mu\text{-}OCH_3)_2Cl_2]FeCl_4 \cdot H_2O$ (**2**) with an asymmetric quasi-linear triiron(III) core. In addition, solvated mononuclear complexes $Fe(\mathbf{L2})Cl_2 \cdot H_2O$ (**3a**), $Fe(\mathbf{L2})Cl_2 \cdot THF$ (**3b**) and $Fe(\mathbf{L3})Cl_2 \cdot THF$ (**3c**) were obtained by solvent-dependent reaction between **1** and $FeCl_3$. Using CH_3CN and H_2O as a mixed solvent, **3a** was formed; diffusion of THF into the CH_3CN reaction solution gave **3b**; when THF was diffused into the mixed CH_3CN/CH_3OH reaction solution, product **3c** was generated.

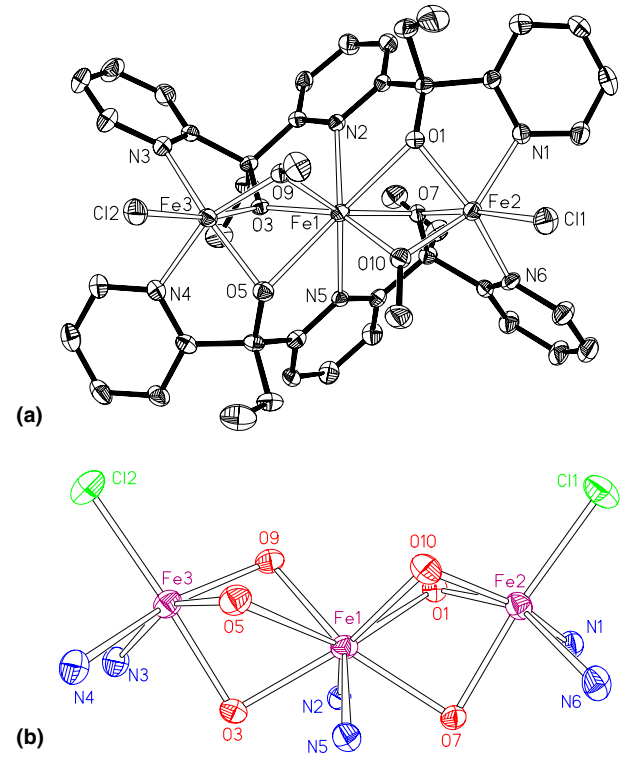


Fig. 3. (a) The quasi-linear asymmetric triiron(III) cation in complex **2**. Hydrogen atoms are omitted for clarity. (b) Saddle-like molecular skeleton composed of fused coordination polyhedra. The atoms are shown as 30% probability ellipsoids.

Table 3
Selected bond lengths (Å) and angles (°) in the triiron(III) core of complex **2**

Fe(1)–O(10)	2.016(4)	Fe(2)–O(1)	1.955(4)
Fe(1)–O(9)	2.027(4)	Fe(2)–O(7)	2.097(3)
Fe(1)–O(3)	2.087(4)	Fe(2)–N(6)	2.122(5)
Fe(1)–O(7)	2.104(3)	Fe(2)–N(1)	2.161(5)
Fe(1)–N(5)	2.254(5)	Fe(2)–Cl(1)	2.253(2)
Fe(1)–N(2)	2.255(5)	Fe(3)–O(5)	1.950(4)
Fe(1)–O(1)	2.375(4)	Fe(3)–O(9)	1.960(4)
Fe(1)–O(5)	2.463(4)	Fe(3)–O(3)	2.053(4)
Fe(1)–Fe(2)	2.897(1)	Fe(3)–N(4)	2.161(6)
Fe(1)–Fe(3)	2.916(1)	Fe(3)–N(3)	2.174(5)
Fe(1)–C(39)	3.054(6)	Fe(3)–Cl(2)	2.276(2)
Fe(2)–O(10)	1.945(4)		
O(10)–Fe(1)–O(9)	97.3(2)	O(1)–Fe(2)–N(6)	154.4(2)
O(10)–Fe(1)–O(3)	152.0(2)	O(7)–Fe(2)–N(6)	76.0(2)
O(9)–Fe(1)–O(3)	78.2(2)	O(10)–Fe(2)–N(1)	157.6(2)
O(10)–Fe(1)–O(7)	79.8(2)	O(1)–Fe(2)–N(1)	78.00(2)
O(9)–Fe(1)–O(7)	152.4(2)	O(7)–Fe(2)–N(1)	89.4(2)
O(3)–Fe(1)–O(7)	116.6(1)	N(6)–Fe(2)–N(1)	97.8(2)
O(10)–Fe(1)–N(5)	86.6(2)	O(10)–Fe(2)–Cl(1)	99.1(1)
O(9)–Fe(1)–N(5)	135.0(2)	O(1)–Fe(2)–Cl(1)	109.3(1)
O(3)–Fe(1)–N(5)	78.0(2)	O(7)–Fe(2)–Cl(1)	172.0(1)
O(7)–Fe(1)–N(5)	72.5(2)	N(6)–Fe(2)–Cl(1)	96.1(1)
O(10)–Fe(1)–N(2)	136.1(2)	N(1)–Fe(2)–Cl(1)	92.7(1)
O(9)–Fe(1)–N(2)	86.7(2)	O(5)–Fe(3)–O(9)	81.4(2)
O(3)–Fe(1)–N(2)	71.7(2)	O(5)–Fe(3)–O(3)	80.7(2)
O(7)–Fe(1)–N(2)	77.3(2)	O(9)–Fe(3)–O(3)	80.5(1)
N(5)–Fe(1)–N(2)	120.5(2)	O(5)–Fe(3)–N(4)	78.0 (2)
O(10)–Fe(1)–O(1)	69.2(2)	O(9)–Fe(3)–N(4)	158.7(2)
O(9)–Fe(1)–O(1)	83.5(1)	O(3)–Fe(3)–N(4)	90.8(2)
O(3)–Fe(1)–O(1)	136.2(1)	O(5)–Fe(3)–N(3)	154.2(2)
O(7)–Fe(1)–O(1)	69.8(1)	O(9)–Fe(3)–N(3)	104.0(2)
N(5)–Fe(1)–O(1)	138.0(2)	O(3)–Fe(3)–N(3)	75.5(2)
N(2)–Fe(1)–O(1)	67.9(2)	N(4)–Fe(3)–N(3)	92.5(2)
O(10)–Fe(1)–O(5)	83.7(2)	O(5)–Fe(3)–Cl(2)	109.6(1)
O(9)–Fe(1)–O(5)	68.4(2)	O(9)–Fe(3)–Cl(2)	98.4(1)
O(3)–Fe(1)–O(5)	68.9(1)	O(3)–Fe(3)–Cl(2)	169.5(1)
O(7)–Fe(1)–O(5)	137.3(2)	N(4)–Fe(3)–Cl(2)	93.5(1)
N(5)–Fe(1)–O(5)	67.5(2)	N(3)–Fe(3)–Cl(2)	94.8(1)
N(2)–Fe(1)–O(5)	136.6(2)	Fe(2)–O(1)–Fe(1)	83.4(1)
O(1)–Fe(1)–O(5)	138.1(1)	Fe(3)–O(3)–Fe(1)	89.6(1)
Fe(2)–Fe(1)–Fe(3)	152.63(3)	Fe(3)–O(5)–Fe(1)	81.8(1)
O(10)–Fe(2)–O(1)	80.2(2)	Fe(2)–O(7)–Fe(1)	87.2(1)
O(10)–Fe(2)–O(7)	81.6(2)	Fe(3)–O(9)–Fe(1)	94.0(2)
O(1)–Fe(2)–O(7)	78.7(2)	Fe(2)–O(10)–Fe(1)	94.0(2)
O(10)–Fe(2)–N(6)	99.8(2)		

3.3. Crystal structure of complexes

The cation in compound **2** consists of a quasi-linear array of three iron(III) atoms bridged by two *cis*-related deprotonated di-hemiketals **L1** and two methoxide groups, with a terminal chloro ligand at each end (Fig. 3 and Table 3). All non-cyclic triiron cores reported to date are almost exactly linear [21], whereas in **2**, due to the steric bulk and disposition of the pair of pentadentate ligand **L1**, the Fe2···Fe1···Fe3 angle is 152.63(3)°, and the non-bonding distances between the central to the outer iron(III) atoms are significantly different, being 2.897(1) and 2.916(1) Å [22]. The Fe1 atom is surrounded by two *cis*-related **L1** ligands each employing its central pyridyl N and pair of hemiketal O atoms, as well as a pair of bridging methoxide groups. Owing to the steric effect, the distances between Fe1 and O1/O5 in $[Fe_3(\mathbf{L1})_2(\mu\text{-}OCH_3)_2Cl_2]^+$ are much longer at 2.375(4)/2.463(4) Å as compared to commonly observed iron(III)–oxygen bonds in the range 1.945–2.104 Å. Nevertheless, the central Fe atom can still be considered to be eight-coordinate in a highly distorted FeN_2O_6 dodecahedral coordination environment, in contrast to the distorted octahedral geometry of the outer Fe2 and Fe3 atoms. The Fe–X (X = N or O) bond distances in known eight-coordinate iron complexes are very different: in $Ph_4As[Fe(NO_3)_4]$ reported by Logan and coworkers [27b], the average distance of the Fe–O bonds is 2.13(3) Å; in $Fe(1,8\text{-naphthyridine})_4(ClO_4)_2$ reported by Bernal and coworkers [28,29], the Fe–N distances range from 2.18 to 2.76 Å; in the work of Krüger and coworkers [27a], the Fe–N distances lie in the range of 2.29–2.39 and 2.21–2.33 Å for iron(II) and iron(III) complexes, respectively; and Meier and Rihs [30] have observed a mean Fe–O bond length of 2.40 Å in their iron(II)–crown ether complex. In the present triiron complex **2**, the Fe–X distances range from 1.95 to 2.46 Å. The mean Fe–X distance of the central Fe(III) atom (excluding two unusually long ones) is significantly longer than that of the side Fe(III) atoms, which may be attributed to the difference in their coordination geometries. The trinuclear cation has approximate C_2 molecular symmetry, and its skeletal configuration resembles a saddle (Fig. 3(b)), which has not been observed in reported linear triiron complexes. To our knowledge, only two eight-coordinate Fe(III) complexes have been

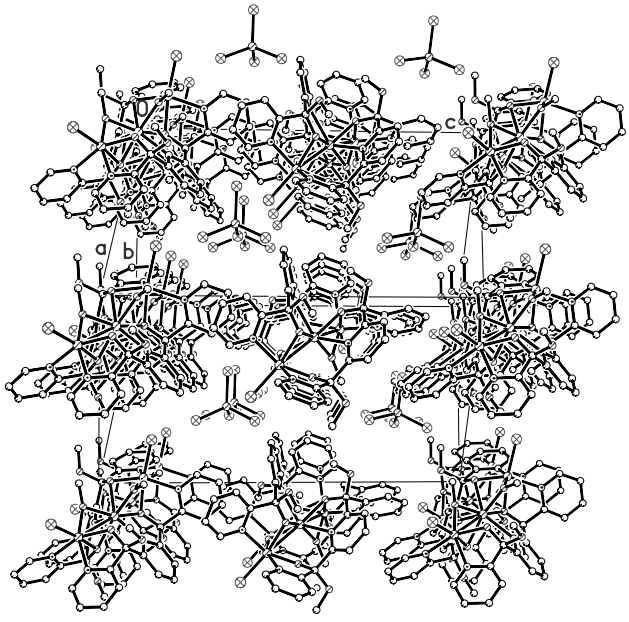


Fig. 4. Packing diagram of compound **2** viewed along $[1\,\bar{1}\,0]$. Hydrogen atoms are omitted for clarity.

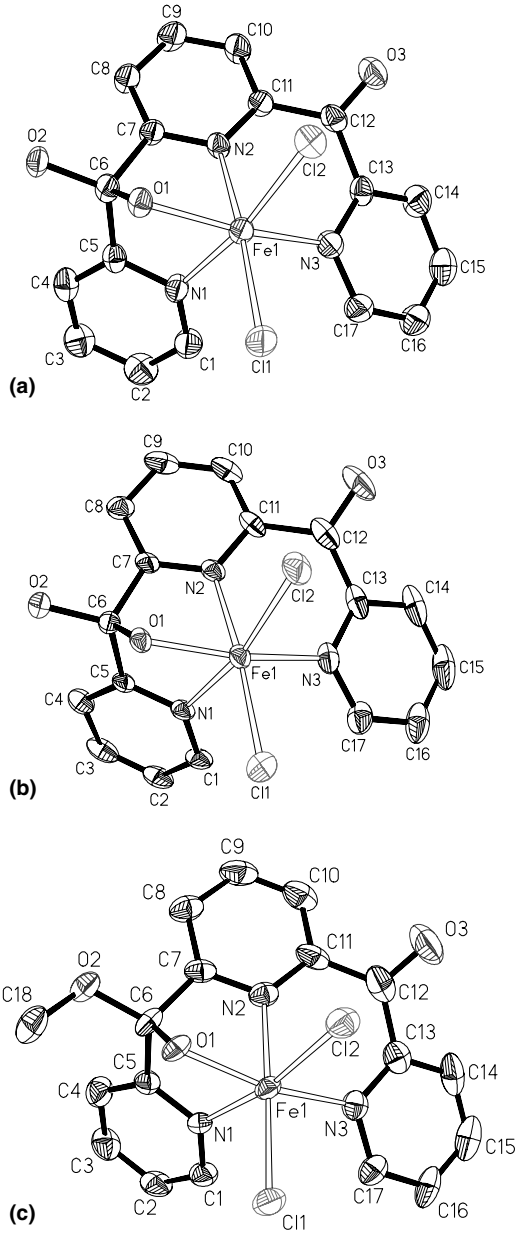


Fig. 5. The cationic monoiron(III) core in **3a** (a), **3b** (b) and **3c** (c). Hydrogen atoms are omitted for clarity. The lattice water molecule in **3a** and THF solvate molecules in **3b** and **3c** are omitted for clarity.

elucidated by X-ray analysis [27] among the few reported examples that commonly bear bidentate, tetradentate or octadentate ligands [27–31].

In the crystal structure of **2**, the trinuclear cations and tetrahedral $FeCl_4^{2-}$ anions are packed in separate columns parallel to the $[1\,\bar{1}\,0]$ direction (Fig. 4). Also present in the crystal are very weak π–π stacking interactions that have a center-to-center separation of ca. 4.00 Å between two almost parallel pyridine rings from adjacent cations that make a dihedral angle of 16.6°.

The neutral complexes **3a**, **3b** and **3c** have similar molecular structures, all containing a six-coordinate Fe(III) center with a pair of *cis*-chloro ligands (Fig. 5). In both hydrated **3a** and THF solvated **3b**, hydrolysis occurs at one carbonyl group of ligand L, whereas in THF solvated **3c** the corresponding carbonyl group undergoes methanolysis. Complexes **3b** and **3c** constitute a nearly isomorphous pair. In the monoiron core, the Fe–O bond length in **3c** (1.905 Å) is significantly longer than those in **3a** (1.952 Å) and **3b** (1.941 Å); consistent with this, the Fe–N bond distances in **3a** are shorter than those in **3b** and **3c**. Selected bond lengths and angles of complexes **3a**, **3b** and **3c** are listed in Table 4 for comparison. Our previous paper has reported the complete solvolysis of ligand **1** in its Cu(II) complex, just like that in complex **2** [23]. However, in the formation of the mononuclear compounds **3a**–**3c**, **1** involves either hydration or methanol addition at only one carbonyl group while the other remains intact. Although the influence of solvent in the formation of coordination complexes is less well understood and systematic studies are few, one can conclude from the preparation of **3a** and **3b** that H_2O is more effective in stabilizing the crystal lattice as compared to THF. When a mixture of CH_3CN, THF and H_2O was used as the solvent, only compound **3a** was deposited.

3.4. Magnetic susceptibility of complex 2

The variable-temperature magnetic susceptibilities of **2** were measured on a polycrystalline sample with a Quantum Design SQUID susceptometer operating at a magnetic field of 0.1 T in the temperature range of 2–300 K. The diamagnetic corrections were evaluated from Pascal's constants for all the constituent atoms. The magnetic behavior of **2** in the form of μ_{eff} versus T plots is illustrated in Fig. 6. At room temperature, the effective moment has a value of 13.62 μ_B; taking the

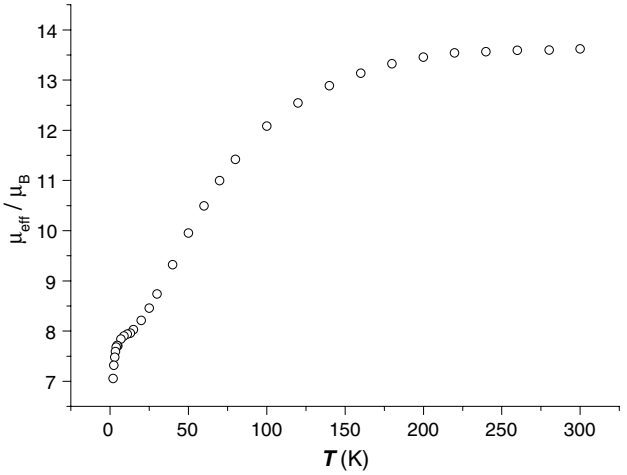


Fig. 6. μ_{eff}–T plot of complex **2**.

Table 4
Selected bond lengths (Å) and angles (°) of complexes **3a**, **3b** and **3c**

3a		**3b**		**3c**	
Fe(1)–O(1)	1.952(5)	Fe(1)–O(1)	1.941(3)	Fe(1)–O(1)	1.905(5)
Fe(1)–N(2)	2.171(6)	Fe(1)–N(2)	2.190(4)	Fe(1)–N(2)	2.224(6)
Fe(1)–N(3)	2.200(7)	Fe(1)–N(3)	2.206(5)	Fe(1)–N(3)	2.213(6)
Fe(1)–N(1)	2.232(6)	Fe(1)–N(1)	2.255(4)	Fe(1)–N(1)	2.242(6)
Fe(1)–Cl(1)	2.268(2)	Fe(1)–Cl(1)	2.261(2)	Fe(1)–Cl(1)	2.260(2)
Fe(1)–Cl(2)	2.303(2)	Fe(1)–Cl(2)	2.323(2)	Fe(1)–Cl(2)	2.315(2)
O(1)–Fe(1)–N(2)	77.8(2)	O(1)–Fe(1)–N(2)	77.8(2)	O(1)–Fe(1)–N(3)	154.2(2)
O(1)–Fe(1)–N(3)	157.0(2)	O(1)–Fe(1)–N(3)	156.8(2)	O(1)–Fe(1)–N(2)	77.5(2)
N(2)–Fe(1)–N(3)	82.1(2)	N(2)–Fe(1)–N(3)	82.1(2)	N(3)–Fe(1)–N(2)	79.4(2)
O(1)–Fe(1)–N(1)	76.7(2)	O(1)–Fe(1)–N(1)	75.7(1)	O(1)–Fe(1)–N(1)	75.5(2)
N(2)–Fe(1)–N(1)	79.8(2)	N(2)–Fe(1)–N(1)	78.8(2)	N(3)–Fe(1)–N(1)	89.1(2)
N(3)–Fe(1)–N(1)	89.0(2)	N(3)–Fe(1)–N(1)	89.3(2)	N(2)–Fe(1)–N(1)	79.3(2)
O(1)–Fe(1)–Cl(1)	101.8(2)	O(1)–Fe(1)–Cl(1)	100.6(1)	O(1)–Fe(1)–Cl(1)	105.0(2)
N(2)–Fe(1)–Cl(1)	172.7(2)	N(2)–Fe(1)–Cl(1)	171.1(1)	N(3)–Fe(1)–Cl(1)	96.1(2)
N(3)–Fe(1)–Cl(1)	96.8(2)	N(3)–Fe(1)–Cl(1)	97.5(2)	N(2)–Fe(1)–Cl(1)	170.4(2)
N(1)–Fe(1)–Cl(1)	92.9(2)	N(1)–Fe(1)–Cl(1)	92.3(1)	N(1)–Fe(1)–Cl(1)	92.2(2)
O(1)–Fe(1)–Cl(2)	100.3(2)	O(1)–Fe(1)–Cl(2)	100.0(1)	O(1)–Fe(1)–Cl(2)	100.1(2)
N(2)–Fe(1)–Cl(2)	88.4(2)	N(2)–Fe(1)–Cl(2)	87.8(1)	N(3)–Fe(1)–Cl(2)	90.6(2)
N(3)–Fe(1)–Cl(2)	90.0(2)	N(3)–Fe(1)–Cl(2)	90.6(1)	N(2)–Fe(1)–Cl(2)	88.7(2)
N(1)–Fe(1)–Cl(2)	168.2(2)	N(1)–Fe(1)–Cl(2)	166.4(1)	N(1)–Fe(1)–Cl(2)	167.8(2)
Cl(1)–Fe(1)–Cl(2)	98.9(1)	Cl(1)–Fe(1)–Cl(2)	101.14(7)	Cl(1)–Fe(1)–Cl(2)	99.92(9)

structure into account, this is based on the sum of contributions from the trinuclear Fe(III) cation and the isolated $[FeCl_4]^-$ complex anion. Upon cooling, it smoothly decreases to attain a value of 12.88 μ_B at 140 K, and then quickly decreases to 7.05 μ_B at 2 K. These global features indicate a significant antiferromagnetic couple in the Fe(III) complex and the very sharp decrease below 20 K is due to the zero-field splitting effect.

4. Summary

In summary, we have taken advantage of the in situ generation of the *gem*-diol, hemiketal and di-hemiketal forms of **1** under solvent-controlled reaction conditions to obtain mononuclear and quasi-linear trinuclear iron(III) complexes. The doubly deprotonated di-hemiketal form of **1** functions as a pentadentate bridging ligand in **2**, whereas the mono-deprotonated *gem*-diol or hemiketal form of **1** acts as a tetradentate chelating ligand in **3a**, **3b** and **3c**. A significant antiferromagnetic couple in the trinuclear Fe(III) complex **2** was observed.

Acknowledgment

This work is supported by the Hong Kong Research Grants Council (Earmarked Grant Ref. No. CUHK 402003).

Appendix A. Supplementary data

Supplementary crystal data are available from the CCDC, 12 Union Road, Cambridge CB2 1EZ, UK (fax: +44 1223 336033; e-mail: deposit@ccdc.cam.ac.uk or www: http://www.ccdc.cam.ac.uk) on request by quoting the deposition numbers: CCDC 238015–238020 for **1a**, **1b**, **2**, **3a**, **3b** and **3c**, respectively. Supplementary data associated with this article can be found, in the online version, at doi:10.1016/j.poly.2005.02.004.

References

[1] G.S. Papaefstathiou, S.P. Perlepes, Comments Inorg. Chem. 23 (2002) 249, and references therein.
[2] C. Dendrinou-Samara, M. Alexiou, C.M. Zaleski, J.W. Kampf, M.L. Kirk, D.P. Kessissoglou, V.L. Pecoraro, Angew. Chem. Int. Ed. 42 (2003) 3763.
[3] C.J. Milios, E. Kefalloniti, C.P. Raptopoulou, A. Terzis, R. Vicente, N. Lalioti, A. Escuer, S.P. Perlepes, Chem. Commun. (2003) 819.
[4] G. Crundwell, B.L. Westcott, R. Coffey, M. Zeller, A.D. Hunter, Inorg. Chim. Acta 355 (2003) 432.
[5] M. Bakir, I. Hassan, O. Green, J. Mol. Struct. 657 (2003) 75.
[6] A.K. Boudalis, F. Dahan, A. Bousseksou, J.P. Tuchagues, S.P. Perlepes, Dalton Trans. (2003) 3411.
[7] G.S. Papaefstathiou, A. Escuer, M. Font-Bardia, S.P. Perlepes, X. Solans, R. Vicente, Polyhedron 21 (2002) 2027.
[8] S. Hiraoka, T. Yi, M. Shiro, M. Shionoya, J. Am. Chem. Soc. 124 (2002) 14510.
[9] R. Grommen, P. Manikandan, Y. Gao, T. Shane, J.J. Shane, R.A. Schoonheydt, B.M. Weckhuysen, D. Goldfarb, J. Am. Chem. Soc. 122 (2000) 11488.
[10] S. Aoki, M. Shiro, T. Koike, E. Kimura, J. Am. Chem. Soc. 122 (2000) 576.
[11] A. Kamiyama, T. Noguchi, T. Kajiwara, T. Ito, Cryst. Eng. Commun. 5 (2003) 231.
[12] J.F. Ma, J.F. Liu, Y. Xing, H.Q. Jia, Y.H. Lin, J. Chem. Soc., Dalton Trans. (2000) 2403.
[13] L. Pan, X.Y. Huang, J. Li, Y.G. Wu, N.W. Zheng, Angew. Chem. Int. Ed. 39 (2000) 527.
[14] L.-P. Zhang, W.-J. Lu, T.C.W. Mak, Chem. Commun. (2003) 2830.
[15] J.D. Bois, T.J. Mizoguchi, S.J. Lippard, Coord. Chem. Rev. 200–202 (2000) 443.
[16] D.M. Kurtz, Chem. Rev. 90 (1990) 585.
[17] S.J. Lippard, Angew. Chem. Int. Ed. 27 (1988) 344.
[18] J.K. McCusker, C.A. Christmas, P.M. Hagen, R.K. Chadha, D.F. Harvey, D.N. Hendrickson, J. Am. Chem. Soc. 113 (1991) 6114, and references therein.
[19] L. Que, W.B. Tolman, Angew. Chem. Int. Ed. 41 (2002) 1114.
[20] J. Kuzelka, S. Mukhopadhyay, B. Spingler, S.J. Lippard, Inorg. Chem. 42 (2003) 6447.
[21] (a) R.L. Rardin, A. Bino, P. Poganiuch, W.B. Tolman, S. Liu, S.J. Lippard, Angew. Chem. Int. Ed. 29 (1990) 812;
(b) M.A. Walters, J.C. Dewan, Inorg. Chem. 25 (1986) 4889;
(c) V.A. Vankai, M.G. Newton, D.M. Kurtz, Inorg. Chem. 31 (1992) 341;
(d) K.H. Pannell, A.J. Mayr, D. VanDerveer, J. Am. Chem. Soc. 105 (1983) 6186;
(e) F.A. Cotton, C.A. Murillo, X.P. Wang, Inorg. Chem. Commun. 1 (1998) 281;
(f) G. Vos, R.A.G. de Graaff, J.G. Haasnoot, A.M. van der Kraan, P. de Vaal, J. Reedijk, Inorg. Chem. 23 (1984) 2905;
(g) M. Thomann, O. Kahn, J. Guilhem, F. Varret, Inorg. Chem. 33 (1994) 6029;
(h) J.J.A. Kolnaar, G. van Dijk, H. Kooijman, A.L. Spek, V.G. Ksenofontov, P. Gütlich, J.G. Haasnoot, J. Reedijk, Inorg. Chem. 36 (1997) 2433.
[22] (a) G. Psomas, N. Bréfuel, F. Dahan, J.-P. Tuchagues, Inorg. Chem. 43 (2004) 4590;
(b) E.M. Rumberger, S. Hill, R.S. Edwards, W. Wernsdorfer, L.N. Zakharov, A.L. Rheingold, G. Christou, D.N. Hendrickson, Polyhedron 22 (2003) 1865.
[23] X.-D. Chen, T.C.W. Mak, Inorg. Chim. Acta 358 (2005) 1107.
[24] Bruker, SMART 5.0 and SAINT 4.0 for Windows NT, Area Detector Control and Integration Software, Burker Analytical X-ray Systems Inc., Madison, WI, 1998.
[25] G.M. Sheldrick, SADABS: Program for Empirical Absorption Correction of Area Detector Data, University of Göttingen, Göttingen, Germany, 1996.
[26] G.M. Sheldrick, SHELXTL 5.1 for Windows NT: Structure Determination Software Programs, Bruker Analytical X-ray Systems, Inc., Madison, WI, 1997.
[27] (a) W.O. Koch, A. Barbieri, M. Grodzicki, V. Schüenemann, A.X. Trautwein, H.J. Krüger, Angew. Chem., Int. Ed. Engl. 35 (1996) 422;
(b) T.J. King, N. Logan, A. Morris, S.C. Wallwork, J. Chem. Soc., Chem. Commun. (1971) 554.
[28] P. Singh, A. Clearfield, I. Bernal, J. Coord. Chem. 1 (1971) 29.
[29] A. Clearfield, P. Singh, I. Bernal, J. Chem. Soc., Chem. Commun. (1970) 389.
[30] K. Meier, G. Rihs, Angew. Chem., Int. Ed. Engl. 24 (1985) 858.
[31] M. Di Vaira, F. Mani, P. Stoppioni, J. Chem. Soc., Dalton Trans. (1992) 1127.

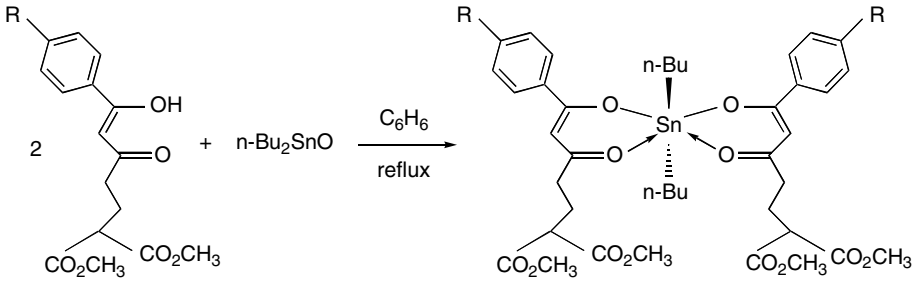


Fig. 1. Synthesis of di-*n*-butyltin(IV) enolates **2a**–**2d**.

synthesis of new di-*n*-butylhydroxytin(IV)enolates, which exhibit higher states of aggregation in solution at low temperature and their FAB mass spectra showed a dimer structure [27]. Our current interest in the synthesis of organotin(IV) compounds [28–31] prompted us to extend our investigations to the synthesis of new organotin(IV) enolates, which could have biological properties [32]. This paper describes the synthesis of four new di-*n*-butyl[bis{dimethyl-2-(3-oxo-5-phenyl(4-subtituted)penten-5-ato)malonates}]tin(IV) **2a**–**2d** by the reaction of di-*n*-butyl(IV) oxide and 1,3-diketone malonates **1a**–**1d** in a 1:2 molar ratio, in which **1a**–**1d** exist as enolates [33,34] (Fig. 1). All compounds were characterized by ^{1}H, ^{13}C, ^{119}Sn NMR, HMQC, HMBC, infrared spectroscopy and mass spectrometry (FAB). The compound **2d** was also characterized by solid state ^{13}C and ^{119}Sn NMR and its structure was further established by a single crystal X-ray diffraction study at 168 K.

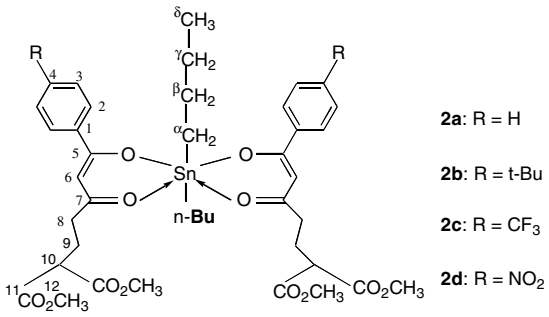
2. Results and discussion

The reaction of 1,3-diketone malonates **1a**–**1d** with di-*n*-butyltin(IV) oxide in a 2:1 ratio, led to di-*n*-butyltin(IV)enolates **2a**–**2d** (Fig. 1). The compounds **2a**–**2c** were obtained as oils, while **2d** was a solid. The ^{1}H NMR spectra in $CDCl_3$ of all the compounds **2a**–**2d** show only one set of signals for each magnetically equivalent H nucleus, thus both $(n\text{-}Bu)_2Sn$ protons and those of the ligands are in a 1:2 ratio, respectively. This can indicate the formation of a unique species or a fast-exchanging equilibrium on the NMR timescale. The H6 and H8 protons appeared as broad signals (0.1 and 0.19 ppm) at higher field with respect to the free ligands (**1a**–**1d**), which suggests a shielding of these protons upon coordination [16], giving evidence for the formation of a Sn–O bonded enolate moiety and a C═O → Sn coordination bond, while the broadening of these signals can suggest a fluxionality between the possible isomers [16,19]. ^{1}H NMR data are summarized in Table 1. The ^{13}C NMR data for compounds **2a**–**2d** are summarized in Table 2. For all compounds the assignment of the *n*-butyl moieties are based on ^{1}H–^{13}C HMQC and ^{1}H–^{13}C HMBC experiments. Thus α and β carbons correlate with the broad signal around 1.5 ppm of Hα and Hβ. The γ-carbon correlates with the signal around 1.27 ppm and δ-carbon correlates with the triplet signal of the methyl group.

The unambiguous assignment of Hβ and Hγ are based on ^{1}H–^{13}C HMBC, where the signal of the γ-carbon correlates with the signal around 1.27 ppm. All these compounds exhibit $^{1}J(^{119}Sn–^{13}C)$, $^{2}J(^{119}Sn–^{13}C)$ and $^{3}J(^{119}Sn–^{13}C)$ coupling constants within the range of *trans* six-coordinated tin compounds [16,17,19–21,26,38]. In particular, $^{1}J(^{119}Sn–^{13}C)$ values for compounds **2a**–**2d** are 872, 879, 866 and 860 Hz, respectively and on the basis of the empirical equation of Holecek and Lycka [39], it was possible to determine θ(C–Sn–C) of these compounds in $CDCl_3$ solution: the calculated values are 160.2° for **2a**, 160.9° for **2b**, 159.7° for **2c** and 159.1° for **2d**, which indicate that the tin atom is in a skewed trapezoidal bipyramidal environment, where the trapezoidal plane is defined by four oxygen atoms derived from two asymmetrically coordinating enolate ligands and the tin-bound organo substituents are orientated over the weakly bound oxygen atoms [17,21]. The value calculated for **2d** agrees well with the angle of 157.1(3)° found in the crystal structure.

The ^{119}Sn NMR spectra of **2a**–**2c** at 19 °C and for **2d** at 25 °C in chloroform show only one peak, which can indicate a unique species or a fast exchanging equilibrium on the NMR time scale (Table 3). Their chemical shifts are within the range of di-*n*-butyltin(IV) hexacoordinated compounds [19,23,35–38]. In order to obtain more information about the structure of these compounds, a variable-temperature NMR study of **2a**–**2d**

Table 1
^{1}H NMR data for compounds **2a**–**2d**



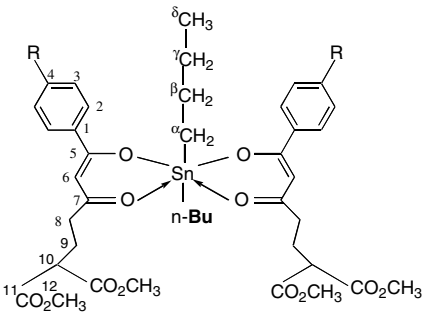
Compound	*n*-BuSn	H8	H9	H10	H12	H6	Harom
2a	H_{δ}: 0.78 (t) J = 7.2 H_{γ}: 1.27 (se) J = 7.2 $H_{\alpha,\beta}$: 1.48 (m)	2.42 (b)	2.26 (q) J = 7.4	3.50 (t) J = 7.4	3.72 (s)	5.97 (s)	7.41 (m) 7.87 (d) J = 7.5
2b	H_{δ}: 0.78 (t) J = 7.2 H_{γ}: 1.25 (se) J = 7.2 $H_{\alpha,\beta}$: 1.44 (m)	2.42 (b)	2.26 (q) J = 7.4	3.52 (t) J = 7.4	3.71 (s)	5.97 (s)	7.42 (d) 7.82 (d) J = 8.2
2c	H_{δ}: 0.79 (t) J = 7.3 H_{γ}: 1.28 (se) J = 7.3 $H_{\alpha,\beta}$: 1.50 (m)	2.47 (b)	2.27 (q) J = 7.3	3.50 (t) J = 7.3	3.73 (s)	5.99 (s)	7.69 (d) 7.98 (d) J = 8.4
2d	H_{δ}: 0.78 (t) J = 7.3 H_{γ}: 1.29 (se) J = 7.3 $H_{\alpha,\beta}$: 1.50 (b)	2.49 (bt) J = 7.3	2.27 (q) J = 7.3	3.50 (t) J = 7.3	3.73 (s)	6.00 (s)	8.02 (d) 8.26 (d) J = 8.8

δ (^{1}H) relative to $Si(CH_3)_4$; δ (^{119}Sn) relative to $Sn(CH_3)_4$; solvent $CDCl_3$.
The protons of the *t*-Bu group exhibit a singlet at 1.34 ppm.
b: broad; bt: broad triplet; d: doublet; m: unresolved pattern; q: quartet; s: singlet; t: triplet; se: sextet and $|J|$ Hz.

was undertaken from 45 to −25 °C for **2a**–**2c** and in the case of **2d** until −45 °C. Thus the spectra at 45 °C exhibit one signal within the range typical of hexacoordinated tin(IV) compounds, the same result was observed upon lowering the temperature to −5 °C for **2a** and **2b**, but not for **2c** and **2d**, which showed two absorptions with slightly different chemical shifts but equal intensity, indicating the presence of both *trans syn*- and *anti*-isomers, in which the alkyl groups must be *trans*, and the isomerism is attributed to a different arrangement of the two ligands as shown in Fig. 2 [19,21]. The same result is found for compound **2d** at 5 °C in which the signals are in ca. 1:4 ratio. All compounds show these two signals at −25 °C, with equal intensity for **2a** and **2b**, while for **2c** and **2d** in ca. 1:1.5 ratio. The spectrum of **2d** at −35 °C showed three signals in a ca. 1:2:4 ratio, the first one at δ −183.54 associated to a five-coordinate species and the other two to the six-coordinate species, this result suggests the existence of an equilibrium between *trans* isomers through a five-coordinate species. Its spectrum at −45 °C exhibited only the signals that belong to the *trans* isomers in ca. 1:2 ratio.

These results show the existence of the mixture of *trans* isomers in solution at low temperature, where chemical shifts of the major isomers for **2c** and **2d** are at lower frequency. The solid state ^{119}Sn NMR spectrum of **2d** (Fig. 3) at room temperature exhibits two signals at −386.07 and −402.10 in a ca. 1:1.5 ratio, as was observed at −25 °C in solution. Its solid state ^{13}C NMR spectrum at room temperature exhibits a set of signals for each magnetically equivalent C nucleus, except for C_5 and C_7, which exhibit two signals each, at δ 200.76, 199.00 and 177.30, 174.40, respectively. The chemical shifts of the major isomer are at a lower frequency than those on the minor isomer, in approximately 0.8:1 ratio (Fig. 4). This result can be attributed again to a different arrangement of the two ligands, giving evidence of the existence of the two *trans*-isomers.

Table 2
^{13}C NMR data for compounds **2a**–**2d**



2a: R = H

2b: R = t-Bu

2c: R = CF_3

2d: R = NO_2

	Compound			
	2a	**2b**	**2c**	**2d**
C_1	139.30	136.17	144.84	144.86
C_2	128.41	127.31	127.62	128.25
C_3	127.43	125.41	125.37	123.59
C_4	131.55	155.11	149.40	149.40
C_5	183.32	183.41	181.04	179.61
C_6	96.71	96.35	97.08	97.71
C_7	193.74	193.28	195.19	195.89
C_8	38.62	38.31	38.73	38.85
C_9	25.17	25.17	24.90	24.81
C_{10}	50.75	50.78	50.71	50.70
C_{11}	169.69	169.69	169.51	169.47
C_{12}	52.49	52.64	52.58	52.61
C_α	27.83 [872/834]	27.71 [879/842]	28.08 [866/828]	28.22 [860/824]
C_β	27.22 [41]	27.19 [40]	27.12 [41]	27.04 [46]
C_γ	26.36 [133]	26.39 [132]	26.27 [129]	26.16 [126]
C_δ	13.80	13.74	13.74	13.68

Chemical shifts in ppm with respect to TMS, $^nJ(^{13}C–^{119/117}Sn)$ coupling constant between square brackets.

Table 3
^{119}Sn NMR variable-temperature data for compounds **2a**–**2d**

	Compound			
	2a	**2b**	**2c**	**2d**
45 °C	−382.93	−385.37	−379.12	−377.15
35 °C				−377.44
19 °C	−383.74	−385.97	−379.66	−377.59[a]
15 °C				−378.09
5 °C				−377.25[1]
				−379.61[4]
−5 °C	−384.39	−386.45	−379.90[1]	−376.46[1]
			−381.07[1]	−379.61[1]
−15 °C				−376.56[1]
				−380.01[1]
−25 °C	−383.81[1]	−386.54[1]	−379.07[1]	−376.60[1]
	−385.08[1]	−386.84[1]	−381.74[1.5]	−380.16[1.5]
−35 °C				−183.54[1]
				−376.60[2]
				−380.16[4]
−45 °C				−376.60[1]
				−380.21[2]

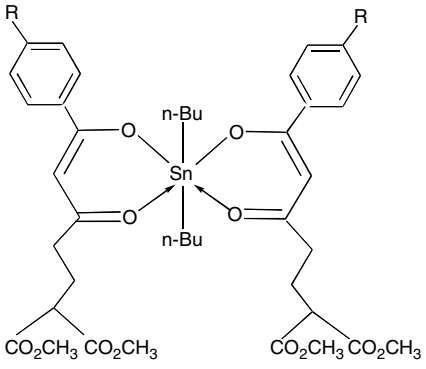
δ: (ppm); solvent $CDCl_3$.
[a] Spectrum obtained at 25 °C [ratio].

The IR data are summarized in Table 4. The spectra exhibit two $\nu_{(C=O)}$ carbonyl oxygen bands, one of them assigned to the CO_2CH_3 groups in the range between 1740 and 1734 cm^{-1} and the other one to the enolate group between 1615 and 1540 cm^{-1}. Also a broad band due to Sn–O is observed between 434 and 302 cm^{-1}.

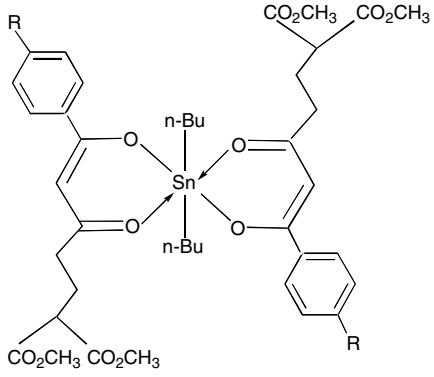
The FAB mass spectra for **2a**–**2d** exhibit the molecular ion, which by the loss of one *n*-Bu group give the base peaks. Therefore, the fragment ion corresponding to the loss of one ligand from the molecular ion is observed. The spectra show others fragment ions and a possible fragmentation pattern is given in Fig. 5.

Compound **2d** was recrystallized from methanol to provide suitable colourless crystals for X-ray diffraction. Intensity data were collected at 168 K and the crystal structure corresponds to one of the two isomers seen in solution and solid state. An ORTEP view of the compound with the numbering scheme is given in Fig. 6.

Bond distances are listed in Table 5. The tin atom is six-coordinate, showing the metal in skewed trapezoidal bipyramidal arrangement (STB), where four O atoms from two ligands, and two C atoms from the *n*-butyl groups form the coordination polyhedron. This is a distorted octahedron characterized by two different sets of



Trans-syn



Trans-anti

Fig. 2. *trans*-isomers for compound **2a**–**2d**.

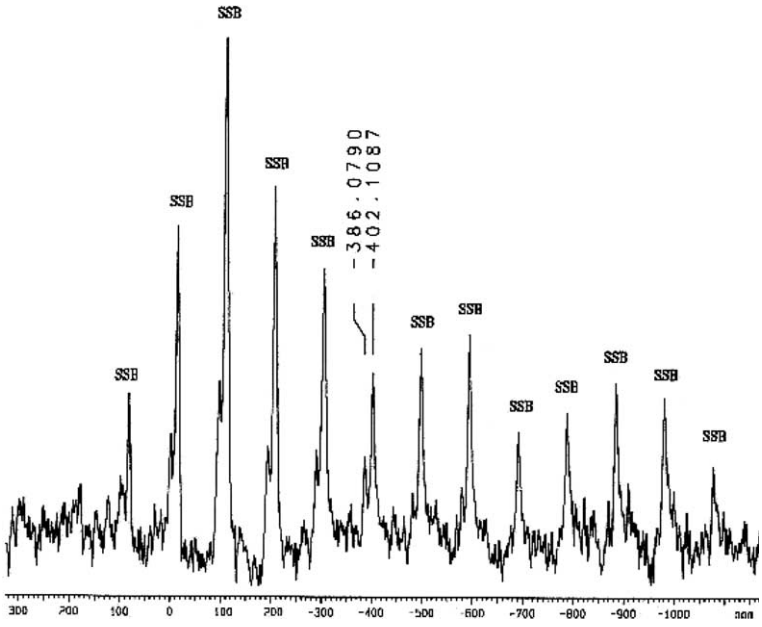


Fig. 3. Solid state ^{119}Sn NMR spectrum for compound **2d**.

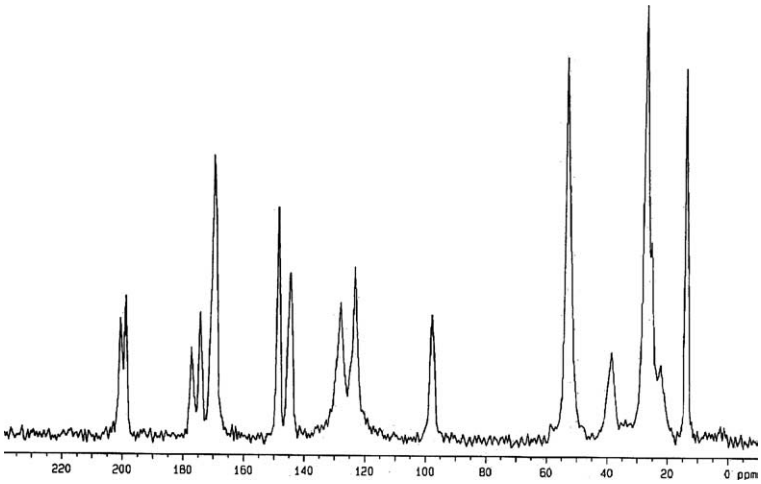


Fig. 4. Solid state ^{13}C NMR spectrum for compound **2d**.

Table 4
IR data for compounds **2a**–**2d**

Compound	C–H$_{arom}$	C–H$_{aliph}$	C=O	C=C–C–O	Sn–O
2a[a]	3062	2954	1734	1594	440–304
		2868		1559	
				1540	
2b[a]	3032	2956	1740	1615	434–302
		2868		1543	
2c[a]	3036	2956	1736	1598	436–318
		2870		1560	
2d[b]	3080	2954	1738	1610	450–312
		2928		1570	
		2870			

ν (cm^{-1}), [a] Net liquid, [b] Film.

Sn–O bond. In this context, one ligand has a short bond length Sn_1–O_1 = 2.112(4) Å (primary bond) and a longer one, Sn_1–O_2 = 2.292(5) Å (secondary bond). For the other ligand, the corresponding values are Sn_1–O_3 = 2.115(3) Å and Sn_1–O_4 = 2.349(4) Å. The *n*-Bu groups are *trans* to each other although a strong distortion from 180° is found and the angle is 157.1(3)°. This asymmetry in bond length is a result of the asymmetric nature of the ligand, as well as the presence of the following intermolecular contacts: NO(6)···H(191)$_{arom}$ 2.5827(0.0065), C=O(13)···H(31)$_{arom}$ 2.2576(0.0088), C=O(9)···H(281)$_{methynic}$, 2.5862(0.0101), C=O(15)···H(121)$_{methynic}$ 2.5252(0.0158) and C=O(13)···H(81)$_{vinylic}$ 2.3372(0.0077) Å. Besides the intermolecular contacts,

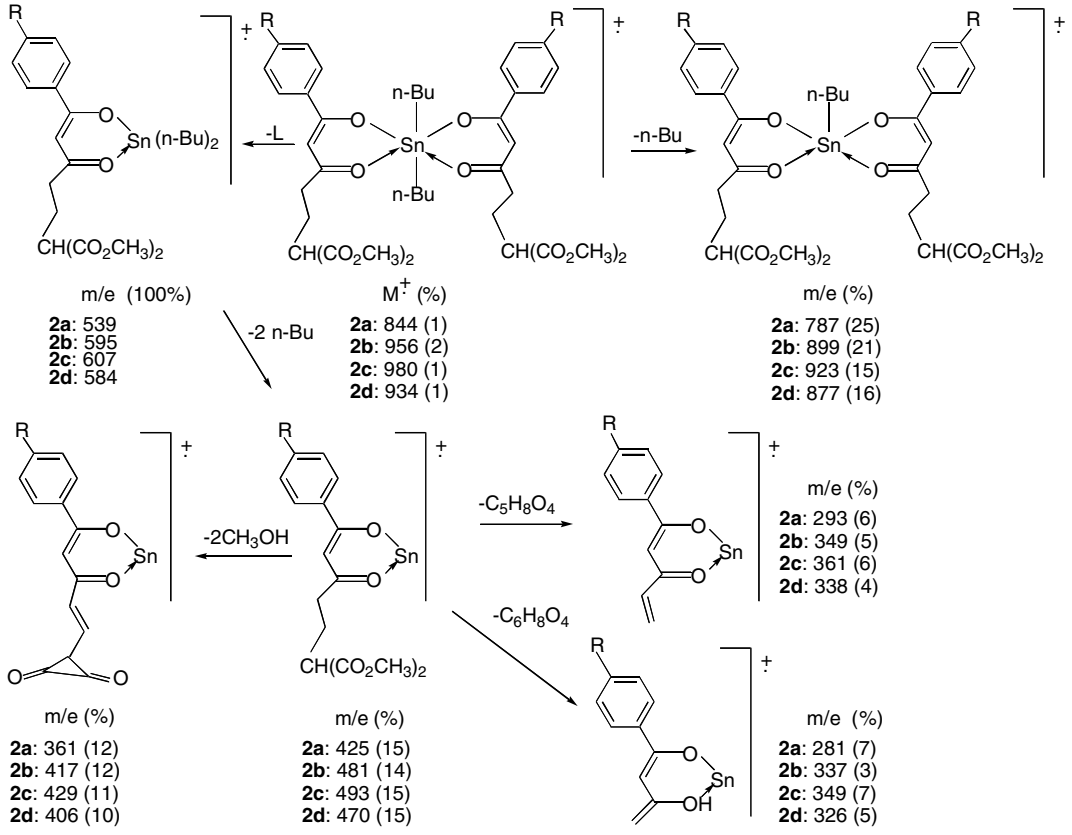


Fig. 5. FAB mass spectra for compounds **2a**–**2d**.

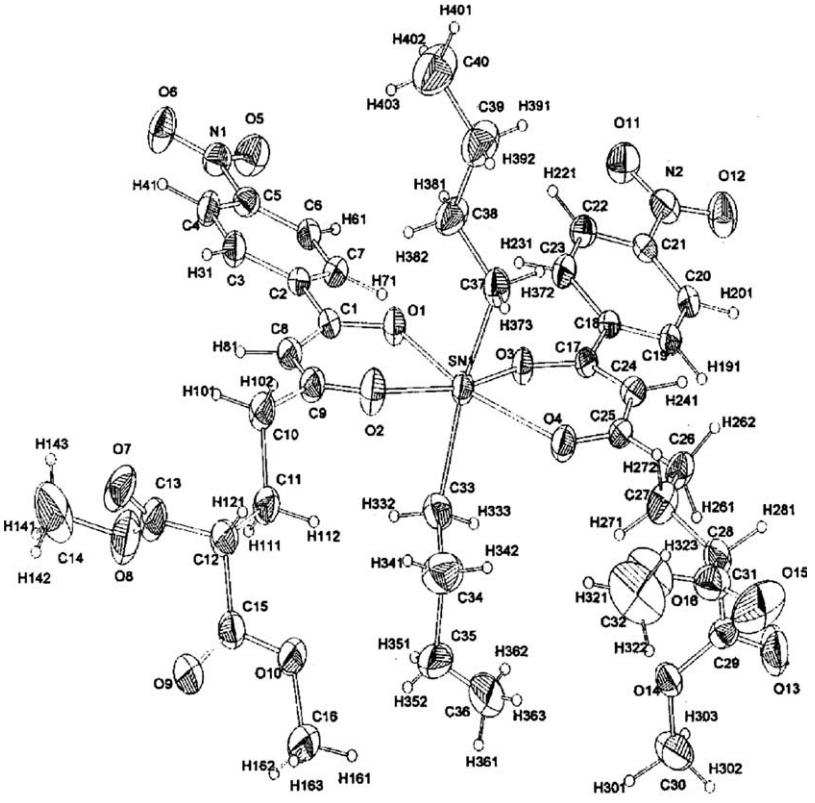


Fig. 6. Molecular structure of $C_{40}H_{50}N_2O_{16}Sn$ and crystallographic numbering scheme.

Table 5
Bond distances selected (Å) for $C_{40}H_{50}N_2O_{16}Sn$ (**2d**)

Sn(1)–O(1)	2.112(4)	C(1)–C(8)	1.387(9)
Sn(1)–O(2)	2.292(5)	C(8)–C(9)	1.396(10)
Sn(1)–O(3)	2.115(4)	C(9)–O(2)	1.261(9)
Sn(1)–O(4)	2.349(4)	O(3)–C(17)	1.289(7)
Sn(1)–C(33)	2.133(9)	C(17)–C(24)	1.380(9)
Sn(1)–C(37)	2.134(8)	C(24)–C(25)	1.416(9)
O(1)–C(1)	1.307(7)	O(4)–C(25)	1.257(8)

there are the following intramolecular contacts: NO(6)···$H(41)_{arom}$ 2.4553(72), NO(5)···$H(61)_{arom}$ 2.3962(72), C–O(7)···$H(121)_{methynic}$ 2.4265(84), NO(11)···$H(221)_{arom}$ 2.4682(65), NO(12)···$H(201)_{arom.}$ 2.4576(74), C=O(15)···$H(281)_{methynic}$ 2.5368(101) and C–O(14)···$H(271)_{methylenic}$ 2.5674(61) Å, which are significantly shorter than the sum of van der Waals radii of oxygen and hydrogen (2.70 Å) [40].

The six-membered ring Sn(1), O(1), C(1), C(8), C(9), O(2) adopts an intermediate between envelope and screw-boat conformation, while the ring Sn(1), O(3), C(17), C(24), C(25), O(4) adopts an intermediate envelop and twist conformation, from their puckering parameters calculated according to Cremer and Pople [41,42], which are: $Q = 0.261$, $\theta = 60.35°$, $\phi = 10.56°$ and $Q = 0.241$, $\theta = 62.06°$, $\phi = 10.64°$, respectively. Therefore the out of-plane displacements calculated for the atoms of each ring are: Sn(1), −0.178(3); O(1), 0.091(6); C(1), 0.034(8); C(8), −0.073(8); C(9), −0.014(9); O(2), 0.139(7) and Sn(1), −0.166(3); O(3), 0.122(6); C(17), −0.001(8); C(24), −0.075(8); C(25), 0.030(8); 0(4), 0.090(6) Å, which give evidence that the six-membered rings do not lie in a plane [43]. In addition, the equatorial plane made by the four O atoms has the oxygen atoms associated with the primary bonds, O(1) and O(3), closer to each other than those associated with the secondary bond, O(2) and O(4), as shown by the corresponding angles O(3)–Sn(1)–O(1) = 79.51(16)° and O(4)–Sn(1)–O(2) = 118.60(17)°, as well as O(1)–O(3) and O(2)–O(4) intramolecular distances of 2.7034(63) and 3.9915(74) Å, respectively. Therefore, bond angle values for C(33)–Sn(1)–O(1), C(33)–Sn(1)–O(3), C(37)–Sn(1)–O(1), C(37)–Sn(1)–O(3) are 99.80(3)°, 97.10(3)°, 99.90(2)° and 97.90(2)°, which are bigger than those of C(33)–Sn(1)–O(2) 85.20(3)°, C(33)–Sn(1)–O(4) 84.50(3)°, C(37)–Sn(1)–O(2) 86.40(3)° and C(37)–Sn(1)–O(4) 80.90(2)°, indicating that the *n*-Bu groups are folded towards the side of the secondary bonds.

3. Conclusion

The new diorganotin(IV) compounds **2a**–**2d** were obtained as enolate derivatives. The tin atom is hexacoordinated in a skewed trapezoidal bipyramidal (STB) geometry according to their spectroscopic data in solution. Their ^{119}Sn variable-temperature NMR studies provide information of the existence of *anti* and *syn* trans isomers, the *syn* isomer being in the major proportion at low temperature. The same result was observed in the solid state ^{13}C and ^{119}Sn NMR for compound **2d**, while its X-ray diffraction study at 168 K shows only the *syn* species, which exhibits interesting intermolecular contacts, NO(6)···$H(191)_{arom.}$, C=O(13)···$H(31)_{arom.}$, C=O(15)···$H(121)_{methynic}$, C=O(9)···$H(281)_{methynic}$ and C=O(13)···$H(81)_{vinylic}$.

The solid state NMR data, as well as low-temperature NMR studies should mirror more closely the structure deduced from the X-ray crystal structure analysis at 168 K where the molecules are effectively locked into place by intermolecular forces, therefore it is possible determine that the major product corresponds to the *trans-syn* isomer and the minor to the *trans-anti* isomer.

4. Experimental

4.1. General procedure and measurements

The reagents were purchased from Aldrich Co. 1,3-Diketone malonates **1a**–**1d** were prepared according to the literature [33,34]. ^{1}H, ^{13}C and ^{119}Sn NMR spectra were recorded on Jeol GLX-270, Jeol Eclipse-400 and Bruker Avance 300-DPX spectrometers, $CDCl_3$ was used as solvent. The solid state ^{119}Sn and ^{13}C CP-MAS NMR spectra for compound **2d** were obtained on a Bruker ASX300 at 10.7 and 10.73 KHz, respectively. High resolution mass spectra (FAB) were obtained with a Jeol JMS-AX 505 mass spectrometer, and infrared spectra were recorded on a Perkin–Elmer 16F PC FT-IR spectrometer. The melting point for compound **2d** was measured in an open capillary tube on a Gallemkamp MFB-595 apparatus and it was uncorrected.

4.2. Preparation of compounds *2a*–*2d*

The procedure outlined below is general for the preparation of compounds **2a**–**2d**.

4.2.1. Synthesis of di-n-butyl[bis{dimethyl-2-(3-oxo-5-phenylpenten-5-ato) malonate}]tin(IV) (*2a*)

A solution of 63.6 mg (0.20 mmol) of **1a** in 10 ml of benzene was placed in a flask equipped with a magnetic stirrer and Dean-Stark trap and 25.7 mg (0.1 mmol) of di-*n*-butyltin(IV) oxide were added. The suspension was refluxed for 8 h. After being cooled to room temperature, the solvent was evaporated under vacuum. The residue was treated with chloroform, the solution was filtered and the solvent was evaporated under

vacuum to yield 41 mg (49%) of compound **2a** as a yellow oil.

4.2.2. Synthesis of di-n-butyl[bis{dimethyl-2-(5-[4-tertbutylphenyl]-3-oxo-penten-5-ato)-malonate}]tin(IV) (2b)

57 mg (0.16 mmol) of compound **1b** and 20.3 mg (0.08 mmol) of di-*n*-butyltin(IV) oxide gave 60 mg (78%) of compound **2b** as a yellow oil.

4.2.3. Synthesis of di-n-butyl[bis{dimethyl-2-(5-[4-trifluoromethylphenyl]-3-oxo-penten-5-ato)-malonate}]tin(IV) (2c)

81.7 mg (0.22 mmol) of compound **1c** and 27.3 mg (0.11 mmol) of di-*n*-butyltin(IV) oxide gave 95 mg (88%) of compound **2c** as a yellow oil.

4.2.4. Synthesis of di-n-buty[bis{dimethyl-2-(5-[4-nitropheny]-3-oxo-penten-5-ato)-malonate}]tin(IV) (2d)

131.2 mg (0.37 mmol) of compound **1d** and 46.6 mg (0.19 mmol) of di-*n*-butyltin(IV) oxide gave a solid, which was recrystallized from methanol to yield 95 mg (54%) of compound **2d**, m.p. 93–94 °C.

4.3. Crystal structure determination of compound 2d

Diffraction data from compound **2d** were collected on an Enraf-Nonius Kappa CCD diffractometer at 168 K. Compound **2d**, $C_{40}H_{50}N_2O_{16}Sn$ (MW 933.53), crystallized in the space group $P\bar{1}$, triclinic, from methanol as yellow light rectangular prisms, size: $0.45 \times 0.33 \times 0.21$ mm^3 with $a = 10.0920(2)$, $b = 13.0880(4)$, $c = 17.3920(2)$ Å, $V = 2142.38(17)$ Å^3, $\alpha = 75.432(10°)$, $\beta = 86.744(15°)$, $\gamma = 74.502(11°)$; $\rho = 1.447$ g/cm^3, $Z = 2$, $\mu = 0.668$ mm^{-1}, $F(0\,0\,0) = 964$. Data collection: a total of 32 417 reflections were measured ($2° > \theta > 26°$), 9831 were independent and of these 3885 were considered observed [$F_o > 4.0\sigma(F_o)$]. Solution and refinement: direct methods, all non hydrogen atoms were refined anisotropically, $R = 0.0606$, $Rw = 0.0570$, $w = 1/\sigma^2$, GoF = 1.1308, largest residual electron density peak/hole in the final difference map: 0.79/−0.50 e Å^{-3}. Atomic scattering factors were taken from the International Tables for X-ray Crystallography [44]. Data reduction were performed by Denzo [45]. All calculations were carried out using the CRYSTALS program package [46] and the molecular graphics by the CAMERON program [47,48].

Acknowledgements

The authors thank the "Consejo Nacional de Ciencia y Tecnología" (Conacyt-México) for financial support and for a research scholarship to D.A.N.A. We also acknowledge the help of Luis Velasco for recording the FAB-MS, Marco Antonio Leyva for X-ray crystallography and Dr. Bárbara Gordillo for reading the manuscript and for her helpful comments.

Appendix A. Supplementary data

Crystallographic data for **2d** has been deposited at the Cambridge Crystallographic Data Center, CCDC No. 223635. Copies of this information may be obtained free of charge from The Director, CCDC, 12 Union Road, Cambridge CB2 1EZ, UK (Fax: +44-1223-366-033; e-mail: deposit@ccdc.cam.ac.uk or http://www.ccdc.cam.ac.uk). Supplementary data associated with this article can be found in the online version at doi:10.1016/j.poly.2005.02.024.

References

[1] J.G. Noltes, H.M.J.C. Creemers, G.J.M. van der Kerk, J. Organomet. Chem. 11 (1968) 21.
[2] S.S. Labadie, J.K. Stille, Tetrahedron 40 (1984) 2329.
[3] Y. Yamamoto, H. Yataggi, K. Maruyama, J. Chem. Soc., Chem. Commun. 162 (1981).
[4] Y. Odic, M. Pereyre, J. Organomet. Chem. 55 (1973) 273.
[5] M.E. Jung, R.B. Blum, Tetrahedron Lett. 43 (1977) 3791.
[6] M. Kosugi, I. Hagiwara, T. Sumiya, T. Migita, Bull. Chem. Soc. Jpn. 57 (1984) 242.
[7] M. Fosugi, I. Hagiwara, T. Migita, Chem. Lett. (1983) 839.
[8] M. Kosugi, M. Koshiba, A. Atoh, H. Sano, T. Migita, Bull. Chem. Soc. Jpn. 59 (1986) 677.
[9] M. Pereyre, B. Bellegarde, J. Mendelsohn, J. Valade, J. Organomet. Chem. 11 (1968) 97.
[10] I.F. Lutsenko, Y.I. Baukov, J. Yu Balavin, J. Organomet. Chem. 24 (1970) 359.
[11] K. Kobayashi, M. Kawanisi, I. Hitomi, S. Kozima, Chem. Lett. (1984) 497.
[12] M. Yasuda, Y. Katoh, I. Shibata, A. Baba, H. Matsuda, N. Sonada, J. Org. Chem. 59 (1994) 4386.
[13] M. Pereyre, J.P. Quintard, A. Rahm, A Tin in Organic Synthesis, Butterworth, London, 1987.
[14] I. Shibata, A. Baba, Org. Prep. Proced. Int. 26 (1994) 87.
[15] J.A.S. Smith, E.J. Wilkins, J. Chem. Soc. (A) (1966) 1749.
[16] B. Bovio, A. Cingolani, F. Marchetti, C. Pettinari, J. Organomet. Chem. 458 (1993) 39.
[17] C. Pettinari, F. Marchetti, A. Cingolani, D. Leonesi, E. Mundorff, M. Rossi, F. Caruso, J. Organomet. Chem. 557 (1998) 187.
[18] W. Ralph Jr., R. Jones, C. Fay, Inorg. Chem. 12 (1973) 2599.
[19] C. Pettinari, G. Rafaiani, G.G. Lobbia, A. Lorenzotti, F. Bonati, B. Bovio, J. Organomet. Chem. 405 (1991) 75.
[20] C. Pettinari, F. Marchetti, A. Gregori, A. Cingolani, J. Tanski, M. Rossi, F. Caruso, Inorg. Chem. Acta 257 (1997) 37.
[21] C. Pettinari, F. Marchetti, A. Cingolani, A. Lorenzotti, E. Mundorff, M. Rossi, F. Caruso, Inorg. Chem. Acta 262 (1997) 33.
[22] F. Caruso, M. Rossi, F. Marchetti, C. Pettinari, Organometallics 18 (1999) 2398.
[23] J.J. Otera, Organomet. Chem. 221 (1981) 57.
[24] J. Otera, T. Hinoishi, Y. Kawabe, R. Okawara, Chem. Lett. (1981) 273.
[25] S.K. Brama, W.H. Nelson, Inorg. Chem. 21 (1982) 4077.
[26] W.F. Howard Jr., R.W. Crecely, W.H. Nelson, Inorg. Chem. 24 (1985) 2204.

[27] D.A. Nieto-Álvarez, F. Jiménez-Cruz, T. Mancilla, Polyhedron 21 (2002) 417.
[28] T. Mancilla, N. Farfán, D. Castillo, L. Molinero, A. Meriem, R. Willem, B. Mahieu, M. Gielen, Main Group Met. Chem. XII (1989) 213.
[29] T. Mancilla, L. Carrillo, Main Group Met. Chem. 17 (1994) 363.
[30] T. Mancilla, D. Castillo, L. Carrillo, N. Farfán, Heteroatom Chem. 10 (1999) 133.
[31] T. Mancilla, L. Carrillo, L.S. Zamudio-Rivera, C. Camacho-Camacho, D. de Vos, R. Kiss, F. Darro, B. Mahieu, E.R. Tiekink, H. Rahier, M. Gielen, M. Kemmer, M. Biesemans, R. Willem, Appl. Organometal. Chem. 15 (2001) 593.
[32] A.J. Crowe, in: M. Gielen (Ed.), Metal-based Anti-tumour Drugs, Freund Publishing House LTD, England, 1988, p. 141.
[33] F. Jiménez-Cruz, L.A. Maldonado, R. Cetina, Tetrahedron Lett. 39 (1998) 2685.
[34] F. Jiménez-Cruz, L.A. Maldonado, R. Cetina, H. Rios-Olivares, Synth. Commun. 30 (2000) 3439.
[35] J. Jurkschat, C. Mügge, A. Tzschach, A. Zschunke, F.M. Larin, V.A. Pestunovich, M.G. Voronokov, J. Organomet. Chem. 139 (1977) 279.
[36] J. Holecek, M. Nadvornik, K. Handlir, A. Lycka, J. Organomet. Chem. 315 (1986) 299.
[37] A. Lycka, J. Holecek, M. Nadvornik, Main Group Met. Chem. 12 (1989) 169.
[38] B. Wrackmeyer, in: G.A. Webb (Ed.), Ann. Rep. NMR Spectroscopy, vol. 16, Academic Press, New York, 1985, pp. 73–186.
[39] J. Holecek, A. Lycka, Inorg. Chim. Acta 118 (1986) L15.
[40] A. Bondi, J. Phys. Chem. 68 (1964) 441.
[41] D. Cremer, J.A. Pople, J. Am. Chem. Soc. 97 (1975) 1354.
[42] A.Y. Zotov, V.A. Palyulin, N.S. Zefirov, J. Chem. Inf. Comput. Sci. 37 (1997) 766.
[43] (a) Platon/Pluton A.L. Spek, Acta Crystallogr. A46 (1990) C34; (b) A.L. Spek, Platon, A multipurpose Crystallography Tool, Utrecht University, Utrecht, The Netherlands, 1998.
[44] D.T. Cromer, I.T. WaberInternational Tables for X-ray Crystallography, vol. IV, Kynoch Press, England, 1974.
[45] Z. Otwinowski, W. Minor, in: C.W. Carter, R.M. Sweet (Eds.), R.M., Processing of X-ray Diffraction Data Collected in Oscillation Mode, Academic Press, Prince, E, 1996, Methods Enzymol. 276 (1997) 307–326.
[46] P.W. Betteridge, J.R. Carruthers, R.I. Cooper, K. Prout, D.J. Watkin, J. Appl. Cryst. 36 (2003) 1487.
[47] D.J. Watkin, Acta Crystallogr. A50 (1994) 411.
[48] D.J. Watkin, C.K. Prout, L.J. Pearce, CAMERON, Chemical Crystallography Laboratory, Oxford, UK, 1996.

biphosphine monoxide of metals such as nickel, palladium, rhenium, rhodium and platinum has been extensively described and some species have been found to be efficient catalysts in oligomerization reactions [7,8]. On the other hand various ruthenium complexes with O, P ligands such as keto-phosphine, ether-phosphine, ester-phosphine and *o*-phenylenobis(methyl(phenyl)-phosphine) have been reported, showing the coordination modes P ∼ O: η^1-P and P ∩ O: η^2-O,P [9]. Some of these compounds are regarded as holding interesting properties in catalytic reactions [10].

The present study reports on the synthesis of Ru(II) complexes with the hemilabile biphosphine monoxide ligand $PPh_2(CH)_2P(O)Ph_2$ (dppmO). The behavior of the *tcc*-[$RuCl_2(\eta^2$-dppmO$)_2$] complex – chlorine ions in *trans* positions, phosphorus and oxygen atoms in *cis* positions – towards carbon monoxide was also investigated and proved to be consistent with the predicted hemilabile character of the ligand.

The dppmO ligand presents two chemically different phosphorus atoms and the characterization of the synthesized species through ^{1}H and ^{31}P NMR, reported here, was a very effective tool in disclosing the phosphorus–phosphorus spin coupling systems. The reaction of the biphosphine monoxide ligand with a Ru(III) precursor yielded the *mer*-$RuCl_3(\eta^1,\eta^2$-dppmO$)_2$ complex. The crystallographic structure of the latter was determined by X-ray analysis, identifying a species analogous to the *mer*-$RuCl_3(\eta^1,\eta^2$-$Ph_2PCH_2C(O)Oet)_2$ complex described in the literature [9d].

2. Experimental

All manipulations were performed under an inert atmosphere of purified argon using Schlenk techniques. The solvents were purified according to standard procedures. The $RuCl_2(PPh_3)_3$ [11] and $[RuCl_2(COD)]_2$ [12] complexes as well as the $PPh_2(CH)_2P(O)Ph_2$ [7d] ligand were prepared according to the procedures described in the literature. CO was generated from HCO_2H with H_2SO_4. All the NMR spectra were obtained in a 9.4 T BRUKER DRX400 spectrometer at 298 K, using TMS and H_3PO_4 85% as internal and external references for ^{1}H and ^{31}P (161 MHz), respectively. The IR spectra were recorded as CsI pellets in a Bomen Hartmann and Braun MB Series model spectrometer in the 4000–200 cm^{-1} region. The elemental analysis was performed in a Fison EA 1108 model.

The electrochemical experiments were performed at room temperature in freshly distilled dichloromethane containing 0.1 mol/L TBAP under argon atmosphere (1 atm), using EG/PARC 273A electrochemical equipment. A three-electrode system was used. The working and auxiliary electrodes were a stationary platinum foil and the reference electrode was Ag/AgCl 0.1 mol/L TBAP in CH_2Cl_2, a medium in which ferrocene is oxidized at 0.43 V, with all potentials referred to this electrode.

2.1. *tcc*-[$RuCl_2(\eta^2$-dppmO$)_2$] (t = Cl) (**1**)

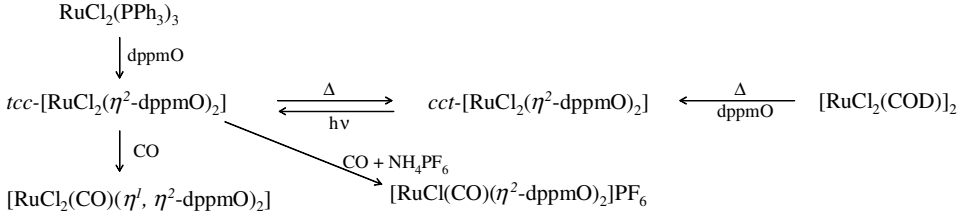
$RuCl_2(PPh_3)_3$ (0.050 g, 0.050 mmol) and $PPh_2CH_2P(O)Ph_2$ (0.042 g, 0.10 mmol) were dissolved in acetone (10 mL) and the mixture was stirred for 1 h at room temperature. During this time the color of the solution changed from dark brown to light pink and precipitation of a small amount of solid with the same color occurred. To increase the precipitation ethyl ether was added. The solid was then filtered and washed with ethyl ether. Yield: 0.045 g (94%). *Anal.* Calc. for $C_{50}H_{44}P_4O_2Cl_2Ru$: C, 61.74; H, 4.56. Found: C, 61.69; H, 4.57%. IR (CsI) (RuCl) 317 cm^{-1}; ν(P═O) 1140 cm^{-1}. See Scheme 1.

2.2. *cct*-[$RuCl_2(\eta^2$-dppmO$)_2$] (t = O) (**2**)

$PPh_2CH_2P(O)Ph_2$ (0.23 g, 0.60 mmol) and $[RuCl_2(COD)]_2$ (0.10 g, 0.30 mmol) were added to a solution of dichloromethane/methanol 1:3 (15 mL). The mixture was stirred for 18 h. At the end of this period the solvents were evaporated until only around 3 mL were left and then ethyl ether was added. A light brown solid was obtained, which was then filtered and dried under vacuum. Yield: 0.205 g (70%). *Anal.* Calc. for $C_{50}H_{44}P_4O_2Cl_2Ru$: C, 61.74; H, 4.56. Found: C, 60.85; H, 4.85%. IR (CsI). ν(P═O) 1132 cm^{-1}.

2.3. [$RuCl_2(CO)(\eta^1,\eta^2$-dppmO$)_2$] (**3**)

tcc-[$RuCl_2(\eta^2$-dppmO$)_2$], complex (**1**), was dissolved in 15 mL of dichloromethane and stirred under an atmosphere of CO at room temperature. After 10 min the



Scheme 1. Summary of the reactions for Ru(II) complexes with the dppmO ligand.

light pink color of the solution turned to light yellow. After the removal of around 10 mL of the solvent under vacuum, ethyl ether was added, observing the formation of a pale yellow solid which was then filtered and dried under vacuum. This complex had its structure determined by ^{1}H and ^{31}P NMR. IR (CsI) ν(RuCl) 320 cm^{-1}; $\nu(P_B{=}O)$ 1097 cm^{-1}; $\nu(P_D{=}O)$ 1166 cm^{-1}; ν(CO) 1975 cm^{-1}.

2.4. *[RuCl(CO)(η^2-dppmO)$_2$]PF$_6$ (**4**)*

tcc-[RuCl$_2$(η^2-dppmO)$_2$] (0.015 g, 0.015 mmol) and NH_4PF_6 (0.0244 g, 0.154 mmol) were dissolved in 1:1 methanol/dichloromethane and stirred under a CO atmosphere at room temperature. After 12 h, precipitation of a bright yellow solid occurred. The solid was then washed several times with methanol, filtered and dried under vacuum. Yield: (60%). *Anal*. Calc. for $C_{51}H_{44}P_5O_3F_6ClRu$: C, 55.17; H, 3.99%. Found: C, 54.99; H, 4.19. IR (CsI) ν(RuCl) 320 cm^{-1}; ν(P=O) 1131 cm^{-1}; ν(CO) 1946 cm^1.

2.5. *mer-RuCl$_3$(η^1,η^2-dppmO)$_2$ (**5**)*

$PPh_2CH_2P(O)Ph_2$ (0.13 g, 0.325 mmol) was added to a solution (15 mL) of methanol/dichloromethane (1:3) containing $RuCl_3 \cdot 3H_2O$ (0.04 g, 0.15 mmol). The procedure was conducted under an inert atmosphere to prevent ligand oxidation. After being stirred for 2 h, the mixture was evaporated until a volume of approximately 5 mL remained. A light orange precipitate was obtained with the addition of 15 mL of ether. The compound obtained was then filtered and dried under vacuum. Recrystallization was obtained in a mixture of ethanol/dichloromethane. Yield: 0.083 g (55%). *Anal*. Calc. for $C_{50}H_{44}P_4O_2Cl_3Ru$: C, 58.57; H, 4.33. Found: C, 59.23; H, 4.34%. EPR (experimental) g_y 2.347 and g_z 1.833. EPR (simulated) g_x 2.415, g_y 2.359 and g_z 1.833.

2.6. *X-ray crystallographic analyses of complexes **1** and **5***

Crystals were obtained through slow evaporation of methanol solvent containing the dissolved complexes, at room temperature. A single crystal of approximate dimensions of $0.25 \times 0.2 \times 0.16$ mm^3 for *tcc*-[RuCl$_2$(η^2-dppmO)$_2$] (**1**) and $0.30 \times 0.27 \times 0.20$ mm^3 for *mer*-[RuCl$_3$(η^1,η^2-dppmO)$_2$] (**5**) were used for the data collections and unit cell determinations in an Enraf Nonius CAD-4 diffractometer at room temperature. The data collections were made using the CAD-4 [13] program and the data reductions were performed with the XCAD4 [14] program. The data were corrected for Lorentz, polarization and absorption. The structures were solved using direct methods with SHELXS-97 [15]. The models were refined by full-matrix least-squares procedures on F^2 using SHELXL-97 [16]. The WINGX [17] program was used to analyze and prepare the data for publication. Crystal data, data collection procedures, structure determination

Table 1
Crystallographic data for *tcc*-RuCl$_2$(η^2-dppmO)$_2$ and *mer*-RuCl$_3$(η^1,η^2-dppmO)$_2$

Complex	*tcc*-RuCl$_2$(η^2-dppmO)$_2$	*mer*-RuCl$_3$(η^1,η^2-dppmO)$_2$
Empirical formula	$[C_{50}H_{44}O_2Cl_2P_4Ru] \cdot 1/2H_2O$	$[C_{50}H_{44}O_2Cl_3P_4Ru] \cdot 3/4H_2O$
Formula weight	981.71	1021.66
Wavelength (Å)	0.71073	1.54184
Crystal system	monoclinic	monoclinic
Space group	$P2_1/c$	Cc
Unit cell dimensions		
a (Å)	11.030(1)	13.913(1)
b (Å)	17.500(2)	18.092(2)
c (Å)	23.113(2)	21.307(2)
β (°)	97.797(9)	92.384(8)
Volume (Å^3)	4419.8(7)	5358.6(9)
Z	4	4
D_{calc} (Mg m^{-3})	1.475	1.266
Absorption coefficient (mm^{-1})	0.663	5.158
$F(000)$	2012	2090
Ranges	$0 \leqslant h \leqslant 13$; $0 \leqslant k \leqslant 20$; $-27 \leqslant l \leqslant 27$	$0 \leqslant h \leqslant 16$; $0 \leqslant k \leqslant 22$; $-25 \leqslant l \leqslant 25$
Reflections collected	8196	10516
Independent reflections [R_{int}]	7760 [0.0390]	5244 [0.0309]
θ Maximum (°)	25	70.0
Completeness to theta maximum (%)	100.0	99.3
Absorption correction	empirical (DIFABS) [20]	analytical [19]
Maximum/minimum transmission	0.8524/0.5280	0.472/0.3101
Data/restraints/parameters	7760/541	5244/2/551
Goodness-of-fit on F^2	1.008	1.024
Final R indexes [$I > 2\sigma(I)$]	$R_1 = 0.0390$, $wR_2 = 0.0853$	$R_1 = 0.0371$, $wR_2 = 0.0996$
R indexes (all data)	$R_1 = 0.1164$, $wR_2 = 0.1057$	$R_1 = 0.0372$, $wR_2 = 0.0999$
Largest difference in peak and hole (e Å^{-3})	0.380 and −0.492	0.721 and −0.813

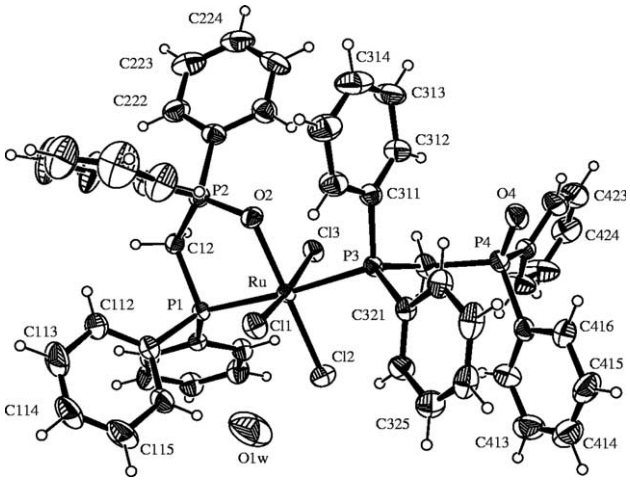


Fig. 1. ORTEP[18] type view of *mer*-$RuCl_3(\eta^1,\eta^2\text{-dppmO})_2$.

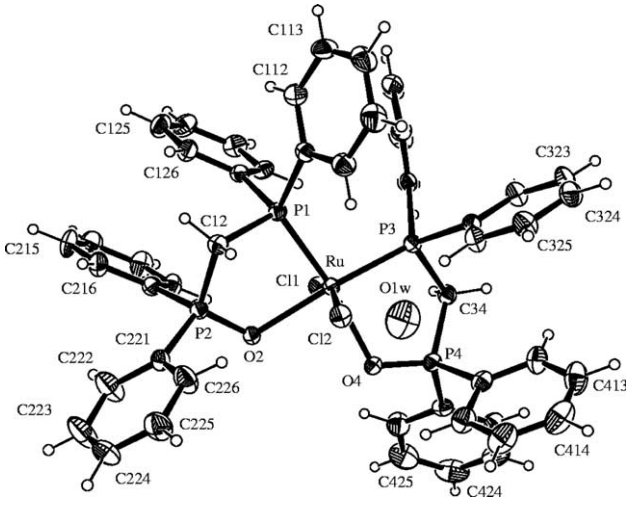


Fig. 2. ORTEP[18] type view of *tcc*-$RuCl_2(\eta^2\text{-dppmO})_2$.

methods and refinement results are summarized in Table 1. Figs. 1 and 2 were prepared using ORTEP-3 for Windows [18]. All non-H atoms were refined anisotropically. Hydrogen atoms were stereochemically positioned and refined using the riding model [21]. The aromatic and methylene H atoms were assigned a thermal parameter 20% greater than that of the equivalent isotropic thermal parameter of the associated C atom. Selected bond lengths and angles are shown in Table 2.

3. Results and discussion

The metal coordination of the *mer*-$[RuCl_3(\eta^1,\eta^2\text{-dppmO})_2]$ species (Fig. 1) may be described as a distorted octahedron with three chlorine atoms in a meridional arrangement, two phosphorus atoms in *trans* positions and the oxygen atom from one of the two phosphine moieties occupying the sixth coordination site. The distortion observed is mainly due to the steric

Table 2
Selected bond lengths (Å) and angles (°)[a]

tcc-$RuCl_2(\eta^2\text{-dppmO})_2$		*mer*-$RuCl_3(\eta^1,\eta^2\text{-dppmO})_2$	
Ru–O(2)	2.214(3)	Ru–O(2)	2.076(4)
Ru–O(4)	2.193(3)	Ru–Cl(1)	2.337(1)
Ru–Cl(1)	2.407(1)	Ru–Cl(1)	2.333(2)
Ru–Cl(2)	2.421(1)	Ru–Cl(3)	2.373(1)
Ru–P(1)	2.239(1)	Ru–P(1)	2.372(1)
Ru–P(3)	2.236(1)	Ru–P(3)	2.396(1)
P(2)–O(2)	1.502(3)	P(2)–O(2)	1.505(4)
P(4)–O(4)	1.493(3)	P(4)–O(4)	1.495(5)
O(2)–Ru–Cl(1)	85.67(8)	O(2)–Ru–Cl(1)	86.9(1)
O(2)–Ru–Cl(2)	83.84(8)	O(2)–Ru–Cl(2)	177.8(1)
O(2)–Ru–P(1)	85.59(8)	O(2)–Ru–Cl(3)	85.4(1)
O(2)–Ru–P(3)	171.00(8)	O(2)–Ru–P(1)	85.6(1)
O(4)–Ru–O(2)	86.8(1)	O(2)–Ru–P(3)	89.9(1)
O(4)–Ru–Cl(1)	82.14(9)	Cl(1)–Ru–Cl(3)	171.99(6)
O(4)–Ru–Cl(2)	84.89(9)	Cl(1)–Ru–P(1)	92.71(5)
O(4)–Ru–P(1)	171.79(9)	Cl(1)–Ru–P(3)	88.27(5)
O(4)–Ru–P(3)	87.90(9)	Cl(2)–Ru–Cl(1)	94.89(6)
Cl(1)–Ru–Cl(2)	163.73(5)	Cl(2)–Ru–Cl(3)	92.88(5)
P(1)–Ru–Cl(1)	100.35(5)	Cl(2)–Ru–P(2)	93.09(5)
P(1)–Ru–Cl(2)	91.22(5)	Cl(2)–Ru–P(3)	91.38(5)
P(3)–Ru–Cl(1)	86.40(5)	Cl(3)–Ru–P(3)	89.62(4)
P(3)–Ru–Cl(2)	102.93(5)	P(1)–Ru–Cl(3)	88.79(5)
P(3)–Ru–P(1)	100.04(5)	P(1)–Ru–P(3)	175.33(5)

[a] Estimated standard deviations are given in parentheses.

constraints caused by the chelate ring formed between the phosphine ligand and the metal center. Braunstein and coworkers described the X-ray structure of the *mer*-$[RuCl_3(\eta^1,\eta^2\text{-}(PPh_2CH_2C(O)OEt)_2]$ complex, analogous to the one synthesized here [9d]. In their study the Ru(III)–O distance [2.143(5) Å] is reported to be the shortest one encountered in similar complexes, being just slightly longer than the sum of the two covalent radii. For the *mer*-$[RuCl_3(\eta^1,\eta^2\text{-dppmO})_2]$ species an even shorter Ru(III)–O distance was found [2.076(4) Å]. This fact may be attributed to the greater hard acid character of the oxygen atom, which is directly connected to a phosphorus atom through a double bond system.

The EPR spectrum of *mer*-$RuCl_3(\eta^1,\eta^2\text{-dppmO})_2$ in a dichloromethane frozen solution (at −160 °C) showed a well resolved $g_\perp$ signal of 1.833. The other two g values are very close to each other, with $g_\parallel = 2.388$ and 2.347. This fact indicates the presence of an octahedral configuration with slightly rhombic distortions, consistent with the crystallographic structure shown in Fig. 1.

The structure of the *tcc*-$[RuCl_2(\eta^2\text{-dppmO})_2]$ complex was also determined by single crystal X-ray diffraction, showing both chlorine atoms in *trans* positions and the phosphorus and oxygen atoms of the two ligands in *cis* positions, respectively (Fig. 2). The configuration observed at the metal center is also a distorted octahedron in which the angle between the axial chlorines is smaller than 180°, and the chelate rings show O–Ru–P angles close to 85°. The Ru–Cl distances of ca. 2.4 Å are typical of ruthenium (II) complexes, but the Ru–P bonds are comparatively shorter than those found in simple

biphosphine ligands probably due to the presence of the oxygen atom, which makes the phosphorus atoms harder [22–29].

The IR spectra of the *tcc*-$RuCl_2(\eta^2\text{-dppmO})_2$ and *cct*-$RuCl_2(\eta^2\text{-dppmO})_2$ isomers revealed a P=O band dislocated 40–50 cm^{-1} to a region of lower energy, compared to the free ligand [30]. This is indicative of the coordination, through the oxygen atom, of the mono-oxidated ligand to the metal. The Ru–Cl stretching band appears in the region of 310–340 cm^{-1} for these isomeric complexes.

The Ru(II) complexes studied had their structures investigated by NMR, resulting in a very interesting set of data. For this reason, two-dimensional NMR techniques were also applied in order to obtain a deeper understanding of the complexes. The ^1H NMR multiplicity spectral analysis became difficult due to the coupling between ^1H and ^{31}P. In order to eliminate this interaction a $^1H\{^{31}P\}$ spectrum was run, enabling the assignment of the methylene hydrogens between the two phosphorus of the dppmO ligand and the *ortho* hydrogens of the two kinds of aromatic rings (A and B, see Scheme 2). From the integral values it was possible to identify all the other hydrogen chemical shifts. To confirm this assignment a ^1H–^{31}P HMBC was also run using 2 and 8 Hz. In these spectra, it was possible to observe the correlation between the phosphorus and the hydrogen atoms positioned at 2, 3 and 4 bonds, corresponding to *ortho*, *meta* and *para* hydrogens of the phenylic rings A and B. In the $^{13}C\{^1H\}$ spectrum, all the ^{13}C chemical shifts were identified and most of the ^{13}C–^{31}P coupling constants were observed. A ^1H–^{13}C HMCB spectrum enabled the correlation between all the hydrogens and the respective carbons of the phenylic rings. Based on the ^1H–^{31}P HETCOR NMR spectrum, it is possible to conclude that the most deshielded hydrogens pertaining to the phenylic ring correlate to the more shielded phosphorus type (P_A) and not the opposite, as one could expect. These data are presented in the supplemental section.

The ^{31}P chemical shifts and coupling constants of the *tcc*-$RuCl_2(\eta^2\text{-dppmO})_2$ and *cct*-$RuCl_2(\eta^2\text{-dppmO})_2$ isomers are summarised in Table 3 and the phosphorus nuclei are considered as an AA′XX′ spin system. The values for N and M are actually the sum or difference of the former coupling constants J, where $N = [^2J(P_AP_B) + {}^4J(P_AP_{B'})]$, and $M = [^2J(P_AP_{A'}) + {}^4J(P_BP_{B'})]$. Abraham [31] and Harris [32] consider the $^4J(P_BP_{B'})$ coupling constant to be equal to zero in the simple AA′XX′ systems, which makes the value of the constant M basically the coupling between P_A and $P_{A'}$ corresponding, in our case, to the coupling between the two phosphorus atoms in the *cis* position.

Table 3
$^{31}P\{^1H\}$ NMR of the *tcc*-$RuCl_2(\eta^2\text{-dppmO})_2$ and *cct*-$RuCl_2(\eta^2\text{-dppmO})_2$ isomers

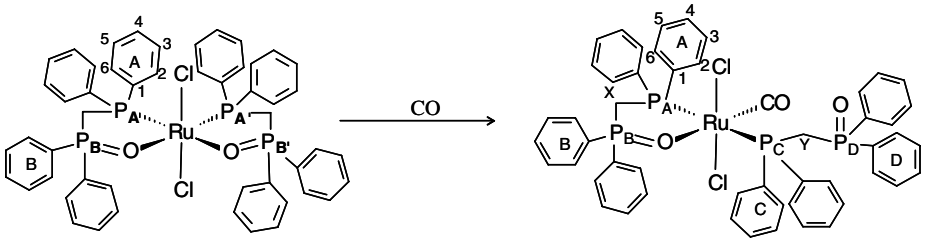
Complexes	δ	M	N	L
tcc-$RuCl_2(\eta^2\text{-dppmO})_2$	P_A 52.1 P_B 53.8	43.8	17.1	3.6
cct-$RuCl_2(\eta^2\text{-dppmO})_2$	P_A 48.5 P_B 59.2	n.o.	16.0	4.9

n.o., not observable; $N = [^2J(P_AP_B) + {}^4J(P_AP_{B'})]$, in Hz; $M = [^2J(P_AP_{A'}) + {}^4J(P_BP_{B'})]$, in Hz; $L = [^2J(P_AP_B) + {}^3J(P_AP_{B'})]$; δ ppm, in relation to H_3PO_4 85%.

The reaction of *tcc*-$RuCl_2(\eta^2\text{-dppmO})_2$ with CO generates the $RuCl_2(CO)(\eta^1,\eta^2\text{-dppmO})_2$ species, which shows a weak band at 320 cm^{-1} related to νRu–Cl, suggesting a *trans* position chlorides, and two strong bands (at 1097 and at 1166 cm^{-1}) attributed to stretching P=O bonds. A very intense band at 1975 cm^{-1} for νC≡O is also observed.

For $RuCl_2(CO)(\eta^1,\eta^2\text{-dppmO})_2$ (**3**) the $^{31}P\{^1H\}$ NMR spectrum shows four different phosphorus atoms. From ^{31}P–^{31}P COSY (Fig. 3) the deshielded chemical shift was attributed to phosphorus P_B (see Scheme 2) based on the fact that it is coordinated to the metal through oxygen, having a similar chemical environment to the P_B phosphorus in complex **1**. For complex **3**, it was possible to attribute unequivocally all the phosphorus atoms of the molecule (see Table 4). The P_A and P_C signals, with δ 40.8 and 27.2, respectively, are double double doublets due to three possible couplings. Thus, P_A couples with P_C with a coupling constant about 10 times the value of a *cis* coupling, in the 30–40 Hz range [33]. This is characteristic of *trans* position phosphorus atoms and $^2J(P_CP_A)$ = 375.8 Hz.

With the data obtained from ^1H–^{31}P HMBC, using 8 and then 2 Hz for the coupling constants in the NMR experiment, it was possible to finally see the connection



Scheme 2. Structures of *tcc*-$RuCl_2(\eta^2\text{-dppmO})_2$ and $RuCl_2(CO)(\eta^1,\eta^2\text{-dppmO})_2$.

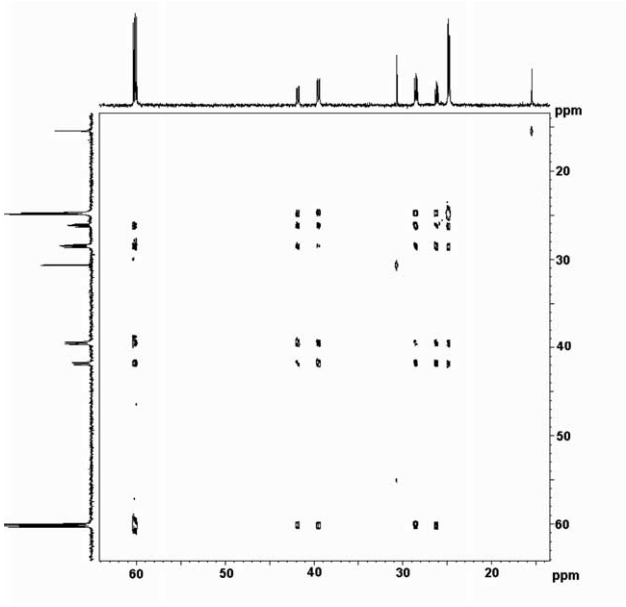


Fig. 3. ^{31}P–^{31}P COSY NMR spectrum in $CDCl_3$ of $RuCl_2(CO)(\eta^1,\eta^2\text{-dppmO})_2$.

between the *ortho* hydrogen from the phenylic ring, as well as the methylene hydrogen atoms of the ligand, to the corresponding phosphorus atoms (data reported in the supplemental section). In the spectrum where 2 Hz was used, the correlation with hydrogens in *meta* and *para* positions with the respective phosphorus was established. In addition ^1H–^{13}C gHSQC and $^{31}C\{^1H\}$ spectra were also acquired enabling the assignment of all carbon chemical shifts related to the hydrogens of rings A, B, C and D and most of the $J_{13C-31P}$ coupling constants.

A new mono-carbonyl cationic complex was obtained through the reaction of *tcc*-$RuCl_2(\eta^2\text{-dppmO})_2$ with NH_4PF_6 in the presence of CO. The $[RuCl(CO)(\eta^2\text{-dppmO})_2]PF_6$ complex was also characterized by IR and NMR spectroscopy. The IR spectrum of this new species displays an intense band at 1946 cm^{-1} attributed to $\nu C{\equiv}O$ and a broad band at 1131 cm^{-1} related to the P═O group coordinated to the metal center. A band at 840 cm^{-1} due to the presence of PF_6^- as a counter ion was also observed.

The $^{31}P\{^1H\}$ NMR spectrum of $[RuCl(CO)(\eta^2\text{-dppmO})_2]PF_6$ is very similar to the spectrum of $RuCl_2(CO)(\eta^1,\eta^2\text{-dppmO})_2$, except that in this case both phosphorus atoms bonded to the oxygen atoms have chemical shifts in the low field region, at 71.3 and 64.1 ppm, respectively (see Table 4). These facts suggest that for this molecule the two P═O groups of the phosphine ligand are coordinated to the metal. The two double double doublets with δ 40.3 and 25.7 were assigned to P_A and P_C, respectively. These two phosphorus atoms are *trans* to one another, therefore they have a coupling constant of ca. 300 Hz.

Cyclic voltammetric measurements of the *tcc*-$RuCl_2(\eta^2\text{-dppmO})_2$ and *cct*-$RuCl_2(\eta^2\text{-dppmO})_2$ isomers showed reversible processes, attributed to the redox pair RuIII/II. The $E_{1/2}$ value for the *cct* species (Cl atoms in the *cis* position) is more anodic than the value found for the *tcc* complex (Table 5). This fact is due to the *trans* cooperative effect, which describes a rise in the magnitude of the retrodonation metal → ligand in *cis* isomers of $MCl_2(dppm)_2$ (M = Ru and Os) complexes [34,35]. As expected, the carbonyl complexes $RuCl_2(CO)(\eta^1,\eta^2\text{-dppmO})_2$ and $[RuCl(CO)(\eta^2\text{-dppmO})_2]PF_6$ presented much more anodic $E_{1/2}$ values, even for a reversible $1e^-$ process, as determined by differential pulse voltammetry. It is interesting to observe that when the CO molecule displaces a Cl instead of an O atom of the O,P ligand, as in the case of the cationic species $[RuCl(CO)(\eta^2\text{-dppmO})_2]PF_6$, the redox potential is appreciably increased, as compared to the case in the $RuCl_2(CO)(\eta^1,\eta^2\text{-dppmO})_2$ complex.

We find that the *tcc*-$RuCl_2(\eta^2\text{-dppmO})_2$ isomer can be easily and quantitatively converted into the *cct*-$RuCl_2(\eta^2\text{-dppmO})_2$ isomer by thermolysis (heating at reflux in CH_2Cl_2) and the opposite conversion is reached by photolysis of *cct*-$RuCl_2(\eta^2\text{-dppmO})_2$ in CH_2Cl_2

Table 4
^{31}P NMR Chemical Shifts (δ) and J coupling constants (Hz) for $RuCl_2(CO)(\eta^1,\eta^2\text{-dppmO})_2$ and $[RuCl(CO)(\eta^2\text{-dppmO})_2]PF_6$ complexes

	δ[a]	J[b]
$RuCl_2(CO)(\eta^1,\eta^2\text{-dppmO})_2$		
P_A	40.8ddd	J_{AC} = 375.80; J_{AB} = 35,00; J_{AD} = 8.90
P_B	60.1dd	J_{AB} = 35.00; J_{BC} = 20.80
P_C	27.2ddd	J_{CA} = 375.80; J_{CD} = 27.60; J_{BC} = 20.80
P_D	24.2dd	J_{DC} = 27.60; J_{DA} = 8.90
$[RuCl(CO)(\eta^2\text{-dppmO})_2]PF_6$		
P_A	40.3ddd	J_{AC} = 354.2; J_{AB} = 33.3; J_{AD} = 16.6
P_B	64.1dd	J_{BA} = 33.3; J_{BC} = 21.5
P_C	25.7ddd	J_{CA} = 354.2; J_{CD} = 31.3; J_{CB} = 21.5
P_D	71.3dd	J_{DC} = 31.3; J_{DA} = 16.6
PF_6^-	−143.4q	$J_{31P-19F}$ = 712.8

[a] δ ppm, in relation to H_3PO_4.
[b] In Hz.

Table 5
$E_{1/2}$ (RuIII/II) potentials for complexes **1**–**4**

Complexes	$E_{1/2}$ (RuIII/II)[a]
tcc-$RuCl_2(\eta^2\text{-dppmO})_2$	0.40
cct-$RuCl_2(\eta^2\text{-dppmO})_2$	0.53
$RuCl_2(CO)(\eta^1,\eta^2\text{-dppmO})_2$	1.10
$[RuCl(CO)(\eta^2\text{-dppmO})_2]PF_6$	1.51

[a] In V.

solution with white light, resulting in a quantitative conversion to *tcc*-$RuCl_2(\eta^2\text{-dppmO})_2$. These processes were followed by cyclic voltammetric and $^{31}P\{^1H\}$ measurements. Similar conversions were observed for the *cis*- and *trans*-$M(dppm)_2Cl_2$ ($M = Os^{II}$, Ru^{II}) complexes [35]. Since the $^{31}P\{^1H\}$ NMR experiments during the isomerization process show free dppmO it is possible to infer that a dissociative mechanism is involved.

As mentioned in the experimental section, the *cct*-$RuCl_2(\eta^2\text{-dppmO})_2$ isomer is light brown while the *tcc*-$RuCl_2(\eta^2\text{-dppmO})_2$ isomer is pink. Our hypotheses is that the pink color of *tcc*-$RuCl_2(\eta^2\text{-dppmO})_2$ is due to the MLTC transition at 502 nm of the ruthenium metal to the oxygen atoms of the P=O groups *trans* to phosphorus atoms. In this case, this transition could easily occur (at low energy) since the phosphorus atoms are good π acceptors and could make the oxygen atoms harder and better electron acceptors. It is worth mentioning that complexes such as $RuCl_2(dppm)_2$ (with the absence of an oxygen atom in the ligand) are yellow or light brown and show MLTC transitions below 400 nm [35]. *cct*-$RuCl_2(\eta^2\text{-dppmO})_2$ shows a MLTC transition at 340 nm ($\varepsilon \approx 10^3$ $M^{-1}\,cm^{-1}$). On the other hand *tcc*-$RuCl_2(\eta^2\text{-dppmO})_2$ presents two shoulders (at about 340 and 400 nm) and a well defined band at 502 nm ($\varepsilon \approx 10^2$ $M^{-1}\,cm^{-1}$). Thus the isomerization process can be followed by UV–Vis spectroscopy in CH_2Cl_2.

Acknowledgments

The authors acknowledge the Brazilian agencies CAPES, CNPq and FAPESP for the financial support given to this research.

Appendix A. Supplementary data

Supplementary data associated with this article can be found in the online version at doi:10.1016/j.poly.2005.02.026.

References

[1] H. Yang, M. Alvarez-Gressier, N. Lugan, R. Mathieu, Organometallics 16 (1997) 1401.
[2] I. Le Gall, P. Laurent, E. Soulier, J.-Y. Salaün, H. des Abbayes, J. Organomet. Chem. 567 (1998) 13.
[3] S. Borns, R. Kadyrov, D. Heller, W. Baumann, A. Splannenberg, R. Kempe, J. Holz, A. Börner, Eur. J. Inorg. Chem. 9 (1998) 1291.
[4] C.S. Slone, D.A. Weinberger, Prog. Inorg. Chem. 48 (1999) 233.
[5] A. Bader, E. Lindner, Coord. Chem. Rev. 108 (1991) 27.
[6] V.V. Grushin, Chem. Rev. 104 (2004) 1629.
[7] (a) I. Brassat, U. Englert, W. Keim, D.P. Kertel, S. Killat, G.P. Suranna, R. Wang, Inorg. Chim. Acta 280 (1998) 150;
(b) R.J. Coyle, Y.L. Slovokhotov, M.Y. Antipin, V.V. Grushin, Polyhedron 17 (1998) 3059;
(c) X.L.R. Fontaine, E.H. Fowles, T.P. Layzell, B.L. Shaw, M. Thornton-Pett, J. Chem. Soc., Dalton Trans. (1991) 1519;
(d) S.J. Higgins, R. Taylor, B.L. Shaw, J. Organomet Chem. 325 (1987) 285.
[8] I. Brassat, W. Keim, S. Killat, M. Möthrath, P. Mastrorilli, C.F. Nobile, G.P. Suranna, J. Mol. Catal. 157 (2000) 41.
[9] (a) B. Demerseman, R. Le Legadec, B. Guilbert, C. Renouard, P. Crochet, P.H. Dixneuf, Organometallics 13 (1994) 2269;
(b) E. Lindner, A. Möckel, H.A. Mayer, H. Kuehbauch, R. Fawzi, M. Steimann, Inorg. Chem 32 (1993) 1266;
(c) E. Lindner, M. Haustein, H.A. Mayer, H. Kühbauch, K. Urieze, B. Klerk-Engels, Inorg. Chim. Acta 215 (1994) 165;
(d) P. Braunstein, D. Matt, D. Nobel, S. Bouaoud, B. Carluer, D. Grandjean, P. Lemoine, J. Chem. Soc., Dalton Trans (1986) 415;
(e) S.R. Hall, B.W. Skelton, A.H. White, Aust. J. Chem. 36 (1983) 267.
[10] (a) E. Lindner, S. Pautz, R. Fawzi, M. Steinmann, Organometallics 17 (1998) 3006;
(b) E. Valls, J. Suades, R. Mathieu, Organometallics 18 (26) (1999) 5475.
[11] T.A. Stephenson, G. Wilkinson, J. Inorg. Nucl. Chem. 28 (1966) 945.
[12] J.P. Genêt, C. Pinel, Tetrahedron: Asymmetry 5 (1994) 665.
[13] Enraf–Nonius CAD-4, Enraf–Nonius, Delft, The Netherlands, 1993.
[14] K. Harms, S. Wocadlo, XCAD-4, Program for Processing CAD-4 Diffractometer Data, University of Marburg, Marburg, Germany, 1995.
[15] G.M. Sheldrick, SHELXS-97, Program for Crystal Structure Resolution, University of Göttingen, Göttingen, Germany, 1997.
[16] G.M. Sheldrick, SHELXL-97, Program for Crystal Structures Analysis, University of Göttingen, Göttingen, Germany, 1997.
[17] L.J. Farrugia, WinGX, J. Appl. Cryst. 32 (1999) 837.
[18] L.J. Farrugia, ORTEP-3 for Windows, J. Appl. Cryst. 30 (1997) 565.
[19] J. de Meulenaar, H. Tompa, Acta Cryst. A19 (1965) 1014.
[20] N. Walker, D. Stuart, Acta Cryst. A39 (1983) 158.
[21] R.F. Stewart, E.R. Davidson, W.T. Simpson, J. Chem. Phys. 42 (1965) 3175.
[22] J.C. Jeffrey, T.B. Rauchfuss, Inorg. Chem. 18 (1979) 2658.
[23] E. Lindner, U. Shober, R. Fawzi, W. Hiller, U. Englert, P. Wegner, Chem. Ber. 120 (1987) 1621.
[24] P. Braunstein, D. Matt, Y. Dusausoy, Inorg. Chem. 22 (1983) 2043.
[25] J.G. Verkade, Coord. Chem. Rev 9 (1972/1973) 1.
[26] M.R.M. Fontes, G. Oliva, L.A.C. Cordeiro, A.A. Batista, J. Coord. Chem. 30 (1993) 125.
[27] A.A. Batista, L.A.C. Cordeiro, G. Oliva, O.R. Nascimento, Inorg. Chim. Acta 258 (1997) 131.
[28] A.A. Batista, M.O. Santiago, C.L. Donnici, I.S. Moreira, P.C. Healy, S.J. Berners-Price, S.L. Queiroz, Polyhedron 20 (2001) 2123.
[29] N.P.G. Roeges, A Guide to the Interpretation of Infrared Spectra of Organic Structures, Wiley, England, 1994.
[30] (a) R.W. Wegman, A.G. Abatjoglou, A.M. Harrison, Chem. Commun. (1987) 1891;

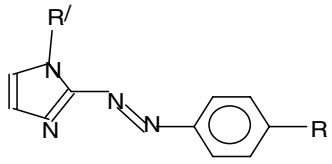
(b) E. Lindner, S. Meyer, P. Wegner, Chem. Ber. 119 (1986) 2616;
(c) K. Nakamoto, Infrared and Raman Spectra of Inorganic and Coordination, Wiley, New York, 1986.
[31] R.J. Abraham, The Analysis of High Resolution NMR Spectra, Elsevier, Amsterdam, 1971.
[32] R.K. Harris, Can. J. Chem. 42 (1964) 2275.
[33] J.C. Briggs, C.A. McAuliffe, G.J. Dyer, Chem. Soc., Dalton Trans. (1984) 423.
[34] A.A. Batista, L.A.C. Cordeiro, G. Oliva, O.R. Nascimento, Inorg. Chim. Acta 258 (1997) 131.
[35] B.P. Sullivan, T.J. Meyer, Inorg. Chem. 21 (1982) 1037.

favorable situation with completely filled bonding e-orbitals (Td) versus not yet filled bonding t_{2g}–orbitals for the Oh situation in the high spin Co(II) system. This idea has prompted us to carry out the reaction between $Zn(RaaiR')Cl_2 \cdot H_2O$ and $Co(ClO_4)_2 \cdot 6H_2O$ under ambient conditions. The product characterization by single-crystal X-ray diffraction showed tetrahedral coordination of the complex in which the four imidazole-N from four RaaiR′ ligands coordinates to Co(II). The product isolated from the direct reaction of $Co(ClO_4)_2 \cdot 6H_2O$ and RaaiR′ is chemically and structurally identical with the product obtained from the transmetallation reaction. The reaction of pseudohalide (N_3^- and NCS^-) with $Co(RaaiR')_4^{2+}$ has forced the pendant azo function to chelate Co(II) along with the expulsion of two ligand molecules to synthesise octahedral $Co(RaaiR')_2X_2$. The pseudo-octahedral complexes may exist as five geometrical isomers [6]. In the present case, one isomer has been isolated and characterized by X-ray diffraction.

2. Results and discussion

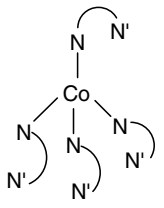
2.1. Synthesis and formulation

1-Alkyl-2-(arylazo)imidazole [RaaiR′, where R = H (**a**), Me (**b**); R′ = Me (**1**), Et (**2**)], is an unsymmetrical *N*,*N*′-bidentate chelator where *N* and *N*′ refer to N(imidazole) and N(azo) donor centers, respectively. It can also act as a monodentate ligand coordinating through imidazole-N to the metal ion [12–17]. A methanolic solution of $Co(ClO_4)_2 \cdot 6H_2O$ and RaaiR′ (in mole proportions of 1:2, 1:3, 1:4 or 1:6) have isolated brown crystalline products of the same composition, $[Co(RaaiR')_4](ClO_4)_2 \cdot H_2O$ (**3**,**4**). Transmetallation of $[Zn(RaaiR')Cl_2 \cdot H_2O]$ with $Co(ClO_4)_2 \cdot 6H_2O$ in the presence of $NaClO_4$ has also isolated $[Co(RaaiR')_4](ClO_4)_2 \cdot H_2O$ (**3**,**4**). In these complexes, RaaiR′ coordinates through the imidazole-N in a tetrahedral arrangement around Co(II). Microanalytical data support the composition of the complexes and single-crystal X-ray diffraction of one of the complexes has been established as tetrakis 1-methyl-2-(*p*-tolylazo)imidazole cobalt(II) perchlorate (**3b**).

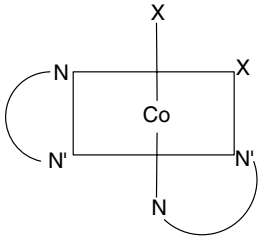


RaaiR′

R = H (**a**), Me (**b**); R′ = Me (**1/3/6**), Et (**2/4/7**)



3, **4**



5 (X = N_3), **6/7** (X = NCS)

The complexes **3** and **4** are 1:2 electrolytes (Λ_M = 160–170 Ω^{-1} cm^2 mol^{-1} in MeCN). In search of the reactivity of $[Co(RaaiR')_4](ClO_4)_2 \cdot H_2O$, we have examined the reaction of N_3^- (NaN_3), NCS^- (NH_4NCS) with a representative compound, $[Co(HaaiMe)_4](ClO_4)_2 \cdot H_2O$ (**3a**), and the products have been characterized as $Co(HaaiMe)_2X_2$ [X = N_3^-(**5**), NCS^-(**6**/**7**)]. A mixture of $Co(ClO_4)_2 \cdot 6H_2O$, NaN_3 (NH_4SCN) and HaaiMe in 1:2:2 mole proportion in methanol solution under stirring conditions in air has also isolated $Co(HaaiMe)_2(X)_2$ (X = N_3, NCS).

2.2. Structure description

2.2.1. *[Co(MeaaiMe)$_4$](ClO$_4$)$_2$ · H$_2$O* (*3b*)

The molecular structure is shown in Fig. 1. Selected bond parameters are given in Table 1. The cationic complex $[Co(MeaaiMe)_4]^{2+}$ consists of a central cobalt atom surrounded by two pairs of MeaaiMe in which each pair is symmetry related as evident from bond lengths and angles. The Co atom sits at the center of a tetrahedron. The ligand, MeaaiMe acts as a monodentate ligand and binds through the imidazole-N donor center. The coordination environment of Co is compressed along the crystallographic *c*-axis in such a way that two of the N–Co–N angles are higher than the tetrahedral angle

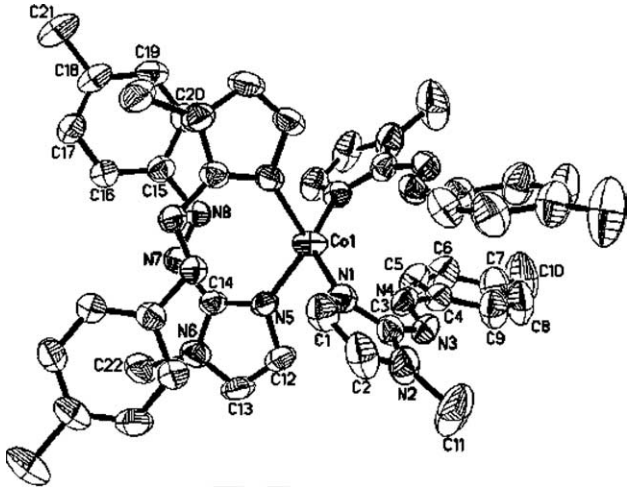


Fig. 1. ORTEP view of $[Co(MeaaiMe)_4]^{2+}$ (**3b**).

Table 1
Bond distances (Å) and bond angles (°) of [Co(MeaaiMe)$_4$](ClO$_4$)$_2$ · H$_2$O (**3b**)

Bond distance (Å)		Bond angle (°)	
Co(1)–N(1/1a)	2.045(3)	N(1)–Co(1)–N(1a)	139.51(17)
Co(1)–N(5/5a)	2.079(3)	N(1a)–Co(1)–N(5a)	96.53(11)
N(1)–C(3)	1.329(5)	N(1/1a)–Co(1)–N(5a/5)	102.90(12)
N(3)–N(4)	1.272(4)	N(1)–Co(1)–N(5)	96.53(11)
N(5)–C(14)	1.330(4)	N(5a)–Co(1)–N(5)	121.75(16)
N(7)–N(8)	1.257(4)	N(4)–N(3)–C(3)	112.5(3)
Cl(1)–O(1)	1.315(3)	N(8)–N(7)–C(14)	113.0(3)
Cl(1)–O(2)	1.314(3)	O(2)–Cl(1)–O(3)	109.46(9)
Cl(1)–O(3)	1.314(3)	O(2)–Cl(1)–O(4)	109.41(9)
Cl(1)–O(4)	1.314(3)	O(2)–Cl(1)–O(1)	109.58(9)
N(1)–C(3)	1.329(5)	O(3)–Cl(1)–O(1)	109.51(9)
		O(4)–Cl(1)–O(1)	109.45(9)

with a value of N(1)–Co(1)–N(1a) 139.51(17)° and N(5)–Co(1)–N(5a), 121.75(16)°. Two other N–Co–N angles show a lower value, each of them, N(1)–Co(1)–N(5) and N(1a)–Co(1)–N(5a), being 96.53(11)°. The remaining N–Co–N angles [N(1)–Co(1)–N(5a) or N(1a)–Co(1)–N(5)] are 102.90(12)°. The angular distortion may be due to steric crowding provided by the pendant *p*-tolylazo group. Two types of Co–N bond lengths are Co(1)–N(1), 2.045(3); Co(1)–N(5), 2.079(3) Å. The N=N bond lengths are N(3)–N(4), 1.272(4) and N(7)–N(8), 1.257(4) Å. The free ligand N=N distance is 1.250(1) Å [22,23]. This suggests that one of the N=N groups in the coordinated ligand may participate in a $d\pi(Co) \rightarrow \pi^*$ transition.

2.2.2. [Co(HaaiMe)$_2$(NCS)$_2$] (*6a*)

The single-crystal X-ray structure of Co(HaaiMe)$_2$(NCS)$_2$ (**6a**) is shown in Fig. 2 and bond parameters are set out in Table 2. HaaiMe acts as an unsymmetric bidentate chelator of N-imidazole(N) and N-azo(N′). The other two coordination sites are occupied by two *N*CS groups (underlined atom refers to the donor center). Thus, the molecule shows an octahedral arrangement about Co(II) with *cis*-N(imidazole), N(imidazole); *cis*-N(azo), N(azo) and *cis*-*N*CS, *N*CS donor centers, and has been abbreviated thereafter *cis*–*cis*–*cis*-[Co(HaaiMe)$_2$(NCS)$_2$]. The N–Co–N bond angles subtended by the chelating HaaiMe are N(2)–Co–N(5), 65.8(5)°, N(6)–Co–N(9), 70.42(10)°. The two angles differ widely and deviate significantly from the ideal 90° for a regular octahedral geometry. Observed chelate angles in platinum metal complexes (Ru^{II}, Os^{II}, Pd^{II}, Pt^{II}) of arylazoimidazole [5–11] lie at 76 ± 2° while in the series of 3d transition metal complexes (Mn^{II}, Co^{II}, Ni^{II}, Cu$^{I/II}$) [24–27] the angle is 70 ± 2°. The chelate complexes of Group 12 metals (Zn^{II}, Cd^{II}, Hg^{II}) [12–17] show even lower chelate angles, 65 ± 2°. The chelate angles in the present complex appear in the reported range 65–76°. The *trans* angle values also support the structural distortion [N(2)–Co–N(9), 172.67(10)° while N(6)–Co–N(10), 135.77(11)° and N(1)–Co–N(5) 158.6(6)°], exhibiting severe distortion. The chelate plane consisting of Co, N(2), C(9), N(4), N(5) (plane-1) shows severe distortion from the mean plane while the other chelate plane consisting of Co, N(6), C(14), N(8), N(9) is a good plane (plane-2) (mean deviation ⩽0.02 Å). A closer look to the molecular structure shows that the chelate plane-2 constitutes a part of the molecular plane consisting of Co, N(6), N(9), N(10) and N(2). The pendant phenyl group is no longer planar and makes a dihedral angle of 55–76° with the respective chelate plane. The azo-N(5) is placed at an axial position. Azo-N stereochemically demands larger space

Table 2
Bond distances (Å) and bond angles (°) of [Co(HaaiMe)$_2$(NCS)$_2$] (**6a**)

Bond distance (Å)		Bond angle (°)	
Co–N(1)	2.000(3)	N(1)–Co–N(2)	92.84(11)
Co–N(2)	2.073(3)	N(1)–Co–N(6)	106.97(13)
Co–N(6)	2.020(3)	N(1)–Co–N(9)	84.81(11)
Co–N(9)	2.487(3)	N(1)–Co–N(10)	108.71(13)
Co–N(10)	1.976(3)	N(2)–Co–N(6)	103.79(11)
Co–N(5)	2.73(2)	N(2)–Co–N(9)	172.67(10)
S(1)–C(4)	1.623(4)	N(2)–Co–N(10)	99.71(11)
N(1)–C(4)	1.158(5)	N(6)–Co–N(9)	70.42(10)
N(4)–N(5)	1.259(4)	N(6)–Co–N(10)	135.77(11)
N(8)–N(9)	1.261(4)	N(9)–Co–N(10)	87.63(10)
		Co–N(1)–C(4)	160.6(3)
		Co–N(2)–C(2)	131.5(2)
		Co–N(2)–C(9)	123.0(2)
		Co–N(6)–C(1)	135.1(2)
		Co–N(6)–C(14)	119.0(2)
		Co–N(9)–N(8)	113.23(19)
		Co–N(9)–C(3)	132.6(2)
		N(1)–Co–N(5)	158.6(6)
		N(2)–Co–N(5)	65.8(5)
		N(6)–Co–N(5)	78.6(6)
		N(5)–Co–N(9)	116.1(9)
		N(5)–Co–N(10)	77.6(1)

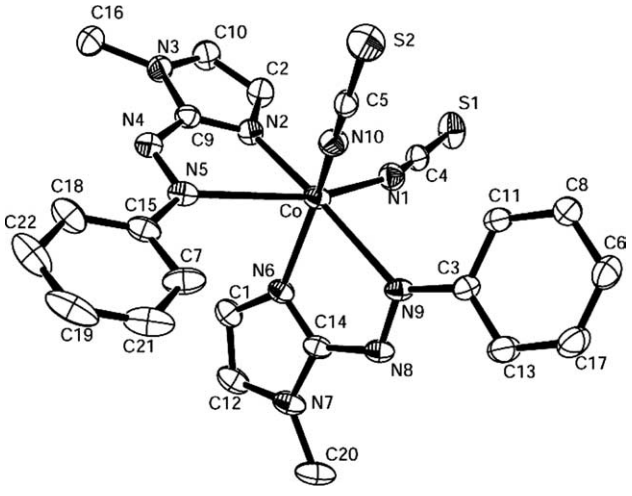


Fig. 2. ORTEP view of [Co(HaaiMe)$_2$(NCS)$_2$] (**6a**).

and becomes unfavourable at an axial position. The distortion is thus manifested by elongation of the Co–N(5) distance (2.73(2) Å) and smaller chelate bite angle (N(2)–Co–N(5), 65.8(5)°). However, the sum of the van der Waals radii of Co(II) and azo-N are greater than the Co–N(5) bond length and warrants a covalent interaction [28]. The Co–N(9) bond length (N(9) is an azo-N) is shorter ($\Delta d \sim 0.2$ Å) than Co–N(5) and supports stronger covalency. The six Co–N bond lengths are expectedly unequal for a distorted octahedral geometry. The shortest length is observed for Co–N(NCS) (Co–N(10), 1.976(3); Co–N(1), 2.000(3) Å) and the longest one are exhibited by Co–N(azo) (Co–N(9), 2.487(3); Co–N(5), 2.732(1) Å). The Co–N(imidazole) distances lie in between them: Co–N(2), 2.073(3) Å and Co–N(6), 2.020(3) Å. The distortion in chelate plane-2 (vide supra) may be the reason for the elongation of the Co–N(2) bond length. The shortening of the Co–N(imidazole) bond distances (Co–N(2/6)) relative to Co–N(azo) (Co–N(5/9)) suggest preferential binding of N(imidazole) to Co(II). The N=N distances are longer than the free ligand values [22,23]. The elongation may be due to the combined effect of the steric requirement of the chelated azoimine group as well as d(Co) → π*(azo) charge transference.

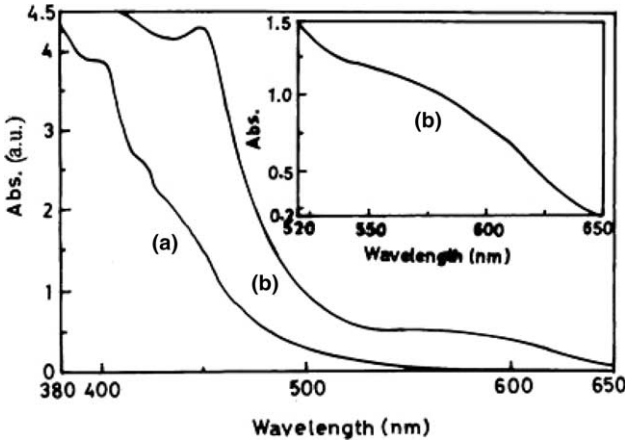


Fig. 3. UV–Vis spectra of (a) $[Co(MeaaiMe)_4](ClO_4)_2 \cdot H_2O$ (**3b**) [0.21×10^{-3} M] and (b) $[Co(HaaiMe)_2(NCS)_2]$ (**6a**) [2.1×10^{-3} M] in MeCN solvent.

2.3. Spectra and magnetism

The IR stretchings of the complexes are assigned on comparing with the free ligand data [6,24]. Not all the bands have been assigned and some significant vibrations are compared. The broad band appearing at 3414–3416 cm^{-1} is due to $\nu(H_2O)$. The strong band at 1085–1093 cm^{-1} with a weak stretch at 624–627 cm^{-1} are due to $\nu(ClO_4)$ for complexes **3** and **4**. The complexes upon exposure to heat treatment in a thermostatic oven at 80° for 10 min do not show $\nu(H_2O)$ (~3415 cm^{-1}). This shows water loss during the thermal program. The complexes absorb water reversibly on cooling in air, which is evident from the reappearance of $\nu(H_2O)$ in the IR spectra. However, we could not study the complete thermal behaviour because of explosive ClO_4^- in the complexes. The strong sharp band at 2076–2079 cm^{-1} is due to ν(CN) of –NCS for complex **6**. Moderately intense stretchings at 1583–1600 and 1438–1452 cm^{-1} are due to ν(C=N) and ν(N=N), respectively, for all the complexes [8–10].

Solution electronic spectra (Fig. 3) of the complexes were recorded in acetonitrile solution in the UV/Vis region (250–900 nm). The data are listed in Table 3. The complexes **3** and **4** show intense bands at >400 nm which may be due to MLCT transitions. The electronic spectra support the tetrahedral structure of the complexes [29]. For the complexes **6** and **7**, three transitions in the range 470–640 nm are observed. The intensity

Table 3
UV–Vis spectra,[a] cyclic voltammetric[b] and magnetic moment (μ) data

Compound	UV–Vis spectral data (λ_{max}/nm) ($10^{-3}\varepsilon$ M^{-1} cm^{-1})	CV data E^0 (V) (ΔE_P, mV)				μ (BM)
		Co(III)/Co(II)	Ligand reductions[c]			
$[Co(HaaiMe)_4](ClO_4)_2 \cdot H_2O$ (**3a**)	442 (8.2), 434 (10.83), 400 (9.12)	1.00 (120)	−0.28 (120)	−0.60 (140)	−1.15 (200)	4.78
$[Co(HaaiEt)_4](ClO_4)_2 \cdot H_2O$ (**4a**)	446 (5.74), 432 (10.61), 402 (15.03)	0.95 (150)	−0.30 (120)	−0.58 (140)	−1.16 (200)	4.81
$[Co(MeaaiMe)_4](ClO_4)_2 \cdot H_2O$ (**3b**)	448 (6.32), 432 (11.61), 400 (16.51)	1.09 (130)	−0.24 (110)	−0.55 (140)	−1.10 (180)	4.53
$[Co(MeaaiEt)_4](ClO_4)_2 \cdot H_2O$ (**4b**)	440 (9.68), 434 (12.53), 402 (15.06)	1.043 (100)	−0.31 (110)	−0.64 (120)	−1.18 (220)	4.68
$[Co(HaaiMe)_2(NCS)_2]$ (**6a**)	608 (0.29), 564 (0.46), 452 (6.43)	0.87 (150)	−0.20 (100)	−0.58 (130), −1.55 (150)	−1.25 (200)	4.34
$[Co(MeaaiMe)_2(NCS)_2]$ (**6b**)	606 (0.32), 562 (0.48), 450 (5.96)	0.94 (125)	−0.28 (120)	−0.65 (140)	−1.22 (180)	4.53
$[Co(HaaiEt)_2(NCS)_2]$ (**7a**)	612 (0.34), 564 (0.49), 454 (5.58)	0.86 (110)	−0.30 (80)	−0.54 (140), −1.34 (200)	−1.15 (150)	4.45
$[Co(MeaaiEt)_2(NCS)_2]$ (**7b**)	610 (0.28), 566 (0.45), 455 (6.89)	0.98 (135)	−0.26 (120), −0.55 (170)	−1.32 (180)	−1.20 (140)	4.43

[a] Solvent: MeCN.
[b] Solvent: dry MeCN; Pt-disk working electrode, Pt-wire auxiliary and SCE, TBAP as supporting electrolyte, scan rate 50 mV s^{-1}, potential $E_{1/2} = (E_{pa} + E_{pc})/2$ in V, $\Delta E_p = |E_{pa} - E_{pc}|$ in mV.
[c] E_{pc} in V.

pattern of the bands are different; the transition at 450–455 nm is of high intensity ($\varepsilon \sim 10^4$ M^{-1} cm^{-1}) and sharp while the other two transitions, 520–575 and 605–620 nm, are weak ($\varepsilon \sim 10^2$–10^3 M^{-1} cm^{-1}) and broad. Based on the low intensity and low energy nature the bands are considered to be d–d transitions. The high intense transition at 450–455 nm may be assigned to MLCT transitions. The spectral pattern and the intensity support tetrahedral-Co in **3**, **4** and octahedral-Co in **6**, **7** [29].

Bulk magnetic moment (μ) measurements of both $[Co(RaaiR')_4](ClO_4)_2 \cdot H_2O$ (**3**, **4**) and $[Co(RaaiR')_2(X)_2]$ (X = N_3 (**5**), NCS (**6**/**7**)) complexes at room temperature (300 K) suggest high spin mononuclear ones (Table 3). $[Co(RaaiR')_4](ClO_4)_2 \cdot H_2O$ exhibit μ in the range 4.5–4.8 BM and $[Co(RaaiR')_2(NCS)_2]$ exhibit μ in the range 4.3–4.4 BM, slightly greater than the spin only value [30].

2.4. Electrochemistry

Redox properties of the complexes were examined by cyclic voltammetry in MeCN solution in the potential range ±1.6 V versus a SCE electrode. A representative voltammogram is shown in Fig. 4 and data are given in Table 3. $Co(RaaiR')_4(ClO_4)_2$ exhibit a couple on scanning in the positive direction ($0.0 \rightarrow -1.6$ V) at 0.9–1.2 V and peak-to-peak separation $\Delta E_P > 80$ mV, which shows quasireversibility of the voltammogram. On scanning in the negative direction ($0.0 \rightarrow -1.6$ V) three redox responses were observed at −0.2 to −0.3; −0.5 to −0.6 and −1.0 to −1.2 V. These three couples are quasireversible ($\Delta E_P \geqslant 100$ mV). The current height of the third couple is about double that of the first or second couple. Redox response at positive to reference is oxidative in nature and may be assigned to a Co(III)/Co(II) type. Redox couples at negative to SCE are reductive responses. There are four dangling azo groups in the imidazole-N coordinated RaaiR′ and may show, in principle, four azo reductions [–N=N–] $\rightarrow$ [–N^{-}–N–]$^{-}$. This is indeed observed. The third and fourth reductions may overlap at high negative potential. However, the potential is very close to the free ligand redox data [6].

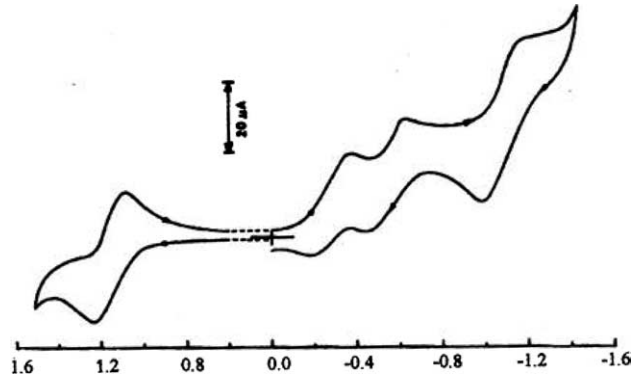


Fig. 4. Cyclic voltammogram of $[Co(MeaaiMe)_4](ClO_4)_2 \cdot 2H_2O$ (**3b**) in MeCN solvent.

Cyclic voltammograms of $Co(RaaiR')_2(NCS)_2$ also record similar observations. The Co(III)/Co(II) couple appears at 0.8–0.9 V and four reductive responses at −0.2 to −0.3, −0.5 to −0.6, −1.2 to −1.3, −1.5 to −1.6 V. Reductions refer to accommodation of electrons into the LUMOs dominated by the azo groups. Ligand reductions appear at less negative values for $Co(RaaiR')_2(NCS)_2$ compared to $[Co(RaaiR')_4](ClO_4)_2$ which may be due to better stability of the chelated azoimine fragment in the former. The higher Co(III)/Co(II) redox potential for $Co(RaaiR')_4^{2+}$ compared to $Co(RaaiR')_2(NCS)_2$ suggests fairly stable Co(II) in the Td geometry compared to that of the Oh geometry. The electrostatic effects in the tetrahedral compounds, which are already in +2 state $(Co(RaaiR')_4^{2+}$, means they are hard to oxidize, where as oxidation of the octahedral complexes $Co(RaaiR')_2(NCS)_2$ is easier because they are neutral.[1]

3. Conclusion

We have synthesized cobalt(II) complexes of 1-alkyl-2-(arylazo)imidazole (RaaiR′) and one of the complexes has been structurally characterized as tetrahedral tetrakis $[Co(RaaiR')_4](ClO_4)_2 \cdot H_2O$. The structure shows that RaaiR′ act as monodentate imidazole-N donor ligands. The reaction of N_3^- or SCN^- with $[Co(RaaiR')_4](ClO_4)_2 \cdot H_2O$ has synthesized $Co(RaaiR')_2(X)_2$ ($X = N_3^-, SCN^-$). The structural characterization shows pseudooctahedral *cis*-N(azo), N(azo); *cis*-N(imidazole), N(imidazole) and *cis*-X,X configuration. Their spectral, magnetic and electrochemical study confirms the structure of the complexes.

4. Experimental

4.1. Materials

$Co(ClO_4)_2 \cdot 6H_2O$ was prepared by treatment of cobalt carbonate (E. Merck, India) with perchloric acid (E. Merck, India) followed by slow evaporation on a steam bath, filtration through a fine glass-frit and preservation in a desiccator containing concentrated sulfuric acid for subsequent use. 1-Alkyl-2-(arylazo)imdazoles (RaaiR′) were prepared following the literature procedures [24]. All other chemicals and solvents are reagent grade. Solvents are used after drying.

[1] Explanation is thankfully received from one of the referees.

4.2. Physical measurements

Microanalyses (C, H, N) were performed using a Perkin–Elmer 2400 CHNO/S elemental analyzer. Spectroscopic measurements were carried out using the following instruments: UV–Vis spectra, reflectance spectra, JASCO UV–Vis/NIR model V-570; IR spectra (KBr disk, 4000–200 cm^{-1}), JASCO FT-IR model 420. Room temperature magnetic moments were measured using a vibrating sample 155 magnetometer at 298 K. Molar conductances (Λ_M) were measured in a Systronics conductivity meter 304 model using ca. 10^{-3} M solutions in MeOH. Electrochemical measurements were carried out with the use of a computer controlled EG&G PARC VersaStat model 250 electrochemical instrument using a Pt-disk working electrode and Pt-wire auxiliary electrode. The reported results are referenced to SCE in acetonitrile and are uncorrected for junction potential. Cyclic voltammograms of the complexes were drawn within the potential range +1.6 to −1.6 versus SCE. Estimation of cobalt and manganese were carried out by the complexometric titration method [31].

4.3. Preparation of $[Co(MeaaiMe)_4](ClO_4)_2 \cdot H_2O$ (**3b**)

4.3.1. Direct reaction

1-Methyl-2-(*p*-tolylazo)imidazole (MeaaiMe) (0.1 g, 0.50 mmol) in MeOH (10 ml) was added dropwise to a stirred solution of $Co(ClO_4)_2 \cdot 6H_2O$ (0.045 g, 0.125 mmol) in MeOH (10 ml) at 298 K. The red-orange solution was stirred for 15 min, filtered and left undisturbed for two weeks. Bright red-orange crystals were obtained. They were washed with a cold water–methanol mixture and ether. Finally, they were dried in vacuo. The yield was 0.10 g (75%). The microanalytical data of the complex is as follows, $[Co(MeaaiMe)_4](ClO_4)_2 \cdot H_2O$ (**3b**): *Anal*. Calc. for $C_{44}H_{50}N_{16}Cl_2O_9Co$: C, 49.07; H, 4.64; N, 20.82; Co, 5.48. Found: C, 49.15; H, 4.58; N, 20.91; Co, 5.43%. IR (KBr disk) (cm^{-1}): $\nu(H_2O)$ 3416 (m); $\nu(ClO_4^-)$ 1085(s), 624(w); ν(C=N) 1597(m), ν(N=N) 1445(m).

All the other complexes were prepared by the same procedure. In all cases, crystalline products were obtained. The yield varied from 75% to 80% and microanalytical and IR data of the complexes are as follows. $[Co(HaaiMe)_4](ClO_4)_2 \cdot H_2O$ (**3a**): *Anal*. Calc. for $C_{40}H_{42}N_{16}Cl_2O_9Co$: C, 47.06; H, 4.12; N, 21.96; Co, 5.78. Found: C, 47.18; H, 4.03; N, 21.82; Co, 5.58%. IR (KBr disk) (cm^{-1}) $\nu(H_2O)$ 3416 (m); $\nu(ClO_4^-)$ 1085(s), 624(w); ν(C=N) 1587(m); ν(N=N) 1444(m). $[Co(HaaiEt)_4]_4(ClO_4)_2 \cdot H_2O$ (**4a**) *Anal*. Calc. for $C_{44}H_{50}N_{16}Cl_2O_9Co$: C, 49.07; H, 4.64; N, 20.82; Co, 5.48. Found: C, 49.17; H, 4.59; N, 20.87; Co, 5.45%. IR (KBr disk) (cm^{-1}) $\nu(H_2O)$ 3414 (m); $\nu(ClO_4^-)$ 1089(s), 626(w); ν(C=N) 1598(m); ν(N=N) 1446(m). $[Co(MeaaiEt)_4](ClO_4)_2 \cdot H_2O$ (**4b**): *Anal*. Calc. for $C_{48}H_{58}N_{16}Cl_2O_9Co$: C, 50.88; H, 5.12; N, 19.79; Co, 5.21. Found: C, 50.79; H, 5.21; N, 19.70; Co, 5.19%. IR (KBr disk) (cm^{-1}) $\nu(H_2O)$ 3416 (m); $\nu(ClO_4^-)$ 1089(s), 627(w); ν(C=N) 1598(m); ν(N=N) 1446(m).

Reactions under identical conditions with $Co(ClO_4)_2 \cdot 6H_2O$ and MeaaiMe in different mole proportions, 1:2, 1:3, 1:6, have isolated complexes of same composition.

4.3.2. Transmetallation reaction

To a solution of $[Zn(MeaaiMe)(H_2O)Cl_2]$ (0.18 g, 0.50 mmol) in methanol $Co(ClO_4)_2 \cdot 6H_2O$ (0.1 g, 0.25 mmol) was added in the same solvent and stirred for 1 h. The solution was slowly evaporated in air from which bright orange-red crystals were separated. They were then filtered, washed with cold methanol and dried over $CaCl_2$.

4.4. Reaction of NCS^- with $[Co(HaaiMe)_4](ClO_4)_2 \cdot H_2O$

4.4.1. Method I

To a methanolic suspension of $[Co(HaaiMe)_4](ClO_4)_2 \cdot H_2O$ (0.25 g, 0.25 mmol), NH_4SCN (0.07 g, 1 mmol) was added and refluxed. Within a few minutes the suspension became clear orange-red and the refluxing was continued for 2 h. Bright brown crystals were deposited on slow cooling and collected by filtration. They were then dried in a $CaCl_2$ dessicator and the yield was 0.09 g. The composition of the complex has been supported by microanlytical, spectral and magnetic data. $Co(HaaiMe)_2(NCS)_2$ (**7a**). *Anal*. Calc. for $C_{22}H_{20}N_{10}S_2Co$: C, 48.26; H, 3.65; N, 25.60. Found: C, 48.39; H, 3.71; N, 25.56%. IR (KBr disk) (cm^{-1}) ν(C=N) 1595(m); ν(N=N) 1436(m); ν(SCN) 2076(s).

Similarly, the reaction of NaN_3 with $[Co(HaaiMe)_4](ClO_4)_2 \cdot H_2O$ in a 4:1 mole ratio in MeOH under identical reaction conditions has isolated $Co(HaaiMe)_2(N_3)_2$ (**5a**). *Anal*. Calc. for $C_{20}H_{20}N_{14}Co$: C, 46.60; H, 3.88; N, 38.06. Found: C, 46.72; H, 3.93; N, 37.95; Co, 11.04%. IR (KBr disk) (cm^{-1}) ν(C=N) 1589(m); ν(N=N) 1434(m); $\nu(N_3)$ 2044(s).

4.4.2. Method II

1-Methyl-2-(phenylazo)imidazole (HaaiMe) (0.09 g, 0.5 mmol) in MeOH (15 ml) was added dropwise to a stirred solution of $Co(ClO_4)_2 \cdot 6H_2O$ (0.25 g, 0.25 mmol) in the same solvent (10 ml) at 298 K. The brown solution was stirred for 15 min followed by the addition of NH_4SCN (0.04 g, 0.5 mmol) in MeOH (10 ml). The solution colour intensified. It was then filtered and left undisturbed for a week. A dark brown

crystal was obtained. It was washed with water and then by methanol. Finally, it was dried in vacuum. Yield was 65%.

4.5. Synthesis of $Co(HaaiMe)_2X_2$ [X = N_3 (5), NCS (6/7)]

These complexes were prepared by a common procedure and the reaction conditions had been settled following the synthesis of $Co(MeaaiMe)_2(N_3)_2$ [24].

To a methanolic solution (20 ml) of $CoCl_2 \cdot 6H_2O$ (0.06 g, 0.25 mmol), HaaiMe (0.09 g, 0.50 mmol) in the same solvent was added dropwise and stirred under ambient conditions for 4 h. The solution was evaporated slowly in air to half of the original volume and an excess of NaN_3 (0.06 g, 1 mmol) in MeOH was added. The solution was kept in a freezer. Crystals were deposited then separated by filtration, washed with cold methanol and dried over $CaCl_2$ in a dessicator. Yield: 35%.

Other products were also prepared following a similar procedure by adding NH_4SCN in place of NaN_3. The yield was 60%. The microanalytical data of the complexes are as follows: $Co(HaaiMe)_2(NCS)_2$ (**6a**). *Anal.* Calc. for $C_{22}H_{20}N_{10}S_2Co$: C, 48.26; H, 3.65; N, 25.60. Found: C, 48.34; H, 3.74; N, 25.52%. IR (KBr disk) (cm^{-1}) ν(C=N) 1587(m); ν(N=N) 1436(m); ν(NCS) 2076(s). $Co(MeaaiMe)_2(NCS)_2$ (**6b**). *Anal.* Calc. for $C_{24}H_{24}N_{10}S_2Co$: C, 50.09; H, 4.17; N, 24.35, Co, 10.24%. Found: C, 50.01; H, 4.20; N, 24.21; Co, 10.22%. IR (KBr disk) (cm^{-1}) ν(C=N) 1589(m); ν(N=N) 1434(m); ν(NCS) 2078(s). $Co(HaaiEt)_2(NCS)_2$ (**7a**). *Anal.* Calc. for $C_{24}H_{24}N_{10}S_2Co$: C, 50.09; H, 4.17; N, 24.35; Co, 10.24. Found: C, 50.00; H, 4.22; N, 24.24; Co, 10.21%. IR (KBr disk) (cm^{-1}) ν(C=N) 1587(m); ν(N=N) 1436(m); ν(NCS) 2079(s). $Co(HaaiEt)_2(NCS)_2$ (**7b**). *Anal.* Calc. for $C_{26}H_{28}N_{10}S_2Co$: C, 51.74; H, 4.64; N, 23.21; Co, 9.77. Found: C, 51.68; H, 4.67; N, 23.15; Co, 9.68%. IR (KBr disk) (cm^{-1}) ν(C=N) 1589(m); ν(N=N) 1434(m); ν(NCS) 2079(s).

4.6. X-ray crystal structure analysis

Suitable single crystals of complexes **3b** and **6a** were mounted on a Siemens CCD diffractometer equipped with graphite monochromated Mo Kα (λ = 0.711073 Å) radiation at 293 K for **3b** and 294 K for **6a**. The crystallographic data are listed in Table 4. Unit cell parameters were determined from least squares refinements of setting angles of 6372 reflections for **3b** and 2875 for **6a** with 2θ in the range $3.06° \leqslant 2\theta \leqslant 58.84°$ and $3.4° \leqslant 2\theta \leqslant 56.6°$, respectively. The intensity data were corrected for Lorentz and polarisation effects and an empirical absorption correction was also employed using the SAINT program for complexes. A total of 17268 [unique data, 6372] and 5909 [unique data, 2875] reflections were measured for complexes **3b** and **6a**, respectively. All these structures were solved by direct methods and followed by successive Fourier and difference Fourier syntheses. Full-matrix least-squares refinements on F_o^2 were carried out using SHELXL-97 with anisotropic displacement parameters for all non-hydrogen atoms. Hydrogen atoms were constrained to ride on the respective carbon or nitrogen atoms with isotropic displacement parameters equal to 1.2 times the equivalent isotropic displacement of their parent atom in all cases. All calculations were carried out using SHELXS-97, SHELXL-97, PLATON-99 and ORTEP-3 programs.

Table 4
Summarised crystallographic data for $[Co(MeaaiMe)_4](ClO_4)_2 \cdot H_2O$ (**3b**) and $[Co(HaaiMe)_2(NCS)_2]$ (**6a**)

Complex	$[Co(MeaaiMe)_4(ClO_4)_2] \cdot H_2O$ (**3b**)	$[Co(HaaiMe)_2(NCS)_2]$ (**6a**)
Empirical formula	$C_{44}H_{48}Cl_2O_9N_{16}Co$	$C_{22}H_{22}N_{10}S_2Co$
Formula weight	1074.81	547.53
T (K)	293	294
Crystal system	monoclinic	monoclinic
Space group	$C2/c$	$P2_1/c$
Crystal size (mm)	$0.50 \times 0.36 \times 0.26$	$0.2 \times 0.1 \times 0.1$
Unit cell dimensions		
a (Å)	19.9333(9)	9.0718(7)
b (Å)	18.3672(8)	15.1015(11)
c (Å)	14.3379(6)	19.0573(15)
β (°)	103.313(1)	91.999(2)
V (Å)^3	5108.3(4)	2609.2(3)
Z	4	4
λ (Å)	0.71073	0.71073
μ (Mo Kα) (mm^{-1})	0.510	0.849
D_{calc} (Mg m^{-3})	1.398	1.394
Refinement parameters	331	316
Total reflections	17268	5909
Unique data	6372	2875
R_1[a] [$I > 2\sigma(I)$]	0.0751	0.0462
wR_2[b]	0.2058	0.1025
Goodness-of-fit	0.936	0.913
$\Delta\rho_{max}$ and $\Delta\rho_{min}$ (e Å^{-3})	0.851 and −0.829	0.530 and −0.198

[a] $R = \sum|F_o - F_c|/\sum F_o$.
[b] $wR = [\sum w(F_o^2 - F_c^2)^2/\sum wF_o^4]^{1/2}$ are general but w are different, $w = 1/[\sigma^2(F^2) + (0.1186P)^2]$ for **3b** and $w = 1/[\sigma^2(F_o^2) + (0.0600P)^2]$ for **5a** where $P = (F_o^2 + 2F_c^2)/3$.

5. Supplementary material

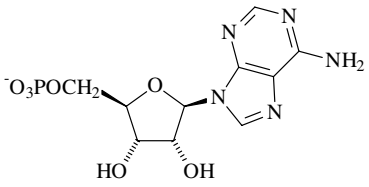
Crystallographic data for the structures have been deposited with the Cambridge Crystallographic data center, CCDC No. 243841 for $[Co(MeaaiMe)_4](ClO_4)_2 \cdot H_2O$ (**3b**) and CCDC No. 244230 for $[Co(HaaiMe)_2(NCS)_2]$ (**6a**). Copies of this information may be obtained free of charge from the Director, CCDC, 12 Union Road, Cambridge CB2 1EZ, UK (e-mail: deposit@ccdc.cam.ac.uk or www: http://www.ccdc.cam.ac.uk).

Acknowledgments

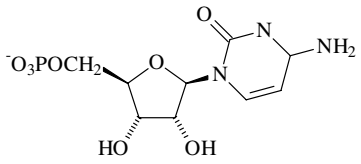
Financial support from the Council of Scientific and Industrial Research, New Delhi is gratefully acknowledged. One of us (U.S.R.) thanks to UGC, for a fellowship.

References

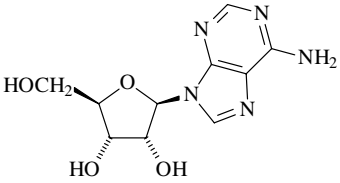
[1] C. Place, J.-L. Zimmermann, E. Mulliez, G. Guillot, C. Bois, J.-C. Chottard, Inorg. Chem. 37 (1998) 4030.
[2] J.M. Dominguez-Vera, A. Rodriguez, R. Cuesta, R. Kivekas, E. Colacio, J. Chem. Soc., Dalton Trans. (2002) 561.
[3] S. Nagasato, Y. Sunatsuki, S. Ohsato, T. Kido, N. Matsumoto, M. Kojima, Chem. Commun. (2002) 14.
[4] T.K. Misra, D. Das, C. Sinha, Polyhedron 16 (1997) 4163.
[5] P. Byabartta, J. Dinda, P.K. Santra, C. Sinha, K. Paneerselvam, F.-L. Liao, T.-H. Lu, J. Chem. Soc., Dalton Trans. (2001) 2825.
[6] T.K. Misra, D. Das, C. Sinha, P. Ghosh, C.K. Pal, Inorg. Chem. 37 (1998) 1672.
[7] S. Pal, T.K. Misra, C. Sinha, A.M.Z. Slawin, J.D. Woollins, Polyhedron 19 (2000) 1925.
[8] P. Chattopadhyay, B.K. Dolui, C. Sinha, Indian J. Chem. A 36 (1997) 429.
[9] D. Das, A.K. Das, C. Sinha, Anal. Lett. 32 (1999) 567.
[10] S. Pal, D. Das, C. Sinha, C.H.L. Kennard, Inorg. Chim. Acta 313 (2001) 21.
[11] S. Pal, D. Das, P. Chattopadhyay, C. Sinha, K. Paneerselvam, T.-H. Lu, Polyhedron 19 (2000) 1263.
[12] B.G. Chand, U.S. Ray, J. Chang, T.-H. Lu, C. Sinha, Polyhedron 22 (2003) 1213.
[13] B.G. Chand, U.S. Ray, G. Mostafa, T.-H. Lu, C. Sinha, J. Coord. Chem. 57 (2004) 627.
[14] B.G. Chand, U.S. Ray, G. Mostafa, T.-H. Lu, L.R. Falvello, T. Soler, M. Tomás, C. Sinha, Polyhedron 22 (2003) 3161.
[15] B.G. Chand, U.S. Ray, G. Mostafa, T.-H. Lu, C. Sinha, Polyhedron 23 (2004) 1669.
[16] B.G. Chand, U.S. Ray, P.K. Santra, G. Mostafa, T.-H. Lu, C. Sinha, Polyhedron 22 (2003) 1205.
[17] B.G. Chand, U.S. Ray, J. Cheng, T.-H. Lu, C. Sinha, unpublished result.
[18] L. Wang, C. Bailly, A. Kumar, D. Ding, M. Bajic, W.D. Wilson, Proc. Natl. Acad. Sci. USA 97 (2002) 12.
[19] N. Lambercht, K. Munson, O. Vagin, G. Sachs, J. Biol. Chem. 275 (2000) 4041.
[20] W.R. Rypniewski, S. Managani, S. Bruni, P.L. Orioli, M. Casati, K. Wilson, J. Mol. Biol. 251 (1995) 282.
[21] J.E. Huheey, E.A. Keiter, R.L. Keiter, Inorganic Chemistry, fourth ed., Harper Collins/Addison-Wesley, New York/Reading, MA, 2000.
[22] D. Das, Ph.D. Thesis, Burdwan University, Burdwan, 1998.
[23] A. Saha, C. Das, S. Goswami, S.-M. Peng, Indian J. Chem. A 40 (2001) 198.
[24] U.S. Ray, B.G. Chand, G. Mostafa, J. Chang, T.-H. Lu, C. Sinha, Polyhedron 22 (2003) 2587.
[25] U.S. Ray, Sk. Jasimuddin, B.K. Ghosh, M. Monfort, J. Ribas, G. Mostafa, T.-H. Lu, C. Sinha, Eur. J. Inorg. Chem. (2004) 250.
[26] J. Dinda, U.S. Ray, G. Mostafa, T.-H. Lu, A. Usman, I.A. Razak, S. Chantrapromma, H.-K. Fun, C. Sinha, Polyhedron 22 (2003) 247.
[27] U.S. Ray, D. Banerjee, G. Mostafa, T.-H. Lu, C. Sinha, unpublished result.
[28] A.G. Orpen, L. Brammar, F.H. Allen, O. Kennard, D.G. Watson, R. Taylor, J. Chem. Soc., Dalton Trans. (1989) S I.
[29] A.B.P. Lever, Inorganic Electronic Spectroscopy, Elsevier, Amsterdam, 1984.
[30] R.L. Dutta, A. Syamal, Elements of Magnetochemistry, second ed., Affiliated East-west Press, New Delhi, 1993, p. 150.
[31] A.I. Vogel, A Text-book of Quantitative Inorganic Analysis, third ed., ELBS, Longman, London, 1975, p. 433.



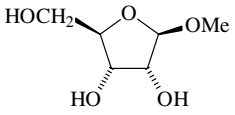
AMP



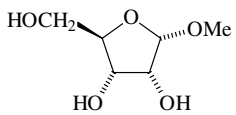
CMP



Adenosine



β-Rib1Me



α-Rib1Me

2. Experimental

2.1. Materials

Adenosine 5′-monophosphate (sodium salt, Sigma, >99%), cytidine 5′-monophosphate (sodium salt, Sigma, >98%), adenosine (Sigma, 99%), methyl α- and β-D-ribofuranoside (Sigma, 100%), L-cysteine (Cys, Sigma, 98%), sodium chromate (Merck), were used without further purification. $Na[CrO(ehba)_2]\cdot H_2O$ was synthesized from 2-ethyl-2-hydroxybutanoic acid (ehba, Aldrich, 99%), and sodium dichromate (Merck) in acetone (Merck, AR grade) according to the literature method [17]. Water was deionized and doubly distilled from $KMnO_4$. 4-(2-Hydroxyethyl)-1-piperazineethanesulfonic acid (HEPES, Research Organics) was added to adjust the pH value of the solution to 7.5. Acetate buffer (made from Merck, AR, reagents) was used for experiments at pH 5.5.

Warning: Cr^{VI} and Cr^{V} compounds are toxic and carcinogens [18].

2.2. EPR Measurements

EPR Spectra were obtained on a Bruker EMX spectrometer. The microwave frequency was generated with a Bruker 04 ER (9-10 GHz) and measured with a Bruker EMX 048T frequency meter. The magnetic field was measured with a Bruker EMX 035M NMR-probe gaussmeter. Reactions were carried out by addition of $Na[Cr^{V}O(ehba)_2]$ (1.0 mM), or Na_2CrO_4 (1.0 mM) and Cys (1.0 mM), to solutions of nucleotide, nucleoside or riboside, (2.00 to 150 mM) in Ar-saturated HEPES buffer (100 mM, pH 7.5 ± 0.1) at 20 ± 1 °C. Stock solutions were: $Na[Cr^{V}O(ehba)_2]$ (100 mM) in DMF; Na_2CrO_4 (100 mM) in H_2O; and Cys (100 mM) in H_2O (kept under Ar). EPR Spectra were simulated with the program PEST WINSIM [19], using 100% Lorentzian lineshapes. The spectral parameters for each Cr^{V} species were consistent within all simulations, with maximum deviations in the g_{iso} values being ±0.0001 units. In the simulations, values for ^{1}H a_{iso} were included only where the ^{1}H a_{iso} value is greater than the line width (LW) of the Cr^{V} species, since the signal is not significantly affected where the ^{1}H a_{iso} value is $\leqslant$LW.

3. Results

The one-electron reduction of Cr^{VI} by Cys at pH 7.5 generates Cr^{V}, which rapidly disproportionates [20]. When this reaction is performed in the presence of excess ribonucleotide, Cr^{V} can be stabilized by formation of Cr^{V}/nucleotide complexes. These Cr^{V} species can be followed by EPR spectroscopy, where strong isotropic signals are observed at room temperature in the X-band spectra. In HEPES (pH 7.5) buffer, the reaction of chromate with Cys (1:1 ratio) in the presence of 100-times excess of AMP or CMP, gives the Cr^{V} EPR spectra shown in Fig. 1(a) and (b). The best fit of the spectra affords one quintet at $g_{iso} = 1.9803$ and one quartet at $g_{iso} = 1.9798/7$ (signals were deconvoluted by fitting the spectra to Lorentzian derivatives, correlation $R > 0.99$), with four ^{53}Cr (9.55% abundance, $I = 3/2$) hyperfine peaks at 16.2×10^{-4} cm^{-1} spacing (Table 1).

The reaction of 20 mM adenosine, 1 mM Cr^{VI} and 1 mM Cys at pH 7.4 gives the spectrum shown in Fig. 1(c). Deconvolution of the EPR signal affords one quintet at $g_{iso} = 1.9803$ and one quartet at $g_{iso} = 1.9798$ with hyperfine coupling constants listed in Table 1. This signal had been previously proposed to consist of only one component with Cr^{V} coupled to four equivalent carbin-

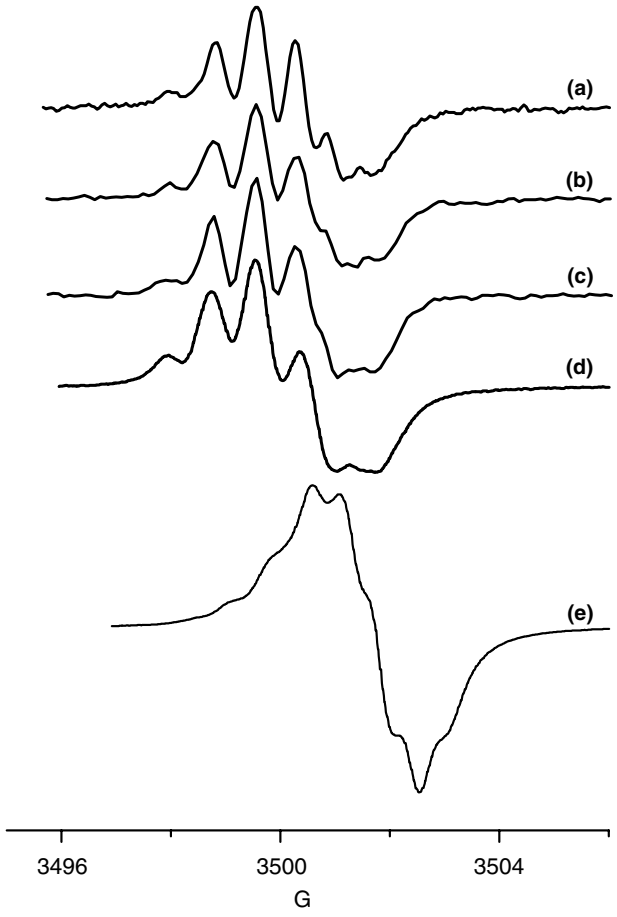


Fig. 1. X-band EPR spectra of mixtures 1 mM Cys + 1 mM Cr^{VI} and: (a) 100 mM AMP, pH 7.5, t = 7 min; (b) 100 mM CMP, pH 7.5, t = 7 min; (c) 20 mM adenosine, pH 7.4, t = 2 h; (d) 150 mM β-Rib1Me, pH 7.5, t = 24 h; (e) 100 mM α-Rib1Me, pH 5.5, t = 24 h. Frequency = 9.7 GHz, mod. ampl. = 0.2 G.

olic protons [21], however, such a model does not reproduce the signal pattern. The mixture of β-Rib1Me, Cr^{VI} and Cys (150:1:1) at pH 7.5 (or pH 5.5) also affords EPR spectra composed of one quintet at 1.9803 and one quartet at 1.9798 (Fig. 1(d)), while the Cr^{V} EPR spectra generated by reaction of 100 mM α-Rib1Me, 1 mM Cr^{VI} and 1 mM Cys in acetate buffer (pH 5.5) consist of two quintets at g_{iso} = 1.9793 and 1.9791 (Fig. 1(e), Table 1).

Alternatively, Cr^{V}/nucleotide complexes were obtained by the ligand-exchange reaction of $[Cr^{V}O(ehba)_2]^-$. At pH 7.5 and room temperature, $[Cr^{V}O(ehba)_2]^-$ is not stable [22], but in the presence of excess ribonucleotide rapid ehba substitution takes place and the ligand-exchange products can be easily observed by EPR spectroscopy. The EPR spectra of ribonucleotide/$[Cr^{V}O(ehba)_2]^-$ mixtures show a quintet at g_{iso} = 1.9803, a quartet at g_{iso} = 1.9798/7 and two triplets at g_{iso} = 1.9792 and 1.9788, besides the singlet of the starting Cr^{V} complex at g_{iso} = 1.9783. The relative intensity of these signals depends on the nucleotide to Cr^{V} mole ratio and the reaction time. Spectra taken 5 min after mixing AMP or CMP with $[Cr^{V}O(ehba)_2]^-$ in 2-5:1 mole ratio are dominated by the signal at g_{iso} = 1.9783 (>50%) (Figs. 2(b), (c) and 3(a)) while for ribonucleotide:Cr^{V} mole ratio $\geqslant$20:1, only the signals of the ehba-exchanged products are observed (Figs. 2(d) and 3(b)). When a 100:1 mole ratio is used, the Cr^{V} signals at g_{iso} = 1.9803 and 1.9798/7 are the dominant EPR features in the spectra (Figs. 2(e) and 3(c)). The final spectra of these ligand-exchange reactions are superimposable to those of the AMP (or CMP), Cr^{VI} and Cys (100:1:1) mixtures, although they are 200-times more intense than the latter ones.

Table 1
EPR Spectral parameters

Cr^{V} species	g_{iso}	^{53}Cr $A_{iso}/10^4$ cm^{-1}	$a_H/10^4$ cm^{-1}
$[Cr(O)(O^{2\prime},O^{3\prime}\text{-AMP})_2]^-$	1.9803	16.2	0.85, 0.81,0.78, 0.77
	1.9798		0.78, 0.73, 0.44
$[Cr(O)(O^{2\prime},O^{3\prime}\text{-AMP})(ehba)]^-$	1.9792	ND	0.78, 0.71
	1.9788		0.76, 0.52
$[Cr(O)(O^{2\prime},O^{3\prime}\text{-CMP})_2]^-$	1.9803	16.2	0.77, 0.76, 0.73, 0.72
	1.9797		0.72, 0.70, 0.41
$[Cr(O)(O^{2\prime},O^{3\prime}\text{-CMP})(ehba)]^-$	1.9792	ND	0.73, 0.68
	1.9788		0.66, 0.40
$[Cr(O)(O^{2\prime},O^{3\prime}\text{-adenosine})_2]^-$	1.9803	16.2	0.76, 0.76, 0.72, 0.70
	1.9798		0.72, 0.65, 0.40
$[Cr(O)(O^{2},O^{3}-\beta\text{-Rib1Me})_2]^-$	1.9803	16.1	0.85, 0.82, 0.75, 0.67
	1.9798		0.88, 0.64, 0.50
$[Cr(O)(O^{2},O^{3}-\alpha\text{-Rib1Me})_2]^-$	1.9793	16.1	0.79, 0.71, 0.59, 0.44
	1.9791		060, 0.60, 0.45, 0.43

ND, not determined.

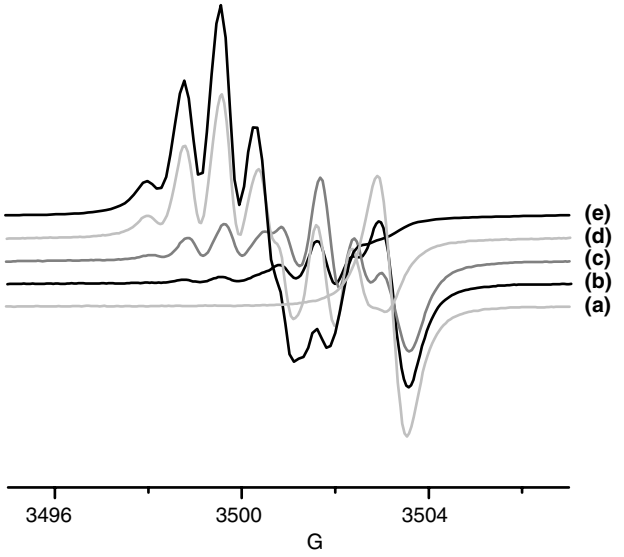


Fig. 2. X-band EPR spectra of (a) $[Cr^{V}O(ehba)_2]^-$; and mixtures of 1 mM $[Cr^{V}O(ehba)_2]^-$ with: (b) 2 mM AMP, $t = 4$ min; (c) 5 mM AMP, $t = 4$ min; (d) 20 mM AMP, $t = 19$ min; (e) 100 mM AMP, $t = 10$ min. Frequency = 9.7 GHz, pH 7.5, mod. ampl. = 0.2 G.

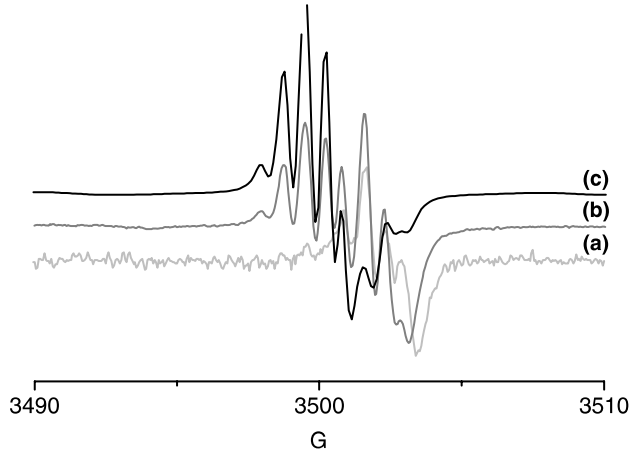


Fig. 3. X-band EPR spectra from mixtures of 1 mM $[Cr^{V}O(ehba)_2]^-$ and: (a) 2 mM CMP, $t = 19$ min; (b) 20 mM CMP, $t = 19$ min; (c) 100 mM CMP, $t = 12$ min. Frequency = 9.7 GHz, pH 7.5, mod. ampl. = 0.2 G.

Reactions of 20 mM of the following nucleotides, nucleosides and nucleic bases: 2′-deoxyadenosine, adenine, 2′-deoxythymidine 5′-monophosphate (dTMP), 2′-deoxythymidine, thymine, guanine, 2′-deoxyguanosine, 3′,5′-CMP, 3′,5′-dTMP, 3′,5′-AMP, guanosine 3′,5′-monophosphate, with 1.0 mM Cr^{VI} and 1.0 mM Cys in Ar-saturated 200 mM HEPES buffer (pH 7.4 ± 0.1) at 20 °C, for 1.5–2 h, gave no EPR signal.

4. Discussion

The most common means of characterizing Cr^{V} complexes in solution is EPR spectroscopy. The EPR spectral parameters, g_{iso} and A_{iso} values, together with the proton shf coupling, are useful in determining the binding modes of ligands to the Cr^{V} centre [8,16]. An empirical relationship between the nature and number of donor groups and the EPR spectral parameters of Cr^{V} complexes has been established [16,23]. Thus, we used the isotropic EPR parameters (g_{iso} and A_{iso} values) and the shf pattern of the signal to characterize the Cr^{V}/AMP and Cr^{V}/CMP species formed in the reaction of AMP (or CMP) with either Cr^{VI} and Cys or $[Cr^{V}O(ehba)_2]^-$.

The two EPR signals at $g_{iso} = 1.9803$ (quintet) and 1.9798/7 (quartet) (A_{iso} (16.2×10^{-4} cm^{-1})) observed in the Cr^{VI}/Cys reaction performed in the presence of excess AMP or CMP, at pH 7.5, have g_{iso} and A_{iso} values consistent with those calculated for five-coordinate oxo-Cr^{V} complexes with four alcoholato donors ($g_{calc} = 1.9800$, $A_{calc} = 16.5 \times 10^{-4}$ cm^{-1}) [8,23]. The simulation of the shf pattern indicates that the EPR signal is a composite of two oxo-Cr^{V}-ribonucleotide$_2$ species with four (two from each chelate ring) and three carbinolic protons coupled to the Cr^{V} electronic spin, respectively (Table 1, Figs. 4(a) and 5(a)). This shf pattern is consis-

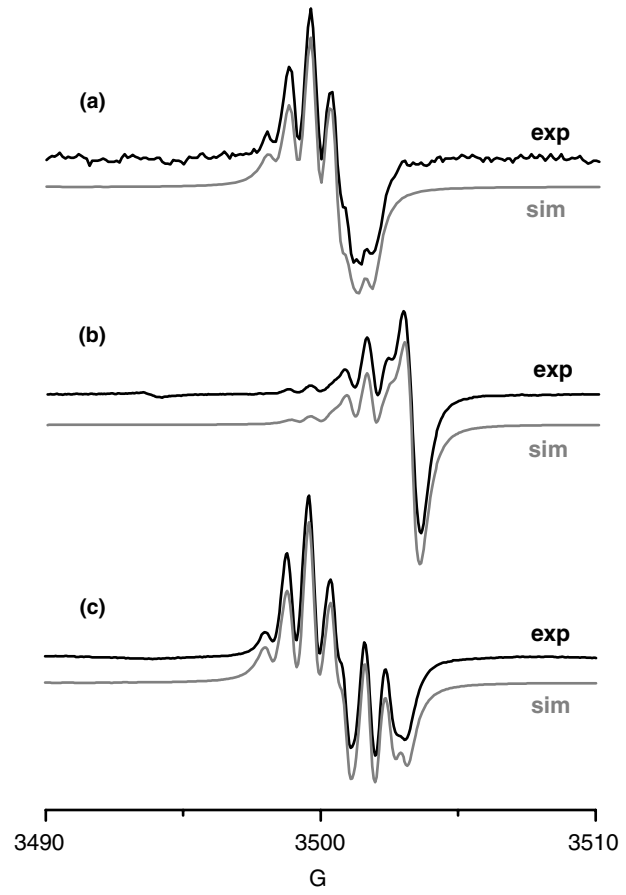


Fig. 4. Experimental and simulated X-band EPR spectra from mixtures of: (a) AMP + Cr^{VI} + Cys (100:1:1); (b) AMP + $[Cr^{V}O(ehba)_2]^-$ (2:1), $t = 4$ min; (c) AMP + $[Cr^{V}O(ehba)_2]^-$ (20:1), $t = 19$ min. LW = 0.35 G.

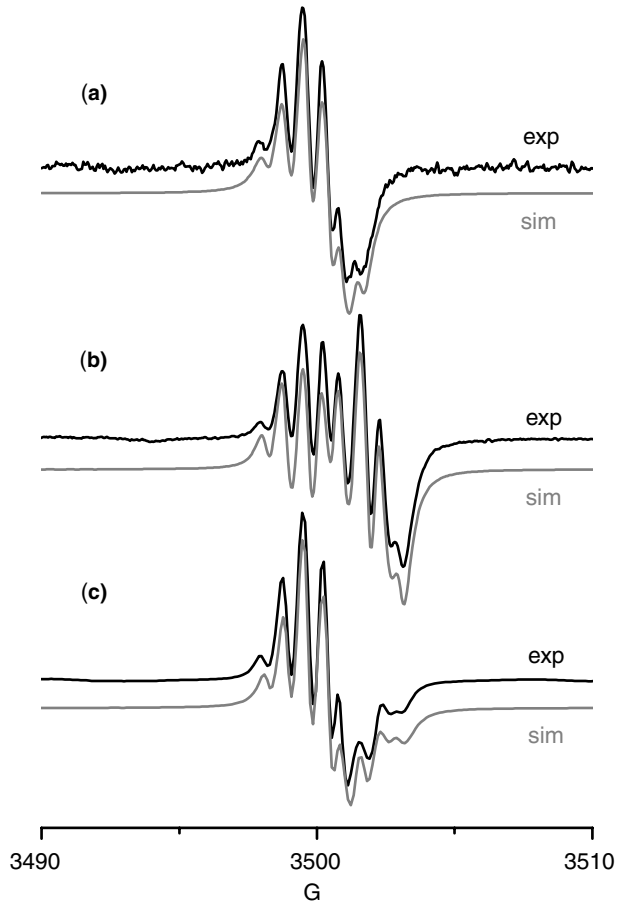


Fig. 5. Experimental and simulated X-band EPR spectra from mixtures of: (a) CMP + Cr^{VI} + Cys (100:1:1); (b) CMP + $[Cr^{V}O(ehba)_2]^-$ (20:1), $t = 20$ min; (c) CMP + $[Cr^{V}O(ehba)_2]^-$ (100:1), $t = 12$ min. LW = 0.35 G.

tent with that previously observed for oxo-Cr^{V} bischelates formed with 1,2-cyclopentanediol [24].

The values of the shf coupling constants (^1H a_{iso}) are maximal when the carbinolic protons lay near the Cr^{V}-ligand plane ($a_{Heq} \sim 1 \times 10^{-4}$ cm^{-1}), and decrease as the carbinolic protons move away this plane to reach the minimal values at the largest angles ($a_{Hax} \sim 0.35 \times 10^{-4}$ cm^{-1}) [24–26]. The EPR spectra of the Cr^{V} species formed with both AMP and CMP show two Cr^{V} components split by non equivalent carbinolic protons coupled to the Cr^{V} electronic spin: one Cr^{V} component with four protons disposed at angles in between the "pseudo-axial/equatorial" orientations, and a second Cr^{V} species with two "pseudo-axial" protons (^1H a_{iso} 0.41×10^{-4} cm^{-1}, <LW (AMP) and 0.40×10^{-4} cm^{-1}, <LW (CMP)), and two protons protruding at intermediate angles. This EPR pattern is very close to that found for the average conformations of the two geometric isomers of $[Cr^{V}(O)(1,2\text{-cyclopentanediolato})_2]^-$ [24]. So that, in the present case, the two Cr^{V} components can be attributed to the two geometric isomers of $[Cr^{V}(O)$–$O^{2\prime},O^{3\prime}$-ribonucleotide$_2]^-$ (**I** and **II** in Fig. 6). The fact that the shf coupling constants obtained for $[CrO(O^{2\prime},O^{3\prime}$-AMP$)_2]^-$ and $[CrO(O^{2\prime},O^{3\prime}$-CMP$)_2]^-$ are only slightly different (Table 1), indicates that the Cr^{V} complexes formed with the two nucleotides adopt a similar conformation.

The ligand-exchange reactions of $[Cr^{V}O(ehba)_2]^-$ with AMP or CMP result in five Cr^{V} EPR signals with $g_{iso} = 1.9803$ (quintet), 1.9798/7 (quartet), 1.9792 (triplet), 1.9788 (triplet) and 1.9783 (singlet) (Figs. 4(b), (c) and 5(b), (c)). The quintet and quartet correspond to the two geometric isomers of $[CrO(O^{2\prime},O^{3\prime}$-ribonucleotide$)_2]^-$ as discussed above for the nucleotide/Cys/Cr^{VI} system. The g_{iso} values and the multiplicity of the signals at $g_{iso} = 1.9792$ and 1.9788 are consistent with those expected for the two geometric isomers of $[Cr^{V}O(ehba)$-$(O^{2\prime},O^{3\prime}$-ribonucleotide$)]^-$ (**III**–**IV** in Fig. 6) [9]. The singlet at $g_{iso} = 1.9783$ is due to $[Cr^{V}O(ehba)_2]^-$ and is observed at low nucleotide:Cr^{V} mole ratios (Fig. 4(b)) or very short reaction times. When more than 20-times

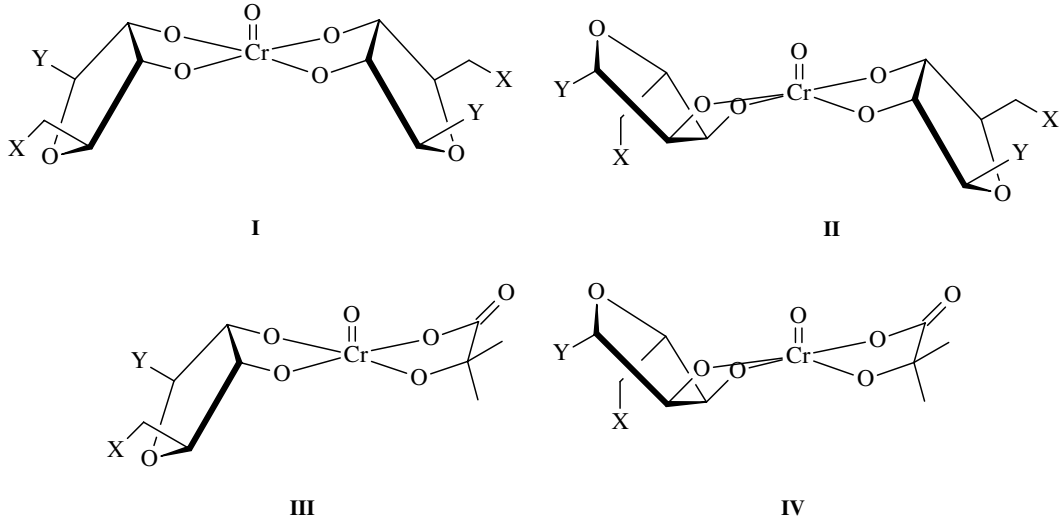


Fig. 6. Structures of Cr^{V} complexes of β-ribose derivatives (X = OPO_3 or OH; Y = nucleic base or OMe).

excess of nucleotide over Cr^V is used, the oxo-Cr^V-$O^{2'},O^{3'}$-ribonucleotide$_2$ isomers dominate the EPR spectra (Fig. 5(c)).

The reaction of adenosine with Cr^{VI}/Cys (20:1:1) at pH 7.5 affords EPR spectra analogous to those of the AMP/Cr^{VI}/Cys mixtures. The kinetic profiles for the formation of these Cr^V species in both reactions are essentially the same, and the EPR spectra are superimposable at any time. This reveals that the 5′-O-monophosphate functionality has no influence on either the chelating properties of the nucleotide or the structure of the resulting Cr^V bischelate.

The reaction of β-Rib1Me with Cr^{VI}/Cys gives EPR spectra with the same pattern as observed for the Cr^V/nucleotide and Cr^V/nucleoside systems: a quintet at g_{iso} 1.9803 and a quartet at g_{iso}1.9798. The ^1H a_{iso} values of $[CrO(O^2,O^3\text{-Rib1Me})_2]^-$ are only slightly different from those of $[CrO(O^{2'},O^{3'}\text{-ribonucleotide})_2]^-$, giving EPR signals with the same spectral features. This means that the Cr^V species formed with the β-1-substituted D-ribose derivatives have very close conformations, with a similar spatial orientation of the coupled carbinolic protons. Unlike β-Rib1Me, α-Rib1Me affords differently featured EPR spectra (Fig. 1(e), Table 1): g_{iso} values lower than observed for Cr^V species formed with the β-derivatives, and a different shf splitting of the signal that reveals a substantial modification of the Cr^V-bischelate conformation.

Other modifications in the ribose moiety, such as replacement of the 2′-hydroxyl by hydrogen or esterification of the 3′-hydroxyl with phosphate groups, suppress completely the chelating properties of the nucleotide. These results reveal that OH groups in both the 2′ and 3′ positions of the ribose ring are required for stabilization of Cr^V.

5. Conclusions

The common EPR spectral pattern found for Cr^V complexes of adenosine, AMP, CMP and β-Rib1Me reveals that the shape of the Cr^V EPR signal is not affected by groups oriented *anti* to the 2,3-diolato moiety of the ribofuranosic ring. Small differences in the ^1H a_{iso} coupling constants of the Cr^V bischelates formed with these ligands reflect the adoption of very similar conformations for the four β-ribose derivatives under study. The shf pattern of these Cr^V bischelates differs from that of the Cr^V species formed with α-Rib1Me – in which the methoxy group is *syn* to the 2,3-diolato donor site. This observation indicates that the α- and β-derivatives of ribose afford Cr^V-bischelates with different geometries, and thus, different spatial orientations of the carbinolic protons in the chelate ring. Another important difference concerns the g_{iso} values: α-Rib1Me affords Cr^V complexes with g_{iso} values lower than the β-isomer, revealing that the spatial orientation of the 1-substituent influences the strength of the diolato-Cr^V linkage. Therefore, EPR spectra can be used as an easy means to distinguish between Cr^V complexes formed with α- and β-1-subtituted-D-ribose derivatives bound to Cr^V through the 2,3-diolato group.

Acknowledgements

We thank the National Research Council of Argentina (CONICET), the National Agency for Sciences Promotion (ANPCyT), the National University of Rosario (UNR), the International Foundation for Sciences (IFS) and ANTORCHAS Foundation, for financial support. P.A.L. gratefully acknowledges support from the Australian Research Council (ARC Discovery and Large grants) and an Australian Professorial Fellowship. The ARC is also acknowledged for support for EPR measurements through a LIEF grant.

References

[1] C.B. Klein, in: L.W. Chang (Ed.), Toxicology of Metals, CRC-Lewis Publishers, New York, 1996, p. 205.
[2] P.C. Grevat, Toxicological Review of Hexavalent Chromium (CAS No. 18540-29-9), U.S. Environmental Protection Agency, Washington DC, 1998.
[3] A. Levina, R. Codd, C.T. Dillon, P.A. Lay, Prog. Inorg. Chem. 51 (2003) 145.
[4] C.T. Dillon, P.A. Lay, A.M. Bonin, M. Cholewa, G.J.F. Legge, T.J. Collins, K.L. Kostka, Chem. Res. Toxicol. 11 (1998) 119.
[5] X. Shi, N.S. Dalal, V. Vallyathan, Arch. Biochem. Biophys. 280 (1991) 381.
[6] X. Shi, Z. Dong, N.S. Dalal, P.M. Gannett, Biochim. Biophys. Acta 1226 (1994) 65.
[7] X. Shi, N.S. Dalal, Arch. Biochem. Biophys. 277 (1990) 342.
[8] R. Codd, C.T. Dillon, A. Levina, P.A. Lay, Coord. Chem. Rev. 216/217 (2001) 537.
[9] M. Rizzotto, A. Levina, M. Santoro, S. García, M.I. Frascaroli, S. Signorella, L.F. Sala, P.A. Lay, J. Chem. Soc., Dalton Trans. (2002) 3206.
[10] S. Signorella, R. Lafarga, V. Daier, L.F. Sala, Carbohydr. Res. 324/2 (2000) 127.
[11] S. Signorella, V. Daier, S. García, R. Cargnello, J.C. González, M. Rizzotto, L.F. Sala, Carbohydr. Res. 316 (1999) 14.
[12] V. Daier, S. Signorella, M. Rizzotto, M.I. Frascaroli, C. Palopoli, C. Brondino, J.M. Salas-Peregrin, L.F. Sala, Can. J. Chem. 77 (1999) 57.
[13] A. Levina, P.A. Lay, Coord. Chem. Rev. 249 (2005) 281;
R. Codd, J.A. Irwin, P.A. Lay, Curr. Opinion Chem. Biol. 7 (2003) 213.
[14] D.M.L. Goodgame, P.B. Hayman, D.E. Hathway, Polyhedron 1 (1982) 497.
[15] M. Rizzotto, V. Moreno, S. Signorella, V. Daier, L.F. Sala, Polyhedron 19 (2000) 417.
[16] S. Signorella, J.C. González, L.F. Sala, J. Argentine Chem. Soc. 90 (2002) 1.
[17] M. Krumpolc, J. Roček, Inorg. Synth. 20 (1980) 63.
[18] International Agency for Research on Cancer (IARC), IARC Monogr. Eval. Carcinog. Risk Chem. Hum. Suppl. 7 (1987) 165.
[19] WINSIM EPR Calculations for MS-Windows, Version 0.96, National Institute of Environmental Health Sciences, 1995.

[20] P.A. Lay, A. Levina, Inorg. Chem. 35 (1996) 7709.
[21] M. Quirós, D.M.L. Goodgame, Polyhedron 11 (1992) 1.
[22] A. Levina, P.A. Lay, N.E. Dixon, Inorg. Chem. 39 (2000) 385.
[23] G. Barr-David, M. Charara, R. Codd, R.P. Farrell, J.A. Irwin, P.A. Lay, R. Bramley, S. Brumby, J.-Y. Ji, G.R. Hanson, J. Chem. Soc., Faraday Trans. 91 (1995) 1207.
[24] S. Signorella, V. Daier, M. Santoro, S. García, C. Palopoli, L. Korecz, A. Rockenbauer, L.F. Sala, Eur. J. Inorg. Chem. (2001) 1829.
[25] R. Codd, P.A. Lay, J. Am. Chem. Soc. 121 (1999) 7864.
[26] M. Branca, G. Micera, U. Segre, A. Dessi, Inorg. Chem. 31 (1992) 2404.

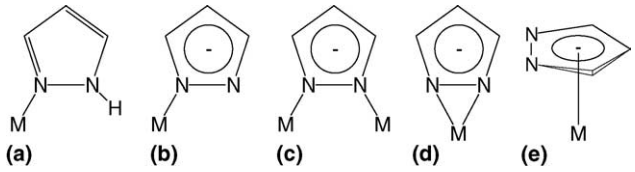
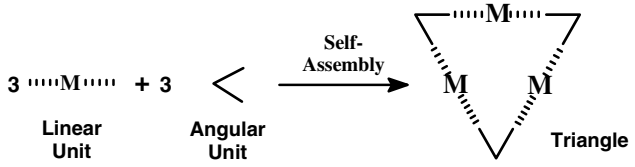
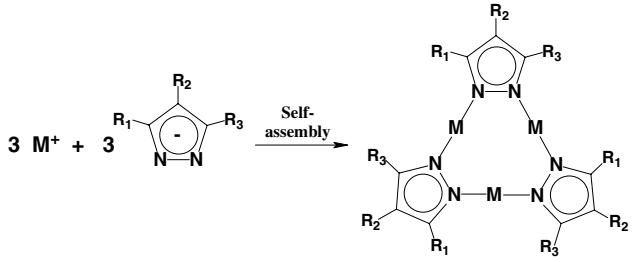


Fig. 1. Coordination modes of pyrazole ligand.



Scheme 1. The construction of molecular triangles.



Scheme 2. Trimers self-assembled from 3,5-diphenylpyrazolate (dpPz) and M = Ag^+ or Au^+.

the geometry at the metal centres. In addition, the presence of other ligands in the same coordination sphere also plays an important role in the resulting structure. Particularly, different supramolecular assemblies involving stacking interactions as well coordination and/or hydrogen bond motifs can be observed when pyrazoles and pseudohalides (e.g. azide and thiocyanate) are combined with transition metal ions. For instance, coordination bonds are responsible for the formation of a 1-D linear chain structure in $[Ni(\mu_2\text{-}1,3\text{-}N_3)(5\text{-}HmPz)_4]_n(ClO_4)_n$ [14] (5-HmPz = 5-methylpyrazole) whereas intermolecular hydrogen bonds between pyrazoles and pseudohalides result in supramolecular species composed by monomers of the type $[MX_2(HPz^*)_4]$ (M = Mn(II), Ni(II); $X = N_3^-$, SCN^-; HPz* = pyrazole, 3-substituted pyrazole [15–17]) or $[Pd(SCN)_2(HdmPz)_2]$ (HdmPz = 3,5-dimethylpyrazole) [18].

An interesting situation arises when azide anion and pyrazolate group act simultaneously as bridges, yielding the $M(\mu\text{-}1,1\text{-}N_3)(\mu\text{-pyrazolato})M$ core (M = d^8 electronic systems). The crystal packing of $[(CO)_2Rh(\mu_2\text{-}1,1\text{-}N_3)(\mu\text{-pyrazolato})Pd(\eta^3\text{-}C_3H_5)]$ shows a 1-D columnar stacking arrangement of heterobimetallic units with extended Rh–Rh interactions [19].

This work was developed on the basis of our earlier studies on the spontaneous formation of a coordination polymer from the reaction among $[PdCl_2(MeCN)_2]$, pyrazole (HPz), and azide group [20]. This prompted us to initiate a research program based on the supramolecular pyrazole-pseudohalide systems. In this paper we wish to report the syntheses and spectroscopic studies of a new class of coordination polymer having a backbone composed of palladium atoms bridged simultaneously by pyrazolato and azido groups: $[(N_3)(HL)Pd\{Pd_3(\mu\text{-}N_3)(\mu\text{-}L)_5\}_{10}(\mu\text{-}L)_2Pd(L)(HL)]$ {L = Pz^- (**1**); mPz^- (**2**), IPz^- (**3**)} and $[(N_3)(HPz)Pd\{Pd_6(\mu\text{-}N_3)_2(\mu\text{-}Pz)_5(\mu\text{-}L)_5\}_{10}(\mu\text{-}L)_2Pd(Pz)(HPz)]$ {L = mPz^- (**4**), $dmPz^-$ (**5**); IPz^- (**6**) {L = pyrazolate (Pz^-), 4-methylpyrazolate (mPz^-), 4-iodopyrazolate (IPz^-), 3,5-dimethylpyrazolate ($dmPz^-$)}.

2. Experimental

2.1. General comments

The materials used in the syntheses were all commercially available and were used without purification. All solvents were dried and kept over molecular sieves prior to use. Literature procedures were followed for the synthesis of $[PdCl_2(MeCN)_2]$ [21].

2.2. Synthesis of *1–3*

To a deep orange solution of $[PdCl_2(MeCN)_2]$ (0.39 mmol) in 10 mL of MeOH, the appropriate pyrazolyl ligand (0.81 mmol) dissolved in 2 mL of methanol was added dropwise. After stirring the resulting mixture for 5 min, NaN_3 (0.81 mmol) dissolved in 2 mL of water was added dropwise yielding a yellow suspension, which was filtered off and the obtained solid was washed with methanol and dried under vacuum. Yield 75%.

2.3. Synthesis of *4–6*

Pyrazole (0.43 mmol) and the corresponding substituted pyrazolyl ligand (0.43 mmol), dissolved in 2 mL of methanol, were added dropwise to a deep orange solution of $[PdCl_2(MeCN)_2]$ (0.39 mmol) in 10 mL of MeOH. After stirring the resulting mixture for 5 min, NaN_3 (0.81 mmol) dissolved in 2 mL of water was added affording a yellow suspension, which was filtered off and the obtained solid was washed with methanol and dried under vacuum. Yield 70%.

2.4. Instrumentation

The C, H and N analyses were carried out with a CE Instruments EA1110 CHNS-O microanalyzer. The molecular weight determinations were performed by vapor phase osmometry, using chloroform as solvent, in the Analytische Laboratorien Gmbh, Malissa und Reuter, D-51789 Lindlar Germany. Infrared spectra were

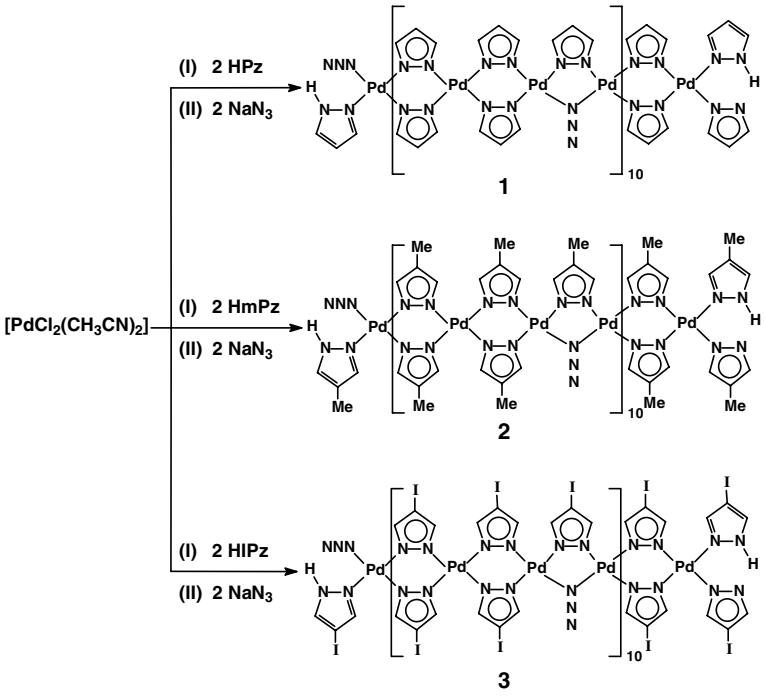
Table 1
Results of chemical analyses and molecular weight data of the compounds **1**–**6**

Compound	M_w (g mol^{-1})		Carbon (%)		Nitrogen (%)		Hydrogen (%)	
	Found	Calc.	Found	Calc.	Found	Calc.	Found	Calc.
$C_{165}H_{167}N_{143}Pd_{32}$ (**1**)	7600	7558	25.9	26.2	26.2	26.5	2.2	2.2
$C_{220}H_{277}N_{143}Pd_{32}$ (**2**)	8600	8330	31.9	31.7	23.4	23.4	4.1	4.0
$C_{165}H_{112}N_{143}I_{55}Pd_{32}$ (**3**)		14483	13.5	13.7	13.5	13.6	0.9	0.8
$C_{367}H_{421}N_{273}Pd_{62}$ (**4**)	15400	15254	29.3	28.9	24.9	25.1	3.0	2.8
$C_{419}H_{525}N_{273}Pd_{62}$ (**5**)	16200	15983	31.6	31.5	23.9	23.6	3.5	3.6
$C_{315}H_{262}N_{273}I_{52}Pd_{62}$ (**6**)		21071	17.9	18.0	17.8	18.1	1.3	1.3

recorded as KBr pellets or $CHCl_3$ solution in KBr window on a Nicolet FTIR-Impact 400 spectrophotometer (range 4000–400 cm^{-1}). ^{1}H and $^{13}C\{^1H\}$ NMR spectra were recorded in $CDCl_3$ solutions at room temperature on a Brucker AC-200 spectrophotometer working at 200 MHz for hydrogen and 50 MHz for carbon, using $SiMe_4$ as internal standard. Electronic absorption spectra were obtained in chloroform solution with a Perkin–Elmer Lambda 14 P spectrometer.

3. Results and discussion

During our investigations on some mononuclear pyrazolyl complexes of Pd(II) containing pseudohalides [18,22–24], we have obtained physical, analytical and spectroscopic evidences of the formation of an unusual coordination polymer when azide and pyrazole were employed in the reaction (compound **1**) [20]. Elemental analysis results together with osmometry data of samples obtained from repeated syntheses were consistent with a $C_{165}H_{167}N_{143}Pd_{32}$ formulation. Compound **1** was obtained as an air stable amorphous powder, soluble in chloroform and toluene, giving rise to non-conducting solutions. The solution behavior of **1** closely parallels those of some organic polymers, showing two stages of dissolution. First, it is observed a swollen and solvated mass which broke up, in a second stage, affording a solution. In addition, thin molecular films can be obtained by slow solvent evaporation. Encouraged by these observations, we synthesized a series of analogous compounds employing 4-methylpyrazole (**2**) and 4-iodopyrazole (**3**) as well mixed species with two distinct pyrazole ligands (**4**, **5**, and **6**). The analytical data obtained for the compounds are listed in Table 1. The aim was to search for trends in the spectroscopic and structural aspects as a function of pyrazole ligand. In this way, compounds **4**–**6** were successfully synthesized under identical experimental conditions used for **1**. It is important to point out that these mixed polymers are structurally similar to **1**–**3** (see Scheme 3), but have random distributions of pyrazole ligands. The obtained



Scheme 3. Syntheses of **1**–**3**.

solids are thermally stable up to 250 °C, air stable and, with exception of **3** and **6**, are soluble in chloroform.

Crystallographic studies on the polymers via X-ray diffraction of single crystals or Rietveld method were not performed due to their amorphous nature. For this reason the challenging task of this work was to present a consistent structural proposal for these systems based on physical, analytical and spectroscopic evidences.

3.1. Infrared spectroscopy

The most important bands observed in the IR spectra of the complexes along with their tentative assignments are presented in Table 2. It has been shown that the coordination mode of pyrazole-type ligands can be inferred on basis of IR data [25]. In principle the absence of an intense and broad νNH band (ca. 3300 cm^{-1}) cannot distinguish unambiguously between the anionic monodentate (C_s) and exobidentate (C_{2v}) coordination modes. However, the presence of exobidentate pyrazolato groups, clearly detected in the spectra of **1**–**6**, could be inferred by other IR evidences. Firstly it was observed the shift to lower frequency (1491–1558 cm^{-1}) of the band attributed to the ring breathing mode when compared with the free ligand (1533–1596 cm^{-1}) (see Table 2). The number of bands assigned to γCH vibrational modes can be also used as diagnosis for pyrazole coordination. The appearance of the expected two γCH bands at 870 and 742 cm^{-1} for **1** strongly supports the exobidentate character of pyrazole instead of three ones for monodentate pyrazole complexes [25]. Concerning the 4-substituted-pyrazolyl derivatives two γCH bands are expected for monodentate mode. In this work the presence of only one absorption in the spectra of **2** and **3** (819–827 cm^{-1} region) reveals exobidentate coordination. With regard to the mixed species **4**–**6** the simultaneous coordination of two distinct bridging pyrazolates was confirmed by IR spectra.

A strong $\nu_{as}N_3$ band appeared in the 2081–2087 cm^{-1} region in all IR spectra, shifted about 40 cm^{-1} to higher frequencies with respect to Pd(II) compounds containing terminal azido groups [18,20,22–24], being therefore consistent of bridging azide [26]. The ν_sN_3 mode occurs as a medium-weak band in the range 1250–1360 cm^{-1} and is only IR active when azido group acts in a terminal or asymmetrical bridging (*end-on*) fashion [27]. For this reason the presence of the ν_sN_3 band in the IR spectra of **1**–**6** in the 1248–1253 cm^{-1} region strongly suggests the existence of azido group coordinated in an *end-on* fashion. It is worth mentioning that IR spectra of the soluble polymers were also obtained in chloroform solution and exhibited the same pattern of those registered in solid state. Therefore it seems plausible suggest that the structures of the polymers in the solid state are retained in solution.

3.2. Molecular weight determinations

Osmometry data obtained for the soluble polynuclear complexes (see Table 1) revealed a value of $n = 10$ ($\overline{M_w} = 7600$ g mol^{-1}, **1**; $\overline{M_w} = 8600$ g mol^{-1}, **2**; $\overline{M_w} = 15400$ g mol^{-1}, **4**; $\overline{M_w} = 16200$ g mol^{-1}, **5**), indicating a low degree of polymerization. It is important to point out that additional IR results showed a good agreement with these molecular weight data since end-group bands associated to terminal azide (2035–2040 cm^{-1}, $\nu_{as}N_3$) and neutral monodentate pyrazole (ca. 3300 cm^{-1}, νNH) are also indicative of the formation of low-weight polymers.

3.3. NMR spectroscopy

NMR experiments carried out for compounds **1**, **2**, **4**, and **5** exhibited a series of broad signals being consistent with their oligomeric or polymeric structures. The spectra displayed characteristic resonances corresponding to

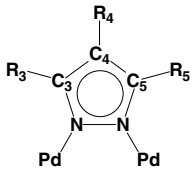
Table 2
Selected vibrational data (cm^{-1}) for palladium(II) azide complexes

Compounds						Band assignment
1	**2**	**3**	**4**	**5**	**6**	
3299 w	3302 w	3310 w	3298 w	3311 w	3296 w	νNH
3121 w	3126 w	3123 w	3133 w	3126 w	3124 w	νCH
2086 s	2085 s, 2038 sh	2081 s, 2035 m	2087 s, 2032 sh	2086 s, 2040 m	2081 s, 2035 m	$\nu_{as}N_3$
1491 m	1558 w	1490 w	1491 w	1533 w[c], 1491 w[a]	1485 w	Ring breathing
1384 m	1379 m	1379 m	1385 s	1385 m	1381 m	$\nu_{ring} + \beta_{ring}$
1248 m	1252 m	1250 w	1253 m	1252 w	1250 m	ν_sN_3
1062 s	1079 s	1064 s	1069 s	1063 m	1065 m	βCH
870 w, 742 s	819 s	825 m	821 s[b], 747 s[a]	747 m[a]	827 s[d], 754 s[a]	γCH
622 m	624 m	609 m	626 w	624 w	611 m	γ_{ring}
460 w, 398 w	461 m	440 m	460 m	459 w 399 w	445 w, 429 sh	νPdN

[a] Pz band.
[b] mPz band.
[c] dmPz band.
[d] IPz band.

hydrogen and carbon pyrazolate atoms of the inner-chain repeating units of the polymers and low-intensity signals originated from pyrazolyl end-groups (Table 3).

Therefore, it becomes evident from NMR the formation of low-molecular weight coordination polymers in agreement with osmometry and IR spectroscopy. Moreover, the ^{1}H NMR spectra display two distinct pyrazolate environments in a 2:1 ratio, which we attributed to the six-membered ring Pd(μ-L)$_2$Pd and the Pd(μ-N$_3$)(μ-L)Pd metallocycle, respectively. Such assumption is also supported by $^{13}C\{^{1}H\}$ NMR spectra. For instance, the spectrum of **1** clearly shows the typical ^{13}C signals of the Pd(μ-Pz)$_2$Pd moiety [28] centered at 140.55 ppm (C$_3$/C$_5$), 107.12 and 106.25 ppm (C$_4$) whereas the Pd(μ-N$_3$)(μ-Pz)Pd core is associated to the resonances at 139.05 (C$_3$/C$_5$) and 104.81 ppm (C$_4$) (see Scheme 4).



Pyrazolate ligand	R$_3$	R$_4$	R$_5$
pyrazolate (Pz$^-$)	H	H	H
4-methylpyrazolate (mPz$^-$)	H	Me	H
3,5-dimethylpyrazolate (dmPz$^-$)	Me	H	Me

Scheme 4. Numbering scheme of pyrazolate groups.

3.4. Structural propositions

Although proposals for the structures of compounds **1**–**6** on the basis of elemental analyses, molecular weight determinations and spectroscopic data are not a trivial matter, some models are suggested in this work from comparisons with structurally characterized compounds containing the boat-shaped M(μ-Pz)$_2$M [28] and M(μ-Pz)(μ-N$_3$)M frameworks (M = d^8 electronic systems; Pz = pyrazolate). According to earlier reports [19,29–31] the five-membered M(μ-Pz)(μ-X)M core (X = OH$^-$, Cl$^-$, N$_3^-$) adopts a nearly planar conformation which is suitable to columnar stacking, giving rise to 1-D polymeric structures. Therefore one of our assumptions involves the existence of such arrangement along the polymeric backbones of this series, in which the bidentate (Pz)$_2$Pd(Pz)$_2$ fragment acts as U-shaped spacer-chelator groups keeping the Pd(μ-Pz)(μ-N$_3$)Pd rings stacked above one another, along a given axis, yielding a polymeric structure with sinusoidal conformation. Another structural possibility take into account that the (Pz)$_2$Pd(Pz)$_2$ fragment adopts an inverted configuration compared to the U-shaped one, giving rise to a linear polymeric chain. In order to illustrate the suggested structural models, we choose compound **1** to represent the isostructural series, as can be seen in Fig. 2.

It is worth mentioning that other alternative structures are possible depending on the sequence of Pd(μ-L)(μ-N$_3$)Pd units (e.g. alternate "up and down") in the polymeric chain as well the ligands disposition in the (L)$_2$Pd(L′)$_2$ unit of the mixed-species. Thus, all these coordination polymers are likely to be correctly formulated as random copolymers.

3.5. UV–Vis spectroscopy

The UV–Vis results (Table 4) agree with the proposed structural models for the complexes. The most striking feature of electronic spectra was the presence of low-intensity absorptions at ca. 410–460 and 733–759 nm which do not appear in the spectra of the mononuclear complexes [Pd(N$_3$)$_2$(L)$_2$] (L = 1-phenyl-3-methylpyrazole, 3,5-dimethylpyrazole), being suggestive of the polynuclear nature of these compounds. These bands can be assigned to 4dz^2 (a_{1g}) → 5pz (a_{2u}) transitions whose energies strongly depend on intrachain metal–metal separation: on decreasing Pd–Pd distance there is an enhancement of the 4dz^2 → 5pz interaction causing a red-shift in this transition [32]. Many authors have ascribed the dz^2–pz transition as evidence of columnar stacking of square-planar d^8 complexes via metal–metal interactions in the solid state [33–35]. In addition it was also observed in the electronic spectra intense UV bands in the spectral range of 258–291 nm attributed to d–d transitions ($^{1}A_{1g} \rightarrow {}^{1}E_g$), which are typical of d^8 square-planar systems [36]. In **1** it can also be observed

Table 3
^{1}H and ^{13}C NMR chemical shifts (ppm)[a] for compounds **1**, **2**, **4**, and **5**

Compounds	^{1}H		^{13}C		
	R$_3$/R$_5$	R$_4$	C$_3$/C$_5$	C$_4$	R
1	7.96*, 7.58, 7.31, 6.91, 6.62, 6.48	6.14	140.55, 139.05	107.12, 106.25, 104.81	
2	7.38, 6.78, 6.48	2.11*, 2.01			
4	7.62[a], 7.36[a], 7.03[b], 6.81[b]	6.17[a], 2.11*,[b], 1.98[b]			
5	7.45[a], 7.02[a], 2.64[c], 2.33[c], 2.26[c]	6.12[a], 5.82*,[c], 5.73[c]	149.48[c], 144.35*,[c], 140.23[a]	105.73; 104.26*	14.02[c], 13.48[c], 12.07*,[c]

For labeling pyrazolate protons, see Scheme 4. Values found for the signals at room temperature in $CDCl_3$. Coupling constants could not be determined due to the broadening of signals.

[a] Pz signals.
[b] mPz signals.
[c] dmPz signals.
* Signal of chain termini.

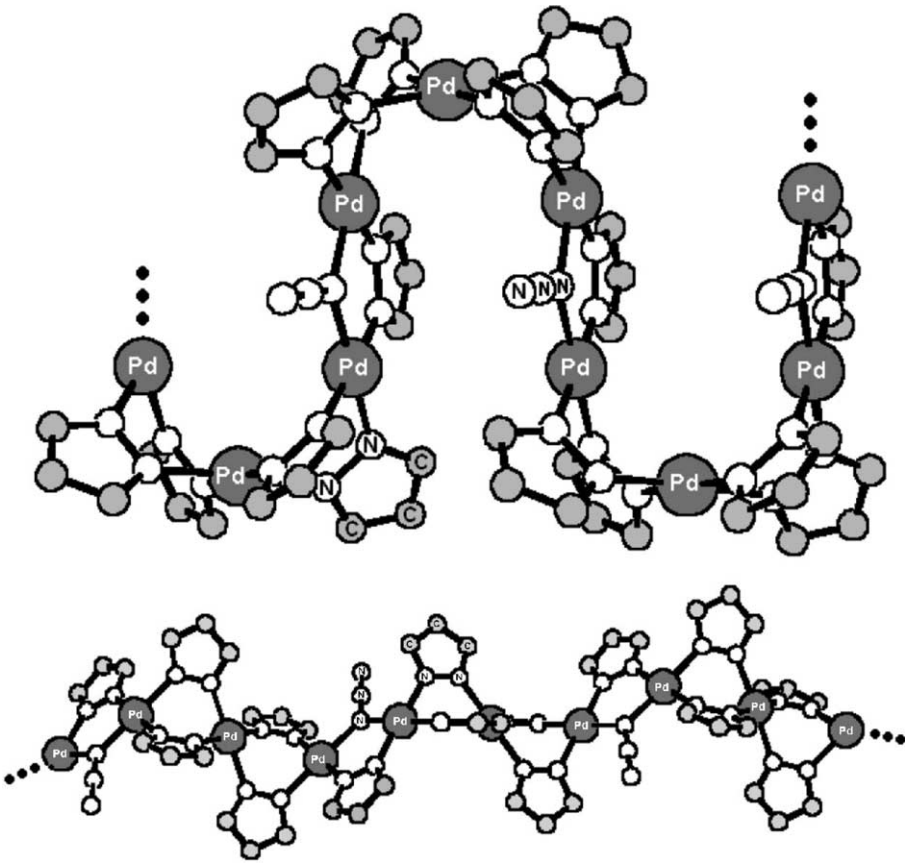


Fig. 2. Proposed structures for **1**, where the large black circles represent palladium, gray circles carbon and clear circles nitrogen atoms. The hydrogen atoms are not shown.

a $^1A_{1g} \rightarrow {}^1A_{2g}$ band near 307 nm. A LMCT transition, assigned to $\pi_{N3} \rightarrow b_{1g}Pd$ excitation, is also found in the 354–364 nm range [37,38].

4. Final remarks

We show in this article the synthetic, analytical and spectroscopic investigations of coordination polymers comprising palladium(II), unsubstituted and substituted pyrazolates and azido group. Some key points of this exciting chemistry deserve further comments. First, the polymerization reactions are extremely dependent on the pseudohalide group as well on the R groups of the pyrazolate ring. In fact, our previous results showed that, under identical experimental conditions, the use of thiocyanate, instead of azide, gave rise to the mononuclear *trans*-$[Pd(SCN)_2(HPz)_2]$ [22–24] whereas replacement of pyrazole by 3,5-dimethylpyrazole yielded the H-bonded polymer *trans*-$[Pd(N_3)_2(HdmPz)_2]$ [18]. Therefore we concluded that the self-assembly reaction via coordinative bonds only takes place combining palladium(II), pyrazole or 4-substituted pyrazoles and azide ion. Another point of interest is the spontaneous deprotonation of the pyrazole molecule to the pyrazolate without the need of any base. Such behavior has already been reported in the presence of soft metals (e.g. Ag^+) [39]. A hypothesis could be postulated taking into account the strength of azide as a Brönsted-Lowry base ($pK_b = 9.08$) [40], which could deprotonate pyrazole directly or by means of a hydrolysis. Further studies on the properties of these systems, e.g. host–guest chemistry and manufacturing of thin molecular films, as well the synthesis involving self-assembly reactions among pyrazoles, azide, and another transition metals are also underway in our laboratory.

Table 4
UV–Vis electronic data (nm)[a] of the complexes

Compound	Band assignments		
	$^1A_{1g} \rightarrow {}^1E_g$	$\pi_{N3} \rightarrow b_{1g}Pd$	$4dz^2\ (a_{1g}) \rightarrow\ 5pz\ (a_{2u})$
1	264 s; 288 s	354 m	460 m; 737 vw
2	258 s; 288 s	364 m	410 m; 459 sh; 733 vw
4	259 s; 287 s	360 m	447 m; 739 vw
5	262 s; 291 s	364 m	433 m; 757 vw

[a] Relative intensities.

Acknowledgments

We thank Prof. Dominique Matt from Université Louis Pasteur, Strasbourg, France, for his assistance

with the molecular weight determinations. Financial support by the *FAPESP*, *Capes and CNPq* are gratefully acknowledged.

References

[1] H.K. Chae, D.Y. Siberio-Pérez, J. Kim, Y. Go, M. Eddaoudi, A.J. Matzger, M. O'Keeffe, O.M. Yaghi, Nature 427 (2004) 523.
[2] N.L. Rosi, J. Eckert, M. Eddaoudi, D.T. Vodak, J. Kim, M. O'Keeffe, O.M. Yaghi, Science 300 (2003) 1127.
[3] O. Ohmori, M. Kawano, M. Fujita, J. Am. Chem. Soc. 126 (2004) 16292.
[4] S.R. Seidel, P.J. Stang, Acc. Chem. Res. 35 (2002) 972.
[5] B. Moulton, M.J. Zaworotko, Chem. Rev. 101 (2001) 1629.
[6] S. Trofimenko, Prog. Inorg. Chem. 34 (1986) 115.
[7] G. La Monica, G.A. Ardizzoia, Prog. Inorg. Chem. 46 (1997) 151.
[8] J. Reedijk, Recl. Trav. Chim. Pays. Bas. 90 (1971) 117.
[9] G. Yang, R.G. Raptis, Inorg. Chem. 42 (2003) 261.
[10] P.J. Stang, B. Olenyuk, Acc. Chem. Res. 30 (1997) 502.
[11] G. Yang, R.G. Raptis, Inorg. Chim. Acta 352 (2003) 98.
[12] R.G. Raptis, H.H. Murray III, J.P. Fackler Jr., J. Chem. Soc., Chem. Commun. (1987) 737.
[13] N. Masciocchi, G.A. Ardizzoia, S. Brenna, G. La Monica, A. Maspero, S. Galli, A. Sironi, Inorg. Chem. 41 (2002) 6080.
[14] C.S. Hong, Y. Do, Angew. Chem. Int. Ed. Engl. 38 (1999) 193.
[15] C. Zhang, C. Janiak, H. Brombacher, Z. Naturforsch b 56 (2001) 1205.
[16] Y.J. Sun, X.Y. Chen, P. Cheng, S.P. Yan, D.Z. Liao, Z.H. Jiang, P.W. Shen, J. Mol. Struct. 613 (2002) 167.
[17] M.A.S. Goher, F.A. Mautner, M.A.M. Abu-Youssef, Transit. Met. Chem. 24 (1999) 29.
[18] A.V.G. Netto, R.C.G. Frem, A.E. Mauro, E.T. de Almeida, A.M. Santana, J. de Souza Jr., R.H.A. Santos, Inorg. Chim. Acta 350 (2003) 252.
[19] F.H. Cano, C. Foces-Foces, L.A. Oro, M.T. Pinillos, C. Tejel, Inorg. Chim. Acta 128 (1987) 75.
[20] A.V.G. Netto, R.C.G. Frem, A.E. Mauro, Mol. Cryst. Liq. Cryst. 374 (2002) 255.
[21] R.F. Heck, Palladium Reagents in Organic Synthesis: Best Synthetic Methods, Academic Press, London, 1985.
[22] A.V.G. Netto, A.E. Mauro, R.C.G. Frem, A.M. Santana, R.H.A. Santos, J.R. Zoia, J. Coord. Chem. 54 (2001) 129.
[23] A.V.G. Netto, R.C.G. Frem, A.E. Mauro, R.H.A. Santos, J.R. Zoia, Transit. Met. Chem. 27 (2002) 279.
[24] A.V.G. Netto, P.M. Takahashi, R.C.G. Frem, A.E. Mauro, H.E. Zorel Jr., J. Anal. Appl. Pyrolysis 72 (2004) 183.
[25] J.G. Vos, W.L. Groeneveld, Transit. Met. Chem. 4 (1979) 137, and see references therein.
[26] T.M. Klapötke, K. Polborn, T. Schütt, Z. Anorg. Allg. Chem. 626 (2000) 1444.
[27] S. Martín, M.G. Barandika, L. Lezama, J.L. Pizarro, Z.E. Serna, J.I.R. Larramendi, M.I. Arriortua, T. Rojo, R. Cortés, Inorg. Chem. 40 (2001) 4109.
[28] A. Boixassa, J. Pons, X. Solans, M. Font-Bardia, J. Ros, Inorg. Chem. Commun. 6 (2003) 922, and see references therein.
[29] S. Komeda, M. Lutz, A.L. Spek, M. Chikuma, J. Reedijk, Inorg. Chem. 39 (2000) 4230.
[30] W.C. Deese, D.A. Johnson, A.W. Cordes, Inorg. Chem. 20 (1981) 1519.
[31] B.M. Louie, S.J. Rettig, A. Storr, J. Trotter, Can. J. Chem. 63 (1985) 688.
[32] H.B. Gray, C.J. Ballhausen, J. Am. Chem. Soc. 85 (1963) 260.
[33] P.W. DeHaven, V.L. Goedken, Inorg. Chem. 18 (1979) 827.
[34] L.M. Vallarino, S.W. Sheargold, Inorg. Chim. Acta 36 (1979) 243.
[35] K.R. Mann, J.G. Gordon II, H.B. Gray, J. Am. Chem. Soc. 97 (1975) 3553.
[36] E. Francke, C.R. Acad. Sc. Paris B 274 (1972) 659, In: A.B.P. Lever, Inorganic Electronic Spectroscopy, second ed., Elsevier, Amsterdam, 1984.
[37] H.H. Schmidtke, D. Garthoff, J. Am. Chem. Soc. 89 (1967) 1317.
[38] T.W. Bitner, J.I. Zink, Inorg. Chem. 40 (2001) 3252.
[39] G.A. Ardizzoia, G. La Monica, S. Cenini, M. Moret, N. Masciocchi, J. Chem. Soc., Dalton Trans. (1996) 1351.
[40] A.M. Golub, H. Kohler, V.V. Skopenko, Chemistry of Pseudohalides, Elsevier, Amsterdam, 1986.

roles in the structures of the zinc amides. Zinc amides with less-sterically demanding amido ligands are prone to yield bridging dimers in the solid state, as demonstrated by $\{Zn[N(SiMe_3)Ph]_2\}_2$ [11], $[Zn(NPh_2)]_2$ [12] and $\{ZnN[Si(CH_3)_2CH_2CH_2Si(CH_3)_2]_2\}_2$ [15]. Zinc amides derived from significantly more sterically bulky amido ligands, however, are generally found as monomers in the solid state, as exemplified by $Zn[N(SiMe_3)(2,6\text{-}Me_2C_6H_3)]_2$, $Zn[N(SiMe_3)(2,6\text{-}{}^iPr_2C_6H_3)]_2$, $Zn[N(SiMe_3)(2,5\text{-}{}^tBu_2C_6H_3)]_2$ and $Zn[N(SiMePh_2)_2]_2$ [11,13]. However, mercury amides always appear to be monomeric in the solid state, no matter whether bulky amido ligands are used or not. A search of the Cambridge Structural Database maintained by the Cambridge Crystallographic Database Centre (CCDC) indicates that the N–Hg–N angle in two-coordinate R_2N–Hg–NR_2 compounds range from ca. 172° to 180°. We also note that the use of silylamides as supporting ligands in these structurally characterized two coordinate Hg compounds is extremely limited [15]. This does not mean that all Hg amides are linear or only two coordinate. Supporting donor or solvent ligands can also be present to create three- or higher coordinate Hg complexes, which causes obvious deviations from the nearly linear geometry seen in the two coordinate Hg compounds. An additional strategy used in keeping the two coordinate Hg species monomeric is the presence of highly electronegative groups, either in the σ- (e.g., CF_3, TeF_5 and SF_5) and/or π-sense (e.g., $SiMe_3$), which are bonded to the nitrogen atom to reduce the electron donation of the amido ligands [18]. In our laboratory, we have synthesized and begun to report numerous main group metal (bis)amides based on various bulky silylamido ligands of the formula [N($SiMe_3$)(R)] [9,19]. This survey of preparative main group chemistry has led us to our current interest in the bulky silylamides of Zn and Hg.

In this report, we continue looking at the synthesis and structural characterization of main group bis(amides) by preparing new zinc and mercury complexes containing the bulky silyamido ligands – [N($SiMe_3$)(R)], where R is either –$SiPh_2{}^tBu$ or adamantyl (Ad). These compounds have been characterized by X-ray diffraction and have been shown to be monomeric in the solid state, containing approximately linear N–M–N bonds. Additionally, we have reacted solutions of these two coordinate Zn and Hg monomers with gaseous CO_2 and have begun to determine the reaction products obtained.

2. Experimental

2.1. General considerations

All manipulations were carried out in an Ar-filled glovebox or by using standard Schlenk techniques [20]. Anhydrous solvents were purchased from Aldrich or Fisher Scientific Company, after which they were stored in the glovebox over 4 Å molecular sieves. Anhydrous $ZnCl_2$, $HgBr_2$, Me_3SiNCO, $Me_3SiN{=}C{=}NSiMe_3$ and ^{n}BuLi (2.5 M in hexanes) were purchased from Aldrich. The ligands (Me_3Si)(R)NH (R = –$SiPh_2{}^tBu$ and Ad) were synthesized by the literature procedures [21]. ^{1}H and ^{13}C NMR spectra were obtained on a Bruker AMX 250 spectrometer using C_6D_6 or $CDCl_3$ as a solvent. GC/MS data of the organic products after reactions with CO_2 were obtained on a Hewlett–Packard Model 5890 GC equipped with an HP Model 5972 mass selective detector. Elemental analyses for carbon, hydrogen and nitrogen content were measured in sealed volatile sample pans using a Perkin–Elmer series II CHNS/O 2400 analyzer, or performed commercially by Desert Analytics, Tucson, Arizona.

2.2. $Zn[N(SiMe_3)(SiPh_2{}^tBu)]_2$ (**1**)

In a glovebox, a solution of ^{n}BuLi (3.1 ml, 7.7 mmol) was added slowly to (Me_3Si)($^tBuPh_2Si$)NH (2.50 g, 7.6 mmol) in 50 ml diethyl ether at room temperature, and the reaction mixture was stirred for 3 h. Anhydrous $ZnCl_2$ (0.52 g, 3.8 mmol) was added in small portions via a solid addition funnel. The mixture was stirred overnight and then the solvents removed. The residue was held in vacuo for 2 h and was then extracted with 60 ml hexanes, and filtered through Celite filter aid. Hexane was removed under reduced pressure to yield **1** as a white solid (2.11 g, 77%). An analytical sample was obtained by recrystallization from a saturated hexane solution at −20 °C to afford **1** as colorless crystals. ^{1}H NMR (C_6D_6): δ 0.12 (s, 18H, –SiMe_3), 1.07 (s, 18H, –Si(CMe_3)), 7.15 (m, 16H, C_6H_5), 7.62 (m, 4H, C_6H_5). ^{13}C NMR (C_6D_6): δ 6.09 (–SiMe_3), 20.18 (–Si(CMe$_3$)), 29.13 (–Si(CMe_3)), 128.21 (C_6H_5), 129.62 (C_6H_5), 136.06 (C_6H_5), 139.63 (C_6H_5). *Anal.* Calc. for $C_{38}H_{56}N_2Si_4Zn$: C, 63.52; H, 7.86; N, 3.99. Found: C, 63.55; H, 7.32; N, 4.48%.

2.3. $Hg[N(SiMe_3)(SiPh_2{}^tBu)]_2$ (**2**)

Similarly to the preparation of **1**, [(Me_3Si)($^tBuPh_2$-Si)N]Li was generated in situ from the reaction of (Me_3Si)($^tBuPh_2Si$)NH (2.00 g, 6.1 mmol) and ^{n}BuLi (2.5 ml, 6.2 mmol) in 50 ml of diethyl ether at room temperature. The Li salt was treated with anhydrous $HgBr_2$ (1.10 g, 3.1 mmol) over a 24-h period to form a white precipitate, which after extraction and removal of solvent led to **2** (2.14 g, 82%) as a white solid. Recrystallization from a saturated hexane solution at −20 °C afforded **2** as colorless crystals. ^{1}H NMR (C_6D_6): δ 0.05 (s, 18H, –SiMe_3), 1.14 (s, 18H, –Si(CMe_3)), 7.15 (m, 16H, C_6H_5), 7.77 (m, 4H, C_6H_5). ^{13}C NMR (C_6D_6): δ 5.95 (–SiMe_3), 19.73 (–Si(CMe$_3$)), 29.19 (–Si(CMe_3)),

128.39 (C_6H_5), 129.51 (C_6H_5), 136.18 (C_6H_5), 139.63 (C_6H_5). *Anal.* Calc. for $C_{38}H_{56}N_2Si_4Hg$: C, 53.46; H, 6.61; N, 3.28. Found: C, 52.44; H, 6.51; N, 3.22%.

2.4. Zn[N(SiMe$_3$)(Ad)]$_2$ (3)

Analogously to the preparation of **1**, [(Me_3Si)(Ad)N]-Li was generated in situ from (Me_3Si)(Ad)NH (2.23 g, 10.0 mmol) and ^{n}BuLi (4.0 ml, 10.0 mmol) in 50 ml diethyl ether at room temperature. $ZnCl_2$ (0.68 g, 5.0 mmol) was added via solid addition funnel and allowed to react overnight. The precipitate was extracted and filtered to give **3** (1.88 g, 74%) as a white solid. An analytically pure sample of **3** was obtained by recrystallization from saturated hexane solution at −20 °C as colorless crystals. ^{1}H NMR (C_6D_6): δ 0.29 (s, 18H, –SiMe_3), 1.51 (m, 12H, –CH_2–), 1.79 (m, 12H, –CH_2–), 1.96 (m, 6H, –CH–). ^{13}C NMR (C_6D_6): δ 5.87 (–SiMe_3), 31.05 (–CH$_2$–), 36.58 (–CH$_2$–), 51.98 (–CH–), 53.40 (–CN). *Anal.* Calc. for $C_{26}H_{48}N_2Si_2Zn$: C, 61.20; H, 9.48; N, 5.49. Found: C, 61.13; H, 9.52; N, 5.49%.

2.5. Hg[N(SiMe$_3$)(Ad)]$_2$ (4)

As in **3**, [(Me_3Si)(Ad)N]Li, generated in situ from (Me_3Si)(Ad)NH (2.50 g, 11.2 mmol) and ^{n}BuLi (4.5 ml, 11.2 mmol), was treated with $HgBr_2$ (2.02 g, 5.6 mmol) in 50 ml diethyl ether at room temperature. After reacting for 24 h, workup of the reaction as above yielded **4** as a white solid (2.89 g, 80%). An analytically pure sample was obtained by recrystallization from saturated hexane solution at −20 °C to afford **4** as colorless crystals. ^{1}H NMR (C_6D_6): δ 0.33 (s, 18H, –SiMe_3), 1.50 (m, 12H, –CH_2–), 1.86 (m, 12H, –CH_2–), 1.99 (m, 6H, –CH–). ^{13}C NMR (C_6D_6): δ 6.26 (–SiMe_3), 31.01 (–CH$_2$–), 36.54 (–CH$_2$–), 52.10 (–CH–), 54.96 (–CN). *Anal.* Calc. for $C_{26}H_{48}N_2Si_2Hg$: C, 48.38; H, 7.50; N, 4.34. Found: C, 48.58; H, 7.54; N, 4.39%.

2.6. Reactions with CO_2

Two different procedures were used in the treatment of **1**–**4** with gaseous CO_2. In the first route, a hexane solution of the metal amide was placed in a flask under inert atmosphere, and CO_2 was simply bubbled through the solution for approximately an hour. The reaction contents were heated to ca. 60 °C and held for additional time if no reaction was apparent at room temperature. Any organic products were identified by GC/MS. In a second procedure, more forcing conditions were used. A closed, glass Fischer–Porter (F–P) bottle reactor system was used in order to hold the contents under pressure (60 psig) and temperature (60 °C) [22]. Again, the metal amide was added as a hexane solution into the F–P bottle, and CO_2 was added to a pressure of 60 psig and then allowed to react at 60 °C for an hour. Careful depressurization of the F–P reactor in a hood was followed by analysis of the organic solution by GC–MS. Identification and quantification of the Me_3Si–NCO and/or $Me_3SiN{=}C{=}NSiMe_3$, if formed, was possible by comparison to authentic purchased samples.

2.7. X-ray crystallography

Crystallographic data and details of X-ray studies for **1**–**4** are given in Table 1. As all of the compounds are extremely air-sensitive the crystals were always handled under an inert atmosphere, covered with oil and immediately transferred to the N_2 stream of the diffractometer. Data were collected at low temperatures on a Bruker P4/CCD diffractometer using λ (Mo Kα) = 0.71073 Å radiation. The structures were solved using the direct methods, completed by subsequent difference Fourier syntheses, and refined by full matrix least-squares procedures on F^2. SADABS absorption corrections were applied to all data. All non-hydrogen atoms were refined with anisotropic displacement coefficients. All H atoms in **1** and the H atoms of Me groups in **4** were found on the residual densities and refined with isotropic thermal parameters. Other H atoms in **4** and all H atoms in **2** and **3** were treated as idealized contributions. Both Ad groups in the crystal structure of **3** and one Ad group in **4** are disordered over two positions (in ratios 76/24, 63/37 and 68/32, respectively) related by rotation around the N–C bond by ca. 60°. The Flack parameters for **1** and **2** are 0.003(8) and 0.082(8), respectively. All software and sources of scattering factors are contained in the SHELXTL (6.10) program package (G. Sheldrick, Bruker XRD, Madison, WI) [23,24].

3. Results and discussion

Compounds **1**–**4** were directly synthesized via metathesis reactions of two equivalents of the lithium amides [(Me_3Si)(^{t}BuPh_2Si)]NLi or [(Me_3Si)(Ad)]NLi with one equivalent of $ZnCl_2$ or $HgBr_2$. While the $ZnCl_2$ reactions occurred immediately as shown by the production of LiCl, the reactions of $HgBr_2$ with lithium amides were more sluggish, requiring longer times for the reaction to reach completion. Colorless crystals of **1**–**4** suitable for X-ray diffraction analysis were obtained via recrystallization of a saturated hexane solution at −20 °C.

3.1. Complexes containing the –[N(SiMe$_3$)(SiPh$_2$^{t}Bu)] ligand

X-ray diffraction analysis reveals that in the solid-state Zn[N($SiMe_3$)($SiPh_2$^{t}Bu)]$_2$ (**1**) is monomeric with a two coordinate Zn center (Fig. 1). The sp hybridized Zn atom is bonded to two nitrogen atoms in an

Table 1
Crystallographic data and parameters for complexes **1**–**4**

	Complex **1**	Complex **2**	Complex **3**	Complex **4**
Empirical formula	$C_{38}H_{56}N_2Si_4Zn$	$C_{38}H_{56}N_2Si_4Hg$	$C_{26}H_{48}NSi_2Zn$	$C_{26}H_{48}NSiHg$
Formula weight	718.58	853.80	510.21	645.43
Crystal size (mm)	$0.25 \times 0.20 \times 0.15$	$0.30 \times 0.25 \times 0.05$	$0.40 \times 0.35 \times 0.25$	$0.30 \times 0.25 \times 0.05$
T (K)	218(2)	218(2)	218(2)	218(2)
Crystal system	orthorhombic	orthorhombic	triclinic	monoclinic
Space group	$P2_12_12_1$	$Pca2_1$	$P\bar{1}$	$P2_1/c$
a (Å)	13.7118(8)	21.5234(15)	9.7545(6)	11.8526(8)
b (Å)	17.0799(10)	11.0835(8)	11.4733(7)	12.8793(8)
c (Å)	17.3076(9)	33.986(3)	13.2709(8)	18.0078(12)
α (°)	90	90	86.377(1)	90
β (°)	90	90	86.719(1)	91.987(1)
γ (°)	90	90	72.233(1)	90
Volume (Å^3)	4053.4(4)	8108(2)	1410.4(2)	2747.3(3)
Z, Z'	4, 1	8, 2	2, 1	4, 1
Calculated density (g/cm^3)	1.178	1.399	1.201	1.560
μ (mm^{-1})	0.751	3.942	0.971	5.706
Measured reflections	25596	57283	8934	19839
Independent reflections (R_{int})	9624 (0.0339)	19156 (0.0885)	5856 (0.0194)	6517 (0.0364)
Observed reflections	7977	12760	5152	5754
Absorption correction (T_{max}/T_{min})	SADABS (0.896/0.835)	SADABS (0.827/0.384)	SADABS (0.793/0.697)	SADABS (0.763/0.279)
R_1, wR_2 (all data)	0.0499, 0.0915	0.0865, 0.1385	0.0417, 0.1101	0.0316, 0.0681
R_1, wR_2 [$I > 2\sigma(I)$]	0.0398, 0.0881	0.0580, 0.1298	0.0372 0.1069	0.0269, 0.0657
Goodness-of-fit on F^2	0.964	0.898	1.043	1.034

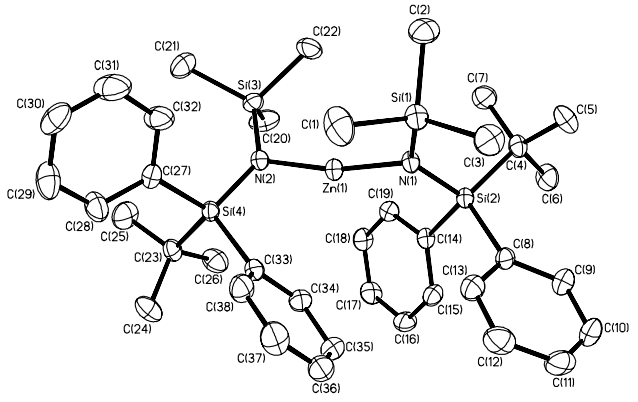


Fig. 1. Molecular structure of **1** (30% ellipsoids), the H atoms are omitted for clarity.

approximate linear arrangement. We presume that owing to the increased steric hindrance presented by the –[N(SiMe$_3$)(SiPh$_2$^{t}Bu)] ligands, the N–Zn–N angle (167.87(10)°) is forced to be significantly deviated from linearity. This is in stark contrast to the strictly linear structures found in Zn[N(SiMe$_3$)(2,6-Me$_2$C$_6$H$_3$)]$_2$, Zn[N(SiMe$_3$)(2,5-^{t}Bu$_2$C$_6$H$_3$)]$_2$ and Zn[N(SiMe$_3$)(2,6-^{i}Pr$_2$-C$_6$H$_3$)]$_2$ (N–Zn–N angles are 177.18°, 179.56° and 180°, respectively) [11]. The Zn–N bond distances in **1** (1.853(2) and 1.858(2) Å) are slightly longer than those found in Zn[N(SiMe$_3$)(^{t}Bu)]$_2$ (1.82 Å) and Zn[N(SiMe$_3$)$_2$]$_2$ (1.82 Å, by gas-phase electron diffraction) [14,17], but equivalent to that found in Zn[N(SiMePh$_2$)]$_2$ (1.85 Å) [13]. Compared to the N(1)–Si(2) distance of 1.718(2) Å, a relatively longer N(1)–Si(1) bond length of 1.732(2) Å is observed; both are comparable to the N–Si bond lengths found in Zn[N(SiMe$_3$)-(2,6-^{i}Pr$_2$C$_6$H$_3$)]$_2$ (1.728(14) Å) and Zn[N(SiMe$_3$)(2,5-^{t}Bu$_2$C$_6$H$_3$)]$_2$ (1.731(4) Å) [11]. Interestingly, the Si(2)–N(1)–Zn(1) angle of 116.06(11)° is significantly larger than the Si(4)–N(2)–Zn(1) angle of 111.46(11)°, while the Si(2)–N(1)–Si(1) angle of 129.77(12)° is substantially smaller than the Si(4)–N(2)–Si(3) angle of 132.97(13)°. Both ligand nitrogen atoms are located in nearly ideal trigonal–planar environments, within the $ZnSi_2$ planes. Important bond distances and angles for **1** and **2** are shown in Table 2.

Compound **2** (Fig. 2) features similar structural characteristics. The complex is again monomeric with the Hg atom attached to two ligand nitrogen atoms. No solvent ligands are coordinated to the Hg atom. Compared to the N–Zn–N arrangement in **1**, the N–Hg–N angle found in **2** (176.1(3)°) is much closer to linearity, likely due to the larger size of the Hg atom relative to Zn. The N–Hg–N angle in the related structures Hg[N(Si-Me$_3$)(2,6-^{i}Pr$_2$C$_6$H$_3$)]$_2$ and {HgN[Si(CH$_3$)$_2$CH$_2$CH$_2$Si-(CH$_3$)$_2$]$_2$}$_2$ show no deviation from linearity (180°) [11,15]. The Hg–N distances found in **2** (2.034(7), 2.015(7) and 2.026(7), 2.034(7) Å for two independent molecules) are close to those seen in bis[2,3,4,5-tetrakis(trifluoromethylthio)pyrrolyl]mercury {Hg[N(CSC-F$_3$)$_4$]$_2$} (2.02 Å) [25], but slightly shorter than in Hg(N=SF$_2$)$_2$ (2.05 Å) [26], Hg[N(SO$_2$CH$_3$)$_2$]$_2$ (2.07 Å) [27], Hg[PhC(NSiMe$_3$)$_2$]$_2$ (2.07 Å) [28] or Hg[N(SiMe$_3$)-C(Ph)NC(Ph)=C(SiMe$_3$)$_2$]$_2$ (2.065 Å) [29]. The larger Hg atom in **2** also leads to substantially longer Hg–N

Table 2
Selected bond lengths (Å) and angles (°) for complexes **1** and **2**

	1, M = Zn	**2**, M = Hg[a]
M(1)–N(1)	1.853(2)	2.034(7) (2.026(7))
M(1)–N(2)	1.858(2)	2.015(7) (2.034(7))
N(1)–Si(1)	1.732(2)	1.729(9) (1.714(9))
N(1)–Si(2)	1.718(2)	1.713(9) (1.740(8))
N(2)–Si(3)	1.732(2)	1.724(9) (1.721(9))
N(2)–Si(4)	1.710(2)	1.728(9) (1.708(9))
Si(2)–N(1)–Si(1)	129.77(12)	134.0(5) (133.6(5))
Si(2)–N(1)–M(1)	116.06(11)	115.6(4) (114.0(4))
Si(1)–N(1)–M(1)	114.15(11)	109.5(4) (111.1(4))
Si(4)–N(2)–Si(3)	132.97(13)	126.1(5) (127.3(5))
Si(4)–N(2)–M(1)	111.46(11)	121.0(5) (120.5(4))
Si(3)–N(2)–M(1)	115.28(12)	112.9(4) (112.2(4))
N(1)–M(1)–N(2)	167.87(10)	176.1(3) (176.1(3))

[a] The values for two symmetrically independent molecules are given.

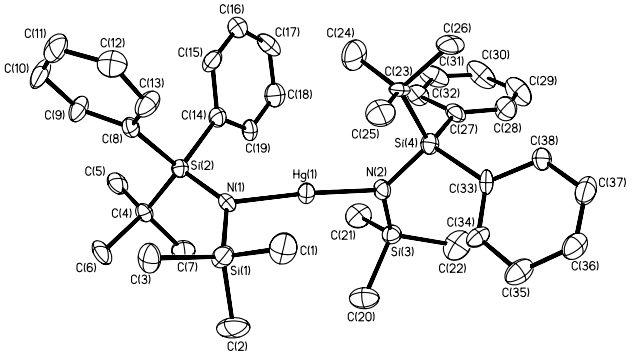


Fig. 2. Molecular structure of **2** (30% ellipsoids). Only one of two symmetrically independent molecules is shown. The H atoms are omitted for clarity.

bonds relative to the Zn–N bonds in **1** (increase of 0.17 Å) and thus to a less-crowded molecule. An interesting feature present in the structure of **2** is that the Si–N–Si angles found in the two –N[(SiMe$_3$)(SiPh$_2$^{t}Bu)] groups attached to Hg are significantly different – the Si(2)–N(1)–Si(1) angle of 134.0(5)° (133.6(5)°) is opened up considerably relative to its counterpart Si(4)–N(2)–Si(3) angle of 126.1(5)° (127.3(5)°) in both independent molecules. This naturally causes the other angles around N(1) to diminish in order to maintain a trigonal planar geometry at the nitrogen atom. This indicates that the two –N[(SiMe$_3$)(SiPh$_2$^{t}Bu)] ligands are attached to the Hg atom with different arrangements. We find no apparent close interactions in the crystal structure between Hg and the ligand periphery that might contribute to the opening up of one Si–N–Si angle relative to the other.

3.2. Complexes containing the –[N(SiMe$_3$)(Ad)] ligand

We have also prepared Zn (**3**) and Hg (**4**) complexes utilizing the somewhat less sterically hindered ligand –[N(SiMe$_3$)(Ad)]. The structure of **3** is shown in Fig. 3, while the structure of **4** appears in Fig. 4. Pertinent bond

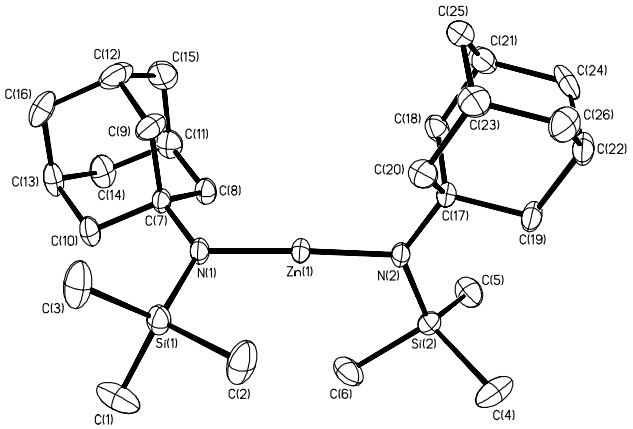


Fig. 3. Molecular structure of **3** (30% ellipsoids). For clarity, the H atoms are omitted and only one of two possible positions for both disordered Ad groups is shown.

lengths and angles are given in Table 3. Both Ad groups in the crystal structure of **3** and one Ad group in **4** are disordered over two positions related by rotation around the N–C bond by an angle of ca. 60°. Only one position for these Ad groups is shown in Fig. 3 and 4. The use of this ligand allows the N–Zn–N angle (177.46(6)°) in **3** to be much closer to the idealized linear arrangement. Similar to **1**, the zinc atom is coordinated to two ligand nitrogen atoms in a solvent-free, monomeric structure. Quite interestingly, the crystal structure indicates that the two adamantyl groups located on the two amido ligands are *syn* to each other, that is they lie on the same side of the N–Zn–N line. Looking down the N–Zn–N coordinate (Fig. 5) it can be seen that the N–C(Ad) bonds of the two ligands (N(1)–C(7) and N(2)–C(17)) have a torsion N(1)–C(7)···N(2)–C(17) angle of 77.6°. Obviously, with the adamantyl groups being arranged in a *syn*-like geometry, this causes the two –SiMe$_3$ groups bound to N also to be roughly

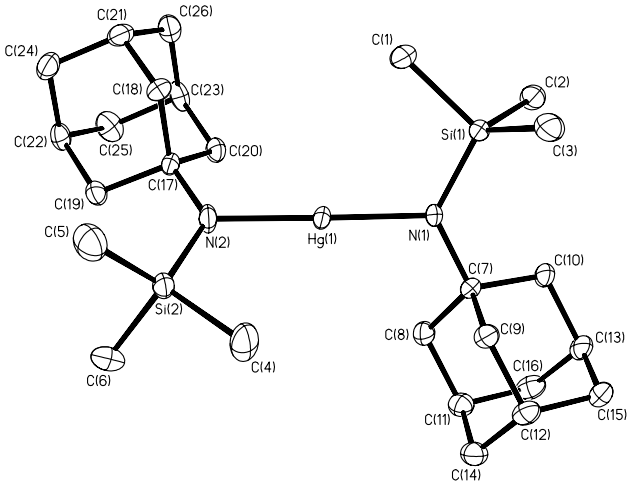


Fig. 4. Molecular structure of **4** (25% ellipsoids). For clarity, the H atoms are omitted and only one of two possible positions for the disordered Ad group is shown.

Table 3
Selected bond lengths (Å) and angles (°) for complexes **3** and **4**

	3, M = Zn	**4**, M = Hg
M(1)–N(1)	1.827(2)	2.004(3)
M(1)–N(2)	1.828(14)	2.009(3)
N(1)–Si(1)	1.715(2)	1.717(3)
N(2)–Si(2)	1.713(2)	1.712(3)
N(1)–C(7)	1.467(3)	1.478(4)
N(2)–C(17)	1.472(2)	1.476(4)
N(1)–M(1)–N(2)	177.46(6)	178.80(10)
Si(1)–N(1)–M(1)	114.75(9)	116.22(14)
Si(2)–N(2)–M(1)	115.51(8)	116.64(16)
C(7)–N(1)–Si(1)	127.11(12)	126.1(2)
C(7)–N(1)–M(1)	118.05(12)	116.32(19)
C(17)–N(2)–Si(2)	127.49(11)	126.9(2)
C(17)–N(2)–M(1)	116.95(11)	116.4(2)

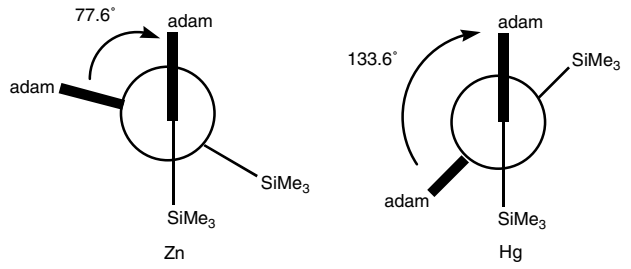


Fig. 5. View down the N–M–N axis for **3** (M = Zn) and **4** (M = Hg) showing the difference in location of the adamantyl groups on the amido ligands.

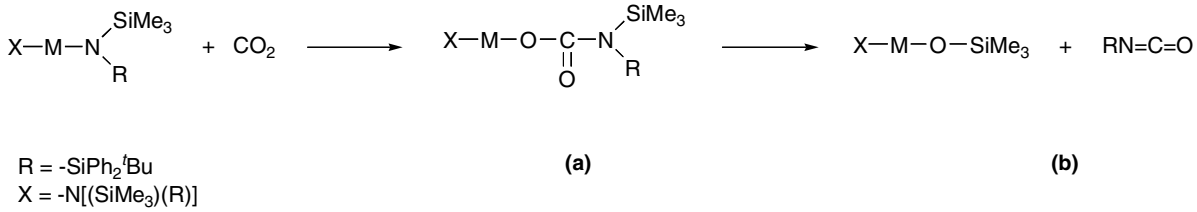
syn. The torsion angle N(1)–Si(1)···N(2)–Si(2) between the –N–$SiMe_3$ groups is 75.1°. Both Zn–N distances of 1.827(15) and 1.828(14) Å are found to be identical and marginally shorter than those observed in **1** (ave. 1.856(4) Å). Although not imposed by crystallography, this suggests that the two ligands reside symmetrically on both sides of the zinc atom. This is confirmed by the negligible differences seen in the Si(1)–N(1)–Zn(1) (114.75(9)°) and Si(2)–N(2)–Zn(1) (115.51(8)°) angles, as well as the C(7)–N(1)–Si(1) (127.11(12)°) and C(17)–N(2)–Si(2) (127.49(11)°) angles.

Compound **4**, containing the same –[$N(SiMe_3)$(Ad)] ligand, also adopts an almost linear structure with a N–Hg–N bond angle of 178.80(10)°. Despite being prepared in diethyl ether, again no coordinated solvent is present. In contrast to the arrangement of the ligands in **3**, the crystal structure reveals that the adamantyl and –$SiMe_3$ groups of each –[$N(SiMe_3)$(Ad)] ligand reside in a configuration that is an *anti* arrangement, rather than the *syn* geometry seen in **3**. The torsion angle C(7)–N(1)···N(2)–C(17) for the two N–C(Ad) bonds is 133.6° (a perfect *anti* configuration would be 180°) and the torsion angle Si(1)–N(1)···N(2)–Si(2) for the two N–$Si(Me_3)$ bonds is 120.6°. An *anti*-like arrangement similar to this has been seen previously in the structure of the mercury amide $Hg[N(CF_3)TeF_5]_2$, where the –TeF_5 groups have opposite locations relative to the N–Hg–N coordinate [18]. The two Hg–N bond lengths in **4** (2.004(3) and 2.009(3) Å) are close each other, but slightly shorter than those in **2** (ave. 2.027(9) Å). The N–Si bond lengths in **4** (1.715(2) and 1.713(2) Å) are comparable to the corresponding lengths found in **2**. As in **3**, although not rigorously imposed by crystallography, the essentially identical angles between the pairs Si(1)–N(1)–Hg(1) (116.22(14)°) and Si(2)–N(2)–Hg(1) (116.64(16)°), C(7)–N(1)–Si(1) (126.1(2)°) and C(17)–N(2)–Si(2) (126.9(2)°), and C(7)–N(1)–Hg(1) (116.32(19)°) and C(17)–N(2)–Hg(1) (116.4(2)°), indicate that the two –$N(SiMe_3)$(Ad) ligands are symmetrically coordinated to the Hg atom. Neither of the two ligand nitrogen atoms shows any deviation from trigonal planar geometry.

3.3. Attempted reactions of *1–4* with CO_2

One of our primary interests in these complexes involves their possible interactions with carbon dioxide. More specifically, we are interested in determining under what conditions bis(silylamido) species of the *s* and *p* block elements either (a) directly insert CO_2 (and stop) to yield isolable metal carbamates as final products, or (b) after insertion, in a subsequent reaction produce silyl-isocyanates via elimination from these metal carbamato intermediates (Scheme 1) [30]. The driving force for the elimination reaction is believed to be the formation of a strong Si–O bond as shown. With **1**–**4** it is not possible to predict beforehand whether CO_2 will react with the complexes to form species of type (a) or (b) above, or even react at all.

Complexes **1**, **2** and **4** were all unreactive towards gaseous CO_2 under a variety of conditions. Initial experiments simply bubbling CO_2 through solutions of the



Scheme 1. Possible route to either (a) metal carbamates, or (b) isocyanates, from a metal bis(silylamide).

metal bis(amides) at atmospheric pressure indicated no reaction, and so more severe conditions were used. Using the Fisher–Porter bottle and raising the reaction temperature to 60 °C and the CO_2 pressure to 60 psig also did not cause any reaction as evidenced by CO_2 uptake (monitored by loss of CO_2 pressure) or precipitation of any solids. GC/MS analysis of the solution did not indicate the presence of any new organic species. The ^1H and ^{13}C NMR spectra of the final solutions were consistent with the presence of unreacted starting bis(amides).

Compound **3**, however, appeared to react with CO_2 under mild conditions. Upon bubbling CO_2 through the hexane solution of **3** an immediate reaction was seen to occur as evidenced by a slight evolution of heat as well as the formation of a white precipitate A. GC/MS analysis of the hexane solution indicated that neither Me_3SiNCO nor $Me_3SiN{=}C{=}NSiMe_3$ had formed. As well, (Ad)NCO was not seen in the GC/MS analysis. However, removal of the hexane solvent afforded a white solid B that could be conclusively identified as (Ad)N=C=N(Ad) by high resolution mass spectroscopy and ^1H NMR. By inference, this indicates that the initial white precipitate A formed upon CO_2 addition and isocyanate/carbodiimide elimination could possibly be (a) $[Zn(OSiMe_3)_2]_2$, an expected by-product from the formation of (Ad)N=C=N(Ad), (b) $\{Zn[N(Ad)(SiMe_3)](OSiMe_3)\}_x$, also expected if the reaction is not complete, or a mixture of the two compounds. The white solid A is only sparingly soluble in a variety of solvents. The ^1H NMR spectrum obtained in $CDCl_3$ is consistent with the presence of both adamantyl and trimethylsilyl groups, but in a variety of environments, indicating an oligomeric structure and/or a mixture of products. The ^{13}C NMR spectrum does not provide more definitive information – particularly telling is that no low-field carbamato type peak is seen; however, this peak can be difficult to observe even when the metal carbamate is extremely soluble. It is not surprising that the product remaining from the Zn/CO_2 reaction may be oligomeric as we have shown earlier that alkyl Zn amides can insert CO_2 to give either tetrameric or dimeric products [19b]. Sita has reported in a similar case that the reaction product of $Pb[N(SiMe_3)_2]_2$ and CO_2 gives a white product with similar difficulties with characterization, and it is indicated that the compound is likely oligomeric [31]. We speculate that the lack of reaction of **1** or **2** with CO_2 can be attributed to the sterically crowded nature of the metal–N[$(SiMe_3)(SiPh_2{}^tBu)$] moiety. This lack of reactivity is similar to the situation seen earlier by Sita when he treated $Sn[N(SiMe_3)(2,6\text{-}{}^iPr_2C_6H_3)]_2$ with CO_2 [32]. While the metal–nitrogen bonds in **3** and **4** are less sterically constrained than in **1** or **2**, the lack of reactivity of **4** versus **3** may be attributed to the lower oxophilicity of Hg relative to its more oxophilic congener Zn, which readily undergoes insertion of CO_2 [3,19b].

4. Summary

The utilization of sterically demanding ligands, [N-$(SiMe_3)(R)$] (R = –$SiPh_2{}^tBu$ and adamantyl), can stabilize two coordinate complexes of zinc and mercury. No coordinating solvents are found in any of these species. Compounds **1**–**4** have been synthesized and their solid-state geometry established by X-ray diffraction analyses. The crystal structures for **1**–**4** indicate that zinc and mercury bis(silylamides) form monomeric, two coordinate compounds of roughly linear N–M–N arrangement, with $Zn[N(SiMe_3)(SiPh_2{}^tBu)]_2$ (**1**) deviating most significantly from linearity. A quite unusual feature seen is the difference in solid-state structures shown by **3** and **4**. While in the solid state $Zn[N(SiMe_3)(Ad)]_2$ (**3**) is found with a *syn* arrangement of the adamantyl ligands, the Hg analog **4** adopts an arrangement that is *anti*. **1**, **2** and **4** do not react with CO_2, even at 60 °C and 60 psig pressure, while **3** reacts readily with CO_2 to give (Ad)N=C=N(Ad).

5. Supplementary data

Crystallographic data for the structural analysis have been deposited with the Cambridge Crystallographic Data Centre, CCDC Nos. 256302–256305 for the compounds **1**–**4**. Copies of this information may be obtained free of charge from The Director, CCDC, 12 Union Road, Cambridge CB2 1EZ, UK (fax: +44-1223-336033; e-mail: deposit@ccdc.cam.ac.uk or www: http://www.ccdc.cam.ac.uk).

Acknowledgments

We thank the National Science Foundation, Grant No. CHE-0213165 for financial support. Sandia is a multiprogram laboratory operated by Sandia Corporation, a Lockheed Martin Company, for the US Department of Energy's National Nuclear Security Administration under Contract DE-AC04-94-AL85000.

References

[1] A. Wolk, J.W. Ager, K.J. Duxstad, E.E. Haller, N.R. Taskar, D.R. Dorman, D.J. Olego, Appl. Phys. Lett. 63 (1993) 2756.
[2] A. Kamata, H. Mitsuhashi, H. Fujita, Appl. Phys. Lett. 63 (1993) 3353.
[3] D.B. Dell'Amico, F. Calderazzo, L. Labella, F. Marchetti, G. Pampaloni, Chem. Rev. 103 (2003) 3857.
[4] M.B. Hursthouse, M.A. Malik, M. Motevalli, P. O'Brien, Chem. Commun. (1991) 1690.
[5] D.C. Bradley, M.B. Hursthouse, A.A. Ibrahim, K.M. Abdul Malik, M. Motevalli, R. Möseler, H. Powell, J.D. Runnacles, A.C. Sullivan, Polyhedron 9 (1990) 2959.
[6] R.A. Bartlett, P.P. Power, J. Am. Chem. Soc. 109 (1987) 7563.

[7] H. Chen, R.A. Bartlett, H.V.R. Dias, M.M. Olmstead, P.P. Power, J. Am. Chem. Soc. 111 (1989) 4338.
[8] R.A. Bartlett, M.M. Olmstead, P.P. Power, Inorg. Chem. 33 (1994) 4800.
[9] Y. Tang, A.M. Felix, L.N. Zakharov, A.L. Rheingold, R.A. Kemp, Inorg. Chem. 43 (2004) 7239.
[10] R.A. Andersen, D.H. Templeton, A. Zalkin, Inorg. Chem. 17 (1978) 2317.
[11] H. Schumann, J. Gottfriedsen, S. Dechert, F. Girgsdies, Z. Anorg. Allg. Chem. 626 (2000) 747.
[12] M.A. Putzer, A. Dashti-Mommertz, B. Neumüller, K. Dehnicke, Z. Anorg. Allg. Chem. 624 (1998) 263.
[13] P.P. Power, K. Ruhlandt-Senge, S.C. Shoner, Inorg. Chem. 30 (1991) 5013.
[14] W.S. Rees Jr., D.M. Green, W. Hesse, Polyhedron 11 (1992) 1697.
[15] O. Just, D.A. Gaul, W.S. Rees Jr., Polyhedron 20 (2001) 815.
[16] H. Bürger, W. Sawodny, U. Wannagat, J. Organomet. Chem. 3 (1965) 113.
[17] A. Haaland, K. Hedberg, P.P. Power, Inorg. Chem. 23 (1984) 1972.
[18] J.S. Thrasher, J.B. Nielsen, S.G. Bott, D.J. McClure, S.A. Morris, J.L. Atwood, Inorg. Chem. 27 (1988) 570.
[19] (a) Y. Tang, L.N. Zakharov, A.L. Rheingold, R.A. Kemp, Organometallics 23 (2004) 4788;
(b) Y. Tang, W.S. Kassel, L.N. Zakharov, A.L. Rheingold, R.A. Kemp, Inorg. Chem. 43 (2004), ASAP.
[20] D.F. Shriver, The Manipulation of Air-sensitive Compounds, McGraw-Hill, New York, 1986.
[21] (a) J.R. Bowser, R.H. Neilson, R.L. Wells, Inorg. Chem. 17 (1978) 1882;
(b) V.F. Miranov, N.S. Fedotov, Zh. Obshch. Khim. 42 (1972) 166.
[22] L. Messerle, ACS Symp. Ser. 357 (1987) 198.
[23] G.M. Sheldrick, SADABS (2.01), Bruker/Siemens Area Detector Absorption Correction Program, Bruker AXS, Madison, WI, USA, 1998.
[24] G.M. Sheldrick, SHELXTL: Program Package for Structure Solution and Refinement, Bruker AXS, Madison, WI, USA, 1997.
[25] D.J. Bauer, Acta Crystallogr. B 35 (1979) 1770.
[26] B. Krebs, E. Meyer-Hussein, O. Glemser, R. Mews, J. Chem. Soc., Chem. Commun. (1968) 1578.
[27] A. Blaschette, P.G. Jones, A. Michalides, K. Linoh, Z. Anorg. Allg. Chem. 619 (1993) 392.
[28] A. Zinn, K. Dehnicke, D. Fenske, G. Baum, Z. Anorg. Allg. Chem. 596 (1991) 47.
[29] P.B. Hitchcock, M.F. Lappert, M. Layh, J. Chem. Soc., Dalton Trans. (1998) 3113.
[30] L.R. Sita, J.R. Babcock, R. Xi, J. Am. Chem. Soc. 118 (1996) 10912.
[31] C.S. Weinert, I.A. Guzei, A.L. Rheingold, L.R. Sita, Organometallics 17 (1998) 498.
[32] J.R. Babcock, L. Liable-Sands, A.L. Rheingold, L.R. Sita, Organometallics 18 (1999) 4437.

isolated, their stability was low in the reaction medium. The copper(II) nitrate–TMEDA 1:1 complex became turbid in aqueous solution due to disproportionation reaction and form a more stable 1:2 complex. Previously, it has been shown that dimers of the chelate complexes tend to show negligible catalytic activity [11]. In order to better define the coordination chemistry of substituted diamines with copper(II), mixed ligand complexes of oxalate and diamines have been synthesized and discussed.

2. Experimental

$CuSO_4$, $K_2(C_2O_4)$ and diamines were used as purchased from Aldrich company Limited. $Cu(C_2O_4)\cdot 1/2H_2O$ was prepared according to the reported method [12].

2.1. Preparation of Cu(TMEDA)oxalate·4H$_2$O (1)

To a stirred solution of TMEDA (0.48 ml, 3.2 mmol) in water (2 ml), finely powdered $Cu(C_2O_4)\cdot 1/2H_2O$ (0.25 g, 1.6 mmol) was added. Unreacted copper oxalate was removed by filtration. Ethanol (2 ml) was added to the filtrate and the solution was allowed to stand. After several days, a mixture of colourless and blue crystals formed. The blue crystals of **1** were separated for analysis; m.p. 232 °C; yield, 79%. *Microanal*. Calc. for $CuC_8H_{22}O_8N_2$: C, 28.3, H, 7.1, N, 8.2. Found: C, 28.3, H, 7.3, N, 8.1%. IR bands: 3407 (s), 2926 (m), 1673 (s), 1046 (m), 520 (m). UV/Vis bands: $\lambda_{max} = 15.0 \times 10^3$ cm^{-1} with a shoulder at 9.8×10^3 cm^{-1}.

2.2. Preparation of Cu(TriMPDA)oxalate (2)

To a stirred solution of *N*,*N*,*N*′-trimethyl-1,3-propanediamine (0.37 ml, 1.6 mmol) in water (4 ml) was added $Cu(C_2O_4)\cdot 1/2H_2O$ (0.25 g, 6.4 mmol). The excess copper oxalate was removed by filtration. The addition of ethanol immediately precipitated a blue solid which was dissolved in water (2 ml) and allowed to stand for crystallization. After several days blue crystals of **2** were formed which were separated by filtration, dried, m.p. 240 °C; yield, 68%. *Microanal*. Calc. for $CuC_8H_{16}O_4N_2$: C, 35.9, H, 6.0, N, 10.5. Found: C, 35.8, H, 5.8, N, 10.6%. IR bands: 3443 (m), 2930 (m), 1619 (s), 1044 (m), 495 (m). UV/Vis bands: $\lambda_{max} = 13.6 \times 10^3$ cm^{-1} with a shoulder at 9.6×10^3 cm^{-1}.

2.3. Preparation of Cu(TriMEDA)oxalate (3)

To a stirred solution of $Cu(C_2O_4)\cdot 1/2H_2O$ (0.5 g, 3.2 mmol) in ethanol (5 ml) and water (5 ml), was added *N*,*N*,*N*′-trimethylethylenediamine (0.81 ml, 6.4 mmol). The resulting solution was allowed to stand. Blue/violet crystals of **3** were grown after a few days; m.p. >240 °C; yield, 77%. *Microanal*. Calc. for $CuC_7H_{14}O_4N_2$: C, 33.1, H, 5.5, N, 11.0. Found: C, 33.2, H, 5.4, N, 11.4%. IR bands: 3424 (m), 2927 (m), 1619 (s), 1055 (m), 790 (s), 490 (m). UV bands: $\lambda_{max} = 18.4 \times 10^3$ cm^{-1}.

Table 1
Crystal data and structural refinement parameters

Compound	$C_8H_{24}N_2CuO_8$ (**1**)	$C_8H_{16}N_2CuO_4$ (**2**)	$C_7H_{14}N_2CuO_4$ (**3**)
F_w	339.83	267.77	253.74
Temperature (K)	298(2)	298(2)	298(2)
Crystal system	triclinic	orthorhombic	orthorhombic
Space group	$P\bar{1}$	*Pbca*	$Pca2_1$
a (Å)	7.362(2)	11.368(3)	10.994(3)
b (Å)	8.891(8)	9.844(6)	8.557(10)
c (Å)	11.841(4)	18.639(7)	10.752(3)
α (°)	101.44(6)	90	90
β (°)	98.08(3)	90	90
γ (°)	92.53(8)	90	90
Volume (Å^3)	750.0(7)	2085(2)	1011.5(4)
Z	2	8	4
d_{calc} (Mg/m^3)	1.505	1.705	1.666
Absorption coefficient (mm^{-1})	1.490	2.091	2.151
Index ranges	$-8 \leqslant h \leqslant 8$ $0 \leqslant k \leqslant 10$ $-14 \leqslant I \leqslant 13$	$-4 \leqslant h \leqslant 13$ $-11 \leqslant k \leqslant 0$ $-7 \leqslant I \leqslant 22$	$-3 \leqslant h \leqslant 13$ $-10 \leqslant k \leqslant 1$ $-6 \leqslant I \leqslant 12$
Collected/unique	2887/2621	1875/1823	969/945
Data/restraints/parameters	2621/0/214	1823/0/144	945/2/134
Goodness-of-fit on F^2	1.078	0.940	1.020
R_1, wR_2 [$I > 2\sigma(I)$]	0.0565, 0.1696	0.0321, 0.0936	0.0231, 0.0656
R_1, wR_2 (all data)	0.0605, 0.1720	0.0407, 0.0969	0.0277, 0.067
Differential peak, hole (e Å^{-3})	1.639, −1.285	0.469, −0.638	0.222, −0.359

Table 2
Selected bond lengths (Å) and angles (°) in complex **1**

Cu(1)–O(4)	2.383(5)
Cu(1)–O(1)	2.00(3)
Cu(1)–N(1)	2.050(4)
Cu(1)–N(2)	2.054(3)
Cu(1)–O(2)	2.347(3)
Cu(1)–O(3)	1.999(3)
N(1)–C(5)	1.471(6)
N(2)–C(6)	1.495(8)
O(1)–C(1)	1.257(5)
O(4)–C(2a)	1.254(5)
O(5)–C(6)	1.453(9)
O(3)–Cu(1)–N(1)	173.51(11)
O(1)–Cu(1)–N(2)	174.50(12)
O(1)–Cu(1)–O(2)	76.66(12)
O(3)–Cu(1)–O(4)	75.48(15)
O(2)–Cu(1)–O(4)	156.90(12)
C(5)–N(1)–Cu(1)	106.3(3)
C(6)–N(2)–Cu(1)	104.8(3)

2.4. Physical measurements

Infrared spectra were recorded on a Perkin–Elmer FT-IR 1720X spectrometer in the range 4000–200 cm^{-1}. Samples were examined as nujol mulls between caesium iodide plates or as potassium bromide discs. Melting points were determined using a Gallenkamp melting-point apparatus. A Philips PU 8710 spectrophotometer was used to carry out the optical measurements, the samples were placed in silica cuvettes (1 cm path length). Elemental analyses were obtained from the microanalytical laboratory at University College London. Single-crystal X-ray diffraction data for the compounds were collected with a CAD-4 diffractometer and Mo Kα radiation ($\lambda = 0.71069$ Å) using ω–2θ scan. The unit cell parameters were determined by least-squares refinement on diffractometer angles ($9.99° \leqslant \theta \leqslant 12.51°$) for 25 automatically centered reflections. The structures were solved by heavy-atom method using DIRDIF-99 programs, refined anisotropically (non-hydrogen atoms) by full-matrix least-squares on F^2 using SHELXL-97 program [13]. Crystallographic details and selected interatomic distances and angles are given in Tables 1–4.

Table 3
Selected bond lengths (Å) and angles (°) in complex **2**

Cu(1)–O(3)	1.978(18)
Cu(1)–O(1)	2.017(2)
Cu(1)–O(2)	2.379(19)
Cu(1)–O(4)	2.396(18)
O(1)–C(1)	1.259(3)
Cu(1)–N(2)	2.093(2)
N(1)–C(3)	1.481(3)
N(2)–C(5)	1.498(4)
C(1)–C(2)	1.561(3)
O(3)–C(4)	1.509(5)
C(4)–C(5)	1.504(5)
O(3)–Cu(1)–O(1)	87.78(9)
O(1)–Cu(1)–O(2)	74.67(6)
O(3)–Cu(1)–O(4)	76.05(6)
O(1)–Cu(1)–O(4)	94.62(7)
O(2)–Cu(1)–O(4)	168.05(6)
C(6)–C(5)–C(4)	114.9(3)
N(1)–Cu(1)–O(2)	91.33(9)

Table 4
Selected bond lengths (Å) and angles (°) in complex **3**

Cu(1)–O(2)	1.922(3)
Cu(1)–O(3)	1.948(3)
Cu(1)–N(2)	1.952(4)
Cu(1)–N(1)	2.000(3)
N(1)–C(4)	1.486(7)
N(2)–C(3)	1.454(6)
N(1)–C(6)	1.489(7)
O(2)–C(1)	1.272(5)
O(3)–C(2)	1.275(6)
O(1)–C(2)	1.211(6)
O(4)–C(1)	1.224(5)
C(3)–C(4)	1.503(7)
C(1)–C(2)	1.557(7)
Cu(1)–O(2)–C(1)	113.1(3)
N(2)–Cu(1)–O(3)	178.24(15)
N(1)–Cu(1)–O(2)	178.10(15)
N(2)–Cu(1)–N(1)	86.95(15)
C(3)–N(2)–C(7)	112.1(4)
C(3)–N(2)–Cu(1)	109.5(3)
C(4)–N(1)–Cu(1)	105.3(3)
C(4)–C(1)–O(2)	124.0(4)
O(1)–C(2)–O(3)	127.0(4)

3. Results and discussion

The compounds have been characterized by IR, UV, elemental analysis and X-ray single crystallography. All three compounds have ratios of 1:1:1 for the copper, oxalate and diamine ligand but the common structure of compounds **1**, **2** is not shared by compound **3**.

Both compounds **1** and **2** have a six coordinate $CuN_2O_2O'_2$ chromophore with an elongated, rhombic, octahedral structure. The neutral Cu(L)ox units where L = diamine and ox = oxalate, involve bridging oxalate anions which gives a zig-zag polymeric chain structure. In **1**, the water molecules are not coordinated to the copper atom but are present as lattice water (Fig. 1). The water molecules are hydrogen bonded to each other and to oxygen atoms, O(2) and O(4), of the oxalate groups (Fig. 2). In the IR spectrum of compound **1**, ν(OH) has a single broad band at 3407 cm^{-1}, indicating hydrogen bonding to other water molecules and to the oxygen of the bridging oxalate group [14]. In **2**, hydrogen bonding between H(1) of the secondary amine group and the oxygen O(4) of the oxalate group within the chain, at a distance of 2.323 Å, has been suggested. Compound **2** contains no water. Generally, the diamine

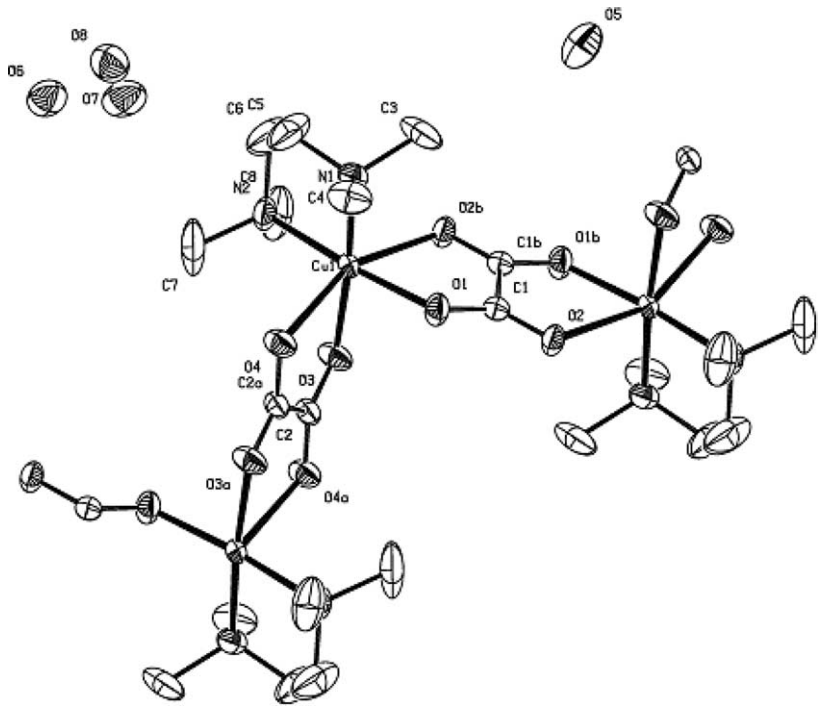


Fig. 1. X-ray single crystal structure of compound **1**.

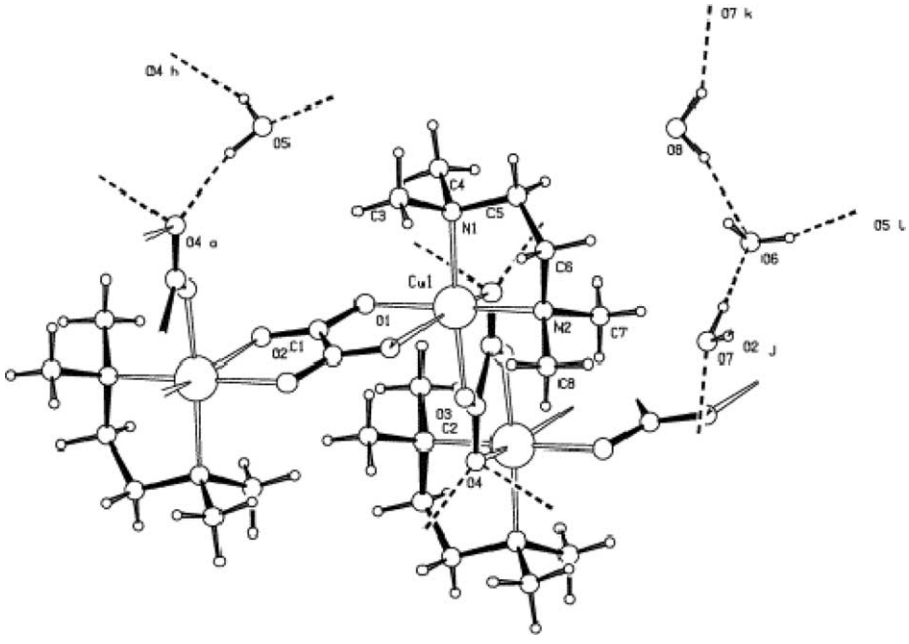


Fig. 2. Hydrogen bonding within complex **1**.

ligand is coordinated to the metal and the two oxalate ligands are asymmetrically coordinated with one long Cu–O bond and one short Cu–O bond (Fig. 3).

Table 2 shows selected bond lengths and angles in compound **1**. Compound **1** has a symmetrically coordinated TMEDA (mean Cu–N 2.052 Å) and two asymmetrically coordinated bridging oxalate (Cu–O (1.999–2.383 Å)) that are centrosymmetric (Fig. 1). Cu–O bond lengths are comparable to those reported (1.940–2.345 Å) for $[Cu(DMEDA)ox(H_2O)]_2$ $[Cu(DMEDA)_2](ClO_4)_2$ [15]. Compound **2** has an asymmetrically coordinated TriMPDA (Cu–N(1) 2.048 Å and Cu–N(2) 2.093 Å), the shorter bond being to the least substituted nitrogen N(1) and two asymmetrically coordinated

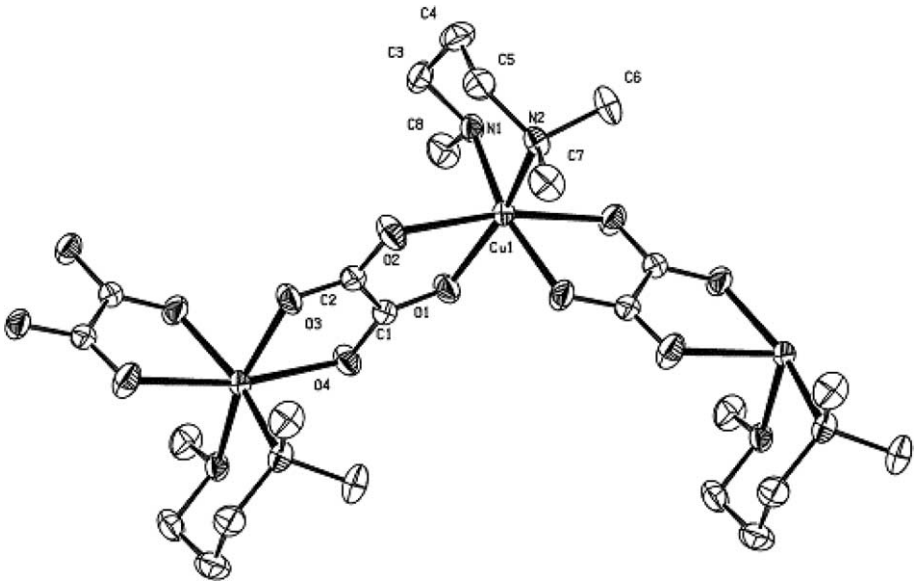


Fig. 3. X-ray single crystal structure of compound **2**.

bridging oxalate groups (shorter bonds Cu–O(1) 2.017 Å, Cu–O(3) 1.978 Å and longer bonds Cu–O(2) 2.379 Å, Cu–O (4) 2.396 Å) (Fig. 3). The oxalate groups are involved in an asymmetric bridging role between copper atoms. Selected bond lengths and angles of compound **2** are shown in Table 3.

The mean O–C–O angles within the oxalate in complex **1** is 125.8° and in complex **2** 125.9° [16–18]. Similarly, the bond lengths and angles associated with TMEDA are normal for such complexes [19]. In complex **2**, the six-membered ring Cu–N(1)–C(3)–C(4)–C(5)–N(2)– is in a chair conformation. The mean C–N bond length, (1.49 Å) in complex **2** is noticeably longer than the average C–N bond length of (1.47 Å). The mean C–N bond length of complex **1** is 1.481 Å. This difference is attributed to the increase in the size of ring from five- in **1** to six-membered in **2** [20].

The bite angle of TMEDA at copper is 86.1° which compares well with that observed in $(Cu(TMEDA)Cl_2)_2$, where the angle is 85.3° [19]. The bite angles of the two oxalate groups in compound **1** are 75.48° and 76.66°, which are significantly different to each other. These angles compare well with those observed in **2** and in $Cu(bipy)ox\cdot 2H_2O$, where the oxalate bite angles are 77.4° and 77.9° [12]. The bite angle of TriMPDA at the copper center is 91.33° and those of the oxalate groups in compound **2** are 74.67° and 76.05° which are similar to those reported elsewhere [21].

In compound **1**, the N(1), N(2), O(1), O(2) atoms are distorted from a planar arrangement. The O(2)–Cu–O(4) angle of 156.90° is significantly reduced from 180°. Previously, this distortion has been attributed to the small bite angle of the oxalate groups [12]. In compound **2**, the N(1), N(2), O(1), O(3) atoms are again distorted from a planar arrangement. The O(2)–Cu–O(4) angle of 168.05° is reduced from 180° but not to the same extent as in **1**.

In compound **3**, the copper is described as square planar with two nitrogen atoms from the diamine and two oxygen atoms from the oxalate (Fig. 4). Table 4 shows selected bond lengths and angles of compound **3**. The copper deviates slightly out of the O(2), O(3), N(1), N(2) plane by ca. 0.031 Å. The TriMEDA is almost symmetrically coordinated with the bond lengths for Cu–N(1) and Cu–N(2) being 2.001 and 1.952 Å and the bite angle is 86.95°. This compares well with the reported bite angle of 86.4° for the diamine ligand in oxalato(*N*,*N*′-dimethylethylenediamine)copper(II) monohydrate [22]. This shortening of the bond to the least substituted nitrogen has been noted previously [23,24]. The C(4)–N(1)–Cu(1) angle of 105.3° and C(3)–N(2)–Cu(1) of 109.5°,

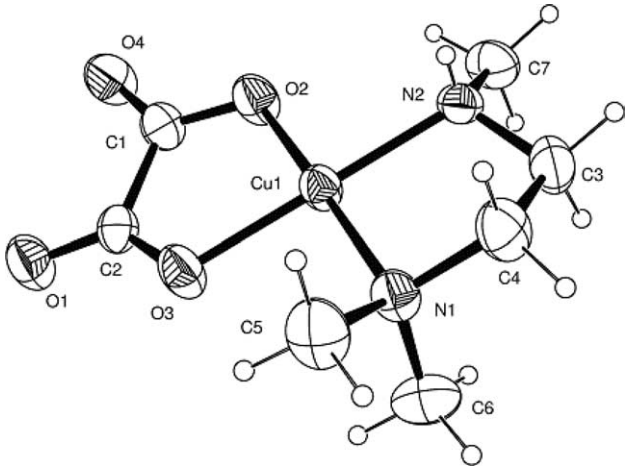


Fig. 4. X-ray single crystal structure of compound **3**.

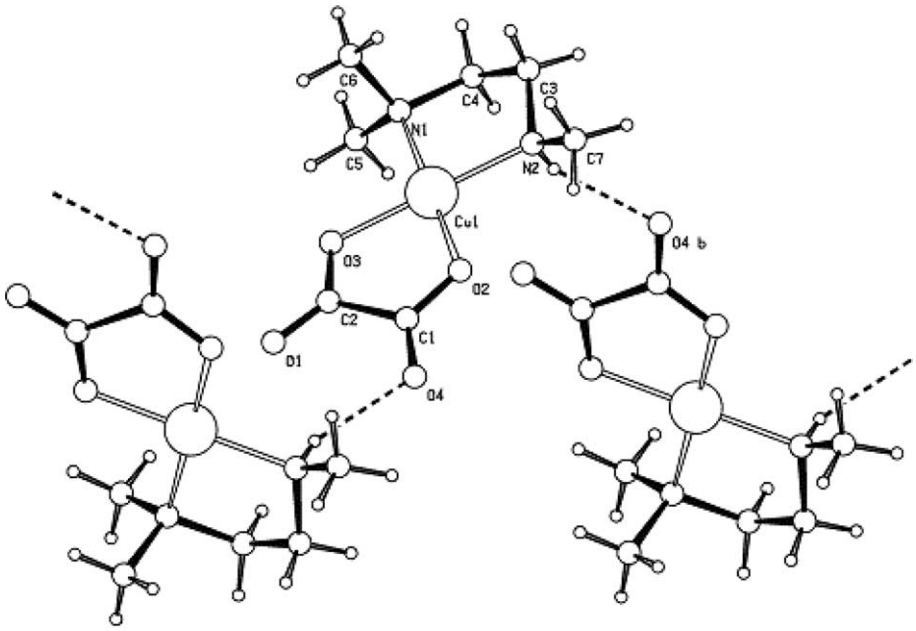


Fig. 5. Hydrogen bonding within complex **3**.

reflect the substitution on the nitrogen, with the largest angle at the least substituted nitrogen. The oxalate group is almost symmetrically coordinated to the copper through two oxygen atoms with Cu–O bond lengths of 1.922 and 1.948 Å in 1,2-*cis*-conformation. This contrasts with the asymmetry of the oxalate groups observed in compounds **1** and **2**. Within the oxalate group, the C–C bond length of 1.555 Å and the average C–O bond length of 1.247 Å are in accord with those previously reported [21]. Two long and two short bond lengths have been observed. This reflects the difference between those that are chelating (mean C–O length 1.274 Å) and those that are terminal (mean C–O 1.218 Å). The O–C–O angles are unequal. The O(1)–C(2)–O(3) moiety, where only one of the oxygen interacts with a copper, has an angle of 127.0°. This agrees well with the value of 126–128° observed in the free ion and oxalic acid [16–18]. In the O(4)–C(2)–O(1) moiety, the angle is reduced to 124.0°. Both oxygen atoms are involved in interactions, O(2) with Cu and O(4) in hydrogen bonding. The bite angle of the oxalate group is 84.53°. This compares well with the value of 84.2°, reported for oxalate(*N*,*N*′-dimethylethylenediamine)copper(II) [23]. The Cu(L)(C_2O_4) units are linked together by hydrogen bonding between the hydrogen H(1) bonded to N(1) and an oxygen, O(4), of an oxalate group in a neighbouring unit to from winding chains (Fig. 5).

4. Electronic properties

The diffuse reflectance spectra of complexes **1**, **2** and **3** were recorded between 8000 and 50 000 cm^{-1}. The compounds **1** and **2** have a main band with a shoulder and compound **3** have a single broad band.

The reflectance spectra of **1** had previously been reported [25]. Fukuda et al. recorded the spectra between 10 000 and 29 400 cm^{-1}. They reported a band at λ_{max} = 14 030 cm^{-1}. However, they failed to report a shoulder at this main band at lower frequency because their scan range was to too narrow.

Complex **1** has a main band at $\lambda_{max} = 15 \times 10^3$ cm^{-1} with a shoulder at 9.8×10^3 cm^{-1}. Similarly, the spectrum of complex **2** has a main band at $\lambda_{max} = 13.6 \times 10^3$ cm^{-1} with a shoulder at 9.6×10^3 cm^{-1}. These two-band spectra are common to the compounds that are isostructural. The spectrum of complex **3** has a single broad absorption at 18.4×10^3 cm^{-1}.

This sensitivity of the electronic spectra to the two modes of coordination has been previously reported in compounds of type Cu(L)(C_2O_4)·xH_2O where L = bipy and 1,10-phen [12,26,27]. The first modes contains an axially elongated N_2O_4 chromophore consisting of one bipy and two *catena* bridging oxalates which is comparable to complex **1** containing TMEDA and complex **2** containing TriMPDA. The second mode has an N_2O_2 chromophore of an oxalate and one bipy in a square plane at copper(II) which is comparable to complex **3** with TriMEDA. It can be concluded that the observation of two bands is consistent with the elongated tetragonal distortion seen in complexes **1** and **2**. The electronic broad band for complex **3** is consistent with an N_2O_2, ca. square planar chromophore.

The electronic reflectance spectra of complexes **1** and **2** are clearly different from complex **3**. This difference is associated with the local molecular structure of the

Table 5
ESR values for compounds **1**–**3**

Complex	ESR Spectra		
	g_1	g_2	g_3
Cu(TMEDA)oxalate·$4H_2O$ (**1**)	2.080	2.224	2.334
Cu(TriMPDA)oxalate (**2**)	2.108	2.232	2.315
Cu(TriMEDA)oxalate (**3**)	2.119		

complex. This local structure is shared by complexes **1** and **2** but not complex **3** and is best seen by the presence of the low energy shoulder in **1** and **2**.

The compounds were also analyzed by electron spinning resonance (ESR) and observed g values for the crystalline samples lie in the range 2.08–2.34, with no absorptions at high or low fields (Table 5). The ESR spectra for both complexes **1** and **2** are clearly axial but a small rhombic component is indicated. This suggests a non-square planar geometry for complexes **1** and **2** as shown by the crystal structures obtained. The lowest observed g values for the complexes are greater than 2.08 and this is consistent with a $d_{x^2-y^2}$ or d_{xy} ground state.

5. Conclusion

Three new copper complexes have been synthesized and characterized by spectroscopic and X-ray single crystallographic methods. The structures of compound **1** and **2** are based on polymers where oxalato ligand is chelating and bridging between the metal centers. Both compounds share a common zig-zag structure with copper in a distorted octahedral configuration. Compound **3** is a monomer where oxalate is chelating only mode and the geometry around copper can be described as distorted square planar. Difference between the monomeric and polymeric structures was also shown by diffuse reflectance spectroscopy and ESR spectroscopy.

6. Supplementary material

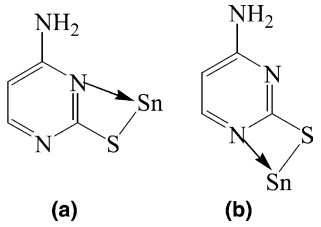
Crystallographic data for the structural analysis have been deposited with the Cambridge Crystallographic Data Center, CCDC No. 262838 for compound **1**, 262839 for compound **2** and 262840 for compound **3**. Copies of this information may be obtained free of charge on application to CCDC, 12 Union Road, Cambridge CB2 1EZ, UK (fax: +44 1223 336 033; e-mail: deposit@ccdc.cam.ac.uk or http://www.ccdc.cam.ac.uk).

Acknowledgments

The authors thank MOD (UK) for funding this project.

References

[1] H. Sigel, Angew. Chem. Int. Ed. Engl. 15 (1975) 394.
[2] K. Stone, S. Utsuno, T. Ogura, J. Inorg. Nucl. Chem. 31 (1969) 117.
[3] I.M. Proctor, B.J. Hathaway, P.G. Hodgson, J. Inorg. Nucl. Chem. 34 (1972) 3689.
[4] G. Arena, R.P. Bonomo, E. Rizzarelli, A. Seminara, Inorg. Chem. 30 (1978) 13.
[5] D.P. Murtha, R.A. Walton, Inorg. Chim. Acta 8 (1974) 279.
[6] J. Michel, R.A. Walton, J. Inorg. Nucl. Chem. 37 (1975) 71.
[7] W.L. Kwik, K.P. Ang, G. Chen, J. Inorg. Nucl. Chem. 42 (1980) 303.
[8] R.C. Courtney, R.L. Gustafson, S.J. Westerbeck, H. Hyyatianen, S.C. Chabereck, A.E. Martell, J. Am. Chem. Soc. 79 (1957) 3030.
[9] S.C. Chabereck, A.E. Martell, R.L. Gustafson, Adv. Catal. L34 (1956).
[10] D.N. Marjit, U.S. Sharma, Ind. J. Chem. 28 (1988) 958.
[11] R.L. Gustafson, A.E. Martell, J. Am. Chem. Soc. 84 (1962) 2309.
[12] W. Fitzgerald, J. Foley, D. McSweeney, D. Ray, D. Sheahan, S. Tyagi, B. Hathaway, P. O'Brien, J. Chem. Soc., Dalton Trans (1982) 1117.
[13] G. Sheldrick, SHELXL-97, University of Göttingen, 1997.
[14] N.F Curtis, J. Chem. Soc. (1968) 1584.
[15] Z. Smékal, J. Kameníček, P. Klasová, P. Wrzeszcz, Z. Šindelář, P. Kopel, Z. Žák, Polyhedron 21 (2002) 1203.
[16] M. Currie, J.C. Speakman, N.A. Curry, J. Chem. Soc. (A) (1967) 1862.
[17] D.J. Haas, Acta Crystallogr. 17 (1964) 1511.
[18] H. Kuppers, Acta Crystallogr. (B) 29 (1972) 318.
[19] E. Dixon Estes, W.E. Estes, W.E. Hatfield, D.J. Hodgson, Inorg. Chem. 14 (1975) 106.
[20] R. Sadaghat-Herati, S.P. McManus, J.M. Harris, J. Org. Chem. 53 (1988) 2539.
[21] F.S. Stephens, J. Chem. Soc. (A) (1969) 2493.
[22] J. Korvenranta, Suomen Kemistilehti B 46 (1973) 296.
[23] R. Hamalainen, A. Pajunen, Suomen Kemistilehti B 46 (1973) 285.
[24] R. Hamalainen, Suomen Kemistilehti B 46 (1973) 237.
[25] Y. Fukuda, K. Sone, Bull. Chem. Soc. Jpn. 45 (1972) 465.
[26] P. O'Brien, J. Chem. Soc., Dalton Trans. (1981) 1540.
[27] P. O'Brien, C. Stafford, L.C. Young, Inorg. Chim. Acta 147 (1988) 3.



Scheme 1. Two possible coordination modes of HSapym.

2. Experimental

2.1. Materials and measurements

All reagents and solvents were purchased commercially and used without further purification unless otherwise noted. The melting points were obtained on a Kofler micro melting point apparatus and are uncorrected. ^{1}H NMR spectra were obtained on a Varian Mercury Plus 400 MHz NMR spectrometer. Chemical shifts are given in ppm relative to Me_4Si in $CDCl_3$ as solvent. Elemental analyses were performed with a PE-2400 II elemental analyser.

2.2. Syntheses of the compounds *1–6*

2.2.1. *[Me_2SnCl(Spym)] (1)*

Under a dry nitrogen atmosphere, 2-mercaptopyrimidine (0.112 g, 1 mmol) and sodium ethoxide (0.068 g, 1 mmol) were added in benzene (20 ml) to a Schlenk flask and stirred for about 10 min. Then dimethyltin dichloride (0.220 g, 1 mmol) was added to the flask, and stirring was continued for 14 h at 40 °C. After filtration, the filtrate was gradually evaporated until a solid product was obtained. The solid was recrystallized from diethylether–petroleum ether. Transparent colourless crystals of compound **1** were formed. Yield: 79%; m.p. > 200 °C (dec.). *Anal*. Calc. for $C_6H_9ClN_2SSn$: C, 24.40; H, 3.07; N, 9.49. Found: C, 24.24; H, 3.18; N, 9.61%. ^{1}H NMR ($CDCl_3$): 8.44–7.18 (m, 3H, aromatic-H); 1.12 (s, 6H).

2.2.2. *[Bu_2SnCl(Spym)] (2)*

The procedure was the same as that of compound **1** and the crystalline compound **2** was formed in diethylether–petroleum ether. Yield: 82%; m.p. 120–125 °C. *Anal*. Calc. for $C_{12}H_{21}ClN_2SSn$: C, 37.97; H, 5.58; N, 7.38. Found: C, 37.86; H, 5.54; N, 7.56%. ^{1}H NMR ($CDCl_3$): 7.06–8.38 (m, 3H), 0.79–0.90 (s, 18H). ^{1}H NMR ($CDCl_3$): 7.34–7.90 (m, 3H, aromatic-H); 0.92–1.10, 1.05–1.28 (m, 18H).

2.2.3. *[Ph_2ClSn(Sapym)] · EtOH (3)*

The procedure was the same as that of compound **1** and crystalline compound **3** was formed in ethanol. Yield: 83%; m.p. 112–114 °C. *Anal*. Calc. for $C_{18}H_{20}ClN_3OSSn$: C, 44.98; H, 4.19; N, 8.74. Found: C, 43.16; H, 4.32; N, 8.59%. ^{1}H NMR ($CDCl_3$): 6.94–8.07 (m, 12H, aromatic-H); 6.02 (s, 2H); 4.65 (s,1H); 3.51 (q, 2H); 0.92 (t, 3H).

2.2.4. *[($PhCH_2$)$_2$Sn(Spym)$_2$] (4)*

Under a dry nitrogen atmosphere, 2-mercaptopyrimidine (0.224 g, 2 mmol) and sodium ethoxide (0.136 g, 2 mmol) were added in benzene (20 ml) to a Schlenk flask and stirred for about 10 min. Then dibenzyltin dichloride (0.371 g, 1 mmol) was added to the flask, and stirring was continued for 14 h at 40 °C. After filtration, the filtrate was gradually evaporated until a solid product was obtained. The solid was recrystallized from diethylether–petroleum ether. Yield: 84%; m.p. 164–166 °C. *Anal*. Calc. for $C_{22}H_{20}N_4S_2Sn$: C, 50.49; H, 3.85; N, 10.71. Found: C, 50.56; H, 3.78; N, 10.62%. ^{1}H NMR ($CDCl_3$): 6.86–8.42 (m, 18H, aromatic-H); 3.20 (s, 4H).

2.2.5. *[Bu_2Sn(Sapym)$_2$] · 2MeOH (5)*

The procedure was the same as that of compound **4** and in methyl alcohol crystals of compound **5** were obtained. Yield: 84%; m.p. 170 °C. *Anal*. Calc. for $C_{18}H_{34}N_6O_2S_2Sn$: C, 39.35; H, 6.24; N, 15.30. Found: C, 39.29; H, 6.31; N, 15.38%. ^{1}H NMR ($CDCl_3$): 6.42–7.96 (m, 12H, aromatic-H); 6.02 (s, 2H); 4.50 (s, 1H); 3.39 (s, 3H); 0.92–1.10, 1.05–1.28 (m, 18H).

2.2.6. *[($PhCH_2$)$_2$Sn(Sapym)$_2$] · 3MeOH (6)*

The procedure was the same as that of compound **4** and in methyl alcohol crystals of compound **6** were obtained. Yield: 84%; m.p. 95–97 °C. *Anal*. Calc. for $C_{25}H_{54}N_6O_3S_2Sn$: C, 44.84; H, 8.13; N, 12.55. Found: C, 44.76; H, 8.18; N, 12.62%. ^{1}H NMR ($CDCl_3$): 6.34–7.89 (m, 18H, aromatic-H); 6.02 (s, 2H); 4.50 (s, 1H); 3.39 (s, 3H); 3.26 (s, 4H).

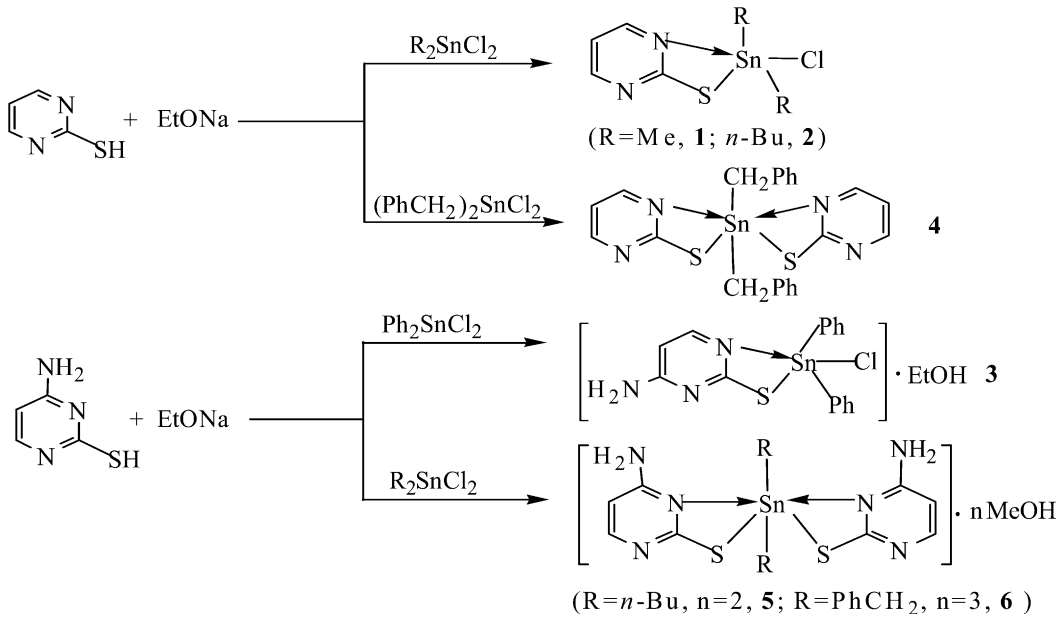
2.3. X-ray crystallographic studies of compounds *1–6*

All X-ray crystallographic data were collected with graphite-monochromated Mo Kα radiation (λ = 0.71073 Å) at 298(2) K on a Bruker SMART CCD 1000 diffractometer. The structures were solved by direct methods and refined by a full-matrix least squares procedure based on F^2 using the SHELXL-97 program system. The positions of hydrogen atoms were calculated, and their contributions were included in structural factor calculations.

3. Results and discussion

3.1. Syntheses of the compounds *1–6*

The synthesis procedure was as in Scheme 2.



Scheme 2.

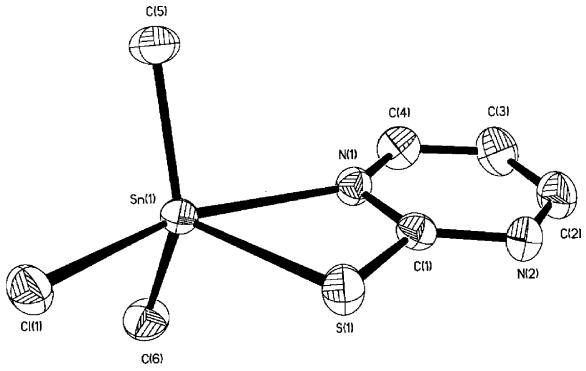


Fig. 1. Molecular structure of compound **1**.

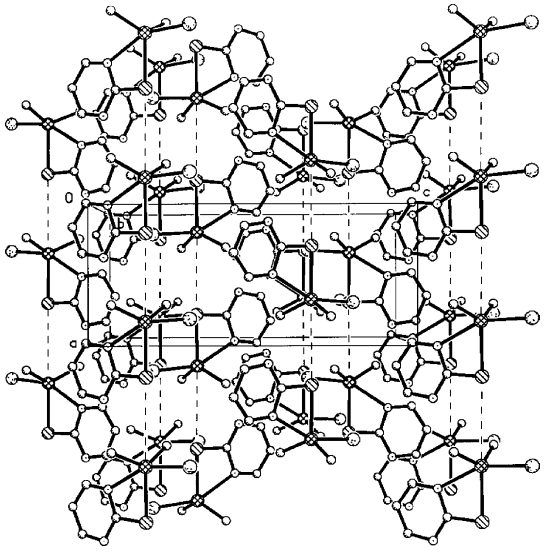


Fig. 2. Cell packing of compound **1**.

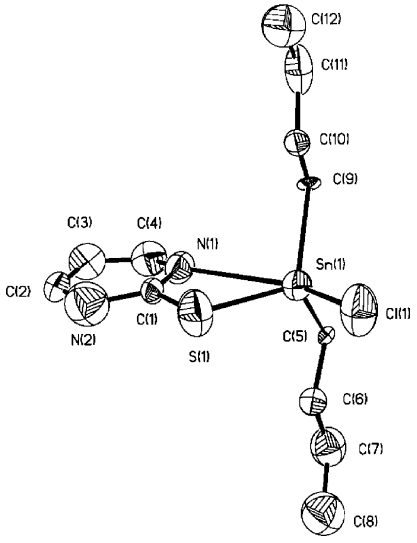


Fig. 3. Molecular structure of compound **2**.

3.2. ^1H NMR data of the compounds 1–6

^1H NMR data showed that the signal of the –SH proton in the spectrum of the ligand is absent in compounds **1**–**6**, indicating the removal of the –SH proton and the formation of Sn–S bonds. Moreover, the signal (4.65 ppm for compound **3**, 4.50 ppm for both **5** and **6**) further prove the existence of different solvent molecules in these compounds.

3.3. Crystal structures of compounds 1–6

The crystal structures and crystal packing of compounds **1**–**6** are shown in Figs. 1–9. All H atoms have

been omitted for clarity. Table 1 lists the crystal data and structure refinement parameters for compounds **1**–**6**, and their selected bond lengths and angles are shown in Tables 2–7, respectively. In general, each of compounds **1**–**3** has a penta-coordinated tin atom (Scheme 3a) and for compound **3**, the ligand HSapym

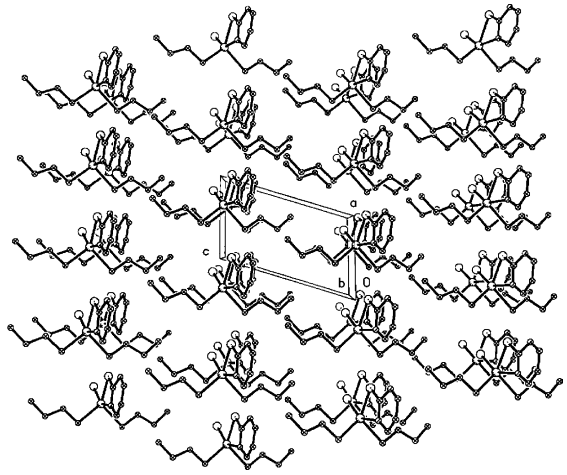


Fig. 4. Cell packing of compound **2**.

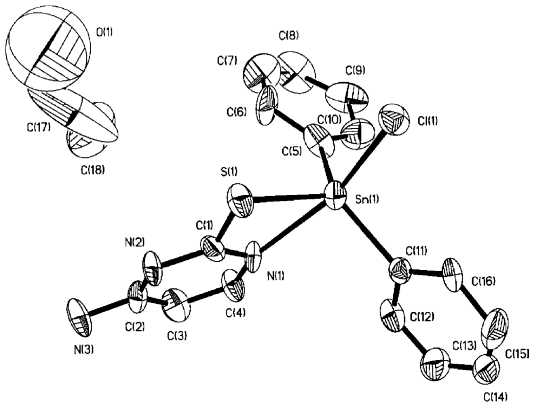


Fig. 5. Molecular structure of compound **3**.

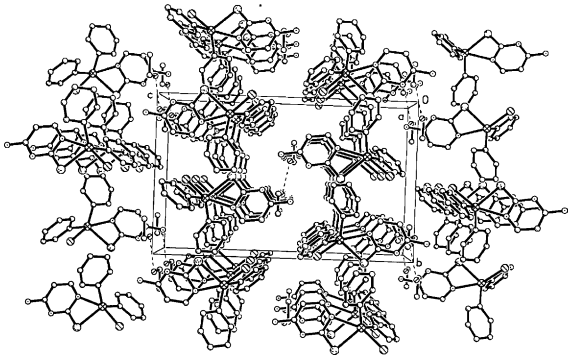


Fig. 6. Cell packing of compound **3**.

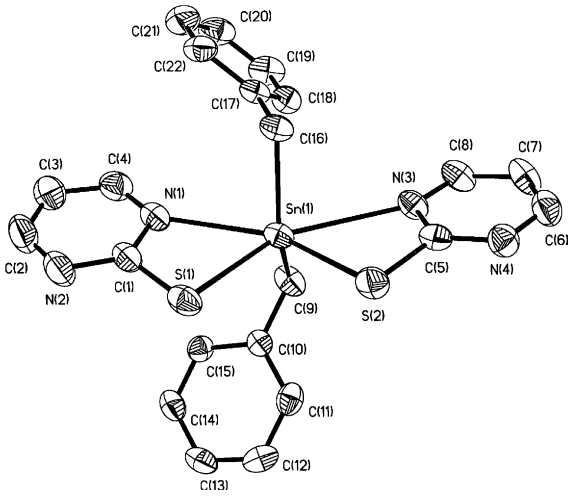


Fig. 7. Molecular structure of compound **4**.

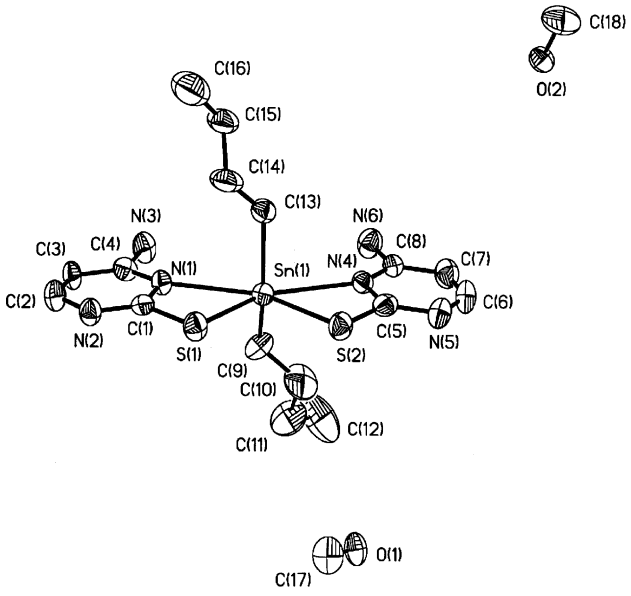


Fig. 8. Molecular structure of compound **5**.

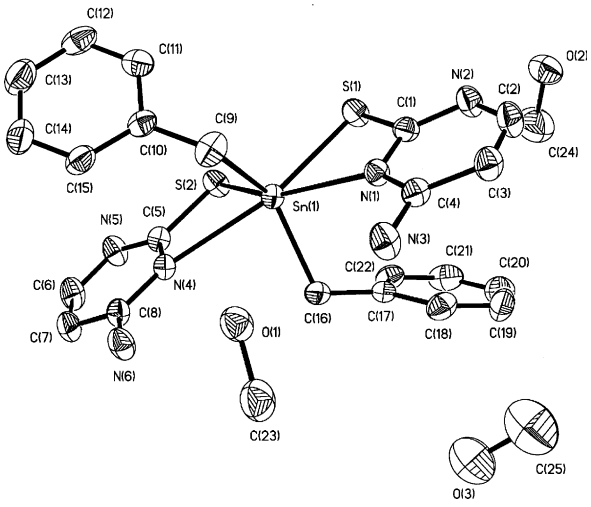


Fig. 9. Molecular structure of compound **6**.

Table 1
Crystal data and structure refinement parameters for complexes **1**–**6**

	Complex **1**	Complex **2**	Complex **3**	Complex **4**	Complex **5**	Complex **6**
Empirical formula	$C_6H_9ClN_2SSn$	$C_{12}H_{21}ClN_2SSn$	$C_{22}H_{20}N_4S_2Sn$	$C_{18}H_{34}N_6O_2S_2Sn$	$C_{25}H_{54}N_6O_3S_2Sn$	$C_{18}H_{20}ClN_3OSSn$
Formula weight	295.35	379.51	523.23	549.32	669.5	480.57
Crystal system	orthorhombic	triclinic	orthorhombic	monoclinic	orthorhombic	monoclinic
Space group	$P2_12_12_1$	$\bar{P}$	*Pbca*	$P2_1/c$	*Pbca*	$P2_1/c$
Unit cell dimensions						
a (Å)	6.423(4)	6.199(6)	17.121(7)	10.756(2)	13.932(6)	9.028(4)
b (Å)	10.913(6)	9.91(1)	14.105(6)	14.158(3)	20.901(8)	11.951(6)
c (Å)	14.772(8)	9.93(1)	18.740(8)	16.017(3)	21.033(9)	19.32(1)
α (°)	90	84.42(2)	90	90	90	90
β (°)	90	71.80(1)	90	94.91(3)	90	92.81(1)
γ (°)	90	71.86(1)	90	90	90	90
V (Å^3)	1035(1)	550(1)	4526(3)	2430.2(8)	6125(4)	2082(2)
Z	4	1	8	4	8	4
D_c (g cm^{-3})	1.895	1.145	1.536	1.501	1.452	1.533
Crystal size (mm)	$0.22 \times 0.17 \times 0.12$	$0.45 \times 0.12 \times 0.10$	$0.43 \times 0.29 \times 0.18$	$0.32 \times 0.19 \times 0.09$	$0.42 \times 0.35 \times 0.13$	$0.21 \times 0.15 \times 0.09$
F(000)	568	190	2096	1128	2816	960
Total reflections	5410	2453	22502	12581	30748	10422
Independent reflections	1825	2020	4006	4258	5404	3638
Data/restraints/parameters	1825/0/100	2020/94/154	4006/0/262	4258/16/270	5404/25/364	3638/10/226
Final *R* indices [$I > 2\sigma(I)$]	$R_1 = 0.0216$	$R_1 = 0.0743$	$R_1 = 0.0354$	$R_1 = 0.0660$	$R_1 = 0.0300$	$R_1 = 0.0736$
	$wR_2 = 0.0495$	$wR_2 = 0.1274$	$wR_2 = 0.0603$	$wR_2 = 0.0748$	$wR_2 = 0.0808$	$wR_2 = 0.1260$
R indices (all data)	$R_1 = 0.0254$	$R_1 = 0.1997$	$R_1 = 0.0780$	$R_1 = 0.1575$	$R_1 = 0.0603$	$R_1 = 0.2082$
	$wR_2 = 0.0508$	$wR_2 = 0.1632$	$wR_2 = 0.0675$	$wR_2 = 0.0877$	$wR_2 = 0.1017$	$wR_2 = 0.1611$
Goodness-of-fit	0.993	0.847	0.998	0.968	1.010	0.777
Theta range for data collection (°)	2.32–25.02	4.33–25.02	2.16–25.02	1.92–25.03	1.94–25.03	2.00–25.02
Absorption coefficient (mm^{-1})	2.872	1.365	1.329	1.248	1.007	1.466
Largest difference peak and hole (e Å^{-3})	0.510 and −0.331	0.281 and −0.209	0.615 and −0.548	0.640 and −0.882	0.764 and −0357	0.770 and −0.443

Table 2
Selected bond lengths (Å) and angles (°) of complex **1**

Sn(1)–C(5)	2.107(5)
Sn(1)–N(1)	2.450(3)
Sn(1)–S(1)	2.473(2)
S(1)–C(1)	1.749(4)
Sn(1)–Cl(1)	2.457(2)
Sn(1)–C(6)	2.104(4)
N(1)–C(1)	1.340(5)
N(1)–Sn(1)–Cl(1)	155.30(9)
C(6)–Sn(1)–S(1)	110.1(2)
N(1)–Sn(1)–S(1)	63.51(9)
C(5)–Sn(1)–S(1)	112.3(2)
C(5)–Sn(1)–C(6)	133.7(2)

Table 3
Selected bond lengths (Å) and angles (°) of complex **2**

Sn(1)–C(5)	2.33(1)
Sn(1)–N(1)	2.90(2)
Sn(1)–S(1)	2.39(1)
S(1)–C(1)	1.74(1)
Sn(1)–Cl(1)	2.388(8)
Sn(1)–C(9)	2.34(1)
N(1)–C(1)	1.34(2)
N(1)–Sn(1)–Cl(1)	149.4(4)
N(1)–Sn(1)–S(1)	61.2(4)
C(9)–Sn(1)–S(1)	118.9(4)
C(5)–Sn(1)–S(1)	121.6(4)
C(5)–Sn(1)–C(9)	95.0(4)

Table 4
Selected bond lengths (Å) and angles (°) of complex **3**

Sn(1)–C(5)	2.05(1)
Sn(1)–N(1)	2.39(1)
Sn(1)–S(1)	2.452(3)
Sn(1)–C(11)	2.13(1)
Sn(1)–Cl(1)	2.446(4)
N(1)–C(1)	1.36(1)
S(1)–C(1)	1.72(1)
N(1)–Sn(1)–Cl(1)	157.0 (3)
C(11)–Sn(1)–S(1)	118.0(3)
C(11)–Sn(1)–C(5)	125.6(6)
S(1)–Sn(1)–C(5)	110.6(5)
S(1)–Sn(1)–N(1)	65.4(3)

coordinates to the Sn atom in coordination mode **b**. However, for compounds **4**–**6**, the tin environment is six-coordinated (Scheme 3b), and for compounds **5** and **6**, the ligand HSapym chelates the Sn atom in coordination mode **a**. The detailed description is as follows.

*3.3.1. Structures of compounds **1**, **2** and **3***

The structures of compounds **1**–**3** are all penta-coordinated with R_2ClSn chelated by the thiol S and heterocyclic N atoms of the same ligand. The structure for each complex is distorted *cis*-trigonal bipyramidal with the Cl and N atoms in axial sites and two C atoms and one S atom occupying the equatorial plane. The Cl–Sn–N angles are 156.8(1)°, 149.4(4)° and 157.0(3)° for compounds **1**, **2** and **3**, respectively.

Table 5
Selected bond lengths (Å) and angles (°) of complex **4**

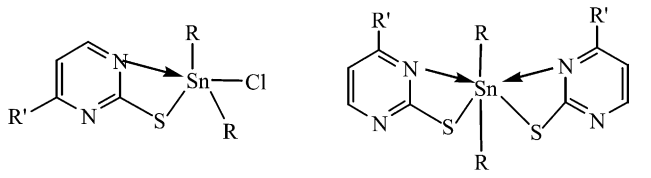
Sn(1)–C(16)	2.147(4)
Sn(1)–N(1)	2.627(4)
Sn(1)–S(1)	2.475(1)
Sn(1)–C(9)	2.150(4)
N(3)–C(5)	1.333(5)
Sn(1)–S(2)	2.487(1)
Sn(1)–N(3)	2.799(4)
N(1)–C(1)	1.337(5)
S(1)–C(1)	1.737(5)
S(2)–C(5)	1.748(4)
N(1)–Sn(1)–S(1)	61.60(9)
N(3)–Sn(1)–S(2)	59.60(8)
C(16)–Sn(1)–C(9)	128.3(2)
S(1)–Sn(1)–S(2)	91.75(4)
N(3)–Sn(1)–N(1)	147.2(1)

Table 6
Selected bond lengths (Å) and angles (°) of complex **5**

Sn(1)–C(9)	1.968(7)
Sn(1)–N(1)	2.596(6)
Sn(1)–S(1)	2.492(2)
Sn(1)–C(13)	2.081(7)
N(4)–C(5)	1.301(9)
Sn(1)–S(2)	2.487(2)
Sn(1)–N(4)	2.673(7)
N(1)–C(1)	1.340(9)
S(1)–C(1)	1.742(8)
S(2)–C(5)	1.734(9)
N(1)–Sn(1)–S(1)	61.14(7)
N(4)–Sn(1)–S(2)	59.6(2)
C(13)–Sn(1)–C(9)	131.6(3)
S(1)–Sn(1)–S(2)	89.86(8)
N(4)–Sn(1)–N(1)	149.4(2)

Table 7
Selected bond lengths (Å) and angles (°) of complex **6**

Sn(1)–C(9)	2.156(4)
Sn(1)–N(1)	2.566(3)
Sn(1)–S(1)	2.5053(4)
Sn(1)–C(16)	2.157(4)
N(4)–C(5)	1.345(4)
Sn(1)–S(2)	2.497(1)
Sn(1)–N(4)	2.655(3)
N(1)–C(1)	1.337(4)
S(1)–C(1)	1.755(4)
S(2)–C(5)	1.750(4)
N(1)–Sn(1)–S(1)	61.77(7)
N(4)–Sn(1)–S(2)	61.05(6)
C(16)–Sn(1)–C(9)	131.1(2)
S(1)–Sn(1)–S(2)	90.52(3)
N(4)–Sn(1)–N(1)	146.59(9)



3a **3b**

(R=Me, *n*-Bu, Ph or $PhCH_2$; R'=H or NH_2)

Scheme 3.

The Sn–S bond lengths (2.473(2) Å for compound **1**, 2.39(1) Å for compound **2** and 2.452(3) Å for compound **3**), approaching the sum of the covalent radii of Sn and S atoms (2.42 Å) [14], indicate typical Sn–S covalent bonds. Concerning the Sn–N bond lengths, there exists some obvious differences. For compounds **1** and **2**, derived from HSpym, the Sn–N bond lengths are 2.450(3) and 2.90(2) Å, respectively, indicating the different bulkiness of the alkyl groups. In contrast, for compound **3**, the diphenyltin(IV) derivative of HSapym, the Sn–N bond length (2.39(1) Å) is much shorter than those in compounds **1** and **2**, which evidences the influence of the amino group to strengthen the coordination bond of N to Sn.

Especially, there exists a weak intermolecular Sn···S non-bonded interaction in crystals of compound **1**, stabilizing its infinite 1D chain structure. The Sn···S distance is 3.95 Å, similar to that of $Ph_3Sn(MNBT)$ (3.97 Å) and $Ph_2Sn(SCH_2CH_2S)$ (3.89 Å) but shorter than that in tribenzyl(2-thiolatopyridine-*N*-oxide)tin(IV) (4.15 Å) [12,14–16]. For compound **3**, there is an intermolecular N···H hydrogen bonding between the amino group and the heterocyclic N that does not coordinate to Sn, leading to the formation of a dimer. The N···H distance is 2.15 Å.

*3.3.2. Structures of compounds **4**, **5** and **6***

The three compounds are all six-coordinated with the R_2Sn moiety coordinated by two thiol S and two heterocyclic N atoms from two deprotonated ligands. The nitrogen atoms occupy *trans* positions with the N–Sn–N angle ranging from 146.59(9)° to 149.4(2)°. The sulfur atoms occupy *cis* positions with S–Sn–S angles ranging from 89.86(8)° to 91.75(4)°. Thus the structure for each is distorted trapezoidal bipyramid with two C atoms in bent axial positions, the trapezoidal plane being defined by the two Sn–S covalent bonds and two Sn–N secondary interactions. On each side of the central tin atom, the sulfur and nitrogen equatorial ligating atoms belong to the same moiety, so their positions are fixed and the S–Sn–N angles can only admit very little deformation. The sum of the angles between the tin atom and the equatorial ligating atoms (i.e., two N and two S in each case) is 360.14° for **4**, 360.03° for **5** and 359.93° for **6**, indicating that the five atoms almost lie in the same plane.

The Sn–S bond lengths are similar, ranging from 2.475(1) to 2.5053(4) Å, shorter than those in $R_2Sn(MNBT)_2$ (2.49–2.54 Å) [13]. The Sn–N bond lengths, 2.596(6) and 2.673(7) Å for compound **5** and 2.566(3) and 2.655(3) Å for compound **6**, are all shorter than those in compound **4** (2.627(4) and 2.799(4) Å), evidencing the influence of the amino group to strengthen the coordination trend of N to Sn.

It is worth noting that it is by the N(3) atom that the deprotonated HSapym coordinates to the central Sn atom in compounds **5** and **6**. The fact suggests that under the influence of the amino group, the coordination ability of N(3) to Sn is larger than that of N(1). However, in the case of compound **3**, due to the greater steric bulk of the phenyl group, Sn–N coordination occurs between the N(1) and Sn atoms.

4. Conclusions

A series of organotin complexes of derivatives of 2-mercaptopyrimidine and 4-amino-2-mercaptopyrimidine have been synthesized and characterized. Detailed studies on the structures and spectra of these compounds indicate that the structures of mono-chelated diorganotin(IV) chlorides have a distorted trigonal bipyramidal geometry and *cis*-chelated complexes have distorted skew-trapezoidal bipyramid geometry. Besides, both the substituent from the ligand and the stereoconstraints from the R groups of the R_2Sn moiety were found to have great influence on the final coordination mode. The influence of different substituents shows that the coordination capability from N to Sn in HSapym is larger than that in HSpym. Especially for HSapym, the coordination ability of N(3) is greater than N(1).

5. Supplementary material

Crystallographic data for the structural analyses have been deposited with the Cambridge Crystallographic Data Center, CCDC Nos. 233178, 227958, 233183, 235029, 238965 and 238960 for compounds **1**–**6**, respectively. Copies of this information may be obtained free of charge from the Director, CCDC, 12 Union Road, Cambridge, CB2 1EZ, UK (fax: +44 1223 336033; e-mail: deposit@ccdc.cam.ac.uk or www: http://www.ccdc.cam.ac.uk).

Acknowledgements

We thank the National Natural Foundation, PR China (20271025), the Key Teachers Foundation from the State Education Ministry of China and the National Natural Foundation of Shandong Province, PR China for financial support of this work.

References

[1] M. Gielen, Appl. Organomet. Chem. 16 (2002) 481.
[2] A. Jancsó, L. Nagy, E. Moldrheim, E. Sletten, J. Chem. Soc., Dalton Trans. (1999) 1587.
[3] R. Barbieri, A. Silvestri, V. Piro, J. Chem. Soc., Dalton Trans. (1990) 3605.
[4] Q. Li, P. Yang, H. Wang, M. Guo, J. Inorg. Biochem. 64 (1996) 181.
[5] J.D. Cashion, J. Organomet. Chem. 185 (1980) 433.
[6] M.J. Hynes, M. O'Dowd, J. Chem. Soc., Dalton Trans. (1987) 563.
[7] N. Buzas, T. Gajda, E. Kuzmann, A. Vértes, K. Burger, Main Group Met. Chem. 11 (1995) 641.
[8] G. Arena, R. Cali, A. Contino, A. Musumeci, S. Musumeci, R. Purello, Inorg. Chim. Acta 237 (1995) 187.
[9] S.K. Hadjikakou, M.A. Demertzis, M. Kubicki, D. Kovala-Demertzi, Appl. Organomet. Chem. 14 (2000) 727.
[10] C.L. Ma, Q. Jiang, R.F. Zhang, D.Q. Wang, Dalton Trans. 15 (2003) 2975.
[11] C.L. Ma, Q. Jiang, J.H. Zhang, R.F. Zhang, Polyhedron 20 (2003) 2767.
[12] C.L. Ma, Q. Jiang, R.F. Zhang, Polyhedron 23 (2004) 779.
[13] C.L. Ma, Q. Jiang, R.F. Zhang, Appl. Organomet. Chem. 17 (2003) 623.
[14] R.A. Varga, M. Schuermann, C. Silvestru, J. Organomet. Chem. 623 (2001) 161.
[15] A.P.G. de Sousa, R.M. Silva, A. Cesar, J.L. Wardell, J.C. Huffmna, A. Abras, J. Organomet. Chem. 605 (2002) 82.
[16] S.W. Ng, C. Wei, K.V.G. Das, T.C.W. Mak, J. Organomet. Chem. 334 (1987) 283.

[21,22]. These peripheral units are particularly noteworthy as they allow for cation selectivity and complex stability to be enhanced through changing the numbers and types of macrocycle donors [23,24]. The usual purification methods such as crystallization and chromatographic separation cannot be used in most phthalocyanines due to their extreme insolubility [25]. The solubility of phthalocyanines can be enhanced by adding various groups such as a crown ether [26–29], mixed donor macrocycle [30–35] or macropolycycle [36,37] to the benzene rings.

We have described, for the first time, the synthesis and characterization of metal-free phthalocyanine peripherally fused to four spherical or cylindrical macrotricyclic moieties [38]. These compounds may allow new functionalized materials to be prepared, which is of importance for analytical chemistry as a new type of Cs^+ and NH_4^+ extraction agent. On the other hand, the importance of this new type of phthalocyanine may be regarded as an important step in that it may be a viable sensor and molecular material [39].

2. Experimental

2.1. Material

4-(2-{2-[2-(1,7-Dioxa-4,10-diazacyclododecane)ethoxy]ethoxy}ethyl)-1,7-dioxa-4,10-diazacyclododecane [40], 4,10,16,22,27,30-hexaoxa-1,7,13,19-tetraazabicyclo[11.11.8]dotriacontane [41] and 1,2-bis(2-tosyloxyethylmercapto)-4,5-dicyanobenzene [42] were prepared according to the literature procedures. Reagent grade chemicals were used as received. Solvents were purified according to standard methods [43] before use. Silica gel (70–230 mesh) was used for chromatographic separations.

2.2. Measurements

Melting points were determined with an electrothermal apparatus and were uncorrected. The ^1H, ^{13}C NMR and IR spectra were recorded on a Varian XL-200 spectrometer and on a Perkin–Elmer Spectrum One spectrometer with the samples in KBr pellets, respectively. Optical spectra in the UV–Vis region were recorded with a Unicam UV2-100 spectrophotometer, using 1 cm pathlength cuvettes at room temperature. Fast atom bombardment mass spectra were recorded on a Varian MAT 711 and VG Zap-Spec spectrometers using *m*-nitrobenzyl alcohol as the matrix. The elemental analysis and the metal contents of the compounds were determined on a Hewlett-Packard 185 CHN analyzer and on a Unicam 929 AA spectrophotometer.

2.3. Synthesis

2.3.1. 2,3,5,6,8,9,11,12,14,15,17,18,20,21,23,24,26,27-Octadecahydro-4,10:19,25-di(ethanooxyethano)-1,4,7,10,13,16,19,22,25,28-[2′,3′-dicyanobenzo]tetraoxadithiatetraazacyclotriacontine (**4**) or 25,26-(2′,3′-dicyanobenzo)-4,10,13,19,31,36-hexaoxa-24,27-dithia-1,7,16,22-tetraazatricyclo[14. 12.5.5^{7,22}]-octatriacontane (**5**)

A three-necked flask containing dry acetonitrile or propionitrile (200 ml) and fitted with a condenser was evacuated, refilled three times with argon, and connected to a vacuum line. Under argon, the flask was charged with **1** (1.84 g, 4 mmol) and finely ground anhydrous Na_2CO_3 (10.6 g, 100 mmol) and the mixture was stirred at 40 °C for 45 min. Compounds **2** or **3** (3.52 g, 5.2 mmol) were added to this mixture under argon atmosphere and the reaction mixture was heated and stirred at 125 °C for 7 days. The reaction was monitored by thin layer chromatography [silica gel (chloroform:petroleum ether:methanol) (6:3:1) (**4**) or (chloroform:petroleum ether:methanol) (7:2:1) (**5**)]. At the end of this period, the mixture was cooled to room temperature and filtered using Celite as the filtering agent and washed with dichloromethane (50 ml). The major liquor and washing solvents were combined and evaporated to dryness under reduced pressure. The residue was purified in a silica gel column using chloroform/petroleum ether:methanol (6:3:1) (**4**) or chloroform:petroleum ether:methanol (7:2:1) (**5**) as eluents. The appropriate fraction was evaporated, 100 ml of dichloromethane was added, and the mixture was filtered off and washed with methylene chloride. After evaporation of the solvent, the products were obtained as a solid or an oil.

Compound ***4***: Yield: 1.12 g (40%); m.p. 230 °C. *Anal.* Calc. for $C_{34}H_{54}N_6O_6S_2$: C, 57.79; H, 7.64; N, 11.89. Found: C, 55.97; H, 7.81; N, 11.57 %. IR (KBr): ν_{max} (cm^{-1}) 3077 (w, Ar–H), 2932–2865 (vs, CH_2), 2228 (vs, CN), 1582 (s), 1568 (s), 1515 (m), 1469 (s), 1411 (m), 1333 (m), 1268 (s), 1223 (s), 1119 (vs, CH_2–O–CH_2), 1097 (s), 1045 (s), 912 (s), 872 (m), 812 (m), 763 (m), 642 (m). ^1H NMR ($CDCl_3$): δ 7.42 (s, 2H, ArH), 3.47 (m, 24H, OCH_2), 3.24 (m, 24H, NCH_2), 2.69 (m, 4H, SCH_2). ^{13}C NMR ($CDCl_3$): δ, 143.97 (ArCS), 131.53 (ArCH), 115.47 (ArCN), 112.78 (ArC), 71.37–71.18 (OCH_2), 55.33 (NCH_2), 50.33 (NCH_2), 36.40 (SCH_2). MS (FAB positive): *m*/*z* 706.2 $[M]^+$.

Compound ***5***: Yield: 0.85 g (30%); oil. *Anal.* Calc. for $C_{34}H_{54}N_6O_6S_2$: C, 57.79; H, 7.64; N, 11.89. Found: C, 57.55; H, 7.47; N, 12.05%. IR (NaCl disc): ν_{max} (cm^{-1}) 3055 (w, Ar–H), 2918–2850 (vs, CH_2), 2229 (vs, CN), 1594 (s), 1566 (s), 1488 (s), 1456 (s), 1352 (m), 1278 (m), 1262 (m), 1218 (m), 1116 (vs, CH_2–O–CH_2), 1067 (s), 926 (m), 855 (m), 718 (m), 683 (s). ^1H NMR ($CDCl_3$): δ 7.32 (s, 2H, ArH), 3.71 (m, 24H, OCH_2),

3.00 (m, 24H, NCH_2), 2.62 (m, 4H, SCH_2). ^{13}C NMR ($CDCl_3$): δ 135.94 (ArCS), 130.30 (ArCH), 125.84 (ArC), 115.69 (C≡N), 70.29–68.31 (OCH_2), 53.93 (NCH_2), 49.71 (NCH_2), 31.92 (SCH_2). MS (FAB positive): *m/z* 706 $[M]^+$.

*2.3.2. 2,3,5,6,8,9,11,12,14,15,17,18,20,21,23,24,26,27-Octadecahydro-4,10:19,25-di(ethanooxyethano)-1,4,7,10,13,16,19,22,25,28-[2′,3′-diiminoisoindoline]tetraoxadithiatetraazacyclotriacontine (**6**) or 25,26-[2′,3′-diiminoisoindoline]-4,10,13,19,31,36-hexaoxa-24,27-dithia-1,7,16,22-tetraazatricyclo[14.12.5.5^{7,22}]-octatricontane (**7**)*

Compound **4** or **5** (0.57 g, 0.8 mmol) was dissolved under an argon atmosphere in dry and degassed methanol (50 ml) on a vacuum line. Dry sodium methoxide (72 mg, 1.33 mmol) in dry methanol (10 ml) was added to the solution at room temperature and then anhydrous ammonia was bubbled through the reaction mixture for 8 h at reflux temperature, after which time the reaction was complete as shown by thin layer chromatography [silica gel (chloroform:methanol (9.5:0.5)]. The ammonia inlet was stopped and the volume of the solution reduced to 10 ml under reduced pressure and then the residue was placed in a refrigerator at −18 °C overnight. The pale green amorphous solid was separated by filtration and dried in vacuo.

*Compound **6***: 0.46 g (80%); m.p. 265 °C (dec.). *Anal.* Calc. for $C_{34}H_{57}N_7O_6S_2$: C, 56.43; H, 7.88; N, 13.55. Found: C, 56.27; H, 8.02; N, 13.41%. IR (KBr): ν_{max} (cm^{-1}) 3355 (s, NH), 3066 (w, Ar–H), 2911–2857 (vs, CH_2), 1635 (m, C=N), 1604 (w, NH), 1594 (s), 1575 (s), 1503 (m), 1450 (s), 1415 (m), 1355 (s), 1287 (m), 1231 (m), 1142 (m), 1107 (vs, CH_2–O–CH_2), 964 (m), 895 (m), 788 (m), 655 (m). ^1H NMR ($CDCl_3$): δ 8.35 (s, 3H, NH), 7.15 (s, 2H, ArH), 3.57 (m, 24H, OCH_2), 3.28 (m, 24H, NCH_2), 2.58 (m, 4H, SCH_2). ^{13}C NMR ($CDCl_3$): δ 159.67 (C=NH), 139.49 (ArCS), 130.11 (ArCH), 131.75 (ArC), 71.05–68.32 (OCH_2), 54.86 (NCH_2), 51.11 (NCH_2), 35.91 (SCH_2). MS (FAB positive): *m/z* 723.1 $[M]^+$.

*Compound **7***: Yield: 0.5 g (86%); m.p. 280 °C (dec.). *Anal.* Calc. for $C_{34}H_{57}N_7O_6S_2$: C, 56.43; H, 7.88; N, 13.55. Found: C, 56.29; H, 8.04; N, 13.32%. IR (KBr): ν_{max} (cm^{-1}) 3329 (m, NH), 3048 (w, Ar–H), 2897–2835 (vs, CH_2), 1668 (s, C=N), 1613 (s, NH), 1592 (s), 1574 (s), 1456 (s), 1373 (s), 1352 (s), 1287–1248 (m), 1108 (vs, CH_2–O–CH_2), 1055 (m), 956 (m), 880 (w), 839 (m), 776 (m), 682 (m). ^1H NMR (d_6-DMSO): δ 8.49 (s, 3H, NH), 7.35 (s, 2H, ArH), 3.75 (m, 24H, OCH_2), 3.12 (m, 24H, NCH_2), 2.67 (m, 4H, SCH_2). ^{13}C NMR (d_6-DMSO): δ 164.13 (C=NH), 134.62 (ArCS), 129.23 (ArCH), 124.28 (ArC), 70.03–68.11 (OCH_2), 53.27 (NCH_2), 51.78 (NCH_2), 31.17 (SCH_2). MS (FAB positive): *m/z* 723.3 $[M]^+$.

*2.3.3. Metal-free phthalocyanines (**8**–**9**)*

Compound **6** or **7** (0.36 g, 0.5 mmol) and dry 2-(dimethylamino)ethanol (1 ml) were placed under an argon atmosphere in a standard Schlenk tube and degassed several times. The reaction mixture was refluxed and stirred under argon for 24 h (**8**) or 26 h (**9**). After cooling to room temperature, the solvent was evaporated to dryness under reduced pressure. The residue was solidified by treating with a mixture of diethyl ether:methanol (1:1), filtered off, and then chromatographed on silica gel with chloroform:methanol (9:1) (**8**) or chloroform:petroleum ether:methanol (7:2:1) (**9**) as eluents.

*Compound **8***: Yield: 0.17 g (48%); m.p. >300 °C. *Anal.* Calc. for $C_{136}H_{218}N_{24}O_{24}S_8$: C, 57.74; H, 7.71; N, 11.88. Found: C, 57.55; H, 7.59; N, 12.03%. IR (KBr): ν_{max} (cm^{-1}) 3407 (s, NH), 3027 (w, Ar–H), 2921–2851 (vs, CH_2), 1626 (m, C=N), 1602 (w, NH), 1589 (s), 1560 (m), 1521 (m), 1458 (m), 1444 (m), 1350 (s), 1277 (m), 1220 (m), 1209 (m), 1176 (s), 1108 (vs, CH_2–O–CH_2), 1031 (m), 933 (m), 875 (m), 777 (m), 736 (m), 620 (s). UV–Vis [(in chloroform) λ_{max}/nm 10^{-5} ε (mol^{-1} cm^{-1})]: 714 (4.89), 681 (4.71), 635 (4.58), 353 (4.77), 298 (5.03), 271 (5.24). ^1H NMR ($CDCl_3$): δ 7.22 (s, 8H, ArH), 3.46 (m, 96H, OCH_2), 3.37 (m, 96H, NCH_2), 2.47 (m, 16H, SCH_2), −1.42 (br, 2H, NH). MS (FAB positive): *m/z* 2826.3 $[M]^+$.

*Compound **9***: Yield: 0.134 g (38%); m.p. >300 °C. *Anal.* Calc. for $C_{136}H_{218}N_{24}O_{24}S_8$: C, 57.74; H, 7.71; N, 11.88. Found: C, 57.97; H, 7.81; N, 11.57%. IR (KBr): ν_{max} (cm^{-1}) 3390 (m, NH), 3061 (w, Ar–H), 2921–2849 (vs, CH_2), 1646 (s, C=N), 1603 (w, NH), 1591 (s), 1561 (m), 1496 (m), 1440 (s), 1401 (m), 1316 (m), 1267 (m), 1196 (m), 1105 (vs, CH_2–O–CH_2), 1060 (s), 995 (s), 964 (m), 870 (m), 798 (m), 770 (m), 699 (m), 617 (m). UV–Vis [(in chloroform) λ_{max}/nm 10^{-5} ε (mol^{-1} cm^{-1})]: 711 (4.84), 673 (4.47), 640 (4.59), 367 (4.74), 306 (5.08), 275 (5.21). ^1H NMR ($CDCl_3$): δ 7.16 (m, 8H, ArH), 3.58 (m, 96H, OCH_2), 2.88 (m, 96H, NCH_2), 2.55 (m, 16H, SCH_2). MS (FAB positive): *m/z* 2827.2 $[M + 1]^+$.

*2.3.4. Nickel(II) phthalocyanines (**10**–**11**)*

A mixture of **4** or **5** (0.71 g, 1 mmol), anhydrous $NiCl_2$ (0.13 g, 1 mmol), dry *n*-pentanol (1.5 ml) and 5 drops of DBU was placed in a well-stoppered Schlenk tube under an argon atmosphere. Then the mixture was heated and stirred gently to 150 °C. The mixture was refluxed at this temperature for 24 h. The crude product was cooled to room temperature and diethyl ether was added dropwise to this mixture until precipitation occurred. The resulting dark green precipitate was filtered off, washed with water and ethanol, and then dried. The solid product was purified by column chromatography [silica gel (methanol:chloroform) (9.5:0.5)] (**10**) or [silica gel (chloroform:petroleum ether:methanol) (8:2:1)] (**11**).

Compound ***10***: Yield: 0.23 g (32%); m.p. >300 °C. *Anal*. Calc. for $C_{136}H_{216}N_{24}O_{24}S_8Ni$: C, 56.61; H, 7.49; N, 11.65; Ni, 2.03. Found: C, 56.77; H, 7.35; N, 11.80; Ni, 2.24%. IR (KBr): ν_{max} (cm^{-1}) 3032 (w, Ar–H), 2925–2857 (vs, CH_2), 1618 (m, C=N), 1596 (s), 1555 (m), 1518 (m), 1467 (m), 1445 (s), 1380 (m), 1290 (m), 1224 (m), 1201 (m), 1121 (vs, CH_2–O–CH_2), 1059 (m), 1048 (m), 1017 (m), 946 (m), 866 (m), 790 (s), 658 (vs). UV–Vis [(in pyridine) λ_{max}/nm 10^{-5} ε ($mol^{-1}cm^{-1}$)]: 701 (4.97), 630 (4.38), 348 (4.65), 302 (4.92), 285 (5.29). ^{1}H NMR (d_6-DMSO): δ 7.31 (m, 8H, ArH), 3.57 (m, 96H, OCH_2), 3.44 (m, 96H, NCH_2), 2.52 (m, 16H, SCH_2). MS (FAB positive): *m*/*z* 2882.3 $[M]^+$.

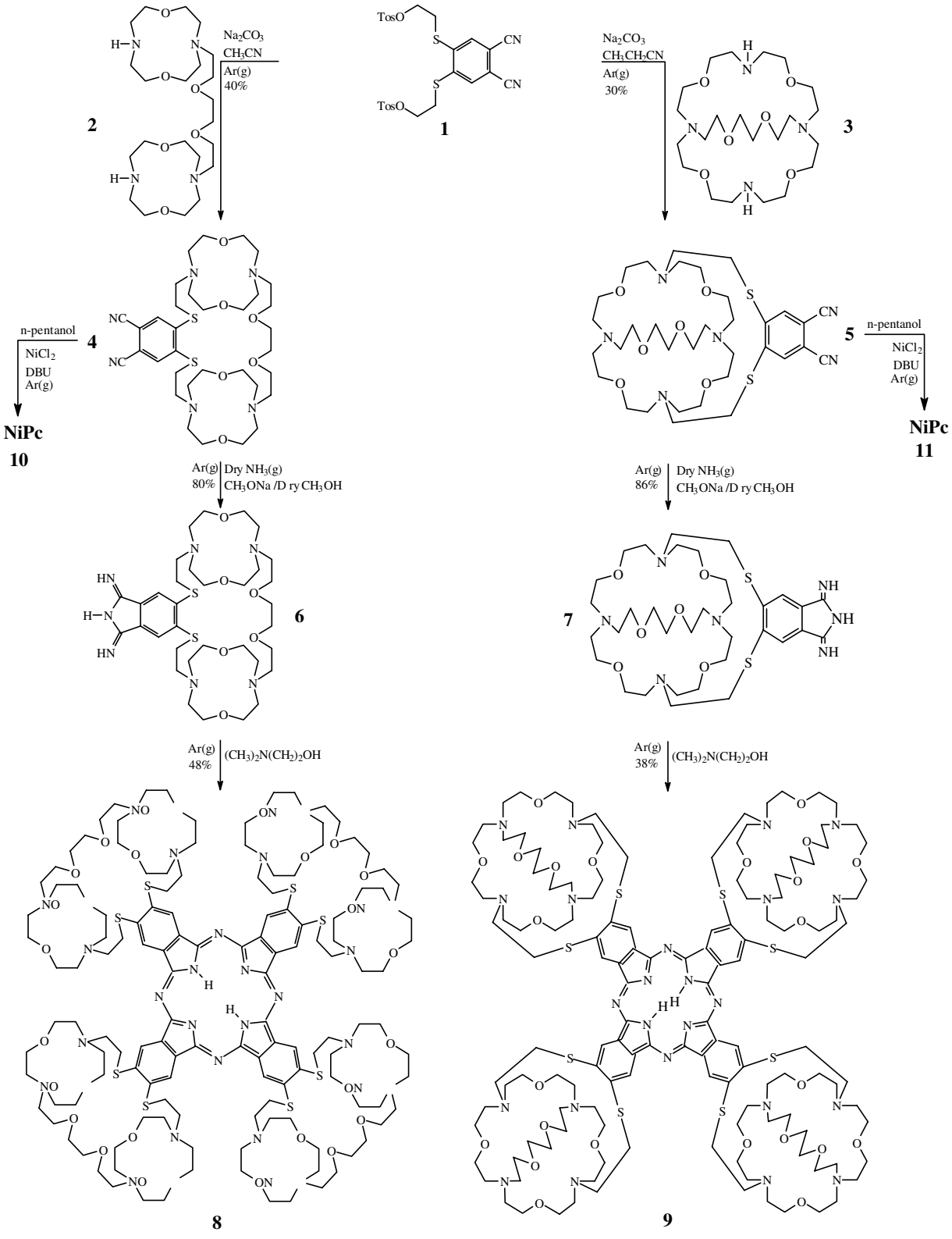
Compound ***11***: Yield: 0.39 g, (55%), m.p. >300 °C. *Anal*. Calc. for $C_{136}H_{216}N_{24}O_{24}S_8Ni$: C, 56.61; H, 7.49; N, 11.65; Ni, 2.03. Found: C, 56.39; H, 7.61; N, 11.80; Ni, 1.89%. IR (KBr): ν_{max} (cm^{-1}) 3059 (w, Ar–H), 2918–2840 (vs, CH_2), 1623 (s, C=N), 1595 (s), 1572 (s), 1501 (m), 1445 (vs), 1394 (s), 1346 (vs), 1300 (m), 1253 (m), 1197 (m), 1185 (m), 1095 (vs, CH_2–O–CH_2), 1070 (s), 1001 (s), 959 (m), 880 (m), 847 (m), 805 (m), 749 (m), 687 (m), 620 (m). UV–Vis [(in pyridine) λ_{max}/nm 10^{-5} ε (mol^{-1} cm^{-1})]: 695 (4.80), 665 (4.59), 628 (4.45), 363 (4.81), 303 (5.12), 273 (5.24). ^{1}H NMR (d_6-DMSO): δ 7.20 (m, 8H, ArH), 3.64 (m, 96H, OCH_2), 2.83 (m, 96H, NCH_2), 2.59 (m, 16H, SCH_2). MS (FAB positive): 2883.5 $[M + 1]^+$.

3. Results and discussion

The synthesis of the cylindrical or spherical macrotricyclic compounds **4**–**5** was performed by starting with 4-(2-{-2[2-(1,7-dioxa-4,10-diazacyclododecane)ethoxy]-ethoxy}ethyl)-1,7-dioxa-4,10-diazacyclododecane **2** [40] or 4,10,16,22,27,30-hexaoxa-1,7,13,19-tetraazabicyclo [11.11.8]dotriacontane **3** [41] and 1,2-bis(2-tosyloxyethylmercapto)-4,5-dicyanobenzene **1** [42] in acetonitrile or propionitrile, respectively, in the presence of Na_2CO_3 for a period of 7 days, affording the asymmetrical cylindrical or spherical macrotricycles **4** or **5**, respectively (Scheme 1). The template effect of sodium cations accounts for the high yield obtained in the desired ring closure. Final purification of the supercryptands by chromatography [silica gel, chloroform:petroleum ether:methanol (6:3:1)] (**5**) or [silica gel, chloroform: petroleum ether:methanol (7:2:1)] afforded **4** in 40% and **5** in 30% yields, for which elemental analyses and FAB mass spectral data were satisfactory: 706.2 $[M]^+$ and 706 $[M]^+$, respectively. ^{1}H NMR spectra of **4** and **5** showed new signals due to aromatic and SCH_2 protons at δ = 7.42–7.32 and 2.69–2.62 ppm, respectively, as expected. The proton-decoupled ^{13}C NMR spectra of the same compounds clearly indicate the presence of nitrile carbon atoms with peaks at δ = 115.47 and 115.69 ppm, respectively. The disappearance of N–H and presence of C≡N stretching vibrations which occur as strong absorptions at 2228 (**4**) and 2229 cm^{-1} (**5**), seen in the IR spectra of these compounds, also confirm the formation of **4** and **5**.

The transformation of the cylindrical and spherical substituted macrotricycle phthalonitriles **4** and **5** into the isoiminoindoline derivatives **6** and **7** was performed by bubbling dry ammonia through a solution of **4** and **5** in dry CH_3OH in the presence of catalytic amounts of CH_3ONa over a period of 8 h [44,45]. In the preparation of metal-free phthalocyanine, the isoiminoindoline route is more convenient than the phthalonitrile route since the reaction conditions employing **8** and **9** are mild in comparison to those employing **4** and **5** [46,47]. In the ^{1}H NMR spectra of **6** and **7**, there are broad signals at δ = 8.35 (**6**) and 8.49 ppm (**7**) due to the imino groups, which can be identified easily owing to deuterium-exchangeable characteristics of these NH protons. In the ^{13}C NMR spectra of **6** and **7**, the disappearance of the C≡N signals, along with the appearance of new peaks at δ = 159.67 (**6**) and 164.13 ppm (**7**) concerning C=NH groups, is in agreement with the proposed structure. In the IR spectra of these compounds, the C≡N stretching vibrations disappeared after conversion of **4** and **5** to isoiminoindolines (**6**,**7**) which show absorptions at 3355 and 3329 cm^{-1} for the N–H groups, respectively, which also suggests the formation of **6** and **7**. In the FAB mass spectra of these compounds, the presence of the characteristic molecular ion peaks at *m*/*z* = 723.1 (**6**) and 723.3 $[M]^+$ (**7**) confirmed the proposed structure.

The first example of a metal-free phthalocyanine containing cylindrical or spherical macrotricyclic moieties was synthesized in good yield according to the previously reported procedure [48–50]. Condensation of four molecules of the isoiminoindoline derivative **6** and **7** into the metal-free phthalocyanine **8** and **9** was carried out in a Schlenk system in 2-(dimethylamino)ethanol at reflux temperature for 22 and 26 h, respectively. In the ^{1}H NMR spectrum of **8**, the typical shielding of inner core protons was seen as a broad signal at around δ = −1.42 ppm which could be attributed to the NH resonances as confirmed by deuterium exchange. However, similar chemical shifts could not be observed in the ^{1}H NMR spectrum of **9**. The signals related to aromatic and aliphatic protons in the cylindrical and spherical macrotricyclic moieties and phthalocyanine skeleton gave significant absorbances characteristic of the proposed structures. This spectrum closely resembles that of the precursor compound (**6**) as expected. A distinct difference encountered in the ^{1}H NMR spectra of phthalocyanines when compared with previously obtained macrocycle substituted derivatives is the sharp signals, which indicates a lower tendency to aggregate even at the concentration used for NMR measurements [51–53]. The IR spectrum of **8** is very similar to that of **6**



Scheme 1. The synthesis of the metal-free and metallophthalocyanines.

and contains the characteristic stretching peaks of aromatic and supercryptand groups. The resonances at 3407–3390 and 1602–1603 cm^{-1}, belonging to N–H stretching and bending vibrations of metal-free phthalocyanines (**8**,**9**), also support the proposed structure. In addition to the results of elemental analysis, the mass

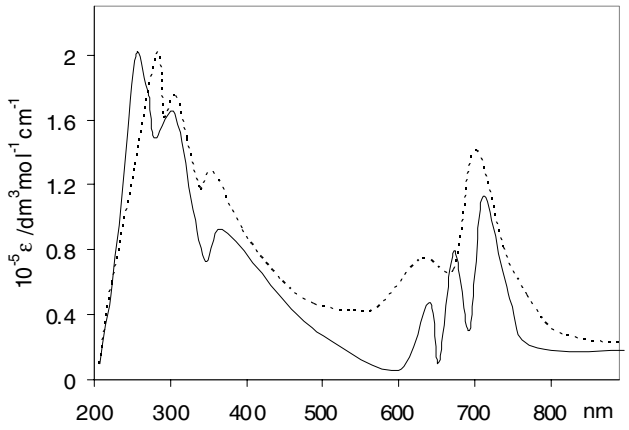


Fig. 1. UV–Vis spectra of **8** (solid line) and **10** (dotted line).

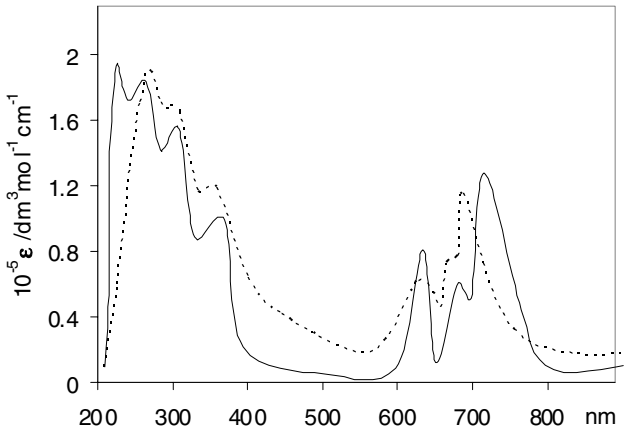


Fig. 2. UV–Vis spectra of **9** (solid line) and **11** (dotted line).

spectra were determined. The molecular ion peaks at $m/z = 2826.3$ $[M]^+$ (**8**) and 2827.2 $[M + 1]^+$ (**9**) were found by the FAB technique (matrix *m*-nitrobenzyl alcohol) for the metal-free phthalocyanines, together with some reasonable ion fragments.

The preparation of metallophthalocyanines (**10**,**11**) from dicyano compounds can be carried out under different reaction conditions [54]. The reactions in the presence of a strong organic base such as 1,8-diazabicyclo[5.4.0]undec-7-ene (DBU) in dry *n*-pentanol at reflux temperature are the most efficient ones in comparison to the other route [55,56]. The metal content of the metallophthalocyanines are in accord with their calculated results. This is also supported by the presence of the characteristic molecular ion peaks in the mass spectrum of **10** at $m/z = 2882.3$ $[M]^+$ and **11** at $m/z = 2883.5$ $[M + 1]^+$. The ^{1}H NMR spectra of these compounds are almost identical with those of the metal-free phthalocyanines, with the absence of the NH protons belonging to the cavity of the phthalocyanine core. Also, it should be mentioned that the peaks of the ^{1}H NMR spectra are broad as encountered in some other soluble phthalocyanines. The aromatic protons are shifted to lower field because of the π-electron ring current of the phthalocyanine core, even after complexation with Ni(II). A common feature of the ^{1}H NMR spectra of the Ni(II) phthalocyanines (**10**,**11**) is the broad absorption when compared with that of the precursor dicyano compounds. In the IR spectra of **10** and **11**, the disappearance of the strong C≡N stretching vibrations of precursors **4** and **5** can be taken as clear evidence for metallophthalocyanine formation. Also, the characteristic vibrations in the IR spectra of **10** and **11** are very similar to those of the metal-free phthalocyanines (**8**,**9**) with the exception of the N–H resonances of the phthalocyanine core. They are in agreement with the structural information.

The UV–Vis absorption spectra of **8** and **9** in a chloroform solution (ca. 1×10^{-5} M) at room temperature are shown in Figs. 1 and 2. In general, phthalocyanines show typical electronic spectra with two strong absorption regions, one in the UV region at about 300–350 nm related to the B band and the other in the visible region at 600–700 nm related to the Q band. The split Q bands in **8** and **9**, which are characteristic for metal-free phthalocyanines, were observed at $\lambda_{max} = 714$, 681, 635 and 711, 673, 640 nm, respectively. These intense Q bands indicate monomeric species, as species with D_{2h} symmetry show two intense absorptions around 700 nm [57–61]. Such split Q band absorptions are due to the $\pi \Rightarrow \pi^*$ transition from the HOMO to the LUMO of the phthalocyanine ring related to the fully conjugated 18π electron system. The presence of strong absorption bands in **8** and **9** in the near UV region at λ_{max} 353, 298, 271 and 367, 306, 275 nm also shows Soret region B bands which have been ascribed to the deeper $\pi \Rightarrow \pi^*$ levels of LUMO transitions [62–64].

UV–Vis absorption spectra of the metallophthalocyanines **10** and **11** in pyridine show intense Q absorptions at 701 and 695 nm (Figs. 1 and 2), with weaker absorptions at 630 and 628 nm, respectively. The single Q bands in metallo derivatives and the split form in their metal-free counterparts are characteristic [65]. These absorptions are generally observed in the case of metallophthalocyanines, indicating the presence of aggregated species together with monomeric ones. Figs. 1 and 2 show that the Q band region is considerably different from **10** and **11**. The observed peaks, as mentioned above, indicate that the symmetry of the molecules have been changed. This result is typical of metal complexes of substituted and unsubstituted *Pc* with D_{4h} symmetry [66,67]. When Ni(II) metal ions are included in the phthalocyanine core of **8** and **9**, the average position of the Q-bands of the resulting metallophthalocyanines (**10**,**11**) is slightly shifted to the blue with respect to the parent metal-free phthalocyanines. B band absorptions of the nickel(II) phthalocyanines (**10**–**11**) were observed at 348, 302, 285 and 363, 302, 275 nm as expected, respectively.

4. Conclusion

We have described for the first time, the synthesis of metal-free and metallophthalocyanines containing cylindrical or spherical subunits. 1,2-Bis(2-tosyloxy-ethyl-mercapto)-4,5-dicyanobenzene (**1**) reacts with macrobicyclic aza-crown moieties (**2**–**3**) in actonitrile or propionitrile under basic conditions to yield the dicyano compounds (**4**–**5**) containing cylindrical or spherical polymacrocyclic units. Compound **1** is a good target for preparing dicyano derivatives. On the other hands, the presence of nitrogen atoms bearing localized electron pairs make compounds **2** and **3** interesting targets for preparing dicyanobenzo units containing cylindrical or spherical macrotricycles. The exhaustive study of the synthesis of the corresponding isoiminoindoline derivative precursor of the metal-free phthalocyanines has been carried out from the dicyano compounds by bubbling through dry ammonia in dry methanol in the presence of CH_3ONa. Starting from **4** and **5**, nickel(II) phthalocyanines (**10**–**11**) were prepared. Unfortunately, all attempts made to grow crystals suitable for X-ray crystallographic studies were unsuccessful. However, ^1H, ^{13}C NMR, IR, elemental analysis, mass spectral data and UV–Vis measurements of the metal-free and the metallophthalocyanines are fully consistent with their identity.

Acknowledgements

This study was supported by the Research Fund of Karadeniz Technical University, Project No. 2002.111.8 (Trabzon/Turkey). We are indebted to Dr. Ayhan Çelik (University of Edinburgh/England) for assistance with some spectral data.

References

[1] J.J. Lehn, Pure Appl. Chem. 49 (1977) 857.
[2] E. Graf, J.-M. Lehn, J. Am. Chem. Soc. 97 (1975) 5022.
[3] H. An, J.S. Bradshaw, R.M. Izatt, Chem. Rev. 92 (1992) 543.
[4] K.E. Krakowiak, J.S. Bradshaw, J. Org. Chem. 60 (1995) 7070.
[5] Y. Murakami, J.I. Kikuchi, T. Ohno, in: G.W. Gokel (Ed.), Advances in Supramolecular Chemistry, JAI Press, Greenwhich, 1990.
[6] J.-M. Lehn, Supramolecular Chemistry, VCH Publishers, Weinheim, 1995.
[7] J.-M. Lehn, in: K.J. Laidler (Ed.), Frontainers of Chemistry, Pergamon Press, New York, 1982, p. 265.
[8] A. Kumar, S. Mageswaran, I.O. Sutherland, Tetrahedron 42 (1986) 3291.
[9] A.E. Pratt, I.O. Sutherland, R.F. Newton, J. Chem. Soc., Perkin Trans 1 (1988) 13.
[10] B. Dietrich, M.W. Hosseini, J.-M. Lehn, R.B. Sessions, J. Am. Chem. Soc. 103 (1981) 1282.
[11] A. Bianchi, M. Micheloni, P. Paoletti, Coord. Chem. Rev. 110 (1991) 17.
[12] C. Bazzicalupi, A. Bencini, A. Bianci, V. Fusi, P. Paoletti, B. Valtancoli, J. Chem. Soc., Perkin Trans. 2 (1994) 815.
[13] B. Dietrich, Pure Appl. Chem. 65 (1993) 1457.
[14] B. Meltz, J.M. Roalky, R. Weiss, J. Chem. Soc., Chem. Commun. (1976) 533.
[15] J.A. Ibers, R.H. Holm, Science 209 (1980) 223.
[16] J.P. Collman, P.C. Herrmann, B. Boitrel, X.M. Zhang, T.A. Eberspacher, L. Fu, J.L. Wang, D.L. Rousseau, E.R. Williams, J. Am. Chem. Soc. 116 (1994) 9763.
[17] R. Guilad, S. Brandes, C. Tardieux, A. Tabard, M. L'Her, C. Miry, P. Gouerec, Y. Knop, J.P. Collman, J. Am. Chem. Soc. 117 (1995) 11721.
[18] T.D. Smith, J.R. Pilbrow, Coord. Chem. Rev. 39 (1981) 295.
[19] D.H. Busch, N.W. Alcock, Chem. Rev. 94 (1994) 585.
[20] J. Simon, T. Toupance, in: D.N. Reinhoudt (Ed.), Comprehensive Supramolecular Chemistry, vol. 10, Pergamon Press, Exeter, 1996.
[21] S.J. Lange, J.W. Sibert, A.G.M. Barrett, B.M. Hoffman, Tetrahedron 56 (2000) 7371.
[22] Ö. Bekaroğlu, J. Porph. Phthalocyan. 4 (2000) 465.
[23] V. Ahsen, E. Ýılmazer, Ö. Bekaroğlu, J. Chem. Soc., Dalton. Trans. (1988) 401.
[24] A.G. Gürek, V. Ahsen, A. Gül, Ö. Bekaroğlu, J. Chem. Soc., Dalton. Trans. (1991) 3367.
[25] Ö. Bekaroğlu, Appl. Organomet. Chem. 10 (1996) 605.
[26] V. Ahsen, E. Ýılmazer, M. Erbaş, Ö. Bekaroğlu, J. Chem. Soc., Dalton Trans. (1988) 401.
[27] V. Ahsen, E. Ýılmazer, Ö. Bekaroğlu, Macromol. Chem. 189 (1988) 2533.
[28] J. Vacus, G. Memetzidis, P. Doppelt, J. Simon, Chem. Commun. (1994) 697.
[29] G. Pawlowski, M. Hanack, Synthesis (1980) 287.
[30] E. Musluoğlu, A.G. Gürek, V. Ahsen, A. Gül, Ö. Bekaroğlu, Chem. Ber. 125 (1992) 2337.
[31] B. Cabezon, E. Quesada, S. Esperanza, T. Torres, Eur. J. Org. Chem. (2000) 2767.
[32] Y. Gök, S.Z. Ýıldız, J. Coord. Chem. 36 (1995) 175.
[33] Y. Gök, S.Z. Ýıldız, Polyhedron 16 (1997) 113.
[34] Y. Gok, S.Z. Ýıldız, Polyhedron 16 (1997) 2335.
[35] H. Kantekin, I. Değirmencioğlu, Y. Gök, Acta Chim. Scand. 53 (1998) 247.
[36] Y. Gök, H. Kantekin, A. Bilgin, D. Mendil, I. Değirmencioğlu, Chem. Commun. (2001) 285.
[37] A. Bilgin, Y. Gök, Tetrahedron Lett. 43 (2002) 5343.
[38] A. Bilgin, B. Ertem, Y. Gök, Tetrahedron Lett. 44 (2003) 6937.
[39] H. Engelkamp, R.J.M. Nolte, J. Porph. Phthalocyan. 4 (2000) 454.
[40] K.E. Krakowiak, J.S. Bradshaw, X. Kou, N.K. Dalley, J. Heterocycl. Chem. 32 (1995) 931.
[41] K.E. Krakowiak, J.S. Bradshaw, J. Org. Chem. 60 (1995) 7070.
[42] A.G. Gürek, Ö. Bekaroğlu, J. Porph. Phthalocyan. 1 (1997) 227.
[43] D.D. Perrin, W.L.F. Armarego, Purification of Laboratory Chemicals, 2nd ed., Pergamon, Oxford, 1989.
[44] J.A. Elvidge, R.P. Linstead, J. Chem. Soc. (1952) 5000.
[45] K. Ohta, L. Jacquemin, C. Sirlin, L. Basio, J. Simon, New J. Chem. (1988) 751.
[46] N. Kobayashi, S. Kondo, S. Nakajima, T. Osa, J. Am. Chem. Soc. 112 (1990) 9640.
[47] K. Kasuga, T. Idehara, M. Handa, K. Isa, Inorg. Chim. Acta 196 (1992) 127.
[48] S. Dabak, Ö. Bekaroğlu, New J. Chem. 21 (1997) 267.
[49] G. Gümüş, A. Gül, Ö. Bekaroğlu, J. Chem. Res. (S) (1994) 430.
[50] A. Bilgin, B. Ertem, Y. Gök, Tetrahedron Lett. 44 (2003) 3829.
[51] E. Musluoğlu, V. Ahsen, A. Gül, Ö. Bekaroğlu, Chem. Ber. 124 (1991) 2531.
[52] S.Z. Ýıldız, H. Kantekin, Y. Gök, J. Porph. Phthalocyan. 5 (2001) 367.
[53] S.Z. Yıldız, Y. Gök, New J. Chem. (1998) 1365.
[54] C.C. Leznoff, A.B.P. Lever (Eds.), Phthalocyanines: Properties and Applications, vol. 1–4, VCH, New York, 1989, 1993, 1996.

[55] H. Tomoda, S. Saito, S. Ogawa, S. Shiraishi, Chem. Lett. (1980) 1277.
[56] D. Wöhrle, G. Schnurpfeil, G. Knothe, Dyes Pigments 18 (1992) 91.
[57] M. Hanack, H. Heckmann, R. Polley, Methods of Organic Chemistry, Georg Thieme Verlag, Stuttgard, 1998, Additional Supplementary Volume, p. 776.
[58] A.G. Gürek, Ö. Bekaroğlu, J. Chem. Soc., Dalton Trans. (1994) 1419.
[59] C.F. van Nastrum, S.J. Pic-ken, A.-J. Schouten, R.J.M. Nolte, J. Am. Chem. Soc. 117 (1995) 9957.
[60] C. Wang, M.R. Bryce, A.S. Batsanow, C.F. Stanley, A. Beeby, J.A.K. Howard, J. Chem. Soc., Perkin Trans. 2 (1997) 1671.
[61] M.T.M. Choi, P.P.S. Li, D.K.P. Ng, Tetrahedron 56 (2000) 3881.
[62] M.J. Stilman, T. Nyokong, in: C.C. Leznoff, A.B.P. Lever (Eds.), Phthalocyanines: Properties and Applications, vol. 1, VCH, New York, 1989 (Chapter 3).
[63] S.J. Lange, J.W. Sibert, A.G.M. Barrett, B.M. Hoffman, Tetrahedron 56 (2000) 7371.
[64] S. Gürsoy, Z.A. Bayır, E. Hamuryudan, Ö. Bekaroğlu, Monatsch. Chem. 131 (2000) 287.
[65] A.E. Pullen, C. Faulmann, P. Cassoux, Eur. J. Inorg. Chem. (2000) 269.
[66] K. Takahashi, M. Kawashima, Y. Tomita, M. Itoh, Inorg. Chim. Acta 232 (1995) 69.
[67] A. Bilgin, B. Ertem, Y. Gök, Supramol. Chem. (in press).

at low concentrations, although the basis for its toxicity it not clearly understood. The concern arises because it accumulates in particular food species, with potential consequences for human health (renal tubular dysfunction, hypertensive disorders, respiratory problems and others). According to the literature, one general mechanism for cadmium detoxification is the chelation of the metal [10,13,14,16].

We have been working for the last year on the synthesis and coordination capability of compounds containing thiazoline rings [15,16] due to their interesting biological properties. Moreover, these compounds are able to form complexes with cadmium [15,17] and could play an important role in its detoxification.

For all these reasons, in this paper, we report the synthesis and the characterization by single crystal X-ray diffraction, elemental analysis and spectroscopic measurement of a novel hydrazone derivative ligand, 2-acetyl-2-thiazoline hydrazone (ATH), and its complex with Cd(II).

2. Experimental

2.1. General procedures

All chemicals were of reagent grade and used without any further purification. 2-Acetyl-2-thiazoline was synthetized according to the method described by Doornbos and Peer [18]. Chemical analyses of carbon, hydrogen, nitrogen and sulfur were performed by microanalytical methods using a Leco CHNS-932 microanalyser. IR spectra were recorded on a Perkin–Elmer FT-IR 1720 spectrophotometer, from KBr pellets in the 4000–370 cm^{-1} range and on a Perkin–Elmer FT-IR 1700X spectrophotometer, from polyethylene pellets in the 500–150 cm^{-1} range. Electronic spectra were measured on a Shimadzu UV-3101 PC using a 10 mm quartz cell. ^1H and ^{13}C NMR spectra were obtained with a Bruker AM 400 instrument at 400 and 100 MHz, respectively. The NMR study has been carried out in D_2O for the complex and $DCCl_3$ for ATH. In addition, the NMR study of ATH has also been carried out in D_2O to be able to compare NMR spectra of both compounds.

2.2. Synthesis of 2-acetyl-2-thiazoline hydrazone (ATH)

A solution of 0.977 g (7 mmol) of 2-acetyl-2-thiazoline and 0.350 g (7 mmol) of hydrazine hydrate in 30 ml ethanol was heated to reflux for 3 h. The solvent was then removed under reduced pressure to obtain a brown oil. 2 ml of absolute ethanol was added and a yellow solid appeared (0.825 g, 76.2%). This solid was recrystallized from water, yielding prismatic crystals of considerable size (ca. 0.4 mm), suitable for X-ray diffraction.

^1H NMR (deuteriochloroform): δ 5.76 (s, 2H, NH_2), 4.38 (t, $J = 8.3$ Hz, 2H, CH_2–N), 3.24 (t, $J = 8.3$ Hz, 2H, CH_2–S), 2.08 (s, 3H, CH_3); ^{13}C NMR (deuteriochloroform): δ 169.90 C(1), 142.45 C(4), 64.87 C(2), 32.07 C(3), 10.39 C(5). Elemental Analysis, Found: C, 42.06; H, 6.35; N, 29.67; S, 22.19%. Calc. for $C_5H_9N_3S$: C, 41.94; H, 6.34; N, 29.33; S, 22.39%. UV–Vis (EtOH): λ_{max}, nm; (ε, L mol^{-1} cm^{-1}) 261 (5859).

2.3. Synthesis of $[Cd(NO_3)_2(ATH)_2]$

This complex was isolated from an 80% ethanol solution (2 mL) of $Cd(NO_3)_2 \cdot 4H_2O$ (216 mg, 0.7 mmol) that was added to an 80% ethanol solution (15 mL) of ATH (100 mg, 0.7 mmol). The resulting solution was allowed to evaporate slowly at room temperature. After a few days, yellow prismatic crystals of considerable size (ca. 0.6 mm) were isolated from the solution (104 mg, 57.0%). The crystals were separated by filtration, washed with cold ether and air-dried. ^1H-NMR (D_2O): 4.31 (t, $J = 8.6$ Hz, 2H, CH_2–N), 3.45 (t, $J = 8.6$ Hz, 2H, CH_2–S), 2.10 (s, 3H, CH_3); ^{13}C-NMR (D_2O): δ 175.22 C(1), 142.71 C(4), 63.64 C(2), 33.69 C(3), 13.48 C(5). Elemental Analysis, Found: C, 23.12; H, 3.41; N, 21.33; S, 11.87%. Calc. for $C_{10}H_{18}CdN_8O_6S_2$: C, 22.97; H, 3.47; N, 21.42; S, 12.27%.

2.4. Crystal structure determinations

X-ray diffraction measurements were performed using a Bruker SMART CCD diffractometer for ATH and a Siemens P4 diffractometer for the complex.

Crystal data, data collection and structure analysis parameters are given in Table 1. For ATH, the first 50 frames were recollected at the end of the data collection to monitor for decay, whereas in the case of complex, the examination of three standard reflections, monitored after 97 scans, showed only a slight change during data collection.

Data reduction was made using the SAINTPLUS program [19] for ATH and the XSCANS program [20] for the complex. Data were corrected for absorption effects using an empirical method based on azimuthal scan data in the case of the ligand. In the same way, absorption corrections were applied using the SADABS program [21] for the complex. The structures were solved by direct methods and subsequent Fourier differences using the SHELXS 97 program [22] included in the WINGX package [23], and refined by full-matrix least-squares analysis with SHELXL 97 [22]. H atoms attached to C and N atoms were positioned geometrically, with U_{iso} values derived from U_{eq} values of the corresponding C and N atoms. In the structure of the complex, one of the two ATH ligands were disordered and were modelled using two sets of positions. For this procedure, the occupancy of the two alternate orientations were constrained to unity

Table 1
Crystal data, data collection and refinement details for ATH and $[Cd(NO_3)_2(ATH)_2]$

	[ATH]	$[Cd(NO_3)_2(ATH)_2]$
Crystal shape	prism	prism
Colour	yellow	yellow
Size (mm)	$0.36 \times 0.17 \times 0.14$	$0.60 \times 0.40 \times 0.30$
Chemical formula	$C_5H_9N_3S$	$C_{10}H_{18}CdN_8O_6S_2$
Formula weight	143.21	522.84
Crystal system	orthorhombic	monoclinic
Space group	$Pc2_1b$	Cc
Unit cell dimensions		
a (Å)	5.601(1)	16.174(2)
b (Å)	9.656(1)	9.288(2)
c (Å)	13.039(1)	13.500(2)
β (°)		107.71(1)
Cell volume (Å^3)	705.1(1)	1931.8(6)
Z	4	4
T (K)	298(2)	298(2)
D_{calc} (g cm^{-3})	1.349	1.798
μ (mm^{-1})	0.371	1.392
$F(000)$	304	1048
Diffractometer	Bruker SMART CCD	Siemens P4
Radiation, λ (Å)	Mo Kα (0.71073)	Mo Kα (0.71073)
Collection method	ϕ–ω	θ–2θ
2θ range (°)	6.2–56.5	5.1–60.0
Index ranges	$-5 \leqslant h \leqslant 7$; $-12 \leqslant k \leqslant 12$; $-14 \leqslant l \leqslant 17$	$-1 \leqslant h \leqslant 22$; $-1 \leqslant k \leqslant 13$; $-18 \leqslant l \leqslant 18$
Decay of standards (%)	0.9	2.5
Independent reflections	1659	3080
Observed reflections	1487[$F > 4.0\sigma(F)$]	2736[$F > 4.0\sigma(F)$]
Refinement method	full-matrix least-squares on F^2	full-matrix least-squares on F^2
Absorption correction	empirical	empirical
Maximum/minimum transmission	0.9499/0.8780	0.6802/0.4889
Number of refined parameters	83	217
R [$F > 4.0\sigma(F)$][a]	0.0309	0.046
wR [all data][b]	0.0844	0.140
The goodness-of-fit[c]	1.04	1.049
$\Delta\rho$ (e Å^{-3})	0.378	2.214
Flack parameter	−0.06(10)	0.08(6)

[a] $R = \sum||F_o| - |F_c||/\sum|F_o|$.
[b] $R = \{\sum[w(F_o^2 - F_c^2)^2]/\sum[w(F_o^2)^2]\}^{1/2}$.
[c] GOF = $\{\sum[w(F_o^2 - F_c^2)^2]/(N_{reflections} - N_{params})\}^{1/2}$.

and soft constraints (with EADP) were applied to the disordered ATH. The refined occupancy was 0.53(1) for the orientation named A and 0.47(1) for the orientation named B. The non-hydrogen atoms were refined with anisotropic displacement parameters excepting atoms involved in disorder which were refined with isotropic displacement parameters. The Flack parameters of ATH and the complex indicate that the crystals did not contain inversion-twins. Diagrams were generated using ORTEP3 for Windows [24].

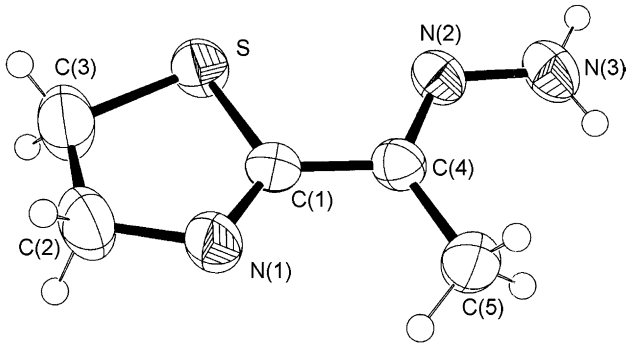


Fig. 1. Crystal structure of ATH, showing the atom-numbering scheme. The thermal ellipsoids are drawn at the 50% probability level.

3. Results and discussion

3.1. Description of the crystal structures

The molecular structure of ATH with the atomic labelling is shown in Fig. 1. Selected bond lengths, angles and hydrogen-bond parameters are given in Table 2.

In the S–C(1)–N(1)–C(2)–C(3) ring, the short endocyclic C=N bond [C(1)–N(1) = 1.270(2) Å] is accompanied

Table 2
Selected bond lengths (Å), angles (°) and hydrogen-bond parameters for ATH

S–C(1)	1.773(2)	S–C(3)		1.803(2)
C(1)–N(1)	1.270(2)	C(1)–C(4)		1.465(2)
C(4)–N(2)	1.295(2)	C(4)–C(5)		1.493(3)
N(2)–N(3)	1.361(2)	N(1)–C(2)		1.467(3)
C(2)–C(3)	1.479(3)			
C(1)–S–C(3)	89.9(1)	N(1)–C(1)–C(4)		123.6(1)
N(1)–C(1)–S	117.4(1)	C(4)–C(1)–S		119.0(1)
N(2)–C(4)–C(1)	114.8(2)	N(2)–C(4)–C(5)		125.0(2)
C(1)–C(4)–C(5)	120.2(1)	C(4)–N(2)–N(3)		117.4(2)
C(1)–N(1)–C(2)	112.6(2)	C(2)–C(3)–S		107.7(2)
N(1)–C(2)–C(3)	112.4(2)			
D–H···A	position of A	D–H (Å)	D···A (Å)	D–H···A (°)
N(3)–H(3B)···N(1)	$-x, y, z-0.5$	0.860(2)	3.093(3)	149.2(2)

by a high N–C–S angle [N(1)–C(1)–S = 117.4(1)°] and a relatively long S^{II}–C(sp^2) bond [S–C(1) = 1.773(2) Å], which is characteristic of a thiazoline ring [25]. It is known that the imino tautomers can exist as two geometrical isomers, *syn* (*Z*) and *anti* (*E*), but in this crystal, only *E* isomers have been observed.

The thiazoline ring is essentially planar, with maximum mean-plane deviation from C(3) (0.031 Å).

The molecular packing is determinated by a hydrogen-bond network N(1)···H(3B)–N(3) of the intermolecular type. A diagram showing this network is given in Fig. 2.

A diagram of the molecular structure of the Cd(II) complex, showing the higher occupancy molecule for simplicity, is shown in Fig. 3. Selected bond lengths, angles and hydrogen bond parameters are given in Table 3.

The structure consists of discrete neutral monomeric units in which the environment around the cadmium(II) atom may be described as a very distorted octahedral geometry. The ligand–metal–ligand bite angles differ from the ideal value of 90°, varying between 65.1(6)° [N(4)–Cd–N(5)] and 136.1(4)° [N(1A)–Cd–O(4)]. The metallic atom is coordinated by two monodentate nitrate oxygen atoms, [Cd–O(1) = 2.334(12) Å; Cd–O(4) = 2.383(12) Å], two thiazolinic nitrogen atoms [Cd–N(1A) = 2.230(12) Å; Cd–N(4) = 2.384(12) Å] and two iminic nitrogen atoms [Cd–N(2A) = 2.414(10) Å; Cd–N(5) = 2.427(14) Å].

The crystal structure of the complex exhibits a positional disorder due to the existence of two quite different orientations from the ATH, numbering C(1)···C(5). In this ligand, the C(1) atom is common in both orientations. A representation of this disorder is shown in Fig. 4, with only the Cd atom and the disordered ligand displayed for simplicity.

The Cd–O distances of the monodentate nitrate groups are comparable with the calculated average value [2.418(82) Å] for 58 six-coordinate cadmium(II) complexes obtained with CONQUEST software [26] from the Cambridge Structural Database (CSD) [27]. Likewise, the Cd–N_{imino} distances are slightly higher than the mean value calculated for 47 six-coordinate cadmium(II) complexes using the data of 47 crystal structures obtained from the CSD: 2.347(87) Å. Moreover, the Cd–$N_{thiazoline}$ bond distances are comparable to

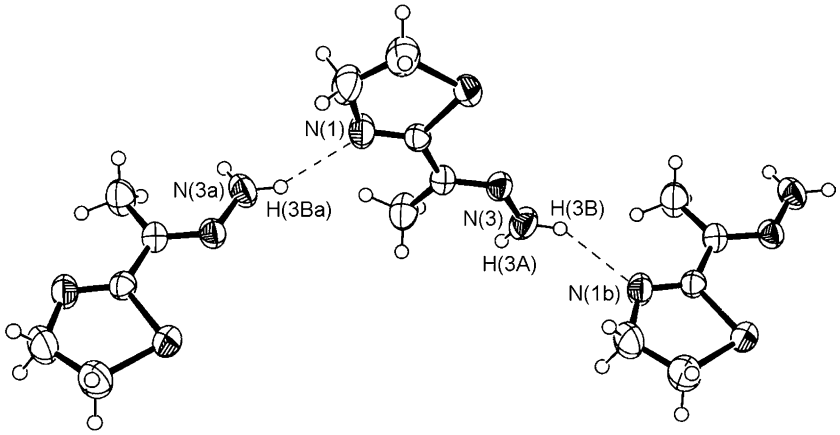


Fig. 2. View of the hydrogen bond network of ATH. Symmetry codes: (a) $-x, y, z+0.5$; (b) $-x, y, z-0.5$.

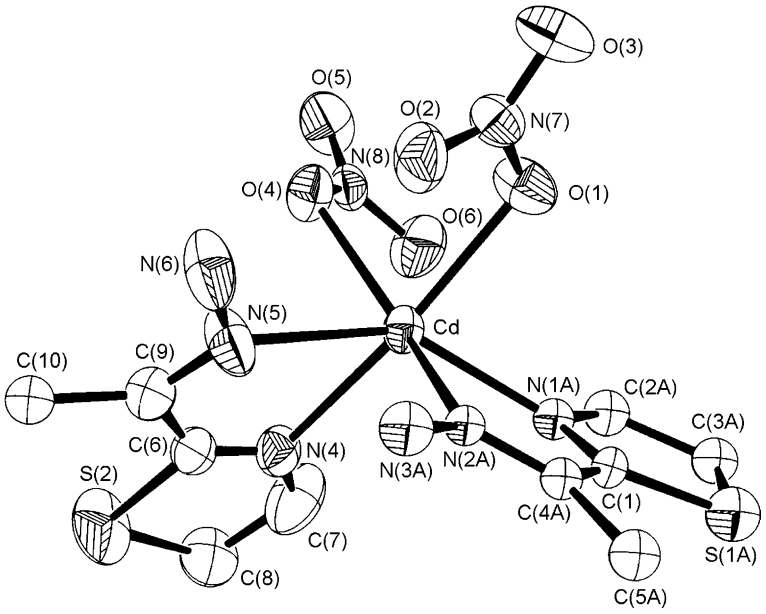


Fig. 3. Molecular structure of $[Cd(NO_3)_2(ATH)_2]$ showing the atom-numbering scheme. The thermal ellipsoids are drawn at the 40% probability level.

Table 3
Selected bond lengths (Å), angles (°) and hydrogen-bond parameters for $[Cd(NO_3)_2(ATH)_2]$

Cd–N(1A)	2.230(12)	Cd–N(2A)		2.414(10)
Cd–N(4)	2.384(12)	Cd–N(5)		2.427(14)
Cd–O(1)	2.334(11)	Cd–O(4)		2.383(12)
C(1)–N(1A)	1.45(2)	C(1)–C(4A)		1.27(2)
C(6)–N(4)	1.16(4)	C(6)–C(9)		1.42(3)
N(6)–N(5)	1.45(2)	N(2A)–N(3A)		1.31(2)
N(5)–C(9)	1.26(2)	N(2A)–C(4A)		1.289(16)
N(1A)–Cd–O(1)	82.5(5)	N(1A)–Cd–N(4)		100.1(5)
O(1)–Cd–N(4)	167.0(5)	N(1A)–Cd–O(4)		136.1(4)
O(1)–Cd–O(4)	80.5(3)	O(1)–Cd–N(5)		120.2(5)
N(4)–Cd–O(4)	89.0(4)	O(1)–Cd–N(2A)		91.7(4)
N(1A)–Cd–N(2A)	70.7(4)	N(4)–Cd–N(2A)		101.1(4)
O(4)–Cd–N(2A)	149.5(4)	N(1A)–Cd–N(5)		141.3(5)
N(4)–Cd–N(5)	65.1(6)	O(4)–Cd–N(5)		81.3(5)
N(2A)–Cd–N(5)	77.3(5)	N(7)–O(1)–Cd		110.1(9)
N(8)–O(4)–Cd	107.2(9)			
D–H···A	position of A	D–H (Å)	D···A (Å)	D–H···A (°)
N(6)–H(6B)···O(2)	x, y, z	0.860(2)	2.775(17)	135.7(9)
N(3A)–H(3A2)···N(6)	x, y, z	0.860(2)	2.927(16)	153.8(8)
N(6)–H(6A)···O(1)	$x, -y, z - 0.5$	0.860(2)	3.066(18)	136.5(9)

those found for $[CdCl_2(HzTz)] \cdot H_2O$ [HzTz = (2-thiazolin-2-yl)hydrazine] [2.241(2) Å] [17], $[Cd(NO_3)_2(PyTT)(H_2O)]$ [2.351(2) Å] and $[CdCl\{(\mu\text{-}Cl)_2CdCl(\mu\text{-}Cl)(\mu\text{-}PyTT)Cd\}_2]_n$ [2.271(2) Å] [16].

The five-membered chelate ring Cd–N(1A)–C(1)–C(4A)–N(2A) is essentially planar with the maximum deviation, in relation to the corresponding mean plane, from C(1) [0.079 Å]. On the contrary, the puckering parameters calculated for the chelate ring Cd–N(4)–C(6)–C(9)–N(5) [$q = 0.135$ Å; $\phi = 173.4°$], according to Cremer and Pople [28], indicate a conformation near to envelope with the Cd atom deviating 0.330 Å from the plane formed by N(4), C(6), C(9) and N(5) [maximum mean-plane deviation from C(6) = 0.019 Å].

The main difference of the organic moiety with respect to the structure of ATH is due to the different degree of rotation of the thiazoline rings around the C(1)–C(4A) and C(6)–C(9) bonds, which does permit the coordination through N(1A) and N(4) [torsion angles S(1A)–C(1)–C(4A)–N(2A) = 175.8° and S(2)–C(6)–C(9)–N(5) = 177.9° in the complex, respectively, 9.7° in ATH].

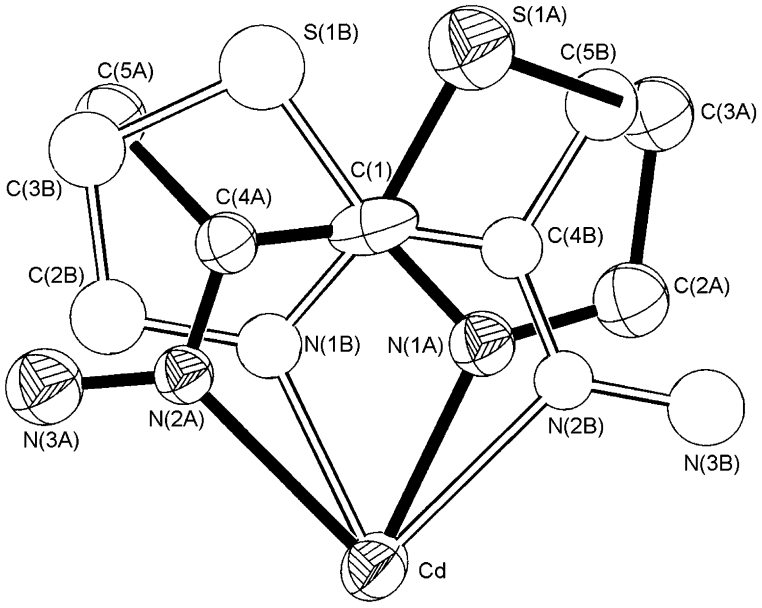


Fig. 4. A drawing demonstrating the disordering of the ATH ligand in the complex.

The thiazoline ring S(1A)–C(1)–N(1A)–C(2A)–C(3A) is essentially planar with maximum mean-plane deviation from S(1A) (0.042 Å). However, the thiazoline ring S(2)–C(6)–N(4)–C(7)–C(8) shows a conformation near to envelope with the apex at C(7). This atom is 0.202 Å out of the plane formed by N(4), C(6), S(2) and C(8) [maximum mean-plane deviation from C(6) = 0.010 Å]. This geometry is proved by the puckering parameters $q = 0.133$ Å and $\phi = 113.7°$ [28].

Focusing our attention on the N(7)–O(1)–Cd and N(8)–O(4)–Cd angles, we see that their values differ significantly from linearity, amounting to 110.1(9)° and 107.2(9)°, respectively. Likewise, the mean plane formed by the atoms O(1), O(2), O(3) and N(7) of one monodentate nitrate ligand forms an angle of 97.0° with the plane constituted by N(2A)–Cd–N(5). In the same way, in the other monodentate nitrate ligand there is an angle of 94.5° between the mean plane formed by O(4), O(5), O(6) and N(8) and the plane N(1A)–Cd–N(4). Both facts may possibly be explained in terms of crystal packaging effects, but as they facilitate the approach from O(2) and O(6) to the central ion, it cannot be excluded that they are conditioned by the existence of weak interactions O(2)–Cd [2.801(15) Å] and O(6)–Cd [2.766(15) Å].

The crystal packing is stabilized by a complicated hydrogen-bond network in which O(1) and O(2) act as hydrogen acceptors, hydrazinic nitrogen N(3A) acts as hydrogen donor and hydrazinic nitrogen N(6) acts on both forms. A diagram showing this network is given in Fig. 5.

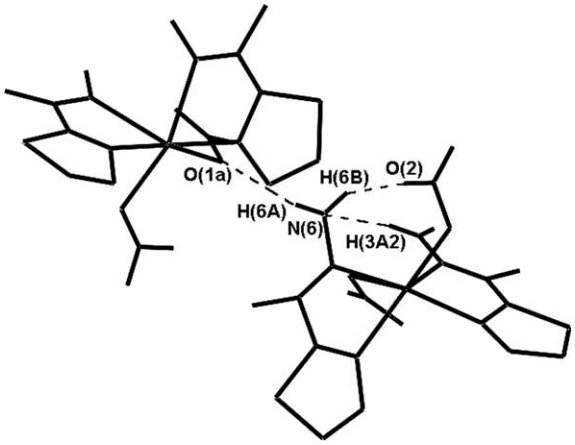


Fig. 5. View of the hydrogen network of $[Cd(NO_3)_2(ATH)_2]$.

3.2. Spectroscopic studies

The IR spectrum of ATH in the 4000–370 cm^{-1} region shows the presence of bands due to thiazoline ring at 1593 (W_1), 1003 (W_2), 915 (W_3), 714 (W_4), 675 (W_5), 657 (W_6), 619 (W_8), 549 (W_7) and 421 (Γ_1) cm^{-1} [29–31].

Moreover, the bands of NH_2 vibrations are detected at 3352, 3317, 3195 [$\nu(NH_2)$], 1567 [$\delta(NH_2)$], 1346 [$\omega(NH_2)$] and 1031 [$r(NH_2)$] cm^{-1} [30,32–34].

Other relevant bands are registered at 1653 cm^{-1} [ν(C=N)] and at 943 cm^{-1} [ν(N–N)] [30,35].

In the IR spectrum of the complex two bands can be observed in the 4000–370 cm^{-1} region at 1641 and 952 cm^{-1}, assigned to ν(C=N) and ν(N–N) vibrations, respectively. Moreover, other bands due to organic moiety vibrations are detected as is shown in Table 4. Bands

Table 4
Infrared bands (cm^{-1}) assigned to organic moiety vibrations of ATH and $[Cd(NO_3)_2(ATH)_2]$

	Assignment	ATH	$[Cd(NO_3)_2(ATH)_2]$
Thiazoline	W_1	1593 (vs)	1605 (s)
	W_2	1003 (s)	1046 (vs)
	W_3	915 (s)	952 (m)
	W_4	714 (m)	734 (m)
	W_5	675 (m)	685 (m)
	W_6	657 (m)	669 (m)
	W_8	619 (m)	629 (m)
	W_7	549 (m)	563 (m)
	Γ_1	421 (m)	424 (w)
Hydrazine	$\nu(NH_2)$	3352 (vs), 3317 (s), 3195 (vs)	3419 (s), 3307 (s), 3246 (s), 3214 (s)
	$\delta(NH_2)$	1567 (vs)	1545 (s)
	$\omega(NH_2)$	1346 (m)	1338 (s)
	$r(NH_2)$	1031 (vs)	1046 (vs)
	ν(N–N)	943 (w)	952 (m)

Abbreviations: s, strong; m, medium; w, weak; v, very.

due to nitrate ligands are registered at 734, 709 and 602 cm^{-1} (ν_4), 818 cm^{-1} (ν_2), 1145 and 1030 cm^{-1} (ν_1) and 1446, 1430 and 1299 cm^{-1} (ν_3) [36].

In addition, in the 1700–1800 cm^{-1} region, the IR spectrum of the complex shows four combination bands due to nitrate groups. Methods to discriminate between bidentate and monodentate bonded nitrate groups have been reported and have been proved reliable. Some of them are based on the pattern or the splitting of the ($\nu_1 + \nu_4$) combination bands [37–40]. The bands registered at 1767 and 1744 cm^{-1} are assigned to ($\nu_1 + \nu_4$) combination bands. The value of the splitting ($\Delta = 23$ cm^{-1}) reveals the presence of one monodentate nitrate group, in agreement with Lever's criteria [38]. In the same way, the bands registered at 1748 and 1733 cm^{-1} ($\Delta = 15$ cm^{-1}) can be assigned to the other monodentate nitrate group.

Four bands assignable to Cd-ligand stretching vibrations are observed in the low frequency range. The band at 185 cm^{-1} is tentatively assigned to the (Cd–ONO_2) vibration due to monodentate nitrate ligands, in accord with the literature data for this type of bond [16,36].

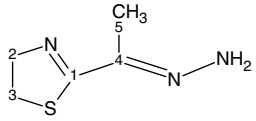
The bands at 221 and 234 cm^{-1} can be assigned to the ν(Cd–$N_{thiazoline}$) vibration [16,30], whereas the band at 302 cm^{-1} is assigned to the ν(Cd–N_{imino}) vibration, according to the literature [16,41].

As usual [42], the coordination to the d^{10} Cd(II) ion shifts the ^{1}H NMR signals of the complexes downfield from those of the free ligand ($\Delta\delta \approx 0.0$–0.2 ppm). A comparison of the chemical shift data for ATH and the complex in Table 5 confirms this statement. The small shift is due to the weak Lewis acidity of this ion. The trends in the ^{13}C NMR shifts are similar. The signals of the carbon atoms 1, 3 and 5 show a slight downfield shift to those of the free ligand ($\Delta \approx 1.1$–3.2 ppm), whereas the C(2) and C(4) suffer an upfield shift ($\Delta\delta \approx -1.4$ and -2.9 ppm, respectively). The chemical shift differences are due to two superimposing effects: the negative inductive effect of the coordinated metal ion leads to a downfield shift and, on the other hand, the interaction of the paired metal d electrons with the organic ligand induces an upfield shift.

4. Supplementary material

CCDC 258903, corresponding to ATH, and CCDC 258904, to $[Cd(NO_3)_2(ATH)_2]$, contain the supplementary crystallographic data for this paper. These data can be obtained free of charge via www.ccdc.cam.ac.uk/conts/retrieving.html (or from the CCDC, 12 Union

Table 5
NMR spectral data for ATH and its Cd complex in D_2O solvent



Compound	^{1}H NMR			^{13}CNMR				
	CH_3	CH_2–S	CH_2–N	C5	C3	C2	C4	C1
ATH	1.99	3.24	4.27	11.89	32.63	65.01	145.64	172.98
$[Cd(NO_3)_2(ATH)_2]$	2.10	3. 45	4.31	13.48	33.69	63.64	142.71	175.22

Road, Cambridge CB2 1EZ, UK; fax: +44 1223 336033; e-mail: deposit@ccdc.cam.ac.uk).

Acknowledgements

We thank the Junta de Extremadura (Consejería de Educación, Ciencia y Tecnología) and the FEDER [Project 2PR02A098] for financial support. M.A. Maldonado-Rogado thanks the Spanish Ministerio de Ciencia y Tecnología and E. Viñuelas-Zahínos thanks the Junta de Extremadura (Consejería de Educación, Ciencia y Tecnología) and the FEDER for their Ph.D. fellowships.

References

[1] C.G. Bonde, N.J. Gaikwad, Bioorgan. Med. Chem. 12 (2004) 2151.
[2] S.H. Kim, H. Son, G. Nam, D.Y. Chi, J.H. Kim, Bioorg. Med. Chem. Lett. 10 (2000) 1143.
[3] L.M. Cañedo, J.A. de la Fuente, C. Gesto, M.J. Ferreiro, C. Jimenez, R. Riguera, Tetrahedron Lett. 40 (1999) 6841.
[4] M.C. Rodríguez-Argüelles, M. Belicchi Ferrari, F. Bisceglie, C. Pelizzi, G. Pelosi, S. Pinelli, M. Sassi, J. Inorg. Biochem. 98 (2004) 313.
[5] P.B. Sreeja, A. Sreekanth, C.R. Nayar, M.R. Prathapachandra Kurup, A. Usman, I.A. Razak, S. Chantrapromma, H.K. Fun, J. Mol. Struct. 645 (2003) 221.
[6] K. Langemann, D. Heineke, S. Rupprecht, K.N. Raymond, Inorg. Chem. 35 (1996) 5663.
[7] A. Ino, A. Murabayashi, Tetrahedron 57 (2001) 1897.
[8] G.L. Mislin, A. Burger, M.A. Abdallah, Tetrahedron 60 (2004) 12143.
[9] C. Wang, M. Zhao, J. Yang, X. Li, S. Peng, Toxicol. Appl. Pharm. 200 (2004) 229.
[10] O. Andersen, Chem. Rev. 99 (1999) 2683.
[11] D. Caiazza, S.F. Lincoln, A.D. Ward, Inorg. Chim. Acta 357 (2004) 716.
[12] M. Dakanali, E.T. Kefalas, C.P. Raptopoulou, Inorg. Chem. 42 (2003) 2531.
[13] P.D.B. Adamis, D.S. Gomes, M.L.C.C. Pinto, A.D. Panek, E.C.A. Eleutherio, Toxicol. Lett. 154 (2004) 81.
[14] S.C. Swain, K. Keusekotten, R. Baumeister, S.R. Stürzenbaum, J. Mol. Biol. 341 (2004) 951.
[15] F.J. Barros-García, A. Bernalte-García, F.J. Higes-Rolando, F. Luna-Giles, R. Pedrero-Marín, E. Viñuelas-Zahínos, Inorg. Chim. Acta 357 (2004) 1457.
[16] F.J. Barros-García, A. Bernalte-García, F.J. Higes-Rolando, F. Luna-Giles, M.A. Maldonado-Rogado, E. Viñuelas-Zahínos, Inorg. Chim. Acta 357 (2004) 3574.
[17] A. Bernalte-García, M.A. Díaz-Diez, F.J. García-Barros, F.J. Higes-Rolando, A.M. Pizarro-Galán, J.D. Martín-Ramos, C. Valenzuela-Calahorro, Polyhedron 16 (1997) 297.
[18] T. Doornbos, H.G. Peer, Recl. Trav. Chim. Pays-Bas. 91 (1972) 711.
[19] Bruker AXS Inc SAINTPLUS, version 6.22 Bruker AXS Inc., Madison, WI, 2001.
[20] Siemens XSCANS, X-ray Single Crystal Analysis System, Siemens Analytical X-ray Instruments Inc., Madison, WI, USA, 1994.
[21] Bruker AXS Inc SADABS, version 2.03 Bruker AXS Inc., Madison, WI, 2001.
[22] G.M. Sheldrick, SHELX-97, Programs for Crystal Structure Analysis, University of Göttingen, Germany, 1997.
[23] L.J. Farrugia, J. Appl. Cryst. 32 (1999) 837.
[24] L.J. Farrugia, J. Appl. Cryst. 30 (1997) 565.
[25] C. Cohen-Addad, Acta Crystallogr. B 38 (1982) 1753.
[26] F.H. Allen, Acta Crystallogr. B 58 (2002) 380.
[27] I.J. Bruno, J.C. Cole, P.R. Edington, M. Kessler, C.F. Macrae, P. McCabe, J. Pearson, R. Taylor, Acta Crystallogr. B 58 (2002) 389.
[28] D. Cremer, J.A. Pople, J. Am. Chem. Soc. 97 (1975) 1354.
[29] A. Bernalte-García, F.J. García-Barros, F.J. Higes-Rolando, F. Luna-Giles, Polyhedron 18 (1999) 2907.
[30] A. Bernalte-García, F.J. García-Barros, F.J. Higes-Rolando, A.M. Pizarro-Galán, C. Valenzuela-Calahorro, Thermochim. Acta 339 (1999) 95.
[31] G. Mille, J.L. Meyer, J. Chouteau, J. Mol. Struct. 50 (1978) 247.
[32] K.C. Patil, J.P. Vital, J. Chem. Soc., Dalton Trans. (1992) 2291.
[33] D.N. Sathayanarayana, D. Nicholls, Spectrochim. Acta 34A (1978) 263.
[34] K.C. Patil, R. Soundararajan, V.R.P. Verneker, Inorg. Chem. 18 (1979) 1969.
[35] R.T. Conley, in: Espectroscopía Infrarroja, Alhambra, Madrid, 1979.
[36] J.R. Ferraro, Low-frequency Vibrations of Inorganic and Coordination Compounds, Plenum Press, New York, 1971.
[37] K. Nakamoto, Infrared and Raman Spectra of Inorganic and Coordination Compound, 5th ed., Wiley, New York, 1997.
[38] A.B.P. Lever, E. Mantovani, B.S. Ramaswamy, Can. J. Chem. 49 (1971) 1957.
[39] C.C. Addison, D. Suttom, Prog. Inorg. Chem. 8 (1967) 195.
[40] B.N. Gaterhouse, S.E. Livingstone, R.S. Nyholm, J. Chem. Soc. (1957) 4222.
[41] M.M. Mostafa, M.A. Khattab, K.M. Ibrahim, Polyhedron 2 (1983) 583.
[42] C. Janiak, S. Deblon, H.P. Wu, M.J. Kolm, P. Küflers, H. Piotrowski, P. Mayer, Eur. J. Inorg. Chem. (1999) 1507.

complexes [24]. In this paper, we report the spectral characteristics of four copper(II) complexes derived from di-2-pyridyl ketone *N*(4)-methyl-*N*(4)-phenylthiosemicarbazone (Hdptsc) (Fig. 1). The crystal structures of two complexes formulated as $[Cu(dptsc)Br]_2$ (**2**) and $[Cu(dptsc)(\mu\text{-}N_3)]_2$ (**3**) are also described.

2. Experimental

2.1. Materials

Di-2-pyridyl ketone (Fluka) was used as received. $CuCl_2 \cdot 2H_2O$, $CuBr_2$, $Cu(OAc)_2 \cdot H_2O$, $Cu(NO_3)_2 \cdot 2.5H_2O$ and NaN_3 were commercial products of higher grade (Merck) and solvents were purified according to standard procedures. Elemental analyses were carried out using a Heraeus Elemental Analyzer and the molar conductance measurements of the complexes were carried out in DMF solvent at 28 ± 2 °C on a Century CC-601 digital conductivity meter with dip type cell and platinum electrode. Approximately 10^{-3} M solutions were used. The magnetic susceptibility measurements were made using a simple Gouy balance at room temperature using mercury tetrathiocyanatocobaltate(II), $Hg[Co(NCS)_4]$ as calibrant. Infrared spectral measurements were done on a Shimadzu DR 8001 series FTIR instrument using KBr pellets for spectra in the region 4000–400 cm^{-1}, and far IR spectra were recorded using polyethylene pellets in the 500–100 cm^{-1} region on a Nicolet Magna 550 FTIR instrument. An Ocean Optics SD 2000 Fiber Optic Spectrometer was used to measure solid-state reflectance spectra in the range 200–900 nm. ^1H NMR spectra were recorded using AMX 400 MHz FT-NMR Spectrometer with $CDCl_3$ as solvent and TMS as the internal standard. EPR spectral measurements were carried out on a Varian E-112 X-band spectrometer using TCNE as standard.

2.2. Synthesis of ligand

The ligand, Hdptsc was synthesized as reported earlier [24]. A solution of di-2-pyridyl ketone (1.84 g, 10 mmol) in 5 ml methanol was treated with *N*(4)-methyl, *N*(4)-phenylthiosemicarbazide (1.81 g, 10 mmol) in 25 ml methanol and refluxed for 2 h. On slow evaporation at room temperature, bright yellow crystals of Hdptsc separated out. These crystals were collected, washed with methanol and dried over P_4O_{10} in vacuo.

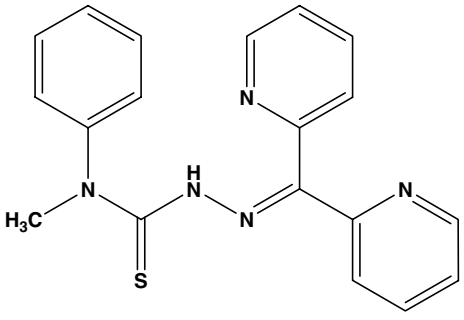


Fig. 1. Structure of Hdptsc.

2.3. Synthesis of $Cu(dptsc)Cl]_2 \cdot 3H_2O$ (**1**)

Methanolic solutions of Hdptsc (0.347 g, 1 mmol) and $CuCl_2 \cdot 2H_2O$ (0.171 g, 1 mmol) were mixed and heated under reflux for 2 h. Dark blue-green crystals of complex **1** were obtained, which were separated, washed with methanol followed by ether and dried over P_4O_{10} in vacuo. Yield: 0.25 g (52%).

2.4. Synthesis of $[Cu(dptsc)Br]_2$ (**2**)

Hdptsc (0.347 g, 1 mmol) was dissolved in methanol (15 ml) and refluxed with a solution of $CuBr_2$ (0.223 g, 1 mmol) in 1:1 methanol–chloroform mixture. Blue crystals separated out, which were filtered, washed with methanol followed by ether and dried in vacuo. Colourless single crystals suitable for X-ray diffraction were grown by slow evaporation of a 1:1:1 solution of methanol, chloroform and dichloromethane of the complex. Yield: 0.175 g (33%).

2.5. Synthesis of $[Cu(dptsc)(\mu\text{-}N_3)]_2$ (**3**)

$Cu(OAc)_2 \cdot H_2O$ (0.199 g, 1 mmol) dissolved in methanol (15 ml) was added to Hdptsc (0.347 g, 1 mmol) and refluxed. NaN_3 (0.0651 g, 1 mmol) was then added to the solution and further refluxed for 3 h. Dark blue crystals of **3** separated out, which were collected and dried in vacuo. Single crystals for X-ray diffraction were grown by slow evaporation of a 1:1:1 solution of methanol, chloroform and dichloromethane of the complex. Yield: 0.35 g (56%).

2.6. Synthesis of $[Cu(dptsc)(NO_3)]_2 \cdot H_2O$ (**4**)

A solution of $Cu(NO_3)_2 \cdot 2.5H_2O$ (0.233 g, 1 mmol) in a methanol–chloroform mixture (20 ml, v/v) was added to Hdptsc (0.347 g, 1 mmol) and refluxed for 2 h. The resulting crystals were washed with methanol, followed by ether and dried in vacuo. Yield: 0.35 g (65%).

2.7. X-ray crystallography

Single crystal X-ray diffraction measurements were carried out on a Bruker Smart Apex CCD diffractometer equipped with a fine-focused sealed tube. The unit cell parameters were determined and the data collections were performed using graphite-monochromated Mo Kα

Table 1
Elemental analyses, colours and molar conductivities of the Cu(II) complexes

Compound	Colour	Composition % (Found/Calc.)			λ_M[a]	μ_{eff}[b] (BM)
		Carbon	Hydrogen	Nitrogen		
$[Cu(dptsc)Cl]_2 \cdot 3H_2O$ (**1**)	Blue	48.54 (48.30)	3.65 (4.05)	14.71 (14.82)	32	1.63
$[Cu(dptsc)Br]_2$ (**2**)	Blue	46.63 (46.58)	3.32 (3.29)	14.35 (14.30)	27	2.24
$[Cu(dptsc)(\mu\text{-}N_3)]_2$ (**3**)	Blue	50.53 (50.49)	3.62 (3.57)	24.82 (24.79)	27	1.98
$[Cu(dptsc)(NO_3)]_2 \cdot H_2O$ (**4**)	Blue	46.67 (47.44)	3.45 (3.56)	17.98 (17.47)	24	2.56

[a] Molar conductivity, 10^{-3} M DMF at 298 K.
[b] Magnetic susceptibility.

($\lambda = 0.71073$ Å) radiation. Both the crystals were found to be monoclinic with a $P2_1/c$ space group. Least square refinements of 17855 and 17083 reflections were done for compounds **2** and **3**, respectively. The data collected were reduced using the SAINT program [25]. The trial structures were obtained by direct methods [26] using SHELXS-86, which revealed the position of all non-hydrogen atoms and refined by full-matrix least squares on F^2 (SHELXL-97) [27] and the graphic tool was DIAMOND for windows [28]. All non-hydrogen atoms were refined anisotropically, while the hydrogen atoms were treated with a mixture of independent and constrained refinements.

3. Results and discussion

3.1. Synthesis of complexes

Compounds **1**, **2** and **4** were prepared by direct reaction between the ligand and the corresponding metal salts, while compound **3** was prepared by the displacement of the acetate in $Cu(OAc)_2 \cdot H_2O$ by the azide ion. The complexes are mostly blue or blue-green coloured, as expected with thiosemicarbazone coordination, resulting from the ligand to copper charge transfer bands [29]. Elemental analyses (C, H, N) data (Table 1) of the complexes are consistent with the 1:1:1 ratio of metal:thiosemicarbazone:gegenion and also reveals that compounds **1** and **4** are hydrated. Conductivity measurements in DMF solution (10^{-3} M) indicate that all the complexes are non-electrolytes suggesting anionic coordination to the metal centre.

3.2. Crystal structures of $[Cu(dptsc)Br]_2$ and $[Cu(dptsc)(\mu\text{-}N_3)]_2$

Structural studies of compound **2** reveal a three-dimensional copper-thiosemicarbazone network consisting of two units of [Cudptsc] with a distorted square pyramidal geometry around Cu(II), with the basal plane

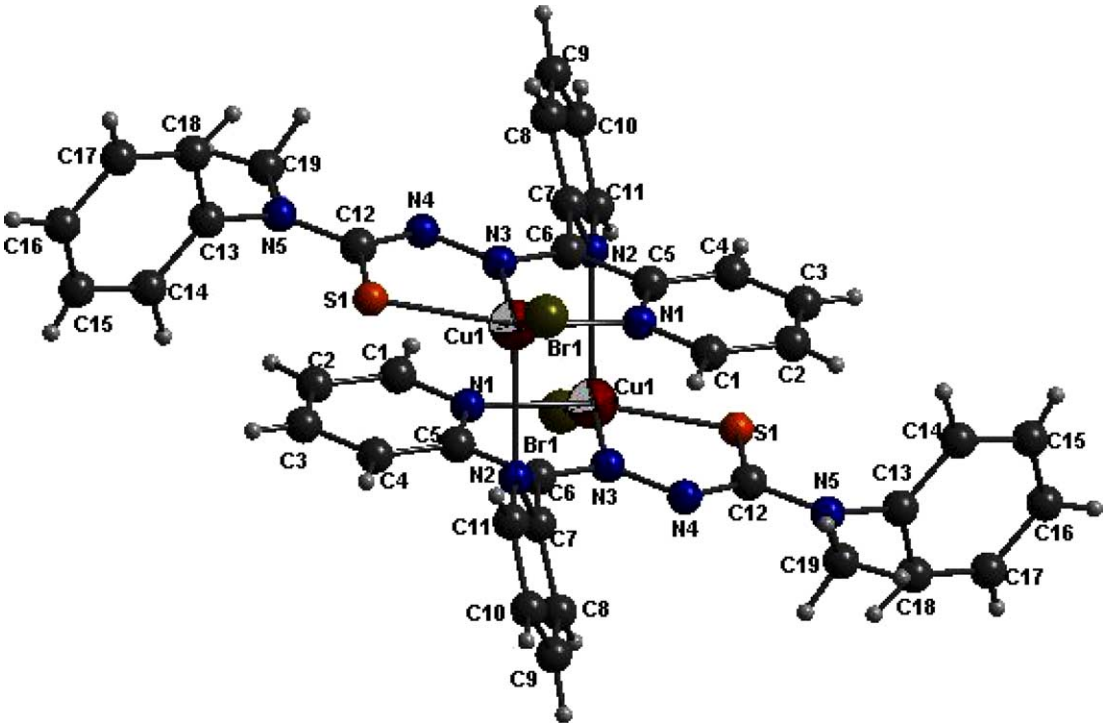


Fig. 2. Molecular structure of complex **2**.

consisting of one of the pyridyl nitrogens, azomethine nitrogen, thiolate sulfur and the bromine atom, while the pyridyl nitrogen of the second ligand unit occupies the apical position. A labelled representation of **2** is depicted in Fig. 2 along with the structural data refinements (Table 2) and selected bond distances and angles (Table 3). The bite angles N(1)–Cu(1)–N(3) (80.05°), Br(1)–Cu(1)–N(1) (96.81°), Br(1)–Cu(1)–S(1) (95.22°) and S(1)–Cu(1)–N(3) (83.60°) also support the distortion from square pyramidal geometry. The basal plane consisting of N(1), N(3), Br(1), S(1) and Cu(1) shows a maximum mean deviation of −0.3411 Å at N3. The Cu(II) atom is deviated at a distance of 0.3002 Å out of the mean plane towards the apical position. The thiosemicarbazone moiety comprising of N(5), C(12), S(1), N(4) and N(3) atoms and the pyridyl ring, Cg(3), make dihedral angles of 18.73° and 18.58°, respectively, with the metal chelate CuN_2BrS square plane. The loss of the proton bound to N(4) in Hdptsc produces a negative charge, which is delocalized on the thiosemicarbazone moiety. Delocalization of electron density over the entire thiosemicarbazone moiety is evidenced by the little marginal change in the C(6)–N(3) and N(3)–N(4) bond distances in **2**, compared to that of the uncomplexed thiosemicarbazone [30]. The bond distance S(1)–C(12) is longer and C(12)–N(4) is shorter than the corresponding values in the free ligand, which support thiolate formation in the ligand on complexation [31].

The structural pattern of the discrete binuclear complex, $[Cu(dptsc)(\mu\text{-}N_3)]_2$ (**3**) is best viewed as two end-on $\mu_{1,1}$-azido bridged quasi-square pyramids. Each *Hdptsc* unit acts as a tridentate chelate, coordinating through one of the pyridyl nitrogens, azomethine nitrogen and the thiolate sulfur to a single Cu(II) center which is involved in a $\mu_{1,1}$-azido bridging to an identical coordination network, thus materializing a penta-coordinated environment (Fig. 3). The base of each distorted square pyramidal unit is occupied by N(1), N(3), N(6) and S(1) atoms, with the apical position occupied by the N(6) atom of the second azido group. Each azido ligand functions as an electron donor to the coordination network through an end-on azido bridging mode. The centrosymmetric nature of the structure is revealed by an inversion center with the two azido-bridged angles, Cu–N–Cu (92.94°) and N–Cu–N (87.06°), being the same in both the units. The intramolecular Cu–Cu distance is found to be 3.303 Å and the axial Cu(1)–N(6)

Table 2
Crystal data, data collection and structure refinement parameters for $[Cu(dptsc)Br]_2$ and $[Cu(dptsc)(N_3)]_2$

Parameters	$[Cu(dptsc)Br]_2$	$[Cu(dptsc)(N_3)]_2$
Empirical formula	$C_{19}H_{16}BrCuN_5S$	$C_{19}H_{16}CuN_8S$
Formula weight (M)	489.88	452.00
Temperature, T (K)	293(2)	293(2)
Wavelength (Mo Kα) (Å)	0.71073	0.71073
Crystal system	monoclinic	monoclinic
Space group	$P2_{1/c}$	$P2_{1/c}$
Lattice constants		
a (Å)	9.029(4)	12.845(8)
b (Å)	17.279(8)	12.512(7)
c (Å)	13.217(6)	13.014(8)
α (°)	90.00	90
β (°)	97.228(8)	107.753(10)
γ (°)	90.00	90.00
Volume, V (Å^3)	2045.6(16)	1992(2)
Z	4	4
Calculated density, ρ (Mg m^{-3})	1.591	1.507
Absorption coefficient, μ (mm^{-1})	3.136	1.224
$F(0\,0\,0)$	980	924
Crystal size (mm)	$0.41 \times 0.13 \times 0.11$	$0.30 \times 0.12 \times 0.09$
θ Range for data collection	2.36–27.98	1.66–28.04
Limiting indices	$-11 \leqslant h \leqslant 11$, $-22 \leqslant k \leqslant 22$, $-17 \leqslant l \leqslant 16$	$-16 \leqslant h \leqslant 16$, $-16 \leqslant k \leqslant 16$, $-16 \leqslant l \leqslant 16$
Reflections collected	17 855	17 083
Unique reflections	4877 [R_{int} = 0.0207]	4682 [R_{int} = 0.0265]
Completeness to θ (%)	27.98 (99.2)	28.04 (97.1)
Maximum and minimum transmission	0.7242 and 0.3596	0.8978 and 0.7102
Refinement method	full-matrix least-squares on F^2	full-matrix least-squares on F^2
Data/restraints/parameters	4877/0/296	4682/0/326
Goodness-of-fit on F^2	1.025	1.074
Final R indices [$I > 2\sigma(I)$]	R_1 = 0.0431, wR_2 = 0.1202	R_1 = 0.0375, wR_2 = 0.0859
R indices (all data)	R_1 = 0.0558, wR_2 = 0.1296	R_1 = 0.0490, wR_2 = 0.0908
Largest difference peak and hole (e Å^{-3})	1.455 and −0.538	0.418 and −0.218

Table 3
Comparison of selected bond lengths (Å) and bond angles (°) of Hdptsc, $[Cu(dptsc)Br]_2$ and $[Cu(dptsc)(N_3)]_2$

	Hdptsc	$[Cu(dptsc)Br]_2$	$[Cu(dptsc)(N_3)]_2$
S(1)–C(12)	1.668	1.721	1.744
N(3)–C(6)	1.295	1.298	1.299
N(3)–N(4)	1.361	1.354	1.370
N(4)–C(12)	1.377	1.343	1.326
N(5)–C(12)	1.350	1.344	1.354
Cu(1)–S(1)		2.2565	2.2603
Cu(1)–N(1)		2.019	2.027
Cu(1)–N(3)		1.979	1.964
Cu(1)–N(2)		2.352	
Cu(1)–Br(1)		2.4134	
Cu(1)–N(6)			1.9561
Cu(1)–N(6)a			2.5628
C(6)–N(3)–N(4)	120.87	118.9	120.36
N(3)–N(4)–C(12)	118.72	111.1	111.68
N(5)–C(12)–N(4)	113.74	115.6	115.02
N(5)–C(12)–S(1)	123.48	118.9	119.09
N(4)–C(12)–S(1)	122.77	125.4	124.89
N(1)–Cu(1)–N(3)		80.05	80.56
S(1)–Cu(1)–N(1)		163.28	160.88
S(1)–Cu(1)–N(3)		83.60	84.95
S(1)–Cu(1)–N(2)		100.88	
N(2)–Cu(1)–N(1)		89.00	
N(2)–Cu(1)–N(3)		113.93	
Br(1)–Cu(1)–S(1)		95.22	
Br(1)–Cu(1)–N(1)		96.81	
Br(1)–Cu(1)–N(2)		97.60	
Br(1)–Cu(1)–N(3)		148.15	
S(1)–Cu(1)–N(6)			100.81
S(1)–Cu(1)–N(7)			81.74
S(1)–Cu(1)–N(6)a			104.53
N(1)–Cu(1)–N(6)			94.28
N(1)–Cu(1)–N(7)			112.12
N(1)–Cu(1)–N(6)a			87.77
N(3)–Cu(1)–N(6)			173.80
N(3)–Cu(1)–N(7)			166.63
N(3)–Cu(1)–N(6)a			89.29
N(6)–Cu(1)–N(7)			19.40
N(6)–Cu(1)–N(6)a			87.06
N(7)–Cu(1)–N(6)a			95.25
Cu(1)–N(6)–Cu(1)a			92.94

distance is found to be 2.5628 Å. The nitrogen atoms N(3) and N(6) are closer to the Cu(II) center with bond distances Cu(1)–N(3) (1.964 Å) and Cu(1)–N(6) (1.956 Å) compared to Cu(1)–N(1) (2.027 Å) and Cu(1)–S(1) (2.2603 Å). A maximum deviation of 0.1649 Å at N(1) is revealed at the base of the square pyramid with the central Cu(II) atom positioned 0.0689 Å above the mean plane. The pyridyl ring Cg(1) is less deviated from the basal plane (the dihedral angle between the two least square planes is 3.00°), when compared to the thiosemicarbazone moiety, which deviates more, at a dihedral angle of 13.51° from the basal CuN_3S plane. The dimer is located on an inversion centre and the bridging Cu_2N_2 network is perfectly planar. Similar to **2** above, the C(6)–N(3) and N(3)–N(4) bond distances in **3** reveal extensive delocalization over the entire binuclear coordination framework.

The diverse π–π stacking, C–H---π and ring–metal interactions give rise to polymeric chains in the unit cells of **2** and **3** (Figs. 4 and 5). The shortest π–π interactions are perceived at 3.3631 Å for $Cg(2)–Cg(2)^{i}$ [i = $1-x$, $1-y$, $1-z$] in **2**. Ring–metal interactions $Cg(2)---Cu(1)^{iii}$ [iii = x, $1/2-y$, $1/2+z$] are observed in **3** at a distance of 3.774 Å. Two C–H---π interactions each are shown in the unit cells of **2** and **3**. They are $C(8)–H(8)---Cg(1)^{iv}$ [d_{H---Cg} = 3.0853 Å; iv = $-1+x$, y, z] and $C(10)–H(10)---Cg(5)^{v}$ [d_{H---Cg} = 2.6471 Å; v = $-1+x$, $1/2-y$, $-1/2+z$] for **2** and $C(10)–H(10)---Cg(3)^{vi}$ [d_{H---Cg} = 2.9888 Å; vi = $1-x$, $-y$, $1-z$] and $C(15)–H(15)---Cg(2)^{vii}$ [d_{H---Cg} = 2.9537 Å; v = $1-x$, $-1/2+y$, $1/2-z$] for compound **3**.

3.3. Spectrochemical studies

The ν_a(N–H) vibrations of the imino group are observed at ca. 3428 cm^{-1} in the IR spectrum of Hdptsc. In the ^1H NMR spectrum, the N(4)H resonance, at a downfield value of 14.68 ppm, is consistent with the intramolecular N(4)–H---N(2) hydrogen bonding revealed by its crystal structure [30]. A strong band at 1580 cm^{-1} in the IR spectrum of Hdptsc corresponds to ν(N3–C6) stretching, which suffers a positive shift on complexation due to a change in bond order [31,32] (Table 4). The absence of a ν(S–H) band around 2565 cm^{-1} supports the predominant thione form of the ligand in the solid state, while the lack of an (N–H) stretching in the spectra of the complexes endorses the ligand coordination to Cu(II) ion in the deprotonated thiolate form. A medium band around 644 cm^{-1} indicates out-of-plane pyridyl ring vibrations ρ(py) of Hdptsc, which suffers a positive shift in all complexes. The IR bands observed at 1360 and 793 cm^{-1} in the ligand have significant contributions from C=S stretching and bending vibrations, and are shifted to lower wavenumbers on complexation [33]. Solid state reflectance spectrum of the ligand shows an absorption maximum in the region 37000 cm^{-1} attributed to intra-ligand $\pi^* \leftarrow \pi$ transitions of the pyridyl ring and imine function of the thiosemicarbazone moiety (Table 5). The peaks at ca. 27 000 and 30 030 cm^{-1} indicate $\pi^* \leftarrow$ n transitions of the thioamide function, which are shifted to higher energy values upon complexation. As expected, the Cu(II) ← S charge transfer transitions [34] are observed at ca. 23 000 cm^{-1}. For all the compounds, the peaks observed at ca. 17 000 and 14 000 cm^{-1} are assigned to d_{xz}, $d_{yz} \leftarrow d_{x^2-y^2}$ and $d_z^2 \leftarrow d_{x^2-y^2}$ transitions in an elongated square based pyramidal geometry [35,36]. Magnetic moment values for the bromo (**2**) and nitrato (**4**) complexes are greater than the spin only value for a dimeric system, since a larger Cu–Cu distance, revealed by the crystal structure in **2**, render the electron spins parallel resulting

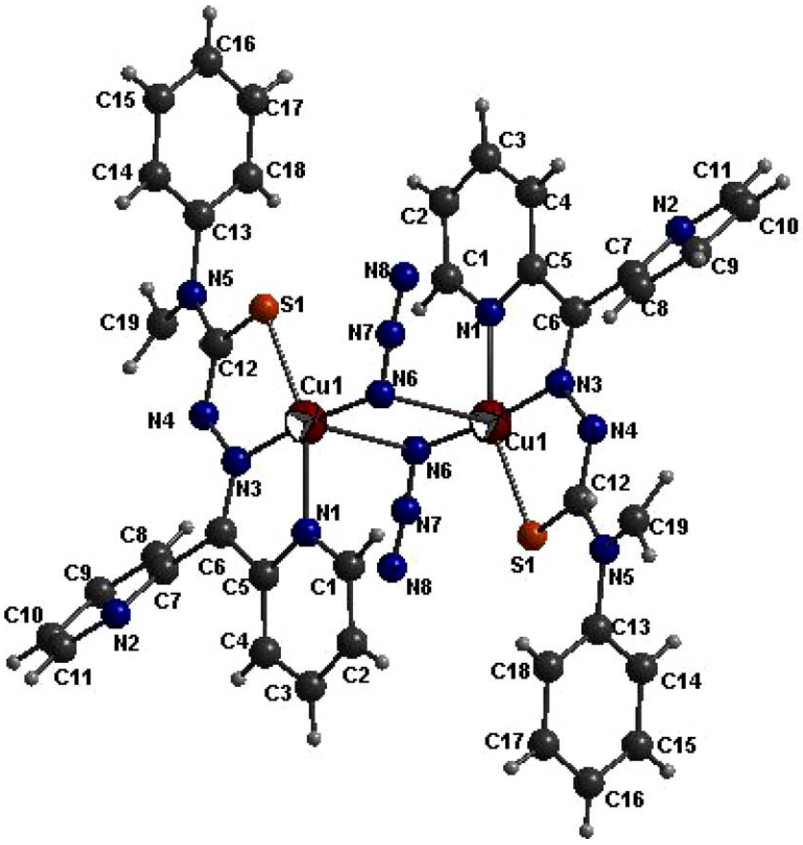


Fig. 3. Molecular structure of complex **3**.

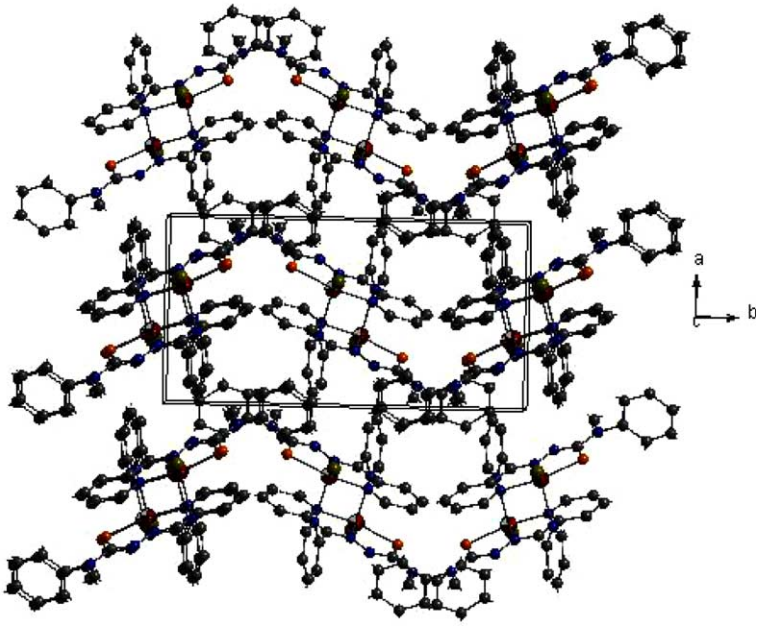


Fig. 4. Molecular packing diagram of **2** viewed down the '*c*' axis.

in a high magnetic moment. The azido (**3**) and the chloro complex (**1**) show magnetic moment values close to the spin only value per copper for a dimer, suggesting the absence of spin–orbit coupling and anti-ferromagnetic interactions. A medium band at 245 cm^{-1} in the IR spectrum of **2** is indicative of the coordinated bromine.

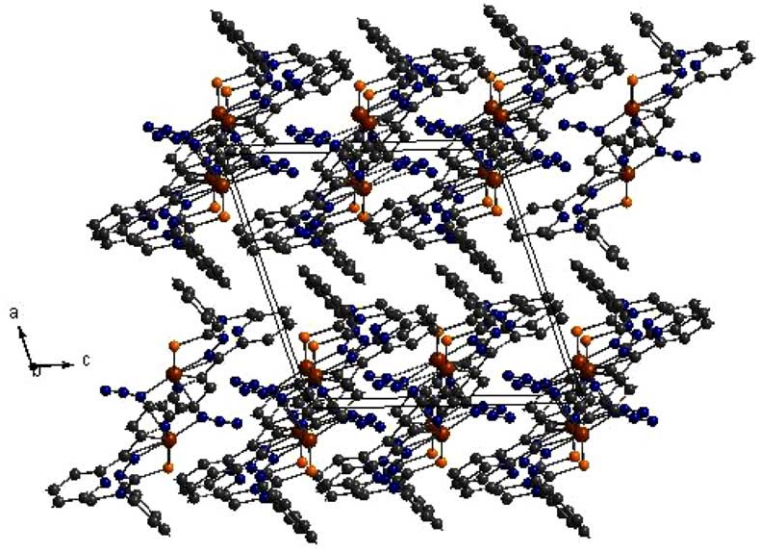


Fig. 5. Molecular packing diagram of **3** viewed down the '*b*' axis.

Table 4
Selected IR bands (cm^{-1}) with tentative assignments for the complexes

Compound	ν(C=N) + ν(N=C)	ν(N–N)	ν(C=S)	δ(C=S)	δ (o.p)	ν(Cu–N)	ν(Cu–S)	ν(Cu–N) py	ν(Cu–X$^{\#}$)
Hdptsc	1580 s	1051 w	1360 s	793 m	644 m				
$[Cu(dptsc)Cl]_2 \cdot 3H_2O$ (**1**)	1592 m	1004 w	1305 m	781 w	683 w	419 s	325 s	353 m	303 m
$[Cu(dptsc)Br]_2$ (**2**)	1590 w	1002 w	1306 m	781 m	692 m	419 s	328 m	350 m	245 m
$[Cu(dptsc)(\mu\text{-}N_3)]_2$ (**3**)	1594 m	1011m	1310 sh	778 w	699 m	444 s	332 sh	351 m	315 m
$[Cu(dptsc)(NO_3)]_2 \cdot H_2O$ (**4**)	1592 w	1005 m	1308 m	775 m	692 m	416 s	325 m	355 m	444 w

Table 5
Electronic spectral data (cm^{-1}) of Hdptsc and the complexes

Compound	d–d	C T	$\pi^* \leftarrow n$	$\pi^* \leftarrow \pi$
Hdptsc			26882 s, 30030 sh	 37543 s, 32787 sh
$[Cu(dptsc)Cl]_2 \cdot 3H_2O$ (**1**)	17636 sh, 14084 sh	24814 sh, 23201 s	32154 s 30395 b	37313 s
$[Cu(dptsc)Br]_2$ (**2**)	17699 sh, 14556 sh	28169 sh 23310 sh, 22831 s,b	 32467 s, 31648 sh	 37453 s
$[Cu(dptsc)(\mu\text{-}N_3)]_2$ (**3**)	17211 sh, 144450 sh	26882 sh, 22676 s	32573 sh, 30864 sh	
$[Cu(dptsc)(NO_3)]_2 \cdot H_2O$ (**4**)	17007 sh, 14104 sh	23095 s,b, 16949 sh	 30487 s,b	 38314 sh

Compound **3** exhibits strong bands at 2041 and 1310 cm^{-1} corresponding to the ν_a and ν_s of the coordinating azido group [37]. The prominent bands at 699 cm^{-1} and a weak band at 444 cm^{-1}, assigned to δ(NNN) and ν(Cu–N), suggest a non-linear Cu–N–N–N bond [34]. Bands corresponding to ν_1, ν_2, ν_4 at 1010, 1284 and 1385 cm^{-1}, respectively, are observed in **4** whereas a $\nu_1 + \nu_4$ combination band at ca. 1750 cm^{-1} indicates monocoordinated nitrato group [37]. Magnetic moment measurement of **4** supports its potential dimeric disposition where the magnetic susceptibility value is found to be higher than that of a coupled Cu(II) ion pair, which is presumed with the association of small amounts of paramagnetic impurities in the compounds [38].

3.4. Electron paramagnetic resonance spectra

EPR spectra of the samples with 100-kHz field modulation at room temperature were recorded in the X-band. An isotropic spectrum with a broad signal is obtained for **3** and the remaining complexes gave axial spectra in the solid state at room temperature. The copper(II) ion, with a d^9 configuration, has an effective spin of $S = 1/2$ and is associated with a spin angular momentum $m_s = \pm 1/2$, leading to a doubly degenerate spin state in the absence of a magnetic field. In a magnetic field the degeneracy is lifted between these states and the energy difference between them is given by $E = h\nu = g\beta H$, where h is Planck's constant, ν is the frequency, g is the Lande's splitting factor (equal to 2.0023 for a free electron), β is the Bohr magneton and H is the magnetic field. For the case of a $3d^9$ copper(II) ion, the appropriate spin Hamiltonian assuming a B_{1g} ground state [36] is given by:

$$\hat{H} = \beta[g_{\parallel}H_zS_z + g_{\perp}(H_xS_x + H_yS_y)] + A_{\parallel}I_zS_z + A_{\perp}(I_xS_x + I_yS_y)$$

The EPR spectra of the compounds **1**, **2** and **4** in the polycrystalline state at 298 K show typical axial spectra with slightly different $g_{\parallel}$ and $g_{\perp}$ features. The variations in g values indicate that the geometry of the compound is affected by the nature of the coordinating gegenions (Table 6). The spectrum of compound **3** in the polycrystalline state (298 K) shows a broad signal indicating only one g value, 2.0638, due to dipolar broadening and enhanced spin lattice relaxation.

The geometric parameter G calculated as $G = (g_{\parallel} - 2.003)/(g_{\perp} - 2.003)$ is a measure of the exchange interaction between copper centers in the polycrystalline compound. It is perceived that, if $G > 4$, the exchange interaction is negligible and vice versa in the complexes. All complexes with $g_{\parallel} > g_{\perp} > 2.003$ and G values falling within the range of 2–4 are consistent with a $d_{x^2-y^2}$ ground state in a square planar or square pyramidal geometry. The g values are found to be lower than those reported for copper(II) complexes prepared from a substituted 2-benzoylpyridine thiosemicarbazone [39], indicating a stronger metal-ligand bonding. Absence of half field signals for the compounds reinforces the assumption of very weak super exchange interactions.

The solution spectra of complexes **1** and **4** were recorded in DMF at 298 K. They are isotropic in nature with well-resolved four hyperfine lines. The hyperfine splitting is due to the interaction of the electron spin with the copper nuclear spin (^{65}Cu, $I = 3/2$). There are indications of nitrogen superhyperfine splitting in the high field component in some spectra. The A_{iso} and g_{iso} values show variations in **1** and **4**, their values indicating dissimilarity in bonding in the complexes.

The spectra of complexes **1**, **3** and **4** in DMF at 77 K show rhombic features with three g values g_1, g_2, and g_3 where $g_3 > g_2 > g_1$. It is observed that the g values for complexes in the solid state at 298 K and in DMF at 77 K are not much different from each other, hence the geometry around the copper(II) ion is unaffected on cooling the solution to liquid nitrogen temperature. In the low field region, the chloro and nitrato complexes show six hyperfine lines that are moderately resolved and perpendicular features overlapping with seventh one suggesting a dimeric state with two copper centers. The g_3 values of the complexes are less than 2.3 and they assign considerable covalent character to the M–L bonds [40]. For the compounds **1**, **3** and **4**, the lowest g value (g_1) is less than 2.04 indicating a compressed rhombic symmetry with all axes aligned parallel and is consistent with distorted trigonal bipyramidal stereochemistry or a compressed axial symmetry or rhombic symmetry with slight misalignment of the axes. In the spectra with $g_3 > g_2 > g_1$, rhombic spectral values $R = (g_2 - g_1)/(g_3 - g_2)$ may be significant. If $R > 1$, a predominant d_{z^2} ground state is present. If $R < 1$, a predominant $d_{x^2-y^2}$ ground state is present and when $R = 1$, then the ground state is approximately an equal mixture of d_{z^2} and $d_{x^2-y^2}$, the structure is intermediate between square planar and trigonal bipyramidal geometries. All the present complexes have values $R < 1$ suggesting a distorted square based pyramidal geometry with a $d_{x^2-y^2}$ ground state. These observations are consistent with g values of the corresponding complexes in the polycrystalline state at 298 K and further supports the distorted square pyramidal geometry around copper(II) ion in these complexes.

Spin Hamiltonian parameters are calculated from the frozen state EPR and electronic spectra (Table 7). The

Table 6
EPR spectral assignments (experimental) for the copper(II) complexes

Compound	Solid (298 K)			DMF(298 K)			DMF (77 K)					
	$g\|\|$	g_{iso}	$g_{\perp}$	g_{iso}	A_{iso}	A_N	$g_3/g\|\|$	g_2	$g_1/g_{\perp}$	g_{av}	$A\|\|$[a]	$A_{\perp}(N)$[a]
$[Cu(dptsc)Cl]_2 \cdot 3H_2O$ (**1**)	2.1422		2.0576	2.0446	43.33	15	2.2224	2.0597	1.9808	2.0876	63.33	11.66
$[Cu(dptsc)Br]_2$ (**2**)	2.1349		2.0602				2.1423		2.0612	2.0882		
$[Cu(dptsc)(\mu\text{-}N_3)]_2$ (**3**)		2.0638					2.1961	2.0631	1.9868	2.0820	175	22
$[Cu(dptsc)(NO_3)]_2 \cdot H_2O$ (**4**)	2.1484		2.0384	2.1047	48.33	20	2.1816	2.0341	1.9723	2.0627		

[a] A values in 10^{-4} cm^{-1}.

Table 7
Spin Hamiltonian and orbital reduction parameters of the complexes **1** and **4**

Compound	$[Cu(dptsc)Cl]_2 \cdot 3H_2O$ (**1**)	$[Cu(dptsc)(NO_3)]_2 \cdot H_2O$ (**4**)
$g_{\|/gzz}(g_3)$	2.2224	2.1816
$g_{yy}(g_2)$	2.0597	2.0341
$g_{xx}(g_1)$	1.9808	1.9723
$g_{av\ (77k)}$	2.0876	2.0627
g_{av} (solid)	2.0858	2.0750
R[a]	0.404	0.98
$K_{\|}$	0.6686	0.6357
$K_{\perp}$	0.6534	0.6030

[a] $R = (g_2 - g_1)/(g_3 - g_2)$.

orbital reduction factors were estimated using the following expressions [41].

$$K_{\|}^2 = (g_{\|} - 2.0023)\Delta E(d_{xy} - d_{x^2-y^2})/8\lambda_0,$$

$$K_{\perp}^2 = (g_{\perp} - 2.0023)\Delta E(d_{xz,yz} - d_{x^2-y^2})/2\lambda_0,$$

where λ_0 is the spin–orbit coupling constant and has a value of $-828\ cm^{-1}$ for Cu(II) d^9 systems.

According to Hathaway [42], $K_{\|} = K_{\perp} = 0.77$ for pure σ bonding and $K_{\|} < K_{\perp}$ for in-plane bonding, while for out-of-plane bonding $K_{\|} > K_{\perp}$. It is seen that for complexes **1** and **4** $K_{\|} > K_{\perp}$, indicating stronger out-of-plane π bonding.

4. Supplementary data

Crystallographic data for structural analysis has been deposited with the Cambridge Crystallographic Data center, CCDC 231110 for compound $[Cu_2(dptsc)_2Br_2]$ (**2**) and CCDC 231109 for compound $[Cu_2(dptsc)_2(N_3)_2]$ (**3**). Copies of this information may be obtained free of charge from The Director, CCDC, 12 Union Road, Cambridge, CB2 IEZ, UK (fax: +44-1223-336-033; e-mail: deposit@ccdc.cam.ac.uk or http://www.ccdc.cam.ac.uk).

Acknowledgements

The authors are thankful to the Regional Sophisticated Instrumentation Center, CDRI, Lucknow, India, for the elemental analysis and Sophisticated Instruments Facility, IISc Bangalore for NMR measurements.

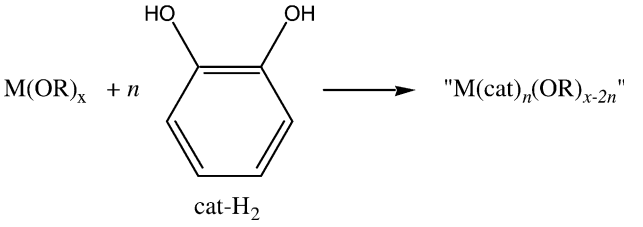
References

[1] S.P.J. Albracht, Biochim. Biophys. Acta 111 (1993) 317.
[2] D.L. Klayman, J.P. Scovill, J.F. Bartosevich, J. Bruce, J. Med. Chem. 26 (1983) 35, and references therein.
[3] G.Z. Bahr, Allg. Chem. 268 (1952) 351A.
[4] G.Z. Bahr, Allg. Chem. 273 (1952) 325A.
[5] A.G. Quiroga, J.M. Perez, E.I. Montero, D.X. West, C. Alonso, C.N. Ranninger, J. Inorg. Biochem. 75 (1999) 293.
[6] F.A. French, E.J. Blanz Jr., J. Med. Chem. 9 (1996) 585.
[7] A.S. Dobek, D.L. Klayman, E.T. Dickson, J.P. Scovill, E.C. Tramont, Antimicrob. Agents Chemother. 18 (1980) 27.
[8] D.L. Klayman., A.J. Lin, J.W. McCall, J. Med. Chem. 34 (1991) 1422.
[9] C. Shipman Jr., H. Smith, J.C. Drach, D.L. Klayman, Antiviral Res. 6 (1986) 197.
[10] P.J. Blower, T.C. Castle, A.R. Cowley, J.R. Dilworth, P.S. Donnelly, E. Labisbal, F.E. Sowrey, S.J. Teat, M.J. Went, J. Chem. Soc., Dalton Trans. (2003) 4416.
[11] R.I. Maurer, P.J. Blower, J.R. Dilworth, C.A. Reynolds, Y. Zheng, G.E.D. Mullen, J. Med. Chem. 45 (2002) 1420.
[12] P. Bindu, M.R.P. Kurup, T.R. Satyakeerthy, Polyhedron 18 (1999) 321.
[13] R.P. John, A. Sreekanth, M.R.P. Kurup, A. Usman, I.A. Razak, H.K. Fun, Spectrochim. Acta 59A (2003) 1349.
[14] M.R.P. Kurup, M. Joseph, Synth. React. Inorg. Met.-Org. Chem. 33 (2003) 1275.
[15] A. Sreekanth, S. Sivakumar, M.R.P. Kurup, J. Mol. Struct. 655 (2003) 47.
[16] A. Sreekanth, U.L. Kala, C.R. Nayar, M.R.P. Kurup, Polyhedron 23 (2004) 41.
[17] A. Sreekanth, M.R.P. Kurup, Polyhedron 23 (2004) 969.
[18] C. Duan, B. Wu, T.C. Mak, J. Chem. Soc., Dalton Trans. (1996) 3485.
[19] C. Duan, X. You, T.C. Mak, Acta Crystallogr. C54 (1935) 1935.
[20] C. Duan, X. You, T.C. Mak, Acta Crystallogr. C54 (1935) 1937.
[21] J.K. Swearingen, D.X. West, Transition Met. Chem. 26 (2001) 252.
[22] J.K. Swearingen, W. Kaminsky, D.X. West, Transition Met. Chem. 27 (2002) 724.
[23] A. Usman, I.A. Razak, S. Chantrapromma, H.K. Fun, V. Philip, A. Sreekanth, M.R.P. Kurup, Acta Crystallogr. C58 (2002) 0652.
[24] V. Philip, V. Suni, M.R.P. Kurup, M. Nethaji, Polyhedron 23 (2004) 1225.
[25] Siemens, SMART and SAINT, Area Detector Control and Integration Software, Siemens Analytical X-ray Instruments Inc., Madison, Wisconsin, USA, 1996.
[26] G.M. Sheldrick, Acta Crystallogr. A46 (1990) 467.
[27] G.M. Sheldrick, SHELXS-97 Program for the Solution of Crystal Structures, University of Göttingen, Göttingen, Germany, 1997.
[28] K. Brandenburg, H. Putz, DIAMOND version 3.0, Crystal Impact, GbR, Postfach 1251, D-53002 Bonn, Germany, 2004.
[29] B.N. Figgis, Introduction to Ligand Field, Wiley Interscience, New York, 1976.
[30] V. Philip, V. Suni, M.R.P. Kurup, Acta Crystallogr. C60 (2004) o856.
[31] B.S. Garg, M.R.P. Kurup, S.K. Jain, Y.K. Bhoon, Transition Met. Chem. 16 (1991) 111.
[32] M.J.M. Campbell, Coord. Chem. Rev. 15 (1975) 279.
[33] R. Mayer, in: M. Jansen (Ed.), Organosulfur Chemistry, Interscience, New York, 1967.
[34] R.P. John, A. Sreekanth, M.R.P. Kurup, S.M. Mobin, Polyhedron 21 (2002) 2515.
[35] B.J. Hathaway, A.A.G. Tomlinson, Coord. Chem. Rev. 5 (1970) 24.

[36] M.A. Ali, M.T.H. Tarafdar, J. Inorg .Nucl .Chem. 39 (1977) 1785.
[37] K. Nakamoto, Infrared and Raman Spectra of Inorganic and Coordination Compounds, 5th ed., Wiley, New York, 1997.
[38] Y. Journaux, J. Sletten, O. Kahn, Inorg. Chem. 24 (1985) 4063.
[39] A. Sreekanth, M.R.P. Kurup, Polyhedron 22 (2003) 3321.
[40] D. Kivelson, R. Neiman, J. Chem. Phys. 35 (1961) 149.
[41] K.D. Karlin, J. Zubieta, Copper Coordination Chemistry – Biological and Inorganic Perspectives, Adenine Press, New York, 1983.
[42] B.J. Hathaway, G. Wilkinson, R.D. Gillard, J.A. McCleverty (Eds.), Comprehensive Coordination Chemistry, Pergamon, Oxford, 1987.

esterification that causes uncontrolled reactivity, forming larger clusters [5–7]. To circumvent this, we have investigated alternative polydentate alcohol ligands [8].

From the commercially available ligands of interest, we have begun an investigation of the bidentate catechol (cat-H_2, Eq. (1)). Catechol is of interest since it has a number of applications ranging from biology, electrochemistry and catalytic investigations. In addition, it is reported that transition metal species that utilize the cat ligand favor chelation over a bridging mode of bonding. This will allow us to selectively reduce the more easily hydrolyzable monodentate ligands and thus garner control over the condensation process of these very reactive species. The metal cations we are interested in involve Group 4 and 5 cations due to their wide spread use in materials production.



(1)

We undertook the synthesis and characterization of Group 4 and 5 metal alkoxides derivatized with cat-H_2 (see Eq. (1)). Since, literature reports indicate that the fully substituted species could not be isolated [9–11], we chose to investigate the highest degree of substitution we could invoke. Therefore, two equivalents of cat-H_2 were reacted with the following alkoxides [Ti(μ-ONep)-(ONep)$_3$]$_2$ [12] (ONep = OCH_2CMe_3), [Zr(μ-OPr^i)(ONep)$_3$ · HONep]$_2$ [13] (OPr^i = $OCHMe_2$), $Hf(OEt)_4$ (OEt = OCH_2Me), and three equivalents with $M(OEt)_5$ (M = Nb or Ta). The resulting modified precursors were structurally identified as $Ti_3(\mu_3\text{-}O)(\mu\text{-cat})_3(cat)(cat\text{-}H)_2$ (**1**), $Zr_4(\mu_4\text{-}O)(\mu\text{-cat})_6(\mu\text{-cat-}H)_2(py)_4$ (**2**), $Hf_4(\mu_4\text{-}O)$-$(\mu\text{-cat})_6(\mu\text{-cat-}H)_2(py)_4$ (**3**), $M(cat)_2(cat\text{-}H)(py)$ (M = Nb (**4**); Ta (**5**)). The synthesis and characterization of these compounds in relationship to existing catechol derivatives is presented in the following discussion. In addition, the utility of these precursors as potential nanoparticle precursors to Group 4 and 5 ceramic materials was undertaken using **1**–**5**. Details of the process to synthesize these materials are also presented.

2. Experimental

All reactions were performed under a dry, inert atmosphere using standard Schlenk line and glovebox techniques. The following chemicals were purchased from Aldrich and used without further purification: cat-H_2, HONep, Ti(OPr^i)$_4$, Zr(OPr^i)$_4$ · HOPr^i, $Hf(OEt)_4$, $M(OEt)_5$ (M = Nb, Ta). All solvents used were used as received as anhydrous solvents (sure-sealed). [Ti(μ-ONep)-(ONep)$_3$]$_2$ [12] and [Zr(μ-OPr$_i$)(ONep)$_3$(HONep)]$_2$ [13] were synthesized according to literature routes wherein Ti(OPr^i)$_4$ or Zr(OPr^i)$_4$(HOPr^i) complex were reacted with HONep.

FT-IR spectral data were obtained on a Bruker Vector 22 spectrometer using KBr pellets pressed and handled under an atmosphere of flowing nitrogen. Elemental analysis was performed on a Perkin–Elmer 2400 CHN-S/O elemental analyzer. Thermal gravimetric analysis/Differential thermal analysis (TGA/DTA) data were performed on a Universal V3.0G TA Instrument by heating from room temperature to 650 °C at a ramp rate of 5°/min under an argon atmosphere. Solution NMR spectra were obtained on a Bruker DRX400 using a 5 mm broadband solution probe: ^1H (399.8 MHz) and $^{13}C\{^1H\}$ (100.6 MHz). Chemical shifts were referenced to the residual proton signal from the solvent in the ^1H NMR spectra or to the deuterated solvent resonance in the ^{13}C NMR spectra. Solid-state ^{13}C CPMAS NMR data were collected on a Bruker Avance400 using standard experimental conditions with a 4mm magic angle spinning (MAS) NMR probe and two pulse phase modulated (TPPM) high power ^1H decoupling. Typical acquisition conditions included 2 ms contact time, 1024 or 2048 scans, 10 kHz MAS spinning speed and 5 s recycle delay. The chemical shift was referenced to the carbonyl resonance (δ = 176 ppm) of the standard glycine with respect to TMS (δ = 0 ppm). For NMR analysis the rotors were packed with crystalline material under an atmosphere of argon.

2.1. $Ti_3(O)(cat)_4(cat\text{-}H)_2$ (*1*)

In a vial, cat-H_2 (0.171 g, 1.55 mmol) was added to a stirring solution of $Ti(ONep)_4$ (0.311 g, 0.777 mmol) dissolved in THF (~2 mL) and heated (~65 °C) for 5 min. After the reaction cooled to room temperature, the volatile material was removed by rotary evaporation, forming an off red powder. This powder was redissolved in pyridine and then set aside to slowly evaporate until crystals formed. Yield: 52% (0.328 g). FT-IR (KBr, cm^{-1}): 3132(s), 3062(m), 3019(s), 2958(s), 2928(s), 2857(s), 1654(s), 1635(s), 1607(s), 1534(s), 1508(s), 1484(w), 1326(m), 1245(w), 1205(m), 1099(m), 1016(m), 885(m), 863(m), 823(w), 808(w), 744(w), 678(w), 666(w), 648(w), 623(w), 605(w), 582(m), 562(s), 545(m), 536(m), 507(w). Elemental *Anal*. Calc. for $C_{50}H_{45}N_2O_{14}Ti_3$: C, 74.58; H, 5.5; N, 3.45. Found: C, 66.05; H, 4.89; N, 9.69%.

2.1.1. General synthesis

Due to the similarity of the synthesis of **2**–**5**, a general description will be provided. The appropriate amount of cat-H_2 dissolved in pyridine was added via pipette to a stirring solution of $M(OR)_x$ in py. After 1 h, if the

reaction mixture was not homogeneous, it was warmed slightly until a clear solution was obtained. The reactions were then set aside to slowly evaporate over an extended period of time.

2.2. $Zr_4(O)(cat)_6(cat\text{-}H)_2(py)_4$ (**2**)

Used $[Zr(\mu\text{-}OPr_i)(ONep)_3(HONep)]_2$ (0.439 g, 0.467 mmol), cat-H_2 (0.205 g, 1.862 mmol). Yield: 16% (0.118 g). FT-IR (KBr, cm^{-1}): 3052(m), 3019(s), 2959(s), 2927(s), 2869(s), 1635(s), 1606(s), 1580(m), 1544(s), 1486(w), 1448(w), 1438(m), 1328(m), 1315(m), 1253(w), 1215(m), 1192(m), 1100(m), 1023(m), 876(m), 809(w), 741(w), 701(m), 683(m), 607(w), 580(m), 503(m). Elemental *Anal.* Calc. for $C_{68}H_{52}N_4O_{17}Zr_4$: C, 52.49; H, 3.34; N, 3.57. Found: C, 54.07; H, 4.21; N, 3.76%.

2.3. $Hf_4(O)(cat)_6(cat\text{-}H)_2(py)_4$ (**3**)

Used $Hf(OEt)_4$ (0.101 g, 0.282 mmol), cat-H_2 (0.062 g, 0.563 mmol). Yield: 31% (0.162 g). FT-IR (KBr, cm^{-1}): 3053(m), 3021(s), 2960(s), 2927(s), 2871(s), 1635(s), 1608(s), 1580(m), 1543(s), 1488(w), 1449(w), 1329(m), 1270(w), 1252(w), 1215(m), 1193(m), 1149(s), 1100(m), 1069(s), 1042(s), 1024(m), 878(m), 810(w), 740(w), 696(m), 683(s), 609(w), 527(s), 508(s). Elemental *Anal*. Calc. for $C_{68}H_{52}N_4O_{17}Hf_4$: C, 42.93; H, 2.73; N, 2.92. Found: C, 48.96; H, 3.47; N, 4.84%.

2.4. $Nb(cat)_2(cat\text{-}H)(py)$ (**4**)

Used $Nb(OEt)_4$ (0.308 g, 0.968 mmol), cat-H_2 (0.320 g, 2.91 mmol). Yield: 95% (0.450 g). FT-IR (KBr, cm^{-1}): 3134(s), 3065(m), 3015(s), 2962(s), 1599(s), 1577(s), 1545(s), 1508(s), 1473(w), 1452(m), 1437(m), 1333(m), 1248(w), 1205(m), 1096(m), 1064(m), 1014(m), 869(m), 836(m), 806(w), 766(w), 741(w), 703(s), 678(m), 637(w), 620(w), 604(w), 515(w). ^1H NMR (399.8 Hz, py-d_5) δ 6.78 (br s, $O_2C_6H_4$). ^{13}C NMR (100.6 MHz, py-d_5) δ 159.9, 119.9, 113.9 ($O_2C_6H_3$). Elemental *Anal*. Calc. for $C_{23}H_{17}N_1O_6Nb$: C, 55.86; H, 3.43; N, 2.80. Found: C, 53.69; H, 3.44; N, 4.64%.

2.5. $Ta(cat)_2(cat\text{-}H)(py)$ (**5**)

Used $Ta(OEt)_4$ (0.508 g, 1.25 mmol), cat-H_2 (0.413 g, 3.751 mmol). Yield: 91.4% (0.758 g). FT-IR (KBr, cm^{-1}): 3131(s), 3067(m), 3050(m), 3023(m), 2965(s), 1636(s), 1609(m), 1580(s), 1541(s), 1482(w), 1449(w), 1420(s), 1337(m), 1317(s), 1293(m), 1252(w), 1211(m), 1197(m), 1155(s), 1100(m), 1070(m), 1044(s), 1016(m), 872(m), 812(w), 744(w), 692(m), 675(m), 630(w), 606(w), 529(w). ^1H NMR (399.8 Hz, py-d_5) δ 6.82 (br s, $O_2C_6H_4$), 6.74 (br s, $O_2C_6H_4$). ^{13}C NMR (100.6 MHz, py-d_5) δ 159.9, 119.8, 114.9 ($O_2C_6H_3$). Elemental *Anal*. Calc. for $C_{28}H_{22}N_2O_6Ta$: C, 57.80; H, 3.78; N, 4.77. Found: C, 62.71; H, 4.48; N, 6.22%.

2.5.1. General X-ray crystal structure information[1]

Each crystal was mounted onto a thin glass fiber from a pool of Fluorolube™ and immediately placed under a liquid N_2 stream, on a Bruker AXS diffractometer. The radiation used was graphite monochromatized Mo Kα radiation ($\lambda = 0.7107$ Å). The lattice parameters were optimized from a least-squares calculation on carefully centered reflections. Lattice determination and data collection were carried out using SMART Version 5.054 software. Data reduction was performed using SAINT Version 6.01 software. The structure refinement was performed using XSHELL 3.0 software. The data were corrected for absorption using the SADABS program within the SAINT software package.

Each structure was solved using direct methods. This procedure yielded the heavy atoms, along with a number of the C, N and O atoms. Subsequent Fourier synthesis yielded the remaining atom positions. The hydrogen atoms were fixed in positions of ideal geometry and refined within the XSHELL software. These idealized hydrogen atoms had their isotropic temperature factors fixed at 1.2 or 1.5 times the equivalent isotropic U value of the C atoms to which they were bonded. The final refinement of each compound included anisotropic thermal parameters on all non-hydrogen atoms. Additional information concerning the data collection and final structural solutions of **1**–**5** can be found in the supplemental information. Any variations from standard structural solution associated with the representative compounds are discussed below. All CIF files were checked for errors using the free on-line Checkcif service provided by the International Union of Crystallography (available on the Web at http://www.iucr.org/acs/checkcif.html).

3. Results and discussion

Since cat-H_2 is commercially available, inexpensive, stable and can act as a chelating ligand, it is an attractive ligand for a variety of applications and has lead to extensive reports of transition metal complexes. As mentioned previously, we are interested in the Group 4 and 5 cations for materials synthesis; however, for our systems, non-oxygen anions (i.e., halides, sulfides, etc.) can have deleterious effects on the properties of the materials of interest and therefore are avoided.

Several cationic species where the Group 4 cations use the cat ligand without the afore-mentioned anions

[1] The listed Versions of SAINT, SMART, XSHELL, and SADABS Software from Bruker Analytical X-ray Systems Inc., 6300 Enterprise Lane, Madison, WI 53719 were used in analysis.

have been reported, including the following for Ti species: $[Et_3NH]_2[Ti(cat)_3]$ [14], $K_4[TiO(cat)_2]\cdot 9H_2O$ [14], along with several neutral species including $[Ti_6O_4(OPr^i)_4(cat)_4\{(CO)_9Co_3CCO_2\}_4]$ and $[Ti_6O_4(OBu^n)_{10}(O_2CCH_3)_8]$ (note several reports indicate that species with molar ratios of catechol:Ti greater than 1 were unsuccessful) [9–11]. Zirconium cat adducts have also been reported including: $[Zr_3(acac)_4(cat)_4(MeOH)_2]$, $[Zr(acac)_2(DBcat)]_2$ (H_2DBcat = 3,5-di-*tert*-butylcatechol) and $[Zr_4(\mu_4\text{-}O)(acac)_4(DBcat)_3(OMe)_4(MeOH)]$ [15]. Only one Hf derivative, $Na[Hf(cat)_4]\cdot H_2O$ [16,17], has been reported.

For Group 5 a similar set of cationic and neutral species have been isolated for vanadium, including: $[V(cat)_3][Z]\cdot solv$, where $Z\cdot solv = NHEt_3\cdot MeN$; $K\cdot H_2O$, $K[V(O)(cat)]\cdot(H_2O)(EtOH)$ [18], V(O)(DBcat)(DBBQ) (where DBBQ = 3,5-di-*t*-butyl-1,2-benoquinone) [19], $[Na(\mu\text{-}cat)_2V(cat)(MeOH)_2]_2\cdot MeOH$ [20,21], V(O)(cat)(SEI) where SEI = (4-(2-(salicylideniimino)ethyl)imidazole) [22,23], $[V(O)_2(DBcat)][NHEt_3]$ [24], $[(MeOH)Na(\mu\text{-}DBcat)_2V(\mu\text{-}DBcat\text{-}H)(\mu_3\text{-}OMe)\text{-}V(MeOH)_2]_2\cdot MeOH$ [25], V(O)(cat-H)(SDC), V(O)(DBcat-H)(SDC) and V(O)(DBcat)(SDC) where SDC = *N*-salicylideneglycinato-*N*,*O*,*O*′) [26], $V(DBcat)_2(bipy)\cdot$ toluene [27]. However, surprisingly, there are no species reported for Nb or Ta metals with the cat ligand. It is of note that there are numerous structurally characterized species that possess both cat and halide ligands, and as previously mentioned, the latter anions can be a derisive contamination in the materials we have interest in.

From the above collection of structures, no fully substituted catecholate complexes for Group 4 or 5 compounds have been reported. Therefore, we chose to synthesize and characterize this family of compounds. While the $OCHMe_2$ (OPr^i) derivatives are commercially available, the ONep derivatives have several characteristics that make them more attractive than the OPr^i derivatives. Initially, we used $[Ti(\mu\text{-}ONep)(ONep)_3]_2$ [12] and $[Zr(\mu\text{-}OPr^i)(ONep)_3\cdot HONep]_2$ [13] to study the fully substituted cat-H_2 Group 4 species. As we observed the full exchange was accessible, we proceeded to use the commercially available ethoxide derivatives for the Hf, V and Ta catechol derivatives. The synthesis and characterization of **1**–**5** are discussed below.

3.1. Synthesis

The simple alcoholysis reactions were investigated according to Eq. (1) to generate fully cat-substituted Group 4 species. The reaction was undertaken using pyridine (py) as the solvent to maintain solubility of the final products. For the Ti system, after heating to solubilize the reaction mixture, the color changed from clear to red and a small precipitate formed that was removed by centrifugation. Additional investigations with other alkoxides showed the same product was isolated independent of the pendant alkoxy chain. Therefore, we used commercially available alkoxide species for the remainder of experiments where applicable. For the Zr and Hf reactions the colors changed from clear to yellow but did not require any heating. The Hf reaction was similar to the Zr reaction, turning from clear to yellow with no precipitate and no heating required. For Group 5 species, the appropriate amount of cat-H_2 dissolved in pyridine was added via pipette to a stirring solution of $M(OEt)_5$ OET = ethoxidein pyridine in pyridine. Color changes were noticeable for the clear solutions of niobium and tantalum, going to deep red and yellow, respectively. Again, py proved to be the best solvent for generating the cleanest products. For each reaction, X-ray quality crystals were grown by slow evaporation. The resulting modified precursors were structurally identified as **1**–**5** shown in Figs. 1–5, respectively, and show that full substitution of the alkoxide for cat ligands had occurred for each reaction.

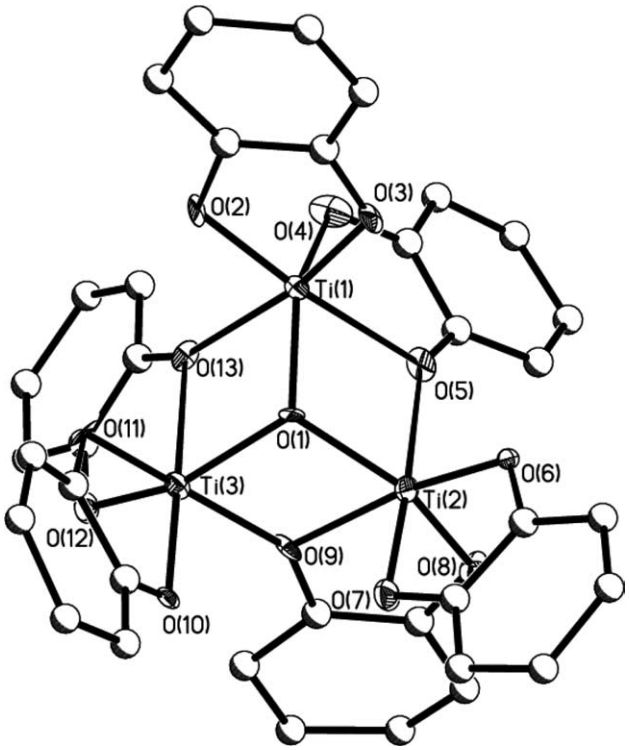


Fig. 1. Structure plot of **1**. Thermal ellipsoids of heavy atoms drawn at 30% level. Carbon atoms are drawn as ball and stick representations. *Selected representative distances (Å):* Ti(1)–O(4) 1.903(5); Ti(1)–O(3) 1.906(4); Ti(1)–O(2) 1.926(5); Ti(1)–O(1) 1.954(4); Ti(1)–O(13) 2.033(4); Ti(1)–O(5) 2.082(5). *Selected representative angles (°):* O(4)–Ti(1)–O(3) 99.7(2); O(4)–Ti(1)–O(2) 99.9(2); O(3)–Ti(1)–O(2) 81.21(19); O(4)–Ti(1)–O(1) 147.9(2); O(3)–Ti(1)–O(1) 99.25(19); O(2)–Ti(1)–O(1) 108.5(2); O(4)–Ti(1)–O(13) 91.6(2); O(3)–Ti(1)–O(13) 163.2(2); O(2)–Ti(1)–O(13) 84.59(19); O(1)–Ti(1)–O(13) 76.73(18); O(4)–Ti(1)–O(5) 77.7(2); O(3)–Ti(1)–O(5) 92.34(19); O(2)–Ti(1)–O(5) 172.71(19); O(1)–Ti(1)–O(5) 75.78(18); O(13)–Ti(1)–O(5) 102.30(19).

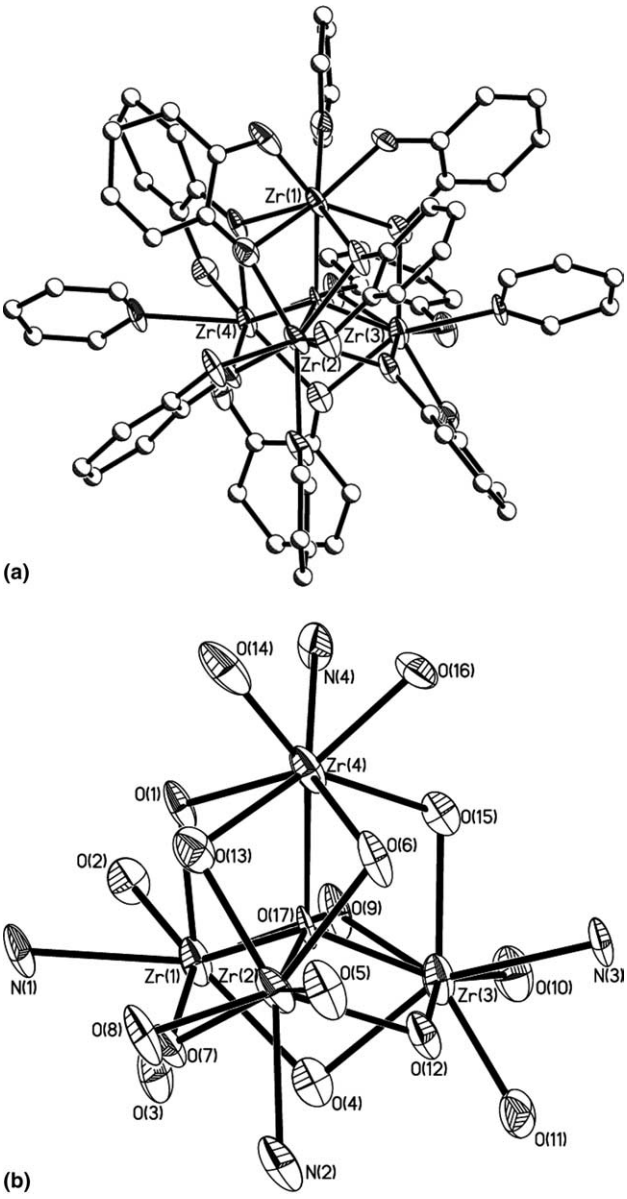


Fig. 2. Structure plot of **2** (a) full structure and (b) central core. Thermal ellipsoids of heavy atoms drawn at 30% level. Carbon atoms are drawn as ball and stick representations. *Selected representative distances (Å):* Zr(1)–O(3) 2.064(10); Zr(1)–O(17) 2.161(5); Zr(1)–O(2) 2.179(7); Zr(1)–O(1) 2.209(8); Zr(1)–O(9) 2.235(7); Zr(1)–O(7) 2.253(7); Zr(1)–O(4) 2.274(8); Zr(1)–N(1) 2.418(10); Zr(1)–Zr(2) 3.6111(15). *Selected representative angles (°)*: O(3)–Zr(1)–O(17) 140.5(3); O(3)–Zr(1)–O(2) 77.3(3); O(17)–Zr(1)–O(2) 134.7(3); O(3)–Zr(1)–O(1) 148.0(3); O(17)–Zr(1)–O(1) 70.9(2); O(2)–Zr(1)–O(1) 72.0(3); O(3)–Zr(1)–O(9) 99.4(3); O(17)–Zr(1)–O(9) 69.8(2); O(2)–Zr(1)–O(9) 82.1(3); O(1)–Zr(1)–O(9) 85.0(3); O(3)–Zr(1)–O(7) 96.9(3); O(17)–Zr(1)–O(7) 68.8(2); O(2)–Zr(1)–O(7) 146.2(3); O(1)–Zr(1)–O(7) 103.7(3); O(9)–Zr(1)–O(7) 131.6(3); O(3)–Zr(1)–O(4) 71.5(3); O(17)–Zr(1)–O(4) 69.2(3); O(2)–Zr(1)–O(4) 132.7(3); O(1)–Zr(1)–O(4) 137.9(3); O(9)–Zr(1)–O(4) 69.4(3); O(7)–Zr(1)–O(4) 73.4(3); O(3)–Zr(1)–N(1) 83.7(4); O(17)–Zr(1)–N(1) 123.7(3); O(2)–Zr(1)–N(1) 71.9(3); O(1)–Zr(1)–N(1) 78.6(3); O(9)–Zr(1)–N(1) 152.5(3); O(7)–Zr(1)–N(1) 74.4(3); O(4)–Zr(1)–N(1) 136.0(3); O(3)–Zr(1)–Zr(2) 126.6(2); O(17)–Zr(1)–Zr(2) 33.35(14); O(2)–Zr(1)–Zr(2) 153.9(2); O(1)–Zr(1)–Zr(2) 82.53(16); O(9)–Zr(1)–Zr(2) 101.67(18); O(7)–Zr(1)–Zr(2) 35.87(17); O(4)–Zr(1)–Zr(2) 71.24(19); N(1)–Zr(1)–Zr(2) 98.1(3).

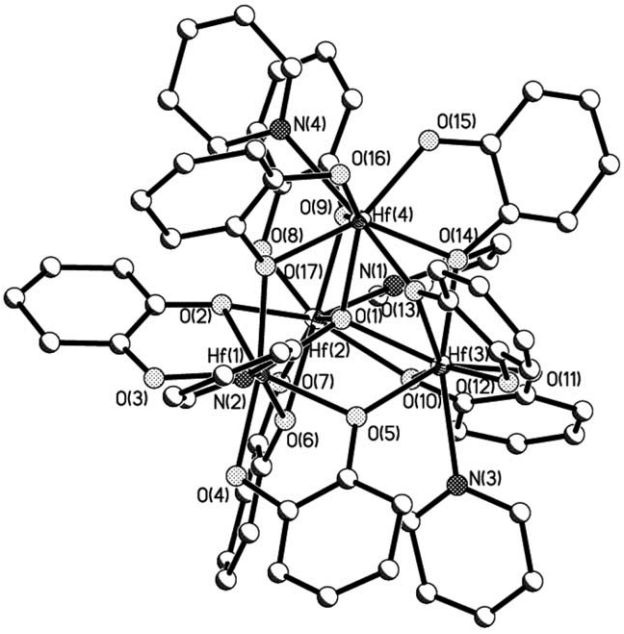


Fig. 3. Structure plot of **3**. Thermal ellipsoids of heavy atoms drawn at 30% level. Carbon atoms are drawn as ball and stick representations. *Selected representative distances (Å):* Hf(1)–O(3) 2.076(15); Hf(1)–O(1) 2.110(12); Hf(1)–O(4) 2.147(15); Hf(1)–O(5) 2.194(15); Hf(1)–O(6) 2.221(14); Hf(1)–O(17) 2.243(13); Hf(1)–O(2) 2.302(15); Hf(1)–N(2) 2.369(19). *Selected representative angles (°):* O(3)–Hf(1)–O(1) 141.0(6); O(3)–Hf(1)–O(4) 75.4(6); O(1)–Hf(1)–O(4) 137.3(5); O(3)–Hf(1)–O(5) 148.9(6); O(1)–Hf(1)–O(5) 69.8(5); O(4)–Hf(1)–O(5) 74.8(6); O(3)–Hf(1)–O(6) 100.6(6); O(1)–Hf(1)–O(6) 71.3(5); O(4)–Hf(1)–O(6) 82.2(6); O(5)–Hf(1)–O(6) 84.1(6); O(3)–Hf(1)–O(17) 96.2(5); O(1)–Hf(1)–O(17) 68.0(5); O(4)–Hf(1)–O(17) 145.0(5); O(5)–Hf(1)–O(17) 103.1(5); O(6)–Hf(1)–O(17) 132.7(5); O(3)–Hf(1)–O(2) 71.7(5); O(1)–Hf(1)–O(2) 69.6(5); O(4)–Hf(1)–O(2) 131.6(5); O(5)–Hf(1)–O(2) 137.1(5); O(6)–Hf(1)–O(2) 70.3(6); O(17)–Hf(1)–O(2) 73.7(5); O(3)–Hf(1)–N(2) 83.6(7); O(1)–Hf(1)–N(2) 121.6(7); O(4)–Hf(1)–N(2) 72.3(6); O(5)–Hf(1)–N(2) 79.0(6); O(6)–Hf(1)–N(2) 152.3(6); O(17)–Hf(1)–N(2) 73.0(6); O(2)–Hf(1)–N(2) 135.7(6).

3.1.1. Crystal structure

For **1**, the species isolated was trinuclear using a μ_3-O to bind the three Ti metal centers together in a corner missing cube arrangement (see Fig. 1). Each metal center is octahedrally coordinated using one cat ligand as a chelating ligand and one as a bridging chelating ligand. While py molecules are present in the lattice, none were found bound to the metal centers. Based on charge balance, two of the cat ligands can have one hydroxide (cat-H) present; however, the protons could not be located and are assumed to be disordered over the entire molecule for all of the following molecules discussed.

An alternative location of the H atom may be in that a pyridimium molecule is formed, generating $[py\text{-}H]^{+-}[Ti(cat)_3]$. The FTIR spectrum indicates the presence of an OH but due to overlapping stretches it is difficult to identify the presence of pyridimium ion [28]. A search of the structurally characterized pyridimium ions

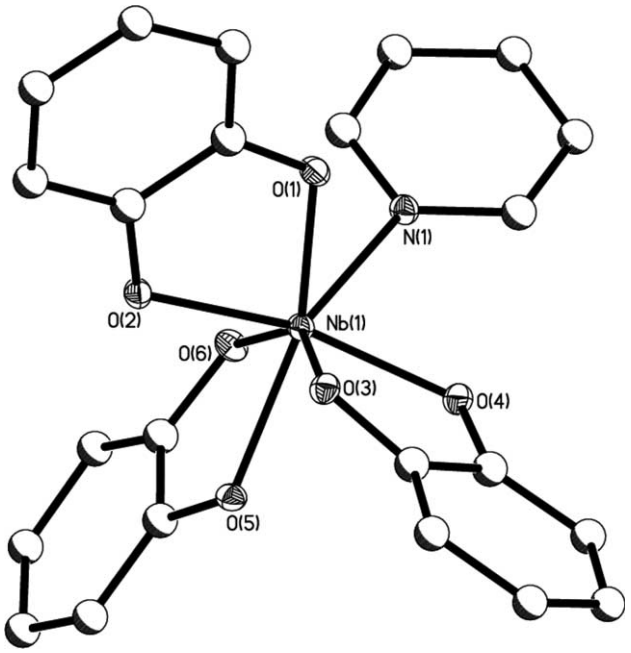


Fig. 4. Structure plot of **4**. Thermal ellipsoids of heavy atoms drawn at 30% level. Carbon atoms are drawn as ball and stick representations. *Selected representative distances (Å):* Nb(1)–O(4) 1.995(2); Nb(1)–O(6) 2.003(2); Nb(1)–O(1) 2.003(2); Nb(1)–O(2) 2.035(2); Nb(1)–O(3) 2.046(2); Nb(1)–O(5) 2.124(2); Nb(1)–N(1) 2.326(3). *Selected representative angles (°):* O(4)–Nb(1)–O(6) 107.09(9); O(4)–Nb(1)–O(1) 108.30(9); O(6)–Nb(1)–O(1) 121.17(9); O(4)–Nb(1)–O(2) 158.19(9); O(6)–Nb(1)–O(2) 87.34(9); O(1)–Nb(1)–O(2) 76.02(9); O(4)–Nb(1)–O(3) 75.93(9); O(6)–Nb(1)–O(3) 149.59(9); O(1)–Nb(1)–O(3) 84.51(9); O(2)–Nb(1)–O(3) 83.39(9); O(4)–Nb(1)–O(5) 87.50(9); O(6)–Nb(1)–O(5) 74.38(9); O(1)–Nb(1)–O(5) 150.81(9); O(2)–Nb(1)–O(5) 80.63(8); O(3)–Nb(1)–O(5) 75.55(9); O(4)–Nb(1)–N(1) 76.10(9); O(6)–Nb(1)–N(1) 72.20(9); O(1)–Nb(1)–N(1) 72.71(9); O(2)–Nb(1)–N(1) 124.77(10); O(3)–Nb(1)–N(1) 135.75(9); O(5)–Nb(1)–N(1) 136.08(9).

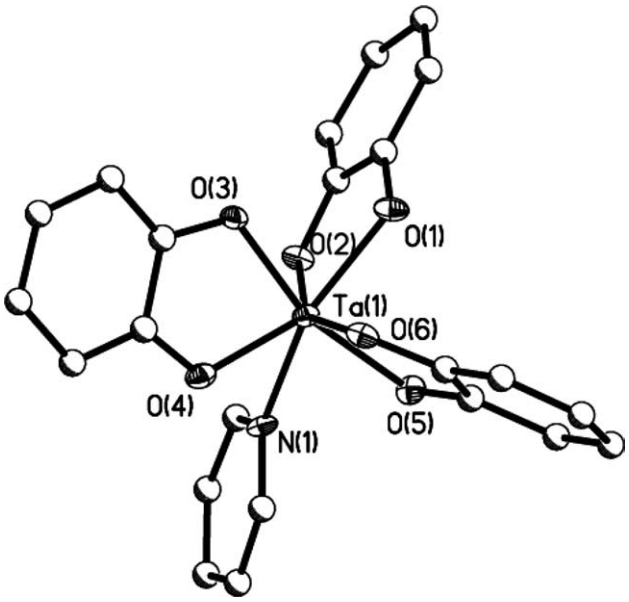


Fig. 5. Structure plot of **5**. Thermal ellipsoids of heavy atoms drawn at 30% level. Carbon atoms are drawn as ball and stick representations. *Selected representative distances (Å):* Ta(1)–O(4) 2.003(5); Ta(1)–O(6) 2.005(5); Ta(1)–O(3) 2.017(5); Ta(1)–O(2) 2.018(5); Ta(1)–O(1) 2.023(5); Ta(1)–O(5) 2.084(5); Ta(1)–N(1) 2.308(6). *Selected representative angles (°):* O(4)–Ta(1)–O(6) 122.5(2); O(4)–Ta(1)–O(3) 76.8(2); O(6)–Ta(1)–O(3) 87.4(2); O(4)–Ta(1)–O(2) 80.94(19); O(6)–Ta(1)–O(2) 155.0(2); O(3)–Ta(1)–O(2) 90.3(2); O(4)–Ta(1)–O(1) 125.14(19); O(6)–Ta(1)–O(1) 94.8(2); O(3)–Ta(1)–O(1) 149.9(2); O(2)–Ta(1)–O(1) 75.28(19); O(4)–Ta(1)–O(5) 74.89(19); O(6)–Ta(1)–O(5) 75.56(18); O(3)–Ta(1)–O(5) 131.0(2); O(2)–Ta(1)–O(5) 123.08(19); O(1)–Ta(1)–O(5) 78.16(19); O(4)–Ta(1)–N(1) 145.4(2); O(6)–Ta(1)–N(1) 75.8(2); O(3)–Ta(1)–N(1) 75.0(2); O(2)–Ta(1)–N(1) 79.5(2); O(1)–Ta(1)–N(1) 76.5(2); O(5)–Ta(1)–N(1) 139.62(19).

with Group 4 cations necessarily contain halide anions.[2] Attempts to observe the pyridium ion using high speed ^{1}H solid state NMR investigations revealed cat resonances but no resonance could be conclusively assigned to a pyridimium ion and there are no transition metal pyridimium ion chemical shift reports available in the literature; however, organic pyridimium ions have been reported at 7–8 ppm [29] which overlap with the solid state cat resonances observed. Based on these data, we feel the more traditional disordered OH for metal alkoxides [1–3] is the actual structure and have used this notation throughout this work; however, the pyridimium ion cannot be fully ruled out at this point.

Both **2** and **3** possess similar central cores to each other, best described as a tetrahedral arrangement of four Zr or Hf atoms around a μ_4-O (see Figs. 2 and 3, respectively). Each metal is eight coordinated adopting a distorted bicapped trigonal prismatic structure through the additional binding of two chelating bridging cat ligands and a terminal py solvent molecule. Two of the cat ligands must be cat-H in order to balance the charge of the molecule, but again the protons were not located in the structural solution.

In contrast, the Group 5 species (**4** and **5** shown in Figs. 4 and 5, respectively) adopted mononuclear species. Similar complexes are formed, independent of the cation. Each metal has three cat ligands binding in a chelating manner, but based on charge balance one of the cat ligands must possess a hydroxy group. This H atom was not located in the final structure and must be disordered over several sites. Each Group 5 metal finishes its 7-coordination by binding a py molecule to formally form what appears to be a capped octahedral geometry. Bond distances and angles are in agreement with literature values [9–11,14–27].

3.1.2. Bulk characterization

The FTIR spectra show the stretches of **1**–**5** are consistent with the cat ligand as would be expected for the full substitution. The alkyl stretches and bends associated with the OEt, OPr^i and/or ONep ligands are absent,

[2] A search of the Cambridge Data Crystal Data Base (Version 1.6 – Feb 21, 2005 update) reveals 10 references that contain a pyridiumium ion with a Group 4 metal center, but all possess halide ligands.

indicating complete exchange, but there are some sharp stretches observed around 3000 cm^{-1} that are consistent with the residual OH groups present for each sample. As expected from their similar crystal structures, the spectra of **2** and **3** are nearly indistinguishable from each other, as are the spectra of **4**–**5**. For **1**, the FTIR spectrum looks similar to **2** and **3** with the notable additional stretches around 600 cm^{-1} that are consistent with the Ti–O stretches [1–3].

Elemental analyses of the bulk powders of **1**–**5** do not agree with the crystal structures obtained. The variations are often attributed to "trapped" and bound solvent that is often labile enough to cause variations and thus make meaningful data impossible to collect [30–32]. Therefore, alternative methods were necessary to prove the identify of the bulk powder.

TGA/DTA data was collected for **1**–**5** under an argon atmosphere. For compound **2**, there are two weight step losses but only one exothermal event. This occurs at ~350 °C. The first weight loss can be associated with loss of the py and the subsequent thermal events with the cat ligands. Surprisingly, the thermal decomposition of the Hf analog **3** is different in comparison to **2**. For **2** there is a steady weight with a very broad but small exothermal thermal event (<400 °C) across the weight loss process. For **4**, there is an endotherm associated with a slight weight loss that is consistent with loss of py. At higher temperatures an exotherm starting around 400 °C is associated with the largest weight loss consistent with the loss of catechol ligands. Similar TGA/DTA data are recorded for **5**. The calculations for weight loss of the bulk powders for Group 4 species **1** (21.1%), **2** (27.9%), **3** (32.6%) are consistent with the observed values of 21.0%, 26.0%, 31.8%, respectively, indicating that the bulk powders are in general agreement with the single crystal structures. For the Group 5 species, the experimental weight loss for **4** (24.5%) and **5** (35.5%) were substantially more than what was calculated at 18.0% and 33.2%, respectively. This again may be a reflection of the amount of solvent located in the lattice (Tables 1 and 2).

Table 2
Data collection parameters for **4**–**5**

Compound	**4**	**5**
Chemical formula	$C_{38}H_{32}N_4NbO_6$	$C_{28}H_{22}N_2O_6Ta$
Formula weight	733.59	663.43
Temperature (K)	168(2)	273(2)
Space group	monoclinic *P*2(1)/*c*	triclinic $P\bar{1}$
Unit cell dimensions		
a (Å)	9.9941(12)	10.5834(15)
b (Å)	10.3747(12)	11.7465(16)
c (Å)	31.784(4)	20.504(3)
α (°)	90	105.338(2)
β (°)	97.730(2)	92.582(2)
γ (°)	90	95.276(2)
V (Å^3)	3265.6(7)	2441.4(6)
Z	4	4
D_{calc} (Mg/m^3)	1.492	1.805
μ (Mo Kα) (mm^{-1})	4	4
R_1[a] (%) (all data)	4.77 (7.52)	3.96 (5.27)
wR_2[b] (%) (all data)	11.43 (13.04)	8.03 (8.64)

[a] $R_1 = \sum||F_o| - |F_c||/\sum|F_o| \times 100$.
[b] $wR_2 = [\sum w(F_o^2 - F_c^2)^2/\sum(w|F_o|^2)^2]^{1/2} \times 100$.

Solid-state ^{13}C NMR spectra were collected on the crystalline materials of **1**–**5** to further investigate the identity of the bulk powder. Fig. 6 shows the solid state NMR spectra for **1**–**5** and Table 3 metrically lists this data. The resulting solid-state ^{13}C NMR spectra of **1** reveals numerous aromatic peaks with no alkoxide resonances. For the crystal structure of **1**, two types of cat ligands are present (chelating and unidentate bridging) which should lead to 12 types of carbon resonances. There are numerous overlapping ^{13}C resonances observed between δ 170 and 110 ppm, with the overlap

Table 1
Data collection parameters for **1**–**3**

Compound	**1**	**2**	**3**
Chemical formula	$C_{54}H_{50}N_2O_{15}Ti_3$	$C_{108}H_{117}N_{12}O_{17}Zr_4$	$C_{68}H_{52}Hf_4N_4O_{17}$
Formula weight	1110.66	2220.02	1911.10
Temperature (K)	168(2)	203(2)	203(2)
Space group	monoclinic *P*2(1)/*c*	monoclinic *P*2(1)/*c*	monoclinic *P*2(1)/*c*
Unit cell dimensions			
a (Å)	15.210(5)	23.432(5)	22.960(8)
b (Å)	16.146(5)	15.464(4)	15.372(5)
c (Å)	21.180(7)	28.175(7)	27.916(10)
β (°)	102.499(7)	98.929(4)	100.058(6)
V (Å^3)	5078(3)	10086(4)	9701(6)
Z	4	4	4
D_{calc}(Mg/m^3)	1.453	1.462	1.308
μ (Mo Kα) (mm^{-1})	0.532	0.475	4.315
R_1[a] (%) (all data)	10.19 (24.31)	11.86 (30.27)	11.20 (14.58)
wR_2[b] (%) (all data)	19.69 (24.19)	18.83 (33.72)	28.54 (30.38)

[a] $R_1 = \sum||F_o| - |F_c||/\sum|F_o| \times 100$.
[b] $wR_2 = [\sum w(F_o^2 - F_c^2)^2/\sum(w|F_o|^2)^2]^{1/2} \times 100$.

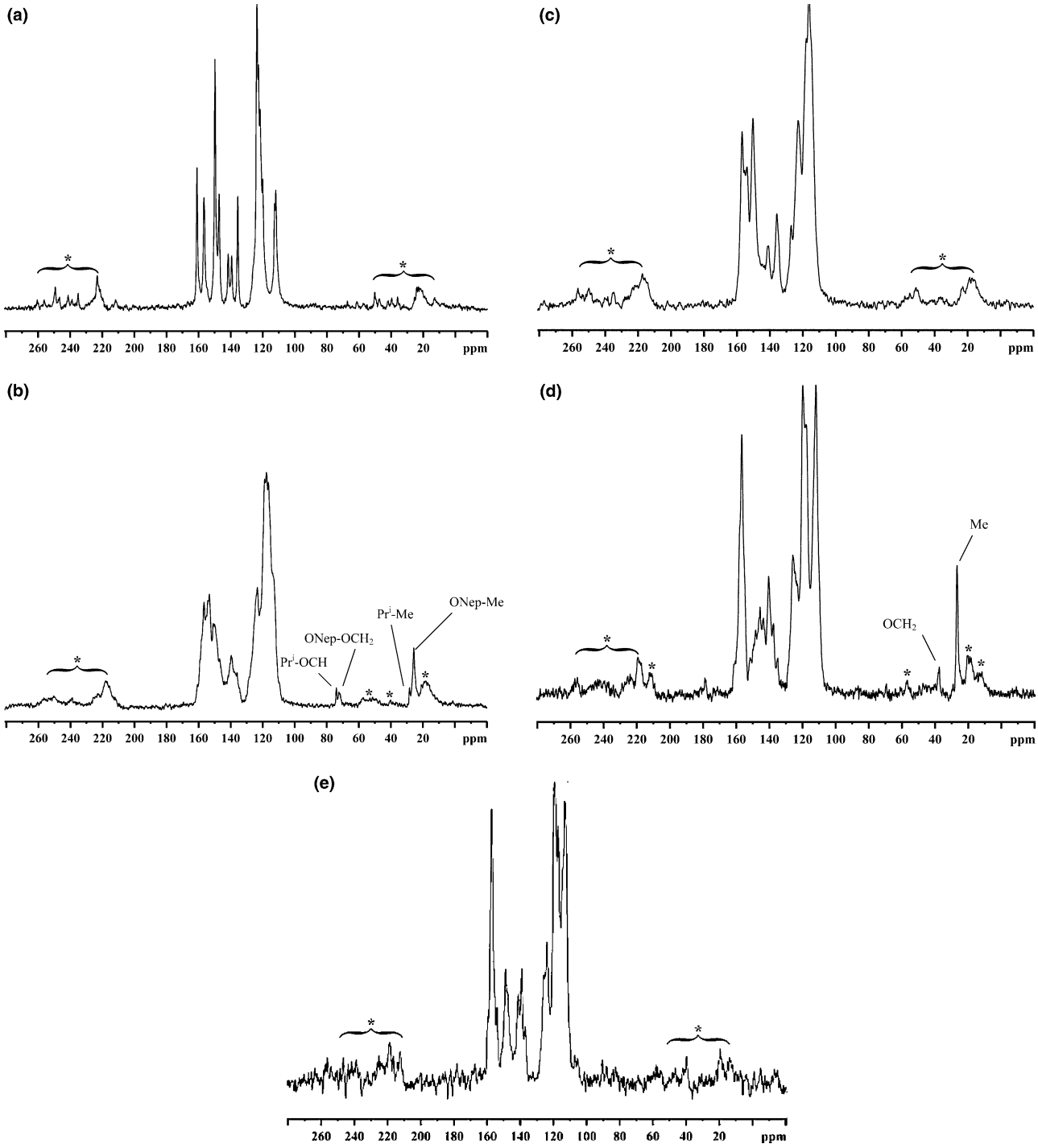


Fig. 6. Solid-state ^{13}C CPMAS NMR spectra for **1**–**5** (a)–(e), respectively.

most likely resulting from crystal packing inequivalancies. However, these data would indicate that the sample investigated is fully substituted with cat ligands and that the simplicity of the aromatic region argues for the bulk of the material to be consistent with the solid state structure.

For **2** and **3**, the solid-state spectra are consistent with each other. The resonances observed fall within the same range observed for **1** but are broader and less defined in comparison to **1**. This is most likely due to the more complex nature of the final structure, wherein, there are three types of cat ligands present (two unidentate bridging and one chelating). Additionally, the bound and trapped py molecules will contribute additional complexity to this region. For **2**, there are some resonances associated with alkoxide ligands, indicating a

Table 3
Solid state ^{13}C NMR data for **1**–**5**

Compound	^{13}C MAS (ppm)
1	166.8, 160.9, 156.7, 149.8, 147.2, 14125, 139.3, 135.6, 130.3, 123.7, 122.7, 121.7, 120.0, 112.7, 111.9
2	156.6, 153.3, 150.9, 146.8, 143.9, 139.7, 135.9, 123.3, 118.8, 117.7, 116.4
3	156.9, 153.7, 140.8, 135.8, 129.0, 122.9, 117.9, 116.5
4	156.5, 148.2, 145.5, 143.5, 140.3, 137.4, 134.8, 125.7, 119.8, 111.9
5	157.2, 153.9, 148.9, 141.0, 139.1, 136.9, 123.9, 119.7, 117.0, 113.0

minor impurity. Some of these have been identified in the spectrum (Fig. 6(b)). This contaminant would be another aspect of the elemental analyses data that is not consistent with the bulk powder. Multiple crystallizations did not remove this impurity.

For **4**–**5**, the ^{13}C MAS NMR spectra are nearly identical. The six carbons of the catechol rings are observed between 165 and 110 ppm but these resonances are split. This splitting is associated with packing inequivalencies and the asymmetry of the rings induced by the presence of the proton. For **4** (Fig. 6(d)), several minor alkoxy peaks have also been noted, as observed for **2**.

3.1.3. Solution state NMR

It is of interest to know the solution behavior of these compounds prior to use as nanoparticle precursors since the nuclearity of the solution compound may play a big role in the nanoparticle formation. Crystalline material of each sample was dissolved in py-d_5 and sealed under vacuum. Compounds **1**–**3** were not soluble enough to obtain meaningful NMR spectra, even at elevated temperatures. Therefore, these have been omitted from the experimental section. Compounds **4** and **5** possess increased solubility in comparison to the Group 4 derivatives. The ^{1}H NMR spectrum for compound **4** displayed one resonance associated with cat (δ 6.78 ppm); however, there was a shoulder present on the broad resonance. For **5**, two ^{1}H NMR resonances were noted at δ 6.82 and 6.74 ppm. The $^{13}C\{^{1}H\}$ NMR spectra show three resonances with slight variations in the chemical shifts of the two species. Based on these data it appears the monomer molecular species are retained in solution.

3.1.4. Materials synthesis

Due to the reduction of clustering wrought by the cat ligand for some of these compounds, it was of interest to determine their utility as MOCVD and/or nanoparticle precursors. It has been previously noted that similar properties of the precursor are desired for both MOCVD and nanoparticle production [33]. Based on the high decomposition temperatures observed in the TGA/DTA data of **2**–**6**, these compounds were eliminated for consideration of further investigation. For **1**, the thermal decomposition temperature was at the upper limit of utility. The compound did not sublime which prevented further investigations using MOCVD techniques. Nanoparticle synthesis was attempted following Stucky et al. [34] methodology. In general, **1** was added to benzyl alcohol and heated to 250 °C for 24 h. After this time, the reaction was allowed to cool to room temperature, and hexanes were added to precipitate the resultant material. The mother liquor was removed by centrifugation and the orange precipitate was washed several times with hexanes. The powder was redispersed in hexanes and a drop of the slurry was placed onto a TEM grid. The TEM image is shown in Fig. 7. While the particles are clustered together, the material consists of polydispersed nanocrystalline ceramic material.

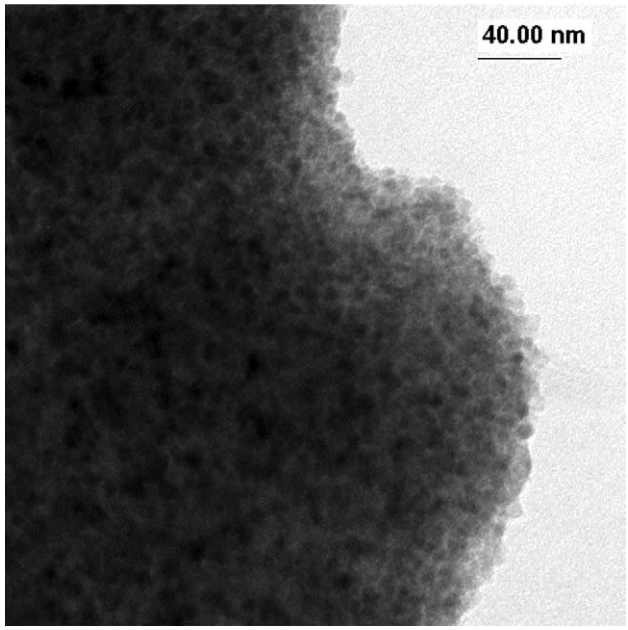


Fig. 7. TEM figures of nanoparticles of **1**.

4. Conclusion

In contrast to initial reports [9–11], we have successfully isolated the first fully substituted catechol derivatives of Group 4 and 5 species. For the Group 4 family of compounds, an oxide formed to link the metals together, the Ti complex being trinuclear and the heavier congeners Zr and Hf being tetranuclear. For the Group 5 species only monomers were isolated. For each compound, due to charge balance, the catechol ligands must have –OH present which was disordered over the entire molecule. The majority of the molecules synthesized and characterized did not display the expected thermal decomposition necessary for MOCVD or nanoparticle synthesis. However, we were successfully in the production of TiO_2 nanoparticles using compound **1**.

Acknowledgements

For support of this research, the authors thank the Office of Basic Energy Science of the Department of Energy and the United States Department of Energy. The authors also acknowledge Dr. Mark A. Rodriguez for assistance on the crystal structure solutions. Sandia is a multiprogram laboratory operated by Sandia Corporation, a Lockheed Martin Company, for the United States Department of Energy under contract DE-AC04-94AL85000.

Appendix A. Supplementary data

X-ray crystallographic files in CIF format for the structures **1**–**5** are available from the Cambridge Data Base under CCDC 267 277-267 281 reference numbers for Polyhedron (0580). These data can be obtained free of charge via www.ccdc.cam.ac.uk/conts/retrieving.html (or from the CCDC, 12 Union Road, Cambridge CB2 1EZ, UK; fax: +44 1223 336033; e-mail: deposit@ccdc.cam.ac.uk). Supplementary data associated with this article can be found, in the online Version, at doi:10.1016/j.poly.2005.03.055.

References

[1] D.C. Bradley, R.C. Mehrotra, D.P. Gaur, Metal Alkoxides, Academic Press, New York, 1978.
[2] D.C. Bradley, R.C. Mehrotra, I.P. Rothwell, A. Singh, Alkoxo and Aryloxo Derivatives of Metals, Academic Press, San Diego, 2001.
[3] M.Y. Turova, E.P. Turevskaya, V.G. Kessler, M.I. Yanovskaya, The Chemistry of Metal Alkoxides, Kluwer Academic Publishers, Boston, 2002.
[4] T.J. Boyle, R.W. Schwartz, R.J. Doedens, J.W. Ziller, Inorg. Chem. 34 (1995) 1110.
[5] T.J. Boyle, R.P. Tyner, T.M. Alam, B.L. Scott, J.W. Ziller, B.G.J. Potter, J. Am. Chem. Soc. 121 (1999) 12104.
[6] T.J. Boyle, N.L. Andrews, T.M. Alam, M.A. Rodriguez, J.M. Santana, B.L. Scott, Polyhedron 21 (2002) 2333.
[7] T.J. Boyle, T.M. Alam, C.J. Tafoya, B.L. Scott, Inorg. Chem. 37 (1998) 5588.
[8] T.J. Boyle, M.A. Rodriguez, T.M. Alam, J. Chem. Soc., Dalton Trans. 24 (2003) 4598.
[9] X. Lei, M. Shang, T.P. Fehlner, Organometallics 115 (1996) 3779.
[10] X. Lei, M. Shang, T.P. Fehlner, Organometallics 16 (1997) 5289.
[11] K. Gigant, A. Rammal, M. Henry, J. Am. Chem. Soc. 123 (2001) 11632.
[12] T.J. Boyle, T.M. Alam, E.R. Mechenbeir, B. Scott, J.W. Ziller, Inorg. Chem. 36 (1997) 3293.
[13] T.J. Boyle, J.J. Gallegos III, D.M. Pedrotty, E.R. Mechenbier, B.L. Scott, J. Coord. Chem. 47 (1999) 155.
[14] B.A. Borgias, S.R. Cooper, Y.B. Koh, K.N. Raymond, Inorg. Chem. (1984) 1009.
[15] Y. Chi, J.-W. Lan, W.-L. Ching, S.-M. Peng, G.-H. lee, J. Chem. Soc., Dalton Trans. (2000) 2923.
[16] S.R. Sofen, S.R. Cooper, K.N. Raymond, Inorg. Chem. 18 (1979) 1611.
[17] G.E. Freeman, K.N. Raymond, Inorg. Chem. 24 (1985) 1410.
[18] S.R. Cooper, Y.B. Koh, K.N. Raymond, J. Am. Chem. Soc. 104 (1982) 5092.
[19] M.E. Cass, D.L. Greene, R.M. Buchanan, C.G. Pierpont, J. Am. Chem. Soc. 105 (1983) 2680.
[20] M.E. Cass, N.R. Gordon, C.G. Pierpont, Inorg. Chem. 25 (1986) 3962.
[21] N.P. Luneva, S.A. Mironova, K.A. Lyssenko, M.Y. Antipin, Koord. Khim. (Russ.) (Coord. Chem.) 23 (1997) 899.
[22] C.R. Cornman, J. Kampf, V.L. Pecoraro, Inorg. Chem. 31 (1992) 1981.
[23] C.R. Cornman, G.J. Colpas, J.D. Hoeschele, J. Kampf, V.L. Pecoraro, J. Am. Chem. Soc. 114 (1992) 9925.
[24] M.J. Manos, A.J. Tasiopouos, C. Paptopoulou, A. Terzis, J.D. Woollins, A.M.Z. Slawin, A.D. Keramidas, T.A. Kabanos, J. Chem. Soc., Dalton Trans. (2001) 1556.
[25] M.P. Luneva, S.A. Mironova, A.E. Shilov, M.Y. Antipin, Angew. Chem., Int. Ed. Engl. 32 (1993) 1178.
[26] B. Bruah, S. Das, A. Chakravorty, Inorg. Chem. 41 (2002) 4502.
[27] T.A. Kabanos, A.M.Z. Slawin, D.J. Williams, J.D. Woollins, J. Chem. Soc., Dalton Trans. (1992) 1423.
[28] K.R. Heier, A.J. Norquist, C.G. Wilson, C.L. Stern, K.R. Poeppelmeier, Inorg. Chem. 37 (1998) 76.
[29] P. Archarya, O. Plashkevych, C. Morita, S. Yamada, J. Chattopadhyaya, J. Org. Chem. 68 (2003) 1529.
[30] T.J. Boyle, T.M. Alam, K.P. Peters, M.A. Rodriguez, Inorg. Chem. 40 (2002) 6281.
[31] T.J. Boyle, D.M. Pedrotty, T.M. Alam, S.C. Vick, M.A. Rodriguez, Inorg. Chem. 39 (2000) 5133.
[32] T.J. Boyle, N.L. Andrews, M.A. Rodriguez, C. Campana, T. Yiu, Inorg. Chem. 42 (2003) 5357.
[33] S.D. Bunge, T.J. Boyle, T.J. Headley, Nano Lett. 3 (2003) 901.
[34] M. Niederberger, M.H. Bartl, G.D. Stucky, J. Am. Chem. Soc. 124 (2002) 13642.

cooperative effects of the metal centers in their chemical interaction with external substrates. Furthermore, this kind of transition metal derivative possesses uncommon catalytic properties, as for instance in the cross-coupling of Grignard reagents of organic bromides and allylic alcohols [14].

Although ESI-MS and ESI-MS^2 have been increasingly used as powerful techniques for structural characterization of organometallic and coordination compounds [2,5,15–24], no similar studies on the characterization of heteropolymetallic complexes, especially those containing a Ru–Sn bond, have been reported. Therefore, the main purpose of this paper is to characterize the novel heterotrimetallic RuCp(dppf)SnX_3 complexes (**1**) as well as their heterobimetallic RuCp(dppf)X precursors (**2**) by ESI-MS and ESI-MS^2.

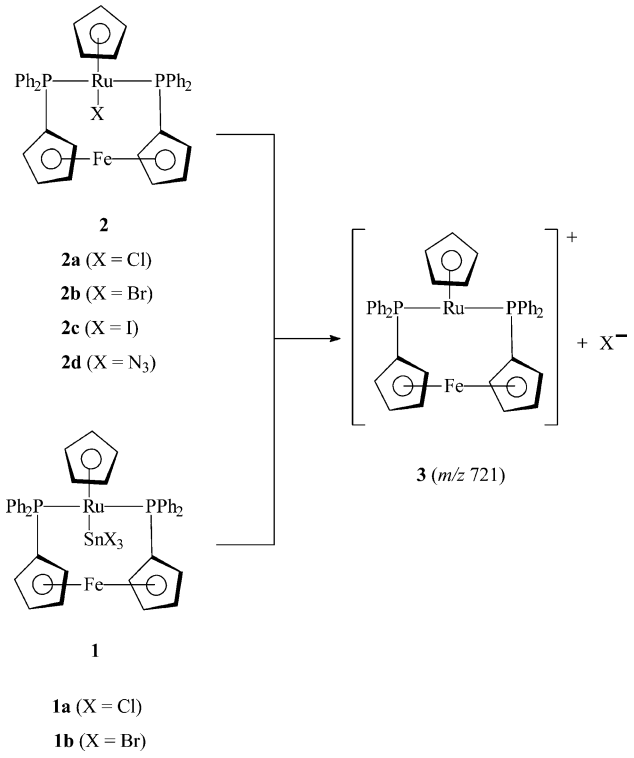
2. Experimental

Complexes **1** [25] and **2** [26] were synthesized following previously described procedures. Acetonitrile solutions of **1** and **2** were prepared in a concentration of 2×10^{-5} mol L^{-1}. All experiments were performed using a commercial LCQ Advantage ion trap mass spectrometer (ThermoElectron, San Jose, CA) equipped with an ESI source and operated in the positive ion mode. The spectra shown represent the average of about 50 scans (0.2 s/scan). Samples were infused into the ESI source with a syringe pump at a flow rate of 3–5 μL min^{-1}. Typical ESI conditions were as follows: capillary temperature, 150 °C; sheath gas (N_2) flow rate, 20 units (roughly 0.50 L min^{-1}); spray voltage 4.5 kV; capillary voltage 25 V; tube lens offset voltage, 25 V. In the MS^n operation mode, the parent ion of interest was first isolated by applying an appropriate waveform across the end cap electrodes of the ion trap to eject all trapped ions by resonance, except those with the *m/z* ratio of interest. The isolated ions were then subjected to a supplementary ac signal for excitation by resonance and collision-induced dissociation (CID). The collision energy was set to a value at which product ions were produced in measurable amounts, i.e. ca. 10%. The isolation width used in the MS^n experiments was 2 units.

3. Results and discussion

Compounds **1** [25] and **2** [26] (Scheme 1) have already been fully characterized both in the solid state and in solution, which facilitates the comparison of their structural solution NMR patterns with ESI-MS and ESI-MS^2.

Fig. 1 shows the ESI(+) mass spectrum of complex **2a** in acetonitrile solution. Very similar ESI(+) mass spectra were obtained for the analogous complexes **2b** and



Scheme 1.

2c (not shown). Through ESI, the cationic species $[Ru(C_5H_5)(dppf)]^+$ (**3**) (Scheme 1) is transferred from solution to the gas phase and detected by mass spectrometry. It is likely that the solution contains mainly neutral **2a**, which is in equilibrium with **3** and Cl^-. Because ruthenium displays seven abundant isotopes, [^{104}Ru (18.6%), ^{102}Ru (31.6%), ^{101}Ru (17.1%), ^{100}Ru (12.6%), ^{99}Ru (12.7%), ^{98}Ru (1.86%)], ^{96}Ru (5.54%)] and iron possesses four isotopes [^{58}Fe (0.28%), ^{57}Fe (2.1%), ^{56}Fe (91.72%) ^{54}Fe (5.9%)] [27], cation **3** is detected by MS as an isotopomeric cluster of singly charged ions centered at *m/z* 721 (for ^{102}Ru and ^{56}Fe), and with an isotopic pattern that matches well to that calculated [28] for $C_{39}H_{33}P_2RuFe$ (Fig. 1). In solution, **3** associates with acetonitrile forming $[\mathbf{3} + CH_3CN]^+$, which is transferred to the gas phase by ESI and detected by MS as a solvent adduct ion centered at *m/z* 762 (Fig. 1).

Fig. 2 shows the positive-ion ESI tandem mass spectrum at *m/z* 721, which is the highest abundance isotope of structure **3**. Upon CID, prominent fragments of *m/z* 657 ($[\mathbf{3} - C_5H_4]^+$), 644 ($[\mathbf{3} - C_6H_5]^+$), 580 ($[\mathbf{3} - C_6H_5{-}C_5H_4]^+$), 536 ($[\mathbf{3} - P(C_6H_5)_2]^+$) and 305 ($[Fe(C_5H_4)P(C_6H_5)_2]^+$) were observed, which is consistent with the structure proposed for **3** (Scheme 1).

The spectrum of **2d** (Fig. 3) obtained under the same electrospray conditions displays two major cations: **3** and $[Ru(C_5H_5)(dppf)N]^+$ (**4**). The latter was detected by MS as an isotopomeric cluster of singly charged ions centered at *m/z* 735 (for ^{102}Ru and ^{56}Fe), and with an

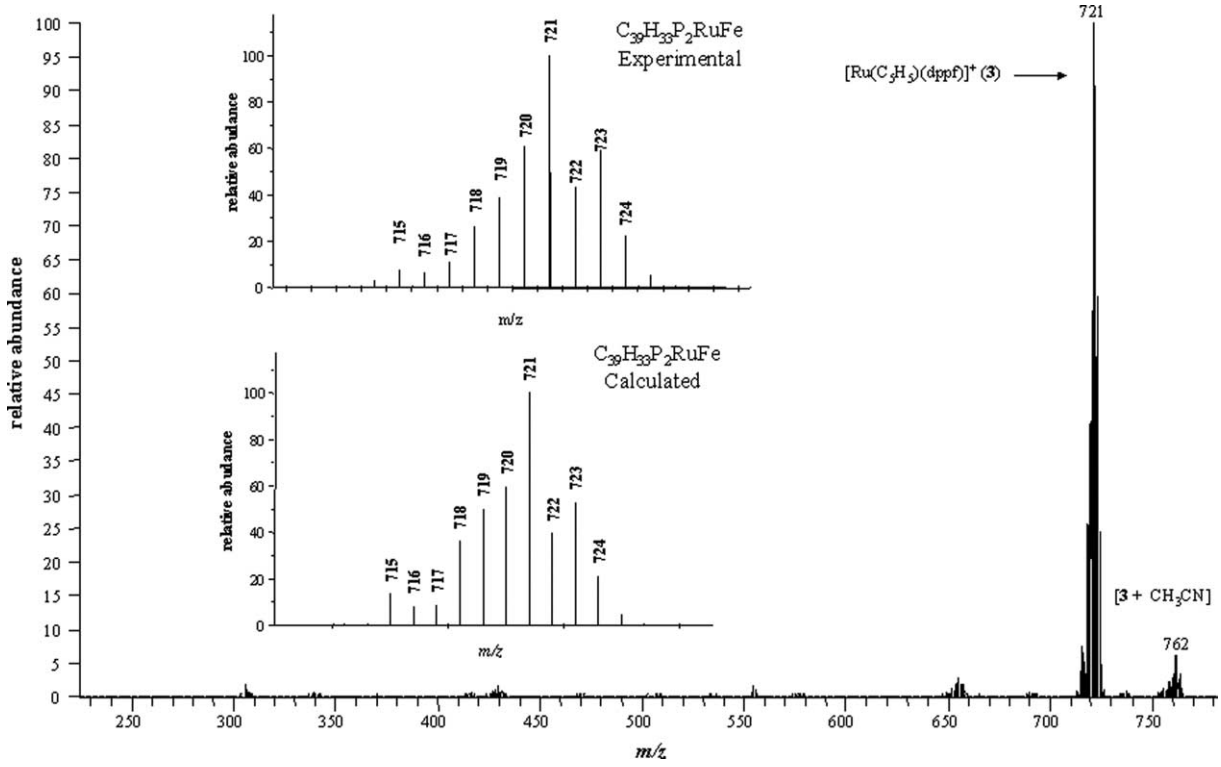


Fig. 1. Positive-ion ESI mass spectrum of the complex $[Ru(C_5H_5)(dppf)]Cl$ (**2a**) in acetonitrile solution. Insets show the ion intensities and the *m/z* distributions (experimental and calculated [28]) of cation **3** ($C_{39}H_{33}P_2RuFe$).

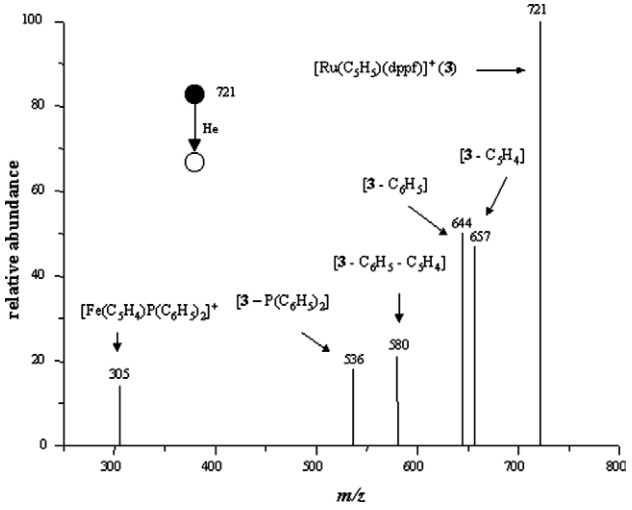


Fig. 2. Positive-ion ESI mass spectrum of mass-selected cation **3** (ionic cluster centered at *m/z* 721). For more details on the ''empty and filled circle'' notation, see [49].

isotopic pattern that fits well to that calculated for $C_{39}H_{33}P_2NRuFe$ [28]. In the positive-ion ESI tandem mass spectrum of the mass-selected ion **4** (not shown), the following most intense fragments are observed: [**4** – C_5H_4] (*m/z* 671), [**4** – C_6H_5] (*m/z* 658), [**4** – FeC_5H_4] (*m/z* 615) and [**4** – $(C_6H_5)_3$] (*m/z* 504).

The formation of ion **4** is suggested to occur in the electrospray ion source via an initial oxidation of the ruthenium atom of **2d** ($Ru^{II} \rightarrow Ru^{III}$) followed by the release of a nitrogen molecule (Scheme 2). We assume that this initial oxidation contributes to the weakening of the N–N bond in the azide moiety, which ultimately causes the formation of cation **4**. In this cation, the remaining nitrogen stays connected to the ruthenium atom, likely via a double Ru–N bond (Scheme 1). This occurs because the filled ruthenium d_{yz} orbital is available to interact with the empty p_z nitrogen orbital, thus allowing the formation of a π Ru → N bond. Moreover, the extra empty orbital in this N atom and its proximity with the Fe atom could suggest a Ru–N–Fe interaction, as represented in Scheme 2. However, additional studies are required to confirm this hypothesis.

Oxidation processes in electrospray ion sources are well known and can occur under certain experimental conditions [29–33]. Similar oxidation processes were also verified to take place for the analogous bimetallic ruthenocenyl ruthenium complex $[Ru(C=CHPh)(\eta^5\text{-}C_5H_5)(dppr)]Cl$ (dppr = $[Ru(\eta^5\text{-}C_5H_4PPh_2)_2]$). In its positive-ion ESI mass spectrum, beside an intense fragment related to the singly charged cation $[Ru(C=CHPh)(\eta^5\text{-}C_5H_5)(dppr)]^+$, a doubly charged cation was also detected at low cone voltages. However, its formation was attributed to the oxidation of the dppr-ruthenium moiety, giving rise to a complex with Ru present in two different oxidation states (Ru^{II} and Ru^{III}) [19]. Based on this example, we can also consider the

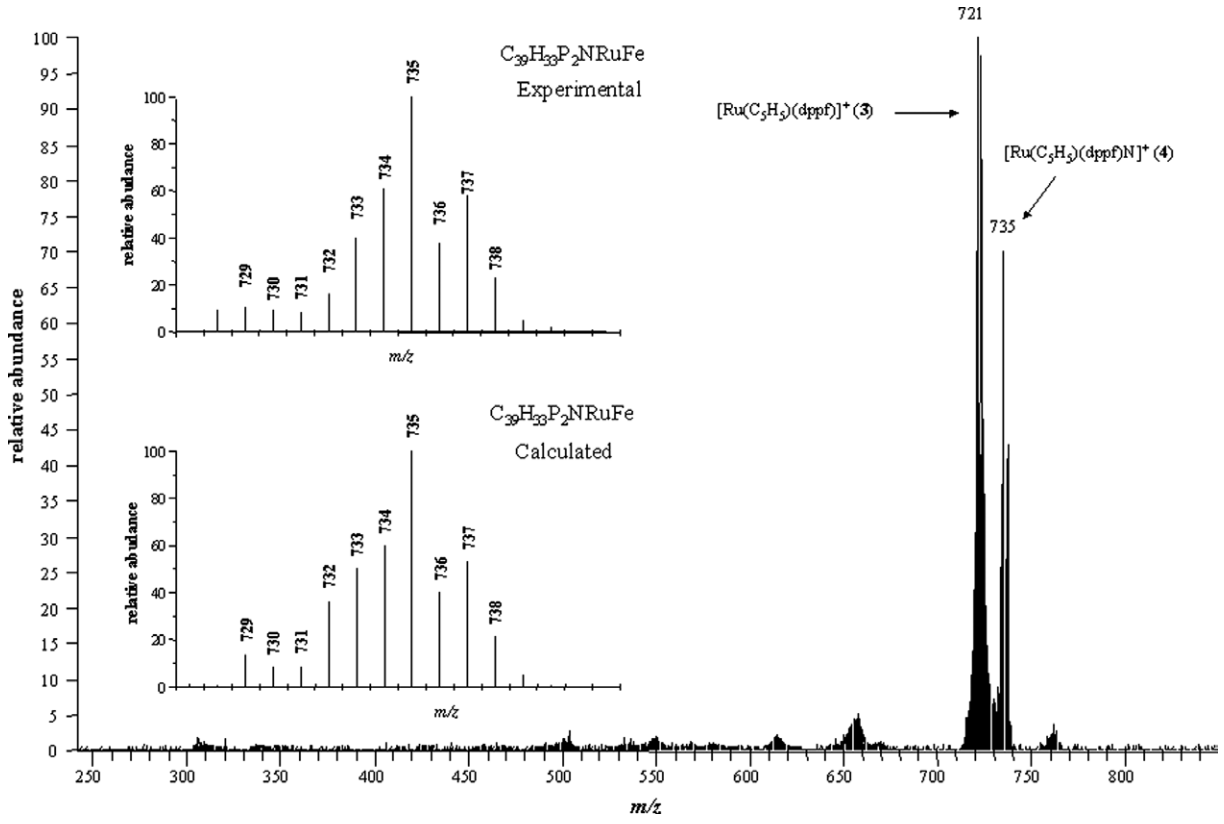
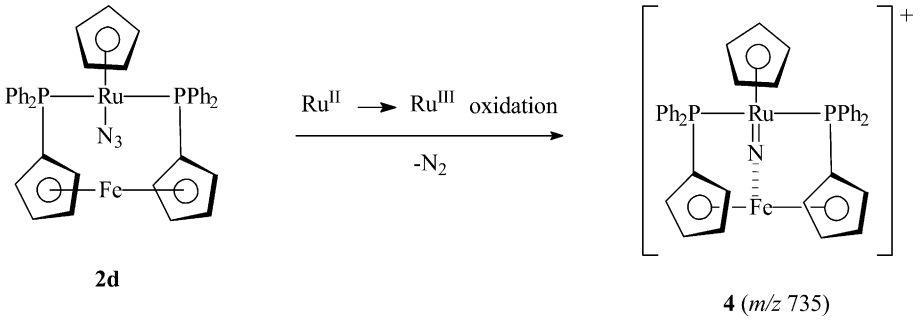


Fig. 3. Positive-ion ESI mass spectrum of the acetonitrile solution of complex $[Ru(C_5H_5)(dppf)]N_3$ (**2d**). Insets show the ion intensities and the *m*/*z* distributions (experimental and calculated [28]) of cation **4** ($C_{39}H_{33}P_2NRuFe$).



2d **4** (*m*/*z* 735)

Scheme 2.

alternative oxidation of the ferrocene centre in **2d** ($Fe^{2+} \rightarrow Fe^{3+}$), a well known and facile process, to yield the cation of *m*/*z* 735 after the release of N_2. Although it is difficult to distinguish between both oxidation processes, i.e. $Ru^{2+} \rightarrow Ru^{3+}$ or $Fe^{2+} \rightarrow Fe^{3+}$, by using only mass spectrometry, electrochemical measurements could elucidate this issue. In fact, cyclic voltammetry experiments are underway in our laboratory and will be the subject of a future publication.

Fig. 4 shows the positive-ion ESI mass spectrum of complex **1a** in acetonitrile solution (a similar mass spectrum was obtained for the analogous complex **1b**). As previously verified for complex **2a**, cation **3** (*m*/*z* 721) is by far the predominant species. Thus, it is likely that in acetonitrile solution, **1a** is in equilibrium with **3** and its negative counterpart $SnCl_3^-$. This is an unexpected result since the presence of electronegative substituents (such as Cl, Br) connected to Sn, which promote the formation of a π RuSn bond and contribute to increase the order of this bond, should impede, or at least strongly inhibit, such a dissociation. Other minor clusters centered at *m*/*z* 756, $[Ru(C_5H_5)(dppf)Cl]^+$ (**5**), *m*/*z* 911, $[Ru(C_5H_5)(dppf)SnCl_2]^+$ (**6**) and *m*/*z* 946, $[Ru(C_5H_5)(dppf)SnCl_3]^+$ (**7**) are also observed in this spectrum. The formation of these cations is tentatively explained in Scheme 3. For instance, cation **5** is likely formed via the previously described $Ru^{II} \rightarrow Ru^{III}$ oxidation followed by the loss of a neutral $SnCl_2$ molecule. On the

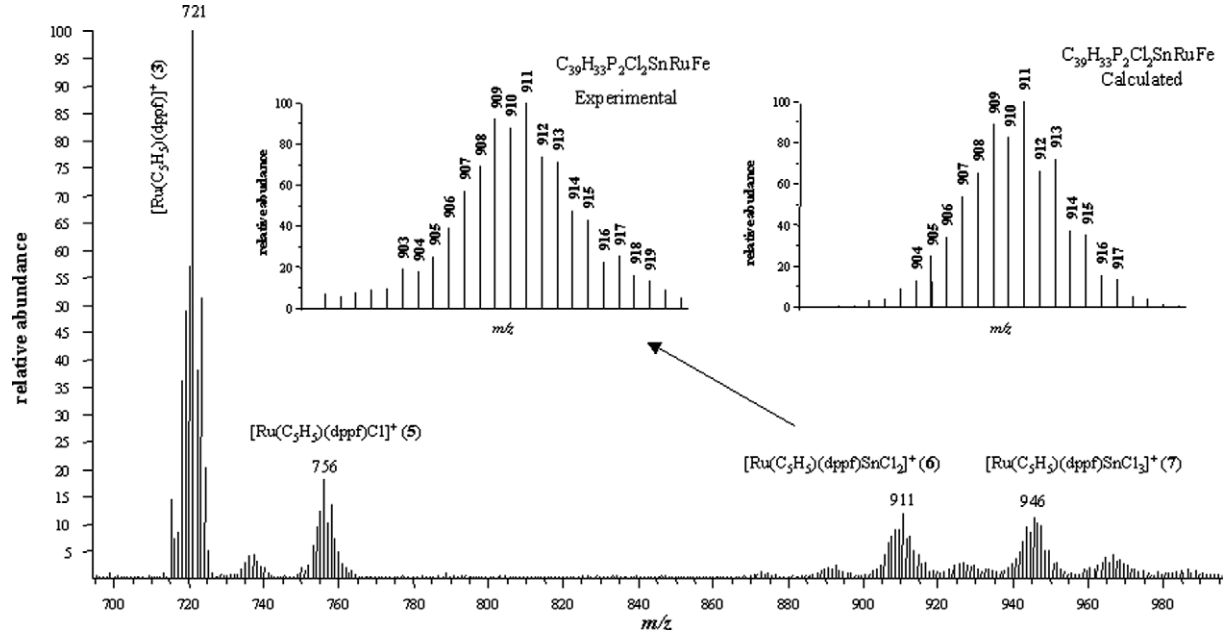
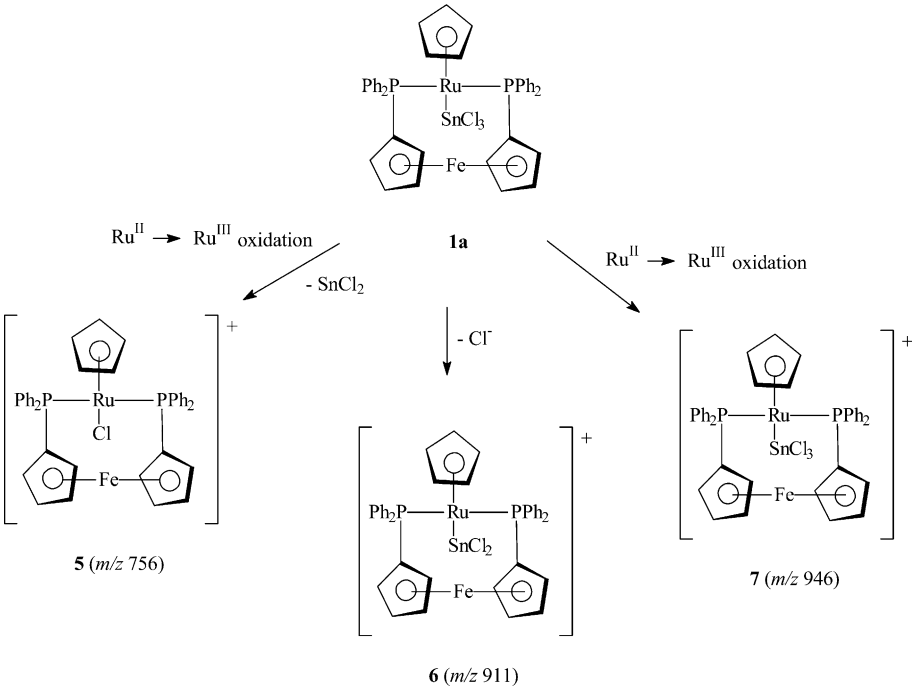


Fig. 4. Positive-ion ESI mass spectrum of the acetonitrile solution of complex $[Ru(C_5H_5)(dppf)]SnCl_3$ (**1a**). Insets show the ion intensities and the *m*/*z* distributions (experimental and calculated [28]) of cation **6** ($C_{39}H_{33}P_2Cl_2$ SnRuFe).

other hand, cation **6** is produced via a simple release of Cl^- from **1a**, whereas cation **7** corresponds to the singly charged intact complex **1a**, likely formed upon $Ru^{II} \rightarrow Ru^{III}$ oxidation. The experimental isotopic patterns of these cations fit well to those calculated for $C_{39}H_{33}P_2ClRuFe$ (**5**), $C_{39}H_{33}P_2Cl_2SnRuFe$ (**6**) (Fig. 4) and $C_{39}H_{33}P_2Cl_3SnRuFe$ (**7**) [28]. The mass-selection and CID of **5** characteristically display the loss of a chlorine atom, giving rise to the fragment of *m*/*z* 721 as cation **3** (spectrum not shown). The positive-ion ESI tandem mass spectrum of the mass-selected ion **6** (not shown) furnishes exclusively cation **3** (*m*/*z* 721) via the release of a neutral $SnCl_2$ molecule. Finally, the mass selection and fragmentation of ion **7** also yields exclu-



Scheme 3.

sively the *m*/*z* 721 fragment via the $SnCl_3$ radical loss (spectrum not shown).

3.1. Detection of catalytically active species

It has been verified that complexes **2** and **1** [34] as well as similar heterotrimetallic Ru(II)–Sn(II) complexes [35,36] and $RuCl_3$–SnX_2 composite systems [37] are effective catalysts in the conversion of methanol to acetic acid [38]. The mechanism of this reaction has been studied [35,37,39,40] but is not yet fully understood. Thus, taking into account that ESI is able to transfer ions from solution to the gas phase [6,8,41–44], and most importantly, the composition of ESI-generated ions often closely reflects that of the solution [5,16,17,41,45,46], we hypothesize that cation **3**, undoubtedly detected in acetonitrile solutions of complexes **2** and **1** (Scheme 1), could be the catalytically active species in this conversion. This hypothesis is based on several studies [47,48] describing the use of ESI-MS to detect cationic species likely to be involved in catalytic processes. For instance, Dyson and coworkers [48] verified that in the electrospray ionization mass spectrum of $[Ru_4\ (\eta^6\text{-}C_6H_6)_4\text{-}(OH)_4]^{4+}$, the main species present in aqueous solution are the intact cubane tetramer and the dimer $[Ru_2\text{-}(\eta^6\text{-}C_6H_6)_2(OH)_2]^{2+}$ and proposed that the latter is an active benzene hydrogenation catalyst.

4. Conclusion

ESI proved to be a suitable and efficient technique for the characterization of heterotrimetallic $Ru(\eta^5\text{-}C_5H_5)(dppf)SnX_3$ (**1**) complexes, containing a Ru–Sn bond, and their heterobimetallic $Ru(\eta^5\text{-}C_5H_5)(dppf)X$ (**2**) precursors. The formation of cation **3**, likely the catalytically active species in the single step conversion of methanol to acetic acid, from **2** and **1** seems to be a general tendency for these ruthenium complexes.

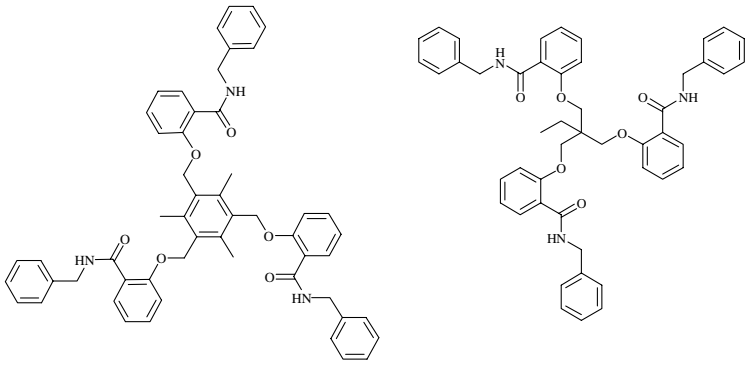
Acknowledgments

This work had financial support from FAPEMIG (Fundação de Amparo à Pesquisa do Estado de Minas Gerais, Brazil) and CNPq (Conselho Nacional de Desenvolvimento Científico e Tecnológico, Brazil).

References

[1] N.B. Cech, C.G. Enke, Mass Spectrom. Rev. 20 (2001) 362.
[2] R. Colton, A. DAgostino, J.C. Traeger, Mass Spectrom. Rev. 14 (1995) 79.
[3] T.G. Spence, T.D. Burns, G.B. Guckenberger, L.A. Posey, J. Phys. Chem. A 101 (1997) 1081.
[4] T.D. Burns, T.G. Spence, T.A. Mooney, L.A. Posey, Chem. Phys. Lett. 258 (1996) 669.
[5] R.M.S. Pereira, V.I. Paula, R. Buffon, D.M. Tomazela, M.N. Eberlin, Inorg. Chim. Acta 357 (2004) 2100.
[6] J. Griep-Raming, S. Meyer, T. Bruhn, J.O. Metzger, Angew. Chem., Int. Ed. 41 (2002) 2738.
[7] R. Arakawa, S. Tachiyashiki, T. Matsuo, Anal. Chem. 67 (1995) 4133.
[8] E.C. Meurer, A.A. Sabino, M.N. Eberlin, Anal. Chem. 75 (2003) 4701.
[9] D.V. Augusti, F. Carazza, A.A. Okuma, R. Augusti, Rapid Commun. Mass Spectrom. 17 (2003) 1084.
[10] D.A. Plattner, Int. J. Mass Spectrom. 207 (2001) 125.
[11] R. Bertani, R. Seraglia, D. Favretto, R.A. Michelin, M. Mozzon, S.M. Sbovata, A. Sassi, Inorg. Chim. Acta 356 (2003) 357.
[12] A.M. Bond, R. Colton, A. Dagostino, J. Harvey, J.C. Traeger, Inorg. Chem. 32 (1993) 3952.
[13] T.J. Cardwell, R. Colton, N. Lambropoulos, J.C. Traeger, P. Marriott, J. Anal. Chim. Acta 280 (1993) 239.
[14] T. Hayashi, M. Konishi, M. Kumada, J. Organomet. Chem. 186 (1980) C1.
[15] R. Colton, K.L. Harrison, Y.A. Mah, J.C. Traeger, Inorg. Chim. Acta 231 (1995) 65.
[16] S.H. Toma, S. Nikolaou, D.M. Tomazela, M.N. Eberlin, H.E. Toma, Inorg. Chim. Acta 357 (2004) 2253.
[17] S.H. Toma, M. Uemi, S. Nikolaou, D.M. Tomazela, M.N. Eberlin, H.E. Toma, Inorg. Chem. 43 (2004) 3521.
[18] J.M. Slocik, K.V. Somayajula, R.E. Shepherd, Inorg. Chim. Acta 320 (2001) 148.
[19] S.P. Yeo, W. Henderson, T.C.W. Mak, T.S.A. Hor, J. Organomet. Chem. 575 (1999) 171.
[20] J.V. Iribarne, P.J. Dziedzic, B.A. Thomson, Int. J. Mass Spectrom. 50 (1983) 331.
[21] C.M. Whitehouse, R.N. Dreyer, M. Yamashita, J.B. Fenn, Anal. Chem. 57 (1985) 675.
[22] V. Katta, S.K. Chowdhury, B.T. Chait, J. Am. Chem. Soc. 112 (1990) 5348.
[23] R.D. Smith, C.J. Barinaga, H.R. Udseth, Anal. Chem. 60 (1988) 1948.
[24] M. Yamashita, J.B. Fenn, J. Phys. Chem. A 88 (1984) 4451.
[25] L.A. Paim, E.M. Moura, H.G.L. Siebald, G.M. de Lima, A.C. Doriguetto, J. Ellena, Spectrochim. Acta A 60 (2004) 2383.
[26] M.I. Bruce, I.R. Butler, W.R. Cullen, G.A. Koutsantonis, M.R. Snow, E.R.T. Tiekink, Aust. J. Chem. 41 (1988) 963.
[27] E. de Hoffmann, V. Stroobant, Mass Spectrometry Principles and Applications, second ed., Wiley, Chichester, UK, 2002.
[28] Theoretical fits were carried out using the University of Sheffield software, which is available at <http://www.shef.ac.uk/chemistry/chemputer/isotopes.html>.
[29] G.J. Vanberkel, S.A. Mcluckey, G.L. Glish, Anal. Chem. 64 (1992) 1586.
[30] C.E.C.A. Hop, D.A. Saulys, D.F. Gaines, J. Am. Soc., Mass Spectrom. 6 (1995) 860.
[31] G.J. Van Berkel, F. Zhou, Anal. Chem. 67 (1995) 3958.
[32] X.M. Xu, S.P. Nolan, R.B. Cole, Anal. Chem. 66 (1994) 119.
[33] C.E.C.A. Hop, J.T. Brady, R. Bakhtiar, J. Am. Soc. Mass Spectrom. 8 (1997) 191.
[34] L.A. Paim, H.G.L. Siebald, Unpublished results.
[35] T. Yamakawa, M. Hiroi, S. Shinoda, J. Chem. Soc., Dalton Trans. 15 (1994) 2265.
[36] P.A. Robles-Dutenhefner, E.M. Moura, G.J. Gama, H.G.L. Siebald, E.V. Gusevskaya, J. Mol. Catal. A 164 (2000) 39.
[37] L.C. Yang, T. Yamakawa, S. Shinoda, J. Mol. Catal. A 130 (1998) 249.
[38] S. Shinoda, T. Yamakawa, J. Chem. Soc., Chem. Commun. (1990) 1511.

[39] T. Ohnishi, T. Yamakawa, S. Shinoda, J. Chem. Soc., Dalton Trans. 5 (1997) 789.
[40] H. Einaga, T. Yamakawa, S. Shinoda, J. Mol. Catal. A 97 (1995) 35.
[41] R.G. Cooks, D.X. Zhang, K.J. Koch, F.C. Gozzo, M.N. Eberlin, Anal. Chem. 73 (2001) 3646.
[42] K.J. Koch, F.C. Gozzo, S.C. Nanita, Z. Takats, M.N. Eberlin, R.G. Cooks, Angew. Chem., Int. Ed. 41 (2002) 1721.
[43] A.A. Sabino, A.H.L. Machado, C.R.D. Correia, M.N. Eberlin, Angew. Chem., Int. Ed. 43 (2004) 2514.
[44] S. Meyer, J.O. Metzger, Anal. Bioanal. Chem. 377 (2003) 1108.
[45] D.M. Tomazela, F.C. Gozzo, G. Ebeling, P.R. Livotto, M.N. Eberlin, J. Dupont, Inorg. Chim. Acta 357 (2004) 2349.
[46] Z. Takats, S.C. Nanita, R.G. Cooks, Angew. Chem., Int. Ed. 42 (2003) 3521.
[47] J.A. Kenny, K. Versluis, A.J.R. Heck, T. Walsgrove, M. Wills, Chem. Commun. (2000) 99.
[48] P.J. Dyson, K. Russell, T. Welton, Inorg. Chem. Commun. 4 (2001) 571.
[49] M.N. Eberlin, Mass Spectrom. Rev. 16 (1997) 113.



L **L_1**

Scheme 1. The chemical formula of the ligands **L** and $\mathbf{L}_1$.

arms, the solid complex is still highly luminescent. In order to study the influence of the skeleton of the amide type tripodal ligand on the structure and luminescence properties of rare earth complexes, recently we prepared another new amide type tripodal ligand, 1,3,5-trimethyl-2,4,6-tris{[(2′-benzylaminoformyl)phenoxyl]methyl}-benzene (**L**) (Scheme 1), and investigated the reaction of **L** with rare earth nitrates. Interestedly, the crystal structure of $[Sm(NO_3)_3\mathbf{L}]_n$ demonstrates a (10,3)-a net type coordination polymeric structure. To our best knowledge, it is the first example of a (10,3)-a net directed by rare earth ions. Although there are some examples found in coordination polymers of (10,3)-a nets, a unique type of three-connected 3-D net [6,7], nearly all of them are directed by transition metal ions with nitrogen-donor ligands [8]. This is partly due to the tendency of transition metals to have a relatively low coordination number.

As a part of our systematic studies, in this paper we report the preparation, properties and structure of complexes of rare earth nitrates with 1,3,5-trimethyl-2,4,6-tris{[(2′-benzylaminoformyl)phenoxyl]methyl}benzene (**L**).

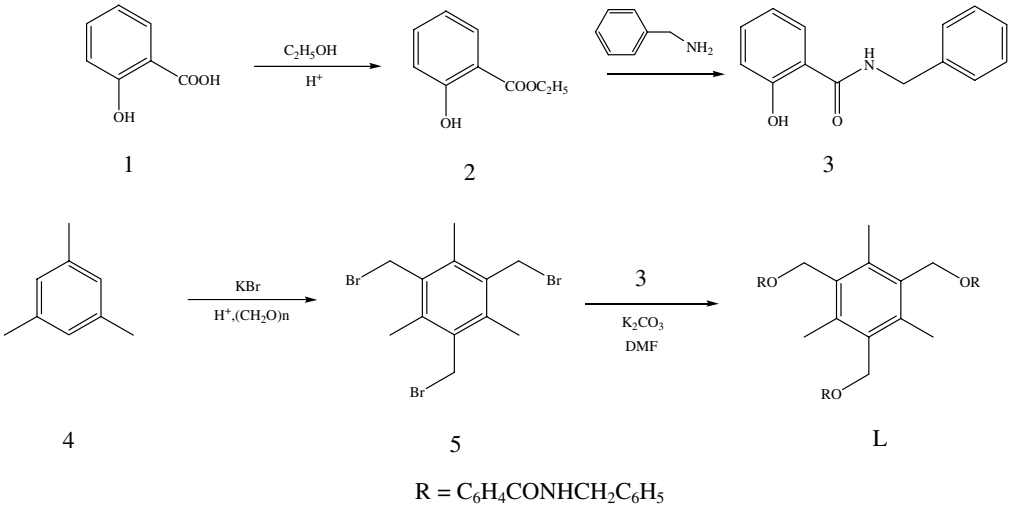
2. Experimental

2.1. Materials

N-Benzylsalicylamide (**3**) [9] and 1,3,5-tribromomethyl-2,4,6-trimethylbezene (**5**) [10] were prepared according to the literature methods. Other chemicals were obtained from commercial sources and used without further purification.

2.2. Preparation of tripodal ligand *L*

The synthetic route for the tripodal ligand is shown in Scheme 2. *N*-Benzylsalicylamide (0.58 g, 2.57 mmol), potassium carbonate (0.5 g, 3.6 mmol) and DMF (10 cm^3) were warmed to ca 80 °C and 1,3,5-tribromomethyl-2,4,6-trimethylbenzene (0.5 g, 0.85 mmol) was



R = $C_6H_4CONHCH_2C_6H_5$

Scheme 2. The synthetic route for the tripodal ligand **L**.

added. The reaction mixture was stirred at 80–90 °C for 5 h. After cooling down, the mixture was poured into water (100 cm^3). The resulted solid was treated by column chromatography on silica gel [petroleum ether:-ethyl acetate (3:1)] to get tripodal ligand **L**, yield 65%; m.p. 74–76 °C; ^1H NMR ($CDCl_3$, 300 MHz) δ: 2.17 (s, 9H), 4.34 (d, $J = 6$ Hz, 6H), 4.94 (s, 6H), 6.90–8.31 (m, 27H), $H_{(N-H)}$ not detected; IR (KBr) ν: 3390, 1652, 1530, 1478, 1293, 1217, 754 cm^{-1} ; *Anal*. Calc. for $C_{54}H_{51}N_3O_6$: C, 76.33; H, 6.01; N, 4.95. Found: C, 76.19; H, 5.92; N, 4.94%.

2.3. Preparation of the complexes

A solution of 0.1 mmol **L** in 10 cm^3 of ethyl acetate was added dropwise to a solution of 0.1 mmol rare earth nitrates (RE = La, Pr, Nd, Sm, Eu, Gd, Tb, Ho, Y) in 10 cm^3 of ethyl acetate. The mixture was stirred at room temperature for 4 h. The precipitated solid complex was filtered, washed with ethyl acetate and dried in vacuo over P_4O_{10} for 48 h and submitted for elemental analysis, yield 60%. Analytical data and molar conductance values of the complexes are given in Table 1. Slow diffusion of diethyl ether into the DMF solution of the samarium complex afforded colorless rhombic crystals.

2.4. Chemical and physical measurements

The RE(III) ion was determined by EDTA titration using xylenol-orange as an indicator. Carbon, nitrogen and hydrogen were determined using an Elementar Vario EL (see Table 1). The IR spectra were recorded in the 4000–400 cm^{-1} region using KBr pellets and a Nicolet Nexus 670 FTIR spectrometer (see Table 4). Thermal analyses (TG and DTA) were performed on a Beijing WCT-2A thermobalance using about 10 mg powder sample and working at a heating rate of 5 °C min^{-1} in static air. ^1H NMR spectra were measured on a Varian Mercury 300 spectrometer in $CDCl_3$ solutions, with TMS as an internal standard. Luminescence spectra were obtained on a Hitachi M-850 fluorescence spectrophotometer.

2.5. Crystal structure determination

For the samarium complex, X-ray measurements were performed on a Siemens P4 four-circle diffractometer with graphite-monochromatized Mo Kα radiation ($\lambda = 0.71073$ Å) at 295 ± 2 K. The structure was solved by full-matrix least-squares techniques with anisotropic thermal factors for all non-hydrogen atoms. Theoretical models fixed the hydrogen atoms of the compound. All calculations were performed using the program package SHELXTL-97.

3. Results and discussion

The analytical data for the newly synthesized complexes, listed in Table 1, indicate that the nine complexes conform to a 1:1 metal-to-ligand stoichiometry. All the complexes are soluble in DMSO and DMF and are sparingly soluble in ordinary organic solvents such as methanol, ethanol, acetonitrile, acetone, chloroform, benzene and cyclohexane.

3.1. Crystal structure of $[Sm(NO_3)_3\mathbf{L}]_n$

A summary of the crystallographic data and details of the structure refinements are listed in Table 2. Selected bond lengths and bond angles are given in Table 3.

The single-crystal X-ray analysis of the complex $[Sm(NO_3)_3\mathbf{L}]_n$ reveals that each Sm atom is coordinated with nine oxygen donor atoms, six of which belong to three bidentate nitrate groups and the remaining three to carbonyl groups from three tripodal ligands (Fig. 1). The coordination polyhedron around Sm is a distorted monocapped square antiprism. At the same time, each ligand binds to three Sm(III) ions using its three oxygen atoms of the amide groups (Fig. 2(a)). So the whole structure consists of an infinite array of trigonal Sm(III) ions bridged by tridentate ligands and a (10,3)-a net is formed. A schematic view of this 3-D net is shown in Fig. 2(b). Characteristic features of a

Table 1
Analytical data for $[RE(NO_3)_3\mathbf{L}]\cdot 2H_2O$

Complex	Found (Calc.)			
	%C	%H	%N	%RE
$[La(NO_3)_3\mathbf{L}]\cdot 2H_2O$	54.49 (54.11)	4.80 (4.62)	6.68 (7.01)	11.44 (11.58)
$[Pr(NO_3)_3\mathbf{L}]\cdot 2H_2O$	54.14 (54.00)	4.64 (4.61)	7.19 (7.00)	11.89 (11.73)
$[Nd(NO_3)_3\mathbf{L}]\cdot 2H_2O$	54.06 (53.86)	4.40 (4.60)	7.13 (6.98)	11.60 (11.97)
$[Sm(NO_3)_3\mathbf{L}]\cdot 2H_2O$	54.03 (53.58)	4.70 (4.58)	6.96 (6.94)	12.01 (12.43)
$[Eu(NO_3)_3\mathbf{L}]\cdot 2H_2O$	53.65 (53.51)	4.37 (4.57)	7.24 (6.93)	12.38 (12.54)
$[Gd(NO_3)_3\mathbf{L}]\cdot 2H_2O$	52.98 (53.28)	4.44 (4.55)	7.05 (6.90)	12.68 (12.91)
$[Tb(NO_3)_3\mathbf{L}]\cdot 2H_2O$	53.23 (53.47)	4.19 (4.37)	7.17 (6.89)	13.01 (13.04)
$[Ho(NO_3)_3\mathbf{L}]\cdot 2H_2O$	52.97 (52.94)	4.63 (4.52)	6.97 (6.86)	13.40 (13.46)
$[Y(NO_3)_3\mathbf{L}]\cdot 2H_2O$	56.26 (56.45)	4.62 (4.82)	7.38 (7.31)	7.50 (7.74)

Table 2
Crystal data and structure refinement for the complex $[Sm(NO_3)_3L]_n$

Empirical formula	$C_{54}H_{48}N_6O_{15}Sm$
Formula weight	1171.33
Temperature (K)	295(2)
Crystal system	orthorhombic
Space group	$P2_12_12_1$
a, b, c (Å)	13.312(2), 19.119(4), 21.075(6)
α, β, γ (°)	90.00, 90.00, 90.00
V (Å^3)	5364(2)
Z	4
D_{calc} (g cm^{-3})	1.450
μ(Mo Kα) (mm^{-1})	1.168
F(000)	2384
Crystal size (mm)	$0.50 \times 0.48 \times 0.26$
Range (°)	1.81–27.00
Index ranges	$-15 \leqslant h \leqslant 16$; $-22 \leqslant k \leqslant 24$; $-25 \leqslant l \leqslant 26$
Reflection collected	12406
Independent reflections [R_{int}]	7681 [0.0222]
Absorption correction	empirical
Refinement method	full-matrix least-squares on F^2
Data/restraints/parameters	7681/717/58
Goodness-of-fit on F^2	0.935
Final R indices	$R = 0.0446$, $wR = 0.0882$

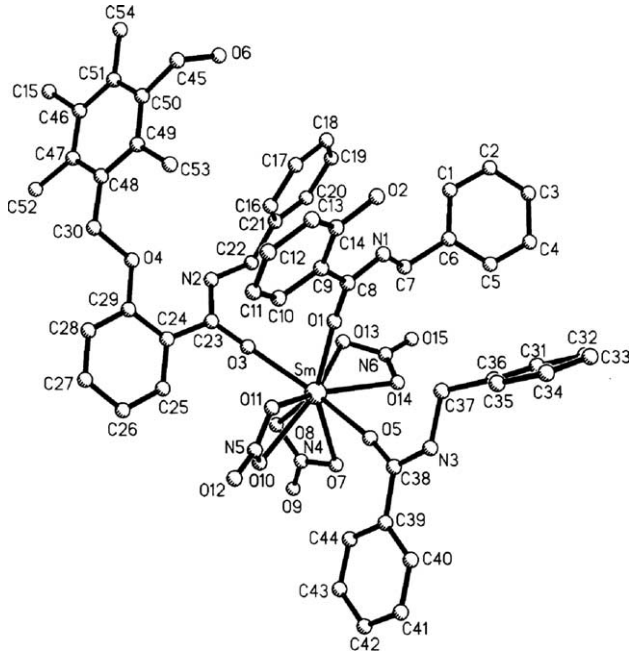


Fig. 1. Coordinated environment of the Sm atoms in $[Sm(NO_3)_3L]_n$.

single (10,3)-a net are 4_1 helices [6,7], all of the same handedness, running parallel to the cubic cell edges. In contrast to its prototypal frame, this complex contains two types of alternating centers, so that the original interconnected 4_1 helical chains become 2_1–Sm–L–Sm–L–helixes, which happen to be left handed. In addition, all the counter ions, NO_3^-, do not fill the formed channels, but bind to the Sm(III) ions. So the whole frame is a completely neutral network.

The conformation of the ligand in the complex is interesting. The three arms are so long that their terminal groups can "fold back". Through intra-molecular π–π interactions, two benzyl groups wrap around the central benzene ring, one above and the other below, forming the "folding-shape" of the ligand. The three parallel phenyl rings are separated by 3.699 Å (a and b) and 3.746 Å (a and c) (Fig. 3). The dihedral angle between (a) and (b) is 13.6°, and 15.7° between (a) and (c). Two oxygen atoms of the carbonyl groups in the ligand, namely, O1 and O5, are located in the outer part of the whole ligand molecule (Fig. 3). This conformation is necessary for the ligand to bind three Sm(III) ions simultaneously.

In general, a net of the (10,3)-a type exhibits large channels of octagonal section, and their dimension is related to the length of the rods connecting the centers [8]. The large channels are usually filled by the counter ions, such as Sr^{2+} in $SrSi_2$ (rod length 2.39 Å), PF_6^- in [Ag(hmt)] $PF_6 \cdot H_2O$ (rod length 3.85 Å) [8b] and SbF_6^- in $[Ag_2(2,3\text{-}Me_2pyz)_3][SbF_6]_2$ (rod length 7.16–7.58 Å) [8d]. Some of the nets exhibit interpenetration, in the same handedness or the opposite handedness. In fact,

Table 3
Selected bond lengths (Å) and angles (°) for the complex $[Sm(NO_3)_3L]_n$

Sm–O5	2.328(4)	Sm–O3	2.337(4)	Sm–O1	2.361(4)
Sm–O13	2.493(4)	Sm–O11	2.498(5)	Sm–O8	2.513(4)
Sm–O10	2.525(4)	Sm–O14	2.534(5)	Sm–O7	2.539(4)
O5–Sm–O3	154.4(2)	O5–Sm–O1	88.11(2)	O3–Sm–O1	80.03(14)
O5–Sm–O13	121.6(2)	O3–Sm–O13	79.27(2)	O1–Sm–O13	81.61(2)
O5–Sm–O11	73.68(2)	O3–Sm–O11	81.40(15)	O1–Sm–O11	75.91(15)
O13–Sm–O11	152.5(2)	O5–Sm–O8	125.3(2)	O3–Sm–O8	71.36(14)
O1–Sm–O8	146.0(15)	O13–Sm–O8	75.50(15)	O11–Sm–O8	116.2(15)
O5–Sm–O10	81.42(15)	O3–Sm–O10	87.38(13)	O1–Sm–O10	126.2(15)
O13–Sm–O10	146.6(15)	O11–Sm–O10	50.47(13)	O8–Sm–O10	71.25(15)
O5–Sm–O14	71.73(2)	O3–Sm–O14	128.8(2)	O1–Sm–O14	84.50(15)
O13–Sm–O14	50.18(2)	O11–Sm–O14	140.53(2)	O8–Sm–O14	99.20(2)
O10–Sm–O14	138.6(2)	O5–Sm–O7	77.08(2)	O3–Sm–O7	121.5(15)
O1–Sm–O7	154.0(13)	O13–Sm–O7	88.05(2)	O11–Sm–O7	118.9(2)
O8–Sm–O7	50.20(14)	O10–Sm–O7	73.05(2)	O14–Sm–O7	70.67(2)

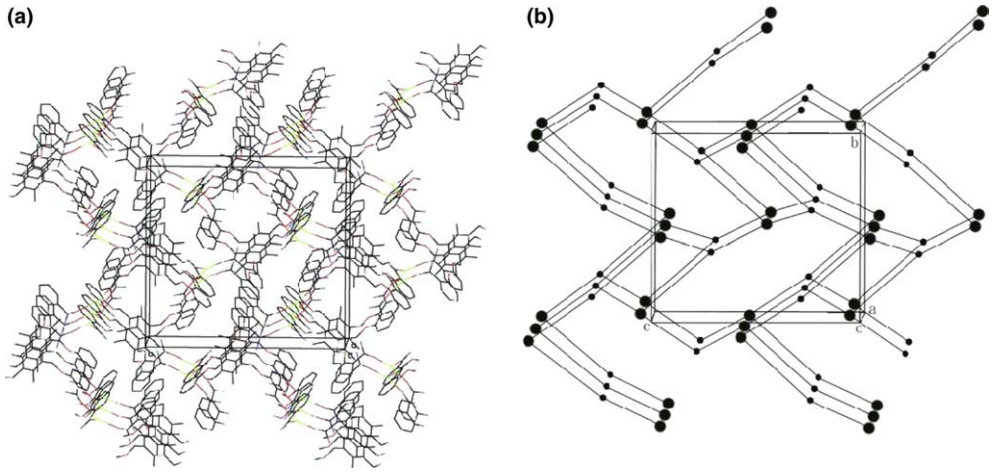


Fig. 2. (a) Structure view of $[Sm(NO_3)_3L]_n$ down the *a* axis. All the nitrates and the benzyl groups are omitted for clarity. (b) Schematic view of the framework in $[Sm(NO_3)_3L]_n$ (small balls, Sm ions; large balls, centers of the central benzene rings of the ligands).

the main problem encountered in constructing molecular-based microporous materials is the obstruction formed by self-interpenetration of networks. So interpenetration should be avoided in preparing the porous materials. It is noteworthy that although the rods are long (length 9.15–9.49 Å), no interpenetration is observed in this complex. But unfortunately, the ligands fill the channels themselves with their "thick" rods and large terminal groups (Fig. 4). It seems like a contradiction. So there is much to do to find well-designed molecular materials with large channels or holes, especially in (10,3)-a nets, which have chiral channels [11].

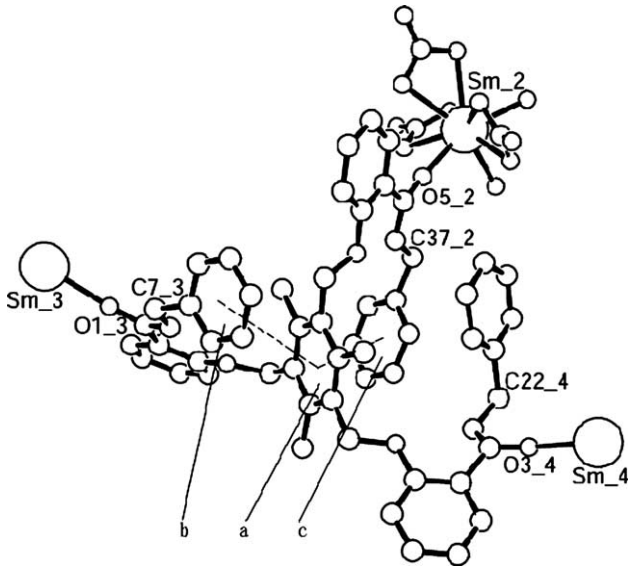


Fig. 3. The intra-molecular π–π interaction (indicated by dashed lines).

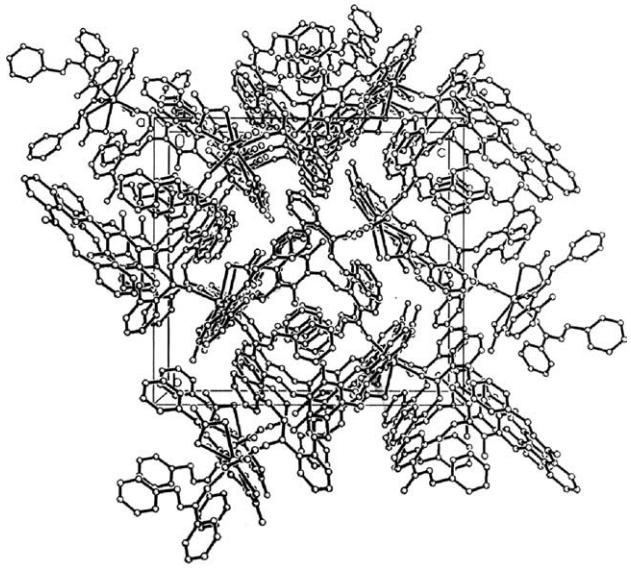


Fig. 4. The molecular packing arrangement.

3.2. Infrared spectra

The most important IR peaks of the ligand and the complexes are reported in Table 4.

The "free" ligand **L** exhibit two absorption bands at 1652 and 1217 cm^{-1} which are assigned to ν(C=O) and ν(C–O–C), respectively. In the complexes, the low-energy band remains unchanged, but the high-energy band red shifts to about 1610 cm^{-1} ($\Delta\nu = 42\ cm^{-1}$) as compared to its counterpart for the "free" ligand, indicating that only the oxygen atom of C=O takes part in coordination to the metal ions.

The characteristic frequencies of the coordinating nitrate groups (C_{2v}) appear at ca 1500 (ν_1), 1300 (ν_4), 1030 (ν_2) and 815 (ν_3) cm^{-1} [12], and the

Table 4
The IR spectra data (cm^{-1})

Compound	ν(C=O)	ν(C–O–C)	$\nu(NO_3^-)$				
			ν_1	ν_4	ν_2	ν_5	$\nu_1 - \nu_4$
L	1652s	1217s					
$[La(NO_3)_3\mathbf{L}]\cdot 2H_2O$	1611s	1219s	1480s	1283s	1026	817w	197
$[Sm(NO_3)_3\mathbf{L}]\cdot 2H_2O$	1611s	1225s	1484s	1301s	1028	816w	183
$[Eu(NO_3)_3\mathbf{L}]\cdot 2H_2O$	1611s	1225s	1483s	1302s	1028	815w	181
$[Tb(NO_3)_3\mathbf{L}]\cdot 2H_2O$	1612s	1224s	1482s	1302s	1028	815w	180
$[Y(NO_3)_3\mathbf{L}]\cdot 2H_2O$	1613s	1223s	1490s	1305s	1030	816w	185

difference between two strongest absorptions (ν_1 and ν_4) of the nitrate groups is about 190 cm^{-1}, clearly establishing that the NO_3^- groups in the solid complexes coordinate to the rare earth ion as bidentate ligands [13]. Additionally, no bands at 1380, 820 and 720 cm^{-1} in the spectra of complexes indicates that free nitrate groups (D_{3h}) are absent. This is in agreement with the results of the structural analyses discussed above.

In the IR spectra of the complexes, broad bands at 3450 cm^{-1} occur from the O–H stretching vibrations of water and the absence of a band for $\rho_r(H_2O)$ at ca 590 cm^{-1} shows that the water molecules in the complexes are not coordinated water [13]. This inference is verified by the result of TG-DTA analysis.

3.3. Thermal analysis

The TG and DTA curves for the Y complex show that the complex has no melting point and the water molecules contained in the complex are all crystallized water molecules, because only one endothermic peak appears at ca 104 °C and the percent of water is consistent with the result of the elemental analysis. The complex is stable up to ca 218 °C and then decomposes in the temperature range 218–800 °C, producing three exothermic peaks.

3.4. Luminescence properties of the complexes

Ligand-based excitations cause structural emission of rare earth complexes and the ligand luminescence is quenched showing that ligand-to-metal energy transfer occurs [14]. The ability to transfer energy from being ligand-centered to metal-centered is important in the design of rare earth(III) supramolecular photonic devices [15]. The luminescence spectra of the ligand and the Eu^{3+} and Tb^{3+} complexes in the solid state were recorded at room temperature. The emission spectra of the complexes are shown in Fig. 5.

On excited by the absorption band at 320 nm, the "free" ligand exhibits broad emission bands (λ_{max} = 450 nm). It is shown in Fig. 5 that the complexes show the characteristic emissions of Eu^{3+} or Tb^{3+}. This indicates that the tripodal ligand **L** is a good organic chelator to absorb energy and transfer it to the metal ions. In the spectrum of the Eu^{3+} complex, the relative intensity of $^5D_0 \rightarrow {}^7F_2$ is more intense than that of $^5D_0 \rightarrow {}^7F_1$ showing that the Eu(III) ion does not lie in a centrosymmetric coordination site [16], in agreement with the crystal structure analysis. In addition, the emission bands at ca 450 nm in the complexes are still visible, indicating that the energy transfer in these complexes is not so effective. An intramolecular energy transfer from the triplet state of the ligand to the resonance level of the

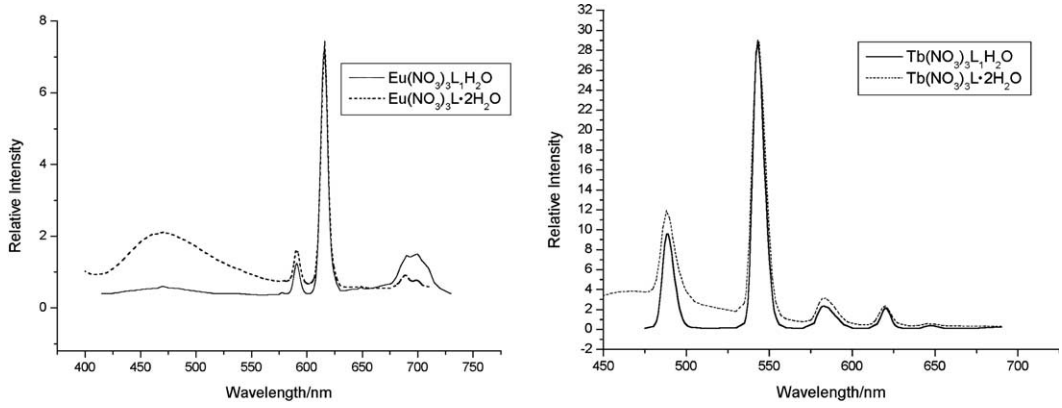


Fig. 5. Emission spectra of complexes in the solid state (excited at 320 nm).

RE(III) ion is one of the most important processes having influence on the RE(III) luminescence quantum yields of RE(III) chelates [17]. So considering the emission spectra of the complexes, we can conclude that the triplet energy of **L** is not at a very appropriate level.

4. Conclusions

In this paper, we report the preparation, properties and crystal structure of the complexes of rare earth nitrates with 1,3,5-trimethyl-2,4,6-tris{[(2′-benzylaminoformyl)phenoxyl]methyl}benzene (**L**). The complex $[Sm(NO_3)_3\mathbf{L}]_n$ is the first example determined by X-ray structure analysis, showing a (10,3)-a net constructed by RE(III) ions and a flexible tripodal ligand. We deduce that there may be two reasons for this interesting result. Firstly, NO_3^-, as a suitable counter ion was chosen. The coordination number provided by the ligand is only three, which is not sufficient for high coordinated rare earth ions. An additional three bidentate nitrates make the total coordinated number nine, satisfying the need of high coordination number. The other reason is the "folding-shaped" conformation of the ligand in the structure, which makes it easy for the oxygen atom to coordinate with the rare earth ions. This is one of the key triggers for the construction of the backbone of the 3-C, 3-D network. In addition, this structure is very different from the structure of the rare earth complex of 1,1,1-tris{[(2′-benzylaminoformyl)phenoxyl]methyl}propane ($\mathbf{L}_1$) [5], which is a 1-D coordination polymer with a H-bonded 3-D network. Comparing the luminescence spectra of the complex $[Eu(NO_3)_3\mathbf{L}]\cdot 2H_2O$ with the complex of europium(III) nitrate with $\mathbf{L}_1$, we found that the tripodal ligand $\mathbf{L}_1$ is more effective in energy-transfer than **L**. The complexes of ligand $\mathbf{L}_1$ show no emission bands from the ligand at ca 450 nm, but the emission bands in the complexes of ligand **L** are still visible (Fig. 5). This may be due to the suitable lowest triplet energy of $\mathbf{L}_1$ in its rare earth nitrate complexes. So the skeleton of the tripodal ligand is very essential in determining the structure and luminescent properties of the rare earth complexes.

5. Supplementary data

Supplementary data are available from The Director, CCDC, 12 Union Road, Cambridge, CB2 IEZ, UK (fax: +44 1223 336033; e-mail: deposit@ccdc.cam.ac.uk or www: http://www.ccdc.cam.ac.uk) on request, quoting the deposition number CCDC-177276.

Acknowledgment

This work was supported by the Doctoral Research Foundation of Lanzhou University.

References

[1] P. Guerriero, S. Tamburini, P.A. Vigato, Coord. Chem. Rev. 139 (1995) 17.
[2] (a) M. Watanabe, T. Nankawa, T. Yamada, T. Kimura, K. Namiki, M. Murata, H. Nishihara, S. Tachimori, Inorg. Chem. 42 (2003) 6977;
(b) V.M. Mukkala, J.J. Kankare, Helv. Chim. Acta 75 (1992) 1578;
(c) B. Alpha, J.-M. Lehn, G. Mathgis, Angew. Chem., Int. Ed. Engl. 26 (1987) 266;
(d) X.P. Yang, C.Y. Su, B.S. Kang, X.L. Feng, W.L. Wang, H.Q. Liu, J. Chem. Soc., Dalton Trans. (2000) 3253.
[3] (a) D.L. Reger, R.F. Serneniuc, M.D. Smith, Inorg. Chem. 42 (2003) 8137;
(b) M. Fujita, S.Y. Yu, T. Kusukawa, H. Funaki, K. Orgura, K. Yamaguchi, Angew. Chem., Int. Ed. Engl. 37 (1998) 2082;
(c) S.L. James, D.M.P. Mingos, A.J.P. White, D.J. Williams, Chem. Commun. (1998) 2323.
[4] B. Tümmler, G. Maass, F. Vögtle, J. Am. Chem. Soc. 101 (1979) 2588.
[5] J. Zhang, Y. Tang, N. Tang, M.Y. Tan, W.S. Liu, K.B. Yu, J. Chem. Soc., Dalton Trans. (2002) 832.
[6] A.F. Wells, Three-dimensional Nets and Polyhedra, Wiley-Interscience, New York, 1977.
[7] A.F. Wells, Further studies of three-dimensional nets, ACA Monogragh No. 8, American Crystallographic Association, 1979.
[8] (a) S. Decurtins, H.W. Schmalle, P. Schneuwly, H.R. Oswald, Inorg. Chem. 32 (1993) 1888;
(b) L. Carlucci, D.M. Proserpio, A. Sironi, G. Ciani, J. Am. Chem. Soc. 117 (1995) 12861;
(c) B.F. Abrahams, S.R. Batten, H. Haunt, F. Hoskins, R. Robson, Chem. Commun. (1996) 1313;
(d) L. Carlucci, G. Ciani, D.M. Proserpio, A. Sironi, Chem. Commun. (1996) 1393.
[9] K. Michio, Bull. Chem. Soc. Jpn. 49 (1976) 2679.
[10] Z. Jiri, P. Magdalena, H. Petr, T. Miloš, Synthesis 110 (1994) 1132.
[11] B.F. Abrahams, R. Robson, P.A. Jackson, Angew. Chem., Int. Ed. Engl. 37 (1998) 2656.
[12] W. Carnall, S. Siegel, J. Ferrano, B. Tani, E. Gebert, Inorg. Chem. 12 (1973) 560.
[13] K. Nakamoto, Infrared and Raman Spectra of Inorganic and Coordination Compounds, 3rd ed., John Wiley, New York, 1978, p. 227.
[14] C. Piguet, G. Hopfgartner, A. Williams, J.-C. Bünzli, Chem. Commun. (1995) 491.
[15] (a) S. Aime, M. Botta, M. Fasano, E. Terreno, Chem. Soc. Rev. 27 (1998) 19;
(b) P. Caro, in: P.R. Saez (Ed.), Basic and Applied Aspects of Rare Earths, Springer, New York, 1997.
[16] W.S. Liu, M.Y. Tan, X. Wang, S.Y. Zhang, Acta Chim. Sin. 48 (1990) 1090.
[17] M. Latva, H. Takalo, V.-M. Mukkala, C. Marachescu, J.-C. Rodriguez-Ubis, J. Kankare, J. Lumin. 75 (1997) 149.

is inert to the oxidation of glycine. Two electrons within the complex are transferred to Au(III) from glycine to form a Au(I)-imine intermediate, which being unstable undergoes hydrolysis to NH_4^+ and glyoxylic acid. An excess of $[AuCl_4]^-$ oxidizes glyoxylic acid to CO_2 and Au(o) through the intermediate formation of formic acid. Since the rate law was not given (dependence of the rate on [glycine], $[H^+]$ and $[Cl^-]$), it was of interest to study the kinetics of the oxidation of histidine, another amino acid.

2. Experimental

2.1. Chemicals and solutions

The solutions of $AuCl_4^-$ (Johnson and Matthey) were freshly prepared in perchloric acid (E. Merck, GR), though such solutions are stable over 24 h. The concentrations were determined from the optical density measured at 310 nm on a HP 8452A diode array spectrophotometer using carefully determined $\varepsilon = 4.82 \times 10^3\ dm^3\ mol^{-1}\ cm^{-1}$, which compared well with the lit. value [19–21] $4.86 \times 10^3\ dm^3\ mol^{-1}\ cm^{-1}$. The solutions of L-histidine (BioChemika Micro Select, Fluka) and D-histidine (Puriss, Fluka) were freshly prepared by weighing the samples. $LiClO_4$ solution for adjusting the ionic strength (μ) was prepared and standardised as described earlier [22]. All other chemicals were used as received. The solutions were prepared in water, distilled twice, and purged by nitrogen.

2.2. Reaction products

At the end of the reaction, the metal ion from the reaction mixture was removed using an ion exchange method. A portion of the filtrate was treated with a saturated solution of 2,4-dinitrophenylhydrazine and the same was left overnight in a refrigerator. The precipitated 2,4-dinitrophenylhydrazone was separated by filtration and recrystallised from a mixture of ethyl acetate and light petroleum. The melting point of the precipitated hydrazone, 190 ± 0.5 °C, was characteristic of β-imidazolyl pyruvic acid, indicating that the seat of the reaction is not the imidazole ring since it remained intact. Another portion of the eluent on treatment with Nessler's reagent confirmed the presence of the NH_4^+ ion.

2.3. Stoichiometry

Several reaction mixtures having excess of $AuCl_4^-$ over known histidine concentrations were prepared. The optical density of the reaction mixtures was measured at 310 nm at room temperature until a constant value was recorded. The mean of several such estimates yielded $\Delta[AuCl_4^-]/\Delta[\text{Histidine}] = 1.07 \pm 0.10$. Hence, in view of the characterised products and the stoichiometry ratio, the equation of the reaction is expressible by Eq. (1).

$$H_2O + C_3H_3N_2CH_2CH(NH_2)COOH + AuCl_4^- \rightarrow C_3H_3N_2CH_2COCOOH + AuCl_4^{3-} + NH_4^+ + H^+ \quad (1)$$

2.4. Kinetics

The reaction mixtures were prepared so as to conform to the pseudo-first-order conditions (excess of histidine over Au(III) ion) for studying the rate of the reaction that was followed at 360 nm (Beer's law was obeyed) with a Spectrochem MK II colorimeter fitted with a thermostated reaction cell. The pseudo first order rate constants k_{obs} were calculated from the slopes of the plots between $\log(A_t - A_\infty)$ against time "t", which were linear for more than two half-lives (80–90%) where A_t and A_∞ are the optical densities of the reaction mixture at any time "t" and infinite time, respectively. These linear plots indicated the monophasic character of the reaction and that the products did not interfere with the rate profile of the reaction. There was no trace of metallic gold in the reaction mixture at the time of measuring A_∞ after several half-lives. The EXCEL program was used for plotting the $\log(A_t - A_\infty)$-time data and evaluating the least square values of the slopes and intercepts of the linear plots. The pseudo first order rate constants, k_{obs} were generally reproducible within 5%.

The repetitive spectra of the reaction mixtures for several concentrations of histidine, recorded on a HP8451A spectrophotometer, had not shown any change from the spectral characteristics of the control solution of $AuCl_4^-$. The absorbance of the spectra decreased with time and no isosbestic points appeared, indicating that the spectra of the products of the reaction do not overlap with that of the $AuCl_4$ solution. The absence of any transient absorbance peaks in the spectra over a period of time, therefore, suggests that the intermediates, if formed, are weak or only weak bridged complexes are formed.

2.5. Test for free radical

The addition of acrylonitrile (6% v/v) to the reaction mixture, degassed with nitrogen, produced cloudiness due to the formation of polyacrylonitrile, indicating the formation of free radicals. A similar solution of acrylonitrile when added to similarly degassed blank solutions of $AuCl_4$ and histidine did not produce any cloudiness.

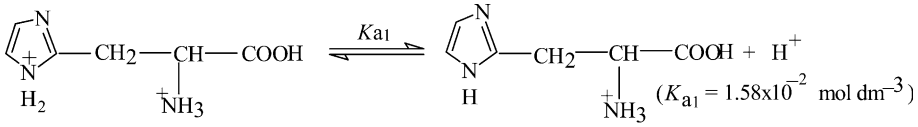
3. Results

k_{obs} increased proportionately with [Histidine] at constant [H^+], [Cl^-] and ionic strength (Table 1). The plot of k_{obs} against [Histidine]$_0$ was linear and passed through the origin, suggesting a first order dependence in histidine. The decreasing k_{obs} with increasing [Cl^-] and [H^+], at constant concentrations of the other, is reported in Tables 1 and 2, respectively. The correlations between k_{obs} and [H^+] or [Cl^-] at constant concentration of the other, are shown in Figs. 1 and 2, respectively. These plots indicate the absence of a linear correlation between k_{obs} and the respective concentrations of H^+ and Cl^- ions. A later analysis of the respective data indicated that a linear correlation between k_{obs} and [H^+] or [Cl^-] is consistent with the empirical rate law, Eq. (2), where $k_2 = k_{obs}$/[Histidine] and X is a constant. These results suggested the presence of an equilibria between species that differ by a single proton and a [Cl^-] ion

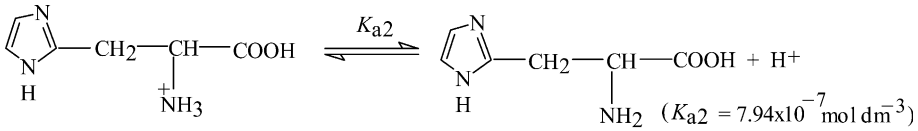
$$k_2 \cdot X = a + b[H^+]^{-1}[Cl^-]^{-1}. \quad (2)$$

k_{obs} decreased with an increase in the ionic strength, Table 3, and the plot, in accordance with Eq. (3) [23,24], is linear with a negative slope, Fig. 5, suggesting the reactive species have opposite charges

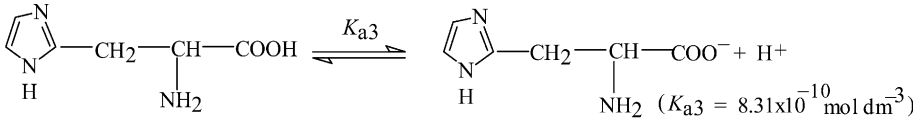
$$\log k_{obs} = \log k_0 + 1.02 Z_a Z_b \left(\frac{\sqrt{\mu}}{1+\sqrt{\mu}} - 0.05\mu \right). \quad (3)$$



(4)



(5)



(6)

4. Mechanism and discussion

The following equilibria between various histidine species, A^{2+}, B^+, C and D^- (the charge shown is the net total charge on that species), and the respective equilibrium constants [25] are known. The retarding effect of the H^+ ion could be due to any one or all the equilibria shown in Eqs. (4)–(6). However, these equilibria have no bearing on the retarding effect of the Cl^- ion. For an initial [Histidine] = 0.002 and [H^+] = 0.02 mol dm^{-3}, the calculated [B^+] is 8.5×10^{-4} mol dm^{-3} using the given K_{a1} value The concentrations of C and D^-, using the respective K_{a2} and K_{a3} values, can be shown to be negligibly small compared to [B^+]. The equilibria (7)–(9), involving Au(III) species [19,26,27], can also explain the retarding effect of both H^+ and Cl^- ions.

$$AuCl_4^- + H_2O \overset{K_{hy}}{\rightleftharpoons} AuCl_3H_2O + Cl^- \quad (7)$$

$$AuCl_3H_2O \overset{K_a}{\rightleftharpoons} AuCl_3OH^- + H^+ \quad (8)$$

$$AuCl_3(OH)^- + H_2O \overset{K_{aq}}{\rightleftharpoons} AuCl_2(H_2O)(OH) + Cl^- \quad (9)$$

The equilibrium (9) is excluded from consideration because the calculated [$AuCl_2(H_2O)(OH)$] is negligibly small. The equilibria (7) and (8) can be combined to a single equilibrium (10). A consequence of equilibrium (10) is that the likely reactive Au(III) species are $AuCl_4^-$ and $AuCl_3OH^-$ ions. The equilibrium constant K ($=K_{hy}K_a$) can be calculated from the known K_{hy} and K_a values. The rate constants tend to limiting values at the higher end of the [H^+] (Fig. 1) and [Cl^-] (Fig. 2) because the equilibrium constant K has a very small value. The reactivity of $AuCl_4^-$ and $AuCl_3OH^-$ ions is consistent with the analysis of the rate data that indicated two parallel reactions. The reactivity of $AuCl_3OH^-$ is $\approx 10^3$ times the reactivity of $AuCl_4^-$(aq) (Table 4). The

participation of a hydroxo species, $AuCl_3OH^-$, is consistent with the inverse dependence of the rate on $[H^+]$, that is suggestive of an inner-sphere mechanism [28].

$$AuCl_4^-(aq) + H_2O \overset{K}{\rightleftharpoons} AuCl_3OH^- + Cl^- + H^+ \quad (10)$$

$$AuCl_4^- + R\text{-}CH_2CH(N^+H_3)COOH \xrightarrow{k} \underset{\mathbf{C}}{[AuCl_4^-R\text{-}CH_2CH(NH_2)COOH]^{\ddagger}} + H^+ \quad (11)$$

$$AuCl_3OH^- + R\text{-}CH_2CH(N^+H_3)COOH \xrightarrow{k_1} \underset{\mathbf{C_1}}{[AuCl_3R\text{-}CH_2CH(NH_2)COOH]^{\ddagger}} + H_2O \quad (12)$$

$$[AuCl_4^-R\text{-}CH_2CH(NH_2)COOH]^{\ddagger} \xrightarrow{fast} R\text{-}CH_2C^{\bullet}(NH_2)COOH + AuCl_4^{2-} + H^+ \quad (13)$$

$$[AuCl_3R\text{-}CH_2CH(NH_2)COOH]^{\ddagger} \xrightarrow{fast} R\text{-}CH_2C^{\bullet}(NH_2)COOH + AuCl_3^- + H^+ \quad (14)$$

$$R\text{-}CH_2C^{\bullet}(NH_2)COOH + Au(II) \xrightarrow{fast} R\text{-}CH_2CH(N^+H)COOH + Au(I) \quad (15)$$

$$R\text{-}CH_2C^{\bullet}(NH_2)COOH + Au(III) \xrightarrow{fast} R\text{-}CH_2CH(N^+H)COOH + Au(II) \quad (15A)$$

$$R\text{-}CH_2CH(N^+H)COOH + H_2O \xrightarrow{fast} R\text{-}CH_2COCOOH + NH_4^+ \quad (16)$$

$$2Au(II) \xrightarrow{fast} Au(III) + Au(I) \quad (17)$$

Scheme 1.

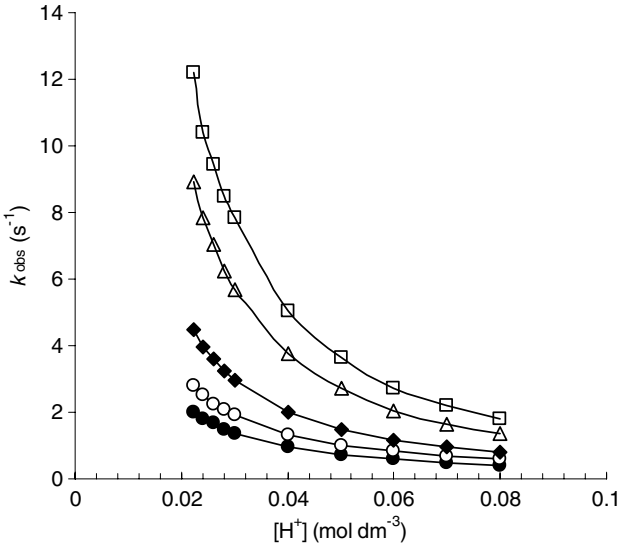


Fig. 1. The plots of k_{obs} against $[H^+]$, at constant $[Cl^-]$, at 27 °C (●), 31 °C (○), 35 °C (♦), 40 °C (△) and 45 °C (□).

Table 1
The dependence of k_{obs} (s^{-1}) on [L-Histidine] and $[Cl^-]$at 31 °C $10^4[AuCl_4^-] = 2.0$, $[H^+] = 0.026$ and $\mu = 0.4$ mol dm^{-3}

S. No.	[L-Histidine]	$[Cl^-]$	10^3k_{obs}
1	0.002	0.013	0.234
2	0.005	0.013	0.569
3	0.011	0.013	1.23
4	0.020	0.013	2.25
5	0.050	0.013	5.68
6	0.100	0.013	10.4
7	0.150	0.013	16.1
8	0.200	0.013	23.9
9	0.250	0.013	28.3
10	0.300	0.013	33.1
11	0.400	0.013	46.4
12	0.020	0.013	2.34
13	0.020	0.020	1.83
14	0.020	0.025	1.66
15	0.020	0.030	1.49
16	0.020	0.050	1.31
17	0.020	0.062	1.21
18	0.020	0.074	1.18
19	0.020	0.084	1.13
20	0.020	0.094	1.10
21	0.020	0.150	1.05
22	0.020	0.200	1.02

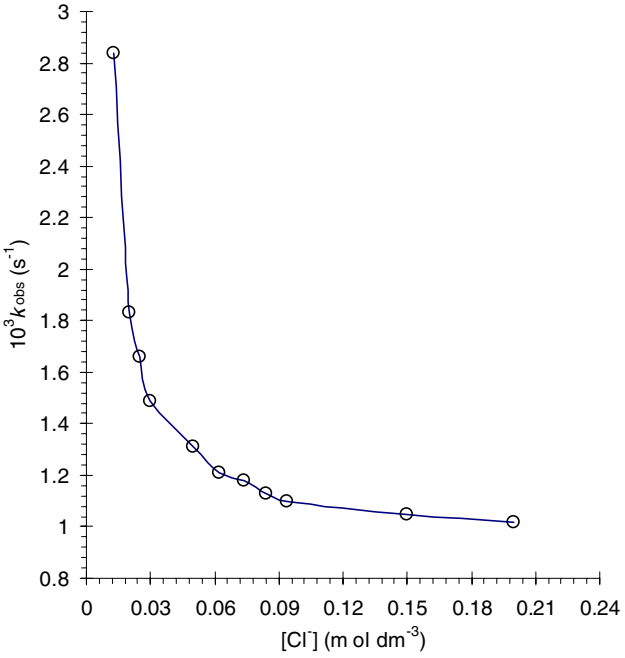


Fig. 2. The plot of k_{obs} against $[Cl^-]$ at constant $[H^+]$ at 31 °C.

Table 2
The dependence of k_{obs} (s^{-1}) on $[H^+]$ at different temperatures

$[H^+]$ (mol dm^3):	0.022	0.024	0.026	0.028	0.030	0.040	0.050	0.060	0.070
10^3k_{obs}, 27 °C	2.02	1.81	1.67	1.47	1.35	0.943	0.731	0.582	0.494
10^3k_{obs}, 31 °C	2.79	2.53	2.25	2.07	1.92	1.31	1.02	0.821	0.696
10^3k_{obs}, 35 °C	4.50	3.98	3.62	3.26	2.97	2.01	1.50	1.15	0.946
10^3k_{obs}, 40 °C	8.93	7.86	7.04	6.23	5.67	3.76	2.72	2.06	1.66
10^3k_{obs}, 45 °C	12.2	10.4	9.44	8.49	7.85	5.03	3.66	2.71	2.21

$10^4[AuCl_4^-] = 2.0$, [L-Histidine] = 0.02, $[Cl^-] = 0.013$ and $\mu = 0.4$ mol dm^{-3}.

Table 3
The effect of the ionic strength ($LiClO_4$) on the rate of the reaction at 35 °C

μ (mol dm^{-3})	0.1	0.20	0.40	0.60	1.00	1.20
$10^3 k_{obs}$ (s^{-1})	3.49	3.29	3.20	3.10	3.01	2.96

$10^4[AuCl_4^-] = 1.0$, [Histidine] = 0.005, $[H^+] = 0.01$ mol dm^{-3}.

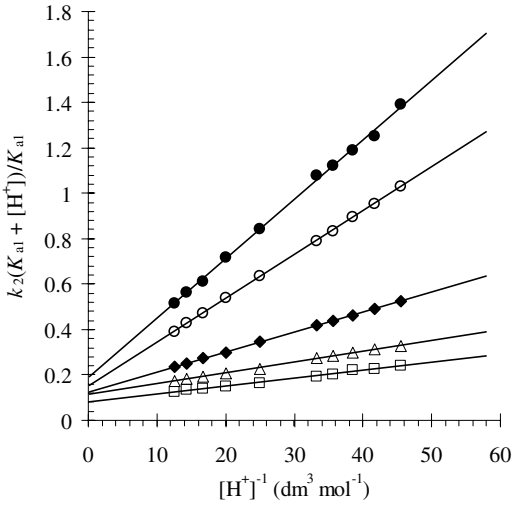


Fig. 3. The linear plot of $k_2(K_a + [H^+])K_a^{-1}$ against $[H^+]^{-1}$ at constant $[Cl^-] = 0.13$ mol dm^{-3}, consistent with the Eq. (21), at temperatures 27 °C (□), 31 °C (△), 40 °C (○) and 45 °C (●).

Table 4
The values of k and k_1 at different temperatures and the related thermodynamic parameters

Temperature (°C):	27	31	35	40	45
k_c (dm^3 mol^{-1} s^{-1})	0.0813	0.114	0.125	0.151	0.189
$10^{-2} k_{c1}$ (mol dm^{-3} s^{-1})	1.10	1.38	2.33	4.59	5.62
10^7 K (mol^2 dm^{-6})	4.12	4.51	4.91	5.46	6.04

$\Delta H_k^{\ddagger} = 32 \pm 2$ kJ mol^{-1}; $\Delta H_{k_1}^{\ddagger} = 76 \pm 5$ kJ mol^{-1}; $\Delta S_k^{\ddagger} = -159 \pm 8$ J K^{-1} mol^{-1}; $\Delta S_{k_1}^{\ddagger} = 48 \pm 17$ J K^{-1} mol^{-1}.

Though the formation of intermediates between Au(III) and histidine is not indicated by the spectral study of the reaction mixture in the UV region, their formation in the proposed mechanism would be reasonable in view of the NMR studies on glycine [1a], glycylglycyl-L-histidine [17]. The observation that the imidazole ring is not the seat of reaction because it is present in the final oxidation product of the reaction is consistent with the view that the binding of a proton or a metal ion is very unfavourable at the pyrrole nitrogen of histidine [17].

The results of the spectral studies would not be in contradiction to the assumption of the formation of transient intermediates in the rate-determining step. The mechanism in Scheme 1 is based on this assumption.

The probable free radical is R-$CH_2C^{\cdot}(NH_2)$COOH where R is the imidazole ring. The presence of a free radical is indicative of the one electron reduction of Au(III) in the rate determining step. Transient Au(II) is reported in several redox reactions [29–35]. The unstable Au(II) can oxidise the free radical instantaneously to the imine (15). Imines with a proton on N are seldom stable and undergo fast hydrolysis to the NH_4^+ ion and the final product (17).

Alternately, Au(II) may disproportionate to Au(III) and Au(I) instantaneously, reaction (17), because the rate of disproportionation [36], 1.67×10^8 dm^3 mol^{-1} s^{-1}, is very near to the rate of diffusion. Au(II) is, therefore, very likely removed through disproportionation that makes the reactions (15) most unlikely. The rate law, deduced from reactions (10)–(17), is expressible by Eq. (18) which changes to Eq. (21) on substituting the proper values of $[AuCl_4^-]$ and $[\mathbf{B}^+]$ (R–$CH_2CH(N^+H_3)$COOH), given by Eqs. (19) and (20), respectively, and applying the inequality $K \ll [H^+][Cl^-]$ in view of $[H^+]$and $[Cl^-]$ used where $k_2 = k_{obs}/[\text{Histidine}]_0$

$$\frac{-\mathrm{d}[\mathrm{Au(III)}]}{\mathrm{d}t} = \left(k + \frac{k_1 K}{[H^+][Cl^-]}\right)[AuCl_4^-][\mathbf{B}^+], \tag{18}$$

$$[AuCl_4^-] = \frac{[\mathrm{Au(III)}][H^+][Cl^-]}{K + [H^+][Cl^-]}, \tag{19}$$

$$[\mathbf{B}^+] = \frac{K_{a1}[\text{Histidine}]_0}{K_{a1} + [H^+]}, \tag{20}$$

$$\frac{k_2(K_{a1} + [H^+])}{K_{a1}} = \left(k + \frac{k_1 K}{[H^+][Cl^-]}\right). \tag{21}$$

The reactivity of the species $\mathbf{B}^+$ in outer-sphere oxidation with $[Co(III)W]^{5-}$ ($E^0 = 1.01$ V [37],) and $[Mncdta]^-$ ($E^0 = 0.81$ V [38],) ions [39] is of the same order as are the respective E^0 values of these ions, and so is the reactivity of the species $\mathbf{D}^-$ with $[Mncdta]^-$ and $Fe(CN)_6^{3-}$ ($E^0 = 0.36$ V) ions [40]. Though E^0 (=0.95 V [41],) for the $AuCl_4^-/AuCl_2$ couple is between the E^0 values of $[Co(III)W]^{5-}$ and $[Mncdta(OH_2)]^-$ ions, the reactivity of the species $\mathbf{B}^+$ with the Au(III) ion is greater than that with the $[Co(III)W]^{5-}$ ion. This is probably because the present reaction is inner-sphere.

The slope value, −0.3, of the plot in Fig. 5 is less than the expected slope of −1 considering that the reactive histidine species B^+ has a net single positive charge and the reactive Au(III) species have a single negative charge. The deviation from the expected value could be due to the spreading of the net single positive charge over the entire histidine molecule.

The Eq. (21) is consistent with the linear plots of the left hand side against $[H^+]^{-1}$ at constant $[Cl^-]$ (Fig. 3), and $[Cl^-]^{-1}$ at constant $[H^+]$ (Fig. 4) with intercepts on the rate axis. The values of k (0.120 dm^3 mol^{-1} s^{-1}) and k_1 (139 dm^3 mol^{-1} s^{-1}) obtained from the plot in Fig. 4 are in close agreement with those (k = 0.114 dm^3 mol^{-1} s^{-1}; k_1 = 15.6 dm^3 mol^{-1} s^{-1}) obtained from the plot in Fig. 3 at 31 °C. This close agreement

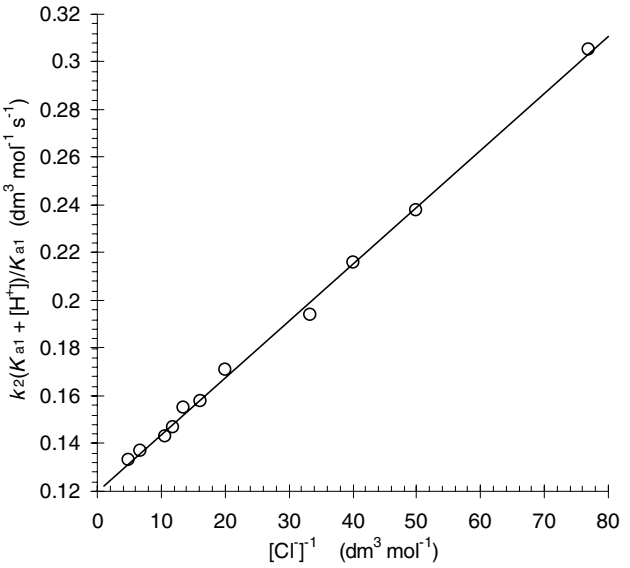


Fig. 4. The linear plot of $k_2(K_a + [H^+])K_a^{-1}$ against $[Cl^-]^{-1}$ at constant $[H^+]$, consistent with the Eq. (21), at 31 °C.

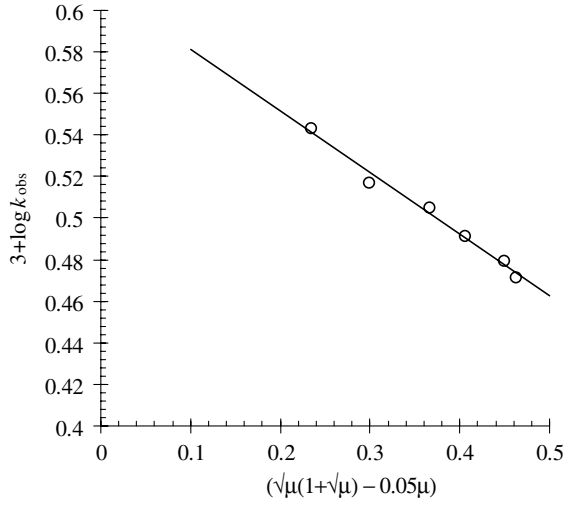
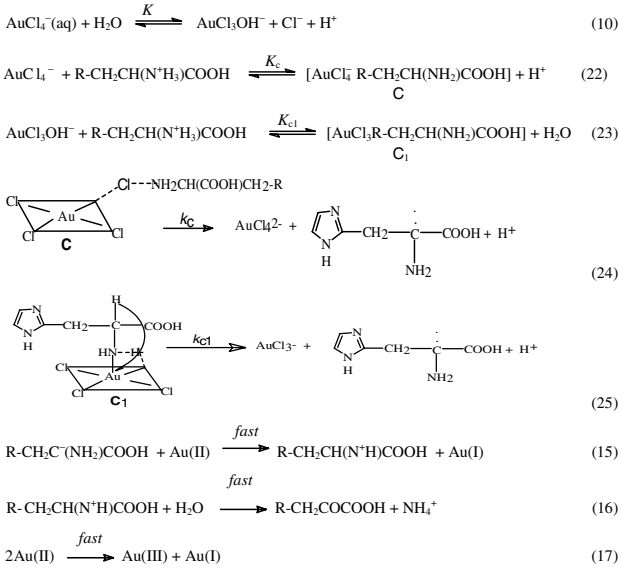


Fig. 5. The linear plot of log k_{obs} against $\{\mu/(1 + \sqrt{\mu}) - 0.05\mu\}$ has an intercept of −0.3. The ionic strength is varied using $LiClO_4$.

between the values of k and k_1 obtained from two different plots, not only support the validity of the rate law but that of the proposed mechanism too. The values of k and k_1 at different temperatures are in Table 4. The values of K_{a1} [25], and K [20] (Table 4) at different temperatures, were estimated from the published data. The large difference in the values of k and k_1 ($k_1 \approx 10^3 k$) reflect the ease of formation of the respective transient species.

The two intermediates are formed by equatorial coordination of histidine with the respective Au^{3+} species. The rate of formation of the intermediate formed by elimination of a water molecule is obviously faster than that formed through a chloride bridge. This mechanism is unlikely to show any difference in the rates of oxidation of H^1-histidine and H^2-histidine (deuteriated molecule). Since an authentic sample of H^2-histidine was



Scheme 2.

unprocurable from a reliable source, the rates of H^2-histidine were not measurable. However, the most disturbing aspect of the mechanism is the value of k_1 (110 dm^3 mol^{-1} s^{-1} at 27 °C) which is inadmissible for a process in which a water molecule is eliminated because of the reaction between H^+ and OH^- ions. The rate of such a process is diffusion controlled. This indicated the presence of some other factor with k_1 and thus a modification in the mechanism is required.

The alternate mechanism presumes the formation of the intermediates in equilibrium steps rather than in the rate-limiting steps. The intermediates so formed could be of a transitory nature defying spectrometric detection if the rates of the formation and decomposition of the intermediates to the products approach the rate of the backward reaction of the equilibrium, so that there is no accumulation of the intermediates over a period of time. Yet another reason for the intermediates defying spectrometric detection could be that the molar absorptivity coefficient of the transition complexes might not be very different from that of tetrachloroaurate(III) solution. The mechanism so modified is considered in Scheme 2 in which the reaction (15A) is eliminated for the reasons given earlier.

The rate law, based on Scheme 2, is in Eq. (26). The transformed form of (26) is Eq. (27) which is identical with Eq. (21) where $k = k_c K_c$ and $k_1 = k_{c1} K_{c1}$

$$\frac{-\mathrm{d}[\mathrm{Au(III)}]}{\mathrm{d}t} = \left(k_c K_c + \frac{k_{c1} K_{c1} K}{[H^+][Cl^-]}\right)[AuCl_4^- -][B^+], \tag{26}$$

$$\frac{k_2(K_{a1} + [H^+])}{K_{a1}} = \left(k_c K_c + \frac{k_{c1} K_{c1} K}{[H^+][Cl^-]}\right) = \left(k + \frac{k_1 K}{[H^+][Cl^-]}\right). \tag{27}$$

The square planar $AuCl_4^-$ is isoelectronic with the square planar $[Ag(OH)_4]^-$ ion. The latter is reported to form intermediates with the $H_2PO_2^-$ ion [42] and several others [43–50] in which the ligand is axially coordinated. The high rates of S(IV) oxidation with the $AuCl_4^-$ ion is attributed to the axially coordinated SO_2^{2-} and HSO_4^- ions in the intermediates [1e]. Therefore histidine can coordinate with Au(III) either axially (**C1**) or equatorially (**C**). In the equatorial coordination, the amide nitrogen can coordinate with $AuCl_4^-$ through a chloride bridge [1e] though glycine substitutes for one of the chlorines. It may be mentioned that it is not clear if glycine had two simultaneous paths of oxidation as observed presently. Since the nature of coordination in the two intermediates is different, their rate of decomposition are obviously expected to be different and there is no direct removal of OH^- by a proton as in Scheme 1.

In conclusion, histidine forms transitory intermediates with $AuCl_4^-$ and $AuCl_3OH^-$, preferring an equatorial coordination with the $AuCl_4^-$ ion, and the substitution is likely to be through a chloride bridge whereas an axial coordination is preferred with the $AuCl_3OH^-$ ion despite the sterically hindered large histidine molecule. Since this coordinated species may be under strain it obviously has an overall high rate of decomposition compared to strain free equatorially coordinated species. The intermediates defy spectrometric detection either because the total rates of formation and decomposition to the products have approached the rate of the backwards reaction of the equilibrium step so that there is no accumulation of the intermediates over a period of time or the molar absorptivity coefficient of the transition complexes is not very different from that of the tetrachloroaurate(III) solution.

Acknowledgement

Sponsorship of this work by the University Grants Commission (F.12-59/97 and F.12-147/01) is gratefully acknowledged.

References

[1] (a) J. Zou, Z. Guo, J.A. Parkinson, Y. Chen, P.J. Sadler, Chem. Commun. (1999) 1359;
(b) A. Ericson, J.C. Arthur, R.S. Coleman, L.I. Elding, S.K.C. Elmroth, J. Chem. Soc., Dalton Trans. (1998) 1687;
(c) A. Ericson, L.I. Elding, S.K.C. Elmroth, J. Chem. Soc., Dalton Trans. (1997) 1159;
(d) S.K.C. Elmroth, L.I. Elding, Inorg. Chem. 35 (1996) 2337;
(e) J. Berglund, L.I. Elding, Inorg. Chem. 34 (1995) 513.
[2] (a) S. Elmroth, L.H. Skibsted, L.I. Elding, Inorg. Chem. 28 (1989) 2703;
(b) L. Drougge, L.I. Elding, Inorg. Chem. 26 (1987) 1073;
(c) L.I. Elding, L.H. Skibsted, Inorg. Chem. 25 (1986) 4084;
(d) L.I. Elding, L.F. Olsson, Inorg. Chem. 21 (1982) 779.
[3] (a) L.H. Skibsted, Adv. Inorg. Bioinorg. Mech. 4 (1986) 137;
(b) L.I. Elding, A.-B. Gröning, Ö. Gröning, J. Chem. Soc., Dalton Trans. (1981) 1093;
(c) R. Ettore, J. Chem. Soc., Dalton Trans. (1983) 2329.
[4] Refs. [1e–9] cited therein.
[5] Refs. [2b,12].
[6] G. Nord, L.H. Skibsted, A.S. Halonin, Acta Chem. Scand. A29 (1975) 505.
[7] A. Ericson, L.I. Elding, S.K.C. Elmroth, J. Chem. Soc., Dalton Trans. (1997) 1159.
[8] L.I. Elding, L.F. Olsson, Inorg. Chem. 21 (1982) 779.
[9] S. Elmroth, L.H. Skibsted, L.I. Elding, Inorg. Chem. 28 (1989) 2703.
[10] C.F. Shaw, M.P. Cancro, P.L. Witkiewicz, J.E. Eldridge, Inorg. Chem. 19 (1980) 3198.
[11] P.L. Wikiewicz, C.F. Shaw, J. Chem. Soc., Chem. Commun. (1981) 1111.
[12] W.E. Smith, J. Reglinski, Perspect. Bioinorg. Chem. 1 (1991) 183.
[13] E. Bordignon, L. Catallini, G. Natile, A. Scatturi, J. Chem. Soc., Chem. Commun. (1973) 878.
[14] G. Natile, E. Bordignon, L. Catallini, Inorg. Chem. 15 (1976) 246.
[15] A.A. Isab, P.J. Sadler, Biochim. Biophys. Acta 492 (1979) 322.
[16] M. Wienken, B. Lippert, E. Zangrando, L. Randaccio, Inorg. Chem. 31 (1992) 1983.
[17] S.L. Best, T.K. Chattopadhyay, M.I. Djuran, R.A. Palmer, P.J. Sadler, J. Chem. Soc., Dalton Trans. (1997) 2587.
[18] A.A. Cornejo, A. Catineiras, A.I. Yanovsky, K.B. Nolan, Inorg. Chim. Acta 349 (2003) 91.
[19] K.K. Sengupta, A. Sanyal, P.K. Sen, Transition Met. Chem. 19 (1994) 534.
[20] F.H. Fry, G.A. Hamilton, J. Turkevich, Inorg. Chem. 5 (1966) 1943.
[21] P. van Z. Bekker, W. Robb, Inorg. Chim. Acta 8 (1972) 849.
[22] A. Prakash Rekha, Raj N. Mehrotra, Can. J. Chem. 71 (1991) 2164.
[23] C.W. Davies, Ion Association, Butterworths, London, 1962, p. 39.
[24] C.W. Davies, Ion association, J. Chem. Soc. (1938) 2093.
[25] A.E. Martell, R.M. Smith, Critical Stability Constants, vol. 5, Plenum, New York, 1982, p. 31 (First supplement).
[26] W. Robb, Inorg. Chem. 6 (1967) 382.
[27] B.I. Peshchevitskii, V.I. Belevantsev, N.V. Kubatova, Russ. J. Inorg. Chem. (Engl. Transl.) 16 (1971) 1007.
[28] R.G. Wilkins, Kinetics and Mechanism of Reactions of Transition Metal Complexes, 2nd ed., VCH, Weinheim, 1991, p. 262.
[29] K.K. Sengupta, B. Basu, Transition Met. Chem. 8 (1983) 6.
[30] K.K. Sengupta, B. Basu, S. Sengupta, S. Nandi, Polyhedron 2 (1983) 983.
[31] K.K. Sengupta, B. Basu, Polyhedron 3 (1984) 805.
[32] K.K. Sengupta, S. Das, S. Sengupta, Transition Met. Chem. 13 (1988) 261.
[33] A. Brown, W.C.E. Higginson, J. Chem. Soc., Dalton Trans. (1972) 166.
[34] H.G. Foresberg, H. Widdel, L.G. Erwall, J. Chem. Educ. 37 (1960) 44.
[35] F. Basalo, R.G. Pearson, Mechanism of Inorganic Reactions, 2nd ed., Wiley Eastern, New Delhi, 1977, p. 414.
[36] R.L. Rich, H. Taube, J. Phys. Chem. 58 (1954) 6.
[37] L. Eberson, J. Am. Chem. Soc. 105 (1983) 3192.
[38] R.E. Hamm, M.A. Suwyn, Inorg. Chem. 6 (1967) 139.
[39] S. Gangopadhyaya, M. Ali, P. Banerji, J. Chem. Soc., Perkin Trans. 2 (1992) 781.
[40] D. Laloo, M.K. Mahanti, J. Chem. Soc., Dalton Trans. (1990) 311.
[41] R.L. Rich, H. Taube, J. Phys. Chem. 58 (1954) 1.

[42] Raj N. Mehrotra, L.J. Kirschenbaum, Inorg. Chem. 28 (1989) 4327.
[43] L.J. Kirschenbaum, J.D. Rush, Inorg. Chem. 24 (1985) 744.
[44] L.J. Kirschenbaum, J. Inorg. Nucl. Chem. 38 (1976) 881.
[45] Kouadio, L.J. Kirschenbaum, Raj N. Mehrotra, J. Chem. Soc., Dalton Trans. (1990) 1929.
[46] R.K. Panda, L.J. Kirschenbaum, J. Chem. Soc., Dalton Trans. (1989) 217.
[47] L.J. Kirschenbaum, L. Mrozowski, Inorg. Chem. 17 (1978) 3718.
[48] Kouadio, L.J. Kirschenbaum, Raj N. Mehrotra, J. Chem. Soc., Perkin Trans. 2 (1990) 2123.
[49] Y. Sun, L.J. Kirschenbaum, Issifou Kouadio, J. Chem. Soc., Dalton Trans. (1991) 2311.
[50] L.J. Kirschenbaum, Y. Sun, Inorg. Chem. 30 (1991) 2360.

is adjacent to the oximic α-carbon. Far now, this particular oxime and their complexes with copper(II) and nickel(II) ions have been studied in solution (potentiometric, UV–Vis, EPR studies) only [8]. It is known that this class of oximes predominantly coordinates to metals via the nitrogen atom (mainly transition metal ions) or via the oxygen atom (s-, p-metal ions). Additionally, deprotonation of the **1a** oximic group allows formation of dimeric species where the nitrogen and oxygen atoms act as metal donors [8–11].

In the present work, the focus is on elucidating molecular structures of mentioned-above **1a** complexes in solid state based on molecular spectroscopy methods (IR, RA and EPR). To give detailed assignment of vibrational spectra and consequently to solve molecular structures we applied quantum-mechanical calculations at the DFT level of theory. Additionally, we performed potential energy distribution calculations (PED) to show a detailed description of vibrational modes and atomic charge distribution to give an explanation of the **1a** anionic nature (the APT population analysis).

2. Experimental

2.1. Preparation

2.1.1. Na–*1a*

The sodium salt of 2-cyano-2-(hydroxyimino)acetic acid was synthesized by the reported procedure [7]. Elemental analysis (C, H, N) was conducted at the Faculty of Pharmacy of Jagiellonian University according to standard microanalytical procedures (*Anal.* Calc. for $Na_2C_3H_{0.7}N_2O_{3.35}$: C, 21.9; H, 0.4; N, 17.0. Found: C, 22.2; H, 0.7; N, 16.7%). In the microcrystalline sample, the sodium-to-**1a** molar ratio (2:1) was confirmed by a standard analytical procedure (AAS).

2.1.2. Cu–*1a* and Ni–*1a*

The complexes were prepared as described below using 1:2 molar ratio of metal ions to **1a**. An aqueous solutions of $Cu(NO_3)_2 \cdot 2.5H_2O$ and $NiCl_2 \cdot 6H_2O$ (21.9 and 21.4 mg in 5 ml H_2O, respectively) were added to Na–**1a** (25 mg) dissolved in water (5 ml). In case of the Cu–**1a** complex the clear dark green solution was stirred (20 min) with heating (~35 °C) and treated dropwise with 0.5 M HNO_3 (to pH 2). The resulting green solution was still heated and stirred (1 h) then filtered and concentrated by evaporation at room temperature. Dark green microcrystalline precipitate began to form within a week. The procedure for the Ni–**1a** complex was analogues. The $NiCl_2 \cdot 6H_2O$–**1a** mixture was clear straw-colored and after treating with 1 M KOH (to pH 8) the solution became dark red. Finally, after a few days dark red microcrystalline powder was obtained. Despite of co-precipitation of the synthesized complexes with nitrate and chloride ions, respectively, elemental analyses indicated clearly that the metal-to-**1a** molar ratio is about (1:2).

2.2. Spectroscopy

For FT-Raman measurements, a few milligrams of the compound was placed in capillary tube and measured directly; 512 and 3000 scans were collected (with a resolution of 4 cm^{-1}) for the sodium and the transition metal ions compounds, respectively. Fourier transform mid-infrared (FT-MIR, 256 scans) and Fourier transform far-infrared (FT-FIR, 512 scans) spectra were run in KBr and low molecular weight polyethylene discs, respectively. Resolution was set at 4 cm^{-1} (MIR) and 2 cm^{-1} (FIR). Sodium–**1a** salt FT-Raman spectrum was recorded on a Bio-Rad step-scan spectrometer (FTS 6000) combined with a Bio-Rad Raman Accessory (FTS 40). Excitation at 1064 nm was made by a Spectra-Physics Topaz T10-106c cw Nd:YAG laser. Raman spectra of the copper and nickel complexes were collected on a Jobin Yvon spectrometer model T6400 equipped with an argon ion laser (excitation at 514.5 nm) and a CCD camera as a detector (Princeton Instruments). FT-IR spectra were measured on Bruker (IFS 48) and Bio-Rad (FTS 60V) spectrometers in the mid and far IR regions, respectively. The accuracy of the readings was ±1 cm^{-1}.

EPR spectrum of the Cu–**1a** complex (the microcrystalline powder sample) was recorded on a Bruker spectrometer ELEX SYS X500 [X-band (9.5 GHz)] at 298 K.

3. Computational details

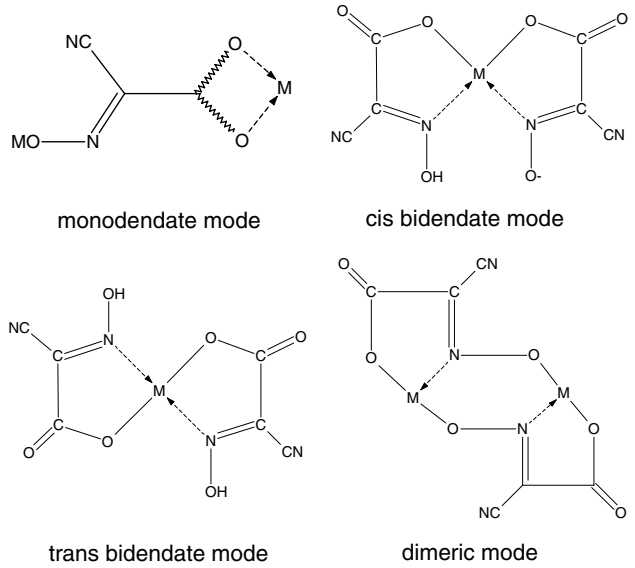
B3LYP [12,13] calculations with 6-311++G(d,p) and LanL2DZ [14,15] basis sets (for the sodium salt and the transition metals complexes, respectively) were carried out using the quantum-mechanical GAUSSIAN-98 set of programs [16]. Optimum geometries and harmonic frequencies were determined by using SGI 2800 computer in the Academic Computer Center "Cyfronet" in Krakow and on a Cray SV1ex-1-32 computer in Interdisciplinary Center for Mathematical and Computational Modeling in Warsaw. No symmetry constraints were imposed during the optimization process. At the B3LYP/6-311++G(d,p) level a scaling factor of 0.983 was applied to the most harmonic frequencies [except to ν(OH) modes (0.953)] in order to yield the best fit to the experimental data, as suggested by Michalska and co-workers [17]. Raman intensities were determined by RAINT program [18] using values of Raman scattering activities obtained from the Gaussian outputs. The potential energy distributions (PED) were obtained from the Veda program [19], while atomic charge

calculations were performed using APT population analysis (GAPT, Generalized Atomic Polar Tensor) [20]. For the latter, the optimized geometries at the B3LYP/LanL2DZ level of theory were used.

4. Results and discussion

The **1a** complexes can exist as variety of geometrical isomers, where a metal ion is chelated by the ligand in the bidentate mode via the carboxylic oxygen and oximic nitrogen atoms or in the monodentate fashion via either the carboxylate ion or the oximato fragment (Scheme 1). Potentiometric and UV–Vis studies have suggested that the copper complex exists as $[CuHL_2]^-$ species at pH 2, while the nickel complex is present in the $[NiL_2]^{2-}$ form at pH range of 6–10. In these complexes, two ligand molecules are located to each other in the *trans* configuration. However, crystallographic data of Cu(II) complex showed the dimeric structure [8]. All discussed above molecular structures of **1a** complexes are presented in Scheme 1.

In order to identify the molecular structures of the **1a** complexes obtained in this work we used theoretical simulation of their vibrational spectra. It should be emphasized that this method allows to predict a general coordination pattern only but it is very valuable in the case of the lack of crystallographic data. However, this is more than enough to distinguish between *cis* and *trans* conformation of the metallocomplex with information whether coordinated ligands are protonated or not. Thus, for the purpose of this work, we considered as models bis-chelate square planar molecules with different conformation of the ligand (*cis* $[MHL_2]^-$ and *trans* with the protonated $[MH_2L_2]$ as well as deprotonated oximic group $[ML_2]^{2-}$). However, for the sodium complex we assumed that sodium ions can be coordinated to either oximate or carboxylate moieties [MHL] or to both of them simultaneously $[M_2L]$ (see Scheme 1).



Scheme 1.

In case of the nickel–**1a** complex, frequency calculations at equilibrium geometries yield only real values; hence all models correspond to local minima. The comparison of theoretical and experimental IR spectra in the range of 1000–1800 cm^{-1} showed (Fig. 1) that $[NiL_2]^{2-}$ model reproduces the best obtained experimental data, where Ni(II) coordinates to deprotonated **1a** ligands in *trans* configuration (Fig. 2). The deprotonation of both ligand molecules is confirmed by the detailed analysis of the oximic vibrations as it is discussed below. It is clear that there has to be a counter cation for the dianionic form of 2-cyano-2-(hydroxyimino)acetic acid in this structure. It is known, from our previous works [22,24], that the type as well as the binding site of a counterion do not effect significantly experimental and theoretical vibrational spectra. Hence, in our models the presence of the counterion is neglected.

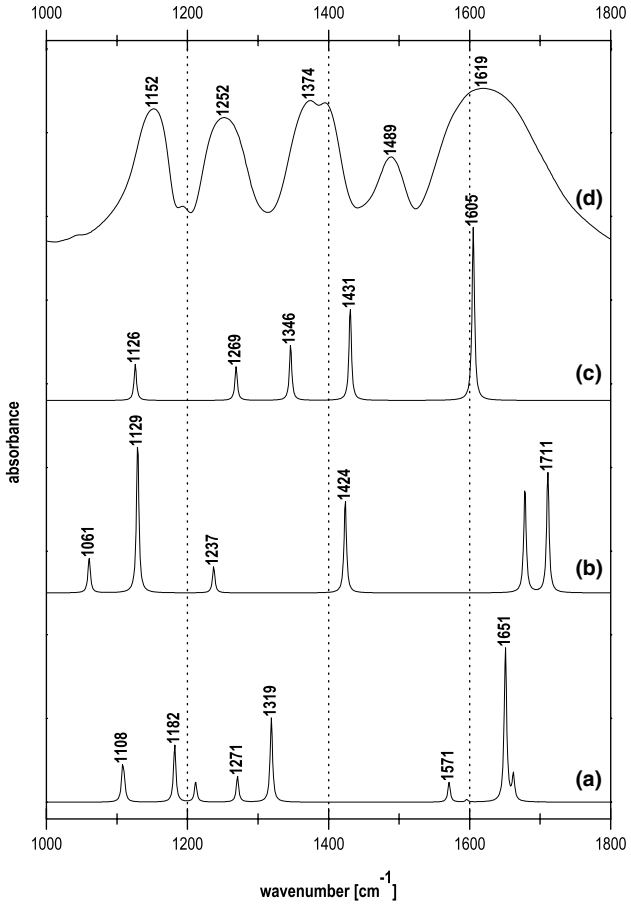


Fig. 1. Comparison of theoretical and experimental IR spectra (1000–1800 cm^{-1}) of the **1a** nickel complex: (a) *cis* $[NiHL_2]^-$, (b) *trans* $[NiH_2L_2]$, (c) *trans* $[NiL_2]^{2-}$ and (d) experimental spectrum.

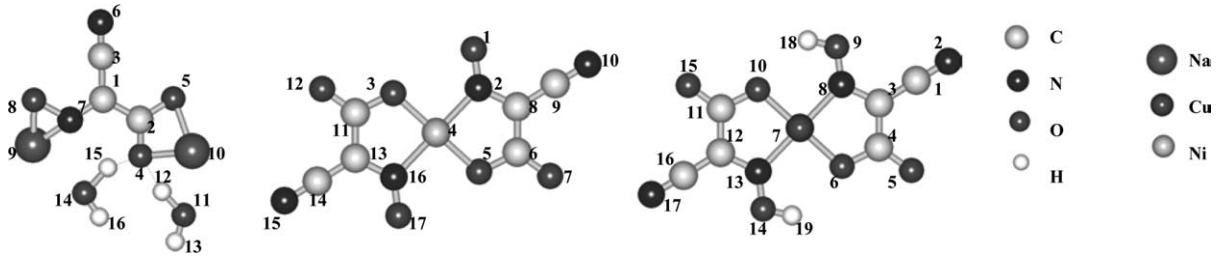


Fig. 2. Model structures of **1a** complexes with the atom numbering used in calculations.

The same procedure was applied to determinate the structure of the **1a** complex with Cu(II) ions. The dimeric species can be ruled out based on the EPR spectrum typical for a complex with orthorhombic symmetry ($g_1 = 2.249$, $g_2 = 2.188$ and $g_3 = 2.051$; cf. Fig. 3). Frequency analysis of *trans* $[CuL_2]^{2-}$ showed one imaginary value what indicated this model to be a transition state and excluded it finally from further studies. Moreover, the differences in experimental IR and Raman spectra of the nickel and copper complexes evidently indicates that these compounds are not isostructural. Additionally, the comparison of the calculated vibrational spectra of the other copper complex models with experimental IR and Raman clearly indicates that *trans* $[CuH_2L_2]$ form exists in solid state (see Figs. 2 and 4). Also, the presence of the protonated oximic groups has been established by their positions in the vibrational spectra (Section 4.3).

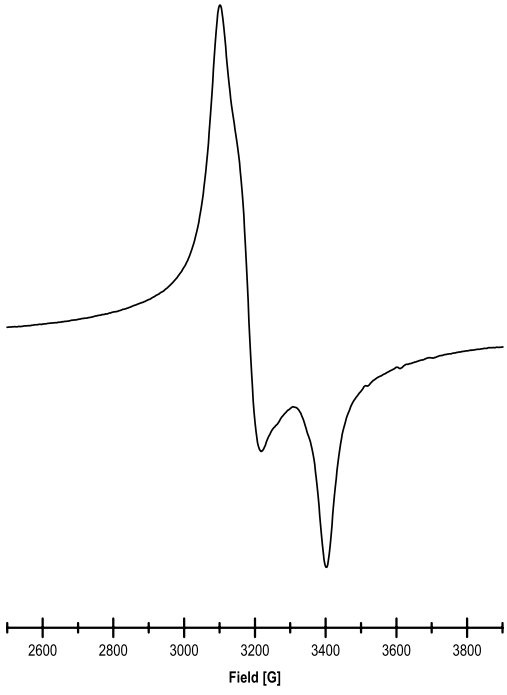


Fig. 3. Microcrystalline EPR spectra of the **1a** copper complex at the X band frequency at 298 K.

In case of the sodium–**1a**, several structures with different binding of this metal ion to the carboxylic and/or oximic groups were taken into consideration. As mention in Section 2 two sodium atoms are present in this complex of **1a**. Furthermore, despite of the elemental analysis results (water-to-Na–**1a** molar ratio is 1:3), two water molecules were added to the model structure to mimic H-bond presented in experimental IR spectrum (see Fig. 5). Finally, the comparison of experimental and simulated vibrational spectra showed that both NOH and COOH have to be deprotonated to allow coordination of two sodium ions ($[Na_2L] \cdot 2H_2O$; cf. Fig. 2).

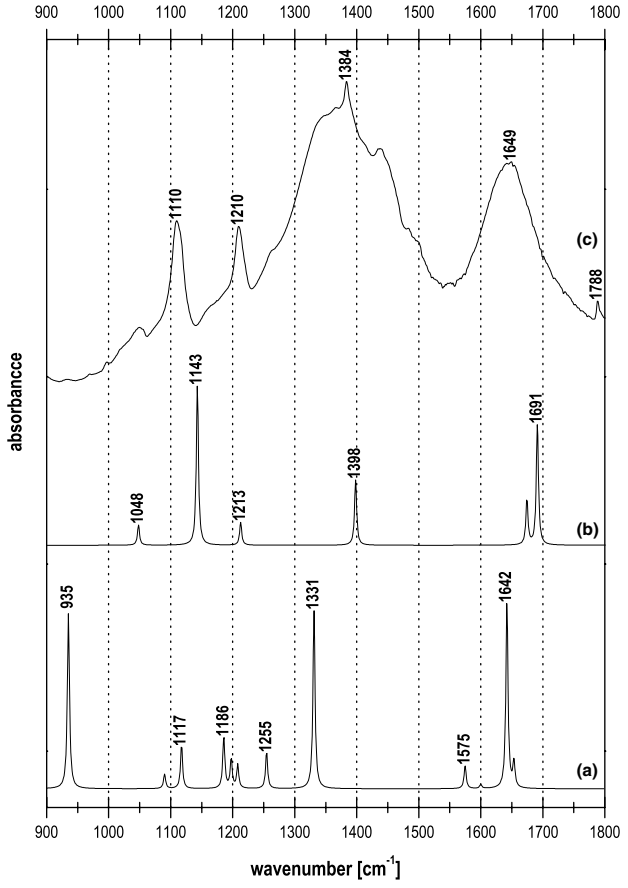


Fig. 4. Comparison of theoretical and experimental IR spectra (900–1800 cm^{-1}) of the **1a** copper complex: (a) *cis* $[CuHL_2]^-$, (b) *trans* $[CuH_2L_2]$ and (c) experimental spectrum.

Geometrical parameters, charge distribution and vibrational spectra for assigned molecular structures of **1a** complexes are discussed below.

4.1. Geometry

Computed bond lengths obtained for structures of E-isomer [H_2L] of **1a** and its complexes with metal ions present here are shown in Table 1. The comparison between bond length values in all studied complexes with the uncoordinated protonated **1a** molecule shows differences mainly in "functional" groups coordinating to the metal ions. The carbonyl bonds in the complexes lengthen considerably (0.04–0.06 Å) after the coordination, whereas the C—O bond involved in metal ion binding shorten slightly in the transition metal complexes (~0.01 Å) and over 0.05 Å in the sodium salt. This results probably from the bidentate coordination of the sodium ion by carboxylate group. The observed trend of changes in bond lengths for this group is typical for many oxocarboxylic acid oximic complexes [3,7,21,23,24].

The oximic NO and CN bonds in the sodium and nickel compounds are close to those reported for the N-coordinated deprotonated oxime group [3–5,23]. This indicates that the CNO^- moiety exists in the nitroso-form (C—N=O). The lengths of the oximic bonds in the protonated copper complex are longer than those in the **1a** molecule, contrary to the deprotonated complexes, where the C=N bond is elongated and the N—O bond is shortened upon coordination. The latter effect was observed for the *cis* complex of 2-hydroxyiminopropanoic acid [H_3C—C(COOH)=NOH, hpa] with Cu(II) ion regardless of the ligand protonation state [22]. Besides, in the **1a** copper complex the elongation of the oximic bonds supports the *trans* configuration of the investigated compound like it was found for the *trans* nickel hpa complex.

Table 1
Selected computed bond lengths [Å] for **1a** and its complexes with Na(I), Ni(II) and Cu(II) ions

Bond	H_2L 6-311 ++G(d,p)	$[Na_2L]\cdot 2H_2O$ 6-311++G(d,p)	$[NiL_2]^{2-}$ LanL2DZ	$[CuH_2L_2]$ LanL2DZ
C=O	1.199	1.254	1.263	1.236
C—O	1.347	1.298	1.339	1.342
C=N	1.287	1.316	1.357	1.305
N—O	1.359	1.292	1.300	1.393
C≡N	1.154	1.157	1.189	1.181
C_{ox}–C_{car}	1.506	1.481	1.496	1.559
C_{ox}–C_{cya}	1.433	1.427	1.423	1.428
M—O		2.256[a]	1.883[b]	1.920[b]
		2.197[b]		
		2.439[b]		
M—N		2.236	1.935	1.962

Functional groups are denoted as: ox – oximic, car – carboxylic, cya – cyano groups and M as metal ion. Upper symbols are denoted as: $[H_2L]$ – the fully protonated ligand; $[CuH_2L_2]$, $[Na_2L]\cdot 2H_2O$, $[NiL_2]^{2-}$ – applied models of complexes.
[a] The oximic oxygen atom.
[b] The carboxylic oxygens.

Regarding the cyano group, its bond lengthens upon the complexation with all metal ions studied here. Interestingly, coordination of the alkali ion causes a slight change of the C≡N length (0.003 Å), whereas for transition metal ions the elongation is rather significant (~0.03 Å). Besides, the deprotonation of the oximic group causes the decrease of the electron density of the cyano bond, and consequently, its lengthening. The B3LYP/LanL2DZ method predicted this bond to be too long (cf. Table 1), but it is still close enough to those observed in related cyanoxime complexes (1.13–1.15 Å) [3–5,7].

The metal–ligand bond distances were calculated in the range comparable to other complexes. For sodium salt of **1a**, the distances between sodium and carboxylic oxygen atoms were calculated at 2.20 and 2.44 Å. These values are consistent with the range of 2.01–2.59 Å found for other oximic complexes with alkali metal ions. Similarly, the Na–N_{oximic} bond length is 2.24 Å, while its typical value is observed in the 2.22–2.54 Å range [21,25,26]. However, the comparison of calculated

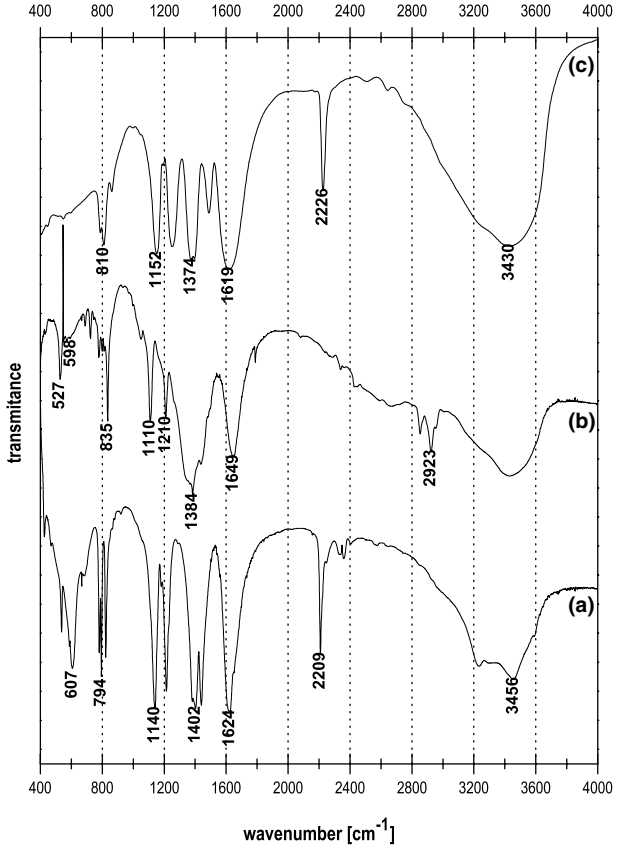


Fig. 5. Mid-IR spectra (400–4000 cm^{-1}) of (a) the **1a** sodium complex, (b) the **1a** copper complex and (c) the **1a** nickel complex.

metal–ligand bond lengths for proposed structures (*trans* $[NiL_2]^{2-}$ and $[CuH_2L_2]$) indicates the stronger binding of Ni(II) than Cu(II) ion to **1a**. It seems that the transition metal ion rather than the deprotonation state of the oximic group is responsible for this effect. As calculated for *trans* $[NiH_2L_2]$ isomer, the metal–nitrogen bond lengths (Ni—N = 1.855 Å, Ni—O = 1.851 Å) are still shorter than respective bonds in $[CuH_2L_2]$. All calculated metal–ligand bond lengths are in the range of the oximic complexes studied so far [3–5,7,22–26].

4.2. Atomic charges

The atomic charges at all atoms in **1a** at the different protonation stages and its complexes studied here are given in Table 2. The effective charges at the metal ions are reduced up on binding ligand and are +1.06 [(Cu(II)], +0.91 and +0.86 [Na(I), for the ion bonded to the carboxylate and oximato groups, respectively], +0.72 a.u. [Ni(II)]. The smallest change of the charge value in the sodium ion is consistent with the weakest metal–ligand interaction.

As expected, the electron density on the oxygen atoms in the deprotonated carboxylic group of **1a** (denoted in Table 2 as $[HL]^-$) is almost equal on both oxygens. The further deprotonation of the oximic group (see data for $[L]^{2-}$) causes only a charge increase at the carboxylic oxygens by ~ -0.1 a.u. Upon coordination of the copper ion, the withdrawal of electronic charge towards O-atom bonded to the metal ion is expected and observed. The similar distribution of the electron density on the carboxylic group is found for the sodium salt. The difference between charges on the O-atoms for the sodium compound is lower than for $[CuH_2L_2]$. It results from the fact that Na(I) ion coordinates to both oxygen atoms. Interestingly, a reverse trend is observed for the nickel complex. It appears that the deprotonation of the oximic group reduces the electron density at the carboxylic O-atom and shifts it towards the Ni-atom.

In the oximic group, the electron density is systematically shifted toward the oxygen atom. The deprotonation of the carboxylic proton causes an increase of negative charge at the NOH moiety (see data for $[HL]^-$ form of **1a**). After coordination of Cu(II), the negative charge density is accumulated on the N-atom and partially moved towards the metal ion. Upon the removal of the oximic proton the distribution of electron density changes significantly. The C and O atoms become strongly negative, whereas positive charge is accumulated on the N atom. This affects the C=N and N—O bond lengths as discussed above. These changes of the charge distribution follow the coordination of the sodium and nickel ions to the fully deprotonated ligand. Again, the largest withdrawal of the electronic charge from the N-atom towards the metal ion is observed in $[NiL_2]^{2-}$.

It is worth to look at the charge distribution of the cyano group. Upon the deprotonation of the carboxylic proton, the negative charge of the N-atom increases by 0.18 a.u. whereas a charge at the C-atom decreases by 0.13 a.u., due to the withdrawing electron character of C≡N. After coordination of Cu(II), the electron density flows from the N-atom through the cyano carbon towards the remaining fragment of the ligand. However, the deprotonation of the oximic proton causes more ionic character of the cyano bond than in the $[HL]^-$ form. This group behaves as an electron donating substituent in coordination of sodium and nickel ions. Regardless the coordination mode and the type of a metal ion, the same effective charge (−0.08 a.u.) is shifted from C≡N towards the adjacent oximic C-atom. Furthermore, the difference between the effective charges at the carbon and nitrogen atoms in C≡N follows the trend: $[CuH_2L_2]$ (0.03 a.u.), $[Na_2L]\cdot 2H_2O$ (0.55 a.u.) and $[NiL_2]^{2-}$ (0.99 a.u.). It worth to note that this differ-

Table 2
Computed atomic charges [APT population analysis (GAPT)] of **1a** forms and its complexes with metal ions [M=Na(I), Ni(II) and Cu(II)][a]

Atom	$[H_2L]$	$[HL]^-$	$[CuH_2L_2]$	$[L]^{2-}$	$[Na_2L]\cdot 2H_2O$	$[NiL_2]^{2-}$
$O_{carboxylic}$	−0.726	−0.873	−1.010	−0.968	−1.229	−0.871
$C_{carboxylic}$	+1.195	+1.199	+1.266	+1.206	+1.433	+1.264
$O_{carbonyl}$	−0.678	−0.887	−0.750	−0.979	−1.052	−0.925
$H_{carboxylic}$	+0.349					
C_{oximic}	−0.008	−0.007	+0.210	−0.518	−0.413	−0.535
N_{oximic}	+0.251	+0.163	+0.079	+0.332	+0.376	+0.611
O_{oximic}	−0.543	−0.610	−0.521	−0.779	−0.792	−0.694
H_{oximic}	+0.333	+0.254	+0.415			
C_{cyano}	−0.003	+0.131	−0.125	+0.405	+0.169	+0.388
N_{cyano}	−0.185	−0.370	−0.094	−0.699	−0.381	−0.599
M			+1.059		+0.911	+0.724
					+0.858	

Upper symbols are denoted as: $[HL]^-$ – ligand with the deprotonated carboxylic group; $[L]^{2-}$ – the fully deprotonated ligand.
[a] Geometry by B3LYP/LanL2DZ for all models.

ence for models $[CuL_2]^{2-}$ and $[NiH_2L_2]$ are 0.97 and 0.01 a.u., respectively. It clearly indicates that polarization of the cyano group strongly depends on the deprotonation of the oximic group only. That can be traced in vibrational properties of this group as will be shown below.

4.3. Vibrational spectra

The calculated and experimental vibrational frequencies and assignments of the characteristic modes for all investigated complexes are summarized in Table 3 (full description of the internal coordinates and vibrational spectra are given in the Supplementary Material, Tables I–VI). Experimental (IR and Raman) spectra of the complexes are shown in Figs. 5–7. It should be emphasized that the simulated spectra refer to the isolated molecule at 0 K, whereas the assignments are made for the vibrational spectra of the solid state. Thus, some differences in the calculated versus experimental frequencies or intensities are most probably caused by intermolecular interactions (crystal packing) or by anharmonicity of vibrations. Vibrational modes which are of great importance in the determination of discussed molecular structures are shown below.

4.3.1. $\nu(OH)$ and $\delta(OH)$

The IR spectra of all compounds exhibit broad absorption bands with maxima at 3456 and 3234 [Na–**1a**], 3450 [Cu–**1a**] and 3430 cm^{-1} [Ni–**1a**] (cf. Fig. 5). These are assigned to the stretch vibration of the oximic OH (in the copper complex) as well as free or weakly H-bonded hydrated water molecules in the other complexes. Calculations for the applied models predict the presence of those vibrations at 3720, 3719, 3265 and 2983 cm^{-1} [$\nu(OH)_{H_2O}$] for the sodium salt (cf. Fig. 2) and at 3496 and 3499 cm^{-1} [$\nu(OH)_{ox}$] for the copper complex. Additionally, calculations of vibrational spectra for Ni and Cu complexes with hydrated waters showed that $\nu(OH)_{H_2O}$ should appear in the mentioned-above experimental range (data not shown). Moreover, bands at ~1620 cm^{-1} are characterized by significant values of FWHM resulting from the presence of bending modes of H_2O [$\delta(OH)$]. Hence, we can conclude that water molecules are not directly coordinated to the complex structures. Furthermore, the absence of IR absorptions characteristic for water molecules located in the first coordination sphere of a complex confirms this assumption (at ~900 and ~770 cm^{-1}, the rocking and the wagging vibrations of the OH group, respectively).

4.3.2. $\nu(C{\equiv}N)$

The stretches modes of cyano bond in the IR and Raman spectra of the **1a** complexes (cf. Table 3) definitely indicate the shortening of this bond in the following order: Na–**1a**, Ni–**1a** and Cu–**1a**. The mode frequencies of the sodium and nickel compounds are typical for their coordination motifs [3,5]. However, a participation of the C≡N group in the metal binding may be suggested by the high-shift of the C≡N stretch (2242 cm^{-1}, Raman spectrum, see Fig. 7(b)) for the cooper complex comparing to the latter. Surprisingly, IR and Raman intensities for this complex are very low, in the contrary to the other complexes. That is due to the electron density distribution. As showed above, the smallest polarization of the cyano bond is observed for $[CuH_2L_2]$.

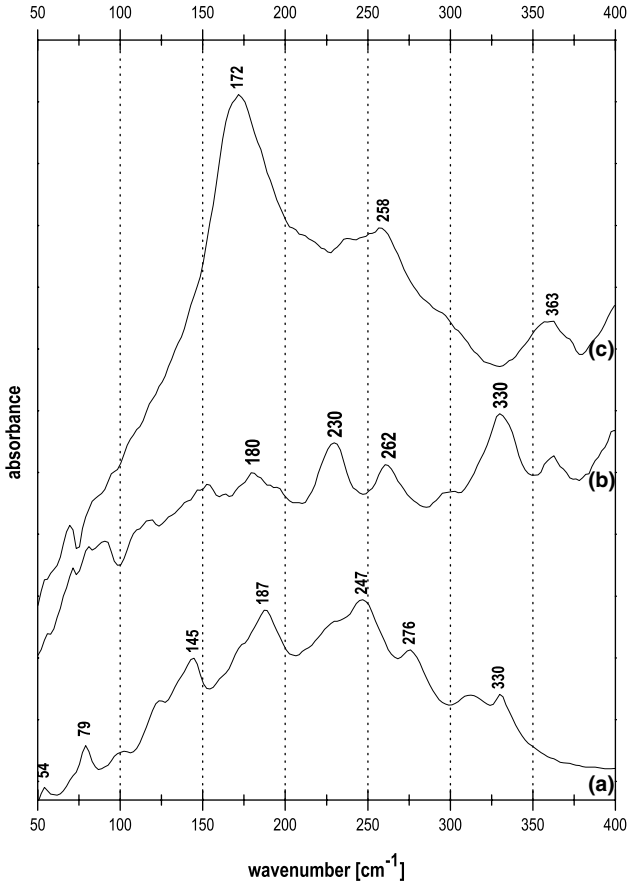


Fig. 6. Far-IR spectra (50–400 cm^{-1}) of (a) the **1a** sodium complex, (b) the **1a** copper complex and (c) the **1a** nickel complex.

4.3.3. $\nu_{as}(COO)$ and $\nu_s(COO)$

A characteristic features of the vibrational spectra of the **1a** complexes is the lowering of frequencies of the asymmetric carboxylate stretching [ν_{as}(COO)] down to ~1610 cm^{-1}. Thus, the change in these mode frequencies can be attributed to the deprotonation of the carboxylic group as well as the ability to bind the metal centers. The position of this band in the sodium complex is typical for the alkali complexes of hpa [21]. That clearly indicates the absence of a significant influence of the withdrawing electron cyano group on the coordination fashion by the carboxylate anion. Furthermore, a

Table 3
Computed [with potential energy distribution (PED, %)] and experimental IR and Raman frequencies (in cm^{-1}) of the selected stretching modes for sodium, nickel and copper complexes of **1a**

Mode	Na–**1a** (exp.)		$[Na_2L] \cdot 2H_2O$ (calc.)	$[NiL_2]^{2-}$ (exp.)		$Ni(\mathbf{1a})_2$ (calc.)		Cu–**1a** (exp.)		$[CuH_2L_2]$ (calc.)	
	IR	Raman	IR/Raman	IR	Raman	IR	Raman	IR	Raman	IR	Raman
ν(C≡N)	2209	2208	2275 [90]	2226	2229	2210 [63][a]	2212 [62][b]		2242	2281 [86][a]	2281 [86][b]
ν_{as}(COO)	1613	1611	1538 [81]	1619	1645	1605 [84][a]	1614 [81][b]	1649	1668	1691 [64][a]	1695 [83][b]
ν_s(COO)	1383	1381	1359 [36]	1152	1160	1126 [22][a]	1130 [36][b]	1110	1165	1154 [56][a]	1143 [60][b]
	1140	1144	1136 [30]								
ν(C=N)	1440	1444	1454 [69]	1489	1496	1431 [73][a]	1423 [74][b]	1649	1650	1674 [48][a]	1678 [66][b]
ν(NO)	1214	1211	1260 [70]	1252	1263	1269 [42][a]	1275 [45][b]	1050	1045	1048 [53][a]	1038 [56][b]
ν(M–N)	307		294 [32]	357		373 [46][a]	202 [12][b]	330		344 [41][a]	156 [53][b]
ν(M–O)	330[c]	330[c]	337 [46][c]								
	307[d]		294 [23][d]	408	356	427 [48][a]	316 [18][b]	363		376 [39][a]	290 [41][b]
	161[d]	162[d]	165 [19][d]								

[a] In-counter-phase.
[b] In-phase.
[c] The oximic oxygen atom.
[d] The carboxylic oxygens.

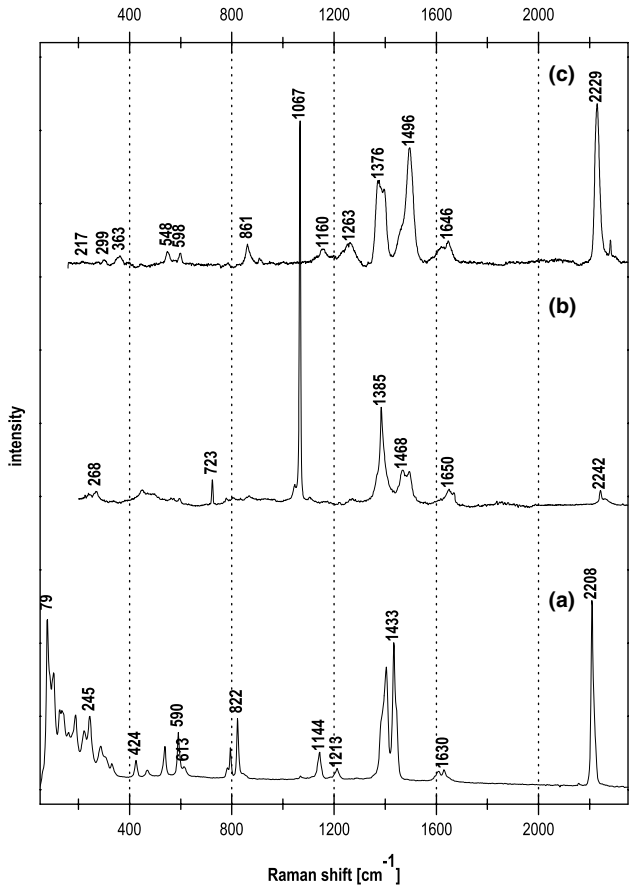


Fig. 7. Raman spectra (50–2500 cm^{-1}) of (a) the **1a** sodium complex, (b) the **1a** copper complex, (c) the **1a** nickel complex.

smaller low-frequency shifts of this vibration for 3-d metal ions complexes support bidentate coordination of the 2-cyano-2-(hydroxyimino)acetate anion to metal center. Similar behavior has been found previously for other transition metals oximates [22]. Additionally, the vibrational spectra of those complexes exhibit the splitting of the COO stretching vibration. The in-counter-phase modes are observed in IR whereas the in-phase counterparts are present in the Raman spectrum. That is consistent with the proposed model where two ligands in *trans* configuration coordinate to the metal ion (see Table 3). Moreover, the deprotonation of the oximic group but not a metal ion [Cu(II) versus Ni(II)] seems to be responsible for the lower shift-frequency of the ν_{as}(COO) in the nickel complex. The IR frequency of the latter is almost the same as for the sodium salt with the deprotonated C=NO.

According to the DFT results, the symmetric stretching mode [ν_s(COO)] appears mainly in the range of 1165–1110 cm^{-1} with its relatively small contribution in the normal mode (22–60% PED). Merely, the spectra of Na–**1a** exhibit additional bands in the typical frequency range for ν_s(COO), at ~1381 cm^{-1} with 36% participation of this vibration.

4.3.4. ν(C=N) and ν(N—O)

The positions of the ν(C=N) and ν(NO) vibrations in IR and Raman spectra are dependent to a great extend on the oxime or nitroso character of this group in a particular compound and are reflected by the coordination mode. The vibrational spectra of the sodium and nickel complexes exhibit a significant shift of ν(C=N) to lower frequencies, at ~1440 and ~1490 cm^{-1}, for Na–**1a** and Ni–**1a**, respectively. That clearly indicates that **1a** appears in these complexes as a nitroso-containing anion. The lower shift of the band of the sodium salt results primarily from a participation in coordination of the oximic oxygen atom. DFT fully confirms this assignment (1454 cm^{-1}, 69% PED). The ν(C=N) of the nickel complex is found in our experiment in the similar range as for the Ir(III) and Ru(II) complexes of other α-hydroxyiminocarboxylic acids with the deprotonated oximic group (1515–1495 cm^{-1}) [23]. On the other hand, the C=N stretch vibration of the copper complex is assigned to the band at 1650 cm^{-1} in the Raman spectrum [1678 cm^{-1} (66% PED) calculated]. This frequency indicates that oximic not nitroso group takes part in Cu(II) coordination.

The high-frequency shift of the ν(NO) modes in the vibrational spectra of Na(I) and Ni(II) compounds confirms additionally that these metal ions are bonded to the ligand by the nitrogen atom of the nitroso group (cf. Table 3). B3LYP predicts positions of this mode very well, with an error less than 4.0%. Additionally, the simulated spectra of the nickel complex exhibit the different position of the mode in IR (1269 cm^{-1}) and Raman (1275 cm^{-1}) spectra, respectively. The same has been observed in the experimental spectra and results from the *trans* ligand conformation. The difference is equal to 9 cm^{-1}. The most pronounced feature of vibrational spectra of the copper complex is in their very low frequencies of the ν(NO) vibrations (1050 and 1045 cm^{-1} in IR and Raman, respectively) comparing to Na–**1a** and Ni–**1a**. Thus, the positions of these bands are consistent with the protonated *trans* structure.

4.3.5. Metal–ligand vibrations

The frequency region below 500 cm^{-1} provides information on the metal–ligand stretch vibrations. The far IR and Raman spectra of the complexes present here in this particular range are shown in Figs. 6 and 7. The IR absorptions at 307, 330 and 357 cm^{-1} are assigned to the metal–nitrogen stretching vibration of Na, Cu(II) and Ni(II) complexes, respectively. The contribution of this vibration to the normal modes is less than 50%, as predicted by calculated PEDs (cf. Table 3). As expected, the coordination by the oximic nitrogen atom of the s-type metal ions is considerably weaker. Similar observation has been found for the metal-carboxylic oxygen stretch modes. Moreover, the comparison of frequencies of Na–O_{oximic} with Na–$O_{carboxylic}$ indicates the stronger coordination this alkali ion by the nitroso moiety than by the carboxylate anion.

5. Conclusions

The experimental IR and Raman spectra of solid state supported by the DFT calculations have shown that the transition metal complexes of 2-cyano-2-(hydroxyimino)acetic acid have *trans* bidendate square-planar geometry with the different protonation state of the oximic group. This is similar to their structures in solution determined previously by our potentiometric and spectroscopic studies [8]. However, two sodium ions are bonded to the carboxylate as well as oximate moieties. Vibrational analysis has clearly indicated the binding nature of the oximic and carboxylic oxygen atoms and the oximic nitrogen atom. It also shows the presence of the nitroso form of the oximic group in Ni–**1a** and Na–**1a**. Furthermore, the latter effects the coordination strength in all complexes presented. Namely, this causes the increase of the stability of the nickel complex comparing to the copper one and the binding ability of the oximic group comparing to the carboxylic one in Na–**1a**. The magnitude of all stretch vibrations has been shown to be well correlated with the atomic charge distribution. The calculations of atomic charges have suggested that the deprotonation of the carboxylic group does not change significantly the electronic distribution in the **1a** molecule, whereas the removal of the oximic proton causes the accumulation of the positive charge on the oximic nitrogen. Moreover, the electron density is shifted from the metal ion towards the carboxylic oxygens in the copper and sodium complexes in reverse to Ni–**1a**. And in the oximic group, the N-atom is an electron donor for metal ions.

Acknowledgments

The authors thank Academic Computer Centre CYFRONET of the University of Science and Technology in Krakow (grant no. KBN/SPP/UJ/027/1999) and Interdisciplinary Center for Mathematical and Computational Modeling of Warsaw University in Warsaw (grant no. G25-8) for the possibility to perform necessary calculations.

Appendix A. Supplementary data

Supplementary data associated with this article can be found, in the online version at doi:10.1016/j.poly.2005.04.007.

References

[1] H.A. Kirst, E.F. Szymanski, D.E. Doman, J.L. Occolowitz, N.D. Jones, M.O. Chaney, R.L. Hamill, M.M. Hoehn, J. Antibiot. 28 (1975) 286.

[2] H. Nakamura, Y. Iitaka, H. Sakakibara, H. Umezawa, J. Antibiot. 27 (1974) 894.

[3] V.V. Ponomareva, N.K. Halley, X. Kou, N.N. Gerasimchuk, K.V. Domasevich, J. Chem. Soc. Dalton Trans. (1996) 2351.

[4] A.A. Mokhir, K.V. Domasevich, N.K. Dalley, X. Kou, N.N. Gerasimchuk, O.A. Gerasimchuk, Inorg. Chim. Acta 284 (1999) 85.

[5] K.V. Domasevich, N.N. Gerasimchuk, A.A. Mokhir, Inorg. Chem. 39 (2000) 1227.

[6] A. Gupta, R.K. Sharma, R. Bohra, V.K. Jain, J.E. Drake, M.B. Hursthouse, M.E. Light, J. Organomet. Chem. 645 (2002) 118.

[7] T.Y. Sliva, A.M. Duda, T. Glowiak, I.O. Fritsky, V.M. Amirkhanov, A.A. Mokhir, H. Kozlowski, J. Chem. Soc. Dalton Trans. (1997) 273.

[8] T.Y. Sliva, A. Dobosz, L. Jerzykiewicz, A. Karaczyn, A.M. Moreeuw, J. Świa˛tek-Kozłowska, T. Głowiak, H. Kozłowski, J. Chem. Soc. Dalton Trans. (1998) 1863.

[9] Ch.O. Onindo, T.Y. Sliva, T. Kowalik-Jankowska, I.O. Fritsky, P. Buglyo, L.D. Pettit, H. Kozlowski, T. Kiss, J. Chem. Soc. Dalton Trans. (1995) 3911.

[10] A.A. Mokhir, E. Gumienna-Kontecka, J. Świa˛tek-Kozłowska, E.G. Petkova, I.O. Fritsky, L. Jerzykiewicz, A.A. Kapshuk, T.Y. Sliva, Inorg. Chim. Acta 329 (2002) 113.

[11] T.Y. Sliva, T. Kowalik-Jankowska, V.M. Amirkhanov, T. Głowiak, Ch.O. Onindo, I.O. Fritsky, H. Kozlowski, J. Inorg. Biochem. 65 (1997) 287.

[12] C. Lee, W. Yang, R.G. Parr, Phys. Rev. B 37 (1988) 785.

[13] A.D. Becke, J. Chem. Phys. 98 (1993) 5648.

[14] P.J. Hay, W.R. Wadt, J. Chem. Phys. 82 (1985) 299.

[15] P.J. Hay, W.R. Wadt, J. Chem. Phys. 82 (1985) 270.

[16] M.J. Frisch, G.W. Trucks, H.B. Schlegel, G.E. Scuseria, M.A. Robb, J.R. Cheeseman, V.G. Zakrzewski, J.A. Montgomery, R.E. Stratmann, J.C. Burant, S. Dapprich, J.M. Millam, A.D. Daniels, K.N. Kudin, M.C. Strain, O. Farkas, J. Tomasi, V. Barone, M. Cossi, R. Cammi, B. Mennucci, C. Pomelli, C. Adamo, S. Clifford, J. Ochterski, G.A. Petersson, P.Y. Ayala, Q. Cui, K. Morokuma, D.K. Malick, A.D. Rabuck, K. Raghavachari, J.B. Foresman, J. Cioslowski, J.V. Ortiz, B.B. Stefanov, G. Liu, A. Liashenko, P. Piskorz, I. Komaromi, R. Gomperts, R.L. Martin, D.J. Fox, T. Keith, M.A. Al-Laham, C.Y. Peng, A. Nanayakkara, C. Gonzalez, M. Challacombe, P.M.W. Gill, B. Johnson, W. Chen, M.W. Wong, J.L. Andres, C. Gonzalez, M. Head-Gordon, E.S. Replogle, J.A. Pople, Gaussian 98 (Revision A.6), Gaussian Inc., Pittsburgh, PA, 1998.

[17] D. Michalska, W. Zierkiewicz, D.C. Bienko, W. Wojciechowski, Th. Zeegers-Huyskens, J. Phys. Chem. A105 (2001) 8734.

[18] D. Michalska, R. Wysokinski, Chem. Phys. Lett. 403 (2005) 211.

[19] M.H. Jamroz, Vibrational Energy Distribution Analysis: Veda 3.0 Program, Drug Institute, Warsaw, Poland, 2000.

[20] J. Cioslowski, J. Am. Chem. Soc. 111 (1989) 8333.

[21] A.W. Apblett, G.D. Georgieva, J.T. Mague, Inorg. Chem. 36 (1997) 2656.

[22] K. Malek, PhD dissertation, Jagiellonian University, Krakow, 2003.

[23] R. Bergs, R. Lampeka, C. Robl, W. Beck, Z. Naturforsch. b 49 (1994) 483.

[24] K. Malek, M. Vala, J. Swiatek-Kozlowska, L.M. Proniewicz, New. J. Chem. 28 (2004) 477.

[25] T. Adatia, J. Chakrabarti, O. Carugo, C.B. Castellani, Polyhedron 15 (1996) 1331.

[26] G.P. Voutsas, K.G. Keramidas, M. Lalia-Kantouri, Polyhedron 15 (1996) 147.

species was observed. Adducts such as $Cu_2(TFA)_4L_2$ [L = MeCN [7a], quinoline [7b], 2-hydroxypyridine (2-pyOH)] and $Cu(TFA)_2L_4$ [L = H_2O] [7a], 3-hydroxypyridine (3-PyOH) [7c] or mixed-ligand species such as $Cu(TFA)_2(3\text{-pyOH})_2(THF)_2$ were also reported. A number of $Ba(TFA)_2$ complexes with O- and N-donor polydentate ligands have been described [8,9]. The complex with 15-crown-5 has been used for $MTiO_3$ films (M = Ba, Sr) [8,9].

We wish to report herein the synthesis and characterization in the solid state as well as in solution of various adducts of copper(II) and barium(II) fluorinated carboxylates. Indications about their stability and reactivity are given as well.

2. Experimental

All manipulations were routinely performed under nitrogen using Schlenk tubes and vacuum line techniques. Solvents were purified by standard methods. Trifluoroacetic (TFAH), perfluorobutyric (PFBH) and difluoroacetic acids (Aldrich) were stored over molecular sieves. $[Cu(OMe)_2]_\infty$ was prepared by anodic dissolution of the metal [10]. FT-IR spectra were recorded as Nujol mulls on an IR-FTS 45 Perkin–Elmer spectrometer. Elemental analyses were done at the Centre de Microanalyses du CNRS. FT-IR data and general characteristics are collected in Table 1. ESR spectra (X-band), were obtained at rt on powders with a Bruker spectrometer (microwave power of 10 mW, modulation frequency of 100 kHz). DPPH (diphenylpicrylhydrazyl) was used as reference (g = 2.0036).

2.1. Syntheses

2.1.1. $[Cu_2(TFA)_4(THF)_2]$ (1) and $Cu(O_2CCHF_2)_2(THF)$ (2)

TFAH (1.6 ml, 20.6 mmol) was added to a THF/toluene (1:3, 40 ml) suspension of $[Cu(OMe)_2]_\infty$ (1.30 g, 10.3 mmol). The dark green solution obtained after stirring overnight and filtration, concentration yielded green crystals of **1** at −20 °C (2.20 g, 59%). *Anal.* Calc. for $C_8H_8F_6O_5Cu$: C, 26.57; H, 2.23. Found: C, 26.14; H, 2.16%. Additional crops of crystals were contaminated with $Cu_2(TFA)_4(MeOH)_2$ (IR and analytical evidence).

The same procedure applied to CHF_2CO_2H (0.46 ml, 7.27 mmol), $[Cu(OMe)_2]_\infty$ (0.458 g, 3.63 mmol) and THF (30 ml) gave green crystals of **2** at −20 °C (0.65 g, 55%) by addition of toluene. *Anal.* Calc. for $C_8H_{10}O_5F_4Cu$: C, 29.50; H, 3.09. Found: C, 29.45; H, 2.92%.

2.1.2. $[Cu(TFA)(OAc)]_m(THF)_{0.25m}$ and $Cu_2(PFB)_4(THF)_2$ (3)

TFAH (0.25 ml, 3.30 mmol) was added to a suspension of $Cu(OAc)_2$ (0.30 g, 1.65 mmol) in THF (15 ml). After 3 h, the green solution was concentrated. Addition of toluene gave a green-blue solid at −20 °C (0.32 g, 76%). *Anal.* Calc. for $C_5H_5F_3O_{4.25}Cu$: C, 23.68; H, 1.99. Found: C, 23.97; H, 1.58%.

The same procedure applied to perfluorobutyric acid (0.45 ml, 3.43 mmol), $Cu(OAc)_2$ (0.284 g, 1.56 mmol) in THF (20 ml) gave green crystals of **3** (0.57 g, 65%). *Anal.* Calc. for $C_{12}H_8F_{14}O_5Cu$: C, 25.66; H, 1.44. Found: C, 25.75; H, 1.53%. Sublimation at 190 °C/2×10^{-4} Torr gave the very hygroscopic $[Cu(PFB)_2]_m$.

2.1.3. $Cu_2(TFA)_4(^iPrOC_2H_4OH)_2$ (4)

2-Isopropoxyethanol (1.1 ml, 9.35 mmol) was added to **1** (0.678 g, 2.08 mmol) in toluene (20 ml). After stirring for 12 h at rt, concentration afforded green crystals (0.66 g, 81%). *Anal.* Calc. for $C_9H_{12}F_6O_4Cu$: C, 27.46; H, 3.06. Found: C, 27.65; H, 3.36%. ESR: $\langle g \rangle$ = 2.0834.

2.1.4. $Cu(TFA)_2(Me_2NC_2H_4NMeC_2H_4NMe_2)$ (5)

$Me_2NC_2H_4NMeC_2H_4NMe_2$ (1.0 ml, 4.80 mmol) was added to **1** (0.690 g, 2.12 mmol) in toluene (15 ml). The solution was stirred at rt overnight and evaporated. Recrystallization in THF gave blue crystals (0.90 g, 92%). *Anal.* Calc. for $C_{13}H_{23}F_6N_3O_4Cu$: C, 33.73; H, 5.01; N, 9.08. Found: C, 33.26; H, 5.15; N, 8.81%. ESR: $\langle g \rangle$ = 2.1039.

2.1.5. $[Cu(TFA)(OC_2H_4NMe_2)]_4$ (6)

N,*N*′-Dimethylaminoethanol (0.84 ml, 8.4 mmol) was added to $Cu(TFA)_2(MeOH)$ (0.81 g, 2.8 mmol) in toluene (15 ml). Afer stirring at rt overnight, evaporation to dryness, recrystallization in THF gave blue crystals (1.12 g, 85%). *Anal.* Calc. for $C_{24}H_{40}F_{12}N_4O_{12}Cu_4$: C, 27.23; H, 3.81; N, 5.29. Found: C, 27.35; H, 3.86; N, 5.32%. ESR: $\langle g \rangle$ = 2.090. The monocrystals displayed 0.25 lattice THF molecules per tetramer.

2.1.6. $Cu_2(PFB)_4(^iPrOC_2H_4OH)_2$ (7)

2-Isopropoxyethanol (0.31 ml, 2.7 mmol) was added to **2** (0.500 g, 0.90 mmol) in THF (10 ml). Stirring at rt overnight, evaporation to dryness and recrystallization in toluene yielded green crystals (0.40 g, 75%). *Anal.* Calc. for $C_{13}H_{12}F_{14}O_6Cu$: C, 26.53; H, 2.02. Found: C, 26.30; H, 2.04%.

2.1.7. $Ba(O_2CCHF_2)_2 \cdot 0.5MeOH$ (8)

CHF_2CO_2H (0.72 ml, 11.4 mmol) was added to a suspension of BaH_2 (0.794 g, 5.71 mmol) in THF (30 ml) at −40 °C. After stirring overnight at rt, the suspension was evaporated to dryness. Recrystallization in MeOH gave **8** at −20 °C (1.30 g, 61%). *Anal.* Calc. for $C_{5.5}H_7F_4O_{5.5}Ba$: C, 15.74; H, 1.17. Found: C, 15.76;

Table 1
FT-IR data (cm^{-1}) of the Cu(II) and Ba fluorinated carboxylate adducts

Compound	$\nu(CO_2)$		ν(M–O)	ν(OH)	Observation[a]
	$\nu_{as}(CO_2)$	$\nu_s(CO_2)$			
$Cu_2(TFA)_4(THF)_2$ (**1**)	1684 s	1684 s, 1620 sh	500 m[b]		hygroscopic
$[Cu(TFA)(OAc)]_m$	1684 s, 1620 sh	1438 m, 1430 w	518 m, 420 m[b]		hygroscopic
$Cu(O_2CCHF_2)_2(THF)$ (**2**)	1674 s	1460 m	629 w, 604 w, 526 w, 489 w		green; very hygroscopic. THF s, toluene ss, hexane in
$Cu_2(PFB)_4(THF)_2$ (**3**)	1684 s	1418 m	529 br m[b]		green; air-stable for a few hours
$Cu_2(TFA)_4(^iPrOC_2H_4OH)_2$ (**4**)	1706 s	1464 m	628 w, 538 w, 528 w, 505 w	3176 br	air-stable for some hours; toluene, s; EtOH, ss; hexane, H_2O, in
$Cu(TFA)_2(Me_2NC_2H_4NMeC_2H_4NMe_2)$ (**5**)	1704 s	1424 m	606 w, 585 w, 520 w, 501 w, 480 w, 461 w		blue, turn purple in air; THF, H_2O, EtOH, s; toluene, in
$[Cu(TFA)(OC_2H_4NMe_2)]_4$ (**6**)	1691 s	1420 m	637 w, 614 w, 523 w, 496 w, 472 w		air-stable for some hours; toluene, THF, s; EtOH, ss; Et_2O, hexane, in
$Cu_2(PFB)_4(^iPrOC_2H_4OH)_2$ (**7**)	1698 s	1437 m	656 w, 601 w, 530 w, 494 w, 455 w	3166 br	air-stable for some hours; toluene, s; EtOH, ss; hexane, H_2O, in
$Ba(O_2CCHF_2)_2 \cdot 0.5MeOH$ (**8**)	1652 s	1460 m	599 m, 525 m	3333 br, 3196 br	hygroscopic, THF, ss; MeOH, s
$Ba(TFA)_2\{MeN(C_2H_4OH)_2\}_3$ (**9**)	1677 s	1463 w	600 w, 564 w, 542 w, 518 w	3317 br, 3184 br	air-stable for some hours, THF, s; MeOH, s; $CHCl_3$, s
$Ba(TFA)_2(N(C_2H_4OH)_3)_2$ (**10**)	1682 s	1434 m	599 w, 567 w, 521 w	3354 br	Air stable for some hours; THF, s; MeOH, s; $CHCl_3$, s

[a] s, soluble; ss, slightly soluble; in, insoluble.
[b] IR spectra on NaCl (products react with KBr).

H, 1.23%. ^{1}H NMR (CD_3OD): 5.96 t (J_{H-F} = 53.10 Hz, 2H, CH), 3.5 s (Me, 1.5H).

2.1.8. $Ba(TFA)_2\{MeN(C_2H_4OH)_2\}_3$ (9)

N-Methyldiethanolamine (0.7 ml, 6.04 mmol) was added to a solution of $Ba(TFA)_2$ (0.549 g, 1.51 mmol) in THF (20 ml). After stirring overnight at rt and concentration, colorless needles were obtained (0.475 g, 44%). *Anal*. Calc. for $C_{19}H_{39}F_6N_3O_{10}Ba$: C, 31.66; H, 5.45; N, 5.83. Found: C, 31.53; H, 5.45; N, 5.79%. ^{1}H NMR ($CDCl_3$): 5.10 br (6H, OH), 3.70 (J = 4.4 Hz, 12H, OCH_2), 2.5 t (J = 4.4 Hz, 12H, NCH_2), 2.22 s (9H, NMe).

2.1.9. $Ba(TFA)_2\{N(C_2H_4OH)_3\}_2$ (10)

Same procedure as for **9** applied to triethanolamine (0.4 ml, 3.10 mmol) and $Ba(TFA)_2$ (0.564 g, 1.55 mmol) gave **10** (0.89 g, 87%). *Anal*. Calc. for $C_{14}H_{30}F_6O_{10}Ba$: C, 26.37; H, 4.74; N, 4.39. Found: C, 26.55; H, 4.86; N, 4.45%. ^{1}H NMR ($CDCl_3$): 3.4 t (J = 4.4 Hz, 24H, OCH_2), 2.72 t (J = 4.4 Hz, 24H, NCH_2), 4.9 br (6H, OH).

All Cu compounds were soluble in THF. Complexes **4** and **7** were more soluble in toluene than in ethanol. The Ba–TFA complexes with polyols were soluble in solvents such as $CHCl_3$.

2.1.10. Crystallography of 3, 4, 6 and 9

Suitable crystals of **3** and **9** were grown directly from the reaction medium, those of **4** and **6** were obtained by recrystallization in toluene/hexane and in THF, respectively. X-ray single-crystal diffraction data were collected at low temperature (160 K) with a Nonius Kappa CCD diffractometer equipped with a normal monochromatized focus X-ray tube having a molybdenum target. The data were collected using the COLLECT software [11a] then were processed through the DENZO reduction software [11b]. The structures were solved and refined on F^2 using the SHELXTL software [12]. All non-hydrogen atoms were refined with anisotropic thermal parameters. The hydrogen atoms were included in the final refinement model in calculated positions with isotropic thermal parameters. Crystal structure and refinement data are summarized in Table 2. For compound **3** the quality of the crystal did not allow a high resolution and a high data to parameters ratio required for full unrestrained anisotropic refinement. Therefore the C–F and C–C bond length were restrained to acceptable values and all non-hydrogen anisotropic displacement parameters (ADP) were restrained so that their Uij approximate to isotropic behaviour. For **6**, some CF_3 groups were disordered over two positions and lattice THF molecules were found and refined with 0.25 occupation. For compound **9**, one of the fluorine

Table 2
Crystallographic and refinement data

Compound	3	4	6	9
Empirical formula	$C_{12}H_8CuF_{14}O_5$	$C_{18}H_{24}Cu_2F_{12}O_{12}$	$C_{25}H_{42}Cu_4F_{12}N_4O_{12.25}$	$C_{19}H_{29}BaF_6N_3O_{10}$
Formula weight	561.72	787.45	1076.79	710.79
Space group	$P\bar{1}$	$P\bar{1}$	$P2_1/c$	$P2_12_12_1$
Crystal system	triclinic	triclinic	monoclinic	orthorhombic
a (Å)	10.0464(5)	8.6038(2)	14.0473(2)	10.3244(3)
b (Å)	12.0225(6)	9.2394(2)	21.4557(3)	16.9143(5)
c (Å)	15.8136(9)	10.0941(2)	14.1960(2)	17.3474(3)
α (°)	77.021(2)	100.727(1)	90	90
β (°)	89.659(2)	98.964(1)	105.300(1)	90
γ (°)	89.661(2)	110.045(1)	90	90
V (Å^3)	1861.16(17)	719.39(3)	4126.95(10)	3029.38(14)
Z	4	1	4	4
T (K)	160(2)	160(2)	163(2)	163(2)
μ (Mo Kα) (mm^{-1})	1.334	1.611	2.145	1.397
θ Range (°)	3.97–27.43	2.79–27.51	2.56–27.48	1.68–28.69
hkl Ranges	−13–11, −13–15, −20–20	−11–11, −11–11, −13–13	−18–18, −27–27, −18–18	−13–13, −22–22, −23–23
Number of reflections collected	11 577	5637	16 249	7184
Number of unique reflections (R_{int})	7651 (0.0664)	3252 (0.0203)	9235 (0.0264)	7184 (0.0000)
Data/restraints/parameters	7651/764/577	3252/0/199	9235/0/631	7184/12/326
Goodness-of-fit on F^2	1.181	1.210	1.035	1.055
R_1, wR_2 [$I > 2\sigma(I)$][a]	0.1175, 0.3043	0.0385, 0.1108	0.0517, 0.1381	0.0638, 0.1741
R_1, wR_2 (all data)	0.2157, 0.3748	0.0470, 0.1499	0.0800, 0.1562	0.0832, 0.1921
Residual electron density (e Å^{-3})	1.869 and −0.951	0.969 and −0.750	0.711, 0.832	1.516 and −1.748

[a] $R_1 = \sum\|F_o| - |F_c\|/\sum|F_o|$, $wR_2 = [\sum[w(F_o^2 - F_c^2)^2]/\sum[w(F_o^2)^2]]^{1/2}$.

atoms of one CF_3 group was splitted over two positions with half occupancies factors.

3. Results and discussion

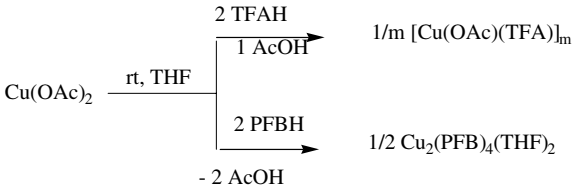
Synthetic routes and reactivity, namely stabilisation by Lewis bases of Cu(II) and Ba trifluoroacetates were investigated. The various compounds were isolated in high yields and were characterized by elemental analysis, FT-IR, ^{1}H NMR or ESR and for $Cu_2(PFB)_4(THF)_2$ **3**, $Cu_2(TFA)_4(OHC_2H_4O^iPr)_2$ **4**, $Cu_4(TFA)_4(OC_2H_4N\text{-}Me_2)_4$ **6** and $Ba(mdeaH_2)_3(TFA)_2$ **9**, by single crystal X-Ray diffraction.

3.1. Synthesis and characterization

3.1.1. Copper(II) fluorocarboxylates

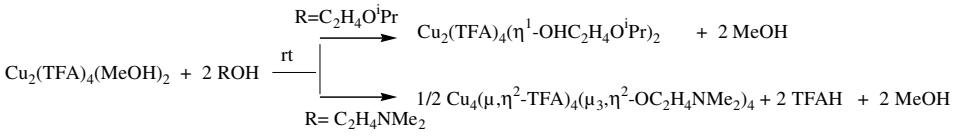
The synthesis of anhydrous of Cu(II) trifluoroacetate, $[Cu(TFA)_2]_m$, was reported by reacting the acid with Cu_2O in the presence of dioxygen, trifluoroacetic anhydride being added to remove the by-product, water [13]. Ligand exchange between $Cu(TFA)_2(H_2O)_x$ and acetone, followed by heating (135–145 °C) under reduced pressure was reported as another way to ligand free $Cu(TFA)_2$, characterized as $[Cu_2(TFA)_4]_\infty$ [6].

We have investigated various alternative routes to anhydrous Cu(II) trifluoroacetate. The reaction between copper(II) methoxide $[Cu(OMe)_2]_\infty$ and TFAH in THF afforded the $Cu_2(TFA)_4(THF)_2$ (**1**) adduct. If the reaction was conducted in methanol, a $Cu(TFA)_2$ methanol adduct was obtained, the methanol ligands could not be exchanged by THF at rt. The difluoroacetate $Cu(O_2CCHF_2)_2(THF)$ (**2**) could be prepared from $[Cu(OMe)_2]_\infty$ and CHF_2CO_2H in THF. Its lower Lewis acidity, as compared to that of the trifluoroacetate **1**, precluded contamination by methanol as ligand which was observed for the last crops in the synthesis of **1**. Attempts to prepare $Cu(TFA)_2$ from $Cu(OAc)_2$ at rt afforded an heteroleptic derivative, $[Cu(TFA)(OAc)]_m(THF)_{0.25m}$. In contrast, the homoleptic perfluorobutyrate $Cu_2(PFB)_4(THF)_2$ (**3**) was easily obtained, in similar conditions, from anhydrous $Cu(OAc)_2$ and perfluorobutyric acid (PFBH = $CF_3C_2F_4CO_2H$) (Eq. (1)).



(1)

Ligand exchange reactions at rt applied to **1** and **3** with isopropoxyethanol afforded $Cu_2(TFA)_4(^iPrO\text{-}C_2H_4OH)_2$ (**4**) and $Cu_2(PFB)_4(^iPrOC_2H_4OH)_2$ (**7**), respectively. $Cu(TFA)_2(Me_2NC_2H_4NMeC_2H_4NMe_2)$ (**5**) was obtained from **1** in the presence of *N*,*N*,*N*′,*N*″,*N*″-pentamethyldiethyltriamine. The TFA ligands of **1** or $Cu(TFA)_2(MeOH)$ appeared labile, even at rt, in the presence of dimethylaminoethanol and a tetranuclear carboxylatoaminoalkoxide $[Cu(TFA)(OC_2H_4\text{-}NMe_2)]_4$ (**6**) was obtained in high yield (characterized by X-ray – see below – with lattice THF molecules) (Eq. (2)).



(2)

Compounds **1**, **2**, and **3** are hygroscopic. Compound **1** either as solid or in solution gave hydroxide species (ν(OH) = 3641, 3595, 3336, 3191 cm^{-1}) after several weeks in air. The same species was obtained by reacting $Cu(OH)_2$ and one equivalent of TFAH in THF. However, no single crystals could be obtained so far by either route. Cu(II) carboxylatohydroxides $Cu_2(OH)_3(O_2CR)$ (R = C_mH_{2m+1}, m = 5–10) have been reported as 2D-magnetic materials [14].

3.1.2. Barium fluorinated carboxylates

The reaction between BaH_2 and CF_3CO_2H in THF was reported as a clean route to anhydrous, ligand free $[Ba(TFA)_2]_m$, the driving force being the elimination of dihydrogen [8,9]. We have investigated its reactivity toward various ligands mostly functional alcohols which might be used as media for the MOD deposition of high Tc superconductors.

No reaction was observed even on refluxing for 5 h in THF between $[Ba(TFA)_2]_m$ and excess (>4 equivalents) of bidentate ligands such as TMEDA or functional alcohols such as $Me_2NC_2H_4OH$ or $^iPrOC_2H_4OH$. In contrast, polyols such as *N*-methyldiethanolamine $MeN(C_2H_4OH)_2$ ($mdeaH_2$) and triethanolamine $N(C_2H_4OH)_3$ ($teaH_3$) were able to achieve depolymerization of $[Ba(TFA)_2]_m$ in THF even at rt giving, respectively,

$Ba(TFA)_2\{MeN(C_2H_4OH)_2\}_3$ (**9**) and $Ba(TFA)_2\{N(C_2H_4OH)_3\}_2$ (**10**). These adducts were more soluble than $[Ba(TFA)_2]_m$ in methanol. The difluorinated acetate $[Ba(O_2CCHF_2)_2]_m$ was prepared from BaH_2 and CHF_2CO_2H. Its solubility in THF is lower than that of the trifluoroacetate oligomer but comparable in methanol. As observed for $[Ba(TFA)_2]_m$ [8,9] and expected for the less acidic difluoroacetate, no adduct was formed with MeOH. Its recrystallization in methanol yielded $[Ba(O_2CCHF_2)_2]_m \cdot 0.5mMeOH$ (**8**) but the methanol molecules were in the lattice as evidenced by the absence of shift in the FT-IR with respect to the free ligand.

3.2. Spectroscopic characterization and physicochemical properties

The FT-IR spectra of the various compounds (Table 1) display very intense broad absorption bands around 1290–1100 cm^{-1} corresponding to the C–F vibrations. Additional sharp bands due to the coordinated Lewis base are present as well, they are shifted to lower frequencies with respect to those of the free ligand. The absorption bands characteristic of the carboxylate ligands appear generally around 1704–1674 cm^{-1} for the asymmetric $\nu_{as}(CO_2)$ vibration and around 1464–1420 cm^{-1} for the symmetric ones. The values of the difference $\Delta = \nu_{as}(CO_2) - \nu_s(CO_2)$ around 240 cm^{-1} suggest that the TFA ligands are bridging in the copper(II) species [15]. FT-IR spectra of $Ba(TFA)_2\{MeN(C_2H_4OH)_2\}_3$ (**9**) and $Ba(TFA)_2\{N(C_2H_4OH)_3\}_2$ (**10**) display comparable features but their $\nu_{as}(CO_2)$ absorption bands are observed at lower frequencies than those of the Cu(II) fluorocarboxylates. The value of Δ is 214 cm^{-1} for **9** where the trifluoroacetates are identified as non-coordinated anions by X-Ray diffraction (see below). Its $\nu_{as}(CO_2)$ vibration occurs at 1677 cm^{-1} while a frequency of 1694 cm^{-1} (Δ = 212 cm^{-1}) is recorded for $Ba(\eta^1\text{-}TFA)_2(mdeaH_2)_2$ [15] making it difficult to rely on the IR data for deciding about the coordination behavior of TFA on barium centers. The ν(OH) absorption bands of the copper species **4** and **7** correspond to alcohol ligands while those of **8** account for lattice alcohol molecules. In contrast, the absence of ν(OH) absorption bands for **6** supports a trifluoroacetatoalkoxide formula. The strong, broad bands at 3317, 3184 cm^{-1} of **9** and 3354 cm^{-1} of **10** account for the absence of deprotonation of the polyols. ^1H NMR spectra of the Ba derivatives in $CDCl_3$ are rather uninformative although they confirmed the presence of the polyols in the metal coordination sphere. The ESR data of the Cu(II) species are in agreement with the literature body [17].

The high Lewis acidity of fluorinated carboxylates makes them extremely prone to hydration. In general, the compounds are more stable in the solid state than in solution (THF or MeOH media). The Cu adducts with O-donor ligands are also more stable toward ambient atmosphere than those based on N-donor Lewis bases. Indeed, **5**, the $Cu(TFA)_2$ adduct with pentamethyldiethylenetriamine (pmedta) turns rapidly into a purple species in air. The barium species are hygroscopic, they appear less soluble in organic media than the copper(II) ones but more than the Y trifluoroacetate derivatives [18].

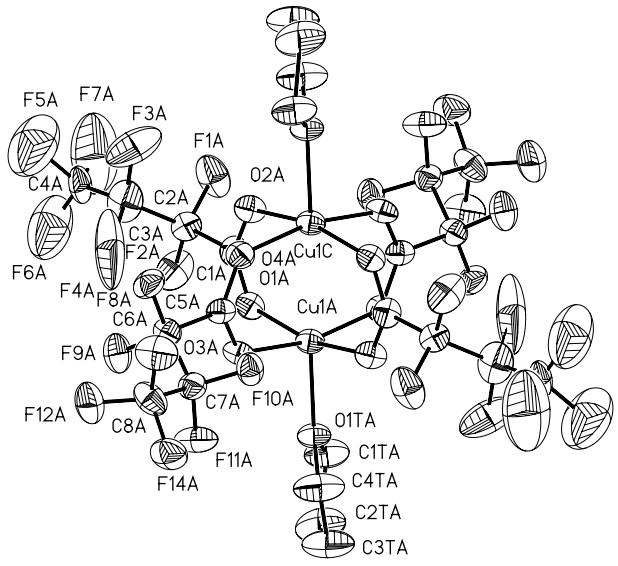


Fig. 1. Molecular structure of **3a** showing the atom numbering scheme (thermal ellipsoids at 30%).

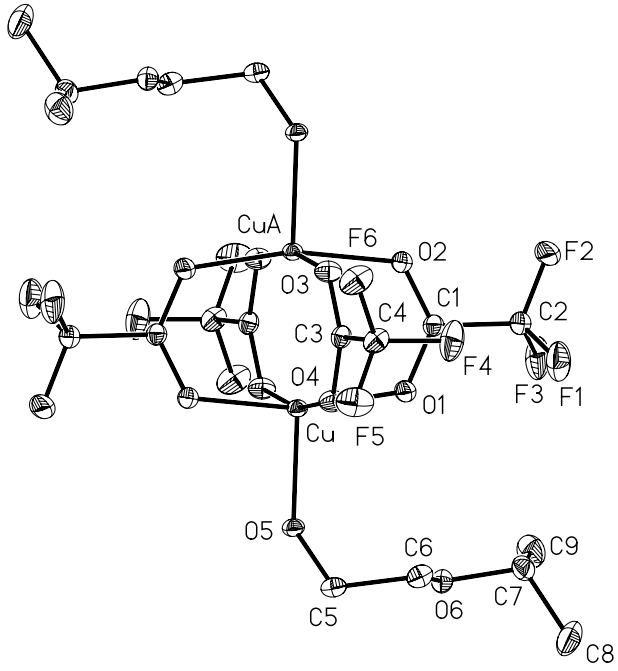


Fig. 2. Molecular structure of **4** showing the atom numbering scheme (thermal ellipsoids at 30% probability).

Table 3
Selected bond lengths (Å) and angles (°) for **3**

3a		**3b**	
Bond lengths (Å)			
Cu1A–O4A#1	1.979(8)	Cu1B–O1B	1.961(7)
Cu1A–O3A	1.968(8)	Cu1B–O3B	1.972(7)
Cu1A–O2A#1	1.956(8)	Cu1B–O2B#2	1.970(7)
Cu1A–O1A	1.958(7)	Cu1B–O4B#2	1.980(7)
Cu1A–O1TA	2.093(7)	Cu1B–O1TB	2.093(6)
Cu1A···Cu1A#1	2.706(2)	Cu1B···Cu1B#2	2.713(2)
Bond angles (°)			
O4A#1–Cu1A–O3A	166.8(3)	O1B–Cu1B–O3B	87.8(3)
O4A#1–Cu1A–O2A#1	89.9(3)	O1B–Cu1B–O2B#2	166.5(3)
O3A–Cu1A–O2A#1	89.2(3)	O3B–Cu1B–O2B#2	90.7(3)
O4A#1–Cu1A–O1A	88.2(3)	O1B–Cu1B–O4B#2	89.6(3)
O3A–Cu1A–O1A	89.5(3)	O3B–Cu1B–O4B#2	166.1(3)
O2A#1–Cu1A–O1A	166.3(3)	O2B#2–Cu1B–O4B#2	88.7(3)
O4A#1–Cu1A–O1TA	96.4(3)	O1B–Cu1B–O1TB	97.7(3)
O3A–Cu1A–O1TA	96.8(3)	O3B–Cu1B–O1TB	97.3(3)
O2A#1–Cu1A–O1TA	93.0(3)	O2B#2–Cu1B–O1TB	95.7(3)
O1A–Cu1A–O1TA	100.7(3)	O4B#2–Cu1B–O1TB	96.5(3)

Symmetry transformations used to generate equivalent atoms: #1: $-x$, $-y$, $-z$; #2: $-x$, $-y+1$, $-z+1$.

The coordination of the copper(II) fluorocarboxylates by organic ligands provides solubility in solvents such as THF or even toluene. Compounds **4** and **7** are more soluble in toluene than in ethanol. The order of solubility in methanol, the solvent the most used for the deposition of high Tc superconductors, is in the favour of the perfluorobutyrate, the order being $Cu_2(PFB)_4(THF)_2 \gg Cu_2(O_2CCF_3)_4(THF)_2 \approx Cu_2(O_2CCHF_2)_4(THF)_2$. Compound **6** is the least soluble Cu species in methanol among those reported here.

The various copper trifluoroacetate derivatives as well as $Cu_2(O_2CCHF_2)_4(THF)_2$ have poor volatility. Only ~10% sublimation is observed for $Cu_2(TFA)_4(THF)_2$ (250 °C/2×10^{-4} Torr) for instance whereas no sublimation occurs at all for $Cu_2(O_2CCHF_2)_4(THF)_2$ or $Cu_2(TFA)_4(MeOH)_2$. In contrast, **3** sublimes completely at 190 °C/2×10^{-4} Torr as a ligand free, extremely hygroscopic $[Cu(PFB)_2]_m$ species. Thermogravimetric analysis (N_2, 1 atm) of **3** shows the loss of THF between 170 and 240 °C whereas decomposition of the carboxylate ligands occurs at 240–310 °C. The amount of residue (10%) is lower than the value expected for copper(II) oxide (14%) due to partial volatility under the TGA conditions [2].

Table 4
Selected bond lengths (Å) and angles (°) for **4**

Bond lengths (Å)			
Cu–O1	1.973(2)	Cu–O4	1.974(2)
Cu–O3#1	1.979(2)	Cu–O2#1	1.984(2)
Cu–O5	2.082(2)	Cu···Cu#1	2.7293(6)
Bond angles (°)			
O1–Cu–O4	88.3(1)	O1–Cu–O3#1	90.1(1)
O4–Cu–O3#1	166.30(9)	O1–Cu–O2#1	166.10(9)
O4–Cu–O2#1	90.7(1)	O3#1–Cu–O2#1	87.6(1)
O1–Cu–O5	99.02(9)	O4–Cu–O5	98.84(9)
O3#1–Cu–O5	94.84(9)	O2#1–Cu–O5	94.83(9)

Symmetry transformations used to generate equivalent atoms: #1: $-x$, $-y$, $-z$.

The TFA ligands of some copper derivatives are extremely labile. Complexes **1**, **3** and $[Cu(OAc)(TFA)]_m$, react with the KBr plates for the IR spectra (as Nujoll mulls) giving dark green–brown Cu(II) bromide derivatives. In contrast, FT-IR spectra could be obtained with NaCl plates. The exchange between TFA ligands with aminoethanol giving **6** provides a rare example of a high yield synthesis of a metal alkoxide starting from a carboxylate. The reaction between the monofluoroacetate adduct $Cu_2(O_2CCFH_2)_4(H_2O)_2$ and 2-diethylaminoethanol was reported to afford the $[Cu_2(\mu,\eta^2\text{-}O_2CCFH_2)_4(\eta^1\text{-}O_2CCFH_2)_2]^{2-}$ anion, the counter-ion, protonated aminoethanol $Et_2NHC_2H_4OH$, interacts via H-bonding [19]. This illustrates the versatility of the behaviour of fluorinated carboxylates in the presence of nitrogen donor ligands [16,18].

3.3. Molecular structures of Cu(II) and Ba fluorocarboxylates

The copper TFA or PFB adducts **4** and **3** are discrete dinuclear species in the solid displaying the typical paddle-wheel structures found for other carboxylate adducts with four bridging carboxylates having syn-syn conformation [7]. The Lewis bases occupy the axial position of a distorted tetragonal pyramid of the five-coordinate metal centres. Their structures are depicted in Figs. 1

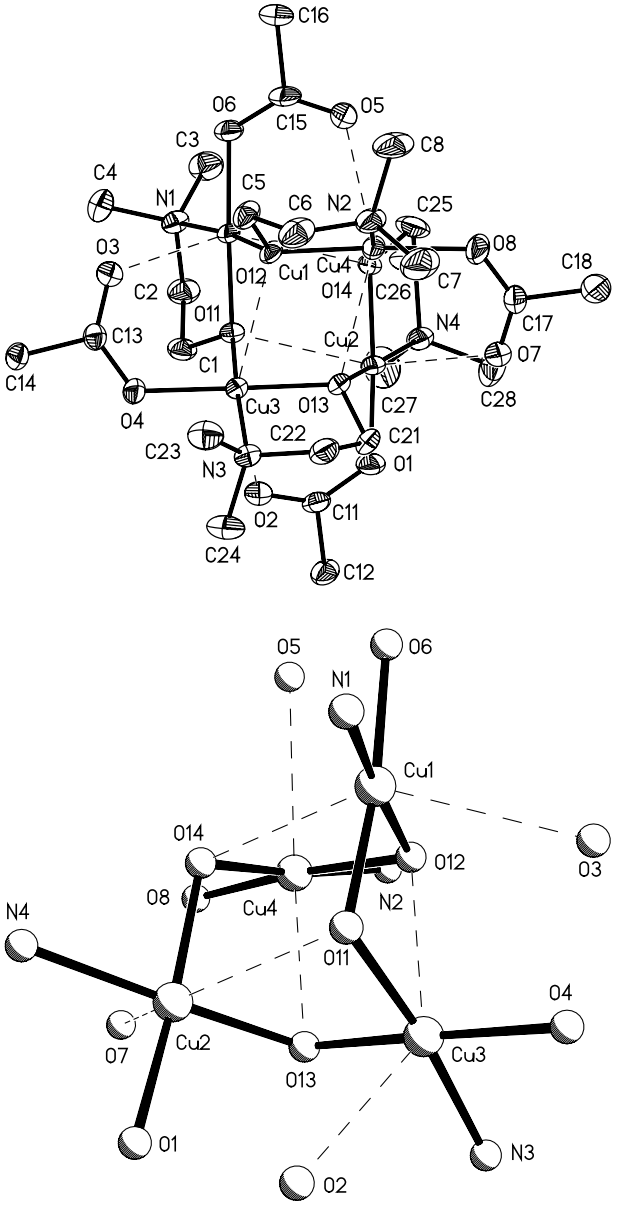


Fig. 3. (a) Molecular structure of **6** showing the atom numbering scheme (thermal ellipsoids at 30% probability). The fluorine atoms on C14, C16 and C18 are disordered over two positions. The dotted lines indicate the long axial Cu–O bonds, (b) drawing of the copper–oxygen core showing the long Cu–O interactions (>2.69 Å).

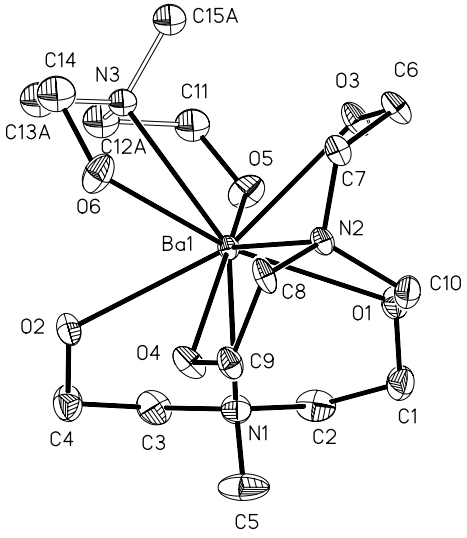


Fig. 4. Molecular structure of the $[Ba(mdeaH_2)_3]^{2+}$ cation of compound **9** showing the atom numbering scheme. (thermal ellipsoids at 30% probability).

and 2, respectively, selected bond lengths and bond angles being collected in Tables 3 and 4. The overall structure of **4** is similar to that of the other structurally characterized $Cu_2(TFA)_4L_2$ adducts (L = quinoline, acetonitrile) [7], the functional alcohol being only monodentate in contrast to its behaviour in $Y_2(TFA)_6$-(η^2-$OHC_2H_4O^iPr)_2$ [16]. Two independent molecules **3a** and **3b** are found in the asymmetric unit cell for $Cu_2(O_2CCF_2CF_2CF_3)_4(THF)_2$. Their basal Cu–O bonds have comparable lengths [1.956(8)–1.980(7) Å] as also observed for $Cu_2(TFA)_4(\eta^1$-$OHC_2H_4O^iPr)_2$, (1.973(2)–1.984(2) Å). As expected, the coordination bonds, Cu–O(THF) or Cu–O(OHR), are longer with values of 2.093(6)–2.093(7) Å in agreement with the literature body [20]. The Cu···Cu distances 2.706(2) and 2.713(2) Å in the perfluorobutyrate **3** are shorter than for the analogous trifluoroacetate adduct **4** or for $Cu_2(TFA)_4(MeCN)_2$ 2.766(1) Å or $[Cu_2(TFA)_4]_\infty$ 3.086(2) Å. The Cu···Cu distance has been reported to be very sensitive to the nature of the R substituent of the carboxylate as well as to that of the apical, neutral ligand [6,7]. The Cu···Cu distance increases with the electron-withdrawing ability of the R group of either terminal or bridging carboxylates whereas axial coordination tends to shorten it. The Cu···F distances are larger than 4.50 Å for **3** and **4** excluding thus any interaction in the solid.

Compound **6** corresponds to a copper(II) trifluoroacetatoaminoalkoxide with lattice THF molecules. The structure of the tetranuclear unit was previously reported without any other characterization or yield of the compound [21]. In this structure, the CF_3 groups and three of the aminoethoxide ligands were disordered. Our results are based on a low temperature [163(2) K] versus rt data collection and more reflections were taken into account (9235 versus 3584). The disorder is thus limited to three CF_3 groups and the metric parameters are more precise, especially for the Cu–N bond distances [2.039(3)–2.048(2) versus 2.052(12)–2.062(13) Å]. Its molecular structure corresponds to a tetranuclear $[Cu(\mu,\eta^2$-TFA$)(\mu_3,\eta^2$-$OC_2H_4NMe_2)]_4 \cdot 0.25THF$ species (Fig. 3). The four metal form an eight-membered ring folded into a boat like configuration as observed for $Cu_4(teaH)_4 \cdot 2teaH_3$ [22]. The copper atoms are square planar coordinated with three oxygens and one nitrogen

with a deviation of the atom from the CuO_3N mean plane less than 0.3 Å. The Cu–O and Cu–N bond lengths spread over the range 1.927(1)–1.956(2) and 2.039(3)–2.052(2) Å, respectively (Table 5). Moreover, for each copper atom, two longer Cu···O contacts are found in apical positions with distances comprised in the range 2.690(2)–2.741(2) Å and involving one of the oxygens of a TFA ligand as well as that of the aminoethoxide. The copper stereochemistry may thus be described as an elongated octahedron. This is probably the result of the Jahn-Teller effect and folding of the Cu_4 ring [16]. It results in an important distorsion for the axial ligation (∠O–Cu–O ∼ 148°) as well as to a highly dissymmetrical Cu–μ,η^2-TFA coordination (1.952 av. versus 2.721 av. Å). In contrast, the Cu-μOR bridges are only slightly dissymmetrical. The Cu···Cu distances of 3.172 Å av. are quite long as compared to the paddle-wheel type compounds probably as a result of the bridging aminoethoxide ligand. No short Cu···F or N···F distances were found in the solid state. A number of copper(II) carboxylatoalkoxides have been structurally characterized [20]. They are mostly based on tetranuclear units associated into polymers. Typical examples are $[Cu_4(OAc)_6(bdmap)(H_2O)_6]_\infty$ (bdmapH=1,3-bis(dimethylamino)propanol) or $[Cu_4(\mu,\eta^2\text{-}OAc)_4(O\text{-}Me)_4]_\infty$ associated rerspectively by H-bonding involving the H_2O molecules [23], or via acetate ligands [24] or $[Cu_4(\mu,\eta^2\text{-}OAc)_4\{MeN(C_2H_4O)(C_2H_4OH)\}_4]_\infty$ in which the four copper are linked in an anti-tricyclo[4.2.0.$0^{2,5}$]octane-like fashion [25].

Compound **9** $[Ba(mdeaH_2)_3](TFA)_2$ (Fig. 4) obtained by reaction between $Ba(TFA)_2$ and *N*-methyldiethanolamine at rt is ionic (Eq. (3)). The Ba···O(TFA) distances are larger than 4.83 Å and the trifluoroacetates act thus as counter-ions. The Ba^{2+} cation is surrounded by three tridendate *N*-methyldiaminoethanol ligands and is thus nine-coordinate, as often observed for that metal. Complex **9** represents, to the best of our knowledge, the first example of an anionic Ba trifluoroacetate. The transanular Ba–N coordination bonds [2.899(7)–2.954(8) Å] are longer than the Ba–O(H) ones [2.740(6)–2.836(6) Å] (Table 6). By contrast to fluorinated alkoxides or fluorinated β-diketonates which form neutral adducts [26–28], no short Ba···F distances are observed. The structure of $Ba(\eta^1\text{-}TFA)_2\{MeN(C_2H_4OH)_2\}_2$ (**11**) has

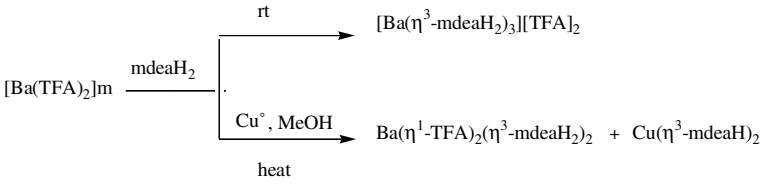
Table 5
Selected bond lengths (Å) and angles (°) for **6**

Bond lengths (Å)			
Cu1–O11	1.927(1)	Cu1–O12	1.947(2)
Cu1–O6	1.950(2)	Cu1–N1	2.048(2)
Cu1–O14	2.733(2)	Cu1–O3	2.738(2)
Cu2–O14	1.933(2)	Cu2–O13	1.940(2)
Cu2–O1	1.956(2)	Cu2–N4	2.044(2)
Cu2–O7	2.715(3)	Cu2–O11	2.729(2)
Cu3–O13	1.927(2)	Cu3–O11	1.937(2)
Cu3–O4	1.945(2)	Cu3–N3	2.052(2)
Cu3–O12	2.704(2)	Cu3–O2	2.741(2)
Cu4–O12	1.934(2)	Cu4–O14	1.939(2)
Cu4–O8	1.958(2)	Cu4–N2	2.039(3)
Cu4–O5	2.690(2)	Cu4–O13	2.696(2)
Bond angles (°)			
O11–Cu1–O12	90.26(7)	O11–Cu1–O6	172.54(9)
O12–Cu1–O6	95.35(8)	O11–Cu1–N1	85.83(8)
O12–Cu1–N1	173.37(9)	O6–Cu1–N1	89.03(9)
O11–Cu1–O14	74.45(6)	O12–Cu1–O14	69.86(7)
O6–Cu1–O14	102.86(7)	N1–Cu1–O14	114.03(8)
O11–Cu1–O3	82.32(6)	O12–Cu1–O3	80.29(7)
O6–Cu1–O3	103.46(7)	N1–Cu1–O3	93.87(8)
O14–Cu1–O3	141.61(6)	O14–Cu2–O13	90.47(7)
O14–Cu2–O1	171.56(9)	O13–Cu2–O1	95.73(8)
O14–Cu2–N4	85.54(8)	O13–Cu2–N4	172.35(9)
O1–Cu2–N4	88.93(8)	O14–Cu2–O7	82.41(8)
O13–Cu2–O7	80.72(8)	O1–Cu2–O7	104.21(8)
N4–Cu2–O7	92.26(9)	O14–Cu2–O11	74.46(6)
O13–Cu2–O11	69.80(6)	O1–Cu2–O11	102.31(7)
N4–Cu2–O11	115.18(8)	O7–Cu2–O11	141.89(6)
O13–Cu3–O11	90.68(7)	O13–Cu3–O4	172.99(9)
O11–Cu3–O4	94.86(8)	O13–Cu3–N3	86.25(9)
O11–Cu3–N3	173.29(8)	O4–Cu3–N3	88.67(9)
O13–Cu3–O12	74.13(6)	O11–Cu3–O12	70.34(6)
O4–Cu3–O12	103.71(7)	N3–Cu3–O12	114.36(8)
O13–Cu3–O2	82.60(7)	O11–Cu3–O2	80.48(7)
O4–Cu3–O2	102.53(8)	N3–Cu3–O2	93.20(8)
O12–Cu3–O2	141.98(6)	O12–Cu4–O14	90.71(8)
O12–Cu4–O8	173.1(1)	O14–Cu4–O8	94.7(1)
O12–Cu4–N2	85.80(9)	O14–Cu4–N2	173.82(9)
O8–Cu4–N2	89.2 (1)	O12–Cu4–O5	81.36(7)
O14–Cu4–O5	80.71(7)	O8–Cu4–O5	103.7(1)
N2–Cu4–O5	93.70(9)	O12–Cu4–O13	74.23(6)
O14–Cu4–O13	70.64(6)	O8–Cu4–O13	103.59(8)
N2–Cu4–O13	113.13(9)	O5–Cu4–O13	141.65(6)

Table 6
Selected bond lengths (Å) and angles (°) for for $[Ba(mdeaH_2)_3](TFA)_2$ (**9**)

Bond lengths (Å)			
Ba1–O4	2.740(6)	Ba1–O5	2.759(6)
Ba1–O O2	2.789(6)	Ba1–O3	2.803(5)
Ba1–O6	2.828(7)	Ba1–O1	2.836(6)
Ba1–N2	2.899(7)	Ba1–N3	2.932(8)
Ba1–N1	2.954(8)		
Bond angles (°)			
O4–Ba1–O5	155.1(2)	O4–Ba1–O2	72.1(2)
O5–Ba1–O2	89.4(2)	O4–Ba1–O3	120.0(2)
O5–Ba1–O3	82.4(2)	O2–Ba1–O3	161.2(2)
O4–Ba1–O6	72.1(2)	O5–Ba1–O6	120.4(2)
O2–Ba1–O6	76.2(2)	O3–Ba1–O6	93.3(2)
O4–Ba1–O1	105.3(2)	O5–Ba1–O1	69.3(2)
O2–Ba1–O1	120.3(2)	O3–Ba1–O1	72.5(2)
O6–Ba1–O1	162.3(2)	O4–Ba1–N2	59.9(2)
O5–Ba1–N2	140.3(2)	O2–Ba1–N2	130.2(2)
O3–Ba1–N2	60.2(2)	O6–Ba1–N2	77.5(2)
O1–Ba1–N2	86.0(2)	O4–Ba1–N3	129.0(2)
O5–Ba1–N3	60.3(2)	O2–Ba1–N3	79.7(2)
O3–Ba1–N3	81.6(2)	O6–Ba1–N3	60.3(2)
O1–Ba1–N3	125.6(2)	N2–Ba1–N3	120.7(2)
O4–Ba1–N1	78.7(2)	O5–Ba1–N1	77.7(2)
O2–Ba1–N1	60.4(2)	O3–Ba1–N1	133.0(2)
O6–Ba1–N1	133.4(2)	O1–Ba1–N1	60.7(2)
N2–Ba1–N1	117.3(2)	N3–Ba1–N1	121.8(2)

been recently reported by us [16]. It cocrystallizes in the asymmetric unit cell with $[Cu\{MeN(C_2H_4O)(C_2H_4OH)\}_2]$ in a reaction aimed to provide heterometallic Ba–Cu trifluoroacetate derivatives. The Ba species **11** is actually an intermediate to the formation of the ionic Ba–TFA derivatives **9**. Oxidation of copper and partial deprotonation of *N*-methyldiethanolamine appears to preclude the formation of this species.



(3)

Although various heterometallic fluorocarboxylates are known [29], no reaction is observed by mixing the $Cu(TFA)_2$ adducts with THF or isopropoxyethanol and barium trifluoroacetate at rt in THF, methanol or isopropoxyethanol media. In contrast, heterometallic Ba–Cu(II) species could easily be obtained by mixing barium trifluoroacetate and copper(II) alkoxides [16].

4. Conclusions

A number of adducts of copper(II) and barium fluorocarboxylates have been prepared as possible precursors for MOD of high Tc superconductors and characterized. O-donors are better able to stabilize copper(II) fluorocarboxylates toward ambient atmosphere than N-donor Lewis bases. In contrast to alcohols such as methanol or isopropoxyethanol, polyols such as *N*-methyldiethanolamine and triethanolamine could form stable adducts of $Ba(TFA)_2$ by depolymerization of the oligomer. These derivatives are ionic but remain soluble in organic media.

5. Supplementary material

Tables of coordinates, of thermal parameters, of bond lengths and angles have been deposited at the Cambridge Crystallographic Data Base Centre. CCDC reference numbers for **3**, **4**, **6** and **9** are 227439, 227442, 227443 and 227446, respectively.

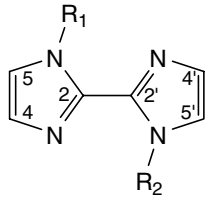
Acknowledgements

Financial support from the EEC (GRDCT 2001 00550) and Rhône-Alpes (project RUBIS) are acknowledged.

References

[1] C. Ruessel, J. Non-Cryst. Solids 153 (1993) 161.
[2] D.A. Edwards, R.M. Harker, M.F. Mahan, K.C. Molloy, Inorg. Chim. Acta 328 (2002) 134, and references cited therein.
[3] V.I. Saloutin, L.A. Brusnitsyna, L.N. Pushkina, I.A. Piterskikh, G.A. Kitaev, K.I. Pashkevich, V.V. Sidorov, Patent URXXAF SU 857106 A1 19810823, CAN 96:60903.
[4] S.A. Krupoder, V.S. Danilovitch, A.O. Miller, G.G. Furin, Zh. Org. Khim. 30 (1994) 1185.
[5] T. Araki, I. Hirabayashi, Sup. Sci. Technol. 16 (2003) R71.
[6] F.A. Cotton, E.V. Dikorev, M.A. Petrukhina, Inorg. Chem. 39 (2000) 6072.
[7] (a) E.V. Karpova, A.I. Boltalin, M.A. Zakharov, N.I. Sorokina, Y.M. Korenev, Z. Anorg. Allg. Chem. 624 (1998) 741;
(b) E. Szlyk, I. Szymanska, R. Kucharek, G. Wrzeszcz, F. Rozploch, Pol. J. Chem. 75 (2001) 215;
(c) S. Kawazta, S.R. Breeze, S. Wang, J.E. Greedan, N.P. Raju, Chem. Commun. (1997) 717.
[8] W.A. Wojtczak, P. Atanassova, M.J. Hampden-Smith, E. Duesler, Inorg. Chem. 35 (1996) 6995.
[9] W.A. Wojtczak, M.J. Hampden-Smith, E.N. Duesler, Inorg. Chem. 37 (1998) 1781.
[10] J.S. Banait, P.K. Pahil, Synth. React. Inorg. Met-Org. Chem. 16 (1986) 1217.
[11] (a) B.V. Nonius, Collect Software, 1997–2000;
(b) Z. Otwinowski, W. Minor, in: C.W. CarterJr., R.M. Sweet (Eds.), Methods in Enzymology: Macromolecular Crystallography, Part A, vol. 276, Academic Press, New York, 1997, pp. 307–326.
[12] G.M. Sheldrick, SHELXTL: Program for the Refinement of Crystal Structures, University of Göttingen, Göttingen, Germany, 1997 (Bruker AXS, Madison, WI, USA).
[13] F. Calderazzo, N. Donati, U. Englert, F. Marchetti, G. Pampaloni, V. Pasarelli, Inorg. Chim. Acta 346 (2003) 100.
[14] W. Fujita, K. Awaga, T. Yokoyama, Appl. Clay Sci. 15 (1999) 281.
[15] D.H. Gibson, Y. Ding, R.L. Miller, B.A. Slead, M.S. Mashuta, J.F. Richardson, Polyhedron 18 (1999) 1189.
[16] J. Zhang, L.G. Hubert-Pfalzgraf, D. Luneau, Inorg. Chem. Commun. 7 (2004) 979.
[17] C.F.G.C. Geraldes, M.P.M. Marques, B. de Castro, E. Pereira, Eur. J. Inorg. Chem. (2000) 559.
[18] J. Zhang, S. Morlens, L.G. Hubert-Pfalzgraf, D. Luneau, Eur. J. Inorg. Chem., in press.
[19] K. Smolander, Inorg. Chim. Acta 114 (1986) 1.
[20] W. Melnik, M. Kabesova, M. Koman, L. Macaskowa, C.E. Holloway, J. Coord. Chem. 45 (1998) 147.
[21] M. Ahlgren, U. Turpeinen, R. Hamalainen, Acta Crystallogr., Sect. B 38 (1982) 429.
[22] L.G. Hubert-Pfalzgraf, M.C. Massiani, J.C. Daran, J. Vaissermann, Better Ceramics Through Chemistry V, vol. 271, Material Research Proceedings, San Diego, USA, 1992, p. 135.
[23] S. Wang, Polyhedron 17 (1998) 831.

[24] I.A. Koval, P. Gomez, O. Roubeau, W.L. Driessen, M. Lutz, A.L. Spek, J. Reedijk, Inorg. Chem. 42 (2003) 868.
[25] W. Saalfrank, I. Bernt, F. Hampel, Angew. Chem. Int. Ed. 40 (2001) 1700.
[26] L.G. Hubert-Pfalzgraf, Coord. Chem. Rev. 178–180 (1998) 967, and references cited therein.
[27] H. Vincent, F. Labrize, L.G. Hubert-Pfalzgraf, Polyhedron 13 (1994) 3223.
[28] L.G. Hubert-Pfalzgraf, H. Guillon, Appl. Organomet. Chem. 12 (1998) 321.
[29] K.S. Gravilenko, A. Vertes, L.F. Kiss, A.W. Addison, T. Weyhermuller, V.V. Pavlishchuck, Eur. J. Inorg. Chem. (2002) 3347.



$R_1 = R_2 = H$; 2,2'-Biimidazole (H_2bim)

$R_1 = Me$, $R_2 = H$; N-Methyl-2,2'-biimidazole (MeHbim)

$R_1 = -EtOH$; $R_2 = H$; N-hydroxyethyl-2,2´-biimidazole (HOEtHbim)

$R_1 = R_2 = Me$; N,N'-Dimethyl-2,2'-biimidazole (Me_2bim)

Scheme 1.

2. Experimental

2.1. Materials and instrumentation

Ammonia (30%, from Normasolv), glyoxal (40%, from Merck), activated carbon (from Panreac), sodium hydride (60% dispersion in mineral oil, from Aldrich), methyl iodide (98%, from Aldrich), dimethyl sulfate (99%, from Probus) and sodium hexachloroplatinate(IV) hexahydrate (98%, from ABCR) were used as supplied. Solvents were reagent grade.

Elemental chemical analyses were performed on a Fisons EA1108CHNS-O microanalyser. Melting points (m.p.) were determined using a Büchi apparatus. The IR spectra of samples included in KBr discs (4000–400 cm^{-1}) or in Nujol mulls between polythene sheets (400–100 cm^{-1}) were recorded on a Bruker IFS66V FT-IR spectrometer, and Raman spectra of polycrystalline samples were recorded on the same spectrometer using an FRA-106 accessory (IR and Raman bands are reported using the following abbreviations: s: strong, m: medium, w: weak, sh: shoulder, v: very). ^1H and ^{13}C NMR spectra (see Scheme 1 for numbering scheme) were obtained in DMF-d_7 at room temperature (293 K) on a Bruker AMX 300 spectrometer and referred to $SiMe_4$, and ^{195}Pt NMR spectra were obtained in the same solvent at room temperature on a Bruker AMX 500 spectrometer and referred to a 1 M solution of Na_2PtCl_6. NOE experiments and ^1H–^{13}C HMBC and HMQC experiments were run at 293 K, and 223 K for MeHbim, on a Bruker AMX 500 apparatus. All physical measurements reported were made by the RIAIDT services of the University of Santiago de Compostela (http://www.ti.usc.es/riaidt/index.htm).

2.2. Synthesis of the ligands

In an attempt to improve the yields of previously published methods for the preparation and purification of some of the ligands [8], these methods were modified slightly as follows.

2.2.1. H_2bim

Glyoxal (98 mL, 0.86 mol) and ammonia (100 mL, 1.56 mol) were reacted for 22 h at 4 °C. The brown solid recovered by filtration was extracted with DMF in a soxhlet apparatus, and the extract was decoloured with activated carbon and then concentrated to dryness, affording a beige solid. Yield: 15%. M.p. >300 °C. *Anal.* Calc. for $C_6H_6N_4$: C, 53.7; H, 4.5; N, 41.8. Found: C, 53.9; H, 4.4; N, 41.8%. ^1H NMR (ppm): 12.67 (s,vb, N–H); 7.22 (s,b, H5/H5′) and 7.02 (s,b, H4/H4′).

2.2.2. MeHbim

A solution of NaH (29.8 mmol) in dry DMF (50 mL) was added under argon to a suspension of H_2bim (4.0 g, 29.8 mmol) in 50 mL of the same solvent. After 7 h reaction at room temperature, followed by a further hour at 100 °C, MeI (1.86 mL, 29.8 mmol) was added and reaction was continued for a further 24 h at room temperature. The reaction mixture was filtered. The filtrate was concentrated and the solid was work-up as in [8]. Yellow solid. Yield: 20%. M.p. 146–147 °C. *Anal.* Calc. for $C_7H_8N_4$: C, 56.7; H, 5.4; N, 37.8. Found: C, 56.8; H, 5.3; N, 37.9%. ^1H NMR (ppm), $T = 293$ K: 12.77 (s,vb, N–H), 7.24 (s, H5), 7.18. (s,b, H5′/H4′), 6.98 (s, H4), 4.11 (s, N–CH_3); $T = 223$ K: 13.27 (s, N–H), 7.39 (s, H5′); 7.34 (s, H5), 7.11 (s, H4′), 7.00 (s, H4), 4.07 (s, N–CH_3). ^{13}C NMR (ppm), $T = 293$ K: 140.3 (C2′), 139.5 (C2), 128.0 (C4), 123.6 (C5), 35.0 (N–CH_3); $T = 223$ K: 140.1 (C2′), 139.1 (C2), 129.2 (C4′), 127.9 (C4), 123.8 (C5), 118.0 (C5′), 35.0 (N–CH_3).

2.2.3. HOEtHbim

A solution of H_2bim (4.0 g, 29.8 mmol) in a mixture of 96% EtOH (30 mL), 20% NaOH (7.5 mL) and 2-chloroethanol (0.52 mL, 7.8 mmol) was refluxed for 6 h, allowed to cool to room temperature and neutralized with 37% HCl, and the solid recovered by filtration of the reaction mixture was washed with hot ethanol. Recrystallization from water afforded a yellow solid. Yield: 13%. M.p. 134–136 °C. *Anal.* Calc. for $C_8H_{10}N_4O$: C, 53.9; H, 5.7; N, 31.4. Found: C, 53.3; H, 5.5; N, 31.2%. ^1H NMR (ppm): 12.70 (s,vb, N–H), 7.30 (d, H5), 7.26 (s,b, H5′), 7.07 (s,b, H4′), 6.98 (d, H4), 4.68 and 3.86 (t, N–CH_2–CH_2–OH). ^{13}C NMR (ppm): 138.7 (C2′), 137.2 (C2), 125.5 (C4′), 124.2 (C4), 122.8 (C5), 120.8 (C5′), 63.3 and 50.5 (N–CH_2–CH_2–OH).

2.2.4. Me_2bim

Prepared by methylation of H_2bim with Me_2SO_4 [8]. Yellow solid. Yield: 74%. M.p. 113-114 °C. *Anal.* Calc. for $C_8H_{10}N_4$: C, 59.2; H, 6.2; N, 34.6. Found: C, 59.1;

H, 6.2; N, 34.5%. ^{1}H NMR (ppm): 7.28 (d, H5/H5′), 7.03 (d, H4/H4′), 4.02 (s, N–CH_3). ^{13}C NMR (ppm): 139.2 (C2/C2′), 127.8 (C4/4′), 123.6, (C5/5′), 35.3 (N–CH_3).

2.3. Synthesis of the complexes

2.3.1. [$PtCl_4(H_2bim)$]

A solution of H_2bim (0.120 g, 0.89 mmol) in water (35 mL) was added to a solution of $Na_2PtCl_6 \cdot 6H_2O$ (0.500 g, 0.89 mmol) in 25 mL of the same solvent. After stirring for 72 h at 70 °C, the mixture was filtered and the filtrate concentrated to dryness, leaving a yellow solid that was washed with water and dried under reduced pressure. Yield: 48%. *Anal.* Calc. for $C_6H_6N_4Cl_4Pt$: C, 15.3; H, 1.3; N, 11.9. Found: C, 15.3; H, 1.3; N, 11.6%. IR (Raman) data (cm^{-1}): 356sh (356m), 346s (346m), 332sh (330vs), 309m (309m), *ν*(Pt–Cl); 232w (231w), 218w (219w), *ν*(Pt–N). ^{1}H NMR (ppm): 7.89 (d, H5/H5′, $^4J_{Pt-H}$ = 8.2 Hz), 7.69 (d, H4/H4′, $^3J_{Pt-H}$ = 10.5 Hz). ^{13}C NMR (ppm): 138.1 (C2/C2′, $^2J_{Pt-C}$ = 27.7 Hz), 125.0 (C4/C4′, $^2J_{Pt-C}$ = 26.9 Hz), 121.7 (C5/C5′, $^3J_{Pt-C}$ = 24.7 Hz); ^{195}Pt NMR (ppm): $\delta = -171$.

2.3.2. [$PtCl_4(MeHbim)] \cdot H_2O$

Preparation as for [$PtCl_4(H_2bim)$], but using 0.132 g (0.89 mmol) of MeHbim in 20 mL of water, 0.500 g (0.89 mmol) of $Na_2PtCl_6 \cdot 6H_2O$ in 25 mL of water, and 17 h stirring at 70 °C. Yellow solid. Yield: 20%. *Anal.* Calc. for $C_7H_{10}N_4OCl_4Pt$: C, 16.7; H, 2.0; N, 11.1. Found: C, 16.6; H, 2.1; N, 10.7%. IR (Raman) data (cm^{-1}): 344s (346s), 328m (330s), 303w, 285m (279w), *ν*(Pt–Cl); 254sh (257m), *ν*(Pt–N). ^{1}H NMR (ppm): 7.96 (d, H5′, $^4J_{Pt-H}$ = 8.0 Hz), 7.92 (d, H5, $^4J_{Pt-H}$ = 8.6 Hz), 7.71 (d, H4′, $^3J_{Pt-H}$ = 10.9 Hz), 7,64 (d, H4, $^3J_{Pt-H}$ = 11.6 Hz), 4.43 (s, CH_3). ^{13}C NMR (ppm): 138.8 (C2′), 137.4 (C2, $^2J_{Pt-C}$ = 28.3 Hz), 125.4 (C4′, $^2J_{Pt-C}$ = 23.2 Hz), 124.7 (C4, $^2J_{Pt-C}$ = 26.1 Hz), 124.5 (C5, $^3J_{Pt-C}$ = 26.1 Hz), 122.2 (C5′, $^3J_{Pt-C}$ = 25.4 Hz), 36.3 (N–CH_3); ^{195}Pt NMR (ppm): $\delta = -171$.

2.3.3. [$PtCl_4(HOEtHbim)$]

Preparation as for [$PtCl_4(H_2bim)$], but using 0.100 g (0.56 mmol) of HOEtHbim in 15 mL of water, 0.300 g (0.53 mmol) of $Na_2PtCl_6 \cdot 6H_2O$ in 10 mL of water, and 24 h stirring at room temperature. Work-up included a final wash of the yellow solid product with ethanol. Yield: 38%. *Anal.* Calc. for $C_8H_{10}N_4OCl_4Pt$: C, 18.7; H, 2.0; N, 10.9. Found: C, 19.2; H, 2.1; N, 11.0%. IR (Raman) data (cm^{-1}): 343vs (343s), 325sh (330vs), 300sh (283w), *ν*(Pt–Cl); 254w (253w), *ν*(Pt–N).

2.3.4. [$PtCl_4(Me_2bim)$]

Preparation as for [$PtCl_4(H_2bim)$], but using 0.072 g (0.44 mmol) of Me_2bim in 10 mL of water, 0.250 g (0.44 mmol) of $Na_2PtCl_6 \cdot 6H_2O$ in 10 mL of water, and 48 h stirring at room temperature. Concentration of the filtered reaction mixture to dryness under vacuum at 65 °C afforded an oil that was washed with chloroform and mixed with water, upon which a yellow solid precipitated out. Yield: 31%. *Anal.* Calc. for $C_8H_{10}N_4Cl_4Pt$: C, 19.2; H, 2.0; N, 11.2. Found: C, 19.1; H, 2.2; N, 10.9%. IR (Raman) data (cm^{-1}): 350sh (354sh), 342m (344m), 324s (326s), 290w (295w), *ν*(Pt–Cl); 262w (263w), 254w, *ν*(Pt–N). ^{1}H NMR (ppm): 7.97 (d, H5/H5′), 7.69 (d, H4/H4′, $^4J_{Pt-H}$ = 13.4 Hz), 4.61 (s, N–CH_3). ^{13}C NMR (ppm): 138.5 (C2/C2′), 127.0 (C4/C4′, $^2J_{Pt-C}$ = 23.5), 124.7 (C5/C5′, $^3J_{Pt-C}$ = 21.9), 38.9 (N–CH_3); ^{195}Pt NMR (ppm): $\delta = -224$. Crystallization from DMF afforded crystals suitable for single-crystal X-ray crystallography.

2.4. Crystallography

2.4.1. X-ray data collection and reduction

Data were collected from a prismatic crystal of [$PtCl_4(Me_2bim)$] mounted on a glass fibre in an Enraf Nonius MACH3 automatic diffractometer [9]. Cell constants and an orientation matrix for data collection were obtained by least-squares refinement of the data for 25 reflections in the range $11.093° < \theta < 21.182°$. Data were collected at 293(2) K using Mo K_α radiation (λ = 0.71073 Å) and the ω-scan technique, and were corrected for Lorentz and polarization effects [10]. A semi-empirical absorption correction (ψ scan) was also made [11].

2.4.2. Structure solution and refinement

The structure was solved by the Patterson method [12] and subsequent difference Fourier maps, and was refined on F^2 by a full-matrix least-squares procedure using anisotropic displacement parameters [13], with all hydrogen atoms riding at calculated positions (C–H = 0.93–0.97 Å). The Flack x parameter (absolute structure parameter) was calculated to be 0.00(2) for the present structure and 0.98(2) for the inverted structure, thus providing strong evidence that the absolute structure has been assigned correctly [14]. Atomic scattering factors were taken from International Tables for Crystallography [15]. Molecular graphics were drawn using PLATON [16]. The crystal data, experimental details and refinement results are summarized in Table 1.

2.5. In vitro cytotoxicity studies

2.5.1. Cell lines and growth conditions

The human ovarian cancer cell line A2780 and its cisplatin-resistant mutant A2780cis (both from the European Collection of Cell Cultures through Sigma–Aldrich) were grown at 37 °C under humidified 5:95 CO_2/air in RPMI 1640 medium (Sigma–RBI, Spain) supplemented with 10% fetal bovine serum (FBS,

Table 1
Crystal and structure refinement data for [$PtCl_4(Me_2bim)$]

Formula weight	499.09
Temperature (K)	293(2)
Wavelength (Å)	0.71073
Crystal size (mm^3)	$0.40 \times 0.30 \times 0.25$
Crystal system	orthorhombic
Space group	$P2_12_12_1$
Unit cell dimensions (Å)	
a	8.6155(13)
b	10.3534(13)
c	15.528(2)
Volume ($Å^3$)	1385.1(3)
Z	4
Calculated density (Mg/m^3)	2.393
Absorption coefficient (mm^{-1})	10.884
F(000)	928
θ range for data collection (°)	2.36 to 27.95
Index ranges	$-11 \leqslant h \leqslant 0$, $0 \leqslant k \leqslant 13$, $0 \leqslant l \leqslant 20$
Reflections collected/unique	1918/1918 [R_{int} = 0.0000]
Maximum and minimum transmission	0.978 and 0.438
Data/parameters	1918/155
Goodness-of-fit on F^2	1.060
Final *R* indices [$I > 2\sigma(I)$]	
R_1	0.0308
wR_2	0.0746
R indices (all data)	
R_1	0.0420
wR_2	0.0781
Absolute structure parameter	0.00(2)
Largest difference peak and hole (e $Å^{-3}$)	1.799 and −1.702

Sigma–RBI, Spain) and 2 mM L-glutamine (Sigma–RBI, Spain).

2.5.2. In vitro chemosensitivity assay

Cells were seeded into 96-well plates (Beckton–Dickinson, Spain) in volumes of 100 μL (containing 4000 cells/well), and after incubation for 24 h were treated with the platinum complexes dissolved in TE–NaCl buffer (pH 7.5) containing 10 mM tris(hydroxymethylamino)methane hydrochloride (Tris–HCl), 0.1 mM disodium ethylenediaminetetraacetate (EDTA) and 50 mM NaCl. After a further 96 h incubation the cells were fixed by 15 min treatment with 10 μL of 11% glutaraldehyde per well, the fixative was removed, the cells were washed four times with deionized water, and cell biomass was determined by staining with crystal violet [17], and measuring the optical density at 595 nm, for which a Tecan Ultra Evolution microplate reader was used. IC_{50} (the drug concentration that inhibits cell growth by 50% with respect to controls) was determined graphically using Prism 2.01 (GraphPad Software Inc.).

For comparison, the cytotoxicity of cisplatin was evaluated under the same experimental conditions. All compounds were tested in two independent experiments with quadruplicate points. These experiments were performed in the Screening Unit of the Institute for Industrial Pharmacy, University of Santiago de Compostela.

3. Results and discussion

3.1. Synthesis

Our modifications of previously published methods for the preparation of H_2bim, MeHbim and HOEtbim failed to achieve significant improvements in yield. The yield of the dimethylation reaction was more satisfactory, 74%. Those of the complexation reactions ranged from 20% to 50%. Only in the case of the MeHbim derivative did the complex contain water of crystallization.

3.2. Solid state structure of [$PtCl_4(Me_2bim)$]

Crystals of [$PtCl_4(Me_2bim)$] consist of discrete molecules, the structure of which is shown in Fig. 1 together with the atomic numbering scheme used. The Pt atom is coordinated to the two unmethylated N atoms of the biimidazole ligand and to four Cl atoms in a distorted octahedral environment, the main distortion of which is the N(1)–Pt–N(3) bite angle, 79.0(3)°. The Pt atom lies only 0.0162 Å from the Cl(1)N(1)N(3)Cl(2) plane. The two rings of the Me_2bim ligand are both planar, and make a dihedral angle of 10.0(5)° with each other, and dihedral angles of 5.4(4)° [the N(1) ring] and 11.5(4)° [the N(3) ring] with the Cl(1)N(1)N(3)Cl(2) plane.

The Pt–N bond lengths (Table 2) are similar to those found in other complexes in which Pt(IV) forms a PtN_2C_2 ring with an *N*,*N*′-bidentate ligand. In particular, the geometry around the Pt atom is close to those found in [$PtCl_4$(bipy)] [18] (bipy = 2,2′-bipyridyl) and [$PtCl_4$(bpym)] · MeOH [19] (bpym = 2,2′-bipyrimidine), in which the bite angles are 81.3° and 80.3°, respectively. Among these three complexes, the angle opposite the bite [Cl(1)–Pt–Cl(2)] widens as the bite angle narrows,

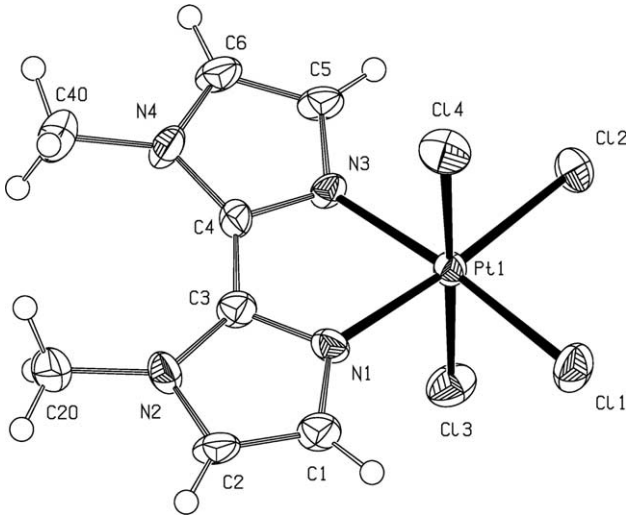


Fig. 1. ORTEP representation of the molecular structure of [$PtCl_4(Me_2bim)$], showing the numbering scheme. Thermal ellipsoids are drawn at the 50% probability.

Table 2
Selected bond lengths (Å) and angles (°) in [$PtCl_4(Me_2bim)$]

Bond lengths (Å)	
Pt(1)–N(1)	2.018(8)
Pt(1)–N(3)	2.030(7)
Pt(1)–Cl(2)	2.306(2)
Pt(1)–Cl(1)	2.311(2)
Pt(1)–Cl(4)	2.311(2)
Pt(1)–Cl(3)	2.324(2)
Bond angles (°)	
N(1)–Pt(1)–N(3)	79.0(3)
N(1)–Pt(1)–Cl(2)	174.0(2)
N(3)–Pt(1)–Cl(2)	95.0(2)
N(1)–Pt(1)–Cl(1)	93.7(2)
N(3)–Pt(1)–Cl(1)	172.6(2)
Cl(2)–Pt(1)–Cl(1)	92.28(10)
N(1)–Pt(1)–Cl(4)	89.2(2)
N(3)–Pt(1)–Cl(4)	87.1(2)
Cl(2)–Pt(1)–Cl(4)	90.31(10)
Cl(1)–Pt(1)–Cl(4)	91.42(10)
N(1)–Pt(1)–Cl(3)	90.3(2)
N(3)–Pt(1)–Cl(3)	91.5(2)
Cl(2)–Pt(1)–Cl(3)	90.07(10)
Cl(1)–Pt(1)–Cl(3)	89.97(10)
Cl(4)–Pt(1)–Cl(3)	178.53(10)

being 89.1°, 90.18° and 92.28° for the bipy, bpym and Me_2bim derivatives, respectively. The Cl–Pt–Cl angle involving the Cl atoms *cis* to the N atoms is 178.3° in [$PtCl_4(bipy)$], 177.6° in [$PtCl_4(bpym)$] and 178.53° in [$PtCl_4(Me_2bim)$].

In the bipy and bpym complexes the influence of the N atoms makes the *trans*-Pt–Cl bonds shorter than the *cis*-Pt–Cl bonds [2.301(2)–2.307(3) Å as against 2.316(3)–2.335(2) Å]. This structural *trans* influence is not so strong in the Me_2bim derivative, in which one of the *cis*-Pt–Cl bonds is the same length as one of the *trans*-Pt–Cl bond distances, 2.311(2) Å, a situation similar to that found in [$PtCl_4(dpk)$] (dpk = di-2-pyridyl ketone) [20] (in which there are *trans*- and *cis*-Pt–Cl distances of 2.301 and 2.302 Å, respectively) and close to that found in Pt(IV) complexes in which two N-coordinated monodentate imidazole rings occupy *cis* positions [21].

Comparison of the PtN_2C_2 ring of [$PtCl_4(Me_2bim)$] with those of the two Pt-complexes of biimidazole derivatives for which structures have been described previously, [$PtCl_2(MeHbim)] \cdot Et_4NCl$ [22] and [PtI_2-(Me_2bim)] [23] shows no significant differences. In particular, the Pt–N distances are practically indifferent to the redox state of the metal atom.

3.3. Spectral characteristics

The IR and Raman bands of the biimidazole ligands undergo small shifts upon coordination. With regard to those of the ring stretching vibrations (1600–1300 cm^{-1}) the four complexes are similar to each other and to those previously described complexes of these ligands [7,24], which suggest that these ligands have similar coordination modes in all these compounds.

For [$PtCl_4(LL)$] compounds with an ideal C_{2v} $PtCl_4N_2$ framework four ν(Pt–Cl) bands are expected in their IR and Raman spectra: two A_1, B_1 and B_2. In general these bands are found in the spectra of the new complexes at positions close to those reported for similar compounds [25], suggesting that all have the same $PtCl_4N_2$ structure. As in the case of [$MCl_2(LL)$] compounds (LL = 2,2′-biimidazole or *N*,*N*′-dimethyl-2,2′-biimidazole) [7], the ligand bands hinder a rigorous identification of the expected two ν(Pt–N) bands.

3.4. Studies in solution

The ligands and complexes were characterized by NMR spectroscopy in DMF-d_7. When necessary, assignments were corroborated by NOE and two-dimensional NMR experiments.

The ^{1}H NMR spectrum of H_2bim shows two broad singlets for the ring protons at nearly the same positions as those of two doublets that appear in the spectrum of the *N*,*N*′-dimethyl derivative. By contrast, the spectrum of MeHbim at room temperature (293 K) shows two signals for the protons of the methylated ring but, probably owing to the fast exchange of the iminic proton, only one broad signal for H5′ and H4′. At 223 K this latter signal splits into two singlets. In the ^{13}C NMR spectra the C4′ and C5′ signals are not observable at 293 K but are present at 223 K. No such room temperature tautomerism is observed in the ^{1}H and ^{13}C NMR spectra of HOEtbim, the signals of which were identified on the basis of the MeHbim spectra obtained at 223 K.

The low solubility of [$PtCl_4(HOEtHbim)$] in DMF led to a poor quality ^{1}H NMR spectrum which makes identification of its signals impossible. In the NMR spectra of the other platinum complexes, all the ^{1}H signals are shifted to lower field than in the spectrum of the free ligand, and the ^{13}C signals show that coordination to Pt(IV) deshielded C5/5′ and N–CH_3 carbons, and shielded C2/2′ and C4/4′ carbons. For example, the ^{1}H spectrum of [$PtCl_4(H_2bim)$] shows two doublets that are both 0.67 ppm downfield of their positions in the spectrum of the free ligand. As in the Pt(II) complex of this ligand [7] the value of $^3J_{HH}$ is approximately 1.5 Hz. The poor solubility of free H_2bim makes it impossible to obtain its ^{13}C NMR spectrum in DMF, but the above-noted shifts in carbon signals may be deduced from its ^{13}C CP/MAS spectrum, which shows signals at 139.1, 129.1, 126.8, 120.8 and 118.6 ppm for carbons 2, 2′, 4, 4′, 5 and 5′ (the splitting of the signals being due to the asymmetrically hydrogen bonded structure of solid H_2bim [26]).

The above data and the observation of platinum-hydrogen and platinum-carbon couplings and of δ

Table 3
Cytotoxicity (IC_{50}) of the the prepared compounds and cisplatin against human ovarian cancer cell lines

Compound	IC_{50} (μM)		RF[a]
	A2780	A2780cis	
$[PtCl_4(H_2bim)]$	16.7 ± 0.5	25.6 ± 0.4	1.5
$[PtCl_4(MeHbim)] \cdot H_2O$	11.4 ± 0.3	16.8 ± 0.5	1.5
$[PtCl_4(HOEtHbim)]$	20.6 ± 0.4	67.9 ± 0.6	3.3
$[PtCl_4(Me_2bim)]$	30 ± 4	16 ± 5	0.5
Cisplatin	0.38 ± 0.4	3.5 ± 0.5	9.2

[a] The resistance factor: RF = IC_{50}(A2780cis)/IC_{50}(A2780).

(^{195}Pt) values similar to those found for other compounds with a *cis*-$PtCl_4N_2$ kernel [27], confirm the persistence of this kernel in DMF solution.

3.5. Cytotoxicity

Table 3 lists the results of testing the new compounds and cisplatin for cytotoxicity against the human ovarian cancer cell line A2780 and the cisplatin-resistant line A2780cis. Against A2780 the new compounds had IC_{50} values in the low micromolar range but were in general less active than other Pt(IV) [28–30] or dinuclear Pt(II) [31] complexes that have recently been described and were far less active than cisplatin.

The cisplatin resistance of A2780cis line is known to be multifactorial, a combination of decreased accumulation, enhanced DNA repair tolerance and elevated glutathione levels [28]. The ability of all the new compounds except the HOEtHbim derivative to circumvent cisplatin-induced resistance is suggested by their having values <2 for the resistance factor RF (the ratio of the values of IC_{50} against the resistant and parent lines) [28]. The RF value of $[PtCl_4(Me_2bim)]$, 0.5, seems particularly promising.

4. Supplementary data

Crystallographic data have been deposited with The Director, CCDC, 12 Union Road, Cambridge CB21EZ, UK (fax: +44 1223 366033; e-mail: deposit@ccdc.cam.ac.uk or http:www.ccdc.cam.ac.uk) and are available on request, quoting the deposition number 252712.

Acknowledgment

We thank the Xunta de Galicia (Spain) for financial support under Project XUGA 20318B96.

References

[1] B. Lippert (Ed.), Cisplatin. Chemistry and Biochemistry of a Leading Anticancer Drug, Wiley-VCH, Weinheim, 1999.
[2] (a) E. Wong, C.M. Giandomenico, Chem. Rev. 99 (1999) 2451;
(b) L.R. Kelland, N. Farrell (Eds.), Platinum-based Drugs in Cancer Chemotherapy, Humana Press, Tatowa, 2000;
(c) M.A. Fuertes, C. Alonso, J.M. Pérez, Chem. Rev. 103 (2003) 646.
[3] (a) B.K. Keppler (Ed.), Metal Complexes in Cancer Chemotherapy, VCH, Weinheim, 1993;
(b) G. Berthon (Ed.), Handbook of Metal Ligand Interactions in Biological Fluids, vol. 2, Marcel Dekker, New York, 1995;
(c) M.J. Clarke, F. Zhu, D.R. Frasca, Chem. Rev. 99 (1999) 2511.
[4] (a) M.D. Hall, T.W. Hambley, Coord. Chem. Rev. 232 (2002) 49;
(b) W.H. Ang, I. Khalaila, C.S. Allardyce, L. Juillerat-Jeanneret, P.J. Dyson, J. Am. Chem. Soc. 127 (2005) 1382.
[5] M.D. Hall, G.J. Foran, M. Zhang, P.J. Beale, T.W. Hambley, J. Am. Chem. Soc. 125 (2003) 7524.
[6] M.D. Hall, C.T. Dillon, M. Zhang, P. Beale, Z. Cai, D. Lai, A.P.J. Stampfl, T.W. Hambley, J. Biol. Inorg. Chem. 8 (2003) 726.
[7] J.S. Casas, A. Castiñeiras, Y. Parajó, M.L. Pérez-Parallé, A. Sánchez, A. Sánchez-González, J. Sordo, Polyhedron 22 (2003) 1113.
[8] (a) P. Melloni, E. Dradi, W. Logemann, I. de Carneri, F. Trane, J. Med. Chem. 15 (1972) 926;
(b) P. Melloni, D. Fusar-Bassini, E. Dradi, C. Confaloneri, J. Heterocycl. Chem. 11 (1974) 731;
(c) A. Abushamleh, H.A. Goldwin, Aust. J. Chem. 32 (1979) 513.
[9] B.V. Nonius, CAD4-Express Software, Ver. 5.1/1.2, Enraf Nonius, Delft, The Netherlands, 1994.
[10] M. Kretschmar, GENHKL Program for the Reduction of CAD4 Diffractometer Data, University of Tübingen, Germany, 1997.
[11] A.C.T. North, D.C. Phillips, F.S. Mathews, Acta Crystallogr. A 24 (1968) 351.
[12] G.M. Sheldrick, Acta Crystallogr. A 46 (1990) 467.
[13] G.M. Sheldrick, SHELXL-97. Program for the Refinement of Crystal Structures, University of Göttingen, Germany, 1997.
[14] H.D. Flack, Acta Crystallogr. A 39 (1983) 876.
[15] International Tables for Crystallography, vol. C, Kluwer Academic Publishers, Dordrecht, The Netherlands, 1995.
[16] A.L. Spek, PLATON. A Multipurpose Crystallographic Tool. Utrecht University, The Netherlands, 2000. Available from: <http://www.cryst.chem-uu.nl/platon>.
[17] W. Kueng, E. Silber, U. Eppenberger, Anal. Biochem. 182 (1989) 16.
[18] T.W. Hambley, Acta Crystallogr. C 42 (1986) 49.
[19] A. Gaballa, C. Wagner, H. Schmidt, D. Steinborn, Z. Anorg. Allg. Chem. 629 (2003) 703.
[20] K.N. Crowder, S.J. García, R.L. Burr, J.M. North, M.H. Wilson, B.L. Conley, P.E. Fanwick, P.S. White, K.D. Sienerth, R.M. Granger II, Inorg. Chem. 43 (2004) 72.
[21] J. Kuduk-Jaworska, M. Kubiak, T. Glowiak, B. Jezowska-Tuzebiatowska, Acta Crystallogr. C 46 (1990) 2046, and references therein.
[22] S. Karentzopoulos, H. Engelking, B. Bremer, N. Paschke, B. Krebs, Acta Crystallogr. C 53 (1997) 172.
[23] J.S. Casas, A. Castiñeiras, Y. Parajó, J. Sordo, J.M. Varela, Acta Crystallogr. C 54 (1998) 1777.
[24] (a) A. Sánchez-González, J.S. Casas, J. Sordo, U. Russo, M.I. Lareo, B.J. Regueiro, J. Inorg. Biochem. 39 (1990) 227;
(b) C. López, A. Sánchez-González, M.E. García, J.S. Casas, J. Sordo, R. Graziani, U. Casellato, J. Organomet. Chem. 434 (1992) 261;
(c) P. Alvarez Boo, J.S. Casas, M.D. Couce, E. Freijanes, A. Furlani, V. Scarcia, J. Sordo, U. Russo, M. Varela, Appl. Organomet. Chem. 11 (1997) 963.
[25] H. Juniche, K. Schenzel, F.W. Heinemann, K. Pelz, H. Bögel, D. Steinborn, Z. Anorg. Allg. Chem. 623 (1997) 603.
[26] (a) S. Takasu, H. Takai, T. Takagi, H. Fujisuma, Anal. Sci. 7 (1991) 845;

(b) D.T. Cromer, R.R. Ryan, C.B. Storm, Acta Crystallogr. C 43 (1987) 1435.
[27] U. Bierbach, T.W. Hambley, J.D. Roberts, N. Farrell, Inorg. Chem. 35 (1996) 4865.
[28] J.M. Pérez, L.R. Kelland, E.I. Montero, F.E. Boxall, M.A. Fuertes, C. Alonso, C. Navarro-Ranninger, Mol. Pharm. 63 (2003) 933, and references therein.
[29] R. Song, S.Y. Park, Y.S. Kim, S.J. Kim, B.T. Ahn, Y.S. Sohn, J. Inorg. Biochem. 96 (2003) 339.
[30] M.D. Hall, S. Amjadi, M. Zhang, P.J. Beale, T.W. Hambley, J. Inorg. Biochem. 98 (2004) 1614.
[31] B.A.J. Jansen, P. Wielaard, G.V. Kalayda, M. Ferrari, C. Molenaar, H.J. Tanke, J. Brouwer, J. Reedijk, J. Biol. Inorg. Chem. 9 (2004) 403.

one-electron oxidation with PbO_2 was especially very interesting for us [6a,6d,6e,6f,6g]. While upon oxidation they are easily generate relatively stable M(II)-phenoxyl radical complexes [6], the proceeding unexpected oxidative C–C coupling in bis-salicylaldimine Cu^{II} complexes [6b] and reduction via radical intermediates of Cu^{II} and Pd^{II} bis-salicylaldiminates upon treatment with PPh_3 were also observed [6d,6e,6f,6g].

In this context recently, we have described some bulky *N*-aryl-3,5-di-*t*-butylated salicylaldimine metal(II) chelates, which *t*-butyl groups are introduced into salicylic moiety [7]. Our preliminary studies revealed that while the above ligands easily coordinate with Cu(II), Co(II) and Pd(II) ions, the preparation of Ni^{II}, Mn^{II}, Zn^{II}, VO^{IV} metal ions complexes with above ligands were unsuccessful [7].

In the present paper, we report the synthesis, spectroscopic and redox behaviors of a new series of bis[*N*-alkyl-3,5-Bu^t_2-salicylideneiminato]copper(II) complexes, CuL^x_2, derived from 3,5-DTBS and alkylamines RNH_2 R = CH_3(L^1H), C_2H_5 (L^2H), *n*-C_3H_7(L^3H), *n*-C_4H_9-(L^4H), *iso*-C_4H_9(L^5H), *t*-C_4H_9(L^6H), C_5H_{11}(L^7H), *neo*-C_5H_{11}(L^8H), *n*-C_6H_{13}(L^9H), *cyclo*-C_6H_{11}(L^{10}H). The copper(II) complexes are abbreviated as **1**, **2**, **3**, **4**, **5**, **6**, **7**, **8**, **9** and **10**, correspondingly.

2. Experimental

2.1. Measurements

C, H and N analyses were performed with a LECO CHNS 932 elemental analyzer. Electronic absorption spectra were recorded on a Shimadzu 1601 UV–Vis spectrophotometer in the range 1100–200 nm. IR spectra were recorded on a Perkin–Elmer FTIR spectrometer using KBr disks. The room temperature (r.t.) magnetic susceptibility measurements were performed by the Gouy balance using a tube calibrated with Hg[Co(NCS)$_4$]. Diamagnetic corrections were made using Pascal's constant. ESR spectra were taken on a Varian E109 C X-band spectrometer. The field and frequency calibration were made using DPPH (g = 2.0037) powder. Errors for g- and A-parameters of the complexes and g-factor of radicals are ±0.001, ±0.5G and ±0.0002, respectively.

Electrochemical measurements were recorded on a PC-controlled Eco Chemie-Autolab-12 potentiostat/galvanostat in nitrogen degassed acetonitrile (MeCN) solutions of ca. 10^{-3}–10^{-4} M **X** containing 0.05 M Et_4NBF_4 as the supporting electrolyte. The three-electrode cell contained a platinum working and counter electrodes and an Ag/AgCl reference electrode. The potentials are referred to Ag/AgCl in the potential range +2.0 to −1.5 V. All solutions were purged with N_2 for about 5 min prior to each set of experiment.

2.2. Materials

All the chemicals and solvents were of analytical grade and were used without further purification. Cu$(AcO)_2 \cdot H_2O$, 2,4-di-*tert*-butylphenol, all alkylmines ($CH_3NH_2 \cdot HCl$, $C_2H_5NH_2 \cdot HCl$, *n*-$C_3H_7NH_2$, *n*-$C_4H_9NH_2$, *iso*-$C_4H_9NH_2$, *t*-$C_4H_9NH_2$, *n*-$C_5H_{11}NH_2$, *neo*-$C_5H_{11}NH_2$, *n*-$C_6H_{13}NH_2$, *cyclo*-$C_6H_{11}NH_2$) and $(NH_4)_2Ce(NO_3)_6$ abbreviated as ACN, were obtained from Aldrich Chemical Co. 3,5-di-*t*-butylsalicylaldehyde was prepared by standard methods [8].

2.3. Preparation of ligands

All salicylaldimines, L^xH, were prepared in high yields (80–96%) via condensation of the 3,5-di-*t*-butylsalicylaldehyde with the corresponding alkyl amines (1:1 molar ratio) in methanol/ethanol at reflux for 5–6 h in the presence of 3–5 drops of formic acid and recrystallized from methanol or hexane. Except *t*-butyl-, *neo*-pentyl- and *cyclo*-hexylamines, all other amine Schiff bases were obtained as yellow viscous oils and used without further purification for the preparation of the complexes. The crude oil samples were purified using a column chromatography technique (SiO_2 column, eluent hexane–MeOH (5:1)).

2.4. Synthesis of the complexes

The **X** complexes were prepared by following general procedure. To a solution of 1 mmol of the appropriate ligand in MeOH (80–90 ml) was added, with stirring at 50–60 °C, 100 mg (0.5 mmol) Cu$(AcO)_2 \cdot H_2O$ in MeOH (10–15 ml) solution and the mixture was refluxed on a water bath for 1.5–2.0 h. Then the solution volume evaporated to 15–20 ml and left to cool to room temperature. The precipitated product was filtered and washed with cold MeOH, *n*-hexane and dried in air. Recrystallization from $CHCl_3$–methanol yielded **X** as microcrystalline powder (76–91%). Analytical, and spectroscopic data for the **X** are given in the Tables 1, 4, 5 and 6.

3. Results and discussion

All of the *N*-alkyl-3,5-Bu^t_2-salicylaldimines studied were prepared in high yields as a yellow oils or crystalline solids (L^6H, L^8H, L^{10}H) by the condensation of 3,5-DTBS with the appropriate alkyl amine in refluxing methanol and in the presence of a catalytic amount of formic acid. Satisfactory elemental analyses were obtained for all of L^xH ligands and **X** chelates (Table 1). We also tried to prepare Ni^{II}, Co^{II}, Mn^{II}, VO^{IV} and Zn^{II} complexes with L^xH by using the method similar to that for preparation of Cu^{II}. But in spite of all our repeated

Table 1
Physico-chemical, analytical data of the L^xH ligands and their ML^x_2 complexes

Compound	M.p. (°C)	Yield (%)	μ_{eff}, BM	Formula	Found (Calcd.) (%)		
					C	H	N
L^6H	100	72		$C_{19}H_{31}NO$	75.43(78.84)	11.08(10.79)	4.58(4.84)
L^8H	98	56		$C_{20}H_{33}NO$	78.76(79.16)	11.14(10.96)	4.43(4.61)
$L^{10}H$	95	74		$C_{21}H_{33}NO$	80.36(79.95)	10.29(10.54)	4.54(4.44)
1	259	86	2.03	$C_{32}H_{48}N_2O_2Cu$	68.23(69.09)	8.56(8.69)	4.89(5.03)
2	175	78	1.76	$C_{34}H_{52}N_2O_2Cu$	70.12(69.88)	8.89(8.96)	4.68(4.79)
3	132	56	1.76	$C_{36}H_{56}N_2O_2Cu$	69.78(70.61)	9.58(9.22)	4.53(4.57)
4	189	71	1.76	$C_{38}H_{60}N_2O_2Cu$	71.57(71.26)	9.78(9.44)	4.65(4.37)
5	162	75	1.77	$C_{38}H_{60}N_2O_2Cu$	72.14(71.26)	8.86(9.44)	4.45(4.37)
6	177	67	1.78	$C_{38}H_{60}N_2O_2Cu$	70.34(71.26)	9.12(9.44)	4.08(4.37)
7	113	56	1.77	$C_{40}H_{64}N_2O_2Cu$	72.48(71.92)	8.89(9.65)	4.45(4.19)
8	155	79	1.86	$C_{40}H_{64}N_2O_2Cu$	72.87(71.92)	8.83(9.65)	4.26(4.19)
9	193	75	1.74	$C_{42}H_{68}N_2O_2Cu$	73.63(72.42)	9.64(9.83)	3.12(4.02)
10	151	62	1.82	$C_{42}H_{64}N_2O_2Cu$	74.62(72.63)	10.18(9.58)	4.05(4.03)

attempts, we have not succeeded in preparing their complexes under above conditions.

3.1. Infrared spectra

The spectra of viscous oil L^xH samples unlike polycrystallic L^6H, L^8H and $L^{10}H$ ligands together with bands in the 1626–1648 cm^{-1} region due to ν(C=N) stretch, also display a stronger bands at 1728–1731 cm^{-1} assignable to ν(C=O), which clearly indicates that the oil samples the ligands consist of enol-imine and keto-amine tautomer forms (Table 2). While the spectra of polycrystallic L^6H, L^8H and $L^{10}H$ samples according their IR spectra predominantly of enol-imine tautomer (Table 2), their $CHCl_3$ solution spectra together with imine bands (1625–1630 cm^{-1}) also exhibit a band at 1728–1731 cm^{-1}, supporting that in solution these ligands are exist in both enol-imine and keto-amine tautomer forms. The IR spectra of the complexes show the ν(C=N) stretching shifted to 1610–1626 cm^{-1}, while the ν(OH) stretching (2600–2800 cm^{-1} due to intramolecularly H-bonded OH in L^xH) and ν(C=O) disappears in all the complexes, indicating that the ligands are coordinated in their phenol-imine tautomer form. New bands, which are absent in the spectra of all the free lignds, were observed at 1530 and 1547 cm^{-1}, attributable to the coordinated ν(C–O) mode [10], and in the 450–660 cm^{-1} region assigned to the M–O and M–N bonds.

3.2. Electronic spectra

The electronic spectral data of L^xH in ethanol are collected in Table 2. The absorption bands appeared in the UV region and at around 408–420 nm can be assigned to intraligand $\pi \rightarrow \pi^*$ and $n \rightarrow \pi^*$ transitions in L^xH, and $n \rightarrow \pi^*$ transitions in dipolar zwitterionic or keto-amine tautomer structures, respectively [11]. All **X** complexes in chloroform solution along with nearly identical intraligand bands in the 273–387 nm region, also exhibit an intense band at ca. 460–500 assigned to Cu(II) (dπ)-to-(equatorial) phenolate (pπ) MLCT transition and low intense band appeared as a shoulder at 630–790 nm (Table 3), originated from $d_{xy} \rightarrow d_{x^2-y^2}$ transition in a distorted planar geometry of Cu^{II} compounds, respectively [11,12].

Table 2
IR and electronic spectral data for *N*-alkyl-3,5-Bu^t_2-salicylaldimines (L^xH)

R	L^xH	IR-spectra, cm^{-1}		Electronic spectra, λ_{max} (nm)
		$\nu_{(C=N)}$	$\nu_{(C=O)}$	
Methyl	(L^1H)	1648	1728	207, 224, 265, 340, 420[a]
Ethyl	(L^2H)	1648	1728	208, 224, 265, 336, 410
n-Propyl	(L^3H)	1634	1733	261, 328, 408
n-Butyl	(L^4H)	1633	1729	261, 328, 404
sec-Butyl	(L^5H)	1631	1728	260, 329, 408[a]
[b]*t*-Butyl	(L^6H)	1626		220[a], 233, 262, 329, 417
n-Pentyl	(L^7H)	1634	1731	261, 328, 416
[b]*t*-Amyl	(L^8H)	1625		220[a], 235, 263, 328, 416
n-Hexyl	(L^9H)	1633	1731	261, 349, 416
[b]*cyclo*-Hexyl	($L^{10}H$)	1630		208, 265, 345, 420

[a] Shoulder.
[b] Solid samples.

Table 3
Magnetic, IR and electronic spectral data for **X** complexes and **X** + $(NH_4)_2Ce(NO_3)_6$ systems

Complex	IR spectra, cm^{-1}		Electronic spectra, λ/nm (ε, $M^{-1}cm^{-1}$)	λ_{max}/nm for oxidized complexes
	ν(C=N)	ν(C–O)		**X** + $(NH_4)_2Ce(NO_3)_6$
1	1626	1547	325, 382, 500[a], 620[a](154)	642, 800[b]
2	1621	1548	273, 328, 385, 490[a], 620[a](128)	645, 800[b]
3	1622	1547	277, 327, 384, 490[a], 620[a](172)	636, 830[a]
4	1615	1547	337, 396, 520[a], 630[a](169)	642, –
5	1625	1547	328, 386, 480[a], 640[a](195)	640, 820[a]
6	1610	1547	282, 329, 385, 480[a], 795[a](86)	709, –
7	1615	1548	335, 398, 520[a], 640[a](169)	641, 820[a]
8	1619	1527	277, 328, 387, 460[a], 660[a](131)	700, –
9	1619	1548	276[a], 328, 383, 490[a], 640[a](166)	636, 800[a]
10	1620	1547	276, 328, 385, 480[a], 650[a](133)	648, 830[a]

[a] Shoulder.
[b] A very weak shoulder.

3.3. Magnetic measurements

The r.t. μ_{eff} values of **X** except **1**, **8** and **10** are lie in the range 1.74–1.78 BM (Table 3). Despite the fact that the presented chelates are more bulky than their planar non-di-*tert*-butylated *N*-alkyl-salicylaldiminato copper(II) analogs [9a], the μ_{eff} values of the former are significantly lower than those reported for the latter (1.86–1.92 BM) [13]. The reason of this probably associated with the existence of complexes in the magnetically diluted state due to bulkiness salicylic moiety. As reported by Hathaway in the magnetically dilute copper(II) complexes, when the copper ions are well separated from each other (>5 Å), then the μ_{eff} may be given by the spin-only vale of 1.73 BM [15a].

3.4. ESR investigation

3.4.1. Solid-state spectra

The solid state and solution spin Hamiltonian parameters of **X** complexes estimated from ESR spectra are listed in Table 4. The ESR spectra of powder samples of all **X** were obtained at 300 K. No half-field $\Delta M_s = \pm 2$ lines typical for binuclear triplet-state species [14a,14b] were observed. The polycrystalline ESR spectra of **X** are typical of monomeric distorted tetragonal copper(II) complexes with a $d_{x^2-y^2}$ ground state ($g_\parallel > g_\perp > g_e$) [15]. Selected spectra are shown in Fig. 1. The polycrystalline ESR spectra of the complexes **1**, **3** and **5** exhibit only one an exchange-averaged broad signal (Fig. 1(a) and (b)), which is attributable to dipolar interaction between crystallographycally non-equivalent Cu^{II} centers in the solid [15]. The ESR spectrum of powder samples all of other **X** complexes display three copper hyperfine lines in the parallel region ($g_\parallel$ = 2.159–2.229, $A_\parallel^{Cu}$ = 128–168 *G*) (Table 4, Fig. 1(c) and (d)). This fact indicates that the complexes are monomeric in the polycrystalline state with $|J| \leqslant 0.2\ cm^{-1}$ [14c]. It is interesting that the spectrum of *N*-cyclohexyl substituted **10**, besides three resolved $g_\parallel$ components also exhibits low intensity lines at the low-field (g = 2.559) and high-field (g = 1.915) sides of the monomeric signal (Fig. 1(d) and (e)), indicating the presence of the exchange-coupled binuclear species in polycrystalline state for this complex [15]. The exchange-coupling term G, estimated from the $G = (g_\parallel - 2.0023)/$

Table 4
ESR[a] parameters of bis(*N*-alkyl-3,5-Bu^t_2-salicylideneiminato)Cu(II) complexes

(**X**)	Solid state spectra		Solution spectra							
	$g_\parallel(A_\parallel)$	$g_\perp$	g_{iso}	$g_\parallel$	$g_\perp$	A_{iso}	$A_\parallel$	$A_\perp$	G	$g_\parallel/A_\parallel$, cm
1	g_{av} = 2.092		2.116	2.223	2.063	75	168	25.5	3.62	143
2	2.159(140)	2.062	2.117	2.223	2.067	72	168	22.5	3.41	143
3	g_{av} = 2.075		2.118	2.223	2.067	71	166	23.5	3.41	145
4	2.233(168)	2.048	2.119	2.223	2.067	71	164	24.5	3.41	146
5	g_{av} = 2.065		2.119	2.226	2.066	67	160	20.5	3.51	150
6	2.212(140)	2.069	2.126	2.265	2.056	70	132	37.5	4.85	185
7	2.212(160)	2.056	2.118	2.227	2.063	68	166	21.0	3.70	145
8	2.224(160)	2.062	2.062	2.224	1.981		160		3.63	150
9	2.229(168)	2.054	2.117	2.223	2.064	69	164	21.5	3.58	146
10	2.189(125)	2.092	2.118	2.238	2.058	70	144	33	4.23	168

[a] The values of copper hyperfine constants (A) are given in *G*.

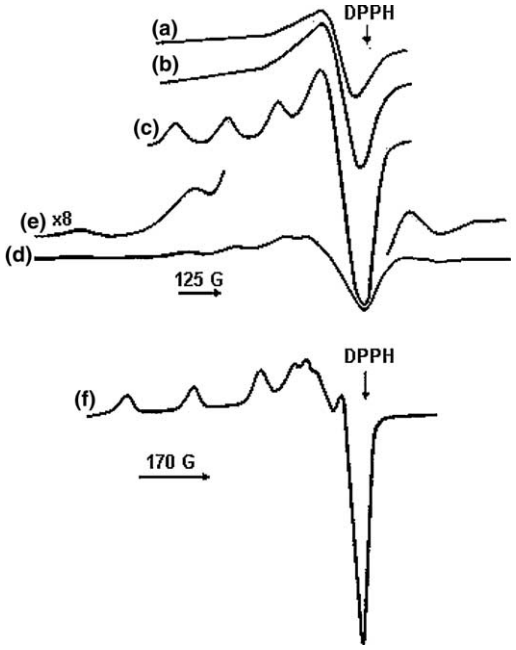


Fig. 1. Powder ESR spectra (X-band, r.t.); (a) **1**, (b) **3**, (c) **4** and (d) **10**; (f) $CHCl_3$ glass spectrum of **3** at 153 K.

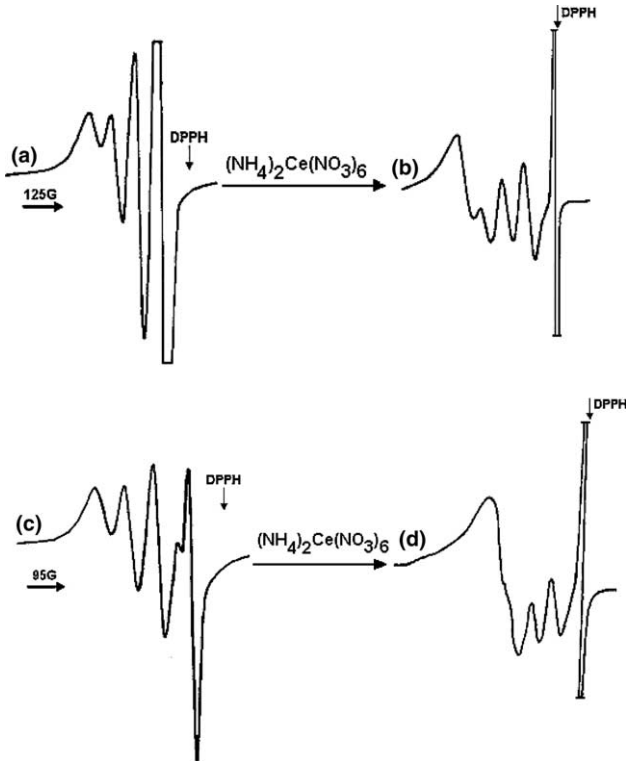


Fig. 2. ESR spectra of **5** (a) and **6** (c) complexes in $CHCl_3$ at r.t. and for systems obtained by the oxidation of **5** (b) and **6** (d) with 8-fold excess of $(NH_4)_2Ce(NO_3)_6$.

($g_\perp - 2.0023$), lying within 2.63–3.78 < 4 suggests the presence of a exchange coupling between Cu^{II} centers and the misalignment is appreciable [15] except **4** and **9** for all **X** complexes, respectively. The **4** and **9** complexes which have $G > 4$, (4.48 for **4** and 4.38 for **9**), suggest that the local tetragonal axes are aligned parallel and the exchange coupling effects are not operative for theses complexes [15].

3.4.2. Solution ESR spectra

The room temperature ESR spectra of **X** exhibit in toluene/$CHCl_3$ solutions in generally show well resolved four-line hyperfine patterns without ^{14}N-shfs resolutions on the high-field copper components (Fig. 2(a) and (c)). The frozen-solution ESR spectra at 153 K (Fig. 1(f)) are indicative of a $d_{x^2-y^2}$ ground state ($g_\parallel > g_\perp > 2.03$) (Table 4) and thus suggest a dominantly tetragonal component in the solution stereochemistry [12,14,15]. As it is expected for **6**, the lowest $A_\parallel$ (132 G) and highest $g_\parallel$ (2.265) values, due to tetrahedral distortion of Cu(II) geometry as a result of steric hindrance between bulky *N*-Bu^t and salicylic Bu^t groups, were observed. An increased distortion from a planar geometry to distorted tetrahedral with increasing in bulkiness of R is also reflected in the large $g_\parallel/A_\parallel$ values; $g_\parallel/A_\parallel = 150$, 168 and 185 cm were observed for **8**, **10** and **6**, respectively (Table 4) [16]. It is interesting that with increasing of tetrahedral distortion in Cu(II) geometry the gradually decreasing in the value of in-plane σ-bonding parameter, α^2(0.66–0.72), evaluated using the expression $\alpha^2 = |A|/0.036 + (g_\parallel - 2.0023) + 3/7(g_\perp - 2.0023) + 0.04$ [17], indicate that there is a substantial in the in-plane σ-bonding in these complexes. The values of the exchange-coupling parameters, *G*, of 3.41–3.63 estimated from frozen glass ESR spectra of **X,** except **6** and **10**, were <4.0 (Table 4), suggesting the presence of an exchange interaction in these complexes at frozen-glass state [15a,15b].

3.5. Chemical oxidation of X with $(NH_4)_2$ $Ce(NO_3)_6$

The present investigation of the oxidative behavior of **X** complexes, revealed that when they are treated with the "mild" oxidant $(NH_4)_2Ce(NO_3)_6$(ACN) in $CHCl_3$ at r.t., along with significantly decreasing signal of intensity of **X**, the generation of radical signals with $g = 2.0048 - 2.0086$ and the appearance of a new broad singlet centered at $g = 2.116 - 2.194$ were also observed (Fig. 2(b) and (d)). Note that very poor solubility of ACN in $CHCl_3$, the reaction mixture periodically was stirred for 4–5 s before of each scanning. Upon addition of 8–10-fold excess ACN to $CHCl_3$ solutions of **5**, **6**, **7**, **8** and **10** and stirring a color simultaneously turned from dark brown to green. In the ESR spectra of these oxidized complexes besides significantly decreasing in the intensity of the initial spectra, the appearance of strong radical signals ($g = 2.0071 - 2.0086$) and a new broad signal centered at $g = 2.116$, 2.182, 2.185, 2.194 and 2.172, respectively, were observed. The observed *g*

values are slightly greater than that observed free phenoxyl radicals (2.004–2.005). It is more likely that there is contribution of metal orbitals to the molecular orbital that contain the unpaired electron. Under similar conditions the oxidation of **1**, **2**, **3**, **4** was rather difficult than that for **5**, **6**, **7**, **8** and **10** complexes. Although the broad line near $g = 2.18$, observed in the spectra of oxidized **X**, may be originate from aggregated Cu(II) intermediates, a detailed explanation of the observed spectral changes is not possible at present. It is noteworthy that when oxidation of **5**, **6**, **7**, **8** and **10** complexes was carried out with a twofold excess ACN while the decreasing in the intensity of the initial spectra and generation of a strong radical signal were appeared, but no new signal assignable to Cu(II) species was detected (Fig. 3). The detection of radical signals for **X** + ACN systems undoubtedly supports the generation of the coordinated phenoxyl radical because of one electron oxidation of the coordinated phenolate oxygen atoms in **X**. The decreasing in the ESR signal intensity of the oxidized **X** probably results from an antiferromagnetic coupling between unpaired d^9 copper electron and coordinated radical center in Cu^{II}–PhO$^{\cdot}$ radical species. It is necessary to note that radical species generated from free L^8H and $L^{10}H$ are too unstable and their spectra can be detected only at 130 K as unresolved singlets at $g = 2.0049$ and 2.0053, respectively. Note that the generation of coordinated radical species recently were observed in the oxidation of bis(*N*-aryl-3,5-Bu^t_2-salicylaldiminato)copper(II) complexes [7a]. It is interesting in the oxidation of bis(*N*-aryl-3,5-Bu^t_2-salicylaldiminato)palladium(II) along with coordinated Pd^{II}–phenoxyl radical species the generation of nitroxide radical species also were detected [7b]. In addition, our unpublished complexes with similar ligands bis(*N*-cyclohexyl-3,5-But_2-salicylaldiminato) cobalt(II) and bis(*N*-3,5-Bu^t_2-phenyl-3,5-But_2-salicylaldiminato)cobalt(II) in the chemical oxidation under above conditions also affords generation of radical species, in which ESR spectra exhibit octets of doublets with $g = 2.0027$, $A^{Co} = 9.25G$, $A^{H} = 3.65G$ and $g = 2.0037$, $A^{Co} = 9.0G$, $A^{H} = 3.75G$, respectively, clearly indicating the presence of a coordinated phenoxyl radical of Co(III). We take this as good evidence that the chemical oxidation of above complexes yields phenoxyl or semiquinone coordinated Co(III) species.

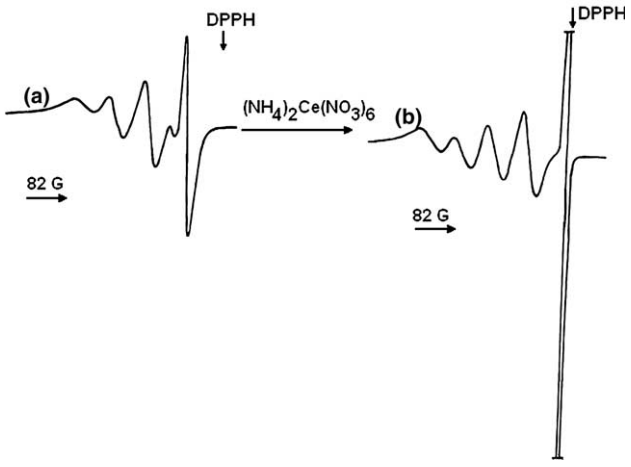


Fig. 3. ESR spectra of **8** (a) in $CHCl_3$ and oxidized **8** (b) generated by twofold excess of ACN.

The spectral changes for **X** + ACN systems was monitored by UV–Vis spectroscopy during the progress of the oxidation of **X** complexes with ACN in $CHCl_3$. When 8–10-fold excess ACN is added to the solution of **X** in $CHCl_3$, the dark brown solution turns to green or light green with the decreasing in the absorbance of a d–d shoulder bands of **X** and the appearance of new absorption maxima at 630–709 nm and a very weak shoulders at 800–830 nm for some of them were observed (Tables 3 and 5). Changes in the values of the absorbances and wavelengths of the d–d bands detected during oxidation processes of **X** are summarized in Table 5. As can be seen from Table 5, after each stirring of the heterogeneous reaction mixtures increase in the wavelength and in the absorbance values of the absorption maxima takes place. The green color and absorbance of the oxidized *n*-alkyl substituted **X** practically did not change during 40–50 min. At the same time, upon oxidation of **X** complexes bearing R = *t*-butyl, *t*-amyl and cyclohexyl groups, the color simultaneously turned to dark green and a red shift in λ_{max} was detected (Table 5). The green color of these systems after about 1 h gradually converted to light yellow with the disappearing of d–d bands in the electronic spectra. It is thought that the appearance of new maximums at about 640–800 nm and their red shifts during oxidation may be related with the changes in the coordination sphere around the Cu(II) in the oxidized **X**. Although a new appeared bands are similar to the d–d bands of Cu^{II} ions [14,17], the similar visible absorptions also have been identified in many M^{II}–phenoxyl radical complexes, which has been attributed to MLCT or LMCT transitions involving the phenoxyl radical [18].

3.6. Cyclic voltammetry

The redox behavior of some **X** complexes has been examined by cyclic voltammetry (CV) under nitrogen in acetonitrile solution in the potential range +1.85 to −2.0 V versus Ag/AgCl reference, and the results are summarized in Table 6. CV of *N*-cyclohexyl-3,5-Bu^t_2-salicylaldimine ligand exhibits a quasi-reversible anodic processes ($E_{1/2} = 0.985$ V) attributable to the phenolate/phenoxyl radical couple. Cathodic scans of this sample in the region of 0.0 to −1.5 V exhibit an irreversible reduction wave at −1.173 V associated with reduction of the imine group [19] and a reversal anodic

Table 5
Changes in λ of the lowest d-d absorption bands and absorbances (A) of **X** + ACN systems in $CHCl_3$ during oxidation processes

Complex	Electronic spectra for (X) + ACN systems λ_{max} (A) (nm)
1 + ACN	639(0.896), 641(0.942), 641(1,02), 642(1.08), 643(1.09), 641(1.128), [a]281, 324, 382, 642(0.9097), 820[b](0.265)
2 + ACN	623(0.985), 631(1.018), 633(1.045), 638(1.066), 640(1.028), 641(0.969) [a]277, 326, 379, 641(0.9697), 800[b](0.383)
3 + ACN	636(0.592), 639(0.586), 639(0.603), 642(0.713), [a]283, 324, 385, 642(0.617), 800[b](0.254)
4 + ACN	668(0.569), 680(0.539), 688(0.519), 690(0.499), 693(0.484), 701(0.363) [a]270[b], 311, 373, 703(0.288)
5 + ACN	635(0.677), 641(0.641), 641(0.625), 642(0.623), 643(0.628), 830[b](0.262), [a]282, 327, 380[b], 420[b], 641(0.624)
6 + ACN	792[b](0.610), 785[b](0.536), 630[b](0.488), 634(0.358), 639(0.361), 654(0.395), 671(0.516), 681(0.532), 693(0.656), 700(0.731), 709(1.007), [a]262, 326, 400, 433[b], 709(1.003)
7 + ACN	657(0.623), 668(0.581), 678(0.528), 683(0.0.479), 690(0.378), 689(0.326),[a]275, 311, 373, 689(0.326)
8 + ACN	680[b](0.557), 650[b](0.479), 635[b](0.461), 654(0.438), 682(0.423), 698(0.367), 701(0.0.468), 705(0.511), 708(0.787), [a]265, 334, 420[b], 707(0.786)
9 + ACN	640(0.665), 646(0.654), 651(0.685), 652(0.739) [a]383, 324, 378, 655(0.252)
10 + ACN	635(0.638), 641(0.555), 645(0.541), 647(0.566), 654(0.424), 659(0.363)[a]284, 313, 330[b], 380[b], 440[b], 659(0.359)

[a] Wavelength of the oxidized **X** recorded at the end of the oxidation processes.
[b] Shoulder.

Table 6
Cyclic voltammetric redox potentials (vs. Ag/AgCl) for some **X** complexes in MeCN

Compound	$[L]^- \rightarrow L^{\cdot} + e E_{pa}$ (E_{pc}) (V)	[a]Secondary processes E_{pa} (E_{pc}) (V)	$Cu^{II/I}$ couple $E_{pa}(E_{pc})$ (V)	$Cu^{I/0}$ couple $E_{pa}(E_{pc})$ (V)
1	1.048(0.857)	1.170(1.048)	−0.213(−0.459)	−0.661(−1.355)
2	1.204(0.994)	1.035(0.947)	−0.224(−0.422)	−0.776(−1.272)
6	1.072(0.825)		−0.226(−0.705)	
8	1.121(0.801)	1.643[a]	−0.219(−0.958)	
10	1.204(0.994)			

Irreversible.
[a] Secondary processes means the process related with oxidation of radical species or other decomposition products.

oxidation at −0.626 V probably originated from of the reduction products. The CV of some X complexes recorded in the potential range of 0.0–1.85 V show one or two quasireversible oxidation waves (Fig. 4(b) and (c)). In generally, the oxidation potentials [$E_{1/2} = 1/2 (E_{pa} + E_{pc})$] of the **X** complexes are less sensitive to the involved change in alkyl groups directly attached to the imine nitrogen (Table 6), suggesting that the anodic oxidation processes are associated with the phenolic moieties of the ligands and can be assigned to a quasi-reversible Cu(II)–phenoxide/Cu(II)–phenoxyl couples. At the same time, the values of the first and second reduction potentials ($E_{1/2}$) of an irreversible Cu^{II}/Cu^{I} and Cu^{I}/Cu^{0} redox couples, scanned at a negative potentials in the range 0.0 to −2.0 V versus Ag/AgCl, are very sensitive to the bulkiness of alkyl groups and shifts towards anodically from CH_3 to Bu^t (Table 6) (Fig. 4), i.e., in order of an increase of the tetrahedral distortion around copper(II). Practically all of studied complexes except **10** exhibit virtually identical anodic stripping wave at $-0.213 \div 0.226$ V. First anodic and first cathodic waves are ill-defined. The reason of these probably originates from unstability of the reduction products i.e. the presence of decomposition or disproportion reactions. The cathodic CV of **1** and **2** displays two reduction peaks with $E_{1/2}$, of −1.008, −0.336 and −1.024, −0.323 V versus Ag/AgCl, respectively (Fig. 4(a)). In the reverse anodic scan one anodic stripping peak at $E_{pa} = -0.213$ V for **1** and $E_{pa} = -0.224$ V for **2** due to Cu(0)/Cu(II) oxidation couple, is observed. Complexes **6** and **8** having bulky *t*-butyl and *t*-amyl groups on the imines nitrogen, exhibit only a single quasi-reversible reduction for Cu(II)/Cu(I) couple with $E_{1/2}$ of −0.465 and −0.596 V, respectively. As can be seen from Table 6, the oxidation potentials $E_{1/2}$ of the complexes are not appreciable affected by the distortion of the coordination geometry of Cu(II) ion. The absence of the reduction peaks of imine groups in the complexes during cathodic scans probably indicates that the reduction potentials of the monoanionic ligands have been shifted beyond the lower limit of the potential interval considered in the experimental measurements [20].

Thus, the present work demonstrates that the sterically bulky *N*-alkyl-3,5-di-*tert*-butylsalicylaldimine ligands unlike Ni^{II}, Zn^{II}, Mn^{II}, VO^{IV} and Co^{II} metal ions are readily complexing with Cu^{II}. The stereochemistry and redox behavior of copper(II) complexes have been characterized using ESR, UV–Vis and electrochemical methods. Their ligand centered oxidation potentials are less sensitive to bulkiness of alkyl groups. Chemical oxidation of some complexes leads to the

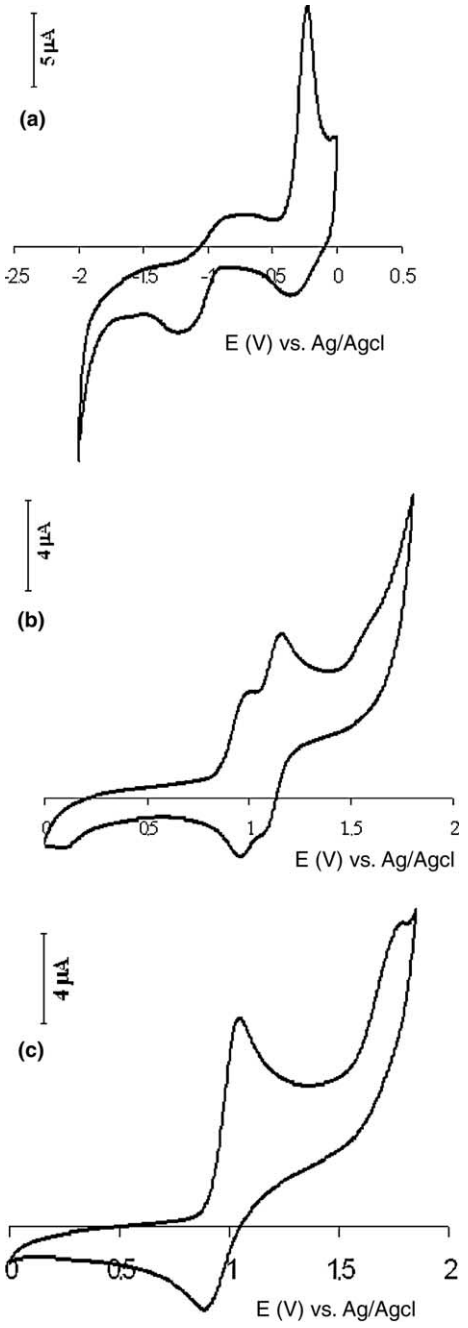


Fig. 4. Cyclic voltammograms of some complexes in acetonitrile (0.05 M Et_4NBF_4) at 25 °C . (a) **1** in the range of 0.0 to −2.0 V; (b) **1** in the range of 0.0–1.85 V; (c) **6** in the range of 0.0–1.5 V. Scan rate, 0.2 V s^{-1}.

formation of the directly coordinated Cu(II)–phenoxyl radical species.

Acknowledgement

Financial support of this research by the Harran University Research Fund (HUBAK, Grant No: 275) is gratefully acknowledged.

References

[1] (a) H. Taube, Electron Transfer Reactions of Complex Ions in Solution, Academic Press, London, 1970;
(b) T.J. Meyer, Progr. Inorg. Chem. 30 (1983) 389;
(c) W. Kaim, J. Chem. Soc., Dalton Trans. (2003) 761.
[2] (a) M.M. Wittaker, Y.-Y. Chuang, J.W. Wittaker, J. Am. Chem. Soc. 115 (1993) 10029;
(b) P.F. Knowles, N. Ito, Perspectives in Bioinorganic Chemistry, Jai Press Ltd, London, 1994, vol. 2, pp. 207–244.
[3] (a) C. Stevens, Z.B. Ogel, J.N. Keen, K.D.S. Yadav, P.F. Knowles, Nature 350 (1991) 87;
(b) N. Ito, S.E. Phllipps, K.D.S. Yadav, P.F. Knowles, J. Mol. Biol. 238 (1994) 794.
[4] (a) J.-L. Pierre, Chem. Soc. Rev. 29 (2000) 251;
(b) B.A. Jazdewski, W.B. Tolmen, Coord. Chem. Rev. 200–202 (2000) 833;
(c) F. Thomas, G. Gellon, I. Gautier-Luneau, E. Saint-Aman, J.-L. Pierre, Angew .Chem., Int. Ed. 41 (2002) 3047.
[5] (a) P. Chaudhuri, M. Hess, U. Flörke, K. Wieghardt, Angew. Chem., Int. Ed. 37 (1998) 2217;
(b) P. Chaudhuri, M. Hess, T. Weyhermüller, K. Wieghardt, Angew. Chem., Int. Ed. 38 (1999) 1095;
(c) P. Chaudhuri, M. Hess, J. Müller, K. Hildebrand, E. Bill, T. Weyhermüller, K. Wieghardt, J. Am. Chem. Soc. 121 (1999) 9599;
(d) C.G. Pierpont, C.W. Lnge, Prog. Inorg. Chem. 41 (1994) 331.
[6] (a) A.A. Medjidov, V.T. Kasumov, H.S. Mamedov, Koord. Khim. 7 (1981) 66;
(b) M.K. Guseyinova, A.A. Medjidov, V.T. Kasumov, J. Struct. Chem. 23 (1982) 114;
(c) V.T. Kasumov, A.A. Medjidov, Russ. J. Coord. Chem. 16 (1990) 1355;
(d) V.T. Kasumov, A.A. Medjidov, R.Z. Rzaev, I.A. Golubeva, Russ. J. Coord. Chem. 19 (1993) 933;
(e) V.T. Kasumov, A.A. Medjidov, R.Z. Rzaev, D.I. Mirzai, R.D. Kasumov, Russ. J. Coord. Chem. 21 (1995) 209;
(f) V.T. Kasumov, A.A. Medjidov, R.D. Kasumov, Russ. J. Coord. Chem. 22 (1996) 938;
(g) V.T. Kasumov, Spectrochim. Acta A 57 (2001) 1649.
[7] (a) V.T. Kasumov, F. Köksal, R. Köseoğlu, J. Coord. Chem. 57 (2004) 591;
(b) V.T. Kasumov, E. Taş, F. Köksal, Şeniz Özalp-Yaman, Polyhedron 24 (2005) 319;
(c) V.T. Kasumov, M. Özdemir, E. Taş, O. Şahin, Trans. Met. Chem. 30 (2005) 191.
[8] J.F. Larrow, E.N. Jacobsen, Y. Gao, Y. Hong, X. Nie, C.M. Zeppe, J. Org. Chem. 59 (1994) 1939.
[9] (a) L. Sacconi, Coord. Chem. Rev. 1 (1966) 126;
(b) R.H. Holm, M.J. O'Conner, Prog. Inorg. Chem. 14 (1971) 241;
(c) S. Yamada, A. Takeuchi, Coord. Chem. Rev. 43 (1982) 187;
(d) G.V. Panova, N.K. Vikulova, V.M. Potapov, Russ. Chem. Rev. 49 (1980) 655;
(e) S. Yamada, Coord. Chem. Rev. 190–192 (1999) 537.
[10] (a) S.J. Gruber, C.M. Harris, E. Sinn, J. Inorg. Nucl. Chem. 30 (1968) 1805;
(b) M. Nakamura, H. Okawa, S. Kida, Inorg. Chim. Acta 62 (1982) 201.
[11] (a) P.W. Alexander, R.J. Sleet, Aust. J. Chem. 23 (1970) 1183;
(b) G.L. Estiu, A.H. Jubert, J. Costamagna, J. Vargas, J. Molec. Struct. (Theochem.) 367 (1996) 97.
[12] A.R. Amundsen, J. Whelan, B. Bosnich, J. Am. Chem. Soc. 99 (1977) 6730.
[13] L. Sacconi, M. Ciampolini, J. Chem. Soc. (1964) 276.
[14] (a) R.H. Dunhill, J.R. Pilbrow, T.D. Smith, J. Chem. Phys 45 (1966) 1474;
(b) N.D. Chasteen, R.L. Belford, Inorg. Chem. 9 (1970) 169;

(c) A. Takeuchi, S. Yamada, H. Yokoi, Bull. Chem. Soc. Jpn. 58 (1985) 2987.
[15] (a) B.J. Hathaway, A.A.G. Tomlinson, Coord. Chem. Rev. 5 (1970) 1;
(b) I.M. Procter, B.J. Hathaway, P. Nicholls, J. Chem. Soc. (A) (1968) 1678;
(c) S. Antosik, N.M.D. Brown, A.A. McConnel, A.L. Porte, J. Chem. Soc. A (1969) 545;
(d) F.J. Boas, R.H. Dunhill, J.R. Pilbrow, R.C. Sirvastava, T.D. Smith, J. Chem. Soc. A (1969) 94.
[16] U. Sakaguchi, A.W. Addison, J. Chem. Soc., Dalton Trans. (1979) 600.
[17] A.H. Maki, B.R. McGarvey, J. Chem. Phys. 29 (1958) 35.
[18] (a) M.L. McGlashen, D.D. Edas, T.G. Spiro, J.W. Wittaker, J. Phys. Chem. 99 (1995) 4918;
(b) J.A. Halfen, B.A. Jazdzewski, S. Mahapatra, L.M. Berreau, E.C. Wilkinson, L. Que, W.B. Tolmen, J. Am. Chem. Soc. 119 (1997) 8217;
(c) O. Seneque, M. Campion, B. Douziech, Y.L. Mest, O. Reinaud, J. Chem. Soc., Dalton Trans. (2003) 4216;
(d) M.A. Halcrow, L.M.L. Chia, X. Liu, E.J.L. McInnes, L.J. Yellowless, F.E. Mabbs, J.E. Davies, J. Chem. Soc., Chem. Commun. (1998) 2465.
[19] (a) J.M.V. Scott, W.H. Jura, Can. J. Chem. 45 (1967) 2375;
(b) C.P. Andrieux, J.M. Saveant, J. Electrochem. Soc. 33 (1971) 1849;
(c) H. Ohmori, A. Matsumoto, M. Masui, H. Sayo, J. Electrochem. Soc. 124 (1977) 1849.
[20] A.A. Isse, A. Gennaro, E. Vianello, Electrochem. Acta 42 (1997) 2065.

been described for the intramolecular addition of carboxylic acid to alkynes to afford enol lactones, by activation of the alkyne [7].

Theoretical studies on these cuboidal heterobimetallic systems suggest a crucial dependence of the reactivity at the heterometal site from the coordination environment around the molybdenum atoms [8]. It is well known that phosphanes occupy a unique role in the design and development of transition metal catalysts. These facts have prompted us to investigate the synthesis, structure, redox properties and reactivity of phosphane substituted $[M_3NiS_4]$ (M = Mo, W) cluster complexes.

2. Experimental

2.1. General remarks

All reactions were carried out under nitrogen atmosphere using standard Schlenk techniques. The solids $\{Mo_3S_7Cl_4\}_n$, $\{Mo_3S_7Br_4\}_n$ and $\{W_3S_7Br_4\}_n$, as well as the homometallic clusters $[Mo_3S_4Cl_3(dmpe)_3]PF_6$, $[Mo_3S_4Br_3(dmpe)_3]PF_6$, $[W_3S_4Br_3(dmpe)_3]PF_6$ and $[Mo_3S_4Cl_3(dppe)_3]PF_6$ (dmpe = 1,2-bis(dimethylphosphanyl)ethane) were obtained according to literature methods [9]. $[Ni(cod)_2]$ (cod = 1,5-cyclooctadiene) was purchased from Strem Chemicals. Solvents for synthesis and electrochemical measurements were dried and degassed by standard methods before use. Chromatographic work was performed on silica gel 60 Å.

Elemental analyses were performed on an EA 1108 CHNS microanalyzer at the Universidad de La Laguna. $^{31}P\{^1H\}$ NMR spectra were recorded with a reference of 85% H_3PO_4 on a Varian 300 MHz. IR spectra were recorded on a Perkin–Elmer System 2000 FT-IR using KBr pellets. Electronic absorption spectra were obtained on a Perkin–Elmer Lambda-19 spectrophotometer. Electrospray mass spectra (ESI-MS) were recorded with a Micromass Quattro LC instrument. Nitrogen was employed as a drying and nebulizing gas. Cone voltage was typically varied from 20 to 100 V in order to investigate the effect of higher voltages on the fragmentation pathways of the parent ions. Isotope experimental patterns were compared with theoretical patterns obtained using the MassLynx 3.5 program. Cyclic voltammetry experiments were performed with an Echochemie Pgstat 20 electrochemical analyzer. All measurements were carried out at room temperature with a conventional three-electrode configuration consisting of platinum working and auxiliary electrodes and an Ag/AgCl reference electrode containing aqueous 3 M KCl. Dichloromethane was used in all experiments and dried and degassed by standard methods. The supporting electrolyte was 0.1 M tetrabutylammonium hexafluorophosphate. $E_{1/2}$ values were determined as 1/2 ($E_a + E_c$), where E_a and E_c are the anodic and cathodic peak potentials, respectively. All potentials reported are not corrected for the junction potential.

2.2. Syntheses

2.2.1. $[Mo_3NiS_4Cl_3(dmpe)_3(CH_3CN)]PF_6$ ([1]PF_6)

To a green solution of $[Mo_3S_4Cl_3(dmpe)_3]PF_6$ (0.4 g, 0.36 mmol) in CH_3CN (40 mL) was added an excess of $[Ni(cod)_2]$ (0.153 g, 0.56 mmol) under nitrogen without any apparent colour change. After stirring for 48 h, the resulting solution was taken to dryness and the solid was redissolved in CH_2Cl_2 and adsorbed in a silica gel column. After washing the column with CH_2Cl_2, elution with acetone/CH_2Cl_2 (1/3) afforded a very concentrated green solution. Finally, the resulting solution was taken to dryness to give an air stable green solid characterized as $[Mo_3NiS_4Cl_3(dmpe)_3(CH_3CN)]PF_6$ [**1**]PF_6 (0.346 g, 79%). *Anal.* Calc. for $C_{20}H_{51}Cl_3F_6Mo_3NNiP_7S_4$: requires C, 19.73; H, 4.22; N, 1.15; S, 10.53. Found: C, 19.79; H, 4.17; N, 0.76; S, 11.03%; λ_{max}/nm (CH_2Cl_2) 650, 463, 330 (sh), 260 (sh) and 237; δ_P(CH_2Cl_2): −145.00 (1P, sept, ^1J(P–F) 704.0 Hz), 17.74 (3P, dd) and 25.26 (3P, dd); *m*/*z* (CH_2Cl_2): 1074 (M^+), 1033 ($M^+ - CH_3CN$) and 882 ($M^+ - CH_3CN$ − dmpe).

2.2.2. $[Mo_3NiS_4Br_3(dmpe)_3(CH_3CN)]PF_6$ ([2]PF_6)

This compound was prepared following the general procedure described for [**1**]PF_6, except that $[Mo_3S_4Br_3(dmpe)_3]PF_6$ (0.300 g, 0.24 mmol) was used instead of $[Mo_3S_4Cl_3(dmpe)_3]PF_6$. This compound was reacted with an excess of $[Ni(cod)_2]$ (0.101 g, 0.37 mmol). The air stable green product obtained was characterized as $[Mo_3NiS_4Br_3(dmpe)_3(CH_3CN)]PF_6$ [**2**]PF_6 (0.120 g, 31%). *Anal.* Calc. for $C_{20}H_{51}Br_3F_6Mo_3NNiP_7S_4$: requires C, 17.78; H, 3.81; N, 1.04; S, 9.49. Found: C, 17.89; H, 3.72; N, 0.75; S, 9.06%; λ_{max}/nm (CH_2Cl_2): 656, 470 (sh), 270 (sh) and 240; δ_P (CH_2Cl_2): −145.00 (1P, sept, ^1J(P–F) 704.0 Hz), 10.95 (3P, dd) and 22.90 (3P, dd); *m*/*z* (CH_2Cl_2): 1207 (M^+), 1166 ($M^+ - CH_3CN$) and 1016 ($M^+ - CH_3CN$ − dmpe).

2.2.3. $[Mo_3NiS_4Cl_3(dppe)_3(CH_3CN)]PF_6$ ([3]PF_6)

This compound was prepared following the general procedure described for [**1**]PF_6 except that $[Mo_3S_4Cl_3(dppe)_3]PF_6$ (0.500 g, 0.27 mmol) was used instead of $[Mo_3S_4Cl_3(dmpe)_3]PF_6$. This compound was reacted with an excess of $[Ni(cod)_2]$ (0.110 g, 0.40 mmol) during 4 h. The air stable green product obtained was characterized as $[Mo_3NiS_4Cl_3(dppe)_3(CH_3CN)]PF_6$ [**3**]PF_6 (0.078 g, 15%). *Anal.* Calc. for $C_{80}H_{75}Cl_3F_6Mo_3NNiP_7S_4$ requires C, 48.96; H, 3.85; N, 0.71; S, 6.54. Found: C, 49.09; H, 4.10; N, 1.20; S, 6.07%; λ_{max}/nm (CH_2Cl_2): 646, 500 (sh) and 240; δ_P (CH_2Cl_2): −145.00 (1P, sept, ^1J(P–F) 704.0 Hz), 26.59 (3P, t, ^3J(P–P_{trans}) 9.1 Hz) and 33.74 (3P, t, ^3J(P–P_{trans}) 10.0 Hz); *m*/*z* (CH_2Cl_2): 1818 (M^+), 1777 ($M^+ - CH_3CN$) and 1379 ($M^+ - CH_3CN$ − dppe).

*2.2.4. [$Mo_3NiS_4Cl_3(dmpe)_3(NC_5H_5)$]$PF_6$ ([**4**]PF_6)*

Compound [**1**]PF_6 (0.075 g, 0.06 mmol) was dissolved in 30 mL of CH_2Cl_2. Excess of pyridine (2 mL, 24.50 mmol) was added with fast stirring for 24 h. The resulting solution was adsorbed in a silica gel column and excess of pyridine was eluted with CH_2Cl_2. Elution with acetone/CH_2Cl_2 (1/3) afforded a very concentrated green solution of the product which was taken to dryness to give an air stable deep green solid characterized as [$Mo_3NiS_4Cl_3(dmpe)_3(NC_5H_5)$]$PF_6$ [**4**]PF_6 (0.070 g, 91%). *Anal.* Calc. for $C_{23}H_{53}Cl_3F_6Mo_3NNiP_7S_4$ requires C, 22.00; H, 4.25; N, 1.12; S, 10.21. Found: C, 22.01; H, 4.10; N, 1.54; S, 9.77. λ_{max}/nm (CH_2Cl_2): 680, 480, 341, 305, 270 (sh) and 239; δ_P (CH_2Cl_2): −145.00 (1P, sept, ^1J(P–F) 704.0 Hz), 18.98 (3P, dd) and 24.80 (3P, dd); *m*/*z* (CH_2Cl_2): 1112 (M^+), 1033 ($M^+ - NC_5H_5$) and 882 ($M^+ - NC_5H_5$ − dmpe).

*2.2.5. [$Mo_3NiS_4Cl_3(dmpe)_3(SC_4H_8)$]$PF_6$ ([**5**]PF_6)*

This compound was synthesized following the same procedure as used for compound [**4**]PF_6, taking 0.075 g (0.06 mmol) of cluster [**1**]PF_6 and using an excess of tetrahydrothiophene (15 mL, 168.40 mmol) instead of pyridine. The air stable deep green product obtained was identified as compound [$Mo_3NiS_4Cl_3(dmpe)_3(SC_4H_8)$]$PF_6$ [**5**]PF_6. (0.065 g, 83%). *Anal.* Calc. for $C_{22}H_{56}Cl_3F_6Mo_3NiP_7S_5$ requires C, 20.89; H, 4.46; S, 12.68. Found: C, 20.98; H, 4.18; S, 12.20%; λ_{max}/nm (CH_2Cl_2): 650, 524, 470, 330 (sh), 290 (sh) and 241; δ_P (CH_2Cl_2): −145.00 (1P, sept, ^1J(P–F) 704.0 Hz), 18.34 (3P, dd) and 24.44 (3P, dd); *m*/*z* (CH_2Cl_2): 1121 (M^+), 1033 ($M^+ - SC_4H_8$) and 882 ($M^+ - SC_4H_8$ − dmpe).

*2.2.6. [$Mo_3NiS_4Cl_3(dmpe)_3(CO)$]$PF_6$ ([**6**]PF_6)*

Compound [**1**]PF_6 (0.075 g, 0.06 mmol) was dissolved in 10 mL of CH_2Cl_2 adding 1 mL of MeOH. CO was bubbled through the solution for 60 min. The solution was kept in a CO atmosphere for one day. The resulting brown solution was taken to dryness giving a compound characterized as [$Mo_3NiS_4Cl_3(dmpe)_3(CO)$]$PF_6$ [**6**]PF_6 (0.074 g, 100%). *Anal.* Calc. for $C_{19}H_{48}Cl_3F_6Mo_3NiOP_7S_4$ requires C, 18.95; H, 4.02; S, 10.65. Found: C, 19.40; H, 4.11; S, 10.14%; ν_{CO}/cm^{-1} (KBr): 2038; λ_{max}/nm (CH_2Cl_2): 520 (sh), 390 (sh), 312, 260 (sh) and 236; δ_P (CH_2Cl_2): −145.00 (1P, sept, ^1J(P–F) 704.0 Hz), 17.74 (3P, dd) and 23.72 (3P, dd); *m*/*z* (CH_2Cl_2): 1061 (M^+), 1033 ($M^+ - CO$) and 882 ($M^+ - CO$ − dmpe).

*2.2.7. [$W_3NiS_4Br_3(dmpe)_3(CH_3CN)$]$PF_6$ ([**7**]PF_6)*

This compound was prepared following the general procedure described for [**1**]PF_6 except that [$W_3S_4Br_3(dmpe)_3$]PF_6 (0.350 g, 0.23 mmol) was used instead of [$Mo_3S_4Cl_3(dmpe)_3$]PF_6. The complex was reacted with an excess of [Ni(cod)$_2$] (0.103 g, 0.37 mmol). The air stable green product obtained was characterized as [$W_3NiS_4Br_3(dmpe)_3(CH_3CN)$]$PF_6$ [**7**]PF_6 (0.227 g, 61%). *Anal.* Calc. for $C_{20}H_{51}Br_3F_6NNiP_7S_4W_3$ requires C, 14.88; H, 3.18; N, 0.87; S, 7.94. Found: C, 14.90; H, 3.03; N, 0.81; S, 7.51%; λ_{max}/nm (CH_2Cl_2): 604, 410 (sh), 310 (sh), 275, 245 and 236; δ_P (CH_2Cl_2): −145.00 (1 P, sept, ^1J(P–F) 704.0 Hz), −10.55 (3P, s, ^1J(P–W) 191.8 Hz) and −8.55 (3P, s, ^1J(P–W) 170.5 Hz); *m*/*z* (CH_2Cl_2): 1471 (M^+), 1430 ($M^+ - CH_3CN$), 1280 ($M^+ - CH_3CN$ − dmpe).

*2.2.8. [$W_3NiS_4Br_3(dmpe)_3(NC_5H_5)$]$PF_6$ ([**8**]PF_6)*

Compound [**7**]PF_6 (0.075 g, 0.05 mmol) was dissolved in 30 mL of CH_2Cl_2. Excess of pyridine (8 mL, 98.10 mmol) was added with fast stirring for 24 h. The resulting solution was adsorbed in a silica gel column and excess of pyridine was eluted with CH_2Cl_2. Elution with acetone/CH_2Cl_2 (1/3) afforded a very concentrated green solution of the product which was taken to dryness to give an air stable deep green solid characterized as [$W_3NiS_4Br_3(dmpe)_3(NC_5H_5)$]$PF_6$ [**8**]PF_6 (0.068 g, 88%). *Anal.* Calc. for $C_{23}H_{53}Br_3F_6NNiP_7S_4W_3$ requires C, 16.71; H, 3.23; N, 0.85; S, 7.76. Found: C, 16.93; H, 3.16; N, 0.79; S, 7.40%; λ_{max}/nm (CH_2Cl_2): 631, 480 (sh), 370 (sh), 284, 253 and 231; δ_P (CH_2Cl_2): −145.00 (1P, sept, ^1J(P–F) 704.0 Hz), −9.06 (3P, s, ^1J(P–W) 190.1 Hz) and −8.51 (3P, s, ^1J(P–W) 190.1 Hz); *m*/*z* (CH_2Cl_2): 1509 (M^+), 1430 ($M^+ - NC_5H_5$) and 1280 ($M^+ - NC_5H_5$ − dmpe).

*2.2.9. [$W_3NiS_4Br_3(dmpe)_3(SC_4H_8)$]$PF_6$ ([**9**]PF_6)*

This compound was synthetized following the same procedure as used for compound [**8**]PF_6, taking 0.100 g (0.06 mmol) of cluster [**7**]PF_6 and using an excess of tetrahydrothiophene (15 mL, 168.40 mmol) instead of pyridine. The air stable deep green product obtained was identified as compound [$W_3NiS_4Br_3(dmpe)_3(SC_4H_8)$]$PF_6$ [**9**]PF_6 (0.080 g, 78%). *Anal.* Calc. for $C_{22}H_{56}Br_3F_6NiP_7S_5W_3$ requires C, 15.90; H, 3.40; S, 9.65. Found: C, 15.94; H, 3.31; S, 9.17%; λ_{max}/nm (CH_2Cl_2): 592, 473, 405 (sh), 305 (sh), 285, 253 and 235; δ_P (CH_2Cl_2): −145.00 (1 P, sept, ^1J(P–F) 704.0 Hz), −10.01 (3 P, s, ^1J(P–W) 195.0 Hz) and −8.69 (3 P, s, ^1J(P–W) 160.4 Hz); *m*/*z* (CH_2Cl_2): 1518 (M^+), 1430 ($M^+ - SC_4H_8$) and 1280 ($M^+ - SC_4H_8$ − dmpe).

*2.2.10. [$W_3NiS_4Br_3(dmpe)_3(CO)$]PF_6 ([**10**]PF_6)*

Compound [**7**]PF_6 (0.075 g, 0.05 mmol) was dissolved in 10 mL of CH_2Cl_2 adding 1 mL of MeOH. CO is bubbled through the solution for 30 min. The colour changes from green to brown within 5 min. The solution was kept in a CO atmosphere for one day and was taken to dryness giving a compound characterized as [$W_3NiS_4Br_3(dmpe)_3(CO)$]PF_6 [**10**]PF_6 (0.074 g, 100%). *Anal.* Calc. for

$C_{19}H_{48}Br_3F_6NiOP_7S_4W_3$ requires C, 14.25; H, 3.02; S, 8.01. Found: C, 14.27; H, 2.95; S, 7.75%; ν_{CO}/cm^{-1} (KBr): 2017; λ_{max}/nm (CH_2Cl_2): 570 (sh), 442, 309 and 234; δ_P (CH_2Cl_2): −145.00 (1P, sept, ^1J(P–F) 704.0 Hz), −10.67 (3P, s, ^1J(P–W) 200.0 Hz) and −9.21 (3P, s, ^1J(P–W) 142.9 Hz); *m/z* (CH_2Cl_2): 1458 (M^+), 1430 ($M^+ - CO$) and 1280 ($M^+ - CO - dmpe$).

2.2.11. X-ray crystallography

Suitable crystals for X-ray diffraction characterization of the tetraphenylborate salt of $[\mathbf{1}]^+$ were grown by slow diffusion of MeOH into a CH_2Cl_2 solution. Replacement of the PF_6^- anion in [**1**]PF_6 was done by addition of an excess of $NaBPh_4$ to a methanol solution of [**1**]PF_6 that precipitates the desired tetraphenylborate salt of the tetranuclear cation $[\mathbf{1}]^+$. Suitable crystals of compound [**10**]PF_6 were grown by slow evaporation of a CH_2Cl_2 solution. The air stable crystals were mounted on a glass fibre with the use of epoxy cement. X-ray diffraction experiments were carried out on a Bruker SMART CCD diffractometer using Mo Kα radiation (λ = 0.71073 Å). The data were collected with a frame width of 0.3° in Ω and a counting time of 20 s for [**1**]BPh_4 and 15 s for [**10**]PF_6 per frame at a crystal to detector distance of 4 cm. The software SAINT [10] was used for integration of intensity reflections and scaling and SADABS [11] for absorption correction. Final cell parameters were obtained by global refinement of reflections obtained from integration of all the frame data. The crystal parameters and basic information relating data collection and structure refinement for compounds [**1**]BPh_4 and [**10**]PF_6 are summarized in Table 1. The structures were solved by direct methods and refined by full-matrix methods based on F^2 using the SHELXTL software package [12].

The compounds [**1**]BPh_4 and [**10**]PF_6 crystallized in centro-symmetric space groups *P*2(1)/*c* and P2(1)/*n*, respectively. Their structures are formed by racemic mixtures of the chiral cluster cations $[\mathbf{1}]^+$ and $[\mathbf{10}]^+$. In both cases the non-hydrogen atoms of the cationic clusters were refined anisotropically; the positions of all hydrogen atoms were generated geometrically, assigned isotropic thermal parameters and allowed to ride on their respective parent carbon atoms. The PF_6^- anion in the structure of [**10**]PF_6 was refined as a rigid group with the phosphorus as pivot atom. The fluorine atoms rotate about the phosphorus atom and the same translational shifts are applied to all atoms. Anisotropic thermal parameters were assigned to phosphorus and isotropic to fluorine atoms.

2.2.12. Catalytic test

A typical experimental procedure for the hydrodesulfurization reaction of 1-octanethiol is described. The cluster compound (20 mg) was dissolved in 15 mL of methanol for [**1**]PF_6 or acetone for [**2**]PF_6, [**3**]PF_6 and [**7**]PF_6, and 10 mg of 1-octanethiol was added. The reactions were carried out in an autoclave at 160–180 °C under a hydrogen pressure of 25 bar at 20 °C (≈42 bar at reaction temperature) for 16 h. The resulting products were identified by GC-MS (Agilent Technologies 5973 Mass Selective Detector) and analysed with a chromatograph (Agilent Technologies 6890 Plus) equipped with a HP Ultra-1 capillary column (25 m × 200 μm × 0.33 μm film thickness).

Table 1
Crystallographic data for $[Mo_3NiS_4Cl_3(dmpe)_3(CH_3CN)]BPh_4$ ([**1**]BPh_4) and for $[W_3NiS_4Br_3(dmpe)_3(CO)]PF_6$ ([**10**]PF_6)

Compound	[**1**]BPh_4	[**10**]PF_6
Empirical formula	$C_{44}H_{68}BCl_3Mo_3NNiP_6S_4$	$C_{19}H_{48}Br_3F_6NiOP_7S_4W_3$
Formula weight	1388.74	1601.59
Crystal system	monoclinic	monoclinic
a (Å)	19.724(6)	12.687(3)
b (Å)	11.371(3)	16.335(4)
c (Å)	26.399(8)	21.086(5)
β (°)	95.399(8)	90.617(6)
V (Å^3)	5894(3)	4369.6(17)
T (K)	293(2)	298(2)
Space group	*P*2(1)/*c*	*P*2(1)/*n*
Z	4	4
μ (Mo Kα) (mm^{-1})	1.409	11.530
θ range (°)	1.04–26.37	1.58–24.71
Reflections collected	36600	23925
Unique reflections (R_{int})	12045/0.0749	7445/0.0770
R_1[a]/wR_2[b] ($I > 2\sigma$)	0.0438/0.0887	0.0557/0.1417
R_1[a]/wR_2[b] (all data)	0.0917/0.1101	0.0948/0.1581
Maximum shift/esd	0.006	0.005
Residual *ρ* (e Å^{-3})	0.723/−0.733	4.374/−1.972

[a] $R_1 = \sum||F_o| - |F_c||/\sum F_o$.
[b] $wR_2 = [\sum[w(F_o^2 - F_c^2)^2]/\sum[w(F_o^2)^2]]^{1/2}$.

3. Results and discussion

3.1. Synthesis

Clusters with $[M_3NiS_4]^{4+}$ cores (M = Mo, W) have been prepared with various ligands on the group 6 metal (aqua, nta, dppe, Cp derivatives) and on the nickel atom (CO, PPh_3, organic sulfides, phenylsulfinate) [13–15]. Most synthesis strategies started from the aqua clusters $[M_3S_4(H_2O)_9]^{4+}$, which are reacted with Ni metal in acidic media or with divalent nickel salts under reducing conditions to give rise to the heterobimetallic $[Mo_3NiS_4]$ core. Ligand substitutions on the group 6 metal or the nickel atom afford various cluster complexes. Another strategy begins with substitution of the aqua ligands of the trinuclear $[Mo_3S_4(H_2O)_9]^{4+}$ cluster by Cp or Cp′ (Cp′ = Me-Cp) that in a second step incorporates the nickel atom from a Ni^0 complex in an organic solution.

We have shown that $[M_3S_4X_3(diphos)_3]^+$ cluster cations, which are synthesized by scission of polymeric $\{M_3S_7X_4\}_n$ solids with dmpe or dppe, are versatile building blocks for the synthesis of heterobimetallic thiocubane clusters by incorporation of copper or cobalt atoms in organic media [16,17]. The reaction of $[M_3S_4X_3(diphos)_3]^+$ with an excess of $[Ni(cod)_2]$ in acetonitrile affords the $[M_3NiS_4X_3(diphos)_3(CH_3CN)]^+$ clusters as their PF_6^- salts in yields that range from 15% to 79% for molybdenum complexes and 61% yield for $[W_3NiS_4Br_3(dmpe)_3(CH_3CN)]PF_6$, as shown in Scheme 1 [18].

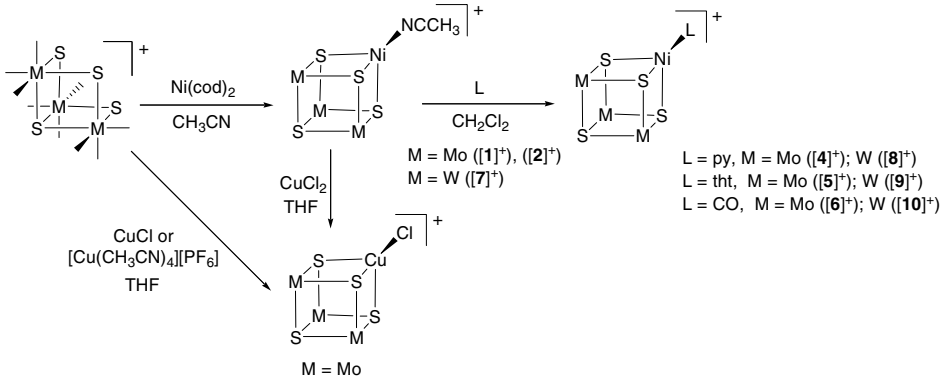
The compounds [**1**]PF_6 and [**7**]PF_6 exchange almost quantitatively the acetonitrile ligand on the nickel atoms by addition of pyridine, tetrahydrothiophene or carbon monoxide in CH_2Cl_2 solutions at room temperature. This substitution did not take place with less nucleophilic ligands such as water, methanol, benzenethiol, furane or pyrrol. Fragmentation of the tetranuclear cluster is observed when [**1**]PF_6 is treated with an excess of triphenylphosphine or dmpe. Reaction of $[Mo_3NiS_4Cl_3(dmpe)_3(CH_3CN)]PF_6$ with divalent $CuCl_2$ in THF affords $[Mo_3CuS_4Cl_3(dmpe)_3Cl]PF_6$ by replacement of a $Ni(CH_3CN)$ cluster fragment by CuCl [18]. This transmetallation reaction does not take place with Cu(I) salts such as CuCl or $[Cu(CH_3CN)_4]PF_6$. The compound $[Mo_3CuS_4Cl_3(dmpe)_3Cl]PF_6$ has been also prepared by reaction of the trimetallic cluster $[Mo_3S_4Cl_3(dmpe)_3]PF_6$ with Cu^I salts, but no reaction has been observed between the triangular cluster and divalent copper salts [16]. These facts are in agreement with the following reaction scheme proposed by Sykes et al. for transmetallation of the aqua cluster $[Mo_3FeS_4(H_2O)_{10}]^{4+}$ (see Scheme 2) [19].

$$[Mo_3FeS_4(H_2O)_{10}]^{4+} + 2\,Cu^{2+} \longrightarrow [Mo_3S_4(H_2O)_9]^{4+} + Fe^{2+} + 2\,Cu^{+}$$

$$[Mo_3S_4(H_2O)_9]^{4+} + Cu^{+} \longrightarrow [Mo_3CuS_4(H_2O)_{10}]^{5+}$$

Scheme 2.

The $^{31}P\{^1H\}$ NMR spectra of $[M_3S_4NiX_3(diphos)_3L]PF_6$ (M = Mo, W; X = Cl, Br; diphos = dmpe, dppe; L = NC_5H_5, SC_4H_8, CO) ([**1**]PF_6–[**10**]PF_6) show two signals corresponding to the three phosphorus atoms above and below the trimetallic plane. In the molybdenum dmpe series, the phosphorus signals are displayed at 11–19 and 23–25 ppm with a doublet of doublets pattern characteristic of an AA′A″BB′B″ second order system. For the dppe derivatives, the signals are triplets and are displayed at lower fields (27 and 34 ppm) than the dmpe derivatives. The singlet signals in the tungsten derivatives are displayed at ca. −9 and −10 ppm, with the characteristic satellites of ^{31}P–^{183}W coupling (^{183}W has 14.4% natural abundance). Incorporation of a nickel atom causes a high field shift of the signals of ca. 8 ppm, but the lineshape of the spectra remains unaltered. This fact has been described previously for the copper cluster cations $[M_3S_4CuX_3(diphos)_3X]^+$ [16]. The averaged 25 ppm high field shift for the resonances of the tungsten clusters in comparison with the analogous molybdenum clusters indicate an increase of



Scheme 1.

electron density at the phosphorus atom caused by a higher electron density of tungsten atoms.

The UV/Vis spectra of reported compounds show a blue-shift of all bands going from Mo ([**1**]PF_6, [**4**]PF_6, [**5**]PF_6) to W ([**7**]PF_6–[**9**]PF_6) of 45–60 nm for the band of lowest energy. A similar hypsochromic shift to Mo/W containing cluster was previously reported for heterobimetallic cluster anions $[\{(OC)_3Re\}_3S_4M(S)]^-$ (M = Mo, W) and was ascribed to the stronger electron accepting ability of the molybdenum compared to tungsten [20]. The substitution of acetonitrile for pyridine or tetrahydrothiophene does not cause any colour change, but upon coordination of CO to clusters [**1**]PF_6 and [**7**]PF_6, a colour change is observed from green to brown. The same effect has been described for the aqua cluster $[M_3NiS_4(H_2O)_9]^{4+}$, (M = Mo, W) [21], and a bathochromic shift of 50 nm of the band at lowest energy is observed going from [**6**]PF_6 to [**10**]PF_6.

The IR carbonyl stretching frequencies in the reported $[M_3NiS_4]$ aqua clusters (2060 cm^{-1} for $[Mo_3NiS_4(H_2O)_9(CO)]^{4+}$ [22] and 2045 cm^{-1} for $[W_3NiS_4(H_2O)_9(CO)]^{4+}$ [21]) have been interpreted based on the Ni^{2+} metal oxidation state which implies an oxidation of the heterometal upon incorporation on the trinuclear molybdenum or tungsten cluster. However, these high frequency values are explained based on Fenske–Hall MO calculations through a competition between the M–Ni^0 bond formation and and the π-backbonding to the CO ligand [8]. The IR spectra of [**6**]PF_6 and [**10**]PF_6 show carbonyl bands at 2038 and 2017 cm^{-1}, respectively, which ranges between those of the aqua and Cp compounds (2020 cm^{-1} for $[Mo_3NiS_4Cp_3(CO)]^+$ and 2032 cm^{-1} for $[Mo_3NiS_4Cp_3'(CO)]^+$). This fact is explained by the electron donating ability of the diphosphine ligand, which is better than that of the aqua ligand, but worse than that of the Cp ligands [23,24,22].

3.2. Structure

The crystal structure analyses of [**1**]BPh_4 and [**10**]PF_6 confirm the presence of cubane-like $[M_3NiS_4]^{4+}$ cluster cores whose innermost part is formed by a tetrahedral arrangement of three molybdenum or tungsten atoms and one nickel atom. Each tetrahedral face is capped by a μ_3-coordinated sulfido ligand, thus generating the cubane-like structure (Fig. 1).

The group 6 metals have an octahedral configuration (if metal–metal bonds are neglected), formed by three sulphur atoms, two phosphorus atoms from the dmpe ligand and one halogen atom. The M–M average bond distances are 2.795 Å for $[\mathbf{1}]^+$ and 2.784 Å for $[\mathbf{10}]^+$. The M–Ni bond distances of 2.672 and 2.735 Å for $[\mathbf{1}]^+$ and $[\mathbf{10}]^+$, respectively, are consistent with the presence of metal–metal single bonds. Selected bond lengths of the cubane complexes and of their trinuclear precursors are listed in Table 2 and selected bonds lengths of previously reported $[M_3NiS_4]$ clusters are listed in Table 3 for comparison.

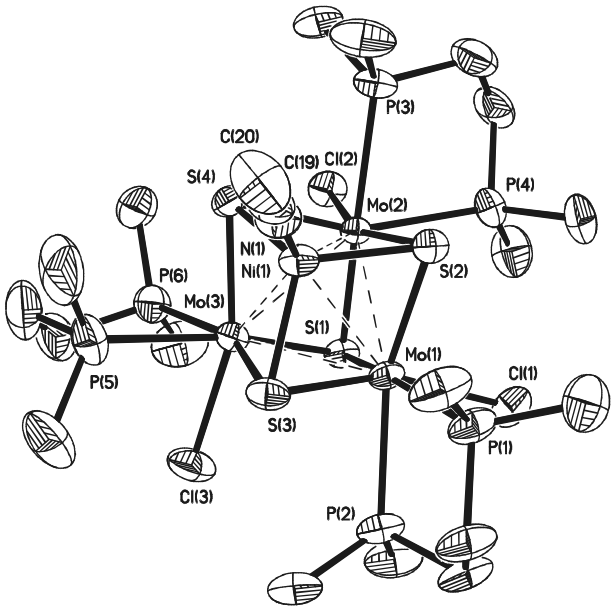


Fig. 1. ORTEP diagram of the cation $[\mathbf{1}]^+$ with 50% thermal ellipsoids and atom numbering scheme. Hydrogen atoms have been removed for clarity.

The molybdenum–molybdenum and tungsten–tungsten bond lengths are very similar to the corresponding distances in $[M_3NiS_4Cp_3']^+$ (M = Mo, W) clusters and slightly longer than the distances in $[M_3NiS_4]^{4+}$ aqua complexes. The molybdenum–nickel bond lengths follow a different tendency which is similar to that reported for aqua complexes and slightly shorter than those reported for $[Mo_3NiS_4Cp_3']^+$ clusters. These differences can be explained based on the electron-accepting properties of the ligands. The fact that diphosphine ligands are better electron-accepting ligands than aqua ligands can cause a weakening of the metal–metal bond. On the other hand, acetonitrile is a poorer electron-accepting ligand than 4,4′-bipy or PPh_3 and, consequently, it decreases the Mo–Ni distance. Owing to the differences in the bond distances between M–M and M–Ni, the cubane-like cluster framework is distorted with respect to the Ni vertex of the cluster cube. This fact is apparent by the size of the S–M–S angles, which lie in a range of 99.5–106.9° for $[\mathbf{1}]^+$ and $[\mathbf{10}]^+$, and of the S–Ni–S angles, which are around 109.5° for $[\mathbf{1}]^+$ and 107° for $[\mathbf{10}]^+$. This difference in the S–Ni–S angles reflects the smaller difference between metal bond distances in $[\mathbf{10}]^+$ as compared to $[\mathbf{1}]^+$. The stability of the M_3NiS_4 cluster core is evidenced by mass spectroscopy. The base peak in the mass spectra of [**1**]PF_6–[**10**]PF_6 are the molecular cations, followed by the loss of the ligand on the nickel atom. In the analogous copper clusters, the M–Cu bond is larger

Table 2
Selected average bond distances (Å) for compounds and trinuclear precursors

Compound/Dist (Å)	M–M	M–Ni	M–S(1)	M–S(#)[a]	M–S(#)[b]	Ni–S(2)	M–X	M–P(1)	M–P(2)
$[Mo_3S_4Cl_3(dmpe)_3]^+$	2.7666(4)		2.360(9)	2.290(7)	2.336(7)		2.473(7)	2.534(8)	2.605(8)
$[Mo_3NiS_4Cl_3(dmpe)_3(CH_3CN)]^+$ ([**1**]PF_6)	2.795[17]	2.672[5]	2.365[5]	2.343[16]	2.368[3]	2.206[6]	2.506[6]	2.541[10]	2.585[13]
$[W_3S_4Br_3(dmpe)_3]^+$	2.763[6]		2.379[25]	2.271[41]	2.311[32]		2.640[22]	2.509[37]	2.607[23]
$[W_3NiS_4Br_3(dmpe)_3(CO)]^+$ ([**10**]PF_6)	2.784[3]	2.735[5]	2.385[6]	2.332[8]	2.367[2]	2.228[9]	2.637[15]	2.526[3]	2.595[8]

[a] Mo–S(#), (S(#) sulphurs atoms labelled as 2, 3 and 4) *trans* distance to Mo–X bond.
[b] Mo–S(#), (S(#) sulphurs atoms labelled as 2, 3 and 4) *trans* distance to Mo–P(2) bond.

Table 3
Comparison of intermetallic bond distances lengths for $[M_3NiS_4]$ cubane clusters

Compound	M–M	M–M′	M′–L	References
$[Mo_3NiS_4(H_2O)_{10}]^{4+}$	2.755[10]	2.640[9]	1.964(11)	[28]
$[Mo_3NiS_4(H_2O)_9(CO)]^{4+}$	2.744[8]	2.677[7]		[20]
$[\{Mo_3NiS_4Cp_3'\}_2(\mu\text{-}C_4H_8S_2)]^{2+}$	2.819[13]	2.71[1]	2.210[2]	[3]
$[\{Mo_3NiS_4Cp_3'\}_2(\mu\text{-}(4,4'\text{-bipy})]^{2+}$	2.83[1]	2.711[4]	1.937[4]	[3]
$[Mo_3NiS_4Cl_3(dmpe)_3(CH_3CN)]^+$ ([**1**]PF_6)	2.795[17]	2.672[5]	1.913[5]	this work
$[Mo_3PtS_4Cl_4(dppe)_3]$	2.817[5]	2.755[12]	2.388[8]	[26]
$[Mo_3NiS_4(Hnta)(nta)_2Cl]^{5-}$	2.775[3]	2.668[6]	2.240[2]	[28]
$[Mo_3NiS_4Cp_3'(PPh_3)]^+$	2.831[2]	2.718[8]	2.160[2]	[29]
$[W_3NiS_4Br_3(dmpe)_3(CO)]^+$ ([**10**]PF_6)	2.784[3]	2.735[5]	1.75[2]	this work
$[W_3NiS_4Cp_3'(PPh_3)]^+$	2.809[1]	2.733[9]	2.143[3]	[30]
$[W_3NiS_4(H_2O)_9(C_2H_4)]^{4+}$	2.7137[9]	2.701[2]		[22]
$[\{W_3NiS_4(H_2O)_9\}_2]^{8+}$	2.747[7]	2.66[4]		[22]

than the M–M bond and in MS spectra, fragments without the Cu atom have been detected [16].

Among the bond distances between the molybdenum or tungsten atoms and the μ_3-S ligands capping the M_2Ni faces, those at the *trans* position to the M–P bond are by 0.02–0.03 Å longer than the other M–S distances. This may be attributed to the *trans* influence of the phosphane ligand being stronger than the one of the halogen ligands.

The nickel atom is, in all cases, tetrahedrally bonded to three μ_3-sulfur atoms and one ligand (acetonitrile or CO in $[\mathbf{1}]^+$ and $[\mathbf{10}]^+$, respectively). In the structure of [**10**]PF_6, a very regular tetrahedron around Ni is observed. In the structure of [**1**]PF_6, a distortion of the Ni environment is observed due to a bending of the CH_3CN away from the threefold axis through the cluster core, the S–Ni–C angle varying between 104.9(1)° and 114.9(1)°.

3.3. Electrochemical properties of $[Mo_3NiS_4]$

The electrochemical behaviour of compounds [**1**]PF_6–[**10**]PF_6 have been studied by cyclic voltammetry, the results from which are collected in Table 4 together with the previously reported data of triangular precursors [9]. The cyclic voltammogram of [**1**]PF_6–[**10**]PF_6 complexes are broadly similar, with two quasi-reversible oxidation waves and three or two irreversible reduction processes for molybdenum or tungsten derivatives, respectively. On the basis of the relative heights and by comparison with $[M_3NiS_4Cp_3'PPh_3]^+$ [24] and the aqua complexes $[M_3NiS_4(H_2O)_{10}]^{4+}$ [25], all processes seem to be one-electron processes. Compared to the W analogues the Mo clusters are more difficult to oxidize (ca. 0.20 V) and more easily reducible.

The incomplete cubane precursor $[M_3S_4X_3(diphos)_3]^+$ undergoes a chemically quasi-irreversible two electrons reduction ($M_3^{IV} \rightarrow M^{IV}M_2^{III}$) followed by an irreversible one-electron reduction ($M^{IV}M_2^{III} \rightarrow M_3^{III}$) (Fig. 2) [9]. The addition of a Ni–L fragment exerts an important electronic effect, the detection of two oxidation waves and the split into two irreversible processes of the quasi-reversible two-electrons reduction (Fig. 3). Nickel incorporation seems to produce an electronic communication inside the heterocubane core. This fact may complicate the assignment of oxidation states for the metal atoms [8,13,25,26] Similar effects have been described for platinum and copper incorporation to incomplete cuboidal clusters [16], whereas palladium insertion does not cause the split of the reduction wave [24]. Recent calculations based on topological AIM theories show that the incorporation of nickel or copper in the trinuclear $[Mo_3S_4X_3(PH_3)_6]^+$ complex does not produce changes in molybdenum charges.

The electronic structure of the 16 metal electron $[M_3M'S_4]$ (M = transition metal) cubane clusters is characterized by three bonding M–M′ orbitals, three weakly antibonding M–M′ orbitals and two non-bonding orbitals primarily located at the transition metal [8]. The first oxidation process of [**1**]PF_6–[**10**]PF_6 appears at

Table 4
Redox potentials of $[M_3NiS_4]$ clusters [**1**]PF_6–[**10**]PF_6 and their incomplete cubane-type precursors in dichloromethane[a]

Compound	Oxidation				Reduction		
	$E_{1/2}$ (V)	ΔE (V)	$E_{1/2}$ (V)	ΔE (V)	E_c (V)	E_c (V)	E_c (V)
$[Mo_3S_4Cl_3(dmpe)]PF_6$[b]					−0.69 (0.068)	−1.38	
$[Mo_3NiS_4Cl_3(dmpe)_3(CH_3CN)]PF_6$ ([**1**]PF_6)	0.80	0.035	0.43	0.075	−1.27	−1.61	−1.77
$[Mo_3NiS_4Cl_3(dmpe)_3(NC_5H_5)]PF_6$ ([**4**]PF_6)	0.80	0.086	0.44	0.062	−1.21	−1.50	−1.69
$[Mo_3NiS_4Cl_3(dmpe)_3(C_4H_8S)]PF_6$ ([**5**]PF_6)	0.85	0.088	0.45	0.045	−1.148	−1.44	−1.59
$[Mo_3NiS_4Cl_3(dmpe)_3(CO)]PF_6$ ([**6**]PF_6)	1.17	0.102	0.44	0.067	−1.16	−1.43	−1.69
$[Mo_3S_4Br_3(dmpe)]PF_6$[b]					−0.56 (0.102)	−1.20	
$[Mo_3NiS_4Br_3(dmpe)_3(CH_3CN)]PF_6$ ([**2**]PF_6)	0.79	0.077	0.45	0.077	−1.25	−1.70	−1.87
$[Mo_3S_4Br_3(dppe)_3]PF_6$					−0.50 (0.068)	−1.34	
$[Mo_3NiS_4Br_3(dppe)_3(CH_3CN)]PF_6$ ([**3**]PF_6)	0.94	0.085	0.56	0.065	−1.18	−1.47	−1.74
$[W_3S_4Br_3(dmpe)]PF_6$[b]	1.19 (0.08)				−0.95 (0.110)	−1.34	
$[W_3NiS_4Br_3(dmpe)_3(CH_3CN)]PF_6$ ([**7**]PF_6)	0.60	0.075	0.25	0.055		−1.57	−1.63
$[W_3NiS_4Br_3(dmpe)_3(NC_5H_5)]PF_6$ ([**8**]PF_6)	0.55	0.071	0.23	0.034		−1.49	−1.76
$[W_3NiS_4Br_3(dmpe)_3(C_4H_8S)]PF_6$ ([**9**]PF_6)	0.62	0.081	0.24	0.055		−1.45	−1.61
$[W_3NiS_4Br_3(dmpe)_3(CO)]PF_6$ ([**10**]PF_6)	0.97	0.087	0.23	0.066		−1.48	−1.69

[a] $E_{1/2}$ (ferrocene/ferrocene$^+$) = 0.44 V (ΔE = 66 mV).
[b] Electrochemical data in acetonitrile.

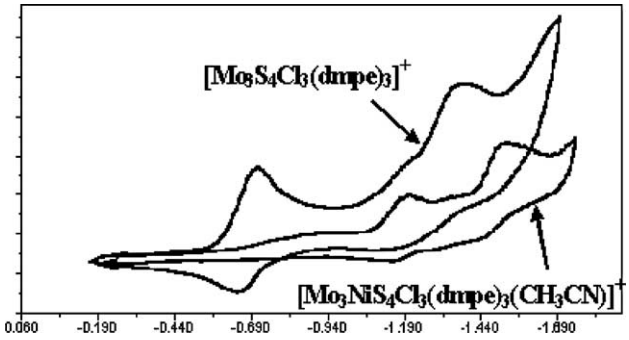


Fig. 2. Cyclic voltammogram (reduction region) for the compound [**1**]PF_6 and the precursor complex $[Mo_3S_4Cl_3(dmpe)_3]PF_6$ (scan rate 100 mV s^{-1}).

the same potential, ca. 0.44 or 0.23 V for Mo or W derivatives, respectively, and it is unaffected by the nature of the ligands (diphosphanes, halogens) or the ligands on the nickel atoms. However, the second oxidation potentials are mainly affected by the nature of the ligand on the nickel atom. A previous study on the electrochemical properties of $[Mo_3PtS_4(dppe)_3Cl_4]$ and $[Mo_3NiS_4(dppe)_3Cl_4]$ only reports one reversible oxidation wave at ca. 0.65 V (vs. SCE) [26]. Consequently, the substitution of CH_3CN in [**3**]PF_6 by the Cl^- ligand does not substantially change the oxidation capability of these clusters.

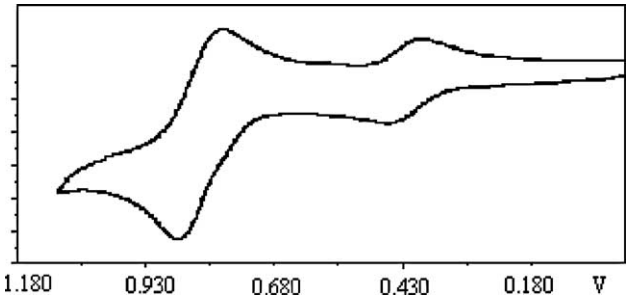


Fig. 3. Cyclic voltammogram (oxidation region) for the compound [**5**]PF_6 (scan rate of 100 mV s^{-1}).

3.4. Catalysis

Cuboidal heterobimetallic clusters have been used as model systems for the active sites of the industrial HDS catalysts. However, their application in catalysis for other organic reactions is largely unexplored, an exception being $[Mo_3PdS_4]$ and $[Mo_3S_4Ni]$-based systems which catalyse the addition of methanol or carboxylic acids to electron deficient alkynes [7].

The CO adsorbtion capacity has often taken as a measure of the HDS activity of a heterogeneous catalyst. In our case, 16 electron clusters [**1**]PF_6 and [**7**]PF_6 react with CO to afford [**6**]PF_6 and [**10**]PF_6, respectively. These clusters also react with organosulfur and -nitrogen molecules in CH_2Cl_2. The ability of the heterometal atom to bind CO in the $[M_3M'Q_4]^{n+}$ (Q = S, Se) depends strongly of the number of electrons, but also the coordination environment around the group 6 atoms. The clusters [**1**]PF_6–[**3**]PF_6 and [**7**]PF_6 have been tested as catalyst in the desulfuration of 1-octanethiol in experimental conditions at which a commercial heterogeneous Ni–MoS_2 catalyst desulfurizes 1-octanethiol completely. Experiments afforded in all cases a brown precipitate originating from partial decomposition of the cluster and a considerable amount of dioctyldisulfide, but no homogeneous HDS activity was detected. When acetone was taken as solvent, a great amount of aldol condensation products of acetone were obtained. However, it was shown in a blind experiment without the cluster that

aldol condensation of acetone was thermally induced and not related to the presence of the cluster.

No catalytic activity was detected in the addition of methanol to methyl propiolate taking $[Mo_3NiS_4Cl_3(dmpe)_3(CH_3CN)]PF_6$ as catalyst, in the conditions described previously by Hidai et al. for the addition of alcohols to alkynic acid esters catalysed by $[Mo_3PdS_4(tacn)_3Cl]PF_6$ (tacn = 1,4,7-triazacyclononane) [27].

4. Supplementary material

CCDC reference numbers 251825 and 251826 contains the supplementary crystallographic data for this paper. These data can be obtained free of charge via the Cambridge Crystallographic Data Centre, 12 Union Road, Cambridge CB2 1EZ, UK; fax: +44 1223 336 033, e-mail deposit@ccdc.cam.ac.uk or on the web http://www.ccdc.cam.ac.uk.

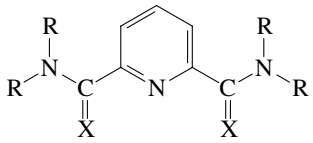
Acknowledgements

Financial support from the Ministry of Science and Technology of Spain (grants BQU2002-00313) is gratefully acknowledged. We are most indebted to Servei Central d'Instrumentació Científica (SCIC) of the University Jaume I for providing us the mass spectrometry, nuclear resonance and X-ray facilities and to the University of La Laguna for performing the elemental analyses.

References

[1] B.K. Burgess, D.J. Lowe, Chem. Rev. 96 (1996) 2983.
[2] U. Riaz, O.J. Curnow, M.D. Curtis, J. Am. Chem. Soc. 116 (1994) 4357.
[3] K. Herbst, M. Monari, M. Brorson, Inorg. Chem. 41 (2002) 1336.
[4] M. Taniguchi, Y. Ishii, T. Murata, T. Tatsumi, M. Hidai, Chem. Commun. (1995) 2533.
[5] M. Taniguchi, D. Imamura, H. Ishige, Y. Ishii, T. Murata, M. Hidai, T. Tatsumi, J. Catal. 187 (1999) 139.
[6] T. Tatsumi, M. Tanaguchi, H. Ishige, Y. Ishii, T. Murata, M. Hidai, Appl. Surf. Sci. 121–122 (1997) 500.
[7] I. Takei, Y. Wakebe, K. Suzuki, Y. Enta, T. Suzuki, Y. Mizobe, M. Hidai, Organometallics 22 (2003) 4639.
[8] C.S. Bahn, A. Tan, S. Harris, Inorg. Chem. 37 (1998) 2770.
[9] F. Estevan, M. Feliz, R. Llusar, J.A. Mata, S. Uriel, Polyhedron 20 (2001) 527.
[10] B.A.X.-R. Systems. SAINT; Bruker Analytical X-Ray Systems, Madison, WI, 1996.
[11] G.M. Sheldrick, SADABS Empirical Absorption Program, University of Göttingen, 1996.
[12] G.M. Sheldrick, SHELXTL; Bruker Analytical X-Ray Systems, Madison, WI, 1997.
[13] D.M. Saysell, C.D. Borman, C.-H. Kwak, A.G. Sykes, Inorg. Chem. 35 (1996) 173.
[14] R. Hernandez-Molina, A.G. Sykes, Coord. Chem. Rev. 187 (1999) 291.
[15] M.N. Sokolov, R. Hernández-Molina, D.N. Dybtsev, E.V. Chubarova, S.F. Solodovnikov, N.V. Pervukhina, C. Vicent, R. Llusar, V. Fedin, Z. Anorg. Allg. Chem. 628 (2002) 2335.
[16] M. Feliz, J.M. Garriga, R. Llusar, S. Uriel, M.G. Humphrey, N.T. Lucas, M. Samoc, B. Luther-Davies, Inorg. Chem. 40 (2001) 6132.
[17] M. Feliz, R. Llusar, S. Uriel, C. Vicent, E. Coronado, C.I. Gomez-Garcia, Chem. Eur. J. 10 (2004) 4308.
[18] M. Feliz. Ph.D. thesis, Universitat Jaume I, Castelló, 2003.
[19] M. Nasreldin, Y.-J. Li, E.M. Frank, A.G. Sykes, Inorg. Chem. 33 (1994) 4283.
[20] F. Hornung, M. Wanner, K.W. Klinkhammer, W. Kaim, J. Fiedler, Z. Anorg. Allg. Chem. 627 (2001) 2430.
[21] I. Schmidt, J. Hyldtoft, J. Hjortkjær, C.J. Jacobsen, Acta Chem. Scand. 50 (1996) 871.
[22] T. Shibahara, S. Mochida, G. Sakane, Chem. Lett. (1993) 89.
[23] I. Takei, K. Suzuki, Y. Enta, K. Dohki, T. Suzuki, Y. Mizobe, M. Hidai, Organometallics 22 (2003) 1790.
[24] K. Herbst, P. Zanello, M. Corsini, N. D'Amelio, L. Dahlenburg, M. Brorson, Inorg. Chem. 42 (2003) 974.
[25] T. Shibahara, G. Sakane, Y. Naruse, K. Taya, H. Akashi, A. Ichimura, H. Adachi, Bull. Chem. Soc. Jpn. 68 (1995) 2769.
[26] D. Masui, Y. Ishii, M. Hidai, Bull. Chem. Soc. Jpn. 73 (2000) 931.
[27] T. Murata, Y. Mizobe, H. Gao, Y. Ishii, T. Wakabayashi, F. Nakano, T. Tanase, S. Yano, M. Hidai, I. Echizen, H. Nanikawa, S. Motomura, J. Am. Chem. Soc. 116 (1994) 3389.
[28] T. Shibahara, M. Yamasaki, H. Akashi, T. Katayama, Inorg. Chem. 30 (1991) 2693.
[29] K. Herbst, L. Dahlenburg, M. Brorson, Inorg. Chem. 40 (2001) 1989.
[30] K. Herbst, B. Rink, L. Dahlenburg, M. Brorson, Organometallics 20 (2001) 3655.

in the study of *N*,*N*,*N*′,*N*′-tetraalkylpyridine-2,6-dicarboxamide ligands has been twofold: firstly, to study the effect of steric congestion brought by employing isopropyl or phenyl groups at the terminal carboxamide side arms, i.e., R = $-CH(CH_3)_2$ or $-C_6H_5$ and secondly to investigate the effect of change in the donor set of atoms in the two side arms on the coordination geometry adopted by the complexes. In our recent studies, it has been shown that substitution of the donor atoms by atoms of different size and electronegativity is reflected by major changes in the coordination geometries and solid state structures adopted by the corresponding complexes [7]. Crystal structures of Cu_2Cl_4(S-dept) and $CuCl_2$(O-deap) have shown important differences between the two complexes. Cu_2Cl_4(S-dept) is a tetranuclear copper(II) complex, formed by a cationic $[Cu_2Cl_2\{\mu\text{-(S-dept)}\}_2]^{2+}$ and an anionic dinuclear complex $[Cu_2Cl_4(\mu\text{-}Cl)_2]^{2-}$ [7c]. On the other hand, $CuCl_2$(O-deap) is a five coordinated trigonally distorted rectangular pyramidal complex [7a]. Similarly, complexes of $CoCl_2$ with S-dept and O-deap have revealed different structures [7b]. This paper describes the comparative X-ray diffraction, IR and visible spectra and magnetic properties of the nickel(II) thiocyanate complexes of tridentate *SNS* and *ONO* donor ligands S-dept and O-deap. Stabilization of the metal–ligand complexes of O-deap in the solid state critically depends upon the solvent used for crystallization. The role of coordinating solvents like acetonitrile and ethanol in the lattice stabilization of the complex is discussed in the paper. It was also of interest to investigate the different thiocyanate bonding modes present in these complexes.



X=S; R= Et (S-dept)
X=O; R= Et (O-deap)

2. Experimental

2.1. Materials

All reactions were carried out in anhydrous solvents. Solvents were dried using standard techniques. Absolute ethanol (AR quality, Hayman Ltd.) and pyridine-2,6-dicarboxylic acid (Fluka) were used as supplied. Anhydrous $NiCl_2$ was prepared by boiling the hydrated salt under reflux with freshly distilled $SOCl_2$ for about 4 h. The anhydrous $NiCl_2$ was filtered, washed with dry benzene and dried in vacuo.

2.2. Preparation of *N*,*N*,*N*′,*N*′-tetraethylpyridine-2,6-dicarboxamide (O-deap) and *N*,*N*,*N*′,*N*′-tetraethylpyridine-2,6-dithiocarboxamide (S-dept)

O-deap was prepared as described earlier [5]. S-dept was obtained by refluxing a mixture of O-deap (8.26 g, 0.03 mol) and P_2S_5 (4.13 g, 0.018 mol) in benzene (50 mL) for 8 h. The reaction mixture was filtered to remove unreacted P_2S_5. Crude sample of S-dept was recovered by removal of the solvent under vacuum. Pure product was obtained as shinning yellow crystals on crystallization from hot ethanol (yield: 7.37 g, 80%). M.p. 130 °C. *Anal*. Calc. for $C_{15}H_{23}N_3S_2$: C, 58.25; H, 7.44; N, 13.59. Found: C, 58.10; H, 7.56; N, 13.48%.

2.3. Ni(S-dept)(NCS)$_2$ (**1**)

A solution of 3 mmol of anhydrous $NiCl_2$ in 20 mL of ethanol was added to a solution of 6 mmol of KSCN in 20 mL of ethanol. The filtrate after removal of quantitative amount of KCl was refluxed with 3 mmol of S-dept for 4 h. Dark brown precipitates of **1** separated out at room temperature. Recrystallization from ethanol gave dark-brown crystals. Yield: 1.26 g (87%); m.p. 226 °C. *Anal*. Calc. for $C_{34}H_{46}N_{10}S_8Ni_2$: C, 42.17; H, 4.75; N, 14.47; S, 26.5; Ni, 12.1. Found: C, 41.76; H, 5.03; N, 14.26; S, 26.1; Ni, 12.0%. Molar conductance [Λ_M, Ω cm^2 mol^{-1}]: 12.0 (CH_3CN) (expected range for 1:1 electrolytes: 120–160 Ω cm^2 mol^{-1}). IR (KBr pellet, cm^{-1}): 2087, 2007, 1602, 1581, 1518, 1469, 1450, 1388, 1360, 1316, 1282, 1260, 1186, 1145, 1094, 1017, 811, 722, 625, 474. Visible spectral data [λ_{max}, nm (ε, M^{-1} cm^{-1})] in methanol: 406 (265), 661 (8.1), 727 sh (6.5), 1092 (7.6). FAB mass [(*m*-nitrobenzyl alcohol): (M^+, 966)], *m*/*z*: 734 [Ni_2(S-dept)$_2$], 676 [Ni(S-dept)$_2$]$^+$, 425 [Ni_2(S-dept)]$^+$, 367 [Ni(S-dept)]$^+$ (base peak), 338 [Ni(S-dept)-C_2H_5]$^+$, 310 [Ni(S-dept)-C_2H_5-C_2H_4]$^+$, 278 [Ni(S-dept)-C_2H_5-C_2H_4-S]$^+$.

2.4. [Ni(NCS)$_2$(O-deap)(CH_3CN)] · CH_3CN (**2**)

This was prepared by the procedure adopted for **1**, except CH_3CN was used as the medium and O-deap as ligand. Recrystallization from acetonitrile gave green crystals. Yield: 1.47 g (91%); m.p. 220 °C. *Anal*. Calc. for $C_{21}H_{29}N_7O_2S_2Ni$: C, 47.19; H, 5.43; N, 18.35; S, 12.0; Ni, 11.0. Found: C, 47.58; H, 5.87; N, 17.97; S, 11.7; Ni, 10.7%. Molar conductance [Λ_M, Ω cm^2 mol^{-1}]: 18 (CH_3CN). IR (KBr pellet, cm^{-1}): 2315, 2287, 2092, 1600, 1561, 1315, 1270, 1198, 1098, 1069, 1046, 1030, 947, 829, 758, 723, 698, 656, 511, 447. Visible spectral data [λ_{max}, nm (ε, M^{-1} cm^{-1})] in methanol: 390 (13.1), 670 (1.7), 742 (1.9), 1071 (1.4).

2.5. [Ni(NCS)$_2$(O-deap)(C$_2$H$_5$OH)] (3)

This complex was prepared by the same procedure but anhydrous ethanol was used as the reaction medium. Yield: 1.20 g (90%); m.p. 200 °C. *Anal.* Calc. for $C_{19}H_{29}N_5O_3S_2Ni$: C, 45.78; H, 5.82; N, 14.05; S, 12.8; Ni, 11.8. Found: C, 45.24; H, 5.64; N, 14.02; S, 12.4; Ni, 11.3%. Molar conductance [Λ_M, Ω cm^2 mol^{-1}]: 6.0 (C_2H_5OH) (expected range for 1:1 electrolytes: 30–45 Ω cm^2 mol^{-1}). IR (KBr pellet, cm^{-1}): 3196, 2100, 1600, 1562, 1316, 1272, 1198, 1098, 1070, 1049, 1030, 947, 830, 762, 722, 705, 657, 510, 442. Visible spectral data [λ_{max}, nm (ε, M^{-1} cm^{-1})] in ethanol: 370 sh (14.2), 664 (4.4), 728 (4.5), 1080 (4.8).

2.6. Physical methods

Elemental analysis (C, H, N) were performed on a Perkin–Elmer Model 2400 CHN analyzer at RSIC, Panjab university, Chandigarh. IR spectra were recorded as Nujol/hcb mulls on KBr plates on a Perkin–Elmer RX-1 FTIR spectrophotometer. The UV–Vis spectra were recorded on a JASCO V-530 UV–Vis spectrophotometer. Reflectance spectra were recorded on an integrating sphere Hitachi model 330 using $MgCO_3$. The FAB mass spectra were recorded on a JEOL SX 102/DA-6000 Mass Spectrometer/Data System using Argon/Xenon (6 kV, 10 mA) as the FAB gas. *m*-Nitrobenzyl alcohol (NBA) was used as the matrix. Variable temperature (34–300 K)[1] solid state magnetic susceptibility measurements were done using a locally built Faraday balance [2].

2.7. X-ray crystallography

The crystals of complexes **1** and **3** were grown from ethanol and **2** from acetonitrile by a method of slow evaporation at room temperature. The data were collected on a Siemens P4 single crystal diffractometer using graphite monochromatized Mo Kα radiation (0.71073 Å). Table 1 shows the unit cell parameters and data measurement details. Data collection and cell refinement were done with XSCANS [10]. Data were corrected for Lorentz and polarization effects but no absorption correction was performed for **1**. Structure was solved by direct methods and refined anisotropically by full matrix least squares methods. All the hydrogens were fixed geometrically as riding atoms with a displacement parameter equal to 1.2 (CH, CH_2) or 1.5 (CH_3) times that of the parent atoms. Data reduction, structure solutions, refinement and molecular graphics were performed using SHELXLTL-PC [11]. During refinement the terminal ethyl groups of the dithioamide ligand showed disorder in terms of abnormal bond lengths and high thermal parameters. The disorder could be resolved successfully for C8, C10, C13, C15 methyl and C9, C12 methylene carbon atoms. Each of their atomic positions was split into two peaks with a total site occupancy of 1.000. These atoms were refined isotropically with restraints using fixed C–C (1.510 Å) and C–N (1.456 Å) distances. All other atoms were refined anisotropically. Torsion angles and least squares planes were calculated by using PARST [12]. The data collection procedure,structure solution and refinement for **2** and **3** were as follows, **2**: 40 reflections ($9.685° < 2\theta < 29.236°$) for accurate cell parameter determination, a total of 26.56 h of X-ray exposure time, $R = 0.0307$, $wR = 0.0780$, $a = 0.0471$ and $b = 0.22$ [in the weighting scheme]. **3**: 40 reflections ($10.207° < 2\theta < 29.936°$) for accurate cell parameter determination, a total of 39.65 h of X-ray exposure time, $R = 0.0465$, $wR = 0.1178$, $a = 0.0627$ and $b = 7.53$ [in the weighting scheme]. CCDC numbers for the complexes **1**, **2** and **3** are 261983, 261984 and 261985, respectively.

3. Results and discussion

Complexes **1**–**3** were obtained in good yield by refluxing $Ni(NCS)_2$ and the S-dept or O-deap ligand. These complexes are air and moisture stable and readily dissolved in common organic solvents. Conductance values in CH_3CN and C_2H_5OH did not show dissociation into ionic species [13]. No molecular ion peak corresponding to the dinuclear nickel species [{Ni(S-dept)(SCN)$_2$}$_2$] (*m*/*z*, 966) was observed in the FAB mass spectrum of **1**. However, some structurally important nickel containing ions were observed (see Section 2). Instability of M^+ ion may be attributed to the facile loss of 2 moles of $(NCS)_2$; the driving force for the formation of [Ni$_2$(S-dept)$_2$] may be the formation of Ni–Ni bond. Thermal analysis (TGA) of complex **1** in air shows that the weight loss of 27.0% between 230 and 320 °C corresponds to the removal of $(SCN)_2$ and ethylene. On heating above 320 °C, it loses the entire organic mass to yield NiO. TGA of **2** did not show the formation of any stable intermediates. The complex on heating above 60 °C loses all the organic components to yield a stable residue of NiO at 680 °C. The μ_{eff} values at 300 K for **1, 2** and **3** (per Ni atom) are 2.98, 2.82 and 2.88 μ_B, respectively. The magnetic moment of **1** was measured over the temperature range 300–34 K[1] (Fig. 1). The $\chi_M T$ value is almost constant (2.205 cm^3 mol^{-1} K) in the range 300–200 K. Below this temperature, $\chi_M T$ decreases slowly to 2.006 cm^3 mol^{-1} K upto 100 K. Between 100 and 34 K, it decreases to 1.326 cm^3 mol^{-1} K. This behaviour suggests the presence of weak antiferromagnetic interactions. The equations for dimers with two $S = 1$ metal ions (as is the case for dinuclear Ni compounds) is

[1] Due to lack of facilities measurements could not be extended below 34 K.

Table 1
Crystal data and structure refinement for complexes **1**–**3**

Complex	**1**	**2**	**3**
Empirical formula	$C_{17}H_{23}N_5NiS_4$	$C_{21}H_{29}N_7NiO_2S_2$	$C_{19}H_{29}N_5NiO_3S_2$
Formula weight	484.35	534.34	498.30
T (K)	293(2)	293(2)	293(2)
Wavelength (Å)	0.71069	0.71073	0.71073
Crystal system	monoclinic	monoclinic	monoclinic
Space group	$P2_1/c$	$P2_1$	$C2/c$
Unit cell dimensions			
a (Å)	9.623(5)	8.327(1)	29.33(2)
b (Å)	14.361(5)	10.909(1)	13.286(1)
c (Å)	16.284(5)	15.136(1)	15.877(1)
α (°)	90.0	90	90
β (°)	95.4(5)	97.91(1)	121.63(1)
γ (°)	90.0	90	90
V (Å^3)	2240.4(16)	1361.9(2)	5267.9(6)
Z	4	2	8
D_{calc} (Mg/m^3)	1.436	1.303	1.257
Absorption coefficient (mm^{-1})	1.251	0.895	0.921
F(000)	1008	560	2096
Crystal size (mm)	$0.15 \times 0.12 \times 0.10$	$0.21 \times 0.19 \times 0.16$	$0.27 \times 0.24 \times 0.17$
θ Range for data collection (°)	1.89–27.50	2.31–24.01	2.00–24.00
Scan type	2θ–θ	2θ–θ	2θ–θ
Scan speed	variable, 2.0–60.0°/min in ω	variable, 2.0–60.0°/min in ω	variable, 2.0–60.0°/min in ω
Limiting indices	$0 \leqslant h \leqslant 12$, $0 \leqslant k \leqslant 18$, $-21 \leqslant l \leqslant 21$	$0 \leqslant h \leqslant 9$, $0 \leqslant k \leqslant 12$, $-17 \leqslant l \leqslant 17$	$0 \leqslant h \leqslant 33$, $0 \leqslant k \leqslant 15$, $-18 \leqslant l \leqslant 15$
Reflections collected/unique (R_{int})	5456/5152 (0.0691)	2447/2276 (0.0182)	4232/4144 (0.0147)
Refinement method	full-matrix least-squares on F^2	full-matrix least-squares on F^2	full-matrix least-squares on F^2
Data/restraints/parameters	5152/12/238	2276/1/299	4144/0/272
Goodness-of-fit on F^2	0.995	1.027	1.013
Final R indices [$I > 2\sigma(I)$]	$R_1 = 0.0900$, $wR_2 = 0.2015$	$R_1 = 0.0307$, $wR_2 = 0.0780$	$R_1 = 0.0465$, $wR_2 = 0.1178$
R indices (all data)	$R_1 = 0.2189$, $wR_2 = 0.2727$	$R_1 = 0.0344$, $wR_2 = 0.0803$	$R_1 = 0.0654$, $wR_2 = 0.1262$
Largest difference in peak and hole (e Å^{-3})	0.991 and −0.717	0.225 and −0.243	0.763 and −0.523

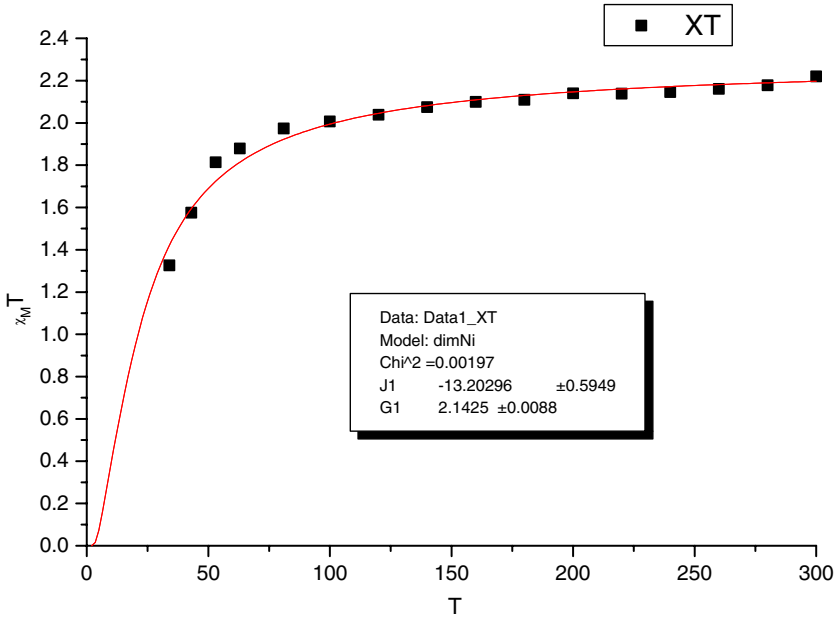


Fig. 1. Showing the variation of $\chi_M T$ with T for complex **1**.

derived from Van Vleck's equation and, by using the spin hamiltonian, $H = -JS_1 \times S_2$, it takes the following form: $\chi T = (Ng^2\beta^2/k)[(2\exp(x) + 10 \times \exp(3x))/(1 + 3\exp(x) + 5\exp(3x))]$, where $x = J/kT$, k being the Boltzman's constant, and J the magnetic coupling constant (in cm^{-1}). The results of the best fit, shown

as the solid line in Fig. 1, were $J = -13.203 \pm 0.595$ cm^{-1}, $g = 2.142 \pm 0.009$.

3.1. Spectroscopic properties

3.1.1. IR spectra

Complex **1** shows two distinct ν(CN) modes for the NCS^- group, at 2087 and 2007 cm^{-1}. The higher frequency band is assigned to the N-bonded terminal thiocyanate group [14], and the lower frequency band at 2007 cm^{-1} strongly indicates the presence of N-bridging thiocyanate ligand joining the two nickel centres. This unusual bridging mode of thiocyanate ligand has been observed for a very limited number of complexes which are listed in Table 3 [15–19]. The position of the C–S stretching frequency in the region 860–690 cm^{-1} is usually employed for differentiating S-bonded from N-bonded terminal thiocyanates [14,20]. However, the ν(CS) modes are obscured by ligand bands in this region which made assignment of the C–S stretches quite uncertain. The peaks attributed to ν(CN) are not perturbed in its solution spectrum thus suggesting that the solid state structure is retained in $CHCl_3$ solution. Complexes 2 and 3 show a single band in the ν(CN) region, at 2092 and 2100 cm^{-1}, respectively, which are assigned to the N-bonded terminal NCS ligands. The carbonyl stretching frequency which appears at 1625 cm^{-1} in the free ligand is shifted to 1600 cm^{-1} suggesting carbonyl coordination to metal centre.

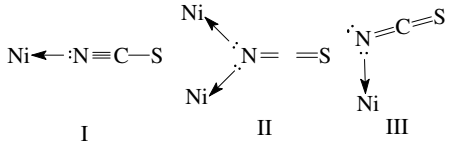
3.1.2. Visible spectra

Complexes **1**–**3** show a close resemblance between absorption in methanol and their reflectance spectra suggesting that the same geometry is retained by the metal ion on dissolution. Complex **1** exhibits three distinct absorption bands at 406, 661 and 1090 with a shoulder band at 738 nm. Similar spectra are observed for **2** and **3**with bands at 390, 670 (sh), 742 and 1080 and 370 (sh), 664, 728 and 1080 nm, respectively. Assuming Oh symmetry for the Ni ions in these compounds, the bands may be assigned to the spin allowed d-d transitions $^3T_{1g}(P) \leftarrow {}^3A_{2g}$, $^3T_{1g}(F) \leftarrow {}^3A_{2g}$ and $^3T_{2g} \leftarrow {}^3A_{2g}$, respectively. The band at about 730 nm may be a consequence of the transition to the ^1E_g level gaining intensity through configurational interaction with the $^3T_{1g}(F)$ level.

3.2. Crystal structures of complexes *1*–*3*

3.2.1. Complex *1*

Crystallization of **1** from ethanol or acetonitrile by slow evaporation of its saturated solution at room temperature afforded good single crystals of $[Ni_2(\mu\text{-}NCS)_2(S\text{-}dept)_2(NCS)_2]$. The bond lengths and angles are listed in Table 2. The complex is a centrosymmetric dimer (Fig. 2). It consists of two distorted octahedrons, one about each Ni^{2+}, which share an edge, formed by the N atoms of the bridging NCS ions. The remaining sites are occupied by two S and one N atoms from the tridentate chelating ligand and from a N atom of the terminally bonded thiocyanate ion. The bond angles around Ni^{2+} are close to that of an ion in an octahedral environment. Both Ni–S bonds are equal and trans to each other. The three M–N bonds in the xy plane are equal with an average M–N distance of 2.028(7) Å. The four nitrogens N1 N4 N5 and $N4^i$ (where i = $-x$, $-y$, $-z + 1$) are almost planar with a deviation of 0.016 Å from a least square plane. The M–N bond lengths for the bridging NCS ligands are Ni–N4 2.022(7) and Ni–$N4^i$ 2.396(8) Å, respectively. This shows that NCS is behaving as an unsymmetrical bridging bidentate ligand through N. The bridging NCS ligands are perpendicular to Ni–Ni^i axis with Ni–N–Ni^i angle of 96.9° (**3**). Ni–Ni distance is 3.316(8) Å, which indicates the absence of any metal–metal bond. Both bridging and terminal NCS ligands are almost linear with small differences in their respective bond distances and angles. The bonding parameters of the terminal NCS ligand fall well within the range generally observed in the literature [15–19,21]. The short N–C distance [N(5)–C(17), 1.151(12) Å] corresponds with structure **I**. The C–S bond distance [C(17)–S(4), 1.631(12) Å] is shorter than the C–S(sp^3) bond distance (1.81 Å) but is close to C=S bond distance (1.61 Å) as given by Pauling [22]. However, it falls well within the range 1.588(13)–1.689(13) Å found for terminally bonded covalent NCS group. The terminal M–NCS linkages in this complex are bent with M–N–C angle 170.8° (8) which fall in the range (141–174°) found for Ni^{2+} having bent terminally bonded NCS anions [6b]. Ni–N5–C17–S4 torsion angle is 15.1°. This non-linearity has been attributed to the steric effects [23] and indicates more electron density localization on N so that **II** becomes the major contributing resonance structure for NCS anion [24].



The C–S bond length [C(16)–S(3), 1.606(10) Å] of the bridging NCS ion is more closer to C=S and is in conformity with structure **II**. As already known [14] this also accounts for the two lone pairs on N atoms directed at the metal ion and the linearity of the group, however, N–C bond [N(4)–C(16), 1.145(10) Å] remains too short to be a double bond. This short N–C bond may be due to inductive effect, which results due to greater flow of electron density from the C–S bond through the C–N bond towards metal ion, as shown in **III**. Bridging through N requires M–NCS linkages to be essentially

Table 2
Important bond lengths (Å) and bond angles (°) for complexes **1**–**3**

Complex ***1***[a]	
Ni–N(5)	2.018(9)
Ni–N(4)	2.022(7)
Ni–N(1)	2.043(6)
Ni–S(2)	2.384(3)
Ni–S(1)	2.388(3)
Ni–(N4)^{i}	2.396(8)
S(1)–C(6)	1.651(9)
S(2)–C(11)	1.656(8)
S(3)–C(16)	1.606(10)
S(4)–C(17)	1.631(12)
N(4)–C(16)	1.145(10)
N(5)–C(17)	1.151(12)
N(5)–Ni–N(4)	95.7(3)
N(5)–Ni–N(1)	91.2(3)
N(4)–Ni–N(1)	173.0(3)
N(5)–Ni–S(2)	91.8(2)
N(4)–Ni–S(2)	95.8(2)
N(1)–Ni–S(2)	84.0(2)
N(5)–Ni–S(1)	93.9(2)
N(4)–Ni–S(1)	96.1(2)
C(16)–N(4)–Ni	149.2(8)
C(16)–N(4)–Ni^{i}	113.8(7)
N(1)–Ni–S(1)	83.3(2)
S(2)–Ni–S(1)	1666.19(10)
N(5)–Ni–N(4)^{i}	178.0(3)
N(4)–Ni–N(4)^{i}	83.1(3)
N(1)–Ni–N(4)^{i}	90.0(3)
S(2)–Ni–N(4)^{i}	86.79(19)
S(1)–Ni–N(4)^{i}	87.81(19)
Ni–N(4)–Ni^{i}	96.9(3)
C(17)–N(5)–Ni	170.8(8)
Complex ***2***	
Ni(1)–N(5)	1.995(3)
Ni(1)–N(6)	2.043(4)
Ni(1)–O(1)	2.098(4)
S(1)–C(18)	1.620(4)
O(1)–C(6)	1.252(5)
N(1)–C(5)	1.337(6)
N(2)–C(6)	1.341(6)
N(2)–C(7)	1.493(6)
N(3)–C(14)	1.470(6)
N(4)–C(16)	1.118(6)
N(6)–C(19)	1.146(7)
Ni(1)–N(1)	2.023(3)
Ni(1)–O(2)	2.085(3)
Ni(1)–N(4)	2.141(4)
S(2)–C(19)	1.632(6)
O(2)–C(11)	1.249(5)
N(1)–C(1)	1.347(6)
N(2)–C(9)	1.481(7)
N(3)–C(11)	1.331(5)
N(3)–C(12)	1.474(6)
N(5)–C(18)	1.155(4)
N(7)–C(20)	1.122(13)
N(5)–Ni(1)–N(1)	177.48(15)
N(1)–Ni(1)–N(6)	90.65(15)
N(1)–Ni(1)–O(2)	77.74(15)
N(5)–Ni(1)–O(1)	103.20(17)
N(6)–Ni(1)–O(1)	94.72(17)
N(5)–Ni(1)–N(4)	88.84(17)
N(6)–Ni(1)–N(4)	179.29(17)

Table 2 (*continued*)

Complex ***2***	
O(1)–Ni(1)–N(4)	84.84(16)
C(11)–O(2)–Ni(1)	114.5(2)
C(5)–N(1)–Ni(1)	117.6(3)
C(6)–N(2)–C(9)	116.8(4)
C(9)–N(2)–C(7)	115.5(4)
C(11)–N(3)–C(12)	126.8(4)
C(16)–N(4)–Ni(1)	177.5(4)
C(19)–N(6)–Ni(1)	162.7(4)
N(1)–C(1)–C(6)	110.1(3)
N(5)–Ni(1)–N(6)	91.81(17)
N(5)–Ni(1)–O(2)	101.63(16)
N(6)–Ni(1)–O(2)	91.00(16)
N(1)–Ni(1)–O(1)	77.16(16)
O(2)–Ni(1)–O(1)	154.30(11)
N(1)–Ni(1)–N(4)	88.71(15)
O(2)–Ni(1)–N(4)	89.16(15)
C(6)–O(1)–Ni(1)	115.7(3)
C(5)–N(1)–C(1)	122.3(3)
C(1)–N(1)–Ni(1)	118.5(3)
C(6)–N(2)–C(7)	127.5(4)
C(11)–N(3)–C(14)	117.2(3)
C(14)–N(3)–C(12)	115.8(4)
C(18)–N(5)–Ni(1)	178.0(5)
N(1)–C(1)–C(2)	119.8(4)
C(2)–C(1)–C(6)	129.9(4)
Complex ***3***	
Ni(1)–N(4)	1.980(3)
Ni(1)–N(5)	2.045(3)
Ni(1)–O(1)	2.123(2)
S(1)–C(16)	1.625(5)
O(1)–C(6)	1.256(4)
O(3)–C(18)	1.414(6)
Ni(1)–N(1)	2.030(3)
Ni(1)–O(3)	2.078(3)
NI(1)–O(2)	2.137(2)
S(2)–C(17)	1.634(4)
O(2)–C(11)	1.254(4)
N(4)–Ni(1)–N(1)	176.85(12)
N(1)–Ni(1)–N(5)	89.67(12)
N(1)–Ni(1)–O(3)	90.20(11)
N(4)–Ni(1)–O(1)	106.16(12)
N(5)–Ni(1)–O(1)	90.07(12)
N(4)–Ni(1)–O(2)	99.55(12)
N(5)–Ni(1)–O(2)	93.07(12)
O(1)–Ni(1)–O(2)	154.03(10)
C(11)–O(2)–Ni(1)	112.9(2)
C(1)–N(1)–Ni(1)	116.6(2)
N(4)–Ni(1)–N(5)	91.08(14)
N(4)–Ni(1)–O(3)	89.07(13)
N(5)–Ni(1)–O(3)	179.67(14)
N(1)–Ni(1)–O(1)	76.90(10)
O(3)–Ni(1)–O(1)	89.60(12)
N(1)–Ni(1)–O(2)	77.35(10)
O(3)–Ni(1)–O(2)	87.20(12)
C(6)–O(1)–Ni(1)	114.4(2)
C(18)–O(3)–Ni(1)	126.6(3)

[a] Symmetry i: $-x, -y, -z + 1$.

angular with M–N–C being 149.2(8)° and 113.8(7)°. The first example of an N-bonded NCS bridging ligand was reported for a mixed valence Re^{III}/Re^{IV} complex [15]. It

Table 3
Various bond lengths (Å) and bond angles (°) found in complexes of NCS anion having bidentate, N-bridging mode of coordination

S. no.	Complex	Type of bond	M–N	C–N	C–S	N–C–S	M–N–C	M–N–M	M–M
1	$[Re_2(NCS)_{10}]^{3-}$ (**2**)	terminal[a]	2.026(8)	1.16(1)	1.59(1)	178.8(9)	171.8(7)	77.4(3)	2.613(1)
		bridging[a]	2.087(8), 2.095(8)	1.17(1)	1.57(1)	178.7(8)	141.5(7)		
2	$[Cd_2(NCS)_4(butrz)_3]_n$ (**3**)	terminal[a]	2.240(3)					100.83(9)	3.6912(4)
		bridging[a]	2.352(3), 2.437(3)						
3	$Ni_3(detrH)_6(NCS)_6$ (**7**)	terminal[a]	2.04(1)	1.15(1)	1.64(1)	177.4(9)	163.3(9)	105.5(5)	3.39(1)
		bridging[a]	2.09(1), 2.18(1)	1.18(1)	1.57(1)	178.8(9)			
4	$[Ni(L^1)(NCS)_2]_2$ (**6**)	terminal[a]							3.03(1)
		bridging[a]							
5	$[Ni_2(L^2)(AcO)_2(NCS)^2(MeOH)]$ (**5**)	terminal[a]	2.105(6)					88.1(2)	2.993(1)
		bridging[a]	2.131(5), 2.172(5)						
6	$[Ni_2(L^2)(NCS)^3(MeOH)]$ (**5**)	terminal[a]	2.008(7)						3.142(2)
		bridging[a]	2.039(7), 2.170(6)						
7	$[Ni(L^2)(NCS)_3(urea)]$ (**5**)	terminal[a]	2.002(6)						3.155(2)
		bridging[a]	2.077(5), 2.197(5)						
8	$[Ni_2(S\text{-}dept)_2(NCS)_4]$ (present work)	terminal[a]	2.018(9)	1.15(1)	1.63(1)	179.2(10)	170.8(8)	96.9(8)	3.316(5)
		bridging[a]	2.022(7), 2.396(8)	1.14(1)	1.60(1)	176.1(9)	149.2(8), 113.8(7)		

[a] Average value of M–N (terminal), C–N, C–S, NCS and MNC are given.

had two equal Re–N bonds with Re–Re bond (Table 3). However, Cd^{II} complex contained slightly different M–N bond lengthsand no M–M bond [16]. In the case of Ni^{2+} this type of bonding has been reported for five complexes [17–19] all of them showed bidentate bridging through N of the NCS anion with Ni–Ni distance ranging between 2.993(1) and 3.39(1) Å. In the present complex, the two M–N bond lengths are significantly different from each other and the shorter Ni–N4 distance is comparable to Ni–N5 distance of the terminally bonded NCS anion. Thus the present complex becomes the first example to show maximum asymmetry in bidentate bridging through N atom of the NCS anion. No M–M bonding has been found in the case of any of the Ni^{2+} complexes yet the M–M distance seems to be dependent upon M–N–M (Table 3).

3.2.2. Complex *2*

Crystallization of $[Ni(NCS)_2(O\text{-}deap)(CH_3CN)]\cdot CH_3CN$ by slow evaporation of its saturated solution in acetonitrile at room temperature yields good single crystals. Fig. 3 displays the ORTEP diagram of **2** which crystallizes in $P2_1$ space group with 2 molecules per unit cell. The coordination around the Ni atom can be best described as octahedral as can be ascertained from the bond lengths and angles (Table 2). However, contrary to the expected value in an octahedral geometry, one of the *trans* ligand–metal–ligand angle is not 180° but deviated to a value of 154.3° (O1–Ni1–O2). This apparent deviation from the ideal value may be attributed to the geometrical constraints of O-deap acting as a tridentate meridonal ligand. The two thiocyanate ligands show a marked difference of approach towards the metal coordination polyhedra. While one of the SCN moiety (i.e., S1–C18–N5, Fig. 3) that is placed parallel to O-deap, approaches the metal almost in a nearly linear arrangement (C18–N5–Ni1 = 178°), the other thiocyanate ligand (i.e., S2–C19–N6, Fig. 3) which is approaching orthogonal to the former is substantially deviated from linearity, the C19–N6–Ni1 angle being 162.7°. Nevertheless, their coordinating strengths are almost same as reflected from their almost equal Ni–N bond lengths of 1.995 and 2.043 Å. It is also noteworthy that this type of subtle deviations can modify the geometry around the metal centre. For example, the two five membered rings formed out of the two carbonyl to the metal centre (⩾C=O1···Ni1 and ⩾C=O2···Ni1, Fig. 3) are not placed parallel, but have taken a wedge shape with a wedge angle of 3.7° (angle between the least square planes of these two five membered rings). Similarly, the planar pyridyl moiety is also bent with respect to these rings, the angle between the planes of aromatic pyridyl moiety and the five membered ring involving O1 (i.e., N1, Ni1, O1, C6 and C1) is 11.6° and that with the other ring containing O2 (i.e., N1, Ni1, O2, C11 and C5) is 14.2°. These type of variations, most probably are not only controlled by electronic effects alone, but also

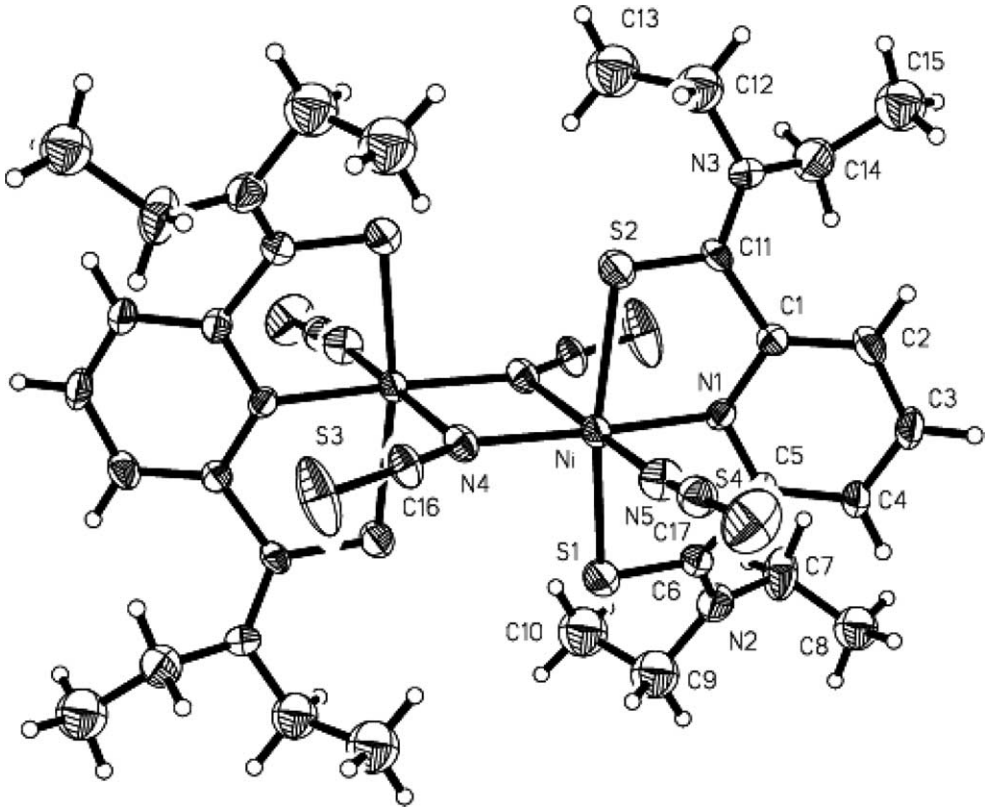


Fig. 2. A perspective view of complex **1** with the atom numbering scheme (thermal ellipsoids are at 50% probability level).

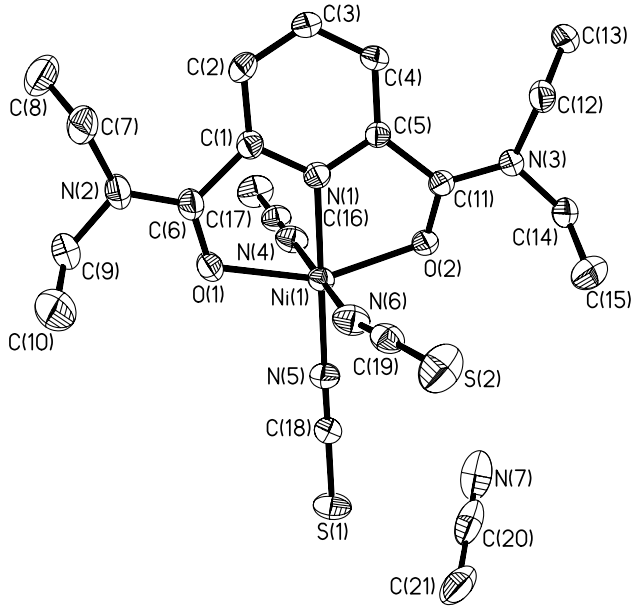


Fig. 3. A perspective view of complex **2** with the atom numbering scheme (thermal ellipsoids are at 50% probability level).

by the subtle steric requirements that are needed for a stable lattice. Such effects which minimize the overall steric congestion are reflected even in the 'coordinating arms' of the ligand. The symmetrically positioned ethyl part of the arms on both sides are placed one 'up' and one 'down' with respect to the meridonal plane of the ligand as evidenced from Fig. 3. The two terminal methyl groups (C10 and C15) that are closer to the coordinating oxygen atoms are 'up' while the other two (C8 and C13) which are away from these oxygen atoms are 'down' (the sense of up and down is with respect to the planar meridonal ligand plane when viewed parallel to Ni(1)–N(1) vector). The sixth coordination of the octahedral geometry is completed by the solvent of crystallization (CH_3CN) itself and its reduced Lewis basicity compared with SCN^- (and hence the weaker coordinating ability) is clear from the higher Ni–N bond length of 2.141 Å. However, the approach towards the metal centre is almost linear, the Ni1–N4–C16 angle being 177.5°.

The role of solvent used for crystallization is twofold in stabilizing the metal ligand complex. Firstly, it completes the coordination around the metal center and imparts stability and secondly, during the packing of molecules in the lattice, the voids generated are filled by these solvent molecules again providing overall stability to the three-dimensional lattice. Packing of this acetonitrile lattice inclusion complex is shown in Fig. 4. Two 'arms' of the neighbouring ligand molecules and the methyl group of the coordinating CH_3CN together generates a cavity and the CH_3CN molecules are occupied in these centres. The stability to this inclusion is imparted through two weak C–H···N interactions of the nitrogen atom of CH_3CN (N7···H12A–

Cl2 = 2.704 and N7···H17C–Cl7 = 2.798 Å) and the other is through a C–H···S interaction of the methyl group of CH_3CN (S1···H21A–C21 = 3.152 Å) and sulphur atom of the thiocyanate moiety. In effect a linear CH_3CN molecule is anchored from both of its terminal ends to the center of the cavity through C–H···N and C–H···S interactions involving the solvent and metal ligand complex. In addition there are three lattice stabilizing C–H···S interactions (involving sulphur atoms of SCN^- moiety) observed in the lattice, S2···H9A–C9 = 2.885, S2···H7A–C7 = 2.922 and S1···H13A–C13 = 3.080 Å.

3.2.3. Complex 3

The structure of **3** obtained after recrystallization in ethanol, is presented in Fig. 5. The coordination around the Ni atom in **3** is also distorted octahedral (Table 2). The difference of 4.3° in the O–Ni–O angle in **2** (154.3°) from **3** (150.0°) shows that O-deap ligand can adopt to subtle geometrical requirements during the complex formation. However, to meet the steric demands, the pyridyl part of O-deap has to undergo a substantial bend from the mean plane of the two five membered rings formed out of the coordination to Ni atom (Fig. 5), the angle being 21.8°. It is interesting that the same deviation in **2** is only 12.7 showing that change in the coordination from acetonitrile to ethanol can have profound influence in the overall topology of the metal ligand complex. As in **2**, the two five membered rings are also wedge shaped, infact the wedge angle has increased to 5.5°. The approach of the two thiocyanate ligands is very similar to that of **2**, the one in the plane of the ligand is linearly placed with respect to the metal (C16–N4–Ni1 = 174.2°), whereas the other orthogonally placed one makes an angle of 163.2° (C17–N5–Ni1). The coordinating arms of the ligand have a very similar up and down conformation as in **2**.

Participation of the amide nitrogen in the coordination process through amide resonance is evident from the very planar nature of N atoms of both **2** and **3** (sum of the angles around nitrogen is 359.8° (**2**) and 359.6° (**3**), respectively). This type of resonance would facilitate more charge on the carbonyl oxygens for better participation in metal–ligand coordination. It is noteworthy that the major difference in the octahedral coordination of Ni in **2** and **3** is that the acetonitrile in **2** is replaced by an ethanol molecule in **3**. Out of the six octahedral metal–ligand bonds in **2**, it is the Ni–N(acetonitrile) that is the longest (2.141 Å, Table 2). However, since enhanced Lewis basicity can be expected for the oxygen atom of ethanol (than that of the nitrogen atom of CH_3CN), the Ni–O(ethanol) is no longer the highest and is reduced to 2.078 Å. In fact it is the shortest among the three Ni–O bonds in **3** (Table 2).

We hypothesised that the sixth coordination of compound **2** can be replaced, if a solvent of similar size (but with equal or higher Lewis basicity) can be used for crystallization. Another motivation was to examine the role

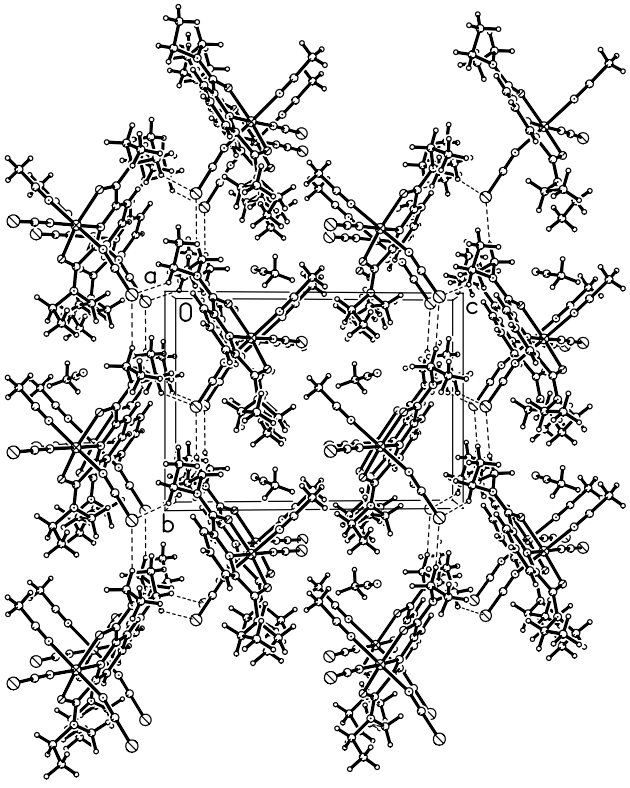


Fig. 4. Packing of complex **2** viewed perpendicular to the *bc* plane.Note the occpancy of solvent acetonitrile (right to the middle of unit cell) in the cavity formed from the arms of the ligand and the methyl group of coordinated CH_3CN. The lattice stabilizing C–H···S interactions are shown by dotted lines.

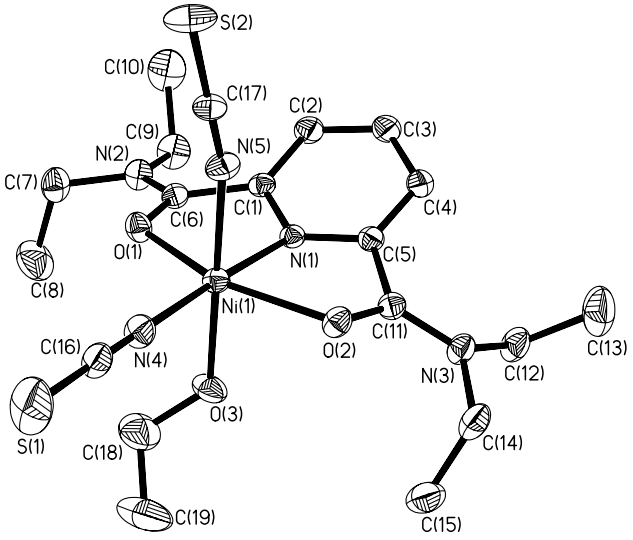


Fig. 5. A perspective view of complex **3** with the atom numbering scheme (thermal ellipsoids are at 50% probability level).

of solvent in stabilizing the three-dimensional lattice, after all, does the solvent play a deciding role in the lattice formation? If so, the compound would display polymorphism, which is of contemporary interest [25]. Ethanol was conceived as appropriate solvent as it satisfies both the condition of size and Lewis basicity. Gratifyingly, compound **3** was successfully crystallized from absolute ethanol with an ethanol occupying the sixth position in the octahedral coordination. But interestingly no solvent of crystallization was included in the lattice and the molecular packing is significantly different from that of **2**. A packing diagram viewed down the *ab* plane is shown in Fig. 6.

In the lattice, one of the thiocyanate groups (i.e., S1–C16–N4) is involved in a lattice stabilizing C–H···S interaction (C10–H10A···S1 = 2.835 Å) whereas the other one (i.e., S2–C17–N5) is hydrogen bonded to the hydrogen atom of the coordinated ethanol (O3–H3A···S2 = 2.431 Å) through a O–H···S hydrogen bond. Thus, as in **2** both the thiocyanate groups are involved in S–H···O/C interactions. In addition, the hydrogen atom at the para position of the pyridyl moiety also takes part in a C–H···O hydrogen bond with one of the carbonyl oxygen atoms (C3–H3B···O2 = 2.448 Å). Thus, our initial hypothesis of obtaining a complex in which the replacement of an acetonitrile with ethanol was realized, but the lack of inclusion of ethanol as a solvent of crystallization amply displays the complex interplay of weak interactions in stabilizing the three-dimensional lattice of these molecules. These observations show that, at molecular level certain predictability can be realized, but the nature of molecular packing is still a complex process to comprehend and indeed it is one of the challenges in crystal engineering [26].

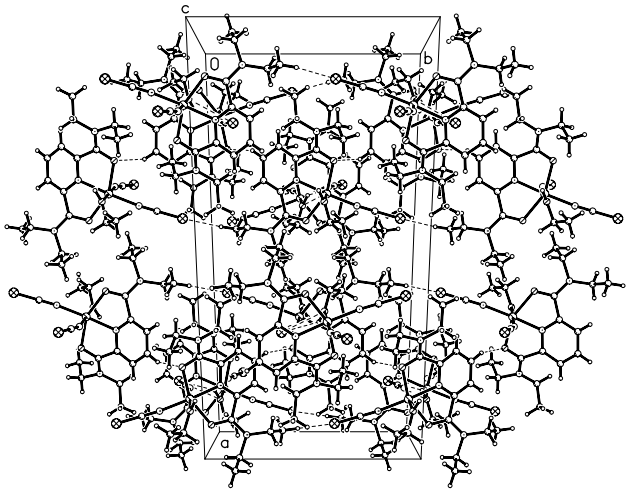


Fig. 6. Packing of complex **3** viewed perpendicular to the *ab* plane. The lattice stabilizing C–H···S interactions are shown by dotted lines.

Acknowledgements

We sincerely thank Professor Rabindranath Mukherjee for his kind help with low temperature magnetic susceptibility measurements on complex **1**. A.K. is grateful to CSIR, New Delhi, India for senior research fellowship.

Appendix A. Supplementary material

Supplementary data associated with this article can be found, in the online version at doi:10.1016/j.poly.2005.04.006.

References

[1] (a) F.A. Chavez, M.M. Olmstead, P.K. Mascharak, Inorg. Chem. 35 (1996) 1410;
(b) F.A. Chavez, M.M. Olmstead, P.K. Mascharak, Inorg. Chem. 36 (1997) 6323;
(c) D.S. Marlin, M.M. Olmstead, P.K. Mascharak, Inorg. Chem. 38 (1999) 3258;
(d) J.C. Noveron, M.M. Olmstead, P.K. Mascharak, J. Am. Chem. Soc. 121 (1999) 3553;
(e) D.S. Marlin, M.M. Olmstead, P.K. Mascharak, Inorg. Chim. Acta 297 (2000) 106;
(f) D.S. Marlin, M.M. Olmstead, P.K. Mascharak, J. Mol. Struct. 554 (2000) 211;
(g) J.C. Noveron, M.M. Olmstead, P.K. Mascharak, J. Am. Chem. Soc. 123 (2001) 3247;
(h) D.S. Marlin, M.M. Olmstead, P.K. Mascharak, Inorg. Chem. 40 (2001) 7003.
[2] (a) A.K. Singh, V. Balamurugan, R. Mukherjee, Inorg. Chem. 42 (2003) 6497;
(b) M. Ray, D. Ghosh, Z. Shirin, R. Mukherjee, Inorg. Chem. 36 (1997) 3568;
(c) A.K. Patra, R. Mukherjee, Inorg. Chem. 38 (1999) 1388.
[3] D.S. Marlin, P.K. Mascharak, Chem. Soc. Rev. 29 (2000) 69.
[4] (a) S.M. Redmore, C.E.F. Rickard, S.J. Webb, L.J. Wright, Inorg. Chem. 36 (1997) 4743;
(b) T. Yano, R. Tanaka, T. Nishioka, L. Kinoshita, K. Isobe, L.J. Wright, T. Collins, J. Chem. Commun. (2002) 1396.
[5] T. Kawamoto, B.S. Hammes, R. Ostrander, A.L. Rheingold, A.S. Borovik, Inorg. Chem. 37 (1998) 3424.
[6] (a) F. Renaud, C. Piguet, G. Bernardinelli, J.C.G. Bunzli, G. Hopfgartner, Chem. Eur. J. 3 (1997) 1646;
(b) T. Le Borgne, J.M. Benech, S. Floquet, G. Bernardinelli, C. Aliprandini, P. Bettens, C. Piguet, J. Chem. Soc., Dalton Trans. (2003) 3856.
[7] (a) P. Kapoor, A. Kumar, J. Nistandra, P. Venugopalan, Transition Met. Chem. 25 (2000) 465;
(b) R. Kapoor, A. Kataria, P. Kapoor, P. Venugopalan, Transition Met. Chem. 29 (2004) 425;
(c) P. Kapoor, A. Kataria, P. Venugopalan, R. Kapoor, M. Corbella, M. Rodriguez, M. Romero, A. Llobet, Inorg. Chem. 43 (2004) 6699.
[8] (a) J.G.H. De Preez, B. van Brecht, J.F. de Wet, J. Koorts, Inorg. Nucl. Chem. Lett. 10 (1974) 935;
(b) J.G.H. de Preez, B.J.A.M. van Brecht, Inorg. Chim. Acta 162 (1989) 49.

[9] (a) J. Garcia-Lozano, M.A. Martinez-Lorento, E. Escriva, R. Ballesteros, Synth. React. Inorg. Met. Org. Chem. 24 (1994) 365;
(b) J. Garcia-Lozano, L. Soto, J.V. Folgado, E. Escriva, Polyhedron 15 (1996) 4003.
[10] Siemens, XSCANS, X-ray Single Crystal System, Version 2.1, Siemens Analytical X-ray Instruments Inc., Madison, WI, USA, 1994.
[11] G.M. Sheldrick, SHELXTL-PC, Release 5.03, Siemens Analytical X-ray Instruments Inc., Madison, WI, USA 1995.
[12] M. Nardelli, PARST, Comput. Chem. (1983) 95.
[13] W.J. Geary, Coord. Chem. Rev. 7 (1971) 81.
[14] (a) P.C.H. Mitchell, R.J.P. Williams, J. Chem. Soc. (1960) 1912;
(b) J. Lewis, R.S. Nyholm, P.W. Smith, J. Chem. Soc. (1961) 4590;
(c) J.L. Burmeister, Coord. Chem. Rev. 1 (1966) 205;
(d) J.L. Burmeister, Coord. Chem. Rev. 3 (1968) 225.
[15] F.A. Cotton, A. Davison, W.H. Ilsley, H.S. Trop, Inorg. Chem. 18 (10) (1979) 2719.
[16] L.R. Groeneveld, G. Vos, G.C. Verschoor, J. Reedijk, J. Chem. Soc., Chem. Commun. (1982) 620.
[17] T. Koga, H. Furutachi, T. Nakamuura, N. Fukita, M. Ohba, K. Takahashi, H. Okawa, Inorg. Chem. 37 (1998) 989.
[18] (a) P.A. Harding, K. Henrick, L.F. Lindoy, M. McPartlin, P.A. Tasker, J. Chem. Soc., Chem. Commun. (1983) 1300;
(b) K.R. Adam, A.J. Leong, L.F. Lindoy, B.J. McCool, A. Ekstrom, I. Liepa, P.A. Harding, K. Henrick, M. McPartlin, P.A. Tasker, J. Chem. Soc., Dalton Trans. 11 (1987) 2537.
[19] G.A. van Albada, R.A.G. de Graff, J.G. Haasnoot, J. Reedijk, Inorg. Chem. 23 (1984) 1404.
[20] D.-T. Wu, C.-S. Chung, Inorg. Chem. 25 (1986) 3584, and references therein.
[21] J.A.A. Mokuolu, J.C. Speakman, Acta Crystallogr., Sect. B 31 (1975) 172, and references therein.
[22] L. Pauling, The Nature of Chemical Bond, Cornell University Press, Ithaca, NY, 1960.
[23] (a) D.V. Naik, W.R. Scheidt, Inorg. Chem. 12 (1973) 272;
(b) M.G.B. Drew, A.H. bin Othman, S.G. McFall, P.D.A. Mcllroy, S.M. Nelson, J. Chem. Soc., Dalton Trans. (1977) 438.
[24] (a) S.E. Livingstone, Quart. Rev. Chem. Soc. 19 (1965) 386;
(b) M.G.B. Drew, A.H. bin Othman, S.M. Nelson, J. Chem. Soc., Dalton Trans. (1976) 1394.
[25] For a special issue on polymorphism in crystals: fundamentals, prediction and industrial practice, see: in: R.D. Rogers (Ed.), Cryst. Growth Des. 3 (6) (2003).
[26] (a) G.R. Desiraju, Crystal engineering: the design of organic solids, Elsevier, Amsterdam, 1989;
(b) J.-M. Lehn, Supramolecular Chemistry: Concepts and Perspectives, VCH, Weinheim, 1995;
(c) D.S. Lawerence, T. Jiang, M. Levett, Chem. Rev. 95 (1995) 2229.

Available online at www.sciencedirect.com
SCIENCE DIRECT®
Polyhedron 24 (2005) 1233
POLYHEDRON
www.elsevier.com/locate/poly

Foreword

Polyhedron Symposia-in-Print, number 27 *Ansa* metallocenes and related compounds

It is well known that the incorporation of substituents on cyclopentadienyl rings may have a profound effect on the reactivity of metallocene compounds by varying both the electronic nature and steric environment of a metal center. In particular, an important class of ring-substituents is one that links the two cyclopentadienyl groups together. Such complexes are called *ansa* metallocenes, a term that is derived from the Latin word *ansa*, meaning "bent handle, attached at both ends". The interest in *ansa* metallocenes stems from the ability of the bridge to displace the cyclopentadienyl rings from their natural positions and thereby provide an additional influence on reactivity. Closely related to *ansa* metallocenes are "half-sandwich" counterparts in which the bridge is between a cylopentadienyl ring and another donor group. Certain molecules in this class have been dubbed "constrained geometry catalysts" because of their excellent ability to catalyze olefin polymerization. The purpose of this Symposium-in-Print is to highlight recent advances pertaining to these *ansa* metallocene and "constrained geometry" systems.

Gerard Parkin
Department of Chemistry
Columbia University
New York, NY 10027
USA
E-mail address: parkin@chem.columbia.edu

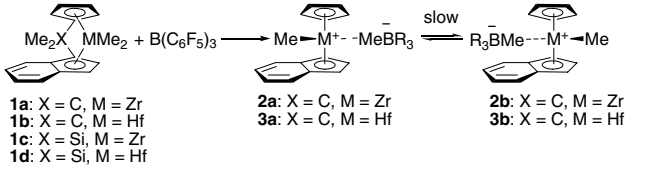
Available online 15 July 2005

doi:10.1016/j.poly.2005.06.001

apolar media in which typical polymerization reactions are conducted.

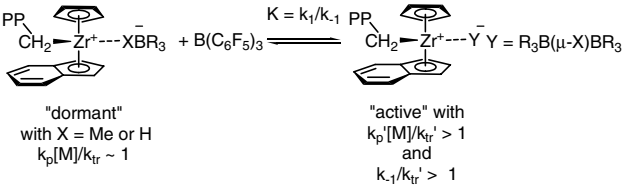
As activity is correlated with the weakness of this interaction, the search for less coordinating anions has focused on dinuclear anions in which two group 13 atoms are linked via an anionic bridge [5]. Some of these dinuclear activators give rise to extremely active catalysts where polymer tacticity is subtly affected by the nature of the counter-anion [5a]. It is therefore interesting to consider the possible role of such species in olefin polymerization using mononuclear activators [5a] particularly when in situ alkylation using aluminum alkyls and activation with such compounds is employed [6]. It is known that aluminum alkyl scavenging agents degrade activators such as $B(C_6F_5)_3$ and $[Ph_3C][B(C_6F_5)_4]$ [7], and it is therefore not always clear as to the nature of the active species produced under these conditions, depending on activation protocol [8].

Recent studies on 1-hexene polymerization using [*rac*-en(Ind)$_2$ZrMe][MeB$(C_6F_5)_3$] in the absence of additives such as alkyl aluminum compounds indicate that excess $B(C_6F_5)_3$ activator has no effect on the kinetics of initiation and propagation [2h]. However, when using $Al(C_6F_5)_3$, pronounced effects on catalyst activity were noted when using two versus one equivalent and various metallocene or constrained geometry catalysts [9]. This was attributed to "double-activation" of the catalyst precursor, based on the X-ray structure of $[Me_2Si(Ind)_2Zr][MeAl(C_6F_5)_3]_2$, although an alternative explanation based on transient formation of $[Me_2Si(Ind)_2ZrMe][(C_6F_5)_3Al(\mu\text{-Me})Al(C_6F_5)_3]$ [9] featuring this more weakly coordinating di-aluminate counter-ion [10] was not excluded. It should be noted in this regard that a related dicationic complex, $[(^tBu_3P{=}N)_2Ti][MeB(C_6F_5)_3]_2$, is *inactive* in olefin polymerization at least in polar media [11]. More recently, the use of excess $[Ph_3C][B(C_6F_5)_4]$ has been reported to significantly increase the rate of a number of metallocene-catalyzed propene polymerizations; only a portion of this activation has been attributed to an increase in active site concentration [12].



(1)

During the course of some mechanistic work involving the activation of $Me_2X(Cp)IndMMe_2$ (**1**; X = C or Si, M = Zr, Eq. (1)) using $B(C_6F_5)_3$ [3c] we had encountered poor reproducibility in propene polymerizations initiated by the ion-pairs that were *pre-formed* using a B:Zr ratio of 1.0–1.2:1 in the presence of the weakly interacting scavenger $MeAl(BHT)_2$ [5e]. Subsequent work has revealed that the steady-state rate of polymerization and rate of initial monomer insertion of these sterically open, metallocene catalysts is very sensitive to the B:Zr stoichiometry used to form these ion-pairs [13]. The enhanced rates of initiation were interpreted as involving double-activation [9] of the ion-pairs **2a**–**b** [3c] formed from **1a** and $B(C_6F_5)_3$, whereas the effect of excess borane on propagation rates were postulated as arising from two forms of the catalyst differing significantly in their polymerization activity, in equilibrium with one another in the presence of excess borane (e.g., Eq. (2)).



(2)

In this paper, we report that the nature of the Zr-containing by-products formed following consumption of monomer is also sensitive to the initial B:Zr stoichiometry used to form these ion-pairs, and possible interpretations of enhanced propagation rates in the presence of excess borane.

2. Results and discussion

2.1. Propene polymerization and reaction of ion-pairs *2a–b* with propene

As shown in Fig. 1(a), the rate of initial propene uptake using catalyst **1a** (X = C, M = Zr) is strongly increased in the presence of excess borane. Moreover, the steady-state rate of propene consumption is also affected in a similar manner. Thus, an excess of borane appears to increase *both* initiation and propagation rates in a qualitatively similar manner. Additional experiments revealed that this effect is observed on addition of excess borane to a catalyst producing polymer after initiation has occurred. Similar behavior is also observed for catalyst **1c** (X = Si) or for C_s-symmetric catalyst $Me_2C(Cp)FluZrMe_2$ [13].

These polymerizations involved pre-contacting the dialkyl with the borane in a small volume of toluene prior to introduction into the reactor saturated with monomer and containing an excess of the scavenging agent $MeAl(BHT)_2$ and small quantities of $AlMe_3$. While it is tempting to attribute this unexpected behavior to the conditions employed, control studies have shown that there is no reaction between the catalyst components (or the derived ion-pairs) and this scavenging agent [3c] nor its degradation product BHT [14] at least on the time scale of these polymerization

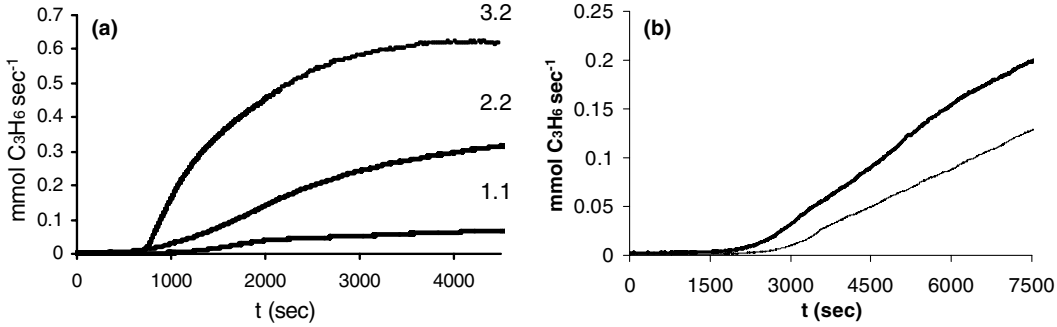


Fig. 1. (a) Propene consumption vs. time for zirconocene **1a** (40 μM) activated by 1.1–3.2 equiv. of $B(C_6F_5)_3$. The induction period observed prior to monomer uptake corresponds to the consumption of dissolved propene so as to produce a pressure drop across the mass flowmeter. (b) Initial rate of monomer uptake using hafnocene **1b** (40 μM) and 3.0 vs. 1.1 equiv. of $B(C_6F_5)_3$.

experiments. Moreover, the activity of Hf analogue **1b** is less affected in the presence of excess borane (Fig. 1(b)), supporting our contention that the observed behavior is intrinsic (i.e., correlated with M–C versus B–C bond strengths), rather than an artifact of the experimental conditions.

With complex **1a**, the microstructure of the PP formed was insensitive to changes in B:Zr stoichiometry over the range studied (1.1:1–70:1), while the MW of the oligomers formed, as judged by the intensity of signals due to vinylidene end groups, increased in the presence of excess borane. The former finding tends to suggest that the nature of the species that is producing polymer is unaffected in the presence of excess borane – there is simply "more" of it.

The change in MW could be consistent with this hypothesis provided excess borane indirectly affects the relative rates of chain-transfer (via β-H elimination with first order rate constant k_{tr}) to propagation (with second order rate constant k_p) as suggested in Eq. (2) [13]. It is easy to show that if the k_p/k_{tr} characteristics of each catalyst state are sufficiently different, and that the rate of isomerization from the more active to the less active state is faster than the rate of chain transfer from the

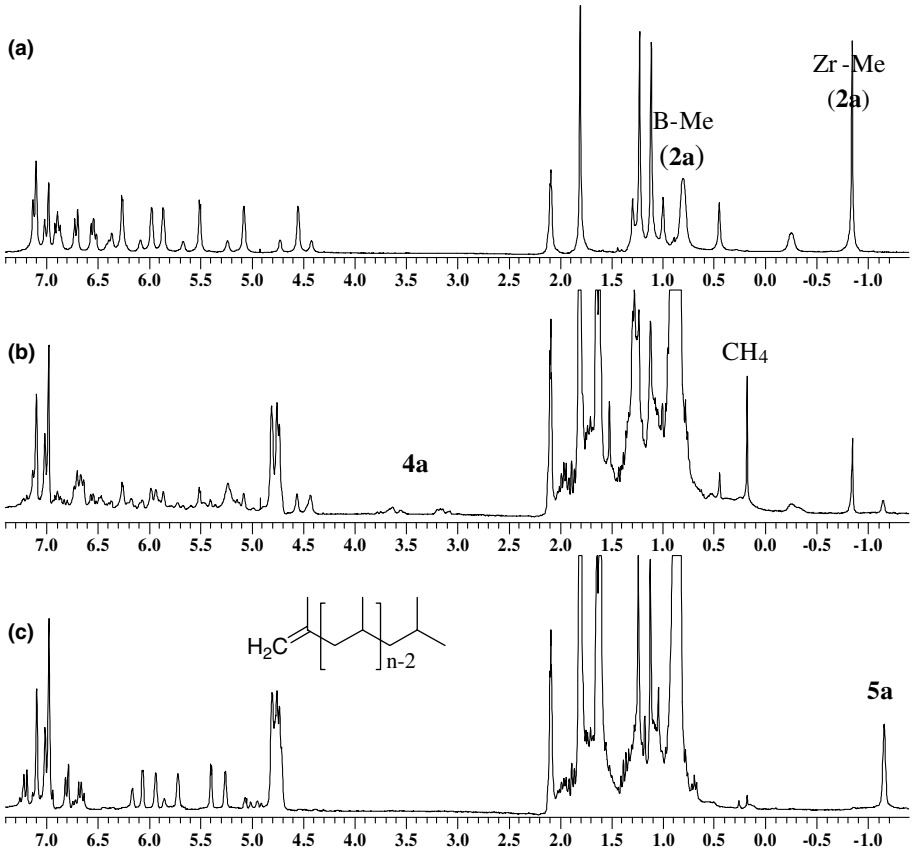


Fig. 2. ^1H NMR spectra (300 MHz, toluene-d_8) of (a) ion-pairs **2a**–**b**, and following the addition of 10.0 equiv. of propene in the presence of (b) 0.0 and (c) 0.2 equiv. of excess $B(C_6F_5)_3$.

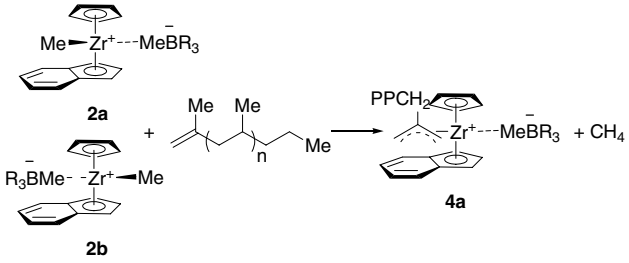
former, the MW of the polymer formed will be dictated by the k_p/k_{tr} characteristics of the less productive state when present in significant quantities at equilibrium [15].

As expected, saturation behavior is observed on the steady-state rate of polymerization as a function of excess borane using both this catalyst and $Me_2C(Cp)FluZrMe_2$ [13] but the interpretation of this observation is rendered difficult in that the chemical nature of both the dormant and active states during propagation is actually unknown as suggested in Eq. (1). In addition, it is not known whether the active state reverts to the dormant state following each insertion; certainly the value of K that was estimated by assuming it *remains* in the active state is sufficiently large (10^4 M^{-1}) so as to suggest to former scenario is likely.

We also examined the reaction of ion-pairs **2a**–**b** (M = Zr, Eq. (1)) and **3a**–**b** (M = Hf) prepared at ratios of 1.0 and 1.2 B:M with fixed amounts of propene using both ^1H and ^{19}F NMR spectroscopy in C_6D_6 at 25 °C. As shown in Fig. 2, it is evident that the isomeric ion-pairs formed from **1a** and 1.2 equiv. $B(C_6F_5)_3$ (Fig. 2(a)) are consumed on addition of 10.0 equiv. of propene (Fig. 2(c)) whereas they are still present in significant amounts when 1.0 equiv. of borane is used (Fig. 2(b)). While mass-transfer effects are undoubtedly important in these NMR experiments, it is clear that there are detectable differences given this limitation.

It is also evident from Fig. 2 that the nature of the by-products formed following consumption of monomer is also sensitive to B:Zr stoichiometry. In particular at a 1:1 stoichiometry, significant quantities of methane are produced and multiple signals appear in the region between 3 and 4 ppm (Fig. 2(b)). On monitoring this mixture for extended periods of time at room temperature, it became evident that methane was being produced as ion-pairs **2a**–**b** were being consumed by reaction with the unsaturated (and soluble) oligomers that form under these conditions.

The nature of the complexes formed was not immediately evident from the spectroscopic data, but given extensive literature precedent for allylic C–H activation of olefins to form stable or transient π-allyl complexes [16], it seemed likely that oligomeric π-allyl complexes **4a** were being produced (Eq. (3)). We will demonstrate that this is indeed the case (vide infra).



(3)

2.2. Formation of borohydride complexes 5 and 6 in the presence of excess borane

In the presence of excess borane, very little methane is detected while two complexes **5a**–**b** are produced (Eq. (4)). The major isomer **5a** features a broadened Zr–Me resonance at −1.2 ppm (Fig. 2(c)), while two sets of resonances are observed in the ^{19}F NMR spectrum of the mixture (Fig. 3). Although the reaction is relatively clean, attempted isolation of these complexes invariably resulted in their decomposition. In concentrated solu-

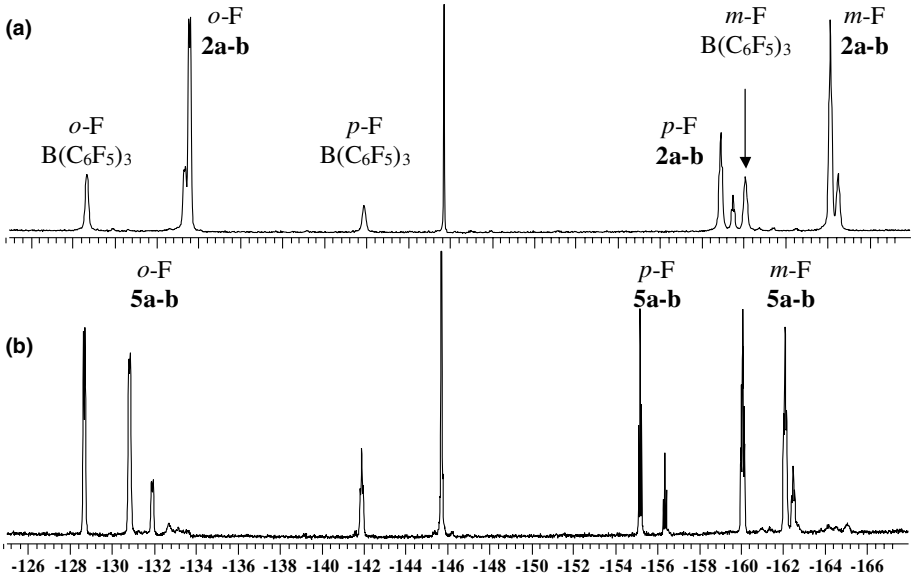
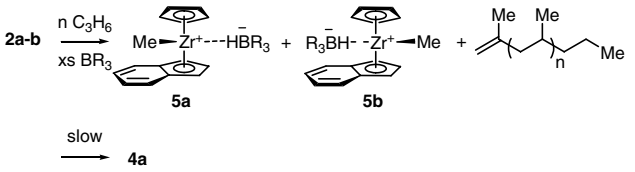


Fig. 3. ^{19}F NMR spectra (282 MHz, toluene-d_8) of (a) ion-pairs **2a**–**b** and 0.2 equiv. of excess $B(C_6F_5)_3$ and (b) following the addition of 10.0 equiv. of propene. All of the signals in (a) are line-broadened due to borane-mediated exchange of isomers **2a** and **2b** [3c,13].

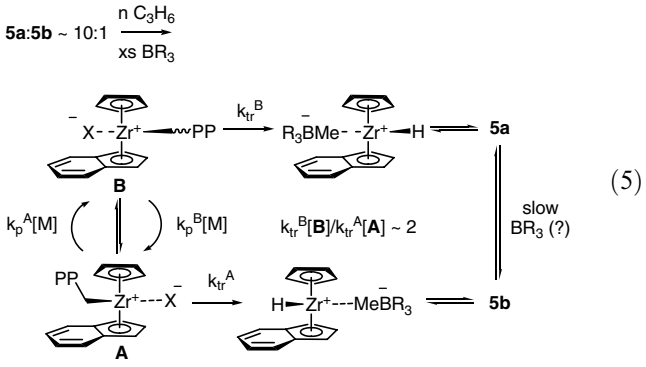
tion these complexes are also reactive towards the unsaturated oligomers present in these mixtures and the products are analogous to those formed from **2a**–**b** (vide infra).



(4)

Depending on how much propene was initially added, and the Zr:B stoichiometry, the relative amounts of these two complexes varied. The minor complex **5b** tended to form in lower amounts when adding small quantities of propene at lower ratios of B:Zr but not in a manner that was easily explained due to the presence of unreacted ion-pairs **2a**–**b** under these conditions. We have since discovered that if sufficient propene is added initially so as to consume all of **2a** and **2b**, that the equilibrium ratio of **5a**:**5b** (ca. 10:1) changes to about 2:1 on addition of more monomer while added oligomer is produced (Fig. 4). In the absence of monomer, this ratio then reverts slowly to the equilibrium ratio by a mechanism which must involve ion-pair reorganization [1b], possibly assisted by excess borane [3c].

In essence, as suggested in Eq. (5), the processes of re-initiation involving **5a**–**b**, subsequent chain growth and chain transfer must afford the (unobserved) cationic hydrides in a 2:1 ratio, presumably via kinetically controlled β-H elimination from the isomeric, propagating ion-pairs **A** and **B**. These then rapidly isomerize (vide infra) to the borohydride complexes which eventually interconvert through an independent mechanism in the absence of monomer.



(5)

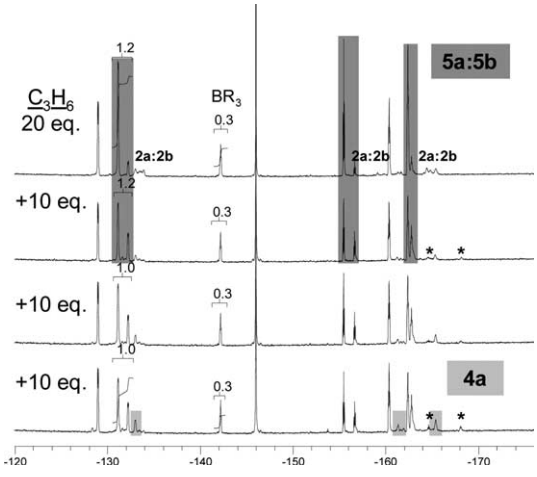


Fig. 4. ^{19}F NMR spectra (282 MHz, toluene-d_8) of ion-pairs **2a**–**b** and 0.2 equiv. of excess $B(C_6F_5)_3$ following the addition of 20 equiv. of propene, and then after three consecutive additions of 10 equiv. of propene. Signals due to borohydride complexes **5a**–**b** are highlighted in dark gray while those due to oligo-π-allyl complexes **4a** are highlighted in light gray. Faint signals marked with an asterisk are due to a weakly coordinating anion with $\delta\Delta \sim 3$ ppm. Tetrafluoro-*p*-xylene added as an internal standard.

The Hf analogues **3a**–**b** were also studied and qualitatively similar behavior was observed. Here, however, consumption of propene was considerably slower under otherwise identical conditions [see Fig. 5(a) (1)–(3)] and as would be expected the oligomers produced were of higher molecular weight. It is interesting to note that a complex **6** analogous to **5a** is present *during* monomer consumption [Fig. 5(a) (2)] and is the sole product present following completion of monomer consumption under these conditions [Fig. 5(a) (3) and Fig. 5(b) (3)]. Unlike its Zr counter-part, complex **6** could be isolated and purified as it was less reactive towards the oligomers produced. We do not know if this differential behavior is intrinsic or simply results from the lower end-group concentrations present [compare Fig. 5(a) (3) versus Fig. 2(c)].

Crystals of complex **6** could be grown from a mixture of hexane and benzene and the molecular structure of this complex is shown in Fig. 6, while crystallographic and refinement data, atomic coordinates and isotropic thermal parameters, and selected bond lengths and angles appear in Tables 1–3, respectively.[1] Complex **6** is an *ansa*-metallocenium ion partnered with a $(C_6F_5)_3BH$ counter-anion where the latter is interacting with the Hf through bridging H and F atoms. We believe this is the first structurally characterized example of this type of complex where the borohydride counter-anion is bridging rather than terminal.

The B–H distance at 1.24(4) Å is somewhat longer than that observed (1.06–1.21 Å) in other structures involving this counter-anion [17] while the Hf–H distance of 2.05(4) Å is only 14% longer than the sum of the single bond covalent radii. The characteristics of the Hf–H–B bridge are consistent with strong, directional bonding where the angle at H is close to linearity

[1] CCDC-257963 contains the supplementary crystallographic data for this structure. These data can be obtained free of charge via www.ccdc.ac.uk/conts/retrieving.html (or from the Cambridge Crystallographic Data Centre, 12 Union Road, Cambridge CB2 1EZ, UK; fax: +44 1223 336 033; or deposit@ccdc.cam.ac.uk).

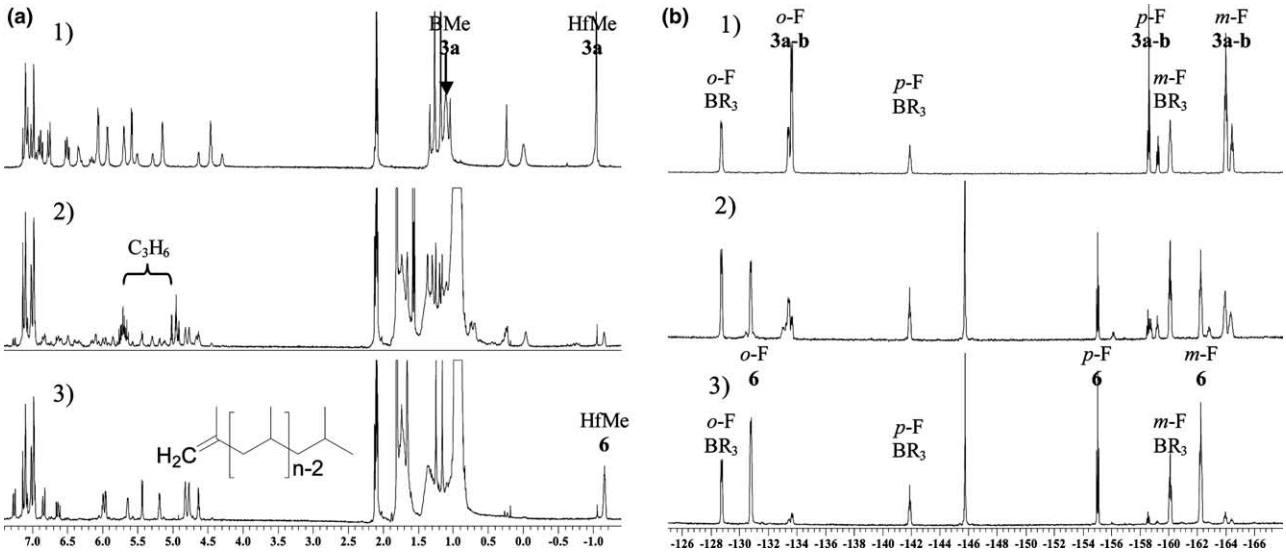


Fig. 5. (a) ^{1}H NMR spectra (300 MHz, toluene-d_8) of hafnocene ion-pairs **3a**–**b** formed from **1b** and excess borane (1) prior to, (2) 5 min and (3) 30 min after the addition of 14.0 equiv. of propene and (b) ^{19}F NMR spectra (282 MHz, toluene-d_8) of hafnocene ion-pairs **3a**–**b** formed from **1b** and excess borane (1) prior to, (2) 5 min and (3) 30 min after the addition of 14.0 equiv. of propene. Tetrafluoro-*p*-xylene added as an internal standard.

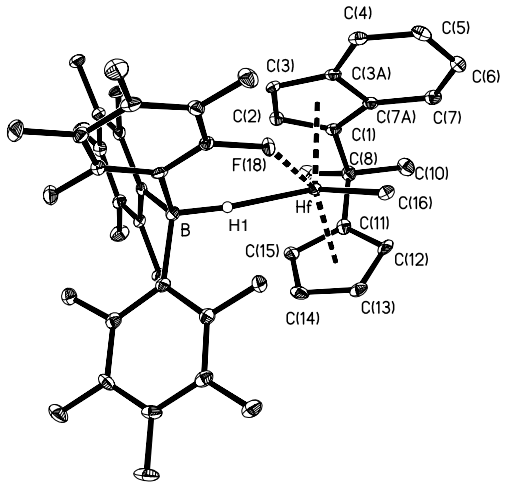


Fig. 6. Molecular structure of borohydride complex **6** with 30% thermal ellipsoids and H-1 depicted.

at 175(3)°. In contrast, the Hf–F interaction is relatively weak at 2.686(2) Å which is about 14% longer than *intramolecular* Zr–F contacts in zwitterionic structures featuring such interactions [2.237(4)–2.423(3) Å] [18], and is even longer than the *intermolecular* Zr–F contacts in $[Cp^*_2ZrH][HB(C_6F_5)_3]$ of 2.416(3) and 2.534(3) Å [17c].

In solution, both of these interactions are maintained. The bridging H atom resonates at δ 0.44 as deduced from the $^1H\{^{11}B\}$ spectrum, in agreement with NMR data reported by Sadow and Tilley [19] for $CpCp^*HfH(\mu\text{-}H)B(C_6F_5)_3$, whereas terminal B–H typically appear at 3–4 ppm in $(C_6F_5)_3BH$ complexes [17]. Furthermore, the Hf–Me signal appears as a line broadened septet at room temperature (J_{HF} = 2.2 Hz) consistent with a time-averaged structure in which all six *o*-F atoms of the counter-anion undergo rapid exchange between terminal and bridging positions. It was not possible to freeze out this process at lower T as has been observed with other complexes [18], consistent with the weakness of the Hf–F interaction observed in the solid state.

It should be noted that complex **6**, once formed, is relatively unreactive towards further insertion of propene. Complexes **5a**–**b** are also much less reactive towards monomer insertion than **2a**–**b** and thus formation of such species is a potential deactivation pathway, at least for complexes where this counter-anion can adopt a bridging mode as is documented here. A similar borohydride complex of unknown structure is produced following 1-hexene or 1-propene polymerization using $[rac\text{-en(Ind)}_2ZrMe][MeB(C_6F_5)_3]$ – it was reactive towards further insertion of propene or 2-methylpentene [2f].

2.3. Reaction of ion-pairs *2a*–*b* with isoalkenes

As mentioned previously, very little of complexes **5** form in the absence of excess borane. The reaction of unreacted ion-pairs **2a**–**b** with the unsaturated oligomers that form is considerably slower and requires about 120 min for completion under the conditions summarized in Fig. 2(b) with [Zr] = 0.025 M and $[C_3H_6]_o \sim 0.25$ M.[2]

[2] The initial end-group concentration is approximately 0.034 M based on integration of the vinylidene signals at δ 4.8 with respect to the Me group of **5a** at δ −1.2 in Fig. 2(c). A similar value can be assumed for the experiment in Fig. 2(b).

Table 1
Crystal data and structure refinement for complexes **4b** and **6**

Complex	**6**	**4b**
Empirical form	$C_{39}H_{27}BF_{15}Hf$	$C_{40}H_{26}BF_{15}Zr$
Formula weight	969.91	893.64
T (K)	100(2)	100(2)
λ (Å)	0.71073	0.71073
Crystal system	triclinic	monoclinic
Space group	$P\bar{1}$	$P2_1/c$
Unit cell dimensions		
a (Å)	10.726 (1)	12.380(2)
b (Å)	12.914(1)	16.843(2)
c (Å)	14.044(2)	16.948(2)
α (°)	68.735(2)	90
β (°)	87.970(2)	102.317(2)
γ (°)	70.778(2)	90
V (Å^3)	1704.0(3)	3452.5(7)
Z	2	4
ρ_{calc} (Mg/m^3)	1.890	1.719
Absorption coefficient (mm^{-1})	3.174	0.432
F(000)	946	1784
Crystal size (mm)	$0.50 \times 0.30 \times 0.30$	$0.35 \times 0.25 \times 0.10$
θ Range (°)	1.56–25.00	1.68–28.28
Number of reflections collected	11 345	28 986
Number of independent reflections (R_{int})	5594 (0.0281)	8153 (0.0563)
Completeness in θ (%)	93.0	95.2
Absorption corrections	semi-empirical	semi-empirical
Maximum/minimum transmission	0.4494/0.275	0.9581/0.8114
Refinement	full-matrix least-squares on F^2	full-matrix least-squares on F^2
Data/parameters	5594/511	8153/526
Goodness-of-fit (F^2)	1.110	1.087
R indices [$I > 2\sigma(I)$]	$R_1 = 0.0276$, $wR_2 = 0.0723$	$R_1 = 0.0444$, $wR_2 = 0.1058$
R indices (all data)	$R_1 = 0.0301$, $wR_2 = 0.0806$	$R_1 = 0.0502$, $wR_2 = 0.1092$
Largest difference peak/hole (e Å^{-3})	1.859/−1.270	0.868/−0.577

We chose to confirm the formation of π-allyl complexes **4a** through the synthesis of discrete complexes of this type using model alkenes. The reaction of ion-pairs **2a**–**b** with both isobutene and 2,4,4-trimethylpentene (TMP) were examined and in each case clean formation of allyl complexes **4b**–**c** was observed.

As illustrated in Scheme 1, complex **4b** is formed via two competing routes, one involving direct C–H activation and the other consisting of a single insertion of isobutene followed by C–H activation to produce neopentane and **4b** [16c]. As neopentane was formed in ca. 3× greater amounts than methane, we conclude that the second pathway is more favorable. With the more sterically hindered TMP only methane production was noted along with the chemoselective formation of **4c** arising from C–H activation at the 2-Me group of TMP.

In the case of complex **4b**, single crystals of this material were obtained by recrystallization from hexane–CH_2Cl_2 and the molecular structure of this compound appears in Fig. 7.[3] This structure features a distorted π-allyl ligand with Zr–C(18), Zr–C(17) and Zr–C(16) distances of 2.372(2), 2.552(2) and 2.598(2) Å, respectively, and a long Zr–C(19) contact of 2.800(4) Å to the counter-anion. The metrical parameters associated with the distorted π-allyl ligand are intermediate between those [2.356(3), 2.580(2), 2.651(2) Å] in the zwitterionic allyl complex [$Cp_2Zr(\eta^3$-2-Me-C_4H_5)–$B(C_6F_5)_3$] [18b], which features a strong Zr–F interaction [2.402(1) Å] in the solid state, and the methallyl complex $Cp^*[\eta^5$-$C_5H_4CMe_2CH_2B(C_6F_5)_3]Zr(\eta^3$-$C_4H_7)$ [16d] [2.412(10), 2.593(8) and 2.513(9)] which features a very long Zr–CH_2–B contact of 3.307(10) Å. Evidently, the interaction of the $MeB(C_6F_5)_3$ anion with the metal center in the present structure, although weak, is of comparable importance to the Zr–F interaction exhibited in the former structure in terms of the extent of distortion of the π-allyl ligand. In agreement with this interpretation, the ^{19}F NMR spectra of **4b** and **4c** in benzene-d_6 are characterized by a smaller separation between the *p*- and *m*-F resonances ($\Delta\delta_{p,m} = 4.5$ ppm) compared with ion-pairs **2a**–**b** ($\Delta\delta_{p,m} = 5.2$–5.4 ppm) but these values are much larger when compared with free $MeB(C_6F_5)_3$ anion ($\Delta\delta_{p,m} = 2.7$ ppm) [20].

The ^{1}H NMR spectra of these π-allyl complexes reveals three signals between 2 and 4 ppm and a single

[3] CCDC-257964 contains the supplementary crystallographic data for this structure. These data can be obtained free of charge via www.ccdc.ac.uk/conts/retrieving.html (or from the Cambridge Crystallographic Data Centre, 12 Union Road, Cambridge CB2 1EZ, UK; fax: +44 1223 336 033; or deposit@ccdc.cam.ac.uk).

Table 2
Atomic coordinates ($Å \times 10^4$) and equivalent isotropic displacement parameters ($Å^2 \times 10^3$) for Complexes **4b** and **6**

	x	y	z	U_{eq}[a]
Complex ***6***				
Hf	4996(1)	1543(1)	7124(1)	14(1)
F(18)	3611(2)	1681(2)	8732(2)	21(1)
F(19)	2685(2)	2149(2)	10370(2)	27(1)
F(20)	313(2)	1963(2)	10982(2)	30(1)
F(21)	−1204(2)	1423(2)	9855(2)	28(1)
F(22)	−301(2)	970(2)	8184(2)	25(1)
F(24)	4445(2)	−724(2)	8819(2)	21(1)
F(25)	5155(2)	−3077(2)	9550(2)	28(1)
F(26)	3633(3)	−4132(2)	9019(2)	32(1)
F(27)	1428(3)	−2786(2)	7679(2)	30(1)
F(28)	724(2)	−444(2)	6910(2)	24(1)
F(30)	2442(2)	378(2)	5565(2)	22(1)
F(31)	1162(2)	1772(2)	3722(2)	29(1)
F(32)	−603(2)	3975(2)	3411(2)	28(1)
F(33)	−1108(2)	4681(2)	5023(2)	24(1)
F(34)	165(2)	3353(2)	6845(2)	22(1)
C(1)	5051(4)	3232(3)	5642(3)	19(1)
C(2)	3706(4)	3368(4)	5765(3)	20(1)
C(3)	3339(4)	3587(3)	6666(3)	18(1)
C(3A)	4465(4)	3652(3)	7108(3)	19(1)
C(4)	4632(4)	3924(4)	7978(3)	22(1)
C(5)	5840(4)	3930(4)	8235(3)	24(1)
C(6)	6919(4)	3672(4)	7641(3)	23(1)
C(7)	6798(4)	3413(4)	6805(3)	22(1)
C(7A)	5549(4)	3404(3)	6495(3)	18(1)
C(8)	5841(4)	2645(4)	4939(3)	21(1)
C(9)	5011(5)	2994(4)	3934(3)	29(1)
C(10)	7128(4)	2900(4)	4670(3)	29(1)
C(11)	6101(4)	1355(4)	5621(3)	20(1)
C(12)	7064(4)	686(4)	6486(3)	22(1)
C(13)	6731(4)	−309(4)	7105(3)	22(1)
C(14)	5558(4)	−250(4)	6651(3)	23(1)
C(15)	5153(4)	772(4)	5752(3)	19(1)
C(16)	6315(4)	1003(4)	8528(3)	21(1)
C(17)	1678(4)	1328(3)	8370(3)	18(1)
C(18)	2381(4)	1628(3)	8968(3)	17(1)
C(19)	1940(4)	1871(4)	9823(3)	20(1)
C(20)	738(4)	1781(4)	10124(3)	21(1)
C(21)	−15(4)	1491(4)	9561(3)	20(1)
C(22)	464(4)	1269(4)	8711(3)	19(1)
C(23)	2576(4)	−468(4)	7798(3)	17(1)
C(24)	3675(4)	−1216(4)	8505(3)	19(1)
C(25)	4055(4)	−2420(4)	8906(3)	22(1)
C(26)	3290(4)	−2955(4)	8626(3)	23(1)
C(27)	2174(4)	−2274(4)	7959(3)	22(1)
C(28)	1843(4)	−1058(4)	7557(3)	20(1)
C(29)	1372(4)	1769(4)	6318(3)	16(1)
C(30)	1561(4)	1450(4)	5469(3)	18(1)
C(31)	924(4)	2149(4)	4501(3)	20(1)
C(32)	36(4)	3262(4)	4334(3)	21(1)
C(33)	−209(4)	3622(4)	5154(3)	19(1)
C(34)	452(4)	2892(4)	6105(3)	18(1)
C(35)	2173(6)	4068(5)	1851(5)	53(2)
C(36)	1616(6)	4758(6)	763(5)	52(2)
C(37)	215(6)	4779(5)	556(4)	46(1)
B	2229(4)	947(4)	7418(3)	17(1)

Table 2 (*continued*)

	x	y	z	U_{eq}[a]
Complex ***4b***				
Zr	3633(1)	7435(1)	2231(1)	13(1)
F(22)	1777(1)	5700(1)	3401(1)	24(1)
F(23)	1181(1)	4549(1)	4272(1)	28(1)
F(24)	−985(1)	4391(1)	4405(1)	27(1)
F(25)	−2509(1)	5470(1)	3658(1)	25(1)
F(26)	−1926(1)	6630(1)	2758(1)	20(1)
F(28)	−1150(1)	5469(1)	1619(1)	26(1)
F(29)	−2368(1)	5415(1)	147(1)	39(1)
F(30)	−2530(2)	6691(1)	−864(1)	47(1)
F(31)	−1261(2)	8005(1)	−373(1)	43(1)
F(32)	−2(1)	8078(1)	1114(1)	26(1)
F(34)	−1779(1)	8104(1)	1868(1)	24(1)
F(35)	−2130(1)	9409(1)	2635(1)	30(1)
F(36)	−743(1)	9849(1)	4037(1)	31(1)
F(37)	1000(1)	8884(1)	4687(1)	35(1)
F(38)	1377(1)	7556(1)	3938(1)	25(1)
C(1)	4191(2)	6834(1)	1069(1)	16(1)
C(2)	3013(2)	6875(1)	872(1)	16(1)
C(3)	2658(2)	7671(1)	743(1)	17(1)
C(3A)	3612(2)	8149(1)	810(1)	18(1)
C(4)	3739(2)	8980(1)	688(1)	22(1)
C(5)	4776(2)	9293(2)	799(2)	27(1)
C(6)	5731(2)	8804(2)	1026(2)	27(1)
C(7)	5648(2)	8005(2)	1146(2)	22(1)
C(7A)	4580(2)	7648(1)	1035(1)	17(1)
C(8)	4827(2)	6100(1)	1454(1)	18(1)
C(9)	6004(2)	6040(2)	1310(2)	25(1)
C(10)	4207(2)	5338(1)	1139(2)	24(1)
C(11)	4808(2)	6248(1)	2340(1)	18(1)
C(12)	3912(2)	6058(1)	2709(1)	19(1)
C(13)	4036(2)	6497(2)	3442(1)	21(1)
C(14)	4987(2)	6961(2)	3521(1)	22(1)
C(15)	5453(2)	6836(2)	2837(1)	20(1)
C(16)	2631(2)	8718(1)	2535(2)	22(1)
C(17)	3655(2)	8702(1)	3059(1)	20(1)
C(18)	4613(2)	8603(1)	2733(2)	21(1)
C(19)	3711(2)	8656(2)	3964(2)	27(1)
C(20)	1491(2)	6952(1)	2300(2)	17(1)
C(21)	−55(2)	6220(1)	3010(1)	15(1)
C(22)	688(2)	5666(1)	3423(1)	18(1)
C(23)	403(2)	5054(1)	3884(2)	21(1)
C(24)	−678(2)	4980(1)	3959(2)	21(1)
C(25)	−1451(2)	5525(1)	3581(1)	19(1)
C(26)	−1121(2)	6122(1)	3129(1)	17(1)
C(27)	−548(2)	6803(1)	1474(1)	17(1)
C(28)	−1147(2)	6132(2)	1168(1)	20(1)
C(29)	−1796(2)	6083(2)	391(2)	27(1)
C(30)	−1860(2)	6721(2)	−121(2)	31(1)
C(31)	−1236(2)	7385(2)	125(2)	29(1)
C(32)	−591(2)	7405(2)	902(2)	22(1)
C(33)	−126(2)	7773(1)	2824(1)	15(1)
C(34)	−1021(2)	8276(1)	2549(1)	18(1)
C(35)	−1231(2)	8964(1)	2934(2)	20(1)
C(36)	−539(2)	9186(1)	3648(2)	21(1)
C(37)	337(2)	8699(2)	3972(1)	22(1)
C(38)	515(2)	8015(1)	3564(1)	18(1)
B	188(2)	6932(2)	2404(2)	14(1)

[a] U_{eq} is defined as one third of the trace of the orthogonalized U^{ij} tensor.

Table 3
Bond lengths (Å) and angles (°) for complexes **4b** and **6**

Bond lengths (Å)		Bond angles (°)	
Complex ***6***			
Hf–Cp[a]	2.155(4)	Cp–Hf–Ind	117.5(3)
Hf–Ind[b]	2.176(4)	C(16)-Hf–F(18)	68.2(1)
Hf–H(1)	117(1)	F(18)–Hf–H(1)	60(1)
Hf–C(1)	2.424(4)	C(16)–Hf–F(18)	68.2(1)
Hf–C(2)	2.427(4)	C(18)–F(18)–Hf	132.8(2)
Hf–C(3)	2.510(4)	C(17)–B–C(23)	107.3(3)
Hf–C(3A)	2.585(4)	C(17)–B–C(29)	115.5(3)
Hf–C(7A)	2.504(4)	C(23)–B–C(29)	118.0(4)
Hf–C(11)	2.434(4)	C(17)–B–H(1)	104(2)
Hf–C(12)	2.431(4)	C(23)–B–H(1)	106(2)
Hf–C(13)	2.509(4)	C(29)–B–H(1)	104(2)
Hf–C(14)	2.516(4)	Hf–H(1)–B	175(3)
Hf–C(15)	2.447(4)		
Hf–C(16)	2.219(4)		
Hf–F(18)	2.687(2)		
Hf–H(1)	2.05(4)		
C(17)–B	1.615(6)		
C(23)–B	1.618(6)		
C(29)–B	1.622(6)		
B–H(1)	1.24(4)		
Complex ***4b***			
Zr–Cp[a]	2.197(2)	Cp–Zr–Ind	117.1(2)
Zr–Ind[b]	2.240(2)	C(18)–Zr–C(17)	33.2(1)
Zr–C(1)	2.441(2)	C(18)–Zr–C(16)	57.9(1)
Zr–C(2)	2.455(2)	C(17)–Zr–C(16)	31.2(1)
Zr–C(3)	2.584(2)	C(17)–C(16)–Zr	72.6(1)
Zr–C(3A)	2.687(2)	C(16)–C(17)–Zr	76.3(1)
Zr–C(7A)	2.574(2)	C(18)–C(17)–Zr	66.4(1)
Zr–C(11)	2.455(2)	C(19)–C(17)–Zr	120.3(2)
Zr–C(12)	2.456(2)	C(17)–C(18)–Zr	80.3(1)
Zr–C(13)	2.553(2)	C(16)–C(17)–C(18)	118.6(2)
Zr–C(14)	2.581(2)	C(16)–C(17)–C(19)	119.1(2)
Zr–C(15)	2.482(2)	C(18)–C(17)–C(19)	121.6(2)
Zr–C(16)	2.598(2)	B–C(20)–Zr	163.9(2)
Zr–C(17)	2.552(2)	C(20)–B–C(21)	113.0(2)
Zr–C(18)	2.372(2)	C(20)–B–C(27)	104.6(2)
Zr–H(20A)	2.57(3)	C(21)–B–C(27)	111.1(2)
Zr–H(20B)	2.54(3)	C(20)–B–C(33)	110.4(2)
Zr–H(20C)	2.90(3)	C(21)–B–C(33)	105.2(2)
Zr–C(20)	2.800(3)	C(27)–B–C(33)	112.7(2)
C(16)–C(17)	1.385(4)		
C(17)–C(18)	1.422(4)		
C(20)–B	1.660(3)		
C(21)–B	1.647(3)		
C(27)–B	1.658(3)		
C(33)–B	1.669(3)		

[a] Cp is the centroid of the cyclopentadienyl ligand in each structure.
[b] Ind is the centroid of five-membered ring of the indenyl ligand.

tons through a combination of 2D COSY, and NOESY spectra. These and other chemical shift assignments are summarized in Section 4. The high field signal is due to the allyl proton closest to the indenyl ring in complexes **4b**–**c**. It can be seen by comparing the spectrum of complexes **4a** and **4b** in bromobenzene-d_5 (Fig. 8) that there is a 1:1 correspondence between the ^{1}H signals of the latter with the former mixture of complexes. Multiple signals appear in the spectrum of the former, presumably due to a combination of stereoisomers (the oligomers are basically atactic and regio-irregular) and different chain-lengths being present.

Thus, there is little question that complexes **4a** possess the indicated structure and given the chemoselectivity observed in the formation of **4c** it seems likely that this C–H activation reaction also occurs predominantly at the Me carbon of the vinylidene end-group.

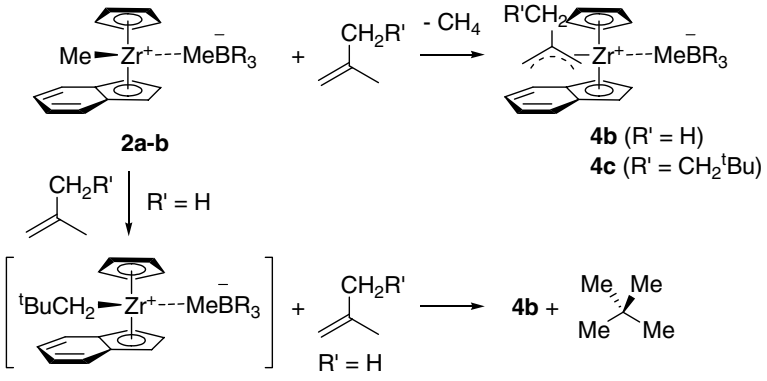
As mentioned previously, borohydride complexes **5a** and **5b** also (slowly) react with unsaturated oligomers in concentrated solution to produce π-allyl complexes **4a** and surprisingly, the counter-anion formed is not $HB(C_6F_5)_3$ but $MeB(C_6F_5)_3$ (i.e., the products are *identical*). This suggests that **5a**–**b** are in equilibrium with the corresponding cationic hydride complexes (Eq. (5) and Scheme 2) and the latter complexes are also reactive towards C–H activation.

By analogy to the reaction of **2a**–**b** with isobutene, it seems probable in this case that this process involves (reversible) insertion into Zr–H by one molecule of oligomer [2f] followed by C–H activation of a second molecule. However, we cannot exclude direct formation of **4a** with elimination of H_2 (this was not detected but could have been obscured by the Me resonances of the oligomers which form) as has been proposed to occur in propene polymerization using other metallocene catalysts [21,22].

3. Conclusions

As summarized above, in the presence of excess borane, initiation involving ion-pairs **2a**–**b** is efficient and the principal by-products are borohydride complexes **5** (or **6** in the case of Hf-analog **3a**–**b**). In the absence of excess borane, and with fixed quantities of propene, any unreacted ion-pairs undergo slow C–H activation to form π-allyl complexes **4**. Thus, the principal effect of having excess borane present is that initiation is increased relative to propagation [13] resulting in more efficient conversion of the starting ion-pairs to **5** and polymer or oligomer.

We do not view the C–H activation reaction of ion-pairs **2a**–**b** (or for that matter **5** which are less reactive – Scheme 2) with the oligomers produced as being very relevant to catalysis as this reaction is quite slow even at high catalyst concentrations (i.e., 120 min at 25 mM [Zr] and 34 mM $H_2C{=}CR_2$ groups for complete conversion of **2a**–**b**). One can estimate from this data that under conditions summarized in Fig. 1, even at $[H_2C{=}CR_2] = 0.2$ M (corresponds to about 50 g of 500 M_n polymer dissolved in 0.5 L of toluene), that this reaction would be ca. 100× slower (i.e., ~8 days for completion at 25 °C!).



Scheme 1.

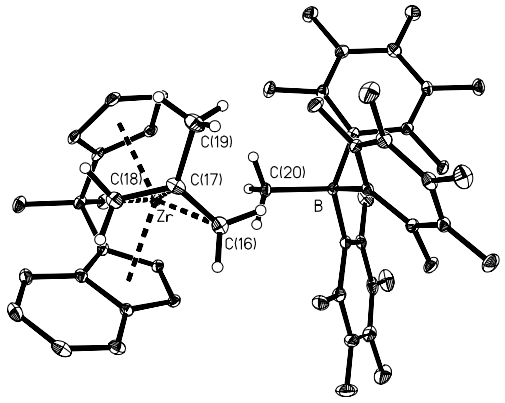


Fig. 7. Molecular structure of π-methallyl complex **4b** with 30% thermal ellipsoids and selected H-atoms depicted. The numbering scheme for the C-atoms of the *ansa*-ligand is the same as shown in Fig. 5.

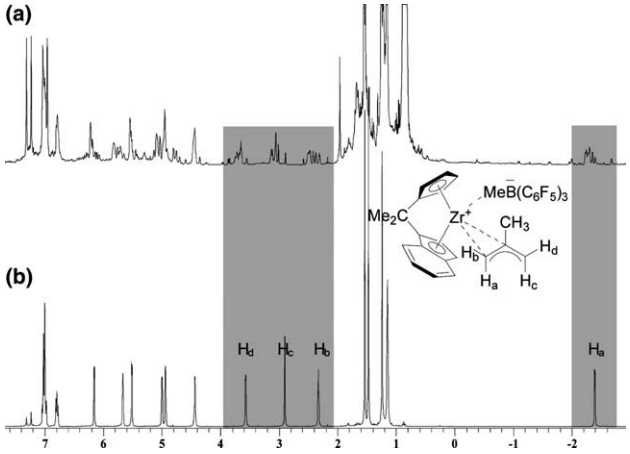


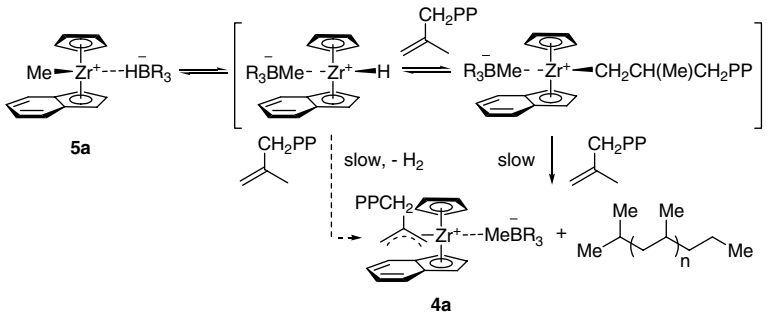
Fig. 8. ^{1}H NMR Spectra (400 MHz, C_6D_5Br) of (a) oligo-π-allyl complexes **4a** formed from ion-pairs **2a**–**b** and propene oligomers and (b) π-methallyl complex **4b** with selected ^{1}H assignments shown and highlighted in gray.

On the other hand, there is indirect evidence of this process occurring in propene polymerization using other metallocene catalysts [21,22] and it is known from model studies [16b] that these π-allyl complexes will undergo further insertion, although sluggishly compared with alkyls. Thus, it is possible that following chain transfer to metal (or to coordinated monomer) that this C–H activation reaction will be more competitive, as the unsaturated oligomer would be coordinated to the metal center [21,22] and direct C–H activation would furnish **4a** and either H_2 (or *n*-propane) as by-products.

It is difficult to reconcile this hypothesis with the observed product distribution here, as in both the presence and absence of excess borane, **5** is the principle product formed following chain transfer and the only volatile product detected is methane. Perhaps, in systems with more weakly coordinating counter-ions, or in sterically hindered metallocenes where formation of **5** is less favorable, this C–H activation reaction is more competitive.

Complex **6** and **5** are the products of chain transfer followed by isomerization (Eq. (5)). This intramolecular isomerization process has been examined theoretically using DFT and QM/MM techniques in a [bis(pyrrolide-imine)TiH][$MeB(C_6F_5)_3$] complex [23] and has a low barrier of 10 kcal mol^{-1} [24]. As we have suggested, and others have indicated with [$en(Ind)_2ZrMe$][$HB(C_6F_5)_3$] [2f], the process appears reversible with metallocene complexes. However, in the present case the equilibrium must be quite unfavorable (perhaps due to strong interaction of the counter-anion with the metal in **5** and **6**) since complexes **5**–**6** are relatively unreactive towards monomer insertion, and thus the formation of these complexes represents a reversible deactivation process. It is likely, following *initial* chain transfer in a reactor continuously supplied with monomer, that complexes **5** (or **6**) thus represent dormant states and that the function of excess borane in polymerizations involving **1** (or other catalysts of this type) is to reactivate species analogous to **5** towards insertion.

This could involve irreversible formation of [Me_2C(Cp)$IndZr(CH_2CHMe)_nR$][$MeB(C_6F_5)_3$], by analogy to the chemistry depicted in Scheme 2, where the $MeB(C_6F_5)_3$ anion is rendered less coordinating as a result of the high-



Scheme 2.

er alkyl group on the metal [2f]. Alternately, the species $[Me_2C(Cp)IndZrR][(C_6F_5)_3B(\mu\text{-}H)B(C_6F_5)_3]$, featuring a more weakly coordinating dinuclear anion [5] could form in situ as suggested in Eq. (2).

The latter counter-anion has not been reported before but does appear to form in situ from $[Bu_4N][(C_6F_5)_3BH]$ [25] and $B(C_6F_5)_3$.[4] A species with an ^{19}F NMR signature very similar to this anion is also present in trace quantities during consumption of propene by borohydride complexes **5a**–**b** (Fig. 4). However, the chemical shifts are also close to those of $[Bu_4N][(C_6F_5)_3BMe]$[4] in which the $MeB(C_6F_5)_3$ anion is non-coordinating [20]. Future work will concentrate on exploring the validity of these hypotheses.

4. Experimental

All manipulations of air- and moisture-sensitive materials were undertaken using standard vacuum and Schlenk techniques or in a glovebox under an atmosphere of nitrogen. Unless otherwise noted, all reagents were obtained from commercial sources and purified as required. All synthetic reactions were carried out in glassware under N_2 using Schlenk techniques or in a glove-box. Tetrahydrofuran, diethyl ether, hexane, toluene and dichloromethane were dried and deoxygenated by passage through columns of A-2 alumina (12×32 mesh) and Engelhard CU-0226s (Q-5) deoxo catalyst under N_2 prior to use, as described in the literature [26]. $MeAl(BHT)_2$ (MAD, [27]), $B(C_6F_5)_3$ [28], the ligands $Me_2X(IndH)CpH$ (X = C, Si) [29], $M(NMe_2)_4$ (M = Zr, Hf) [30], $Me_2X(Ind)CpMMe_2$ complexes (X = C, Si; M = Zr, Hf) [3c,31] and $Me_2C(Cp)FluZrMe_2$ [32] were prepared via the literature procedures.

Routine ^1H, ^{13}C or ^{19}F NMR spectra were obtained on either Varian Mercury or Gemini 300 MHz instruments. All ^1H NMR spectra were referenced with respect to residual protonated solvent while ^{13}C NMR spectra were referenced with respect to deuterated solvent. ^{19}F NMR spectra were referenced with respect to tetrafluoro-*p*-xylene (δ −145.69 toluene-d_8) or external $CFCl_3$. Benzene-d_6 and toluene-d_8 were dried by distillation from potassium and benzophenone under N_2 (g) and stored over activated 4 Å molecular sieves. Variable temperature ^1H, ^{13}C and ^{19}F NMR spectra were recorded on Varian Inova 400 or Unity+ 750 MHz instruments, the thermocouples of which had been calibrated to within 5% of the actual temperature using a methanol standard [33].

4.1. Polymerization procedure

Propylene polymerizations were conducted in either a 1 L Autoclave Engineers Zipperclave reactor. The temperature of the reactor was controlled using a Neslab RTE-110 constant temperature bath by circulation of coolant (50:50 v/v ethylene glycol:water) through an external jacket. The consumption of monomer (propylene) during the course of polymerization was monitored using a calibrated Matheson mass flow meter, which was controlled by a Matheson Dynablender Model 8219 power supply/readout device. The progress of polymerization was monitored using Labtech Acquire data acquisition software, which converted the digital input reading to the desired value (mmol/s of monomer) using appropriate conversion factors.

Prior to each polymerization, the reactor was conditioned by evacuation for ~4 h at 100 °C, and then cooled under nitrogen after three refill-evacuation cycles. About 480 mg of MAD (1 mmol) were dissolved in 25 mL of a stock solution of Me_3Al in toluene (0.4 mM) and the solution was transferred to the reactor via sampling bomb using a known amount of toluene (225 mL) to flush the contents of the sample bomb into the reactor (final concentration of [MAD] = 4 mM and

[4] S. Collins, A. Al-Humydi, R. Gonzales, unpublished results. $[Bu_4N][(C_6F_5)_3B(\mu\text{-}H)B(C_6F_5)_3]$: ^{19}F NMR (282 MHz, C_6D_6) −133.8 (br d, *o*-F) −164.9 (br t, *p*-F) −167.9 (m, *m*-F). $[Bu_4N][MeB(C_6F_5)_3]$: ^{19}F NMR (282 MHz, C_6D_6) −133.4 (br d, *o*-F) −165.6 (br t, *p*-F) −168.3 (m, *m*-F).

[Me_3Al] = 40 μM). The solvent was allowed to saturate with monomer at the 30 psi g and 30 °C while stirring. This procedure has been found to reduce the length of time needed for effective scavenging while effectively sequestering any residual Me_3Al to extremely low levels, through (quasi-irreversible) formation of Me_2AlBHT [27,34].

Stock solutions were prepared in the glove box by dissolving 20 mg of the metallocene complex **1** (0.058 mmol) in 25 mL toluene (2.3 mM) and 300 mg borane (0.598 mmol) in 25 mL toluene (23 mM). A stock solution of the ion-pair and excess borane was then prepared by adding a known volume of the former to the latter solution at 25 °C. Polymerizations were initiated by adding a known volume of the resulting stock solution of the ion-pair to the reactor via gas-tight syringe through a septum port. Temperature control was generally ±1 °C following catalyst introduction and catalyst concentrations were chosen so as to avoid exothermic conditions. Polymerization reactions were typically conducted for periods of time corresponding to attainment of steady state as revealed by a stable mass flow profile and then for an additional period = the length of time required to reach steady state in most cases.

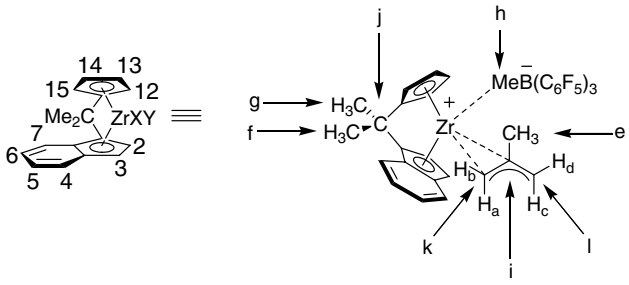
Fig. 1 depicts typical flow profiles observed under various conditions summarized in the text. The lag period observed prior to detectable uptake corresponds to consumption of dissolved propene so as to produce a small pressure drop across the mass flow meter – the length of this period is thus sensitive to catalyst activity (and absolute [Met]) as well as the extent of saturation of the solution with propene prior to catalyst introduction.

Reactions were halted by venting the monomer and emptying the reactor contents into methanol. Solvent was partially evaporated to dryness in vacuo and then the syrup was transferred to an aluminum pie plate. Solvent was allowed to further evaporate at room temperature in a hood and then at 60 °C in a vacuum oven (~1 mmHg). Polymer characterization procedures have been reported in detail elsewhere [35].

4.2. Formation of ion-pairs **2a**–**b** from complex **1a** and $B(C_6F_5)_3$ in toluene-d_8

Stock solutions of $Me_2C(Ind)CpZrMe_2$ (0.10 M) and $B(C_6F_5)_3$ (0.10 M) in toluene-d_8 were mixed in a 1:1 ratio at 25 °C in a glove box. Upon adding the metallocene to the $B(C_6F_5)_3$ solution, an immediate color change from colorless to orange red indicated a rapid reaction at this temperature. The ^1H and ^{19}F NMR spectra of the resulting solution show two sets of signals in a roughly 1:3.5 at ambient temperature due to different stereoisomers. ^1H and ^{19}F NMR spectra are depicted in Figs. 2 and 3, respectively.

4.3. [$Me_2C(Cp)IndZr(\eta^3$-$C_4H_7)$][$MeB(C_6F_5)_3$] (**4b**)

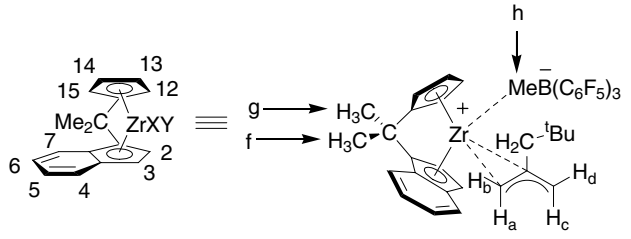


Inside the glove box, to a 25 mL round bottom flask, was added 86 mg (0.168 mmol) of $B(C_6F_5)_3$, dissolved in 1 mL of benzene-d_6. A solution of *ansa*-zirconocene complex **1a** (50 mg, 0.146 mmol) in 1 mL of benzene-d_6 was added to the $B(C_6F_5)_3$ solution at 25 °C to form an orange-red solution of the *ansa*-zirconocenium ion-pair **2a**–**b**. Outside the glove box, isobutene was bubbled into the ion-pair solution while stirring the reaction mixture for ~30 min. To ensure complete consumption of ion-pair, the reaction mixture was monitored by ^1H or ^{19}F NMR spectroscopy. At complete consumption of the ion-pair, the ^1H and ^{19}F NMR spectra indicated that the reaction was very clean and the product was stable at 25 °C. After completion of reaction, the reaction mixture was then pumped down in vacuo to dryness. The allyl complex produced was washed with hexane and crystals were obtained by redissolving the solid in minimal dichloromethane and then layering it with hexane (in 1:1 mixture) and placing this mixture in a −30 °C freezer in the dry box, overnight. The product was isolated as a yellow-orange crystals (114 mg, 91% yield). ^1H NMR (bromobenzene-d_5, 400 MHz, 25 °C): δ 6.99 (m, 3H, H_4, H_6, and H_7), 6.79 (ddd, J = 8.8, 6.2, 1.6, 1H, H_5), 6.15 (dd, J = 3.5, 1.1 Hz, 1H, H_3), 5.66 (dm, J = 3.7 Hz, 1H, H_{13}), 5.51 (d, J = 3.7 Hz, 1H, H_2), 4.99 (dm, J = 3.7 Hz, 1H, H_{14}), 4.94 (m, 1H, H_{12}), 4.44 (dd, J = 4.8, 2.7 Hz, 1H, H_{15}), 3.57 (dm, J = 4.5 Hz, 1H, H_a), 2.90 (t, J = 1.1 Hz, 1H, H_c), 2.33 (t, J = 4.0 Hz, 1H, H_b), 1.54 (s, 3H, Me_f), 1.47 (s, 3H, Me_e), 1.24 (s, 3H, Me_g), 1.14 (b, 3H, Me_h), −2.39 (dt, J = 3.7, 1.1 Hz, H, H_d). ^{13}C NMR (bromobenzene-d_5, 100 MHz, 25 °C): δ 153.3 (C_i), 148.9 (dm, J_{C-F} = 236.6 Hz, *o*-C, $B(C_6F_5)_3$), 137.8 (dm, J_{C-F} = 244.0 Hz, *p*-C, $B(C_6F_5)_3$), 136.8 (dm, J_{C-F} = 246.9 Hz, *m*-C, $B(C_6F_5)_3$), not observed $B(C_6F_5)_3$ (*ipso*-C), 128.5, 128.3, 126.7, 126.0, 122.6, 120.0, 118.5, 113.4, 110.7, 108.1, 103.1, 99.5, 97.6, 97.1 (Cp and indenyl), 89.3 (C_l), 69.0 (C_k), 38.0 (C_j), 26.5 (C_e), 25.0 (C_g), 24.0 (C_f), 11.2 (C_h). ^{19}F NMR (bromobenzene-d_5, 282 MHz, standard: tetrafluoro-*p*-xylene, −145.71 ppm): δ −133.1 (br d, J = 24.4 Hz, *o*-*F*), −160.7 (t, J = 21.4 Hz, *p*-*F*), −165.2 (m, *m*-*F*). IR (Nujol, KBr plates, cm^{-1}): 1642 (w), 1514 (w), 1088 (w), 970 (w), 910 (w), 820 (w). Elec-

trospray ionization mass spectrometry: positive-ion at *m/z* 365.1 (M^+, Zr^{90}), negative-ion at *m/z* 526.8 (M^-, B^{11}). Elemental *Anal*. Calc. for $C_{40}H_{26}BF_{15}Zr$: C, 53.76; H, 2.93. Found: C, 53.18; H, 2.93%.

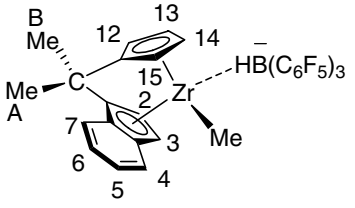
A crystal of dimensions $0.35 \times 0.25 \times 0.10$ mm was coated with Paratone oil and mounted on Cryoloops™ and placed on the goniometer head of a Bruker Apex CCD diffractometer. The reflections were collected at 100(2) K using ψ and ω scans. The diffraction source was graphite-monochromated Mo Kα radiation ($\lambda = 0.71073$ Å). Unit cell determination was achieved by using reflections from three different orientations. Data integration was accomplished using SAINT. An empirical absorption correction and other corrections were done using multi-scan SADABS. Structure solution, refinement and modeling were accomplished using the Bruker SHELXTL package. The structure was obtained by full-matrix least-squares refinement of F^2 and the selection of the appropriate atoms from the generated difference map. Hydrogen atoms of the borate anion were found from the difference map, U_{iso}(H) values fixed according to a riding model, and their positions refined. All other hydrogen positions were calculated and their U_{iso}(H) values fixed according to a riding model.

4.4. [$Me_2C(Cp)IndZr(\eta^3$-2-($CH_2{}^tBu)C_4H_4$)][$MeB(C_6F_5)_3$] (**4c**)



Inside the glove box, to a 25 mL round bottom flask, was added 82 mg (0.160 mmol) of $B(C_6F_5)_3$ dissolved in 1 mL of benzene-d_6. A solution of *ansa*-zirconocene complex **1a** (50 mg, 0.146 mmol) in 1 mL of benzene-d_6 was added to the borane solution at 25 °C to form an orange-red solution of the *ansa*-zirconocenium ion-pair **2a**–**b**. Outside the glove box, excess 2,4,4-trimethyl-1-pentene (140 μL, 0.883 mmol) was added via microsyringe to the ion-pair solution with magnetic stirring, and the reaction mixture stirred for ~1 h to ensure complete consumption of ion-pair, as monitored by NMR spectroscopy. At complete consumption of ion-pair, the ^{1}H and ^{19}F NMR spectra indicated that the reaction was clean and the product was stable at 25 °C. After completion of reaction, the reaction mixture was then pumped down. The allyl complex produced was washed with hexane (2×5 mL) and the orange-red solid further dried in vacuo to dryness (109 mg, 81% yield). ^{1}H NMR (benzene-d_6, 300 MHz, 25 °C): δ 6.64 (m, 3H, H_4, H_6, and H_7), 6.40 (ddd, $J = 9.1$, 4.9, 2.8 Hz, 1H, H_5), 6.18 (dd, $J = 3.3$, 0.6 Hz, 1H, H_3), 5.93 (d, $J = 3.3$ Hz, 1H, H_2), 5.36 (dd, $J = 5.2$, 2.7 Hz, 1H, H_{13}), 5.19 (dd, $J = 5.2$, 2.7 Hz, 1H, H_{14}), 5.15 (dd, $J = 5.2$, 2.7 Hz, 1H, H_{12}), 4.34 (dd, $J = 5.2$, 2.7 Hz, 1H, H_{15}), 3.54 (dm, $J = 3.85$ Hz, 1H, H_a), 3.17 (s, 1H, H_c), 1.85 (t, $J = 4.39$ Hz, 1H, H_b), 1.24 (s, 3H, Me_f), 1.23 (s, 2H, CH_2), 1.22 (s, 3H, Me_g), 0.79 (s, 9H, ^{t}Bu), −0.24 (b, 3H, Me_h), −2.53 (dt, $J = 3.5$, 1.1 Hz, H, H_d). ^{19}F NMR (benzene-d_6, 282 MHz): δ −133.0 (br d, $J = 18.3$ Hz, *o-F*), −160.9 (t, $J = 21.4$ Hz, *p-F*), −165.1 (m, *m-F*). IR (Nujol, KBr plates, cm^{-1}): 1642 (w), 1512 (m), 1273 (w), 1089 (m), 970 (m), 803 (w). Electrospray ionization mass spectrometry: positive-ion at *m/z* 421.2 (M^+, Zr^{90}), negative-ion at *m/z* 526.9 (M^-, B^{11}).

4.5. Reaction of propylene with zirconocenium ion-pairs **2a**–**b**; formation of borohydride complexes **5a**–**b**



The reaction was conducted in screw cap NMR tubes. Stock solutions of $Me_2C(Ind)CpZrMe_2$ (0.05 M) and $B(C_6F_5)_3$ (0.05 M) in toluene-d_8 were mixed in a 1:1.2 or 1:1 ratio at 25 °C in a glove box. There was an immediate color change from colorless to orange red. Outside the glove box, 10 equiv. of propylene was added to the ion-pair solution in each NMR tube using a vortex mixer. The ^{1}H and ^{19}F NMR spectra obtained are summarized in Figs. 2 and 3. ^{1}H NMR of the major isomer **5a** (benzene-d_6, 300 MHz): δ 7.23 (d, $J = 8.5$ Hz 1H,H_4), 6.96 (m, 1H, H_5), 6.78 (dm, $J = 9.1$ Hz, 1H, H_7), 6.65 (m, 1H, H_6), 6.09 (d, $J = 3.0$ Hz, 1H, H_3), 5.91 (dd, $J = 5.5$, 3.3 Hz, 1H, H_{14}), 5.73 (dd, $J = 4.4$, 2.2 Hz, 1H, H_{13}), 5.42 (d, $J = 3.3$ Hz, 1H, H_2), 5.28 (dd, $J = 5.5$, 2.7 Hz, 1H, H_{12}), 4.75 (dd, $J = 5.5$, 2.7 Hz, 1H, H_{15}), 1.20 (s, 3H, Me_A), 1.09 (s, 3H, Me_B), −1.10 (septet, $^3J_{H-F} = 2.2$ Hz, 3H, Me–Zr).^{19}F NMR (benzene-d_6, 282 MHz): δ −131.0 (br d, $J = 18.3$ Hz, *o-F*), −155.0 (t, $J = 21.4$ Hz, *p-F*), −162.0 (m, *m-F*). ^{1}H NMR spectrum of the minor isomer **5b** (benzene-d_6, 300 MHz): δ 0.27 (s, 3H, Me–Zr) other signals due to this isomer could not be assigned and/or overlapped with those of **5a**.^{19}F NMR (benzene-d_6, 282 MHz): δ −132.2 (br d, $J = 18.3$ Hz, *o-F*), −156.5 (t, $J = 21.4$ Hz, *p-F*), −162.8 (m, *m-F*).

4.6. $Me_2C(Cp)IndHfMe(\mu\text{-}H)B(C_6F_5)_3$ (**6**)

Inside the glove box, to a 25 mL round bottom flask, was added 180 mg (0.351 mmol) of $B(C_6F_5)_3$, dissolved in 2 mL toluene. A solution of *ansa*-hafnocene complex **1b** (100 mg, 0.233 mmol) in 2 mL of toluene was added to the solution of $B(C_6F_5)_3$ at 25 °C, and a bright yellow solution of the *ansa*-hafnocenium ion-pair was formed. Outside the glove box, propylene was bubbled into the ion-pair solution with magnetic stirring. The solution became orange and the reaction mixture was stirred for ~30 min. To ensure complete consumption of the starting ion-pair, the reaction mixture was monitored by ^1H or ^{19}F NMR spectroscopy, and if needed, additional propylene was added. At complete consumption of the ion-pair, the ^1H and ^{19}F NMR spectra indicated that the reaction was very clean (Fig. 5) and the product was stable at 25 °C for more than one day. After completion of the reaction, the reaction mixture was then pumped down in vacuo and the mixture was dissolved in 2 mL of hexane and recrystallized at −30 °C to form yellow crystals (192 mg, 89% yield). ^1H NMR (benzene-d_6, 300 MHz): δ 7.28 (d, J = 8.8 Hz, 1H, H_4), 6.97 (dm, J = 6.6 Hz, 1H, H_5), 6.82 (ddd, J = 9.1, 1.7, 0.9 Hz, 1H, H_7), 6.60 (dm, J = 6.6 Hz, 1H, H_6), 5.99 (d, J = 3.3 Hz, 1H, H_3), 5.95 (dd, J = 5.2, 3.3 Hz, 1H, H_{14}), 5.65 (dd, J = 5.2, 2.7 Hz, 1H, H_{13}), 5.45 (d, J = 3.3 Hz, 1H, H_2), 5.20 (dd, J = 5.2, 2.7 Hz, 1H, H_{12}), 4.60 (dd, J = 5.2, 2.7 Hz, 1H, H_{15}), 1.19 (s, 3H, Me_A), 1.11 (s, 3H, Me_B), −1.10 (septet, $^3J_{H-F}$ = 2.2 Hz, 3H, Me–Hf). In the $^1H\{^{19}F\}$ NMR spectrum (benzene-d_6, 750 MHz) the signal at δ −1.10 collapsed to a singlet. In the $^1H\{^{11}B\}$ NMR spectrum (benzene-d_6, 400 MHz) the signal associated with μ-H appeared at δ 0.44. ^{13}C NMR (bromobenzene-d_5, 100 MHz, 25 °C): δ 148.9 (dm, J_{C-F} = 240 Hz, *o*-C, $B(C_6F_5)_3$), 141.3 (dm, J_{C-F} = 241 Hz, *p*-C, $B(C_6F_5)_3$), 138.1 (dm, J_{C-F} = 244 Hz, *m*-C, $B(C_6F_5)_3$), not observed $B(C_6F_5)_3$ (*ipso*-C), 128.0, 127.6, 127.5, 126.3, 122.6, 120.2, 118.2, 115.0, 114.0, 110.0, 107.4, 104.0, 99.9, 96.3 (Cp and indenyl), 40.9 (C-bridged), 38.6 (Hf–Me), 26.1 and 24.2 (2C, Me_A, Me_B). ^{19}F NMR (benzene-d_6, 282 MHz) δ −130.7 (d, J = 24.4 Hz, *o-F*), −155.0 (t, J = 21.4 Hz, *p-F*), −162.2 (m, *m-F*). IR (Nujol, KBr plates, cm^{-1}): 2095 (br), 1646 (m), 1516 (s), 1287 (m), 1112 (m), 964 (m), 910 (w), 818 (w), 789 (w), 728 (w). Electrospray ionization mass spectrometry: positive-ion at *m*/*z* 415.2 (M^+, Hf^{180}), negative-ion at *m*/*z* 512.8 (M^-, B^{11}). Elemental *Anal*. Calc. for $C_{36}H_{20}BF_{15}Hf \cdot 1/2C_6H_{14}$: C, 48.30; H, 2.81. Found: C, 50.46; H, 2.89%.

A crystal of dimensions $0.50 \times 0.30 \times 0.30$ mm was coated with Paratone oil and mounted on Cryoloops™ and placed on the goniometer head of a Bruker Apex CCD diffractometer. The reflections were collected at 100(2) K using ψ and ω scans. The diffraction source was graphite-monochromated Mo Kα radiation (λ = 0.71073 Å). Unit cell determination was achieved by using reflections from three different orientations. Data integration was accomplished using SAINT. An empirical absorption correction and other corrections were done using multi-scan SADABS. Structure solution, refinement and modeling were accomplished using the Bruker SHELXTL package. The structure was solved by direct methods and refined by full-matrix least-squares refinement of F^2 and the selection of the appropriate atoms from the generated difference map. Hydrogen atoms of the borate anion were found from the difference map, U_{iso}(H) values fixed according to a riding model, and their positions refined. All other hydrogen positions were calculated and their U_{iso}(H) values fixed according to a riding model.

4.7. Reaction of propylene with borohydride complexes **5a–b**

The reaction was conducted in a 5 mm screw cap NMR tube equipped with a septum. Stock solutions of $Me_2C(Ind)CpZrMe_2$ (167 μL, 0.025 M) and $B(C_6F_5)_3$ (200 μL, 0.025 M) in toluene-d_8 were mixed in a 1:1.2 ratio at 25 °C in a glove box in the NMR tube, while a stock solution of propene in toluene-d_8 (ca. 0.5 M) was prepared outside the box by bubbling propene through toluene-d_8 at 25 °C and 1 atm. Outside the box, ~20 equiv. (ca. 170 μL) of propylene was added to the ion-pair solution via syringe and then the tube mixed using a vortex mixer and then was transported to the NMR laboratory (5–10 min) and spectra recorded. The ^1H and ^{19}F NMR spectra revealed the nearly complete consumption of ion-pairs **2a–b** and formation borohydride complexes **5a–b** in about a 10:1 ratio. Three more additions of 85 μL each of the propene stock solution were conducted and spectra recorded after each addition. The ^{19}F NMR spectra appear in Fig. 4 while the ^1H NMR spectra are available from the authors on request.

Acknowledgments

The authors thank the Natural Sciences and Engineering Research Council of Canada, Nova Chemicals Ltd. of Calgary, Alberta, The University of Akron and the National Science Foundation for financial support of this work.

References

[1] (a) M. Bochmann, S.J. Lancaster, M.D. Hannant, A. Rodriguez, M. Schormann, D.A. Walker, T.J. Woodman, Pure Appl. Chem. 75 (2003) 1183;
(b) E.X.-Y. Chen, T.J. Marks, Chem. Rev. 100 (2000) 1391.

[2] For recent quenched flow kinetic and related mechanistic studies on olefin polymerization using discrete ion-pairs, see (a) C.R. Landis, D.R. Sillars, J.M. Batterton, J. Am. Chem. Soc. 126 (2004) 8890;
(b) A. Rodriguez-Delgado, M.D. Hannant, S.J. Lancaster, M. Bochmann, Macromol. Chem. Phys. 205 (2004) 334;
(c) F. Song, R.D. Cannon, M. Bochmann, Chem. Commun. (2004) 542;
(d) F. Song, M.D. Hannant, R.D. Cannon, M. Bochmann, Macromol. Symp. 213 (2004) 173;
(e) D.R. Sillars, C.R. Landis, J. Am. Chem. Soc. 125 (2003) 9894;
(f) C.R. Landis, K.A. Rosaaen, D.R. Sillars, J. Am. Chem. Soc. 125 (2003) 1710;
(g) C.R. Landis, K.A. Rosaaen, J. Uddin, J. Am. Chem. Soc. 124 (2002) 12062;
(h) Z. Liu, E. Somsook, C.B. White, K.A. Rosaaen, C.R. Landis, J. Am. Chem. Soc. 123 (2001) 11193;
(i) Z. Liu, E. Somsook, C. White, C.R. Landis, J. Am. Chem. Soc. 123 (2001) 2915;
(j) J. Zhou, S.J. Lancaster, D.A. Walker, S. Beck, M. Thornton-Pett, M. Bochmann, J. Am. Chem. Soc. 123 (2001) 223.

[3] (a) M. Chen, J.A. Roberts, T.J. Marks, J. Am. Chem. Soc. 126 (2004) 4605;
(b) V. Busico, R. Cipullo, F. Cutillo, M. Vacatello, V. Van Axel Castelli, Macromolecules 36 (2003) 4258;
(c) M. Mohammed, M. Nele, A. Al-Humydi, S. Xin, R. Stapleton, S. Collins, J. Am. Chem. Soc. 125 (2003) 7930;
(d) M. Mohammed, S. Xin, M. Nele, A. Al-Humydi, S. Collins, Polym. Prepr. (Am. Chem. Soc., Div. Polym. Chem.) 43 (2002) 305;
(e) M. Chen, T.J. Marks, J. Am. Chem. Soc. 123 (2001) 11803;
(f) E. Chen, M.V. Metz, L. Li, C.L. Stern, T.J. Marks, J. Am. Chem. Soc. 120 (1998) 6287;
(g) J.C. Chien, W. Song, M.D. Rausch, J. Polym. Sci. A 32 (1994) 2387;
(h) J. Ewen, in: K. Soga, M. Terano (Eds.), Catalyst Design for Tailor-made Polyolefins, Elsevier, Tokyo, 1994, p. 405;
(i) J.C. Chien, W. Song, M.D. Rausch, Macromolecules 26 (1993) 3239;
(j) N. Herfert, G. Fink, Makromol. Chem., Rapid Commun. 14 (1993) 91;
(k) M.A. Giardello, M.S. Eisen, C.L. Stern, T.J. Marks, J. Am. Chem. Soc. 115 (1993) 3326.

[4] For recent theoretical work incorporating the counter-anion, see
(a) K. Vanka, Z. Xu, T. Ziegler, Macromol. Symp. 213 (2004) 275;
(b) K. Vanka, Z. Xu, T. Ziegler, Organometallics 23 (2004) 2900;
(c) Z. Xu, K. Vanka, T. Ziegler, Macromol. Symp. 206 (2004) 457;
(d) K. Vanka, Z. Xu, T. Ziegler, Can. J. Chem. 81 (2003) 1413;
(e) Z. Xu, K. Vanka, T. Ziegler, Organometallics 23 (2004) 104;
(f) K. Vanka, Z. Xu, T. Ziegler, Israel J. Chem. 42 (2003) 403;
(g) Z. Xu, K. Vanka, T. Firman, A. Michalak, E. Zurek, C. Zhu, T. Ziegler, Organometallics 21 (2002) 2444;
(h) G. Lanza, I.L. Fragala, T.J. Marks, Organometallics 21 (2002) 5594;
(i) G. Lanza, I.L. Fragala, T.J. Marks, Organometallics 20 (2001) 4006;
(j) G. Lanza, I.L. Fragala, T.J. Marks, J. Am. Chem. Soc. 122 (2000) 12764;
(k) G. Lanza, I.L. Fragala, T.J. Marks, J. Am. Chem. Soc. 120 (1998) 8257.

[5] (a) M. Chen, J.A. Roberts, T.J. Marks, Organometallics 23 (2004) 932;
(b) S.J. Lancaster, A. Rodriguez, A. Lara-Sanchez, M.D. Hannant, D.A. Walker, D.H. Hughes, M. Bochmann, Organometallics 21 (2002) 451;
(c) R.E. LaPointe, G.R. Roof, K.A. Abboud, J. Klosin, J. Am. Chem. Soc. 122 (2000) 9560;
(d) V.C. Williams, G.J. Irvine, W.E. Piers, Z. Li, S. Collins, W. Clegg, M.R.J. Elsegood, T.B. Marder, Organometallics 19 (2000) 1619;
(e) V.C. Williams, C. Dai, Z. Li, S. Collins, W.E. Piers, W. Clegg, M.R.J. Elsegood, T.B. Marder, Angew. Chem., Int. Ed. 38 (1999) 3695;
(f) S.J. Lancaster, D.A. Walker, M. Thornton-Pett, M. Bochmann, Chem. Commun. (1999) 1533;
(g) K. Koehler, W.E. Piers, A.P. Jarvis, S. Xin, Y. Feng, A.M. Bravakis, S. Collins, W. Clegg, G.P.A. Yap, T.B. Marder, Organometallics 17 (1998) 3557;
(h) L. Jia, X. Yang, C. Stern, T.J. Marks, Organometallics 13 (1994) 3755.

[6] See inter alia (a) M. Vathauer, W. Kaminsky, Polymer 42 (2001) 4017;
(b) S. Beck, H.H. Brintzinger, J. Suhm, R. Mülhaupt, Macromol. Rapid Commun. 19 (1998) 235;
(c) I. Kim, R.F. Jordan, Macromolecules 29 (1996) 489;
(d) Y.-X. Chen, M.D. Rausch, J.C.W. Chien, Organometallics 13 (1994) 748, and references cited therein.

[7] (a) J. Klosin, G.R. Roof, E.X.-Y. Chen, K.A. Abboud, Organometallics 19 (2000) 4684;
(b) M. Bochmann, M.J. Sarsfield, Organometallics 17 (1998) 5908.

[8] For recent mechanistic work in the absence of monomer, see C. Gotz, A. Rau, J. Luft, J. Mol. Catal. A 184 (2002) 95.

[9] E.X.-Y. Chen, W.J. Kruper, G. Roof, D.R. Wilson, J. Am. Chem. Soc. 123 (2001) 745.

[10] S. Feng, G.R. Roof, E.X.-Y. Chen, Organometallics 21 (2002) 832.

[11] F. Guerin, D.W. Stephan, Angew. Chem., Int. Ed. 39 (2000) 1298.

[12] F. Song, R.D. Cannon, S.J. Lancaster, M. Bochmann, J. Mol. Catal. A 218 (2004) 21.

[13] A. Al-Humydi, J.C. Garrison, W.J. Youngs, S. Collins, Organometallics 24 (2005) 193.

[14] R.A. Stapleton, B.R. Galan, S. Collins, R.S. Simons, J.C. Garrison, W.J. Youngs, J. Am. Chem. Soc. 125 (2003) 9246.

[15] M. Nele, S. Collins, M.L. Diaz, J.C. Pinto, S. Lin, R.M. Waymouth, Macromolecules 33 (2000) 7249.

[16] (a) G. Moscardi, L. Resconi, Organometallics 20 (2001) 1918;
(b) S. Lieber, M. Prosenc, H.H. Brintzinger, Organometallics 19 (2000) 377;
(c) A.G. Carr, D.M. Dawson, M. Pett, M. Bochmann, Organometallics 18 (1999) 2933;
(d) H.V. Heijden, B. Hessen, A.G. Orpen, J. Am. Chem. Soc. 120 (1998) 1112;
(e) D.E. Richardson, N.G. Alameddin, M.F. Ryan, T. Hayes, J.R. Eyler, A.R. Siedle, J. Am. Chem. Soc. 118 (1996) 11244;
(f) A.D. Horton, Organometallics 15 (1996) 2675.

[17] (a) S. Liu, F. Liu, G. Renkes, S.G. Shore, Organometallics 20 (2001) 5717;
(b) F. Liu, J. Liu, E. Meyers, S.G. Shore, J. Am. Chem. Soc. 122 (2000) 6106;
(c) X. Yang, C.L. Stern, T.J. Marks, Angew. Chem., Int. Ed. Engl. 31 (1992) 1375.

[18] (a) Y. Sun, R.E. Spence, W.E. Piers, M. Parvez, G.P. Yap, J. Am. Chem. Soc. 119 (1997) 5132;
(b) J. Karl, G. Erker, R. Frochlich, J. Am. Chem. Soc. 119 (1997) 11165.

[19] This complex was not structurally characterized A.D. Sadow, T.D. Tilley, Organometallics 22 (2003) 3577, and references cited therein.

[20] M. Niehues, G. Erker, G. Kehr, P. Schwab, R. Frolich, O. Blacque, H. Berke, Organometallics 21 (2002) 2905.

[21] L. Resconi, L. Cavallo, A. Fait, F. Piemontesi, Chem. Rev. 100 (2000) 1253.

[22] L. Resconi, J. Mol. Catal. A 146 (1999) 167.
[23] (a) K. Vanka, Z. Xu, T. Ziegler, Organometallics 23 (2004) 2900;
(b) T. Matsugi, S. Matsui, S. Kojoh, Y. Takagi, Y. Imoue, T. Nakano, T. Fujita, N. Kashiwa, Macromolecules 35 (2002) 4880;
(c) M. Mitani, J. Mohri, Y. Yoshida, J. Saito, S. Ishii, K. Tsuru, S. Matsui, R. Furuyama, T. Nakano, H. Tanaka, S. Kojoh, T. Matsugi, K. Norio, T. Fujita, J. Am. Chem. Soc. 124 (2002) 3327;
(d) Y. Yoshida, S. Matsui, Y. Takagi, M. Mitani, T. Nakano, H. Tanaka, N. Kashiwa, T. Fujita, Organometallics 20 (2001) 4793;
(e) S. Matsui, M. Mitani, J. Saito, Y. Tohi, H. Makio, N. Matsukawa, Y. Takagi, K. Tsuru, M. Nitabaru, T. Nakano, H. Tanaka, N. Kashiwa, T. Fujita, J. Am. Chem. Soc. 123 (2001) 6847;
(f) Y. Yoshida, S. Matsui, Y. Takagi, M. Mitani, M. Nitabaru, T. Nakano, H. Tanaka, T. Fujita, Chem. Lett. (2000) 1270.
[24] (a) K. Vanka, Ph.D. Thesis, The University of Calgary, 2004;
(b) K. Vanka, Z. Xu, T. Ziegler, Organometallics 24 (2005) 419.
[25] J.M. Blackwell, D.J. Morrison, W.E. Piers, Tetrahedron 58 (2002) 8247.
[26] A.B. Pangborn, M.A. Giardello, R.H. Grubbs, R.K. Rosen, F.J. Timmers, Organometallics 15 (1996) 1518.
[27] A.P. Shreve, R. Mulhaupt, W. Fultz, J. Calabrese, W. Robbins, S.D. Ittel, Organometallics 7 (1988) 409.
[28] A. Massey, A. Park, J. Organomet. Chem. 2 (1964) 245.
[29] (a) W.J. Gauthier, J.F. Corrigan, N.J. Taylor, S. Collins, Macromolecules 28 (1995) 3771;
(b) M.L.H. Green, N. Ishihara, J. Chem. Soc., Dalton Trans. (1994) 657.
[30] G.M. Diamond, S. Rodewald, R.F. Jordan, Organometallics 14 (1995) 5.
[31] W.A. Hermann, M.J.A. Morawietz, T. Priemeier, J. Organomet. Chem. 506 (1996) 351.
[32] A. Razavi, U. Thewalt, J. Organomet. Chem. 445 (1993) 111.
[33] C. Amman, P. Meier, A.E. Merbach, J. Magn. Reson. 46 (1982) 319.
[34] R.A. Stapleton, A. Al-Humydi, S. Collins, in preparation.
[35] A.M. Bravakis, L.E. Bailey, M. Pigeon, S. Collins, Macromolecules 31 (1998) 1000.

3,4,5-trimethoxybenzaldehyde were obtained commercially from Aldrich Chemical Co. THF and toluene were dried over and distilled from Na/benzophenone prior to use. Cyclopentadiene was collected under an atmosphere of nitrogen from freshly cracked dicyclopentadiene and pyrrolidine was distilled under argon prior to use. Manipulation of air and moisture sensitive compounds was carried out using standard Schlenk techniques under an argon atmosphere. NMR spectra were measured on a Varian 300 MHz spectrometer. Chemical shifts are reported in ppm and are referenced to TMS. IR spectra were recorded on a Perkin–Elmer Paragon 1000 FT-IR Spectrometer employing a KBr disk.

The GCMS spectrum for fulvene **1** was measured on a FINNIGAN TRACE GCMS 2000 Series (70 eV) and 1×10^{-5} M solutions in ethyl acetate were used.

For mass spectrometric analysis of titanocene **2**, a stock solution of the sample was prepared by dissolving the compound in 0.5 ml dichloromethane. A 10-fold dilution of these solutions was made in acetonitrile and electrospray mass spectrometry was performed on a quadrupole tandem mass spectrometer (Quattro Micro, Micromass/Waters Corp., USA) in a negative ion mode.

With a view to elucidate the structures, spectroscopic data, bonding properties and energies of formation, the application of theoretical methods is advantageous. For this purpose, the GAUSSIAN 98 Revision A11 [24] running under Red Hat Linux was used. DFT calculations were performed at the B3LYP level using the 6-31G* basis set for the species of interest.

2.1. 6-(3′,4′,5′-Trimethoxyphenyl)fulvene (*1*)

The synthesis of fulvene **1** was carried out under argon as outlined in reference [25]. Pyrrolidine (2.5 ml, 30.0 mmol) was added to a solution of 3,4,5-trimethoxybenzaldehyde (3.9 g, 20.0 mmol) and cyclopentadiene (4.1 ml, 60.0 mmol) in 30 ml of methanol. After this addition the solution turned from colourless to deep red. When TLC analysis (silica/dichloromethane) showed only one product band after 2 h, acetic acid (1.8 ml, 32.0 mmol) was added. The reaction mixture was partitioned between 20 ml of ether and 40 ml water and extracted with a total of 3×20 ml ether. The combined organic extracts were washed with a saturated aqueous NaCl solution. The organic solution was dried over magnesium sulfate and the solvent removed under reduced pressure. The crude product was triturated with pentane. After solvent removal under reduced pressure a deep red/orange product was obtained. 3.8 g (85% yield wrt 3,4,5-trimethoxybenzaldehyde); m.p. 41.0–43.0 °C.

^{1}H NMR (δppm $CDCl_3$): 6.75, 6.65, 6.40 (C_5H_4, 4H m); 6.95 (C_6H_2, 2H s); 3.95 (*p*-OCH_3 and *o*-OCH_3, 9H s); 7.20 (Ph-C*H*-Cp, 1H s).

^{13}C NMR (δppm $CDCl_3$): 153.3, 144.7, 139.4, 138.3, 135.5, 132.3, 130.6, 127.3, 120.0, 108.0 (C_5H_4 and C_6H_2); 61.0 (*o*-OCH_3); 56.2 (*m*-OCH_3).

IR absorptions (cm^{-1} KBr): 3001 (m), 2937 (m), 1576 (s), 1503 (m), 1417 (m), 1329 (s), 1242 (m).

GCMS: 244.2 (M^+ 70%), 229.1 ($M^+ - CH_3$ 50%), 213.1 ($M^+ - OCH_3$ 40%), 201.2 ($M^+ - COCH_3$ 13%), 155.1($M^+ - CCH(C_5H_4)$ 17%), 115.1 ($M^+ - COCH_3)_3$ 100%).

Anal. Calc. for $C_{15}H_{16}O_3$: C, 73.75; H, 6.60; Found: C, 72.31; H, 6.50%.

2.2. [1,2-Di(cyclopentadienyl)-1,2-di(3′-4′-5′-trimethoxyphenyl)-ethanediyl] titanium dichloride [1,2-(3′,4′,5′-(MeO)$_3$-C_6H_2)$_2$$C_2H_2${$\eta^5$-$C_5H_4$}$_2$]$TiCl_2$ (*2*)

$TiCl_4$ (6.25 mmol, 1 M in toluene) was added to 90 ml of dry toluene and 10 ml dry THF. The solution turned immediately from colourless to pale yellow. The solution was stirred and cooled down to −78 °C, and then was treated dropwise with *n*BuLi (7.8 ml, 12.5 mmol). The solution turned from yellow to brown during the addition. After this addition, the mixture was allowed to warm up slowly to r.t. and the solution finally turned black. After 20 h stirring, a solution of **1** (3.05 g, 12.5 mmol) in dry toluene was added to the solution of $TiCl_2 \cdot 2THF$ at r.t. under argon. It was then stirred under reflux for another 16 h. The solvent was removed under vacuum. The resulting black solid was extracted with 3×20 ml of chloroform and filtered on celite. The solvent was removed under vacuum and the residue dissolved in 8 ml of chloroform and filtered twice through Whatman No. 1 filter paper. The solvent was removed again under vacuum and the residue triturated with a total of 40 ml pentane to give 2.5 g (66% yield) black solid. The ratio of *trans* and *cis* isomers was 58–42%. The mixture cannot be purified or separated by column chromatography or crystallisation; therefore the elemental analysis shows some discrepancy between measured and calculated values and an X-ray crystal structure is not available.

^{1}H NMR (δppm $CDCl_3$): 6.36 (*cis*-C_6H_2, 4H s); 6.33 (*trans*-C_6H_2, 4H s); 7.23–6.00 (C_5H_4, 8H m); 5.34 (*trans*-PhC*H* Cp, 2H s); 4.63 (*cis*-PhC HCp, 2H); 3.80 (*cis-m*-CH_3, 6H s); 3.78 (*cis-m*-CH_3, 12H s); 3.74 (*trans-p*-CH_3, 6H s); 3.67 (*trans-m*-CH_3, 12H s).

^{13}C NMR (δppm $CDCl_3$): 153.3, 153.1, 152.8, 137.5, 137.0, 136.5, 135.8, 133.9, 129.0, 126.6, 120.3, 117.4, 116.5, 115.4, 109.7, 106.5, 105.9, 105.2 (*cis* and *trans*-C_6H_3 and C_5H_4); 60.9, 60.8 (*cis* and *trans-o*-O(CH_3)$_2$), 56.3, 56.2 (*cis* and *trans-m*-O(CH_3)$_2$); 54.4, 52.2 (*cis* and *trans*-PhCHCp).

IR absorptions (cm^{-1} KBr): 3104 (m), 2991 (s), 2976 (m), 2965 (s), 1583 (m), 1461 (m), 1412 (m), 1120 (m), 1000 (m), 821 (m).

MS: 641.0 ($M + Cl^-$).

Anal. Calc. for $C_{30}H_{32}Cl_2O_6Ti$: C, 58.94; H, 5.31; Found: C, 57.74; H, 5.19%.

2.3. MTT-based cytotoxicity tests

The pig kidney carcinoma cell line, LLC-PK, was obtained from the American Tissue Culture Collection.

The cytotoxic activity of titanocene **2** was determined using an MTT-based assay. In more detail, cells were seeded into a 96-well plate (5000 cells/well) and allowed to attach for 24 h. Subsequently, the cells were treated with various concentrations of the cytotoxic agents. In order to prepare drug solutions, **2** was first dissolved in DMSO, followed by dilution with medium to the required maximum concentration of 1.5×10^{-3} M, with a final concentration of DMSO not exceeding 0.7%. From this stock solution, solutions with lower concentrations were prepared by further dilution with medium. Care was taken that the drug solutions were applied within 1 h on the cells to avoid interference with already hydrolysed compounds. After 48 h, the relevant drug was removed, the cells were washed twice with PBS and fresh medium was added for another 24 h for recovery. Viability of cells was determined by treatment with MTT in medium (5 mg/11 ml) for 3 h. The purple formazan crystals formed were dissolved in DMSO and absorbance measured at 540 nm using a VICTOR^2 multilabel plate reader (Wallac). IC_{50} (inhibitory concentration 50%) values were determined from the drug concentrations that induced a 50% reduction in light absorbance.

3. Results and discussion

3.1. Synthesis

Fulvene **1** (Scheme 1) was synthesised according to reference [23], by reacting the corresponding benzaldehyde with cyclopentadiene in the presence of pyrrolidine as a base. Afterwards titanocene **2** (Fig. 2) could be obtained by a reductive dimerisation of fulvene **1** with titanium dichloride (Scheme 1). $TiCl_2$ was synthesised by reduction of $TiCl_4$ with *n*BuLi as described in the literature [17,18] (Scheme 1). The determined *cis–trans* ratio at the bridge is 58:42 for **2**.

3.2. Theoretical studies

Density functional theory calculations were carried out for fulvene **1** and titanocene **2** at the B3LYP level using the 6-31G** basis set.

Selected bond lengths of the optimised structure of fulvene **1** (Fig. 2, for the atom numbering scheme see

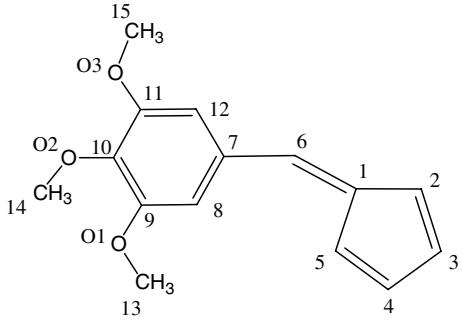


Fig. 1. Structure of fulvene **1**.

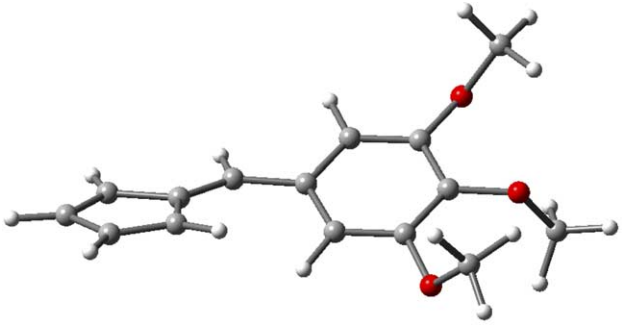
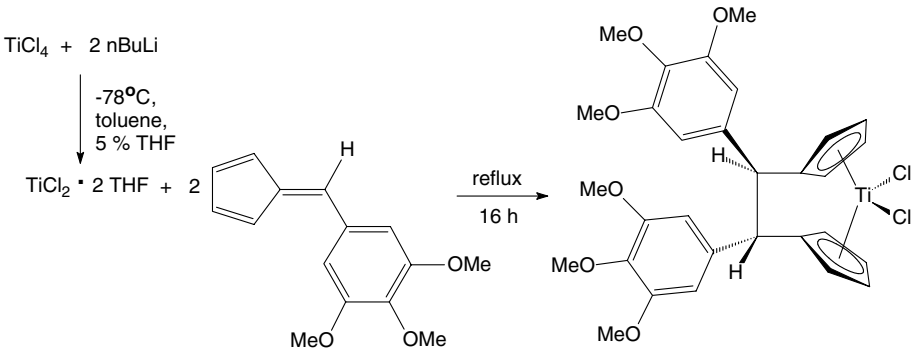


Fig. 2. Gaussview plot of the optimised structure of fulvene **1**.



Scheme 1. Synthesis of titanocene **2**.

Table 1
Selected bond lengths of the DFT-calculated structure of **1**

	1: Bond length [pm]
C(1)–C(2)	148.1
C(2)–C(3)	136.4
C(3)–C(4)	147.5
C(1)–C(6)	136.4
C(6)–C(7)	146.4
C(7)–C(8)	141.2
C(8)–C(9)	139.6
C(9)–C(10)	140.8
C(9)–O(1)	139.9
C(10)–O(2)	140.0
O(1)–C(13)	147.5
O(2)–C(14)	148.0

Fig. 1) can be found in Table 1. As expected, the carbon–carbon bond lengths in the cyclopentadiene system of this fulvene vary significantly, demonstrating the flexibility of the resonance system within the five-membered ring. This is confirmed by the length of the regular exocyclic double bond C(1)–C(6), calculated as 136.4 pm, and the single bond carrying the aryl substituent C(6)–C(7) is calculated as 146.4 pm (Table 1). For fulvene **1**, a distortion from planarity is seen with a dihedral angle between the phenyl ring and the five-membered dienyl ring of 25.5°. In the calculated structure of **1**, the three methyl groups are oriented alternating up and down relative to the plane of the phenyl ring.

Optimised structures were also calculated for titanocene **2** (Fig. 3, for the atom numbering scheme see Scheme 2) at the B3LYP level using the 6-31G** basis set. Selected bond lengths of this structure are listed in Table 2.

The length of the bonds between the metal centre and the carbon atoms of the cyclopentadienyl rings bound to the metal ion vary between 236.4 and 245.3 pm and are in the range of bond lengths found in previous calculations for comparable *ansa*-titanocenes (236.4–245.4 pm) [20–23]. The carbon–carbon bonds of the cyclopentadienyl rings have values of 140.3–143.0 pm. These values suggest that the titanocene has no plane of symmetry bisecting the Cl–Ti–Cl plane and that the calculated structures exhibit C_2 symmetry. The titanium–chlorine bond length is 234.5 pm. These values are in agreement with the corresponding values calculated previously for (1,2-diphenyl-1,2-dicyclopentadienyl)ethanediyl} titanium dichloride [20]. The bridge length [C(6)–C(6′)] is 157.1 pm and is slightly elongated in comparison to (1,2-diphenyl-1,2-dicyclopentadienyl)-ethanediyl} titanium dichloride (153.6 pm) [20]. The steric bulk of the subsituted phenyl rings attached to the bridging carbon centres causes a lengthening of the bond, in order to relieve the resultant steric strain.

The $TiCl_2$ angle was calculated for **2** to be 97.7°. The dihedral angle between the aryl rings was calculated as

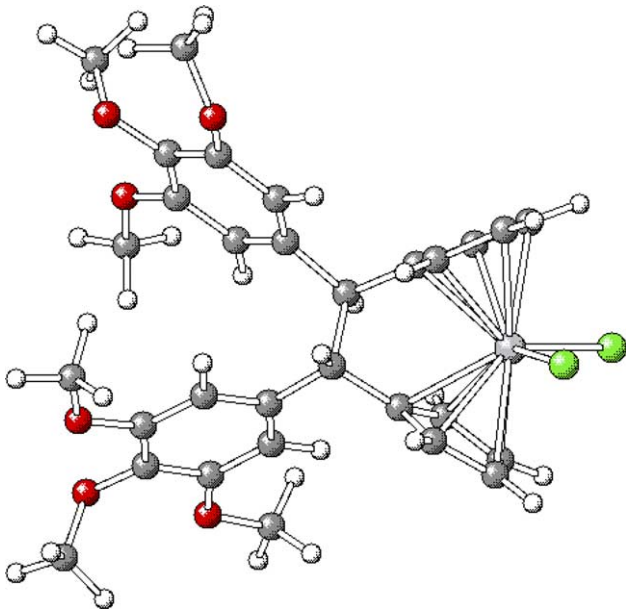
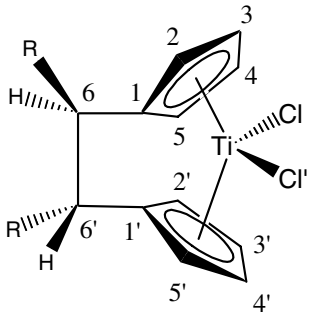


Fig. 3. Gaussview plot of the optimised structure of titanocene **2**.



Scheme 2. Numbering scheme for structural discussion of titanocenes **2**.

58.1°, whereas the dihedral angle between the cyclopentadienyl rings is −46.4°. The angle formed by the bonds between C(1), C(6) and C(6′) takes a value of 107.4°, between C(7), C(6), and C(6′) a value of 113.6°, and between C(7), C(6) and C(1) a value of 114.5°. All these angles are in agreement with the corresponding values calculated previously for comparable *ansa*-titanocenes prepared by our group [20–23].

3.3. Cytotoxicity studies

The in vitro cytotoxicity of compound **2** was determined by an MTT-based assay [26] involving a 48 h drug exposure period, followed by 24 h of recovery time. The compound was tested for its activity on pig kidney carcinoma (LLC-PK) cells. The IC_{50} value found for **2** is 9.0×10^{-4} M [Fig. 4] and this is slightly worse with respect to the inhibition value found previously for [1,2-di(cyclopentadienyl)-1,2-di(4-*N*,*N*-dimethylaminophe-

Table 2
Selected bond lengths from the DFT-calculated structure of complex **2**

	2: Bond length [pm]
Ti–C(1)	242.3
Ti–C(2)	236.7
Ti–C(3)	243.2
Ti–C(4)	245.1
Ti–C(5)	241.4
Ti–C(1′)	241.5
Ti–C(2′)	236.4
Ti–C(3′)	243.7
Ti–C(4′)	245.3
Ti–C(5′)	241.9
C(1)–C(2)	142.6
C(2)–C(3)	142.3
C(3)–C(4)	140.3
C(4)–C(5)	142.4
C(5)–C(1)	141.7
C(1′)–C(2′)	143.0
C(2′)–C(3′)	142.1
C(3′)–C(4′)	140.4
C(4′)–C(5′)	142.3
C(5′)–C(1′)	141.5
Ti–Cl	234.5
C(6)–C(6′)	157.1
C(1)–C(6)	251.1

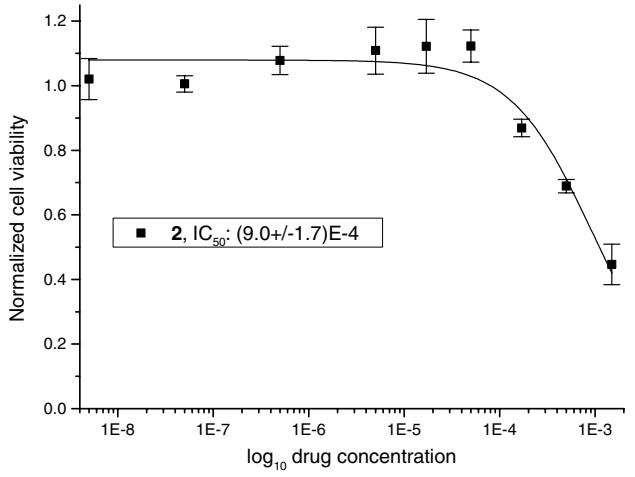


Fig. 4. Cytotoxicity curve from typical MTT assays showing the effect of compound **2** on the viability of pig kidney carcinoma (LLC-PK) cells.

nyl)ethanediyl] titanium dichloride, which has an IC_{50} value of 2.7×10^{-4} M [21]. Under identical conditions, *cis*-platin showed an IC_{50} value of 3.3×10^{-6} M, whereas Cp_2TiCl_2 is found at 2.0×10^{-3} M [21].

4. Conclusion and outlook

Compound **2** has an IC_{50} value against LLC-PK cells in the upper 10^{-4} M range, which is slightly more cytotoxic than unsubstituted titanocene dichloride, for which Phase I/II clinical trials have been performed. The use of three methoxy substituents has improved the water solubility quite well, but the observed cytotoxicity is not impressing. It is intended to perform further in vitro cellular tests with the compound to evaluate its potential for testing in animal models and additionally to search for differently substituted titanocenes also derived from fulvenes.

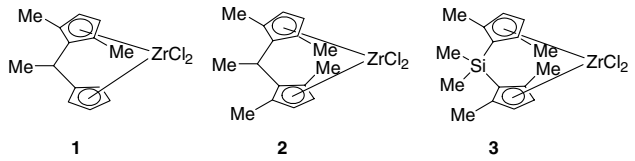
Acknowledgements

The authors thank the Higher Education Authority (HEA) and the Centre for Synthesis and Chemical Biology (CSCB) for funding through the HEA PRTLI cycle 3. In addition funding from Science Foundation Ireland (SFI/04/BRG/C0682) and COST D20 (WG 0001) was granted.

References

[1] A. Gelasco, S.J. Lippard, Top. Biol. Inorg. Chem. 1 (1999) 1.
[2] E.R. Jamieson, S.J. Lippard, Chem. Rev. 99 (1999) 2467.
[3] N. Farrell, Y. Qu, J.D. Roberts, Top. Biol. Inorg. Chem. 1 (1999) 99.
[4] P. Köpf-Maier, H. Köpf, Chem. Rev. 87 (1987) 1137.
[5] P. Köpf-Maier, H. Köpf, Struct. Bond. 70 (1988) 105.
[6] C.V. Christodoulou, D.R. Ferry, D.W. Fyfe, A. Young, J. Doran, T.M. Sheehan, A. Eliopoulos, K. Hale, J. Baumgart, G. Saß, D.J. Kerr, J. Clin. Oncol. 16 (1998) 2761.
[7] A. Korfel, M.E. Scheulen, H.J. Schmoll, O. Grundel, A. Harstrick, M. Knoche, M. Fels, M. Skorzec, F. Bach, J. Baumgart, G. Saß, S. Seeber, E. Thiel, W.E. Berdel, Clin. Cancer Res. 4 (1998) 2701.
[8] G. Lummen, H. Sperling, H. Luboldt, T. Otto, H. Rubben, Cancer Chemother. Pharmacol. 42 (1998) 415.
[9] N. Kröger, U.R. Kleeberg, K. Mross, L. Edler, G. Saß, D.K. Hossfeld, Onkologie 23 (2000) 60.
[10] G. Mokdsi, M.M. Harding, Metal-Based Drugs 5 (1998) 207.
[11] O.R. Allen, L. Croll, A.L. Gott, R.J. Knox, P.C. McGowan, Organometallics 23 (2004) 288.
[12] R.J. Boyles, M.C. Baird, B.G. Campling, N. Jain, J. Inorg. Biochem. 84 (2001) 159.
[13] R. Teuber, G. Linti, M. Tacke, J. Organomet. Chem. 545–546 (1997) 105.
[14] F. Hartl, L. Cuffe, J.P. Dunne, S. Fox, T. Mahabiersing, M. Tacke, J. Mol. Struct. 559 (2001) 331.
[15] M. Tacke, J.P. Dunne, S. Fox, G. Linti, R. Teuber, J. Mol. Struct. 570 (2001) 197.
[16] S. Fox, J.P. Dunne, D. Dronskowski Schmitz, M. Tacke, Eur. J. Inorg. Chem. (2002) 3039.
[17] J.J. Eisch, S. Xian, F.A. Owuor, Organometallics 17 (1998) 5219.
[18] J.J. Eisch, F.A. Owuor, S. Xian, Organometallics 18 (1999) 1583.
[19] K.M. Kane, P.J. Shapiro, A. Vij, R. Cubbon, A.L. Rheingold, Organometallics 16 (1997) 4571.
[20] S. Fox, J.P. Dunne, M. Tacke, J.F. Gallagher, Inorg. Chim. Acta 357 (2004) 225.

[21] M. Tacke, L.T. Allen, L.P. Cuffe, W.M. Gallagher, Y. Lou, O. Mendoza, H. Müller-Bunz, F.-J.K. Rehmann, N. Sweeney, J. Organomet. Chem. 689 (2004) 2242.
[22] F.-J.K. Rehmann, L.P. Cuffe, O. Mendoza, D.K. Rai, N. Sweeney, K. Strohfeldt, W.M. Gallagher, M. Tacke, Appl. Organomet. Chem. 19 (2005) 293.
[23] M. Tacke, L.P. Cuffe, W.M. Gallagher, Y. Lou, O. Mendoza, H. Müller-Bunz, F.-J.K. Rehmann, N. Sweeney, J. Inorg. Biochem. 98 (2004) 1987.
[24] GAUSSIAN Inc., Carnegie Office Park, Building 6, Suite 230, Carnegie, PA 15106 USA.
[25] K.J. Stone, R.D. Little, J. Org. Chem. 49 (1984) 1849.
[26] T. Mosmann, J. Immunol. Meth. 65 (1983) 55.

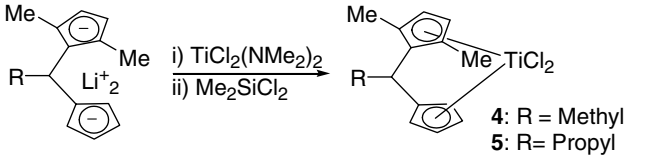


1 2 3

2. Results and discussion

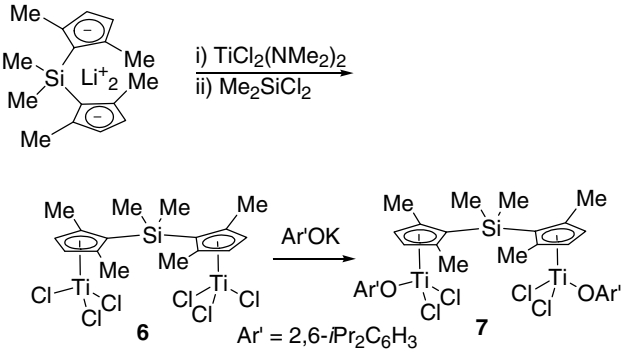
2.1. Syntheses and characterizations

The C1-bridged *ansa*-titanocene complex [Me(H)C(η^5-C_5H_4)(η^5-2,5-$Me_2C_5H_2$)]$TiCl_2$ (**4**) was prepared using the ligand of *ansa*-zirconocene complex **1** [3]. Thus, the reaction of the dilithium salt with $TiCl_2(NMe)_2$ in pyridine afforded the desired bis(dimethylamido)titanium complex which was transformed to the dichloride complex **4** by treatment with Me_2SiCl_2 (Eq. (1)). The overall yield from the dilithium salt was rather low (28%). The ^1H and ^{13}C NMR spectra are in agreement with the structure. Two doublet signals are observed for Me_2Cp–H protons at 6.67 and 6.64 ppm (J = 3.6 Hz) and four Cp–H signals are observed at 6.67, 6.83, 5.45 and 5.18 ppm in the ^1H NMR spectrum. The bridge-CH signal is observed at 3.90 ppm as a quartet. The complex is sparingly soluble in benzene or toluene. Complex [($CH_3CH_2CH_2$)(H)-C(η^5-C_5H_4)(η^5-2,5-$Me_2C_5H_2$)]$TiCl_2$ (**5**) was synthesized by almost the same method and conditions applied for the synthesis of **4**. The overall yield from the dilithium salt was 50%. The complex is freely soluble in toluene. The Cp–H and Me_2Cp–H signal pattern is identical to that observed for **4** and the bridge-CH signal is observed at 3.60 ppm as a triplet.



(1)

Attempts to prepare the *ansa*-titanocene complex using the ligand of **3** were unsuccessful. The major product is a dinuclear complex when equimolar amount of the dilithium salt and $TiCl_2(NMe_2)_2$ are reacted even under fairly dilute conditions (Eq. (2)). Only four singlet signals are observed at 5.80 (Cp–H), 3.11 (NCH_3), 2.01 (CH_3) and 1.03 ($SiCH_3$) ppm with an integration ratio of 2:12:6:3 in the ^1H NMR spectrum. The integration ratio strongly supports the formation of a dinuclear complex. The same kind of dinuclear titanium complex was obtained when the dilithium salt of methylene-bridged 2,5-dimethylcyclopentadienyl indenyl ligand was reacted with an equimolar amount of $TiCl_2(NMe_2)_2$ [5]. Because unbridged cyclopentadienyl phenoxy titanium dichloride complexes have been reported to serve effectively as catalysts for olefin polymerizations [7], the dinuclear Me_2Si[(η^5-2,5-$Me_2C_5H_2$)Ti{O(2,6-*i*$Pr_2C_6H_3$)}Cl_2]$_2$ (**7**) has been prepared (Eq. (2)). Recently, dinuclear CGC-type complexes have drawn extensive attention because of their enhanced reactivity compared to the mononuclear counterparts [8]. Thus, addition of two equivalents of $TiCl_2(NMe_2)_2$ to the dilithium salt provides cleanly the desired dinuclear complex, Me_2-Si[(η^5-2,5-$Me_2C_5H_2$)Ti(NMe_2)$_2$Cl]$_2$, which is cleanly transformed to the trichloride complex by treatment with Me_2SiCl_2 (overall yield from the dilithium salt, 75%). Addition of 2,6-diisopropylphenoxypotassium to the trichloride complex affords the desired complex **7** in 86% yield. The ^1H and ^{13}C NMR spectra and the elemental analysis data are in agreement with the structure.



(2)

Attempts to prepare the *ansa*-titanocene complex using the ligand of **2** were unsuccessful. The main product of the reaction between the ligand and $TiCl_2(NMe_2)_2$ was a dinuclear bis(dimethylamido)(chloro)titanium complex, as observed for the ligand of **3**. This failure might be attributed to the repulsion between the methyls attached on each cyclopentadienyl ring. The repulsion between the methyls was observed even in the solid structure of zirconium complex **2** [3]. Because the titanocene complexes have smaller metal–Cp distances, more severe repulsion is expected for the desired *ansa*-titanocene complex, which may hamper the formation of the *ansa*-complex. In the case of *ansa*-titanocene complexes **4** and **5**, that kind of repulsion does not exist due to the presence of methyl groups on only one cyclopentadienyl ligand, consequently allowing formation of the desired *ansa*-complexes.

Single crystals of **4** suitable for Xray crystallography were deposited in the reaction pot when the bis(dimethylamido) titanium complex was reacted with Me_2SiCl_2 in the absence of stirring and its structure was confirmed by X-ray crystallographic studies. The ORTEP drawing with selected bond distances and angles are shown in Fig. 1. It shows a characteristic strained *ansa*-metallocene structure: small angle of Cp(c)–Ti–Cp(c) (Cp(c), centroid of Cp), deviation of C_b–C–C_b (C_b, bridgehead carbon on Cp) angle from the ideal tetrahedral value

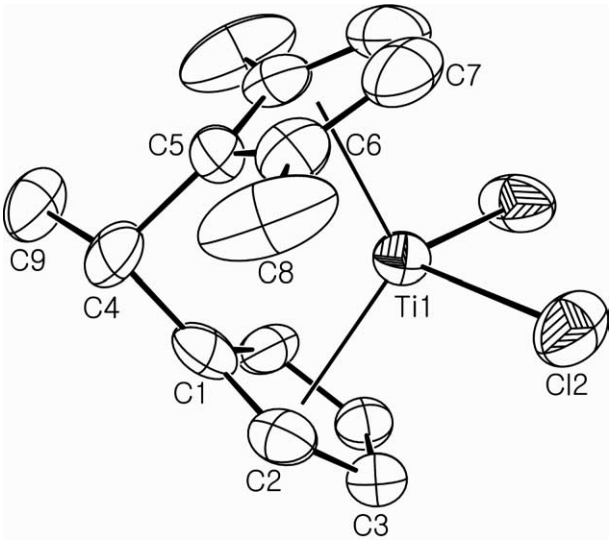


Fig. 1. Thermal ellipsoid plot (30% probability level) of the structure of **4**. Selected bond distances (Å) and angles (°): Ti–C(1), 2.355(18); Ti–C(2), 2.336(11); Ti–C(3), 2.408(13); Ti–C(5), 2.323(17); Ti–C(6), 2.371(13); Ti–C(7), 2.411(15); Ti–Cl, 2.343(4); Cp(c)–Ti, 2.043; Me_2Cp(c)–Ti, 2.060; Cl–C–Cl, 98.7(2); Me_2Cp(c)–Ti–Cp(c), 120.4; C(1)–C(4)–C(5), 95.5(12).

of 109.5°, increase of C–Ti bond distances on going from bridgehead carbon to peripheral carbons. The Cp(c)–Ti and Me_2Cp–Ti distances (2.043 and 2.060 Å, respectively) are smaller than those observed for the corresponding zirconium complex **1** (2.188 and 2.186 Å, respectively) [3]. The Me_2Cp(c)–Ti–Cp(c) angle, which measures how far the metal is displaced from the cyclopentadienyl ligand, is smaller (120.4°) in **4** than the corresponding angle in **1**, indicating that the titanium atom is displaced more closely to the mouth of the cyclopentadienyl ligands and that, consequently, the reaction site is opened less in **4**. The Cl–Ti–Cl angle is smaller (98.2(7)°) than that observed for **1** (102.11(7)°). The C_b–C(bridge)–C_b angle (95.5(12)°) is more strained in **4** than the corresponding angle is in **1** (100.7(4)°). The methyl group attached on the cyclopentadienyl is out of the cyclopentadienyl plane as much as the methyl is in **1** (the H_3C–C–Cp(c) angle for **1** and **4**, 175.5° and 176.0°, respectively).

Table 1
Ethylene polymerization results of **1**–**7** and CGC[a]

Complex	Time (min)	Temperature (°C)[b]	Activity (10^{-6} g/mol h)	M_w	M_w/M_n
1	10	80	15	183 000	12
2	10	80	36	68 000	4.0
3	2.5	93	288	232 000	2.8
4	5	89	100	796 000	2.4
5	2.5	87	125	770 000	3.1
6	10	80	negligible		
7	10	80	negligible		
CGC	10	80	20	129 000	2.5

[a] Polymerization conditions: 100 psig ethylene, 30 mL toluene, 0.25 μmol catalyst, Al/Zr = 6000, initial temperature 80 °C.
[b] Final temperature.

2.2. Polymerization studies

The complexes **1**–**7** were studied for ethylene polymerization after activation with MAO (Table 1). The C1-bridged zirconocene complexes **1** and **2** show similar activities to [Me_2Si(Me_4C_5)(N*t*Bu)]$TiCl_2$ (CGC), but the titanocene complexes **4** and **5** show much higher activities than CGC. The Me_2Si-bridged complex **3** shows extremely high activity for ethylene polymerization. The activity is 15 times higher than that observed for CGC under the same conditions. The dinuclear complexes **6** and **7** show negligible activity under the same conditions. Interestingly, the molecular weights of the polymers obtained by the titanocene complexes **4** and **5** are significantly higher (M_w, ~800 000) than those of

Table 2
Ethylene/1-hexene copolymerization results of **3**, **5** and **CGC**[a]

Entry	Complex	1-Hexene (mol/L)	Time (min)	Temperature (°C)[b]	T_m (°C)	Activity (10^{-6} g/mol h)	M_w	M_w/M_n
1	**3**	0.10	5	93	117	132	210 000	3.0
2	**3**	0.20	5	96	115	139	191 000	2.9
3	**3**	0.30	5	96	105[c]	150	160 000	2.4
4	**3**	0.40	5	94	104	139	152 000	2.6
5	**3**	0.50	5	95	102	143	174 000	2.8
6	**5**	0.10	5	79	120	35	537 000	2.2
7	**5**	0.20	5	82	107	37	356 000	2.3
8	**5**	0.30	5	82	105[d]	36	291 000	2.2
9	**5**	0.40	5	80	106	32	281 000	3.2
10	**5**	0.50	10	79	105	31	237 000	2.3
11	**CGC**	0.30	5	87	n.d.[e]	35	279 000	2.4

[a] Polymerization conditions: 60 psig ethylene, 30 mL toluene, 0.25 μmol catalyst, Al/Zr = 8000, initial temperature 80 °C.
[b] Final temperature.
[c] 3 mol% of 1-hexene content by the ^{13}C NMR analysis.
[d] 4 mol% of 1-hexene content by the ^{13}C NMR analysis.
[e] 14 mol% of 1-hexene content by the ^{13}C NMR analysis.

polymers obtained by the zirconocene complexes **1**, **2** and CGC.

The ethylene/1-hexene copolymerization reactivities were investigated for the highly active complexes **3** and **5** (Table 2). Complex **3** shows still higher activity than CGC but in the case of the titanocene complex **5**, the activity reduces to the level of CGC by the addition of 1-hexene. The 1-hexene incorporation ability of **3** and **5** is inferior to that of CGC. Polymers containing 3 and 4 mol% of 1-hexene are obtained by **3** and **5**, respectively, but CGC gives a polymer containing 14 mol% of 1-hexene under the same conditions (entries 3, 8 and 11) [9]. The T_m value is correlated with the 1-hexene incorporation. With the initial increase of the 1-hexene feeding amount, the T_m value decreases but a plateau is observed above 0.3 M of 1-hexene feeding for both **3** and **5**, which implies that the 1-hexene incorporation is limited to some extent and that it cannot be easily increased above that value merely by increasing the 1-hexene feed amount. The molecular weight is reduced not only by the addition of 1-hexene but also with the increase of the 1-hexene feeding for complex **5**, implying 1-hexene acts as a chain transfer agent in this catalyst system.

3. Conclusion

C1-bridged 2,5-dimethylcyclopentadienyl *ansa*-titanocene complexes, [Me(H)C(η^5-C_5H_4)(η^5-2,5-$Me_2C_5H_2$)]-$TiCl_2$ (**4**) and [($CH_3CH_2CH_2$)(H)C(η^5-C_5H_4) (η^5-2,5-$Me_2C_5H_2$)]$TiCl_2$ (**5**) show much higher activity for ethylene polymerization than the corresponding *ansa*-zirconocene complex [Me(H)C(η^5-C_5H_4)(η^5-2,5-$Me_2C_5H_2$)]-$ZrCl_2$ (**1**) and the molecular weights of the obtained polymers are significantly higher (M_w, ~800 000) than those of polymers obtained with the zirconocene complex **1**. The Me_2Si-bridged complex [Me_2Si(η^5-2,5-$Me_2C_5H_2$)$_2$]$ZrCl_2$ (**3**) shows extremely high activity for ethylene polymerization and the activity is 15 times higher than that of [$Me_2Si(Me_4C_5)$(N*t*Bu)]$TiCl_2$ (CGC). However, Complexes **3** and **5** are inferior to CGC in terms of comonomer incorporation ability in ethylene/1-hexene copolymerization.

4. Experimental

4.1. General considerations

All manipulations were performed under an inert atmosphere using standard glove box and Schlenk techniques. Toluene, pentane, THF and C_6D_6 were distilled from benzophenone ketyl. Pyridine was dried over CaH_2. Toluene used for polymerization reactions was purchased from Aldrich (anhydrous grade) and purified further over Na/K alloy. Ethylene was purchased from Conley Gas (99.9%) and purified by contact with molecular sieves and copper overnight under a pressure of 150 psig. Methylaluminoxane (MAO) was purchased as a solution in toluene from Akzo (7.6 wt% of Al, MMAO type 4). $TiCl_2(NMe_2)_2$ was prepared according to the literature method [10]. NMR spectra were recorded on a Varian Mercury plus 400 or Bruker spectrometer. Elemental analyses were carried out at the Inter-University Center Natural Science Facilities, Seoul National University. Gel permeation chromatograms (GPC) were obtained at 140 °C in trichlorobenzene using Waters Model 150-C+ GPC and the data were analyzed using a polystyrene analyzing curve. Differential scanning calorimetry (DSC) was performed on a Thermal Analysis 3100.

4.2. Synthesis of [Me(H)C(η^5-C_5H_4)(η^5-2,5-$Me_2C_5H_2$)]$TiCl_2$ (**4**)

$TiCl_2(NMe_2)_2$ (0.209 g, 1.01 mmol) and the dilithium salt [Me(H)C(C_5H_4)(2,5-$Me_2C_5H_2$)]Li_2 (0.200 g, 1.01 mmol) were weighed in a vial inside a glove box. Cold pyridine (2.5 mL, −20 °C) was added and the resulting mixture was stirred for 3 min at room temperature. The solvent was removed to give a residue which was dissolved in benzene. The solution was filtered and the solvent was removed by vacuum to give a red oily residue which was used for the next reaction without further purification. ^{1}H NMR (pyridine-d_5): δ 6.44 (quartet, J = 2.0 Hz, 1H, Cp–H), 6.37 (quartet, J = 2.0 Hz, 1H, Cp–H), 6.18 (d, J = 3.2 Hz, 1H, Me_2Cp–H), 6.12 (d, J = 3.2 Hz, 1H, Me_2Cp–H), 5.48 (quartet, J = 2.0 Hz, 1H, Cp–H), 5.17 (quartet, J = 2.0 Hz, 1H, Cp–H), 3.86 (quartet, J = 7.2 Hz, 1H, C*H*CH_3), 2.98 (s, 6 H, NCH_3), 2.97 (s, 6H, NCH_3), 2.07 (s, 3H, CH_3), 1.95 (s, 3H, CH_3), 1.61 (d, J = 7.2 Hz, 3H, CHCH_3) ppm. The bis(dimethylamido)titanium complex was dissolved in benzene (1.5 mL) and Me_2SiCl_2 (0.39 mL, 3.0 mmol) was added. The solution was stirred for 1 h to give dark brown precipitates, which were collected by filtration. The solid was pure by analysis of the ^{1}H and ^{13}C NMR spectra (0.085 g; overall yield, 28%). Single crystals suitable for X-ray crystallography were deposited when the bis(dimethylamido) complex was reacted with Me_2SiCl_2 in the absence of stirring. ^{1}H NMR (C_6D_6:pyridine-d_5, 10:1): δ 6.76 (quartet, J = 2.8 Hz, 1H, Cp–H), 6.83 (quartet, J = 2.8 Hz, 1H, Cp–H), 6.67 (d, J = 3.6 Hz, 1H, Me_2Cp–H), 6.64 (d, J = 3.6 Hz, 1H, Me_2Cp–H), 5.45 (dd, J = 3.6, 2.8 Hz, 1H, Cp–H), 5.18 (dd, J = 3.6, 2.8 Hz, 1H, Cp–H), 3.90 (quartet, J = 7.2 Hz, 1H, C*H*CH_3), 1.83 (s, 3H, CH_3), 1.67 (s, 3H, CH_3), 1.40 (d, J = 7.2 Hz, 1H, CHCH_3) ppm. ^{13}C NMR (C_6D_6:pyridine-d_5, 10:1): δ 133.88, 132.32, 131.58, 129.95, 126.70, 124.89, 111.91, 111.36, 109.28, 102.59, 32.43, 18.78,

16.22, 15.87 ppm. *Anal.* Calc. for $C_{14}H_{16}Cl_2Ti$: C, 55.48; H, 5.33. Found: C, 55.11; H, 5.53%.

4.3. Synthesis of [(CH$_3$CH$_2$CH$_2$)(H)C(η^5-C$_5$H$_4$)-(η^5-2,5-Me$_2$C$_5$H$_2$)]TiCl$_2$ (5)

$TiCl_2(NMe_2)_2$ (1.80 g, 8.70 mmol) was dissolved in toluene (10 mL) and the dilithium salt [$(CH_3CH_2CH_2)$-$HC(C_5H_4)(2,5\text{-}Me_2C_5H_2)$]$Li_2(THF)_{2.25}$ (3.38 g, 8.70 mmol) was dissolved in a cosolvent of toluene (25 mL) and pyridine (7 mL). After the two solutions were cooled in a refrigerator (−20 °C), they were rapidly combined. The combined solution was stirred for 20 min at room temperature and the solvent was removed by vacuum. The bis(dimethylamido) complex was extracted with pentane. Removal of the solvent gave a red residue which was pure by analysis of the ^{1}H NMR spectrum. The residue was used for the next reaction without further purification. ^{1}H NMR (C_6D_6): δ 6.38 (s, 1H, Cp–H), 6.32 (s, 1H, Cp–H), 6.13 (d, J = 2.8 Hz, 1H, Me_2Cp–H), 6.08 (d, J = 2.8 Hz, 1H, Me_2Cp–H), 5.22 (s, 1H, Cp–H), 5.03 (s, 1H, Cp–H), 3.61 (t, J = 7.8 Hz, 1H, bridge-CH), 3.01 (s, 6H, NCH_3), 2.98 (s, 6H, NCH_3), 2.05–1.93 (m, 2H, $CH_2CH_2CH_3$), 1.95 (s, 3H, CH_3), 1.82 (s, 3H, CH_3), 1.46 (dq, J = 14.4, 7.2 Hz, 2H, $CHCH_2CH_2$), 0.97 (t, J = 7.6 Hz, 3H, CH_2CH_3). The residue was dissolved in pentane (35 mL) and Me_2SiCl_2 (2.25 g, 17.3 mmol) was added. The solution was stirred for 30 min. The solvent was decanted and product was dissolved in toluene. Some impurities were deposited from the solution when the solution was stored at room temperature for 1 day. The precipitates were removed by filtration over Celite. Removal of solvent gave a brown solid (1.44 g, overall 50%). ^{1}H NMR (C_6D_6): δ 6.73 (quartet, J = 2.8 Hz, 1H, Cp–H), 6.65 (quartet, J = 2.8 Hz, 1H, Cp–H), 6.63 (d, J = 4.0 Hz, 1H, Me_2Cp–H), 6.60 (d, J = 4.0 Hz, 1H, Me_2Cp–H), 5.15 (dd, J = 5.2, 3.2 Hz, 1H, Cp–H), 4.99 (dd, J = 4.8, 2.4 Hz, 1H, Cp–H), 3.59 (t, J = 8.4 Hz, 1H, bridge-CH), 1.75–1.60 (m, 2 H, CH_2CH_3), 1.70 (s, 3H, CH_3), 1.55 (s, 3H, CH_3), 1.22 (dq, J = 14.4, 7.2 Hz, 2H, $CHCH_2CH_2$), 0.83 (t, J = 7.6 Hz, 3H, CH_2CH_3). ^{13}C NMR (C_6D_6): δ 133.99, 132.36, 131.90, 129.84, 127.10, 124.52, 111.69, 111.38, 109.25, 102.03, 38.48, 32.09, 21.13, 18.63, 16.11, 14.19 ppm. *Anal.* Calc. for $C_{16}H_{20}Cl_2Ti$: C, 58.04; H, 6.11. Found: C, 57.67; H, 6.20%.

4.4. Synthesis of Me$_2$Si[(η^5-2,5-Me$_2$C$_5$H$_2$)TiCl$_3$]$_2$ (6)

$TiCl_2(NMe_2)_2$ (0.341 g, 1.65 mmol) was dissolved in toluene (14 mL) and the dilithium salt $Me_2Si[(2,5\text{-}Me_2\text{-}C_5H_2)]Li_2 \cdot (THF)_2$ (0.300 g, 0.820 mmol) was dissolved in a cosolvent of toluene (2 mL) and pyridine (2 mL). After the two solutions were cooled in a refrigerator (−20 °C), they were rapidly combined. The combined solution was stirred for 3 h at room temperature and solvent was removed by vacuum. Toluene (10 mL) was added and the solution was filtered over Celite. Removal of solvent gave a red residue which was triturated in pentane. The obtained solid was pure by the analysis of the ^{1}H and ^{13}C NMR spectra. ^{1}H NMR (C_6D_6): δ 5.80 (s, 4H, Cp–H), 3.11 (s, 24H, NCH_3), 2.01 (s, 12H, CH_3), 1.03 (s, 6H, $SiCH_3$). ^{13}C NMR (C_6D_6): δ 134.68, 123.33, 116.47, 48.60, 17.23, 3.50. The residue was dissolved in toluene (10 mL) and excess Me_2SiCl_2 (~2 mL) was added. The solution was stirred for 3 h. The solvent was removed by vacuum to give a red residue which was triturated in pentane (0.340 g, 75%). ^{1}H NMR (C_6D_6:pyridine-d_5, 10:1): δ 6.45 (s, 4H, Cp–H), 2.05 (s, 12H, CH_3), 0.79 (s, 6H, $SiCH_3$). ^{13}C NMR (C_6D_6:pyridine-d_5, 10:1): δ 147.63, 135.44, 128.80, 19.95, 1.76. *Anal.* Calc. for $C_{16}H_{22}Cl_6Ti_2Si$: C, 34.88; H, 4.03. Found: C, 34.52; H, 4.22%.

4.5. Synthesis of Me$_2$Si[(η^5-2,5-Me$_2$C$_5$H$_2$)Ti{O(2,6-iPr$_2$C$_6$H$_3$)}Cl$_2$]$_2$ (7)

To a flask containing **6** (0.247 g, 0.448 mmol) and cold toluene (5 mL, −20 °C) was added KO(2,6-iPr$_2$C$_6$H$_3$) (0.165 g, 0.896 mmol), which was prepared by treatment of KH with the corresponding alcohol in THF. The solution was stirred for 2 h and filtered over Celite. The solvent was removed by vacuum to give a yellow residue which was triturated in pentane. The yield was 0.320 g (86%). ^{1}H NMR (C_6D_6): δ 7.10–6.98 (m, 6H), 5.66 (s, 4H, Cp–H), 3.48 (septet, J = 6.4 Hz, 4H, CH), 2.22 (s, 12H, CH_3), 1.28 (d, J = 6.4 Hz, 24H, $CH(CH_3)$), 1.19 (s, 6H, $SiCH_3$). ^{13}C NMR (C_6D_6): δ 164.49, 145.20, 138.51, 131.21, 124.90, 123.80, 122.94, 27.45, 24.08, 19.74, 2.16. *Anal.* Calc. for $C_{40}H_{56}Cl_4O_2SiTi_2$: C, 57.57; H, 6.76. Found: C, 57.25; H, 6.58%.

4.6. Crystallographic studies

A crystal of **4**, coated with grease (Apiezon N), was mounted inside a thin glass tube with epoxy glue and placed on an Enraf-Nonius CCD single crystal X-ray diffractometer. The structures were solved by direct methods (SHELXL-97) [11] and refined against all F^2 data (SHELXL-97). All non-hydrogen atoms were refined with anisotropic thermal parameters. The hydrogen atoms were treated as idealized contributions. Detailed structural data are given in the supplementary information. *Crystal data for* **4:** $C_{14}H_{16}Cl_2$ Ti, M = 303.07, a = 10.962(4) Å, b = 13.744(5) Å, c = 9.000(3) Å, Z = 4, d = 1.485 g/cm^3, orthorhombic, space group *Pnma*, crystal size 0.20 × 0.15 × 0.15 mm, T = 293(2) K, $2.71 \leqslant \Theta \leqslant 25.44$, $-12 \leqslant h \leqslant 13$, $-16 \leqslant k \leqslant 15$, $-10 \leqslant l \leqslant 10$, 4914 measured reflections, 1281 independent reflections (R_{int} = 0.2039), μ = 0.999 mm^{-1}, R_1 [$F^2 > 2\sigma(F^2)$] = 0.1142, ωR_2 = 0.2456.

4.7. Polymerization

In a dry box, to a dried 70 mL glass reactor was added 30 mL of toluene or 1-hexene solution in toluene. The reactor was assembled and brought out from the dry box. The reactor was heated to a given temperature by mantle. After an activated catalyst, prepared by mixing 0.25 μmol of catalyst and MAO (Akzo, MMAO type 4, 6.4 wt% of Al, 0.63 g (Al/Zr, 6000) or 0.84 g (Al/Zr, 8000)), was added via a syringe, ethylene (100 psig) was fed immediately. After polymerization had been conducted for a given time, the ethylene was vented and acetone was added to the reactor to give white precipitates which were collected by filtration and dried under vacuum.

5. Supplementary material

Crystallographic data for structural analysis have been deposited with the Cambridge Crystallographic Data Center (**4**: CCDC No. 259500). Copies of this information may be obtained free of charge from The Director, CCDC, 12 Union Road, Cambridge CB2 1EZ, UK (fax: +44 1223 336033; e-mail: deposit@ccdc.cam.ac.uk or http://www.ccdc.cam.ac.uk).

Acknowledgments

Authors give thanks for financial support from the Whang Pill Sang research fund.

References

[1] (a) Recent progress L.J. Irwin, J.H. Reibenspies, S.A. Miller, J. Am. Chem. Soc. 126 (2004) 16716;
(b) C.R. Baar, C.J. Levy, E.Y.-J. Min, L.M. Henling, M.W. Day, J.E. Bercaw, J. Am. Chem. Soc. 126 (2004) 8216;
(c) M.D. LoCoco, R.F. Jordan, J. Am. Chem. Soc. 126 (2004) 13918;
(d) J.W. Strauch, J.-L. Faure, S. Bredeau, C. Wang, G. Kehr, R. Fröhlich, H. Luftmann, G. Erker, J. Am. Chem. Soc. 126 (2004) 2089;
(e) C.R. Landis, D.R. Sillars, J.M. Batterton, J. Am. Chem. Soc. 126 (2004) 8890;
(f) E.Y.-X. Chen, R.E. Campbell Jr., D.D. Devore, D.P. Green, B. Link, J. Soto, D.R. Wilson, K.A. Abboud, J. Am. Chem. Soc. 126 (2004) 42;
(g) M.-C. Chen, J.A.S. Roberts, T.J. Marks, J. Am. Chem. Soc. 126 (2004) 4605;
(h) C. Zuccaccia, N.G. Stahl, A. Macchioni, M.-C. Chen, J.A. Roberts, T.J. Marks, J. Am. Chem. Soc. 126 (2004) 1448;
(i) M.B. Harney, R.J. Keaton, L.R. Sita, J. Am. Chem. Soc. 126 (2004) 4536;
(j) M.W. McKittrick, C.W. Jones, J. Am. Chem. Soc. 126 (2004) 3052;
(k) W.-L. Nie, G. Erker, R. Fröhlich, Angew. Chem. Int. Ed. 43 (2004) 310;
(l) C. Karafilidis, H. Hermann, A. Rufiska, B. Gabor, R.J. Mynott, G. Breitenbruch, C. Weidenthaler, J. Rust, W. Joppek, M.S. Brookhart, W. Thiel, G. Fink, Angew. Chem. Int. Ed. 43 (2004) 2444;
(m) C.J. Miller, D. O'Hare, Chem. Commun. (2004) 1710.

[2] (a) E. Wasserman, in: I.T. Horvath (Ed.), Encyclopedia of Catalysis, vol. 4, Wiley-Interscience, New Jersey, 2003, p. 725;
(b) H.G. Alt, A. Köppl, Chem. Rev. 100 (2000) 1205;
(c) W. Kaminsky, Macromol. Chem. Phys. 197 (1996) 3907.

[3] E.S. Cho, U.G. Joung, B.Y.L.H. Lee, Y.-W. Park, C.H. Lee, D.M. Shin, Organometallics 23 (2004) 4693.

[4] (a) Y.C. Won, H.Y. Kwon, B.Y. Lee, Y.-W. Park, J. Organomet. Chem. 677 (2003) 133;
(b) T.H. Kim, Y.C. Won, B.Y. Lee, D.M. Shin, Y.K. Chung, Eur. J. Inorg. Chem. (2004) 1522;
(c) Y.C. Won, U.G. Joung, E.S. Cho, B.Y. Lee, H. Lee, Y.-W. Park, K.H. Song, Synthesis (2004) 1052;
(d) B.Y. Lee, Y.H. Kim, Y.C. Won, J.W. Han, W.H. Suh, I.S. Lee, Y.K. Chung, K.H. Song, Organometallics 21 (2002) 1500.

[5] E.S. Cho, Y.C. Won, S.Y. Lee, B.Y. Lee, D.M. Shin, Y.K. Chung, Inorg. Chim. Acta 357 (2004) 2301.

[6] (a) S.-J. Kim, Y.-J. Lee, E. Kang, S.H. Kim, J. Ko, B.Y. Lee, M. Cheong, I.-H. Suh, S.O. Kang, Organometallics 22 (2003) 3958;
(b) S. Xu, X. Deng, B. Wang, X. Zhou, L. Yang, Y. Li, Y. Hu, F. Zou, Y. Li, Macromol. Rapid Commun. 22 (2001) 708.

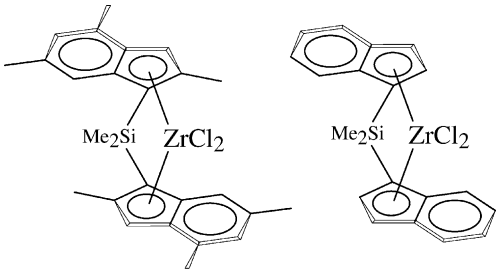
[7] (a) D.J. Byun, A. Fudo, A. Tanaka, M. Fujiki, K. Nomura, Macromolecules 37 (2004) 5520;
(b) K. Nomura, Y. Hatanaka, H. Okumura, M. Fujiki, K. Hasegawa, Macromolecules 37 (2004) 1693.

[8] (a) H. Li, L. Li, T.J. Marks, Angew. Chem. Int. Ed. 43 (2004) 4937;
(b) N. Guo, L. Li, T.J. Marks, J. Am. Chem. Soc. 126 (2004) 6542;
(c) J. Wang, H. Li, N. Guo, L. Li, C.L. Stern, T.J. Marks, Organometallics 23 (2004) 5112;
(d) H. Li, L. Li, T.J. Marks, L. Liable-Sands, A.L. Rheingold, J. Am. Chem. Soc. 125 (2003) 10788;
(e) L. Li, M.V. Metz, H. Li, M.-C. Chen, T.J. Marks, L. Liable-Sands, A.L. Rheingold, J. Am. Chem. Soc. 124 (2002) 12725.

[9] H.N. Cheng, Polym. Bull. 26 (1991) 325.

[10] E. Benzing, W. Kornicker, Chem. Ber. 94 (1961) 2263.

[11] G.M. Sheldrick, SHELXL-97, Program for the Refinement of Crystal Structures, University of Göttingen, Germany, 1997.



1 2

Chart 1.

certain extent, but isospecificity and regioselectivity of the catalyst becomes poorer [12]. Much of the literature deal with modifying the structure of the metallocene itself, because this is the most effective way to regulate polymerization behavior and polymer structure [2,13,14].

Keeping in view these factors, we report in this paper another member of *ansa*-zirconocene catalysts, namely *rac*-dimethylsilyl-bis(2,4,6-trimethyl-1-indenyl)zirconium dichloride (**1**) (see Chart 1). The influence of polymerization temperature (T_p) on polypropylene microstructure has been studied and the results are compared with the *rac*-dimethylsilylbis(indenyl)zirconium dichloride (**2**) congener under identical conditions.

2. Results and discussion

2.1. Polymerization kinetics

The results of propylene polymerization by catalyst **1** are shown in Table 1. As can be seen from the table, the activity of catalyst **1** was strongly affected by T_p. Low catalytic activity was observed at low T_p, which increased to a maximum at 70 °C and then decreased. A similar behavior has been observed with most Ziegler–Natta catalysts. This was interpreted as slow chain propagation at low temperature and rapid catalyst deactivation at elevated temperatures [15]. Catalyst **2** showed a different activity behavior. A sharp decrease in activity was observed with increase in T_p and the maximum activity was observed at 40 °C. Compared to **2**, catalyst **1** shows better stability at high temperature.

The influence of T_p on the kinetic profiles of propylene polymerization was also investigated (Fig. 1). As can be seen from the figure, all polymerizations performed by **1** have a short induction period followed by rate decay after the maximum rate is reached. It can also be seen that the extent of rate decay increases with increasing T_p. At 50 °C the rate decayed to about 1/3 of the maximum rate after 60 min of polymerization, while the rate decayed to only about 1/5 of the maximum value when T_p was 90 °C. This means that deactivation of the catalyst was accelerated at higher temperature.

The molecular weight of the produced isotactic polypropylene (PP) was also affected by T_p. It can be seen from Table 1 that for catalyst **1**, increasing T_p from 30 to 90 °C caused a drop in M_η from 63 300 to 5930. The same trend was observed for complex **2** but the molecular weight was lower than in the case of **1**. In general, a decrease in molecular weight of polypropylene with T_p is a typical phenomenon found in the propylene polymerization by metallocene/MAO catalysts. Usually, the activation energies of chain termination by β-H elimination (the most frequent chain termination reaction in

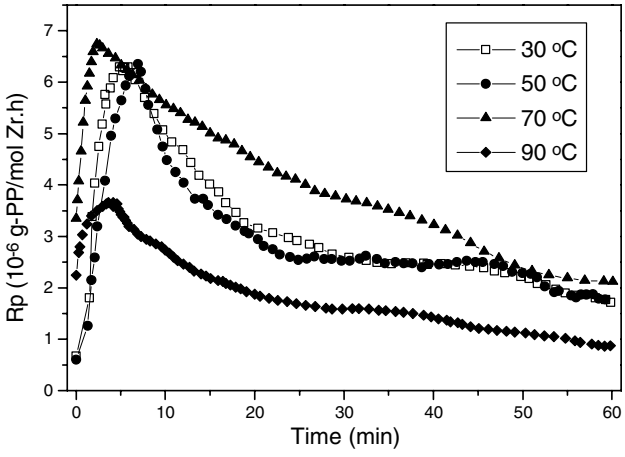


Fig. 1. Effect of temperature on rate profiles of propylene polymerization with **1**/MAO; [Zr] = 20 μmol/l, Al/Zr = 2000. Al/Zr = 2000.

Table 1
Effect of polymerization temperature (T_p) on catalytic activity and polymer properties

Run no.	Catalyst	T_p (°C)	Yield (g)	Activity (kg-PP/mol-Zr h)	$M_\eta \times 10^{-4}$	T_m (°C)	ΔH_f (J/g)
1	**1**	30	6.15	3070	6.33	149	80.6
2	**1**	50	6.28	3141	2.02	146	86.2
3	**1**	70	8.20	4100	1.28	128	65.9
4	**1**	90	3.38	1690	0.59	84	9.3
5	**2**	40	10.54	5270	1.73	140	83.0
6	**2**	50	8.98	4490	1.89	134	79.2
7	**2**	60	2.56	1280	1.12	128	57.6
8	**2**	70	0.76	380	0.99	116	50.0

Polymerization conditions; [Zr] = 20 μmol/l, toluene = 100 ml, Al/Zr = 2000.

metallocene complexes) or other chain transfer reactions are higher than that of propagation. The high polymer molecular weight produced by **1** compared to **2** can be explained by the presence of 2-methyl in the former system, which suppresses chain termination by β-H elimination reaction [1].

2.2. Polymer microstructure

The microstructure of the polypropylene produced by **1** at different T_p was analyzed by ^{13}C NMR spectroscopy. The ^{13}C NMR spectra of PP by **1** are shown in Fig. 2, and the measured methyl pentad intensities at

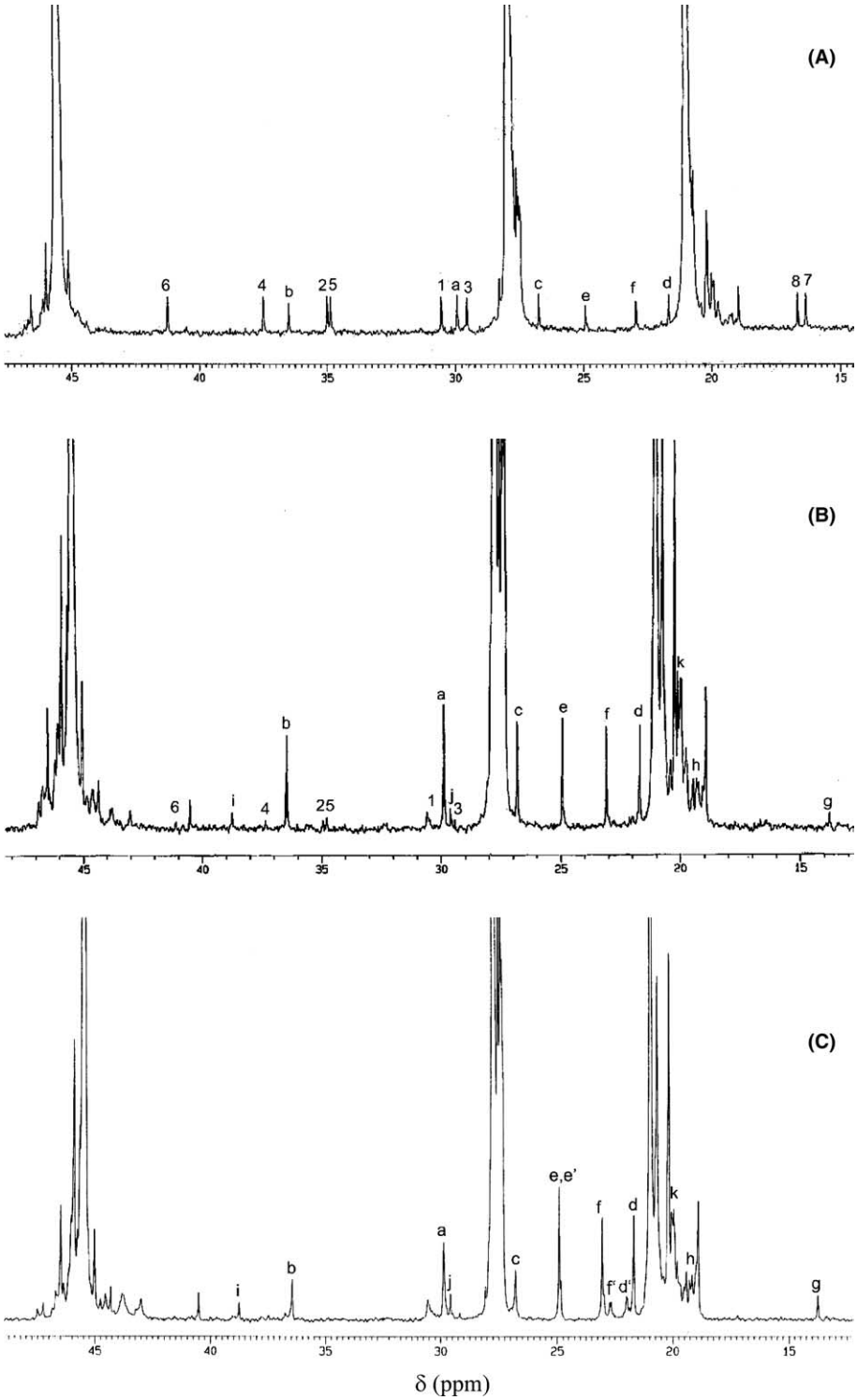


Fig. 2. ^{13}C NMR spectra of polypropylene produced by **1**/MAO at various polymerization temperatures (A) 50 °C; (B) 70 °C; (C) 90 °C.

Table 2
Microstructure of polypropylene determined by ^{13}C NMR

Catalyst	T_p (°C)	Methyl pentad distributions (%)								
		mmmm	mmmr	rmmr	mmrr	mmrm + rmrr	mrmr	rrrr	mrrr	mrrm
1	50	91.6	2.3	0.7	2.5	0.9	0.7	0.3	0.3	0.7
1	70	72.0	8.9	1.4	6.0	4.3	2.7	1.2	0.9	2.5
1	90	50.7	15.2	2.7	12.8	4.2	3.7	3.0	1.8	5.9
2	50	82.0	9.1	0.0	5.2	1.5	0.1	0.0	0.1	2.0

Polymerization conditions are the same as in Table 1.

different T_p are summarized in Table 2. Under similar polymerization conditions, the isotacticity of PP produced by **1** is higher than that of **2**, and it is very sensitive to T_p. For catalyst **1**, the [mmmm] pentad percentage dropped from 92% to 51% and the melting temperature from 149 to 84 °C as the T_p increased from 30 to 90 °C. Comparing the two metallocenes **1** and **2** at the same T_p, it is clear that introducing the methyl groups in the former greatly improves the isotacticity and melting temperature. At T_p = 50 °C, **1** gives PP with [mmmm] = 92% and T_m = 146 °C, while catalyst **2** displays [mmmm] of 82% and T_m of 134 °C under the same conditions.

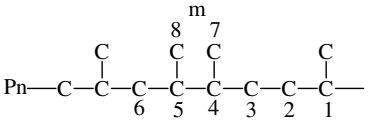
The increase of stereoirregular pentads [mmmr], [mmrr] and [mrrm] with T_p can be explained by the acceleration of chain epimerization at high temperature [2]. Low propylene concentration at high T_p is also a factor favoring epimerization. It can be seen in Table 2 that there are also strong increases of the pentads [mmrm]+[rmrr], [mrrr] and [rrrr] with T_p. These pentads are formed when successive mis-insertion happens. So it means that the active site control over the chain propagation is partly lost when T_p increases, and chain-end control begins to play an important role. Therefore, possible change of the catalyst's configuration from racemic to mesomeric at elevated temperature may also play an important role in influencing the stereochemical structure of PP. An evidence for this change is the loss of the catalyst's stability at high temperature.

2.3. Regioselectivity

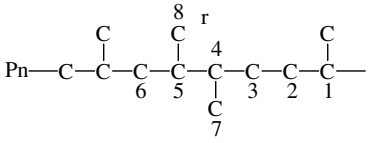
The dominating mechanism in isospecific polymerization is 1,2-insertion (also called primary insertion). But polypropylene produced by isospecific zirconocenes shows incomplete regioregularity [16,17] caused by occasional insertions of isolated secondary (2,1 meso and racemic) units.

^{13}C NMR is a powerful tool for studying regioregularity in polypropylene, and the amount of regioerrors in the PP chain can be calculated from the relative intensities of the peaks arising from the regioirregular structures. In Fig. 2 a series of ^{13}C NMR signals were assigned to various regioirregular structures, including the structures formed by 2,1-insertion and 1,3-insertion (see Chart 2). According to the literature, the 1,3-enchainment is formed by the transformation of a part of the 2,1-insertion through β-hydrogen exchange [16]. The amount of regioirregular structures in PP obtained by **1** at different T_p is listed in Table 3. It is seen that the total number of regioirregular insertions increases with increase in T_p. Table 3 also shows that for catalyst **1**, only 2,1-insertion in the *m*-configuration is observed and no 2,1-insertion in the *r*-configuration is found, while catalyst **2** produces PP with 2,1-insertions both in the *m*-configuration and the *r*-configuration. The total amount of regioirregular structures is higher in catalyst system **2**/MAO than in **1**/MAO. The higher regiospecificity of catalyst **1** than **2** can possibly be attributed to the substitution pattern of the indenyl ligand in the former system. On the other hand, **1** shows higher stereospecificity when a 2,1-insertion happens, namely, **1** does not produce any 2,1-*r*-insertion.

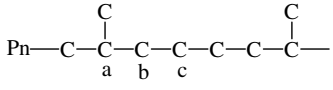
It has been reported in the literature that 2,1-insertion units will reduce the molecular weight, because the rate of β-hydrogen transfer, after a secondary insertion, is higher than after a primary insertion [18]. The slightly higher molecular weight of PP by **1**/MAO than **2**/MAO may also be explained based on lower 2,1-insertion



2,1-*m*-insertion



2,1-*r*-insertion



1,3-insertion

Chart 2. Regioirregular structures.

Table 3
Regioerrors in isotactic polypropylene prepared at different T_p

Run no.	T_p (°C)	Catalyst	2,1 m-in (%)	2,1 r-in (%)	1,3-in (%)	Total (%)
1	30	**1**	0.37	0.00	0.00	0.37
2	50	**1**	0.42	0.00	0.16	0.58
3	70	**1**	0.10	0.00	0.52	0.62
4	90	**1**	0.00	0.00	0.71	0.71
6	50	**2**	0.44	0.10	0.19	0.73

Polymerization conditions are the same as in Table 1.

and 1,3-insertion rates in the former. However, it is still unclear if there are direct connections between the low rate of β-hydrogen transfer (high molecular weight) and low rate of mis-insertions (high regioregularity) when we try to explain the effect of changing the ligand structure in *ansa*-zirconocenes. On the other hand, the proportion of 1,3-insertion in iPP produced by **1** increases rapidly with increasing T_p. This phenomenon means that the β-hydrogen transfer becomes faster at higher temperature. Usually, 1,3-insertion can help to overcome the hindrance to chain growth caused by a 2,1-insertion via a β-hydride shift initiated transformation of the Zr-chain bond. The higher activity of **1**/MAO than **2**/MAO at 70 °C and higher temperatures might be partly the result of this effect.

2.4. End group analysis

As can be seen from Table 1, the molecular weight of PP decreases with increasing T_p. By ^{13}C NMR analysis (Fig. 2), the changes of chain end groups and thus the chain transfer reactions with T_p can be clearly seen. Three types of chain end groups, namely isopropyl, *n*-propyl and vinylidene groups were observed in PP synthesized by **1**/MAO at T_p values from 30 to 90 °C (see Chart 3).

As shown in Fig. 2(A), in PP produced by **1**/MAO at 50 °C, only isopropyl end groups (represented by the signals d, e and f) can be found. This kind of end group should be produced when the polymer chain was transferred to $AlMe_3$ in MAO. This chain transfer in propylene polymerization will produce the isopropyl end group either from Al–polymer connection or by the insertion of a propylene unit into the metal–methyl group. Therefore, isopropyl end groups are formed either at the initiated or the terminated polymer chains through the chain transfer reaction by MAO.

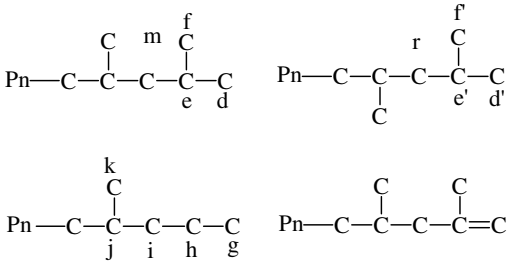


Chart 3. Chain-end structures.

The ^{13}C NMR spectra of PP obtained at 70 and 90 °C (Fig. 2B and C) still display strong peaks of the isopropyl end groups, meanwhile weak signals of the *n*-propyl end group (the peaks g, h, i, j and k) and the vinylidene group (peaks at 111.0 and 136.5 ppm, not shown in Fig. 2) are also detected. These end groups are formed by either β-H transfer or chain transfer to the monomer. Because the molar ratio of the (isopropyl end groups)/(*n*-propyl end groups) is high at all temperatures, the main chain transfer reaction is still by the cocatalyst in the **1**/MAO catalyst system.

It is worth noting that in the ^{13}C NMR spectra of PP obtained at 90 °C, an isopropyl end group with a racemic configuration between the last and the second last monomer units is also detected, which are represented by the signals d′ and f′. This is consistent with the low stereospecificity of the polymerization at such a high temperature.

In conclusion, the influences of T_p on activity and molecular weight in the **1**/MAO catalyzed propylene polymerization are similar to those observed by Kaminsky et al. [9] in *rac*-dimethylsilylbis(2,4,7-trimethyl-1-indenyl)zirconium dichloride. Under our experimental conditions, catalyst **1**/MAO shows better stereochemical and regiochemical control than $Me_2Si(2,4,7\text{-}Me_3Ind)_2ZrCl_2$ and gives PP with higher stereospecificity. The reason might be the steric hindrance caused by 7-methyl in $Me_2Si(2,4,7\text{-}Me_3Ind)_2ZrCl_2$. This methyl is moved to position 6 in **1**, which is quite far from the bridge and opposite the indenyl and thus causes less hindrance. As compared to **2**, which is less reactive and produces low molecular weight polypropylene, catalyst **1** polymerizes propylene with high activity to afford PP with higher molecular weight, higher isotacticity and higher regioregularity. Another beneficial feature of catalyst **1** is its higher stability at elevated temperature. Because the main chain transfer reaction in the **1**/MAO catalyst system is by the cocatalyst, it is foreseeable that the molecular weight of polymer can be further increased when higher monomer concentration is applied.

An important feature relating to catalyst **1** is its easy preparation in terms of starting material and reaction route (the main starting substances for preparing

2,4,6-trimethylindene are *m*-xylene and methacrylic acid [19]), and at the same time its relatively good performance for synthesizing isotactic polypropylene, in many aspects similar to the already industrialized *rac*-Me_2Si(2-Me-4,5-Benz[e]Ind)$_2ZrCl_2$ [20].

3. Experimental

All manipulations were carried out under a dry argon atmosphere using standard Schlenk techniques. Toluene was purified by refluxing over Na-benzophenone ketyl under argon atmosphere and distilled prior to use. Methylaluminoxane (MAO, 10% w/w toluene solution, Albemarle Co.) was used as obtained.

3.1. Synthesis of the ligand and catalyst

2,4,6-trimethylindene was prepared according to an established method [19]. The yield of 2,4,6-trimethylindene was 47%. It is an oil of light yellow color.

For the preparation of dimethylsilylbis(2,4,6-trimethylindene), 15.8 g (0.1 mol) of 2,4,6-trimethylindene was dissolved in 250 ml of tetrahydrofuran in a three-neck flask equipped with magnetic stirrer, a dropping funnel and a condenser. The mixture was cooled to −15 °C and 47.4 ml (2.11 M) of *n* -butyllithium solution in n-hexane was slowly added through dropping funnel. The reaction mixture was stirred for 4 h, then the temperature of the lithium salt was lowered to −78 °C and 6.1 ml (0.05 mol) of dichlorodimethyl silane [$(CH_3)_2SiCl_2$] was added. After this the reaction mixture was slowly warmed to room temperature and stirred for 24 h. Then the mixture was quenched with water, and the organic layer was separated. The aqueous layer was extracted three times with diethyl ether. The combined organic layer was dried over Na_2SO_4, the solvent was removed and the residue was crystallized from methanol:diethyl ether (2:1) to collect 3.7 g of product [21].[1]

For the synthesis of Me_2Si(2,4,6-Me_3Ind)$_2ZrCl_2$, in a three-neck flask 2.82 g (7.5 mmol) of dimethylsilylbis(2,4,6-trimethylindene) was dissolved in 250 ml of dry *n*-hexane at 30 °C and reacted with 8.2 ml (1.84 M) of *n*-butyllithium. After 4 h, the solvent was removed and the lithium salt was dried under vacuum. Then this salt was added to 1.75 g (7.5 mmol) of $ZrCl_4$ in 100 ml of CH_2Cl_2 at −78 °C. The reaction mixture was stirred for 12 h and the solvent was removed. The residue was extracted with hot toluene (100 °C) and 0.35 g of the pure racemic isomer of Me_2Si(2,4,6-Me_3Ind)$_2ZrCl_2$ was obtained by fractional crystallization at −20 °C [21].[2]

3.2. Polymerization procedure

Polymerization was carried out in toluene in a 250 ml glass reactor equipped with a propylene inlet and a magnetic stirrer. Polymerization grade propylene was further purified by passing over activated 4 Å molecular sieves. Toluene (100 ml) was introduced into the reactor and was saturated with propylene of 0.98 atm pressure. Calculated amounts of MAO and metallocene in toluene were added, respectively. After one hour, polymerization was stopped by adding acidified ethanol and the product was poured into an excess of ethanol. The resulting polymer was separated by filtration, washed and dried in vacuum at 60 °C to constant weight.

3.3. Polymer analysis

The intrinsic viscosity [η] of the polymer sample was measured with an Ubbelhode type viscometer using decahydronaphthalene as solvent at 135 ± 0.1 °C. M_η of the polymer was calculated according to the equation: $[\eta] = KM_\eta^\alpha$ ($K = 1.10 \times 10^{-4}$, $\alpha = 0.80$) [22]. ^{13}C NMR spectra of the polymers were recorded on a Bruker Avance 500 spectrometer at 120 °C in *o*-dichlorobenzene-D_4. Hexamethyldisiloxane (HMDS) was added as internal standard. Differential scan calorimetry (DSC) analysis of the polymer sample was performed in a Perkin–Elmer DSC-7 instrument to determine the melting temperature and heat of fusion of the polymer.

Acknowledgment

Support from the National Natural Science Foundation of China (Grant Nos. 29734144, 20274037) is gratefully acknowledged.

References

[1] H.H. Brintzinger, D. Fisher, R. Mulhaupt, B. Rieger, R.M. Waymouth, Angew. Chem., Int. Ed. Engl. 34 (1995) 1143.
[2] L. Resconi, L. Cavallo, A. Fait, F. Piemontesi, Chem. Rev. 100 (2000) 1253.
[3] O. Olabisi, M. Atiqullah, W. Kaminsky, Macromol. Chem. Phys. 37 (1997) 519.
[4] W. Spaleck, F. Kueber, A. Winter, J. Rohrmann, B. Bachmann, M. Antberg, V. Dolle, E.F. Paulus, Organometallics 13 (1994) 954.

[1] ^1H NMR (Bruker DMX-500, $CDCl_3$, 25 °C) dimethylsilylbis (2,4,6-trimethylindene) $\delta = 7.08$ (s, 2H), 6.65 (s, 2H), 6.65 (s, 2H), 3.65 (s, 2H), 2.39 (S, 6H), 2.32 (s, 6H), 2.19 (S, 6H), −0.31 (s, 6H).

[2] ^1H NMR (Bruker DMX-500, $CDCl_3$, 25 °C) racemic isomer ($CDCl_3$, 25 °C) $\delta = 7.22$ (s, 2 H), 6.96 (s, 2H), 6.71 (s, 2H), 2.32 (s, 6H), 2.28 (s, 6H), 2.19 (s, 6H), 1.28 (s, 6H).

[5] F.R.W.P. Wild, M. Wasiucionek, G. Huttner, H.H. Brintzinger, J. Organomet. Chem. 88 (1985) 63.
[6] W.A. Herrmann, J. Rohrman, E. Herdtweck, W. Spaleck, A. Winter, Angew. Chem., Int. Ed. Engl. 28 (1989) 1511.
[7] W. Spaleck, M. Antberg, J. Rohrman, A. Winter, B. Bachmann, P. Kiprof, J. Behm, W.A. Herrmann, Angew. Chem., Int. Ed. Engl. 31 (1992) 1347.
[8] W. Spaleck, A. Winter, B. Bachmann, V. Dolle, F. Kuber, J. Rohrman, in: MetCon'93, Proceedings, May 27, 1993.
[9] W. Kaminsky, O. Rabe, A.M. Schauwienold, G.U. Schupfner, J. Hanss, J. Kopf, J. Organomet. Chem. 497 (1995) 181.
[10] F. Forlini, Z.Q. Fan, I. Tritto, P. Locatelli, M.C. Sacchi, Macromol. Chem. Phys. 198 (1997) 2397.
[11] Z.Q. Fan, Y.H. Zhang, Q. Wang, L.X. Feng, Chin. Chem. Lett. 9 (1998) 83.
[12] D. Arrowsmith, W. Kaminsky, A. Laban, U. Weingarten, Macromol. Chem. Phys. 202 (2001) 2161.
[13] Z.Q. Fan, T. Yasin, L.X. Feng, J. Polymer Sci., Part A 38 (2000) 4299.
[14] Z.Q. Fan, T. Yasin, L.X. Feng, Chin. Chem. Lett. 11 (2000) 167.
[15] J.C.W. Chien, J. Polym. Sci., Part A 1 (1963) 1839.
[16] K. Soga, T. Shiono, S. Takemura, W. Kaminsky, Makromol. Chem., Rapid Commun. 8 (1987) 305.
[17] A. Grassi, A. Zambelli, L. Resconi, E. Albizzati, R. Mazzocchi, Macromolecules 21 (1988) 617.
[18] L. Resconi, F. Piemontesi, L. Camurati, D. Balboni, A. Sironi, M. Moret, H. Rychlicki, R. Ziegler, Organometallic 15 (1996) 5046.
[19] T. Yasin, Z.Q. Fan, L.X. Feng, Chem. Res. Chinese Univ. 5 (1999) 281.
[20] S. Jungling, R. Mulhaupt, U. Stehling, H.H. Brintzinger, D. Fisher, F. Langhauser, J. Polymer Sci., Part A 33 (1995) 1305.
[21] T. Yasin, Ph.D. Dissertation, Zhejiang University, Hanzhou, China, 2000.
[22] J.B. Kinsinger, R.E. Hugres, J. Phys. Chem. 63 (1959) 2001.

control properties such as density of polyethylene [10], AO was used in a ternary system with ethylene/norbornene/AO only for enhancement of norbornene insertion [11] or alternatively as a chain transfer agent to introduce terminal vinyl groups [12].

Recently, we reported the novel *ansa*-zirconocene catalyst, [methylenebis(2,5-dimethylcyclopentadienyl)]zirconium dichloride $[H_2C(Me_2C_5H_2)_2]ZrCl_2$ (**1**), which demonstrated excellent ENC activity. Thus, the careful catalyst design with permethylation adjacent to the *ansa*-bridge lowered the steric hindrance while retaining electronic properties [13]. We have performed preliminary studies on copolymerization of norbornene with AO, revealing that catalyst **1** has adequate activity despite substrate bulkiness. More importantly, this was the first time the AO content in the AO/norbornene copolymer, was calculated using the extended calculation method for ENC [14].

2. Experimental

2.1. Materials

Catalyst **1** was prepared according to the literature procedure [13a]. The cocatalyst methylaluminoxane (MAO) was purchased from Akzo as 8.2 wt% solution in toluene. The monomers, ethylene, propylene, norbornene (bicyclo[2,2,1]hept-2-ene), 1-hexene and 1-octene, were purchased commercially and purified over molecular sieves, CuO and Al_2O_3.

2.2. Polymerization

2.2.1. Copolymerization of ethylene/norbornene or propylene/norbornene

All manipulations were performed in an inert atmosphere using standard Schlenk techniques in conjunction with a VAC dry-box. The copolymerization was carried out using a 500 mL jacketed stainless steel reactor, equipped with a mechanical stirrer. Norbornene was dissolved in toluene to obtain 150 mL solution with the desired mol%. The solution was passed through a purification column and injected into the reactor. After the reactor temperature was stabilized at 70 °C, the MAO toluene solution (Al/Zr = 2000, 6.0 mL, 12.0 mmol, 8.2 wt% in toluene) was injected into the reactor and the reaction mixture was stirred for 15 min. The catalyst (**1**) in toluene (6×10^{-6} mol/L) was added to the reactor and polymerization began as gaseous ethylene or propylene was added to the reactor at a constant pressure. The polymerization time was measured from the moment stirring began. After polymerization occurred, the reactor was vented and the reaction mixture was added into ca. 2 L of acetone. The precipitated white polymer was filtered, washed with acetone several times and dried in a vacuum oven at 80 °C.

2.2.2. Copolymerization of 1-hexene or 1-octene AO/norbornene

All polymerization runs were performed with a 250 mL Schlenk flask immersed in an oil thermostat at 70 °C since the AO is a liquid. With vigorous stirring with a magnetic stirrer, the norbornene and appropriate amount of 1-hexene or 1-octene was dissolved in toluene to obtain 150 mL of a desired mol% solution and then the MAO toluene solution (Al/Zr = 2000, 5.0 mL, 10.0 mmol, 8.2 wt% in toluene) was added to the flask. After ca. 30 min of mixing, polymerization was initiated by addition of the catalyst **1** in toluene (5×10^{-6} mol/L). After polymerization occurred, the reaction mixture was quantitatively transferred into 2 L of acetone. The precipitated white polymer was filtered, washed with smaller quantities of acetone several times and finally dried in a vacuum oven at high temperature.

2.3. Characterization of copolymers

The glass transition temperatures (T_g) were measured with a TA DSC 2010 instrument. The sample was first heated to 300 °C, then cooled to 30 °C at a rate of 20 °C/min, and reheated to 250 °C at a rate of 20 °C/min. The data used in this work was taken from the second heating. The average molecular weights (M_w) and the molecular weight distributions were determined by a Waters/Wyatt GPC-MALLS system at

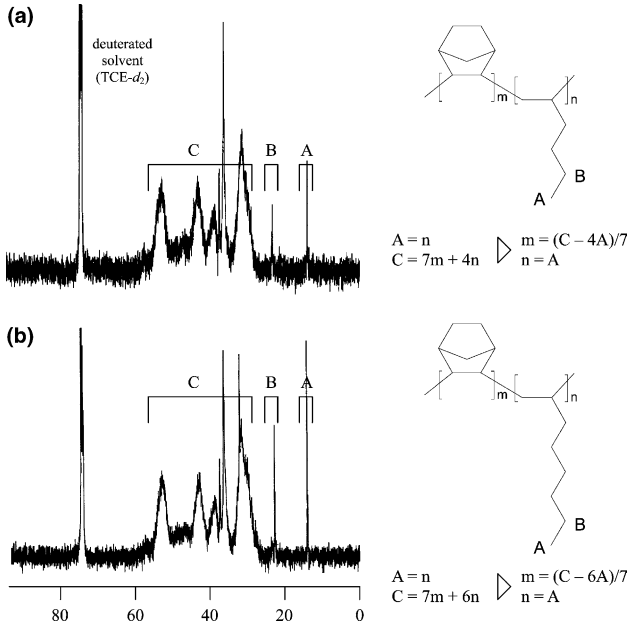


Fig. 1. Representative ^{13}C NMR spectra of (a) 1-hexene/norbornene copolymer (entry 7) and (b) 1-octene/norbornene copolymer (entry 10). Calculation of each monomer incorporation ratio, *m* and *n*, from the peak integration is presented to the right. TCE = 1,1,2,2-tetrachloroethane.

40 °C with chloroform as an eluent. These values were used without further correction. The ^{13}C NMR spectra were recorded by a Bruker Advance 400 FT NMR spectrometer in 1,1,2,2-tetrachloroethane-d_2, at 100 °C, in a 5 mm NMR tube, using inverse gated proton decoupling. Chemical shifts were referenced using the internal solvent resonance which was set to δ 74.0. The AO's content in the copolymers was calculated by ^{13}C NMR spectroscopy as illustrated in Fig. 1.

3. Results and discussion

Monomer composition, thermal property and molecular weight of the resulting polymers were investigated by altering the AO/norbornene feed ratio. The copolymerization results are summarized in Table 1 along with previous copolymerization results involving ethylene/norbornene and propylene/norbornene [13c]. The polymerization activity decreases as the accompanying norbornene monomer goes from ethylene to the bulkier 1-octene. However, within 1-hexene or 1-octene α-olefins, the activity change was not differentiated by the [*N*]/[AO] feed ratio. It ranged from 0.9 to 1.1 kg (polymer)/mmol(Zr) h. On the contrary, Tritto and co-workers [8b] reported the activity for the copolymerization of propylene/norbornene under another *ansa*-metallocene, *rac*-Et(indenyl)$ZrCl_2$/MAO, was decreased as the [*N*]/[*P*] feed ratio was increased. The polymer's glass transition temperature (T_g) is greatly dependent on the AO feed ratio and hence on its mole fraction in the polymer. Use of 1-hexene feed compositions of 39% and 75% result in polymer T_g's of 223.9 and 98.2 °C, respectively. In the case of 1-octene, uses of 30% and 51% result in T_g's of 207.8 and 166.8 °C, respectively.

The monomer composition of the polymer was determined by using ^{13}C NMR spectroscopy in 1,2-dideutero-1,1,2,2-tetrachloroethane with a pulse sequence of inversely gated proton decoupling for correct integration in order to achieve the relationship between polymer T_g and comonomer content. Fig. 1 shows representative ^{13}C NMR spectra of each AO/norbornene copolymer, demonstrating that AO's are incorporated in the polymer. The terminal CH_3 and its adjacent CH_2 carbon peaks for pendant alkyls of each AO are observed at ca. δ 14 and δ 23 (integrations A and B), respectively. The other peaks ranging from δ 26–60 (integration C) are assigned to the remaining carbon atoms. So the AO content in the polymers can be calculated from measuring peak integrations and equations illustrated to the right side of each spectrum in Fig. 1. This calculation method has been used to determine the norbornene content in ENC and to elucidate the microstructure of the copolymer in the literature. In addition it is demonstrated that the experimental calculation and theoretical prediction are very closely matched [15]. However, it should be mentioned that the composition percentage of norbornene calculated by ^1H NMR spectroscopy gives a lower value for AO content than that of ^{13}C NMR, with approximately a 10% difference.

Table 1
Results of α-olefin/norbornene copolymerization

Run no.[a]	AO[b]	NB feed (g)	AO feed (psi) or (g)	AO feed mol ratio[c](%)	Time (h)	AO in the polymer[d] (%)	Yield[e] (g)	A[f]	T_g[g] (°C)	M_w[h] (kg/mol)	PDI[h]
1	C_2	76.0	30	4.8	0.33	13.1	15.7	23.6	251	117	1.67
2		76.0	60	7.7	0.33	20.2	57.3	34.2	228	109	1.63
3		76.0	100	11.4	0.33	20.8	52.8	79.2	226	94	1.71
4	C_3	90.0	70	19	0.33	3.0	7.1	3.6	239	17.3	1.26
5		45.0	60	35	1.0	19.0	13.6	2.3	165	7.3	1.29
6		22.5	50	55	1.0	63.0	11.6	1.9	96	5.9	1.19
7	C_6	25.0	14.2	39	1.0	9.5	4.80	0.96	224	15.8	1.66
8		17.0	11.4	43	13.5	21.8	15.0	0.22	145	10.2	1.62
9		9.9	26.8	75	1.0	35.6	5.54	1.11	98	5.5	1.35
10	C_8	24.8	15.4	34	1.0	12.5	5.43	1.09	208	17.2	1.68
11		17.1	20.9	51	1.0	21.1	4.54	0.91	167	6.7	1.49
12		16.2	20.0	51	12	34.4	11.7	0.20	85	8.5	1.51

[a] Polymerization conditions: total volume 150 mL of toluene, 2.0 μmol of catalyst **1** for the runs 1–3, 6.0 μmol of catalyst **1** for the runs 4–6, 5.0 μmol of catalyst **1** for the runs 7–12, Al/Zr = 2000, P_{temp} = 70 °C.
[b] AO, α-olefin; C_2, ethylene, C_3, propylene, C_6, 1-hexene, C_8, 1-octene.
[c] The feed ratios [*E*]/[*N*] and [*P*]/[*N*] were converted by Henry's law.
[d] Determined by ^{13}C NMR spectroscopy.
[e] Yield is defined as the weight of copolymer obtained.
[f] A, polymerization activity in kg(polymer)/mmol(Zr) h.
[g] Determined by DSC.
[h] Determined by MALLS (multi-angle laser light scattering).

There is an approximate linear relationship between the polymer T_g at °C (T_g) and norbornene content in mol% of the polymer (NB) (Fig. 2), described in Eq. (1).

$$NB = T_g/5 + 47. \quad (1)$$

The relationship is adopted for both the copolymers of 1-hexene and 1-octene, ignoring effects of molecular weights or polymer non-uniformity induced by long polymerization time. According to the experimental data, reduction of the norbornene mole fraction (or, increase of the AO mole fraction) by 1% lowers the T_g of the polymer by 5 °C. This is distinguished from a relationship, $NB = T_g/4 + 14$, applied for the ENC copolymer produced by other *ansa*-metallocenes, rac-ethylene(indenyl)$ZrCl_2$,[15b] and a relationship for propylene/norbornene copolymer, $NB = T_g/2.7 + 5$, derived from the work of Henschke et al. [8].

The polymer T_g decreases along with the polymerization time, as observed in entries 7 and 9 for 1-hexene, and in entries 10 and 11 for 1-octene (Table 1). The 1-octene content in the polymer increases from 21% to 34% upon extension of the polymerization time from 1 to 12 h (entries 11 and 12). The corresponding result for 1-hexene appears in entries 7 (39% AO feed, 1 h) and 8 (43% AO feed, 13.5 h) in which the AO contents are greatly changed in spite of small differences in its initial feed ratio. These results indicate that norbornene inserts more rapidly than the AO, causing a comonomer composition drift to higher concentration of α-olefin, and consequently a polymer of high AO content with an extension of polymerization time.

The molecular weight, determined by multi-angle laser light scattering (MALLS), was dependent on α-olefin monomer feed ratio, but not on the kind of α-olefin monomer. On increasing the 1-hexene feed from 39% to 75%, the M_w decreased from 15800 to 5500 g/mol. Additionally, increase of 1-octene feed from 34% to 51% diminished the M_w from 17500 to 6700 g/mol. According to these observations, coordination of AO to the active site of the catalyst seems to render the growing polymer chain susceptible to chain transfer reaction.

We are currently investigating methods to increase the copolymer molecular weight and to effect terpolymerization of ethylene/AO/norbornene with catalyst **1**.

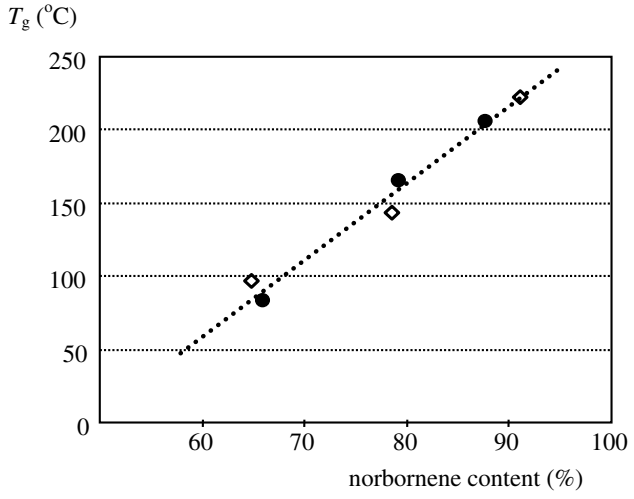


Fig. 2. Relationship between T_g's of AO/norbornene copolymers and norbornene content for AO = 1-hexene (◇) and AO = 1-octene (●).

4. Conclusions

We have found that the methylene bridged *ansa*-metallocene $[H_2C(Me_2C_5H_2)_2]ZrCl_2$ is a very effective catalyst especially for the copolymerization of 1-hexene/norbornene or 1-octene/norbornene. The α-olefin content in the copolymer, characterized and calculated by ^{13}C NMR spectroscopy and reported for the first time, greatly affected the glass transition temperature in such a way that increase of AO mole fraction by 1% lowers the polymer T_g by ca. 5 °C. The molecular weight of the copolymer was drastically decreased upon increase of AO feed.

Acknowledgements

We gratefully thank Ms. Sunyoung Park for the GPC-MALLS analysis and LG Chem./Research Park for the financial support. Prof. David G. Churchill of KAIST (Daejeon, Republic of Korea) has been very helpful in the written preparation of this manuscript.

References

[1] (a) W. Kaminsky, R. Steiger, Polyhedron 7 (1988) 2375;
(b) H. Lasarov, K. Monkkonene, T.T. Pakkanen, J. Appl. Polym. Sci. 77 (2000) 2291;
(c) B.-G. Jeong, D.-W. Nam, S.-D. Hong, S.-G. Lee, Y.-W. Park, K.H. Song, Korean J. Chem. Eng. 20 (2003) 22;
(d) C.H. Bergström, J.V. Seppälä, J. Appl. Polym. Sci. 63 (1997) 1063;
(e) M. Arndt, I. Beulich, Makromol. Chem. Phys. 199 (1998) 1221.
[2] (a) H.-R.H. Damrau, A. Geyer, M.-H. Prosenc, A. Weeber, F. Schaper, H.-H. Brintzinger, J. Organomet. Chem. 553 (1998) 331;
(b) H. Lee, P.J. Desrosiers, I. Guzei, A.L. Rheingold, G. Parkin, J. Am. Chem. Soc. 120 (1998) 3255;
(c) W. Kaminsky, R. Spiehl, Makromol. Chem. 19 (1989) 515;
(d) W. Kaminsky, A. Bark, M. Arndt, Makromol. Chem. Macromol. Symp. 47 (1991) 83;
(e) W. Kaminsky, G. Schupfner, Macromol. Symp. 177 (2002) 61;
(f) W. Kaminsky, I. Beulich, M. Arndt-Rosenau, Macromol. Symp. 173 (2001) 211.
[3] (a) C. Wang, S. Friedrich, T.R. Younkin, R.T. Li, R.H. Grubbs, D.A. Bansleben, M.W. Day, Organometallics 17 (1998) 3149;

(b) T.R. Younkin, E.F. Conner, J.I. Henderson, S. Friedrich, R.H. Grubbs, D.A. Bansleben, Science 287 (2000) 460;
(c) F. Bauers, S. Mecking, Macromolecules 34 (2001) 1165;
(d) R. Soula, J.P. Broyer, M.F. Llauro, A. Tomov, R. Spitz, J. Claverie, X. Drujon, J. Malinge, T. Saudemont, Macromolecules 34 (2001) 2438.

[4] G.M. Benedikt, B.L. Goodall, H.A. Kalamarides, L.H. McIntosh III, L.F. Rhodes, K.T. Selvy, C. Andes, K. Oyler, A. Sen, Macromolecules 35 (2002) 8978.

[5] (a) E. Brock, F. Osan, MetCon 98: "Polymers in Transition", June 10–11, The catalyst group, Inc., Houston, TX, USA, 1998;
(b) R.R. Lamonte, D. McNally, Adv. Mater. Process (2001), March;
(c) A.H. Tullo, Chem. Eng. News 80 (20) (2002) 13.

[6] S.L. Mukerjee, V.L. Kyllingstad, Nippon Zeon Co. Ltd, US Patent 6342621, 2002.

[7] (a) D. Ruchatz, G. Fink, Macromolecules 31 (1998) 4674;
(b) D. Ruchatz, G. Fink, Macromolecules 31 (1998) 4684;
(c) C.H. Bergström, J. Routoistenmäki, E.T. Aitola, J.V. Seppälä, J. Appl. Polym. Sci. 77 (2000) 1108.

[8] (a) O. Henschke, F. Köller, M. Arnold, Macromol. Rapid Commun. 18 (1997) 617;
(b) L. Boggioni, F. Bertini, G. Zannoni, I. Tritto, P. Carbone, M. Ragazzi, D.R. Ferro, Macromolecules 36 (2003) 882.

[9] W. Kaminsky, M. Arndt-Rosenau, in: J. Scheirs, W. Kaminsky (Eds.), Metallocene-based Polyolefins, vol. II, Wiley, Chichester, 2000, p. 91.

[10] (a) K. Kunz, G. Erker, G. Kehr, R. Fröhlich, H. Jacobsen, H. Berke, O. Blacque, J. Am. Chem. Soc. 124 (2002) 3316;
(b) W. Kaminsky, C. Piel, J. Mol. Catal. A 213 (2004) 15.

[11] D.H. Lee, J.H. Lee, H.J. Kim, W.S. Kim, K.E. Min, L.S. Park, K.H. Seo, I.K. Kang, Polymer (Korea) 25 (2001) 468.

[12] W. Hatke, F. Osan, A.G. Hoechst, US Patent 5610253, 1997.

[13] (a) B.Y. Lee, Y.H. Kim, Y.C. Won, J.W. Han, W.H. Suh, I.S. Lee, Y.K. Chung, K.H. Song, Organometallics 21 (2002) 1500;
(b) Y.C. Won, U.G. Joung, E.S. Cho, B.Y. Lee, H. Lee Y.-W. Park, K.H. Song, Synthesis (2004) 1052;
(c) H. Lee, S.-D. Hong, Y.-W. Park, B.-G. Jeong, D.-W. Nam, H.Y. Jung, M.W. Jung, K.H. Song, J. Organomet. Chem. 689 (2004) 3402.

[14] G. Xu, E. Ruckenstein, Macromolecules 31 (1998) 4724.

[15] (a) I. Tritto, C. Marestin, L. Boggioni, L. Zetta, A. Provasoli, D.R. Ferro, Macromolecules 33 (2000) 8931;
(b) D. Ruchatz, G. Fink, Macromolecules 31 (1998) 4681;
(c) R.A. Wendt, R. Mynott, G. Fink, Macromol. Chem. Phys. 203 (2002) 2531;
(d) M. Arndt-Rosenau, I. Beulich, Macromolecules 32 (1999) 7386.

of $[Nb(C_5H_4SiMe_2Cl)Cl_2(N^tBu)]$ with $LiNH^tBu$ [11]. Finally, Chen and co-workers [25] observed that the imido compound $[Ta(C_5Me_4H)Cl_2(N^tBu)]$ was obtained on treating $TaCl_5$ with the aminosilyl-cyclopentadiene $C_5Me_4H(SiMe_2NH^tBu)$. From these results, it is clear that the thermodynamic stability of the M-imido bond is much higher than that of the bridging cyclopentadienyl-silyl-η-amido-M system (M = group 5 metal).

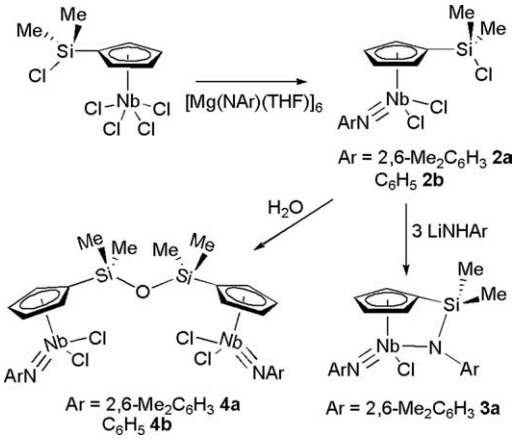
Most of these group 5 metal compounds containing the cyclopentadienyl-silyl-η-amido ligand were isolated as oily products. It has been suggested that aryl-imido ligands provide more crystalline solids [26]. Consequently, we decided to extend our research on Si–Cl functionalized monocyclopentadienyl niobium complexes [11,27,28] to isolate new aryl-imido derivatives using the organomagnesium compounds $[Mg(NAr)(THF)]_6$ (Ar = 2,6-$Me_2C_6H_3$, **1a**; Ph, **1b**) as imido transfer reagents. This method was first published by Power and co-workers [29] to obtain titanium and zirconium imido compounds. The main advantage of the organomagnesium compounds is their lower tendency to promote reduction of the metal centre than their lithium analogues. The reactivity of the Si–Cl bond of these imido complexes and the first X-ray structure of a group 5 metal silyl-η-amido complex is reported.

2. Results and discussion

The magnesium imide compound $[Mg(NAr)(THF)]_6$ (Ar = 2,6-$Me_2C_6H_3$, **1a**) was synthesized following the method reported [29] for the analogous phenyl derivative $[Mg(NPh)(THF)]_6$ (**1b**). Hence, reaction of $[MgBu_2]$ with 1 equivalent of the corresponding aniline $ArNH_2$ (Ar = 2,6-$Me_2C_6H_3$) in THF at −78 °C gave $[Mg(NAr)(THF)]_6$ (**1a**) as a scarcely soluble white solid in high yield (Eq. (1)). Compound **1a** was identified by ^1H NMR, but its instability prevented suitable elemental analysis being obtained, and the hexameric structure was proposed by analogy with the phenyl derivative **1b**, for which X-ray structure had been determined [29].

$$\underset{\text{Ar=2,6-Me}_2\text{C}_6\text{H}_3}{MgBu_2} + H_2NAr \xrightarrow[-2BuH]{THF} \underset{\mathbf{1a}}{[Mg(NAr)(THF)]_6} \qquad (1)$$

These magnesium imide compounds $[Mg(NAr)(THF)]_6$ (Ar = 2,6-$Me_2C_6H_3$, **1a**; Ph, **1b**) can be used to transfer the imido ligand when reacted with the monocyclopentadienyl niobium complex $[NbCp^{Cl}Cl_4]$ (Cp^{Cl} = $C_5H_4(SiMe_2Cl)$) (Scheme 1). Reaction of the niobium complex with 1 equivalent of the magnesium imides gave the new imido compounds $[NbCp^{Cl}Cl_2(NAr)]$ (Ar = 2,6-$Me_2C_6H_3$, **2a**; Ph, **2b**) as red oils after 3 h in diethylether at room temperature. Compared with the analogous reaction with the alkaline amide compound LiNHAr, this procedure prevents the formation of the corresponding amine NH_2Ar as a by-product,



Scheme 1.

which is difficult to eliminate because its solubility is close to that of compounds **2**, although the same compounds can also be obtained using the lithium amide LiNHAr (Ar = 2,6-$Me_2C_6H_3$, Ph). Also, this procedure seems to be a faster way to isolate the imido compounds and demonstrates the remarkable stability of the Nb-imido bond, formation of which is preferred to a bridging silyl-η-amido system between the cyclopentadienyl ring and the niobium centre.

The presence of a silicon–chlorine bond in compounds **2** moved us to try the synthesis of the silyl-η-amido complexes using the same magnesium imide to transfer the [NAr] moiety, but unfortunately decomposition was observed. However, reaction of **2a** with excess LiNHAr (Ar = 2,6-$Me_2C_6H_3$) in diethylether afforded the desired compound $[Nb(\eta^5\text{-}C_5H_4SiMe_2\text{-}\eta^1\text{-}NAr)Cl(NAr)]$ (**3a**) in moderate yield, whereas the same reaction for Ar = Ph was unsuccessful. We have observed that using more than two equivalents of the lithium amide compound is required although we have never detected the substitution of the remaining chlorine atom by another amido group, probably due to the steric hindrance of the [2,6-$Me_2C_6H_3$] substituent. However, the related diamido compound $[NbCp(NAr)(NHAr)_2]$ (Ar = 2,6-$Me_2C_6H_3$) was obtained through an analagous procedure [26]. This is the same method reported previously for introducing a bridging amido group between the metal atom and the silylcyclopentadienyl ligand in similar niobium complexes [11].

The dinuclear Si–O–Si bridged compounds $[\{NbCl_2(NAr)\}_2\{(\eta^5\text{-}C_5H_4SiMe_2)_2(\mu\text{-}O)\}]$ (Ar = 2,6-$Me_2C_6H_3$, **4a**; Ph, **4b**) were obtained in low yields upon addition of a stoichiometric amount of H_2O to toluene solutions of compounds **2a** and **2b**, respectively. The selective hydrolysis of the Si–Cl bond with formation of a Si–O–Si bridge was the expected behaviour for this type of niobium compound [11,27]. In contrast, it was observed [6,30–33] that the hydrolysis reactions of related monocyclopentadienyl group 4 metal complexes with

the chloro-silylcyclopentadienyl ligand afforded Si–O–M bridges. Attempts to produce further hydrolysis of Nb–Cl bonds failed and led to decomposition products with elimination of the corresponding amine.

The molecular structure of compound **3a** was determined by X-ray diffraction studies on a single crystal. Fig. 1 shows a view of the molecular structure of complex **3a** and Table 1 summarizes selected bond distances and angles. The coordination around the niobium centre is typical of half-sandwich imido complexes and could be described as a pseudo-tetrahedral structure with the centroid of the cyclopentadienyl ring, the chloro ligand, the imido nitrogen and the nitrogen of the bridging silyl-η-amido system occupying the four coordination sites.

The most remarkable feature of this structure is the distorted geometry due to the presence of this silyl-η-amido group bridging the cyclopentadienyl ring and the niobium atom. The Cg–Nb–N(1) (amido-silyl) bond angle (Cg = centroid of the Cp ring) of 100.76° for compound **3a** is the closest angle reported for amido ligands, which showed values in the range 106.60° and 116.67°

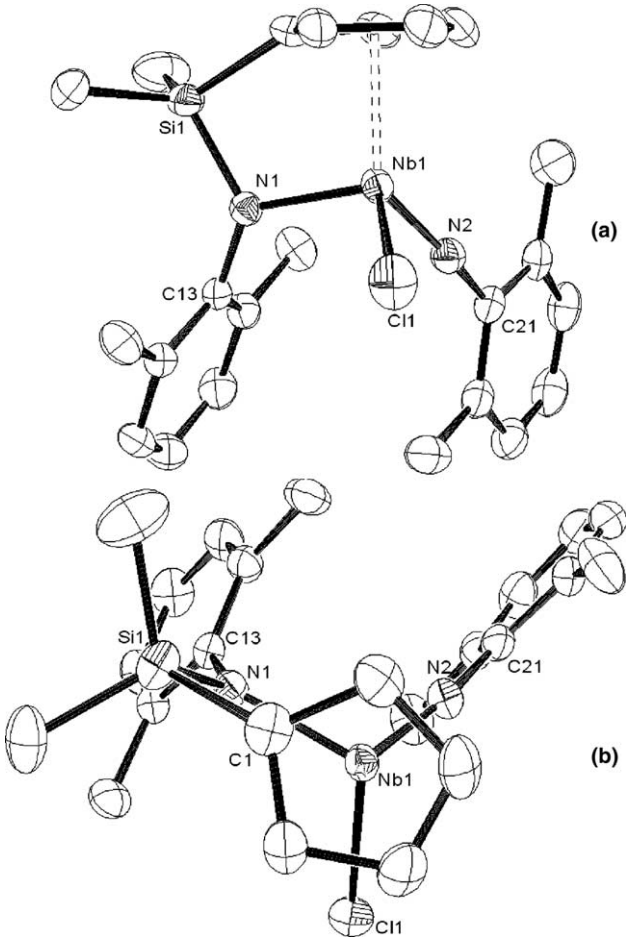


Fig. 1. Molecular structure of compound **3a**. (a) ORTEP ellipsoids are drawn at the 50% probability level and hydrogen atoms are omitted for clarity. (b) View perpendicular to the cyclopentadienyl ring plane.

Table 1
Selected bond distances (Å) and bond angles (°) of compound **3a**

Bond lengths (Å)	
N(1)–Nb	2.016(2)
N(2)–Nb	1.786(2)
N(1)–Si	1.754(2)
Nb–Cg	2.1474
Cl–Nb	2.3796(9)
Bond angles (°)	
Cg–Nb–Cl	112.85
Cg–Nb–N(1)	100.76
Cg–Nb–N(2)	130.20
N(2)–Nb–N(1)	102.3(1)
N(2)–Nb–Cl	101.05(8)
N(1)–Nb–Cl	107.83(7)
N(1)–Si–C(1)	91.9(1)
Si–N(1)–Nb	108.9(1)
C(13)–N(1)–Si	126.6(2)
C(13)–N(1)–Nb	124.7(8)
C(21)–N(2)–Nb	172.8(2)

Cg is the centroid of the cyclopentadienyl ring.

for unbridged ligands [11,21,26,34,35], and in addition is smaller than those reported for constrained silyl-η-amido group 4 metal complexes (105–108°) [7,36]. Moreover, the Cg–Nb–N(2) (imido ligand) bond angle of 130.20° is the most open observed for half-sandwich imido complexes [11,21,26,34,35], for which the expected value is in the range 119.24–124.15°, whereas the Cg–Nb–Cl bond angle of 112.85° and the angles formed by the three N(1), N(2) and Cl substituents about the niobium atom are in the usual range found for this type of half-sandwich imido compound.

As a consequence of the constrained bridging situation, the silicon atom presents a distorted tetrahedral environment (C(1)–Si–N(1) = 91.9(1)°) and the N(1) a distorted planar environment (Si–N(1)–Nb = 108.2(1)°). Furthermore, the N(1)–Nb and N(1)–Si bond distances of 2.016(2) and 1.754(2) Å are, respectively, slightly longer than the related Nb–N(amide) and Si–N(amide) bonds found in monoamide complexes of the type $[NbCp^RCl(NHR)(NR)]$ [26,37] and in the non-bridged aminosilyl compound $[NbCp^RCl_2(N^tBu)]$ ($Cp^R = C_5H_4(SiMe_2NH^tBu)$, Si–N = 1.719(9) Å) [11]. This is an indication of the lower N–Nb and N–Si π-bonding contribution. These data together with the co-planarity of the Nb, N(1), C(13) and Si atoms are consistent with the behaviour known for group 4 metal constrained geometry cyclopentadienylsilyl-η-amido complexes [7,18].

Regarding the cyclopentadienyl ring, the C–C bond distances are in the range 1.401–1.432 Å, indicating a preference for η^5-coordination in contrast to other half-sandwich group 5 metal imido and group 4 metal constrained geometry complexes, for which significant contribution of a η^3-allyl-η^2-olefin structure is proposed [7,21]. On the other hand, the Nb–C bond lengths, 2.382–2.519 Å, show two bonds clearly longer,

Nb–C(4) and Nb–C(5), corresponding to the C–C bond opposite to the imido ligand, as typically found for imido complexes [21,35]. Also, the Nb–C(1) bond supporting the bridge is not the shortest one as found in group 4 metal constrained geometry complexes [7,38]. This could be related with the location of the C(1) atom with respect to the imido ligand.

Another notable feature found in the structure of complex **3a** is that the imido-aryl group is almost perpendicular to the Cp ring, whereas in the other 2,6-disubstituted aryl-imido half-sandwich complexes the aromatic ring is almost coplanar with the cyclopentadienyl ligand, regardless of the nature of the other ligands present [21,26,35,37,39]. Moreover, the silyl group does not occupy the *trans* position with respect to the imido ligand as in the silylcyclopentadienyl imido compounds [$NbCp^RCl_2(NR)$] ($Cp^R = C_5H_4(SiMe_2NH^t$-Bu) [11], $C_5H_4(SiMe_3)$ [34]). Finally, the Nb–N(2) bond distance of 1.786(2) Å and the almost linear Nb–N(2)–C(21) bond angle of 172.8 (2)° of the imido ligand correspond to a typical triple bond of a 4-electron-donor ligand [23].

3. Experimental

All manipulations were performed under argon atmosphere, using standard Schlenk techniques or a glovebox. Solvents used were previously dried and freshly distilled under argon: diethylether and tetrahydrofuran from sodium benzophenone, ketyl and hexane from sodium–potassium amalgam. Deuterated solvents from Scharlau were degassed and stored over molecular sieves. NMR spectra were recorded on a Varian Unity FT-300 and chemical shifts are given in ppm (δ). C, H and N microanalyses were performed on a Perkin–Elmer 240B microanalyzer. Unless otherwise stated, reagents were obtained from commercial sources and used as received. $ArNH_2$ (Ar = 2,6-$Me_2C_6H_3$, Ph) (Aldrich) were distilled before use and stored under argon. LiNHAr was prepared in tetrahydrofuran in almost quantitative yield from $ArNH_2$ and ^{n}BuLi (Aldrich, 1.6 M in hexane) and the resulting product was washed with hexane (2 × 10 mL). $[Mg(NPh)(THF)]_6$ (**1b**) [29] and $[Nb[\eta^5\text{-}C_5H_4(SiClMe_2)]Cl_4]$ [27] were prepared according to the literature procedures.

3.1. [Mg(NAr)(THF)]$_6$ (Ar = 2,6-$Me_2C_6H_3$, **1a**)

Compound **1a** was isolated as a white solid following the procedure reported for $[Mg(NPh)(THF)]_6$ (**1b**) [29], from $ArNH_2$ (5.00 g, 41.25 mmol) and $[MgBu_2]$ (41.25 mmol) in THF (8.45 g, 95% yield). Data for **1a**: ^{1}H NMR: 6.71 (d, J = 7.6 Hz, 2H, $Me_2C_6H_3$), 6.62 (t, J = 7.6 Hz, 1H, $Me_2C_6H_3$), 3.55 (m, 4H, OCH_2), 2.34 (s, 6H, $Me_2C_6H_3$), 1.40 (m, 4H, CH_2).

3.2. [Nb{η^5-$C_5H_4(SiMe_2Cl)$}Cl_2(NAr)] (Ar = 2,6-$Me_2C_6H_3$, **2a**)

Diethylether (50 mL) was added to a solid mixture of $[Nb\{\eta^5\text{-}C_5H_4(SiMe_2Cl)\}Cl_4]$ (1.00 g, 2.54 mmol) and $[Mg(NAr)(THF)]_6$ (**1a**) (0.54 g, 0.42 mmol) at room temperature and the reaction mixture was stirred for 3 h. Over this time the mixture became dark red and the solvent was removed to half volume under reduced pressure. Hexane (20 mL) was added and the solution was filtered. The volatiles were completely removed to give a dark red oil which was characterized as **2a** (1.11 g, 90%). Data for **2a**: ^{1}H NMR: 6.78 (d, J = 7.1 Hz, 2H, $Me_2C_6H_3$), 6.67 (t, J = 7.1 Hz, 1H, $Me_2C_6H_3$), 6.25 (m, 2H, C_5H_4), 5.81 (m, 2H, C_5H_4), 2.34 (s, 6H, $Me_2C_6H_3$), 0.53 (s, 6H, $SiMe_2$). ^{13}C NMR: 154.1 (C_i, $Me_2C_6H_3$), 135.1 ($Me_2C_6H_3$), 129.8 ($Me_2C_6H_3$), 126.1 ($Me_2C_6H_3$), 123.1 (C_5H_4), 122.0 (C_i, C_5H_4), 113.3 (C_5H_4), 19.3 ($Me_2C_6H_3$), 2.3 ($SiMe_2$). *Anal.* Calc. for $C_{15}H_{19}Cl_3NNbSi$: C, 40.88; H, 4.35; N, 3.18. Found: C, 41.09; H, 4.45; N, 3.12%.

3.3. [Nb{η^5-$C_5H_4(SiMe_2Cl)$}Cl_2(NAr)] (Ar = C_6H_5, **2b**)

Compound **2b** was prepared from $[Nb\{\eta^5\text{-}C_5H_4(SiMe_2Cl)\}Cl_4]$ (1.00 g, 2.54 mmol) and $[Mg(NAr)(THF)]_6$ (**1b**) (0.47 g, 0.42 mmol) following the method given for **2a** and was obtained as a red oil (0.94 g, 90% yield). Data for **2a**: ^{1}H NMR: 7.02–6.80 (m, 5H, C_6H_5), 6.28 (m, 2H, C_5H_4), 5.86 (m, 2H, C_5H_4), 0.49 (s, 6H, $SiMe_2$). ^{13}C NMR: 156.0 (C_i, C_6H_5), 129.6 (C_6H_5), 128.7 (C_6H_5), 126.5 (C_6H_5), 124.5 (C_5H_4), 122.2 (C_i, C_5H_4), 114.4 (C_5H_4), 2.5 ($SiMe_2$). *Anal.* Calc. for $C_{13}H_{15}Cl_3NNbSi$: C, 37.84; H, 3.66; N, 3.39. Found: C, 37.12; H, 3.49; N, 3.46%.

3.4. [Nb(η^5-$C_5H_4SiMe_2$-η^1-NAr)Cl(NAr)] (Ar = 2,6-$Me_2C_6H_3$, **3a**)

A solution of **2a** (1.06 g, 2.40 mmol) in diethylether (30 mL) was treated dropwise with a solution of LiNHAr (Ar = 2,6-$Me_2C_6H_3$) (0.91 g, 7.21 mmol) in diethylether (30 mL) and the mixture was stirred for 16 h at room temperature. After addition of hexane (30 mL), the solution was filtered and the solvents were removed under vacuum to ca. 30 mL. The remaining solution was cooled to −38 °C to give complex **3a** as a yellow crystalline solid (0.70 g, 60% yield). Data for **3a**: ^{1}H NMR: 6.96–6.69 (m, 6H, $Me_2C_6H_3$), 6.46 (m, 2H, C_5H_4), 6.33 (m, 1H, C_5H_4), 6.23 (m, 1H, C_5H_4), 2.23 (s, 3H, $Me_2C_6H_3$), 2.12 (s, 6H, $Me_2C_6H_3$), 1.94 (s, 3H, $Me_2C_6H_3$), 0.28 (s, 3H, $SiMe_2$), 0.07 (s, 3H, $SiMe_2$). ^{13}C NMR: 132.1, 130.1, 124.3, 121.1, 118.2, 112.3, 112.0 and 109.5 ($Me_2C_6H_3$ and C_5H_4, C_{ipso} not observed), 19.4 ($Me_2C_6H_3$), 19.3 ($Me_2C_6H_3$), 17.5

($Me_2C_6H_3$), 0.2 (SiMe_2), −1.3 (SiMe_2). *Anal.* Calc. for $C_{23}H_{28}ClN_2NbSi$: C, 56.50; H, 5.77; N, 5.73. Found: C, 55.90; H, 5.43; N, 5.59%.

3.5. [{$NbCl_2(NAr)$}$_2${(η^5-C_5H_4)$_2$($Me_2SiOSiMe_2$)}] (Ar = 2,6-$Me_2C_6H_3$, **4a**)

Distilled water (0.02 mL, 1.20 mmol) was added to a mixture of **2a** (1.06 g, 2.40 mmol) and NEt_3 (0.33 mL, 2.40 mmol) in toluene (60 mL). After stirring for 24 h at room temperature, the solution was filtered and the volatiles removed under vacuum to give **4a** as a brown solid (0.40 g, 40% yield). Data for **4a**: ^{1}H NMR: 6.78 (m, 4H, $Me_2C_6H_3$), 6.73 (m, 2H, $Me_2C_6H_3$), 6.35 (m, 4H, C_5H_4) 5.91 (m, 4H, C_5H_4), 2.39 (s, 12H, $Me_2C_6H_3$), 0.37 (s, 12H, SiMe_2). *Anal.* Calc. for $C_{30}H_{38}Cl_4N_2Nb_2OSi_2$: C, 43.60; H, 4.63; N, 3.39. Found: C, 42.91; H, 4.29; N, 3.05%.

3.6. [{$NbCl_2(NAr)$}$_2${(η^5-C_5H_4)$_2$($Me_2SiOSiMe_2$)}] (Ar = C_6H_5, **4b**)

This compound was prepared as above from **2b** (1.00 g, 2.42 mmol), NEt_3 (0.34 mL, 2.42 mmol) and distilled water (0.02 mL, 1.21 mmol) to yield **4b** (0.37 g, 40%). Data for **4b**: ^{1}H NMR: 6.92–6.70 (m, 10H, C_6H_5), 6.40 (m, 4H, C_5H_4) 5.96 (m, 4H, C_5H_4), 0.33 (s, 12H, SiMe_2). *Anal.* Calc. for $C_{26}H_{30}Cl_4N_2Nb_2OSi_2$: C, 40.54; H, 3.93; N, 3.64. Found: C, 39.88; H, 3.81; N, 3.47%.

3.7. X-ray crystallographic study of **3a**

Suitable single crystals for the X-ray diffraction study were grown by standard techniques from a saturated solution of **3a** ($C_{23}H_{28}ClN_2NbSi$) in diethylether. A light yellow crystal, $0.31 \times 0.30 \times 0.16$ mm, monoclinic, space group $P2_1/n$ was used. Data collection were performed at 200 K on a Kappa-CCD area detecting diffraction system using a Mo Kα radiation. The unit cell dimensions were determined from 110 reflections between $\theta = 3.102°$ and 21.448°. Unit cell parameters were $a = 8.3381(5)$ Å, $b = 21.597(2)$ Å, $c = 12.751(1)$ Å, $\beta = 92.549(7)°$, $V = 2294.0(3)$ Å^3, $Z = 4$. X-ray data were collected within the θ-range of $3.01° < \theta < 27.51°$ to a completeness of 0.998. An empirical absorption correction was applied, and symmetry equivalent and multiple measured reflections were averaged with the program SORTAV [40]. A total of 19118 reflections were collected and merged ($R_{int} = 0.0688$) to give 5271 unique reflections of which 3884 were observed with $I > 2\sigma(I)$. The crystal structure was solved by direct methods and refined using full-matrix least squares on F^2 [41]. All non-hydrogen atoms were anisotropically refined. Hydrogen atoms were geometrically placed and left riding on their parent atoms. The final cycle of full-matrix least-squares refinement based on 5271 reflections and 253 parameters converged to final values of $R_1(F^2 > 2\sigma(F^2)) = 0.0388$, $wR_2(F^2 > 2\sigma(F^2)) = 0.0927$, $R_1(F^2) = 0.0668$, $wR_2(F^2) = 0.1014$ and goodness-of-fit = 1.011. Final difference Fourier maps showed no peaks higher than 0.513 nor deeper than −0.453 e Å^{-3}. Geometrical calculations were made with PLATON [42]. The crystallographic plots were made with ORTEP-3. All calculations were made at the University of Alcalá.

4. Supplementary material

Crystallographic data for the structural analysis for **3a** have been deposited with the Cambridge Crystallographic Data Centre, CCDC No. 259073. Copies of this information may be obtained free of charge from The Director, CCDC, 12 Union Road, Cambridge CB2 1EZ, UK (fax: +44 1223 366 033; e-mail: deposit@ccdc.cam.ac.uk or http://www.ccdc.cam.ac.uk).

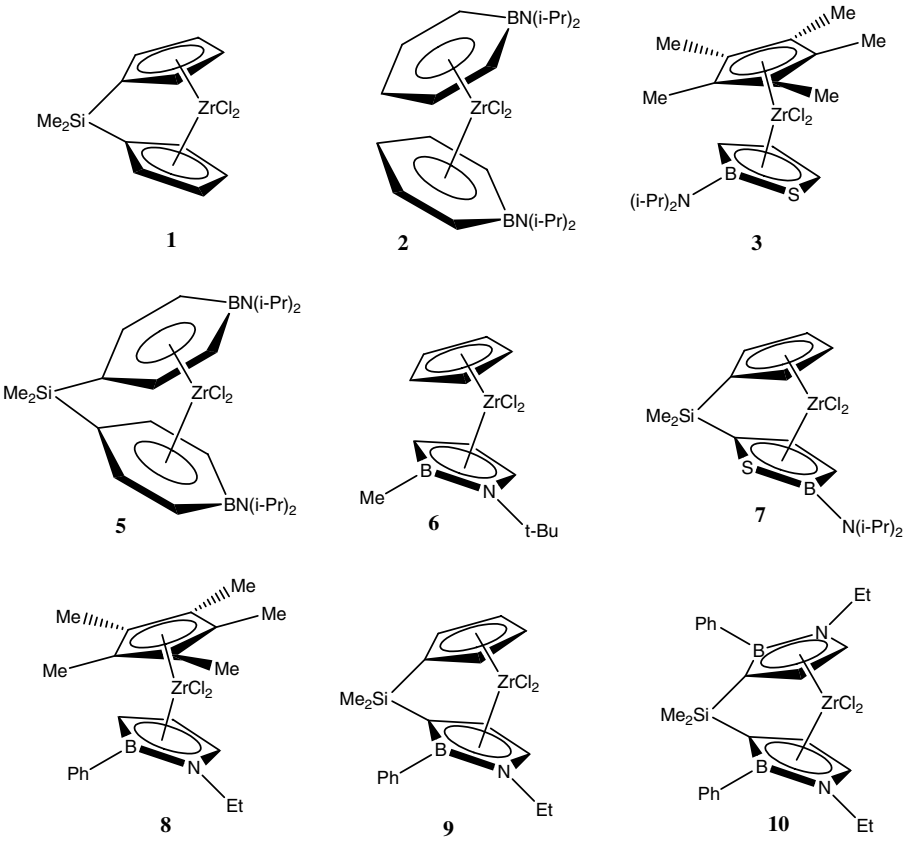
Acknowledgments

We gratefully acknowledge the Ministerio de Educación y Ciencia (Project MAT2004-02614) and DGUI-Comunidad de Madrid (Project GR/MAT/0622/2004) (Spain) for financial support. R.A.-M. acknowledges MCyT for a fellowship.

References

[1] T. Cuenca, P. Royo, Coord. Chem. Rev. 195 (1999) 447.
[2] M. Antberg, H. Lüker, L. Böhm, Eur. Patent. Appl. EP 293815A1, Hoechst, 1998.
[3] G.G. Hlatky, Chem. Rev. 100 (2000) 1347.
[4] R.M. Kasi, E.B. Coughlin, Organometallics 22 (2003) 1534.
[5] K.Q. Yu, M.W. McKittrick, C.W. Jones, Organometallics 23 (2004) 4089.
[6] S. Ciruelos, T. Cuenca, R. Gómez, P. Gómez-Sal, A. Manzanero, P. Royo, Organometallics 15 (1996) 5577.
[7] R. Gómez, P. Gómez-Sal, A. Martín, A. Núñez, P.A. del Real, P. Royo, J. Organomet. Chem. 564 (1998) 93.
[8] S. Ciruelos, A. Sebastián, T. Cuenca, P. Gómez-Sal, A. Manzanero, P. Royo, J. Organomet. Chem. 604 (2000) 103.
[9] G. Jiménez, E. Rodríguez, P. Gómez-Sal, P. Royo, T. Cuenca, M. Galakhov, Organometallics 20 (2001) 2459.
[10] G. Jiménez, P. Royo, T. Cuenca, E. Herdtweck, Organometallics 21 (2002) 2189.
[11] M.I. Alcalde, M.P. Gómez-Sal, P. Royo, Organometallics 18 (1999) 546.
[12] A.L. McKnight, R.M. Waymouth, Chem. Rev. 98 (1998) 2587.
[13] H.G. Alt, A. Reb, W. Milius, A. Weis, J. Organomet. Chem. 628 (2001) 169.
[14] V.C. Gibson, S.K. Spitzmesser, Chem. Rev. 103 (2003) 283.
[15] N. Guo, L.T. Li, T.J. Marks, J. Am. Chem. Soc. 126 (2004) 6542.

[16] J. Okuda, T. Eberle, Half-sandwich Complexes as Metallocene Analogues in Metallocenes: Synthesis, Reactivity, Applications, vol. 1, Wiley–VCH, Weinheim, 1998.
[17] J. Cano, P. Royo, M. Lanfranchi, M.A. Pellinghelli, A. Tiripicchio, Angew. Chem. Int. Ed. 40 (2001) 2495.
[18] J. Cano, P. Royo, H. Jacobsen, O. Blacque, H. Berke, E. Herdtweck, Eur. J. Inorg. Chem. (2003) 2463.
[19] M. Sudupe, J. Cano, P. Royo, E. Herdtweck, Eur. J. Inorg. Chem. (2004) 3074.
[20] F. Hannig, R. Fröhlich, K. Bergander, G. Erker, J.L. Petersen, Organometallics 23 (2004) 4495.
[21] D.N. Williams, J.P. Mitchell, A.D. Poole, U. Siemeling, W. Clegg, D.C.R. Hockless, P.A. O'Neil, V.C. Gibson, J. Chem. Soc., Dalton Trans. (1992) 739.
[22] M.C.W. Chan, J.M. Cole, V.C. Gibson, J.A.K. Howard, C. Lehmann, A.D. Poole, U. Siemeling, J. Chem. Soc., Dalton Trans. (1998) 103.
[23] D.E. Wigley, Prog. Inorg. Chem. 42 (1994) 239.
[24] W.A. Herrmann, W. Baratta, J. Organomet. Chem. 506 (1996) 357.
[25] S.G. Feng, G.R. Roof, E.Y.X. Chen, Organometallics 21 (2002) 832.
[26] M.J. Humphries, M.L.H. Green, R.E. Douthwaite, L.H. Rees, J. Chem. Soc., Dalton Trans. (2000) 4555.
[27] M.I. Alcalde, P. Gómez-Sal, A. Martín, P. Royo, Organometallics 17 (1998) 1144.
[28] M.I. Alcalde, M.P. Gómez-Sal, P. Royo, Organometallics 20 (2001) 4623.
[29] W.J. Grigsby, M.M. Olmstead, P.P. Power, J. Organomet. Chem. 513 (1996) 173.
[30] S. Ciruelos, T. Cuenca, P. Gómez-Sal, A. Manzanero, P. Royo, Organometallics 14 (1995) 177.
[31] B. Royo, P. Royo, L.M. Cadenas, J. Organomet. Chem. 551 (1998) 293.
[32] O. Buitrago, G. Jiménez, T. Cuenca, J. Organomet. Chem. 683 (2003) 70.
[33] A.B. Vázquez, P. Royo, E. Herdtweck, J. Organomet. Chem. 683 (2003) 155.
[34] J.M. Benito, E.d. Jesús, F.J.d.l. Mata, J.C. Flores, R. Gómez, P. Gómez-Sal, J. Organomet. Chem. 664 (2002) 258.
[35] M.V. Galakhov, M. Gómez, G. Jiménez, M.A. Pellinghelli, P. Royo, A. Tiripicchio, Organometallics 13 (1994) 1564.
[36] D.W. Carpenetti, L. Kloppenburg, J.T. Kupec, J.L. Petersen, Organometallics 15 (1996) 1572.
[37] M.J. Humphries, M.L.H. Green, M.A. Leech, V.C. Gibson, M. Jolly, D.N. Williams, M.R.J. Elsegood, W. Clegg, J. Chem. Soc., Dalton Trans. (2000) 4044.
[38] J. Okuda, T. Eberle, T.P. Spaniol, Chem. Ber.-Recl. 130 (1997) 209.
[39] J. Gavenonis, T.D. Tilley, Organometallics 23 (2004) 31.
[40] R.H. Blessing, Acta Crystallogr. 51 (1995) 33.
[41] G.M. Sheldrick, SHELXL-97, University of Gottingen, Gottingen, 1997.
[42] A.L. Spek, PLATON, Utrecht University, Utrecht, The Netherlands, 2000.



2. Experimental

2.1. General methods

^{1}H, $^{11}B\{^{1}H\}$, and $^{13}C\{^{1}H\}$ NMR spectra were recorded on Varian INOVA-400 or 500 MHz spectrometers. The solvents used were chloroform-d_1 ($CDCl_3$), benzene-d_6 (C_6D_6), or tetrahydrofuran-d_8 (THF-d_8) as indicated. Chemical shifts (δ) are reported in parts per million (ppm). Proton and carbon chemical shifts are relative to respective solvent internal standards: 7.27 (for proton), 77.23 (for carbon) ($CDCl_3$): 7.16, 128.39 (C_6D_6): 3.58, 67.40 (THF-d_8). Boron-11 chemical shifts are relative to prospective external reference: δ 0.00 (BF_3/Et_2O 1.0 M LiCl in D_2O). The coupling constants (J) are reported in Hz. The following abbreviations are used to describe peak patterns: "s" for singlet, "d" for doublet, "t" for triplet. "q" for quartet, "m" for multiplet, and "br" for broad peak. Data are presented as follows: chemical shift (multiplicity, integrated intensity, coupling constant, and assignment). High-resolution mass spectra (HRMS) were recorded on a VG-250S spectrometer with electron-impact spectra at 70 eV. Elemental analyses were conducted on a Perkin–Elmer 240 CHN analyzer by the analytical service in the Department of Chemistry at the University of Michigan, Ann Arbor. Melting points were recorded on a Laboratory Devices MEL_TEMP melting point apparatus with an uncorrected thermometer.

Solvents were freshly distilled prior to use. THF and diethyl ether were distilled from sodium and benzophenone ketyl under N_2. Pentane and hexane were distilled from sodium. All reagents were purchased from the commercial vendors and were used as received or distilled if necessary. All reactions were conducted under an inert atmosphere of argon or in the glovebox under nitrogen unless otherwise specified.

2.2. Syntheses

2.2.1. (*N*-allyl-*N*-ethylamino)vinylphenylborane (**12**)

A solution of *N*-allyl-*N*-ethylamine (3.61 g, 42.5 mmol) in 10 mL of CH_2Cl_2 was added to a solution of phenylvinylboron chloride [10] (6.4 g, 42.7 mmol) in 20 mL of CH_2Cl_2 at −78 °C with stirring. The mixture was stirred for 1 h. Triethylamine (4.3 g, 42.6 mmol) was then added and a white precipitate formed immediately. The reaction mixture was allowed to warm to 25 °C with stirring for 3 h. The solid was removed by filtration and the solvent was removed in vacuo. Vacuum distillation of the residue gave the product as a clear colorless liquid (84%), bp 67–70 °C at 0.05 torr. The ^{1}H NMR and ^{13}C NMR spectra were consistent with it existing as two B–N

rotomers with a ratio of 1:1. ^{1}H NMR (C_6D_6, 400 MHz): δ 7.42 (d, 4 H, J = 8.0 Hz, ArH), 7.31–7.19 (m, 6H, ArH), 6.64 (dd, 1H, J = 19.0, 13.2 Hz, BCH), 6.57 (dd, 1H, J = 19.0, 13.2 Hz, BCH′), 6.02 (bt, 2H, J = 13.2 Hz, alkene), 5.80–5.50 (m, 4H, alkene), 5.12–4.91 (m, 4H, alkene), 3.68 (dt, 2H, J = 5.2, 1.7 Hz, $=CCH_2$), 3.51 (dt, 2H, J = 5.2, 1.7 Hz, $=CCH'_2$), 3.12 (q, 2H, J = 7.1 Hz, Et), 2.93 (q, 2H, J = 7.1 Hz, Et′), 0.99 (t, 3H, J = 7.1 Hz, Et), 0.81 (t, 3H, J = 7.1 Hz, Et′). ^{13}C NMR (C_6D_6, 100.6 MHz): shows two sets of signals. ^{11}B NMR (C_6D_6, 115.5 MHz): δ 39.4 HRMS (EI, *m*/*z*): calc. for $C_{13}H_{18}{}^{11}BN$ (M^+), 119.1532; found 119.1528. *Anal.* Calc. for $C_{13}H_{18}BN$: C, 78.42; H, 9.11; N, 7.03. Found: C, 78.28; H, 8.59; N, 6.50%.

2.2.2. 1-Ethyl-2,5-dihydro-2-phenyl-1H-1,2-azaborole (*13*)

A solution of **12** (17.2 g, 86.4 mmol) in 20 mL of CH_2Cl_2 was added to a solution of bis (tricyclohexylphosphine)benzylidene ruthenium(IV) dichloride (Grubbs catalyst) (3.55 g, 4.31 mmol) in 40 mL of CH_2Cl_2 at 25 °C. The mixture was stirred at 25 °C for 10 h after which the color had changed from purple-red to dark brown. The solvent was removed in vacuo giving the product (12.6 g, 85%) as a clear colorless liquid, bp 60 °C at 0.05 torr. ^{1}H NMR (C_6D_6, 400 MHz): δ 7.75 (d, 2H, J = 8.0 Hz, ArH), 7.33 (t, 2H, J = 8.0 Hz, ArH), 7.25 (t, 1H, J = 8.0 Hz, ArH), 6.93 (d, 1H, J = 8.1 Hz, vinyl), 6.60 (d, 1H, J = 8.1 Hz, vinyl), 3.51 (m, 2H, $NCH_2CH=$), 3.26 (q, 2H, J = 7.0 Hz, Et), 0.94 (t, 3H, J = 7.0 Hz, Et). ^{13}C NMR (C_6D_6, 100.6 MHz): δ 148.5, 134.1, 132.3, 123.1, 128.9, 128.1, 127.6, 60.3 ($NCH_2C=$), 41.4 (Et), 16.7 (Et). ^{11}B NMR (C_6D_6, 115.5 MHz): δ 39.4. HRMS (EI, *m*/*z*): Calc. for $C_{11}H_{14}{}^{11}BN$ (M^+), 171.1219; found, 171.1224. *Anal.* Calc. for $C_{11}H_{14}BN$: C, 77.24; H, 8.25; N, 8.19. Found: C, 77.83; H, 8.45; N, 7.68%.

2.2.3. Lithium 1-ethyl-2-phenyl-1H-1,2-azaborolide (*14*)

1-Ethyl-2,5-dihydro-2-phenyl-1*H*-1,2-azaborole (5.0 g, 29.2 mmol) was dissolved in 15 mL of ether at −78 °C. To this was added a solution of LDA (3.13 g, 29.2 mmol) in 15 mL of ether. The mixture was stirred at −78 °C for 2 h and at 25 °C for 10 h. After removal of the solvent the residue was washed with 3 × 20 mL of pentane. The residue was dried under vacuum to give the product as a light yellow powder (3.9 g, 77%). ^{1}H NMR (THF-d_8, 400 MHz): δ 7.51 (d, 2H, J = 8.0 Hz, ArH), 7.05 (t, 2H, J = 8.0 Hz, ArH), 6.87 (t, 1H, J = 8.0 Hz, ArH), 5.91 (m, 1H, H_4), 5.86 (m, 1H, H_5), 4.16 (m, 1H, H_3), 3.78 (q, 2H, J = 7.0 Hz, Et), 1.27 (t, 3H, J = 7.0 Hz, Et). ^{13}C NMR (THF-d_8, 100.6 MHz): δ 133.9, 127.2, 123.8, 112.8, 111.9, 86.5 (br), 43.2 (Et), 19.6 (Et). ^{11}B NMR (THF-d_8, 115.5 MHz): δ 29.4.

2.2.4. (η-1-Ethyl-2-phenyl-1H-1,2-azaborolyl)(η-pentamethylcyclopentadienyl)zirconium(IV) dichloride (*8*)

A solution of lithium 1-ethyl-2-phenyl-1*H*-1,2-azaborolide (0.42 g, 2.37 mmol) in 10 mL of ether was added to a suspension of pentamethylcyclopentadienylzirconium trichloride (0.78 g, 2.34 mmol) in 10 mL of ether at −78 °C. Stirring was maintained for 12 h as the mixture was slowly warmed to 25 °C. The solvent was removed in vacuo and the residue was washed with pentane and dried, affording the product (0.54 g, 56%) as a yellow powder. The product could be recrystallized from CH_2Cl_2/pentane to afford yellow crystals. ^{1}H NMR (400 MHz, C_6D_6): δ 7.79 (dd, J = 8.2, 1.4 Hz, 2H, ArH); 7.29 (t, J = 7.3 Hz, 2H, ArH); 7.19 (t, J = 7.4 Hz, 1H, ArH),; 6.24 (t, J = 2.6 Hz, 1H ring CH); 5.33 (dd, J = 4.9, 2.7 Hz, 1H, ring CH); 4.62 (dd, J = 4.9, 2.7 Hz, 1H, ring CH); 4.06 (dq, J = 14.0, 7.0 Hz, 1H, NCH); 3.86 (dq, J = 14.0, 7.0 Hz, 1H, NCH′); 1.77 (s, 15H, CpMe) 0.89 (t, J = 7.3 Hz, 3H, NCH_2CH_3). ^{13}C NMR (100.6 MHz): δ 134.5, 128.5, 127.7, 127.5, 123.5, 114.1, 44.1, 16.8, 12.1. ^{11}B NMR (115.6 MHz, C_6H_6): δ 33.7. HRMS: Calc. for $C_{21}H_{28}{}^{11}B^{35}Cl_2N^{90}Zr$, 465.0740. Found: 465.0740. *Anal.* Calc. for $C_{21}H_{28}BCl_2N^{90}Zr$: C, 53.96; H, 6.05; N, 3.00. Found: C, 52.52; H, 6.41; N, 2.79%.

2.2.5. 1-Ethyl-3-chlorodimethylsilyl-2,3-dihydro-2-phenyl-1H-1,2-azaborole (*15*)

A solution of Me_2SiCl_2 (0.69 mL, 0.73 g, 5.65 mmol) in 15 mL of ether was added dropwise to a solution of lithium 1-ethyl-2-phenyl-1*H*-1,2-azaborolide (1.0 g, 5.65 mmol) in 25 mL of ether at −78 °C. When the addition was complete, the mixture was warmed slowly to 25 °C and stirred for 10 h. The solvent was removed under reduced pressure and the residue was extracted with pentane. The extracts were filtered through celite and the solvent was removed in vacuo leaving the product as an orange oil (1.38 g, 92%). ^{1}H NMR (400 MHz, $CDCl_3$): δ 7.40 (dd, J = 7.7, 1.8 Hz, 2H, ArH), 7.23 (m, 3H, ArH); 6.32 (dd, J = 3.8, 1.3 Hz, 1H, ViH); 5.70 (dd, J = 3.8, 2.4 Hz, 1H, ViH); 3.30 (m, 1H, NCH); 3.12 (m, 1H, NCH′); 2.64 (br s, 1H, BCH); 0.94 (t, J = 7.1 Hz, 3H, CMe), 0.14 (s, 3H, SiMe′), 0.09 (s, 3H, SiMe′). ^{13}C NMR (100.6 MHz, C_6D_6): δ 139.1, 133.5 (Ph), 128.8 (Ph), 127.9 (Ph), 122.2, 41.1 (NCH_2), 39 (br, BCH), 17.3 (CMe), 2.4 (SiMe), 0.2 (SiMe′). ^{11}B NMR (115.5 MHz, C_6D_6): δ 44.6. HRMS: Calc. for $C_{13}H_{19}{}^{11}B^{35}ClNSi$: 263.1068. Found: 263.1078. *Anal.* Calc. for $C_{13}H_{19}BClNSi$: C, 59.21; H, 7.28; N, 5.31. Found: C, 59.04; H, 7.12; N, 5.46%.

2.2.6. 1-Ethyl-3-(cyclopentadienyldimethylsilyl)-2,3-dihydro-2-phenyl-1H-1,2-azaborole (*16*)

A solution of cyclopentadienyl lithium (0.16 g, 2.27 mmol) in 10 mL of THF was added slowly to

a solution of 1-ethyl-3-chlorodimethylsilyl-2-3-dihydro-2-phenyl-1*H*-1,2-azaborole (0.60 g, 2.27 mmol) in 10 mL of THF at −50 °C. The reaction mixture was slowly warmed to 25 °C and stirred for 12 h. The solvent was removed in vacuo and the residue was extracted with pentane. Solvent was removed from the extracts leaving the desired product as a brown oil (0.58 g, 87%). ^{1}H NMR (400 MHz, C_6D_6): δ 7.40 (dd, J = 7.9, 1.2 Hz, 2H, ArH); 7.16 (t, J = 7.0 Hz, 2H, ArH); 7.10 (t, J = 7.0 Hz, 1H, ArH); 6.54 (br s, 2H, Cp); 6.50 (br s, 2H, Cp), 6.28 (dd, J = 4.0, 1.1 Hz, 1H, ViH); 5.54 (dd, J = 3.9, 2.8 Hz, 1H, ViH); 3.30 (m, 1H, NCH); 3.22 (br s, 1H, Cp); 3.10 (m, 1H, N CH′), 2.45 (dd, J = 2.6, 1.1 Hz, 1H, BCH); 0.92 (t, J = 7.1 Hz, 3H, CMe); −0.13 (s, 3H, SiMe); −0.35 (s, 3H, SiMe′). ^{13}C NMR (C_6D_6, 100.6 mHz): δ 137.8, 133.5, 133.0, 130.4, 128.6; 128.0, 127.7, 113.4, 67.5, 41.1, 37.4 (br), 25.6, 17.5, −4.8, −4.9. ^{11}B NMR (115.5 Hz, C_6D_6): δ 45.0. HRMS: Calc. for $C_{18}H_{24}{}^{11}BNSi$: 293.1771. Found: 293.1774.

2.2.7. [(η^5-cyclopentadien-1-yl)(η^5-1-ethyl-2-phenyl-1H-1,2-azaborol-3-yl)dimethylsilane]zirconium dichloride (**9**)

A solution of lithium diisopropylamide (0.66 g, 6.20 mmol) in THF (20 mL) was added to a solution of 1-ethyl-3-[cyclopentadienyldimethylsilyl]-2,3-dihydro-2-phenyl-1*H*-1,2-azaborole (0.91 g, 3.10 mmol) in 20 mL of THF at −78 °C. The mixture was slowly warmed to 25 °C and allowed to stir for 12 h. After removal of the solvent in vacuo the residue was washed with pentane. The solid was dissolved in 20 mL of toluene and added to a suspension of $ZrCl_4$ (0.69 g, 3.00 mmol) in 10 mL of toluene at −50 °C. When the addition was complete, the mixture was allowed to warm to 25 °C with stirring for 12 h. The solvent was removed under reduced pressure and the product was extracted with ether, which was then filtered through celite. Removal of solvent left a yellow solid, which was recrystallized from CH_2Cl_2/pentane to give yellow needles. The yield was 0.80 g (59%). ^{1}H NMR (300 MHz, $CDCl_3$): δ 7.57 (m, 2H, ArH); 7.38 (d, J = 2.5 Hz, 1H, C_3H_2BN), 7.26 (m, 3H, ArH), 6.98 (M, 1H, Cp); 6.87 (m, 1H, Cp); 6.00 (m, 1H, Cp); 5.92 (d, J = 2.5 Hz, 1H, C_3H_2BN); 5.88 (m, 1H, Cp); 4.08 (dq, J = 13.7, 7.1 Hz, 1H, NCH); 3.75 (dq, J = 13.7, 7.1 Hz, NCH); 1.21 (t, J = 7.3 Hz, 3H, CH_3C); 0.62 (s, 3H, SiMe); 0.37 (s, 3H, SiMe′). ^{13}C NMR (100.6 MHz, $CDCl_3$): δ 140.4, 135.6, 129.5, 128.6, 127.3, 120.9, 120.6, 112.5, 110.4, 44.1, 16.8, −2.3, −3.5. ^{11}B NMR (115.6 MHz, $CDCl_3$): δ 34.6. HRMS: Calc. for $C_{18}H_{22}{}^{11}B^{35}Cl_2NSi^{90}Zr$: 451.0039. Found: 451.0016. *Anal.* Calc. for $C_{18}H_{22}B^{35}Cl_2NSi^{90}Zr$: C, 47.68; H, 4.90; N, 3.09. Found: C, 47.92; H, 5.17; N, 3.11%.

2.2.8. Bis(1-ethyl-2,3-dihydro-2-phenyl-1H-1,2-azaborol-3-yl)dimethylsilane (**17**)

The title compound was prepared in the same manner as (**16**) from lithium 1-ethyl-2-phenyl-1*H*-1,2-azaborolide (0.41 g, 2.31 mmol) in 15 mL of THF and 1-ethyl-3-chlorodimethylsilyl-2,3-dihydro-2-phenyl-1*H*-1,2-azaborole (0.01 g, 2.31 mmol) in 15 mL of THF. The product was obtained as a yellow oil (0.85 g, 92%). ^{1}H NMR (400 MHz, C_6D_6): δ 7.41 (dd, J = 8.0, 1.5 Hz, 4H, ArH); 7.18 (t, J = 7.3 Hz, 4H, ArH); 7.12 (t, J = 7.3 Hz, 2H, ArH); 6.29 (dd, J = 4.0, 1.1 Hz, 2H, ViH); 5.58 (dd, J = 3.6, 1.1 Hz, 2H, ViH); 3.26 (m, 2H, NCH); 3.11 (m, 2H, NCH); 2.43 (dd, J = 2.6, 1.1 Hz, 2H, BCH); 0.89 (t, J = 7.0 Hz, 6H, CMe); −0.18 (s, 3H, SiMe); −0.42 (s, 3H, SiMe). ^{13}C NMR (100.6 MHz, $CDCl_3$); δ 137.4, 133.5 (Ph); 128.3 (Ph); 127.7 (Ph), 113.7, 41.2 (NCH_2), 37.2 (br, BCH), 17.9 (CMe), −4.3 (SiMe), −4.4 (SiMe). ^{11}B ($CDCl_3$, 115.5 MHz): δ 45.2. HRMS: Calc. for $C_{24}H_{32}{}^{11}B_2N_2Si$: 398.2520. Found: 398.2516.

2.2.9. Rac-(bis(η^5-1-ethyl-2-phenyl-1H-1,2-azaborol-3-yl)dimethylsilane)zirconium dichloride (**10**)

A solution of lithium diisopropylamide (0.46 g, 4.26 mmol) in 10 mL of THF was added to a solution of bis (1-ethyl-2,3-dihydo-2-phenyl-1*H*-1,2-azaborol-3-yl)dimethylsilane (0.85 g, 2.13 mmol) in 10 mL of THF at −78 °C. The mixture was slowly warmed to 25 °C and stirred for 8 h. The solvent was removed in vacuo and the residue was washed with 3 × 10 mL of pentane. The solid was dissolved in 10 mL of toluene and the resulting solution was added to a suspension of $ZrCl_4$ (0.49 g, 2.143 mmol) in 10 mL of toluene at −50 °C. Stirring was continued for 12 h and the mixture was warmed slowly to 25 °C. The solvent was removed in vacuo and the product was dissolved in ether which was filtered through celite. Removal of the solvent under reduced pressure gave an orange solid which was recrystallized from CH_2Cl_2 to give orange crystals of product (0.80 g, 68%). ^{1}H NMR (300 MHz, C_6D_6): δ 7.70 (dd, J = 8.1, 1.5 Hz, 4H, ArH); 7.25 (t, J = 7.6 Hz, 4H, ArH); 7.15 (t, J = 7.4 Hz, 2H, ArH); 6.83 (d, J = 2.5 Hz, 2H, C_3H_2BN); 5.86 (d, J = 2.5 Hz, 2H, C_3H_2BN); 3.75 (dq, J = 13.4, 6.9 Hz, 2H, NCH); 3.38 (dq, J = 13.4, 6.9 Hz, 2H, NCH′); 0.64 (t, J = 7.2 Hz, 6H, CH_3), 0.32 (s, 6H, SiMe). ^{13}C NMR (100.6 MHz, $CDCl_3$): δ 135.6, 131.4, 128.5, 127.6, 119.7, 44.7, 17.2, −1.0. ^{11}B (115.6 MHz, $CDCl_3$): δ 31.8. HRMS: Calc. for $C_{24}H_{30}{}^{11}B_2{}^{35}Cl_2N_2Si^{90}Zr$: 556.0788. Found: 556.0770. *Anal.* Calc. for $C_{24}H_{30}B_2Cl_2N_2SiZr$: C, 51.62; H, 5.43; N, 5.02. Found: C, 51.32; H, 5.39; N, 5.08%.

2.3. X-ray data collection

X-ray quality crystals of **8**, **9**, and **10** were crystallized from dichloromethane at room temperature. A suitable crystal was mounted on a standard Bruker SMART CCD-based X-ray diffractometer equipped with a normal focus Mo-target X-ray tube ($\lambda = 0.71073$ Å) operated at 2000 W power (50 kV, 40 mA). The X-ray intensities were measured at 158(2) K; the detector was placed at a distance of 4.959 cm from the crystal. Analysis of the data showed negligible decay during data collection; the data were processed with SADABS [11] and corrected for absorption. The structure was solved and refined with the Bruker SHELXTL [12] (version 5.10) software package. All non-hydrogen atoms were refined anisotropically with the hydrogen atoms located on a difference Fourier map and allowed to refine isotropically. Additional details are presented in Table 1 and are given as Supplementary materials as CIF files.

2.4. Polymerization conditions

A 2 L reactor was charged with mixed alkane solvent and 1-octene. Hydrogen was added by differential pressure expansion from a 75 mL addition tank from 2.1 MPa to near 1.9 MPa. The reaction and container were heated to 140 °C and saturated with ethylene at 3.4 MPa. In an inert atmosphere glovebox the appropriate quantities of zirconium complex and MAO (1:1000 m) were combined and this solution was transferred to a catalyst addition tank. The polymerization were initiated by injecting this catalyst solution into the reactor. The polymerization condition were maintained for 15 min with ethylene provided on demand at 3.4 MPa. The polymer solution was removed from the reactor and combined with a hindered phenol antioxidant and isopropanol. Volatile components were removed from the polymer in a vacuum oven set at 140 °C for about 20 h. The dried polymers were weighed and analyzed. Additional details are given in [13].

Table 1
Crystallographic data for complexes **8**, **9**, and **10**

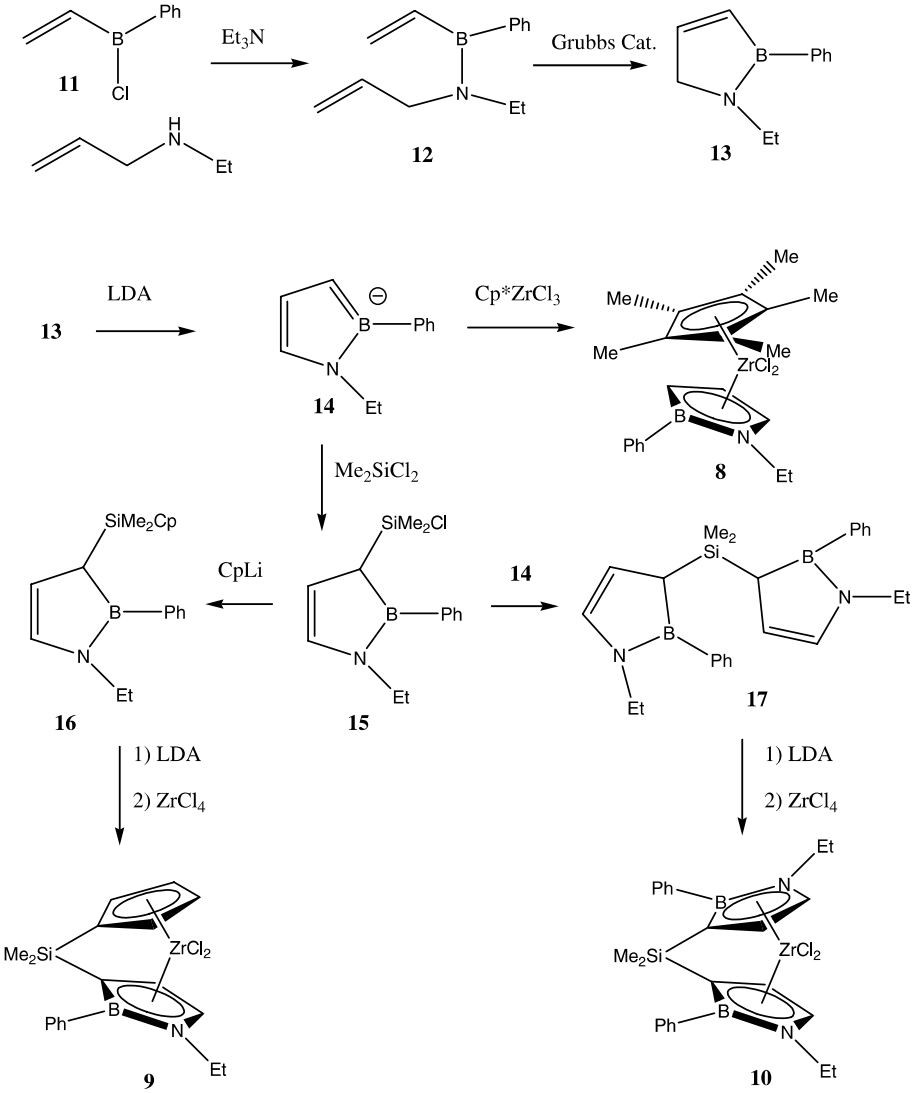
	8	**9**	**10**
Empirical formula	$C_{21}H_{28}BCl_2NZr$	$C_{18}H_{22}BCl_2NSiZr$	$C_{24}H_{30}B_2Cl_2N_2Zr(CH_2Cl_2)$
Formula weight	467.37	453.39	643.26
Temperature (K)	158(2)	158(2)	158(2)
Wavelength (Å)	0.71073	0.71073	0.71073
Crystal system	monoclinic	monoclinic	triclinic
Space group	*P*2(1)/*c*	*P*2(1)/*n*	*P*1
Unit cell dimensions			
a (Å)	8.7474(11)	7.4420(6)	9.6792(13)
b (Å)	16.566(2)	12.9009(11)	12.780(2)
c (Å)	15.2556(19)	21.2678(18)	13.276(2)
α (°)			89.419(2)
β (°)	105.790(2)	93.1030(10)	79.316(2)
γ (°)			88.605(2)
Volume (Å^3)	2125.8(5)	2038.9	1446.7(4)
Z	4	4	2
$D_{calc.}$ (Mg/m^3)	1.460	1.477	1.477
Absorption coefficient (mm^{-1})	0.774	0.860	0.809
F (000)	960	920	656
Crystal size (mm)	$0.22 \times 0.28 \times 0.42$	$0.10 \times 0.16 \times 0.44$	$0.28 \times 0.28 \times 0.38$
θ range for data (%)	1.85–26.40	1.85–26.38	1.56–26.39
Collection index range	$-10 \leqslant h \leqslant 10$, $-20 \leqslant k \leqslant 20$, $-19 \leqslant l \leqslant 19$	$-9 \leqslant h \leqslant 9$, $-16 \leqslant k \leqslant 16$, $-26 \leqslant l \leqslant 26$	$-10 \leqslant h \leqslant 10$, $-15 \leqslant k \leqslant 15$, $-16 \leqslant l \leqslant 16$
Reflections collected/unique	19920/4350	20075/4184	15766/5850
Completeness to $\theta = 26.40$	99.8%	99.9	98.9
Absorption correction	semi-empirical from equivalents	semi-empirical from equivalents	semi-empirical from equivalents
Max. and min. transmission	0.911 and 0.821	0.942 and 0.818	0.879 and 0.786
Refinement method	full-matrix least-square on F^2	full-matrix least-square on F^2	full-matrix least-square on F^2
Data/restraints/parameters	4350/0/348	4184/0/307	5850/0/432
GOF on F^2	1.049	1.042	1.044
Final *R* indices [$I > 2\sigma(I)$]	$R_1 = 0.0216$, $wR_2 = 0.0581$	$R_1 = 0.204$, $wR_2 = 0.0515$	$R_1 = 0.279$, $wR_2 = 0.0735$
R indices (all data)	$R_1 = 0.0241$, $wR_2 = 0.0595$	$R_1 = 0.0254$, $wR_2 = 0.0526$	$R_1 = 0.0305$, $wR_2 = 0.0753$
Largest differential peaks and hole (e Å^{-3})	0.0352 and −0.273	0.287 and −0.278	0.639 and −0.850

3. Results and discussion

3.1. Synthesis

The 1,2-azaborolyl ring system has been prepared by several routes [10,14–16]. In our hands a synthesis via a ring closing metathesis from B-vinyl-*N*-allyl-aminoboranes is particularily convenient. The B-phenyl-*N*-ethyl azaborolyl **14** was easily prepared by this route (Scheme 1) which had previously been used to prepare the corresponding B-phenyl-*N*-methyl derivative **14a** [10]. The reaction of phenylvinylboron chloride [11] with allylethylamine in pentane containing triethylamine gave a 84% yield of aminoborane **12**. The ^{1}H and ^{13}C NMR spectra of **12** are complex indicating that it exists as a 1:1 mixture of rotomers about the B–N bond. The appreciable π-bond character of this B–N bond makes the rotation about this bond slow on the NMR time scale [17]. On treatment of **12** with 5 mol% Grubbs catalyst in CH_2Cl_2 at 25 °C for 12 h, cyclization occurred to afford a 74% yield of the ring closed product **13**. The reaction of **13** with LDA in ether gave the lithium 1,2-azaborolide **14** which was isolated as a pale yellow powder in 96% yield. The ^{1}H, ^{11}B, and ^{13}C NMR chemical shift values of the ring atoms of **14** are very similar to those previously reported for corresponding N-methyl derivative **14a** [10] and other 1,2-azaborolides [14]. The reaction of **14** with Cp^*ZrCl_3 in ether gave the expected **8** as yellow crystals in 56% yield.

The dimethylsilyl-bridged mixed 1,2-azaborolyl cyclopentadienyl zirconium complex **9** was prepared by a straightforward route outlined in Scheme 1. Silylation of **14** with an excess of dichlorodimethylsilane afforded the 3-chlorodimethylsilyl isomer **15** as an orange oil in 96% yield. Compound **15** was not detectably contaminated with the possible 5-regio isomer. It seems probable



Scheme 1. Synthesis of lithium 1-ethyl-2-phenyl-1,2-azaborolide (**14**) and its conversion to zirconium complexes **8**, **9**, and **10**.

that C(3) of **14** is more nucleophilic than C(5) due to its larger negative charge density which is indicated by the higher field signal for C(3) in the ^{13}C NMR spectrum [18a]. The sequential reaction of **15** with CpLi followed by LDA and then $ZrCl_4$ gave **9** or yellow crystals in 59% yield.

The reaction of **15** with lithium azaborolide **14** afforded the dimethylsilyl derivative **17** as a yellow oil in 92% yield. As was the case from **16**, it was not detectably contaminated by regioisomers. The reaction of **17** with LDA followed by $ZrCl_4$ gave **10** as a yellow crystalline product in 68% yield. The ^{1}H and ^{13}C NMR spectra of **10** suggested that it was a single diastereomer. A subsequently obtained X-ray crystal structure showed that it is the racemic isomer.

3.2. Structure

The molecular structures of **8**, **9**, and **10** are illustrated in Figs. 1–3, respectively. Selected bond distances and angles are compared in Table 2. These compounds are the first structurally characterized monocyclic 1,2-azaborolyl zirconium complexes although we have previously reported structures for zirconium complexes of fused ring 1,2-azaborolyls [18b]. Prior crystallographic work on both early and late transition metal 1,2-azaborolyl complexes shows that the ligand usually binds in an unsymmetrical η^5-manner [15,19]. Compounds **8**, **9**, and **10** conform to this pattern. In each case the 1,2-azaborolyl ring is largely coplanar. The B–Zr distances (2.68 Å, ave) are somewhat longer than the C–Zr and N–Zr distances (2.44–2.54 Å, range). The longer boron–metal distances are consistent with the larger atomic radius of boron compared to that of carbon and nitrogen. A similar pattern is found in the structures of most metal π-coordinated complexes of boron heterocycles [20].

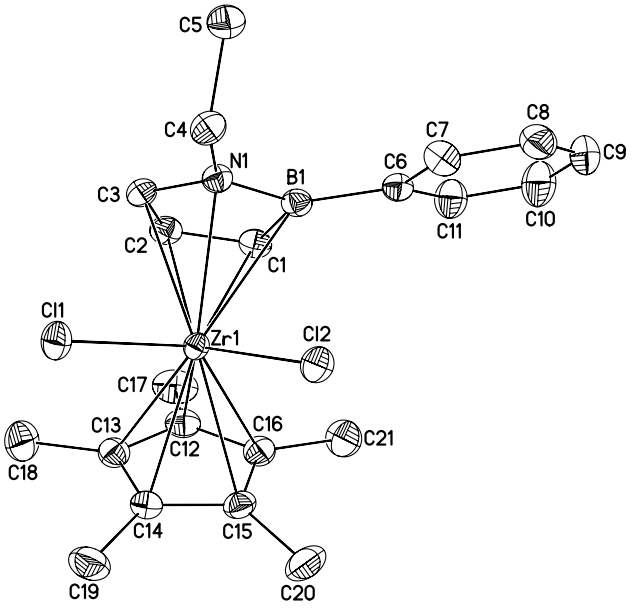


Fig. 1. Molecular structure of **8** (ORTEP). Thermal ellipsoids are at the 50% probability level. Hydrogen atoms have been omitted for clarity.

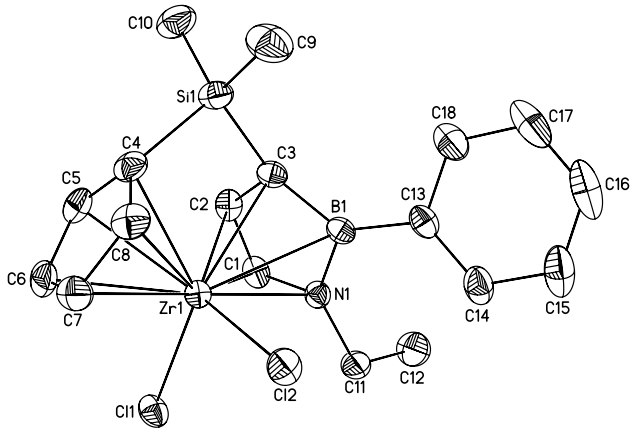


Fig. 2. Molecular structure of **9** (ORTEP). Thermal ellipsoids are at the 50% probability level. Hydrogen atoms have been omitted for clarity.

Comparison of the structures of **8**, **9**, and **10** shows that the corresponding intraring 1,2-azaborolyl distances vary by no more than ±0.02 Å. Similarly the distance of Zr atoms to the corresponding ring atoms vary by no more than ±0.05 Å. Thus the bridges in **9** and **10** exert little perturbation on the structure found for **8**.

The structures of **8**, **9**, and **10** can also be compared with those of similar zirconocene dichlorides. The Cp planes of Cp_2ZrCl_2 intersect an angle of 52° [21]. The mean plane of the 1,2-azaborolyl ring of **8** intersects its Cp* plane at an angle of 52.5(1)°. In the dimethylsilyl bridged **1** the Cp planes intersect at 57° [22]. The corresponding Cp/1,2-azaborolyl planes of **9** intersect at 60.1(1)° and the 1,2-azaborolyl/1,2-azaborolyl planes of **10** intersect at 57.3(1)°. Thus, all three *ansa*-complexes have very similar open wedges to the Zr atoms.

3.3. Polymerization studies

On activation by a 10^3 molar excess of MAO in a hydrocarbon solvent the 1-ethyl-2-phenyl-1,2-azaborolyl zirconium complexes **8**, **9**, **10** form active catalysts for the polymerization of mixtures of ethylene and 1-octene. The results are summarized in Table 3. In all cases, the product was polyethylene with the incorporation of approximately 1% 1-octene. All three 1,2-azaborolyl complexes are significantly better catalysts than 1-diisopropylamino-1-boratabenzene zirconium complexes **2** [5a,6a] and **5** [7] and 1-diisopropylamino-1,2-thiaborolyl zirconium complex **3** [6a] under identical conditions. MAO activated **2** has previously been found to have

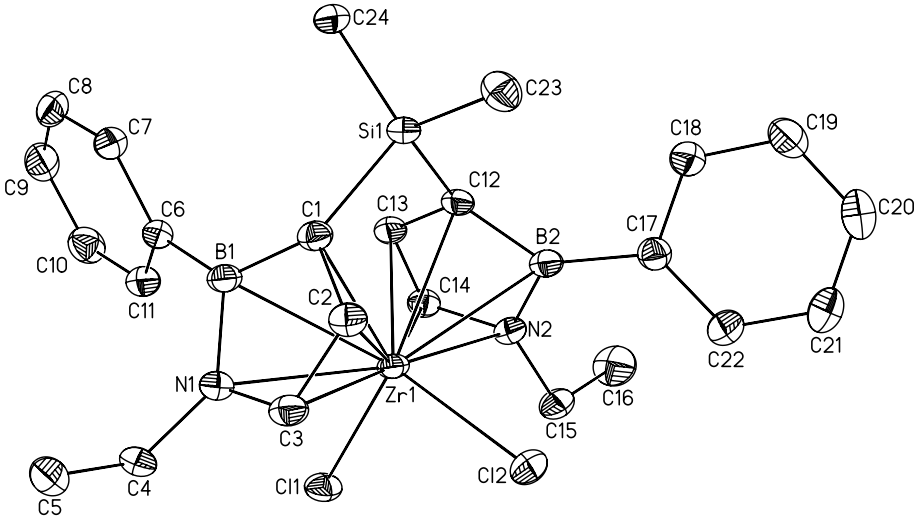


Fig. 3. Molecular structure of **10** (ORTEP). Thermal ellipsoids are at the 50% probability level. Hydrogen atoms have been omitted for clarity.

Table 2
Comparison of selected distances (Å) and angles (°) from **8**, **9**, and **10**

	8	**9**	**10**[a]
B–Cα[b]	1.510(2)	1.520(2)	1.537(3), 1.530(3)
Cα–Cβ[b]	1.432(2)	1.456(2)	1.438(2), 1.455(2)
Cβ–Cγ[b]	1.372(2)	1.363(2)	1.391(3), 1.384(3)
Cγ–N[b]	1.396(2)	1.393(2)	1.391(2), 1.395(2)
B–N	1.482(2)	1.485(2)	1.471(2), 1.492(2)
Zr–B	2.681(2)	2.688(2)	2.632(2), 2.679(2)
Zr–Cα[b]	2.479(2)	2.471(2)	2.478(2), 2.478(2)
Zr–Cβ[b]	2.404(2)	2.442(2)	2.459(2), 2.454(2)
Zr–Cγ[b]	2.491(2)	2.485(2)	2.504(2), 2.503(2)
Zr–N	2.531(1)	2.525(1)	2.576(2), 2.522(2)
PL (ring 1)/ PL (ring 2)	52.5(1)	60.1(1)	57.3(1)

[a] The first distance refers to ring B1C1C2C3N1. The second distance refers to ring B2C12C13C14N2.

[b] Cα, Cβ, Cγ designate the carbon atoms of the 1,2-azaboroyl rings which are 1,2 or 1,3 or 1,4 to the boron atom, respectively.

approximately the same ethylene polymerization activity as Cp_2ZrCl_2, albeit under somewhat different conditions [5a]. Thus we can safely conclude that **8**, **9**, and **10** are significantly more active than Cp_2ZrCl_2 from the polymerization of ethylene.

Table 3
Comparison of the efficiency of ethylene/1-octene polymerization of **8**, **9**, and **10** with selected other complexes

Complex	Efficiency (g polymer/mol Zr atom)	Reference
8	234×10^4	this work
9	66×10^4	this work
10	126×10^4	this work
2	20.4×10^4	[6c]
3	6.0×10^4	[6a]
5	2.4×10^4	[7]

The η^5-1,2-azaborolyl ligands of **8**, **9**, and **10** are nearly isostructural with the η^5-Cp groups of zirconocene dichlorides. Furthermore, the degree of canting of the rings of **8**, **9**, and **10** is nearly identical to that found in the corresponding zirconocenes. Therefore, it is unlikely that the greater reactivity of the 1,2-azaborolyl zirconium complexes is due to steric efforts. Fu and co-workers [15] found that the 1,2-azaborolyl ligand in Fe(II) complexes is more electron-rich than Cp. Thus, it is likely that electron density at Zr is higher for **8**, **9**, and **10** than it is for the corresponding zirconocenes. It may be that the higher catalytic activity of the 1,2-azaborolyl zirconium complexes is associated with the greater electron density and lower electrophilicity at the active metal center. It has previously been observed that electron withdrawing groups decrease the activity of zirconium-based Ziegler–Natta catalysts [23].

Contrary to our expectations the dimethylsilyl bridging in **9** and **10** led to a small decrease rather than an increase is the polymerization activity relative to **8**. It may be that the lack of conformational mobility enforced by the bridge holds that 1-ethyl and 2-phenyl substituents in positions which interfere with the propagation steps. A similar but larger drop-off in activity was observed between **2** and **5** [7].

4. Conclusion

In summary, we have developed an efficient synthetic route to Me_2Si-bridged and non-bridged (1,2-azaborolyl) zirconium(IV) dichlorides **8**, **9**, and **10**. The 1,2-azaborolyl is an electron rich surrogate for Cp and the structure of its zirconium complexes closely resemble those of the corresponding zirconocenes. On activation by excess MAO, **8**, **9**, and **10** form highly active catalysts for the polymerization of ethylene.

5. Supplementary material

Crystallographic data for the structural analyses have been deposited with the Cambridge Crystallographic Data Centre, CCDC Nos. 262648, 262649, and 262650 for compounds **8**, **9**, and **10**, respectively. Copies of this information may be obtained from the Director, CCDC, 12 Union Road, Cambridge CB2 1EZ, UK (fax: +44 1233 336 033; e-mail: deposit@ccdc.cam.ac.uk, or http://www.ccdc.cam.ac.uk).

Acknowledgments

This work was supported by the National Science Foundation and the Dow Chemical Company. We are grateful to the Dow Chemical Company for running the polymerization experiments. We are also grateful to the Boulder Scientific Company from a generous gift of the Grubbs catalyst.

References

[1] (a) H.H. Brintzinger, D. Fischer, R. Mülhaupt, B. Rieger, R.M. Waymouth, Angew. Chem., Int. Ed. Engl. 34 (1995) 1143;
(b) G. Fink, R. Mülhaupt, H.H. Brintzinger (Eds.), Ziegler Catalysts, Spinger, Berlin, Germany, 1995;
(c) J.A. Gladysz, Chem. Rev. 100 (2000) 1167.
[2] L. Resconi, L. Cavallo, A. Fait, F. Piemontesi, Chem. Rev. 100 (2000) 1253.
[3] W.A. Herrmann, J. Rohrmann, E. Herdtweck, W. Spaleck, A. Winter, Angew. Chem., Int. Ed. Engl. 28 (1989) 1511.
[4] W. Spaleck, M. Antberg, J. Rohrmann, A. Winter, B. Bachmann, P. Kiprof, J. Behm, W.A. Herrmann, Angew. Chem., Int. Ed. Engl. 31 (1992) 1347.
[5] (a) G.C. Bazan, G. Rodriguez, A.J. Ashe, III, S. Al-Ahmad, C. Müller, J. Am. Chem. Soc. 118 (1996) 2291;
(b) G.C. Bazan, G. Rodriguez, A.J. Ashe III, S. Al-Ahmad, J.W. Kampf, Organometallics 16 (1997) 2492.
[6] (a) A.J. Ashe III, X. Fang, J.W. Kampf, Organometallics 19 (2000) 4935;
(b) A.J. Ashe III, J.W. Kampf, M. Schiesher, Organometallics 19 (2000) 4681;
(c) A.J. Ashe III, X. Fang, J.W. Kampf, Organometallics 18 (1999) 1821.
[7] A.J. Ashe III, S. Al-Ahmad, X. Fang, J.W. Kampf, Organometallics 17 (1998) 3883.
[8] S. Nagy, R. Krishnamurti, B.P. Etherton, PCT Int. Appl (1996) WO96 34,021; Chem. Abstr. 126 (1997) 19432j.
[9] A.J. Ashe, III, H. Yang, F.J. Timmers PCT Int. Appl (2003) WO 2003 087114 A1 20031023; Chem. Abstr. 139 (2003) 323949.
[10] A.J. Ashe III, X. Fang, Org. Lett. 2 (2000) 2089.
[11] G.M. Sheldrick, SADABS Program for Empirical Absorption Correction of Area Detector Data, University of Göttingen, Göttingen, Germany, 1996.
[12] G.M. Sheldrick, SHELXTL, v. 5.10 Brucker Analytical X-ray, Madison, WI, 1999.
[13] A.J. Ashe III, X. Fang, A. Hokky, J.W. Kampf, Organometallics 23 (2004) 2197.
[14] (a) G. Schmid, in: I. Shinkai (Ed.), Comprehensive Heterocyclic Chemistry II, vol. 3, Elsevier, Oxford, UK, 1996 (Chapter 3.17);
(b) G. Schmid, Comments Inorg. Chem. 4 (1985) 17.
[15] S-Y. Liu, M.M.-C. Lo, G.C. Fu, Angew. Chem., Int. Ed. 41 (2001) 174.
[16] J. Pan, J.W. Kampf, A.J. Ashe III, Organometallics 23 (2004) 5626.
[17] (a) D. Imbery, A. Jaeschke, H. Friebolin, Org. Magn. Reson. 2 (1970) 271;
(b) H. Friebolin, R. Rensch, H. Wendel, Org. Magn. Reson. 8 (1976) 287.
[18] (a) A.J. Ashe, III, X. Fang, X. Fang, J.W. Kampf, Organometallics 20 (2001) 5413;
(b) A.J. Ashe III, H. Yang, X. Fang, J.W. Kampf, Organometallics 21 (2002) 4578.
[19] (a) G. Schmid, O. Boltsch, D. Bläser, R. Boese, Z. Naturforsch. B 39 (1984) 1082;
(b) G. Schmid, D. Kampmann, W. Meyer, R. Boese, P. Paetzold, K. Delpy, Chem. Ber. 118 (1985) 2418;
(c) G. Schmid, F. Schmidt, R. Boese, Chem. Ber. 118 (1985) 1949;
(d) G. Schmid, B. Kilanowski, R. Boese, D. Bläser, Chem. Ber. 126 (1993) 899;
(e) G. Schmid, S. Haske, D. Zaika, R. Boese, D. Bläser, Chem. Ber. 127 (1994) 73.
[20] J. Chen, X. Fang, Z. Bajko, J.W. Kampf, A.J. Ashe III, Organometallics 23 (2004) 5088.
[21] (a) K. Prout, S.T. Cameron, R.A. Forder, S.R. Critchley, B. Denton, G.V. Rees, Acta Crystallogr. B 30 (1977) 2290;
(b) J.Y. Corey, X.-H. Zhu, L. Brammer, N.P. Rath, Acta Crystallogr. C 51 (1995) 565.
[22] C.S. Bajgur, W. Tikkanen, J.L. Petersen, Inorg. Chem. 24 (1985) 2539.
[23] (a) N. Piccolrovazzi, P. Pino, G. Consiglio, A. Sironi, M. Moret, Organometallics 9 (1990) 3098;
(b) I-M. Lee, W.J. Gauthier, J.M. Ball, B. Iyengar, S. Collins, Organometallics 11 (1992) 2115;
(c) M.P. Thornberry, N.T. Reynolds, P.A. Deck, F.R. Fronczek, A.L. Rheingold, L.M. Liable-Sands, Organometallics 23 (2004) 1333.

examples will be described and discussed in this account to illustrate such recent developments in *ansa*-metallocene chemistry.

2. Attempts via metallacyclopentane formation

It is well known that the reduced zirconocenes or titanocenes [$Cp_2M(II)$] add two equivalents of alkenes or alkynes to form the respective five-membered metallacycles [6]. It was tempting to try to use a variant of this rather general reaction type in *ansa*-metallocene synthesis. We have made such an attempt by reducing the ω-pentenyl-substituted *rac*-*ansa*-zirconocene dichloride complex **1** with sodium-amalgam in THF. The expected doubly trimethylene-linked zirconacyclopentane derivative **2** was actually formed in high yield (95% isolated) and characterized by X-ray diffraction (see Fig. 1) [7]. We expected that subsequent treatment of **2** with, e.g., HCl would yield the respective doubly bridged *ansa*-zirconocene dichloride by protonolytic cleavage of both Zr–$C(sp^3)$ σ-bonds. However, we obtained the mono-alkenyl system **4** instead, which indicated a much preferred reaction of the reactive η^2-alkene-type complex **3** to take place under our typical reaction conditions (see Scheme 1). K. Mach et al. subsequently showed that *ansa*-metallocene bridges can actually be formed by the metallacyclopentane route, but the reaction is apparently limited to specific cases, where the protonolysis reaction of the five-membered metallacycle is sufficiently preferred over the alternative cleavage pathway via concerted ring opening. In K. Mach's case, the linked titanacyclopentane **6** was formed by Mg-reduction from

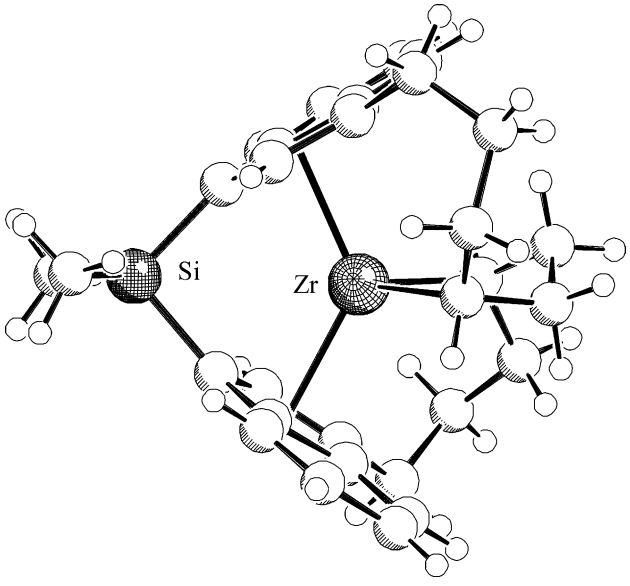
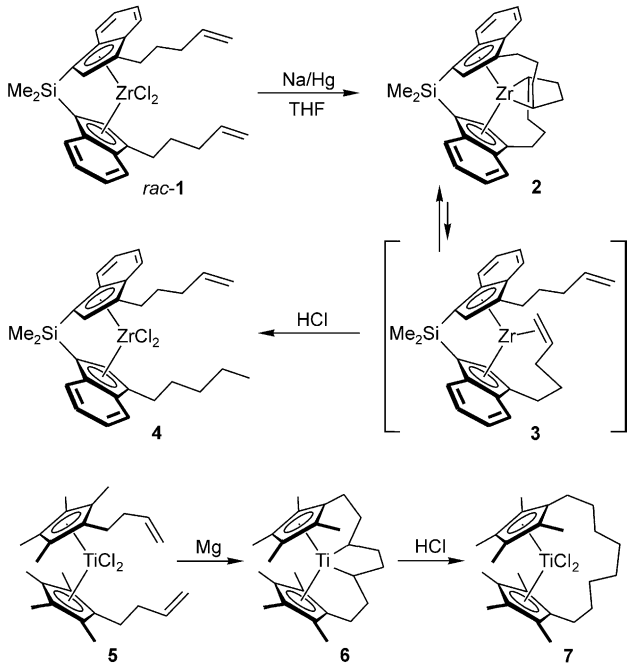


Fig. 1. A view of the molecular structure of the *ansa*-zirconacyclopentane derivative **2**.



Scheme 1.

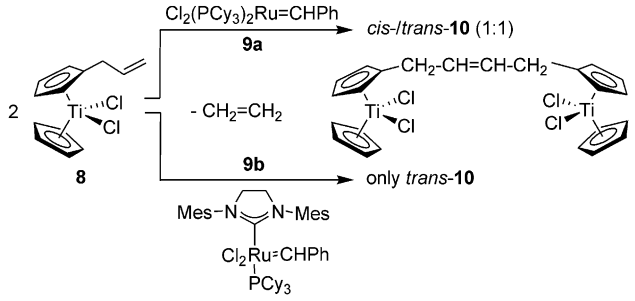
5 and subsequently gave the octamethylene-bridged *ansa*-titanocene **7** upon treatment with HCl [8].

3. *ansa*-Metallocene formation by olefin metathesis

The olefin metathesis reaction has found increasing use in organic synthesis in recent years [9]. This is, among other reasons, due to the availability of a variety of metal alkylidene catalysts that allow the metathetical transformation of organic substrates in the presence of a great number of organic functional groups. Therefore, it was tempting to also employ the catalytic olefin metathesis reaction for selective transformations at (suitably substituted) Group 4 bent metallocenes and related systems, hoping that even these otherwise reactive organometallic functionalities would prove stable and largely inert toward the typical metathesis conditions. This actually turned out to be the case for a variety of typical Cp-zirconium and -titanium systems when treated with the typical Ru-based olefin metathesis catalysts.

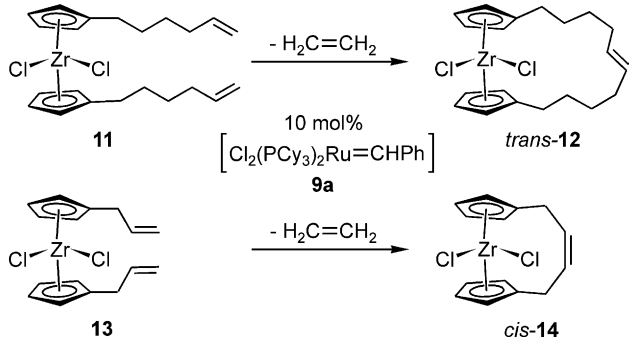
Here is a typical example. The alkyl-Cp-containing titanocene dichloride complex **8** undergoes an intermolecular metathetical coupling reaction in the presence of ca. 3 mol% of $(PCy_3)_2Cl_2Ru{=}CHPh$ (**9a**) to give a ca. 50% isolated yield of a ca. 1:1 mixture of *cis*- and *trans*-**10**. Similar treatment of **8** with the more active second generation Grubbs catalyst (**9b**) gave almost pure *trans*-**10** (see Scheme 2) [10].

We have applied related intramolecular olefin metathesis reactions for the synthesis of *ansa*-metallocenes. Treatment of sodium cyclopentadienide with



Scheme 2.

ω-hexenyl bromide followed by deprotonation (MeLi) and transmetallation gave the bis-hexenyl-functionalized zirconocene dichloride complex **11** (isolated in 38% yield). Its treatment with 10 mol% of $(PCy_3)_2Cl_2$-Ru=CHPh (**9a**) under high dilution conditions using a syringe pump resulted to the formation of a sizeable amount of the corresponding intramolecular olefin metathesis coupling product **12**. Crystallization from a toluene solution furnished this large *ansa*-zirconocene dichloride as the pure *trans*-isomer (*trans*-**12**) in 25% yield (see Scheme 3 and Fig. 2) [11].



Scheme 3.

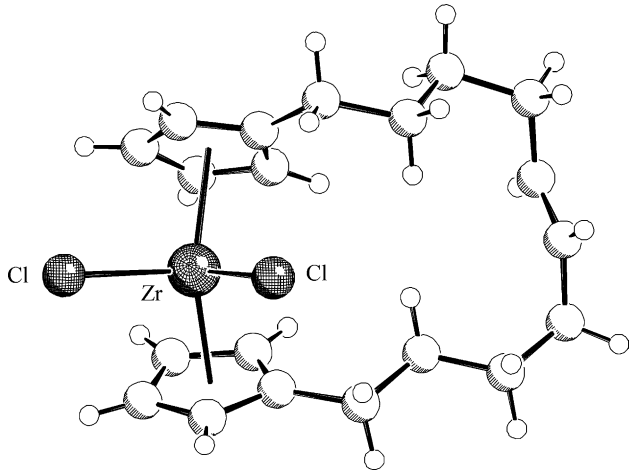
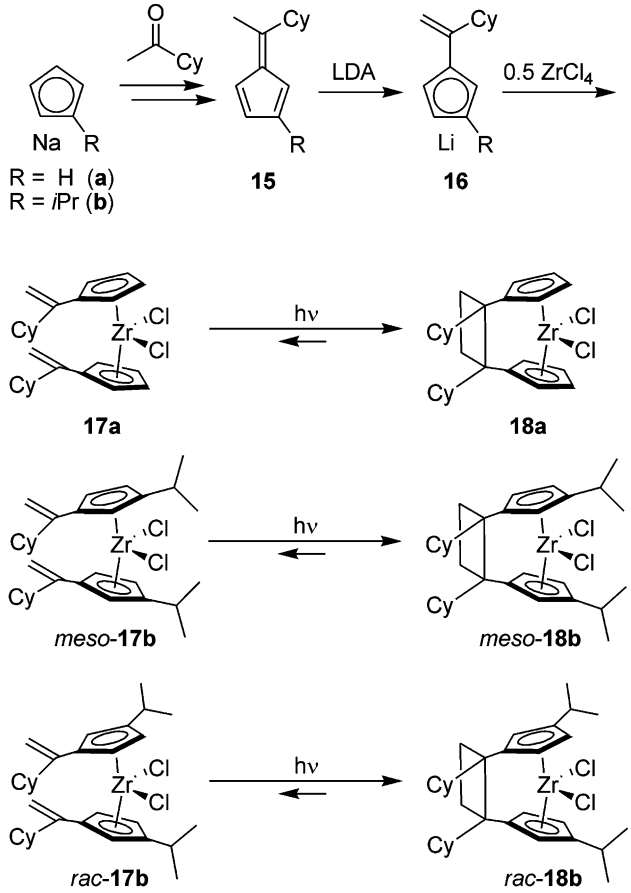


Fig. 2. A view of the large *ansa*-metallocene *trans*-**12**.

Ring closing metathesis of bis(allyl-Cp)zirconium dichloride (**13**), that was prepared by a similar route, occurs readily upon treatment with the Ru-carbene catalyst **9a** under similar conditions, as we [11] and Hayashi and coworkers [12] have found independently. We isolated the product *cis*-**14** in ca. 50% yield from the reaction mixture. The *ansa*-metallocene *cis*-**14** was characterized by X-ray diffraction and its conformational behavior characterized by dynamic NMR spectroscopy [11].

4. Ring closure by intramolecular photochemical [2 + 2]cycloaddition

Alkenyl-substituted Cp-ligands can conveniently be prepared by means of fulvene routes. The reaction sequence starting with the condensation reaction between Na-cyclopentadienide with methylcyclohexylketone to yield the fulvene **15a** marks a typical example. Treatment of **15a** with LDA results in a clean selective deprotonation at the fulvene methyl group to yield the alkenyl cyclopentadienide **16a**. Subsequent transmetallation then gave the corresponding zirconocene complex **17a** (see Scheme 4). Irradiation of the metallocene **17a** rapidly resulted in an intramolecular [2 + 2]cycloaddition



Scheme 4.

reaction with formation of the cyclobutylene-bridged *ansa*-zirconocene **18a**. This reaction is wavelength dependent. With 300–350 nm UV-light we observed a photostationary equilibrium of **18a**:**17a** ≈ 70:30, that was reached and maintained after 4 h of irradiation in a Pyrex NMR tube in benzene-d_6 at ambient temperature [13]. Using a 450 nm light source we achieved a rapid (1 h) and almost complete (>98%) conversion of **17a** to **18a** (see Scheme 4).

Similarly, the doubly substituted alkenyl-cyclopentadienide **16b** was obtained by treatment of isopropylcyclopentadienide with methylcyclohexyl-ketone followed by LDA deprotonation. Transmetallation with $ZrCl_4$ in this case gave ca. a 1:1 mixture of the *meso*-**17b** and *rac*-**17b** diastereoisomers, that we were able to separate by fractional crystallization. Each of these diastereoisomeric metallocenes was intramolecularly [2 + 2] coupled by 450 nm irradiation to yield the corresponding *ansa*-metallocenes *meso*-**18b** and *rac*-**18b**, respectively. The [2 + 2]cycloaddition product *meso*-**18b** was characterized by X-ray diffraction [13a]. A number of related examples were investigated using a variety of substituent combinations. The eventually resulting photostationary equilibrium in some cases turned out to be quite sensitive to the specific substituents used [13b]. The [2 + 2]cycloaddition method has increasingly been used in the coupling of "*ansa*-bridges" in more complicated cases [14].

An extension to a series of related alkenyl-functionalized bis(indenyl)zirconium complexes gave an interesting result. For this study the 2-alkenyl indenes (**19**) were synthesized by a Ni-catalyzed cross-coupling reaction of 2-bromoindene with the respective 1-alkenyl-*Grignard* reagents (see Scheme 5), or in the case of **19b** by alkenyl-*Grignard* addition to 2-indanone followed by H^+-catalyzed dehydrogenation. Subsequent deprotonation followed by transmetallation then gave the corresponding bis(2-alkenylindenyl)$ZrCl_2$ complexes **20**. These systems form the respective *ansa*-metallocenes very easily. Thus, irradiation (HPK 125, Pyrex filter) rapidly resulted in the practically complete conversion to the *ansa*-metallocenes **21** that were isolated as crystalline solids from the reaction mixtures in fair yields [15,16]. The complexes **21a** (R = CH_3) and **21b** (R = cyclohexyl) were both characterized by X-ray diffraction which has revealed the remarkable structural features of these systems. As depicted in Fig. 3 the cyclobutylidene bridge in the complexes **21** is located at the narrow back side of the bent metallocene wedge. Consequently the indenyl phenylene subunits are both pointing toward the open front side, thus featuring their aromatic π-systems oriented above and below the σ-ligand system. There is indication that suitable ligands bonded to the metal at the front side of the bent metallocene can potentially interact electronically with this "π-electron box". This was shown for the corresponding (η^4-s-*trans*-butadiene)metallocene complex **22a** that features a butadiene *meso*-H/π-indenyl interaction. In the ^{1}H NMR spectrum of **22a** this leads to a shifting of the ^{1}H NMR H-*meso* resonance to strongly negative δ-values (ca. δ −1.5 in benzene-d_6) [15,16]. This corresponds to an "upfield" shift of Δδ ≈ −2.9 relative to the parent compound (η^4-s-*trans*-butadiene)$ZrCp_2$ [17].

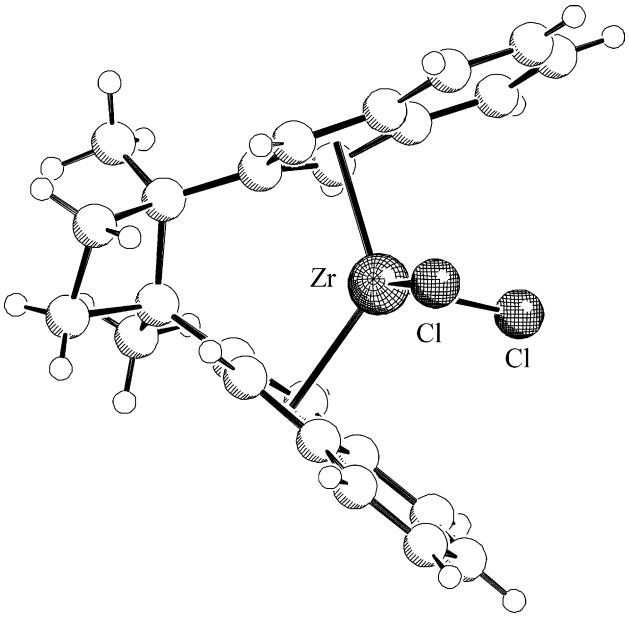
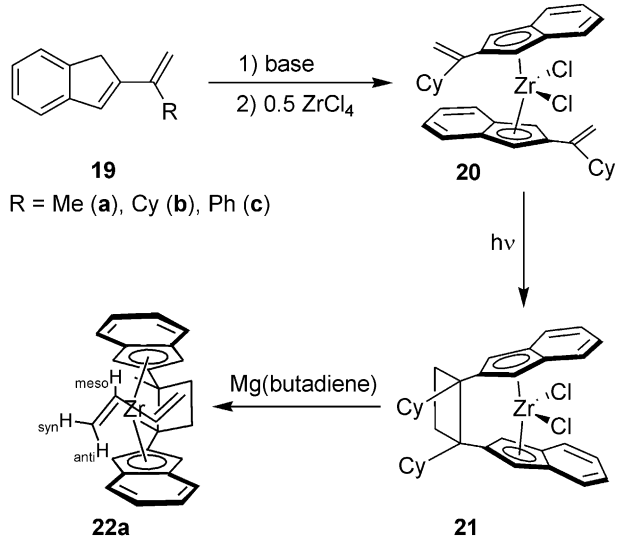


Fig. 3. Molecular structure of complex **21a**.



Scheme 5.

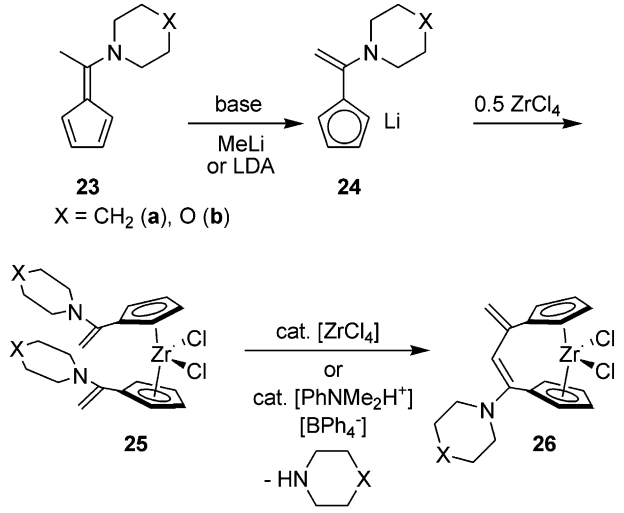
5. Intramolecular Mannich coupling at the metallocene framework

The fulvene route has also been used to prepare a variety of Group 4 metallocene complexes bearing

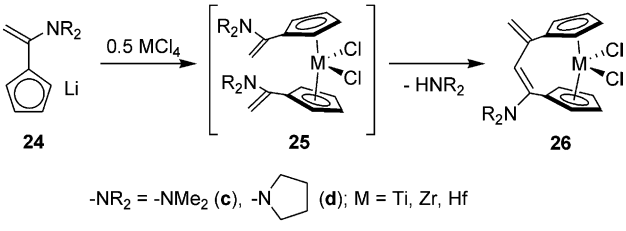
enamino substituents at their Cp-ligands. The synthesis made use of the readily available amino fulvenes (**23**) that were prepared by the method of Hafner et al. [18] by condensation of activated dialkylacetamides with cyclopentadienide. Deprotonation with a suitable base furnished the substituted aminoethenylcyclopentadienides (**24**) [19]. Transmetallation with $ZrCl_4$ gave the bis(enamino-Cp)$ZrCl_2$ complexes that in some cases (e.g., **25a**, **25b**) could be isolated [20] (see Scheme 6).

Treatment of **25a** or **25b** with catalytic amounts of $ZrCl_4$ or a *Brønsted* acid resulted in a rapid intramolecular *Mannich*-type condensation reaction to yield the C_3-bridged *ansa*-zirconocene complexes **26(a,b)** with extrusion of one equivalent of piperidine or morpholine, respectively. It must be assumed that protonation of one of the enamino substituents of the starting material **25** generates a reactive iminium ion that is then intramolecularly attacked by the adjacent enamino-carbon-nucleophile to make the essential new carbon–carbon bond of the *ansa*-bridge. Amine elimination and deprotonation then closes the catalytic cycle to give the observed coupling products (**26**) (see Scheme 7).

In many cases the synthesis of the *ansa*-metallocenes can conveniently be carried out as a one-pot reaction starting from the respective enamino-Cp reagent. This is especially very convenient in the case of the dimethyla-



Scheme 6.



Scheme 7.

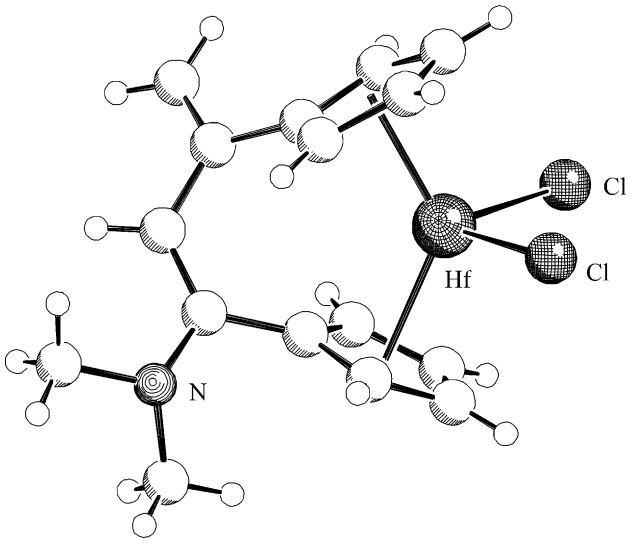


Fig. 4. A projection of the molecular geometry of the *ansa*-hafnocene complex **26c′**.

mino-ethenyl systems (**24c**) or their pyrrolidino-ethenyl analogues (**24d**). We must assume that the reaction of these reagents with the respective Group 4 metal halides initially also leads to the formation of the corresponding substituted bis(enamino-Cp) Group 4 metal complexes. With these (small) enamino substituents, however, these intermediates rapidly react further with the *Lewis* acidic metal halide components to enter the catalyzed *Mannich*-type condensation reaction. In many of these cases, the corresponding unsaturated C_3-bridged Group 4 ansa-metallocenes (**26**) were obtained in good yields [21–24]. Many examples were characterized by X-ray diffraction. A typical example (**26c′**, M = Hf) is depicted in Fig. 4. Some of these complexes were used as precursors for the generation of active homogeneous *Ziegler–Natta* olefin polymerization catalysts [21,22].

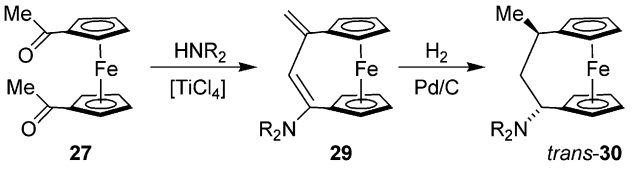
6. Use of the intramolecular Mannich reaction in [3]ferrocenophane chemistry

A variety of [*n*]ferrocenophanes can readily be prepared by a number of conventional methods [25,26]. Nevertheless, our intramolecular *Mannich*-type coupling reaction turned out to be so convenient that it was adapted and modified for the synthesis of a series of [3]ferrocenophane systems, some of which have turned out to be well suited frameworks for the preparation of some useful chelate ligands [27].

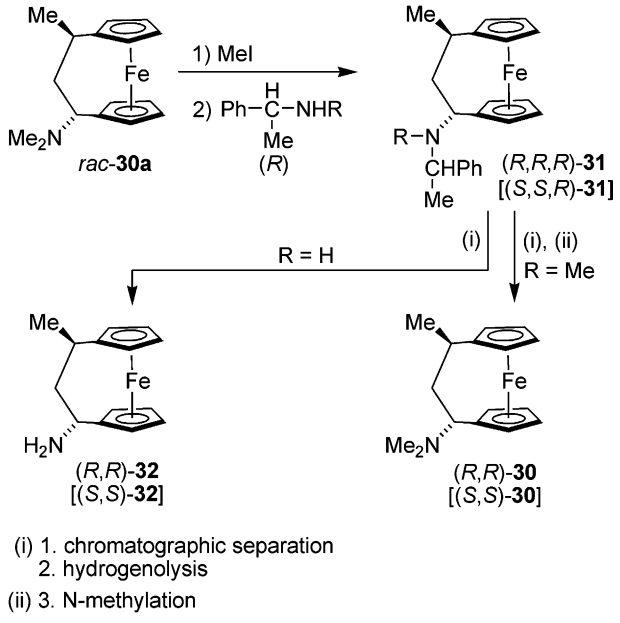
For the synthesis of the unsaturated [3]ferrocenophanes (**29**) it was convenient to start from the readily available 1,1′-diacetylferrocene (**27**). Its treatment with excess dimethylamine in the presence of the *Lewis* acid $TiCl_4$ [28] rapidly resulted in the formation of the intramolecular coupling product **29a** ($-NMe_2$), which was probably formed by a *Mannich*-type condensation

reaction via a bis(enamino)ferrocene intermediate (**28**) [29]. Subsequent catalytic hydrogenation (Pd/C, H_2) gave the saturated [3]ferrocenophane-amines (**30**), that contain two newly formed chiral centers (see Scheme 8). Both the *cis*- and the *trans*-diastereoisomers of the products **30** are formed, but in all cases investigated so far it was the *trans*-**30** product that was formed predominantly, with *trans*-/*cis*-**30** ratios ranging from 5:1 to ca. 7:1. The *trans*-products were obtained pure by crystallization. We have obtained a variety of products with various $–NR_2$ substituents, either introduced directly or by exchange at the amino[3]ferrocenophane stage **30** [29]. In the latter cases, it was shown that the amine exchange reactions proceeded with overall retention of configuration at the α-carbon center, i.e., by a two-step sequence involving the nucleophilic iron center as a very efficient neighboring group [30,31]. The three-carbon bridge fits almost perfectly between the pair of ferrocene Cp-rings, both in the unsaturated systems **29** as well as the saturated [3]ferrocenophane systems **30**, which is illustrated in Fig. 5 for a pair of representative examples ($–NEt_2$, **29b**, **30b**).

The enantiomerically pure *trans*-**30** [3]ferrocenophanylamines were obtained each in ca. 25% yield (from a possible 50%) by treatment of the *trans*-**30a** racemate ($–NMe_2$) with a Ph–CH(Me)–NHMe enantiomer. The



Scheme 8.



Scheme 9.

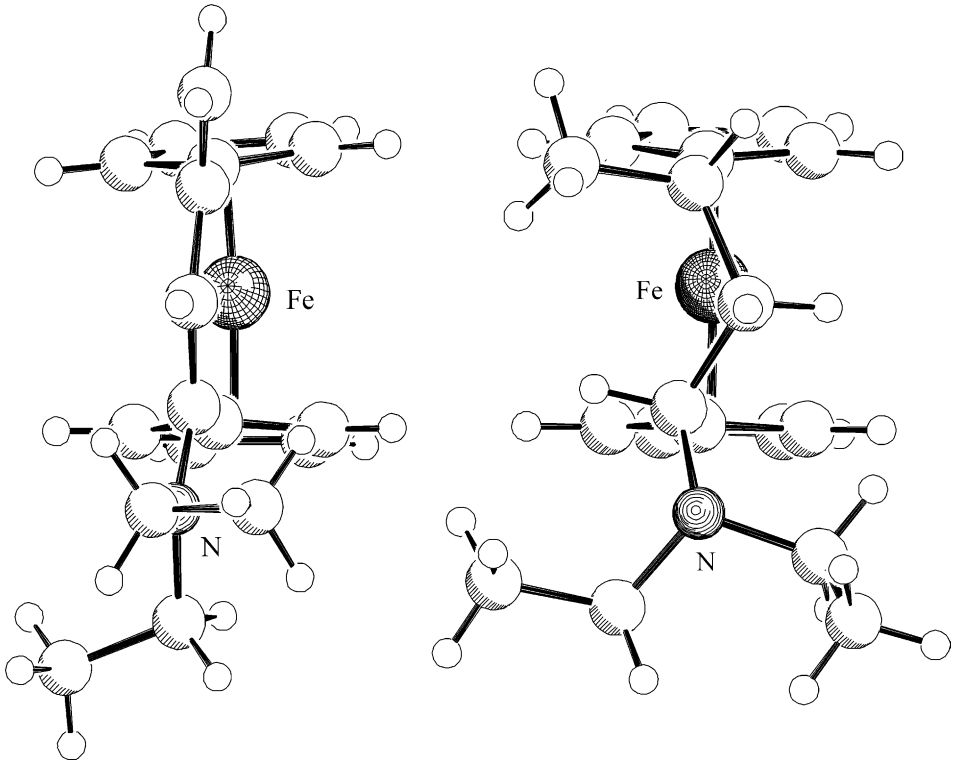


Fig. 5. Back side view of the diethylamino-substituted [3]ferrocenophane examples **29b** and *trans*-**30b**.

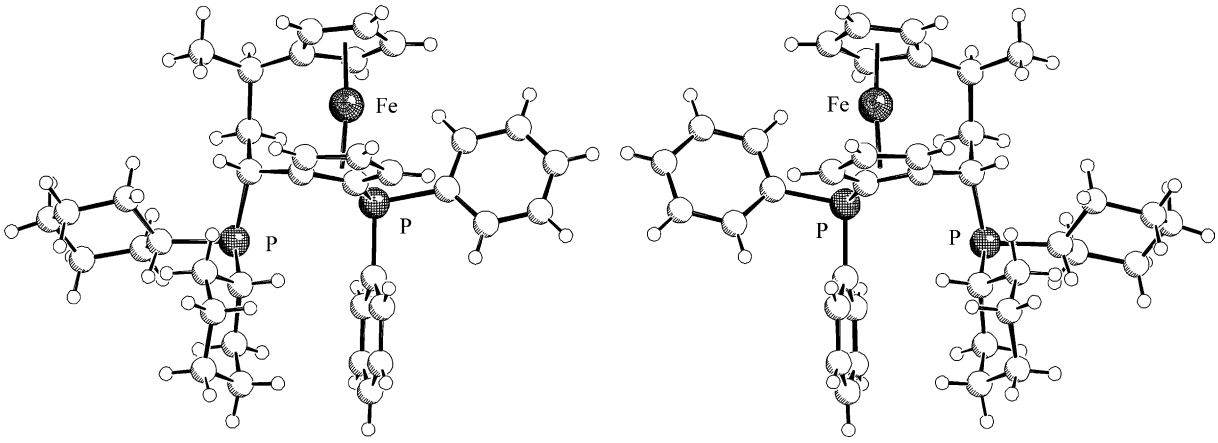


Fig. 6. A view of the molecular structures of the separately prepared enantiomers of **35**.

diastereomeric amine-exchange products, e.g., (*R*,*R*,*S*)-**31** and (*S*,*S*,*S*)-**31**, were readily separated by column chromatography and then the chiral auxiliary was selectively removed by catalytic hydrogenation. Subsequently, *N*-methylation eventually yielded the (*R*,*R*)- and (*S*,*S*)-**30** enantiomers (see Scheme 9) [32]. The parent amino[3]ferrocenophane system (**32**), exhibiting a free $-NH_2$ substituent at the α-position of the saturated bridge, was obtained optically pure by means of a variant of this route employing the Ph–CH(Me)–NH_2 enantiomers as the resolving chiral auxiliaries [33].

Treatment of each of the **30a** ($-NMe_2$) enantiomers with butyl lithium followed by $ClPPh_2$ resulted in a directed metallation with subsequent formation of the enantiomerically pure (*P*,*N*)-[3]ferrocenophane chelate systems **33**. Stereospecific exchange of the $-NMe_2$ group by treatment with $HPPh_2$ or $HPCy_2$ furnished the corresponding (*P*,*P*)-[3]ferrocenophane chelates **34** and **35**, respectively [27,34,35] (see Fig. 6). The Pd(II) complex

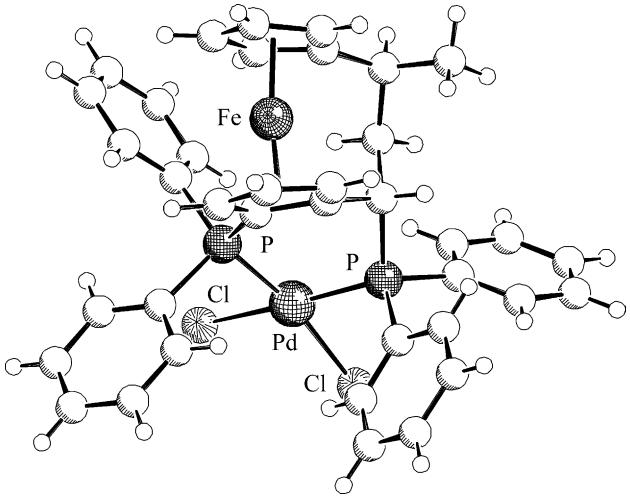
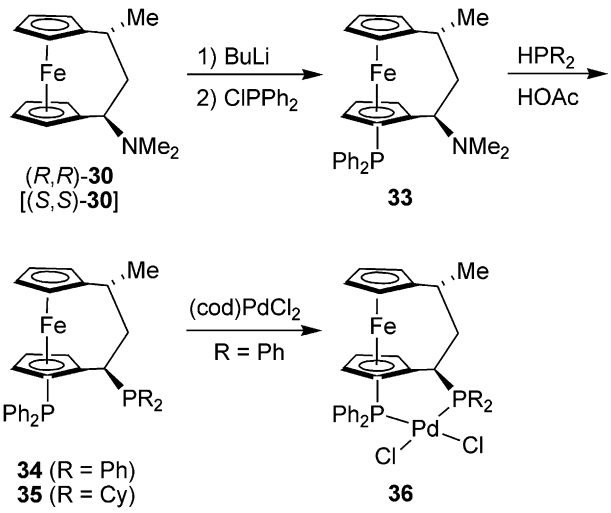


Fig. 7. A view of the molecular structure of the (*P*,*P*)-[3]ferrocenophane chelate–Pd complex **36**.



Scheme 10.

36 (see, e.g. Fig. 7) gave an active catalyst for alternating CO/1-alkene copolymerization after suitable electrophilic activation. The $-PCy_2$-derived chelate ligand (**35**) gave a Pd-catalyst that showed a high asymmetric induction in alternating CO/propene copolymerization and its $-PPh_2$ analogue (**34**) gave an effective Rh-catalyst for asymmetric hydrogenation of dimethylitaconate (95% ee) [27] (see Scheme 10).

7. Some conclusions

Carrying out carbon–carbon coupling reactions at the framework of the sensitive Group 4 bent metallocenes had been notoriously difficult. It took some time until some limited organic functional group chemistry begun to appear in Group 4 metallocene chemistry, other than the well established procedures of introducing various types of substituents via attachment at the free ligand state prior to the final transmetallation step. It seems that useful developments toward carrying out

typical organic functional group transformations at the bent metallocene stage are increasingly emerging from the literature. It has been shown that a number of carbon–carbon coupling reactions can indeed be performed at the Group 4 bent metallocene frameworks by a variety of procedures from the current repertoire of synthetic organic chemistry, if care is taken that these methods are adapted to the specific needs and features of the rather sensitive bent metallocenes of the oxophilic Group 4 transition metals. Many examples originating from my research group as well as from others have demonstrated this, such as the, e.g., formation of ansa-metallocenes via metallacyclopentane formation, by means of intramolecular photochemical alkenyl [2 + 2]cycloaddition or catalyzed intramolecular Mannich-type coupling, or, last but not least, by application of the olefin metathesis reaction catalyzed by ruthenium carbene complexes. Especially, these latter examples nicely demonstrate the increasing importance of catalytic procedures for the preparation of novel organometallic systems. Since these organometallic products are themselves often valuable precursors for the generation of new catalysts, some examples described in this article illustrate an interesting current development to use catalytic pathways to generate new catalysts.

Acknowledgements

G.E. thanks his coworkers and collaborators, whose names are given in the references, for their valuable contributions to this chemistry. He also acknowledges the generous financial support from the Deutsche Forschungsgemeinschaft, the Fonds der Chemischen Industrie, and the Alexander von Humboldt foundation for the investigations that were carried out in his group at the University of Münster.

References

[1] (a) E. Negishi, T. Takahashi, Aldrichim. Acta 18 (1985) 31;
(b) E. Negishi, T. Takahashi, Synthesis (1988) 1;
(c) C.L. Buchwald, R.B. Nielsen, Chem. Rev. 88 (1988) 1047;
(d) E. Negishi, T. Takahashi, Acc. Chem. Res. 27 (1994) 124;
(e) P. Wipf, H. Jahn, Tetrahedron 52 (1996) 12853;
(f) D.V. Kondakov, E. Negishi, J. Am. Chem. Soc. 118 (1996) 1577;
(g) K.H. Shaughnessy, R.M. Waymouth, Organometallics 17 (1998) 5728;
(h) E. Negishi, T. Takahashi, Bull. Chem. Soc. Jpn. 71 (1998) 755;
(i) S. Ribe, R.K. Kondru, D.N. Beratan, P. Wipf, J. Am. Chem. Soc. 122 (2000) 4608;
(j) A. Gansäuer, H. Bluhm, M. Pierobon, M. Keller, Organometallics 20 (2001) 914;
(k) P. Wipf, C. Kendall, Org. Lett. 3 (2001) 2773;
(l) P. Wipf, C. Kendall, Chem. Eur. J. 8 (2002) 1778.

[2] (a) Reviews: H.-H. Brintzinger, D. Fischer, R. Mülhaupt, B. Rieger, R. Waymouth, Angew. Chem. 107 (1995) 1255;
(b) H.-H. Brintzinger, D. Fischer, R. Mülhaupt, B. Rieger, R. Waymouth, Angew. Chem., Int. Ed. Engl. 34 (1995) 1143;
(c) M. Bochmann, J. Chem. Soc., Dalton Trans. (1996) 255;
(d) G.W. Coates, Chem. Rev. 100 (2000) 1223.

[3] (a) F.R.W.P. Wild, L. Zsolnai, G. Huttner, H.H. Brintzinger, J. Organomet. Chem. 232 (1982) 233;
(b) F.R.W.P. Wild, W. Wasiucionek, G. Huttner, H.H. Brintzinger, J. Organomet. Chem. 288 (1985) 63;
(c) J.A. Ewen, R.L. Jones, A. Razawi, J.D. Ferrara, J. Am. Chem. Soc. 110 (1988) 6255;
(d) B. Rieger, X. Mu, D.T. Mallin, M.D. Rausch, J.C.W. Chien, Macromolecules 23 (1990) 3559.

[4] (a) J. Wonnemann, M. Oberhoff, G. Erker, R. Fröhlich, K. Bergander, Eur. J. Inorg. Chem. (1999) 1111;
(b) D. Kunz, G. Erker, R. Fröhlich, G. Kehr, Eur. J. Inorg. Chem. (2000) 409;
(c) D. Hüerländer, R. Fröhlich, G. Erker, J. Chem. Soc., Dalton Trans. (2002) 1513;
(d) D. Harmsen, G. Erker, R. Fröhlich, G. Kehr, Eur. J. Inorg. Chem. (2002) 3156;
(e) M. Hill, G. Kehr, R. Fröhlich, G. Erker, Eur. J. Inorg. Chem. (2003) 3583;
(f) B. Meyer von Berstenhorst, G. Erker, G. Kehr, J.-C. Wasilke, J. Müller, H. Redlich, J. Pyplo-Schnieders, Eur. J. Inorg. Chem. (2005) 92.

[5] (a) G. Erker, G. Kehr, R. Fröhlich, J. Organomet. Chem. 689 (2004) 1402;
(b) G. Erker, G. Kehr, R. Fröhlich, Coord. Chem. Rev., in press.

[6] T. Takahashi, R. Fischer, Z. Xi, K. Nakajima, Chem. Lett. (1996) 357.

[7] T.H. Warren, G. Erker, R. Fröhlich, B. Wibbeling, Organometallics 19 (2000) 127.

[8] L. Lukešová, P. Štěpnička, K. Fejfarová, R. Gyepes, I. Císařová, M. Horáček, J. Kubišta, K. Mach, Organometallics 21 (2002) 2639.

[9] (a) M. Schuster, S. Blechert, Angew. Chem. 109 (1997) 2124;
(b) M. Schuster, S. Blechert, Angew. Chem., Int. Ed. Engl. 36 (1997) 2036;
(c) R.H. Grubbs, S. Chang, Tetrahedron 54 (1998) 4413;
(d) A. Fürstner, Angew. Chem. 112 (2000) 3140;
(e) A. Fürstner, Angew. Chem., Int. Ed. Engl. 39 (2000) 3013;
(f) T. Trnka, R.H. Grubbs, Acc. Chem. Res. 34 (2001) 18;
(g) A.J. Locke, C. Jones, C.J. Richards, J. Organomet. Chem. 637–639 (2001) 669;
(h) J. Ruwwe, J.M. Martín-Alvarez, C.R. Horn, E.B. Bauer, S. Szafert, T. Lis, F. Hampel, P.C. Cagle, J.A. Gladysz, Chem. Eur. J. 7 (2001) 3931;
(i) C.R. Horn, J.M. Martín-Alvarez, J.A. Gladysz, Organometallics 21 (2002) 5386.

[10] J. Cano Sierra, D. Hüerländer, M. Hill, G. Kehr, G. Erker, R. Fröhlich, Chem. Eur. J. 9 (2003) 3618.

[11] D. Hüerländer, N. Kleigrewe, G. Kehr, G. Erker, R. Fröhlich, Eur. J. Inorg. Chem. (2002) 2633.

[12] M. Ogasawara, T. Nagano, T. Hayashi, J. Am. Chem. Soc. 124 (2002) 9068.

[13] (a) G. Erker, S. Wilker, C. Krüger, R. Goddard, J. Am. Chem. Soc. 114 (1992) 10983;
(b) G. Erker, S. Wilker, C. Krüger, M. Nolte, Organometallics 12 (1993) 2140.

[14] (a) N. Iwama, T. Kato, T. Sugano, Organometallics 23 (2004) 5813;
(b) Review: T.E. Bitterwolf, J. Organomet. Chem. 689 (2004) 3939.

[15] W.-L. Nie, G. Erker, G. Kehr, R. Fröhlich, Angew. Chem. 116 (2004) 313.

[16] W.-L. Nie, G. Erker, G. Kehr, R. Fröhlich, Angew. Chem., Int. Ed. Engl. 43 (2004) 310.

[17] (a) G. Erker, J. Wicher, K. Engel, F. Rosenfeldt, W. Dietrich, C. Krüger, J. Am. Chem. Soc. 102 (1980) 6344;
(b) H. Yasuda, Y. Kajihara, K. Mashima, K. Nagasuna, K. Lee, A. Nakamura, Organometallics 1 (1982) 388;
(c) G. Erker, J. Wicher, K. Engel, C. Krüger, Chem. Ber. 115 (1982) 3300;
(d) G. Erker, K. Engel, C. Krüger, A.-P. Chiang, Chem. Ber. 115 (1982) 3311;
(e) G. Erker, C. Krüger, G. Müller, Adv. Organomet. Chem. 24 (1985) 1;
(f) H. Yasuda, K. Tatsumi, A. Nakamura, Acc. Chem. Res. 18 (1985) 120;
(g) G. Erker, G. Kehr, R. Fröhlich, Adv. Organomet. Chem. 51 (2004) 109;
(h) A. Nakamura, K. Mashima, J. Organomet. Chem. 689 (2004) 4552.
[18] (a) K. Hafner, K.H. Vöpel, G. Ploss, C. König, Liebigs Ann. Chem. 661 (1963) 52;
(b) H. Meerwein, K. Hafner, G. Schulz, K. Wagner, Liebigs Ann. Chem. 678 (1964) 39;
(c) K. Hafner, K.H. Vöpel, G. Ploss, C. König, Org. Synth. 47 (1967) 52;
(d) K. Hafner, K.H. Vöpel, G. Ploss, C. König, Org. Synth. Coll. Vol. V (1973) 431.
[19] S. Venne-Dunker, G. Kehr, R. Fröhlich, G. Erker, Organometallics 22 (2003) 948.
[20] S. Knüppel, C. Wang, G. Kehr, R. Fröhlich, G. Erker, J. Organomet. Chem. 690 (2005) 14.
[21] S. Knüppel, G. Erker, R. Fröhlich, Angew. Chem. 111 (1999) 2048.
[22] S. Knüppel, G. Erker, R. Fröhlich, Angew. Chem., Int. Ed. Engl. 38 (1999) 1923.
[23] S.-D. Bai, X.-H. Wei, J.-P. Guo, D.-S. Liu, Z.-Y. Zhou, Angew. Chem. 111 (1999) 2051.
[24] S.-D. Bai, X.-H. Wei, J.-P. Guo, D.-S. Liu, Z.-Y. Zhou, Angew. Chem., Int. Ed. Engl. 38 (1999) 1926.
[25] (a) A. Eisenstadt, M. Cais, Isr. J. Chem. 5 (1967) 37;
(b) T.D. Turbitt, W.E. Watts, J. Organomet. Chem. 46 (1972) 109;
(c) P. Dodey, B. Gautheron, C.R. Seance, Acad. Sci. Ser. C (1975) 1113;
(d) W. Crawford, T.D. Turbitt, W.E. Watts, J. Organomet. Chem. 105 (1976) 341;
(e) M. Sališová, Š. Toma, E. Sołčániová, J. Organomet. Chem. 132 (1977) 419;
(f) E. Gyepes, T. Glowiak, Š. Toma, J. Soldánová, J. Organomet. Chem. 276 (1984) 209;
(g) E. Gyepes, T. Glowiak, Š. Toma, J. Organomet. Chem. 316 (1986) 163.
[26] T. Sturm, W. Weissensteiner, F. Spindler, K. Mereiter, A.M. López-Agenjo, B.R. Manzano, F.A. Jalón, Organometallics 21 (2002) 1766.
[27] P. Liptau, L. Tebben, G. Kehr, R. Fröhlich, G. Erker, F. Hollmann, B. Rieger, Eur. J. Org. Chem. (in press).
[28] W.A. White, H. Weingarten, J. Org. Chem. 32 (1967) 213.
[29] (a) S. Knüppel, R. Fröhlich, G. Erker, J. Organomet. Chem. 586 (1999) 218;
(b) S. Knüppel, R. Fröhlich, G. Erker, J. Organomet. Chem. 595 (2000) 307;
(c) P. Liptau, S. Knüppel, G. Kehr, O. Kataeva, R. Fröhlich, G. Erker, J. Organomet. Chem. 637–639 (2001) 621.
[30] P. Liptau, M. Neumann, G. Erker, G. Kehr, R. Fröhlich, S. Grimme, Organometallics 23 (2004) 21.
[31] (a) D. Marquarding, H. Klusacek, G. Gokel, P. Hoffmann, I. Ugi, J. Am. Chem. Soc. 92 (1970) 5389;
(b) G. Gokel, D. Marquarding, I. Ugi, J. Org. Chem. 37 (1972) 3052;
(c) G. Tainturier, K. Chhor y Sok, B. Gautheron, C.R. Acad. Sci. Paris C (1973) 1269;
(d) K. Chhor y Sok, G. Tainturier, B. Gautheron, Tetrahedron Lett. 25 (1974) 2207;
(e) K. Chhor y Sok, G. Tainturier, B. Gautheron, J. Organomet. Chem. 132 (1977) 173;
(f) T. Hayashi, T. Mise, M. Fukushima, M. Kagotani, N. Nagashima, Y. Hamada, A. Matsumoto, S. Kawakami, M. Konishi, K. Yamamoto, M. Kumada, M. Bull. Chem. Soc. Jpn. 53 (1980) 1138;
(g) E.M. Caynela, L. Xiao, T. Sturm, B.R. Manzano, F.A. Jalón, W. Weissensteiner, Tetrahedron: Asymmetry 11 (2000) 861;
(h) B.R. Manzano, F.A. Jalón, F. Gómez-de la Torre, A.M. López-Agenjo, A.M. Rodríguez, K. Mereiter, W. Weissensteiner, T. Sturm, Organometallics 21 (2002) 789;
(i) Review: W.E. Watts, J. Organomet. Chem. Library 7 (1979) 399;
(j) A.J. Pearson, Metallo-Organic Chemistry, Wiley, New York, 1985, 319–322.
[32] P. Liptau, L. Tebben, G. Kehr, B. Wibbeling, R. Fröhlich, G. Erker, Eur. J. Inorg. Chem. (2003) 3590, 4261.
[33] L. Tebben, G. Kehr, R. Fröhlich, G. Erker, Synthesis 12 (2004) 1971.
[34] P. Liptau, D. Carmona, L.A. Oro, F.J. Lahoz, G. Kehr, G. Erker, Eur. J. Inorg. Chem. (2004) 4586.
[35] P. Liptau, T. Seki, G. Kehr, A. Abele, R. Fröhlich, G. Erker, S. Grimme, Organometallics 22 (2003) 2226.

1. Introduction

The catalytic activity of group 4 metallocene complexes in the polymerization of olefins has been the principal reason for the dramatic growth in interest towards these compounds [1]. The main focus of this research field is centred on the design of metallocene complexes towards the goal of "made to measure" catalysts that can direct the catalytic reaction in producing polymers with desired physical properties. *ansa*-Cyclopentadienyl systems are now widely recognized to afford better catalytic activity and selectivity in the polymerization of olefins than their non-*ansa* counterparts [2]. Recent studies have demonstrated that the incorporation of the *ansa*-bridge may have a profound influence on the chemical behaviour of these complexes [3].

Industry requirements for the development of supported metallocene polymerization catalysts, that can offer homogeneous single-site selectivity in a heterogeneous medium, is presently of utmost importance. Several studies on immobilized catalysts have recently been published [4]. The immobilization of the catalyst is normally achieved by the introduction of functional groups in the ligand system and their interaction with the surface of an inorganic oxide with the metallocene framework remaining, in most cases, unaltered [5].

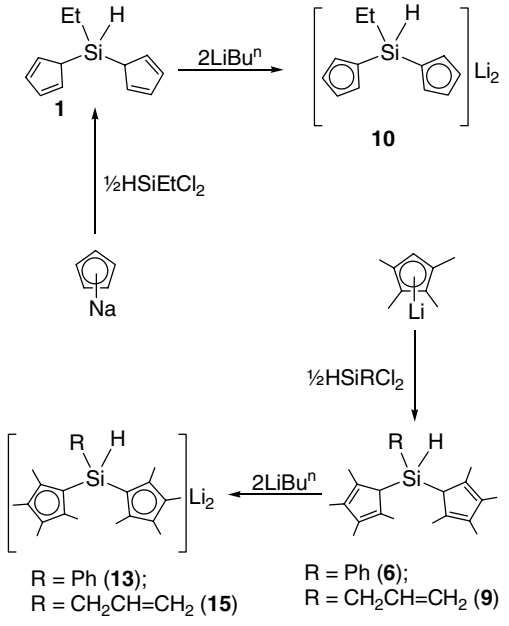
Suzuki et al. [5d] have reported the hydrosilylation of *ansa*-zirconocene complexes with vinyl substituents at the silicon *ansa* bridge to give derivatives which were subsequently supported on silica. In a similar manner O'Hare and co-worker [5e] have reported the immobilization on silica of an *ansa*-bisindenyl complex. Alt et al. [6] have also recently published their work relating to the modification by hydrosilylation of *ansa*-cyclopentadienyl ligands and their subsequent incorporation in group 4 metallocene systems. Collins and co-workers [5a] have reported the anchoring, on modified silica surfaces, of *ansa*-metallocene complexes via hydrosilylation reactions. Seyferth and Wyrwa [7] have also carried out work incorporating group 4 metallocene fragments in organosilicon dendrimers.

As part of our ongoing studies in *ansa*-metallocene complexes [8], we recently published our initial results on the modification of the *ansa*-ligand framework via hydrosilylation reactions [9]. As a continuation of this work we now report the synthesis of new group 4 *ansa*-metallocene complexes and the reactivity of the *ansa*-bridge Si–H bond in the hydrosilylation of unsaturated silane substrates. We also describe the hydrosilylation of vinyl or allyl substituents at the silicon *ansa* bridge of group 4 metallocene complexes. The catalytic activity of the *ansa*-zirconocene complexes in the polymerization of ethylene is included.

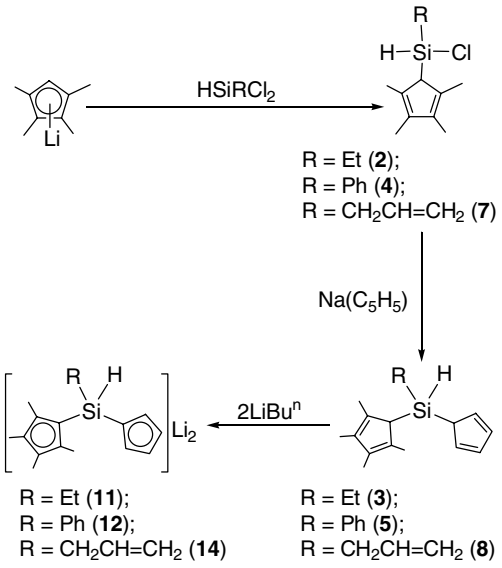
2. Results and discussion

The ligand systems, $Et(H)Si(C_5H_5)_2$ (**1**), $Et(H)Si(C_5HMe_4)Cl$ (**2**), $Et(H)Si(C_5HMe_4)(C_5H_5)$ (**3**), $Ph(H)Si(C_5HMe_4)Cl$ (**4**), $Ph(H)Si(C_5HMe_4)(C_5H_5)$ (**5**), $Ph(H)Si(C_5HMe_4)_2$ (**6**), $CH_2{=}CHCH_2(H)Si(C_5HMe_4)$-Cl (**7**), $CH_2{=}CHCH_2(H)Si(C_5HMe_4)(C_5H_5)$ (**8**) and $CH_2{=}CH$-$CH_2(H)Si(C_5HMe_4)_2$ (**9**) were prepared as yellow oils following previously reported synthetic protocols (Schemes 1 and 2) and isolated as mixtures of the double bond position isomers [8,9]. In the preparation of **2** and **4**, an excess of the dichlorosilane reagent was used in order to favour monosubstitution. **1**–**9** were characterized by ^1H NMR spectroscopy and electron impact mass spectrometry (see Section 5). The *ansa*-biscyclopentadiene compounds, **1**, **3**, **5**, **6**, **8** and **9** were lithiated in the traditional manner with *n*-butyllithium, to give the dilithium derivates, $Li_2\{Et(H)Si(C_5H_4)_2\}$ (**10**), $Li_2\{Et(H)Si(C_5Me_4)(C_5H_4)\}$ (**11**), $Li_2\{Ph(H)Si(C_5Me_4)$-$(C_5H_4)\}$ (**12**), $Li_2\{Ph(H)Si(C_5Me_4)_2\}$ (**13**), $Li_2\{CH_2{=}$ $CHCH_2$-$(H)Si(C_5Me_4)(C_5H_4)\}$ (**14**) and $Li_2\{CH_2{=}CH$-$CH_2(H)$-$Si(C_5Me_4)_2\}$ (**15**), in high yields.

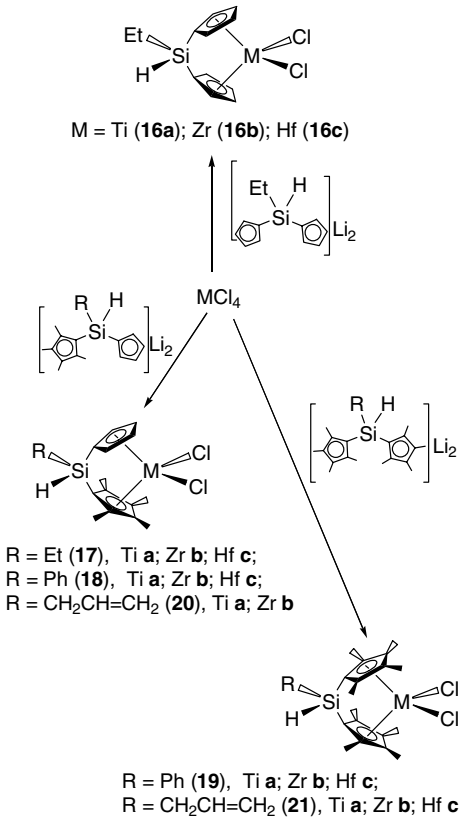
The reaction of **10**–**15** with either $[TiCl_4(THF)_2]$, $ZrCl_4$ or $HfCl_4$, yielded the corresponding *ansa*-metallocene (IV) dichloride complexes, $[M\{Et(H)Si(\eta^5$-$C_5H_4)_2\}$-$Cl_2]$ (M = Ti (**16a**), Zr (**16b**), Hf (**16c**)), $[M\{Et(H)Si(\eta^5$-$C_5Me_4)(\eta^5$-$C_5H_4)\}Cl_2]$ (M = Ti (**17a**), Zr (**17b**), Hf (**17c**)), $[M\{Ph(H)Si(\eta^5$-$C_5Me_4)(\eta^5$-$C_5H_4)\}Cl_2]$ (M = Ti (**18a**), Zr (**18b**), Hf (**18c**)), $[M\{Ph(H)Si(\eta^5$-$C_5Me_4)_2\}Cl_2]$ (M = Ti (**19a**), Zr (**19b**), Hf (**19c**)), $[M\{CH_2{=}$ $CHCH_2(H)Si(\eta^5$-$C_5Me_4)(\eta^5$-$C_5H_4)\}Cl_2]$ (M = Ti (**20a**), Zr (**20b**)) and $[M\{CH_2{=}$ $CHCH_2(H)Si(\eta^5$-$C_5Me_4)_2\}Cl_2]$ (M = Ti (**21a**), Zr (**21b**), Hf (**21c**)) (Scheme 3).



Scheme 1.



Scheme 2.



Scheme 3.

16–**21** were isolated as crystalline solids and characterized spectroscopically.[1] The ^{1}H NMR spectra for **16** showed the expected signals, namely 4 multiplets in the region δ 6.0–7.2, corresponding to the C_5 ring protons, and two multiplets, at ca. δ 1.1 and 1.4, assigned to the ethyl group. A triplet, at ca. δ 5.1, was observed for the proton bonded directly to the silicon atom. The mixed cyclopentadienyl chiral complexes **17**, **18** and **20** gave eight signals assigned to the four protons of the unsubstituted cyclopentadienyl moiety and to the four methyl groups of the tetramethylcyclopentadienyl fragment. For **17** the α-protons of the ethyl unit are diastereoscopic and give rise to two overlapping multiplet signals (δ 1.4) with a further multiplet being observed for the β-protons (δ 1.5). The Si–H proton resonates (δ 5.2) as a pseudo-triplet due to its coupling with the two inequivalent α-protons of the ethyl group. For **18** three multiplets for the phenyl moiety (δ 7.3, 7.6 and 8.0) and a singlet (δ 5.9) assigned to the Si–H proton were observed. For **20** the α-protons of the allyl unit are again diastereoscopic and were observed as an unresolved multiplet (δ 2.5) arising from both geminal and vicinal couplings. Further multiplets were observed for the central CH (δ 6.1) and terminal olefinic protons (δ 5.2 and 5.3, *cis* and *trans*, respectively, with respect to H_β). As in the case of **17**, the Si–H signal in **20** was observed as a pseudo-triplet (δ 5.2). The C_s symmetric complexes **19** and **21** gave in the ^{1}H NMR spectra, four singlets, in the region δ 1.6–2.2, corresponding to the per-methyl substituted *ansa*-ligand. For **19**, three multiplets for the phenyl moiety (δ 7.3, 7.5 and 8.0) and a singlet for the Si–H proton (δ 6.0) were also observed. For **21**, the ^{1}H NMR spectra were completed with the assignment of four multiplets (δ 2.6, 5.2, 5.3 and 6.1) and a triplet (δ 5.3) to the allyl and Si–H protons, respectively. The $^{13}C\{^{1}H\}$ NMR spectra for **16**–**21** showed the expected signals for the different ligand systems present (see Section 5). Signals for the allyl carbons of **20** and **21** were observed in the ^{13}C NMR spectra at ca. δ 20, 132 and 117 corresponding to the silicon bonded, central and terminal carbons, respectively. The signal due to the *ansa*-bridge silicon atom in **16**–**21** was observed in the ^{29}Si NMR spectra with the nature of this signal depending on the substituents present; **16**, **17**, **20** and **21** a doublet of multiplets and **18** and **19** a doublet. The multiplicity of the signal corresponds to the coupling of the silicon atom with its hydride substituent and the α-protons of the ethyl or allyl group.

The molecular structures of **21b** and **21c** were established by single crystal X-ray diffraction studies. The molecular structures and atomic numbering schemes are shown in Figs. 1 and 2. Selected bond lengths and angles for **21b** and **21c** are given in Table 1. In the case of **21c**, there are two distinct molecules in the asymmetric unit. A disordered toluene molecule was also located in the asymmetric unit.

For **21b** and **21c**, the usual bent metallocene conformation is observed with the geometry around the metal atom being pseudo-tetrahedral. The *ansa* ligand chelates

[1] We were unable to obtain the hafnium derivative of 20 with sufficient purity.

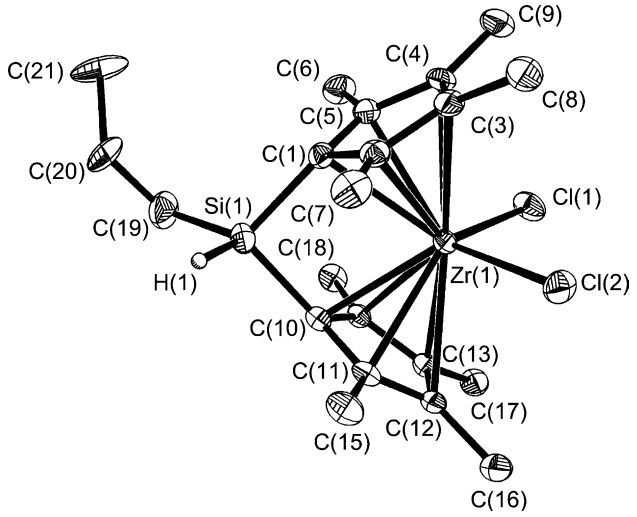


Fig. 1. Molecular structure and atom-labelling scheme for $[Zr\{CH_2{=}CHCH_2(H)Si(\eta^5\text{-}C_5Me_4)_2\}Cl_2]$ (**21b**) with thermal ellipsoids at 30% probability.

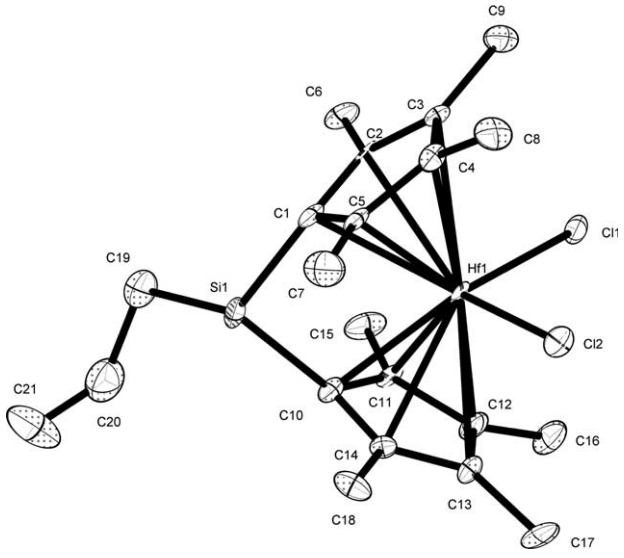


Fig. 2. Molecular structure and atom-labelling scheme for $[Hf\{CH_2{=}CHCH_2(H)Si(\eta^5\text{-}C_5Me_4)_2\}Cl_2]$ (**21c**) with thermal ellipsoids at 50% probability.

the zirconium or hafnium atom and both C_5 rings are bound to the metal in an η^5 mode. The centroids of the tetramethylcyclopentadienyl rings form an angle with the metal atom of 128.5° **21b** and 129.05° and 128.65° **21c**, which is typical for dichloride group 4 *ansa*-metallocene complexes. In **21b** the hydrogen atom (H(1)) bonded to the silicon atom was located in the difference map. The carbon atoms of the allyl moiety in **21b** are disordered, therefore we make no reference to the bond distances and angles of this fragment. However, in **21c** the allyl carbon atoms were clearly resolved and exhibit bond distances of C(19)–C(20) 1.51(1) and 1.53(1) Å and C(20)–C(21) 1.33(1) and 1.26(1) Å which

Table 1
Selected bond lengths (Å) and angles (°) for **21b** and **21c**

	21b	**21c**	
M–Cent(1)	2.229	2.219	2.202
M–Cent(2)	2.217	2.206	2.209
av M–C(Cent(1))[a]	2.531	2.522	2.513
av M–C(Cent(2))[a]	2.522	2.517	2.516
M–Cl(1)	2.425(3)	2.402(2)	2.413(2)
M–Cl(2)	2.413(3)	2.412(2)	2.416(2)
Si(1)–C(19)	1.864(8)	1.835(8)	1.879(8)
Si(1)–H(1)	1.597		
C(19)–C(20)		1.51(1)	1.53(1)
C(20)–C(21)		1.33(1)	1.26(1)
Cent(1)–M–Cent(2)	128.5	129.05	128.65
Si(1)–C(1)–Cent(1)	160.7	161.37	160.87
Si(1)–C(10)–Cent(2)	162.7	161.19	161.27
C(1)–Si(1)–C(10)	96.5(2)	96.2(3)	95.9(3)
Cl(1)–M–Cent(1)	106.5	105.70	105.99
Cl(1)–M–Cent(2)	106.3	106.50	106.02
Cl(2)–M–Cent(1)	106.7	106.22	106.58
Cl(2)–M–Cent(2)	107.0	106.23	107.78
Cl(1)–M–Cl(2)	97.54(8)	99.33(6)	97.51(6)
H(1)–Si(1)–C(1)	106.6		
H(1)–Si(1)–C(11)	106.3		
H(1)–Si(1)–C(21)	112.0		
Si(1)–C(19)–C(20)		108.7(5)	109.4(5)
C(19)–C(20)–C(21)		124.8(9)	126.3(9)

Cent(1) and Cent(2) are the centroids of C(1)–C(5) and C(10)–C(14), respectively.

[a] Refers to the average bond distance between Zr or Hf and the carbon atoms of the C_5 ring of the corresponding cyclopentadienyl moiety.

are typical for carbon carbon single (C(19)–C(20)) and double bonds (C(20)–C(21)), respectively. The angles Si(1)–C(19)–C(20) 108.7(5)° and 109.4(5)° and C(19)–C(20)–C(21) 124.8(9)° and 126.3(9)° indicate that C(19) and C(20) are sp^3 and sp^2 hybridized, respectively. Selected structural data of **21b** and **21c** can be compared with similar *ansa*-metallocene complexes using Table 2.

We have previously reported the modification of *ansa*-metallocene systems via hydrosilylation processes [9] and in order to gain a better understanding into the possible electronic or steric factors that may influence the outcome of these reactions we have tested **16**–**21** as hydrosilylation reagents. The hydrosilylation of $Si(CH{=}CH_2)_4$ by **16**–**21** in the presence of the Karstedt catalyst (divinyltetramethylsiloxane Pt(0)) was attempted. The per-methyl substituted *ansa*-complexes **19** and **21** did not react, inferring that the Si–H bond is not sufficiently reactive (even at high temperatures) to participate in the hydrosilylation reaction. This may be due to electronic effects caused by the electrodonating nature of the methyl ring substituents which translates to a less reactive Si–H bond [13]. The mixed cyclopentadienyl complexes (with four fewer methyl substituents) **17**, **18** and **20** did react with $Si(CH{=}CH_2)_4$ giving the product formed by the reaction of only one of the double bonds of the silane substrate. Only in the case of **17a** and **17b** were we able to isolate the final product with high purity

Table 2
Selected structural data of some *ansa*-zirconocene and hafnocene complexes

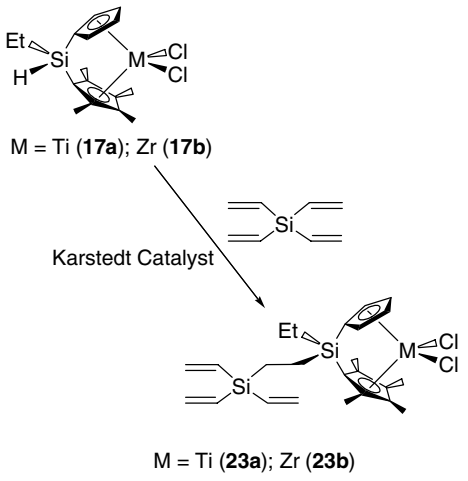
Complex	M–Cp (Å)[a]	M–Cl (Å)	Cp–M–Cp (°)	Cl–M–Cl (°)	$C_{(cp)}$–Si–$C_{(cp)}$ (°)	Reference
[Zr{CH_2=$CHCH_2$(H)Si(η^5-C_5Me_4)$_2$}Cl_2] (**21b**)	2.223	2.419	128.5	97.54(8)	96.5(2)	this work
[Zr{Me(H)Si(η^5-C_5Me_4)$_2$}Cl_2]	2.230	2.427	128.5	98.85(6)	96.15(19)	[9]
[Zr{Me_2Si(η^5-C_5Me_4)$_2$}Cl_2]	2.329	2.4334(7)	128.6	92.28	95.7(1)	[10]
[Zr{Me(CH_2=CH)Si(η^5-C_5Me_4)$_2$}Cl_2]	2.220	2.418	128.76	99.32(7)	95.8(2)	[8e]
[Zr{(CH_2=CH)$_2$Si(η^5-C_5Me_4)$_2$}Cl_2]	2.235	2.4333	128.7	99.24(3)	96.3(1)	[11]
[Hf{CH_2=$CHCH_2$(H)Si(η^5-C_5Me_4)$_2$}Cl_2] (**21c**)	2.213	2.407	129.05	99.33(6)	96.2(3)	this work
	2.206	2.415	128.65	97.51(6)	95.9(3)	
[Hf{Me_2Si(η^5-C_5Me_4)$_2$}Cl_2]	2.223	2.407(2)	129.2	98.0(1)	95.1(3)	[12]
[Hf{Et_2Si(η^5-C_5Me_4)$_2$}Cl_2]	2.224	2.407		98.75(8)	95.3(2)	[12]
[Hf{(CH_2=CH)$_2$Si(η^5-C_5Me_4)$_2$}Cl_2]	2.217	2.405	129.2	97.98(7)	96.5(2)	[12]

	C–C (Å)	C=C (Å)	Si–C–C (°)	C–C=C (°)	Reference
[Zr{Me(CH_2=$CHCH_2$)Si(η^5-C_5H_4)$_2$}Cl_2]	1.49(3)	1.26(5)	111.6(8)	124(5)	[8e]
[Zr{Me(CH_2=$CHCH_2$)Si(η^5-C_5Me_4)(η^5-C_5H_4)}Cl_2]	1.49(1)	1.32(1)	113.8(7)	123(1)	[8e]
[Hf{CH_2=$CHCH_2$(H)Si(η^5-C_5Me_4)$_2$}Cl_2] (**21c**)	1.51(1)	1.33(1)	108.7(5)	124.8(9)	this work
	1.53(1)	1.26(1)	109.4(5)	126.3(9)	

[a] Cp refers to the C_5Me_4 moiety.

and although the experimental conditions were directed towards the polyhydrosilylation of the silane substrate only the monohydrosilylation derivative, [M{(CH_2=CH)$_3$SiCH_2CH_2(Et)Si(η^5-C_5Me_4)(η^5-C_5H_4)}Cl_2] (M = Ti (**23a**), Zr (**23b**)), was obtained (Scheme 4). This fact may be due to steric hindrance in the hypothetical tetra-substitution of the silane substrate by four metallocene units. However, Alt et al. [6a] have recently prepared tetranuclear complexes via the hydrosilylation of *ansa*-cyclopentadienyl ligands and their subsequent incorporation in group 4 *ansa*-metallocene systems. Our synthetic strategy differs from that used by Alt in that in our case the reactivity takes place at the group 4 *ansa*-metallocene complex and not from previous modification of the organic ligand.

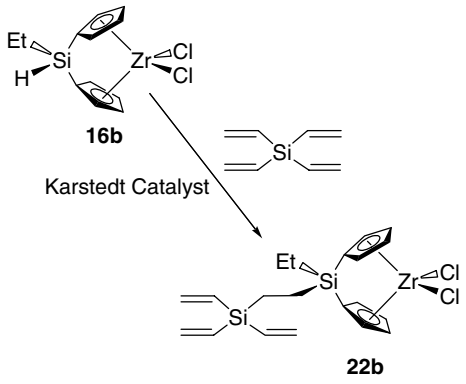
23a and **23b** were isolated as red and yellow oils, respectively, and characterized by NMR spectroscopy. The ^{1}H NMR spectra showed the expected signals for the cyclopentadienyl moieties namely four singlets and four multiplets. The three unreacted vinyl groups of the silane gave an ABX system in the ^{1}H NMR spectra and signals at ca. δ 133 (C_α) and 136 (C_β) in the ^{13}C{^{1}H} NMR spectra. The –CH_2CH_2– fragment, resulting from the hydrosilylation of the vinyl group, gave a complex set of multiplets with geminal and vicinal couplings in the ^{1}H NMR spectra. Two signals were observed in the ^{29}Si{^{1}H} NMR spectra at ca. δ −18 and −9, corresponding to the vinyl substituted and *ansa* bridge silicon atoms, respectively. The hydrosilylation reaction can also give the alternative regioisomer, [M{(CH_2=CH)$_3$Si(CH_3)CH(Et)Si(η^5-C_5Me_4)(η^5-C_5H_4)}Cl_2], via α-addition [14]. This minor product was detected, in quantities of ca. 5–10%, by ^{1}H NMR spectroscopy.



Scheme 4.

The *ansa*-metallocene complex without ring substituents **16b** was also tested in this reaction. It was hoped that the complete absence of electrodonating ring substituents would aid in the polyhydrosilylation of the tetravinylsilane. However, only the monohydrosilylation product, [Zr{(CH_2=CH)$_3$SiCH_2CH_2(Et)Si(η^5-C_5H_4)$_2$}Cl_2] (**22b**), was detected (Scheme 5). Nevertheless the Si–H bond in **16b** was shown to be more reactive than its methyl substituted counterparts **17**–**21** with the reaction of hydrosilylation being complete after 3 h at room temperature whereas for **23a** and **23b** the experimental conditions required were 100 °C and 40 h reaction time. **22b** was isolated as a yellow oil and characterized by NMR spectroscopy giving data similar to **23a** and **23b** (see Section 5).

Similar reactions have been carried out between **17a** and **17b** and dimethyldivinylsilane and gave the products [M{(CH_2=CH)Me_2SiCH_2CH_2(Et)Si(η^5-C_5Me_4)(η^5-C_5H_4)}Cl_2] (M = Ti (**24a**), Zr (**24b**)), as red and yellow oils, respectively, formed by the hydrosilylation of only one of the double bonds of the silane substrate



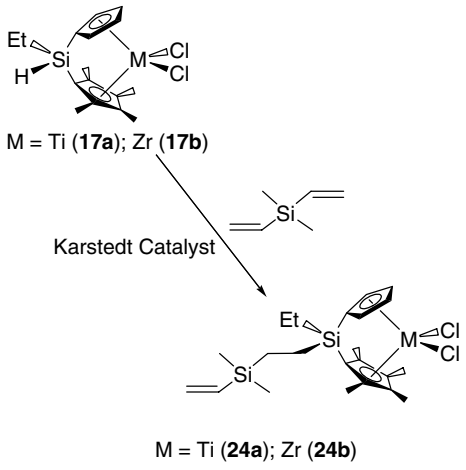
Scheme 5.

(Scheme 6). The NMR spectra of **24a** and **24b** are similar in all aspects to those previously discussed for **22** and **23** and showed in addition the presence of the minor regioisomer produced by α-addition (5–10%).

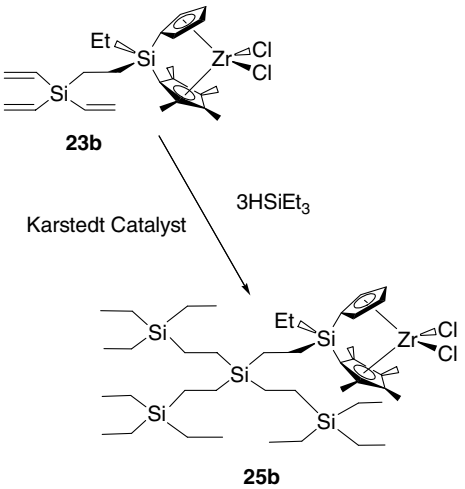
Further hydrosilylation of the vinyl groups of **22**–**24** was not possible when the hydrogen–silicon bond corresponded to the *ansa*-metallocene complexes. It appears that the reaction of one of the vinyl groups with the *ansa*-metallocene complex deactivates the remaining vinyl groups towards hydrosilylation by the Si–H of the *ansa* bridge. This may be attributed to electronic and/or steric effects. However, with triethylsilane, hydrosilylation took place at all the remaining vinyl groups of **23b** and **24b**, to give [Zr{$(Et_3SiCH_2CH_2)_3SiCH_2CH_2$(Et)Si($\eta^5$-$C_5Me_4$)($\eta^5$-$C_5H_4$)}$Cl_2$] (**25b**) and [Zr{$(Et_3SiCH_2CH_2)Me_2SiCH_2CH_2$(Et)Si($\eta^5$-$C_5Me_4$)($\eta^5$-$C_5H_4$)}$Cl_2$] (**26b**) (Schemes 7 and 8).

25b and **26b** were isolated as yellow oils and characterized by NMR spectroscopy. The reaction was deemed to have gone to completion by the absence of any signals in ^1H and $^{13}C\{^1H\}$ NMR spectroscopy corresponding to the vinyl groups of the parent complexes. The ^1H NMR spectra showed the expected signals for the C_5H_4 and C_5Me_4 moieties. In addition two multiplets, assigned to the ethyl groups of $SiEt_3$, and a complex set of multiplets, corresponding to the two distinct $-CH_2CH_2-$ fragments, were observed. The presence of the minor α-addition regioisomers was again detected (5–10%). $^{29}Si\{^1H\}$ NMR spectra revealed three signals corresponding to the three distinct silicon atoms present.

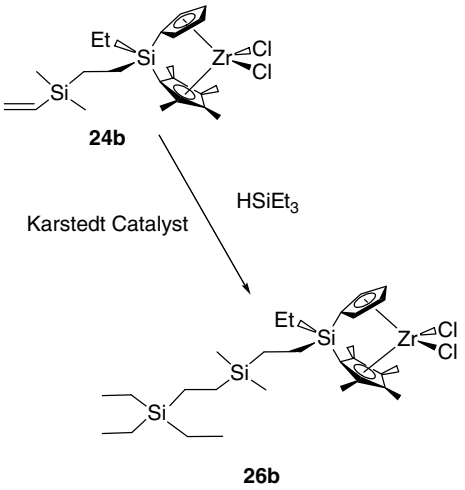
The hydrosilylation of the previously reported complexes [M{CH_2=CH(Me)Si(η^5-C_5Me_4)$_2$}Cl_2] (M = Ti (**27a**), Zr (**27b**)) and [Zr{CH_2=$CHCH_2$(Me)Si(η^5-C_5Me_4)$_2$}Cl_2] (**28b**) [8e], by $HSiMeCl_2$ has successfully been carried out. The reaction, in the presence of the Karstedt catalyst, gave after two hours reaction time the β-hydrosilylation products [M{$Cl_2MeSiCH_2CH_2$(Me)Si(η^5-C_5Me_4)$_2$}Cl_2] (M = Ti (**29a**), Zr (**29b**)) and [Zr{$Cl_2MeSiCH_2CH_2CH_2$(Me)Si(η^5-C_5Me_4)$_2$}Cl_2] (**30b**)



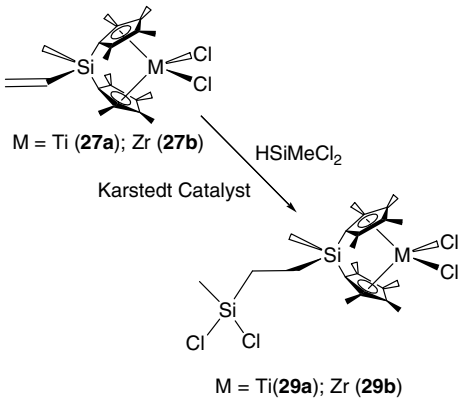
Scheme 6.



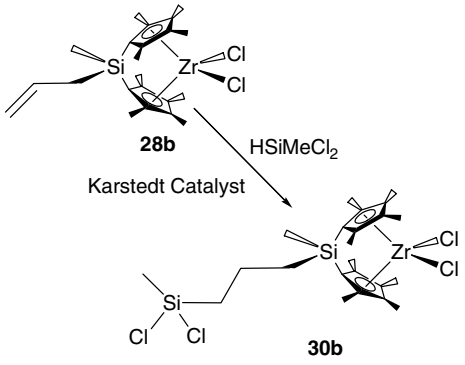
Scheme 7.



Scheme 8.



Scheme 9.



Scheme 10.

(Schemes 9 and 10). The presence of the minor α-addition regioisomer was also detected (5–10%).

29 and **30** were isolated as yellow solids and characterized by NMR spectroscopy. In the ^{1}H NMR spectra the presence of signals due to the vinyl or allyl protons of the starting products, **27** and **28**, was not observed. In the region of δ 0.5–1.8 multiplet signals were observed, two in the case of **29** (–$SiCH_2CH_2Si$–) and three for **30** (–$SiCH_2CH_2CH_2Si$–). For **29** and **30** a singlet at δ 0.4 was observed corresponding to the methyl protons of the dichloromethylsilyl fragment. Two signals were recorded in the $^{29}Si\{^1H\}$ NMR for **29** and **30** at ca. δ −10 and 32 and assigned to the *ansa* bridge and chloride bonded silicon atoms, respectively. In the $^{29}Si\{^1H\}$ NMR spectra of the vinyl and allyl substituted *ansa*-metallocene precursors of **29** and **30** a unique signal was observed for the *ansa* bridge silicon atom at δ −21.2, −22.7 and −15.6 for **27a**, **27b** and **28b**, respectively [15].

3. Polymerization studies

The polymerization of ethylene using the zirconium derivatives described in this paper as catalysts has been carried out. The polymerization experiments were conducted with a MAO–metal catalyst ratio of 3000:1, at 20 °C and at olefin pressure of 2 bar for 15 min. Polymerization was also carried out with the reference compound $[Zr(\eta^5\text{-}C_5H_5)_2Cl_2]$, under the same experimental conditions. The catalytic activities and polymer molecular weight and distribution values are given in Table 3.

Complex **29b** proved to be the most active catalyst of the series. A slightly lower value was recorded for the reference complex $[Zr(\eta^5\text{-}C_5H_5)_2Cl_2]$. The low catalytic activities observed for **22**, **23b** and **25** may be due to steric factors as proposed previously by De Jesús and co-workers [16] for similar modified metal-

Table 3
Ethylene polymerization results for **16**–**30** and $[Zr(\eta^5\text{-}C_5H_5)_2Cl_2]$[a]

Catalyst	Activity[b]	M_w	M_w/M_η
$[Zr(\eta^5\text{-}C_5H_5)_2Cl_2]$	23750	1014670	2.1
$[Zr\{Et(H)Si(\eta^5\text{-}C_5H_4)_2\}Cl_2]$ (**16b**)	11100	210200	3.2
$[Zr\{Et(H)Si(\eta^5\text{-}C_5Me_4)(\eta^5\text{-}C_5H_4)\}Cl_2]$ (**17b**)	8760	186200	3.1
$[Zr\{Ph(H)Si(\eta^5\text{-}C_5Me_4)(\eta^5\text{-}C_5H_4)\}Cl_2]$ (**18b**)	7053	185240	3.3
$[Zr\{(CH_2{=}CHCH_2)(H)Si(\eta^5\text{-}C_5Me_4)(\eta^5\text{-}C_5H_4)\}Cl_2]$ (**20b**)	3120	133500	4.1
$[Zr\{Ph(H)Si(\eta^5\text{-}C_5Me_4)_2\}Cl_2]$ (**19b**)	15967	194650	3.4
$[Zr\{(CH_2{=}CHCH_2)(H)Si(\eta^5\text{-}C_5Me_4)_2\}Cl_2]$ (**21b**)	6373	156800	4.0
$[Zr\{(CH_2{=}CH)_3SiCH_2CH_2(Et)Si(\eta^5\text{-}C_5H_4)_2\}Cl_2]$ (**22b**)	3307	139460	4.0
$[Zr\{(CH_2{=}CH)_3SiCH_2CH_2(Et)Si(\eta^5\text{-}C_5Me_4)(\eta^5\text{-}C_5H_4)\}Cl_2]$ (**23b**)	5513	420000	3.1
$[Zr\{(CH_2{=}CH)Me_2Si(CH_2CH_2)(Et)Si(\eta^5\text{-}C_5Me_4)(\eta^5\text{-}C_5H_4)\}Cl_2]$ (**24b**)	7213	141300	3.1
$[Zr\{(Et_3SiCH_2CH_2)_3SiCH_2CH_2(Et)Si(\eta^5\text{-}C_5Me_4)(\eta^5\text{-}C_5H_4)\}Cl_2]$ (**25b**)	3367	717000	4.7
$[Zr\{(Et_3SiCH_2CH_2)Me_2SiCH_2CH_2(Et)Si(\eta^5\text{-}C_5Me_4)(\eta^5\text{-}C_5H_4)\}Cl_2]$ (**26b**)	10147	669000	3.1
$[Zr\{CH_2{=}CH(Me)Si(\eta^5\text{-}C_5Me_4)_2\}Cl_2]$ (**27b**)	15510	236000	5.4
$[Zr\{CH_2{=}CHCH_2(Me)Si(\eta^5\text{-}C_5Me_4)_2\}Cl_2]$ (**28b**)	16472	136790	3.0
$[Zr\{Cl_2MeSiCH_2CH_2(Me)Si(\eta^5\text{-}C_5Me_4)_2\}Cl_2]$ (**29b**)	26898	483000	4.8
$[Zr\{Cl_2MeSiCH_2CH_2CH_2(Me)Si(\eta^5\text{-}C_5Me_4)_2\}Cl_2]$ (**30b**)	17707	558000	4.6

[a] At 20 °C, 2 bar monomer pressure, 200 mL toluene, $[Al] = 9 \times 10^{-2}$ mol L^{-1}, $[Zr] = 3 \times 10^{-5}$ mol L^{-1}, $t_{Pol} = 15$ min.
[b] In kg Pol (mol Zr h)$^{-1}$.

locene systems. In general, but not always, the complexes that contain a carbon carbon double bond substituent give low catalytic activities. This is most probably due to the fact that during the polymerization of ethylene, the vinyl or allyl groups of the *ansa*-ligand co-polymerize with the monomer thus immobilizing the metallocene complex on the polymer chain to give a pseudo-heterogeneous catalyst. This phenomenon with similar *ansa*-metallocene complexes has previously been reported [17].

4. Conclusions

In this paper we have reported the synthesis and catalytic activity of new *ansa*-metallocene complexes containing a Si–H bond which can be exploited in reactions of hydrosilylation to modify the ligand framework. The potential of translating this reactivity to the immobilization of *ansa*-metallocene catalysts on distinct substrates should be of great interest.

5. Experimental

All reactions were performed using standard Schlenk tube techniques in an atmosphere of dry nitrogen. Solvents were distilled from the appropriate drying agents and degassed before use. $C_5H_2Me_4$, $[TiCl_4(THF)_2]$, $ZrCl_4$, $HfCl_4$, $HSiMeCl_2$,$Si(CH{=}CH_2)_4$, $SiMe_2(CH{=}CH_2)_2$ and $HSiEt_3$ were purchased from Aldrich, $HSiEtCl_2$ and $HSiPhCl_2$ from Fluka and $HSi(CH_2CH{=}CH_2)Cl_2$ and the Karstedt catalyst from ABCR. All the commercial reagents were used directly. $Na(C_5H_5)$ [18], **27a**, **27b** and **28b** [8e] were prepared as previously described. IR spectra were recorded on a Thermo Nicolet Avatar 330 FT-IR spectrophotometer. ^1H, ^{13}C and ^{29}Si NMR spectra were recorded on a Varian Mercury FT-400 spectrometer. Microanalyses were carried out with a Perkin–Elmer 2400 or LECO CHNS-932 microanalyser. Mass spectroscopic analyses were preformed on a Hewlett–Packard 5988A (*m/z* 50–1000) instrument. Polymer molecular weights and distribution were determined by GPC (Waters 150C Plus or Alliance GPC-2000) in 1,2,4-trichlorobenzene at 150 °C.

5.1. Synthesis of $Et(H)Si(C_5H_5)_2$ (*1*)

$Et(H)SiCl_2$ (3.66 g, 28.38 mmol) was added to a solution of $Na(C_5H_5)$ (5.00 g, 56.76 mmol) in THF (50 mL) at −78 °C. The reaction mixture was allowed to warm to room temperature and stirred for 15 h. Solvent was removed in vacuo and hexane (150 mL) was added to the resulting orange oil. The mixture was filtered and solvent removed from the filtrate under reduced pressure to yield the title compound as a dark orange oil (4.54 g, 85%). ^1H NMR (400 MHz, $CDCl_3$) (for the predominant isomer): δ −0.38 (2H), 0.96 (3H) (m, Si*Et*), 3.07 (m, 2H, *H*C_5), 3.47 (m, 1H, Si*H*), 5.52 (2H), 6.00 (2H), 6.64 (2H), 6.97 (2H) (m, C_5H_4). MS electron impact (*m/e* (relative intensity)): 188 (25) $[M^+]$, 159 (19) $[M^+ - Et]$, 123 (62) $[M^+ - C_5H_5]$, 93 (100) $[M^+ - C_5H_5, -Et]$.

The preparation of **2**–**9** was carried out in an identical manner to **1**.

5.2. $Et(H)Si(C_5HMe_4)Cl$ (*2*)

From $Et(H)SiCl_2$ (5.02 g, 39.00 mmol) and $Li(C_5HMe_4)$ (2.50 g, 19.50 mmol). Yield: 3.57 g, 94%. ^1H NMR (400 MHz, $CDCl_3$) (for the predominant isomer): δ −0.54 (2H), 0.94 (3H) (m, Si*Et*), 1.85 (6H), 1.99 (3H), 2.04 (3H) (s, C_5Me_4), 3.24 (m, 1H, *H*C_5), 4.73 (m, 1H, Si*H*). MS electron impact (*m/e* (relative intensity)): 214 (18) $[M^+]$, 122 (100) $[M^+ - Et(H)SiCl]$, 91 (52) $[M^+ - C_5HMe_4]$.

5.3. $Et(H)Si(C_5HMe_4)(C_5H_5)_2$ (*3*)

From $Et(H)Si(C_5HMe_4)Cl$ (**2**) (2.00 g, 9.31 mmol) and $Na(C_5H_5)$ (0.82 g, 9.31 mmol). Yield: 2.05 g, 90%. ^1H NMR (400 MHz, $CDCl_3$) (for the predominant isomer): δ −0.48 (2H), 0.95 (3H) (m, Si*Et*), 1.88 (3H), 1.90 (3H), 1.96 (3H), 2.07 (3H) (s, C_5Me_4), 2.90 (1H), 3.01 (1H) (m, *H*C_5), 3.42 (m, 1H, Si*H*), 6.57 (1H), 6.59 (1H), 6.66 (1H), 6.83 (1H) (m, C_5H_4). MS electron impact (*m/e* (relative intensity)): 244 (18) $[M^+]$, 215 (28) $[M^+ - Et]$, 179 (100) $[M^+ - C_5H_5]$, 123 (52) $[M^+ - C_5HMe_4]$, 121 (41) $[M^+ - Et(H)SiC_5H_5]$.

5.4. $Ph(H)Si(C_5HMe_4)Cl$ (*4*)

From $Ph(H)SiCl_2$ (6.92 g, 39.00 mmol) and $Li(C_5HMe_4)$ (2.50 g, 19.50 mmol). Yield: 4.66 g, 91%. ^1H NMR (400 MHz, $CDCl_3$) (for the predominant isomer): δ 1.63 (3H), 1.68 (3H), 1.96 (3H), 2.02 (3H) (s, C_5Me_4), 3.43 (m, 1H, *H*C_5), 5.14 (m, 1H, Si*H*), 7.30 (2H), 7.38 (2H), 7.74 (1H) (m, Si*Ph*). MS electron impact (*m/e* (relative intensity)): 262 (74) $[M^+]$, 227 (26) $[M^+ - Cl]$, 141 (23) $[M^+ - C_5HMe_4]$, 122 (100) $[M^+ - Ph(H)SiCl]$.

5.5. $Ph(H)Si(C_5HMe_4)(C_5H_5)_2$ (*5*)

From $Ph(H)Si(C_5HMe_4)Cl$ (**4**) (2.00 g, 7.61 mmol) and $Na(C_5H_5)$ (0.67 g, 7.61 mmol). Yield: 1.96 g, 88%. ^1H NMR (400 MHz, $CDCl_3$) (for the predominant isomer): δ 1.65 (3H), 1.71 (3H), 1.72 (3H), 1.91 (3H) (s, C_5Me_4), 3.06 (1H), 3.13 (1H) (m, *H*C_5), 3.60 (m, 1H,

Si*H*), 6.63 (1H), 6.67 (1H), 6.73 (1H), 6.95 (1H) (m, C_5H_4), 7.29 (2H), 7.33 (2H), 7.46 (1H) (m, Si*Ph*). MS electron impact (*m/e* (relative intensity)): 292 (24) [M^+], 262 (28) [$M^+ - 2\times Me$], 227 (100) [$M^+ - C_5H_5$], 171 (55) [$M^+ - C_5HMe_4$].

5.6. $Ph(H)Si(C_5HMe_4)_2$ (6)

From $Ph(H)SiCl_2$ (1.73 g, 9.75 mmol) and Li(C_5HMe_4) (2.50 g, 19.50 mmol). Yield: 2.05 g, 90%. ^{1}H NMR (400 MHz, $CDCl_3$) (for the predominant isomer): δ 1.62 (6H), 1.68 (6H), 1.85 (6H), 1.99 (6H) (s, C_5Me_4), 3.27 (m, 2H, HC_5), 4.06 (m, 1H, Si*H*), 7.03 (2H), 7.17 (2H), 7.22 (1H) (m, Si*Ph*). MS electron impact (*m/e* (relative intensity)): 348 (9) [M^+], 227 (100) [$M^+ - C_5HMe_4$], 121 (14) [$M^+ - Ph(H)SiC_5HMe_4$], 105 (17) [$M^+ - 2\times C_5HMe_4$].

5.7. $CH_2{=}CHCH_2(H)Si(C_5HMe_4)Cl$ (7)

From $CH_2{=}CHCH_2(H)SiCl_2$ (2.74 g, 19.50 mmol) and Li(C_5HMe_4) (2.50 g, 19.50 mmol). Yield: 3.57 g, 94%. ^{1}H NMR (400 MHz, $CDCl_3$) (for the predominant isomer): δ 1.52 (m, 2H, $CH_2CH{=}CH_2$), 1.81 (6H), 1.82 (3H), 1.86 (3H) (s, C_5Me_4), 2.74 (m, 1H, HC_5), 4.77 (m, 1H, Si*H*), 4.93 (m, 2H, $CH_2CH{=}CH_2$), 5.59 (m, 1H, $CH_2CH{=}CH_2$). MS electron impact (*m/e* (relative intensity)): 226 (1) [M^+], 121 (100) [$M^+ - CH_2CH{=}\ CH_2(H)SiCl$], 103 (46) [$M^+ - C_5HMe_4$].

5.8. $CH_2{=}CHCH_2(H)Si(C_5HMe_4)(C_5H_5)$ (8)

From $CH_2{=}CHCH_2(H)Si(C_5HMe_4)Cl$ (**7**) (2.00 g, 8.81 mmol) and Na(C_5H_5) (0.78 g, 8.81 mmol). Yield: 1.78 g, 79%. ^{1}H NMR (400 MHz, $CDCl_3$) (for the predominant isomer): δ 1.50 (m, 2H, $CH_2CH{=}CH_2$), 1.66 (3H), 1.74 (3H), 1.80 (3H), 1.91 (3H) (s, C_5Me_4), 2.73 (1H), 3.03 (1H) (m, HC_5), 4.64 (m, 1H, Si*H*), 4.94 (m, 2H, $CH_2CH{=}CH_2$), 6.49 (m, 1H, $CH_2CH{=}CH_2$), 5.95 (2H), 6.41 (2H), (m, C_5H_4). MS electron impact (*m/e* (relative intensity)): 256 (5) [M^+], 215 (7) [$M^+ - CH_2CH{=}CH_2$], 191 (19) [$M^+ - C_5H_5$], 149 (100) [$M^+ - CH_2CH{=}CH_2, -C_5H_5, -H$].

5.9. $CH_2{=}CHCH_2(H)Si(C_5HMe_4)_2$ (9)

From $CH_2{=}CHCH_2(H)SiCl_2$ (1.37 g, 9.75 mmol) and Li(C_5HMe_4) (2.50 g, 19.50 mmol). Yield: 2.86 g, 94%. ^{1}H NMR (400 MHz, $CDCl_3$) (for the predominant isomer): δ 1.48 (m, 2H, $CH_2CH{=}CH_2$), 1.83 (12H), 1.92 (6H), 1.97 (6H) (s, C_5Me_4), 2.70 (m, 2H, HC_5), 3.98 (m, 1H, Si*H*), 4.88 (m, 2H, $CH_2CH{=}CH_2$), 5.67 (m, 1H, $CH_2CH{=}CH_2$). MS electron impact (*m/e* (relative intensity)): 312 (21) [M^+], 191 (85) [$M^+ - C_5HMe_4$], 149 (100) [$M^+ - CH_2CH{=}CH_2, -C_5HMe_4$], 121 (98) [$M^+ - CH_2CH{=}CH_2(H)SiC_5HMe_4$].

5.10. Synthesis of $Li_2\{Et(H)Si(C_5H_4)_2\}$ (10)

LiBu^n (1.6 M in hexane) (13.3 mL, 21.24 mmol) was added dropwise to a solution of $Et(H)Si(C_5H_5)_2$ (**1**) (2.00 g, 10.62 mmol) in hexane (100 mL) at −78 °C. The mixture was allowed to warm to 25 °C and stirred for 15 h. Solvent was removed in vacuo to give a white solid which was washed with hexane (2 × 50 mL) and dried under vacuum to yield a free flowing white solid of the title complex (2.06 g, 97%). *Anal.* Calc. for $C_{12}H_{14}Li_2Si$: C, 71.99; H, 7.05. Found: C, 71.58; H, 7.00%.

The preparation of **11**–**15** was carried out in an identical manner to **10**.

5.11. $Li_2\{Et(H)Si(C_5Me_4)(C_5H_4)\}$ (11)

From $Et(H)Si(C_5HMe_4)(C_5H_5)_2$ (**3**) (2.00 g, 8.18 mmol) and LiBu^n (1.6 M in hexane) (10.2 mL, 16.36 mmol). Yield: 1.89 g, 90%. *Anal.* Calc. for $C_{16}H_{22}Li_2Si$: C, 74.98; H, 8.65. Found: C, 74.49; H, 8.60%.

5.12. $Li_2\{Ph(H)Si(C_5Me_4)(C_5H_4)\}$ (12)

From $Ph(H)Si(C_5HMe_4)(C_5H_5)_2$ (**5**) (2.00 g, 6.83 mmol) and LiBu^n (1.6 M in hexane) (8.6 mL, 13.66 mmol). Yield: 1.83 g, 88%. *Anal.* Calc. for $C_{20}H_{22}Li_2Si$: C, 78.93; H, 7.29. Found: C, 78.66; H, 7.27%.

5.13. $Li_2\{Ph(H)Si(C_5Me_4)_2\}$ (13)

From $Ph(H)Si(C_5HMe_4)_2$ (**6**) (2.00 g, 5.73 mmol) and LiBu^n (1.6 M in hexane) (7.2 mL, 11.46 mmol). Yield: 1.69 g, 82%. *Anal.* Calc. for $C_{24}H_{30}Li_2Si$: C, 79.97; H, 8.39. Found: C, 79.45; H, 8.31%.

5.14. $Li_2\{CH_2{=}CHCH_2(H)Si(C_5Me_4)(C_5H_4)\}$ (14)

From $CH_2{=}CHCH_2(H)Si(C_5HMe_4)(C_5H_5)$ (**8**) (2.00 g, 7.80 mmol) and LiBu^n (1.6 M in hexane) (9.8 mL, 15.60 mmol). Yield: 1.73 g, 83%. *Anal.* Calc. for $C_{17}H_{22}Li_2Si$: C, 76.10; H, 8.26. Found: C, 75.89; H, 8.22%.

5.15. $Li_2\{CH_2{=}CHCH_2(H)Si(C_5Me_4)_2\}$ (15)

From $CH_2{=}CHCH_2(H)Si(C_5HMe_4)_2$ (**9**) (2.00 g, 6.40 mmol) and LiBu^n (1.6 M in hexane) (8.0 ml, 12.80 mmol). Yield: 1.70 g, 78%. *Anal.* Calc. for $C_{21}H_{30}Li_2Si$: C, 77.74; H, 9.32. Found: C, 77.44; H, 9.28%.

5.16. Synthesis of [Ti{Et(H)Si(η⁵-C₅H₄)₂}Cl₂] (16a)

THF (50 mL) was added to a solid mixture of $[TiCl_4(THF)_2]$ (1.67 g, 4.99 mmol) and $Li_2\{Et(H)Si(\eta^5\text{-}C_5H_4)_2\}$ (**10**) (1.00 g, 4.99 mmol). The resulting solution was stirred for 15 h. Solvent was removed in vacuo and toluene added (75 mL) to the resulting solid. The mixture was filtered and the filtrate concentrated (10 mL) and cooled to −30 °C to yield crystals of the title complex (0.78 g, 51%). IR (ZnSe): ν_{Si-H} 2187 cm^{-1}. ^1H NMR (400 MHz, $CDCl_3$): δ 1.11 (3H), 1.37 (2H) (m, Si*Et*), 5.05 (t, 1H, Si*H*) ($^3J(^1H–^1H)$ 3.3 Hz), 6.02 (2H), 6.08 (2H), 7.22 (2H), 7.25 (2H) (m, C_5H_4). $^{13}C\{^1H\}$ NMR (100 MHz, $CDCl_3$): δ 1.5, 7.3 (Si*Et*), 101.7 (C^{ipso}), 118.2, 120.4, 134.7, 136.2 (C_5H_4). ^{29}Si NMR (79.49 MHz, $CDCl_3$): δ −24.0 (doublet of multiplets) ($^1J(^{29}Si–^1H)$ 214.7 Hz). MS electron impact (*m/e* (relative intensity)): 304 (74) [M^+], 268 (32) [M^+ − Cl], 240 (37) [M^+ − Cl, −Et], 176 (100) [M^+ − Cl, −Et, $-C_5H_4$]. *Anal.* Calc. for $C_{12}H_{14}Cl_2SiTi$: C, 47.24; H, 4.63. Found: C, 47.11; H, 4.59%.

The preparation of **16b**–**32** was carried out in an identical manner to **16a**.

5.17. [Zr{Et(H)Si(η⁵-C₅H₄)₂}Cl₂] (16b)

From $ZrCl_4$ (1.16 g, 4.99 mmol) and $Li_2\{Et(H)Si(C_5H_4)_2\}$ (**10**) (1.00 g, 4.99 mmol). Yield: 0.63 g, 36%. IR (ZnSe): ν_{Si-H} 2177 cm^{-1}. ^1H NMR (400 MHz, $CDCl_3$): δ 1.17 (3H), 1.37 (2H) (m, Si*Et*), 5.07 (t, 1H, Si*H*) ($^3J(^1H–^1H)$ 3.3 Hz), 6.02 (2H), 6.11 (2H), 6.97 (2H), 7.00 (2H) (m, C_5H_4). $^{13}C\{^1H\}$ NMR (100 MHz, $CDCl_3$): δ 1.7, 7.3 (Si*Et*), 104.6 (C^{ipso}), 113.7, 116.0, 127.8, 129.3 (C_5H_4). ^{29}Si NMR (79.49 MHz, $CDCl_3$): δ −24.2 (doublet of multiplets) ($^1J(^{29}Si–^1H)$ 213.4 Hz). MS electron impact (*m/e* (relative intensity)): 348 (70) [M^+], 316 (25) [M^+ − Et], 282 (39) [M^+ − Cl, −Et], 253 (45) [M^+ − Et, $-C_5H_4$]. *Anal.* Calc. for $C_{12}H_{14}Cl_2SiZr$: C, 41.36; H, 4.05. Found: C, 41.05; H, 4.04%.

5.18. [Hf{Et(H)Si(η⁵-C₅H₄)₂}Cl₂] (16c)

From $HfCl_4$ (1.60 g, 4.99 mmol) and $Li_2\{Et(H)Si(C_5H_4)_2\}$ (**10**) (1.00 g, 4.99 mmol). Yield: 0.67 g, 31%. IR (ZnSe): ν_{Si-H} 2166 cm^{-1}. ^1H NMR (400 MHz, $CDCl_3$): δ 1.11 (3H), 1.36 (2H) (m, Si*Et*), 5.06 (t, 1H, Si*H*) ($^3J(^1H–^1H)$ 3.3 Hz), 5.95 (2H), 6.03 (2H), 6.88 (2H), 6.90 (2H) (m, C_5H_4). $^{13}C\{^1H\}$ NMR (100 MHz, $CDCl_3$): δ 1.8, 7.5 (Si*Et*), 106.1 (C^{ipso}), 111.5, 113.9, 126.4, 127.9 (C_5H_4). ^{29}Si NMR (79.49 MHz, $CDCl_3$): δ −24.9 (doublet of multiplets) ($^1J(^{29}Si–^1H)$ 215.1 Hz). MS electron impact (*m/e* (relative intensity)): 436 (26) [M^+], 407 (16) [M^+ − Et], 250 (65) [M^+ − Et(H)Si(C_5H_4)$_2$]. *Anal.* Calc. for $C_{12}H_{14}Cl_2HfSi$: C, 33.08; H, 3.24. Found: C, 32.99; H, 3.19%.

5.19. [Ti{Et(H)Si(η⁵-C₅Me₄)(η⁵-C₅H₄)}Cl₂] (17a)

From $[TiCl_4(THF)_2]$ (1.30 g, 3.90 mmol) and $Li_2\{Et(H)Si(C_5Me_4)(C_5H_4)\}$ (**11**) (1.00 g, 3.90 mmol). Yield: 0.89 g, 63%. IR (ZnSe): ν_{Si-H} 2172 cm^{-1}. ^1H NMR (400 MHz, $CDCl_3$): δ 1.38 (3H), 1.48 (2H) (m, Si*Et*), 1.87 (3H), 1.90 (3H), 2.15 (3H), 2.16 (3H) (s, C_5Me_4), 5.21 (dd, 1H, Si*H*) ($^3J(^1H–^1H)$ 4.4 Hz), 5.59 (1H), 5.62 (1H), 7.17 (1H), 7.22 (1H) (m, C_5H_4). $^{13}C\{^1H\}$ NMR (100 MHz, $CDCl_3$): δ 3.3, 7.8 (Si*Et*), 13.7, 15.7, 15.8 (C_5Me_4), 95.3 (C^{ipso}), 115.2, 117.0, 132.3, 134.3 (C_5H_4), 99.7, 129.8, 131.7, 144.0, 144.5 (C_5Me_4). ^{29}Si NMR (79.49 MHz, $CDCl_3$): δ −25.5 (doublet of multiplets) ($^1J(^{29}Si–^1H)$ 210.6 Hz). MS electron impact (*m/e* (relative intensity)): 360 (48) [M^+], 324 (100) [M^+ − Cl, –H], 288 (91) [M^+ − 2 × Cl, −H]. *Anal.* Calc. for $C_{16}H_{22}Cl_2SiTi$: C, 53.20; H, 6.14. Found: C, 53.01; H, 6.09%.

5.20. [Zr{Et(H)Si(η⁵-C₅Me₄)(η⁵-C₅H₄)}Cl₂] (17b)

From $ZrCl_4$ (0.91 g, 3.90 mmol) and $Li_2\{Et(H)Si(C_5Me_4)(C_5H_4)\}$ (**11**) (1.00 g, 3.90 mmol). Yield: 0.73 g, 46%. IR (ZnSe): ν_{Si-H} 2168 cm^{-1}. ^1H NMR (400 MHz, $CDCl_3$): δ 1.36 (3H), 1.46 (2H) (m, Si*Et*), 2.03 (3H), 2.07 (3H), 2.08 (6H) (s, C_5Me_4), 5.20 (dd, 1H, Si*H*) ($^3J(^1H–^1H)$ 4.4 Hz), 5.71 (1H), 5.78 (1H), 6.99 (1H), 7.04 (1H) (m, C_5H_4). $^{13}C\{^1H\}$ NMR (100 MHz, $CDCl_3$): δ 3.6, 7.9 (Si*Et*), 12.3, 12.4, 14.4, 14.9 (C_5Me_4), 95.1 (C^{ipso}), 112.1, 113.9, 126.4, 127.8 (C_5H_4), 102.5, 124.7, 126.0, 135.7, 136.2 (C_5Me_4). ^{29}Si NMR (79.49 MHz, $CDCl_3$): δ −26.7 (doublet of multiplets) ($^1J(^{29}Si–^1H)$ 207.6 Hz). MS electron impact (*m/e* (relative intensity)): 402 (88) [M^+], 366 (100) [M^+ − Cl], 338 (86) [M^+ − Cl, −Et]. *Anal.* Calc. for $C_{16}H_{22}Cl_2SiZr$: C, 47.50; H, 5.48. Found: C, 47.33; H, 5.48%.

5.21. [Hf{Et(H)Si(η⁵-C₅Me₄)(η⁵-C₅H₄)}Cl₂] (17c)

From $HfCl_4$ (1.25 g, 3.90 mmol) and $Li_2\{Et(H)Si(C_5Me_4)(C_5H_4)\}$ (**11**) (1.00 g, 3.90 mmol). Yield: 0.82 g, 43%. IR (ZnSe): ν_{Si-H} 2164 cm^{-1}. ^1H NMR (400 MHz, $CDCl_3$): δ 1.34 (3H), 1.45 (2H) (m, Si*Et*), 2.03 (3H), 2.07 (3H), 2.08 (6H) (s, C_5Me_4), 5.18 (dd, 1H, Si*H*) ($^3J(^1H–^1H)$ 4.4 Hz), 5.67 (1H), 5.73 (1H), 6.91 (1H), 6.97 (1H) (m, C_5H_4). $^{13}C\{^1H\}$ NMR (100 MHz, $CDCl_3$): δ 3.6, 7.8 (Si*Et*), 12.1, 12.2, 14.0, 14.5 (C_5Me_4), 97.0 (C^{ipso}), 109.5, 111.5, 125.0, 126.9 (C_5H_4), 104.6, 121.5, 123.3, 133.8, 134.3 (C_5Me_4). ^{29}Si NMR (79.49 MHz, $CDCl_3$): δ −27.3 (doublet of multiplets) ($^1J(^{29}Si–^1H)$ 207.2 Hz). MS electron impact (*m/e* (relative intensity)): 492 (85) [M^+], 456 (100) [M^+ − Cl, −H], 428 (19) [M^+ − Cl, −Et]. *Anal.* Calc. for $C_{16}H_{22}Cl_2HfSi$: C, 39.07; H, 4.51. Found: C, 39.00; H, 4.46%.

5.22. [Ti{Ph(H)Si(η^5-C_5Me_4)(η^5-C_5H_4)}Cl_2] (**18a**)

From $[TiCl_4(THF)_2]$ (1.10 g, 3.28 mmol) and $Li_2\{Ph(H)Si(C_5Me_4)(C_5H_4)\}$ (**12**) (1.00 g, 3.28 mmol). Yield: 0.82 g, 61%. IR (ZnSe): ν_{Si-H} 2167 cm^{-1}. ^{1}H NMR (400 MHz, $CDCl_3$): δ 1.49 (3H), 2.00 (3H), 2.11 (3H), 2.22 (3H) (s, C_5Me_4), 5.85 (s, 1H, Si*H*), 5.68 (1H), 5.81 (1H), 7.21 (2H) (m, C_5H_4), 7.31 (2H), 7.55 (2H), 7.95 (1H) (m, Si*Ph*). ^{13}C{^{1}H} NMR (100 MHz, $CDCl_3$): δ 13.5, 13.8, 15.9, 16.8 (C_5Me_4), 94.5 (C^{ipso}), 115.2, 118.0, 134.7, 135.9 (C_5H_4), 98.4, 128.5, 129.8, 143.0, 146.0 (C_5Me_4), 128.8, 130.9, 131.2, 133.1 (Si*Ph*). ^{29}Si NMR (79.49 MHz, $CDCl_3$): δ −32.4 (d) ($^1J(^{29}Si–^1H)$ 215.4 Hz). MS electron impact (*m*/*e* (relative intensity)): 408 (26) [M^+], 372 (41) [$M^+ - Cl, -H$], 336 (100) [$M^+ - 2\times Cl, -H$]. *Anal.* Calc. for $C_{20}H_{22}Cl_2SiTi$: C, 58.70; H, 5.42. Found: C, 58.44; H, 5.34%.

5.23. [Zr{Ph(H)Si(η^5-C_5Me_4)(η^5-C_5H_4)}Cl_2] (**18b**)

From $ZrCl_4$ (0.77 g, 3.28 mmol) and $Li_2\{Ph(H)Si(C_5Me_4)(C_5H_4)\}$ (**12**) (1.00 g, 3.28 mmol). Yield: 0.82 g, 55%. IR (ZnSe): ν_{Si-H} 2155 cm^{-1}. ^{1}H NMR (400 MHz, $CDCl_3$): δ 1.60 (3H), 2.04 (3H), 2.12 (3H), 2.13 (3H) (s, C_5Me_4), 5.88 (s, 1H, Si*H*), 5.81 (1H), 5.98 (1H), 7.05 (1H), 7.13 (1H) (m, C_5H_4), 7.28 (2H), 7.57 (2H), 7.95 (1H) (m, Si*Ph*). ^{13}C{^{1}H} NMR (100 MHz, $CDCl_3$): δ 12.3, 12.4, 14.5, 15.1 (C_5Me_4), 94.2 (C^{ipso}), 125.0, 128.7, 134.6, 135.1 (C_5H_4), 101.0, 112.2, 114.7, 128.9, 131.0 (C_5Me_4), 124.4, 128.6, 129.0, 134.2 (Si*Ph*). ^{29}Si NMR (79.49 MHz, $CDCl_3$): δ −37.9 (d) ($^1J(^{29}Si–^1H)$ 214.5 Hz). MS electron impact (*m*/*e* (relative intensity)): 452 (34) [M^+], 414 (57) [$M^+ - Cl, -H$], 105 (100) [$M^+ - H, -Zr(C_5Me_4)(C_5H_4)Cl_2$]. *Anal.* Calc. for $C_{20}H_{22}Cl_2SiZr$: C, 53.07; H, 4.90. Found: C, 52.96; H, 4.87%.

5.24. [Hf{Ph(H)Si(η^5-C_5Me_4)(η^5-C_5H_4)}Cl_2] (**18c**)

From $HfCl_4$ (1.05 g, 3.28 mmol) and $Li_2\{Ph(H)Si(C_5Me_4)(C_5H_4)\}$ (**12**) (1.00 g, 3.28 mmol). Yield: 0.74 g, 42%. IR (ZnSe): ν_{Si-H} 2172 cm^{-1}. ^{1}H NMR (400 MHz, $CDCl_3$): δ 1.66 (3H), 2.06 (3H), 2.13 (3H), 2.19 (3H) (s, C_5Me_4), 5.84 (s, 1H, Si*H*), 5.77 (1H), 5.93 (1H), 6.98 (1H), 7.06 (1H) (m, C_5H_4), 7.27 (2H), 7.55 (2H), 7.95 (1H) (m, Si*Ph*). ^{13}C{^{1}H} NMR (100 MHz, $CDCl_3$): δ 12.1, 12.2, 14.2, 14.8 (C_5Me_4), 95.9 (C^{ipso}), 109.7, 112.5, 128.2, 130.9 (C_5H_4), 103.1, 121.6, 124.2, 133.3, 135.6 (C_5Me_4), 124.4, 128.6, 129.0, 134.2 (Si*Ph*). ^{29}Si NMR (79.49 MHz, $CDCl_3$): δ −38.5 (d) ($^1J(^{29}Si–^1H)$ 214.1 Hz). MS electron impact (*m*/*e* (relative intensity)): 540 (9) [M^+], 502 (6) [$M^+ - Cl$], 315 (5) [$M^+ - Ph(H)Si(C_5Me_4)(C_5H_4)$], 123 (100) [$M^+ - Hf(C_5H_4Si(H)Ph)Cl_2$]. *Anal.* Calc. for $C_{20}H_{22}Cl_2HfSi$: C, 44.49; H, 4.11. Found: C, 44.03; H, 4.08%.

5.25. [Ti{Ph(H)Si(η^5-$C_5Me_4)_2$}Cl_2] (**19a**)

From $[TiCl_4(THF)_2]$ (0.92 g, 2.77 mmol) and $Li_2\{Ph(H)Si(C_5Me_4)_2\}$ (**13**) (1.00 g, 2.77 mmol). Yield: 0.80 g, 62%. IR (ZnSe): ν_{Si-H} 2155 cm^{-1}. ^{1}H NMR (400 MHz, $CDCl_3$): δ 1.59 (6H), 1.93 (6H), 2.11 (6H), 2.18 (6H) (s, C_5Me_4), 6.06 (s, 1H, Si*H*), 7.26 (2H), 7.53 (2H), 7.98 (1H) (m, Si*Ph*). ^{13}C{^{1}H} NMR (100 MHz, $CDCl_3$): δ 13.9, 16.1, 17.2 (C_5Me_4), 88.4, 125.2, 130.8, 143.2, 144.5 (C_5Me_4), 128.1, 128.4, 130.9, 135.0 (Si*Ph*). ^{29}Si NMR (79.49 MHz, $CDCl_3$): δ −41.3 (d) ($^1J(^{29}Si–^1H)$ 210.1 Hz). MS electron impact (*m*/*e* (relative intensity)): 464 (12) [M^+], 428 (22) [$M^+ - Cl$], 413 (25) [$M^+ - Cl, -Me$], 105 (100) [$M^+ - Ti(C_5Me_4)_2Cl_2$]. *Anal.* Calc. for $C_{24}H_{30}Cl_2SiTi$: C, 61.94; H, 6.50. Found: C, 61.55; H, 6.42%.

5.26. [Zr{Ph(H)Si(η^5-$C_5Me_4)_2$}Cl_2] (**19b**)

From $ZrCl_4$ (0.67 g, 2.77 mmol) and $Li_2\{Ph(H)Si(C_5Me_4)_2\}$ (**13**) (1.00 g, 2.77 mmol). Yield: 0.66 g, 47%. IR (ZnSe): ν_{Si-H} 2169 cm^{-1}. ^{1}H NMR (400 MHz, $CDCl_3$): δ 1.70 (6H), 2.04 (6H), 2.07 (6H), 2.13 (6H) (s, C_5Me_4), 6.02 (s, 1H, Si*H*), 7.26 (2H), 7.52 (2H), 7.94 (1H) (m, Si*Ph*). ^{13}C{^{1}H} NMR (100 MHz, $CDCl_3$): δ 12.6, 12.7, 14.9, 16.1 (C_5Me_4), 89.0, 124.9, 125.2, 136.0, 136.9 (C_5Me_4), 128.3, 130.3, 130.7, 135.0 (Si*Ph*). ^{29}Si NMR (79.49 MHz, $CDCl_3$): δ −43.0 (d) ($^1J(^{29}Si–^1H)$ 208.5 Hz). MS electron impact (*m*/*e* (relative intensity)): 508 (86) [M^+], 471 (40) [$M^+ - Cl$], 455 (89) [$M^+ - Cl, -Me$], 105 (100) [$M^+ - Zr(C_5Me_4)_2Cl_2$]. *Anal.* Calc. for $C_{24}H_{30}Cl_2SiZr$: C, 56.66; H, 5.94. Found: C, 56.12; H, 5.91%.

5.27. [Hf{Ph(H)Si(η^5-$C_5Me_4)_2$}Cl_2] (**19c**)

From $HfCl_4$ (0.89 g, 2.77 mmol) and $Li_2\{Ph(H)Si(C_5Me_4)_2\}$ (**13**) (1.00 g, 2.77 mmol). Yield: 0.64 g, 39%. IR (ZnSe): ν_{Si-H} 2116 cm^{-1}. ^{1}H NMR (400 MHz, $CDCl_3$): δ 1.77 (6H), 2.09 (6H), 2.12 (6H), 2.16 (6H) (s, C_5Me_4), 5.99 (s, 1H, Si*H*), 7.18 (2H), 7.50 (2H), 7.95 (1H) (m, Si*Ph*). ^{13}C{^{1}H} NMR (100 MHz, $CDCl_3$): δ 12.5, 12.6, 14.8, 16.0 (C_5Me_4), 91.1, 121.8, 123.4, 134.3, 135.3 (C_5Me_4), 128.2, 130.3, 130.5, 134.9 (Si*Ph*). ^{29}Si NMR (79.49 MHz, $CDCl_3$): δ −43.7 (d) ($^1J(^{29}Si–^1H)$ 208.7 Hz). MS electron impact (*m*/*e* (relative intensity)): 596 (29) [M^+], 561 (3) [$M^+ - Cl$], 545 (12) [$M^+ - Cl, -Me$], 105 (100) [$M^+ - Hf(C_5Me_4)_2Cl_2$]. *Anal.* Calc. for $C_{24}H_{30}Cl_2HfSi$: C, 48.37; H, 5.07. Found: C, 48.00; H, 5.02%.

*5.28. [Ti{CH$_2$=CHCH$_2$(H)Si(η^5-C$_5$Me$_4$)-(η^5-C$_5$H$_4$)}Cl$_2$] (**20a**)*

From [TiCl$_4$(THF)$_2$] (1.24 g, 3.73 mmol) and Li$_2${CH$_2$=CHCH$_2$(H)Si(C$_5$Me$_4$)(C$_5$H$_4$)} (**14**) (1.00 g, 3.73 mmol). Yield: 0.85 g, 61%. IR (ZnSe): ν_{Si-H} 2166, ν_{CH} 3081, $\nu_{CH=CH_2}$ 1625 cm^{-1}. ^{1}H NMR (400 MHz, CDCl$_3$): δ 1.90 (6H), 2.16 (6H) (s, C$_5$*Me*$_4$), 2.47 (m, 2H, C*H*$_2$CH=CH$_2$), 5.23 (dd, 1H, Si*H*) (^3J(^{1}H–^{1}H) 4.4 Hz), 5.17 (1H) (*cis*), 5.26 (1H) (*trans*) (dd, CH$_2$CH=C*H*$_2$) ($^3J_{cis}$(^{1}H–^{1}H) 10.0, $^3J_{trans}$(^{1}H–^{1}H) 17.1 Hz), 6.06 (m, 1H, CH$_2$C*H*=CH$_2$), 5.63 (1H), 6.06 (1H), 7.18 (1H), 7.24 (1H) (m, C$_5$*H*$_4$). ^{13}C{^{1}H} NMR (100 MHz, CDCl$_3$): δ 13.8, 15.8, 16.5 (C$_5$*Me*$_4$), 18.1 (*C*H$_2$CH=CH$_2$), 95.0 (C^{ipso}), 115.1, 116.9, 132.1, 134.4 (*C*$_5$H$_4$), 95.2, 129.5, 130.7, 143.8, 144.5 (*C*$_5$Me$_4$), 117.1 (CH$_2$CH=*C*H$_2$), 131.6 (CH$_2$*C*H=CH$_2$). ^{29}Si NMR (79.49 MHz, CDCl$_3$): δ −30.0 (doublet of multiplets) (^1J(^{29}Si–^{1}H) 217.0 Hz). MS electron impact (*m*/*e* (relative intensity)): 372 (48) [M$^+$], 336 (100) [M$^+$ − Cl, −H], 295 (44) [M$^+$ − Cl, −H, −CH$_2$CH=CH$_2$], 123 (100) [M$^+$ − Ti(C$_5$H$_4$Si(H)CH$_2$CH=CH$_2$)Cl$_2$]. *Anal.* Calc. for C$_{17}$H$_{22}$Cl$_2$SiTi: C, 54.71; H, 5.94. Found: C, 54.35; H, 5.94%.

*5.29. [Zr{CH$_2$=CHCH$_2$(H)Si(η^5-C$_5$Me$_4$)(η^5-C$_5$H$_4$)}-Cl$_2$] (**20b**)*

From ZrCl$_4$ (0.87 g, 3.73 mmol) and Li$_2${CH$_2$=CHCH$_2$(H)Si(C$_5$Me$_4$)(C$_5$H$_4$)} (**14**) (1.00 g, 3.73 mmol). Yield: 0.79 g, 51%. IR (ZnSe): ν_{Si-H} 2170, ν_{CH} 3080, $\nu_{CH=CH_2}$ 1626 cm^{-1}. ^{1}H NMR (400 MHz, CDCl$_3$): δ 2.00 (3H), 2.06 (3H), 2.07 (6H) (s, C$_5$*Me*$_4$), 2.45 (m, 2H, C*H*$_2$CH=CH$_2$), 5.22 (dd, 1H, Si*H*) (^3J(^{1}H–^{1}H) 4.4 Hz), 5.14 (1H) (*cis*), 5.25 (1H) (*trans*) (dd, CH$_2$CH=C*H*$_2$) ($^3J_{cis}$(^{1}H–^{1}H) 10.1, $^3J_{trans}$(^{1}H–^{1}H) 17.1 Hz), 6.04 (m, 1H, CH$_2$C*H*=CH$_2$), 5.74 (1H), 5.78 (1H), 7.00 (2H) (m, C$_5$*H*$_4$). ^{13}C{^{1}H} NMR (100 MHz, CDCl$_3$): δ 12.3, 13.9, 14.4, 15.1 (C$_5$*Me*$_4$), 18.3 (*C*H$_2$CH=CH$_2$), 94.9 (C^{ipso}), 112.0, 113.9, 125.9, 128.0 (*C*$_5$H$_4$), 102.0, 124.4, 126.4, 136.0, 136.3 (*C*$_5$Me$_4$), 116.9 (CH$_2$CH=*C*H$_2$), 131.1 (CH$_2$*C*H=CH$_2$). ^{29}Si NMR (79.49 MHz, CDCl$_3$): δ −31.1 (doublet of multiplets) (^1J(^{29}Si–^{1}H) 215.1 Hz). MS electron impact (*m*/*e* (relative intensity)): 416 (22) [M$^+$], 378 (23) [M$^+$ − Cl, −H], 337 (20) [M$^+$ − Cl, −H, −CH$_2$CH=CH$_2$], 303 (5) [M$^+$ − 2 × Cl, −H, −CH$_2$CH=CH$_2$]. *Anal.* Calc. for C$_{17}$H$_{22}$Cl$_2$SiZr: C, 49.01; H, 5.32. Found: C, 48.88; H, 5.28%.

*5.30. [Ti{CH$_2$=CHCH$_2$(H)Si(η^5-C$_5$Me$_4$)$_2$}Cl$_2$] (**21a**)*

From [TiCl$_4$(THF)$_2$] (0.98 g, 2.93 mmol) and Li$_2${CH$_2$=CHCH$_2$(H)Si(C$_5$Me$_4$)$_2$} (**15**) (1.00 g, 2.93 mmol). Yield: 0.81 g, 64%. IR (ZnSe): ν_{Si-H} 2169, ν_{CH} 3076, $\nu_{CH=CH_2}$ 1627 cm^{-1}. ^{1}H NMR (400 MHz, CDCl$_3$): δ 1.83 (6H), 1.87 (6H), 2.12 (12H) (s, C$_5$*Me*$_4$), 2.59 (m, 2H, C*H*$_2$CH=CH$_2$), 5.37 (t, 1H, Si*H*) (^3J(^{1}H–^{1}H) 5.2 Hz), 5.17 (1H) (*cis*), 5.28 (1H) (*trans*) (dd, CH$_2$CH=C*H*$_2$) ($^3J_{cis}$(^{1}H–^{1}H) 9.9, $^3J_{trans}$(^{1}H–^{1}H) 16.9 Hz), 6.10 (m, 1H, CH$_2$C*H*=CH$_2$). ^{13}C{^{1}H} NMR (100 MHz, CDCl$_3$): δ 13.7, 13.9, 16.0, 16.7 (C$_5$*Me*$_4$), 19.5 (*C*H$_2$CH=CH$_2$), 89.5, 129.0, 130.0, 143.4, 143.6 (*C*$_5$Me$_4$), 116.7 (CH$_2$CH=*C*H$_2$), 131.6 (CH$_2$*C*H=CH$_2$). ^{29}Si NMR (79.49 MHz, CDCl$_3$): δ −34.7 (doublet of multiplets) (^1J(^{29}Si–^{1}H) 213.9 Hz). MS electron impact (*m*/*e* (relative intensity)): 428 (78) [M$^+$], 392 (100) [M$^+$ − Cl], 387 (44) [M$^+$ − CH$_2$CH=CH$_2$], 351 (22) [M$^+$ − Cl, −CH$_2$CH=CH$_2$]. *Anal.* Calc. for C$_{21}$H$_{30}$-Cl$_2$SiTi: C, 58.75; H, 7.04. Found: C, 58.52; H, 7.01%.

*5.31. [Zr{CH$_2$=CHCH$_2$(H)Si(η^5-C$_5$Me$_4$)$_2$}Cl$_2$] (**21b**)*

From ZrCl$_4$ (0.68 g, 2.93 mmol) and Li$_2${CH$_2$=CHCH$_2$(H)Si(C$_5$Me$_4$)$_2$} (**15**) (1.00 g, 2.93 mmol). Yield: 0.72 g, 52%. IR (ZnSe): ν_{Si-H} 2182, ν_{CH} 3076, $\nu_{CH=CH_2}$ 1631 cm^{-1}. ^{1}H NMR (400 MHz, CDCl$_3$): δ 1.93 (6H), 1.97 (6H), 2.07 (12H) (s, C$_5$*Me*$_4$), 2.55 (m, 2H, C*H*$_2$CH=CH$_2$), 5.34 (t, 1H, Si*H*) (^3J(^{1}H–^{1}H) 5.2 Hz), 5.14 (1H) (*cis*), 5.25 (1H) (*trans*) (dd, CH$_2$CH=C*H*$_2$) ($^3J_{cis}$(^{1}H–^{1}H) 10.0, $^3J_{trans}$(^{1}H–^{1}H) 17.0 Hz), 6.07 (m, 1H, CH$_2$C*H*=CH$_2$). ^{13}C{^{1}H} NMR (100 MHz, CDCl$_3$): δ 12.5, 12.7, 14.8, 15.6 (C$_5$*Me*$_4$), 19.9 (*C*H$_2$CH=CH$_2$), 90.3, 124.5, 125.5, 136.0, 136.2 (*C*$_5$Me$_4$), 116.5 (CH$_2$CH=*C*H$_2$), 131.8 (CH$_2$*C*H=CH$_2$). ^{29}Si NMR (79.49 MHz, CDCl$_3$): δ −36.0 (doublet of multiplets) (^1J(^{29}Si–^{1}H) 209.2 Hz). MS electron impact (*m*/*e* (relative intensity)): 472 (80) [M$^+$], 435 (44) [M$^+$ − Cl], 419 (100) [M$^+$ − Cl, −Me]. *Anal.* Calc. for C$_{21}$H$_{30}$Cl$_2$SiZr: C, 53.36; H, 6.40. Found: C, 53.31; H, 6.39%.

*5.32. [Hf{CH$_2$=CHCH$_2$(H)Si(η^5-C$_5$Me$_4$)$_2$}Cl$_2$] (**21c**)*

From HfCl$_4$ (0.94 g, 2.93 mmol) and Li$_2${CH$_2$=CHCH$_2$(H)Si(C$_5$Me$_4$)$_2$} (**15**) (1.00 g, 2.93 mmol). Yield: 0.71 g, 43%. IR (ZnSe): ν_{Si-H} 2165, ν_{CH} 3077, $\nu_{CH=CH_2}$ 1629 cm^{-1}. ^{1}H NMR (400 MHz, CDCl$_3$): δ 2.01 (6 H), 2.04 (6H), 2.09 (6H), 2.10 (6H) (s, C$_5$*Me*$_4$), 2.54 (m, 2H, C*H*$_2$CH=CH$_2$), 5.30 (t, 1H, Si*H*) (^3J(^{1}H–^{1}H) 5.1 Hz), 5.13 (1H) (*cis*), 5.24 (1H) (*trans*) (dd, CH$_2$CH=C*H*$_2$) ($^3J_{cis}$(^{1}H–^{1}H) 10.0, $^3J_{trans}$(^{1}H–^{1}H) 17.1 Hz), 6.06 (m, 1H, CH$_2$C*H*=CH$_2$). ^{13}C{^{1}H} NMR (100 MHz, CDCl$_3$): δ 12.4, 12.5, 14.6, 15.4 (C$_5$*Me*$_4$), 19.9 (*C*H$_2$CH=CH$_2$), 92.3, 121.6, 122.6, 134.5, 134.7 (*C*$_5$Me$_4$), 116.4 (CH$_2$CH=*C*H$_2$), 131.9 (CH$_2$*C*H=CH$_2$). ^{29}Si NMR (79.49 MHz, CDCl$_3$): δ −36.6 (doublet of multiplets) (^1J(^{29}Si–^{1}H) 208.9 Hz). MS electron impact (*m*/*e* (relative intensity)): 560 (40) [M$^+$], 519 (53) [M$^+$ − CH$_2$CH=CH$_2$], 504 (20) [M$^+$ − Me, −CH$_2$CH=CH$_2$]. *Anal.* Calc. for C$_{21}$H$_{30}$Cl$_2$HfSi: C, 45.04; H, 5.40. Found: C, 45.02; H, 5.36%.

The experimental procedure described for **22**–**24** relates to the optimized synthesis of the monohydrosilylation product.

5.33. Synthesis of [Zr{(CH$_2$=CH)$_3$SiCH$_2$CH$_2$(Et)Si(η^5-C$_5$H$_4$)$_2$}Cl$_2$] (**22b**)

Two drops of the Karstedt catalyst (divinyltetramethylsiloxane Pt(0) in xylene (3–3.5%)) were added to a solution of tetravinylsilane (0.059 g, 0.43 mmol) in toluene (5 mL) and the mixture was stirred for 5 min at room temperature. To this solution was added dropwise [Zr{Et(H)Si(η^5-C$_5$H$_4$)$_2$}Cl$_2$] (**16b**) (0.15 g, 0.31 mmol) in toluene (10 mL) and the reaction mixture was stirred for 40 h at 100 °C and then allowed to cool to room temperature. The mixture was filtered and volatiles were removed from the filtrate under reduced pressure to give the title product as a dark yellow oil (0.19 g, 92%). IR (KBr): ν_{CH} 3046, $\nu_{CH=CH_2}$ 1599 cm^{-1}. ^{1}H NMR (400 MHz, CDCl$_3$) (for the major isomer): δ 1.31 (3H), 1.43 (2H) (m, Si*Et*), 0.95 (2H), 1.28 (2H) (m, C*H*$_2$C*H*$_2$), 5.96 (2H), 6.00 (2H), 6.98 (4H) (m, C$_5$*H*$_4$), 5.86 (m, 3H, CH$_2$=C*H*), 6.19 (m, 6H, C*H*$_2$=CH). ^{13}C{^{1}H} NMR (100 MHz, CDCl$_3$) (for the major isomer): δ 1.5, 7.5 (Si*Et*), 2.9, 4.3 (*C*H$_2$*C*H$_2$), 108.3 (C^{ipso}), 114.3, 115.0, 133.2, 136.0 (*C*$_5$H$_4$), 133.5, 135.3 (*C*H=*C*H$_2$). ^{29}Si{^{1}H} NMR (79.49 MHz, CDCl$_3$) (for the major isomer): δ −18.2 (*Si*CH=CH$_2$), −10.7 (*Si*C$_5$H$_4$). MS electron impact (*m*/*e* (relative intensity)): 484 (15) [M$^+$], 447 (7) [M$^+$ − Cl], 310 (40) [M$^+$ − Cl, −CH$_2$CH$_2$Si(CH=CH$_2$)$_3$], 109 (100) [M$^+$−Zr{CH$_2$CH$_2$Si(Et)(C$_5$H$_4$)$_2$}Cl$_2$]. *Anal.* Calc. for C$_{20}$H$_{26}$Cl$_2$Si$_2$Zr: C, 49.56; H, 5.41. Found: C, 49.09; H, 5.36%.

The preparation of **23**–**26** was carried out in an identical manner to **22b**.

5.34. [Ti{(CH$_2$=CH)$_3$SiCH$_2$CH$_2$(Et)Si(η^5-C$_5$Me$_4$)(η^5-C$_5$H$_4$)}Cl$_2$] (**23a**)

From Si(CH=CH$_2$)$_4$ (0.056 g, 0.41 mmol) and [Ti{Et(H)Si(η^5-C$_5$Me$_4$)(η^5-C$_5$H$_4$)}Cl$_2$] (**17a**) (0.15 g, 0.41 mmol). Yield: 0.20 g, 98%. IR (KBr): ν_{CH} 3050, $\nu_{CH=CH_2}$ 1592 cm^{-1}. ^{1}H NMR (400 MHz, CDCl$_3$) (for the major isomer): δ 1.31 (3H), 1.41 (2H) (m, Si*Et*), 0.99 (2H), 1.25 (1H), 1.35 (1H) (m, C*H*$_2$C*H*$_2$), 1.84 (3H), 1.88 (3H), 2.14 (3H), 2.15 (3H) (s, C$_5$*Me*$_4$), 5.55 (1H), 5.58 (1H), 7.18 (2H) (m, C$_5$*H*$_4$), 5.84 (m, 3H, CH$_2$=C*H*), 6.18 (m, 6H, C*H*$_2$=CH). ^{13}C{^{1}H} NMR (100 MHz, CDCl$_3$) (for the major isomer): δ 4.0, 4.9 (Si*Et*), 4.3, 7.0 (*C*H$_2$*C*H$_2$), 13.6, 13.7, 16.2, 16.3 (C$_5$*Me*$_4$), 103.8 (C^{ipso}), 116.0, 116.3, 132.8, 133.5 (*C*$_5$H$_4$), 98.5, 131.1, 131.7, 144.0, 144.3 (*C*$_5$Me$_4$), 133.3, 135.3 (*C*H=*C*H$_2$). ^{29}Si{^{1}H} NMR (79.49 MHz, CDCl$_3$) (for the major isomer): δ −18.2 (*Si*CH=CH$_2$), −7.8 (*Si*C$_5$H$_4$). MS electron impact (*m*/*e* (relative intensity)): 496 (23) [M$^+$], 460 (13) [M$^+$ − Cl], 109 (100) [M$^+$ − Ti{CH$_2$CH$_2$Si(Et)(C$_5$Me$_4$)(C$_5$H$_4$)}Cl$_2$]. *Anal.* Calc. for C$_{24}$H$_{34}$Cl$_2$Si$_2$Ti: C, 57.94; H, 6.89. Found: C, 57.88; H, 6.85%.

5.35. [Zr{(CH$_2$=CH)$_3$SiCH$_2$CH$_2$(Et)Si(η^5-C$_5$Me$_4$)(η^5-C$_5$H$_4$)}Cl$_2$] (**23b**)

From Si(CH=CH$_2$)$_4$ (0.051 g, 0.37 mmol) and [Zr{Et(H)Si(η^5-C$_5$Me$_4$)(η^5-C$_5$H$_4$)}Cl$_2$] (**17b**) (0.15 g, 0.37 mmol). Yield: 0.20 g, 99%. IR (KBr): ν_{CH} 3050, $\nu_{CH=CH_2}$ 1591 cm^{-1}. ^{1}H NMR (400 MHz, CDCl$_3$) (for the major isomer): δ 1.30 (3H), 1.40 (2H) (m, Si*Et*), 0.96 (2H), 1.23 (1H), 1.33 (1H) (m, C*H*$_2$C*H*$_2$), 1.93 (3H), 1.96 (3H), 2.05 (3H), 2.06 (3H) (s, C$_5$*Me*$_4$), 5.66 (1H), 5.70 (1H), 7.01 (2H) (m, C$_5$*H*$_4$), 5.85 (m, 3H, CH$_2$=C*H*), 6.18 (m, 6H, C*H*$_2$=CH). ^{13}C{^{1}H} NMR (100 MHz, CDCl$_3$) (for the major isomer): δ 4.0, 4.6 (Si*Et*), 4.4, 6.9 (*C*H$_2$*C*H$_2$), 12.4, 15.1, 15.2 (C$_5$*Me*$_4$), 106.4 (C^{ipso}), 112.6, 112.9, 126.6, 127.0 (*C*$_5$H$_4$), 98.0, 125.8, 126.2, 135.9, 136.1 (*C*$_5$Me$_4$), 133.6, 135.2 (*C*H=*C*H$_2$). ^{29}Si{^{1}H} NMR (79.49 MHz, CDCl$_3$) (for the major isomer): δ −18.2 (*Si*CH=CH$_2$), −8.7 (*Si*C$_5$H$_4$). MS electron impact (*m*/*e* (relative intensity)): 538 (25) [M$^+$], 503 (8) [M$^+$ − Cl], 109 (100) [M$^+$ − Zr{CH$_2$CH$_2$Si(Et)(C$_5$Me$_4$)(C$_5$H$_4$)}Cl$_2$]. *Anal.* Calc. for C$_{24}$H$_{34}$Cl$_2$Si$_2$Zr: C, 53.30; H, 6.34. Found: C, 53.10; H, 6.31%.

5.36. [Ti{(CH$_2$=CH)Me$_2$SiCH$_2$CH$_2$(Et)Si(η^5-C$_5$Me$_4$)(η^5-C$_5$H$_4$)}Cl$_2$] (**24a**)

From SiMe$_2$(CH=CH$_2$)$_2$ (0.037 g, 0.41 mmol) and [Ti{Et(H)Si(η^5-C$_5$Me$_4$)(η^5-C$_5$H$_4$)}Cl$_2$] (**17a**) (0.15 g, 0.41 mmol). Yield: 0.18 g, 93%. IR (KBr): ν_{CH} 3050, $\nu_{CH=CH_2}$ 1599 cm^{-1}. ^{1}H NMR (400 MHz, CDCl$_3$) (for the major isomer): δ 0.18 (s, 6H, Si*Me*$_2$), 1.30 (3H), 1.41 (2H) (m, Si*Et*), 0.82 (2H), 1.28 (1H), 1.38 (1H) (m, C*H*$_2$C*H*$_2$), 1.86 (3H), 1.88 (3H), 2.15 (3H), 2.16 (3H) (s, C$_5$*Me*$_4$), 5.56 (1H), 5.58 (1H), 7.18 (2H) (m, C$_5$*H*$_4$), 5.76 (m, 1H, CH$_2$=C*H*), 6.11 (m, 2H, C*H*$_2$=CH). ^{13}C{^{1}H} NMR (100 MHz, CDCl$_3$) (for the major isomer): δ −3.8 (Si*Me*$_2$), 3.9, 4.4 (Si*Et*), 7.0, 7.1 (*C*H$_2$*C*H$_2$), 13.6, 13.7, 16.2, 16.3 (C$_5$*Me*$_4$), 104.0 (C^{ipso}), 116.1, 116.3, 132.8, 133.3 (*C*$_5$H$_4$), 98.6, 131.1, 131.7, 144.0, 144.2 (*C*$_5$Me$_4$), 132.5, 137.7 (*C*H=*C*H$_2$). ^{29}Si{^{1}H} NMR (79.49 MHz, CDCl$_3$) (for the major isomer): δ −7.9 (*Si* C$_5$H$_4$), −3.4 (*Si*CH=CH$_2$). MS electron impact (*m*/*e* (relative intensity)): 472 (38) [M$^+$], 436 (40) [M$^+$ − Cl], 85 (100) [M$^+$ − Ti{CH$_2$CH$_2$Si(Et)(C$_5$Me$_4$)(C$_5$H$_4$)}Cl$_2$], 59 (87) [M$^+$ − CH=CH$_2$, −Ti{CH$_2$CH$_2$Si(Et)(C$_5$Me$_4$)(C$_5$H$_4$)}Cl$_2$]. *Anal.* Calc. for C$_{22}$H$_{34}$Cl$_2$Si$_2$Ti: C, 55.81; H, 7.24. Found: C, 55.55; H, 7.14%.

5.37. [Zr{(CH_2=CH)Me_2SiCH_2CH_2(Et)Si-(η^5-C_5Me_4)(η^5-C_5H_4)}Cl_2] (**24b**)

From $SiMe_2(CH{=}CH_2)_2$ (0.042 g, 0.37 mmol) and [Zr{Et(H)Si(η^5-C_5Me_4)(η^5-C_5H_4)}Cl_2] (**17b**) (0.15 g, 0.37 mmol). Yield: 0.19 g, 98%. IR (KBr): ν_{CH} 3047, $\nu_{CH=CH_2}$ 1591 cm^{-1}. ^{1}H NMR (400 MHz, $CDCl_3$) (for the major isomer): δ 0.18 (s, 6H, Si*Me*$_2$), 1.30 (3H), 1.41 (2H) (m, Si*Et*), 0.80 (2H), 1.22 (1H), 1.31 (1H) (m, C*H*$_2$C*H*$_2$), 1.94 (3H), 1.97 (3H), 2.06 (6H) (s, C_5Me_4), 5.67 (1H), 5.71 (1H), 7.02 (2H) (m, C_5H_4), 5.75 (m, 1H, CH_2=C*H*), 6.13 (m, 2H, C*H*$_2$=CH). ^{13}C{^{1}H} NMR (100 MHz, $CDCl_3$) (for the major isomer): δ −3.8 (Si*Me*$_2$), 4.1, 4.5 (Si*Et*), 6.9, 7.0 (*C*H$_2$*C*H$_2$), 12.4, 12.5, 15.0, 15.1 (C_5Me_4), 106.0 (C^{ipso}), 112.6, 112.9, 126.5, 127.0 (C_5H_4), 98.2, 125.7, 126.3, 135.9, 136.1 (C_5Me_4), 132.4, 137.8 (*C*H=*C*H$_2$). ^{29}Si{^{1}H} NMR (79.49 MHz, $CDCl_3$) (for the major isomer): δ −8.8 (*Si*C_5H_4), −3.5 (*Si*CH=CH_2). MS electron impact (*m*/*e* (relative intensity)): 516 (17) [M^+], 478 (5) [M^+ − Cl], 85 (100) [M^+ − Zr{$CH_2CH_2Si(Et)(C_5Me_4)(C_5H_4)$}$Cl_2$], 59 (89) [$M^+$ − CH=CH_2, −Zr{$CH_2CH_2Si(Et)(C_5Me_4)(C_5H_4)$}$Cl_2$]. *Anal.* Calc. for $C_{22}H_{34}Cl_2Si_2Zr$: C, 51.13; H, 6.63. Found: C, 51.09; H, 6.61%.

5.38. [Zr{(Et_3SiCH_2CH_2)$_3$SiCH_2CH_2(Et)Si-(η^5-C$_5$-Me$_4$)(η^5-C_5H_4)}Cl_2] (**25b**)

From $HSiEt_3$ (0.098 g, 0.84 mmol) and [Zr{(CH_2=CH)$_3$SiCH_2CH_2(Et)Si(η^5-C_5Me_4)(η^5-C_5H_4)}Cl_2] (**23b**) (0.15 g, 0.28 mmol). Yield: 0.24 g, 97%. ^{1}H NMR (400 MHz, $CDCl_3$) (for the major isomer): δ 0.55 (q, 18H, SiC*H*$_2$CH$_3$), 0.97 (t, 27H, SiCH$_2$C*H*$_3$), 1.28 (3H), 1.42 (2H) (m, CpSi*Et*), 0.4–1.4 (m, 16H, SiC*H*$_2$C*H*$_2$Si), 1.97 (3H), 1.98 (3H), 2.07 (6H) (s, C_5Me_4), 5.66 (1H), 5.72 (1H), 7.02 (2H) (m, C_5H_4). ^{13}C{^{1}H} NMR (100 MHz, $CDCl_3$) (for the major isomer): δ 3.6, 4.9 (CpSi*Et*), 3.0, 7.7 (Si*Et*$_3$), 2.9, 3.3, 3.6, 6.9 (*C*H$_2$*C*H$_2$), 12.4, 15.0, 15.1 (C_5Me_4), 106.6 (C^{ipso}), 112.5, 113.0, 125.5, 126.2 (C_5H_4), 98.3, 125.6, 127.0, 135.8, 136.2 (C_5Me_4). ^{29}Si{^{1}H} NMR (79.49 MHz, $CDCl_3$) (for the major isomer): δ −9.1 (*Si*C_5H_4), 8.1 (*Si*Et$_3$), 9.6 (*Si*CH$_2$CH$_2$). MS chemical ionization with CH_4 (*m*/*e* (relative intensity)): 886 (1) [M^+], 121 (34) [M^+ − Zr{$Et_3Si(CH_2CH_2)_3SiCH_2CH_2(Et)Si(C_5H_4)$}$Cl_2$], 115 (100) [$SiEt_3^+$], 87 (33) [$SiEt_2^+$]. *Anal.* Calc. for $C_{42}H_{82}Cl_2Si_5Zr$: C, 56.70; H, 9.29. Found: C, 56.66; H, 9.30%.

5.39. [Zr{(Et_3SiCH_2CH_2)Me_2SiCH_2CH_2(Et)Si-(η^5-C_5Me_4)(η^5-C_5H_4)}Cl_2] (**26b**)

From $HSiEt_3$ (0.034 g, 0.29 mmol) and [Zr{(CH_2=CH)Me_2SiCH_2CH_2(Et)Si(η^5-C_5Me_4)(η^5-C_5H_4)}Cl_2] (**24b**) (0.15 g, 0.29 mmol). Yield: 0.17 g, 91%. ^{1}H NMR (400 MHz, $CDCl_3$) (for the major isomer): δ 0.07 (s, 6H, Si*Me*$_2$), 0.54 (q, 6H, SiC*H*$_2$CH$_3$), 0.96 (t, 9H, SiCH$_2$C*H*$_3$), 1.27 (3H), 1.40 (2H) (m, CpSi*Et*), 0.4–1.1 (m, 8H, SiC*H*$_2$C*H*$_2$Si), 1.96 (3H), 1.97 (3H), 2.06 (6H) (s, C_5Me_4), 5.67 (1H), 5.70 (1H), 7.02 (2H) (m, C_5H_4). ^{13}C{^{1}H} NMR (100 MHz, $CDCl_3$) (for the major isomer): δ −4.3 (Si*Me*$_2$), 4.0,4.6 (CpSi*Et*), 3.0, 7.6 (Si*Et*$_3$), 3.3, 6.1, 6.8, 6.9 (*C*H$_2$*C*H$_2$), 12.3, 12.4, 15.0, 15.1 (C_5Me_4), 106.7 (C^{ipso}), 112.6, 112.9, 126.5, 126.0 (C_5H_4), 98.3, 125.6, 126.3, 135.9, 136.1 (C_5Me_4). ^{29}Si{^{1}H} NMR (79.49 MHz, $CDCl_3$) (for the major isomer): δ −9.0 (*Si*C_5H_4), 6.3 (*Si*CH$_2$CH$_2$), 8.2 (*Si*Et$_3$). MS electron impact (*m*/*e* (relative intensity)): 630 (1) [M^+], 595 (2) [M^+ − Cl], 515 (2) [M^+ − Et_3Si], 481 (4) [M^+ − Cl, −Et_3Si], 115 (74) [$SiEt_3^+$], 93 (100) [M^+ − Zr(C_5Me_4)Cl_2, −$CH_2CH_2SiMe_2(CH_2CH_2SiEt_3)$, −Et]. *Anal.* Calc. for $C_{28}H_{50}Cl_2Si_3Zr$: C, 53.12; H, 7.96. Found: C, 53.44; H, 8.08%.

5.40. Synthesis of [Ti{Cl_2MeSiCH_2CH_2(Me)Si-(η^5-$C_5Me_4)_2$}Cl_2] (**29a**)

Two drops of the Karstedt catalyst (divinyltetramethylsiloxane Pt(0) in xylene (3–3.5%)) were added to a solution of [Ti{CH_2=CH(Me)Si(η^5-$C_5Me_4)_2$}Cl_2] (0.30 g, 0.70 mmol) in toluene (10 mL) and the mixture was stirred for 10 min at room temperature. To this solution was added dropwise $HSiMeCl_2$ (0.08 g, 0.70 mmol) and the reaction mixture was stirred for 2 h. The mixture was filtered and volatiles removed from the filtrate under reduced pressure to give the title product as a red crystalline solid (0.37 g, 97%). ^{1}H NMR (400 MHz, $CDCl_3$) (for the major isomer): δ 0.43 (s, 3H, CpSi*Me*), 0.55 (s, 3H, Cl_2Si*Me*), 1.00 (2H), 1.31 (2H) (m, C*H*$_2$C*H*$_2$), 1.64 (6H), 1.65 (6H), 2.06 (6H), 2.09 (6H) (s, C_5Me_4). ^{13}C{^{1}H} NMR (100 MHz, $CDCl_3$) (for the major isomer): δ 0.0 (CpSi*Me*), 2.4 (Cl_2Si*Me*), 4.4, 9.5 (*C*H$_2$*C*H$_2$), 14.1, 14.2, 16.3, 16.5 (C_5Me_4), 92.1, 128.5, 128.7, 143.2, 143.4 (C_5Me_4). ^{29}Si{^{1}H} NMR (79.49 MHz, $CDCl_3$) (for the major isomer): δ −9.5 (Cp*Si*Me), 33.0 (Cl_2*Si*Me). MS electron impact (*m*/*e* (relative intensity)): 546 (11) [M^+], 508 (23) [M^+ − Cl], 493 (100) [M^+ − Cl, −Me], 349 (13) [M^+ − $CH_2CH_2SiMeCl_2$, −Cl, −Me], 321 (22) [M^+ − $CH_2CH_2SiMeCl_2$, −Cl, −3 × Me], 286 (22) [M^+ − $CH_2CH_2SiMeCl_2$, −2 × Cl, −3 × Me]. *Anal.* Calc. for $C_{22}H_{34}Cl_4Si_2Ti$: C, 48.54; H, 6.30. Found: C, 48.33; H, 6.28%.

The preparation of **29b** and **30** was carried out in an identical manner to **29a**.

5.41. [Zr{Cl_2MeSiCH_2CH_2(Me)Si(η^5-$C_5Me_4)_2$}Cl_2] (**29b**)

From $HSiMeCl_2$ (0.11 g, 0.10 mmol) and [Zr{CH_2=CH(Me)Si(η^5-$C_5Me_4)_2$}Cl_2] (0.45 g, 0.10 mmol). Yield: 0.55 g, 96%. ^{1}H NMR (400 MHz, $CDCl_3$) (for the major

isomer): δ 0.42 (s, 3H, CpSi*Me*), 0.55 (s, 3H, Cl_2Si*Me*), 0.99 (2H), 1.32 (2H) (m, CH_2CH_2), 1.75 (6H), 1.76 (6H), 1.99 (6H), 2.02 (6H) (s, C_5Me_4). $^{13}C\{^1H\}$ NMR (100 MHz, $CDCl_3$) (for the major isomer): δ 0.1 (CpSi*Me*), 0.5 (Cl_2Si*Me*), 4.6, 10.0 (*C*H_2*C*H_2), 13.0, 13.1, 15.5, 15.6 (C_5Me_4), 93.0, 124.5, 125.2, 136.1, 136.2 (C_5Me$_4$). $^{29}Si\{^1H\}$ NMR (79.49 MHz, $CDCl_3$) (for the major isomer): δ −11.0 (Cp*Si*Me), 33.1 (Cl_2*Si*Me). MS electron impact (*m*/*e* (relative intensity)): 586 (35) [M^+], 549 (12) [M^+ − Cl], 535 (23) [M^+ − Cl, −Me], 445 (15) [M^+ − $CH_2CH_2SiMeCl_2$], 304 (100) [M^+ − Zr(C_5Me_4)Cl_2], 280 (40) [M^+ − C_5Me_4Si(Me)-$CH_2CH_2SiMeCl_2$]. *Anal.* Calc. for $C_{22}H_{34}Cl_4Si_2Zr$: C, 44.96; H, 5.83. Found: C, 44.58; H, 5.76%.

5.42. [Zr{$Cl_2MeSiCH_2CH_2CH_2(Me)Si(\eta^5$-$C_5Me_4)_2$}-$Cl_2$] (**30b**)

From $HSiMeCl_2$ (0.12 g, 0.11 mmol) and [Zr{CH_2=CHCH_2(Me)Si(η^5-$C_5Me_4)_2$}Cl_2] (0.52 g, 0.11 mmol). Yield: 0.61 g, 92%. ^{1}H NMR (400 MHz, $CDCl_3$) (for the major isomer): δ 0.38 (s, 3H, CpSi*Me*), 0.67 (s, 3H, Cl_2Si*Me*), 0.91 (2H), 0.93 (2H), 1.27 (2H) (m, CH_2CH_2CH_2), 1.75 (6H), 1.82 (6H), 2.00 (6H), 2.01 (6H) (s, C_5Me_4). $^{13}C\{^1H\}$ NMR (100 MHz, $CDCl_3$) (for the major isomer): δ 0.2 (CpSi*Me*), 2.2 (Cl_2Si*Me*), 17.2, 22.2, 25.9 (*C*H_2*C*H_2*C*H_2), 13.0, 13.1, 15.6, 15.7 (C_5Me_4), 93.0, 124.5, 125.3, 136.1, 136.2 (C_5Me$_4$). $^{29}Si\{^1H\}$ NMR (79.49 MHz, $CDCl_3$) (for the major isomer): δ −13.5 (Cp*Si*Me), 31.5 (Cl_2*Si*Me). MS electron impact (*m*/*e* (relative intensity)): 598 (100) [M^+], 564 (14) [M^+ − Cl], 549 (24) [M^+ − Cl, −Me], 486 (13) [M^+ − $SiMeCl_2$], 445 (23) [M^+ − $CH_2CH_2CH_2SiMeCl_2$]. *Anal.* Calc. for $C_{23}H_{36}Cl_4Si_2Zr$: C, 45.91; H, 6.03. Found: C, 45.44; H, 6.00%.

5.43. Polymerization of ethylene

The zirconocene catalyst (6 μmol), MAO (10% in toluene) (1800 μmol) and toluene (200 mL) were mixed together for 15 min in a 1 L glass autoclave. The N_2 pressure inside the autoclave was reduced by applying a vacuum. Ethylene pressure of 2 bar was then applied and maintained to the autoclave and stirring of the mixture commenced (1000 rpm). After exactly 15 min, stirring was halted and the ethylene pressure released. Excess MAO was then destroyed by adding cautiously a mixture of methanol/HCl (90:10). The polymer was isolated by filtration and washed with ethanol and dried under vacuum at 90 °C for 16 h.

5.44. X-ray structure determination of [Zr{CH_2=CH-$CH_2(H)Si(\eta^5$-$C_5Me_4)_2$}Cl_2] (**21b**)

Data were collected on a Bruker SMART CCD-based diffractometer operating at 50 kV and 30 mA, using ω/2θ scan-technique. Absorption corrections were applied using the SADABS program (maximum and minimum transmission coefficients 0.9608 and 0.7384). The structure was solved using the Bruker SHELXTL-PC software by direct methods and refined by full-matrix least-squares methods on F^2. All non-hydrogen atoms were refined anisotropically. Hydrogen atoms were included in calculated positions (except H(1) which was located in a difference map), and refined in the riding mode. Weights were optimized in the final cycles. Crystallographic data are given in Table 4.

5.45. X-ray structure determination of [Hf{CH_2=CH-$CH_2(H)Si(\eta^5$-$C_5Me_4)_2$}Cl_2] (**21c**)

Data were collected on a Bruker SMART CCD-based diffractometer operating at 50 kV and 100 mA, using ω/2θ scan-technique. The structure was solved using the SHELXS-97 software by direct methods and refined by full-matrix least-squares methods on F^2. All non-hydrogen atoms were refined anisotropically. Hydrogen atoms were included in calculated positions, and refined in the riding mode. Weights were optimized in the final cycles. Crystallographic data are given in Table 4.

Table 4
Crystal data and structure refinement for **21b** and **21c**

	21b	**21c**
Formula	$C_{21}H_{30}Cl_2SiZr$	$C_{24.5}H_{34}Cl_2HfSi$
Formula weight	472.66	606.022
T (K)	298(2)	100(2)
Crystal system	monoclinic	monoclinic
Space group	*C*2/*c*	*P*2(1)/*c*
a (Å)	30.62(3)	18.43380(10)
b (Å)	8.851(10)	10.01510(10)
c (Å)	17.175(18)	26.2604(2)
β (°)	110.58(7)	91.9560(10)
V (Å^3)	4357(8)	4845.27(7)
Z	8	8
D_c (g cm^{-3})	1.441	1.650
μ (mm^{-1})	0.807	10.513
F(000)	1952	2376
Crystal dimensions (mm)	0.40 × 0.15 × 0.05	0.25 × 0.20 × 0.12
θ range (°)	2.41 to 25.92	2.40 to 70.48
hkl ranges	$-37 \leqslant h \leqslant 36$, $-9 \leqslant k \leqslant 10$, $-14 \leqslant l \leqslant 21$	$-19 \leqslant h \leqslant 22$, $-10 \leqslant k \leqslant 11$, $-30 \leqslant l \leqslant 30$
Data/parameters	4177/256	8816/495
Goodness-of-fit on F^2	0.987	1.026
Final *R* indices [$I > 2\sigma(I)$]	R_1 = 0.0465, wR_2 = 0.1026	R_1 = 0.0509, wR_2 = 0.1146
R indices (all data)	R_1 = 0.0905, wR_2 = 0.1182	R_1 = 0.0543, wR_2 = 0.1171
Largest difference peak and hole (e Å^{-3})	0.507/−0.375	5.825/−4.816

$R_1 = \sum ||F_o| - |F_c|| / \sum |F_o|$;
$wR_2 = \{\sum[w(F_o^2 - F_c^2)^2] / \sum[w(F_o^2)^2]\}^{0.5}$.

6. Supplementary material

Crystallographic data for the structural analyses of **21b** and **21c** have been deposited with the Cambridge Crystallographic Data Centre, CCDC 261467 and 261468. Copies of this information may be obtained free of charge from The Director, CCDC, 12 Union Road, Cambridge CB2 1EZ, UK (Fax: +44 1223 336 033; e-mail: deposit@ccdc.cam.ac.uk or http//www.ccdc.cam.ac.uk).

Acknowledgements

We gratefully acknowledge financial support from the Ministerio de Educación y Ciencia, Spain (Grants No. BQU2002-04638-C02-01 and MAT2003-05345), the Junta de Comunidades de Castilla-La Mancha (PAC-02-003 and PAI-02-010), the Comunidad de Madrid (GR/MAT/0929/2004) and the Universidad Rey Juan Carlos (GVC-2004-12). We also thank Repsol-YPF for their assistance in the polymer analysis.

References

[1] See for example: (a) H.G. Alt, A. Köppl, Chem. Rev. 100 (2000) 1205;
(b) G.W. Coates, Chem. Rev. 100 (2000) 1223;
(c) L. Resconi, L. Cavallo, A. Fait, F. Piemontesi, Chem. Rev. 100 (2000) 1253;
(d) H.H. Brintzinger, D. Fischer, R. Mülhaupt, B. Reiger, R.M. Waymouth, Angew. Chem., Int. Ed. Engl. 36 (1995) 1143.

[2] (a) E.W. Abel, F.G.A. Stone, G. Wilkinson, M.F. Lappert (Eds.), 2nd ed., Comprehensive Organometallic Chemistry, 4, Pergamon Press, Oxford, 1995;
(b) B. Rieger, G. Jany, R. Fawzi, M. Steimann, Organometallics 13 (1994) 647.

[3] See for example: (a) S.L.J. Conway, T. Dijkstra, L.H. Doerrer, J.C. Green, M.L.H. Green, A.H.H. Stephens, J. Chem. Soc., Dalton Trans. (1998) 2689;
(b) J.H. Shin, G. Parkin, Chem. Commun. (1999) 887;
(c) H. Lee, B.M. Bridgewater, G. Parkin, J. Chem. Soc., Dalton Trans. (2000) 4490;
(d) P.J. Shapiro, Coord. Chem. Rev. 231 (2002) 67;
(e) C.E. Zachmanoglou, A. Docrat, B.M. Bridgewater, G. Parkin, C.G. Brandow, J.E. Bercaw, C.N. Jardine, M. Lyall, J.C. Green, J.B. Keister, J. Am. Chem. Soc. 124 (2002) 9525;
(f) L. Labella, A. Chernega, M.L.H. Green, J. Chem. Soc., Dalton Trans. (1995) 395.

[4] (a) G.C. Hlatky, Chem. Rev. 100 (2000) 1347;
(b) B.Y. Lee, J.S. Oh, Macromolecules 33 (2000) 3194;
(c) M. Galan-Fereres, T. Koch, E. Hey-Hawkins, M.S. Eisen, J. Organomet. Chem. 580 (1999) 145;
(d) B.Y. Lee, J.S. Oh, J. Organomet. Chem. 552 (1998) 313.

[5] See for example: (a) J. Tian, Y. Soo-Ko, R. Metcalf, Y. Feng, S. Collins, Macromolecules 34 (2001) 3120;
(b) L.K. Van Looveren, D.F. Geysen, K.A. Vercruysse, B.H. Wouters, P.J. Grobet, P.A. Jacobs, Angew. Chem., Int. Ed. 37 (1998) 517;
(c) J. Tudor, D. O'Hare, Chem. Commun. (1997) 603;
(d) N. Suzuki, J. Yu, N. Shioda, H. Asami, T. Nakamura, T. Huhn, A. Fukuoka, M. Ichikawa, M. Saburi, Y. Wakatsuki, Appl. Catal. A 224 (2002) 63;
(e) C.J. Miller, D. O'Hare, Chem. Commun. (2004) 1710.

[6] (a) H.G. Alt, R. Ernst, I. Böhmer, J. Mol. Catal. A 191 (2003) 177;
(b) H.G. Alt, R. Ernst, Inorg. Chim. Acta 350 (2003) 1;
(c) H.G. Alt, R. Ernst, J. Mol. Catal. A 195 (2003) 11.

[7] D. Seyferth, R. Wyrwa, US Pat. 5969073, 1999.

[8] (a) A. Antiñolo, I. López-Solera, I. Orive, A. Otero, S. Prashar, A.M. Rodríguez, E. Villaseñor, Organometallics 20 (2001) 71;
(b) A. Antiñolo, I. López-Solera, A. Otero, S. Prashar, A.M. Rodríguez, E. Villaseñor, Organometallics 21 (2002) 2460;
(c) C. Alonso-Moreno, A. Antiñolo, I. López-Solera, A. Otero, S. Prashar, A.M. Rodríguez, E. Villaseñor, J. Organomet. Chem. 656 (2002) 129;
(d) A. Antiñolo, R. Fernández-Galán, I. Orive, A. Otero, S. Prashar, Eur. J. Inorg. Chem. (2002) 2470;
(e) A. Antiñolo, M. Fajardo, S. Gómez-Ruiz, I. López-Solera, A. Otero, S. Prashar, A.M. Rodríguez, J. Organomet. Chem. 683 (2003) 11;
(f) A. Antiñolo, R. Fernández-Galán, B. Gallego, A. Otero, S. Prashar, A.M. Rodríguez, Eur. J. Inorg. Chem. (2003) 2626;
(g) A. Antiñolo, R. Fernández-Galán, A. Otero, S. Prashar, I. Rivilla, A.M. Rodríguez, M.A. Maestro, Organometallics 23 (2004) 5108.

[9] A. Antiñolo, M. Fajardo, S. Gómez-Ruiz, I. López-Solera, A. Otero, S. Prashar, Organometallics 23 (2004) 4062.

[10] T. Koch, S. Blaurock, F.B. Somoza, A. Voigt, R. Kirmse, E. Hey-Hawkins, Organometallics 19 (2000) 2556.

[11] C. Takayama, Y. Yamaguchi, T. Mise, N. Suzuki, J. Chem. Soc., Dalton Trans. (2001) 948.

[12] N. Suzuki, Y. Masubuchi, Y. Yamaguchi, T. Kase, T.K. Miyamoto, A. Horiuchi, T. Mise, Macromolecules 33 (2000) 754.

[13] (a) J.L. Speier, Adv. Organomet. Chem. 17 (1979) 407;
(b) L.N. Lewis, J. Am. Chem. Soc. 112 (1990) 5998.

[14] S.W. Krska, D. Seyferth, J. Am. Chem. Soc. 120 (1998) 3604.

[15] S. Gómez-Ruiz, Doctoral Thesis, Univ. Rey Juan Carlos, 2004.

[16] R. Andrés, E. de Jesús, F.J. de la Mata, J.C. Flores, R. Gómez, Eur. J. Inorg. Chem. (2002) 2281.

[17] H. Zhu, G.-X. Jin, N. Hu, J. Organomet. Chem. 655 (2002) 167.

[18] T.K. Panda, M.T. Gamer, P.W. Roesky, Organometallics 22 (2003) 877.

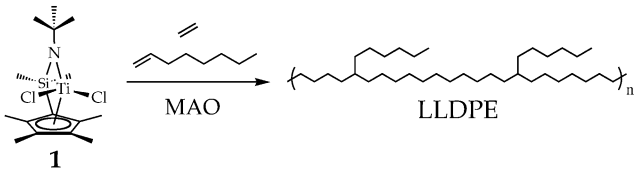


Fig. 1. The titanium *ansa*-tetramethylcyclopentadienyl-amido precatalyst **1**, upon activation with methylaluminoxane (MAO), readily copolymerizes ethylene and α-olefins to form linear low density polyethylene (LLDPE).

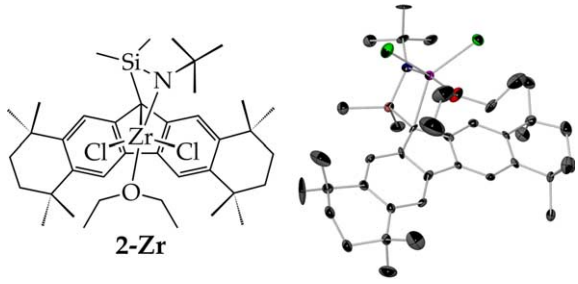


Fig. 2. The first CGC with η^1 ligation to the carbon-based five-membered ring [26]. X-ray structure of **2-Zr** with thermal ellipsoids drawn at 50% probability and hydrogen atoms omitted.

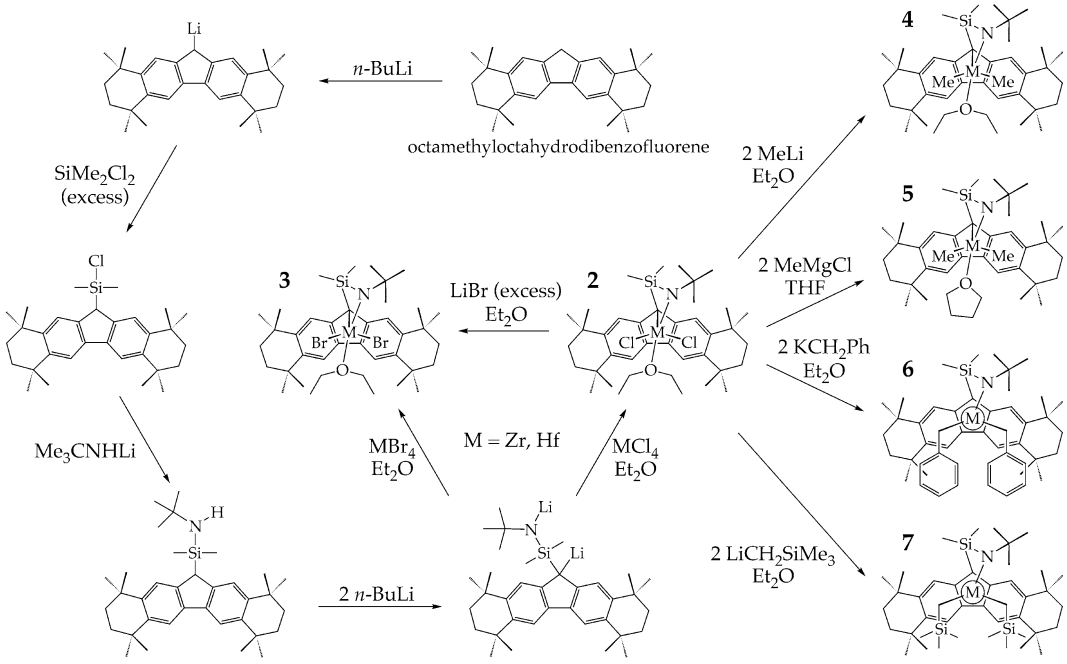
contain the η^1-Oct motif. These structures are compared to alkylated derivates with normal η^5-Oct binding in the context of quantifying and understanding this variable hapticity, which may be related to the unusual preference toward α-olefins over ethylene that **2-Zr**/MAO can exhibit.

2. Results and discussion

2.1. Synthesis of Zr and Hf complexes

The synthesis of zirconium and hafnium Oct-amido complexes (Scheme 1) parallels that of Okuda for the synthesis of zirconium fluorenyl-amido complexes [18]. Octamethyloctahydrodibenzofluorene [27] is deprotonated with *n*-butyllithium [25,28] and transferred into a hexane solution containing excess dimethyldichlorosilane. Subsequent reaction with Me_3CNHLi, followed by double deprotonation with *n*-butyllithium and combination with $ZrCl_4$ or $HfCl_4$ provides **2-Zr** or **2-Hf**. Interestingly, these five steps can be performed in two flasks (OctLi must be added to excess $SiMe_2Cl_2$), without isolation of the intermediates or their separation from salts, to yield 17 g of **2-Zr** as yellow microcrystals in 31.6% overall yield. The dibromide **3-Zr** was obtained from $ZrBr_4$. Additionally, we have shown that **3-Zr** and **3-Hf** can be synthesized from the dichlorides **2-Zr** and **2-Hf** via direct halide exchange with an excess of LiBr in diethyl ether.

2-Zr and **2-Hf** are readily derivatized with alkylating agents. The use of methyllithium with diethyl ether as solvent provides diethyl ether adducts **4-Zr** and **4-Hf**, whereas with methylmagnesium chloride in the presence of tetrahydrofuran, THF adducts **5-Zr** and **5-Hf** are obtained. The use of larger alkylating agents does not afford ethereal adducts. The dibenzyl species **6-Zr** and **6-Hf** are made from benzyl potassium and the bis(trimethylsilylmethyl) species **7-Zr** and **7-Hf** are made from trimethylsilylmethyllithium.



Scheme 1. Synthetic route to zirconium and hafnium *ansa*-Oct-amido complexes **2**–**7**.

2.2. X-ray crystallography of Zr and Hf complexes

Crystals suitable for X-ray crystallography were obtained for complexes **3-Zr**, **3-Hf,** and **5-Zr** by cooling saturated diethyl ether solutions. Crystals of **6-Zr** and **6-Hf** were grown by vapor diffusion of diethyl ether into saturated dichloromethane solutions, while crystals of **7-Zr** were obtained by cooling a saturated pentane solution. Fig. 3 depicts the structural results of the X-ray crystallography.

It is readily apparent that ethereal solvents remain bound to the metal in **3-Zr**, **3-Hf**, and **5-Zr**, resulting in a trigonal bipyramid with oxygen and nitrogen in the apical positions. This trigonal bipyramid structure is unprecedented for fluorenyl-amido complexes; even the remarkably similar $Me_2Si(\eta^5\text{-}2,7\text{-}^tBu_2\text{-}C_{13}H_6)(\eta^1\text{-}N\text{-}^tBu)ZrCl_2$ [29,30] and $Me_2Si(\eta^5\text{-}3,6\text{-}^tBu_2\text{-}C_{13}H_6)(\eta^1\text{-}N\text{-}^tBu)ZrCl_2$ [23,31] adopt the η^5, pseudotetrahedral geometry. Apparently there is an important difference between a 2,3,6,7-*tetra*-substituted fluorenyl ligand (Oct) and a *di*-substituted fluorenyl ligand. **3-Zr** and **3-Hf** are isomorphic, and only **5-Zr** cocrystallizes with solvent, packing one diethyl ether molecule into the cleft of each Oct ligand. In this case, note the selectivity of the metal to bind THF despite the use of diethyl ether as the crystallization solvent.

6-Zr, **6-Hf**, and **7-Zr**, which bear the larger benzyl or trimethylsilylmethyl groups, crystallize as ether-free species with a pseudotetrahedral coordination sphere and η^5 ligation to Oct. **6-Zr** and **6-Hf** are isomorphic and each of these structures contains one benzyl group that is arguably η^2. The M–CH_2Ph bond length is 2.295 Å for **6-Zr** (2.299 Å for **6-Hf**) and the M–(C_{ipso}) distance is 2.793 Å for **6-Zr** (2.871 Å for **6-Hf**). The structure of **7-Zr** is quite similar to that published for the parent fluorenyl-containing compound, $Me_2Si(\eta^5\text{-}C_{13}H_8)(\eta^1\text{-}N\text{-}^tBu)Zr(CH_2SiMe_3)_2$ [18].

Table 1 lists selected bond lengths and angles for **2-Zr** [26], **3-Zr**, **3-Hf**, **5-Zr**, **6-Zr**, **6-Hf**, and **7-Zr**. In the η^1

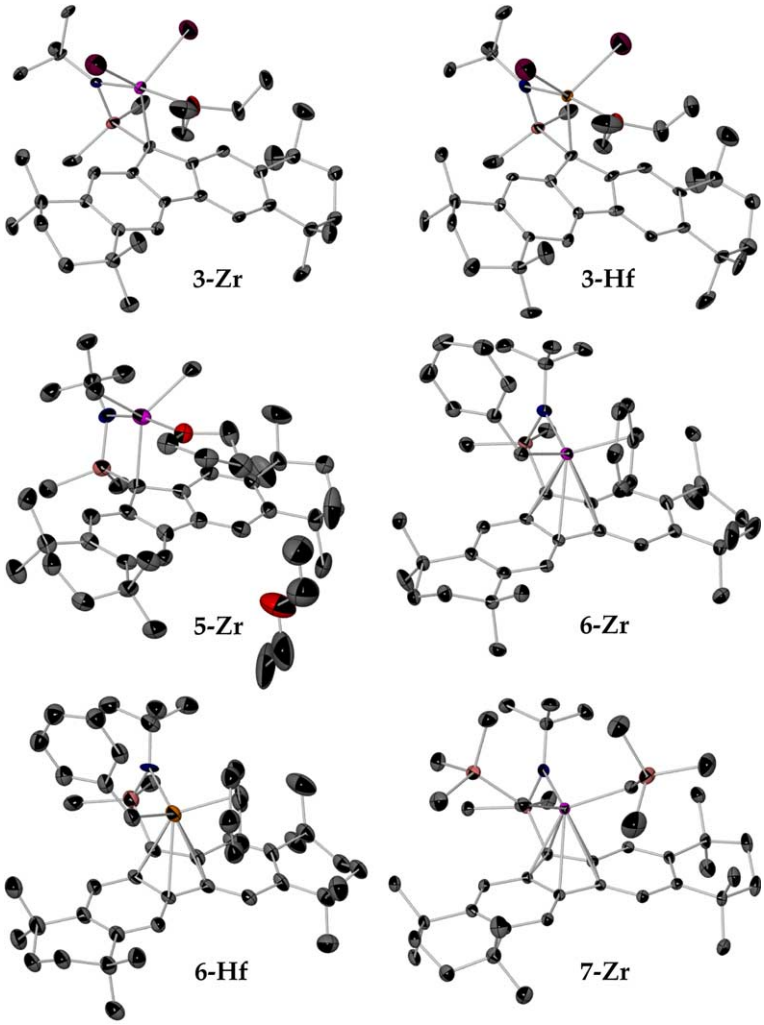


Fig. 3. X-ray structures of **3-Zr**, **3-Hf**, **5-Zr**, **6-Zr**, **6-Hf**, and **7-Zr** with thermal ellipsoids drawn at 50% probability and hydrogen atoms omitted.

Table 1
Selected bond lengths (Å) and angles (°)

Complex	M–C(1)	M–N	M–X(1)	M–X(2)	M–O	*cent*-C(1)–Si[a]	Si–N–M	X–M–X	N–M–O
2-Zr ($Cl_2 \cdot Et_2O$)	2.299(7)	2.013(5)	2.4155(19)	2.3918(18)	2.330(5)	203.67	99.1(2)	112.92(7)	169.87(19)
3-Zr ($Br_2 \cdot Et_2O$)	2.300(8)	2.019(6)	2.5427(13)	2.5387(13)	2.322(6)	202.78	99.0(3)	112.31(5)	169.6(2)
3-Hf ($Br_2 \cdot Et_2O$)	2.281(8)	2.022(7)	2.5112(14)	2.4974(15)	2.297(6)	204.90	98.8(3)	111.93(5)	167.1(3)
5-Zr ($Me_2 \cdot THF$)	2.330(5)	2.068(4)	2.240(6)	2.274(5)	2.280(4)	197.86	99.3(2)	111.8(2)	167.05(16)
6-Zr ($(CH_2Ph)_2$)	2.397(2)	2.052(2)	2.295(2)	2.316(2)		156.80	103.47(9)	116.20(9)	
6-Hf ($(CH_2Ph)_2$)	2.373(1)	2.087(8)	2.299(9)	2.305(11)		155.80	99.9(4)	111.6(4)	
7-Zr ($(CH_2SiMe_3)_2$)	2.390(2)	2.0648(18)	2.249(2)	2.265(2)		156.46	102.85(9)	107.30(8)	

[a] *cent* is defined as the centroid of the five-membered ring of the Oct ligand.

trigonal bipyramidal structures, the metal–C(1) bond lengths are consistently shorter (2.281–2.330 Å) than the corresponding bond lengths in the η^5 pseudotetrahedral structures (2.373–2.397 Å). The shortening of the remaining M–C bond upon η^5 to η^1 ring-slip is typical for cyclopentadienyl [32] and indenyl ligands [33]. In *ansa*-metallocenes and cyclopentadienyl-amido complexes, the $C_{5centroid}$–C(1)–Si angle is always less than 180°; examples are *rac*-$Me_2Si(\eta^5\text{-}C_9H_6)_2ZrCl_2$ (163.7°) [34] and $Me_2Si(\eta^5\text{-}C_5Me_4)(\eta^1\text{-}N\text{-}^tBu)TiCl_2$ (152.3°) [35]. For the η^5 complexes in Table 1, this angle is ~156°, a typical value. Strikingly, the $C_{5centroid}$–C(1)–Si angles for the η^1 complexes are considerably larger than 180° and range from 197.9° to 204.9°. Thus, *the silicon atom and the metal are on opposite sides of the Oct ligand.* This results in the most sterically open class of CGCs reported.

2.3. Hapticity analysis of Zr and Hf complexes by X-ray crystallography

While η^5-fluorenyl ligands are the most common [36–40], a number of η^3-fluorenyl examples have also been documented [41–46]. In contrast, η^1-fluorenyl ligands are quite rare. The first definitive examples were found with octahedral mid-transition metal species such as $Mn(\eta^1\text{-}C_{13}H_9)(CO)_3(P(n\text{-}Bu)_3)_2$ [47], $Mn(\eta^1\text{-}C_{13}H_9)(CO)_3(PEt_3)_2$ [48], and $Re(\eta^1\text{-}C_{13}H_9)(CO)_5$ [49,50]. Later, examples were found with early transition metal species such as pseudotetrahedral $(\eta^5\text{-}C_5H_4Me)_2Zr(\eta^1\text{-}C_{13}H_9)Cl$, $(\eta^5\text{-}C_5H_5)_2Zr(\eta^1\text{-}C_{13}H_9)_2$ [51], and pseudotrigonal bipyramidal $Me_2C(\eta^5\text{-}C_5H_4)(\eta^1\text{-}C_{13}H_8)TaMe_3$ [52].

The assignment of hapticity can sometimes be arbitrary [53], but the metrical parameters cataloged in

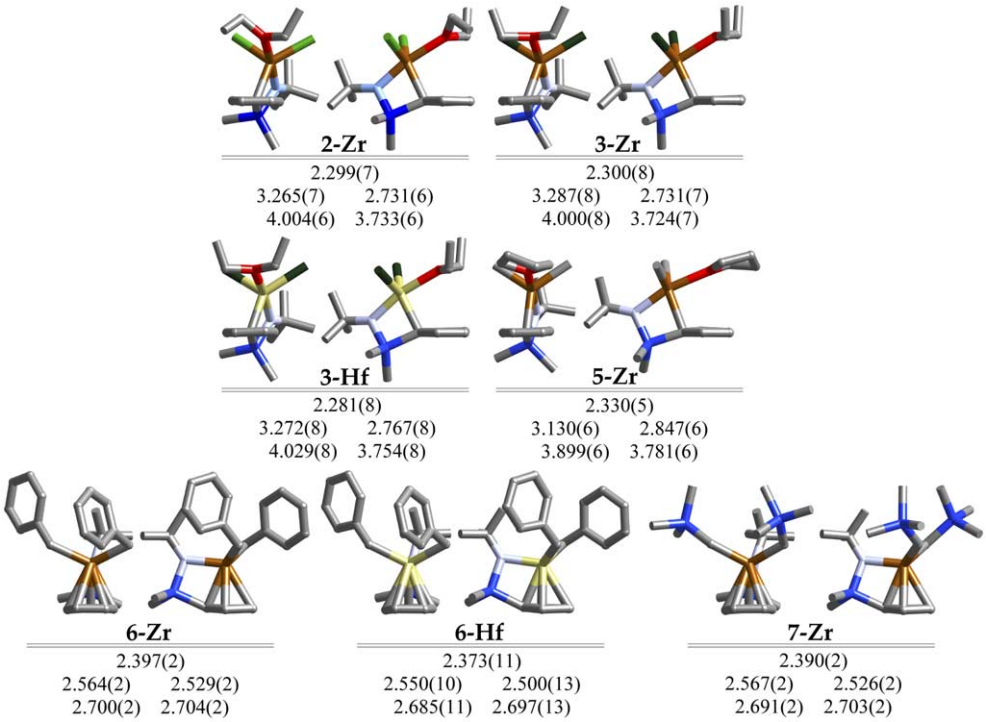


Fig. 4. Structures of **2-Zr**, **3-Zr**, **3-Hf**, **5-Zr**, **6-Zr**, **6-Hf**, and **7-Zr** with the Oct ligand truncated to the five-membered ring. Bond lengths and interatomic distances (Å) correspond to the metal–Oct interaction, moving clockwise from the C(1) carbon.

Fig. 4 largely support the conclusion that **2-Zr**, **3-Zr**, **3-Hf**, and **5-Zr** are η^1, while **6-Zr**, **6-Hf**, and **7-Zr** are η^5. Assignments from the literature place the threshold for zirconium–carbon bonding between 2.65 and 2.81 Å [41,54]. For example, the two "non-bonded" carbons in $(\eta^5\text{-}C_{13}H_9)(\eta^3\text{-}C_{13}H_9)ZrCl_2$ are 2.801 and 2.807 Å from the metal while the remaining eight "bonded" carbons are between 2.395 and 2.645 Å away [42]. In $Re(\eta^1\text{-}C_{13}H_9)(CO)_5$ the bonded carbon is 2.307 Å from rhenium while the four unequivocally non-bonded carbons are between 3.193 and 4.149 Å from the metal [50]. In structures **2-Zr**, **3-Zr**, **3-Hf**, and **5-Zr**, the bonded carbon is between 2.281 and 2.330 Å from the metal. Each structure has one metal–carbon interatomic distance between 2.731 and 2.847 Å, which is at the upper limit of the bonding range. The remaining three distances for each structure are at least 3.130 Å, considerably beyond normal zirconium–carbon or hafnium–carbon bond lengths.

An alternative method for assessing hapticity is by measurement of the carbon–carbon bond lengths of the five-membered ring. In octamethyloctahydrodibenzofluorene, long bonds are found connecting the sp^3 carbon to the aromatic rings (1.515 Å) and short bonds are found as part of the aromatic rings (1.401 Å) [26]. The parameter δ can be defined as the difference between these bond lengths – or average difference for non-symmetrical species – as defined in Fig. 5. Table 2 lists carbon–carbon bond lengths and the calculated parameter δ for a variety of fluorenyl- and Oct-containing compounds. The entries are listed in order of *decreasing* δ, which corresponds to *increasing* hapticity since the carbon–carbon bond lengths are predicted to become more similar as an η^5, aromatic cyclopentadienide core is approached.

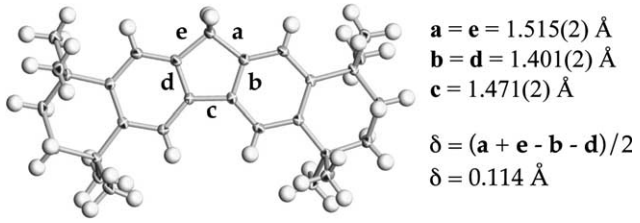


Fig. 5. The bond length difference parameter δ is 0.114 Å for octamethyloctahydrodibenzofluorene and is predicted to decrease with increasing hapticity.

The largest value of δ (0.095 Å) is found for $Re(\eta^1\text{-}C_{13}H_9)(CO)_5$, an electronically ($18e^-$) and coordinatively (octahedral) saturated compound that cannot increase its η^1 hapticity with the fluorenyl ligand. Although $(\eta^5\text{-}C_5H_4Me)_2Zr(\eta^1\text{-}C_{13}H_9)Cl$ and $Me_2C(\eta^5\text{-}C_5H_4)(\eta^1\text{-}C_{13}H_8)TaMe_3$ are not electronically saturated, sterics probably dissuade a greater hapticity, resulting in a high δ value (0.081 for both). The next three species are **3-Hf**, **3-Zr**, and **5-Zr**, which have δ values of 0.069, 0.066, and 0.047 Å, respectively, which still indicate significant carbon–carbon bond length differences. This last value is also found for a complex reported as η^3, $Mo(\eta^3\text{-}C_{13}H_9)(\eta^3\text{-}C_3H_5)_3$. The remaining twelve compounds, including **6-Zr**, **7-Zr**, and **6-Hf**, have δ values of 0.030 Å or less and are predicted to be η^5. Three anomalies exist in this range: $(\eta^5\text{-}C_{13}H_9)(\eta^3\text{-}C_{13}H_9)ZrCl_2$ ($\delta = 0.025$), which is reported as η^3; **2-Zr** ($\delta = 0.021$), which is reported as η^1; and fluorenylLi$(Et_2O)_2$ ($\delta = -0.018$), which is reported as η^2. It

Table 2
Carbon–carbon bond lengths of the fluorenyl or Oct five-membered ring along with the bond length difference parameter $\delta = (a + e - b - d)/2$ in Å

Compound	*a*	*b*	*c*	*d*	*e*	δ	References
OctH ($C_{29}H_{38}$)	1.515(2)	1.401(2)	1.471(2)	1.401(2)	1.515(2)	0.114	[26]
Fluorene ($C_{13}H_{10}$)	1.504(2)	1.397(2)	1.472(3)	1.397(2)	1.504(2)	0.107	[55]
$Re(\eta^1\text{-}C_{13}H_9)(CO)_5$	1.506	1.405	1.451	1.417	1.505	0.095	[50]
$(\eta^5\text{-}C_5H_4Me)_2Zr(\eta^1\text{-}C_{13}H_9)Cl$	1.505(5)	1.415(5)	1.461(5)	1.405(5)	1.477(5)	0.081	[51]
$Me_2C(\eta^5\text{-}C_5H_4)(\eta^1\text{-}C_{13}H_8)TaMe_3$	1.502(4)	1.417(5)	1.448(4)	1.417(4)	1.493(4)	0.081	[52]
3-Hf ($Br_2 \cdot Et_2O$)	1.485(10)	1.410(10)	1.479(11)	1.409(10)	1.472(12)	0.069	this work
3-Zr ($Br_2 \cdot Et_2O$)	1.474(11)	1.439(10)	1.449(11)	1.383(11)	1.479(12)	0.066	this work
5-Zr ($Me_2 \cdot THF$)	1.459(8)	1.428(7)	1.445(8)	1.417(8)	1.480(7)	0.047	this work
$Mo(\eta^3\text{-}C_{13}H_9)(\eta^3\text{-}C_3H_5)_3$	1.476(3)	1.407(3)	1.465(4)	1.433(3)	1.458(3)	0.047	[43]
$Me_2Si(\eta^5\text{-}3,6\text{-}^tBu_2\text{-}C_{13}H_6)(\eta^1\text{-}N\text{-}^tBu)ZrCl_2$	1.46(1)	1.43(1)	1.46(1)	1.42(1)	1.45(1)	0.030	[23]
6-Zr ($(CH_2Ph)_2$)	1.455(3)	1.426(3)	1.447(3)	1.430(3)	1.459(3)	0.029	this work
7-Zr ($(CH_2SiMe_3)_2$)	1.453(3)	1.426(3)	1.454(3)	1.421(3)	1.448(3)	0.027	this work
6-Hf ($(CH_2Ph)_2$)	1.454(14)	1.416(12)	1.447(14)	1.445(14)	1.459(13)	0.026	this work
$(\eta^5\text{-}C_{13}H_9)(\eta^3\text{-}C_{13}H_9)ZrCl_2$	1.50	1.41	1.47	1.43	1.39	0.025	[42]
2-Zr ($Cl_2 \cdot Et_2O$)	1.468(9)	1.431(8)	1.434(8)	1.437(9)	1.441(9)	0.021	[26]
$Me_2Si(\eta^5\text{-}C_{13}H_8)(\eta^1\text{-}N\text{-}^tBu)Zr(CH_2SiMe_3)_2$	1.450(4)	1.426(4)	1.442(4)	1.431(4)	1.442(4)	0.018	[18]
$Me_2C(\eta^5\text{-}C_5H_4)(\eta^5\text{-}C_{29}H_{36})ZrCl_2$	1.449(5)	1.431(5)	1.434(5)	1.440(5)	1.443(5)	0.011	[56]
$Ph_2C(\eta^5\text{-}C_5H_4)(\eta^5\text{-}C_{29}H_{36})ZrCl_2$	1.457(6)	1.430(6)	1.443(6)	1.458(6)	1.447(6)	0.008	[25]
$(\eta^5\text{-}C_{13}\mathbf{H}_9)(\eta^3\text{-}C_{13}H_9)ZrCl_2$	1.44	1.42	1.44	1.44	1.43	0.005	[42]
$Me_2C(\eta^5\text{-}C_5H_4)(\eta^5\text{-}C_{13}H_8)ZrCl_2$	1.45(1)	1.44(1)	1.43(1)	1.44(1)	1.43(1)	0.000	[57]
FluorenylLi$(Et_2O)_2$	1.424(4)	1.443(4)	1.434(4)	1.443(5)	1.426(5)	−0.018	[40]

Table 3
Selected ^{1}H NMR and ^{13}C NMR chemical shifts (ppm) for Oct–Zr species: aromatic C–*H* in the 1 and 4 positions; M–*C*(1); and aromatic *C* (in C_6D_6 except **7-Zr**, recorded in $CDCl_3$)

Compound	*H*	*H*	*C*(1)	*C*	*C*	*C*	*C*	*C*	*C*	References
OctH ($C_{29}H_{38}$)	7.46	7.98	36.5	117.5	123.3	140.3	141.4	143.4	143.6	this work
2-Zr ($Cl_2 \cdot Et_2O$)	8.01	8.24	71.9	121.5	123.2	125.3	134.8	145.6	148.9	[26]
3-Zr ($Br_2 \cdot Et_2O$)	8.01	8.27	72.0	122.0	124.0	126.0	134.6	146.0	148.8	this work
4-Zr ($Me_2 \cdot Et_2O$)	7.93	8.23	70.8	120.6	122.7	123.7	135.0	142.6	146.7	this work
5-Zr ($Me_2 \cdot THF$)	7.82	8.15	86.3	117.4	118.5	133.6	137.6	139.7	141.9	this work
6-Zr ($(CH_2Ph)_2$)	8.15	8.16	73.9	120.1	122.0	122.7	134.1	145.7	147.0	this work
7-Zr ($(CH_2SiMe_3)_2$)	7.92	8.17	71.1	120.1	122.5	123.2	133.9	142.7	146.1	this work
$Me_2Si(\eta^1\text{-}C_{29}H_{36})(\eta^1\text{-N-}^t\text{Bu})ZrCl_2 \cdot THF$	7.94	8.02	96.5	117.6	119.1	135.8	138.7	139.7	143.0	this work
$Me_2Si(\eta^1\text{-}C_{29}H_{36})(\eta^1\text{-N-}^t\text{Bu})ZrBr_2 \cdot NCMe$	8.03	8.03	93.0	117.0	121.2	134.6	139.6	141.4	142.8	this work

should be noted that δ is an *indirect* measure of hapticity. It only measures carbon–carbon bond length distortions that occur in response to a metal's location and bonding. Thus, δ and hapticity are reasonably correlative, but the exceptions remind us that hapticity is best determined by measuring metal–carbon interatomic distances.

2.4. Hapticity analysis of Zr complexes in solution by NMR

The solution ^{1}H NMR spectra of the diethyl ether complexes (**2-Zr**, **2-Hf**, **3-Zr**, **3-Hf**, **4-Zr**, and **4-Hf**) show sharp resonances for the ethereal protons, a trait usually attributed to unbound ether species. Thus suggests solution species with η^5-Oct ligation. The THF adducts, however, provide somewhat broad resonances for the ethereal protons, indicating that THF coordination and low Oct hapticity are maintained in solution. Careful inspection of the ^{1}H and ^{13}C NMR chemical shifts of compounds **2-Zr** through **7-Zr** indeed reveals unusual chemical shifts for only the THF adduct **5-Zr** (Table 3). The aromatic C–H protons in the 1 and 4 positions of the Oct moiety are the most upfield of this group at 7.82 and 8.15 ppm. The M–C(1) carbon is the most downfield (86.3 ppm) and, of the aromatic carbons, two have comparatively high chemical shifts (133.6 and 137.6 ppm) and four have comparatively low chemical shifts (117.4, 118.5, 139.7 and 141.9 ppm). These unusual chemical shifts for **5-Zr** are mirrored in $Me_2Si(\eta^1\text{-}C_{29}H_{36})(\eta^1\text{-N-}^t\text{Bu})ZrCl_2 \cdot THF$ and $Me_2Si(\eta^1\text{-}C_{29}H_{36})(\eta^1\text{-N-}^t\text{Bu})ZrBr_2 \cdot NCMe$ (see Table 3), suggesting that each of these also maintains η^1-Oct ligation in solution.

3. Conclusions

A series of sterically expanded *ansa*-fluorenyl-amido zirconium and hafnium complexes with the general formula $Me_2Si(\eta^n\text{-}C_{29}H_{36})(\eta^1\text{-N-}^t\text{Bu})MX_2 \cdot L_m$ was synthesized and characterized. Incorporation of the octamethyloctahydrodibenzofluorenyl (Oct) ligand effected ethereal binding in the solid-state when the remaining ligands were small (X = Cl, Br, or Me). Ether-free species were observed when larger ligands (X = benzyl or trimethylsilylmethyl) were present. X-ray crystallography established that an unusual trigonal bipyramidal η^1-Oct structure accompanied ethereal binding ($n = 1$, $m = 1$), while the ether-free species adopted the anticipated pseudotetrahedral η^5-Oct structure ($n = 5$, $m = 0$). The hapticity assignments were made largely by analyzing the relevant metal–carbon distances, but a correlation between hapticity and converging carbon–carbon bond lengths of the five-membered ring was also identified.

4. Experimental

4.1. General remarks

All air sensitive procedures were carried out under a purified atmosphere of nitrogen in a glove box equipped with a −35 °C freezer, or by using standard Schlenk line techniques. Solvents were dried and distilled under nitrogen into Straus flasks and stored until needed. Diethyl ether and tetrahydrofuran were distilled from sodium/benzophenone; *n*-heptane and dichloromethane were distilled from calcium hydride; and toluene was distilled from elemental sodium.

The commercially available reagents *n*-butyllithium (Acros, 2.5 M in hexanes or Alfa Aesar, 2.87 M in hexanes), $LiCH_2SiMe_3$ (Aldrich, 1.0 M in pentane), MeLi (Aldrich, 1.6 M in diethyl ether), MeMgCl (Aldrich, 3.0 M in tetrahydrofuran), zirconium tetrachloride (Strem, 99.5+%), hafnium tetrachloride (Strem, 99.9+%), zirconium tetrabromide (Strem, 98%), and lithium bromide (Aldrich, 99.995+%) were used as received, unless otherwise noted. Both KCH_2Ph [58] and the ligand $Me_3CNHSiMe_2(C_{29}H_{37})$ [26] were prepared according to literature procedures.

All NMR chemical shifts are given in ppm and were recorded on a Mercury-300BB spectrometer (^{1}H, 299.91 MHz; ^{13}C {^{1}H}, 75.41 MHz) using the residual

protonated solvent peak as an internal standard ($CDCl_3$: ^1H, 7.27 ppm; ^{13}C, 77.0 ppm. C_6D_6: ^1H, 7.15 ppm; ^{13}C, 128.0 ppm).

4.2. Syntheses

4.2.1. Synthesis of $Me_2Si(\eta^1\text{-}C_{29}H_{36})(\eta^1\text{-}N\text{-}^tBu)ZrCl_2 \cdot OEt_2$ (**2-Zr**)

In the glove box $Me_3CNHSiMe_2(C_{29}H_{37})$ (3.00 g, 6.26 mmol) was charged into a 100 ml pear-shaped round bottom and then attached to a 3 cm swivel frit. The frit was then evacuated and diethyl ether (50 ml) was vacuum transferred in. Next, *n*-butyllithium (5.51 ml, 13.77 mmol, 2.5 M in hexanes) was syringed in. The orange slurry was stirred for 20 h and then the diethyl ether was removed under vacuum. $ZrCl_4$ (1.46 g, 6.26 mmol) was added in the glove box and diethyl ether (40 ml) was vacuum transferred in on the line. After slowly warming to room temperature and stirring the light brown slurry for 48 h, the LiCl was filtered off and the cake was extracted until colorless. The slurry was concentrated to about 10 ml and the precipitated solid was collected by filtration. The cake was washed once to remove a brown oil and then evacuated until dry. This yielded 1.42 g (31.8%) of product as a neon yellow solid. Large rod-shaped crystals can be grown by cooling a saturated diethyl ether solution to −35 °C. ^1H NMR (C_6D_6): δ 0.86 (s, 6H, $(CH_3)_2Si$), 1.10 (t, $^3J_{HH}$ = 7.0 Hz, 6H, ether–CH_3), 1.26 (s, 9H, –$C(CH_3)_3$), 1.28, 1.35, 1.38, 1.39 (s, 24H, Oct–CH_3), 1.62 (m, 8H, Oct–CH_2), 3.25 (q, $^3J_{HH}$ = 7.0 Hz, 4H, ether–CH_2), 8.01, 8.24 (s, 4H, Oct–CH_1). ^{13}C {^1H} NMR (C_6D_6): δ 5.9, 15.5, 32.3, 32.6, 32.8, 32.9, 33.4, 34.95, 35.02, 35.3, 35.4, 56.4, 66.0, 71.9, 121.5, 123.2, 125.3, 134.8, 145.6, 148.9. Elemental analysis: *Anal.* Calc.: C, 62.44; H, 8.13; N, 1.87; Cl, 9.45. Found: C, 61.40; H, 8.24; N, 1.81; Cl, 9.45%.

4.2.2. Synthesis of $Me_2Si(\eta^1\text{-}C_{29}H_{36})(\eta^1\text{-}N\text{-}^tBu)HfCl_2 \cdot OEt_2$ (**2-Hf**)

2-Hf was prepared in a manner analogous to **2-Zr** except that $HfCl_4$ (3.34 g, 10.43 mmol) was utilized yielding 3.30 g (39.5%) of **2-Hf** as a yellow solid. ^1H NMR (C_6D_6): δ 0.84 (s, 6H, $(CH_3)_2Si$), 0.99 (t, $^3J_{HH}$ = 6.0 Hz, 6H, ether–CH_3), 1.31, 1.34, 1.39, 1.42 (s, 24H, Oct–CH_3), 1.37 (s, 9H, –$C(CH_3)_3$), 1.65 (app. s, 8H, Oct–CH_2), 3.19 (q, $^3J_{HH}$ = 6.0 Hz, 4H, ether–CH_2), 7.99, 8.22 (s, 4H, Oct–CH_1).

4.2.3. Synthesis of $Me_2Si(\eta^1\text{-}C_{29}H_{36})(\eta^1\text{-}N\text{-}^tBu)ZrBr_2 \cdot OEt_2$ (**3-Zr**)

3-Zr was prepared in a manner analogous to **2-Zr** except that $ZrBr_4$ (2.57 g, 6.26 mmol) was utilized yielding 1.30 g (24.8%) of **3-Zr** as a bright yellow powder. Large rod-shaped crystals can be grown by cooling a saturated diethyl ether solution to −35 °C. ^1H NMR (C_6D_6): δ 0.86 (s, 6H, $(CH_3)_2Si$), 1.11 (t, $^3J_{HH}$ = 7.0 Hz, 6H, ether–CH_3), 1.27, 1.34, 1.39, 1.41 (s, 24H, Oct–CH_3), 1.31 (s, 9H, –$C(CH_3)_3$), 1.61 (m, 8H, Oct–CH_2), 3.26 (q, $^3J_{HH}$ = 7.0 Hz, 4H, ether–CH_2), 8.01, 8.27 (s, 4H, Oct–CH_1). ^{13}C {^1H} NMR (C_6D_6): δ 5.8, 15.5, 32.1, 32.7, 33.0, 34.98, 35.0, 35.3, 35.4, 56.9, 65.9, 72.0, 122.0, 124.0, 126.0, 134.6, 146.0, 148.8.

4.2.4. Synthesis of $Me_2Si(\eta^1\text{-}C_{29}H_{36})(\eta^1\text{-}N\text{-}^tBu)HfBr_2 \cdot OEt_2$ (**3-Hf**)

In the glove box, **2-Hf** (0.13 g, 0.16 mmol) was charged into a 100 ml pear-shaped round bottom flask followed by the addition of anhydrous LiBr (4.90 g, 56.42 mmol). Next, the flask was attached to a 3 cm swivel frit and brought out to the line where diethyl ether (60 ml) was vacuum transferred in. The slurry was then stirred for 2 days after which time the solvent was removed under vacuum and pentane (30 ml) was vacuum transferred in. All insoluble material was removed via filtration and the cake was extracted until colorless. Concentration of the filtrate to 5 ml followed by filtration yielded 0.07 g (69.0%) of **3-Hf** as an orange-yellow powder. Large rod-shaped crystals can be grown by cooling a saturated diethyl ether solution to −35 °C. X-ray crystallography suggested that complete salt metathesis of the Hf–Cl bonds had been achieved. This was further supported by ^1H NMR via a characteristic shift of the aromatic Oct–CH_1 protons from 8.22 ppm (**2-Hf**) to 8.26 ppm (**3-Hf**). A similar shift is observed between **2-Zr** and **3-Zr**. ^1H NMR (C_6D_6): δ 0.89 (s, 6H, $(CH_3)_2Si$), 1.03 (t, $^3J_{HH}$ = 6.0 Hz, 6H, ether–CH_3), 1.28, 1.31, 1.35, 1.36 (s, 24H, Oct–CH_3), 1.32 (s, 9H, –$C(CH_3)_3$), 1.63 (m, 8H, Oct–CH_2), 3.19 (q, $^3J_{HH}$ = 6.0 Hz, 4H, ether–CH_2), 8.00, 8.26 (s, 4H, Oct–CH_1).

4.2.5. Synthesis of $Me_2Si(\eta^1\text{-}C_{29}H_{36})(\eta^1\text{-}N\text{-}^tBu)ZrMe_2 \cdot OEt_2$ (**4-Zr**)

In the glove box **2-Zr** (0.50 g, 0.67 mmol) was charged into a 100 ml pear-shaped round bottom flask, which was then attached to a 3 cm swivel frit. The frit was evacuated on the vacuum line and diethyl ether (50 ml) was then vacuum transferred in. Next, a LiBr-free diethyl ether solution of CH_3Li (0.83 ml, 1.33 mmol, 1.6 M in diethyl ether) was slowly syringed into the yellow solution while vigorously stirring. The solution began to bleach and acquire a very pale fluorescent yellow color. (Note: Extended exposure to excess CH_3Li leads to a dark brown/black solution and complete decomposition of the product in a matter of hours.) After 2 h the precipitated LiCl was removed via filtration and extracted until colorless. Concentration of the filtrate to 10 ml and collection of the precipitated product on the frit led to 0.42 g (89.0%) of product as a pale yellow solid. ^1H NMR (C_6D_6): δ −0.59 (s, 6H, $Zr(CH_3)_2$), 0.89 (s, 6H, $(CH_3)_2Si$), 1.10 (t, $^3J_{HH}$ = 7.0 Hz, 6H, ether–CH_3), 1.32, 1.37 (s, 24H,

Oct–CH_3), 1.33 (s, 9H, –C(CH_3)$_3$), 1.64 (m, 8H, Oct–CH_2), 3.24 (q, $^3J_{HH}$ = 7.0 Hz, 4H, ether–CH_2), 7.93, 8.23 (s, 4H, Oct–CH_1). ^{13}C {^{1}H} NMR (C_6D_6): δ 6.6, 15.5, 32.6, 32.8, 32.9, 33.2, 34.5, 34.8, 35.2, 35.55, 35.57, 39.4, 55.0, 65.9, 70.8, 120.6, 122.7, 123.7, 135.0, 142.6, 146.7.

4.2.6. Synthesis of $Me_2Si(\eta^1\text{-}C_{29}H_{36})(\eta^1\text{-}N\text{-}^tBu)HfMe_2 \cdot OEt_2$ (**4-Hf**)

4-Hf was prepared in a manner analogous to **4-Zr** except that **2-Hf** (0.40 g, 0.49 mmol) was utilized yielding 0.23 g (60.5%) of **4-Hf** as a pale yellow powder. ^{1}H NMR (C_6D_6): δ −0.16 (s, 6H, Hf(CH_3)$_2$), 0.84 (s, 6H, (CH_3)$_2$Si), 1.02 (t, $^3J_{HH}$ = 6.0 Hz, 6H, ether–CH_3), 1.34, 1.35, 1.36, 1.38 (s, 24H, Oct–CH_3), 1.37 (s, 9H, –C(CH_3)$_3$), 1.66 (app. s, 8H, Oct–CH_2), 3.17 (q, $^3J_{HH}$ = 6.0 Hz, 4H, ether–CH_2), 7.84, 8.21 (s, 4H, Oct–CH_1).

4.2.7. Synthesis of $Me_2Si(\eta^1\text{-}C_{29}H_{36})(\eta^1\text{-}N\text{-}^tBu)ZrMe_2 \cdot THF$ (**5-Zr**)

In the glove box, **2-Zr** (5.00 g, 6.67 mmol) was charged into a 100 ml pear-shaped round bottom flask. The flask was then attached to a 3 cm swivel frit and diethyl ether (80 ml) was vacuum transferred in on the line. Next, while the flask was still cold, MeMgCl (4.44 ml, 13.33 mmol, 3.0 M in THF) was slowly added via syringe. A large quantity of white precipitate immediately formed. The contents of the flask were stirred for 2 h before the precipitated salt was removed by filtration. The cake was extracted until the eluent was colorless. The solvent was then removed under vacuum and the frit was brought into the box where the off-white product was recrystallized by cooling a saturated diethyl ether solution to −35 °C, yielding 2.98 g (63.0%) of product as nearly white crystals which were suitable for X-ray diffraction. ^{1}H NMR (C_6D_6): δ 0.02 (s, 6H, Zr(CH_3)$_2$), 0.77 (s, 6H, (CH_3)$_2$Si), 1.14 (br, 4H, THF–CH_2), 1.34, 1.37, 1.40, 1.43 (s, 24H, Oct–CH_3), 1.52 (s, 9H, –C(CH_3)$_3$), 1.69 (m, 8H, Oct–CH_2), 2.81 (br, 4H, THF–CH_2), 7.82, 8.15 (s, 4H, Oct–CH_1). ^{13}C {^{1}H} NMR (C_6D_6): δ 3.9, 15.5, 32.6, 32.7, 32.9, 33.3, 34.5, 34.8, 35.0, 35.9, 36.0, 39.7, 57.2, 65.8, 86.3, 117.4, 118.5, 133.6, 137.6, 139.7, 141.9.

4.2.8. Synthesis of $Me_2Si(\eta^1\text{-}C_{29}H_{36})(\eta^1\text{-}N\text{-}^tBu)HfMe_2 \cdot THF$ (**5-Hf**)

5-Hf was prepared in a manner analogous to **5-Zr** except that **2-Hf** (0.43 g, 0.54 mmol) was utilized yielding 0.43 g of **5-Hf** as an off-white solid (>95% yield, some persistent THF). ^{1}H NMR (C_6D_6): δ 0.29 (s, 6H, Hf(CH_3)$_2$), 0.70 (s, 6H, (CH_3)$_2$Si), 1.01 (br, 4H, THF–CH_2), 1.33, 1.40, 1.45, 1.48 (s, 24H, Oct–CH_3), 1.67 (s, 9H, –C(CH_3)$_3$), 1.73 (m, 8H, Oct–CH_2), 2.41 (br, 4H, THF–CH_2), 7.67, 8.13 (s, 4H, Oct–CH_1). ^{13}C {^{1}H} NMR (C_6D_6): δ 3.8, 15.9, 25.8, 33.0, 33.03, 33.3, 33.7, 34.9, 35.4, 35.5, 36.2, 36.4, 51.4, 66.2, 71.6, 117.5, 118.8, 126.6, 133.8, 137.9, 142.0.

4.2.9. Synthesis of $Me_2Si(\eta^5\text{-}C_{29}H_{36})(\eta^1\text{-}N\text{-}^tBu)Zr(CH_2Ph)_2$ (**6-Zr**)

In the glove box, **2-Zr** (4.00 g, 5.33 mmol) was charged into a 100 ml pear-shaped round bottom flask followed by the addition of KCH_2Ph (1.39 g, 10.66 mmol). The flask was then attached to a 3 cm swivel frit and brought out onto the line where diethyl ether (60 ml) was vacuum transferred in. The contents were allowed to slowly warm to room temperature and then stir for 2 h before the salt was removed by filtration and the cake extracted until colorless. Concentration of the slurry to 20 ml, followed by filtration, led to the desired product as a yellow solid (3.21 g, 76.5%). Large block-like crystals were grown by the vapor diffusion of diethyl ether into dichloromethane saturated with **6-Zr**. ^{1}H NMR (C_6D_6): δ −0.48, 0.86 (d, $^2J_{HH}$ = 10.5 Hz, 4H, Zr–CH_2), 0.99 (s, 9H, –C(CH_3)$_3$), 1.01 (s, 6H, (CH_3)$_2$Si), 1.34, 1.38, 1.39, 1.42 (s, 24H, Oct–CH_3), 1.62 (m, 8H, Oct–CH_2), 6.69 (m, 4H, Zr–$CH_2C_6H_5$), 6.89 (m, 2H, Zr–$CH_2C_6H_5$), 7.16 (m, 4H, Zr–$CH_2C_6H_5$), 8.15, 8.16 (s, 4H, Oct–CH_1). ^{13}C {^{1}H} NMR ($CDCl_3$): δ 6.2, 32.4, 32.6, 32.8, 33.0, 33.5, 34.8, 35.06, 35.08, 35.09, 56.9, 61.3, 73.1, 119.8, 121.2, 122.2, 123.1, 127.5, 128.8, 133.4, 143.5, 145.5, 146.8. ^{13}C {^{1}H} NMR (C_6D_6): δ 6.4, 32.57, 32.6, 33.06, 33.1, 33.6, 34.9, 35.2, 35.26, 35.3, 57.2, 61.9, 73.9, 120.1, 122.0, 122.7, 123.6, 128.3, 129.3, 134.1, 143.7, 145.7, 147.0

4.2.10. Synthesis of $Me_2Si(\eta^5\text{-}C_{29}H_{36})(\eta^1\text{-}N\text{-}^tBu)Hf(CH_2Ph)_2$ (**6-Hf**)

6-Hf was prepared in a manner analogous to **6-Zr** except that **2-Hf** (1.50 g, 1.87 mmol) was utilized yielding 0.42 g (25.8%) of **6-Hf** as a yellow-orange solid. Large block-like crystals were grown by the vapor diffusion of diethyl ether into dichlormethane saturated with **6-Hf**. ^{1}H NMR (C_6D_6): δ −0.30, 0.66 (d, $^2J_{HH}$ = 7.2 Hz, 4H, Hf–CH_2), 0.95 (s, 6H, (CH_3)$_2$Si), 1.01 (s, 9H, –C(CH_3)$_3$), 1.33, 1.34, 1.35, 1.36 (s, 24H, Oct–CH_3), 1.57 (m, 8H, Oct–CH_2), 6.65 (m, 4H, Hf–$CH_2C_6H_5$), 6.82 (m, 2H, Hf–$CH_2C_6H_5$), 7.12 (m, 4H, Hf–$CH_2C_6H_5$), 8.04, 8.26 (s, 4H, Oct–CH_1). ^{13}C {^{1}H} NMR ($CDCl_3$): δ 6.2, 32.5, 32.6, 33.0, 33.6, 33.7, 34.9, 35.0, 35.08, 35.1, 55.9, 70.4, 71.4, 120.0, 121.1, 122.4, 122.7, 127.5, 128.0, 134.1, 143.5, 146.5, 147.4.

4.2.11. Synthesis of $Me_2Si(\eta^5\text{-}C_{29}H_{36})(\eta^1\text{-}N\text{-}^tBu)Zr(CH_2SiMe_3)_2$ (**7-Zr**)

In the glove box, **2-Zr** (0.50 g, 0.67 mmol) was charged into a 100 ml pear-shaped round bottom flask. The flask was then attached to a 3 cm swivel frit and brought out to the vacuum line where pentane (50 ml) was vacuum transferred in. Next, $LiCH_2SiMe_3$ (1.40 ml, 1.40 mmol, 1.0 M in pentane) was slowly

Table 4
Crystallographic data summary

Compound	**3-Zr** ($Br_2 \cdot Et_2O$)	**3-Hf** ($Br_2 \cdot Et_2O$)	**5-Zr** ($Me_2 \cdot THF$)	**6-Zr** ($(CH_2Ph)_2$)	**6-Hf** ($(CH_2Ph)_2$)	**7-Zr** ($(CH_2SiMe_3)_2$)
Empirical formula	$C_{39}H_{61}Br_2NOSiZr$	$C_{39}H_{61}Br_2NOSiHf$	$C_{45}H_{75}NO_2SiZr$	$C_{49}H_{65}NSiZr$	$C_{49}H_{65}NSiHf$	$C_{43}H_{73}NSi_3Zr$
Formula weight	839.02	926.29	781.36	787.33	874.60	779.53
Temperature (K)	110(2)	110(2)	110(2)	110(2)	110(2)	110(2)
Wavelength (Å)	1.54184	0.71073	1.54184	0.71073	1.54184	0.71073
Crystal system	monoclinic	monoclinic	monoclinic	monoclinic	monoclinic	monoclinic
Space group	*Cc*	*Cc*	$P2_1/c$	$P2_1/n$	P_1/n	$P2_1$
a (Å)	24.122(3)	24.094(10)	12.564(7)	14.6594(14)	14.630(3)	12.980(4)
b (Å)	11.7263(11)	11.765(5)	25.347(8)	16.0990(15)	16.103(3)	20.326(5)
c (Å)	15.0453(16)	15.069(7)	14.555(6)	18.1773(17)	18.162(4)	17.152(5)
α (°)	90	90	90	90	90	90
β (°)	109.000(6)	108.847(7)	107.60(3)	95.952(2)	95.410(9)	93.840(4)
γ (°)	90	90	90	90	90	90
Volume (Å^3)	4023.9(7)	4042(3)	4418(3)	4271.9(7)	4259.6(14)	4515(2)
Z	4	4	8	4	4	5
D_{calc} (g cm^{-3})	1.385	1.522	1.175	1.224	1.364	1.147
μ (mm^{-1})	5.059	4.616	2.548	0.319	5.033	0.351
Crystal size (mm^3)	$0.50 \times 0.01 \times 0.01$	$0.22 \times 0.21 \times 0.08$	$0.10 \times 0.05 \times 0.05$	$0.42 \times 0.39 \times 0.27$	$0.20 \times 0.20 \times 0.05$	$0.60 \times 0.40 \times 0.20$
Reflections	22767	15407	41117	48123	31312	42757
Independent reflections	5158	6476	6237	9745	6016	19672
Data/restraints/parameters	5158/314/445	6476/17/434	6237/1/461	9745/0/491	6016/349/470	19672/1/866
GOF (F^2)	1.005	1.078	1.037	1.215	1.020	1.066
R_1 [$I > 2\sigma(I)$]	0.0489	0.0381	0.0592	0.0540	0.0595	0.0310
wR_2 [$I > 2\sigma(I)$]	0.1192	0.0990	0.1262	0.1312	0.1148	0.0790
R_1 (all data)	0.0620	0.0409	0.1078	0.0645	0.1594	0.0325
wR_2 (all data)	0.1257	0.1009	0.1425	0.1498	0.1381	0.0800
Largest differential peak, hole (e Å^{-3})	0.676, −0.0943	1.792, −1.381	0.819, −1.428	2.320, −0.655	1.634, −1.517	0.713, −0.356

syringed into the still cold solution in the flask. The contents were allowed to stir for 1 h before the LiCl was removed by filtration and the salt was extracted until colorless. The solvent was removed under vacuum yielding a yellow foam. This was brought into the box where 5 ml of pentane was added causing the precipitation of a neon yellow powder. The solvent was decanted and the powder collected and dried under vacuum yielding 0.35 g (67.0%) of **7-Zr**. Pentane (5 ml) was then saturated with **7-Zr** and stored in a −35 °C freezer for one month, resulting in the formation of large block-like crystals. ^{1}H NMR (C_6D_6): δ −1.32, −0.77 (d, $^2J_{HH}$ = 12.3 Hz, 4H, Zr–CH_2), 0.17 (s, 18H, –Si(CH_3)$_3$), 0.89 (s, 6H, (CH_3)$_2$Si), 1.31 (s, 9H, –C(CH_3)$_3$), 1.39, 1.41, 1.41, 1.49 (s, 24H, Oct–CH_3), 1.68 (m, 8H, Oct–CH_2), 7.92, 8.17 (s, 4H, Oct–CH_1). ^{13}C {^{1}H} NMR ($CDCl_3$): δ 3.3, 6.3, 32.2, 32.9, 33.1, 33.3, 34.3, 34.9, 35.08, 35.1, 35.3, 55.0, 55.9, 71.1, 120.1, 122.5, 123.2, 133.9, 142.7, 146.1.

4.2.12. Synthesis of $Me_2Si(\eta^5\text{-}C_{29}H_{36})(\eta^1\text{-}N\text{-}^tBu)Hf(CH_2SiMe_3)_2$ (7-Hf)

7-Hf was prepared in a manner analogous to **7-Zr** except that **2-Hf** (0.40 g, 0.49 mmol) was utilized yielding 0.24 g (54.5%) of **7-Hf** as a yellow powder. ^{1}H NMR ($CDCl_3$): δ −2.09, −1.38 (d, $^2J_{HH}$ = 12.0 Hz, 4H, Hf–CH_2), −0.11 (s, 18H, –Si(CH_3)$_3$), 0.89 (s, 6H, (CH_3)$_2$Si), 1.33, 1.35, 1.46, 1.49 (s, 24H, Oct–CH_3), 1.37 (s, 9H, –C(CH_3)$_3$), 1.79 (app. s, 8H, Oct–CH_2), 7.72, 8.02 (s, 4H, Oct–CH_1).

4.3. Crystallographic studies

Crystals were mounted at room temperature in mineral oil, and affixed to a glass fiber. X-ray crystallographic data were obtained using a Bruker SMART 1000 three-circle diffractometer operating at 50 kV and 40 mA, Mo Kα (λ = 0.71073 Å) with a graphite monochromator and a CCD-PXL-KAF2 detector or a Bruker GADPS instrument operating at 40 kV and 40 mA, Cu Kα (λ = 1.54578 Å) with a graphite monochromator and a CCD-PXL-KAF2 detector. Details of the crystallographic data collection and refinement are summarized in Table 4. The molecular structures were solved by direct methods and were refined employing the SHELXS-97 [59] and SHELXL-97 programs [60].

5. Supplementary material

Crystallographic data for **3-Zr** (CCDC 260056), **3-Hf** (CCDC 260057), **5-Zr** (CCDC 260058), **6-Zr** (CCDC

260055), **6-Hf** (CCDC 260059), and **7-Zr** (CCDC 260060) have been deposited with the Cambridge Crystallographic Data Centre. These data can be obtained free of charge via www.ccdc.cam.ac.uk/data_request/cif, or by emailing data_request@ccdc.cam.ac.uk, or by contacting The Cambridge Crystallographic Data Centre, 12, Union Road, Cambridge CB2 1EZ, UK; fax: +44 1223 336033.

Acknowledgements

This research is supported by grants from The Robert A. Welch Foundation (No. A-1537) and the Texas Advanced Technology Program (No. 010366-0196-2003).

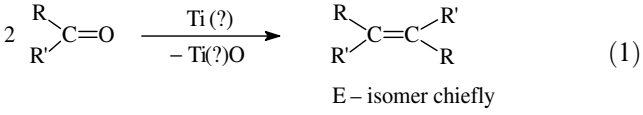
References

[1] Chemical Market Associates, Inc. (CMAI), 2003 World polyolefins analysis. Available from: www.cmaiglobal.com.
[2] K.W. Swogger, in: G.M. Benedikt (Ed.), Metallocene Technology in Commercial Applications, Plastics Design Library, Norwich, New York, 1999, pp. 283–291.
[3] C.S. Bajgur, S. Sivaram, Current Sci. 78 (2000) 1325.
[4] J. Scheirs, W. Kaminsky (Eds.), Metallocene-based Polyolefins: Preparation, Properties and Technology, John Wiley and Sons, New York, 2000.
[5] A.O. Patil, G.G. Hlatky (Eds.), Beyond Metallocenes: Next-generation Polymerization Catalysts, American Chemical Society, Washington, DC, 2003.
[6] A.L. McKnight, R.M. Waymouth, Chem. Rev. 98 (1998) 2587.
[7] J.C. Stevens, F.J. Timmers, D.R. Wilson, G.F. Schmidt, P.N. Nickias, R.K. Rosen, G.W. Knight, S.Y. Lai, Eur. Patent Appl. EP 416815-A2, 1991.
[8] J.M. Canich, Eur. Patent Appl. EP 420436-A1, 1991.
[9] D.D. Devore, F.J. Timmers, D.L. Hasha, R.K. Rosen, T.J. Marks, P.A. Deck, C.L. Stern, Organometallics 14 (1995) 3132.
[10] P.S. Chum, W.J. Kruper, M.J. Guest, Adv. Mater. 12 (2000) 1759.
[11] P.J. Shapiro, E. Bunel, W.P. Schaefer, J.E. Bercaw, Organometallics 9 (1990) 867.
[12] P.J. Shapiro, W.D. Cotter, W.P. Schaefer, J.A. Labinger, J.E. Bercaw, J. Am. Chem. Soc. 116 (1994) 4623.
[13] R.E. LaPointe, J.C. Stevens, P.N. Nickias, M.H. McAdon, Eur. Pat. Appl. 0520732A1, 1992.
[14] P.N. Nickias, M.H. McAdon, J.T. Patton, PCT Int. Appl. WO 97/15583 (1997).
[15] A.L. McKnight, M.A. Masood, R.M. Waymouth, D.A. Straus, Organometallics 16 (1997) 2879.
[16] E. Ruckenstein, G. Xu, Macromolecules 31 (1998) 4724.
[17] G. Xu, D. Cheng, Macromolecules 34 (2001) 2040.
[18] J. Okuda, F.J. Schattenmann, S. Wocadlo, W. Massa, Organometallics 14 (1995) 789.
[19] H.V.R. Dias, Z. Wang, S.G. Bott, J. Organomet. Chem. 508 (1996) 91.
[20] H.V.R. Dias, Z. Wang, J. Organomet. Chem. 539 (1997) 77.
[21] G. Xu, Macromolecules 31 (1998) 2395.
[22] H.G. Alt, K. Fottinger, W. Milius, J. Organomet. Chem. 572 (1999) 21.
[23] A. Razavi, U. Thewalt, J. Organomet. Chem. 621 (2001) 267.
[24] E. Kirillov, L. Toupet, C.W. Lehmann, A. Razavi, J.-F. Carpentier, Organometallics 22 (2003) 4467.
[25] S.A. Miller, J.E. Bercaw, Organometallics 23 (2004) 1777.
[26] L.J. Irwin, J.H. Reibenspies, S.A. Miller, J. Am. Chem. Soc. 126 (2004) 16716.
[27] R. Guilhemat, M. Pereyre, M. Petraud, Bull. Soc. Chim. Fr. 2 (1980) 334.
[28] S.A. Miller, J.E. Bercaw, US Patent 6,469,188, 2002.
[29] A. Razavi, US Patent 6,448,349, 2002.
[30] A. Razavi, V. Bellia, Y. De Brauwer, K. Hortmann, L. Peters, S. Sirole, S. Van Belle, U. Thewalt, Macromolecular Symposia 213 (2004) 157.
[31] A. Razavi, D. Baekelmans, V. Bellia, Y. De Brauwer, K. Hortmann, M. Lambrecht, O. Miserque, L. Peters, M. Slawinski, S. Van Belle, in: R. Blom, A. Follestad, E. Rytter, M. Tilset, M. Ystenes (Eds.), Organometallic Catalysts and Olefin Polymerization, Springer, Berlin, 2001, pp. 267–279.
[32] J.L. Calderon, F.A. Cotton, P. Legzdins, J. Am. Chem Soc. 91 (1969) 2528.
[33] C. Sui-Seng, G.D. Enright, D. Zargarian, Organometallics 23 (2004) 1236.
[34] V.A. Dang, L.-C. Yu, D. Balboni, T. Dall'Occo, L. Resconi, P. Mercandelli, M. Moret, A. Sironi, Organometallics 18 (1999) 3781.
[35] J. Zemánek, P. Stepnicka, K. Fejfarova, R. Gyepes, I. Cisarová, M. Horácek, J. Kubista, V. Varga, K. Mach, Collect. Czech. Chem. Commun. 66 (2001) 605.
[36] J.A. Ewen, R.L. Jones, A. Razavi, J.D. Ferrara, J. Am. Chem. Soc. 110 (1988) 6255.
[37] A. Razavi, D. Vereecke, L. Peters, K. Den Dauw, L. Nafpliotis, J.L. Atwood, in: G. Fink, R. Mülhaupt, H.-H. Brintzinger (Eds.), Ziegler Catalysts, Recent Scientific Innovations and Technological Improvements, Springer, Berlin, 1995, pp. 111–147.
[38] L. Resconi, L. Cavallo, A. Fait, F. Piemontesi, Chem. Rev. 100 (2000) 1253.
[39] A brief review of the various binding modes of the fluorenyl ligand can be found in: E. Kirillov, L. Toupet, C.W. Lehmann, A. Razavi, S. Kahlal, J.-Y. Saillard, J.-F. Carpentier, Organometallics 22 (2003) 4038.
[40] Various binding modes for fluorenyllithium have been addressed computationally: M. Hakansson, C.-H. Ottosson, A. Boman, D. Johnels, Organometallics 17 (1998) 1208.
[41] C. Kowala, P.C. Wailes, H. Weigold, J.A. Wunderlich, J. Chem. Soc. Chem. Commun. 23 (1974) 993.
[42] C. Kowala, J. Wunderlich, Acta Cryst. B32 (1976) 820.
[43] O. Andell, R. Goddard, S. Holle, P.W. Jolly, C. Krueger, Y.H. Tsay, Polyhedron 8 (1989) 203.
[44] M. Bochmann, S.J. Lancaster, M.B. Hursthouse, M. Mazid, Organometallics 12 (1993) 4718.
[45] M.J. Calhorda, I.S. Goncalves, E. Herdtweck, C.C. Romao, B. Royo, L.F. Veiros, Organometallics 18 (1999) 3956.
[46] M.J. Calhorda, I.S. Goncalves, B.J. Goodfellow, E. Herdtweck, C.C. Romao, B. Royo, L.F. Veiros, New J. Chem. 26 (2002) 1552.
[47] L.N. Ji, M.E. Rerek, F. Basolo, Organometallics 3 (1984) 745.
[48] R.N. Biagioni, I.M. Lorkovic, J. Skelton, J.B. Hartung, Organometallics 9 (1990) 547.
[49] K.M. Young, T.M. Miller, M.S. Wrighton, J. Am. Chem. Soc. 112 (1990) 1529.
[50] A.L. Mejdrich, T.W. Hanks, Synth. React. Inorg. Met.-Org. Chem. 28 (1998) 953.
[51] M.A. Schmid, H.G. Alt, W. Milius, J. Organomet. Chem. 541 (1997) 3.
[52] P.J. Chirik, Ph.D. Thesis, California Institute of Technology, 2000.
[53] J.M. O'Connor, C.P. Casey, Chem. Rev. 87 (1987) 307.
[54] L. Resconi, R.L. Jones, A.L. Rheingold, G.P.A. Yap, Organometallics 15 (1996) 998.
[55] R.E. Gerkin, A.P. Lundstedt, W.J. Reppart, Acta Cryst. C40 (1984) 1892.

[56] L.J. Irwin, J.H. Reibenspies, S.A. Miller, unpublished results.
[57] A. Razavi, J. Ferrara, J. Organomet. Chem. 435 (1992) 299.
[58] M. Schlosser, J. Hartmann, Angew. Chem. Int. Ed. 12 (1973) 508.
[59] G.M. Sheldrick, SHELXS-97, Program for the Solution of Crystal Structures, Universität Göttingen, 1997.
[60] G.M. Sheldrick, SHELXL-97, Program for the Solution of Crystal Structures, Universität Göttingen, 1997.

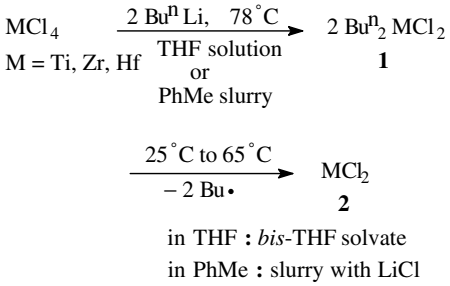
1. Introduction

Over the last decade we have been interested in applying the diverse chemical reactions of subvalent transition metal salts to the methodology of organic synthesis [1–4]. Our attention was especially drawn to the salts of Group 4 metals by the reports of the novel reductive dimerization of carbonyl derivatives to olefins by subvalent titanium reductants of unspecified oxidation state and composition (Eq. (1)).



(1)

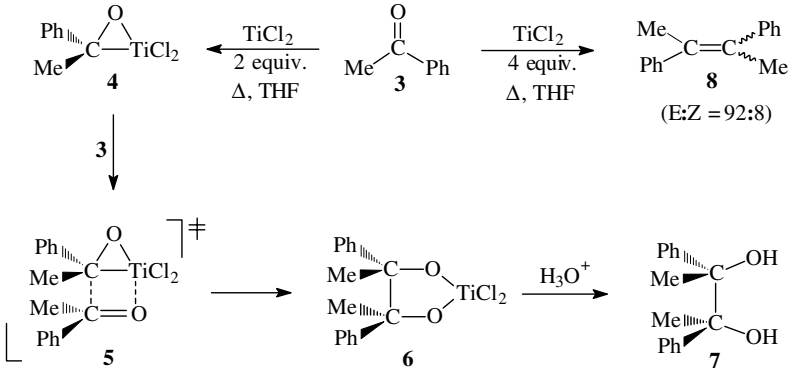
Such reports have issued independently from three different research groups where each utilized an empirical combination of a Ti(III) or Ti(IV) salt with a main-group metal or metal hydride [5–7]. This transformation, which has come to be termed the McMurry coupling after one of its discoverers, has found many valuable applications in organic synthesis [8–10]. But the use of such empirical reductants either in mechanistic studies of the McMurry coupling itself or in the synthesis of transition metal organometallics has up to now proved to be impractical. Hence, the recent discovery of a convenient, low-temperature route to the Group 4 dichlorides, MCl_2, as bis-THF solvates in THF, or as slurries with LiCl in toluene, has proved crucial for a systematic study of reductive dimerizations [2–4]. In a process termed alkylative reduction the MCl_4 is dialkylated with *n*-butyllithium at −78 °C to form intermediate **1**; warming **1** to 25 °C and above causes the reductive elimination of butyl groups (as butane and butene) and the high-yielding production of **2** (Eq. (2)).



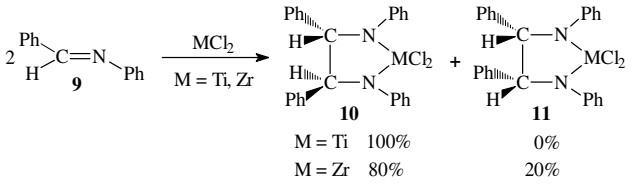
(2)

By the use of such reagents as **2** of well-defined valence and stoichiometry, considerable control could be exerted on both the extent and stereochemistry of the reductive coupling of ketones [2]. Acetophenone (**3**), for example, reacts with 2 equiv. of $TiCl_2$ in refluxing THF to give upon hydrolysis 83% of the *racemic*-2,3-diphenyl-2,3-butanediol (**7**) only, while with 4 equiv. of $TiCl_2$ the ketone gives 88% of olefin **8** as a 92:8 mixture of *E* and *Z* isomers. The exclusive formation of *racemic* **7** is consistent with the likely intermediacy of the three-membered ring **4** and the sterically controlled transition state **5** for the insertion of the second ketonic unit to form **6** (Scheme 1) [3,4].

Accordingly, the stereoselective reductive coupling of carbonyl derivatives by $TiCl_2$ depicted in Scheme 1 and the analogous reductive coupling subsequently observed with imines, such as *N*-benzylideneaniline (**9**), as mediated by $TiCl_2$ or $ZrCl_2$ (Scheme 2), have provided excellent model systems with which to assess steric effects in forming C–C bonds in such *ansa*-bridged systems, such as **6** and **10** and **11** (where the bridging O–CH_2–CH_2–O and NPh–CHPh–CHPh–NPh linkages can be envisaged as providing a "handle" (L. *ansa*) on the metal center). In all three systems these intermediate metallocycles can readily be hydrolyzed and the ratio of the resulting *racemic*:*meso* glycols (**7**) or diamines [$(PhCH–NHPh)_2$ from **10** and **11**] can be determined by ^1H NMR spectroscopy. Alternatively, the ratio of the metallocycles **10** and **11** can be estimated directly from their ^1H NMR spectra.

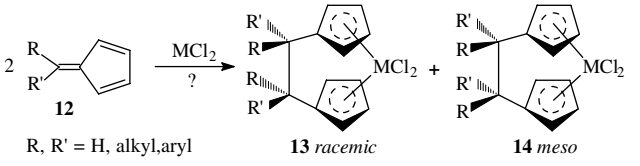


Scheme 1.



Scheme 2.

Because of the foregoing success with the efficient and stereoselective reductive dimerizations of both ketones and imines with Group 4 metal dichlorides, we were inspired to attempt a similar dimerization of 6-substituted fulvenes (**12**) with the hope of producing thereby novel *ansa*-metallocenes having some stereochemical preference for the substituents on the *ansa*-bridge (ratio of **13**:**14**) (Eq. (3)) [11,12]. Were such a dimerization to succeed, it would represent a radical departure from established routes to bridged or *ansa*-metallocenes and offer a new approach to stereochemical isomers of such systems as **13** and **14** [12].



(3)

2. Results

2.1. Initial attempts with 6,6-dimethylfulvene (*15*) and Group 4 metal dihalides

The reactions of 6,6-dimethylfulvene (**15**) with the Group 4 metal dichlorides, $TiCl_2$ (**16**), $ZrCl_2$ (**17**) or $HfCl_2$ (**18**), were initially examined in THF, a solvent in which such salts are readily prepared at room temperature according to Eq. (2) (e.g., $TiCl_2 \cdot 2THF$) [11]. Although *ansa*-metallocene formation (**19**–**21**) was observed in refluxing THF, such reductive dimerization was slow (Scheme 3). Accordingly, individual slurries in toluene of **16**, **17** and **18** admixed with LiCl by-product were prepared according to Eq. (2) and allowed to react with 2 equiv. of fulvene **15** at reflux. Although the fulvene was largely consumed and the *ansa*-metallocenes **19**–**21** formed in good to high yield, moderate to fair yields of unbridged substituted metallocenes (**25**–**27**) were also obtained. The source of the unbridged metallocenes **25**–**27** as side-products was traced to the presence of undecomposed Bu_2MCl_2 (**22**–**24**) in the MCl_2 formed in toluene at 25 °C . Clearly Bu_2MCl_2 performed a bis-hydrometallation by transfer of two moles of fulvene **15** [13].

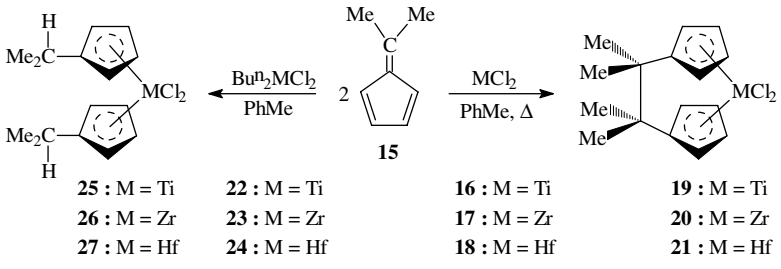
2.2. Preparation of tetramethylethylene-bis(cyclopentadienyl)metal dichlorides *19*, *20* and *21*

In light of this insight complete conversion of any Bu_2MCl_2 remaining in the toluene suspension to MCl_2 could be assured by heating the reagent at reflux for several hours. Then the reaction of such purified MCl_2 gave yields of over 90% for *ansa*-metallocenes **19**–**21**, as well as pure product by Soxhlet extraction or flash column chromatography in 80–85% yield.

2.3. Preparation of bis(isopropylcyclopentadienyl)metal dichlorides *25*, *26* and *27*

The discovery of the interesting bis-hydrozirconation by Bu_2MCl_2 leading to unbridged metallocenes **25**–**27** prompted us to attempt to maximize this course of reaction by generating the individual $Bu^n{}_2MCl_2$ at −78 °C in toluene (Eq. (1)) and immediately thereupon adding the 2 equiv. of 6,6-dimethylfulvene. The resulting reaction was warmed to 25 °C and then heated at 65 °C for several hours. This procedure was most effective in producing 75–85% yields of bis(isopropylcyclopentadienyl)-zirconium dichloride (**26**) and bis(isopropylcyclopentadienyl)hafnium dichloride (**27**), which products were shown to be free of the corresponding *ansa*-derivatives (**20** and **21**, respectively) by NMR criteria [13].

However, in the reaction of $TiCl_4$ with *n*-butyllithium in toluene at −78 °C, minutes after admixing the reagents the solution turned black, which signaled formation of $TiCl_2$. Even though the fulvene **15** was then



Scheme 3.

added at −78 °C, subsequent warming of the mixture to 25 °C and then to 65 °C led to an inseparable mixture of bis(isopropylcyclopentadienyl)titanium dichloride (**25**) and tetramethylethylene-bis(cyclopentadienyl)titanium dichloride (**19**), formed in approximately equal amounts.

2.4. ansa-Zirconocenes from 6-substituted fulvenes and zirconium dichloride

In order to investigate steric effects on the stereochemistry of *ansa*-bridge formation a trio of 6-arylfulvenes (**28**–**30**), where Ar = phenyl, 1-naphthyl or 9-anthryl, was subjected to reductive coupling by pure $ZrCl_2$ (free of $Bu^n{}_2ZrCl_2$, cf. supra). In each reaction *ansa*-bridge formation occurred in satisfactory yield but with different ratios of *racemic*- and *meso*-isomers (Scheme 4). A random ratio of *racemic*:*meso*-isomers was obtained with Ar equals phenyl (**28a**:**28b** = 50:50), a great preference with Ar equals 1-naphthyl (**29a**:**29b** = 83:17) and an exclusive formation of *racemic*-isomer (**30a**) with Ar = 9-anthryl.

In order to learn whether the covalent radii of Ti (132 pm) and Zr (145 pm) would have any effect on the *racemic–meso*-isomer ratio of *ansa*-bridged product, the reductive dimerization of 6-phenylfulvene (**28**) was also performed with pure $TiCl_2$. In this case, *ansa*-derivative formation also occurred efficiently in 75% yield but again the ratio of *racemic*- and *meso*-isomers obtained was 50:50 (analogous to **28a** and **28b**, with Zr replaced by Ti).

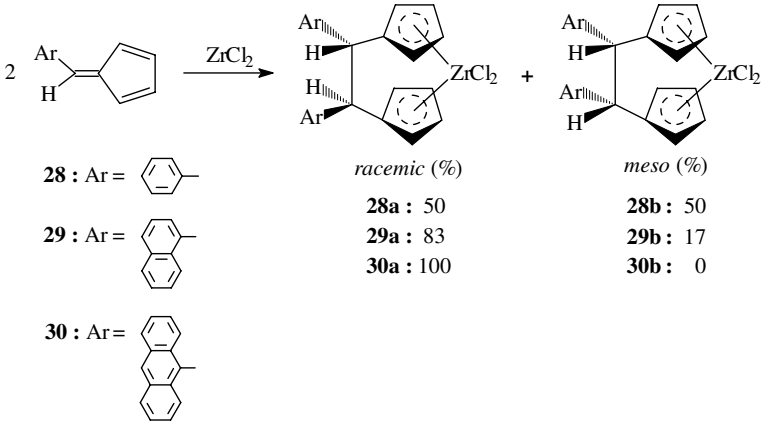
2.5. Structure assignments of the resulting ansa-metallocenes and the unbridged substituted metallocenes

The ultimate structure determination usually is achieved by an XRD analysis of a single crystal of a substance. Although not yet achieved with any of the present metallocenes, partly refined electron-diffraction data however were obtained on the major isomer resulting from the coupling of two units of 6-(1-naphthyl)fulvene by $ZrCl_2$. By plotting such data this 1,2-di(1-naphthyl)ethylene-bis(cyclopentadienyl)zirconium dichloride has been shown unambiguously to be the *racemic*-isomer (**29a**) and that furthermore two chlorine atoms are also bonded to the zirconium center. This structural evidence confirms the assignment made in Section 4.7.4. of the ratio of *racemic*-(**29a**) to *meso*-(**29b**) isomers formed by integration of the methine H singlets at 6.28 and 6.20 ppm in the ^1H NMR spectrum of the isomeric mixture.

To substantiate the presence of the MCl_2 group in these metallocenes, two representative metallocenes, tetramethylethylene-bis(cyclopentadienyl)titanium dichloride (**19**) and tetramethylethylene-bis(cyclopentadienyl)zirconium dichloride (**20**), were subjected to mass spectrometry by the electrospray technique with NaI. Both **19** and **20** yielded mass spectra having prominent peaks for parent ions containing $^{35}Cl_2$, $^{35}Cl^{37}Cl$ and $^{37}Cl_2$ mass contributions, respectively, in the expected intensity ratios. Therefore, based on the XRD of **29a** and the MS data for **19** and **20**, we can be confident that all these metallocenes resulting from the interaction of 2 equiv. of a fulvene with 1 equiv. of either MCl_2 or $Bu^n{}_2MCl_2$ contain the atomic grouping of MCl_2 (details in Sections 4.3, 4.6.1 and 4.7.1).

Further structural specification for the individual metallocenes is completely corroborated by NMR spectroscopic data (cf. Section 4.3): (1) the individual ^1H NMR spectrum has the proper integral ratio of protons, with each proton having the expected chemical shift and proton–proton coupling; and (2) the individual ^{13}C NMR spectrum of the pure metallocene or isomeric mixture displays exactly the proper number of singlets with the expected chemical shifts; moreover, the ^{13}C NMR spectrum in a DEPT experiment shows the expected number of quaternary C and methine C (C–H) centers.

On the basis of the foregoing array of instrumental analyses we judge that the structures assigned to these novel metallocenes are dependably correct.

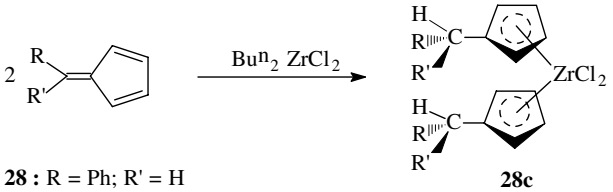


Scheme 4.

2.6. Attempted synthesis of tetraphenylethylene-bis(cyclopentadienyl)zirconium dichloride (32) and the generalized hydrozirconation of fulvenes

Since 6,6-dimethylfulvene (**15**) undergoes efficient reductive dimerization to *ansa*-derivatives **19**, **20** and **21** with the respective metal dichloride, we were curious to determine whether 6,6-diphenylfulvene (**31**) would react similarly (Scheme 5). To an organic chemist, *ansa*-product **32** would have a structure closely similar to the unknown hexaphenylethane, $Ph_3C–CPh_3$, which if fleetingly formed would be expected rapidly to dissociate into stable trityl radicals [14]. When reductive coupling of **31** with $ZrCl_2$ was attempted, no *ansa*-derivative was isolable.

Instead, substituted zirconocene **34** was obtained in 25% yield. Because a number of 6-substituted fulvenes, such as **28**, **29**, **30** and **31**, undergo satisfactory hydrozirconation with $Bu^n{}_2ZrCl$ (Eq. (4)), an authentic sample of **34**, prepared in an unambiguous manner, was available for spectral comparison and positive identification of product **34** resulting from the attempted synthesis of **32**.



28 : R = Ph; R' = H — **28c**

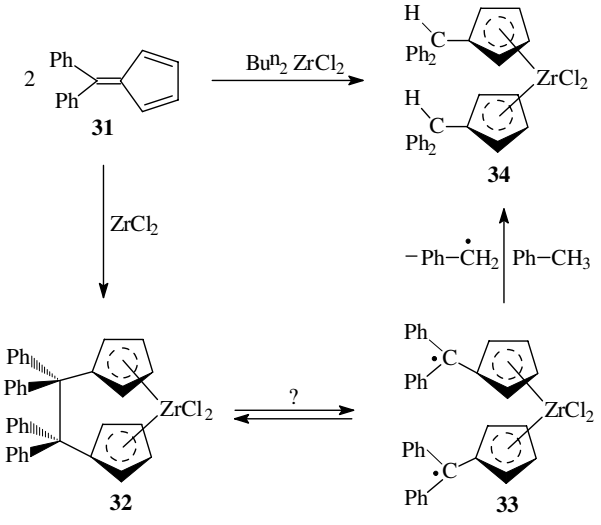
29 : R = 1-Naphthyl; R' = H — **29c**

30 : R = 9-Anthryl; R' = H — **30c**

31 : R = Ph; R' = Ph — **31c = 34**

(4)

Accordingly, it is reasonable to conclude that the F-strain [15] imposed on the *ansa*-C–C bond of **32** by the near eclipsing of neighboring phenyl groups causes dissociation of **32** into stabilized biradical **33**. Eventual H-atom abstraction by **33** from toluene would result in product **34**.



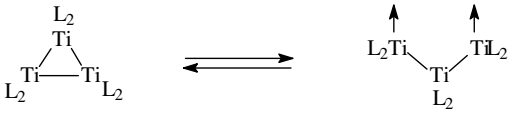
Scheme 5.

3. Discussion

3.1. Mechanism of the reductive dimerization of the model system, benzylideneaniline (9), with Group 4 metal dichlorides

In considering the reactivity of $TiCl_2$ (**16**), $ZrCl_2$ (**17**) or $HfCl_2$ (**18**) toward a carbonyl (Scheme 1), an imine (Scheme 2) or a fulvene substrate (Eq. (3)), it is important to realize that the monomeric MCl_2 unit delivered must first be detached from a highly associated aggregate $[MCl_2]_x$. For unsolvated MCl_2 generated in toluene such an aggregate could resemble the layer lattice of $TiCl_2$, for example, where infinite layers of Ti atoms are sandwiched between two layers of Cl atoms. But the MCl_2 formed in Eq. (2) clearly can exist in much smaller, oligomeric aggregates. In THF solution the complex $TiCl_2 \cdot 2THF$ (**35**) has been shown to form [2]. Although the degree of association of such a complex is not known, its ready solution in toluene would not be consistent with a polymeric aggregate. Furthermore, such a solution of $TiCl_2$ is diamagnetic and does not show an EPR signal even at low temperatures.

Fortunately, information on the state of aggregation of titanium(II) salts has been obtained from a study of the properties of titanium(II) isopropoxide (**36b**), which can be prepared analogous to $TiCl_2$ (Eq. (2)), by treating $Ti(OPr^i)_4$ with 2 equiv. of *n*-butyllithium. Even when prepared in THF, complex **36b** can be completely freed of THF in vacuo and redissolved in toluene. Such solutions of **36b** exhibit a strong EPR signal indicative of a biradical and hence the presence of two unpaired electrons. The strength of the signal coupling is best in accord with the unpaired electrons being on titanium centers located 1,3 to each other (**36b**), rather than on vicinal or the same Ti center(s) (Eq. (5)) [16,17]. The bulky nature of the isopropoxy ligands may strain the three-membered ring (**36a**) and favor the biradical **36b**. With much smaller chloro ligands the diamagnetic ring in **35a** should be much less strained. There would likely be sufficient room about each Ti atom in **35a** to accommodate two THF units and thereby permit octahedral coordination.



35a : L = Cl — **35b :** L = Cl

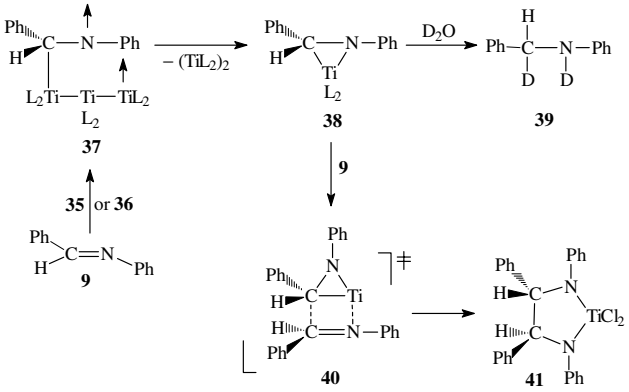
36a : L = OPr^i — **36b :** L = OPr^i

(5)

The process of forming a three-membered ring or epimetallated product, like **4** for carbonyl substrates or **38** for imines such as **9**, could be viewed as in Scheme 6. Attack of **35** (or **36**) on **9** would lead to biradical **37**, which would close the most rapidly to **38** by intramolecular radical displacement [18]. The presence of **38** in such reductive coupling was corroborated by work-up of the reaction mixture with D_2O and finding the *N*-phenylbenzylamine dideuterated (**39**).

The observed stereochemistry of reductive coupling can be readily understood by postulating the insertion of a second **9** into the C–Ti bond of **38** via transition state **40** where the phenyl groups would minimize steric repulsion by forming the *racemic* dimer **41** [19]. With little modification the less stereoselective coupling of **9** by $ZrCl_2$ (*racemic*:*meso* = 80:20) can follow from the longer C–M bond in the Zr intermediate analogous to **38**. The larger covalent radius of Zr over Ti, 145 versus 132 pm, would mean that the two carbon centers would be farther apart in the transition state (similar to **40**) and thus not as sensitive to the steric effects of the phenyl groups.

The only remaining puzzling observation is that made in the attempted transfer-hydrozirconation of **9** by $Bu^n_2ZrCl_2$ (**23**).[1] From our experience with other substrates in hydrozirconation [13], the expected major product should have been *N*-phenylbenzylamine (**43**), formed via **42**. Although **43** was in fact obtained in 49% yield, yet comparable amounts (51%) of an 80:20 mixture of *racemic*- and *meso*-1,2-dianilinoethanes (**47** and **48**) were also formed, products expected to arise from the reductive coupling of **9** by $ZrCl_2$ (cf. supra). However, at the temperature of reaction, 25 °C, $ZrCl_2$ had not yet formed from the decomposition of



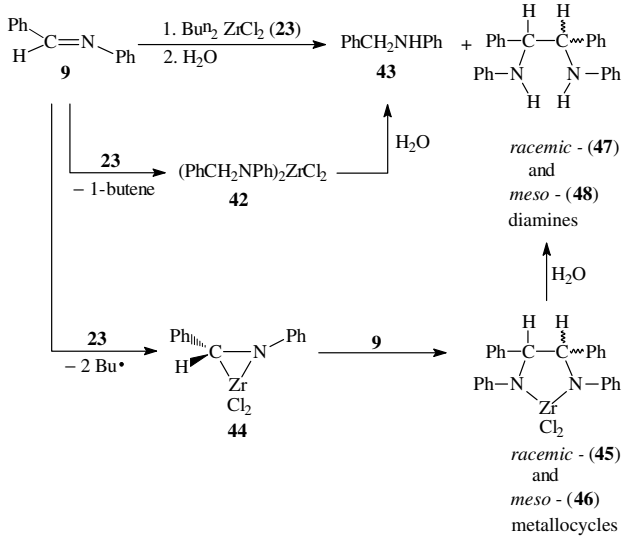
Scheme 6.

$Bu^n_2ZrCl_2$ in toluene. We are forced to conclude therefore that epimetallated zirconium intermediate **44** has been formed from **23** by the process of the transfer-epimetallation of **9** (Scheme 7).[1] The generation of the *racemic*- and *meso*-metallocycles (**45** and **46**) would ensue as with the titanium analog (**38** → **41**, Scheme 6). Transfer-epititanation of a wide variety of unsaturated substrates by $Bu^n_2TiCl_2$ (**22**) has been amply demonstrated to be an important process in the functionalization of alkenes and alkynes [20,21], in the Kulinkovich cyclopropanol synthesis [22] and in olefin polymerization [23,24].

3.2. Transfer-hydrometallation of fulvenes and the synthesis of unbridged substituted bis(cyclopentadienyl)metal dichlorides

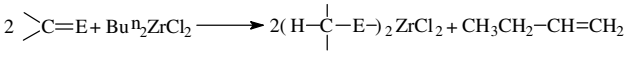
3.2.1. Chemical and physical properties of fulvenes (12)

Fulvenes (**12**) are colored nonaromatic hydrocarbons possessing a dipole moment and a high degree of chemical reactivity by virtue of their uneven π-electron

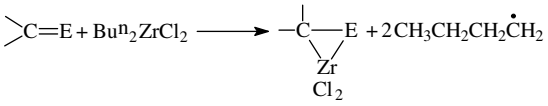


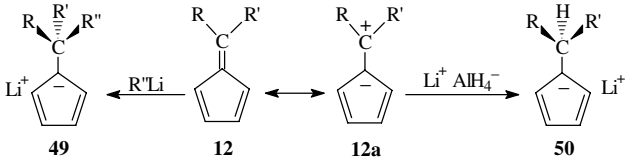
Scheme 7.

[1] The generalized reactions discussed in this section, "transfer-hydrometallation" and "transfer-epimetallation", as well as their metal-specific counterparts, "transfer-epititanation, transfer-epizirconation, transfer-hydrotitanation and transfer-hydrozirconation, are reactions that have been studied and established in previous publications of our research group. Transfer-hydrozirconation as described in [13] refers to the transfer of zirconium dichloride dihydride from di-*n*-butylzirconium dichloride to an unsaturated substrate C = E (carbonyl, imine or fulvene) with release of 1-butene:



Analogously, transfer-epizirconation as described in [20] and [21] refers to the transfer of zirconium dichloride from di-*n*-butylzirconium dichloride to C = E (carbonyl, imine or fulvene) with release of two butyl radicals (or as butane and 1-butene):



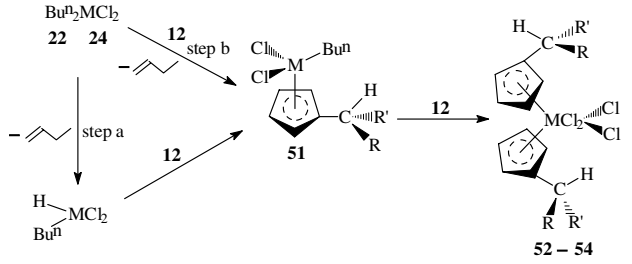


Scheme 8.

distribution (**12a** and its resonance structures). Especially for our present purposes, the long-known addition reactions of fulvenes with organolithium reagents (RLi) [25] and with $LiAlH_4$ [26] are especially relevant (Scheme 8). In the formation of adducts **49** and **50** the regioselectivity is driven by the aromatic stabilization attained with the formation of the cyclopentadienyl anion.

3.2.2. Transfer-hydrometallation of fulvenes

Whether the elimination of 1-butene from $Bu^n{}_2MCl_2$ (**22**–**24**) *precedes* the interaction of $Bu^n{}_2MCl_2$ with the fulvene to produce H_2MCl_2 (step a) or *accompanies* such an interaction with the fulvene (step b) cannot be decided at present (Scheme 9). Either path produces the "open-face sandwich" (**51**). π-Complexation of **51** with a second **12**, so that the RR′HC-groups on the ring are *anti* to each other, would yield the final metallocenes (**52**–**54**) with minimal steric hindrance.



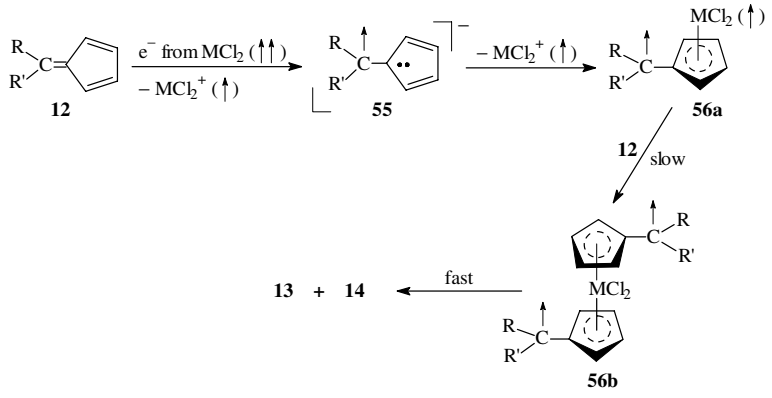
Scheme 9.

3.3. Reductive coupling of fulvenes by union with biradicals

Analogous to the mechanistic insight gained from the reductive dimerization of ketones or of benzylideneaniline by Group 4 metal(II) dichlorides (Schemes 1 and 2), we propose the analogous biradical "open-face sandwich" **56** (Scheme 10), which could be formed via radical-anion **55** by SET from biradical $MCl_2(\uparrow\uparrow)$. Interaction of **56a** with a second fulvene **12** would surely be sensitive to steric factors during the formation of the *ansa*-C–C bond. But if the rate of formation of the final *ansa*-complexes **13** and **14** is determined by the complexation of biradical **56a** with a second fulvene **12** to form **56b**, then the subsequent C–C bonding would be fast and steric hindrance would have only an attenuated effect on the *ansa-racemic*- and *meso*-isomeric ratio. Whether R = phenyl and R′ = H or whether M = Ti or Zr in **56b** would then have no large steric effect. Only when R = 1-naphthyl or 9-anthryl and R′ = H would a steric effect become unavoidable. This effect may have nothing to do with steric bias in the relatively rapid *ansa*-C–C bond formation but rather in the rate of complexation of **56a** with the prochiral π-electron cloud surface of the second fulvene.

3.4. Comparative polymerization of ethylene by ansa-metallocene and unbridged metallocene procatalysts with MAO cocatalysis

A complete survey of all the *ansa*- and unbridged catalysts synthesizable from fulvenes has not yet been made. However, the preliminary results obtained thus far and presented in Table 1 permit us to propose three valuable trends in reactivity: first, *ansa*-metallocenes are much more active polymerization catalysts than their unbridged counterparts: for Ti, consider runs 1, 2 and 3; for Zr, compare runs 4, 5 and 6 as well as runs 7 and 9; second, the normal order of polymerization activity for unbridged metallocenes, Zr > Ti > Hf, is changed



Scheme 10.

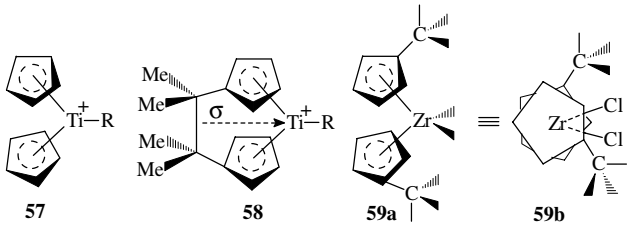
Table 1
Comparative polymerization of ethylene with metallocene procatalysts and MAO cocatalysts

Run	Metallocene	Polymerization activity[a] (g PE/g M h atm)
1	Tetramethylethylene-bis(cyclopentadienyl)titanium dichloride (**19**)	2640
2	Titanocene dichloride	1100
3	*racemic*- and *meso*-1,2-Diphenylethylene-*bis*(cyclopentadienyl)titanium dichloride, 1:1 mixture (titanium analogue of **28a** and **28b**)	3170
4	*racemic*- and *meso*-1,2-(Diphenylethylene-*bis*(cyclopenta-dienyl)zirconium dichloride (**28a** and **28b**), 1:1 mixture	360
5	Bis(benzylcylcopentadienyl)zirconium dichloride (**28c**)	242
6	Bis[(diphenylmethyl)cyclopentadienyl)]zirconium dichloride (**34**)	62
7	Bis[(1-naphthylmethyl)cyclopentadienyl)]zirconium dichloride (**29c**)	126
8	1,2-Di-[(1-naphthylethylene)-cyclopentadienyl]titanium dichloride (titanium analogue of **29a**)	313
9	1,2-Di-[(1-naphthylethylene)-cyclopentadienyl]zirconium dichloride (83:17 mixture of **29a** and **29b**)	52
10	Bis(isopropylcyclopentadienyl)hafnium dichloride	182

[a] All runs were conducted in toluene at ambient temperature with uncontrolled exotherm employing 0.2–1.0 mmol of metallocene and 50 equiv. of MAO. Comparisons of polymerization activity are reported per grams of metal in the catalyst and are measured for polymerizations proceeding under a constant pressure of ethylene, under the spontaneous exotherm of polymerization and in a reaction mixture turning rapidly from homogeneous to heterogeneous. Therefore, this empirical measure of activity, widely used in industry, cannot be expected to rank polymerization rates of catalysts in an absolute and accurate series. But as employed here, such measurements can readily distinguish among catalysts of high activity, intermediate activity and low activity. Finally, it should be noted that the accurate measurement of initial polymerization rates (the only reliable measure of intrinsic catalyst activity) is a most difficult procedure to carry out in a reproducible and reliable manner (cf. Fischer, D. "Untersuchungen zur Propenpolymerisation an Homogenen Zirconocen/Methylaluminoxan Ziegler-Natta Katalysatoren", *Doctoral Dissertation*, Albert-Ludwig University, Freiburg (Breisgau), Germany, 1992.

for *ansa*-metallocenes, where Ti > Zr > Hf; and third, unbridged substituted zirconocenes have depressed activities, as the steric size of the cyclopentadienyl ring substituent increases: note runs 5, 6 and 7.

The usual reason for the lesser polymerization activity of unbridged titanocenes over analogous zirconocenes is the lower kinetic stability of the titanocenium cation **57**, which has been proposed as the active polymerization site [27]. The greater reactivity for *ansa*-titanocenes over *ansa*-zirconocenes or *ansa*-hafnocenes, therefore, may arise from the greater stabilization of cation **58**. A source of such stabilization of the titanium cation in **58** could be the σ-bond hyperconjugation provided to the backside of the empty sp^3-hybridized orbital of the cationic Ti center (**58**).[2] Since such stabilization would be more important in *ansa*-titanocenes than in *ansa*-zirconocenes (better orbital-energy match and shorter distance between the metal center and the σ-electrons of the C–C bond), *ansa*-titanocenes should show a larger increase in polymerization activity than *ansa*-zirconocenes.



Finally, the reduced polymerization activity of bis(substituted cyclopentadienyl)zirconium dichlorides (with substituents of $PhCh_2$-, Ph_2CH- and 1-naphthylmethyl (runs 5, 6 and 7)) can be attributed to the favoring of those conformers where the substituents project out of the wider gap between the tilted rings (**59a** and **59b**). Such substituents thereby impede the interaction of such zirconocenes with the MAO cocatalyst and the approach of the ethylene to the zirconocenium cation in the active site.

4. Experimental

4.1. Starting reagents and solvents

Cyclopentadiene was freshly cracked from commercially available dicyclopentadiene and distilled under an atmosphere of dry argon directly before use. 6,6-Dimethylfulvene, 6,6-diphenylfulvene, 1-naphthaldehyde, 9-anthraldehyde, benzylideneaniline, titanium(IV), zirconium(IV) and hafnium(IV) chlorides and *n*-butyllithium in hexane were obtained from

[2] Such σ-bond hyperconjugation is widely recognized as stabilizing carbenion ions β to silicon as in $R_3Si–CH_2–CH_2+$ (W. Hanstein, H.J. Berwin, T.G. Trayler, J. Am. Chem. Soc. 92 (1970) 829) and in promoting the facile ring-opening of the cyclopropyl carbenium ion to the allyl cation (S.F. Cristol, R.M. Segueira, C.H. DePuy, J. Am. Chem. Soc. 87 (1965) 4007). Since the ansa-C–C bond is closer to the titanium cation, σ-bond hyperconjugation is more likely to be the operative effect than some inductive release of electron density from the *ansa*-carbon centers to the titanium centers but operative through the π-bonding of the rings.

commercial sources in at least 98% purity and were used directly. All solvents employed with organometallic reagents or anhydrous metal salts were dried and distilled from a sodium metal–benzophenone ketyl mixture prior to use [28].

4.2. General procedures

All procedures involving the purification of reaction solvents, the individual preparation of Group 4 metal dialkylmetal dichlorides, Group 4 metal dichlorides and their subsequent reactions leading to metallocenes and their purification were conducted under an atmosphere of anhydrous, oxygen-free argon. The drying and deoxygenation of argon were carried out by means of a purification apparatus previously described [28]. Nonhydrolytic workup of certain reactions to recover the organic ligand was achieved with 3 N aqueous HCl.

4.3. Instrumentation and analysis

After purification the reaction products were routinely subjected to IR and ^{1}H and ^{13}C NMR spectroscopic and, in some cases, mass spectrometric analysis. Since such data served to corroborate the structures assigned to the metallocenes satisfactorily, elemental analyses were considered unnecessary. The IR spectra were recorded with a Perkin–Elmer instrument (model 457) and samples were measured under argon either as mineral oil mulls or as KBr films. The NMR spectra (^{1}H and ^{13}C) were recorded under argon with a Bruker spectrometer (model EM-360) and tetramethylsilane (Me_4Si) was used as the internal standard. The chemical shifts reported are expressed on the δ scale in parts per million (ppm) from the Me_4Si reference signal. No data on J_{HH} coupling constants exhibited in the ^{1}H NMR spectra have been included because such values are in all cases in the expected range and unexceptional. However, it is worth noting that DEPT measurements in the ^{13}C NMR spectra reported here were able to distinguish quaternary carbon centers (C) from methine–carbon (C–H) centers. The latter but not the former carbon signals underwent resonance with inversion of signal. The number of quaternary C signals and methine–carbon signals observed fit the assigned structure in every case.

The gas chromatographic analyses were carried out with a Hewlett–Packard instrument (model 5880) provided with a 2-m OV-101 packed column or with a Hewlett–Packard instrument (model 4890) having a 30 m SE-30 capillary column. Melting points were determined on a Thomas-Hoover Unimelt capillary melting point apparatus and are uncorrected.

The mass spectral measurements were performed at the Mass Spectrometry & Proteomics Facility at the Ohio State University and employed a Micromass ESI-Tof™ mass spectrometer (Micromass, Wythenshawe, UK) equipped with an orthogonal electrospray source (Z spray) operated in a positive ion mode. The samples were prepared in a solution containing acidified methanol and sodium iodide as an internal mass standard.

4.4. Preparation of Group 4 metal dichlorides

4.4.1. Titanium dichloride (*16*)

The preparation of titanium dichloride in THF and its isolation as the LiCl-free and analytically supported complex, $TiCl_2 \cdot 2THF$ (**35**), has been described elsewhere [2]. The complex **35** was analyzed after removal of the THF in vacuo and found to have retained two moles of solvated THF per Ti unit. However, the solvate-free titanium dichloride (**16**), prepared in hydrocarbon slurry with LiCl, has proved more effective in the following reductive dimerizations of fulvenes. A colorless solution of $TiCl_4$ (5.5 mL, 5.5 mmol) in 20 mL of THF was prepared at −78 °C to avoid cleavage of the THF. Then 6.9 mL of *n*-butyllithium 1.6 M in hexane (11 mmol) was added dropwise at −78 °C causing the formation of a red-brown solution. The dark red solution was brought to RT, stirred for 12 h and then heated at reflux for 3 h. After solvent removal in vacuo the dark residue was diluted with 30 mL of toluene to give a black solution of **16** (5.5 mmol) with suspended LiCl.

4.4.2. Zirconium dichloride (*17*)

Zirconium dichloride can likewise be prepared in THF and isolated as the LiCl-free and analytically pure complex, $ZrCl_2 \cdot 2THF$ (**17**). Again, here the complex **17** in toluene slurried with LiCl has proved more effective in *ansa*-metallocene preparations. Thus a clear solution of $ZrCl_4$ (0.20 g, 0.86 mmol), prepared in 20 mL of THF at −78 °C, was treated with 1.1 mL of 1.6 M *n*-butyllithium in hexane (1.72 mmol). The dark red solution was brought to RT, stirred for 12 h and then heated at reflux for 3 h. After solvent removal in vacuo the black residue was treated with 20 mL of toluene to give a black solution of **17** (0.86 mmol) with suspended LiCl.

In a similar manner a suspension of $ZrCl_2$ (5.89 mmol) and LiCl in hexane alone was prepared from 5.89 mmol of $ZrCl_4$ and 11.8 mmol of *n*-butyllithium in a total of 40 mL of hexane.

4.4.3. Hafnium dichloride (*18*)

Hafnium dichloride (**18**) prepared in THF appears to form the solvate, $HfCl_2 \cdot 2THF$, as well but the solvate is not stable upon removal of the THF in vacuo. Thus a clear solution of $HfCl_4$ (3.73 g, 11.6 mmol) in 80 mL of THF at −78 °C was treated with 15 mL of 1.6 M *n*-butyllithium (23.2 mmol). The pale yellow solution was then stirred for 12 h at RT and then heated at reflux for 5 h. The dark brown solution was freed of solvent in

vacuo and the residue of $HfCl_2$ (**18**) and LiCl was suspended in 60 mL of toluene.

4.5. Synthesis of fulvenes

4.5.1. 6-Phenylfulvene (*28*)

To a solution of freshly distilled benzaldehyde (distilled under argon, 0.40 mL, 4.0 mmol) and freshly cracked cyclopentadiene (0.82 mL, 10 mmol) in 4.0 mL of methanol was added 0.5 mL of pyrrolidine. After 15-min stirring a 0.4 mL-portion of acetic acid was added and the solution stirred for a further 15 min. A mixture of ether and water was added and the organic layer separated and dried over solid $MgSO_4$. Ether removal from the organic layer left pure 6-phenylfulvene (**28**), 584 mg (89%) of dark orange crystals, mp. 33–34 °C. The reaction could be run on a 20-fold scale with little decrease in yield. *Anal*. Calc. for $C_{12}H_{10}$: C, 93.46; H, 6.54. Found: C, 93.65; H, 6.49%.

^{1}H NMR ($CDCl_3$): 7.59–9.56 (m, 2H), 7.42–7.30 (m, 3H), 7.20 (s, 1H), 6.71–6.64 (m, 2H), 6.52–6.49 (m, 1H), 6.33–6.31 (m, 1H). ^{13}C NMR ($CDCl_3$): 145.3, 138.2, 136.8, 136.4, 130.8, 130.7, 129.0, 128.6, 127.2, 120.3.

4.5.2. 6-(1-Naphthyl)fulvene (*29*)

To a solution of 1-naphthaldehyde (9.1 g, 58.2 mmol) in 50 mL of methanol was added the fresh cyclopentadiene (12.0 mL, 0.146 mol). After 15-min stirring 7.30 mL of pyrrolidine was introduced, causing the mixture to turn orange during 4 h-stirring at RT. Addition of 5.3 mL of acetic acid, further stirring for 20 min and dilution of the reaction mixture with water and ether yielded a biphasic system. The organic layer was separated, dried over $MgSO_4$ and freed of solvent to provide the crude **29**. Its purification by flash column chromatography on silica gel with a hexane–ethyl acetate eluent gave orange crystals of **29** (9.93 g, 84%), m.p. 52–54 °C.

Anal. Calc. for $C_{16}H_{12}$: C, 93.71; H, 6.29. Found: C, 93.84; H, 6.18%.

^{1}H NMR ($CDCl_3$): 8.11 (d, 1H), 7.90 (t, 3H), 7.76 (d, 1H), 7.53 (t, 3H), 6.69 (d, 2H), 6.56 (s, 1H), 6.50 (s, 1H). ^{13}C NMR ($CDCl_3$): 147.1, 135.7, 134.9, 133.8, 133.4, 132.0, 131.8, 130.0, 129.4, 128.6, 126.6, 126.2, 126.1, 125.4, 124.4, 121.5.

4.5.3. 6-(9-Anthryl)fulvene (*30*)

In a procedure analogous to the foregoing, a solution of 9-anthraldehyde (15.0 g, 82.8 mmol) and cyclopentadiene (15.0 mL, 0.182 mol) in 75 mL of methanol was treated with 9.1 mL of pyrrolidine and worked up with water and ether. The crude **30** was purified by flash column chromatography to give orange crystals of **30** (12.6 g, 68%), m.p. 100–101 °C.

Anal. Calc. for $C_{20}H_{14}$: C, 94.45; H, 5.55. Found: C, 94.22; H, 5.60%.

^{1}H NMR ($CDCl_3$): 8.5 (s, 1H), 8.16–8.13 (m, 2H), 8.06–8.01 (m, 2H), 7.94 (s, 1H), 7.51–7.44 (m, 4H), 6.65–6.60 (m, 2H), 6.52–6.49 (m, 1H), 5.89 (d, 1H). ^{13}C NMR ($CDCl_3$): 150.3, 134.5, 134.3, 132.4, 131.2, 130.6, 130.1, 128.5, 127.7, 126.3, 125.8, 125.4, 125.3, 122.5.

4.6. ansa-Metallocene dichlorides of titanium

4.6.1. From 6,6-dimethylfulvene (*15*)

To a black solution of 10.0 mmol of $TiCl_2 \cdot 2THF$ (**16**) in 30 mL of toluene (cf. Section 4.4.1) were added 20.0 mmol (2.41 mL) of 6,6-dimethylfulvene (**15**) and the resulting mixture heated at reflux for 6 h. Thereupon, the suspension was filtered and the black solid was washed twice with chloroform. The filtrate was freed of volatiles in vacuo to give red-brown **19**, spectrally quite pure, consistently in >90% yield in duplicate runs. Alternatively, the solvent was removed in vacuo, and the solid residue transferred under argon to the thimble of a Soxhlet extraction apparatus. Extraction with hexane over 20 h gave a hexane solution of 1,1,2,2-tetramethylethylene-bis(cyclopentadienyl)titanium dichloride (**19**). By solvent removal, washing with cold pentane and vacuum-drying, product **19** was isolated as a reddish brown solid (2.81 g, 85%). Further purification could be achieved by flash column chromatography with a gradient of hexane–chloroform, starting from pure hexane and ranging to pure chloroform. This metallocene is oxygen- and moisture-sensitive, turning yellowish green in moist air. ^{1}H NMR ($CDCL_3$): 6.90 (t, 4H), 6.25 (t, 4H), 1.45 (s, 12H). ^{13}C NMR ($CDCl_3$): 145.5, 128.5, 112.5, 45.5, 28.0. MS (electrospray in ESI with N_2 gas; capillary voltage 3000 V, source temperature 110 °C, cone voltage 55 V) prominent parent ion + Na peaks (intensity) at 297 (10), 299 (5), 301 (1), corresponding to the theoretical masses and intensities of $C_{12}H_{12}{}^{35}Cl_2TiNa$, $C_{12}C_{12}{}^{35}Cl^{37}ClTiNa$ and $C_{12}C_{12}{}^{37}Cl_2TiNa$, respectively.

4.6.2. From 6-phenylfulvene (*28*)

In a similar manner, a solution of 6-phenylfulvene (**28**, 1.54 g, 10.0 mmol) and a solution slurry of $TiCl_2 \cdot 2THF$ (**16**, 5.0 mmol) with the suspended LiCl in 50 mL of toluene were heated at reflux for 6 h. The reaction suspension was filtered and the black filter cake washed twice with chloroform. Removing volatiles from the filtrate gave >90% of a spectrally pure 1:1 mixture of *meso*- and *racemic*-isomers. Alternatively, analogous Soxhlet extraction and subsequent workup provided 85% of a brown-red 1:1 mixture of the *meso-ansa*- and the *racemic-ansa*-isomers of 1,2-diphenylethylene-bis(cyclopentadienyl)titanium dichloride. The conclusion that both isomers are present in such product is drawn from the ^{13}C NMR spectrum, which displays 18 sp^2-carbon and 2 sp^3-carbon

(methine carbon) signals. The ^{1}H NMR signals also come in signal packets of 10:4:4:1:1, consistent with the presence of both *meso*- and *racemic*-isomers. The equal intensity of the methine singlets at 4.85 and 4.35 ppm confirm the presence of a 1:1 mixture. The signal at 4.35 ppm is assigned to the *racemic*-isomer, since its methine H should be shielded by the π-cloud of the adjacent phenyl group. The *meso*- and *racemic*-isomers could be separated by flash column chromatography with a hexane–chloroform gradient. ^{1}H NMR ($CDCl_3$): 7.16–6.80 (m, 10H), 5.88–5.85 (m, 4H), 5.77–5.76 (m, 4H), 4.85 (s, 1H), 4.35 (s, 1H). ^{13}C NMR ($CDCl_3$): 140.8, 139.2, 137.4, 136.9, 134.0, 130.6, 129.3, 129.1, 128.8, 128.5, 127.8, 127.5, 126.9, 126.9, 117.7, 116.7, 113.2, 109.4, 53.9, 51.1.

The greater thermal lability and reactivity of the other *ansa*-metallocenes made their isolation more difficult, so a more extensive study of *ansa*-metallocenes was undertaken with zirconium analogues.

4.7. ansa-Metallocene dichlorides of zirconium

4.7.1. From 6,6-dimethylfulvene (*15*)

A solution of 6,6-dimethylfulvene (**15**, 1.20 mL, 10 mmol) in 60 mL of toluene was combined with a solution slurry of ZrCl2 (**17**, 5.0 mmol, cf. Section 4.4.2.) and LiCl in 50 mL of toluene and the mixture stirred at reflux for 8 h. Filtration of the reaction mixture and washing of the filtered cake twice with chloroform gave an extract, from which volatiles were removed in vacuo. The off-white **20** was spectrally pure and isolated in >90% yield. Alternatively, nonhydrolytic workup and Soxhlet extraction provided 1.31 g of colorless tetramethylene-bis(cyclopentadienyl)zirconium dichloride (**20**) in 70% yield. ^{1}H NMR ($CDCl_3$): 6.70 (t, 4H), 6.20 (t, 4H), 1.45 (s, 12H). ^{13}C NMR ($CDCl_3$): 143.5, 123.3, 108.8, 45.2, 28.4. MS (electrospray in ESI with N_2 gas; capillary voltage 3000 V, source temperature 110 °C, cone voltage 55 V) the three most prominent parent ion + Na peaks (intensity) at 339 (1.5), 341 (1.5) and 343 (1.0), corresponding to the theoretical intensities of $C_{12}C_{12}{}^{35}Cl_2ZrNa$, $C_{12}C_{12}{}^{35}Cl^{37}ClZrNa$ and $C_{12}C_{12}{}^{37}Cl_2ZrNa$, respectively.

4.7.2. From 6,6-diphenylfulvene (*31*), (attempted)

Heating a suspension of $ZrCl_2$ (**17**, 9.5 mmol) and LiCl with a solution of 6,6-diphenylfulvene (**31**, 2.20 g, 9.5 mmol) in 60 mL of toluene for 18 h gave upon usual nonhydrolytic workup an off-white, air- and moisture-sensitive solid in about 25% yield that proved to be bis(diphenylmethyl(cyclopentadienyl))zirconium dichloride (**34**), rather than the expected *ansa*-metallocene **32**. The presence of a singlet signal for the methine hydrogen at 5.64 ppm provided decisive evidence against the presence of **32**. Moreover, the straightforward hydrozirconative coupling of **31** by dibutylzirconium dichloride (**23**) (Section 4.9.5) provided an authentic sample of **34** for confirming the structure of this reaction product. ^{1}H NMR ($CDCl_3$): 7.28–7.09 (m, 20H), 6.05 (t, 4H), 5.78 (t, 4H), 5.64 (s, 2H). ^{13}C NMR ($CDCl_3$): 143.4, 136.3, 129.0, 128.4, 126.7, 116.0, 115.2, 51.5.

4.7.3. From 6-phenylfulvene (*28*)

A suspension of $ZrCl_2$ (**17**, 10.0 mmol) and LiCl in 30 mL of toluene was heated at reflux with 6-phenylfulvene (3.08 g, 20 mmol) for 8 h. Work-up by filtration gave >90% of essentially pure **28a** and **28b**. Alternatively, nonhydrolytic workup and Soxhlet extraction gave 3.53 g (75%) of a colorless 1:1 mixture of the *meso-ansa*-(**28b**) and *racemic-ansa*-(**28a**) isomers of 1,2-diphenylethylene-bis(cyclopentadienyl)zirconium dichloride. Spectral evidence for such a composition of these isomers and the assignment of the methine H at 4.28 ppm to the *racemic*-isomer follow the arguments given in Section 4.6.2. for the titanium analogue. ^{1}H NMR ($CDCl_3$): 7.16–6.90 (m, 20H), 5.90 (t, 4H), 5.85–5.70 (m, 4H), 4.91 (s, 1H), 4.28 (s, 1H). ^{13}C NMR ($CDCl_3$): 141.6, 139.8, 135.6, 129.5, 129.0, 128.7, 127.8, 127.6, 127.0, 113.5, 113.3, 110.7, 106.1, 54.4, 51.3.

4.7.4. From 6-(1-naphthyl)fulvene (*29*)

In a similar procedure, a solution of 6-(1-naphthyl)fulvene (**29**, 352 mg, 1.72 mmol) in 30 mL of toluene was heated at reflux with $ZrCl_2$ (**17**, 0.86 mmol) for 4 h. The reaction mixture was filtered and the filter cake washed repeatedly with toluene. The solvent was removed from the combined filtrate and washings in vacuo to give 369 mg (75%) of off-white *meso-ansa*-(**29b**) and *racemic-ansa*-(**29a**) isomers. The spectral evidence for the presence of both *meso*- and *racemic*-isomers is: (1) the presence of 30 sp^2-C signals; and (2) the presence of 2 sp^3-C signals and of 2 ^{1}H methine singlets. The ratio of the *meso*:*racemic*-isomers can be obtained by integrating the ^{1}H methine singlets at 6.20 and 6.28 ppm and obtaining a ratio of 6.20:6.28 signals of 17:83. Noting that the *racemic* methine H should be more shielded (Section 4.6.2), we can conclude that the *racemic-ansa*-isomer (**29a**) is the major isomer. Upon recrystallization of mixture **29a** and **29b** from a toluene–hexane pair a colorless product was recovered; its ^{1}H NMR spectrum now lacked the singlet at 6.20 ppm and its ^{13}C NMR spectrum had no signal at 45.5. Hence, the recrystallized product consisted of essentially the *racemic-ansa*-isomer. Crystal samples submitted thus far to Professor A.L. Rheingold (then of the University of Delaware and now of the University of California at San Diego) for single-crystal X-ray determination have led to the unambiguous determination that this isomer has the *racemic* structure (**29a**). However, better crystals will be required, in order to refine the data to attain $R < 10\%$.

^{1}H NMR ($CDCl_3$): 8.56 (d, 4H), 7.99 (d, 2H), 7.79–7.66 (m, 6H), 7.52–7.18 (m, 8H), 6.85 (m, 4H), 6.52

(m, 4H), 6.44 (s, 2H), 6.20–6.28 (2s, total of 2H). ^{13}C NMR ($CDCl_3$): 136.58, 136.12, 134.94, 134.57, 133.87, 131.63, 129.21, 129.13, 128.98, 128.17, 128.05, 127.86, 127.51, 127.21, 126.40, 125.72, 125.64, 125.55, 125.50, 125.25, 124.46, 1223.13, 123.02, 122.16, 121.52, 120.00, 113.43, 113.24, 110.28, 106.66, 48.30, 45.46.

4.7.5. From 6-(9-anthryl)fulvene (30)

A solution of 6-(9anthryl)fulvene (**30**, 2.23 g, 8.8 mmol) in 30 mL of toluene was stirred with a suspension of $ZrCl_2$ (14.4 mol) and LiCl in 20 mL of toluene at RT for 12 h and then at reflux for 6 h. The cooled reaction mixture was filtered and the filtrate cake washed thrice with 20-mL portions of toluene. The combined filtrate and washings were freed of solvent in vacuo to give 1.92 g (65%) of light brown *racemic*-1,2-(di-9-anthryl)ethylene-bis(cyclopentadienyl)zirconium dichloride (**30a**). Recrystallization from a toluene–hexane gave colorless, air- and moisture-sensitive **30a**. ^1H NMR ($CDCl_3$): 7.95 (d, 2H), 7.74 (d, 4H), 7.65 (d, 2H), 7.44–7.15 (m, 10H), 6.81 (m, 4H), 6.47 (m, 2H), 6.40 (s, 2H), 6.16 (s, 2H). ^{13}C NMR ($CDCl_3$): 137.8, 136.1, 134.6, 133.9, 131.7, 129.2, 129.0, 128.2, 128.1, 127.6, 126.4, 125.9, 125.6, 125.3, 124.5, 123.1 spectrum (6.16) and in the ^{13}C spectrum (48.4) are consonant with only one *ansa*-isomer. Steric control decisively supports the *racemic* structure (**30a**) for that single isomer.

4.8. ansa-Metallocene dichlorides of hafnium

4.8.1. From 6,6-dimethylfulvene (15)

A mixture of 6,6-dimethylfulvene (**15**, 1.00 mL, 8.7 mmol) and a suspension of $HfCl_2$ (11.6 mmol) and LiCl in 60 mL of toluene was heated at reflux for 12 h. The cooled reaction mixture was freed of solvent in vacuo and the residue subjected to Soxhlet extraction with 10% chloroform in hexane to yield 1.83 g (90%) of colorless, air- and moisture-sensitive tetramethylene-bis(cyclopentadienyl)hafnium dichloride (**21**). ^1H NMR ($CDCl_3$): 6.57 (t, 4H), 6.02 (t, 4H), 1.46 (s, 12H). ^{13}C NMR ($CDCl_3$): 141.6, 121.7, 106.7, 44.7, 28.5.

4.9. Hydrometallations of fulvenes

4.9.1. Hydrotitanation of 6,6-dimethylfulvene (15), (attempted)

Attempts to generate di-*n*-butyltitanium dichloride (**22**) at −78 °C just before adding 6,6-dimethylfulvene (**15**) to such a reagent failed because of the instability of **22** even at such low temperatures. Thus to a solution of $TiCl_4$ (4.0 mL, 4.0 mmol) in 30 mL of toluene at −78 °C were slowly added 2 equiv. of *n*-butyllithium (5.0 mL of 1.6 M in hexane, 8.0 mmol). During 30 min the progression of a colorless reaction mixture to yellow to green to brown and then to black signaled decomposition of **22** to $TiCl_2$ (**16**). Addition of 2 equiv. of 6,6-dimethylfulvene and warming to RT and finally 65 °C led to the formation of a mixture of tetramethylethylene-bis(cyclopentadienyl)titanium dichloride (**19**) (NMR spectral data in Section 4.6.1) and bis(isopropylcyclopentadienyl)titanium dichloride (**25**), readily identifiable by a 12H doublet at 1.45 and a 2H septet at 3.25 ppm.

4.9.2. Hydrozirconation of 6,6-dimethylfulvene (15)

To a white suspension of $ZiCl_4$ (2.12 g, 9.1 mmol) in 50 mL of toluene at −78 °C were slowly added 2 equiv. of *n*-butyllithium (18.2 mmol, 11.4 mL of 1.6 M), whereupon the solution turned light brown as it was warmed to RT. After 6 h 6,6-dimethylfulvene (**15**, 1.97 g, 18.6 mmol) was added and the reaction continued for 1 h at RT and 6 h at 65 °C. Filtration of the cooled reaction mixture and removal of volatiles in vacuo gave the light-brown bis(isopropylcyclopentadienyl)zirconium dichloride (**26**) consistently in >90% yield. Extraction with hexane in a Soxhlet apparatus over 1 h gave colorless **26** in 75% yield. ^1H NMR ($CDCl_3$): 6.60 (t, 4H), 6.45 (t, 4H), 3.25 (septet, 2H), 1.45 (d, 12H). ^{13}C NMR ($CDCl_3$): 142.0, 114.6, 112.0, 28.3, 23.2.

4.9.3. Hydrozirconation of 6-phenylfulvene (28)

A mixture of 6-phenylfulvene (**28**, 860 mg, 5.6 mmol) and di-*n*-butylzirconium dichloride (**23**, 2.8 mmol, cf. Section 4.9.2) in 40 mL of toluene was allowed to react at RT for 1 h and at reflux for 2 h. Solvent removal in vacuo and the solid washed well with pentane to remove any residual **28**. The residue was slurried again with toluene and the LiCl filtered off. The filtrate was freed of volatiles in vacuo to give 282 mg (95%) of light brown bis(benzylcyclopentadienyl)zirconium dichloride (**28c**). Further purification by Soxhlet extraction gave 75% of colorless **28c**. ^1H NMR (C_6D_6): 715–6.99 (m, 10H), 5.89 (t, 4H), 5.69 (t, 4H), 3.98 (s, 4H). ^{13}C NMR ($CDCl_3$): 140.71, 133.81, 129.59, 129.16, 127.03, 117.51, 112.96, 36.07.

4.9.4. Hydrozirconation of 6-(1-naphthyl)fulvene (29)

A mixture of 6-(1-naphthyl)fulvene (**29**, 1.9 g, 9.2 mmol) and $Bu^n{}_2ZrCl_2$ (**23**, 4.6 mmol) in 40 mL of toluene was allowed to react for 1 h at RT and 3 h at 65 °C. The cooled mixture was filtered to remove the LiCl. The filtrate was freed of solvent in vacuo and the residue was extracted with methylene chloride in a Soxhlet apparatus. In this way a 55% yield of almost colorless bis(1-naphthylmethyl(cyclopentadienyl))zirconium dichloride (**29c**) was obtained. ^1H NMR ($CDCl_3$): 8.05 (m, 3H), 7.88 (m, 4H), 7.76 (m, 3H), 7.44 (m, 4H), 6.21 (m, 4H), 6.16 (m, 4H), 4.52 (s, 4H). ^{13}C NMR ($CDCl_3$): 142.5, 136.0, 133.9, 128.8, 127.4, 127.0, 126.1, 125.9, 125.7, 124.7, 124.0, 117.5, 112.4, 47.7.

4.9.5. Hydrozirconation of 6,6-diphenylfulvene (31)

A mixture of 6,6-diphenylfulvene (**31**, 202 g, 8.84 mmol) and $Bu^n{}_2ZrCl_2$ (**23**, 4.42 mmol) in 40 mL of

toluene was allowed to react for 1 h at RT and 3 h at 65 °C. The cooled reaction mixture was freed of solvent in vacuo and the residue extracted with methylene chloride in a Soxhlet apparatus. The filtrate was freed of volatiles to give a light brown residue of bis(diphenylmethyl(cyclopentadienyl))zirconium dichloride (**31c**) (65% yield). Washing with pentane gave an off-white sample of **31c**, whose ^{1}H and ^{13}C NMR spectra were identical with the product obtained in Section 4.7.2.

*4.9.6. Hydrohafniation of 6,6-dimethylfulvene (**15**)*

A mixture of 6,6-dimethylfulvene (**15**, 1.7 mL, 14.2 mmol) and $Bu^{n}_{2}HfCl_{2}$ (**24**, 7.1 mmol, made analogous to $Bu^{n}_{2}ZrCl_{2}$ from $HfCl_{4}$ and 2 equiv. of *n*-butyllithium) in 40 mL of toluene was allowed to react for at RT for 1 h and at 65–70 °C for 4 h. The toluene was removed from the reaction mixture and the residue extracted with hexane in a Soxhlet apparatus. The hexane yielded 2.44 g (73%) of red-brown bis(isopropylcyclopentadienyl)hafnium dichloride (**27**). ^{1}H NMR ($CDCl_{3}$): 6.30 (t, 3H), 6.12 (t, 4H), 3.14 (septet, 2H), 1.14 (d, 12H). ^{13}C NMR ($CDCl_{3}$): 141.3, 113.1, 110.7, 27.0, 22.6.

4.10. Comparative polymerizations of ethylene with metallocene catalysts

*4.10.1. Typical polymerization run for tetramethylethylene-bis(cyclopentadienyl)titanium dichloride (**19**)*

Polymerizations were conducted in 250 mL resin-coated glass pressure (Fisher-Porter) bottle provided with magnetic stirring and equipped with a metal head (polymer coated on the inside) bearing a pressure gauge, an outlet for gas and reagents by syringe, and a stopcock for evacuation. The metallocene procatalysts, tetramethylethylene-bis(cyclopentadienyl)titanium dichloride (**19**, 0.560 mmol), in 100 mL of predried and deoxygenated toluene was treated with 28 mmol of MAO in toluene (Al:Ti = 50:1) and the bottle purged with anhydrous ethylene to initiate the polymerization. Under an ethylene overpressure of 40 psi the polymerizations are allowed to proceed for 10 min. Usual quench with aqueous HCl and filtration with a methanol-wash allow the polyethylene to be isolated. In this case the polymerization activity (PA) in grams of polyethylene (PE) per gram of Ti, per atmosphere was calculated as 2640. Such polyethylene generally melted over 135 °C.

4.10.2. Analogous polymerization with bis(cyclopentadienyl)titanium dichloride

An analogous polymerization of ethylene using 0.53 mmol of titanocene dichloride and 28 mmol (50 equiv.) of MAO for 10 min gave a PA = 1100 g PE/g Ti h atm.

*4.10.3. Analogous polymerization with bis(isopropylcyclopentadienyl)hafnium dichloride (**27**)*

A parallel polymerization of ethylene using 1.02 mmol of **27** and 50 equiv. of MAO for 30 min gave a PA = 182 g PE/g Hf h atm.

*4.10.4. Analogous polymerization with bis(benzylcyclopentadienyl)zirconium dichloride (**28c**)*

With 0.85 mmol of **28c** and 50 equiv. of MAO for 15 min of ethylene purge, a PA of 242 g PE/g Zr h atm was obtained.

*4.10.5. Analogous polymerization with bis(diphenylmethyl(cyclopentadienyl))zirconium dichloride (**31c**)*

With 0.18 mmol of **31c** and 50 equiv. of MAO for 10 min of ethylene purge, a PA of 62 g PE/g Zr h atm was obtained.

*4.10.6. Analogous polymerization with bis(1-naphthylmethyl(cyclopentadienyl))zirconium dichloride (**29c**)*

With 0.79 mmol of **29c** and 50 equiv. of MAO for 15 min of ethylene purge, a PA of 126 g PE/g Zr h atm was obtained.

4.10.7. Analogous polymerization with 1:1 racemic- and meso-1,2-diphenylethylene-bis(cyclopentadienyl) titanium dichloride

With 0.45 mmol of this metallocene and 50 equiv. of MAO for 10 min of ethylene purge, a PA of 3170 g PE/g Zr h atm was obtained.

4.10.8. Analogous polymerization with racemic- and meso-1,2-di(1-naphthyl)ethylene-bis(cyclopentadienyl)-titanium dichloride

With 0.20 mmol of this catalyst and 50 equiv. of MAO for 10 min of ethylene purge, a PA of 313 g PE/g Zr h atm was obtained.

*4.10.9. Analogous polymerization with 1:1 racemic- and meso-1,2-diphenylethylene-bis(cyclopentadienyl)-zirconium dichloride (**28a** and **28b**)*

With 0.75 mmol of this catalyst and 50 equiv. of MAO for 10 min of ethylene purge, a PA of 360 g PE/g Zr h atm was obtained.

*4.10.10. Analogous polymerization with 83:17 mixture of racemic- and meso-1,2-di(1-naphthyl)ethylene-bis(cyclopentadienyl)zirconium dichloride (**29a** and **29b**)*

With 0.22 mmol of this mixture and 50 equiv. of MAO for 15 min of ethylene purge, a PA of 52 g PE/g Zr h atm was obtained.

*4.11. Reductive dimerizations of N-benzylideneaniline (**9**)*

4.11.1. With titanium dichloride

To 15 mmol of $TiCl_{2}$ (**16**) in 40 mL of toluene (free of $Bu^{n}_{2}TiCl_{2}$, Eq. (2)) but containing the LiCl by-product

was added 5.40 g (30 mmol) of *N*-benzylideneaniline (**9**) at 25 °C. The mixture was heated at reflux for 2 h to form a dark khaki-colored suspension. Hydrolysis with 1 N aqueous HCl and separation of the organic layer, which was dried over $MgSO_4$ and freed of solvent in vacuo, provided 5.10 g (94% recovery) of products, which by ^1H NMR spectroscopy and comparison with spectral data of authentic samples to consist of 15% of *N*-phenylbenzylamine (**39**, but without D atoms) and 85% of *racemic*-1,2-dianilino-1,2-diphenylethane. After exchange with D_2O, the *racemic*-isomer showed a sharp C–H peak at 4.6 ppm. The corresponding CH peak for the *meso*-isomer at 5.0 ppm was absent [29].

When an identical reaction run was worked up with DCl in D_2O, the *N*-phenylbenzylamine (**39**) was monodeuteriated in the methylene group (^1H NMR peak at 4.29 and the N–H peak at 3.97 ppm was absent), the changes of which are consistent with the structure, Ph–CHD–ND–Ph (**39**).

*4.11.2. With zirconium dichloride (**17**)*

Similar to the foregoing, a mixture of *N*-benzylideneaniline (**9**) (6.00 g, 33 mmol) and freshly prepared $ZrCl_2$ (**17**, 16.3 mmol) free of $Bu^n{}_2ZrCl_2$ but containing LiCl was heated to reflux for 4 h. Hydrolytic work-up gave a 90% conversion to a mixture of *N*-phenylbenzylamine (20%) and an 80:20 mixture of *racemic*-1,2-dianilinoethane and *meso*-1,2-dianilinoethane (85%). The proportion of *racemic* to *meso*-isomers was determined by integration of C–H proton peaks at 4.6 and 5.0 ppm.

*4.11.3. With di-n-butylzirconium dichloride (**23**)*

N-Benzylideneaniline (**9**, 2.1 g, 11.4 mmol) and a slurry of $Bu^n{}_2ZrCl_2$ (**23**, 5.7 mmol) and LiCl in 40 mL were mixed at 25 °C to form a dark brown suspension in an exothermic reaction. After being stirred for 1 h at RT the reaction mixture was heated at reflux for 2 h and then subjected to the usual hydrolytic work-up. In 85% recovery, the reaction products consisted of *N*-phenylbenzylaniline (49%) and an 80:20 mixture of *racemic*- and *meso*-1,2-dianilino-1,2-diphenylethane (51%). Although the *N*-phenylbenzylaniline could have resulted either from transfer-hydrozirconation or epizirconation, formation of the *racemic*- and *meso*-1,2-dianilinoethanes require epizirconation, either directly by $ZrCl_2$ or by transfer (cf. discussion in Section 3.1).

*4.11.4. With zirconium dichloride (**17**) and the isolation of the mixture of racemic- and meso-1,1-dichloro-2,3,4,5-tetraphenyl-2,5-diazaazirconacyclopentanes (**10** and **11** with M = Zr)*

The experiment described in Section 4.11.2 but instead of a hydrolytic work-up the reaction mixture was cooled to RT and filtered to remove the LiCl. The filtrate was freed of toluene in vacuo and the dark tan washed repeatedly to give a mixture of *racemic*- and *meso*-isomers **10** and **11**, calculated to be a 70% yield and present in a 80:20 ratio. This product could be recrystallized from a toluene–hexane pair. ^1H NMR (THF-d_8) of **10** and **11**: 7.60–7.00 (m), 6.93–6.88 (m), 6.56–6.46 (m), 4.90 (s, *meso*-CH), 4.55 (s, *racemic*-CH); ^{13}C NMR (THF-d_8): 65.3 (*racemic*-CH), 63.3 (*meso*-CH).

*4.11.5. Polymerization with the mixture of racemic- and meso-1,1-dichloro-2,3,4,5-tetraphenyl-2,5-diazazirconacyclopentanes (**10** and **11** with M = Zr)*

Analogous to the foregoing polymerizations a mixture of **10** and **11** (160 mg, 0.29 mmol) in 100 mL of toluene was treated with 28 mmol (50 equiv.) of MAO was treated with ethylene at 40 psi for 15 min. Usual work-up gave 9.45 g of polyethylene for a PA = 129 PE/g Zr h atm.

Acknowledgments

The authors hereby thank the US National Science Foundation and Akzo Corporate Research America for supporting the initiation of this research, the Solvay Corporation of Brussels, Belgium for its continuation and the Boulder Scientific Company of Mead, Colorado for bringing this project to ultimate fruition. Former group members, Drs. Adetenu A. Adeosun, John N. Gitua and Peter O. Otieno have contributed valuable orienting experiments to the research approach herein described.

References

[1] J.J. Eisch, A.A. Adeosun, S. Dutta, P.O. Fregene, Eur. J. Org. Chem. (2005), in press.
[2] J.J. Eisch, X. Shi, J. Lasota, Z. Naturforsch. 50b (1995) 342.
[3] J.J. Eisch, X. Shi, J.R. Alila, S. Thiele, Chem. Ber./Recl. 130 (1997) 1175.
[4] J.J. Eisch, X. Shi, F.A. Owuor, in: W. Kaminsky (Ed.), Metalorganic Catalysts for Synthesis and Polymerization, Springer, Berlin, 1999, p. 248.
[5] T. Mukaiyama, T. Sato, J. Hanna, Chem. Lett. (1973) 1041.
[6] S. Tyrlik, I. Wolochowicz, Bull. Soc. Chim. Fr. (1973) 2147.
[7] J.E. McMurry, M.P. Fleming, J. Am. Chem. Soc. 96 (1974) 4708.
[8] J.E. McMurry, Chem. Rev. 89 (1989) 1513.
[9] J.E. McMurry, Acc. Chem. Res. 16 (1983) 405.
[10] Reductive coupling on a broad spectrum of carbonyl and azomethine derivatives has been the subject of many recent investigations, exemplified by the following:
(a) A. Fürstner, A. Hupperts, A. Ptock, E. Janssen, J. Org. Chem. 59 (1994) 5215;
(b) A. Fürstner, A. Hupperts, J. Am. Chem. Soc. 117 (1995) 4468;
(c) A. Fürstner, G. Seidel, B. Gabor, C. Kopiske, C. Krüger, R. Mynott, Tetrahedron 51 (1995) 8875;
(d) A.R. Katritzky, J. Li, J. Org. Chem. 62 (1997) 238;
(e) J. Gao, M.-Y. Hu, J.-X. Chen, S. Yuan, W.-X. Chen, Tetrahedron Lett. (1993) 1617;
(f) D.-Q. Shi, J.-X. Chen, W.-Y. Chai, W.-X. Chen, T.-Y. Kao, Tetrahedron Lett. (1993) 2963;
(g) J.-X Chen, W.-Y. Chai, J.-L. Zhu, J. Gao, W.-X. Chen, T.-Y. Kao, Synthesis (1993) 87;

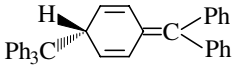
(h) R. Dams, M. Malinowski, I. Westdop, H. Geise, J. Org. Chem. 46 (1981) 2407;
(i) Y. Okude, S. Hirano, T. Hiyama, H. Nozaki, J. Am. Chem. Soc. 99 (1977) 3179;
(j) A. Fürstner, N. Shi, J. Am. Chem. Soc. 118 (1996) 12349.

[11] J.J. Eisch, X. Shi, F.A. Owuor, Oganometallics 17 (1998) 5219: the preliminary communication of the synthesis of *ansa*-metallocenes by reductive dimerization of fulvenes.

[12] For previously known methods of metallocene synthesis, the following references may be helpful:
(a) R.B. King, in: J.J. Eisch, R.B. King (Eds.), Organometallic Syntheses , vol. 2, Academic Press, New York, 1966 , p. 64;
(b) K.M. Kane, P.J. Shapiro, A. Vij, R. Cubbon, A.L. Rheingold, Organometallics 16 (1997) 4567;
(c) N.J. Long, Metallocenes – An introduction to sandwich complexes, Blackwell Science, Oxford, 1998, 285 pp.

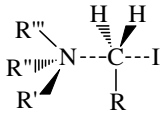
[13] J.J. Eisch, F.A. Owuor, X. Shi, Organometallics 18 (1999) 1583: the preliminary communication of the synthesis of Group 4 bis(substituted-cyclopentadienyl)metal dichlorides by the transfer-hydrometallation of fulvenes.

[14] Since Moses Gomberg's discovery of the trityl radical it was believed that the reassociation of trityl radicals would form hexaphenylethane, until NMR measurements revealed that the dimer actually has the structure shown in **a** (telltale sp^3 C–H in ^1H NMR spectrum) H. Lankamp, W.T. Nauta, C. MacLean, Tetrahedron Lett. (1968) 249,



a

[15] In organic chemistry Front or F-Strain can refer to the retardation of the quaternization of tertiary amines by alkyl iodides in S_N2 reactions, where the steric hindrance between substituents in such backside-attack raises the energy of the transition state (below). Also in equilibria of Lewis acid–Lewis base complexation, such as in $R_3'N - BR_3$ adduct formation, greater F-strain between the R and R′ groups promotes complex dissociation. Cf. M.S. Newman (Ed.), Steric Effects in Organic Chemistry, Wiley, New York, 1956, (Chapters 2 and 13).



Repulsions between R–R' and R–R" in T.S.

[16] J.N. Gitua, Doctoral Dissertation, State University of New York at Binghamton, 2005.

[17] J.J. Eisch, J.N. Gitua, D.C. Doetschman (manuscript in preparation).

[18] In the ring formation of cyclic amines from the reaction, $Br–(CH_2)_n–NH_2 \rightarrow (CH_2)_nNH \cdot HBr$, the rate of closure to the aziridine ($n = 2$) is faster by 100-fold than the closure to the azetidine ($n = 3$): G. Salomon, Helv. Chim. Acta 19 (1936) 743.

[19] Related to the proposed reactions of **38** or its zirconocene analogue with imine **9** are the interesting insertion reactions of zirconaziridines, $Cp_2Zr\text{-}\eta^2\text{-}[N(R^1)CH(R^2)](THF)$ with carbodiimides: J.A. Tunge, C.J. Czerwinski, D.A. Gately, J.R. Norton, Organometallics 20 (2001) 254.

[20] J.J. Eisch, J.N. Gitua, Organometallics 22 (2003) 24.

[21] J.J. Eisch, J.N. Gitua, Organometallics 22 (2003) 4172.

[22] J.J. Eisch, A.A. Adeosun, J.N. Gitua, Eur. J. Org. Chem. (2003) 4721.

[23] J.J. Eisch, J.N. Gitua, P.O. Otieno, A.A. Adeosun, Macromol. Symp. 213 (2004) 187.

[24] J.J. Eisch, P.O. Otieno, Eur. J. Org. Chem. (2004) 3269.

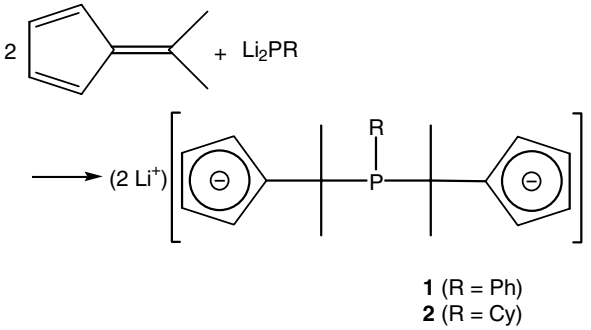
[25] K. Ziegler, W. Schaefer, Liebigs Ann. Chem. 511 (1934) 101.

[26] K. Ziegler, H.G. Gellert, H. Martin, K. Nagel, J. Schneider, Liebigs Ann. Chem. 589 (1954) 91.

[27] J.J. Eisch, A.M. Piotrowski, S.K. Brownstein, E.J. Gabe, F.L. Lee, J. Am. Chem. Soc. 107 (1985) 7219.

[28] J.J. Eisch, in: J.J. Eisch, R.B. King (Eds.), Organometallic Syntheses, vol. 2, Academic Press, New York, 1981, p. 1.

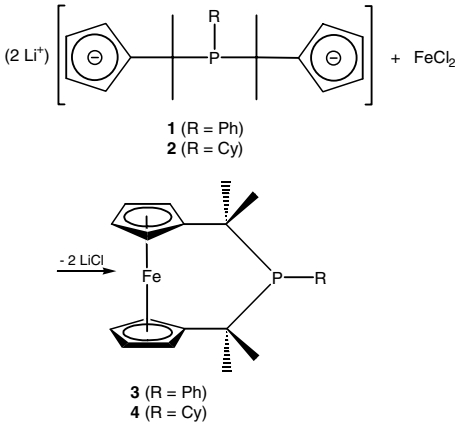
[29] J.J. Eisch, D. Drew, C.J. Peterson, J. Org. Chem. 31 (1966) 453.



(1)

The compounds Li[$(C_5H_4)CMe_2PHR$] (R = Ph, Cy) are always obtained as by-products in ca. 40% yield. We assume that Li_2PR attacks the methyl groups of 6,6-dimethylfulvene to give LiPHR, which then reacts with dimethylfulvene to give the observed by-products. The amount of Li[$(C_5H_4)CMe_2PHR$] was determined by ^{31}P NMR spectroscopy and a corresponding amount of ^{n}BuLi was added followed by 6,6-dimethylfulvene to give **1** in high yield and purity (97%) and **2** as a mixture with the monolithio salt (ca. 70% purity).

Attempts to further purify **2** failed. Therefore, preparation of the [3]ferrocenophane was carried out with the mixture of **2** and Li[$(C_5H_4)CMe_2PHR$], and [3]ferrocenophane **4** was purified by recrystallisation from toluene, while **3** was obtained from pure **1** and $FeCl_2$ in THF (Eq. (2)). The [3]ferrocenophanes are obtained as orange-yellow powders.



(2)

2.2. Spectroscopic properties of $Li_2[\{(C_5H_4)CMe_2\}_2PR]$ [R = Ph (**1**), Cy (**2**)] and of $[Fe\{(C_5H_4)CMe_2\}_2PR]$ [R = Ph (**3**), Cy (**4**)]

Compound **1** was characterised by ^{1}H, ^{13}C, ^{31}P and ^{7}Li NMR spectroscopy, and **2** only by ^{31}P NMR spectroscopy. In the ^{1}H NMR spectrum, the methyl groups of the CMe_2 group in **1** are inequivalent and exhibit different chemical shifts and coupling constants (0.95 ppm, $^{3}J_{P-H}$ = 15.5 Hz and 1.79 ppm, $^{3}J_{P-H}$ = 2.6 Hz). Two multipletts are observed at 5.21 and 5.52 ppm for the expected AA′BB′ coupling pattern of the C_5H_4 rings. In the ^{13}C NMR spectrum, a large P–C coupling constant is observed for the *ipso* carbon atom and two signals for the *ortho* carbon atoms of the phenyl ring. The latter suggest hindered rotation about the P–C(Ph) bond.

In the ^{1}H NMR spectra of **3** and **4**, two doublets with different $^{3}J_{P-H}$ coupling constants [1.09 ppm, $^{3}J_{P-H}$ = 16.8 Hz and 1.65 ppm, $^{3}J_{P-H}$ = 2.8 Hz (**3**); 1.39 ppm, $^{3}J_{P-H}$ = 15.0 Hz and 1.55 ppm, $^{3}J_{P-H}$ = 2.4 Hz (**4**)] are observed for the two inequivalent methyl groups, one of which has a *trans* and the other a *cis* orientation to the lone pair of electrons of the phosphorus atom.

2.3. Molecular structures of $[Fe\{(C_5H_4)CMe_2\}_2PR]$ [R = Ph (**3**), Cy (**4**)]

Yellow needles of **3** and **4** were obtained after recrystallisation from *n*-hexane. Compound **3** (Fig. 1) crystallises in the monoclinic space group $P2_1/n$ with four molecules in the unit cell, and compound **4** (Fig. 2) in the monoclinic space group $C2/c$ with eight molecules in the unit cell. Selected bond lengths and angles are given in Table 1. In both [3]ferrocenophanes, the cyclopentadienyl rings are almost synperiplanar and are nearly parallel [deviation 3.9° (**3**) and 4.6° (**4**)]. The small deviation from being parallel is presumably caused by the phosphanylalkyl bridge. The two methyl groups are inequivalent; one has a *trans* and the other a *cis* orientation to the lone pair of electrons of the phosphorus atom. In **3** the phenyl ring and the cyclopentadienyl rings are almost parallel (deviations: 9.6° and 8.0°).

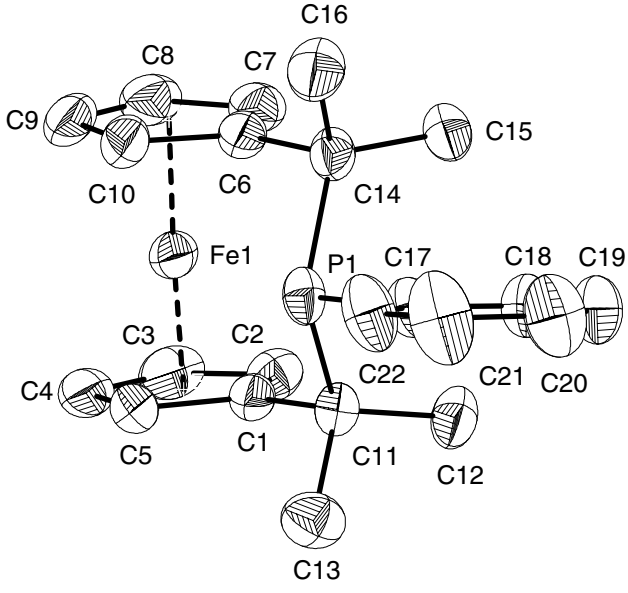


Fig. 1. Molecular structure of [Fe({(η^5-C_5H_4)CMe_2}$_2$PPh)] (**3**) showing the atom-numbering scheme employed (ORTEP plot, 50% probability, SHELXTL PLUS; XP). Hydrogen atoms are omitted for clarity.

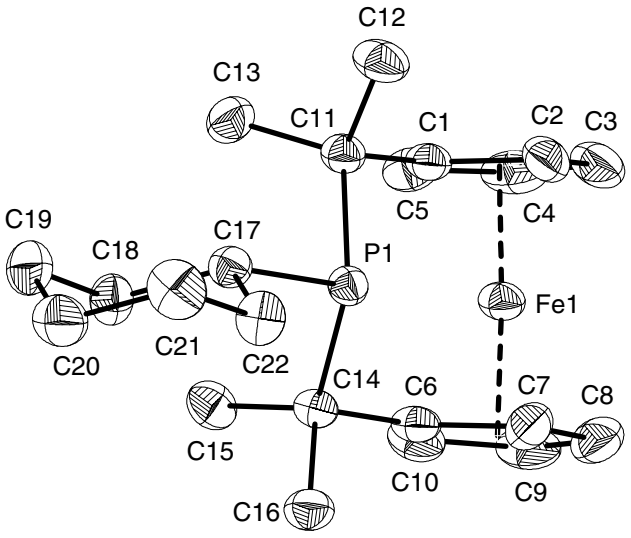


Fig. 2. Molecular structure of [Fe({(η^5-C_5H_4)CMe_2}$_2$PCy)] (**4**) showing the atom-numbering scheme employed (ORTEP plot, 50% probability, SHELXTL PLUS; XP). Hydrogen atoms are omitted for clarity.

2.4. Electrochemistry

Fig. 3 shows the cyclic voltammetric behaviour of [Fe{(η^5-C_5H_4)CMe_2}$_2$PPh] (**3**) in CH_2Cl_2 solution.

As expected for a monoferrocene complex, it undergoes an oxidation process ($E^{o\prime}$ = +0.37 V, versus SCE) with features of chemical reversibility. In fact, analysis of the cyclic voltammetric responses with scan rate increasing from 0.02 to 2.0 V s^{-1} shows that: (i) the current function $i_{pa} \cdot v^{-1/2}$ decreases by about 10% for each 10-fold increase of the scan rate; (ii) the current ratio i_{pc}/i_{pa} remains constantly equal to 1; and (iii) the peak-to-peak separation progressively increases from 76 to 182 mV. These parameters are diagnostic for an electrochemically quasireversible one-electron process which is chemically reversible on the short timescale of cyclic voltammetry [40]. In reality, as deducible from Fig. 3(b)–(d), in the longer timeframe of controlled potential coulometry (E_w = +0.7 V) the process is accompanied by the formation of a new species which in turn undergoes oxidation at higher potential ($E^{o\prime}$ = +0.80 V). On stepwise oxidation, the original yellow solution (λ_{max} = 440 nm) tends to become blue after consumption of 0.7 electrons per molecule (λ_{max} = 690 nm) (Fig. 4); then, after consumption of about 1 electron per molecule, the solution remains blue but the band shows overlap of two close absorptions (λ_{max} = 660 and 690 nm); finally, after consumption of 1.1 electrons per molecule the solution again takes on a yellow colour but absorbs at different wavelengths from the original solution (λ_{max} = 360 nm). On further exhaustive oxidation in correspondence of the second anodic process (E_w = +1.0 V), about two electrons per molecule are consumed. The final solution turns blue again and the spectrum only shows an absorption at λ_{max} = 690 nm.

Table 1
Selected distances (Å) and bond angles (°) for **3** and **4**

3	
Fe(1)–C(2)	2.034(2)
Fe(1)–C(10)	2.035(2)
Fe(1)–C(7)	2.035(2)
Fe(1)–C(6)	2.034(2)
Fe(1)–C(4)	2.037(2)
Fe(1)–C(5)	2.039(2)
Fe(1)–C(9)	2.040(2)
Fe(1)–C(8)	2.042(3)
Fe(1)–C(1)	2.045(2)
Fe(1)–C(3)	2.045(2)
P(1)–C(17)	1.844(2)
P(1)–C(11)	1.899(2)
P(1)–C(14)	1.900(2)
C(1)–C(5)	1.430(3)
C(1)–C(2)	1.435(3)
C(1)–C(11)	1.516(3)
C(2)–C(3)	1.421(3)
C(4)–C(5)	1.431(4)
C(14)–C(15)	1.534(3)
C(14)–C(16)	1.544(3)
C(6)–C(10)	1.428(3)
C(6)–C(7)	1.437(3)
C(6)–C(14)	1.516(3)
C(7)–C(8)	1.422(3)
C(8)–C(9)	1.402(4)
C(9)–C(10)	1.425(4)
C(11)–C(12)	1.524(3)
C(11)–C(13)	1.549(3)
C(17)–C(22)	1.389(3)
C(17)–C(18)	1.402(3)
C(18)–C(19)	1.382(3)
C(19)–C(20)	1.369(4)
C(20)–C(21)	1.380(4)
C(21)–C(22)	1.387(4)
C(1)–C(11)–C(13)	108.2(2)
C(12)–C(11)–C(13)	107.2(2)
C(6)–C(14)–C(15)	110.3(2)
C(6)–C(14)–C(16)	108.6(2)
C(10)–C(6)–C(7)	106.5(2)
C(8)–C(7)–C(6)	108.8(2)
C(9)–C(8)–C(7)	107.7(2)
C(19)–C(18)–C(17)	121.3(2)
C(5)–C(1)–C(2)	106.6(2)
C(4)–C(3)–C(2)	107.9(2)
C(3)–C(4)–C(5)	108.8(2)
C(1)–C(5)–C(4)	107.9(2)
C(15)–C(14)–C(16)	107.7(2)
C(10)–C(6)–C(14)	126.3(2)
C(7)–C(6)–C(14)	127.2(2)
C(22)–C(17)–C(18)	117.2(2)
C(19)–C(20)–C(21)	119.3(3)
C(6)–C(10)–C(9)	108.2(3)
C(2)–C(1)–C(11)	126.9(2)
C(1)–C(11)–C(12)	110.9(2)
C(8)–C(9)–C(10)	108.9(2)
C(11)–P(1)–C(14)	109.16(9)
C(12)–C(11)–P(1)	119.2(2)
C(13)–C(11)–P(1)	104.5(2)
C(15)–C(14)–P(1)	118.5(2)
C(22)–C(17)–P(1)	115.2(2)
C(17)–P(1)–C(11)	106.26(9)

Table 1 (*continued*)

3	
C(21)–C(22)–C(17)	121.1(2)
C(3)–C(2)–C(1)	108.8(2)
C(20)–C(19)–C(18)	120.6(2)
C(5)–C(1)–C(11)	126.4(2)
C(1)–C(11)–P(1)	106.3(1)
C(6)–C(14)–P(1)	106.5(1)
C(16)–C(14)–P(1)	104.8(2)
C(18)–C(17)–P(1)	127.5(2)
C(17)–P(1)–C(14)	103.44(9)
4	
Fe(1)–C(4)	2.031(2)
Fe(1)–C(2)	2.031(2)
Fe(1)–C(7)	2.033(2)
Fe(1)–C(10)	2.035(2)
Fe(1)–C(3)	2.038(2)
Fe(1)–C(5)	2.040(2)
Fe(1)–C(8)	2.046(2)
Fe(1)–C(9)	2.046(2)
Fe(1)–C(1)	2.051(2)
P(1)–C(17)	1.887(2)
P(1)–C(14)	1.905(2)
P(1)–C(11)	1.907(2)
C(14)–C(6)	1.518(3)
C(14)–C(15)	1.527(3)
C(14)–C(16)	1.548(3)
C(17)–C(18)	1.535(3)
C(6)–C(10)	1.441(3)
C(3)–C(4)	1.393(4)
C(1)–C(2)	1.433(3)
C(1)–C(5)	1.434(3)
C(7)–C(8)	1.426(3)
C(9)–C(8)	1.404(4)
C(9)–C(10)	1.428(3)
C(2)–C(3)	1.422(3)
C(18)–C(19)	1.527(3)
C(11)–C(12)	1.547(3)
C(20)–C(21)	1.514(4)
C(22)–C(21)	1.528(3)
C(17)–C(22)	1.534(3)
C(5)–C(4)	1.422(3)
C(11)–C(1)	1.515(3)
C(11)–C(13)	1.530(3)
C(1)–C(11)–C(13)	111.3(2)
C(1)–C(11)–C(12)	107.2(2)
C(13)–C(11)–C(12)	107.5(2)
C(1)–C(11)–P(1)	108.5(1)
C(13)–C(11)–P(1)	116.9(1)
C(12)–C(11)–P(1)	104.9(1)
C(7)–C(6)–C(10)	106.5(2)
C(7)–C(6)–C(14)	126.8(2)
C(10)–C(6)–C(14)	126.7(2)
C(21)–C(22)–C(17)	112.2(2)
C(6)–C(14)–C(15)	109.5(2)
C(6)–C(14)–C(16)	107.4(2)
C(15)–C(14)–C(16)	108.8(2)
C(19)–C(18)–C(17)	111.6(2)
C(18)–C(17)–C(22)	109.6(2)
C(17)–P(1)–C(11)	102.95(8)
C(6)–C(14)–P(1)	106.1(1)
C(15)–C(14)–P(1)	119.0(1)
C(16)–C(14)–P(1)	105.4(1)
C(19)–C(20)–C(21)	110.8(2)
C(4)–C(3)–C(2)	108.1(2)

Table 1 (*continued*)

4	
C(2)–C(1)–C(5)	106.0(2)
C(8)–C(9)–C(10)	108.4(2)
C(2)–C(1)–C(11)	126.1(2)
C(5)–C(1)–C(11)	127.9(2)
C(8)–C(7)–C(6)	108.6(2)
C(9)–C(8)–C(7)	108.3(2)
C(9)–C(10)–C(6)	108.2(2)
C(3)–C(2)–C(1)	108.8(2)
C(3)–C(4)–C(5)	108.6(2)
C(4)–C(5)–C(1)	108.5(2)
C(20)–C(21)–C(22)	111.9(2)
C(20)–C(19)–C(18)	111.3(2)
C(14)–P(1)–C(11)	108.89(8)
C(17)–P(1)–C(14)	108.50(8)
C(18)–C(17)–P(1)	121.3(1)
C(22)–C(17)–P(1)	109.6(1)

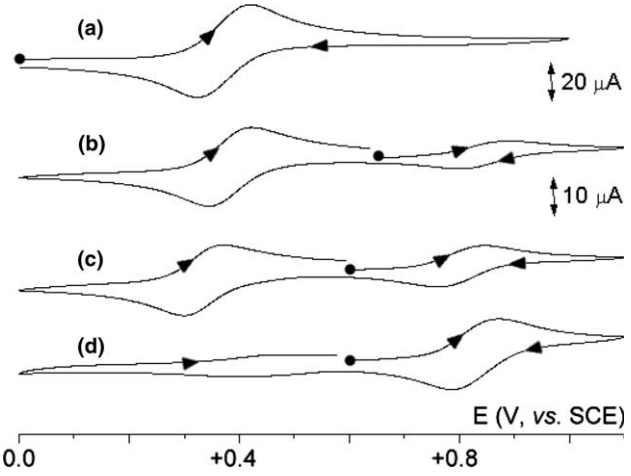


Fig. 3. Cyclic voltammetric responses recorded at a platinum electrode for a CH_2Cl_2 solution of $[Fe\{(\eta^5\text{-}C_5H_4)CMe_2\}_2PPh]$ (**3**) (1.9×10^{-3} mol dm^{-3}) before and after controlled potential coulometry. $[NBu_4][PF_6]$ (0.2 mol dm^{-3}) supporting electrolyte. (a) Original solution; (b) after consumption of 0.7 electrons per molecule; (c) after consumption of 0.9/1.0 electrons per molecule; (d) after consumption of 1.1 electrons per molecule. (●) Starting potential. Scan rate: 0.2 V s^{-1}.

In an attempt to account for such electrochemical behaviour, it is useful to note that the formation of uncharacterised products was also observed in the irreversible oxidation of both the [1]ferrocenophane $[Fe(\eta^5\text{-}C_5H_4)_2PPhMe]^+$ [41] and the [5]ferrocenophane $[Fe\{(\eta^5\text{-}C_5H_4)CH_2CH_2\}_2PPh]$ [13]. In particular, in the latter case, this has been attributed to a dimerisation reaction (with formation of a P–P bond) rather than to formation of the corresponding phosphine oxide $[Fe\{(\eta^5\text{-}C_5H_4)CH_2CH_2\}_2P(O)Ph]$ [13], since the oxidation potential of the by-product arising from the primary process $[Fe\{(\eta^5\text{-}C_5H_4)CH_2CH_2\}_2PPh]^{0/+}$ looks different from that of a crystallographically characterised sample of $[Fe\{(\eta^5\text{-}C_5H_4)CH_2CH_2\}_2P(O)Ph]$. We

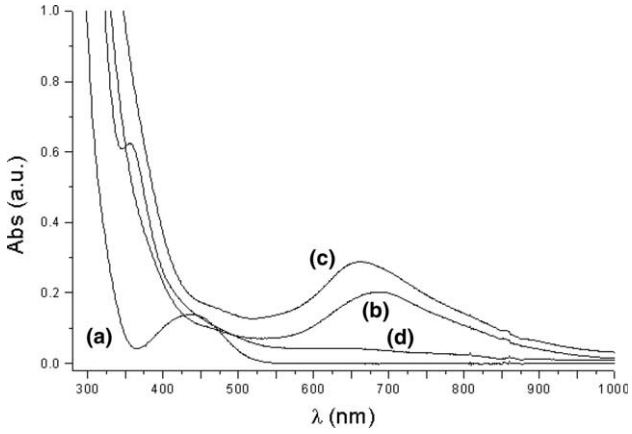


Fig. 4. UV/Vis spectral profiles obtained on stepwise oxidation of $[Fe\{(\eta^5\text{-}C_5H_4)CMe_2\}_2PPh]$ (**3**) (1.9×10^{-3} mol dm^{-3}) in correspondence of the primary anodic process. CH_2Cl_2 solution containing $[NBu_4][PF_6]$ (0.2 mol dm^{-3}) as supporting electrolyte. (a) Original solution; (b) after 0.7 electrons/molecule; (c) after 0.9/1.0 electrons/molecule; (d) after 1.1 electrons/molecule.

note, however, that the comparison of the two oxidation processes was done in different solvents. In our case we are inclined to assign the secondary step as due to the process $[Fe\{(\eta^5\text{-}C_5H_4)CMe_2\}_2P(O)Ph]^{0/+}$, since $[Fe\{(\eta^5\text{-}C_5H_4)CMe_2\}_2PPh]$, even in the solid state, proved to be air-sensitive. This assumption is also supported by the observation that a powdered sample that was not maintained under strictly anaerobic conditions (for about one month) also showed this second oxidation step.

Table 2
Crystal data and structure refinement for **3** and **4**

	3	**4**
Empirical formula	$C_{22}H_{25}FeP$	$C_{22}H_{31}FeP$
M_r	376.24	382.29
Temperature (K)	220(2)	210(2)
Crystal system	monoclinic	monoclinic
Space group	$P2_1/n$	$C2/c$
Unit cell dimensions		
a (Å)	15.7183(6)	35.053(5)
b (Å)	8.5450(3)	6.386(5)
c (Å)	15.7434(6)	18.088(5)
β (°)	117.916(1)	111.124(5)
V (Å^3)	1868.5(1)	3777(3)
Z	4	8
$\rho_{calc.}$ (Mg m^{-3})	1.337	1.345
$F(000)$	792	1632
Crystal size (mm)	$0.50\times0.30\times0.20$	$0.40\times0.20\times0.10$
Absorption coefficient (mm^{-1})	0.892	0.884
Θ range (°)	1.51–28.28	1.25–28.95
Reflections collected	11 382	14 839
Independent reflections	4446	4628
R_{int}	0.0255	0.0332
Parameters	317	341
$R[I > 2\sigma(I)]$	0.0362	0.0314
wR_2 (all data)	0.1124	0.0978
$\Delta/\rho_{min.}$ (e Å^{-3})	0.475	0.299
$\Delta/\rho_{max.}$ (e Å^{-3})	−0.743	−0.356

Table 3
Formal electrode potentials (V, vs. SCE) for the one-electron oxidation of different phosphaferrocenophanes

Complex	$E^{o\prime}$	Solvent	Ref.
$[Fe(C_5Me_4)_2PPh]$	+0.37	CH_2Cl_2	[45]
	+0.50	THF	[45]
$[Fe(C_5H_4)_2PPhMe]^+$	+1.11[a]	CH_2Cl_2	[41]
$[Fe\{(C_5Me_4)(C_5H_4)\}CH_2PPh]$	+0.26	CH_2Cl_2	[12]
$[Fe\{(C_5H_4)CMe_2\}_2PPh]$	+0.37	CH_2Cl_2	[b]
$[Fe\{(C_5H_4)CH_2CH_2\}_2PPh]$	+0.04[a]	MeCN	[13]
$[Fe(C_5H_5)_2]$	+0.39	CH_2Cl_2	[b]

[a] Peak potential for irreversible processes.
[b] This work.

On this basis, a tentative explanation of the electrochemical data would be that the primarily generated ferrocenium ion $[\mathbf{3}]^+$ reacts with traces of air (or water from the nominally anhydrous solvent) to give $[Fe\{(\eta^5\text{-}C_5H_4)CMe_2\}_2P(O)Ph]^+$, which, because of the inappropriate potential, is reduced to the corresponding ferrocene $[Fe\{(\eta^5\text{-}C_5H_4)CMe_2\}_2P(O)Ph]$; on application of the proper potential, the latter is again oxidised to the corresponding monocation.

Table 3 compiles the redox potentials for the ferrocene/ferrocenium process in a series of phosphaferrocenophanes.

We note that the oxidation of methylated derivatives such as $[Fe\{(C_5H_4)CMe_2\}_2PPh]$, $[Fe(C_5Me_4)_2PPh]$ and $[Fe\{(C_5Me_4)(C_5H_4)\}CH_2PPh]$ occurs at potentials similar to that of unsubstituted ferrocene, and this suggests that the electron-donating ability of the bridging carbon atoms or the cyclopentadienyl methyl groups is attenuated by the electron-withdrawing ability of the PPh group.

3. Experimental

3.1. General

All experiments were carried out under purified dry nitrogen. Solvents were dried and freshly distilled under argon. The NMR spectra were recorded with an AVANCE DRX 400 spectrometer (Bruker), ^{1}H NMR: internal standard TMS; ^{13}C NMR: internal standard TMS; ^{31}P NMR: external standard 85% H_3PO_4. The IR spectra were recorded on an FT-IR spectrometer Perkin–Elmer System 2000 in the range 350–4000 cm^{-1}. MS: MAT 8230 (Finnigan) 70 eV. The melting points were determined in sealed capillaries under nitrogen and are uncorrected (BOETIUS). Materials and apparatus for electrochemistry and spectroelectrochemistry have been described elsewhere [42]. Potential values are referred to the saturated calomel electrode (SCE).

Li_2PR (R = Ph, Cy) were prepared from PH_2R and two equivalents of MeLi. $FeCl_2$ is commercially available.

3.2. Synthesis of dilithiumphenylphosphinobis(dimethylmethylcyclopentadienide), $Li_2[\{(C_5H_4)CMe_2\}_2PPh]$ (**1**)

6,6-Dimethylfulvene (4.33 ml, 36 mmol) was added dropwise to a suspension of Li_2PPh (2.2 g, 18 mmol) in 50 ml of Et_2O and stirred for at least 12 h, during which time the yellow suspension turned colourless. The solid was isolated by filtration, washed 3 times with 30 ml of Et_2O and dried in vacuo. The amount of $Li[(C_5H_4)CMe_2PHPh]$ was determined by ^{31}P NMR spectroscopy. The mixture was dissolved in 30 ml of THF and the appropriate amount of $^{n}BuLi$ (corresponding to the amount of $Li[(C_5H_4)CMe_2PHPh]$) was added. The solvent was evaporated, the residue was suspended in Et_2O and the appropriate amount of 6,6-dimethylfulvene was added. After stirring for 12 h the colourless solid was isolated by filtration, washed with Et_2O and *n*-hexane and dried. Yield: 4.9 g (81.5%) of **1** as a colourless air-sensitive powder. M.p.: 256 °C (decomp.).

^1H NMR (THF-d_8): δ 0.95 (d, $^3J_{P-H}$ = 15.5, 6H, CH_3 in CMe_2), 1.79 (d, $^3J_{P-H}$ = 2.6, 6H, CH_3 in CMe_2), 5.21 (m, 4H, C*H* in C_5H_4), 5.52 (m, 4H, C*H* in C_5H_4), 7.26 (m, 3H, *o*- and *p*-C*H* in Ph), 7.93 (m, 2H, *m*-C*H* in Ph). $^{13}C\{^1H\}$ NMR (THF-d_8): δ 26.20 (d, $^2J_{P-C}$ = 4.1, C–CH_3), 35.50 (d, $^2J_{P-C}$ = 26.5, C–CH_3), 37.40 (d, $^1J_{P-C}$ = 39.4, *C*–CH_3), 102.30 (s, *m*-*C* in C_5H_4), 104.10 (d, $^3J_{P-C}$ = 6.6, *o*-*C* in C_5H_4), 127.58 (d, $^2J_{P-C}$ = 14.1, *ipso*-*C* in C_5H_4), 127.64 (d, $^3J_{P-C}$ = 8.4, *m*-*C* in Ph), 128.50 (s, *p*-*C* in Ph), 136.00 (d, $^2J_{P-C}$ = 14.1, *o*-*C* in Ph), 138 (d, br, $^2J_{P-C}$ = 14.0, *o*-*C* in Ph), 143.80 (d, $^1J_{P-C}$ = 41.9, *ipso*-*C* in Ph). ^{31}P NMR (THF-d_8): δ 42.9, s. ^7Li NMR (THF-d_8): δ = −7.2, s. IR $\tilde{\nu}$ (cm^{-1}): 3074 w (ν(CH) aryl), 2864 m ($\nu(CH_3)$), 1462–1360 m ($\delta(CH_3)$).

3.3. Synthesis of dilithiumcyclohexylphosphinobis-(dimethylmethylcyclopentadienide), $Li_2[\{(C_5H_4)CMe_2\}_2PCy]$ (**2**)

Analogously to the synthesis of **1** from Li_2PCy (1 g, 7.8 mmol) in 50 ml Et_2O and 6,6-dimethylfulvene (1.9 ml, 15.6 mmol). The amount of $Li[(C_5H_4)CMe_2PHCy]$ was determined by ^{31}P NMR spectroscopy. The mixture was dissolved in 30 ml of THF and the appropriate amount of $^{n}BuLi$ (corresponding to the amount of $Li[(C_5H_4)CMe_2PHCy]$) was added. The solvent was evaporated, the residue suspended in Et_2O and the appropriate amount of 6,6-dimethylfulvene added. After stirring for 12 h the colourless solid was isolated by filtration, washed with Et_2O and *n*-hexane and dried. Yield: 2.5 g of **2** (m.p.: 257 °C (decomp.)) as a colourless air-sensitive powder, which contained ca. 30% of $Li[(C_5H_4)CMe_2PHCy]$. Attempts to further purify **2** failed. Therefore the mixture was employed in the synthesis of **4**.

^{31}P NMR (THF-d_8): δ 54.0, s.

3.4. Synthesis of [bis(cyclopentadienyldimethylmethyl)-phenylphosphino]ferrocenophane, $[Fe\{(C_5H_4)CMe_2\}_2PPh]$ (**3**)

Solid **1** (1.2 g, 3.6 mmol) was added in small portions to a suspension of $FeCl_2$ (0.46 g, 3.6 mmol) in 50 ml of THF. The solution turned yellow to brown. After stirring overnight the solvent was evaporated and 50 ml of Et_2O was added to the remaining brown oil, giving a brown solid and an orange solution. The solution was filtered over dry Al_2O_3, and the residue washed repeatedly with Et_2O until the washings were colourless. The Et_2O fractions were combined and the solvent evaporated. Fifty millilitres of hexane was added to the residue, filtered and the hexane evaporated leaving 1.0 g (74%) of **3** as an orange powder. Yellow crystals were obtained from a concentrated solution of **3** in *n*-hexane at −20 °C. M.p.: 143 °C.

^1H NMR ($CDCl_3$): δ 1.09 (d, $^3J_{P-H}$ = 16.8, 6H, CH_3 in CMe_2), 1.65 (d, $^3J_{P-H}$ = 2.8, 6H, CH_3 in CMe_2), 4.05 (s, 2H, C*H* in C_5H_4), 4.16 (s, 2H, C*H* in C_5H_4), 4.19 (s, 2H, C*H* in C_5H_4), 4.41 (s, 2H, C*H* in C_5H_4), 7.42 (m, 3H, *o*- and *p*-C*H* in Ph), 7.86 (m, 2H, *m*-C*H* in Ph). $^{13}C\{^1H\}$ NMR ($CDCl_3$): δ 24.3 (d, $^2J_{P-C}$ = 5.0, C–CH_3), 31.7 (d, $^2J_{P-C}$ = 33.9, C–CH_3), 32.1 (d, $^1J_{P-C}$ = 22.3, *C*–CH_3), 67.0 (d, $^4J_{P-C}$ = 2.1, *C*H in C_5H_4), 67.2 (d, $^4J_{P-C}$ = 2.5, *C*H in C_5H_4), 68.8 (d, $^3J_{P-C}$ = 6.2, *C*H in C_5H_4), 95.0 (d, $^2J_{P-C}$ = 12.4, *ipso*-*C* in C_5H_4), 127.8 (d, $^3J_{P-C}$ = 8.3, *m*-*C* in Ph), 129.0 (s, *p*-*C* in Ph), 136.7 (d, $^2J_{P-C}$ = 23.9, *o*-*C* in Ph), 137.8 (d, $^1J_{P-C}$ = 34.7, *ipso*-*C* in Ph). ^{31}P NMR ($CDCl_3$): δ = 50.5, s. IR (KBr), $\tilde{\nu}$ (cm^{-1}): 3077 m (ν(CH) aryl), 2969 s ($\nu(CH_3)$), 1431 br, m ($\delta(CH_3)$), 1359 m (ν(CC) in C_5H_4). EI-MS: *m*/*z* = 376 (100%, M^+), 268 (69%, M^+ − PPh), and fragmentation products thereof. *Anal.* Calc. for $C_{22}H_{25}PFe$ (376): C, 70.2; H, 6.7; P, 8.2. Found: C, 70.1; H, 5.1; P, 7.6%.

3.5. Synthesis of [bis(cyclopentadienyldimethylmethyl)-cyclohexylphosphino]ferrocenophane, $[Fe\{(C_5H_4)CMe_2\}_2PCy]$ (**4**)

The mixture containing **2** (0.50 g, 1.47 mmol) and $Li[(C_5H_4)CMe_2PHCy]$ (0.15 g, 0.65 mmol), obtained as described above, was added as a solid in small portions to a suspension of $FeCl_2$ (0.23 g, 1.8 mmol) in 25 ml of THF. The solution turned yellow, then brown and finally almost black. After stirring overnight the solvent was evaporated and 50 ml of Et_2O was added to the remaining black oil giving a brown solid and an orange solution. The solution was filtered over dry Al_2O_3, and the residue washed repeatedly with Et_2O until the washings were colourless. The Et_2O fractions were combined and the solvent evaporated. The residue was recrystallised from 10 ml of *n*-hexane giving 0.27 g (48%) of **4** as yellow crystals. M.p.: 188 °C.

^{1}H NMR ($CDCl_3$): δ 1.2–1.9 (br, m, 11H, C*H* and CH_2 in Cy), 1.39 (d, $^3J_{P-H}$ = 15.0, 6H, CH_3 in CMe_2), 1.55 (d, $^3J_{P-H}$ = 2.4, 6H, CH_3 in CMe_2), 3.99 (s, 2H, C*H* in C_5H_4), 4.04 (s, 2H, C*H* in C_5H_4), 4.09 (s, 2H, C*H* in C_5H_4), 4.27 (s, 2H, C*H* in C_5H_4). $^{13}C\{^1H\}$ NMR ($CDCl_3$): δ 24.92 (d, $^2J_{P-C}$ = 4.2, C–*C*H_3), 26.49 (s, *C*4 in Cy), 28.85 (d, $^3J_{P-C}$ = 9.3, *C*3 in Cy), 32.43 (d, $^2J_{P-C}$ = 31.9, C–*C*H_3), 32.65 (d, *C*–CH_3, $^2J_{P-C}$ = 26.5), 34.40 (d, J_{P-C} = 15.2, *C*2 in Cy), 38.84 (d, $^1J_{P-C}$ = 35.0, *C*1 in Cy), 66.37 (d, $^4J_{P-C}$ = 2.7, *C*H in C_5H_4), 66.86 (d, $^4J_{P-C}$ = 2.0, *C*H in C_5H_4), 68.66 (d, $^3J_{P-C}$ = 8.4, *C*H in C_5H_4), 68.75 (s, *C*H in C_5H_4), 96.2 (d, $^2J_{P-C}$ = 11.3, *ipso-C* in C_5H_4). ^{31}P NMR ($CDCl_3$): δ 67.8, s. IR (KBr), $\tilde{\nu}$ (cm^{-1}): 2970 s ($\nu(CH_3)$), 1444 br, m ($\delta(CH_3)$), 1359 m (ν(CC) in C_5H_4). EI-MS: *m*/*z* = 382 (26%, M^+), 267 (100%, M^+ – PCy), and fragmentation products thereof. *Anal*. Calc. for $C_{22}H_{31}PFe$ (382): C, 69.1; H, 8.2. Found: C, 68.5; H, 7.3%.

3.6. Data collection and structural refinement of **3** and **4**

Data (λ(Mo Kα) = 0.71073 Å) were collected with a Siemens CCD (SMART) diffractometer. All observed reflections were used for refinement (SAINT) of the unit cell parameters. Empirical absorption correction was applied with SADABS [43]. The structures were solved by direct methods (SHELXTL PLUS) [44]. Fe, P and C atoms were refined anisotropically; H atoms were located by difference maps and refined isotropically. Table 2 lists crystallographic details.

4. Supplementary material

CCDC 266919 (**3**) and 266918 (**4**) contain the supplementary crystallographic data for this paper. These data can be obtained free of charge from the Cambridge Crystallographic Data Centre (CCDC), 12 Union Road, Cambridge CB2 1EZ, UK via www.ccdc.cam.ac.uk/data_request/cif, e-mail: deposit@ccdc.cam.ac.uk.

Acknowledgement

P.Z. gratefully acknowledges the financial support from the University of Siena (PAR 2003).

References

[1] A. Togni, T. Hayashi, Ferrocenes, VCH, Weinheim, 1995.
[2] M. Herberhold, F. Hertel, W. Milius, B. Wrackmeyer, J. Organomet. Chem. 582 (1999) 352.
[3] I.R. Butler, W.R. Cullen, F.W.B. Einstein, S.J. Rettig, A.J. Willis, Organometallics 2 (1983) 128.
[4] H. Stoeckli-Evans, A.G. Osborne, R.H. Whiteley, J. Organomet. Chem. 194 (1980) 91.
[5] I.R. Butler, W.R. Cullen, S.J. Rettig, Organometallics 6 (1987) 872.
[6] T. Mizuta, T. Yamasaki, K. Miyoshi, Chem. Lett. (2000) 924.
[7] C.E.B. Evans, A.J. Lough, H. Grondey, I. Manners, New J. Chem. Nouv. J. Chim. 24 (2000) 447.
[8] T. Mizuta, M. Onishi, K. Miyoshi, Organometallics 19 (2000) 5005.
[9] H. Brunner, J. Klankermayer, M. Zabel, J. Organomet. Chem. 601 (2000) 211.
[10] C.H. Honeyman, D.A. Foucher, F.Y. Dahmen, R. Rulkens, A.J. Lough, I. Manners, Organometallics 14 (1995) 5503.
[11] T. Mizuta, T. Yamasaki, H. Nakazawa, K. Miyoshi, Organometallics 15 (1996) 1093.
[12] R. Resendes, J.M. Nelson, A. Fischer, F. Jäkle, A. Bartole, A.J. Lough, I. Manners, J. Am. Chem. Soc. 123 (2001) 2116.
[13] J.J. Adams, O.J. Curnow, G. Huttner, S.J. Smail, M.M. Turnbull, J. Organomet. Chem. 577 (1999) 44.
[14] C. Charrier, F. Mathey, Tetrahedron Lett. 19 (1978) 2407.
[15] Review: P. Jutzi, T. Redeker, Eur. J. Inorg. Chem. (1998) 663.
[16] H. Butenschön, Chem. Rev. 100 (2000) 1527.
[17] A.M. Bensley Jr., E.A. Mintz, J. Organomet. Chem. 353 (1988) 93 (and references therein).
[18] R.T. Kettenbach, W. Bonrath, H. Butenschön, Chem. Ber. 126 (1993) 1657.
[19] B.E. Bosch, G. Erker, R. Fröhlich, O. Meyer, Organometallics 16 (1997) 5449.
[20] C. Charrier, F. Mathey, J. Organomet. Chem. 170 (1979) C41.
[21] T. Kauffmann, J. Ennen, H. Lhotak, A. Rensing, F. Steinseifer, A. Woltermann, Angew. Chem. 92 (1980) 321.
[22] T.-F. Wang, J.-P. Juang, Y.-S. Wen, J. Organomet. Chem. 503 (1995) 117.
[23] J. Szymoniak, J. Besançon, A. Dormond, C. Moïse, J. Org. Chem. 55 (1990) 1429.
[24] N.E. Schore, J. Am. Chem. Soc. 101 (1979) 7410.
[25] N.E. Schore, L.S. Benner, B.E. LaBelle, Inorg. Chem. 20 (1981) 3200.
[26] N.E. Schore, S. Sundar, J. Organomet. Chem. 184 (1980) C44.
[27] S.R. Iyer, D.R. Tueting, N.E. Schore, J. Organomet. Chem. 320 (1987) 339.
[28] N.E. Schore, B.E. LaBelle, J. Org. Chem. 46 (1981) 2306.
[29] T.A. Mobley, R.G. Bergman, J. Am. Chem. Soc. 120 (1998) 3253.
[30] D.M. Bensley Jr., E.A. Mintz, S.J. Sussangkarn, J. Org. Chem. 53 (1988) 4417.
[31] Y. Kataoka, Y. Saito, K. Nagata, K. Kitamura, A. Shibahara, K. Tani, Chem. Lett. (1995) 833.
[32] M.D. Fryzuk, S.S.H. Mao, M.J. Zaworotko, L.R. MacGillivray, J. Am. Chem. Soc. 115 (1993) 5336.
[33] T. Kauffmann, J. Olbrich, Tetrahedron Lett. 25 (1984) 1967.
[34] B. Antelmann, U. Winterhalter, G. Huttner, B.C. Janssen, J. Vogelgesang, J. Organomet. Chem. 545–546 (1997) 407.
[35] O.J. Curnow, G. Huttner, S.J. Smail, M.M. Turnbull, J. Organomet. Chem. 524 (1996) 267.
[36] Review: T. Cuenca, P. Royo, Coord. Chem. Rev. 193–195 (1999) 447.
[37] Review: C.S. Slone, D.A. Weinberger, C.A. Mirkin, Prog. Inorg. Chem. 48 (1999) 233.
[38] T. Koch, E. Hey-Hawkins, Polyhedron 18 (1999) 2113.
[39] T. Koch, S. Blaurock, F.B. Somoza Jr., A. Voigt, R. Kirmse, E. Hey-Hawkins, Organometallics 19 (2000) 2556.
[40] P. Zanello, Inorganic Electrochemistry. Theory, Practice and Application, RS.C, Cambridge, United Kingdom, 2003.
[41] T.J. Peckham, A.J. Lough, I. Manners, Organometallics 18 (1999) 1030.
[42] F. Fabrizi de Biani, M. Corsini, P. Zanello, H. Yao, M.E. Bluhm, R.N. Grimes, J. Am. Chem. Soc. 126 (2004) 11360.
[43] G.M. Sheldrick, SADABS – A Program for Empirical Absorption Correction, Göttingen, 1998.
[44] SHELXTL PLUS, Siemens Analyt. X-ray Inst. Inc., XS: Program for Crystal Structure Solution, XL: Program for Crystal Structure Determination, XP: Interactive Molecular Graphics, 1990.
[45] M. Viotte, B. Gautheron, M.M. Kubicki, Y. Mugnier, R.V. Parish, Inorg. Chem. 34 (1995) 3465.

copolymer results in significant increase in viscoelastic, mechanical properties and compatibility of ES copolymers with LLDPE [7]. Additionally, ES copolymers contain syndiotactic styrene dyads, which enhance the thermal properties, as syndiotactic polystyrene is known to have a T_m of 273 °C.

Other discoveries put forth regarding piano-stool catalysts include the effect that substitution of alkyl groups on the cyclopentadienyl ring and of the halides on the titanium catalyst center for various substituents has on the copolymerization of ethylene and α-olefins. Most significant to this work are Nomura's publications on the aryloxy substituted $CpTi(R)_2OAr$ complexes [8–13]. The authors found that by substituting one of the halide groups on the Ti catalyst center with an aryloxy group, polyethylene, poly(ethylene-*co*-1-butene), and poly(ethylene-*co*-styrene) could be obtained with reasonable activity, molecular weight, polydispersity, and comonomer distribution [8–13].

There is a significant commercial drive to combine the inherent advantages of SSC catalysts (high activity, control over monomer reactivity and polymer structure control) with the attributes of supported catalyst technology (morphology and high bulk density control) [14]. With this in mind, piano-stool catalysts have been supported on a variety of substrates including, but not limited to, lightly cross-linked polystyrene beads [15], alumina or $MgCl_2$ [14], butyl ethylmagnesium treated silica [14], mesoporous silica [16], and (4-hydroxystyrene)-styrene (HPS) copolymers [17].

In this work, various piano-stool catalysts were reacted with a (4-hydroxystyrene) styrene copolymer (HPS), in essence creating bulky aryloxy substituents (macroligand). We have previously shown that the presence of the macroligand is vital for the production of butyl branched polyethylene produced during ethylene homopolymerization [18]. More importantly, the support should be regarded as a part of the ligand–metal environment. Hence, chemical and structural changes to the support affect the overall performance of the piano-stool complex bound to the HPS support [18]. In this paper, the use of macroligated catalysts for the copolymerization of ethylene with 1-octene and styrene has been explored. The effect of using the macroligated catalysts with appropriate cocatalysts for ethylene/α-olefin copolymerization on the molecular weight, branch content, melting temperature, degree of crystallinity, and copolymer microstructure has been analyzed in detail.

2. Experimental

2.1. Reagents and general techniques

All reactions were performed under nitrogen in Schlenk glassware or in an inert atmosphere dry box. All solvents used were obtained from a solvent manifold [19]. Titanium tetrachloride, bis(trimethylsilyl)cyclopentadiene, 2,5,5-tris(trimethylsilyl)-1,3-cyclopentadiene, cyclopentadienyltitanium trichloride, pentamethyl-cyclopentadienyltitanium trichloride, styrene, 4-acetoxy styrene, AIBN, tetrahydrofuran, and hydrazine hydrate were obtained from Aldrich. AIBN was recrystallized from acetone, and styrene was distilled over calcium hydride. Methyl aluminoxane (MAO, 30 wt% (4.7 M) in toluene) was generously supplied by Albemarle. The copolymerizations were performed using heavy-walled glass reactors and a polymerization manifold [20]. The styrene-*co*-hydroxy styrene (HPS, macroligand) and the supported aryloxy cyclopentadienyltitanium trichloride complexes were synthesized as previously reported [18].

2.2. Instrumentation

^{13}C NMR spectra of the polyolefins in tetrachloroethylene-d_2 were recorded at 150 MHz on an Avance DPX 600 using a quantitative pulse program for solution NMR at 135 °C. Gel permeation chromatography (GPC) of the polyolefins was performed with a Polymer Laboratories PL-220 high temperature GPC equipped with a Wyatt MiniDawn (620 nm diode laser) high temperature light scattering detector and refractive index detector. Experiments were performed at 135 °C using 1,2,4-trichlorobenzene as solvent, and results were based on calibration with polystyrene standards. The dn/dc value for polyethylene used was −0.11. Thermal analyses were performed using a TA differential scanning calorimeter (DSC) 2910 equipped with liquid nitrogen cooling accessory unit. Experiments were performed under a continuous nitrogen purge (50 mL/min) with a heating and cooling scan rate of 10 °C/min.

3. General procedure for supported catalyst preparation (HPS-Ti-1 to -4)

Synthesis of the support matrix poly(styrene-*r*-4-hydroxystyrene (HPS)) and subsequent assembly of the aryloxy piano stool complex on HPS was carried out in the glovebox using precursor catalysts (**1**–**4**) as previously reported [18,21]. The support contains 0.3 mol% hydroxystyrene, as determined by ^1H NMR. The supported catalysts were analyzed via elemental analysis in order to determine the weight percent of Ti, as well as the ratio of Cl:Ti. For all cases, it was determined that the Cl:Ti ratio was between 1 and 2, meaning that the most prevalent forms of the supported catalysts were Form A and Form B (Fig. 1). Although a Form C (containing three bonds to the macroligand) is not ruled out, the authors believe that this form would be sterically hindered. The reaction of the homogeneous

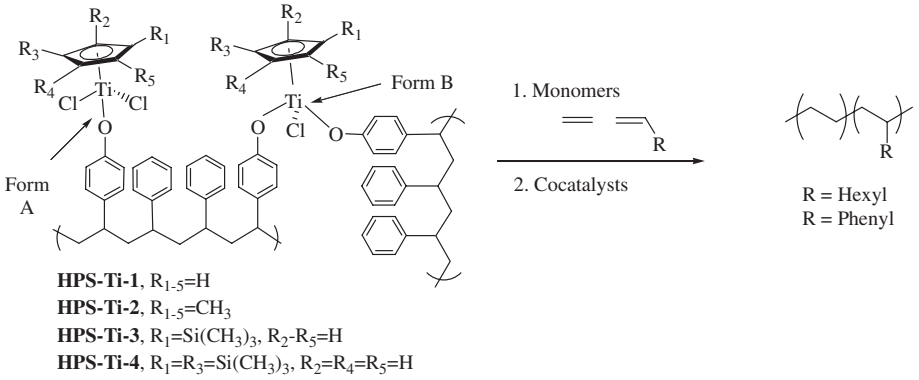


Fig. 1. Synthesis of ethylene/α-olefin random copolymers using supported aryloxy piano stool complexes.

catalysts with the support was observed to form a gel, which further supports the crosslinked structure outlined in Fig. 1. Independent confirmation of the proposed supported structure was obtained via ^{1}H and ^{13}C NMR. The ^{1}H NMR displays a downfield shift for the trimethylsilyl protons from δ 0.2 for the precursor of **HPS-Ti-4** to δ 0.4 ppm for **HPS-Ti-4**. Further confirmation of the presence of Forms A and B was obtained from the ^{13}C NMR of **HPS-Ti-4**, which displays two peaks in the trimethylsilyl region at δ −0.1 (Form A) and δ 1.5 ppm (Form B).

4. Synthesis of mono(phenoxy)(trimethylsilylcyclopentadienyl) titanium(IV) dichloride (5)

To a mixture of 10.0 mL of dichoromethane and (trimethylsilyl)cyclopentadienyltitanium trichloride (**3**, 102 mg, 0.34 mmol), phenol (32 mg, 0.35 mmol) was added slowly with constant stirring, The reaction was allowed to proceed at room temperature for a period of 12 h. The solvent was removed in vacuo, affording an orange solid (110 mg, 82% yield).

^{1}H NMR ($CDCl_3$): 0.4 (s, 9H, $Si(CH_3)_3$), 6.8 (t, 2H), 7.1 (t, 2H), 7.0–7.4 (m, 5H, C_6H_5).

^{13}C NMR ($CDCl_3$, CPD): −0.2, 118.8, 124.6, 123.9, 126.9, 128.6, 129.8, 137.5, 168.3.

5. Synthesis of bis(phenoxy)(trimethylsilyl-(cyclopentadienyl)) titanium(IV) chloride (6)

To a solution of 10.0 mL of toluene and (trimethylsilyl)cyclopentadienyltitanium trichloride (**3**, 102 mg, 0.34 mmol), phenol (75 mg, 0.7 mmol) was added slowly with constant stirring, and the reaction mixture was refluxed for a period of 1 day. The solvent was removed in vacuo, affording a red solid in 90% yield.

^{1}H NMR ($CDCl_3$): 0.3 (s, 9H, $Si(CH_3)_3$), 6.6–7.4 (m,14H, C_6H_5, C_5H_4).

^{13}C NMR ($CDCl_3$, CPD): 0.0, 115.7, 118.9, 121.5, 123.2, 126.3, 130.1, 133.7, 167.6.

6. Copolymerization of ethylene and 1-octene

To a mixture of 10.0 mL of toluene and 1.7 mL of 30 wt% of MAO in toluene in a polymerization reactor, 38.2 mg of **HPS-Ti-1** was added. To this system, 1-octene (5 mL) was added, and ethylene (60 psig) was supplied for 15 min with stirring. The ethylene supply was stopped and the reactor was vented to remove excess ethylene, the reaction mixture was quenched with 10% hydrochloric acid–methanol mixture and the polymer was collected by filtration and dried in vacuo overnight resulting in ethylene/1-octene copolymer (Table 1,

Table 1
Ethylene/1-octene copolymerization using macroligated catalysts in conjunction with MAO

Entry	Catalysts	Al:Ti	Activity (kg/mol Ti h atm)	T_m[a] (°C)	1-Octene incorporation (mol%)[a,b]	M_w[c] ($\times 10^{-3}$)	PDI[c]
1	**HPS-Ti-1**	511	48	116.4	2.5	268	broad
2	**HPS-Ti-2**	665	17	119.8	2.5	177	2.4
3	**HPS-Ti-3**	1710	42	105.1	3.8	407	2.2
4	**HPS-Ti-4**	1613	10	123.3	2.0	501	broad
5	**3**[d]	660	5	134.9		n.d	n.d.
6	**5**	780	60	114.1	3.0	400	2.0
7	**6**	765	71	115.3	3.0	110	1.9

[a] DSC *first* scan.
[b] Calculated from depression in melting point [26] and ^{13}C NMR measurements.
[c] Determined through GPC at 135 °C in TCB using light scattering detectors calibrated with PS standards.
[d] (Trimethylsilyl)cyclopentadienyltitanium(IV) chloride.

entry 1). For copolymerizations catalyzed with an unsupported catalyst, conditions were identical to the supported catalyst systems, however, only 3–5 mg of the catalyst were used (Table 1, entries 5–7).

7. Homopolymerization of styrene

To 50 mL round bottom flasks equipped with magnetic stirbars, 10.5 mL of distilled toluene, 25–30 mg of the supported catalyst, and 1.7 mL of MAO were added. (Al:Ti ratios for **HPS-Ti-1** and **HPS-Ti-2** were 600, while **HPS-Ti-3** was 1000 and **HPS-Ti-4** was 1400. The amount of MAO was increased for **HPS-Ti-3** and **-4**, as we knew that the homogeneous precursors were much less active.) After sealing with septa, the charged flasks were removed from the glovebox and placed on magnetic stirrers. At zero minutes reaction time, 3.0 mL (0.026 mol) of distilled styrene (which had been loaded in syringes in the glovebox) were added to each flask. If gelation did not occur within a few minutes, the reaction was allowed to proceed for 50–60 min. The reaction mixture was quenched with 10% hydrochloric acid–methanol mixture, and the polymer was collected by filtration and dried in vacuo overnight.

8. Copolymerization of ethylene and styrene

To a 12 fluid ounce glass reactor, 75 mL of distilled toluene, 25–30 mg of supported catalyst, and 1.7 mL of MAO were added. (Al:Ti ratios were the same as for the styrene polymerization.) The reactor was then fitted with the mechanical stirring apparatus and reactor head. To a 25 mL side-port on the reactor head, 21.5 mL (0.188 mol) of distilled styrene were added. The entire closed system was then removed from the glove box and attached to a medium pressure line and mechanical stirrer [20]. After flushing the system, the reactor was pressurized to 60 psig with ethylene gas. At this point, the styrene was added by back-pressuring the side port of the reactor with nitrogen. The nitrogen line was then detached from the reactor, and the excess nitrogen in the reactor was vented out of the side port. The reactor was then repressurized with ethylene, and the reaction was allowed to proceed for 1.5 h. The reaction mixture was quenched with 10% hydrochloric acid–methanol mixture and the polymer was collected by filtration and dried in vacuo overnight.

9. Results and discussions

We have designed synthetic schemes to tether pianostool complexes on hydroxy-functionalized polystyrene supports (HPS) in order to study the influence of the support matrix on the catalyst performance and the properties of the resulting polyolefin [18]. Additionally, we studied how the substituents on the cyclopentadienyl ring affect both the amount of comonomer incorporated into the copolymer and also the microstructure of the copolymer. These effects on polymer yield, activity, weight average molecular weight (M_w), polydispersity index (PDI), melting point (T_m), and percent comonomer incorporation are outlined in Tables 1–3.

Table 2
Homopolymerization of styrene

Entry	Catalyst	Activity (kg/mol Ti h)	T_m[a] (°C)	ΔH (J/g)	M_w ($\times 10^{-3}$)	PDI
8	**HPS-Ti-1**	962	261	15	17	[b]
9	**HPS-Ti-2**	6	260 271	1.5 14	132	2.31
10	**HPS-Ti-3**	1946	260 271	2.1 9.2	135	2.34
11	**HPS-Ti-4**	114	260 271	4.0 17	52	2.35

[a] Second scan.
[b] Chromatogram is multimodal.

Table 3
Copolymerization of ethylene and styrene results

Entry	Catalyst	Activity (kg/mol Ti h atm)	T_m[a] (°C)	ΔH (J/g)	M_w ($\times 10^{-3}$)	PDI
12	**HPS-Ti-1**	26.6	114 247	30.4 2.2	412	2.10[b]
13	**HPS-Ti-2**	18.0	117	38.7	341	2.42[b]
14	**HPS-Ti-3**	4.6	128 255	24.8 6.2	478	2.22[c]
15	**HPS-Ti-4**	2.7	259 270	2.2 11.3	340	1.95[c]

[a] Second scan.
[b] Chromatogram is multimodal.
[c] Chromatogram contains a low molecular weight shoulder.

9.1. Ethylene/1-octene copolymers

During ethylene homopolymerizations, the supported aryloxy complexes (**HPS-Ti-1** to **-4**), in conjunction with different cocatalysts (MAO, tris(pentafluorophenyl)borane, dimethylanilinium borate, trityl borate), afford linear or branched polyethylenes from an ethylene only feed. The production of butyl branched polyethylene from an ethylene only feed has been attributed to 1-hexene produced from an ethylene trimerization process triggered by the use of macroligated catalysts [18]. In order to determine the effect of the macroligand on the properties of LLDPE, ethylene and 1-octene copolymerizations were performed using the macroligated catalysts (**HPS-Ti-1**–**4**) and MAO as the cocatalyst. It was

observed that for the ethylene/1-octene copolymers, **HPS-Ti-3** and **HPS-Ti-1** show higher activity than **HPS-Ti-2** and **HPS-Ti-4**. Also, **HPS-Ti-3** affords higher levels of 1-octene incorporation compared to the other three macroligated catalysts. The copolymers synthesized from these supported catalysts are of moderately high molecular weights (Table 1, entries 1–4).

For 1-octene incorporation, the trend followed **HPS-Ti-3** > **HPS-Ti-2** > **HPS-Ti-4**. The trend in the molecular weight of the ethylene/1-octene copolymer was found to be **HPS-Ti-4** > **HPS-Ti-3** > **HPS-Ti-1** > **HPS-Ti-2**. The trends observed in the activity and the molecular weight of the copolymer produced from the macroligated catalysts agree well with the results obtained by Nomura and co-workers. These authors have shown that in the case of non-bridged cyclopentadienyl aryloxy titanium species like ^{t}BuCp, $(CH_3)_5$Cp, and $(^{t}Bu)_2$Cp, the Cp–Ti–O bond angle changes from 117.6°, 120.5° and 119.3° [9,22,23]. For 1-hexene incorporation, the activity of the substituents has been shown to follow the trend: ^{t}Bu Cp > $(CH_3)_5$Cp > $(^{t}Bu)_2$Cp. On the other hand, the molecular weight for the copolymer is highest for $(^{t}Bu)_2$Cp followed by the ^{t}Bu and the $(CH_3)_5$Cp analogues. Nomura and co-workers [9,22,23] have attributed the observed trends in activity and molecular weight of the ethylene/hexene copolymer produced to the rotational flexibility of the subsituents on the cyclopentadienyl ring.

Another interesting feature is that the formation of ethylene/octene-based copolymers using supported aryloxy-based cyclopentadienyl complexes can also be used as additional evidence for the presence of the tethered aryloxy moiety. A previous control polymerization performed with complex **3**, MAO as the cocatalyst, and ethylene and 1-octene in the monomer feed produced HDPE (Table 2, entry 5). On the other hand, the use of small molecular analogues **5** and **6** with MAO resulted in the formation of ethylene/1-octene copolymers (LLDPE) from ethylene and 1-octene copolymerization (Table 1, entries 6 and 7, respectively).

9.2. Copolymer microstructure analysis of ethylene/octene copolymers obtained from macroligated catalysts

In order to determine the copolymer composition of the copolymers synthesized, ^{13}C NMR of the copolymers was performed at 135 °C. The ^{13}C NMR resonances of the copolymer synthesized from complex **HPS-Ti-1** were analyzed. The spectrum is similar to that reported by Cavagna [24,25], and hence low level of octene incorporations were expected. The nomenclature for carbon assignments, monomer sequence distribution and equations relating signal intensity to the sequences as reported by Randall were used to identify the branches in ^{13}C NMR of the polyolefin [25]. The ^{13}C peak resonances were assigned as 14.19 ($1s + 1B_6$, CH_3, EOE + EOO + OOE + OOO), 22.85 ($2s + 2B_6$,

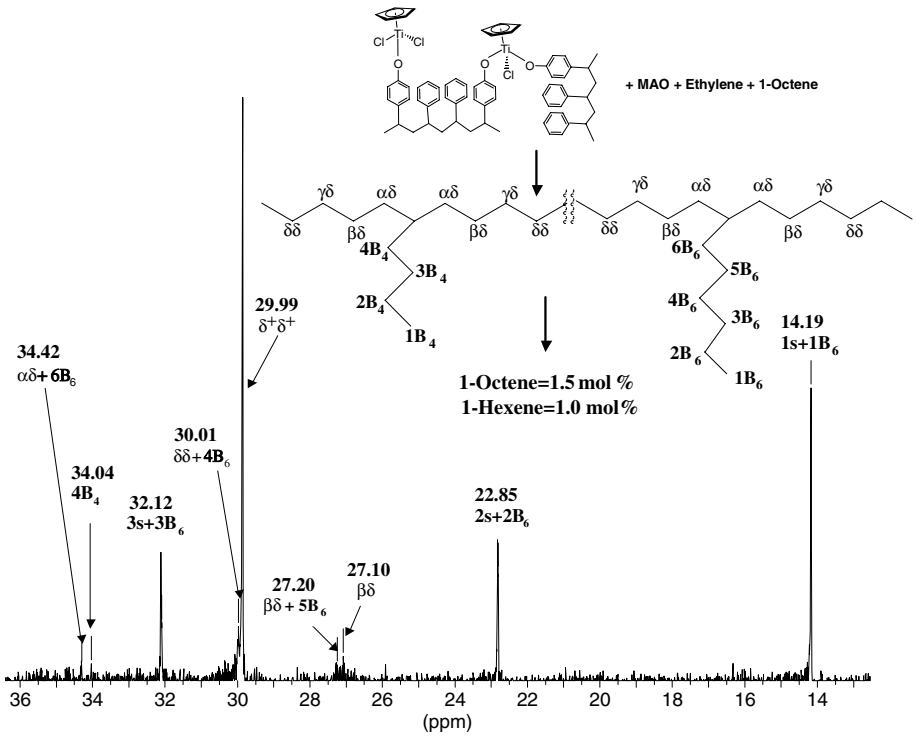


Fig. 2. ^{13}C NMR composite pulse decoupling (CPD) spectrum of ethylene/octene copolymer synthesized from complex **HPS-Ti-1** with MAO as the cocatalyst.

EOE + EOO + OOE + OOO), 27.10 (βδ, OOEE + EEOO), 27.20 (βδ + $5B_6$, EOE), 29.99 (δδ, EEE), 30.01 (δδ + $4B_6$, EEE), 32.12 (3s + $3B_6$, EOE), 34.04 ($4B_4$, EHE), 34.42 (αδ + $6B_6$, EOEE + EEOE), and 38.01 (CH, EOO + OOE, methine), as shown in Fig. 2. A quantitative relationship between signal intensity to monomer sequences was established to quantify the 1-octene incorporated in the copolymer [25]. The 1-octene content, calculated from the ratio of the sum of the octene-centered sequences to that of all the sequences, was determined to be 1.5 mol%. The presence of a $4B_4$ branch (butyl branch) was also observed. This can be attributed to the 1-hexene formed by ethylene trimerization and further incorporation of 1-hexene into the copolymer. The resonances $4B_4$ and (αδ + $6B_6$) were used to quantify the ratio of hexene (1.0 mol%) and octene (1.5 mol%) incorporated into the ethylene chain.

The microstructure of ethylene/octene copolymer obtained from complexes **HPS-Ti-2** and **HPS-Ti-3** were also analyzed and assigned as δ 14.22 (1s + $1B_6$, EOE + EOO + OOE + OOO), 22.87 (2s + $2B_6$, EOE + EOO + OOE + OOO), 26.95 (βδ, OOEE + EEOO), 27.05 (βδ + $5B_6$, EOE), 29.97 (δδ, EEE), 32.21 (3s + $3B_6$, EOE), 34.51 (αδ + $6B_6$, EOEE + EEOE), and 38.04 (CH, methine). The α-olefin incorporation in the copolymers obtained from **HPS-Ti-2** and **HPS-Ti-3** were estimated to be 2.5 and 3.8 mol%, respectively, as established by ^{13}C NMR. These values are corroborated by the observed depression in melting point. The microstructure of ethylene/octene copolymers from the macroligated catalysts (**HPS-Ti-1** to **3**) is similar to the microstructure of copolymers obtained from non-bridged cyclopentadienyl aryloxy complexes [23].

9.3. Ethylene/styrene copolymers

Homopolymerizations of styrene with the supported catalysts **HPS-Ti-1** to **-4** and assorted cocatalysts (MAO, tris(pentafluorophenyl)borane, dimethylanilinium borate, trityl borate) were performed in order to determine any differences between the catalysts and to discern if they would yield syndiotactic polystyrene as do the unsupported analogues. Table 2 shows that these polymerizations did indeed yield syndiotactic polystyrene with varying activities, molecular weights and polydispersities. Overall, polymerizations cocatalyzed with MAO display higher yields than those polymerized with a borane as the cocatalyst. The DSC results show that runs with **HPS-Ti-2**, **-3**, and **-4** contain the expected melting temperature at 270 °C, which is associated with syndiotactic polystyrene. The polystyrene obtained with **HPS-Ti-1**, however, lacks the melting transition around 270 °C. Also, the GPC data indicates significantly lower molecular weight and a multimodal distribution. The data indicate that the polystyrene produced with catalyst **HPS-Ti-1** is neither completely syndiotactic nor does it have uniform molecular weight. This may be due to leaching of the precursor catalyst from the supported catalyst, **HPS-Ti-1**. As the precursor to this supported catalyst ($CpTiCl_3$) is known to produce syndiotactic polystyrene in high yield and purity, the macroligand form of the catalyst displays an obvious and significant effect on the polymer properties.

Xu et al. [17] reported similar styrene polymerization results with $CpTiCl_3$, which had been supported onto a polystyrene terpolymer containing hydroxy and methoxy moieties. While our reaction conditions are comparable, it is apparent that the melting point data that we obtained for entry 8 corresponds to the production of polystyrene with higher syndiotactic content. This further supports our argument that the use of macroligated catalysts is an additional tuning parameter in dictating the characteristics of the resulting polymer.

Additionally, entry 9 displays that the polystyrene produced with **HPS-Ti-2** was obtained with activity that was two to three orders of magnitude lower than the rest of the catalysts. It is widely known and accepted that the precursor, Cp^*TiCl_3, produces syndiotactic polystyrene in high yield and activity. This phenomenon further illustrates the effect that the macroligand imparts on the catalyst's ability to polymerize styrene. Polymerizations with the borane cocatalyst system produced very similar results with respect to catalyst activity, polymer yield, and melting behavior, thereby ensuring this result is neither an anomaly nor dependent upon the cocatalyst system employed.

Polymerization of ethylene and styrene with the supported catalysts **HPS-Ti-1** to **-4** and MAO catalyst system produced very interesting results, Table 3. As with the styrene homopolymerization, very similar results were obtained with the borane cocatalyst system. It is evident that activity shows a marked decrease with the introduction of the ethylene comonomer. Although no trend is evident from yield and activity results with respect to cyclopentyl substituents, it is apparent from the DSC analysis that each supported catalyst produced very different polymers. In entries 12 and 14, the data is consistent with the presence of a reactor blend of polyethylene and syndiotactic polystyrene. Entry 13, however, suggests that only polyethylene is produced. A degree of crystallinity of 13.4% was calculated by dividing the heat of fusion value for the polyethylene melting by the total heat of fusion for a perfect polyethylene crystal (293 J/g) [26]. Finally, data in entry 15 suggest that only syndiotactic polystyrene is produced. This can also be seen in the DSC chromatogram (Fig. 3).

Analysis of the homopolymerizations of ethylene and styrene sheds some light on the polymer composition of entries 13 and 15. For the homopolymerization of styrene, **HPS-Ti-2** is clearly a poor performer, as the activity of this polymerization is two to three orders lower

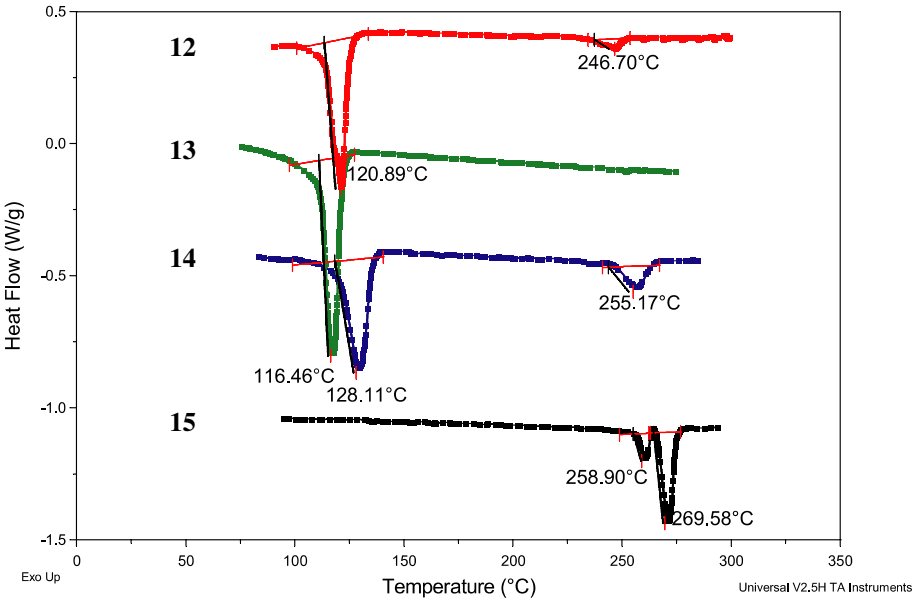


Fig. 3. Differential scanning calorimetry chromatograms of entries 12–15 (before extraction).

than that of the other catalysts employed. For this reason, it is expected that **HPS-Ti-2** would preferentially polymerize ethylene in copolymerization conditions with styrene. Indeed, the DSC chromatogram of the polymer obtained with **HPS-Ti-2** in the presence of ethylene and styrene monomers is consistent with the production of polyethylene.

Similarly, **HPS-Ti-4** displays a remarkably lower activity for the homopolymerization of ethylene than the other catalysts employed in this study [18]. Using this information in conjunction with the styrene homopolymerization results from Table 2, it is possible to predict that **HPS-Ti-4** would only polymerize styrene in copolymerization conditions with ethylene. As predicted, the entry 15 data and the DSC chromatogram display a preferential polymerization of styrene.

HPS-Ti-1 and **HPS-Ti-3** display sufficiently high activities in homopolymerizations of ethylene and styrene, and therefore it is conceivable that they would produce either a copolymer or a reactor blend of two homopolymers. Evidence of such a blend of homopolymers was detected through DSC and NMR analyses.

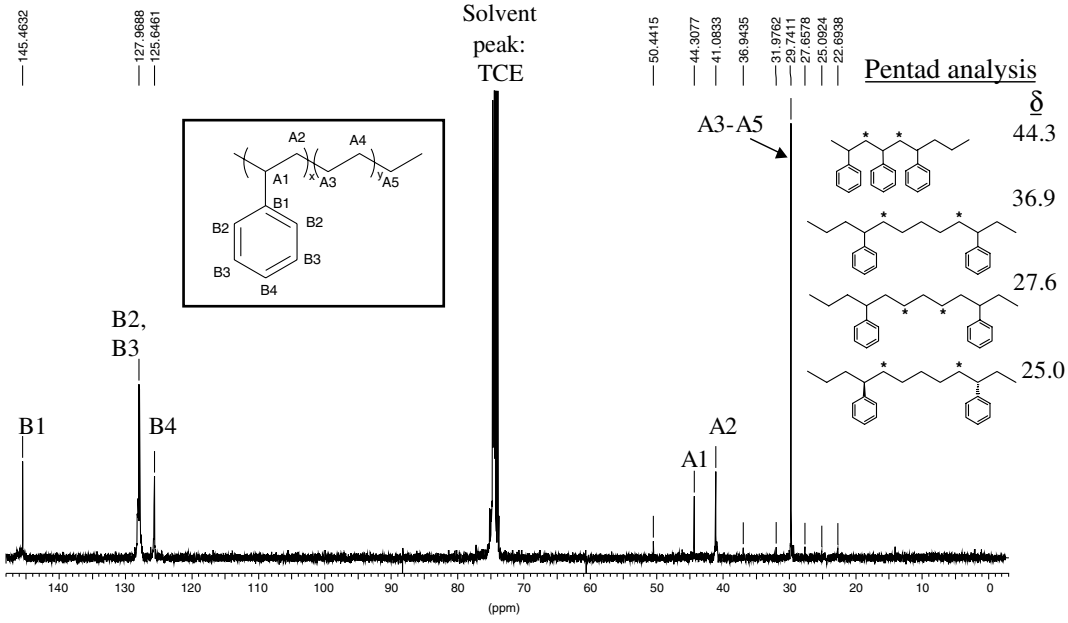


Fig. 4. ^{13}C NMR of entry 14.

Sequential Soxhlet extractions in methyl ethyl ketone (MEK) and tetrahydrofuran (THF) were performed on the entry 12 sample, in order to determine the relative amounts of atactic polystyrene, random ethylene/styrene copolymer, and polyethylene that were present. These results indicate that there is a significant amount of atactic polystyrene (MEK-soluble, >50%), random ES copolymer (THF-soluble, 11%), and polyethylene (THF-insoluble, 32%, $T_m = 132$ °C). Entry 14 was analyzed via ^{13}C NMR, as insufficient yield did not allow for Soxhlet extraction. As shown in Fig. 4, significant resonances in the NMR were consistent with syndiotactic polystyrene and polyethylene. Peaks consistent with the presence of an ES copolymer are of very low intensity, suggesting that an insignificant amount of the sample consists of random ES copolymer. The NMR and DSC data of entry 14 indicate the presence of two homopolymers: syndiotactic polystyrene and polyethylene.

Due to insufficient yield quantities, Soxhlet extractions could not be performed on entries 13 or 15. While DSC results of entry 15 are consistent with syndiotactic polystyrene, DSC results of entry 13 cannot conclusively determine whether or not a significant portion of the sample contains atactic polystyrene.

In summary, there seems to be a notable macroligand effect on the homopolymerization of styrene and the copolymerization of ethylene and styrene. This is clearly demonstrated in the decrease of the melting temperatures for the polystyrene. For the copolymerizations, it is evident that although the variety of substituents on the cyclopentadienyl ring does not have a correlation with the polymer composition, there is clearly another effect that causes these catalysts to produce different copolymer compositions. This effect is demonstrated through the supported catalysts behavior in homopolymerizations of styrene and ethylene. As the results are mirrored with the borane cocatalyst system, we believe that they are true results and not merely anomalies.

10. Conclusions

In order to study the influence of the support matrix on the catalyst performance and the properties of the resulting polyolefin, macroligated aryloxy titanium complexes (**HPS-Ti**) were prepared. In this paper, the effect of the macroligand on ethylene and α-olefin (1-octene or styrene) copolymerization using aryloxycyclopentadienyl macroligated catalysts were studied.

LLDPE has been synthesized from ethylene and 1-octene feed using supported aryloxycyclopentadienyltitanium complexes. The activity of the supported catalysts for copolymerization and the amount of 1-octene incorporated into the copolymer is dependent upon the substituents on the cyclopentadienyl ring. The microstructure of the copolymers was determined using ^{13}C NMR and shows random incorporation of the octene comonomer. The formation of ethylene/1-octene copolymers using supported aryloxy-based cyclopentadienyl complexes can also be used as additional evidence for the presence of the tethered aryloxy moiety, since the precursor piano-stool complex affords HDPE during attempted copolymerization. (Due to the incorporation of the comonomer, the melting points (T_m) and the enthalpy of fusion (ΔH) of the copolymers is depressed as determined by DSC.)

We have also explored the effect of supported single-site catalysts on styrene and ethylene/styrene polymerizations. Polymerizations with each of the supported catalysts, (**HPS-Ti-1** to **-4**) were carried out with MAO and borane cocatalysts. The MAO and borane cocatalyst systems produced very similar results.

DSC analysis displayed that **HPS-Ti-1** produced polystyrene with lower syndiotactic content than the precursor catalyst, indicating the presence of a strong macroligand effect. DSC analysis also showed that polymer composition varies greatly with the specific supported catalyst. Polymerizations of ethylene and styrene via **HPS-Ti-1** and **HPS-Ti-3** display both polyethylene and syndiotactic polystyrene melting behavior, while polymerizations of ethylene and styrene via **HPS-Ti-2** and **HPS-Ti-4** produce melting temperatures consistent with polyethylene or syndiotactic polystyrene, respectively. Based on homopolymerization data with styrene and ethylene, the phenomenon of different catalysts producing vastly different polymer compositions in copolymerization conditions was proscribed to the fact that certain supported catalysts preferentially polymerize ethylene or styrene.

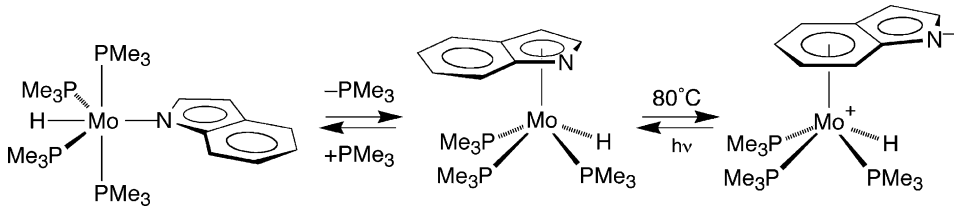
Acknowledgements

This material is based on work supported by the National Science Foundation under Grant No. CHE-0113643, and the Army Research Laboratory Polymer Materials Center of Excellence (DAAD19-01-2-0002 P00005). Central analytical facilities utilized used in these studies were supported by the NSF-sponsored Materials and Research Science and Engineering Center on Polymers at UMass Amherst (DMR-0213695).

References

[1] R.W. Barnhart, G.C. Bazan, T. Mourey, J. Am. Chem. Soc. 120 (1998) 1082.
[2] S.D. Ittel, L.K. Johnson, M. Brookhart, Chem. Rev. 100 (2000) 1169.
[3] A.L. McKnight, R.M. Waymouth, Chem. Rev. 98 (1998) 2587.
[4] G. Melillo, L. Izzo, M. Zinna, C. Tedesco, L. Oliva, Macromolecules 35 (2002) 9256.

[5] C. Pellecchia, D. Pappalardo, G.J. Gruter, Macromolecules 32 (1999) 4491.
[6] G.J.P. Britovsek, V.C. Gibson, D.F. Wass, Angew. Chem. Int. Ed. 38 (1999) 428.
[7] P.S. Chum, W.J. Kruper, M.J. Guest, Adv. Mater. 12 (2000) 1759.
[8] K. Nomura, N. Naga, M. Miki, K. Yanagi, A. Imai, Organometallics 17 (1998) 2152.
[9] K. Nomura, N. Naga, M. Miki, K. Yanagi, Macromolecules 31 (1998) 7588.
[10] K. Nomura, K. Oya, T. Komatsu, Y. Imanishi, Macromolecules 33 (2000) 3187.
[11] K. Nomura, T. Komatsu, Y. Imanishi, Macromolecules 33 (2000) 8122.
[12] K. Nomura, K. Oya, Y. Imanishi, J. Mol. Catal. A 17 (2001) 127.
[13] K. Nomura, H. Okumura, T. Komatsu, N. Naga, Macromolecules 35 (2002) 5388.
[14] G.G. Hlatky, Chem. Rev. 100 (2000) 1347.
[15] S.B. Roscoe, J.M.J. Frechet, J.F. Walzer, A.J. Dias, Science 280 (1998) 270.
[16] K. Kageyama, J. Tamazawa, T. Aida, Science 285 (1999) 2113.
[17] J. Xu, J. Ouyang, Z. Fan, D. Chen, L. Feng, J. Polym. Sci. A 38 (2000) 127.
[18] R.M. Kasi, E.B. Coughlin, Macromolecules 36 (2003) 6300.
[19] A.B. Pangborn, M.A. Giardello, R.H. Grubbs, R.K. Rosen, F.J. Timmers, Organometallics 15 (1996) 1518.
[20] G.S. Constable, R.A. Gonzalez-Ruiz, R.M. Kasi, E.B. Coughlin, Macromolecules 35 (2002) 9613.
[21] J.M. Nasrullah, S. Raja, K. Vijayakumaran, R. Dhamodharan, J. Polym. Sci. Polym. Chem. 38 (2000) 453.
[22] K. Nomura, T. Komatsu, M. Nakamura, Y. Imanishi, J. Mol. Catal. A 164 (2000) 131.
[23] K. Nomura, T. Komatsu, Y. Imanishi, J. Mol. Catal. A 152 (2000) 249.
[24] F. Cavagna, Macromolecules 14 (1981) 215.
[25] J.C. Randall, J. Macromol. Sci.-Rev. Macromol. Chem. Phys. C29 (1989) 201.
[26] H.Y. Chen, S.P. Chum, A. Hiltner, E. Baer, J. Polym. Sci. B 39 (2001) 1578.



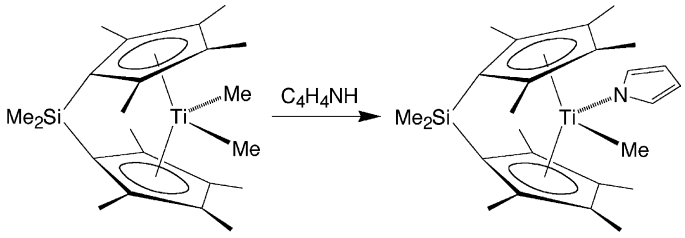
Scheme 1.

$Cp_2Ti(NC_4H_4)_2$ [8] are monodentate because the cyclopentadienyl ligand coordinates more effectively in an η^5-mode than does the pyrrolyl ligand, an observation attributed to the sp^2-lone pair electrons on nitrogen being higher in energy than those involved in the π-system of the pyrrolyl anion [4b,9,10]. In this paper we provide further examples of this uncommon class of molecules that feature the Ti—NC_4H_4 moiety by describing the synthesis, structure and reactivity of a series of *ansa* titanocene complexes, namely $[Me_2Si(C_5Me_4)_2]Ti(NC_4H_4)X$ (X = H, Me, Cl, NC_4H_4) and $[Me_2Si(C_5Me_4)(C_5Me_3CH_2)]Ti(NC_4H_4)$.

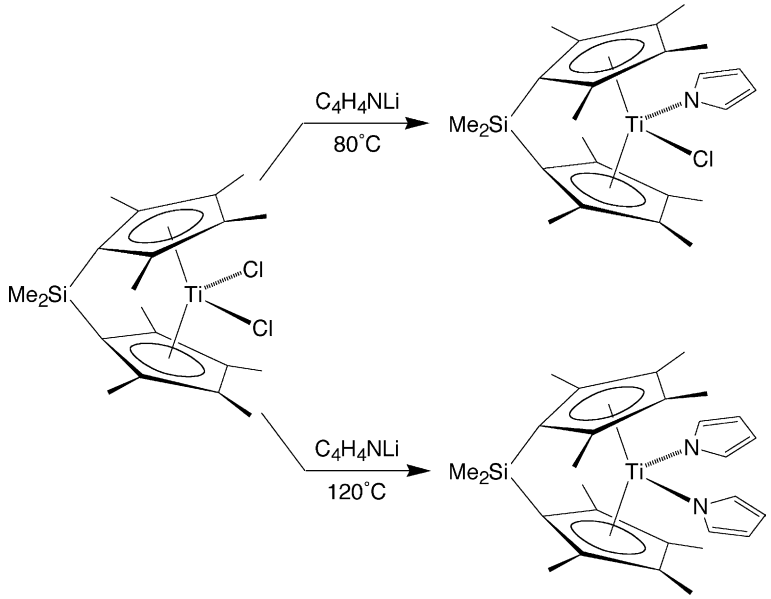
2. Results and discussion

2.1. Synthesis and structural characterization of $[Me_2Si(C_5Me_4)_2]Ti(NC_4H_4)X$ (X = Me, Cl, NC_4H_4)

As noted above, there is a paucity of well-defined titanium pyrrolyl compounds, with the only structurally characterized Ti—NC_4H_4 compound listed in the Cambridge Structural Database [11] being $Cp_2Ti(NC_4H_4)_2$ [8a]. Access to a series of *ansa* titanocene pyrrolyl compounds is, however, readily provided via two synthetic procedures, namely (i) the reaction of



Scheme 2.



Scheme 3.

the dimethyl compound $[Me_2Si(C_5Me_4)_2]TiMe_2$ [12] with pyrrole, C_4H_4NH (Scheme 2) and (ii) the reaction of the dichloride $[Me_2Si(C_5Me_4)_2]TiCl_2$ [13] with the lithium derivative $LiNC_4H_4$ (Scheme 3). Thus, $[Me_2Si(C_5Me_4)_2]TiMe_2$ reacts with C_4H_4NH at 120 °C to give $[Me_2Si(C_5Me_4)_2]Ti(NC_4H_4)Me$, while $[Me_2Si(C_5Me_4)_2]TiCl_2$ reacts with $LiNC_4H_4$ to give sequentially $[Me_2Si(C_5Me_4)_2]Ti(NC_4H_4)Cl$ and $[Me_2Si(C_5Me_4)_2]Ti(NC_4H_4)_2$. The molecular structures of $[Me_2Si(C_5Me_4)_2]Ti(NC_4H_4)Me$, $[Me_2Si(C_5Me_4)_2]Ti(NC_4H_4)Cl$ and $[Me_2Si(C_5Me_4)_2]Ti(NC_4H_4)_2$ have been determined by X-ray diffraction, as illustrated in Figs. 1–3, respectively. The incorporation of an *ansa* bridge into a metallocene system often facilitates a shift of the cyclopentadienyl rings towards a reduced hapticity [14–16] and thereby provides a possible mechanism for modifying the coordination mode of the ancillary ligand. However, it is evident from the structures of $[Me_2Si(C_5Me_4)_2]Ti(NC_4H_4)Me$, $[Me_2Si(C_5Me_4)_2]Ti(NC_4H_4)Cl$ and $[Me_2Si(C_5Me_4)_2]Ti(NC_4H_4)_2$ that this perturbation is sufficiently small that it does not promote a shift towards η^5-coordination of the pyrrolyl ligand.

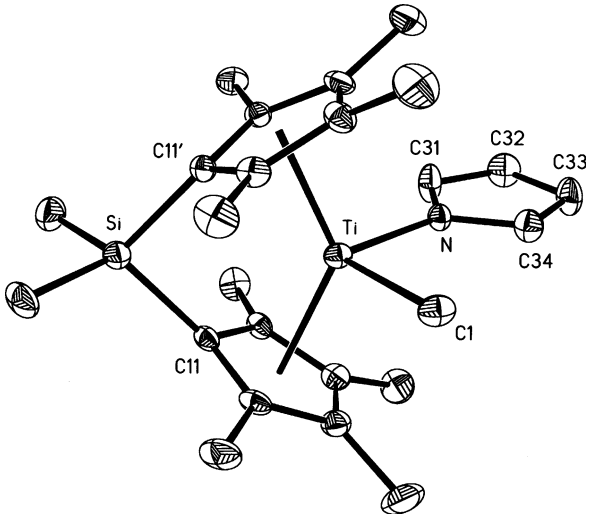


Fig. 1. Molecular structure of $[Me_2Si(C_5Me_4)_2]Ti(NC_4H_4)Me$.

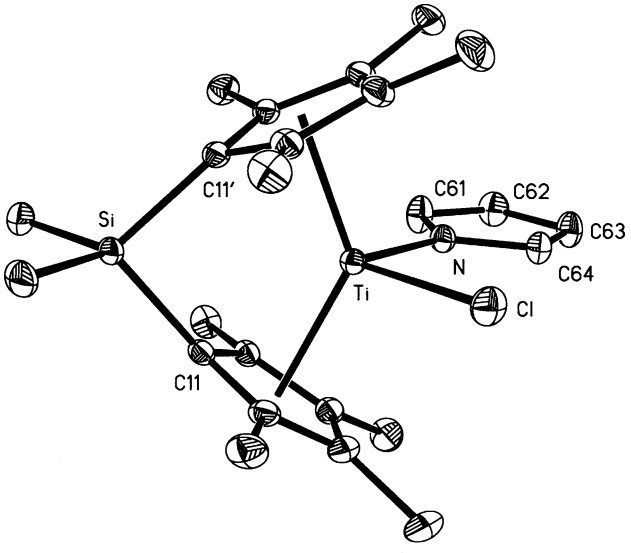


Fig. 2. Molecular structure of $[Me_2Si(C_5Me_4)_2]Ti(NC_4H_4)Cl$.

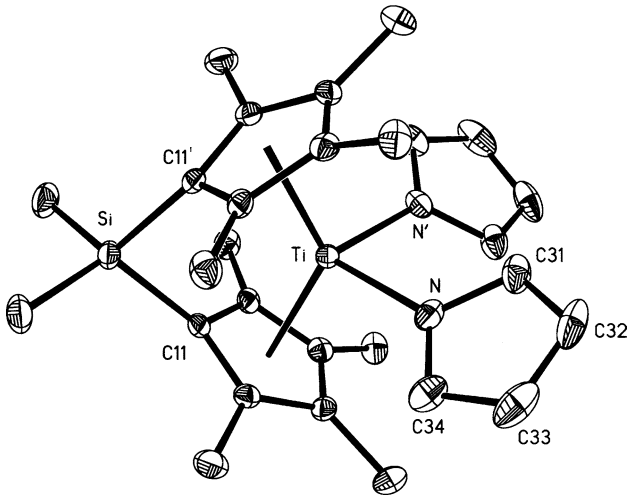
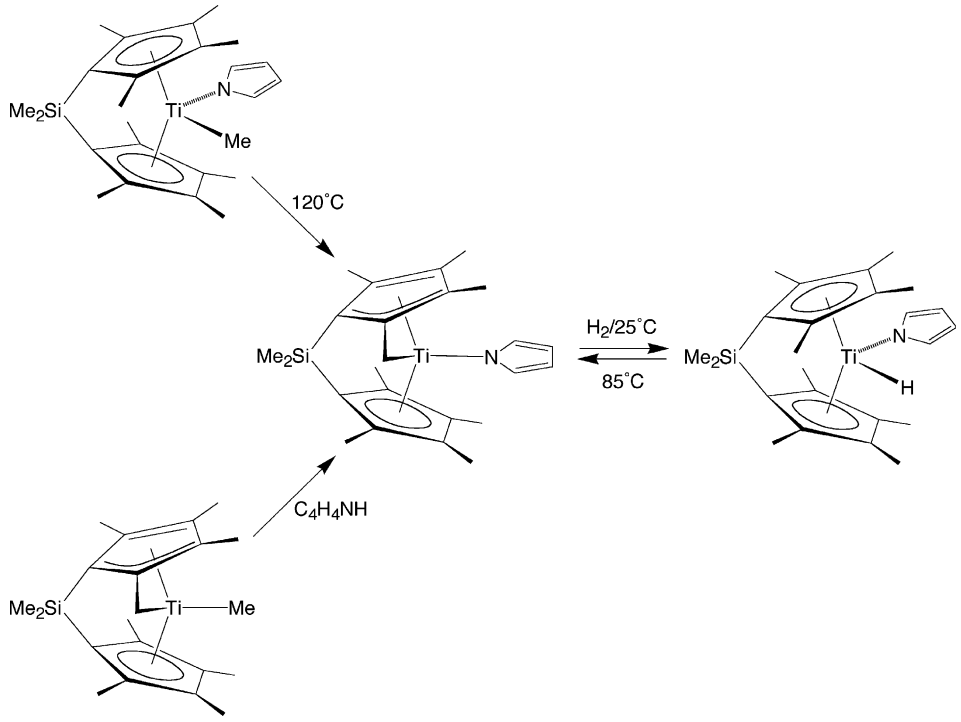


Fig. 3. Molecular structure of $[Me_2Si(C_5Me_4)_2]Ti(NC_4H_4)_2$.

2.2. Synthesis and structural characterization of the fulvene complex $[Me_2Si(C_5Me_4)(C_5Me_3CH_2)]Ti(NC_4H_4)$

The methyl complex $[Me_2Si(C_5Me_4)_2]Ti(NC_4H_4)Me$ provides a pathway to two other pyrrolyl compounds, namely the fulvene complex $[Me_2Si(C_5Me_4)(C_5Me_3CH_2)]Ti(NC_4H_4)$ and the hydride derivative $[Me_2Si(C_5Me_4)_2]Ti(NC_4H_4)H$ (Scheme 4). Thus, $[Me_2Si(C_5Me_4)_2]Ti(NC_4H_4)Me$ eliminates methane upon prolonged heating at 120 °C to give a fulvene complex $[Me_2Si(C_5Me_4)(C_5Me_3CH_2)]Ti(NC_4H_4)$ that is derived by formal abstraction of a hydrogen atom from a ring methyl group. Support for the formation of a fulvene ligand is provided by NMR spectroscopy which indicates the presence of a CH_2 group by observation of (i) two doublets at δ 1.89 and 2.83 ($^2J_{HH}$ = 4 Hz) in the ^{1}H NMR spectrum and (ii) a doublet of doublets signal at δ 86.2 ($^1J_{CH}$ = 151 and 154 Hz) in the ^{13}C NMR spectrum. While NMR spectroscopy indicates that one of the methyl groups has been activated and transformed into the methylene group of a fulvene moiety, it does not indicate from which of the methyl groups the hydrogen atom was abstracted. Definitive evidence is, nevertheless, provided by an X-ray diffraction study on $[Me_2Si(C_5Me_4)(C_5Me_3CH_2)]Ti(NC_4H_4)$ (Fig. 4), which demonstrates that it is a ring methyl group adjacent to the $[Me_2Si]$ bridge that is activated; the structure is, therefore, analogous to that of the phenyl counterpart $[Me_2Si(C_5Me_4)(C_5Me_3CH_2)]TiPh$ [12]. In this regard, $[Me_2Si(C_5Me_4)(C_5Me_3CH_2)]Ti(NC_4H_4)$ may also be



Scheme 4.

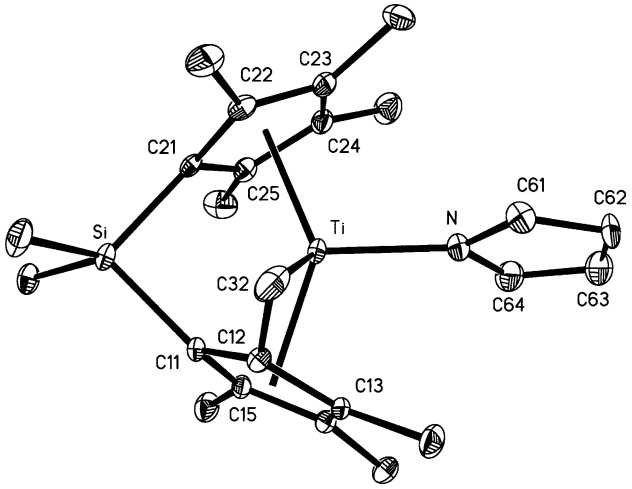


Fig. 4. Molecular structure of $[Me_2Si(C_5Me_4)(C_5Me_3CH_2)]$-$Ti(NC_4H_4)$. Selected bond lengths (Å): Ti—C11 2.263(5), Ti—C12 2.162(6), Ti—C13 2.393(5), Ti—C14 2.583(5), Ti—C15 2.503(5), Ti—C32 2.356(7).

obtained by reaction of $[Me_2Si(C_5Me_4)(C_5Me_3CH_2)]$-TiMe [12] with C_4H_4NH at 120 °C (Scheme 4). The preferential reactivity of pyrrole with the Ti—Me bond is noteworthy in light of the fact that the Ti—C bond involving the *exo*-methylene group is often more reactive. For example, $Cp^*(C_5Me_4CH_2)ZrPh$ reacts with H_2 and H_2O to give $Cp^*{}_2Zr(Ph)H$ and $Cp^*{}_2Zr$-(Ph)OH, respectively [17].

With respect to the coordination mode of the fulvene moiety [18], the principal interaction is with only four carbon atoms, namely those of the *exo* double bond and the two adjacent atoms, with Ti—C bond lengths in the range 2.16–2.39 Å; the carbon atoms of the *endo* double bond are much further from the titanium center, with bond lengths of 2.502(5) and 2.583(5) Å. As such, the complex may be viewed as a trialkylidenemethane, i.e. $C(CR_2)_3$, derivative supplemented by a weaker titanium–olefin interaction (Fig. 5). In this regard, although fulvene complexes are common, the bonding is typically discussed in terms of whether the interaction is better described as coordination of a neutral η^6-fulvene (i.e. a "diene-olefin") or as that of a dianionic η^1,η^5-ligand (Fig. 5) [18–20]. We first described the trialkylidenemethane coordination mode for $[Me_2Si(C_5Me_4)(C_5Me_3$-$CH_2)]TiPh$ [12] and this mode has now been reported for several other complexes, including $Cp^*[C_4H_4$-$(CHR)]TiCl$ [21] and $[C_5Me_4CH_2]Ta(cb)_2X$ (cb = carbazolyl; X = Cl, CH_2SiMe_3, CH_2Ph) [3a].

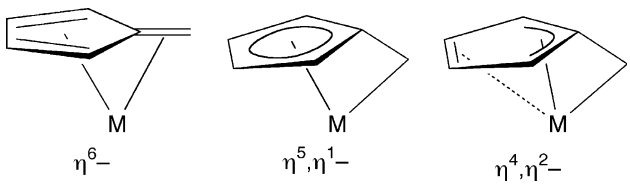


Fig. 5. Coordination modes of fulvene ligands.

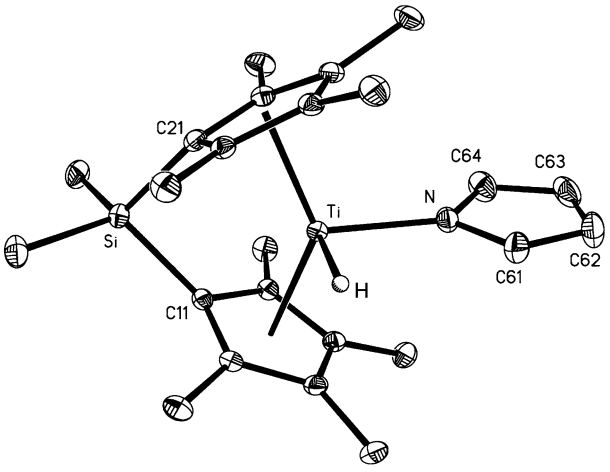


Fig. 6. Molecular structure of $[Me_2Si(C_5Me_4)_2]Ti(NC_4H_4)H$.

2.3. Synthesis and structural characterization of the hydride complex $[Me_2Si(C_5Me_4)_2]Ti(NC_4H_4)H$

The fulvene complex $[Me_2Si(C_5Me_4)(C_5Me_3CH_2)]$-$Ti(NC_4H_4)$ serves as a useful precursor for the pyrrolyl–hydride complex $[Me_2Si(C_5Me_4)_2]Ti(NC_4H_4)H$ via reaction with H_2 at room temperature (Scheme 4). The molecular structure of $[Me_2Si(C_5Me_4)_2]Ti(NC_4H_4)H$ has been determined by X-ray diffraction (Fig. 6), while the [Ti—H] moiety is characterized spectroscopically by an absorption at 1601 cm^{-1} in the IR spectrum and a signal at δ 4.62 in the ^1H NMR spectrum. Interestingly, the formation of $[Me_2Si(C_5Me_4)_2]Ti(NC_4H_4)H$ is reversible, with elimination of H_2 and regeneration of $[Me_2$-$Si(C_5Me_4)(C_5Me_3CH_2)]Ti(NC_4H_4)$ occurring at 85 °C. In accord with this reversibility, treatment of $[Me_2Si(C_5$-$Me_4)_2]Ti(NC_4H_4)H$ with D_2 at 80 °C results in incorporation of deuterium into the hydride and one ring methyl group (δ 1.80) of each cyclopentadienyl ring of the $[Me_2Si(C_5Me_4)_2]$ ligand.

2.4. Nature of the titanium–pyrrolyl interaction in ansa-titanocene complexes

As noted above, the pyrrolyl ligand is considered to be a less effective π-donor ligand than dialkylamido counterparts. Evidence in support of this notion is provided by consideration of the Ti—NC_4H_4 bond lengths in $[Me_2Si(C_5Me_4)_2]Ti(NC_4H_4)X$ (X = H, Me, Cl, NC_4H_4) and $[Me_2Si(C_5Me_4)(C_5Me_3CH_2)]Ti(NC_4H_4)$, as summarized in Table 1. Thus, the average Ti—NC_4H_4 bond length of 2.08 Å is approximately 0.2 Å longer than the mean value of 1.89 Å for the Ti—NMe_2 bond length in structurally characterized complexes listed in the Cambridge Structural Database [11]. While this comparison furnishes excellent evidence that the pyrrolyl ligand is a less effective π-donor than is the Me_2N ligand, it provides no indication as to whether there is any π-character associated with the Ti—NC_4H_4 interaction. In this regard, the use of Ti—NC_4H_4 bond lengths to evaluate whether or not there exists any π-character requires knowledge of the hypothetical Ti—NC_4H_4 bond length in the absence of π-donation, and an estimate of this value in this system may be obtained by consideration of the Ti—Ph bond length of $[Me_2Si(C_5Me_4)_2]Ti(Ph)Cl$ (Fig. 7). Thus, since (i) the Ti—Ph bond is expected to possess negligible π-character and (ii) the planar phenyl and pyrrolyl ligands have a comparable size, an estimate of the Ti—NC_4H_4 bond length in the absence of π-donation may be obtained by adjusting the Ti—Ph bond length of $[Me_2Si$-$(C_5Me_4)_2]Ti(Ph)Cl$ [2.172(3) Å] by the difference in covalent radii of carbon (0.77 Å) and nitrogen (0.73 Å) [22,23]. On this basis, a Ti—NC_4H_4 bond length of 2.14 Å would be predicted for $[Me_2Si(C_5Me_4)_2]$-$Ti(NC_4H_4)X$ in the absence of π-donation.

The experimentally observed average Ti—NC_4H_4 bond length of 2.08 Å for the various titanium pyrrolyl compounds is, therefore, intermediate between the values for the hypothetical value in the absence of π-donation (2.14 Å) and the average value for Ti—NMe_2 bond lengths (1.89 Å). However, while it is intermediate, it is evident that the average Ti—NC_4H_4 bond length is much closer to the hypothetical value in the absence of π-donation. In this regard, it is pertinent to note that, because the frontier orbitals of a metallocene reside in

Table 1
Ti—N bond lengths of pyrrolyl complexes

	d (Ti—N) (Å)
$[Me_2Si(C_5Me_4)_2]Ti(NC_4H_4)Cl$	2.090(3)
$[Me_2Si(C_5Me_4)_2]Ti(NC_4H_4)Me$	2.090(7)
$[Me_2Si(C_5Me_4)_2]Ti(NC_4H_4)_2$	2.086(3)
$[Me_2Si(C_5Me_4)_2]Ti(NC_4H_4)H$	2.058(2)
$[Me_2Si(C_5Me_4)(C_5Me_3CH_2)]Ti(NC_4H_4)$	2.072(4)

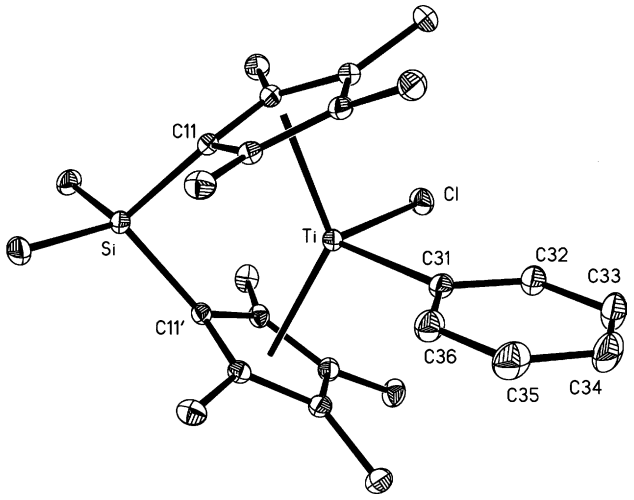


Fig. 7. Molecular structure of $[Me_2Si(C_5Me_4)_2]Ti(Ph)Cl$.

the equatorial plane [24], the pyrrolyl ligand would be required to be orthogonal if it were to act as an effective π-donor ligand.

A further relevant comparison of bond lengths is provided by substituted pyrrolyl compounds. Specifically, the 2,4-diphenylpyrrolyl complex $[pyr^{Ph_2}]Ti(NMe_2)_3$ has been shown by X-ray diffraction to exhibit η^1-coordination of the $[pyr^{Ph_2}]$ ligand, and the two independent Ti—$NC_4Ph_2H_2$ bond lengths [2.052(4) Å and 2.038(4) Å; average = 2.045 Å] are ca. 0.16 Å longer than the Ti—NMe_2 bond lengths [1.881(4)–1.898(4) Å; average = 1.888 Å] [25]. In accord with this observation, the Ti—NC_4H_4 bond length in the hypothetical compound $[\eta^1$-$NC_4H_4]Ti(NMe_2)_3$ (1.99 Å) is calculated to be 0.15 Å longer than the Ti—NMe_2 bond lengths (1.84 Å) [26]. Thus, in all titanium pyrrolyl compounds which exhibit η^1-coordination, the Ti—N bond length indicates that there is little π-character associated with the bond.

A final noteworthy aspect of the series of pyrrolyl compounds $[Me_2Si(C_5Me_4)_2]Ti(NC_4H_4)X$ (X = H, Me, Cl, NC_4H_4) pertains to rotation of the pyrrolyl ligand about the Ti—N bond. Of these complexes, only the chloride derivative exhibits ^1H and ^{13}C NMR spectra consistent with hindered rotation on the NMR timescale at room temperature (Fig. 8). For example, at 290 K, the pyrrolyl ligand of $[Me_2Si(C_5Me_4)_2]Ti(NC_4H_4)Cl$ is characterized by 4 distinct signals (A–D). Upon raising the temperature, however, the signals broaden in a manner that is consistent with rotation about the Ti-pyrrolyl bond, with interconversion of A/D and B/C pairs. The coalescence temperature for the interconversion of B and C is 300 K, from which values of $k = 31\ s^{-1}$ and $\Delta G^{\ddagger} = 15.5$ kcal mol^{-1} may be obtained for the barrier to rotation. This value also serves as an upper limit for the rotation of the pyrrolyl ligand in $[Me_2Si(C_5Me_4)_2]Ti(NC_4H_4)X$ (X = H, Me, NC_4H_4). With respect to the greater barrier for the chloride derivative, it is pertinent to note that the barrier to rotation about the Zr—Ph bond is also greatest for the chloride derivative in a series of related zirconocene phenyl compounds, namely $[Me_2Si(C_5Me_4)_2]Zr(Ph)X$ (X = Ph, H, Cl) [27].

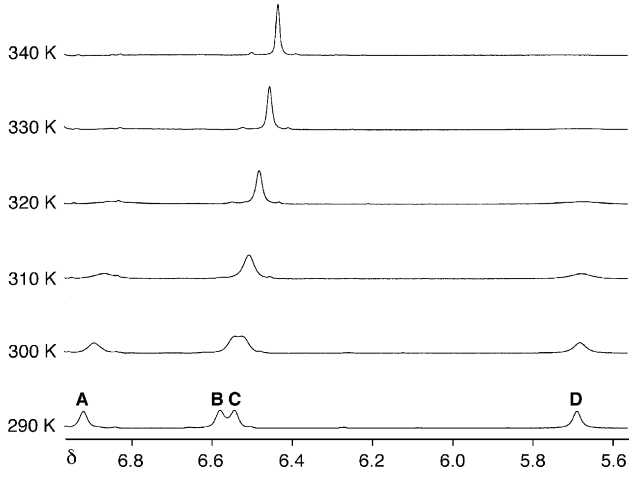


Fig. 8. Variable temperature ^1H NMR spectra of $[Me_2Si(C_5Me_4)_2]Ti(NC_4H_4)Cl$ in d^8-toluene, focusing on the four signals of a static pyrrolyl ligand. At 330 K only the B/C pair of protons have coalesced, with the signal for the A/D pair remaining in the base line due to the much greater frequency difference for the A and D signals compared to that for B and C.

3. Conclusions

In summary, a series of titanium–pyrrolyl compounds, namely $[Me_2Si(C_5Me_4)_2]Ti(NC_4H_4)X$ (X = H, Me, Cl, NC_4H_4) and $[Me_2Si(C_5Me_4)(C_5Me_3CH_2)]Ti(NC_4H_4)$ has been synthesized and structurally characterized by X-ray diffraction. Consideration of the Ti—NC_4H_4 bond lengths indicates that the pyrrolyl ligand does not act as an efficient π-donor in this system, such that the experimentally observed average Ti—NC_4H_4 bond length of 2.08 Å is much closer to the hypothetical value in the absence of π-donation (2.14 Å) than the average value of Ti—NMe_2 bond lengths (1.89 Å).

4. Experimental

4.1. General considerations

All manipulations were performed using a combination of glovebox, high-vacuum and Schlenk techniques under a nitrogen or argon atmosphere. Solvents were purified and degassed by standard procedures. ^1H and ^{13}C NMR spectra were measured on Bruker 300 DRX, Bruker 400 DRX, and Bruker Avance 500 DMX spectrometers. Chemical shifts are reported in ppm relative to $SiMe_4$ ($\delta = 0$) and were referenced internally with respect to the protio solvent impurity (δ 7.15 for C_6D_5H) and ^{13}C resonances (δ 128.0 for C_6D_6). Coupling constants are given in hertz. Infrared spectra were recorded on Perkin–Elmer 1430 and 1600 spectrometers and are reported in cm^{-1}. $LiNC_4H_4$ [8c], $[Me_2Si(C_5Me_4)_2]TiCl_2$ [13], $[Me_2Si(C_5Me_4)_2]TiMe_2$ [12], and $[Me_2Si(C_5Me_4)(C_5Me_3CH_2)]TiMe$ [12] were prepared by the literature methods.

4.2. Synthesis of $[Me_2Si(C_5Me_4)_2]Ti(NC_4H_4)Cl$

Toluene (15 mL) was added to a mixture of $[Me_2Si(C_5Me_4)_2]TiCl_2$ (0.12 g, 0.29 mmol) and $LiNC_4H_4$ (0.063 g, 0.86 mmol) in an ampoule. The mixture was stirred at 80 °C for ca. 24 h, after which period the volatile components were removed in vacuo. The residue was extracted into pentane (ca. 100 mL), concentrated to ca. 10 mL, and placed at −78 °C giving

$[Me_2Si(C_5Me_4)_2]Ti(NC_4H_4)Cl$ as a dark green solid, which was isolated by filtration and dried in vacuo (0.05 g, 35%). Anal. Calc. for $C_{24}H_{34}NSiClTi$: C, 64.4; H, 7.6; N, 3.1. Found: C, 64.6; H, 7.6; N, 2.7%. IR Data (KBr pellet, cm^{-1}): 2958 (m), 2905 (s), 2212 (w), 1656 (w), 1441 (s), 1381 (s), 1322 (m), 1252(s), 1206 (w), 1148 (m), 1087 (vs), 1033 (s), 909 (w), 818 (s), 769 (s), 721 (s), 677 (s), 653 (m), 568 (w), 475 (s). ^1H NMR data (C_6D_6): 0.54 [s, 1Me of $(CH_3)_2Si\{C_5(CH_3)_4\}_2$], 0.68 [s, 1Me of $(CH_3)_2Si\{C_5(CH_3)_4\}_2$], 1.27 [s, 2Me of $(CH_3)_2Si\{C_5(CH_3)_4\}_2$], 1.67 [s, 2Me of $(CH_3)_2Si\{C_5(CH_3)_4\}_2$], 1.91 [s, 2Me of $(CH_3)_2Si\{C_5(CH_3)_4\}_2$], 2.16 [s, 2Me of $(CH_3)_2Si\{C_5(CH_3)_4\}_2$], 5.73 [br s, 1H of NC_4H_4], 6.66 [s, 2H of NC_4H_4], 7.05 [br s, 1H of NC_4H_4]. ^{13}C NMR data (C_6D_6): 2.6 [q, $^1J_{C-H}$ = 121, 1Me of $(CH_3)_2Si\{C_5(CH_3)_4\}_2$], 3.1 [q, $^1J_{C-H}$ = 120, 1Me of $(CH_3)_2Si\{C_5(CH_3)_4\}_2$], 10.4 [q, $^1J_{C-H}$ = 127, 2Me of $(CH_3)_2Si\{C_5(CH_3)_4\}_2$], 13.8 [q, $^1J_{C-H}$ = 127, 2Me of $(CH_3)_2Si\{C_5(CH_3)_4\}_2$], 15.4 [q, $^1J_{C-H}$ = 127, 2Me of $(CH_3)_2Si\{C_5(CH_3)_4\}_2$], 16.7 [q, $^1J_{C-H}$ = 127, 2Me of $(CH_3)_2Si\{C_5(CH_3)_4\}_2$], 95.1 [s, 2C of $(CH_3)_2Si\{C_5(CH_3)_4\}_2$], obscured by solvent [2C of $(CH_3)_2Si\{C_5(CH_3)_4\}_2$], 109.4 [d, $^1J_{C-H}$ = 168, 1CH of NC_4H_4], obscured by solvent [1CH of NC_4H_4], 111.0 [d, $^1J_{C-H}$ = 167, 1CH of NC_4H_4], 121.9 [d, $^1J_{C-H}$ = 175, 1CH of NC_4H_4], 133.9 [s, 2C of $(CH_3)_2Si\{C_5(CH_3)_4\}_2$], 141.2 [s, 2C of $(CH_3)_2Si\{C_5(CH_3)_4\}_2$], 147.6 [s, 2C of $(CH_3)_2Si\{C_5(CH_3)_4\}_2$].

4.3. Synthesis of $[Me_2Si(C_5Me_4)_2]Ti(NC_4H_4)_2$

Toluene (20 mL) was added to a mixture of $[Me_2Si(C_5Me_4)_2]TiCl_2$ (0.24 g, 0.58 mmol) and $LiNC_4H_4$ (0.168 g, 2.30 mmol) in an ampoule. The mixture was stirred at 120 °C for ca. 24 h, after which period the volatile components were removed in vacuo. The product was extracted into pentane (ca. 100 mL), concentrated to ca. 10 mL, and placed at −78 °C giving $[Me_2Si(C_5Me_4)_2]Ti(NC_4H_4)_2$ as a dark green solid, which was isolated by filtration and dried in vacuo (0.14 g, 50%). Anal. Calc. for $C_{28}H_{38}N_2SiTi$: C, 70.3; H, 8.0; N, 5.9. Found: C, 70.2; H, 8.0; N, 5.5%. IR Data (KBr pellet, cm^{-1}): 3110 (w), 2913 (s), 2203 (w), 1543 (w), 1442 (s), 1379 (s), 1326 (m), 1259 (m), 1190 (w), 1147 (m), 1077 (vs), 1025 (vs), 837 (s), 772 (m), 716 (vs), 680 (s), 649 (m), 615 (w), 568 (w), 471 (m). ^1H NMR data (C_6D_6): 0.65 [s, 2Me of $(CH_3)_2Si\{C_5(CH_3)_4\}_2$], 1.45 [s, 2Me of $(CH_3)_2Si\{C_5(CH_3)_4\}_2$], 1.85 [s, 2Me of $(CH_3)_2Si\{C_5(CH_3)_4\}_2$], 6.57 ["t", $^3J_{H-H}$ = 2, 4H of 2 NC_4H_4], 6.74 [br s, 4H of 2 NC_4H_4]. ^{13}C NMR data (C_6D_6): 2.7 [q, $^1J_{C-H}$ = 120, 2Me of $(CH_3)_2Si\{C_5(CH_3)_4\}_2$], 12.3 [q, $^1J_{C-H}$ = 127, 4Me of $(CH_3)_2Si\{C_5(CH_3)_4\}_2$], 16.2 [q, $^1J_{C-H}$ = 127, 4Me of $(CH_3)_2Si\{C_5(CH_3)_4\}_2$], 98.6 [s, 2C of $(CH_3)_2Si\{C_5(CH_3)_4\}_2$], 108.4 [d, $^1J_{C-H}$ = 172, 4CH of 2 NC_4H_4], 128.4 [d, $^1J_{C-H}$ = 176, 4CH of 2 NC_4H_4], 130.0 [s, 4C of $(CH_3)_2Si\{C_5(CH_3)_4\}_2$], 145.6 [s, 4C of $(CH_3)_2Si\{C_5(CH_3)_4\}_2$].

4.4. Synthesis of $[Me_2Si(C_5Me_4)_2]Ti(NC_4H_4)Me$

A solution of $[Me_2Si(C_5Me_4)_2]TiMe_2$ (0.30 g, 0.80 mmol) in toluene (15 mL) was treated with freshly dried pyrrole (0.21 g, 3.20 mmol). The mixture was stirred at 120 °C for ca. 24 h, after which period the volatile components were removed in vacuo. The residue was extracted into pentane (ca. 10 mL) and placed at −78 °C to deposit $[Me_2Si(C_5Me_4)_2]Ti(NC_4H_4)Me$ as a red crystalline solid. The crystals were washed with cold pentane (2.3 mL) and dried in vacuo (0.22 g, 64%). Anal. Calc. for $C_{25}H_{37}NSiTi$: C, 70.2; H, 8.7; N, 3.3. Found: C, 70.8; H, 8.6; N, 3.2%. IR Data (KBr pellet, cm^{-1}): 2948 (m), 2901 (m), 2874 (m), 1477 (w), 1460 (w), 1440 (m), 1408 (w), 1379 (s), 1354 (m), 1325 (s), 1249 (s), 1205 (w), 1151 (w), 1129 (w), 1084 (s), 1053 (w), 1035 (s), 1016 (s), 910 (w), 839 (vs), 812 (vs), 766 (s), 716 (vs), 675 (vs), 658 (s), 569 (w), 542 (w), 476 (vs). ^1H NMR data (C_6D_6): 0.43 [s, 1Me of $(CH_3)_2Si\{C_5(CH_3)_4\}_2$], 0.61 [s, 1Me of $(CH_3)_2Si\{C_5(CH_3)_4\}_2$], 0.72 [s, 1Me of $TiCH_3$], 1.36 [s, 2Me of $(CH_3)_2Si\{C_5(CH_3)_4\}_2$], 1.46 [s, 2Me of $(CH_3)_2Si\{C_5(CH_3)_4\}_2$], 1.97 [s, 2Me of $(CH_3)_2Si\{C_5(CH_3)_4\}_2$], 2.04 [s, 2Me of $(CH_3)_2Si\{C_5(CH_3)_4\}_2$], 5.94 [br s, 2H of NC_4H_4], 6.61 [t, $^3J_{H-H}$ = 2, 2H of NC_4H_4]. ^{13}C NMR data (C_6D_6): 2.8 [q, $^1J_{C-H}$ = 123, 1Me of $(CH_3)_2Si\{C_5(CH_3)_4\}_2$], 3.1 [q, $^1J_{C-H}$ = 121, 1Me of $(CH_3)_2Si\{C_5(CH_3)_4\}_2$], 10.3 [q, $^1J_{C-H}$ = 127, 2Me of $(CH_3)_2Si\{C_5(CH_3)_4\}_2$], 13.0 [q, $^1J_{C-H}$ = 127, 2Me of $(CH_3)_2Si\{C_5(CH_3)_4\}_2$],15.1 [q, $^1J_{C-H}$ = 127, 2Me of $(CH_3)_2Si\{C_5(CH_3)_4\}_2$], 15.2 [q, $^1J_{C-H}$ = 126, 2Me of $(CH_3)_2Si\{C_5(CH_3)_4\}_2$], 60.8 [q, $^1J_{C-H}$ = 124, 1Me of $TiCH_3$], 94.6 [s, 2C of $(CH_3)_2Si\{C_5(CH_3)_4\}_2$], 109.4 [d, $^1J_{C-H}$ = 168, 2CH of NC_4H_4], 123.3 [d, $^1J_{C-H}$ = 176, 2CH of NC_4H_4], 125.7 [s, 2C of $(CH_3)_2Si\{C_5(CH_3)_4\}_2$], 127.1 [s, 2C of $(CH_3)_2Si\{C_5(CH_3)_4\}_2$], 135.5 [s, 2C of $(CH_3)_2Si\{C_5(CH_3)_4\}_2$], 140.9 [s, 2C of $(CH_3)_2Si\{C_5(CH_3)_4\}_2$].

4.5. Synthesis of $[Me_2Si(C_5Me_4)(C_5Me_3CH_2)]Ti(NC_4H_4)$

(a) A solution of $[Me_2Si(C_5Me_4)_2]Ti(NC_4H_4)Me$ (ca. 20 mg) in benzene (ca. 0.8 mL) was heated at 120 °C for 7 days. The quantitative formation of green $[Me_2Si(C_5Me_4)(C_5Me_3CH_2)]Ti(NC_4H_4)$ was demonstrated by ^1H NMR spectroscopy. The solvent was removed by lyophilization to give $[Me_2Si(C_5Me_4)(C_5Me_3CH_2)]Ti(NC_4H_4)$ as a solid. (b) A solution of $[Me_2Si(C_5Me_4)(C_5Me_3CH_2)]TiMe$ (ca. 5 mg) in benzene (ca. 0.8 mL) was treated with pyrrole and heated at 120 °C for ca. 24 h. The quantitative formation of $[Me_2Si(C_5Me_4)(C_5Me_3CH_2)]Ti(NC_4H_4)$ was demonstrated by ^1H NMR spectroscopy. Anal. Calc. for $C_{24}H_{33}NSiTi$:

C, 70.1; H, 8.1; N, 3.4. Found: C, 70.1; H, 8.1; N, 3.1%. IR Data (KBr pellet, cm^{-1}): 3086 (w), 2959 (s), 2910 (s), 2865 (s), 1616 (m), 1442 (s), 1380 (s), 1330 (s), 1252 (s), 1201 (w), 1154 (s), 1130 (m), 1070 (s), 1053 (m), 1029 (s), 918 (w), 838 (s), 813 (s), 776 (br s), 656 (s), 626 (m), 570 (w), 497 (w), 459 (w). ^{1}H NMR data (C_6D_6): 0.03 [s, 1Me of $(CH_3)_2Si\{C_{10}(CH_3)_7(CH_2)\}$], 0.31 [s, 1Me of $(CH_3)_2Si\{C_{10}(CH_3)_7(CH_2)\}$], 1.30 [s, 1Me of $(CH_3)_2Si\{C_{10}(CH_3)_7(CH_2)\}$], 1.61 [s, 1Me of $(CH_3)_2Si\{C_{10}(CH_3)_7(CH_2)\}$], 1.73 [s, 1Me of $(CH_3)_2Si\{C_{10}(CH_3)_7(CH_2)\}$], 1.76 [s, 1Me of $(CH_3)_2Si\{C_{10}(CH_3)_7(CH_2)\}$], 1.77 [s, 1Me of $(CH_3)_2Si\{C_{10}(CH_3)_7(CH_2)\}$], 1.84 [s, 1Me of $(CH_3)_2Si\{C_{10}(CH_3)_7(CH_2)\}$], 1.89 [d, $^2J_{H-H}$ = 4, 1H of $(CH_3)_2Si\{C_{10}(CH_3)_7(CH_2)\}$], 2.15 [s, 1Me of $(CH_3)_2Si\{C_{10}(CH_3)_7(CH_2)\}$], 2.83 [d, $^2J_{H-H}$ = 4, 1H of $(CH_3)_2Si\{C_{10}(CH_3)_7(CH_2)\}$], 5.65 [br s, 2H of NC_4H_4], 6.46 [t, $^3J_{H-H}$ = 2, 2H of NC_4H_4]. ^{13}C NMR data (C_6D_6): 0.7 [q, $^1J_{C-H}$ = 120, 1Me of $(CH_3)_2Si\{C_{10}(CH_3)_7(CH_2)\}$], 3.1 [q, $^1J_{C-H}$ = 120, 1 Me of $(CH_3)_2Si\{C_{10}(CH_3)_7(CH_2)\}$], 10.6 [q, $^1J_{C-H}$ = 126, 1Me of $(CH_3)_2Si\{C_{10}(CH_3)_7(CH_2)\}$], 12.6 [q, $^1J_{C-H}$ = 126, 1Me of $(CH_3)_2Si\{C_{10}(CH_3)_7(CH_2)\}$], 12.86 [q, $^1J_{C-H}$ = 124, 1Me of $(CH_3)_2Si\{C_{10}(CH_3)_7(CH_2)\}$], 12.92 [q, $^1J_{C-H}$ = 126, 1Me of $(CH_3)_2Si\{C_{10}(CH_3)_7(CH_2)\}$], 13.9 [q, $^1J_{C-H}$ = 126, 1Me of $(CH_3)_2Si\{C_{10}(CH_3)_7(CH_2)\}$], 14.3 [q, $^1J_{C-H}$ = 126, 1Me of $(CH_3)_2Si\{C_{10}(CH_3)_7(CH_2)\}$], 16.5 [q, $^1J_{C-H}$ = 126, 1Me of $(CH_3)_2Si\{C_{10}(CH_3)_7(CH_2)\}$], 86.2 [d of d, $^1J_{C-H}$ = 151, 154, 1C of $(CH_3)_2Si\{C_{10}(CH_3)_7(CH_2)\}$],95.5 [s, 1C of $(CH_3)_2Si\{C_{10}(CH_3)_7(CH_2)\}$], 104.6 [s, 1C of $(CH_3)_2Si\{C_{10}(CH_3)_7(CH_2)\}$],106.5 [d, $^1J_{C-H}$ = 166, 2CH of NC_4H_4], 117.7 [s, 1C of $(CH_3)_2Si\{C_{10}(CH_3)_7(CH_2)\}$], 121.1 [d, $^1J_{C-H}$ = 173, 2CH of NC_4H_4], 128.9 [s, 1C of $(CH_3)_2Si\{C_{10}(CH_3)_7(CH_2)\}$],129.5 [s, 1C of $(CH_3)_2Si\{C_{10}(CH_3)_7(CH_2)\}$], 130.7 [s, 1C of $(CH_3)_2Si\{C_{10}(CH_3)_7(CH_2)\}$],134.4 [s, 1C of $(CH_3)_2Si\{C_{10}(CH_3)_7(CH_2)\}$], 137.2 [s, 1C of $(CH_3)_2Si\{C_{10}(CH_3)_7(CH_2)\}$],139.0 [s, 1 C of $(CH_3)_2Si\{C_{10}(CH_3)_7(CH_2)\}$], 142.4 [s, 1C of $(CH_3)_2Si\{C_{10}(CH_3)_7(CH_2)\}$].

4.6. Synthesis of $[Me_2Si(C_5Me_4)_2]Ti(NC_4H_4)H$

A solution of $[Me_2Si(C_5Me_4)(C_5Me_3CH_2)]Ti(NC_4H_4)$ (ca. 20 mg) in benzene (ca. 0.8 mL) was treated with H_2 (ca. 1 atm) and stirred at room temperature for 12 h, after which period the quantitative formation of red brown $[Me_2Si(C_5Me_4)_2]Ti(NC_4H_4)H$ was demonstrated by ^{1}H NMR spectroscopy. The solvent was removed by lyophilization to give $[Me_2Si(C_5Me_4)_2]Ti(NC_4H_4)H$ as a solid. IR Data (KBr pellet, cm^{-1}): 3093 (m), 2911 (s), 2728 (w), 2230 (w), 1703 (w), 1655 (w), 1601 (m), 1441 (s), 1378 (s), 1317 (m), 1252 (s), 1202 (w), 1152 (s), 1130 (m), 1076 (s), 1028 (s), 913 (w), 837 (vs), 768 (s), 719 (vs), 675 (vs), 598 (w), 481 (m). ^{1}H NMR data (C_6D_6): 0.46 [s, 1 Me of $(CH_3)_2Si\{C_5(CH_3)_4\}_2$], 0.57 [s, 1 Me of $(CH_3)_2Si\{C_5(CH_3)_4\}_2$], 1.35 [s, 2 Me of $(CH_3)_2Si\{C_5(CH_3)_4\}_2$], 1.81 [s, 2Me of $(CH_3)_2Si\{C_5(CH_3)_4\}_2$], 1.94 [s, 2Me of $(CH_3)_2Si\{C_5(CH_3)_4\}_2$], 2.19 [s, 2Me of $(CH_3)_2Si\{C_5(CH_3)_4\}_2$], 4.62 [s, 1H of Ti*H*], 6.09 [br s, 2H of NC_4H_4], 6.66 [t, $^3J_{H-H}$ = 2, 2H of NC_4H_4]. ^{13}C NMR data (C_6D_6): 3.0 [q, $^1J_{C-H}$ = 121, 1Me of $(CH_3)_2Si\{C_5(CH_3)_4\}_2$], 3.1 [q, $^1J_{C-H}$ = 121, 1Me of $(CH_3)_2Si\{C_5(CH_3)_4\}_2$], 10.8 [q, $^1J_{C-H}$ = 127, 2Me of $(CH_3)_2Si\{C_5(CH_3)_4\}_2$], 13.8 [q, $^1J_{C-H}$ = 127, 2Me of $(CH_3)_2Si\{C_5(CH_3)_4\}_2$], 14.0 [q, $^1J_{C-H}$ = 127, 2Me of $(CH_3)_2Si\{C_5(CH_3)_4\}_2$], 16.7 [q, $^1J_{C-H}$ = 127, 2Me of $(CH_3)_2Si\{C_5(CH_3)_4\}_2$], 95.5 [s, 2C of $(CH_3)_2Si\{C_5(CH_3)_4\}_2$], 108.7 [d, $^1J_{C-H}$ = 162, 2CH of NC_4H_4], 118.5 [d, $^1J_{C-H}$ = 180, 2CH of NC_4H_4], 123.6 [s, 2C of $(CH_3)_2Si\{C_5(CH_3)_4\}_2$], obscured by solvent [2C of $(CH_3)_2Si\{C_5(CH_3)_4\}_2$], 133.2 [s, 2C of $(CH_3)_2Si\{C_5(CH_3)_4\}_2$], 139.9 [s, 2C of $(CH_3)_2Si\{C_5(CH_3)_4\}_2$].

4.7. Synthesis of $[Me_2Si(C_5Me_4)_2]Ti(Ph)Cl$

A solution of $[Me_2Si(C_5Me_4)_2]TiCl_2$ (0.50 g, 1.2 mmol) in Et_2O (15 mL) was treated with PhMgCl (1.44 mL of 2.0 M in THF; 2.9 mmol) and stirred at room temperature for ca. 16 h. After this period, the volatile components were removed under reduced pressure and the residue was extracted into pentane (ca. 150 mL). The pentane extract was concentrated to ca. 10 mL and placed at −78 °C, giving $[Me_2Si(C_5Me_4)_2]Ti(Ph)Cl$ as a red crystalline solid which was isolated by filtration. The isolated crystals were washed with cold pentane (2.5 mL) and dried in vacuo (0.24 g, 44%). Anal. Calc. for $C_{26}H_{35}SiTiCl$: C, 68.0; H, 7.7. Found: C, 68.0; H, 8.0%. IR Data (KBr pellet, cm^{-1}): 3036 (s), 2988 (s), 2954 (s), 2898 (vs), 1941 (w), 1870 (w), 1813 (w), 1638 (w), 1594 (w), 1562 (m), 1477 (s), 1439 (s), 1410 (s), 1380 (vs), 1321 (s), 1253 (s), 1127 (m), 1018 (s), 840 (vs), 812 (s), 767 (s), 724 (s), 702 (s), 676 (s), 625 (w), 572 (w), 488 (s), 469 (m). ^{1}H NMR data (C_6D_6): 0.58 [s, 1Me of $(CH_3)_2Si\{C_5(CH_3)_4\}_2$], 0.62 [s, 1Me of $(CH_3)_2Si\{C_5(CH_3)_4\}_2$], 1.38 [s, 2Me of $(CH_3)_2Si\{C_5(CH_3)_4\}_2$],1.75 [s, 2Me of $(CH_3)_2Si\{C_5(CH_3)_4\}_2$], 1.80 [s, 2Me of $(CH_3)_2Si\{C_5(CH_3)_4\}_2$], 2.25 [s, 2Me of $(CH_3)_2Si\{C_5(CH_3)_4\}_2$], 6.11 [d, $^3J_{H-H}$ = 8, 1H of C_6H_5], 6.95 [t, $^3J_{H-H}$ = 8, 1H of C_6H_5], 7.06 [t, $^3J_{H-H}$ = 8, 1H of C_6H_5], 7.13 [d, $^3J_{H-H}$ = 8, 1H of C_6H_5 (partially obscured by solvent)], 7.63 [d, $^3J_{H-H}$ = 8, 1H of C_6H_5]. ^{13}C NMR data (C_6D_6): 2.8 [q, $^1J_{C-H}$ = 121, 1Me of $(CH_3)_2Si\{C_5(CH_3)_4\}_2$], 3.3 [q, $^1J_{C-H}$ = 121, 1Me of $(CH_3)_2Si\{C_5(CH_3)_4\}_2$], 12.7 [q, $^1J_{C-H}$ = 127, 2Me of $(CH_3)_2Si\{C_5(CH_3)_4\}_2$], 13.9 [q, $^1J_{C-H}$ = 127, 2Me of $(CH_3)_2Si\{C_5(CH_3)_4\}_2$], 14.9 [q, $^1J_{C-H}$ = 127, 2Me of $(CH_3)_2Si\{C_5(CH_3)_4\}_2$], 16.7 [q, $^1J_{C-H}$ = 127, 2Me of $(CH_3)_2Si\{C_5(CH_3)_4\}_2$], 91.0 [s, 2C of $(CH_3)_2Si\{C_5(CH_3)_4\}_2$],124.0 [d of t, $^1J_{C-H}$ = 158, $^2J_{C-H}$ = 7, 1C of of C_6H_5], 125.3 [s, 2C of $(CH_3)_2Si\{C_5(CH_3)_4\}_2$], 126.9 [d of d, $^1J_{C-H}$ = 155,

$^2J_{C-H}$ = 7, 1C of C_6H_5], 128.9 [d of d, $^1J_{C-H}$ = 156, $^2J_{C-H}$ = 7, 1C of C_6H_5], 132.3 [d of t, $^1J_{C-H}$ = 152, $^2J_{C-H}$ = 8, 1C of C_6H_5], 133.1 [s, 2C of $(CH_3)_2Si\{C_5(CH_3)_4\}_2$], 138.3 [s, 2C of $(CH_3)_2Si\{C_5(CH_3)_4\}_2$], 138.9 [d of t, $^1J_{C-H}$ = 159, $^2J_{C-H}$ = 7, 1C of C_6H_5], 140.5 [s, 2C of $(CH_3)_2Si\{C_5(CH_3)_4\}_2$], 204.2 [*ipso*, s, 1C of C_6H_5].

4.8. X-ray structure determinations

X-ray diffraction data were collected on a Bruker P4 diffractometer equipped with either a point detector or a SMART CCD detector and crystal data, data collection and refinement parameters are summarized in Table 2. The structures were solved using direct methods and standard difference map techniques, and were refined by full-matrix least-squares procedures on F^2 with SHELXTL (Version 5.10) [28]. The crystallographic data for $[Me_2Si(C_5Me_4)_2]Ti(NC_4H_4)H$ (CCDC #262716), $[Me_2Si(C_5Me_4)_2]Ti(NC_4H_4)Me$ (CCDC #262718), $[Me_2Si(C_5Me_4)_2]Ti(NC_4H_4)Cl$ (CCDC #262719), $[Me_2Si(C_5Me_4)_2]Ti(NC_4H_4)_2$ (CCDC #262717), $[Me_2Si(C_5Me_4)(C_5Me_3\text{-}CH_2)]Ti(NC_4H_4)$ (CCDC #262720), and $[Me_2Si(C_5Me_4)_2]$- Ti(Ph)Cl (CCDC #262721) have

Table 2
Crystal, intensity collection and refinement data

	$[Me_2Si(C_5Me_4)_2]Ti(NC_4H_4)H$	$[Me_2Si(C_5Me_4)_2]Ti(NC_4H_4)Me$	$[Me_2Si(C_5Me_4)_2]Ti(NC_4H_4)Cl$
Lattice	triclinic	monoclinic	monoclinic
Formula	$C_{24}H_{35}NSiTi$	$C_{25}H_{37}NSiTi$	$C_{24}H_{34}ClNSiTi$
Formula weight	413.52	427.55	447.96
Space group	$P\bar{1}$	$C2/m$	$C2/m$
a (Å)	8.5435(6)	17.078(7)	17.064(18)
b (Å)	9.3181(7)	10.981(5)	10.898(12)
c (Å)	15.403(1)	13.495(5)	13.465(14)
α (°)	78.017(1)	90	90
β (°)	80.372(2)	114.27(2)	113.61(3)
γ (°)	68.106(1)	90	90
V (Å^3)	1107.5(1)	2307(2)	2295(4)
Z	2	4	4
Temperature (K)	218	293	228
Radiation (λ, Å)	0.71073	0.71073	0.71073
ρ (calcd.) (g cm^{-3})	1.240	1.231	1.297
μ (Mo Kα) (mm^{-1})	0.449	0.433	0.552
θ max (°)	28.3	22.5	28.3
Number of data	4907	1124	2691
Number of parameters	259	143	149
R_1	0.0411	0.0484	0.0450
wR_2[a]	0.1069 (0.1152)	0.1253 (0.1331)	0.1265 (0.1372)
Goodness-of-fit	1.021	1.138	1.109
	$[Me_2Si(C_5Me_4)_2]Ti(NC_4H_4)_2$	$[Me_2Si(C_5Me_4)(C_5Me_3CH_2)]Ti(NC_4H_4)$	$[Me_2Si(C_5Me_4)_2]Ti(Ph)Cl$
Lattice	tetragonal	triclinic	orthorhombic
Formula	$C_{28}H_{38}N_2SiTi$	$C_{24}H_{33}NSiTi$	$C_{26}H_{35}ClSiTi$
Formula weight	478.59	411.50	458.98
Space group	$P4_32_12$	$P\bar{1}$	$Pnma$
a (Å)	11.2367(6)	8.715(1)	15.6864(8)
b (Å)	11.2367(6)	9.025(1)	11.0445(5)
c (Å)	19.998(2)	15.187(2)	13.7809(7)
α (°)	90	77.098(4)	90
β (°)	90	82.230(3)	90
γ (°)	90	68.577(2)	90
V (Å^3)	2525.0(3)	1081.9(2)	2387.5(2)
Z	4	2	4
Temperature (K)	293	218	208
Radiation (λ Å)	0.71073	0.71073	0.71073
ρ (calcd.) (g cm^{-3})	1.259	1.263	1.277
μ (Mo Kα) (mm^{-1})	0.405	0.460	0.531
θ max (°)	25.0	28.2	28.3
Number of data	2209	4807	2958
Number of parameters	152	254	152
R_1	0.0497	0.0927	0.0367
wR_2[a]	0.0982 (0.1106)	0.1275 (0.1620)	0.0927 (0.1021)
Goodness-of-fit	1.025	1.049	1.045

[a] $I > 2\sigma(I)$; value in parentheses for all data.

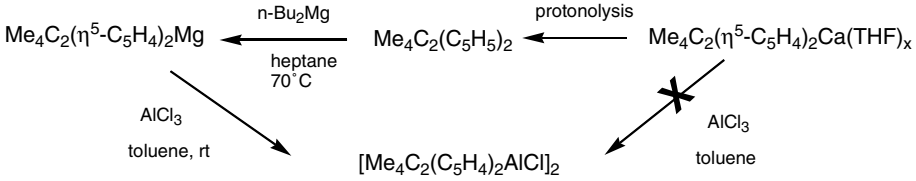
been deposited with the Cambridge Crystallographic Data Centre.

Acknowledgement

We thank the US Department of Energy, Office of Basic Energy Sciences (DE-FG02-93ER14339) for support of this research.

References

[1] D.C. Bradley, M.H. Chisholm, Acc. Chem. Res. 9 (1976) 273.
[2] C.C. Cummins, Prog. Inorg. Chem. 47 (1998) 685.
[3] See, for example:
(a) P.N. Riley, J.R. Parker, P.E. Fanwick, I.P. Rothwell, Organometallics 18 (1999) 3579;
(b) P.N. Riley, P.E. Fanwick, I.P. Rothwell, J. Chem. Soc., Dalton Trans. (2001) 181;
(c) S.A. Harris, J.T. Ciszewski, A.L. Odom, Inorg. Chem. 40 (2001) 1987;
(d) J.M. Tanski, G. Parkin, Organometallics 21 (2002) 587;
(e) M.R. Mason, B.F. Fneich, K. Kirschbaum, Inorg. Chem. 42 (2003) 6592;
(f) M.R. Mason, D. Ogrin, B. Fneich, T.S. Barnard, K. Kirschbaum, J. Organomet. Chem. 690 (2005) 157.
[4] See, for example:
(a) F. Nief, Eur. J. Inorg. Chem. (2001) 891;
(b) D.L. Kershner, F. Basolo, Coord. Chem. Rev. 19 (1987) 279.
[5] G. Zhu, J.M. Tanski, D.G. Churchill, K.E. Janak, G. Parkin, J. Am. Chem. Soc. 124 (2002) 13658.
[6] D.C. Bradley, K.J. Chivers, J. Chem. Soc. (A) (1968) 1967.
[7] For other examples of η^5-pyrrolyl titanium compounds (including substituted pyrroles), see:
(a) N. Kuhn, S. Stubenrauch, R. Boese, D. Bläser, J. Organomet. Chem. 440 (1992) 289;
(b) A.R. Dias, A.M. Galvao, A.C. Galvão, M.S. Salema, J. Chem. Soc., Dalton Trans. (1997) 1055;
(c) A.K. Sharma, N.K. Kaushik, Chimica Hungarica 116 (1984) 361;
(d) G.S. Sodhi, A.K. Sharma, N.K. Kaushik, J. Organomet. Chem. 238 (1982) 177;
(e) G.S. Sodhi, A.K. Sharma, N.K. Kaushik, Synth. React. Inorg. Met.-Org. Chem. 12 (1982) 947;
(f) A.R. Dias, A.M. Galvão, A.C. Galvão, J. Organomet. Chem. 632 (2002) 157;
(g) R. Boese, D. Bläser, N. Kuhn, S.Z. Stubenrauch, Kristallogr. 209 (1994) 188.
[8] (a) R.V. Bynum, W.E. Hunter, R.D. Rogers, J.L. Atwood, Inorg. Chem. 19 (1980) 2368;
(b) K. Issleib, G.Z. Bätz, Anorg. Allg. Chem. 369 (1969) 83;
(c) D. Tille, Z. Naturforsch. B 25 (1970) 1358.
[9] η^1-Coordination of pyrrolyl ligands is also promoted by using it as a component of a multidentate ligand. See, for example, Ref. [(3c)] and:
(a) Y. Li, Y. Shi, A.L. Odom, J. Am. Chem. Soc. 126 (2004) 1794;
(b) Y. Shi, C. Cao, A.L. Odom, Inorg. Chem. 43 (2004) 275;
(c) W.S. Seo, Y.J. Cho, S.C. Yoon, J.T. Park, Y. Park, J. Organomet. Chem. 640 (2001) 79;
(d) Y. Shi, C. Hall, J.T. Ciszewski, C. Cao, A.L. Odom, Chem. Commun. (2003) 586;
(e) A. Novak, A.J. Blake, C. Wilson, J.B. Love, Chem. Commun. (2002) 2796;
(f) G. Solari, E. Solari, G. Lemercier, C. Floriani, A. Chiesi-Villa, C. Rizzoli, Inorg. Chem. 36 (1997) 2691;
(g) R. Crescenzi, E. Solari, C. Floriani, A. Chiesi-Villa, C. Rizzoli, Organometallics 15 (1996) 5456.
[10] For a recent discussion of η^1- and η^5-pyrrolyl coordination in zirconium chemistry, see: A.R. Dias, A.P. Ferreira, L.F. Veiros, Organometallics 22 (2003) 5114.
[11] CSD Version 5.25. 3D Search and Research Using the Cambridge Structural Database, F.H. Allen, O. Kennard, Chemical Design Automation News 8 (1) (1993) 1.
[12] H. Lee, J.B. Bonanno, J. Cordaro, J.M. Hahn, G. Parkin, J. Chem. Soc., Dalton Trans. (1999) 1365.
[13] P. Jutzi, R. Dickbreder, Chem. Ber. 119 (1986) 1750.
[14] C.E. Zachmanoglou, A. Docrat, B.M. Bridgewater, G. Parkin, C.G. Brandow, J.E. Bercaw, C.N. Jardine, M. Lyall, J.C. Green, J.B. Keister, J. Am. Chem. Soc. 124 (2002) 9525.
[15] For examples of ansa metallocene compounds with η^5,η^1-coordination modes, see:
(a) W.A. Herrmann, M.J.A. Morawietz, T. Priermeier, Angew. Chem. Int. Ed. Engl. 33 (1994) 1946;
(b) W.A. Herrmann, W. Baratta, E. Herdtweck, J. Organomet. Chem. 541 (1997) 445;
(c) A.N. Chernega, M.L.H. Green, A.G. Suarez, Can. J. Chem. 73 (1995) 1157.
[16] η^1-Coordination modes have also been observed in metallocenes of the type $[Me_2Si(NR)(ring)]MX_2$. See, for example:
(a) L.J. Irwin, J.H. Reibenspies, S.A. Miller, J. Am. Chem. Soc. 126 (2004) 16716;
(b) L.J. Irwin, J.H. Reibenspies, S.A. Miller, Polyhedron, this issue.
[17] L.E. Schock, T.J. Marks, J. Am. Chem. Soc. 110 (1988) 7701.
[18] For a discussion of bonding in fulvene complexes, see:
(a) J.A. Bandy, V.S.B. Mtetwa, K. Prout, J.C. Green, C.E. Davies, M.L.H. Green, N.J. Hazel, A. Izquierdo, J.J. Martin-Polo, J. Chem. Soc. Dalton Trans. (1985) 2037;
(b) A.Z. Kreindlin, M.A. Rybinskaya, Russ. Chem. Rev. 73 (2004) 417.
[19] For further comparison, the longest Ti—C bond length in the Ti(III) complex $Cp^*(C_5Me_4CH_2)Ti$ is 2.47 Å. See: J.M. Fischer, W.E. Piers, V.G. Young Jr., Organometallics 15 (1996) 2410.
[20] (a) L.E. Schock, C.P. Brock, T. Marks, J. Organometallics 6 (1987) 232;
(b) A.R. Bulls, W.P. Schaefer, M. Serfas, J.E. Bercaw, Organometallics 6 (1987) 1219.
[21] R. Beckhaus, A. Lutzen, D. Haase, W. Saak, J. Stroot, S. Becke, J. Heinrichs, Angew. Chem. Int. Ed. Engl. 40 (2001) 2056.
[22] S.S. Batsanov, Russ. Chem. Bull. 44 (1995) 2245.
[23] Chisholm has previously put forth this argument to predict M–NMe_2 bond lengths in the absence of π-donation by consideration of M-alkyl (sp^3) bond lengths. See: M.H. Chisholm, L.-S. Tan, J.C. Huffman, J. Am. Chem. Soc. 104 (1982) 4879.
[24] (a) J.W. Lauher, R. Hoffmann, J. Am. Chem. Soc. 98 (1976) 1729;
(b) Z. Lin, M.B. Hall, Coord. Chem. Rev. 123 (1993) 149;
(c) J.C. Green, M.L.H. Green, C.K. Prout, J. Chem. Soc., Chem. Commun. (1972) 421.
[25] It is worth noting that the average Ti—N bond length in $Cp^*Ti(NMe_2)_3$ (1.91 Å), with an η^5-coordinated Cp* ligand is marginally longer than that in $[pyr^{Ph_2}]Ti(NMe_2)_3$. See: A. Martín, M. Mena, C. Yélamos, R. Serrano, P.R. Raithby, J. Organomet. Chem. 467 (1994) 79.
[26] A.R. Dias, A.M. Galvao, A.C. Galvao, Coll. Czech. Chem. Commun. 63 (1998) 182.
[27] H. Lee, B.M. Bridgewater, G. Parkin, J. Chem. Soc., Dalton Trans. (2000) 4490.
[28] G.M. Sheldrick, SHELXTL, An Integrated System for Solving, Refining and Displaying Crystal Structures from Diffraction Data, University of Göttingen, Göttingen, 1981.



Scheme 1.

compounds of p-block elements have been reported to date, $Me_4C_2(C_5H_4)_2Sn$ and $Me_4C_2(C_5H_4)_2Pb$ [25],[1] which were isolated in only 2% yield and were not characterized crystallographically.

Although cyclopentadienylaluminum compounds containing a tethered amine [26,27] and amide ligand [28] have been reported, no *ansa*-aluminocene compounds containing two bridged cyclopentadienyl rings have yet been described. Our motivation for pursing these compounds is multifold. We anticipated that the interannular ("*ansa*") bridge would slow the haptotropic rearrangements of the cyclopentadienyl–aluminum bonds to the extent that they could be studied on the NMR time scale. We also expect the constraints of the bridge on the coordination geometry of the cyclopentadienyl rings to increase the Lewis acidity of the aluminum in the same way that it increases the Lewis acidity of early transition metals [29–32]. Finally, we plan to develop chiral *ansa*-aluminocene compounds for application as asymmetric catalysts of Lewis acid-promoted reactions.

In this report, we describe the synthesis and characterization of $[Me_4C_2(C_5H_4)_2Al\text{-}\mu\text{-}Cl]_2$ (**2**), and its Lewis base adducts $[\{Me_4C_2(C_5H_4)\}Al(THF)Cl]$ (**3**) and $[\{Me_4C_2(C_5H_4)\}Al(CN\text{-}t\text{-}Bu)Cl]$ (**4**). The molecular structures of all three compounds were determined by single crystal X-ray crystallography. Whereas migration of aluminum over its cyclopentadienyl ring(s) is normally too rapid to be followed on the NMR time scale, the tetramethylethano bridge in compounds **2**–**4** impedes the migration to the extent that it can be studied for the first time using dynamic NMR methods.

2. Results and discussion

2.1. Synthesis and characterization of $[Me_4C_2(C_5H_4)_2Al\text{-}\mu\text{-}Cl]_2$ (2)

Initial efforts to prepare an *ansa*-aluminocene compound by transmetallation of the ligand framework from $[Me_4C_2(\eta^5\text{-}C_5H_4)_2Ca(THF)_x]$ [13] to $AlCl_3$ were unsuccessful. No reaction occurred, even upon heating the mixture to 80 °C in toluene. Since magnesocenes have been used successfully in the synthesis of cyclopentadienylaluminum compounds [33–37], we prepared the corresponding *ansa*-magnesocene compound $[Me_4C_2(\eta^5\text{-}C_5H_4)_2Mg]$ (**1**) in the manner described by Brintzinger and coworkers [14] for related *ansa*-magnesocene compounds. Compound **1** does react with $AlCl_3$ at room temperature in toluene to afford the *ansa*-aluminocene compound $[Me_4C_2(C_5H_4)_2AlCl]_2$ (**2**) (Scheme 1).

The *ansa*-aluminocene compound was isolated in 47% yield as an air-sensitive, off-white powder. Decomposition of the compound after one day at room temperature under an N_2 atmosphere is accompanied by its discoloration to dark blue. The compound is stable for months when stored in a −30 °C freezer. Interestingly, compound **2** is stable in toluene for over a week at room temperature but is not stable in benzene solution, in which its turns dark blue over 24 h. Despite the instability of **2** in benzene, single crystals of the compound that were suitable for an X-ray structure determination were grown by evaporation of benzene from a saturated solution. The molecular structure of the dimer is shown in Fig. 1(a) along with a view down the backbone of the bridge (Fig. 1(b)). Crystallographic data and selected bond lengths and angles are listed in Tables 1 and 2, respectively.

The dimer sits on a center of inversion in the unit cell, so the geometries of each half of the dimer are identical with one σ-coordinated (η^1) and one η^5 cyclopentadienyl ring. The C–C bonds in the η^1 cyclopentadienyl ring are localized, with two double bonds at C(8)–C(12) and C(10)–C(11) and three single bonds at C(9)–C(8), C(9)–C(10), and C(11)–C(12). The aluminum adopts a highly distorted tetrahedral geometry with a narrow Cl(1)–Al(1)–Cl(1A) bond angle of 85.07(3)° and a much wider C(9)–Al(1)-centroid angle of 117.6°. The geometry of the aluminum center is similar to that found in another dimeric cyclopentadienylaluminum chloride compound, $[(EtMe_4C_5)(Ph)Al\text{-}\mu\text{-}Cl]_2$, reported by Roesky and coworkers [38]. The Al-centroid distance of 1.939 Å for the η^5 ring is longer than the corresponding bonds in $[(\eta^5\text{-}C_5H_5)(2,6\text{-}t\text{-}Bu\text{-}4\text{-}Me\text{-}C_6H_2O)_2Al]$ (1.920 Å) [39] and $[(\eta^5\text{-}C_5H_5)\{(2,6\text{-}i\text{-}Pr_2C_6H_3)N\}Al]_2$ (1.886 Å) [40]. The Al–C(9) distance for the η^1 ring is within the 1.976–2.080 range reported for other η^1-cyclopentadienylaluminum(III) compounds

[1] During the publication of this paper, a communication describing the synthesis and structural characterization of a C_2-symmetric *ansa*-stannocene complex appeared in print (C.J. Pilotto, E.P. Roth, G.M. Canfield, J.E.B. Johnson, B.J. Balaich, L.N. Zakharov, A.L. Rheingold, Organometallics 24 (2005) 1806).

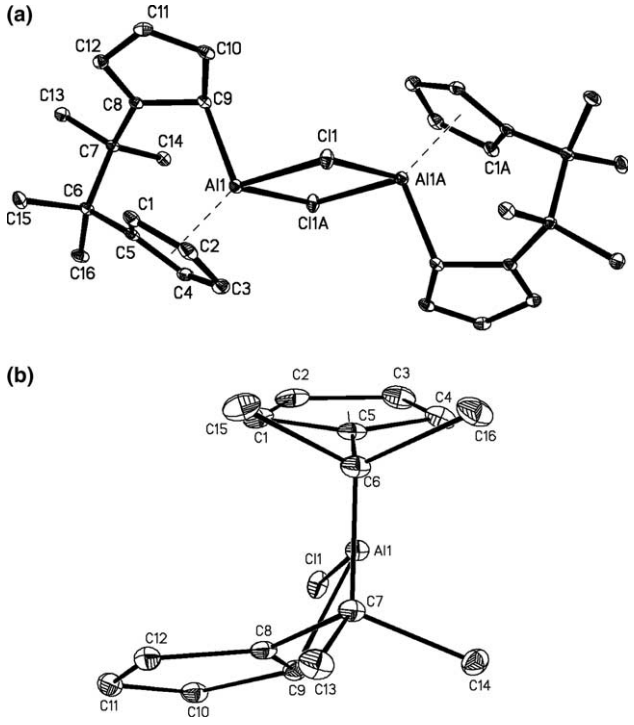


Fig. 1. Thermal ellipsoid drawings of **2** (30%) with atom numbering scheme: (a) side view of dimer; (b) rear view of one *ansa*-aluminocene fragment. Hydrogen atoms have been omitted for clarity.

[35–37,41–44]. The torsion angle between the bonds connecting the ethano bridge to the cyclopentadienyl rings (C(5)–C(6)–C(7)–C(8), −43.18(15)°) is somewhat larger in magnitude than the corresponding angle in bis-η^5 *ansa*-metallocene complexes (29–32°) containing a similar ligand framework [45,46]. The larger torsion angle allows the methyl substituents on the bridge to be fully staggered.

2.2. NMR spectroscopic characterization of the fluxional properties of 2

The room temperature ^{1}H NMR spectrum of a 50 mM solution of **2** (Fig. 2) in toluene-d_8 exhibited only two resonances for the cyclopentadienyl rings at δ 5.13 and δ 6.16 and only one resonance at δ 1.01 for the methyl groups on the ethano bridge due to a dynamic process that averages the proton environments. As the sample was cooled, the high field cyclopentadienyl resonance broadened and separated into two new signals at δ 6.15 and δ 4.36. The δ 6.15 signal is attributable to protons attached to non-coordinated sp^2-hybridized (olefinic) ring carbons and the 4.36 signal is characteristic of protons attached to sp^3-hybridized (allylic) carbons σ-coordinated to aluminum. The lower field

Table 1
Crystallographic data for compounds **2**, **3**, and **4**

Compound	**2**	**3**	**4**
Formula	$C_{32}H_{40}Al_2Cl_2$	$C_{20}H_{28}AlClO$	$C_{21}H_{29}AlClN$
Molecular weight	549.50	346.85	357.88
Crystal system	monoclinic	triclinic	triclinic
Space group	$P2_1/c$	$P\bar{1}$	$P\bar{1}$
a (Å)	13.525(3)	7.0281(14)	9.6197(19)
b (Å)	8.0997(16)	9.919(2)	13.390(3)
c (Å)	13.419(3)	13.662(3)	16.691(3)
α (°)	90	100.49(3)	99.25(3)
β (°)	105.11(3)	99.55(3)	99.66(3)
γ (°)	90	103.45(3)	99.08(3)
V (Å^3)	1419.2(6)	888.9(4)	2053.8(8)
Z	2	2	4
T (K)	83(2)	83(2)	83(2)
λ (Å)	0.71073	0.71073	0.71073
ρ_{calc} (Mg/m^3)	1.286	1.296	1.157
μ (mm^{-1})	0.311	0.267	0.231
F(0 0 0)	584	372	768
Crystal size (mm^3)	0.39 × 0.38 × 0.06	0.37 × 0.22 × 0.2	0.75 × 0.40 × 0.23
θ Range (°)	1.56–27.50	2.17–27.50	1.57–25.00
Index ranges	$-17 \leqslant h \leqslant 17$; $-10 \leqslant k \leqslant 10$; $-17 \leqslant l \leqslant 17$	$-9 \leqslant h \leqslant 9$; $-12 \leqslant k \leqslant 12$; $-17 \leqslant l \leqslant 17$	$-11 \leqslant h \leqslant 11$; $-15 \leqslant k \leqslant 15$; $0 \leqslant l \leqslant 19$
Number of reflections collected	17 346	13 415	27 010
Number of independent reflections (R_{int})	3265 (0.0298)	4065 (0.0221)	7229 (0.0314)
Data/restraints/parameters	3265/0/167	4065/3/213	7229/0/447
Goodness-of-fit	1.095	1.057	1.041
R^a [$I > 2\sigma$ (I)]	0.0354	0.0374	0.0552
wR^a [$I > 2\sigma(I)$]	0.0904	0.0949	0.1389
Largest differential peak and hole (e Å^{-3})	0.449, −0.241	0.379, −0.379	1.651, −0.363

[a] $R_1 = \sum |F_o| - |F_c| / \sum |F_o|$; $wR_2 = \{\sum[w(F_o^2 - F_c^2)^2] / \sum[w(F_o^2)^2]\}^{1/2}$.

Table 2
Selected bond lengths (Å) and bond angles (°) for **2**

Al(1)–C(9)	1.9886(15)
Al(1)–C(1)	2.3840(17)
Al(1)–C(2)	2.2167(16)
Al(1)–C(3)	2.1321(16)
Al(1)–C(4)	2.2537(15)
Al(1)–C(5)	2.4231(16)
Al(1)–Cl(1)	2.3221(7)
Al(1)–Cl(1A)	2.4078(8)
C(1)–C(2)	1.413(2)
C(2)–C(3)	1.421(2)
C(3)–C(4)	1.431(2)
C(4)–C(5)	1.417(2)
C(5)–C(1)	1.420(2)
C(8)–C(12)	1.358(2)
C(8)–C(9)	1.4936(19)
C(9)–C(10)	1.4884(19)
C(10)–C(11)	1.347(2)
C(11)–C(12)	1.449(2)
Al(1)-centroid	1.939
C(9)–Al(1)-centroid	117.6
Al(1)–Cl(1)–Al(1)A	94.93(3)
Cl(1)–Al1–Cl(1A)	85.07(3)
C(10)–C(9)–Al(1)	109.02(9)
C(8)–C(9)–Al(1)	113.40(9)
C(10)–C(9)–C(8)	103.60(11)
C(5)–C(6)–C(7)–C(8)	−43.18(15)

cyclopentadienyl resonance decoalesced at a lower temperature into two more closely spaced signals at δ 6.40 and δ 6.33. The methyl resonance broadened and shifted downfield by more than 0.1 ppm, but it did not decoalesce by −94 °C, at which point the toluene-d_8 became too viscous to permit recording NMR spectra on further cooling. No further change in the spectrum was observed upon cooling a 50 mM solution of **2** in methylcyclohexane-d_{14} to −124 °C.

Interestingly, for more dilute solutions of **2**, the methyl proton resonances *did* decoalesce (Fig. 3). The separation between the two methyl signals increased with increasing dilution of the sample. The chemical shifts of the downfield pair of cyclopentadienyl proton resonances also varied considerably with the concentration of the sample.

We considered the possibility that this concentration dependence of the coalescence behavior was due to a monomer–dimer equilibrium. Efforts to determine the degree of aggregation of **2** in solution by measuring the colligative properties of the solutions were unsuccessful. The poor thermal stability of **2** over days at room temperature in cyclohexane precluded a molecular weight determination using the Signer ebulliometric method [50], and we were unable to obtain reliable freezing point depression data from a cyclohexane solution of the compound. Variable temperature $^{13}C\{^1H\}$ and ^{27}Al NMR spectra (Supporting Information) offered no additional insight into this behavior.

A −94 °C ROESY experiment (Supporting Information) revealed that the cyclopentadienyl protons resonating at δ 4.36 and δ 6.15 are nearest the bridge and, therefore, on carbons α to the *ipso* ring carbons. A −94 °C COSY experiment (Supporting Information) showed cross peaks between all four cyclopentadienyl ^1H NMR signals, indicating that each resonance corre-

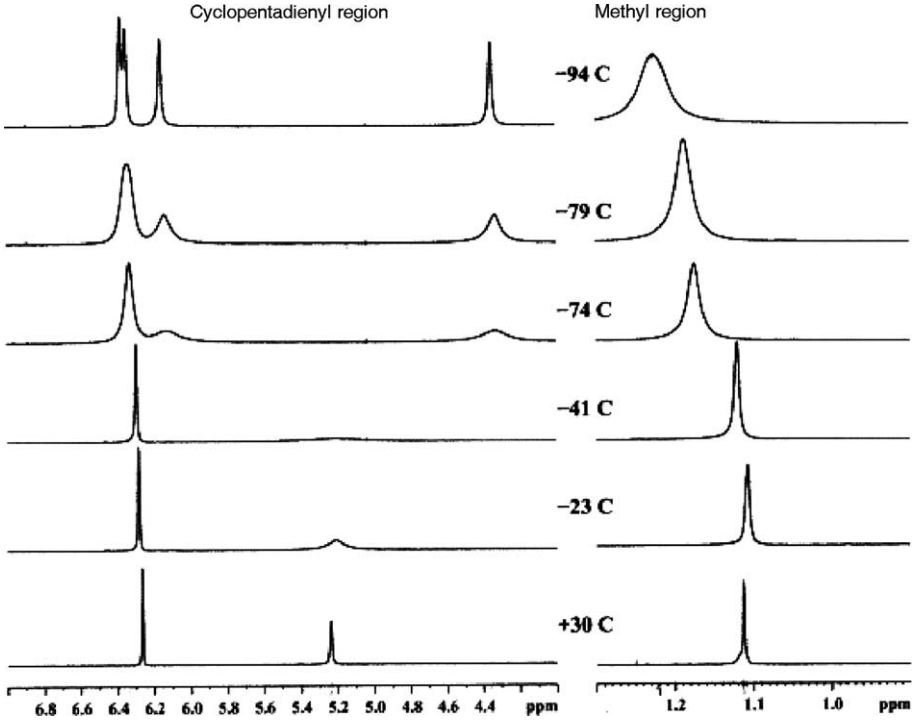


Fig. 2. Variable temperature ^1H NMR spectra of a 50 mM solution of **2** in toluene-d_8.

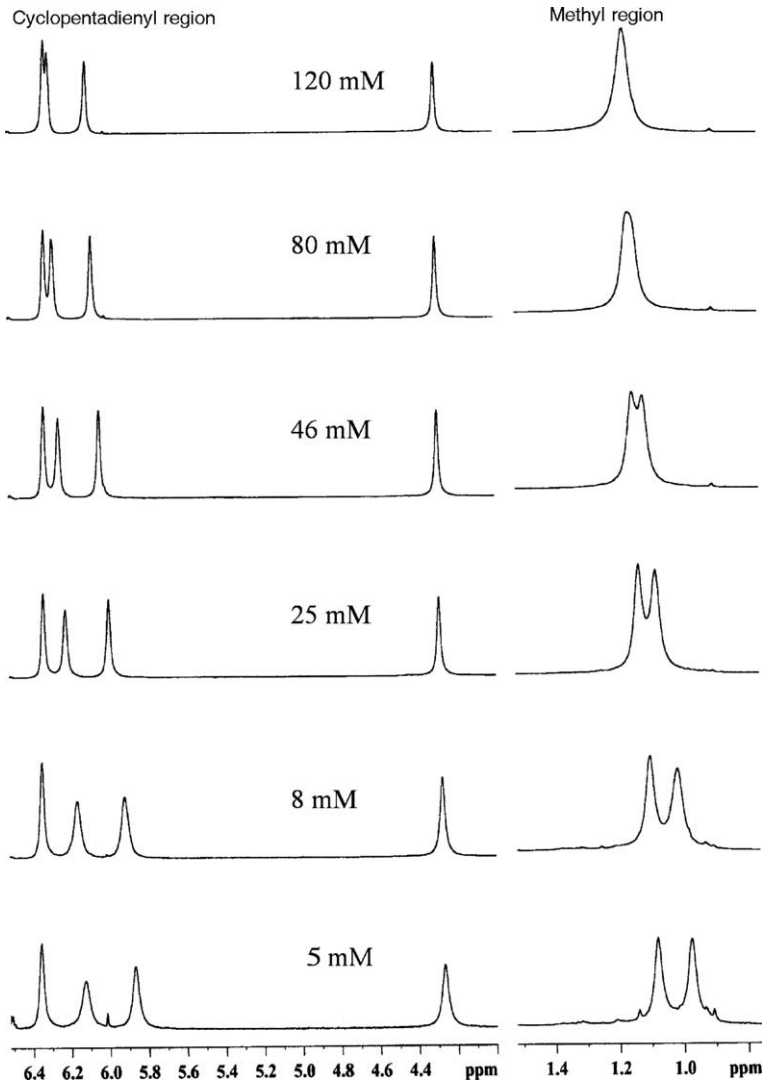


Fig. 3. ^{1}H NMR spectra of samples of **2** at different concentrations in toluene-d_8 at −94 °C.

sponds to two protons at equivalent positions on opposite rings and that the coordination geometries of the rings are equivalent. The presence of only two ^{1}H NMR resonances for the methyl groups, one ^{13}C NMR signal for the two cyclopentadienyl *ipso* carbons, and one ^{13}C NMR signal for the two quarternary carbons of the ethano bridge in the −94 °C ^{1}H and ^{13}C{^{1}H} NMR spectra (Supporting Information) further support this conclusion. The combined NMR data are consistent with η^1 geometries for both cyclopentadienyl rings. Fig. 4 illustrates two possible bonding arrangements of the cyclopentadienyl ligand framework.

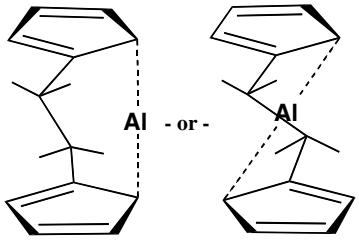


Fig. 4. Possible geometries of the dicyclopentadienyl ligand framework in **2**.

It is not possible to identify with certainty the fluxional pathways responsible for the signal averaging exhibited by **2** from the variable temperature ^{1}H and ^{13}C NMR spectra; however, the chemical shifts and coalescence behavior of the ^{1}H and ^{13}C NMR resonances rule out a circumambulatory type migration of the aluminum about the periphery of its cyclopentadienyl rings through either an $\eta^2 \rightarrow \eta^3 \rightarrow \eta^2$ migration [47] or a series of 1,5 sigmatropic shifts [48] since only the α carbons and their protons exhibit the high field chemical shifts indicative of localized coordination to aluminum. Possible rearrangement pathways include $\eta^1 \leftrightarrow \eta^5$ shifts, $\eta^1 \leftrightarrow \eta^3$ shifts, and 1,3-migration of the aluminum between the two α carbons of the ring. The last alternative is symmetry-forbidden unless it proceeds with stereo-

chemical inversion at aluminum [49]. Our findings with compound **4** (vide infra), suggest that this type of inversion could, in fact, play a role in the rearrangements of these compounds.

^{27}Al NMR spectroscopy is a useful tool for probing the coordination environment of aluminum, and Benn et al. [51–55] have shown that the chemical shifts of inorganic and organo-aluminum compounds can be correlated to the coordination number of the aluminum. In general, the ^{27}Al NMR chemical shifts increase as the coordination number of the aluminum decreases. The room temperature ^{27}Al NMR spectrum of **2** in toluene-d_8 exhibited a single broad signal at δ −2, which broadened into the baseline as the temperature of the sample was reduced to −50 °C (Supporting Information). An ^{27}Al NMR chemical shift of δ −2 is at a considerably higher field than that of other di- and tricyclopentadienylaluminum(III) compounds, which usually appear in the 52–118 ppm range [55]. In fact, it is more characteristic of cyclopentadienylaluminum(III) compounds containing at least one η^5 cyclopentadienyl ring. We believe that the δ −2 chemical shift of **2** reflects the contribution of a bis-η^5 geometry to the average structure of the compound at the fast exchange limit at room temperature. As the dynamic exchange slows, the line broadens into the baseline. Temperature-dependent quadrupole broadening effects undoubtedly contribute to this line broadening.

Rate constants for the dynamic averaging of the ^{1}H and ^{13}C NMR signals for **2** were determined over a >50 °C temperature range by line shape analysis of cyclopentadienyl and methyl signals in the variable temperature ^{1}H and ^{13}C NMR spectra. Both 75 and 5 mM solutions of **2** in toluene-d_8 were examined in order to check for concentration effects on the rate of rearrangement. Eyring plots of the data are shown in Fig. 5. An excellent linear fit of the kinetic data was found for both concentrations. Similar values (within error) for the activation parameters were obtained from the two Eyring plots: 75 mM (5 mM): $\Delta H^{\neq} = 8.7 \pm 0.7$ (7.7 ± 1.1) kcal mol^{-1}, $\Delta S^{\neq} = -3 \pm 5$ (-7.6 ± 3) cal K^{-1} mol^{-1}. Thus, sample concentration has little, if any, effect on the rearrangement process.

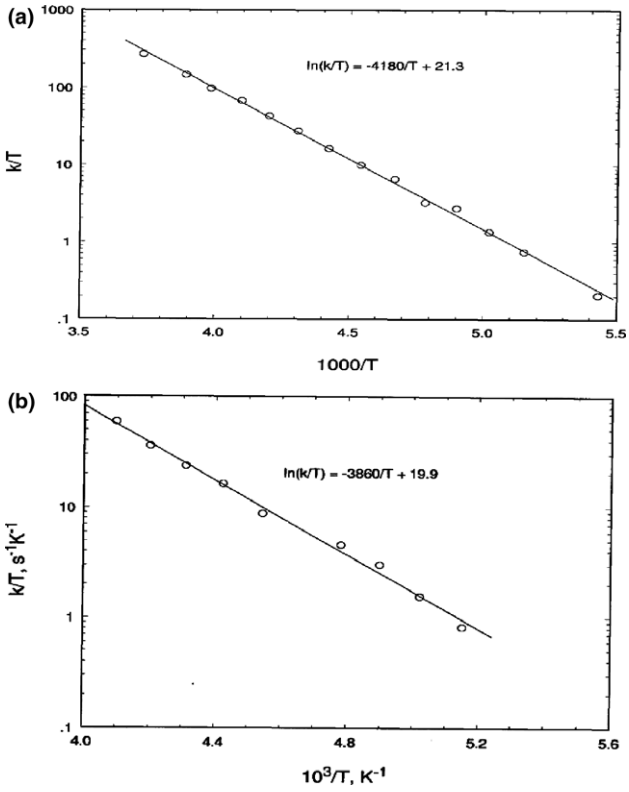


Fig. 5. Eyring plots of rate constants for the fluxional rearrangement of **2** at 75 mM (a) and 5 mM (b) concentrations in toluene-d_8.

2.3. Lewis base adducts of *2*

2.3.1. Synthesis and characterization of *{Me$_4$C$_2$(C$_5$H$_4$)$_2$}AlCl(THF) (3)*

We prepared Lewis base adducts of **2** in order to reduce the symmetry of the complex so that the fate of each individual cyclopentadienyl proton and carbon could be examined in order to elucidate the haptotropic rearrangement(s) of the system.

[{Me$_4$C$_2$(C$_5$H$_4$)$_2$}AlCl(THF)] (**3**) was obtained in 94% yield as a white powder by dissolving **2** in THF and then removing the excess solvent under reduced pressure. Unlike **2**, compound **3** is stable for more than a week in the solid state at room temperature in the absence of air. X-ray quality crystals of **3** were grown from benzene solution by slow evaporation of the solvent. Rear and side views of the molecular structure are shown in Fig. 6. X-ray crystallographic data and selected bond distances and angles are listed in Tables 1 and 3, respectively. As in the structure of **2**, one cyclopentadienyl ring is η^1 coordinated at an α carbon and contains localized single and double C–C bonds with double bonds at C(2)–C(3) and C(4)–C(5) and single bonds at C(1)–C(2), C(3)–C(4) and C(1)–C(5). The second ring is η^3. The η^3 interaction involves both β ring carbons (C(10) and C(11)) and one α ring carbon (C(12)), with C(10) more distant from Al(1) than C(11) and C(12), which are on the same side as the THF moiety. The tighter coordination of C(11)–C(12) is reflected in its bond length, which is significantly longer than the other C–C bonds in the ring. C18 and C19 are disordered in the THF molecule with occupancies of 66% and 33%. The Al(1)–Cl(1) bond distance in **3** (2.1925(8) Å) is shorter than the bonds between aluminum and the bridging chlorides in **2** (2.3221(7) and 2.4078(8) Å), and the O(1)–Al(1)–Cl(1) angle of 96.47(5)° is wider than the Cl(1)–Al–Cl(1A) angle of 85.07(3)° in **2**. The torsion angle (C(5)–C(6)–C(7)–C(8), 46.60(6)°) associated with the conformation of the bridge is larger in magnitude than the corresponding angle in compound **2**.

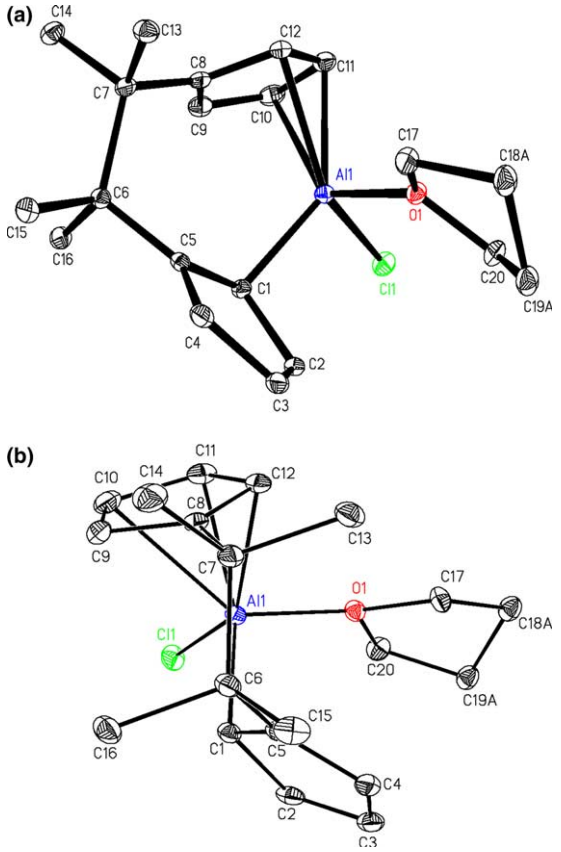


Fig. 6. Thermal ellipsoid drawings of **3** (30%) ((a) side and (b) rear views) with atom numbering scheme: Hydrogen atoms have been omitted for clarity.

Table 3
Selected bond lengths (Å) and bond angles (°) of **3**

Al(1)–C(1)	2.0239(15)
Al(1)–C(10)	2.4521(17)
Al(1)–C(11)	2.1089(16)
Al(1)–C(12)	2.2630(16)
Al(1)–O(1)	1.9110(13)
Al(1)–Cl(1)	2.1926(8)
C(1)–C(2)	1.4782(19)
C(2)–C(3)	1.353(2)
C(3)–C(4)	1.443(2)
C(4)–C(5)	1.367(2)
C(5)–C(1)	1.486(2)
C(8)–C(9)	1.416(2)
C(9)–C(10)	1.396(2)
C(10)–C(11)	1.420(2)
C(11)–C(12)	1.439(2)
C(8)–C(12)	1.412(2)
O(1)–Al(1)–Cl(1)	96.47(5)
C(1)–Al1–Cl(1)	102.98(5)
C(5)–C(6)–C(7)–C(8)	46.60(16)

Cyclopentadienyl and methyl regions of the variable temperature ^{1}H NMR spectra of **3** are shown in Fig. 7. Variable temperature ^{1}H NMR spectra of the THF proton resonances are included in the Supporting Information. As the sample was cooled, the two cyclopentadienyl resonances split into eight resonances (peaks 1–8 in the −99 °C spectrum in Fig. 7). The single resonance for the methyl groups split into four peaks.

The presence of only two cyclopentadienyl proton resonances and one methyl group resonance in the 43 °C ^{1}H NMR spectrum of **3** indicated that the aluminum center was epimerizing. Dynamic exchange between free and bound THF was evident in the VT ^{1}H NMR spectra of a solution of **3** to which excess THF had been added (Supporting Information). This suggests that THF dissociation is responsible for the epimerization of the aluminum, although we cannot rule out intramolecular inversion at aluminum as the cause. It is noteworthy that excess THF did not influence the rate of signal averaging in the VT ^{1}H NMR spectra, contrary to the effect of excess *t*-BuNC on the rate of signal averaging for compound **4** (vide infra).

The COSY (Fig. 8) and ROESY spectra (Figs. 9–11) allowed us to assign the absolute positions of the cyclopentadienyl protons relative to the tetramethylethano bridge and the THF ligand and to assign a solution structure for the compound (Fig. 12) that is similar to the structure found in the solid state, except that one cyclopentadienyl ring is η^2 instead of η^3. The ^{27}Al NMR chemical shift of compound **3** (δ 78) is consistent with this geometry. A complete analysis of the spectra is provided in the Supporting Information.

Although, we were able to identify the structure of **3** in solution from the low-temperature 1-D and 2-D ^{1}H NMR data, it was not possible to elucidate the nature of the cyclopentadienyl ring rearrangements on aluminum from the ^{1}H NMR coalescence pattern due to the involvement of multiple dynamic processes.

*2.3.2. Synthesis and characterization of {Me$_4$C$_2$(C$_5$H$_4$)$_2$}AlCl(CN-t-Bu) (**4**)*

In order to eliminate the NMR signal averaging associated with Lewis base dissociation, and possibly make the NMR coalescence patterns easier to interpret, we prepared compound **4** with the expectation that *t*-butyl isocyanide would coordinate the aluminum irreversibly.

Crystallographic analysis of a single crystal of **4** revealed two unique molecules in the unit cell. Each molecule bears two η^1 cyclopentadienyl rings. Since they are structurally similar, only one of the molecules is shown in Fig. 12. Crystallographic data and selected bond lengths and angles are listed in Tables 1 and 4. Each cyclopentadienyl ring exhibits localized single and double C–C bonds like the η^1 rings of **2** and **3**. Although Al1–C17 (2.1089(16) Å) is slightly longer, C17–N1 (1.143(3) Å) is comparable in length to the corresponding bonds in Cp$_3$Al(CN-*t*-Bu) (2.067(6) and 1.152(7) Å, respectively) [35]. Al(1)–Cl(1) is slightly shorter than the corresponding bond in **3** and significantly shorter than the Al–Cl bonds in **2**. Angle C(17)–Al(1)–Cl(1) is

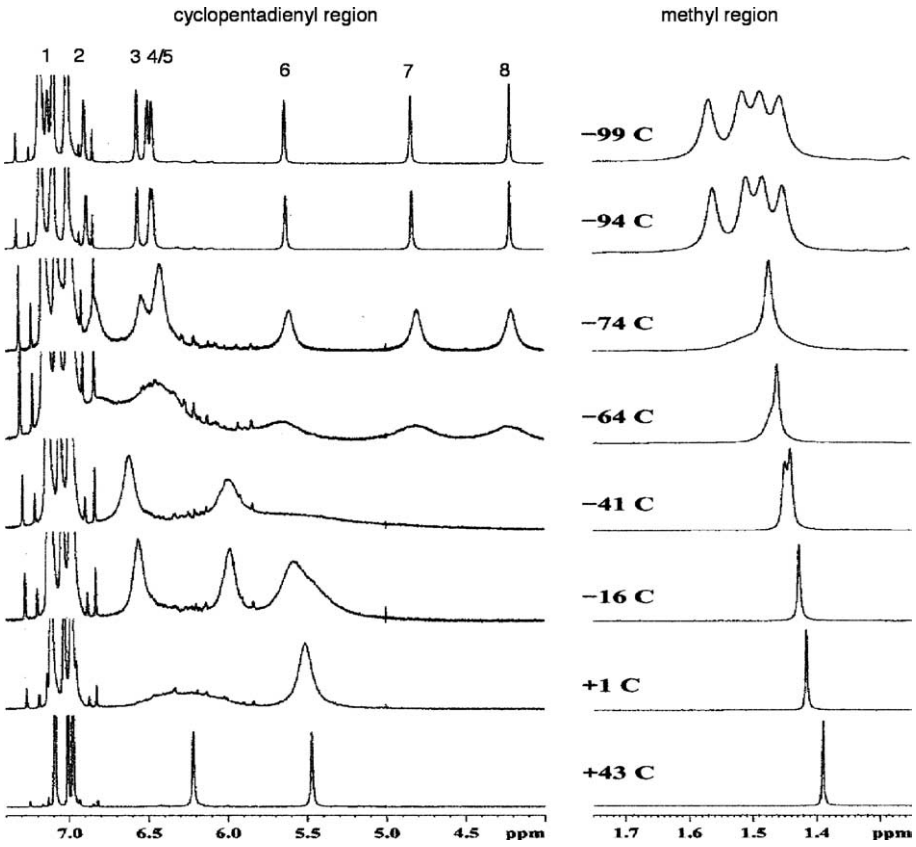


Fig. 7. Variable temperature ^{1}H NMR spectra of a solution of **3** in toluene-d_8.

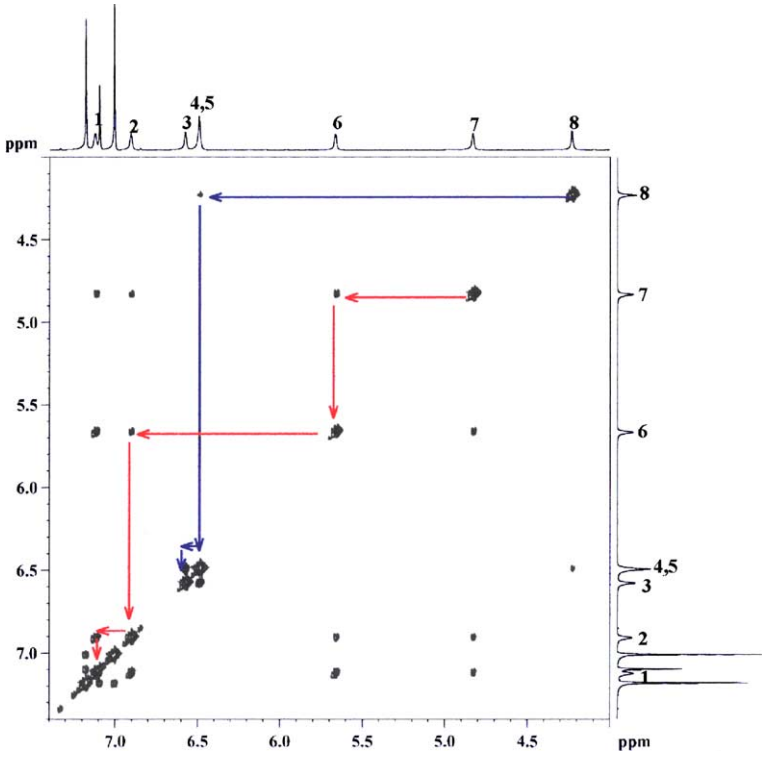


Fig. 8. Partial COSY spectrum of **3** at −94 °C in toluene-d_8 showing coupling between cyclopentadienyl protons.

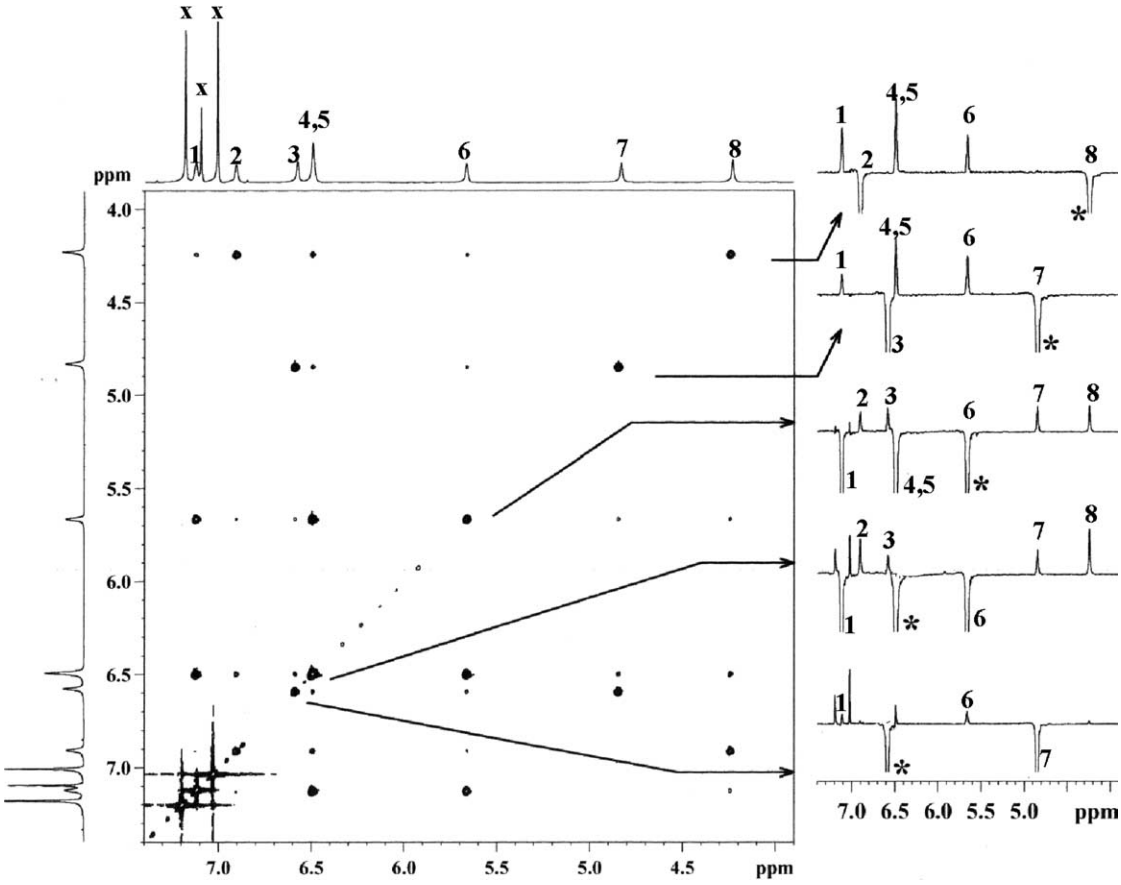


Fig. 9. Partial −94 °C ROESY spectrum of **3** in toluene-d_8 showing the cyclopentadienyl proton interactions. Positive cross peaks represent coupling and negative cross peaks represent exchange (∗ labels diagonal peaks, X labels solvent peaks).

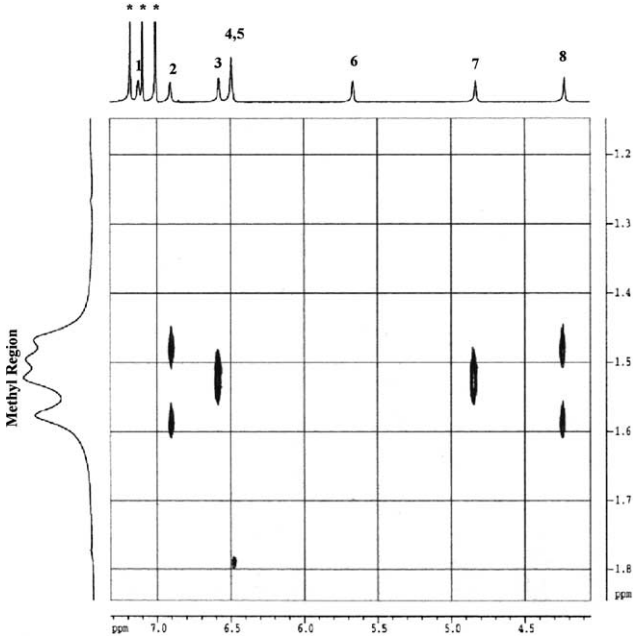


Fig. 10. Partial ROESY spectrum of **3** (−94 °C in toluene-d_8) showing coupling between the cyclopentadienyl and methyl protons (∗ labels solvent peaks).

much wider than Cl(1)–Al(1)–Cl(1A) in **2** and O1–Al(1)–Cl(1) (96.47(5)°) in **3**, which is consistent with the tighter coordination of the chloride and isocyanide ligands. The torsion angle C5–C6–C7–C8 (−45.4(2)°) of the bridge is between that of **2** and **3** in magnitude (see Fig. 13).

Variable temperature ^{1}H NMR spectra of **4** in toluene-d_8 are shown in Fig. 14. The appearance of only two cyclopentadienyl resonances at δ 5.5 and 6.6 and one methyl resonance from the tetramethylethano bridge at δ 1.41 in the 30 °C spectrum indicates that epimerization of the aluminum center occurs in addition to cyclopentadienyl ring rearrangement. By −41 °C, each cyclopentadienyl resonance decoalesced into two signals and the methyl resonance decoalesced into two signals. As the sample was cooled further, these signals broadened again but did not decoalesce by −94 °C.

A ROESY experiment was performed at −40 °C (Fig. 15) since this appeared to be the slow exchange region for one dynamic process. The ROESY spectrum revealed that peaks a and b correspond to the four cyclopentadienyl protons nearest the ethano bridge.

Addition of a small amount of methylcyclohexane-d_{14} (ca. 25% by volume) to a toluene-d_8 solution of **4**

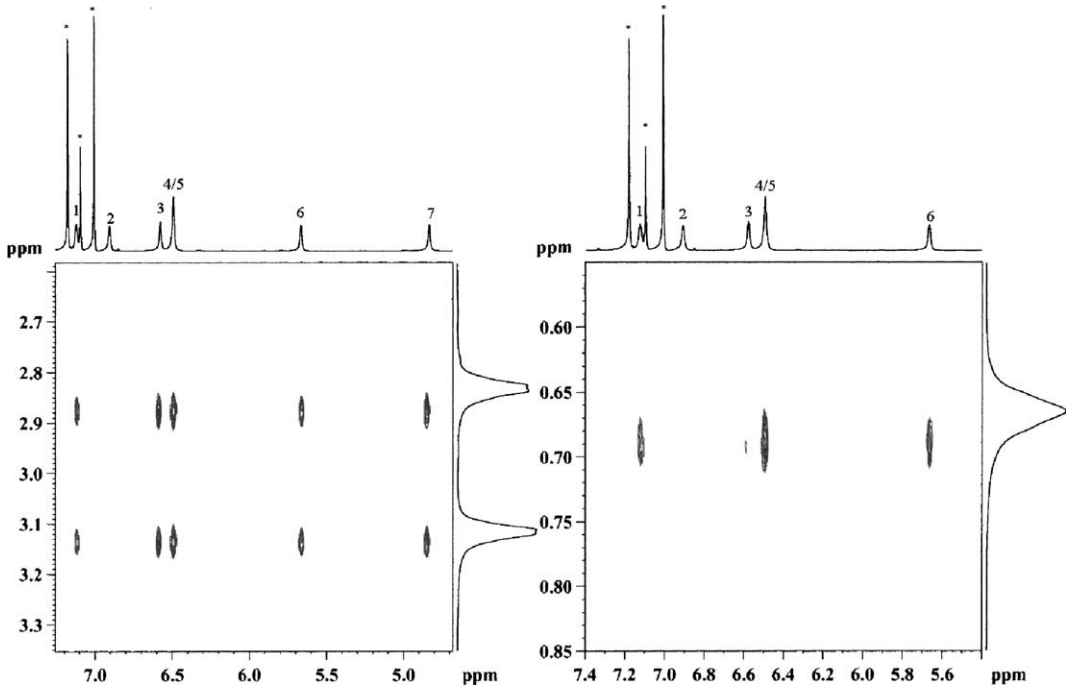


Fig. 11. Partial ROESY spectrum of **3** (−94 °C in toluene-d_8) showing coupling between the cyclopentadienyl and THF protons (∗ labels solvent peaks).

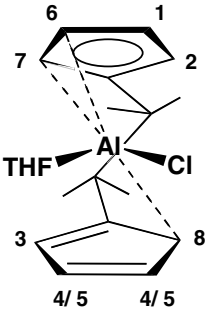


Fig. 12. Proposed solution structure for **3**. Numbering of cyclopentadienyl carbon positions corresponds to numbering of ^{1}H NMR peaks in Fig. 7.

allowed the sample to be cooled to −114 °C so that further decoalescence of the ^{1}H NMR signals could be achieved. Partial −114 °C COSY and ROESY spectra of **4** are shown in Fig. 16. We were surprised to find that the two protons corresponding to "allylic-type" signals (7 and 8) belong to the *same* cyclopentadienyl ring. Cross peaks in the −114 °C ROESY spectrum indicate that signals 1, 2, 7, and 8 correspond to one cyclopentadienyl ring and signals, 3, 4, 5, and 6, belong to the other one. The data are consistent with the solution structure shown in Fig. 17, in which one cyclopentadienyl ring is η^3 and the other is η^5. Curiously, the room temperature ^{27}Al NMR chemical shift of the compound (δ 104) is more consistent with the bis-η^1 geometry of the rings found in the crystal. Perhaps, as suggested for **2**, the average solution structure at room temperature differs from the low temperature structure. We suspect that the solvent may play a role in this behavior. Notably, the ^{1}H NMR chemical shift profile of **4** in pure methylcyclohexane-d_{14} at −114 °C (Supporting Information) is considerably different from that seen in Fig. 15.

At least two different processes are responsible for the dynamic averaging of the ^{1}H NMR signals of **4**. On process exchanges the coordination geometries of the

Table 4
Selected bond lengths (Å) and bond angles (°) of **4**

Al(1)–C(1)	2.009(2)
Al(1)–C(12)	2.014(2)
Al(1)–C(17)	2.1089(16)
Al(1)–Cl(1)	2.153(10)
C(17)–N(1)	1.143(3)
C(1)–C(2)	1.457(3)
C(1)–C(5)	1.464(3)
C(2)–C(3)	1.359(3)
C(3)–C(4)	1.426(3)
C(4)–C(5)	1.378(3)
C(8)–C(9)	1.378(3)
C(8)–C(12)	1.471(3)
C(9)–C(10)	1.423(3)
C(10)–C(11)	1.361(3)
C(11)–C(12)	1.459(3)
C(1)–Al(1)–C(12)	114.79(9)
C(1)–Al(1)–C(17)	105.82(9)
C(12)–Al(1)–C(l7)	106.96(9)
C(1)–Al(1)–Cl(1)	108.29(7)
C(1)2–Al(1)–Cl(1)	113.80(7)
C(17)–Al(1)–Cl(1)	106.56(7)
C(5)–C(6)–C(7)–C(8)	−45.4(2)

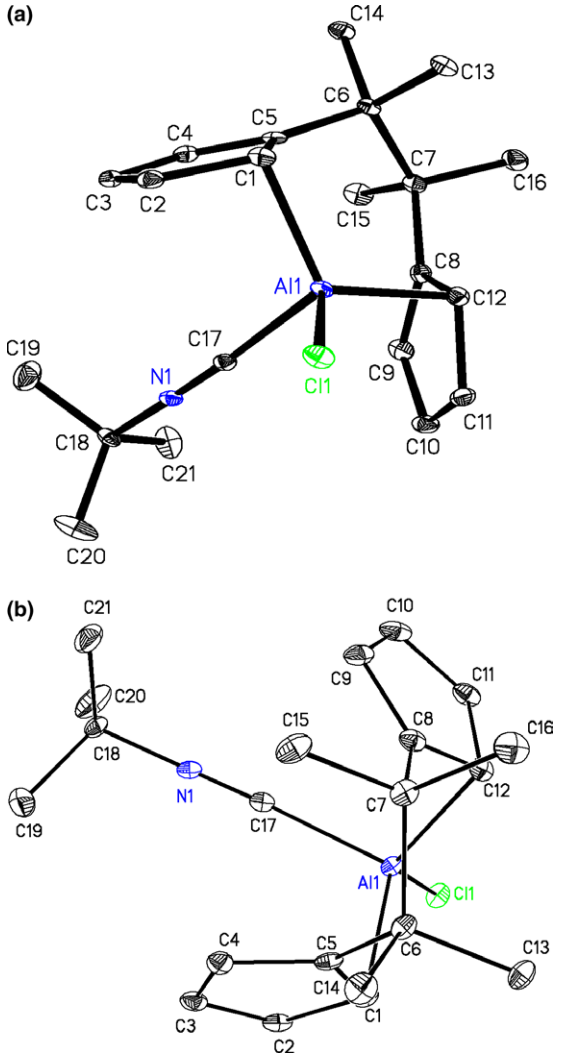


Fig. 13. Thermal ellipsoid drawing of **4** (30%) ((a) side and (b) rear views) with atom numbering scheme. Hydrogen atoms have been omitted for clarity.

cyclopentadienyl rings. The other process exchanges the positions of the chloride and isocyanide ligands. Based on the low temperature solution structure of **4**, slippage of the cyclopentadienyl rings between η^3 and η^5 geometries would be the shortest pathway for accomplishing the first process, which appears to be "frozen out" by −41 °C in the variable temperature ^{1}H NMR spectra (Fig. 14). Further cooling leads to a slowing of the second process to the extent that the different chemical shifts for left and right cyclopentadienyl protons on each ring begin to be resolved.

To rule out the involvement of isocyanide ligand dissociation in the second process, we examined the effect of excess *t*-butyl isocyanide on the ^{1}H NMR and ^{13}C{^{1}H} NMR spectra of **4** in toluene-d^8 (Supporting Information). Both revealed separate peaks for free and bound *t*-butyl isocyanide, indicating that *t*-butyl isocyanide dissociation *does not* occur on the timescale of the signal averaging and some other process is responsible for the exchange between chloride and isocyanide ligand positions. Unlike THF (vide infra), excess isocyanide ligand *did* increase the rate of the signal averaging, however, an effect that is dependent on isocyanide ligand concentration. The effect of free *t*-butylisocyanide on the rate of signal averaging suggested an associative process involving a five-coordinate aluminum. The room temperature ^{27}Al NMR spectrum of a solution of **4** in the presence of a 20-fold excess of *t*-butyl isocyanide revealed no change in the chemical shift of the compound, however.

3. Summary and conclusions

Calculations at the ab inito level show that the potential energy surface for the rearrangement of cyclopentadienylaluminum between different haptotropes is extremely shallow with barriers ranging from 1 to 5 kcal mol [14,55]. Due to these low barriers, the actual pathway(s) by which the cyclopentadienylaluminum compounds rearrange have never been established experimentally since the rearrangements have been too rapid to capture on the NMR time scale. We have shown that introduction of an interannular bridge between the cyclopentadienyl rings of a dicyclopentadienylaluminum compound increases the barrier to rearrangement to $\sim$8 kcal mol^{-1}, in the case of compound **2**, making it possible to "freeze-out" the process in the ^{1}H and ^{13}C NMR spectra of the compound at experimentally accessible temperatures.

We suspect that the geometry of the bridge and the hapticity of the cyclopentadienyl rings on aluminum are intimately linked and that the rate of ring rearrangement is limited by the barrier to conformational rearrangement of the bridge. Indeed, in bis-η^5 *ansa*-metallocene complexes [56], fluctuation of the bridge between right and left zig-zag conformations is accompanied by a swiveling of the η^5 cyclic polyene ligands between two different orientations.

While the variable temperature NMR data ruled out a circumambulatory migration pathway for the aluminum in compound **2**, it did not allow us to pinpoint the actual dynamic processes responsible for the signal averaging. Coordination of THF to aluminum complicated the analysis with the competing dynamic process of THF site exchange, which probably occurs via reversible THF dissociation.

A different mechanism, possibly stereochemical inversion at aluminum, is responsible for the rapid exchange between the chloride and *t*-butyl isocyanide coordination sites in compound **4**. Such an inversion has been invoked to explain the enantiomerization of chiral tetrahedral chelate complexes of Be, B, Cd, Zn, and Hg [57]. The "freezing-out" of the epimerization process

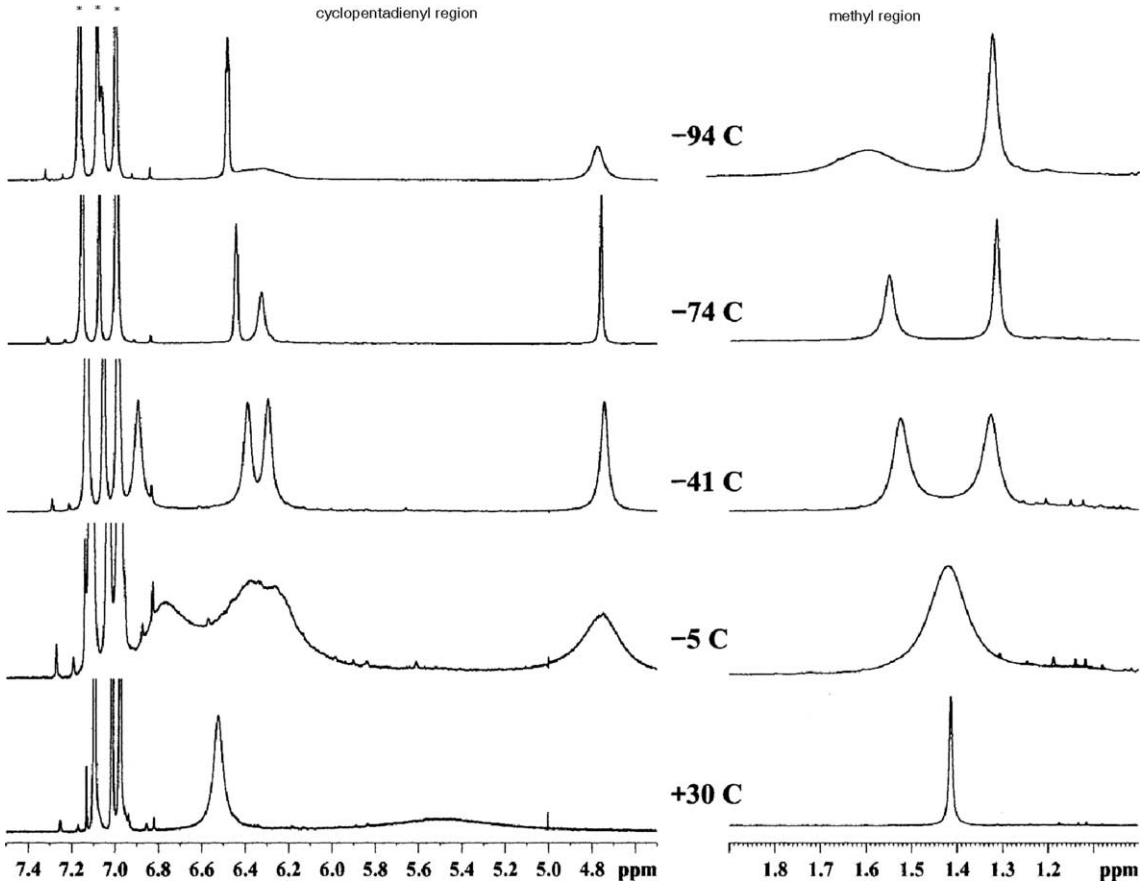


Fig. 14. Variable temperature ^{1}H NMR spectra of **4** in toluene-d_8 (* labels solvent peaks).

in the ^{1}H NMR spectrum of **4** occurs at a lower temperature than the cyclopentadienyl ring rearrangements. Ongoing work includes modeling the variable temperature ^{1}H NMR spectra of this system in order to extract out the kinetic parameters for the two fluxional processes. We will continue to investigate the role of excess *t*-butyl isocyanide in accelerating the dynamic averaging of the cyclopentadienyl ligand environments in **4**. We will also continue to investigate the possible involvement of stereochemical inversion at aluminum in the rearrangement of these pseudo-tetrahedral *ansa*-aluminocene compounds.

4. Experimental

4.1. General considerations

All experiments were performed under inert atmosphere conditions using a combination of glovebox, high vacuum and Schlenk techniques. Non-deuterated solvents were dried over alumina columns and stored in line-pots over sodium/benzophenone. Deuterated solvents were dried over 4A molecular sieves. Argon was purified by passage over an oxytower BASF catalyst (Aldrich) and 4A molecular sieves. NMR spectra were recorded on Bruker Avance 300 MB (300 MHz ^{1}H; 75.4 MHz, ^{13}C; 78 MHz, ^{27}Al) and Bruker Avance 500 (500 MHz, ^{1}H; 125 MHz, ^{13}C; 130 MHz, ^{27}Al) spectrometers. All chemical shifts are reported in ppm and referenced to residual protons in the solvent (^{13}C, ^{1}H) or $Al(OH)_3$ (^{27}Al external reference, 0 ppm). IR spectra were recorded on a Perkin–Elmer-Spectrum 1000 FT-IR Spectrometer. Elemental analyses were determined by Desert Analytics (Tuscon, AZ).

6,6-Dimethylfulvene was prepared according to the literature procedure [58]. Solid $MeAlCl_2$ was obtained by removing the solvent from a 1.0 M hexane solution from Aldrich under vacuum.

4.2. $[(CH_3)_4C_2(C_5H_5)_2]$

This molecule has been described previously [59,60]. The route that we used for its preparation is described below.

To a suspension of activated calcium (5.50 g, 137 mmol) [13] in 250 mL of THF was added 33 mL of 6,6-dimethylfulvene (274 mmol). The solution turned brown while being stirred overnight at room temperature. The solution was transferred slowly via a cannula

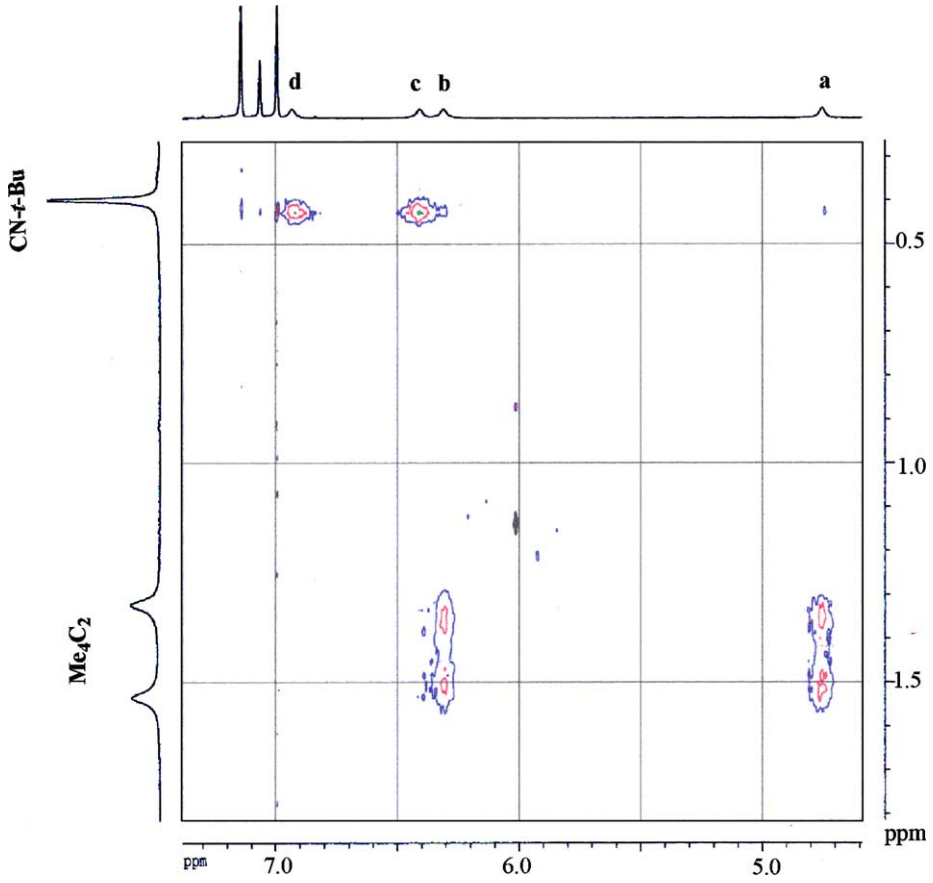


Fig. 15. Partial −40 °C ROESY spectrum of **4** in toluene-d_8.

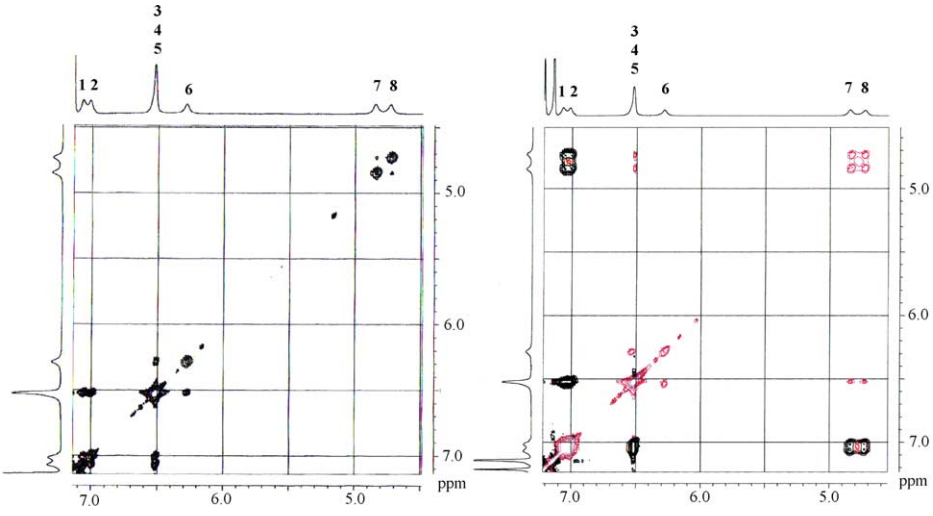


Fig. 16. Partial COSY (left) and partial ROESY (right) spectra of a solution of **4** in ~3:1 toluene-d_8:methyl-cyclohexane-d_{14} at −114 °C. Pink shading of peaks in ROESY spectrum indicates exchange.

to another flask containing 200 mL of distilled water. The resulting bright yellow solution was stirred an additional hour at room temperature. (Workup of the reaction mixture did not involve air free procedures.) The volume of the solution was increased to 600 mL with distilled water, and the solution was acidified with concentrated HCl to a pH of 2 and diluted with ether (200 mL). The aqueous portion was extracted with ether (2×100 mL), and the combined organic phases were washed with water (100 mL) and dried over $MgSO_4$. The solution was concentrated to 100 mL under reduced pressure and stored at −60 °C. Bright yellow crystals

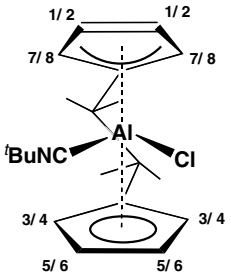


Fig. 17. Proposed solution structure for **4**. Numbering of cyclopentadienyl ring positions corresponds to number of 1H NMR peaks in Fig. 15.

formed after 20 h. The product was separated by filtration and dried under vacuum (6 h, 100 mTorr) to afford 6.67 g (23%) of free ligand.

4.3. [$Me_4C_2(C_5H_4)_2Mg$] (**1**)

16 mL (16.3 mmol) of a 1.0 M heptane solution of dibutylmagnesium was syringed into a solution of [$Me_4C_2(C_5H_5)_2$] (3.4 g, 16.0 mmol) in 50 mL heptane. The mixture was heated to 70 °C and stirred overnight under argon. White solid precipitated from the mixture. The white precipitate was isolated by filtration, washed with petroleum ether, and then dried under vacuum (yield 1.52 g, 40%). ^{1}H NMR (300 MHz, 297 K, THF-d_4): δ 1.08 (s, 12H, (CH_3)$_4$); δ 5.76 (s, 4H, C_5H_4); δ 5.99 (s, 4H, C_5H_4).

4.4. [$Me_4C_2(C_5H_4)_2Al$-μ-$Cl]_2$ (**2**)

Aluminum trichloride (1.15 g, 8.45 mmol) was added from a solid dispenser to a solution of **1** (2.0 g, 8.46 mmol) in 50 mL toluene. The mixture appeared yellow orange color and was stirred overnight at room temperature. The yellow solution was filtered to remove $MgCl_2$. The toluene then was removed from the filtrate under reduced pressure leaving a yellow oil. Addition of 25 mL petroleum ether to the oil precipitated a yellow-tinged white powder that was collected by filtration and dried under vacuum (yield 1.12 g, 48%). ^{1}H NMR (500 MHz, 297 K, toluene-d_8): δ 1.01 (s, 12H, (CH_3)$_4$); δ 5.13 (s, 4H, C_5H_4); δ 6.16 (s, 4H, C_5H_4); ^{13}C{^{1}H} NMR (125 MHz, 297 K, toluene-d_8): δ 24 C_2(CH_3)$_4$; δ 97 (C_5H_4); δ 117 (C_5H_4); δ 148 (quaternary, C_5H_4); ^{27}Al NMR (130 MHz, 297 K, toluene-d_8): δ −2. *Anal.* Calc. for $C_{14}H_{16}AlCl$: C, 69.98; H, 7.28. Found: C, 68.18; H, 7.42%.

4.5. [$Me_4C_2(C_5H_4)_2AlCl(THF)$] (**3**)

THF (10 mL) was condensed onto 0.3 g of **2** $Me_4C_2Cp_2AlCl$ at −78 °C and the mixture was warmed to room temperature. The compound dissolved immediately and the solution was stirred for 30 min. THF was then removed under reduced pressure and the white product was washed with 10 mL pentane and dried under vacuum to afford 0.35 g (94% yield) of **3** as a white powder. ^{1}H NMR (500 MHz, 297 K, toluene-d_8): δ 1.39 (s, 12H, (CH_3)$_3$); δ 1.09 (t, THF); δ 3.4 (t, THF); δ 5.5 (s, 4H, C_5H_4), δ 6.25 (s, 4H, C_5H_4); ^{13}C{^{1}H} NMR (125 MHz, 297 K, toluene-d_8): δ 24.8, 26.2 (CH_3)$_4$; δ 42.8 THF; δ 72 THF; δ 98 C_5H_4; δ 117 C_5H_4; δ 150 (quaternary, C_5H_4); ^{27}Al NMR (130 MHz, 297 K, toluene-d_8): δ 78.

4.6. [$Me_4C_2(C_5H_4)_2AlCl(CN^tBu)$] (**4**)

t-Butylisocyanide (0.5 mL, 1.09 mmol) was syringed into a solution of 0.3 g (1.09 mmol) $Me_4C_2Cp_2AlCl$ in 20 mL benzene at room temperature under argon. The mixture was stirred for 2 h. Volatiles were removed under vacuum to afford a white solid. The solid product was washed with 10 mL pentane and was dried under reduced pressure to yield 0.19 g (53% yield) of **4**. ^{1}H NMR (500 MHz, 297 K, toluene-d_8): δ 0.53 (s, 9H, (CNC(CH_3)$_3$); δ 1.41 (s, 12H, (CH_3)$_4$; δ 5.5 (s, very broad, 4H, C_5H_4); δ 6.6 (s, 4H, C_5H_4); ^{13}C{^{1}H} NMR (125 MHz, 297 K, toluene-d_8): δ 27.3 (CH_3)$_4$; 27.5 (CNC(CH_3)$_4$); δ 42.8 $CH(Me)_2$; δ 122.8 C_5H_4; δ 149.3 (quaternary, C_5H_4); ^{27}Al NMR (130 MHz, 297 K, toluene-d_8) δ 104; IR(Nujol mull/NaCl plates: (ν N≡C) 2258 cm^{-1}.

5. X-ray crystal structure determinations

Crystals were removed from their container and covered with a layer of hydrocarbon oil. A suitable crystal was selected, attached to a glass fiber and placed in the low-temperature nitrogen stream [61]. Data for **2** were collected at 83(2) K, **3** at 85(2) K, **4** at 84(2) K using a Bruker/Siemens SMART APEX instrument (Mo Kα radiation, λ = 0.71073 Å) equipped with a Cryocool NeverIce low temperature device. Data were measured using omega scans of 0.3° per frame for 10 s (**2**) and 5 s (**3**, **4**), and a full sphere of data was collected for each A total of 2132 (**2**) and 2450 (**3**, **4**) frames were collected with a final resolutions of 0.77 Å (**2**, **3**) and 0.84 Å (**4**). The first 50 frames were recollected at the end of data collection to monitor for decay. Cell parameters were retrieved using SMART [62] software and refined using SAINTPLUS [63] on all observed reflections. Data reduction and correction for Lp and decay were performed using the SAINTPLUS software. Absorption corrections were applied using SADABS [64]. Structures were solved by direct methods and refined by least squares method on F^2 using the SHELXTL program package [65]. Structures were solved in the space groups $P2_1/c$ (**2**) and $P\bar{1}$ (**3**, **4**). All non-hydrogen atoms were refined anisotropically. The THF molecule in **3** is disordered

with a majority occupancy of 66% for C18 and C19. A large residual of 1.651 e $Å^{-3}$ remains 0.93 Å from Cl(2) in **4**. This is due to crystal size (cutting led to loss of crystallinity) and absorption problems and could not be modeled or eliminated. No decomposition was observed during data collection. Details of the data collection and refinement are given in Table 1. Further details are provided in the Supporting Information.

Acknowledgments

We are grateful to the donors of The Petroleum Research Fund, administered by the ACS and the Idaho NSF EPSCoR program (EPS-0132626) for support of this research. We thank Professor Richard V. Williams for his helpful advice.

Appendix A. Supplementary data

Additional variable temperature 1-D NMR spectra, COSY and ROESY spectra of compounds **2**–**4** (13 pages). CCDC 262014, 262015, 240803 contain the supplementary crystallographic data for this paper. These data can be obtained free of charge via www.ccdc.cam.ac.uk/data_request/cif, by emailing data_request@ccdc.cam.ac.uk, or by contacting The Cambridge Crystallographic Data Centre, 12, Union Road, Cambridge CB2 1EZ, UK; fax: +44 1223 336033. Supplementary data associated with this article can be found, in the online version, at doi:10.1016/j.poly.2005.04.014.

References

[1] W. Kaminsky, K. Külper, H.H. Brintzinger, F.R.W.P. Wild, Angew. Chem., Int. Ed. Engl. 204 (1985) 507.
[2] G. Fink, R. Mulhaupt, H.H. Brintzinger (Eds.), Ziegler Catalysts: Recent Scientific Innovations and Technological Improvements, Springer-Verlag, Berlin, 1995.
[3] L. Resconi, L. Cavallo, A. Failt, F. Piemontesi, Chem. Rev. 100 (2000) 1253.
[4] H.H. Brintzinger, D. Fischer, R. Mülhaupt, B. Rieger, R.M. Waymouth, Angew. Chem., Int. Ed. Engl. 34 (1995) 1143.
[5] A.H. Hoyveda, J.P. Morken, Angew. Chem., Int. Ed. Engl. 35 (1996) 1262.
[6] A.H. Hoveyda, Trans. Metal Org. Synth. 1 (1998) 195.
[7] M.V. Troutman, D.H. Appella, S.L. Buchwald, J. Am. Chem. Soc. 121 (1999) 4916.
[8] C.A. Willoughby, S.L. Buchwald, J. Am. Chem. Soc. 116 (1994) 11703.
[9] R.L. Halterman, C. Zhu, Z. Chen, M.S. Dunlap, M.A. Khan, K.M. Nicholas, Organometallics 19 (2000) 3824.
[10] R.D. Broene, S.L. Buchwald, J. Am. Chem. Soc. 115 (1993) 12569.
[11] M. Beller, C. Bolm, Catalytic Enantioselective Alkylation of Alkenes by Chiral Metallocenes, Wiley-VCH Verlag GMbH, Weinheim, 1998.
[12] R. Littger, N. Metzler, H. Nöth, M. Wagner, Chem. Ber. 127 (1994) 1901.
[13] M. Rieckhoff, U. Pieper, D. Stalke, F.T. Edelmann, Angew. Chem., Int. Ed. Engl. 32 (1993) 1079.
[14] H.-R.H. Damrau, A. Geyer, M.-H. Prosenc, A. Weeber, F. Schaper, H.H. Brintzinger, J. Organomet. Chem. 553 (1998).
[15] S. Harder, M. Lutz, S.J. Obert, Organometallics 18 (1999) 1808.
[16] S. Harder, M. Lutz, A.W.G. Straub, Organometallics 16 (1997) 107.
[17] S. Harder, M.-H. Prosenc, U. Rief, Organometallics 15 (1996) 118.
[18] R. Littger, N. Metzler, M. Wagner, Chem. Ber. 27 (1994) 1901.
[19] R. Littger, N. Metzler, H. Noeth, M. Wagner, Chem. Ber. 127 (1994) 1901.
[20] E.P. Roth, B.K. O'Keefe, B. Keelin, J.Z. Fernandez, G.M. Graziano, J.E.B. Johnson, G.J. Balaich, N.E. Heimer, in: ACS National Meeting, Anaheim, CA, 2003.
[21] P.-J. Sinnema, B. Höhn, R.L. Hubbard, P.J. Shapiro, B. Twamley, A. Blumenfeld, A. Vij, Organometallics 21 (2002) 182.
[22] K.M. Kane, P.J. Shapiro, R. Cubbon, A. Vij, A.L. Rheingold, Organometallics 16 (1997) 4567.
[23] P.-J. Sinnema, B. Twamley, P.J. Shapiro, Acta Crystallogr. E57 (2001) m438.
[24] P.J. Sinnema, P.J. Shapiro, B. Hoehn, B. Twamley, J. Organomet. Chem. 676 (2003) 73.
[25] M. Tacke, Organometallics 13 (1994) 4124.
[26] P. Jutzi, M. Bangel, B. Neumann, H.-G. Stammler, J. Am. Chem. Soc. 15 (1996) 4559.
[27] P. Jutzi, Dahlhaus, B. Neumann, H.-G. Stammler, Organometallics 15 (1996) 747.
[28] J.M. Pietryga, J.D. Gorden, C.L.B. Macdonald, A. Voigt, R.J. Wiacek, A.H. Cowley, J. Am. Chem. Soc. 123 (2001) 7713.
[29] D. Churchill, J.H. Shin, T. Hascall, J.M. Hahn, B.M. Bridgewater, G. Parkin, Organometallics 18 (1999) 2403.
[30] D.G. Churchill, B.M. Bridgewater, G. Parkin, J. Am. Chem. Soc. 122 (2000) 178.
[31] H. Lee, P.J. Desrosier, I. Guzei, A.L. Rheingold, G. Parkin, J. Am. Chem. Soc. 120 (1998) 3255.
[32] J.H. Shin, G. Parkin, Chem. Commun. (1999) 887.
[33] C. Dohmeier, C. Robl, M. Tacke, H. Schnöckel, Angew. Chem., Int. Ed. Engl. 103 (1991) 594.
[34] C. Dohmeier, C. Robl, M. Tacke, H. Schnöckel, Angew. Chem., Int. Ed. Engl. 30 (1991) 564.
[35] J.D. Fisher, M.-Y. Wei, R. Willett, P.J. Shapiro, Organometallics 13 (1994) 3324.
[36] J.D. Fisher, P.H.M. Budzelaar, P.J. Shapiro, R.J. Staples, G.P.A. Yap, A.L. Rheingold, Organometallics 16 (1997) 871.
[37] J.D. Fisher, J.T. Golden, P.J. Shapiro, G.P.A. Yap, A.L. Rheingold, Main Group Met. Chem. 19 (1996).
[38] S. Schulz, H.W. Roesky, M. Noltemeyer, H.-G. Schmidt, J. Organomet. Chem. 493 (1995) 69.
[39] J.D. Fisher, P.J. Shapiro, P.H.M. Budzelaar, R.J. Staples, Inorg. Chem. (1997).
[40] J.D. Fisher, P.J. Shapiro, G.P.A. Yap, A.L. Rheingold, Inorg. Chem. 35 (1996) 271.
[41] S. Szumacher, I. Madura, J. Zachara, A.R. Kunicki, J. Organomet. Chem. 613 (2000) 119.
[42] A. Kunicki, R. Sadowski, J. Zachara, J. Organomet. Chem. 508 (1996) 249.
[43] A. Kunicki, J. Topczewski, S. Szumacher, A. Cebulski, Main Group Met. Chem. 23 (2000) 773.
[44] S. Szumacher, I. Madura, J. Zachara, A.R. Kunicki, A. Cebulski, L. Jerzykiewicz, J. Organomet. Chem. 669 (2003) 64.
[45] P. Burger, K. Hortmann, D. J., H.-H. Brintzinger, J. Organomet. Chem. 417 (1991) 9.
[46] B. Dorer, J. Diebold, O. Weyand, H.-H. Brintzinger, J. Organomet. Chem. 427 (1992) 245.

[47] D.A. Drew, A. Haaland, J. Chem. Soc., Chem. Commun. (1972) 1300.
[48] P. Jutzi, Chem. Rev. 86 (1986) 983.
[49] M.A. McKinney, D.T. Haworth, J. Chem. Ed. 52 (1980) 110.
[50] B.J. Burger, J.E. Bercaw, in: A.L. Wayda, M.Y. Darensbourg (Eds.), Experimental Organometallic Chemistry, American Chemical Society, Washington, DC, 1987, p. 94.
[51] R. Benn, E. Janssen, H. Lehmkuhl, A. Rufinska, J. Organomet. Chem. 333 (1987) 155.
[52] R. Benn, E. Janssen, H. Lehmkuhl, A. Rufinska, K. Angermund, P. Betz, R. Goddard, C. Krüger, J. Organomet. Chem. 411 (1991) 37.
[53] R. Benn, A. Rufinska, Angew. Chem., Int. Ed. Engl. 25 (1986) 861.
[54] R. Benn, A. Rufinska, H. Lehmkuhl, E. Janssen, C. Krüger, Angew. Chem., Int. Ed. Engl. 22 (1983) 779.
[55] P.J. Shapiro, Coord. Chem. Rev. 189 (1998) 1.
[56] F. Piemontesi, I. Camurati, L. Resconi, D. Balboni, A. Sironi, M. Moret, R. Ziegler, N. Picolrovazzi, Organometallics 14 (1995) 1256.
[57] A.L. Nivorozhkin, E.V. Sukholenko, L.E. Nivorozhkin, N.I. Borisenko, V.I. Minkin, Polyhedron 8 (1989) 569 (references therein).
[58] K.J. Stone, R.D. Little, J. Org. Chem. 49 (1984) 1849.
[59] H. Schwemlein, H.H. Brintzinger, J. Organomet. Chem. 254 (1983) 69.
[60] M. Tacke, J.P. Dunne, S. Fox, G. Linti, R. Teuber, J. Mol. Struct. 570 (2001) 197.
[61] H. Hope, Prog. Inorg. Chem. 41 (1995) 1.
[62] SMART: v.5.626, Bruker Molecular Analysis Research Tool, Bruker AXS, Madison, WI, 2002.
[63] SAINTPLUS: v. 6.22, Data Reduction and Correction Program, Bruker AXS, Madison, WI, 2001.
[64] G.M. Sheldrick, SADABS: V.2.01, an Empirical Absorption Correction Program, Bruker AXS Inc., Madison, WI, 2001.
[65] G.M. Sheldrick, SHELXTL: V. 6.10, Structure Determination Software Suite, Bruker AXS Inc., Madison, WI, 2001.

This paper describes computational work on a doubly silicon-bridged *ansa*-metallocene, $[W(\eta^5\text{-}C_5H_3)_2\text{-}(SiMe_2)_2]$, ($a$-$Si_2Cp_2W$), that is shown to have the lowest singlet state of comparable energy to the lowest triplet state.

2. Computational methods

DFT calculations, using the ADF code version 2004 [18], were performed using Vosko, Wilke and Nusair's local functional [19], with the Becke 88 [20,21] and the Perdew 86 [22] non-local exchange and correlation gradient corrections. The basis sets used were uncontracted triple-ζ Slater-type orbitals (STOs). Hydrogen, carbon and silicon were given extra polarization functions (2p on H, 3d on C, and 4d on Si). The cores of atoms were frozen, C up to the 1s level, Si up to 2p, and W up to 4d. Scalar ZORA relativistic corrections [23–26] were used. The calculations used gradient corrections applied after the SCF convergence.

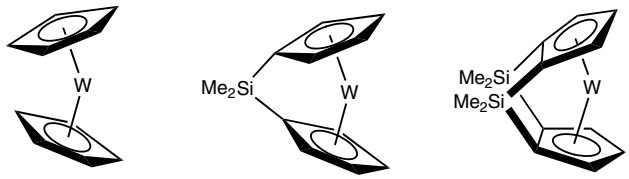
The SCF energy surface for methane addition to **3** and release from **6** was scanned to identify maxima and minima. These were then confirmed as stationary points by frequency calculations. Structures **4** and **5** showed additional imaginary frequencies of -5i and -25i cm^{-1} corresponding to rotation of methyl groups on the bridging Si. These are considered negligible.

Total energies given in Table 1 are referenced with respect to atomic fragments with zero spin as calculated by the ADF program. They represent relative SCF energies and give only this component of the energy surface. Neither zero-point energies nor thermal contributions to enthalpy, or entropy are given here.

Orbital surfaces were calculated using Molekel and represent a surface with value ±0.03.

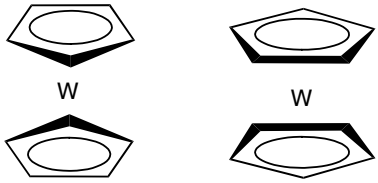
3. Results

Geometries were optimized for **1**–**3** with the spin set at 0 and 1 and no symmetry constraints.



1 **2** **3**

1 was also optimized with C_{2v} symmetry imposed; two optimizations were carried out under this constraint, where the ring conformation was set to orientations **A** and **B**. In these cases, only a spin of 0 was employed.



A **B**

Total energies and the angle between the ring planes are given in Table 1.

Stationary points for the addition of CH_4 to a-Si_2Cp_2W, **3**, were computed with spin 0. These comprised **3** + CH_4, a methane σ-complex, **4**, the transition state for oxidative addition, **5**, and the methyl hydride product, **6**. SCF energies are given in Table 1. Table 1 also reports the energies of the LUMO, HOMO and HOMO − 1 for **1**–**4** ($S = 0$).

In the case of **1** and **2**, the $S = 1$ optimization gave the lower total SCF energy. For **3**, the SCF energies of both multiplicities were the same within computational error. When **1** was optimized with no symmetry constraints and spin 0 the structure was found to be significantly bent. The minimum SCF energy structure was found to be virtually identical to **1A** where the rings were constrained to have four carbons lie at the back of the

Table 1
Energies (eV) and inter-ring angles, α (°) for **1**–**6**

Compound	$S = 0$		$S = 1$		$4a_1$	$2b_1$	$3a_1$
	Energy	α	Energy	α			
1	−131.034	30.6	−131.43	0	−3.20	−3.73	−3.60
1A	−131.024	29.9			−3.24	−3.55	−3.79
1B	−131.035	31.9			−3.16	−3.71	−3.58
2	−168.65	37.2	−169.02	40.1	−3.17	−3.59	−3.95
3	−205.93	44.4	−205.95	47.5	−3.17	−3.85	−3.82
CH_4	−23.71						
4	−230.02	47.0			−1.07	−3.55	−3.76
5	−229.99	48.5					
6	−230.94	51.6					

Orbital energies (eV) of the LUMO, HOMO and HOMO − 1 of **1**–**3** with $S = 0$.

metallocene wedge. The total SCF energies of **1A** and **1B** were found to be very close.

Conformations **1A** and **1B** were found to have different HOMOs, that of the former being of b_1-symmetry and that of the latter a_1-symmetry. In line with this result, **2**, which has ring conformation **A**, has a b_1-symmetry type HOMO, while **3** with a **B** type ring conformation has an a_1-symmetry type HOMO. For all compounds, the LUMO is of a_1-symmetry.

Stationary point SCF energies on the pathway to methane addition to **3** are given in Table 1. The methane σ-complex, **4**, is stabilized by 0.38 eV relative to **3** and methane, and no barrier was found to binding on the singlet surface. The methyl hydride **6** was 1.3 eV more stable than the reactants and the SCF energy barrier to oxidative addition from the σ-complex was 0.03 eV.

4. Discussion

Addition of methane to tungstenocenes is overall enthalpically favourable, though entropically unfavourable. The entropy is similar for all tungstenocenes as it is dominated by the gas phase entropy of methane. The thermal decomposition temperature of a tungstenocene methyl hydride is therefore controlled by the size of the enthalpy change. Thus, a study of addition and decomposition should in principle be carried out on a Gibbs free energy surface as a function of temperature. This is not currently possible and current practice is to compute reaction pathways on an SCF energy surface to identify minima, as models for intermediates, and saddle points, as models for transition states. The benefit of this approach is that it illuminates crucial electronic factors that control reactivity.

The Cartesian system assumed for the metallocenes is given in Fig. 1. For a C_{2v} structure, z is the C_2 axis and xz is the metallocene plane in which further ligands may be bound.

For a group 6 metallocene four d electrons are accommodated in the frontier orbitals. The relevant ones are two of a_1-symmetry and one of b_1-symmetry. To concur with an earlier review [15], they are numbered $3a_1$, $2b_1$ and $4a_1$. The calculations indicate that the ground state of **1** is a triplet and has a parallel ring structure as established experimentally [12,13]. The lowest singlet state is bent and is 0.4 eV higher in energy, with a configuration of $3a_1^2 2b_1^2$. The ring orientation makes very little difference to the total energy but does affect the orbital ordering, in that conformation **A** has the $2b_1$ orbital as the HOMO whereas conformation **B** has $3a_1$ as the highest occupied orbital. Both these orbitals have the bonding role of back-donation to a linear combination of the cyclopentadienyl ring e_2 orbitals. The metal lies closest to the carbons at the back of the metallocene wedge, so the overlap with these carbons is crucial to determining the degree of stabilization. The nodal characteristics maximize the stabilization of the $3a_1$ orbital in conformation **A** and the $2b_1$ orbital in conformation **B**. Hence the reversal of orbital ordering between the two conformations. These interactions are illustrated by the orbital surface plots in Fig. 2. The energy separation between the $3a_1$ and $2b_1$ orbitals is greater for conformation **A** than conformation **B**. Also the $3a_1$ orbital in conformation **A** is the lowest energy found for a frontier orbital in either conformation, suggesting that this conformation is favoured by a d^2 metal system, which has been found to be the case [16,27].

The $4a_1$ orbital is significantly destabilized by bending as a result of anti-bonding interaction with the rings. Thus, to achieve a diamagnetic ground state a large

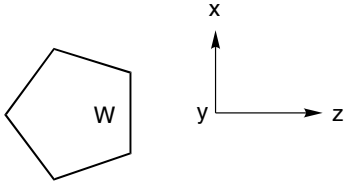


Fig. 1. Coordinate system employed for a bent metallocene unit.

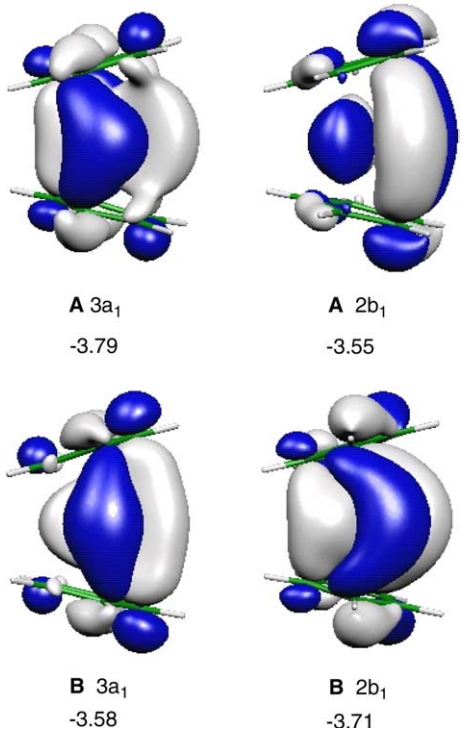


Fig. 2. Isosurfaces and energies (eV) of the $3a_1$ and $2b_1$ MO of **1** with conformations **A** and **B**, showing that for **A** the $3a_1$ orbital maximises interaction with the closest carbons and for **B** the $2b_1$ orbital maximizes interaction with the closest carbons.

inter-ring angle is needed. It is also desirable to maximize the HOMO–LUMO separation. In the unsubstituted case, this is achieved by adopting conformation **B**.

Thus, it seemed a good idea to test whether the doubly Si-bridged metallocene **3** would have a singlet ground state. The inter-ring angle calculated for **3** is 44.4°. This is less than the 60–65° found for tungstenocene structures with a single carbon *ansa*-bridge. For these, the triplet metallocene was found to be 0.14 eV lower in energy than the singlet structure. However, a single bridge holds the rings in the less favourable **A** conformation. For the double Si-bridged compound **3**, the singlet and triplet states are of very similar energy.

For comparison purposes the singlet and triplet energies of **2**, where there is a single Si bridge, were also calculated. In this case, the triplet was 0.37 eV lower in energy. The $3a_1$ and $2b_1$ orbital surfaces of both **2** and **3** are shown in Fig. 3. The stabilization by back donation is greater for the $3a_1$ orbital for **2** and for the $2b_1$ orbital for **3**. As a consequence, the HOMO–LUMO gap is larger for **3** so in this case the cost of going high spin is greater.

In order to establish the likely energy profile for oxidative addition of methane geometries were optimized for the stationary points on the reaction surface. The structure for the methane σ-complex, **4**, the oxidative addition transition state, **5**, and the methyl hydride product, **6**, are shown in Fig. 4. They resemble previously calculated structures for oxidative addition to tungstenocenes [7,9,11]. These stationary points were

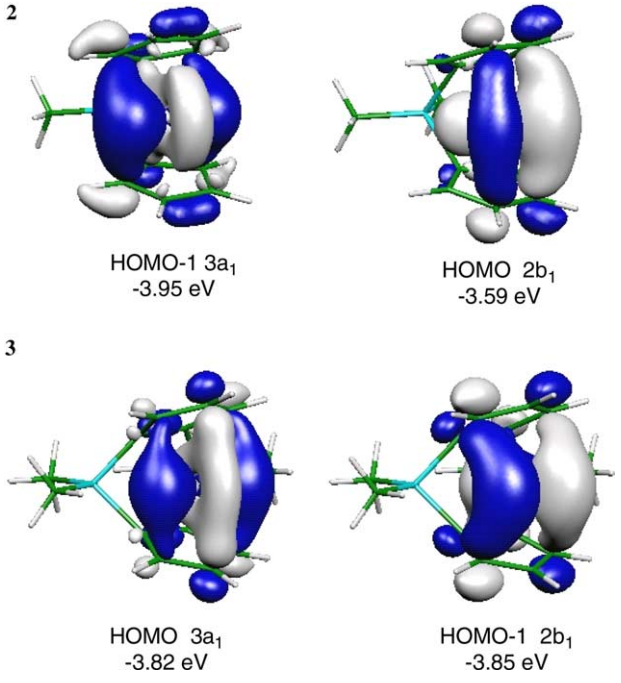


Fig. 3. Isosurfaces and energies (eV) of the $3a_1$ and $2b_1$ orbitals of **2** and **3**.

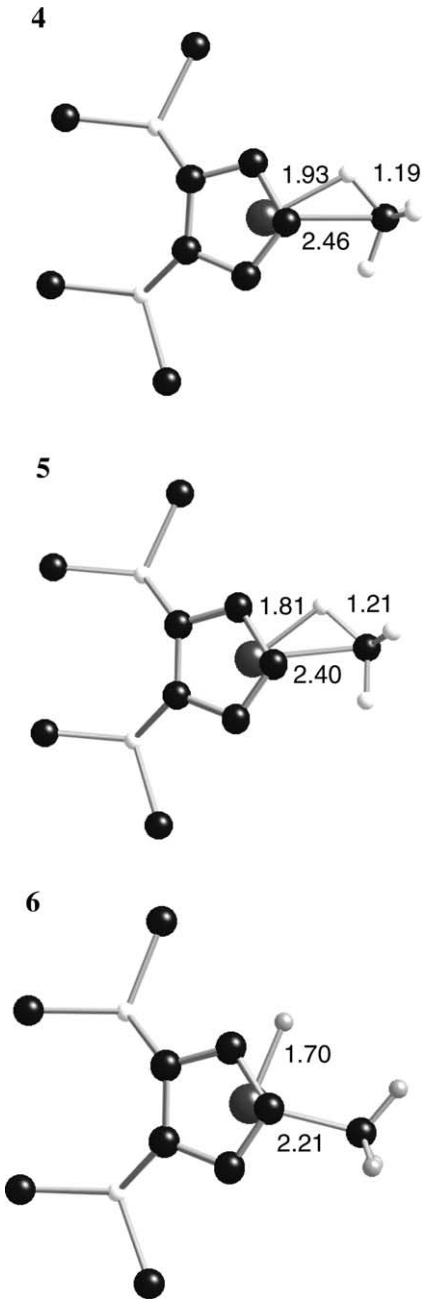


Fig. 4. Calculated structures of stationary points found for methane addition to **3**. (Hydrogens of the metallocene unit have been omitted in the interest of clarity.)

verified by frequency calculations. Transition state **5** had an imaginary vibration of $-352i\ cm^{-1}$ that showed motion of the hydride moving from the metal to the methyl carbon. In addition, both **5** and **6** gave very small imaginary frequencies corresponding to rotation of methyl groups attached to the Si bridges. These are considered to be negligible.

Intermediate **4** shows very little change in the energy of the $3a_1$ and $2b_1$ orbitals when compared with **3** (Table 1). Orbital $4a_1$ is significantly destabilized

and has an anti-bonding interaction with the methane. Search of the energy manifold in the energy region of the methane t_2 orbitals revealed one with a small W contribution at −11.06 eV that was 0.2 and 0.4 eV more stable than the other two. None of these three orbitals were exclusively localized on methane but that was their predominant character, and the most stable corresponds to σ donation from the methane.

One point of interest is a reorientation of the cyclopentadienyl rings during the course of oxidative addition. The structure of **4** shows the rings in orientation **B** with the methane coordinated opposite the pair of bridges. In the transition state **5** there is a slight twist of the rings. When the oxidative addition is complete, the rings have changed to a conformation close to **A**. The bisector of the W–CH_3 and W–H vectors points to only one of the Si bridging atoms. Examination of the rings shows that the carbons connected to this Si have an inter-atomic distance of 2.65 Å while the other two *ipso* carbons are 2.79 Å apart. Fig. 5 shows a rear view of **6**. The methane complex **4** is formally d^4. On oxidative addition two electrons are provided by the metal for bond formation, and the metal configuration changes to d^2. The calculations discussed above demonstrate the superiority of the **A** conformation in stabilizing just two electrons in the $3a_1$ orbital. Thus, the reorientation of the rings facilitates back donation in the oxidized complex. A similar ring reorientation was found between a d^0 Mo complex, $[Mo(\eta^5C_5H_5)_2H_3]^+$, which has conformation **B**, and the d^2 transition state for hydrogen exchange, which has ring conformation **A** [27].

The SCF energetics of the addition are represented graphically in Fig. 6. There was no barrier on the SCF energy surface to methane binding from the singlet state of **3**. The methane σ-complex, **4**, has a binding energy of −37 kJ mol^{-1} and the methyl hydride is exo-energetic by −125 kJ mol^{-1}. The SCF energy barrier found for oxidative addition from **4** was very small as has been calculated to be the case with other tungstenocene systems [9,11].

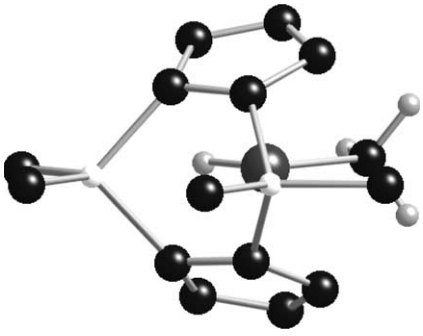


Fig. 5. View of **6** showing **A** type conformation of the rings for the d^2 methyl hydride.

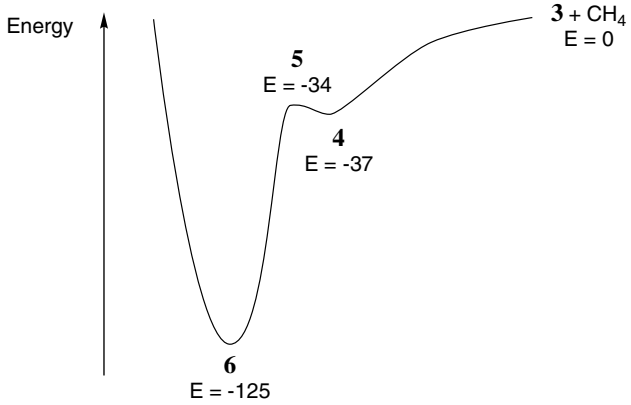


Fig. 6. Energetics of the addition of methane to **3**. Energies are given in kJ mol^{-1}.

5. Conclusions

The orbital energies of metallocene frontier orbitals may be tuned by introduction of *ansa*-bridges. Single *ansa*-bridges favour a ring conformation that stabilizes the $3a_1$ orbital. In contrast double *ansa*-bridges favour a ring conformation that stabilizes the $2b_1$ orbital.

In the latter cases, the $3a_1$ orbital is the HOMO and the gap between this and the $4a_1$ orbital is maximized, leading to an orbital splitting that makes a low spin configuration more competitive for a d^4 configuration. For $[W(\eta^5\text{-}C_5H_3)_2(SiMe_2)_2]$ the singlet and triplet states are of comparable energy with the consequence that binding of methane encounters no barrier on an SCF energy surface.

Acknowledgement

I thank the Oxford Supercomputing Centre (O.S.C.) for provision of computational facilities and considerable assistance.

References

[1] N.J. Cooper, M.L.H. Green, R. Mahtab, J. Chem. Soc., Dalton Trans. (1979) 1557.
[2] R.M. Bullock, C.E.L. Headford, K.M. Hennessy, S.E. Kegley, J.R. Norton, J. Am. Chem. Soc. 111 (1989) 3897.
[3] G. Parkin, J.E. Bercaw, Organometallics 8 (1989) 1172.
[4] L. Labella, A. Chernega, M.L.H. Green, J. Chem. Soc., Dalton Trans. (1995) 395.
[5] A. Chernega, J. Cook, M.L.H. Green, L. Labella, S.J. Simpson, J. Souter, A.H.H. Stephens, J. Chem. Soc., Dalton Trans. (1997) 3225.
[6] D. Churchill, K. Janak, J. Wittenberg, G. Parkin, J. Am. Chem. Soc. 125 (2003) 1403.
[7] J.C. Green, C.N. Jardine, J. Chem. Soc., Dalton Trans. (1998) 1057.
[8] M.-D. Su, S.-Y. Chu, J. Phys. Chem. A 105 (2001) 3591.

[9] J.C. Green, J.N. Harvey, R. Poli, J. Chem. Soc., Dalton Trans. (2002) 1861.
[10] K. Janak, D. Churchill, G. Parkin, Chem. Commun. (2003) 22.
[11] J.-L. Carreon-Macedo, J.N. Harvey, R. Poli, Eur. J. Inorg, Chem. (in press).
[12] J. Chetwynd-Talbot, P. Grebnik, R.N. Perutz, Inorg. Chem. 21 (1982) 3647.
[13] P.A. Cox, P. Grebnik, R.N. Perutz, M.D. Robinson, R. Grinter, D.R. Stern, Inorg. Chem. 22 (1983) 3614.
[14] A. Shilov, G.B. Shul'pin, Chem. Rev. 97 (1997) 2879.
[15] J.C. Green, Chem. Soc. Rev. 27 (1998) 263.
[16] C.E. Zachmanoglou, A. Docrat, B.M. Bridgewater, G. Parkin, G. Brandow, J.E. Bercaw, C.N. Jardine, M. Lyall, J.C. Green, J.B. Keister, J. Am. Chem. Soc. 124 (2002) 9525.
[17] L.J. Ackerman, M.L.H. Green, J.C. Green, J.E. Bercaw, Organometallics 22 (2003) 188.
[18] E.J. Baerends, J.A. Autschbach, A. Berces, C. Bo, P.M. Boerringter, L. Cavallo, D.P. Chong, L. Deng, R.M. Dickson, D.E. Ellis, L. Fan, T.H. Fischer, C. Fonseca-Guerra, S.J. van Gisbergen, J.A. Groeneveld, O.V. Gritsenko, M. Grüning, F.E. Harris, P. van den Hoek, H. Jacobsen, G. van Kessel, F. Kootstra, E. van Lenthe, V.P. Osinga, S. Patchkovskii, P.H.T. Philipsen, D. Post, C.C. Pye, W. Ravenek, P. Ros, P.R.T. Schipper, G. Schreckenbach, J.G. Snijiders, M. Sola, M. Swart, D. Swerhone, G. te Velde, P. Vernooijis, L. Versluis, O. Visser, E. van Wezenbeek, G. Wiesenekker, S.K. Wolff, T.K. Woo, T. Ziegler, in: ADF 2002.03, Vrije Universiteit, Amsterdam, 2002.
[19] S.H. Vosko, L. Wilk, M. Nusair, Can. J. Phys. 58 (1980) 1200.
[20] A.D. Becke, Phys. Rev. A 38 (1988) 3098.
[21] A.D. Becke, J. Chem. Phys. 88 (1988) 1053.
[22] J.P. Perdew, Phys. Rev. B 33 (1986) 8800.
[23] E. van Lenthe, E.J. Baerends, J.G. Snijders, J. Chem. Phys. 99 (1993) 4597.
[24] E. van Lenthe, E.J. Baerends, J.G. Snijders, J. Chem. Phys. 101 (1994) 9783.
[25] E. van Lenthe, J.G. Snijders, E.J. Baerends, J. Chem. Phys. 105 (1996) 6505.
[26] E. van Lenthe, R. van Leeuwen, E.J. Baerends, J.G. Snijders, Int. J. Quantum Chem. 57 (1996) 281.
[27] V. Pons, S. Conway, M. Green, J. Green, B. Herbert, D. Heinekey, Inorg. Chem. 43 (2004) 3475.

described [W{(η-C_5H_4)CMe_2(η-C_5H_4)}Cl_2] [1] and the zinc dialkyl compounds [Zn{$(CH_2)_nCH_3$}$_2$] (n = 1, 2 or 3) in toluene at low temperatures [2,3]. In a typical reaction, the mixture was stirred at room temperature for 12 h and then the excess of the dialkylzinc reagent was cautiously hydrolysed by the addition of H_2O, prior to passing the toluene soluble mixture down an alumina column and then eluting with toluene. The compounds **2** and **3** were extracted into pentane and isolated as yellow crystalline solids by cooling the solution to −80 °C. The compound **3** is new and has been characterised by elemental analyis, FAB mass spectrometry and ^{1}H and ^{13}C{^{1}H} NMR spectroscopy. The characterising data for **3** and all the other new compounds described in this work are given in Table 1. In most cases assignments of the ^{1}H NMR spectra were assisted by ^{1}H–^{1}H NMR COSY experiments [6].

Treatment of [W{(η-C_5H_4)CMe_2(η-C_5H_4)}Cl_2] with di(*n*-butyl)zinc [Zn{$(CH_2)_3CH_3$}$_2$] in toluene at low temperature affords a mixture of the σ-*n*-butyl compounds [W{(η-C_5H_4)CMe_2(η-C_5H_4)}{$(CH_2)_3CH_3$}$_2$] (**4**) and [W{(η-C_5H_4)CMe_2(η-C_5H_4)}{$(CH_2)_3CH_3$}Cl] (**5**). The yellow σ-*n*-butyl compounds **4** and **5** can be separated by fractional recrystallisation from a 1:1 toluene/pentane solution in 16% and 41% yield, respectively. Unexpectedly the NMR data showed the peak due to the hydrogens in the α-CH_2, methylene group relative to the metal is not the highest field resonance of the hydrogens of the *n*-butyl ligand. In the σ-ethyl compound [W{(η-C_5H_4)CMe_2(η-C_5H_4)}{$(CH_2CH_3$}I] the peak due to the α-CH_2 methylene hydrogens is also found at a lower field relative to the β-methyl hydrogens [2]. The *n*-pentyl-chloride compound [W{(η-C_5H_4)-CMe_2(η-C_5H_4)}{$(CH_2)_4CH_3$}Cl] (**6**) was prepared by the reaction between [W{(η-C_5H_4)CMe_2(η-C_5H_4)}Cl_2] and [Zn{$(CH_2)_4CH_3$}$_2$]. The compound **6** is obtained as a pale orange/red solid in 29% yield following passage in diethyl ether down an alumina column. The corresponding di-*n*-pentyl compound [W{(η-C_5H_4)CMe_2-(ηC_5H_4)}{$(CH_2)_4CH_3$}$_2$] (**7**) was isolated in the same reaction as a very minor product (ca. 1%). It was characterised by ^{1}H NMR spectroscopy only. The di-*n*-hexyl compound [W{(η-C_5H_4)CMe_2(η-C_5H_4)}{$(CH_2)_5CH_3$}$_2$] (**8**) was prepared by the reaction between [W{(η-C_5H_4)-CMe_2(η-C_5H_4)}Cl_2] and [Zn{$(CH_2)_5CH_3$}$_2$].

Treatment of the di-*n*-propyl compound [W{(η-C_5H_4)-CMe_2(η-C_5H_4)}{$(CH_2)_2CH_3$}$_2$] (**3**) with NH_4I in THF at 65 °C gave the compound [W{(η-C_5H_4)CMe_2(η-C_5H_4)}{$(CH_2)_2CH_3$}I] (**9**) as a pale red solid in 47% yield. The compound [W{(η-C_5H_4)CMe_2(η-C_5H_4)}-{$(CH_2)_2CH_3$}I] (**9**) was treated with [Na{AlH_2(OCH_2O-CH_2CH_3)$_2$}] at low temperature to give, after cautious hydrolysis of excess of [Na{AlH_2($OCH_2CH_2OCH_3$)$_2$}], the *n*-propyl-hydride compound [W{(η-C_5H_4)CMe_2(η-C_5H_4)}{$(CH_2)_2CH_3$}H] (**10**) as a yellow crystalline solid in ca. 50% yield.

Table 1
Analytical and spectroscopic data

Compound[a]	NMR data[b]
[W{(η-C_5H_4)CMe_2-(η-C_5H_4)}{$(CH_2)_2CH_3$}$_2$] (**3**). Yellow solid: C, 50.9 (51.8); H, 6.5 (6.4). MS: *m/z* = 440 $(M)^+$ 45%, *m/z* = 355 $(M–2\{(CH_2)_2$- $CH_3\})^+$ 100%.	^{1}H: 4.28 (m., 4H, C_5H_4) 4.19 (m., 4H, C_5H_4) 1.45 (m., 4H, $CH_2CH_2CH_3$) 1.21 (t., 6H, $CH_2CH_2CH_3$) 0.55 (m., 4H, $CH_2CH_2CH_3$) 0.43 (m., 6H, CMe_2) ^{13}C{^{1}H}: 104.26 (s., C_5H_4) 67.19 (s., C_5H_4) 51.43 (s., C_{ipso} C_5H_4) 31.13 (s., CMe_2) 22.32 (s., CMe_2) 22.19 (s., $(CH_2)_2CH_3$) 5.83 (s., $(CH_2)_2CH_3$) 1.04 (s., $(CH_2)_2CH_3$)
[W{(η-C_5H_4)CMe_2-(η-C_5H_4)}{$(CH_2)_3$-CH_3}$_2$] (**4**). Yellow solid: C, 53.6 (53.9); H, 6.7 (6.9). MS: *m/z* = 468 $(M)^+$ 86%, *m/z* = 411 $(M–\{(CH_2)_3CH_3\})^+$ 20%, *m/z* = 355 $(M–2\{(CH_2)_3CH_3\})$ 100%.	^{1}H: 4.31 (m., 4H, C_5H_4) 4.22 (m., 4H, C_5H_4) 1.52 (m., 8H, $CH_2(CH_2)_2CH_3$) 1.16 (t., 6H, $CH_2(CH_2)_2CH_3$) 0.56 (m., 4H, $CH_2(CH_2)_2CH_3$) 0.42 (s., 6H, CMe_2) ^{13}C{^{1}H}: 104.29 (s., C_5H_4) 67.20 (s., C_5H_4) 51.70 (s., $C_{ipso}C_5H_4$) 40.72 (s., $(CH_2)_3CH_3$) 30.38 (s.,CMe_2) 30.35 (s., $(CH_2)_3CH_3$) 22.20 (s., CMe_2) 5.92 (s., $(CH_2)_3CH_3$) 1.73 (s., $(CH_2)_3CH_3$)
[W{(η-C_5H_4)CMe_2-(η-C_5H_4)}{$(CH_2)_3$-CH_3}Cl] (**5**). Pale red solid: C, 46.2 (45.7); H, 5.5 (5.2). MS: *m/z* = 446 $(M)^+$ 55%, *m/z* = 411 $(M–Cl)^+$ 25%, *m/z* = 389 $(M–\{(CH_2)_3CH_3\})^+$ 100%.	^{1}H: 5.20 (m., 2H, C_5H_4) 4.71 (m., 2H, C_5H_4) 4.68 (m., 2H, C_5H_4) 3.96 (m., 2H, C_5H_4) 1.55 (m., 2H, $CH_2CH_2CH_2CH_3$) 1.37 (m., 2H, $CH_2CH_2CH_2CH_3$) 1.31 (t., 2H, $CH_2CH_2CH_2CH_3$) 1.15 (t., 3H, $CH_2CH_2CH_2CH_3$) 0.35 (s., 3 H, CMe_2) 0.03 (s., 3H, CMe_2) ^{13}C{^{1}H}: 115.76 (s., C_5H_4) 106.44 (s., C_5H_4) 70.15 (s., C_5H_4) 69.59 (s., C_5H_4) 57.92 (s., C_{ipso} C_5H_4) 39.69 (s., $(CH_2)_3CH_3$) 29.59 (s., $(CH_2)_3CH_3$) 22.39 (s., $(CH_2)_2CH_3$) 21.76 (s., CMe_2) 21.61 (s., CMe_2) 14.12 (s., $(CH_2)_3CH_3$)
[W{(η-C_5H_4)CMe_2-(η-C_5H_4)}{$(CH_2)_4$-CH_3}Cl] (**6**). Pale red solid: C, 46.3 (46.9); H, 5.8 (5.5); Cl, 7.2 (7.7). MS: *m/z* = 462 $(M)^+$ 18%, *m/z* = 389 $(M–\{(CH_2)_4CH_3\})^+$ 100%.	^{1}H: 5.19 (m., 2H, C_5H_4) 4.70 (m., 4H, C_5H_4) 3.97 (m., 2H, C_5H_4) 1.55 (m., 2H, $CH_2CH_2CH_2CH_3$) 1.53 (m., 2H, $CH_2CH_2CH_2CH_2CH_3$) 1.42 (t., 2H, $CH_2CH_2CH_2CH_3$) 1.29 (m., 2H, $CH_2CH_2CH_2CH_2CH_3$) 1.11 (t., 3H, $CH_2CH_2CH_2CH_3$) 0.35 (s., 3H, CMe_2) 0.05 (s., 3H, CMe_2) ^{13}C{^{1}H}: 115.57 (s., C_5H_4)

(*continued on next page*)

Table 1 (*continued*)

Compound[a]	NMR data[b]
	106.17 (s., C_5H_4) 70.18 (s., C_5H_4) 69.48 (s., C_5H_4) 57.93 (s., C_{ipso} C_5H_4) 39.03 (s., $(CH_2)_4CH_3$) 36.88 (s., $(CH_2)_4CH_3$) 29.42 (s., CMe_2) 22.72 (s., $(CH_2)_4CH_3$) 21.78 (s., CMe_2) 21.62 (s., CMe_2) 14.48 (s., $(CH_2)_4CH_3$) 1.38 (s., $(CH_2)_4CH_3$)
[W{(η-C_5H_4)CMe_2-(η-C_5H_4)}{$(CH_2)_5CH_3$}$_2$] (**8**). Yellow solid: C, 56.5 (57.3); H, 7.5 (7.7). MS: *m/z* = 524 $(M)^+$ 85%, *m/z* = 439 $(M–\{(CH_2)_5CH_3\})^+$ 17%, *m/z* = 355 $(M–2\{(CH_2)_5CH_3\})^+$ 100%.	^{1}H: 4.35 (m., 4H, C_5H_4) 4.25 (m., 4H, C_5H_4) 1.52 (m., 16H, $CH_2(CH_2)_4CH_3$) 1.06 (t., 6H, $CH_2(CH_2)_4CH_3$) 0.58 (m., 4H, $CH_2(CH_2)_2CH_3$) 0.44 (s., 6H, CMe_2) $^{13}C\{^1H\}$: 104.25 (s., C_5H_4) 67.23 (s., C_5H_4) 51.48 (s., C_{ipso} C_5H_4) 38.08 (s., $(CH_2)_5CH_3$) 37.29 (s., $(CH_2)_5CH_3$) 32.07 (s., $(CH_2)_5CH_3$) 30.78 (s., CMe_2) 23.28 (s., $(CH_2)_5CH_3$) 22.19 (s., CMe_2) 14.28 (s., $(CH_2)_5CH_3$) 2.15 (s., $(CH_2)_5CH_3$)
[W{(η-C_5H_4)CMe_2-(η-C_5H_4)}{$(CH_2)_2CH_3$}I] (**9**). Pale red solid: C, 36.8 (36.7); H, 4.3 (4.1). MS: *m/z* = 524 $(M)^+$ 62%, *m/z* = 481 $(M–\{(CH_2)_2CH_3\})^+$ 85%.	^{1}H: 5.57 (m., 2H, C_5H_4) 4.39 (m., 2H, C_5H_4) 4.37 (m., 2H, C_5H_4) 3.83 (m., 2H, C_5H_4) 1.53 (m., 2H, $CH_2CH_2CH_3$) 1.18 (m., 2H, $CH_2CH_2CH_3$) 1.15 (t., 3H, $CH_2CH_2CH_3$) 0.22 (s., 3H, CMe_2) 0.09 (s., 3H, CMe_2) $^{13}C\{^1H\}$: 111.55 (s., C_5H_4) 105.58 (s., C_5H_4) 70.62 (s., C_5H_4) 68.38 (s., C_5H_4) 57.32 (s., C_{ipso} C_5H_4) 32.62 (s., $(CH_2)_2CH_3$) 22.39 (s., $(CH_2)_2CH_3$) 22.21 (s., CMe_2) 21.83 (s., CMe_2) −0.53 (s., $(CH_2)_2CH_3$)
[W{(η-C_5H_4)CMe_2-(η-C_5H_4)}{$(CH_2)_2$-CH_3}H] (**10**). Yellow solid: C, 47.8 (47.3); H, 6.1 (5.6).	^{1}H: 5.10 (m., 2H, C_5H_4) 4.48 (m., 2H, C_5H_4) 4.29 (m., 2H, C_5H_4) 3.78 (m., 2H, C_5H_4) 1.36 (m., 2H, $CH_2CH_2CH_3$) 1.13 (t., 3H, $CH_2CH_2CH_3$) 1.04 (m., 2H, $CH_2CH_2CH_3$) 0.56 (s., 3H, CMe_2) 0.29 (s., 3H, CMe_2) −6.47 (m.,$^1J_{WH}$ = 50 Hz, 1H, WH_2) $^{13}C\{^1H\}$: C_6D_6 125 MHz 103.79 (s., C_5H_4) 86.89 (s., C_5H_4) 70.21 (s., C_5H_4) 62.82 (s., C_5H_4)

Table 1 (*continued*)

Compound[a]	NMR data[b]
	57.32 (s., C_{ipso} C_5H_4) 33.30 (s., $(CH_2)_2CH_3$) 22.35 (s., $(CH_2)_2CH_3$) 22.02 (s., CMe_2) 21.96 (s., CMe_2) −14.99 (s., $(CH_2)_2CH_3$)
[W{(η-C_5H_4)CMe_2-(η-C_5H_4)}{$(CH_2)_3CH_3$}H] (**11**). Yellow solid: C, 49.5 (49.5); H, 5.9 (5.8).	^{1}H: 5.10 (m., 2H, C_5H_4) 4.48 (m., 2H, C_5H_4) 4.29 (m., 2H, C_5H_4) 3.78 (m., 2H, C_5H_4) 1.45 (m., 2H, $CH_2CH_2CH_2CH_3$) 1.36 (m., 2H, $CH_2CH_2CH_2CH_3$) 1.11 (t., 3H, $CH_2CH_2CH_2CH_3$) 1.02 (m., 2H, $CH_2CH_2CH_2CH_3$) 0.55 (s., 3H, CMe_2) 0.29 (s., 3H, CMe_2) −6.46 (m.,$^1J_{WH}$ = 50 Hz, 1H, WH_2) $^{13}C\{^1H\}$: C_6D_6 125 MHz 103.94 (s., C_5H_4) 86.81 (s., C_5H_4) 70.25 (s., C_5H_4) 62.77 (s., C_5H_4) 53.88 (s., $C_{ipso}C_5H_4$) 42.75 (s., $(CH_2)_3CH_3$) 30.50 (s., $(CH_2)_2CH_3$) 22.03 (s., CMe_2) 21.95 (s., CMe_2) 14.08 (s., $(CH_2)_3CH_3$) −12.15 (s., $(CH_2)_3CH_3$)
[W{(η-$_5H_4$)CMe_2(η-C_5H_4)}-{$(CH_2)_4CH_3$}H] (**12**). Yellow solid: C, 49.7 (50.7); H, 5.9 (6.2). MS: *m/z* = 426 $(M–H)^+$25%, *m/z* = 355 $(M–\{(CH_2)_4CH_3\}–H)^+$ 100%.	^{1}H: 5.12 (m., 2H, C_5H_4) 4.51 (m., 2H, C_5H_4) 4.32 (m., 2H, C_5H_4) 3.80 (m., 2H, C_5H_4) 1.49 (m., 2H, $CH_2CH_2CH_2CH_2CH_3$) 1.38 (m., 2H, $CH_2CH_2CH_2CH_2CH_3$) 1.36 (m., 2H, $CH_2CH_2CH_2CH_2CH_3$) 1.07 (t., 3H, $CH_2CH_2CH_2CH_2CH_3$) 1.01 (m., 2H, $CH_2CH_2CH_2CH_2CH_3$) 0.46 (s., 3H, CMe_2) 0.20 (s., 3H, CMe_2) $^{13}C\{^1H\}$: C_6D_6 125 MHz 103.78 (s., C_5H_4) 86.84 (s., C_5H_4) 70.20 (s., C_5H_4) 62.74 (s., C_5H_4) 53.88 (s., C_{ipso} C_5H_4) 40.10 (s., $(CH_2)_4CH_3$) 40.04 (s., $(CH_2)_4CH_3$) 31.70 (s., CMe_2) 22.78 (s., $(CH_2)_4CH_3$) 22.05 (s., CMe_2) 21.96 (s., CMe_2) 14.51 (s., $(CH_2)_4CH_3$) −11.83 (s., $(CH_2)_4CH_3$)
[W{(η-C_5D_4)$C(CD_3)_2$-(η-C_5D_4)}Cl_2] (**13d**). Purple solid	^{2}H: 5.96 (br. s., 4D, C_5D_4) 5.44 (br. s., 4D, C_5D_4) 0.70 (s., 6D, $C(CD_3)_2$)
[W{(η-C_5D_4)$C(CD_3)_2$-(η-C_5D_4)}{CH_2CH_3}$_2$] (**14d**). Yellow solid	^{1}H: 1.59 (t., 6H, CH_2CH_3) 0.58 (q., 4H, CH_2CH_3) ^{2}H:4.30 (s., 4D, C_5D_4) 4.26 (s., 4D, C_5D_4) 0.33 (s., 6D, $C(CD_3)_2$)

Table 1 (*continued*)

Compound[a]	NMR data[b]
[W{(η-C_5D_4)$C(CD_3)_2$-(η-C_5D_4)}{CH_2CH_3}I] (**15d**). Pale red solid	^{1}H: 1.59 (q., 2H, CH_2CH$_3$) 1.14 (t., 3H, CH$_2$CH_3) ^{2}H: 5.54 (m., 2D, C_5D_4) 4.39 (m., 2D, C_5D_4) 4.37 (m., 2D, C_5D_4) 3.67 (m., 2D, C_5D_4) 0.20 (s., 3D, $C(CD_3)_2$) 0.07 (s., 3D, $C(CD_3)_2$)
[W{(η-C_5D_4)$C(CD_3)_2$-(η-C_5D_4)}{CH_2CH_3}D] (**16d**). Yellow solid	^{1}H: 1.58 (t., 3H, CH$_2$CH_3) 1.12 (q., 2H, CH_2CH$_3$) ^{2}H: 5.08 (s., 2D, C_5D_4) 4.48 (s., 2D, C_5D_4) 4.28 (s., 2D, C_5D_4) 3.75 (s., 2D, C_5D_4) 0.46 (s., 3D, $C(CD_3)_2$) 0.19 (s., 3D, $C(CD_3)_2$) −6.44 (s., 1D, WD)
[W{(η-C_5D_4)$C(CD_3)_2$-(η-C_5D_4)}{$(CH_2)_2$-CH_3}$_2$] (**3d**). Yellow solid	^{1}H: 1.46 (m., 4H, CH$_2$CH_2CH$_3$) 1.21 (t., 6H, CH$_2$CH$_2$CH_3) 0.54 (m., 4H, CH_2CH$_2$CH$_3$) ^{2}H: 4.24 (br. S., 8D, C_5D_4) 0.42 (s., 6D, $C(CD_3)_2$)
[W{(η-C_5D_4)$C(CD_3)_2$-(η-C_5D_4)}{$(CH_2)_2$-CH_3}I] (**9d**). Pale red solid	^{1}H: 1.52 (m., 2H, CH$_2$CH_2CH$_3$) 1.17 (m., 2H, CH_2CH$_2$CH$_3$) 1.14 (t., 3H, CH$_2$CH$_2$CH_3) ^{2}H: 5.55 (m., 2D, C_5D_4) 4.39 (m., 4D, C_5D_4) 3.82 (m., 2D, C_5D_4) 0.18 (s., 3D, $C(CD_3)_2$) 0.07 (s., 3D, $C(CD_3)_2$)
[W{(η-C_5D_4)$C(CD_3)_2$-(η-C_5D_4)}{$(CH_2)_2$-CH_3}D] (**10d**). Yellow solid	^{1}H: 1.37 (m., 2H, CH$_2$CH_2CH$_3$) 1.16 (t., 3H, CH$_2$CH$_2$CH_3) 1.04 (m., 2H, CH_2CH$_2$CH$_3$) ^{2}H: 5.09 (s., 2D, C_5D_4) 4.51 (s., 2D, C_5D_4) 4.29 (s., 2D, C_5D_4) 3.77 (s., 2D, C_5D_4) 0.52 (s., 3D, $C(CD_3)_2$) 0.26 (s., 3D, $C(CD_3)_2$) −6.44 (s., 1D, WD)
[W{(η-C_5D_4)$C(CD_3)_2$-(η-C_5D_4)}{$(CH_2)_3$-CH_3}Cl] (**5d**). Pale red solid	^{1}H: 1.55 (m., 2H, CH$_2$CH$_2$CH_2CH$_3$) 1.37 (m., 2H, CH$_2$CH_2CH$_2$CH$_3$) 1.28 (t., 3H, CH_2CH$_2$CH$_2$CH$_3$) 1.15 (t., 3H, CH$_2$CH$_2$CH$_2$CH_3) ^{2}H: 5.20 (s., 2D, C_5D_4) 4.73 (s., 2D, C_5D_4) 4.68 (s., 2D, C_5D_4) 3.98 (s., 2D, C_5D_4) 0.38 (s., 3D, $C(CD_3)_2$) 0.06 (s., 3D, $C(CD_3)_2$)
[W{(η-C_5D_4)$C(CD_3)_2$-(η-C_5D_4)}{$(CH_2)_3$-CH_3}D] (**11d**). Yellow solid	^{1}H: 1.43 (m., 2H, CH$_2$CH$_2$CH_2CH$_3$) 1.35 (m., 2H, CH$_2$CH_2CH$_2$CH$_3$) 1.16 (t., 3H, CH$_2$CH$_2$CH$_2$CH_3) 1.01 (m., 2H, CH_2CH$_2$CH$_2$CH$_3$) ^{2}H: 5.05 (s., 2D, C_5D_4) 4.47 (s., 2D, C_5D_4) 4.26 (s., 2D, C_5D_4) 3.77 (s., 2D, C_5D_4) 0.56 (s., 3D, $C(CD_3)_2$) 0.27 (s., 3D, $C(CD_3)_2$) −6.45 (s., 1D, WD)

Table 1 (*continued*)

Compound[a]	NMR data[b]
[W{(η-C_5D_4)$C(CD_3)_2$-(η-C_5D_4)}{$(CH_2)_4$-CH_3}$_2$] (**7d**). Yellow solid	^{1}H: 1.59 (m., 4H, CH$_2$CH_2CH$_2$CH$_2$CH$_3$) 1.50 (m., 4H, CH$_2$CH$_2$CH_2CH$_2$CH$_3$) 1.42 (m., 4H, CH$_2$CH$_2$CH$_2$CH_2CH$_3$) 1.09 (t., 6H, CH$_2$CH$_2$CH$_2$CH$_2$CH_3) 0.75 (m., 4H, CH_2CH$_2$CH$_2$CH$_2$CH$_3$) ^{2}H: 4.31 (s., 4D, C_5D_4) 4.27 (s., 4D, C_5D_4) 0.38 (s., 3D, $C(CD_3)_2$) 0.19 (s., 3D, $C(CD_3)_2$)
[W{(η-C_5D_4)$C(CD_3)_2$-(η-C_5D_4)}{$(CH_2)_4$-CH_3}I] (**17d**). Pale red solid	^{1}H: 1.56 (m., 2H, CH$_2$CH$_2$CH$_2$CH_2CH$_3$) 1.53 (m., 2H, CH$_2$CH$_2$CH_2CH$_2$CH$_3$) 1.40 (t., 2H, CH$_2$CH_2CH$_2$CH$_3$) 1.29 (m., 2H, CH_2CH$_2$CH$_2$CH$_2$CH$_3$) 1.09 (t., 3H, CH$_2$CH$_2$CH$_2$CH$_2$CH_3) ^{2}H 5.19 (s., 2D, C_5D_4) 4.70 (s., 4D, C_5D_4) 3.96 (s., 2D, C_5D_4) 0.35 (s., $C(CD_3)_2$) 0.05 (s., $C(CD_3)_2$)
[W{(η-C_5D_4)$C(CD_3)_2$-(η-C_5D_4)}{$(CH_2)_4$-CH_3}D] (**12d**). Yellow solid	^{1}H:1.54 (m., 2H, CH$_2$CH$_2$CH$_2$CH_2CH$_3$) 1.42 (m., 2H, CH$_2$CH$_2$CH_2CH$_2$CH$_3$) 1.30 (m., 2H, CH$_2$ CH_2CH$_2$CH$_2$CH$_3$) 1.10 (t., 3H, CH$_2$CH$_2$CH$_2$CH$_2$CH_3) 1.05 (m., 2H, CH_2CH$_2$CH$_2$CH$_2$CH$_3$) ^{2}H: 5.11 (m., 2D, C_5D_4) 4.46 (m., 2D, C_5D_4) 4.32 (m., 2D, C_5D_4) 3.80 (m., 2D, C_5D_4) 0.47 (s., 3D, $C(CD_3)_2$) 0.24 (s., 3D, $C(CD_3)_2$) −6.52 (s. 1D, WD)
[W{(η-C_5H_4)CMe_2-(η-C_5H_4)}{CD_2-CD_3}$_2$] (**18**). Yellow solid	^{1}H: 4.27 (m., 4H, C_5H_4) 4.19 (m., 4H, C_5H_4) 0.44 (s., 6H, CMe_2) ^{2}H: 1.60 (s., 6D, CD_2CD_3) 0.62 (s., 4D, CD_2CD_3)
[W{(η-C_5H_4)CMe_2-(η-C_5H_4)}{CD_2-CD_3}I] (**19**). Pale red solid	^{1}H: 5.56 (s., 2H, C_5H_4) 4.38 (s., 4H, C_5H_4) 3.84 (s., 2H, C_5H_4) 0.17 (s., 3H, CMe_2) 0.04 (s., 3H, CMe_2) ^{2}H: 1.57 (s., 2D, CD_2CD_3) 1.34 (s., 3D, CD_2CD_3)
[W{(η-C_5H_4)CMe_2-(η-C_5H_4)}{CD_2-CD_3}H] (**20**). Yellow solid	^{1}H: 5.11 (s., 2H, C_5H_4) 4.48 (s., 2H, C_5H_4) 4.29 (s., 2H, C_5H_4) 3.77 (s., 2H, C_5H_4) 0.53 (s., 3H, CMe_2) 0.29 (s., 3H, CMe_2) −6.47 (s. ^{1}H, $^1J_{WH}$ = 31 Hz, WH) ^{2}H: 1.58 (s., 3D, CD_2CD_3) 1.13 (s., 2D, CD_2CD_3)

All IR data are expressed in wave numbers (cm^{-1}).

For the FAB mass spectrometry data, the characteristic isotope patterns were observed.

[a] Microanalytical data given as: element, found(calc.), %.

[b] NMR data are given as chemical shift (δ) [relative intensity, coupling, multiplicity, assignment] at 298 K unless otherwise stated. In C_6D_6 unless otherwise stated. ^{1}H NMR at 500 MHz, $^{13}C\{^1H\}$ at 125 MHz and ^{2}H at 76.75 MHz.

The *n*-butyl-hydride and *n*-pentyl-hydride compounds; [W{(η-C_5H_4)CMe_2(η-C_5H_4)}{$(CH_2)_nCH_3$}H] (*n* = 3, **11**; 4, **12**) were prepared similarly by treatment of the corresponding *n*-alkyl-chloride compounds [W{(η-C_5H_4)CMe_2(η-C_5H_4)}{$(CH_2)_nCH_3$}Cl] (*n* = 3, **5**; 4, **6**) with [Na{$AlH_2(OCH_2CH_2OCH_3)_2$}] as yellow crystalline solids in 42% and 49% yields, respectively.

The isolation and thermal stability at ambient temperatures of the *n*-alkyl-hydrides [W{(η-C_5H_4)CMe_2(η-C_5H_4)}{$(CH_2)_nCH_3$}H] (*n* = 2, **10**; 3, **11**; 4, **12**) in both the solid state and in solution confirmed our expectation the there would be an increased stability of Group 6 *ansa*-metallocene alkyl-hydrides with respect to reductive alkane elimination as a consequence of the presence of the single carbon *ansa*-bridge.

In order to study hydrogen exchange processes between alkyl and hydride ligands in *n*-alkyl hydride species it was necessary to prepare appropriately isotopically labelled compounds, namely [W{(η-C_5H_4)-CMe_2(η-C_5H_4)}{$(CH_2)_nCH_3$}D], where *n* = 0–4. It had been shown previously that treatment of [W{(η-C_5H_4)-CMe_2(η-C_5H_4)}{CH_2CH_3}I] with [Li{$AlD_2(OCH_2CH_2$-$OCH_3)_2$}] gave a mixture of the desired ethyl-deuteride [W{(η-C_5H_4)CMe_2(η-C_5H_4)}{CH_2CH_3)}D] together with the mono-deuterated C_5-ring ethyl-hydride species [W{(η-C_5H_3D)CMe_2(η-C_5H_4)}{CH_2CH_3}H] [2].

A reasonable mechanism for the formation of the mono-deuterated C_5-ring compound has been proposed [7] and is shown in Fig. 1.

When the *n*-alkyl-halide compounds [W{(η-C_5H_4)-CMe_2(η-C_5H_4)}{$(CH_2)_nCH_3$}X] (X = I and *n* = 2, **9** or X = Cl, *n* = 3, **5**; 4, **6**) were reacted with [Li{AlD_2-$(OCH_2CH_2OCH_3)_2$}] then only the undesired mono-deuterated C_5-ring *n*-alkyl hydride species [W{(η-C_5-H_3D)CMe_2(η-C_5H_4)}{$(CH_2)_nCH_3$}H] are formed, as shown by ^{1}H and ^{2}H NMR spectroscopy. There was no evidence for the desired tungsten alkyl-deuteride species [W{(η-C_5H_4)CMe_2(η-C_5H_4}{$(CH_2)_n$-CH_3}D]. It seems that as the length and effective bulk of the *n*-alkyl chain is increased from ethyl to *n*-propyl and longer, the direct attack of deuteride at the metal centre is increasingly disfavoured compared to *exo* attack at the cyclopentadienyl rings of the equilibrium dissociated cations (see Fig. 1).

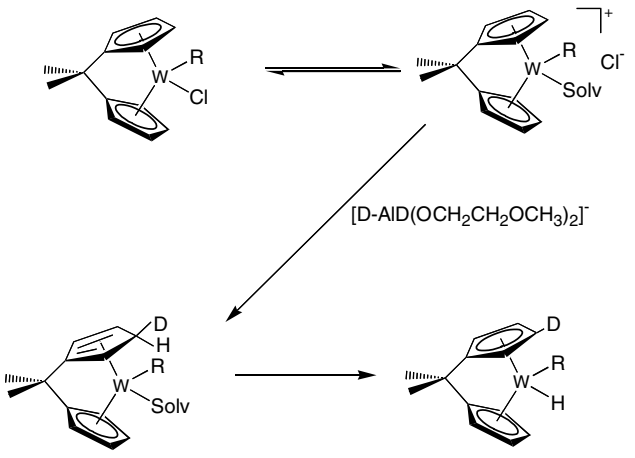


Fig. 1. Mechanism proposed for deuteration of the cyclopentadienyl ring in [W{(η-$C_5H_{4-x}D_x$)CMe_2(η-$C_5H_{4-x}D_x$)}(R)H] [7].

Various alternative routes to the desired compounds [W{(η-C_5H_4)CMe_2(η-C_5H_4)}{$(CH_2)_nCH_3$}D] (*n* = 2–4) were investigated but none were successful. For example, attempts to deprotonate [W{(η-C_5H_4)CMe_2(η-C_5H_4)}-{$(CH_2)_nCH_3$}H] using KH in the presence of 18-crown-6, followed by quenching of the anticipated salts [K(18-crown-6)][W{(η-C_5H_4)CMe_2(η-C_5H_4)}-{$(CH_2)_nCH_3$}] [8] with D_2O, gave no tractable products. Alternative deuteride reagents such as $NaBD_4$ or Li-BEt_3D again gave only the ring deuterated *n*-alkyl-hydride compounds. Finally, it was decided to prepare suitable alkyl-deuterides by starting with ring-perdeuterated *ansa*-metallocene alkyl-halides [W{(η-C_5D_4)-$C(CD_3)_2$(η-C_5D_4)}{$(CH_2)_nCH_3$}X] (*n* = 1–4; X = Cl or I). Treatment of these with [Li{$AlD_2(OCH_2CH_2OCH_3)_2$}] should result in the *exo* attack of D^- and then the *endo*-deuterium should transfer to the tungsten centre to give the desired W–D group (see Fig. 2).

The perdeuterated *ansa*-ligand [Li_2{$(C_5D_4)C(CD_3)_2$-(C_5D_4)}] and the perdeuterated *ansa*-metallocene dichloride compound [W{(η-C_5D_4)$C(CD_3)_2$(η-C_5D_4)}Cl_2] (**13d**) (where **d** indicates a perdeuterated ansa ligand system) were prepared by a slightly modified procedure to that used for the analogous protio compounds [9] (see Section 3 and Fig. 3).

The compound **13d** was characterised by ^{2}H NMR spectroscopy and by its subsequent reactions. The extent of deuteration of the metallocene fragment was determined to be >95%.

The deuterated di-*n*-alkyl compounds [W{(η-C_5D_4)-$C(CD_3)_2$(η-C_5D_4)}{$(CH_2)_nCH_3$}$_2$] (*n* = 1, **14d**; 2, **3d**; 4, **6d**) and the corresponding *n*-alkyl-halide compounds [W{(η-C_5D_4)$C(CD_3)_2$(η-C_5D_4)}{$(CH_2)_nCH_3$}X], (X = I, *n* = 1, **15d**; *n* = 2, **9d**; *n* = 4 **7**; X = Cl, *n* = 3, **5d**) were then prepared [2]. Due to the small amount of compound **13d** available these deuterated *ansa*-metallocenes were characterised by ^{1}H and ^{2}H NMR spectroscopy only. The extent of deuteration of the fragment [W{(η-C_5D_4)$C(CD_3)_2$(η-C_5D_4)}] in all the compounds containing that fragment was shown by NMR data to be 95 ± 2% see Fig. 4.

Addition of [Li{$AlD_2(OCH_2CH_2OCH_3)_2$}] to a solution of [W{(η-C_5D_4)$C(CD_3)_2$(η-C_5D_4)}{CH_2CH_3}I] (**15d**) in toluene at low temperature afforded the ethyl-deuteride compound [W{(η-C_5D_4)$C(CD_3)_2$(η-C_5D_4)}-{CH_2CH_3}D] (**16d**) as a yellow crystalline solid. Compound **16d** was characterised by ^{1}H and ^{2}H NMR spectroscopy. The ^{1}H NMR spectrum of compound **16d** consists of a triplet and a quartet at δ 1.58 and

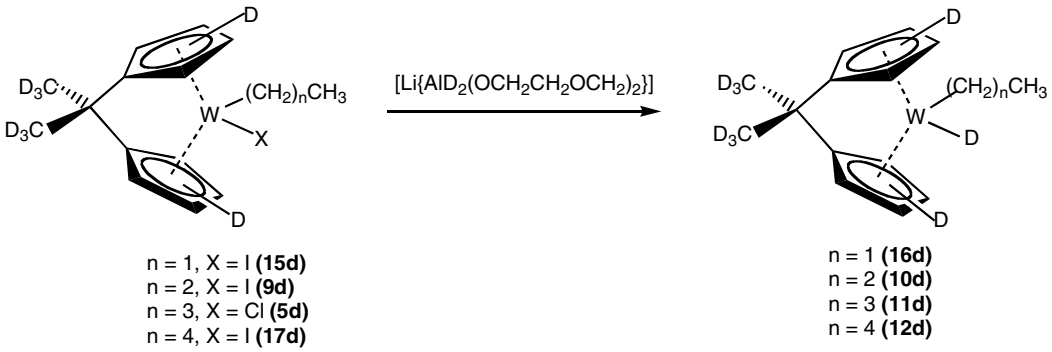


Fig. 2. Proposed route for the synthesis of the tungsten alkyl-deuterides [W{(η-C_5D_4)$C(CD_3)_2$(η-C_5D_4)}{$(CH_2)_nCH_3$}D] where = 1–4.

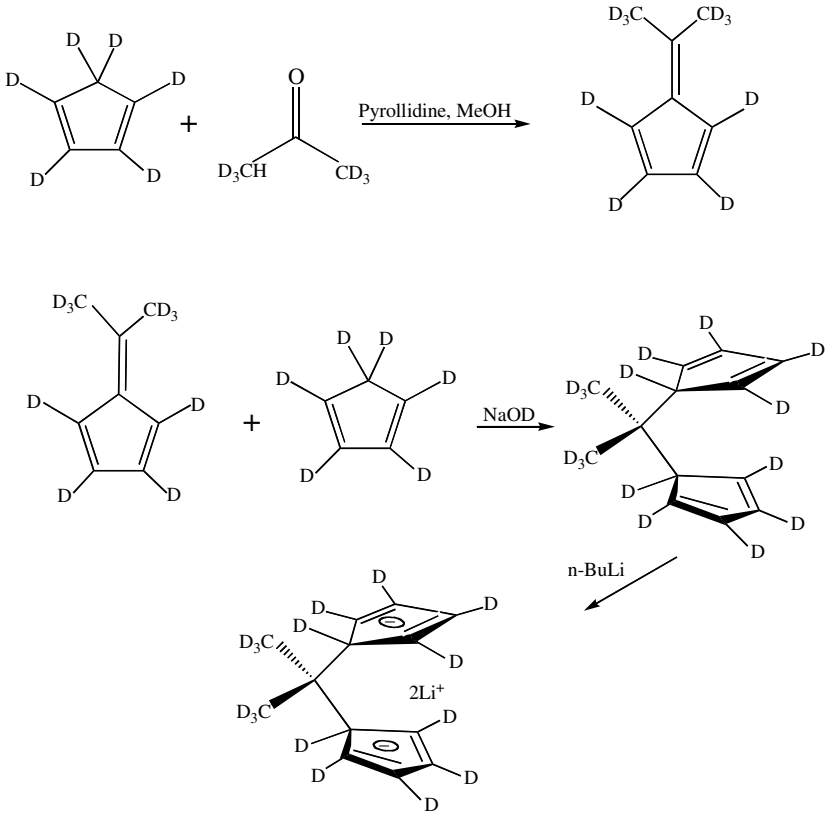


Fig. 3. Synthesis of the perdeuterated ligand precursor {$[Li]_2[(C_5D_4)C(CD_3)_2(C_5D_4)]$}.

1.12 ppm, respectively, corresponding to the protons of the ethyl ligand. Residual cyclopentadienyl proton peaks (5% H) are located at δ 5.12, 4.50, 4.31 and 3.78 ppm. The ^{2}H NMR spectrum of the compound **16d** shows the four deuterium atoms attached to the cyclopentadienyl rings are located at δ 5.08, 4.48 4.28 and 3.75 ppm. Two singlets at δ 0.46 and 0.19 ppm correspond to the deuterium atoms of the $C(CD_3)_2$ bridging unit. A singlet at δ −6.44 ppm is assigned to deuterium attached to the metal. In the ^{1}H NMR spectrum of the corresponding ethyl-hydride compound [W{(η-C_5H_4)CMe_2(η-C_5H_4)}{CH_2CH_3}H] the hydride resonance is found at δ −6.46 ppm [2].

The higher *n*-alkyl-deuteride compounds [W{(η-C_5D_4)$C(CD_3)_2$(η-C_5D_4)}{$(CH_2)_nCH_3$}D] (n = 2, **10d**; 3, **11d**; 4, **12d**) were prepared by the reaction between [W{(η-C_5D_4)$C(CD_3)_2$(η-C_5D_4)}{$(CH_2)_nCH_3$}X] (X = I, n = 2, **9d**; 4, **7**; X = Cl, n = 3, **5d**) and [Li{AlD_2(OCH_2-CH_2OCH_3)$_2$}]. Again all compounds were obtained as pale yellow solids and characterised by ^{1}H and ^{2}H NMR spectroscopy. We note that for all the *n*-alkyl-deuterides there was no evidence for intramolecular

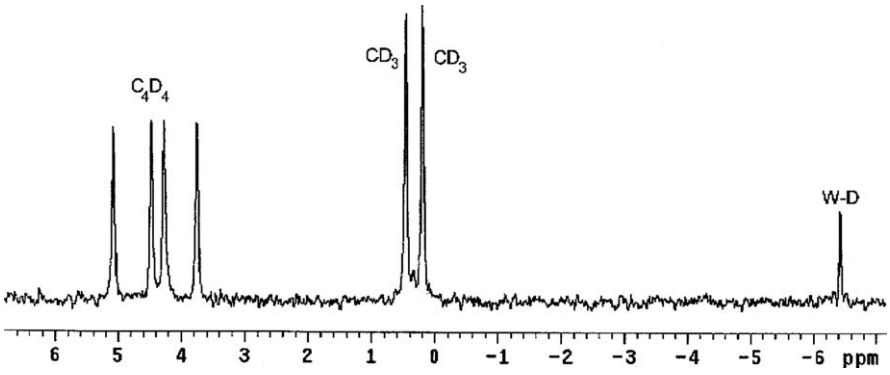


Fig. 4. ^{2}H NMR spectrum of the compound [W{(η-C_5D_4)C(CD_3)$_2$(η-C_5D_4)}{CH_2CH_3}D] (**16d**) in C_6H_6.

H/D scrambling between alkyl and W–D atoms at room temperature even after prolonged storage.

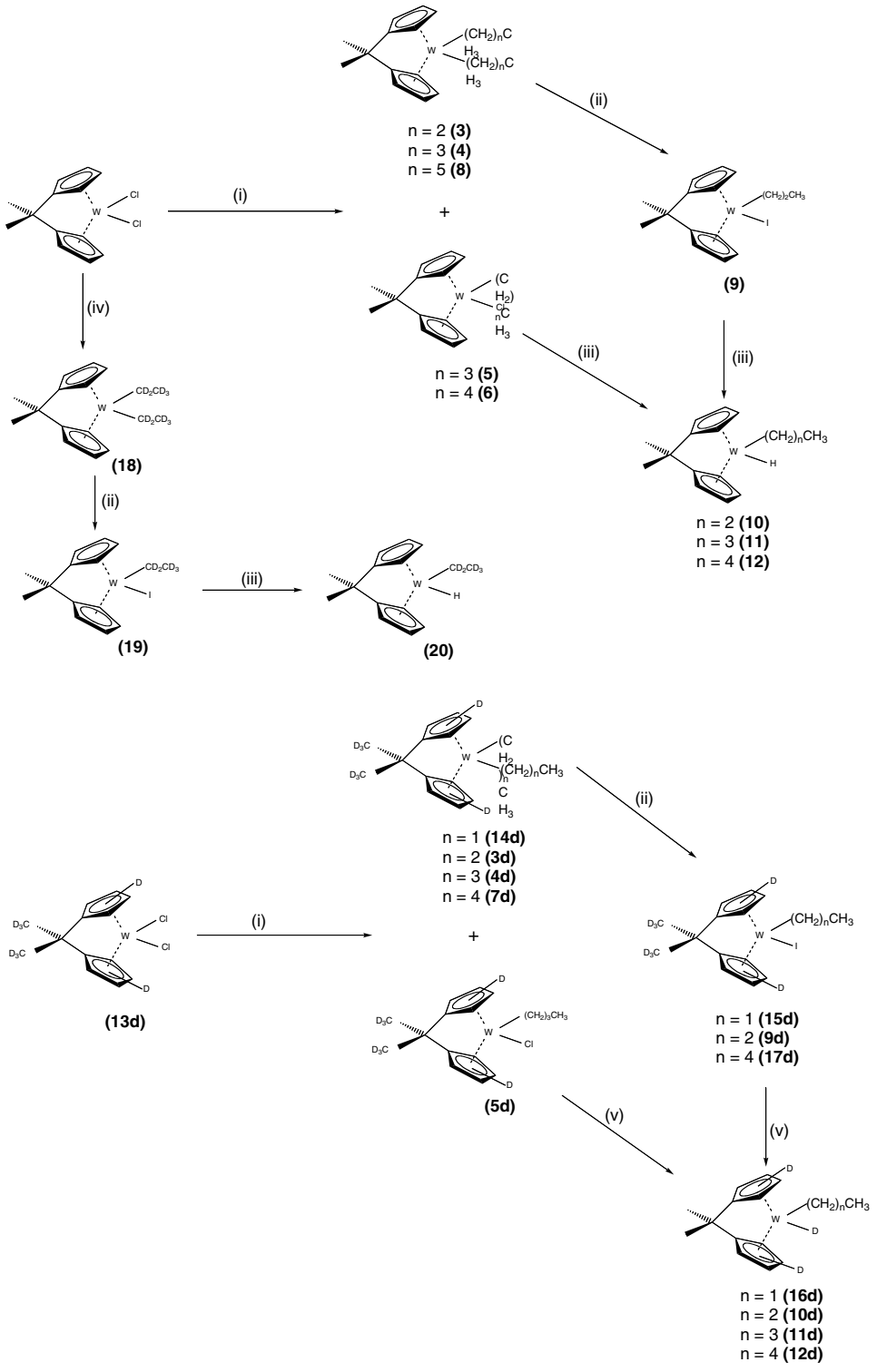
An alternative approach by which to study H/D scrambling in *ansa*-metallocene *n*-alkyl hydride compounds would be to prepare species in which the *n*-alkyl group was deuterated, as in [W{(η-C_5H_4)CMe_2(η-C_5H_4)}{$(CD_2)_nCD_3$}]. Indeed the H/D scrambling process in [W{(η-C_5H_4)CMe_2(η-C_5H_4)}(CD_3)H] has been described [2]. Perdeuterated diethylzinc [Zn{CD_2CD_3}$_2$] was prepared by the condensation of d^5-iodoethane onto a Zn/Cu couple in a thick walled-glass tube. The tube was sealed under reduced pressure and heated at 140 °C overnight. [Zn{CD_2CD_3}$_2$] was freed from impurity by low pressure distillation and obtained as a pyrophoric colourless liquid. Treatment of a toluene suspension of the compound [W{(η-C_5H_4)CMe_2(η-C_5H_4)}Cl_2] with a 0.4 M solution of [Zn{CD_2CD_3}$_2$] in toluene gave a dark red suspension from which the compound [W{(η-C_5H_4)CMe_2(η-C_5H_4)}{CD_2CD_3}$_2$] (**18**) was isolated. The compound **18** was characterised by ^{1}H and ^{2}H NMR spectroscopy. The ^{2}H NMR spectrum shows two peaks at δ 1.60 and 0.62 ppm corresponding to the β-methyl and α-methylene deuterium of the ethyl ligands respectively.

Reaction of the compound [W{(η-C_5H_4)CMe_2(η-C_5H_4)}{CD_2CD_3}$_2$] (**18**) with NH_4I in THF at 65 °C gives the compound [W{(η-C_5H_4)CMe_2(η-C_5H_4)}-{CD_2CD_3}I] (**19**), as a pale red solid in 47% yield. The compound [W{(η-C_5H_4)CMe_2(η-C_5H_4)}{CD_2CD_3}I] (**19**) was reacted with [Na{$AlH_2(OCH_2OCH_2CH_3)_2$}] at low temperature to give, after cautious hydrolysis of excess [Na{$AlH_2(OCH_2CH_2OCH_3)_2$}], the compound [W{(η-C_5H_4)CMe_2(η-C_5H_4)}{CD_2CD_3}H] (**20**) as a yellow crystalline solid (see the Scheme 1).

The compound **20** was characterised by ^{1}H and ^{2}H NMR spectroscopy. In the ^{1}H NMR were four singlets at δ 5.11, 4.48, 4.29 and 3.77 ppm corresponding to the hydrogens of the cyclopentadienyl rings and a pair of singlets at δ 0.53 and 0.29 ppm corresponding to the protons of the CMe_2 bridging unit, the singlet at δ −6.47 ppm is assigned to the hydride proton. Associated with this singlet are the characteristic ^{183}W satellites ($^{1}J_{WH}$ = 31 Hz). The ^{2}H NMR spectrum of the compound **20** shows two peaks at δ 1.58 and 1.13 ppm corresponding to the CD_3 and α-CD_2 groups of the ethyl ligand. The spectroscopic data for the compound **20** are in agreement with that reported for the perprotio compound [W{(η-C_5H_4)CMe_2(η-(C_5H_4)}{CH_2CH_3}H] [2].

The thermolysis of the partially ring deuterated ethyl-deuteride [W{(η-C_5H_4)CMe_2(η-C_5H_4)}{CH_2CH_3}D] has been described previously [2] but quantitative kinetic data for the observed intramolecular hydrogen scrambling processes could not be obtained. Therefore, the perdeutero-*ansa*-tungstenocene ethyl-deuteride [W{(η-C_5D_4)C(CD_3)$_2$(η-C_5D_4)}{CH_2CH_3}D] (**16d**) was prepared and H/D scrambling was reinvestigated. A 8 mM solution of the compound **16d** in C_6H_6 and a 6 mM solution of the compound **16** in C_6D_6 were prepared and sealed in separate NMR tubes. ^{1}H and ^{2}H NMR spectra show that at room temperature there had been no observable scrambling between alkyl and deuterium sites. The samples were heated at 65 °C and ^{1}H and ^{2}H NMR spectra were recorded periodically. After ca. 8 h, the ^{2}H NMR spectra showed a peak at δ 1.10 ppm which grew with time (Fig. 5). Simultaneously, the intensity of the W–D peak at δ −6.44 ppm decreased. The ^{1}H NMR spectra shows there is a decrease in intensity of the quartet at δ 1.12 ppm due to the α-methylene hydrogens compared to the triplet at δ 1.58 ppm corresponding to the β-methyl hydrogens of the ethyl ligand.

Additionally a peak at δ −6.45 ppm corresponding to a tungsten-hydrogen group appeared. These NMR data are fully consistent with H/D exchange between the W–D and the α-CH_2 hydrogens of the ethyl group. No evidence for scrambling of deuterium into the β-methyl hydrogens of the compound **16** was observed. Scrambling of deuterium into this position should be indicated by a peak growing in at, or close to, δ 1.58 ppm, by analogy to the ^{1}H NMR spectrum of the compound **16**. No peak in this region ($\delta \pm 0.15$ ppm) was observed. This



Scheme 1. Conditions (i) $[Zn\{(CH_2)_nCH_3\}_2]$ in toluene. (ii) NH_4I in THF, 65 °C. (iii) $[Na\{AlH_2(OCH_2CH_2OCH_3)_2\}]$ in toluene. (iv) $[Zn\{CD_2CD_3\}_2]$ in toluene. (v) $[Li\{AlD_2(OCH_2CH_2OCH_3)_2\}]$ in toluene. When **d** is placed after a compound number this indicates the ansa-bis-cyclopendadienyl ligand is perdeuterated.

conclusion contrasts with that previously reported for studies on $[W\{(\eta\text{-}C_5H_4)CMe_2(\eta\text{-}C_5H_4)\}\{CH_2CH_3\}D]$ where scrambling into the β-position was suggested to occur and further that it occurred at a faster rate than for the α-methylene hydrogens [2]. The quality of the earlier data was significantly worse than for this work and we assume the earlier results were erroneous due to the presence of decomposition products see Fig. 6.

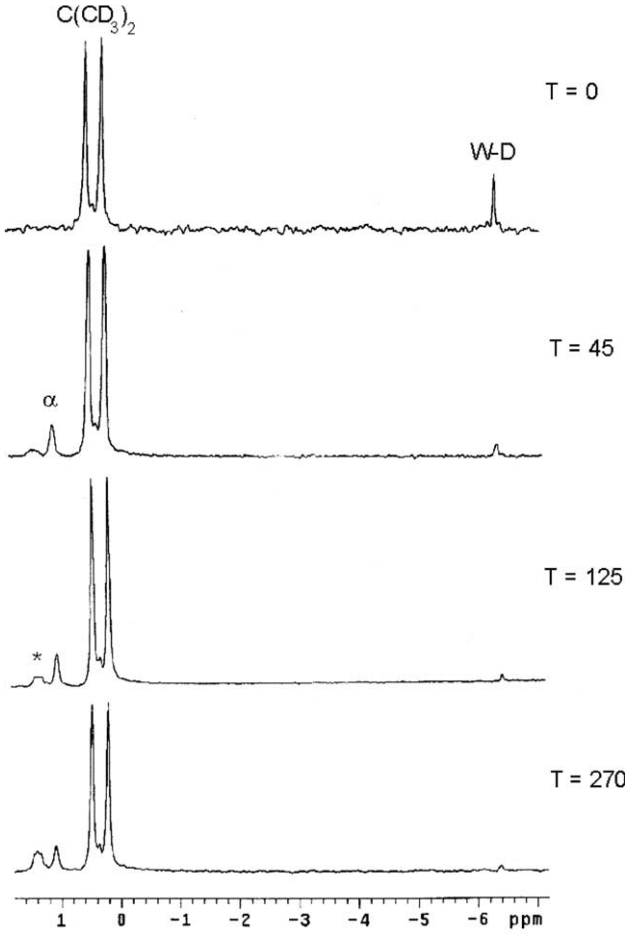


Fig. 5. Partial ^{2}H NMR spectrum of the compound [W{(η-C_5D_4)C$(CD_3)_2$(η-C_5D_4)}{CH_2CH_3}D] (**16d**) in C_6H_6 at 65 °C (*T* in h). The peak marked α corresponds to deuterium in the α-methylene position of the *n*-propyl ligand. * Denotes a decomposition product.

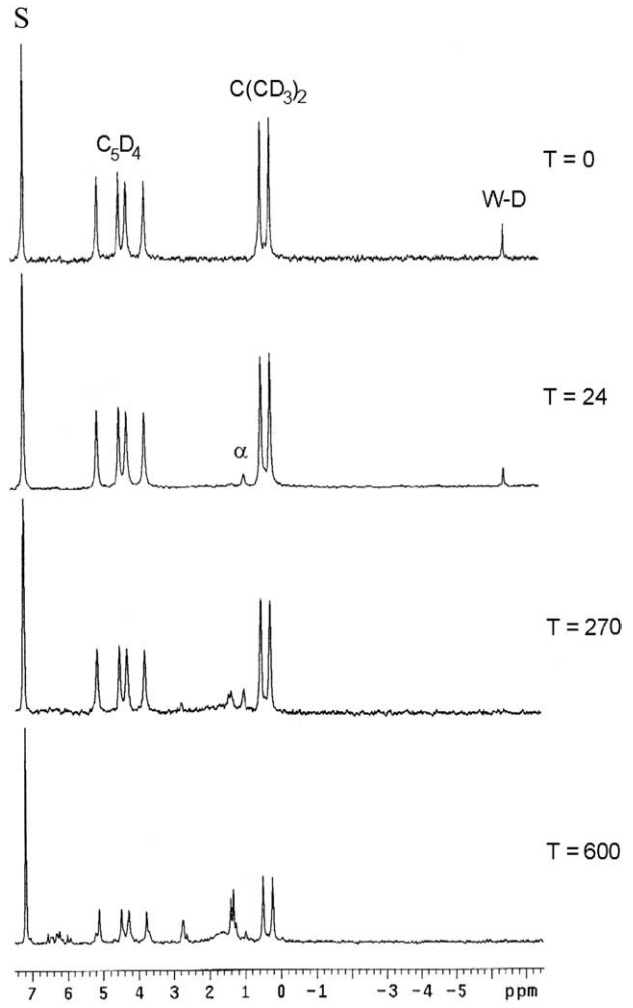


Fig. 6. ^{2}H NMR spectrum of the compound [W{(η-C_5D_4)C$(CD_3)_2$(η-C_5D_4)}{$(CH_2)_2CH_3$}D] (**10d**) in C_6H_6 at 65 °C (*T* in h). The peak marked α corresponds to deuterium in the α-methylene position of the *n*-propyl ligand. S denotes the residual solvent peak.

Apart from the H/D scrambling there is evidence for slow thermal decomposition of the compound **16**. After 45 h; the ^{2}H NMR spectra show new peaks in the cyclopentadienyl region δ 6.65–5.32 ppm and broad peaks at δ 2.71 and 1.38 ppm. These new peaks grow in intensity over time while the intensity of all the peaks of the compound **16d** decrease. The ^{1}H NMR spectra of the partially decomposed compound **16** in C_6D_6 showed no ethane was present. Also, there is no evidence in either the ^{1}H or ^{2}H NMR spectra of the partially decomposed solution of compound **16d** for the formation of new W–D or W–H groups. Attempts to identify the nature the new compounds were unsuccessful due to the very small quantity of alkyl-hydride and -deuteride compounds available.

Further, accurate kinetic data for the scrambling of deuterium from the metal to the α-position of the ethyl group in the compound **16** compared to related alkyl-deuteride species could not be obtained due to the presence of the competing decomposition reactions.

The thermolysis of the d^5-ethyl hydride compound [W{(η-C_5H_4)CMe_2(η-C_5H_4)}{CD_2CD_3}$_2$H] (**20**) was studied. A 10 mM solution of the compound **20** in C_6D_6 was sealed in a NMR tube and heated at 65 °C for a prolonged period and the ^{1}H NMR spectra were recorded periodically. After 8 h a peak at δ 1.11 ppm appeared corresponding to hydrogen in the α-methylene group. The increase in the intensity of this resonance was accompanied by a decrease in the intensity of the singlet at δ −6.47 ppm corresponding to the tungsten-hydrogen.

After heating the sample of **20** at 65 °C for 77 h a number of new peaks appeared and grew in intensity in the cyclopentadienyl region of the spectrum together with complex peaks in the region δ 2.65–1.35 ppm. We assign these new peaks to one or more decomposition products. There were no peaks at or close to δ 1.58 ppm implying that H/D scrambling into the β-CD_3

group of the d^5-ethyl ligand does not occur, as found for the studies on **16d**.

A 4 mM solution of the *n*-propyl-deuteride [W{(η-C_5D_4)$C(CD_3)_2$(η-C_5D_4)}{$(CH_2)_2CH_3$}D] (**10d**) in C_6H_6 and a 3 mM solution of the compound **10a** in C_6D_6 were prepared in separate NMR tubes. The ^1H and ^2H NMR spectra showed that at room temperature there had been no observable H/D crambling between *n*-propyl and W–D groups. The samples of **10d** were heated at 65 °C and the ^1H and ^2H NMR spectra recorded periodically. After ca. 12 h the ^2H NMR spectrum showed a new and growing peak at δ 1.02 ppm. We note that the compound **10d** has a peak in the ^1H NMR spectrum of due to the α-CH_2 hydrogens at δ 1.04 ppm. Also, the ^2H NMR spectra showed the peak due to W–D at δ −6.44 ppm decreased. Correspondingly, the relative intensity of the peak due to the α-CH_2 hydrogens in the ^1H NMR spectrum of the compound **10d** decreased compared to the resonance due to the β-CH_2 and γ-CH_3 hydrogens of the *n*-propyl group. Additionally, a peak at δ 6.47 ppm corresponding to a W–H group grew in intensity. These spectra are consistent with scrambling of W–D with only the α-CH_2 hydrogens of the *n*-propyl group. The NMR spectra of the thermolysed solutions of **10d** also showed evidence for one or more new compounds and a relative decrease of intensity of all bands associated with **10d**. The rate of scrambling into the α-position is faster than the rate of formation of decomposition products. Attempts to characterise the decomposition products were unsuccessful. Also, attempts to observe C–D coupling in $^{13}C\{^1H\}$ NMR spectrum of the compound **10d** were thwarted by lack of the of material.

The *n*-butyl-deuteride compound [W{(η-C_5D_4)-$C(CD_3)_2$(η-C_5D_4)}{$(CH_2)_3CH_3$}D] (**11d**) also showed H/D scrambling between the W–D and the α-CH_2 hydrogens of the *n*-butyl group. Thus, an 8 mM solution of the compound **11d** in C_6H_6 and a 5 mM solution of the compound **11d** in C_6D_6 were prepared, sealed in NMR tubes were heated at 65 °C. In the ^2H NMR spectra the resonance due to the W–D group at δ −6.45 ppm decreases while a peak at δ 1.01 ppm appears and grows in intensity. In the ^1H NMR spectrum the relative intensity of the peak at δ 1.01 ppm corresponding to the hydrogens of the α-CH_2 of the *n*-butyl compound decreases and a peak at δ −6.46 ppm appears and grows in intensity. Again the rate of this α-hydrogen scrambling process was faster than the decomposition reaction which gives rise to one or more new compounds, the nature of which have not been determined. No evidence of scrambling into other positions of the *n*-butyl group was observed.

Scrambling of deuterium into the α-position of the *n*-pentyl compound [W{(η-C_5D_4)$C(CD_3)_2$(η-C_5D_4)}-{$(CH_2)_4CH_3$}D] (**12d**) is observed on heating a 6 mM solution in C_6H_6 and a 4 mM solution in C_6D_6 at 65 °C. In both cases a peak at δ 1.04 ppm appeared in the ^2H NMR spectra along with a decrease in the resonance due to the W–D (δ −6.49 ppm). This scrambling process was accompanied by the slow formation of decomposition products. No evidence for scrambling

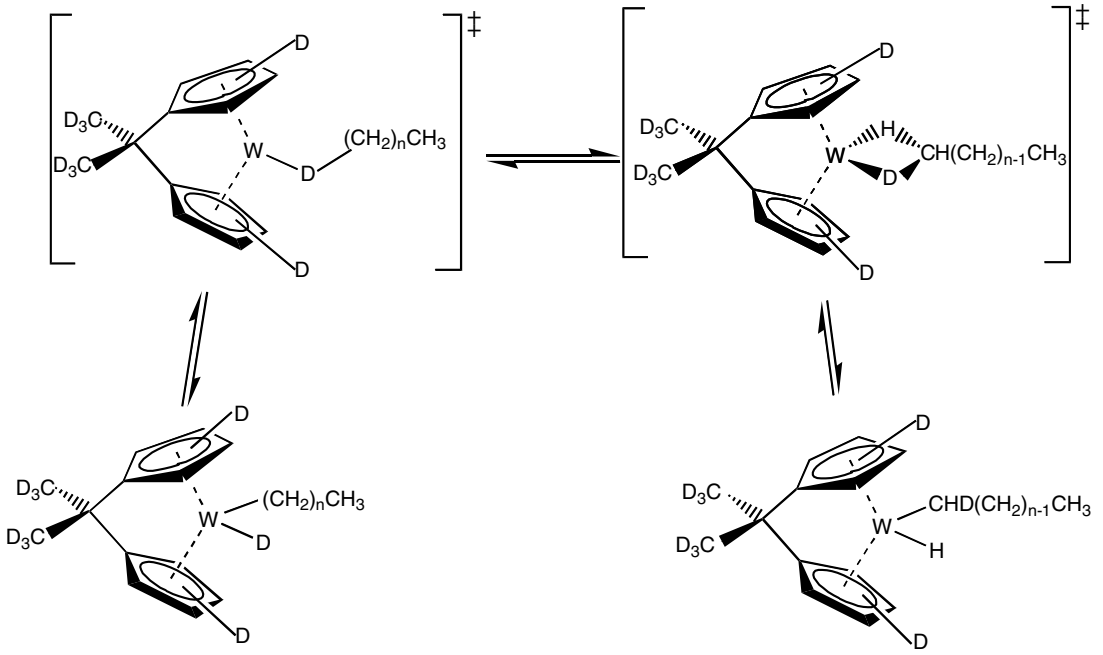


Fig. 7. Intramolecular hydrogen scrambling in the compounds [W{(η-C_5D_4)$C(CD_3)_2$(η-C_5D_4)}{$(CH_2)_nCH_3$}D] (n = 1–4) via η^1-H and η^2-H,H-σ-complexes.

into other positions of the *n*-pentyl chain was observed by ^1H or ^2H NMR spectroscopy.

In summary, thermolysis of the *n*-alkyl-deuteride compounds $[W\{(\eta\text{-}C_5D_4)C(CD_3)_2(\eta\text{-}C_5D_4)\}\{(CH_2)_n\text{-}CH_3)_2D\}]$ ($n = 1$–4) and $[W\{(\eta\text{-}C_5H_4)CMe_2(\eta\text{-}C_5H_4)\}\text{-}\{CD_2CD_3)H]\}$ shows intramolecular hydrogen/deuterium exchange between the α-methylene hydrogens of the *n*-alkyl ligand and the W–D group. Exchange into other positions of the *n*-alkyl ligand was not observed for any of the compounds $[W\{(\eta\text{-}C_5D_4)C(CD_3)_2(\eta\text{-}C_5D_4)\}\{(CH_2)\}_nCH_3)_2D]$ ($n = 1$–4). Similarly, H/D scrambling onto the α-methylene position was also observed by NMR spectroscopy for the d^5-ethyl-hydride compound $[W\{(\eta\text{-}C_5H_4)CMe_2(\eta\text{-}C_5H_4)\}CD_2CD_3)_2H]$. Whereas the methyl-deuteride compound $[W\{(\eta\text{-}_5H_4)\text{-}CMe_2(\eta\text{-}C_5H_4)\}(CH_3)D]$ is stable at 110 °C, the higher *n*-alkyl-deuteride compounds $[W\{(\eta\text{-}C_5D_4)C(CD_3)_2(\eta\text{-}C_5D_4)\}\{(CH_2)_nCH_3)_2D]\}$ ($n = 1$–4) decompose slowly above ca. 65 °C.

We propose that the H/D exchange into the α-methylene hydrogens proceeds by an intramolecular mechanism with an intermediate or transition state agostic alkane (see Fig. 7) by analogy with H/D the intermolecular exchange process proposed for the methyl compound $[W\{(\eta\text{-}C_5H_4)C(CH_3)_2(\eta\text{-}C_5H_4)\}\text{-}CH_3D]$ and related studies [2,3,10–26]. Subsequent to this work [6] there have been two reports of migration of transition metal along metal-alkyl chains of the kind hoped for in these studies [27,28]. Also there he been an elegant stdy by Ball et al. [29] in which alkane-σ-transition metal complexes are observed in solution by NMR studies.

3. Experimental

All manipulations of air and/or moisture sensitive materials were performed under an inert atmosphere of dry dinitrogen using standard Schlenk line techniques or in an inert atmosphere dry box containing dinitrogen [30]. Inert gases were purified firstly by passage through columns filled with activated molecular sieves (4 Å) and then either manganese (II) oxide suspended on vermiculite, for the Schlenk line, or BASF catalyst, for the dry box. Celite® filtration aid was purchased from Fluka Chemie and oven-dried at 100 °C prior to use.

Solvents were pre-dried over activated 4 Å molecular sieves and then distilled from Na/K alloy (light petroleum ether (b.p. 40–60 °C), diethyl ether, pentane and DME), from sodium (petroleum ether (b.p. 100–120 °C) and toluene), from potassium (THF) or from calcium hydride (acetonitrile, dichloromethane and TMEDA), under a slow continuous stream of dinitrogen. DMSO and d^1-methanol were used without drying. Deuterated NMR solvents were dried over potassium (benzene, toluene and THF) or calcium hydride (acetone, chloroform, dichloromethane and pyridine), distilled and degassed by the freeze–pump–thaw technique prior to use. $CDFCl_2$ was prepared by the literature method [31]. WCl_6 (99%), $LiAlH_4$ (95%), $LiAlD_4$ (96%), \D Super-Hydride® $LiBEt_3H$ (1.0 M solution in THF), dimethylzinc (2.0 M solution in hexanes), diethylzinc (1.0 M solution in hexanes), ^{t}BuLi (1.7 M solution in pentane), ^{n}BuLi (2.5 M solution in light petroleum ether (b.p. 40–60 °C)), $[Na\{AlH_2(OCH_2\text{-}CH_2OCH_3)_2\}]$ (2.5 M solution in toluene), HCl (1.0 M solution in diethyl ether), HBF_4 (54+ wt% solution in diethyl ether), NH_4I, 1-chloro-*n*-propane, 1-chloro-*n*-butane, 1-chloro-*n*-pentane, 1-chloro-*n*-hexane, d^5-ethanol, pyrrolidine, Me_2SiCl_2 and D_2 were purchased from Aldrich Chemical Company and used without further purification. $ZnCl_2$ was bought from Aldrich Chemical Company and dried in refluxing thionyl chloride for 6 h. Magnesium turnings were preactivated by the addition of a small amount (ca. 2 wt%) of dibromoethane to a suspension in THF and then washed with THF.

The compounds $[W\{(\eta\text{-}C_5H_4)CMe_2(\eta\text{-}C_5H_4)\}Cl_2]$ [1,2] and $[Li\{AlD_2(OCH_2CH_2OCH_3)_2\}]$ [26], were prepared using standard literature methods. NMR spectra were recorded out on a Varian Unity *Plus* 500 spectrometer (^1H, ^2H, and ^{13}C spectra were recorded at 499.868, 76.750, and 125.703 MHz, respectively). The spectra were referenced internally relative to the residual protio-solvent (^1H), residual deutero-solvent (^2H) and solvent (^{13}C) resonances relative to tetramethylsilane (^1H, ^2H, ^{13}C; $\delta = 0$ ppm). Chemical shifts (δ) are expressed in ppm and coupling constants (J) in Hz. Mass spectra (FAB) were recorded by the EPSRC Mass Spectrometry Service at the University College of Swansea.

IR spectra were recorded on a Mattson Polaris FTIR spectrometer or a Perkin–Elmer 1710 FTIR spectrometer. Samples were prepared as a Nujol mull between NaCl plates. Data are quoted in cm^{-1}.

Elemental analysis data were obtained from the Microanalysis Department of the Inorganic Chemistry Laboratory, Oxford.

3.1. Preparation of $[Zn\{CD_2CD_3\}_2]$

A thick-walled glass tube was charged with a finely ground mixture of zinc powder (7 g, 107.1 mmol) and copper powder (1.7 g, 26.8 mmol). Anti-bumping granules were added and the admixture was dried by heating under reduced pressure at 200 °C for 2 h. d^5-Iodoethane (7.9 g, 49.1 mmol) was transferred to the tube via low pressure distillation and the tube was sealed under reduced pressure, prior to heating overnight at 140 °C. The tube was connected to a Schlenk line, carefully scored and then broken. Volatiles were collected and the compound $[Zn\{CD_2CD_3\}_2]$ obtained as an extremely pyrophoric colourless liquid. Yield of $[Zn\{CD_2\text{-}CD_3)\}_2]$ = 0.55 g, 9%.

3.2. The compounds $[Zn\{(CH_2)_nCH_3\}_2]$

1-Chloro-*n*-propane (19.9 g, 250 mmol) was added dropwise to a suspension 3 of activated magnesium turnings (12 g, 490 mmol) in diethyl ether (150 cm^3) at such a rate to maintain a vigorous reaction. The reaction mixture was stirred for 2 h and a colourless solution was then isolated by filtration. Anhydrous $ZnCl_2$ (17 g, 120 mmol) was added to this ethereal solution via a solid addition tube in a slightly exothermic reaction. The resulting white suspension was stirred overnight and a colourless solution was then separated by filtration. Removal of volatiles under reduced pressure yielded $[Zn\{(CH_2)_2CH_3\}_2]$ as a pyrophoric colourless oil. Yield of $[Zn\{(CH_2)_2CH_3\}_2]$ (based on 1-chloro-*n*-propane) = 5.34 g, 28%. The compounds $[Zn\{(CH_2)_3CH_3\}_2]$ (yield [based on 1-chloro-*n*-butane] = 12.06 g, 42%), $[Zn\{(CH_2)_4CH_3\}_2]$ (yield [based on 1-chloro-*n*-pentane] = 14.32 g, 61%) and $[Zn\{(CH_2)_5CH_3\}_2]$ (yield [based on 1-chloro-*n*-hexane] = 25.05 g, 85%) were prepared via an analogous procedure.

3.3. Preparation of d^6-cyclopentadiene

To a flask containing D_2O (560 cm^3) at 3 °C, elemental sodium (65 g, 2.83 mol) was added in small portions over 2 h. A portion of the resulting solution of NaOD in D_2O (85 cm^3) was transferred to a flask containing DMSO (100 cm^3) and stirred vigorously at 0 °C. Freshly distilled cyclopentadiene monomer (125 cm^3, 1.58 mol) was added to the reaction mixture and stirring continued at 0 °C for 1 h. Cyclopentadiene monomer was transferred from the reaction mixture to a Schlenk tube, at −196 °C, under reduced pressure, allowed to warm to −78 °C and then added to a flask containing fresh NaOD in D_2O (85 cm^3) and DMSO (100 cm^3). This procedure was repeated for a total of 5 exchanges. d^6-Cyclopentadiene was stored at −80 °C. Yield of d^6-cyclopentadiene, 46.1 g, 94% D, 40%.

3.4. Preparation of d^{12}-6,6-dimethylfulvene

To a flask containing d^6-acetone (28.4 cm^3, 386 mmol) in d^1-methanol (100 cm^3) at 0 °C was added freshly distilled d^6-cyclopentadiene monomer (27 g, 94% D, 390 mmol). Pyrrolidine (41.7 cm^3, 500 mmol) was added and the reaction mixture immediately turned deep orange. The reaction mixture was stirred at 0 °C for 0.75 h. Glacial acetic acid (50 cm^3) and D_2O (50 cm^3) were added and the organic layer extracted into pentane (3×40 cm^3). The organic extracts were combined, washed with D_2O (50 cm^3) and dried over anhydrous $MgSO_4$. A pale orange solution was isolated by filtration and volatiles removed under reduced pressure to afford d^{12}-6, 6-dimethylfulvene as dark orange liquid, which was stored at −80 °C. Yield d^{12}-6, 6-dimethylfulvene, 31.6 g, 95% D, 74%.

3.5. Preparation of $[(C_5D_5)C(CD_3)_2(C_5D_5)]$

THF (350 cm^3) was added to a flask charged with NaOD (20 g, 500 mmol), prepared as described above, and the resulting suspension stirred at room temperature for 1 h. Freshly distilled d^6-cyclopentadiene monomer (15.7 g, 94% D, 232 mmol) was added to the reaction mixture which was stirred for 0.5 h to give a pale pink suspension. A solution of d^{12}-6, 6-dimethylfulvene (26.1 g, 95% D, 232 mmol) in THF (40 cm^3) was added dropwise over 0.5 h and the reaction mixture stirred overnight. An orange solution was isolated by filtration, washed with D_2O (50 cm^3) and dried over $MgSO_4$, prior to separation by filtration. Removal of volatiles under reduced pressure afforded the compound $[(C_5D_5)C(CD_3)_2(C_5D_5)]$ as a pale yellow oil. Yield of $[(C_5D_5)C(CD_3)_2(C_5D_5)]$, 22.7 g, 93% D, 55%.

3.6. Preparation of $[Li_2\{(C_5D_4)C(CD_3)_2(C_5D_4)\}]$

A solution of ^{n}BuLi (40 cm^3, 2.5 M, 100 mmol) in light petroleum ether (b.p. 40–60 °C) was added dropwise to a solution of $[(C_5D_5)C(CD_3)_2(C_5D_5)]$ (11.3 g, 94% D, 62.3 mmol) in light petroleum ether (b.p. 40–60 °C) (100 cm^3) at −78 °C. A flocculent white precipitate immediately formed and the reaction mixture was allowed to warm to room temperature and then stirred overnight. A white solid was isolation by filtration, washed with light petroleum ether (b.p. 40–60 °C) (100 cm^3) and diethyl ether (2×50 cm^3) and then dried under reduced pressure. Yield of $[Li_2\{(C_5D_4)C(CD_3)_2(C_5D_4)\}]$,10.8 g, 95% D, 93%.

3.7. Preparation of $[W\{(\eta\text{-}C_5H_4)CMe_2(\eta\text{-}C_5H_4)\}\{(CH_2)_2CH_3\}_2]$ (**3**)

To a suspension of $[W\{(\eta\text{-}C_5H_4)CMe_2(\eta\text{-}C_5H_4)\}Cl_2]$ (0.6 g, 1.2 mmol) in toluene (40 cm^3) a solution of $[Zn\{(CH_2)_2CH_3\}_2]$ (3.5 cm^3, 1.85 M, 6.5 mmol) in toluene was added slowly at −78 °C. The reaction mixture was allowed to warm to room temperature and stirred overnight. The dark red suspension was hydrolysed via the cautious addition of H_2O (0.6 cm^3) to remove excess $[Zn\{(CH_2)_2CH_3\}_2]$. The reaction mixture was filtered and the filtrate passed down a column containing activated alumina by elution with toluene. The resulting yellow solution was collected and volatiles removed under reduced pressure to give an oily yellow solid. The residue was extracted into pentane (15 cm^3). The solution was cooled to −80 °C to afford $[W\{(\eta\text{-}C_5H_4)CMe_2(\eta\text{-}C_5H_4)\}\{(CH_2)_2CH_3\}_2]$ **3** as a yellow solid. Yield: 0.23 g, 44%.

3.8. Preparation of [W{(η-C_5D_4)$C(CD_3)_2$(η-C_5D_4)}-{{$(CH_2)_2CH_3$}$_2$]} (**3d**)

The compound [W{(η-C_5D_4)$C(CD_3)_2$(η-C_5D_4)}{{$(CH_2)_2CH_3$}$_2$]} **3d** was prepared by the reaction between the compound **13** (0.44 g, 1.0 mmol) and a solution of [Zn{$(CH)_2CH_3$}$_2$](1 cm^3, 1.1 M, 1.10 mmol) in toluene The compound **3d** was obtained as a yellow solid. Yield: 0. 11 g, 23%.

3.9. Preparation of [W{(η-C_5H_4)CMe_2(η-C_5H_4)}-{$(CH_2)_3CH_3$}$_2$] (**4**) and [W{(η-C_5H_4)CMe_2(η-C_5H_4)}-{$(CH_2)_3CH_3$}Cl] (**5**)

To a suspension of [W{(η-C_5H_4)CMe_2(η-C_5H_4)}Cl_2] (0.3 g, 0.6 mmol) in toluene (40 cm^3) a solution of [Zn{$(CH_2)_3CH_3$}$_2$] (3.0 cm^3, 1.5 M, 4.5 mmol) in toluene was added slowly at −78 °C. The reaction mixture was allowed to warm to room temperature and stirred overnight. The dark red suspension was hydrolysed via the cautious addition of H_2O (0.5 cm^3) to remove excess [Zn{$(CH_2)_3CH_3$}$_2$]. The reaction mixture was filtered and volatiles removed under reduced pressure. The resulting orange solid was extracted into pentane (15 cm^3) to yield a yellow solution. The residue was extracted into a 1:1 mixture of toluene/pentane (20 cm^3). Cooling of the pentane solution to −80 °C afforded the compound [W{(η-C_5H_4)CMe_2(η-C_5H_4)}{$(CH_2)_3CH_3$}$_2$] (**4**) as a yellow solid. Yield: 0.045 g, 16%. Cooling of the toluene/pentane solution to −80 °C afforded the compound [W{(η-C_5H_4)CMe_2(η-C_5H_4)}{$(CH_2)_3CH_3$}Cl] (**5**) as a yellow solid. Yield: 0.11 g, 41%.

3.10. Preparation of [W{(η-C_5D_4)$C(CD_3)_2$(η-C_5D_4)}-{$(CH_2)_3CH_3$}Cl] (**5d**)

The compound **5d** was prepared by the reaction between the compound **13** (0.24 g, 0.55 mmol) and a solution of [Zn{$(CH_2)_3CH_3$}$_2$] (4 cm^3, 1.5 M, 6 mmol) in toluene in a procedure analogous to that used to prepare the compound **5** and was obtained as an yellow solid. Yield: 0.099 g, 39%.

3.11. Preparation of [W{(η-C_5H_4)CMe_2(η-C_5H_4)}-{$(CH_2)_4CH_3$}Cl] (**6**) and [W{(η-C_5H_4)CMe_2(η-C_5H_4)}-{$(CH_2)_4CH_3$}$_2$] (**7**)

To a suspension of [W{(η-C_5H_4)CMe_2(η-C_5H_4)}Cl_2] (1.0 g, 2.34 mmol) in toluene (40 cm^3) a solution of [Zn{$(CH_2)_4CH_3$}$_2$] (7.0 cm^3, 1.86 M, 13.0 mmol) in toluene was added slowly at −78 °C. The reaction mixture was allowed to warm to room temperature and stirred overnight. The dark red suspension was hydrolysed via the cautious addition of H_2O (0.6 cm^3) to remove excess [Zn{$(CH_2)_4CH_3$}$_2$]. The reaction mixture was filtered and the filtrate passed down a column containing activated alumina by elution with toluene to give a yellow solution. Further elution with diethyl ether gave an orange solution which was collected separately. Removal of diethyl ether under reduced pressure afforded the compound [W{(η-C_5H_4)CMe_2(η-C_5H_4)}-{$(CH_2)_4CH_3$}Cl] (21) (**6**) as a pale red solid. Yield: 0.31 g, 29%.

Removal of volatiles under reduced pressure from the yellow toluene solution yielded a yellow solid. Extraction into pentane (5 cm^3) prior to cooling to −80 °C afforded a yellow solid in very low yield (ca. 0.01 g, 1%) which was characterised by ^{1}H NMR spectroscopy as [W{(η-C_5H_4)CMe_2(η-C_5H_4)}{$(CH_2)_4CH_3$}$_2$] (**7**).

3.12. Preparation of [W{(η-C_5D_4)$C(CD_3)_2$(η-C_5D_4)}-{$(CH_2)_4CH_3$}$_2$] (**6d**)

To a suspension of the compound **13d** (0.27 g, 95% D, 0.58 mmol) in toluene (50 cm^3) a solution of [Zn-{$(CH_2)_4CH_3$}$_2$] (3.0 cm^3, 1.5 M, 4.5 mmol) in toluene was added dropwise at −78 °C. The reaction mixture was allowed to warm to room temperature and stirred overnight. Excess [Zn{$(CH_2)_4CH_3$}$_2$] was hydrolysed by the cautious addition of D_2O (0.4 cm^3). The resulting solid was extracted into pentane (30 cm^3). Cooling of the pentane solution to −80 °C afforded the compound 6a as a yellow crystalline solid. Yield: 0.098 g, 33%.

3.13. Preparation of [W{(η-C_5H_4)CMe_2(η-C_5H_4)}-{$(CH_2)_5CH_3$}$_2$] (**8**)

To a suspension of [W{(η-C_5H_4)CMe_2(η-C_5H_4)}Cl_2] (0.33 g, 0.6 mmol) in toluene (40 cm^3) a solution of [Zn{$(CH_2)_5CH_3$}$_2$] (2.0 cm^3, 5.3 M, 10.6 mmol) in toluene was added dropwise at −78 °C. The reaction mixture was allowed to warm to room temperature and stirred overnight. Excess [Zn{$(CH_2)_5CH_3$}$_2$] was hydrolysed via the cautious addition of H_2O (0.5 cm^3). The reaction mixture was filtered and the filtrate passed down a column containing activated alumina by elution with a 1:1 mixture of diethyl ether/toluene. The resulting yellow solution was collected and volatiles removed under reduced pressure to give an orange/yellow solid, prior to extraction into pentane (15 cm^3) to yield a yellow solution. The residue was extracted into a 1:1 mixture of toluene/pentane (20 cm^3). Cooling of the pentane solution to −80 °C afforded the compound [W{(η-C_5H_4)CMe_2(η-C_5H_4)}{$(CH_2)_5CH_3$}$_2$] (**8**) as a yellow solid. Yield: 0.095 g, 18%. Cooling of the toluene/pentane solution to −78 °C afforded a small amount (ca. 0.025 g, 9%) of a pale red solid characterised by ^{1}H NMR spectroscopy as [W{(η-C_5H_4)CMe_2(η-C_5H_4)}-{$(CH_2)_5CH_3$}Cl].

3.14. Preparation of [W{(η-C_5H_4)CMe_2(η-C_5H_4)}{$(CH_2)_2CH_3$}I] (9)

A mixture of the compound **3**(0.06 g, 0.13 mmol) and NH_4I (0.05 g, 0.34 mmol) in THF (25 cm^3) was heated at 65 °C for seven days in a Rotaflo® ampoule. A gradual colour change from yellow to pale red was observed. The solution was isolated by filtration and volatiles were removed under reduced pressure. The resulting red–orange solid was washed with pentane (20 cm^3) to remove any unreacted compound **3** prior to extraction into a 1:4 mixture of toluene/pentane. Cooling of the red–orange solution to −80 °C afforded the compound [W{(η-C_5H_4)CMe_2(η-C_5H_4)}{$(CH_2)_2CH_3$}I] (**9**) as a pale red solid. Yield: 0.032 g, 47%.

3.15. Preparation of [W{(η-C_5D_4)$C(CD_3)_2$(η-C_5D_4)}{$(CH_2)_2CH_3$}I] (9d)

The compound [W{(η-C_5H_4)$C(CD_3)_2$(η-C_5D_4)}{$(CH_2)_2CH_3$}I] (**9d**) was prepared by the reaction between the compound **3d** (0.11 g, 0.24 mmol) and NH_4I (0.07 g, 0.48 mmol) in a procedure analogous to that employed to prepare the compound **9** and was obtained as a pale red solid. Yield: 0.057 g, 44%.

3.16. Preparation of [W{(η-C_5H_4)CMe_2(η-C_5H_4)}{$(CH_2)_2CH_3$}H] (10)

To a solution of the compound **23** (0.03 g, 0.06 mmol) in toluene (20 cm^3) was added a solution of [Na{$AlH_2(OCH_2CH_2OCH_3)_2$}] (0.2 cm^3, 2.5 M, 0.5 mmol) in toluene at −78 °C. The reaction mixture was allowed to warm to room temperature and stirred overnight during which time the colour of the solution changed from orange to pale yellow. Excess [Na{$AlH_2(OCH_2CH_2OCH_3)_2$}] was hydrolysed by the cautious addition of H_2O (0.1 cm^3). Volatiles were removed and the reaction mixture dried under reduced pressure for 2 h. The yellow residue was extracted into pentane (2×20 cm^3) and the volume subsequently reduced to 10 cm^3 prior to cooling to −80 °C. The compound [W{(η-C_5H_4)CMe_2 (η-C_5H_4)}{$(CH_2)_2CH_3$}H] (**10**) was obtained as a yellow crystalline solid. Yield: 0.012 g, 50%.

3.17. Preparation of [W{(η-C_5D_4)$C(CD_3)_2$(η-C_5D_4)}{$(CH_2)_2CH_3$}D] (10d)

The compound [W{(η-C_5D_4)$C(CD_3)_2$(η-C_5D_4)}{$(CH_2)_2CH_3$}D] (**10d**) was prepared by the reaction between the compound **9d** (0.020 g, 0.04 mmol) and a solution of [Li{$AlD_2(OCH_2CH_2OCH_3)_2$}] (1 cm^3, 1.5 M, 1.5 mmol) in toluene in a procedure analogous to that used to prepare the compound **16** and was obtained as a yellow solid. Since only a small amount of compound was obtained, and in order to utilise all of the compound prepared, the Yield: **10d** was not calculated.

3.18. Preparation of [W{(η-C_5H_4)CMe_2(η-C_5H_4)}{$(CH_2)_3CH_3$}H] (11)

The compound [W{(η-C_5H_4)CMe_2(η-C_5H_4)}{$(CH_2)_3CH_3$}H] (**11**) was prepared by the reaction between the compound **5** (0.1 g, 0.22 mmol) and a solution of [Na{$AlH_2(OCH_2CH_2OCH_3)_2$}] (2 cm^3, 2.5 M, 5 mmol) in toluene in a procedure analogous to that employed to prepare the compound **10** and was obtained as a yellow solid. Yield: 0.038 g, 42%.

3.19. Preparation of [W{(η-C_5D_4)$C(CD_3)_2$(η-C_5D_4)}{$(CH_2)_3CH_3$}D] (11d)

The compound **11d** was prepared by the reaction between the compound **5d** (0.035 g, 0.08 mmol) and a solution of [Li{$AlD_2(OCH_2CH_2OCH_3)_2$}] (1.5 cm^3, 1.0 M, 1.5 mmol) in toluene in a procedure analogous to that used to prepare the compound **16** and was obtained as a yellow solid. Since only a small amount of compound was obtained, and in order to utilise all of the compound prepared, the Yield: **11d** was not determined.

3.20. Preparation of [W{(η-C_5H_4)CMe_2(η-C_5H_4)}{$(CH_2)_4CH_3$}H] (12)

The compound [W{(η-C_5H_4)CMe_2(η-C_5H_4)}{$(CH_2)_4CH_3$}H] (**12**) was prepared by the reaction between the chloro compound **6** (0.05 g, 0.11 mmol) and a solution of [Na{$AlH_2(OCH_2CH_2OCH_3)_2$}] (1 cm^3, 2.5 M, 2.5 mmol) in toluene in a procedure analogous to that employed to prepare the compound **11d** and was obtained as a yellow solid. Yield: 0.023 g, 49%.

3.21. Preparation of [W{(η-C_5D_4)$C(CD_3)_2$(η-C_5D_4)}{$(CH_2)_4CH_3$}D] (12d)

The compound [W{(η-C_5D_4)$C(CD_3)_2$(η-C_5D_4)}{$(CH_2)_4CH_3$}D] (**12d**) was prepared by the reaction between the iodo compound **17d** (0.022 g, 0.05 mmol) and a solution of [Li{$AlD_2(OCH_2CH_2OCH_3)_2$}] (1.0 cm^3, 1.5 M, 1.5 mmol) in toluene in a procedure analogous to that used to prepare the compound **30** and was obtained as a yellow solid. Since only a small amount of compound was obtained and in order to utilise all of the compound prepared the Yield: **12d** was not calculated.

3.22. Preparation of [W{(η-C_5D_4)$C(CD_3)_2$(η-C_5D_4)}Cl_2] (13d)

The two solids $WCl_4 \cdot DME$ [32] (10.5 g, 25.2 mmol) and [Li_2{$(C_5D_4)C(CD_3)_2(C_5D_4)$}] (5.5 g, 95%, 27.7 mmol) were stirred together in the absence of solvent

to give a good admixture. Diethyl ether (100 cm^3) was added and the resulting brown suspension stirred for two days. The liquid phase was removed by filtration and DME (50 cm^3) was added to the remaining solid. The resulting dark brown suspension was stirred for 0.5 h and a brown solid isolated by filtration. The residue was washed with ethanol (50 cm^3) and then diethyl ether (3×30 cm^3) until the washings were colourless. After drying under reduced pressure, the resulting pale brown solid was extracted into dichloromethane (2×250 cm^3) to give a deep red/brown solution. Removal of volatiles under reduced pressure afforded the compound $[W\{(\eta\text{-}C_5D_4)C(CD_3)_2(\eta\text{-}C_5D_4)\}Cl_2]$ (**13d**) as a purple solid. Yield: 1.25 g, 95% D, 11.3%.

*3.23. Preparation of $[W\{(\eta\text{-}C_5D_4)C(CD_3)_2(\eta\text{-}C_5D_4)\}\{CH_2CH_3\}_2]$ (**14d**)*

To a suspension of the compound **13d** (0.1 g, 95% D, 0.22 mmol) in toluene (50 cm^3) a solution of $[Zn\{CH_2CH_3\}_2]$ (5.0 cm^3, 1.0 M, 5.0 mmol) in hexanes was added dropwise at −78 °C. The reaction mixture was allowed to warm to room temperature and stirred overnight. Volatiles were removed under reduced pressure and collected in a trap containing propan-2-ol at −196 °C. Excess $[Zn\{CH_2CH_3\}_2]$ can be readily removed in this way. The resulting solid was extracted into pentane (20 cm^3). Cooling of the pentane solution to −80 °C afforded the compound $[W\{(\eta\text{-}C_5D_4)C(CD_3)_2(\eta\text{-}C_5D_4)\}\{CH_2CH_3\}_2]$ (**14d**) as a yellow crystalline solid. Yield: 0.042 g, 46%. Preparation of $[W\{(\eta\text{-}C_5D_4)C(CD_3)_2(\eta\text{-}C_5D_4)\}\{CH_2CH_3\}I]$ (**15d**). The compound $[W\{(\eta\text{-}C_5H_4)C(CD_3)_2(\eta\text{-}C_5D_4)\}\{CH_2CH_3\}I]$ (**15d**) was prepared by the reaction between the compound **14d** (0.03 g. 0.07 mmol) and NH_4I (0.02 g, 0.14 mmol) in a procedure analogous to that employed to prepare the compound **2** and was obtained as a pale red solid. Yield: 0.037 g, 67%.

*3.24. Preparation of $[W\{(\eta\text{-}C_5D_4)C(CD_3)_2(\eta\text{-}C_5D_4)\}\{CH_2CH_3\}D]$ (**16d**)*

To a solution of the compound **15d** (0.03 g, 0.06 mmol) in toluene (20 cm^3) was added a solution of $[Li\{AlD_2(OCH_2CH_2OCH_3)_2\}]$ (0.5 cm^3, 1.1 M, 0.55 mmol) in toluene at −78 °C. The reaction mixture was allowed to warm to room temperature and stirred overnight during which time the colour of the solution changed from orange to pale yellow. Excess $[Li\{AlD_2(OCH_2CH_2OCH_3)_2\}]$ was hydrolysed by the cautious addition of D_2O (0.35 cm^3). Volatiles were removed, and the reaction mixture dried, under reduced pressure. The yellow residue was extracted into pentane (20 cm^3) and the volume subsequently reduced to 10 cm^3 prior to cooling to −80 °C. The compound **16d** was obtained as a yellow crystalline solid. Since only a small amount of compound was obtained, and in order to utilise all of the compound prepared, the Yield of **16d** was not determined.

*3.25. Preparation of $[W\{(\eta\text{-}C_5D_4)C(CD_3)_2(\eta\text{-}C_5D_4)\}\{(CH_2)_4CH_3\}I]$ (**17d**)*

The compound $[W\{(\eta\text{-}C_5H_4)C(CD_3)_2(\eta\text{-}C_5D_4)\}\{(CH_2)_4CH_3\}I]$ (**17d**) was prepared by the reaction between the compound **7d** (0.05 g, 0.098 mmol) and NH_4I (0.015 g, 0.11 mmol) in a procedure analogous to that employed to prepare the compound **9** and was obtained as a pale red solid. Yield: 0.026 g, 47%.

*3.26. Preparation of $[W\{(\eta\text{-}C_5H_4)CMe_2(\eta\text{-}C_5H_4)\}\{CD_2CD_3\}_2]$ (**18**)*

The compound **18** was prepared by the reaction between the compound $[W\{(\eta\text{-}C_5H_4)CMe_2(\eta\text{-}C_5H_4)\}Cl_2]$ (0.47 g, 1.1 mmol) and a solution of $[Zn\{CD_2CD_3\}_2]$ (5 cm^3, 0.4 M, 2 mmol) in toluene in a procedure analogous to that used to prepare the compound **3** and was obtained as a yellow solid. Yield: 0.24 g, 52%.

*3.27. Preparation of $[W\{(\eta\text{-}C_5H_4)CMe_2(\eta\text{-}C_5H_4)\}\{CD_2CD_3\}I]$ (**19**)*

The compound $[W\{(\eta\text{-}C_5H_4)CMe_2(\eta\text{-}C_5H_4)\}\{CD_2CD_3\}I]$ (**19**) was prepared by the reaction between the compound **18** (0.04 g, 0.09 mmol) and NH_4I (0.025 g, 0.17 mmol) in a procedure analogous to that employed to prepare the compound **9** and was obtained as a pale red solid. Yield: 0.032 g, 69%.

*3.28. Preparation of $[W\{(\eta\text{-}C_5H_4)CMe_2(\eta\text{-}C_5H_4)\}\{CD_2CD_3\}H]$ (**20**)*

The compound **20** was prepared by the reaction between the compound **19** (0.027 g, 0.05 mmol) and a solution of $[Na\{AlH_2(OCH_2CH_2OCH_3)_2\}]$ (0.5 cm^3, 2.5 M, 1.25 mmol) in toluene in a procedure analogous to that used to prepare the compound **10**. The compound **20** was obtained as a yellow solid. Yield: 0.012 g, 62%.

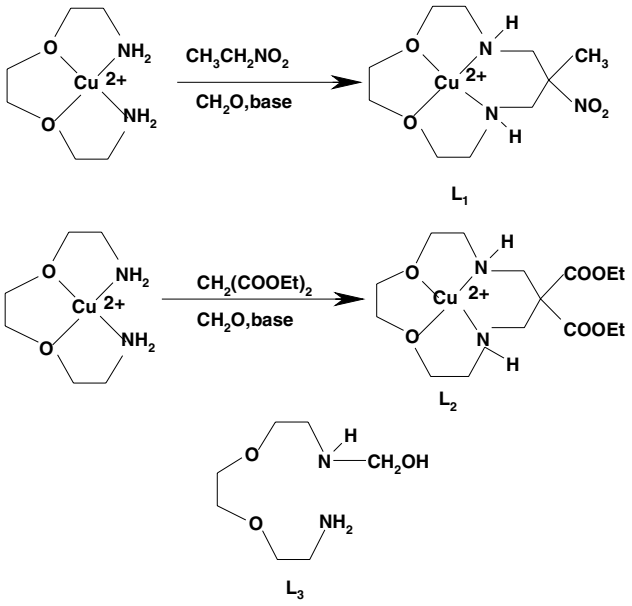
Acknowledgements

We thank the EPSRC for a studentship (to S.L.J. Conway) and St John's College for a Junior Research Fellowship (to L.H. Doerrer).

References

[1] L. Labella, A. Chernega, M.L.H. Green, J. Chem. Soc., Dalton Trans. (1995) 395.

[2] A. Chernega, J. Cook, M.L.H. Green, L. Labella, S.J. Simpson, J. Souter, A.H.H. Stephens, J. Chem. Soc., Dalton Trans. (1997) 3225.
[3] J.C. Green, C.N. Jardine, J. Chem. Soc., Dalton Trans. (1998) 1057.
[4] A.H. Janowicz, R.G. Bergman, J. Am. Chem. Soc. 104 (1982) 352.
[5] R.G. Bergman, Science 223 (1984) 902.
[6] S.L.J. Conway, D. Phil. thesis, Oxford, 2000.
[7] R.M. Bullock, C.E.L. Headford, K.M. Hennessy, S.E. Kegley, J.R. Norton, J. Am. Chem. Soc. 111 (1989) 3897.
[8] A. Berry, M.L.H. Green, J.A. Bandy, K. Prout, J. Chem. Soc., Dalton Trans. (1991) 2185.
[9] I.E. Nifant'ev, P.V. Ivchenko, M.V. Borzov, J. Chem. Res. (S) (1992) 162.
[10] V. Pons, S.L.J. Conway, M.L.H. Green, J.C. Green, B.J. Herbert, B/M/ Heinekey, Inorg. Chem. 43 (2004) 3475.
[11] S.L.J. Conway, T. Dijkstra, L.H. Doerrer, J.C. Green, M.L.H. Green, A.H.H. Stephens, J. Chem. Soc., Dalton Trans. (1998) 2689.
[12] W.J. Carter, S.J. Okrasinski, J.R. Norton, Organometallics 4 (1985) 1376.
[13] G. Parkin, J.E. Bercaw, Organometallics 8 (1989) 1172.
[14] J.M. Buchanan, J.M. Stryker, R.G. Bergman, J. Am. Chem. Soc. 108 (1986) 1537.
[15] R.A. Periana, R.G. Bergman, J. Am. Chem. Soc. 108 (1986) 7332.
[16] B.A. Arndtsen, R.G. Bergman, T.A. Mobley, T.H. Petersen, Acc. Chem. Res. 28 (1995) 1995.
[17] R.G. Bergman, Science 278 (1997) 260.
[18] C. Hall, R.N. Perutz, Chem. Rev. 96 (1996) 3125.
[19] D.M. Heinekey, G.L. Gould, J. Am. Chem. Soc. 111 (1989) 550216.
[20] C.L. Gross, G.S. Girolami, J. Am. Chem. Soc. 120 (1998) 6605.
[21] R.L. Martin, J. Am. Chem. Soc. 121 (1999) 9459.
[22] R.N. Perutz, J.J. Turner, Inorg. Chem. 14 (1975) 262.
[23] G.R. Dobson, P.M. Hodges, M.A. Healy, M. Poliakoff, J.J. Turner, S. Firth, K.J. Asali, J. Am. Chem. Soc. 1091 (1987) 4218.
[24] C.E. Brown, Y. Ishikawa, P.A. Hackett, D.M. Rayner, J. Am. Chem. Soc. 112 (1990) 2530.
[25] D.R. Evans, T. Drovetskaya, R. Bau, C.A. Reed, P.D.W. Boyd, J. Am. Chem. Soc. 119 (1997) 3633.
[26] S. Geftakis, G.E. Ball, J. Am. Chem. Soc. 120 (1998) 9953.
[27] T.O. Northcutt, D.D. Wick, A.J. Vetter, W.D. Jones, J. Am. Chem. Soc 123 (2001) 7257.
[28] T.C. Flood, J.K.eE. Janak, M. Iimura, H. Zhen., J. Am. Chem. Soc. 122 (2000) 6783.
[29] D.E.J. Lawes, S. Geftakis, G.E. Ball, J. Am. Chem. Soc. 127 (2005) 4134–4135.
[30] D.F. Shriver, M.A. Drezdzon, The Manipulation of Air-sensitive Compounds, Wiley-Interscience, New York, 1986.
[31] R.M. Bullock, C.E.L. Headford, K.M. Hennessy, S.E. Kegley, J.R. Norton, J. Am. Chem. Soc. 111 (1989) 3897.
[32] A. Chernega, J. Cook, M.L.H. Green, L. Labella, S.J. Simpson, J. Souter, A.H.H. Stephens, J. Chem. Soc., Dalton Trans. (1997) 3225.



Scheme 1.

cane and decaazacyclooctadecane as ligands by the template condensation. In this paper, we report the synthesis, characterization and properties of new copper(II) complexes of (12-methyl-12-nitro-4,7-dioxa-1,10-diazacyclotridecane), $[Cu(L_1)]^{2+}$, and (12,12-dicarboxyethyl-4,7-dioxa-1,10-diazacyclotridecane), $[Cu(L_2)]^{2+}$, with perchlorate, hexafluorophosphate and tetrachlorozincate as counter ions. The mononuclear copper(II) complexes were prepared from the template condensation of (1,8-diamino-3,6-dioxaoctane), formaldehyde with the carbon acids nitroalkane or diethylmalonate in the presence of a metal ion (Scheme 1).

2. Experimental

2.1. Materials and measurements

Safety note. Perchlorate salts of transition metal complexes with organic ligands are often explosive and should be handled with caution. All chemicals and solvents used in the syntheses were of reagent grade and were used without further purification. For the spectroscopic measurements, water was distilled and organic solvents were purified according to the literature method [29]. Electronic absorption spectra were obtained with a Shimadzu UV–Vis scanning spectrophotometer (Model 2101 PC), FTIR (KBr, cm^{-1}) spectra with a Shimadzu Varian 4300 spectrophotometer and conductance measurements with a Metrohm Herisau conductometer E 518. The elemental analysis (carbon, hydrogen and nitrogen) of the complexes was obtained from a Carlo ERBA Model EA 1108 analyser. Magnetic moments were calculated from magnetic susceptibility data obtained using a Johnson Matthey MK-1 magnetic susceptibility balance. Atomic Absorption Spectra (AAS) were recorded on a Perkin–Elmer 4100–1319 spectrophotometer. The electrochemical data were obtained in acetonitrile with 0.1 M $(n\text{-}Bu)_4NClO_4$ as the supporting electrolyte. The working electrode was a platinum disk, the auxiliary electrode was a coiled platinum wire and the reference electrode was $Ag/AgClO_4$ (0.1 M in CH_3CN), which showed +0.24 V versus SCE.

2.2. Preparation of (12-methyl-12-nitro-4, 7-dioxa-1, 10-diazacyclotridecane)copper(II) perchlorate, $[Cu(L_1)](ClO_4)_2$

1,8-Diamino-3,6-dioxaoctane (21.7 mmol, 3.22 g) was added to a solution of $Cu(NO_3)_2 \cdot 2.5H_2O$ (21.9 mmol, 5.19 g) in methanol (150 ml). The resulting blue solution was warmed to ca. 40 °C. Then nitroethane (21.9 mmol, 1.34 g), triethylamine (21.7 mmol, 2.2 g) and excess formaldehyde (12 ml, 36% aqueous, 1.57 mmol) were added. After heating for 60 min, the solution was diluted with a large volume of water, sorbed onto a column of SP-Sephadex C-25 (Na^+ form) resin (25×4 cm) and eluted with 0.2 mol dm^{-3} $NaClO_4$. Only one major purple band was observed and collected, reduced in volume, and the product crystallized by slow evaporation. The complex was isolated as a blue-purple solid, further crystallization was achieved, but with some contamination from the electrolyte. *Anal.* Calc. for $C_{10}H_{21}Cl_2CuN_3O_{12}$: Cu, 12.46; C, 23.56; H, 4.15; N, 8.24%. Found: Cu, 12.34; C, 23.42; H, 4.04; N, 8.30%.

2.3. Preparation of (12-methyl-12-nitro-4,7-dioxa-1, 10-diazacyclotridecane)copper(II) tetrachlorozincate, $[Cu(L_1)][ZnCl_4]$

The perchlorate salt, $[Cu(L_1)](ClO_4)_2$, was dissolved in a small volume of water and an excess of zinc chloride was added, followed by acetone until the solution became turbid. The blue-purple product was collected after 24 h, washed with ethanol, and then recrystallized from hot methanol–propane-2-ol. *Anal.* Calc. for $C_{10}H_{21}Cl_4CuN_3O_4Zn$: Cu, 12.24; Zn, 12.8; C, 23.13; H, 4.05; N, 8.10%. Found: Cu, 12.09; Zn, 12.68; C, 23.02; H, 3.89; N, 8.25%.

2.4. Preparation of (12-methyl-12-nitro-4,7-dioxa-1, 10-diazacyclotridecane)copper(II) hexafluorophosphate, $[Cu(L_1)](PF_6)_2$

To an acetonitrile (50 ml) suspension of $[Cu(L_1)](ClO_4)_2$ (0.5 g) was added excess NH_4PF_6. $[Cu(L_1)](ClO_4)_2$ went into the solution, and white precipitates

of NH_4ClO_4 were formed. NH_4ClO_4 was filtered off, and the filtrate was concentrated to 25 ml. Water (25 ml) was added to the solution, and the mixture was kept in a refrigerator. A yellow Cu(II) complex was prepared, filtered, washed with a 6:1 mixture of water and acetonitrile, and dried in vacuum. *Anal.* Calc. for $CuC_{10}H_{21}N_3O_4P_2F_{12}$: Cu, 10.58; C, 19.99; H, 3.52; N, 6.99. Found: Cu, 10.41; C, 19.76; H, 3.41; N, 7.12%.

2.5. Preparation of (12,12-dicarboxyethyl-4,7-dioxa-1,10-diazacyclotridecane) copper(II) perchlorate, $[Cu(L_2)](ClO_4)_2$

Tetradentate 1,8-diamino-3,6-dioxaoctane (21.7 mmol, 3.22 g) was added to $Cu(NO_3)_2 \cdot 2.5H_2O$ (21.7 mmol, 5.19 g) in methanol (200 ml). The resulting blue solution was warmed, then diethylmalonate (21.7 mmol, 3.2 g), triethylamine (21.7 mmol, 3 ml) and formaldehyde (13.1 mol, 37% aq, 10 ml) were added. After heating for a further 2 h, the solution was left at room temperature overnight. The solution was diluted with water, sorbed onto SP Sephadex C-25 resin (25×4 cm column) and eluted with 0.25 M $NaClO_4$ adjusted to pH $\sim$ 3. Three significant blue bands were collected. The first failed to crystallize readily, proved to be acid-sensitive and hence non-cyclic (L_3), and was discarded. The third band on concentration and standing gave a blue powder. Rapid and essentially complete loss of colour of a solution of this material on acid addition is indicative of a non-cyclic product; the diester macrocycle does not decolourize readily in aqueous acid. Spectroscopy (IR and UV–Vis) indicated a similarity to the precursor, and the micro-analysis indicated a C:N ratio of 7:2, although an acceptable fit for all elements to presumed structures was not forthcoming. Clearly, this material does not arise from a condensate involving diethylmalonate, and complete identification was not pursued. The second band, on concentration, gave blue-purple solids, which were collected, washed with alcohol and ether, and air-dried to give the diester product. *Anal.* Calc. for $C_{15}H_{28}Cl_2CuN_2O_{14}$: Cu, 10.68; C, 30.28; H, 4.74; N, 4.71%. Found: Cu, 10.52; C, 30.08; H, 4.66; N, 4.89%.

2.6. Preparation of (12,12-dicarboxyethyl-4,7-dioxa-1,10-diazacyclotridecane) copper(II) tetrachlorozincate, $[Cu(L_2)][ZnCl_4]$

The perchlorate salt, $[Cu(L_2)](ClO_4)_2$, was dissolved in a small volume of water and an excess of zinc chloride was added, followed by acetone until the solution became turbid. The blue product was collected after 24 h, washed with ethanol, and then recrystallized from hot methanol-propane-2-ol. *Anal.* Calc. for $C_{15}H_{28}Cl_4CuN_2O_6Zn$; Cu, 10.53; Zn, 10.84; C, 29.86; H, 4.68; N, 4.64%. Found: Cu, 10.45; Zn, 10.68; C, 29.69; H, 4.50; N, 4.78%.

2.7. Preparation of (12,12-dicarboxyethyl-4,7-dioxa-1,10-diazacyclotridecane) copper(II) hexafluorophosphate, $[Cu(L_2)](PF_6)_2$

A solution of 3.1 mmol NH_4PF_6 in 5 ml of H_2O was added to a solution of 1.2 mmol $[Cu(L_2)](ClO_4)_2$ in 10 ml of H_2O. The blue-purple product precipitate was filtered, washed with H_2O, and dried in air. *Anal.* Calc. for $CuC_{15}H_{28}N_2O_6P_2F_{12}$: Cu, 9.26; C, 26.27; H, 4.11; N, 4.08. Found: Cu, 9.11; C, 26.08; H, 3.95; N, 4.23%.

3. Results and discussion

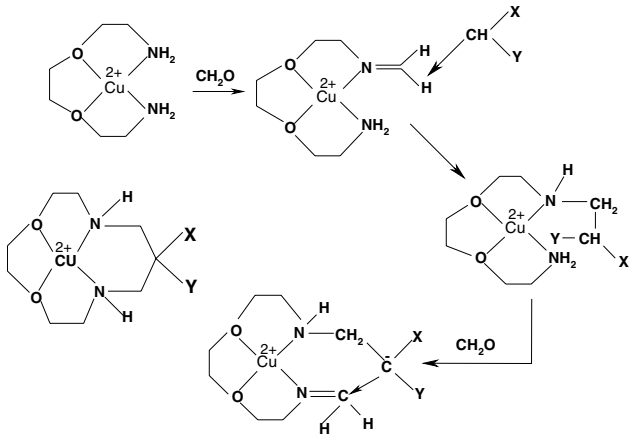
Reaction of copper(II) nitrate, 1,8-diamino-3,6-dioxaoctane, formaldehyde and nitroethane proceeds readily in warm methanol containing triethylamine as a non-coordinating base, with the product macrocycle 12-methyl-12-nitro-4,7-dioxa-1,10-diazacyclotridecane (L_1) actually crystallizing as the copper(II) complex during the reaction without any extensive attempts to refine the conditions, and yields of the isolated solid of 65% have been obtained routinely. Chromatography of a reaction mixture on SP-Sephadex C-25 cation exchange resin indicate that $[Cu(L_1)]^{2+}$ accounts for >84% of copper in the product mixture. The IR spectra of the complexes (Table 1) show a single absorption around 3230 cm^{-1}, which is attributed to ν_{N-H} of the coordinated secondary amines. A much higher ν_{N-H} value (for $[Cu(L_1)](ClO_4)_2$), than that of (6-methyl-6-nitro-1,4,8,

Table 1
Spectral and conductance data for 13-membered diaaza dioxa macrocyclic copper (II) complexes at 25 °C in water unless otherwise specified

Complex	IR (KBr, cm^{-1})				Electronic spectra λ_{max} (cm^{-1} (ε, $m^{-1}cm^{-1}$))	Λ_M ($\Omega^{-1}cm^{-2}M^{-1}$)	μ_B
	ν_{N-H}	$\nu_{s(NO_2)}$	$\nu_{a(NO_2)}$	ν_{ester}			
$[Cu(L_1)](ClO_4)_2$	3230	1355	1555		17301(105), 38168(8100)	245	1.70
$[Cu(L_1)](PF_6)_2$	3231	1357	1556		17450(109), 38356(8150)	246	1.71
$[Cu(L_1)](ZnCl_4)_2$	3232	1359	1555		17560(116), 38259(8210)	249	1.69
$[Cu(L_2)](ClO_4)_2$	3235			1731	17452(110), 37175(7520)	248	1.72
$[Cu(L_2)](PF_6)_2$	3236			1733	17480(113), 37190(7560)	246	1.71
$[Cu(L_2)](ZnCl_4)_2$	3235			1730	17468(118), 37186(7657)	245	1.70

11-tertraazacyclotetradecane)copper(II) perchlorate, (12-methyl-12-nitro-1,4,7,10-tetraazacyclotridecane) copper(II) perchlorate and (10-methyl-10-nitro-1,4,8,12-tetraazacyclopentadecane)copper(II) perchlorate indicates that the Cu–N interaction in the 13-membered diazadioxa is much stronger than in 13-membered tetraaza complexes [16–24]. The products exhibit a characteristic IR vibration for the nitro group, with v_{asym} (NO_2) at 1555 cm^{-1} and v_{sym} (NO_2) at 1355 cm^{-1}. Voltammetry in water defined a Cu(II)–(I) couple at −0.73 V (versus Ag/AgCl) and a multielectron irreversible nitro group reduction at −0.92 V. The product is also extremely resistant to dissociation in aqueous acid. Spectroscopic and electrochemical properties are similar to those reported for other well-characterized analogues [16–24]. The molar conductance values of 245 $\Omega^{-1}\,M^{-1}\,cm^{-2}$, measured in water, correspond to 1:2 electrolytes. The magnetic moments (1.69–1.72 μ_B) of the copper(II) complexes measured in the solid state correspond to a square-planar coordination geometry of the complexes. The electronic spectra (Table 1) of the copper(II) complexes are comparable to those of square-planar copper(II) complexes with other macrocycles, indicating that the 13-membered dioxadiaza ligands of this study do not differ significantly from the tetraaza ligands with respect to the ligand field strength [16–24]. Evidently, the reaction, via Schemes 1 and 2, proceeds to the essential exclusion of other reactions, the formation of the new five-membered ring being favored entropically. We are currently pursuing this type of reaction with a range of nitroalkanes and amine complexes, as well as looking at complexes of the pendant amine ligands resulting from nitro group reduction. It is clear that the experimental method represents a facile and probably general route to a new range of macromonocyclic ligands.

When the identical reaction to that described above was performed with diethylmalonate as the carbon



Scheme 2.

acid, it was not possible to crystallize any product directly. Chromatography on SP-Sephadex C-25 resin indicated that several products were present. The major band, from which a blue solid was crystallized, did not contain a cyclic ligand, decomposing readily in aqueous acid. Spectroscopy and microanalysis best fit a simple structure such as L_3, rather than the required compound L_2. A complex of the latter compound was isolated in low yield from the second band, and despite attempts to vary the outcome by altering the reaction conditions, the result was always similar. The only macrocyclic complex isolated, which amounted to less than 15% of the total copper and was crystallized in no better than 3% yield, proved to contain the macrocycle L_2. The IR spectrum showed a strong band at 1731 cm^{-1} characteristic of an ester. The complex was stable in aqueous acid, indicative of a macrocyclic complex. Voltammetry yielded a well defined reversible copper(II)–(I) couple at a potential of −0.84 V, with an irreversible wave at −1.36 V associated with electron addition to the ester substituents and in a similar position to waves assigned to this process in several macrocyclic complexes with ester substituents [6–15]. The likely reaction of the putative monoimine intermediate (product of the first step in Scheme 1) with hydroxide ion to ultimately form L_3, rather than reaction with the $(EtOOC)_2CH^-$ nucleophile, is not unreasonable since there was no attempt to exclude water form the reaction mixture. The pK_a of diethylmalonate is about 5 units higher than that of nitroethane, strictly limiting the concentration of the anion in the former case. Possibly in stringently anhydrous conditions, reactions involving carbon acids with higher pK_a values may prove more successful. We are pursuing this prospect. Evidently, nitroalkane carbon acids are for more successful reactants than diester alkenes carbon acids under the conditions described. All efforts to obtain the free ligands from the complexes by treating the complexes with excess NaCN, H_2S gas, or strong acid were unsuccessful.

4. Conclusions

Square-planar copper(II) complexes of 13-membered dioxa diaza macrocyclic ligands (12-methyl-12-nitro-4,7-dioxa-1,10-diazacyclotridecane), $[Cu(L_1)]^{2+}$, and (12,-12-dicarboxyethyl-4,7-dioxa-1,10-diazacyclotridecane), $[Cu(L_2)]^{2+}$, with perchlorate, hexafluorophosphate and tetrachlorozincate as counter ions have been prepared by the one-pot template reactions of formaldehyde, 1,8-diamino-3,6-dioxaoctane, with the carbon acids nitroalkane or diethylmalonate in the presence of the copper(II) ion. The spectra of the complexes show that the two nitrogen and two oxygen atoms are coordinated to the copper(II) ion.

References

[1] J.B. Harrowfield, A.J. Herbit, P.A. Lay, A.M. Sargeson, A.M. Bond, J. Am. Chem. Soc. 105 (1983) 5503.

[2] (a) S.G. Kang, M.S. Kim, K. Ryu, Polyhedron 15 (1996) 1835;
(b) B. Korybut-Daszkiewicz, J. Coord. Chem. 19 (1988) 101;
(c) R.W. Hay, M.P. Pujari, B. Korybut-Dasz-Kiewicz, G. Ferguson, B. Ruhl, J. Chem. Soc., Dalton Trans. (1989) 85;
(d) B. Korybut-Daszkiewicz, J. Chem. Soc., Dalton Trans. (1992) 1673.

[3] M. Rossignoli, P.V. Bernhardt, G.A. Lawrance, M. Maeder, Aust. J. Chem. 50 (1997) 529, and references therein.

[4] (a) I. Murase, I. Ueda, N. Marubayashi, S. Kida, N. . Matsumoto, M. Kudo, M. Toyohara, K. Hiate, M. Mikuriya, J. Chem. Soc., Dalton Trans. (1990) 2763;
(b) E. Asato, S. Kida, I. Murase, Inorg. Chem. 61 (1989) 2666.

[5] K.P. Wainwright, Coord. Chem. Rev. 166 (1997) 35, and references therein.

[6] G.A. Lawrence, M.A. O'Leary, Polyherdon 6 (1987) 1291.

[7] M.P. Suh, W. Shin, D. Kim, S. Kim, Inorg. Chem. 23 (1984) 618.

[8] M.P. Suh, D. Kim, S. Kim, Inorg. Chem. 24 (1985) 3712.

[9] M.P. Suh, W. Shin, H. Kim, C.H. Koo, Inorg. Chem. 26 (1987) 1846.

[10] M.P. Suh, S.-G. Kang, Inorg. Chem. 27 (1988) 2544.

[11] M.P. Suh, W. Shin, S.-G. Kang, M.S. Lah, T.-M. Chung, Inorg. Chem. 28 (1989) 1602.

[12] S.-K. Jung, S.-G. Kang, M.P. Suh, Bull. Korean Chem. Soc. 10 (1989) 362.

[13] M.P. Suh, S.-G. Kang, V.L. Goedken, S.-H. Park, Inorg. Chem. 30 (1991) 365.

[14] M.P. Suh, D. Kim, Inorg. Chem. 24 (1985) 3712.

[15] M.P. Suh, W. Shin, H. Kim, C.H. Koo, Inorg. Chem. 26 (1987) 1846.

[16] G. Pattrick, M.P. Ngwenya, S.M. Dobson, R.D. Hancock, J. Chem. Soc., Dalton Trans. (1991) 1295.

[17] (a) R.D. Hancock, Acc. Chem. Res. 23 (1990) 253;
(b) R.D. Hancock, S.M. Dobson, A. Evers, P.W. Wade, M.P. Ngwenya, J.C.A. Boeyens, K.P. Wainwright, J. Am. Chem. Soc. 110 (1988) 2788;
(c) R.D. Hancock, M.P. Ngwenya, P.W. Wade, J.C.A. Boeyens, S.M. Dobson, Inorg. Chim. Acta 164 (1989) 73.

[18] (a) P. Comba, N.F. Curtis, G.A. Lawrence, M.A. O'Leary, B.W. Skelton, A.H. White, J. Chem. Soc., Dalton Trans. (1988) 2145;
(b) P. Comba, N.F. Curtis, G.A. Lawrence, A.M. Sargeson, B.W. Skelton, A.H. White, Inorg. Chem. 25 (1986) 4260;
(c) P. Comba, N.F. Curtis, G.A. Lawrence, M.A. O'Leary, B.W. Skelton, A.H. White, J. Chem. Soc., Dalton Trans. (1988) 497.

[19] (a) P.V. Bernhart, G.A. Lawrence, T.W. Hambley, J. Chem. Soc., Dalton Trans. (1990) 235;
(b) P.V. Bernhart, G.A. Lawrence, T.W. Hambley, J. Chem. Soc., Dalton Trans. (1989) 1059.

[20] T.W. Hambley, G.A. Lawrence, M. Maeder, E.N. Wikes, J. Chem. Soc., Dalton Trans. (1992) 1283.

[21] N.F. Curtis, in: G.A. Melson (Ed.), Coordination Chemistry of Macrocyclic Complexes, Plenum Press, New York, 1982, pp. 219–344.

[22] P.V. Bernhart, G.A. Lawrence, Coord. Chem. Rev. 93 (1990) 297.

[23] R.D. Hancock, A.E. Martell, Chem. Rev. 89 (1989) 1875.

[24] N.F. Curtis, Coord. Chem. Rev. 3 (1963) 3.

[25] W.P. Jencks, J. Regenstein, in: H.A. Sobar (Ed.), Ionization Constants of Acids and Bases, 2nd ed., Handbook of Biochemistry, Chemical Rubber, Cleveland, 1970.

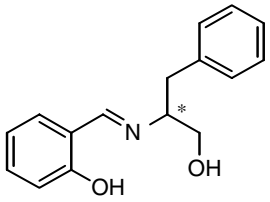
[26] (a) M. Salavati-Niasari, M. Rezai Adaryani, Polyhedron 23 (2004) 1325;
(b) M. Salavati-Niasari, Chem. Lett. 34 (2005) 244;
(c) M. Salavati-Niasari, J. Mol. Catal. A 229 (2005) 159;
(d) M. Salavati-Niasari, Inorg. Chem. Commun. 8 (2005) 174.

[27] M. Salavati-Niasari, H. Najafian, Polyhedron 22 (2003) 263.

[28] M. Salavati-Niasari, Inorg. Chem. Commun. 7 (2004) 698.

[29] D.D. Perrin, W.L.F. Armarego, D.R. Perrin, Purification of Laboratory Chemicals, 2nd ed., Pergamon Press, Headington Hill Hall, Oxford, London, England, 1980.

H_2L:



2. Experimental

2.1. General methods

Microanalytical (C, H, N) data were obtained with a FLASH EA 1112 Series CHNS Analyzer. A SHIMADZU 3101-PC UV/Vis/NIR spectrophotometer was used to record the electronic spectra. Infrared spectra were recorded on KBr pellets with a JASCO-5300 FT-IR spectrophotometer. ^{1}H spectra of the ligand in $CDCl_3$ solution were recorded on a Bruker 400 MHz spectrometer using $Si(CH_3)_4$ as an internal standard. The room temperature solid-state magnetic susceptibility was measured by using a Sherwood Scientific magnetic susceptibility balance. A CH-Instruments Model 620A electrochemical analyzer was used for cyclic voltammetric experiment on an acetonitrile solution of the complex containing tetrabutylammonium perchlorate (TBAP) as the supporting electrolyte. The three-electrode measurement was carried out at 298 K under a dinitrogen atmosphere with a glassy carbon disc working electrode, a platinum wire auxiliary electrode and a saturated calomel reference electrode (SCE). The CD spectra were measured with a JASCO J-810 spectropolarimeter. EPR spectra were recorded on a JEOL JES-FA200 spectrometer.

2.2. Materials

L-Phenylalaninol [(*S*)-(−)-2-amino-3-phenyl-1-propanol] and salicylaldehyde were purchased from Lancaster and used as received. TBAP, used as the supporting electrolyte in electrochemical measurement, was purchased from Acros, India. Solvents were purified by standard methods. All other chemicals were of analytical grade and were used without further purification.

2.3. Synthesis of ligand H_2L

L-Phenylalaninol [(*S*)-(−)-2-amino-3-phenyl-1-propanol] (0.151g, 1 mmol) and salicylaldehyde (0.122 g, 1 mmol) were stirred together in methanol (15 mL) for 1 h at room temperature. The resulting yellow solution was filtered and the filtrate was kept for 2 days in an open beaker for slow evaporation. The yellow precipitate of H_2L thus obtained was washed with hexane and dried at room temperature. Yield: 0.196 g (77%). Elemental *Anal.* Calc. for $C_{16}H_{17}NO_2$: C, 75.27; H, 6.71; N, 5.49. Found: C, 74.98; H, 6.67; N, 5.65%. IR (KBr, cm^{-1}): 3246.49 (ν_{O-H}), 1631.93 ($\nu_{C=N}$). ^{1}H NMR (400 MHz, $CDCl_3$): δ 2.94 (m, 2H, CH_2–Ph), 3.54 (m, 1H, CH), 3.814 (m, 2H, CH_2–OH), 6.838–7.340 (m, 9H, Ar), 8.1 (s, 1H, HC=N). UV/Vis [CH_3CN; λ_{max}/nm (ε)]: 315 (4689), 255 (13 647), 225 (16 640).

2.4. Synthesis of complex $\mathbf{1}\cdot 2DMF$

To a methanolic solution (15 mL) of ligand H_2L (0.255 g, 1 mmol) was added $Mn(CH_3COO)_2\cdot 4H_2O$ (0.245 g, 1 mmol). The mixture was allowed to stir at room temperature in air for 3 h. The resultant dark brown solution was evaporated to dryness using a rotavapor and a vacuum pump. The solid, thus obtained, was dissolved in dichloromethane, washed twice with water, once with brine solution (using a separating funnel) and dried over anhydrous Na_2SO_4. The resulting dark brown solution, on slow evaporation, gave a brown microcrystalline solid of $[Mn^{IV}L_2]$ (**1**). Yield: 0.381g (68%). This microcrystalline product was recrystallized from DMF–CH_3CN (1:1) to yield single crystals of $\mathbf{1}\cdot 2$DMF, suitable for crystal structure determination. Elemental *Anal.* Calc. for $C_{38}H_{44}N_4O_6Mn$ ($\mathbf{1}\cdot 2$DMF): C, 64.49; H, 6.27; N, 7.92. Found: C, 64.17; H, 6.21; N, 8.01%. IR (KBr, cm^{-1}): 1616.49 ($\nu_{C=N}$). UV/Vis [CH_3CN; λ_{max}/nm (ε)]: 540 (250), 404 (8252), 344 (sh), 294 (sh).

2.5. X-ray crystallography

Data were measured at 298(2) K on a Bruker SMART APEX CCD area detector system [λ(Mo Kα) = 0.71073 Å], graphite monochromator, 1315 frames were recorded with an ω scan width of 0.3°, each for 8 s, crystal-detector distance 60 mm, collimator 0.5 mm. Data reduction was by SAINTPLUS [10], the structure solution used SHELXS-97 [11] and was refined using SHELXL-97 [12]. All non-hydrogen atoms were refined anisotropically. Hydrogen atoms were introduced in calculated positions and included in the refinement riding on their respective parent atoms. Additional details of the data collection parameters and refinement are collected in Table 1. The absolute configuration for the compound molecule was successfully determined by refining the Flack parameter (0.03(3)) [13]. The final Fourier difference synthesis showed minimum and maximum peaks of −0.434 and +0.690 e $Å^{-3}$.

Table 1
Crystallographic data for **1** · 2DMF

Chemical formula	$C_{32}H_{30}MnN_2O_4 \cdot 2DMF$
Formula weight	707.71
Crystal system	orthorhombic
Space group	$P2_12_12_1$
λ (Å)	0.71073
a (Å)	9.8290(11)
b (Å)	10.2640(12)
c (Å)	36.308(4)
V (Å^3)	3663.0(7)
Z	4
μ (mm^{-1})	0.410
ρ_{calc} (g cm^{-3})	1.283
T (°C)	25
Scan type	ω
Number of independent reflections (R_{int})	22714 (0.0582)
Number of observed reflections [$F > 4\sigma(F)$]	5198
Number of parameters	446
S_{gof} on F^2	1.043
R_1[a] [$F > 4\sigma(F)$]	0.0668
wR_2[b]	0.1453

[a] $R_1 = \sum||F_o| - |F_c||/\sum|F_o|$.
[b] $wR_2 = [\sum\{(F_o^2 - F_c^2)^2\}/\sum\{w(F_o^2)^2\}]^{1/2}$.

3. Results and discussion

3.1. Synthesis

The ligand H_2L, obtained as a yellow solid by Schiff base condensation (Scheme 1), was reacted with manganese(II) acetate tetrahydrate at room temperature in methanol to afford the mononuclear complex [$Mn^{IV}L_2$] (**1**), in moderate yield. Atmospheric oxygen is the possible oxidizing agent here, which oxidizes the Mn(II) center directly to Mn(IV). This rather easy oxidation is assisted by the fact that the tridentate ligand (L^{2-}), containing phenolate and alkoxide oxygens, effectively stabilizes the +4 oxidation state of manganese. Stabilization of Mn(IV) species by phenolate and alkoxide oxygens is well established [4a,8a].

3.2. Description of the structure

Single crystals of **1** · 2DMF, suitable for X-ray crystallography, were grown by slow evaporation of a 1:1 mixture of dimethyl formamide (DMF) and acetonitrile solution of the compound. Compound **1** · 2DMF crystallizes in the non-centrosymmetric orthorhombic space group $P2_12_12_1$. The asymmetric unit contains one molecule of the complex and two molecules of DMF. The ORTEP drawing of the complex with the atom labelling scheme is shown in Fig. 1. Selected bond lengths and bond angles are listed in Table 2. The geometry around the metal is six coordinated with an N_2O_4 core. The chiral H_2L ligand is dianionic in the complex and acts as a meridional ONO donor using imine nitrogen, phenolate and alkoxide oxygen atoms to bind the metal. The chiral centers are shown by asterisk marks in Fig. 1. The resulting MnN_2O_4 coordination sphere has a nearly planar O_4 equator with respect to which the two N atoms are located in virtually ideal trans positions. The angles at the metal center show deviations from the ideal octahedral values of 90° and 180°, resulting in a distorted octahedral geometry around Mn. The distortion from octahedral geometry is reflected in the acute bite angles between the alkoxide O atom and the imine N atom of the $[ONO]^{2-}$ ligand: [O2–Mn–N1, 82.79(13)° and O4–

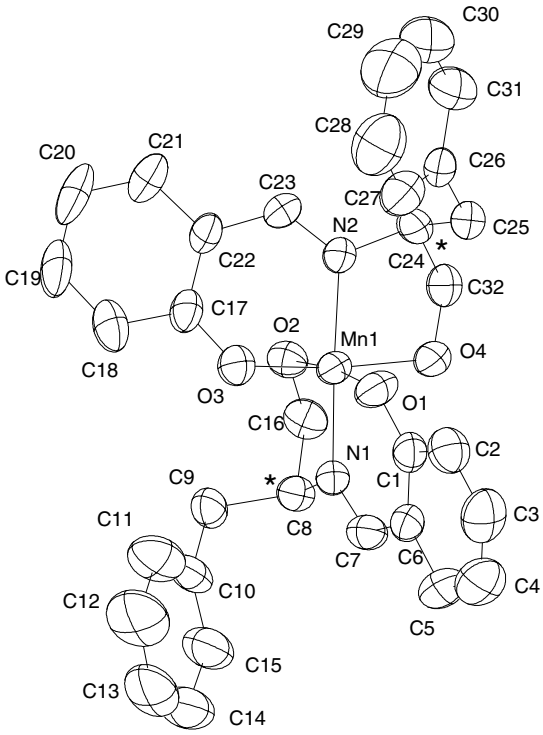
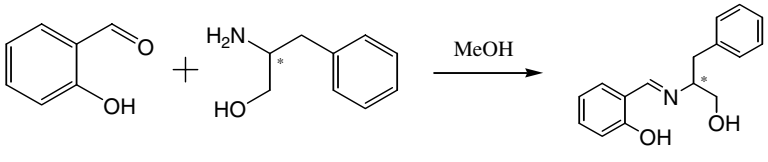


Fig. 1. Thermal ellipsoid plot for complex **1**. Hydrogen atoms are not shown for clarity. The asterisk marks indicate chiral centers.



H_2L

Scheme 1.

Table 2
Selected bond lengths (Å) and bond angles (°) for **1**

Bond length (Å)	
Mn(1)–O(1)	1.906(3)
Mn(1)–O(2)	1.834(3)
Mn(1)–N(1)	1.973(3)
Mn(1)–O(3)	1.915(3)
Mn(1)–O(4)	1.854(3)
Mn(1)–N(2)	1.975(3)
N(1)–C(7)	1.297(5)
N(2)–C(23)	1.275(5)
O(1)–C(1)	1.319(5)
O(3)–C(17)	1.290(5)
Bond angle (°)	
O(2)–Mn(1)–O(1)	172.48(13)
O(4)–Mn(1)–O(3)	172.27(14)
O(2)–Mn(1)–O(4)	93.50(14)
O(4)–Mn(1)–O(1)	90.49(14)
O(2)–Mn(1)–O(3)	90.70(14)
O(1)–Mn(1)–O(3)	86.09(14)
O(2)–Mn(1)–N(1)	82.79(13)
O(4)–Mn(1)–N(1)	90.45(13)
O(1)–Mn(1)–N(1)	90.81(13)
O(3)–Mn(1)–N(1)	96.52(13)
O(2)–Mn(1)–N(2)	89.58(14)
O(4)–Mn(1)–N(2)	83.89(13)
O(1)–Mn(1)–N(2)	97.19(14)
O(3)–Mn(1)–N(2)	89.66(13)
N(1)–Mn(1)–N(2)	170.22(15)

Mn–N2, 83.89(13)°]. This deviation can be attributed mainly to the rigidity of the Schiff base ligand. Similar distortions from ideal octahedral geometry have been reported by Chakravorty et al. [8h] in Mn(IV) complexes of tridentate ONO donor Schiff base ligands. Thus, the overall geometry around the manganese ion is best described as a distorted meridional octahedron. The average $Mn–O_{phenolate}$, $Mn–O_{alkoxide}$ and Mn–N bond distances of 1.9105(3), 1.884(3) and 1.974(3) Å, respectively, fall in the range of those reported for structurally characterized mononuclear manganese(IV) complexes [8b,8h,8l].

In the crystal structure, there are intermolecular C–H···O hydrogen bonding interactions among $[MnL_2]$ (**1**) complexes resulting in a supramolecular hydrogen bonding network. This consists of hydrogen bonded chain-like arrangements via C(13)–H(13)···O(2) bonds (relevant H-bonding parameters: 0.93, 2.33, 3.195(7), 155.3), that are further interlinked via C(9)–H(9B)···O(4) bonds (relevant H-bonding parameters: 0.97, 2.57, 3.350(5), 137.0) into an intricate hydrogen bonded framework as shown in Fig. 2. Along the chain, each complex MnL_2 is additionally hydrogen bonded to a DMF solvent molecule (not shown in Fig. 2 for clarity). Interestingly, the packing of the chiral complexes in the crystal results in the formation of helical channels, when viewed down the crystallographic *a*-axis (Fig. 3). DMF solvent molecules are accommodated in the alternate channels. We believe that the formation of such helical channels is induced by the chirality of the complex $[MnL_2]$.

3.3. IR spectroscopy

The IR peak due to *ν*(OH), which occurs as a broad feature around 3260 cm^{-1} for the free ligand, is missing in the complex indicating that on complexation the phenol character of the ligand has been lost. The C=N peak of the ligand at 1632 cm^{-1} is shifted to 1616 cm^{-1} in the complex indicating complexation of the imine nitrogen with the metal center.

3.4. Electrochemistry

The cyclic voltammogram of **1** · 2DMF in 0.1 M TBAP/CH_3CN (glassy carbon working electrode, 298 K) shows two reduction responses as shown in Fig. 4. A nearly reversible reduction occurs at $E_{1/2} = -0.47$ V versus SCE ($\Delta E = 0.11$ V), which can be assigned to the $[Mn^{IV}L_2] + e^- \leftrightarrow [Mn^{III}L_2]^{1-}$ couple. Another quasi-reversible reduction is observed at $E_{1/2} = -0.89$ V,

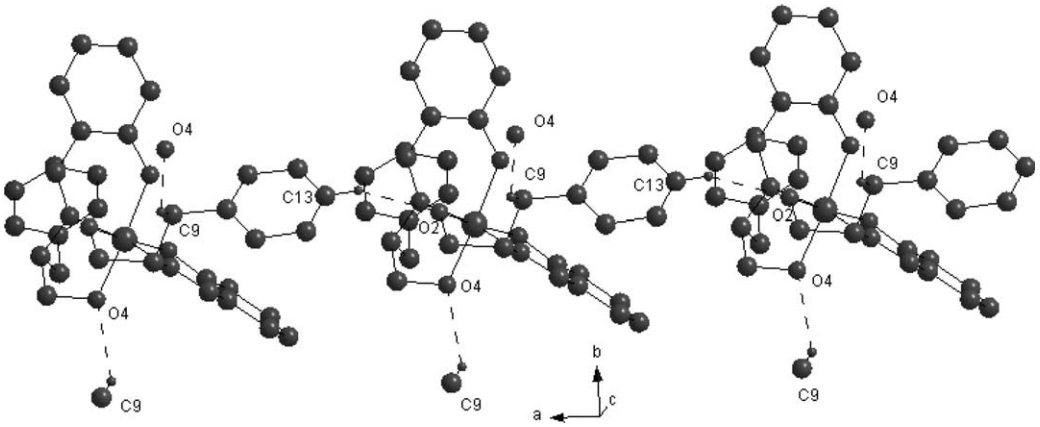


Fig. 2. Inter molecular association via C–H···O type hydrogen bonds into a chain-like structure and its mode of linking to adjacent chains.

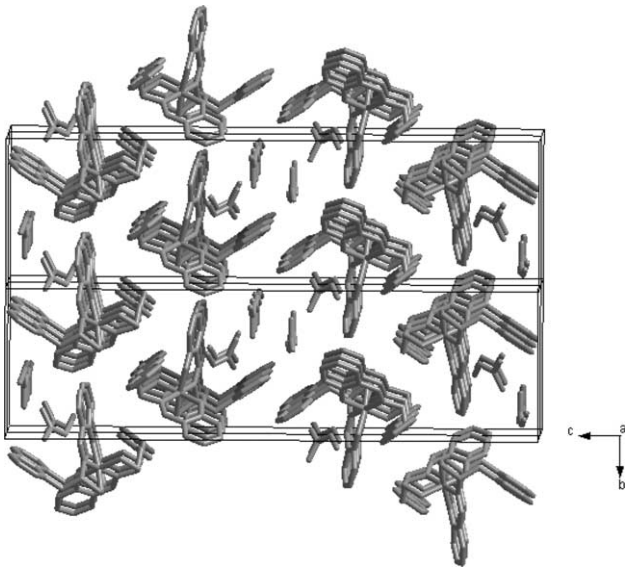


Fig. 3. Packing diagram of **1** · 2DMF showing helical channels when viewed down the crystallographic *a*-axis. The channels are alternatively filled by solvent DMF molecules.

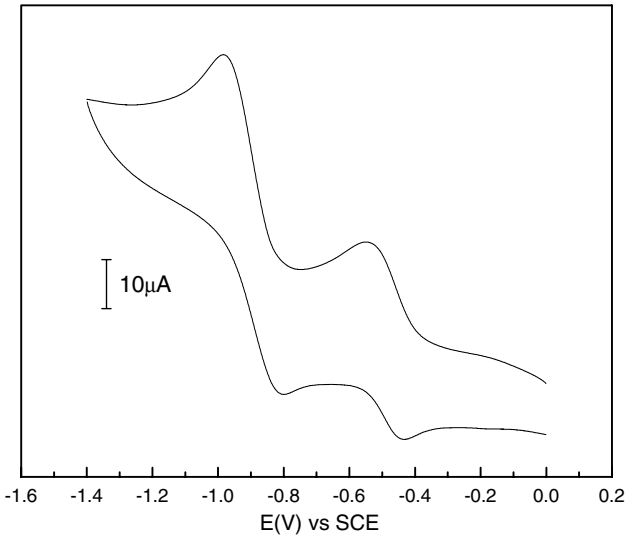


Fig. 4. Cyclic volotammogram of $\sim 10^{-3}$ M acetonitrile solution of **1** · 2DMF at 298 K (0.1 M TBAP, scan rate 100 mV s^{-1}, glassy carbon electrode).

corresponding to the Mn^{III}/Mn^{II} reduction ($\Delta E = 0.18$ V). The rather negative reduction wave at −0.47 V for the Mn^{IV}/Mn^{III} couple indicates a relatively stable Mn(IV) complex which in turn justifies the easy formation of **1** · 2DMF from H_2L and Mn(II) salt in the presence of air at room temperature.

Ligands having alkoxide groups are reported to be efficient in stabilizing the higher oxidation state Mn(IV), thus causing a negative reduction potential for the Mn^{IV}/Mn^{III} couple. For example, Pecoraro et al. [8l] reported quasi-reversible one-electron reductions at $E_{pc} = -0.32$ and −0.46 V (versus Ag/AgCl) in Mn(IV) complexes such as $Mn(SALAHP)_2$ and $Mn(SALA-DHP)_2$, respectively, which are prepared from hydroxyl rich Schiff base ligands.

3.5. Electronic and circular dichroism spectra

The electronic spectrum of the ligand H_2L in acetonitrile is characterized by three intraligand charge transfer transitions, judging from their molar extinction coefficient values [225 nm ($\varepsilon = 16640$ $cm^{-1}M^{-1}$), 255 nm ($\varepsilon = 13647$ $cm^{-1}M^{-1}$), 315 nm ($\varepsilon = 4689$ $cm^{-1}M^{-1}$)] as shown in Fig. 5. The UV visible spectrum of the manganese complex **1** · 2DMF in acetonitrile is dominated by an absorption band at 404 nm ($\varepsilon = 8252$ cm^{-1} M^{-1}) and two shoulders at ∼344 and ∼294 nm (possibly charge transfers in origin). Also a broad absorption band is observed in the visible region around 550 nm, which can be associated with d–d transitions, judging from its intensity.

The circular dichroism spectrum of the ligand H_2L shows two negative bands (ILCT) around 315 and 255 nm as shown in Fig. 5. These peaks correspond to the UV absorption peaks observed around 315 and 255 nm. The CD spectrum of the manganese complex **1** · 2DMF also shows three peaks, but at shifted positions (as negative cotton effects) corresponding to the UV (charge transfer) transitions at 404, 344 and 294 nm. Also the complex shows one broad CD band

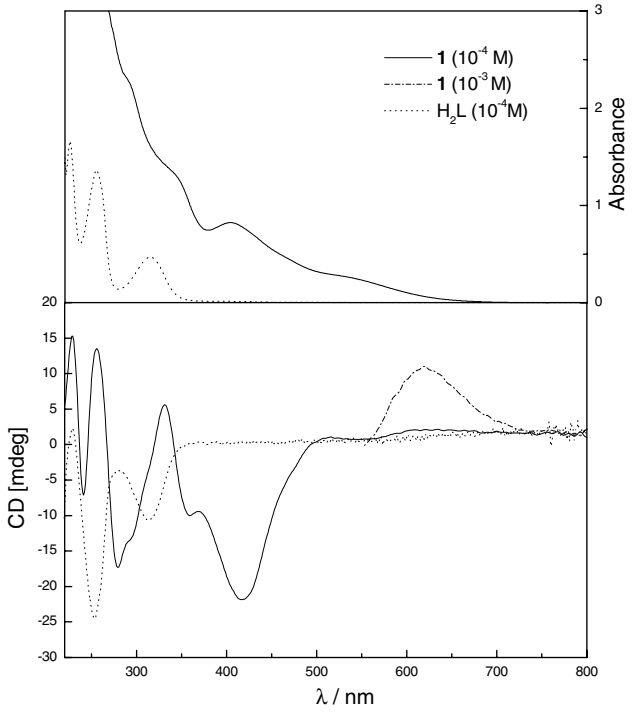


Fig. 5. Electronic (above) and circular dichroism (below) spectra of **1** · 2DMF and ligand H_2L in acetonitrile solution.

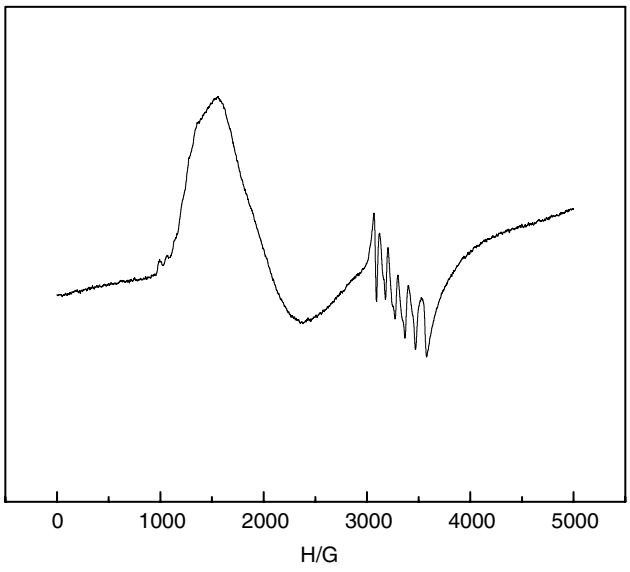


Fig. 6. X-band EPR spectrum of **1** · 2DMF in ethanol solution at liquid nitrogen temperature.

around 600 nm (at a relatively higher concentration, see Fig. 5), which can be assigned as d–d transitions.

3.6. EPR spectroscopy

The EPR measurement of **1** · 2DMF was done at the X-band frequency at liquid nitrogen temperature and the spectrum is shown in Fig. 6. As expected, the spectrum indicates a paramagnetic d^3 system. The EPR features of a d^3 species depend upon the axial (D) and rhombic (E) zero-field splitting parameters. In an axial field ($E/D = 0$), the spectrum is dependent on the magnitude of the zero-field splitting parameters. Two limiting cases are defined when the value of the axial field ($2D$) is either much larger than or much smaller than $h\nu$ (0.31 cm^{-1}). In the first case a strong signal at $g \sim 4$ and a weak signal at $g \sim 2$ are observed. Whereas in the second case a weak signal at $g \sim 4$ and a strong signal at $g \sim 2$ are found [14,8j].

The X-band EPR spectrum of the complex **1** · 2DMF in ethanol solution at liquid nitrogen temperature displays a strong absorption near $g \sim 4$ and a weak but resolved response at $g \sim 2$. This type of spectral profile is characteristic of a d^3 system in which $2D$ is much larger than the microwave frequency, [$2D \gg h\nu$]. The magnitude of the ^{55}Mn hyperfine coupling of 90 G is consistent with that of previous reports for the Mn(IV) complexes [8m,9]. The room temperature magnetic susceptibility of **1** · 2DMF in the solid state is 3.9 BM, which is close to the spin only value (3.87) for a high spin d^3 system. This experimental μ_{eff} value clearly indicates that the complex **1** · 2DMF is a Mn(IV) system, which is in complete agreement with X-ray and EPR results.

4. Conclusions

We have reported here the synthesis, crystal structure and properties of a new mononuclear manganese(IV) chiral complex. In the crystal, the complexes get interlinked into a supramolecular hydrogen bonded network. The chirality of the complex is established by circular dichroism (CD) studies. The complex exhibits two redox waves in the cyclic voltammogram corresponding to Mn^{IV}/Mn^{III} and Mn^{III}/Mn^{II} couples. The EPR spectral feature (an absorption near $g \sim 4$ and a weak but resolved response at $g \sim 2$) is consistent with a Mn(IV) complex.

5. Supplementary material

Crystallographic data for the structural analysis have been deposited with the Cambridge Crystallographic Data Centre, CCDC No. 262962 for compound **1** · 2DMF. Copies of this information may be obtained free of charge from the Director, CCDC, 12 Union Road, Cambridge CB2 1EZ, UK (fax: +44 1223 336 033; e-mail: deposit@ccdc.cam.ac.uk or www: http://www.ccdc.cam.ac.uk).

Acknowledgements

We acknowledge the Department of Science and Technology, Government of India, for financial support. X-ray crystallographic data were obtained from the National Single Crystal Diffractometer Facility (established by the Department of Science and Technology, New Delhi) at the School of Chemistry, University of Hyderabad. We are grateful to UGC, New Delhi, for infrastructure facility at the University of Hyderabad under a UPE grant. C.P.P thanks UGC, Government of India, for a fellowship.

References

[1] (a) V.L. Pecoraro (Ed.), Manganese Redox Enzymes, VCH, New York, 1992;
(b) V.K. Yachandra, V.J. DeRose, M.J. Latimer, I. Mukerji, K. Sauer, M.P. Klein, Science 260 (1993) 675;
(c) R. Manchanda, G.W. Brudvig, R.H. Crabtree, Coord. Chem. Rev. 144 (1995) 1;
(d) R.J. Debus, Biochim. Biophys. Acta 1102 (1992) 269;
(e) J. Cole, Y.K. Yachandra, R.D. Guiles, A.E. McDermott, R.D. Britt, S.L. Dexheimer, K. Sauer, M.P. Klein, Biochim. Biophys. Acta 890 (1987) 395;
(f) J.L. Zimmermann, A.W. Rutherford, Biochemistry 25 (1986) 395.
[2] O.R. Hansson, R. Aasa, T. Vanngard, Biophys. J. 51 (1987) 825.
[3] (a) A. Zouni, H.T. Witt, J. Kern, P. Fromme, N. Kraub, W. Saenger, P. Orth, Nature 409 (2001) 739;

(b) N. Kamiya, J.R. Shen, Proc. Natl. Acad. Sci. USA 100 (2003) 98;
(c) K.N. Ferreira, T.M. Iverson, K. Maghlaoui, J. Barber, S. Iwata, Science 303 (2004) 1831.
[4] (a) V.C. Quee-Smith, L. DelPizzo, S.H. Jureller, J.L. Kerschner, R. Hage, Inorg. Chem. 35 (1996) 6461;
(b) J.T. Groves, M.K. Stern, J. Am. Chem. Soc. 109 (1987) 3812;
(c) J.A. Smegal, C.L. Hill, J. Am. Chem. Soc. 105 (1983) 2920;
(d) J.A. Smegal, B.C. Schardt, C.L. Hill, J. Am. Chem. Soc. 105 (1983) 3510;
(e) J.A. Smegal, C.L. Hill, J. Am. Chem. Soc. 105 (1983) 3515.
[5] (a) E.N. Jacobsen, A. Pfaltz, H. Yamamoto (Eds.), Comprehensive Asymmetric Catalysis, Springer, New York, 1999;
(b) T. Katsuki, in: I. Ojima (Ed.), Catalytic Asymmetric Synthesis, VCH, New York, 2000.
[6] W. Adam, C. Mock-Knoblauch, C.R. Saha-Moller, M. Herderich, J. Am. Chem. Soc. 122 (2000) 9685.
[7] (a) A.V. Lakshmi, N.R. Sangeetha, S. Pal, Indian J. Chem. A 36 (1997) 844;
(b) S. Pal, J. Chem. Res. (S) (1995) 236;
(c) V. Manivannan, S. Dutta, P. Basu, A. Chakravorty, Inorg. Chem. 32 (1993) 769;
(d) S. Pal, P. Ghosh, A. Chakravorty, Inorg. Chem. 24 (1985) 3704;
(e) T. Matsushita, T. Shono, Polyhedron 2 (1983) 613;
(f) D.T. Richens, D.T. Sawyer, J. Am. Chem. Soc. 101 (1979) 3681;
(g) M. Koikawa, H. Okawa, S. Kida, J. Chem. Soc., Dalton Trans. (1988) 641;
(h) M. Fujiwara, T. Matsushita, T. Shono, Polyhedron 4 (1985) 1895;
(i) H. Okawa, M. Nakamura, S. Kida, Bull. Chem. Soc. Jpn. 55 (1982) 466;
(j) R.Y. Saleh, D.K. Straub, Inorg. Chem. 13 (1974) 3017.
[8] (a) T. Weyhermuller, T.K. Paine, E. Bothe, E. Bill, P. Chaudhuri, Inorg. Chim. Acta 337 (2002) 344;
(b) T.M. Rajendiran, J.W. Kampf, V.L. Pecoraro, Inorg. Chim. Acta 339 (2002) 497;
(c) P. Perez-Lourido, J. Romero, L. Rodriguez, J.A. Garcia-Vazquez, J. Castro, A. Sousa, J.R. Dilworth, O.R. Nascimento, Inorg. Chem. Commun. 5 (2002) 337;
(d) H. Asada, M. Ozeki, M. Fujiwara, T. Matsushita, Chem. Lett. (1999) 525;
(e) M. Mikuriya, D. Jie, Y. Kakuta, T. Tokii, Bull. Chem. Soc. Jpn. 66 (1993) 1132;
(f) R.O.C. Hart, S.G. Bott, J.L. Atwood, S.R. Cooper, J. Chem. Soc., Chem. Commun. (1992) 894;
(g) S.M. Saadeh, M.S. Lah, V.L. Pecoraro, Inorg. Chem. 30 (1991) 8;
(h) S. Dutta, P. Basu, A. Chakravorty, Inorg. Chem. 30 (1991) 4031;
(i) S.K. Chandra, S.B. Choudhury, D. Ray, A. Chakravorty, J. Chem. Soc., Chem. Commun. (1990) 474;
(j) S.K. Chandra, P. Basu, D. Ray, S. Pal, A. Chakravorty, Inorg. Chem. 29 (1990) 2423;
(k) P. Deplano, E.F. Trogu, F. Bigoli, M.A. Pellingheli, J. Chem. Soc., Dalton Trans. (1987) 2407;
(l) D.P. Kessissoglou, X. Li, W.M. Butler, V.L. Pecoraro, Inorg. Chem. 26 (1987) 2487;
(m) D.P. Kessissoglou, W.M. Butler, V.L. Pecoraro, J. Chem. Soc., Chem. Commun. (1986) 1253;
(n) P.S. Pavacik, J.C. Huffman, G. Christou, J. Chem. Soc., Chem. Commun. (1986) 43;
(o) M. Tirant, T.D. Smith, Inorg. Chim. Acta 121 (1986) 5;
(p) J.R. Hartman, B.M. Foxman, S.R. Cooper, Inorg. Chem. 23 (1984) 1381;
(q) D.H. Chin, D.T. Sawyer, W.P. Schaefer, C.J. Simmons, Inorg. Chem. 22 (1983) 752;
(r) M.J. Camenzind, F.J. Hollander, C.L. Hill, Inorg. Chem. 22 (1983) 3776;
(s) C.G. Howard, G.S. Girolami, G. Wilkinson, M. Thornton-Pett, M.B. Hursthouse, J. Chem. Soc., Chem. Commun. (1983) 1163;
(t) M.J. Camenzind, F.J. Hollande, C.L. Hill, Inorg. Chem. 21 (1982) 4301;
(u) K.L. Brown, R.M. Golding, P.C. Healy, K.J. Jessop, W.C. Tennant, Aust. J. Chem. 27 (1974) 2075.
[9] C.P. Pradeep, T. Htwe, P.S. Zacharias, S.K. Das, New J. Chem. 28 (2004) 735.
[10] Software for the CCD Detector System, Bruker Analytical X-ray Systems Inc., Madison, WI, 1998.
[11] G.M. Sheldrick, Program for Structure Solution, University of Göttingen, Göttingen, Germany, 1997.
[12] G.M. Sheldrick, Program for Crystal Structure Analysis, University of Göttingen, Göttingen, Germany, 1997.
[13] H.D. Flack, Acta Crystallogr., Sect A 39 (1983) 876.
[14] (a) E. Pederson, H. Toftlund, Inorg. Chem. 13 (1974) 1603;
(b) D.C. Bradley, R.G. Copperthwaite, S.A. Cotton, K.D. Sales, J.F. Gibson, J. Chem. Soc., Dalton Trans. (1973) 191;
(c) J.C. Hempel, L.O. Morgan, W.B. Lewis, Inorg. Chem. 9 (1970) 2064;
(d) L.S. Singer, J. Chem. Phys. 23 (1955) 379.

method of self-consistent field (SCF) [8]. Thus, the theoretically calculated cluster species reported as being As_2 [9,10], As_3 [11] and As_4 [10,12,13] and also their formation has been proved experimentally.

Subsequently, Bowen et al. [14] determined the electron affinities of several As_n^- ($n = 1–5$) clusters using negative ion photoelectron spectroscopy. The confirmation of the evidence of several other metals' negatively charged cluster species, other than arsenic, was achieved using the pulsed UV laser ablation technique [15].

Lately, electron level theoretical calculations based on DFT and the prediction of infrared and Raman spectra of fullerene-like arsenic cages have been reported [16]. The work of Baruah et al. [16] concluded that clusters of As_n [$n = 4, 8, 20, 28, 32, 36, 60$] would be unstable and would dissociate into As_4 units except for a suggested As_{20} cluster.

Recently, in our laboratory, we have successfully applied commercial MALDI-TOF mass spectrometric instrumentation (MALDI-TOF-MS) for the generation of tellurium, selenium, phosphorus, or sulfur clusters and many new compounds [17–20]. In this work, the possibilities of laser desorption ionization (LDI) and/or laser ablation as a promising approach towards the generation of As_n and As_nS_m clusters are studied.

2. Experimental

2.1. Chemicals and reagents

Elemental gray arsenic of 99.997% purity was purchased from Sigma Aldrich (Steinheim, Germany). Elemental sulfur of 99.98% purity was obtained from Aldrich Chemical Co., Milwaukee, USA. The arsenic sulfides As_2S_2, As_2S_3 and As_2S_5 of 99.99% purity were purchased from Aldrich Chemical Co., Milwaukee, USA, as well. For the calibration of the mass spectrometer 2,5-dihydroxybenzoic acid (gentisic acid, DHBA) of analytical grade purity purchased from Sigma (Steinheim, Germany) was used. The experiments on the generation of As_n clusters with matrix assisted laser desorption/ionisation were done using as matrices *trans*-2-[3-(4-*tert*-butylphenyl)-2-methyl-2-propenylidene]-malononitrile (AnorgPro) from Fluka (Buchs, Switzerland), 2-(4′-hydroxybenzolazo)-benzoic acid (HABA) from Sigma Aldrich (Steinheim, Germany) and α-cyano-4-hydroxycinnamic acid from Sigma Aldrich (Steinheim, Germany). C_{60} fullerene was purchased from Merck (Darmstadt, Germany). All the above mentioned chemicals were used as received without further purification.

2.2. Apparatus

Mass spectrometric measurements were performed on the commercial AXIMA CFR mass spectrometer from Kratos Analytical (Manchester, United Kingdom) equipped with a nitrogen laser emitting on the wavelength of 337 nm. For the calibration of the mass spectrometer in the linear positive and reflectron positive mode, molecular ions $[M + H]^+$ of DHBA were used. In the case of the linear negative and reflectron negative mode, the calibration of the mass spectra was achieved using molecular ions $[M - H]^-$ of DHBA as well. Laser desorption/ionization mass spectra acquired for this work were obtained from at least 400 laser pulses per spectrum and the recorded spectra of all the laser shots were summed.

All the recorded spectra of post-source decay (PSD) measurement were obtained by setting the mass range windows 15 Da at least.

2.3. Sample preparation

Arsenic as well as arsenic sulfides and elemental sulfur are not soluble in any MALDI sample plate 'friendly' solvent. Because of that, the studied samples were placed directly on a spot of the MALDI sample plate and thoroughly milled in a mortar with a glass stick and mixed if necessary. In the case of matrix assisted generation of cluster species, the quick and dirty standard preparation technique was used. Thus, a suspension of arsenic powder in toluene at a concentration of 1 mg ml^{-1} was prepared. The matrices solutions were prepared by dissolving each matrix in toluene and then acidifying by adding 0.1 ml of 0.1% TFA to obtain a concentration of 20 mg ml^{-1} in a vial. A volume of 0.5 μl of both arsenic suspension and matrix were deposited onto a sample plate and air-dried at room temperature.

3. Results and discussion

3.1. The use of MALDI matrices

The investigation on the possibility of using matrices for the generation of homopolyatomic As_n cluster species was considered here. Several different matrices were examined including DHBA, HABA, AnorgPro matrix and C_{60} in order to examine the possibility of the MALDI approach for the cluster(s) production. Such an approach is rare, although recently its application has been described for gold cluster generation [21]. Also, we have tried the generation of cluster species from specially fabricated graphite crucibles as described thoroughly in a previous work [20].

However, it was found that for all the studied matrices, including the AnorgPro matrix especially recommended for inorganic samples by the producer, we were not able to produce arsenic clusters. Moreover, the presence of fragments of matrices in the mass spectra made their evaluation quite difficult and the signals of arsenic species

were suppressed. We have also observed this phenomenon at high laser energies when graphite crucibles were used where, in addition, carbon clusters became co-ablated and were detected in the mass spectra.

3.1.1. Generation of positively charged homopolyatomic As_n^+ clusters via the LDI approach

Because As_n clusters were not generated using MALDI matrices, we have turned to the laser desorption ionisation (LDI) approach.

An example of a mass spectrum of elemental arsenic obtained in the linear positive mode is shown in Fig. 1(a). In the mass spectra the formation of positively charged As_n^+ ($n = 2-7$) clusters has been observed only after applying sufficiently high laser energy, of at least 3 mW, to the solid sample of elemental arsenic. The values of *m/z* corresponding to As_3^+, As_4^+, As_5^+, and As_7^+ clusters clearly indicated their formation (cf. Fig. 1(a), peaks at *m/z* values equal to 224.94, 299.94, 374.73 and 524.48 Da). In the mass spectra the signal corresponding to As_2^+ has also been observed as a peak of relatively low signal intensity (cf. Fig. 1(a), peak at *m/z* value 150.42 Da), while the signal for the As_6^+ cluster was not observed.

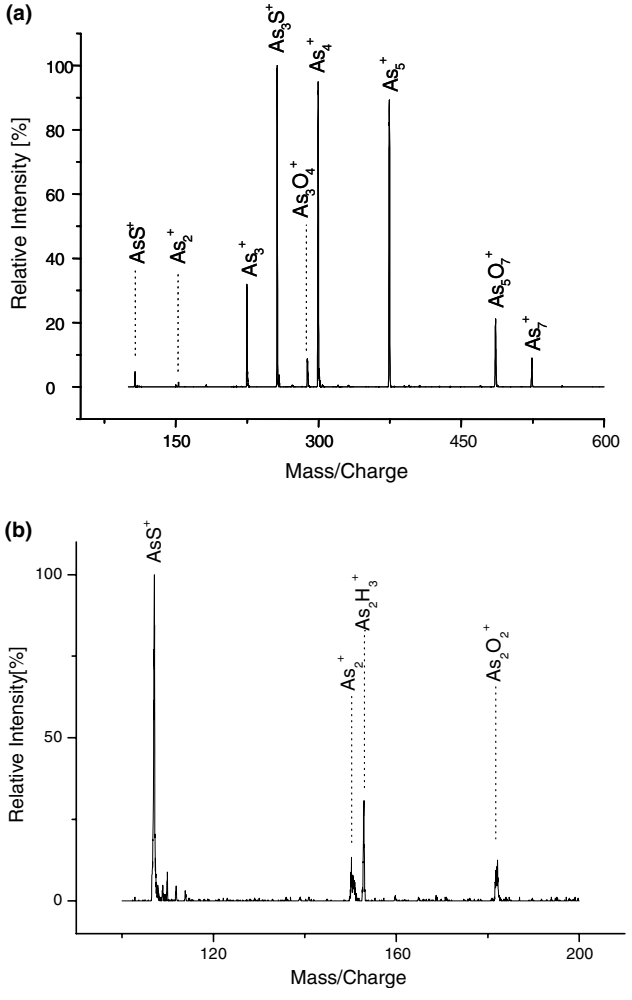


Fig. 1. The positive linear mode mass spectra concerning laser ablation of elemental arsenic. (a) An example of spectra displaying As_n^+ clusters and several other peaks reflecting the evidence of trace impurities contained in highly pure elemental arsenic (purity 99.997%). (b) Detailed view of the range 100–200 *m/z* showing the presence of AsS^+, $As_2^+$and As-hydride $As_2H_3^+$ derived from di-arsan (As_2H_4).

The PSD spectra of detected clusters did not show any signs of decomposition, even at the highest possible laser power (6 mW). In the mass spectra measured in the positive mode, peaks corresponding to AsS^+, As_2^+ and $As_2O_2^+$ are observed (cf. Fig. 1(b), *m/z* values at 107.26, 150.42 and 182.36 Da), while another peak of relatively weak intensity (cf. Fig. 1(b), *m/z* value at 153.14 Da) was assigned to $As_2H_3^+$, according to isotopic pattern modelling. Even if non-dissociative chemisorption of large amounts of H_2 on metal cluster anions has been recently reported [22], we rather suggest that in this case the species was "a chemical compound derived from arsan (AsH_3) or other As-hydrides". We are suggesting that possibly, even in the highly pure arsenic product used in this work, a low but detectable amount of arsan was present and could be detected.

In addition to the peaks of As_n^+ clusters, there were others which were identified using isotopic pattern modelling as arsenic oxides As_nO_m and/or arsenic sulfides As_nS_m, even though elemental gray arsenic of high purity (99.997%) was used. In the case of arsenic sulfides, it can be suggested that the major source of contamination, according to the producer's Certificate of Guarantee, is sulfur, with a content of up to 0.003%. This corresponds to a sulfur molar content of 0.3 mmol kg^{-1} in the pure arsenic used in this work. In reality, such a concentration is very high, as usually in MALDI-TOF-MS a sample concentration of 10^{-5} to 10^{-6} mol l^{-1} is commonly used (by the way, the limit of detection in MALDI is often 10^{-15} mol or even less). Consequently, taking into consideration the previous comments, we have detected and identified the following species: AsS^+ and As_3S^+. Concerning arsenic oxides, it is

Table 1
Review of As_n species generated via laser ablation of metallic arsenic and identified from mass spectra

Cluster	Theoretical *m/z*	Observed *m/z*	References
As^+	74.92159	75.01	[27]
As_2^+	149.84318	150.42	[9]
As_3^+	224.76477	224.94	[11]
As_4^+	299.68636	299.93	[16]
As_5^+	374.60795	374.73	this work
As_6^+	449.52954	449.64	this work
As_7^+	524.45113	524.48	this work
As^-	74.92159	not observed	[14]
As_2^-	149.84318	not observed	[14]
As_3^-	224.76477	not observed	[14]
As_4^-	299.68636	not observed	[14]
As_5^-	374.60795	not observed	[14]
As_6^-	449.52954	not observed	not described
As_7^-	524.45113	not observed	not described

interesting to note that the presence of As_nO_m species such as As_3O_4, and As_5O_7 (cf. Fig. 1(b), peaks at *m/z* values equal to 288.43, and 486.17 Da) were observed in the mass spectra obtained in the positive linear and reflectron modes as well as in both negative modes, in accordance with the literature [23].

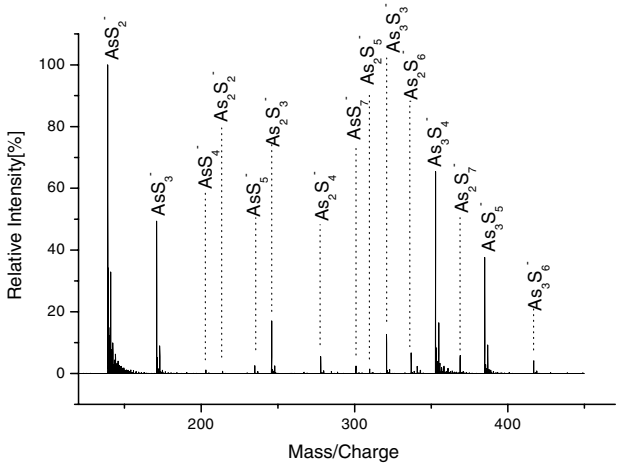


Fig. 2. An example of arsenic sulfide mass spectra recorded in the reflectron negative mode from laser ablation of As_2S_5 powder.

Not only As_2^+, As_3^+, As_4^+, As_5^+ and As_7^+, species of positively charged sulfide clusters, such as AsS^+ and As_3S^+, but also positively charged species such as $As_3O_4^+$, and $As_5O_7^+$ were observed as well. In addition, the $As_2H_3^+$ species derived from di-arsan was detected under the experimental conditions.

3.1.2. Generation of negatively charged As_n^- clusters

The formation of negatively charged As_n^- clusters was suggested theoretically by Zhao et al. [22] and species As^-, As_2^-, As_3^-, As_4^-, As_5^- have already been proved by photoelectron spectroscopy [14]. Therefore, in this chapter we examine the possibility to generate As_n^- clusters by the LDI approach.

The formation of negatively charged As_n^- ($n = 2$–7) clusters has not been observed even when applying a maximal laser power of at least 6 mW to the solid sample of the elemental arsenic. Also, the mass spectra measured in the linear negative and in the reflectron negative mode were represented only by a low number of signals corresponding to $As_nS_m^-$ (S_3^-, AsS^-, AsS_2^-) and/or $As_nO_m^-$ (AsO^-, $As_3O_5^-$, $As_5O_7^-$) species. The stoichiometries were confirmed according to isotopic pattern modelling.

Table 2
Review of As_nS_m species generated via laser ablation of fine As_2S_2 powder and identified from mass spectra of both negative and positive modes

	m	*n*			
		0	1	2	3
As_nS_m	0				
	1	S^+ S^-	AsS^+ AsS^-[a]	As_2S^+[a]	
	2	S_2^+ S_2^-[a]	AsS_2^+ AsS_2^-	AsS_2^+ AsS_2^-[a]	
	3	S_3^+ S_3^-	AsS_3^+ AsS_3^-[a]	$As_2S_3^+$ $As_2S_3^-$[a]	[b,c]$As_3S_4^+$ $As_3S_4^-$
	4	S_4^+ S_4^-[a]	AsS_4^-	$As_2S_4^-$	[b,c]$As_3S_4^+$ $As_3S_4^-$
	5		AsS_5^-		$As_3S_5^-$
	6				
	7				

[a] As_nS_m species were found under [24] as neutral molecules.
[b] [25].
[c] [26].

Table 3
Review of As_nS_m species generated via laser ablation of fine As_2S_2 powder and identified from mass spectra of both negative and positive modes

	m	*n*			
		0	1	2	3
As_nS_m	0				
	1	S^+ S^-	AsS^+ AsS^-[a]	As_2S^+[a]	[c]As_3S^+
	2	S_2^+ S_2^-[a]	AsS_2^+ AsS_2^-	AsS_2^+ AsS_2^-[a]	[b,c]$As_3S_2^+$
	3	S_3^+ S_3^-	AsS_3^+ AsS_3^-[a]	$As_2S_3^+$ $As_2S_3^-$[a]	[b,c]$As_3S_4^+$ $As_3S_4^-$
	4	S_4^+ S_4^-[a]	AsS_4^-	$As_2S_4^-$	[b,c]$As_3S_4^+$ $As_3S_4^-$
	5		AsS_5^-		$As_3S_5^-$
	6				$As_3S_6^-$
	7				

[a] As_nS_m species were found under [24] as neutral molecules.
[b] [25].
[c] [26].

Table 4
Review of As_nS_m species generated via laser ablation of fine As_2S_5 powder and identified from mass spectra recorded in the linear and reflectron positive, as well as both negative modes

	m	*n*			
		0	1	2	3
As_nS_m	0				
	1	S^+ S^-	AsS^+ AsS^-[a]	As_2S^+[a]	
	2	S_2^+ S_2^-[a]	AsS_2^+ AsS_2^-	$As_2S_2^+$ $As_2S_2^-$[a]	[b,c]$As_3S_2^+$ $As_3S_2^-$
	3	S_3^+ S_3^-	AsS_3^+ AsS_3^-[a]	$As_2S_3^+$ $As_2S_3^-$[a]	[b,c]$As_3S_3^+$ $As_3S_3^-$
	4	S_4^+ S_4^-[a]	AsS_4^-	$As_2S_4^-$	[b,c]$As_3S_4^+$ $As_3S_4^-$
	5		AsS_5^-	$As_2S_5^-$[a]	$As_3S_5^-$
	6		AsS_6^-	$As_2S_6^-$	$As_3S_6^-$
	7		AsS_7^-	$As_2S_7^-$	$As_3S_7^-$

[a] As_nS_m species were found under [24] as neutral molecules.
[b] [25].
[c] [26].

It is well known that the ionization potential (IP) (first IP of sulfur 10.4 eV and of arsenic 9.8 eV) and electron affinity (EA) (first EA of sulfur 200 kJ mol^{-1} and of arsenic 78 kJ mol^{-1}) are important physico-chemical properties of atoms. This suggests that atoms with high positive values of ionization potential and high positive values of electron affinity would form, in the negative mode, more stable negatively charged species. Therefore, we conclude that the substantially different relative abundance of As_n and/or As_nS_m species in positive and negative modes under the LDI condition is due to preferred formation of As_nS_m species over singly charged As_n^- species as expected.

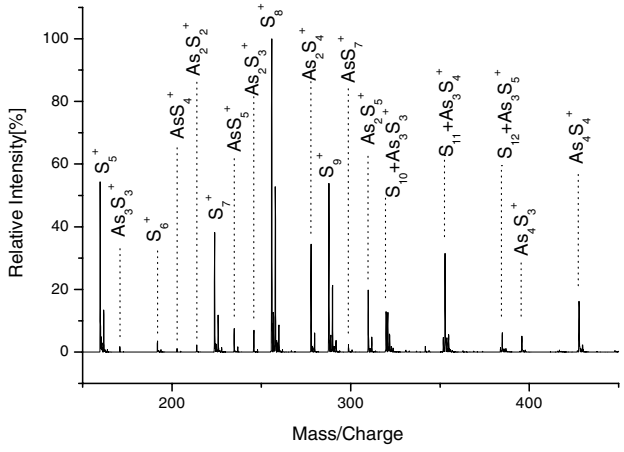


Fig. 3. An example of linear positive mode mass spectra obtained from an As_2S_2 and S_8 mixture used as a precursor for mixed As_nS_m species generation.

The complete summary of both negatively and positively charged arsenic cluster species described and/or identified is given in Table 1.

3.2. Arsenic-sulfur clusters

In the second part of this work we have studied the formation of arsenic sulfide clusters from various precursors. The following possibilities were examined: (i) laser ablation generation from As_2S_2, As_2S_3 and As_2S_5 sulfides, (ii) generation of sulfides from As–S mixtures.

Table 5
Review of As_nS_m species generated via laser ablation of fine $As_2S_2 + S_8$ powder and identified from mass spectra of both negative and positive modes

	m	*n*				
		0	1	2	3	4
As_nS_m	0					
	1	S^+ S^-	AsS^+ AsS^-[a]			
	2	S_2^+ S_2^-[a]	AsS_2^+ AsS_2^-	$As_2S_2^+$ $As_2S_2^-$[a]	[b,c]$As_3S_2^+$ $As_3S_2^-$	
	3	S_3^+ S_3^-	AsS_3^+ AsS_3^-[a]	$As_2S_3^+$ $As_2S_3^-$[a]	[b,c]$As_3S_3^+$ $As_3S_3^-$	[b]$As_4S_3^+$ $As_4S_3^-$
	4	S_4^+ S_4^-[a]	AsS_4^+ AsS_4^-	$As_2S_4^+$ $As_2S_4^-$	[b,c]$As_3S_4^+$ $As_3S_4^-$	[b]$As_4S_4^+$ $As_4S_4^-$
	5	S_5^+ S_5^-	AsS_5^+ AsS_5^-	$As_2S_5^+$ $As_2S_5^-$[a]	[b]$As_3S_5^+$ $As_3S_5^-$	
	6	S_6^+ S_6^-[a]	AsS_6^+ AsS_6^-	$As_2S_6^+$ $As_2S_6^-$	[b]$As_3S_6^+$ $As_3S_6^-$	
	7	S_7^+ S_7^-[a]	AsS_7^+ AsS_7^-	$As_2S_7^-$	[b]$As_3S_7^+$ $As_3S_7^-$	
	8	S_8^+ S_8^-[a]	AsS_8^-			
	9	S_9^+ S_9^-[a]				
	10	S_{10}^+ S_{10}^-[a]				
	11	S_{11}^+ S_{11}^-[a]				
	12	S_{12}^+ S_{12}^-[a]				

[a] As_nS_m species were found under [24] as neutral molecules.
[b] [25].
[c] [26].

3.2.1. Laser ablation of As_2S_2, As_2S_3 and As_2S_5 sulfides

The generation of As_nS_m species was achieved from thoroughly milled precursors placed directly on the MALDI plate as described elsewhere [17]. The experimental conditions of equal distribution of analysed molecules throughout the spot on the sample plate was strictly abided with the purpose of avoiding the co-ablation of the sample plate surface and formation of unexpected mixed cluster species. The arsenic-sulfur composite clusters were observed both in linear positive, linear negative as well as in the corresponding reflectron modes. Fig. 2 shows an example of a mass spectrum concerning As_nS_m species generated from the arsenic sulfide precursor. The stoichiometries were confirmed using isotopic pattern modelling. The summary of all identified compounds generated from the As_2S_2, As_2S_3 and As_2S_5 sulfides, used as precursors, is given in Tables 2–4, respectively.

Species (both negative and positive) such as AsS_2, AsS_4, AsS_5, AsS_6, AsS_7, As_2S_4, As_2S_6 have been described for the first time and the richest generation of new heteroatomic arsenic-sulfur clusters was observed in the case of As_2S_5 sulfide.

3.2.2. Generation of As_nS_m species from a mixture of the elements

In the previous chapter, we have suggested that the increasing sulfur content in the studied arsenic sulfide precursors leads to a rich laser ablation synthesis of new members of the composite cluster species family.

Table 6
Review of As_nS_m species generated via laser ablation of fine $As_2S_3 + S_8$ powder and identified from mass spectra of both negative and positive modes

	m	*n*				
		0	1	2	3	4
As_nS_m	0					
	1	S^+ S^-	AsS^+ AsS^-[a]			
	2	S_2^+ S_2^-[a]	AsS_2^+ AsS_2^-	$As_2S_2^+$ $As_2S_2^-$[a]	[b,c]$As_3S_2^+$ $As_3S_2^-$	
	3	S_3^+ S_3^-	AsS_3^+ AsS_3^-[a]	$As_2S_3^+$ $As_2S_3^-$[a]	[b,c]$As_3S_3^+$ $As_3S_3^-$	
	4	S_4^+ S_4^-[a]	AsS_4^+ AsS_4^-	$As_2S_4^+$ $As_2S_4^-$	[b,c]$As_3S_4^+$ $As_3S_4^-$	[b]$As_4S_4^+$ $As_4S_4^-$
	5	S_5^+ S_5^-	AsS_5^+ AsS_5^-	$As_2S_5^+$ $As_2S_5^-$[a]	[b]$As_3S_5^+$ $As_3S_5^-$	
	6	S_6^+ S_6^-[a]	AsS_6^+ AsS_6^-	$As_2S_6^-$	[b]$As_3S_6^+$ $As_3S_6^-$	
	7	S_7^+ S_7^-[a]	AsS_7^+ AsS_7^-		[b]$As_3S_7^+$ $As_3S_7^-$	
	8	S_8^+ S_8^-[a]	AsS_8^-			
	9	S_9^+ S_9^-[a]				
	10	S_{10}^+ S_{10}^-[a]				
	11	S_{11}^+ S_{11}^-[a]				
	12	S_{12}^+ S_{12}^-[a]				

[a] As_nS_m species were found under [24] as neutral molecules.
[b] [25].
[c] [26].

Table 7
Review of As_nS_m species generated via laser ablation of fine $As_2S_5 + S_8$ powder and identified from mass spectra recorded in the linear and reflectron positive, as well as both negative modes

	m	*n*				
		0	1	2	3	4
As_nS_m	0					
	1	S^+ S^-	AsS^+ AsS^-[a]	As_2S^+[a]	[c]As_3S^+	
	2	S_2^+ S_2^-[a]	AsS_2^+ AsS_2^-	$As_2S_2^+$ $As_2S_2^-$[a]	[b,c]$As_3S_2^+$ $As_3S_2^-$	
	3	S_3^+ S_3^-	AsS_3^+ AsS_3^-[a]	$As_2S_3^+$ $As_2S_3^-$[a]	[b,c]$As_3S_3^+$ $As_3S_3^-$	
	4	S_4^+ S_4^-[a]	AsS_4^+ AsS_4^-	$As_2S_4^+$ $As_2S_4^-$	[b,c]$As_3S_4^+$ $As_3S_4^-$	
	5	S_5^+ S_5^-	AsS_5^+ AsS_5^-	$As_2S_5^+$ $As_2S_5^-$[a]	[b]$As_3S_5^+$ $As_3S_5^-$	
	6	S_6^+ S_6^-[a]	AsS_6^+ AsS_6^-	$As_2S_6^-$	[b]$As_3S_6^+$ $As_3S_6^-$	
	7	S_7^+ S_7^-[a]	AsS_7^+ AsS_7^-	$As_2S_7^-$	$As_3S_7^-$	
	8	S_8^+ S_8^-[a]				
	9	S_9^+ S_9^-[a]				
	10	S_{10}^+ S_{10}^-[a]				
	11	S_{11}^+ S_{11}^-[a]				
	12	S_{12}^+ S_{12}^-[a]				

[a] As_nS_m species were found under [24] as neutral molecules.
[b] [25].
[c] [26].

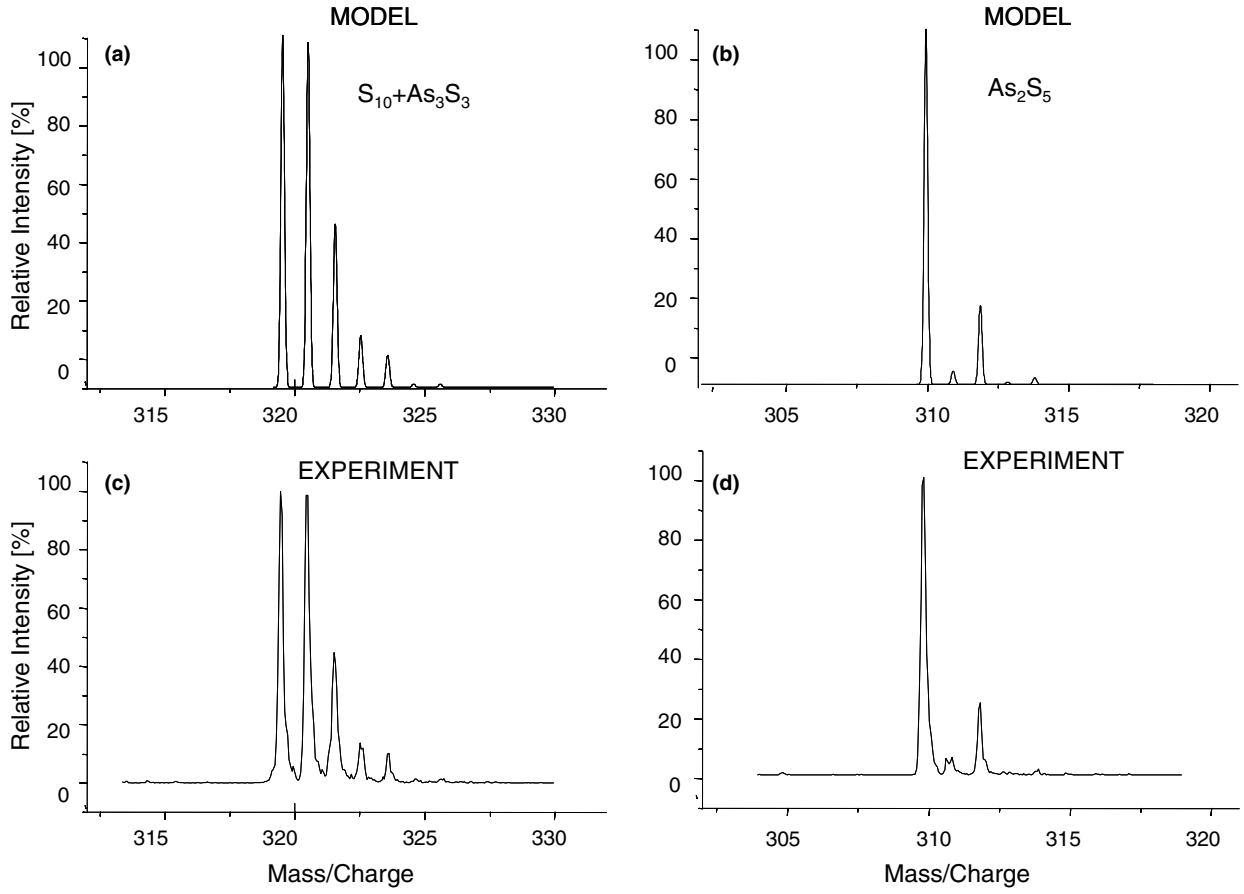


Fig. 4. Comparison of theoretical mass spectra reflecting the isotopic pattern of S_{10} + As_3S_3 and As_2S_5 species (a, b) with experimental spectra (c, d).

Therefore, the effect of sulfur as a possible MALDI matrix for the generation of As_nS_m species was considered and the possibility of different arsenic sulfide cluster generation from mixtures with sulfur was studied.

An example of the measured mass spectra is given in Fig. 3 and the overview of all newly identified stoichiometries generated from the mixture of elemental sulfur and the As_2S_2, As_2S_3 and As_2S_5 sulfides is given in Tables 5–7. All stoichiometries were confirmed according to isotopic pattern modelling and an example of the isotopic pattern confirmation is given in Fig. 4.

The effect of sulfur as a MALDI matrix in the synthesis of mixed arsenic-sulfur clusters was confirmed and, in addition to previous experiments, clusters such as As_4S_3 and As_4S_4 were detected. The richest arsenic-sulfur cluster generation was observed from the mixture of As_2S_2 arsenic sulfide with elemental sulfur. On the other hand, a high excess of sulfur leads to the generation of various sulfur species only.

4. Conclusions

The generation of As_n^+ (n = 2–7) clusters, except As_6^+, has been successfully achieved in the positive mode. The As_6^+ cluster was observed in a few cases only, with an intensity equal to 5 mV, and we confirm here that it is formed in a low abundance and this cluster is most probably unstable. No As_n^- clusters were detected in the negative mode. Clusters with intensity lower or equal than three-times the level of threshold (≈1.2 mV) were considered as non-detected. The stability of arsenic clusters was confirmed in the post-source decay. However, the existence of arsenic fullerene-like cages As_n (n = 20, 28, 32, 36, 60) was not proved. In addition, laser ablation synthesis also leads to the formation of several arsenic oxide ions (AsO, As_3O_4, As_3O_5, As_5O_7) and a positively charged $As_2H_3^+$ arsenic hydride.

New single negatively and positively charged species were generated and identified: AsS_2, AsS_4, AsS_5, AsS_6, AsS_7, AsS_8, As_2S_4, As_2S_6, As_2S_7. All stoichiometries were confirmed using isotopic pattern modelling.

Many new cluster species previously not described in the literature and/or suggested from quantum chemistry calculations were generated via laser ablation synthesis and identified. In pure arsenic, As_nS_m cluster species were detected in the positive mode (AsS and As_3S) and in the negative mode (S_3, AsS, AsS_2). We have also shown that LDI and/or laser ablation mass spectrometry

is a suitable method for the rapid identification of low sulfur impurities in metallic arsenic. Thus, this approach can be used for the detection of super-low impurities found in arsenic for industrial purposes.

Acknowledgements

The authors are grateful to the Ministry of Education, Youth and Sports, Projects No. MSM 143 1000 11 and MSM 0021622411 for financial support. E.M. Peña-Méndez gives thanks to Dirección General de Universidades (Canarian Government, Spain) for financial support. English has been kindly revised by Mr. Philip G. Watson.

References

[1] A.A. Duker, E.J.M. Carranza, M. Hale, Int. J. Health Geogr. 3 (2004) 19.
[2] J.A. Jay, N.K. Blute, H.F. Hemond, J.L. Durant, Water Res. 38 (2004) 1155.
[3] WHO, Guidelines for drinking water quality 1, 1993.
[4] J. Punčochářová, Z. Kafka, Chem. Listy 96 (2002) 611.
[5] V.Q. Nguyen, B. Cole, J. Am. Ceram. Soc. 85 (2002) 2056.
[6] J. Kobelke, A. Jetschke, J. Schwuchow, K. Kirchhof, K. Schuster, J. Non-Cryst, Solids 326/327 (2003) 446.
[7] P. Ballone, R.O. Jones, J. Chem. Phys. 100 (1994) 4941.
[8] G. Igel-Mann, H. Stoll, H. Preuss, Mol. Phys. 80 (1993) 325.
[9] K. Balasubramanian, J. Mol. Spetrosc. 121 (1987) 465.
[10] U. Meier, D. Peyerimhoff, F. Grein, Chem. Phys. 150 (1991) 331.
[11] K. Balasubramanian, K. Sumathi, D. Dai, J. Chem. Phys. 95 (1991) 3494.
[12] M. Shen, H.F. Schaefer, J. Chem. Phys. 101 (1994) 2261.
[13] K. Balasubramanian, H. Zhang, D. Dai, J. Chem. Phys. 97 (1992) 3437.
[14] T.P. Lippa, S.J. Xu, S.A. Lyapustina, J.M. Nilles, K.H. Bowen, J. Chem. Phys. 109 (1998) 10727.
[15] C. Stoemer, J. Friedrich, M.M. Kappes, Int. J. Mass. Spectrom. 206 (2001) 63.
[16] T. Baruah, M.R. Pederson, R.R. Zope, M.R. Beltrán, Chem. Phys. Lett. 387 (2004) 476.
[17] O. Šedo, M. Alberti, J. Havel, Polyhedron 22 (2003) 2601.
[18] O. Šedo, Z. Voráč, M. Alberti, J. Havel, Polyhedron 23 (2004) 1199.
[19] O. Šedo, M. Alberti, J. Havel, Polyhedron 24 (2005) 639.
[20] O. Šedo, M. Alberti, J. Havel, Shimadzu News 3 (2004) 2.
[21] S. Kéki, L. Nagy, G. Deák, M.J. Zsuga, J. Am. Soc. Mass Spectrom. 15 (2004) 1455.
[22] Y. Zhao, X. Wenguo, L. Qianshu, X. Yaoming, H.F. Schaeffer, J. Comput. Sci. 25 (2003) 907.
[23] P.B. Kelly, T.M. Allen, C.H. Smith, E.M.. McCauley, Anal. Chem. 68 (1996) 4052.
[24] N.N. Greenwood, A. Earnshaw, Chemistry of the Elements, 2nd ed., Linacre House, Oxford, UK, 1992, pp. 578–583.
[25] T.T. Martin, Solid State Commun. 47 (1983) 111.
[26] V.S. Ban, B.E. Knox, J. Chem. Phys. 52 (1970) 248.
[27] C.W. Wetzel, J.A.C. Broekaert, G.M. Hieftje, Spectrochim. Acta, Part B 57 (2002) 1009.

due to the possibility of producing attractive novel topologies and intriguing frameworks [1–4]. The major factor for the design of such polymers is in the choice of metal atoms, which allow a wide range of geometries and coordination numbers, ligands, which provide multifunctional abilities, and anions, which can exhibit several possible coordination modes. The fascination of heterometallic compounds is that the presence of two diverse metal centres concurrently can potentially give rise to interesting physical properties and intricate entanglement of coordination networks. Consequently a large number of new and exciting heterometallic structures have been reported to date [5–7]. The introduction of two different anions into mixed-metal systems can also potentially vary the resulting structures, and with a rational selection of anionic pairs, the dimensionality of inorganic solids can be regulated. It is well known that ethylenediamine (en) is a strong coordination agent and has widely been applied in supramolecular design [8–11]. Due to the particularly flexible coordination spheres of copper(II) and cadmium(II), the usage of these dissimilar transition metals conjointly in the preparation of coordination polymers will promote the structural diversity of complexes and their more complicated physico-chemical properties. Moreover, employment of various types of anions, which function as the essential element of the coordination polyhedra, such as carboxylate and halide (or pseudohalide) ligands, may lead to a more gripping series of coordination compounds. The carboxylate group represents a wide variety of binding geometries [12–14], while halide or thiocyanate anions display their rigid nature and can coordinate to the metal centres as terminal or bridging ligands [15–18]. Despite intensive progress in the construction of polymeric solids there is no example of a heterometallic coordination polymer that contains both carboxylate and halide (or pseudohalide) anions.

As we reported earlier, various coordination compounds of unusual stoichiometry and structure can be prepared easily through a "one-pot" reaction using a metal powder or metal oxide as an initial reagent, with a complex-forming agent in non-aqueous solution in air [19]. The synthetic strategy is to construct two kinds of building blocks, by adding en to a first metal atom and attaching anions of different types to a second, which are joined into heterometallic polymeric structures yielded a series of new Cu/M (M = Zn [20], Cd [21]) coordination polymers, revealing zigzag, quasi linear and helical types of chain crystal structures, of the general formula $[Cu(en)_2MX_4]\cdot n$Solv (X = Cl, I, Br, NCS, O_2CMe; Solv = dmf, dmso, CH_3CN, H_2O; n = 0, 0.5, 1). Using this approach, we have also obtained, and structural characterized, 2D polymeric Cu/Cd complexes, which are distinguished by the unique polymeric ladder-like anion $[Cd_2(O_2CMe)_6]_n^{2-}$ [22] and the rather rare $Cd(NCS)_6^{4-}$ fragment with N-bonded thiocyanate groups [21]. An attempt to prepare mixed-anion Cu/Cd heterometallic polymers employing dicyanamide (dca) and thiocyanate bridges has successfully resulted in a 2D Cu/Cd polymer featuring the unique mixed-anion $Cd(dca)_2(SCN)_2^{2-}$ fragment [23]. In the present investigation, we have replaced dca by the acetate ligand and used NCS and halide as the second anions. We also propose an efficient route to influence individual crystal structures and to regulate the dimensionality of the polymeric architectures by using different anion pairs based on the acetate group. In the preparation of mixed-anion heterometallic polymers we used copper powder, cadmium acetate and ammonium halide or thiocyanate as starting materials and investigated the interaction in the following system:

$$Cu^0\text{–}Cd(O_2CMe)_2\text{–}NH_4X\text{–en–Solv} \qquad X = Cl, Br, I, NCS;$$
$$Solv = dmf, dmso, CH_3OH, CH_3CN$$

This paper elucidates the isolation and crystal structures of three novel heterometallic coordination polymers: 1D chain compounds $[Cu(en)_2Cd(\mu\text{-}Cl)(\mu\text{-}O_2CMe)Cl(O_2CMe)]_n$ (**1**) and $[Cu(en)_2CdI_{1.64}(O_2CMe)_{2.36}]_n$ (**2**), and the 2D $[Cu_2(en)_4Cd_2(NCS)_2(NCS)_4(O_2CMe)_2]_n$ (**3**), that have a number of interesting features. To the best of our knowledge this is the first report of heterometallic complexes with mixed-anion $Cd(\mu\text{-}Cl)(\mu\text{-}O_2CMe)Cl(O_2CMe)^{2-}$, $Cd(\mu\text{-}O_2CMe)_2I(O_2CMe)^{2-}$ or $Cd(\mu\text{-}I)(\mu\text{-}O_2CMe)I(O_2CMe)^{2-}$ building blocks and $Cd_2(NCS)_6(O_2CMe)_2^{2-}$ fragments, which are supported by the X-ray structures.

2. Experimental

2.1. General details

Commercial reagents were used without further purification, all experiments were carried out in air. Elemental analyses for metals were performed by atomic absorption spectroscopy and by standard titrimetric methods for anions by the Department of Chemistry, National Taras Shevchenko University of Kyiv and with a Carlo Erba Strumentazion Analyzer (for C, H and N) by the L.V. Pisarzhevskii Institute of Physical Chemistry. Infrared spectra were recorded as KBr discs and in Nujol mulls on a UR-10 spectrophotometer in the 4000–400 cm^{-1} region using conventional techniques. The EPR spectra were recorded on a Bruker ESP 300E (Bruker, Germany) spectrometer operating at X-band and equipped with the Bruker NMR gaussmeter ER 035M and the Hewlett–Packard microwave frequency counter HP 5350B. EPR parameters were calculated by computer simulation of the experimental spectra using Bruker's WIN-EPR SimFonia Software Version 1.25. Magnetic measurements in the temperature range 4.5–300 K were

performed using a Quantum Design SQUID magnetometer (type MPMS XL-5). All susceptibility measurements were made at a field of 5 KGs. The corrections for diamagnetism of the constituent atoms were calculated from the Pascal constants [24].

2.2. Preparations

2.2.1. $[Cu(en)_2Cd(\mu\text{-}Cl)(\mu\text{-}O_2CMe)Cl(O_2CMe)]_n$ (1)

Copper powder (0.16 g, 0.0025 mol), $Cd(O_2CMe)_2$ (0.57 g, 0.0025 mol), NH_4Cl (0.27 g, 0.005 mol), dmso (20 cm^3) and ethylenediamine (0.35 cm^3, 0.005 mol) were heated to 50–60 °C and stirred magnetically until total dissolution of the copper metal was observed (40 min). Dark violet microcrystals of **1** were obtained from the violet reaction mixture in the presence of Pr^iOH after three days. They were collected by filter-suction and dried in vacuo. Yield: 0.36 g, 29.5%. *Anal.* calc. for $C_8H_{22}CuCdCl_2N_4O_4$: Cu, 13.10; Cd, 23.17; Cl, 14.62; C, 19.81; H, 4.57; N, 11.55. Found: Cu, 13.2; Cd, 23.3; Cl, 15.0; C, 19.9; H, 4.6; N, 11.5%. IR (KBr, cm^{-1}): 3300vs ν_{as}(NH), 3170 s ν_s(NH), 1600vs ν_{as}(CO), 1440vs ν_s(CO), 1050vs ν(CN).

2.2.2. $[Cu(en)_2CdI_{1.64}(O_2CMe)_{2.36}]_n$ (2)

Copper powder (0.32 g, 0.005 mol), $Cd(O_2CMe)_2$ (1.73 g, 0.0075 mol), NH_4I (0.72 g, 0.005 mol), dmf (20 cm^3) and ethylenediamine (0.7 cm^3, 0.01 mol) were heated to 50–60 °C and stirred magnetically until total dissolution of the copper metal was observed (40 min). In the course of the reaction a light brown powder, later found to be cadmium(II) oxide, precipitated. The resulting reaction mixture was filtered and dark violet crystals suitable for X-ray crystallography were formed after three days from the violet solution. Yield: 1.15 g, 35%. *Anal.* calc. for $C_{8.73}H_{23.095}CuCdI_{1.635}N_4O_{4.73}$: Cu, 9.86; Cd, 17.45; I, 32.20; C, 16.27; H, 3.62; N, 8.70. Found: Cu, 9.9; Cd, 17.6; I, 32.1; C, 16.3; H, 3.7; N, 8.8%. IR (KBr, cm^{-1}): 3300vs ν_{as}(NH), 3240s ν_s(NH), 1580vs ν_s(CO), 1410s ν_s(CO), 1045vs ν(CN).

2.2.3. $[Cu_2(en)_4Cd_2(NCS)_6(O_2CMe)_2]_n$ (3)

Copper powder (0.32 g, 0.005 mol), $Cd(O_2CMe)_2$ (1.15 g, 0.005 mol), NH_4NCS (1.14 g, 0.015 mol), CH_3OH (20 cm^3) and ethylenediamine (0.7 cm^3, 0.01 mol) were heated to 50–60 °C and stirred magnetically until total dissolution of the copper metal was observed (90 min). After cooling the reaction mixture, white crystals of ammonium acetate precipitated. The solution was filtered, and after successive additions of Pr^iOH into the resulting violet solution, dark violet crystals suitable for X-ray crystallography were deposited over a period of one month. Yield: 1.38 g, 52%. *Anal.* calc. for $C_{18}H_{38}Cu_2Cd_2N_{14}O_4S_6$: Cu, 12.00; Cd, 21.23; C, 20.42; H, 3.62; N, 18.52. Found: Cu, 11.6; Cd, 21.6; C, 20.8; H, 3.7; N, 18.9%. IR (KBr, cm^{-1}): 3320s ν_{as}(NH), 3150m ν_s(NH), 2090vs $\nu(CN_{NCS})$, 1530s ν_{as}(CO), 1430m ν_s(CO), 1040s $\nu(CN_{en})$, 790w ν(CS).

The compounds are sparingly soluble in dmso and dmf and (except for **1**) insoluble in water. All the complexes are indefinitely stable in air.

2.3. X-ray crystallography

Details of the data collection and processing, structure analysis and refinement are summarized in Table 1. Diffraction experiments were performed on a Bruker SMART CCD diffractometer (ω rotation scans with

Table 1
Crystal data and structure refinement for **1**–**3**

Complex	**1**	**2**	**3**
Formula	$C_8H_{22}CdCl_2CuN_4O_4$	$C_{8.73}H_{23.095}CdCuI_{1.635}N_4O_{4.73}$	$C_{18}H_{38}Cd_2Cu_2N_{14}O_4S_6$
Formula weight	485.15	644.35	1058.9
Crystal size (mm)	$0.22 \times 0.20 \times 0.15$	$0.19 \times 0.17 \times 0.08$	$0.24 \times 0.20 \times 0.13$
Crystal system	monoclinic	monoclinic	orthorhombic
Space group	$P2_1/n$	$P2_1/n$	$Pmc2_1$
a (Å)	8.3080(10)	9.7840(10)	12.3360(10)
b (Å)	13.634(2)	11.978(2)	8.6381(9)
c (Å)	15.144(2)	16.428(2)	16.824(2)
β (°)	100.751(2)	105.278(2)	90
V (Å^3)	1685.3(4)	1857.2(4)	1792.8(3)
Z	4	4	2
T (K)	150(2)	150(2)	150(2)
F(000)	964	1221.2	1052
μ (mm^{-1})	2.855	5.053	2.738
R_{int}	0.029	0.065	0.065
Measured/independent reflections	16354/4212	17497/4277	33031/3396
Data used [$F > 4.00\sigma(F)$]	3684	3309	2978
$\Delta\rho_{min,max}$ (e Å^{-3})	−0.60, 1.49	−1.16, 1.36	−2.14, 1.48
R	0.029	0.049	0.051
wR	0.038	0.070	0.066

narrow frames) equipped with graphite monochromated Mo Kα radiation ($\lambda = 0.71073$ Å). The data were corrected for the effects of absorption using the multi-scan method. The structures were solved by direct methods and refined by full-matrix least-squares methods on F using XTAL 3.7 [25]. The non-hydrogen atoms were refined anisotropically, hydrogen atoms being included at ideal positions but not refined. For **2**, two of the bridging ligand sites were found to be occupied partly by acetate and partly by iodide; the site occupancies being refined to (acetate and iodide) 0.670(3) and $1 - 0.670(3)$ for C(022)C(021)O(021)O(022) and I(2) (group 2) and 0.595(2) and $1 - 0.595(2)$ for C(032)-C(031)O(031)O(032) and I(3) (group 3). The atoms C(021) and C(031) of the acetate groups were refined with isotropic displacement parameters. For **3** the refined absolute structure parameter was 0.04(3).

3. Results and discussion

3.1. Synthesis and spectroscopic characterization

The reaction of copper powder, cadmium acetate and NH_4X (X = Cl, I, NCS) with ethylenediamine in dmso (**1**), dmf (**2**) or CH_3OH (**3**), in open air, using a molar ratio of $Cu:Cd(O_2CMe)_2:NH_4X:en = 1:1:2:2$ (for **1**, X = Cl), 2:3:2:4 (for **2**, X = I) or 1:1:3:2 (for **3**, X = NCS) gave heterometallic compounds which show analytical data accounting for the presence of Cu(II) and Cd(II) in a 1:1 stoichiometry. The title compounds could also be isolated from CH_3OH (in case **1**), dmso (in case **2**) or from dmf and CH_3CN (in case **3**) solutions. Their formation can be understood if one considers the following reaction schemes:

$$Cu^0 + Cd(O_2CMe)_2 + 2NH_4Cl + 2en + 1/2O_2 \rightarrow [Cu(en)_2Cd(\mu\text{-}Cl)(\mu\text{-}O_2CMe)Cl(O_2CMe)] + 2NH_3 + H_2O \quad (1)$$

$$2Cu^0 + 3Cd(O_2CMe)_2 + 2NH_4I + 4en + O_2 \rightarrow 2[Cu(en)_2Cd(\mu\text{-}O_2CMe)_2I(O_2CMe)] + CdO + 2NH_3 + H_2O \quad (2)$$

$$2Cu^0 + 2Cd(O_2CMe)_2 + 6NH_4NCS + 4en + O_2 \rightarrow [Cu_2(en)_4Cd_2(NCS)_6(O_2CMe)_2] + 4NH_3 + 2NH_4O_2CMe + 2H_2O \quad (3)$$

The structural features of these complexes were determined by IR, EPR spectroscopy and single-crystal X-ray diffraction studies.

The IR spectra of all complexes confirmed that ethylenediamine was present. The characteristic ligand peaks: ν(N–H), ν(C–H), ν(C–N) and ν(C–C) in the ranges 3300–3140, 2990–2890, 1050–1040 and 990–980 cm^{-1}, respectively, can be easily identified, although $\delta(NH_2)$ frequencies of en, observed for **3** (1580 cm^{-1}), were obscured by stretching vibrations of the carboxylate group for **1** and **2**. Two strong and broad absorption bands found for acetate groups in **1** and **2** (1600–1580 cm^{-1} and 1440–1410 cm^{-1}) lead to the Δ value [$\nu_{as}(COO) - \nu_s(COO)$] in the range 160–170 cm^{-1}, which can be used as evidence of bridging unidentate or asymmetrical chelating acetate coordination [26]. In the spectrum of **3**, the difference in wavenumbers, $\Delta = 100$ cm^{-1}, between the asymmetric (1530 cm^{-1}) and symmetric (1430 cm^{-1}) COO^- stretching frequencies demonstrate the existence of chelating carboxylate ligands [27], confirmed by the X-ray structure determination. The coordinated thiocyanate groups in **3** are confirmed by the presence of the sharp intense ν(CN) absorption peak at 2090 cm^{-1} and the weak ν(CS) vibration at 790 cm^{-1}.

3.2. Description of the structure of *1*

The structure of compound **1** consists of an infinite 1D helical chain comprised of cationic $Cu(en)_2^{2+}$ and mixed-ligand anionic $Cd(\mu\text{-}Cl)(\mu\text{-}O_2CMe)Cl(O_2CMe)^{2-}$ building blocks, linked together through one bridging chlorine atom and an oxygen atom of the chelating (and also bridging) bidentate acetate ligand (Fig. 1). Selected bond lengths and angles are listed in Table 2. The copper(II) atoms in the $Cu(en)_2^{2+}$ moiety are in a distorted octahedral coordination environment consisting of four nitrogen atoms of ethylenediamine molecules, forming the basal plane (Cu–N distances are in the range 2.010(3)–2.019(3) Å), and with the chlorine atom (Cu–Cl(2) = 2.9902(9) Å) and the oxygen atom of the bridging acetate group (Cu–O(011) = 2.364(2) Å) occupying the apical positions. The bond distances and angles in the chelate rings are similar to those found in the literature [28,29]. The Cd atom is six coordinate; the coordination sphere consisting of two acetate groups, one of which is weakly bidentate [Cd–O(021) = 2.181(2) Å and Cd–O(022) = 2.907(3) Å], the other one being bidentate [through O(011) and O(012)] and bridging unidentate [through O(011)] with Cd–O distances equal to 2.460(3) and 2.356(3) Å. Each of the Cd(II) centres is further coordi-

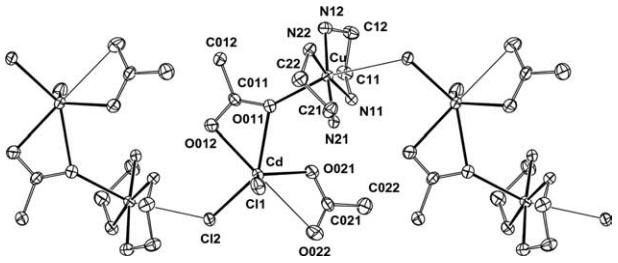


Fig. 1. The 1D helical chain in compound **1** along with its numbering scheme. The hydrogen atoms are omitted for clarity.

Table 2
Selected bond distances (Å) and angles (°) for **1**

Cd–Cl(1)	2.4711(8)
Cd–Cl(2)	2.4668(8)
Cd–O(011)	2.460(3)
Cd–O(012)	2.356(3)
Cd–O(021)	2.181(2)
Cd–O(022)	2.907(3)
Cu–N(11)	2.019(3)
Cu–N(12)	2.010(3)
Cu–N(21)	2.016(3)
Cu–N(22)	2.018(3)
Cu–O(011)	2.364(2)
Cu–Cl(2)[a]	2.9902(9)
Cl(1)–Cd–Cl(2)	105.40(3)
Cl(1)–Cd–O(011)	91.26(5)
Cl(1)–Cd–O(012)	101.33(6)
Cl(1)–Cd–O(021)	121.74(6)
Cl(1)–Cd–O(022)	96.62(6)
Cl(2)–Cd–O(011)	141.72(5)
Cl(2)–Cd–O(012)	88.82(7)
Cl(2)–Cd–O(021)	113.94(7)
Cl(2)–Cd–O(022)	85.34(6)
O(011)–Cd–O(012)	53.75(8)
O(011)–Cd–O(021)	83.52(8)
O(011)–Cd–O(022)	127.41(8)
O(012)–Cd–O(021)	120.02(9)
O(012)–Cd–O(022)	162.01(8)
O(021)–Cd–O(022)	48.64(9)
N(11)–Cu–N(12)	84.85(11)
N(11)–Cu–N(21)	96.28(10)
N(11)–Cu–N(22)	173.21(11)
N(11)–Cu–O(011)	84.79(9)
N(11)–Cu–Cl(2)[a]	88.42(8)
N(12)–Cu–N(21)	174.89(11)
N(12)–Cu–N(22)	93.44(11)
N(12)–Cu–O(011)	99.93(9)
N(12)–Cu–Cl(2)[a]	92.32(8)
N(21)–Cu–N(22)	84.85(11)
N(21)–Cu–O(011)	85.15(9)
N(21)–Cu–Cl(2)[a]	82.74(8)
N(22)–Cu–O(011)	101.99(10)
N(22)–Cu–Cl(2)[a]	85.07(8)
O(011)–Cu–Cl(2)[a]	165.38(6)

[a] Symmetry transformation used to generate equivalent atoms: $1/2 - x$, $1/2 + y$, $1/2 - z$.

nated by one terminal and one bridging chlorine atom [Cd–Cl(1) = 2.4711(8) Å and Cd–Cl(2) = 2.4668(8) Å, respectively] to form a CdO_4Cl_2 distorted octahedron. The chains of Cu–Cl(2)–Cd–O(011) atoms reveal a helical shape with angles: Cl(2)–Cd–O(011) = 141.72(5)°, Cl(2)–Cu–O(011) = 165.38(6)°, Cu–Cl(2)–Cd = 111.75(3)°, Cu–O(011)–Cd = 128.18(10)°, Cu–Cd–Cu = 134.71(1)° and Cd–Cu–Cd = 111.97(1)°. The intrachain Cu···Cu and Cd···Cd distances are 8.183(1) Å and 7.350(1) Å, respectively. The chains are additionally strengthened by strong hydrogen bonds [N(11)–H(11aN)···O(021); D–A = 2.940(1) Å, D–H···A = 174(3)°. N(21)–H(21aN)···O(012); D–A = 2.968(1) Å, D–H···A = 164(3)°]. Moreover, two sets of hydrogen bonds assemble the chains, related by crystallographic glide planes, into a

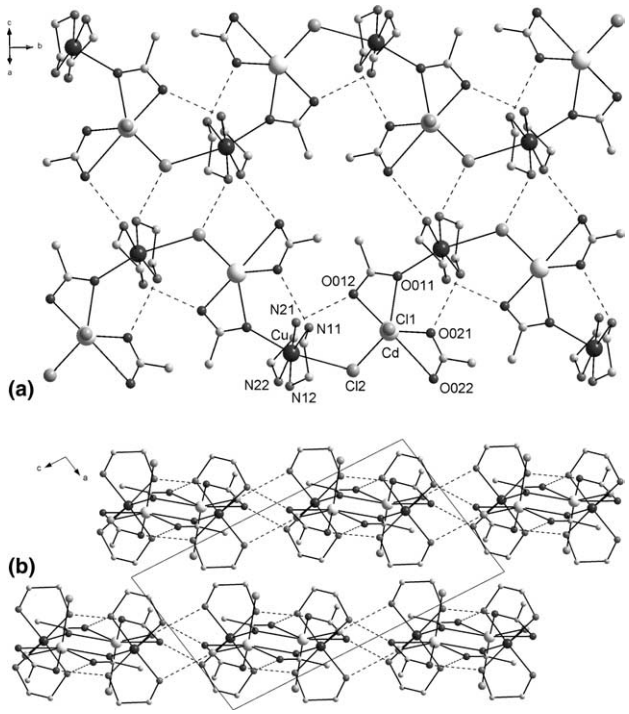


Fig. 2. A fragment of the 2D sheet (a) and a view of the layer arrangement (b) in the structure **1**. The hydrogen atoms are omitted for clarity.

2D structure (Fig. 2). The first set, N(22)–H(22aN)···O(022), involves a hydrogen atom of the NH_2 group of ethylenediamine and an oxygen atom of a weakly chelating bidentate acetate group [D–A = 2.946(1) Å, D–H···A = 160(3)°]. The second set, N(12)–H(12aN)···Cl(2), involves a hydrogen atom of the NH_2 group of ethylenediamine and the bridging chlorine atom [D–A = 3.274(2) Å, D–H···A = 158(4)°]. The nearest interlayer Cu···Cu and Cd···Cd separations are in the range 6.2882(8)–9.696(1) and 8.1307(7)–9.507(1) Å, respectively.

3.3. Description of the structure of **2**

The complex **2** is basically a 1D helical chain structure formed by $Cu(en)_2^{2+}$ and $Cd(\mu\text{-}O_2CMe)_2I(O_2CMe)^{2-}$ building blocks, which are joined through the oxygen atoms from a weakly bidentate chelate acetate ligand and also through the oxygen atoms of the other acetate group which is bridging unidentate and bidentate (Fig. 3). However, both bridging acetate sites are also partially occupied by iodide ions, the site occupancies of the acetate and iodide being refined to 0.670(3) and 1 − 0.670(3) for group 2 and 0.595(2) and 1 − 0.595(2) for group 3. Thus, as well as bridging $Cd(\mu\text{-}O_2CMe)_2I(O_2CMe)^{2-}$ units, there is also a minor component of $[Cu(en)_2Cd(\mu\text{-}I)(\mu\text{-}O_2CMe)I(O_2CMe)]$, there being two possibilities corresponding to the two crystallographically distinct acetate/iodide groups 2 and 3. There may also be some $[Cu(en)_2Cd(\mu\text{-}I)_2$-

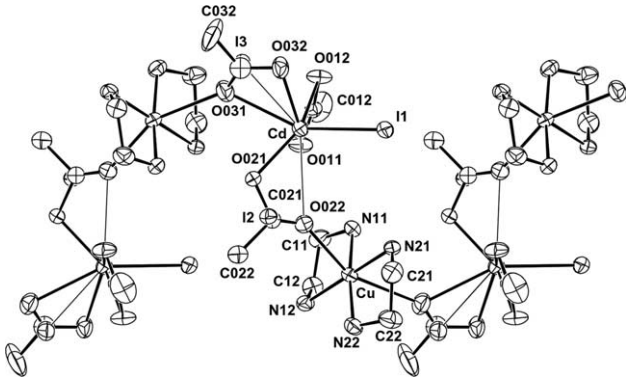


Fig. 3. Perspective view of a helical chain of complex **2** together with the atom numbering. The hydrogen atoms are omitted for clarity.

$I(O_2CMe)$], corresponding the replacement of both bridging acetates. Selected bond lengths and angles for **2** are tabulated in Table 3. For the major component, the environment around the copper(II) atom in the $Cu(en)_2^{2+}$ unit can be best described as a distorted octahedron with four nitrogen atoms of ethylenediamines forming the basal plane [Cu–N distances are in the range 1.994(7)–2.018(6) Å] and with two oxygen atoms of acetate groups [Cu–O(022) = 2.420(9) Å, Cu–O(031) [at $3/2 - x$, $1/2 + y$, $1/2 - z$] = 2.579(10) Å] occupying the apical positions. The cadmium atom in the complex has {6 + 1} coordination and a IO_6 donor set. Each Cd(II) ion is coordinated by one terminal iodine atom [Cd–I(1) = 2.7728(9) Å] and three acetate groups with different coordination modes: one is very asymmetric bidentate and bridging [Cd–O(021) = 2.214(7) Å and Cd–O(022) = 2.948(8) Å], one bidentate [through O(032) and O(031)] and also bridging unidentate [through O(031)] with Cd–O distances equal to 2.288(12) and 2.567(10) Å and the last is bidentate with Cd–O bond lengths equal to 2.263(6) and 2.617(5) Å. The chains of Cu–O(031)–Cd–O(022) atoms present a helical type with angles: O(022)–Cd–O(031) = 118.9(3)°, O(022)–Cu–O(031) = 155.8(3)°, Cu–O(031)–Cd = 126.8(5)°, Cu–O(022)–Cd = 132.9(3)°, Cu–Cd–Cu = 107.16(2)° and Cd–Cu–Cd = 107.52(2)°. The Cu···Cu and Cd···Cd separations within the chains are 7.668(2) and 7.686(1) Å, respectively. Hydrogen bonds also link the chains to form a 2D structure. In **2** only one nitrogen atom from an NH_2 group of en takes part in the intrachain hydrogen bonding with oxygen atoms of the acetate ligands [N(11)–H(11aN)···O(021); D–A = 2.991(9) Å, D–H···A = 152.5(5)°. N(11)–H(11bN)···O(011); D–A = 3.078(9) Å, D–H···A = 148.7(4)°], in contrast with two N_{en} atoms that participated in hydrogen bonding in **1**. Furthermore, only one type of hydrogen bonding interaction, that involves a hydrogen atom of an NH_2 group of en and an oxygen atom of a bidentate acetate group, facilitates the formation of 2D sheets [N(22)–H(22aN)···O(012);

Table 3
Selected bond distances (Å) and angles (°) for **2**

Cd–I(1)	2.7728(9)
Cd–I(2)	2.905(10)
Cd–I(3)	2.743(3)
Cd–O(011)	2.263(6)
Cd–O(012)	2.617(5)
Cd–O(021)	2.214(7)
Cd–O(022)	2.948(8)
Cd–O(031)	2.567(10)
Cd–O(032)	2.288(12)
Cu–O(022)	2.420(9)
Cu–N(11)	2.018(6)
Cu–N(12)	2.012(7)
Cu–N(21)	1.994(7)
Cu–N(22)	2.001(6)
Cu–O(031)[a]	2.579(10)
I(1)–Cd–I(2)	104.6(2)
I(1)–Cd–I(3)	122.40(7)
I(1)–Cd–O(011)	109.83(16)
I(1)–Cd–O(012)	94.00(15)
I(1)–Cd–O(021)	119.43(18)
I(1)–Cd–O(022)	87.54(16)
I(1)–Cd–O(031)	146.9(3)
I(1)–Cd–O(032)	94.5(2)
I(2)–Cd–I(3)	115.3(2)
I(2)–Cd–O(011)	86.0(2)
I(2)–Cd–O(012)	138.3(2)
I(2)–Cd–O(031)	96.8(3)
I(2)–Cd–O(032)	127.2(3)
I(3)–Cd–O(011)	112.67(16)
I(3)–Cd–O(012)	83.00(16)
I(3)–Cd–O(021)	91.0(2)
I(3)–Cd–O(022)	138.93(17)
O(011)–Cd–O(012)	52.4(2)
O(011)–Cd–O(021)	98.1(3)
O(011)–Cd–O(022)	76.2(2)
O(011)–Cd–O(031)	96.5(3)
O(011)–Cd–O(032)	132.7(3)
O(012)–Cd–O(021)	142.9(2)
O(012)–Cd–O(022)	125.8(2)
O(012)–Cd–O(031)	86.2(3)
O(012)–Cd–O(032)	87.1(3)
O(021)–Cd–O(022)	48.1(3)
O(021)–Cd–O(031)	74.4(3)
O(021)–Cd–O(032)	104.4(3)
O(022)–Cd–O(031)	118.9(3)
O(022)–Cd–O(032)	146.9(3)
O(031)–Cd–O(032)	52.5(4)
O(022)–Cu–N(11)	85.3(3)
O(022)–Cu–N(12)	101.1(3)
O(022)–Cu–N(21)	77.9(3)
O(022)–Cu–N(22)	104.3(3)
O(022)–Cu–O(031)[a]	155.8(3)
N(11)–Cu–N(12)	84.8(3)
N(11)–Cu–N(21)	96.9(3)
N(11)–Cu–N(22)	170.4(3)
N(11)–Cu–O(031)[a]	85.5(3)
N(12)–Cu–N(21)	177.9(3)
N(12)–Cu–N(22)	93.7(3)
N(12)–Cu–O(031)[a]	100.3(3)
N(21)–Cu–N(22)	84.9(3)
N(21)–Cu–O(031)[a]	81.0(3)
N(22)–Cu–O(031)[a]	85.5(3)

[a] Symmetry transformation used to generate equivalent atoms: $3/2 - x$, $1/2 + y$, $1/2 - z$.

D–A = 3.046(10) Å, D–H···A = 136.3(4)°, N(12)–H(12bN)··· O(012); D–A = 2.878(9) Å, D–H···A = 167.9(5)°, N(22)–H(22bN)···O(032); D–A = 3.12(1) Å, D–H··· A = 140.4(5)°] where all these interactions are related by a cell translation on *a* to the adjacent sheet (Fig. 4). Thus, these hydrogen bonding interactions are to layers where the chains are not translated (Fig. 4).

For the minor component of **2** where the acetate ligands C(022)C(021)O(021)O(022) or C(032)C(031)-O(031)O(032) have been replaced by iodide ions, the building blocks containing the Cd atom now become $Cd(\mu\text{-}I)(\mu\text{-}O_2CMe)I(O_2CMe)^{2-}$. The Cd atom is 6-coordinate and contains an IO_5 donor set. For I(2) and I(3) the distances to the Cd atom are Cd–I(2) = 2.905(1) and Cd–I(3) = 2.743(3) Å with the copper atom now weakly bonded at Cu–I(2) 3.49(1) and Cu–I(3) 3.598(3) Å. The angles at the bridging iodine atoms are Cd–I(2)–Cu = 100.4(3)° and Cd–I(3)–Cu [at $3/2 - x$, $y - 1/2$, $1/2 - z$] = 92.1(1)°. The nearest interlayer metal-metal distances are in the range 7.807(2)–9.784(2) and 8.464(1)–9.784(1) Å for Cu···Cu and Cd···Cd, respectively.

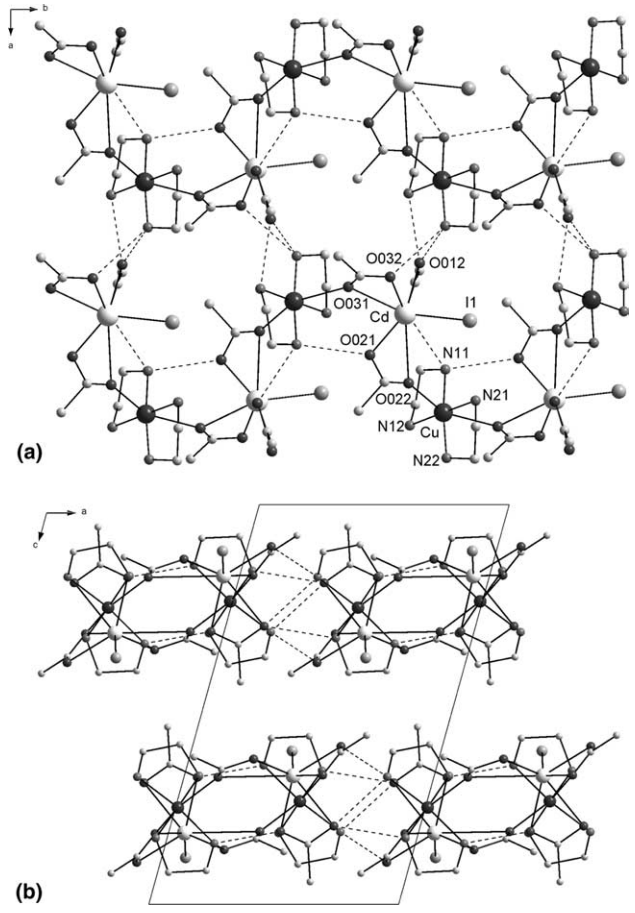


Fig. 4. A view of a fragment of the 2D layer (a) and the packing diagram of the polymeric sheets (b) of major component of complex **2**. The hydrogen atoms are omitted for clarity.

3.4. Description of the structure of *3*

X-ray analysis reveals a 2D wave-like polymeric network for complex **3**, the crystal structure of which consists of 1D anionic chains of $Cd_2(NCS)_6(O_2CMe)_2^{4-}$ and $Cu(en)_2^{2+}$ units. The view of the 1D anionic chain motif together with the atom numbering scheme is presented in Fig. 5, while Fig. 6 shows the perspective view of a 2D sheet. The molecular packing of complex **3**, projected onto the *cb* plane, is represented in Fig. 7.

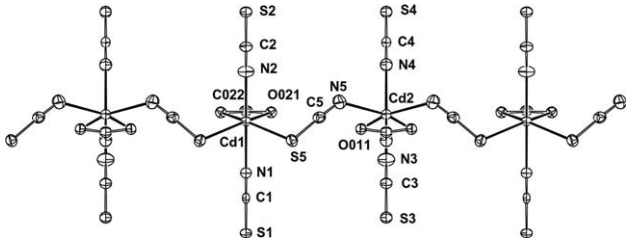


Fig. 5. The view of the 1D anionic chain motif of complex **3** together with the atom numbering scheme. The hydrogen atoms are omitted for clarity.

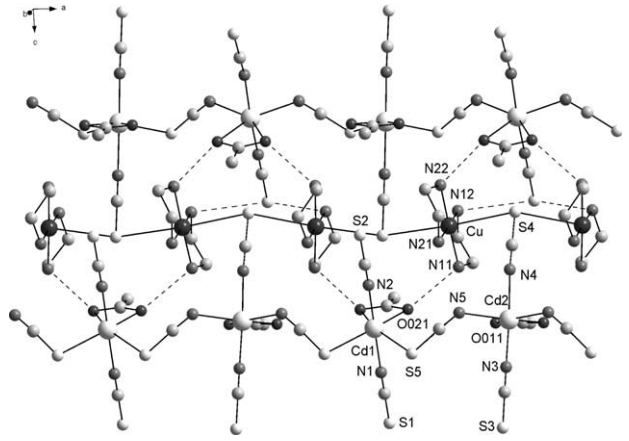


Fig. 6. Perspective view of a sheet in complex **3**. The hydrogen atoms are omitted for clarity.

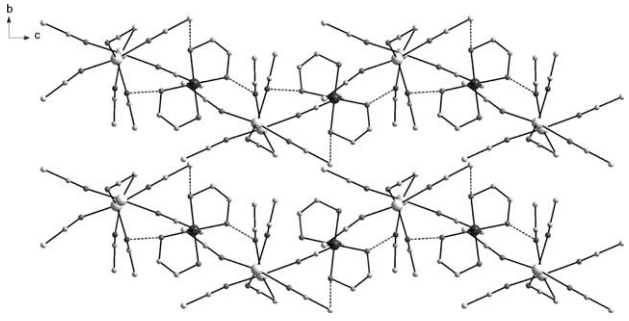


Fig. 7. Molecular packing of complex **3** projected onto the *cb* plane showing the undulating character of the polymeric layers. The hydrogen atoms are omitted for clarity.

Table 4
Selected bond distances (Å) and angles (°) for **3**

Cd(1)–N(1)	2.348(12)
Cd(1)–N(2)	2.221(15)
Cd(1)–S(5)[a]	2.666(3)
Cd(1)–O(021)	2.369(7)
Cd(2)–N(3)	2.205(16)
Cd(2)–N(4)	2.240(15)
Cd(2)–N(5)[b]	2.333(11)
Cd(2)–O(011)[b]	2.392(7)
Cu–S(4)	3.1467(14)
Cu–N(11)	2.015(8)
Cu–N(12)	2.014(8)
Cu–N(21)	2.011(9)
Cu–N(22)	2.018(9)
Cu–S(1)[c]	3.1113(12)
N(1)–Cd(1)—N(2)	177.7(5)
N(1)–Cd(1)–S(5)[a]	84.3(2)
N(1)–Cd(1)–O(021)	81.6(3)
N(2)–Cd(1)–S(5)[a]	97.2(3)
N(2)–Cd(1)–O(021)	96.3(4)
S(5)[a]–Cd(1)–O(021)	101.21(17)
S(5)–Cd(1)–S(5)[a]	98.69(8)
S(5)–Cd(1)–O(021)	154.3(2)
O(021)–Cd(1)–O(021)[a]	55.5(2)
N(3)–Cd(2)–N(4)	169.0(6)
N(3)–Cd(2)–N(5)[b]	90.0(3)
N(3)–Cd(2)–O(011)[b]	101.0(4)
N(4)–Cd(2)–N(5)[b]	84.8(4)
N(4)–Cd(2)–O(011)[b]	88.7(4)
N(5)[b]–Cd(2)–O(011)[b]	89.8(3)
N(5)–Cd(2)–N(5)[b]	124.0(4)
N(5)–Cd(2)–O(011)[b]	144.6(3)
O(011)–Cd(2)–O(011)[b]	55.2(2)
N(5)–Cd(2)–O(011)[b]	89.8(3)
S(4)–Cu–N(11)	93.9(3)
S(4)–Cu–N(12)	89.0(2)
S(4)–Cu–N(21)	93.3(2)
S(4)–Cu–N(22)	84.4(2)
S(4)–Cu–S(1)[c]	176.16(11)
N(11)–Cu–N(12)	85.5(4)
N(11)–Cu–N(21)	93.8(4)
N(11)–Cu–N(22)	177.9(3)
N(11)–Cu–S(1)[c]	90.0(3)
N(12)–Cu–N(21)	177.6(3)
N(12)–Cu–N(22)	95.6(4)
N(12)–Cu–S(1)[c]	91.7(2)
N(21)–Cu–N(22)	85.2(4)
N(21)–Cu–S(1)[c]	86.0(2)
N(22)–Cu–S(1)[c]	91.8(2)

Symmetry transformation used to generate equivalent atoms: [a] $1-x$, y, z; [b] $2-x$, y, z; [c] $1-x$, $1-y$, $z-1/2$.

The selected bond lengths and angles are shown in Table 4. Both copper(II) and cadmium(II) atoms are joined through '–Cu–SCN–Cd–' linkages. The copper(II) atom has an elongated octahedral environment with an N_4S_2 donor set; the equatorial positions are occupied by four nitrogen atoms from two ethylenediamine bidentate chelate ligands with Cu–N distances in the range 2.011(9)–2.018(9) Å, with the axial positions occupied by the sulfur atoms from the bridging thiocyanate ligands. The bond distances of Cu–S, 3.1113(12) and 3.1467(14) Å, are shorter than the sum of the van der Waals radii of the Cu and S atoms (3.4 Å) [30] and similar to the values found in other complexes in which the S atoms adopt an axial position in a distorted octahedron around copper(II) [31–33]. The polymers contains two crystallographically independent cadmium atoms, Cd(1) and Cd(2), both of which are six coordinate with $CdS_2N_2O_2$ and CdN_4O_2 distorted octahedral geometries, respectively. Both Cd(II) atoms are coordinated by one chelating bidentate acetate group, one terminal thiocyanate ligand, one $\mu_{1,3}$-NCS group, which connect the copper(II) and cadmium(II) atoms in the 2D layer, and another two $\mu_{1,3}$-NCS groups, which serves to bridge between the metal centres. The Cd(1)–N distances are 2.221(15) and 2.348(12) Å, and Cd(2)–N bond lengths vary between 2.205(16) and 2.333(11) Å. The N(1)–Cd(1)–N(2) angle is 177.7(5)°, while the N–Cd(2)–N bond angles lie in the range 84.8(4)–169.0(6)°. The S–C distances of the thiocyanates are in the range 1.607(15)–1.652(11) Å and the C–N distances vary between 1.157(15) and 1.19(2) Å, which is in accordance with the values observed in other thiocyanato-containing metal complexes [34,35]. The polymeric mixed-anion –NCS–$Cd(NCS)_2(O_2CMe)$–SCN–$Cd(NCS)_2(O_2CMe)$–NCS– chains are almost linear with angles between the three cadmium(II) atoms of 172.01(2)°. The adjacent Cd···Cd distance within the chain is 6.1830(5) Å. The resulting 2D sheets consist of 18-membered [$Cd_3(\mu_{1,3}$-$NCS)_4Cu_2S_{NCS}$] rings folded in a wave-like manner with a dihedral angle of 115.84(2)° between adjacent planes along the c axis. The copper(II) atoms in the layer are located on a straight line as a result of the mirror planes, with the intermetallic Cu···Cu separations through the S_{NCS} atom of 6.165(2) and 6.171(2) Å. The nearest Cu···Cu distances between neighboring –Cu–S–Cu–S– lines are 8.455(2) Å, while the shortest Cu···Cu separation between adjacent 2D sheets is 8.638(2) Å. In addition, a network of intramolecular hydrogen bonds [N(22)–H(22aN)···O(011) [x, $1-y$, $z-1/2$]; D–A = 3.00(1) Å, D–H···A = 151.9(6)°; N(11)–H(11bN)··· O(021), D–A = 2.98(1) Å, D–H···A = 166.1(6)°; N(12)– H(12bN)··· S(3), D–A = 3.629(8) Å, D–H···A = 148.2(5)°] is responsible for the stabilization of the overall 2D architecture.

3.5. Magnetic properties

Magnetic data for **1**–**3** are shown in Fig. 8 as μ_{eff} versus T plots, which indicate that the magnetic behaviour is in general paramagnetic in accordance with the crystal structures of the compounds (the closest intrachain Cu···Cu separations are 8.183(1) Å for **1** and 7.668(2) Å for **2**, and the nearest intralayer Cu···Cu distance is 6.165(2) Å for **3**). The room temperature magnetic moment for each copper atom, ca. 1.8 μ_B, is in the normal range for isolated $S = 1/2$ ions. The drop in the effective magnetic moment below 5 K indicates

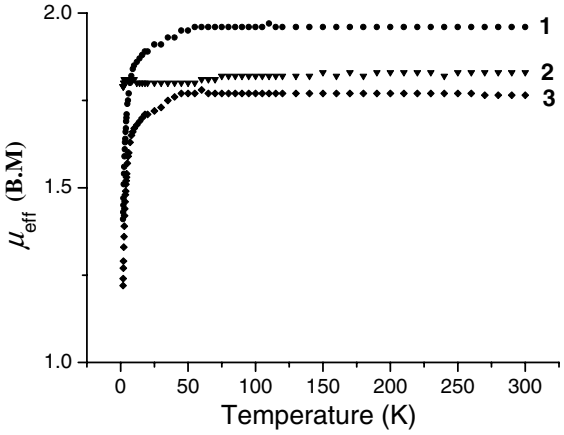


Fig. 8. Plots of the effective magnetic moment vs. temperature for **1**, **2** and **3**.

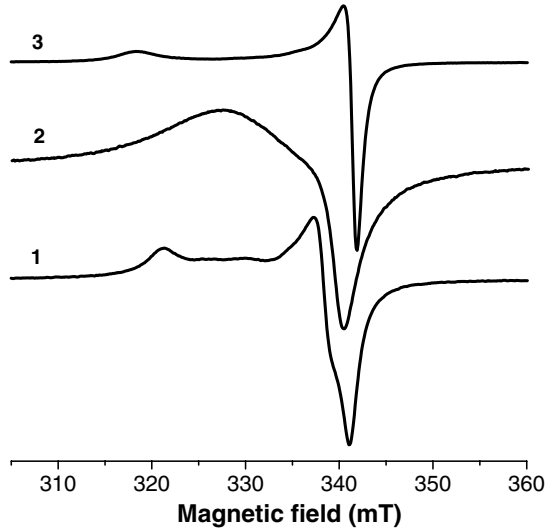


Fig. 9. EPR spectra of polycrystalline complexes **1**–**3** measured at 77 K.

the onset of a weak antiferromagnetic coupling: this is not unexpected for the systems in which hydrogen bond contacts are important. It can be concluded that –Cl–Cd–O– (for **1**), –O–Cd–O– (for **2**) and S_{NCS} (for **3**) bridges effectively prevent any exchange interactions between copper centres.

The EPR spectra of polycrystalline samples exhibit different patterns: axial for **3** (with distinctly resolved g components) and **2**, and rhombic for **1** (Fig. 9). The absence of the signals due to $S = 1$ transitions between 77–295 K support the paramagnetic character of the Cu(II) centres. The spectra remain unchanged upon lowering of the temperature to 77 K. Generally, the EPR spectra of concentrated Cu(II) complexes are affected by interactions between the paramagnetic centres leading, in the case of non-parallel aligned complexes, to the coupling of g tensor components [36]. The crystal g^c values are: $g_1^c = 2.173$, $g_2^c = 2.064$, $g_3^c = 2.045$ for **1**, $g_1^c \sim 2.16$, $g_2^c = g_3^c = 2.058$ for **2** and $g_\parallel^c = 2.193$, $g_\perp^c = 2.046$ for **3**. The $Cu(en)_2^{2+}$ cations immobilized in the matrix of organic polymers exhibits axial g and A. The following EPR spectral parameters, $g_\parallel = 2.210$, $g_\perp = 2.048$, $A_\parallel = 186$ G and $A_\perp = 20$ G [37] are typical for square planar or elongated octahedral geometries for a coordination sphere composed of four nitrogen atoms from two ligands forming aliphatic chelate rings in the Cu(II) plane. Comparison of the molecular EPR parameters with those observed for the complexes present in the studied compounds reveals that the g values of **1** and **2** are greatly modified due to cooperative interactions compared to those for **3**. It is remarkable that diamagnetic Cd(II) complexes are not able to efficiently separate Cu(II) centres, and copper hyperfine splitting is not detected. The observed change of the EPR spectral patterns with cooperative effects should be mainly assigned to the differences in the solid state structures. The studied complexes consist of similar $Cu(en)_2^{2+}$ units with two en ligands coordinated in the Cu(II) plane which are dissimilarly arranged and interact with different donors at the Cu(II) axial positions, although the effect of misalignment of the $Cu(en)_2^{2+}$ units seems to be the more important. The angle between the N_4 planes of two neighboring Cu(II) complexes are 43.84(3)°, 83.3(2)° and 12.5(2)° for **1**, **2** and **3**, respectively. The smallest angle corresponds to the weakest cooperative interactions from the results of the EPR parameters.

4. Conclusions

The reactions of copper powder, cadmium acetate, ethylenediamine and ammonium salts in dmso, dmf and CH_3OH, yield the formation of three novel 1D and 2D polymeric Cu/Cd complexes with unique mixed-anion $Cd(\mu\text{-}Cl)(\mu\text{-}O_2CMe)Cl(O_2CMe)^{2-}$, $Cd(\mu\text{-}O_2CMe)_2I(O_2CMe)^{2-}$, $Cd(\mu\text{-}I)(\mu\text{-}O_2CMe)I(O_2CMe)^{2-}$ and $Cd_2(NCS)_6(O_2CMe)_2^{2-}$ fragments. Evidently for these three systems, a key difference lies in the nature of the X^- anion of NH_4X and our results shows that the type of counterion is of crucial importance in determining the dimensionality and structure of the Cu/Cd polymers formed. Variable-temperature magnetic susceptibility measurements of **1**–**3** show weak antiferromagnetic coupling between the copper centres.

Acknowledgement

The work was supported in part by the INTAS (Project 03–51–4532).

Appendix A. Supplementary data

Crystallographic data for the structures **1**–**3** in this paper have been deposited with the Cambridge Crystallographic Data Centre as supplementary publication nos. CCDC 250874–250876. Copies of the data can be obtained, free of charge, on application to CCDC, 12 Union Road, Cambridge CB2 1EZ, UK (fax: +44 1223 336 033 or e-mail: deposit@ccdc.cam.ac.uk or on the web http://www.ccdc.cam.ac.uk). Supplementary data associated with this article can be found, in the online version at doi:10.1016/j.poly.2005.03.091.

References

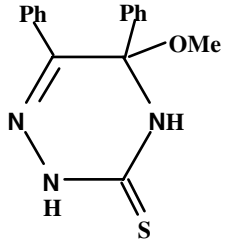
[1] M. Clemente-Leon, E. Coronado, J.R. Galan-Mascaros, C.J. Gomez-Garsia, Th. Woike, J.M. Clemente-Juan, Inorg. Chem. 40 (2001) 87.
[2] E. Colacio, F. Lloret, R. Kivekas, J. Suarez-Varela, M.R. Sundberg, R. Uggla, Inorg. Chem. 42 (2003) 560.
[3] B.-Z. Lin, Y.-M. Chen, P.-D. Liu, J. Chem. Soc., Dalton Trans. (2003) 2474.
[4] J. Zhang, L.G. Hubert-Pfalzgraf, D. Luneau, Inorg. Chem. Commun. 7 (2004) 979.
[5] R. Gheorghe, M. Andruh, A. Muller, M. Schmidtmann, Inorg. Chem. 41 (21) (2002) 5314.
[6] A. Bach, M. Hoyer, H. Hartl, Z. Naturforsch. 52b (1997) 1497.
[7] J. Gao, A.E. Martell, J. Reibenspies, Inorg. Chim. Acta 329 (2002) 122.
[8] T. Iwamoto, Supramolecular Chemistry in Cyanometallate Systems, in: D.D. MacNicol, F. Toda, R. Bishop (Eds.), Comprehensive Supramolecular Chemistry, Pergamon Press, Oxford, 1996.
[9] A. Yuan, J. Zou, B. Li, Z. Zha, C. Duan, Y. Liu, Z. Xu, S. Keizer, Chem. Commun. (2000) 1297.
[10] N. Fukita, M. Ohba, H. Okawa, K. Matsuda, H. Iwamura, Inorg. Chem. 37 (5) (1998) 842.
[11] D.B. Leznoff, B.Y. Xue, R.J. Batchelor, F.W.B. Einstein, B.O. Patrick, Inorg. Chem. 40 (23) (2001) 6026.
[12] R.C. Mehrotra, R. Bohra, Metal Carboxylate, Academic, New York, 1983.
[13] B.-H. Ye, X.-M. Chen, F. Xue, L.-N. Ji, T.C.W. Mak, Inorg. Chim. Acta 299 (2000) 1.
[14] S. Adam, A. Bauer, O. Timpe, U. Wild, G. Mestl, W. Bensch, R. Schlogl, Chem. Eur. J. 4 (8) (1998) 1458.
[15] D.M. Ciurtin, M.D. Smith, H.-C. zur Loye, Chem. Commun. (2002) 74.
[16] D.M. Ciurtin, M.D. Smith, H.-C. zur Loye, J. Chem. Soc., Dalton Trans. (2003) 1245.
[17] L. Shen, Y.-Z. Xu, J. Chem. Soc., Dalton Trans. (2001) 3413.
[18] H. Zhang, X. Wang, K. Zhang, B.K. Teo, Coord. Chem. Rev. 183 (1999) 157.
[19] A.D. Garnovskii, B.I. Kharissov (Eds.), Direct Synthesis of Coordination and Organometallic Compounds, Elsevier Science, Amsterdam, 1999.
[20] O.V. Pryma, S.R. Petrusenko, V.N. Kokozay, B.W. Skelton, O.V. Shishkin, T.S. Teplytska, Eur. J. Inorg. Chem. (2003) 1426.
[21] O.V. Pryma, S.R. Petrusenko, V.N. Kokozay, O.V. Shishkin, M.V. Zhigalko, W. Linert, Z. Naturforsch. 58b (2003) 1117.
[22] O.V. Pryma, S.R. Petrusenko, V.N. Kokozay, O.V. Shishkin, M.V. Zhigalko, Inorg. Chem. Commun. 6 (2003) 896.
[23] O.V. Nesterova (Pryma), S.R. Petrusenko, V.N. Kokozay, B.W. Skelton, W. Linert, Inorg. Chem. Commun. 7 (2004) 450.
[24] E. König, Magnetic Properties of Coordination and Organometallic Transition Metal Complexes, Springer, Berlin, 1966.
[25] S.R. Hall, D.J. du Boulay, R. Olthof-Hazekamp (Eds.), XTAL 3.7 System, University of Western Australia, 2000.
[26] G.B. Deacon, R.J. Phillips, Coord. Chem. Rev. 33 (1980) 227.
[27] K. Nakamoto, Infrared and Raman Spectra of Inorganic and Coordination Compounds, 4th ed., Wiley, New York, 1986.
[28] Brian J. Hathaway, in: G. Wilkinson, R.D. Gillard, J.A. McCleverty (Eds.), Comprehensive Coordination Chemistry: Copper, Pergamon Press, Oxford, 1987.
[29] A.F. Wells, Structural Inorganic Chemistry, 5th ed., Clarendon Press, Oxford, 1986.
[30] L. Pauling, The Nature of the Chemical Bond, 3rd ed., Cornell University Press, Ithaca, 1960, p. 260.
[31] J. Ribas, C. Diaz, X. Solans, M. Font-Bardia, Inorg. Chim. Acta 231 (1995) 229.
[32] R. Vicente, A. Escuer, E. Penalba, X. Solans, M. Font-Bardia, Inorg. Chim. Acta 255 (1997) 7.
[33] S. Ferlay, G. Francese, H.W. Schmalle, S. Decurtins, Inorg. Chim. Acta 286 (1999) 108.
[34] M. Kabešová, R. Boca, M. Melník, D. Valigura, M. Dunaj-Jurco, Coord. Chem. Rev. 140 (1995) 115.
[35] A. Golub, H. Kohler, V. Skopenko (Eds.), Chemistry of Pseudohalides, Elsevier Science, Amsterdam, 1986.
[36] G. Plesch, C. Friebel, O. Švajlenová, J. Krätsmár-Šmogrovič, Polyhedron 14 (1995) 1185.
[37] B.N. Kolarz, A.W. Trochimczuk, D. Jermakowicz-Bartkowiak, J. Jezierska, Polymer 43 (2002) 1061.

coordination preferences, the ligand can show different coordination behaviour.

Although Zn(II) has a preference for tetrahedral coordination [11], there are many complexes with coordination numbers 5 and 6, which in many cases are induced by conformational requirements of the ligands. The same situation is found in the case of Cd(II), but with a greater preference for high coordination numbers than zinc (II) [10,12]. Pb(II) can adopt many different geometries in its complexes, allowing a degree of tolerance for ligand configuration which is not seen, for example, in d-block elements. Coupled with the ability to bind well both hard and soft donor atoms, these properties make Pb(II) an interesting metal to study, forming as it often does complexes different from those that might be conventionally expected. In the case of Ni(II), square planar complexes with strong field ligands are very stable, although octahedral complexes are also common. When cobalt (II) complexes are synthesised, oxidation to Co(III) is possible, specially in alkali medium in the presence of N-donor ligands. Co(II) complexes can adopt different geometries, while Co(III) complexes are virtually all low-spin and octahedral.

In previous works we have reported the synthesis and characterization of some coordination compounds with ligands derived from benzil and thiosemicarbazide: an open chain thiosemicarbazone, which shows the versatile chelating behaviour of TSC ligands [13], as well as the title ligand with some organotin (IV) derivatives. In this case complexes with 1:1 and 1:2 stoichiometries can be obtained, depending on the counter ion, in which the triazine acts always as a NS chelate. In the 1:2 complexes the ligands occupy the equatorial positions in a distorted octahedral arrangement [14].

In this paper we report the synthesis and characterisation of cadmiun, zinc, lead, cobalt and nickel derivatives of the ligand LH_2OCH_3 (Scheme 1). In these complexes, depending on the preference for a coordinated donor atom and the geometry for the metal ion, the triazine acts as a bidentate ligand and as a bidentate and bridging ligand.



Scheme 1. Drawing of LH_2OCH_3.

2. Experimental

2.1. Physical measurements

Microanalyses were carried out using a Perkin–Elmer 2400 II CHNS/O Elemental Analyser. IR Spectra in the 4000–400 cm^{-1} range were recorded as KBr pellets on a Jasco FT/IR-410 spectrophotometer. ^1H, ^{13}C and ^{113}Cd NMR spectra were recorded on a Bruker AMX-300 spectrophotometer using $CDCl_3$, DMSO-d_6 and DMF/$CDCl_3$ as solvents and TMS or 0.1 M aqueous $Cd(ClO)_4$ as references. ^{13}C CP/MAS NMR spectra were obtained at 298 K on a Bruker avance-400 spectrometer, using a standard cross-polarisation pulse sequence [15–18]. The external magnetic field was 9.4 T, and the sample was spun at 4–4.5 kHz around an axis inclined 54°44′ with respect to this field. Spectrometer frequencies were set to 100.63 MHz. For the recorded spectra a contact time of 1 ms was used. The number of scans were about 4000. The analysis was done with the WINFIT program. In this program the principal values of the chemical shift anisotropy tensor were determined from the intensity of the sidebands with the Herzfeld and Berger's method [19]. Fast atom bombardment (FAB) mass spectra were recorded on a VG Auto Spec instrument using Cs as the fast atom and *m*-nitrobenzilalcohol (*m*NBA) as the matrix. Matrix assisted laser desorption ionisation-time of flight (MALDI-TOF) mass spectra were recorded using a Bruker Reflex III mass spectrometer equipped with a nitrogen laser emitting at 337 nm, using ditranol as matrix. UV–Vis Spectra in DMF solution were registered on an Ati-Unicam UV2 spectrophotometer and the solid reflectance spectra on a Pye-Unicam SP-8-100. Conductivity data were measured using freshly prepared DMF solutions (ca. 10^{-3} M) at 25 °C with a Metrohm Herisau model E-518 instrument. Electrochemical measurements were performed with a BAS CV 27 voltammograph and a BAS A-4 XY register using glassy carbon (∅ 5 mm) as the working electrode, a platinum wire as the auxiliary electrode, and a double junction with a porous ceramic wick, Ag/AgCl as the reference electrode, standardized for the redox couple ferricinium/ferrocene ($E_{1/2}$ = +0.400 V, ΔE_p = 60 mV). Cyclic voltammetry studies of LH_2OCH_3 and the complexes were carried out on 0.01 M solutions in dimethylformamide containing 0.1 M $[NBu_4][PF_6]$ as the supporting electrolyte. The range of potential studied was between +1.4 and −2.2 V. All solutions were purged with nitrogen steam for 5 min before measurement and the working electrode was polished before each experiment with diamond paste. The procedure was performed at room temperature and a nitrogen atmosphere was maintained over the solution during the measurements. Magnetic susceptibilities of powder samples were

measured in the range 2–293 K with a SQUID magnetometer (MPMS, Quantum Design) in a 1-T external magnetic field.

2.2. Crystallography

A crystal of compound **1a** was mounted on a glass fibre and transferred to a Bruker SMART 6K CCD area-detector three-circle diffractometer with a MAC Science Co., Ltd. Rotating Anode (Cu Kα radiation, $\lambda = 1.54178$ Å) generator equipped with Goebel mirrors at settings of 50 kV and 110 mA. X-ray data were collected at 296 K, with a combination of six runs at different φ and 2θ angles, 3600 frames. The data were collected using 0.3° wide ω scans and a crystal-to-detector distance of 4.0 cm.

The substantial redundancy in data allows empirical absorption corrections (SADABS) [20] to be applied using multiple measurements of symmetry-equivalent reflections (ratio of minimum to maximum apparent transmission: 0.566680). The unit cell parameters were obtained by full-matrix least-squares refinements of 10487 reflections.

The raw intensity data frames were integrated with the SAINT [21] program, which also applied corrections for Lorentz and polarization effects.

The software package SHELXTL [22] version 6.10 was used for space group determination, structure solution and refinement. The space group determination was based on a check of the Laue symmetry and systematic absences and was confirmed using the structure solution. The structure was solved by direct methods (SHELXS-97) [23], completed with difference Fourier syntheses, and refined with full-matrix least squares using SHELXL-97 [24] minimizing $\omega(F_o^2 - F_c^2)^2$. Weighted R factors (R_w) and all goodness of fit (S) are based on F^2; conventional R factors (R) are based on F. All non-hydrogen atoms were refined with anisotropic displacement parameters. All scattering factors and anomalous dispersions factors are contained in the SHELXTL 6.10 program library. The H atoms were introduced in calculated positions with fixed C–H distances. The coordinated DMF molecules were found to be greatly disordered, which was modelled. The occupation factors for each position are 43% for O1 and 57% for O2; 36% for C32A and 64% for C32B; and 36% for C33A and 64% for C33B.

2.3. Syntheses

All reagents and other solvents were obtained from standard commercial sources and were used as received. $Pb(NO_3)_2$ was synthesised from $Pb(SCN)_2$ and nitric acid, according to the procedure described in the literature.

2.4. Methoxy-5,6-diphenyl-4,5-dihydro-2H-[1,2,4]triazine-3-thione, LH_2OCH_3 [25]

Selected spectroscopic data: IR/cm^{-1}: 3184s and 3131s (NH); 1608w (C=N), 1550s (thioamide I), 846w (thioamide IV). ^{1}H NMR (300 MHz, $CDCl_3$, 25 °C): $\delta = 3.1$ (s, 3H, OCH_3), 7.4–7.2 (m, 8H, Ph), 7.5 (m, 2H, Ph), 10.0 (d, 1H, NH), 12.1 (d, 1H, NH). ^{13}C NMR (300 MHz, $CDCl_3$, 25 °C): 83.2 (CR_4), 50.7 (CH_3O), 126.5, 129.3, 133.7, 141.7 (Ph), 142.4 (CN), 169.7 (CS).

2.5. $[Cd(H_2O)L_2]_2$ (**1**)

A mixture of LH_2OCH_3 (0.50 g, 1.70 mmol) and $LiOH \cdot H_2O$ (0.07 g, 1.70 mmol) was dissolved in methanol (25 mL). Then a solution of $Cd(NO_3)_2 \cdot 4H_2O$ (0.52 g, 1.70 mmol) in the same solvent (25 mL) was added. The mixture was stirred for 6 h at room temperature and the yellow solid formed was filtered off, washed with methanol and dried "in vacuo". Yield: 40%; m.p. 200 °C. $[(CdH_2O)L_2]_2$ (1329.4): *Anal.* Calc. C, 54.68; H, 3.34; N, 12.76; S, 9.72. Found: C, 54.92; H, 3.32; N, 13.05; S, 9.53%. Λ_M (DMF, Ω^{-1} cm^2 mL^{-1}): 5. *m/z* (FAB+): 643.0 ($[CdL_2 + 1]^+$, 7%), 752.9 ($[Cd_2L_2 - 1]^+$, 3%), 1017.9 ($[Cd_2L_3]^+$, 15%). Selected spectroscopic data: IR (KBr, cm^{-1}): 1600w, 1573w (C=N), 1490s (NCS), 812w (thioamide IV). ^{1}H NMR (300 MHz, DMSO-d_6, 25 °C): 7.3–7.5 (m, Ph). ^{13}C NMR (300 MHz, DMSO-d_6, 25 °C): 128.3, 128.5, 128.8, 129.0, 129.6, 130.4, 135.6, 135.8 (Ph), 150.8, 155.1 (CN), 180.7 (CS). ^{113}Cd NMR (300 MHz, DMF/$CDCl_3$, 25 °C): 202.0. Yellow crystals of complex **1a**, with the formula $[Cd(DMF)L_2]_2 \cdot 2DMF \cdot 1/4H_2O$, suitable for X-ray analysis, were grown by slow evaporation of a dimethylformamide solution of complex **1**.

2.6. $[Zn(H_2O)L_2]_2$ (**2**)

$Zn(NO_3)_2 \cdot 6H_2O$ (0.25 g, 0.85 mmol) dissolved in methanol (10 mL) was added to a solution of LH_2OCH_3 (0.25 g, 0.85 mmol) and $LiOH \cdot H_2O$ (0.04 g, 0.95 mmol) in methanol (40 mL). The mixture was stirred under reflux during 4 h. Then the yellow solid formed was filtered off, washed with methanol and vacuum dried. Yield: 51%; m.p. >260 °C. $[Zn(H_2O)L_2]_2$ (1228.8): *Anal.* Calc. C, 57.20; H, 3.81; N, 13.35; S, 10.17. Found: C, 56.90; H, 3.44; N, 13.35; S, 10.14%. Λ_M (DMF, Ω^{-1} cm^2 mL^{-1}): 9. *m/z* (MALDI-TOF): 923.7 ($[Zn_2L_3]^+$). Selected spectroscopic data: IR (KBr, cm^{-1}): 1598w, 1578w (C=N), 1495s (NCS), 807w (thioamide IV). ^{13}C CP/MAS NMR: 126.0, 128.5, 130.3, 134.5 (Ph), 151.4, 155.1 (CN), 177.6 (CS).

2.7. $[PbL_2]_2$ (3)

To a solution containing LH_2OCH_3 (0.50 g, 1.68 mmol) and $LiOH \cdot H_2O$ (0.07 g, 1.67 mmol) in methanol (50 mL) was added a solution of $Pb(NO_3)_2$ (0.56 g, 1.69 mmol) in distilled water (5 mL). The mixture was stirred under reflux for 6 h and the brown solid formed was filtered off, washed with methanol, then distilled water and vacuum dried. Yield: 68%; m.p. 222 °C with decomposition. $[PbL_2]_2$ (1470.4): *Anal.* Calc. C, 34.21; H, 2.49; N, 14.97, S, 11.40. Found: C, 34.48; H, 2.55; N, 14.84; S, 11.46%. Λ_M (DMF, $\Omega^{-1}\,cm^2\,mL^{-1}$): 7. *m/z* (FAB+): 472.0 ($[PbL + 1]^+$, 100%), 737.1 ($[PbL_2 + 1]^+$, 4%), 1207.1 ($[Pb_2L_3]^+$, 35%). Selected spectroscopic data: IR (KBr, cm^{-1}): 1599w, 1581w (C=N), 1486s (NCS), 812 (thioamide IV). ^1H NMR (300 MHz, DMSO-d_6, 25 °C): 7.1–7.5 (m, Ph). ^{13}C NMR (300 MHz, DMSO-d_6, 25 °C): 128.4, 129.0, 129.6, 130.1, 136.6 (Ph), 151.9, 154.2 (CN), 178.7 (CS).

2.8. $[CoL_3]$ (4)

A solution of $Co(NO_3)_2 \cdot 6H_2O$ (0.46 g, 1.58 mmol) in methanol (25 mL) was added to a solution of LH_2OCH_3 (0.47 g, 1.58 mmol) and $LiOH \cdot H_2O$ (0.07 g, 1.67 mmol) in methanol (25 mL). The mixture was stirred at room temperature for 6 h. Then the green solid formed was filtered off, washed with methanol and dried "in vacuo". Yield: 33%; m.p. 200 °C. $[CoL_3]$ (850.9): *Anal.* Calc. C, 63.46; H, 3.52; N, 14.80; S, 11.52. Found: C, 63.09; H, 3.38; N, 14.58; S, 11.52%. Λ_M (DMF, $\Omega^{-1}\,cm^2\,mL^{-1}$): 8. *m/z* (FAB+): 587.9 ($[CoL_2 + 1]^+$, 15%), 852.2 ($[CoL_3 + 1]^+$, 25%). Selected spectroscopic data: IR (KBr, cm^{-1}): 1600w, 1579w (C=N), 1480s (NCS), 815w (thioamide IV). ^1H NMR (300 MHz, DMSO-d_6, 25 °C): 7.1–7.6 (m, Ph). ^{13}C NMR (300 MHz, DMSO-d_6, 25 °C): 128.73, 128.78, 128.81, 128.89, 128.95, 129.00, 129.11, 129.51, 129.56, 129.87, 130.01, 130.13, 130.25, 130.34, 130.37, 130.40, 131.31, 131.81, 131.85, 134.81, 134.83, 135.06, 135.13, 135.17, 135.42, 135.46 (Ph), 153.11, 153.25, 154.46, 154.63, 159.91, 160.13, 160.23, 160.36 (CN), 182.57, 183.27, 184.35, 184.70 (CS).

2.9. $[NiL_2]$ (5)

To a solution of LH_2OCH_3 (1.00 g, 3.40 mmol) and $LiOH \cdot H_2O$ (0.07 g, 1.67 mmol) in methanol (130 mL) was added $Ni(NO_3)_2 \cdot 6H_2O$ (0.50 g, 1.70 mmol) dissolved in the same solvent (15 mL). The mixture was stirred at room temperature for 8 h and the brown solid formed was filtered off, washed with methanol and dried "in vacuo". Yield: 39%; m.p. >260 °C. $[NiL_2]$ (586.7): *Anal.* Calc. C, 61.36; H, 3.41; N, 14.32; S, 10.91. Found: C, 61.03; H, 3.52; N, 14.16; S, 10.87%. Λ_M (DMF, $\Omega^{-1}\,cm^2\,mL^{-1}$): 11. *m/z* (MALDI-TOF): 587.0 ($[NiL_2 + 1]^+$. Selected spectroscopic data: IR (KBr, cm^{-1}): 1600w, 1579w (C=N), 1485s (NCS), 817w (thioamide IV).

3. Results and discussion

The complexes were obtained in methanol in the presence of a basic medium, which induces the loss of the methoxy group as a methanol molecule, probably due to an acid–base reaction with the relatively highly acidic N–H bond, yielding LH, according to a mechanism previously published [14].

Analytical data of complexes show 1:2 metal/ligand stoichiometries for all the derivatives, except for complex **4** where the ratio is 1:3, and the absence of nitrate groups. These indicate that in all the complexes the ligand acts as a monoanion L and that in complex **4** the cobalt has been oxidised to Co(III). Oxidation of Co(II) salts in the presence of thiosemicarbazone ligands in ethanol, methanol and chloroform is documented [26–28]. The possibility of oxidation increases with the presence of a basic medium. Measurements of magnetic susceptibility for complex **4** indicate that $\mu_{eff} = 0$ BM, so the complex is diamagnetic, which confirms the oxidation of the metal and the existence of a low-spin octahedral complex. Conductivity measurements in DMF indicate the presence of non-ionic species in this solvent [29]. In the mass spectra of complexes **1**, **2** and **3** (Fig. 1) a peak corresponding to the fragment $[M_2L_3]^+$ can be observed, which indicates the presence of a dinuclear species. Due to the analytical data indicating the absence of nitrate groups, if the complexes contain two metal ions they must contain four ligands to get neutrality, and one of them is lost to form a monopositive ion. The way to get a dinuclear species could be due to the formation of sulfur bridges, as occurs in many thiosemicarbazone complexes [30–32]. Moreover the spectra show peaks corresponding to different fragmentations of the complexes, owing to the loss of L or M. The mass spectrum of complex **4** exhibits a peak corresponding to the fragment $[CoL_3 + 1]^+$ pointing out the presence of a complex containing one cobalt and three deprotonated ligands. Mass spectra of complex **5** shows a peak corresponding to the fragment $[NiL_2 + 1]^+$, which indicates the presence of a species containing one metal ion and two deprotonated ligands. Experimental isotopic distributions show the same patterns as the theoretical ones for all compounds.

The electronic spectrum of complex **4** shows a band centred at ca. 17.241 cm^{-1} and reflectance spectrum shows two bands at 16.667 and 20.000 cm^{-1}, which is consistent with a octahedral low-spin Co(III) complex. The spectrum of complex **5** shows a band at 20.000 cm^{-1}, which agrees with a square-planar environment [33].

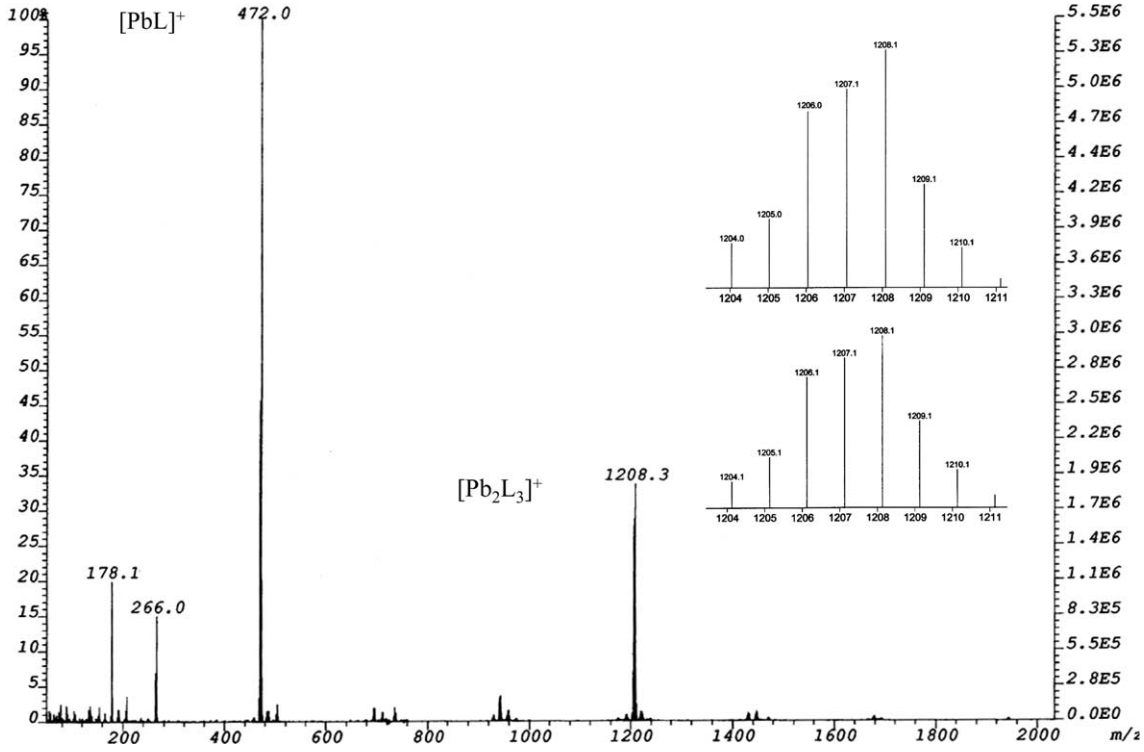


Fig. 1. FAB + spectrum of $[PbL_2]_2$ (**3**).

3.1. Crystal structure of $[Cd(DMF)L_2]_2 \cdot 2DMF \cdot 1/4H_2O$

Crystallographic data of complex **1a** are summarised in Table 1.

The crystal structure of the cadmium complex is formed of discrete $[Cd(DMF)L_2]$ entities linked through one sulfur atom of another thiosemicarbazone ligand, which leads to the dinuclear centrosymmetric $[Cd(DMF)L_2]_2$ species. The molecular structure is shown in Fig. 2 and selected bond distances and angles are summarised in Table 2. In the complex the Cd(II) ion is in a distorted octahedral arrangement formed by two amine nitrogen atoms, three sulfur atoms and the oxygen of a DMF molecule. The two water molecules present in complex **1** have been substituted by solvent molecules, which present great disorder. The coordination mode of the ligand affords four four-member chelate rings. The triazine rings are almost planar with a maximum deviation of 0.0749 Å for C(1) and 0.055 Å for C(16). S(1) is 0.318 Å under this plane and S(2) 0.2487 Å above. So the triazine that contains N(4), N(5) and N(6) is more planar than the one that contains N(1), N(2) and N(3). The aromatic rings form with respect to these planes dihedral angles of 35.75° for C(3)–C(8), 44.77° for C(10)–C(15), 42.55° for C(18)–C(23) and 38.63° for C(25)–C(30). Cd–N bond distances are slightly different (2.322 and 2.306 Å), the one belonging to the ligand that acts as a bridge being shorter. The Cd–S bond distance with the monodentate sulfur atom is shorter than those with the bridging sulfurs, which moreover are quite different (2.6342 and 2.8932 Å).

Table 1
Crystal data and structure refinement for complex **1a**

	1a
Formula	$C_{72}H_{68.5}N_{16}CdO_2S_4O_{4.25}Cd_2$
Molecular weight	1579.00
Crystal system	tetragonal
Space group	*P4/n*
Unit cell dimensions	
a (Å)	23.4137(4)
b (Å)	23.4137(4)
c (Å)	13.8831(3)
α (°)	90
β (°)	90
γ (°)	90
V (Å^3)	7610.7(2)
Z	4
D_c (Mg m^{-3})	1.376
Absorption coefficient (mm^{-1})	5.963
F(000)	32166
Goodness-of-fit on F^2	1.070
Reflections collected	48038
Independent reflections (R_{int})	7188 (0.0389)
Completeness to theta = 70.53°	98.3%
Absorption correction	SADABS v. 2.03
Refinement method	full-matrix least-squares on F^2
Final R_1 and wR_2 [$I > 2\sigma(I)$]	$R_1 = 0.0437$, $wR_2 = 0.1277$
R indices (all data)	$R_1 = 0.0484$, $wR_2 = 0.1322$

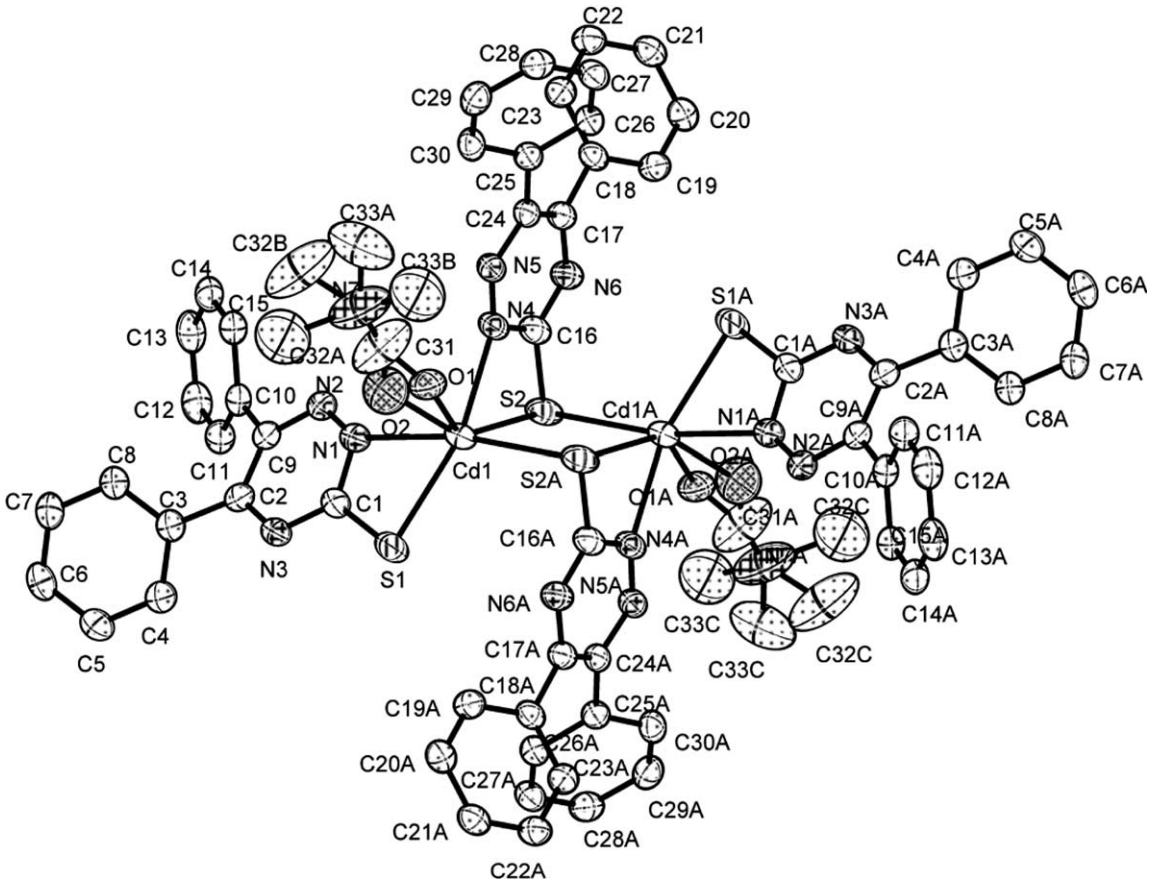


Fig. 2. Molecular structure of $[Cd(DMF)L_2]_2 \cdot 2DMF \cdot 1/4H_2O$ (**1a**). Thermal ellipsoids are shown at 50% probability. Hydrogen atoms are omitted for clarity.

In the complex, owing to the deprotonation, there is a considerable electronic delocalisation through the thiosemicarbazone backbone. As a consequence all the C–N bonds have almost the same length (Table 2), which does not occur in LH_2OCH_3 (1.28–1.459 Å). In the complex the thione bonds are longer than in the precursor ligand (1.628 Å in LH_2OCH_3) and they are intermediate between the theoretical C–S single and double bonds, as is also the case of the N–N bonds [34]. In addition the N(3)–C(2)–C(3) and N(3)–C(8)–C(1) angles are close to 120°, as would be expected for sp^2 hybridisation, while in LH_2OCH_3 the corresponding angle is 108°, corresponding to sp^3 hybridisation.

3.2. IR Spectroscopy

The IR spectrum of LH_2OCH_3 is reported in Section 2. The absence of a band in the 2600 cm^{-1} region in any complex suggests the absence of a thiol tautomer [35]. In the spectra of all complexes there are no bands in the 3000–3300 cm^{-1} region, which indicates the absence of N–H bonds. Moreover bands attributable to the nitrate group are not observed. The absence of these bands confirms that the ligand acts as a monoanion L in all complexes. The band corresponding to the CS moiety is shifted to lower frequencies, indicating coordination of the sulfur to the metal ion. The presence of two bands attributable to C=N bonds could indicates the formation of a new imine group, due to the loss of the methoxy group of the ligand LH_2OCH_3, although the great electronic delocalisation in the ring probably leads to there being only one C=N band and the new band could be due to the hydrazinic CN. These imine nitrogen atoms are not coordinated to the metal ion.

3.3. NMR Spectroscopy

The NMR assignments for LH_2OCH_3 are listed in Section 2. The low solubility of complexes **2** and **5** made it impossible to obtain ^1H and ^{13}C NMR spectra. In addition, the ^{13}C CP/MAS NMR of complex **5** was recorded, but it did not show any clear signal, probably due to a high heterogeneity in the sample. The ^1H NMR spectra of all the complexes only show a multiplet in the aromatic region, corresponding to the phenyl rings of the ligand. The absence of any signal corresponding to amine protons supports the ligand deprotonation. The absence of the singlet attributable to the

Table 2
Selected bond lengths (Å) and angles (°) for complex **1a**

Cd(1)–N(4)	2.306(2)
Cd(1)–O(2)	2.310(9)
Cd(1)–O(1)	2.346(5)
Cd(1)–N(1)	2.522(3)
Cd(1)–S(1)	2.5300(9)
Cd(1)–S(2)#1	2.6342(9)
Cd(1)–S(2)	2.8932(9)
C(1)–N(3)	1.349(5)
C(1)–N(1)	1.353(4)
C(1)–S(1)	1.732(4)
C(2)–N(3)	1.332(5)
C(2)–C(9)	1.418(5)
C(9)–N(2)	1.338(4)
C(16)–N(4)	1.342(4)
C(16)–N(6)	1.347(4)
C(16)–S(2)	1.738(3)
C(17)–N(6)	1.325(4)
C(17)–C(24)	1.420(5)
C(24)–N(5)	1.332(4)
N(1)–N(2)	1.332(4)
N(4)–N(5)	1.334(4)
S(2)–Cd(1)#1	2.6342(9)
N(4)–Cd(1)–O(2)	89.3(3)
N(4)–Cd(1)–O(1)	83.92(14)
O(2)–Cd(1)–O(1)	23.3(3)
N(4)–Cd(1)–N(1)	95.23(9)
O(2)–Cd(1)–N(1)	83.6(5)
O(1)–Cd(1)–N(1)	106.7(3)
N(4)–Cd(1)–S(1)	157.44(7)
O(2)–Cd(1)–S(1)	91.2(3)
O(1)–Cd(1)–S(1)	104.66(17)
N(1)–Cd(1)–S(1)	62.43(7)
N(4)–Cd(1)–S(2)#1	91.12(7)
O(2)–Cd(1)–S(2)#1	108.6(5)
O(1)–Cd(1)–S(2)#1	86.0(2)
N(1)–Cd(1)–S(2)#1	166.38(7)
S(1)–Cd(1)–S(2)#1	110.05(3)
N(4)–Cd(1)–S(2)	59.20(7)
O(2)–Cd(1)–S(2)	146.9(2)
N(2)–N(1)–Cd(1)	145.1(2)
C(1)–N(1)–Cd(1)	95.4(2)
N(1)–N(2)–C(9)	119.5(3)
C(2)–N(3)–C(1)	117.0(3)
N(5)–N(4)–C(16)	119.7(3)
N(5)–N(4)–Cd(1)	129.9(2)
C(16)–N(4)–Cd(1)	108.2(2)
O(1)–Cd(1)–S(2)	141.33(16)
N(1)–Cd(1)–S(2)	89.17(7)
S(1)–Cd(1)–S(2)	113.89(3)
S(2)#1–Cd(1)–S(2)	83.75(3)
N(3)–C(1)–N(1)	123.5(3)
N(3)–C(1)–S(1)	120.8(3)
N(1)–C(1)–S(1)	115.6(3)
N(3)–C(2)–C(9)	119.3(3)
N(3)–C(2)–C(3)	116.5(3)
N(2)–C(9)–C(2)	120.0(3)
N(2)–C(9)–C(10)	115.3(3)
N(4)–C(16)–N(6)	123.2(3)
N(4)–C(16)–S(2)	115.8(2)
N(6)–C(16)–S(2)	121.0(3)
N(6)–C(17)–C(24)	120.0(3)
N(5)–C(24)–C(17)	119.8(3)
N(2)–N(1)–C(1)	118.5(3)
C(24)–N(5)–N(4)	119.1(3)
C(17)–N(6)–C(16)	117.1(3)
C(1)–S(1)–Cd(1)	86.33(12)
C(16)–S(2)–Cd(1)#1	93.76(10)
C(16)–S(2)–Cd(1)	76.55(11)
Cd(1)#1–S(2)–Cd(1)	96.25(3)

Symmetry transformations used to generate equivalent atoms: #1 $-x$, $-y+1$, $-z$.

methoxy group at 3.3 ppm confirms the loss of the inserted methoxy group and the formation of a new C=N bond.

In the ^{13}C NMR spectra the signals corresponding to the methoxy group and the tetrasubstituted carbon atom have disappeared and a new signal corresponding to an imine group is observed. The imine groups are not bonded to the metal ion, as the X-ray diffraction has established for complex **1a**. In addition the signal corresponding to the thione group is deshielded in all complexes, suggesting the presence of metal–sulfur bonds.

The ^{13}C NMR spectrum of complex **4** shows four signals corresponding to CS groups, four to CN and 26 corresponding to aromatic carbon atoms. Two isomers of octahedral complexes with asymmetric chelating ligands are possible. In the *fac* isomer, the A end of each ligand is *trans* to the B end, and the three ligands are equivalent. In the *mer* form, which has a triple statistical probability, two of the A ends are *trans* to each other, and all three ligands are chemically distinct [36]. Thus, if there is an isomer mixture four sets of carbon resonances must be observed, as occurs. So we can establish there is a mixture of *fac* and *mer* isomers.

The ^{113}Cd NMR spectrum of complex **1** in a DMF/$CDCl_3$ solution shows a peak at 202.04 ppm, which indicates a coordination number of six for the cadmium ion. Sulfur ligands are most strongly deshielding, while nitrogen and oxygen donor ligands have a weaker deshielding effect on the Cd(II) ion [37]. Taking this into account and by comparison with the complex $[CdLH_6(NO_3)_2]$ ($\delta = 177.8$ ppm), with the ligand benzilbisthiosemicarbazone LH_6 in which the metal is in a distorted octahedral arrangement with a $N_2S_2O_2$ environment [38], the value of the ^{113}Cd chemical shift is in agreement with a N_2S_3O environment for cadmium ions.

In sight of the data found, and taking into account the results obtained with some organotin derivatives [14], we can assume that the ligand L acts in all complexes as at least as a NS chelate. The structure of complex **2** could consist of a monomer, in which two sulfur and two nitrogen atoms of two ligands occupy the base of a square-base pyramid and with the oxygen of the water molecule in the apex, or a dinuclear one as

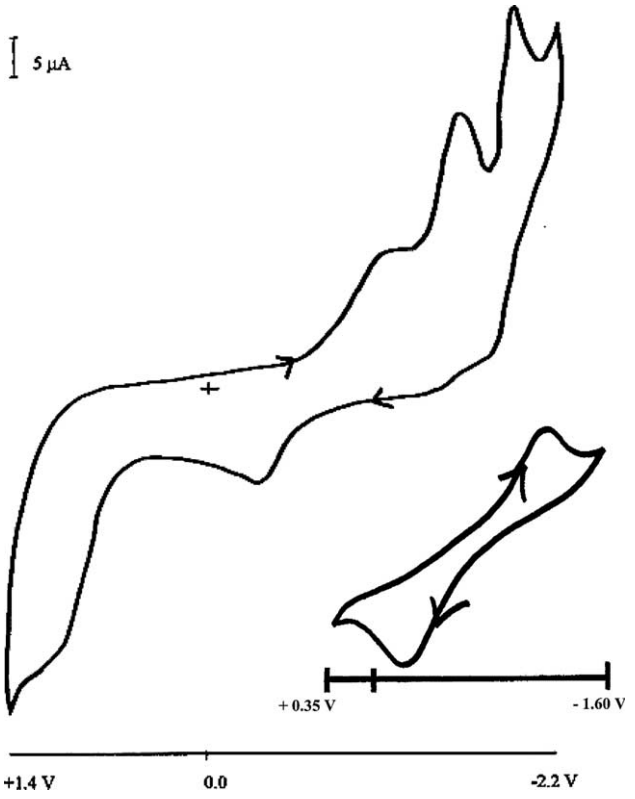


Fig. 3. Cyclic voltammogram of complex $[Cd(H_2O)L_2]_2$ (**1**) in DMF; $v = 100$ mV/s. Inset: the redox couple.

complex **1** shows. Complexes **1a** and **2** show the same spectroscopic characteristics and the same pattern in the mass spectra. In particular, the mass fragment $[Zn_2L_3]^+$ would be difficult to explain without the presence of a dimeric species (molecular association during the experiment would lead to the fragment $[Zn_2L_4 + 1]^+$). Hence the structure of complex **1** could be expected for complex **2**, with Zn(II) in a distorted octahedral arrangement formed by two amine nitrogen atoms, an oxygen of a water molecule and three sulfur atoms, two of them acting as bridge, a structure that has been found in other Zn(II) complexes with N_2S ligands, with a dimeric structure via sulfur bridges [39]. In complex **3** a dimeric structure is also expected, where two of the four ligands act also as bridges, so Pb(II) is in a N_2S_3 environment in a pentacoordinate geometry. However, the structure of complex **3** may be considered as octahedral if the lone pair is considered as "occupying" one position, as is quite common for Pb(II) complexes. Complex **4** presents the expected octahedral geometry for Co(III), with a N_3S_3 environment for the metal ion. In complex **5** the Ni(II) ion is in a square-planar arrangement with the two ligands bonded through the sulfur atom and the amine nitrogen, so the Ni(II) environment is N_2S_2. By comparison with other metal derivatives previously published by us with this ligand [14], we expect the formation of the *cis* isomer.

3.4. Electrochemical behaviour

The cyclic voltammogram of LH_2OCH_3 in DMF only shows an irreversible cathodic wave at −1.897 V, which can be attributed to the reduction of the groups present in the ligand.

The cyclic voltammogram of complex **1** between 1.4 and −2.2 V (Fig. 3) exhibits three cathodic waves at −0.892, −1.482 and −1.847 V and an anodic one at −0.261 V, related to the one at −0.892 V. This redox couple, with $E_{1/2} = -0.576$ V, corresponds to Cd(II)/Cd(I) process. The morphology of the first cathodic peak is similar to that of the Cd(II)/Cd(I) process in $Cd(NO_3)_2 \cdot 4H_2O$ in DMF, although it is shifted to more negative potentials.

On scanning from 1.0 to −2.2 V, the cyclic voltammogram of complex **4** (Fig. 4) shows a redox couple at $E_{1/2} = -0.150$ V, corresponding to a Co(III)/Co(II) process, and two irreversible cathodic peaks corresponding to ligand reduction processes. Analysis of the redox couples of complexes **1** and **4** in the interval 25–800 mV/s shows a linear variation of i_{pc} versus $v^{1/2}$. A small dependence of the potential peak with the scan rate is observed, and the i_{pa}–i_{pc} ratio is close to unity. These

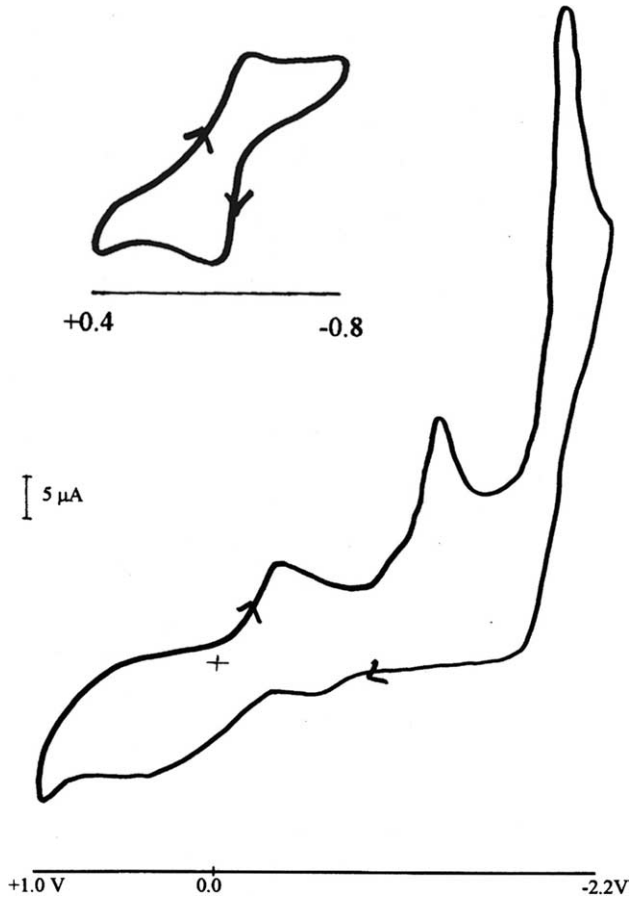


Fig. 4. Cyclic voltammogram of complex $[CoL_3]$ (**4**) in DMF; $v = 100$ mV/s. Inset: the redox couple.

results suggest diffusion controlled quasirreversible processes [40].

4. Conclusions

Reaction of the ligand LH_2OCH_3 with divalent metals leads to the formation of the corresponding coordination compounds, where the ligand has lost the methoxy group and acts as a monoanion. The presence of basic medium is necessary to get all the metal derivatives.

In all the complexes the ligand acts as bidentate and bonds to metal ions through the sulfur atom and the deprotonated amine nitrogen, giving a four-member chelate ring. The structure of the complexes is determined by the structural preferences of the metal ions as well as by the ligand configuration. Complexes **1**, **2** and **3** are dinuclear species, in which the sulfur atom of two thiosemicarbazone ligands acts as a bridge between the metal ions. Complexes **4** and **5** are monomeric compounds.

Preliminary electrochemical results confer good prospects for complex **1** to be a lead compound in the discovery of new sensors for the toxic Cd(II) ion.

Acknowledgements

We thank César J. Pastor and Beatriz Souto Pérez, of the "Servicio Interdepartamental de Investigación, Universidad Autónoma de Madrid" for the X-ray diffraction and Prof. Regino Sáez and Dr. Julio Romero of the "Universidad Complutense de Madrid" for the magnetic susceptibility measurements. We also thank DGICYT for financial support (Project BQU2001-0151).

Appendix A. Supplementary data

CCDC 256951 for complex **1a** contains the supplementary crystallographic data for this paper. These data can be obtained free of charge from the Cambridge Crystallographic Data Centre, 12 Union Road, Cambridge CB2 1EZ, UK, fax: (internat.) +44 1223 336 033; e-mail: deposit@ccdc.cam.ac.uk, or on the web www.ccdc.cam.ac.uk/conts/retrieving.html. Supplementary data associated with this article can be found, in the online version at doi:10.1016/j.poly.2005.03.093.

References

[1] D.X. West, A.E. Liberta, S.B. Padhye, R.C. Chikate, P.B. Sonawane, A.S. Kumbhar, R.G. Yeranda, Coord. Chem. Rev. 123 (1993) 49, and references therein.
[2] A.E. Liberta, D.X. West, Biometals 5 (1992) 121.
[3] D.X. West, S.B. Padhye, P.B. Sonawane, Struct. Bond. 76 (1991) 1.
[4] J.G. Cory, A.H. Cory (Eds.), International Encyclopaedia of Pharmacology and Therapeutics, Pergamon Press, New York, 1989.
[5] J. Ruipérez, M.A. Mendiola, M.T. Sevilla, J. Rodríguez-Procopio, L. Hernández, Electroanalysis 14 (2002) 532.
[6] M.J. Gismera, M.A. Mendiola, J. Rodríguez-Procopio, M.T. Sevilla, Anal. Chim. Acta 385 (1999) 143.
[7] G. Giacomelli, A. Porcheddu, L. Luca, Curr. Org. Chem. 8 (2004) 1497.
[8] Z. Brzozowski, F. Saczewski, M. Gdaniec, Eur. J. Med. Chem. 35 (2000) 1053.
[9] J.S. Casas, A. Castiñeiras, M.C. Rodríguez-Argüelles, A. Sánchez, J. Sordo, A. Vázquez-López, E.M. Vázquez-López, J. Chem. Soc., Dalton Trans. (2000) 2267.
[10] J.S. Casas, M.S. Tasende, J. Sordo, Coord. Chem. Rev. 209 (2000) 197.
[11] M. Melnik, K. Györyová, J. Skorsepa, C.E. Holloway, J. Coord. Chem. 35 (1995) 179.
[12] E. Labisbal, A. Sousa-Pedrares, A. Castiñeiras, J.K. Swearingen, D.X. West, Polyhedron 21 (2002) 1553.
[13] E. López-Torres, M.A. Mendiola, C.J. Pastor, B. Souto Pérez, Inorg. Chem. 43 (2004) 5222.
[14] E. López-Torres, M.A. Mendiola, C.J. Pastor, J.R. Procopio, Eur. J. Inorg. Chem. (2003) 2711.
[15] R.A. Santos, E.S. Gruff, S.A. Koch, G.S. Harbison, J. Am. Chem. Soc. 112 (1990) 9257.
[16] S.R. Hartmann, E.L. Hahn, Phys. Rev. 128 (1962) 2042.
[17] A. Pines, M.G. Gibby, J.S. Waugh, J. Chem. Phys. 59 (1973) 569.
[18] P.D. Murphy, W.C. Stevens, T.T.P. Cheung, S. Lacelle, B.C. Gerstein, D.M. Kurtz Jr., J. Am. Chem. Soc. 103 (1981) 4400.
[19] J. Herzfeld, A.E. Berger, J. Chem. Phys. 73 (1980) 6021.
[20] G.M. Sheldrick, SADABS Version 2.03, Program for Empirical Absorption Correction, Universität Göttingen, 1997–2001.
[21] G.M. Sheldrick, SAINT + NT (version 6.04) *SAX* Area-Detector Integration Program, Bruker AXS, Madison, WI, 1997–2001.
[22] Bruker AXS SHELXTL (version 6.10) Structure Determination Package, Bruker AXS, Madison, WI, 2000.
[23] SHELXS-97, Program for Structure Solution G.M. Sheldrick, Acta Crystallogr., Sect. A 46 (1990) 467.
[24] SHELXL-97, Program for Crystal Structure Refinement, Universität Göttingen, 1997.
[25] E. Franco, E. López-Torres, M[a].A. Mendiola, M[a].T. Sevilla, Polyhedron 19 (2000) 441.
[26] R.P. John, A. Sreekanth, M.R. Prathapachandra Kurup, S.M. Mobin, Polyhedron 21 (2002) 2515.
[27] D.K. Sau, R.J. Butcher, S. Chaudhuri, N. Saha, Polyhedron 23 (2004) 5.
[28] N.C. Saha, R.J. Butcher, S. Chaudhuri, N. Saha, Polyhedron 22 (2003) 383.
[29] W.J. Geary, Coord. Chem. Rev. 7 (1971) 81.
[30] E. Bermejo, A. Castiñeiras, R. Domínguez, R. Carballo, C. Maichle-Mössmer, J. Strähle, D.X. West, Z. Anorg. Allg. Chem. 625 (1999) 961, and references therein.
[31] E. Bermejo, A. Castiñeiras, I. García, D.X. West, Polyhedron 22 (2003) 1147.
[32] P. Gómez-Saiz, J. García-Tojal, M.A. Maestro, J. Mahía, F.J. Arnaiz, L. Lezama, T. Rojo, Eur. J. Inorg. Chem. (2003) 2639.
[33] A.B.P. Lever, Inorganic Electronic Spectroscopy, second ed., Elsevier, Amsterdam, 1984.
[34] E. Sutton, Tables of Interatomic Distances, Configuration in Molecules and Ions (Supplement), The Chemical Society, London, 1965.
[35] D.E. Fenton, D.H. Cook, J. Chem. Soc., Chem. Commun. (1977) 714.

[36] E.A.V. Ebsworth, D.W.H. Rankin, S. Cradock, Structural Methods in Inorganic Chemistry, Blackwell Scientific Publications, Oxford, 1987.
[37] J.S. Casas, M.V. Castaño, E.E. Castellano, M.S. García-Tasende, A. Sánchez, L.M. Sanjuán, J. Sordo, Eur. J. Inorg. Chem. (2000) 83, and references therein.
[38] E. López-Torres, M.A. Mendiola, J. Rodríguez-Procopio, M.T. Sevilla, E. Colacio, J.M. Moreno, I. Sobrados, Inorg. Chim. Acta 323 (2001) 130.
[39] U. Brand, H. Vahrenkamp, Inorg. Chim. Acta 308 (2000) 97.
[40] B.W. Rossiter, J.F. Hamilton, 2nd ed.Electrochemical Methods, vol. II, John Wiley & Sons, New York, 1986.

The complexes were prepared by adding the appropriate picoline (0.2 ml) to the solution of $[RuCl_2(PPh_3)_3]$ (0.2 g) in methanol (100 ml). The reaction mixture was stirred for 4 h. The solvent was then removed in vacuo and the crude residue was crystallized from methanol. Crystals of $[RuCl_2(\beta\text{-pic})_4]$, suitable for X-ray analysis, were obtained by slow evaporation of the methanolic solution.

2.1. $[RuCl_2(\alpha\text{-pic})_4]$

Yield 60%. *Anal*. Calc. for $C_{24}H_{28}Cl_2N_4Ru$: C, 52.94; H, 5.18; N, 10.29. Found: C, 52.42; H, 5.12; N, 5.04%. IR (KBr): 3052 (ν_{CH}), 2974 (ν_{CH}), 1604 ($\nu_{C=N}$), 1481 (ν_{ring}), 1435 ($\nu_{C=C}$), 1303 (ν_{ring}), 1187 (δ_{CH}), 1093 (δ_{CH}), 696 (δ_{ring}), 536 (ν_{M-N}). ^{1}H NMR (δ, $CDCl_3$): 8.36 (dd H6 pic), 7.23 (t H5 pic), 7.56 (td H4 pic), 7.27 (d H3 pic), 2.59 (CH_3). UV–Vis (CH_2Cl_2): 645.8 (1.90), 386.0 (3.81), 265.6 (4.74), 228.4 (5.32), 215.8 (5.03).

2.2. $[RuCl_2(\beta\text{-pic})_4]$

Yield 63%. *Anal*. Calc. for $C_{24}H_{28}Cl_2N_4Ru$: C, 52.94; H, 5.18; N, 10.29. Found: C, 52.72; H, 5.22; N, 5.14%. IR (KBr): 3077 (ν_{CH}), 3050 (ν_{CH}), 1615 ($\nu_{C=N}$), 1484 (ν_{ring}), 1420 ($\nu_{C=C}$), 1335 (ν_{ring}), 1195 (δ_{CH}), 1051 (δ_{CH}), 650 (δ_{ring}), 556 (ν_{M-N}). ^{1}H NMR (δ, $CDCl_3$): 8.87 (H2 pic), 7.31 (d H4 pic), 7.31 (dd H5 pic), 8.81 (d H6 pic), 2.18 (CH_3). UV–Vis (CH_2Cl_2): 513.4 (1.92), 427.0 (3.48), 381.8 (3.91), 244.4 (4.20), 222.2 (5.32), 215.8 (5.34).

2.3. $[RuCl_2(\gamma\text{-pic})_4]$

Yield 67%. *Anal*. Calc. for $C_{24}H_{28}Cl_2N_4Ru$: C, 52.94; H, 5.18; N, 10.29. Found: C, 52.47; H, 5.18; Nn 5.12%. IR (KBr): 3049 (ν_{CH}), 3023 (ν_{CH}), 1614 ($\nu_{C=N}$), 1481 (ν_{ring}), 1432 ($\nu_{C=C}$), 1385 (ν_{ring}), 1209 (δ_{CH}), 1088 (δ_{CH}), 724 (δ_{ring}), 531 (ν_{M-N}). ^{1}H NMR (δ, $CDCl_3$): 8.50 (d H2, H6 pic), 7.25 (d H3, H5 pic), 2.23 (CH_3). UV–Vis (CH_2Cl_2): 527.1 (1.91), 431.6 (3.77), 352.0 (4.22), 272.6 (4.81), 228.2 (5.21), 214.6 (5.05).

2.4. Physical measurements

Infrared spectra were recorded on a Nicolet Magna 560 spectrophotometer in the spectral range 4000–400 cm^{-1} with the samples in the form of KBr pellets. Electronic spectra were measured on a spectrophotometer Lab Alliance UV–Vis 8500 in the range 800–180 nm in deoxygenated dichloromethane solution. Elemental analyses (C, H, N) were performed on a Perkin–Elmer CHN-2400 analyzer. The ^{1}H NMR spectra were recorded on a Bruker DRX-400 spectrometer in $CDCl_3$ solutions.

2.5. Crystal structure determination and refinement

A rectangular prism crystal was mounted on a KM-4-CCD automatic diffractometer equipped with CCD detector, and used for data collection. X-ray intensity data were collected with graphite monochromated Mo Kα radiation ($\lambda = 0.71073$ Å) at a temperature of 293.0(2) K, with the ω scan mode. A 12 s exposure time was used and all the Ewald sphere was collected up to $2\theta = 50.22°$. The unit cell parameters were determined from least-squares refinement of the setting angles of 5589 strongest reflections. Details concerning crystal data and refinement are given in Table 1. Examination of 98 reflections on two reference frames monitored after each 20 frames measured showed 2.61% loss of the intensity. During the data reduction, the above decay correction coefficient was taken into account. The orange, transparent crystal used for the data collection did not change its appearance. Lorentz, polarization and numerical absorption [19] corrections were applied. The structure was solved by direct methods and subsequently completed by difference Fourier recycling. All the non-hydrogen atoms were refined anisotropically using the full-matrix, least-squares technique on F^2. All the hydrogen atoms were found from difference Fourier synthesis after four cycles of anisotropic refinement, and refined as ''riding'' on the adjacent carbon atom with an individual isotropic temperature fac-

Table 1
Crystal data and structure refinement details of $[RuCl_2(\beta\text{-pic})_4]$

Empirical formula	$C_{24}H_{28}Cl_2N_4Ru$
Formula weight	544.47
Temperature (K)	293(2)
Crystal system	tetragonal
Space group	*P*4*nc*
Unit cell dimensions	
a (Å)	11.1792(6)
b (Å)	11.1792(6)
c (Å)	10.1596(6)
Volume (Å^3)	1269.69(12)
Z	2
Calculated density (Mg/m^3)	1.424
Absorption coefficient (mm^{-1})	0.846
F(000)	556
Crystal dimensions (mm)	$0.572 \times 0.349 \times 0.274$
θ Range for data collection (°)	3.65–25.11
Index ranges	$-13 \leqslant h \leqslant 13$, $-13 \leqslant k \leqslant 13$, $-12 \leqslant l \leqslant 12$
Reflections collected	16633
Independent reflections [R_{int}]	1133 [0.0373]
Data/restraints/parameters	1133/1/74
Goodness-of-fit on F^2	1.119
Final *R* indices [$I > 2\sigma(I)$]	$R_1 = 0.0373$, $wR_2 = 0.1037$
R indices (all data)	$R_1 = 0.0389$, $wR_2 = 0.1054$
Largest difference in peak and hole (e Å^{-3})	0.282 and −0.297

tor equal to 1.2 times the value of the equivalent temperature factor of the aromatic parent carbon atom and equal to 1.5 times the value of the equivalent temperature factor of the methyl parent carbon atom. The methyl group was allowed to rotate during refinement about its local threefold axis. SHELXS 97 [20], SHELXL 97 [21] and SHELXTL [22] programs were used for all the calculations. Atomic scattering factors were those incorporated in the computer programs.

2.6. Computational details

The GAUSSIAN 03 program [23] was used in the calculations. The geometry optimization was carried out with the DFT method with the use of the B3LYP functional [24,25]. The electronic spectrum was calculated with the TDDFT method [26]. Two basis set were used in the calculation. The Lanl2dz basis set [27] was used on the ruthenium atom, 6-31G(d) on the chlorine, nitrogen, oxygen and carbon atoms and 6-31G basis on the hydrogen atoms in the first calculations. The second one was performed using the DZVP basis set [28] with f functions with exponents 1.94722036 and 0.748930908 on the ruthenium atom and polarization and diffuse functions to all other atoms: 6-31+g(2d,p)–chlorine, 6-31+g** – carbon, nitrogen and 6-31g(d,p) on hydrogen atoms. The results obtained from the calculations were compared.

3. Results and discussion

2,3 and 4-Methylpyridine react in methanolic solutions with $[RuCl_2(PPh_3)_3]$ giving complexes of the general formula $[RuCl_2(L)_4]$, where L is the appropriate picoline, with good yields.

Infrared spectra of the complexes exhibit characteristic bands due to picoline ring vibrations. The $\nu_{C=N}$ band in the complexes appears around 1615 (complex with β and γ-picoline) and 1604 cm^{-1} ($[RuCl_2(\alpha\text{-pic})_4]$). The $\nu_{C=C}$ absorption bands are visible at 1435 and 1420 cm^{-1} respectively. The absorption bands at 536 cm^{-1} (complex with α-picolne), 556 cm^{-1} (β-picoline) and 531 (γ-picoline) are due to ν_{Ru-N}. The ^1H NMR spectra of the complexes confirm the presence of picoline molecules in the coordination spheres. The positions of the ^1H NMR signals and their assignments are given in the experimental part of the paper.

The obtained complexes were recrystallized from methanolic solution, but only the complex with β-picoline gave well-shaped crystals suitable for X-ray analysis.

The $[RuCl_2(\beta\text{-pic})_4]$ complex crystallises in the tetragonal space group *P4nc* (no. 104). The molecular structure of the compound is shown in Fig. 1 (a structural drawing of the complex is presented in Fig. 2). Selected bond lengths and angles are listed in Table 2. The asymmetric unit includes a quarter of the molecule. The Ru and Cl atoms lie on fourfold axis (special positions *a* of *P4nc* space group at 0, 0, *z* [29]) and rest of the atoms lie in general positions. The ruthenium atom has an

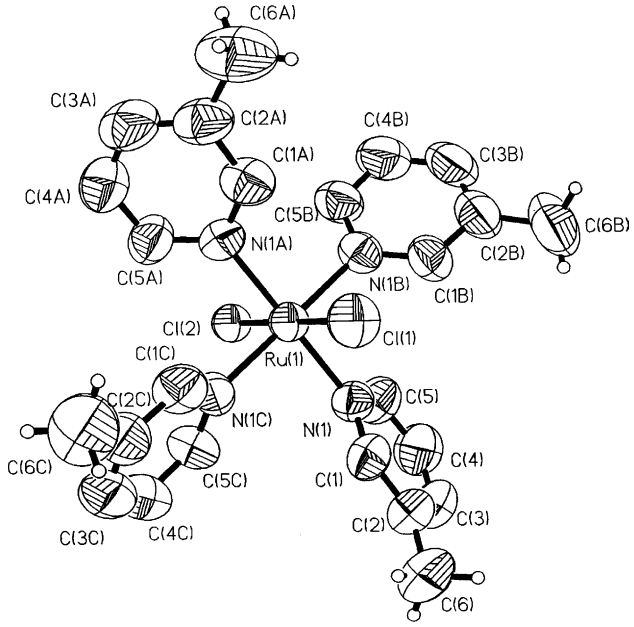


Fig. 1. ORTEP drawing of $[RuCl_2(\beta\text{-pic})_4]$ with 50% probability thermal ellipsoids.

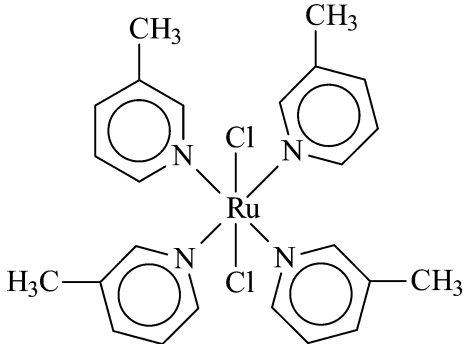


Fig. 2. Structural drawing of $[RuCl_2(\beta\text{-pic})_4]$.

Table 2
Selected bond lengths (Å) and angles (°) for $[RuCl_2(\beta\text{-pic})_4]$

Bond lengths (Å)	
Ru(1)–N(1)	2.087(3)
Ru(1)–Cl(1)	2.430(6)
Ru(1)–Cl(2)	2.390(5)
Bond angles (°)	
N(1)–Ru(1)–N(1A)	179.5(6)
N(1)–Ru(1)–N(1B)	89.999(1)
N(1)–Ru(1)–N(1C)	90
Cl(1)–Ru(1)–Cl(2)	180.0
N(1)–Ru(1)–Cl(1)	90.2(3)
N(1)–Ru(1)–Cl(2)	89.8(3)

Symmetry transformations used to generate equivalent atoms: A. $1-y,x,z$; B. $1-x,1-y,z$; C. $y,1-x,z$.

octahedral geometry (4 + 2) with *trans* chlorine atoms (Cl(1)–Ru(1)–Cl(2)–180°). The β-picoline ligands are in a square–planar disposition. The angles between N–Ru–Cl are close to 90° (89.8(3)–90.2(3)°), and the N–Ru–N angles are 179.5(6)° and 89.999(1)°. The Ru–ligand distances, such as Ru–Cl 2.430(6), 2.390(5), and Ru–N 2.087(3) Å, are normal and comparable with distances in other ruthenium complexes containing nitrogen heterocyclic ligands [2,30–33]. The bond valences were computed as $v_{ij} = \exp[(R_{ij} - d_{ij})/0.37]$ [34–36], where R_{ij} is the bond-valence parameter (in the formal sense R_{ij} is the single-bond length between i and j atoms) [37]. The R_{Ru-N}, R_{Ru-Cl} values were taken as 1.656 and 1.932 Å [38], respectively. The computed bond valences of the ruthenium complex are $v_{Ru-N(1)} = 0.312$, $v_{Ru-Cl(1)} = 0.260$ and $v_{Ru-Cl(2)} = 0.290$ v.u. (valence units) which means that picoline is the strongest bonded subsituent, and the Ru–Cl(1) bond is the weakest one.

3.1. Geometry and electronic structure

The optimized geometry parameters for the studied complexes are given in Table 3. The calculated bond lengths and angles for $[RuCl_2(\beta\text{-pic})_4]$ agree well with the experiment, the largest difference are found for the ruthenium–chlorine bonds, but the relative differences in these bond lengths are reproduced in the calculations. The geometry calculated by using both basis sets is comparable. The geometries of the complexes with α- and γ-picoline were calculated with the DFT method using the small basis sets (Lanl2dz on the ruthenium atom). The complexes are depicted in Fig. 3. The Ru–N and Ru–Cl distances in the complex with α-picoline are longer than the corresponding bond lengths in complexes with β-and γ-picoline. For the complexes with α- and γ-picoline the frequency calculations were performed and compared with experimental IR spectra. An agreement between the calculated and experimental spectra indicates that the calculated geometry corresponds to the real structure. Several calculated frequencies (experimental values are given in parentheses) of $[RuCl_2(\gamma\text{-pic})_4]$ are 3102 (3049) ν_{CH}, 3047 (3023) ν_{CH}, 1672 (1614) $\nu_{C=N}$, 1545 (1481) ν_{ring}, 1468 (1432) $\nu_{C=C}$, 1374 (1385) ν_{ring}, 1245 (1209) δ_{CH}, 1092 (1088) δ_{CH}, 735 (724) δ_{ring}, 543 (531) ν_{Ru-N} and for $[RuCl_2(\alpha\text{-pic})_4]$ 3068 (3052) ν_{CH}, 3062 (2974) ν_{CH}, 1622 (1604) $\nu_{C=N}$, 1504 (1481) ν_{ring}, 1469 (1435) $\nu_{C=C}$, 1343 (1303) ν_{ring}, 1194 (1187) δ_{CH}, 1098 (1093) δ_{CH}, 737 (696) δ_{ring}, 559

Table 3
Optimized geometry of $RuCl_2(picoline)_4]$

	Lanln2dz	DZVP		Lanl2dz	DZVP
Bond lengths (Å)			Bond angles (°)		
[RuCl₂(β-pic)₄]					
Ru(1)–Cl(1)	2.522	2.472	Cl(1)–Ru(1)–Cl(2)	180.00	180.00
Ru(1)–Cl(2)	2.514	2.468	N(1)–Ru(1)–Cl(1)	90.05	90.02
Ru(1)–N(1)	2.134	2.133	N(1)–Ru(1)–Cl(2)	89.95	89.98
			N(1)–Ru(1)–N(1A)	179.90	179.96
			N(1)–Ru(1)–N(1B)	90.00	90.00
			N(1)–Ru(1)–N(1C)	90.00	90.00
[RuCl₂(γ–pic)₄]					
Ru(1)–Cl(1)	2.522		Cl(1)–Ru(1)–Cl(2)	179.97	
Ru(1)–Cl(2)	2.520		N(1)–Ru(1)–Cl(1)	90.03	
Ru(1)–N(1)	2.136		N(1)–Ru(1)–Cl(2)	89.99	
			N(1)–Ru(1)–N(2)	179.97	
			N(1)–Ru(1)–N(3)	90.00	
			N(1)–Ru(1)–N(4)	90.04	
[RuCl₂(α–pic)₄]					
Ru(1)–Cl(1)	2.592		Cl(1)–Ru(1)–Cl(2)	174.08	
Ru(1)–Cl(2)	2.606		N(1)–Ru(1)–Cl(1)	88.94	
Ru(1)–N(1)	2.204		N(2)–Ru(1)–Cl(1)	85.71	
Ru(1)–N(2)	2.234		N(3)–Ru(1)–Cl(1)	89.88	
Ru(1)–N(3)	2.234		N(4)–Ru(1)–Cl(1)	95.55	
Ru(1)–N(4)	2.209		N(1)–Ru(1)–Cl(2)	95.45	
			N(2)–Ru(1)–Cl(2)	90.39	
			N(3)–Ru(1)–Cl(2)	85.45	
			N(4)–Ru(1)–Cl(2)	88.06	
			N(1)–Ru(1)–N(2)	88.95	
			N(1)–Ru(1)–N(3)	175.56	
			N(1)–Ru(1)–N(4)	94.59	
			N(2)–Ru(1)–N(4)	176.25	
			N(2)–Ru(1)–N(3)	86.70	
			N(3)–Ru(1)–N(4)	89.77	

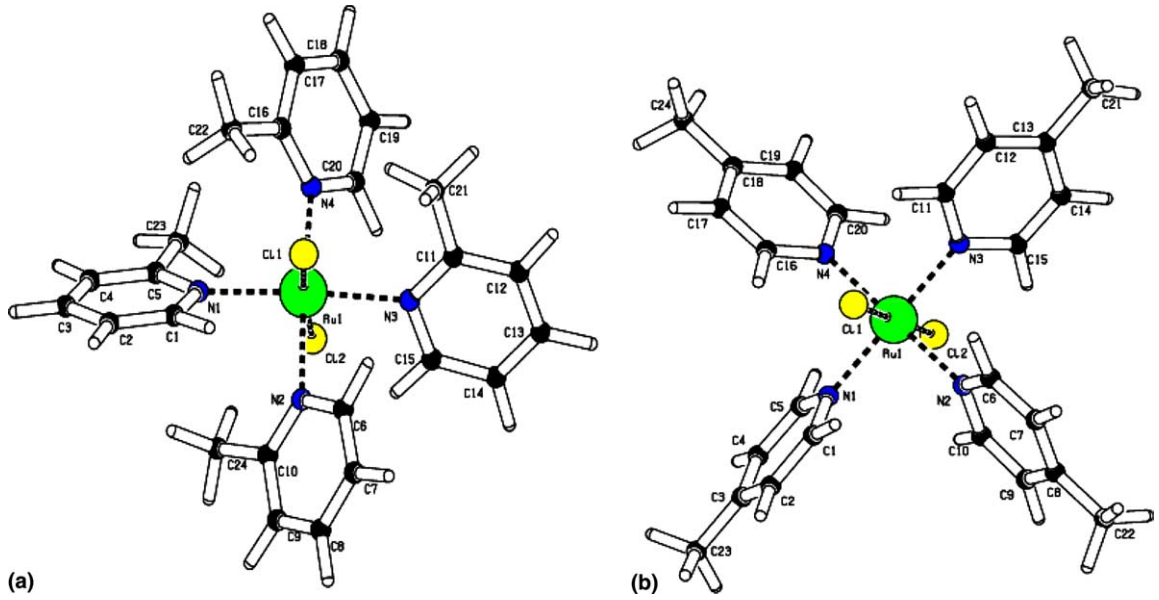


Fig. 3. The idealized geometry of $[RuCl_2(\alpha\text{-pic})_4]$ and $[RuCl_2(\gamma\text{-pic})_4]$.

(536) ν_{Ru-N}. The maximum error between the calculated and experimental values is about 5.7%.

In Table 4 the energies of several HOMO and LUMO orbitals of $[RuCl_2(\beta\text{-pic})_4]$ are gathered. The charge of ruthenium calculated from natural population analysis is smaller than 1 (0.525-Lanl2dz; 0.831-DZVP). This results from charge donation from chloride ions, which act as σ-donors (the charges of Cl ligands are −0.633, −0.627 – Lanl2dz and −0.653, −0.649 – DZVP). The charge on the picoline nitrogen atom bonded with ruthenium is negative (−0.423 Lanl2dz and −0.451 DZVP).

The doubly degenerate HOMO and HOMO − 3 orbitals are d_π (d_{xz}, d_{yz} and d_{yz}, d_{xz}) metal orbital with the admixture of chlorine π orbitals and πC. The HOMO − 1 orbital is created from $d_{x^2-y^2}$ and πC of picoline ligands. The lower lying orbitals are π orbitals of the picoline and chlorine ligands.

The LUMO orbital is composed of β-picoline rings. The d ruthenium orbitals hold small shares in LUMO + 1 (d_{xz}, d_{yz}) and LUMO + 2 ($d_{x^2-y^2}$) molecular orbitals. The LUMO + 5 MO is a combination of d_z^2 and σCl. The LUMO + 7 orbital is d_{xy} with an antibonding

Table 4
The energy and character of the upper valence MO for $[RuCl_2(\beta\text{-pic})_4]$

MO	*E* (eV)		Character
	Lanl2dz	DZVP	
H-8	−7.78	−7.94	61.78% πC + 30.65% πN
H-7(a)(b)	−7.00	−7.17	78.13% πC + 15.59% πCl
H-6	−6.99	−7.00	90.65% πC
H-5	−6.82	−6.89	93.49% πC
H-4	−6.68	−6.76	85.02% πCl
H-3(a)(b)	−6.60	−6.72	16.05% d_{yz}(a) d_{xz}(b) + 65.57% πCl + 10.73% πC
H-2(a)(b)	−6.28	−6.35	80.07% πCl + 17.12% πC
H-1	−4.87	−5.03	82.19% $d_{x^2-y^2}$ + 17.01% πC
H(a)(b)	−4.60	−4.66	74.47% d_{xz}(a) d_{yz}(b) + 19.54% πCl
L	-0.90	−1.21	65.84% πC + 26.13% πN
L+1(a)(b)	−0.88	−1.19	60.95% πC + 26.01% πN + 2.80% d_{xz}(a) d_{yz}(b)
L+2	−0.68	−1.02	59.61% πC + 27.82% πN + 7.78% $d_{x^2-y^2}$
L+3	−0.32	−0.62	89.33% πC
L+4(a)(b)	−0.09	−0.39	93.32% πC
L+5	−0.05	−0.37	49.21% d_z^2 + 29.03% σCl
L+6	0.02	−0.10	93.37% πC
L+7	0.96	0.04	42.53% d_{xy} + 22.00% σN + 19.90% σC
L+8(a)(b)	1.32	0.17	32.72% πC
L+9	1.51	0.30	26.12% πC + 6.79% πCl

H, HOMO; L, LUMO.

contribution σ (lone pairs) of nitrogen picoline and σ carbon orbitals.

The energy of appropriate HOMO and LUMO orbitals calculated with the DZVP basis set on the ruthenium atom, and diffuse and polarization functions on the other atoms is lower than that obtained from calculation with the Lanl2dz basis on the Ru atom. The HOMO–LUMO gap in both calculations is similar (the difference is 0.25 eV).

The character of the MO orbitals for the complexes with α- and γ-picoline are close to, mentioned above, $[RuCl_2(\beta\text{-pic})_4]$. The d_π metal orbitals (d_{xz}, d_{yz} and d_{yz},

Table 5
Calculated electronic transitions for $[RuCl_2(pic)_4]$ with the TDDFT method

Most important configurations		E (V)	λ (nm)	f	Exp. λ (nm)(E [eV])log ε
$[RuCl_2(\beta\text{-pic})_4]$					
H → L+5		2.44	509.0	0.0006	513.4 (2.41) 1.92
H → L+1		2.88	430.3	0.0003	
H → L	H-1 → L+1	2.92	424.2	0.0184	442.0 (2.81) 3.48
H → L +2	H-1 → L+1	3.02	410.7	0.0055	
H-1 → L+1	H → L+2	3.28	377.9	0.2302	381.8 (3.25) 3.91
H → L+6	H → L+7	3.85	322.2	0.0047	
H → L+7		3.89	318.5	0.0110	
H-2 → L		4.71	263.2	0.0032	
H-2 → L+1		4.73	261.9	0.0081	244.4 (5.07) 4.20
H-3 → L		4.99	248.4	0.0070	
H-2 → L+5		5.17	239.8	0.0078	
H-2 → L+3	H-3 → L+3	5.35	231.8	0.0256	
H-5 → L+1	H-3 → L+3	5.37	230.9	0.0417	222.2 (5.58) 5.32
H-7 → L+1	H-6 → L	5.42	228.9	0.0737	
H-6 → L+1	H-5 → L+1; H-7 → L	5.47	226.6	0.0135	215.8 (5.75) 5.34
H-2 → L+4		5.61	221.0	0.0008	
$[RuCl_2(\gamma\text{-pic})_4]$					
H → L+5		2.38	520.4	0.0006	527.1 (2.35) 1.91
H → L	H-1 → L	2.84	436.6	0.0193	427.0 (2.90) 3.77
H → L+2	H-1 → L+2	2.93	422.7	0.0070	
H-1 → L+7		3.14	394.5	0.0035	
H-1 → L+1		3.21	386.2	0.2536	352.0 (3.52) 4.22
H → L+7		3.73	332.4	0.0198	
H-1 → L+5		3.81	325.1	0.0046	
H-2 → L+1		4.64	267.4	0.0060	
H-5 → L		4.88	253.9	0.0106	272.6 (4.55) 4.81
H-6 → L+1		4.99	248.4	0.0066	
H-3 → L+3	H-5 → L+1	5.09	243.8	0.0503	
H-3 → L+5		5.31	233.4	0.0365	228.2 (5.43) 5.21
H-4 → L+3	H-4 → L+6	5.33	232.7	0.0032	
H-4 → L+3	H-3 → L+4; H-5 → L+5	5.50	225.6	0.0076	
H-7 → L+4		5.69	217.8	0.0141	214.6 (5.78) 5.05
$[RuCl_2(\alpha\text{-pic})_4]$					
H → L+4		1.98	626.9	0.0001	645.8 (1.92) 1.90
H → L	H → L+1	2.92	424.5	0.0069	
H → L+1	H → L+9	2.95	420.8	0.0185	
H → L+3	H-1 → L; L+9	3.00	413.8	0.0328	
H-2 → L	H-1 → L+9	3.25	381.7	0.0119	
H-2 → L+1	H-1 → L+3	3.35	370.3	0.0911	386.0 (3.21) 3.81
H-2 → L+2	H-1 → L+9	3.39	365.3	0.0817	
H-1 → L+6	H → L+6	3.68	336.5	0.0046	
H-4 → L+1	H-3 → L	4.45	278.5	0.0062	
H-6 → L	H-4 → L+3	4.68	265.1	0.0104	
H-5 → L+3		4.82	257.1	0.0131	265.6 (4.67) 4.74
H-4 → L+5	H-3 → L+5	5.05	245.6	0.0102	
H-9 → L	H-5 → L+5	5.29	234.4	0.0266	
H-3 → L+8		5.35	230.2	0.0272	228.4 (5.43) 5.32
H-11 → L	H-10 → L	5.51	225.2	0.0135	
H-11 → L+1	H-10 → L+2	5.55	223.5	0.0136	
H-6 → L+7		5.59	221.8	0.0265	215.8 (5.75) 5.03
H-5 → L+8		5.64	219.9	0.0093	

d_{xz}) are visible in the HOMO and HOMO − 2 molecular orbitals of $[RuCl_2(\alpha\text{-pic})_4]$ and $[RuCl_2(\gamma\text{-pic})_4]$. The HOMO − 1 orbital is created from $d_{x^2-y^2}$ and πCl. For the $[RuCl_2(\alpha\text{-pic})_4]$ complex in the LUMO MO, the d ruthenium orbitals hold shares in LUMO + 1 (d_{xz}) LUMO + 2 (d_{yz}) and LUMO+3 ($d_{x^2-y^2}$). The LUMO + 4 MO is a combination of d_z^2 and σCl. The LUMO + 9 orbital is d_{xy} with an antibonding σ contribution (lone pairs) of nitrogen picoline.

The HOMO–LUMO gaps are 3.55, 3.70 and 3.76 eV for $[RuCl_2(\alpha\text{-pic})_4]$, $[RuCl_2(\beta\text{-pic})_4]$ and $[RuCl_2(\gamma\text{-pic})_4]$ complexes, respectively.

3.2. Electronic spectrum

The spin-allowed, singlet transitions were calculated with the TDDFT method. The calculated electronic transitions are gathered in Table 5. The calculated and experimental spectra of $[RuCl_2(pic)_4]$ are depicted in Fig. 4. Each calculated transition in Fig. 4 is represented by a gaussian function with the height equal to the oscillator strength and width equal to 0.05. The spectrum of complex with β-picoline was calculated using the Lanl2dz (dashed line in the Fig. 4) and DZVP basis set (dotted line). Both Lanl2dz and DZVP calculations predict the experimental spectrum of the complex with similar accuracy, but using the DZVP basis set on the ruthenium atom to calculation the UV–Vis spectrum gave better results for the higher energy of transitions than the Lanl2dz basis set.

The experimental spectrum of $[RuCl_2(\beta\text{-pic})_4]$ shows bands at 513.4, 442.0, 381.8, 244.4, 222.2 and 215.8 nm. We ascribe the first experimental bands at 513.4 nm to the calculated transition at 509.0 with small oscillator strengths. This is a d → d transition. The experimental bands at 442.0 nm and 381.8 nm are assigned to the transitions calculated between 430.3 and 377.9 nm. These transitions are of d → π^*_{pic} excitation of MLCT character.

The experimental band at 244.4 nm is ascribed to the transitions calculated between 263.2 and 239.8 nm. The transition is mainly from chlorine ligands orbitals to π^*_{pic} (LLCT character) with the admixture of MLCT transition (H-3 → L) and LMCT (H-2 → L + 5). The calculated transitions between 231.8 and 221.0 are assigned to experimental bands 222.2 and 215.8. They are of LLCT type (interligand transitions) and intraligand ($\pi_{pic} \rightarrow \pi^*_{pic}$ transitions).

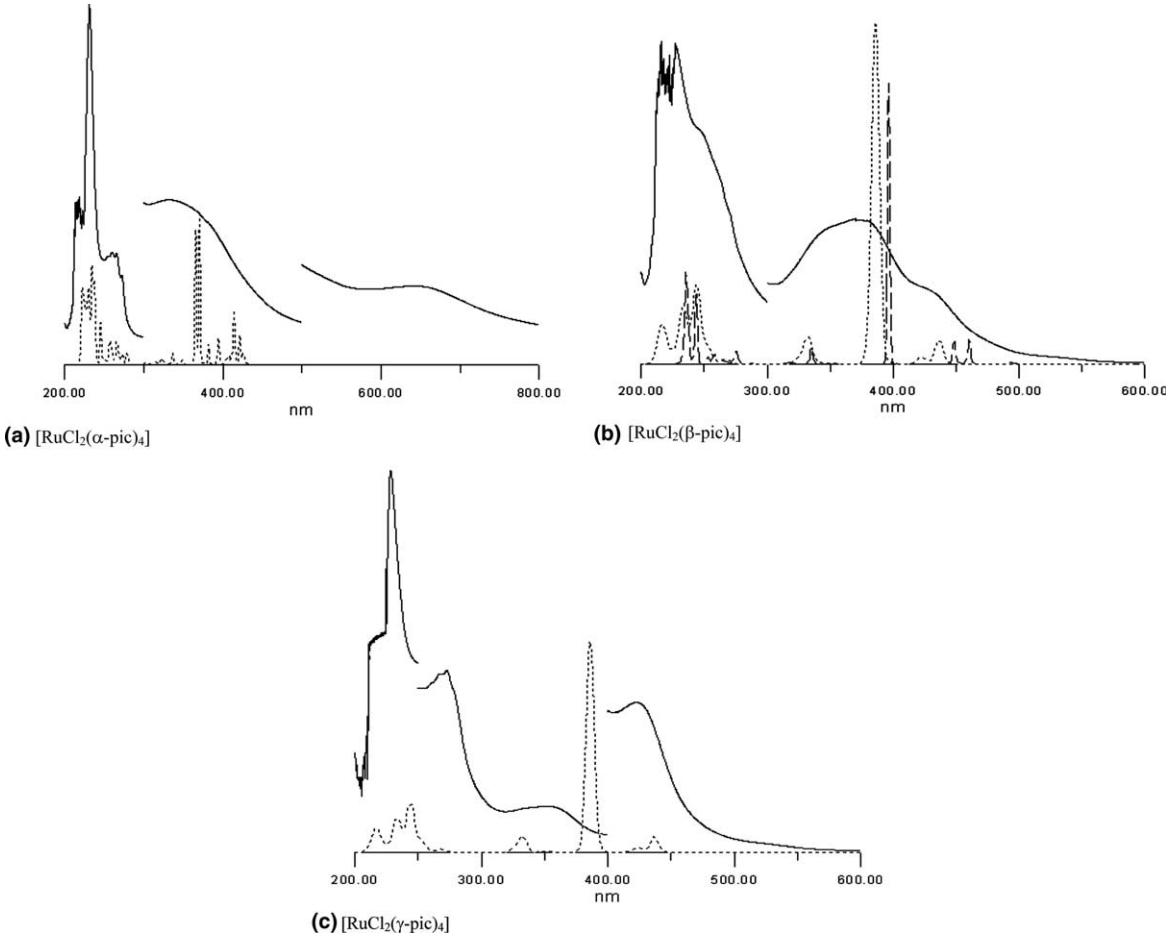


Fig. 4. The calculated and experimental spectra of $[RuCl_2(picoline)_4]$.

The UV–Vis spectrum of $[RuCl_2(\gamma\text{-pic})_4]$ is similar to the electronic spectrum of the β-picoline complex and shows bands at 527.1, 427.0, 352.0, 272.6, 228.2 and 214.6 nm. Based on the calculated geometry of this complex, the spectrum was computed using the DZVP basis set on ruthenium and polarization and diffuse functions on the other atoms. The first experimental band is due to $d \rightarrow d$ transitions and was calculated at 520.0 nm with 0.0006 oscillator strengths. The calculated transitions at 436.61 and 436.50 nm are assigned to the experimental band at 427.0 nm. The transition is of $d \rightarrow \pi^*_{pic}$ (HOMO − 1, HOMO → LUMO) excitation of MLCT character. The next experimental band at 352.0 has the same character and was calculated in the range 386.16 and 332.36 nm.

The experimental band at 272.6 nm is ascribed to the transitions calculated between 268.3 and 240.7 nm. The transition is mainly from chlorine ligands orbitals to π^*_{pic} (LLCT character) with the admixture of MLCT and LMCT transitions. The LLCT type inter- and intraligand transitions ($\pi_{pic} \rightarrow \pi^*_{pic}$) were calculated between 233.4 and 206.9, and are assigned to experimental bands 228.2 and 214.6 nm.

The electronic spectrum of $[RuCl_2(\alpha\text{-pic})_4]$ shows bands at 645.8, 386.0, 265.6, 228.4 and 215.8 nm. The first band, with a small oscillator strength, is of $d \rightarrow d$ type and was calculated at 626.9 nm. The next asymmetric band, with a maximum at 386.0 nm, was calculated in the range 420.8–365.3 nm and is of $d \rightarrow d$ character with an admixture of MLCT transition ($d \rightarrow \pi^*_{pic}$, π^*_{Cl}). The transition from chlorine ligands orbitals to π^*_{pic} (LLCT character) with the admixture of MLCT transitions were calculated between 278.5 and 245.6 nm and are assigned to the band at 265.6 nm. The excitations calculated between 234.4 and 225.2 nm are LLCT type (inter- and intraligand) and are ascribed to the band at 228.4 nm. The experimental band at 215.8 is LLCT and MLCT type and is attributed to the calculated transitions between 223.5 and 219.9 nm.

4. Supplementary data

More details of the crystal structure determination have been deposited with the Cambridge Crystallographic Data Centre with the deposition number: CCDC 248944. Copies of the data can be obtained, free of charge, on application to CCDC, 12 Union Road, Cambridge CB2 1EZ, UK, fax: +44 1223 336 033 or deposit@ccdc.cam.ac.uk or on the www: http://www.ccdc.cam.ac.uk.

Acknowledgements

The Crystallographic part was financed by funds allocated by the Ministry of Scientific Research and Information Technology to the X-ray Crystallography and Crystal Chemistry Group, Institute of General and Ecological Chemistry, Lodz University of Technology. The GAUSSIAN 03 calculations were carried out in the Wrocław Centre for Networking and Supercomputing, WCSS, Wrocław, Poland under calculational Grant No. 51/96.

References

[1] F. Porta, S. Tollari, C. Bianchi, S. Recchia, Inorg. Chim. Acta 249 (1996) 79.
[2] S.L. Queiroz, A.A. Batista, G. Olivia, M.T. do, P. Gambardella, R.H.A. Santos, K.S. MacFarlane, S.J. Rettig, B.R. James, Inorg. Chim. Acta 267 (1998) 209.
[3] I.R. Butler, U. Griesbach, P. Zanello, M. Fontani, D. Hibbs, B.M. Hursthouse, J. Organomet. Chem. 565 (1998) 243.
[4] J.G. Małecki, J.O. Dziêgielewski, R. Kruszynski, T.J. Bartczak, Inorg. Chem. Commun. 6 (2003) 721.
[5] A.A. Batista, I.S. Thorburn, B.R. James, S.J. Rettig, R.G. Ball, Proc. 6th Int. Symp. Homogeneous Catalysis, Vancouver, Canada, 1988, p. 123.
[6] R. Riuz-Ramirez, T.A. Stephenson, E.S. Switkes, J. Chem. Soc., Dalton Trans. (1973) 1770.
[7] P.C. Hohenberg, W. Kohn, L.J. Sham, Adv. Quantum Chem. 21 (1990) 7.
[8] W. Kohn, A.D. Becke, R.G. Parr, J. Phys. Chem. 100 (1996) 12974.
[9] R.G. Parr, W. Yang, Ann. Rev. Phys. Chem. 46 (1995) 701.
[10] E.J. Baerends, O.V. Gritsenko, J. Phys. Chem. A 101 (1997) 5383.
[11] T. Ziegler, Chem. Rev. 91 (1991) 651.
[12] M.E. Casida, in: D.P. Chong (Ed.), Recent Advances in Density Functional Methods, vol. 1, World Scientific, Singapore, 1995.
[13] M.E. Casida, in: J.M. Seminario (Ed.), Recent Developments and Applications of Modern Density Functional Theory, Theoretical and Computational Chemistry, vol. 4, Elsevier, Amsterdam, 1996, p. 391.
[14] M.E. Casida, C. Jamorski, K.C. Casida, D.R. Salahub, J. Chem. Phys. 108 (1998) 4439.
[15] C. Adamo, V. Barone, Theor. Chem. Acta 105 (2000) 169.
[16] S.J.A. van Gisbergen, J.A. Groeneveld, A. Rosa, J.G. Snijders, E.J. Baerends, J. Phys. Chem. A 103 (1999) 6835.
[17] A. Rosa, E.J. Baerends, S.J.A. van Gisbergen, E. van Lenthe, J.A. Groeneveld, J.G. Snijders, J. Am. Chem. Soc. 121 (1999) 10356.
[18] T.A. Stephenson, G. Wilkonson, J. Inorg. Nucl. Chem. 28 (1966) 945.
[19] X-RED. Version 1.18. STOE & Cie GmbH, Darmstadt, Germany, 1999.
[20] G.M. Sheldrick, Acta Cryst. A 46 (1990) 467.
[21] G.M. Sheldrick, SHELXL 97. Program for the Solution and Refinement of Crystal Structure, University of Göttingen, Germany, 1997.
[22] G.M. Sheldrick, SHELXTL: release 4.1 for Siemens Crystallographic Research Systems (1990).
[23] R. Mukherjee, Coord. Chem. Rev. 203 (2000) 151.
[24] M.J. Frisch, G.W. Trucks, H.B. Schlegel, G.E. Scuseria, M.A. Robb, J.R. Cheeseman, J.A. Montgomery Jr., T. Vreven, K.N. Kudin, J.C. Burant, J.M. Millam, S.S. Iyengar, J. Tomasi, V. Barone, B. Mennucci, M. Cossi, G. Scalmani, N. Rega, G.A. Petersson, H. Nakatsuji, M. Hada, M. Ehara, K. Toyota, R. Fukuda, J. Hasegawa, M. Ishida, T. Nakajima, Y. Honda, O. Kitao, H. Nakai, M. Klene, X. Li, J.E. Knox, H.P. Hratchian, J.B. Cross, C. Adamo, J. Jaramillo, R. Gomperts, R.E. Strat-

mann, O. Yazyev, A.J. Austin, R. Cammi, C. Pomelli, J.W. Ochterski, P.Y. Ayala, K. Morokuma, G.A. Voth, P. Salvador, J.J. Dannenberg, V.G. Zakrzewski, S. Dapprich, A.D. Daniels, M.C. Strain, O. Farkas, D.K. Malick, A.D. Rabuck, K. Raghavachari, J.B. Foresman, J.V. Ortiz, Q. Cui, A.G. Baboul, S. Clifford, J. Cioslowski, B.B. Stefanov, G. Liu, A. Liashenko, P. Piskorz, I. Komaromi, R.L. Martin, D.J. Fox, T. Keith, M.A. Al-Laham, C.Y. Peng, A. Nanayakkara, M. Challacombe, P.M.W. Gill, B. Johnson, W. Chen, M.W. Wong, C. Gonzalez, J.A. Pople, GAUSSIAN 03, Revision B.03, Gaussian Inc., Pittsburgh, PA, 2003.

[25] A.D. Becke, J. Chem. Phys. 98 (1993) 5648.

[26] C. Lee, W. Yang, R.G. Parr, Phys. Rev. B 37 (1988) 785.

[27] M.E. Casida, in: J.M. Seminario (Ed.), Recent Developments and Applications in Modern Density Functional Theory, Theoretical and Computational Chemistry, vol. 4, Elsevier, Amsterdam, 1996.

[28] N. Godbout, D.R. Salahub, J. Andzelm, E. Wimmer, Can. J. Chem. 70 (1992) 560.

[29] T. Hahn (Ed.), International Tables for Crystallography, vol. I, D. Reidel Publishing Company, Dordrecht, Holland, 1983, p. 382.

[30] P.J. Hay, W.R. Wadt, J. Chem. Phys. 82 (1985) 299.

[31] M. Jahnecke, A. Neels, H. Stoeckli-Evans, G. Süss-Fink, J. Organomet. Chem. 561 (1998) 227.

[32] S. Elgafi, L.D. Field, B.A. Messerle, I.E. Buys, T.W. Hambley, J. Organomet. Chem. 538 (1997) 119.

[33] Wing-Tak Wong, TAa-Cnu Lau, Acta Cryst. C 50 (1994) 1406.

[34] I.D. Brown, Acta Cryst. B 48 (1992) 553.

[35] I.D. Brown, Acta Cryst. B 53 (1997) 381.

[36] M. O'Keeffe, N.E. Brese, J. Am. Chem. Soc. 113 (1991) 3226.

[37] L. Sieron, M. Bukowska-Strzyzewska, Acta Cryst. C 55 (1999) 1230.

[38] J.G. Małecki, J.O. Dzigielewski, M. Jaworska, R. Kruszynski, T.J. Bartczak, Polyhedron 23 (5) (2004) 885.

C(O)NHCH$_2$C(O)OEt, (CH$_2$)$_3$C(O)OH, (CH$_2$)$_3$C(O)OEt groups are known [6].

This paper presents the syntheses and spectroscopic properties of the [Re(4-NC$_6$H$_4$NH$_2$)X$_3$(PPh$_3$)$_2$] (X = Cl and Br) complexes, obtained in the reaction of [ReOX$_3$(PPh$_3$)$_2$] with 1,4-diaminobenzene. The crystal and molecular structure of [Re(4-NC$_6$H$_4$NH$_2$)Cl$_3$(PPh$_3$)$_2$] has been determined, and its molecular diagram has been calculated with the density functional theory (DFT). Additional information about the binding in the [Re(4-NC$_6$H$_4$NH$_2$)Cl$_3$(PPh$_3$)$_2$] complex has been obtained by NBO analysis. The spin-allowed singlet–singlet electronic transitions of [Re(4-NC$_6$H$_4$NH$_2$)Cl$_3$(PPh$_3$)$_2$] have been calculated with the time-dependent DFT method (TDDFT), and the UV–Vis spectrum has been discussed on this basis.

2. Experimental

2.1. General procedure

All synthetic manipulations were carried out open to the atmosphere. All solvents were of reagent grade and used as received. Ammonium perrhenate, triphenylphosphine and 1,4-diaminobenzene were purchased from Aldrich. The [ReOX$_3$(PPh$_3$)$_2$] complexes were prepared according to the literature methods [16].

Infrared spectra were recorded on a Nicolet Magna 560 spectrophotometer in the spectral range 4000–400 cm^{-1}, with the samples in the form of potassium bromide pellets. Electronic spectra were measured on a spectrophotometer Lab Alliance UV–Vis 8500 in the range 900–200 nm in deoxygenated dichloromethane solution. ^{1}H NMR spectra were obtained in CDCl$_3$ using an INOVA 300 spectrometer. Magnetic susceptibility was measured at 296 K by the Faraday method. Elemental analysis (C, H, N) was performed on a Perkin–Elmer CHN-2400 analyzer.

2.2. Preparation of [Re(4-NC$_6$H$_4$NH$_2$)Cl$_3$(PPh$_3$)$_2$] · PPh$_3$

A mixture of *trans*-[ReOCl$_3$(PPh$_3$)$_2$] (0.83 g, 1 mmol), 1,4-diaminobenzene (0.43, 4 mmol) and acetone (100 ml) was stirred for 2 days, and then 50 ml of acetone was distilled off. [Re(4-NC$_6$H$_4$NH$_2$)Cl$_3$(PPh$_3$)$_2$] was filtered off, washed with ethanol, diethyl ether and dried. Yield: 60%.

IR (KBr, cm^{-1}) 3466 (m), 3360 (s), 3050 (w), 1614 (s), 1588 (s), 1482(m), 1433 (s), 1365 (s), 1327 (m), 1169 (s), 1089 (m), 832 (w), 749 (s), 696 (s), 606 (w), 560 (w), 522 (s), 480 (w).

^{1}H NMR (CDCl$_3$, ppm): δ = 7.26 (s, 2H, NH$_2$); 7.38–7.46 (m, 30H, coordinated PPh$_3$ ligands); 7.77–7.81 (m, 4H of imido ligand and 15H of uncoordinated PPh$_3$).

Anal. Calc. for C$_{60}$H$_{51}$Cl$_3$N$_2$P$_3$Re: C, 60.79; H, 4.34; N, 2.36. Found: C, 60.85; H, 4.40; N, 2.30%.

2.3. Preparation of [Re(4-NC$_6$H$_4$NH$_2$)Br$_3$(PPh$_3$)$_2$]

A procedure similar to that for the chloro analogue was used with *trans*-[ReOBr$_3$(PPh$_3$)$_2$] (0.97 g, 1 mmol) and 1,4-diaminobenzene (0.43, 4 mmol). Yield: 55%.

IR (KBr, cm^{-1}) 3452 (w), 3334 (s), 3047 (w), 1613 (s), 1587 (s), 1483 (m), 1434 (m), 1369 (s), 1327 (m), 1163 (s), 1091 (m), 838 (w), 745 (m), 695 (s), 602 (w), 999 (m), 520 (s), 505 (sh), 480 (w).

^{1}H NMR (CDCl$_3$, ppm): δ = 7.274 (s, 2H, NH$_2$); 7.270–7.254 (m, 4H of imido ligand and 30H of coordinated PPh$_3$ ligands).

Anal. Calc. for C$_{42}$H$_{36}$Br$_3$N$_2$P$_2$Re: C, 47.74; H, 3.43; N, 2.65. Found: C, 47.87; H, 3.55; N, 2.55%.

2.4. Crystal structure determination and refinement

Crystals suitable for X-ray investigation were obtained by recrystallization from acetonitrile. The X-ray intensity data of the title complex were collected on a KM-4-CCD automatic diffractometer equipped with a CCD detector with 40 s exposure time, and all reflections of the Ewald sphere were collected up to θ = 25°. The unit cell parameters were determined from least-squares refinement of the setting angles of the 6795 strongest reflections. Details concerning crystal data and refinement are given in Table 1. Lorentz polarization and numerical absorption corrections [17] were applied. The structure was solved by the Patterson method and subsequently completed by difference Fourier recycling. All the non-hydrogen atoms were refined anisotropically using the full-matrix least-squares technique. All the hydrogen atoms were found from difference Fourier synthesis after four cycles of anisotropic refinement, and refined as ''riding'' on the adjacent atom with an individual isotropic temperature factor equal to 1.2 times the value of the equivalent temperature factor of the parent atom. Carbon-bonded hydrogen atom positions were idealized after each cycle of refinement [d(C–H) = 0.96 Å]. SHELXS-97 [18], SHELXL-97 [19] and SHELXTL [20] programs were used for all the calculations. Atomic scattering factors were those incorporated in the computer programs.

2.5. Computational details

The GAUSSIAN-03 program [21] was used in the calculations. The geometry optimization was carried out with the DFT method with the use of the B3LYP functional [22,23]. The electronic spectrum was calculated with the TDDFT method [24].

In the calculations, the LANL2DZ basis set [25] with additional d (α = 0.3811) and f (α = 0.2033) functions

Table 1
Crystal data and structure refinement for $[Re(4\text{-}NC_6H_4NH_2)Cl_3(PPh_3)_2]\cdot PPh_3$.

Empirical formula	$C_{60}H_{51}Cl_3N_2P_3Re$
Formula weight	1185.49
T (K)	293(2)
λ (Å)	0.71073
Crystal system	monoclinic
Space group	$P2_1/n$
Unit cell dimensions	
a (Å)	11.0688(5)
b (Å)	32.6510(16)
c (Å)	14.7331(7)
β (°)	91.114(4)
V (Å^3)	5323.6(4)
Z	4
D_{calc} (Mg/m^3)	1.479
Absorption coefficient (mm^{-1})	2.564
$F(000)$	2384
Crystal size (mm)	$0.22\times0.05\times0.05$
θ Range for data collection (°)	2.95–25.11
Index ranges	$-13\leqslant h\leqslant 13$, $-38\leqslant k\leqslant 38$, $-17\leqslant l\leqslant 17$
Reflections collected	56075
Independent reflections (R_{int})	9473 (0.0716)
Completeness to 2θ (%)	97.8
Maximum and minimum transmission	0.8804 and 0.6061
Data/restraints/parameters	9473/0/623
Goodness-of-fit on F^2	1.161
Final R indices [$I>2\sigma(I)$]	$R_1 = 0.0598$, $wR_2 = 0.0659$
R indices (all data)	$R_1 = 0.0906$, $wR_2 = 0.0726$
Largest difference in peak and hole (e Å^{-3})	0.499 and −0.717

was used on the rhenium atom, 6-31G(d) on the chlorine, nitrogen, phosphorous and carbon atoms and 6-31G basis on the hydrogen atoms.

Natural bond orbital (NBO) calculations were performed with the NBO code [26] included in GAUSSIAN-03.

3. Results and discussion

3.1. Synthesis

The reaction of *trans*-$[ReOX_3(PPh_3)_2]$ with an excess of 1,4-diaminobenzene in acetone leads to the formation of $[Re(4\text{-}NC_6H_4NH_2)X_3(PPh_3)_2]$ in good yield (Eq. (1)).

$$[ReOX_3(PPh_3)_2] + H_2N\text{–}C_6H_4\text{–}NH_2 \rightarrow [Re(4\text{-}NC_6H_4NH_2)X_3(PPh_3)_2] + H_2O \quad (1)$$

The complexes are air stable. Their solubilities in most polar solvents are low, but they can be crystallized from acetonitrile. Room temperature magnetic susceptibility measurements show the complexes to be diamagnetic. The lack of paramagnetic broadening or shifts of resonances in the ^{1}H NMR spectra of $[Re(4\text{-}NC_6H_4NH_2)X_3(PPh_3)_2]$ also confirms diamagnetism of the complexes. $[Re(4\text{-}NC_6H_4NH_2)X_3(PPh_3)_2]$ are formally rhenium(V) compounds with the arylimido unit as a dianionic NR^{2-} ligand.

3.2. Description of the structure of $[Re(4\text{-}NC_6H_4NH_2)Cl_3(PPh_3)_2]\cdot PPh_3$

The $[Re(4\text{-}NC_6H_4NH_2)Cl_3(PPh_3)_2]$ complex crystallizes as the $[Re(4\text{-}NC_6H_4NH_2)Cl_3(PPh_3)_2]\cdot PPh_3$ adduct in the monoclinic space group $P2_1/n$. The starting oxo complex is synthesized using a large excess of triphenylphosphine, and $[ReOCl_3(PPh_3)_2]$ can be impure with PPh_3. It explains the presence of PPh_3 in the adduct. There are no significant contacts between the uncoordinated triphenylphosphine and the imido complex. Table 1 presents crystal data and structural refinement for $[Re(4\text{-}NC_6H_4NH_2)Cl_3(PPh_3)_2]\cdot PPh_3$.

A displacement ellipsoids plot of $[Re(4\text{-}NC_6H_4NH_2)Cl_3(PPh_3)_2]$ is shown in Fig. 1. The rhenium atom of $[Re(4\text{-}NC_6H_4NH_2)Cl_3(PPh_3)_2]$ is in a distorted octahedral environment with the chloride ions in a *meridional* geometry and two mutually *trans*-triphenylphosphine ligands, and the shortest Re···Re distance is equal to 9.678(1) Å (the second Re atom is obtained by $-x$, $-y$, $-z+1$ symmetry transformation).

The weak intramolecular hydrogen bonds; C(12)–H(12)···Cl(1) [D···A distance = 3.393(2) Å and D–H···A angle = 147.0°], C(24)–H(24)···Cl(2) [D···A distance = 3.548(6) Å and D–H···A angle = 154.0°], C(32)–H(32)···Cl(2) [D···A distance = 3.527(2) Å and D–H···A angle = 134.2°] and C(32)–H(32)···Cl(3) [D···A distance = 3.378(2) Å and D–H···A angle =

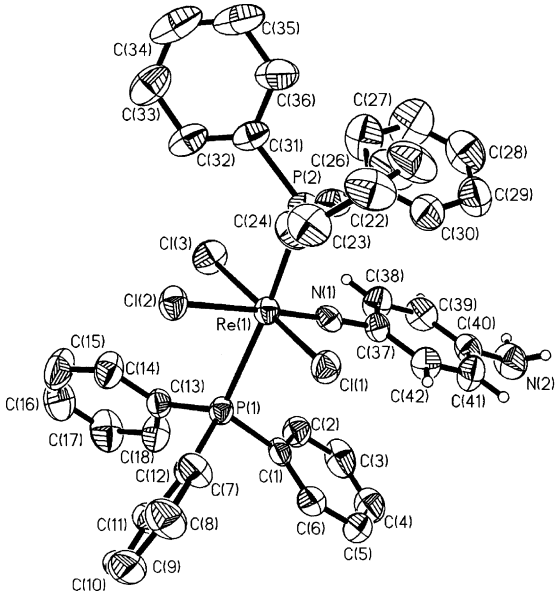


Fig. 1. A displacement ellipsoid plot of $[Re(4\text{-}NC_6H_4NH_2)Cl_3(PPh_3)_2]$ showing the atom numbering scheme (50% probability ellipsoids). The hydrogen atoms of the phenyl rings are omitted for clarity.

126.1°] provide additional conformational stabilization of the [Re(4-$NC_6H_4NH_2$)$Cl_3(PPh_3)_2$] molecule [27,28].

The most important bond lengths and angles for [Re(4-$NC_6H_4NH_2$)$Cl_3(PPh_3)_2$] are reported in Table 2. The Re(1)–N(1)–C(37) bond angle [177.2(4) Å] agrees with the linear coordination mode of the 4-$NC_6H_4NH_2$ ligand, and the Re–N(1) distance [1.719(4) Å] is typical for Re≡NR of rhenium(V) complexes [6]. Similar to the d^2 complexes *mer*,*trans*-[Re(NR)$Cl_3(PEt_2Ph)_2$] (R = C_6H_4-4-OMe or C_6H_4-4-COMe) [29] and *mer*, *trans*-[Re(NMe)$Cl_3(PEt_2Ph)_2$] [30], no structural *trans* effect of the imido ligand is observed in [Re(4-$NC_6H_4NH_2$)$Cl_3(PPh_3)_2$]. The Re–P bond distances fall within the normal range of Re–P distances observed in six-coordinate tertiary phosphine complexes – 2.45–2.51 Å [31].

The bond valences were computed as $v_{ij} = \exp[(R_{ij} - d_{ij})/b]$ [32–34], where R_{ij} is the bond-valence parameter (in the formal sense the R_{ij} parameter value can be considered as the idealized single-bond length between *i* and *j* atoms). The R_{Re-N}, R_{Re-P}, R_{Re-Cl} were taken as 2.06, 2.46 and 2.23 [34], respectively, and *b* was taken as 0.37 [33]. The computed bond valences of rhenium are $v_{Re-N} = 2.513$; $v_{Re-P} = 0.905$ and 0.915; $v_{Re-Cl} = 0.554$, 0.552 and 0.602 v.u. (valence units), which means that the Re–P bonds are two times stronger than the Re–Cl bonds, the Re–N bond is the strongest one and in a formal sense can be considered as a triple bond.

Table 2
The experimental and optimized bond lengths (Å) and bond angles (°) for [Re(4-$NC_6H_4NH_2$)$Cl_3(PPh_3)_2$]

	Experimental	Optimized
Bond length (Å)		
Re(1)–N(1)	1.719(4)	1.715
Re(1)–Cl(1)	2.4554(13)	2.506
Re(1)–Cl(2)	2.4498(12)	2.496
Re(1)–Cl(3)	2.4180(14)	2.508
Re(1)–P(1)	2.4969(14)	2.549
Re(1)–P(2)	2.4929(14)	2.549
Bond angle (°)		
N(1)–Re(1)–Cl(1)	90.31(13)	90.70
N(1)–Re(1)–Cl(2)	177.97(14)	179.75
N(1)–Re(1)–Cl(3)	92.71(14)	90.45
N(1)–Re(1)–P(1)	92.39(13)	94.58
N(1)–Re(1)–P(2)	93.78(13)	94.68
Cl(1)–Re(1)–P(1)	91.00(5)	90.41
Cl(1)–Re(1)–P(2)	88.61(5)	89.36
Cl(2)–Re(1)–Cl(1)	88.26(4)	89.55
Cl(2)–Re(1)–P(1)	86.19(4)	85.42
Cl(2)–Re(1)–P(2)	87.63(4)	85.32
Cl(3)–Re(1)–Cl(1)	176.70(5)	178.85
Cl(3)–Re(1)–Cl(2)	88.76(5)	89.30
Cl(3)–Re(1)–P(1)	90.19(5)	89.46
Cl(3)–Re(1)–P(2)	89.87(5)	89.46
P(2)–Re(1)–P(1)	173.82(4)	170.74
Re(1)–N(1)–C(37)	177.2(4)	179.66

3.3. Optimized geometry and charge distribution

The geometry of the [Re(4-$NC_6H_4NH_2$)$Cl_3(PPh_3)_2$] complex was optimized in a singlet state using the DFT method with the B3LYP functional. The optimized geometric parameters are gathered in Table 2. The calculated bond lengths and angles are in agreement with the values based upon the X-ray crystal structure data, and the general trends observed in the experimental data are well reproduced in the calculations.

Table 3 presents the atomic charges from the natural population analysis (NPA) for [Re(4-$NC_6H_4NH_2$)$Cl_3(PPh_3)_2$]. The calculated charge on the rhenium atom is considerably lower than the formal charge of +5. The populations of the d_{xy}, d_{xz}, d_{yz}, $d_{x^2-y^2}$ and d_{z^2} orbitals of the central atom are 1.300, 1.957, 0.904, 1.145 and 1.042, respectively. This is a result of significant charge donation from the imido ligand, chloride ions and triphenylphosphine molecules. Small differences in values of charges can be noticed between the chloride ion in the *trans* position to the imido group and two mutually *trans* Cl(1) and Cl(3) ligands. The Cl(2) ligand is less negative, which indicates higher electron density delocalization towards the rhenium atom.

3.4. Electronic structure

The rhenium atom of [Re(4-$NC_6H_4NH_2$)$Cl_3(PPh_3)_2$] possesses a d^2 configuration, the highest MO of this compound is of d_{xz} type with antibonding contributions from p_π chloride orbitals. The remaining four d-type orbitals of the rhenium are found among the unoccupied MOs. The d_{yz}, d_{xy}, d_{z^2} and $d_{x^2-y^2}$ orbitals of the central atom constitute mainly the LUMO, LUMO + 1, LUMO + 2 and LUMO + 10, respectively. The d_{yz} and d_{xy} rhenium orbitals bear antibonding character towards the p_π nitrogen orbitals of the imido ligand; the LUMO, LUMO + 1 can be considered as $\pi^*_{Re\equiv NR}$ orbitals.

3.5. NBO analysis

Table 4 presents the occupancies and natural atomic orbital compositions (NAO) of the calculated NBOs

Table 3
Atomic charges from the natural population analysis (NPA) of [Re(4-$NC_6H_4NH_2$)$Cl_3(PPh_3)_2$]

Atom	Atomic charge
Re(1)	0.326
Cl(1)	−0.481
Cl(2)	−0.463
Cl(3)	−0.482
P(1)	1.415
P(2)	1.414
N(1)	−0.234
N(2)	−0.806

Table 4
The selected results of the NBO analysis of [Re(4-$NC_6H_4NH_2$)-$Cl_3(PPh_3)_2$]

Bond orbital BD	Occupancy	NAO composition		
Re(1)–N(1) (σ)	1.95644	% Re	26.20	s(23.28%) d(76.52%)
		% O	73.80	s(53.61%) p(46.35%)
Re(1)–N(1) (π)	1.97310	% Re	39.38	d(99.49%)
		% O	60.62	p(99.98%)
Re(1)–N(1) (π)	1.93278	% Re	48.46	(98.95%)
		% O	51.54	p(99.97%)
Re(1)–Cl(1) (σ)	1.95214	% Re	26.29	s(30.29%) d(69.17%)
		% Br	73.71	s(16.84%) p(83.03%)
Re(1)–P(1) (σ)	1.87547	% Re	35.48	s(43.37%) d(56.43%)
		% Br	64.52	s(26.63%) p(73.20%)

between the rhenium and the donor ligand atoms for [Re(4-$NC_6H_4NH_2$)$Cl_3(PPh_3)_2$]. Some of the Re–L bonds were not detected indicating predominant Coulomb-type interactions between the central ion and the ligands.

The NBO analysis confirms the presence of a triple bond between the rhenium and the imido ligand in [Re(4-$NC_6H_4NH_2$)$Cl_3(PPh_3)_2$]. The Re–N bond orbital of σ-character is strongly polarized towards the nitrogen atom (ca. 74% at N), and the s and p nitrogen orbitals and s and d rhenium orbitals take part in the bond formation. The Re–N bond orbitals of π-character are the result of overlapping of the empty d_{xy} and d_{yz} rhenium orbitals with the occupied p_x and p_z orbitals of the deprotonated nitrogen of the imido ligand.

The NBO analysis also takes into consideration all possible interactions between 'filled' (donor) Lewis-type NBOs and 'empty' (acceptor) non-Lewis NBOs and estimates their energetic importance by second-order perturbation theory. Since these interactions lead to a loss of occupancy from the localized NBOs of the idealized Lewis structure into the empty non-Lewis orbitals, they are referred to as 'delocalization' corrections to the zeroth-order natural Lewis structure. The stabilization energy $E(2)$ associated with delocalization is estimated as

$$E(2) = \Delta E_{ij} = q_i(F(i,j)^2)/(\varepsilon_j - \varepsilon_i),$$

where q_i is the donor orbital occupancy, ε_i, ε_j are diagonal elements (orbital energies) and $F(i,j)$ is the off-diagonal NBO Fock matrix element [35].

Table 5 summarizes the most important delocalizations in [Re(4-$NC_6H_4NH_2$)$Cl_3(PPh_3)_2$] with their stabilization energy $E(2)$ values. Some of them concern the imido ligand. The electron density of the lone pair of the Cl(2) ligand (in the *trans* position to the imido ligand) is delocalized into the $\sigma^*_{Re(1)-N(1)}$ bond orbital. A significant loss of occupancy concerns the p_π orbital of the C(37) atom in the imido group. The electron density of this orbital is delocalized into the $\pi^*_{Re(1)-N(1)}$ bond orbital and π^*_{C-C} bond orbitals of the imido ring.

3.6. Spectroscopic properties

The IR spectra of [Re(4-$NC_6H_4NH_2$)$Cl_3(PPh_3)_2$] and [Re(4-$NC_6H_4NH_2$)$Br_3(PPh_3)_2$] are characterized by strong absorptions at 1169 and 1163 cm^{-1}, respectively, which is within the region (1000–1200 cm^{-1}) expected for a linearly coordinated phenylimido moiety with a triple bond [36]. The absorption bands at ~3400 cm^{-1} correspond to the N–H stretching vibrations and confirm the presence of the uncoordinated NH_2-group.

The experimental and calculated electronic spectra of the chloro complex are represented graphically in Fig. 2. Each calculated transition in Fig. 2 is represented by a

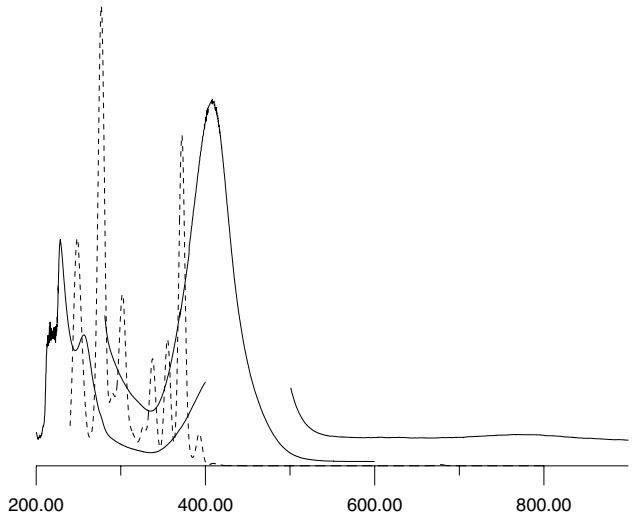


Fig. 2. The experimental (——) and calculated (------) electronic absorption spectrum of [Re(4-$NC_6H_4NH_2$)$Cl_3(PPh_3)_2$].

Table 5
The most important delocalizations observed for [Re(4-$NC_6H_4NH_2$)$Cl_3(PPh_3)_2$] and their stabilization energies (kcal/mol)

Donor natural bond orbital	Occupancy of donor NBO	Acceptor natural bond orbital	Occupancy of acceptor NBO	Stabilization energy
LP of Cl(2) (σ)	1.66073	σ* of Re(1)–N(1)	0.40280	137.39
p_π of C(37)	1.08447	π* of Re(1)–N(1)	0.37253	171.49
p_π of C(37)		π* of C(38)–C(39)	0.27819	64.81
p_π of C(37)		π* of C(41)–C(42)	0.27864	64.90
LP of Cl(3) (σ)	1.55618	σ* of Re(1)–Cl(1)	0.44406	136.88
LP of P(2)	1.33608	σ* of Re(1)–P(1)	0.51972	139.84

LP, lone pair.

Table 6
The energy and molar absorption coefficients of experimental absorption bands and the electronic transitions calculated with the TDDFT method for $[Re(4\text{-}NC_6H_4NH_2)Cl_3(PPh_3)_2]$

The most important orbital excitations	Character	λ (nm)	E (eV)	f	Experimental Λ (nm) (E (eV)) ε
H → L + 1	d → d	678.4	1.83	*0.0007*	790.0 (1.60) 25
H → L + 2	d → d	431.9	2.87	*0.0001*	419.2 (2.96) 19 800
H-1 → L + 1	π(imido)/π(Cl) → d	409.0	3.03	*0.0015*	
H-3 → L	π(Ph)/π(Cl) → d	392.6	3.16	*0.0219*	
H-1 → L	π(imido)/π(Cl) → d	372.1	3.33	*0.2250*	
H-5 → L	π(Ph)/π(Cl) → d	355.0	3.49	*0.0836*	
H-3 → L + 1	π(Ph)/π(Cl) → d	337.4	3.67	*0.0506*	
H-7 → L	π(Ph) → d	336.8	3.68	*0.0183*	
H-5 → L + 1	π(Ph)/π(Cl) → d	326.6	3.80	*0.0098*	
H-7 → L	π(Ph) → d	326.3	3.80	*0.0125*	
H-9 → L + 1	π(Cl) → d	302.5	4.10	*0.0822*	256.2 (4.84) 24 600
H → L + 7	d → π*(Ph)	301.6	4.11	*0.0141*	
H-17 → L	π(Ph)/π(Cl) → d	297.9	4.16	*0.0291*	
H-13 → L + 1	π(Cl)/π(Cl)/σ(Cl) → d	290.4	4.27	*0.0128*	
H-11 → L + 1	π(Ph) → d				
H-1 → L + 2	π(imido)/π(Cl) → d	288.5	4.30	*0.0207*	
H-2 → L + 2	n(P)/π(Cl) → d	277.3	4.47	*0.2661*	
H → L + 11	d → π*(Ph)	274.1	4.52	*0.0410*	
H-17 → L	π(Ph)/π(Cl) → d	273.1	4.54	*0.0108*	
H-3 → L + 2	π(Ph)/π(Cl) → d	265.5	4.67	*0.0135*	
H-5 → L + 2	π(Ph)/π(Cl) → d	255.6	4.85	*0.0106*	
H-1 → L + 10	π(imido)/π(Cl) → d	250.0	4.96	*0.0243*	
H-6 → L + 2	π(Ph) → d	249.2	4.97	*0.0160*	
H → L + 15	d → π*(Ph)	249.0	4.98	*0.0196*	
H-2 → L + 6	n(P)/π(Cl) → π*(Ph)	248.7	4.98	*0.0257*	228.4 (5.43) 42 700
H-1 → L + 7	π(imido)/π(Cl) → π*(Ph)	247.5	5.01	*0.0229*	
H-3 → L + 3	π(Ph)/π(Cl) → π*(Ph)	245.0	5.06	*0.0232*	
H-2 → L + 7	n(P)/π(Cl) → π*(Ph)	244.5	5.07	*0.0135*	
					216.4 (5.73) 27 000

H, HOMO; L, LUMO.

Gaussian function with the height equal to the oscillator strength and width equal to 0.04. The shape of the UV–Vis spectrum of $[Re(4\text{-}NC_6H_4NH_2)Br_3(PPh_3)_2]$ is the same as for the chloro analogue; the absorption bands of the bromo complex were recorded at 788.0, 421.0, 267.4, 237.0 and 224.8 nm.

Table 6 shows the energy and molar absorption coefficients of the experimental absorption bands of $[Re(4\text{-}NC_6H_4NH_2)Cl_3(PPh_3)_2]$ and the spin-allowed singlet–singlet electronic transitions calculated with the TDDFT method. Except for the low energy part of the spectrum, only transitions with oscillator strengths larger than 0.01 are listed in Table 6.

The investigated complex is of large size, and the number of basis functions is equal to 812. Eighty electron transitions calculated by the TDDFT method do not comprise all the experimental absorption bands. The UV–Vis spectrum of $[Re(4\text{-}NC_6H_4NH_2)Cl_3(PPh_3)_2]$ was calculated to ~240 nm, so the shortest wavelength experimental band is not assigned to the calculated transitions, and the assignment of the band at 228.4 nm is probably not complete. Considering that the solution spectra of PPh_3 and 1,4-diaminobenzene exhibit intense absorption bands in 250–200 nm region, some additional intraligand and interligand transitions are expected to be found at higher energies in the calculations for $[Re(4\text{-}NC_6H_4NH_2)Cl_3(PPh_3)_2]$.

The longest wavelength experimental band at 790 nm may be attributed to the transition of d → d character with small oscillator strength, calculated at 678.4 nm.

The absorption band at 419.2 nm corresponds to the LMCT transitions calculated in the range 432–326 nm. These transitions occur from the chloride, imido and phosphine ligand orbitals to the d rhenium orbitals.

The next experimental band at 256.2 nm may be assigned to the transitions calculated between 305 and 249 nm with large oscillator strengths. These are LMCT transitions from the chloride, imido and phosphine ligand orbitals to the d rhenium orbitals and MLCT transitions from the d_{Re} to the acceptor orbitals of PPh_3.

The absorption band at 228.4 nm is attributed to the LLCT transitions with large oscillator strengths. They comprise intra- and interligand transitions.

4. Supplementary data

Supplementary data for $C_{60}H_{51}Cl_3N_2P_3Re$ are available from the CCDC, 12 Union Road, Cambridge CB2 1EZ, UK (fax: +44 1223 336 033; e-mail:

deposit@ccdc.cam.ac.uk or www: http://www.ccdc.cam.ac.uk) on request, quoting the deposition number: 263918.

Acknowledgements

The GAUSSIAN-03 calculations were carried out in the Wrocław Centre for Networking and Supercomputing, WCSS, Wrocław, Poland under calculational Grant No. 51/96.

The crystallographic part was financed by funds allocated by the Ministry of Scientific Research and Information Technology to the Institute of General and Ecological Chemistry, Technical University of Łódź.

References

[1] W.A. Nugent, B.L. Haymore, Coord. Chem. Rev. 31 (1980) 123.
[2] W.A. Nugent, J.M. Mayer, Metal–ligand Multiple Bonds, Wiley, New York, 1988, pp. 184–185.
[3] D.E. Wigley, Prog. Inorg. Chem. 42 (1994) 407.
[4] L.H. Gade, P. Mountford, Coord. Chem. Rev. 216–217 (2001) 65.
[5] A.A. Danopolous, J.C. Green, M.B. Hursthouse, J. Organomet. Chem. 591 (1999) 36.
[6] R.A. Eikey, M.M. Abu-Omar, Coord. Chem. Rev. 243 (2003) 83, and references cited therein.
[7] T.R. Cundari, J. Am. Chem. Soc. 114 (1992) 7879.
[8] M.T. Benson, T.R. Cundari, E.W. Moody, J. Organomet. Chem. 504 (1995) 1.
[9] K.R. Birdwhistell, J. Lanza, J. Pasos, J. Organomet. Chem. 584 (1999) 200.
[10] P.J. Walsh, A.M. Baranger, R.G. Bergman, J. Am. Chem. Soc. 114 (1992) 1708.
[11] P.L. McGrane, M. Jensen, T. Livinghouse, J. Am. Chem. Soc. 114 (1992) 5459.
[12] P.J. Walsh, F.J. Hollander, R.G. Bergman, J. Am. Chem. Soc. 110 (1988) 8729.
[13] K.M. Doxsee, K.B. Farahi, H. Hope, J. Am. Chem. Soc. 113 (1991) 8889.
[14] B. Coutinho, D. Dawson, J.R. Dilworth, J.R. Miller, M. Rosser, C.M. Archer, J.D. Kelly, in: M. Nicolini, G. Bandoli, U. Mazzi (Eds.), Technetium and Rhenium in Chemistry and Nuclear Medicine, 4, vol. 3, S.G. Editoriali, Padova, 1995.
[15] M.T. Ahmet, B. Coutinho, J.R. Dilworth, J.R. Miller, S.J. Parrott, Y. Zheng, Polyhedron 15 (1996) 2041.
[16] G. Rouschias, G. Wilkinson, J. Chem. Soc. A (1966) 465.
[17] STOE & Cie, X-RED: Version 1.18. STOE & Cie GmbH, Darmstadt, Germany, 1999.
[18] G.M. Sheldrick, Acta Crystallogr., Sect. A 46 (1990) 467.
[19] G.M. Sheldrick, SHELXL-97: Program for the Solution and Refinement of Crystal Structures, University of Göttingen, Göttingen, Germany, 1997.
[20] G.M. Sheldrick, SHELXTL: Release 4.1 for Siemens Crystallographic Research Systems, 1990.
[21] M.J. Frisch, G.W. Trucks, H.B. Schlegel, G.E. Scuseria, M.A. Robb, J.R. Cheeseman, J.A. Montgomery Jr., T. Vreven, K.N. Kudin, J.C. Burant, J.M. Millam, S.S. Iyengar, J. Tomasi, V. Barone, B. Mennucci, M. Cossi, G. Scalmani, N. Rega, G.A. Petersson, H. Nakatsuji, M. Hada, M. Ehara, K. Toyota, R. Fukuda, J. Hasegawa, M. Ishida, T. Nakajima, Y. Honda, O. Kitao, H. Nakai, M. Klene, X. Li, J.E. Knox, H.P. Hratchian, J.B. Cross, C. Adamo, J. Jaramillo, R. Gomperts, R.E. Stratmann, O. Yazyev, A.J. Austin, R. Cammi, C. Pomelli, J.W. Ochterski, P.Y. Ayala, K. Morokuma, G.A. Voth, P. Salvador, J.J. Dannenberg, V.G. Zakrzewski, S. Dapprich, A.D. Daniels, M.C. Strain, O. Farkas, D.K. Malick, A.D. Rabuck, K. Raghavachari, J.B. Foresman, J.V. Ortiz, Q. Cui, A.G. Baboul, S. Clifford, J. Cioslowski, B.B. Stefanov, G. Liu, A. Liashenko, P. Piskorz, I. Komaromi, R.L. Martin, D.J. Fox, T. Keith, M.A. Al-Laham, C.Y. Peng, A. Nanayakkara, M. Challacombe, P.M.W. Gill, B. Johnson, W. Chen, M.W. Wong, C. Gonzalez, J.A. Pople, GAUSSIAN-03: Revision B.03, Gaussian, Inc., Pittsburgh, PA, 2003.
[22] A.D. Becke, J. Chem. Phys. 98 (1993) 5648.
[23] Lee, W. Yang, R.G. Parr, Phys. Rev. B 37 (1988) 785.
[24] M.E. Casida, in: J.M. Seminario (Ed.), Recent Developments and Applications in Modern Density Functional Theory: Theoretical and Computational Chemistry, vol. 4, Elsevier, Amsterdam, 1996.
[25] P.J. Hay, W.R. Wadt, J. Chem. Phys. 82 (1985) 299.
[26] E.D. Glendening, A.E. Reed, J.E. Carpenter, F. Weinhold, NBO (version 3.1).
[27] G.A. Jeffrey, W. Saenger, Hydrogen Bonding in Biological Structures, Springer, Berlin, 1994.
[28] G.R. Desiraju, T. Steiner, The Weak Hydrogen Bond in Structural Chemistry and Biology, Oxford University Press, Oxford, 1999.
[29] D. Bright, J.A. Ibers, Inorg. Chem. 7 (1968) 1099.
[30] D. Bright, J.A. Ibers, Inorg. Chem. 8 (1969) 703.
[31] R. Hübner, U. Abram, J. Strähle, Acta Crystallogr., Sect. C 51 (1995) 1284.
[32] I.D. Brown, Acta Crystallogr., Sect. B 48 (1992) 553.
[33] I.D. Brown, Acta Crystallogr., Sect. B 53 (1997) 381.
[34] M. O'Keeffe, N.E. Brese, J. Am. Chem. Soc. 113 (1991) 3226.
[35] A.E. Reed, L.A. Curtiss, F. Weinhold, Chem. Rev. 88 (1988) 899.
[36] M. Bakir, J.A.M. McKenzie, B.P. Sullivan, Inorg. Chim. Acta 254 (1997) 9.

azobenzene chromophore, 4-[di(biphenyl-4-yl)amino]-azobenzene and 4,4′-bis[bis(4-*tert*-butylbiphenyl-4-yl)-amino]-azobenzene have been used as photochromic amorphous molecular materials [10]. Other azobenzene-based amorphous molecular materials, with a spiro-linked bifluorene, have been synthesized and their photoinduced behavior such as optically induced birefringence, diffraction efficiency and surface relief gratings (SRGs) were investigated in relation to their unique molecular structures [11].

Based on our knowledge, only a few coordination or organometallic compounds have been reported as amorphous molecular materials. Platinum 5-fluorouridine green sulfate is a typical example of an amorphous coordination compound [12]. A polycrystalline sample of titanyl phthalocyanine was vacuum evaporated at ca. 10^{-5} Torr to form an amorphous thin film. Photovoltaic devices consisting of an amorphous thin film of titanyl phthalocyanine and *N*,*N*-dimethyl-3,4:9,10-perylenebis (dicarboximide), sandwiched between ITO and Au electrodes, demonstrated a response to light over the whole visible wavelength region from 400 to 900 nm [13]. Shirota and co-workers [8a] have synthesized copper and titanyl phthalocyanines containing triarylamine moieties. These compounds are soluble in common organic solvents and readily form stable amorphous glasses with high glass transition temperatures. Bazan and co-workers [14] have synthesized Iridium complexes with fluorene-modified phenylpyridine ligands that are resistant to crystallization and can be used in the fabrication of single layer light emitting diodes. It is worth mentioning that the introduction of a metal center into organic systems in order to form coordination or organometallic molecular materials can introduce extra parameters such as color, magnetism and birefringence in amorphous molecular materials. Besides the metal center can improve the electroluminescent properties of coordination molecular materials.

In this work, we report the synthesis and investigation of glass-forming properties of new bis[5-((4-^{n}dodecyloxyphenyl)azo)-*N*-(4-^{n}alkoxyphenyl)-salicylaldiminato]-nickel (II) complex homologues (see Scheme 1).

2. Experimental

2.1. Reagents

All reagents and solvents used were supplied by Merck chemical company and used without further purification. 4-Alkoxynitrobenzene homologues were obtained by reaction between 4-nitrophenol with 1-bromoctan or 1-bromododecane in DMF as solvent and K_2CO_3 as base by refluxing for 3 h [15] and then crude 4-alkoxy nitrobenzene homologues were purified by recrystallization from ethanol. 4-Alkoxyaniline homologues prepared by reduction of the corresponding 4-alkoxynitrobenzene as described in the literature [16].

2.2. Physical measurements

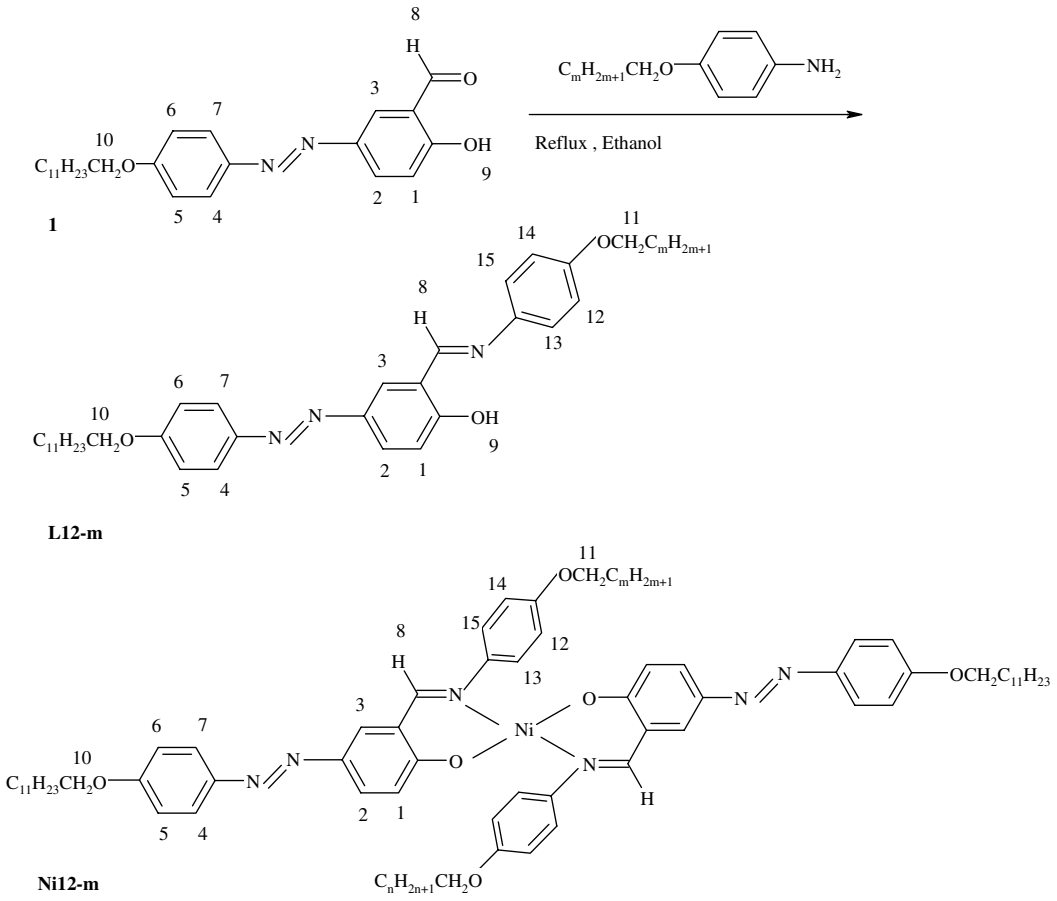
Elemental (C, H and N) analyses were carried out on a Perkin–Elmer automatic equipment model 240B. Electron impact (70 eV) mass spectra were recorded on a Finnigan-mat GC–MS–DS spectrometer model 8430. Infrared spectra were taken with a Bruker FT-IR spectrometer model vector 22, using KBr pellets in the 400–4000 cm^{-1} range. The DSC thermograms of the compounds were obtained on a Mettler–Toledo DSC 822e module, which was calibrated with indium metal ($T = 156.6 \pm 0.3$, $\Delta H = 28.45 \pm 0.6$ J g^{-1}). Samples of 2–5 mg in the solid form were placed in aluminum pans (40 μl) with a pierced lid, and heated or cooled at a scan rate of 10 °C min^{-1} under a nitrogen flow. TGA was carried out on a Mettler–Toledo TGA 851e at a heating rate of 10 °C min^{-1} under a nitrogen atmosphere. X-ray powder diffraction patterns were recorded on a Bruker D8 powder diffractometer (Cu Kα: 1.541 Å). The optical observations were made with a Zeiss polarizing microscope equipped with a Linkam THMSG 600 heating and cooling stage and Linkam THMS 93 programmable temperature-controller. ^{1}H NMR spectra were obtained in deutrated chloroform as solvent on a Bruker FT-NMR AC-400 (400 MHz) spectrometer. All chemical shifts are reported in δ (ppm) relative to tetramethylsilane as an internal standard.

2.3. Materials

*5-(4-Dodecyloxyphenylazo)salicylaldehyde (**1**).* This compound was prepared as described in the literature [17]. Yellow, yield 80%, m.p. 123 °C. MS *m/z* (relative intensity): 411.6 (M + 1,15), 410.6 (M, 45), 242.5 (M − $C_{12}H_{25}$, 25), 121.6 (M − $C_{12}H_{25}OC_6H_4N_2$, 100). *Anal.* Calc. for $C_{25}H_{34}N_2O_3$: C, 73.15; H, 8.35; N, 6.83. Found: C, 72.73; H, 8.14; N, 6.47%. ^{1}H NMR (400 MHz, $CDCl_3$) δ 11.26 (s, H-9), 10.02 (s, H-8), 8.15 (d, $J = 2.8$ Hz, H-3), 8.13 (dd, $J = 2.9$, 8.2 Hz, H-2), 7.89 (dd, $J = 3.0$, 7.9 Hz, H-4, H-7), 7.11 (d, $J = 8.1$ Hz, H-1), 7.01 (dd, $J = 3.2$, 7.9 Hz, H-5, H-6), 4.04 (t, $J = 6.7$ Hz, H-10), 1.84–0.87 (23H, alkyl chain).

3. Syntheses of the ligands

All homologue materials were prepared similarly. Thus, 0.026 mol of the related amine (4-alkoxy aniline) and 0.026 mol of 5-(4-^{n}dodecyloxyphenylazo)salicylaldehyde were dissolved in 100 ml absolute ethanol with a few drops of glacial acetic acid as a catalyst. The



Compound No.	m
L12-8	7
L12-12	11
L12-16	15
Ni12-8	7
Ni12-12	11
Ni12-16	15

Scheme 1.

solution was refluxed for 1 h and then left at room temperature. After cooling, the ligands were obtained as yellow micro crystals. The micro crystals were filtered off, washed with 15 ml of cold absolute ethanol and then recrystallized several times in ethanol–chloroform (1:3, v/v).

L12-8. Yellow, yield 85%. MS *m*/*z* (relative intensity): 614.8 (M + 1,15), 613.8 (M, 65), 443.7 (M − $C_{12}H_{25}$, 23), 324.7 (M − $C_{12}H_{25}OC_6H_4N_2$, 100). *Anal.* Calc. for $C_{39}H_{55}N_3O_3$: C, 76.30; H, 9.03; N, 6.85. Found: C, 76.0; H, 8.8; N, 6.6%. ^{1}H NMR (400 MHz, $CDCl_3$) δ 13.99 (s, H-9), 8.72 (s, H-8), 7.97 (dd, J = 3, 6.7 Hz, H-2), 7.95 (d, J = 6.7 Hz, H-3), 7.87 (dd, J = 3, 6.8 Hz, H-4, H-7), 7.30 (dd, J = 3.1, 7.9 Hz, H-5, H-6), 7.10 (d, J = 8.7 Hz, H-1), 6.99 (dd, J = 2, 8.9 Hz, H-13, H-15), 6.95 (dd, 1.9, 8.8 Hz, H-12, H-14), 4.03 (t, J = 6.5 Hz, H-10), 3.98 (t, J = 6.5 Hz, H-11), 1.85–0.86 (38H, alkyl chain).

L12-12. Yellow, yield 87%. MS *m*/*z* (relative intensity): 670.7 (M + 1,13), 669.7 (M, 60), 500.6 (M − $C_{12}H_{25}$, 25), 380.5 (M − $C_{12}H_{25}OC_6H_4N_2$, 100). *Anal.* Calc. for $C_{43}H_{63}N_3O_3$: C, 78.02; H, 9.59; N, 6.35. Found: C, 77.8; H, 9.4; N, 6.2%. ^{1}H NMR (400 MHz, $CDCl_3$) δ 13.99 (s, H-9), 8.73 (s, H-8), 7.97 (dd, J = 3, 6.8 Hz, H-2), 7.95 (d, J = 2.9 Hz, H-3), 7.88 (dd, J = 3, 6.9 Hz, H-4, H-7), 7.31 (dd, J = 3.0, 7.8 Hz, H-5, H-6), 7.11 (d, J = 8.8 Hz, H-1), 7.00 (dd, J = 1.9, 8.9 Hz, H-13, H-15), 6.95 (dd, 1.9, 8.8 Hz, H-12, H-14), 4.04 (t, J = 6.6 Hz, H-10), 3.99 (t, J = 6.5 Hz, H-11), 1.85–0.87 (46H, alkyl chain).

L12-16. Yellow, yield 87%. MS *m*/*z* (relative intensity): 726.8 (M + 1,12), 725.8 (M,63), 556.7 (M − $C_{12}H_{25}$, 26), 433.7 (M − $C_{12}H_{25}OC_6H_4N_2$, 100). *Anal.* Calc. for $C_{47}H_{71}N_3O_3$: C, 78.62; H, 9.97; N, 5.85. Found: C, 77.1; H, 9.5; N, 5.5%. ^{1}H NMR (400 MHz,

$CDCl_3$) δ 13.99 (s, H-9), 8.73 (s, H-8), 7.97 (dd, J = 3, 6.8 Hz, H-2), 7.95 (d, J = 6.8 Hz, H-3), 7.89 (dd, J = 3, 6.8 Hz, H-4, H-7), 7.30 (dd, J = 3.0, 7.6 Hz, H-5, H-6), 7.12 (d, J = 8.8 Hz, H-1), 7.00 (dd, J = 1.9, 8.8 Hz, H-13, H-15), 6.96 (dd, 2.0, 8.7 Hz, H-12, H-14), 4.04 (t, J = 6.6 Hz, H-10), 3.99 (t, J = 6.5 Hz, H-11), 1.85–0.87 (54H, alkyl chain).

Syntheses of the nickel complexes. The nickel complexes were prepared in a similar manner as described by Nejati et al. [17]. Thus, a solution of 4 mmol of $Ni(CH_3COO)_2{\cdot}4H_2O$ in 10 ml of ethanol was added to an ethanol–chloroform (1:1 v/v) solution containing 8 mmol of ligand, and the resulting solution was refluxed for 2 h. The obtained solution was left at room temperature. The nickel complexes were obtained as yellow-green micro crystals. The micro crystals were filtered off, washed with absolute ethanol and then recrystallized in ethanol–chloroform (1:3 v/v).

Ni12-8. Yellow-green, yield 80%. *Anal.* Calc. for $C_{78}H_{108}N_6O_6Ni$: C, 72.94; H, 8.48; N, 6.54. Found: C, 72.4; H, 8.0; N, 6.2%. ^{1}H NMR (400 MHz, $CDCl_3$) δ 8.13 (s, H-8), 7.97 (dd, J = 2.9, 6.9 Hz, H-2), 7.94 (d, J = 6.6 Hz, H-3), 7.84 (dd, J = 3, 6.8 Hz, H-4, H-7), 7.28 (dd, J = 3.1, 7.9 Hz, H-5, H-6), 7.13 (d, J = 8.5 Hz, H-1), 7.00 (dd, J = 2, 8.8 Hz, H-13, H-15), 6.93 (dd, 1.9, 8.7 Hz, H-12, H-14), 4.24 (t, J = 6.1 Hz, H-11), 4.02 (t, J = 6.5 Hz, H-10), 1.81–0.84 (76H, alkyl chain).

Ni12-12. Yellow-green, yield 85%. *Anal*. Calc. for $C_{86}H_{124}N_6O_6Ni$: C, 74.26; H, 8.95; N, 6.02. Found: C, 73.9; H, 8.6; N, 5.8%. ^{1}H NMR (400 MHz, $CDCl_3$) δ 8.12 (s, H-8), 7.97 (dd, J = 3, 6.8 Hz, H-2), 7.93 (d, J = 6.7 Hz, H-3), 7.85 (dd, J = 2.9, 6.7 Hz, H-4, H-7), 7.27 (dd, J = 3.0, 7.8 Hz, H-5, H-6), 7.12 (d, J = 8.3 Hz, H-1), 7.01 (dd, J = 2.1, 8.6 Hz, H-13, H-15), 6.94 (dd, 2, 8.5 Hz, H-12, H-14), 4.24 (t, J = 6.1 Hz, H-11), 4.02 (t, J = 6.5 Hz, H-10), 1.82–0.82 (92H, alkyl chain).

Ni12-16. Yellow-green, yield 80%. *Anal*. Calc. for $C_{94}H_{140}N_6O_6Ni$: C, 74.82; H, 9.35; N, 5.57. Found: C, 74.4; H, 8.9; N, 5.2%. ^{1}H NMR (400 MHz, $CDCl_3$) δ 8.13 (s, H-8), 7.96 (dd, J = 3, 6.9 Hz, H-2), 7.92 (d, J = 6.8 Hz, H-3), 7.84 (dd, J = 3, 6.8 Hz, H-4, H-7), 7.28 (dd, J = 3.0, 7.7 Hz, H-5, H-6), 7.13 (d, J = 8.1 Hz, H-1), 7.02 (dd, J = 2.2, 8.5 Hz, H-13, H-15), 6.95 (dd, 2, 8.6 Hz, H-12, H-14), 4.23 (t, J = 6.2 Hz, H-11), 4.01 (t, J = 6.4 Hz, H-10), 1.83–0.81 (108H, alkyl chain).

4. Results and discussion

4.1. Synthesis

The Schiff base ligands were synthesized in a four-step process, in which the hydroxy group in 4-nitrophenol is first replaced by an alkoxy chain followed by reduction of nitro group to an amine. In the third step, salicylaldehyde is coupled with the diazonium chloride obtained from the 4-dodecyloxyaniline and finally the Schiff base ligands were obtained by reaction of 5-(4-dodecyloxyphenylazo)salicylaldehyde with an appropriate 4-alkoxyaniline (Scheme 1) by refluxing in absolute ethanol, using a few drops of acetic acid as a catalyst. The Schiff-bases, **2a**–**2c**, were purified by repeated crystallization in an ethanol/chloroform mixture. The 5-(4-^{n}dodecyloxyphenylazo)salicylaldehyde and ligand homologues were characterized by IR, ^{1}H NMR, mass spectroscopy and elemental analyses. The Ni complexes were characterized by C, H, N elemental analyses, ^{1}H NMR and IR spectroscopy. Some physical and characterization data for the ligands and the complexes are given in the experimental section and selected IR data are reported in Table 1. The IR spectra of the nickel complexes show that the stretching frequency of the C=N bond was shifted to lower wavenumbers (ca. 15 cm^{-1}) in comparison with the free ligand after coordination. This shift is due to the reduction of the double bond character of the C=N bond, which is caused by the coordination of nitrogen to the metal center and is in agreement with the results obtained from the other similar complexes described previously [17–19]. On the other hand, the disappearance of the OH band of the free ligands in the spectra of the metal complexes indicates that the OH group has been deprotonated and coordinates to the metal ion as $-O^-$. In addition, a comparison of the ^{1}H NMR spectra of the ligands and the Ni complexes indicates that the proton signal corresponding to the OH group of the free ligands has disappeared in the nickel complexes and a large shielding occurrs for the imine proton H-8 ($\Delta\delta = \delta_{ligand} - \delta_{complex} = 0.7$ ppm). Based on these observations and elemental analyses results, we concluded that the Schiff-base ligands are coordinated to the metal center as bidentate (N–O) ligands in a 2:1 ratio.

Table 1
Selected IR data for the Schiff base ligands and the metal complexes

Compound	ν (cm^{-1})					
	O–H	C–H (aromatic)	C–H (aliphatic)	C=N	C–O (etheric)	C=O
1	3185(br, m)	3070-75(m)	2950-2850(s)		1241-4(s)	1663(s)
L12-m	3445-60(br, m)	3050-55(m)	2950-2865(s)	1625-30(s)	1250-80(s)	
Ni12-m		3040-47(m)	2922-2848(s)	1615-18(s)	1240-48(s)	

s, strong; m, medium; br, broad.

We recently reported the crystal structure of bis-[5-((4-^{n}propyloxyphenyl)azo)-*N*-(^{n}-pentyl-salicylaldiminato)] Ni(II) [20], which has a similar coordination environment to that of the title complex of this work. In these kinds of complexes, the Schiff base ligands have an approximately *trans*-planar configuration around the Ni central ion and the structure is square planar. Therefore, we propose that the Ni(II) complexes have square planar or nearly square planar coordination geometry.

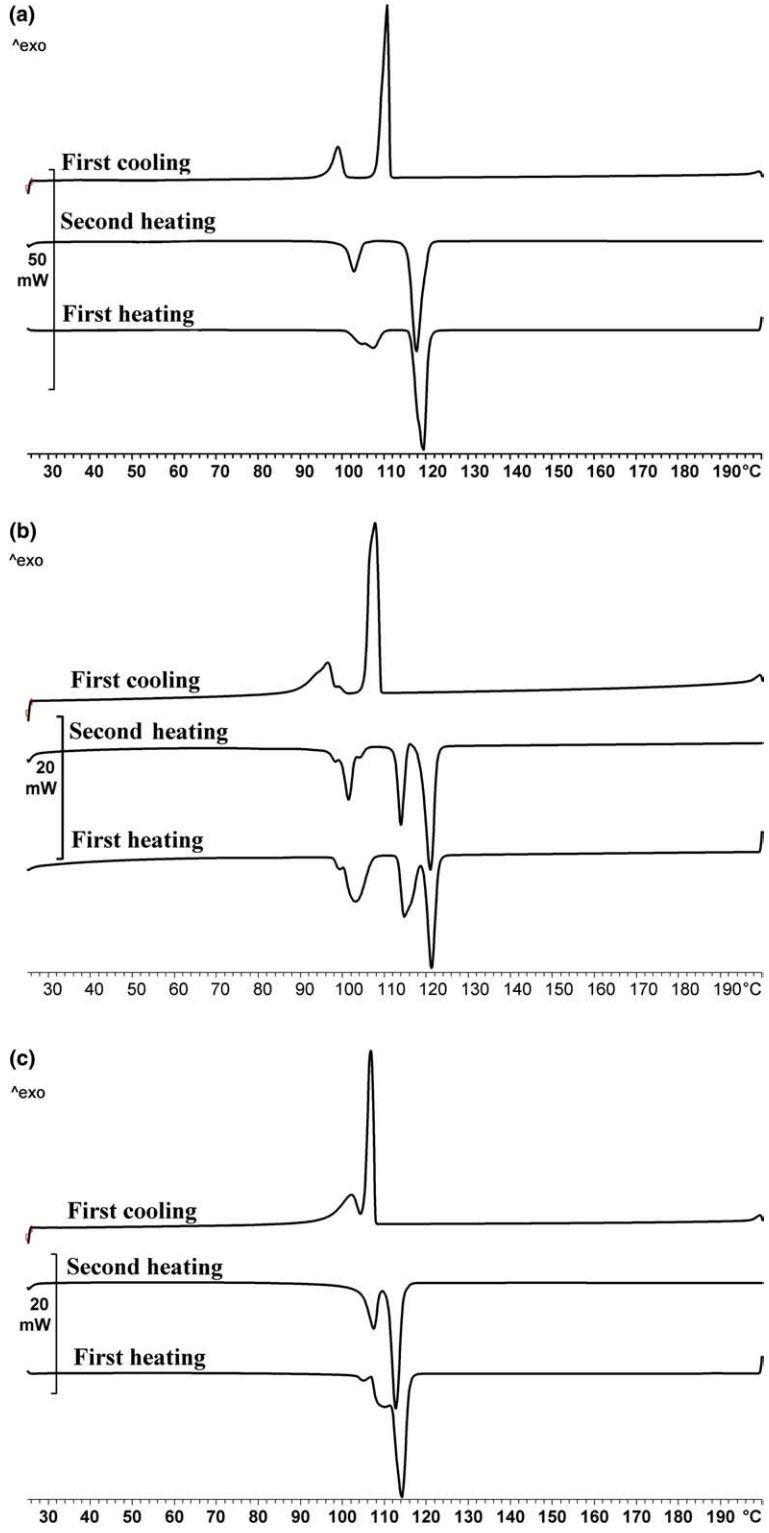


Fig. 1. DSC thermograms of: (a) **L12-8**, (b) **L12-12** and (c) **L12-16**.

4.2. Glass formation

The thermal stability of these materials was checked by thermogravimetric analysis (TGA) at first. All other thermal characterizations were then carried out below the decomposition temperature. Glass forming properties of the Schiff base ligands and the related Ni(II) complexes were studied by differential scanning calorimetry, polarizing optical microscopy (POM) observations utilizing a heating–cooling stage and X-ray diffraction (XRD). The transition temperatures of the ligands and the complexes were measured by DSC. Fig. 1(a)–(c)

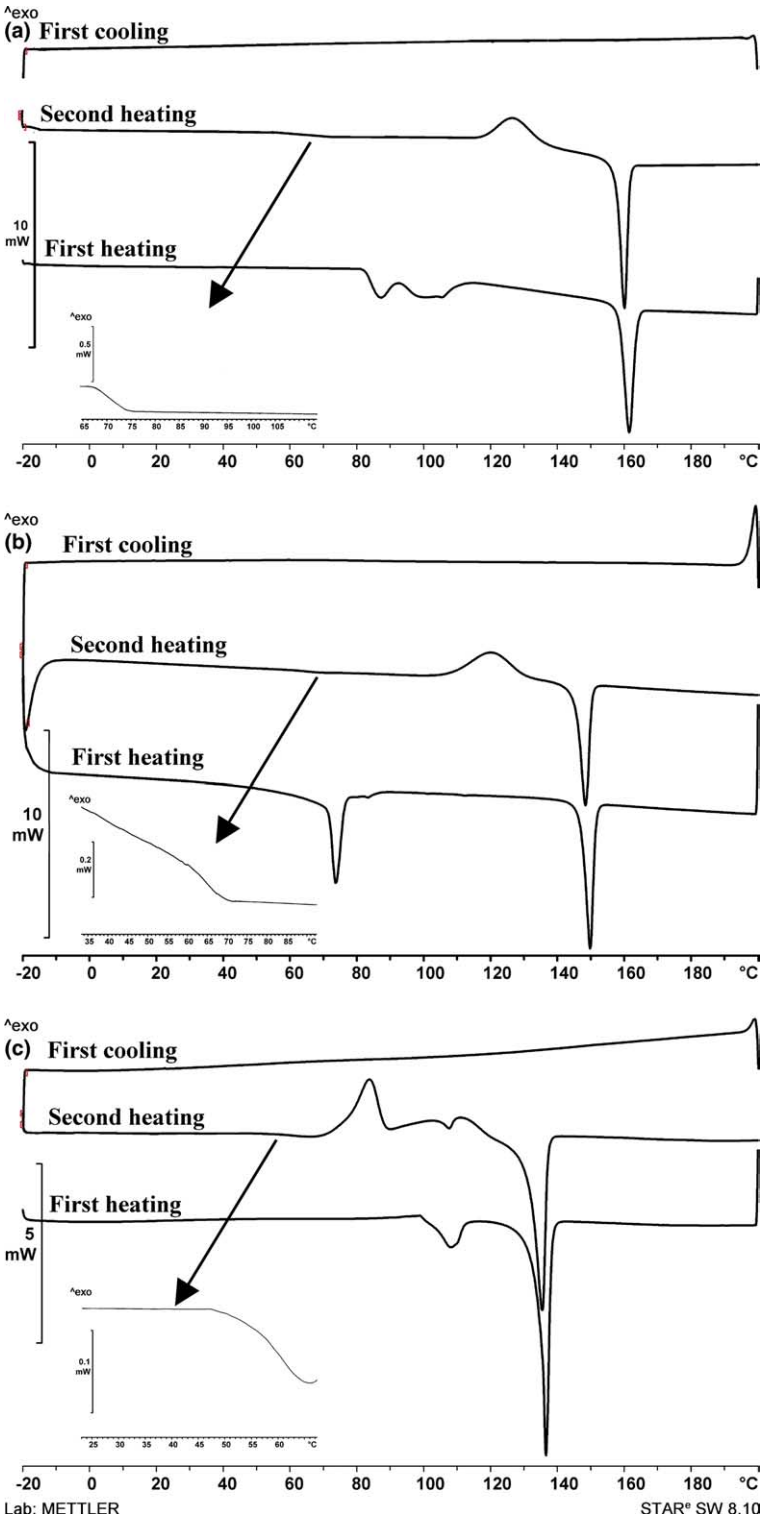


Fig. 2. DSC thermograms of: (a) **Ni12-8**, (b) **Ni12-12** and (c) **Ni12-16**, heating and cooling rate: 10 K min^{-1}.

shows the DSC curves of the ligands. The thermal behaviors of the ligands were similar as it is apparent from the DSC curves; therefore we describe here the behavior of compound **L12-12** as a representative. In the first heating scan, **L12-12** showed four endothermal peaks at 99.1, 102.9, 114.3 and 120.5 °C (Fig. 1(b)). In the second heating scan, four endothermal peaks at 98.1, 101.0, 113.4 and 120.2 °C were observed. When the isotropic melt of **L12-12** was cooled at a cooling rate of 10 K min^{-1}, two exothermal peaks at 108.7, and 99.5 °C were observed (see Fig. 2). The powder XRD patterns of **L12-12** recorded at room temperature prior to heating and after cooling from the isotropic liquid indicated a typical crystalline phase. Therefore, the peaks at 120.5 °C (in the first and second heating scan) are attributed to melting, the peak at 108.7 °C on the cooling step due to crystallization and other peaks may be related to solid–solid phase transitions. The melting peak is narrow and the enthalpy of fusion amounts to 40 kJ mol^{-1}. Such a high value of the enthalpy of fusion is in agreement with the presence of a perfect crystalline state of the compound as found by X-ray analyses [3a]. Melting to the isotropic liquid and crystallization of the isotropic liquid of **L12-12** are confirmed by polarizing optical microscopy and are in agreement with the DSC measurements. On the basis of these observations we can conclude that, due to little difference between melting and crystallization temperatures, the Schiff base ligands do not have a tendency towards supercooling and do not form a glassy state. The tendency of Ni(II) complexes towards glass formation was analyzed using differential scanning calorimetry, POM and XRD. We here again describe the glass-forming behavior of **Ni12-12** as a representative; because the other complexes behave similarly. When a polycrystalline sample of **Ni12-12** obtained by recrystal-

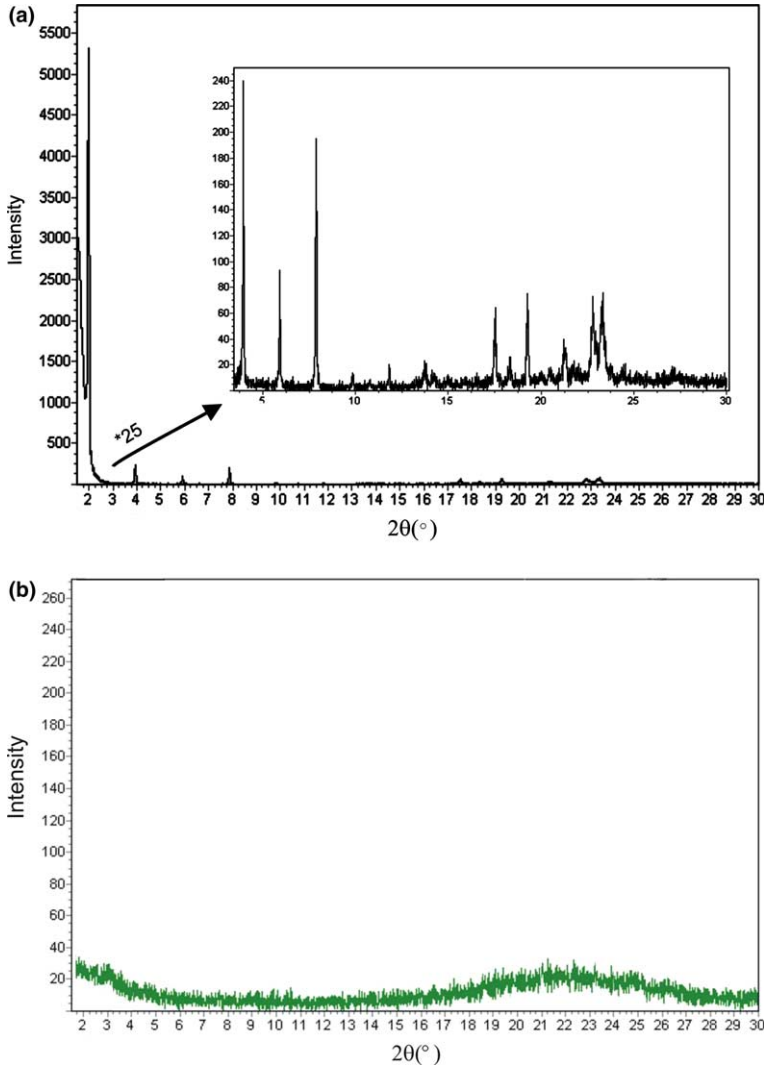


Fig. 3. X-ray diffraction patterns of **Ni12-12**; (a) virgin sample crystallized from ethanol/chloroform, (b) after heating the sample above the melting point and cooling to room temperature.

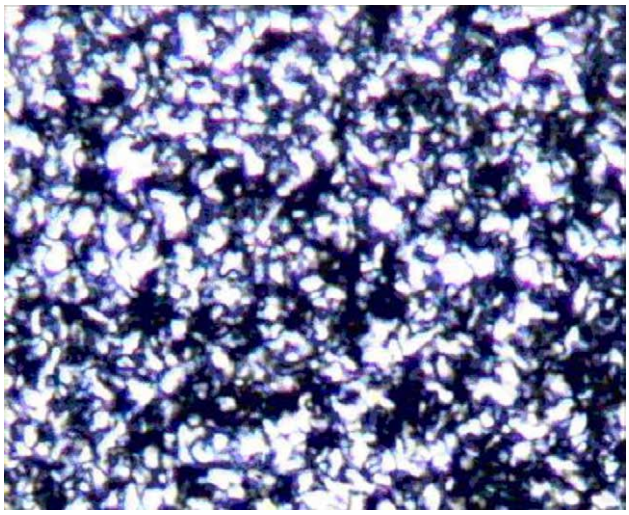


Fig. 4. Optical texture of **Ni12-12** after annealing the isotropic glass phase at room temperature for 7 days between crossed polarizers.

lisation from ethanol/chloroform (1:1 v/v) was heated, two endothermic peaks at 90 and 150 °C due to solid–solid transition and melting were observed. In the cooling cycle no exothermal peaks were observed. When the isotropic liquid was cooled down at the same cooling rate by DSC under polarizing microscopy, a transparent glass was formed via a supercooled liquid. When the amorphous glass sample was again heated, a glass transition phenomenon was observed at 64 °C. On further heating above the glass transition, an exothermic peak was observed at 120 °C due to crystallization producing the same crystals obtained by recrystallization from solution, which melted at 150 °C. Fig. 3 shows the XRD patterns of **Ni12-12**. The powder XRD pattern from virgin crystals of **Ni12-12** (Fig. 3(a)) indicates a crystalline state. In order to determine the amorphous state of **Ni12-12**, the XRD pattern of a sample upon cooling from the isotropic liquid was recorded at room temperature. The XRD pattern of **Ni12-12** after cooling from the isotropic liquid is given in Fig. 3(b). No sharp Bragg peaks were observed in the diffraction pattern of **Ni12-12** and only a broad diffraction hump was observed, indicating an amorphous state. The crystallization process of **Ni12-12** was confirmed by XRD. XRD patterns of **Ni12-12** after annealing the amorphous material at 120 °C for 30 min. and virgin sample are similar, which indicates that the two crystalline phases are identical. Moreover, the high value of the enthalpy of fusion of **Ni12-12** (29.9 kJ mol^{-1}) is in agreement with the presence of a perfect crystalline state of **Ni12-12** as confirmed by the X-ray analyses.

Upon cooling the isotropic liquid of the nickel complexes, only a black field under POM was observed throughout the cooling process even when the temperature reached below −20 °C, which confirms the existence of the amorphous state. However, anisotropic glass phases were found while annealing samples for a long time. When the samples were annealed at room temperature for several days, a schlieren optical texture was formed. Fig. 4 shows the photomicrograph of **Ni12-12** as an example, indicating the formation of a discotic nematic (N_d) mesophase [21]. To further confirm the structure of the mesophase, we carried out XRD experiments. The XRD pattern obtained exhibits only a peak in the small angle area and a broad halo with a wide angle (Fig. 5). On the basis of these observations we can conclude that an anisotropic glass has been formed. Formation of a discotic nematic mesophase in the Ni complexes is in agreement with the discotic structure of the complexes [22]. Thermodynamic data for the Schiff-base ligands and the related Ni complexes are tabulated in Table 2.

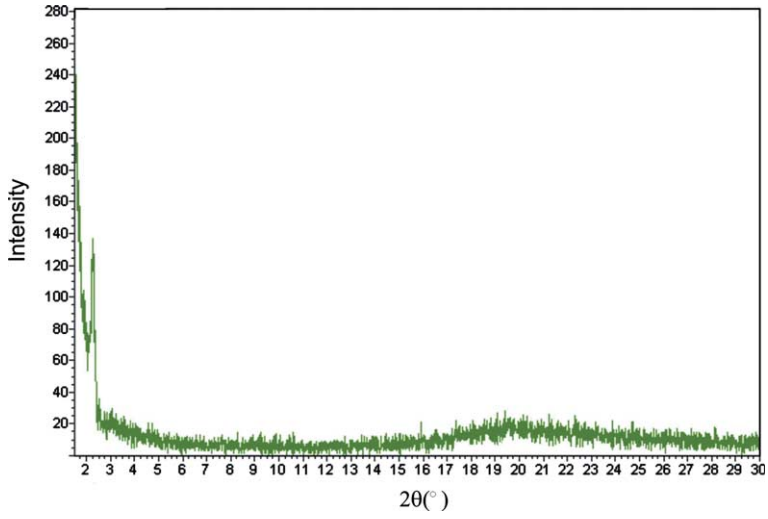


Fig. 5. X-ray diffraction pattern after annealing **Ni12-12** at room temperature for 7 days.

Table 2
Thermal transitions and thermodynamic data of the ligands and the Ni complexes, heating and cooling rate: 10 °C min^{-1}

Compound	Phase transitions (°C) and corresponding enthalpies (kJ mol^{-1}, in parentheses)[a]		
	First heating scan	First cooling scan	Second heating scan
L12-8	K104.0,105.5(2.7)[b]K107.7(7)K118.2(61.3)I	I112.3(59.3)K99.4(15.1)K	K102.4(16.7)K116.7(58.70)
L12-12	K99.1,102.9[b](18.6)K114.3(21.3)K120.5(26.9)I	I108.7(56.0)K99.5(14.5)K	K98.1,99.6,101.1[b](10.6)K113.4(17.0)K120.2(40.30)I
L12-16	K104.9,108.1[b](6.1)K113.4(31.3)I	I107.7(34.6)K102.2(10.7)K	K107.1(10.9)K112.0(33.7)I
Ni12-8	K86.8(8.5),105.1(11.6)[b],160.8(35.6)I		G65.1[c],126.4(−24.2)K159.4(33.3)I
Ni12-12	K73.4(16.1),83.2(0.2),149.1(29.9)I		G66.5[c],119.9(−19.7)K147.7(25.8)I
Ni12-16	K107.7(9.7),136.2(41.5)I		G58.1[c],83.7(−19.3)K107.7(1.0)K135.1(39.4)

[a] K, crystal; G, glass; I, isotropic.
[b] Overlapped with a previous transition.
[c] Glass transition.

From the above results, it is apparent that the Schiff base ligands do not show any tendency towards glass formation and go to a crystalline phase when cooled from the isotropic liquid, but the related Ni(II) complexes have a great tendency for glass forming and after several days change to an anisotropic glassy state. Some structural requirements such as non-planarity of molecular structure, bulkiness and weight of substitutions and number of conformers of the molecule in the fluid state are responsible for glass formation in organic compounds. Furthermore, the enlargement of molecular size is an important factor for the achievement of the stability of a glassy state [1a]. On the other hand, another requirement is that the molecular system should have a weak tendency towards crystallization despite strong intermolecular attractions [5]. From a structural point of view, the nickel complex is essentially non-planar. It is well known that azobenzene and its *p*,*p*′-substituted derivatives are essentially planar, but the azomethine part of the structure is non-planar. As the X-ray analyses indicates in the crystalline state, in this kind of compound, the two benzene rings (phenylimine and salicylidenic ring) are twisted with respect to the azomethine group plan [23]. The Ni(II) complexes, in comparison with the ligands, have all of the structural requirements to form a glassy state. It is notable that the phenomenon of polymorphism, which is observed for the Ni(II) complexes and suggests the existence of different conformers, is responsible for the formation of the glassy state [1a].

5. Conclusion

In this work, we have prepared a series of nickel complex homologues derived from 5-((4-^{n}alkoxyphenyl)azo)-*N*-(4-^{n}alkoxyphenyl)-salicylaldimine homologues. For the first time, we report the glass forming properties of azo-containing salicylaldimine complexes of nickel. While the Schiff base ligands do not show any glass forming properties, the nickel complexes have a resistance to crystallization and form a glassy state.

Acknowledgements

We thank professor Yasuhiko Shirota, The University of Osaka, Japan for useful comments and suggestions. Financial support from Azarbaijan University of Tarbiat Moallem research council is greatly appreciated.

References

[1] (a) Y. Shirota, J. Mater. Chem. 10 (2000) 1;
(b) R.H. Friend, R.W. Gymer, A.B. Holmes, J.H. Burroughes, R.N. Marks, C. Taliani, D.D.C. Bradley, D.A. Dos Santos, J.L. Bredas, M. Lugdlund, M.W.R. Salanek, Nature 397 (1999) 121;
(c) J.R. Sheats, P.F. Babara, Acc. Chem. Res. 32 (1999) 191.
[2] (a) K. Naito, A. Miura, J. Phys. Chem. 97 (1993) 6240;
(b) K. Naito, Chem. Mater. 6 (1994) 2343.
[3] (a) I. Alig, D. Braun, R. Langendrof, H.O. Wirth, M. Voigt, J.H. Wendrof, J. Mater. Chem. 8 (1998) 847;
(b) W. Wedler, D. Demus, H. Zaschke, K. Mohr, W. Schafer, W. Weissflog, J. Mater. Sci 1 (1991) 347.
[4] (a) Y. Shirota, T. Kobata, N. Noma, Chem. Lett. (1989) 145;
(b) W. Ishikawa, H. Inada, H. Nakano, Y. Shirota, Mol. Crys. Liq. Crys. 211 (1992) 431;
(c) W. Ishikawa, H. Inada, H. Nakano, Y. Shirota, Chem. Lett. (1991) 1731;
(d) H. Inada, Y. Shirota, J. Mater. Chem 3 (1993) 319.
[5] D. Braun, R. Langendrof, J. Parkt. Chem. 341 (1999) 128.
[6] D. Braun, R. Langendrof, J. Parkt. Chem. 342 (2000) 80.
[7] J.C. Ostrowski, R.A. Hudack Jr., R. Robinson, S. Wang, G.C. Bazan, Chem. Eur. J. 7 (2001) 4500.
[8] (a) M. Ottmar, T. Ichisaka, L.R. Subramanian, M. Hanack, Y. Shirota, Chem. Lett. (2001) 788;
(b) M. Brewis, G.J. Clarkson, M. Helliwell, A.M. Holder, N.B. McKeown, Chem. Eur. J. 6 (2000) 4630.
[9] H. Nishihara, Bull. Chem. Soc. Jpn. 77 (2004) 407.
[10] Y. Shirota, K. Moriwaki, S. Yoshikawa, T. Ujike, H. Nakano, J. Mater. Chem. 8 (1998) 2579.
[11] C. Chun, Mi.-J. Kim, D. Vak, D.U. Kim, J. Mater. Chem. 13 (2003) 2904.
[12] V. Etelaniemi, R. Serimaa, T. Laitalainen, T. Paakkari, J. Chem. Soc., Dalton Trans. (1998) 3001.
[13] N. Hirota, N. Noma, Y. Shirota, K. Iuchi, H. Miazaki, Kubanshi Ronbunsh 47 (1990) 839.
[14] J.C. Ostrowski, M.R. Robinson, A.J. Heeger, G.C. Bazan, Chem. Commun. 7 (2002) 784.
[15] R.V. Deun, K. Binnemans, J. Alloys Compd 303–304 (2000) 146.
[16] E.C. HorningOrganic Syntheses, Collective, vol. III, Wiley, New York, 1955, p. 130.

[17] K. Nejati, Z. Rezvani, New J. Chem. 27 (2003) 1665.
[18] A.A. Khandar, Z. Rezvani, Polyhedron 18 (1998) 129.
[19] M. Lee, Y.S. Yoo, M.G. Chol, Macromolecules 32 (1999) 2777.
[20] A.A. Khandar, Z. Rezvani, K. Nejati, A.I. Yanovsky, J.M. Martinez, Acta Chim. Slov. 49 (2002) 733.
[21] Y. Geng, A. Fechtenkotter, K. Mullem, J. Mater. Chem. 11 (2003) 1634.
[22] C.K. Lai, C.-H. Chang, C.-H. Tsai, J. Mater. Chem. 8 (1998) 599.
[23] H. Kelker, R. Hatz, Handbook of Liquid Crystals, Verlag, Chemie, Weinheim, 1980.

$[Os_3Ru(\mu\text{-}H)_2(CO)_{12}(PPh_2H)]$. The reactions of secondary phosphines with $[M_3(CO)_{10}(\mu\text{-dppm})]$ (**1**, M = Ru; **2**, M = Os) have been reported by Azam et al. [14] and Böttcher et al. [15]. The products formed were shown to be dependent on both the metal and steric demands of the phosphines. For example, compound **2** reacts with Ph_2PH in refluxing toluene at 110 °C to give the simple substitution product $[Os_3(CO)_9(\mu\text{-dppm})(Ph_2PH)]$ and the dihydrido–diphosphido compound $[H(\mu\text{-}H)Os_3(CO)_7(\mu\text{-dppm})(\mu\text{-}PPh_2)_2]$ [14], whereas $^tBu_2PH$ gives exclusively the electron deficient compound $[(\mu_3\text{-}H)(\mu\text{-}H)Os_3(CO)_5(\mu\text{-dppm})(\mu\text{-}P^tBu_2)_2]$ [15]. A similar reaction of $[Ru_3(CO)_{10}(\mu\text{-dppm})]$ with $^tBu_2PH$ in refluxing heptane gives the corresponding electron deficient compound $[(\mu_3\text{-}H)(\mu\text{-}H)Ru_3(\mu\text{-}CO)(CO)_4(\mu\text{-dppm})(\mu\text{-}P^tBu_2)_2]$ which contains a bridging CO ligand, unlike the homologous osmium isomer [16]. Interestingly, the reaction of **1** with the less bulkyphosphine Cy_2PH leads to the electronically saturated compound $[(\mu\text{-}H)_2Ru_3(CO)_6(\mu\text{-dppm})(\mu\text{-}PCy_2)_2]$ [16]. Recently, we have reported the phosphido and phosphinido clusters $[(\mu\text{-}H)Ru_3(\mu\text{-}PHPh)(CO)_8(\mu\text{-dppm})]$ and $[(\mu\text{-}H)_2Ru_3(\mu_3\text{-}PPh)(CO)_7(\mu\text{-dppm})]$ from the reaction of **1** with $PhPH_2$ in refluxing THF at 66 °C [17]. However, attempts to extend these syntheses to diphenylphosphido bridge complexes did not give the analogous products. We report here that, instead, triruthenium complexes with phosphido, hydrido, CH_2PPh, PPh_2CH_2PPh and PPh ligands were formed via some interesting transformations such as P–C and P–H bonds activations. A part of this work has been described briefly [18].

2. Experimental

All the reactions were performed under a nitrogen atmosphere using standard Schlenk techniques. Solvents were dried and distilled prior to use by standard methods. The starting clusters $[Ru_3(CO)_{10}(\mu\text{-dppm})]$ (**1**) [19] and $[Ru_3(CO)_9\{\mu_3\text{-}\eta^2\text{-}Ph_2PCH_2P(C_6H_4)\}]$ (**7**) [8b] were prepared according to known procedures. Infrared spectra were recorded on a Shimadzu FT-IR 8101 spectrophotometer. ^1H and $^{31}P\{^1H\}$ NMR spectra were recorded on a Bruker DPX 400 spectrometer. Chemical shifts for the $^{31}P\{^1H\}$ NMR spectra are relative to 85% H_3PO_4. Fast atom bombardment mass spectra were obtained on a JEOL SX-102 spectrometer using 3-nitrobenzyl alcohol as matrix and CsI as calibrant.

2.1. Reaction of $[Ru_3(CO)_{10}(\mu\text{-dppm})]$ (1) with PPh_2H

To a heptane solution (100 mL) of **1** (0.458 g, 0.473 mmol) was added PPh_2H (0.176 g, 0.945 mmol) and the reaction mixture was refluxed for 1.5 h. The solvent was removed under reduced pressure and the residue chromatographed by TLC on silica gel. Elution with cyclohexane/CH_2Cl_2 (3:2, v/v) developed four bands. The first band gave $[Ru_3(CO)_6(\mu\text{-}CO)(\mu_3\text{-}CH_2PPh)(\mu\text{-}PPh_2)_2]$ (**3**), (0.094 g, 20%) as pink crystals from hexane/CH_2Cl_2 at −20 °C . IR (ν(CO), CH_2Cl_2): 2052s, 2014s, 2001s, 1964m, 1951m cm^{-1}; $^{31}P\{^1H\}$ NMR ($CDCl_3$): δ 47.6 (dd, 1P, J = 19.7, 78.3 Hz), 270.6 (dd, 1P, J = 19.7, 165.9 Hz), 275.9 (dd, 1P, J = 78.3, 165.9 Hz), 19.30 (dd, 1P, J = 25.5, 121.6 Hz). Compound **3** has been characterized by comparing the spectroscopic data with those reported [18]. The second band afforded $[(\mu\text{-}H)Ru_3(CO)_6(\mu_3\text{-}\eta^3\text{-}PPhCH_2PPh_2)(\mu\text{-}PPh_2)_2]$ (**4**) (0.044 g, 8%) as red crystals after recrystallization from hexane/CH_2Cl_2 at −4 °C. *Anal.* Calc. for $C_{49}H_{38}O_6P_4Ru_3$: C, 51.17; H, 3.34. Found: C, 51.29; H, 3.45%. IR (ν(CO), CH_2Cl_2): 2028s, 2000vs, 1967w, 1955m, 1943w cm^{-1}; ^1H NMR ($CDCl_3$): δ 7.24 (m, 35H), 3.04(dd, 2H), −12.25 (virtual dddd, 1H); $^{31}P\{^1H\}$ NMR ($CDCl_3$): δ 254.5 (ddd, 1P, J = 15.5, 25.3, and 127.5 Hz), 210.10 (dd, 1P, J = 73.7, 127.4 Hz), 51.4 (ddd, 1P, J = 15.7, 73.7, 121.6 Hz), 19.30 (dd, 1P, J = 25.5, 121.6 Hz); FAB MS: m/z 1149 (M^+). The third band gave $[(\mu\text{-}H)_2Ru_3(CO)_5(\mu\text{-dppm})(\mu_3\text{-PPh})(\mu\text{-}PPh_2)_2]$ (**5**) (0.062 g, 10%) as red crystals from hexane/CH_2Cl_2 at −4 °C. *Anal.* Calc. for $C_{60}H_{49}O_5P_5Ru_3$: C, 55.08; H, 3.78. Found: C, 55.31; H, 3.95%. IR (ν(CO), CH_2Cl_2): 2057vs, 2019vs, 2003s, 1961m cm^{-1}; ^1H NMR ($CDCl_3$): δ 7.50–7.12 (m, 40 H), 5.81 (m, 1H), 4.89 (m, 1H), −16.12 (m, 1H), −16.99 (m, 1H); $^{31}P\{^1H\}$ NMR ($CDCl_3$): δ 258.8 (m, 1P), 164.9 (m, 1P), 160.9 (m, 1P), 24.5 (m, 1P), 12.8 (m, 1P); FAB MS: m/z 1307 (M^+). The fourth band gave $[(\mu\text{-}H)_2Ru_3(CO)_6(\mu\text{-dppm})(\mu\text{-}PPh_2)_2]$ (**6**) (0.041 g, 7%) as red crystals from hexane/CH_2Cl_2 at −4 °C. *Anal.* Calc. for $C_{55}H_{44}O_6P_4Ru_3$: C, 53.79; H, 3.62. Found: C, 53.99; H, 3.78%. IR (ν(CO), KBr): 2007vs, 1988s, 1934s, 1934m, 1902m cm^{-1}; ^1H NMR ($CDCl_3$): δ 7.65–7.12 (m, 40H), 4.80 (m, 1H), 4.0 (m, 1H), −16.20 (m, 1H), −17.11 (m, 1H); Mass spectrum: m/z 1227 (M^+).

2.2. Reaction of $[Ru_3(CO)_9\{\mu_3\text{-}\eta^3\text{-}PPhCH_2P(Ph)(C_6H_4)\}]$ (7) with PPh_2H

To a THF solution (35 mL) of **7** (0.150 g, 0.174 mmol) was added PPh_2H (0.0649 g, 0.348 mmol) and dppm (0.1803 g, 0.469 mmol). The reaction mixture was heated to reflux for 1 h. The solvent was removed under reduced pressure and the residue chromatographed by TLC on silica gel. Elution with cyclohexane/CH_2Cl_2 (4:1, v/v) developed several bands. The major band afforded the compound $[(\mu\text{-}H)Ru_3(CO)_6\{\mu_3\text{-}\eta^3\text{-}PPhCH_2PPh_2\}(\mu\text{-}PPh_2)]$ (**4**) (0.070 g, 35%) as red crystals. The minor bands were too small for complete characterization.

2.3. X-ray crystallography

Red crystals of **4** and **5** suitable for diffraction analysis were grown by slow evaporation from a hexane/methylene chloride solution at −4 °C. Crystallographic data were collected at 150 K, using a Bruker-Nonius CCD area detector diffractometer and Mo Kα radiation (λ = 0.71073 Å). The crystal to detector distance was 32 mm, and Ø and Ω scans (1.2° increments, 15 s exposure time) were carried out to fill the Ewald sphere. Data collection and processing were carried out using the program COLLECT [20] and DENZO [21]. Empirical absorption corrections were applied to the data set using multiple and symmetry related data measurements via the program SORTAV [22,23]. The unit cell was indexed on low angle reflections and refined from 25 reflections in a θ range of 12–13°. The structure was solved by direct methods (SHELXS-96) [24] and refined on F^2 by full matrix least squares (SHELXS-97) [25] using all unique data. All non-hydrogen atoms were refined anisotropically. Hydrogen atoms were included in calculated positions (riding model) with U_{iso} set at 1.2 times the U_{eq} of the parent atom. However, due to the poor quality of the crystals of **5**, we are as yet unable to obtain an *R* factor better than 13%. Nevertheless, the connectivities are clearly established and are in agreement with spectroscopic characterization. The crystal data, data collection parameters and refinement results are summarized in Table 1. Selected bond lengths and angles for **4** and **5** are given in Tables 2 and 3, respectively.

Table 1
Crystallographic data and structure refinement parameters[a] for **4** and **5**

	4	**5**
Empirical formula	$C_{49}H_{37}O_6Ru_3P_4$	$C_{60}H_{47}O_5Ru_3P_5$
Formula weight	1148.88	1306.04
Crystal system	monoclinic	monoclinic
Space group	*P*2(1)/*n*	*P*2(1)/*c*
Unit cell dimensions		
a (Å)	12.2330(8)	18.3232(6)
b (Å)	26.3357(18)	12.8481(4)
c (Å)	15.1213(11)	23.5826(7)
α (°)	90	90
β (°)	104.692(4)	101.758(2)
γ (°)	90	90
V (Å^3)	4712.3(6)	5435.3(3)
Z	4	4
D_{calc} (g cm^{-3})	1.619	1.596
μ(Mo Kα) (mm^{-1})	1.132	1.019
F(000)	2284	2616
Crystal size (mm)	0.22 × 0.18 × 0.15	0.25 × 0.22 × 0.20
θ Range (°)	2.31–25.00	1.76–25.00
Limiting indices	$-14 \leqslant h \leqslant 12$, $-31 \leqslant k \leqslant 31$, $-16 \leqslant l \leqslant 16$	$-21 \leqslant h \leqslant 21$, $-15 \leqslant k \leqslant 15$, $-28 \leqslant hl \leqslant 28$
Reflections collected	18584	7683
Independent reflections [R_{int}]	5818 [0.0549]	9565 [1.0634]
Maximum and minimum transmission factor	0.8485 and 0.7887	0.8221 and 0.7847
Data/restraints/parameters	5818/24/559	9565/6/659
Goodness-of-fit on F^2	1.090	1.164
Final *R* indices	R_1 = 0.0554	R_1 = 0.1315
[$I > 2\sigma(I)$]	wR_2 = 0.1383	wR_2 = 0.3647
R indices (all data)	R_1 = 0.0903	R_1 = 0.1527
	wR_2 = 0.1533	wR_2 = 0.3797
Largest difference in peak and hole (e Å^{-3})	0.808 and −758	3.493 and −2.130

[a] Details in common: X-radiation, Mo Kα (λ = 0.71073 Å), temperature (K) 150(2), refinement method: full-matrix least-squares on F^2.

3. Results and discussion

The reaction of [$Ru_3(CO)_{10}$(μ-dppm)] (**1**) with PPh_2H in refluxing heptane for 1.5 h followed by the usual workup and chromatographic separation afforded four triruthenium compounds, [$Ru_3(CO)_6$(μ-CO)-

Table 2
Selected bond distances (Å) and angles (°) for [(μ-H)$Ru_3(CO)_6$-(μ-PPh_2)$_2${μ_3-η^2-$PPh_2CH_2P(Ph)$}] (**4**)

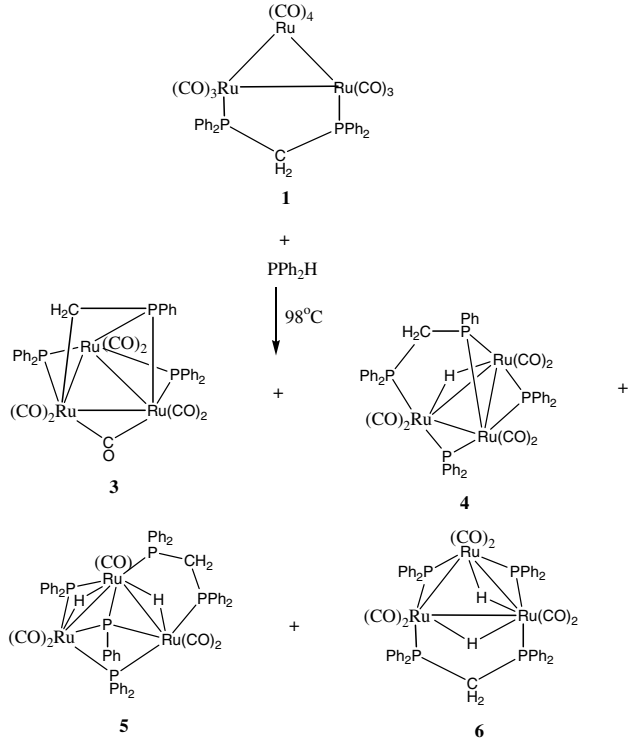
Ru(1)–Ru(2)	2.8562(10)
Ru(1)–Ru(3)	2.9120(9)
Ru(2)–Ru(3)	2.9862(9)
Ru(3)–P(4)	2.302(2)
Ru(3)–P(2)	2.393(2)
P(2)–C(14)	1.836(8)
Ru(1)–P(1)	2.359(2)
Ru(1)–P(3)	2.276(2)
Ru(2)–P(4)	2.351(2)
Ru(2)–P(1)	2.373(2)
Ru(2)–P(3)	2.384(2)
P(2)–C(13)	1.815(8)
P(3)–Ru(1)–P(1)	79.34(8)
P(3)–Ru(1)–Ru(2)	53.92(6)
P(1)–Ru(1)–Ru(2)	53.10(6)
P(3)–Ru(1)–Ru(3)	113.70(6)
P(1)–Ru(1)–Ru(3)	76.93(5)
Ru(2)–Ru(1)–Ru(3)	62.35(2)
P(4)–Ru(2)–P(1)	97.12(8)
P(4)–Ru(2)–P(3)	157.07(8)
P(1)–Ru(2)–P(3)	76.95(8)
P(4)–Ru(2)–Ru(1)	108.29(6)
P(1)–Ru(2)–Ru(1)	52.64(6)
P(3)–Ru(2)–Ru(1)	50.50(6)
P(4)–Ru(2)–Ru(3)	49.36(6)
P(1)–Ru(2)–Ru(3)	75.24(5)
P(3)–Ru(2)–Ru(3)	107.95(6)
Ru(1)–Ru(2)–Ru(3)	59.74(2)
P(4)–Ru(3)–P(2)	94.32(8)
P(4)–Ru(3)–Ru(1)	107.90(6)
P(2)–Ru(3)–Ru(1)	87.07(5)
P(4)–Ru(3)–Ru(2)	50.80(5)
P(2)–Ru(3)–Ru(2)	99.46(6)
Ru(1)–Ru(3)–Ru(2)	57.91(2)
Ru(1)–P(1)–Ru(2)	74.26(7)
Ru(1)–P(3)–Ru(2)	75.58(7)
Ru(3)–P(4)–Ru(2)	79.83(7)
C(1)–Ru(1)–Ru(3)	137.2(3)
C(5)–Ru(3)–Ru(1)	144.2(3)

Table 3
Selected bond distances (Å) and angles (°) for $[(\mu\text{-H})_2Ru_3(CO)_5(\mu\text{-PPh}_2)_2(\mu\text{-dppm})(\mu_3\text{-PPh})]$ (**5**)

Ru(1)–Ru(2)	2.817(2)
Ru(1)–Ru(3)	3.019(2)
Ru(1)–P(1)	2.275(5)
Ru(1)–P(4)	2.326(5)
Ru(1)–P(3)	2.341(5)
Ru(2)–P(3)	2.367(5)
Ru(2)–P(4)	2.376(5)
Ru(2)–P(5)	2.403(5)
Ru(3)–P(4)	2.391(5)
Ru(3)–P(2)	2.413(5)
Ru(3)–P(5)	2.436(5)
P(1)–Ru(1)–P(4)	99.75(19)
P(1)–Ru(1)–P(3)	117.03(19)
P(4)–Ru(1)–P(3)	79.46(18)
P(1)–Ru(1)–Ru(2)	151.71(15)
P(4)–Ru(1)–Ru(2)	54.01(13)
P(3)–Ru(1)–Ru(2)	53.68(13)
P(1)–Ru(1)–Ru(3)	92.34(14)
P(4)–Ru(1)–Ru(3)	51.14(13)
P(3)–Ru(1)–Ru(3)	126.85(14)
Ru(2)–Ru(1)–Ru(3)	79.07(6)
P(3)–Ru(2)–P(4)	77.94(18)
P(3)–Ru(2)–P(5)	138.97(19)
P(4)–Ru(2)–P(5)	74.93(17)
P(3)–Ru(2)–Ru(1)	52.83(13)
P(4)–Ru(2)–Ru(1)	52.39(13)
P(5)–Ru(2)–Ru(1)	86.16(13)
P(4)–Ru(3)–P(2)	94.70(18)
P(4)–Ru(3)–P(5)	74.06(17)
P(2)–Ru(3)–P(5)	168.51(19)
P(4)–Ru(3)–Ru(1)	49.27(12)
P(2)–Ru(3)–Ru(1)	89.67(13)
P(5)–Ru(3)–Ru(1)	81.21(13)
Ru(1)–P(3)–Ru(2)	73.49(16)
Ru(1)–P(4)–Ru(2)	73.59(15)
Ru(1)–P(4)–Ru(3)	79.59(16)
Ru(2)–P(4)–Ru(3)	102.54(19)
Ru(2)–P(5)–Ru(3)	100.43(19)
P(1)–C(18)–P(2)	112.2(10)

$(\mu_3\text{-CH}_2\text{PPh})(\mu\text{-PPh}_2)_2]$ (**3**), $[(\mu\text{-H})Ru_3(CO)_6(\mu_3\text{-}\eta^2\text{-PPh}_2\text{CH}_2\text{PPh})\text{-}(\mu\text{-PPh}_2)_2]$ (**4**), $[(\mu\text{-H})_2Ru_3(CO)_5\text{-}(\mu\text{-dppm})\text{-}(\mu_3\text{-PPh})(\mu\text{-PPh}_2)_2]$ (**5**) and $[(\mu\text{-H})_2Ru_3(CO)_6\text{-}(\mu\text{-dppm})\text{-}(\mu\text{-PPh}_2)_2]$ (**6**) in 20%, 8%, 10% and 7% yields, respectively (Scheme 1). Compounds **3**–**6** are different from the thermolysis products of **1** which include the triruthenium compound $[Ru_3(CO)_9\{\mu_3\text{-}\eta^2\text{-Ph}_2\text{PCH}_2\text{P-}(C_6H_4)\}]$ (**7**) [8b] and two isomeric binuclear complexes $[Ru_2(CO)_6\{\mu\text{-CH}_2\text{PPh}(C_6H_4)\text{PPh}\}]$ [26] and $[Ru_2(CO)_6\text{-}\{\mu\text{-}(C_6H_4)\text{PPhCH}_2\text{PPh}\}]$ [27].

The new compounds have been characterized by elemental analysis, infrared, ^{1}H NMR, ^{31}P{^{1}H} NMR and mass spectroscopic data together with single crystal X-ray diffraction studies for **4** and **5**. The structure of compound **3**, which contains two bridging PPh_2 groups and a triply bridging $PhPCH_2$ ligand has been discussed previously, and therefore no further comments are needed [18]. The molecular structure of **4** is depicted in



Scheme 1.

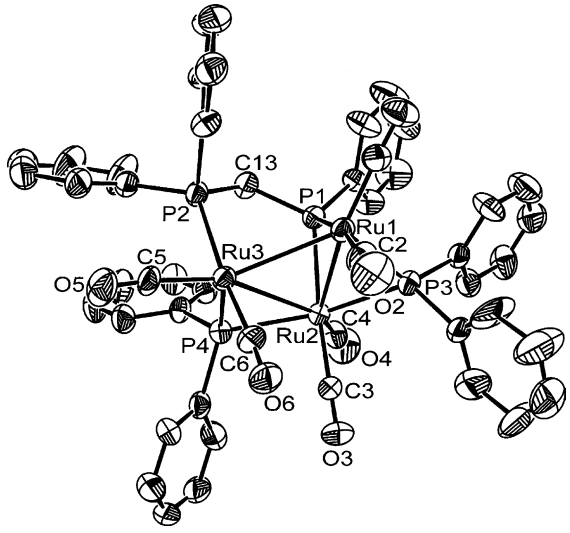


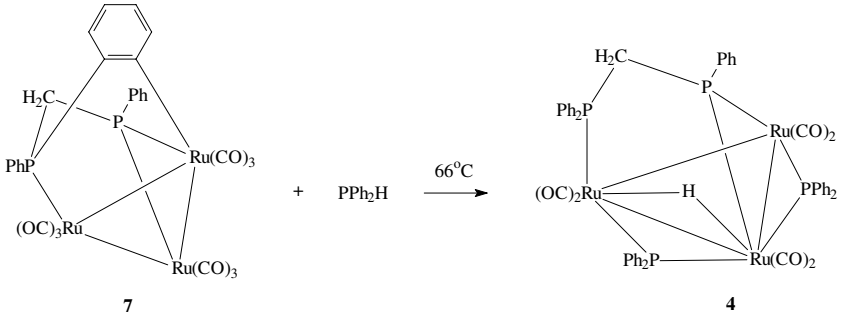
Fig. 1. ORTEP drawing of $[(\mu\text{-H})Ru_3(CO)_6(\mu\text{-PPh}_2)_2\{\mu_3\text{-}\eta^2\text{-PPh}_2\text{CH}_2\text{P(Ph)}\}]$ (**4**). Thermal ellipsoids are drawn at the 50% probability level.

Fig. 1, crystal data are collected in Table 1 and selected bond distances and angles are given in Table 2. The structure consists of a triangular cluster of ruthenium atoms with two elongated metal–metal bonds {Ru(2)–Ru(3) = 2.9862(9) and Ru(1)–Ru(3) = 2.9120(9) Å}, one comparatively shorter metal–metal bond {Ru(1)–Ru(2) = 2.8562(10) Å} and six terminal CO ligands, two bonded to each ruthenium atom. The molecule

contains one triply bridging PPh_2CH_2PPh moiety, two bridging PPh_2 groups and a bridging hydride ligand. The PPh_2CH_2PPh moiety is most probably derived from $PPh_2CH_2PPh_2$ by the cleavage of a P–C bond in **1**, with reductive elimination of a phenyl group as benzene, and the PPh_2 groups are derived from the PPh_2H ligand by P–H bond activation. The longest metal–metal edge is asymmetrically bridged by a PPh_2 ligand, {Ru(2)–P(4) = 2.351(2), Ru(3)–P(4) = 2.302(2) Å}, while the shortest edge is also asymmetrically bridged by the other μ-PPh_2 ligand {Ru(1)–P(3) = 2.276(2), Ru(3)–P(2) = 2.393(2) Å}. The PPh_2 ligands lie on the same plane as the Ru_3 triangle and the Ru–P distances are comparable to those in related phosphido bridged triruthenium clusters [12b,12c,14]. The two Ru–P–Ru angles {Ru(3)–P(4)–Ru(2) = 79.83(7)°, Ru(1)–P(3)–Ru(2) = 75.58(7)°} are nearly the same and comparable to the Ru-P-Ru angles in the phosphido bridged compound $[(\mu\text{-H})_2Ru_3(CO)_8(\mu\text{-}PPh_2)_2]$ [12b]. The bidentate phosphine ligand, PPh_2CH_2PPh sits on the top of the $(\mu\text{-H})Ru_3(CO)_6$ fragment so that the P(2) atom is bonded to the Ru(3) atom while the other P(1) atom bridges Ru(1) and Ru(2) atoms, thus capping one face of the metal framework forming two five-membered Ru(3)–P(2)–C(13)–P(1)–Ru(1) and Ru(3)–P(2)–C(13)–P(1)–Ru(2) metallacycles. A similar bonding mode of the PPh_2CH_2PPh ligand was found in $[(\mu\text{-H})Ru_3(CO)_9(\mu_3\text{-}\eta^2\text{-}PPh_2CH_2PPh)]$, which was obtained from the thermolysis of **7** in the presence of H_2 at 80 °C [8b]. The Ru–P distances involving the diphosphine ligand {Ru(3)–P(2) = 2.393(2), Ru(1)–P(1) = 2.359(2), Ru(2)–P(1) = 2.373(2), Å} are comparable to the corresponding distances in $[(\mu\text{-H})Ru_3(CO)_9(\mu_3\text{-}\eta^2\text{-}PPh_2CH_2PPh)]$ [8b]. The position of the hydride ligand in **4** could not be reliably located and refined crystallographically but its presence along the longest Ru(2)–Ru(3) edge is on the basis of its bond lengthening effect on the metal triangle [13,28]. This conclusion is further supported by the carbonyl ligands arrangement, in particular the large C(4)–Ru(2)–Ru(3) angle of 145.7(3)° and C(5)–Ru(3)–Ru(2) angle of 157.3(3)° to accommodate the bridging hydride ligand. Compound **4** contains 48 valence electrons, as expected for an electron precise trinuclear cluster containing three metal–metal bonds, and each metal atom can achieve an 18-electron configuration. The formation of compound **4** most probably proceeds via the intermediate formation of the orthometallated compound **7** followed by oxidative addition of two molecules of PPh_2H. To test this hypothesis, we performed the reaction of an authentic sample of **7** (prepared from the thermolysis of **1** by refluxing in cyclohexane at 80 °C [8b]), with PPh_2H in refluxing THF and obtained **4** in 35% yield (Scheme 2).

The spectroscopic data of **4** are in accord with the solid state structure. The mass spectrum shows the molecular ion peak at *m*/*z* 1149. The infrared spectrum shows υ(CO) bands due to the terminal carbonyl ligands. The ^1H NMR spectrum in the hydride region contains a 16 line multiplet at δ −12.25 due to coupling to four non-equivalent ^{31}P nuclei. The $^{31}P\{^1H\}$ NMR spectrum contains four equal intensity signals, two doublet of double doublets at δ 254.5 (J = 15.5, 25.3, 127.5 Hz) and 51.4 (J = 15.7, 73.7, 121.6 Hz) and two doublet of doublets at δ 210.10 (J = 73.7, 127.4 Hz) and 19.30 (J = 25.5, 121.6 Hz) for the four magnetically non-equivalent phosphorus atoms. The strongly deshielded resonances at δ 254.5 and 210.10 are as expected for arylphosphide ligands bridging metal–metal bonds while the resonances at δ 51.4 and 19.30 are consistent with the terminal phosphorus atoms of the PPh_2CH_2PPh ligand [29]. The cross peaks in the ^{31}P–^{31}P COSY spectrum confirms the assignment of the ^{31}P resonances.

The molecular structure of **5** is shown in Fig. 2, crystal data are collected in Table 1 and selected bond distances and angles are given in Table 3. The structure consists of an open cluster of three ruthenium atoms with two metal–metal bonds {Ru(1)–Ru(3) = 3.019(2), Ru(1)–Ru(2) = 2.817(2) Å} and a non-bonded separation of 3.569 Å, along the Ru(2)–Ru(3) edges and five terminal CO ligands distributed as shown in Fig. 2. It contains one μ_3-PPh, two μ-PPh_2, two bridging hydrides and a bridging dppm ligand. The bridging hydrides were not located in the structural analysis but both are believed to bridge the same Ru(1)–Ru(3) vector as the dppm ligand. Thus, the Ru(1)–Ru(3) edge {3.019(2) Å} is significantly longer than the unbridged Ru(1)–Ru(2) edge {2.817(2) Å}. The two phosphorus



7 **4**

Scheme 2.

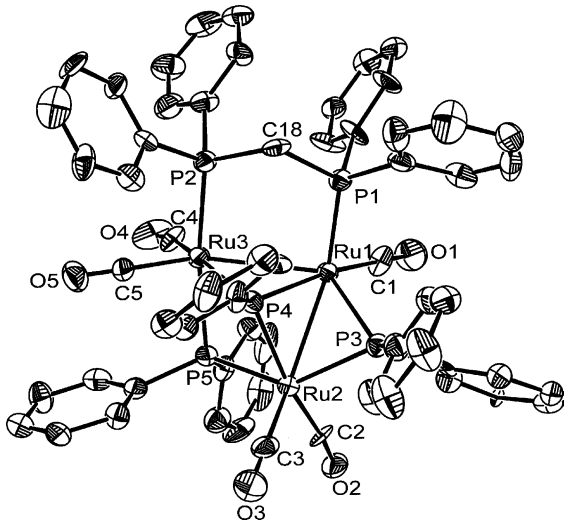


Fig. 2. ORTEP drawing of $[(\mu\text{-H})_2Ru_3(CO)_5(\mu\text{-PPh}_2)_2(\mu\text{-dppm})(\mu_3\text{-PPh})]$ (**5**). Thermal ellipsoids are drawn at the 50% probability level.

atoms, P(1) and P(2), of the dppm ligand are axially bound to Ru(1) and Ru(3) respectively forming a five-membered Ru(1)–Ru(3)–P(2)–C(18)–P(1) metallacycle vertically orientated on the molecular plane. The Ru–P distances involving the dppm ligand {Ru(1)–P(1) = 2.275(5), Ru(2)–P(3) = 2.367(5) Å} are slightly shorter than those found in **1** [30]. Of the two μ-PPh_2 groups, one asymmetrically bridges the closed Ru(1)–Ru(2) edge {Ru(1)–P(3) = 2.341(5), Ru(2)–P(3) = 2.367(5) Å} while the other asymmetrically bridges the open Ru(2)–Ru(3) edge {Ru(2)–P(5) = 2.403(5), Ru(3)–P(5) = 2.436(5) Å}. These values are similar to those found in **4**. As expected the Ru(2)–P(5)–Ru(3) angle of 100.43(19)° is significantly greater than the Ru(1)–P(3)–Ru(2) angle of 73.49(16)° due to metal–metal bonding in the latter. The phosphinidene ligand, PPh, asymmetrically caps the Ru_3 triangle {Ru(1)–P(4) = 2.326(5), Ru(2)–P(4) = 2.376(5), Ru(3)–P(4) = 2.391(5) Å}. As usual, the triply bridging μ_3-PPh ligand acts as a five-electron donor, two μ-PPh_2 ligands donate six electrons and the dppm donates four electrons to the cluster which results in a total of 50 valence electrons. The observation of two formal Ru–Ru bonds present in the trinuclear framework is consistent with the electron count.

The analytical and spectroscopic data of **5** are consistent with the solid-state structure. The IR spectrum of **5** indicates that all the carbonyl groups are terminal. In addition to the usual phenyl resonances, the ^{1}H NMR spectrum in the aliphatic region exhibits two multiplets at δ 5.81 and 4.89 due to methylene protons of the dppm ligand. The hydride region of the ^{1}H NMR spectrum contains two multiplets at δ −16.12 and −16.99 indicating the presence of two bridging hydride ligands. The $^{31}P\{^1H\}$ NMR spectrum shows five multiplets at δ 258.8, 164.9, 160.9, 24.5 and 12.8 due to the five non-equivalent ^{31}P nuclei associated with the cluster. The multiplet at δ 258.8 is assigned to the capping phosphinidene ligand, while the two multiplets at δ 164.9 and 160.9 are due to two μ-PPh_2 ligands and the high field multiplets at δ 24.5 and 12.8 account for the terminal phosphorous atoms of the dppm ligand. The FAB mass spectrum exhibits a molecular ion peak at *m*/*z* 1307 corresponding to the molecular formula of **5**, and fragmentation peaks due to the sequential loss of five carbonyl ligands.

We were unable to obtain X-ray quality crystals of **6** therefore characterization was based on spectroscopic data. The IR spectrum of **6** in KBr indicates that all the carbonyl groups are of a terminal type. In addition to the usual phenyl resonances, the ^{1}H NMR spectrum in the aliphatic region exhibits two multiplets at δ 4.80 and 4.0 due to methylene protons of the dppm ligand. The hydride region of the ^{1}H NMR spectrum contains two equal intensity multiplets at δ −16.20 and −17.11 indicating the presence of two bridging hydride ligands. The spectroscopic data of **6** are very similar to the osmium analogue $[(\mu\text{-H})_2Os_3(CO)_6(\mu\text{-dppm})(\mu\text{-PPh}_2)_2]$ which was obtained from the thermolysis of $[Os_3(CO)_8(\mu\text{-dppm})(PPh_2H)_2]$ and characterized crystallographically [13]. The FAB mass spectrum shows the molecular ion peak at *m*/*z* 1227 consistent with the formulation of **6**, and fragmentation peaks due to the sequential loss of six carbonyl ligands.

4. Conclusion

We have shown that the reaction of **1** with PPh_2H in refluxing heptane afforded the four triruthenium compounds $[Ru_3(CO)_6(\mu\text{-CO})(\mu_3\text{-CH}_2\text{PPh})(\mu\text{-PPh}_2)_2]$ (**3**), $[(\mu\text{-H})Ru_3(CO)_6(\mu_3\text{-}\eta^2\text{-PPh}_2CH_2PPh)(\mu\text{-PPh}_2)_2]$ (**4**), $[(\mu\text{-H})_2Ru_3(CO)_5(\mu\text{-dppm})(\mu_3\text{-PPh})(\mu\text{-PPh}_2)_2]$ (**5**) and $[(\mu\text{-H})_2Ru_3(CO)_6(\mu\text{-dppm})(\mu\text{-PPh}_2)_2]$ (**6**). The X-ray analysis reveals that compound **4** is a closed triangular cluster bearing one bidentate μ_3-η^2-PPh_2CH_2PPh and two μ-PPh_2 ligands whereas compound **5** is an open triangular cluster possessing one μ_3-PPh, two μ-PPh_2 and one dppm ligand. In compound **4**, most probably, the bidentate PPh_2CH_2PPh moiety has been derived from $PPh_2CH_2PPh_2$ by the cleavage of a P–C bond in **1**, and concomitant reductive elimination of benzene via H transfer from a Ph_2PH ligand, simultaneously producing the PPh_2 ligand via oxidative cleavage of the P–H bond. Compound **4** can also be obtained in moderate yield from the reaction of the orthometallated compound **7** with PPh_2H in refluxing THF (66 °C). Compound **5** may be considered as being derived from **1** by the oxidative cleavage of the P–H bond of 3 molecules of PPh_2H to give the three μ-PPh_2 ligands, one of which in turn underwent P–C bond activation to give the μ_3-PPh moiety. The dppm ligand remained intact

during this transformation. Compound **6** is the result of simple oxidative addition of 2 molecules of PPh_2H to **1**.

Acknowledgment

The support of this research by the Ministry of Science and Technology, Government of the Peoples Republic of Bangladesh is gratefully acknowledged.

Appendix A. Supplementary data

Crystallographic data for the compounds have been-deposited with the Cambridge Crystallographic Data-Centre, CCDC Nos. 260929 (**3**) and 260930 (**4**). Copies of this information may be obtained free of charge from The Director, CCDC, 12 Union Road, Cambridge, CB2 1EZ, UK (fax: +44-1223-3360333 or e-mail: deposit@ccdc.cam.ac.uk or www: http://www.ccdc.cam.ac.uk). Supplementary data associated with this article can be found, in the online version at doi:10.1016/j.poly.2005.03.095.

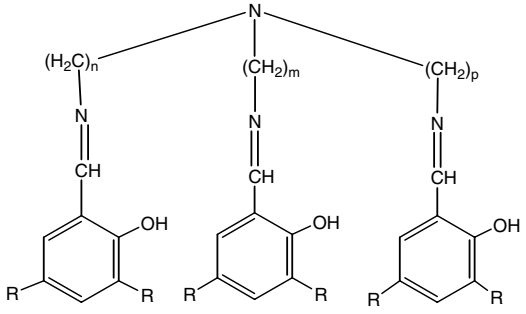
References

[1] R.J. Puddephatt, Chem. Soc. Rev. 12 (1983) 99.
[2] F.A. Cotton, B. Hong, Prog. Inorg. Chem. 40 (1992) 179.
[3] (a) J.N.L. Dennett, A.L. Gillon, K. Heslop, D.J. Hyett, J.S. Fleming, C.E. Lloyd-Jones, A.G. Orpen, P.G. Pringle, D.F. Wass, J.N. Scutt, R.H. Weatherhead, Organometallics 23 (2004) 6078;
(b) J.L. Kuiper, P.A. Shapley, C.M. Rayner, Organometallics 23 (2004) 3814.
[4] I. Albers, E. Álvarez, J. Cámpora, C.M. Maya, P. Palma, L.J. Sánchez, E. Passaglia, J. Organomet. Chem. 689 (2004) 833.
[5] A.K. Smith, in: E.W. Abel, F.G.A. Stone, G. Wilkinson (Eds.), Comprehensive Organometallic Chemistry II, Pergamon Press, Oxford, 1995, p. 747 (and references therein).
[6] E. Sappa, in: E.W. Abel, F.G.A. Stone, G. Wilkinson (Eds.), Comprehensive Organometallic Chemistry II, Pergamon Press, Oxford, 1995, p. 804 (and references therein).
[7] A.J. Deeming, in: E.W. Abel, F.G.A. Stone, G. Wilkinson (Eds.), Comprehensive Organometallic Chemistry II, Pergamon Press, Oxford, 1995, p. 684 (and references therein).
[8] (a) G. Lavigne, N. Lugan, J.J. Bonnet, Organometallics 1 (1982) 1040;
(b) G. Lavigne, N. Lugan, J.A. Ibers, J. Am. Chem. Soc. 107 (1985) 4484;
(c) C. Bergounhou, J.J. Bonnet, P. Fompeyrine, G. Lavigne, N. Lugan, F. Mansilla, Organometallics 5 (1986) 60.
[9] F.A. Cotton, J.A.M. Canich, R.I. Luck, K. Vidyasagar, Organometallics 10 (1991) 352.
[10] P.E. Garrou, Chem. Rev. 85 (1985) 171.
[11] (a) M.E. Garcia, V. Riera, M.T. Rueda, M.A. Ruiz, D. Saez, Organomatallics 21 (2002) 5515;
(b) M.E. Garcia, V. Riera, M.T. Rueda, M.A. Ruiz, M. Lanfranchi, A. Tiripicchio, J. Am. Chem. Soc. 121 (1999) 4060;
(c) M.E. Garcia, V. Riera, M.T. Rueda, M.A. Ruiz, S. Halut, J. Am. Chem. Soc. 121 (1999) 1960.
[12] (a) E. Keller, H. Vahrenkamp, Chem. Ber. 114 (1981) 1124;
(b) V.D. Patal, A.A. Cherkas, D. Nucclarone, N.J. Taylor, A.J. Carty, Organometallics 4 (1985) 1792;
(c) M. Graf, K. Merzweiler, C. Bruhn, H.-C. Bottcher, J. Organomet. Chem. 533 (1998) 371, and references therein;
(d) F. Iwasaki, M.J. Mays, P.R. Raithby, P.L. Taylor, P.J. Wheattey, J. Organomet. Chem. 213 (1981) 185;
(e) J.S. Field, R.J. Haines, M.H. Moore, D.N. Smith, L.M.S. Steer, Afr. J. Chem. (1984) 37;
(f) A.M. Arif, T.A. Bright, R.A. Bright, R.A. Jones, C.M. Nunn, J. Am. Chem. Soc. 110 (1988) 6894.
[13] F.J. Safarowic, D.J. Bierdeman, J.B. Kiester, J. Am. Chem. Soc. 118 (1996) 11805.
[14] K.A. Azam, M.B. Hursthouse, M.R. Islam, S.E. Kabir, K.M.A. Malik, R. Miah, C. Sudbrake, H. Vahrenkamp, J. Chem. Soc., Dalton Trans. (1998) 1997.
[15] F.W. Heinemann, H.-C. Bottcher, J. Organomet. Chem. 526 (1996) 145.
[16] H.-C. Böttcher, H. Thönnessen, P.G. Jones, R. Schmutzler, J. Organomet. Chem. 520 (1996) 15.
[17] A.J. Deeming, C.S. Forth, M.I. Hyder, S.E. Kabir, E. Nordlander, F. Rodgers, B. Ullmann Eur. J. Inorg. Chem. (communicated).
[18] S.E. Kabir, M. Karim, K.M.A. Malik, T.A. Siddiquee, Inorg. Chem. Commun. 2 (1999) 128.
[19] M.I. Bruce, B.K. Nicholson, M.L. Williams, Inorg. Synth. 28 (1990) 225.
[20] R. Hooft, COLLECT Data Collection Software, Nonius BV, Delft, The Netherlands, 1998.
[21] Z. Otwinowski, W. Minor, in: C.W. CarterJr., R.M. Sweet (Eds.), Macromolecular Crystallography, Academic Press, New York, 1997, pp. 307–326.
[22] R.H. Blessing, Acta Crystallogr. A51 (1995) 33.
[23] R.H. Blessing, J. Appl. Crystallogr. 30 (1997) 421.
[24] G.M. Sheldrick, Acta Crystallogr. A61 (1990) 467.
[25] G.M. Sheldrick, SHELXL-97, Program for Crystal Structure Refinement, University of Göttingen, Germany, 1997.
[26] M.I. Bruce, J.R. Hinchliffe, R. Surynt, B.W. Skelton, A.H. White, J. Organomet. Chem. 469 (1994) 89.
[27] K.A. Azam, M. Bhowmick, G.M.G. Hossain, S.E. Kabir, K. Kundu, K.M.A. Malik, S. Pervin, J. Chem. Crystallogr. 31 (2001) 63.
[28] Y.K. Au, K.K. Cheung, W.T. Wong, J. Chem. Soc., Dalton Trans. (1995) 1047.
[29] (a) B.K. Park, M.A. Miah, G. Lee, Y.-J. Cho, K. Lee, S. Park, M.-G. Choi, J.T. Park, Angew. Chem. Int. Ed. 43 (2004) 1712;
(b) A.J. Carty, S.A. McLaughlin, D. Nucciarone, in: J.G. Verkade, L.D. Quin, (Eds.), VCH, Deerfield Beach, FL, 1987 (Chapter 16).
[30] A.W. Coleman, D.F. Jones, P.H. Dixneuf, C. Brisson, J.–J. Bonnet, G. Lavigne, Inorg. Chem. 23 (1984) 952.

shown that the similar complexes of first row transition metals are usually six-coordinate [15–19]. The existence of complexes of lanthanides with larger coordination numbers is a natural consequence of their large size, and of the predominantly ionic character of their bonding.

In contrast to tren Schiff bases, there has been less attention to potentially heptadentate Schiff base ligands derived from condensation reactions of other tripodal tetraamines such as tris(3-aminopropyl)amine (tpt or trpn) and corresponding asymmetrical tetraamines with appropriate aldehydes or ketones. We have reported the synthesis and characterization of some complexes of fully condensed potentially heptadentate N_7 and N_4O_3 tripodal Schiff base ligands, derived from template and/or direct condensation reactions of tpt with acetylpyridine and salicylaldehyde, respectively [20–22]. However, herein we report the synthesis and characterization of two new potentially heptadentate Schiff base ligands, H_3L^1 and H_3L^2 (Figs. 1(a) and (c)), together with the synthesis of their gadolinium(III) and samarium(III) complexes (Fig. 3). We report also the synthesis of a gadolinium(III) complex of the previously known ligand H_3L^3 (Fig. 1(e)).

Although, the behavior of the potentially heptadentate N_4O_3 Schiff bases derived from tren as a function of metal ion size has been already investigated by X-ray crystal structure analysis of a series of lanthanide complexes [10–14], the effect of the size of the ligand cavity on encapsulation of a metal ion has been never reported. Therefore, ab initio RHF and density functional B3LYP calculations on La(III) complexes of H_3L^1, H_3L^2 and H_3L^3 ligands as well as their unsubstituted analogues are also reported. In our knowledge, no ab initio or DFT theoretical studies on complexes of potentially heptadentate N_4O_3 ligands have yet been reported.



(a) H_3L^1: R=*t*-Bu, n=m=p=3 **(b)** $H_3L^{1'}$: R=H, n=m=p=3

(c) H_3L^2: R=*t*-Bu, n=m=3, p=2 **(d)** $H_3L^{2'}$: R=H, n=m=3, p=2

(e) H_3L^3: R=*t*-Bu, n=m=p=2 **(f)** $H_3L^{3'}$: R=H, n=m=p=2

Fig. 1. Structures of the tripodal heptadentate ligands investigated here.

2. Experimental

2.1. General information

Tris(2-aminoethyl)amine (tren) and the hydrated metal salt were obtained from Aldrich and were used without further purification. The tripodal tetraamine ligands, tris(3-aminopropyl)amine (tpt or trpn) and bis(3-aminopropyl)(2-aminoethyl)amine (ppe), were prepared according to the literature methods [23,24]. 3,5-Di-*tert*-butylsalicylaldehyde (SATBU) [25] and tris-[2-(3,5-di-*tert*-butylsalicylideneimino)-ethyl]amine (H_3L^3) [26] were also prepared as previously described. IR, UV–Vis, and NMR spectra were measured on FT-IR Bomem MB 100, UV-265 FW and Bruker 500 FT-NMR spectrometers, respectively. Conductivity measurements were determined at room temperature in chloroform and toluene solutions (10^{-4} M) on a Metrohm 712 conductometer.

2.2. Theoretical calculations

It is well known that the inclusion of a relativistic effect is essential for heavy-metal complexes, such as second and third row transition metals. Effective core potentials (ECPs) can be used in conventional ab initio methods and in density functional theory, and both methods are most important tools for theoretical calculations of transition metal complexes. Scalar relativistic effects, which replace the chemically inert core electrons by means of a set of parameterized functions that are derived from relativistic calculations, have been included in relativistic ECPs. In addition, the electron-correlation effect is considered in the DFT method itself. In the present work, the geometries of all the Lanthanum complexes were fully optimized at both the restricted Hartree–Fock (RHF) and DFT (B3LYP) [27] levels of theory using the GAUSSIAN 98 program [28] on a Pentium-PC computer with a 2400 MHz processor. At first, all complexes were optimized using the standard LanL2MB basis set [29] and then the resulting structures were used for further calculations using the standard 6-31G* basis set for nitrogen and oxygen donor atoms, 3-21G* basis set for carbon and hydrogen atoms and LanL2DZ for the metal ion [30–32]. Therefore, all complexes were optimized with four different methods. It should be noted that the calculation at a higher level (for example using 6-31G* for all ligand atoms) will be too expensive especially for bulky substituted complexes which consist of 135–144 different atoms.

Vibrational frequency analyses, calculated at the same level of theory, indicate that the optimized structures are at the stationary points corresponding to local minima without any imaginary frequency. A starting molecular

mechanics structure for the ab initio calculations was obtained using the HyperChem 5.02 program [33].

2.3. Ligand synthesis

2.3.1. $\{N[(CH_2)_3N{=}CH(2\text{-}OH\text{-}3,5\text{-}t\text{-}Bu_2C_6H_2)]_3\}\cdot H_2O$ ($H_3L^1\cdot H_2O$)

To a solution of 3,5-di-*tert*-butyl salicylaldehyde (SATBU) (1.4 g, 5.9 mmol) in absolute ethanol (25 ml) was added tpt (0.69 g, 1.98 mmol) in the same solvent (20 ml). The resulting yellow solution was stirred at room temperature for about 45 min. Slow evaporation of the solvent afforded a yellow solid, which was collected by filtration, washed with absolute ethanol and dried in vacuum. Yield: 1.4 g (84%); m.p. 112–114 °C. *Anal*. Calc. for $C_{54}H_{84}N_4O_3(H_2O)$: C, 75.8; H, 10.1; N, 6.5. Found: C, 76.0; H, 10.0; N, 6.6%. IR (cm^{-1}, Nujol): 1633 (s, νC=N).

2.3.2. $\{N[(CH_2)_3N{=}CH(2\text{-}OH\text{-}3,5\text{-}t\text{-}Bu_2C_6H_2)]_2[(CH_2)_2N{=}CH\text{-}(2\text{-}OH\text{-}3,5\text{-}t\text{-}Bu_2C_6H_2)]\}$ (H_3L^2)

A procedure similar to that for H_3L^2 was followed using SATBU (1 g, 4.27 mmol) and ppe (0.52 g, 1.42 mmol). Yield: 1 g (86%); m.p. 139–141 °C. *Anal*. Calc. for $C_{53}H_{82}N_4O_3$: C, 77.3; H, 10.0; N, 6.8. Found: C, 77.0; H, 10.0; N, 6.8%. IR (cm^{-1}, Nujol): 1634 and 1610sh (νC=N).

2.4. Synthesis of the gadolinium complexes

2.4.1. $[Gd(L^1)]$ (**1**)

To a solution of H_3L^1 (0.3 g, 0.358 mmol) in methanol (25 ml) and chloroform (5 ml) was added $Gd(NO_3)_3\cdot 6H_2O$ (0.161 g, 0.358 mmol) in methanol (5 ml). After addition of NaOH (0.058 g, 1.43 mmol) in methanol (5 ml), the solution was refluxed for 6 h. The resulting mixture was filtered to give a yellow powder. This powder was washed with small amounts of methanol and chloroform. Recrystallization in toluene afforded a microcrystalline solid, which was collected by filtration, washed with cold toluene and dried in vacuum. Yield: 0.26 g (70%); m.p. > 200 °C dec. *Anal*. Calc. for $C_{54}H_{81}GdN_4O_3(C_7H_8)_{0.75}$: C, 66.5; H, 8.3; N, 5.3. Found: C, 67.1; H, 7.9; N, 5.0%. IR (cm^{-1}, Nujol): 1615 (s, νC=N).

2.4.2. $[Gd(L^2)]$ (**2**)

This complex was prepared analogously using $Gd(NO_3)_3\cdot 6H_2O$ (0.164 g, 0.364 mmol) and H_3L^2 (0.3 g, 0.364 mmol). The solution was filtered and the filtrate was left standing at room temperature, where slow evaporation yielded a yellow powder. This powder was washed with small amounts of methanol and chloroform. Recrystallization in toluene afforded a microcrystalline solid. Yield: 0.2 g (54.0%); m.p. > 200 °C dec. *Anal*. Calc. for $C_{53}H_{79}GdN_4O_3(C_7H_8)_{0.75}$: C, 66.8; H, 8.2; N, 5.4. Found: C, 66.7; H, 8.2; N, 5.1%. IR (cm^{-1}, Nujol):1616 (s, νC=N).

2.4.3. $[Gd(L^3)]$ (**3**)

This complex was prepared analogously using $Gd(NO_3)_3\cdot 6H_2O$ (0.0835 g, 0.185 mmol) and H_3L^3 (0.147 g, 0.185 mmol). The resulting mixture was filtered to give a yellow powder. This powder was washed with small amounts of methanol and chloroform. Recrystallization in toluene afforded a microcrystalline solid. Yield: 0.19 g (49%); m.p. > 200 °C dec. *Anal*. Calc. for $C_{51}H_{75}GdN_4O_3(C_7H_8)_{0.5}$: C, 65.8; H, 8.0; N, 5.6. Found: C, 65.6; H, 7.9; N, 5.4%. IR (cm^{-1}, Nujol): 1616 (s, νC=N).

2.5. Synthesis of samarium complexes

2.5.1. $[Sm(L^1)]$ (**4**)

To a solution of H_3L^1 (0.3 g, 0.358 mmol) in methanol (25 ml) and chloroform (5 ml) was added $Sm(CH_3COO)_3$ (0.117 g, 0.358 mmol) in DMF (5 ml). After addition of NaOH (0.058 g, 1.43 mmol) in methanol (5 ml), the solution was refluxed for 6 h. The resulting mixture was filtered to give a yellow powder. Recrystallization in toluene afforded a microcrystalline solid, which was collected by filtration, washed with cold toluene and dried in vacuum. Yield: 0.19 g (55%); m.p. > 200 °C dec. *Anal*. Calc. for $C_{54}H_{81}SmN_4O_3(C_7H_8)_{0.5}$: C, 66.7; H, 8.3; N, 5.4. Found: C, 66.5; H, 8.1; N, 5.2%. IR (cm^{-1}, Nujol): 1617 (s, νC=N).

2.5.2. $[Sm(L^2)]$ (**5**)

This complex was prepared analogously using $Sm(CH_3COO)_3$ (0.119 g, 0.364 mmol) and H_3L^2 (0.3 g, 0.364 mmol). The resulting mixture was filtered to give a yellow powder. This powder was washed with small amounts of chloroform and methanol, recrystallized in toluene and dried in vacuum. Yield: 0.16 g (45%); m.p. > 200 °C dec. *Anal*. Calc. for $C_{53}H_{79}SmN_4O_3(C_7H_8)_{0.5}$: C, 66.5; H, 8.2; N, 5.5. Found: C, 66.3; H, 8.1; N, 5.3%. IR (cm^{-1}, Nujol): 1615 (s, νC=N).

3. Results and discussion

3.1. Ligands synthesis

Two new potentially heptadentate tripodal Schiff base ligands H_3L^1 and H_3L^2 have been easily prepared from the reaction of tripodal tetraamine ligands tpt and ppe with 3 equiv. of SATBU. These tribasic lipophilic ligands have two *tert*-butyl groups at the 3- and 5-positions of the salicylidene group and are soluble in slightly polar solvents such as chloroform and methanol, and are insoluble in water. The analytical

Table 1
^{1}H NMR and ^{13}C{^{1}H} NMR spectral assignments for H_3L^1 and H_3L^2 recorded at 500 MHz in $CDCl_3$

Hydrogen atoms	δ_H (ppm)	J (Hz)	Carbon atoms	δ_C (ppm)
H_3L^1				
H_1 (6H)	2.591(bt)		C_1 (3C)	51.898
H_2 (6H)	1.882(bm)		C_2 (3C)	28.812
H_3 (6H)	3.643(t)	$^3J(H_3, H_2) \approx 6.4$	C_3 (3C)	57.944
H_4 (3H)	8.382(s)		C_4 (3C)	166.368
H_8 (3H), H_{10} (3H)	7.091(d), 7.389(d)	$^4J(H_8, H_{10}) \approx 2$	C_5 (3C), C_6 (3C)	118.268, 158.629
H_{12} (27H), H_{14} (27H)	1.321(s), 1.460(s)		C_7 (3C), C_9 (3C)	137.056, 140.296
OH (3H)	13.960(s)		C_8 (3C), C_{10} (3C)	126.164, 127.152
			C_{11} (3C), C_{13} (3C)	34.560, 35.465
			C_{12} (9C), C_{14} (9C)	29.863, 31.972
H_3L^2				
H_1 (4H)	2.634(t)	$^3J(H_1, H_2) \approx 6.6$	C_1 (2C)	52.004
H_2 (4H)	1.876(m)		C_2 (2C)	28.935
H_3 (4H)	3.630(t)	$^3J(H_3, H_2) \approx 6.3$	C_3 (2C)	57.500
$H_{1'}$ (2H)	2.805(t)	$^3J(H_{1'}, H_{3'}) \approx 6.2$	$C_{1'}$ (1C)	54.922
$H_{3'}$ (2H)	3.682(t)	$^3J(H_{3'}, H_{1'}) \approx 6.0$	$C_{3'}$ (1C)	58.038
H_4 (2H)	8.356(s)		C_4 (2C)	166.476
$H_{4'}$ (1H)	8.373(s)		$C_{4'}$ (1C)	167.028
H_8 (2H), $H_{8'}$ (1H)	7.058(d),	$^4J(H_8, H_{10}$ or $H_{8'}, H_{10'}) \approx 2.0$	C_5 (3C)	118.324
H_{10} (2H), $H_{10'}$ (1H)	7.380(bd)		C_6 (3C)	158.687
H_{12} (18H), H_{14} (18H)	1.308(s), 1.464(s)		C_7 (3C), C_9 (3C)	137.064, 140.300
$H_{12'}$ (9H), $H_{14'}$ (9H)	1.298(s), 1.458(s)		C_8 (2C), C_{10} (2C)	126.187, 127.139
OH (3H)	14.021(s)		$C_{8'}$ (1C), $C_{10'}$ (1C)	126.249, 127.189
			C_{11} (3C), C_{13} (3C)	34.581, 35.502
			C_{12} (6C), $C_{12'}$ (3C); C_{14} (6C), $C_{14'}$ (3C)	29.928, 32.008

s, singlet; d, doublet; t, triplet; m, multiplet; b, broad.

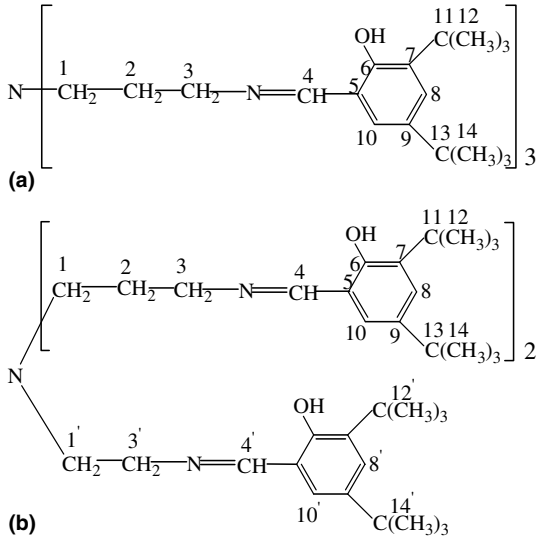


Fig. 2. NMR numbering for (a) H_3L^1 and (b) H_3L^2.

and spectral data are completely consistent with the proposed formulation. The ^{1}H NMR and ^{13}C{^{1}H} NMR spectral assignments for H_3L^1 and H_3L^2 are given in Table 1. The NMR numbering of the atoms is shown in Fig. 2. It should be noted that the H_3L^2 is first example of an asymmetrical tripodal heptadentate N_4O_3 ligand, which is derived from an asymmetrical tripodal tetraamine.

3.2. Gadolinium and samarium complexes

Three new gadolinium(III) complexes, [Gd(L^{1-3})], and two new samarium(III) complexes, [Sm(L^{1-2})], have been synthesized from the reaction of 1 equiv. of each potentially heptadentate tripodal Schiff base ligands with 1 equiv. of the appropriate metal salt in the presence of 4 equiv. of sodium hydroxide. For all resulting complexes, which are insoluble in water, conductivity data in toluene and chloroform show non-ionic behavior, consistent with a neutral product. Furthermore, IR spectra as well as elemental analysis do not show any counter ion or coordinating nitrate anion in any

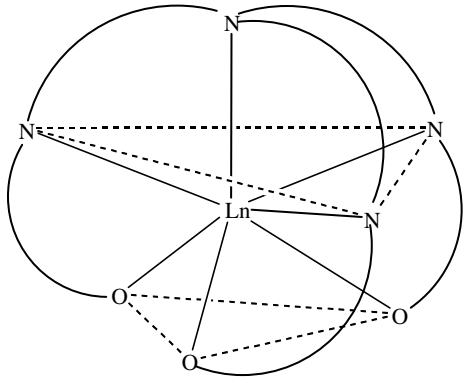


Fig. 3. The simplified proposed structure around the lanthanide ion of [Ln(L^{1-3})] (Ln = Gd or Sm) complexes.

of the complexes and are consistent with the [Ln(L)] formulation. A simplified geometrical structure for these complexes is illustrated in Fig. 3.

3.2.1. IR spectra

The IR spectra of the synthesized complexes contain strong bands characteristic of imine C=N bands, confirming the complexation of the lanthanide ions and absence of ligand hydrolysis. Upon coordination to the metal center, the imine C=N stretch in the IR spectra dropped from 1633, 1634 and 1630 cm^{-1} in the free ligands, H_3L^1, H_3L^2 and H_3L^3, respectively, to 1615, 1616 and 1616 cm^{-1} in the related gadolinium(III) complexes and to 1617 and 1615 cm^{-1} in the related samarium complexes. A similar observation was reported for [Sm(L^3)] and [Nd(L^3)] complexes [11]. Deprotonation of all phenolic functions is confirmed by the lack of O–H stretching bands in the IR region 2500–3500 cm^{-1} for all the complexes. The full IR spectral data (1700–500 cm^{-1}) for complexes **1**, **3** and **4** are compared in Table 2 with those of the previously known complex [Sm(L^3). As can be seen, the IR spectra of the gadolinium complexes are very similar to each other and to those of the corresponding samarium complexes thus indicating that all complexes have the same structure and symmetry.

3.2.2. Electronic spectra

Electronic absorption data for all complexes together with those of the related Schiff base ligands are shown in Table 3. The electronic absorption spectrum of H_3L^3 and the related gadolinium(III) complex are compared in Fig. 4, other compounds described here have similar spectra. As can be seen upon coordination of the ligand to metal, the electronic absorption band of the imine bond (above 300 nm) and even that of the phenolic ring (below 300 nm) are changed in position and intensity. This, in addition to the IR data, confirms the coordination of both latter moieties to the metal ion.

Table 3
Electronic spectroscopy data (nm) for H_3L^{1-3} and related complexes

Compound	λ_{max} (solution, $CHCl_3$–CH_3CN)[a]		
	ν_1	ν_2	ν_3
H_3L^1	234(29000)	260(29900)	325(11500)
H_3L^2	233(27500)	260(24010)	325(9070)
H_3L^3	234(30130)	259(29600)	324(10870)
[Gd(L^1)]	230–270(>30000)		370(16660)
[Gd(L^2)]	~242(~33333)	260(23111)[b]	372(10440)
[Gd(L^3)]	~246(~34444)	270(26600)[b]	370(18820)
[Sm(L^1)]	~243(40600	260(26000)	374(12480)
[Sm(L^2)]	240–280(>34000)		380(9110)

[a] Figures in parentheses are extinction coefficients ($dm^3\ mol^{-1}\ cm^{-1}$).
[b] Shoulder.

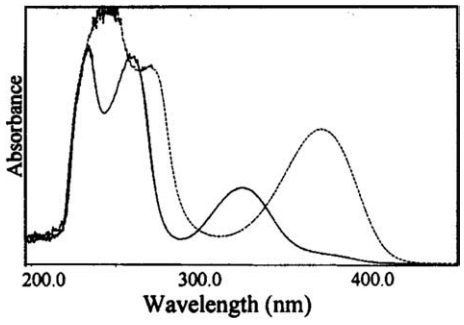


Fig. 4. Comparison of the electronic absorption spectra of H_3L^3 (solid line) and [Gd(L^3)] (dashed line).

Table 2
Comparison of IR data (cm^{-1}) for [Ln(L^1)] and [Ln(L^3)] (Ln = Gd or Sm) complexes

[GdL^1]	[SmL^1]	[GdL^3]	[SmL^3][a]
1615(s), 1549(m),	1617(s), 1542(m),	1616(s), 1547(m),	1617(s), 1549(m),
1531(s), 1463(s),	1533(s), 1464(s),	1532(s), 1461(s),	1533(s), 1466(s),
1436(s), 1410(m),	1437(s), 1412(m),	1436(s), 1410(m),	1439(s), 1412(m),
1384(m), 1357(m),	1389(m), 1358(m),	1391(m), 1359(m),	1390(m), 1362(m),
1329(s),	1327(s),	1327(s),	1335(s), 1323(s)
1274(s), 1253(s),	1274(s), 1254(s),	1274(s), 1255(s),	1273(s), 1255(s),
1232(m), 1219(w),	1232(m), 1220(w),	1233(m),	1234(m),
1197(m),	1200(m),	1200(m),	1201(m),
1165(s), 1132(m),	1164(s), 1131(m),	1165(s), 1135(m),	1165(s), 1136(m),
1068(m), 1040(m),	1068(m), 1039(m)	1058(m),	1078(m), 1039(m)
1026(w), 998(w), 980(w),	1020(w), 1002(w), 980(w),	1024(w), 980(w),	1022(w), 981(w),
917(w), 875(m),	917(w), 875(m),	904(m), 875(m),	906(m), 875(m),
842(s), 824(w), 809(w),	842(s), 823(w), 807(w),	840(s),	837(s),
788(m), 744(s),	788(m), 744(s),	809(w),	810(w),
698(w), 638(w),	698(w), 639(w),	789(m), 745(s),	791(m), 744(s),
612(w),	611(w),	695(w), 638(w),	702(w), 640(w),
523(m)	524(m)	523(m)	523(m)

[a] Ref. [11].

3.2.3. X-ray crystal structure of similar complexes

Although the spectral and analytical data show that new neutral lanthanide complexes with the general formula [Ln(L)] are formed, there is this question: is the tertiary nitrogen atom of the new ligands described here normally coordinated to the metal ion?

Essig and co-workers [11] have recently reported the synthesis and X-ray crystal structures of the complexes $[Ln(L^3)](C_7H_8)_{0.5}$ (Ln = Sm, Nd). X-ray diffraction of these complexes shows that the geometry about the metal centers is distorted capped octahedral, and the metal atoms are coordinated by a triply deprotonated N_4O_3 heptadentate ligand. In $[Sm(L^3)]$, Sm–N distances are of two types; an average of 2.556(3) Å to the three imine nitrogen atoms, and a significantly longer interaction of 2.818(4) Å with the apical amine nitrogen. In [Nd(L1)], Nd–N distances are also of two types, an average of 2.586(5) Å to the three imine nitrogens, and a 2.811(5) Å contact with the apical amine nitrogen. Furthermore, X-ray crystal structures of some lanthanide derivatives of a range of similar Schiff base ligands of the type $\{N[CH_2CH_2N{=}CH(2\text{-}OH\text{-}3\text{-}t\text{-}BuC_6H_3)]_3\}$ (H_3L) have also been reported [8–14]. In these neutral 1 + 1 metal–ligand complexes [ML] (M = La, Ce, Sm, Tb, Y, Lu), the apical amine nitrogen–metal distance is in the range of 2.984(4)–2.658(2) Å. Therefore, it is obvious that all reported neutral complexes of lanthanide ions with Schiff bases derived from condensation reactions of tren with various ring substituted salicylaldehydes are seven-coordinate. Thus, it is clear that the structure of $[Gd(L^3)]$ should be similar to $[Sm(L^3)]$ and the above complexes. On the other hand, because of the similar spectroscopic and analytical data for $[Gd(L^{1-3})]$ and $[Sm(L^{1-3})]$ complexes, the structures of $[Ln(L^{1-2})]$ (Ln = Gd, Sm) complexes are probably the same as $[Gd(L^3)]$ and $[Sm(L^3)]$. Therefore, we believe that the gadolinium and samarium atoms in the neutral Schiff base complexes under consideration here, like the above complexes, are completely enclosed by the triply deprotonated N_4O_3 Schiff base ligands and the coordination geometry is probably capped octahedral (or distorted capped trigonal antiprism) (Fig. 3).

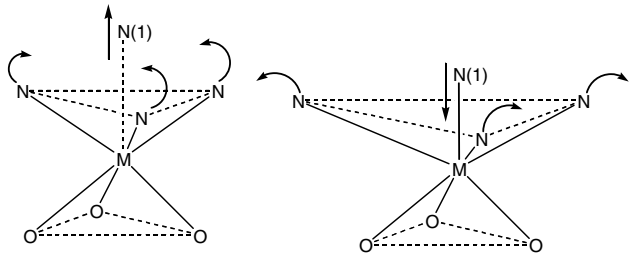


Fig. 5. Illustration of the expansion of the triangular face defined by imine nitrogen atoms, and increasing the sizes of N_{im}–M–N_{im} and N(1)–M–N_{im} bond angles upon coordination of the tertiary nitrogen atom to the metal.

Unfortunately there is only one reported X-ray crystal structure analysis for complexes of potentially heptadentate tripodal Schiff bases derived from tpt [21]. It has been confirmed that in contrast to Schiff base complexes derived from tren, $[M(py_3\ tren)]^{2+}$ (M = Mn, Fe, Co, Ni, Cu, Zn, Cd) which are all six-coordinate [34], $[Cd(py_3\ tpt)]^{2+}$, $[Cd\{N[(CH_2)_3N{=}C(CH_3)\text{-}(C_5H_4N)]_3\}]^{2+}$, is seven-coordinate. The Cd(II)-unique nitrogen distance, 2.486 Å, in the latter complex is about the weighted mean of the other Cd–N distances, 2.425 Å. and is even shorter than one of the Cd–N_{py}

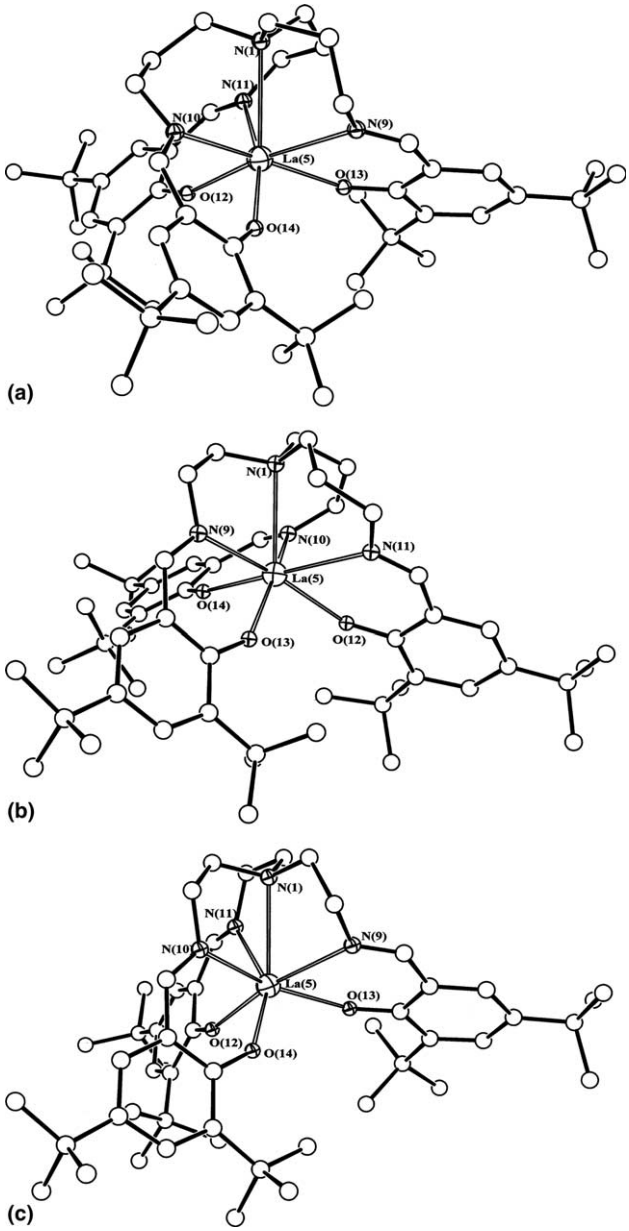


Fig. 6. Calculated molecular structure of (a) $[La(L^1)]$, (b) $[La(L^2)]$ and (c) $[La(L^3)]$ complexes, at the B3LYP level of theory, using the standard 6-31G* basis set for nitrogen and oxygen donor atoms, 3-21G* basis set for carbon and hydrogen atoms and LanL2DZ for the metal ion. Hydrogen atoms are omitted for clarity.

distances, 2.572 Å. This is probably due to the great intrinsic flexibility of propylene chains, in the latter complex. But from this single experimental observation it is not obvious that we will meet similar results in coordination of the tren and trpn Schiff bases to large metals such as lanthanides.

3.3. Ab initio and DFT studies

We were interested to study the relative capability of potentially heptadentate (N_4O_3) ligands, described here to encapsulate lanthanide ions. Unfortunately due to SCF convergence problems we were not able to optimize the gadolinium(III) and samarium(III) complexes synthesized here. This was due to inherent complications, first, to electronic effects, resulting from partially filled f-orbitals, and second, to the size of these bulky molecules. Thus we decided to choose La(III) complexes of H_3L^1, H_3L^2 and H_3L^3 as well as their unsubstituted analogs for ab initio studies. La(III) is an ion with a closed shell configuration and its stereochemistry is similar to Gd(III) and Sm(III) metal ions. On the other hand it is well known that calculations on closed shell configurations are less expensive than that of open shell configurations. Therefore, considering La(III) as the central lanthanide ion, the comparison of the capability of these ligands to encapsulate the lanthanide ion will make less expensive calculations. Although the parameters obtained for the [La($L^{1–3}$)] and [La($L^{1'–3'}$)] complexes at the different levels of theory described here are not identical, all calculations show that the three imine and the unique tertiary nitrogen donor atoms as well as the three phenolate oxygen donor atoms arranged at apices of a distorted capped octahedral (Figs. 6(a)–(c)). Selected bond lengths and bond angles of all complexes calculated with the LanL2MB basis set are compared in Table 4 and those calculated with the standard 6-31G* basis set for nitrogen and oxygen donor atoms, 3-21G* basis set for carbon and hydrogen atoms and LanL2DZ for the metal ion are given in Table 5. As can be seen in Table 4, the considerable difference between the parameters obtained from RHF/LanL2MB calculations relative to those from B3LYP/LanL2MB is in La–N and La–O bond lengths, where La–N bond lengths are slightly longer and La–O bond lengths are always slightly shorter in the former calculation. On the other hand, the significant difference between the parameters obtained from LanL2MB calculations (Table 4) with those derived from calculations at a higher level of theory (Table 5) is only in La–O bond lengths and therefore in calculated values for T_O. The mean of bond lengths and bond angles about the metal center in the substituted and unsubstituted derivatives are almost same, and thus the introduction of bulky *tert*-butyl substituents seems to have essentially no significant effect upon the geometry of the LaN_4O_3 core. In all bulky substituted complexes the La–tertiary nitrogen distance, La–N(1), is usually slightly longer than other bonds. As

Table 4
Selected theoretical bond lengths (Å) and bond angles (°) of the calculated structures using the LanL2MB basis set

	[La(L^1)]		[La($L^{1'}$)]		[La(L^2)]		[La($L^{2'}$)]		[La(L^3)]		[La($L^{3'}$)]	
Bond lengths												
La–N(1)	2.88	**2.85**	2.86	**2.83**	2.82	**2.80**	2.82	**2.79**	2.82	**2.79**	2.76	**2.73**
La–N(9)	2.69	**2.67**	2.72	**2.70**	2.70	**2.69**	2.72	**2.70**	2.66	**2.65**	2.77	**2.73**
La–N(10)	2.74	**2.72**	2.78	**2.75**	2.75	**2.73**	2.77	**2.76**	2.71	**2.69**	2.77	**2.73**
La–N(11)	2.76	**2.75**	2.80	**2.78**	2.75	**2.73**	2.76	**2.74**	2.71	**2.70**	2.77	**2.73**
La–O(12)	2.21	**2.25**	2.19	**2.23**	2.20	**2.24**	2.19	**2.23**	2.24	**2.27**	2.20	**2.24**
La–O(13)	2.20	**2.24**	2.19	**2.23**	2.22	**2.25**	2.20	**2.24**	2.22	**2.26**	2.20	**2.24**
La–O(14)	2.21	**2.24**	2.19	**2.23**	2.21	**2.25**	2.19	**2.23**	2.21	**2.24**	2.20	**2.24**
T_N	13.39	**13.35**	13.61	**13.57**	13.34	**13.39**	13.46	**13.42**	12.34	**12.36**	12.78	**12.71**
T_O	9.91	**9.95**	9.82	**9.80**	9.94	**9.98**	9.90	**9.91**	10.09	**10.12**	9.65	**9.69**
Bond angles												
N(1)–La–N(9)	71.5	**72.3**	72.4	**73.6**	64.6	**65.2**	63.57	**64.53**	62.4	**63.3**	62.6	**63.7**
N(1)–La–N(10)	71.8	**72.4**	72.3	**73.4**	73.0	**73.9**	73.20	**74.2**	62.9	**63.9**	62.6	**63.7**
N(1)–La–N(11)	70.6	**71.4**	71.2	**72.1**	75.2	**76.8**	75.13	**75.9**	63.4	**64.0**	62.6	**63.7**
N(1)–La–O(12)	121.8	**123.1**	121.9	**123.6**	125.4	**126.6**	125.1	**126.9**	125.0	**126.2**	122.3	**123.7**
N(1)–La–O(13)	113.8	**114.5**	114.3	**115.3**	125.7	**127.1**	122.6	**124.5**	109.4	**110.4**	122.3	**123.5**
N(1)–La–O(14)	125.0	**126.7**	125.2	**127.8**	108.2	**109.3**	110.8	**111.6**	122.8	**124.4**	122.3	**123.7**
N(9)–La–N(10)	98.3	**97.9**	98.4	**98.3**	121.4	**122.5**	116.4	**118.0**	87.0	**87.9**	100.5	**102.0**
N(9)–La–N(11)	118.4	**119.6**	119.5	**121.1**	100.4	**101.4**	102.6	**103.5**	113.9	**115.3**	100.5	**101.8**
N(10)–La–N(11)	113.3	**114.4**	114.1	**115.4**	106.0	**106.9**	108.9	**109.0**	99.5	**100.2**	100.5	**102.0**
O(12)–La–O(13)	101.2	**100.0**	100.5	**98.7**	93.5	**93.0**	95.6	**93.1**	101.2	**99.5**	94.1	**92.3**
O(12)–La–O(14)	93.6	**91.5**	93.6	**90.5**	103.6	**102.9**	102.7	**101.0**	92.8	**90.9**	94.1	**92.1**
O(13)–La–O(14)	96.1	**94.8**	95.7	**93.6**	95.1	**94.2**	94.5	**92.8**	101.6	**100.4**	94.1	**92.6**

The parameters obtained at the HF level are given as plain text, those for the B3LYP level are in bold. T_N and T_O are the sum of the calculated lengths of the sides of the triangle defined by imine nitrogen atoms and oxygen atoms, respectively.

Table 5
Selected theoretical bond lengths (Å) and bond angles (deg) of the calculated structures using the standard 6-31G* basis set for nitrogen and oxygen donor atoms, 3-21G* basis set for carbon and hydrogen atoms and LanL2DZ for the metal ion

	[La(L^1)]		[La($L^{1'}$)]		[La(L^2)]		[La($L^{2'}$)]		[La(L^3)]		[La($L^{3'}$)]	
Bond lengths												
La–N(1)	2.85	**2.81**	2.86	**2.82**	2.83	**2.81**	2.87	**2.84**	2.85	**2.82**	2.77	**2.75**
La–N(9)	2.71	**2.69**	2.73	**2.71**	2.75	**2.72**	2.74	**2.71**	2.70	**2.67**	2.80	**2.75**
La–N(10)	2.77	**2.74**	2.80	**2.75**	2.75	**2.72**	2.77	**2.73**	2.75	**2.71**	2.80	**2.76**
La–N(11)	2.79	**2.76**	2.82	**2.79**	2.79	**2.74**	2.77	**2.74**	2.75	**2.72**	2.80	**2.76**
La–O(12)	2.37	**2.36**	2.36	**2.36**	2.35	**2.35**	2.36	**2.36**	2.38	**2.38**	2.36	**2.36**
La–O(13)	2.37	**2.36**	2.36	**2.36**	2.37	**2.37**	2.37	**2.36**	2.37	**2.37**	2.36	**2.36**
La–O(14)	2.37	**2.37**	2.36	**2.36**	2.37	**2.37**	2.37	**2.37**	2.36	**2.36**	2.36	**2.36**
T_N	13.37	**13.30**	13.48	**13.36**	13.37	**13.23**	13.20	**13.10**	12.41	**12.38**	12.76	**12.70**
T_O	10.94	**10.80**	11.03	**10.90**	11.03	**10.90**	11.19	**11.04**	10.90	**10.73**	10.7	**10.5**
Bond angles												
N(1)–La–N(9)	69.2	**70.0**	69.1	**70.1**	63.8	**64.6**	61.1	**62.0**	61.0	**62.1**	61.4	**62.5**
N(1)–La–N(10)	70.1	**70.7**	69.6	**70.1**	71.2	**71.6**	68.9	**69.6**	62.1	**63.4**	61.4	**62.5**
N(1)–La–N(11)	69.1	**70.1**	68.8	**69.6**	73.1	**73.6**	72.5	**73.2**	62.5	**63.5**	61.4	**62.5**
N(1)–La–O(12)	118.0	**120.5**	117.0	**118.0**	119.2	**121.9**	119.0	**121.0**	124.5	**126.3**	119.6	**121.4**
N(1)–La–O(13)	111.5	**112.3**	109.9	**110.7**	124.9	**126.4**	119.8	**121.8**	107.4	**108.3**	119.6	**121.1**
N(1)–La–O(14)	122.4	**122.5**	121.5	**123.6**	103.3	**105.5**	104.2	**104.9**	122.0	**124.2**	119.6	**121.3**
N(9)–La–N(10)	97.7	**98.8**	96.8	**95.9**	117.8	**118.7**	113.0	**114.6**	87.9	**88.8**	98.9	**100.1**
N(9)–La–N(11)	115.5	**116.2**	115.7	**117.5**	99.3	**101.5**	98.2	**98.9**	111.7	**113.6**	98.9	**100.5**
N(10)–La–N(11)	111.4	**112.1**	111.1	**112.4**	106.3	**104.9**	106.5	**106.4**	97.1	**98.6**	98.9	**100.4**
O(12)–La–O(13)	105.7	**103.0**	107.3	**106.9**	100.4	**97.7**	101.4	**99.0**	101.2	**99.6**	97.7	**95.3**
O(12)–La–O(14)	97.4	**96.5**	98.6	**96.3**	110.9	**107.4**	110.1	**108.4**	92.8	**89.9**	97.7	**95.6**
O(13)–La–O(14)	99.1	**98.2**	100.6	**98.7**	95.3	**93.7**	100.9	**99.4**	106.1	**104.4**	97.7	**95.5**

The parameters obtained at the HF level are given as plain text, those for the B3LYP level are in bold. T_N and T_O are the sum of the calculated lengths of the sides of the triangle defined by imine nitrogen atoms and oxygen atoms, respectively.

can be expected, the N(1)–La–N(imine) and N(imine)–La–N(imine) bond angles are greater for [La(L^1)] and [La(L^2)] complexes and also their unsubstituted analogs, in which the tertiary nitrogen atom, N(1), is connect to imine nitrogen atoms through propylene chains. On the other hand, in all complexes, the size of the triangle defined by the oxygen atoms is always much smaller than that of imine nitrogen atoms. Obviously, upon coordination of a tertiary nitrogen atom to the metal atom the triangular face defined by the other coordinated nitrogen atoms is expanded and the three N(1)–La–N(imine) bond angles as well as the three N(imine)–La–N(imine) bond angles are increased (Fig. 5). The expansion of this triangular face in these complexes can be readily compared by the sum of the calculated lengths of the sides of the triangle defined by the imine nitrogen atoms, T_N (see Tables 4 and 5). The results show that the latter expansion for [La(L^1)] and [La($L^{1'}$)] is more significant. The mean of the bond lengths and bond angles about the metal center for the calculated structure of [La(L^3)] and the corresponding experimental data for previously known lanthanide complexes, [Sm(L^3)] and [Nd(L^3)] [11], are compared in Table 6. It seems that the results of B3LYP calculations are more reliable than those of RHF calculations. The mean of the bond angles about the central metal atom for La, Nd and Sm complexes is very similar, indicating that the chemical structure of these complexes strongly depends on the structure of these tripodal ligands. The

Table 6
A comparison between the mean of bond lengths (Å) and bond angles (°) for the calculated structure of [La(L^3)] and corresponding experimental values for the [Nd(L^3)] and [Sm(L^3)] complexes

	La		Nd	Sm
Bond lengths				
Ln–N(1)	2.85	**2.82**	2.81	2.82
Ln–N_{im}	2.73	**2.70**	2.59	2.55
Ln–O	2.37	**2.37**	2.24	2.22
Bond angles				
N(1)–Ln–N_{im}	61.9	**63.0**	65.2	65.2
N(1)–Ln–O	118.0	**119.6**	121.1	121.3
N_{im}–Ln–N_{im}	98.9	**100.3**	103.6	103.7
O–Ln–O	100.0	**98.0**	95.7	95.5

The theoretical data are derived from Table 5 and the experimental values are obtained from [11].

La–N_{im} and La–O bond lengths, as we expect, are considerably greater than similar bond lengths in Sm and Nd complexes. On the other hand there is no significant difference between the Ln–N(1) bond length in these complexes. Note that the Nd–N(1) bond length is even smaller than Sm–N(1) indicating that the comparison of metal–N(1) bond lengths based on the ionic radii of the central metal ions is incorrect. The latter conclusion was supported by the observation that most of the similar complexes of the first row transition metals involve an N_3O_3 donor set of the ligands, with the tertiary nitrogen atom, (N(1)), remaining uncoordinated [15–19].

4. Conclusions

Two new bulky tripodal Schiff base ligands and the related neutral gadolinium(III) and samarium(III) complexes as well as the gadolinium(III) complex of one previously known ligand were synthesized and characterized with various spectroscopic methods. We believe that gadolinium and samarium atoms in these neutral complexes are coordinated by an apical nitrogen atom, three imino groups and three phenolate oxygen donor atoms. The results of this work, as well as previous observations, show that the introduction of bulky *tert*-butyl substituents seems to have essentially no significant effect upon the geometry of the LaN_4O_3 core. The present ab initio study as well as experimental data also confirm that the potentially heptadentate tripodal Schiff bases, derived from a condensation reaction of trpn and ppe with salicylaldehyde derivatives, the same as similar Schiff bases derived from tren, can effectively encapsulate the lanthanide ions and enforce a seven-coordinate geometry. Obviously, the tertiary nitrogen atom of these tripodal ligands will coordinate to the metal atom if the triangular face defined by the other coordinated nitrogen atoms is expanded, and the present data show that by increasing the number of propylene chains, from the complexes of L^3 to L^1 tripodal ligands, this expansion will be more considerable.

Acknowledgment

We are grateful to the Bu-Ali Sina University, Sharif University of Technology and the Ministry of Science, Research & Technology of Iran, for financial support.

References

[1] A.D. Garnovskii, A.L. Nivorozhkin, V.I. Minkin, Coord. Chem. Rev. 1 (1993) 126.
[2] V. Alexander, Chem. Rev. 95 (1995) 273.
[3] R.B. Lauffer, Chem. Rev. 87 (1987) 901.
[4] P. Caravan, J.J. Ellison, T.J. Mcmurry, R.B. Lauffer, Chem. Rev. 99 (1999) 2293.
[5] D.J. Clevette, D.M. Lyster, W.M. Nelson, T.J. Rihela, G.A. Webb, C. Orvig, Inorg. Chem. 29 (1990) 667.
[6] L. Thunus, R. Lejeune, Coord. Chem. Rev. 184 (1999) 125.
[7] C.S. Cutler, C.J. Smith, G.J. Ehrhardt, T.T. Tyler, S.S. Jurisson, E. Deutsch, Cancer Biother. Radiopharm. 15 (2000) 531.
[8] S. Liu, L. Gelmini, S.J. Rettig, R.C. Thompson, C. Orvig, J. Am. Chem. Soc. 114 (1992) 6081.
[9] M. Kanesato, T. Yokoyama, O. Itabashi, T.M. Suzuki, M. Shiro, Bull. Chem. Soc. Jpn. 69 (1996) 1297.
[10] M. Kanesato, T. Yokoyama, Chem. Lett. (1999) 137.
[11] M.W. Essig, D.W. Keogh, B.L. Scott, J.G. Watkin, Polyhedron 20 (2001) 373.
[12] B.M. Flanagan, P.V. Bernhardt, E.R. Krausz, S.R. Luthi, M.J. Riley, Inorg. Chem. 41 (2002) 5024.
[13] S. Mizukami, H. Houjou, M. Kanesato, K. Hiratani, Chem. Eur. J. 9 (2003) 1521.
[14] M. Kanesato, S. Mizukima, H. Houjou, H. Tokuhisa, E. Koyama, Y. Nagawa, J. Alloy Compd. 374 (2004) 307.
[15] N.W. Alcock, D.F. Cook, E.D. McKenzie, J.M. Worthiugton, Inorg. Chim. Acta 38 (1980) 107.
[16] K. Ramesh, R. Mukherjee, J. Chem. Soc., Dalton Trans (1991) 3259.
[17] K. Ramesh, D. Bhuniya, R. Mukherjee, J. Chem. Soc., Dalton Trans (1991) 2917.
[18] S.K. Chandra, P. Chakraborty, A. Chakraborty, J. Chem. Soc., Dalton Trans (1993) 863.
[19] D.F. Cook, D. Cummins, E.D. Mckenzie, J. Chem. Soc., Dalton Trans (1976) 1369.
[20] H. Keypour, S. Salehzadeh, R.G. Pritchard, R.V. Parish, Transition Met. Chem. 23 (1998) 605.
[21] H. Keypour, S. Salehzadeh, R.G. Pritchard, R.V. Parish, Polyhedron 19 (2000) 1633.
[22] H. Keypour, S. Salehzadeh, R.V. Parish, Molecules 7 (2002) 140.
[23] H. Keypour, D.A. Stotter, Inorg. Chim. Acta 33 (1979) 141.
[24] H. Keypour, S. Salehzadeh, Transition Met. Chem. 25 (2000) 205.
[25] G. Casiraghi, G. Casnati, G. Puglia, G. Sartori, G. Terenghi, J. Chem. Soc., Perkin Trans. 1 (1980) 1862.
[26] J. Parr, A.T. Ross, A.M.Z. Slawin, Main Group Chem. 2 (1998) 243.
[27] A.D. Becke, J. Chem. Phys. 98 (1993) 5648.
[28] M.J. Frisch, G.W. Trucks, H.B. Schlegel, G.E. Scuseria, M.A. Robb, J.R. Cheeseman, V.G. Zakrazewski, J.A. Montgomery Jr., R.E. Startmann, J.C. Burant, S. Dapprich, J.M. Millam, A.D. Daniels, K.N. Kudin, M.C. Strain, O. Farkas, J. Tomasi, V. Barone, M. Cossi, R. Cammi, B. Mennucci, C. Adamo, S. Clifford, J. Ochterski, G.A. Petersson, P.Y. Ayala, Q. Cui, K. Morokuma, D.K. Malik, A.D. Rabuck, K. Raghavachar, J.B. Foresman, J. Cioslowski, J.V. Ortiz, B.B. Stefanov, G. Liu, A. Liashenko, P. Piskorz, I. Komaromi, R. Gomperts, R.L. Martin, D.J. Fox, T. Keith, M.A. Al-Laham, C.Y. Peng, A. Nanyakkara, C. Gonzalez, M. Challacombe, P.M.W. Gill, B. Johnson, W. Chen, M.W. Wong, J.L. Andres, M. Head-Gordon, E.S. Replogle, J.A. Pople, GAUSSIAN 98, Revision A.6, Gaussian Inc., Pittsburgh, PA, USA, 1998.
[29] P.J. Hay, W.R. Wadt, J. Chem. Phys. 82 (1985) 270.
[30] P.C. Hariharan, J.A. Pople, Theor. Chim. Acta 28 (1973) 213.
[31] K.D. Dobbs, W.J. Hehre, J. Comp. Chem. 8 (1987) 880.
[32] P.J. Hay, W.R. Wadt, J. Chem. Phys. 82 (1985) 299.
[33] HyperChem, Release 5.02, hypercube, Inc., Gainesville, 1997.
[34] R.M. Kirchner, C. Mealli, M. Bailey, N. Howe, L.P. Torre, L.J. Wilson, L.C. Andrews, N.J. Rose, E.C. Lingafelter, Coord. Chem. Rev. 77 (1987) 89.

for $Ag[Gd(dipic)_2(H_2O)_3] \cdot 3H_2O$ [8], $[M(dipicH_2)(OH_2)_3][Ce(dipic)_3] \cdot nH_2O$ [5b,c] (M = Ca, $n = 5$; M = Sr, $n = 6$), $[Ln(dipic)_3Mn_{1.5}(H_2O)_3] \cdot nH_2O$ [9] (Ln = Pr, $n = 2$; Ln = Gd, $n = 3.5$; Ln = Er, $n = 3$) and $[Yb(dipic)_3Mn_{1.5}(H_2O)_m] \cdot nH_2O$ [10] ($m = 3$, $n = 1.5$; $m = 6$, $n = 6$). Studies involving $dipicH_2$, Ce^{4+} and Ba^{2+} show that different novel chains and networks can be obtained depending on the conditions of crystallization. These are reported in the present paper.

2. Experimental

2.1. Materials

$BaCl_2 \cdot 2H_2O$ and $(NH_4)_2Ce(NO_3)_6$ were purchased from Ranbaxy Chemicals. $DipicH_2$ was purchased from Lancaster Chemicals.

2.2. Preparation of $Ba(dipicH_2)(OH_2)_4Ce(dipic)_3 \cdot 4.6H_2O$ (1)

To a 5 mL aqueous solution of $BaCl_2 \cdot 2H_2O$ (0.245 g, 1.00 mmol) and $(NH_4)_2Ce(NO_3)_6$ (0.549 g, 1.00 mmol), 40 mL methanolic solution of $dipicH_2$ (0.668 g, 4.00 mmol) was added slowly while stirring. As the methanolic solution was being added, the color changed from deep red to orange to pale yellow. After stirring for about 5 min, a small amount of precipitate formed was removed by filtration. The clear filtrate gave yellow crystalline material. Yield: 0.701 g (0.640 mmol, 64%). Recrystallization from hot water yielded pale yellow single crystals of **1** suitable for X-ray data collection. *Anal.* Calc. for $C_{28}H_{31.2}BaCeN_4O_{24.6}$ (MW 1094.83): C, 30.72; H, 2.87; N, 5.12. Found: C, 31.30; H, 1.91; N, 5.44%. IR (KBr disk, cm^{-1}): 3428, 1607, 1568, 1441, 1375, 1275, 1188, 1082, 1018, 916, 727, 682.

Table 1
Crystallographic data for **1**, **2** and **3**

	1	**2**	**3**
Formula	$C_{28}H_{31.20}BaCeN_4O_{24.60}$	$C_{21}H_{21}BaCeN_3O_{18}$	$C_{21}H_{21}BaCeN_3O_{18}$
Formula weight	1094.83	880.86	880.86
Colour	pale yellow	yellow	yellow
Crystal system	triclinic	trigonal	monoclinic
Unit cell dimensions			
a (Å)	11.050(6)	13.0370(11)	11.2287(7)
b (Å)	12.940(4)	13.0370(11)	10.9693(10)
c (Å)	16.4970(17)	9.1886(6)	11.3137(8)
α (°)	96.926(16)	90	90
β (°)	103.57(2)	90	92.322(6)
γ (°)	112.25(3)	120	90
V (Å^3)	2063.9(13)	1352.49(18)	1392.38(18)
Z	2	2	2
Space group	$P\bar{1}$	$P31c$	$P2/n$
T (°C)	20	20	20
λ (Å)	0.71073	0.71073	0.71073
D_{calc} (g cm^{-3})	1.762	2.163	2.101
μ (mm^{-1})	2.129	3.201	3.110
$F(000)$	1076	852	852
Crystal size (mm)	$0.61 \times 0.37 \times 0.20$	$0.50 \times 0.30 \times 0.28$	$0.34 \times 0.30 \times 0.28$
θ Range for data collection (°)	1.92–25.13	2.86–27.51	2.51–27.37
$h/k/l$	−13,12/−15,15/0,19	−16,16/−16,16/0,11	−14,14/−14,0/−14,14
Reflections collected/unique [R_{int}]	7294/7294 [0]	6084/1105 [0.0405]	6353/3155 [0.0767]
Completeness to $2\theta = 25.00$(%)	98.9	100	99.6
Maximum and minimum transmission	0.655 and 0.346	0.409 and 0.359	0.418 and 0.367
Refinement method	full-matrix least squares on F^2	full-matrix least squares on F^2	full-matrix least squares on F^2
Data/restraints/parameters	7294/13/569	1105/4/134	3155/0/212
Goodness of fit on F^2	1.037	1.051	1.137
Final R indices [$I > 2\sigma(I)$]			
R_1	0.0575	0.0166	0.0364
wR_2	0.1487	0.0333	0.0771
R indices (all data)			
R_1	0.0759	0.0172	0.0380
wR_2	0.1675	0.0335	0.0780
Extinction coefficient		0.0301(8)	0.0243(10)
Largest difference peak and hole (e Å^{-3})	2.803, −3.655	0.540, −0.796	2.133, −2.669

Table 2
Selected bond lengths (Å) and angles (°) for (**1**)[a]

Cerium coordination	
Ce–O9	2.318(6)
Ce–O11	2.346(6)
Ce–N1	2.487(6)
Ce–O1	2.321(6)
Ce–O7	2.361(6)
Ce–N2	2.522(6)
Ce–O3	2.343(5)
Ce–O5	2.364(6)
Ce–N3	2.525(6)
O9–Ce–O1	86.8(2)
O9–Ce–O11	127.1(2)
O9–Ce–O7	146.8(2)
O11–Ce–O7	79.0(2)
O3–Ce–O5	76.3(2)
O9–Ce–N1	74.6(2)
O11–Ce–N1	138.7(2)
O9–Ce–N2	138.7(2)
O11–Ce–N2	71.8(2)
N1–Ce–N2	117.4(2)
O3–Ce–N3	137.0(2)
O5–Ce–N3	75.2(2)
O9–Ce–O3	80.1(2)
O1–Ce–O11	81.2(2)
O1–Ce–O7	76.5(2)
O9–Ce–O5	79.9(2)
O11–Ce–O5	85.3(2)
O1–Ce–N1	63.95(19)
O7–Ce–N1	72.3(2)
O1–Ce–N2	134.4(2)
O7–Ce–N2	63.0(2)
O9–Ce–N3	63.7(2)
O11–Ce–N3	63.4(2)
N1–Ce–N3	121.7(2)
O1–Ce–O3	128.14(19)
O3–Ce–O11	144.1(2)
O3–Ce–O7	87.9(2)
O1–Ce–O5	149.7(2)
O7–Ce–O5	127.2(2)
O3–Ce–N1	64.19(19)
O5–Ce–N1	135.8(2)
O3–Ce–N2	72.4(2)
O5–Ce–N2	64.2(2)
O1–Ce–N3	74.5(2)
O7–Ce–N3	135.2(2)
N2–Ce–N3	120.9(2)
Barium coordination	
Ba–O6	2.662(8)
Ba–OW4A	2.715(18)
Ba–OW3	2.794(12)
Ba–OW4B	3.01(2)
Ba–OW2	2.704(12)
Ba–O15	2.738(7)
Ba–OW1	2.842(8)
Ba–O2#2	2.706(6)
Ba–O13	2.762(7)
Ba–N4	2.879(7)
O6–Ba–OW2	74.2(3)
O6–Ba–O2#2	145.4(2)
OW2–Ba–O2#2	76.2(3)
OW2–Ba–OW4A	119.7(6)
O6–Ba–O15	71.0(2)

Table 2 (*continued*)

Barium coordination	
O2#2–Ba–O15	84.0(2)
O6–Ba–O13	141.4(2)
O2#2–Ba–O13	70.4(2)
O15–Ba–O13	113.6(2)
OW2–Ba–OW3	62.2(4)
OW4A–Ba–OW3	67.4(6)
O13–Ba–OW3	98.9(3)
OW2–Ba–OW1	143.7(3)
OW4A–Ba–OW1	60.8(5)
O13–Ba–OW1	72.0(2)
O6–Ba–N4	111.2(2)
O2#2–Ba–N4	71.24(19)
O15–Ba–N4	56.84(18)
OW3–Ba–N4	146.8(3)
O6–Ba–OW4B	60.3(6)
O2#2–Ba–OW4B	144.8(6)
O15–Ba–OW4B	129.9(6)
OW3–Ba–OW4B	69.2(7)
N4–Ba–OW4B	131.6(6)
O6–Ba–OW4A	86.4(7)
O2#2–Ba–OW4A	124.3(6)
OW2–Ba–O15	74.2(3)
OW4A–Ba–O15	149.6(6)
OW2–Ba–O13	144.3(3)
OW4A–Ba–O13	72.1(6)
O6–Ba–OW3	101.8(3)
O2#2–Ba–OW3	79.4(3)
O15–Ba–OW3	135.8(4)
O6–Ba–OW1	69.6(2)
O2#2–Ba–OW1	136.5(2)
O15–Ba–OW1	91.6(3)
OW3–Ba–OW1	127.8(4)
OW2–Ba–N4	122.6(3)
OW4A–Ba–N4	117.6(5)
O13–Ba–N4	57.05(18)
OW1–Ba–N4	70.3(2)
OW2–Ba–OW4B	101.7(6)
OW4A–Ba–OW4B	27.3(6)
O13–Ba–OW4B	98.4(6)
OW1–Ba–OW4B	62.0(6)

[a] Symmetry transformation used to generate equivalent atoms: (#1) $x-1, y-1, z$; (#2) $x+1, y+1, z$.

2.3. Preparation of $Ba(OH_2)_6Ce(dipic)_3$ (**2**)

To a 10 mL aqueous solution of $BaCl_2 \cdot 2H_2O$ (0.499 g, 2.04 mmol) and $(NH_4)_2Ce(NO_3)_6$ (1.109 g, 2.022 mmol), 60 mL methanolic solution of dipicH_2 (1.000 g, 5.983 mmol) was added slowly while stirring. As the methanolic solution was being added, the color changed from deep red to orange to pale yellow. After stirring continuously for 3 h a pale yellow precipitate formed, which was separated by filtration, washed with cold methanol and dried. Yield: 1.165 g (1.322 mmol, 66%). Recrystallization from hot water yielded yellow needles of **2** suitable for X-ray data collection. *Anal.* Calc. for $C_{21}H_{21}BaCeN_3O_{18}$ (MW 880.86): C, 28.63; H, 2.40; N, 4.77. Found: C, 29.14; H, 2.50; N, 4.29%. IR (KBr disk, cm^{-1}): 3437, 1618, 1427, 1338, 1186, 1080, 1024, 920, 770, 731, 667.

Table 3
Bond lengths (Å) and angles (°) for (**2**)[a]

Cerium coordination	
Ce–O1	2.351(2)
Ce–O3	2.364(2)
Ce–N1	2.524(2)
Ce–O1#1	2.351(2)
Ce–O3#1	2.364(2)
Ce–N1#1	2.524(2)
Ce–O1#2	2.351(2)
Ce–O3#2	2.364(2)
Ce–N1#2	2.524(2)
O3–Ce–O3#1	80.91(9)
O1–Ce–O1#2	81.97(10)
O1–Ce–O3	127.17(8)
O1–Ce–N1	63.79(8)
O3–Ce–N1	63.39(8)
N1–Ce–N1#1	119.995(2)
O3–Ce–N1#2	137.65(9)
O1–Ce–O3#2	83.01(9)
O1–Ce–N1#2	72.56(8)
O1–Ce–O3#1	144.59(8)
O1–Ce–N1#1	139.34(10)
O3#1–Ce–N1	137.65(9)
O3–Ce–N1#1	72.04(8)
Barium coordination	
Ba–OW1#3	2.770(3)
Ba–OW2#5	2.868(3)
Ba–OW2	2.960(3)
Ba–OW1#4	2.770(3)
Ba–OW2#6	2.868(2)
Ba–OW2#3	2.960(3)
Ba–OW1	2.770(3)
Ba–OW2#7	2.868(2)
Ba–OW2#4	2.960(3)
OW1#3–Ba–OW1	118.36(3)
OW1–Ba–OW2#7	67.22(8)
OW2#5–Ba–OW2#7	65.54(8)
OW1–Ba–OW2	64.23(8)
OW2#5–Ba–OW2	165.26(9)
OW2#7–Ba–OW2	108.37(8)
OW1–Ba–OW2#5	121.21(8)
OW1–Ba–OW2#6	64.29(8)
OW1#3–Ba–OW2	127.11(8)
OW1#4–Ba–OW2	98.05(8)
OW2#6–Ba–OW2	125.55(8)
OW2–Ba–OW2#3	63.26(8)

[a] Symmetry transformation used to generate equivalent atoms: (#1) $-x+y+1, -x+1, z$; (#2) $-y+1, x-y, z$; (#3) $-x+y+1, -x+2, z$; (#4) $-y+2, x-y+1, z$; (#5) $-x+2, -x+y+1, z+1/2$; (#6) $x-y+1, -y+2, z+1/2$; (#7) $y, x, z+1/2$.

2.4. Preparation of $Ba(OH_2)_4Ce(dipic)_3 \cdot 2H_2O$ (**3**)

Compound **2** (0.735 g, 0.834 mmol) was dissolved in 75 mL hot water and filtered. The pH of the solution was adjusted to about 2 by adding a few drops of 0.1 N HNO_3 and it was refluxed at 100 °C for 3 days and concentrated to 25 mL on a water bath. The filtered solution was kept for slow evaporation at room temperature. Yellow prisms of **3** were collected after 5 days.

Table 4
Bond lengths (Å) and angles (°) for (**3**)[a]

Cerium coordination	
Ce–O1	2.352(2)
Ce–O5	2.353(2)
Ce–N2	2.513(3)
Ce–O1#1	2.352(2)
Ce–O3#1	2.357(2)
Ce–N1	2.520(2)
Ce–O5#1	2.353(2)
Ce–O3	2.357(2)
Ce–N1#1	2.520(2)
O1#1–Ce–O1	146.07(10)
O1–Ce–O5	87.87(9)
O1–Ce–O3#1	80.23(8)
O1–Ce–O3	127.22(7)
O3#1–Ce–O3	83.54(12)
O5–Ce–N2	64.02(5)
O1–Ce–N1	63.56(7)
O3–Ce–N1	63.84(8)
O1–Ce–N1#1	135.49(8)
O3–Ce–N1#1	75.89(7)
O1–Ce–O5#1	77.38(8)
O5#1–Ce–O5	128.04(10)
O5–Ce–O3#1	146.92(8)
O5–Ce–O(3)	79.37(8)
O1–Ce–N2	73.04(5)
O3–Ce–N2	138.23(6)
O5–Ce–N1	71.18(8)
N2–Ce–N1	117.32(5)
O5–Ce–N1#1	136.45(9)
N1–Ce–N1#1	125.35(10)
Barium coordination	
Ba–O6#2	2.722(2)
Ba–O2#4	2.843(2)
Ba–O8A	2.778(6)
Ba–O8B#4	2.754(8)
Ba–O6#3	2.722(2)
Ba–O7	2.802(3)
Ba–O8A#4	2.778(6)
Ba–O2	2.843(2)
Ba–O7#4	2.802(3)
Ba–O8B	2.754(8)
O6#2–Ba–O6#3	137.72(11)
O6#3–Ba–O8B	66.3(2)
O6#2–Ba–O8A	71.94(14)
O8B–Ba–O8A	30.1(4)
O8A–Ba–8A#4	101.8(3)
O6#3–Ba–O7	75.76(8)
O8B–Ba–O7#4	128.2(4)
O8A–Ba–O7#4	99.97(18)
O6#2–Ba–O2	121.59(8)
O8B–Ba–O2	90.8(4)
O(7)–Ba–O(2)	75.71(8)
O8B–Ba–O2#4	133.9(4)
O2–Ba–O2#4	134.98(12)
O6#2–Ba–O8B	74.6(2)
O8B–Ba–O8B#4	44.9(8)
O6#3–Ba–O8A	81.69(17)
O8B#4–Ba–8A	72.5(5)
O6#2–Ba–O7	142.60(8)
O8B–Ba–O7	141.9(2)
O8A–Ba–O7	141.76(13)
O7–Ba–O7#4	81.01(12)

(*continued on next page*)

Table 4 (*continued*)

Barium coordination	
O6#3–Ba–O2	75.66(8)
O8A–Ba–O2	68.96(13)
O7#4–Ba–O2	70.41(8)
O8A–Ba–O2#4	147.32(13)

[a] Symmetry transformations used to generate equivalent atoms: (#1) $-x+3/2,\ y,\ -z+1/2$; (#2) $x-1/2,\ -y+1,\ z+1/2$; (#3) $-x+2,\ -y+1,\ -z+1$; (#4) $-x+3/2,\ y,\ -z+3/2$.

Yield: 0.440 g (0.500 mmol, 59%). *Anal*. Calc. for $C_{21}H_{21}BaCeN_3O_{18}$ (MW 880.86): C, 28.63; H, 2.40; N, 4.77. Found: C, 29.71; H, 2.46; N, 5.56%. IR (KBr disk, cm^{-1}): 3393, 1624, 1427, 1363, 1265, 1178, 1074, 1024, 922, 856, 825, 767, 733.

2.5. X-ray crystallography

X-ray data were collected for compounds **1**, **2** and **3** on an Enraf Nonius CAD-4 diffractometer using graphite monochromated Mo Kα radiation. The data were reduced using XTAL 3.4 [11] and absorption corrections (refdelf [12] or psi-scan [13]) were applied. The structures were solved by a combination of heavy atom and direct methods and refined (over F^2) by least squares techniques using SHELXL-97 [14]. Drawings were made using ORTEP-III [15] and RASMOL 2.6 [16]. One of the four coordinated water molecules in **1** was disordered in two positions, while seven out of eight lattice water sites were refined with occupation factor less than unity. In **3**, two of the four coordinated water molecules were disordered in two positions. The crystal data for the three compounds are presented in Table 1, and selected interatomic distances and angles are in Tables 2–4.

Powder diffractograms were measured using a PW3710 model Philips Analytical X-ray diffractometer.

3. Results and discussion

3.1. Synthesis

The formation of the three compounds **1**, **2** and **3** is controlled by a subtle balance of reaction conditions (solvent, temperature and pH). It was found that the variations in the relative amounts of starting materials used, within reasonable limits, do not play a decisive role in determining the product formed. In order to

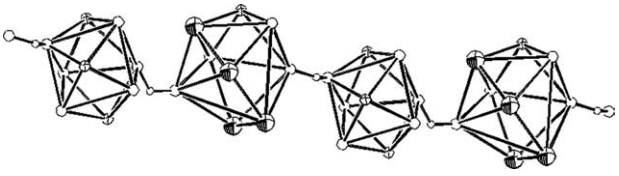


Fig. 2. Perspective view of a segment of the polymeric chain formed by the linking of coordination polyhedra in **1**. Three $dipic^{2-}$ nitrogen atoms (footballs) cap the trigonal prism formed by carboxylate oxygen atoms (large open circles) around Ce. The trigonal prism around Ba is formed by four water molecules (large shaded footballs), one $dipicH_2$ nitrogen atom and four carboxylate oxygen atoms. The alternating $BaNO_8$ and CeN_3O_6 polyhedra are linked by carboxylate groups (C1 and C21, small open circles). The Ba and Ce atoms are not shown.

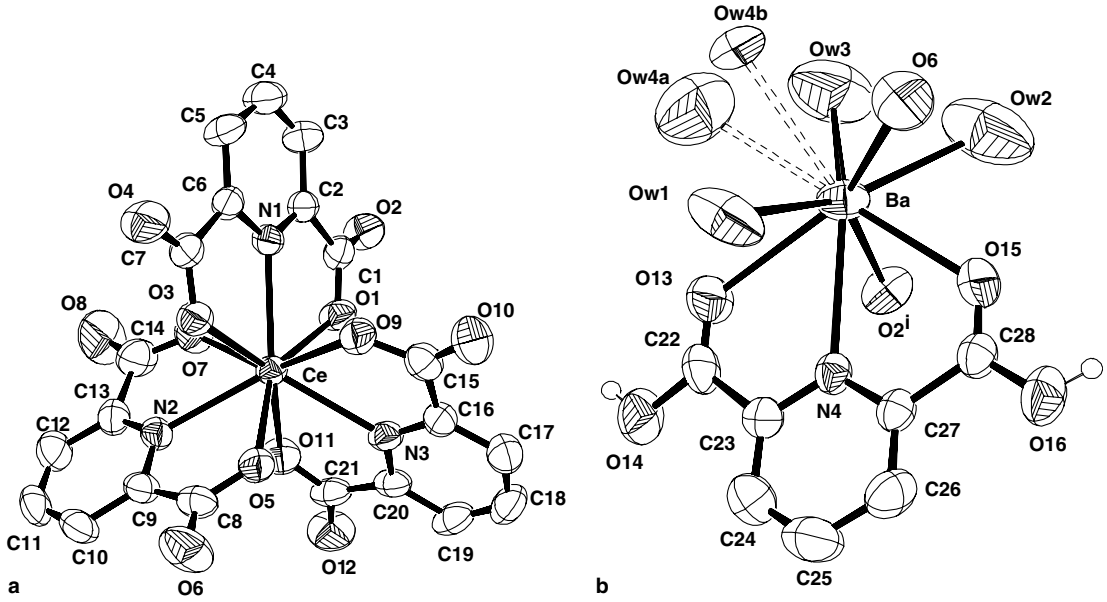


Fig. 1. ORTEP view of the coordination environment of (a) Ce^{4+} and (b) Ba^{2+} in **1**. In this and later ORTEP drawings, atoms are represented as 50% probability ellipsoids and ring and water hydrogens have been omitted for clarity. Symmetry code: (i) $x+1,\ y+1,\ z$. In (b), bonds to disordered atoms are indicated by broken lines.

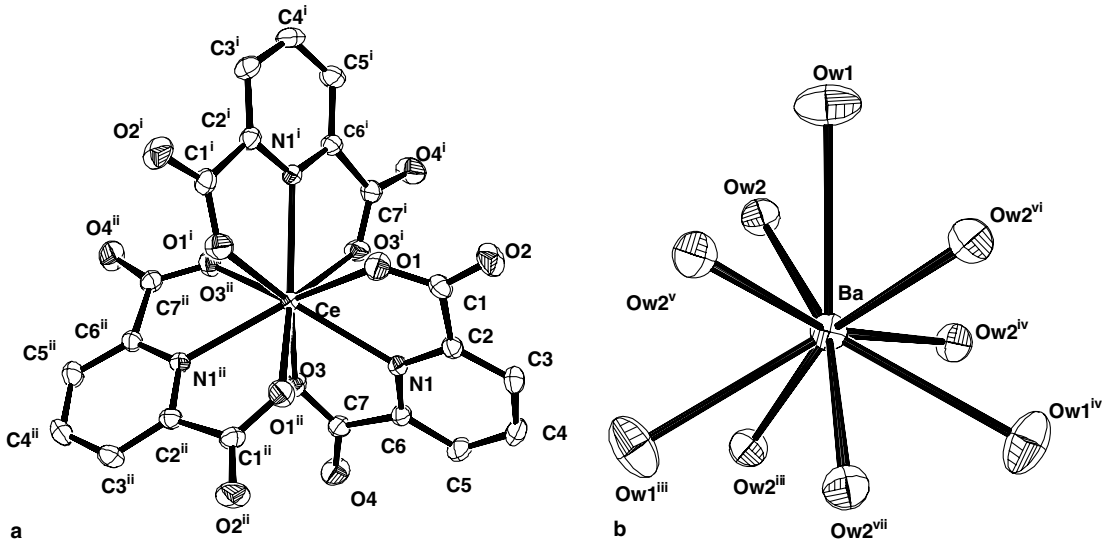


Fig. 3. ORTEP view of the coordination environment of (a) Ce^{4+} and (b) Ba^{2+} in **2**. Symmetry code: (i) $-x + y + 1, -x + 1, z$; (ii) $-y + 1, x - y, z$; (iii) $-x + y + 1, -x + 2, z$; (iv) $-y + 2, x - y + 1, z$; (v) $-x + 2, -x + y + 1, z + 1/2$; (vi) $x - y + 1, -y + 2, z + 1/2$; (vii) $y, x, z + 1/2$.

relate the precipitate obtained to the crystalline compounds as well as to establish that the X-rayed single crystal represents the bulk sample, the experimental powder diffractograms were compared with diffractograms calculated [17] based on the crystal structures.

Prolonged stirring of the initial methanol–water solution produces a precipitate, which is essentially compound **2**. On the other hand, if the methanol–water solution is allowed to evaporate slowly, a pure crystalline form of **1** is obtained in good yield. The precipitate of **2** formed upon stirring the initial preparative solution, can be crystallized from hot water to yield **2** in the pure form. Much of the crystallization in this case is complete by the time the hot aqueous solution cools to room temperature. Compound **3** was obtained as a minor side product from this solution. It crystallizes only after the second crop of **2** is removed, and the solution is reduced to about

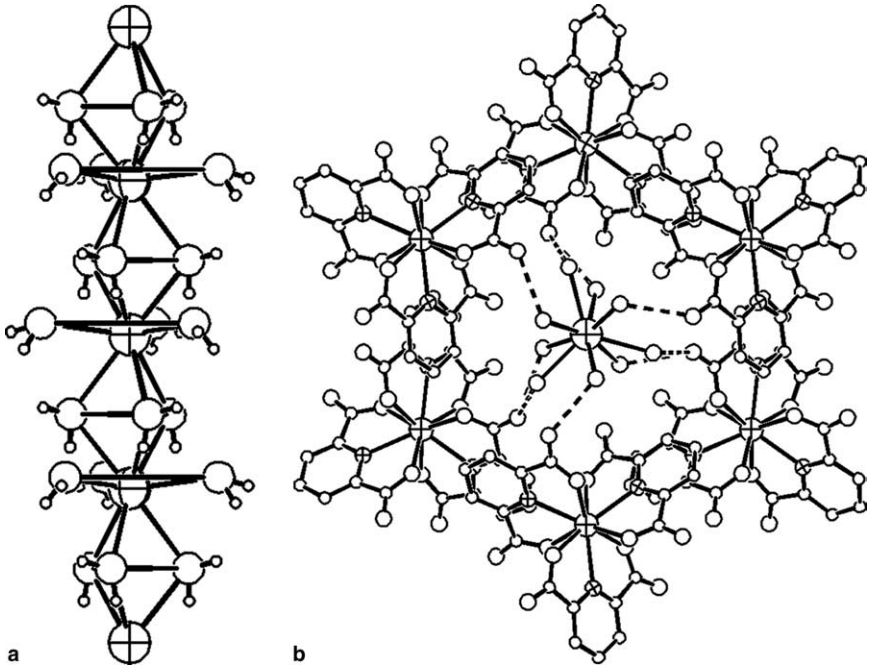


Fig. 4. (a) The polymeric chain of $Ba(OH_2)_6$ units in **2**. Ba atoms are shown as footballs. Water oxygens are represented as open circles. (b) The trigonal arrangement of $Ce(dipic)_3^{2-}$ units. The $Ba(OH_2)_6$ unit is sitting in the trigonal channel. Ba, Ce, and N atoms are shown as footballs in decreasing order of size. C and carboxylate O atoms are shown as open circles. Hydrogen bonds between carboxylate oxygens and water molecules are shown as broken lines.

5% of the initial volume. After several trials it was found that **3** could be obtained in good yield if the pH of the aqueous solution of the initial precipitate of **2** is adjusted to about 2 and the solution is refluxed for several hours, followed by slow evaporation to a small volume at room temperature. Taking into account the loss of material during filtration, the conversion of **2** to **3** is nearly quantitative when done in the above manner. The reverse transformation of **3** to **2** was not observed. Repeated recrystallization of **3** from water even with pH adjustment always produced only crystals of **3**. Crystals of **1** and **3** tend to slowly lose the water of hydration on keeping, this efflorescent nature being mainly responsible for the discrepancy in the elemental analysis values.

3.2. Structure of $Ba(dipicH_2)(OH_2)_4Ce(dipic)_3 \cdot 4.6H_2O$ (1)

The structure of **1** is similar to that observed in the previously reported $Ce(dipic)_3Ca(dipicH_2)(OH_2)_3 \cdot 5H_2O$ [5b] and $Ce(dipic)_3Sr(dipicH_2)(OH_2)_3 \cdot 6H_2O$ [5c]. The coordination around Ce^{4+} and Ba^{2+} is shown in Fig. 1. Both Ce^{4+} and Ba^{2+} are nine-coordinate with distorted tricapped trigonal prismatic coordination geometries. The Ba^{2+} coordination polyhedron is made up of one

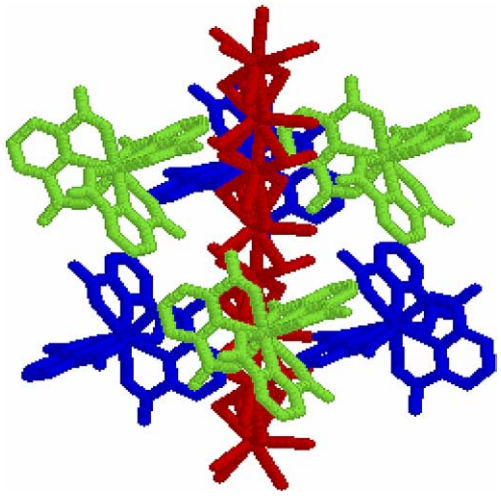


Fig. 5. Stick representation of **2** showing the polymer chain of $Ba(H_2O)_6^{2+}$ passing through the trigonal channels of $Ce(dipic)_3^{2-}$.

$dipicH_2$, four water molecules and two bridging carboxylate oxygen atoms from neighboring Ce^{4+} units. The resulting structure is a one-dimensional chain of alternating nine coordinate Ce^{4+} and nine coordinate Ba^{2+} polyhedra (Fig. 2). Along the chain, the Ce···Ba

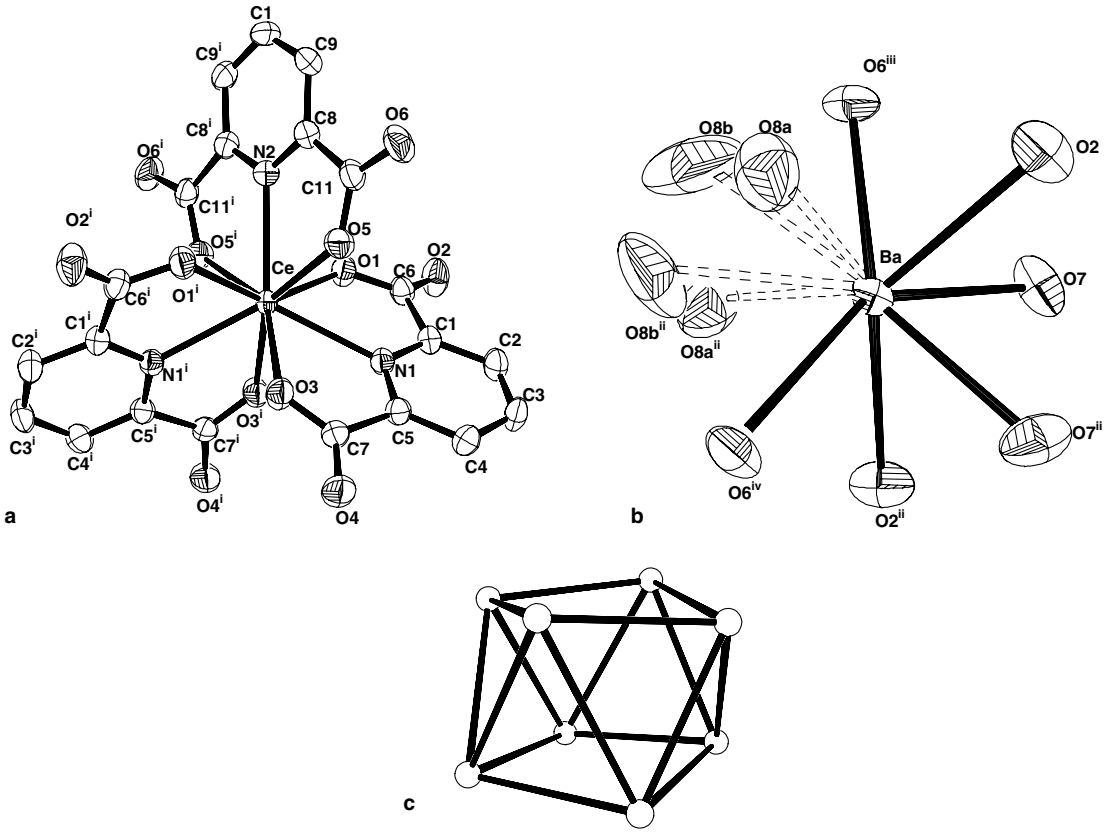


Fig. 6. ORTEP view of the coordination environment of (a) Ce^{4+}, (b) Ba^{2+} and polyhedral drawing (c) showing the distorted square antiprismatic geometry around Ba^{2+} in **3**. In (b), bonds to disordered atoms are indicated by broken lines. In (c), only the major component of the disordered atom (O8) is included. Symmetry code: (i) $-x + 3/2$, y, $-z + 1/2$; (ii) $x - 1/2$, $-y + 1$, $z + 1/2$; (iii) $-x + 2$, $-y + 1$, $-z + 1$; (iv) $-x + 3/2$, y, $-z + 3/2$.

distances alternate between 6.509(3) and 7.027(4) Å. Selected bond lengths and angles are in Table 2.

3.3. Structure of $Ba(OH_2)_6Ce(dipic)_3$ (2)

The structure of **2** is rather different from that of **1**. While the Ce coordination environment (Fig. 3(a)) is the same as that observed in **1**, the Ba coordination environment is made up of water molecules only (Fig. 3(b)). Ce^{4+} is situated on a threefold axis and is coordinated to three symmetry related ligands, resulting in a distorted tricapped trigonal prismatic coordination as observed in **1**. Ba^{2+} is also situated on a threefold axis and coordinated to nine water molecules, again with a tricapped trigonal prismatic geometry. Among the nine water molecules, three lie in the basal plane and the other six are shared with neighboring Ba^{2+} units lying above and below the basal plane, forming a chain (Fig. 4(a)). Ba–O distances (Table 3) are slightly longer (about 0.1 Å) than the distances in **1**. In the crystal, the $Ce(dipic)_3^{2-}$ units pack in a trigonal fashion (Fig. 4(b)). The $Ba(H_2O)_6^{2+}$ polymer chain passes through the trigonal channels created by the anionic units (Fig. 5). Along the chain, the Ba atoms are separated by 9.189(1) Å. The coordinated water molecules are involved in hydrogen bonding with the carboxylate O atoms of the $Ce(dipic)_3^{2-}$ units, with H···O distances in the range 1.7–2.6 Å. The polymer chain of $Ba(H_2O)_6^{2+}$ is similar to the polymer chain structure observed in $SrCl_2 \cdot 6H_2O$ [18]. This type of chain structure is observed in all the hexahydrates of Ca and Sr halides. However, such a hydrate is not known for $BaCl_2$, while $BaI_2 \cdot 6H_2O$ [18a] shows the same structure as the other hexahydrates mentioned above.

3.4. Structure of $Ba(OH_2)_4Ce(dipic)_3 \cdot 2H_2O$ (3)

In **3** also, the coordination of Ce^{4+} is the same as observed in the above two cases. The coordination environments around Ce^{4+} and Ba^{2+} are shown in Fig. 6. As opposed to the above two cases, here Ba^{2+} is eight coordinate. The coordination polyhedron in the present case consists of four water molecules and four carboxylate oxygens from neighboring $Ce(dipic)_3^{2-}$ units, giving a distorted square antiprismatic geometry (Fig. 6(c)). The Ce–O, N and Ba–O distances (Table 4) are similar to those observed in **1** and **2**. If one looks at only the arrangement of Ce and Ba atoms, each Ce is found to be surrounded by four Ba units. All the five atoms are arranged in a square pyramidal geometry with Ce at the apex and the four Ba atoms in the basal plane. The Ce deviates by 2.72 Å from the mean plane defined by its surrounding Ba atoms. Similarly, each Ba is surrounded by four Ce atoms in a distorted tetrahedral fashion. This type of coordination around Ce and Ba units, gives rise to a corrugated sheet structure (Fig. 7). These sheets assemble as layers in the crystal. The water molecules are involved in strong hydrogen bonding with the carboxylate oxygens, the H···O distances lying in the range 1.9–2.5 Å, and connect the layers. Two different

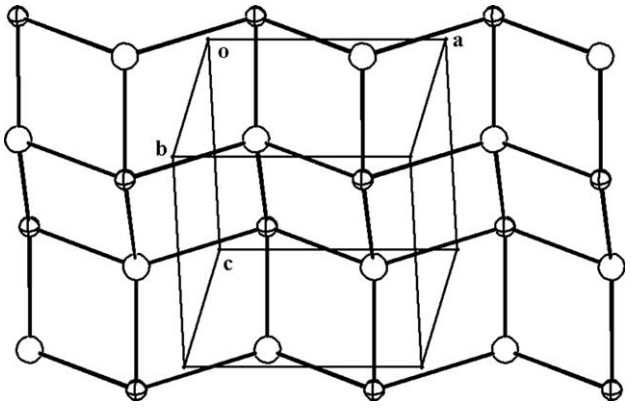


Fig. 7. Corrugated sheet structure made of Ce and Ba atoms in **3**. Footballs represent Ce atoms and open circles Ba atoms.

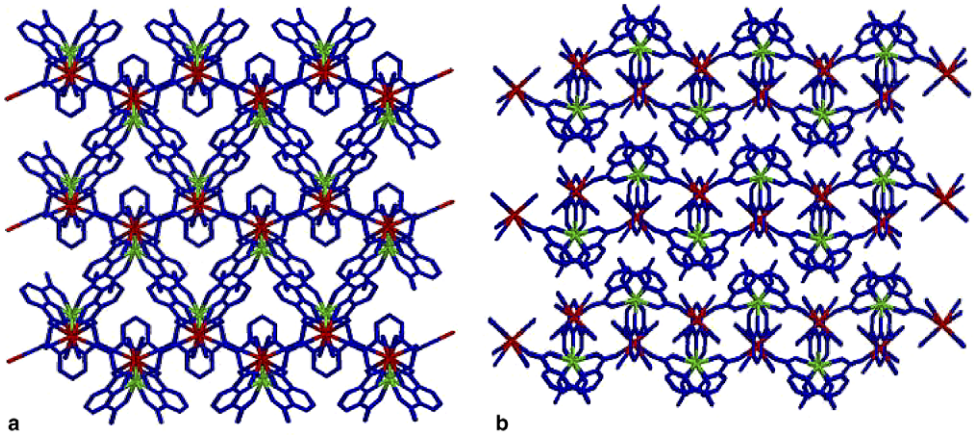


Fig. 8. Different views of the packing in **3**: (a) *ab* plane; (b) *bc* plane.

views of the packing of the cationic and anionic units in the crystal are shown in Fig. 8.

The layer structure observed in the present case may be related to the (4,4) nets of the AX type, seen in the structure of PbO [19]. In the red form of PbO (as well as one polymorph of SnO), the Pb (Sn) atoms are at the apex of a square pyramid with the O atoms forming the base of the pyramid while the O atoms are tetrahedrally surrounded by Pb (Sn) atoms forming AX type layers with A = O and X = Pb (Sn). In the present structure, A and X stand for Ba and Ce coordination polyhedra, respectively.

4. Conclusions

(i) The formation of **1** from methanol–water solution is in keeping with the previous observation with Ce–Ca–dipicH_2 and Ce–Sr–dipicH_2 systems [5b,c]. All the three structures consist of 1-D coordination polymers with alternating Ce and alkaline earth polyhedra. The only difference is that the Ba in **1** is nine-coordinate while Ca and Sr were eight-coordinate. However structures analogous to **2** and **3** were not obtained in the case of Ca and Sr. These differences have to do with the relative size of the cations. Ba^{2+}, being larger than Ce^{4+}, can expand its coordination shell to accommodate 9 or even 10 oxygen ligands.

(ii) The Ce–Ba–dipicH_2 system is delicately balanced with regard to the formation of different polymeric compounds, which are stoichiometrically very similar but structurally very different. The two polymorphs, **2** and **3**, form entirely different network structures.

(iii) Conversion of **2** to **3** is dependent on the pH and thermal aging of the crystallization solution. The fact that the prolonged boiling of the pH adjusted solution of **2** is necessary to crystallize it out as **3** probably means that the oligomeric precursors of the layered structure of **3** are already formed in the boiling solution. It is remarkable that the reverse transformation of **3** to **2** in aqueous solution is not observed.

(iv) **2** and **3** are metal organic analogs of $SrCl_2 \cdot 6H_2O$ and PbO, respectively. This comparison greatly helps in understanding the network in **3**.

(v) Finally, it is to be noted that only a handful of structures are known for alkaline earth–rare earth heteronuclear coordination polymers [5] and clusters [20]. Since alkaline earth ions are optically and magnetically silent, they have the potential to be used as ''binders' for assembling networks of rare earth ions with characteristic solid state properties. The present study shows that multiple networks may be produced from a given set of starting materials by varying the crystallization conditions.

5. Supplementary material

The crystal structure data of complexes **1**, **2** and **3** have been deposited at the Cambridge Crystallographic Data Centre and allocated the deposition numbers CCDC 253800 for **1**, CCDC 253801 for **2** and CCDC 253802 for **3**. Copies of this information can be obtained free of charge from The Director, CCDC, 12 Union Road, Cambridge, CB2 IEZ, UK, fax: +44 1223 336 033, e-mail: deposit@ccdc.cam.ac.uk or on the web http://www.ccdc.cam.ac.uk.

Acknowledgments

We thank a referee for helpful comments on the refinement of the structure of compound **3**. We thank the DST (India) for the X-ray diffractometer facility and the UGC (India) for infra-structural support (UPE program). This work was supported by CSIR, India. T.K.P. and S.S. thank the CSIR for award of research fellowships.

References

[1] (a) C.-T. Chen, K.S. Suslick, Coord. Chem. Rev. 128 (1993) 293;
(b) L. Brunsveld, B.J.B. Folmer, E.W. Meijer, R.P. Sijbesma, Chem. Rev. 101 (2001) 4071.

[2] See for example, S.A. Bourne, J. Lu, A. Mondal, B. Moulton, M.J. Zaworotko, Angew. Chem. Int. Ed. 40 (2001) 2111.

[3] (a) L. Ma, O.R. Evans, B.M. Foxman, W. Lin, Inorg. Chem. 38 (1999) 5837;
(b) X.-J. Zheng, L.-P. Jin, S.-Z. Lu, Eur. J. Inorg. Chem. 12 (2002) 3356;
(c) Y. Wan, L. Jin, K. Wang, L. Zhang, X. Zheng, S. Lu, New J. Chem. 26 (2002) 1590;
(d) S.J. Dalgarno, C.L. Raston, Chem. Commun. (2002) 2216;
(e) Z. Wang, C.-M. Jin, T. Shao, Y.-Z. Li, K.-L. Zhang, H.-T. Zhang, X.-Z. You, Inorg. Chem. Commun. 5 (2002) 642;
(f) A. Thirumurugan, S.K. Pati, M.A. Green, S. Natarajan, J. Mater. Chem. 13 (2003) 2937;
(g) Y.-H. Wan, L.-P. Zhang, L.-P. Jin, J. Mol. Struct. 658 (2003) 253;
(h) Y. Wan, L. Zhang, L. Jin, S. Gao, S. Lu, Inorg. Chem. 42 (2003) 4985;
(i) H.T. Xu, N.W. Zheng, X.L. Jin, R.Y. Yang, Z.Q. Li, J. Mol. Struct. 654 (2003) 183;
(j) Y.-H. Wan, L.-P. Jin, K.-Z. Wang, J. Mol. Struct. 649 (2003) 85;
(k) S.J. Dalgarno, M.J. Hardie, J.L. Atwood, C.L. Raston, Inorg. Chem. 43 (2004) 6351;
(l) S. Neogi, G. Savitha, P.K. Bharadwaj, Inorg. Chem. 43 (2004) 3771;
(m) C. Serre, N. Stock, T. Bein, G. Ferey, Inorg. Chem. 43 (2004) 3159;

(n) M. Dan, J.N. Behera, C.N.R. Rao, J. Mater. Chem. 14 (2004) 1257;
(o) Z. Spichal, M. Necas, J. Pinkas, J. Novosad, Inorg. Chem. 43 (2004) 2776;
(p) W.-J. Lu, L.-P. Zhang, H.-S. Chan, T.-L. Chan, T.C.W. Mak, Polyhedron 23 (2004) 1089;
(q) Y.-F. Zhou, F.-L. Jiang, Y. Xu, R. Cao, M.-C. Hong, J. Mol. Struct. 691 (2004) 191;
(r) Z. Liu, D. Zhang, C. Liu, D. Zhu, Chem. Lett. 33 (2004) 180;
(s) A. Thirumurugan, S. Natarajan, Inorg. Chem. Commun. 7 (2004) 395;
(t) S.J. Dalgarno, M.J. Hardie, C.L. Raston, Cryst. Growth Des. 4 (2004) 227;
(u) J.-Y. Niu, M.-L. Wei, J.-P. Wang, D.-B. Dang, Eur. J. Inorg. Chem. 1 (2004) 160.

[4] (a) R. Murugavel, K. Baheti, G. Anantharaman, Inorg. Chem. 40 (2001) 6870;
(b) L. Pan, T. Frydel, M.B. Sander, X. Huang, J. Li, Inorg. Chem. 40 (2001) 1271;
(c) D.A. Lenev, K.A. Lyssenko, R.G. Kostyanovsky, Eur. J. Inorg. Chem. 16 (2003) 2979;
(d) B.H. Hamilton, K.A. Kelly, W. Malasi, C.J. Ziegler, Inorg. Chem. 42 (2003) 3067;
(e) M.L.G. Salido, P.A. Mascaros, R.L. Garzon, M.D.G. Valero, J.N. Low, J.F. Gallagher, C. Glidewell, Acta Crystallogr., Sect. B 60 (2004) 46.

[5] (a) C.K. Schaver, O.P. Anderson, J. Chem. Soc., Dalton Trans. (1989) 185;
(b) G. Swarnabala, M.V. Rajasekharan, Inorg. Chem. 37 (1998) 1483;
(c) S. Sailaja, M.V. Rajasekharan, Acta Crystallogr., Sect. E 57 (2001) m341;
(d) B.D. Chandler, A.P. Cote, D.T. Cramb, J.M. Hill, G.K.H. Shimzu, Chem. Commun. (2002) 1900.

[6] Y.-B. Dong, M.D. Smith, H.-C.Z. Loye, Inorg. Chem. 39 (2000) 1943.

[7] (a) J. Albertsson, Acta Chem. Scand. 24 (1970) 1213;
(b) J. Albertsson, Acta Chem. Scand. 26 (1972) 985;
(c) J. Albertsson, Acta Chem. Scand. 26 (1972) 1005;
(d) J. Albertsson, Acta Chem. Scand. 26 (1972) 1023.

[8] D.M.L. Goodgame, T.E. Müller, D.J. Williams, Polyhedron 11 (1992) 1513.

[9] B. Zhao, P. Cheng, Y. Dai, C. Cheng, D.-Z. Liao, S.-P. Yan, Z.-H. Jiang, G.-L. Wang, Angew. Chem. Int. Ed. 42 (2003) 934.

[10] B. Zhao, P. Cheng, X. Chen, C. Cheng, W. Shi, D. Liao, S. Yan, Z. Jiang, J. Am. Chem. Soc. 126 (2004) 3012.

[11] S.R. Hall, G.S.D. King, J.M. Stewart, XTAL 3.4, University of Western Australia, Perth, Australia, 1995.

[12] N. Walker, D. Stuart, Acta Crystallogr., Sect. A 39 (1983) 153.

[13] A.C.T. North, D.C. Phillips, F.S. Mathews, Acta Crystallogr., Sect. A 24 (1968) 351.

[14] G.M. Sheldrick, SHELXS-97 and SHELXL-97, University of Gottingen, Gottingen, Germany, 1997.

[15] M.N. Burnett, C.K. Johnson, ORTEP-III, Oak Ridge Thermal Ellipsoid Plot Program for Crystal Structure Illustrations, Oak Ridge National Laboratory Report ORNL-6895, Oak Ridge, USA, 1996.

[16] R. Sayle, E.J. Milner-White, Trends Biochem. Sci. 20 (1995) 374.

[17] W. Kraus, G. Nolze, Powder Cell for WINDOWS Version 2.3, Federal Institute Materials Research and Testing, Berlin, Germany, 1999.

[18] (a) A.F. Wells, Structural Inorganic Chemistry, 4th ed., Oxford University Press, Oxford, UK, 1979, pp. 556;
(b) R.B. English, L.R. Nassimbeni, Acta Crystallogr., Sect. C 40 (1984) 580.

[19] A.F. Wells, Structural Inorganic Chemistry, 4th ed., Oxford University Press, Oxford, UK, 1979, pp. 110.

[20] (a) P. Starynowicz, Acta Crystallogr., Sect. C 47 (1991) 32;
(b) W. Wu, M. Chen, P. Zhou, Organometallics 10 (1991) 98;
(c) C. Sun, G. Wei, Z. Jin, W. Chen, J. Organomet. Chem. 453 (1993) 61;
(d) L.G. Hubert-Pfalzgraf, C. Sirio, C. Bois, Polyhedron 17 (1998) 821;
(e) J. Lin, Z. Wang, J. Organomet. Chem. 589 (1999) 127;
(f) W.J. Evans, D.G. Giarikos, M.A. Greci, J.W. Ziller, Eur. J. Inorg. Chem. 2 (2002) 453.

obtained on a DuPon TGA 2050. Differential scanning calorimetry (DSC) measurements were carried on a DuPon DSC Q-10.

2.2. Starting materials

The reagents $Cu(OAc)_2\cdot H_2O$ and $CuSO_4\cdot 5H_2O$ were purchased from Merck Co. and used as received. The ligands 1,2-bis(4-pyridyl)ethane (bpa) and *trans*-bis-(4-pyridyl)ethene (bpen) were purchased from Aldrich Chemical Co. and also used as received.

2.3. Preparation of $[Cu_2(OAc)_4(bpa)\cdot 2H_2O]_n$ (**1**)

$Cu(OAc)_2\cdot H_2O$ (0.40 g, 2 mmol) and bpa (0.18 g, 1 mmol) were placed in a flask containing 10 ml CH_3OH. The mixture was stirred at room temperature for 30 min to yield a blue-green precipitate. The blue-green solid was then filtered off and washed with CH_3OH and then dried under vacuum. Yield: 0.47 g (82%). *Anal.* Calc. for $C_{20}H_{28}Cu_2N_2O_{10}$: C, 41.16; H, 4.83; N, 4.80. Found: C, 41.09; H, 4.85; N, 4.76%. IR (KBr disk): 3177(br), 1616(m), 1558(m), 1418(m), 1225(s), 1074(s), 1032(s), 833(s), 682(s), 548(s), 418(s). Crystals suitable for X-ray diffraction were grown by layering a H_2O solution of $Cu(OAc)_2\cdot H_2O$ with bpa in CH_3OH for several weeks.

2.4. Preparation of $[Cu(bpen)(H_2O)_3(SO_4)\cdot 4H_2O]_n$ (**2**)

$CuSO_4\cdot 5H_2O$ (0.25 g, 1 mmol) and bpen (0.18 g, 1 mmol) were placed in a flask containing 10 ml CH_3OH. The mixture was stirred at room temperature for 30 min to yield a blue precipitate. The blue solid was then filtered off and washed with CH_3OH and then dried under vacuum. Yield for **2**: 0.34 g (79%). *Anal.* Calc. for $C_{12}H_{24}CuN_2O_{11}S$: C, 30.80; H, 5.17; N, 5.98. Found: C, 30.51; H, 5.29; N, 5.70%. IR (KBr disk): 3246(br), 1614(m), 1509(m), 1430(m), 1300(s), 1099(m), 1026(m), 981(m), 839(m), 618(m), 560(s). Blue crystals suitable for X-ray diffraction were grown by layering a H_2O solution of $CuSO_4\cdot 5H_2O$ with bpen in CH_3OH for 3 days.

3. X-ray crystallography

The diffraction data for complexes **1** and **2** were collected at 25 °C on a Bruker AXS P4 diffractometer,

Table 1
Crystal data for **1** and **2**

	1	**2**
Formula	$C_{20}H_{28}Cu_2N_2O_{10}$	$C_{12}H_{24}CuN_2O_{11}S$
F_w	583.52	467.93
Crystal system	monoclinic	monoclinic
Space group	$C2/c$	$P2_1/c$
a (Å)	24.95(2)	7.3681(9)
b (Å)	13.180(6)	11.329(2)
c (Å)	8.714(7)	23.190(7)
β (°)	90.38(7)	91.51(1)
V (Å^3)	2857(3)	1935.0(7)
Z	4	4
d_{calc} (g/cm^3)	1.357	1.606
F(000)	1200	972
Crystal size (mm)	$0.2\times 0.6\times 0.2$	$0.1\times 0.6\times 0.4$
μ(Mo Kα) (mm^{-1})	1.536	1.294
Data collection instrument	Bruker AXS P4	Bruker AXS P4
Radiation monochromated in incident beam (λ(Mo Kα), Å)	0.71073	0.71073
Range (2θ) for data collection (°)	$5.64 \leqslant 2\theta \leqslant 50.08$	$3.54 \leqslant 2\theta \leqslant 50.00$
Limiting indices	$-29 \leqslant h \leqslant 1$, $-1 \leqslant k \leqslant 15$, $-10 \leqslant l \leqslant 10$	$-1 \leqslant h \leqslant 8$, $-1 \leqslant k \leqslant 13$, $-27 \leqslant l \leqslant 27$
Reflections collected	2896	4703
Independent reflections [R_{int}]	2479 [0.0730]	3397 [0.0224]
Refinement method	full-matrix least-squares on F^2	full-matrix least-squares on F^2
Data/restraints/parameters	2479/0/158	3397/0/248
Quality-of-fit indicator[c]	1.060	1.025
Final R indices [$I > 2\sigma(I)$][a,b]	$R_1 = 0.0765$, $wR_2 = 0.1823$	$R_1 = 0.0459$, $wR_2 = 0.1321$
R indices (all data)	$R_1 = 0.1366$, $wR_2 = 0.2473$	$R_1 = 0.0538$, $wR_2 = 0.1392$
Largest differential peak and hole (e/Å^3)	1.259 and −2.217	1.020 and −0.655

[a] $R_1 = \sum\|F_o| - |F_c\|/\sum|F_o|$.

[b] $wR_2 = [\sum w(F_o^2 - F_c^2)^2/\sum w(F_o^2)^2]^{1/2}$. $w = 1/[\sigma^2(F_o^2) + (ap)^2 + (bp)]$, $p = [\max(F_o^2 \text{ or } 0) + 2(F_c^2)]/3$. $a = 0.0909$, $b = 53.3855$ for **1**; $a = 0.0811$, $b = 3.999$ for **2**.

[c] Quality-of-fit $= [\sum w(|F_o^2| - |F_c^2|)^2/(N_{observed} - N_{parameters})]^{1/2}$.

which was equipped with graphite-monochromated Mo Kα ($\lambda\alpha$ = 0.71073 Å) radiation. Data reduction was carried out by standard methods with the use of well-established computational procedures [6]. The structure factors were obtained after Lorentz and polarization correction. The positions of some of the heavier atoms, including the copper atom, were located by the direct methods. The remaining atoms were found in a series of alternating difference Fourier maps and least-square refinements [7]. The hydrogen atoms were placed at calculated positions and fixed as riding models during the least-square refinements, and the C–H···π distances were calculated based on the default SHELX C–H bond distances. The final residuals of the final refinement were $R_1 = 0.0765$, $wR_2 = 0.1823$ for **1**. The crystallographic procedures for **2** were similar to those for **1** and the final residuals of the final refinement were $R_1 = 0.0459$, $wR_2 = 0.1321$ for **2**. Basic information pertaining to crystal parameters and structure refinement is summarized in Table 1.

4. Results and discussion

4.1. Synthesis and spectroscopic studies

The complex $[Cu_2(OAc)_4(bpa)\cdot 2H_2O]_n$ (**1**) (bpa = 1,2-bis(4-pyridyl)ethane) was prepared by reaction of $Cu(OAc)_2\cdot H_2O$ with bpa in methanol, while the complex $[Cu(bpen)(H_2O)_3(SO_4)\cdot 4H_2O]_n$ (bpen = *trans*-bis(4-pyridyl)ethene) (**2**) was prepared by reaction of $CuSO_4\cdot 5H_2O$ with bpen in methanol. Their structures have been determined by spectroscopic methods and by X-ray crystallography. The IR spectrum for **1** displays the characteristic bands of the acetate anions at 1616 cm^{-1} for $\nu_{asym(COO)}$, 1418 cm^{-1} for $\nu_{sym(COO)}$ and 682 cm^{-1} for $\delta_{(OCO)}$. The difference between $\nu_{asym(COO)}$ and $\nu_{sym(COO)}$ ($\Delta\nu$) is 198 cm^{-1}, indicating that the acetate groups, which are coordinated to the metal ions in a symmetrical bridging mode (*syn*,*syn*-η^1:η^1:μ_2), are in agreement with the paddle-wheel type structures [8].

4.2. Structure of $[Cu_2(OAc)_4(bpa)\cdot 2H_2O]_n$

The structure of **1** was solved in the space group *C*2/*c*. Fig. 1(a) shows the local coordination of the copper center in **1**. Selected bond distances and angles are listed in Table 2. The copper metal center adopts a slightly distorted square pyramidal coordination geometry with the bond angles only deviating slightly from 90° or 180° (Table 2). The Cu(II) atom is bonded to four oxygen atoms of the bridging carboxylate groups (Cu–O = 1.941(6)–1.960(6) Å) in the basal plane. The Cu(II) atom is also bonded to one bpa ligand (Cu–N = 2.169(6) Å) in the axial position to complete the distorted square-pyramidal coordination geometry.

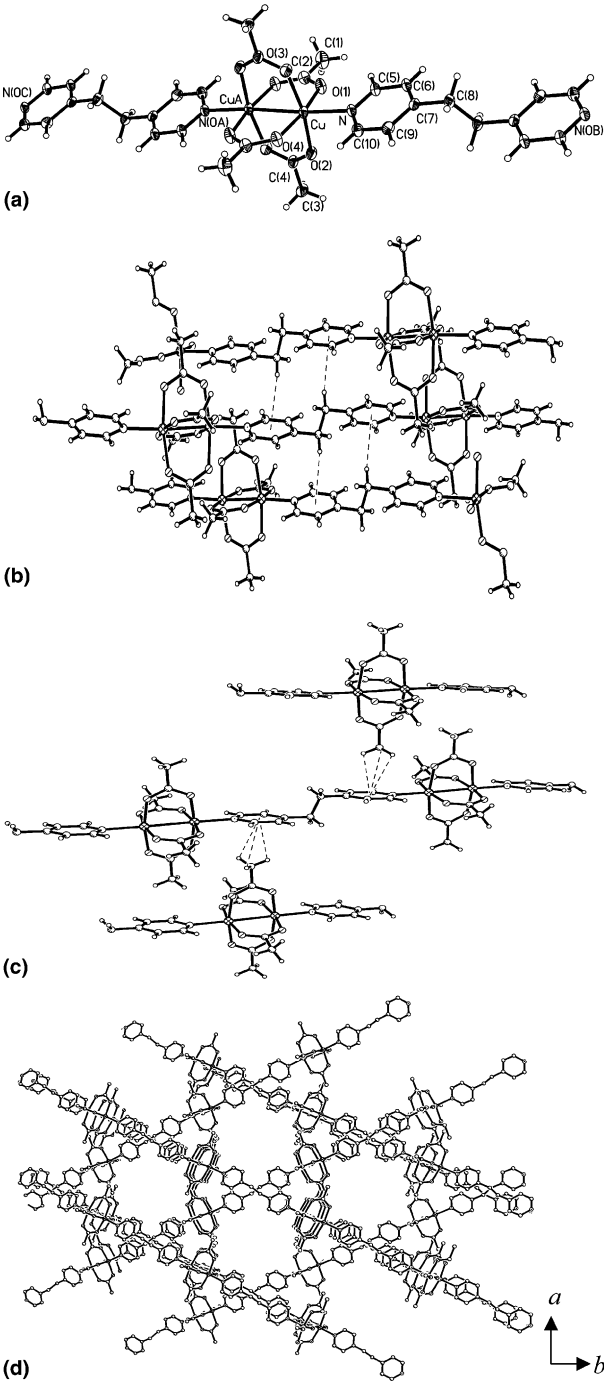


Fig. 1. (a) An ORTEP drawing showing the local coordination of Cu in **1**. (b) An ORTEP drawing showing C–H···π interactions from the methylene hydrogen atoms of the bpa ligand to the center of the pyridyl ring of the other chain. (c) An ORTEP drawing showing C–H···π interactions from the alkyl hydrogen atoms of the acetate ligand to the center of the pyridyl ring of the other chain. (d) An ORTEP drawing showing infinite 1-D chains for **1**, which are interlinked through C–H···π interactions looking down the *c*-axis. Hydrogen atoms are omitted for clarity.

The Cu···Cu separation in the $Cu_2(OAc)_4$ core is 2.605(3) Å while that in the molecular chain separated by the bridging bpa is 13.477 Å. The bpa ligand in

complex **1** adopts an *anti*-conformation with a dihedral angle of −180° (C7–C8–C8B–C7B). Two types of C–H···π interactions were found in the structure. The first one is from the methylene hydrogen atoms of the bpa ligand to the center of the pyridyl ring of the other chain (2.942 Å), Fig. 1(b), while the other is from the methyl hydrogen atoms of the acetate ligands to the center of the pyridyl ring of the other chain (3.025–3.436 Å), Fig. 1(c). It is noted that the C–H···π interactions to the methylene hydrogen atoms appear to link chains that cross each other, whereas those to the methyl hydrogen atoms of the acetate ligands involve parallel chains. The most striking feature in complex **1** is that the molecular chains are interlinked through these C–H···π interactions to form a porous structure, Fig. 1(d). It is seen that the molecular chains are packed in an AB fashion, where the molecular chains in the A layer are positioned over the B layer with an angle of 63.9° to form rhombic channels. The dimensions of the rhombic pores, which are defined as the distances between the midpoints of the ligands, are 13.18 Å for the short and 26.87 Å for the long diagonal lengths. The cavities are occupied by the water molecules.

4.3. Structure of $[Cu(bpen)(H_2O)_3(SO_4)\cdot 4H_2O]_n$

The structure of **2** was solved in the space group $P2_1/c$. Fig. 2(a) shows the local coordination of the copper center in **2**, while Fig. 2(b) shows its infinite 1-D chains consisting of copper(II) ions, bpen ligands and SO_4^{2-} anions. Selected bond distances and angles are listed in Table 2. Fig. 2(b) shows that complex **2** is a coordination polymer of $[Cu(bpen)(H_2O)_3(SO_4)\cdot 4H_2O]_n$, forming a 1-D linear chain. The copper metal center adopts a slightly distorted octahedral coordination geometry with the bond angles only deviating slightly from 90° or 180° (Table 2). The Cu atom is bonded to two *trans* pyridyl nitrogen atoms (Cu–N(1) = 2.028(3) Å and Cu–N(2) = 2.031(3) Å) and two *trans* oxygen atoms of aqua molecules (Cu–O(2) = 1.969(3) Å and Cu–O(3) = 2.005(3) Å) in the equatorial plane. The Cu(II) atom is also bonded to one oxygen atom of an aqua molecule (Cu–O(1) = 2.405(3) Å) and one oxygen atom of the sulfate ligand (Cu–O(6) = 2.471(3) Å) in the axial positions to complete the distorted octahedral coordination geometry. The Cu···Cu distance in the molecular chain separated by the bridging bpen is 13.396 Å. The bidentate ligand bpen

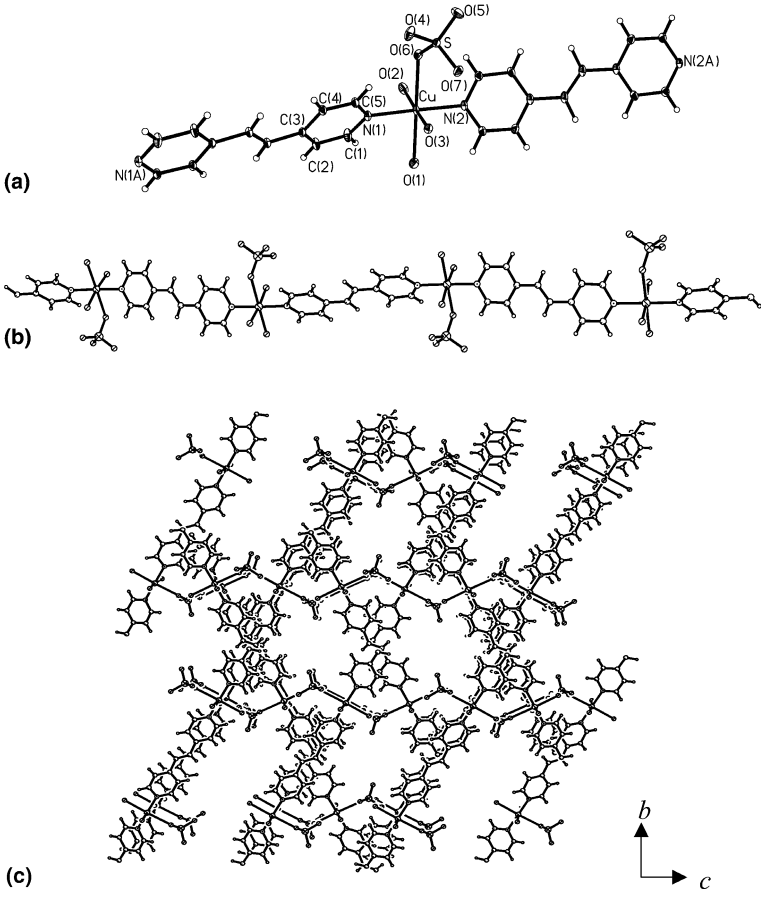


Fig. 2. (a) An ORTEP drawing showing the local coordination of Cu in **2**. (b) An ORTEP drawing showing infinite 1-D chains for **2**. (c) A view looking down the *a*-axis for complex **2**, where the infinite 1-D chains are interlinked through extensive O–H···O and C–H···O hydrogen bondings and π–π interactions to form porous structures. The water molecules which occupy the vacancies are omitted for clarity.

Table 2
Selected bond distances (Å) and angles (°) for complexes **1** and **2**

Complex ***1***	
Cu–O(4)	1.941(6)
Cu–O(1)	1.951(6)
Cu–N	2.169(6)
Cu–O(3)	1.949(6)
Cu–O(2)	1.960(6)
Cu···Cu(A)	2.605(3)
O(4)–Cu–O(3)	89.2(3)
O(3)–Cu–O(1)	89.7(3)
O(3)–Cu–O(2)	168.1(2)
O(4)–Cu–N	98.2(2)
O(1)–Cu–N	93.6(2)
O(4)–Cu–O(1)	168.1(2)
O(4)–Cu–O(2)	88.1(3)
O(1)–Cu–O(2)	90.5(3)
O(3)–Cu–N	93.4(2)
O(2)–Cu–N	98.4(2)
Complex ***2***	
Cu–O(2)	1.969(3)
Cu–N(1)	2.028(3)
Cu–O(1)	2.405(3)
Cu–O(3)	2.005(3)
Cu–N(2)	2.031(3)
Cu–O(6)	2.471(3)
O(2)–Cu–O(3)	173.56(13)
O(3)–Cu–N(1)	87.00(12)
O(3)–Cu–N(2)	90.61(12)
O(2)–Cu–O(1)	93.91(13)
N(1)–Cu–O(1)	88.06(12)
O(6)–Cu–O(3)	176.67(12)
O(6)–Cu–N(1)	91.03(11)
O(6)–Cu–N(2)	89.28(12)
O(2)–Cu–N(1)	91.04(13)
O(2)–Cu–N(2)	91.38(13)
N(1)–Cu–N(2)	177.57(13)
O(3)–Cu–O(1)	92.15(11)
N(2)–Cu–O(1)	91.60(12)
O(2)–Cu–O(6)	89.22(11)
O(1)–Cu–O(6)	84.74(13)

Symmetry transformations used to generate equivalent atoms: (A) $-x + 3/2$, $-y + 1/2$, $-z + 2$ for **1**.

in the structure **2** is flat with a dihedral angle of 0° between the planes of the two pyridyl rings, while the dihedral angle of py–Cu–py is 51.8°.

The most striking feature in complex **2** is that the molecules are interlinked through extensive O–H···O and C–H···O hydrogen bondings and π–π interactions to form a porous structure, as shown in Fig. 2(c). It is seen that the molecular chains are also packed in an AB fashion, where the molecular chains in the A layer are positioned over the B layer with an angle of 51.3°, to form rhombic pores. The cavities are occupied by the water molecules. The dimensions of the rhombic pores, which are defined as the distances between the midpoints of the ligands, are 11.32 Å for the short and 24.15 Å for the long diagonal lengths. The H_2O molecules and SO_4^{2-} anions link the adjacent chains through extensive O–H···O and/or C–H···O hydrogen bondings. The O–H···O distances are in the range from 2.625 to 2.895 Å. The C–H···O distances are in the range from 2.435 to 2.556 Å with C–H···O angles in the range from 124.2° to 134.7°. The distance of the π–π interactions is 3.829 Å.

Complex **2** is in marked contrast to the structure of $[Cu(bpen)(H_2O)(SO_4)]_n$, which was prepared from the reaction mixture of $CuSO_4\cdot 5H_2O$, bpen and H_2O in the mole ratio 1:1:111 at 120 °C. The structure of $[Cu(bpen)(H_2O)(SO_4)]_n$ consists of 1-D $[Cu(bpen)(H_2O)]^{2+}$ cationic chains covalently bonded by the SO_4^{2-} anions to form a 3-D framework [5i].

4.4. Thermal properties

Complexes **1** and **2** are very stable in air at ambient temperature and almost insoluble in common solvents such as water, alcohol, acetonitrile, chloroform, methanol and acetone. Thermal gravimetric analyses (TGA) were carried out to examine the thermal stability of **1** and **2**. The samples were heated in air at 1 atm pressure with a heating rate of 10 °C min^{-1}. The TGA curve shows that **1** is stable up to 114 °C. A total weight loss of 6.4% occurred in the temperature range 114–223 °C, presumably due to the removal of the water molecules per formula unit (calc. 6.2%). A weight loss occurred in the temperature range 223–280 °C, corresponding to the removal of bpa ligands and decomposition of the framework. The TGA curve shows that **2** is stable up to 110 °C. A total weight loss of 47.1% occurred in the temperature range 110–278 °C, mainly corresponding to the removal of the cocrystallized and the bonded H_2O and the sulfate molecules per formula unit (calc. 47.2%). Another weight loss occurred in the temperature range 278–380 °C, consistent with the removal of bpen ligands and decomposition of the framework. Their T_m values have been measured by using differential scanning calorimetry (DSC), which are 247 and 263 °C for complexes **1** and **2**, respectively.

5. Conclusions

The synthesis and structures of two complexes $[Cu_2(OAc)_4(bpa)\cdot 2H_2O]_n$ (**1**) and $[Cu(bpen)(H_2O)_3(SO_4)\cdot 4H_2O]_n$ (**2**) have been successfully accomplished. Complexes **1** and **2** form molecular chains which are packed in AB fashions through C–H···π interactions, π–π interactions and hydrogen bondings, to form porous structures with rhombic channels. Complexes **1** and **2** make interesting comparisons with the complex $\{Cu_2(OAc)_4(bpp)\}_n$ (bpp = 1,3-bis(4-pyridyl)propane) [9]. While bpa and bpp are flexible ligands with two and three backbone carbon atoms, respectively, which can adopt several conformations, and bpen is a rigid ligand, all three ligands adopt the *anti* conformation and the related *trans* (bpen) conformation to show

similar structures with infinite channels. Weak interactions like C–H···π interactions, π–π interactions and hydrogen bondings may play an important role in the self-assembly of these types of structures.

6. Supplementary material

Crystallographic data (CIF files) for the complexes **1** and **2** have been deposited with the Cambridge Crystallographic Data Centre, CCDC Nos. 243076 and 243075. Copies of this information may be obtained free of charge from The Director, CCDC, 12 Union Road, Cambridge, CB2 1EZ, UK (fax: +44 1223 336 033; e-mail: deposit@ccdc.cam.ac.uk or www: http://www.ccdc.cam.ac.uk).

Acknowledgments

We thank the Nanya Institute of Technology and the National Science Council of the Republic of China for support.

References

[1] (a) G.R. Desiraju, Angew. Chem., Int. Ed. Engl. 34 (1995) 2311;
(b) G.R. Desiraju, Chem. Commun. (1997) 1475;
(c) J.M. Lehn, Supramolecular chemistry, VCH, Weinheim, 1995.
[2] (a) A.J. Blake, N.R. Champness, P. Hubberstey, W.-S. Li, M.A. Withersby, M. Schröder, Coord. Chem. Rev. 183 (1999) 117;
(b) S. Muthu, J.H.K. Yip, J.J. Vittal, J. Chem. Soc., Dalton Trans. (2002) 4561.
[3] (a) C.-W. Su, C.-P. Wu, J.-D. Chen, L.-S. Liou, J.-C. Wang, Inorg. Chem. Commun. 5 (2002) 215;
(b) S.-H. Liu, J.-D. Chen, L.-S. Liou, J.-C. Wang, Inorg. Chem. 40 (2001) 6499;
(c) Y.-F. Hsu, J.-D. Chen, Eur. J. Inorg. Chem. (2004) 1488.
[4] (a) Y.-B. Dong, M.D. Smith, R.C. Layland, H.-C. zur Loye, Inorg. Chem. 38 (1999) 5033;
(b) D. Visinescu, G.I. Pascu, M. Andruh, J. Magull, H.W. Roesky, Inorg. Chim. Acta 340 (2002) 201;
(c) K.N. Power, T.L. Hennigar, M.J. Zaworotko, Chem. Commun. (1998) 595;
(d) L. Carlucci, G. Ciani, D.M. Proserpio, S. Rizzato, Chem. Commun. (2001) 1198;
(e) D. Hagrman, R.C. Haushalter, J. Zubieta, Chem. Mater. 10 (1998) 361;
(f) Q.-M. Wang, G.-C. Guo, T.C.W. Mak, Chem. Commun. (1999) 1849;
(g) H.-X. Zhang, B.-S. Kang, Z.-Y. Zhou, A.S.C. Chan, Z.-N. Chen, C. Ren, J. Chem. Soc., Dalton Trans. (2001) 1664;
(h) S. Sain, T.K. Maji, G. Mostafa, T.-H. Lu, N.R. Chaudhuri, New J. Chem. 27 (2003) 185.
[5] (a) S.R. Batten, B.F. Hoskins, R. Robson, Chem. Eur. J. 6 (2000) 156;
(b) D.J. Chesnut, D. Plewak, J. Zubieta, J. Chem. Soc., Dalton Trans. (2001) 2567;
(c) S.R. Batten, A.R. Harris, P. Jensen, K.S. Murray, A. Ziebell, J. Chem. Soc., Dalton Trans. (2000) 3829;
(d) S.R. Batten, J.C. Jeffery, M.D. Ward, Inorg. Chim. Acta 292 (1999) 231;
(e) A.J. Blake, S.J. Hill, P. Hubberstey, W.-S. Li, J. Chem. Soc., Dalton Trans. (1998) 909;
(f) J.M. Knaust, S.W. Keller, Inorg. Chem. 41 (2002) 5650;
(g) A. Blake, N.R. Brooks, N.R. Champness, M. Crew, R. Hanton, P. Hubberstey, S. Parsons, M. Schröder, J. Chem. Soc., Dalton Trans. (1999) 2813;
(h) J.Y. Lu, A.M. Babb, Inorg. Chem. 40 (2001) 3261;
(i) D. Hagrman, R.P. Hammond, R.C. Haushalter, J. Zubieta, Chem. Mater. 10 (1998) 2091;
(j) A. Blake, N.R. Champness, S.S.M. Chung, W.-S. Li, M. Schröder, Chem. Commun. (1997) 1005;
(k) J.M. Knaust, S. Lopez, S.W. Keller, Inorg. Chim. Acta 324 (2001) 81;
(l) D. Visinescu, M. Andruh, A. Müller, M. Schmidtmann, Y. Journaux, Inorg. Chem. Commun. 5 (2002) 42.
[6] (a) XSCANS, Release, 2.1, Siemens Energy and Automation, Inc, Madison, WI, 1995;
(b) SMART/SAINT/ASTRO ASTRO, Release, 4.03, Siemens Energy and Automation, Inc, Madison, WI, 1995.
[7] SHELXTL 5.10. Bruker Analytical X–ray Instruments Inc., Karlsruche, Germany, 1997.
[8] M.V. Marinho, M.I. Yoshida, K.J. Guedes, K. Krambrock, A.J. Bortoluzzi, M. Hörner, F.C. Machado, W.M. Teles, Inorg. Chem. 43 (2004) 1539.
[9] W.J. Belcher, C.A. Longstaff, M.R. Neckenig, J.W. Steed, Chem. Commun. (2002) 1602.

cleave DNA in the presence of hydrogen peroxide [10].[1] Extensive literature already reports inert cationic cobalt(III) complexes with intercalating ligands (i.e., planar aromatic ligands such as 1,10-phenanthroline or those with aromatic pendant substituents) having the ability to bind to DNA and having nucleolytic ability upon activation by UV irradiation [11–15]. Although without an overall positive charge or intercalating ligand, neutral chelated amino acid complexes can still bind to DNA via hydrogen bonding and van der Waals' interactions. Here, we report additional characterization of the meridional cobalt(III) complex of β-alanine, *mer*-[Co(β-ala)$_3$], and its nuclease activity.

2. Experimental

2.1. Materials

The β-alanine and 30% aqueous H_2O_2 were purchased from Merck and Baker respectively. Ascorbic acid (H_2A), cobalt(II) chloride hexahydrate and sodium hydroxide were obtained from Fisher Scientific. Linear λ-DNA (in storage buffer: Tris–HCl, NaCl, EDTA) was obtained from Invitrogen. All compounds and reagents were used as supplied.

2.2. Physical measurements

Infrared spectra of all the compounds were recorded as KBr pellets using a Perkin–Elmer 1000 FT-IR spectrometer in the frequency range 4000–450 cm^{-1}. C, H and N microanalysis was carried out with a Perkin–Elmer 2400. The magnetic susceptibility measurement at room temperature was obtained with a Sherwood Magnetic Susceptibility Balance MSB Mk1 which was calibrated with Hg[Co(SCN)$_4$]. UV–Vis spectroscopic measurement of the aqueous solution of the complex was carried out on a Shimadzu UV-160 spectrophotometer. The electrospray ionisation mass spectrum of an aqueous solution of the complex was obtained by using a MAT LCQ bench top quadrupole ion trap mass spectrometer with a spray voltage of 4.5 kV, cone voltage of 15 V and desolvation temperature of 250 °C.

The voltammetric experiments were performed with a BAS (Bioanalytical Systems, West Lafayette, IN, USA): CV-50W electrochemical workstation. A conventional three electrode potentiostat system was used at 25 ± 2 °C with a 3 mm gold working electrode, a platinum wire (1 mm diameter) counter electrode and a Ag/Ag$^+$ reference electrode. The complex was dissolved in TN buffer pH 8.3 (TN is Tris–NaCl; Tris = Tris (hydroxymethyl)aminomethane); the resulting solution was purged with oxygen-free nitrogen gas for 15 min prior to the cyclic voltammetric measurements.

2.3. Synthesis of *mer*-[Co(β-ala)$_3$]

The purple *mer*-[Co(β-ala)$_3$] was prepared by a slight modification of a previously published procedure [16]. Slightly excess fresh cobalt(III) hydroxide was added to an aqueous solution of β-alanine and the resultant mixture was heated in a water-bath at 60 °C with continuous aeration. Unreacted cobalt(III) hydroxide was filtered, and the aeration of the dark red filtrate in the water-bath was continued to concentrate the solution. Cooling this solution initially yielded less soluble pure pink crystals. Repeated aeration with heating in the water-bath and subsequent cooling yielded different batches of products. These included mixtures of varying ratios of pink and violet crystals, and the pure purple crystals. Repeated synthesis of *mer*-[Co(β-ala)$_3$] yielded crystals suitable for X-ray diffraction. *Anal.* Calc. for $C_9H_{18}O_6N_3Co \cdot 2H_2O$: C, 30.09; H, 6.17; N, 11.70. Found: C, 30.65; H, 6.61; N, 11.58%. IR(cm^{-1}): 3398(s), 3254(s), 1609(vs), 1559(vs, doublet), 1468(w), 1409(s), 1378(m), 1319(w), 1279(m), 1214(w), 1179(w), 1147(w), 1078(w), 1031(w), 987(w), 901(m), 768(m), 698(w), 642(m).

2.4. Structure determination

X-ray data on a purple crystal of size 0.40 × 0.18 × 0.10 mm was collected at 295 K with a Bruker AXS SMART APEX area-detector diffractometer using graphite-monochromated Mo Kα radiation (λ = 0.71073 Å). SHELXS-97 and SHELXL-97 were used to solve and refine the structure [17,18]. The refinement converged at $R = 0.0973$ and $wR = 0.2726$ values for 2406 reflections $F_o > 4\sigma(F_o)$. Crystal data, selected bond lengths and angles are tabulated in Tables 1 and 2. Hydrogen bonding distances and angles are given in Table 3.

2.5. DNA cleavage studies

The electrophoresis experiments were performed on a horizontal gel electrophoresis system. Agarose gel electrophoresis experiments were carried out on linearized λ-DNA (viral; 48.5 kb). All samples in TBE buffer pH 8.3 (90 mM Tris–borate, 2.5 mM Na_2H_2EDTA) were incubated at 37 °C for 2 h, and then electrophoresed on 1% agarose gel for 2 h at 80 V. Essentially samples with an increasing concentration of complex with a given concentration of DNA (0.015 or 0.25 μg/μl) for each sample were incubated in the absence or presence of various component(s). The resultant bands for each set of

[1] Preliminary accounts of the cleavage of DNA by copper(II) complexes of glycine, L-threonine, L-proline and *N*,*N*-dimethylglycine were presented at the Malaysian Scientific and Technological Congress (Sept. 2003), Kuala Lumpur, Malaysia.

Table 1
Crystal data and structure refinement parameters for *mer*-[Co(β-ala)$_3$] · 2H$_2$O

Empirical formula	$C_9H_{22}N_3O_8Co$
Formula weight	359.23
Temperature (K)	295(2)
Wavelength (Å)	0.71073
Crystal system	monoclinic
Space group	$P2_1n$
Unit cell dimensions	
a (Å)	5.6924(4)
b (Å)	12.7041(8)
c (Å)	22.0366(14)
α (°)	90
β (°)	90.924(2)
γ (°)	90
Volume (Å^3)	1593.41(18)
Z	4
D_{calc} (Mg m^{-3})	1.497
Absorption coefficient (mm^{-1})	1.116
$F(000)$	752
Crystal color	purple
Crystal size (mm)	0.40 × 0.18 × 0.10
θ Range for data collection (°)	1.85–25.00
Index ranges	$-6 \leqslant h \leqslant 6$, $-15 \leqslant k \leqslant 15$, $-26 \leqslant l \leqslant 24$
Reflections collected/unique [R_{int}]	2791/2406 [0.0521]
Refinement method	full-matrix least-square on F^2
Data/restraint/parameters	2406/0/199
Goodness-of-fit on F^2	1.179
Final R indices [$F_o > 4\sigma(F_o)$]	$R_1 = 0.0973$, $wR_2 = 0.2726$
R indices (all data)	$R_1 = 0.1075$, $wR_2 = 0.2784$
Largest difference peak and hole (e Å^{-3})	1.19 and −0.54

experiments were photographed under UV light by using a Polaroid camera, GelCam, fixed with an electrophoresis hood.

3. Results and discussion

3.1. Structural characterization and solution properties

The crystal structure of the complex shows that it is the *mer*-isomer of tris(β-alaninato)cobalt(III), *mer*-[Co(β-ala)$_3$] (Fig. 1). One of the two water molecules in the crystal lattice shows disorder. Microanalysis results of the same sample, from which a crystal was used for crystal structure analysis, support the formulation of the complex as $Co(C_3H_6NO_2)_3 \cdot 2H_2O$. Hydrogen bonding links the complex molecules (via use of amino nitrogen protons and carboxylate oxygen atoms) and lattice water molecules into an interlinking network (Table 3). The present complex has some differences with a previously synthesized *mer*-[Co(β-ala)$_3$] which has been shown by crystal structure analysis to be the tetrahydrate [19]. Both structures show that the α-carbon and the carboxylate –COO$^-$ atoms are coplanar and this may allow partial insertion between the base pairs in the major groove of DNA. Unlike the twist-boat conformation of six-member chelate rings in *mer*-[Co(β-ala)$_3$] · 4H$_2$O [19], all the chelate rings in the present complex have a half-chair conformation with the β-carbon atom at the apex of the triangular 'flap' while the other atoms of the ring form an approximately flat seat of the chair.

Magnetic susceptibility determination of this purple needle-shaped complex shows that it is diamagnetic, confirming the starting cobalt(II) has been successfully oxidized to cobalt(III) in the final complex. The pink crystals are paramagnetic and should contain the unoxidized cobalt(II).

The purple *mer*-[Co(β-ala)$_3$] readily dissolves in water. The UV–Vis spectrum shows three bands with absorption maxima values of $\lambda_1 = 575$ nm ($\varepsilon_1 = 97$ M^{-1} cm^{-1}), with a shoulder at 500 nm, $\lambda_2 = 374$ nm ($\varepsilon_2 = 71$ M^{-1} cm^{-1}) attributed to d–d transitions, and $\lambda_3 = 245$ nm ($\varepsilon_3 = 18\,380$ M^{-1} cm^{-1}; UV region) attributed to a LMCT transition. The λ_1 and λ_2 values of the present complex agree well with those of previously synthesized *mer*-[Co(β-ala)$_3$] [λ_{max} (nm)/ε_{max} (M^{-1} cm^{-1}) values are 574/101 and 373/71, respectively [20,21].

In contrast, similar purple *mer*-isomers of [Co(gly)$_3$] (λ_1, 545 nm; λ_2, 373 nm; λ_3, 220 nm) and [Co(L-ala)$_3$] (λ_1, 540 nm; λ_2, 372 nm; λ_3, 221 nm) exhibit shorter λ_1 and λ_3 values [16]. In general, it appears that Co(α-aa)$_3$ complexes of α-amino acid ligands forming five-membered chelate rings have shorter λ_1 values (519–542 nm) than Co(β-ala)$_3$ complexes with six-membered chelate rings [20,21]. This suggests that the β-alaninate ligand interacts less strongly with the cobalt(III) and is therefore a comparatively weaker ligand than α-aminoacidates.

Dissolving the *mer*-[Co(β-ala)$_3$] complex in TN buffer pH 7 and TBE buffer pH 8.3 does not cause any shift in wavelength of the spectral bands (values in TN buffer are $\lambda_1 = 576$, $\varepsilon_1 = 82$; $\lambda_2 = 374$, $\varepsilon_2 = 59$; $\lambda_3 = 245$, $\varepsilon_3 = 16426$ while those in TBE buffer are $\lambda_1 = 576$, $\varepsilon_1 = 86$; $\lambda_2 = 375$, $\varepsilon_2 = 62$; $\lambda_3 = 245$, $\varepsilon_3 = 17483$). This suggests the species in the aqueous and buffer solutions are the same. An aqueous solution of this complex, which is kept over about two weeks, does not show appreciable change in absorbance, and this indicates its high stability in aqueous solution. A strong ESI-MS peak (positive ion mode) of m/z 323.9 (52%) shows the neutral complex species exists in aqueous solution. A full analysis of the ESI-MS spectrum shows presence of a dimer (63%), trimer (94%) and tetramer (34%), besides various β-alanine containing polymetallic complex species (Table 4). These latter species may be due to a combination of hydrogen bonding, bridging by amino acid and an aggregation process.

Analysis of the voltammogram of the complex gives the cathodic reduction peak, E_{pc}, and current, i_{pc}, as

Table 2
Selected bond distances (Å), bond angles (°) and torsion angles (°)

Bond distances (Å)	
Co(1)–O(1)	1.915(7)
Co(1)–N(1)	1.935(8)
Co(1)–O(3)	1.929(7)
Co(1)–N(2)	1.963(8)
Co(1)–O(5)	1.904(7)
Co(1)–N(3)	1.955(8)
Bond angles (°)	
O(1)–Co(1)–N(1)	94.1(3)
O(1)–Co(1)–N(2)	92.5(3)
O(1)–Co(1)–O(3)	88.3(3)
O(3)–Co(1)–N(2)	93.1(3)
O(3)–Co(1)–O(5)	90.4(3)
N(1)–Co(1)–N(2)	89.3(3)
O(5)–Co(1)–N(3)	94.7(3)
O(5)–Co(1)–O(1)	178.4(3)
N(1)–Co(1)–N(3)	93.6(3)
N(2)–Co(1)–N(3)	176.9(4)

Atoms for ligand 1[a]	Ligand 1 (N1)	Ligand 2 (N2)	Ligand 3 (N3)
Torsion angles			
N(1)–Co(1)–O(1)–C(1)	−1.7	−18.8	17.7
Co(1)–O(1)–C(1)–C(2)	11.8	11.1	−7.4
O(1)–C(1)–C(2)–C(3)	−44.3	35.5	−37.7
C(1)–C(2)–C(3)–N(1)	67.1	−70.9	69.4
C(2)–C(1)–O(1)–Co(1)	11.8	11.1	−7.4
C(3)–N(1)–Co(1)–O(1)	25.2	−16.1	15.4

Table 3
Hydrogen bonding distances and angles

D–H	Distance (Å) D–H	Distance (Å) H···A	Angle (°) D–H···A	A	Symmetry operation
O1W–H1W1	0.923	1.838	162.74	04	
O1W–H1W1	0.923	2.471	138.40	O3	
O1W–H1W2	0.734	2.039	161.31	O6	$x + 1, y, z$
02W′–H2W3	1.423	1.817	173.01	O2W	
N1–H11	0.900	2.049	154.83	O1W	$-x + 1/2, y - 1/2, -z + 1/2$
N1–H12	0.900	2.117	173.51	O2	$x - 1, y, z$
N2–H21	0.900	2.139	172.92	O2	$-x + 1, -y, -z$
N2–H22	0.900	2.378	129.56	O2	$x - 1, y, z$
N2–H22	0.900	2.418	174.03	O1	$x - 1, y, z$
N3–H31	0.900	2.165	142.27	O1W	$-x + 11/2, y - 1/2, -z + 1/2$
N3–H32	0.900	2.313	145.96	O6	$x + 1, y, z$
N3–H32	0.900	2.493	142.70	O5	$x + 1, y, z$

−680 mV and −3.375 μA. The anodic oxidation peak, E_{pa}, and current, i_{pa}, values are −567 mV and 3.375 μA, respectively. The anodic to cathodic peak separation, $\Delta E_p = E_{pa} - E_{pc}$, is 113 mV, and this indicates a quasi-reversible one-electron transfer process [22]. The half-wave potential $E_{1/2}$, taken as $(E_{pc} + E_{pa})/2$, is −624 mV, and this value is lower than those of Co^{III} hexamine complexes which range from −640 to −860 mV [23]. In the latter complexes, the six ligating atoms in the octahedral coordination sphere are nitrogen atoms. The lower reduction potential for *mer*-[Co(β-ala)$_3$] shows that it is more easily reduced. In contrast, a series of Co(III) ternary complexes, [Co(NO$_3$-L$_1$)(NO-L$_2$)], containing NO$_3$-type tripodal tetradentate ligands and NO-type bidentate α-amino acids exhibit irreversible redox waves with ΔE_p of ~1 V and E_{pc} values which ranges from −340 to −1080 mV [24]. These differences are relevant here because some cobalt(III) complexes can be reduced by ascorbic acid while others cannot, and this has been ascribed to differences in their redox potentials [25].

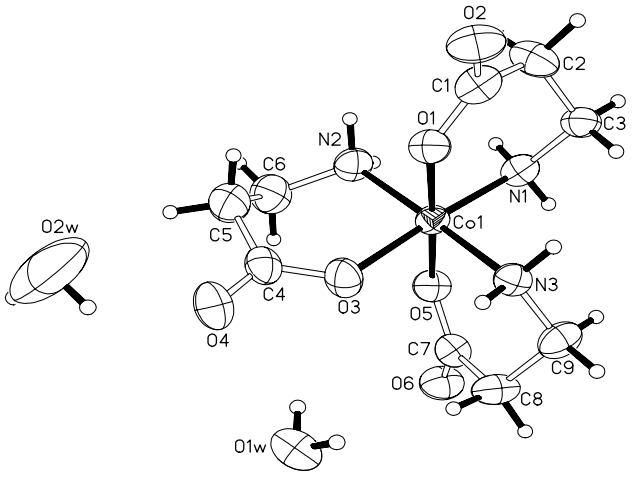


Fig. 1. Ortep plot of *mer*-[Co(β-ala)$_3$] · 2H$_2$O.

Table 4
Assignment of ESI-MS mass peaks (positive ion mode) of the complex

Relative abundance (%)	Peaks	Assignment	Calculated mass
52	323.9	Co(β-ala)$_3$ (monomer)	323.19
24	382.1	Co$_2$(β-ala)$_3$	382.12
34	468.8	Co$_2$(β-ala)$_4$	470.21
79	558.0	Co$_2$(β-ala)$_5$	558.29
24	613.7	Co$_3$(β-ala)$_5$	617.23
63	646.8	Co$_2$(β-ala)$_6$ (dimer)	646.38
31	791.8	Co$_3$(β-ala)$_7$	793.40
16	792.8	Co$_3$(β-ala)$_7$	793.40
100	880.8	Co$_3$(β-ala)$_8$	881.48
19	881.7	Co$_3$(β-ala)$_8$	881.48
94	969.7	Co$_3$(β-ala)$_9$ (trimer)	969.57
21	970.7	Co$_3$(β-ala)$_9$ (trimer)	969.57
18	1203.6	Co$_4$(β-ala)$_{11}$	1204.67
34	1292.6	Co$_4$(β-ala)$_{12}$ (tetramer)	1292.76

3.2. DNA cleavage studies

When *mer*-[Co(β-ala)$_3$] was incubated with λ-DNA in TBE buffer pH 8.3 in the presence of H$_2$O$_2$, there was no apparent degradation of the DNA (Fig. 2, lanes 5–7). However, CoCl$_2$ is a potent nuclease for DNA, cleaving it oxidatively (Fig. 2, lane 4); a recent study has shown that a low concentration of CoCl$_2$ (6 μM) has promoted selective oxidation of Z-DNA at every guanine in

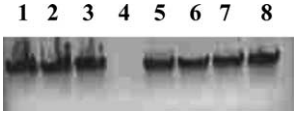


Fig. 2. Results of gel electrophoresis experiment for racemic *mer*-[Co(β-ala)$_3$] and CoCl$_2$ (4 mM) with λ-DNA (0.05 mg/μL) in the presence of 0.5 mM H$_2$O$_2$ in TBE buffer pH 8.3. Lane 1, DNA alone; lane 2, λ-DNA + H$_2$O$_2$; lane 3, λ-DNA + 4 mM complex; lane 4, λ-DNA + 4 mM CoCl$_2$ + H$_2$O$_2$; lanes 5–8, λ-DNA + H$_2$O$_2$ + increasing concentration of complex (200 μM, 2 mM, 3 mM, 4 mM respectively).

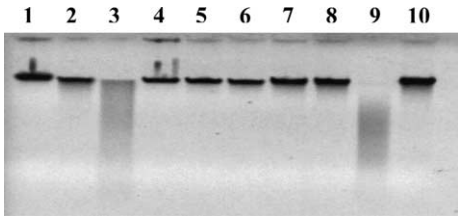


Fig. 3. Agarose gel electrophoresis banding patterns. Reaction of λ-DNA (0.5 μg/μl) with different component(s): Lane 1, λ-DNA + ascorbic acid, AsA (8 mM); lane 2, λ-DNA + H$_2$O$_2$ (2 mM) + H$_2$A (8 mM); lane 3, λ-DNA + complex (4 mM) + H$_2$A (8 mM); lane 4, λ-DNA + CoCl$_2$ (1 mM); and lane 5, λ-DNA + complex (4 mM) + H$_2$O$_2$ (2 mM). λ-DNA (0.5 μg/ml) reacted with same concentration of complex (4 mM) in the presence of 2 mM H$_2$O$_2$, TBE buffer pH 8.3 and various concentration of ascorbic acid: lane 6, H$_2$A (0.1 mM); lane 7, H$_2$A (0.5 mM); lane 8, H$_2$A (1 mM); lane 9, H$_2$A (4 mM); and lane 10, H$_2$A (6 mM).

the presence of the stronger oxidant, KHSO$_5$ [26]. This result for the present complex differs from those of bis(α-aminoacidato)copper(II) complexes, which cleave the DNA in the presence of the weaker oxidant H$_2$O$_2$ in the mM range [10].[1] In addition, it was found that a cationic ternary cobalt(II) complex, [(DOTA)Co(II)-(TPY)](ClO$_4$)2 (DOTA = 1,4,7,10-tetraza-cyclododecane which is an oligopeptide, TPY = 2,2′:6′,2″-terpyridine) binds to DNA strongly and shows anti-tumor properties [27]. In contrast, the neutral, racemic *mer*-[Co(β-ala)$_3$] apparently does not show any nucleolytic property in the absence or presence of H$_2$O$_2$ (Fig. 2, lanes 3 and 5–8) under our experimental conditions.

However when the DNA was reacted with *mer*-[Co-(β-ala)$_3$] in the presence of a reductant, ascorbic acid (H$_2$A), the complex shows high nuclease activity (Fig. 3, lane 3). The combination of this complex with H$_2$O$_2$ and ascorbic acid does not exhibit good nuclease activity except when the H$_2$O$_2$: H$_2$A mole ratio increases to 1:2 (Fig. 3, lane 9); a lower mole ratio or higher mole

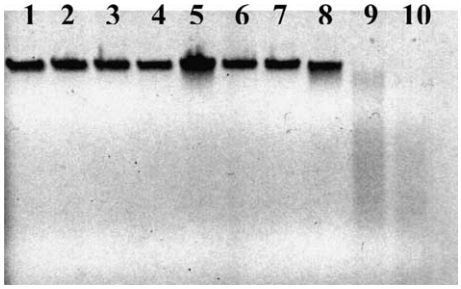


Fig. 4. Agarose gel electrophoresis results. Reactions λ-DNA (0.25 μg/μl) with different component(s) in TBE buffer pH 8.3: lane 1, DNA alone; lane 2, DNA + H$_2$O$_2$ (2 mM); lane 3, DNA + H$_2$A (8 mM); lane 4, DNA + complex (4 mM); lane 5, DNA + CoCl$_2$ (2 mM) + H$_2$A (8 mM); and lane 6, DNA + CoCl$_2$ (2 mM) + H$_2$O$_2$ (2 mM). Reactions of λ-DNA (0.25 μg/μl) with different concentrations of complex in the presence of H$_2$A (8 mM): lane 7, complex (1 mM); lane 8, complex (2 mM); lane 9, complex (3 mM); and lane 10, complex (4 mM).

ratio than this shows reduced cleavage or none. Under our experimental conditions, it is found that the complex alone or ascorbic acid alone cannot cause cleavage of DNA (Fig. 4, lanes 3 and 4). A close parallel may be drawn between this complex and the pro-cancer drugs, platinum(IV) complexes, which are activated by reduction to the platinum(II) analogues by biological reductants such as ascorbic acid and thiols [28,29]. Both the complex and ascorbic acid are required. The effect of the composition of these two reagents has been investigated. It is found that cleavage requires an ascorbic acid: complex mole ratio <4:1 (i.e., the number of moles of ascorbic acid is 2.7× and 2.0× more than that of the complex; Fig. 4, lanes 9 and 10); for mole ratios of 8:1 and 4:1 there is no apparent cleavage (Fig. 4, lanes 7 and 8). Thus, the amount of ascorbic acid required should not be excessively more than the complex, otherwise it can have an inhibitory effect. A similar effect by ascorbic acid has been previously reported where a daily intake of 50 mg afforded a protective effect in cells of people exposed to cobalt chloride [30].

The nucleolytic ability of $[Co(\beta\text{-ala})_3]$ in the presence of ascorbic acid has to result from the reduction of the complex by ascorbic acid. Substituted inert cobalt(III) complexes are known to be easily reduced by ascorbate ions, HA^- and A^{2-} [28]. This reduction can be monitored by UV–Vis spectroscopy as we have found that the absorption maxima decrease without a shift in wavelengths. Previous kinetic and mechanistic studies of the reaction of various cationic and anionic cobalt(III) complexes with ascorbic acid have revealed differences in the reductive ability of its various species, and this reductive order is $H_2A < HA^- < A^{2-}$; the ensuing redox reactions produce ascorbate free radicals [31–33]. As the present investigation involves incubating the complex with ascorbic acid in TBE buffer pH 8.3, the present cobalt(III) complex should be easily reduced by the substantial amount of the more potent ascorbate anion, A^{2-}. Thus, the nucleolytic ability of $[Co(\beta\text{-ala})_3]$ can be attributed to ascorbate free radicals. Such a role of ascorbate radicals as a DNA damaging agent has previously been acknowledged [28]. Although oxidative modification and cleavage of DNA by other free radicals have been widely reported [34,35], this is the first by a neutral cobalt(III) chelated amino acid–ascorbic acid system.

Using an MTT assay, preliminary studies revealed anti-cancer properties of $CoCl_2$ (IC_{50} = 0.06 mM), *mer*-$[Co(\beta\text{-ala})_3]$ (IC_{50} = 2.06 mM) and {*mer*-$[Co(\beta\text{-ala})_3]$ +0.20 mM H_2A system} (IC_{50} = 1.61 mM) towards lung cancer cell line PC9 [36]. The variation in anti-cancer potency parallels their nucleolytic efficiency. The order of nucleolytic efficiency is *mer*-$[Co(\beta\text{-ala})_3]$ < {*mer*-$[Co(\beta\text{-ala})_3] + H_2A$} < $CoCl_2$. These results suggest that a substance or mixture with good nucleolytic ability can be a potential anti-cancer agent.

4. Supplementary data

Full crystallographic data have been deposited with the Cambridge Crystallography Data Center, CCDC No. 248783. Copies of this data can be obtained free of charge from The Director, CCDC, 12 Union Road, Cambridge CB2 1EZ, UK, fax: +44 1223 336 033, e-mail: deposit@ccdc.cam.ac.uk. or on the www.ccdc.cam.ac.uk/conts/retrieving.html.

Acknowledgements

The authors thank Universiti Tunku Abdul Rahman, Tunku Abdul Rahman College, Universiti Putra Malaysia, Universiti Sains Malaysia and the National University of Singapore for financial assistance and use of facilities.

References

[1] D. Yang, H.-J. Andrew Wang, Prog. Biophys. Molec. Biol. 66 (1996) 81.
[2] H. Devlin, P. Geary, D. Pavanlangston, Z. Dori, E.C. Dunkel, Inv. Opthth-V 34 (1993) 1348.
[3] A. Böttcher, T. Takeuchi, M.L. Simon, T.J. Meade, H.B. Gary, J. Inorg. Biochem. 59 (1995) 221.
[4] S. Osinsky, L. Levitin, L. Bubnovskaya, A. Sigan, L. Ganusevich, V. Michailenko, A. Kovelskaya, Exp. Oncol. 22 (2000) 39.
[5] R. Tabakman, P. Lazarovici, R. Kohen, J. Neurosci. Res. 68 (2001) 463.
[6] G. Aldini, P. Granata, M. Carini, J. Mass Spec. 37 (2002) 1219.
[7] V.M. Gutiérrez-García, G. Reyes-Rangel, O. Muñoz-Muñiz, E. Juaristi, J. Braz. Chem. Soc. 12 (2001) 652.
[8] Z. Ma, Y. Zhao, N. Jian, J. Wang, Tetrahedron Lett. 43 (2002) 3209.
[9] A.E. Lurain, P.J. Walsh, J. Am. Chem. Soc. 125 (2003) 10677.
[10] C.H. Ng, H.K. Alan Ong, Y.K. Ling, K.K. Su, S.G. Teoh, S.W. Ng, submitted for publication.
[11] C.V. Sastri, D. Eswaramoorthy, L. Giribabu, B.G. Maiya, J. Inorg. Biochem. 94 (2003) 138.
[12] Q.-L. Zhang, J.-G. Liu, H. Xu, H. Li, J.-Z. Liu, H. Zhou, L.-H. Qu, L.-N. Ji, Polyhedron 20 (2001) 3049.
[13] S. Arounaguiri, D. Easwaramoorthy, A. Ashokkumar, A. Dattagupta, B.G. Maiya, Proc. Indian Acad. Sci. 112 (2000) 1.
[14] S. Moghaddas, P. Hendry, R.J. Geue, C. Qin, A.M.T. Bygott, A.M. Sargeson, N.E. Dixon, J. Chem. Soc., Dalton Trans. (2000) 2085.
[15] L. Fin, P. Yang, J. Inorg. Biochem. 68 (1997) 79.
[16] M. Mori, M. Shibata, E. Kyuno, M. Kanaya, Bull. Chem. Soc. Jpn. 34 (1961) 1837.
[17] G.M. Sheldrick, SHELXS-97, Program for Crystal Structure Solution, Göttingen University, Germany, 1997.
[18] G.M. Sheldrick, SHELXL-97, Program for Crystal Structure Refinement, Göttingen University, Germany, 1997.
[19] H. Soling, Acta Chem. Scand. A 32 (1978) 361.
[20] H. Kumita, K. Jitsukawa, H. Masuda, H. Einaga, Inorg. Chim. Acta 283 (1998) 160.
[21] Y. Yoshimura, Bull. Chem. Soc. Jpn. 75 (2002) 741.
[22] R. Abdel-Hamid, H.M. El-Sagher, A.M. Abdel-Mawgoud, A. Nafady, Polyhedron 17 (1998) 4535.

[23] B. Korybut-Daszkiewicz, J. Taraszewska, K. Zieba, K. WoŸniak, D. Kamiñski, Eur. J. Inorg. Chem. 2003 (2003) 1741.
[24] H. Kumita, K. Jitsukawa, H. Masuda, H. Einaga, Inorg. Chim. Acta 283 (1998) 160.
[25] M.B. Davies, Polyhedron 11 (1992) 285.
[26] N. Tang, J.G. Miller, C.J. Burrows, S.E. Rokita, Biochemistry 38 (1999) 16648.
[27] J. Giao, J.H. Reibenspies, A.E. Martell, J. Inorg. Biochem. 94 (2003) 272.
[28] R.N. Bose, E.L. Weaver, J. Chem. Soc., Dalton Trans. (1997) 1797.
[29] K. Lemma, A.M. Sargeson, L.J. Elding, J. Chem. Soc., Dalton Trans. (2000) 1167.
[30] G.N. L'vova, I.V. Chopikashvili, G.D. Zasukhina, Genetika 26 (1990) 1316.
[31] D.A. Dixon, T.P. Dasgupta, N.P. Sadler, J. Chem. Soc., Dalton Trans. (1997) 1903, and literature cited therein.
[32] K. Tsukahara, Y. Yamamoto, Bull. Chem. Soc. Jpn. 54 (1981) 2642.
[33] M. Kimura, M. Yamamoto, S. Yamabe, J. Chem. Soc., Dalton Trans. (1982) 423.
[34] C.J. Burrows, J.G. Muller, Chem. Rev. 98 (1998) 1109.
[35] W.K. Pogozelski, T.D. Tullius, Chem. Rev. 98 (1998) 1089.
[36] C.H. Ng, Y.T. Teong, Y.M. Lim, K.C. Lim, unpublished results.

complexes [6–14]. A novel aspect is a correlation of the magnetic anisotropy with structural distortion [15].

2. Experimental

2.1. Ligands

All chemicals were of analytical grade. The ligands were prepared according to the literature recipes [16,17]. The starting furan-2-carbaldehydes (**a**) were subjected to the Doebner condensation resulting in the corresponding acids (**b**) (Fig. 1). The acylazides were prepared by treatment of (**b**) with ethyl chloroformate and sodium azide in a one-pot reaction, and then were transformed by thermal cyclization in dowtherm with tributylamine to give the 4,5-dihydropyridines (**c**). Refluxing (**c**) with phosphorus oxychloride and then reduction of the obtained chloro-derivatives yielded furo[3,2-*c*]pyridines (**d**).

2.2. Preparation of the complexes

An ethanol solution of $NiCl_2 \cdot 6H_2O$ (0.04 mol in 100 cm^3) was combined with powdered KNCS (0.08 mol). The precipitated KCl was filtered off and 0.16 mol of the ligand (L^1 = furo[3,2-*c*]pyridine, L^2 = 2-methylfuro[3,2-*c*]pyridine, L^3 = 2,3-dimethylfuro[3,2-*c*]-pyridine, L^4 = benzo[4,5]furo[3,2-*c*]pyridine and L^5 = isoquinoline) was added to the pure solution. Small crystals were formed within 2–3 days at room temperature; these were washed with ethanol and recrystallized

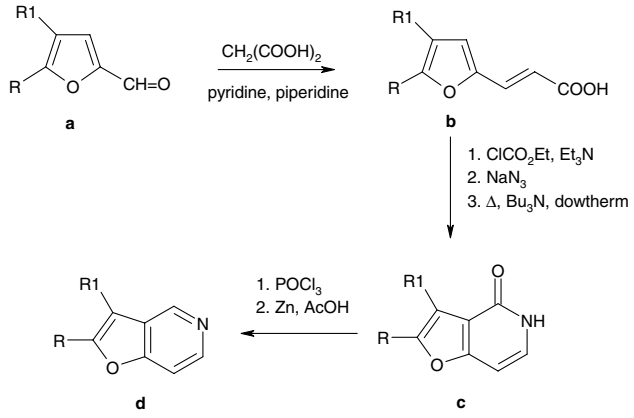


Fig. 1. Preparation of the furo[3,2-*c*]pyridines. L^1, R = R1 = H; L^2, R = CH_3, R1 = H; L^3, R = R1 = CH_3; L^4, R–R1 = CH═CH—CH═CH.

from tetrahydrofuran (THF) (**1**), ethanol (**2**) and CH_2Cl_2/diethylether (**3**–**5**). The composition of the obtained complexes $[Ni(L^1)_4(NCS)_2]\cdot THF$ (**1**), $[Ni(L^2)_4(NCS)_2]\cdot 1.29H_2O$ (**2**), $[Ni(L^3)_4(NCS)_2]\cdot 6.6H_2O$ (**3**), $[Ni(L^4)_4(NCS)_2]\cdot 2H_2O$ (**4**) and $[Ni(L^5)_4(NCS)_2]\cdot CH_2Cl_2$ (**5**) was confirmed by elemental analysis. X-ray structure analysis was performed for compounds **2**, **4** and **5**, since structural data on **1** and **3** can be retrieved from the literature [5].

2.3. Analytical methods and equipment

Elemental C–H–N analysis was carried out with a commercial analyzer (Carlo Erba, 1108). The nickel

Table 1
Summary of X-ray crystallographic data for $[NiL_4(NCS)_2]\cdot sol$

Ligand L	Mefupy	Bzfupy	iqu
Compound	**2**	**4**	**5**
Formula	$C_{34}H_{30.57}N_6NiO_{5.29}S_2$	$C_{46}H_{32}N_6NiO_6S_2$	$C_{39}H_{30}Cl_2N_6NiS_2$
Formula weight	730.61	887.61	776.42
Crystal system	orthorhombic	monoclinic	monoclinic
Space group	$P2_12_12_1$	$P2/c$	$P2_1/n$
Cell parameters			
a (Å)	14.270(2)	7.2975(7)	13.607(2)
b (Å)	15.750(2)	17.5924(18)	17.466(3)
c (Å)	16.243(2)	18.4265(19)	16.053(2)
α (°)	90.00	90.00	90.00
β (°)	90.00	97.018(2)	104.901(3)
γ (°)	90.00	90.00	90.00
V (Å^3)	3650.6(9)	2347.9(4)	3686.6(10)
Z	4	2	4
Density, D_c (g cm^{-3})	1.329	1.256	1.399
Absorption coefficient (mm^{-1})	0.694	0.553	0.822
F(000)	1515	916	1600
Reflections collected	16855	8307	22356
Refinement method		full matrix least squares on F^2	
Data/restraints/parameters	6832/0/460	3345/0/279	8356/0/451
Final R indices	R_1 = 0.0754	R_1 = 0.0493	R_1 = 0.0483
	wR_2 = 0.2065	wR_2 = 0.1308	wR_2 = 0.0824
CCDC code	257365	257363	257364

content was determined by a complexometric titration on murexide. IR spectra were obtained with a FTIR spectrometer (Philips, PU 9800). Electron spectra were measured in the range 9000–40 000 cm^{-1} (Perkin–Elmer, 450).

Diffraction data were collected on a 3-circle-platform diffractometer (Bruker, SMART 1K CCD). The frame data were acquired with the SMART software at 300 K using Mo Kα radiation ($\lambda = 0.71073$ Å). The structures were solved by direct methods (SHELXS 97) and refined by the least-squares method on F^2 (SHELXL 93, incorporated SHELXTL v5.1). Hydrogen atoms were geometrically positioned and left riding on their parent atoms during structure refinement. The structural data are listed in Table 1.

The magnetic data were collected using the SQUID apparatus (Quantum Design) in the temperature range 2–300 K at the applied field of $B = 0.1$ T. The magnetic susceptibility has been corrected for the underlying diamagnetism using a set of Pascal constants.

3. Results and discussion

3.1. X-ray structure

All five complexes under study possess a molecular structure: they are formed by *trans*-$[NiL_4(NCS)_2]$ units with the solvent molecules embodied in the crystal lattice. The chromophore $\{NiN_4N'_2\}$ is nearly octahedral and approximately forms a compressed tetragonal bipyramid. The ORTEP drawings of the X-ray determinations are in the supporting material.

Compound **2** is non-centrosymmetric so that we are left with six different Ni–N bond lengths. The two Ni–NCS bond lengths, Ni1–N1 2.023(13) and Ni1–N2 2.072(12), average to 2.048 whereas the four equatorial N-donor heterocycles exhibit bond lengths to the metal centre between 2.108 and 2.224 with an average of 2.163 (all distances in Å). The bond angles deviate only slightly from octahedral vertices and can be easily retrieved from the corresponding *cif*-file deposited in the CCDC. The *trans* NCS groups are arranged in a way so that the dihedral angle SC–N...N–CS is −119°. This differs from the previously determined structures for **1** and **3**, where that angle amounts to −14° and 180°, respectively. The planes of the aromatic rings are turned in a way so that their dihedral angle with the Ni1–N2 vector is −35°, −17°, +35°, +2°. The ring arrangement is irregular: three oxygen atoms of the furan ring point to the same side whereas just one is opposite (Fig. 2).

Compound **4** is centrosymmetric and there are three different Ni–N bond lengths. The Ni–NCS bond lengths are Ni1–N1 2.084(4) whereas the equatorial N-donor heterocycles exhibit bond lengths to the metal centre 2.143(3) and 2.146(3) with an average of 2.144. The

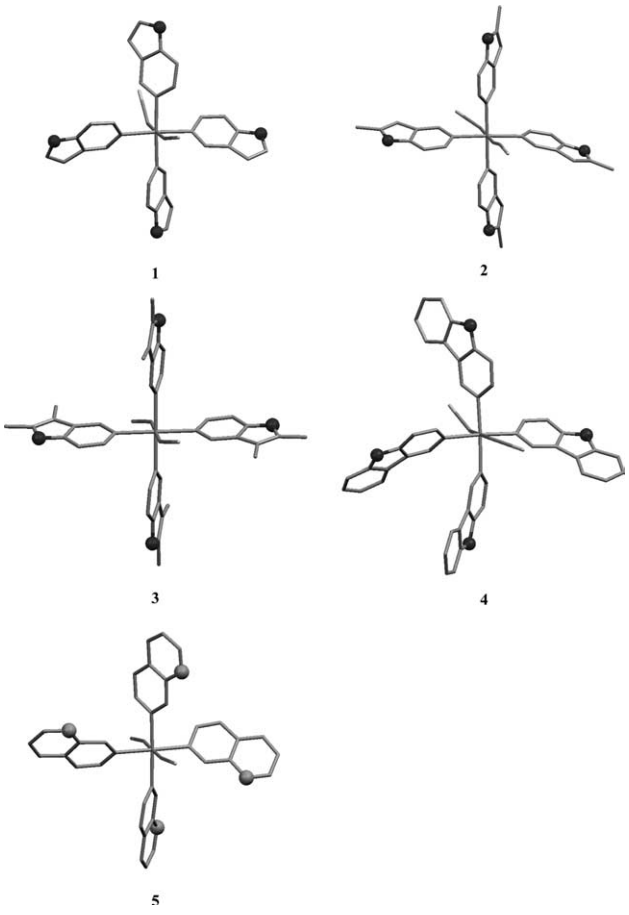


Fig. 2. The molecular structures of compounds **1**–**5**. The oxygen atoms of the furan rings are marked by balls (and the corresponding carbon atom in the isoquinoline complex **5**).

dihedral angle of *trans* NCS, SC–N...N–CS, is −133°. This is nearly the same as for compound **2**. The orientation of the planes of the aromatic rings is described by their dihedral angles relative to the Ni1–N2 vector: +32°, +34°, +41°, +32°. The ring arrangement is regular: opposite oxygen atoms of the furan rings point to different sides. Such an arrangement is not found in the remaining compounds.

Compound **5** is non-centrosymmetric and we can observe six different Ni–N bond lengths. Two Ni–NCS bond lengths, Ni1–N1 2.044(4) and Ni1–N2 2.051(4), average to 2.0475 while four equatorial N-donor heterocycles exhibit bond lengths to the metal centre from 2.133 to 2.160 with an average of 2.143. Dihedral angle of *trans* NCS, SC–N...N–CS, is 162°, which is between angles of compounds **1**, **3** and **2**, **4**. The dihedral angle of the planes of the aromatic rings relative to the Ni1–N2 vector is +35°, +46°, +25°, +49°. The ring arrangement is analogous to compound **2**.

The geometrical distortion has been characterized by two asymmetry parameters using the metal–ligand distances: the axial distortion $D_{str} = d_z - (d_x + d_y)/2$, and the rhombic distortion $E_{str} = (d_x - d_y)/2$. The

Cartesian axes have been chosen with a recipe well-known in magnetochemistry and ESR so that E is positive and $-1/3 < E/D < +1/3$. These data are in Table 2 along with the metal–ligand distances within the chromophore.

3.2. Spectral data

The bands observed in the electronic absorption spectra (Table 3) can be assigned to the three spin allowed transitions $^3T_{2g} \leftarrow {}^3A_{2g}$, $^3T_{1g}(F) \leftarrow {}^3A_{2g}$ and $^3T_{1g}(P) \leftarrow {}^3A_{2g}$ in O_h symmetry. The maxima of the absorption bands for the complexes under study are within the interval usually found for pseudooctahedral nickel(II) complexes [18]. A possible splitting, due to the symmetry lowering to D_{4h} symmetry, is not resolved. It can be concluded that the ligand-field strengths 10 Dq are effectively identical for the furopyridine derivatives and the thiocyanate group.

The mode of coordination of the NCS groups in these complexes has been investigated by means of the infrared absorption spectra. It follows from the literature data [19] that the main criterion of the M–NCS and M–SCN bonding is the band position corresponding to the C–S stretching vibration. The region from 770 to 860 cm^{-1} is assigned to M–NCS bonding, and that between 690 and 730 cm^{-1} to the M–SCN bonding mode. The C–N vibrations of analogous compounds span the region 2080–2110 cm^{-1} and they refer to M–NCS bonding whereas vibrations occurring in the region of 2100–2130 indicate the M–SCN bonding mode. For a bridging thiocyanate group 2130–2180 cm^{-1} values are typical. Thus the NCS groups in the studied complexes are terminally coordinated (ν_{CN} below 2100 cm^{-1}), through the nitrogen donor atom (the absence of ν_{CS} in the region 690–730 cm^{-1}).

3.3. Magnetic data

The magnetic susceptibility of the complexes under study increases monotonously on cooling. The effective magnetic moment keeps almost constant value except at very low temperatures when its decrease reflects a small zero-field splitting (Figs. 3 and 4).

Table 2
Metal–ligand bond lengths (Å) in the studied complexes

Compound	d_z(Ni–NCS)	d_x,d_y(Ni–L)	SC–N...N–CS (°)	D_{str}, E_{str}[a]	Reference
1	Ni–N2 2.073(2) Ni–N1 2.078(2)	Ni–N3 2.126(2) Ni–N5 2.134(2) Ni–N6 2.135(2) Ni–N4 2.155(2)	−14	−0.0620, 0.0075	[5]
2	Ni–N1 2.023(13) Ni–N2 2.072(12)	Ni–N5 2.108(11) Ni–N3 2.122(11) Ni–N6 2.198(11) Ni–N4 2.224(11)	−119	−0.1155, 0.0480	this work
3	Ni–N1 2.051(2)	Ni–N2 2.195(2) Ni–N3 2.172(2)	180	−0.1325, 0.0115	[5]
4	Ni–N1 2.084(4)	Ni–N2 2.146(3) Ni–N3 2.143(3)	−133	−0.0605, 0.0015	this work
5	Ni–N1 2.044(4) Ni–N2 2.051(4)	Ni–N5 2.133(4) Ni–N3 2.137(4) Ni–N6 2.142(4) Ni–N4 2.160(4)	162	−0.0955, 0.0080	this work

[a] The tetragonal distortion is $D_{str} = d_z - (d_x + d_y)/2$; the rhombic distortion equals $E_{str} = (d_x - d_y)/2$.

Table 3
Electronic and infrared absorption spectra of isothiocyanate nickel(II) complexes with furopyridines

Complex	Electronic transitions (cm^{-1})	Vibrational transitions (cm^{-1})	
		$\tilde{\nu}_{CN}$	$\tilde{\nu}_{CS}$
1, $[Ni(fupy)_4(NCS)_2]\cdot THF$	10200, 16400, 27200	2072	798
2, $[Ni(Mefupy)_4(NCS)_2]\cdot 1.29H_2O$	10300, 16700, 27000	2071	801
3, $[Ni(Me_2fupy)_4(NCS)_2]\cdot 6.6H_2O$	10100, 16500, 27100	2074	803
4, $[Ni(Bzfupy)_4(NCS)_2]\cdot 2H_2O$	10300, 16600, 27000	2069	796
5, $[Ni(iqu)_4(NCS)_2]\cdot CH_2Cl_2$	10700, 17300		

Restricting ourselves only to the axial zero-field splitting, the spin Hamiltonian becomes

$$\hat{H} = \hbar^{-2} D(\hat{S}_z^2 - \hat{S}^2/3) + \hbar^{-1} B\mu_B g \hat{S}_\alpha \quad (1)$$

($\alpha = x$ and z). The spin-Hamiltonian formalism offers another constraint among the magnetic parameters [14]

$$D = \lambda(g_z - g_x)/2, \quad (2)$$

where λ is the spin–orbit splitting parameter: $\lambda/hc = -315\ \mathrm{cm}^{-1}$. Thus we are left with two free parameters (g_z and g_x), and eventually the temperature-independent paramagnetism (the van Vleck term) α. Since the D value could be small, the closed formulae for the susceptibility are inappropriate so that we are left with the diagonalization of the spin Hamiltonian for a number of reference fields [20]. The susceptibility and magnetization data were treated simultaneously, by minimizing a joint functional

$$F(g_z, g_x, \chi_{TIP}) = w_1 \frac{\sum_{n=1}^{N} |\chi_n^o - \chi_n^c|}{(1/N)\sum_{n=1}^{N} |\chi_n^o|} + w_2 \sum_{m=1}^{M} (M_m^o - M_m^c)^2 \quad (3)$$

(c – calculated, o – observed data, weights $w_1 = w_2 = 0.5$). Such a choice guarantees that the center of the susceptibility data and the highest-field magnetization data are preferentially recovered by the fitting procedure. The calculated magnetic parameters are listed in Table 4.

As expected, the axial zero-field splitting parameter D adopts only small values. Its negative sign means that the ground state $|S, M_S\rangle$ is the Kramers doublet $M_S = \pm 1$. Therefore the effective magnetic moment on extrapolation to the zero temperature approaches a constant value of about $\mu_{eff} \approx 1.7\ \mu_B$ For nearly octahedral complexes the spin-Hamiltonian formalism offers a set of formulae [21]

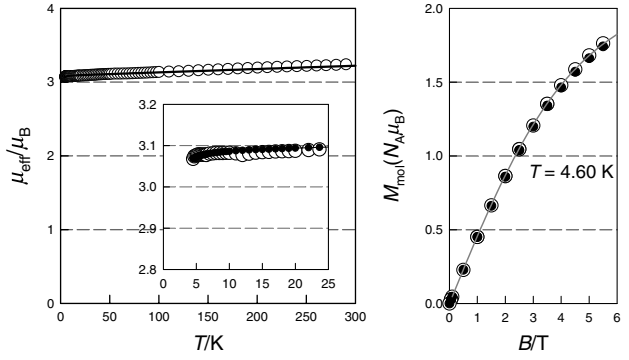


Fig. 4. The effective magnetic moment (left) and magnetization (right) for **5**.

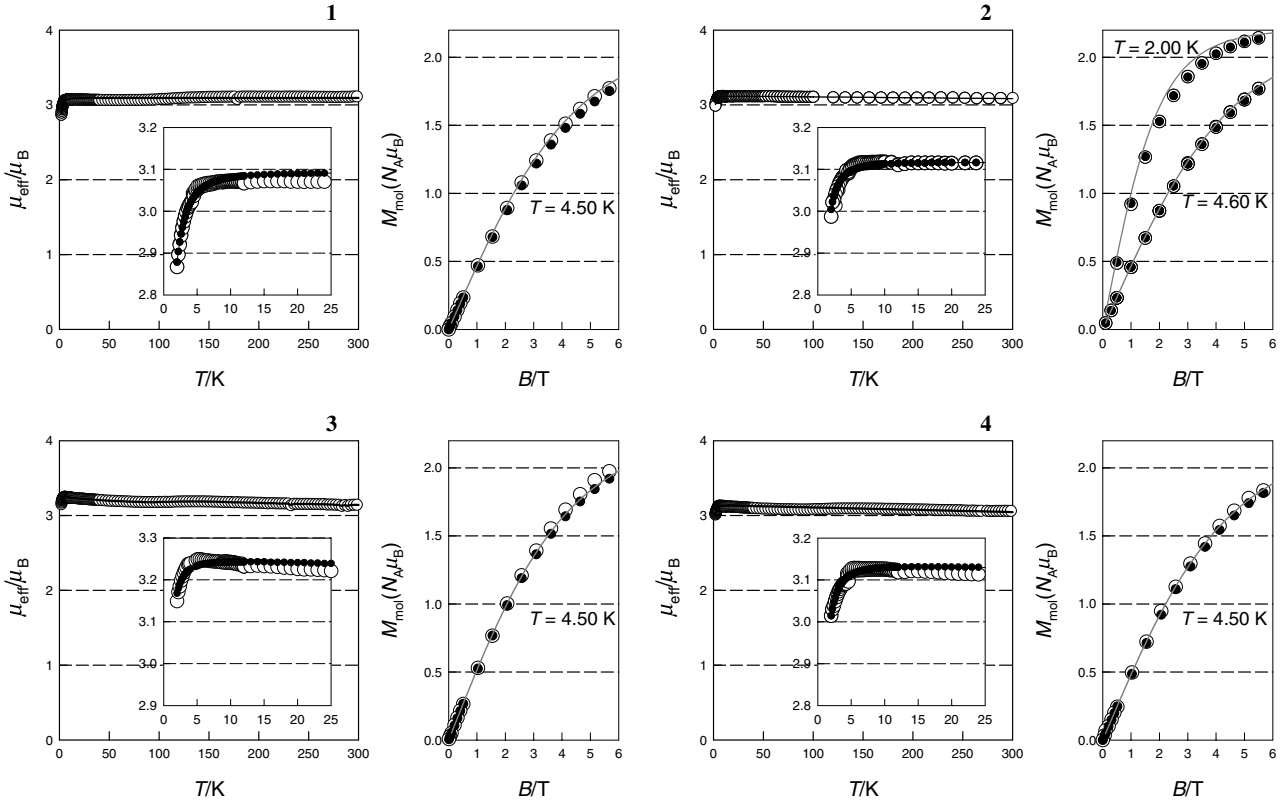


Fig. 3. The effective magnetic moment (left) and magnetization (right) for complexes **1**, **2**, **3** and **4**. Solid line – the Brillouin function for g_{av} and experimental temperature.

Table 4
Calculated magnetic parameters

Compound	g_z	g_x	D/hc (cm^{-1})	α (10^9 m^3 mol^{-1})	R (%)[a]	D_{str} (10^{-10} m)	κ_x/κ_z
1, $[Ni(fupy)_4(NCS)_2]\cdot THF$	2.199	2.180	−2.96		0.46	−0.0620	0.90
2, $[Ni(Mefupy)_4(NCS)_2]\cdot 1.29H_2O$	2.213	2.201	−1.91	−1.2	0.66	−0.1165	0.97
3, $[Ni(Me_2fupy)_4(NCS)_2]\cdot 6.6H_2O$	2.305	2.294	−1.52	−4.8	0.68	−0.1325	0.98
4, $[Ni(Bzfupy)_4(NCS)_2]\cdot 2H_2O$	2.227	2.214	−1.99	−3.0	0.46	−0.0605	0.94
5, $[Ni(iqu)_4(NCS)_2]\cdot CH_2Cl_2$	2.188	2.178	−1.58	+4.5	0.23	−0.0955	0.95

[a] Conventional discrepancy factor on the magnetic susceptibility. Estimated standard deviation of g-parameters: 0.002.

$$D = 4\lambda^2(\kappa_x^2 - \kappa_z^2)/\Delta_0, \quad (4)$$

$$g_z = g_e - 8\lambda\kappa_z^2/\Delta_0 > g_e, \quad (5)$$

$$g_x = g_e - 8\lambda\kappa_x^2/\Delta_0 > g_e, \quad (6)$$

where $\Delta_0 = 10$ Dq matches the first electronic transition $^3A_{2g} \rightarrow {}^3T_{2g}$. With $D < 0$ the orbital reduction factors are interrelated as $\kappa_x < \kappa_z$ so that the equatorial bond Ni–N is more covalent than the axial bond Ni–NCS (which is more polar). The above formulae yield another relationship

$$\frac{\kappa_x}{\kappa_z} = \left(\frac{g_x - g_e}{g_z - g_e}\right)^{1/2} \quad (7)$$

and these data are involved in Table 4. We tried to correlate the magnetochemical D-values with those from the structural data and the corresponding plot is presented in Fig. 5. One can see that a correlation surely exists.

With the inequivalent equatorial and axial ligands (D_{4h} symmetry) we arrive at a modified spin-Hamiltonian formula [22]

$$D = 4\lambda^2[\kappa_x^2/\Delta_{xy}(^3B_{1g} \rightarrow {}^3E_g) - \kappa_z^2/\Delta_z(^3B_{1g} \rightarrow {}^3B_{2g})], \quad (8)$$

where two close-lying transition energies (experimentally unresolved) occur. This formula, however, contains too many parameters which makes their determination and discussion very complex. On ignoring covalence effects (the orbital reduction factors $\kappa = 1$), a calculation has been performed in the complete space spanned by the d^8 term-functions by involving the electron repulsion, crystal-field and the spin–orbit coupling operators [21,22]. The splitting of the lowest crystal-field multiplets

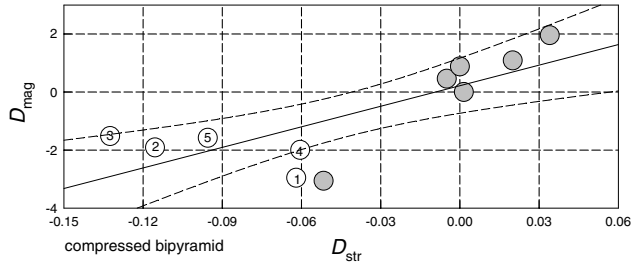


Fig. 5. Correlation of the magnetic D-values with structural D_{str} ones. White points – this work, gray – homoleptic Ni(II) complexes with six imidazole ligands [15]. Dashed – 95% confidence intervals.

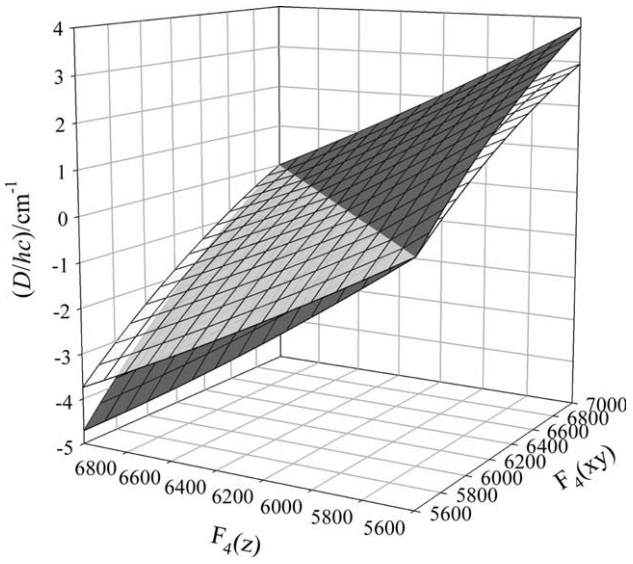


Fig. 6. Calculated D-parameters for Ni(II) systems at different tetragonal crystal fields. Two sets of D-values refer to the spin-Hamiltonian approach (dark) and the exact multiplet splitting (white). The crystal-field quadrupolar integrals are interrelated to the conventional crystal-field parameters through 10 Dq = $(10/6)F_4(xy)$ and $Dt = (2/21)[F_4(xy) - F_4(z)]$.

matches the zero-field splitting parameter $D = E(\Gamma_5) - E(\Gamma_4)$ where the Bethe notation is applied for irreducible representations of the D_4' double group. The modelling in the relevant crystal-field strengths (around 10 Dq = 10 000 cm^{-1} corresponding to $F_4 = 6000$ cm^{-1}) is shown in Fig. 6. It can be concluded that a negative value of the D-parameter is obtained for the compressed tetragonal bipyramid or, more exactly, for the crystal-field quadrupolar integrals obeying a relationship $F_4(xy) < F_4(z)$.

4. Conclusions

In this work, we report on the synthesis, structure, spectral and magnetic properties of five compounds of the formulae $[Ni(fupy)_4(NCS)_2]\cdot THF$, $[Ni(Mefupy)_4(NCS)_2]\cdot 1.29H_2O$, $[Ni(Me_2fupy)_4(NCS)_2]\cdot 6.6H_2O$, $[Ni(Bzfupy)_4(NCS)_2]\cdot 2H_2O$ and $[Ni(iqu)_4(NCS)_2]\cdot CH_2Cl_2$. The chromophore $\{NiN_4N_2'\}$ refers to a slightly compressed tetragonal bipyramid, giving rise to a negative tetragonality parameter D_{str} The electron spectra show

almost identical 10 Dq parameters with unresolved tetragonal splitting. This, however, is evidenced from the magnetic data yielding a negative zero-field splitting parameter D. The greater the (negative) structural distortion, the more negative D-value was observed.

Acknowledgements

Slovak Grant Agencies (VEGA-1/2453/05, APVT-20-005204, VEGA-1/0069/03) are acknowledged for financial support. Dr. Raphael G. Raptis (University of Puerto Rico) is gratefully acknowledged for providing access to the X-ray diffractometer.

Appendix A. Supplementary data

Crystallographic data (excluding structure factors) for the structural analysis have been deposited with the Cambridge Crystallographic Data Centre, CCDC Nos. 257365, 257363 and 257364 for **2**, **4** and **5**. Copies of this information may be obtained free of charge from The Director, CCDC, 12 Union Road, Cambridge, CB2 1EZ, UK (fax: 44 1223 336 033; e-mail: deposit@ccdc.cam.ac.uk or www: http://www.ccdc.cam.ac.uk). Supplementary data associated with this article can be found, in the online version, at doi:10.1016/j.poly.2005.03.103.

References

[1] J.S. New, W.L. Christopher, J.P. Yewich, R. Butler, R.F. Schlemmer Jr., C.P. van der Maelen, J.A. Cipolline, J. Med. Chem. 32 (1989) 1147.
[2] A. Krutošíková, M. Dandárová, Heterocycles 37 (1994) 1695.
[3] M. Bencková, A. Krutošíková, Monatsh. Chem. 126 (1995) 753.
[4] A. Krutošíková, R. Sleziak, Collect. Czech. Chem. Commun. 61 (1996) 1627.
[5] J. Miklovič, A. Krutošíková, P. Baran, Acta Crystallogr. C60 (2004) m227.
[6] R. Boča, P. Baran, L. Dlháň, M. Hvastijová, G. Wltschek, Chem. Phys. Lett. 284 (1998) 254.
[7] A. Mašlejová, R. Boča, L'. Dlháň, B. Papánková, I. Svoboda, H. Fuess, Chem. Phys. Lett. 347 (2001) 397.
[8] A. Mašlejová, M. Gembický, I. Svoboda, R. Boča, Solid State Phenom. 90–91 (2003) 171.
[9] J. Paharová, J. Černák, R. Boča, Z. Žák, Inorg. Chim. Acta 346 (2003) 25.
[10] R. Boča, L'. Dlháň, W. Haase, R. Herchel, A. Mašlejová, B. Papánková, Chem. Phys. Lett. 373 (2003) 402.
[11] A. Mašlejová, R. Boča, L'. Dlháň, R. Herchel, J. Magn. Magn. Mater. 272–276 (2004) 380.
[12] R. Boča, M. Boča, M. Gembický, R. Herchel, L. Jäger, C. Wagner, H. Fuess, Polyhedron 23 (2004) 2337.
[13] A. Tomkiewicz, R. Boča, M. Nahorskaa, J. Mrozinski, J. Mol. Struct. 734 (2004) 143.
[14] R. Boča, Coord. Chem. Rev. 248 (2004) 757.
[15] A. Mašlejová, R. Ivaniková, I. Svoboda, B. Papánková, L. Dlháň, H. Fuess, R. Boča, Polyhedron (submitted).
[16] F. Eloy, A. Deryckere, J. Heterocyclic Chem. 8 (1971) 57.
[17] V. Bobošík, A. Krutošíková, U. Jordis, Monatsh. Chem. 126 (1995) 747.
[18] A.B.P. Lever, Inorganic Electronic Spectroscopy, 2nd ed., Elsevier, Amsterdam, 1984.
[19] K. Nakamoto, Infrared Spectra of Inorganic and Coordination Compounds, 2nd ed., Wiley, New York, 1970.
[20] R. Boča, Theoretical Foundations of Molecular Magnetism, Elsevier, Amsterdam, 1999.
[21] R. Boča, Struct. Bond. 117 (2005) 1.
[22] R. Boča, in: M. Melnik, A. Sirota (Eds.), Progress in Coordination and Bioinorganic Chemistry, STU Press, Bratislava, 2003, p. 227.

theory [6]. As far as we know, the oxidation of $[Fe(phen)_3]^{2+}$ by $[H_6Co^{III}Mo_6O_{24}]^{3-}$ is the only study reported so far [8]. The standard reduction potential (E^0) and the self-exchange rate constant (k_{22}) for the $[H_6Co^{III}Mo_6O_{24}]^{3-}/[H_6Co^{II}Mo_6O_{24}]^{4-}$ couple in perchloric acid, not having been reported so far, are being reported now. The redox potential is measured directly and the self-exchange rate constant is estimated indirectly in a manner used in some recent studies [9,10], The iodide ion is selected as the substrate to test the Marcus cross-relation since a good number of rates for its oxidation by a number of oxidants are available [11].

2. Experimental

2.1. Materials

$[NH_4]_4[H_6Co^{II}Mo_6O_{24}]\cdot 4H_20$, was prepared by adding 100 ml of a solution of $CoCl_2\cdot 6H_2O$ (4.76 g, 0.02 mol), drop by drop, to 150 ml of a solution of $[NH_4]_6[Mo_7O_{24}]\cdot 4H_2O$ (24.72 g, 0.02 mol) followed by solid NH_4Cl (2 g) to have a pH of 4–4.5. The details of the other procedures were similar to those described [12]. The isolated crystals of $[H_6Co^{II}Mo_6O_{24}]^{4-}$ are stable indefinitely [12]. The Co(III)-complex, $K_3[H_6Co^{III}Mo_6O_{24}]$, was prepared by the oxidation of the corresponding Co(II)-complex ion by $[2KHSO_5\cdot KHSO_4\cdot K_2SO_4]$, oxone [12] (Dupont).

$[H_6Co^{III}Mo_6O_{24}]$ was also prepared by adding a solution of carbonatotetraamminecobalt(III) nitrate (15 g, 500 ml), in small portions, to an equal volume of a boiling solution of $[NH_4]_6Mo_7O_{24}\cdot 4H_2O$ (72 g, 500 ml). The solution was evaporated to about 150 ml and filtered. The addition of NH_4Cl to the hot filtrate produced a precipitate of $[NH_4]_3[H_6Co^{III}Mo_6O_{24}]$ and a small amount of dark olive-green [13] $[NH_4]_3[H_6Co^{III}Mo_5O_{21}]$. Because the olive-green (dimeric) species has a greater solubility, the blue-green monomeric $[NH_4]_3[H_6Co^{III}Mo_6O_{24}]$ was easily separated. The potassium salt, $K_3[H_6Co^{III}Mo_6O_{24}]$, was prepared by adding a saturated KCl (Fluka, Puriss) solution to the $[NH_4]_3[H_6Co^{III}Mo_6O_{24}]$ solution until the potassium salt precipitated. The filtered precipitate was dissolved in a minimum volume of hot distilled water and the decanted solution was allowed to cool at the room temperature when a mixture of blue-green and olive-green crystals separated out. These crystals were air-dried. The stock solution was prepared by dissolving the crystals in a dilute perchloric acid solution. The resulting green solution, believed to contain the monomeric species, $[H_6Co^{III}Mo_6O_{24}]^{3-}$, because the dimeric species, $[H_4(CoMo_5O_{19})_2]^{6-}$, is unstable in acidic solutions, was stable for several weeks [13].

The purity of the prepared Co(III)-hetero ion was checked by recording the UV–Vis spectra of the aqueous solution on a HP 8452A spectrophotometer (bandwidth 2 nm). The solution had λ_{max} at 410 nm (ε, 28.7 $dm^3\ mol^{-1}\ cm^{-1}$) and 602 nm (ε, 19.6 $dm^3\ mol^{-1}\ cm^{-1}$) [8].

Solutions of lithium and sodium perchlorate were prepared as described earlier [14] by neutralising lithium hydroxide (Sigma) and sodium carbonate (E. Merck, GR) by perchloric acid (E. Merck, GR). The solutions of sodium iodide (Puriss, Fluka) were freshly prepared by weighing before the kinetic runs. The other chemicals were of high purity and used as received. Double distilled water, once from an all glass still, was used throughout.

2.2. Repetitive scans of the mixture of $[H_6Co^{III}Mo_6O_{24}]^{3-}$ and H^+

The repetitive scans of an aqueous solution of $[H_6Co^{III}Mo_6O_{24}]^{3-}$ (5×10^{-4} mol dm^{-3}) in 0.05 and 0.5 mol dm^{-3} $HClO_4$ were studied at 410 nm and 8 °C using a Union Giken RA-401 stopped-flow spectrophotometer, dead time of 2 ms, connected to a RA-415 rapid scan attachment. The scans were over 96 nm (selected wavelength ± 48 nm). The reference was an aqueous solution of $[H_6Co^{III}Mo_6O_{24}]^{3-}$ of the same concentration. The gate time was 10 ms (the scan over 96 nm is completed in this time) and the interval time was zero (there is no time lag between the two sequential scans). Thus the first scan was completed between 2 and 12 ms and the second scan was completed between 12 and 22 ms, and so on after the solutions are pushed into the reaction cell. The peaks were blue shifted to 396 nm. The saturation in the absorbance, $[H^+] = 0.05$ mol dm^{-3},[1] was reached between 52 and 62 ms whereas the same absorbance was reached between 32 and 42 ms when $[H^+]$ was 0.5 mol dm^{-3}. Hence, it is rational to assume that the Co(III) and Co(II) species present in acid solution are $H_7Co^{III}Mo_6O_{24}^{2-}$ and $H_7Co^{II}Mo_6^{3-}$, which hereafter are represented as $HCo^{III}Mo_6^{2-}$ and $HCo^{II}Mo_6^{3-}$, respectively.

2.3. Reduction potential of the $HCo^{III}Mo_6^{2-}/HCo^{II}Mo_6^{3-}$ couple

The reduction potential of the cells having different $[HCo^{III}Mo_6^{2-}]/[HCo^{II}Mo_6^{3-}]$ ratios in varying $[H^+]$ (0.01–0.05 mol dm^{-3}) was measured using a platinum electrode against a calomel electrode prepared in saturated KCl solution. The plots of the measured potentials against $\log([HCo^{III}Mo_6^{2-}]/[HCo^{II}Mo_6^{3-}])$ at each $[H^+]$ were linear with intercepts in accordance with the Nernst Eq. (1). The least square values of the intercepts of each plot were calculated using the EXCEL program and the mean value of the intercept was 0.81 V. Hence,

[1] The caption of Fig. 1 of [8] should read correctly $[HClO_4] = 0.05$ mol dm^{-3} in place of 0.5 mol dm^{-3}.

the standard potential (E^0) of the $HCo^{III}Mo_6^{2-}$/$HCo^{II}Mo_6^{3-}$ couple is 1.05 V because the potential of the calomel electrode used was 0.24 V

$$E = E^0 + 0.0591 \log \frac{[HCo^{III}Mo_6^{2-}]}{[HCo^{II}Mo_6^{3-}]}. \quad (1)$$

2.4. Kinetic measurements

The rates were studied under pseudo first-order conditions ($[I^-] \geqslant 10[HCo^{III}Mo_6]^{2-}$) at constant ionic strength ($\mu = 1.0$ mol dm^{-3}, $LiClO_4$) in term of the appearance of the I_3^- ion at 353 nm ($\varepsilon = 2.64 \times 10^4$ dm^3 mol^{-1} cm^{-1} [15],), using a Union-Giken RA-401 stopped-flow spectrophotometer. The other species are transparent at this wavelength. The solutions of desired $[H^+]$, $[LiClO_4]$ and $[HCo^{III}Mo_6^{2-}]$, and $[I^-]$ and $[LiClO_4]$ were stored in separate storage cylinders which, along with the reaction cell, are maintained at the desired temperature (±0.1 °C) by circulating water from a Haake D8G circulatory water bath. The temperature of the solutions in storage cylinders was treated as the temperature of the reaction. The other experimental details were similar to those described earlier [16]. The k_{obs} values, reported in the Tables, are the mean values from at least 8–10 runs and the individual k_{obs} value from each run was reproducible within 5–8% of the mean value. The replacement of $LiClO_4$ by $NaClO_4$ for adjusting the ionic strength did not change the rate constant under identical conditions. However, $LiClO_4$ was used for adjusting the ionic strength.

2.5. Test for free radical

Two milliliters of acrylonitrile was added to the $HCo^{III}Mo_6^{2-}$ solution before adding the iodide solution. Both solutions had been previously purged with nitrogen. A white curdy precipitate of polymeric acrylonitrile appeared in the reaction mixtures, suggesting the formation of a free radical during the reaction. The control solutions of $HCo^{III}Mo_6^{2-}$ and I^-, taken separately, did not induce the polymerisation of the monomer.

2.6. Stoichiometry

The stoichiometry of the reaction was determined under kinetic condition, $[I^-]$ in large excess, by estimating $[I_3^-]$. The I_3^- was extracted with three 10 ml portions of carbon tetrachloride and the concentration was determined at 518 nm ($\varepsilon_{518} = 945$ dm^3 mol^{-1} cm^{-1}) [17]. The results indicated that the mean $\Delta[I_2]/\Delta[HCo^{III}Mo_6^{2-}]$ was 0.502 ± 0.004. Hence the stoichiometry of the reaction is represented by

$$2HCo^{III}Mo_6^{2-} + 2I^- \rightarrow 2HCo^{II}Mo_6^{3-} + I_2 \quad (2)$$

2.7. Characterisation of $HCo^{II}Mo_6^{3-}$

The liberated I_2 from the reaction mixture ($[HCo^{III}Mo_6^{2-}] = [I^-] = 5 \times 10^{-3}$ and $[H^+] = 0.1$ mol dm^{-3}) was removed with several aliquots of CCl_4. A known volume of the remaining solution was heated to remove the traces of iodine and then was treated with a slight excess of oxone ($[2KHSO_5 \cdot KHSO_4 \cdot K_2SO_4]$). The resulting solution was cooled to room temperature and made to the original volume. The estimated concentration of this solution (410 nm, $\varepsilon = 28.7$ dm^3 mol^{-1} cm^{-1}) agreed with that of the starting $HCo^{III}Mo_6^{2-}$ within ±2–3%. Hence, it is concluded that the iodide ion reduces the molybdocobaltate(III) ion to the molybdocobaltate(II) ion.

3. Results

The constancy of the k_{obs} values (1.03 ± 0.02 s^{-1}; $10^2[I^-] = 5.0$, $10^3[H^+] = 5.0$ and $\mu = 1.0$ mol dm^{-3}, 20 °C) at an initial $[HCo^{III}Mo_6^{2-}] = (5.0–50.0) \times 10^{-4}$ mol dm^{-3} indicated a first-order dependence in $HCo^{III}Mo_6^{2-}$. The average $k_{obs}/[I^-]$ is 20.6 ± 0.3 dm^3 mol^{-1} s^{-1} and the passage of the linear plot of the k_{obs} against $[I^-]$ through the origin indicated a first-order dependence in $[I^-]$ ($10^4[Co^{III}Mo_6]^{3-} = 5.0$, $[I^-] = (5.0–100.0) \times 10^{-3}$ mol dm^{-3}, $[H^+] = 0.005$ and $\mu = 1$ mol dm^{-3}). The k_{obs} increased with $[H^+]$, Table 1, and the passing of the linear plots of k_{obs} against $[H^+]$ through the origin, Fig. 1, indicated a first-order dependence in H^+. The k_{obs} (1.03 ± 0.02 s^{-1}) is independent of the initially added $HCo^{II}Mo_6^{3-}$ ($10^4[HCo^{III}Mo_6^{2-}] = 5.0$, $10^4[HCo^{II}Mo_6^{3-}] = (0.2–2.0)$, $10^2[I^-] = 5.0$, $[H^+] = 0.005$, $\mu = 1$ mol dm^3, 20 °C). It indicates that the rate-determining electron-transfer is not a reversible reaction.

4. Mechanism and discussion

There is significant difference in the oxidation of I^- ion by $[Co^{III}W_{12}O_{40}]^{5-}$ and $[H_6Co^{III}Mo_6]^{3-}$ ions. The

Table 1
The dependence of k_{obs} on the initial $[H^+]$ at different temperatures

	Temperature (°C):	10	15	20	25	30
	$[H^+]$ (mol dm^{-3})	k_{obs} (s^{-1})				
1.	0.002	0.00436	0.0117	0.0414	0.115	0.336
2.	0.005	0.0106	0.0311	0.104	0.326	0.817
3.	0.010	0.0223	0.0638	0.206	0.627	1.76
4.	0.015	0.0344	0.109	0.324	0.925	2.42
5.	0.020	0.0469	0.138	0.418	1.22	3.28
6.	0.025	0.0571	0.166	0.516	1.54	3.86
7.	0.030	0.0692	0.217	0. 636	1.78	5.12
8.	0.035	0.0783	0.254	0.727	2.15	5.85
9.	0.050	0.117	0.344	1.01	3.05	8.18
10.	0.060	0.134	0.408	1.28	3.71	9.92

$10^4[Co(III)Mo]^{3-} = 2.0$, $10^3[I^-] = 5.0$ and $\mu = 1$ mol dm^{-3}.

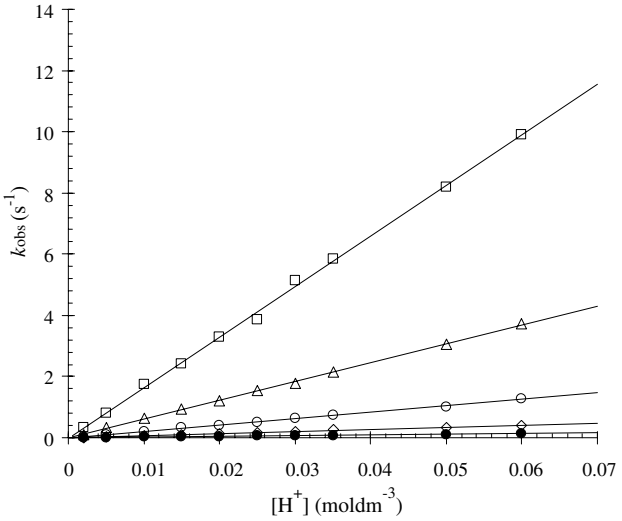


Fig. 1. The linear plots of k_{obs} against [H^+] at temperatures (°C) (10) ●, (15) ◇, (20) ○, (25) △ and (30) □. The linear plots pass through the origin.

k_{obs} in the $[Co^{III}W_{12}O_{40}]^{5-}$ oxidation is independent of [H^+] whereas a first order dependence is observed in the $HCo^{III}Mo_6{}^{2-}$ oxidation. This is due to the fact that the $[Co^{III}W_{12}O_{40}]^{5-}$ ion is not protonated in buffered [18] and perchloric acid solutions [19] whereas $[H_6Co^{III}Mo_6O_{24}]^{3-}$ ion is protonated as evident from the rapid scans of $[H_6Co^{III}Mo_6O_{24}]^{3-}$ and H^+ ion [8], described in the early part of the paper. The proton is probably added to oxygen atoms of low basicity in the shell of the molybdenum octahedra which are exposed to the solution [20] or to the water molecules occupying uncoordinated centres on the shell [21]. The protonated species of $[H_6Co^{III}Mo_6O_{24}]^{3-}$ is $[H_7Co^{III}Mo_6O_{24}]^{2-}$, which is abbreviated as the $[HCo^{III}Mo_6]^{2-}$ ion.

The most likely mechanism of the reaction, in view of the first-order dependence in each of [H^+], [I^-] and $[H_6Co^{III}Mo_6O_{24}]^{3-}$ and the fact that the rate is unaffected by $[H_6Co^{II}Mo_6O_{24}]^{4-}$ ions, is expressed by the most probable reactions (3)–(9)

$$[H_6Co^{III}Mo_6O_{24}]^{3-} + H^+ \overset{K}{\rightleftharpoons} [HH_6Co^{III}Mo_6O_{24}]^{2-} \quad (3)$$

$$[H_6Co^{III}Mo_6O_{24}]^{3-} + I^- \overset{k_4}{\rightarrow} [H_6Co^{II}Mo_6O_{24}]^{4-} + I^{\bullet} \quad (4)$$

$$[HH_6Co^{III}Mo_6O_{24}]^{2-} + I^- \overset{k_5}{\rightarrow} [HH_6Co^{II}Mo_6O_{24}]^{3-} + I^{\bullet} \quad (5)$$

$$I^{\bullet} + I^- \underset{k_{-6}}{\overset{k_6}{\rightleftharpoons}} I_2{}^{-\bullet} \quad (6)$$

$$I^{\bullet} + I^{\bullet} \overset{k_7}{\rightarrow} I_2 \quad (7)$$

$$[HH_6Co^{III}Mo_6O_{24}]^{2-} + I_2{}^{-\bullet} \overset{k_8}{\rightarrow} I_2 + [HH_6Co^{II}Mo_6O_{24}]^{3-} \quad (8)$$

$$I_2 + I^- \underset{k_{-9}}{\overset{k_9}{\rightleftharpoons}} I_3{}^- \quad (9)$$

Reactions (4) and (5) are rate determining. Reactions (6) and (9) are diffusion controlled. Reaction (6) is preferred over (7) for the dissipation of the $I^{\bullet}$ radical because the estimated value [22] of k_6 is 1.3×10^{10} $dm^3\ mol^{-1}\ s^{-1}$ and the equilibrium constant K_6 is [23] 1.1×10^5 $dm^3\ mol^{-1}$. The value [24] of k_9 is $\sim 10^{10}$ $dm^3\ mol^{-1}\ s^{-1}$ and the equilibrium constant K_9 is 720 $dm^3\ mol^{-1}$ [25]. Reactions (6), (8) and (9) are consistent with the observed stoichiometric ratio in Eq. (2).

The rate of disappearance of $[H_6Co^{III}Mo_6O_{24}]_0{}^{3-}$ in view of the reactions (3)–(9) is given by Eq. (10). The passing of the plots of k_{obs} against [H^+] through the origin indicate $1 \gg K\,[H^+]$ and therefore Eq. (10) is reduced to Eq. (11). Further, the species $[H_6Co^{III}Mo_6O_{24}]^{3-}$ are probably inactive or do not react with the iodide ion on the stopped-flow timescale, which is supported by the fact that the plots of k_{obs} against [H^+] have no intercepts combined with the fact that the stopped-flow traces of the reaction are monophasic. Hence, Eq. (11) is reduced to Eq. (12), which is consistent with the plots of k_{obs} against [I^-] and k_{obs} against [H^+] with zero intercepts

$$\frac{d[I_2]}{dt} = \frac{-d[H_6Co^{III}Mo_6O_{24}]_0}{2dt} = \frac{(k_4 + k_5K[H^+])[H_6Co^{III}Mo_6O_{24}][I^-]}{1 + K[H^+]}, \quad (10)$$

$$k_{obs} = 2(k_4 + k_5K[H^+])[I^-], \quad (11)$$

$$k_{obs} = 2k_5K[H^+][I^-]. \quad (12)$$

The activation parameters corresponding to the k_{obs} values at all the [H^+] (Table 1) were calculated by plotting $\ln(k_{obs}/2[I^-])$ against T^{-1}. It was found that the calculated values[2] of ΔE^{I}_{12}, ΔS^{I}_{12} and ΔG^{I}_{12} were independent of the initial [H^+]. Hence, Eq. (12) could be expressed by Eq. (13) where $k_{12} = k_5K[H^+]$. The estimated value of ΔG^{I}_{11} from the use of the ΔG^{I}_{12} value is thus independent of [H^+] and so would be the value of k_{11} deduced from ΔG^{I}_{11}

$$k_{obs} = 2k_{12}[I^-]. \quad (13)$$

The species $[H_2Co^{III}Mo_3O_{12}(HSO_5)]^{3-}$, resulting from the intramolecular electron transfer in the oxidation of $[H_6Co^{II}Mo_6O_{24}]^{4-}$ by the $HSO_5{}^-$ ion [12], has a coordinated $HSO_5{}^{2-}$ radical. A similar coordination complex is unlikely in the oxidation of I^- since the coordination sites in $[HH_6Co^{III}Mo_6O_{24}]^{2-}$ are saturated. However, an outer-sphere precursor complex between I^- and $[HH_6Co^{III}Mo_6O_{24}]^{2-}$ is likely for which K_{os} is the formation constant. The precursor complex is weak because k_{obs} has not shown signs of saturation [26] even

[2] $\Delta H^{\ddagger}_{12} = 151.6 \pm 2.2$ kJ mol^{-1}; $\Delta S^{\ddagger}_{12} = 301 \pm 7$ J K^{-1} mol^{-1} and $\Delta G^{\ddagger}_{12} = 61.7 \pm 2.6$ kJ mol^{-1}.

at high $[I^-]$ and k_{obs} is linearly dependent on $[I^-]$. Hence $k_{obs} = k_{et}K_{os}[I^-]$ where k_{et} is the rate constant for the electron transfer.

K_{os} is expected to be small because species of similar charges are involved. It can be estimated from the extended Fuoss equation [27] (14), where N is the Avagadro's number, $a = r_i + r_j$ (r_i and r_j are the radii of the ions i and j) and w_{ij} is the electric work term required to bring the reactants i and j to a distance a in the precursor complex and is given by Eq. (15). It arises from the Debye–Hückel interionic potential to allow for the effect of ionic strength [27], where z_i and z_j are the charges on the ions i and j, ε_0 and ε are the permittivity in vacuum and the bulk medium and κ is given by the Eq. (16) where k_B is the Boltzmann constant

$$K_{os} = \frac{4}{3}\pi N a^3 \exp(-w_{ij}/RT), \tag{14}$$

$$w_{ij} = \frac{z_i z_j e_0^2 N}{4\pi\varepsilon_0\varepsilon a(1+\kappa a)}, \tag{15}$$

$$\kappa = \sqrt{\frac{2e_0^2 N\mu}{\varepsilon_0\varepsilon k_B T}}. \tag{16}$$

The radius of $[Co^{III}W_{12}O_{40}]^{5-}$ is 0.5 nm and that of $[Ce^{IV}Mo_{12}O_{42}]^{8-}$ is 0.56 nm [28], therefore the radius of $[H_6Co^{III}Mo_6O_{24}]^{3-}$, is likely to be smaller than the radii of both the ions for the ionic radius of Mo^{6+} (0.062 nm) is less than that of W^{6+} (0.068 nm). The assumed value of the radius of $[H_6Co^{III}Mo_6O_{24}]^{3-}$ is 0.40 nm and that of iodide ion is 0.216 nm [29].

4.1. Calculation of k_{et}

The estimated value of κ is 3.28×10^9 m^{-1}, w_{12} is 1.90 kJ and K_{os} is 2.74×10^{-4} dm^3 mol^{-1}. The small value of K_{os} is due to the reaction between similarly charged ions. The calculated value of k_{et}, from the relation $k_{12} = k_{et}K_{os}$, is 1.2×10^3 s^{-1} at $[H^+] = 0.005$ mol dm^{-3} and 1.35×10^4 at $[H^+] = 0.06$ mol dm^{-3} at 25 °C. The corresponding value, calculated for the oxidation by the $[Co^{III}W_{12}O_{40}]^{5-}$ ion [30],[3] is 2.76×10^5 s^{-1} and is independent of $[H^+]$ because k_{12} is independent of $[H^+]$.

4.2. Calculation of exchange rate of $[HCo^{III}Mo_6]^{2-}$–$[HCo^{II}Mo_6]^{3-}$ ions

The unknown self exchange rate of $[HH_6Co^{III}Mo_6O_{24}]^{2-}$/$[HH_6Co^{II}Mo_6O_{24}]^{3-}$ can be calculated using the relations, based on simple Marcus theory [6], given in Eqs. (17)–(20). The method has been used recently to estimate the self-exchange rate of the $[Fe(CN)_5(NO_2)]^{3-}$–$[Fe(CN)_5(NO_2)]^{4-}$ couple [9], and the H_2NCSNH_2–$(H_2N)_2CSSC(NH_2)_2$ couple [10]

$$\Delta G_{12}^{\ddagger} = 0.5(\Delta G_{11}^{\ddagger} + \Delta G_{22}^{\ddagger} + \Delta G_{12}^{0} + \Delta w), \tag{17}$$

$$\Delta G_{12}^{0} = -nF(E_{11}^{0} - E_{22}^{0}), \tag{18}$$

$$\Delta w = w_{12} + w_{21} - w_{11} - w_{22}, \tag{19}$$

$$k_{ij} = K_B T h^{-1} \exp(-G_{ij}^{\ddagger}/RT), \tag{20}$$

where K_B is the Boltzmann constant, h is Planck's constant and T is the Kelvin temperature. ΔG_{12}^0, $\Delta G_{11}^{\ddagger}$, $\Delta G_{22}^{\ddagger}$ are, respectively, the free energy for the cross-reaction and the self exchange reactions of oxidant and reductant couples and $\Delta G_{12}^{\ddagger}$ is the free energy of activation for the cross-reaction.

The experimentally estimated E_{11}^0 for the $[HH_6Co^{III}Mo_6O_{24}]^{2-}$/$[HH_6Co^{II}Mo_6O_{24}]^{3-}$ couple is 1.05 V and is found to be independent of $[H^+]$. The E_{22}^0 value for the $I^{\cdot}/I^-$ couple has been adjusted [31] to 1.33 V from variously reported values [32–34]. This value, used previously in the oxidation by *trans*-$[Ru(tmc)O_2]^{2+}$ (tmc = 1,4,8,11-tetramethyl-1,4,8,11-tetraaza-cyclotetradecane) [35], is used in this paper. The self-exchange rate constant k_{22} for the $I^-/I^{\cdot}$ couple is reported [33,34] to have a value of 7×10^7 dm^3 mol^{-1} s^{-1} and is used presently.

The experimentally determined $\Delta G_{12}^{\ddagger}$ (kJ mol^{-1}) is 61.7 and the estimated ΔG_{12}^0, $\Delta G_{22}^{\ddagger}$ and $\Delta G_{11}^{\ddagger}$ are 27, 28 and 70, respectively, and $w = -1.76$ kJ mol^{-1} ($w_{22} = w_{21} = 0$, $w_{12} = 1.90$ and $w_{11} = 3.66$). $k_{11} = 3.5$ dm^3 mol^{-1} s^{-1} at 25 °C and $\mu = 1.0$ mol dm^{-3} is obtained from the estimated $\Delta G_{11}^{\ddagger}$ and is independent of $[H^+]$ because $\Delta G_{12}^{\ddagger}$ is fortunately independent of $[H^+]$. The k_{11} value for the $[Co^{III}W_{12}O_{40}]^{5-}$/$[Co^{II}W_{12}O_{40}]^{6-}$ couple is 1.7 dm^3 mol^{-1} s^{-1} at the same ionic strength and temperature [36]. Thus the two values are of the same order of magnitude. The small k_{11} value for the $[Co^{III}W_{12}O_{40}]^{5-}$/$[Co^{II}W_{12}O_{40}]^{6-}$ couple [4] is considered to be due to the tungstate environment surrounding the central Co atom. The somewhat higher value for the $[HH_6Co^{III}Mo_6O_{24}]^{2-}$/$[HH_6Co^{II}Mo_6O_{24}]^{3-}$ couple could be due to a more compact environment surrounding the Co atom.

In a recent article Swaddle and co-workers [37] pointed out that the exchange rate of the $[Fe(CN)_6]^{3-}$–$[Fe(CN)_6]^{4-}$ couple reported in the literature is in fact equal to $k'_K[K^+]$ where k'_K ($= k_{ex}/[K^+]_{total}$) is about 60% larger than k_K, the rate constant in the presence of the uncomplexed K^+ ion. k_{ex} is the observed rate constant when $[K^+]$ was controlled with 18-crown-6. Hence, the measured exchange rates in which a cation has a catalytic effect on the rates are larger than the rates predicted by Marcus theory for the reason that the ion pairing by the hydrated cation lowers the anionic–anionic repulsion. The ionic strength as such has only a small effect.

The present reaction is catalysed by the hydrogen ion. It has been shown that the molybdocobaltate species are protonated. Thus the hydrogen ion is not ion pairing with the anionic oxidant and does not act as a bridge between the anionic species. This is supported by the

[3] $\kappa = 3.282\times10^9$ m^{-1}, $w_{12} = 3.694$ kJ, $K_{os} = 6.258\times10^{-4}$ dm^3 mol^{-1} and $k_2 = 172.5$ dm^3 mol^{-1} s^{-1}.

fact that replacement of Li^+ by Na^+ had no perceptible effect on the measured rate. Hence, we are inclined to believe that the estimated exchange rate constant may not be the apparent rate constant. It is to be remembered that the parameters used in the estimation of the self-exchange rate constant were not dependent on $[H^+]$.

The outer-sphere oxidation of I^- by $[HH_6Co^{III}Mo_6O_{24}]^{2-}$ can be supported by estimating the rate constant k_{12} using the simple Marcus cross-relation [6] given by Eqs. (21)–(23)

$$k_{12} = (k_{11}k_{22}K_{12}f_{12})^{0.5}, \tag{21}$$

$$\log f_{12} = \frac{(\log K_{12})^2}{4\log\left(\frac{k_{11}k_{22}}{Z^2}\right)}, \tag{22}$$

$$\log K_{12} = n\Delta E/0.0591. \tag{23}$$

The use of the estimated values of $f_{12} = 0.38$ ($Z^2 = 10^{22}$), $K_{12} = 1.8 \times 10^{-5}$, $k_{11} = 3.54$ and $k_{22} = 7 \times 10^7$ dm^3 mol^{-1} s^{-1} in Eq. (21) leads to a value of $k_{12} = 41.2$ dm^3 mol^{-1} s^{-1} which is in reasonable agreement with the experimental value of 32.6 dm^3 mol^{-1} s^{-1}. Since the f value is dependent on Z^2, a value of $f = 0.29$ is obtained using $Z^2 \approx 10^{19}$ since Z is [38] $\approx 3 \times 10^9$. The value of k_{12} is thus modified to 36 dm^3 mol^{-1} s^{-1} which is in close agreement with the experimental value. Thus the reaction is outer-sphere.

4.3. Application of the modified Marcus' theory

Next the cross-reaction data, Table 2, is considered in terms of a modification [39,40] of the Marcus relationship expressed by the Eqs. (24)–(26) where $Z = 10^{11}$ dm^3 mol^{-1} s^{-1} [31]

$$k_{12} = (k_{11}k_{22}K_{12}f_{12})^{0.5}W_{12}, \tag{24}$$

$$\ln f_{12} = \frac{(\ln K_{12} + \frac{w_{12}-w_{21}}{RT})^2}{4[\ln\left(\frac{k_{11}k_{22}}{Z^2}\right) + \frac{w_{11}+w_{22}}{RT}]}, \tag{25}$$

$$W_{12} = \exp[-(w_{12} + w_{21} - w_{11} - w_{22})/2RT], \tag{26}$$

$$2\ln k_{12} - \ln f_{12} - 2\ln W_{12} - \ln k_{11} = \ln k_{22} + \ln K_{12}. \tag{27}$$

Table 2
The LFER and Marcus calculations using Eqs. (24)–(26); values of E^0, K_{12}, k_{12} and other parameters

	Oxidant	μ	E^0_{11} (V)	r_{11} (Å)	$2\ln k_{12}$	$-\ln f_{12}$	$2\ln W_{12}$	$\ln k_{11}$	$-\ln K_{12}$	L.H.S. of Eq. (27)
1	$[Os(phen)_3]^{3+}$	1.0	0.84 [44]	6.7 [44]	6.49 [34]	8.03	1.21	21.42 [45]	19.07	−8.11
2	$[Os(bpy)_3]^{3+}$	1.0	0.84 [46]	6.8 [46]	5.62 [34]	7.99	1.18	21.42 [46]	19.07	−8.99
3	$[Os(bpy)_3]^{3+}$	0.1	0.84 [46]	6.8 [46]	8.24 [34]	8.52	1.82	21.42 [46]	19.07	−6.48
4	$[Mo(CN)_8]^{3-}$	0.0	0.75 [47]	4.8 [48]	−2.16 [49]	4.53	−0.93	10.31 [50]	22.57	−7.01
5	$[IrBr_6]^{2-}$	0.1	0.84 [31]	4.5 [46]	7.09 [51]	6.11	−0.06	19.11 [31]	19.07	−5.85
6	$[IrCl_6]^{2-}$	0.1	0.89 [52]	4.4 [46]	12.03 [31]	3.17	−0.04	12.21 [53]	17.12	3.03
7	$[IrCl_6]^{2-}$	0.5	0.89 [52]	4.4 [46]	13.07 [33]	3.34	0.39	12.21 [53]	17.12	3.81
8	$[Fe(bpy)_3]^{3+}$	1.0	1.06 [54]	7.0 [33]	20.46 [33]	2.26	1.13	20.03 [55]	10.51	1.56
9	$[Fe(bpy)_3]^{3+}$	1.0	1.06 [54]	7.0 [33]	23.03 [31]	2.26	1.13	20.03 [55]	10.51	4.13
10	$[Fe(phen)_3]^{3+}$	1.0	1.09 [54]	7.0 [33]	22.5 [33]	1.81	1.13	20.03 [55]	9.34	3.15
11	$[Fe(5,6\text{-}Me_2\text{-}phen)_3]^{3+}$	1.0	0.97 [55]	7.0 [33]	18.19 [33]	3.92	1.13	20.03 [55]	14.01	0.95
12	$[Fe(4,7\text{-}Me_2\text{-}phen)_3]^{3+}$	1.0	0.87 [55]	7.0 [33]	11.06 [33]	6.29	1.13	20.03 [55]	17.90	−3.81
13	$[Fe(3,4,7,8\text{-}Me\text{-}phen)_3]^{3+}$	1.0	0.81 [55]	7.0 [33]	8.09 [33]	7.98	1.13	20.03 [55]	20.24	−5.09
14	$[Fe(4,4'\text{-}Me_2\text{-}bpy)_3]^{3+}$	1.0	0.88 [33]	7.0 [33]	9.84 [33]	6.03	1.13	20.03 [55]	17.51	−5.29
15	$[Cu(H_{-2}Aib_3)]$[a]	1.0	0.66 [56]	4.5[b]	−9.21 [57]	7.60	0	10.91 [58]	26.08	−12.52
16	$[Cu(H_{-2}A_3)]$	1.0	0.81 [56]	4.5[b]	1.61 [57]	4.58	0	10.91 [58]	20.24	−4.72
17	$[Cu(H_{-2}DGEN)]^+$	1.0	0.81 [56]	4.5[b]	1.61 [57]	4.73	0.34	10.91 [58]	20.24	−4.91
18	$[Cu(H_{-2}L_3)]$	1.0	0.77 [56]	4.5[b]	0.506 [57]	5.31	0	10.91 [58]	21.80	−5.09
19	$[Cu(H_{-3}G_{4a})]$	1.0	0.68 [56]	4.5[b]	−4.33 [57]	6.84	0	9.90 [58]	25.30	−7.39
20	$[Cu(H_{-3}G_4)]^-$	1.0	0.63 [56]	3.6[b]	−5.99 [57]	8.05	0.16	9.90 [58]	27.24	−8.0
21	$[Ni(9\text{-}ane)N_3]^{3+}$	1.0	0.947 [59]	3.8 [59]	9.12 [59]	2.87	2.83	8.70 [59]	14.91	0.46
22	$[Ni(cyclam)]^{3+}$	1.0	0.99 [60]	3.6 [61]	14.7 [61]	2.24	3.06	7.60 [60]	13.23	6.28
23	$[NiM_m]^{3+}$ [41]	1.0	0.995	3.8	15.2	2.26	2.83	8.87	13.03	5.76
24	$[NiM_r]^{3+}$ [41]	1.0	1.115	3.8	15.8	0.88	2.83	5.30	8.37	8.55
25	$[NiE_m]^{3+}$ [41]	1.0	0.99	3.8	17.0	2.46	2.83	10.1	13.23	6.53
26	$[Ni(tet\text{-}c)]^{3+}$ [41]	1.0	1.24	3.8	24.4	0.20	2.83	3.43	3.50	18.3
27	$[Co^{III}W_{12}]^{5-}$	1.0	1.07 [62]	5.0	10.3 [62]	0.67	3.51	0.53 [63,64]	10.12	6.93
28	$[HH_6Co^{III}Mo_6O_{24}]^{2-}$[c]	1.0	1.05	4.0	6.97	0.82	1.80	1.26	10.90	4.73
29	$[HH_6Co^{III}Mo_6O_{24}]^{2-}$[d]	1.0	1.05	4.0	11.8	0.82	1.80	1.26	10.90	9.56

$E^0(I^{\cdot}/I^-)$ [31] = 1.33 V, $r(I^-)$ [29] = 2.16 Å, $r(I^{\cdot})$ [29] = 1.33 Å, k_{22} [33,34] = 7×10^7 dm^3 mol^{-1} s^{-1}.

[a] Symbols used are: A_3, tri-L-alanine; L_3, tri-L-leucine; G_{4a}, tetraglycinamide; G_4, tetraglycine; Aib_3, tri-α-aminoisobutyric acid; DGEN, *N*,*N*′-diglycyl-1,2-diaminoethane.

[b] J.M. Anast, D.W. Margerum, Inorg. Chem. 21 (1982) 3494, have reported a radius of 4.3 Å for Cu(III)-complexes with $H_{-3}Aib_3a$, $H_{-2}Aib_3$ and 4.1 Å for the Cu(III)($H_{-3}A_3G^-$) complex and the corresponding radii for the Cu(II) complexes being 4.7, 4.7 and 4.9 Å. Hence a mean value, 4.5 Å, is obtained for the Cu(III)/Cu(II)$H_{-2}Aib_3$ complex and has been assumed for the other complexes as well.

[c] This work, $[H^+] = 0.005$ mol dm^{-3}.

[d] This work, $[H^+] = 0.06$ mol dm^{-3}.

Eq. (27), the suitably rearranged logarithmic form of the Eq. (24), indicates that a plot of the left hand side ($2\ln k_{12} - \ln f_{12} - 2\ln W_{12} - \ln k_{11}$) against $\ln K_{12}$ should be linear with a predicted unit slope and the intercept must give the best least-square value of the self-exchange rate k_{22} for the $I^{\cdot}/I^-$ couple. The equation was tested for a number of oxidations of the I^- ion by a variety of oxidants (Table 1). The required linear plot is illustrated in Fig. 2.

The least-squares slope, 1.12, of the linear plot is in excellent agreement with the ideal value of 1.0 for an *outer*-sphere mechanism predicted by Eq. (27). The k_{22} value, estimated from the intercept (18.0), is 6.6×10^7 dm^3 mol^{-1} s^{-1} which is also in excellent agreement with the previously reported values [33,34,41].

4.4. Deviations from earlier observations

The points corresponding to $[Cu(H_{-3}G_{4a})]$, $[Cu(H_{-2}Aib_3)]$ and $Cu(H_{-3}G_4)]^-$ are found to show a greater scatter in the plot of log k_{12} versus $\log(f_{12}k_{22}K_{12})$, constructed by Fairbank and McAuley [41], than shown in Fig. 2. The probable reason for this deviation could be the ignoring of the work term and the radii of $I^{\cdot}$ radical, which is significantly different from that of the I^- ion [29]. However, their contention of an outer-sphere mechanism for the reaction between Cu(III)-peptide complexes and iodide ion is correct.

Another observation for the same reason is related to the position of the nickel complexes, (21)–(26) in Table 2. Fairbank and McAuley [41], report that the points for these complexes were above the least square line in their plot. It was stated that another line having an ideal slope of about 0.5 could be drawn through these points but the intercept value of such a line leads to a self-exchange rate $>10^{10}$ dm^3 mol^{-1} s^{-1} for the $I^{\cdot}/I^-$ couple. Therefore, these authors assigned an inner-sphere mechanism for the oxidation of the I^- ion by these Ni(III) complexes.

It is interesting to note that in Fig. 2, the points (21) ($[Ni(9\text{-ane})N_3]^{3+}$) and (24) ($[NiM_r]^{3+}$) are on the line, the points (22) ($[Ni(cyclam)]^{3+}$), (23) ($[NiM_m]^{3+}$) and (25) ($[NiE_m]^{3+}$) are reasonably near the line and the point (26) ($[Ni(tet\text{-}c)]^{3+}$) for which an outer-sphere mechanism is proposed [41] is a little deviated from the line. We are therefore inclined to assign an outer-sphere mechanism to the oxidation of I^- by the named nickel complexes though linear free energy relationships similar to those observed in the outer-sphere processes have been reported for the inner-sphere reactions also [42,43].

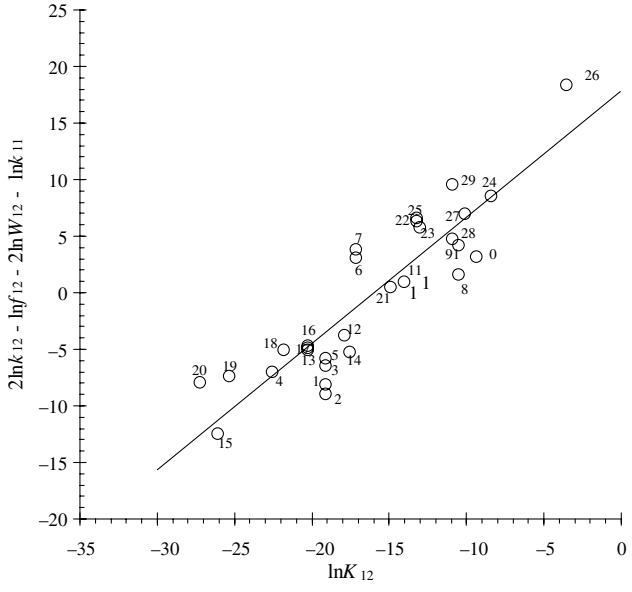


Fig. 2. The linear plot between $2\ln k_{12} - \ln f_{12} - 2\ln W_{12} - \ln k_{11}$ against $\ln K_{12}$ is in agreement with Eq. (27). The points in the plot are labelled according to the numbering of the complexes in Table 2.

4.5. Conclusion

The oxidation of I^- by $[HH_6Co^{III}Mo_6O_{24}]^{2-}$ has a first-order dependence in $[H^+]$ and is therefore different from that of $[Co^{III}W_{12}O_{40}]^{5-}$ oxidation which has zero order dependence in $[H^+]$. The H^+ dependence is caused by the oxidation of I^- by the protonated species $[HH_6Co^{III}Mo_6O_{24}]^{2-}$ whereas the species $[H_6Co^{III}Mo_6O_{24}]^{3-}$ is either inactive or does not react on the time-scale of the stopped flow measurements. The rapid scans of a mixture of H^+ and $[H_6Co^{III}Mo_6O_{24}]^{3-}$ indicated that the protonation equilibrium is attained in a few milliseconds. The measured reduction potential of the $[HH_6Co^{III}Mo_6O_{24}]^{2-}$–$[HH_6Co^{II}Mo_6O_{24}]^{3-}$ couple, 1.05 V, is independent of the initial $[H^+]$. The estimated self exchange rate of the $[HH_6Co^{III}Mo_6O_{24}]^{2-}$–$[HH_6Co^{II}Mo_6O_{24}]^{3-}$ couple is 3.5 dm^3 mol^{-1} s^{-1} since both the Co^{III}–Co^{II} species are likely to exist in the protonated form. The application of the Marcus theory confirms that the reaction is outer-sphere, consistent with the substitution inert nature of the polyoxometalate ions. The application of the Marcus theory, that has taken into consideration the ionic radii of the $I^{\cdot}$ radical and the work term, to the data of the oxidation of the iodide ion by nickel(III) complexes has indicated that these reactions are more likely to be outer-sphere rather than the inner-sphere as suggested in the original study.

Acknowledgement

Thanks are due to the then Head of the Department, Late Prof. R.C. Kapoor for laboratory facilities.

References

[1] P. Carloni, L. Eberson, Acta Chem. Scand. 45 (1991) 373.
[2] C.W. Baker, V.E. Simmons, J. Am. Chem. Soc. 81 (1959) 4744 (report a value 1.04 V).
[3] (a) I.A. Winstock, Chem. Rev. 98 (1998) 113;
(b) S.K. Saha, M. Ali, P. Banerjee, Coord. Chem. Rev. 122 (1993) 41;
(c) Ref. [14];
(d) S. Dholiya, A. Prakash, Raj N. Mehrotra, Indian J. Chem. 36A (1997) 959.
[4] C.H. Brubaker, P.G. Rasmussen, Inorg. Chem. 3 (1964) 977.
[5] Rupa Shah, A. Prakash, Raj N. Mehrotra, Indian J. Chem. 38A (1999) 680.
[6] R.A. Marcus, Discuss. Faraday Soc. 29 (1960) 21;
R.A. Marcus, J. Phys. Chem. 67 (1963) 853;
R.A. Marcus, Annu. Rev. Phys. Chem. 3 (1964) 977.
[7] U.C. Agarawal, Ph.D. Dissertation, Boston University, 1960.
[8] B. Goyal, Manu Mehrotra, A. Prakash, Raj N. Mehrotra, Indian J. Chem. 40A (2001) 965.
[9] A. Wanat, R. van Eldik, G. Stochel, J. Chem. Soc., Dalton Trans. (1998) 2497.
[10] Manu Mehrotra, Raj N. Mehrotra, Dalton Trans. (2003) 3606.
[11] G. Nord, Comments Inorg. Chem. 13 (1992) 221.
[12] A.L. Nolan, R.C. Burns, G.A. Lawrence, J. Chem. Soc., Dalton Trans. (1996) 2629.
[13] L.C.W. Baker, B. Love, T.P. McCutcheon, J. Am. Chem. Soc. 72 (1950) 2374.
[14] S. Dholiya, A. Prakash, N. Raj Mehrotra, J. Chem. Soc., Dalton Trans. (1992) 819.
[15] A.D. Awtrey, R.E. Connick, J. Am. Chem. Soc. 73 (1951) 1341.
[16] Raj N. Mehrotra, Uttra Chandrawat, A. Prakash, Indian J. Chem. 36A (1997) 857.
[17] M. Kimura, G. Wada, Inorg. Chem. 17 (1978) 2239.
[18] Raj N. Mehrotra, S. Dholiya, Kamla Sharma, A. Prakash, Indian J. Chem. 37A (1998) 973.
[19] B. Goyal, A. Prakash, Raj N. Mehrotra, Indian J. Chem. 38A (1999) 541.
[20] (a) M.T. Pope, Heteropoly and Isopoly Oxometalates, Springer-Verlag, Berlin, 1983;
(b) G.A. Tsigdinos, Top. Curr. Chem. 1 (1978) 76.
[21] D.E. Katsoulis, M.T. Pope, J. Am. Chem. Soc. 106 (1984) 2737.
[22] A. Treinin, E. Hayon, Int. J. Radiat. Phys. Chem. 7 (1975) 387.
[23] J.H. Baxendale, P.L.T. Bevan, D.A. Stot, Trans. Faraday Soc. 64 (1984) 2389.
[24] M. Eigen, K. Kustin, J. Am. Chem. Soc. 84 (1962) 1355.
[25] G.S. Laurence, K.J. Ellis, J. Chem. Soc., Dalton Trans. (1972) 2229.
[26] J. Macyk, Rudi van Eldik, J. Chem. Soc., Dalton Trans. (2001) 2288.
[27] P. Hemmes, J. Phys. Chem. 76 (1972) 895.
[28] L. Eberson, L. Johnson, Acta Chem. Scand. B40 (1986) 79.
[29] J.J. Lagowski, Modern Inorganic Chemistry, Marcel-Decker, New York, 1973, p. 111.
[30] M.A. Olatunji, G.A. Ayoko, Polyhedron 3 (1984) 191.
[31] D.M. Stanbury, W.K. Wilmarth, S. Khalaf, H.N. Po, J.E. Byrd, Inorg. Chem. 19 (1980) 2715.
[32] W.H. Woodruff, D.W. Margerum, Inorg. Chem. 12 (1973) 962.
[33] C.O. Adedinsewo, A. Adegite, Inorg. Chem. 18 (1979) 3597.
[34] G. Nord, B. Pederson, O. Farver, Inorg. Chem. 17 (1978) 2233.
[35] T.-Chu Lau, K.W.C. Lau, K. Lau, J. Chem. Soc., Dalton Trans. (1994) 3091.
[36] Z. Amzad, J.-C. Brodovitch, A. McAuley, Can. J. Chem. 55 (1977) 3581.
[37] A. Zahl, R. van Eldik, T.W. Swaddle, Inorg. Chem. 41 (2002) 757.
[38] S.W. Benson, The Foundation of Chemical Kinetics, McGraw-Hill, New York, 1990, p. 233.
[39] N. Sutin, Acc. Chem. Res. 15 (1982) 275.
[40] N. Sutin, Prog. Inorg. Chem. 30 (1983) 441.
[41] M.G. Fairbank, A. McAuley, Inorg. Chem. 26 (1987) 2844.
[42] C.St. Nikolov, Inorg. Chim. Acta 5 (1971) 559.
[43] J.F. Earley, Prog. Inorg. Chem. (1970) 13.
[44] R. Sarala, S.B. Rabin, D.M. Stanbury, Inorg. Chem. 30 (1991) 3999.
[45] B.S. Brunschwig, N. Sutin, Inorg. Chem. 18 (1979) 1731.
[46] R. Sarla, D.M. Stanbury, Inorg. Chem. 29 (1990) 3456.
[47] W.U. Malik, S.I. Ali, Indian J. Chem. 1 (1963) 347.
[48] See Ref. [18] in E. Pelizetti, E. Mentasti, E. Pramauro, Inorg. Chem. 17 (1978) 1688.
[49] M.H. Ford-Smith, J.H. Rawsthorne, J. Chem. Soc., Dalton Trans. (1969) 160.
[50] R. Campion, N. Purdie, N. Sutin, J. Am. Chem. Soc. 85 (1964) 3528.
[51] See [4] in [34].
[52] D.W. Margerum, K.L. Chellappa, F.P. Bossu, G.L. Bruce, J. Am. Chem. Soc. 97 (1975) 6894.
[53] P. Hurwitz, K. Kustin, Trans. Faraday Soc. 62 (1966) 427.
[54] A.A. Schilt, Analytical Applications of 110-phenanthroline and Related Compounds, Pergamon, New York, 1969, p. 36, 107, 122.
[55] I. Ruff, M. Zimonyi, Electrochim. Acta 18 (1973) 515.
[56] F.P. Bossu, K.L. Chellapa, D.W. Margerrum, J. Am. Chem. Soc. 99 (1977) 2198.
[57] J.M.T. Raycheba, D.W. Margerum, Inorg. Chem. 20 (1981) 45.
[58] G.D. Owens, D.A. Phillips, J.J. Czarnecki, J.M.T. Raycheva, D.W. Margerum, Inorg. Chem. 23 (1984) 1345.
[59] P.R. Norman, O. Olubuyide, A. McAuley, J. Chem. Soc., Dalton Trans. (1984) 1501.
[60] D.H. Macartney, A. McAuley, O.A. Olubuyide, Inorg. Chem. 24 (1985) 307.
[61] R.I. Haines, A. McAuley, Inorg. Chem. 19 (1980) 719.
[62] P. Carloni, L. Eberson, Acta Chem. Scand. 45 (1991) 373.
[63] D.G. Rasmussen, C.H. Brubaker, Inorg. Chem. 3 (1964) 977.
[64] cf. D.H. Macartney, N. Sutin, Inorg. Chim. Acta 74 (1983) 221.

complexes with the Schiff bases formed from propane-1, 3-diamine and different pyridine carboxyaldehyde or -ketones [16,17] have prompted us to develop new coordination compounds using azide and thiocyanate ligands. Successfully, we have prepared 12 mononuclear complexes of the type $[Cu(bpap)(N_3/NCS)]ClO_4$ (**1a**–**3b**) and $[Cd(bpap)(N_3/NCS)_2]$ (**4a**–**6b**), characterized on the basis of microanalytical, spectroscopic and other physicochemical properties. X-ray crystallographic studies of $[Cu(bpbp)(N_3)]ClO_4$ (**3a**) and $[Cd(bpbp)(NCS)_2]$ (**6b**) were made to define the coordination sphere. The details of synthesis, structure and luminescence behaviour are described below.

2. Experimental

2.1. Materials

High purity pyridine-2-carboxyaldehyde (Lancaster, UK), 2-acetylpyridine (Lancaster, UK), 2-benzoylpyridine (Lancaster, UK), propane-1,3-diamine (Lancaster, UK), sodium azide (Aldrich, USA), ammoniumthiocyanate (Aldrich, USA) potassium hexafluorophosphate (Fluka, Germany), copper nitrate tetrahydrate (E. Merck, India) and cadmium nitrate tetrahydrate (E. Merck, India) were purchased from their respective concerns and used as received. Copper perchlorate hexahydrate and cadmium perchlorate hexahydrate were prepared by treatment of copper carbonate and cadmium carbonate (E. Merck, India) with perchloric acid (E. Merck, India), respectively, followed by slow evaporation on a steam-bath, filtration through a fine glass-frit, and preservation in a desiccator containing concentrated sulfuric acid (E. Merck, India) for subsequent use. Purification of MeOH (E. Merck, India) and preparation of the supporting electrolyte ($[Et_4N][ClO_4]$) for electrochemical work were executed following a reported method [18]. All other chemicals and solvents were AR grade and were used as received.

Caution! Perchlorate and azido compounds of metal ions are potentially explosive, especially in the presence of organic ligands. Only a small amount of material should be prepared and it should be handled with care.

2.2. Physical measurements

Elemental analyses (carbon, hydrogen and nitrogen) were performed on a Perkin–Elmer 2400 CHNS/O Elemental Analyzer. IR spectra (KBr discs, 4000–300 cm^{-1}) were recorded using a JASCO FTIR model 420 spectrometer. Molar conductances were measured using a Systronics conductivity meter where the cell constant was calibrated with 0.01(M) KCl solution, and dry MeOH was used as the solvent. Ground state absorption and steady-state fluorescence measurements were made with a Shimadzu model UV-1601PC UV–Vis spectrophotometer and Hitachi model F-4500 spectrofluorimeter equipped with polarization accessory and low temperature unit (77 K). The temperature of the solution was kept to within ±0.1 K by circulating water through a HETO HOLTEN system. Room-temperature solid phase magnetic susceptibilities were measured at 298 K with a PAR 155 vibrating sample magnetometer with $Hg[Co(SCN)_4]$ as the reference. Mass spectra were obtained with a MAT 8200 (electron ionization, EIMS) instrument. Electrochemical measurements (cyclic voltammetry, CV) were carried out with the use of computer controlled EG&G PARC VersaStat model 270 electrochemical instrument using a platinum disk working electrode as described elsewhere [19]. The solutions were IR compensated and the results were collected at 298 K. The following parameters and relations were used: scan rate (v), 50 $mV\,s^{-1}$; formal potential $E^0 = 0.5(E_{pa} + E_{pc})$ where E_{pa} and E_{pc} are anodic and cathodic peak potentials, respectively; ΔE_p is the peak-to-peak separation. The potentials are referenced to a saturated calomel electrode (SCE) and are uncorrected for junction contributions.

2.3. Preparation of the Schiff bases

The Schiff base chelators, bpfp, bpmp and bpbp, were prepared following a reported [16] procedure with little modification. The details for bpfp are described: Pyridine-2-carboxyaldehyde (0.214 g, 2 mmol) was refluxed with propane-1,3-diamine (0.074 g, 1 mmol) in dehydrated alcohol. After 10 h the reaction solution was evaporated under reduced pressure to yield a gummy mass, which was dried and stored in vacuo over $CaCl_2$ for subsequent use [yield, 0.212 g (80%)]. Bpmp and bpbp were prepared similarly by refluxing for with 10 h 2-acetyl pyridine (0.242 g, 2 mmol) and 2-benzoylpyridine (0.366 g, 2 mmol), respectively, instead of pyridine-2-carboxyaldehyde, with propane-1,3-diamine (0.088 g, 1 mmol) in a 2:1 molar ratio. Yield: (78–80%). *Anal.* calc. for $C_{15}H_{16}N_4$ (bpfp): C, 71.40; H, 6.39; N, 27.20. Found: C, 71.41; H, 7.40; N, 27.23%. Mass spectrum (EI): m/z 252 ($M^+ = L^+$). IR (KBr, cm^{-1}): ν(C=N) 1590. UV–Vis (λ, nm): 240, 370. *Anal.* calc. for $C_{17}H_{20}N_4$(bpmp): C, 77.82; H, 7.19; N, 19.98. Found: C, 77.80; H, 7.20; N, 20.00%. Mass spectrum (EI): m/z 280 ($M^+ = L^+$). IR (KBr, cm^{-1}): ν(C=N) 1592 cm^{-1}. UV–Vis (λ, nm): 243, 370. *Anal.* calc. for $C_{27}H_{24}N_4$ (bpbp): C, 81.10; H, 5.98; N, 13.85. Found: C, 80.05; H, 5.91; N, 13.80%. Mass spectrum (EI): m/z 404 ($M^+ = L^+$). IR (KBr, cm^{-1}): ν(C=N) 1590. UV–Vis (λ, nm): 245, 372.

2.4. Preparation of the complexes

Complexes **1a**–**3b** were prepared from the perchlorate salts of copper(II) using the same mole ratio (1:1:1) of

metal, bpfp/bpmp/bpbp and azide/thiocyanate; these were also isolated using the nitrate salt by finally adding one equivalent sodium perchlorate. **4a**–**6b** were prepared from both cadmium(II) nitrate and/or cadmium(II) perchlorate using a mole ratio of 1:1:2 with bpfp/bpmp/bpbp and azide/thiocyanate. Typical syntheses are described below.

2.4.1. Copper(II)azido complexes

Solid bpfp (0.252 g, 1 mmol) was added pinch by pinch to a solution (10 cm^3) of $Cu(ClO_4)_2 \cdot 6H_2O$ (0.37 g; 1 mmol) in MeOH (15 cm^3) followed by NaN_3 (0.065 g, 1 mmol) with constant stirring. After 30 min the green solution mixture was filtered and the supernatant liquid was kept in air for slow evaporation. After 7 days **1a** was separated, washed with toluene and dried in vacuo over silica gel indicator. Yield: 0.86 g (70%). **2a** and **3a** were prepared by the same procedure using bpmp and bpbp, respectively, instead of bpfp. *Anal.* calc. for $C_{15}H_{16}N_7O_4ClCu$ (**1a**): C, 39.39; H, 3.52; N, 21.44. Found: C, 39.40; H, 3.54; N, 21.46%. IR (KBr, cm^{-1}): ν(C=N) 1637, 1592; $\nu(N_3)$ 2073; $\nu(ClO_4)$ 1080, 622. Mass spectrum (FAB): *m*/*z* 357 ($M^+ = [Cu(bpfp)(N_3)]^+$). Λ_M (MeOH, $\Omega^{-1}\,cm^2\,mol^{-1}$): 130; UV–Vis ($\lambda$, nm): 715, 394. *Anal.* calc. for $C_{17}H_{20}N_7O_4ClCu$ (**2a**): C, 42.06; H, 4.15; N, 20.20. Found: C, 42.08; H, 4.12; N, 20.22%. IR (KBr, cm^{-1}): ν(C=N) 1635, 1592; $\nu(N_3)$ 2072; $\nu(ClO_4)$ 1080, 622. Mass spectrum (FAB): *m*/*z* 385 ($M^+ = [Cu(bpmp)(N_3)]^+$). Λ_M (MeOH, $\Omega^{-1}\,cm^2\,mol^{-1}$): 130; UV–Vis ($\lambda$, nm): 717, 395. *Anal.* calc. for $C_{27}H_{24}N_7O_4ClCu$ (**3a**): C, 53.20; H, 3.97; N, 16.08. Found: C, 53.15; H, 4.21; N, 16.05%. IR (KBr, cm^{-1}): ν(C=N) 1637, 1590; $\nu(N_3)$ 2073; $\nu(ClO_4)$ 1080, 622. Mass spectrum (FAB): *m*/*z* 510 ($M^+ = [Cu(bpbp)(N_3)]^+$). Λ_M (MeOH, $\Omega^{-1}\,cm^2\,mol^{-1}$): 120; UV–Vis ($\lambda$, nm): 720, 402.

2.4.2. Copper(II)thiocyanato complexes

To copper(II) nitrate tetrahydrate (0.241 g, 1 mmol) in methanolic solution (10 cm^3), faint yellow bpbp (0.406 g, 1 mmol) was added dropwise. An methanolic solution (5 cm^3) of ammoniumthiocyanate (0.076 g, 1 mmol) was added with constant stirring. To this solution one equivalent of sodium perchlorate was added slowly drop by drop. The final deep green solution was filtered and left for slow evaporation in air. After a few days fine green crystals of **3b** were separated out, which were filtered, washed with methanol and dried in *vacuo* over $CaCl_2$. Yield: 0.125 g (74%). **1b** and **2b** were prepared by the same procedure using bpfp and bpmp respectively instead of bpbp. *Anal.* calc. for $C_{28}H_{24}N_5SO_4ClCu$ (**3b**): C, 53.76; H, 3.86; N, 11.19. Found: C, 53.72; H, 3.88; N, 11.14%. IR (KBr, cm^{-1}): ν(C=N) 1637,1592; ν(NCS) 2100, 2095; $\nu(ClO_4)$ 1080, 622. Λ_M (MeOH, $\Omega^{-1}\,cm^2\,mol^{-1}$): 130; UV–Vis ($\lambda$, nm): 715, 394. *Anal.* calc. for $C_{16}H_{16}N_5SO_4ClCu$ (**1b**): C, 40.59; H, 3.40; N, 14.79. Found: C, 40.58; H, 3.42; N, 14.77%. IR (KBr, cm^{-1}): ν(C=N) 1635, 1592; ν(NCS) 2092, 2078; $\nu(ClO_4)$ 1080, 622. Λ_M (MeOH, $\Omega^{-1}\,cm^2\,mol^{-1}$): 120; UV–Vis ($\lambda$, nm): 717, 395. Anal. Found: C, 43.12; H, 4.01; N, 13.93. Calc. for $C_{18}H_{20}N_5SO_4ClCu$ (**2b**): C, 43.11; H, 4.02; N, 13.96%. IR (KBr, cm^{-1}): ν(C=N) 1637, 1590; ν(NCS) 2098, 2095; $\nu(ClO_4)$ 1080, 622. Λ_M (MeOH, $\Omega^{-1}\,cm^2\,mol^{-1}$): 120; UV–Vis ($\lambda$, nm): 720, 402.

2.4.3. Cadmium(II)azido complexes

A methanolic solution (5 cm^3) of bpfp (0.252 g, 1 mmol) was added dropwise to a solution of $Cd(ClO_4)_2 \cdot 6H_2O$ (0.311 g; 1 mmol) in the same solvent (10 cm^3) followed by NaN_3 (0.13 g, 2 mmol) in warm methanol (5 cm^3). The green solution was filtered and the supernatant liquid was kept in air for slow evaporation. After a few days **4a** was separated, washed with toluene and dried in vacuo over silica gel indicator. Yield: 0.113 g (70%). **5a** and **6a** were prepared by same procedure using bpmp and bpbp, respectively, instead of bpfp. *Anal.* calc. for $C_{15}H_{16}N_{10}Cd$ (**4a**): C, 40.18; H, 3.59; N, 31.24. Found: C, 40.14; H, 3.64; N, 31.26%. IR (KBr, cm^{-1}): ν(C=N) 1637,1592; $\nu(N_3)$ 2073, 2040. Λ_M (MeOH, $\Omega^{-1}\,cm^2\,mol^{-1}$): 5; UV–Vis ($\lambda$, nm): 335. *Anal.* calc. for $C_{17}H_{20}N_{10}Cd$ (**5a**): C, 42.85; H, 4.23; N, 29.40. Found: C, 42.80; H, 4.22; N, 29.42% IR (KBr, cm^{-1}): ν(C=N) 1635, 1592; $\nu(N_3)$ 2072, 2045. Λ_M (MeOH, $\Omega^{-1}\,cm^2\,mol^{-1}$): 5; UV–Vis ($\lambda$, nm): 336. *Anal.* calc. for $C_{27}H_{24}N_{10}Cd$ (**6a**): C, 53.99; H, 4.02; N, 23.32. Found: C, 53.95; H, 4.06; N, 23.35%. IR (KBr, cm^{-1}): ν(C=N) 1637, 1590; $\nu(N_3)$ 2073, 2040. Λ_M (MeOH, $\Omega^{-1}\,cm^2\,mol^{-1}$): 5. UV–Vis ($\lambda$, nm): 335.

2.4.4. Cadmium(II)thiocyanato complexes

A methanolic solution (5 cm^3) of bpbp (0.406 g, 1 mmol) was added dropwise to a solution of $Cd(ClO_4)_2 \cdot 6H_2O$ (0.311 g; 1 mmol) in the same solvent (10 cm^3) followed by NH_4NCS (0.15 g, 2 mmol) in warm methanol (5 cm^3). The green solution was filtered and the supernatant liquid was kept in air for slow evaporation. After a few days **4b** was separated, washed with toluene and dried in vacuo over silica gel indicator. Yield: 0.242 g (72%). **5b** and **6b** were prepared in the same way using bpmp and bpbp. *Anal.* calc. for $C_{17}H_{16}N_6S_2Cd$ (**4b**): C, 42.48; H, 3.35; N, 17.48. Found: C, 42.47; H, 3.39; N, 17.43%. IR (KBr, cm^{-1}): ν(NCS) 2100, 2095; ν(C=N) 1605. Λ_M (MeOH, $\Omega^{-1}\,cm^2\,mol^{-1}$): 5; UV–Vis (MeOH; λ, nm): 330. *Anal.* calc. for $C_{19}H_{20}N_6S_2Cd$ (**5b**): C, 44.88; H, 3.96; N, 16.53. Found: C, 44.76; H, 3.92; N, 16.57%. IR (KBr, cm^{-1}): ν(C=N) 1635, 1592; ν(NCS) 2100, 2095. Λ_M (MeOH, $\Omega^{-1}\,cm^2\,mol^{-1}$): 5; UV–Vis ($\lambda$, nm): 335. *Anal.* calc. for $C_{29}H_{24}N_6Cd$ (**6b**): C, 55.06; H, 3.82; N, 13.28. Found: C, 55.08; H, 3.86; N, 13.31%. IR (KBr, cm^{-1}): ν(C=N) 1637, 1590; ν(NCS) 2100, 2095. Λ_M (MeOH, $\Omega^{-1}\,cm^2\,mol^{-1}$): 5; UV–Vis ($\lambda$, nm): 332.

2.5. Copper(II)–copper(I) interconversion

2.5.1. $[Cu(bpap)(N_3/NCS)]ClO_4 \rightarrow [Cu(bpap)]ClO_4$

To a methanolic suspension (15 cm^3) of the complexes $[Cu(bpap)(N_3)]ClO_4$ (0.14 g, 0.25 mmol), ascorbic acid (0.045 g, 0.25 mmol) in water (5 cm^3) was added with stirring. The brown suspension quickly changed to deep red-brown and stirring was continued for 30 min, and the precipitated mass was filtered, washed with water and cold methanol. The residue was dried over a $CaCl_2$ desiccator and subjected to column chromatography on a silica gel column prepared in $CHCl_3$. A brownish-red band was eluted by $CHCl_3$–MeOH (4:1, v/v) mixture and dried in air. Crystals were obtained by diffusion of a CH_2Cl_2 solution of the complex to a hexane layer. Yield: 54–57%. The microanalytical data of the complexes are as follows: *Anal*. calc. for $[Cu(bpfp)]ClO_4$: C, 43.43; H, 3.88; N, 13.50. Found: C, 43.40; H, 3.85; N, 13.49%. *Anal*. calc. for $[Cu(bpmp)]ClO_4$: C, 46.10; H, 4.55; N, 12.65. Found: C, 46.09; H, 4.54; N, 12.63%. *Anal*. calc. for $[Cu(bpbp)]ClO_4$: C, 45.48; H, 5.38; N, 12.48. Found: C, 45.47; H, 5.37; N, 12.47%.

2.5.2. $[Cu(bpap)]ClO_4 \rightarrow [Cu(bpap)(N_3/NCS)]ClO_4$

To a methanolic suspension of $[Cu(bpap)]ClO_4$ (0.15 g, 0.25 mmol) an aqueous solution of NaN_3 (0.015 g, 0.25 mmol) was added, air was passed for through the solution for 30 min and from time to time methanol was added to maintain the volume of the solution at 25 ml. The mixture was filtered and kept in a freezer for 4 h. A brown precipitate was filtered and washed with water and cold methanol. The compound was soluble in a mixture of 2-methoxy ethanol and methanol (1:5, v/v) and crystallized by evaporation in air for a week. Yield: 55–60%. The microanalytical data are consistent with complexes **1a**–**3b**.

2.6. X-ray diffraction study

Suitable single crystals of compounds **3a** and **6b** were mounted on a SMART CCD area detector equipped with a graphite monochromotor and Mo Kα(λ = 0.71073) radiation. The intensity data were corrected for Lorentz and polarization effects for all the complexes. Diffraction data for both **3a** and **6b** were measured using the ϕ and ω scan method. The structures were solved by Patterson syntheses using SHELXS-97 [20] and followed by successive Fourier and difference Fourier syntheses. Full-matrix least-squares refinements on F^2 were carried out using SHELXL-97 [21] with anisotropic displacement parameters for all non-hydrogen atoms for the complexes. The hydrogen atoms were fixed geometrically and refined using a riding model. In the final difference Fourier map the residual maxima and minima were 0.395 and −0.262 e $Å^{-3}$ for **3a**, 0.812 and −0.395 e $Å^{-3}$ for **6b**, respectively. All calculations were carried out using PLATON 99 [22] and ORTEP-32 [23]. The crystal data, data collection parameters and the results of analyses of **3a** and **6b** can be found in Table 1.

3. Results and discussion

3.1. Synthesis and formulation

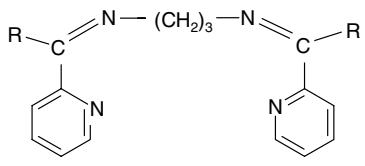
In a one-pot reaction the chelators, the Schiff bases, were prepared by the condensation of one equivalent of propane-1,3-diamine and two equivalents of pyridine-2-carboxyaldehyde/2-acetylpyridine/2-benzoylpyridine in dry alcohol (Scheme 1). The pentacoordinated mononuclear complexes $[Cu(bpap)(N_3/NCS)]ClO_4$ (**1a**–**3b**) initially formed in an MeOH solution containing a 1:1:2 mixture of $Cu(ClO_4)_2 \cdot 6H_2O$, bpap and NaN_3/NH_4NCS; a reactant ratio expected to yield a mononuclear species of the composition $[Cu(pbpa)(N_3/NCS)_2]$. However, microanalyses showed a 1:1:1 ratio of metal, blocking ligand and the pseudohalide, and in the IR spectra the presence of perchlorate bands was noticed. A reactant ratio corresponding to the product stoichiometry afforded better yields of $[Cu(bpap)(N_3/NCS)]ClO_4$ (**1a**–**3b**). In an effort to get $[Cu(bpap)(N_3/NCS)_2]$, the starting material was changed to $Cu(NO_3)_2 \cdot 4H_2O$, and a 1:1:2 molar ratio of nitrate salt, ligand and the pseudohalide produced a gummy mass of indefinite composition. The hexacoordinated mononuclear complexes (**4a**–**6b**) were obtained starting with a 1:1:2 molar ratio of cadmium perchlorate/metal nitrate, bpap and azide/thiocyanate, and conformed in the IR spectra to the absence of perchlorate and/or nitrate bands. The air-stable moisture-insensitive complex salts are highly soluble in common organic solvents like methanol, ethanol, dichloromethane, acetonitrile and dimethylformamide but are insoluble in water. All the complexes were characterized by elemental analysis, electrical conductivity, IR, UV–Vis and reflectance spectra, luminescence behaviour and also magnetic susceptibility, and electrochemistry for the complexes **1a**–**3b**. The results are consistent with the proposed mononuclear formulation. In methanol solutions **1a**–**3b** behave as 1:1 electrolytes [24] as reflected in their Λ_M values (ca. 130 Ω^{-1} cm^2 mol^{-1}) but **4a**–**6b** behave as non-electrolytes as is evident from their low conductivity values (ca. 5 Ω^{-1} cm^2 mol^{-1}). Room-temperature solid-phase magnetic susceptibility measurements show that the copper(II) complexes have magnetic moments close to the spin-only value (S = 1/2), 1.73 BM, as expected from discrete and magnetically non-coupled mononuclear $3d^9$ ions.

3.2. Spectral studies

In the IR spectra, the point of interest is the band due to the azide and thiocyanate in the complexes.

Table 1
Crystal data and structure refinement parameters for **3a** and **6b**

	3a	**6b**
Empirical formula	$C_{27}H_{24}N_7O_4ClCu$	$C_{29}H_{24}N_6S_2Cd$
Formula weight	609.52	633.06
Temperature (K)	296(2)	295(2)
Wavelength (Å)	0.71073	0.71073
Crystal system, space group	monoclinic, *Cc*	triclinic, $P\bar{1}$
a (Å)	22.288(2)	7.8480(5)
b (Å)	12.1157(12)	13.7073(8)
c (Å)	10.1279(10)	14.7229(9)
α (°)	90	62.9370(10)
β (°)	102.636(2)	75.9040(10)
γ (°)	90	83.8340(10)
V (Å^3)	2668.6(5)	1367.92(14)
Z	4	2
D_{calc} (Mg m^{-3})	1.517	1.537
μ (mm^{-1})	0.967	0.981
F(000)	1252	640
Crystal size (mm^3)	$0.36 \times 0.20 \times 0.14$	$0.38 \times 0.30 \times 0.25$
θ ranges (°)	1.87–28.34	1.59–28.27
h/*k*/*l*	−29.22/−9.16/−11.12	−10.10/−18.18/−18.19
Reflections collected	7742	14194
Independent reflections [R_{int}]	4844 [0.0242]	6395 [0.0310]
Completeness to θ (%)	89.8	94.2
T_{max} and T_{min}	0.8693 and 0.7081	0.783 and 0.709
Data/restraints/parameters	4844/2/361	6395/0/343
Goodness-of-fit on F^2	0.995	1.000
Final *R* indices [$I > 2\sigma(I)$]	$R_1 = 0.0555$, $wR_2 = 0.1727$	$R_1 = 0.0295$, $wR_2 = 0.0734$
R indices (all data)	$R_1 = 0.0639$, $wR_2 = 0.1821$	$R_1 = 0.0347$, $wR_2 = 0.0363$
Largest peak and hole (e Å^{-3})	0.395 and −0.262	0.812 and −0.395



R = H, bpfp; R = Me, bpmp; R = Ph, bpbp

Scheme 1.

The spectra exhibit a very strong and sharp absorption band at 2040–2080 cm^{-1} due to asymmetric stretching vibrations [25] of the terminal azide. The presence of ionic perchlorate bands at 1091 and 621 cm^{-1} is noticed for **1a**–**3b**. The complexes **4a**–**6b** show a characteristic strong transmission at 2098–2105 cm^{-1} along with a weak band at 2090–2093 which correspond to $\nu_{asym}(NCS^-)$. The stretching vibrations of the (C=N) band of the Schiff base are seen at 1629 and 1589 cm^{-1}. All other characteristic ligand vibrations are seen in the range 1600–600 cm^{-1}. The solutions of **1a**–**3b** in MeOH are dark green and exhibit absorptions at ca. 720, 400 nm. The transition >700 nm corresponds to a d–d transition of the copper(II) moiety and the band around 400 nm to intramolecular ($n \rightarrow \pi^*$, $\pi \rightarrow \pi^*$) charge transfer transitions [26]. The solutions of the complexes **4a**–**6b** in MeOH are colourless and exhibit absorptions at ca. 330 nm. Reflectance spectra in nujol and electronic spectra in MeOH solutions are akin in each complex, reflecting similar gross structure and electronic structure in the solid state and in solution.

3.3. Electrochemical studies for the copper(II) complexes

Electroactivity of the complexes was studied in MeOH solutions using cyclic voltammetry and coulometry at platinum working electrodes. A one-electron reductive response is observed, presumably due to the electrode reaction:

$$\left[Cu^{II}(L)(N_3)\right]^{1+} + e \rightleftharpoons \left[Cu^{I}(L)(N_3)\right] \quad (1)$$

The electrode process in the CV is reproducible in the potential range of 0.08 to −0.08 V with no trace of decomposition as reflected in smooth cyclic voltammograms. The one-electron stoichiometry of couple 1 was confirmed by a comparison of the current height with that of a standard [27] copper(II)–copper(I) couple, since attempted coulometry at potentials more cathodic than E_{pc} gave a continuous coulomb count due to some unidentified side reactions [28]. The similar pattern in the electron transfer behaviour of all the complexes at about the same potential once again corroborates a similar structure of the cationic units.

3.4. Luminescence properties

Complexes with bpap shows an intense absorption at ca. 405 nm which is assigned to intraligand π–π* transitions. The emission energy of the complexes in MeOH solutions at 298 K is almost same ($\lambda_{max} \approx 475$ nm) and is assignable to intraligand fluorescence [11]. The lifetimes of the complexes are in range 2.55–2.63 ns. In glassy solutions (MeOH at 77 K) both fluorescence and $^3(\pi–\pi^*)$ phosphorescence is observed at 525 nm. In the solid state they show a distinct emission band at 492 nm, differing from their fluorescence spectra in MeOH (Fig. 3).

3.5. X-ray crystal structure

3.5.1. [Cu(bpbp)(N_3)]ClO_4 (**3a**)

In order to define the coordination sphere, a single-crystal X-ray diffraction study was made in one case, viz **3a**. An ORTEP diagram with the atom numbering scheme of the mononuclear unit in **3a** is shown in Fig. 1. Selected interatomic bond lengths and bond angles are listed in Table 2. The crystal lattice consists of $[Cu(bpbd)(N_3)]^+$ cations and ClO_4^- anions. The coordination polyhedron around the metal centre is best described as distorted trigonal bipyramid (tbp) with a CuN_5 chromophore. The coordination includes a tetradentate Schiff base (bpbp), a chelating blocker ligated by two pyridine nitrogens (N5, N7) and two imine nitrogens (N4, N6), and one terminal azide nitrogen (N1). The equatorial positions are occupied by one imine nitrogen (N6), one pyridine nitrogen (N7) and the azide nitrogen (N1) while the axial positions are occupied by the remaining imine (N5) and pyridine (N4) nitrogen atoms. The distortion from ideal tbp geometry is due to the asymmetric nature of the Schiff base and the deviations of the refine angles (90°/120°) formed at the metal centre. The propylenic part of the Schiff base N4–C27–C26–C25–N6 is to some extent puckered due to sp^3 hybridization of the saturated portion of the chelating ligand and deviation [114.6(6)°] from the ideal bond C27–C26–C25 angle of 109°28′ (Fig. 1). The equatorial Cu–N distances [2.005(5)–2.101(5) Å] as well as the bond angles [93.2(2)–133.98(19)°] show significant variations. The axial Cu–N distances [Cu–N4 1.978(4) Å, Cu1–N5 1.994(5) Å] are however close and these are the smaller bond distances than the three equatorial bond distances [9]. The three bite angles N4–Cu–N7, N4–Cu–N6 and N6–Cu–N5 are 79.83(19)°, 92.14(19)° and 80.3(2)°, respectively. The larger bite in N4–Cu–N6 arises due to a six-membered puckered loop formed from the propylenic arm and the lower value of the non-bite angle N5–Cu–N7 [100.6(2)°]. The axial bond angle, N4–Cu–N5 [170.0(2)°], deviates from the ideal value (180°). The sum (359.88°) of the equatorial angles N6–Cu–N7 [133.98(19)°], N1–Cu–N6 [132.7(2)°] and N1–Cu–N7 [93.20(2)° are very close to 360.00°; so the atoms N1, N6, N7 and Cu are almost the same plane. In the terminal azide ligand the N1–N2 distance [1.170(9) Å] is longer than the N2–N3 length [1.152(10) Å] which indicates that the nitrogen (N1) atom of N_3^- is coordinated to the copper(II) centre. The N_3^- ion is coordinated in a linear fashion as seen from its N1–N2–N3 angle [179.0(8)°] [8,10b].

Table 2
Selected bond distances (Å) and angles (°) for **3a**

Bond distances	
Cu–N(4)	1.978(4)
Cu–N(5)	1.994(5)
Cu–N(7)	2.101(5)
N(2)–N(3)	1.152(10)
Cu–N(6)	2.005(5)
Cu–N(1)	2.077(6)
N(1)–N(2)	1.170(9)
Bond angles	
N(4)–Cu–N(5)	170.0(2)
N(4)–Cu–N(6)	92.14(19)
N(5)–Cu–N(1)	95.8(2)
N(5)–Cu–N(6)	80.3(2)
N(4)–Cu–N(1)	94.1(2)
N(6)–Cu–N(1)	132.7(2)
N(4)–Cu–N(7)	79.83(19)
N(5)–Cu–N(7)	100.6(2)
N(6)–Cu–N(7)	133.98(19)
N(1)–Cu–N(7)	93.2(2)
N(2)–N(1)–Cu	118.1(5)
N(3)–N(2)–N(1)	179.0(8)

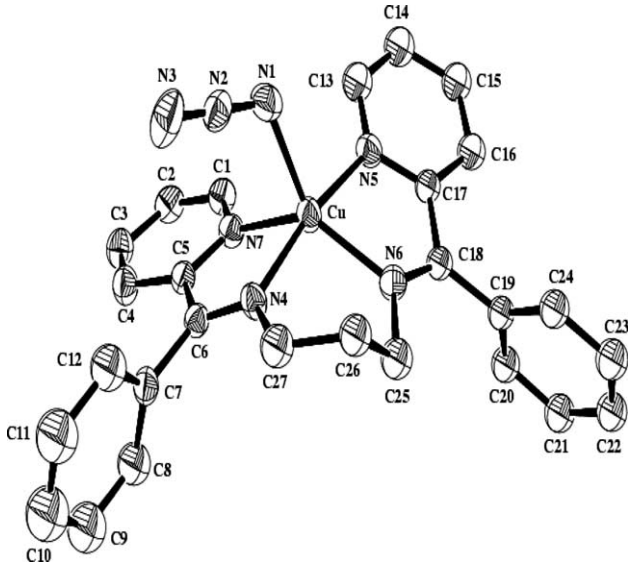


Fig. 1. ORTEP diagram of $[Cu(bpbp)(N_3)]ClO_4$ (**3a**) with the atom numbering scheme and 40% probability ellipsoids for all non-hydrogen atoms.

3.5.2. [Cd(bpbp)(NCS)$_2$] (**6b**)

An ORTEP view with the atom numbering scheme of the mononuclear unit in **6b** is shown in Fig. 2. Selected bond lengths and angles relevant to the coordination sphere are listed in Table 3. The metal centre is best described as a distorted octahedron with a CdN_6 chromophore. Distortion from the ideal octahedral geometry is due to the asymmetric nature of the bound tetradentate Schiff base and the deviations of the refine angles (90°/180°) formed at the metal centre (Table 3). The coordination includes the Schiff base ligated by two pyridine nitrogens (N3, N6) and two imine nitrogens (N4, N5), and two nitrogens (N1, N2) of the thiocyanates. The equatorial positions are occupied by the four nitrogen atoms (N3, N4, N5 and N6) of the tetradentate ligand while the nitrogens (N1, N2) of the isothiocyanato groups are placed at the axial positions. The propylenic part of the Schiff base N5–C17–C16–C5–N4 is to some extent puckered due to sp^3 hybridization of the saturated portion of the chelating ligand and deviation [119.1(2)°] from the ideal C15–C16–C17 bond angle of 109°28′. The four N atoms of the ligand creates hardness in the cadmium(II) centre; so it appears to be a major reason to have preferential N-donation of the ambidentate NCS through its electronegative hard centre. The degrees of distortion from an ideal octahedral (90°) geometry are reflected in the *cisoid* [69.42(6)–119.35(8)°] and the *transoid* angles [141.03(7)–160.23(8)°]. Within the equatorial plane the Cd–N distances are in the range [2.271(2)–2.4486(18) Å], comparable to the corresponding values in similar systems [11]. Axial Cd–N distances [2.301(2)–2.4376(19) Å] indicate stronger coordination of the anionic isothiocyanate over the neutral Schiff base [17]. The angles subtended by the ligand around cadmium in the equatorial plane shows a significant variation [69.42(6)–119.35(8)°] from

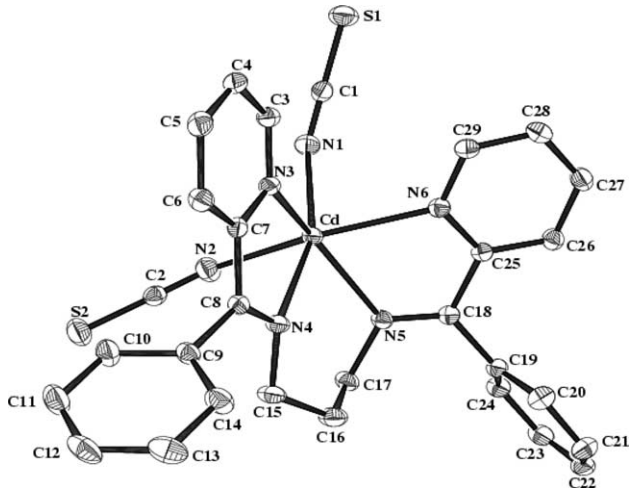


Fig. 2. ORTEP plot of [Cd(bpbp)(NCS)$_2$] (**6b**) with the atom numbering scheme and 40% probability ellipsoids for all non-hydrogen atoms.

Table 3
Selected bond distances (Å) and angles (°) for **6b**

Bond distances	
Cd–N(3)	2.3429(18)
Cd–N(6)	2.4376(19)
Cd–N(1)	2.271(2)
Cd–N(4)	2.4486(18)
S(1)–C(1)	1.620(3)
Cd–N(2)	2.301(2)
Cd–N(5)	2.3157(19)
S(2)–C(2)	1.621(3)
N(1)–C(1)	1.161(3)
N(2)–C(2)	1.158(3)
Bond angles	
N(3)–Cd–N(1)	94.37(8)
N(5)–Cd–N(1)	119.35(8)
N(3)–Cd–N(2)	100.70(8)
N(5)–Cd–N(2)	98.02(8)
N(1)–Cd–N(2)	90.63(9)
N(5)–Cd–N(6)	69.48(6)
N(3)–Cd–N(6)	98.44(6)
N(1)–Cd–N(4)	159.36(8)
N(6)–Cd–N(5)	82.97(7)
N(3)–Cd–N(5)	141.03(7)
N(2)–Cd–N(6)	160.23(8)
N(2)–Cd–N(4)	80.39(8)
N(5)–Cd–N(4)	80.53(6)
N(3)–Cd–N(4)	69.42(6)
N(6)–Cd–N(4)	111.25(6)
N(1)–C(1)–S(1)	179.2(3)
N(2)–C(2)–S(2)	179.2(3)

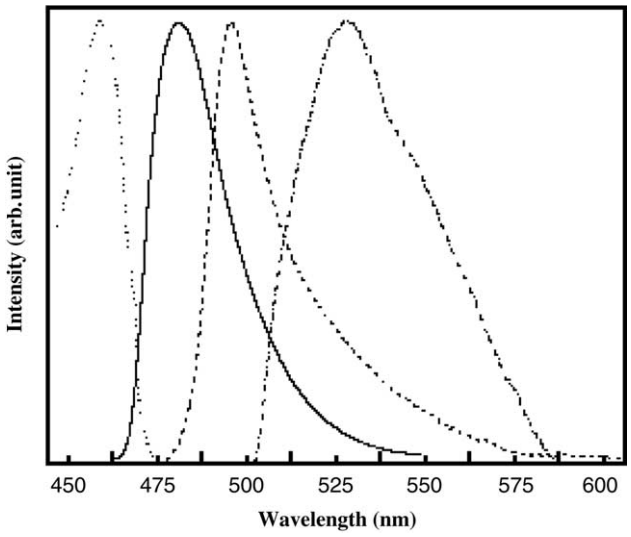


Fig. 3. Emission spectra of **3a**: fluorescence (—), phosphorescence in DMF glassy solution (-·-·-·), solid state at 298 K (-----).

the ideal 90.00°. The *trans* N2–Cd–N6 angle has a value [160.23(8)°], not close to the ideal value of 180.00°. The angles N1–Cd–N3, N3–Cd–N4 and N4–Cd–N5 in the equatorial plane with values 94.37(8)°, 69.42(6)° and 80.53(6)° are much less than the N1–Cd–N5 angle [119.35(8)°], where N3, N6 belong to the two pyridine ends of the Schiff base. Both the isothiocyanate ligands

are almost linear with exact 179.2(3)° angles. N–C [1.158(3)–1.161(3) Å] and C–S [1.620(3)–1.621(3) Å] bond lengths are as expected for N-coordination [11]. All the other bond lengths and angles on the ligand network are close to the expected values [6a].

4. Conclusion

Twelve new complexes are prepared in combination with tetradentate Schiff bases as blockers. In all cases a chelation mode of the Schiff bases is noticeable. The compounds are new example of luminous materials. We are now investigating the congregation [8] behaviour of related tetradentate N-donor Schiff bases with tailoring on the propylenic arm as well as acidic proton(s) on the ligand network towards the preparation of coordination polymers and supramers of varied molecular and crystalline architectures, which may behave as better luminous materials.

5. Supplementary data

Crystallographic data for the structural analysis have been deposited with the Cambridge Crystallographic Data Centre Nos. 260089 for **3a** and 260090 for **6b**. Copies of this information can be had free of charge from The Director, CCDC, 12 Union Road, Cambridge, CB2 IEZ, UK (fax: +44 1223 336 033; e-mail: deposit @ccdc.cam.ac.uk or http://www.ccdc.cam.ac.uk).

Acknowledgement

Financial support from the DST and CSIR, New Delhi, India is gratefully acknowledged.

References

[1] (a) P. Comba, T.W. Hambley, Molecular Modelling of Inorganic and Coordination Compounds, 2nd ed., VCH, Weinheim, 2001;
(b) D.B. Mitzi, Progr. Inorg. Chem. 48 (1999) 1;
(c) B. Moulton, M.J. Zaworotko, Chem. Rev. 101 (2001) 1629.
[2] B. Cornils, W.A. Herrmann, R. Schlogl (Eds.), Catalysis from A to Z: a Concise Encyclopedia, Wiley, New York, 2000.
[3] J.R. Farraro, J.M. Williams, Introduction to Synthetic Electrical Conductors, Academic Press, New York, 1987.
[4] J.S. Miller, M. Drillon (Eds.), Magnetism: Molecules to Materials IV, Wiley–VCH, Weinheim, 2003.
[5] (a) S.R. Marder, J.E. Sohn, G.D. Stucky (Eds.), Materials for Nonlinear Optics: Chemical Perspectives, ACS Symposium Series, Washington, DC, 1991;
(b) O.R. Evans, W. Lin, Acc. Chem. Res. 35 (2002) 511.
[6] (a) M. Mikuriya, Y. Hatano, E. Asato, Bull. Chem. Soc. Jpn. 70 (1997) 2495;
(b) A.D. Garnovskii, A.L. Nivorozkin, V.L. Minkin, Coord. Chem. Rev. 126 (1993) 1;
(c) V. Alexander, Chem. Rev. 95 (1995) 273.
[7] (a) M.K. Saha, D.K. Dey, B. Samanta, A.J. Edwards, W. Clegg, S. Mitra, J. Chem. Soc., Dalton Trans. (2003) 488;
(b) R. Paschke, S. Liebsch, C. Tschierske, M.A. Oakley, E. Sinn, Inorg. Chem. 42 (2003) 8230.
[8] T.K. Karmakar, S.K. Chandra, J. Ribas, G. Mostafa, T.-H. Lu, B.K. Ghosh, Chem. Commun. (2002) 2364, and references therein.
[9] Sk.H. Rahaman, D. Bose, R. Ghosh, H.-K. Fun, B.K. Ghosh, Indian J. Chem. A 43 (2004) 1901.
[10] (a) D. Bose, Sk.H. Rahaman, G. Mostafa, R.D. Bailey Walsh, M.J. Zaworotko, B.K. Ghosh, Polyhedron 23 (2004) 545;
(b) J. Banerjee, D. Bose, Sk.H. Rahaman, M.J. Zaworotko, B.K. Ghosh, Indian J. Chem. A 43 (2004) 1119.
[11] D. Bose, J. Banerjee, Sk.H. Rahaman, G. Mostafa, H.-K. Fun, R.D. Bailey Walsh, M.J. Zaworotko, B.K. Ghosh, Polyhedron 23 (2004) 2045.
[12] (a) A.M. Golub, H. Kohler, V.V. Skopenko (Eds.), Chemistry of Pseudohalides, Elsevier, Amsterdam, 1986;
(b) U. Ray, S. Jasimuddin, B.K. Ghosh, M. Monfort, J. Ribas, G. Mostafa, T.-H. Lu, C. Sinha, Eur. J. Inorg. Chem. (2004) 250.
[13] (a) G. Wilkinson, Comprehensive Coordination Chemistry, vol. 5, Pergamon Press, Oxford, 1987, p. 775;
(b) K.D. Karlin, J. Zubieta (Eds.), Copper Coordination Chemistry, Biochemical and Inorganic Perspectives, Adenine Press, Guilderland, NY, 1983.
[14] (a) G. Mostafa, A. Mondal, A. Ghosh, I.R. Laskar, A.J. Welch, N. Ray Chaudhuri, Acta Crystallogr., Sect. C 56 (2000) 146;
(b) B.G. Chand, U.S. Ray, G. Mostafa, T.-H. Lu, C.R. Sinha, Polyhedron 23 (2004) 1669.
[15] (a) R. Wang, M. Hong, D. Yuan, Y. Sun, L. Xu, J. Luo, R. Cao, A.S.C. Chan, Eur. J. Inorg. Chem. (2004) 37;
(b) X. Shi, G. Zhu, Q. Fang, G. Wu, G. Tian, R. Wang, D. Zhang, M. Xue, S. Qiu, Eur. J. Inorg. Chem. (2004) 185.
[16] (a) C.-M. Liu, R.-G. Xiong, X.-Z. You, Y.-J. Liu, K.-K. Cheung, Polyhedron 15 (1996) 4565;
(b) C.-M. Liu, R.-G. Xiong, X.-Z. You, H.-K. Fun, K. Sivakumar, Polyhedron 16 (1997) 119;
(c) M.S. Ray, R. Bhattacharya, S. Chaudhuri, L. Righi, G. Bocelli, G. Mukhopadhyay, A. Ghosh, Polyhedron 22 (2003) 617.
[17] A. Jäntti, M. Wagner, M. Wagner, R. Suontamo, E. Kolehmainen, K. Rissanen, Eur. J. Inorg. Chem. (1998) 1555.
[18] C.H. Hamann, A. Hammet, W. Vielstich, Electrochemistry, Wiley–VCH, Weinheim, 1998, p. 57.
[19] H. Chowdhury, D. Bose, Sk.H. Rahaman, B.K. Ghosh, Indian J. Chem. A 42 (2003) 2772.
[20] G.M. Sheldrick, SHELXTL V5.1, Software Reference Manual, Bruker AXS, Inc., Madison, WI, USA, 1997.
[21] G.M. Sheldrick, SHELXL-97, Program for Refinement of Crystal Structures, University of Göttingen, Germany, 1997.
[22] A.L. Spek, PLATON 99: Molecular Geometry Program, University of Utrecht, The Netherlands, 1999.
[23] L.J. Farrugia, J. Appl. Crystallogr. 30 (1997) 565.
[24] W.J. Geary, Coord. Chem. Rev. 7 (1971) 81.
[25] K. Nakamoto, Infrared and Raman Spectra of Inorganic and Coordination Compounds, Wiley, New York, 1986, pp.290.
[26] A.B.P. Lever, Inorganic Electronic Spectroscopy, 2nd ed., Elsevier, New York, 1984.
[27] J. Dinda, U. Ray, G. Mostafa, T.-H. Lu, A. Usman, I.A. Razak, S. Chantrapromma, H.-K. Fun, C. Sinha, Polyhedron 22 (2003) 247.
[28] J. Heinze, Angew Chem., Int. Ed. Engl. 23 (1984) 831.

cationic $[Mo(H_2NO)(H_2O)(NO)(terpy)]^{2+}$ complex and CN^- ions [28,29].

It is noticeable that none of the reported cyanonitrosyl complexes of Mo and W have been obtained either from direct synthesis with nitric oxide or from their cyanocomplexes. Our recent investigations on the reactivity of $[M(CN)_4O(L)]^{n-}$ type complexes have revealed their capability of binding of molecular oxygen [30–32]. These reactions proceed via paramagnetic M^V intermediates with the formation of final peroxo complexes, $[M(CN)_4O(O_2)]^{2-}$. The use of NO (instead of O_2), being known for strong coordination to various metals, could facilitate the isolation of the paramagnetic products since nitric oxide can be reduced only in a one-electron process upon coordination. Based on our previous results, we selected $(PPh_4)_2[M(CN)_4O(pz)]\cdot 3H_2O$ salts for the reaction with NO as they have got the weakest M–L bond of all the characterized salts of that class.

In this work we report for the first time the direct reaction between NO and cyanocomplexes of molybdenum(IV) and tungsten(IV). This process is the first example of oxo ligand substitution in the coordination sphere of $[M(CN)_4O(L)]^{n-}$ type complexes. We also describe the X-ray crystal structure and properties of the molybdenum product.

2. Results and discussion

2.1. Reactions with NO

In order to investigate the reactivity of oxocyanocomplexes of Mo(IV) and W(IV) towards NO we have selected the $[M(CN)_4O(pz)]^{2-}$ anions as they have the weakest M–pz bond of all known complexes of that type [$d_{M-N(pz)}$ = 2.569 Å (Mo) and 2.521 Å (W)] [30,33]. We have observed that bubbling nitric oxide through a dioxygen-free dichloromethane solution of the $[M(CN)_4O(pz)]^{2-}$ complexes results in a colour change from green to yellow. IR liquid spectra measured during that process are presented in Fig. 1 in the case of the molybdenum complex and in Fig. 2 in the case of the tungsten one.

The spectra revealed new intense bands at 1692 cm^{-1} (for Mo) and 1653 cm^{-1} (for W) confirming in both cases the coordination of NO. Their relatively low wavenumbers indicate the nitrosyl ligand to be in the form of the NO^- anion [34–36]. The observed bands change subsequently into one intense band at 1712 cm^{-1}, in both cases. The increase of those bands was also accompanied by a decrease of the characteristic M–O band at 974 cm^{-1} (Mo) or 969 cm^{-1} (W) as well as an increase of two new bands at 1222 cm^{-1} (Mo and W) and 1362 cm^{-1} (Mo) or 1355 cm^{-1} (W) (Figs. 1 and 2). The pair of bands (1712 and 1222 cm^{-1}) appearing in the same positions in the reaction of both molybdenum and tungsten complexes

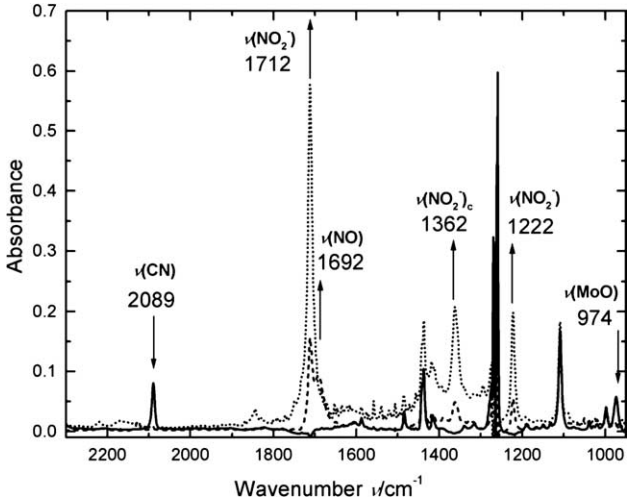


Fig. 1. IR spectra (950–2300 cm^{-1} range) of a deoxygenated dichloromethane solution containing $[Mo(CN)_4O(pz)]^{2-}$ (solid line) after 6 min (dashed line) and 60 min (dotted line) of NO bubbling. Numbers indicate wavenumbers (in cm^{-1}) and the arrows show the direction of the changes.

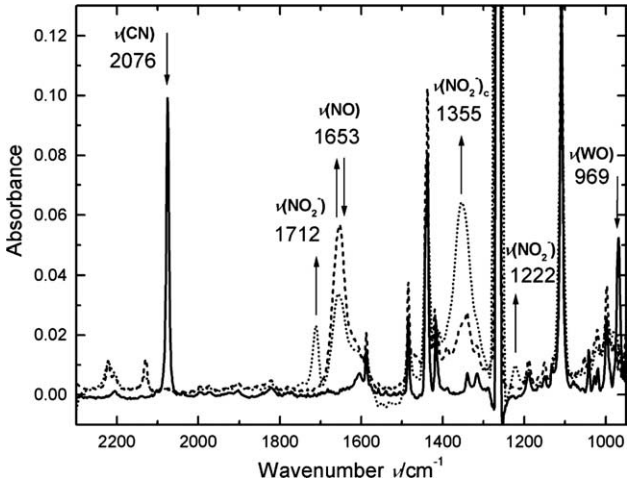


Fig. 2. IR spectra (950–2300 cm^{-1} range) of a deoxygenated dichloromethane solution containing $[W(CN)_4O(pz)]^{2-}$ (solid line) after 8 min (dashed line) and 51 min (dotted line) of NO bubbling. Numbers indicate wavenumbers (in cm^{-1}) and the arrows show the direction of the changes.

was attributed to the stretching vibrations of the NO_2^- group of the uncoordinated nitrites. Such pairs of bands corresponding to stretching N–O vibrations are characteristic of nitrites [4,37]. The formation of NO_2^- anions can be explained by the attack of NO at the oxo ligand in the starting complexes (we observe a decrease of the M–O bands) and subsequent release of a nitrite into solution. After the release of NO_2^-, the resulting complex easily binds other molecules present in solution. In the case of molybdenum at that stage of the reaction the yellow product of the formula $(PPh_4)_4[\{Mo(CN)_5(NO)\}_2(\mu\text{-pz})]\cdot C_4H_9OH\cdot CH_2Cl_2$ (**1a**), was isolated from solution. We have observed that the salt is soluble in

methanol and acetonitrile, and insoluble in such solvents as water, ethanol, butane-1-ol, dichloromethane, acetone and diethyl ether. Its recrystallization in the presence of diethyl ether leads to monocrystals of $(PPh_4)_4[\{Mo(CN)_5(NO)\}_2(\mu\text{-pz})]\cdot 2C_2H_5OC_2H_5$ (**1b**) that were used for X-ray diffraction measurements.

The described reaction of $(PPh_4)_2[M(CN)_4O(pz)]\cdot 3H_2O$ with NO is not the only one proceeding in solution (Figs. 1 and 2). We have observed that if the complex **1a** is not isolated and further NO is passed through the solution, it results in decay of the nitrosyl complex and the IR band appearing at 1362 cm^{-1} (Mo) or 1355 cm^{-1} (W) was assigned to the N–O stretching vibrations of a coordinated NO_2^- ligand. The reported wavenumbers are typical of nitrito ligands [4]. In the case of Mo we have recorded the IR spectrum of the solution confirming the presence only of free and coordinated nitrites.

2.2. Description of the structure of *1b*

The structure of the **1b** anion is presented in Fig. 3, together with the numbering scheme. The selected bond lengths and angles are gathered in Table 1.

The structure is centrosymmetric and the asymmetric unit contains half of the complex anion. In the anion pyrazine forms a bridge between two molybdenum centres, each of which are surrounded by five equatorial cyano ligands and one axial nitrosyl ligand. The central ion exhibits a distorted pentagonal bipyramidal geometry and is slightly displaced out of the equatorial plane towards the NO ligand (the average N6–Mo1–C angle is 93.5°). Similar deformations have been observed for oxocyano complexes with relevance to the oxo ligand. In salt **1b** the displacement towards the NO ligand is smaller than the ones towards oxo ligands, observed in the oxocyano complexes. The Mo1–N6 and N6–O1 bond lengths [1.775(3) and 1.198(4) Å, respectively] are typical for nitrosyl complexes of molybdenum regardless of the coordination number, other ligands or assignment

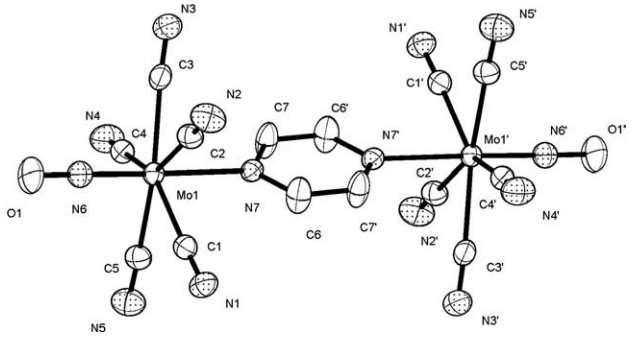


Fig. 3. The structure of the complex anion in $(PPh_4)_4[\{Mo(CN)_5(NO)\}_2(\mu\text{-pz})]\cdot 2C_2H_5OC_2H_5$ with the atom labelling scheme and 50% displacement ellipsoids. The ion is located on a centre of symmetry and primed atoms are generated by $0.5 - x$, $1.5 - y$, $-z$.

Table 1
Selected bond distances and angles of $(PPh_4)_4[\{Mo(CN)_5(NO)\}_2(\mu\text{-pz})]\cdot 2C_2H_5OC_2H_5$ with estimated standard deviations in parentheses

Bond distances (Å)	
Mo1–N6	1.775(3)
Mo1–C1	2.158(3)
Mo1–C2	2.157(3)
Mo1–C3	2.159(4)
Mo1–C4	2.170(4)
Mo1–C5	2.150(3)
N7–C6	1.320(4)
N7–C7	1.325(4)
N6–O1	1.198(4)
Mo1–N7	2.332(3)
C1–N1	1.138(4)
C2–N2	1.142(4)
C3–N3	1.140(4)
C4–N4	1.144(4)
C5–N5	1.138(4)
C6–C7′	1.396(5)
C7–C6′	1.396(5)
Bond angles (°)	
N6–Mo1–C5	92.43(13)
N6–Mo1–C4	94.35(12)
N6–Mo1–C3	96.80(13)
N6–Mo1–C2	90.58(13)
N6–Mo1–C1	93.61(12)
C5–Mo1–C3	143.27(13)
C5–Mo1–C2	142.94(13)
C3–Mo1–C2	72.62(12)
C5–Mo1–C1	71.68(12)
C3–Mo1–C1	142.42(12)
C2–Mo1–C1	71.27(12)
C5–Mo1–C4	72.29(12)
C3–Mo1–C4	71.62(12)
C2–Mo1–C4	144.23(12)
C1–Mo1–C4	143.35(12)
O1–N6–Mo1	178.2(3)
N6–Mo1–N7	177.37(11)
C5–Mo1–N7	89.87(11)
C3–Mo1–N7	82.09(11)
C2–Mo1–N7	86.81(11)
C1–Mo1–N7	85.89(10)
C4–Mo1–N7	87.57(10)
N1–C1–Mo1	178.1(3)
N2–C2–Mo1	177.5(3)
N3–C3–Mo1	175.3(3)
N4–C4–Mo1	178.2(3)
N5–C5–Mo1	177.3(3)
C6–N7–C7	114.3(3)
C6–N7–Mo1	122.8(2)
C7–N7–Mo1	122.7(2)
N7–C6–C7′	123.2(3)
N7–C7–C6′	122.4(3)

of the formal oxidation state of molybdenum [18–20,26]. In particular, the Mo–N(nitrosyl) bond in **1b** is slightly shorter than the analogous bond in the [Mo(CN)(HNO)(NO)(terpy)] complex [d_{Mo-N} = 1.802(7) Å] whereas the NO bonds are the same within experimental errors in both complexes {1.198(4) Å in **1b** versus 1.209(9) Å in [Mo(CN)(HNO)(NO)(terpy)]} [29]. The Mo1–N6–O1 group in **1b** is approximately linear [the

angle is 178.2(3)°] and the same geometries have also been observed for Mo(II) complexes ($\{MNO\}^4$ systems in Enemark's notation). It is consistent with general Enemark's considerations for systems with a low number of {MNO} electrons [38]. According to that formalism, the {MNO} group is considered as a discrete entity and the assignment of the formal metal oxidation state is based upon the treatment of the NO ligand as a neutral species. Thus, in our case we should treat **1b** as a compound with Mo(III) ($\{MNO\}^4$) centres. However, the EPR experiments (vide infra) confirms that the salt is diamagnetic. Hence, based on both structural and spectroscopic data (IR and EPR – vide infra) we propose a Mo(IV)–NO^- assignment of the salt. These data [in particular d_{N6-O1} = 1.198(4) Å (**1b**) greater than 1.154 Å in free NO as well as ν(NO) = 1684 cm^{-1} (**1a**) less than 1875 cm^{-1} in free NO] indicate the predominant $d_{Mo} \rightarrow \pi^*_{NO}$ electron density shift and are consistent with such an assignment [2]. The bonding length of Mo1–N7 (2.332 Å) to the pyrazine, is considerably smaller than in the case of the monomeric $[Mo(CN)_4O(pz)]^{2-}$ oxocyano complex ($d_{Mo-N5(pz)}$ = 2.569 Å) which indicates the stronger bonding of diazine as a bridging ligand. The Mo1–C and C–N bond lengths are similar (in average: d_{Mo1-C} = 2.159 Å and d_{C-N} = 1.140 Å) and the Mo1–C–N groups are approximately linear (the average Mo1–C–N angle is 177.3°). These bond lengths are typical for other Mo(IV) cyano complexes [33]. A similar dimeric structure with a bridging pyrazine has recently been published in the case of the cationic porphyrin complex of iron(III), $[\{Fe(oep)(NO)\}_2(\mu\text{-pz})]^+$ [39]. It contains a near linear Fe–N–O group (the Fe–N–O angle is 176.5°) with a slightly shorter NO bond (d_{N-O} = 1.131 Å) in comparison with the structure of **1b**. Moreover, the bridging pyrazine is considerably closer to the central ions ($d_{Fe-N(pz)}$ = 2.039 Å) than in the molybdenum complex ($d_{Mo1-N7(pz)}$ = 2.332 Å).

2.3. IR and EPR spectra of *1a*

The IR spectrum of solid **1a**, presented in Fig. 4, shows an intense band at 1684 cm^{-1}, assigned to the stretching N–O vibrations of the nitrosyl ligand. Its relatively low wavenumber indicates the anionic form of the ligand, NO^- (the analogous wavenumber in free gaseous nitric monoxide is 1875 cm^{-1}) [2]. The IR spectrum also contains several bands characteristic for pyrazine [40] and tetraphenylphosphonium cations as well as solvent molecules outside the coordination sphere [several bands in the range of 2800–3000 cm^{-1}, corresponding to stretching vibrations in CH_3 and CH_2 groups; a band at 1070 cm^{-1} corresponding to conjugated stretching vibrations of C–O of a C–OH group; a band at 1317 cm^{-1} assigned to ν(OH) deformation; one broad band at 3400 cm^{-1} assigned to stretching vibrations of intermolecularly associated OH groups; and a band at

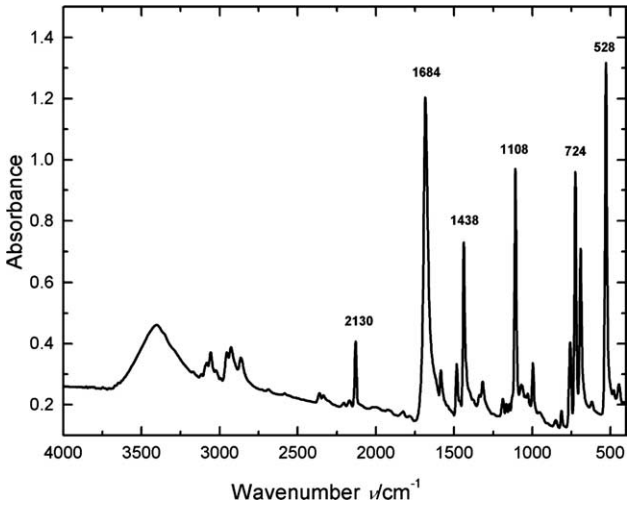


Fig. 4. IR spectrum of $(PPh_4)_4[\{Mo(CN)_5(NO)\}_2(\mu\text{-pz})]\cdot C_4H_9OH \cdot CH_2Cl_2$ in KBr. Numbers indicate wavenumbers (in cm^{-1}) of the most intense bands.

724 cm^{-1} assigned to ν(CCl) overlapping with bands of PPh_4^+ origin] [37]. The spectrum does not contain any bands in the 900–990 cm^{-1} region, which indicates the absence of a MoO group in the analyzed compound. In the CN stretching region the bands at 2130, 2169 and 2205 cm^{-1} confirm the presence of cyano ligands.

The EPR spectrum of **1a** confirms the lack of paramagnetic centres both in the solid state and in solution (MeCN). The diamagnetism is consistent with a formal IV oxidation state of molybdenum as well as with a charged NO^- ligand.

2.4. Mass spectrum

Negative ionization reveals the presence of $\{(PPh_4)[Mo(CN)_5(NO)]\}^-$ fragments in the mass spectrum with the characteristic pattern for molybdenum isotopes [^{100}Mo(9.62%); ^{98}Mo(23.75%); ^{97}Mo(9.45%); ^{96}Mo(16.50%); ^{95}Mo(15.70%); ^{94}Mo(9.12%) and ^{92}Mo(15.86%)] at m/z = 591, 593, 594, 595, 596, 597 and 599 (Fig. 5). The positive ionization results in the appearance of two signals at m/z = 339 and 340 confirming the presence of PPh_4^+ cations.

2.5. Electronic absorption spectra

The UV–Vis spectrum (in the range of 300–500 nm) of **1a** in acetonitrile is presented in Fig. 6. It shows an intense band at λ_{max} = 365 nm (ε_{max} = 2800 mol^{-1} dm^3 cm^{-1}) that was assigned to a MLCT type ($d_{Mo} \rightarrow d_{Mo} \rightarrow \pi^*_{NO}$) transition. Analogous bands have been found for other pyrazine complexes, e.g., in the Creutz-Taube ion, $[\{Ru(NH_3)_5\}_2(\mu\text{-pz})]^{n+}$ (n = 4, 5, 6) with a bridging pz [41,42] or in $[Ru(CN)_5(pz)]^{3-}$ with a monodentate pz [43]. We have observed that this band decreases with time

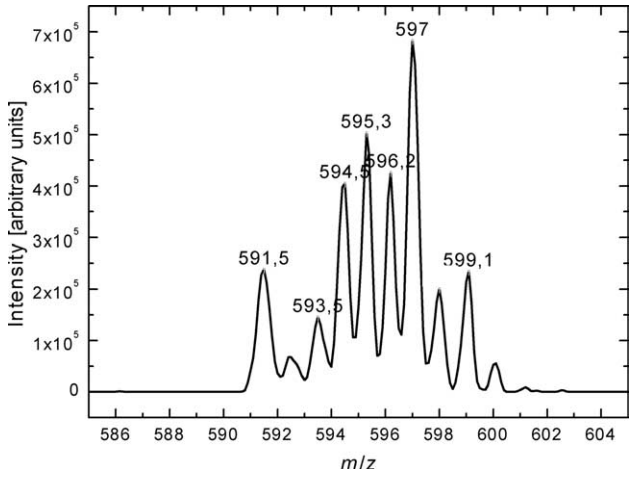


Fig. 5. Mass spectrum of $(PPh_4)_4[\{Mo(CN)_5(NO)\}_2(\mu\text{-pz})]\cdot C_4H_9OH\cdot CH_2Cl_2$ (negative ionization). Numbers indicate peak positions corresponding to several molybdenum isotopes. The other signals appear due to the presence of carbon (^{12}C and ^{13}C) and nitrogen (^{14}N and ^{15}N) isotopes.

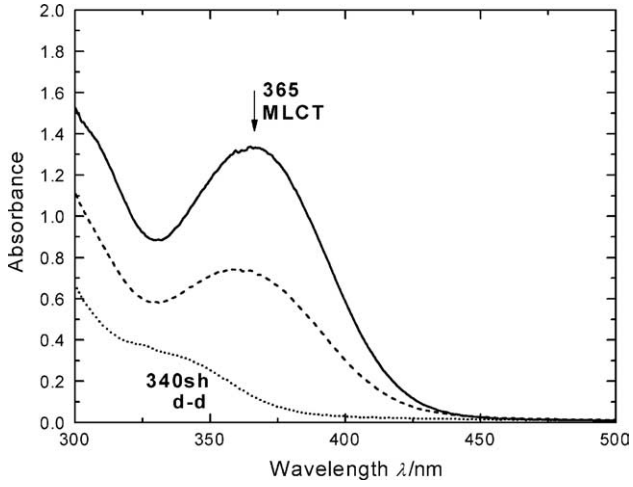


Fig. 6. Electronic absorption spectrum (300–500 nm range) of $(PPh_4)_4[\{Mo(CN)_5(NO)\}_2(\mu\text{-pz})]\cdot C_4H_9OH\cdot CH_2Cl_2$ in acetonitrile (solid line, $c = 4.74\times10^{-4}$ M) and the changes observed with time (dotted line corresponds to final spectrum). Numbers indicate band positions (in nm) and the arrow shows the direction of the changes.

(Fig. 6) simultaneously revealing a band at 340 nm (sh) of a very low intensity which was attributed to a d–d transition. The decrease of the band at 365 nm may be the result of pyrazine being released from the coordination sphere. Apart from the bands at 365 and 340 nm in the UV region, one can observe overlapping bands characteristic for pyrazine ($\pi \rightarrow \pi^*$ or $n \rightarrow \pi^*$) and tetraphenylphosphonium cations ($\pi \rightarrow \pi^*$) [44]. The instability of solutions of **1a** in MeCN, detected by a very slow decrease in intensity of the MLCT band in the UV–Vis spectrum, does not affect the interpretation of solution IR and cyclic voltammetry experiments.

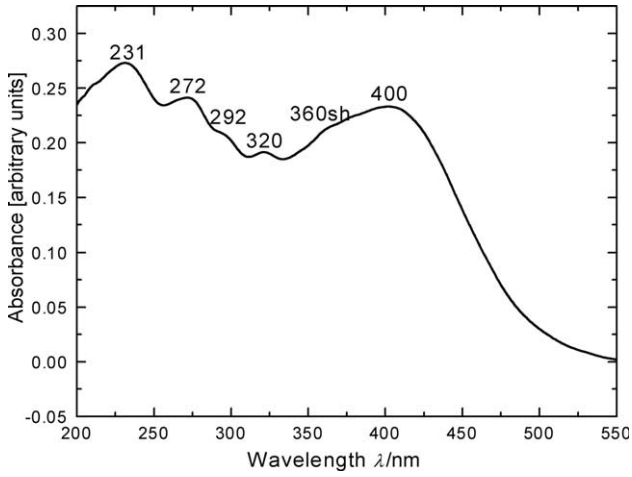


Fig. 7. Diffuse reflectance spectrum of $(PPh_4)_4[\{Mo(CN)_5(NO)\}_2(\mu\text{-pz})]\cdot C_4H_9OH\cdot CH_2Cl_2$. Numbers indicate band positions (in nm).

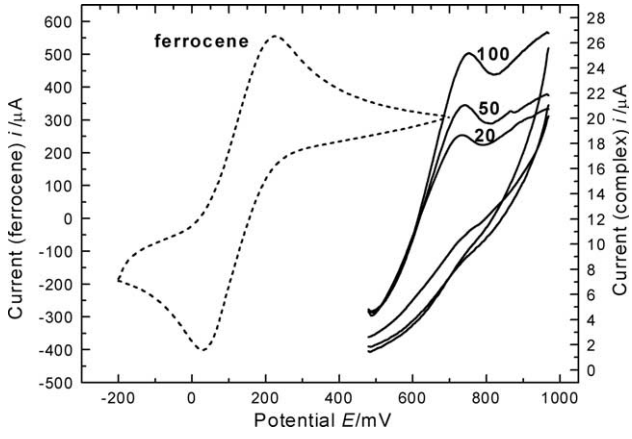


Fig. 8. Cyclic voltammograms of $(PPh_4)_4[\{Mo(CN)_5(NO)\}_2(\mu\text{-pz})]\cdot C_4H_9OH\cdot dot\ CH_2Cl_2$ in acetonitrile (solid lines). Numbers indicate scan speeds (in mV s^{-1}) For comparison the ferrocene curve is given (dashed line).

Similarly to the solution spectrum, the diffuse reflectance spectrum of **1a** exhibits a band at 400 nm (of MLCT character), a shoulder at 360 nm as well as bands of pyrazine and PPh_4^+ origin in the UV region (Fig. 7).

2.6. Cyclic voltammograms

Linear sweep voltammetry measurements revealed that the $[\{Mo(CN)_5(NO)\}_2(\mu\text{-pz})]^{4-}$ complex was irreversibly oxidized at Pt electrodes at $E^0 = 1065$ mV (corresponding to a scan speed of 100 mV s^{-1}) (Fig. 8).

3. Conclusions

We have found that tetraphenylphosphonium salts of oxocyano complexes of molybdenum(IV) and

tungsten(IV), $(PPh_4)_2[M(CN)_4O(pz)]\cdot 3H_2O$ react in anaerobic conditions with NO. The reaction is the first example of direct NO incorporation among cyano complexes of Mo and W and it comprises novel oxo ligand substitution which is released in the form of the NO_2^- anion. It represents a new synthetic route to mixed-ligand cyanonitrosyl complexes of molybdenum(IV) and tungsten(IV), which up until now have been synthesized only in the case of molybdenum in the reaction of hydroxylamine with molybdates(VI) and cyanides.

4. Experimental

4.1. Starting materials and general procedures

Bis(tetraphenylphosphonium) tetracyanooxopyrazine metalates(IV), $(PPh_4)_2[M(CN)_4O(pz)]\cdot 3H_2O$ (M = Mo, W; pz = pyrazine) were synthesized according to the literature method [30]. NO of 99.5% purity was cleaned from trace amounts of higher nitrogen oxides (N_2O_3 and NO_2) by passing through a concentrated KOH solution and an Ascarite II column (NaOH on silica gel, Sigma–Aldrich). Dichloromethane used for the syntheses was purged with argon for 1 h prior to use. All other reagents and solvents were of analytical grade and used without further purification.

Carbon, hydrogen and nitrogen were determined by organic microanalysis on an Euro EA 3000 analyzer. IR spectra of solids were recorded in KBr pellets on a Bruker EQUINOX 55 FT-IR spectrometer whereas the IR spectra of solutions were collected in CaF_2 cuvettes on a Perkin–Elmer 16 PC FT-IR spectrometer. UV–Vis absorption spectra were recorded on a Shimadzu UV 2101PC scanning spectrophotometer. Diffuse reflectance spectra were measured in $BaSO_4$ pellets versus $BaSO_4$ as reference (Shimadzu UV 2101PC equipped with ISR-260 attachment). EPR measurements were carried out on a Bruker ELEXSYS spectrometer operating at X band. The solid samples were examined inside the cavity modulated with a frequency of 100 kHz at −196 °C and room temperature. ESI-MS measurements were performed for acetonitrile solutions on a Bruker ESQUIRE 3000 mass spectrometer using the electrospray negative and positive ionization method. Cyclic voltammetry measurements were carried out in CH_3CN with $[(C_4H_9)_4N]PF_6$ (0.1 M) as the electrolyte using Pt working and counting and Ag/AgCl reference electrodes on a Model EA9 Electrochemical Analyzer. The redox potentials were reported versus ferrocene, which was used as an internal potential standard for measurements in organic solvents to avoid the influence of liquid junction potential. $E_{1/2}$ values were calculated from the average anodic and cathodic peak potentials, $E_{1/2} = 0.5(E_a + E_c)$.

4.2. $(PPh_4)_4[\{Mo(CN)_5(NO)\}_2(\mu\text{-}pz)]\cdot C_4H_9OH\cdot CH_2Cl_2$ (**1a**)

Solid $(PPh_4)_2[Mo(CN)_4O(pz)]\cdot 3H_2O$ (0.30 g, 0.29 mmol) was dissolved in previously deoxygenated dichloromethane (20 cm^3). NO was bubbled through the solution for ca. 7 min until the solution color changed from green to yellow. The volume of obtained solution was reduced to ca. 10 cm^3 by evaporation of the solvent and butane-1-ol was added (12 cm^3). Dichloromethane was then evaporated on a rotary evaporator at 40 °C. The resulting white precipitate was filtered off and the filtrate was left for crystallization at room temperature in air for 5 days. The resulting yellow precipitate was filtered off, washed with a small amount of butane-1-ol and air-dried (yield: 30 mg, 10%). *Anal.* Calc. for $C_{115}Cl_2H_{96}Mo_2N_{14}O_3P_4$: C, 65.50; H, 4.59; N, 9.30. Found: C, 66.1; H, 4.9; N, 9.2%.

The crystals of $(PPh_4)_4[\{Mo(CN)_5(NO)\}_2(\mu\text{-}pz)]\cdot 2C_2H_5OC_2H_5$ (**1b**) suitable for X-ray diffraction were

Table 2
Crystal data and structure refinement for $(PPh_4)_4[\{Mo(CN)_5(NO)\}_2(\mu\text{-}pz)]\cdot 2C_2H_5OC_2H_5$

Empirical formula	$C_{118}H_{104}Mo_2N_{14}O_4P_4$
Formula weight	2098.00
Temperature (°C)	−123(2)
Wavelength (Å)	0.71073
Crystal system	monoclinic
Space group	*C*2/*c*
Unit cell dimensions	
a (Å)	22.9358(13)
b (Å)	23.5318(13)
c (Å)	21.5413(12)
α (°)	90
β (°)	107.880(1)
γ (°)	90
Volume (Å^3)	11 064.8(11)
Z	4
Density (calculated) (g/cm^3)	1.259
Absorption coefficient (mm^{-1})	0.342
F(000)	4344
Crystal size (mm^3)	0.26 × 0.20 × 0.16
Theta range for data collection (°)	1.43–25.00
Index ranges	$-27 \leqslant h \leqslant 27$, $-27 \leqslant k \leqslant 27$, $-25 \leqslant l \leqslant 25$
Reflections collected	40 006
Independent reflections [R_{int}]	9747 [0.0439]
Completeness to theta = 25.00°	99.9%
Absorption correction	empirical
Maximum and minimum transmission	0.928 and 0.825
Refinement method	full-matrix least-squares on F^2
Data/restraints/parameters	9747/0/676
Goodness-of-fit on F^2	0.909
Final *R* indices [$I > 2\sigma(I)$]	$R_1 = 0.0438$, $wR_2 = 0.1288$
R indices (all data)	$R_1 = 0.0587$, $wR_2 = 0.1374$
Largest differential peak and hole (e Å^{-3})	0.815 and −0.369

grown within 2 days by slow diffusion of diethyl ether vapor into the saturated solution of **1a** in CH_3CN at 4 °C.

4.3. X-ray structure determination

Crystal data for **1b** were measured on a Bruker SMART diffractometer with a 2K CCD area detector. All data were collected using graphite monochromated Mo Kα radiation ($\lambda = 0.71073$ Å). An empirical absorption correction, based on comparison of Laue equivalents, was applied to the data. The structure was solved by direct methods and refined by full-matrix least squares cycles on F^2 for all data, using SHELXTL [45]. All non-hydrogen atoms were refined with anisotropic displacements parameters. All hydrogen atoms were included in refinement cycles riding on bonded atoms.

5. Supplementary material

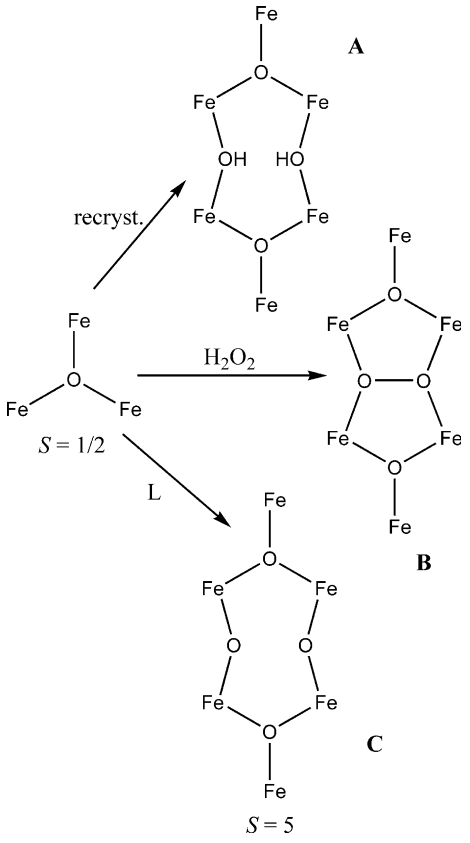
Crystal data for **1b**, and a summary of data collection and structure refinement parameters, are given in Table 2. Full crystallographic data may be obtained from the Cambridge Crystallographic Data Centre, 12 Union Road, Cambridge, CB2 1EZ, UK (fax: 44 1223 336 033; e-mail: deposit@ccdc.cam.ac.uk or www: http://www.ccdc.cam.ac.uk). The CCDC reference number is 236366.

References

[1] G.B. Richter-Addo, P. Legzdins, J. Burstyn, Chem. Rev. 102 (2002) 857.
[2] P.C. Ford, I.M. Lorkovic, Chem. Rev. 102 (2002) 993.
[3] G. Stochel, M. Pawelec, Z. Stasicka, Wiad. Chem. 51 (1997) 163.
[4] G.R.A. Wyllie, W.R. Scheidt, Chem. Rev. 102 (2002) 1067.
[5] P. Coppens, I. Novozhilova, A. Kovalevsky, Chem. Rev. 102 (2002) 861.
[6] M. Wolak, R. van Eldik, Coord. Chem. Rev. 230 (2002) 263.
[7] A. Wanat, M. Wolak, Ł. Orzeł, M. Brindell, R. van Eldik, G. Stochel, Coord. Chem. Rev. 229 (2002) 37.
[8] T.W. Hayton, P. Legzdins, W.B. Sharp, Chem. Rev. 102 (2002) 935.
[9] E.H. Wong, Coord. Chem. Rev. 172 (1998) 247.
[10] M.J. Morris, Coord. Chem. Rev. 172 (1998) 181.
[11] M.J. Morris, Coord. Chem. Rev. 164 (1997) 289.
[12] M.J. Morris, Coord. Chem. Rev. 152 (1996) 309.
[13] M.J. Morris, Coord. Chem. Rev. 146 (1995) 43.
[14] E.H. Wong, Coord. Chem. Rev. 164 (1997) 345.
[15] E.H. Wong, Coord. Chem. Rev. 152 (1996) 251.
[16] K.R. Dunbar, V.P. Saharan, Coord. Chem. Rev. 138 (1995) 39.
[17] M.J. Morris, Coord. Chem. Rev. 138 (1995) 121.
[18] P.T. Bishop, J.R. Dilworth, J. Hutchinson, J. Zubieta, J. Chem. Soc., Dalton Trans. (1986) 967.
[19] P.J. Blower, P.T. Bishop, J.R. Dilworth, T.C. Hsieh, J. Hutchinson, T. Nicholson, J. Zubieta, Inorg. Chim. Acta 101 (1985) 63.
[20] P.T. Bishop, J.R. Dilworth, J. Hutchinson, J. Zubieta, Inorg. Chim. Acta 84 (1984) L15.
[21] M. Green, S.H. Taylor, J. Chem. Soc., Dalton Trans. (1972) 2629.
[22] L. Bencze, J. Kohan, Inorg. Chim. Acta 65 (1982) L17.
[23] F. King, J. Leigh, J. Chem. Soc., Dalton Trans. 5 (1977) 429.
[24] D.H. Svedung, N.G. Vannerberg, Acta Chem. Scand. 22 (1968) 1551.
[25] E. Hejmo, W. Jakób, A. Kanas, Rocz. Chem. 42 (1968) 965.
[26] K. Wieghardt, G. Backes-Dahmann, W. Swiridoff, J. Weiss, Inorg. Chem. 11 (1983) 1221.
[27] N. Machida, S.-I. Ohkoshi, Z.J. Zhong, K. Hashimoto, Chem. Lett. (1999) 907.
[28] K. Wieghardt, W. Holzbach, Angew. Chem., Int. Ed. Engl. 18 (1979) 549.
[29] K. Wieghardt, W. Holzbach, J. Weiss, Z. Naturforsch. 37b (1982) 680.
[30] D. Matoga, J. Szklarzewicz, A. Samotus, J. Burgess, J. Fawcett, D.R. Russell, Polyhedron 19 (2000) 1503.
[31] J. Szklarzewicz, D. Matoga, A. Samotus, J. Burgess, J. Fawcett, D.R. Russell, Croatica Chem. Acta 74 (2001) 529.
[32] D. Matoga, J. Szklarzewicz, A. Samotus, K. Lewiński, J. Chem. Soc., Dalton Trans. (2002) 3587.
[33] A. Samotus, J. Szklarzewicz, D. Matoga, Bull. Pol. Acad. Sci., Chem. 50 (2002) 145.
[34] J.A. McCleverty, Chem. Rev. 79 (1979) 53.
[35] F. Bottomley, Acc. Chem. Res. 11 (1978) 158.
[36] F. Bottomley, W.V.F. Brooks, S.G. Clarkson, S.-B. Tong, J. Chem. Soc., Chem. Commun. 22 (1973) 919.
[37] L.J. Bellamy, The Infra-red Spectra of Complex Molecules, Chapman and Hall, London, 1975 (Chapters 6 and 17).
[38] J.H. Enemark, R.D. Feltham, Coord. Chem. Rev. 13 (1974) 339.
[39] M.K. Ellison, W.R. Scheidt, J. Am. Chem. Soc. 121 (1999) 5210.
[40] B. Klein, J. Berkowitz, J. Am. Chem. Soc. 81 (1959) 5160.
[41] C. Creutz, H. Taube, J. Am. Chem. Soc. 91 (1969) 3988.
[42] C. Creutz, H. Taube, J. Am. Chem. Soc. 95 (1973) 1086.
[43] C.R. Johnson, R.E. Shepherd, Inorg. Chem. 22 (1983) 1117.
[44] UV Atlas of Organic Compounds, vol. II, Butterworths, London, 1966.
[45] G.M. Sheldrick, SHELXL 97, University of Göttingen, Germany, 1997.

described by a $2J$ model (C_{2v} point-group symmetry), assuming the symmetry of an isosceles and not of an equilateral triangle. This has been dubbed the "magnetic Jahn–Teller effect", since the isosceles distortion lifts the 4-fold degeneracy of the $S = 1/2$ ground state in zero field stemming from the equilateral model, and is of theoretical interest. Due to these reasons the physical properties of basic metal carboxylates have been exhaustively studied.

Apart from their interesting physical properties, however, basic metal carboxylates are of special synthetic interest since they can be viewed as building blocks for higher nuclearity molecular species. Focusing further discussion onto iron (III) chemistry, various synthetic routes have been employed to that respect. One such example is the simple recrystallization of the starting material, which has led to the hexanuclear complex $[Fe_6O_2(OH)_2(H_2O)(O_2CPh)_{12}(1,4\text{-dioxane})]$ [6], with an $S = 5$ ground state (Scheme 1, **A**) or to the undecanuclear complex $[Fe_{11}O_6(OH)_6L_{15}]$ [L^- = the anion of 3-(4-methylbenzoyl)-propionic acid] [7]. Reaction with hydrogen peroxide has led to the hexanuclear prismatic anionic complex $[Fe_6(O)_2(O_2)_3(O_2CMe)_9]^-$ presenting an $S = 1$ ground state [8], and to complexes $[Fe_6(O_2)(O)_2(O_2CCMe_3)_{12}L_2]$ (L = Me_3CCO_2H or pyridine) [9], all containing μ_4-peroxo bridges (Scheme 1, **B**).



Scheme 1.

Reactions with various chelating ligands have led to a series of hexanuclear complexes with $S = 5$ ground states (Scheme 1, **C**), and with the general formulae $[Fe_6O_2(OH)_2(O_2CR)_{10}(hep)_2]$ (hep^- = the anion of 2-(2-hydroxyethyl)pyridine and R = Me [10], Ph [11]) or $[Fe_6O_2(OH)_2(O_2CMe)_{10}L_2]$ (L = 1,1-bis(*N*-methyl-imidazol-2-yl)-1-hydroxyethane [12], 2-(*N*-methylimidazol-2-yl)-2-hydroxypropane [10], 6-methyl-(2-hydroxymethyl)pyridine [13]). Such complexes can also be considered as initial steps in the formation process of the mineral core of ferritin.

Ground states higher than $S = 1/2$, which is the rule for basic iron carboxylates, result from competing antiferromagnetic interactions within the cluster, due to its topology.

Azide anions are well known ferromagnetic couplers in their end-on bridging mode. Previous studies [14] have shown that they can replace bridging hydroxides without affecting the total structure of the cluster, but only its magnetic properties. Although end-on azido bridges are extremely rare in iron (III) chemistry [15], we decided to explore the possibility of replacing in situ the hydroxides formed during the recrystallization of a basic iron carboxylate (according to the pathway **A** of Scheme 1) by azides.

Herein, we report the reactivity of basic iron benzoate with azide anions. The reaction product has been characterized structurally, magnetically and spectroscopically (IR, EPR, Mössbauer) and the results of each technique have been correlated to each other. This work can be regarded as the continuation of our research efforts in the cluster chemistry of iron [14c,16].

2. Experimental

2.1. Materials

All reagents and solvents were of analytical grade and used as received, except basic iron (III) benzoate, which was prepared according to a literature procedure [17]. The synthesis was carried out under aerobic conditions. *Warning:* Although no such tendency was observed during the current work, azide salts are potentially explosive and should be handled with caution and in small quantities.

2.2. Synthesis of $[Fe_3O(O_2CPh)_6(EtOH)_2(N_3)]\cdot 2.4EtOH$ (**1**·2.4EtOH)

A paper cone containing solid NaN_3 (0.0162 g, 0.250 mmol) was brought into contact with the surface of a solution of basic iron benzoate (0.262 g, 0.250 mmol) in EtOH (15 mL), in a test tube. After some hours red crystals started to form. The system was left undisturbed and after ca. 1 week dark red prisms of **1**·2.4EtOH were

observed on the test tube walls. These were collected, washed with EtOH and dried in vacuo over silica gel (Yield: 0.15 g, ~50%). The dried sample analysed as **1**·0.7EtOH. *Anal.* Calc. for $C_{47.4}H_{46.2}Fe_3N_3O_{15.7}$: C, 52.88; (52.90), H, 4.33; (4.05), N, 3.90; (4.02). Found: C, 52.90; H, 4.05; N, 4.02% IR bands (KBr, cm^{-1}): 3632 (m), 3400 (m, b), 3064 (m), 2066 (vs), 1602 (vs), 1562 (vs), 1494 (m), 1410 (vs, b), 1178 (m), 1158 (w), 1070 (w), 1026 (m), 840 (w), 820 (w), 718 (vs), 686 (m), 674 (s), 636 (m), 614 (m), 544 (w), 482 (s).

2.3. Physical measurements

Microanalyses were performed by the Microanalytical Laboratory of the Laboratoire de Chimie de Coordination at Toulouse. Infrared spectra (4000–400 cm^{-1}) were recorded as KBr disks on a Perkin–Elmer 16PC spectrometer. Mössbauer measurements were recorded on a constant acceleration conventional spectrometer with a 50-mCi source of ^{57}Co (Rh matrix). The absorber was a powdered sample enclosed in a 20-mm diameter cylindrical, plastic sample-holder, the size of which had been determined to optimize the absorption. Variable-temperature spectra were obtained in the 4.2–300 K range, by using a MD 306 Oxford cryostat, the thermal scanning being monitored by an Oxford ITC4 servocontrol device (±0.1 K accuracy). Recoil [18] programme package or home written routines were used to fit the Mössbauer parameters and determine their standard deviations of statistical origin (given in parentheses). Isomer shift values (δ) are reported relative to iron foil at 300 K. Variable temperature (2–300 K) dc magnetic susceptibility data were collected on powdered microcrystalline solids on a Quantum Design MPMS SQUID susceptometer under a field of 9 kG. Data were corrected with the standard procedure for the contribution of the sample holder and diamagnetism of the sample. Solid state EPR spectra in the 4.2–300 K range were recorded on a Bruker ER 200D-SRC X-band spectrometer equipped with an Oxford ESR 9 cryostat. Simulations of EPR spectra were performed by a program kindly provided to us by Prof. M.P. Hendrich, Department of Chemistry, Carnegie Mellon University [19].

2.4. X-ray crystallography

Crystal data and refinement details for **1**·2.4EtOH are summarized in Table 1.

A crystal of **1**·2.4EtOH, with approximate dimensions of $0.15 \times 0.40 \times 0.50$ mm, was mounted in a capillary, on a Crystal Logic Dual Goniometer diffractometer using graphite-monochromated Mo radiation ($\lambda = 0.71073$ Å). Unit cell dimensions were determined and refined by using the angular settings of 25 automatically centered reflections in the range $11° < 2\theta < 23°$. Intensity data were recorded using a θ–2θ scan to $2\theta_{max} = 45.5°$ with scan speed 1.5° min^{-1} and scan range 2.2 plus $\alpha_1\alpha_2$ separation. Three standard reflections monitored every 97 reflections showed less than 3% variation and no decay. Lorentz, polarization and Ψ-scan absorption corrections were applied using the Crystal Logic software.

Table 1
Crystallographic data for complex **1**·2.4EtOH

Formula	$C_{50.8}H_{56.4}Fe_3N_3O_{17.4}$
Formula weight	1154.94
Crystal system	monoclinic
Space group	*C*2/*c*
T (K)	298
Unit cell dimensions	
a (Å)	42.30(2)
b (Å)	13.662(7)
c (Å)	19.83(1)
α (°)	90
β (°)	92.99(2)
γ (°)	90
V (Å^3)	11446(1)
Z	8
ρ_{calc} (g m^{-3})	1.340
Radiation (Mo Kα), λ (Å)	0.71073
μ (mm^{-1})	0.819
Reflections collected/unique (R_{int})	7958/7690 (0.0383)
Goodness-of-fit (on F^2)	1.100
R_1, wR_2 (all data)	0.1190, 0.2252
R_1, wR_2 ($I > 2\sigma(I)$)	0.0758, 0.1952

The structure was solved by direct methods using SHELXS-97 [20] and refined by full-matrix least-squares on F_o^2 with SHELXL-97 [21] using anisotropic displacement parameters for almost all non-hydrogen atoms. All hydrogen atoms in **1** were introduced at calculated positions as riding on bonded atoms except H(O13) which was located by difference maps. The solvent molecules and the C(62) and C(72) carbon atoms of the coordinated EtOH molecules were refined isotropically with fixed occupation factors.

Scattering factors were taken from [22] The molecular plots were obtained using the ORTEP32 program (see Fig. 1) [23].

CCDC reference number 266618 for **1**.

3. Results and discussion

3.1. Synthesis

Initial investigations of a 1:1 reaction between basic iron benzoate solution and solid NaN_3 in a variety of solvents (MeCN, Me_2CO, EtOH, CH_2Cl_2, and mixtures) under reflux, yielded amorphous yellow solids the IR spectra of which revealed the existence of coordinated azides. The amorphous nature of the solids, however, prevented their characterization by powder

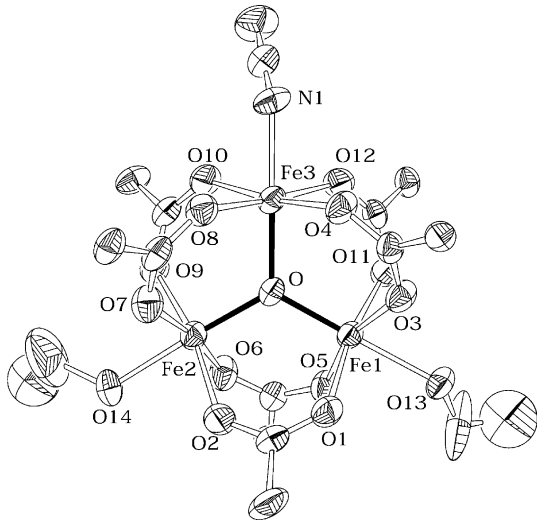


Fig. 1. Partially labelled ORTEP diagram of **1**·2.4EtOH with ellipsoids at the 30% probability level. Hydrogen atoms and phenyl rings have been omitted for clarity.

X-ray diffraction methods, and their very poor solubility in a wide range of solvents hindered our attempts to recrystallize them. Therefore, another crystallization technique was employed for the isolation of X-ray quality single crystals. A paper cone containing the desired amount of solid NaN_3 was inserted into a test tube containing a solution of basic iron benzoate in EtOH. The cone was lowered until its tip touched the free surface of the solution, and then lifted by 1–2 mm, so that only the solvent's meniscus came into contact, without the cone being immersed in the solvent. The low solubility of NaN_3 in EtOH caused a very slow dissolution of the solid, and the slow diffusion led to a very smooth increase of its concentration in solution. This allowed us to obtain X-ray quality crystals of **1**. The reaction that led to this product is summarized by Eq. (1).

$$[Fe_3O(O_2CPh)_6(OH)(H_2O)_2] + NaN_3 + 2EtOH \xrightarrow[20\ ^\circ C]{EtOH} [Fe_3O(O_2CPh)_6(EtOH)_2(N_3)] + NaOH + 2H_2O \quad (1)$$

As confirmed by X-ray crystallography, the reactivity expected was not realized. This can be correlated to the mild conditions employed for the crystallization of the product, with respect to more intense conditions usually employed for other bis-trinuclear complexes [11], and the fact that monatomic bridging modes are very rare for azide anions coordinated to Fe^{III}. However, the presence of a terminal anionic ligand in the trinuclear cluster has serious implications. It leads to a neutral, though non mixed-valent, basic iron carboxylate, a feature that as will be seen affects its solid-state spectroscopic characteristics.

3.2. Description of the structure

The structure of the complex is that of a basic iron benzoate, with six $\eta^1{:}\eta^1{:}\mu_2$-$PhCO_2^-$ ligands and one μ_3 oxide. Two terminal ethanol ligands and a terminal monodentate azido one in the apical positions complete six coordination. The iron atoms are connected by a μ_3-oxide (O), which is coplanar to the Fe_3 plane, with a sum of Fe–O–Fe angles equal to 360.0(3)°. The distances between the Fe^{III} atoms and the donor atoms of the ligands are in the ranges 1.882(5)–2.144(6) Å for Fe1, 1.894(5)–2.116(6) Å for Fe2, and 1.948(5)–2.044(8) Å for Fe3, with the shortest bonds being the Fe–O_{oxo} ones in each case, and the longest being the ones in *trans* respective positions (*trans* effect). The Fe(3)–N_{azido} bond length (2.044(8) Å) is similar with bond lengths found for other six-coordinate iron (III) complexes containing terminal azido ligands (see Table 2) [16e].

Due to the presence of the anionic N_3^- ligand, compound **1** is neutral. Since no counteranions are present, the 3D structure of the complex in the crystal lattice is

Table 2
Selected interatomic distances (Å) and bond angles (°) for complex **1**

Fe(1)–O	1.882(5)	Fe(2)–O	1.894(5)
Fe(1)–O(1)	2.021(6)	Fe(2)–O(2)	2.012(6)
Fe(1)–O(3)	2.000(6)	Fe(2)–O(6)	2.025(6)
Fe(1)–O(5)	2.028(6)	Fe(2)–O(7)	2.009(6)
Fe(1)–O(11)	1.999(6)	Fe(2)–O(9)	1.999(6)
Fe(1)–O(13)	2.144(6)	Fe(2)–O(14)	2.116(6)
Fe(3)–O	1.948(5)	Fe(3)–O(10)	2.026(6)
Fe(3)–O(4)	2.010(5)	Fe(3)–O(12)	2.027(6)
Fe(3)–O(8)	2.017(6)	Fe(3)–N(1)	2.044(8)
Fe(1)···Fe(2)	3.270	Fe(2)···Fe(3)	3.334
Fe(1)···Fe(3)	3.310		
O–Fe(1)–O(1)	94.2(2)	O–Fe(2)–O(14)	177.5(2)
O–Fe(1)–O(11)	95.8(2)	O–Fe(2)–O(2)	95.6(2)
O–Fe(1)–O(13)	176.4(2)	O–Fe(2)–O(6)	94.3(2)
O–Fe(1)–O(3)	97.7(2)	O–Fe(2)–O(7)	95.1(2)
O–Fe(1)–O(5)	98.6(2)	O–Fe(2)–O(9)	96.5(2)
O(1)–Fe(1)–O(11)	169.8(2)	O(2)–Fe(2)–O(14)	82.2(3)
O(1)–Fe(1)–O(13)	84.3(2)	O(2)–Fe(2)–O(6)	87.6(3)
O(1)–Fe(1)–O(3)	88.0(3)	O(2)–Fe(2)–O(7)	90.9(3)
O(1)–Fe(1)–O(5)	89.1(3)	O(2)–Fe(2)–O(9)	167.0(3)
O(3)–Fe(1)–O(11)	91.9(3)	O(6)–Fe(2)–O(14)	84.4(3)
O(3)–Fe(1)–O(13)	79.0(2)	O(6)–Fe(2)–O(7)	170.6(3)
O(3)–Fe(1)–O(5)	163.6(2)	O(6)–Fe(2)–O(9)	87.0(3)
O(5)–Fe(1)–O(11)	88.1(3)	O(7)–Fe(2)–O(14)	86.2(3)
O(5)–Fe(1)–O(13)	84.7(2)	O(7)–Fe(2)–O(9)	92.5(3)
O(11)–Fe(1)–O(13)	85.7(2)	O(9)–Fe(2)–O(14)	85.6(3)
O–Fe(3)–N(1)	178.9(3)	O(4)–Fe(3)–O(8)	86.9(3)
O–Fe(3)–O(10)	93.1(2)	O(8)–Fe(3)–N(1)	87.8(3)
O–Fe(3)–O(12)	91.6(2)	O(8)–Fe(3)–O(10)	92.1(3)
O–Fe(3)–O(4)	94.6(2)	O(8)–Fe(3)–O(12)	175.4(3)
O–Fe(3)–O(8)	93.0(2)	O(10)–Fe(3)–N(1)	86.1(3)
O(4)–Fe(3)–N(1)	86.2(3)	O(10)–Fe(3)–O(12)	88.4(3)
O(4)–Fe(3)–O(10)	172.2(3)	O(12)–Fe(3)–N(1)	87.7(3)
O(4)–Fe(3)–O(12)	92.0(3)		
Fe(1)–O–Fe(2)	120.0(3)	Fe(2)–O–Fe(3)	120.4(2)
Fe(1)–O–Fe(3)	119.6(3)		

primarily defined by intercluster hydrogen-bonding. A hydrogen bond between the hydrogen atom of O(13) (x, y, z) and the N(3′) atom of a neighbouring molecule (′ = x, $-y+1$, $z+1/2$) creates 1D zig-zag chains along the c axis [O(13)···N(3′) = 2.792 Å, O(13)–H(O13) = 0.853 Å, O(13)–H(O13)···N(3′) = 147.28°], see Fig. 2. The closest Fe···Fe separation between two adjacent molecules is 8.061 Å [Fe(1)···Fe(3′)]. This hydrogen-bonding leads to interactions that are too weak to be observed by magnetic susceptibility, but sufficient to influence the spectroscopic properties of the complex in the solid state (see *EPR Spectroscopy*).

Additionally, a series of possible hydrogen bonds between ethanol solvate molecules (OE(3)···OE(1) (x, y, z) 2.881 Å; OE(2)···OE(3) (x, $1-y$, $1/2+z$) 2.518 Å) and between complex and ethanol molecules (OE(1)···N(1) ($1/2-x$, $3/2-y$, $-z$) 2.830 Å; O(14)···OE(2) ($1/2-x$, $-1/2+y$, $1/2-z$) 2.555 Å) form sheets developing parallel to the bc plane (Figure S1).

3.3. IR Spectroscopy

The IR spectrum of dried **1** exhibits two bands characteristic of the antisymmetric and symmetric carboxylate stretching vibrations [ν_{as}(COO) and ν_s(COO)] of the benzoate anions at 1562 and 1410 cm^{-1}, respectively. The difference Δ [$\Delta = \nu_{as}(COO) - \nu_s(COO)$] is 152 cm^{-1}, smaller than that of NaO_2CPh (186 cm^{-1}), as anticipated for a bidentate bridging coordination [24].

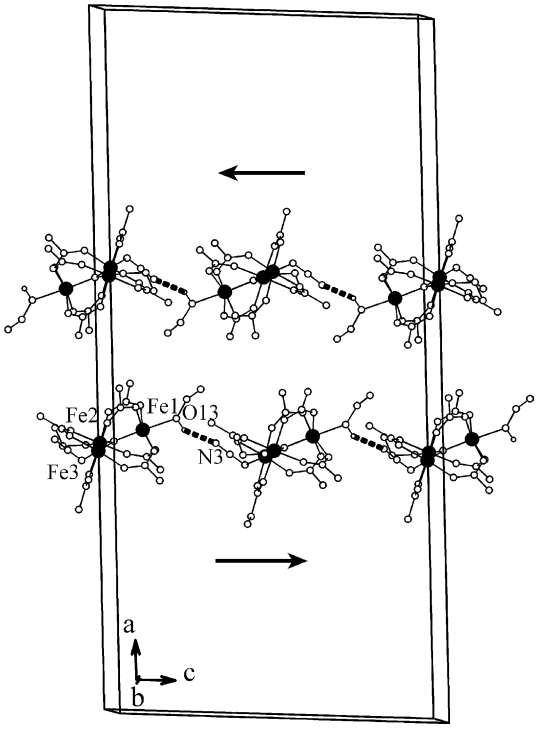


Fig. 2. Crystal packing diagram of **1**, showing the formation of 1D hydrogen-bonded chains along the c axis in opposite directions.

A broad band of medium intensity at 3400 cm^{-1} is attributed to the O–H stretching vibration of the coordinated ethanol molecules. A sharp band at 2066 cm^{-1} is attributed to the antisymmetric stretching vibration [$\nu_{as}(N_3)$] of the terminally bound azide anion. Finally, a strong band at 1602 cm^{-1} is attributed to a ν(C=C) stretching vibration of the aromatic rings, and a medium intensity band at 718 cm^{-1} is attributed to the π(CH) vibration of the aromatic hydrogen atoms.

3.4. Mössbauer spectroscopy

The Mössbauer spectra of complex **1** at six different temperatures between 4.2 and 293 K are shown in Fig. 3. For $T > 80$ K, the spectra consist of an asymmetric composite quadrupole-split doublet, with parameters typical of high-spin iron (III). As described above, the complex contains two iron sites, with FeO_6 [Fe(1) and Fe(2), **A**] and FeO_5N [Fe(3), **B**] chromophores, in a 2:1 ratio. We would expect a higher quadrupole splitting ΔE_Q value for the iron sites with the most distorted octahedral environment. In this case, site **A** has a more homogeneous coordination sphere than **B**, with respect to the type of donor atoms (O_6 versus O_5N environments, respectively), but it presents a higher dispersion of bond lengths [**A**: Fe(1), 1.882(5)–2.144(6) Å and Fe(2), 1.894(5)–2.116(6) Å, **B**: Fe(3), 1.948(5)–2.044(8) Å]. The competition between those two factors is expected to define the relative values of ΔE_{QA} and ΔE_{QB} (see Table 3).

The spectra were fitted with two quadrupole-split doublets. Fitting attempts without any constraint of the variables, yielded for the spectra at 80 and 150 K two doublets in the 2:1 ratio. The higher ratio doublet,

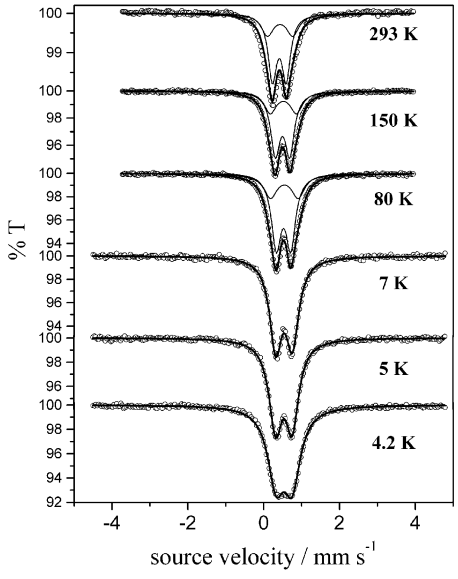


Fig. 3. ^{57}Fe-Mössbauer spectra of **1** in the 4.2–293 K range.

Table 3
Mössbauer parameters for complex **1**

Iron site	T (K)	δ (mm s^{-1})	ΔE_Q (mm s^{-1})	$\gamma_{1/2}$ (mm s^{-1})[a]	Area (%)[a]
1A (FeO_6)	293	0.413(3)	0.363(5)	0.136(4)	*66.7*
1B (FeO_5N)	293	0.43(1)	0.67(3)	*0.20*	*33.3*
1A (FeO_6)	150	0.496(3)	0.38(1)	0.148(9)	68(1)
1B (FeO_5N)	150	0.518(8)	0.69(7)	0.20(2)	32(1)
1A (FeO_6)	80	0.523(2)	0.38(1)	0.153(7)	69(1)
1B (FeO_5N)	80	0.544(7)	0.73(5)	0.21(2)	31(1)
1(average)[b]	7	0.536(3)	0.437(3)	0.20(1)	100
1(average)[b]	5	0.538(3)	0.435(3)	0.21(1)	100
1(average)[b]	4.2	0.537(3)	0.425(3)	0.26(1)	100

[a] Fixed parameters in italics.
[b] Fitted with one quadrupole-split doublet.

which is attributed to site **A**, presents a smaller quadrupole splitting, suggesting that inhomogeneity of donor atoms plays a more significant role to the increase of the electric field gradient than the dispersion of bond lengths. For the 293 K spectrum, initial attempts without constraint led to solutions with area ratios far from the theoretically expected 2:1 one. Thus, in order to avoid local minima without physical meaning, the area ratio was fixed to 2:1 and the $\gamma_{1/2}$ of site **B** was fixed to 0.2 mm s^{-1}, as determined from the 80 and 150 K spectra. A similar differentiation in quadrupole splittings for two distinct iron sites at a 2:1 ratio was observed in the case of the triferric compounds $[Fe_3(\mu_3\text{-}O)(O_2CPh)_5(salox)L_1L_2$ [$L_1 = L_2 =$ MeOH and $L_1 =$ EtOH, $L_2 = H_2O$] [16g].

The decrease of the isomer shift for $T > 80$ K, for both iron sites, is due to second-order Doppler effect [25]. The quadrupole splitting, as expected for high-spin iron (III), does not present an important temperature dependence.

At liquid helium temperatures we obtain relatively symmetric quadrupole-split doublets. The linewidth of these doublets increases on decreasing temperature and the asymmetry due to the different ligand environments of the three ferric sites vanishes. Therefore, we have fitted the spectra with an average quadrupole-split doublet. The broadening of the Mössbauer lines observed at low-temperatures is attributed to the onset of slow relaxation effects.

3.5. Magnetic properties

The $\chi_M T$ product of complex **1** at 300 K, is 4.23 cm^3 mol^{-1} K, is significantly lower than the theoretically expected value for three non-interacting $S = 5/2$ spins (13.14 cm^3 mol^{-1} K for $g = 2$), suggesting antiferromagnetic interactions. Upon cooling, the $\chi_M T$ product decreases without extrapolating to zero as the temperature tends to zero (Fig. 4), which also agrees with the interplay of antiferromagnetic interactions, and a magnetic ground state.

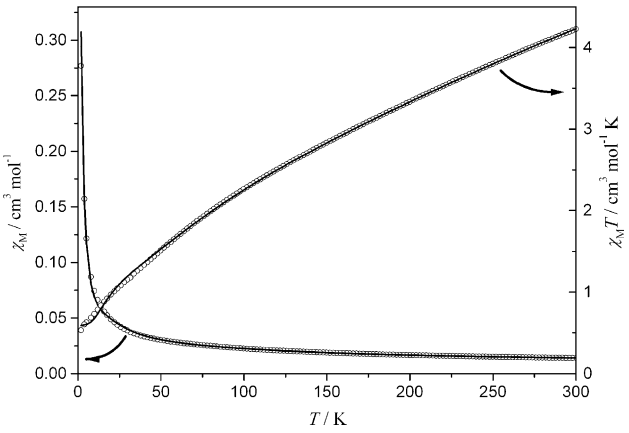


Fig. 4. χ_M vs. T and $\chi_M T$ vs. T experimental data for complex **1**, and theoretical curves based on the Hamiltonian of Eq. (2).

Initial attempts to simulate the magnetic properties of the complex by considering a single J interaction, viewing the complex as an equilateral triangle, did not yield satisfactory results. Inspection of the intermetallic distances, reveals that the Fe–Fe interactions can be grouped into Fe(1)···Fe(3) (3.310 Å) and Fe(2)···Fe(3) (3.334(5) Å) on the one hand, and Fe(1)···Fe(2) (3.270 Å) on the other hand. Thus, the complex is better described by an isosceles triangle, and the exchange parameters can be defined as $J = J_{13} = J_{23}$ and $J' = J_{12}$; the corresponding Hamiltonian is

$$\hat{H} = -2J(\hat{S}_1\hat{S}_3 + \hat{S}_2\hat{S}_3) - 2J'\hat{S}_1\hat{S}_2. \quad (2)$$

The fitting process yielded two solutions of satisfactory quality, with the following sets of parameters **a**: $J = -24.0$ cm^{-1}, $J' = -38.9$ cm^{-1}, $g = 2.0$ ($R = 2.38 \times 10^{-3}$) and **b**: $J = -31.2$ cm^{-1}, $J' = -21.5$ cm^{-1}, $g = 2.0$ ($R = 3.47 \times 10^{-3}$). Small deviations at low temperatures led us to include a paramagnetic impurity (ρ). The best fit parameters were then: **A**: $J = -26.4$ cm^{-1}, $J' = -40.0$ cm^{-1}, $\rho = 1.2\%$, $g = 2.0$ ($R = 2.9 \times 10^{-4}$) and **B**: $J = -33.0$ cm^{-1}, $J' = -24.0$ cm^{-1}, $\rho = 1.2\%$, $g = 2.0$ ($R = 4.2 \times 10^{-4}$). Solution **A** is considered as the most realistic, not only because it presents

the smallest relative error, but also because it is consistent with the structure of the complex. Indeed, Fe(1)–Fe(3) and Fe(2)–Fe(3) pairs present longer intermetallic distances than the Fe(1)–Fe(2) pair, and consequently weaker coupling is expected for them.

Confirmation of the coexistence of two minima was obtained by the calculation of an error surface plot for possible combinations of J and J' values (Fig. 5).

The diagram of energy levels for solution **A** reveals that the first excited $S = 3/2$ state is 25.0 cm^{-1} higher than the ground $S = 1/2$ state, i.e., relatively close to the ground state.

Based on the previously determined parameters, the magnetization M of the complex was calculated as a function of the applied magnetic field. The very good agreement between the calculated values and experimental data confirms the validity of our assumptions (see Fig. 6).

3.6. EPR spectroscopy

The magnetic susceptibility data of powder samples of **1** were well modelled with non-interacting triangular species. Analysis of these data indicates that the complex is characterized by an $S = 1/2$ ground state with an excited state with $S = 3/2$ at 25 cm^{-1}. The EPR spectra of trinuclear transition metal complexes with magnetic properties similar to those of **1** give rise to signals in the $g \sim 2.0$ region. Non-Heisenberg interactions and/or single-ion zero-field splitting result in an anisotropic $S = 1/2$ ground state. Distributions of the magnetic parameters lead to broad features extending to several hundred Gauss at X-band with $g < 2.0$ [26–29].

Fig. 7 shows an EPR spectrum recorded from a powdered sample of 1 at 4.2 K. Broad signals are observed with a prominent feature at $g \sim 2.0$. A weak signal at

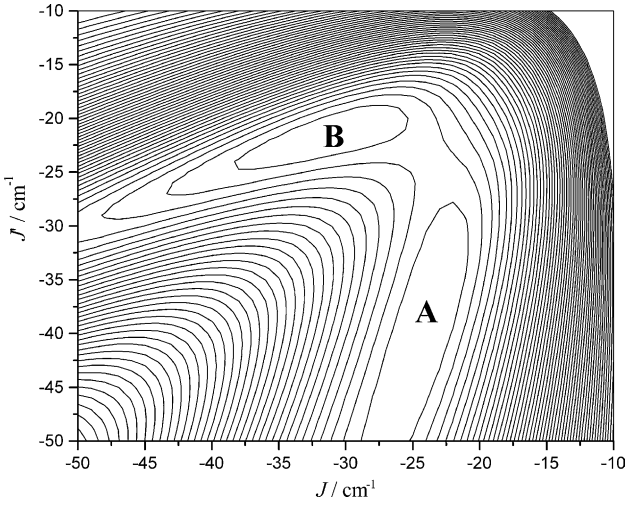


Fig. 5. Surface error plot of J vs. J' (with $g = 2.00$ and $\rho = 1.2\%$) revealing the minima **A** and **B** found by the fitting process.

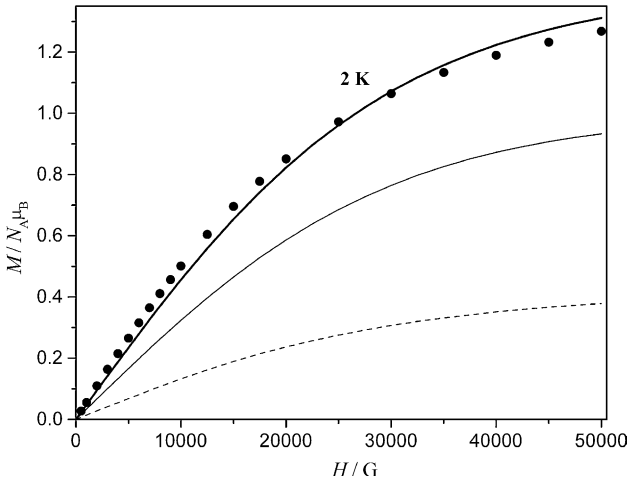


Fig. 6. Variation of the magnetization M vs. the applied field H at 2 K for complex **1**. The dashed, solid and bold lines represent the paramagnetic impurity, the calculated curve according to the parameters of solution **A**, and their sum, respectively.

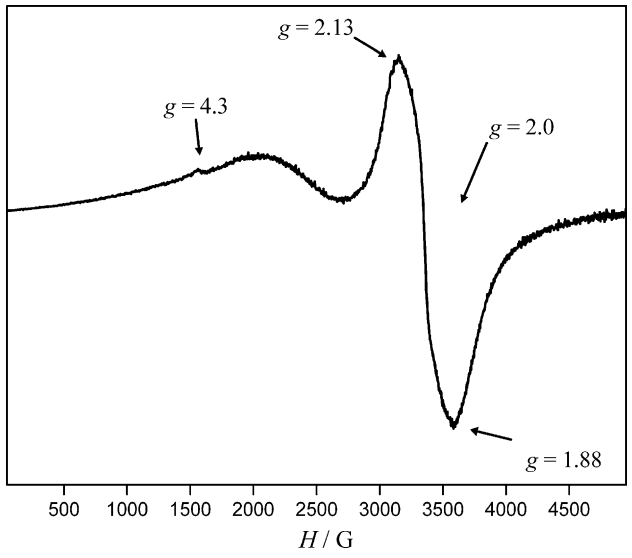


Fig. 7. X-band EPR spectrum of a powder sample of **1** at 4.2 K. EPR conditions: mod. amp. 25 Gpp, microwave power: 36 mW, microwave frequency: 9.41 GHz.

$g \sim 4.3$ is attributed to monomeric Fe^{III} ($S = 5/2$) impurities in agreement with the magnetic susceptibility measurements. The signal at $g \sim 2.0$ consists of an absorption peak at $g \sim 2.13$ a derivative feature at $g \sim 2.0$ and a valley at 1.88. At higher temperatures the intensity of the EPR signals decreases and substantial broadening is observed (not shown) whereas no novel signals attributed to the excited states of the trimer are observed. In the following, we discuss the 4.2 K spectra shown in Fig. 7. These signals cannot be assigned to an isolated $S = 1/2$ species with the assumptions discussed above. Instead, we attribute the observed signals to weak intercluster interactions. This

is supported by the crystal packing depicted in Fig. 2 revealing a one-dimensional arrangement of trimers through hydrogen bonds. We will argue that these interactions are too weak to be discerned in the magnetic susceptibility measurements.

In order to reproduce the main features of the EPR spectrum in the $g \sim 2.0$ region, we assume a weak exchange interaction involving two $S = 1/2$ species with an isotropic g-tensor ($g = 2.0054$) (Eq. (3)),

$$\hat{H}_{\text{inter}} = \hat{S}_1 \tilde{\mathbf{J}}_{\text{inter}} \hat{S}_2 + g\hat{S}_1\mathbf{H} + g\hat{S}_2\mathbf{H}, \quad (3)$$

where $\tilde{\mathbf{J}}_{\text{inter}}$ is a diagonal tensor accounting for the inter-trinuclear interaction. In Eq. (3), $\tilde{\mathbf{J}}_{\text{inter}}$ can be deconvoluted into an isotropic part and a traceless diagonal tensor $\tilde{\mathbf{J}}_{12}$ (Eq. (4)) [30],

$$\tilde{\mathbf{J}}_{\text{inter}} = J_0\mathbf{1} + \tilde{\mathbf{J}}_{12}. \quad (4)$$

In the absence of any inter-trimer interaction, a symmetric derivative is expected from the two $S = 1/2$ species at $g \sim 2.0$ (Fig. 8, thin line). The isotropic part of $\tilde{\mathbf{J}}_{\text{inter}}$ has no effect for such a spectrum. This, however, significantly alters upon involvement of the anisotropic term $\tilde{\mathbf{J}}_{12}$. This interaction induces a splitting of the symmetric line yielding an absorption feature at $g \sim 2.13$, a derivative at $g \sim 2.0$ and a valley at $g \sim 1.88$ for $\mathbf{J}_{12} = [0.03, 0.0, -0.03]$ cm^{-1} (Fig. 8, dashed line). Since the spectra are not sensitive to J_0, this term cannot be determined by EPR. Nevertheless, since the distance between neighbouring trimers is roughly 8 Å in the crystalline sample, J_0 is expected to be small.

The anisotropy of the inter-trimer interaction is mainly of dipolar origin. In the point dipole approximation involving two $S = 1/2$ species, the derived values of $\mathbf{J}_{12}$ correspond to an inter-dipole distance of ~3.4 Å. Also, since isotropic g tensors are involved, an axial $\tilde{\mathbf{J}}_{12}$ tensor is expected [30]. The discrepancy with the experimental results is attributed to the fact that the point-dipole approximation involving two $S = 1/2$ species is an oversimplification of the 1D arrangement of trimers depicted in Fig. 2.

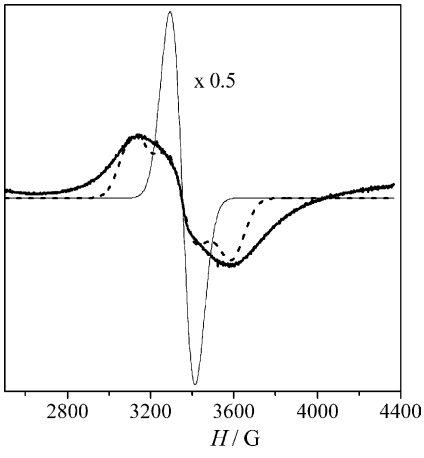


Fig. 8. The experimental EPR spectrum (bold line) of a powder sample of **1** in the $g \sim 2.0$ region and theoretical simulations assuming two non interacting $S = 1/2$ species (thin line) and two $S = 1/2$ species with a weak anisotropic interaction, $\mathbf{J}_{12} = [0.03, 0.0, -0.03]$ cm^{-1} (dashed line). For the simulations, Gaussian line shapes with a 40-G intrinsic line width were considered.

The previous discussion reveals that the EPR spectra of **1** are sensitive to weak inter-trimer interactions. The magnitude of these interactions is too small to be discerned by bulk magnetic susceptibility measurements. We have observed similar behaviour concerning the EPR spectra of powder samples of other trinuclear ferric complexes showing weak 1D or 2D structural interactions [16g].

4. Conclusions

In an attempt to explore the chemistry of iron basic benzoate with sodium azide, we obtained the trinuclear complex **1**, which contains the "iron basic carboxylato" core. From a synthetic viewpoint, it was confirmed that end-on azido bridges are not so easy to obtain in iron (III) carboxylate chemistry, probably due to the increased electrostatic repulsions of Fe^{III}–Fe^{III} pairs, but also due to steric hindrance from the benzoato ligands. Another important factor was the mild conditions used for the crystallization of the product, in contrast to the conditions used to synthesize complexes without azide anion. The terminal azido ligand present in **1** could have future utility as site for facile incorporation of other monoanionic ligands by metathesis. Mössbauer spectroscopy reveals that the inhomogeneity in donor atoms of the environments is more important in influencing the quadrupole-splittings than the geometrical distortions of the ferric sites. The differences in composition of the chromophores for the two types of ferric sites (O_6 and O_5N) are sufficient to distinguish them with Mössbauer spectroscopy. The Mössbauer spectra of complex **1** show asymmetry attributed to the existence of two quadrupole-split doublets, but only well-above liquid helium temperatures. At low temperature the asymmetry vanishes and the quadrupole-split doublets are broadened probably due to slow relaxation effects. Although the magnetic properties of the complex are satisfactorily interpreted with a simple $2J$ model, the 4.2 K EPR spectrum indicates involvement of weak intermolecular interactions. A model involving pair-wise dipolar interactions between neighbouring trimers can reproduce the EPR spectra qualitatively.

Acknowledgements

S.P.P. thanks the Greek General Secretariat of Research and Technology (Grant 99ED139) for support of this work. A.K.B. thanks the European Community for support through a doctoral grant within the frame-

work of the TMR Contract FMRX-CT980174 and the Greek State Scholarship Foundation (IKY) for support through a postdoctoral grant.

Appendix A. Supplementary data

Full crystallographic details have been deposited in CIF format with the Cambridge Crystallographic Data Centre. Copies of the data can be obtained free of charge on request from the CCDC, 12 Union Road, Cambridge CB2 1EZ, UK (fax: +44 1223 3360033; e-mail: deposit@ccdc.cam.ac.uk or www at http://www.ccdc.cam.ac.uk) quoting the deposition number CCDC 266618. A figure showing one hydrogen-bonded sheet of complex **1**·2.4EtOH in the *bc* plane. Supplementary data associated with this article can be found, in the online version, at doi:10.1016/j.poly.2005.04.016.

References

[1] R.C. Mehrotra, R. Bohra, Metal Carboxylates, Academic Press, New York, 1983.
[2] R.L. Rardin, W.B. Tolman, S.J. Lippard, New. J. Chem. 15 (1991) 417.
[3] G. Aromi, S.M.J. Aubin, M.A. Bolcar, G. Christou, H.J. Eppley, K. Folting, D.N. Hendrickson, J.C. Huffman, R.C. Squire, H.-L. Tsai, S. Wang, M.W. Wemple, Polyhedron 17 (1998) 3005.
[4] K. Kambe, J. Phys. Soc. Jpn. 5 (1950) 48.
[5] For example:
(a) R.D. Cannon, R.P. White, Prog. Inorg. Chem. 36 (1988) 195;
(b) A.M. Bond, R.J.H. Clark, D.G. Humphrey, P. Panayiotopoulos, B.W. Skelton, A.H. White, J. Chem. Soc., Dalton Trans. (1998) 1845;
(c) R. Wu, M. Poyraz, F.E. Sowrey, C.E. Anson, S. Wocadlo, A.K. Powell, U.A. Jayasooriya, R.D. Cannon, T. Nakamoto, M. Katada, H. Sano, Inorg. Chem. 37 (1998) 1913.
[6] W. Micklitz, S.J. Lippard, Inorg. Chem. 27 (1988) 3069.
[7] M. Frey, S.G. Harris, J.M. Holmes, D.A. Nation, S. Parsons, P.A. Tasker, S.J. Teat, R.E.P. Winpenny, Angew. Chem., Int. Ed. 37 (1998) 3245.
[8] I. Shweky, L.E. Pence, G.C. Papaefthymiou, R. Sessoli, J.W. Yun, A. Bino, S.J. Lippard, J. Am. Chem. Soc. 119 (1997) 1037.
[9] R. Çelenligil-Çetin, R.J. Staples, P. Stavropoulos, Inorg. Chem. 39 (2000) 5838.
[10] C.A. Christmas, H.-L. Tsai, L. Pardi, J.M. Kesselman, P.K. Gantzel, R.K. Chadha, D.F. Harvey, D.N. Hendrickson, J. Am. Chem. Soc. 115 (1993) 12483.
[11] C. Cañada-Vilalta, T.A. O'Brien, E.K. Brechin, M. Pink, E.R. Davidson, G. Christou, Inorg. Chem. 43 (2004) 5505.
[12] J.K. McCusker, C.A. Christmas, P.M. Hagen, R.K. Chadha, D.F. Havey, D.N. Hendrickson, J. Am. Chem. Soc. 113 (1991) 6114.
[13] C. Cañada-Vilalta, E. Rumberger, E.K. Brechin, W. Wernsdorfer, K. Folting, E.R. Davidson, D.N. Hendrickson, G. Christou, J. Chem. Soc., Dalton Trans. (2002) 4005.
[14] (a) G.S. Papaefstathiou, S.P. Perlepes, A. Escuer, R. Vicente, M. Font-Bardia, X. Solans, Angew. Chem., Int. Ed. 40 (2001) 884;
(b) G.S. Papaefstathiou, A. Escuer, R. Vicente, M. Font-Bardia, X. Solans, S.P. Perlepes, Chem. Commun. (2001) 2414;
(c) A.K. Boudalis, B. Donnadieu, V. Nastopoulos, J.M. Clemente-Juan, A. Mari, Y. Sanakis, J.-P. Tuchagues, S.P. Perlepes, Angew. Chem., Int. Ed. 43 (2004) 2266.
[15] (a) K.R. Reddy, M.V. Rajasekharan, J.-P. Tuchagues, Inorg. Chem. 37 (1998) 5978;
(b) G. De Munno, T. Poerio, G. Viau, M. Julve, F. Lloret, Angew. Chem., Int. Ed. 36 (1997) 1459.
[16] (a) A.K. Boudalis, N. Lalioti, G.A. Spyroulias, C.P. Raptopoulou, A. Terzis, V. Tangoulis, S.P. Perlepes, J. Chem. Soc., Dalton Trans. (2001) 955;
(b) A.K. Boudalis, N. Lalioti, G.A. Spyroulias, C.P. Raptopoulou, A. Terzis, A. Bousseksou, V. Tangoulis, J.-P. Tuchagues, S.P. Perlepes, Inorg. Chem. 41 (2002) 6474;
(c) A.K. Boudalis, F. Dahan, A. Bousseksou, J.-P. Tuchagues, Spyros P. Perlepes, Dalton Trans. (2003) 3411;
(d) A.K. Boudalis, J.-M. Clemente-Juan, F. Dahan, J.-P. Tuchagues, Inorg. Chem. 43 (2004) 1574;
(e) A.K. Boudalis, V. Tangoulis, C.P. Raptopoulou, A. Terzis, J.-P. Tuchagues, S.P. Perlepes, Inorg. Chim. Acta 357 (2004) 1345;
(f) A.K. Boudalis, C.P. Raptopoulou, A. Terzis, S.P. Perlepes, Polyhedron 23 (2004) 1271;
(g) C.P. Raptopoulou, Y. Sanakis, A.K. Boudalis, V. Psycharis, Polyhedron 24 (2005) 711.
[17] A. Earnshaw, B.N. Figgis, J. Lewis, J. Chem. Soc. A (1966) 1656.
[18] K. Lagarec, Recoil, Mössbauer Analysis Software for Windows. Available from: <http://www.physics.uottawa.ca/~recoil>.
[19] A.P. Golombek, M.P.J. Hendrich, J. Magn. Res. 165 (2003) 33.
[20] G.M. Sheldrick, SHELXS-97, Program for Crystal Structure Solution, University of Göttingen, Germany, 1997.
[21] G.M. Sheldrick, SHELXL-97, Program for the Refinement of Crystal Structures from Diffraction Data, University of Göttingen, Germany, 1997.
[22] International Tables for Crystallography, vol. C, Kluwer Academic Publishers, Dordrecht, The Netherlands, 1992, Tables 4.2.6.8 and 6.1.1.4.
[23] ORTEP32 for Windows: L.J. Farrugia, J. Appl. Crystallogr. 30 (1997) 565.
[24] G.B. Deacon, R.J. Phillips, Coord. Chem. Rev. 33 (1980) 227.
[25] N.N. Greenwood, T.C. Gibb, Mössbauer Spectroscopy, Chapman and Hall, London, 1971, pp. 148–164.
[26] A.K., Boudalis et al. Inorg. Chem. (under revision).
[27] Y.V. Rakitin, Y.V. Yablokov, V.V. Zelentzov, J. Magn. Reson. 43 (1981) 288.
[28] A. Caneschi, A. Cornia, A.C. Fabretti, D. Gatteschi, W. Malavasi, Inorg. Chem. 34 (1995) 4660.
[29] Y. Sanakis, A.L. Macedo, I. Moura, J.J.G. Moura, V. Papaefthymiou, E. Munck, J. Am. Chem. Soc. 122 (2000) 11855.
[30] A. Bencini, D. Gatteschi, EPR of Exchange Coupled Systems, Springer, Berlin-Heidelberg, 1990.

$(CH_3OH)_2\}_n$. In this complex, two fluoride atoms link together two Cu(II) metal centres via μ-F bridges. The bimetallic CuF_2Cu moieties are then assembled in an infinite chain via μ_4-SiF_6 anions. The structure is further stabilised by a 3-D network of hydrogen bonds. This compound was obtained by reaction at high temperature (100 °C) in a closed pressure tube from the dipyridylamine ligand and $Cu(BF_4)_2$ in methanol. As reported previously, F^- ions can be formed from gradual ligand-assisted BF_4^- decomposition [23,35] and the hexafluorosilicate ions, by attack of the fluoride ions on the glass surface of the reaction vessel [34]. In the present study, the structure and magnetic properties of a novel SiF_6-bridged polymer are described.

2. Experimental

2.1. Synthesis

All commercially obtained reagents were used without further purification. Copper(II) tetrafluoroborate (20 mg, 0.084 mmol) was added to an equimolar methanolic solution (6 ml) of dipyridylamine. The resulting green limpid solution was allowed to stand at 100 °C for 12 h under autogenous pressure in a sealed tube to form $[Cu_2(\text{dipyridylamine})_2(\mu\text{-}F)_2(\mu_4\text{-}SiF_6)] \cdot (CH_3OH)_2$ as light green prism-shaped crystals. The crystals were filtered off and washed with MeOH. Yield: 35%. *Anal.* Calc.: C, 37.02; H, 3.64; N, 11.77; Cu, 17.80. Found: C, 33.94; H, 3.70; N, 11.89; Cu, 19.10%. Main IR absorption bands (cm^{-1}): multiplet in 3331–3056, 1651, 1591, 1435, 1018, 703, 418. UV–Vis (reflectance, nm) 336, 690. It should be mentioned that a small amount of side product crystallised and was analysed as $[Cu(\text{dipyridylamine})_2(CH_3OH)](SiF_6)$ (the structure will be described elsewhere). The crystals could be separated manually from the main product.

2.2. Physical measurements

Elemental analyses for C, H and N were performed with a Perkin–Elmer 2400 analyser. The Cu analyses were performed with a Vista MPX ICP analyser. IR spectra were recorded with a Perkin–Elmer Paragon 1000 FTIR spectrophotometer, equipped with a Golden Gate ATR device, using the reflectance technique (4000–300 cm^{-1}). Ligand-field spectra were obtained on a Perkin–Elmer Lambda 900 spectrophotometer using the diffuse reflectance technique, with MgO as a reference, over the range 2000–200 nm at room temperature. X-band powder EPR spectra were recorded on a Jeol electron spin resonance spectrometer using DPPH ($g = 2.0036$) as a standard. Magnetic susceptibility measurements were carried out using a Quantum Design MPMS-5 5T SQUID magnetometer at 1000 Oe in the temperature range 2–300 K. Data were corrected for the diamagnetic contributions estimated from the Pascal constants [36].

Table 1
Crystallographic data and refinement details for $[Cu_2(\text{dipyridylamine})_2(\mu\text{-}F)_2(\mu_4\text{-}SiF_6)] \cdot (CH_3OH)_2$

Formula	$C_{22}H_{26}Cu_2F_8N_6O_2Si$
Formula weight ($g\ mol^{-1}$)	713.66
Crystal system	monoclinic
Space group	*C*2/*c*
Unit cell dimensions	
a (Å)	21.5706(7)
b (Å)	7.0919(2)
c (Å)	17.1177(6)
α (°)	90
β (°)	93.572(2)
γ (°)	90
V (Å^3)	2613.52(14)
Z	4
D_{calc} ($g\ cm^{-3}$)	1.814
T (K)	150
λ/Å	0.71073 (Mo Kα)
μ/mm^{-1}	1.765
$F_{(000)}$	1440
Reflections collected/unique	5501/2948 [$R_{int} = 0.0491$]
Final $R^{a,b}$ indices [$I > 2\sigma(I)$]	$R_1 = 0.0397$ $wR_2 = 0.0803$
R indices (all data)	$R_1 = 0.0862$ $wR_2 = 0.0919$
Goodness-of-fit on $F^{2\,c}$	1.033

[a] $R = \Sigma\|F_o| - |F_c\|/\Sigma F_o|$.
[b] $wR_2 = \{\Sigma[w(F_o^2 - F_c^2)^2]/\Sigma[w(F_o^2)^2]\}^{1/2}$.
[c] $S = \{\Sigma[(F_o^2 - F_c^2)^2]/(n/p)\}^{1/2}$, where *n* is the number of reflections and *p* is the total number of parameters refined.

2.3. Crystallographic data collection

Crystal data and refinement parameters for the title compound are listed in Table 1. The careful selected crystal was greased on a glass thread. Diffraction data were collected on a Nonius Kappa CCD diffractometer with area detector at 150(2) K. Cryostream Cooler (Oxford Cryosystems) was used for cooling the sample. A graphite monochromated Mo Kα radiation (λ = 0.71073 Å) was employed. The structure was solved by direct methods implemented in SHELXS-97 [37] and refined by a full-matrix least-squares procedure based on F^2 using SHELXL-97 [38]. All non-hydrogen atoms were refined anisotropically, while the hydrogen atoms were included in the model at geometrically calculated positions and refined using a riding model.

3. Results and discussion

The reaction of dipyridylamine and $Cu(BF_4)_2$ in MeOH in Pyrex tube at 100 °C under autogenous pressure, gave a polymeric compound with $[Cu_2(\text{dipyridylamine})_2(\mu\text{-}F)_2(\mu_4\text{-}SiF_6)] \cdot (CH_3OH)_2$ as repeating unit. Attempts to prepare it under similar conditions, but

using dipyridylamine and $Cu(BF_4)_2$ in CH_3CN or CuF_2 in MeOH, in presence of $Na_2(SiF_6)$, were unsuccessful.

The IR spectrum of the title compound evidences peaks of both the dipyridylamine ligand and the hexafluorosilicate anion. In the 3500–3000 cm^{-1} region, multiple narrow IR absorptions appear. They correspond to the characteristic N–H and C–H vibration bands. Their shape is a proof that hydrogen bonds are present in the material. Below 1650 cm^{-1} several bands can be assigned to the coordinated dipyridylamine ligand, specially the band at 1018 cm^{-1} which is associated with the pyridine ring breathing vibration mode and indicates that all the pyridine rings are coordinated [39]. Below 750 cm^{-1} appear the bands assigned to hexafluorosilicate vibrations. Uncoordinated SiF_6^{2-} is known to have two IR-active vibrations at about 740 and 480 cm^{-1} [40]. These bands, due to the lowering of the anion symmetry upon coordination, are shifted to 703 and 418 cm^{-1} in the present compound. They are assigned to the ν_3 (νSi–F) and ν_4 (δF–Si–F) modes, respectively [41]. On the other hand, not any characteristic signal of the BF_4^- anion are present [23].

4. Structure

An ORTEP view of the repeating unit of the title compound is illustrated in Fig. 1 and selected bond lengths and bond angles are listed in Table 2. This complex is dimeric, consisting of two CuF(dipyridylamine) units related by an inversion centre, these units being connected by two fluoride bridges. In a $[Cu_2(dipyridylamine)_2(\mu\text{-}F)_2]$ moiety, the two dipyridylamine ligand planes are at an angle of ~18°. The copper(II) ions are in an octahedral environment with a coordination sphere defined by two nitrogen atoms of the dipyridylamine ligand (Cu–N 1.982 Å) and two fluoride atoms of the μ-F bridges (Cu–F 1.928 Å) in the equatorial plane, and by two fluoride atoms of the SiF_6^{2-} dianion in axial position (Cu–F 2.399–2.368 Å). It should be highlighted that only a few crystal structures were reported so far showing Cu(II)-based complexes with such N,F environment. In those cases, the F atoms (excluded the ones from the bis-μ-F bridge) come from a BF_4 unit [25,28]. The Cu–N bond distances are considered normal for the Cu(II) ion. The Cu–F bond lengths in the CuF_2Cu moiety are in agreement with those previously reported for related Cu(II) complexes [25–28]. Concerning the Cu–F(SiF_6) bond lengths, they are shorter than in the compounds where the BF_4^- anion is weakly coordinated to the CuF_2Cu unit (Cu–F ~2.50–2.69 Å) [25,28] and they are of the same magnitude range as in polymers where SiF_6^{2-} acts as a μ-SiF_6 bridge between two metal centres (Cu–F 2.225–2.335 Å) [32,42]. Interestingly, it is the first time that coordination of the SiF_6^{2-} anion to a CuF_2Cu moiety occurs via two F atoms. The Cu–F–Cu bond angle (99.85°) is of the same magnitude order as for dinuclear F-bridged copper complexes [25]. The F(SiF_6)–Cu–F(SiF_6) angle (167.33°) is comparable to that in the related BF_4^- containing compounds [25,28].

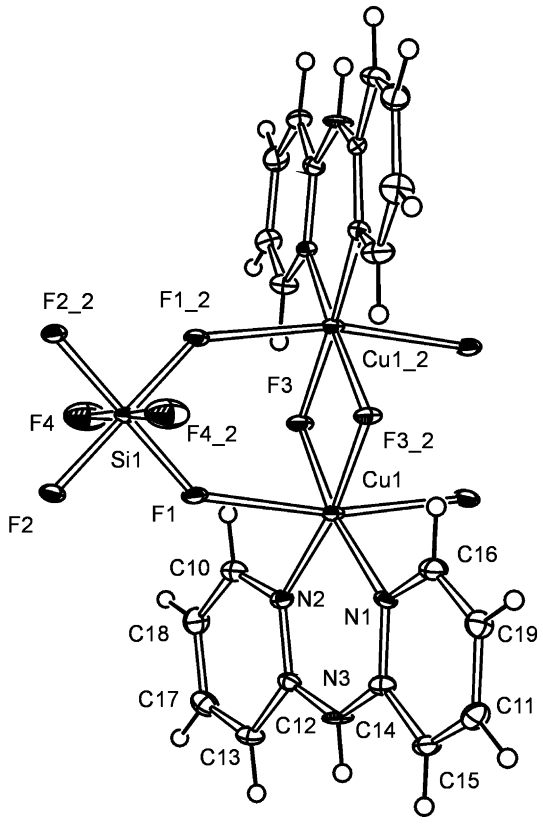


Fig. 1. ORTEP view of the repeating unit of $[Cu_2(dipyridylamine)_2(\mu\text{-}F)_2(\mu_4\text{-}SiF_6)] \cdot (CH_3OH)_2$ with thermal ellipsoids drawn at the 40% probability level. The lattice solvent molecules have been excluded for clarity.

Table 2
Selected bond lengths (Å) and angles (°) for $[Cu_2(dipyridylamine)_2(\mu\text{-}F)_2(\mu_4\text{-}SiF_6)] \cdot (CH_3OH)_2$

Cu1–F1	2.368(2)
Cu1–F2	2.399(2)
Cu1–F3	1.927(2)
Cu1–N1	1.982(3)
Cu1–N2	1.982(3)
Si1–F1	1.693(2)
Si1–F2	1.690(2)
Si1–F4	1.664(2)
Cu1···Cu1_2	2.950
Cu1–F3–Cu1_2	99.85(8)
F3–Cu1–F3_2	80.15(8)
F1–Si1–F1_2	92.06(15)
Si1–F1–Cu1	140.15(11)

As illustrated in Fig. 2, the $[Cu_2(dipyridylamine)_2(\mu\text{-}F)_2]$ motif is repeated along the (0 1 0) direction via the SiF_6^{2-} linker, thus forming an infinite chain running

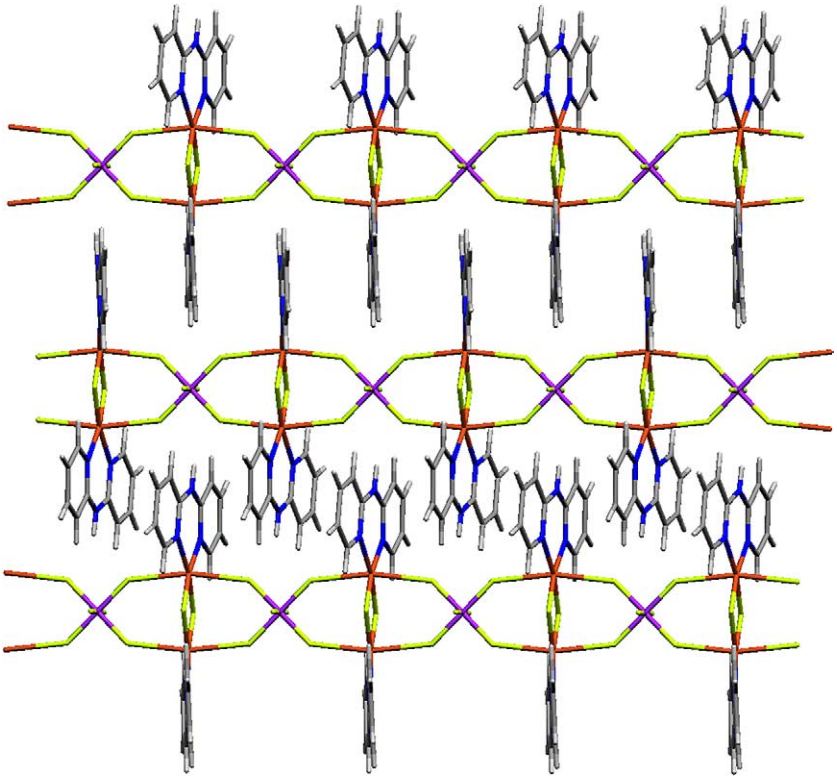


Fig. 2. Stacking diagram of $[Cu_2(dipyridylamine)_2(\mu\text{-}F)_2(\mu_4\text{-}SiF_6)]\cdot(CH_3OH)_2$ along the directions *b* and *c*, evidencing the head-to-tail $\pi\cdots\pi$ interactions between the dipyridylamine ligands (solvent molecules omitted for clarity).

along this direction. These chains are further stacked along the (0 0 1) direction, so that the dipyridylamine ligand planes form interpenetrated columns with $\pi\cdots\pi$ interactions (~3.5–3.8 Å), each dipyridylamine ligand interacting head-to-tail with two dipyridylamine ligands from the adjacent layer. Actually, in view of this stacking, the structure can be best described as inorganic (Cu(II)–Si)-based layers and organic dipyridylamine-based layers, the material thus may be described as a hybrid inorganic/organic material. The structure is stabilised by an important 3-D network of supramolecular contacts, i.e., hydrogen bonds and short contacts. For instance, as illustrated in Fig. 3, the solvent molecules are involved in hydrogen bonding with apical fluoride atoms of hexafluorosilicate anions (O–H$\cdots$F, with O$\cdots$F distances of 2.699 Å). In this scheme are also evidenced interchain interactions between fluoride atoms of hexafluorosilicate anions with amine nitrogen atoms (N–H$\cdots$F, with N$\cdots$F distances in the range of 2.866–2.930 Å).

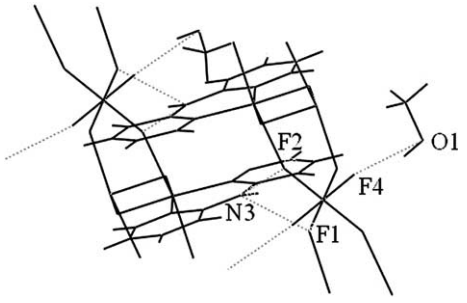


Fig. 3. View of the hydrogen bonds in $[Cu_2(dipyridylamine)_2(\mu\text{-}F)_2(\mu_4\text{-}SiF_6)]\cdot(CH_3OH)_2$ (D$\cdots$A distances: O1$\cdots$ F4 2.699, N3$\cdots$F2 2.866, N3$\cdots$ F1 2.930 Å).

5. Magnetic properties

Fig. 4 shows plots of χ and χT versus T for the title compound where χ is the molar magnetic susceptibility in terms of the repeating unit $[Cu_2(dipyridylamine)_2(\mu\text{-}F)_2(\mu_4\text{-}SiF_6)]\cdot(CH_3OH)_2$. The χT value is 0.621 emu K mol^{-1} at 300 K. This is smaller than the expected value for two uncoupled Cu(II) ions (0.75 emu K mol^{-1}, $g = 2$). Within the temperature range 300–150 K, the χT value is approximately constant, then it decreases reaching a plateau below 20 K. This plateau indicates the presence of a small amount of non-coupled species in the sample, also evidenced by the abrupt increase of the χ at low temperature when cooling. The χT versus temperature behaviour suggests the existence of antiferromagnetic interactions between the metal centres. Given the large separation between the Cu(II) ions imposed by the hexafluorosilicate ion, the non-negligible magnetic pathway arises from the fluoro-bridges in the

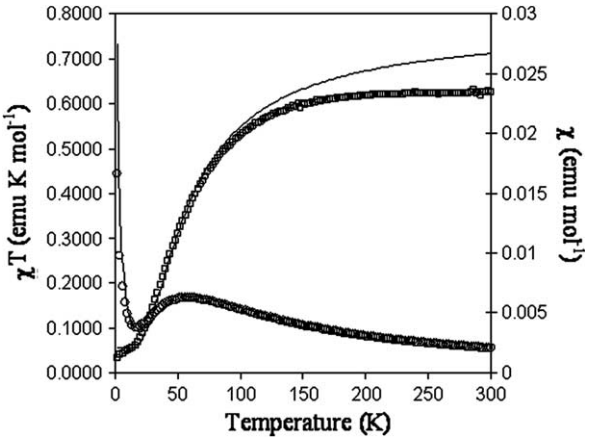


Fig. 4. Temperature dependence of χT (□) and χ(○) for $[Cu_2(dipyridylamine)_2(\mu\text{-}F)_2(\mu_4\text{-}SiF_6)] \cdot (CH_3OH)_2$. The full lines correspond to the best fit to the experimental data.

CuF_2Cu units. Accordingly, the magnetic data were analysed on the basis of the Bleaney-Bowers expression given for dinuclear Cu(II) compounds, modified by Kahn to take into account some paramagnetic impurity due to the presence of a very small amount of non-coupled species in the sample [36]:

$$\chi = \frac{2Ng^2\beta^2}{kT[3 + e^{-\frac{J}{kT}}]}(1-\rho) + \frac{Ng^2\beta^2}{2kT}\rho,$$

where ρ is the molar fraction of the paramagnetic impurity, the other symbols have their usual meanings.

The best fit of the magnetic susceptibility data yielded $J = -74\ cm^{-1}$, $g = 2.04$, $\rho = 0.07$. The J value indicates that strong antiferromagnetic interactions are dominant in the polymer. Correlation of the structural parameters and the J coupling constant are usually established for bridged metal complexes (e.g., with N_3) however, in the present case, such correlation was not attempted yet due to the lack of sufficient CuF_2Cu examples. It can, however, be noted that the magnetic interactions are slightly less stronger in the present compound than in the relatively similar complex $[Cu(mppzH)_2F]_2(BF_4)_2$ where the Cu–F–Cu angle is of 98.9° and the coupling constant is of $-118\ cm^{-1}$ [25]. The strong antiferromagnetic interactions between the two copper centres in the CuF_2Cu unit are confirmed by a quasi-silent solid-state EPR spectrum at room temperature and 77 K. Only a very broad weak band is observed, attributed to a $S = 1$ system in a crystal lattice with other spins nearby.

6. Concluding remarks

The main interest of the present work lies in the isolation and structural characterisation of a unique polymer combining alternating μ-F and μ_4-SiF_6 bridges $\{[Cu_2(dipyridylamine)_2(\mu\text{-}F)_2(\mu_4\text{-}SiF_6)] \cdot (CH_3OH)_2\}_n$. Its magnetic properties were elucidated using a Bleaney-Bowers model for dinuclear Cu(II) complexes, leading to the extraction of a J parameter of $-74\ cm^{-1}$, indicating strong antiferromagnetic interactions in the polymer.

Acknowledgements

The authors thank COST Action D21/003/2001 for allowing regular exchange of preliminary results within a European network before publication and the Dutch National Research School Combination Catalysis (HRSMC and NIOK) for financial support. Travel and exchange with the groups of Profs. E. Hahn and B. Krebs (Westfalische Wilhelms Universität, Münster) through a NWO and DFG Grant in the framework of the Joint Graduierten Kolleg is thankfully acknowledged. The financial support of Ministry of Education, Science and Sport, Republic of Slovenia, through grants MŠZŠ P1-0175-103 and X-2000, all gratefully acknowledged.

Appendix A. Supplementary data

All atom parameters and other crystallographic data have been deposited with the Cambridge Crystallographic Data Center as supplementary material with the deposition number: CCDC 255650. These data can be obtained, free of charge via http://www.ccdc.cam.ac.uk/conts/retrieving.html. Supplementary data associated with this article can be found, in the online version at doi:10.1016/j.poly.2005.04.011.

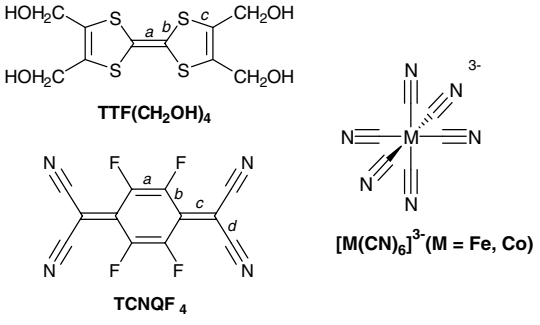
References

[1] J.M. Lehn, Polym. Int. 51 (2002) 825.
[2] B. Moulton, M.J. Zaworotko, Curr. Opin. Solid State Mat. Sci. 6 (2002) 117.
[3] B. Moulton, M.J. Zaworotko, Chem. Rev. 101 (2001) 1629.
[4] G. Leibeling, S. Demeshko, B. Bauer-Siebenlist, F. Meyer, H. Pritzkow, Eur. J. Inorg. Chem. (2004) 2413.
[5] B. Chand, U. Ray, G. Mostafa, T.H. Lu, C. Sinha, Polyhedron 23 (2004) 1669.
[6] D. Bose, J. Banerjee, S.H. Rahaman, G. Mostafa, H.K. Fun, R.D.B. Walsh, M.J. Zaworotko, B.K. Ghosh, Polyhedron 23 (2004) 2045.
[7] D.F. Sun, R. Cao, Y.Q. Sun, W.H. Bi, X.J. Li, Y.Q. Wang, Q. Shi, X. Li, Inorg. Chem. 42 (2003) 7512.
[8] P. Lin, R.A. Henderson, R.W. Harrington, W. Clegg, C.D. Wu, X.T. Wu, Inorg. Chem. 43 (2004) 181.
[9] M.A. Withersby, A.J. Blake, N.R. Champness, P.A. Cooke, P. Hubberstey, A.L. Realf, S.J. Teat, M. Schroder, J. Chem. Soc., Dalton Trans. (2000) 3261.
[10] O. Ohmori, M. Fujita, Chem. Commun. (2004) 1586.
[11] E.Y. Choi, Y.U. Kwon, Inorg. Chem. Commun. 7 (2004) 942.
[12] H.J. Schneider, T.J. Liu, N. Lomadze, Angew. Chem., Int. Edit. 42 (2003) 3544.

[13] S. Shi, in: M. Roundhill, J.P. Kackler Jr. (Eds.), Optoelectronic Properties of Inorganic Compounds, Plenum Press, New York, 1999.
[14] C.L. Chen, C.Y. Su, Y.P. Cai, H.X. Zhang, A.W. Xu, B.S. Kang, H.C. zur Loye, Inorg. Chem. 42 (2003) 3738.
[15] M.K. Saha, F. Lloret, I. Bernal, Inorg. Chem. 43 (2004) 1969.
[16] W.A. Alves, R. Santos, A. Paduan-Filho, C.C. Becerra, A.C. Borin, A. Ferreira, Inorg. Chim. Acta 357 (2004) 2269.
[17] X.M. Liu, J.A. McAllister, M.P. de Miranda, B.J. Whitaker, C.A. Kilner, M. Thornton-Pett, M.A. Halcrow, Angew. Chem., Int. Edit. 41 (2002) 756.
[18] X.H. Bu, M. Du, L. Zhang, Z.L. Shang, R.H. Zhang, M. Shionoya, J. Chem. Soc., Dalton Trans. (2001) 729.
[19] X.M. Liu, J.A. McAllister, M.P. de Miranda, E.J.L. McInnes, C.A. Kilner, M.A. Halcrow, Chem. Eur. J. 10 (2004) 1827.
[20] Z. Smékal, Z. Trávníček, J. Mroziński, J. Marek, Inorg. Chem. Commun. 6 (2003) 1395.
[21] A. Escuer, M. Font-Bardia, S.S. Massoud, F.A. Mautner, E. Penalba, X. Solans, R. Vicente, New J. Chem. 28 (2004) 681.
[22] E.Q. Gao, S.Q. Bai, C.F. Wang, Y.F. Yue, C.H. Yan, Inorg. Chem. 42 (2003) 8456.
[23] G.A. van Albada, O. Roubeau, I. Mutikainen, U. Turpeinen, J. Reedijk, New J. Chem. 27 (2003) 1693.
[24] X.M. Liu, A.C. McLaughlin, M.P. de Miranda, E.J.L. McInnes, C.A. Kilner, M.A. Halcrow, Chem. Commun. (2002) 2978.
[25] W.C. Velthuizen, J.G. Haasnoot, A.J. Kinneging, F.J. Rietmeijer, J. Reedijk, J. Chem. Soc., Chem. Commun. (1983) 1366.
[26] R.R. Jacobson, Z. Tyeklár, K.D. Karlin, J. Zubieta, Inorg. Chem. 30 (1991) 2035.
[27] F.J. Rietmeijer, R.A.G. Degraaff, J. Reedijk, Inorg. Chem. 23 (1984) 151.
[28] D.A. Handley, P.B. Hitchcock, T.H. Lee, G.J. Leigh, Inorg. Chim. Acta 316 (2001) 59.
[29] E.W. Ainscough, A.M. Brodie, J.D. Ranford, J.M. Waters, Inorg. Chim. Acta 236 (1995) 83.
[30] R.A.J. Driessen, F.B. Hulsbergen, W.J. Vermin, J. Reedijk, Inorg. Chem. 21 (1982) 3594.
[31] S. Subramanian, M.J. Zaworotko, Angew. Chem., Int. Edit. Engl. 34 (1995) 2127.
[32] F.S. Keij, R.A.G. Degraaff, J.G. Haasnoot, J. Reedijk, E. Pedersen, Inorg. Chim. Acta 156 (1989) 65.
[33] J.S. Fleming, K.L.V. Mann, S.M. Couchman, J.C. Jeffery, J.A. McCleverty, M.D. Ward, J. Chem. Soc., Dalton Trans. (1998) 2047.
[34] P.J. van Koningsbruggen, J.G. Haasnoot, R.A.G. de Graaff, J. Reedijk, J. Chem. Soc., Dalton Trans. (1993) 483.
[35] J. Reedijk, Comments Inorg. Chem. 1 (1982) 379.
[36] O. Kahn, Molecular Magnetism, VCH Publishers, New York, 1993.
[37] G.M. Sheldrick, SHELXS-97, A Program for Automatic Solution of Crystal Structures, University of Göttingen, Göttingen, Germany, 1997.
[38] G.M. Sheldrick, SHELXS-97, A Program for Crystal Structure Refinement, University of Götingen, Göttingen, Germany, 1997.
[39] P. de Hoog, P. Gamez, M. Luken, O. Roubeau, B. Krebs, J. Reedijk, Inorg. Chim. Acta 357 (2004) 213.
[40] K. Nakamoto, Infrared and Raman Spectra of Inorganic and Coordination Compounds, 5th ed., Wiley, New York, 1997.
[41] A.F. Jalbout, Z.Y. Jiang, A. Ouasri, H. Jeghnou, A. Rhandour, M.C. Dhamelincourt, P. Dhamelincourt, A. Mazzah, Vib. Spectrosc. 33 (2003) 21.
[42] S. Noro, S. Kitagawa, M. Kondo, K. Seki, Angew. Chem., Int. Edit. 39 (2000) 2082.

Pd, Pt, Au, ...) [5]. More recently, cyanide clusters such as $[Re_6Se_8(CN)_6]^{4-}$ [6] or $[Cu_8(i\text{-}mnt)_6]^{4-}$ [7] have also been investigated. Among these anions, the paramagnetic hexacyanometalate $[M(CN)_6]^{3-}$ (M = Fe, Cr) complexes are particularly studied in order to create magnetic interactions between the magnetic moments of the transition metal and the π-electrons of the organic network. Such molecular materials can thus combine both conducting and magnetic properties and lead to multiproperty materials [4,8]. In this prospect, the association of the TTF itself with the hexacyanoferrate anion has been reported [9]. The use of extended molecules such as BEDT-TTF (bis(ethylenedithio)tetrathiafulvalene) [10–14], BET-TTF (bis(ethylenethio) tetrathiafulvalene) [15] or the selenium derivative BEDS-TTF (bis(ethylenediseleno)tetrathiafulvalene) [16], has been also investigated and led to numerous materials. To our knowledge, only two examples with functionalized TTF derivatives have been reported so far. These radical cation salts formulated $(DHET\text{-}DMTTF)_2(Et_4N)[Fe(CN)_6]$ [13a] and $(DHET\text{-}EDTTTF)_2(Et_4N)$ $[Cr(SCN)_6]$ [13b] both incorporate a hydroxyl TTF derivative, either the bis(hydroxyethylenethio)dimethyl-tetrathiafulvalene (DHET-DMTTF) or the bis(hydroxyethylenethio)ethylenedithio-tetrathiafulvalene (DHET-EDTTTF). In these structures, strong hydrogen bonds have been observed between the cyano groups and the hydroxyl groups. Based on this observation, the association of the tetrakis(hydroxymethyl)tetrathiafulvalene ($TTF(CH_2OH)_4$), a TTF derivative bearing four hydroxyl groups, with cyanide anions appeared interesting to investigate.

We report here the synthesis of radical cation salts based on $TTF(CH_2OH)_4$ with either the organic tetrafluorotetracyanoquinodimethane molecule ($TCNQF_4$) or the inorganic paramagnetic $[Fe(CN)_6]^{3-}$ complex (Scheme 1). In order to appreciate the magnetic contribution of the organic part in the resulting salt, the compound incorporating the diamagnetic complex $[Co(CN)_6]^{3-}$ has also been prepared. The synthesis and the crystal structure of the three radical salts formulated $[TTF(CH_2OH)_4][TCNQF_4]$ (**1**) and $[TTF(CH_2OH)_4]_3[18\text{-crown-}6 \subset K][M(CN)_6] \cdot DMF$ with M = Fe (**2a**) and M = Co (**2b**) are reported in this paper, as well as the study of their magnetic properties.



Scheme 1. Molecules studied. The bond labels of the $TTF(CH_2OH)_4$ and $TCNQF_4$ molecules are represented as *a*, *b*, *c* and *d* letters.

2. Experimental

2.1. Synthesis

$TTF(CH_2OH)_4$ was synthesized according to the method described in the literature [17]. The starting compounds $TCNQF_4$, $K_3[Fe(CN)_6]$, $K_3[Co(CN)_6]$ and 18-crown-6 ether were purchased from Aldrich. $TCNQF_4$ was recrystallized twice in acetonitrile prior to use.

Crystals of **1** were obtained by slow diffusion of an acetonitrile (MeCN) solution of 17 mg of $TCNQF_4$ in a dimethylformamide (DMF) solution of 20 mg of $TTF(CH_2OH)_4$ at room temperature. Air-stable dark green crystals were harvested after few days.

Crystals of **2a** and **2b** were grown using the electrocrystallization technique by applying anodic constant current ($I = 0.5$ μA) at platinum wire electrodes ($l =$ 2 cm, $d = 1$ mm) of a two-compartment cell at 25 °C [18]. The supporting electrolyte was a solution of 20 mg of the corresponding potassium hexacyanometalate salt and 50 mg of dried 18-crown-6 ether dissolved in a 5:1 mixture of freshly distilled MeCN and DMF (15 mL). In the anodic compartment 5 mg of $TTF(CH_2OH)_4$ were added. Air-stable black crystals were obtained after 2 weeks.

2.2. X-ray crystallography

Details of data collection and structure refinement are summarized in Table 1. Data were collected at 293 K on a single Φ-axis Stoe-IPDS diffractometer using graphite monochromatized Mo Kα radiation ($\lambda =$ 0.71073 Å). The Stoe software [19] was used for data collection and reduction. No absorption correction was applied due to the low value of the absorption coefficients. Structures were solved by direct-methods and refined by full-matrix least-squares based on F^2, by using the SHELX-97 software package [20].

Hydrogen bonds were detected by the usual but indirect method used for X-ray data, consisting in the observation of short distances between hydrogen bond donor and acceptor [21]. Two types of hydrogen bond, O–H···O and O–H···N are involved in these salts. One singularity of the O–H···O hydrogen bonds lies in the dual hydrogen bond donor and acceptor character of the hydroxyl group. Then even if a hydrogen bond is detected by identifying a short O···O contacts (typically between 2.60 and 2.95 Å) [21,22], the hydrogen atom can be disordered over two positions, each oxygen atom playing alternatively the donor and the acceptor role. Knowing these difficulties, the following process was used for the X-ray structures presented in this paper: (i) identification

Table 1
Crystallographic and structure refinement data for $[TTF(CH_2OH)_4][TCNQF_4]$ (**1**), $[TTF(CH_2OH)_4]_3[18\text{-crown-6} \subset K][Fe(CN)_6] \cdot DMF$ (**2a**) and $[TTF(CH_2OH)_4]_3[18\text{-crown-6} \subset K][Co(CN)_6] \cdot DMF$ (**2b**)

Compound	**1**	**2a**	**2b**
Empirical formula	$C_{22}H_{12}F_4N_4O_4S_4$	$C_{51}H_{67}FeKN_7O_{19}S_{12}$	$C_{51}H_{67}CoKN_7O_{19}S_{12}$
Formula weight	600.60	1561.78	1563.64
Temperature (K)	293(2)	293(2)	293(2)
Crystal system	triclinic	triclinic	triclinic
Space group	$P\bar{1}$	$P\bar{1}$	$P\bar{1}$
a (Å)	7.7797(13)	11.315(2)	11.3273(16)
b (Å)	12.983(2)	12.497(3)	12.4839(15)
c (Å)	13.226(2)	12.790(2)	12.7467(19)
α (°)	63.820(16)	94.08(2)	94.304(16)
β (°)	82.616(2)	96.99(2)	97.075(17)
γ (°)	78.884(18)	108.43(2)	108.363(15)
V (Å^3)	1174.9(3)	1691.4(5)	1685.2(4)
Z	2	1	1
ρ_{calcd} (g cm^{-3})	1.698	1.533	1.553
μ (mm^{-1})	0.477	0.728	0.764
$F(000)$	608	811	802
Crystal size (mm)	$0.36 \times 0.06 \times 0.04$	$0.25 \times 0.16 \times 0.06$	$0.20 \times 0.10 \times 0.06$
θ range (°)	2.70–27.10	1.92–26.03	1.92–26.05
Reflections collected	13380	16380	16843
Independent reflections	4745	5994	6088
R_{int}	0.0609	0.0643	0.0495
Reflections with $I > 2\sigma(I)$	2436	3143	3288
Parameters	287	414	412
Goodness-of-fit on F^2	0.998	1.016	1.007
R_1[a] ($I > 2\sigma(I)$)/wR_2[b]	0.0372/0.0720	0.0549/0.1357	0.0452/0.0992
Largest difference peak/hole (e Å^{-3})	0.240/−0.252	1.102/−0.362	0.926/−0.377

[a] $R_1 = \sum \text{abs}(\text{abs}(F_o) - \text{abs}(F))$.
[b] $wR_2 = [\sum w(F_o^2 - F_c^2)^2 / \sum w(F_o^2)^2]^{0.5}$.

of short donor (O)–acceptor (O) distances, as indication of the presence of a hydrogen bond, followed by (ii) the introduction of hydrogen atoms using riding model. This method gives a plausible position for the hydrogen atoms, but not necessary the only possible one.

In all structures, all non-hydrogen atoms were refined with anisotropic parameters. For **1**, hydrogen atoms were introduced at calculated positions and were not refined (riding model). For **2a**, O2A and O1E atoms were found disordered over two dependent positions with a 0.6:0.4 refined distribution. Thermal ellipsoids on O3A and O4A were found elongated, but attempts to split them on two positions gave unsatisfactory results. These atoms were then ultimately refined with a full occupancy in one position. Hydrogen atoms were introduced at calculated positions and were not refined (riding model), excepted on the minor position of O2A (O2AB) where no hydrogen atom was introduced. For **2b**, O2A and O1E atoms were found disordered over two dependent positions with a 0.6:0.4 refined distribution. As for **2a**, thermal ellipsoids on O3A and O4A were found elongated, but attempts to split them on two positions gave unsatisfactory results. These atoms were then ultimately refined with a full occupancy in one position. Hydrogen atoms were introduced at calculated positions and were not refined, excepted on the minor position of O2A (O2AB) where no hydrogen atom was introduced.

2.3. Magnetic measurements

Magnetic susceptibility measurements were performed on polycrystalline samples (18.35 mg, 13.93 mg and 19.24 mg for **1**, **2a** and **2b**, respectively) on a Quantum Design MPMS-5 SQUID magnetometer in the temperature range 5–300 K at 5000 G. The data were corrected for the sample holder and for the diamagnetic contribution calculated from Pascal constants.

2.4. Theoretical calculations

The overlap interaction energies ($\beta_{HOMO-HOMO}$) were calculated by the extended Hückel method [23]. A modified Wollsberg–Helmholtz formula was used to calculate the $H_{\mu\nu}$ non-diagonal values [24]. Double-ζ orbitals for carbon, sulfur and oxygen atoms were used.

3. Results

3.1. $[TTF(CH_2OH)_4][TCNQF_4]$ (1)

This salt was obtained by chemical oxidation of $TTF(CH_2OH)_4$ by $TCNQF_4$ in a MeCN/DMF mixture. Single crystals suitable for X-ray diffraction were obtained after few days. From the X-ray analysis, this salt

is formulated [TTF(CH$_2$OH)$_4$][TCNQF$_4$]. It crystallizes in a triclinic setting, space group $P\bar{1}$ (No. 2) with one TTF(CH$_2$OH)$_4$ molecule and one TCNQF$_4$ molecule in general position. The geometry of the TTF(CH$_2$OH)$_4$ molecule is similar to the one already observed in the neutral form and in other radical salts [25,26]. The TTF core and the methylene groups are in the same plane whereas all the oxygen atoms of the hydroxyl group lie slightly upper of this plane but on the same side. TTF(CH$_2$OH)$_4$ molecules are assembled in centrosymmetric dimers with an almost bond-over-bond conformation, associated with a short inter-plane distance (3.388(2) Å) and short S···S contacts (3.3916(15) and 3.4362(16) Å). TCNQF$_4$ molecules crystallize planar with a regular geometry, and are also assembled in centrosymmetric dimers with a short inter-plane contact (3.2198(10) Å, shortest intermolecular C···C distance = 3.284(5) Å).

As in all TTF based molecules, intra-molecular bond lengths in TTF(CH$_2$OH)$_4$ are oxidation state sensitive. C–C double bonds (*a* on Scheme 1) and C–S bonds (*b* and *c* on Scheme 1) are, respectively, longer and shorter when oxidation state increases. A similar trend is known for TCNQF$_4$ molecule; double bonds (*a* and especially *c* on Scheme 1) and single bonds (*b* and *d* on Scheme 1) are, respectively, longer and shorter when reduction state increases. Bond distances in TCNQF$_4$ and TTF(CH$_2$OH)$_4$ in **1** are reported in Tables 2 and 3, respectively, as well as those for the corresponding neutral molecule and for known cation radical salts. Bond lengths examination allows to attribute $a+1$ and $a-1$ oxidation state for the TTF(CH$_2$OH)$_4$ and the TCNQF$_4$ molecules, respectively. This is indeed in accordance with the relative redox potentials of both components. The first and the second oxidation of TTF(CH$_2$OH)$_4$ are reported to occur at 0.39 and 0.65 V versus SCE in DMF [17a,27], and the first reduction potential of TCNQF$_4$ at 0.53 V versus SCE in MeCN [28]. Even if it is not an absolute way to conclude, the high potential difference ($\Delta E = 0.14$ V) is in favor of a full charge transfer salt. This is also confirmed by the geometry of the [TTF(CH$_2$OH)$_4$]$_2$ dimer, a bond-over-bond conformation with a short inter-plane contact (<3.5 Å) is usually associated with fully oxidized $(TTF)_2^{2+}$ dimer [7]. The $\beta_{HOMO-HOMO}$ value calculated by the extended Hückel method for the [TTF(CH$_2$OH)$_4$]$_2$ dimer in **1** is 1.116 eV. This high value is in

Table 3
C–C and C–S bond lengths of TTF(CH$_2$OH)$_4$ molecule in its neutral form, in one reported radical cation salt and in **1**, **2a** and **2b** (mean values are in italic)

Compound	C–C (Å)	C–S (Å)		Oxidation state
	a	*b*	*c*	
1	1.394(3)	1.709(3)	1.729(3)	+1
		1.715(3)	1.743(3)	
		1.718(3)	1.744(3)	
		1.720(3)	1.749(3)	
		1.716(5)	*1.741(9)*	
2a				
A	1.380(7)	1.724(5)	1.735(6)	+2/3
		1.726(5)	1.741(5)	
		1.732(5)	1.742(5)	
		1.733(5)	1.743(6)	
		1.729(4)	*1.740(4)*	
C	1.402(11)	1.703(5)	1.735(6)	
		1.729(5)	1.740(6)	
		1.716(18)	*1.738(4)*	
2b				
A	1.373(5)	1.729(4)	1.739(4)	+2/3
		1.729(4)	1.739(4)	
		1.734(4)	1.740(4)	
		1.738(4)	1.741(4)	
		1.733(4)	*1.740(4)*	
C	1.386(8)	1.716(5)	1.744(4)	
		1.728(4)	1.744(4)	
		1.722(8)	*1.744(0)*	
TTF(CH$_2$OH)$_4$ [26]	1.345(10)	*1.756(2)*	*1.758(1)*	0
[TTF(CH$_2$OH)$_4$]$_2$[Mo$_6$O$_{19}$] [25]				
A	1.360	1.731	1.735	+1
		1.726	1.732	
		1.729	*1.734*	
B	1.395	1.714	1.733	
		1.718	1.739	
		1.716	*1.736*	

The corresponding oxidation state in theses salts is also reported. *a*, *b* and *c* bond labels are defined in Scheme 1.

Table 2
C–C bond lengths of TCNQF$_4$ molecule in its neutral form, in one reported radical cation salt and in **1** (mean values are in italic)

Compound	C–C (Å)				Oxidation state
	a	*b*	*c*	*d*	
1	1.359(4)	1.403(4)	1.411(4)	1.421(5)	−1
	1.362(4)	1.411(4)	1.414(4)	1.423(5)	
	1.361(2)	1.416(4)	*1.413(2)*	1.424(5)	
		1.421(4)		1.429(5)	
		1.413(8)		*1.424(3)*	
TCNQF$_4$ [29]	*1.335*	*1.439*	*1.373*	*1.440*	0
[EDO–TTF–CONH$_2$][TCNQF$_4$] [28]	*1.352(4)*	*1.411(4)*	*1.410(4)*	*1.423(5)*	−1

The corresponding oxidation state is also reported. *a*, *b*, *c* and *d* bond labels are defined in Scheme 1.

accordance with those calculated for fully oxidized $[TTF(CH_2OH)_4]_2^{2+}$ dimers in the $[TTF(CH_2OH)_4]_x[Re_6S_{8-n}Cl_{6+n}]$ ($n = 0, 1, 2, 3$) cation radical salts series ($\beta_{HOMO-HOMO}$ ranging from 1.006 to 1.176 eV) [26].

The crystal structure of **1** can be described by focusing on the dimeric units. $[TCNQF_4]_2^{2-}$ dimers stack along the *a* axis with their plane almost perpendicular to this direction. As represented Fig. 1(a), $TTF(CH_2OH)_4$ molecules adopt a ladder-like arrangement in the same direction but this time with their plane parallel to the *a* axis. Nevertheless, this structural feature cannot be associated with a magnetic spin ladder behavior because these dimers are indeed electronically isolated one from the other due to the bulkiness of the CH_2OH groups (inter-dimer S···S contacts > 4.65 Å). The cationic and the anionic ribbons define a distorted cubic lattice in the (*b*, *c*) plane (Fig. 1(b)).

A complex hydrogen bond network occurs in **1**. The cohesion of the $[TTF(CH_2OH)_4]_2^{2+}$ dimer is reinforced by three strong and one weaker O–H···O hydrogen bonds between the hydroxyl groups. As represented Fig. 2, O2A–H12A and O4A–H4A groups act as hydrogen bond donors for O3A and O1A, respectively. Corresponding bond distances and angles are summarized in Table 4 and are in the usual range for this kind of interaction [21,22]. The $[TTF(CH_2OH)_4]_2^{2+}$ dimers are connected with each others by O–H···O hydrogen bonds parallel to the ladder direction with O1A–H11A and O3A–H13A acting this time as hydrogen bond donors for O2A and O4A, respectively (Fig. 2). This results in the formation of cyclic $R_4^4(8)$ motifs [30], where all crystallographically independent hydroxyl groups act as both a donor and an acceptor. The cohesion of the cationic ribbon is then ensured by hydrogen bonding. The hydrogen atom involved in the weakest O–H···O hydrogen bonds, namely H13A (O3A···O4A = 3.008(4) Å, O3A–H13A···O4A = 106.5°) is also hydrogen bonded to a nitrogen atom of a $TCNQF_4$ molecule (N3B on Fig. 2) that thus connects adjacent cationic and anionic ribbons (see Table 4 for bond distances and angles).

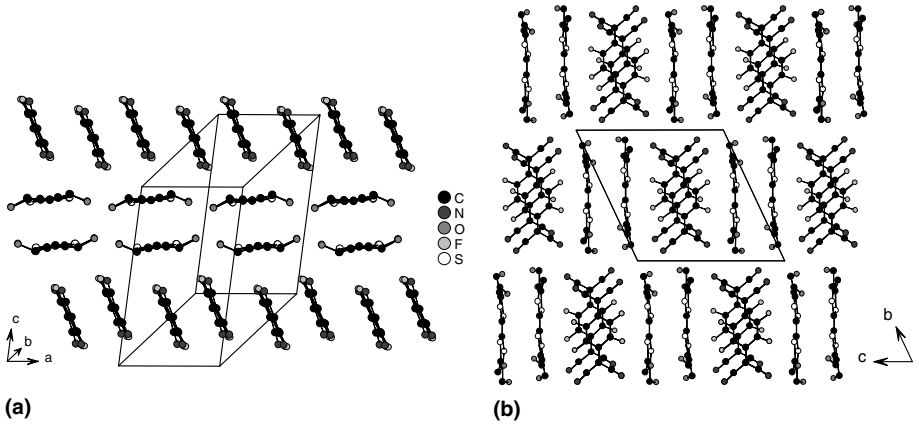


Fig. 1. Crystal structure of **1**. Hydrogen atoms are omitted for clarity. (a) Ribbons of $[TTF(CH_2OH)_4]_2^{2+}$ and $[TCNQF_4]_2^{2-}$ dimers running along the *a* direction, the molecules are viewed along their long axis. (b) Distorted cubic arrangement of the cationic and anionic ribbons in the (*b*,*c*) plane.

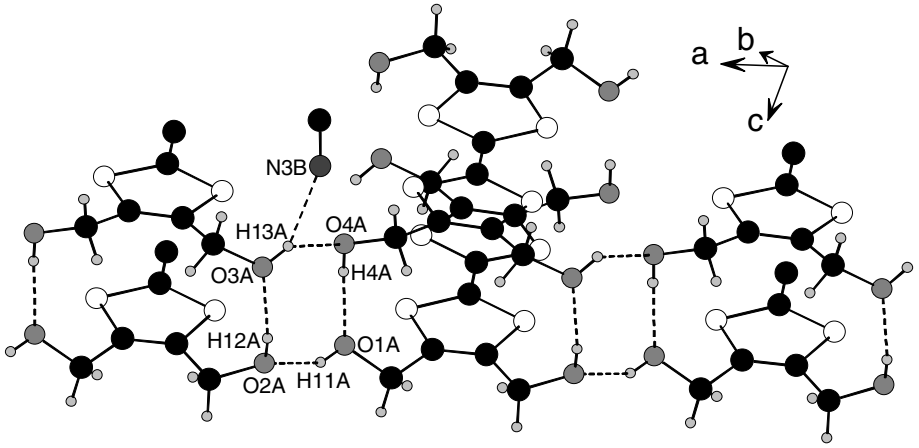


Fig. 2. Hydrogen bond network in **1** represented in dashed lines. Only the central $[TTF(CH_2OH)_4]_2^{2+}$dimer is fully pictured. Only the cyano group of the $TCNQF_4$ molecule involved in the hydrogen bond network is represented.

Table 4
Hydrogen bond distances and angles in **1**, **2a**–**b** salts

Compound	D–H···A	D···A (Å)	H···A (Å)	D–H···A (°)
1	O1A–H1A1···O2A (1 + *x*, *y*, *z*)	2.790(3)	2.071	146.2
	O2A–H2A1···O3A (1 − *x*, 1 − *y*, −*z*)	2.758(4)	1.964	162.6
	O3A–H3A1···N3B (1 − *x*, 1 − *y*, 1 − *z*)	2.967(5)	2.221	151.5
	O3A–H3A1···O4A (1 + *x*, *y*, *z*)	3.008(4)	2.670	106.5
	O4A–H4A1···O1A (1 − *x*, 1 − *y*, −*z*)	2.775(3)	1.963	170.4
2a	O1A–H1A···N2B (−*x*, −*y*, 1 − *z*)	2.789(6)	1.988	165.0
	O2AA–H2AA···O1EA (1 − *x*, 2 − *y*, 1 − *z*)	2.502(10)	1.849	135.6
	O2AB–H2AB···O1EB (1 − *x*, 2 − *y*, 1 − *z*)	2.614(14)	[a]	[a]
	O3A–H3A···O3A (−*x*, 1 − *y*, −*z*)	3.366(23)	3.307	87.13
	O4A–H4A···N3B (*x*, 1 + *y*, *z*)	2.740(7)	1.946	162.9
	O1C–H1C···N1B (*x*, 1 + *y*, *z*)	2.730(6)	171.2	1.917
	O2C–H2C···O1A (1 − *x*, −*y*, 1 − *z*)	2.797(6)	2.046	152.0
	O1C···O2AA (1 − *x*, −*y*, 1 − *z*)	2.708(10)	[a]	[a]
2b	O1A–H1A···N2B (−*x*, −*y*, 1 − *z*)	2.785(5)	1.987	164.12
	O2AA–H2AA···O1EA (1 − *x*, 1−*y*, 1 − *z*)	2.437(8)	1.793	134.26
	O2AB–H2AB···O1EB (1 − *x*, 1 − *y*, 1 − *z*)	2.689(12)	[a]	[a]
	O2AA–H2AA···O1C (1 − *x*, −*y*, 1 − *z*)	2.793(9)	2.859	77.14
	O3A–H3A···O3A (−*x*, 1 − *y*, −*z*)	3.468(19)	3.420	86.55
	O3A–H3A···N1B (*x*, *y*, *z*)	3.414(12)	3.437	81.49
	O4A–H4A···N3B (*x*, 1 + *y*, *z*)	2.740(6)	1.963	157.83
	O1C–H1C···N1B (*x*, −1 + *y*, *z*)	2.737(5)	2.198	123.46
	O2C–H2C···O1A (1 − *x*, −*y*, 1 − *z*)	2.820(5)	2.056	152.92

A and D are the hydrogen bond acceptor and donor, respectively. Values of van der Waals contacts for H···O and H···N are 2.72 and 2.75 Å, respectively.

[a] No hydrogen atom has been introduced on this hydroxyl group during the X-ray elucidation, see Section 2 for details.

The magnetic properties of **1** have been studied by SQUID measurement. The variation of the magnetic susceptibility with the temperature corresponds to a diamagnetic behavior except at low temperature which is attributed to paramagnetic impurities (0.3%). This behavior is in accordance with the presence of fully oxidized, diamagnetic and electronically isolated $[TTF(CH_2OH)_4]_2^{2+}$ and $[TCNQF_4]_2^{2-}$ dimers.

3.2. *[TTF(CH$_2$OH)$_4$]$_3$[18-crown-6 ⊂ K][Fe(CN)$_6$] · DMF (**2a**) and [TTF(CH$_2$OH)$_4$]$_3$[18-crown-6 ⊂ K][Co(CN)$_6$] · DMF (**2b**)*

Electrocrystallization of $TTF(CH_2OH)_4$ with $K_3[Fe(CN)_6]$ or $K_3[Co(CN)_6]$ was performed in a DMF/MeCN mixture. 18-Crown-6 ether was added to the electrolytic solution in order to dissolve the potassium salts. Black air-stable crystals were harvested after 2 weeks. From the X-ray analysis, these salts are isostructural and formulated $[TTF(CH_2OH)_4]_3[18\text{-crown-}6 \subset K][M(CN)_6] \cdot DMF$, with M = Fe (**2a**) or Co (**2b**). They crystallize in a triclinic setting, space group $P\bar{1}$ with one $TTF(CH_2OH)_4$ molecule (**A**) in general position, another molecule (**C**) on an inversion center and one $[M(CN)_6]^{3-}$ anion, one potassium cation, one 6-crown-18-ether molecule and one DMF molecule on inversion centers. The DMF solvent molecule is disordered over two positions.

As represented in Fig. 3, the whole structure can be described as an alternation of cationic and anionic layers stacked in the *c* direction. The anionic layer is composed of hexacyanometalate anions and DMF solvent molecules. In **2a**, $[Fe(CN)_6]^{3-}$ anion adopts a regular octahedral geometry with Fe–C distances and independent C–Fe–C angles ranging from 1.930(5) to 1.947(6) Å and 88.0(2)° to 89.6(2)°, respectively, and C–N distances and Fe–C–N angles ranging from 1.126(7) to 1.145(7) Å and 177.0(6)° to 179.3(5)°, respectively [9–16]. In **2b**, the $[Co(CN)_6]^{3-}$ anion presents also a regular geometry (Co–C = 1.894(5)–1.904(4) Å, C–Co–C = 88.4(2)–89.4(2)°, and C–N = 1.134(5)–1.142(5) Å, Co–C–N = 177.4(4)–178.7(4)°) [10,11].

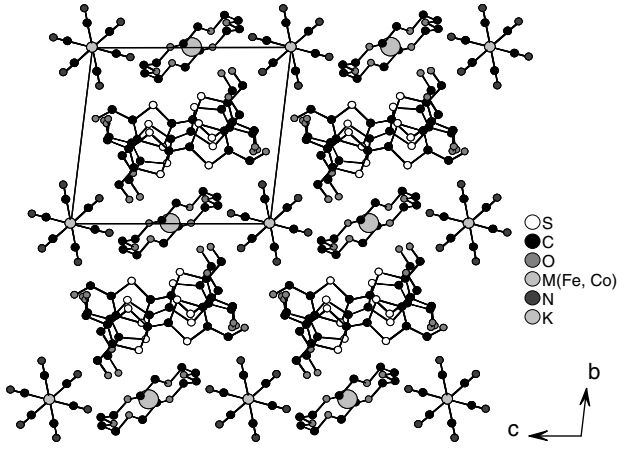


Fig. 3. Crystal structure of **2a** and **2b** viewed along the *a* axis. Hydrogen atoms, DMF solvent molecules and K–O bonds are omitted for clarity.

The cationic layer is built of columns of $TTF(CH_2OH)_4$ molecules (**A** and **C**) developing in the *a* direction, electronically isolated the one to the others by crown-ether-embedded potassium cations (shortest inter-columnar S···S contact > 6.5 Å). The two independent $TTF(CH_2OH)_4$ molecules are planar with the hydroxyl groups pointing slightly outside the TTF plane as already observed in **1**. One of the hydroxyl group (O2A) of the **A** molecule is disordered over two positions with 0.6 : 0.4 refined occupancy. The potassium cation lies in the center of the 18-crown-6 ether molecule with K–O distances ranging from 2.786(4) to 2.819(4) Å in **2a** and from 2.794(3) to 2.815(3) Å in **2b**, as expected for the [18-crown-6 ⊂ K] motif [31]. The coordination sphere of the potassium ion is completed by two oxygen atoms (O2C) of the **C** $TTF(CH_2OH)_4$ molecule (K–O2C = 2.793(4) and 2.804(4) Å in **2a** and **2b**, respectively) defining a 1-D polymeric network along the *b* axis as represented Fig. 4. The potassium cation is thus in a distorted bipyramidal hexagonal coordination environment as commonly observed for alkali cations.

From the salt formulation, namely $[TTF(CH_2OH)_4]_3[18\text{-crown-6} \subset K][M^{III}(CN)_6] \cdot DMF$ (M = Fe, Co), $a + 2/3$ mean oxidation state can be deduced for the $TTF(CH_2OH)_4$ molecules. This charge distribution is in accordance with the geometry of the TTF core. C–S and C=C bond lengths for **A** and **C** molecules (see Table 3) are indeed intermediate between those of the neutral molecule and those of the fully oxidized $[TTF(CH_2OH)_4]^+$ cation. Each column of $TTF(CH_2OH)_4$ molecules is composed of centrosymetric $(\mathbf{ACA})^{2+}$ trimer with a bond-over-bond overlap (shortest S···S contacts are 3.554(2), 3.580(2) and 3.582(2) Å in **2a** and 3.564(2) and 3.592(2) Å in **2b**) and a slight twisting between successive molecules (dihedral angle between the long axis of **A** and **C** molecules is about 10–11°). As shown in Fig. 5, these trimers are packed in a staggered manner with shortest inter-trimer S···S contacts greater than 4 Å (4.060(2) and 4.051(2) Å in **2a** and **2b**, respectively). $\beta_{HOMO-HOMO}$ interactions were calculated by the extended Hückel method and are, respectively, 0.722 and 0.237 eV for the intra- and inter-trimer interactions in **2a**, and 0.746 and 0.239 eV in **2b**. As expected, the HOMO–HOMO overlap in the trimer composed of +2/3 mixed valence $TTF(CH_2OH)_4$ cations is weaker than the one calculated for the fully oxidized $[TTF(CH_2OH)_4]_2^{2+}$ dimer in **1** (0.722 or 0.746 versus 1.116 eV).

As shown in Fig. 5, the cohesion of the $[(TTF(CH_2OH)_4)_3]^{2+}$ trimer is reinforced by O–H···O hydrogen bonds (O2C–H2C···O1A and possibly O1C···O2AA). The corresponding distances and angles are reported in Table 4. Nevertheless, the main interaction occurs between the hydroxyl and the cyano groups of the anions. Each $[Fe(CN)_6]^{3-}$ complex is actually connected to six $TTF(CH_2OH)_4$ molecules by strong O–H···NC hydrogen bonds (O1C–H1C···N1B, O1A–H1A···N2B and O4A–H4A···N3B), as represented in Fig. 6. Geometrical characteristics are summarized in Table 4 and are in the usual range for this kind of interactions [13,32].

On the two remaining hydroxyl groups, one (O2A–H2A) is hydrogen bonded to the carbonyl group of the DMF molecule. This O–H···O hydrogen bond is disordered over two positions (O2AA–H2AA···O1EA

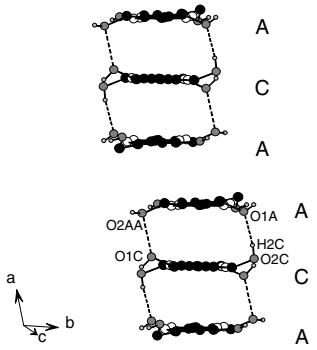


Fig. 5. Stack of $(\mathbf{ACA})^{2+}$ trimers in the *a* direction viewed along the long axis of the $TTF(CH_2OH)_4$ molecules in **2a** and **2b**. Only one of the two disordered position for O2A is pictured. Intra-trimers O–H···O hydrogen bonds are drawn in dashed lines. Hydrogen atoms of CH_2 groups are omitted for clarity.

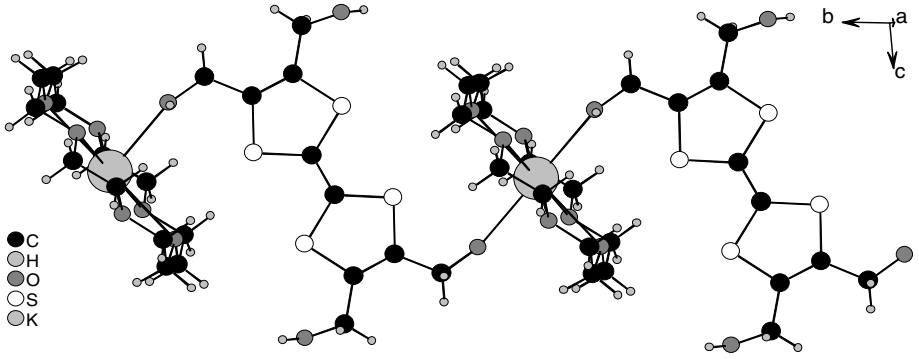


Fig. 4. View of the polymeric chain in **2a** and **2b** composed of $TTF(CH_2OH)_4$ molecules and crown-ether-embedded potassium cations.

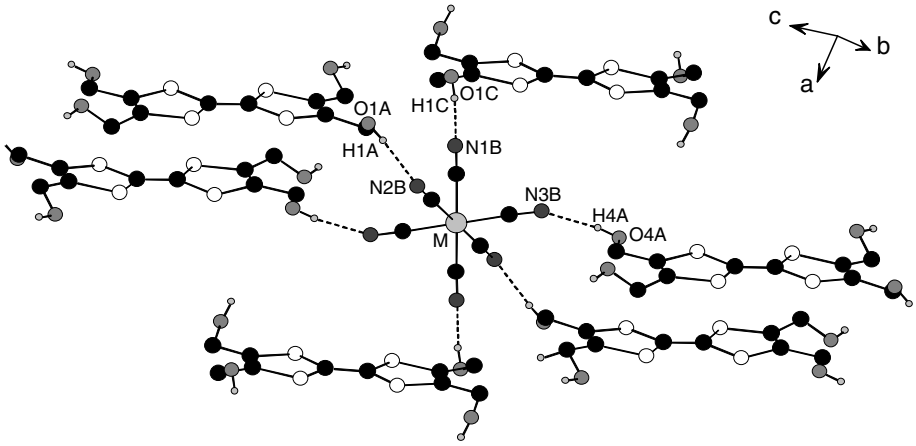
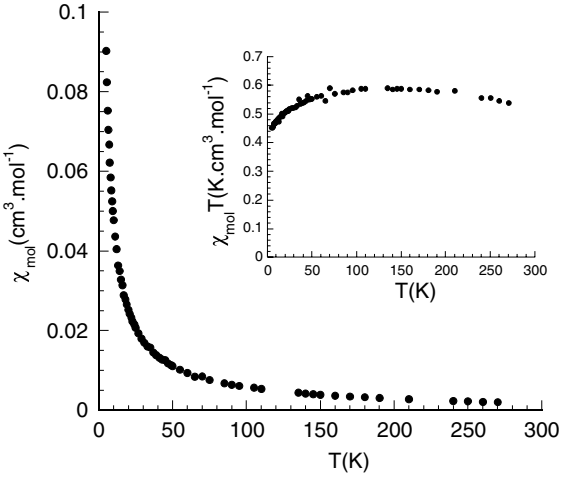


Fig. 6. Hydrogen bonds at the organic-inorganic interface in **2a** and **2b**. $[M(CN)_6]^{3-}$ (M = Fe, Co) anions are involved in six strong O–H···NC hydrogen bonds with $TTF(CH_2OH)_4$ molecules. Only one of the two disordered position for O2A is pictured and hydrogen atoms of CH_2 groups have been omitted for clarity.

and O2AB–H2AB···O1EB) due to the solvent molecule disorder itself. Surprisingly, the latest hydroxyl group (O3A–H3A) does not seem to be involved in any significant hydrogen bond. To summarize, all hydroxyl groups except O3A–H3A act as hydrogen bond donors, either to a cyano group (O1C–H1C, O1A–H1A and O4A–H4A), a hydroxyl group (O2C–H2C) or a carbonyl group (O2A–H2A). This defines a three-dimensional mixed organic-inorganic hydrogen bonded network presenting cavities in which the crown-ether-embedded potassium ions are located.

Magnetic properties have been studied for both salts. Magnetic behavior of **2b** is essentially diamagnetic with a Curie tail at low temperature, certainly due to paramagnetic impurities (4% from fitting with a Curie law). This feature is consistent with the presence of diamagnetic low spin d^6 Co^{III} cation in the complex and diamagnetic $[TTF(CH_2OH)_4]_3^{2+}$ trimers.[2] Compound **2a** being isostructural to **2b**, the same diamagnetic behavior should be observed for the organic part. As shown in Graph 1, the susceptibility curve for **2a** could indeed be fitted by a Curie law ($C = 0.486$ K cm^3 mol^{-1}), which is consistent with isolated paramagnetic $[Fe(CN)_6]^{3-}$ anions with a $S = 1/2$ low spin d^5 state for the Fe^{III} cation (with $g = 2.276$ [33]). Decrease of the susceptibility-temperature product at low temperature may be an indication of weak antiferromagnetic coupling between anions.



Graph 1. Temperature dependence of the SQUID susceptibility of **2a**. Inset: Temperature dependence of χT.

4. Discussion

Here are reported three cation radical salts based on $TTF(CH_2OH)_4$, synthesized either by chemical (**1**) or by electrochemical (**2a**–**b**) oxidation. In these salts, the $TTF(CH_2OH)_4$ molecules are associated in diamagnetic dicationic π-oligomer. In **1**, dimers are formed, as already observed in the $[TTF(CH_2OH)_4]_x[Re_6S_{8-n}Cl_{6+n}]$ ($n = 0, 1, 2, 3$) cation radical salts series [26], whereas trimers are observed in **2a–b**. The later case represents the first mixed valence salt based on $TTF(CH_2OH)_4$ donor. No long range electronic delocalization is however observed due to trimerization and then of course no reasonable conducting properties could be expected. Strong HOMO–HOMO interactions evaluated by extended Hückel calculations, lead in both case to diamagnetic isolated entities, as shown by the magnetic measurements.

In **2a** and **2b**, potassium cations from the reactant $K_3[M(CN)_6]$ (M = Co, Fe) as well as crown-ether molecules are incorporated in the structure. The formation of ternary salts incorporating TTF-based cation radicals

[2] The electronic structure of these trimers can be described by four electrons filling two of the three non-degenerated orbitals generated by the three HOMOs.

and both components of the electrolyte has already been observed with alkaline or alkaline earth cations, especially with the $[M(CN)_6]^{n-}$ anions [10,13,15]. Incorporation of crown ether molecule has also already been reported in the proton-conducting metallic cation radical salts series formulated β''-(BEDT-TTF)$_4$[(H_3O)(Cr$(C_2O_4)_3]_2$[$(H_3O)_2$(18-crown-6)] · $5H_2O$ (M = Cr, Ga, Fe), where H_3O^+ ions are located within the 18-crown-6 ether molecule [34]. In our case, the coordination of the potassium cation by oxygen atoms of TTF$(CH_2OH)_4$ molecules lead to the formation of a polymeric chain.

These three salts, **1** and **2a**–**b** are composed of hydrogen bond donor (and acceptor) organic molecules and on hydrogen bond acceptor cyanide anions. These compounds thus represent another example to study the competition of O–H···O and O–H···NC hydrogen bond, where the cyano group can be either organic (**1**) or inorganic (**2a–b**). In **1**, all hydroxyl groups act as hydrogen bond donors, and three of them are involved as acceptor in moderate O–H···O hydrogen bonding (O1A, O2A and O3A). The last donor (O3A–H3A) interacts with a cyano group of the $TCNQF_4$ molecule. Only one of the four cyano groups is then involved in hydrogen bonding. On the other hand, in **2a**–**b**, all the cyano groups of the $[M(CN)_6]^{3-}$ anion are involved in O–H···NC hydrogen bonds, whereas only one hydroxyl group (O1A–H1A) acts as a good acceptor towards another OH group. Furthermore, O···N distance in **1** appears to be longer than O···O ones (2.97 versus 2.77 Å), whereas in **2a**–**b**, O···N distances seems to be slightly shorter than O···O ones (2.75 versus 2.80 Å, see Table 4). The inorganic cyano group then appears to be a better acceptor than the organic hydroxyl group, and the latter appears to be better acceptor than organic nitrile group. In these specific examples, the following hydrogen bond acceptor strength can thus be proposed: $–CN_{inorganic} > –OH_{organic} > –CN_{organic}$. This is of course consistent the shortening of the O–H···N distances when moving from organic cyano group to inorganic one and with electrostatic considerations: cyano groups are more negatively charged in metallic complexes than in organic molecules, and consequently better acceptors.

5. Conclusion

Three new radical cation salts based on the functionalized organic π-donor TTF$(CH_2OH)_4$ and on cyanide anions have been synthesized. Their crystal structures and magnetic properties have been studied. With the hexacyanometallate $[M(CN)_6]^{3-}$ (M = Fe, Co) anions, ternary salts have been obtained incorporating crown-ether-embedded potassium cations. These cations are coordinated by oxygen atoms of TTF$(CH_2OH)_4$ molecules leading to an original polymeric chain. Despite different oxidation states, in all these three salts the organic molecules are combined in electronically isolated and diamagnetic oligomers, as commonly observed in radical cation salts of TTF derivatives bearing hydroxyl groups.

As expected, complex hydrogen bond networks occur in the structures. The organic molecules are connected to each others via hydrogen bonds but the hydroxyl groups interact also with the cyano groups of the anions. The structural analysis of this salts reveals once again that the inorganic cyano groups of the hexacyanometallate $[M(CN)_6]^{3-}$ anions are better hydrogen bond acceptors than the nitrile groups of $TCNQF_4$ molecule.

This study shows that the association of hydrogen bond acceptor anions to hydrogen bond donor functionalized TTFs is a good strategy to produce new molecular materials with original structural organization where the cationic part interact strongly with the anionic one.

6. Supplementary material

Crystallographic data of **1**, **2a** and **2b** have been deposited with the Cambridge Crystallographic Data Centre with CCDC Nos. 264830, 264831 and 264832, respectively. Copies of the data can be obtained free of charge on application to CCDC, 12 Union Road, Cambridge CB2 1EZ, UK (fax: +44 1223 336033; e-mail: deposit@ccdc.cam.ac.uk or on the web http://www.ccdc.cam.ac.uk).

Acknowledgments

Financial support from the CNRS and University of Nantes is gratefully acknowledged. We thank P. Batail for discussions about functionalized TTF derivatives. Dr. S. Perruchas thanks Dr. T. Devic and Dr. S. Baudron for help and useful discussions.

References

[1] M.R. Bryce, J. Mater. Chem. 5 (10) (1995) 1481, and references therein.
[2] M. Fourmigué, P. Batail, Chem. Rev. 104 (2004) 5379, and references therein.
[3] J.D. Wallis, J.-P. Griffiths, J. Mater. Chem. 15 (2005) 347.
[4] See for example E. Coronado, P. Day, Chem. Rev. 104 (2004) 5419, and references therein.
[5] (a) See for examples R. Kato, Chem. Rev. 104 (2004) 5319; (b) H. Nakajima, M. Katsuhara, M. Ashizawa, T. Kawamoto, T. Mori, Inorg. Chem. 43 (2004) 6075, and references therein.
[6] S.A. Baudron, P. Batail, C. Rovira, E. Canadell, R. Clérac, Chem. Commun. (2003) 1820.
[7] S. Perruchas, K. Boubekeur, P. Auban-Senzier, J. Mater. Chem. 14 (2004) 3509.
[8] L. Ouahab, T. Enoki, Eur. J. Inorg. Chem. (2004) 933.

[9] S. Bouherour, L. Ouahab, O. Peña, J. Padiou, D. Grandjean, Acta Crystrallogr. C 45 (1989) 371.
[10] (a) P. Le Maguerès, L. Ouahab, N. Conan, Solid State Commun. 97 (1996) 27;
(b) R. Swietlik, A. Lapinski, M. Polomska, L. Ouahab, J. Guillevic, Synth. Met. 133–134 (2003) 273.
[11] P. Le Maguerès, L. Ouahab, P. Briard, J. Even, M. Bertault, L. Toupet, J. Rámos, C.J. Gómez-García, P. Delhaès, Mol. Cryst. Liq. Cryst. 305 (1997) 479.
[12] R. Kanehama, Y. Yoshino, T. Ishii, T. Manabe, H. Hara, H. Miyasaka, H. Matsuzaka, M. Yamashita, M. Katada, H. Nishikawa, I. Ikemoto, Synth. Met. 133–134 (2003) 553.
[13] (a) L. Ouahab, S. Golhen, T. Le Hoerff, J. Guillevic, L. Tual, N. Hélou, J. Amiell, P. Delhaès, L. Binet, J.M. Fabre, Synth. Met. 102 (1999) 1642, O···N contacts reported are 2.70(1) and 2.76(1) Å;
(b) F. Thétiot, F. Bérézovsky, S. Triki, J. Sala Pala, C.J. Gómez-Garcia, A.A. Hajem, S. Bouguessa, J.-M. Fabre, C.R. Chimie 6 (2003) 291.
[14] K. Nakata, Y. Yoshino, H. Hara, T. Manabe, T. Ishii, M. Tomohiko, H. Miyasaka, M. Yamashita, H. Matsuzaka, M. Kakada, Mol. Cryst. Liq. Cryst. 380 (2002) 117.
[15] M. Clemente-Léon, E. Coronado, J.R. Galán-Mascarós, C. Giménez-Saiz, C.J. Gómez-García, E. Ribera, J. Vida-Gancedo, C. Rovira, E. Canadell, V. Laukhin, Inorg. Chem. 40 (2001) 3526.
[16] (a) M. Clemente-Léon, E. Coronado, J.R. Galán-Mascarós, C. Giménez-Saiz, C.J. Gómez-García, J.M. Fabre, G.A. Mousdis, G.C. Papavassiliou, J. Solid State Chem. 168 (2002) 616;
(b) M. Clemente-Léon, E. Coronado, J.R. Galán-Mascarós, C. Giménez-Saiz, C.J. Gómez-García, J.M. Fabre, Synth. Met. 103 (1999) 2279;
(c) M. Clemente-Léon, E. Coronado, J.R. Galán-Mascarós, C. Giménez-Saiz, C.J. Gómez-García, E. Martínez-Ferrero, Synth. Met. 120 (2001) 733.
[17] (a) M. Sallé, A. Gorgues, J.-M. Fabre, K. Bechgaard, M. Jubault, F. Texier, J. Chem. Soc., Chem. Commun. (1989) 1520;
(b) M.A. Fox, H. Pan, J. Org. Chem. 59 (1994) 6519.
[18] (a) L.K. Montgomery, Organic conductors, in: J.-P. Farges (Ed.), Fundamentals and Applications, Dekker, NY, 1994, p. 115;
(b) P. Batail, K. Boubekeur, M. Fourmigué, J.-C.P. Gabriel, Chem. Mater. 10 (1998) 3005.
[19] Stoe-IPDS Software Manual V2.87, STOE Darmstadt, Germany, December 1997.
[20] G.M. Sheldrick, University of Gottingen, 1997.
[21] T. Steiner, Angew. Chem., Int. Ed. Engl. 41 (2002) 48.
[22] T. Steiner, W. Saenger, Acta Crystallogr. B 48 (1992) 819.
[23] R. Hoffmann, J. Chem. Phys. 39 (1963) 1397.
[24] J.H. Ammeter, H.-B. Bürgi, J. Thibeault, R. Hoffmann, J. Am. Chem. Soc. 100 (1978) 3686.
[25] A. Dolbecq, A. Guirauden, M. Fourmigué, K. Boubekeur, P. Batail, M.-M. Rhomer, M. Bénard, C. Coulon, M. Sallé, P. Blanchard, J. Chem. Soc., Dalton Trans. (1999) 1241.
[26] S. Perruchas, K. Boubekeur, P. Batail, Cryst. Growth Des., doi: 10.1021/cg0500573.
[27] M. Sallé, A. Gorgues, M. Jubault, K. Boubekeur, P. Batail, Tetrahedron 48 (1992) 3081.
[28] S.A. Baudron, C. Mézière, K. Heuzé, M. Fourmigué, P. Batail, P. Molinié, P. Auban-Senzier, J Solid State Chem. 168 (2002) 668, and references therein.
[29] T.J. Emge, M. Maxfield, D.O. Cowan, T.J. Kirstenmacher, Mol. Cryst. Liq. Cryst. 65 (1981) 161.
[30] M. Etter, Acc. Chem. Res. 23 (1990) 120.
[31] (a) See for examples: K.C.K. Swamy, S. Kumaraswamy, Acta Crystrallogr. C 57 (2001) 1147;
(b) O. Nagano, Y. Sasaki, Acta Crystallogr. B 35 (1979) 2387.
[32] (a) D.S. Reddy, Y.E. Ovchinnikov, O.V. Shishkin, Y.T. Struchkov, G.R. Desiraju, J. Am. Chem. Soc. 118 (1996) 4085;
(b) J.-Y. Le Questel, M. Berthelot, C. Laurence, J. Phys. Org. Chem. 13 (2000) 347.
[33] P.B. Merrithew, A.J. Modestino, J. Am. Chem. Soc. (1972) 3361.
[34] A. Akutsu-Sato, H. Akutsu, S.S. Turner, P. Day, M.R. Probert, J.A.K. Howard, T. Akutagawa, S. Takeda, T. Nakamura, T. Mori, Angew. Chem., Int. Ed. 44 (2005) 292.

2. Experimental

2.1. Synthesis

All manipulations were carried out under dry argon in all-glass reaction and handling vessels that were dried in vacuo. Ammonia (Bayer AG) was made anhydrous by distilling it from sodium and was stored as a sodium–ammonia solution at 195 K. The compound $[Cs_6(PhSb_2)_2]\cdot 11NH_3$ was prepared by placing the starting materials elemental caesium (0.5 g; 3.8×10^{-3} mol) and triphenylantimony (0.268 g, 7.6×10^{-3} mol) into a Schlenk-type reaction tube. Thirty millilitres of ammonia were condensed onto the reaction mixture, which resulted in a blue solution. During three weeks, the colour of the reaction mixture turned brown. After this period, it was possible to isolate dark brown crystals directly from the solution, which were extremely unstable at temperatures above −20 °C or in air.

2.2. Crystallographic analysis

A modification of the method of Kottke and Stalke [16] was used for the isolation, selection and mounting of the crystals. Small amounts of the reaction products were transferred directly from the liquid ammonia into perfluoroether (Galden), which was cooled to 213 K by a stream of cold nitrogen. Single crystals suitable for an X-ray structure analysis were selected with the help of a microscope and collected on the tip of a capillary mounted on a goniometer head. The crystals were then immediately submerged in liquid nitrogen, and transferred to the diffractometer. The structures were solved by direct methods (SHELXS-97) [17] and refined against F^2 (SHELXL-97) [18]. An absorption correction was applied to the data (DELrefABS of the program package PLATON) [19]. The H-atoms were located by difference Fourier synthesis and refined isotropically, all other atoms anisotropically.

Details of the measurement and refinement are given in Table 1. Table 2 contains the resulting atomic parameters. All atoms occupy the general position 2i, except for the nitrogen atom N5, which occupies the special position 1a and is therefore placed on the vertices of the unit cell.

Table 1
Crystallographic data of $[Cs_6(PhSb_2)_2]\cdot 11NH_3$

Empirical formula	$C_{12}H_{43}Sb_4Cs_6N_{11}$
Formula weight (g/mol)	1626.053
Temperature (K)	123(2)
Cell parameters	
a (Å)	6.3126(8)
b (Å)	9.022(1)
c (Å)	18.565(3)
α (°)	80.64(2)
β (°)	83.57(2)
γ (°)	75.05(2)
Cell volume (Å^3)	1005.2(2)
Density (Mg/m^3)	2.686
Formula units per unit cell	1
Crystal system	triclinic
Space group	$P\bar{1}$
X-ray	Mo Kα
Wavelength (Å)	0.71073
Monochromator	graphite
Absorption correction	DELrefABS
Absorption coefficient (mm^{-1})	8.032
R_{int}	0.0375
$R(\sigma)$	0.0289
R_1 ($I > 2\sigma I$)	0.0234
wR_2 ($I > 2\sigma I$)	0.0575
R_1 (all data)	0.0306
wR_2 (all data)	0.0613
Goodness-of-fit	0.998
Completeness to θ (%)	92.8
Maximum residual electron density (e/Å^3)	1.211
Minimum residual electron density (e/Å^3)	−0.800

Table 2
Atomic coordinates (×10^4) and isotropic displacement parameters (Å$^2\times10^3$) of $[Cs_6(PhSbs_2)_2]\cdot 11NH_3$

Atom	x	y	z	U(eq)
Sb1	6695(1)	5124(1)	2270(1)	16(1)
Sb2	7839(1)	2980(1)	1258(1)	16(1)
Cs1	12 482(1)	2665(1)	2776(1)	24(1)
Cs2	1869(1)	5840(1)	943(1)	19(1)
Cs3	4227(1)	9640(1)	1296(1)	26(1)
C1	7021(10)	3567(6)	3309(3)	21(1)
C2	7626(9)	1935(6)	3352(3)	21(1)
C3	6717(16)	4179(8)	3976(4)	51(2)
C4	7854(14)	960(8)	4016(4)	42(2)
C5	6990(30)	3217(11)	4644(4)	110(6)
C6	7560(30)	1598(11)	4656(4)	110(6)
N1	14 205(11)	−1112(6)	3215(3)	37(1)
N2	3406(9)	12 664(5)	−88(3)	24(1)
N3	−117(10)	8601(6)	2051(3)	34(1)
N4	1018(11)	6251(7)	3579(4)	45(2)
N5	0	0	0	112(7)
N6	2210(30)	2676(17)	4669(7)	168(7)

3. Results and discussion

$[Cs_6(PhSb_2)_2]\cdot 11NH_3$ is built from $PhSb_2^{3-}$ anions, Cs^+ cations and ammonia molecules of crystallisation. The approximately planar $PhSb_2^{3-}$ anion (Fig. 1) is an diantimony dumbbell which carries one covalently bound phenyl residue. The threefold negative charge is confirmed by the number of the caesium counter ions per anion in the asymmetric unit. The formal distribution of this charge is easily rationalised by the $(8-N)$ rule [20]: the terminal atom Sb2 has only one covalent bond and is consequently twofold negatively charged, whereas the twofold bound atom Sb1 carries only one formal negative charge. The length of the single Sb–Sb bond in $PhSb_2^{3-}$ is 2.8198(7) Å, which compares well

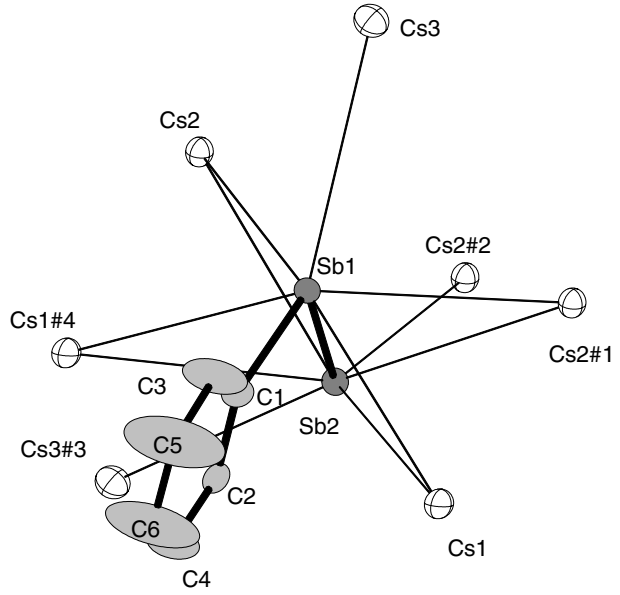


Fig. 1. Caesium coordination sphere of the $PhSb_2^{3-}$-anion in $[Cs_6(PhSb_2)_2] \cdot 11NH_3$. Atomic displacement parameters at 50% probability level. Selected distances (Å) and angles (°): Sb1–Sb2 = 2.8198(7), Sb1–C1 = 2.190(5), C1–C2 = 1.414(8), C2–C4 = 1.392(8), C4–C6 = 1.38(1), C6–C5 = 1.41(1), C5–C3 = 1.39(1), C3–C1 = 1.410(8), Sb1–Cs1 = 3.881(1), Sb2–Cs1 = 4.216(1), Sb1–Cs2#1 = 3.99(1), Sb2–Cs2#1 = 4.0047(8), Sb1–Cs2 = 3.9892(9), Sb2–Cs2 = 4.023(1), Sb1–Cs1#4 = 3.8324(8), Sb2–Cs1#4 = 4.191(1), Sb2–Cs3#3 = 4.210(8), Sb2–Cs2#2 = 4.0466(9), Sb1–Cs3 = 4.154(1); Sb2–Sb1–C1 = 101.1(1), Sb1–C1–C2 = 123.4(4), Sb1–C1–C3 = 120.2(4), C1–C2–C4 = 122.4(5), C2–C4–C6 = 119.2(6), C4–C6–C5 = 120.7(7), C6–C5–C3 = 119.4(7), C5–C3–C1 = 121.5(6). Symmetry operations for the generation of equivalent atoms: #1 = 1 + *x*, *y*, *z*; #2 = 1 − *x*, 1 − *y*, −*z*; #3 = *x*, −1 + *y*, *z*; #4 = − 1 + *x*, *y*, *z*.

to other Sb–Sb single bonds in neutral compounds (i.e., 2.837 Å in Ph_4Sb_2 [21]), but is significantly shorter than the values obtained for Sb_2^{4-}-dumbbells in densely packed ionic solids. In Cs_4Sb_2, the Sb–Sb-distance is 2.923(2) Å [22], in $K_2Ba_3Sb_4$ 2.899(2) Å [23]. This shortening of the single bond in $PhSb_2^{3-}$ may be explained by the lesser charge at the phenyl-substituted Sb atom Sb1, which leads to a reduced repulsion between the Sb atoms. The Sb–Sb bond length of 2.761(1) Å in the $[Sb_3Ph_4]^-$ anion [15] is even shorter.

The Sb atoms of each anion have close contacts to seven surrounding Cs^+ cations, the corresponding Cs–Sb distances range from 3.83(3) to 4.21(3) Å. As can be seen in Fig. 1, four of the Cs^+ cations coordinate to the Sb_2-dumbbell in an η_2-like fashion, which leads to a rectangular arrangement of these cations with the phenyl ring intersecting the larger side of the rectangle. The $PhSb_2^{3-}$ anion is approximately planar, the torsion angle (Sb2–Sb1–C1–C3) is 176.33°.

In the solids Cs_4Sb_2 [22] and $K_2Ba_3Sb_4$ [23], a characteristic trigonal-prismatic environment of the Sb atoms in the Sb_2 dumbbells is observed. If one includes somewhat larger Cs–Sb distances (up to 4.367 Å) into the coordination sphere of Sb, a similar monocapped trigonal prism can be observed for the unsubstituted Sb2 atom in $[Cs_6(PhSb_2)_2] \cdot 11NH_3$ as well (Fig. 2).

Since all three Cs^+ cations in the asymmetric unit of $[Cs_6(PhSb_2)_2] \cdot 11NH_3$ coordinate to two or more Sb atoms of different anions, extended layers parallel to the *ab*-plane are formed (Fig. 3). Between the neutral layers, only Van-der-Waals Contacts via the H atoms of the phenyl rings are observed. Within the layers, the ammonia molecules of crystallisation coordinate to the Cs^+ ions, adding bridging ion-dipole interactions to the ion-pairing interactions comprising the backbone of the layers. Cs–N distances between 3.22 and 3.82 Å were considered for these interactions, the next largest distance being 4.81 Å. The resulting coordination spheres for the Cs^{2+} cations can be deduced from Fig. 3: Cs1 has four contacts to Sb atoms and three contacts to the N atoms of ammonia molecules, one of them serving as a bridging ligand to

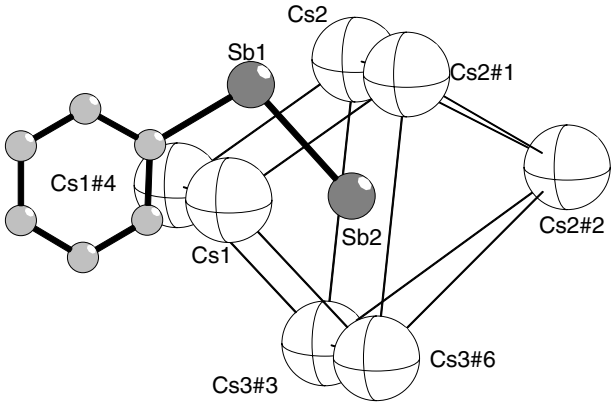


Fig. 2. Monocapped trigonal prismatic environment of Sb2 in $[Cs_6(PhSb_2)_2] \cdot 11NH_3$.

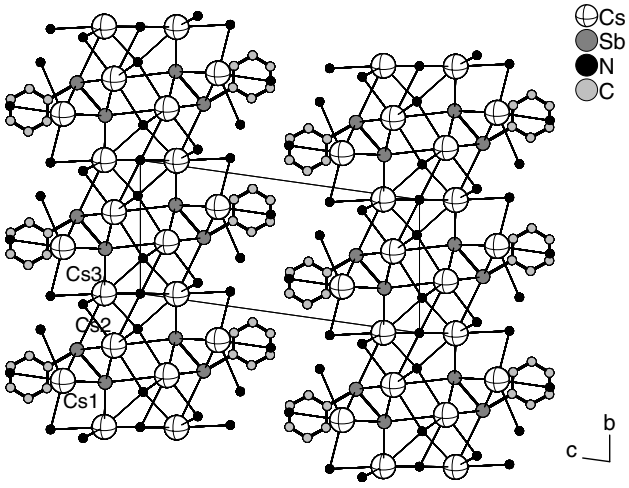


Fig. 3. Projection of the structure of $[Cs_6(PhSb_2)_2] \cdot 11NH_3$ onto the *bc*-plane perpendicular to the layers in the *ab*-direction. H atoms are omitted for clarity.

Cs3. Cs2 has five Sb contacts and four ammonia contacts, all of the latters in bridging coordination to several Cs^+ ions. Finally, Cs3 has a total coordination number of nine, which is the sum of three Sb contacts and six contacts to bridging ammonia ligands.

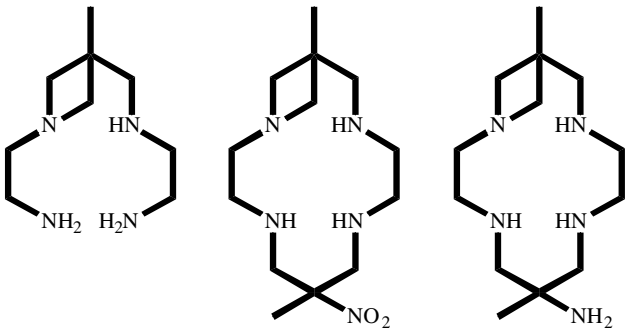
The synthesis of $[Cs_6(PhSb_2)_2] \cdot 11NH_3$ shows that the concept of extending the solution chemistry of Zintl ions by reducing the high charge of the naked ions through the addition of phenyl residues works not only for the tin species already reported but also for antimony. As it is often the case in ammoniates, the stabilisation of the still highly charged anions is further facilitated by extensive ion-pairing.

4. Supplementary data

The crystallographic data have been deposited with the Cambridge Crystallographic Data Centre as Supplementary Publication No. 268483. Copies of the data can be obtained free of charge on application to The Director, CCDC, 12 Union Road, Cambridge CB2 1EZ, UK (fax: int. code +1223 336 033; e-mail: deposit@ccdc.cam.ac.uk or on the web http://www.ccdc.cam.ac.uk).

References

[1] J.D. Corbett, Chem. Rev. (1985) 383.
[2] T.F. Fässler, Coord. Chem. Rev. 215 (2001) 347.
[3] A. Cisar, J.D. Corbett, Inorg. Chem. 16 (1977) 2482.
[4] N. Korber, F. Richter, Angew. Chem., Int. Ed. Engl. 36 (1997) 1512.
[5] F. Kraus, J. Aschenbrenner, N. Korber, Angew. Chem. Int. Ed. 42 (2003) 4030.
[6] N. Korber, M. Reil, Chem. Commun. (2002) 84.
[7] S.C. Critchlow, J.D. Corbett, Inorg. Chem. 23 (1984) 770.
[8] L. Xu, S. Bobev, J. El-Bahraoui, S.C. Sevov, J. Am. Chem. Soc. 122 (2000) 1838.
[9] T. Hanauer, N. Korber, Z. Allg. Anorg. Chem. 630 (2004) 2532.
[10] N. Scotti, U. Zachwieja, H. Jacobs, Z. Anorg. Allg. Chem. 623 (1997) 1503.
[11] E. Zintl, J. Goubeau, W. Dullenkopf, Z. Phys. Chem., Abt. A 154 (1931) 1.
[12] E. Zint, A. Harder, Z. Phys. Chem., Abt. A 154 (1931) 47.
[13] E. Zintl, W. Dullenkopf, Z. Phys. Chem., Abt. B 16 (1932) 183.
[14] K. Wiesler, N. Korber, Z. Kristallogr. 220 (2005) 188.
[15] R.A. Bartlett, H.V. Rasika Dias, H. Hope, B.D. Murray, M.M. Olmstead, P.P. Power, J. Am. Chem. Soc. 108 (1986) 6921.
[16] T. Kottke, D. Stalke, J. Appl. Crystallogr. 26 (1993) 615.
[17] G.M. Sheldrick, SHELXS-97, Programm Zur Lösung Von Kristallstrukturen, Universität Göttingen, Göttingen, 1997.
[18] G.M. Sheldrick, SHELXL-97, Programm Zur Verfeinerung Von Kristallstrukturen, Universität Göttingen, Göttingen, 1997.
[19] A.L. Spek, PLATON, a Multipurpose Crystallographic Tool, Utrecht University, Utrecht, The Netherlands, 2001.
[20] E. Parthé, Acta Crystallogr. 29B (1973) 2808.
[21] L. Balázs, H.J. Breunig, Coord. Chem. Rev. 248 (2004) 603.
[22] C. Hirschle, C. Röhr, Z. Anorg. Allg. Chem. 626 (2000) 1992.
[23] B. Eisenmann, C. Gieck, U. Rößler, Z. Anorg. Allg. Chem. 625 (1999) 1331.



1 2 3

2. Experimental

2.1. Synthesis

Trans-[Co(**1**)Cl_2]ClO_4 and [Cu(**1**)$OClO_3$]ClO_4 were available from earlier work [10,12]. Details of the ion-exchange chromatographic procedures used for complex ion purification and isolation have also been given earlier [9,10,12]. Other reagents were from commercial sources and used as received.

2.1.1. *[Co(**1**)(R,R-chxn)]$^{3+}$ isomers*

Trans-[Co(**1**)Cl_2]ClO_4 (0.54 g) was dissolved in dmso (20 mL), a large excess (~8-fold) of *trans-(R,R)*-cyclohexane-1,2-diamine (chxn, 0.96 g) added and the mixture heated at 70 °C for 3 h. The final red-orange solution was cooled, diluted with water (2 L) and passed through a column (7 × 120 cm) of Na^+-form SP Sephadex C-25 cation exchange resin to absorb the complex cations. Subsequent elution with 0.12 mol L^{-1} trisodium citrate gave three bands, the first and third minor components proving to be hydrolysed starting material and [Co(*R,R*-chxn)$_3$]$^{3+}$, respectively. (The complexes present in the different bands were characterised after conversion to the chlorides by absorption of the citrate eluates on H^+-form Dowex 50W × 2 cation exchange resin and elution with HCl.) Methyl resonances in both the ^{13}C and ^1H nmr spectra (δ ^{13}C 19.95, 20.44; δ ^1H 1.09, 1.12; D_2O solutions) of the material in the second band indicated the presence of at least two isomers of the product. Overlap with cyclohexane methylene resonances rendered integration of the signals in the ^1H spectrum imprecise but the species giving the higher field resonance appeared to be ~3 times as abundant as the other. Analysis (unrecrystallised chloride): *Anal.* Calc. for $C_{15}H_{36}Cl_3CoN_6O_4 \cdot 2.5H_2O$: C, 35.27; H, 8.09; N, 16.45. Found: C, 35.4; H, 7.8; N, 16.3%. On adding $NaClO_4$ to an aqueous solution of the mixture and allowing slow evaporation at ambient temperature, crystals (0.65 g) of the major species, shown by a structure determination to be Δ-*cis*-β-[Co(**1**)(*R,R*-chxn)]$Cl_2(ClO_4)$, were obtained.

2.1.2. *[Co(**1**)(ala)]$^{2+}$ diastereomers*

One mole per liter NaOH was added carefully to a solution of *trans*-[Co(**1**)Cl_2]ClO_4 (2.0 g) and *R*-alanine (= L-alanine = alaH) (0.5 g) in water (50 mL) until a pH ~ 9 was attained. The resulting red solution was heated at 60 °C for 10 h, then cooled and acidified to pH 2 with 1 mol L^{-1} HCl. Chromatography (SP-Sephadex C-25/0.13 mol L^{-1} sodium citrate) separated four red species, the complexes present being recovered as chlorides via Dowex 50W × 2/HCl treatment and evaporation of the effluents. The first-eluted material proved to be simply hydrolysed starting material. Readily identified alanine methine and methyl, and **1** methyl resonances in the ^1H NMR spectra, as well as methyl and carboxyl carbon resonances in the ^{13}C spectra, indicated that all three of the other fractions were mixtures of at least 3 species in each case. Fractional crystallisation of the second band residue as the chloride led to isolation of one species (^1H δ (azetidine CH_3) 1.01, (alanine CH_3) 1.36, 1.38; ^{13}C δ (methyl) 18.42, 20.75, (carboxyl) 184.7), though the crystals obtained were not suitable for a structure determination. Addition of $[NH_4][PF_6]$ to concentrated solutions of the third and fourth band residues, followed by slow evaporation at room temperature led also to precipitation of single species (Third fraction: ^1H δ (azetidine CH_3) 1.05, (alanine CH_3) 1.38, 1.40; ^{13}C δ (methyl) 18.32, 20.64, (carboxyl) 185.1; Fourth fraction: δ (azetidine CH_3) 0.96, (alanine CH_3) 1.33, 1.35; δ (methyl) 18.00, 20.19, (carboxyl) 185.0). In these two instances, the crystals did prove to be suitable for structural studies, on the basis of which their compositions were established as Λ-*cis*-β_1-[Co(**1**)(*R*-ala)]$(PF_6)_2 \cdot H_2O$ and Λ-*cis*-β_2-[Co(**1**)(*R*-ala)] $(PF_6)_2 \cdot H_2O$, respectively.

2.1.3. *[Co(**3**)Cl]Cl[PF_6] · H_2O, obtained via the Cu complex, [Cu(**2**)]Cl_2*

Aqueous formaldehyde (37%, 10 g), nitroethane (2.4 g) and triethylamine (4.5 g) were added to a solution of [Cu(**1**)$(OClO_3)$]ClO_4 (5.4 g) in methanol (200 mL). The mixture was heated at reflux for 24 h, then cooled, diluted to ~1 L with water and acidified to pH 6 by the addition of acetic acid. SP Sephadex/0.3 mol L^{-1} NaCl chromatography showed the presence of a single red component, the eluate for which was collected and taken to dryness under vacuum. The complex was freed of the bulk of associated NaCl by extraction into methanol and the crude [Cu(**2**)]Cl_2 (6.8 g) obtained by evaporating this extract to dryness was used directly in the following step. Thus, Zn powder (8 g) was added to a solution of [Cu(**2**)]Cl_2 (4.5 g) in water (200 mL). Under vigorous stirring, aqueous HCl (6 mol L^{-1}, 100 mL) was added dropwise to this mixture. Stirring was continued for 2 h after the discharge of the red colour was complete. The protonated ligand present (3.0 g) was

recovered via Dowex 50W × 2/HCl chromatography and evaporation of the eluate to dryness. It was redissolved in water (200 mL) and the solution neutralised by the addition of NaOH (1.2 g) before $CoCl_2 \cdot 6H_2O$ (1.6 g) was dissolved in. After aeration for 12 h, the mixture was subjected to Dowex 50W × 2/HCl chromatography to separate three red components, the first eluted proving to be unreacted Co(II), the second containing the bulk (1.24 g) of the product and the third being a very minor (0.07 g) constituent and presumed to be either the species with the pendent amino group uncoordinated or the complex with CH_3 and NH_2 groups exchanged about their attached quaternary centre [15]. Addition of $[NH_4][PF_6]$ to an aqueous solution of the bulk component provided crystals of [Co(**3**)Cl]Cl-$[PF_6] \cdot H_2O$ suitable for a structure determination.

2.2. Crystallography

The data for the four compounds were collected at 100(2) K on a Nonius Kappa-CCD area detector diffractometer [16] using graphite-monochromated Mo Kα radiation (λ 0.71073 Å). The crystals were introduced in glass capillaries with a protecting "Paratone-N" oil (Hampton Research) coating. The unit cell parameters were determined from 10 frames, then refined on all data. A 180° φ-range was scanned with 2° steps during data collection, with a crystal-to-detector distance fixed to 28 mm. The data were processed with DENZO-SMN [17]. The structures were solved by direct methods with SHELXS-97 and subsequent Fourier-difference synthesis and refined by full-matrix least-squares on F^2 with SHELXL-97 [18]. Absorption effects were corrected empirically with the program DELABS from PLATON [19]. The oxygen atoms of the perchlorate ion in Δ-*cis*-β-[Co(**1**)(*R*,*R*-chxn)]$Cl_2(ClO_4)$ are disordered over two sets of positions which have been refined with occupancy parameters constrained to sum to unity and some restraints on bond lengths and displacement parameters. The C8–C9 bond length in Λ-*cis*-β_1-[Co(**1**)(*R*-ala)]$(PF_6)_2 \cdot H_2O$ had also to be restrained to its ideal value. All non-hydrogen atoms were refined with anisotropic displacement parameters, except the disordered perchlorate oxygen atoms. The hydrogen atoms bound to nitrogen and oxygen atoms were found on Fourier-difference maps (except in the first structure, for which their position was calculated) and all the other hydrogen atoms were introduced at calculated positions; all were treated as riding atoms with a displacement parameter equal to 1.2 (NH, NH_2, OH, CH, CH_2) or 1.5 (CH_3) times that of the parent atom. The first three compounds crystallize in chiral space groups, but only for the last two did the Flack parameter [20] enable the correct enantiomer to be

Table 1
Crystal data and structure refinement details

Complex[a]	**A**	**B**	**C**	**D**
Chemical formula	$C_{15}H_{36}Cl_3CoN_6O_4$	$C_{12}H_{30}CoF_{12}N_5O_3P_2$	$C_{12}H_{30}CoF_{12}N_5O_3P_2$	$C_{13}H_{31}Cl_2CoF_6N_5OP$
M (g mol^{-1})	529.78	641.28	641.28	548.23
Crystal system	monoclinic	orthorhombic	orthorhombic	triclinic
Space group	$P2_1$	$P2_12_12_1$	$P2_12_12_1$	$P\bar{1}$
a (Å)	7.7809(6)	9.3066(5)	8.7359(3)	13.4527(11)
b (Å)	11.8084(17)	13.8905(10)	16.1290(7)	13.6087(10)
c (Å)	12.2119(18)	18.1521(12)	16.4818(7)	13.7240(11)
α (°)	90	90	90	80.672(4)
β (°)	91.776(8)	90	90	62.027(4)
γ (°)	90	90	90	76.130(4)
V (Å^3)	1121.5(2)	2346.6(3)	2322.31(16)	2150.7(3)
Z	2	4	4	4
D_{calc} (g cm^{-3})	1.569	1.815	1.834	1.693
μ(Mo Kα) (mm^{-1})	1.157	0.989	0.999	1.187
F(0 0 0)	556	1304	1304	1128
Reflections collected	7549	16183	16118	14938
Independent reflections	3805	4443	4391	7546
"Observed" reflections [$I>2\sigma(I)$]	2999	3621	3753	5122
R_{int}	0.072	0.076	0.068	0.064
Parameters refined	262	318	318	527
R_1	0.077	0.049	0.035	0.060
wR_2	0.196	0.119	0.079	0.162
S	1.036	1.113	1.012	1.067
Flack parameter	0.15(4)	−0.02(3)	−0.019(15)	
$\Delta\rho_{min}$ (e Å^{-3})	−0.62	−0.52	−0.25	−0.58
$\Delta\rho_{max}$ (e Å^{-3})	0.94	0.87	0.39	1.33

[a] **A** = Δ-*cis*-β-[Co(**1**)(*R*,*R*-chxn)]$Cl_2(ClO_4)$; **B** = Λ-*cis*-β_1-[Co(**1**)(*R*-ala)]$(PF_6)_2 \cdot H_2O$; **C** = Λ-*cis*-β_2-[Co(**1**)(*R*-ala)]$(PF_6)_2 \cdot H_2O$; **D** = [Co(**3**)Cl]Cl-$[PF_6] \cdot H_2O$.

Table 2
Environment of the Co(III) atom: selected distances (Å) and angles (°)

	A, X = N6	**B**, X = O1	**C**, X = O1	**D**[a], X = Cl
Bond distances				
Co–N1	1.977(9)	1.949(5)	1.965(3)	1.948(5); 1.960(4)
Co–N2	2.008(9)	1.966(5)	1.997(3)	1.963(5); 1.959(5)
Co–N3	1.994(8)	1.996(5)	1.974(3)	1.938(5); 1.958(5)
Co–N4	1.985(9)	1.967(5)	1.952(3)	1.942(5); 1.962(5)
Co–N5	1.985(7)	1.982(4)	1.971(3)	1.953(5); 1.973(4)
Co–X	1.993(8)	1.906(4)	1.905(2)	2.2440(16); 2.2633(15)
Bond angles				
N1–Co–N2	84.6(4)	86.29(19)	85.86(12)	88.1(2); 88.37(19)
N1–Co–N3	171.0(3)	173.4(2)	175.58(12)	177.3(2); 178.87(19)
N1–Co–N4	89.5(4)	89.90(19)	94.24(12)	92.8(3); 92.75(19)
N1–Co–N5	92.0(3)	90.5(2)	91.97(12)	84.5(2); 84.47(18)
N1–Co–X	91.1(4)	93.36(18)	87.35(11)	88.90(15); 88.53(14)
N2–Co–N3	91.2(3)	91.68(19)	89.74(11)	91.8(2); 91.24(19)
N2–Co–N4	98.6(3)	97.3(2)	94.23(12)	175.0(2); 174.42(19)
N2–Co–N5	91.7(3)	94.3(2)	175.76(11)	93.4(2); 93.42(19)
N2–Co–X	172.8(3)	177.72(19)	92.31(11)	96.03(15); 97.00(14)
N3–Co–N4	83.4(3)	84.14(19)	85.78(12)	87.1(3); 87.5(2)
N3–Co–N5	96.0(3)	95.9(2)	92.45(11)	92.8(2); 94.50(18)
N3–Co–X	93.8(4)	88.91(17)	93.14(11)	93.80(17); 92.57(14)
N4–Co–N5	169.7(3)	168.45(19)	89.56(12)	81.8(2); 81.26(19)
N4–Co–X	87.1(4)	84.98(18)	173.37(11)	88.90(17); 88.50(14)
N5–Co–X	82.7(3)	83.47(17)	83.94(11)	168.31(15); 167.27(14)

(**A**, **B**, **C** and **D** as for Table 1).
[a] Two independent molecules.

identified. Crystal data and structure refinement parameters are given in Table 1 and selected bond lengths and angles in Table 2. The molecular plots were drawn with ORTEP3/PovRay [21]. All calculations were performed on a Silicon Graphics R5000 workstation.

3. Results and discussion

Although the present work was undertaken with the objective of exploring the possibility of using ring opening reactions of a coordinated azetidine in synthesis, it soon became apparent that, even under quite forcing reaction conditions, the azetidine ring of **1** remained intact. For none of the various reaction product fractions presently isolated by ion exchange chromatography did the ^{1}H NMR spectra show evidence of loss of the rather distinctive [9–13] azetidine methylene proton resonances in the δ 3.2–4.0 region (nor loss of ring methylene ^{13}C resonances near δ 57 [13].). Thus, what is defined herein concerns the basic coordination properties of **1**. The ligand is in fact a quadridentate amine of uncommon form in that the azetidine unit not only renders the two 1,2-diamine arms inequivalent but restricts their capacity to chelate a metal ion centre. The complete lack of symmetry in complexes of **1** means simple NMR spectroscopy is of limited use in establishing their stereochemistry and is the reason for the focus in the present work on the use of crystal structure determinations.

When **1** is forced by the presence of a bidentate co-ligand to occupy four non-coplanar sites about an octahedral metal ion such as Co(III), there would appear to be fewer isomeric possibilities than for the "parent" 232-tet ligand, as illustrated for the so-called *cis*-β configuration [5,22] (Fig. 1). Indeed, if the known structures of [Co(**1**)Cl$_2$]ClO$_4$ and Δ-*cis*-β-[Co(**1**)en]Cl$_3$[10] (en = ethane-1,2-diamine) are indicative of the necessity for the azetidine-N to be coplanar with its two adjacent *N*-donors, the *cis*-α form may not be possible and only enantiomers possible for the *trans* form. In the case of en as a chelating co-ligand, the ring it forms may adopt chiral conformations but diastereomers associated with the presence of its two enantiomeric forms within a chiral complex are not usually physically separable, except by chance crystallisation in the solid, because of the very rapid conformational interconversion. This is not so when 1*R*,2*R*-*trans*-cyclohexane-1,2-diamine is the chelate, since chelation is only possible for the diequatorial disposition of the amino groups and this fixes the chelate ring conformation as λ [5,23]. By coincidence, in the particular crystal of Δ-*cis*-β[Co(**1**)en]Cl$_3$ chosen for study earlier [10], the en chelate adopts the λ conformation, as does the five-membered chelate ring involving the azetidine-N, while that involving the 'angular' N is δ.

The cation present in the crystalline lattice of Δ-*cis*-β-[Co(**1**)(*R*,*R*-chxn)]Cl$_2$(ClO$_4$) is shown in Fig. 2. The metal atom is hexa-coordinated, the environment being distorted octahedral (Table 2), in an array of *cis*-β configuration and of Δ chirality. In detail, there are very

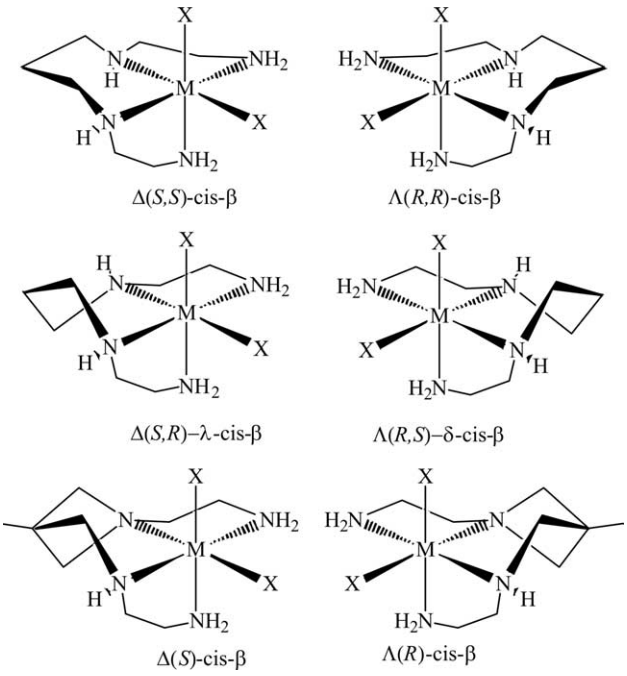


Fig. 1. Binding of a quadridentate amine to an octahedral metal ion – comparison of *cis*-β forms possible for 1,9-diamino-4,7-diazanonane (“232tet”) and **1**, assuming the azetidine-N of the latter cannot occupy an angular site.

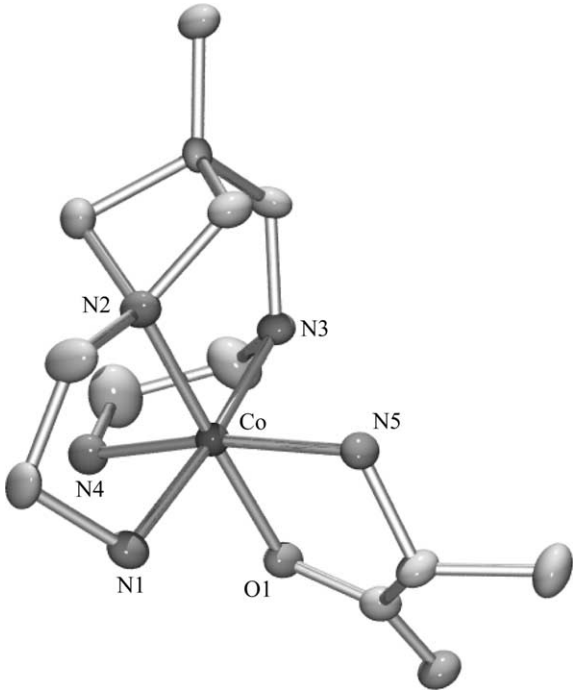


Fig. 3. View of Λ-*cis*-β_1-[Co(**1**)(*R*-ala)]$^{2+}$. Displacement ellipsoids are drawn at the 40% probability level.

close similarities with the structure of Δ-*cis*-β-[Co(**1**)en]$^{3+}$, since not only does the chxn ring match the λ conformation of the en ring but the five-membered ring involving the azetidine-N again is of λ conformation and that involving the ‘angular’ N is δ. The Flack parameter [0.15(4)] seems to indicate racemic twinning, but, since the value is not much larger than three times the error, the result cannot be considered as clear-cut [24]. We presume that the other complex present in the reaction mixture is the Λ-*cis*-β-species and that thus

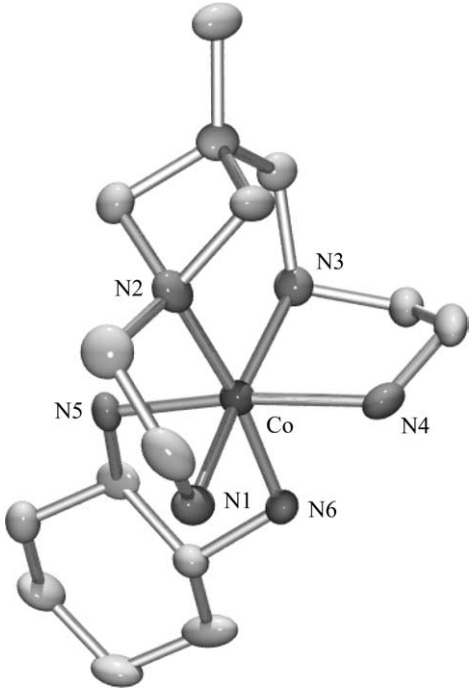


Fig. 2. View of Δ-*cis*-β-[Co(**1**)(*R*,*R*-chxn)]$^{3+}$. Displacement ellipsoids are drawn at the 40% probability level.

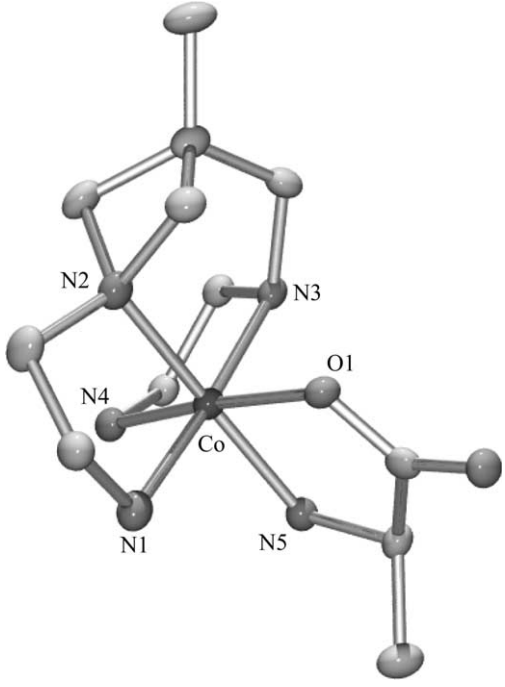


Fig. 4. View of Λ-*cis*-β_2-[Co(**1**)(*R*-ala)]$^{2+}$. Displacement ellipsoids are drawn at the 50% probability level.

there is only a very slight selectivity, be it kinetic or thermodynamic, for *R*,*R*-chxn between the enantiomeric forms of the Co(**1**) unit. Consistent with this, the circular dichroism of the total eluate material is quite weak, with $\Delta\varepsilon_{max} + 0.68\ M^{-1}\ cm^{-1}$ at 463 nm.

The lattice of Δ-*cis*-β-[Co(**1**)(*R*,*R*-chxn)]$Cl_2(ClO_4)$ can be regarded as composed of alternating layers of (cations + chlorides) and perchlorates, the layers lying parallel to the *ab* plane. Cl···HN bonding links cations within layers, while O_3ClO···HN bonding links cations between layers. The packing of the cations is such that the projecting, lipophilic cyclohexano substituents alternate in orientation so as to be rather remote from one another. This arrangement does, however, bring cyclohexano carbon atoms moderately close (3.9–4.0 Å) to both methyl and ethylene carbon atoms of **1**, so that lipophilicity may be of some importance in determining the form of the lattice.

The cations present in the crystal arrays of the two structurally characterised isomers of [Co(**1**)(*R*-ala)]-$(PF_6)_2 \cdot H_2O$ (*R*-ala = *R*-alanine = L-alanine) are shown in Figs. 3 and 4. Both compounds crystallize (with one

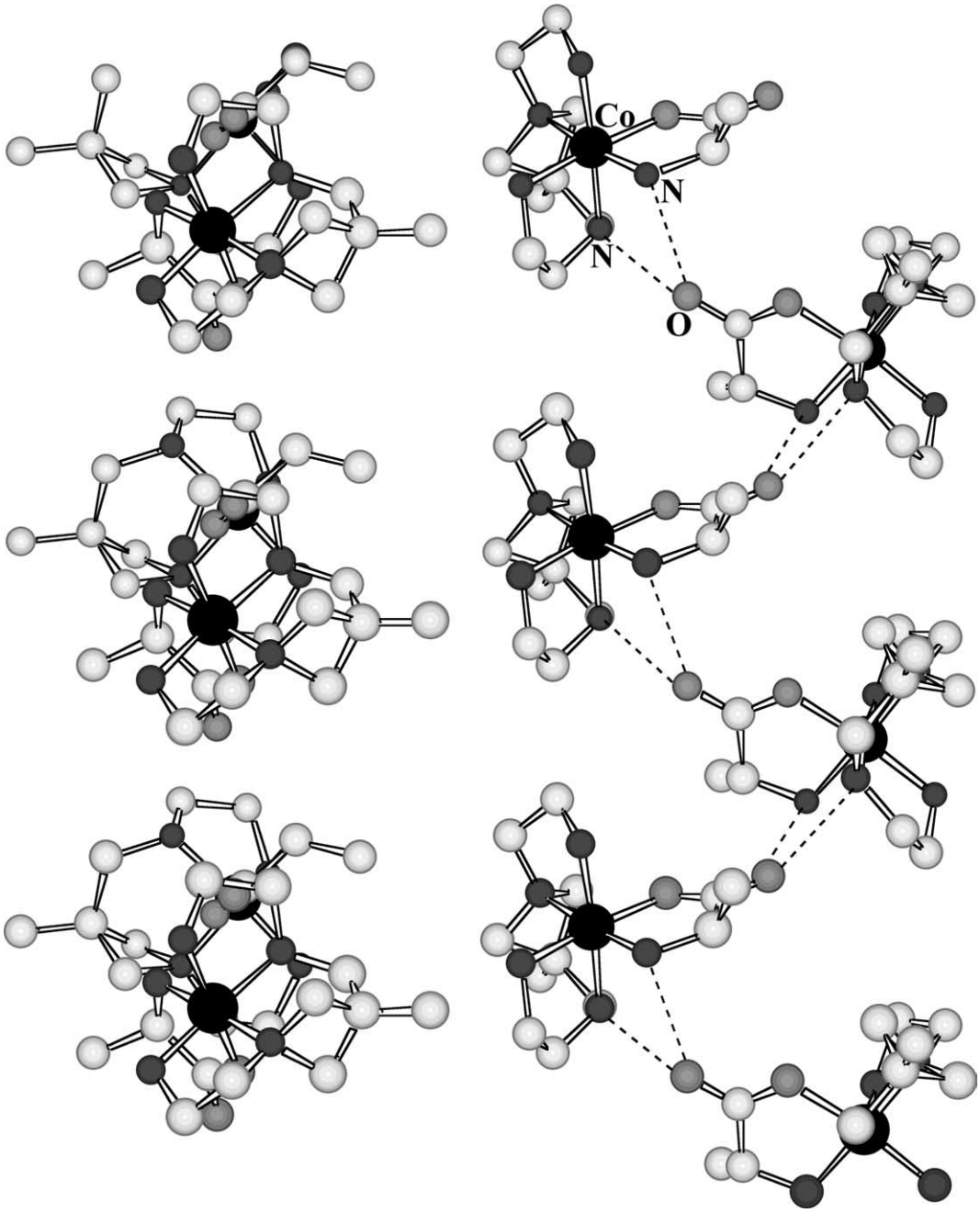


Fig. 5. Simplified view of portions of two adjacent helical arrays of the cations in Λ-*cis*-β_2-[Co(**1**)(*R*-ala)]$(PF_6)_2 \cdot H_2O$, with H-bonding interactions indicated (dashed lines) in one.

water molecule) in the orthorhombic space group $P2_12_12_1$, but with unrelated cell parameters. The variation in cell volume, about 1%, is, however, extremely small. The metal atom in both is in a distorted octahedral N_5O environment, the ligand **1** being quadridentate with the secondary nitrogen donor occupying the "angular" site in the Λ-*cis*-β configuration [22]. Apart from subtle differences in the geometry of ligand **1**, the two cationic species differ only in the position of the alanine chelate unit, with N5 in the crystals isolated from the third fraction, or O1 in those from the fourth, being *trans* to N4, i.e., the β_1 isomer is present in the third and the β_2 in the fourth. As a consequence of this difference in configuration, the intermolecular hydrogen bonding pattern is different in the two compounds, with N1 and N4 acting as donors towards O2 (in a neighbouring complex) and N1 and N5 towards the water oxygen atom in Λ-*cis*-β_1-[Co(**1**)(*R*-ala)]$(PF_6)_2 \cdot H_2O$, whereas, in Λ-*cis*-β_2-[Co(**1**)(*R*-ala)]$(PF_6)_2 \cdot H_2O$, N3 and N5 are bound to O2 (in another complex) and N4 and N5 are bound to the water molecule. In both species, fluorine atoms of the hexafluorophosphate units appear to be involved in H-bonding to both complex-NH and water entities. The NH-bond chelation of uncoordinated carboxylate-*O* (O2) in both cases, again, leads to the formation of polymeric, right-handed helical arrays of the cations. In Λ-*cis*-β_1-[Co(**1**)(*R*-ala)]$(PF_6)_2 \cdot H_2O$, double columns of cations which make up these helices lie in ruffled sheets parallel to the *ab* plane, in such a way that the methyl groups of **1** come into quite close contact (C···C 3.64 Å) with a methylene carbon (the non-azetidine C bound to the quaternary centre) of another ligand **1** in an adjacent helix. In Λ-*cis*-β_2-[Co(**1**)-(*R*-ala)]$(PF_6)_2 \cdot H_2O$, the situation is more complicated in that otherwise identical H-bonded helices can be considered to form an array in planes down *a* and parallel to the *bc* diagonal in which adjacent helices are rotated by 90° about the helix axis relative to one another (Fig. 5). If there are significant contacts to the methyl groups of ligands **1**, these appear to involve fluorine atoms of the anions (C···F 3.29 Å). Presumably by chance, these two complexes contain *R*-alanine and are of the Λ configuration, since the conditions of synthesis, initially hoped to be sufficiently harsh to result in azetidine ring opening, were certainly such as to render possible the racemisation of coordinated alanine [25] and the rather large number of isomeric species detected spectroscopically in the product mixture seems explicable only if both *R*- and *S*-alanine, as well as both configurations around Co(III), were present.

The cation in [Co(**3**)Cl]Cl[PF_6] $\cdot H_2O$ is represented in Fig. 6. The asymmetric unit contains two nearly identical independent molecules, denoted A and B, their form confirming that the expected macrocycle formation and nitro-group reduction reactions [4,12,23] had occurred in the synthesis. The primary amino group and the chlorine atom are in *trans* positions, the overall geometry being distorted octahedral. As is commonly the case with such reactions [4,23], it appears that one product isomer of the ligand is predominant. The Co(III) cation is asymmetric and both enantiomers occur in the lattice, though effectively in centrosymmetric pairs which are bridged by H-bonding either to chloride ions or to water/$[PF_6]^-$ units, explaining the subtly different forms A and B. Differences in geometry between the azetidine rings in A and B are as great as the full range of variation in these rings in all other known complexes of **1** [10,15], suggesting that any differences in reactivity resulting from coordination in different modes to Co(III) or to Cu(II) would be slight.

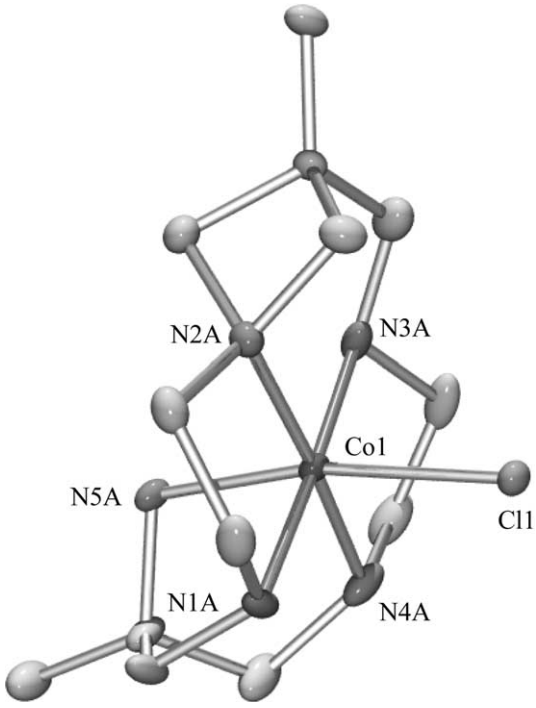


Fig. 6. View of one of the $[Co(\mathbf{3})Cl]^{2+}$ moieties. Displacement ellipsoids are drawn at the 20% probability level.

4. Conclusions

The results of the present and earlier [10,12,13,23] investigations suggest that coordination of an azetidine may in fact be a useful way of protecting it against ring-opening reactions. Thus, while it is of some interest to note that **1** may be stereochemically restrictive in its coordination as a quadridentate ligand, it is of greater interest that it may be efficiently converted to a macrocycle **3** via a familiar template process [5]. Removal of **3** from the metal (as shown presently) should enable free ligand reactions with a variety of nucleophiles to be performed, providing a range of pendent-arm macrocycles through ring-opening processes.

5. Supplementary information

Crystallographic data, in CIF format, have been deposited with the CCDC, deposition numbers 262992–262995. These data may be obtained free of charge via www.ccdc.cam.ac.uk/conts/retrieving.html or from the Cambridge Crystallographic Data Centre, 12 Union Road, Cambridge CB2 1EZ, UK, fax: +44 1223 336 033 or e-mail: deposit@ccdc.cam.ac.uk or on the web www: http://www.ccdc.cam.ac.uk.

Acknowledgement

This work was supported by the Brain Busan 2004 Project and Kosin University.

References

[1] L. Fabbrizzi, F. Foti, M. Licchelli, P.M. Maccarini, D. Sacchi, M. Zema, Chem. Eur. J. 8 (2002) 4965, and references therein.
[2] L.F. Lindoy, Adv. Inorg. Chem. 45 (1998) 75.
[3] M.P. Suh, Adv. Inorg. Chem. 44 (1997) 93.
[4] P.V. Bernhardt, G.A. Lawrance, Coord. Chem. Rev. 104 (1990) 297.
[5] D.A. House, in: G. Wilkinson, J.A. McCleverty, R.D. Gillard (Eds.), Comprehensive Coordination Chemistry, vol. 2, Pergamon Press, New York, 1985, p. 23 (Chapter 13).
[6] C. Hu, T.D. Nguyen, P.S. Wagenknecht, Inorg. Chem. 42 (2003) 742.
[7] T.J. Hubin, N.W. Alcock, M.D. Morton, D.H. Busch, Inorg. Chim. Acta 348 (2003) 33.
[8] R.D. Hancock, M.P. Ngwenya, P.W. Wade, J.C.A. Boeyens, S.M. Dobson, Inorg. Chim. Acta 164 (1989) 73.
[9] P.V. Bernhardt, T.E. Dyahningtyas, S.C. Han, J.M. Harrowfield, I.-C. Kim, Y. Kim, G.A. Koutsantonis, E. Rukmini, P. Thuéry, Polyhedron 23 (2004) 869, and references therein.
[10] J.M. Harrowfield, G.H. Jang, Y. Kim, P. Thuéry, J. Vicens, J. Chem. Soc., Dalton Trans. (2002) 1241.
[11] L.R. Gahan, T.W. Hambley, Inorg. Chem. 26 (1987) 2532.
[12] P.V. Bernhardt, J.M. Harrowfield, Y. Kim, G.A. Koutsantonis, Y.H. Lee, P. Thuéry, Inorg. Chem. 43 (2004) 1681.
[13] R.J. Geue, M.G. McCarthy, A.M. Sargeson, P. Jørgensen, R.T. Hazell, F.K. Larsen, Inorg. Chem. 24 (1985) 2539.
[14] D.C. Ware, B.G. Siim, K.G. Robinson, W.A. Denny, P.J. Brothers, G.R. Clark, Inorg. Chem. 30 (1991) 3750.
[15] J.M. Harrowfield, Y. Kim, G.A. Koutsantonis, Y.H. Lee, P. Thuéry, Inorg. Chem. 43 (2004) 1689.
[16] Kappa-CCD Software, Nonius B.V., Delft, The Netherlands, 1998.
[17] Z. Otwinowski, W. Minor, Meth. Enzymol. 276 (1997) 307.
[18] G.M. Sheldrick, SHELXS-97 and SHELXL-97, University of Göttingen, Germany, 1997.
[19] A.L. Spek, PLATON, University of Utrecht, The Netherlands, 2000.
[20] H.D. Flack, Acta Crystallogr., Sect. A 39 (1983) 876.
[21] L.J. Farrugia, J. Appl. Cryst. 30 (1997) 565.
[22] J.M. Harrowfield, S.B. Wild, in: G. Wilkinson, J.A. McCleverty, R.D. Gillard (Eds.), Comprehensive Coordination Chemistry, vol. 1, Pergamon Press, New York, 1987, pp. 179–212 (Chapter 5).
[23] M.-H. Choi, J.M. Harrowfield, B.J. Kim, I.-C. Kim, S.-H. Kim, Y. Kim, M.-K. Lee, M. Mocerino, E. Rukmini, B.W. Skelton, A.H. White, J. Chem. Soc., Dalton Trans. (2001) 707, and references therein.
[24] H.D. Flack, G.J. Bernardinelli, Appl. Cryst. 33 (2000) 1143.
[25] J.M. Harrowfield, S.-H. Jeong, I.-C. Kim, Y. Kim, B.W. Skelton, A.H. White, Aust. J. Chem. 54 (2001) 63.

their derivatives have aroused considerable interest because of interesting structure and reactivity [9–17], catalytic properties [7–9,18–20], antibacterial and antitumor activity [21–27].

2. Experimental

2.1. Materials

$[Rh_2(OAc)_2(phen)_2(H_2O)_2](OAc)_2$ was prepared according to the literature procedure [25]. ATP (disodium salt) was purchased from Aldrich.

2.2. NMR Spectroscopy

The ^1H, ^{13}C, ^{31}P and ^1H–^{15}N HMBC spectra were recorded on Bruker AMX 300 and Avance 500 spectrometers in D_2O phosphate buffers.

^1H NMR of $[Rh_2(OAc)_2(phen)_2(H_2O)_2](OAc)_2$ (D_2O, $c = 4.70 \times 10^{-3}$ M): 8.42 ppm (d; 2H; $^3J_{2,3} = {}^3J_{8,9} = 5.17$ Hz) – **H 2,9**; 8.19 ppm (d; 2H; $^3J_{3,4} = {}^3J_{7,8} = 8.40$ Hz) – **H 4,7**; 7.63 ppm (s; 2H) – **H 5,6**; 7.53 ppm (dd; 2H; $^3J_{3,4} = {}^3J_{7,8} = 8.40$ Hz; $^3J_{2,3} = {}^3J_{8,9} = 5.17$ Hz) – **H 3,8** (for abbreviations of phen protons see Fig. 1). Increase of complex concentration to $c = 2.24 \times 10^{-2}$ M (approximately 5 times) causes only very small change of chemical shifts (about 0.01 ppm).

^1H–^{15}N two-bond HMBC experiments were performed on a Bruker Avance 500 spectrometer using the standard 4-pulse HMBC sequence with the evolution time of 50 ms and 128 t_1 increments. The number of scans was 35 for pure ATP and 100 for ATP–Rh complex systems. The interpulse delay was 2 s, during which the water resonance was suppressed by low-power irradiation.

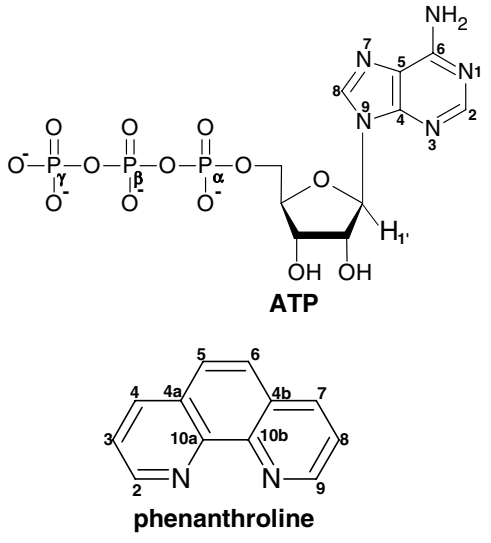


Fig. 1. Abbreviations of carbon, proton, phosphorus and nitrogen atoms in ATP and phenanthroline.

UV–Vis spectra were measured on Beckman DU 7500 spectrometer. The spectra have been recorded in the concentration range $5 \times 10^{-3} - 5 \times 10^{-4}$ M. Difference electronic spectra (Fig. 5) were obtained by subtracting the spectrum of $[Rh_2(OAc)_2(phen)_2(H_2O)_2]^{2+}$ and the spectrum of ATP from the spectrum of the binary system Rh complex/ATP, measured in the same conditions.

The stability constants were determined for D_2O solutions containing $NaNO_3$ ($I = 0.1$ M, 25 °C), to keep ionic strength constant. The pD values were obtaining by adding 0.40 to the pH meter reading [34].

2.3. X-ray crystallographic study

Measurements were performed in low temperature using an Oxford Cryosystem device on Kuma KM4CCD κ-axis diffractometer with graphite-monochromated Mo Kα radiation. Crystals were positioned at 65 mm from the CCD camera. Six hundred and twelve frames were measured at 0.75° intervals with a counting time of 20 s. Accurate cell parameters were determined and refined by least-squares fit of 3750 strong reflections. The data were corrected for Lorentz and polarization effects. Analytical absorption corrections were applied. Data reduction and analysis were carried out with the Oxford Diffraction (Poland) Sp. z.o.o (formerly Kuma Diffraction (Poland) programs. Structures were solved by heavy atom methods (program SHELXS97 [35]) and refined by the full-matrix least-squares method on all F^2 data using the SHELXL97 [36] programs. Nonhydrogen atoms were refined with anisotropic displacement parameters; hydrogen atoms were included from geometry of molecules and $\Delta\rho$ maps. They were fixed during refinement.

3. Results and discussion

3.1. ^1H NMR Spectroscopy

It is well established that stacking interaction of nucleotides with some metal complexes generates the upfield shifts of the ^1H NMR signals of the nucleobase protons due to ring current effects of some heteroaromatic ligands (e.g., bpy or phen) [28,29] which, indeed serve as a clear indication for stack formation.

^1H NMR spectrum of $[Rh_2(OAc)_2(phen)_2(H_2O)_2](OAc)_2$ in D_2O exhibits four signals in aromatic region (see Section 2). This indicates clearly that the corresponding pairs of protons H2,9, H4,7, H5,6 and H3,8 are both chemically and magnetically equivalent, and that protons abbreviated as H5,6 are referred to the A_2 part of the spectrum.

The ^1H NMR spectra for 4.70×10^{-3} and 2.24×10^{-2} M solutions of $[Rh_2(OAc)_2(phen)_2(H_2O)_2](OAc)_2$ in D_2O

show that the positions of all phenanthroline protons are not concentration dependent.

In the presence of ATP substantial changes are observed:

(a) all phenanthroline protons become magnetically nonequivalent after adding ATP and undergo upfield shifts for all ATP to $[Rh_2(OAc)_2(phen)_2(H_2O)_2]^{2+}$ ratios used in experiments;
(b) the observed upfield shifts are concentration dependent, but different phenanthroline protons undergo different shifts. It is important to note, that for all chemically equivalent pairs of protons (H5,6, H4,7, H3,8, H2,9) one proton undergoes larger upfield shift than its chemically equivalent counterpart (Fig. 3). In the case of H5(6) concentration dependent upfield shifts are the largest;
(c) chemical shifts of ATP protons (H8 and H2) are also dependent on concentration and, as for phenanthroline protons, the increase in concentration of ATP (at the same ligand:complex ratio), causes the upfield shift of these protons (Fig. 2);
(d) chemical shifts of both phenanthroline and ATP protons depends on temperature. The increase of temperature causes the downfield shifts of all protons in aromatic region (Fig. 4);

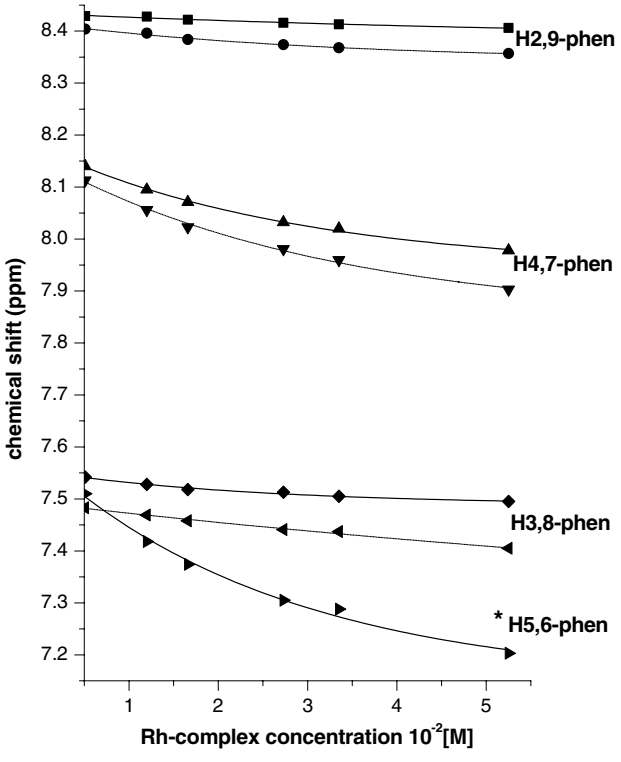


Fig. 3. Concentration dependence of chemical shifts for phenanthroline protons, of $[Rh_2(OAc)_2(phen)_2(H_2O)_2](OAc)_2$ in the presence of ATP, showing that phenanthroline protons became magnetically nonequivalent. *For protons H5,6 (A_2 pattern of spectrum), average chemical shifts are given. (The same solution as for Fig. 2, $T = 298$ K.)

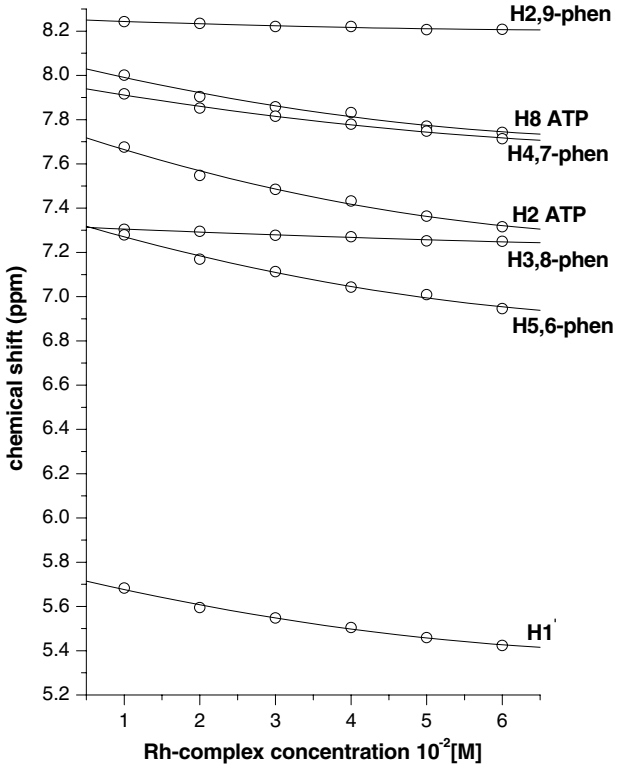


Fig. 2. Concentration dependence of chemical shifts for ATP and phenanthroline protons, of $[Rh_2(OAc)_2(phen)_2(H_2O)_2](OAc)_2$ in the presence of ATP. The spectra were made in buffered D_2O solution at pD 3.35, $T = 283$ K, and ATP:complex = 2:1 (average values of magnetically nonequivalent phenanthroline proton chemical shifts are given).

(e) after NMR measurements, both components (rhodium complex and ATP) can be separated easily. ATP is precipitated with methanol, and after evaporation of the solution the pure rhodium complex is recovered. This has been checked by NMR.

3.2. ^1H–^{15}N NMR HMBC experiments

The well resolved HMBC spectra have been obtained at high concentration of ATP and complex (3.33×10^{-1} M). However at lower concentrations not all nitrogen resonances appear in the spectrum of both ATP and ATP/$[Rh_2(OAc)_2(phen)_2(H_2O)_2]^{2+}$ mixture (ATP:$[Rh_2(OAc)_2(phen)_2(H_2O)_2]^{2+}$ = 1:1, pD 3.35 and concentration of both components equal to 5.25×10^{-2} M). Based on the literature data [30–32], assignment of the four ATP signals (for free ATP) is rather straightforward: N1, −155 ppm; N3, −165 ppm; N7, −149 ppm; and N9, −212 ppm ($c = 5.25 \times 10^{-2}$ M and pD 8.55). At $c = 5.25 \times 10^{-2}$ M and pD 3.35, the nitrogen chemical shifts are as follows: N1, −221 ppm; N3, −159 ppm; N7, – not observed; N9, −204 ppm; If the concentration is higher all nitrogen resonances are observed: N1, −224

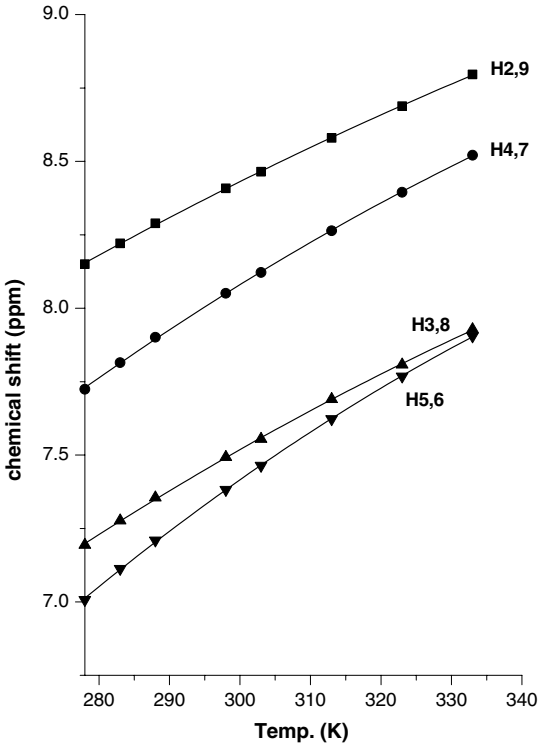


Fig. 4. The example of temperature dependence of chemical shifts of phenanthroline protons. On the plot average values for chemically equivalent protons are given. ATP:complex = 2:1, [compl.] = 2.71×10^{-2} M.

ppm; N3, −161 ppm; N7, −148 ppm; N9, −206 ppm ($c = 3.33 \times 10^{-1}$ M and pD 3.35) (Table 1).

From the above data it can be seen that N1 is very sensitive to pD change ($\Delta\delta$ = 66–68 ppm), while other nitrogens undergo only relatively small changes ($\Delta\delta$ = 1–6 ppm) when pD is changed. The data for the spectra at pD 3.35 at very different concentrations show that the influence of concentration is relatively low (2–3 ppm upfield for the $c = 3.33 \times 10^{-1}$ M as compared with $c = 5.25 \times 10^{-2}$ M) (Table 1).

The value of the pD induced chemical shift change equal 66–68 ppm is in agreement with the well known fact that N1 is the most basic nitrogen in ATP, and therefore this nitrogen atom is protonated in acidic solution. Binding of H^+ makes N1 more shielded, in accordance with the observation by Markowski [30], and up-field shift for protonation is observed.

In the presence of $[Rh_2(OAc)_2(phen)_2(H_2O)_2]^{2+}$ relatively small changes in nitrogen atom chemical shifts of ATP are observed (Table 1). The only substantial change is observed for N1 proton of ATP at pD 3.35. The N1 nitrogen atom which is protonated in the absence of $[Rh_2(OAc)_2(phen)_2(H_2O)_2]^{2+}$, undergoes large downfield shift (53–62 ppm) in the presence of rhodium complex. The values of its chemical shift −162 and −168 ppm, (Table 1) strongly suggests that deprotonation of the N1 atom occurs after interaction with $[Rh_2(OAc)_2(phen)_2(H_2O)_2]^{2+}$. To confirm this information the stability constants of the stacking adducts in three different pH were calculated. In contrast to the numerous literature data the resulted values of log pK are practically the same: 1.27, 1.23, 1.27 at pH 3.40, 5.87 and 7.96, respectively.

When an excess of ATP is added to the solution containing rhodium complex the chemical shift of N1 increases and reaches value of −204 ppm, at pD 3.35

Table 1
^{1}H–^{15}N (HMBC) spectra (N^{15} chemical shifts (ppm) with urea (−300 ppm) as a reference)

pD 3.35; [compl.] = 3.33×10^{-1} M; ATP/compl. = 1:1
ATP (free)
N1 **−224**
N3 **−161**
N7 **−148**
N9 **−206**
ATP + complex
N1(N3) **−162**
N3(N1) **−162**
N7 **−161**
N9 **−209**
N(phen) **−169**
pD 3.35; [compl.] = 3.33×10^{-1} M; ATP/compl. = 5:1
ATP + complex N1
N1 **−204**
N3 **−162**
N7 **−150**
N9 **−208**
N(phen) **−171**
pD 3.35; [compl.] = 5.25×10^{-2} M; ATP/compl. = 1:1
ATP (free)
N1 **−221**
N3 **−159**
N7[a]
N9 **−204**
ATP + complex
N1 **−168**
N3 **−162**
N7[a]
N9[a]
N(phen) **−169**
pD 8.55; [compl.] = 5.25×10^{-2} M; ATP/compl. = 1:1
ATP (free)
N1 **−155**
N3 **−165**
N7 **−149**
N9 **−212**
ATP + complex
N1 **−161**
N3 **−168**
N7 **−157**
N9 **−210**
N(phen) **−169**

[a] Signals are not observed because of low concentrations of ATP.

(ATP:complex = 5:1) (Table 1). This is an average value between the free protonated ATP (−224 ppm) and chemical shift of −168 ppm, in solution where stacking interactions between ATP and complex are observed (ATP:complex = 1:1).

The lack of protonation at pD 3.35 in the presence of rhodium complex may be explained by the formation of hydrogen bonds between N1 atom and the water molecule coordinated to rhodium in axial coordination site. We have found that addition of $NaNO_3$ (to obtain ionic strength of 0.1 M) causes decrease of solubility of rhodium dimer, which finally leads to the crystallization of $[Rh_2(OAc)_2(phen)_2(H_2O)_2](NO_3)_2$. The crystals growth depends on ATP concentration. At higher concentrations of ATP the crystallization process is slower, because of stacking adducts formation in solution. However the resulted crystals do not contain ATP molecule. Crystal structure of the resulted dimer shows the presence of water molecules in axial positions, which is well documented in the literature.

3.3. ^{31}P NMR Spectroscopy

Chemical shifts of phosphorous atoms of ATP undergo only very small changes in the presence of rhodium complex (both for pD 8.45 as well as 3.35). When the terminal γ-phosphate group of ATP participates in complex formation, the chemical shifts for γ-phosporous atom are order of several ppm (see e.g., figures in [33]). The largest difference in the chemical shift after adding of $[Rh_2(OAc)_2(phen)_2(H_2O)_2]^{2+}$ is only 0.3 ppm (for the P_α in acid solution pD 3.35) (Table 2). Phosphorous resonances of ATP were found to be pD dependent in accordance with earlier observations [31]. However no significant variations are observed in the presence of $[Rh_2(OAc)_2(phen)_2(H_2O)_2]^{2+}$.

3.4. ^{13}C NMR Spectroscopy

Chemical shifts for carbon atoms in free ATP, as well as those of pure rhodium complex are only slightly changed when both compounds are mixed together (at 1:1 and 1:2 ATP:Rh complex molar ratios). The changes for ATP carbon atoms are more distinctive (Table 3). Down-field shifts are observed for C2, C4, C6 carbon atoms while C8 signal is up-field shifted.

After adding of ATP to the rhodium complex solution, phenanthroline carbon atoms become chemically nonequivalent, and separate signals with different chemical shifts are observed. The values of the chemical shifts at ATP:complex ratio equal to 1:1 are: C2,9 152.47 ppm (one signal), C3,8 126.46 and 126.35 ppm (0.11 ppm,

Table 2
$^{31}P\{^1H\}$NMR Spectra

ATP	ATP + compl.	$\Delta = P_{compl.} - P_{ATP}$
pD 2.95 $c = 5.25 \times 10^{-2}$ M ATP:compl. = 1:1		
$P_\alpha = -11.2$ ppm	$P_\alpha = -11.5$ ppm	0.3 ppm
$P_\beta = -22.8$ ppm	$P_\beta = -23.0$ ppm	0.2 ppm
$P_\gamma = -10.7$ ppm	$P_\gamma = -10.8$ ppm	0.1 ppm
pD 8.55 $c = 5.25 \times 10^{-2}$ M ATP:compl. = 1:1		
$P_\alpha = -8.1$ ppm	$P_\alpha = -8.3$ ppm	0.2 ppm
$P_\beta = -18.6$ ppm	$P_\beta = -18.7$ ppm	0.1 ppm
$P_\gamma = -3.8$ ppm	$P_\gamma = -3.9$ ppm	0.1 ppm

Table 3
^{13}C NMR Spectra (δ ppm) pD 3.35; [Rh–complex] = 3.33×10^{-1} M

ATP (free)		Rh–complex (free)		ATP[a]		ΔATP[a]	Rh–complex[a]		ΔRh–compl.
ATP:compl. = 1:1									
C2	148.5	C2,9	152.4	C2	151.7	3.2	C2,9	152.5	0.1
C4	145.9	C3,8	126.4	C4	148.9	3.0	C3,8	126.6	0.2
C5	118.5	C4,7	138.6	C5	118.5	0.0	C4,7	138.5	0.1
C6	150.4	C5,6	127.9	C6	155.0	4.6	C5,6	127.6	0.3
C8	142.5	C4a,4b	129.5	C8	140.6	1.9	C4a,4b	129.2	0.3
		C10a,10b	146.5				C10a,10b	146.0	0.5
ATP:compl. = 2:1									
C2	148.5	C2,9	152.4	C2	151.1	2.6	C2,9	152.5	0.1
C4	145.9	C3,8	126.4	C4	148.8	2.9	C3,8	126.6	0.2
C5	118.5	C4,7	138.6	C5	118.5	0.0	C4,7	138.5	0.1
C6	150.4	C5,6	127.9	C6	154.1	3.7	C5,6	127.6	0.3
C8	142.5	C4a,4b	129.5	C8	141.0	1.5	C4a,4b	129.2	0.3
		C10a,10b	146.5				C10a,10b	145.8	0.7

[a] $[Rh_2(OAc)_2(phen)_2(H_2O)_2](OAc)_2$ + ATP.

13.76 Hz), C4,7 138.59 and 138.40 ppm (0.19 ppm, 22.95 Hz), C5,6 127.62 ppm (one signal), C4a,4b 129.27 and 129.22 ppm (0.05 ppm, 5.74 Hz), C10a,10b 145.98 and 145.97 ppm (0.01 ppm, 1.14 Hz) (in parantheses the separations of signals in ppm and Hz are given). The separations between these signals are small: 0.01 – 0.19 ppm (1.14 – 22.95 Hz). When the ATP:compl. ratio = 2:1 the chemical shifts of phenanthroline carbons are as follows: C2,9 152.55 and 152.48 ppm (0.07 ppm, 9.24 Hz), C3,8 126.71 and 126.54 ppm (0.17 ppm, 20.81 Hz), C4,7 138.60 and 138.38 ppm (0.22 ppm, 27.73 Hz), C5,6 127.55 ppm (one signal), C4a,4b 129.21 and 129.11 ppm (0.1 ppm, 11.56 Hz), C10a,10b 145.80 and 145.71 ppm (0.09 ppm, 11.56 Hz), and separations of these peaks are only slightly larger (0.07 – 0.22 ppm) (see also Table 2). In the case of C5,6 and C2,9 only one signal is observed at ATP:compl. = 1:1. When this ratio is 2:1 one signal is observed for C5,6.

3.5. Crystal structure of $[Rh_2(OAc)_2(phen)_2(H_2O)_2](NO_3)_2$

In the presence of $NaNO_3$ (which was added to obtain constant *I*) a crystalline compound appears. The crystallization is more easy in the presence of small amounts of ATP in the system under investigations. At higher concentrations of ATP the crystallization process is much slower. This observation suggests that stacking between ATP and phenanthroline ligands, makes the crystallization more difficult. However no ATP molecules crystallize together with rhodium complex. The crystal structures are shown on Figs. 6 and 7.

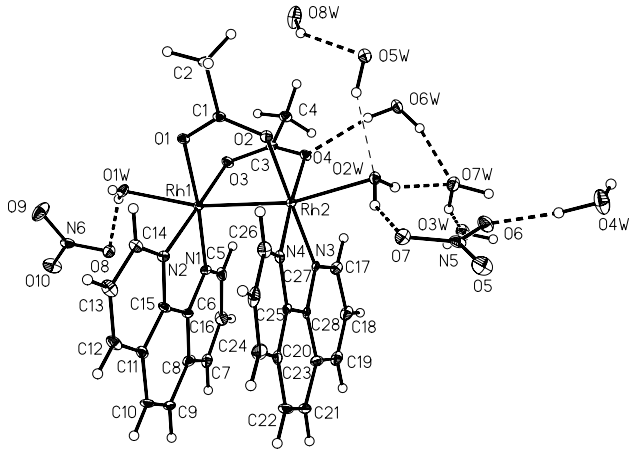


Fig. 6. Structure of $[Rh_2(OAc)_2(phen)_2(H_2O)_2](NO_3)_2$ showing the atom numbering scheme. The atoms are shown as 30% thermal ellipsoids. Selected bond distances (Å): Rh(1)–N(2) 2.003(4), Rh(1)–N(1) 2.021(4), Rh(1)–O(3) 2.037(3), Rh(1)–O(1) 2.052(3), Rh(1)–O(1W) 2.222(3), Rh(1)–Rh(2) 2.5609(3), Rh(2)–N(3) 2.001(3), Rh(2)–N(4) 2.008(4), Rh(2)–O(2) 2.031(3), Rh(2)–O(4) 2.069(3), Rh(2)–O(2W) 2.296(3). Bond angles (°): N(2)–Rh(1)–N(1) 81.67(12), N(2)–Rh(1)–O(3) 174.00(16), N(1)–Rh(1)–O(3) 93.72(16), N(2)–Rh(1)–O(1) 95.12(16), N(1)–Rh(1)–O(1) 175.11(16), O(3)–Rh(1)–O(1) 89.23(11), N(2)–Rh(1)–O(1W) 89.74(13), N(1)–Rh(1)–O(1W) 90.98(13), O(3)–Rh(1)–O(1W) 86.49(12), O(1)–Rh(1)–O(1W) 85.30(12), N(2)–Rh(1)–Rh(2) 98.70(11), N(1)–Rh(1)–Rh(2) 98.96(11), O(3)–Rh(1)–Rh(2) 85.76(10), O(1)–Rh(1)–Rh(2) 85.14(10), O(1W)–Rh(1)–Rh(2) 167.77(7), N(3)–Rh(2)–N(4) 81.57(14), N(3)–Rh(2)–O(2) 176.62(16), N(4)–Rh(2)–O(2) 95.50(15), N(3)–Rh(2)–O(4) 94.28(15), N(4)–Rh(2)–O(4) 175.68(15), O(2)–Rh(2)–O(4) 88.61(11), N(3)–Rh(2)–O(2W) 95.13(12), N(4)–Rh(2)–O(2W) 92.71(13), O(2)–Rh(2)–O(2W) 83.29(11), O(4)–Rh(2)–O(2W) 86.43(11), N(3)–Rh(2)–Rh(1) 95.96(11), N(4)–Rh(2)–Rh(1) 96.46(11), O(2)–Rh(2)–Rh(1) 86.02(10), O(4)–Rh(2)–Rh(1) 85.14(9).

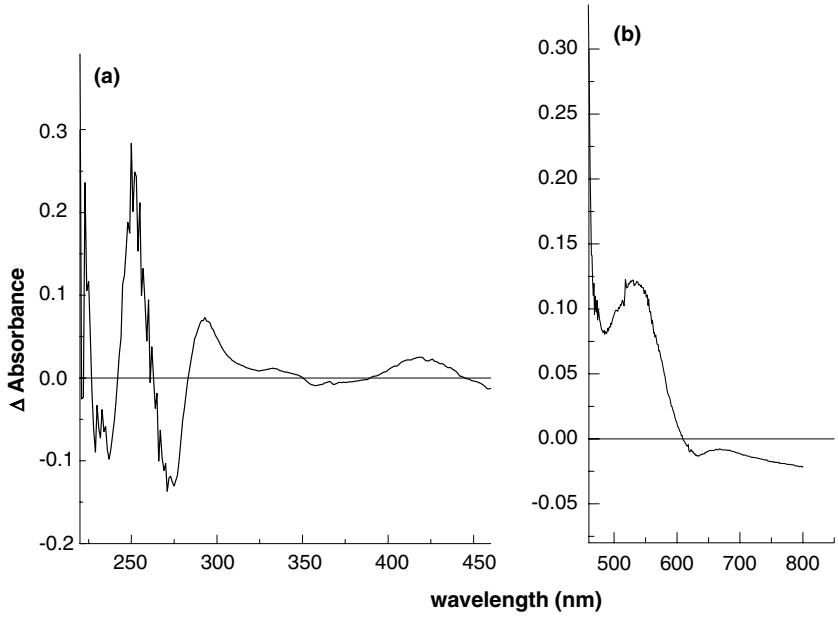


Fig. 5. The difference electronic spectra of $[Rh_2(OAc)_2(phen)_2(H_2O)_2](OAc)_2$/ATP binary systems in water at molar ratio ATP:complex = 1:1 – (a) in 0.1 cm quartz cuvette, [compl.] = 5×10^{-4} M, (b) in 1 cm quartz cuvette, [compl.] = 5×10^{-3} M.

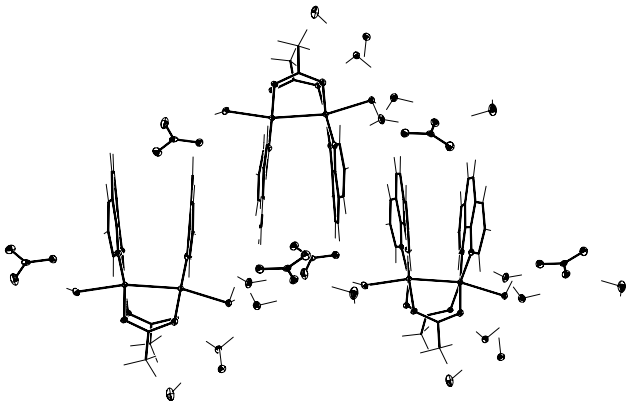


Fig. 7. Crystal structure showing stacking interactions between neighboring dimeric units. The shortest distances between neighboring carbon atoms (from phenanthroline rings) are 3.265–3.371 Å. In solution however no stacking interactions are observed, which was confirmed by NMR.

Fig. 6 shows that the axial positions are occupied by water molecules, which is well known from the literature data of analogous rhodium dimers ([7] and references therein). Difference electronic spectra (Fig. 5) also confirm this observation. This is probably the reason why in the presence of rhodium dimer deprotonation of N1 of the adenine ring takes place as a result of hydrogen bond formation with coordinated water molecule. This also explain why no interaction between rhodium and P_γ is observed in NMR. Fig. 7 shows that in the solid state stacking interactions between neighboring dimeric units occurs. This interaction is not observed in solution.

4. Conclusions

On the basis of above observations it can be concluded:

ATP interacts with $[Rh_2(OAc)_2(phen)_2(H_2O)_2]^{2+}$ by stacking interactions with phenanthroline ligand coordinated with rhodium. This follows especially from the ^1H NMR spectra, which show that in the presence of $[Rh_2(OAc)_2(phen)_2(H_2O)_2]^{2+}$ the ATP proton signals suffer upfield shifts which are ascribable mainly to the ring current effect of coordinated phenanthroline. The largest shift is observed for the H-2 signal. This indicate that this proton is located just above the aromatic rings of the coordinated phenanthroline ligand. The stacking of ATP molecule with coordinated phenanthroline ligand causes magnetic nonequivalence of phenanthroline protons, which also exhibit large upfield shifts. The largest shifts are observed for H5 and H4. This suggests that these protons are located below the six membered pyrimidine aromatic ring of ATP. The chemical shifts of these protons depend on the concentration of compounds and temperature (Figs. 2–4). The H5 and H6 protons, observed in pure rhodium complex at lower fields than H3,8 are shifted towards higher fields in the presence of ATP. As the temperature is increasing the stacking interactions are weaker, which is confirmed by the ^1H NMR spectra. The proton resonances of both phenanthroline and ATP undergo low field shifts when the temperature is increasing (Fig. 4).

The changes of ^{13}C resonances are smaller than in the case of proton resonances. Some signals are shifted towards higher fields and some towards lower fields (Table 3), depending on the relative locations of aromatic rings. However as in the case of proton resonances the phenanthroline carbons became magnetically nonequivalent, and occurs as a doublets (except of C5,6). All carbon atoms in six membered ring of ATP are shifted towards lower fields except of C5 resonance which does not change its position. On the basis of this observations it could be concluded that the largest stacking interactions occur between adenine six membered aromatic ring and phenanthroline rings carbons C4,7 and C5,6 because the protons H5,6 and H4,7 undergo the biggest upfield shift).

In the presence of $[Rh_2(OAc)_2(phen)_2(H_2O)_2]^{2+}$ there are also small changes for nitrogen chemical shifts of ATP apart from the N1 atom at pD 3.35 (Table 1). The signal of this atom observed at −224 ppm for free ATP at pD 3.35 is shifted to −162 ppm for the solution containing ATP and complex at the same acidity. Unexpected is the lack of protonation of N1 nitrogen in the presence of rhodium complex. A reasonable explanation of this is formation of the hydrogen bond N1 and the water molecule coordinated to rhodium in axial position. ^1H NMR Spectra as well as stability constants of the stacking adducts also confirm this observation.

The UV–Vis difference spectra (Fig. 5) as well as ^{13}P (Table 2) spectra suggest additionally that phosphate residue of ATP does not interact with the positively charged $[Rh]^{2+}$ core in axial position. The ^{31}P resonances for P_γ change only of about 0.3 ppm. In the ATP molecule interacting with Zn complexes with phenanthroline- and dipyridine-containing open chain or macrocyclic polyamine ligands analogous shifts for P_γ resonance (downfield) are about 2–3 ppm [32,33].

5. Supplementary material

Crystallographic data (excluding structure factors) for the structure reported in this paper have been deposited with Cambridge Crystallographic Data Centre CCDC No. 264728 Copies of this information may be obtained free of charge from the Director, CCDC, 12 Union Road, Cambridge CB2 1EZ, UK, fax: +44 1223 336 033, e-mail: deposit@ccdc.cam.ac.uk or on the web http://www.ccdc.cam.ac.uk).

References

[1] B. Albert, D. Bray, J. Lewis, M. Raff, K. Roberts, J.D. Watson, Molecular Biology of the Cell, 3rd ed., Garland, New York, 1994, p.89.
[2] A. Bianchi, K. Bowman-James, E. Garcia-Espana (Eds.), Supramolecular Chemistry of Anions, Wiley-VCH, New York, 1997.
[3] H. Sigel, in: D. Banerjca (Ed.), Coordination Chemistry, vol. 20, Pergamon Press (IUPAC), Oxford, 1980, pp. 27–45.
[4] H. Sigel, in: I. Bertini, L. Lunazzi, A. Dei (Eds.), Advances in Solution Chemistry, Plenum Press, New York, 1981, pp. 149–159.
[5] H. Sigel, in: T.D. Tullins (Ed.), Metal–DNA Chemistry, ACS Symposium Series No. 402, American Chemical Society, Washington, DC, 1989, pp. 159–204.
[6] A. Odani, R. Shimata, H. Masuda, O. Yamauchi, Inorg. Chem. 30 (1991) 2133.
[7] F.A. Cotton, R.A. Walton, Multiple Bonds System between Metal Atoms, Clarendon Press, Oxford, 1993.
[8] E.B. Boyar, S.D. Robinson, Coord. Chem. Rev. 50 (1983) 109.
[9] F.P. Pruchnik, Pure Appl. Chem. 61 (1989) 795.
[10] F. Pruchnik, B.R. James, P. Kvintovics, Can. J. Chem. 64 (1989) 936.
[11] F.P. Pruchnik, J. Hanuza, K. Hermanowicz, K. Wajda-Hermanowicz, M. Zuber, Spectrochim. Acta 45A (1989) 835.
[12] T. Głowiak, F.P. Pruchnik, M. Zuber, Pol. J. Chem. 65 (1991) 1749.
[13] A. Szymaszek, F.P. Pruchnik, Pol. J. Chem. 66 (1992) 1859.
[14] F.P. Pruchnik, P. Jakimowicz, Z. Ciunik, K. Stanisławek, L.A. Oro, C. Tejel, M.A. Ciriano, Inorg. Chem. Commun. 4 (2001) 19.
[15] F.P. Pruchnik, P. Jakimowicz, Z. Ciunik, Inorg. Chem. Commun. 4 (2001) 726.
[16] E. Gałdecka, Z. Gałdecki, F.P. Pruchnik, P. Jakimowicz, Transit. Metal Chem. 23 (2000) 315.
[17] L. Trynda-Lemiesz, F.P. Pruchnik, J. Inorg. Biochem. 66 (1997) 187.
[18] J. Halpern, E. Kimura, J. Molin-Case, C.S. Wong, J. Chem. Soc., Chem. Commun. (1971) 1207.
[19] H. Pasternak, E. Lancman, F. Pruchnik, J. Mol. Catal. 29 (1985) 13.
[20] H. Pasternak, F. Pruchnik, K. Wajda-Hermanowicz, M. Zuber, Pol. J. Chem. 63 (1986) 619.
[21] H. Pasternak, F. Pruchnik, Pol. J. Chem. 66 (1992) 865.
[22] P. Jakimowicz, L. Ostropolska, F.P. Pruchnik, Metal-Based Drugs 7 (4) (2000) 201.
[23] J.L. Bear, H.B. Gray Jr., L. Rainen, I.M. Chang, R. Howard, G. Serio, A.P. Kimball, Cancer Chemother. Rep. 59 (1975) 611.
[24] R.A. Howard, A.P. Kimball, J.L. Bear, Cancer Res. 39 (1979) 2568.
[25] F.P. Pruchnik, G. Kluczewska, A. Wilczok, U. Mazurek, T. Wilczok, J. Inorg. Biochem. 65 (1997) 25.
[26] M. Bien, T.M. Lachowicz, A. Rybka, F.P. Pruchnik, L. Trynda, Metal-Based Drugs 4 (2) (1997) 81.
[27] M. Bien, F.P. Pruchnik, A. Seniuk, T.M. Lachowicz, P. Jakimowicz, J. Inorg. Biochem. 73 (1999) 49.
[28] C.E. Johnson Jr., F.A. Borey, J. Chem. Phys. 29 (1958) 1012.
[29] F.A. Borey, Nuclear Magnetic Resonance Spectroscopy, Academic Press, New York, 1969.
[30] V. Markowski, G.R. Sullivan, J.D. Roberts, J. Am. Chem. Soc. 99 (1977) 714.
[31] F. Du, X.-A. Mao, Spectrochim. Acta A 57 (2001) 1711.
[32] L. Jiang, X.-A. Mao, Polyhedron 22 (2003) 611.
[33] C. Bazzicalupi, A. Bencini, E. Berni, A. Bianchi, P. Fornasari, C. Giorgi, C. Marcinelli, B. Valtancoli, J. Chem. Soc., Dalton Trans. (2003) 2564.
[34] P.K. Glasoe, F.A. Long, J. Phys. Chem. 64 (1960) 188.
[35] G.M. Sheldrick, Acta Crystallogr., Sect. A 46 (1990) 467.
[36] G.M. Sheldrick, SHELXL97, Program for Crystal Strucure Refinement, University of Göttingen, 1997.

will HAS be formed [5]. To ensure that $Si(OH)_4$ is the reactant it is important that the solution is both below pH 9.0 (pK_a for $Si(OH)_4$ is about 9.6) and undersaturated with respect to the solubility of $Si(OH)_4$ (it will autocondense at $[Si(OH)_4] > 2.0$ mmol/L). When these criteria are met HAS of distinct stoichiometry and structure are formed and can be precipitated from solution [6]. There are only two basic types of HAS and which of these will form is dependent upon the ratio of $Si(OH)_4$ to Al in the parent solution. When Al is in excess HAS_A is formed. This has a Si:Al ratio of 0.5 and is composed of octahedral assemblies of Al atoms linked to Si through, predominantly, $Q_3(3Al)$ linkages. When $Si(OH)_4$ is present to a twofold excess or more HAS_B is formed. This has a Si:Al ratio of 1.0 and is composed of both octahedral and tetrahedral assemblies of Al atoms, in approximately equal amounts, linked to Si through, predominantly, $Q_3(1\text{-}2Al)$ linkages. The formation of HAS_B involves a dehydroxylation reaction which, at room temperature and pressure, appears to be fuelled by the excess of $Si(OH)_4$ in solution. When the concentrations of Al and $Si(OH)_4$ in parent solutions are either equal or favour $Si(OH)_4$ by less than a factor of two both types of HAS are present in the solid phase. The latter observation prompted the suggestion that HAS_B was formed via the competitive condensation of $Si(OH)_4$ across hydroxyl groups on HAS_A and subsequent research has tended to support this notion [6,7].

Both HAS_A and HAS_B appear to have analogues in the natural environment, protoimogolite and protoimogolite allophane, respectively [8], though their formation and persistence in natural waters has not been demonstrated unequivocally. There have been numerous references to the presence of HAS-like phases in natural environments without any direct confirmation that they are analogous to synthetic HAS. It is our contention that HAS similar in nearly all respects to HAS_A and HAS_B are significant secondary mineral phases which when formed in the natural environment are major players in the biogeochemical cycle of Al and in the biological availability of Al in general [9]. We have recently determined a solubility expression for HAS_B [10] which supports such a notion and will help to explain how Al is successfully retained within the lithospheric cycle and excluded from biota. However, if HAS are formed in nature then it is likely that, unlike in the laboratory, their form and persistence will be influenced by other ligands for Al, both organic such as humic and fulvic acids and inorganic such as fluoride and phosphate. We have taken the first steps to understand how the latter, fluoride and phosphate, when present at equimolar concentrations to $Si(OH)_4$, might influence the formation of synthetic HAS.

2. Experimental

2.1. Preparation of parent solutions

All reagents were of the highest purity available. Each of the parent solutions listed in Table 1 was prepared using ultra pure water (conductivity < 0.067 μS/cm, Elga UK) which included 100 mmol/L KNO_3 as a background electrolyte and was buffered at pH 6.0 with 25 mmol/L of piperazine-N,N′-*bis* (2-ethanesulphonic acid) (PIPES). $Si(OH)_4$ solutions, maximum concentra-

Table 1
Concentrations of silicic acid, aluminium, fluoride and phosphate in parent solutions at the beginning of the experiment and after collection of solid phases and elemental composition of the solid phases

Stoichiometry of solution (mmol/L)				$Si(OH)_4$-dialysis (μmol/L)		Al-dialysis (μmol/L)		F-filtration (μmol/L)		P-filtration (μmol/L)		Soid phase
Si	Al	F	P	Mean	SD[a]	Mean	SD	Mean	SD	Mean	SD	
0.5	2.0			4	0.7	<1						$SiAl_{3.7}$
0.5	2.0	0.5		7	2.1	17	4.1	110	9.7			$SiAl_{4.0}F_{0.47}$
0.5	2.0		0.5	181[b]	2.0	<1				<1		$SiAl_{6.8}P_{1.9}$
1.0	2.0			73	4.0	<1						$SiAl_{2.3}$
1.0	2.0	1.0		141	6.0	66	12	404	9.0			$SiAl_{2.45}F_{0.44}$
1.0	2.0		1.0	798[b]	14	<1				10	0.3	$SiAl_{9.6}P_{6.8}$
1.0	1.0			255	17	<1						$SiAl_{1.6}$
1.0	1.0	1.0		451	4.0	199	11	621	45			$SiAl_{2.0}F_{0.37}$
1.0	1.0		1.0	980[b]	8.0	<1				165	2.0	$SiAl_{33}P_{7.8}$
2.0	1.0			563	72	<1						$SiAl_{1.06}$
2.0	1.0	2.0		937	43	324	27	1349	94			$SiAl_{1.03}F_{0.24}$
2.0	1.0		2.0	1857[b]	8.0	<1				268	4.1	$SiAl_{44}P_{14}$
2.0	0.5			824	45	<1						$SiAl_{0.87}$
2.0	0.5	2.0		1420	61	223	45	1492	80			[c]
2.0	0.5		2.0	1768[b]	13	<1				1209	29	$SiAl_{25}P_8$

[a] Standard deviation, $n = 9$.
[b] Filtration through 0.1 μm Durapore membrane filters.
[c] No solid phase collected.

tion 2.0 mmol/L, were prepared by cation exchange of Na_4SiO_4 and either diluted as required (0.5 and 1.0 mmol/L) or used in place of pure water (2.0 mmol/L). Al was added from a freshly prepared 1 mol/L stock of $Al(NO_3)_3 \cdot 9H_2O$ in 1% HNO_3 and phosphate (HPO_4^{2-}) and fluoride (F^-) were added as $NaH_2PO_4 \cdot H_2O$ and NaF, respectively. We have used an established method of HAS preparation [2] in which the respective constituents of parent solutions are mixed at ca. pH 3.0 and then titrated to pH 6.0 using NaOH. In this way as soon as Al hydrolysis begins and hydroxy-aluminium templates are formed $Si(OH)_4$ will be available to react with them to give HAS.

To determine when any reaction involving the formation of HAS was complete and, therefore, facilitating thereafter the collection of the solid phase by filtration, pilot experiments were run for each parent solution in which the rate of formation of HAS was determined by measuring the change in $[Si(OH)_4]$ over time. One replicate of each solution was prepared in a 1 L PTFE container (Cowie Technology Ltd., UK) and placed in an incubator at 20.0 ± 0.1 °C. The solution was filtered periodically using syringe filters (Millipore) incorporating 0.1 μm polyvinylidene fluoride membrane filters (Durapore) and $[Si(OH)_4]$ determined as molybdate-reactive Si [11]. When $[Si(OH)_4]$ was observed to plateau (see Fig. 1 for representative examples) the reaction was considered complete and the requisite time period was chosen for the full scale experiments. In these the idea was to use the $[Si(OH)_4]$ at equilibrium with the solid phase to discriminate between the different parent solutions. Thus, if F^- were to influence the formation of HAS this might be evident from the equilibrium $[Si(OH)_4]$. To give this idea the greatest possibility of being effective nine replicates of each parent solution were prepared in 200 mL PTFE containers and placed in an incubator at 20.0 ± 0.1 °C. Following incubation of the solutions for the pre-determined time period (ca. 60 days) the equilibrium $[Si(OH)_4]$ was determined in each of the nine replicates though not following filtration (as in the pilot) but by using equilibrium dialysis. A dialysis chamber of volume 500 μL and MWCO 1000 Da (Spectra/Por® DispoDialyzer®) was immersed in the solution and allowed to equilibrate for 72 h. Previous control experiments had shown that $Si(OH)_4$ equilibrated across the membrane in this time interval and that the equilibrium was not influenced by the presence of 2.0 mmol/L F^- but that the same amount of HPO_4^{2-} resulted in an underestimation of the equilibrium $[Si(OH)_4]$. The latter resulted in filtration and not dialysis being used to determine the equilibrium $[Si(OH)_4]$ in parent solutions which included HPO_4^{2-}. Following equilibrium dialysis and the collection of samples for the determination of dialysable $Si(OH)_4$ and Al the solutions were filtered through 0.1 μm membrane filters (Durapore) and the filtered solutions were analysed for F^- and HPO_4^{2-} (see Table 1) whereas the solid phases were dried to a constant weight at 37 °C and stored in a desiccator for subsequent elemental composition by microprobe and solid state NMR.

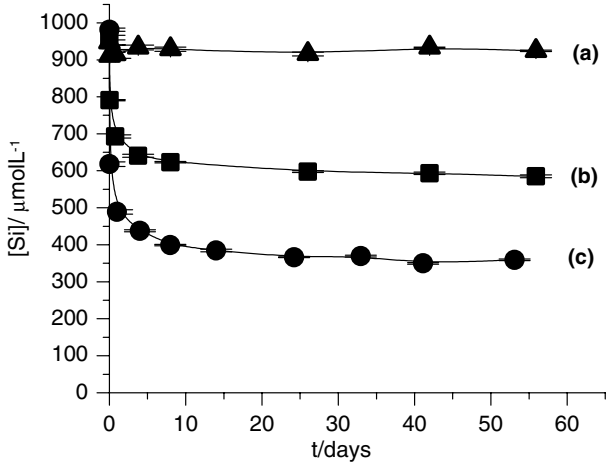


Fig. 1. Change in $[Si(OH)_4]$ during 60 days incubation at 20.0 ± 0.1 °C for: (a) 1 mmol/L $Si(OH)_4$/1 mmol/L Al + 1 mmol/L HPO_4^{2-}; (b) 1 mmol/L $Si(OH)_4$/1 mmol/L Al + 1 mmol/L F^-; and (c) 1 mmol/L $Si(OH)_4$/1 mmol/L Al + no added anion. Mean and SD are plotted, $n = 5$.

2.2. Determination of $Si(OH)_4$, Al, F^- and HPO_4^{2-} in solution

$Si(OH)_4$ was determined spectrophotometrically (λ_{max} 810 nm) as the reduced blue molybdosilicic acid complex [11]. Single use plastic cells of 10 mm pathlength were used. Calibration curves using standards prepared from a certified Si stock solution (1000 mg/L; Perkin–Elmer) were plotted for both semi-micro (1.5 mL) and standard (4.0 mL) cuvettes. Confidence limits (95%) for nine replicates at two different [Si] were: 0.6 mg/L Si – 0.603 ± 0.004 mg/L and 0.2 mg/L Si – 0.194 ± 0.003 mg/L.

Al was determined by graphite furnace atomic absorption spectrometry (GFAAS) using matrix-matched standards and a programme developed by the authors [12].

Total F^- was measured using an ion selective electrode (Sentek, UK) calibrated against standard solutions containing 0.1–100 mg/L F^-. It was measured by the method of standard additions after mixing the sample with total ionic strength adjustment buffer which included 15 g/L *trans*-1,2-diaminocyclohexane-*N*,*N*,*N*′,*N*′-tetraacetic acid monohydrate (CDTA) and 58 g/L NaCl in acetate buffer at pH 5.0.

Total HPO_4^{2-} was measured spectrophotometrically (λ_{max} 880 nm) as the blue heteropoly complex [13].

2.3. Elemental composition of solid phases

Electron microprobe analysis was conducted on a Cameca SX100 electron probe microanalyser. Ground samples were pressed into pellets and the contents of Si, Al, F and P were determined for 20 different 5 μm spots on each pellet. Average atomic percentages were calculated for each sample ($n = 20$, RSD $\leqslant 5\%$ for Al and Si) and normalized to Si = 1 (Table 1).

2.4. Solid state NMR

Solid state magic angle spinning (MAS) NMR was performed on a Varian UNITY Inova spectrometer with a 7.05 T Oxford Instruments magnet. Three probes have been used. The diameters of rotors are: 7.5 mm (Varian; ^{29}Si), 5 mm (Doty Scientific; ^{19}F with proton decoupling) and 4 mm (Varian; ^{27}Al, ^{31}P). Spin rates used were 5 kHz with the 7.5 mm probe, 11.6 kHz for the 5 mm probe and 10–14 kHz for the 4 mm probe. The frequencies for the individual nuclei are: ^{27}Al, 78.1; ^{29}Si, 59.6; ^{19}F, 282.1; ^{31}P, 121.4 MHz. Chemical shifts were referenced to: ^{27}Al, 1 M $AlCl_3$; ^{29}Si, $(CH_3)_4Si$; ^{19}F, $CFCl_3$; ^{31}P, 85% H_3PO_4. All spectra were obtained with direct-polarisation experiments and with 90° excitation pulses except for ^{27}Al where a 20° pulse was used. Recycle delays of 60–120 s were used for the ^{29}Si spectra, 1 s for the ^{19}F, 0.2 s for ^{27}Al and 60 s for ^{31}P.

3. Results

3.1. Influence of fluoride, F^-

Dialysis and membrane filtration were used to discriminate between HAS formed in the absence of F^- and HAS formed in the presence of equimolar F^- and $Si(OH)_4$. For each of the parent solutions the inclusion of F^- significantly increased dialysable $[Si(OH)_4]$ and [Al] whereas $[F^-]$ following filtration were reduced. For example, for parent solutions which included (in mmol/L) 1.0Si/2.0Al ± 1.0F dialysable $[Si(OH)_4]$ and [Al] were, respectively, 73 and < 1 μmol/L in the absence of F^- and 141 and 66 μmol/L in the presence of F^- whereas the $[F^-]$ following filtration had fallen from 1.0 mmol/L to 404 μmol/L (Table 1). Precipitates were collected by filtration from each combination of Al, $Si(OH)_4$ ± F^- except where the stoichiometry of the parent solution was 2.0Si/0.5Al/2.0F where no filterable precipitate was formed. Chemical composition using electron microprobe analysis confirmed the presence of F^- in solid phases (Table 1) and suggested the formation of HAS_A (Si:Al ca. 0.5) and HAS_B (Si:Al ca. 1.0) for parent solutions in which $[Al] \geqslant [Si(OH)_4]$ and $[Al] < [Si(OH)_4]$, respectively [6]. Solid phase Si:Al ratios which were significantly lower than 0.5, for example the parent solution of stoichiometry 0.5Si/2.0Al 0.5F, suggested that precipitates were composed of both HAS_A- and $Al(OH)_{3(s)}$-like phases. Solid state NMR (^{27}Al, ^{29}Si, ^{19}F) of precipitates (Figs. 2–4) identified the formation of $Al(OH)_{3(s)}$ (^{27}Al δ_{max} 0–10 ppm), HAS_A (^{27}Al δ_{max} 0–3.4 ppm and ^{29}Si δ_{max} ca. −78 ppm) and HAS_B (^{27}Al δ_{max} 0–3.4 ppm + ca. 55 ppm and ^{29}Si δ_{max} ca. −90 ppm) [6,14] and the incorporation of F^- (^{19}F δ_{max} −150 and −131 ppm) into solid phases [15] (Table 2).

3.2. Influence of phosphate, HPO_4^{2-}

The concentrations of filtered $Si(OH)_4$ were extremely high in solutions containing equimolar $Si(OH)_4$ and HPO_4^{2-} and, in all but one of the parent solutions

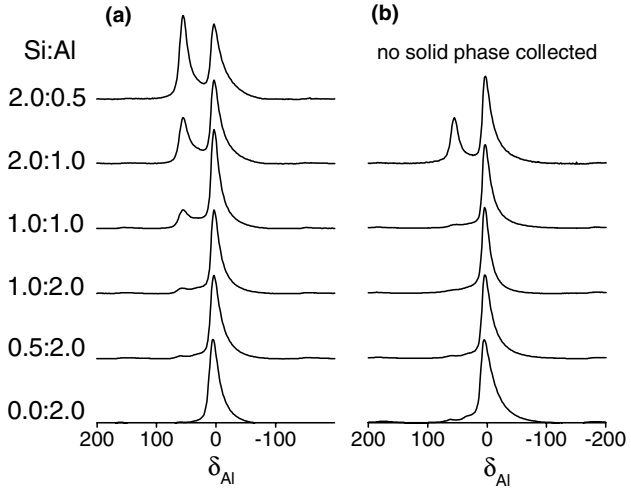


Fig. 2. ^{27}Al MAS NMR spectra of solid phases prepared in the absence (a) and presence (b) of F^-. Si:Al – indicates the concentrations of $Si(OH)_4$ and Al in parent solutions. For (b) $[F^-] = [Si(OH)_4]$ except, if $[Si(OH)_4] = 0$, then $[F^-] = 0.5$ mmol/L.

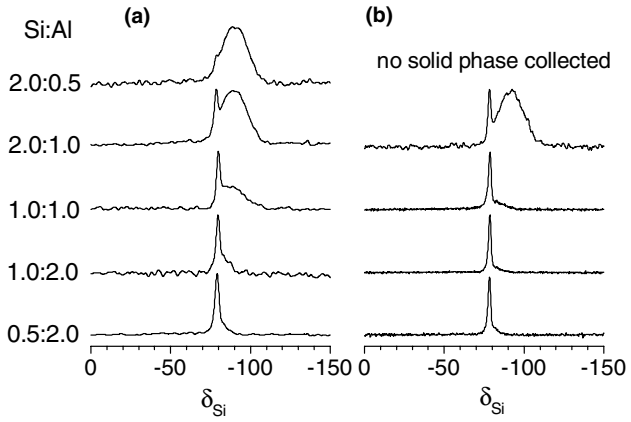


Fig. 3. ^{29}Si MAS NMR spectra of solid phases prepared in the absence (a) and presence (b) of F^-. Si:Al – indicates the concentrations of $Si(OH)_4$ and Al in parent solutions. For (b) $[F^-] = [Si(OH)_4]$.

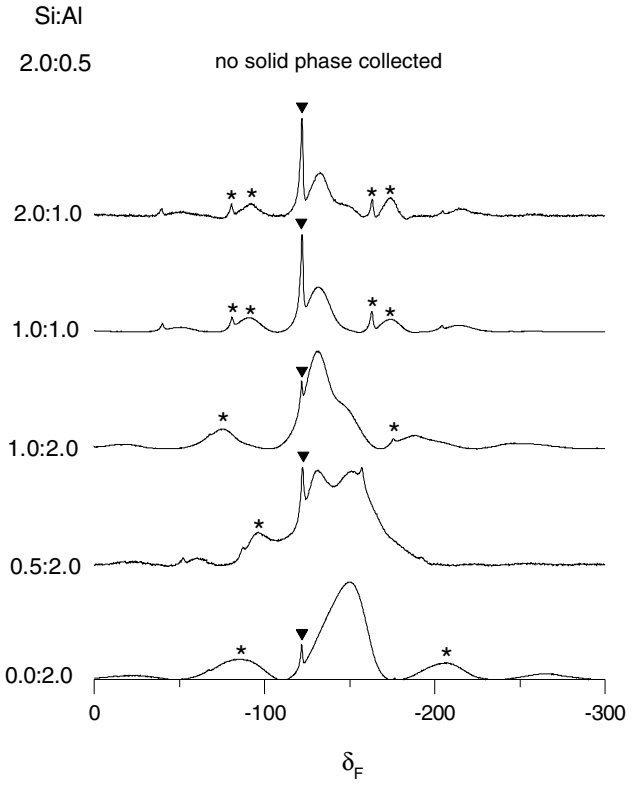


Fig. 4. ^{19}F MAS NMR spectra of solid phases prepared in the presence of F^-. Si:Al – indicates the concentrations of $Si(OH)_4$ and Al in parent solutions. $[F^-] = [Si(OH)_4]$ except, if $[Si(OH)_4] = 0$, then $[F^-] = 0.5$ mmol/L. Asterisks mark positions of sidebands and inverted triangles mark the position of chemical shift corresponding to contaminating PTFE.

(0.5Si/2.0Al/0.5P), showed that very little $Si(OH)_4$ was precipitated in solid phases (Table 1). All Al was precipitated from each of the parent solutions whereas the concentrations of soluble HPO_4^{2-} in equilibrium with solid phases loosely reflected the Al:P ratio of parent solutions. Chemical composition of precipitates using electron microprobe analysis confirmed the results of the solution studies and suggested that Al was precipitated as hydroxyaluminium phosphate from each of the parent solutions (Table 1). Si was only found as a significant component of the solid phase (Si:P ca. 0.5) when the concentration of Al in the parent solution exceeded the combined concentration of $Si(OH)_4$ and HPO_4^{2-} (2.0Si/0.5Al/2.0P). Solid state NMR (^{27}Al, ^{29}Si, ^{31}P) of this precipitate confirmed the formation of an hydroxyaluminium phosphate (^{27}Al δ_{max} 0.4 ppm; ^{31}P δ_{max} −10.6 ppm) and the probable 'contamination' of this phase with a small amount of HAS_A (^{29}Si δ_{max} −78.6 ppm) (Table 2).

4. Discussion

Dialysis demonstrated that HAS formed in the presence of equimolar F^- and $Si(OH)_4$ were in equilibrium with significantly higher concentrations of dialysable $Si(OH)_4$ and Al. The high concentrations of dialysable Al were most probably due to the formation of soluble complexes of aluminium fluoride and, possibly, hydroxyaluminium fluorides [16]. The assumption must be that whilst these complexes remain in solution there will be no opportunity for $Si(OH)_4$ to condense across hydroxyl groups on adjacent Al atoms to form HAS. As such the concomitant higher concentrations of dialysable $Si(OH)_4$ were probably indicative of F^- limiting the availability of hydroxyaluminium templates for the subsequent formation of HAS. The propensity for F^- to react with Al to form soluble complexes and so prevent the formation of HAS was best exemplified in the parent solution which included (in mmol/L) 2.0Si/0.5Al/2.0F in which approximately 50% of the original Al was dialysable and, consequently, no solid phase could be separated following filtration (Table 1). However, this was the only stoichiometry which appeared to prevent the formation of HAS and in each of the other parent solutions the evidence pointed towards the incorporation of F^-

Table 2
Assignments and abundances of ^{27}Al, ^{29}Si, ^{19}F and ^{31}P MAS NMR chemical shifts for each solid phase

Stoichiometry of parent solution (mmol/L)				$\delta^{27}Al$		$\delta^{29}Si$		$\delta^{19}F$		$\delta^{31}P$
Si	Al	F	P	Al^{IV}	Al^{VI}	$Q^3(3Al)$	$Q^3(1\text{-}2Al)$	$Al(OH)_3$–F	HAS–F	PO_4
0.5	2.0				2.5 (100%)	−79.1 (47%)	−81.1 (53%)			
0.5	2.0	0.5			2.7 (100%)	−78.2 (85%)	−82.1 (15%)	−151.1	−131.6	
0.5	2.0		0.5		0.4 (100%)	−78.6 (54%)	−85.0 (46%)			−10.6 (100%)
1.0	2.0				2.5 (100%)	−79.6 (38%)	−82.3 (62%)			
1.0	2.0	1.0			3.4 (100%)	−78.6 (83%)	−81.7 (17%)	−150	−131.1	
1.0	1.0			53.8 (8%)	2.5 (92%)	−79.9 (23%)	−88.8 (77%)			
1.0	1.0	1.0			2.7 (100%)	−78.7 (63%)	−82.1 (37%)		−131.9 (100%)	
2.0	1.0			55.0 (28%)	2.5 (72%)	−78.6 (7%)	−90.3 (93%)			
2.0	1.0	2.0		54.6 (31%)	2.1 (69%)	−78.3 (8%)	−91.7 (92%)		−132.8 (100%)	
2.0	0.5			55.0 (40%)	2.5 (60%)	−78.7 (1%)	−90.9 (99%)			
	2.0				5.0 (100%)					
	2.0	0.5			10.0 (100%)			−150.1 (100%)		

into the solid phase and more particularly into HAS. To understand how F^- influenced HAS formation it is informative to compare solid phases formed for each parent solution stoichiometry in the absence and presence of fluoride.

(i) *0.5Si/2.0Al ± 0.5F* – In the absence of F^- the solid phase was predicted to be a mixture of HAS_A and $Al(OH)_{3(s)}$ and this was borne out by a Si:Al ratio of 0.27 in the solid phase. Further confirmation of the presence of HAS_A was that all Al was present in octahedral geometry (^{27}Al δ_{max} 2.5 ppm) and Si was present in equal mixture of $Q_3(3Al)$ (^{29}Si δ_{max} −79.1 ppm) and $Q_3(2Al)$ (^{29}Si δ_{max} −81.1 ppm). In the presence of F^- the Si:Al ratio of the solid phase was 0.25 which again suggested a mixed phase. Interestingly, the ratios of Si:F and Al:F in the solid phase were ca. 2.0 and 8.5, respectively, and these may prove to be helpful in identifying the location of F in the solid phases. Again all Al was in octahedral geometry (^{27}Al δ_{max} 2.7 ppm) and the presence of HAS_A was confirmed by Si NMR, though this time the proportion of $Q_3(3Al)$ (^{29}Si δ_{max} −78.2 ppm) was very much higher than $Q_3(2Al)$ (^{29}Si δ_{max} −82.1 ppm). ^{19}F NMR gave δ_{max} at −151.1 ppm, which, based upon the chemical shift (^{19}F δ_{max} −150.1 ppm) we obtained for a pure precipitate of aluminium hydroxyfluoride, was probably indicative of F associated with $Al(OH)_{3(s)}$, and −131.6 ppm which we believe showed F associated with HAS_A.

(ii) *1.0Si/2.0Al ± 1.0F* – In the absence of F^- the solid phase was predicted to be primarily HAS_A and this was supported by a Si:Al ratio of 0.43 and characteristic chemical shifts for both ^{27}Al NMR (δ_{max} 2.5 ppm) and ^{29}Si NMR (δ_{max} −79.6 and −82.3 ppm). In the presence of F^- the Si:Al ratio of the solid phase was 0.41 which was indicative of HAS_A and the Si:F and Al:F ratios were ca 2.0 and 5.5, respectively. The lower ratio of Al to F in this phase was probably indicative of a higher $[F^-]$ to [Al] in the parent solution whereas this effect was limited by a significant reduction in the proportion of aluminium hydroxyfluoride in the mixed phase as was suggested by the almost complete disappearance of the ^{19}F NMR chemical shift at ca. −150 ppm. Solid state ^{27}Al, ^{29}Si and ^{19}F NMR showed that this precipitate was almost identical to that isolated from the previous parent solution (0.5Si/2.0Al/0.5F) except that the majority of F was now associated with HAS_A (^{19}F NMR δ_{max} −131.1 ppm).

(iii) *1.0Si/1.0Al ± 1.0F* – In the absence of F^- the solid phase was predicted to be HAS_A with perhaps some HAS_B and the latter was borne out by a Si:Al ratio of 0.63. Again the presence of a proportion of HAS_B was supported by both ^{27}Al NMR, which indicated a small amount of Al in tetrahedral geometry (^{27}Al NMR δ_{max} 53.8), and ^{29}Si NMR which showed that Si was now coordinated through both $Q_3(3Al)$ and $Q_3(1\text{-}2Al)$ linkages [6]. The presence of F^- appeared to reverse the trend towards the formation of HAS_B such that structural (NMR) and compositional (microprobe) analyses of the solid phase showed that it was approximately identical to that precipitated from the previous parent solution (1.0Si/2.0Al/1.0F).

Thus in spite of quite obvious differences in the solid phases formed in the absence of added F^- the structure and composition of HAS formed in its presence were approximately identical, probably an HAS_A-like structure which included F in a single chemical environment (^{19}F NMR δ_{max} ca. −131 ppm) at a Si:F ratio of ca. 2–3 and Al:F ratio of ca. 5–6.

(iv) *2.0Si/1.0Al ± 1.0F* – In the absence of F^- the solid phase was predicted to be predominantly HAS_B and some HAS_A. The Si:Al ratio of the solid phase, ca. 0.94, confirmed the presence of the former and this was supported further by solid state ^{27} Al and ^{29}Si NMR which showed that Al was present in both octahedral (δ_{max} 2.5 ppm) and tetrahedral (δ_{max} 55.0 ppm) geometries and that Si was coordinated primarily through $Q_3(1\text{-}2Al)$ linkages (δ_{max} −90.3 ppm). Microprobe and NMR characterisation of the solid phase which formed in the presence of F^- showed that in respect of both Al and Si it was identical to that formed in the absence of F^-. This was unusual in that for previous parent solutions the additional presence of F^- had always resulted in structural changes manifested as increases in the proportion of $Q_3(3Al)$ linkages relative to $Q_3(1\text{-}2Al)$. No such changes occurred when F was incorporated into the predominantly HAS_B-like phase precipitated from this parent solution. However, the ^{19}F NMR chemical shift at δ_{max} −132.8 ppm was similar to those obtained for substitution of F^- into HAS_A-like structures (−131.6, −131.1 and −131.9 ppm) and this may indicate that F was present in a similar chemical environment in both HAS structures. The solid phase was different from the F-containing HAS_A -like solid phases in that the ratio's of Si:F (ca. 4) and Al:F (ca. 4) showed an increase in Si and a decrease in Al relative to F when compared with HAS_A-F. These apparently contradictory changes in the content of F in the solid phase relative to both Si and Al may actually be informative in respect of the mechanism of formation of HAS_B via HAS_A For example, it was assumed that the solid phase which formed in the absence of F^- was a mixture of HAS_B and HAS_A and this was supported by NMR. However, the Si:Al ratio of this 'mixed' phase was very close to 1.0 and this may indicate that the predominant forms of HAS were actually HAS_B (ca. 60% of the total) and an intermediate form HAS_{AB} (ca. 40% of the total) in which the further incorporation of $Si(OH)_4$ has not yet triggered the dehydroxylation reaction which would result in 50% of its constituent Al switching from an octahedral to a tetrahedral geometry (Fig. 5). It is our understanding to date that the rate at which dehydroxylation takes place is highly dependent upon the $[Si(OH)_4]$ which is free to

exchange with the solid phase. In the presence of F^- the Si:Al ratio of the mixed solid phase was very close to 1.0 whilst the NMR again suggested that Al was predominantly present in octahedral coordination. In addition, the presence of F^- in the parent solution did not influence the coordination of Si in the solid phase. In each of the previous parent solutions the presence of F^- promoted the coordination of Si through Q_3(3Al) as opposed to Q_3(1-2Al) linkages. Considering that this was the first parent solution in which $[F^-] > [Al]$ it is conceivable that a higher proportion of Al–OH will be replaced by Al–F in the solid phase and this would explain the observed increase in the ratio of F to Al. The reason why the F to Si ratio was concomitantly reduced could be that the HAS_B structure only has one potential binding site for F and this is associated with octahedrally coordinated Al in this structure whilst HAS_{AB}, which only includes octahedral Al, retains two potential binding sites for F. In this way, considering the relative proportions of HAS_B and HAS_{AB} in the solid phase, it was possible for the ratio of F to Si to be reduced and the ratio of F to Al to be increased relative to solid phases which were formed from parent solutions in which $[Al] \geqslant [F^-]$, the predominant precipitate would be HAS_A and the lower $[F^-]$ would dictate that Al–OH groups on this phase would only be partially substituted for Al–F.

(v) *2.0Si/0.5Al ± 2.0F* – In the absence of F^- a solid phase was precipitated with a Si:Al ratio of 1.1 and NMR chemical shifts which demonstrated that it was composed of at least 80% HAS_B. We would contend that the remainder was HAS_{AB} and that the higher proportion of tetrahedrally coordinated Al in this mixed phase was the result of an accelerated dehydroxylation reaction which was fuelled by a high concentration of free to exchange $Si(OH)_4$ (ca. 850 μmol/L as compared to ca. 600 μmol/L for the 2.0Si + 1.0Al parent solution). In the presence of F^- we were not able to collect any solid phase and this may have been due to the fourfold excess of F^- preventing the formation of hydroxyaluminium templates required for HAS formation or possibly the substitution of F into preformed HAS_B such that it prevented the aggregation of the solid phase towards a filterable size.

To try to identify the location of F in our HAS we have carried out F–Si CP NMR and we obtained the same spectrum as for DP NMR. The most likely explanation for this is that F was not specifically associated with Si and that the ^{19}F NMR chemical shift in the range −131 to −133 ppm was due to Al–F with Al being linked to Si through varying combinations of Q_3(1-3Al). We obtained further support for this possibility by carrying out F–Al CP NMR which strongly suggested that, not only was F coordinated through Al but that it was only associated with octahedral Al. The association of F with Al and not with Si was again supported by the observation that concomitant with an increase in the Si:Al ratio of the solid phase was an increase in the Si:F ratio and the propensity for F in the solid phase to promote the characteristic HAS_A (^{29}Si NMR δ_{max} −78 ppm) structure. Thus F^- may be competitive with $Si(OH)_4$ in inhibiting/promoting the formation of HAS_B via the putative intermediate HAS_{AB}. This competitive edge to F^- was lost when the rapid formation of HAS_B (via HAS_{AB}) was favoured (i.e., where the $[Si(OH)_4]$ of the parent solution was at least double that of the [Al]) and under these conditions the substitution of F for OH would be limited by the $Si(OH)_4$-directed dehydroxylation reaction in which up to 50% of octahedrally coordinated Al rearranges to give tetrahedrally coordinated Al in the solid phase. The probable role of F^- in the formation of HAS is summarised in the scheme in Table 3. It predicts the formation of a number of different solid phases which though unlikely to be

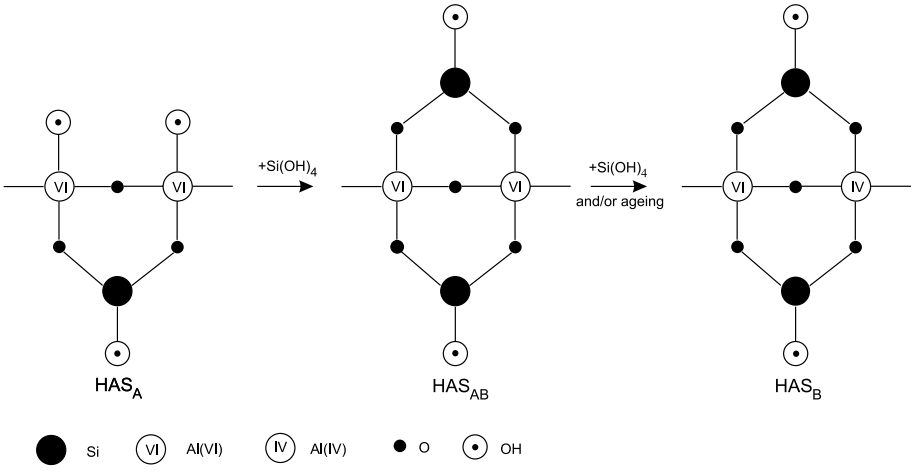


Fig. 5. Suggested scheme for the formation of HAS_B from HAS_A involving a transitional form, HAS_{AB}, which undergoes a dehydroxylation fuelled by either ageing or a significant excess of $Si(OH)_4$.

Table 3
Summary of the suggested role of fluoride in the formation of fluoride-substituted hydroxyaluminosilicates

Conditions	Reactants		Solid phase	Elemental ratio
$[F^-] < [Al]$ $[Si(OH)_4] = 0$	$Al^{3+}_{(aq)} + F^-_{(aq)}$	$\xrightarrow{OH^- \rightarrow pH\ 6.0}$	$Al_4(OH)_{12-x}F_x$	Al:F < 2.0
$[F^-] < [Al]$ $[Si(OH)_4] \leqslant [Al]$	$Al^{3+}_{(aq)} + F^-_{(aq)} + Si(OH)_4$	$\xrightarrow{OH^- \rightarrow pH\ 6.0}$	$(HAS_A)_4F$	Al:F = 8.0 Al:Si = 0.5 Si:F = 4.0
$[F^-] > [Al]$ $[Si(OH)_4] > [Al]$	$Al^{3+}_{(aq)} + F^-_{(aq)} + Si(OH)_4$	$\xrightarrow{OH^- \rightarrow pH\ 6.0}$	$(HAS_{AB})_4F_2$[a]	Al:F = 4.0 Al:Si = 1.0 Si:F = 4.0
$[F^-] < [Al]$ $[Si(OH)_4] > [Al]$	$Al^{3+}_{(aq)} + F^-_{(aq)} + Si(OH)_4$	$\xrightarrow{OH^- \rightarrow pH\ 6.0}$	$(HAS_B)_4F$	Al:F = 8.0 Al:Si = 1.0 Si:F = 8.0

[a] In the presence of an excess of $Si(OH)_4$ this phase will undergo a slow dehydroxylation in which up to 50% of the constituent Al adopts tetrahedral geometry and F will be titrated from the solid phase. The resulting phase will be a mixture of $(HAS_{AB})_4F_{2(s)}$ and $(HAS_B)_4F_{(s)}$.

precipitated as single phases are not too dissimilar in elemental composition and structure to those we have identified and characterised herein (Tables 1 and 2).

Further research will be required to understand fully the mechanism of formation of fluorine-substituted HAS whereas under the conditions used in this study HPO_4^{2-}, when equimolar to $Si(OH)_4$, prevented HAS formation in all but one of the parent solutions. When Al was present to a fourfold excess of HPO_4^{2-} (0.5Si/2.0Al/0.5P) the resulting solid phase included primarily aluminium hydroxyphosphate [17] but it also contained a significant component of HAS_A. Phosphate is a bulky ligand in comparison to F^- and its ligation by Al was generally sufficient to promote the precipitation of an hydroxyphosphate and to prevent any reaction of $Si(OH)_4$ across any remaining Al–OH groups. Whether HPO_4^{2-} would be competitive when $Si(OH)_4$ was present to excess remains to be determined.

In the experiments described herein both F^- and HPO_4^{2-} were present at equimolar concentration to $Si(OH)_4$ and, as such, were given maximal opportunity to influence the formation of HAS. The results have identified the formation of fluorine-substituted HAS, which may have some significance to both the biogeochemistry of Al and also to materials science, and the inhibition of the formation of HAS by HPO_4^{2-}. In the natural environment the concentration of $Si(OH)_4$ is likely to be significantly in excess of both F^- and HPO_4^{2-} and further experiments using more environmentally realistic concentrations of these ligands will be needed to confirm that fluorine-substituted HAS could form in soil and surface waters and similarly that HPO_4^{2-} might prevent or influence HAS formation.

Acknowledgements

This research was funded by NERC. D.C. Apperley is thanked for all his help with the solid state NMR which were obtained through the EPSRC solid state NMR service at Durham. D. Plant is thanked for electron microprobe analyses which were obtained through the NERC-supported Electron Microprobe Facility at Manchester.

References

[1] C. Exley, J.D. Birchall, Polyhedron 11 (1992) 1901.
[2] C. Exley, J.D. Birchall, Polyhedron 12 (1993) 1007.
[3] W.L. Polzer, J.D. Hem, H.J. Gabe, US Geol. Surv. Prof. Paper B 575 (1967) B128.
[4] C. Exley, C. Schneider, F.J. Doucet, Coord. Chem. Rev. 228 (2002) 127.
[5] T.W. Swaddle, Coord. Chem. Rev. 219 (2001) 665.
[6] F.J. Doucet, C. Schneider, S.J. Bones, A. Kretchmer, I. Moss, P. Tekely, C. Exley, Geochim. Cosmochim. Acta 65 (2001) 2461.
[7] F.J. Doucet, M. Rotov, C. Exley, J. Inorg. Biochem. 87 (2001) 71.
[8] P.F. Barron, M.A. Wilson, A.S. Campbell, R.L. Frost, Nature 299 (1982) 616.
[9] C. Exley, J. Inorg. Biochem. 97 (2003) 1.
[10] C. Schneider, F. Doucet, S. Strekopytov, C. Exley, Polyhedron 23 (2004) 3185.
[11] Department of the Environment, Silicon in Waters and Effluents, HMSO, London, 1980.
[12] C. Schneider, C. Exley, J. Inorg. Biochem. 87 (2001) 45.
[13] J. Murphy, J.P. Riley, Anal. Chim. Acta 27 (1962) 31.
[14] S. Hiradate, Soil Sci. Plant Nutr. 50 (2004) 303.
[15] J.M. Miller, Prog. Nucl. Magn. Reson. Spectrosc. 28 (1996) 255.
[16] R.B. Martin, Biochem. Biophys. Res. Commun. 155 (1988) 1194.
[17] L.-O. Öhman, R.B. Martin, Clin. Chem. 40 (1994) 598.

those observed in the humic substances. Previous studies have shown that polyphenols and notably flavonoids are non-negligible components of organic matter [2–5]. For this reason, we have considered the flavonoids' family, belonging to the polyphenolic compounds, which are molecules that occur ubiquitously in plant kingdom. The flavonoids are characterized by a common structure, in C6–C3–C6, in which two benzene rings are connected by a carbonaceous chain C3, different according to nature from the compounds. Thus, the family of flavonoids is subdivided in various groups among which one can quote: flavones and derived, anthocyanes, chalcones, aurones, etc. [6–8]. The basic skeleton common to the elements of the flavones group is constituted of two benzene rings A and B connected to each other by an oxygenated heterocycle: the γ-pyrone ring (C ring). The simplest compound of the group is the flavone (Fig. 1).

These omnipresent molecules in the natural environment are found partially in the beginning of the organic matter of the soil and thus constitute perfect model molecules for the study and the comparison of the different metal complexation sites. The complexes composition obtained from these compounds with a large number of metal ions are reported in the literature [9–18], but so far no information was published concerning the chelation of lead (II). The main chelating sites involving in these compounds are the catechol, α-hydroxy-carbonyl and β-hydroxy-carbonyl functions.

In this work, we report the lead (II) complexation study with three ligands presenting only one binding site: 3-hydroxyflavone (3HF), 5-hydroxyflavone (5HF) and 3′,4′-dihydroxyflavone (3′4′diHF) (Table 1). The goals of this study are: (i) to determine the stoichiometric composition and estimate the stability of each complex obtained with these three ligands; (ii) to class the different sites according to their ability to form chelate with lead (II) in order to obtain complementary information concerning the potential chelating sites of Pb(II) in humic substances; and (iii) to compare the results with those obtained in ours previous studies concerning the chelation of Al(III) [19–23].

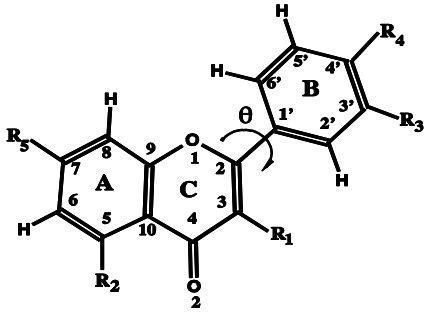


Fig. 1. Structure and atomic numbering (IUPAC nomenclature) of flavonoid.

Table 1
Substitution pattern of studied flavonoids

Compound	Abbreviation	R1	R2	R3	R4	R5
3-Hydroxyflavone	3HF	OH	H	H	H	H
5-Hydroxyflavone	5HF	H	OH	H	H	H
3′,4′-Dihydroxyflavone	3′4′diHF	H	H	OH	OH	H
Quercetin	Q	OH	OH	OH	OH	OH

2. Experimental

2.1. Reagents and methods

Flavonoids (F) were purchased from Extrasynthese (France). Anhydrous lead chloride was used without purification. Because of the very low solubility of flavonoids in water, spectroscopic-grade methanol was used.

The molar ratio method has allowed us to determine the complexes composition in solution from spectrophotometric spectra. For this method, solutions containing a constant concentration (4×10^{-5} M) of F in methanol and variable concentration of $PbCl_2$ (from 4×10^{-7} to 4×10^{-2} M) were prepared. The complexes stoichiometry has also been verified by the method of continuous variation (Job's method).

2.2. Instrumentation

The UV–Vis spectra were recorded on a Cary-l (Varian) spectrophotometer with cells of 1 cm path length, at room temperature. A flow cell was used to allow successive additions of small amounts of lead (II) chloride directly in the flavonoid solution.

2.3. Calculations

The formation constants of the complexes were estimated by using a multivariate data analysis program for modelling and fitting equilibrium titration 3D data sets obtained from the spectrophotometric measurements. The UV–Vis spectra were refined using the Specfit software (version 3.0.32). The set of spectra obtained at variable Pb(II) concentration were treated by evolving factor analysis (EFA) method in order to determine the number of absorbing species in the system and the pure electronic spectrum of each complex [24]. The Specfit software [25] has also been used to estimate the stability constants (β). In order to obtain the best fit between the complexation model and the experimental data, several models of complexes with different stoichiometries have been envisaged for the refinement of the stability constants.

2.4. Methodology

The same methodology which was applied for the study of the complexation of the three ligands is as follows:

(i) The study by UV–Vis spectroscopy of the lead complexation with a ligand (F) in methanol by varying the $[PbCl_2]/[F]$ molar ratio, gives us a set of spectra. The stoichiometry of the formed complexes is determined by the molar ratio method. The curve representing the variation of the absorbance according to the ratio $R = [Pb(II)]/[F]$ at absorption maxima of the complex and the free molecule is representative of the complex composition [26].

(ii) The Job's method was used to validate the molar ratio method. In the Job's method, for a constant volume, one mixes in different proportions equimolar solutions of ligand and lead (II). The sum of the concentrations remains constant, while the molar fraction of the ligand varies. The results obtained from this method provide us one second set of spectra. Here, the stoichiometry corresponds to the change of slope of the variation curve representative to the molar fraction of ligand x_F or the Job's function $[A(\lambda_{max})_{complexed\ solution} - A(\lambda_{max})_F]$ [27].

(iii) From electronic spectra obtained by varying the molar ratio R, the determination of the spectroscopically distinct species is obtained by an experimental data processing by using the EFA method. The result of this calculation allows us to find the pure absorption spectrum of the molecule alone and the complexes. In order to determine the stability constants (β) of successively formed complexes, a numerical processing was carried out on a simple model containing Pb(II) metal, the ligand and the complexes. The stability constant estimation comes from the following reaction equation:

$$a\ Pb + b\ F \Longleftrightarrow Pb_aF_b$$

with the corresponding stability constant

$$\beta_F = \frac{[Pb_aF_b]}{[Pb]^a[F]^b}.$$

Whatever the site implied in the complexation process, a deprotonation of hydroxyl groups occurs in order to allow the coordination to Pb(II). However, this deprotonation has not been taking into account in the constant calculation insofar as the pH notion has no much sense in methanoic medium.

(iv) From these constants and extracted spectra, we simulate a theoretical spectroscopic assay and compare this one with the experimental spectra, so as to validate the initial model. Moreover, if several species are formed, the curves of the concentrations evolution can show if the complexes are formed simultaneously or successively.

3. Results and discussion

3.1. Chelation of lead (II) with hydroxyflavones

Typically, the electronic spectra of flavonoids are characterized by two strong absorption bands: the band I in the long wavelength (320–380 nm) and the band II (240–270 nm) [28].

3-Hydroxyflavone. Fig. 2 illustrates the evolution of the UV–Vis spectra of the 3HF–Pb(II) system for different $[Pb^{2+}]/[3HF]$ molar ratios. The intensity of band I, located at 344 nm, of free 3HF decreases with the amount of $PbCl_2$ added, whereas a new band appears at 405 nm. In the same time, the absorbance at 243 nm increases. The presence of an isosbestic point at 365 nm proves the existence of only two absorbing species in equilibrium. The curve of absorbance versus $[Pb^{2+}]/[3HF]$ molar ratio plotted at 344 nm (λ_{max} of free ligand) and 405 nm (λ_{max} of complex) allow us to find a stoichiometry 1:1 for the complex (Fig. 3). The Job's method of continuous variations has confirmed this result (not shown). To estimate the stability constant of the 1:1 complex, a numerical treatment of the electronic spectra has been carried out. The model best fitting the

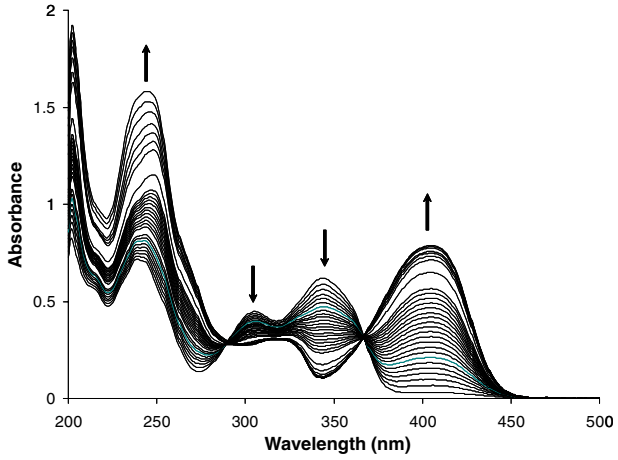


Fig. 2. UV–Vis absorption spectra of 3-hydroxyflavone in methanol in the absence and in the presence of $PbCl_2$. $[Pb^{2+}]/[3HF]$ molar ratios vary from 0 to 3.

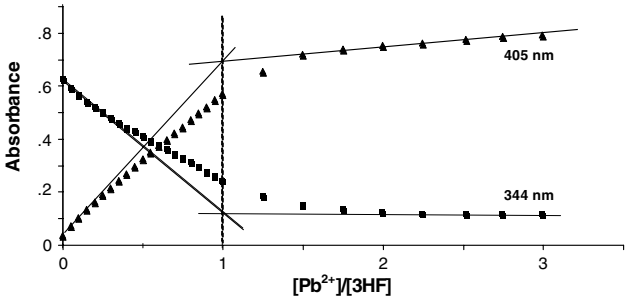


Fig. 3. Absorbance vs. $[PbCl_2]/[3HF]$ molar ratio plots at λ_{max} (3HF) = 344 nm and λ_{max} (complex) = 405 nm.

experimental data gives a stability constant: $\log\beta_{3HF} = 4.97 \pm 4 \times 10^{-6}$. As the chelation of lead occurs at the level of the α-hydroxy-carbonyl group with a complete deprotonation of the hydroxyl group, the formula of the complex is $[(3HF)Pb]^{+}$.

5-Hydroxyflavone. With the addition of lead, the evolution of the electronic spectra of this ligand differs widely from that observed for its homolog the 3HF molecule. The general shape of the free ligand spectrum is not at all modified by the addition of $PbCl_2$, only an increase in the absorbance, more or less important according to the wavelength, is observed (Fig. 4). However, a new band appearing at 241 nm differentiates the spectrum of the complex from that of the free ligand. Both the molar ratio and continuous variations methods give a stoichiometry 1:1 for the complex of 5HF, leading to a chelate $[(5HF)Pb]^{+}$. The treatment of the spectra with Specfit program allows us the determination of the stability constant of this complex: $\log\beta_{5HF} = 4.51 \pm 3 \times 10^{-2}$. So, the comparison of the stability constants indicates that the complex obtained with the 5HF molecule is slightly less stable than the one formed with 3HF.

3′,4′-Dihydroxyflavone. The behaviour of 3′4′diHF in the presence of Pb(II) still differs from that found in the previous compounds. The first spectrum obtained in the absence of Pb(II) is characteristic of the ligand in methanol solution and presents some bands at 343, 306, 244 and 213 nm (Fig. 5). The addition of an increasing quantity of lead chloride to the solution of 3′4′diHF induces a decrease of the intensity of the band at 343 nm relating to the free flavonoid and an appearance of a new band located at 399 nm whose absorbance increases with the quantity of Pb(II) added. The series of spectra does not present a clearly definite isosbestic point, which would tend to mean that several species coexist in solution. The molar ratio plots at 343 and 399 nm (Fig. 6) show inflection at $[Pb^{2+}]/[3'4'diHF] = 0.5$ and 1 (the break at 1 appears clearly on the plot at 399 nm), indicating the formation of two complexes of stoichiometry 1:2 and 1:1. This result is corroborated by the Job's method. From the UV–Vis spectra, the determination of the number of different absorbing species was estimated by the EFA method with the Spectfit software. Three distinct components were found corresponding to the free 3′4′diHF and the two complexed forms $[Pb(3'4'diHF)_2]^{2-}$ and Pb(3′4′diHF). The electronic absorption spectra of these different pure species are presented in Fig. 7. The spectra of the two complexed species are very close, however, an additional intense band located at 237 nm characterizes the Pb(3′4′diHF) form. From these pure species spectra, the stability constants have been estimated and the model which provides the best fit to the experimental data gives: $\log\beta_{3'4'diHF} = 8.82 \pm 0.15$ and $\log\beta_{3'4'diHF} = 5.09 \pm 0.10$ for $[Pb(3'4'diHF)_2]^{2-}$ and Pb(3′4′diHF), respectively. The concentration variations of the free and complexed ligands versus quantity of lead added is illustrated in Fig. 8. The curves show that two complexes are simultaneously formed from the very beginning of the lead addition, however, the Pb(3′4′diHF) species is largely predominant. If the formation of the complex 1:2 is in the minority, it is

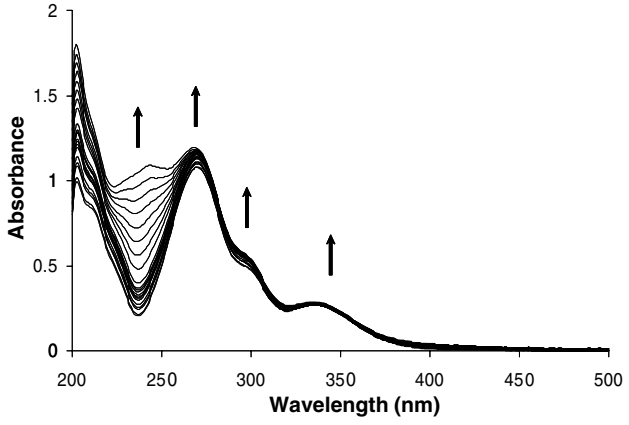


Fig. 4. UV–Vis absorption spectra of 5-hydroxyflavone in methanol in absence and in presence of $PbCl_2$. $[Pb^{2+}]/[5HF]$ molar ratios vary from 0 to 5.

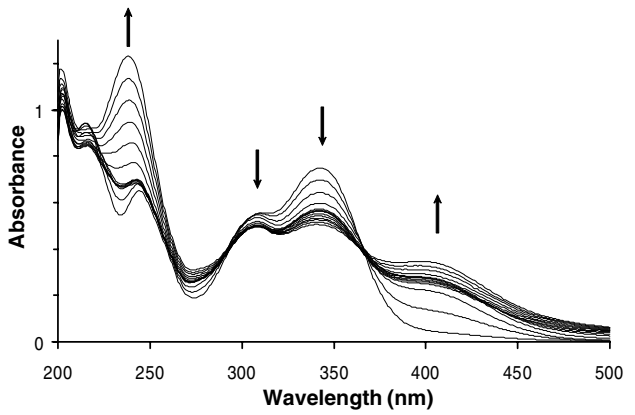


Fig. 5. UV–Vis absorption spectra of 3′,4′-dihydroxyflavone in methanol in absence and in presence of $PbCl_2$. $[Pb^{2+}]/[3'4'diHF]$ molar ratios vary from 0 to 4.

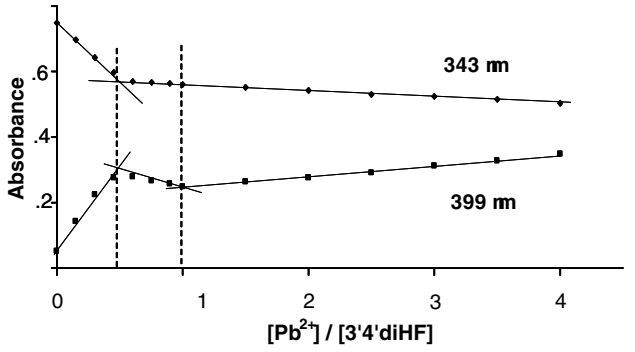


Fig. 6. Absorbance vs. $[PbCl_2]/[3'4'diHF]$ molar ratio plots at λ_{max} (3′4′diHF) = 343 nm and λ_{max} (complex) = 399 nm.

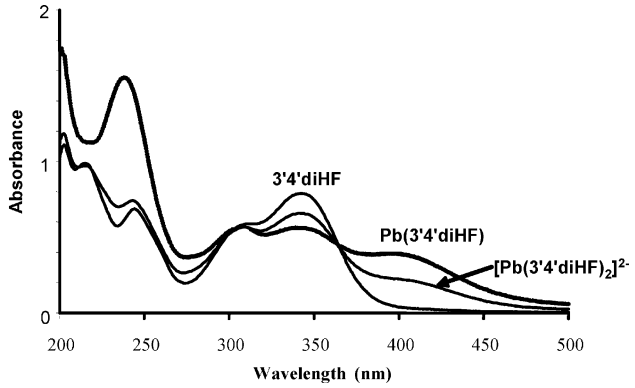


Fig. 7. UV–Vis spectra of the free and two complexed forms of 3′4′diHF extracted using the EFA method.

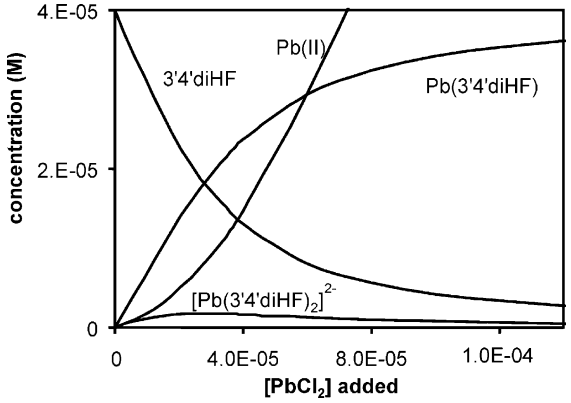


Fig. 8. Distribution curves of the concentration (M) of lead complexes with 3′4′diHF in methanol as a function of $[PbCl_2]$ added.

sufficient to have a significant role in the complexation mechanism of Pb(II) by 3′4′diHF, in particular in the presence of small amounts of lead. The graph also indicates that it remains 32% of free molecules in solution for a molar ratio of 1.

Among the three flavonoids, 3′4′diHF is the only compound which leads to the formation of species of high stoichiometry (1:2) in methanol, and moreover, the stability of its complex 1:1 is higher than those of 3HF and 5HF. These results suggest that the catechol group presents a chelating power with respect to Pb(II) higher than that of other studied functions. Thus, it is possible to classify the three sites of fixation of Pb(II) according to their chelating capacity in the following way: catechol > α-hydroxy-carbonyl > β-hydroxy-carbonyl.

3.2. Comparison of Pb(II)- and Al(III)-hydroxyflavone systems

In a similar way, our preceding works [29] had made it possible to obtain a classification of these three sites with respect to their power of complexation of Al(III), under the same physico-chemical conditions. The comparative results of the two systems are reported in Table 2. It is obviously observed that the behaviour of the three studied sites is very different according to the metal ion implied in the complexation process. With regard to Al(III)-hydroxyflavone systems, it is the α-hydroxy-carbonyl site which presents the greatest affinity for aluminium ion and gives a complex of stoichiometry (metal:ligand) 1:2. The catechol function leads to the formation of a complex 1:1 with Al(III) which has a greater stability than that obtained with the β-hydroxy-carbonyl function. Thus, it is observed that the change of Al(III) by Pb(II) in the system provokes an inversion of the chelating power of the catechol and α-hydroxy-carbonyl sites.

The electronic spectra of the predominant complexes obtained for the three hydroxyflavones with both Al(III) and Pb(II) are presented in Fig. 9. Except for the $[Pb(5HF)]^+$ complex, the electronic spectra of the different complexed species obtained with both Al(III) and Pb(II) exhibit a bathochromic shift of the band I compared to the free molecule spectra. This observation seems to indicate that the complexation mechanism of lead (II) by the β-hydroxy-carbonyl group is very different from that observed with aluminium (III). The hyperchromic effect on the absorption bands of the spectrum of the 5HF solution occurring with the addition of $PbCl_2$ tends to show that low electronic changes at the level of the ligand are generated by complexation. It is interesting to notice that the electronic spectra of the complexes obtained with Al(III) or Pb(II) and the 3HF molecule (which present different stoichiometries but the same charge) are almost similar. That would like to say that the absorption bands of the complexes come from electronic transitions involving only molecular orbitals localized on the ligand, and that no metal–ligand charge transfer is observed.

Table 2
Comparison of the stoichiometry and stability constants of the complexes of hydroxyflavones obtained with Pb(II) and Al(III)

Compounds	λ_{max} (nm)	Pb(II) complexes			Al(III) complexes		
		Pb:L	λ_{max} (nm)	log(β)	Al:L	λ_{max} (nm)	log(β)
3HF	344	1:1	405	4.97	1:2	402	12.3
5HF	270	1:1	268/241	4.51	1:1	397	6.5
3′4′diHF	342	1:2	399	8.82	1:1	384	6.7
		1:1		5.09			

The wavelengths of the band I (in the long wavelength) are given for the free ligand and for all the complexes.

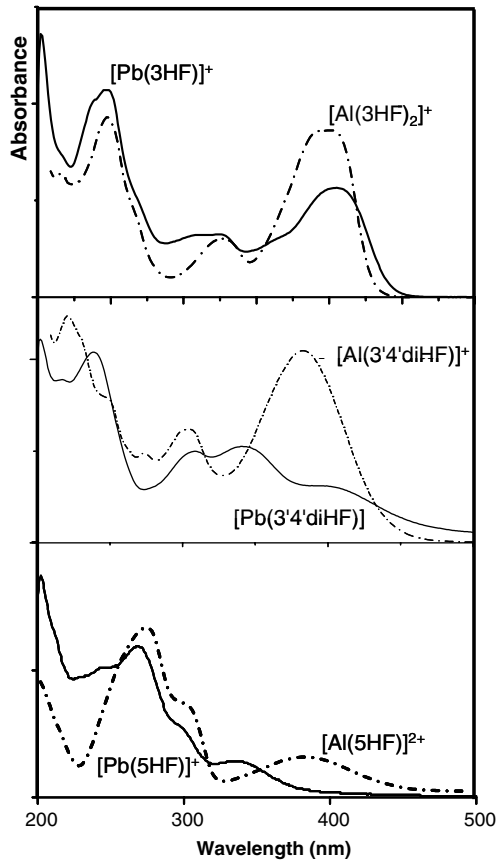


Fig. 9. Comparison of the spectra of the major complexes obtained with Al(III) and lead (II) and hydroxyflavones in methanol.

4. Conclusion

This study made it possible to establish a classification of various chelating sites of humic substances with respect to lead (II) in methanol solution. The interactions between lead (II) and hydroxyflavones had never yet been studied, however, this paper reports the first step of our work. In a second time, we will focus our attention on the complexation mechanism of a molecule presenting simultaneously the functions catechol, α-hydroxy-carbonyl and β-hydroxy-carbonyl: the quercetin molecule (Table 1). That will make it possible to observe if classification obtained with these results remains valid when the three sites are in competition within the same molecule. Moreover, for reasons of solubility this study was carried out in methanol solution. If our preceding studies concerning Al(III) showed that the results obtained in water are comparable with those obtained in methanol, we will study these three molecules in a mixed solvent water–methanol in order to be able to observe the influence of the pH on the capacity of complexation of Pb(II) by these functions.

Acknowledgements

This work is part of the "Programme de Recherche Concertée: Sites et Sols Pollués" supported by the "Région Nord-Pas de Calais" and the "Fonds Européen de Développement Economique des Régions" (FEDER).

References

[1] F.J. Stevenson, Humus Chemistry: Genesis, Composition, Reactions, Wiley, New York, 1982.
[2] C.B. Coulson, R.I. Davies, D.A. Lewis, J. Soil Sci. 11 (1960) 20.
[3] M. Remko, J. Polcin, Collect. Czech. Chem. Commun. 45 (1980) 201.
[4] D.S. Smith, J.R. Kramer, Environ. Int. 25 (1999) 295.
[5] D.S. Smith, J.R. Kramer, Anal. Chim. Acta 416 (2000) 211.
[6] E. Middelton, C. Kandaswami, in: J.B. Harborne (Ed.), The Flavonoids: Advances in Research Since 1986, Chapman & Hall, London, 1994.
[7] L. Bravo, Nutr. Rev. 56 (1998) 317.
[8] E. Middelton, C. Kandaswami, T.C. Theoharides, Pharmacol. Rev. 52 (2000) 673.
[9] G. Speier, V. Fülöp, E. Balogh-Hergovich, Z. Tyeklar, J. Inorg. Biochem. 36 (1989) 329.
[10] G.J. Smith, S.J. Thomsen, K. Markham, C. Andary, D. Cardon, J. Photochem. Photobiol. A 136 (2000) 87.
[11] M. Hauteville, M. Rakotovao, M.C. Duclos, B. Voirin, Phytochemistry 48 (1998) 547.
[12] J. Zhou, L. Wang, J. Wang, N. Tang, J. Inorg. Biochem. 83 (2001) 41.
[13] H. Deng, G.J. Van Berkel, J. Mass Spectrom. 33 (1998) 1080.
[14] J.E. Brown, H. Khodr, R.C. Hider, C.A. Rice-Evans, Biochem. J. 330 (1998) 1173.
[15] P. Hollman, J. Van Trijp, M. Buysman, Anal. Chem. 68 (1996) 3511.
[16] M. Yoshino, K. Murakami, Anal. Biochem. 257 (1998) 40.
[17] M. Katyal, S. Prakash, Talanta 24 (1977) 367.
[18] G. Le Nest, O. Caille, M. Woudstra, S. Roche, F. Guerlesquin, D. Lexa, Inorg. Chim. Acta 357 (2004) 775.
[19] A.C. Boudet, J.P. Cornard, J.C. Merlin, Spectrochim. Acta 56 (2000) 829.
[20] J.P. Cornard, A.C. Boudet, J.C. Merlin, Spectrochim. Acta 57 (2001) 591.
[21] J.P. Cornard, J.C. Merlin, J. Mol. Struct. 569 (2001) 129.
[22] J.P. Cornard, J.C. Merlin, J. Inorg. Biochem. 92 (2002) 19.
[23] J.P. Cornard, J.C. Merlin, Polyhedron 21 (2002) 2801.
[24] H. Gampp, M. Maeder, C.J. Meyer, A. Zuberbühler, Talanta 33 (1986) 943.
[25] Specfit Global Analysis System, Spectrum software Associates, Marlborough, MA, USA.
[26] J.H. Yoe, L. Jones, Ind. Eng. Chem. Anal. Ed. 16 (1944) 11.
[27] P. Job, C. R. Acad. Sci. 180 (1925) 928.
[28] L.J. Porter, K.R. Markham, Phytochemistry 24 (1970) 835.
[29] J.P. Cornard, J.C. Merlin, J. Mol. Struct. 651–653 (2003) 381.

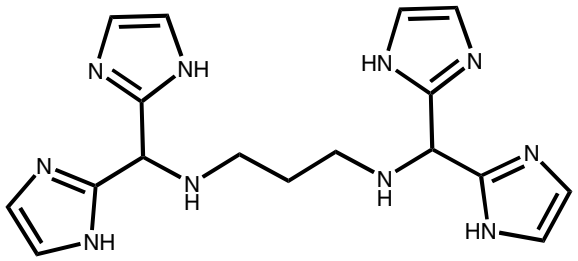


Fig. 1. The molecular structure of the ligand 1,1,7,7-tetrakis(imidazol-2-yl)-2,6 -diazaheptane (H_4L).

field of great interest within the scientific community [6–11].

Since the imidazole is ubiquitous in almost all of the copper proteins, the development of model complexes with imidazole-containing ligands have captured our interest for many years. As a continuation of the study, we present here an investigation of a new copper complex with a potential dinucleating imidazole-containing ligand, 1,1,7,7,-tetrakis(imidazol-2-yl)-2,6-diaza-heptane (H_4L) [12] (see Fig. 1).

Recently, we reported that the reaction of H_4L with $Cu(OAc)_2$ led to an unprecedented imidazolato- and acetato-bridged dodecanuclear complex [12], in which the C–N bonds in the original ligand have been oxidized to C=N bonds upon coordination with copper(II) acetate. However, when $CuCl_2$ is used for the coordination, another interesting 1D tetranuclear-based polymer is formed. In this contribution, the synthesis, crystal structure, spectroscopic and magnetic properties of the copper(II) polymeric compound have been discussed.

2. Results and discussion

The bis(imidazole-2-yl)nitromethane [13] is an interesting intermediate for the synthesis of a variety of new chelating ligands and it can be obtained in five steps by a ring-opening and double ring-closure reaction. Coupling 1,3-diaminopropane with the bis(imidazole-2-yl)-nitromethane intermediate results in the formation of a potential dinucleating ligand H_4L as shown in Fig. 1.

The polynuclear compound of formula $[Cu_4(H_3L)(H_2L)Cl_3(H_2O)_2]Cl_2 \cdot 5H_2O$ was obtained by reaction of one equivalent of the ligand H_4L with three equivalents of copper(II) chloride in acetonitrile. Diethyl ether diffusion into the acetonitrile solution resulted in the formation of blue square crystals suitable for X-ray diffraction analysis. A molecular plot representing one unit of the complex together with the atom-labeling scheme is shown in Fig. 2.

2.1. Description of structure $[Cu_4(H_3L)(H_2L)Cl_3(H_2O)_2]Cl_2 \cdot 5H_2O$

The compound consists of polymeric chains built up by dicationic subunits $[Cu_4(H_3L)(H_2L)Cl_3(H_2O)_2]^{2+}$ containing four metal ions, two nitrogen donor ligands, three coordinated chlorine atoms and two coordinated

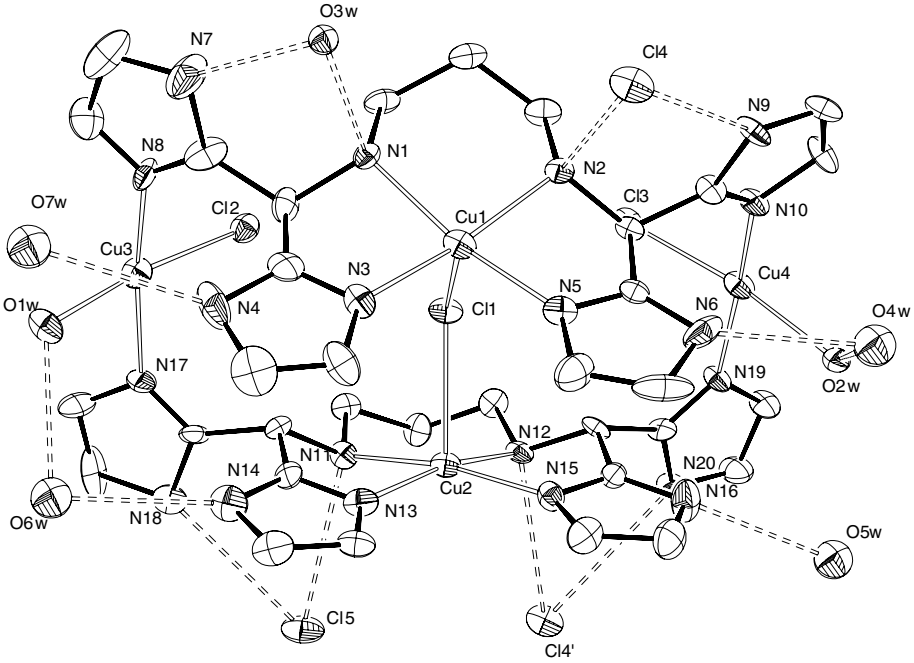


Fig. 2. Thermal ellipsoid plot (20% probability level) of the asymmetric subunit $[Cu_4(H_3L)(H_2L)Cl_3(H_2O)_2]^{2+}$ together with the two chloride counter ions, one chloride ion (Cl4′) from an adjacent subunit and the five crystallization water molecules; the hydrogen atoms have been omitted for clarity. The hydrogen bond network is indicated with dotted double lines.

water molecules. A view of the asymmetric subunit together with the two chloride counter anions and five lattice water molecules is shown in Fig. 2. The Cu1 and Cu2 atoms, both equatorially coordinated by two diamine nitrogens (Cu1–N1 = 2.069(4), Cu1–N2 = 2.061(4) Å; Cu2–N11 = 2.062(4), Cu2–N12 = 2.090(4) Å) and two imidazolate nitrogens (Cu1–N3 = 2.015(4), Cu1–N5 = 1.992(4) Å; Cu2–Nl3 = 2.018(5), Cu2–N15 = 1.986(4) Å), are symmetrically bridged in a square pyramidal configuration by the axial Cl1 chloride (Cu1–Cl1 = 2.576(1) and Cu2–Cl1 = 2.571(2) Å) (N_4Cl donor set, $\tau_1 = 0.013$, $\tau_2 = 0.033$, where $\tau = 0$ and 1 for perfect square-pyramidal and trigonal-bipyramidal geometry [14], respectively). Each ligand bridges to the Cu3 and Cu4 metal ions using two nitrogen atoms of different imidazole rings [Cu3–N8 = 1.959(5), Cu3–N17 = 2.007(5) Å; Cu4–N10 = 1.994(4), Cu4–N19 = 2.015(4) Å] giving rise to a sharing of the two organic ligands between four metal ions. A chloride anion and a water molecule contribute to form an equatorial N_2ClO arrangement around the Cu3 and Cu4 metal centers (Cu3–Cl2 = 2.341(2), Cu3–O1w = 2.244(3) Å; Cu4–Cl3 = 2.320(2), Cu4–O2w = 2.244(3) Å). The coordination environment around Cu3 and Cu4 is completed to square pyramidal by the Cl2 and Cl3 atoms from two neighbouring tetranuclear units (Cu3–Cl2′ = 2.618(2), Cu4–Cl3′ = 2.655(2) Å) (N_2Cl_2O donor set, $\tau_3 = 0.023$ and $\tau_4 = 0.033$). These contacts give rise to a tetranuclear-based polymeric chain. which shows (Fig. 3) an alternate arrangement of dinuclear units in which the copper atoms (Cu1 and Cu2) are connected by a single and symmetric chloride bridge, and other dinuclear units in which the metal centres (Cu3, Cu3′ and Cu4, Cu4′) are linked by two asymmetric chloride bridges. In the dinuclear single bridged moiety the Cu1–Cu2 distance is 4.499(1) Å, while in the dinuclear doubly bridged moieties the copper–copper distance is 3.472(1) Å for Cu3–Cu3′ and 3.491(1) Å for Cu4–Cu4′. The copper atoms Cu1 and Cu2 lie in a plane orthogonal to the planes containing the doubly bridged Cu3–Cu3′ and Cu4–Cu4′ (91.4(1)° and 91.6(1)°, respectively). The Cu···Cu distances between copper ions belonging to different dinuclear moieties, range from 5.843(2) Å to 6.0136(1) Å. Stacking interactions between neutral imidazole rings contribute to the polymeric chain stabilization.

A most unusual feature of the chain of tetranuclear building blocks concerns the charge (and therefore the degree of dehydronation) of the imidazole moieties. In fact (on average, as calculated from 4 Cu(II) ions and 5 chloride ions as much as three H^+ ions from the eight imidazole rings have ionized (all rings involve those coordinated to Cu1 and Cu2). The remaining 5 imidazole acidic hydrogen atoms are disordered and statistically distributed (with SOF = 0.50) over the imidazolate free nitrogens N4 and N6 or N14 and N16. From a stoichiometric point of view in the tetranuclear subunit one ligand is monoanionic and the other is in its dianionic state. It is noteworthy that the imidazolate moieties of the two organic ligands are monodentate. A uninegative behaviour of a ligand similar to that present in our cationic complex, has been reported earlier in the compound $[Cu_6(tidah)_2Cl_{10}(H_2O)_4] \cdot 6H_2O$ where Htidah = 1,1,6,6-tetrakis-(imidazol-2-yl)-2,5-diazahexane [15]. However, in this neutral complex, in which four single and asymmetric chloride bridges play a cooperative role in the metal atoms connection, the dehydronated imidazole ring of each monoanionic tidah ligand acts as a bridging moiety between two copper atoms; all the other undehydronated imidazole rings are monodentate. Bridging behaviours for imidazolate moieties have also been found in the dodecanuclear copper(II) complex $[Cu_{12}(tidhd)_4(MeOH)_8(CH_3COO)_8](MeOH)_{0.8}$ (Htidhd = 1,1,7,7-tetrakis(imidazol-2-yl)-2,6-diaza-1,6-heptadiene) [12] in which all the tidhd ligands are in the dianionic state.

The present polymeric compound is also stabilized by stacking interactions between imidazole moieties and by intermolecular hydrogen bonds. Of the five lattice water

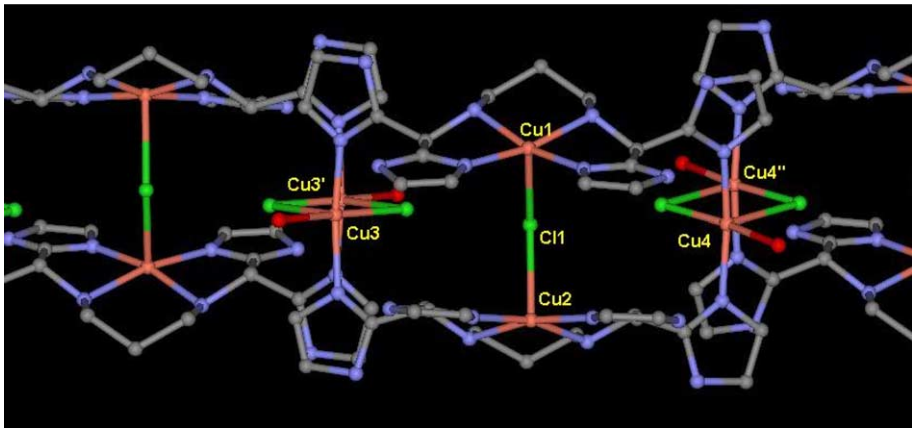


Fig. 3. View of the 1D polymer chains formed by dicationic tetranuclear subunits.

molecules, four interact via O–H···N and O–H···O hydrogen bonds with imidazolate uncoordinated nitrogens (O4w···N6, O5w···N16, O6w···N14, O7w···N4) and coordinated water molecules (O4w···O2w, O6w···O1w). The remaining water molecule and the chloride counter anions are involved, as acceptor atoms, in intermolecular N–H···O and N–H···Cl hydrogen bonds with the N–H groups from amine moieties and undehydronated imidazoles rings (N1···O3w, N7···O3w, N2···Cl4, N9···Cl4, N11···Cl5, N18···Cl5, N12···Cl4′, N20···Cl4′). Weak C–H···Cl interactions contribute to the packing of the chains.

2.2. Electronic properties, ESI-MS and EPR studies

The pattern of the absorption bands in the infrared spectrum of the copper compound is quite different from the free ligand, and some of the ligand bands split or shift as a result of coordination (see Section 2). The diffuse-reflectance spectrum shows a broad band, ca 15.9×10^3 cm^{-1}, and another two bands at 24.4×10^3 and 38.1×10^3 cm^{-1} in agreement with such geometries. The UV–Vis spectrum (25 °C) of the complex dissolved in MeOH shows a shoulder peak at 365 nm (4188 cm^{-1} M^{-1}), and a broad band at 615 nm (308 cm^{-1} M^{-1}). The former peak may be due to the LMCT, while the weak absorption of the latter one is assigned to be d–d transition [16]. The difference between the solid and solution spectra of the complex indicates that the complex may partially dissociate in MeOH.

ESI-MS measurement of the complex has been performed in methanol solution. The observed peak at m/z = 563 g mol^{-1} corresponds to the $[Cu_4(H_3L)(H_2L)Cl_3]^{2+}$ and the most intensive peak at m/z = 428 g mol^{-1} is that with one ligand and one Cu, which indicate that the complex decomposes in MeOH.

X-band EPR spectra of a powdered polycrystalline sample of the complex at room temperature shows a fairly broad isotropic copper(II) signal centered at a g value of 2.11. At 77 K, the signal of the complex becomes sharper, but no resolution of $g_\parallel$ and $g_\perp$ is observed. EPR spectra of the complex dissolved in MeOH shows $g_\parallel = 2.43$, $g_\perp = 2.08$ and $A_\parallel = 120$ mT, which appears to originate from a hexakis(MeOH)Cu(II) species. Another group of signal is quite weak and shows $g_\parallel = 2.38$, $g_\perp = 2.06$ and $A_\parallel = 125$ mT, which must originate from the dissociated mononuclear species.

2.3. Magnetic susceptibility

The magnetic properties of polycrystalline $[Cu_4(H_3L)(H_2L)Cl_3(H_2O)_2]Cl_2 \cdot 5H_2O$ are represented in Fig. 4 as χT versus T plot at 1000 G applied field and M versus field plot at 1.83 K, where $\chi = M/H$ is the molar magnetic susceptibility. The value χT, corresponding to four uncoupled $S = 1/2$ spins with $g \sim 2.2$, remains

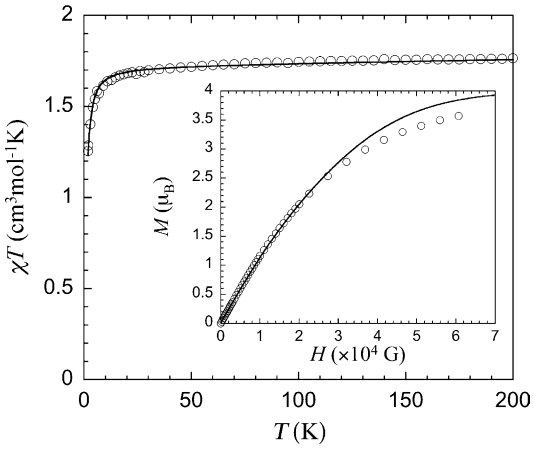


Fig. 4. Temperature dependence of the product χT at 1000 G for the complex $[Cu_4(H_3L)(H_2L)Cl_3(H_2O)_2]Cl_2 \cdot 5H_2O$. Inset: field dependence of the molar magnetization at 1.83 K. Full lines are the best-fit to a model taking into account interactions within Cu(II) pairs and the influence of the applied field (see text).

practically constant at about 1.70–1.76 cm^3 mol^{-1} K down to 30 K. Below 25 K, χT decreases markedly down to 1.25 cm^3 mol^{-1} K at 2 K, indicating the presence of dominant weak antiferromagnetic interactions among the Cu(II) ions in the present complex. The N–C–C–C–N bridges through the ligand L are unlikely to produce any significant magnetic interaction (large Cu–Cu distances, polyatomic unconjugated pathway). The structure of the present complex can be viewed, from the magnetic viewpoint, as pseudo-isolated dinuclear Cu(II) units with either planar dichlorodicopper (Cu4–Cu4′ and Cu3–Cu3′ pairs) or monochlorodicopper bridging pathway (Cu1–Cu2 pair). The former can be expected to be weakly antiferromagnetically coupled on the basis of the ratio of Cu–Cl–Cu angle/Cu–Cl distance, magneto-structural correlations for such topologies [17] and the fact that only one of the Cl$^-$ ions is present in an equatorial position. The monochloro bridged pair, on the other hand, is likely to present extremely small exchange coupling constant, since the bridging chloride ion is in axial coordination site for both Cu1 and Cu2 atoms, at which the electron density is expected to be very small for a square-pyramidal Cu(II) ion. Thus, we have considered the following expression for the magnetization of each Cu(II) pair, derived from the Hamiltonian $\hat{H} = -2J\hat{S}_1 \cdot \hat{S}_2 + g\mu_B H(\hat{S}_1 + \hat{S}_2)$ for a pair of exchanged coupled $S = 1/2$ ions including the effect of the external field, H [18].

$$M = \frac{N_A g \mu_B \sinh(g\mu_B H/k_B T)}{1 + \exp(-2J/k_B T) + 2\cosh(g\mu_B H/k_B T)}. \quad (1)$$

To avoid over-parameterization we have considered only one g-factor for all Cu(II) ion and the same exchange coupling constant J_1 for the two dichloro-bridged pairs (Cu3–Cu3′ and Cu4–Cu4′), J_2

representing the exchange coupling constant for the monochloro bridged (Cu1–Cu2) pair, and fitted the experimental data (with χM/H) to the expression $M = M_1 + M_2$. The best results (corresponding to the full line in Fig. 4) were obtained for $g = 2.25(1)$, $2J_1/k_B = -4.2(7)$ K, $2J_2/k_B = 1.2(9)$ K and a term for Temperature Independent Paramagnetism TIP = $3.3(1) \times 10^{-4}$ cm^3 mol^{-1}, reasonable for four Cu(II) ions. The same set of parameters also fits correctly the magnetization versus field data at 1.83 K (see inset in Fig. 4). Only a slight misfit is observed at high fields, possibly arising from the neglecting of interpair interactions [18]. With the present data, only little significance should be attached to the positive value for $2J_2$. Indeed correct fits can be obtained for $|2J_2|/k_B < 1.2$ K. Overall, these results are in agreement with the structural parameters and show that the magnetic behaviour of $[Cu_4(H_3L)(H_2L)Cl_3(H_2O)_2]Cl_2 \cdot 5H_2O$ is that of weakly antiferromagnetically coupled Cu(II) pairs aside virtually uncoupled Cu(II) ions.

3. Conclusions

In this paper, the synthesis, structure and magnetic properties of a 1D copper(II) polymer have been presented. The results have clearly demonstrated that the potential dinucleating ligand H_4L does not coordinate to copper(II) in the expected way to form a dinuclear copper(II) complex; however, the unique architecture of a tetranuclear-based, chloro-bridged polymer, in which all the imidazolate moieties are monodentate, has been formed by ligand sharing. The chain shows an alternate arrangement of dinuclear units with Cu atoms connected by a single and symmetric chloride bridge, and dinuclear units in which two asymmetric chloride bridges link the metal atoms. Further investigations with ligands containing the bis-(imidazole-2-yl) unit to obtain dinuclear copper complexes are in progress. The ionic ligands can be explained by extensive hydrogen bond interactions in the crystal lattice.

3.1. Synthesis of the ligand and the complex

The ligand 1,1,7,7-tetrakis(imidazol-2-yl)-2,6-diazaheptane (H_4L) was prepared as described in the literature reported by some of us [12].

A solution of the ligand H_4L (36.6 mg, 0.1 mmol) in 5 mL of MeCN was added to a solution of $CuCl_2$ (51 mg, 0.3 mmol) in 5 mL of MeCN. The reaction mixture was stirred at room temperature for 30 min, and it was filtered. Diethyl ether diffusion in to the filtered solution resulted in the formation of blue crystals of sufficient quality for X-ray structure determination. Yield: 30%. *Anal.* Calc. for $C_{34}H_{55}Cu_4N_{20}O_7Cl_5$: C, 31.7; H, 4.2; N, 21.7; Cu, 19.7. Found: C, 31.3; H, 3.8; N, 21.2; Cu, 19.2%. IR (KBr, cm^{-1}): 3420 (s) 3137 (m), 2922 (m), 1618 (m), 1564 (m), 1482 (s), 1384 (m), 1309 (m), 1227 (m), 1135 (w), 1104 (m), 1089 (m), 1018 (s), 960 (m), 756 (s), 665 (m), 571 (w).

3.2. General remarks

All reagents and solvents were purchased from commercial sources and used as received. C, H, N analyses were carried out on a Perkin–Elmer 2400 series II analyzer. Infrared spectra were recorded on a Perkin–Elmer Paragon 1000 spectrophotometer equipped with a Golden Gate Diamond ATR device, using the diffuse reflectance technique. X-Band EPR spectra were recorded at room temperature and at 77 K on a Jeol RE2X electron spin resonance spectrometer using DPPH ($g = 2.0036$) as a standard. The UV/Vis spectrum of the compound was recorded in the 250–800 nm range on a Cary 50 Varian UV/Vis/NIR spectrometer. Electrospray ionization mass spectra (ESI-MS, positive ion) in a methanol solution were recorded on a Thermo Finnigan AQA apparatus. The conductivity measurement was performed using a Philips PW 9526 digital conductivity meter and PW 9551/60 measuring cell with 1 mM solution of the complex in methanol.

The molecular structure of $[Cu_4(H_3L)(H_2L)Cl_3(H_2O)_2]Cl_2 \cdot 5H_2O$ was determined by single-crystal

Table 1
Crystal data of the complex $[Cu_4(H_3L)(H_2L)Cl_3(H_2O)_2]Cl_2 \cdot 5H_2O$

Formula	$C_{34}H_{55}Cl_5Cu_4N_{20}O_7$
Formula weight	1287.39
Crystal system	monoclinic
Space group	*P21/c* (No. 14)
a (Å)	17.133(5)
b (Å)	22.219(5)
c (Å)	19.058(5)
β (°)	112.41(1)
V (Å^3)	6707(3)
Z	4
$D_{calc.}$ (g/cm^3)	1.275
μ (mm^{-1})	1.500
$F(000)$	2624
Crystal size (mm)	$0.18 \times 0.20 \times 0.20$
θ Range for data collection (°)	1.48–25.00
Index ranges	$-20 \leqslant h \leqslant 20$; $-26 \leqslant k \leqslant 26$; $-22 \leqslant l \leqslant 22$
Reflections collected	63035
Independent reflections	11810 [$R_{int} = 0.0288$]
Observed reflections ($I > 2\sigma(I)$)	10613
Data/restraints/parameters	11810/0/606
Final R indices (observed data)[b]	$R_1 = 0.0657$, $wR_2 = 0.1412$
R indices (all data)[b]	$R_1 = 0.0721$, $wR_2 = 0.1421$
Goodness-of-fit on F^2[a]	1.274
Largest different peak and hole (e Å^{-3})	0.412, −0.566

[a] Goodness-of-fit $S = [\sum w(F_o^2 - F_c^2)^2/(n-p)]^{1/2}$, where n is the number of reflections and p the number of parameters.
[b] $R_1 = \sum||F_o| - |F_c||/\sum|F_o|$, $wR_2 = [\sum w(F_o^2 - F_c^2)^2/\sum wF_o^4]^{1/2}$.

Table 2
Bond lengths and angles of $[Cu_4(H_3L)(H_2L)Cl_3(H_2O)_2]Cl_2 \cdot 5H_2O$

Bond lengths (Å)	
Cu1–N5	1.992(4)
Cu1–Cl1	2.576(1)
Cu2–N12	2.090(4)
Cu3–O1w	2.213(4)
Cu4–N19	2.015(4)
Cu1–N3	2.015(4)
Cu2–N15	1.986(4)
Cu2–Cl1	2.571(2)
Cu3–Cl2	2.341(2)
Cu4–O2w	2.244(3)
Cu1–N2	2.061(4)
Cu2–N13	2.018(5)
Cu3–N8	1.959(5)
Cu3–Cl2′	2.618(2)
Cu4–Cl3	2.320(2)
Cu1–N1	2.069(4)
Cu2–N11	2.062(4)
Cu3–N17	2.007(5)
Cu4–N10	1.994(4)
Cu4–Cl3″	2.654(2)
Bond angles (°)	
N5–Cu1–N3	99.8(2)
N3–Cu1–N1	82.6(2)
N2–Cu1–Cl1	90.6(1)
N13–Cu2–N11	80.1(2)
N12–Cu2–Cl1	93.2(1)
N8–Cu3–N17	167.8(2)
N17–Cu3–Cl2	91.7(1)
O1w–Cu3–Cl2′	99.3(1)
N19–Cu4–O2w	86.8(2)
N10–Cu4–Cl3″	95.5(1)
Cu2–Cl1–Cu1	121.9(1)
N5–Cu1–N2	79.8(2)
N2–Cu1–N1	95.0(2)
N1–Cu1–Cl1	90.5(1)
N15–Cu2–N12	82.0(2)
N15–Cu2–Cl1	99.2(1)
N8–Cu3–O1w	87.9(2)
O1w–Cu3–Cl2	169.4(1)
Cl2–Cu3–Cl2′	91.3(1)
N10–Cu4–Cl3	91.4(1)
N19–Cu4–Cl3″	96.2(1)
Cu3–Cl2–Cu3′	88.7(1)
N3–Cu1–N2	167.5(2)
N5–Cu1–Cl1	101.8(1)
N15–Cu2–N13	101.4(2)
N13–Cu2–N12	166.5(2)
N11–Cu2–Cl1	91.8(1)
N17–Cu3–O1w	88.0(2)
N8–Cu3–Cl2′	95.9(1)
N10–Cu4–N19	167.8(2)
N19–Cu4–Cl3	91.9(1)
O2w–Cu4–Cl3″	99.0(1)
Cu4–Cl3–Cu4″	88.9(1)
N5–Cu1–N1	166.6(2)
N3–Cu1–Cl1	101.7(1)
N15–Cu2–N11	168.5(2)
N11–Cu2–N12	94.0(1)
N13–Cu2–Cl1	99.0(1)
N8–Cu3–Cl2	90.3(1)
N17–Cu3–Cl2′	96.0(2)
N10–Cu4–O2w	87.9(2)
Cl3–Cu4 Cl3″	91.1(1)

Symmetry codes: ′ $1-x, -y, 1-z$; ″ $2-x, -y, 2-z$.

Table 3
Hydrogen bonds in $[Cu_4(H_3L)(H_2L)Cl_3(H_2O)_2]Cl_2 \cdot 5H_2O$

Donor-H···Acceptor	H···A (Å)	D···A (Å)	D-H···A (°)
N1–H1···O3w	2.35(1)	3.249(5)	169(1)
N2–H2···Cl4	2.33(1)	3.212(4)	163(1)
N7–H7···O3w	2.30(1)	3.104(7)	155(1)
N9–H9···Cl4	2.45(1)	3.253(4)	155(1)
N11–H11···Cl5	2.25(1)	3.163(5)	176(1)
N12–H12···Cl4^{i}	2.40(1)	3.311(5)	175(1)
N18–H18···Cl5	2.40(1)	3.204(6)	156(1)
N20–H20···Cl4^{i}	2.41(1)	3.251(5)	166(1)
O4w···N6		2.716(9)	
O7w···N4		2.904(11)	
O5w···N16		2.943(12)	
O6w···N14		2.781(9)	
O4w···O2w		2.934(9)	
O6w···O1w		2.732(13)	

Symmetry code: $^{i} = 2-x, 1/2+y, 3/2-z$.

X-ray diffraction methods. Crystallographic and experimental details for the structure are summarized in Table 1. Intensity data and cell parameters were recorded at room temperature (25 °C) on a Bruker AXS Smart 1000 single-crystal diffractometer (Mo Kα radiation) equipped with a CCD area detector. The data reduction was performed using the SAINT [19] and SADABS [20] programs. The structure was solved by Direct Methods using the SIR97 program and refined on F_o^2 by full-matrix least-squares procedures, using the SHELXL-97 program (see Tables 2 and 3).

All non-hydrogen atoms were refined with anisotropic atomic displacements with the exception of the five crystallization water molecules. The H atoms from N–H or C–H groups, including the hydrogen atom statistically distributed (SOF = 0.5) between N4 and N6 or, alternatively, between N14 and N16, were placed in calculated positions and refined riding on the corresponding nitrogen or carbon atoms. The weighting scheme used in the last cycle of refinement was $w = 1/[\sigma^2 F_o^2 + (0.0397P)^2 + 13.3003P]$ (where $P = (F_o^2 + 2F_c^2)/3$). Molecular geometry calculations were carried out using the PARST97 program [21]. Drawings were obtained by ORTEP3 in the WinGX suite [22] and by the program DS ViewerPro 5.0. All calculations were carried out on a DIGITAL Alpha Station 255 computer.

4. Supplementary material

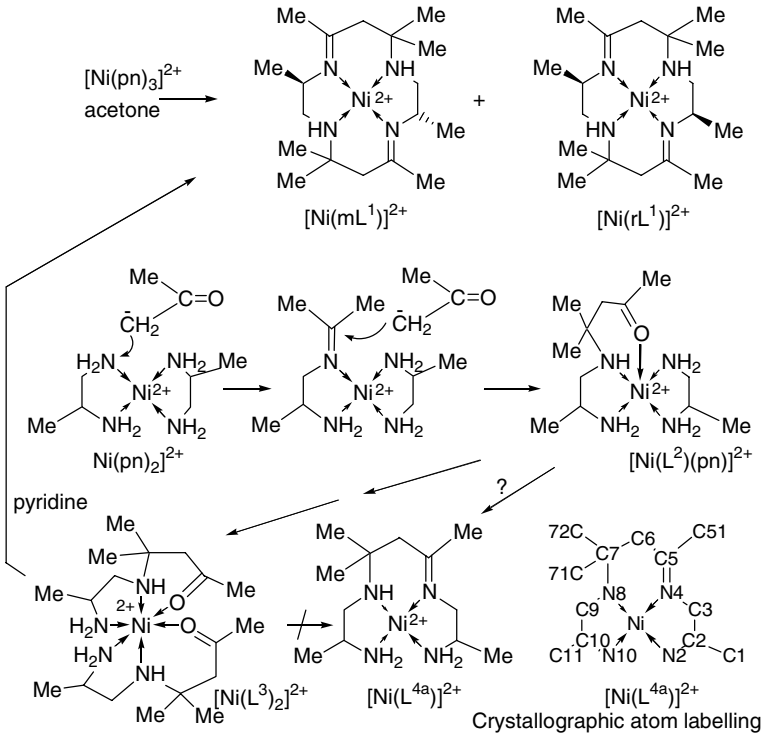
Crystallographic data (excluding structure factors) for the structure reported have been deposited with the Cambridge Crystallographic Data Center as supplementary publication no. CCDC-264342 and can be obtained free of charge on application to the CCDC, 12 Union Road, Cambridge CB2 1EZ, UK. (Fax: (internat.) +44 1223 336 033; e-mail: deposit@ccdc.cam.ac.uk or on the web www: http://www.ccdc.cam.ac.uk.)

Acknowledgements

The work described here has been supported by the Leiden University Study group WFMO (Werkgroep Fundamenteel Materialen-Onderzoek). Support from the NRSC Catalysis (a Research School Combination of HRSMC and NIOK) is kindly acknowledged. The project is financially supported by the Dutch Economy, Ecology, Technology (EET) program, a joint program of the Ministry of Economic Affairs, the Ministry of Education, Culture and Science, and the Ministry of Housing, Spatial Planning and the Environment.

References

[1] J. Reedijk, E. Bouwman, Marcel Dekker, New York & Basel, 1999.
[2] E.I. Solomon, M.J. Baldwin, M.D. Lowery, Chem. Rev. 92 (1992) 521.
[3] K.D. Karlin, Z. Tyeklar, Bioinorganic Chemistry of Copper, Chapman & Hall, New York, 1993.
[4] H.E. Parge, R.A. Hallewell, J. Tainer, Proc. Natl. Acad. Sci. USA 89 (1992) 6109.
[5] J.A. Tainer, E.D. Getzoff, K.M. Beem, J.S. Richardson, D.C. Richardson, J. Mol. Biol. 160 (1982) 181.
[6] N. Kitajima, Y. Moro-oka, Chem. Rev. 94 (1994) 737.
[7] E.I. Solomon, Abstr. Pap. Am. Chem. Soc. 221 (2001) 290.
[8] W.B. Tolman, Acc. Chem. Res. 30 (1997) 227.
[9] L. Casella, L. De Gioia, G.F. Silvestri, E. Monzani, C. Redaelli, R. Roncone, L. Santagostini, J. Inorg. Biochem. 79 (2000) 31.
[10] T.D.P. Stack, V. Mahadevan, M.J. Henson, J.L. DuBois, B. Hedman, K.O. Hodgson, E.I. Solomon, J. Inorg. Biochem. 86 (2001) 442.
[11] Y.F. Song, C. Massera, P. Gamez, A.M.M. Lanfredi, J. Reedijk, Eur. J. Inorg. Chem. (2004) 3025.
[12] Y.F. Song, P. Gamez, A.F. Stassen, M. Lutz, A.L. Spek, J. Reedijk, Eur. J. Inorg. Chem. (2003) 4073.
[13] M. Joseph, T. Leigh, M.L. Swain, Synthesis (1977) 459.
[14] A.W. Addison, T.N. Rao, J. Reedijk, J. van Rijn, G.Ca. Verschoor, J. Chem. Soc., Dalton Trans. (1984) 1349.
[15] G.J.A.A. Koolhaas, W.L. Driessen, P.J. Van Koningsbruggen, J. Reedijk, A.L. Spek, J. Chem. Soc., Dalton Trans. (1993) 3803.
[16] B.J. HathawayComprehensive Coordination Chemistry, vol. 5, Pergamon Press, Oxford, 1987.
[17] W.E. Marsh, K.C. Patel, W.E. Hatfield, D.J. Hodgson, Inorg. Chem. 22 (1983) 511.
[18] B.E. Myers, L. Berger, Friedber Sa, J. Appl. Phys. 40 (1969) 1149.
[19] SAINT, Software Users Guide, Version 6.0; Bruker Analytical X-ray Systems, Madison, WI, 1999.
[20] G.M. Sheldrick, SADABS V2.03: Area-Detector Absorption Correction, University of Göttingen, Germany, 1999.
[21] M. Nardelli, J. Appl. Cryst. 28 (1995) 859.
[22] L.J. Farrugia, J. Appl. Cryst. 30 (1997) 565.



Scheme 1.

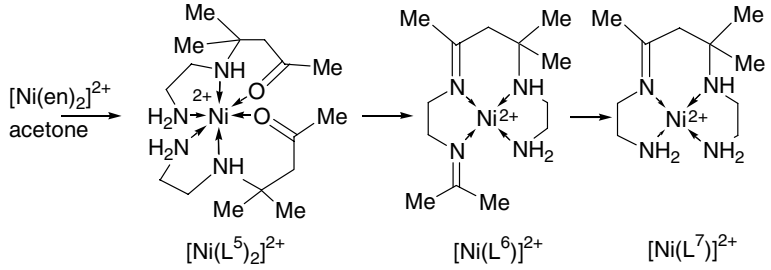
4,8-diazadec-4-ene-2,10-diamine, L^{4d} = 2,4,6,6-tetramethyl-3,7-diazadec-3-ene-1,9-diamine and L^{4e} = 2,4,6,6,8-pentamethyl-3,7-diazanon-3-ene-1,9-diamine are possible, each potentially existing as chiral isomers.

Analogous reactions of $[Ni(en)_2](ClO_4)_2$ with acetone initially form the bis(β-amino ketone) cation $[Ni(L^5)_2]^{2+}$, see Scheme 2. In the presence of ligands that compete with the ketone group for the axial coordination sites, a ketone donor group can be displaced, allowing intramolecular imine formation to occur, giving a tetradentate ligand with one β-aminoketone group [7]. Reverse aldol hydrolysis of this β-aminoketone group would form the tetradentate bis-imine ligand cation $[Ni(L^6)]^{2+}$, for which hydrolysis of the *N*-isopropylidine function would form $[Ni(L^7)]^{2+}$. Reaction of $[Ni(en)_2(NCS)_2]$ with acetone yields $[Ni(L^6)(NCS)_2]$ from which hydrolysis of the *N*-isopropylidine imine group forms $[Ni(L^7)(NCS)_2]$ [8]. Structures have been reported for $[Ni(L^5)_2](ClO_4)_2$, $[Ni(L^6)][ZnCl_4]$ and $[Ni(L^7)(NO_2)]ClO_4$ [7]. Reaction of $[Ni(l\text{-}pn)_2](ClO_4)_2$ with acetone forms $[Ni(l\text{-}L^4)_2](ClO_4)_2$, which cyclizes in pyridine to form $[Ni(ll\text{-}rL^1)]^{2+}$ [9].

In this communication, the reaction of $[Ni(pn)_2(NCS)_2]$ with acetone is described and the structure of the product reported.

2. Results

Reaction of $[Ni(pn)_2(NCS)_2]$ with acetone yields orange, singlet ground state, $[Ni(L^4)](NCS)_2$ for which



Scheme 2.

the structure has been determined. This confirms the ligand as 5,7,7-trimethyl-4,8-diazaundec-4-ene-2,10-diamine, L^{4a}, with both propane-1,2-diamine residue methyl substituents adjacent to the terminal primary amine groups.

In contrast $[Ni(L^7)](NCS)_2]$ exists as a blue-violet, triplet ground state, solid with coordinated thiocyanate. Both $[Ni(L^{4a})](NCS)_2$ and $[Ni(L^7)](NCS)_2]$ form yellow solutions with dissociated thiocyanate in polar solvents (water, lower alcohols, nitromethane, etc.), and blue-violet solutions with coordinated thiocyanate in low-polarity solvents (acetone, acetonitrile, dichloromethane, etc.).

3. Structural study

The structure of a crystal of orange $[Ni(L^{4a})](NCS)_2$, grown from methanol, was determined by X-ray diffractometry, see Section 5.2 for details.

The asymmetric unit consists of the cation (5,7,7-trimethyl-4,8-diazaundec-4-ene-2,10-diamine)nickel(II) and two thiocyanate ions, see Fig. 1. The cation has tetrahedrally twisted square-planar coordination {displacements/Å from the N2, N4, N8, N10 coordination plane: N2 0.0480(5), N4 −0.0472(5), N8 0.0469(5), N10 −0.0477(5), Ni1 −0.0113(6), C2 −0.428(2), C3 0.278(2), C5 −0.049(2), C6 0.204 (2), C7 0.9021(2), C9 0.3709(2), C10 −0.3993(2), C11 −0.0588(2), C51 −0.3284(2), C71 2.3185(2), C72 0.9602(2), with methyl group C71 axially oriented and the other methyl groups equatorially oriented}. The C2–H2 and C7–C71 (axial component of *gem*-dimethyl group) are oriented towards one side of the plane, and N8–H8 and C10–H10 towards the other side. The Ni–N distances (Table 1) are within the usual range for singlet ground state nickel(II), with the bond to the imine nitrogen N4 shorter than the bonds to the amine nitrogen atoms by ca. 0.02 Å, as is usual. The chiral centres C2, N8, C10 all have the *S* configuration.

The thiocyanate ion S2–C32–N32 is located with S32 near the tetragonal axis of the nickel(II) ion (N–Ni1–S32 = 89–92°), on the side of the "molecular plane" opposite to the axial methyl group C71, with Ni1–S32 = 3.0500(5) Å and C32–S2–Ni1 = 100.80(5)°. The closest approach to the nickel on the other side is S2 (x, 1 + y, z) at 4.275 Å. Hydrogen-bond N8–H8···N31 links the cation to the second thiocyanate ion. Other hydrogen bonds form a network (Table 2). The structurally distinct thiocyanate ions give rise to doublet ν(C≡N) absorption in the IR spectrum (see Section 5.1).

Table 1
Selected geometric parameters (Å, °) for (5,7,7-trimethyl-4,8-diazaundec-4-ene-2 10-diamine)nickel(II) thiocyanate

Ni1–N2	1.930(1)
Ni1–N4	1.899(1)
Ni1–N8	1.925(1)
Ni1–N10	1.917(1)
Ni1–S2	3.0500(5)
N4–C5	1.287(2)
S1–C31	1.657(2)
C31–N31	1.159(2)
S2–C32	1.655(2)
C32–N32	1.172(3)
N2–Ni1–N4	86.56(6)
N2–Ni1–N8	176.29(6)
N2–Ni1–N10	91.98(6)
N4–Ni1–N8	94.74(6)
N4–Ni1–N10	177.36(6)
N8–Ni1–N10	86.85(6)
N2–Ni1–S2	92.39(4)
N2–Ni1–N4	86.56(6)
N8–Ni1–S2	91.11(4)
N10–Ni1–S2	88.93(4)
N31–C31–S1	179.3(2)
C32–S2–Ni1	100.82(6)
N32–C32–S2	179.1(2)
N2–Ni1–S2	92.39(4)

Table 2
Hydrogen-bond parameters (Å, °) for (5,7,7-trimethyl-4,8-diazaundec-4-ene-2,10-diamine)nickel(II) thiocyanate

Atoms	D–H	H···A	D···A	D–H···A
N2–H2C···N32i	0.90	2.36	3.231(2)	162
N2–H2D···N32ii	0.90	2.64	3.194(2)	121
N8–H8···N31	0.91	2.10	2.953(2)	156
N10–H10A···N32ii	0.90	2.22	3.058(2)	156

Symmetry codes: (i) x, 1 + y, z; (ii) $-x$, 1/2 + y, 1/2−z.

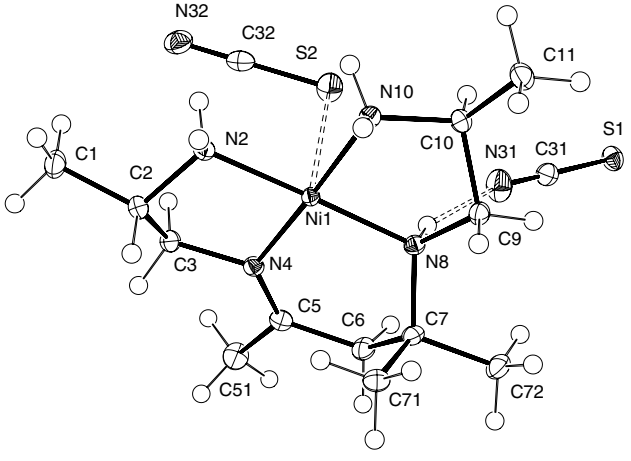


Fig. 1. The asymmetric unit for $[Ni(L^{4a})](NCS)_2$, drawn with probability ellipsoids at the 50% confidence level [10]. Hydrogen atoms are shown as circles of arbitrary radius.

4. Conclusions

Facile reaction of $[Ni(pn)_2(NCS)_2]$ with acetone forms the cation $[Ni(L^{4a})]^{2+}$ with the tetradentate ligand 5,7,7-trimethyl-4,6-diazaundec-4-ene-2,10-diamine, which has the propane-1,2-diamine residue methyl groups remote from the amine–imine bridge group linking these residues. This indicates that the cation $[Ni(L^{4a})]^{2+}$ is not formed via the bis(β-aminoketone) cation $[Ni(L^{3})]^{2+}$ by intramolecular imine formation followed by hydrolysis of one β-aminoketone function. It could be formed via the cation $[Ni(L^{2})(pn)]^{2+}$ by intramolecular imine formation, all reactions occurring at the amine nitrogens remote from the methyl substituents. The cation $[Ni(L^{4a})]^{2+}$ cannot be a precurser of the macrocyle $[Ni(L^{1})]^{2+}$ which has the propane-1,2-diamine methyl substituents adjacent to the imine functions. The overall condensation is stereospecific, forming $[Ni(L^{4a})](NCS)_2$ as the 2*SR*, 8R*S*, 10*SR* isomer.

5. Experimental

5.1. (5,7,7-Trimethyl-4,8-diazaundec-4-ene-2,10-diamine)nickel(II) thiocyanate $[Ni(L^{4a})](NCS)_2$

$[Ni(pn)_2(NCS)_2]$ (5 g) was refluxed in methanol (25 cm^3) and acetone (25 cm^3) for 8 h. The solution was then rotary evaporated and the orange residue recrystallised from methanol/propan-2-ol, yield near quantitative. Visible spectra: the compound forms a yellow, fully dissociated, solution in water {λ_{max}/nm (ε/dm^3 mol^{-1} cm^{-1}), 433 (54)} and a blue-violet solution with coordinated thiocyanate in acetone {539 (12), >900 (c. 9)}. *Anal.* Calc. for $C_{14}H_{28}N_6NiS_2C$, 41.7; H, 7.0; N20.8. Found: C, 41.9; H, 6.7; N, 20.8%. IR spectrum {ν_{max}/cm^{-1}} ν(NH) 3274, 3198, 3081, ν(C≡N) (2052, 2039) vs, ν(N=C) (1658), δ (NH_2) 1996, 1574.

5.2. Structure determination

5.2.1. Crystal data for (5,7,7-trimethyl-4,8-diazaundec-4-ene-2,10-diamine)nickel(II) thiocyanate

$[C_{12}H_{28}N_4Ni](NCS)_2$, $C_{14}H_{28}N_6NiS_2$
Monoclinic, space group $P2_1c$
Mo Kα radiation
a = 16.4051(2) (Å)
b = 6.8106(1) (Å)
c = 18.0205(2) (Å)
β = 107.067(1)°
M_r = 403.25, Z = 4
Orange prism, 0.34 × 0.26 × 0.20 mm
Cell parameters from 8192 reflections
θ = 1.3–27.1°
μ = 1.23 mm^{-1}
T = 190(2) K

5.2.2. Data collection [11]

Siemens CCD diffractomer, ω scans
Absorption correction: multi-scan, [12]
T_{min} = 0.679, T_{max} = 0.791
12152 measured reflections
4213 independent reflections R_{int} = 0.0122
4000 reflections with $I > 2\sigma(I)$
θ_{max} = 27.1°
$h = -20 \rightarrow 20$
$k = 0 \rightarrow 8$
$l = 0 \rightarrow 23$

5.2.3. Refinement [13]

Refinement on F^2
$R[F^2 > 2\sigma(F^2)]$ = 0.020
$wR(F^2)$ = 0.064, S = 1.15
213 parameters, 0 restraints
H-atoms in calculated positions and riding
Calculated weights
$w = 1/[\sigma^2(F_o^2) + (0.0321P)^2 + 0.7112P]$, where $P = (F_o^2 + 2F_c^2)/3$.

Appendix A. Supplementary data

Crystallographic data has been deposited with the Cambridge Crystallographic Data Centre; CDDC 261150. Copies may be obtained free of charge from the Director, CDCC, 12 Union Road, Cambridge, CBZ 1EZ, UK (fax: +44 1223 336 033; e-mail: deposit @ccdc. cam.ac.uk or www:http://www.ccdc.cam.uk). Supplementary data associated with this article can be found, in the online version at doi:10.1016/j.poly.2005.04.021.

References

[1] M.M. Blight, N.F. Curtis, J. Chem. Soc. (1962) 3016.
[2] N.F. Curtis, D.A. Swann, T.N. Waters, I.E. Maxwell, J. Am. Chem. Soc. 91 (1969) 4588.
[3] D.A. Swann, T.N. Waters, N.F. Curtis, J. Chem. Soc., Dalton Trans. (1972) 1115.
[4] T. Ito, D.H. Busch, Inorg. Chem. 13 (1974) 1770.
[5] T. Ito, K. Soma, M. Watanabe, Chem. Lett. (1976) 421.
[6] N.F. Curtis, J. Chem. Soc., Dalton Trans. (1973) 863.
[7] N.F. Curtis, J. Chem. Soc., Dalton Trans. (1972) 1357.
[8] N.F. Curtis, H.K.J. Powell, H. Puschmann, C.E.F. Rickard, J.M. Waters, Inorg. Chim. Acta 355 (2003) 25.
[9] H. Ito, J. Fujita, Bull. Chem. Soc. Japan 44 (1971) 741.
[10] L.J. Farrugia ORTEP-32, J. Appl. Cryst. 30 (1997) 565.

[11] SMART and SAINT, Siemens Analytical Instruments Inc. Madison, WI, USA, 1994.
[12] R.H. Blessing, Acta Crystallogr., Sect. A 51 (1995) 33.
[13] G.M. Sheldrick, SHELXS-97 and SHELXL-97, Programs for the Solution and Refinement of Crystal Structures, University of Göttingen, Germany, 1997.

of the alcohol series Fc–$(CH_2)_m$–OH with $m = 1$–4, Fc–CH(OH)–CH_3 and $Fe(C_5H_4$–CH(OH)–$CH_3)_2$. Results are expressed relative to ferrocene itself and are compared with the related acid series, Fc–$(CH_2)_n$–COOH, $n = 0$–3.

2. Experimental

2.1. Equipment and materials

Ferrocene (**1**, Strem), $LiAlH_4$ (Merck), $AlCl_3$ and other solid reagents (Aldrich) were used without further purification. Dry acetonitrile was obtained by refluxing under nitrogen over CaH_2, distilled onto alumina for storage, and redistilled just prior to use. THF and ether was dried by refluxing under a nitrogen atmosphere over sodium wire and distilled directly before use. Organic solvents were distilled prior to use, water was double distilled. Ferrocene carboxylic acids **2**–**5** [5], **6** [3], the ester **7** [3] and the aldehyde, **8** [6] were synthesised as described before and used as precursors to the alcohols **9**–**12**, Scheme 1. Alcohol **9** was synthesised by $NaBH_4$ reduction of **8** in 90% yield as described by Broadhead [1] but on a 10 times larger scale. The secondary alcohols 1-hydroxyethylferrocene (**13**) and 1,1′-bis(hydroxyethyl)ferrocene (**14**) Fig. 1, was obtained utilising the literature methods [3]. Chromatography was performed on Fluka silica gel 60 grade 60741. The electrolyte tetrabutylammonium tetrakis(pentafluorophenyl)borate was prepared as described [7]. Melting points were determined with a Reichert Thermopan Microscope with a Koffler hot-stage and are uncorrected. ^1H NMR spectra at 20 °C were recorded on a Bruker Advance DPX 300 NMR spectrometer at 300 MHz with chemical shifts presented as δ values referenced to $SiMe_4$ at 0.00 ppm utilising $CDCl_3$ that was made acid free by passing it through basic alumina immediately before use. IR spectra (cm^{-1}) were recorded on a Hitachi spectrophotometer Model 270-50 with data processor. For solid state spectra a KBr matrix was used, while NaCl plates were used for thin films of liquid samples. Elemental analysis was conducted by the Canadian Microanalytical Service, Ltd.

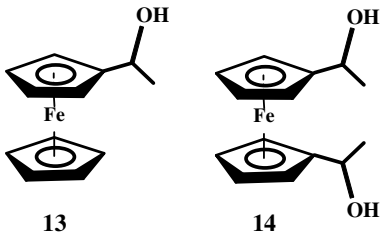
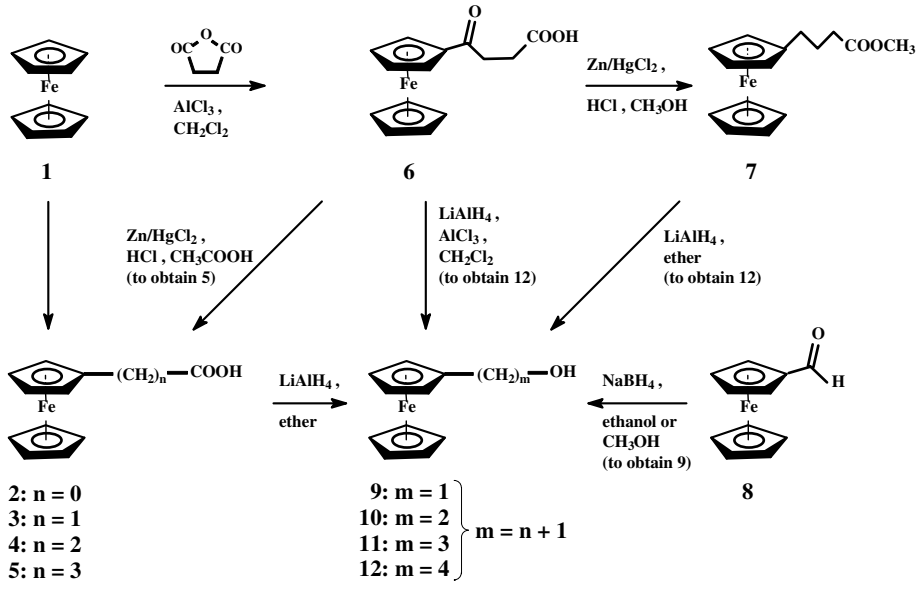


Fig. 1. Structures of secondary alcohols **13** and **14**.

2.2. Synthesis

2.2.1. Fc–$(CH_2)_m$–OH, with m = 1 (9), 2 (10), 3 (11) and 4 (12), utilising $LiAlH_4$ reduction of acids 2–5

The synthesis of 3-ferrocenylpropanol (**11**) may serve as an example. To a $LiAlH_4$ suspension in dry ether (3.42 g, 90 mmol in 100 cm^3) was slowly added a solution of 3-ferrocenylpropanoic acid (**4**, 3 g, 12.6 mmol) in dry ether (110 cm^3) while slight boiling was maintained. After refluxing the mixture for 13 h at 50 °C, a 1:1 ethanol:ether mixture (50 cm^3) was very carefully added to destroy the excess $LiAlH_4$. The reaction mixture was slowly poured into an excess of ice cold 2 M



Scheme 1. Different routes that may be followed to obtain ferrocene-containing alcohols **9**–**12**.

NaOH solution (1 l) and the ether and aqueous phases separated. The aqueous phase was washed with ether after which the combined ether fractions were washed with 1 M NaOH solution (400 cm^3) and twice with equal volumes of water. Drying of the ether layer with $MgSO_4$ and removal of the solvent under reduced pressure gave **11** as a reddish-brown oil (2.86 g, ~100%) that was clean enough for most purposes. A purification column may be employed with ethyl acetate–hexane (1:4) as eluent ($R_f = 0.36$). ^1H NMR (300 MHz, $CDCl_3$): δ_H 4.14 (5H, s, C_5H_5), 4.11 (2H, s, C_5H_4), 4.08 (2H, s, C_5H_4), 3.69 (2H, s, –CH_2–OH), 2.44 (2H, t, Fc–CH_2–), 1.80 (2H, m, –CH_2–). IR (NaCl-discs), ν_{max}/cm^{-1}: 3352 (–OH), 2926 (–CH_2–), 1104 (C–O). $C_{13}H_{16}OFe$ requires: C, 64.0; H, 6.6. Found: C, 63.9; H, 6.3%.

Characterisation data for ***9***: Chromatography on silica with ethyl acetate–hexane (1:4) as eluent ($R_f = 0.28$) gave **9** in 89% yield as a yellow solid, m.p. 76 °C. ^1H NMR (300 MHz, $CDCl_3$): δ_H 4.35 (2H, d, C_5H_4), 4.27 (2H, t, C_5H_4), 4.21 (5H, s, C_5H_5), 4.20 (2H, s, Fc–CH_2–OH). IR (KBr), ν_{max}/cm^{-1}: 3227 (–OH), 2932 (–CH_2–), 1102 (C–O). $C_{11}H_{12}OFe$ requires: C, 61.2; H, 5.6. Found: C, 61.4; H, 5.4%.

Characterisation data for ***10***: Chromatography on silica with ethyl acetate–hexane (1:4) as eluent ($R_f = 0.25$), gave **10** as a low melting solid in 93% yield, m.p. 32–33 °C. ^1H NMR (300 MHz, $CDCl_3$): δ_H 4.13 (9H, m, –C_5H_4 and C_5H_5), 3.75 (2H, m, –CH_2–OH) and 2.62 (2H, t, Fc–CH_2–). IR (NaCl discs), ν_{max}/cm^{-1}: 3408 (–OH), 2935 (C–H), 1038 (C–O). $C_{12}H_{14}OFe$ requires: C, 62.6; H, 6.1. Found: C, 62.6; H, 5.8%.

Characterisation data for ***12***: Chromatography on silica with ethyl acetate–hexane (1:4) as eluent ($R_f = 0.49$), gave **12** as a thick dark yellow liquid in 94% yield. ^1H NMR (300 MHz, $CDCl_3$): δ_H 4.12 (5H, s, C_5H_5), 4.06 (4H, d, C_5H_4), 3.68 (2H, t, CH_2–OH), 2.37 (2H, t, Fc–CH_2), 1.60 (4H, m, $2 \times CH_2$). IR (NaCl-discs), ν_{max}/cm^{-1}: 3346 (–OH), 2800–2900 (C–H), 1104 (C–O). $C_{14}H_{18}OFe$ requires: C, 65.1; H, 7.0. Found: C, 65.3; H, 6.9%.

*2.2.2. Fc–(CH$_2$)$_4$–OH (**12**) utilising LiAlH$_4$/AlCl$_3$ reduction of the γ-ketoacid (**6**)*

To a suspension of $LiAlH_4$ (0.267 g, 6.99 mmol) in dry ether (5 cm^3) was added $AlCl_3$ (0.228 g, 1.63 mmol), also suspended in dry ether (45 cm^3) under nitrogen. 3-Ferrocenoylpropanoic acid (**6**, 0.208 g, 0.699 mmol) was added and additional $AlCl_3$ (0.189 g, 1.39 mmol) suspended in dry ether (9 cm^3) was added over a 5 min interval. The reaction mixture was stirred for 30 min at room temperature and refluxed for 3 h. To the cooled reaction mixture was added water (8 cm^3) and 6 mol dm^{-3} H_2SO_4 (5 cm^3). The mixture was extracted with ether (3×80 cm^3), dried with $MgSO_4$ and solvent removal afforded a yellowish oil of 4-ferrocenylbutanol (**12**) (0.18 g, 97%).

*2.2.3. Fc–(CH$_2$)$_4$–OH (**12**) from LiAlH$_4$ reduction of ester 7*

Solid $LiAlH_4$ (2.7 g, 71 mmol) was added to a solution of **7** (6.32, 22.1 mmol) in 80 cm^3 dry ether over 20 min. The reaction mixture was refluxed for 16 h before the excess $LiAlH_4$ was destroyed by careful addition of a 1:1 ethanol:ether mixture (100 cm^3). The ether layer was washed successively with HCl (2×200 cm^3, 2 mol dm^{-3}), NaOH (200 cm^3, 2 mol dm^{-3}) and water, and dried with $MgSO_4$, to give after solvent removal **12** (5.31 g, 93%).

2.3. Cyclic voltammetry

Cyclic voltammetric (CV) experiments were performed on ca. 1 mM solutions of **9**–**14** in dry CH_3CN/0.100 M $N(^nBu)_4PF_6$, utilising a standard three-electrode cell with a Pt-working electrode of surface area 2.01 mm^2 and pre-treated by polishing on a Beuhler microcloth first with 1 micron and then with 1/4 micron diamond paste, a Pt-wire counter electrode and a Ag/Ag^+ reference electrode (a Ag wire immersed in 0.010 M $AgNO_3$ in CH_3CN utilising a Luggin capillary with vicor tip) under argon at 25.0 °C in a Faraday cage connected to a BAS CV-27 cyclic voltammograph interfaced with a personal computer. Some experiments were also conducted on a glassy carbon electrode of surface area 7.07 mm^2. Obtained formal reduction potentials were essentially the same. Data, uncorrected for junction potentials, were collected with an Adalab-PC™ and Adapt™ data acquisition kit (Interactive Microwave, Inc.) with locally developed software, and analysed with Hyperplot (JHM International, Inc.). All potentials in this study, however, are presented referenced against Fc/Fc^+ as recommended by IUPAC [8]. The Fc/Fc^+ couple exhibited $E^{o'} = 0.087$ V versus Ag/Ag^+, $i_{pc}/i_{pa} = 0.98$, $\Delta E_p = 74$ mV under our experimental conditions. Successive experiments under the same experimental conditions have shown that potentials were reproducible within 3 mV. CV experiments with **9** in CH_2Cl_2/0.100 M $[N(^nBu)_4][B(C_6F_5)_4]$, utilising a glassy carbon electrode of surface area 0.79 mm^2, were experimentally referenced against a Ag/AgCl reference electrode.

3. Results and discussion

3.1. Synthesis

The alcohol series **9**–**12** were synthesised according to Scheme 1. Ferrocenylmethanol (**9**) was synthesised from ferrocenecarboxaldehyde (**8**), utilising $NaBH_4$ as reducing agent in high (~90%) yield. $NaBH_4$ is somewhat safer to use in large quantities than $LiAlH_4$. However, $NaBH_4$ is not a strong enough reducing agent to reduce

carboxylic acids or esters. Hence, for the reduction of **2**–**5** and **7**, $LiAlH_4$ was used. All these reactions were essentially quantitative.

The yield-limiting step in obtaining alcohols **9**–**12** from ferrocene is centred on the success rate in obtaining the acid or other precursors. Hence the preparation of **9** from aldehyde **8** gave a much better overall yield (71% in a two-step syntheses) based on the initial amount of ferrocene used, than the preparation utilising the acid, **2** (ca. 49% yield at least in a three-step syntheses). Because $LiAlH_4$ reduction of the present ferrocene acid series is so facile, there is nothing gained in terms of yields by synthesising alcohols **9**–**12** utilising ester precursors. This is demonstrated for the synthesis of 4-ferrocenylbutanol (**12**) from ester **7**. It is also unnecessary to obtain **5** for the synthesis of **12**, since this alcohol can directly be obtained by the reduction of the γ-ketoacid (**6**). However, in this latter reaction, $LiAlH_4$ does not liberate the alcohol **12** because $LiAlH_4$ does not reduce the γ-keto group of **6** to a CH_2 group. Rather, the formation of an α-alcohol intermediate possessing the molecular fragment Fc–CH(OH)– and follow-up degradation occurs. To obtain **12** from **6**, the use of the mixed reducing system $AlCl_3/LiAlH_4$ leads to simultaneous Clemenson reduction of the γ-keto group to $–CH_2–$ and the carboxylic acid group to $–CH_2–OH$. This reaction is also essentially quantitative. The long term stability of the alcohols with spacers $(CH_2)_m$ and $m = 2$, 3 and 4 is excellent. However, the shelf-life of $Fc–CH_2–OH$ (**9**) and also the secondary alcohols **13** and **14** (Fig. 1), is less impressive. This is the result of the high electron donating power of the ferrocenyl group (group electronegativity of Fc is $\chi_{Fc} = 1.89$ [9,10]), which tend to stabilise ferrocyl cations ($= Fc–CH_2^+$) [11,12]. This promotes decomposition of **9** by water elimination under very mild conditions as follows:

$$Fc–CH_2–OH + H^+ \rightarrow Fc–CH_2–(OH_2)^+ \rightarrow Fc–(CH_2)^+ + H_2O$$

The ferrocenyl group cannot stabilise cations of this nature in **10**–**12**.

3.2. Cyclic voltammetry

CV experiments in dry CH_3CN/0.100 M $N(^nBu)_4PF_6$ indicated reversible electrochemical behaviour for the ferrocenyl group in compounds **10**–**14** with $\Delta E_p = E_{pa} - E_{pc} \leqslant 80$ mV at scan rates up to 250 mV s^{-1} in acetonitrile (Table 1, Fig. 2). Determined peak cathodic/peak anodic current ratios for **10**–**14** were in the range $0.94 < i_{pc}/i_{pa} < 1$ and the formal reduction potentials, $E^{o'} = 1/2\,(E_{pa} + E_{pc})$, were scan rate independent between 50 and 250 mV s^{-1}.

Compound **9**, though, exibited $\Delta E_p = 110$ mV, much larger than for the other alcohols. Close inspection of the CV of **9** hinted on two poorly resolved ferrocene-based waves (Fig. 3) despite the fact that **9** gave satisfactorily elemental analyses and having a clean ^1H NMR spectrum. In an attempt to prove that their really are two peaks associated with the CV of **9**, Osteryoung Square Wave Voltammetry (OSWV) was performed on this complex. The OSWV peaks were certainly broadened, but no clear-cut indication towards two redox peaks could be demonstrated. It then was suspected that the use of the coordinating solvent CH_3CN and 0.100 M $N(^nBu)_4PF_6$ as supporting electrolyte masked some key features of the CV of **9**. Reports by Geiger and co-workers [13] that poorly resolved peaks in CH_3CN/0.100 M $N(^nBu)_4PF_6$ often becomes well resolved in the system dichloromethane utilising the hyper uncoordinative and poorly nucleophylic salt $[N(^nBu)_4][B(C_6F_5)_4]$ as supporting electrolyte, caused us to repeat the CV of **9** in

Table 1
Selected potentials (V) and current (μA) data for ca. 1.0 mM solutions of the indicated compounds in CH_3CN/0.100 M $N(^nBu)_4PF_6$ at 25.0 °C

Compound	E_{pa}	ΔE_p	$E^{o'}$	i_{pa}	i_{pc}/i_{pa}
9 (peak 1)	−0.017[a]	[b]	0.016[c]	[b]	[b]
9 (peak 2)	0.093	[b]	0.060[c]	[b]	[b]
10	−0.011	0.070	−0.046	8.78	0.96
11	−0.016	0.070	−0.052	8.28	0.97
12	−0.017	0.075	−0.054	7.61	0.99
13	0.022	0.066	−0.011	6.47	0.98
14	0.012	0.066	−0.021	8.23	0.95

[a] E_{pc} value.
[b] A poorly defined oxidation wave in peak 1 and reduction wave in peak 2 made current and ΔE_p measurements impossible.
[c] $E^{o'}$ were estimated by assuming $\Delta E_p = 66$ mV, the value obtained for **13** and **14**.

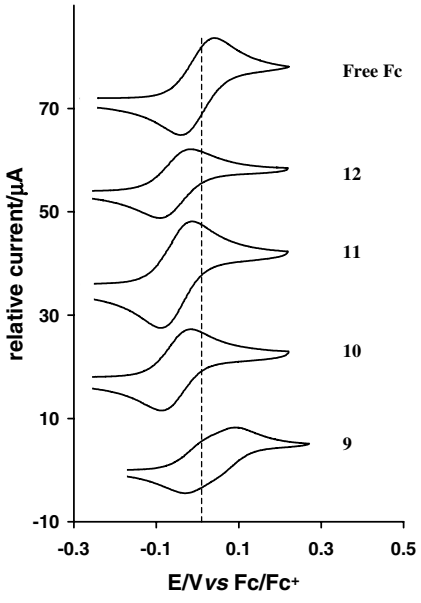


Fig. 2. CV's of **9**–**12** in CH_3CN/0.100 M $N(^nBu)_4PF_6$ at 25.0 °C and a scan rate of 100 mV s^{-1} at a Pt-working electrode.

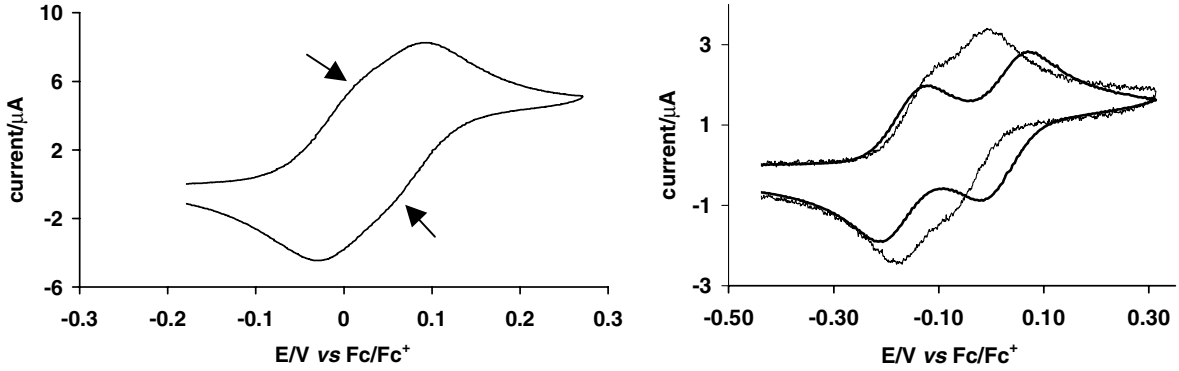


Fig. 3. CV of **9** in CH_3CN/0.100 M $N(^nBu)_4PF_6$ (left) showing two poorly resolved peaks. In CH_2Cl_2/0.100 M $[N(^nBu)_4][B(C_6F_5)_4]$ (right, bold line), two peaks with $\Delta E_p \sim 89$ mV are clearly seen. Upon addition of 0.100 M $N(^nBu)_4PF_6$ to this solution, the CV collapsed into one showing two poorly resolved peaks (right, less bold line).

the system CH_2Cl_2/0.100 M $[N(^nBu)_4][B(C_6F_5)_4]$ with spectacular success.

Fig. 3, right, clearly shows two very well-defined reversible CV waves for **9** in this medium. In a separate test, the stability of **9** in acetonitrile was investigated by ^1H NMR. This compound did not show any degradation within 24 h. The two observed waves in Fig. 3, right, are typical of those associated with a symmetrical dimer, which generates a mixed valent intermediate upon oxidation or reduction. Different formal reduction potentials for side groups on symmetrical complexes in which mixed-valent intermediates are generated are well known in systems that allow electron delocalisation, either through bridge mediated paths or from a direct metal–metal interaction [10,14]. The inequivalence of the ferrocenyl and ferrocenium groups of such a mixed valent intermediate is highlighted in terms of their group electronegativities [9,10]: $\chi_{Fc} = 1.87$, $\chi_{Fc+} = 2.82$. The electron withdrawing power of the ferrocenium group is almost as high as that of the CF_3 group ($\chi_{CF3} = 3.01$). We therefore propose the formation of a dimeric species of **9** in solution that electrochemically are oxidised according to the following electron transfer processes:

$$[2FcCH_2OH \rightleftharpoons (FcCH_2OH)_2] \rightleftharpoons (Fc^+CH_2OH)\text{–}(FcCH_2OH) \rightleftharpoons (Fc^+CH_2OH)_2 \quad (1)$$

It is instructive to observe that **10**–**14** do not show the double peaks in their CV's as **9** had. This implies that the structural effects that was discussed and interpreted above as dimerisation for **9** is absent in **10**–**14**. This observation is consistent with the fact that the longer chain of **10**–**12** introduces so much flexibility into the side chains of these molecules compared to what is expected for **9**, that a dimeric product may not be stable enough to allow its detection in noticeable amounts on a CV time scale. As for **13** and **14**, it is conceivable that the methyl groups in the side chain is bulky enough to impose so much steric constraints on the molecules that dimerisation as it is realised for **9** is not as feasible in **13** and **14**.

The structure of the mixed valent species in Eq. (1) above can only be speculated on at this stage, but in view of the known hydrogen bonding capabilities of alcohols and the fact that the ferrocenyl group are known to interact with protons [15], a hypothetic structure as in Fig. 4 would be consistent with our results.

It would allow a symmetrical dimer to account for the shape of the CV. It would allow communication of the Fe^{II} and Fe^{III} species through space and through conjugation, and it disallows a similar communication pattern of longer chain alcohols in two ways. Firstly, in $–(CH_2)_m–$ chains with $m \geqslant 2$, electron delocalisation through conjugation or inductive effects along the side chains would be very weak indeed. Secondly, through space communication of the Fe^{II} and Fe^{III} species, or the $Fe^{II}\cdots H–O–CH_2–Fc$ interaction in Fig. 4 would be very unlikely over the distances that will be required for the longer side chains.

The lower $E^{o'}$ for **10** compared to **9** (Table 1) clearly indicates that there is much less communication between the hydroxyl group and the ferrocenyl moiety of **10** than in **9**. In particular, for $E^{o'}$ of **10** to be 46 mV more negative than $E^{o'}$ of ferrocene itself, the side-chain of **10**, $–CH_2CH_2OH$, has to become electron-donating relative to H. This is consistent with a conclusion that $–CH_2CH_2–$ and larger alkyl spacers effectively isolates the –OH group from the ferrocenyl

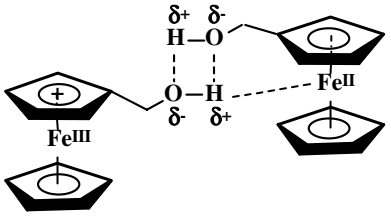


Fig. 4. Possible mixed valent intermediate in the oxidation of **9**.

group, but that a single $–CH_2–$ group does not. This also means that electron-donating properties of the $–CH_2CH_2–$ part of the side-chain in **10** dominates over the electron-withdrawing properties of the –OH moiety of **10**.

Further increases in the side chain length to that of **11** and **12**, lowered the $E^{o'}$ values further, but not nearly as dramatically as did **10**, probably because the $–(CH_2)_m–$ chains became so long that they are very effective isolators: the ferrocenyl group is really existing independent of any through-space or through-bond inductive effects that the OH group may have. The only thing that the slight lowering of the formal reduction potentials of **11** and **12** are thought to imply is a slight increase in the electron donating power of the alkyl chains with increasing chain length.

The $E^{o'}$ of the secondary alcohols **13** and **14** is more negative than that of **9**. This is because they have additional electron-donating methyl groups in the side-chains compared to **9**. It is also instructive to note that our $E^{o'} = -0.011$ V for **13** corresponds very well with the chronopotentiometric determined $E_{1/4} = -0.009$ V value that was reported by Kuwana and co-workers [16]. Alcohol **14** is more easily oxidised than **13** which is what one may expect when the number of electron donating side chains, here two $–CH(CH_3)OH$ groups, are doubled.

Fig. 5 demonstrates a few final key points pertinent to compounds of the type $Fc–(CH_2)_n–COOH$ and $Fc–(CH_2)_m–OH$.

Firstly, it can clearly be seen how the value of $E^{o'}$ decreases as the alkyl chain of the carboxylic acid series **2–5** and the ferrocenylalcohol series **9–12** becomes longer. Secondly, the electron withdrawing properties of both the carbonyl group of –COOH and the OH group in $Fc–(CH_2)_{n/m}$-compounds see to it that $E^{o'}$ are much more drastically affected at short chain length than in compounds with longer side chains. Finally, it can be noted that ferrocenyl alcohols are more easily oxidised than the parent carboxylic acids **2–5**.

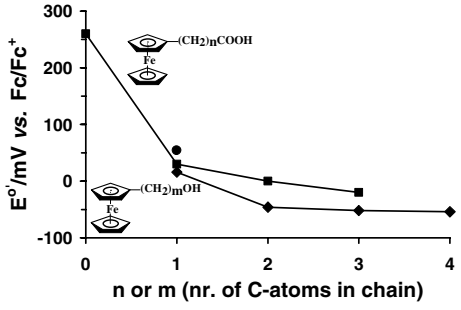


Fig. 5. Graph of $E^{o'}$ vs. number of carbon atoms in the alkyl chain linking the ferrocenyl group with functional groups for $Fc–(CH_2)_n–COOH$ (■) and $Fc–(CH_2)_m–OH$ (♦). The point ● refers to the second couple of **9**.

In conclusion, the yield-limiting step to obtain ferrocenylalcohols is centred in the successful high yield synthesis of suitable precursors. Reduction reactions of these precursors to obtain ferrocenyl alcohols are very efficient. The ferrocenylalcohols under discussion have smaller reduction potentials than the carboxylic acid analogues, and they become easier to oxidise with increasing alkyl chain length. Ferrocenylmethanol undergo solution molecular pairing to a notable extent. A forthcoming publication [17] will provide the details of how more beneficial cytotoxic properties for potential cancer treatment by **9–12** are observed with increasing side chain length and decreasing ferrocenyl formal reduction potential.

Acknowledgements

The authors acknowledge the UFS, CANSA and the MRC for financial support.

References

[1] (a) G.D. Broadhead, J.M. Osgerby, P.L. Pauson, J. Chem. Soc. (1958) 650;
(b) J.K. Lindsay, C.R. Hauser, J. Org. Chem. 92 (1957) 355.
[2] C. Nataro, W.M. Cleaver, C.C. Landry, C.W. Allen, Polyhedron 18 (1999) 1471.
[3] P.J. Swarts, M. Immelman, G.J. Lamprecht, S.E. Greyling, J.C. Swarts, S. Afr. J. Chem. 50 (1997) 208.
[4] J.C. Swarts, D.M. Swarts, D.M. Maree, E.W. Neuse, C. La Madeleine, J.E. van Lier, Anticancer Res. 21 (2001) 2033.
[5] N.F. Blom, E.W. Neuse, H.G. Thomas, Transition Met. Chem. 12 (1987) 301.
[6] D.E. Bublitz, K.L. Rinehart, Org. Reactions 17 (1969) 77.
[7] R.J. LeSuer, C. Buttolph, W.E. Geiger, Anal. Chem. 76 (2004) 6395.
[8] G. Gritzner, J. Kuta, Pure Appl. Chem. 56 (1984) 461.
[9] W.C. Du Plessis, T.G. Vosloo, J.C. Swarts, J. Chem. Soc., Dalton Trans. (1998) 2507.
[10] W.C. Du Plessis, J.J.C. Erasmus, G.J. Lamprecht, J. Conradie, T.S. Cameron, M.A.S. Aquino, J.C. Swarts, Can. J. Chem. 77 (1999) 378.
[11] E.W. Neuse, D.S. Trifan, J. Am. Chem. Soc. 85 (1963) 1952.
[12] J.H. Richards, E.A. Hill, J. Am. Chem. Soc. 81 (1959) 3484.
[13] F. Barriere, R.U. Kirss, W.E. Geiger, Organometallics 10 (1991) 2403, and references therein.
[14] See for example:
(a) C. Creutz, H. Taube, J. Am. Chem. Soc. 91 (1969) 3988;
(b) W.E. Geiger, N. Van Order, D.T. Pierce, T.E. Bitterwolf, A.L. Reingold, N.D. Chasteen, Organometallics 10 (1991) 2403;
(c) N. Van Order, W.E. Geiger, T.E. Bitterwolf, A.L. Reingold, J. Am. Chem. Soc. 109 (1987) 5680;
(d) D.T. Pierce, W.E. Geiger, Inorg. Chem. 33 (1994) 373;
(e) J. Conradie, T.S. Cameron, M.A.S. Aquino, G.J. Lamprecht, J.C. Swarts, Inorg. Chim. Acta 358 (2005) 2530.
[15] T.J. Curphey, J.O. Santer, M. Rosenblum, J.H. Richards, J. Am. Chem. Soc. 82 (1960) 5249.
[16] T. Kuwana, D.E. Bublitz, G. Hoh, J. Am. Chem. Soc. 82 (1960) 5811.
[17] R.F. Shago, J.C. Swarts, Anticancer Res. (2005), accepted.

hydroxylation of monophenol to form *o*-diphenol and subsequent oxidation to *o*-quinone (as a catecholase) [2]. These reactions are of great importance in plant and animal defense systems and signal transfer, which are involved in cuticular melanizations such as coloration of skin and hair, sclerotization of exoskeleton and lignin formation. Recently, it was found that these play a pivotal role in the defense reactions of plants against insect, bacteria, fungi and virus attack and abiostresses [3]. The oxidation of phenols under mild conditions is also of great interest in industrial catalysis and for the degradation of aromatic compounds for environmental ecology [4]. Therefore, there has been sequential interest in the study of PPO model compounds. In this paper we report that the oxidation of pyrogallol and catechol is catalyzed by the model compounds $[Cu_2(EGTB)(H_2O)_2(ClO_4)_2](ClO_4)_2 \cdot 6H_2O$ (I) and $[Co_2(EGTB)Cl_2](ClO_4)_2 \cdot 5H_2O$ (II).

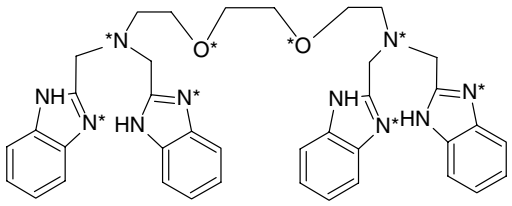
2. Experimental

2.1. Physical measurements

Elemental analyses for C, H and N were carried out on a Perkin–Elmer 2400. Electronic spectra were measured on a Shimadzu UV-265 spectrophotometer. The X-ray data for complexes I and II were collected on a Simens P4 and a Nonius Kappa CCD diffractomer, respectively. The structures were solved by direct methods and refined by least squares method on F^2_{obs} by using the SHELXTL-PC software package. Cyclic voltammetry (CV) was performed with a BAS-100 electrochemical analyzer on a conventional three-electrode cell, i.e., a glassy carbon electrode serving as the working electrode, a platinum wire as the counter electrode and an Ag/AgCl electrode as the reference. The supporting electrolyte, tetrabutylammonium perchlorate (TBAP), was recrystallized twice from methanol and dried overnight in a vacuum. The solvent *N*,*N*-dimethyl formamide (DMF) was sufficiently pure. Electrospray ionization (ESI) mass spectra were recorded on an API 2000 LC/MS/MS system.

2.2. Ligand synthesis

N,*N*,*N*′,*N*′-tetrakis(2′-benzimidazolylmethyl)-1,4-diethylene amino glycol ether (EGTB) was synthesized according to a similar method reported in the literature [5]. Ethylene glycol-bis-(β-aminoethylene)-*N*,*N*,*N*′,*N*′-tetraacetic acid (EGTA) and *o*-phenylenediamine (PDA) in a molar ratio of 1:4 were refluxed in glycol at 180 °C for 6–8 h until no water vapor was evolved. After cooling, a reddish crude product was precipitated by adding water, which was recrystallized a few times in ethanol, yielding a white power or colorless crystals.



EGTB

2.3. Synthesis of the complexes

EGTB (0.67 g, 1.0 mmol) and copper(II) perchlorate (0.74 g, 2.0 mmol) were, respectively, dissolved in methanol, and then were mixed. A blue precipitate formed after stirring at 50 °C for 5 h, and this was collected by filtration. This solid was dissolved in methanol and left standing for several days, yielding a blue crystal suitable for X-ray analysis. *Anal*. Calc. for $[Cu_2(EGTB)(H_2O)_2(ClO_4)_2](ClO_4)_2 \cdot 6H_2O$ (I) ($Cu_2C_{38}H_{56}N_{10}Cl_4O_{26}$): C, 36.02; H, 3.792; N, 11.06. Found: C, 36.47; H, 3.772; N, 11.24. UV–Vis [λ_{max}, nm (ε, $M^{-1}\,cm^{-1}$)] in MeOH: 271(24900), 671(233). CV data: $E_c = 0.026$ V, $E_a = 0.250$ V.

The complex $[Co_2(EGTB)Cl_2](ClO_4)_2 \cdot 5H_2O$ (II) was prepared by a similar method using $CoCl_2 \cdot 6H_2O$ and $NaClO_4 \cdot 6H_2O$ rather than $CoClO_4 \cdot 6H_2O$. *Anal*. Calc. for $Co_2C_{38}H_{50}N_{10}Cl_4O_{15}$: C, 45.60; H, 4.84; N, 14.00. Found: C, 45.57; H, 4.59; N, 14.01. UV–Vis [λ_{max}, nm (ε, $M^{-1}\,cm^{-1}$)] in DMF: 275(21860), 598(643). CV data: $E_a = 0.944$ V.

2.4. Measurements of polyphenol oxidase activities

The kinetics of the reactions were studied spectroscopically. Oxidative reactions of pyrogallol and catechol were carried out in methanol–Tris (i.e., trihydroxymethyl amino methane)–HCl buffer solution. The solution pH value and the reaction temperature were varied in the range 7.3–8.0 and 30–40 °C, respectively. Stock solutions of pyrogallol and catechol were prepared in 0.15 mM phosphoric acid to prevent autooxidation. The assay wavelength of pyrogallol and catechol oxidation were chosen to be 320 and 484 nm, respectively.

3. Results and discussion

3.1. The crystal structures

A summary of the crystallographic parameters and selected bond distances and angles of complex I are listed in Tables 1 and 2, respectively. The crystal structure is shown in Fig. 1. The coordination geometry

around each copper atom is distorted octahedral formed by three nitrogen atoms from the EGTB ligand and a coordinated water molecule in the basal plane, an EGTB ether oxygen and one perchlorate oxygen atom in the axial coordination sites. Cu–N(benzimidazole, bzim) bond lengths are 1.964(2) and 1.961(2) Å, Cu–N(amino) is 2.083(2) Å and the Cu–O(coordinated water) distance is 1.975(2) Å. Axial Cu–O bonds lengths are 2.4070(19) and 2.610(8) Å, which are significantly further away from the central Cu(II) ion than the planar oxygen and nitrogen atoms. Therefore, the axial bindings are weaker. The axial and other bond angles show, respectively, slight departure from 180° and 90°, so the coordination geometry of the copper is a long distorted octahedron. The Cu···Cu distance of the complex is 8.038(8) Å, which is too long to have binuclear coupling.

Table 1
Crystal parameters for complex I

Empirical formula	$C_{38}H_{56}Cl_4Cu_2N_{10}O_{26}$
M	1337.80
Crystal system	triclinic
Space group	$P\bar{1}$
Unit cell dimensions	
a (Å)	9.705(2)
b (Å)	10.665(2)
c (Å)	13.744(2)
α (°)	82.90(1)
β (°)	70.02(1)
γ (°)	89.20(1)
V (Å^3)	1326.1(4)
Z	2
D_c (g cm^{-3})	1.675
$F(000)$	688
Crystal size (mm)	$0.48 \times 0.38 \times 0.38$
θ ranges (°)	1.59–25.25
Reflections collected	5269
Independent reflections	4793
T_{max} and T_{min}	0.9931 and 0.9012
Number of parameters	439
GOF	0.985
Final R indices [$I > 2\sigma(I)$]	$R_1 = 0.0363$, $wR_2 = 0.0874$
R indices (all data)	$R_1 = 0.0515$, $wR_2 = 0.0913$
Largest difference peak and hole (e Å^{-3})	0.608, −0.312

Table 2
Selected bond distances (Å) and angles (°) for complex I

Cu–N(1)	1.964(2)
Cu–N(3)	1.961(2)
Cu–O(1)	2.4070(19)
Cu···Cu	8.038(8)
Cu–O(2)	1.975(2)
Cu–N(5)	2.083(2)
Cu–O(8)	2.610(8)
N(3)–Cu–O(2)	98.27(10)
N(3)–Cu–N(5)	82.00(9)
N(1)–Cu–O(1)	88.81(8)
N(5)–Cu–O(1)	80.46(8)
N(1)–Cu–O(8)	87.07(13)
N(5)–Cu–O(8)	87.53(13)
N(1)–Cu–O(2)	96.43(10)
N(3)–Cu–O(1)	95.14(9)
O(2)–Cu–O(1)	103.03(10)
N(3)–Cu–O(8)	85.73(14)
O(2)–Cu–O(8)	88.94(14)
O(1)–Cu–O(8)	167.71(12)

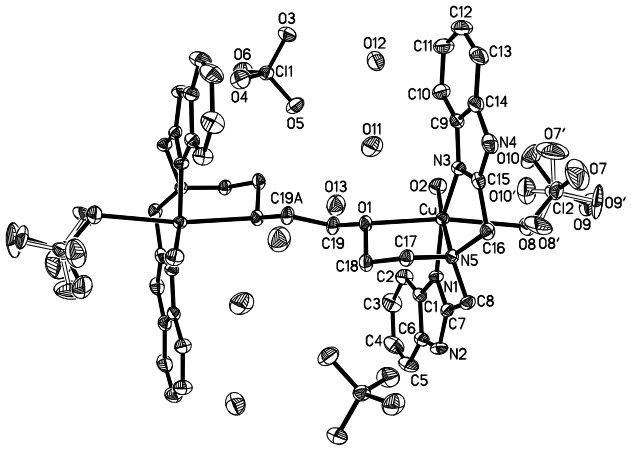


Fig. 1. ORTEP view of complex $[Cu_2(EGTB)(H_2O)_2(ClO_4)_2](ClO_4)_2 \cdot 6H_2O$ (CCDC No. 234479).

As shown in Fig. 2, each cobalt(II) center of complex II has a five coordinated trigonal bipyramidal geometry, which has been reported by us [6]. The average bond lengths of Co–N(bzim), Co–N(amino), Co–O(ether) and Co–Cl are 2.0325, 2.2844, 2.0845 and 2.2937 Å, respectively. The axial positions are occupied by the aliphatic amino nitrogen atom and the chloride ion. The Co···Co distance is 5.7138(10) Å, which is shorter than that of complex I. This internuclear distance may be in the range of negligible binuclear coupling [7].

3.2. CV data

The cyclic voltammogram (CV) of complex I contains a cathodic peak at 0.026 V and an anodic peak at 0.250 V, which are assigned to a two-electron redox process of $Cu(II)_2 \leftrightarrow Cu(I)_2$. For complex II, the $E_a = 0.944$ V is assigned to the oxidative peak of $Co(II)_2 \rightarrow Co(III)_2$.

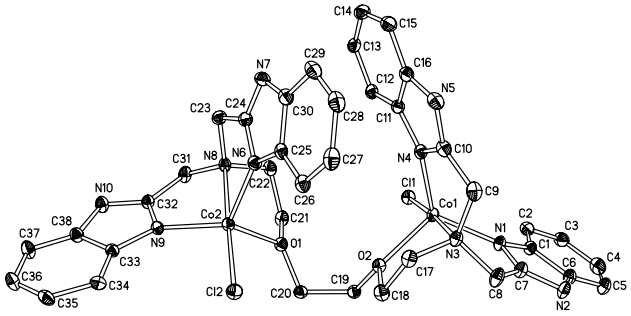


Fig. 2. ORTEP view of complex $[Co_2Cl_2(EGTB)]^{2+}$ (CCDC No. 176342).

Catechol and pyrogallol are sensitive to dioxygen in alkaline solution ($E = -0.23$ and -0.20 V versus SCE, respectively). They are easily oxidized to semiquinone and quinone. The anodic potentials of the two complexes are higher than that of the two substrates, therefore, the two complexes can oxidize catechol and pyrogallol.

3.3. Study on polyphenol oxidase activities

Assuming V_i is the initial velocity, it is found that V_i follows saturation kinetics with respect to substrate concentration [S]. At sufficiently low [S], a plot of V_i versus [S] is linear. When [S] becomes sufficiently high, the catalyst (here is model compound or mimetic enzyme, M) is saturated, the rate of reaction is zero-order and tends toward a limiting value, maximum velocity V_{max}. The kinetics is expressed quantitatively in the Michaelis–Menten equation.

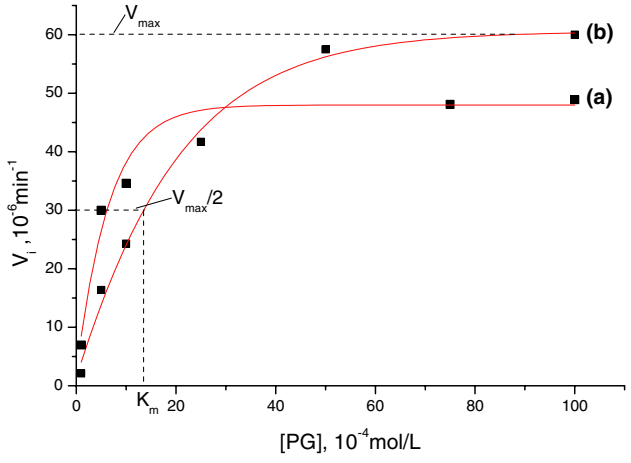


Fig. 3. Plot of initial rate V_i vs. [S]: (a) complex I; (b) complex II: [complex] = 2.5e(−5) mol/L, $T = 30$ °C, pH 8.0.

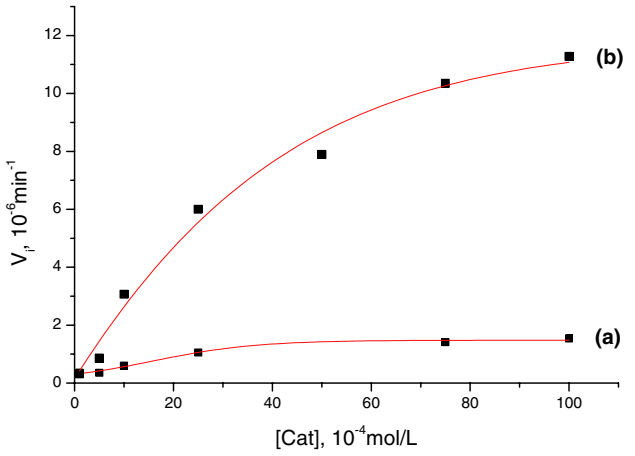


Fig. 4. Plot of initial rate V_i vs. [S]: (a) complex I; (b) complex II: [complex] = 1.0e(−4) mol/L, $T = 40$ °C, pH 8.0.

$$V = \frac{k_{cat}[M][S]}{K_m + [S]} = \frac{V_{max}[S]}{K_m + [S]} \quad \text{here } V_{max} = k_{cat}[M],$$

$$K_m = \frac{k_{-1} + k_2}{k_1} \text{ for reaction } M + S \underset{k_{-1}}{\overset{k_1}{\rightleftharpoons}} MS \xrightarrow{k_2} M + P$$

where k_{cat} is the turnover number, that is the number of moles of substrate converted to product (P) per minute per mole of the model compound. It is a pseudo-first-order rate constant of catalyst–substrate complex MS conversion to products. K_m is the Michaelis constant, k_1, k_{-1} and k_2 are the rate constants for MS formation, dissociation and product formation, respectively.

By applying traditional the Michaelis–Menten approach, values of the kinetic parameters V_{max}, K_m, k_{cat} and k_{cat}/K_m were obtained from the corresponding plot of V_i versus [S] (see Figs. 3, 4 and Table 3). Here k_{cat}/K_m is an apparent constant. It is not a true microscopic rate constant except in the extreme case, in which the rate-determining step in the reaction is dependent on both of catalyst and substrate. For pyrogallol, $k_{cat} = 1.92$(I), 2.42(II) min^{-1} and $K_m = 0.43e - 3$(I),

Table 3
The kinetic data of complexes

Complex	Substrate	T (°C)	pH	k_{cat} (min^{-1})	V_{max} (10^{-6} mol L^{-1} min^{-1})	K_m (10^{-3})	k_{cat}/K_m (min^{-1})
Control	pyrogallol	30	8.0		0.2		
I			8.0	1.92	48.0	0.43	4465
			7.6	1.50	37.5	0.39	3846
			7.3	1.10	27.5	0.35	3142
II			8.0	2.42	60.5	1.34	1805
			7.6	1.72	43.0	1.28	1343
			7.3	0.33	8.25	1.07	308
Control	catechol	40	8.0		0.1		
I			8.0	0.018	1.8	2.15	8.4
			7.6	0.004	0.4	2.03	1.9
			7.3	0.002	0.2	1.98	1.0
II			8.0	0.117	11.7	2.77	42.2
			7.6	0.019	1.9	2.51	7.5
			7.3	0.015	1.5	2.47	6.1

1.34e − 3(II) at pH 8.0 and 30 °C for complex I and II, respectively. While for catechol, k_{cat} = 0.018(I), 0.117(II) min^{-1} and K_m = 2.15e − 3(I), 2.77e − 3(II) at pH 8.0 and 40 °C. In Michaelis–Menten kinetics, the experimentally determined value K_m is considered a constant and is characteristic of catalyst and substrate under specific conditions. It is an apparent dissociation constant and reflects the affinity of the catalyst for the substrate [8]. As described above, the rate constants k_{cat} toward pyrogallol catalyzed by complex II are higher than the corresponding values for complex I. Moreover, K_m (II) values are higher than K_m (I), which suggest that dissociation of MS leaving oxidative products for complex II is easier. Whereas for catechol oxidation, the K_m values are close to each other and the catalytic rate constant k_{cat} of complex I is much lower than that of complex II. This is due to looser unsaturated coordination of the cobalt ion and a short nuclear distance. Moreover, complex II can bind and activate oxygen molecules based on the appearance of an ultraviolet absorption peak at 320 nm, when O_2 was bubbled through a complex-DMF solution for 10 min at room temperature. This peak is assigned to the π^*_σ orbit of the peroxide ion $O_2^{2-} \rightarrow$ Co(II) $d_{x^2-y^2}$ LMCT (ligand to metal charge transfer) transition. However, complex I cannot directly bind and activate oxygen before reduction. A steric match between the substrate and complex is believed to require a close enough binuclear distance (2.9–3.6 Å) in a typical catalysis of binuclear copper tyrosinase, because the first step involves two nuclear bindings with two hydroxyl groups of catechol [9,10]. The lower activity of complex I shows that its binuclear distance is too long to catalyze cooperatively. Moreover, it is found that catalytic activities toward pyrogallol are much higher than those of catechol under the same conditions.

The oxidation rate constants increase with increasing pH values. The rate-determining step of the reactions is considered to be the first proton of a polyphenol being abstracted to form the corresponding semiquinones [11,12], hence, in the pH range 7.3–8.0, the higher the pH value, the better the activities.

3.4. Oxidative mechanisms

In order to approach the oxidative mechanism of pyrogallol (PG) and catechol (Cat), their oxidative products have been checked by ESI mass spectra in the positive mode (see Figs. 5 and 6). The oxidation mechanism of pyrogallol is supposed as shown in Scheme 1. Pyrogallol is first deprontonated and oxidized resulting in quinone(a), further it is followed by cyclo-opening and degradation to produce a formyl ion (m/z = 29) and methyl pentenate (b, m/z = 65) [13]. Then the cyclo-opened intermediate is condensed with a pyrogallol to form purpurogallin [14], which dimerizes to give a dimer (m/z = 436) by linking through hydrogen

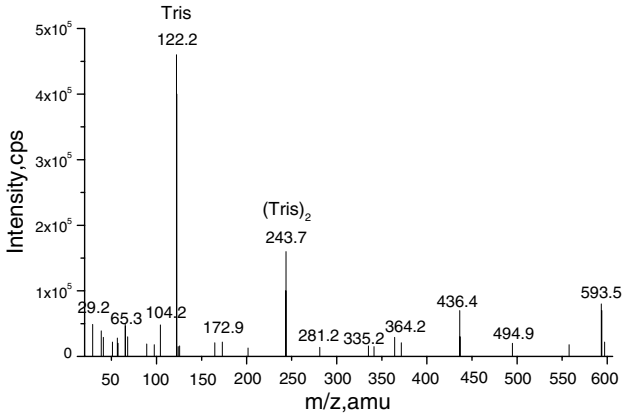


Fig. 5. ESI mass spectra of the oxidative products of pyrogallol catalyzed by complex I.

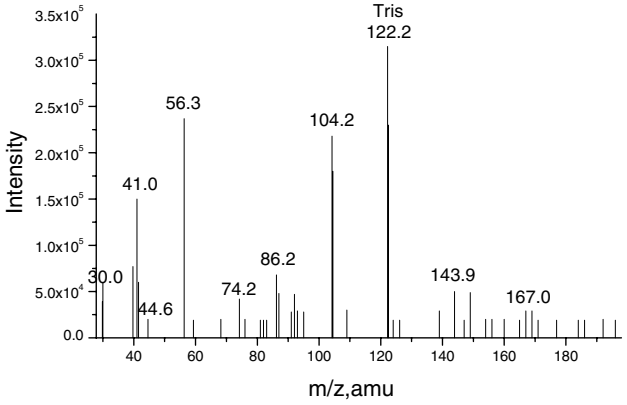
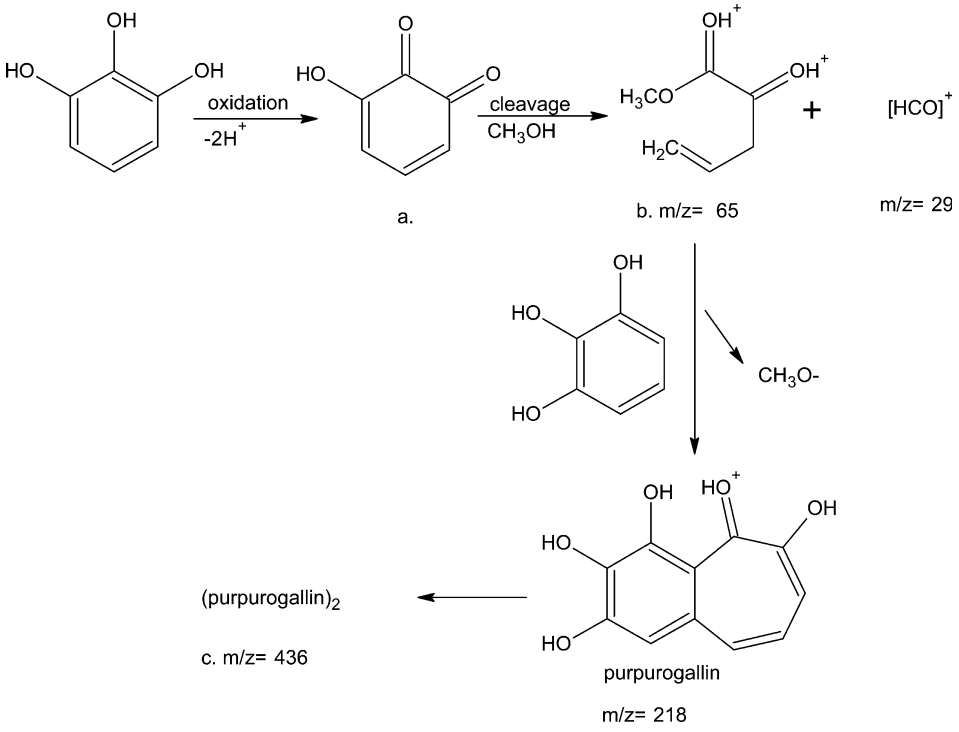


Fig. 6. ESI mass spectra of the oxidative products of catechol catalyzed by complex I.

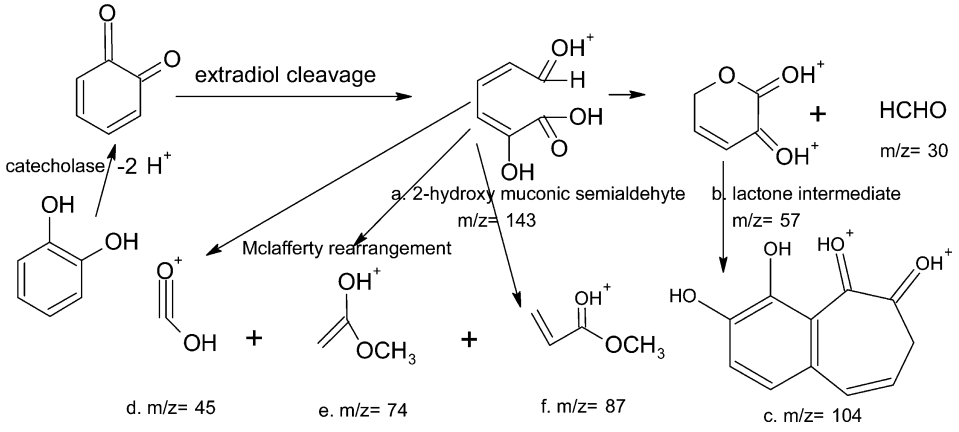
bonds. The molecular ion peaks at m/z = 594 and 495 might be assigned to $[(EGTB)Cu_2(H_2O)_2(ClO_4)_2(PG–O_2)]^{2+}$ and $[(EGTB)Cu_2(H_2O)_2(PG–O_2)]^{2+}$, respectively. Their existences indicate that pyrogallol oxidation may be companied with changes of the coordination structure and oxidative state of the copper ions, such as loss of a coordinated ClO_4^- and formation of a copper(I) complex ion.

The possible mechanism of catechol oxidation is shown in Scheme 2. The formation of *o*-quinone is similar to other reports [15,16], following it is the cyclo-opening which results in 2-hydroxy muconic semialdehyde (a, m/z = 143). It is followed by dehydration and cyclization, forming a lactone intermediate (b, m/z = 57) and formaldehyde (m/z = 30). Then the lactone intermediate is condensed with catechol to form a purpurogallinoid (m/z = 104). All of the processes are similar to the oxidation of pyrogallol. The molecular ion peaks at m/z = 45, 74 and 86 might be produced from the products of a McLafferty rearrangement [17].

The oxidative products of pyrogallol and catechol catalyzed by the two complexes are similar, which



Scheme 1. Proposed mechanism of pyrogallol oxidation.



Scheme 2. Proposed mechanism of catechol oxidation.

indicate that the catalytic mechanisms of the complexes are analogical, i.e., pass an extradiol mechanism [18]. The difference in mechanisms is the first hydrogen atom to be abstracted. For complex I, it may be an hydroxyl ion that abstracts the first proton of polyphenol. The hydroxyl ion is from dissociation of a coordinated water due to a hydrogen bonding interaction with perchlorate or the other water molecule. While complex II abstracts the proton using its bound and activated oxygen, which is a peroxide type ion and a stronger proton acceptor. Hence, the oxidative mechanism of polyphenol catalyzed by complex I is similar to that of the mononuclear non-heme tyrosinase rather than binuclear copper tyrosinase, while the catalytic mechanism of complex II is more similar to coupled binuclear copper tyrosinase.

4. Supplementary data

The crystallographic structural data of the two complexes have been deposited with the Cambridge Crystallographic Data Center as supplementary publication CCDC No. 234479 (I) and CCDC No. 176342 (II). Copies of this information may be obtained free of charge from The Director, CCDC, 12 Union Road, Cambridge, CB2 1EZ, UK, fax: +44 1223 366 033, e-mail: deposit@

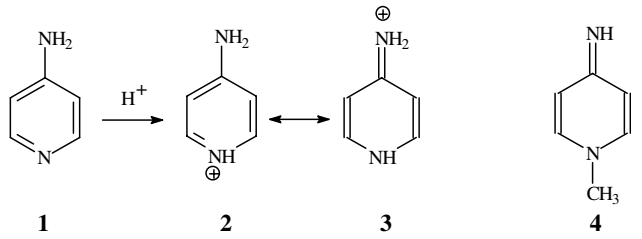
ccdc.ac.uk or on the web www: http://www.ccdc.cam.ac.uk.

Acknowledgments

This research is supported by the Key Fundamental Project of China (2002CCA00500), and partially supported by the College of Chemistry, Peking University.

References

[1] G. Prota, Med. Res. Rev. 8 (1988) 525.
[2] M. Trémolières, J.B. Bieth, Phytochemistry 23 (1984) 501.
[3] D. Strack, W. Schliemann, Angew. Chem. Int. Ed. 40 (2001) 3791.
[4] J. Haggin, Chem. Eng. News 71 (1993) 23.
[5] H.M.J. Hendriks, P.J.M.W.L. Birker, J.V. Rijin, J. Am. Chem. Soc. 104 (1982) 3607.
[6] Li Zhu, Zhan-Ru Liao, Zhe-Ming Wang, Chinese J. Inorg. Chem. 18 (2002) 731.
[7] R. Lontie, Copper Proteins and Copper Enzymes, vol. 2, CRC Press Inc., Boca Raton, FL, 1984, p. 179.
[8] D.B. Northrop, J. Chem. Educ. 75 (1998) 1153.
[9] J. Manzur, A.M. Garcia, V. Rival, A.M. Atria, J. Valenzuela, E. Spondine, Polyhedron 16 (1997) 2299.
[10] J. Reim, B. Krebs, J. Chem. Soc., Dalton Trans. (1997) 3793.
[11] Luc Magnani, Emie M. Gaydou, Jean Claude Hubaud, Anal. Chim. Acta 411 (2000) 209.
[12] Yuan Zhuo-Bin, Gao Ruo-Mei, Chem. J. Chinese Univ. 18 (9) (1997) 1438.
[13] Takashi Tanaka, Chie Mire, Isao Kouno, Tetrahedron 58 (2002) 8851.
[14] Ruo-Mei Gao, Zhuo-Bin Yuan, Zhi-Qiang Zhao, Xiu-Rui Gao, Bioelectrochem. Bioenerg. 45 (1998) 41.
[15] Zhan-Fen Chen, Zhan-Ru Liao, Dong-Feng Li, Wu-Ke Li, X-iang-Gao Meng, J. Inorg. Biochem. 98 (2004) 1315.
[16] Ademir Neves, Viane M. Rossi, Adailton J. Bortoluzzi, Bruno Szpoganicz, Clayton Wiezbicki, Erineu Schwingel, Inorg. Chem. 41 (2002) 1788.
[17] Pe-Cai Fang, J. Mol. Struct. (Theochem) 571 (2001) 83.
[18] Ryo Yamahara, Seiji Ogo, Hideki Masada, Yoshihito Watanabe, J. Inorg. Biochem. 88 (2002) 284.



Scheme 1.

NMR and UV spectroscopy is accomplished, in particular, the linear-dichroic infrared (IR-LD) spectral analysis is applied for the identification of the IR bands corresponding to the structural fragments of the 4-APH$^+$ imino-form. A spectral technique permitting the orientation of the solid samples as a liquid crystal suspension is applied for the measurements by IR polarized light.

2. Experimental

2.1. Synthesis

The complex salt 4-aminopyridinium tetrachloropalladate(II) ($[C_5H_7N_2]_2\cdot[PdCl_4]$) is prepared as follow: 5 ml methanol solution containing 0.8977 g 4-AP (Merck) and 0.0987 g $(NH_4)_2PdCl_4$ (Sigma), corresponding to a molar ratio Pd:4-AP = 1:1, was added to 5×10^{-1} M H_2SO_4 in the same solvent. From the thus produced orange solution, after 10 days brown crystals were obtained, which were filtered, washed with methanol and dried over P_2O_5 in air at 298 K. Yield: 34%. (*Anal.* Calc. for $[C_5H_7N_2]_2[PdCl_4]$: C, 27.3; H, 3.7; N, 12, 7; Cl, 32.2. Found: C, 27.2; H, 3.7; N, 12.8; Cl, 32.2%.) The most intensive signal in the mass spectrum of the protonated salt is the peak at *m*/*z* 95.01, characteristic of the singly charged 4-aminopiridinium cation (4APH$^+$) with a molecule weight of 95.01.

2.2. Methods

The IR spectra were measured on a Bomem-Michelson 100 FT-IR spectrometer (4000–400 cm^{-1}, ±2 cm^{-1} resolution, 150 scans) equipped with a Perkin–Elmer wire-grid polarizer. The non-polarized solid-state IR spectra were recorded using the KBr disk technique. The oriented samples were obtained as a suspension in a nematic 4′-cyano-4′-alkylbicyclohexyl mixture (ZLI 1695 in the Merck notation), mesomorphic at room temperature. The poor IR spectrum makes it possible to record the guest-compound bands in the whole 4000–400 cm^{-1} range. The presence of an isolated nitrile stretching IR band at 2233 cm^{-1} additionally serves as an orientation indicator. The effective orientation of the solid-state sample was achieved through the following procedure: about 5 mg of the compound studied was added to the appropriate liquid crystal substance until a slightly viscous mixture was obtained. The suspension thus prepared was pressed between two KBr-plates rubbed out in advance in one direction by means of fine sandpaper. The grinding of the prepared mull in the rubbing direction promotes an additional orientation of the sample [16,17].

The grounds of the IR-LD spectroscopy and in particular the *difference-reduction* procedure used for polarized IR spectra interpretation is described at length in [18–21]. It consists in subtraction of the perpendicular spectrum (IRs, resulting from 90° angle between the polarized light beam electric vector and the orientation of the sample) from the parallel one (IRp) obtained with a co-linear mutual orientation (Fig. 1). The recorded *difference* (IRp-IRs) spectrum (Fig. 1) divides the corresponding parallel (Ap) and perpendicular (As) integrated absorbancies of each band into positives originating from transition moments which form an average angles with the orientation direction (**n**) between 0° and 54.7° (magic angle), and negative ones corresponding to transition moments between 54.7° and 90°. As the next operation, the perpendicular spectrum, multiplied by the parameter **c**, is subtracted from the parallel one and **c** has to vary until up to a band or set of bands are eliminated. The simultaneous disappearance of bands in the obtained (IRp-cIRs) *reduced* IR-LD spectrum indicates a co-linearity of the corresponding transition moments, thus giving rise to information regarding the mutual disposition of the molecular fragments. This elimination method is graphically carried out using a subtracting procedure attached to the program for processing of IR spectra.

The ^{1}H NMR measurements were made at 298 K with a Bruker DRX-400 spectrometer using 5 mm tubes and D_2O as solvent. The chemical shift reference was sodium 3-(trimethylsilyl)tetradeuteriopropionate. The UV spectra (2.5×10^{-4} aqueous solutions, 1 cm quarz cell) were recorded on a Perkin–Elmer Lambda 15 UV–Vis spectrophotometer.

The X-ray diffraction intensities were measured on a Siemens P4 diffractometer equipped with Mo Kα radiation (λ = 0.71073 Å). The structure was solved by a direct method [22] and refined against – F^2 [23]. An ORTEP plot illustrates the anion and cation structures at the 50% probability level. Relevant structure data and refinement details are presented in Table 1, selected bond distances and angles – in Table 2. The hydrogen atoms were positioned on geometrical grounds in all shown structures.

The elemental analysis was performed by standard procedures for C and H (as CO_2 and H_2O), N by the Dumas method and Cl by titration with $Hg(NO_3)_2$ after wet digestion of the sample. The FAB mass spectra

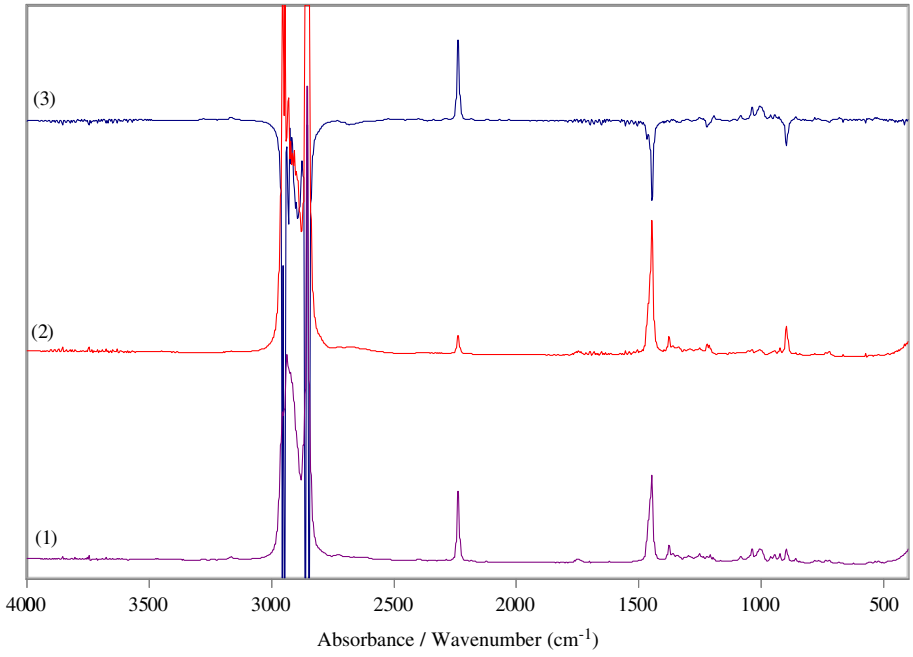


Fig. 1. Parallel (1), perpendicular (2) and difference (3) IR-LD spectra of ZLI 1695.

Table 1
Crystal data, data collection and refinement conditions for $[C_5H_7N_2]_2\cdot[PdCl_4]$

Empirical formula	$C_{10}H_{14}N_4Cl_4Pd$
Formula weight	438.45
Temperature (K)	293(2)
Wavelength (Å)	0.71073
Crystal system, space group	monoclinic, P_2/n
Unit cell dimensions	
a (Å)	7.8440(16)
b (Å)	7.5450(15)
c (Å)	13.608(3)
α (°)	90
β (°)	96.23(3)
γ (°)	90
Volume (Å^3)	800.6(3)
Z	2
Calculated density (Mg/m^3)	1.819
Absorption coefficient (mm^{-1})	1.817
$F(000)$	432
Crystal size (mm)	$0.67 \times 0.59 \times 0.37$
θ range for data collection (°)	2.70–30.02
Limiting indices	$0 \leftarrow h \leftarrow 11$, $-10 \leftarrow k \leftarrow 0$, $-19 \leftarrow l \leftarrow 19$
Reflections collected/unique (R_{int})	2460/2308 (0.0567)
Completeness to $\theta = 30.02$ (%)	98.2
Absorption correction	semi-empirical
Maximum and minimum transmission	0.09956 and 0.05854
Refinement method	full-matrix least-squares on F^2
Data/restraints/parameters	2308/0/89
Goodness-of-fit on F^2	1.008
Final R indices [$I > 2\sigma(I)$]	$R_1 = 0.0451$, $wR_2 = 0.1194$
R indices (all data)	$R_1 = 0.0646$, $wR_2 = 0.1338$
Largest difference peak and hole (e/Å^3)	1.227 and −0.736

Table 2
Selected bond lengths [Å] and angles [°] for $[C_5H_7N_2]_2\cdot[PdCl_4]$

Pd(1)–Cl(1)	2.2940(11)	Cl(1)#1–Pd(1)–Cl(1)	180.0
Pd(1)–Cl(2)	2.3073(14)	Cl(1)#1–Pd(1)–Cl(2)	89.99(5)
C(5)–C(6)	1.359(8)	Cl(1)–Pd(1)–Cl(2)	90.01(5)
C(5)–C(4)	1.378(6)	C(6)–C(5)–C(4)	120.7(5)
N(1)–C(6)	1.304(8)	C(6)–N(1)–C(2)	119.9(6)
N(1)–C(2)	1.336(9)	N(4)–C(4)–C(5)	121.6(5)
C(4)–N(4)	1.316(7)	N(4)–C(4)–C(3)	121.9(5)
C(4)–C(3)	1.428(8)	C(5)–C(4)–C(3)	116.5(5)
C(3)–C(2)	1.339(10)	C(2)–C(3)–C(4)	118.5(6)
		N(1)–C(6)–C(5)	121.6(6)
		N(1)–C(2)–C(3)	122.7(6)

Symmetry transformations used to generate equivalent atoms: # $1-x, -y+1, -z+1$.

utilized for the molecule weight determination were recorded on a Fisons VG Autospect instrument employing 3-nitrobenzyl alcohol as a matrix.

3. Results

3.1. Crystal structure of $[C_5H_7N_2]_2\cdot[PdCl_4]$

The salt is formed by discrete groups consisting of the $PdCl_4^{2-}$ anion and two N_{py} protonated $C_5H_7N_2^+$ cations without appreciable Pd···N interactions (Fig. 2). The coordination around the Pd(II) ion is square planar with Pd–Cl(1) and Pd–Cl(2) bonds 2.2940(11) and 2.3073(14) Å, respectively. The corresponding Cl–Pd–Cl

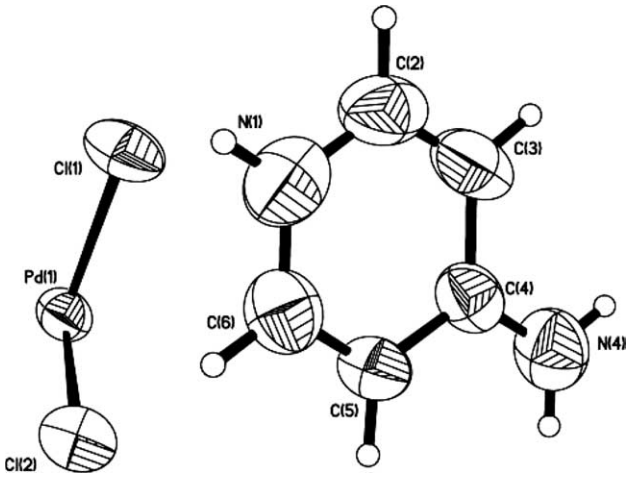


Fig. 2. ORTEP plot of $[C_5H_7N_2]_2[PdCl_4]$ with 50% thermal ellipsoids; hydrogen atoms are shown as spheres of arbitrary radii.

angles are 180.00°, 89.99(5)° and 90.01(5)° (Table 2). The data are similar to those observed for tetrachloropalladate(II) salts of similar organic compounds [13,14]. The corresponding distances and angles for $C_5H_7N_2^+$ (Table 2) are typical of the protonated forms of 4AP derivatives [13–15].

3.2. IR-LD spectral analysis

The IR spectral evidence about the aromatic character of the 4-AP pyridine ring is summarized in our previous papers [17,24]. The most typical features in this respect are the characteristic bands of the pyridine skeleton vibrations at 1602 and 1508 cm^{-1}, and the out-of-plane peak at 824 cm^{-1} (Fig. 3), signed according to Wilson notation [25] as 8a, 19a and 11-γ_{CH}, respectively. These bands are absent in the 4-aminopyridinium tetrachloropalladate(II) IR spectrum, instead three new peaks at 1590, 1530 and 780 cm^{-1} are at hand (Fig. 3). According to [9,10], the first two maxima correspond to mixed $\nu_{C=N+}$ and $\nu_{C=C}$-vibrations of the imino-form (Scheme 1). In the IR spectrum of 1-methyl 1,4-dihydro-4-imino-pyridine (Scheme 1), where this form is fixed, the maxima are observed at 1656 and 1542 cm^{-1} [10]. The band at 780 cm^{-1}, which in our case (Fig. 3) should be assigned to the $\gamma_{=CH}$ out-of-plane mode, exhibits at 806 cm^{-1} in the 4-aminopyridine hydrochloride spectrum [9,10].

To the NH_2-stretching bands in the solid IR of 4-aminopyridine belong the peaks at 3437 ($\nu^{as}{}_{NH_2}$) and 3305, 3085 cm^{-1} ($\nu^{s}{}_{NH_2}$), the doublet $\nu^{s}{}_{NH_2}$-band structure is Fermi resonance provoked as result of $NH\cdots N_{py}$ hydrogen bond formation [17,24]. The analogous maxima in the 4-aminopyridinium tetrachloropalladate(II) spectrum is observed at 3394 ($\nu^{as}{}_{NH_2}$) and 3325, 3120 cm^{-1} ($\nu^{s}{}_{NH_2}$). In this case the Fermi resonance splitting is probably caused by a $(H)N^+–H\cdots Cl$ hydrogen bond (with a $H\cdots Cl$ distance of 2.58 Å). The new band at 3215 cm^{-1} (Fig. 3) should be assigned to a ν_{NH}-vibration created by the protonated N_{py}–H bond (Fig. 2). With regards to the scissoring (δ_{NH_2}) band at 1650 cm^{-1} in the 4-AP spectrum (Fig. 2), the corresponding peak for tetrachloropalladate(II) salt is insignificantly high-frequency shifted to 1656 cm^{-1} (Fig. 3).

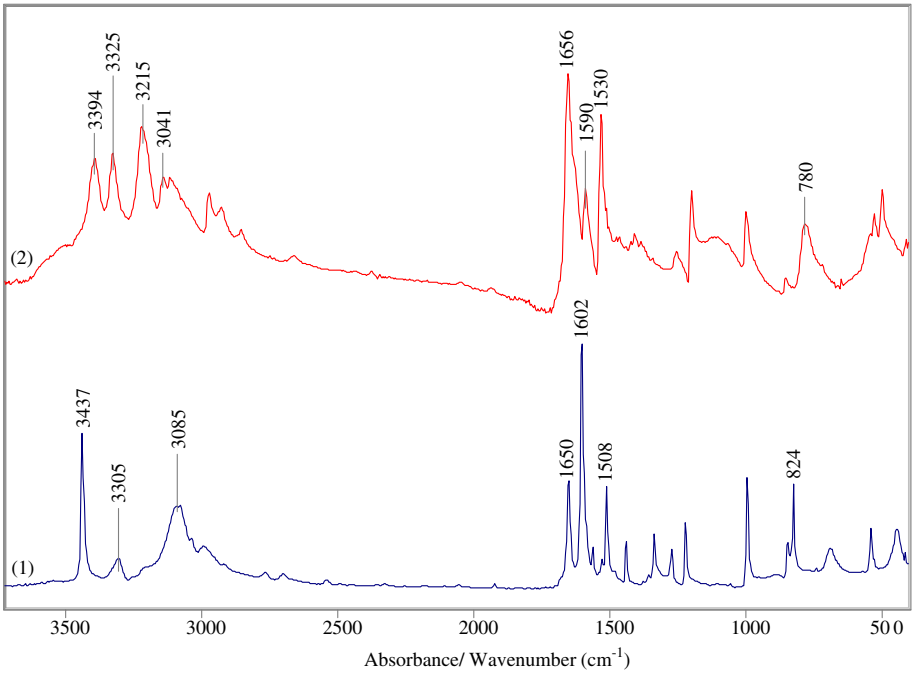
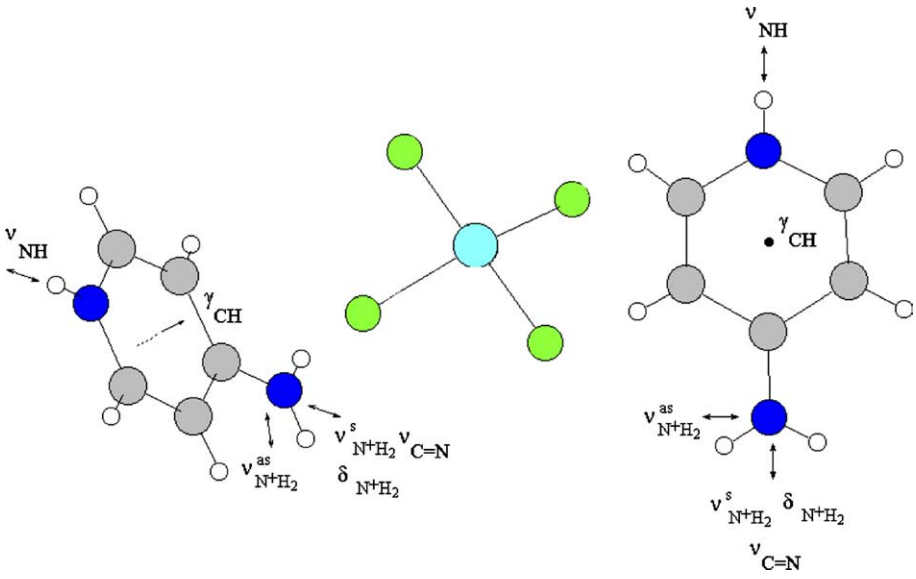


Fig. 3. 4000–400 cm^{-1} solid-state IR spectra of 4-aminopyridine (1) and the 4-aminopyridinium tetrachloropalladate(II) complex salt (2).

The assumed above-characteristic band assignment of the $4APH^+$ structural fragments is confirmed by IR-LD spectral analysis using the difference-reducing procedure described in the experimental part. However, the result interpretation is difficult due to of two different oriented $4APH^+$ moieties in the unit cell of the tetrachhloropalladate(II) lattice (see Table 1, respectively, Scheme 2). This supposed the presence of pairs of corresponding maxima as is shown in Fig. 4, containing the curve-fitted IR spectrum of the tetrachloropalladate(II) salt as a suspension in liquid crystal ZLI 1695. Expecting this precondition, the following results by means of a reducing procedure are obtained. The elimination of the δ_{N+H_2} intensive peak at 1645 cm^{-1} (Fig. 4) must provoke the disappearance of all bands belonging to the transition moments along same direction (Scheme 2). These are the doublet $\nu^s{}_{NH_2}$ band at 3323 and 3143 cm^{-1}, the ν_{NH}-maximum at 3222 cm^{-1}, and also the connected by mixed $\nu_{C=N+}$ and $\nu_{C=C}$-vibration bands at 1632, 1588 and 1532 cm^{-1} (Fig. 4). Simultaneously, the corresponding peaks of the other differently oriented $4APH^+$ cation (Scheme 2) of the same unit cell are revealed (Fig. 4)



Scheme 2.

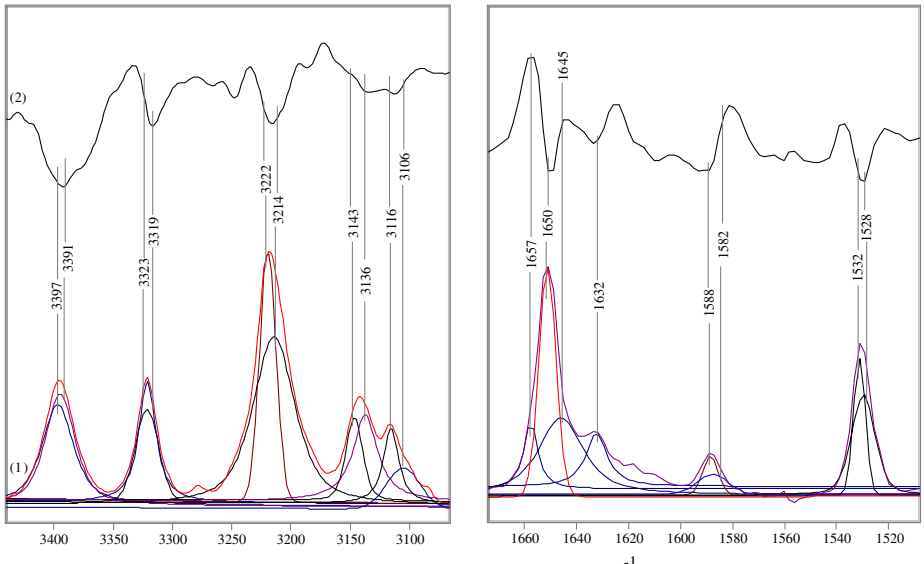


Fig. 4. 3500–3000 and 1700–1500 cm^{-1} IR spectra of the 4-aminopyridinium tetrachloropalladate(II) salt as a suspension in ZLI 1695: non-polarized curve-fitted spectrum (1) and reduced IR-LD spectrum after elimination of the δ_{N+H_2} band at 1650 cm^{-1} (2).

3.3. ^1H NMR data

The suggested imino-tautomeric form of the compound studied is also obtained from ^1H NMR spectra in D_2O. The chemical shifts for the pyridine proton signals of 4-AP, belonging to C(3)H and C(2)H (Fig. 2) are at 6.92 (2H, q) and 8.04 (2H, q) ppm, respectively. The solution of the protonated salt shows two downfield shifted doublet peaks at 7.18 and 8.23 ppm, thus indicating a redistribution of the electron density. The last result is compared to the analogous data of the 4-AP/D_2SO_4 system, characterized by pairs of doublets at 8.44 and 7.22 ppm. The obtained chemical shifts are similar to the previous data of 4-AP salts [10,11] and other protonated aminopyridine derivatives [12].

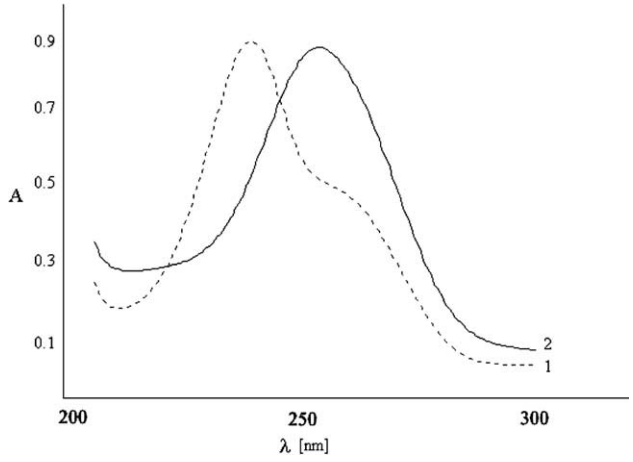


Fig. 5. UV spectra of 4-AP (1) and the 4-aminopyridinium tetrachloropalladate(II) salt (2), aqueous solutions.

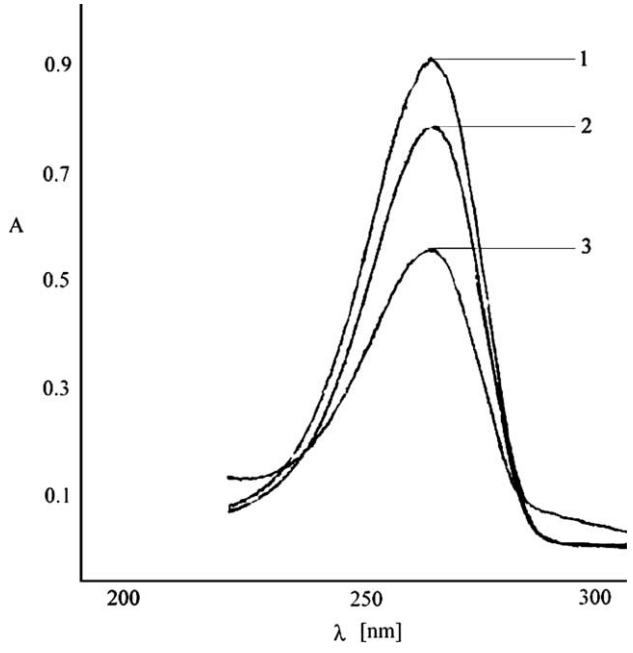


Fig. 6. UV spectra of 4-AP in 10% (1), 40% (2) and 98% H_2SO_4 (3).

3.4. UV spectra

In accordance to the data in the literature [10,12,26], the electronic spectrum of 4-AP shows two characteristic to pyridine aromatic system bands at 246 (ε = 11 056 l mol^{-1} cm^{-1}) and 264^{sh} nm (ε = 788 l mol^{-1} cm^{-1}) (Fig. 5). The spectrum of the protonated compound as an aqueous solution (Fig. 5) contains one broadband at 255 nm (ε = 10 460 l mol^{-1} cm^{-1}), also observed for solutions of neutral 4-AP in 10%, 45% and 98% H_2SO_4 (Fig. 6).

4. Discussion

The X-ray analysis of the 4-aminopyridinium tetrachloropalladate(II) complex salt directly confirms the previous theoretical and experimental data concerning the formation of the 4-AP cation through a proton attached to the ring nitrogen [7,8,13–15]. It is more complicated to reveal its electronic structure and the charge distribution within it. As it is stated above, our IR spectral results are in accordance with the conclusions published in [9,10] which suggest an imino-form stabilization in 4-aminopyridinium hydrochloride with a proton added to the exocyclic nitrogen (see Scheme 1). It is assumed that this charge location is due to the electron-donation effect of the amino group [9,10].

The conclusions thus discussed are grounded on the investigation of solid 4-aminopyridine salts. Like our results, the published ^1H NMR spectral data of solutions of 4-AP in D_2SO_4 or trifluoroacetic acid show a downfield shift for the signals of the pyridine hydrogens [10–12]. This effect is assumed as a redistribution of the electronic structure and a removal of the tautomeric equilibrium to the imino-form.

In this respect the UV spectral study of the 4-aminopyridinium tetrachloropalladate(II) complex salt requires particular discussion. As a rule the protonated aminopyridines are obtained as solutions in strong acids (most often H_2SO_4) and this procedure leads N_{py} monocations being obtained. However, dissolving in concentrated H_2SO_4 stabilized the dication structure and the corresponding effects in the aminopyridine UV and NMR spectra are examined in [10–12]. Although the problem is not clearly discussed, the authors suggest a 4-aminopyridinium monoprotonation in up to 80% H_2SO_4 and only 98% H_2SO_4 caused an additional protonation on the exocyclic nitrogen. Our previous study of the protonated 2-aminopyridine confirms these conclusions [27]. However, the UV spectra of 2-aminopyridinium sulfate dissolved in 10% H_2SO_4 are very close to those of the non-charged 2-aminopyridine, both

exhibiting two maxima at about 230 (π-band) and 290–305 nm range (α-band) [27]. This result indicates a preservation of the aromatic character of the pyridine ring. In concentrated H_2SO_4 2-aminopyridinium sulfate shows only one band at 258 nm ($\varepsilon = 5600\ l\ mol^{-1}\ cm^{-1}$) and this effect is not explain by the formation of the imino-structure, but by eliminations of the n–π conjugation and hypsochromic shift of the π-spectral band, both as a result of the blockage of the amino nitrogen [27] (see also [11]).

The UV spectral data of the 4-aminopyridinium tetrachloropalladata(II) complex salt are different. Its UV spectrum in 0.1 M aqueous solution (equivalent to solution in 40% H_2SO_4) exhibits only the broadband at 255 nm ($10\,460\ l\ mol^{-1}\ cm^{-1}$) (Fig. 5), like the same results obtained for solutions in H_2SO_4 irrespectively of the acid concentration (Fig. 6). The parameters of this absorption maxima are typical for the imino-forms and are very near to those of 1-methyl-1,4-dihydro-4-imino-pyridine (Scheme 1) and 1-methyl-4-amino-pyridinium salts [10,26].

All the presented data assumed a stabilization of the imino-form of the protonated 4-AP in the solid state as well as in solution. These data correlated well also with the known theoretical ones [9,10], also indicating positive charge location on the NH_2-group and stabilization of the thus experimental confirmed imino-form after N_{py}-protonation. Next a more detailed comparative structural investigation of protonated aminopyridines and their derivatives should additionally confirm the conclusions thus suggested.

5. Supplemental materials

Crystallographic data for the structural analysis have been deposited with the Cambridge Crystallographic Data Center, CCDC 220756. Copies of this information may be obtained from the Director, CCDC, 12 Union Road, Cambridge, CB2 1EZ, UK (fax: +44 1223 336 033; e-mail: deposit@ccdc.cam.ac.uk or http://www.ccdc.cam.ac.uk).

Acknowledgment

B. Ivanova is grateful to the Alexander von Humboldt Foundation for a fellowship.

References

[1] P. Gisele, C.A. Carlos, C. Yara, Eur. J. Pharmacol. 469 (2003) 57.
[2] A. Nino, C. Munoz-Caro, Biophys. Chem. 91 (2001) 49.
[3] C. Munoz-Caro, A. Nino, Biophys. Chem. 96 (2002) 1.
[4] S. Akyuz, J. Mol. Struct. 482 (1999) 117.
[5] Y. Buyukmurat, S. Akyuz, J. Mol. Struct. 651 (2003) 533.
[6] B.B. Ivanova, H. Mayer-Figge, J. Coord. Chem. 58 (2005) 653.
[7] H. Konishi, H. Kato, T. Yonezawa, Theoret. Chim. Acta (Berl.) 19 (1970) 71.
[8] J. Fossey, A. Loupy, H. Strzelecka, Tetrahedron 37 (1981) 1935.
[9] E. Spiner, J. Chem. Soc. (1962) 3119.
[10] B.D. Batts, E. Spiner, Aust. J. Chem. 22 (1969) 2595.
[11] Z. Dega-Szafran, A. Kania, B. Nowak-Wydra, M. Szafran, J. Mol. Struct. 322 (1994) 223.
[12] S. Smrckova, K. Juricova, V. Prutianpv, Czech. J. Chem. Soc., Chem. Commun. 59 (1994) 2057.
[13] M. Ranninger, S. Carrera, S. Blanco, Polyhedron 4 (1985) 1379.
[14] H. Sheng-Zhi, Jiegou Huaxue 19 (2000) 234.
[15] J. Sugiyama, J. Meng, T. Matsurra, Acta Crystallogr., Part C 58 (2002) o242.
[16] B.B. Ivanova, M.G. Arnaudov, P.R. Bontchev, Spectrochim. Acta A 60 (2004) 855.
[17] M.G. Arnaudov, B.B. Ivanova, Sh. Dinkov, Vibr. Spectrosc. 37 (2005) 145.
[18] B. Jordanov, R. Nentchovska, B. Schrader, J. Mol. Struct. 297 (1993) 2922.
[19] B. Jordanov, B. Schrader, J. Mol. Struct. 347 (1995) 389.
[20] J. Michl, E.W. Thulstrup, Spectroscopy with Polarized Light. Solute Alignment by Photoselection, in Liquid Crystals, Polymers, and Membranes, VCH, New York, 1986.
[21] E.W. Thulstrup, J.H. Eggers, Chem. Phys. Lett. 1 (1968) 690.
[22] G.M. Sheldrik, SHELXS-97. Program for Crystal Structure Solution, University of Göttingen, Göttingen, Germany, 1997.
[23] G.M. Sheldrik, SHELXL-97. Program for Crystal Structure Solution, University of Göttingen, Göttingen, Germany, 1997.
[24] M.G. Arnaudov, B.B. Ivanova, Sh. Dinkov, Cents. Eur. J. Chem. 2 (2004) 589.
[25] G. Varsanyi, Vibrational Spectra of Benzene Derivatives, Academiai Kiado, Budapest, 1969.
[26] S.F. Mason, J. Chem. Soc. (1960) 219.
[27] Sh. Dinkov, M. Arnaudov, Spectrosc. Lett. 31 (1998) 529.

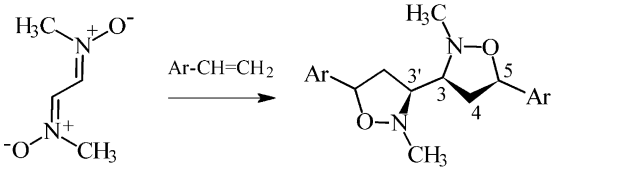
coordination spheres of transition metal ions allows control of the molecule forms and shapes, thus providing selectivity for complexation of isoxazolidine species. The literature precedents for a tetrahedral intermediate consisting of the catalyst with the nitrone around a copper–metal center [7], and a trigonal bipyramidal geometry for the transition structure of a Ni–substrate complex [8] may allow the interpretation of the observed selectivity and it indicates the dependence of catalytic efficiency on the coordination environment at the metal center of the catalyst. However, the ligand properties of the isoxazolidines themselves remain very scarcely investigated [9–11] and some of the isolated species involve only a non-coordinated isoxazolidine frame [12–14].

Even more versatile possibilities are offered by biisoxazolidines, new objects possessing a doubled number of chiral centers. Four adjacent N,O-heteroatoms of the biisoxazolidine frame, especially in combination with donor atoms of functionalized substituents (cf. pyridyl) offer various coordination possibilities for either five- or six-membered chelation of metal ions as well as different monodentate coordination modes. The ability of aryl pendants to afford different π,π-stacked arrays could also be involved in controlling the molecular conformations. In this paper we report experimental details for the synthesis of 3,3′-biisoxazolidines species and a set of metal complexes, targeted to validate their coordination behaviour.

2. Results and discussion

2.1. Synthesis and structure of the ligands

Glyoxal *N*-methylnitrone readily undergoes 3 + 2 1,-3-dipolarophil cycloaddition reactions with styrene and 2-vinylpyridine under mild conditions yielding complicated mixtures of the products. Addition of acetone or 2-propanol into a mixture of the stereoisomeric adducts promotes crystallization of the most symmetrical *cis*-,*cis*-isomer in a pure form that was used for preparation of the coordination compounds. Thus, we will conditionally omit the *cis*-,*cis*-notation for this configuration of the 3,3′-biisoxazolidines and metal complexes thereof.



(mixture of stereoisomers)

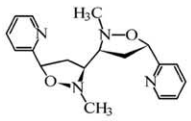
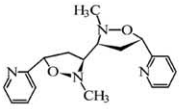
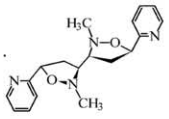
Ar = 2-Py (L^1); Ph (L^2)

Unfortunately, ultraviolet and IR spectroscopy were of little diagnostic value to establish the structure of the biisoxazolidines and to identify the coordination mode of the ligands in the metal complexes. NMR measurements remain most applicable for this purpose and gave abundant information. The positions of the C-5 proton signals at δ 5.1–5.4 ppm as doublet of doublets with close vicinal coupling magnitudes (L^1: $J_{5,4}$ = 8.8 Hz, $J_{5,4'}$ = 8.4 Hz; L^2: $J_{5,4} = J_{5,4'}$ = 8.0 Hz) demonstrate high regioselectivity of the reactions and in turn the formation of a five-substituted isoxazolidine ring. This agrees well with the fact that the direction of dipolarophil cycloaddition is sensitive to the functionality of the dipolarofile (electron withdrawing or donating substituent near the terminal carbon atom) [1,15]. Attribution of H^4 and $H^{4'}$ signals in the spectrum of L^1 was provided by the literature data suggesting that $J_{cis} > J_{trans}$ [1]. Therefore, the signal centered at δ 2.49 ppm corresponds to H^4, while the signal at δ 3.01 ppm corresponds to $H^{4'}$. This observation may be extended for other types of biisoxazolidines. The similarity of the chemical shifts for *cis–cis*-isomers of L^1 and L^2 indicate the close resemblance of the structural features of the compounds. For L^1 the mixture of *cis–trans*- and *trans–trans*-isomers was separated by chromatography on silica gel. The data of ^{1}H NMR spectra gave a possibility to suggest the structure of the biisoxazolidine isomers (Table 1).

The biisoxazolidines crystallize in centrosymmetric space groups and thus the crystal lattices comprise both RSRS and SRSR stereoisomers of the ligands that are related by a crystallographically imposed center of inversion. Compounds L^1 (**1**) and L^2 (**2**) are not isomorphous owing to a different manner of supramolecular aggregation in the crystals (Figs. 1 and 2). Molecules L^2 pack in chains with a set of very weak C–H/π hydrogen bonds ("edge-to-face stacking") [16] between phenyl pendants (H···π 2.84 Å; ∠CH···π 149°), while structure of supramolecular chains in the 2-pyridyl derivative L^1 is supported by a weak slipped π,π-stacking [17] of aromatic groups (Table 2).

The molecular geometries of the biisoxazolidines L^1 (**1**) and L^2 (**2**) are closely related. In both cases the isoxazolidine ring has an envelope conformation. The mean deviation of the atoms from the corresponding mean plane is very similar in both cases and it is approximately 0.153(8) Å. The largest deviation has N1 0.243(8) Å for L^1 and 0.236(2) Å for L^2. The pyridine group is located synclinal with the C3–C4 bond (dihedral angle 68.5°). At the same time the dihedral angle between the planes of the phenyl and isoxazolidine rings is 103.9°, that also corresponds to their synclinal situation. The organic frames possess a *cis–cis*-configuration and the molecules adopt a centrosymmetric structure with two equivalent (aryl)isoxazolidine parts related by a center of

Table 1
^{1}H NMR data for isomeric 3,3′-bi{2-methyl-5-(2-pyridyl)}isoxazolidines

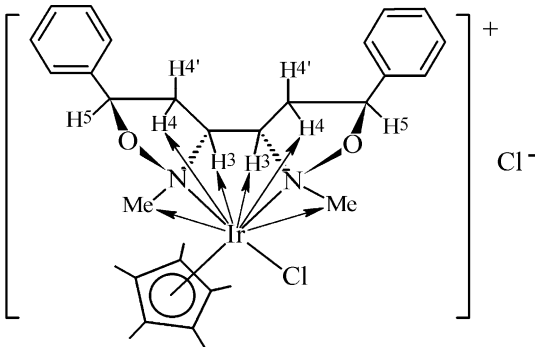
Stereoisomeric compound		Yield (%)	Chemical shifts and multiplicity, δ (ppm)				
			H-5	H-4	H-4′	H-3	NCH_3
	*cis–cis*-L^1	25	5.37 m	2.49 m	3.01 m	3.18 m	2.75 s
	*cis–trans*-L^1	45	5.11 m 5.32 m	2.30 m 2.46 m	2.55 m 2.99 m	2.89 m 3.18 m	2.88 s 2.91 s
	*trans–trans*-L^1	15	5.14 m	2.18 m	2.98 m	3.07 m	2.73 s

inversion (Fig. 1). Thus, the torsion angles N1–C2–C2a–N1a of $\varphi = 180°$ reflect a *trans*-conformation that is not favorable for *N*,*N*-chelate coordination of the biisoxazolidines in metal complexes.

This solid-state geometry of the organic frame agrees well with a semiempirical computational study applying the AM-1 method [18]: the optimal conformation of L^1 molecule is at $\varphi = 180°$ (Fig. 3). However, the relative energies for local minimums corresponding to two *gauche* conformers with φ at ±62–63° are very similar ($\Delta E = 11$ kJ mol$^{-1} \approx 3RT$) and the energy barriers between these three favorable molecule conformations do not exceed 43 kJ mol^{-1}, reflecting ease of rotation around the central C^3–C^3 bond. The energy maximum that occurs at $\varphi = 42°$ corresponds to a maximal interference of *N*-methyl substitutes, the energy barrier between two *gauche* conformations, 73 kJ mol^{-1}, is comparable to the parameter for rotation around a C–N bond in dimethylacetamide ($\Delta E = 75$ kJ mol^{-1}) [19]. The *gauche* conformation N–C–C–N is typical for aliphatic moieties forming five-membered chelates, i.e., ethylenediamine, and thus the calculation suggests conformational flexibility of the biisoxazolidines and their utility as *N*,*N*-chelating ligands in coordination compounds.

2.2. Coordination compounds

^{1}H NMR spectra for the iridium(III) complexes were of use for primary assignment of the coordination modes of the ligands. Thus, NMR spectra of the complex [Cp*Ir(L^2)Cl]Cl feature low-field shifts of almost all the isoxazolidine resonances, excepting $H^{4'}$ signals, as may be compared with data for the non-coordinated ligand. The largest deshielding was observed for H^3 and CH_3 protons ($\Delta\delta$ 1.35 and 0.92 ppm, respectively) that appear to be most closely situated to the nitrogen donor centers, and this indicates bidentate-chelate coordination of the ligand (compare with molecular structure **3**)



In the ^{1}H NMR ($CDCl_3$, 20°) spectrum of [(Cp*$IrCl_2$)$_2${L^1}], the relative intensities for CH_3 signals of Cp* and biisoxazolidine ligands (5:1) are in agreement with the binuclear structure. Significant deshielding for the α-Py proton (δ 8.90 ppm) clearly indicates coordination via the pyridine nitrogen donor and this is also consistent with a low field shift of the H^5 signal as may be compared with the spectrum of L^1 ($\Delta\delta$ 0.28 ppm). The CH_3 and H^3 resonances, which are most sensitive to the coordination of the isoxazolidine-N donor, in the present case remain almost unaffected. Thus, the spectra reflect a bidentate-bridging coordination of the ligand, employing only pyridine-N functions. This conclusion agrees with the NMR spectral assignment of mono-/bidentate coordination modes of 2-methyl-3-ferrocenyl-5-(2-pyridyl)isoxazolidine in palladium chloride complexes [9,10]. However, broadening of α-Py, H^5 and H^3 signals may be suggestive of certain dynamic

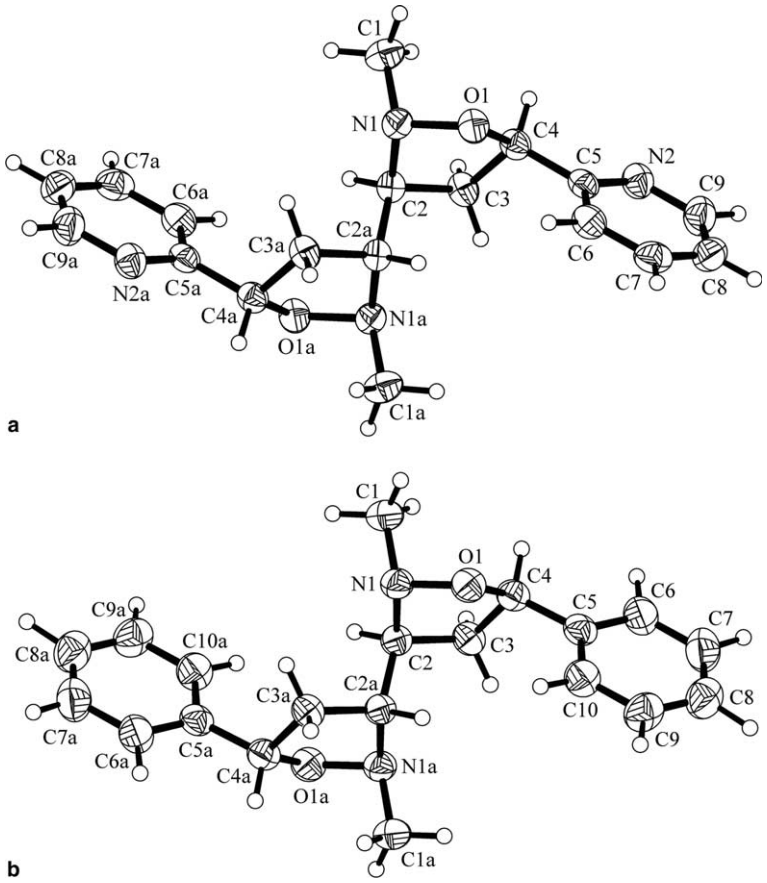


Fig. 1. Molecular structure of biisoxazolidines L^1 (Ar = 2-Py; a) and L^2 (Ar = Ph; b) showing the atom labelling schemes. Thermal ellipsoids are at the 50% probability level. For L^2 only one of the two independent molecules is shown.

processes in the solution which could include elimination of the chloride ligand from the coordination sphere and formation of iridium pyridyl/isoxazolidine chelates. For 2-methyl-3-phenyl-5-(2-pyridyl)isoxazolidine, involving "half" of the L^1 functionality, we were able to stabilize such a coordination mode by replacement of one chloride ligand with a non-coordinating BPh_4^- anion [9].

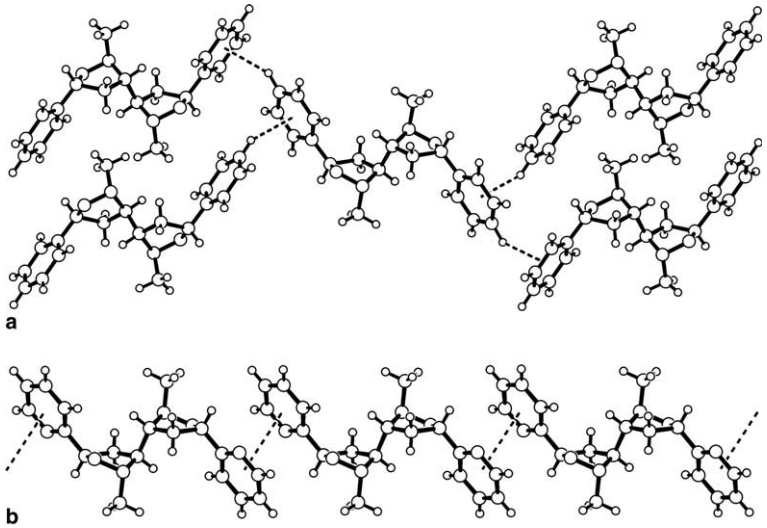


Fig. 2. Supramolecular structure of the biisoxazolidines, which is dominated by CH/π hydrogen bonding for L^2, Ar = Ph (a), and by π,π-stacking between pyridyl groups for L^1 (b).

Table 2
Geometry of π,π-stacking interactions[a]

Compound	Group 1/group 2	ipd (Å)	ccd (Å)	sa (°)
L^1 (**1**)	[N2, C5-9]/[N2, C5-9] (1 − *x*, −*y*, 2 − *z*)	3.462(5)	3.869(4)	26.5(1)
$Cu\{L^2\}Cl_2 \cdot CHCl_3$ (**3**)	(C9-14)/(C9-14) (1 − *x*, −*y*, −*z*)	3.674(6)	4.105(4)	26.5(1)
$[Ni\{L^1\}(H_2O)(NO_3)](NO_3)$ (**4**)	(N4, C14-18)/(N4, C14-18) (−*x*, −*y*, −*z*)	3.385(4)	4.015(4)	32.5(1)

[a] ipd is the interplanar distance (distance from one plane to the neighboring centroid), ccd is the center-to-center distance (distance between ring centroids) and sa is the slippage angle (angle subtended by the intercentroid vector to the plane normal) [17]. In each case the interacting aryl groups are related by inversion and their planes are parallel.

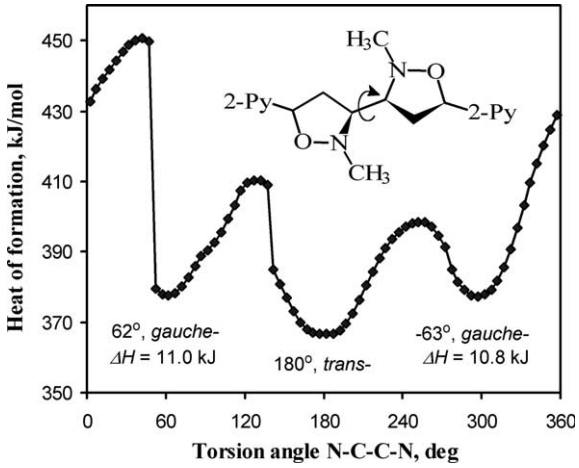


Fig. 3. Energy diagram for rotation around the C(3)–C(3′) bond in a molecule of *cis*-,*cis*-3,3′-bi{2-methyl-5-(2-pyridyl)} isoxazolidine (L^1).

2.3. Crystal structure of the metal complexes

The copper(II) chloride complex $Cu\{L^2\}Cl_2 \cdot CHCl_3$ (**3**) represents a molecular chelate formed by coordination of two isoxazolidine nitrogen atoms to a metal center at typical distances of 2.009(3) and 2.053(3) Å (Table 3, Fig. 4). The organic frame adopts the same configuration as in the structure of the non-coordinated ligands **1** and **2**, while a suitable for chelate function conformation of the molecule is provided by rotation around the 3,3′-carbon–carbon bond. The torsion angle N1–C1–C5–N2 (−52.8°) corresponds to a *gauche* conformation versus centrosymmetric *trans*-conformation for **1** and **2**. A comparable geometry of the chelate fragment was observed for closely related zinc chloride complexes with 2,2′-bipyrrolidine ligands (NCCN −52.8°, NMN 86.9° versus 85.7° for **3**) [20]. The distorted tetrahedral environment of the copper ions is completed with two chlorine atoms situated at 2.203(1) and 2.231(1) Å. Two *N*-methyl groups lie in *cis*-positions in the chelate plane and their steric effect precludes the characteristic dimerization of the complex moieties by secondary Cu···Cl interactions seen in the related structure of the 2-methyl-3-phenyl-5-(2-pyridyl)isoxazolidine ligand [21]. Therefore, there is an evident lack of strong intermolecular interactions and the crystal structure is sustained with a set of weaker slipped π,π-stackings (Table 2) and C–H/π hydrogen bonds (H···π 3.22 Å; ∠CH···π 141°) between the phenyl groups. These interactions arrange the molecules into supramolecular hexa-

Table 3
Selected bond distances (Å) and angles (°) for complexes $Cu\{L^2\}Cl_2 \cdot CHCl_3$ (**3**), $[Ni\{L^1\}(H_2O)(NO_3)](NO_3)$ (**4**) and $[UO_2(CH_3OH)_2(NO_3)_2] \cdot L^1$ (**5**)

*$Cu\{L^2\}Cl_2 \cdot CHCl_3$ (**3**)*	
Cu(1)–N(1)	2.009(3)
Cu(1)–N(2)	2.053(3)
Cu(1)–Cl(1)	2.203(1)
Cu(1)–Cl(2)	2.231(1)
O(1)–N(1)	1.463(4)
O(2)–N(2)	1.440(4)
C(1)–C(5)	1.514(6)
N(1)–Cu(1)–N(2)	85.7(1)
N(1)–Cu(1)–Cl(1)	143.3(1)
N(1)–Cu(1)–Cl(2)	97.2(1)
N(2)–Cu(1)–Cl(2)	135.5(1)
N(2)–Cu(1)–Cl(1)	99.4(9)
Cl(1)–Cu(1)–Cl(2)	103.8(4)
*$[Ni\{L^1\}(H_2O)(NO_3)](NO_3)$ (**4**)*	
Ni(1)–N(1)	2.032(1)
Ni(1)–N(2)	2.030(1)
Ni(1)–N(3)	2.142(1)
Ni(1)–O(3)	2.057(2)
Ni(1)–O(4)	2.091(1)
Ni(1)–O(5)	2.123(1)
O(1)–N(1)	1.465(2)
O(2)–N(3)	1.449(2)
N(2)–Ni(1)–N(1)	94.53(6)
N(1)–Ni(1)–N(3)	83.89(6)
N(2)–Ni(1)–N(3)	92.61(6)
N(1)–Ni(1)–O(3)	89.62(7)
N(2)–Ni(1)–O(3)	92.49(7)
N(2)–Ni(1)–O(4)	164.55(6)
O(3)–Ni(1)–N(3)	172.04(6)
O(4)–Ni(1)–O(5)	61.52(6)
*$[UO_2(CH_3OH)_2(NO_3)_2] \cdot L^1$ (**5**) (a: −x, y, 0.5 − z)*	
U(1)–O(2)	1.767(4)
U(1)–O(6)	2.381(3)
U(1)–O(3)	2.524(4)
U(1)–O(4)	2.529(4)
O(1)–N(1)	1.452(5)
N(1)–C(2)	1.486(6)
O(2)–U(1)–O(2a)	178.6(3)
O(6)–U(1)–O(6a)	70.7(2)
O(3)–U(1)–O(4)	49.8(1)
O(6)–U(1)–O(3)	135.4(1)

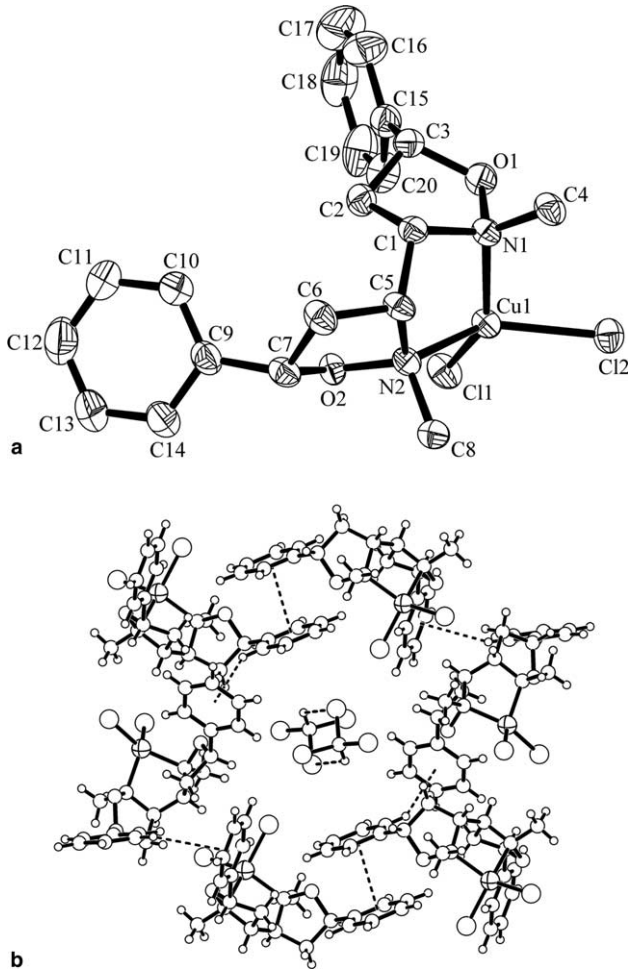
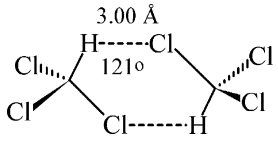


Fig. 4. Molecular structure of the $Cu\{L^2\}Cl_2 \cdot CHCl_3$ (**3**) complex with 50% thermal ellipsoids and the hydrogen atoms omitted for clarity (a); association of $Cu\{L^2\}Cl_2$ molecules into supramolecular hexagons with extensive CH/π hydrogen bonding and π,π-stackings between the phenyl groups and immobilization of a CH···Cl bonded chloroform dimer inside the cage (b).

gons possessing a large internal cavity with inner dimensions 4 × 5 Å [22]. The cage is populated with a hydrogen bonded (CH···Cl 3.58 Å) dimer of chloroform molecules (Fig. 4(b)). Such self-association of chloroform guests held inside the large host voids was observed also for other lattice clathrates [23].



2-Pyridyl functionalized ligand L^1 provides a greater number of possibilities for chelation of metal ions, involving tridentate bis-chelate functions. Therefore, we have examined a complex of the nickel(II) ion that

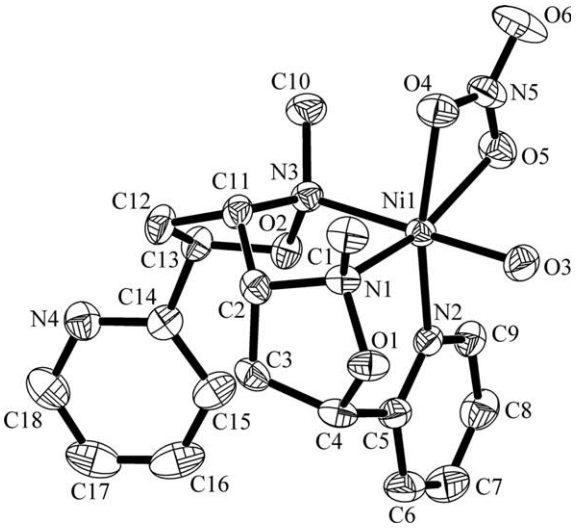


Fig. 5. Structure of the complex cation in $[Ni\{L^1\}(H_2O)(NO_3)]NO_3$ (**4**), with 45% ellipsoids and hydrogen atoms omitted for clarity. Note the facial arrangement of three nitrogen donors within the coordination octahedron and the nearly orthogonal disposition of two pyridyl cycles supporting weak C(15)–H/π hydrogen bonding.

typically supports an octahedral coordination geometry, suitable for a facial arrangement of three nitrogen donors within the coordination sphere. In the $[Ni\{L^1\}(H_2O)(NO_3)]NO_3$ (**4**) complex the ligand wraps around the central atom forming two chelate cycles (Table 3, Fig. 5). Both isoxazolidine nitrogen donors are engaged into coordination forming a five-membered chelate cycle and an additional donor site is provided by one of the 2-pyridyl groups. Thus, three nitrogen atoms occupy MN_3 facial positions in the coordination octahedron, which is a rare feature of flexible tridentates as may be compared with geometrically rigid complexes of 1,4,7-triazacyclodecane [24]. The coordination mode of the organic ligand demonstrates high flexibility of biisoxazolidines and their adaptibility to the coordination preferences of the metal ions. The torsion angle N1–C2–C11–N3 46.8° corresponds to a *gauche* conformation, similar to the one observed for complex **3**. A weak intramolecular C–H/π hydrogen bond between two pyridyl groups (H···π 2.96 Å; ∠CH···π 160°) may also contribute to the stabilization of the ligand conformation (Fig. 5).

The shortest Ni–N separations (2.03 Å) are observed within the six-membered chelate fragment involving pyridyl and isoxazolidine donors, while the coordination interaction with the second isoxazolidine group is slightly weaker (2.14 Å). The distorted octahedral environment of the nickel ions is completed with oxygen atoms of a bidentate nitrate group and of a water molecule. The nitrate ligand is coordinated in an actually isobidentate fashion (Ni–O 2.09 and 2.12 Å), similarly to one found for the *mer*-N_3 octahedral aquanickel(II)

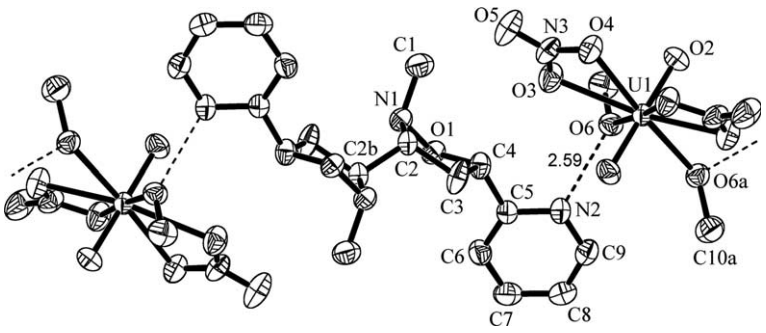


Fig. 6. Fragment of the supramolecular chain in the structure of the adduct $[UO_2(CH_3OH)_2(NO_3)_2]\cdot L^1$ (**5**) employing the centrosymmetric biisoxazolidine molecule as a hydrogen bond acceptor. The ellipsoids are drawn at the 50% probability level and hydrogen atoms are not shown.

nitrate complex with a macrocyclic nitrogen tridentate [25]. The lattice consists of cationic metal–organic complexes $[Ni\{L^1\}(H_2O)(NO_3)]^+$ and non-coordinated nitrate anions. The cations are associated into chains by means of OH···N hydrogen bonds (O···N 2.79 Å, ∠OH···N 175°) involving the non-coordinated pyridyl nitrogen atom and hydrogen atoms of aqua ligands. Weak intermolecular π,π-stacking interactions between these non-coordinated 2-pyridyl groups (Table 2) are also important for the crystal packing.

3,3′-Biisoxazolidine ligands do not form stable coordination compounds with p- and f-block metal ions, though they can afford molecular adducts acting as a hydrogen bond acceptor. Thus, 3,3′-biisoxazolidine (L^1) easily cocrystallizes with uranyl nitrate yielding $[UO_2(CH_3OH)_2(NO_3)_2]\cdot L^1$ (**5**). This associate involves molecular bis-methanol uranyl nitrate moieties and non-coordinated organic ligands (Fig. 6). The uranium atoms have a typical hexagonal bipyramidal eight-fold coordination constituting of two isobidentate nitrate groups (U–O 2.524(4), 2.529(4) Å) and two *cis*-situated methanol molecules in the equatorial plane. This molecular moiety $[UO_2(CH_3OH)_2(NO_3)_2]$ is an unprecedented feature of uranyl nitrate chemistry, as in all known 1:2 uranyl nitrate adducts the neutral ligands are *trans*-situated, for example in $[UO_2(THF)_2(NO_3)_2]$ [26]. The methanol ligands provide hydrogen bond donor sites for interaction with entrapped biisoxazolidine molecules. The latter ones adopt a most symmetrical conformation that is similar to the one observed in structures **1** and **2**, with two identical parts of the molecule related by inversion. The relatively strong OH···N hydrogen bonds (O···N 2.59 Å; ∠OH···N 157°) with 2-pyridyl nitrogen acceptors unite the molecular components into zig-zag chains. Such a discrimination of the isoxazolidine-N versus pyridine-N acceptor sites is predetermined by steric availability and higher basicity of the pyridyl functions. This hydrogen bonded isoxazolidine pattern possibly may be involved also as a model for the bidentate-bridging coordination of the ligand in the $[(Cp^*IrCl_2)_2\{L^1\}]$ complex.

3. Experimental

3.1. Synthesis

Solvents were used as supplied or distilled using standard methods. The reagents were obtained from Aldrich or Fluka. Glyoxal dinitrone was synthesized by condensation of the corresponding aldehyde and *N*-methyl hydroxylamine following a published method [27]. The 3 + 2 dipolarophil cycloaddition reactions of glyoxal dinitrone with styrene or 2-vinylpyridine proceed smoothly yielding arylsubstituted biisoxazolidines. The yields of the products did not change remarkably in view of varying of the solvent (acetonitrile, methanol) and the nitrone/dipolarophile ratio.

3.1.1. 3,3′-Bi{2-methyl-5-(2-pyridyl)}isoxazolidine (L^1)

2-Vinylpyridine (4.8 ml, 43.1 mmol) was added to a hot solution of glyoxal dinitrone (0.50 g, 4.31 mmol) in 20 ml of dry acetonitrile. The mixture was refluxed for 15 h while the reaction was monitored by TLC using an acetone–chloroform (2:1 v/v) mixture as eluent. The solvent was evaporated under reduced pressure yielding a mixture of isomeric 3,3′-biisoxazolidines as was proved by ^{1}H NMR spectra. Addition of 10 ml of acetone to the residue effected crystallization of 0.35 g (25%) of *cis*-,*cis*-3,3′-bi{2-methyl-5-(2-pyridyl)}isoxazolidine as a colorless solid.

The acetone filtrate was evaporated giving a brown oily mixture of *cis–trans*- and *trans–trans*-isomers (ca. 3:1) that was separated by column chromatography (SiO_2, acetone–chloroform 2:1; *cis–trans*-isomer: $R_f = 0.30$; *trans–trans*-isomer: $R_f = 0.45$).

^{1}H NMR data for the three stereoisomers are presented in Table 1. Data for *cis*-,*cis*-3,3′-bi{2-methyl-5-(2-pyridyl)}isoxazolidine: *Anal.* Calc. for $C_{18}H_{22}N_4O_2$: C, 66.24; H, 6.79; N, 17.16. Found: C, 66.85; H, 6.92; N, 17.05%. ^{13}C NMR ($CDCl_3$): δ 42.02 (NCH_3), 48.80 (C^4), 73.70 (C^3), 81.89 (C^5), 123.62 (C^{β}-Py), 125.42 (C^{β}-Py), 139.62 (C^{γ}-Py), 152.08 (C^{α}-Py), 163.52 (ipso-Py).

3.1.2. 3,3′-Bi{2-methyl-5-phenyl}isoxazolidine (L^2)

Styrene (2 ml, 17.2 mmol) was added to a hot solution of glyoxal dinitrone (0.20 g, 1.72 mmol) in dry acetonitrile (10 ml) and the mixture was refluxed for 35 h (TLC: acetone–chloroform 1:1 v/v). The solvent was removed under reduced pressure and the brown oily product was triturated with 5 ml of 2-propanol. This afforded a precipitate of *cis*-,*cis*-3,3′-bi{2-methyl-5-phenyl}isoxazolidine as white flakes (0.084 g, 12%) that was filtered off and recrystallized from ethanol. *Anal*. Calc. for $C_{20}H_{24}N_2O_2$: C, 74.05; H, 7.46; N, 8.63. Found: C, 75.12; H, 7.82; N, 8.43%. ^{1}H NMR ($CDCl_3$): δ 2.28 (m, 1H, H^4), 2.75 (s, 3H, NCH_3), 2.97 (m, 1H, $H^{4'}$), 3.15 (m, 1H, H^3), 5.32 (m, 1H, H^5), 7.25–7.4 (m, 5H, C_6H_5). ^{13}C NMR ($CDCl_3$): δ 44.45 (NCH_3), 48.62 (C^4), 74.87 (C^3), 81.02 (C^5), 129.28 (*p*-Ph), 130.70 (*m*-Ph), 131.46 (*o*-Ph), 143.25 (*ipso*-Ph).

Crystalline *cis–cis*-isomers of $L^1$and L^2 are air-stable and stable in solution, they are soluble in chloroform, acetonitrile and insoluble in 2-propanol, diethyl ether and hexane.

Colorless crystals of *cis–cis*-L^1, suitable for X-ray analysis, were obtained from chloroform–acetonitrile (1:4) solution.

The copper(II) chloride complexes were prepared by reacting the components in methanol/chloroform solutions. In a typical synthesis, solutions of L^1 (0.098 g, 0.3 mmol) in $CHCl_3$ (3 ml) and $CuCl_2 \cdot 2H_2O$ (0.051 g, 0.3 mmol) in 3 ml of methanol were combined and allowed to stand in a vacuum dessicator over $CaCl_2$ for a few days, yielding green needles of the $Cu\{L^1\}Cl_2$ complex. *Anal*. Calc. for $C_{18}H_{22}Cl_2CuN_4O_2$: C, 46.91; H, 4.81; N, 12.16. Found: C, 47.19; H, 4.96; N, 12.03%. For crystallization of a copper(II) chloride complex with L^2 we have used vapour diffusion of 2-propanol into a methanol–chloroform solution of the components (0.039 g, 0.23 mmol $CuCl_2 \cdot 2H_2O$ and 0.147 g, 0.45 mmol L^2), which afforded thin green needles of $Cu\{L^2\}Cl_2 \cdot CHCl_3$ in a period of 5–6 days. *Anal*. Calc. for $C_{21}H_{25}Cl_5CuN_2O_2$: C, 43.63; H, 4.36; N, 4.85. Found: C, 43.91; H, 4.56; N, 5.04%. This chloroform solvate is stable in air for a few days but eventually the crystals became opaque due to the loss of the solvent molecules and disintegration of the structure.

$[Ni\{L^1\}(H_2O)(NO_3)]NO_3$ was prepared using a layering technique. A solution of $Ni(NO_3)_2 \cdot 6H_2O$ (0.037 g, 0.126 mmol) in 2 ml of methanol was layered over a solution of L^1 (0.041 g, 0.126 mmol) in 2 ml of chloroform. Slow interdiffusion of the layers, over a period of 12–15 days, afforded well-developed blue prismatic crystals of the complex (yield 80%). *Anal*. Calc. for $C_{18}H_{24}N_6NiO_9$: C, 41.01; H, 4.59; N, 15.95. Found: C, 41.51; H, 4.87; N, 16.04%.

Unlike this case, 3,3′-bi{2-methyl-5-phenyl}isoxazolidine (L^2) and nickel nitrate gave a mixture of products that were not identified. We were not successful in the preparation of individual compounds for this system.

For the preparation of the pentamethylcyclopentadienyliridium(III) chloride complex, $[Cp^*IrCl]_2Cl_2$ (0.133 g, 0.167 mmol) was dissolved in 10 ml of chloroform and added to a chloroform solution of L^1 (0.109 g, 0.334 mmol). The reaction mixture was stirred at 35 °C for 1.5 h and then the clear solution obtained was evaporated in a vacuum desiccator. Yellow crystals of the $[(Cp^*IrCl_2)_2\{L^1\}]$ complex were obtained in 90% yield, they were washed with hexane and dried in air. ^{1}H NMR ($CDCl_3$): δ 1.55 (s, 15H, Cp*), 2.4 (m, 1H, H^4), 2.82 (s, 3H, NCH_3), 3.15 (m, 1H, $H^{4'}$), 3.2 (m, 1H, H^3), 5.65 (m, 1H, H^5), 7.27 (dd, 1H, Py), 7.72 (m, 2H, Py), 8.9 (d, 1H, Py). $[Cp^*Ir(L^2)Cl]Cl$ was synthesized in a similar fashion. *Anal*. Calc. for $C_{30}H_{39}Cl_2IrN_2O_2$: C, 49.85; H, 5.44; N, 3.88. Found: C, 50.07; H, 5.72; N, 3.54%. H^1 NMR ($CDCl_3$): δ 1.49 (s, 15H, Cp*), 2.60 (m, 1H, H^4), 3.67 (s, 6H, NCH_3), 2.99 (m, 1H, $H^{4'}$), 4.50 (m, 1H, H^3), 5.70 (m, 1H, H^5), 7.1–7.4 (m, 5H, C_6H_5).

Attempted preparation of biisoxazolidine p- and f-block metal complexes failed. However, we have found that L^1 readily forms a molecular complex with uranyl nitrate $[UO_2(CH_3OH)_2(NO_3)_2] \cdot L^1$. A solution of L^1 (0.098 g, 0.3 mmol) in 3 ml of $CHCl_3$ and a solution of $UO_2(NO_3)_2 \cdot 2H_2O$ (0.154 g, 0.3 mmol) in 3 ml of CH_3OH were combined and the mixture was allowed to stand in a vacuum dessicator over $CaCl_2$. The yellow crystalline product was separated, washed with cold methanol and dried in air (yield 70%). *Anal*. Calc. for $C_{20}H_{30}N_6O_{12}U$: C, 30.62; H, 3.85; N, 10.71. Found: C, 30.23; H, 3.64; N, 10.95%. 3,3′-Bi{2-methyl-5-phenyl}isoxazolidine does not co-crystallize with uranyl nitrate under these conditions.

3.2. X-ray crystallography

The measurements for L^1 (**1**), L^2 (**2**) and $Cu\{L^2\}Cl_2 \cdot CHCl_3$ (**3**) were made at 223 K using a Siemens SMART CCD diffractometer (graphite monochromated Mo Kα radiation, $\lambda = 0.71073$ Å, empirical absorption corrections using SADABS [28]). The intensity data for $[Ni\{L^1\}(H_2O)(NO_3)]NO_3$ (**4**) and $[UO_2(CH_3OH)_2(NO_3)_2] \cdot L^1$ (**5**) were collected at 200 K on a Stoe Image Plate Diffraction System (φ oscillation scans 0–188.5°, step $\Delta\varphi = 1°$). The structures were solved by direct methods and refined in the anisotropic approximation using SHELXS-86 and SHELXL-97 [29,30]. In structures **1** and **4** all hydrogen atoms were localized and refined isotropically, while for **3** and **5** the hydrogen atoms were constrained geometrically and considered using the riding model with their isotropic *U* values at 1.2 times the equivalent isotropic *U* value of the atoms to which they are attached. One of two unique biisozaxolidine molecules in structure **2** shows rotational disorder of a phenyl

Table 4
Crystal data for L^1 (**1**), L^2 (**2**), $Cu\{L^2\}Cl_2 \cdot CHCl_3$ (**3**), $[Ni\{L^1\}(H_2O)(NO_3)](NO_3)$ (**4**) and $[UO_2(CH_3OH)_2(NO_3)_2] \cdot L^1$ (**5**)

Compound	**1**	**2**	**3**	**4**	**5**
Formula	$C_{18}H_{22}N_4O_2$	$C_{20}H_{24}N_2O_2$	$C_{21}H_{25}Cl_5CuN_2O_2$	$C_{18}H_{24}N_6NiO_9$	$C_{20}H_{30}N_6O_{12}U$
Molecular weight	326.40	324.41	578.22	527.14	784.53
Crystal system	monoclinic	monoclinic	monoclinic	monoclinic	monoclinic
Space group	$P2_1/n$	$P2_1/c$	$P2_1/c$	$P2_1/n$	$C2/c$
Z	2	4	4	4	4
a (Å)	8.1828(9)	25.439(3)	10.837(1)	9.6552(5)	25.530(2)
b (Å)	7.4161(7)	5.4379(8)	19.304(2)	15.006(1)	8.0859(6)
c (Å)	14.115(1)	12.890(1)	12.293(1)	15.4839(9)	13.3780(11)
β (°)	106.527(2)	104.674(2)	107.233(2)	101.699(7)	99.816(10)
V (Å^3)	821.2(1)	1725.0(4)	2456.3(4)	2196.8(2)	2721.2(4)
μ (Mo Kα) (cm^{-1})	0.89	0.81	14.54	9.47	60.35
D_{calc} (g cm^{-3})	1.320	1.249	1.564	1.594	1.915
$2\theta_{max}$ (°)	55.0	53.4	53.5	55.8	56.2
Measured/unique reflections	4853/1880	8051/3617	13726/4965	17999/5133	12312/3178
R_{int}	0.016	0.029	0.038	0.037	0.071
Parameters refined	153	335	281	403	177
R_1, wR_2 ($I > 2\sigma(I)$)	0.043, 0.099	0.066, 0.213	0.058, 0.137	0.033, 0.081	0.031, 0.072
R_1, wR_2 (all data)	0.051, 0.104	0.079, 0.219	0.085, 0.146	0.047, 0.084	0.051, 0.075
Maximum and minimum peak (e Å^{-3})	0.25 and −0.16	0.27 and −0.15	0.56 and −0.94	0.66 and −0.61	2.44 and −2.51

group with partial contributions of 0.58 and 0.42. The hydrogen atoms of this moiety were not included, while the hydrogen atoms corresponding to the ordered portion were localized and refined isotropically. The maximum of residual electron density in structure **5** (2.44 e Å^{-3}) is located at 0.82 Å from the heavy uranium atom. The crystal data are given in Table 4 and the principal bond lengths and angles are listed in Table 3.

4. Conclusion

The present study demonstrates the potential of geometrically flexible biisoxazolidines as efficient ligands towards metal ions. Coordination preferences of this new ligand system may provide a useful basis for modelling the pathways of metal catalized 1,3-dipolarophil cycloaddition reactions and further transformations of coordinatively immobilized isoxazolidines. They may also be involved in developing strategies for preparative separations of complicated mixtures of cycloaddition products. Our results suggest wider possibilities for designing and fine-tuning the structure and ligand properties of open-chain flexible multidentates and for metal-assisted stabilization of certain molecular conformations.

5. Supplementary data

Crystallographic data (excluding structure factors) for the structures reported in this paper have been deposited with the Cambridge Crystallographic Data Centre as supplementary publication Nos. CCDC-262879–262883 (compounds **1**–**5**). Copies of the data can be obtained free of charge on application to CCDC, 12 Union Road, Cambridge CB2 1EZ, UK (fax: +44 1223 336 033; e-mail: deposit@ccdc.cam.ac.uk or www.http://www.ccdc.cam.ac.uk).

References

[1] K.B.G. Torssell, Nitrile Oxides, Nitrones and Nitronates in Organic Synthesis Novel Strategies in Synthesis, VCH, New York, 1988, p. 75.
[2] K.V. Gothelf, K.A. Jørgensen, Chem. Rev. 98 (1998) 863.
[3] K.V. Gothelf, K.A. Jørgensen, Chem. Commun. (2000) 1449.
[4] K.V. Gothelf, R.G. Hazell, K.A. Jørgensen, J. Am. Chem. Soc. 117 (1995) 4435.
[5] I.M. Mohammed, S.M.A. Hashmi, S.A. Ali, J. Anal. Sci. Spectrosc. 42 (1997) 190.
[6] P. DeShong, C.M. Dicken, J.M. Leginus, R.R. Whittle, J. Am. Chem. Soc. 106 (1984) 5598.
[7] K.B. Jensen, R.G. Hazell, K.A. Jorgensen, J. Org. Chem. 64 (1999) 2353.
[8] S. Kanemasa, Y. Oderaotoshi, J. Tanaka, E. Wada, J. Am. Chem. Soc. 120 (1998) 12355.
[9] A.B. Lysenko, S.V. Shishkina, O.V. Shishkin, E. Peralta-Perez, F. Lopez-Ortiz, R.D. Lampeka, Polyhedron 20 (2001) 957.
[10] R.D. Lampeka, A.B. Lysenko, Zhurn. Obsch. Khim. (Russ.) 70 (2000) 1900.
[11] A.B. Lysenko, O.V. Shishkin, R.D. Lampeka, Z. Naturforsch. B 55 (2000) 373.
[12] C. Mukai, I.J. Kim, W.J. Cho, M. Kido, M. Hanaoka, J. Chem. Soc., Perkin Trans. 1 (1993) 2495.
[13] C. Baldoli, P.D. Buttero, E. Licandro, S. Maiorana, A. Papagni, A. Aibinati, Tetrahedron: Asymmetry 6 (1995) 1711.
[14] G. Roth, H. Fischer, J. Organomet. Chem. 507 (1996) 125.
[15] P. DeShong, C.M. Dicken, R.R. Staib, A.J. Freyer, S.M. Weinreb, J. Org. Chem. 47 (1982) 4397.
[16] G.R. Desiraju, T. Steiner, The Weak Hydrogen Bond in Structural Chemistry and Biology, Oxford University Press, Oxford, 1999.
[17] C. Janiak, J. Chem. Soc., Dalton Trans. (2000) 3885.
[18] M.J.S. Dewar, E.G. Zoebisch, E.F. Healy, J.J.P. Stewart, J. Am. Chem. Soc. 107 (1985) 3902.

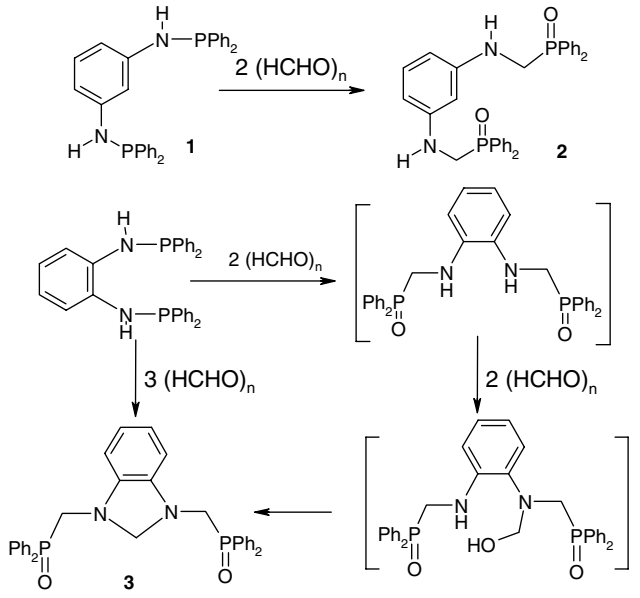
[19] M.B. Robin, F.A. Bovey, H. Basch, in: J. Zabicky (Ed.), The Chemistry of Amides, Interscience, London, 1970 (Chapter 1).
[20] A. Alexakis, A. Tomassini, C. Chouillet, S. Roland, P. Mangeney, G. Bernardinelli, Angew. Chem., Int. Ed. Engl. 39 (2000) 4093.
[21] A.B. Lysenko, K.V. Domasevitch, E. Peralta-Perez, F. Lopez-Ortiz, J.W. Steed, R.D. Lampeka, Polyhedron 21 (2002) 769.
[22] A.L. Spek, PLATON/PLUTON, Jan. 1999, Acta Crystallogr., Sect. A 46 (1990) C-34.
[23] D.V. Soldatov, J.A. Ripmeister, Chem.-Eur. J. 7 (2001) 2979.
[24] B.M.T. Lam, J.A. Halfen, V.G. Young Junior, J.R. Hagadorn, P.L. Holland, A. Lledos, L. Cucurnull-Sanchez, J.J. Novoa, S. Alvarez, W.D. Tolman, Inorg. Chem. 39 (2000) 4059.
[25] C.A. Davis, P.A. Duckworth, A.J. Leong, L.F. Lindoy, A. Bashall, M. McPartin, Inorg. Chim. Acta 273 (1998) 372.
[26] J.G. Reynolds, A. Zalkin, D.H. Templeton, Inorg. Chem. 16 (1977) 3357.
[27] G. Zinner, O. Hantelmann, U. Dybowski, Chem.-Ztg. 97 (5) (1973) 205.
[28] Siemens X-ray Instruments, Madison, WI, 1995.
[29] G.M. Sheldrick, SHELXS-86, Acta Crystallogr., Sect. A 46 (1990) 467.
[30] G.M. Sheldrick, SHELXL-97: A System of Computer Programs for X-ray Structure Determination, University of Göttingen, Göttingen, Germany, 1997.

with aldehydes and ketones. The molecular structures and the complexing ability of some of the bisphosphine oxides thus obtained are also described.

2. Results and discussion

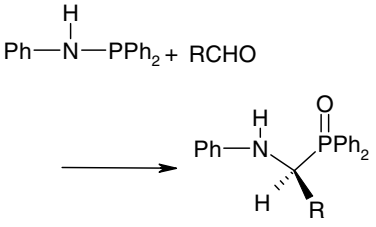
The aminophosphines, $Ph_2PN(H)Ph$, $Ph_2PN(^nBu)PPh_2$ and 1,2-$C_6H_4(N(H)PPh_2)_2$ were prepared as described in the literature (see Section 4). The 1,3-phenylenediamine derivative 1,3-$C_6H_4(N(H)PPh_2)_2$ (**1**) was prepared in 46% yield by reacting chlorodiphenylphosphine with 1,3-phenylenediamine in THF in the presence of a catalytic amount of 4-dimethylaminopyridine. The IR spectrum of **1** shows ν_{NH} at 3218 cm^{-1} and the ^{31}P NMR spectrum of **1** exhibits a single resonance at 35.2 ppm. The structural composition was further confirmed by mass spectral and micro analytical data.

The reaction of **1** with two equivalents of paraformaldehyde affords the P–N bond inserted product, 1,3-$C_6H_4(N(H)CH_2P(O)Ph_2)_2$ (**2**) similar to the analogous reaction of $Ph_2PNC_2H_4NPPh_2$ with paraformaldehyde, reported earlier [7b]. The reaction of **1** with one equivalent of paraformaldehyde did not give a monofunctionalized product of the type $Ph_2PN(H)C_6H_4N(H)CH_2P(O)Ph_2$, instead compound **2** was obtained in 35% yield with half of the reactant **1** left unreacted in the solution. The ^{31}P NMR spectrum of **2** shows a single resonance at 28.7 ppm and the methylene protons appear at 2.39 ppm in its ^1H NMR spectrum. Interestingly, the reaction of 1,2-$C_6H_4(N(H)PPh_2)_2$ with two equivalents of paraformaldehyde afforded a similar product but containing three methylene groups as indicated by its ^1H NMR spectrum (Scheme 1). When the reaction was carried out using three equivalents of paraformaldehyde the yield was almost quantitative indicating the insertion of two methylene groups into two P(III)–N bonds and another one between two nitrogen centers through nucleophilic addition to give a product of the type, 1,2-$C_6H_4\{N(CH_2P(O)Ph_2)(\mu\text{-}CH_2)N(CH_2P(O)Ph_2)\}$ (**3**) in quantitative yield. The ^{31}P NMR spectrum of **3** shows a single resonance at 26.6 ppm. In the ^1H NMR spectrum of **3**, the protons due to the methylene groups inserted into the P–N bonds appear at 3.82 ppm as broad singlets, whereas the bridging methylene protons resonate at 4.96 ppm. When the aminophosphines are treated with aromatic aldehydes, the 'CH(R)' groups insert into the P–N bonds followed by oxidation of the phosphorus from P(III) to P(V), whereas aliphatic aldehydes, such as butylaldehyde, afford an α-hydroxy phosphine oxide through P–N bond cleavage [7b]. The reactions of $Ph_2PN(H)Ph$ with RCHO afford P–N inserted products $Ph_2P(O)CH(R)N(H)Ph$ (R = C_6H_4OH-*o*, **4**; 5-BrC_6H_3OH-*p*, **5**; $(\eta^5\text{-}C_5H_5)Fe(\eta^5\text{-}C_5H_4)$, **6**) in 65–85% yield as shown in Eq. (1).



Scheme 1.

The ^{31}P NMR spectra of compounds **5** and **6** show single resonances at 37.8 and 29.2 ppm, respectively. The ^1H NMR spectrum of **5** shows a doublet at 5.5 ppm for the CH protons with a $^2J_{PH}$ coupling of 5.9 Hz whereas for **6** the analogous signal appears as a broad singlet at 5.1 ppm. The spectroscopic data of **4** is given in our previous report [7b].



(1)

R = C_6H_4OH-*o*, **4**
5-Br-C_6H_3OH-*o*, **5**
$(C_5H_5)Fe(C_5H_4)$, **6**

The structure of $Ph_2P(O)CH(C_6H_4OH\text{-}o)N(H)Ph$ (**4**) was confirmed by single crystal X-ray diffraction studies and is shown in Fig. 1. Crystal data and the details of the structure determination are given in Table 1 while selected bond lengths and inter bond angles are listed in Table 2. The asymmetric unit of compound **4** contains two identical independent molecules but the corresponding bond lengths and bond angles are not significantly different. The P–O bond distances are P(1)–O(1) = 1.522(9), P(2)–O(3) = 1.458(9) Å and the P–C bond distances are in the range 1.720(14)–1.872(11) Å. The geometry around the nitrogen is strictly planar and the sum of the angles is 360°. Although in the lattice the molecules exhibit intra and inter molecular O–H···O type interactions, they are not significantly prominent.

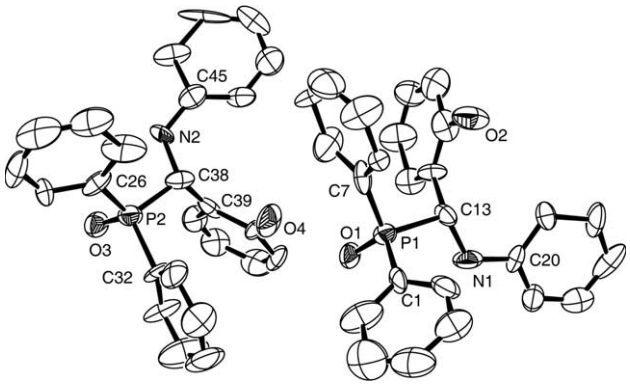


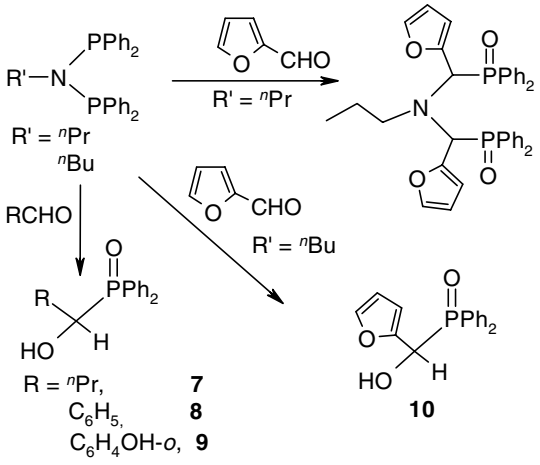
Fig. 1. Molecular structure of $Ph_2P(O)CH(C_6H_4OH\text{-}o)N(H)Ph$ (**4**) with the atom numbering scheme. The ellipsoids are drawn at the 50% probability level.

Table 2
Selected bond distances (Å) and bond angles (°) of **4**

Bond distances			
P(1)–O(1)	1.522(9)	P(2)–O(3)	1.458(9)
P(1)–C(1)	1.721(14)	P(2)–C(26)	1.845(12)
P(1)–C(7)	1.770(13)	P(2)–C(20)	1.762(13)
P(1)–C(13)	1.871(11)	P(2)–C(32)	1.819(9)
C(13)–N(1)	1.449(15)	C(45)–N(2)	1.383(17)
N(1)–C(20)	1.382(16)	N(2)–C(38)	1.470(15)
Bond angles			
O(1)–P(1)–C(1)	111.0(6)	O(3)–P(2)–C(38)	111.7(5)
O(1)–P(1)–C(7)	115.4(5)	O(3)–P(2)–C(32)	113.7(6)
O(1)–P(1)–C(13)	108.8(5)	O(3)–P(2)–C(26)	109.4(6)
C(1)–P(1)–C(13)	109.1(6)	C(32)–P(2)–C(38)	105.5(6)
C(1)–P(1)–C(7)	106.7(6)	C(38)–P(2)–C(26)	108.9(6)
C(7)–P(1)–C(13)	105.4(6)	C(26)–P(2)–C(32)	107.4(6)
C(20)–N(1)–C(13)	120.0(10)	C(45)–N(2)–C(38)	121.3(10)

The reactions of $^nBuN(PPh_2)_2$ with RCHO (R = ^{n}Pr, Ph, $C_6H_4OH\text{-}o$, OC_4H_3) gave α-hydroxy phosphine oxides, $Ph_2P(O)CH(OH)R$ (R = ^{n}Pr, **7**; Ph, **8**; $C_6H_4OH\text{-}o$, **9**; OC_4H_3, **10**) in 40–45% yields (Scheme 2). The formation of these products may be due to the prior cleavage of the P–N bond through the elimination of primary amine to form $Ph_2P(O)H$, which then reacts with the aldehyde to give $Ph_2P(O)CH(OH)R$. Compounds **7**–**10** show ν_{OH} around 3200–3250 cm^{-1} in their IR spectra. The ^{31}P NMR spectra of **7**–**10** show a single resonance in the range of 30–37 ppm and the ^1H NMR spectra show doublets around 4.4–5.5 ppm for the CH proton, with $^2J_{PH}$ couplings in the range of 5–10 Hz.

The structure of $Ph_2P(O)CH(OH)C_6H_4OH\text{-}o$ (**9**) is established by single crystal X-ray diffraction studies and the perspective view of the molecule is shown in Fig. 2. The crystallographic data, selected bond distances and inter bond angles are listed in Tables 1 and 3, respectively. The asymmetric unit contains two identical independent molecules but the corresponding bond distances and bond angles are very similar. The structure of **9** shows a distorted tetrahedral geometry around the phosphorus centers. The P=O bond distance varies



Scheme 2.

Table 1
Crystallographic data for **4**, **9** and **11**

	Compound **4**	Compound **9**	Compound **11**
Empirical formula	$C_{25}H_{22}NO_2P$	$C_{19}H_{17}O_3P$	$C_{18}H_{16}NOP$
Formula weight	399.41	324.30	293.29
Crystal system	orthorhombic	monoclinic	orthorhombic
Space group	$Pbc2_1$ (No. 29)	$P2_1/c$ (No. 14)	$Pca2_1$ (No. 29)
a (Å)	12.567(2)	5.678(1)	9.590(3)
b (Å)	16.452(1)	24.500(2)	9.698(1)
c (Å)	20.968(1)	25.552(4)	16.985(3)
α (°)	90	90	90
β (°)	90	92.06(1)	90
γ (°)	90	90	90
V (Å^3)	4335.2(8)	3552.3(7)	1579.7(6)
Z	8	8	4
D_{calc} (g cm^{-1})	1.224	1.213	1.233
μ (Mo Kα) (mm^{-1})	0.2	0.2	0.2
Theta range (°)	1.62–24.92	1.1–24.9	2.12–24.92
Temperature (K)	293(2)	293	293(2)
R	0.0757	0.084	0.0395
R_w	0.1194	0.281	0.0886

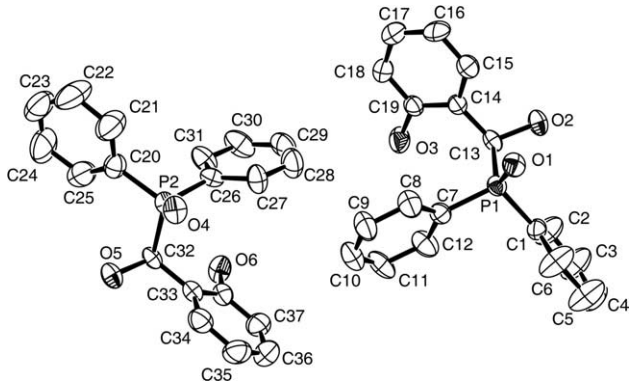


Fig. 2. Molecular structure of $Ph_2P(O)CH(OH)C_6H_4OH$-*o* (**9**) with the atom-numbering scheme.

from 1.486(2) to 1.495(4) Å and the P–C bond distances are in the range of 1.785(5)–1.829(3) Å.

The reactions of the corresponding aminobis(phosphines), $^{n}PrN(PPh_2)_2$ with aldehydes in a 1:2 ratio proceeds in a similar way as described earlier [7b] to give the corresponding α-hydroxy phosphine oxides through P(III)–N bond cleavage, except furfural. The reaction of furfural with the *n*-butyl derivative, $^{n}BuN(PPh_2)_2$, leads to the P(III)–N bond cleavage product, $Ph_2P(O)CH(C_4H_3O)OH$, whereas the *n*-propyl derivative gives the P–N insertion product, $^{n}PrN\{CH(C_4H_3O)P(O)Ph_2\}_2$.

2.1. Reactions of aminophosphines with ketones

The reactions of aminophosphines and aminobis(phosphines) with aldehydes led to the isolation of either P(III)–N bond inserted products or α-hydroxyphosphine oxides via P(III)–N bond cleavage. In order to get more insight into the reactivity of P(III)–N bonds, similar reactions with ketones were carried out with *N*-phenyldiphenylphosphinous amide, $Ph_2PN(H)Ph$ as a representative example.

The reactions of $Ph_2PN(H)Ph$ with aliphatic ketones such as 2-butanone, 4-methyl-2-pentanone and 4-hydroxy acetophenone yielded only the phosphine oxide, $Ph_2P(O)N(H)Ph$ (**11**). The ^{31}P NMR spectrum of **11** shows a single resonance at 18.5 ppm. The structure of **11** was confirmed by a single crystal X-ray structure determination. A perspective view of the molecule **11** is shown in Fig. 3(a) and the selected bond distances and bond angles are given in Table 4. The P–O and P–C distances are comparable with the literature for compounds of a similar type [9–12]. The phosphorus is in a tetrahedral environment as in other phosphine oxides. Compound **11** shows intermolecular P=O...H–N type hydrogen bonding interaction [$d_{H(IN)-O(1)}$ = 2.06(5) Å; $d_{N(1N)-O(1)}$ = 2.807(6) Å; N(1)–H(1N)–O(1) = 169(5)°], thus resulting in a zig-zag arrangement in the lattice as shown in Fig. 3(b).

The reaction of $Ph_2PN(H)Ph$ with benzophenone afforded tetraphenyl diphosphine monoxide $Ph_2PP(O)Ph_2$ (**12**) through P–N bond cleavage as shown in Scheme 3. The formation of product **12** was confirmed

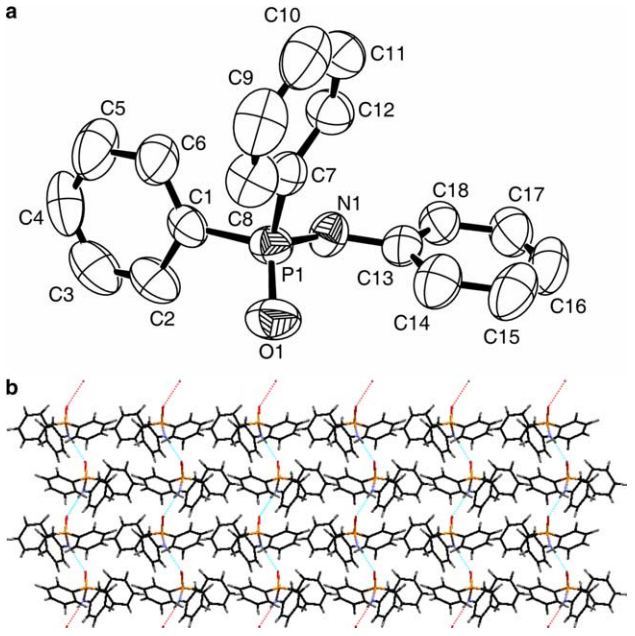


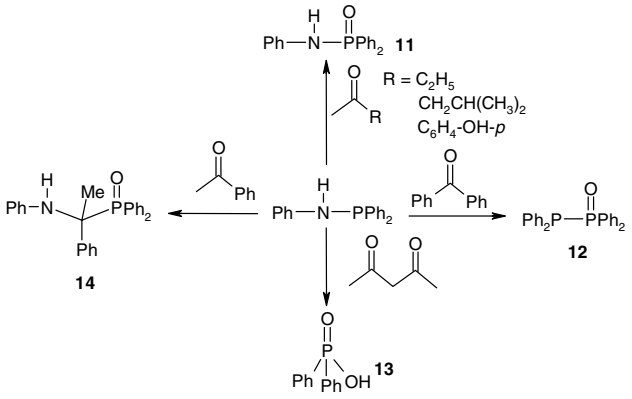
Fig. 3. (a) Molecular structure of $Ph_2P(O)N(H)Ph$ (**11**) with the atom-numbering scheme. (b) Intermolecular hydrogen bonding interaction of P=O of one molecule with N–H of an adjacent molecule in a zig-zag arrangement (view down crystallographic axis *a*).

Table 3
Selected bond distances (Å) and bond angles (°) of **9**

Bond distances			
P(1)–O(1)	1.498(4)	P(1)–C(1)	1.818(5)
P(1)–C(7)	1.785(5)	P(1)–C(13)	1.827(7)
P(2)–O(4)	1.495(4)	P(2)–C(20)	1.794(8)
P(2)–C(26)	1.790(5)	P(2)–C(32)	1.829(6)
Bond angles			
O(1)–P(1)–C(1)	112.1(3)	O(1)–P(1)–C(7)	112.7(3)
O(1)–P(1)–C(13)	110.4(3)	C(1)–P(1)–C(7)	106.7(2)
C(1)–P(1)–C(13)	106.6(3)	C(7)–P(1)–C(13)	108.0(3)
P(1)–C(13)–O(2)	102.3(5)	P(1)–C(13)–C(14)	113.4(4)
O(2)–C(13)–C(14)	112.3(5)	O(4)–P(2)–C(26)	113.7(3)
O(4)–P(2)–C(32)	111.3(3)	O(4)–P(2)–C(20)	110.7(3)
C(20)–P(2)–C(32)	106.8(3)	C(26)–P(2)–C(32)	106.9(3)
C(20)–P(2)–C(26)	107.0(3)	P(2)–C(32)–O(33)	112.6(4)
P(2)–C(32)–O(5)	103.0(4)	O(5)–C(32)–C(33)	112.5(2)

Table 4
Selected bond distances (Å) and bond angles (°) for **11**

Bond distances			
P(1)–O(1)	1.481(4)	P(1)–C(1)	1.794(5)
P(1)–C(7)	1.798(5)	N(1)–C(13)	1.406(6)
P(1)–N(1)	1.642(5)		
Bond angles			
O(1)–P(1)–N(1)	114.5(2)	O(1)–P(1)–C(1)	113.6(2)
O(1)–P(1)–C(7)	109.4(2)	N(1)–P(1)–C(1)	102.6(2)
N(1)–P(1)–C(7)	108.6(2)	P(1)–N(1)–C(13)	127.0(4)
P(1)–N(1)–C(13)	127.0(4)	C(13)–N(1)–H(1N)	119(3)
P(1)–N(1)–H(1N)	114(3)		



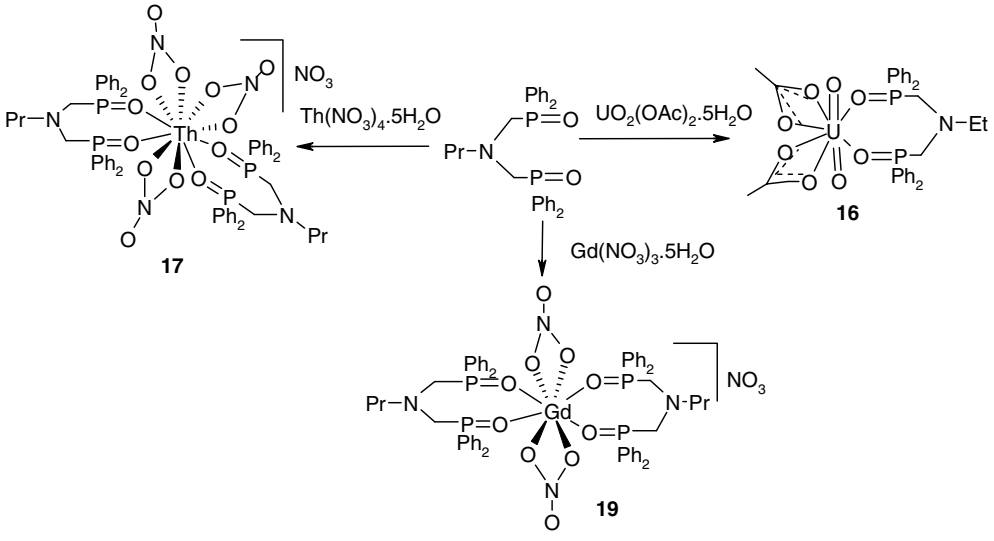
Scheme 3.

by ^{31}P NMR spectral data, which shows two doublets at 36.7 and −21.7 ppm for the P(III) and P(V) centers, respectively with a $^{1}J_{PP}$ coupling of 228 Hz. The reaction of $Ph_2PN(H)Ph$ with acetyl acetone lead to the formation of $Ph_2P(O)OH$ (**13**) through P–N bond cleavage. Compound **13** exhibits a single resonance in its ^{31}P NMR spectrum at 29.6 ppm. When $Ph_2PN(H)Ph$ was treated with acetophenone, insertion of 'C(Me)Ph' into the P–N bond takes place, to afford $Ph_2P(O)C(Me)(Ph)N(H)Ph$ (**14**) in good yield (Scheme 3). The ^{31}P NMR spectrum of **14** shows a single resonance at 29.9 ppm. The structural composition of **14** was further supported by ^{1}H NMR and mass spectral data and by elemental analysis (Scheme 4).

2.2. Coordination chemistry

The phosphine oxides readily react with oxophilic metals to give coordination complexes [13]. The reactions of $Ph_2P(O)CH_2N(H)Ph$ and $(Ph_2P(O)CH_2)_2NEt$ with uranyl acetate in dichloromethane yielded eight-coordinate complexes, *trans*-$[UO_2(OAc)_2\{(Ph_2P(O)CH_2N(H)Ph)_2$-κO,κO$\}]$ (**15**) and *trans*-$[UO_2(OAc)_2\{(Ph_2P(O)CH_2)_2NEt$-κO,κO$\}]$ (**16**), respectively in good yields. The IR spectra of complexes **15** and **16** show a low frequency shift for P=O (∼15 cm^{-1}) compared to the free ligands indicating the coordination to the metal centre. The ^{31}P NMR spectra of complexes **15** and **16** show single resonances at 46.8 and 46.6 ppm, which are considerably deshielded compared to the free ligand values, with coordination shifts of 17.3 and 16.4 ppm, respectively.

The reactions of $(Ph_2P(O)CH_2)_2N^nPr$ with $Th(NO_3)_4 \cdot 5H_2O$ affords a 10-coordinate complex, $[Th(NO_3)_3\{(Ph_2P(O)CH_2)_2N^nPr\}_2](NO_3)$ (**17**). The ^{31}P NMR spectrum of **17** shows a single resonance at 40.1 ppm with a coordination shift of 11 ppm. The IR and ^{1}H NMR spectral data and the micro-analytical data support the proposed structure. The mass spectrum of **17** shows *m*/*z* at 1392 corresponding to the cation. Similarly the reaction of $Ph_2P(O)CH((\eta^5\text{-}C_5H_4)Fe(\eta^5\text{-}C_5H_5))N(H)Ph$ (**6**) with $Th(NO_3)_4 \cdot 5H_2O$ in a 4:1 ratio affords a 10-coordinate complex, $[Th(NO_3)_3\{Ph_2P(O)CH((\eta^5\text{-}C_5H_4)Fe(\eta^5\text{-}C_5H_5))N(H)Ph\}_4](NO_3)$ (**18**). The ^{31}P NMR spectrum of **18** shows two resonances at 23.9 and 28.2 ppm (broad) whereas the free ligand resonates at −29.2 ppm. The IR and ^{1}H NMR spectral data and the micro-analytical data support the proposed structure. The mass spectrum of **18** shows *m*/*z* at 1394 corresponding to the cation. The reaction of $(Ph_2P(O)CH_2)_2N^nPr$ with $Gd(NO_3)_3 \cdot 5H_2O$ affords an 8-coordinate complex, $[Gd(NO_3)_2\{(Ph_2P(O)CH_2)_2N^nPr\}_2](NO_3)$ (**19**). The ^{31}P NMR spectrum of **19** shows a single resonance at 28.1 ppm. The mass spectrum of **19** shows *m*/*z* at 1256 corresponding to the cation.



Scheme 4.

The reaction of two equivalents of $Ph_2P(O)CH((\eta^5\text{-}C_5H_4)Fe(\eta^5\text{-}C_5H_4))N(H)Ph$ (**6**) with $Co(NO_3)_2 \cdot 6H_2O$ gave a purple coloured octahedral complex, $[Co(NO_3)_2\text{-}\{Ph_2P(O)CH((\eta^5\text{-}C_5H_4)Fe(\eta^5\text{-}C_5H_5))NHPh\}_2]$ (**20**) in good yield. The ^{31}P NMR spectra of **20** shows a broad peak around 39 ppm due to the paramagnetic nature of the complex. IR and micro analytical data are consistent with the proposed structure.

3. Conclusions

The reactions of aminophosphines with aldehydes give either P–N inserted products or P–N cleavage products. P–N insertion reactions provide a new route to phosphorus–carbon bond formation whereas P–N cleavage reactions provide α-hydroxy phosphine oxides which can serve as valuable synthons [14] in asymmetric synthesis. Further, P–N inserted products can be used as ligands with oxophilic metal centers. The reactions of both aliphatic and aromatic aldehydes with $^nBuN(PPh_2)_2$ lead to α-hydroxy phosphine oxides via P–N bond cleavage whereas the *n*-propyl derivative gives a P–N inserted product with furfural and α-hydroxy derivatives with other aldehydes. It is observed that these reactions mainly depend on the oxidation state of the phosphorus center and not on the acidic proton present on the nitrogen center. The reactivity also depends on the nature of nitrogen substituents in the aminophosphines. Further investigations to understand the influence of phosphorus substituents on product formation are in progress in our laboratory. Also, this methodology can be adopted to obtain mixed donor ligands which have potential applications in homogeneous catalysis and also in asymmetric synthesis [15].

4. Experimental

All the solvents were purified by conventional procedures and distilled prior to use. $PhN(H)PPh_2$ [16], $RN(PPh_2)_2$ (^nPr, ^nBu [17]) and $1,2\text{-}Ph_2PN(H)C_6H_4\text{-}N(H)PPh_2$ [18] were prepared according to the literature procedures. $Ph_2P(O)CH_2N(H)Ph$ and $[Ph_2P(O)CH_2]_2\text{-}N^nPr$ were prepared as described in our previous report [7b]. 5-Bromo salicylaldehyde was prepared following the reported procedure [19], and all other aldehydes were used after purification except ferrocene carboxaldehyde (Strem). Metal salts were purchased from Loba Chemicals, India and used with out further purification. The ^1H and ^{31}P NMR spectra were recorded using VXR 300 S and Bruker spectrometers; Me_4Si was used as an internal standard for the ^1H NMR and 85% H_3PO_4 as external standard for the ^{31}P NMR. Positive values indicate downfield shifts. IR spectra were recorded on a Nicolet Impact 400 FT IR instrument in KBr disks. Microanalyses were performed on a Carlo Erba model 1112 elemental analyser. The FAB mass spectra were recorded on a JEOL SX 102/DA-6000 mass spectrometer/Data system using Argon/Xenon (6 kV, 10 mA) as the FAB gas. Melting points were recorded in capillary tubes and are uncorrected.

4.1. $1,3\text{-}C_6H_4\{N(H)PPh_2\}_2$ (**1**)

To a solution of *m*-phenylene diamine (1.0 g, 9.24 mmol), Et_3N (1.87 g, 18.4 mmol) and 4-dimethylaminopyridine (0.038 g, 0.31 mmol) in THF (30 mL) at 0 °C, was added dropwise a solution of Ph_2PCl (4.08 g, 18.4 mmol) in THF (20 mL). The reaction mixture was stirred at room temperature for 4 h, the solution was then filtered through celite and the filtrate was concentrated and cooled to give an analytically pure sample of **1**. Yield: 46% (2.02 g, 4.23 mmol), m.p.: 88–92 °C. *Anal*. Calc. for $C_{30}H_{26}N_2P_2$: C, 75.61; H, 5.50; N, 5.88. Found: C, 75.91; H, 5.39; N, 5.83%. FTIR (KBr disk) cm^{-1}: ν_{NH} 3218 s. ^1H NMR ($CDCl_3$): δ 7.21–7.55 (m, *phenyl*). $^{31}P\{^1H\}$ NMR ($CDCl_3$): δ 35.2 (s). MS (HRMS): 476.16 (M^+).

4.2. $1,3\text{-}C_6H_4\{N(H)CH_2P(O)Ph_2\}_2$ (**2**)

A mixture of 1,3-*N*,*N*′-bis(diphenylphosphino)-diaminobenzene (0.20 g, 0.419 mmol) and paraformaldehyde (0.025 g, 0.839 mmol) in 7 mL of toluene was heated under reflux conditions for 10 h and cooled to room temperature. The solvent was removed under reduced pressure and the residue obtained was washed with hexane (4 × 3 mL) and re-dissolved in a mixture of CH_2Cl_2-hexane (2:1) to give the crystalline product **2**. Yield: 72% (0.160 g, 0.298 mmol), m.p.: 133–136 °C. *Anal*. Calc. for $C_{32}H_{30}N_2O_2P_2$: C, 71.62; H, 5.64; N, 5.22. Found: C, 71.92; H, 5.31; N, 5.25%. FTIR (KBr disk) cm^{-1}: ν_{PO} 1174 s. ^1H NMR (CD_2Cl_2): δ 2.39 (s, CH_2, 4H), 7.15–7.99 (m, *phenyl*, 24H). $^{31}P\{^1H\}$ NMR (CD_2Cl_2): δ 28.7 (s). MS (HRMS): 536.18 (M^+).

4.3. $1,2\text{-}C_6H_4NCH_2N(CH_2P(O)Ph_2)_2$ (**3**)

A mixture of 1,2-*N*,*N*′-bis(diphenylphosphino)-diaminobenzene S(0.20 g, 0.419 mmol) and paraformaldehyde (0.037 g, 1.257 mmol) in toluene (7 mL) was refluxed for 10 h. From the cooled reaction mixture, solvent was removed under reduced pressure and the residue obtained was washed with hexane (4 × 3 mL) and redissolved in a mixture of CH_2Cl_2-*n*-hexane (2:1) to give the crystalline product **3**. Yield: 52% (0.120 g, 0.219 mmol), m.p.: 169–172 °C. *Anal*. Calc. for $C_{33}H_{30}N_2O_2P_2$: C, 72.25; H, 5.51; N, 5.11. Found: C, 72.19; H, 5.31; N, 5.17%. FTIR (KBr disk) cm^{-1}: ν_{PO} 1180 s. ^1H NMR ($CDCl_3$): δ 3.82 (br s, P–CH_2–N,

4H), 4.96 (s, N–CH_2–N, 2H), 6.34–8.65 (m, *phenyl*, 24H). $^{31}P\{^1H\}$ NMR ($CDCl_3$): δ 26.6 (s). MS (FAB): 547.21 ($M^+ - 1$).

4.4. General procedure for the preparation of $Ph_2P(O)$-$CH(R)NHPh$ (R = 5-Br-C_6H_3OH-*o*, ferrocenyl)

A mixture of $Ph_2PN(H)Ph$ (0.40 g, 1.44 mmol) and one equivalent of aldehyde, RCHO was stirred at room temperature for 12 h. The resultant slurry was subjected to a vacuum to remove any volatiles and the residue obtained was washed with *n*-hexane (3×5 mL) and crystallized in a mixture of CH_2Cl_2-*n*-hexane (2:1) at 0 °C to give analytically pure products.

4.5. $Ph_2P(O)CH(5\text{-}Br\text{-}C_6H_4OH\text{-}o)N(H)Ph$ (**5**)

Yield: 61% (0.215 g, 0.450 mmol), m.p.: 183–188 °C. *Anal*. Calc. for $C_{25}H_{21}NO_2BrP$: C, 62.78; H, 4.43; N, 2.93. Found: C, 62.79; H, 4.55; N, 2.83%. FTIR (KBr disk) cm^{-1}: ν_{OH} 3382 br s, ν_{NH} 3053 s, ν_{PO} 1150 vs. ^1H NMR ($CDCl_3$): δ 4.68 (br s, N*H*, D_2O exchangeable), 5.49 (dd, C*H*, $^2J_{PH}$ = 5.9 Hz, 1H), 6.60–7.79 (m, *phenyl*, 18H). $^{31}P\{^1H\}$ NMR ($CDCl_3$): δ 37.8 (s).

4.6. $Ph_2P(O)CH\{(\eta^5\text{-}C_5H_5)Fe(\eta^5\text{-}C_5H_4)\}N(H)Ph$ (**6**)

Yield: 66% (0.230 g, 0.500 mmol), m.p.: 175–178 °C. *Anal*. Calc. for $C_{29}H_{26}NOPFe$: C, 70.89; H, 5.33; N, 2.85. Found: C, 70.82; H, 5.36; N, 2.80%. FTIR (KBr disk) cm^{-1}: ν_{NH} 3426 s, ν_{PO} 1173 vs. ^1H NMR ($CDCl_3$): δ 3.90–4.98 (m, *ferrocenyl*, 9H), 5.01 (br s, C*H*, 1H), 6.68–7.72 (m, *phenyl*, 15H). $^{31}P\{^1H\}$ NMR ($CDCl_3$): δ 29.2 (s).

4.7. General procedure for the reaction of $^nBuN(PPh_2)$ ($R = {}^nPr$,) with $R'CHO$ ($R' = {}^nPr$, Ph, OC_4H_3, C_6H_4OH-*o*)

A mixture of $Ph_2PN(^nBu)PPh_2$ (0.400 g, 0.94 mmol) and two equivalents of aldehyde, RCHO (R = ^{n}Pr, Ph, OC_4H_3 and C_6H_4OH-*o*) was stirred at room temperature for 24 h. The resultant slurry was subjected to a vacuum to remove any volatiles and the residue obtained was washed with *n*-hexane (3×5 mL) and crystallized in a mixture of CH_2Cl_2-*n*-hexane (2:1) at 0 °C to give analytically pure products.

4.8. $Ph_2P(O)CH(OH)CH_2CH_2CH_3$ (**7**)

Yield: 42% (0.215 g, 0.784 mmol), m.p.: 116–118 °C. *Anal*. Calc. for $C_{16}H_{19}O_2P$: C, 70.06; H, 6.98. Found: C, 70.67; H, 6.87%. FTIR (KBr disk) cm^{-1}: ν_{OH} 3207 s, ν_{PO} 1179 vs. ^1H NMR ($CDCl_3$): δ 0.85 (t, CH_3, $^3J_{HH}$ = 6.32 Hz, 3H), 1.38 (m, CH_2, 2H), 1.65 (m, CH_2, 2H), 1.73 (br s, O*H*, D_2O exchangeable, 1H), 4.41 (d, C*H*, $^2J_{PH}$ = 10.32 Hz, 2H), 7.43–7.89 (m, *phenyl*, 10H). $^{31}P\{^1H\}$ NMR ($CDCl_3$): δ 31.3 (s).

4.9. $Ph_2P(O)CH(OH)Ph$ (**8**)

Yield: 51% (0.291 g, 0.944 mmol), m.p.: 164–166 °C (dec.). *Anal*. Calc. for $C_{19}H_{17}O_2P$: C, 74.01; H, 5.56. Found: C, 73.86; H, 5.49%. FTIR (KBr disk) cm^{-1}: ν_{OH} 3388 s, ν_{PO} 1163 vs. ^1H NMR ($CDCl_3$): δ 1.83 (br s, OH, D_2O exchangeable), 5.48 (d, C*H*, $^2J_{HH}$ = 5.24 Hz, 1H), 7.13–7.90 (m, *phenyl*, 15H). $^{31}P\{^1H\}$ NMR ($CDCl_3$): δ 30.6 (s).

4.10. $Ph_2P(O)CH(OH)C_6H_4OH$-*o* (**9**)

Yield: 51% (0.311 g, 0.959 mmol), m.p.: 90–92 °C. *Anal*. Calc. for $C_{19}H_{17}O_3P$: C, 70.37; H, 5.28. Found: C, 70.25; H, 5.33%. FTIR (KBr disk) cm^{-1}: ν_{OH} 3229 br s, ν_{PO} 1139 vs. ^1H NMR ($CDCl_3$): δ 4.01 (br s, OH, D_2O exchangeable), 5.45 (d, C*H*, $^2J_{PH}$ = 5.86 Hz, 1H), 6.67–7.82 (m, *phenyl*, 14H), 9.65 (br s, O*H*, D_2O exchangeable). $^{31}P\{^1H\}$ NMR ($CDCl_3$): δ 37.4 (s).

4.11. $Ph_2P(O)CH(OH)(OC_4H_3)$ (**10**)

Yield: 77% (0.313 g, 1.050 mmol), m.p.: 148–151 °C. *Anal*. Calc. for $C_{17}H_{15}O_3P$: C, 68.45; H, 5.06. Found: C, 68.32; H, 4.93%. FTIR (KBr disk) cm^{-1}: ν_{OH} 3380 br s, ν_{PO} 1154 vs. ^1H NMR ($CDCl_3$): δ 4.77 (br s, OH, D_2O exchangeable), 5.59 (d, C*H*, $^2J_{PH}$ = 5.5 Hz, 1H), 6.23–6.29 (m, *furfuryl*, 2H), 7.18–7.88 (m, *phenyl* & *furfuryl*, 11H). $^{31}P\{^1H\}$ NMR ($CDCl_3$): δ 31.5 (s).

5. Reaction of aminophosphines with ketones

5.1. Reaction of $Ph_2PN(H)Ph$ with $CH_3C(O)R$ ($R = C_2H_5$, $CH_2CH(CH_3)_2$, C_6H_4OH-*p*)

A mixture of $Ph_2PN(H)Ph$ (0.400 g, 1.44 mmol) and $CH_3C(O)R$ (1.44 mmol) in toluene (10 mL) was stirred at room temperature for 10 h. The solution was evaporated under reduced pressure and the residue obtained was crystallized from a 1:1 mixture of CH_2Cl_2–petroleum ether at 0 °C to give analytically pure $Ph_2P(O)N(H)Ph$ (**11**). Yield: 47% (0.20 g, 0.682 mmol) (for $R = C_2H_5$); 55% (0.23 g, 0.784 mmol) (for $R = CH_2CH(CH_3)_2$); 50% (0.21 g, 0.716 mmol) (for $R = C_6H_4OH$-*p*), m.p.: ~230 °C (dec.). *Anal*. Calc. for $C_{18}H_{16}NOP$: C, 73.70; H, 5.49; N, 4.78. Found: C, 73.63; H, 5.55; N, 4.59%. FTIR (KBr disk) cm^{-1}: ν_{NH} 3121 s, ν_{PO} 1183 vs. ^1H NMR ($CDCl_3$): δ 4.39 (d, N*H*, D_2O exchangeable, 1H), 6.70–7.13 (m, N*Ph*, 5H), 7.15–7.77 (m, PPh_2, 10H). $^{31}P\{^1H\}$ NMR ($CDCl_3$): δ 18.5 (s).

5.2. Reaction of $Ph_2PN(H)Ph$ with benzophenone

A mixture of $Ph_2PN(H)Ph$ (0.200 g, 0.7 mmol) and benzophenone (0.131 g, 0.7 mmol) was heated to 75–80 °C with stirring. The melt was cooled to room temperature after 4 h and the volatiles were removed under reduced pressure to give a white residue. The residue obtained was crystallized from CH_2Cl_2–petroleum ether (2:1) mixture at 0 °C to get analytically pure $Ph_2PP(O)Ph_2$ (**12**). Yield: 94% (0.131 g, 0.34 mmol), m.p.: 152–154 °C. *Anal.* Calc. for $C_{24}H_{20}OP_2$: C, 74.62; H, 5.22. Found: C, 74.69; H, 5.33%. $^{31}P\{^1H\}$ NMR ($CDCl_3$): δ −21.7 (d), 36.7(d); $^1J_{PP}$ = 228.3 Hz.

5.3. Reaction of $Ph_2PN(H)Ph$ with acetylacetone

To a solution of $Ph_2PN(H)Ph$ (1.00 g, 3.60 mmol) in toluene (10 mL) was added acetylacetone (0.360 g, 3.60 mmol) also in toluene (5 mL) and the reaction mixture was stirred at room temperature for 12 h. The solution was then concentrated to 3 mL, diluted with diethyl ether (7 mL) and on storing the solution at room temperature yielded an analytically pure sample identified as $Ph_2P(O)OH$ (**13**). Yield: 77% (0.590 g, 2.70 mmol), m.p.: 170–172 °C (dec.). FTIR (KBr disk) cm^{-1}: ν_{PO} 1181 s. ^1H NMR ($CDCl_3$): δ 7.45–7.88 (m, *phenyl*). $^{31}P\{^1H\}$ NMR ($CDCl_3$): δ 29.6 (s). MS (FAB): 218.67 (M^+).

5.4. Reaction of $Ph_2PN(H)Ph$ with acetophenone

To a solution of $Ph_2PN(H)Ph$ (0.400 g, 1.44 mmol) in toluene (10 mL), was added acetophenone (0.173 g, 1.44 mmol) and the reaction mixture was allowed to stir at room temperature for 12 h. The solution was then concentrated to 3 mL, diluted with diethyl ether (10 mL) and cooled to 0 °C to give analytically pure $Ph_2P(O)C(CH_3)PhN(H)Ph$ (**14**). Yield: 46% (0.320 g, 0.660 mmol), m.p.: 156–158 °C (dec.). *Anal.* Calc. for $C_{26}H_{24}NOP \cdot CH_2Cl_2$: C, 67.23; H, 5.43; N, 2.90. Found: C, 67.49; H, 5.24; N, 2.79%. ^1H NMR ($CDCl_3$): δ 1.25 (s, CH_3, 3H), 6.91–6.97 (m, *phenyl*, 5H), 7.10–7.92 (m, *phenyl*, 15H). $^{31}P\{^1H\}$ NMR ($CDCl_3$): δ 29.9 (s). MS (FAB): 395 ($M^+ - 2$).

5.5. $[UO_2(CH_3COO)_2(Ph_2P(O)CH_2N(H)Ph)_2]$ (**15**)

Uranyl acetate (0.10 g, 0.23 mmol) in methanol (5 mL) was added to $Ph_2P(O)CH_2N(H)Ph$ (0.146 g, 0.47 mmol) also in methanol (5 mL) and the yellow solution obtained was stirred at room temperature for 2 h. The solvent was evaporated under reduced pressure and the residue was washed with *n*-hexane (2 × 5 mL) and dried to give the crystalline product **15**. Yield: 77% (0.184 g, 0.180 mmol), m.p.: 72–74 °C (dec.). *Anal.* Calc. for $C_{42}H_{42}N_2O_8P_2U$: C, 50.31; H, 4.22; N, 2.79. Found: C, 50.32; H, 4.16; N, 2.67%. FTIR (KBr disk) cm^{-1}: ν_{NH} 3291 s, ν_{CO} 1612 s, ν_{PO} 1138 s. ^1H NMR ($CDCl_3$): δ 0.73 (br s, CH_3, 6H), 4.51 (br s, CH_2, 4H), 6.70–7.60 (m, *phenyl*, 30H). $^{31}P\{^1H\}$ NMR ($CDCl_3$): δ 46.9 (s).

5.6. $[UO_2(CH_3COO)_2\{(Ph_2P(O)CH_2)_2NEt\}]$ (**16**)

A solution of $EtN(CH_2P(O)Ph_2)_2$ (0.056 g, 0.10 mmol) in CH_2Cl_2 (10 mL) was added to $UO_2(OAc)_2$ (0.050 g, 0.10 mmol) also in CH_2Cl_2 (10 mL) and the reaction mixture was stirred at room temperature for 6 h. The solvent was evaporated from the reaction mixture under reduced pressure and the residue obtained was re-crystallized from EtOH–diethyl ether (1:1) at 0 °C to give an analytically pure sample of **16**. Yield: 88% (0.091 g, 0.110 mmol), m.p.: 118–121 °C (dec.). *Anal.* Calc. for $C_{32}H_{35}NO_8P_2U$: C, 44.61; H, 4.09; N 1.63. Found: C, 43.92; H, 3.99; N, 1.51%. FTIR (KBr disk) cm^{-1}: ν_{PO} 1148 s, ν_{CO} 1611 m. ^1H NMR ($CDCl_3$): δ 0.89 (m, CH_3, 6H), 1.25 (s, CH_3, 3H), 2.46 (m, CH_2, 2H), 4.07 (br s, P–CH_2–N, 4H), 7.26–9.92 (m, *phenyl*, 20H). $^{31}P\{^1H\}$ NMR ($CDCl_3$): δ 42.4 (s).

5.7. $[Th(NO_3)_3\{(Ph_2P(O)CH_2)_2N^nPr\}_2]NO_3$ (**17**)

A solution of, $^nPrN(CH_2P(O)Ph_2)_2$ (0.170 g, 0.350 mmol) in ethanol (5 mL) was added to a solution of $Th(NO_3)_4 \cdot 5H_2O$ (0.1 g, 0.175 mmol) also in ethanol (10 mL). The clear solution was allowed to stir at room temperature for 4 h, during which time, the product precipitated out, was filtered and dried. The product was re-crystallized from CH_2Cl_2–diethylether (1:1) mixture. Yield: 76% (0.195 g, 0.121 mmol), m.p.: 109–111 °C (dec.). *Anal.* Calc. for $C_{58}H_{62}N_6O_{16}P_4Th$: C, 47.87; H, 4.29; N, 5.78%. Found: C, 48.11; H, 4.19; N, 5.94%. FTIR (KBr disk) cm^{-1}: ν_{NO3} 1529 vs, ν_{PO} 1138 vs. ^1H NMR ($CDCl_3$): δ 0.26 (t, CH_3, $^3J_{HH}$ = 7.00 Hz, 3H), 0.81(m, CH_2, 2H), 3.15 (m, CH_2, 2H), 3.97 (s, P–CH_2–N, 4H), 6.87–7.73 (m, *phenyl*, 20H). $^{31}P\{^1H\}$ NMR ($CDCl_3$): δ 40.1 (s). MS (FAB): 1392.4 ($M^+ - NO_3$).

5.8. $[Th(NO_3)_3\{Ph_2P(O)CH(C_5H_4FeC_5H_5)N(H)Ph\}_4]NO_3$ (**18**)

A solution of $Ph_2P(O)CH_2N(H)C_5H_4FeC_5H_5$ (0.103 g, 0.021 mmol) in CH_2Cl_2 (5 mL) was added to a solution of $Th(NO_3)_4 \cdot 5H_2O$ (0.03 g, 0.05 mmol) in ethanol (10 mL). The clear solution was allowed to stir at room temperature for 4 h, during which time, the product precipitated out, was filtered and dried. The product was re-crystallized from CH_2Cl_2–diethylether (1:1) mixture. Yield: 64% (0.082 g, 0.034 mmol), m.p.: 152–154 °C. *Anal.* Calc. for $C_{116}H_{104}N_8O_{16}P_4Fe_4Th \cdot 3CH_2Cl_2$: C, 52.93; H, 4.11; N, 4.15. Found: C, 52.74; H, 4.07; N,

4.13%. FTIR (KBr disk) cm^{-1}: ν_{NO_3} 1515 s, ν_{PO} 1138 vs. ^1H NMR ($CDCl_3$): signals are broad, so not incorporated and the ^{31}P signal is also slightly broad in this case. $^{31}P\{^1H\}$ NMR ($CDCl_3$): δ 23.9 (s). MS (FAB): 2382 ($M^+ - 1 - NO_3$).

5.9. $[Gd(NO_3)_2\{(Ph_2P(O)CH_2)_2N^nPr\}_2]NO_3$ (**19**)

A solution of the dioxide, $^nPrN(CH_2P(O)Ph_2)_2$ (0.225 g, 0.460 mmol) in CH_2Cl_2 (5 mL) was added to a solution of $Gd(NO_3)_3 \cdot 5H_2O$ (0.1 g, 0.230 mmol) also in ethanol (10 mL). The clear solution was allowed to stir at room temperature for 4 h, during which time, the product precipitated out, was filtered and dried. The product was washed with diethylether and re-crystallized from MeOH–CH_2Cl_2 (1:1) mixture. Yield: 84% (0.256 g, 0.194 mmol), m.p.: 110–114 °C (dec.). *Anal.* Calc. for $C_{58}H_{62}N_5O_{13}P_4Gd \cdot CH_2Cl_2$: C, 50.50; H, 4.60; N, 4.99. Found: C, 50.37; H, 4.65; N, 4.86%. FTIR (KBr disk) cm^{-1}: ν_{NO_3} 1490 vs, ν_{PO} 1159 s. ^1H NMR (DMSO-d_6): δ 0.29 (br s, CH_3, 3H), 1.78 (br s, CH_2, 2H), 2.51 (br s, CH_2, 2H), 3.57 (br s, DMSO & P–CH_2–N), 7.48–7.79 (br m, *phenyl*, 20H). $^{31}P\{^1H\}$ NMR (DMSO-d_6): δ 28.1 (br s). MS (FAB): 1256 ($M^+ - NO_3$).

5.10. $[Co(O_2NO)_2(Ph_2P(O)CH((\eta^5\text{-}C_5H_4)Fe(\eta^5\text{-}C_5H_5))N(H)Ph)_2]$ (**20**)

To an ethanolic solution (5 mL) of $Co(NO_3)_2 \cdot 6H_2O$ (0.030 g, 0.10 mmol), $Ph_2P(O)CH((\eta^5\text{-}C_5H_4)Fe(\eta^5\text{-}C_5H_5))$-N(H)Ph (0.101 g, 0.20 mmol) also in ethanol (10 mL) was added and the mixture was stirred for 2 h at room temperature. The resultant brown solution was evaporated to dryness and the residue was washed with *n*-hexane (3 × 5 mL) to give the analytically pure product **20**. Yield: 92% (0.110 g, 0.094 mmol), m.p.: 116–120 °C (dec.). *Anal.* Calc. for $C_{58}H_{52}N_4O_8P_2CoFe_2$: C, 59.76; H, 4.49; N, 4.81. Found: C, 59.69; H, 4.56; N, 4.86%. FTIR (KBr disk) cm^{-1}: ν_{NH} 3384 br m, ν_{NO3} 1388 s, ν_{PO} 1143 vs. $^{31}P\{^1H\}$ NMR ($CDCl_3$ &DMSO-d_6): δ 38.7 (br s).

5.11. X-ray Crystallography

Crystals of compounds **4**, **9** and **11** obtained as above were mounted on pyrex resin. A Nonius MACH3 diffractometer was used for the unit cell determination and the intensity data collection. The initially obtained unit cell parameters were refined by accurately centering randomly selected reflections. Periodic monitoring of check reflections showed the stability of the intensity data. Details of crystal and data collection are given in Table 1. The structures were solved by direct methods (SHELXS 97) and refined using SHELXL 97 software [20]. The non-hydrogen atoms were refined with anisotropic thermal parameters. All the hydrogen atoms were geometrically fixed and allowed to refine using a riding model.

6. Supplementary material

Full details of data collection and structure refinement have been deposited with Cambridge Crystallographic Data Center, CCDC reference numbers 245668, 245669 and 245670 for compounds **4**, **9** and **11**, respectively. Copies of this information can be obtained free of charge from the Director, CCDC, 12 Union Road, Cambridge, CB2 1EZ, UK (fax: +44-1223-336033; e-mail: deposit @ccdc.cam.ac.uk or www:http://www.ccdc.cam.ac.uk).

Acknowledgements

We are grateful to the Department of Science and Technology (DST) and CSIR, New Delhi, India for generous support. SP thanks CSIR, New Delhi, India for JRF and SRF fellowships. The X-ray structural studies were carried out at the National Single Crystal X-ray Diffraction Facility, Indian Institute of Technology, Bombay. We also thank RSIC, Mumbai, Sophisticated Instrumentation Facility (SIF), Bangalore, for the spectral facility. The referees' suggestions at the revision stage were very helpful.

References

[1] M.S. Balakrishna, V.S. Reddy, S.S. Krishnamurthy, J.F. Nixon, J.C.T.R. Burckett, St. Laurent, Coord. Chem. Rev. 129 (1994) 1.
[2] M.T. Ashby, Z. Li, Inorg. Chem. 31 (1992) 1321.
[3] M.S. Balakrishna, B.D. Santarsiero, R.G. Cavell, Inorg. Chem. 33 (1994) 3079.
[4] M.G. Newton, R.B. King, M. Chang, J. Gimeno, J. Am. Chem. Soc. 100 (1978) 1632.
[5] A.D. Burrows, M.F. Mahon, M.T. Palmer, M. Varrone, Inorg. Chem. 41 (2002) 1695;
(a) M.S. Balakrishna, S.S. Krishnamurthy, Indian J. Chem. 30A (1991) 356;
(b) S. Priya, M.S. Balakrishna, J.T. Mague, J. Organomet. Chem. 679 (2003) 116;
(c) M.S. Balakrishna, P.P. George, J.T. Mague, J. Organomet. Chem. 689 (2004) 3388.
[6] (a) S. Priya, M.S. Balakrishna, J.T. Mague, Inorg. Chem. Commun. 4 (2001) 437;
(b) S. Priya, M.S. Balakrishna, J.T. Mague, S.M. Mobin, Inorg. Chem. 42 (2003) 1272.
[7] (a) M.S. Balakrishna, K. Ramaswamy, R.M. Abhyankar, J. Organomet. Chem. 560 (1998) 131;
(b) M.S. Balakrishna, R.M. Abhyankar, J.T. Mague, J. Chem. Soc., Dalton Trans. (1999) 1407;
(c) M.S. Balakrishna, R. Panda, J.T. Mague, Inorg. Chem. 40 (2001) 5620;
(d) M.S. Balakrishna, R.M. Abhyankar, M.G. Walawalker, Tetrahedron Lett. 42 (2001) 2733;
(e) M.S. Balakrishna, M.G. Walawalker, J. Organomet. Chem. 628 (2001) 76;

(f) S. Priya, M.S. Balakrishna, S.M. Mobin, R. McDonald, J. Organomet. Chem. 688 (2003) 227;
(g) M.S. Balakrishna, P. Chandrasekaran, P.P. George, Coord. Chem. Rev. 241 (2003) 87;
(h) M.S. Balakrishna, S. Priya, R. Panda, Phosphorus, sulfur, silicon and Rel. Elem. 179 (2004) 911;
(i) S. Priya, M.S. Balakrishna, J.T. Mague, Chem. Lett. 33 (2004) 308;
(j) S. Priya, M.S. Balakrishna, J.T. Mague, J. Organomet. Chem. 689 (2004) 3335.

[8] R.G. Cavell, K.I. The, L. van de Griend, Inorg. Chem. 20 (1981) 3813.

[9] P. Kafarski, P. Mastalerz, Aminophosphonates, Beitrage zur Wirkstofforschung (1984) 1.

[10] J.M. Barendt, R.C. Haltiwanger, C.A. Squier, A.D. Norman, Inorg. Chem. 30 (1991) 2342.

[11] C. Panattoni, G. Bandoli, G. Bortolozzo, D.A. Clemente, U. Croatto, J. Chem. Soc. A (1970) 2778.

[12] K. Aparna, S.S. Krishnamurthy, M. Nethaji, J. Chem. Soc., Dalton Trans. (1995) 2991.

[13] V.V. Grushin, Chem. Rev. 104 (2004) 1629.

[14] (a) D.R. Armstrong, M.G. Davidson, R.P. Davies, H.J. Mitchell, R.M. Oakley, P.R. Raithby, R. Snaith, S. Warren, Angew Chem., Int. Ed. Engl. 35 (1996) 1942;
(b) K.K. Praveen Kumar, S. Kumaraswamy, K.C. Kumaraswamy, Tetrahedron Lett. 42 (2001) 3219;
(c) J. Claydon, E.W. Collington, S. Warren, Tetrahedron Lett. 34 (1993) 1327.

[15] (a) J. Claydon, E.W. Collington, S. Warren, Tetrahedron Lett. 33 (1992) 7043;
(b) D.R. Armstrong, D. Barr, M.G. Davidson, G. Hutton, P. O'Brien, R. Snaith, S. Warren, J. Organomet. Chem. 529 (1997) 29.

[16] W. Wiegraebe, H. Bock, Chem. Ber. 101 (1968) 1414.

[17] H. Noeth, L. Meinel, Z. Anorg. Allg. Chem. 349 (1967) 225.

[18] T.Q. Ly, A.M.Z. Slawin, J.D. Woollins, J. Chem. Soc., Dalton Trans. (1997) 1611.

[19] C.M. Brewster, L.H. Millam, J. Am. Chem. Soc. 55 (1933) 763.

[20] G.M. Sheldrick, SHELXL97. Program for Crystal Structure Refinement, University of Göttingen, Göttingen, Germany, 1997.

Table 1
Selected bond length (Å) and angles (°) for **1**

C(1)–N(1)	1.501(6)
C(5)–N(3)	1.501(6)
C(9)–N(5)	1.504(7)
C(11)–N(6)	1.478(7)
N(1)–Cu(1)	2.043(4)
N(2)–Cu(1)	2.058(5)
N(4)–Cu(1)	2.047(5)
N(5)–Cu(1)	2.047(4)
Cl(1)–Cu(1)	2.6458(7)
Cu(1)#1–Cl(1)–Cu(1)	180.00(1)
N(1)–Cu(1)–N(4)	88.39(18)
N(1)–Cu(1)–N(5)	174.93(17)
N(4)–Cu(1)–N(5)	92.19(18)
N(1)–Cu(1)–N(2)	91.92(17)
N(4)–Cu(1)–N(2)	179.45(18)
N(5)–Cu(1)–N(2)	87.54(17)
N(1)–Cu(1)–Cl(1)	91.03(12)
N(4)–Cu(1)–Cl(1)	88.53(13)
N(5)–Cu(1)–Cl(1)	94.03(13)
N(2)–Cu(1)–Cl(1)	91.02(12)

Symmetry transformations used to generate equivalent atoms: #1 $-x+2, -y+1, -z+2$.

M–X–M link by steric repulsion. One such ligand system we are focusing on is *cis*,*trans*-1,3,5-triaminocyclohexane (*tach*), a multifunctional synthon, that upon protonation can be used to engineer supramolecular solid-state structures. For instance we have recently reported a trinuclear cluster based upon *tach*, $\{(CuCl_2\text{-}(tachH))_3Cl\}$, which incorporates both coordinative and hydrogen bonds; this is because the *tach* ligand can accommodate multiple coordination modes, and its amino groups can act as both hydrogen bond donors and acceptors [11]. Under more basic conditions, the amino groups are not fully protonated and different types of discrete molecular species are formed. We herein report the reaction of *tach* and $CuCl_2$ which produces a dimeric complex of $s = 1/2$ Cu^{II} centers that features a single, linear Cu–Cl–Cu linking group (see Table 1).

2. Experimental

2.1. Materials, measurements, and calculations

cis,*trans*-1,3,5-Triaminocyclohexane (*tach*) was synthesized according to [12]; all other reagents were of analytical grade, purchased commercially and used as obtained. IR spectra were recorded on a Jasco FTIR-410 spectrometer using a *Golden Gate* single reflection diamond ATR setting for solid material. UV/VIS spectra were recorded on a Shimadzu UV-3101PC UV–VIS–NIR Scanning Spectrophotometer. Extended Hückel calculations were performed using the YAEHMOP 3.03 package [13]. The program's default parameters were employed.

2.2. Preparation of [(μ2-chloro)-di-{syn-bis(cis,trans-1,3,5-triaminocyclohexane-κ2-N,N′)-copper(II)}]-trichloride dihydrochloride (1)

A methanolic solution (15 ml) of copper(II) chloride anhydrous (58 mg, 0.43 mmol) was added to a solution of *tach* (110 mg, 0.85 mmol) in methanol (25 ml) giving an instant color change from colorless to dark blue. Reducing the volume to 2 ml and crystallization by diffusion of ether yielded dark blue crystals of **1** suitable for single crystal X-ray analysis. Amorphous material was obtained by addition of ether (10 ml) and filtration. Yield: 14 mg (0.02 mmol, 10% based on Cu) crystals, 54 mg (0.08 mmol, 37%) amorphous solid. M.p. 195 °C (dec.). The identity of **1** was confirmed by IR, UV/Vis spectroscopy and elemental analysis. IR spectrum (in cm^{-1}; s = strong, m = medium): 3217(s), 3116(s), 2920(m), 1609(s), 1558(s), 1458(s), 1346(s), 1165(s), 1119(m), 918(s). UV/Vis (MeOH) $\lambda(\varepsilon)$/nm (M^{-1} cm^{-1}): 247 (3235), 301 (1822, shoulder), 328 (1070, minimum), 355 (1518), 352 (442), 571 (106). MS (ES-TOF+) *m*/*z* (%) 491 (100, $[Cu_2(tach)_2Cl_3]^+$), 419 (5, $[Cu_2(tach)_2Cl - 2H]^+$), 356 (8, $[Cu(tach)_2Cl]^+$), 290 (32, $[Cu_2(tach)Cl - 2H]^+$), 227 (33, $[Cu(tach)Cl]^+$). Elemental analysis for $C_{24}H_{60}Cl_4Cu_2N_{12} \cdot 2HCl \cdot H_2O$ ($M = 948.72$ g mol^{-1}), found (expected) %: C, 33.36 (32.88); H, 8.09 (7.36); N, 18.88 (19.17).

2.3. Single-crystal X-ray structure

Crystallographic data was collected on a Rigaku R-axis image plate area detector (graphite monochromatized Mo Kα radiation, $\lambda = 0.71073$ Å) at 293 K on a needle-shaped single crystal with dimensions $0.3 \times 0.15 \times 0.03$ mm^3. The crystal system was found to be monoclinic, space group $P2_1/n$, $a = 8.726(2)$, $b = 18.500(4)$, $c = 13.341(3)$ Å, $\beta = 96.731(2)°$, $V = 2138.8(9)$ $Å^3$, $Z = 2$, $\rho_c = 1.473$ g cm^{-3}. A total of 9933 reflections were collected.

2.4. Magnetic measurements

Susceptibility data of a polycrystalline sample of **1** were recorded using a Quantum Design MPMS-5 SQUID magnetometer over the temperature range 2–290 K for various magnetic fields (0.1–5.0 T). All susceptibility data were corrected for diamagnetic and temperature-independent paramagnetic contributions ($\chi_{dia/TIP}$(**1**) = -410×10^{-6} emu mol^{-1}). Magnetization measurements at 2.0 and 25 K indicated the presence of a small percentage (1.5%) of an $s = 1/2$ species, which was attributed to disassociated $Cu(tach)_2$ dimer halves. Corresponding $s = 1/2$-Brillouin function fits to the

experimental field-dependence of the magnetization confirmed an isotropic g factor of 2.15. Intermolecular dipole–dipole interactions are negligible due to the large spacing between the dimeric units with closest Cu–Cu distances between neighboring $\{Cu_2Cl\}$ cations of 7.4 Å.

3. Results and discussion

3.1. Synthesis

The *tach* ligand system allows several coordination modes due to its two *cis* and one *trans* positioned amino groups that are connected to the rigid cyclohexane framework [11]. For a stoichiometric *tach*:metal cation ratio of 2:1, the preferred coordination is represented by a chelating binding mode in which the two *cis*-positioned amino groups assume an axial orientation with regard to the cyclohexane framework in its chair conformation, while the third amino group remains uncoordinated in an equatorial position. This coordination mode is targeted in the reaction of the *tach* base with copper(II) chloride in a water/methanol solution at unadjusted pH (11.0), which results in the formation of the partially protonated dinuclear copper(II) complex $[(Cu(tachH)(tach))_2(\mu\text{-}Cl)]^{5+} = \{Cu_2Cl\}^{5+}$ which was isolated as its chloride salt $[(Cu(tachH)(tach))_2(\mu\text{-}Cl)]Cl_5 \cdot H_2O$ (**1**).

3.2. Crystal structure

The single-crystal X-ray structure reveals D_{2h}-symmetric dinuclear Cu^{2+} complexes, consisting of two symmetry-equivalent halves. Two *tach* ligands coordinate to each copper center in a *syn* fashion via *bis*-bidentate coordination of two $-NH_2$ groups per *tach* molecule, with slightly elongated N–C bonds (1.501–1.511 Å) compared to the non-coordinated N–C bonds (1.478–1.500 Å). The cyclohexane ring planes of the two coordinated *tach* ligands are separated by 5.58(6) Å. This coordination mode results in a near-square-planar coordination environment around the copper(II) center (N1–N2 and N4–N5: 2.95 Å, N1–N4 and N2–N5: 2.85 Å) and the Cu position only slightly deviates from the coordination plane. Cu–N bond lengths range from 2.047 to 2.058 Å. Two of the resulting C_{2v}-symmetric Cu(*tach*)$_2$ units are then linked by a linear μ_2-bridging chloro ligand that completes the square pyramidal coordination geometry around the copper(II) centers (Fig. 1). On average, half of the non-coordinated, equatorially oriented amino residues of the *tach* ligands are protonated as shown by elemental analysis and single crystal X-ray diffraction, and **1** may be classified as a di-hydrochloride salt. As discussed above, the linear μ_2-chloro bridging motif between two copper(II) centers is rare and with a copper(II)-chloro distance of 2.646(2) Å, falls in the range observed for the few reported Cu^{II}–Cl–Cu^{II}-type

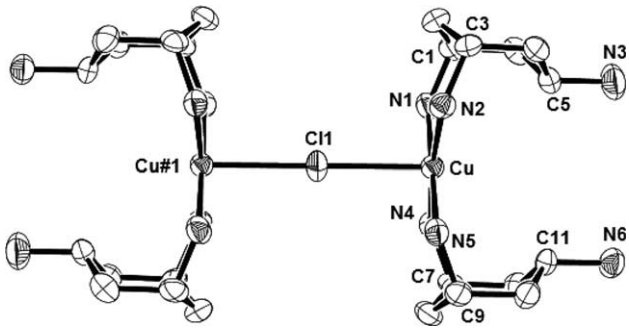


Fig. 1. Thermal ellipsoid (50%) ORTEP-3 representation of the $\{Cu_2Cl\}^{5+}$ cation in **1**, seen along one of the C_2 axes.

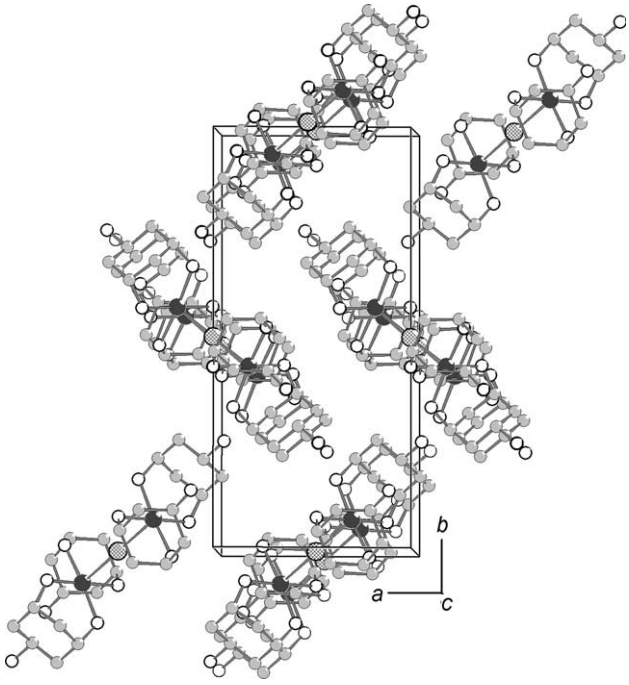


Fig. 2. Schematic representation of the $\{Cu_2Cl\}^{5+}$ dimers' packing in the crystal lattice of **1**, seen approximately along the crystallographic c axis and showing the dimensions of one unit cell (Cu: dark grey, Cl: hatched, C: grey, N: white spheres; counter ions and solvent molecules are omitted).

complexes [6–10]. In the crystal lattice of **1**, the $\{Cu_2Cl\}$ units are stacked along the crystallographic c axis in a fishbone arrangement (Fig. 2), while being hexagonally arranged around the a axis (Fig. 3).

3.3. Magnetic properties

The measured magnetic susceptibility indicates weak antiferromagnetic coupling between the two $s = 1/2$ Cu^{II} centers and follows the Curie–Weiss law with a Weiss temperature of −0.17 K. The situation of a discrete dimer of $s = 1/2$ centers can be modeled using a simple Heisenberg Hamiltonian $\boldsymbol{H} = -J\mathbf{S}_A\mathbf{S}_B$, the eigenstates of which result in the Bleaney–Bowers equation. Here,

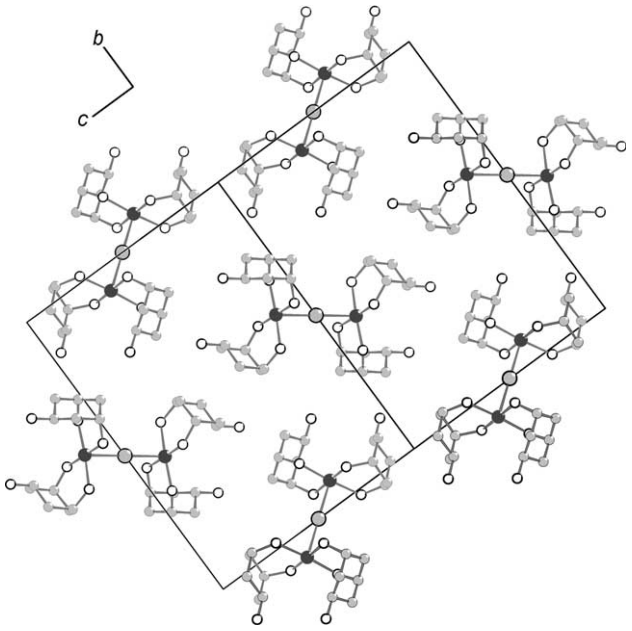


Fig. 3. Crystal packing of **1** along the crystallographic *a* axis. The $\{Cu_2Cl\}^{5+}$ cations are arranged hexagonally around the *a* axis (same codes as in Fig. 2).

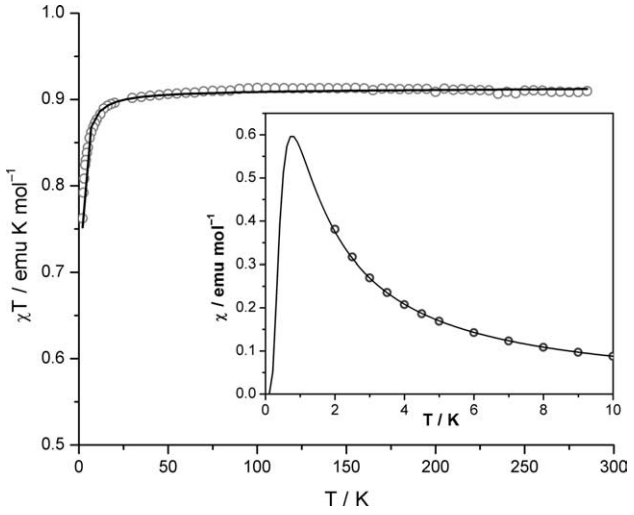


Fig. 4. Temperature dependence of χT for **1** at 0.1 T (experimental data: grey circles, data calculated from least-squares fit: solid line). Inset: the magnetic susceptibility at low temperatures displaying a maximum at 0.8 K (the experimental data was corrected for the determined paramagnetic impurity contribution, the simulated curve is correspondingly calculated for $\alpha = 0$, i.e., representing the pure dimer contribution).

a least-squares fit of the experimentally derived susceptibility data was performed using a modified Bleaney–Bowers equation

$$\chi = \frac{2N_A g^2 \mu_B^2}{kT(3 + e^{-J/kT})}(1-\alpha) + \frac{N_A g^2 \mu_B^2}{2kT}\alpha,$$

where α represents the fraction of an $s = 1/2$ impurity, i.e., dissociated dimer halves. This yielded $J/k = -1.24$ K ($J = -0.86$ cm^{-1}), an isotropic g value of $g_{iso} = 2.15$ (cmp. Section 2.4), and a paramagnetic impurity fraction of $\alpha = 1.5\%$ (Fig. 4). The least-squares fit yielded a correlation factor of 0.994. The relatively high percentage of uncoupled, paramagnetic dimer halves reflects the weak bonding via the Cu-μ-Cl–Cu bridge. The low value of the magnetic exchange can be explained by the axial Jahn–Teller distortion of the Cu^{II} coordination environment, with the nitrogen positions of the coordinating *tach* amino groups providing a strong crystal field and forming an equatorial basal plane to which the Cu–Cl bond vector is oriented perpendicular, defining the pyramidal apex. This causes the two unpaired electrons to reside in molecular orbitals of dominantly Cu(3d) $d_{x^2-y^2}$ character, interacting with the nitrogen ligands, while the (unoccupied) d_{z^2} atomic orbitals of the Cu centers that strongly interact with the Cl(2p) orbitals are only weakly mixed into the magnetic molecular orbitals, thereby limiting the magnetic exchange between the Cu centers. This ligand-field argument is also directly substantiated by simple Extended Hückel-MO calculations that verify the dominating atomic orbital contributions to the magnetically relevant frontier molecular orbitals (Fig. 5).

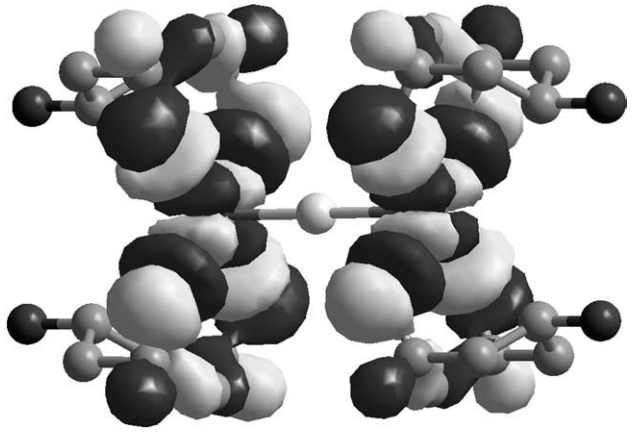


Fig. 5. An overlay representation of one of the two degenerated highest occupied molecular orbitals in the $\{Cu_2Cl\}^{5+}$ cations (omitting all H positions for clarity), illustrating the dominant $d_{x^2-y^2}$ character of these magnetic molecular orbitals.

Acknowledgments

Ames Laboratory is operated for the US Department of Energy by Iowa State University under Contract No. W-7405-Eng-82. L.C. thank the EPSRC for funding.

Appendix A. Supplementary data

Crystallographic data (excluding structure factors) for the structure reported in this paper has been deposited with the Cambridge Crystallographic Data Center as supplementary publication no. CCDC 268-196. Copies

of the data can be obtained free of charge on application to CCDC, 12 Union Road, Cambridge CB2 1EZ, UK [fax: int. code +44 1223 336 033; e-mail: deposit@ccdc.cam.ac.uk; http://www.ccdc.cam.ac.uk]. Supplementary data associated with this article can be found, in the online version, at doi:10.1016/j.poly.2005.05.008.

References

[1] O. Kahn, Molecular Magnetism, VCH, Weinheim, 1993.
[2] K. Fink, R. Fink, V. Staemmler, Inorg. Chem. 33 (1994) 6219.
[3] Ch. Kolczewski, K. Fink, V. Staemmler, Int. J. Quant. Chem. 76 (2000) 137.
[4] C.T. Zeyrek, A. Elmalib, Y. Elerman, Theochem. 680 (2004) 159.
[5] See for example: W.E. Marsh, K.C. Patel, W.E. Hatfield, D.J. Hodgson, Inorg. Chem. 22 (1983) 511, and references therein.
[6] O.P. Gladkikh, N.F. Curtis, Acta Crystallogr., Sect. C: Cryst. Struct. Commun. 52 (1996) 1418.
[7] R. Crescenzi, E. Solari, C. Floriani, A. Chiesi-Villa, C. Rizzoli, J. Am. Chem. Soc. 121 (1999) 1695.
[8] M.H. Choi, B.J. Kim, I.C. Kim, S.H. Kim, Y. Kim, J.M. Harrowfield, M.K. Lee, M. Mocerino, E. Rukmini, B.W. Skelton, A.H. White, J. Chem. Soc., Dalton Trans. 707 (2001).
[9] P.S. Donnelly, J.M. Harrowfield, B.W. Skelton, A.H. White, Inorg. Chem. 39 (2000) 5817.
[10] E.H. Alilou, M. Giorgi, M. Pierrot, M. Reglier, Acta Crystallogr., Sect. C: Cryst. Struct. Commun. 48 (1992) 1612.
[11] G. Seeber, P. Kögerler, B.M. Kariuki, L. Cronin, Chem. Commun. 14 (2004) 1580.
[12] F. Lions, K.V. Martin, J. Am. Chem. Soc. 79 (1957) 1572.
[13] G.A. Landrum, W.V. Glassey, YAEHMOP 3.03 (http://yaehmop.sourceforge.net/).

manganese citrate coordination polymers $\{[Mn^{II}(H_2O)_6][Mn^{II}(C_6H_5O_7)(H_2O)]_2 \cdot 2H_2O\}_n$ [13] and $[Mn(C_6H_6O_7)(H_2O)]_n$ [14] are known so far. Manganese has been known to be involved in the active centers of some metalloenzymes [15]. The participation of manganese in the oxygen-evolving complex (OEC) of photosystem II (PSII) has been proven to be unequivocal and especially important [16]. It is known that the OEC is a bimetallic cluster of 4Mn/Ca, in which calcium is also essential for catalytic activity [17] and the Ca^{2+} ion is believed to be linked by a carboxylic acid residue to the Mn aggregate [18]. Recently, crystallographic data have begun to give the topological arrangement of the Ca ion in the Mn_4 cluster of the OEC [19]. There are three Mn complexes in which calcium exists as a discrete counterion [20]. Recently the Mn/Ca complex $[Mn_{13}Ca_2O_{10}(OH)_2(OMe)_2(O_2CPh)_{18}(H_2O)_4]$, containing the $[Mn_4CaO_4]$ sub-unit, has been reported by Christou [21a] and one Mn/Ca coordination polymer [21b] was also reported. We have also reported several Mn dicarboxylate complexes [22]. In the preparation of novel Mn/Ca (or alkali) bimetallic and Mn citrate complexes, a synthetic system including Mn and Ca (or alkali) metal ions and citric acid has been used. Bimetallic Mn/Ca and Mn/Na citrate and two Mn citrate coordination polymers are obtained and reported in this paper.

2. Experimental

All manipulations were performed under aerobic conditions, and all commercially available reagents were used as received. IR spectra were recorded on a Magna-75-FT-IR spectrophotometer as KBr pellets. The variable temperature susceptibility was measured on a model CF-1 superconducting magnetometer with the crystalline sample kept in a capsule at 5–300 K. Diamagnetic corrections were made with Pascal's constants for all the constituent atoms of the complexes determined. Elemental analyses were performed by Germany Elemental Analyzer Vario EL III.

2.1. $[MnNa(Hcit)]_n$ (1)

To 15 ml of methanolic solution containing CH_3ONa (0.22 g, 4.0 mmol), 0.39 g of $MnCl_2 \cdot 4H_2O$ (2.0 mmol) and 0.42 g of citric acid monohydrate (2.0 mmol) were added. The slurry mixture was sealed into a teflon tube with a space volume of 23 ml and heated for 3 days at 160 °C under autogenous pressure. Prism light red crystals (0.20 g, yield 38%) suitable for X-ray determination were collected. *Anal.* Calc. for $C_6H_5MnNaO_7$: C, 26.99; H, 1.89; Mn, 20.58. Found: C, 27.13; H, 1.98; Mn, 21.23%. IR (KBr, cm^{-1}): 1664(m), 1606(s), 1578(s), 1541(m), 1429(s), 1408(s), 1390(m), 1340(s).

2.2. $[MnCa_2(Hcit)_2(H_2O)_4]_n$ (2)

To 15 ml of H_2O, $MnCO_3$ (0.12 g, 1.0 mmol), $Ca(NO_3)_2$ (0.32 g, 1.95 mmol) and citric acid monohydrate (0.42 g, 2.0 mmol) were added and dissolved. The solution was sealed into a teflon tube with a space volume of 23 ml and heated at 160 °C under autogenous pressure for 3 days. Colorless plate crystals (0.35 g, yield 60%) suitable for X-ray determination were collected. *Anal.* Calc. for $C_{12}H_{18}Ca_2MnO_{18}$: C, 24.62; H, 3.10; Ca, 13.69; Mn, 9.39. Found: C, 24.68; H, 3.12; Ca, 13.71; Mn, 9.35%. IR (KBr, cm^{-1}): 3480(s), 3396(s), 1616(s), 1562(s), 1537(s), 1465(m), 1429(s), 1384(s).

2.3. $[\{Mn(Hcit)(H_2O)_2\}_2Mn(H_2O)_4]_n \cdot 6nH_2O$ (3)

Citric acid (0.42 g, 2.0 mmol) and $Mn(OAc)_2 \cdot 4H_2O$ (0.25 g, 1.0 mmol) were dissolved in 15 ml of MeOH/H_2O (v/v, 2:1), then 0.22 g of MeONa (4.0 mmol) was added. The solution was sealed into a teflon tube with a space volume of 23 ml and heated at 150 °C under autogenous pressure for 3 days. Colorless rhombic crystals (0.078 g, yield 31% based on Mn used) were collected. *Anal.* Calc. for $C_{12}H_{38}Mn_3O_{28}$: C, 18.12; H, 4.82; Mn, 20.73. Found: C, 18.36; H, 4.92; Mn, 20.96%. IR (KBr, cm^{-1}): 3446(br), 3396(s), 1616(s), 1574(s), 1419(s), 1394(s), 1375(s), 525(m).

2.4. $[\{Mn(Hcit)(H_2O)_2\}_2Mn(H_2O)_2]_n \cdot 4nH_2O$ (4)

Citric acid (0.42 g, 2.0 mmol) and $Mn(ClO_4)_2 \cdot 6H_2O$ (0.36 g, 1.0 mmol) were dissolved in 30 ml of DMF and the solution was stirred at room temperature for 2 h. Then 0.27 g of imidazole (4.0 mmol) was added and continuously stirred for 14 h to resulting in a red solution, which was allowed to stand for two months to deposit colorless block crystals of **4** (0.13 g, yield 54% based on Mn used). *Anal.* Calc. for $C_{12}H_{30}Mn_3O_{24}$: C, 19.93; H, 4.18; Mn, 22.79. Found: C, 19.92; H, 4.14; Mn, 22.93%. IR (KBr, cm^{-1}): 3426(br), 3253(w), 1564(s, br), 1439(s), 1417(s), 1389(s), 521(m).

2.5. $[Mn(H_2cit)(H_2O)]_n$ (5)

The synthetic procedure of **2** was utilized in the absence of $Ca(NO_3)_2$, affording colorless insoluble prism crystals which were collected resulting in 0.22 g (yield 84%). *Anal.* Calc. for $C_6H_8MnO_8$: C, 27.39; H, 3.07; Mn, 20.88. Found: C, 27.05; H, 3.16; Mn, 20.65%. IR (KBr, cm^{-1}): 3369(br), 2973(m), 2922(m), 2809(m), 2687(m), 2618(m), 2532(m), 1733(s), 1616(s), 1562(s), 1537(s), 1465(m), 1429(s), 1384(s). The crystal structure was identified by X-ray diffraction and was found to be identical with a known compound [14]. When $MnCO_3$:

$Ca(NO_3)_2$:citric acid = 4–5:1:8, the same product **5** was also isolated.

2.6. X-ray data collection and structure determination

Crystals of **1** and **2** were mounted on a Smart CCD diffractometer and the crystals of **3** and **4** on a Rigaku AFC5R diffractometer with Mo Kα radiation ($\lambda = 0.71073$ Å). Intensity data were corrected for Lorentz and polarization effects. Structure solutions and refinements were performed with the SHELXTL program [23]. Crystallographic data are given in Table 1. Hydrogen atoms were included at calculated positions with isotropic thermal parameters proportional to those of the connected atoms.

3. Results and discussion

3.1. Synthesis

This work has performed the assembly of manganese citrate complexes in which bimetallic Mn/Na or Mn/Ca citrate complexes have been obtained. In order to obtain Mn/Na bimetallic complexes, an excess of NaOMe has been used and has proved to be useful for the entering of the sodium ions into the extended structure of the coordination polymer **1**. Similarly in preparing the Mn/Ca citrate complex, a Mn/Ca mole ratio of 2:1 has been used and the Mn/Ca bimetallic complex **2** has been produced. Interestingly, various Mn salts (chloride, nitrate, sulfate and acetate) have been tried for the Mn/Ca citrate complex, however, our efforts have not yet succeeded except for using $MnCO_3$, which can react with $Ca(NO_3)_2$ in a mole radio of 1:2 leading to the formation of **2**. A similar procedure with a $MnCO_3/Ca(NO_3)_2$ mole radio of 1:1 has also produced the same complex **2** rather than a Mn_1Ca_1 complex, implying the thermodynamic stability of the $MnCa_2$ complex. We have also tried to use larger $MnCO_3/Ca(NO_3)_2$ mole radios of 4:1 or 5:1 for getting the desired Mn_4Ca_1 complex, which is a suitable bimetallic component for the OEC, however only a manganese citrate coordination polymer $[Mn(H_2cit)(H_2O)]_n$ (**5**) has been obtained. It is considered that a large amount of carbonate ions results in the deposition of $CaCO_3$, removing the calcium ion from the reaction system and leading to the lack of the calcium in the product. Another two manganese-only complexes **3** and **4** have been obtained in solvothermal and conventional solution methods, respectively. In the synthesis of **4**, imidazole has been used with the original intention to prepare a Mn citrate complex containing imidazole in the coordination sphere of the manganese. Consequently complex **4** was separated as the only product. Meanwhile for the same reaction system in the absence of imidazole it has proved to be difficult to deposit crystals of complex **4**. Perhaps imidazole is favorable to adjust the acidity of the reaction solution for the separation of **4**.

Table 1
Crystallographic data for complexes **1**–**4**

	Complex **1**	Complex **2**	Complex **3**	Complex **4**
Formula	$C_6H_5MnNaO_7$	$C_{12}H_{18}Ca_2MnO_{18}$	$C_{12}H_{38}Mn_3O_{28}$	$C_{12}H_{30}Mn_3O_{24}$
Formula weight	267.03	585.36	795.23	723.18
Crystal system	monoclinic	orthorhombic	monoclinic	monoclinic
Space group	$P2_1/c$	$P2_12_12_1$	$P2_1/n$	$P2_1/n$
a (Å)	6.0835(2)	5.9065(3)	11.301(2)	9.643(4)
b (Å)	8.7725(3)	10.7039(6)	12.041(2)	8.353(2)
c (Å)	15.8167(1)	29.756 (1)	12.138(2)	15.558(9)
β (°)	99.441(2)		115.71(3)	98.62(5)
V (Å^3)	832.66(4)	1881.2(2)	1488.2(5)	1239(1)
Z	4	4	2	2
D_{calc} (g/cm^3)	2.130	2.067	1.775	1.614
μ (mm^{-1})	1.65	1.347	1.362	1.939
Crystal size (mm)	$0.18 \times 0.14 \times 0.10$	$0.28 \times 0.20 \times 0.16$	$0.50 \times 0.30 \times 0.20$	$0.42 \times 0.32 \times 0.30$
θ_{max} (°)	25.08	25.04	26.02	25.96
Reflections $I > 2\sigma(I)$	1064	2608	1863	1403
Parameter No.	140	338	248	214
R[a]	0.0493	0.0461	0.0517	0.0672
R_w[b]	0.1052	0.1243	0.1149	0.1269
Goodness-of-fit	1.016	1.043	1.076	1.005
Residual density (e Å^{-3})	0.461; −0.696	0.610; −0.401	0.414; −0.415	0.694; −0.676

[a] $R = \sum||F_o| - |F_c||/\sum|F_o|$.

[b] $R_w = \left[\sum w(|F_o| - |F_c|)^2/\sum wF_o^2\right]^{1/2}$ **1**: $w = 1/[S^2(F_o^2) + (0.0607P)^2 + 0.0000P]$; **2**: $w = 1/[S^2(F_o^2) + (0.1000P)^2 + 0.0000P]$; **3**: $w = 1/[S^2(F_o^2) + (0.0283P)^2 + 6.0668P]$ **4**: $w = 1/[S^2(F_o^2) + (0.0493P)^2 + 0.0000P]$, where $P = (F_o^2 + 2F_c^2)/3$.

3.2. Structure

3.2.1. $[NaMn(Hcit)]_n$

The structure of **1** is represented in Fig. 1 with the simplest unit NaMn(Hcit) unit showing the coordination spheres of both Mn and Na ions. Selected bond distances and angles around the metal ions are listed in Table 2. The manganese ion locates at the center of slight distorted octahedron. Each Mn ion is surrounded by four citrates, one of which affords three oxygen atoms from two different carboxylate groups and the hydroxyl, respectively forming five- and six-membered chelating rings sharing a Mn–$O_{hydroxyl}$ edge. The tridentate chelation formed by two carboxylate groups (one central, one terminal) and one hydroxy group is the most common configuration for citrate trianion binding to a metal ion and is also found in all complexes in this work. The other three citrate trianions coordinate to the Mn ion by one carboxylate O atom. The sodium ion links five citrate trianions, each of which affords one carboxylate O atom to construct the distorted trigonal bipyramidal geometry of the sodium ion with an axial O–Na–O angle of 170.6(2)°. Double (μ-$O_{carboxylate}$)($\mu_{1,3}$-OCO) and triple (μ-$O_{carboxylate}$)$_3$ bridges exist between neighboring Mn and Na ions with the shortest Mn···Na separation of 3.223(2) Å in the Mn(μ-$O_{carboxylate}$)$_3$Na unit and 3.512(2) Å in the Mn(μ-$O_{carboxylate}$)(μ-OCO)Na unit. These units are fused to each other by edge-sharing to form a grid-like chain. Citrate trianions span between the chains by both terminal caboxylate groups as shown in Fig. 2. Two neighboring Mn ions are correlated by a carboxylate bridge in a *syn*, *anti*-mode with the shortest Mn···Mn separation of 5.44 Å. Three carboxylate arms of the citrate, together with the hydroxyl, outspread in the lattice space and link 9 metal ions (Scheme 1), constructing a complicated 3-D network structure. This is a novel coordination mode for the citrate trianion and

Table 2
Selected bond distances (Å) and angles (°) for **1**

Bond lengths					
Mn–O1	2.230(3)	Mn–O2A	2.133(3)	Mn–O3	2.196(3)
Mn–O4D	2.128(4)	Mn–O5B	2.134(4)	Mn–O7	2.265(3)
Na–O1	2.361(4)	Na–O2A	2.380(4)	Na–O3E	2.325(4)
Na–O4D	2.705(5)	Na–O6C	2.198(4)	Mn···NaA	3.511(2)
Mn···Na	3.222(2)				
Bond angles					
O4D–Mn–O5B	103.44(15)		O5B–Mn–O1		165.29(13)
O4D–Mn–O2A	87.27(14)		O2A–Mn–O1		80.87(12)
O5B–Mn–O2A	112.43(14)		O3–Mn–O1		86.94(13)
O4D–Mn–O3	168.00(13)		O4D–Mn–O1		82.79(14)
O5B–Mn–O3	85.17(14)		O4D–Mn–O7		98.13(14)
O2A–Mn–O3	97.24(13)		O5B–Mn–O7		88.55(14)
O3–Mn–O7	73.44(13)		O2A–Mn–O7		156.62(13)
O1–Mn–O7	77.31(13)		O1–Na–O4D		68.98(12)
O6C–Na–O3E	85.11(15)		O3E–Na–O2A		148.55(16)
O6C–Na–O1	170.6(2)		O1–Na–O2A		73.32(12)
O3E–Na–O1	94.89(14)		O6C–Na–O4D		104.29(17)
O6C–Na–O2A	111.19(15)		O3E–Na–O4D		133.41(15)
O2A–Na–O4D	70.32(13)				

A: $-x+1, y+1/2, -z+1/2$; B: $-x+1, -y+1, -z$; C: $x-1, -y+1/2, z+1/2$; D: $x-1, y, z$; E: $-x+1, y-1/2, -z+1/2$.

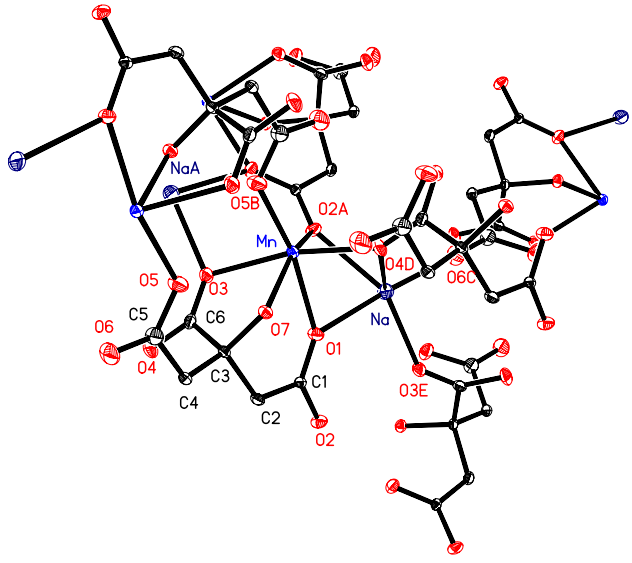


Fig. 1. Structure of **1** with selected atom-labelling scheme, showing the coordination spheres of the Mn and Na ions, thermal ellipsoids were drawn by ORTEP and represent 30% probability surfaces.

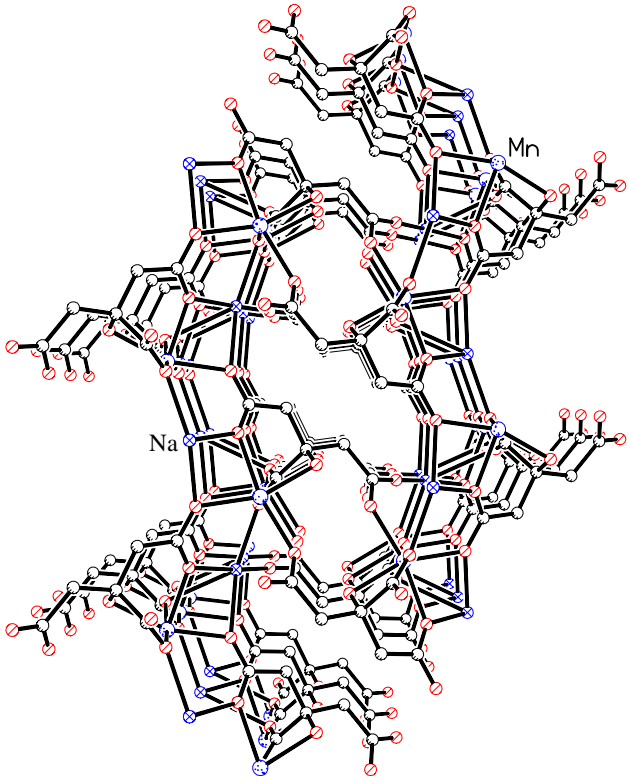
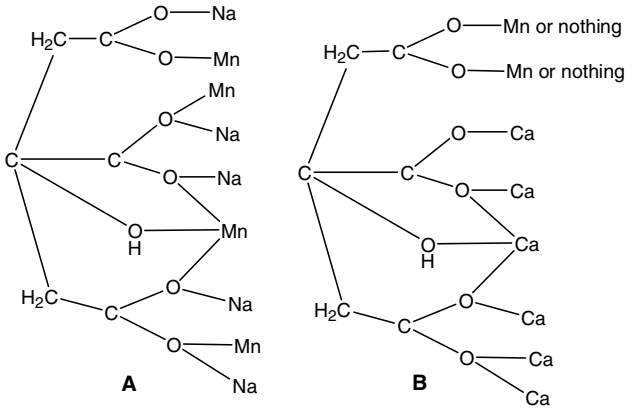


Fig. 2. View of the extended 3-D structure of $[MnNa(C_6H_4O_7)]_n$. Three carboxylate arms of the citrate together with the hydroxyl coordinate to the metal ions and outspread in the lattice space to construct a 3-D network structure.



Scheme 1. Coordination modes of the citrate in complexes **1** and **2**. (A) Nine metal ions are linked by all the seven oxygen donors of the citrate for **1** and (B) 6 Ca ions are linked by hydroxyl and two carboxylate groups leaving a carboxylate free or to link two Mn ions for **2**.

also the maximum number of the metal ions encountered so far around a citrate ligand. In order to identify the oxidation state of the Mn ion in **1**, bond valence sum (BVS) calculations [24] give a value of 2.10 for the Mn ion, indicating a 2+ oxidation state. Meanwhile, The EPR spectrum was recorded on a Bruker-ER420 spectrometer at X-band for the complex at room temperature and 77 K as solid samples, showing a strong signal at $g = 2$. Commonly, the integer spin $S = 2$Mn(III) ion is very difficult to observe with traditional perpendicular polarization EPR spectroscopy at X-band. So this also implies the existence of the Mn(II) ion rather than the Mn(III) ion in the complex. So as to keep the electroneutrality of the compound, the citrate should retain a hydroxyl proton. The Mo–$O_{hydroxyl}$ distance of 2.270(3) Å falls into the normal range found for Mn–$O_{hydroxyl}$ distances (2.166–2.278 Å) of other Mn(II) citrate complexes and is obviously larger than that of the

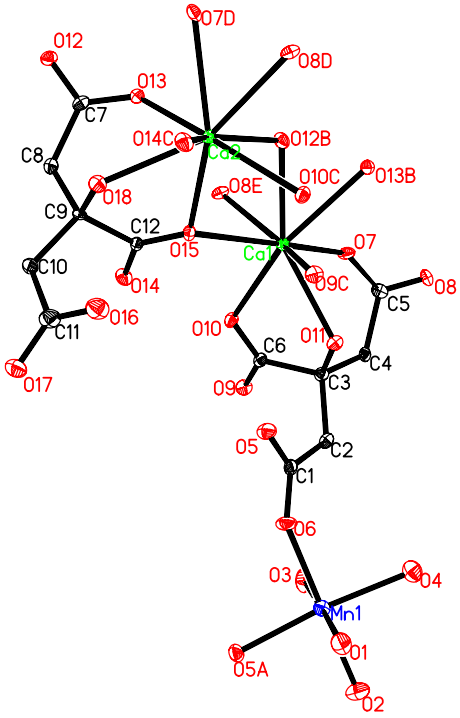


Fig. 3. The unit structure of complex **2** contains two crystallographically unique Ca(II) ions together with a Mn(II) ion in the asymmetric unit.

Mn(III) citrate complex $(NH_4)_5[Mn(C_6H_4O_7)_2]$ (1.885 Å) [12]. Moreover, the absence of characteristic IR absorptions around 1700 cm^{-1}, expected for the vibration of protonated carboxyl (COOH), indicates that all the carboxyl groups in **1** are deprotonated.

3.2.2. $[MnCa_2(Hcit)_2(H_2O)_4]_n$

Complex **2** is the third example of Mn/Ca complexes in which both Mn and Ca are correlated via ligand bridge(s). Only two such Mn/Ca bimetal complexes are

Table 3
Selected bond distances (Å) and angles (°) of complex **2**

Bond lengths					
Mn1–O1	2.165(6)	Mn1–O2	2.213(6)	Mn1–O5A	2.168(5)
Mn1–O3	2.195(6)	Mn1–O4	2.193(5)	Mn1–O6	2.131(5)
Ca1–O7	2.445(4)	Ca1–O8E	2.350(4)	Ca1–O9C	2.432(5)
Ca1–O10	2.430(4)	Ca1–O11	2.484(4)	Ca1–O12B	2.462(5)
Ca1–O13B	2.538(4)	Ca1–O15	2.489(4)	Ca2–O7D	2.564(5)
Ca2–O8D	2.522(5)	Ca2–O10C	2.511(4)	Ca2–O12B	2.337(4)
Ca2–O13	2.425(4)	Ca2–O14C	2.384(5)	Ca2–O15	2.449(4)
Ca2–O18	2.530(5)	Ca1–Ca2	3.889(2)	Ca2-Ca1C	3.882(2)
Bond angles					
O6–Mn1–O1	94.5(2)	O5A–Mn1–O3	91.7(2)	O6–Mn1–O5A	92.8(2)
O4–Mn1–O3	93.9(2)	O1–Mn1–O5A	86.7(2)	O6–Mn1–O2	175.5(2)
O6–Mn1–O4	91.0(2)	O1–Mn1–O2	90.0(2)	O1–Mn1–O4	87.6(2)
O5A–Mn1–O2	88.0(2)	O5A–Mn1–O4	173.3(2)	O4–Mn1–O2	88.6(2)
O6–Mn1–O3	88.3(2)	O3–Mn1–O2	87.2(2)	O1–Mn1–O3	176.9(2)

Symmetry transformations used to generate equivalent atoms: A: $x - 1/2, -y + 1/2, -z$; B: $-x + 2, y - 1/2, -z - 1/2$; C: $x + 1, y, z$; D: $-x + 2, y + 1/2, -z - 1/2$; E: $-x + 1, y + 1/2, -z - 1/2$.

known [21]. Interestingly, the calcium citrate coordination complex has not yet been structurally characterized, though a crystal structure of Ca(H_2citrate) [25] is known in which discrete Ca^{2+} cations and the citrate dianions were found. In the structure of **2** there are two crystallographically unique Ca(II) ions together with a Mn(II) ion in the asymmetric unit. The structure of the unit is shown in Fig. 3 and selected bond distances and angles are listed in Table 3. The two independent Ca1 and Ca2 are eight-coordinate, being enclosed in the center distorted dodecahedrons with eight apices of oxygen atoms from 4–5 citrate ligands, while the coordination sphere of the Mn ion contains 2 caboxylate oxygen atoms and four aqua molecules. The Ca ions are correlated by $\mu_{1,1}$- and $\mu_{1,3}$-carboxylate bridges to create a two-dimensional Ca layer at the a-c face, while the Mn ions are linked by $\mu_{1,3}$-carboxylate bridges in a *syn–anti* configuration to form a helix chain along the *a* axis (Fig. 4 right). The Mn helix chains extend between the neighboring Ca layers. The Mn(II) and Ca(II) ions are connected by the whole citrate backbone using its carboxylate arms and the hydroxyl group, finally constructing a three dimensional architecture of the complex as shown in Fig. 4. Interestingly, both the crystallographically unique citrate ligands use the hydroxyl and two carboxylate groups to link six Ca ions by the aforementioned tridentate chelation and the μ-$O_{carboxylate}$ bridges in the same manner (Scheme 1B). While the third carboxylate group either links two Mn ions by O5 and O6 atoms (Mn1–O5A, 2.168(5) Å; Mn1–O6, 2.131(5) Å) or leaves itself free (O16 and O17 are free). Isometric C11–O17 (1.250(9) Å) and C11–O16 (1.259(10) Å) bonds support the deprotonation of the carboxyl group to which C11 belongs. Meanwhile, the absence of a characteristic COOH absorption ($\sim$1700 cm^{-1}) also implies no proton existing in all carboxyl groups. It should be pointed out that these two coordination modes shown in Scheme 1B are also novel and have not been reported previously.

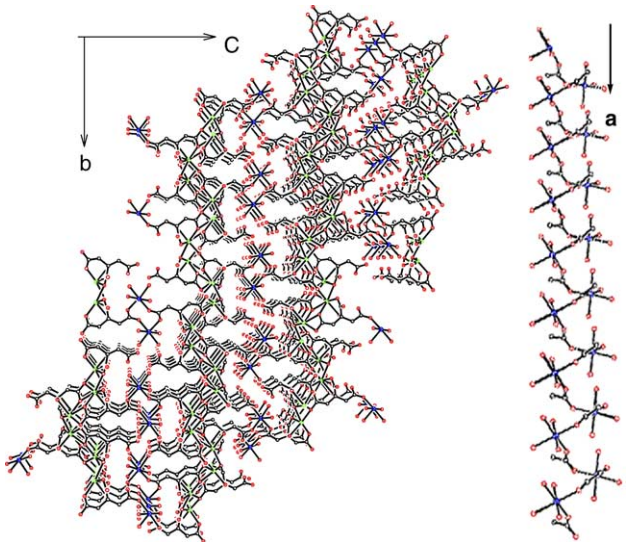


Fig. 4. The packing diagram for complex **2** exhibits a Ca_2Mn citrate sandwich array at the b-c face (left) and a [Mn($\mu_{1,3}$-OCO)]$_n$ helix chain along the *a* axis (right).

3.2.3. [{Mn(Hcit)(H_2O)$_2$}$_2$Mn(H_2O)$_4$]$_n$ · 6nH_2O (**3**) and [{Mn(Hcit)(H_2O)$_2$}$_2$Mn(H_2O)$_2$]$_n$ · 4nH_2O (**4**)

Both complexes **3** and **4** have similar formulas and contain the same Mn(Hcit)(H_2O)$_2$ structural unit with a Hcit tridentate chelation to a Mn ion. Both the Mn(Hcit)(H_2O)$_2$ units are coupled in **3** and **4** by the second terminal carboxylate group to form a centrosymmetrical dimer [Mn(Hcit)(H_2O)$_2$]$_2$ as depicted in Fig. 5. It is noted that a dimeric structure is rare for metal citrate complexes and only a Ni citrate complex [26] has such dimeric structure. In addition, there is another type of Mn ion existing in the octahedral fragments, Mn(H_2O)$_4$($O_{carboxylate}$)$_2$ in **3** and Mn(H_2O)$_2$($O_{carboxylate}$)$_4$ in **4**. In the structure of **3**, the Mn1 ion in the dimer is connected by the carboxylate bridge in a *syn–anti* mode to the Mn2 ion of the Mn(H_2O)$_4$($O_{carboxylate}$)$_2$ fragment. The dimer and the Mn(H_2O)$_4$($O_{carboxylate}$)$_2$ fragment

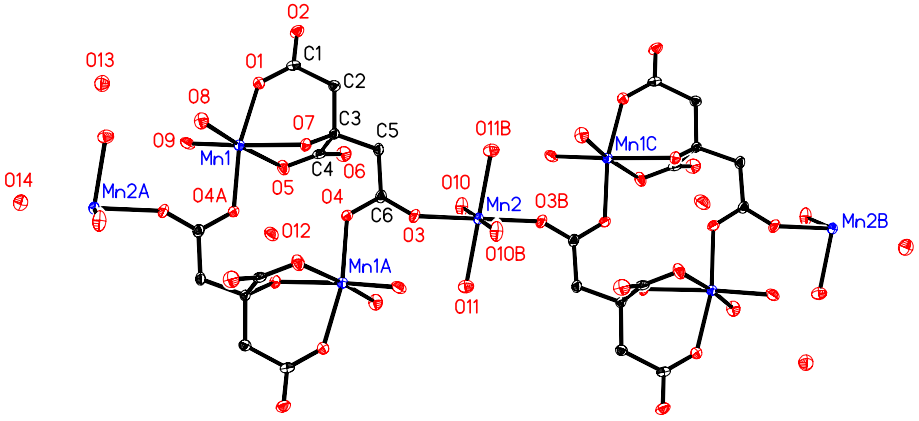


Fig. 5. 1-D unlimited chain structure of complex **3** with selected atom-labelling scheme. The [Mn(Hcit)(H_2O)$_2$]$_2$ dimer and the Mn(H_2O)$_4$-($O_{carboxylate}$)$_2$ unit array alternately to form a 1-D chain.

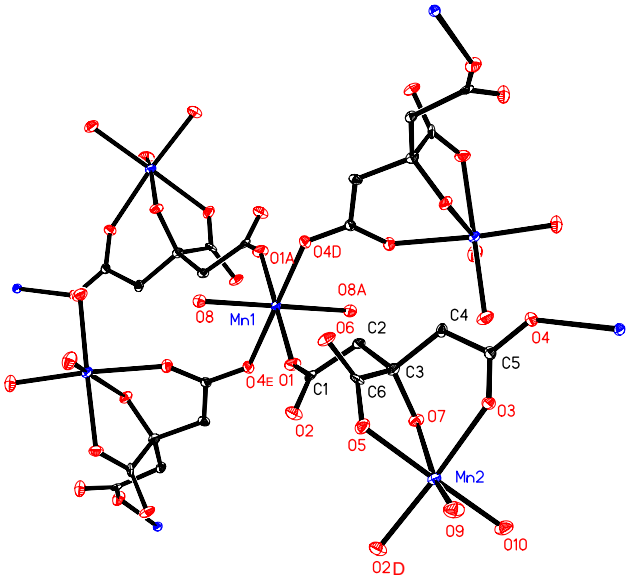


Fig. 6. Structure of **4** with selected atom-labelling scheme. A Mn-$(H_2O)_2(O_{carboxylate})_4$ fragment is enclosed by four $[Mn(Hcit)(H_2O)_2]$ units which are coupled to become the respective $[Mn(Hcit)(H_2O)_2]_2$ dimer (omitted for clarity).

alternately array to construct a one-dimensional chain structure of **3** as shown in Fig. 5. Different from the structure of **3**, complex **4** possesses a 3-D network structure. The Mn1 ions existing in the $Mn(H_2O)_2$-$(O_{carboxylate})_4$ fragment link to the other Mn2 ions at an equatorial plane (O1, O1A, O4D, O4E) as shown in Fig. 6. There are two bridging manners between Mn1 and Mn2 ions, one of which is via the $\mu_{1,3}$-OCO bridges in the *syn–anti* mode along the opposed direction, the other is via the Hcit backbone involving O1, C1, C2, C3 and the hydroxyl. Consequently the $Mn(H_2O)_2$-$(O_{carboxylate})_4$ fragments are surrounded by four dimeric units and extend along various orientations to construct a 3-D network structure (Fig. 7). Selected bond distances and angles are listed in Table 4 for both the complexes, exhibiting unobvious distinction of the same type of bonds, such as Mn–O_{H2O}: 2.154(4)–2.161(5) Å for **3** and 2.153(5)–2.175(6) Å for **4**. The presence of coordinate and solvate H_2O molecules make extensive hydrogen bonding interactions in the lattice of both the complexes. All the hydrogen bonding interactions are listed in Table 5. The hydrogen bonding interactions connect neighboring one-dimensional chains in **3** to become a three-dimensional supramolecular structure.

3.2.4. $[Mn(H_2cit)(H_2O)]_n$ (5)

The structure of **5** has been reported in the literature [14]. In order to account for the magnetic behaviors (vide infra) of the complex it is necessary to point out that the structure is constructed by series of $Mn(\mu_{1,3}$-$OCO)(\mu_{1,1}$-$O_{carboxylate})Mn$ chains, which are connected to each other by extensive hydrogen bonding interactions as shown in Fig. 8.

3.3. IR spectra

IR spectra of these complexes display characteristic features of the coordinated citrate [5,12]. The carbonyls of the citrate ligand exhibit antisymmetric stretching vibrations $\nu_{as}(COO^-)$ in the range from 1664 to 1541 cm^{-1}, and symmetric stretching vibrations $\nu_s(COO^-)$ from 1465 to 1340 cm^{-1}. In comparison with the corresponding vibrations of free citric acid, numerous bands are shifted to lower frequencies, indicating that the coordination of the oxygen donor to the metal ion weakens the C=O bonds. These assignments are in agreement with other reported metal citrate complexes [5,12]. No signal appears in the region between 1700 and 1760 cm^{-1} implying that all the citrate carboxyls in complexes **1**–**4** are deprotonated, while a strong vibration appears at 1734 cm^{-1} indicating a protonated cabboxylate group existing in **5**. This has been confirmed by the X-ray crystal structures of these complexes and is in agreement with other metal citrate complexes [5a,5b]. The carboxylate groups in **1** and **2** are coordinated to both alkali (or alkaline earth) and transition metal ions in various modes (Scheme 1), exhibiting abundant vibrations in the ν_{as}- and ν_s-(COO^-) regions (Table 6). The

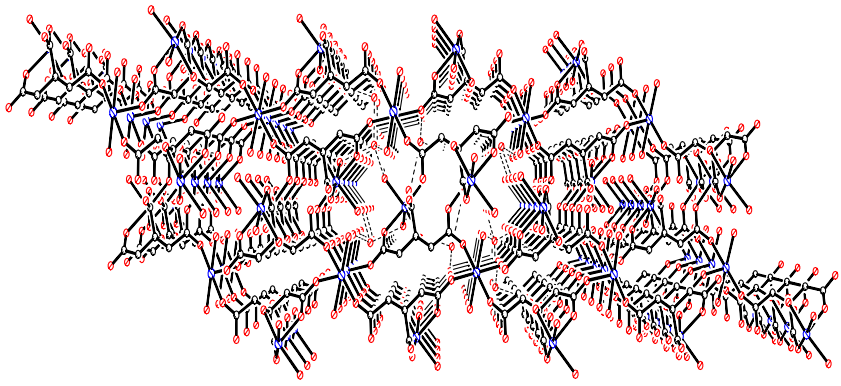


Fig. 7. 3-D structure of complex **4**. Hydrogen bonding interactions are represented by dot lines.

Table 4
Selected bond distances (Å) and angles (°) of complexes **3** and **4**

*Complex **3***					
Mn1–O1	2.156(4)	Mn1–O4A	2.159(4)	Mn1–O5	2.193(4)
Mn1–O7	2.280(4)	Mn1–O8	2.161(5)	Mn1–O9	2.154(4)
Mn2–O3	2.135(4)	Mn2–O10	2.143(5)	Mn2–O11	2.233(4)
O1–Mn1–O4A	168.07(15)	O1–Mn1–O8	92.12(17)	O1–Mn1–O9	91.81(17)
O1–Mn1–O7	80.62(15)	O1–Mn1–O5	86.34(16)	O4A–Mn1–O9	96.98(18)
O4A–Mn1–O8	95.28(18)	O4A–Mn1–O5	85.02(16)	O4A–Mn1–O7	89.02(15)
O8–Mn1–O7	98.52(16)	O8–Mn1–O9	94.01(19)	O8–Mn1–O5	171.95(17)
O9–Mn1–O5	93.94(17)	O9–Mn1–O7	165.57(16)	O5–Mn1–O7	73.44(14)
O3–Mn2–O11	84.02(16)	O3–Mn2–O10B	88.54(18)	O3B–Mn2–O11	95.98(16)
O3–Mn2–O10	91.46(18)	O10–Mn2–O11	92.24(18)	O10B–Mn2–O11	87.76(18)
*Complex **4***					
Mn1–O1	2.217(5)	Mn1–O8	2.178(6)	Mn1–O4C	2.187(5)
Mn2–O3	2.201(5)	Mn2–O5	2.143(5)	Mn2–O7	2.247(5)
Mn2–O9	2.175(6)	Mn2–O10	2.153(5)	Mn2–O2D	2.120(5)
O8–Mn1–O4B	92.4(2)	O8–Mn1–O1	85.7(2)	O8–Mn1–O4C	87.6(2)
O8–Mn1–O1A	94.3(2)	O4B–Mn1–O1	92.6(2)	O4C–Mn1–O1	87.4(2)
O5–Mn2–O10	175.5(2)	O5–Mn2–O9	93.2(2)	O5–Mn2–O2D	89.5(2)
O2D–Mn2–O10	91.1(2)	O2D–Mn2–O3	174.8(2)	O2D–Mn2–O9	89.6(2)
O3–Mn2–O7	75.7(2)	O2D–Mn2–O7	106.3(2)	O9–Mn2–O3	87.4(2)
O10–Mn2–O3	93.2(2)	O9–Mn2–O7	159.1(2)	O10–Mn2–O7	101.8(2)
O5–Mn2–O3	86.4(2)	O10–Mn2–O9	91.2(2)	O5–Mn2–O7	73.8(2)

Symmetry transformations used to generate equivalent atoms: A: $-x+2, -y+1, -z+1$; B: $-x+2, -y+1, -z$ for **3** and A: $-x+1, -y+1, -z$; B: $-x+1/2, y+1/2, -z+1/2$; C: $x+1/2, -y+1/2, z-1/2$; D: $-x, -y, -z$ for **4**.

Table 5
Hydrogen bonding interactions (Å) in compounds **3** and **4**

Complex **3**	(Å)	Symmetry code for latter atom		Complex **4**	(Å)	Symmetry code for latter atom	
O11···O6	2.725	[$x-1/2, -y+1/2, z+1/2$]	$H_2O\cdots COO$	O10···O11	2.748	[$-x-1/2, y-1/2, -z+1/2$]	$H_2O\cdots H_2O$
O10···O14	2.751		$H_2O\cdots H_2O$	O10···O6	2.756	[$x, y-1$, z]	$H_2O\cdots COO$
O9···O7	2.897	[$x+1/2, -y+1/2, z+1/2$]	$H_2O\cdots COO$	O7···O12	2.659	[$x+1/2, -y+1/2, z-1/2$]	$OH\cdots H_2O$
O10···O2	2.701	[$-x+5/2, y+1/2, -z+3/2$]	$H_2O\cdots COO$	O9···O1	2.815	[$-x, -y, -z$]	$COO\cdots H_2O$
O13···O12	2.830	[$-x+5/2, y-1/2, -z+3/2$]	$H_2O\cdots H_2O$	O9···O4	3.251	[$-x-1/2, y-1/2, -z+1/2$]	$H_2O\cdots COO$
O14···O6	2.792	[$x, y, z+1$]	$H_2O\cdots COO$	O12···O5	2.695	[$-x, -y, -z$]	$H_2O\cdots COO$
O12···O1	2.811	[$-x+5/2, y+1/2, -z+3/2$]	$H_2O\cdots COO$	O11···O8	2.789	[$-x, -y+1, -z$]	$H_2O\cdots H_2O$
O8···O13	2.770	[$x-1/2, -y+1/2, z-1/2$]	$H_2O\cdots H_2O$	O12···O4	2.751	[$-x+1/2, y-1/2, -z+1/2$]	$H_2O\cdots COO$
				O8···O6	2.698	[$-x, -y+1, -z$]	$H_2O\cdots COO$
				O8···O5	3.082	[$-x, -y+1, -z$]	$H_2O\cdots COO$

$\Delta(\nu_{as}-\nu_s)$ values are smaller than 200 cm^{-1} for **3** and **4** which is an indication that all the carboxylato groups adopt the μ-OCO bridging coordination mode [27]. Also the $\Delta(\nu_{as}-\nu_s)$ value (<200 cm^{-1}) for **2** is considered to stem from the bridging coordination modes of most carboxylate groups. Complex **5** has the $\Delta(\nu_{as}-\nu_s)$ value being of the order of 300 cm^{-1}, implying the presence of free and unidentately coordinated carboxylato groups, which have been found in its crystal structure [14]. However, complex **1** contains all bridging carboxylate groups but has a larger $\Delta(\nu_{as}-\nu_s)$ value. This contravention would be explained by the involvement of highly unsymmetrical bridging [27] that can be seen as pseudo-unidentate coordination owing to the longer Na–O distances than the sum of atomic covalent radii. In addition, coordinate or solvate H_2O molecules exist in complexes **2**, **3**, **4** and **5**, and exhibit broad signals in the region of 3250–3481 cm^{-1}. Additional medium strong bands for complex **5** were found at 2973–2532 cm^{-1}, originating in the hydrogen-bonded protonated carboxylato groups [5a].

3.4. Magnetic property

The magnetic properties of **1** are illustrated as the temperature dependence of the effective magnetic moments (μ_{eff}) in Fig. 9. At room temperature, μ_{eff} amounts to 5.08 BM, which is lower than the value expected for independent spin $S = 5/2$ (5.92 BM) and close to the value for $S = 2$ (4.90 BM). However the structural parameters and BVS as well as the color of the crystals of **1** did not support the existence of the Mn(III) ion. With the

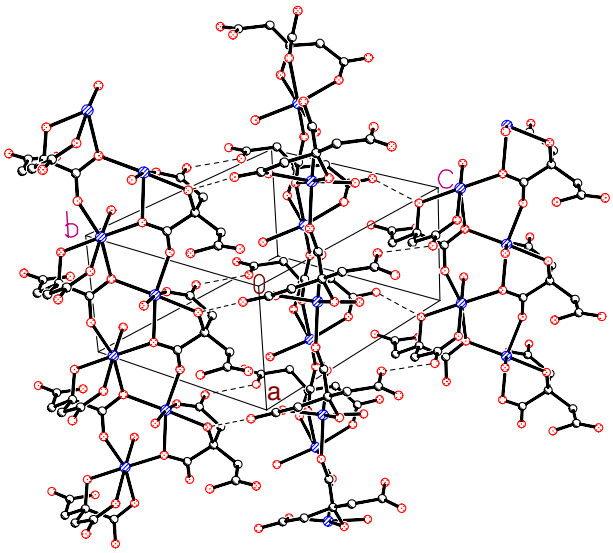


Fig. 8. Structure of complex **5** showing the $[Mn(\mu_{1,3}\text{-}OCO)(\mu_{1,1}\text{-}O_{carboxylate})]_n$ chains along the *a*-axis. Dotted lines show the hydrogen bonding interaction between the chains.

decrease of the temperature in the range of 300–30 K, the μ_{eff} value decreases slightly and turns to rapidly decrease in the further decrease of the temperature, indicating antiferromagnetic interactions between the neighboring Mn(II) ions. In the $1/\chi_M$ versus T plot (insert of Fig. 9), the observed susceptibilities are well-fitted to the Curie–Weiss law with Weiss constants $\theta = -5.23$ K and $C = 3.38$ K cm^3 mol^{-1}.

For complexes **2**, **3** and **5**, their magnetic behaviors as the temperature dependence of the effective magnetic moments (μ_{eff}) are illustrated in Fig. 10. At room temperature, μ_{eff} amounts to 5.79 and 5.50 BM for **2** and **5**, respectively, slightly lower than the value (5.92 BM) expected for an isolated Mn ion ($S = 5/2$), while μ_{eff} amounts to 10.22 BM for **3**, close to the value (10.24 BM) expected for three uncoupled Mn ions ($S = 5/2$). With the temperature decreasing in the range of 300–30 K, the μ_{eff} value decreases slightly and then rapidly decreases with further lower temperatures, indicating antiferromagnetic interactions between the Mn(II) ions for these complexes. To quantitatively analyze the magnetic behavior of **2**, Eq. (1) [28] for a homonuclear uniform chain was used to fit its experimental data, in which J represents the coupling interaction between neighboring paramagnetic centers in the $[Mn(\mu\text{-}CO_2)]_n$ helix chain.

$$\chi_{chain} = \left(\frac{Ng^2\beta^2}{KT}\right)[A + Bx^2][1 + Cx + Dx^3]^{-1}, \quad (1)$$

where $A = 2.9167$, $B = 208.04$, $C = 15.543$, $D = 2707.2$ and $x = |J|/kT$. It is reasonable to ignore the interaction between the helix chains belonging to different $[Ca_2(citrate)_2]_n$ layers. The least-squares fitting of the experimental data led to $J = -0.118$ cm^{-1}, $g = 2.00$ and $R = 3.51 \times 10^{-4}$, showing weak antiferromagnetic interactions within the helix chain. The agreement factor R is defined as $R = \sum[(\chi_M T)^{cal} - (\chi_M T)^{obsd}]^2/\sum[(\chi_M T)^{obsd}]^2$.

A model containing a linear Mn_3 system was used for fitting the experimental magnetic data of **3** by invoking an exchange pathway through the carboxylate bridges, in which the magnetic exchange interaction (J) is considered to exist between neighboring Mn1 and Mn2 sites.

$$Mn1\underline{J}Mn2\underline{J}Mn1A \ldots\ldots ZJ' \ldots\ldots Mn1\underline{J}Mn2\underline{J}Mn1A \ldots\ldots$$

The spin–spin coupling Hamiltonian $\hat{H} = -2J(\hat{S}_{Mn1}\text{-}\hat{S}_{Mn2} + \hat{S}_{Mn2}\hat{S}_{Mn1A})$ was presented and the molar susceptibility expression (Eq. (2)) was used to give the susceptibilities of the trinuclear linear system.

$$\chi_{tri} = \frac{Ng^2\beta^2}{3kT}\left[\frac{A}{B}\right], \quad (2)$$

$$\begin{aligned} A = {} & 2040e^{-32x} + 1860e^{-17x} + 858e^{-4x} + 495e^{7x} + 252e^{16x} \\ & + 105e^{23x} + 1365e^{-27x} + 858e^{-14x} + 495e^{-3x} \\ & + 252e^{6x} + 105e^{13x} + 30e^{18x} + 858e^{-22x} + 492e^{-11x} \\ & + 252e^{-2x} + 105e^{5x} + 30e^{10x} + 3e^{13x} + 252e^{-8x} \\ & + 105e^{-x} + 30e^{4x} + 252e^{-12x} + 105e^{-5x} + 30 + 105e^{-7x}, \\ B = {} & 32e^{-32x} + 48e^{-17x} + 24e^{-4x} + 24e^{7x} + 16e^{16x} \\ & + 12e^{23x} + 28e^{-27x} + 24e^{-14x} + 20e^{-3x} \\ & + 16e^{6x} + 12e^{13x} + 8e^{18x} + 24e^{-22x} + 20e^{-11x} \\ & + 16e^{-2x} + 12e^{5x} + 8e^{10x} + 4e^{13x} + 16e^{-8x} \\ & + 12e^{-x} + 8e^{4x} + 16e^{-12x} + 12e^{-5x} + 8 + 12e^{-7x}, \\ x = {} & \frac{-J}{kT}. \end{aligned}$$

A molecular field approximation [29] was employed to treat the interaction between the trinuclear systems according to Eq. (3).

$$\chi_M = \frac{\chi_{tri}}{1 - (2ZJ'/Ng^2\beta^2)\chi_{tri}}. \quad (3)$$

Table 6
Relevant infrared vibrations (cm^{-1}) for complexes **1**–**5** and citric acid

	Citric acid [5a]	**1**	**2**	**3**	**4**	**5**
OH or H_2O	3495(s), 3448(w), 3298(s,br)		3369(s)	3446(br), 3396(s)	3426(br), 3253(w)	3481(s), 3396(s)
$\nu_{as,COO}$	1750(s), 1704(s)	1664(m), 1606(s), 1578(s), 1541(m)	1616(s), 1562(s), 1537(s)	1616(s, br), 1574(s, br)	1564(s, br)	1734(s), 1595(s)
$\nu_{s,COO}$	1430(s), 1390(s), 1359(s)	1429(s), 1408(s), 1390(m), 1340(s)	1465(m), 1429(s), 1384(s)	1419(s), 1394(s), 1375(s)	1439(s), 1417(s), 1389(s)	1475(m), 1417(s), 1394(s)

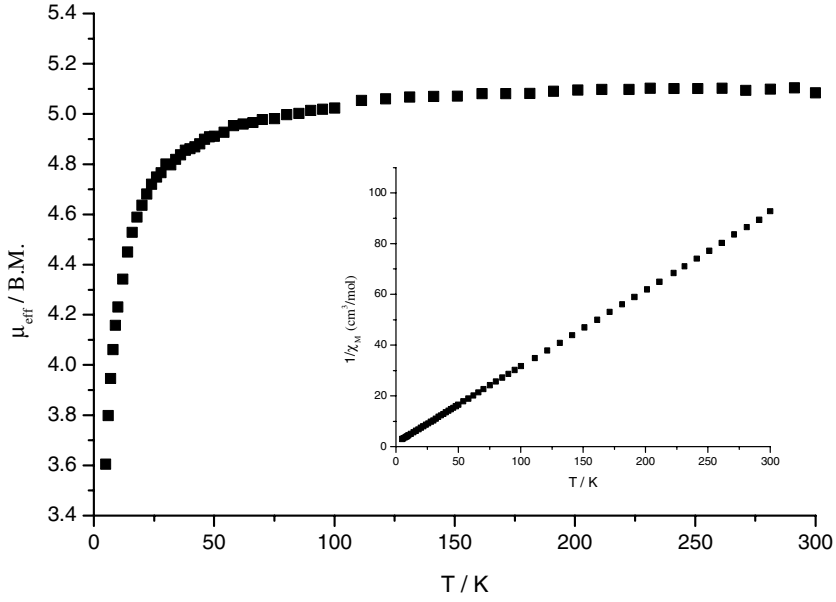


Fig. 9. The temperature dependence of the effective magnetic moments (μ_{eff}) for complex **1**. The insert represents the $1/\chi_M$ versus T plot.

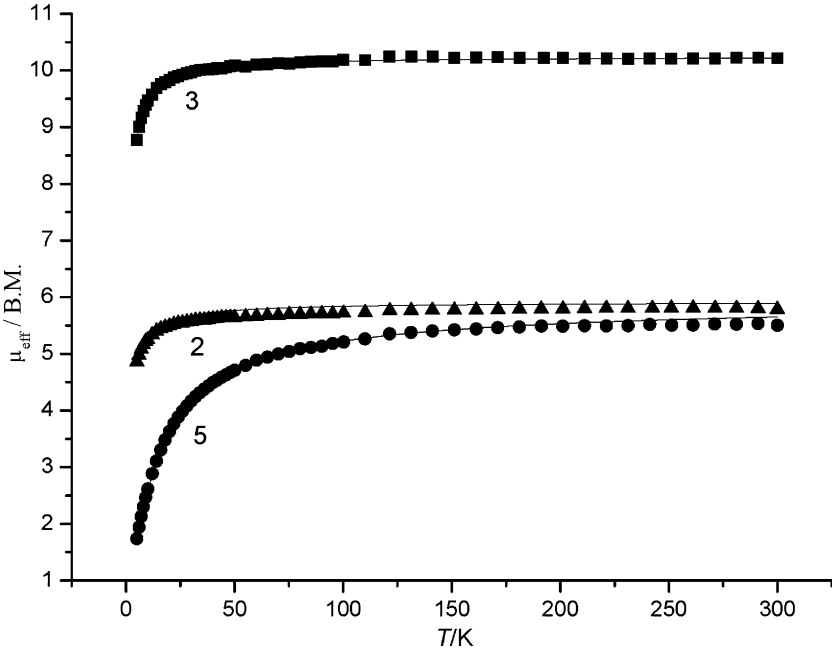


Fig. 10. The temperature dependence of the effective magnetic moments (μ_{eff}) for complexes **2** (triangle), **3** (square) and **5** (circle). The solid lines represent the calculated values.

The best fitting curves are depicted in Fig. 10 for **3**. The best fitting parameters are $g = 2.00$, $J = -0.105$ cm^{-1}, $ZJ' = -2.06 \times 10^{-2}$ cm^{-1} and $R = 8.74 \times 10^{-6}$, showing weak antiferromagnetic exchange interactions between the paramagnetic sites.

According to the structure shown in Fig. 8, Eq. (1) for the model of homonuclear uniform chain was used to treat the magnetic data of **5** as above did for **2**. Also, the molecular field approximation term was applied to estimate the interaction between the chains by using Eq. (3), in which χ_{tri} was revised as χ_{chain}. The best fitting parameters are $g = 2.00$, $J = -1.00$ cm^{-1}, $ZJ' = -4.98 \times 10^{-2}$ cm^{-1} and $R = 2.79 \times 10^{-4}$, showing weak antiferromagnetic exchange interactions between the paramagnetic sites.

All of the negative J values fall in the usual range for bridged carboxylate Mn(II) compounds [30]. The magnitude in the absolute value $|J|$ follows the order: $|J|$

(**2**) ≈ |*J*| (**3**) < |*J*| (**5**). As would be expected on the basis of the respective geometries, there is an efficient overlap between the 3d magnetic orbital of the Mn(II) sites and the 2p magnetic orbital of the oxygen of the carboxylate group in the order *syn–syn* > *anti–anti* > *syn–anti* [31,32]. The smaller |*J*| values of **2** and **3** can be reasonably attributed to the *syn–anti* bridging mode of the carboxylate group, while complex **5** contains both bridging modes: single atomic $\mu_{1,1}$-carboxylate bridging and the *syn–syn* $\mu_{1,3}$-OCO bridging (Fig. 8). Ref. [33] has collected and compared magnetic coupling data in various carboxylate-bridged Mn(II) complexes in an ascending order: *syn–anti* $\mu_{1,3}$-OCO bridge < $\mu_{1,1}$-carboxylato (i.e. monoatomic) bridge < *syn–syn* $\mu_{1,3}$-OCO bridge. So it is expected that complex **5** should have the largest |*J*| value among three Mn(II) complexes. Obviously smaller *ZJ′* values ensure the rationality of using the mean molecular field approximation model [34] and also show that the magnetic interaction via either the citrate backbone in **3** or the hydrogen-bonding supramolecular connect in **5** should be weaker than that via the carboxylate bridges in the respective complexes.

4. Conclusion

Four novel Mn citrate complexes have been reported, in which **1** and **2** are bimetallic citrate coordination polymers containing three novel coordination modes of the citrate trianion and showing 3-dimensional structures. Complexes **3** and **4** contain $[Mn(Hcit)(H_2O)_2]_2$ dimeric units which are connected to $Mn(H_2O)_4$ and $Mn(H_2O)_2$ fragments, respectively, forming a 1D chain in **3** and a 3D network in **4**. These manganese complexes have been characterized by crystal structure, IR spectra and magnetism. It is noteworthy to point out that the Mn/Ca citrate complex **2** belongs to rare Mn/Ca complex family which is attractive because of the involvement of the Mn/Ca cluster in the oxygen-evolving complex (OEC) in PSII. Our attempts to connect both Mn and Ca via a ligand bridge are successful in this work though complex **2** has not been directly relevant to the structure of the OEC. The further research will focus on the preparation and characterization of bimetallic Mn/Ca clusters, in which carboxylate and oxide bridges should be considered as major bridges to link both the Mn and Ca ions for the purpose of obtaining access to the structure of the OEC.

5. Supplementary material

Crystallographic data for the structural analyses have been deposited in the Cambridge Crystallographic Data Centre with CCDC Nos. 257191–257194 for compounds **1**–**4**. Copies of this information may be obtained free of charge from The Director, CCDC, 12 Union Road, Cambridge CB2 1IZ, UK (fax: +44 1223 336033; e-mail: deposit@ccdc.cam.ac.uk or www: http://www.ccdc.cam.ac.uk).

Acknowledgement

This work was supported by NNSFC (No. 20271061, 20273084).

References

[1] (a) S.J. Lippard, J.M. Berg, Principles of Bioinorganic Chemistry, University Science Books, Mill Valley, CA, 1994;
(b) E.M.N. Hamilton, S.A.S. Gropper, The Biochemistry of Human Nutrition, West Publishing Co., St. Paul, MN, 1987;
(c) J. Liang, M. Madden, V.K. Shah, R.H. Burris, Biochemistry 29 (1990) 8577;
(d) H. Beinert, FASEB J. 4 (1990) 2483;
(e) H. Beinert, M.C. Kennedy, Eur. J. Biochem. 186 (1989) 5.

[2] (a) I. Shweky, A. Bino, D.P. Goldberg, S.J. Lippard, Inorg. Chem. 33 (1994) 5161;
(b) J. Strouse, S.W. Layten, C.E. Strouse, J. Am. Chem. Soc. 99 (1977) 562;
(c) A. Bino, I. Shweky, S. Cohen, E.R. Bauminger, S.J. Lippard, Inorg. Chem. 37 (1998) 5168;
(d) I. Gautier-Luneau, C. Fouquard, C. Merle, J.L. Pierre, D.J. Luneau, J. Chem. Soc., Dalton Trans. (2001) 2127;
(e) R. Job, P.J. Kelleher, W.C. Stallings, C.T. Monti, J.P. Glusker, Inorg. Chem. 21 (1982) 3760;
(f) J.-H. Liao, S.-H. Cheng, C.-T. Su, Inorg. Chem. Commun. 5 (2002) 761;
(g) M. Matzapetakis, M. Dakanali, C.P. Raptopoulou, V. Tangoulis, A. Terzis, N. Moon, J. Giapintzakis, A. Salifoglou, J. Biol. Inorg. Chem. 5 (2000) 469;
(h) Z. Zhou, Y. Huang, Y. Jiang, Chinese J. Inorg. Chem. 13 (1997) 385.

[3] (a) R.C. Bott, D.S. Sagatys, D.E. Lynch, G. Smith, C.H.L. Kennard, T.C.W. Mak, Aust. J. Chem. 44 (1991) 1495;
(b) D.S. Sagatys, G. Smith, R.C. Bott, D.E. Lynch, C.H.L. Kennard, Polyhedron 12 (1993) 709.

[4] (a) R. Swanson, W.H. Ilsley, A.G. Stanislowski, J. Inorg. Biochem. 18 (1983) 187;
(b) S. Tsuji, T. Shibata, Y. Ito, S. Fujii, K.I. Tomita, Acta Crystallogr. C 47 (1991) 528;
(c) A.E. Shvelashvili, E.B. Miminoshvili, V.K. Belsky, E.R. Kuteliya, T.N. Sakvarelidze, D.A. Ediberidze, Zh. Neorg. Khim. 46 (2001) 1489.

[5] (a) C. Djordjevic, M. Lee, E. Sinn, Inorg. Chem. 28 (1989) 719;
(b) M. Kaliva, T. Giannadaki, A. Salifoglou, C.P. Raptopoulou, A. Terzis, Inorg. Chem. 41 (2002) 3850;
(c) M. Kourgiantakis, M. Matzapetakis, C.P. Raptopoulou, A. Terzis, A. Salifoglou, Inorg. Chim. Acta 297 (2000) 134;
(d) M. Tsaramyrsi, M. Kaliva, A. Salifoglou, C.P. Raptopoulou, A. Terzis, V. Tangoulis, J. Giapintzakis, Inorg. Chem. 40 (2001) 5772;
(e) M. Tsaramyrsi, D. Kavousanaki, C.P. Raptopoulou, A. Terzis, A. Salifoglou, Inorg. Chim. Acta 320 (2001) 47;
(f) M. Matzapetakis, C.P. Raptopoulou, A. Tsokos, V. Papaefthymiou, N. Moon, A. Salifoglou, J. Am. Chem. Soc. 120 (1998) 13266;
(g) P. O'Brien, H. Salacinski, M. Motevalli, J. Am. Chem. Soc. 119 (1997) 12695;

(h) M. Matzapetakis, C.P. Raptopoulou, A. Terzis, A. Lakatos, T. Kiss, A. Salifoglou, Inorg. Chem. 38 (1999) 618.
[6] (a) Z. Zhou, H. Wan, K. Tsai, Inorg. Chem. 39 (2000) 59;
(b) N.W. Alcock, M. Dudek, R. Grybos, E. Hodorowicz, A. Kanas, A. Samotus, J. Chem. Soc., Dalton Trans. (1990) 707;
(c) J. Flanagan, W.P. Griffith, A.C. Skapski, R.W. Wiggins, Inorg. Chim. Acta 96 (1985) L23;
(d) J.-Q. Xu, X.-H. Zhou, L.-M. Zhou, T.-G. Wang, X.-Y. Huang, B.A. Averill, Inorg. Chim. Acta 285 (1999) 152;
(e) Z.-H. Zhou, H.-L. Wan, K.-R. Tsai, Polyhedron 16 (1997) 75;
(f) Z.-H. Zhou, H.-L. Wan, K.-R. Tsai, J. Chem. Soc., Dalton Trans. (1999) 4289;
(g) E. Llopis, J.A. Ramirez, A. Domenech, A. Cervilla, J. Chem. Soc., Dalton Trans. (1993) 1121;
(h) M. Ti Kakihana, M. Tada, M. Shiro, V. Petrykin, M. Osada, Y. Nakamura, Inorg. Chem. 40 (2001) 891;
(i) M. Quiros, D.M.L. Goodgame, D.J. Williams, Polyhedron 11 (1992) 1343.
[7] (a) M. Matzapetakis, M. Kourgiantakis, M. Dakanali, C.P. Raptopoulou, A. Terzis, A. Lakatos, T. Kiss, I. Banyai, L. Iordanidis, T. Mavromoustakos, A. Salifoglou, Inorg. Chem. 40 (2001) 1734;
(b) T.L. Feng, P.L. Gurian, M.D. Healy, A.R. Barron, Inorg. Chem. 29 (1990) 408;
(c) G.A. Banta, S.J. Rettig, A. Storr, J. Trotter, Can. J. Chem. 63 (1985) 2545.
[8] (a) R. Tacke, J. Heermann, M. Pulm, Organometallics 16 (1997) 5648;
(b) G.R. Willey, U. Somasunderam, D.R. Aris, W. Errington, Inorg. Chim. Acta 315 (2001) 191;
(c) P.R. Deacon, M.F. Mahon, K.C. Molloy, P.C. Waterfield, J. Chem. Soc., Dalton Trans. (1997) 3705.
[9] (a) E. Asato, W.L. Driessen, R.A.G. de Graaff, F.B. Hulsbergen, J. Reedijk, Inorg. Chem. 30 (1991) 4210;
(b) E. Asato, K. Katsura, M. Mikuriya, T. Fujii, J. Reedijk, Chem. Lett. (1992) 1967;
(c) P.J. Barrie, M.I. Djuran, M.A. Mazid, M. McPartlin, P.J. Sadler, I.J. Scowen, H. Sun, J. Chem. Soc., Dalton Trans. (1996) 2417;
(d) E. Asato, K. Katsura, M. Mikuriya, U. Turpeinen, I. Mutikainen, J. Reedijk, Inorg. Chem. 34 (1995) 2447.
[10] (a) D.W. Hartley, G. Smith, D.S. Sagatys, C.H.L. Kennard, J. Chem. Soc., Dalton Trans. (1991) 2735;
(b) G. Smith, D.S. Sagatys, R.C. Bott, D.E. Lynch, Polyhedron 12 (1993) 1491;
(c) G. Smith, D.S. Sagatys, R.C. Bott, D.E. Lynch, C.H.L. Kennard, Polyhedron 11 (1992) 631;
(d) R.C. Bott, G. Smith, D.S. Sagatys, D.E. Lynch, C.H.L. Kennard, Aust. J. Chem. 53 (2000) 917.
[11] (a) D. Mastropaolo, D.A. Powers, J.A. Potenza, H.J. Schugar, Inorg. Chem. 15 (1976) 1444;
(b) E. Asato, K. Katsura, M. Mikuriya, T. Fujii, J. Reedijk, Inorg. Chem. 32 (1993) 5322;
(c) W.A. Herrmann, E. Herdtweck, L.Z. Pajdla, Kristallogr. 198 (1992) 257;
(d) M. Murrie, H. Stoeckli-Evans, H.U. Gudel, Angew. Chem., Int. Ed. Engl. 40 (2001) 1957.
[12] (a) M. Matzapetakis, N. Karligiano, A. Bino, M. Dakanali, C.P. Raptopoulou, V. Tangoulis, A. Terzis, J. Giapintzakis, A. Salifoglou, Inorg. Chem. 39 (2000) 4044;
(b) A.E. Shvelashvili, E.B. Miminoshvili, V.K. Belsky, E.R. Kuteliya, T.N. Sakvarelidze, D.A. Ediberidze, M.G. Tavberidze, Zh. Neorg. Khim. 46 (2001) 927.
[13] H.L. Carrell, J.P. Glusker, Acta Crystallogr. B 29 (1973) 638.
[14] Y.F. Deng, Z.H. Zhou, H.L. Wan, S.W. Ng, Acta Crystallogr. E 59 (2003) m310.
[15] (a) N.A. Law, M.T. Caudle, V.L. Pecoraro, Adv. Inorg. Chem. 46 (1999) 305;
(b) M.L. Ludwig, A.L. Metzger, K.A. Pattridge, W.C. Stallings, J. Mol. Biol. 219 (1991) 335;
(c) Z.F. Kanyo, L.R. Scolnick, D.E. Ash, D.W. Christianson, Nature 383 (1996) 554;
(d) M. Atta, P. Nordlund, A. Aberg, H. Eklund, M. Fontecave, J. Biol. Chem. 267 (1992) 20682.
[16] (a) V.L. Pecoraro, in: V.L. Pecoraro (Ed.), Manganese Redox Enzymes, Verlag Chemie, New York, 1992;
(b) V.L. Pecoraro, M.J. Baldwin, A. Gelasco, Chem. Rev. 94 (1994) 807;
(c) G.C. Dismukes, Chem. Rev. 96 (1996) 2909;
(d) V.K. Yachandra, K. Sauer, M.P. Klein, Chem. Rev. 96 (1996) 7.
[17] C.F. Yocum, in: V.L. Pecoraro (Ed.), Manganese Redox Enzymes, VCH, New York, 1992, pp. 71–83.
[18] (a) P. Ådelroth, K. Lindberg, L.E. Andréasson, Biochemistry 34 (1995) 9021;
(b) T. Noguchi, T.A. Ono, Y. Inoue, Biochim. Biophys. Acta 1228 (1995) 189.
[19] K.N. Ferreira, T.M. Iverson, K. Maghlaoui, J. Barber, S. Iwata, Science 303 (2004) 1831.
[20] (a) R.T. Stibrany, S.M. Gorun, Angew. Chem., Int. Ed. Engl. 29 (1990) 1156;
(b) S.M. Gorun, R.T. Stibrany, A. Lillo, Inorg. Chem. 37 (1998) 836;
(c) S.M. Rocklage, W.P. Cacheris, S.C. Quay, F.E. Hahn, K.N. Raymond, Inorg. Chem. 28 (1989) 477.
[21] (a) A. Mishra, W. Wernsdorfer, K.A. Abboud, G. Christou, Chem. Commun. (2005) 54;
(b) I.G. de Muro, M. Insausti, L. Lezama, M.K. Urtiaga, M.I. Arriortua, T. Rojo, J. Chem. Soc., Dalton Trans. (2000) 3360.
[22] (a) X. Zhang, D. Huang, C. Chen, Q. Liu, D. Liao, L. Li, Inorg. Chem. Commun. 8 (2005) 22;
(b) C. Ma, C. Chen, Q. Liu, F. Chen, D. Liao, L. Li, L. Sun, Eur. J. Inorg. Chem. (2004) 3316;
(c) C. Ma, W. Wang, X. Zhang, C. Chen, Q. Liu, H. Zhu, D. Liao, L. Li, Eur. J. Inorg. Chem. (2004) 3522;
(d) X. Zhang, D. Huang, F. Chen, C. Chen, Q. Liu, Inorg. Chem. Commun. 7 (2004) 662;
(e) C. Chen, D. Huang, X. Zhang, F. Chen, H. Zhu, Q. Liu, C. Zhang, D. Liao, L. Li, L. Sun, Inorg. Chem. 42 (2003) 3540;
(f) C. Ma, C. Chen, Q. Liu, D. Liao, L. Li, Eur. J. Inorg. Chem. (2003) 1227;
(g) C. Ma, C. Chen, Q. Liu, D. Liao, L. Li, L. Sun, New J. Chem. 27 (2003) 890;
(h) C. Chen, H. Zhu, D. Huang, T. Wen, Q. Liu, D. Liao, J. Cui, Inorg. Chim. Acta 320 (2001) 159.
[23] G.M. Sheldrick, SHELXTL-97, Universtät Göttingen, 1997.
[24] (a) H.H. Thorp, Inorg. Chem. 31 (1992) 1585;
(b) I.D. Brown, D. Altermatt, Acta Crystallogr. B 41 (1985) 244.
[25] B. Sheldrick, Acta Crystallogr. B 30 (1974) 2056.
[26] Z.-H. Zhou, Y.-J. Lin, H.-B. Zhang, G.-D. Lin, K.-R. Tsai, J. Coord. Chem. 42 (1997) 131.
[27] G.B. Deacon, R.J. Philips, Coord. Chem. Rev. 33 (1980) 227.
[28] W. Hiller, J. Strähle, A. Datz, M. Hanack, W.E. Hatfield, L.W. ter Haar, P. Gütlich, J. Am. Chem. Soc. 106 (1984) 329.
[29] C.J. O'Connor, Prog. Inorg. Chem. 29 (1982) 203.
[30] (a) C. Ma, C. Chen, Q. Liu, F. Chen, D. Liao, L. Li, L. Sun, Eur. J. Inorg. Chem. (2004) 3316;
(b) C. Ma, W. Wang, X. Zhang, C. Chen, Q. Liu, H. Zhu, D. Liao, L. Li, Eur. J. Inorg. Chem. (2004) 3522;
(c) P.S. Mukherjee, S. Konar, E. Zangrando, T. Mallah, J. Ribas, N.R. Chaudhuri, Inorg. Chem. 42 (2003) 2695;
(d) G. Fernández, M. Corbella, J. Mahia, M.A. Maestro, Eur. J. Inorg. Chem. (2002) 2502;
(e) W.B. Lin, M.E. Chapman, Z.Y. Wang, G.T. Yee, Inorg. Chem. 39 (2000) 4169;

(f) B. Albela, M. Corbella, J. Ribas, I. Castro, J. Sletten, H. Stoeckli-Evans, Inorg. Chem. 37 (1998) 788;
(g) J. Cano, G.D. Munno, J.L. Sanz, R. Ruiz, J. Faus, F. Lloret, M. Julve, A. Caneschi, J. Chem. Soc., Dalton Trans. (1997) 1915;
(h) H. Oshio, E. Ino, I. Mogi, T. Ito, Inorg. Chem. 32 (1993) 5697.

[31] E. Colacio, J.M. Dominguez-Vera, M. Ghazi, R. Kivekäs, M. Klinga, J.M. Moreno, Eur. J. Inorg. Chem. (1999) 441.

[32] (a) M. Inoue, M. Kubo, Inorg. Chem. 9 (1970) 2310;
(b) R.L. Carlin, K. Kopinga, O. Kahn, M. Verdauger, Inorg. Chem. 29 (1990) 4240.

[33] H. Iikura1a, T. Nagata, Inorg. Chem. 37 (1998) 4702.

[34] (a) D.K. Towle, S.K. Hoffmann, W.E. Hatfield, P. Singh, P. Chaudhuri, Inorg. Chem. 27 (1988) 394;
(b) B. Chiari, A. Cinti, L. David, F. Ferraro, D. Gatteschi, O. Piovesana, P.F. Zanazzi, Inorg. Chem. 35 (1996) 7413.

solids [1-(4′-nitrobenzyl)-4-aminopyridinium]-bis(maleonitriledithiolato)nickel([$NO_2BzPyNH_2$][Ni(mnt)$_2$]) (**1**) and [4-aminopyridinium]-bis(maleonitriledithiolato)-platinum ([$NO_2BzPyNH_2$][Pt(mnt)$_2$])(**2**). To the best of our knowledge, a uniform chain exhibiting an unusual magnetic transition is very rare in the Ni(mnt)$_2$ complexes.

2. Experimental

2.1. General materials and techniques

The starting materials, 1-(4′-nitrobenzyl)-4-aminopyridinium bromide ([$NO_2BzPyNH_2$]Br), and disodium maleonitriledithiolate (Na_2mnt) were synthesized following the literature procedures [19,20]. A similar method for preparing [Bu_4N]$_2$[Ni(mnt)$_2$] was utilized to prepare [$NO_2BzPyNH_2$]$_2$[Ni(mnt)$_2$] and [$NO_2BzPyNH_2$]$_2$[Pt(mnt)$_2$] [20].

Elemental analyses were run on a Model 240 Perkin–Elmer C H N instrument. IR spectra were recorded on an IF66V FT-IR (400–4000 cm^{-1} region) spectrophotometer in KBr pellets. Electronic spectra were recorded on a Shimadzu UV-3100 spectrophotometer. All solution concentrations were ca. 10^{-5} mol dm^{-3} in CH_3CN. The electrospray-mass spectra [ESI-MS] were determined on a Finnigan LCQ mass spectrograph, sample concentration ca. 1.0 mmol dm^{-3}. DSC was carried out with a Perkin–Elmer calorimeter. Thermal analyses of crushed polycrystalline samples for **1** placed in an aluminum crucible were performed on warming (rate of 20 K mol^{-1}) from 98 to 293 K. Magnetic susceptibility data on crushed polycrystalline samples of **1** and **2** were collected over the temperature range of 2–300 K using a Quantum Design MPMS-5S super-conducting quantum interference device (SQUID) magnetometer, and the experimental data were corrected for diamagnetism of the constituent atoms estimated from Pascal's constants.

2.2. Syntheses of complexes

2.2.1. [$NO_2BzPyNH_2$]$_2$[Ni(mnt)$_2$] (**1**)

[$NO_2BzPyNH_2$]$_2$[Ni(mnt)$_2$] (0.800 g, 1.0 mmol) was dissolved in 30 cm^3 MeCN, then a MeCN solution (10 cm^3) of I_2 (0.150 g, 0.59 mmol) was slowly added, the mixture was stirred for 1 h, and then 100 cm^3 CH_3OH was added. After the mixture was allowed to stand overnight, 0.508 g dark microcrystals produced were filtered off, washed with CH_3OH and Et_2O, and dried in a vacuum. Yield: 89.3%. *Anal.* Calc. for $C_{20}H_{12}NiN_7S_4O_2$: C, 42.19; H, 2.12; N, 17.22. Found: C, 42.12; H, 2.23; N, 17.16%. IR (cm^{-1}): 3380.4s, 3073.1w, 2207.1s, 1651.3s, 1606.6m, 1565.4m, 1536.6s, 1518.6m, 1454.2s, 1346.1s.

Single crystals suitable for X-ray structure analysis were obtained by evaporating a solution of **1** in a mixed solution of MeCN and *i*-PrOH (1:2 v/v).

2.2.2. [$NO_2BzPyNH_2$][Pt(mnt)$_2$] (**2**)

The procedure for preparing **2** was similar to that for **1**. Yield: 87.5%. *Anal.* Calc. for $C_{20}H_{12}PtN_7S_4O_2$: C, 34.04; H, 1.71; N, 13.89. Found: C, 34.12; H, 1.84; N, 13.76%. IR (cm^{-1}): 3371.9s, 3070.4w, 2205.9s, 1648.2s, 1604.8m, 1564.4m, 1535.2s, 1508.5m, 1449.8s, 1332.8m.

Single crystals suitable for X-ray structure analysis were obtained by evaporating a solution of **2** in a mixed solution of MeCN and *i*-BuOH (1:2 v/v).

2.3. Single-crystal X-ray structure determination

Measurements of the studied complexes **1** and **2** were performed on a Smart APEX CCD area detector using graphite-monochromated Mo Kα radiation ($\lambda = 0.71073$ Å) by the ω scan mode within the angular range $1.87° < \theta < 26.0°$ for **1** and $1.96° < \theta < 25.0°$ for **2**. Space group, lattice parameters and other relevant information are listed in Table 1. The structures were solved by direct methods and refined on F^2 by full-matrix least-squares, employing Bruker's SHELXTL [21]. All non-hydrogen atoms were refined with anisotropic thermal parameters. All H atoms were placed in calculated positions, assigned fixed isotropic displacement parameters 1.2 times the equivalent isotropic U value of the attached atom, and allowed to ride on their respective parent atoms.

3. Results and discussion

3.1. Descriptions of the structures

3.1.1. X-ray structure of **1**

Complex **1** crystallizes in the monoclinic space group $P2_1/c$ at room temperature. Selected bond distances, bond angles and intermolecular Ni···Ni, Ni···S and S···S distances are summarized in Table 2. An ORTEP drawing of **1** with non-hydrogen atomic labelling in an asymmetric unit is shown in Fig. 1. The Ni(III) ion in the [Ni(mnt)$_2$]$^-$ anion is coordinated by four sulfur atoms of two mnt^{2-} ligands, and exhibits square-planar coordination geometry. The CN groups are slightly tipped out of the plane, and the deviations from the plane are −0.4477 Å for N(1), −0.4875 Å for N(2), −0.1285 Å for N(3) and −0.2619 Å for N(4). The average S–Ni–S bond angle within the five-membered ring is 90.0(5)°, and the average Ni–S bond distance is 2.139(1) Å, these values are in agreement with those found in other [Ni(mnt)$_2$]$^-$ complexes [22]. The cation [$NO_2BzPyNH_2$]$^+$, adopts a conformation in which the benzene and pyridine rings are almost perpendicular to the reference plane C(14)–C(15)–N(5) (dihedral angles

Table 1
Crystal data and structure refinements for **1** and **2**

Compound	**1**	**2**
Temperature	293 (2)	293 (2)
Empirical formula	$C_{20}H_{12}NiN_7S_4O_2$	$C_{20}H_{12}PtN_7S_4O_2$
Formula weight	569.32	705.70
Wavelength	0.71073	0.71073
Space group	$P2_1/c$	$P2_1/c$
Crystal system	monoclinic	monoclinic
Unit cell dimensions		
a (Å)	12.331(3)	10.600(3)
b (Å)	26.937(6)	8.376(2)
c (Å)	7.322(2)	27.089(7)
β (°)	105.02(1)	100.84(1)
Volume (Å^3), Z	2349.0(10), 4	2362.2(11), 4
D_{calc} (g/cm^3)	1.610	1.984
Absorption coefficient (mm^{-1})	1.216	6.328
$F(000)$	1156	1356
Crystal size (mm^3)	$0.35 \times 0.30 \times 0.20$	$0.40 \times 0.35 \times 0.25$
Absorption correction	empirical (SHELXA)	empirical (SHELXA)
Maximum and minimum transmission	0.78 and 0.66	0.21 and 0.09
θ Range for data collection (°)	1.87–26.00	1.96–25.00
Limiting indices	$-15 \leqslant h \leqslant 15$, $-33 \leqslant k \leqslant 21$, $-8 \leqslant l \leqslant 8$	$-9 \leqslant h \leqslant 12$, $- \leqslant k \leqslant 9$, $-32 \leqslant l \leqslant 21$
Reflections collected	12474	11200
Independent reflections	4604	4142
R_{int}	0.084	0.047
Refinement method	full-matrix least-squares on F^2	full-matrix least-squares on F^2
Goodness-of-fit on F^2	1.016	1.014
Final R indices [$I > 2\sigma(I)$]	$R_1 = 0.0545$, $wR_2 = 0.1104$	$R_1 = 0.0335$, $wR_2 = 0.0678$
Final R indices (all data)	$R_1 = 0.0973$, $wR_2 = 0.1195$	$R_1 = 0.0431$, $wR_2 = 0.0699$
Largest difference in peak and hole (e Å^{-3})	0.34 and −0.47	1.07 and −0.81

Table 2
Selected bond parameters and intermolecular contacts for **1** and **2**

Compound	**1**		**2**
Bond distances (Å)			
Ni(1)–S(1)	2.134(1)	Pt(1)–S(1)	2.264(2)
Ni(1)–S(2)	2.146(1)	Pt(1)–S(2)	2.253(2)
Ni(1)–S(3)	2.141(1)	Pt(1)–S(3)	2.257(2)
Ni(1)–S(4)	2.136(1)	Pt(1)–S(4)	2.255(2)
S(1)–C(2)	1.716(4)	S(1)–C(2)	1.716(6)
S(2)–C(3)	1.715(4)	S(2)–C(3)	1.699(6)
S(3)–C(6)	1.706(4)	S(3)–C(6)	1.716(6)
S(4)–C(7)	1.702(4)	S(4)–C(7)	1.714(5)
Bond angles (°)			
S(1)–Ni(1)–S(2)	92.50(5)	S(1)–Pt(1)–S(2)	89.88(6)
S(1)–Ni(1)–S(4)	86.63(5)	S(1)–Pt(1)–S(4)	90.71(5)
S(3)–Ni(1)–S(4)	92.23(5)	S(3)–Pt(1)–S(4)	89.95(5)
S(2)–Ni(1)–S(3)	88.60(5)	S(2)–Pt(1)–S(3)	89.46(6)
Intrachain distances (Å)			
Ni···Ni (nearest separation)	3.855	Pt···Pt (nearest separation)	3.511
Ni···S	3.644	Pt···S	4.066
S···S	3.725	S···S	3.488

of 90.4° and 91.0°, respectively). The phenyl ring and the pyridine ring make a dihedral angle of 112.5°. The plane defined by S(1)S(2)Ni(1)S(3)S(4) with the phenyl and pyridine rings make dihedral angles of 17.2° and 113.8°, respectively. The most notable structural feature of **1** is that the anions and cations possess a stacking pattern with well-separated columns along the direction of the c-axis (Fig. 2). Within an anionic column, the nearest Ni···Ni distance is 3.855 Å, and the nearest S···S and Ni···S contacts are 3.725 and 3.664 Å, respectively.

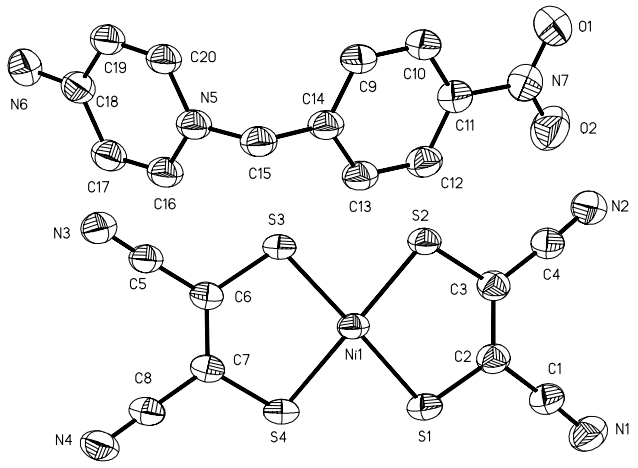


Fig. 1. ORTEP plot (30% probability ellipsoids) showing the molecule structure of **1**.

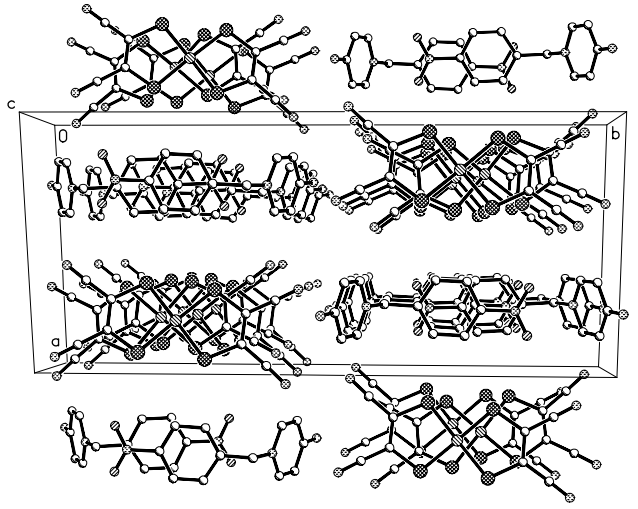


Fig. 2. The packing diagram of a unit cell for **1** as viewed along the *c*-axis.

Therefore, the Ni(III) ions within a $[Ni(mnt)_2]^-$ anionic column form a 1D uniformly spaced chain through intermolecular Ni···S, S···S, Ni···Ni or π···π interactions (Fig. 3(a)). The adjacent cations stack into a column via a boat-type conformation (Fig. 3(b)). The contact distances between the nitrogen atom of the NO_2 group and neighboring phenyl rings are 3.562 and 3.799 Å, respectively. So the cations form a 1D chain via π–π interactions between the NO_2 group and benzene rings. The closest Ni···Ni separation between anionic chains is 12.604 Å, which is significantly longer than that of the Ni···Ni separation within a chain (3.855 Å). Therefore, **1** is an ideal 1D uniform magnetic chain system from the point of view of the structure. There are three intermolecular hydrogen bonds between the anions and cations in the crystal structure of **1** (Table 3).

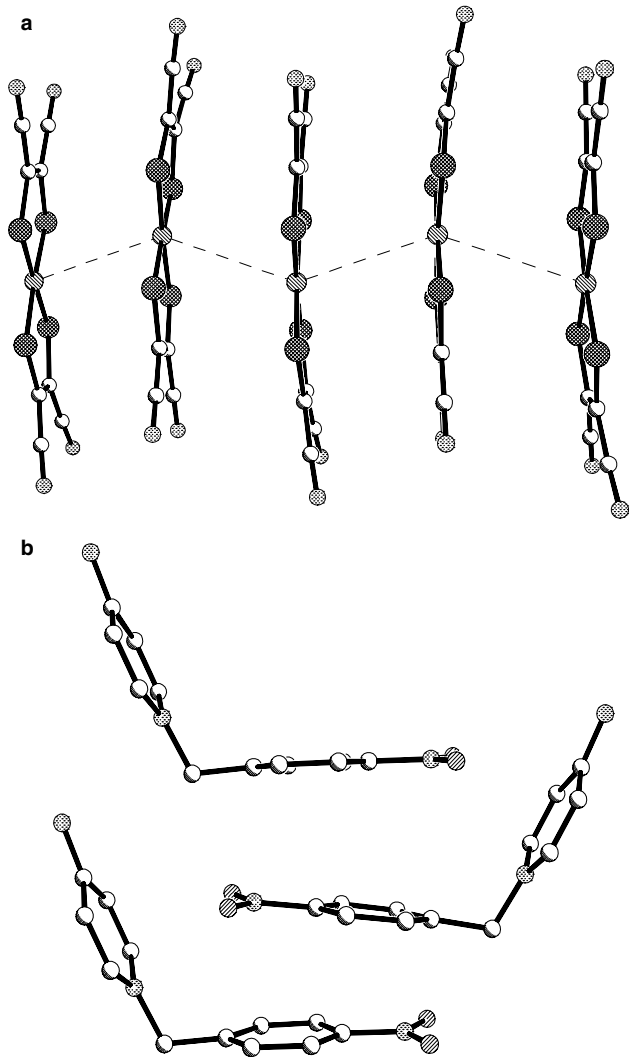


Fig. 3. (a) Side view of the anions stack of **1** showing the uniform space linear-chain of $[Ni(mnt)_2]^-$. (b) Side view of the cations stack of **1**.

3.1.2. *X-ray structure of* **2**

The coordination geometry of the $[Pt(mnt)_2]$ anion is essentially identical to that described above for **1**, while the stacking pattern of the $[Pt(mnt)_2]$ anion and $[NO_2Bz\text{-}PyNH_2]$ cation in **2** is significantly different from that of **1**. Selected bond distances, bond angles and intermolecular Pt···Pt, Pt···S and S···S distances are summarized in Table 2. The cation is situated above the plane of the $[Pt(mnt)_2]$ anion (Fig. 4(a)) in which the dihedral angles between the S(1)S(2)Pt(1)S(3)S(4) plane and phenyl and pyridine rings are 84.8° and 135.6°, respectively. The reference plane defined by C(14)–C(15)–N(5) and the aromatic rings make dihedral angles of 37.4° for the phenyl ring and 115.8 for pyridine ring. The $Pt(mnt)_2^-$ anions of **2** form a dimer with a Pt···Pt distance 3.511 Å and a S···S distance 3.488 Å, which is significantly different from that of **1**. Obviously, the short contacts of M···M, S···S and π–π interactions in **2** are smaller than those of **1**, therefore it is possible that the

Table 3
Hydrogen bonds for **1** and **2** (Å and °)

D–H···A	*d*(D–H)	*d*(H···A)	*d*(D···A)	∠(DHA)
*Complex **1***				
N(6)–H(6A)···N(4)#1	0.86	2.56	3.132(6)	125.0
N(6)–H(6A)···N(1)#2	0.86	2.62	3.323(6)	140.0
N(6)–H(6A)···N(2)#3	0.86	2.43	3.059(6)	131.0
*Complex **2***				
N(6)–H(6A)···N(1)#4	0.86	2.49	3.273(8)	153.0
N(6)–H(6A)···N(3)#5	0.86	2.55	3.207(8)	134.0
C(15)–H(15A)···N(4)#6	0.97	2.55	3.397(8)	146.0
C(16)–H(16A)···O(1)#7	0.93	2.52	3.275(8)	138.0
C(19)–H(19A)···N(2)#8	0.93	2.56	3.310(8)	138.0

Symmetry transformations used to generate equivalent atoms: #1 = $-x+1$, $-y$, $-z+1$; #2 = $x-1$, $-y+1/2$, $z-1/2$; #3 = $-x+1$, $y-1/2$, $-z+1/2$; #4 = $-x+1$, $-y$, $-z+2$; #5 = $-x$, $y-1/2$, $-z+3/2$; #6 = x, $y+1$, z; #7 = $-x+1$, $-y+1$, $-z+2$; #8 = x, $-y+1/2$, $z-1/2$.

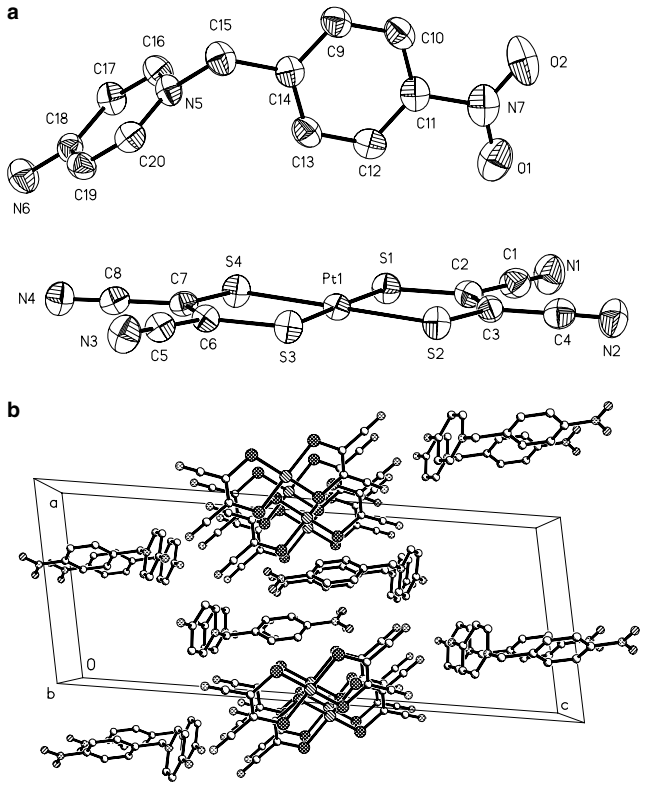


Fig. 4. (a) ORTEP plot (30% probability ellipsoids) showing the molecule structure of **2**. (b) The packing diagram of a unit cell for **2** as viewed along the *b*-axis.

interaction between $M(mnt)_2^-$ anions in **2** may be stronger than that in **1**, and **2** forms a dimer structure (Fig. 4(b)). It is worth noting that five intermolecular hydrogen bonds between anions and cations were observed in the crystal structure of **2**, as listed in Table 3. The anion–anion, anion–cation and cation–cation contacts may play important roles in crystal packing and the stabilization of **2**.

3.2. Infrared spectra

The infrared spectra of the two complexes **1** and **2** are very much consistent with the structural data presented above. The bands at 3380.4(s) and 1651.3(s) cm^{-1} for **1**, and 3371.9 and 1648.2 cm^{-1} for **2** are attributable to N–H stretching and bending of the amino group. The bands at 3073.1 and 3070.4 cm^{-1} are due to the stretching vibration frequencies of C–H in the aromatic ring. The complexes **1** and **2** show one strong band at 2207.1 and 2205.9 cm^{-1}, respectively, which are CN stretching bands. The ν(C=N) and ν(C=C) bands for the pyridine ring and phenyl ring are located at 1606.6, 1565.4 and 1518.6 cm^{-1} for **1**, and 1604.8, 1564.4, and 1508.5 cm^{-1} for **2**. The ν(C=C) band of mnt^{2-} is at 1452.2 cm^{-1} for **1** and 1449.8 cm^{-1} for **2**. The $\nu(NO_2)$ bands of complexes **1** and **2** are presented at 1536.6, 1346.1 cm^{-1} and 1535.2, 1332.8 cm^{-1}.

3.3. Electronic absorption spectra and electrospray mass spectra

The UV–Vis absorption spectra of **1** and **2** were measured in CH_3CN solvent in the region of 230–1200 nm (Table 4). All bands are attributed to the anionic portions of these compounds. The characteristic bands of **1** at 859.6, 473.0, 374.0 and 271.0 nm, are assigned as $L(\pi) \rightarrow M$, $L(\sigma) \rightarrow M$, $L^* \rightarrow L$ and $L(\sigma) \rightarrow M$, respectively, which is basically similar to those of $[(n\text{-}C_4H_9)_4N][Ni(mnt)_2]$ [23]. The bands of **2** are similar to those of **1**. The negative-ion and positive-ion ESI-MS spectra of **1** and **2** in MeCN solution show that the mass spectrum is dominated by the 230.2 peak, which is due to $[NO_2BzPyNH_2]^+$, the peaks at 340.3 and 476.3 are assigned to $[Ni(mnt)_2 + H]^-$ and $[Pt(mnt)_2 + H]^-$, respectively.

3.4. Magnetic properties

The temperature dependence of the magnetic susceptibility for **1** and **2** is measured under an applied field of 1000 Oe in the temperature range 2–300 K. The plot of χ_m versus T for **1** is shown in Fig. 5, where χ_m is the magnetic susceptibility per nickel atom corrected by the diamagnetic contribution. For the complex **1**, the

Table 4
The main UV–Vis spectra (CH_3CN) of **1** and **2**

Complex	λ (nm)	ε (mol^{-1} dm^3 cm^{-1} 10^3)
1	1178.0	0.33
	859.6	0.76
	629.0	0.18
	473.0	0.34
	374.0	7.68
	271.0	133.47
2	1180.0	0.27
	850.0	4.91
	629.0	0.35
	455.0	3.27
	333.6	10.70
	273.0	147.66

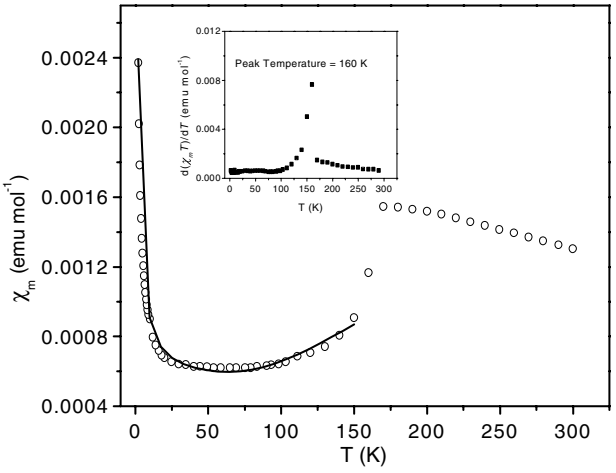


Fig. 5. Plots of χ_m vs. T for **1** (inset: plots of $d(\chi_m T)/dT$ vs. T). The solid line are reproduced from the theoretical calculations and detailed fitting procedure described in the text.

overall magnetic behaviors correspond to a paramagnetic system with an antiferromagnetic coupling interaction. As the temperature decreases, the value of $\chi_m T$ slightly decreases from 0.391 emu K mol^{-1} at 300 K (the value is somewhat higher than that expected for magnetically isolated Ni(III) ions) to 0.187 emu K mol^{-1} at 160 K for **1**. In the LT phase, as the samples are continuously cooled, the magnetic susceptibilities decrease exponentially (Fig. 5), indicating that **1** exhibits the characteristics of a spin gap system [24]. On increasing of temperature back to the original one, the same $\chi_m - T$ curves are obtained without hysteresis effect. These findings indicate that complex **1** undergoes a reversible phase transition. The phase transition temperature is evaluated as the temperature at the maximum of the $d(\chi_m T)/dT$ derivative, that is ~160 K for **1** (inset of Fig. 5).

The spin-gapped system has attracted extensive interest recently [25–28], but it is very rare for Ni(III) complexes [18]. The magnetic susceptibilities of **1** may be estimated by the formula:

$$\chi_m = \alpha \exp\left(-\frac{\Delta}{k_b T}\right)\left(\frac{1}{T}\right) + \frac{C}{T} + \chi_0, \quad (1)$$

where α is a constant value corresponding to the dispersion of the excitation energy, Δ is the magnitude of the spin gap, χ_0 contributes from the core diamagnetism and the possible Van Vleck paramagnetism, and the other symbols have their usual meanings [29]. The best fit curves are shown in Fig. 5, and the corresponding parameters are given as follows: $\alpha = 1.28$, $\Delta/k_b = 494.97$ K, $\chi_0 = -5.3 \times 10^{-4}$ emu mol^{-1}, $C = 3.7 \times 10^{-3}$ emu K mol^{-1} and $R = 2.2 \times 10^{-5}$ (R is defined as $\Sigma(\chi_m^{calcd} - \chi_m^{obsd})^2/(\chi_m^{obsd})^2$). The value of the parameter $2\Delta/k_b T_c$ (T_c is the transition temperature) is estimated to be 7.84 on the basis of the above results, which is higher than the ideal value of 3.53 derived from the BCS formula in a weak coupling regime. These results suggest that the short-range magnetic correlations within a chain are not fully developed and intrinsic magneto elastic instability of a 1D system cannot be considered as a driving force for this transition; that is, the transition is not a pure spin-Peierls transition [18]. The origins of the phase transition for **1** is attributed to cooperative interactions of Ni···S bonding, interplane repulsion of the $[Ni(mnt)_2]^-$ anions, π···π stacking interactions between of adjacent cations, spin–lattice interactions and spin–spin coupled interaction between nearest-neighbor anions [30–32].

Complex **2** is expected to be diamagnetic on account of the dimerized structure.

3.5. Thermodynamic properties

To obtain additional information about the thermodynamic properties of the observed phase transition of **1**, DSC measurements on **1** were performed. The power-compensated DSC traces for **1** from 98 to 293 K at a warming rate of 20 K min^{-1} are displayed in Fig. 6. For **1**, an abruptly endothermic peak in the

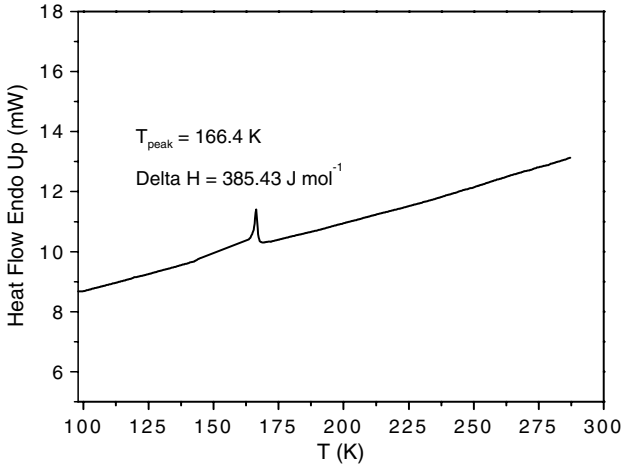


Fig. 6. DSC plot for **1**.

DSC trace is observed, and the phase transition temperature determined from thermal analysis is 166.4 K, close to the value measured from magnetic susceptibility measurements. The endothermic enthalpy change ($\Delta H = 385.43\ \mathrm{J\ mol^{-1}}$) was estimated from the peak area. Therefore, the result of thermal analysis of **1** further confirms that the magnetic phase transition observed is first-order [33,34]. According to the equation $\Delta S = \Delta H/T_c$ and ΔH estimated above, the estimated entropy change from DSC experiments is $2.31\ \mathrm{J\ mol^{-1}}$, which is much less than the magnetic transition entropy ($5.76\ \mathrm{J\ mol^{-1}\ K}$) calculated according to $\Delta S = R\ln[(2S_{HT}+1)/(2S_{LT}+1)$, This is expected from the short-range order effects between nearest-neighbor spins in the HT phase [35].

4. Conclusion

Here, we have reported the syntheses, spectra, crystal structures and magnetic properties of two new ion-pair complexes containing the $M(mnt)_2^-$ anion (M = Ni, Pt). The $Ni(mnt)_2^-$ anions and cations of complex **1** form completely segregated stacking columns, and the Ni(III) ions of **1** forms a 1D zigzag chain with an interatomic Ni···Ni distance of 3.855 Å within a $Ni(mnt)_2^-$ column, while **2** is dimer. The measurement of the temperature dependence of the magnetic susceptibilities reveal that **1** undergoes a magnetic transition around 160 K and exhibits antiferromagnetic interactions in the high-temperature phase and spin gap systems in the low-temperature phase, while **2** is diamagnetic. The phase transition is first order for **1** as determined by DSC analyses. The different magnetic properties of **1** and **2** are associated with the different packing pattern of the $M(mnt)_2^-$ anion in these two complexes.

5. Supplementary materials

The crystallographic data for **1** and **2** have been deposited at the Cambridge Crystallographic Data Center as supplementary publication Nos. CCDC-242502 and 252467. Copies of the data may be obtained free of charge from The Director, CCDC, 12 Union Road, Cambridge, CB2 1EZ, UK (fax: +44 1223 336033; deposit@ccdc.cam.ac.uk or www: http://www.ccdc.cam.ac.uk).

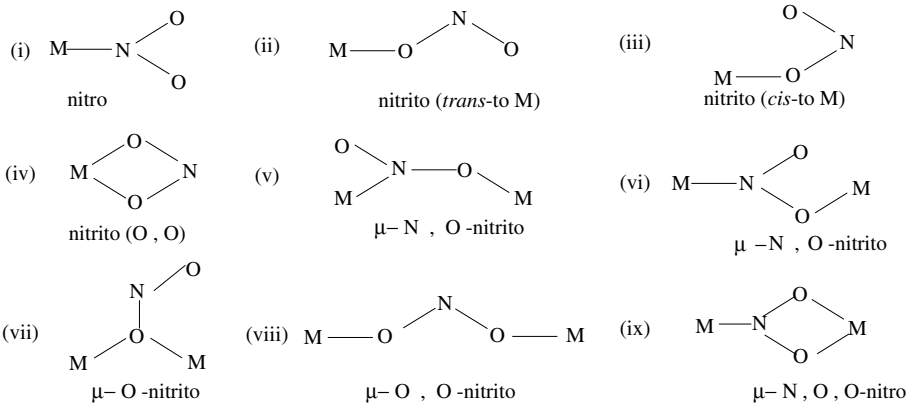
Acknowledgments

The authors thank for financial support from the National Natural Science Foundation (Nos. 20171022, 20490210). The Center of Analysis and Determination of Nanjing University are acknowledged.

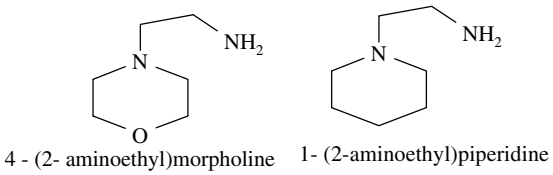
References

[1] N. Robertson, L. Cronin, Coord. Chem. Rev. 227 (2002) 93.
[2] J. Dai, G.Q. Bian, X. Wang, Q.F. Xu, M.Y. Zhou, M. Munakata, M. Maekawa, M.H. Tong, Z.R. Sun, H.P. Zeng, J. Am. Chem. Soc. 122 (2002) 11007.
[3] T. Akutagawa, S. Nishihara, N. Takamatsu, T. Hasegawa, T. Nakamura, T. Inabe, J. Phys. Chem. B 104 (2000) 5871.
[4] A.E. Pullen, C. Faulmann, K.I. Pokhodnya, P. Cassoux, M. Tokumoto, Inorg. Chem. 37 (1998) 6714.
[5] J. Nishijo, E. Ogura, J. Yamaura, A. Miyazaki, T. Enoki, T. Takano, Y. Kuwatani, M. Iyoda, Solid State Commun. 116 (2000) 661.
[6] M. Urichi, K. Yakushi, Y. Yamashita, J. Qin, J. Mater. Chem. 8 (1998) 141.
[7] P.I. Clemenson, A.E. Underhill, M.B. Hursthouse, R.L. Short, J. Chem. Soc., Dalton Trans. (1988) 1689.
[8] J.F. Weiher, L.R. Melby, R.E. Benson, J. Am. Chem. Soc. 86 (1964) 4329.
[9] N. Robertson, C. bergemann, H. Becher, P. Agarwal, S.R. Julian, R.H. Friend, N.J. Hatton, A.E. Underhill, A. Kobayashi, J. Mater. Chem. 9 (1999) 1713.
[10] J. Nishijo, E. Ogura, J. Yamaura, A. Miyazaki, T. Enoki, T. Takano, Y. Kuwatani, M. Iyoda, Synth. Met. 133–134 (2003) 539.
[11] J.L. Xie, X.M. Ren, Y. Song, W.J. Tong, C.S. Lu, Y.G. Yao, Q.J. Meng, Inorg. Chem. Commun. 5 (2002) 395.
[12] A.T. Coomber, D. Beljonne, R.H. Friend, J.L. Brédas, A. Charlton, N. Robertson, A.E. Underhill, M. Kurmoo, P. Day, Nature 380 (1996) 144.
[13] J.L. Xie, X.M. Ren, Y. Song, Y. Zou, Q.J. Meng, J. Chem. Soc., Dalton Trans. (2002) 2868.
[14] J.L. Xie, X.M. Ren, Y. Song, W.W. Zhang, W.L. Liu, C. He, Q.J. Meng, Chem. Commun. (2002) 2346.
[15] J.L. Xie, X.M. Ren, S. Gao, W.W. Zhang, Y.Z. Li, C.S. Lu, C.L. Ni, W.L. Liu, Q.J. Meng, Y.G. Yao, Eur. J. Inorg. Chem. (2003) 2393.
[16] J.L. Xie, X.M. Ren, C. He, Y. Song, Q.J. Meng, R.K. Kremer, Y.G. Yao, Chem. Phys. Lett. 369 (2003) 41.
[17] X.M. Ren, Q.J. Meng, Y. Song, C.L. Lu, C.J. Hu, X.Y. Chen, Z.L. Xue, Inorg. Chem. 41 (2002) 5931.
[18] X.M. Ren, Q.J. Meng, Y. Song, C.S. Lu, C.J. Hu, Inorg. Chem. 41 (2002) 5686.
[19] S.B. Bulgarevich, D.V. Bren, D.Y. Movshovic, P. Finocchiaro, S. Failla, J. Mol. Struct. 317 (1994) 147.
[20] A. Davison, R.H. Holm, Inorg. Synth. 10 (1967) 8.
[21] SHELXTL, Version 5.10. Structure Determination Software Programs, Bruker Analytical X-ray Systems Inc. Madison, WI, USA, 1997.
[22] K. Brunn, H. Endres, J. Weiss, Z. Naturforsch. 42B (1987) 1222.
[23] S.I. Shupack, E. Billig, R.J.H. Clark, R. Williams, H.B. Gray, J. Am. Chem. Soc. 86 (1964) 4594.
[24] C. Rovira, Chem. Eur. J. 6 (2000) 1723.
[25] Y. Fujii, T. Goto, W. Fujita, K. Awaga, Physica B 329–333 (2003) 973.
[26] C. Yasuda, S. Todo, M. Matsumoto, H. Takayama, J. Phys. Chem. Solids 63 (2002) 1607.
[27] S. Nishihara, T. Akutagawa, T. Hasegawa, T. Nakamura, Chem. Commun. (2002) 408.
[28] S. Nishihara, T. Akutagawa, T. Hasegawa, S. Fujiyama, T. Nakamura, J. Solid State Chem. 168 (2002) 661.
[29] L.C. Isett, D.M. Rosso, G.L. Bottger, Phys. Rev. B 22 (1980) 4739.
[30] S. Alvarez, R. Vicente, R. Hoffman, J. Am. Chem. Soc. 107 (1985) 6253.
[31] E. Pytte, Phys. Rev. B 10 (1974) 4637.

[32] M.E. Itkis, X. Chi, A.W. Cordes, R.C. Haddon, Science 296 (2002) 1443.
[33] L. Hatta, S. Nakayama, Thermochim. Acta 318 (1998) 21.
[34] T. Tang, K.M. Gu, Q.q. Cao, D.H. Wang, S.Y. Zhang, Y.W. Du, J. Magn. Magn. Mater. 222 (2002) 110.
[35] R.L. Carlin, Magnetochemistry, Spring, Berlin, 1989.



Scheme 1. Nine possible modes of nitrite ion coordination to metal.



Scheme 2. Molecular structures of the ligands.

as the monodentate nitrito linkage isomers in the solid state. Therefore, the steric and electronic factors of the co-ligand may impart interesting findings in nitrite coordination. For the present study we have chosen 4-(2-aminoethyl)morpholine (Scheme 2) as the co-ligand, which should exert nearly equal steric and electronic effects in comparison with 1-(2-aminoethyl)piperidine (Scheme 2), with the view to obtain some interesting results. We report herein the synthesis and characterization of nitro and nitrito complexes of nickel (II) of 4-(2-aminoethyl)morpholine and the X-ray single crystal structure analysis of the nitro species.

2. Experimental

2.1. Materials

4-(2-Aminoethyl)morpholine was purchased from Aldrich Chemical Company Inc. and used as received. Potassium hexanitronickelate (II) monohydrate was prepared using a standard method [6b]. All other chemicals used were of AR grade.

2.2. Physical measurements

Elemental analyses (carbon, hydrogen and nitrogen) were performed using a Perkin–Elmer 240C elemental analyzer; the nickel (II) content was estimated gravimetrically [12]. The IR spectrum (4000–400 cm^{-1}) was taken at 27 °C using a SHIMADZU FTIR-8400S and KBr was used as the medium. The electronic spectrum (1400–200 nm) was obtained at 27 °C using a SHIMADZU UV-3101PC, and Nujol was used as a medium as well as a reference. The magnetic susceptibility was measured at 27 °C using an EG and G PAR 155 vibrating sample magnetometer, and $Hg[Co(SCN)_4]$ was used as a reference material; diamagnetic corrections were made using Pascal's constants [13]. Molar conductances were measured using a Systronic 304 conductivity meter, where the cell constant was calibrated with 0.02 M KCl solution and dry dichloromethane was used as the solvent.

2.3. Synthesis of the complexes

The nitro $[NiL_2(NO_2)_2]$ (**1a**) and nitrito $[NiL_2(ONO)_2]$ (**1b**) complexes were synthesized by adding the ligand L (2 mmol) in methanol (5 mL) dropwise to a methanolic suspension (10 mL) of potassium hexanitronickelate (II) monohydrate (1 mmol) with vigorous stirring. Initially a clear green solution was formed, but within a few minutes a blue-violet precipitate also appeared. After 1 h of stirring the mixture was filtered and the green colored filtrate part was kept in a $CaCl_2$ desiccator. After a few days, brown-colored crystals (**1a**) separated out from the green solution. Yield 65%. *Anal.* Calc. for $C_{12}H_{28}N_6O_6Ni$: C, 38.0; H, 7.4; N, 22.2; Ni, 15.5. Found: C, 38.0; H, 7.3; N, 22.1; Ni, 15.6%. $\mu_{eff} = 3.2$ μ_M. λ_{max}(Nujol) = 1264, 1182, 535, 371 nm. The blue-violet precipitate part was dissolved in excess methanol, and the resulting green colored solution was kept in a $CaCl_2$ desiccator. After a few days a blue-violet species was deposited at the sidewalls of the beaker and brown crystals were formed at the bottom of the beaker. After crystallization of the blue-violet species, complex **1b** was isolated in pure form. Yield: 25%. *Anal.* Calc. for $C_{12}H_{28}N_6O_6Ni$: C, 38.0; H, 7.4; N, 22.2; Ni, 15.5%. Found: C, 38.1; H, 7.3; N, 22.0; Ni, 15.4%. $\mu_{eff} = 3.2$ μ_M. λ_{max}(Nujol) = 1255, 1192, 588, 412 nm.

2.4. X-ray data collection and structure determination

A single crystal suitable for X-ray data collection was mounted on Bruker SMART CCD diffractometer equipped with a graphite monochromated Mo Kα ($\lambda = 0.71073$ Å) radiation source. The program SMART [14] was used for collecting frames of data, indexing reflection and determination of lattice parameters, SAINT [14] for integration of the intensity of reflections and scaling, and SADABS [15] for absorption correction. A total 2977 reflections were measured and 2366 were assumed observed applying the condition $I > 2\sigma(I)$. The structure was solved by direct methods using the SHELXS-97 [16] computer program and refined by full-matrix least squares methods on F^2, using the SHELXL-97 [17] program with anisotropic displacement parameters for all non-hydrogen atoms. Selected crystallographic data and refinement details are displayed in Table 1. Selected bond lengths and angles are given in Table 2.

3. Results and discussion

When a methanolic solution of L was added to a methanolic suspension of potassium hexanitronickelate (II) monohydrate, a blue-violet precipitate was formed within a few minutes, during the stirring. On filtration a green colored solution was obtained which on keeping yielded complex **1a**. After repeated crystallization of the blue-violet species, complex **1b** was obtained in the pure form. Complex **1a** was the major and thermodynamically controlled product, whereas complex **1b** was the minor and kinetically controlled product. The composition of the complexes **1a** (brown) and **1b** (blue-violet) have been assigned as $NiL_2(NO_2)_2$ on the basis of elemental analyses. Magnetic susceptibility measurements of **1a** and **1b** reveal that nickel (II) is in an octahedral configuration in both complexes and electronic spectral data of the complexes suggest that they have octahedral geometry around the nickel (II) centre. IR spectral studies are observed to be immensely helpful to elucidate the binding mode of the nitrite ion in its complexes. The three fundamental vibrational modes of the nitrite group (C_{2v} symmetry) are all IR active and the band positions are shifted upon coordination. The brown species **1a** exhibits IR bands at 1333, 1310 and 808 cm^{-1} assigned to $\nu_{as}(NO_2)$, $\nu_s(NO_2)$ and $\delta(NO_2)$, respectively. Both $\nu_{as}(NO_2)$ and $\nu_s(NO_2)$ are shifted to higher frequencies as compared to the free nitrite ion (1329 and 1264 cm^{-1}) suggesting that the nitrite ion is coordinated via the N atom [2,11a]. The blue-violet species **1b** shows two sets of bands for $\nu_{as}(NO_2)$ (1365 and 1331 cm^{-1}) and $\nu_s(NO_2)$ (1318 and 1304 cm^{-1}) in its IR spectrum. The complex **1b** may be either the monodentate nitrito species or the nitrito(O,O) species. Generally, nitrito species exhibit $\nu_{as}(NO_2)$ at a higher frequency (observed for **1b**) and $\nu_s(NO_2)$ at a lower frequency (not observed for **1b**) than the free nitrite ion frequencies [11a,18]. On the other hand, nitrito(O,O) species show a lowering of

Table 1
Crystal data and structure refinement of complex **1a**

Empirical formula	$C_{12}H_{28}N_6NiO_6$
Formula weight	411.09
T (K)	293
Mo Kα	0.71073
Crystal system	triclinic
Space group	$P\bar{1}$
a (Å)	7.1761(16)
b (Å)	8.0904(18)
c (Å)	8.3814(19)
α (°)	94.116(3)
β (°)	112.337(2)
γ (°)	101.296(3)
V (Å^3)	435.60(17)
Z	1
D_{calc} (Mg m^{-3})	1.567
$F(000)$	218
μ (mm^{-1})	1.2
θ Range (°)	2.6–28.4
Reflection collected	2977
Independent reflection	2420
Reflection observed	2366 [$I > 2\sigma(I)$]
Goodness of-fit on F^2	1.07
R_{int}	0.013
R	0.0273
wR	0.0698

$w = 1/[\sigma^2(F_o^2) + (0.0469P)^2 + 0.0177P]$, where $P = (F_o^2 + 2F_c^2)/3$.

Table 2
Selected bond lengths (Å) and bond angles (°) of complex **1a**

Ni1–N1	2.069(3)
Ni1–N2	2.336(3)
Ni1–N3	2.032(4)
Ni1–N4	2.372(3)
Ni1–N5	2.135(3)
Ni1–N6	2.101(4)
O1–N5	1.197(5)
O2–N5	1.218(5)
O3–N6	1.276(6)
O4–N6	1.258(5)
N1–Ni1–N2	80.23(12)
N1–Ni1–N3	177.72(14)
N1–Ni1–N4	99.00(13)
N1–Ni1–N5	89.71(13)
N1–Ni1–N6	90.07(15)
N2–Ni1–N3	97.50(12)
N2–Ni1–N4	179.20(13)
N2–Ni1–N5	93.48(12)
N2–Ni1–N6	87.79(14)
N3–Ni1–N4	83.28(13)
N3–Ni1–N5	90.32(14)
N3–Ni1–N6	89.95(15)
N4–Ni1–N5	86.70(13)
N4–Ni1–N6	92.02(14)
N5–Ni1–N6	178.65(15)
O3–N6–O4	114.1(4)
O1–N5–O2	120.3(4)

both $\nu_{as}(NO_2)$ and $\nu_s(NO_2)$ in comparison to free ion frequencies. Therefore, from the IR spectrum of **1b** it is difficult to assign the coordination mode of the nitrite ion in it. Now the electronic spectral and electrolytic conductance studies may impart some light on the mode of nitrite ion coordination especially in **1b**. Electronic spectral data indicate that both **1a** and **1b** possess octahedral geometry around nickel (II) and since they exhibit further splitting in the d–d band in the near-IR region they should have a *trans*-configuration [19]. The electrolytic conductance measurements in dichloromethane suggest that both **1a** and **1b** are non-conducting ($\Lambda_m = 7.1$ and 4.3 Ω^{-1} cm^2 mol^{-1} for **1a** and **1b**, respectively). Since **1b** shows non-electrolytic behavior in non-coordinating solvents like dichloromethane it should be a nitrito species not the nitrito(O,O) species. From the above results it may be assumed that both **1a** and **1b** possess a *trans*-octahedral geometry, and **1a** and **1b** are, respectively, the nitro and nitrito linkage isomers.

The ORTEP view of complex **1a** with the atom numbering scheme has been depicted in Fig. 1. The selected bond lengths and bond angles are shown in Table 2. The hydrogen bonding is presented in Table 3. The structure consists of a discrete $NiL_2(NO_2)_2$ molecule and the nickel atom occupies an inversion center. The coordination polyhedron around the metal atom may be best described as a distorted octahedron. The four nitrogen atoms of the diamine part of the ligands (N1, N2 and their centrosymmetrically related atoms) define the equatorial plane and the two nitrogen atoms belonging to the nitro groups (N5 and its centrosymmetric counter part) coordinate in *trans* axial positions. The Ni–N (amine) distances, ranging between 2.032(4) and 2.372(3) Å, are consistence with the corresponding values observed in similar systems. The discrepancy between the two Ni–N distances is a consequence of the steric constraints imposed by the bulky morpholine group. The crystal packing diagram of **1a**, done by using program PLATON99 [20], is shown in Fig. 2 which reveals a two dimensional infinite chain structure through a hydrogen bonding network.

Table 3
H-bonding list for complex **1a**

D–H···A	D–H	H···A	D···A	∠D–H···A
N1–H1A···O1[a]	0.9001	2.4179	2.869(5)	111.22
N1–H1A···O3[a]	0.9001	2.2971	3.008(6)	135.77
N1–H1B···O4[b]	0.9002	2.4179	2.979(5)	120.67
N1–H1B···O5[b]	0.9002	2.3680	3.164(5)	147.41
N3–H3A···O2[c]	0.8998	2.4347	2.973(5)	118.63
N3–H3A···O6[c]	0.8998	2.4024	3.187(5)	145.74
N3–H3B···O1[d]	0.9005	2.3904	3.085(6)	134.05
N3–H3B···O3[d]	0.9005	2.4847	2.952(6)	112.73
C3–H3D···O3[e]	0.9700	2.4708	3.398(6)	159.89
C4–H4B···N5[e]	0.9709	2.6131	3.198(6)	118.94
C5–H5B···O4[e]	0.9705	2.5920	3.330(5)	132.94
C9–H9A···O1[f]	0.9700	2.5503	3.503(6)	167.43
C10–H10A···N6[f]	0.9693	2.5664	3.155(7)	119.22

[a] Symmetry codes: $1 + x, y, z$.
[b] Symmetry codes: $x, y, -1 + z$.
[c] Symmetry codes: $x, y, 1 + z$.
[d] Symmetry codes: $-1 + x, y, z$.
[e] Symmetry codes: $1 + x, y, 1 + z$.
[f] Symmetry codes: $-1 + x, y, -1 + z$.

The proposition made regarding the structure of complex **1a** and the coordination mode of the nitrite ions in it by routine physicochemical techniques have been established unambiguously through the X-ray single crystal structure analysis of **1a**. Our efforts to synthesize single crystals of **1b** yielded no results. However, routine physicochemical studies suggest that **1b** should be a monodentate nitrito species with a *trans*-octahedral

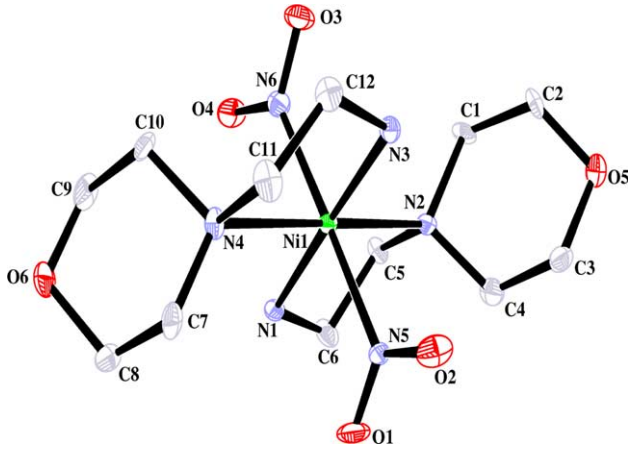


Fig. 1. ORTEP [21] diagram of *trans*-$[NiL_2(NO_2)_2]$ (**1a**) [L = 4-(2-aminoethyl)morpholine] with the atom numbering scheme. Ellipsoids are drawn at 50% probability.

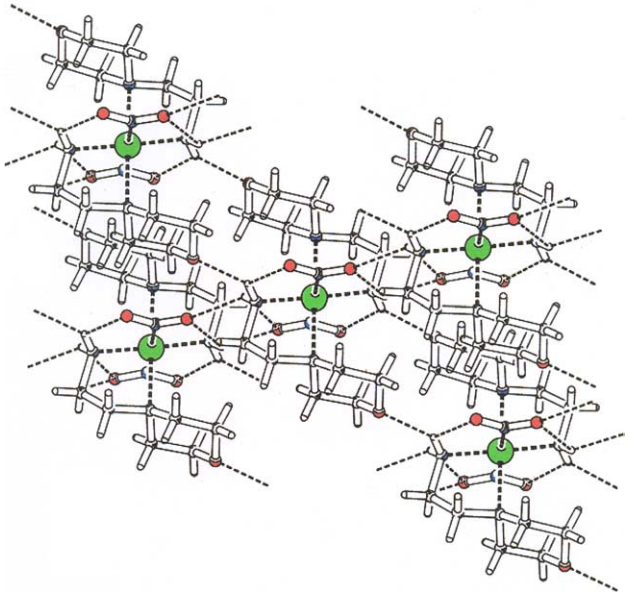


Fig. 2. Crystal packing diagram of *trans*-$[NiL_2(NO_2)_2]$ (**1a**) [L = 4-(2-aminoethyl)morpholine] and H-bonds (-----) in the crystal structure.

configuration. Therefore, the bulkiness of the morpholine moiety in the ligand 4-(2-aminoethyl)morpholine is just the optimum to stabilize both the nitro and nitrito isomers in the solid state as we observed earlier only in one case with the ligand 1-(2-aminoethyl)piperidine.

Acknowledgments

The authors thank the Council of Scientific and Industrial Research, New Delhi (Grant to D.D. & A.M; Project No. 01(1871)/03/EMR-II dated 17/03/2003) for financial support. We (D.D. & A.M.) also thank the Department of Science and Technology (DST), New Delhi for providing FTIR and UV–VIS–NIR spectrophotometers and the networking facility through the DST-FIST program.

Appendix A. Supplementary data

Supplementary data are available from the Cambridge Crystallographic Data Centre, 12, Union Road, Cambridge CB2 1EZ, UK (fax: +44-1223-336033; e-mail: deposit@ccdc.cam.ac.uk) on request, quoting the deposition number CCDC 264274. Supplementary data associated with this article can be found, in the online version, at doi:10.1016/j.poly.2005.04.039.

References

[1] S.M. Jorgensen, Z. Anorg. Chem. 5 (1894) 168.
[2] K. Nakamoto, J. Fujita, H. Murta, J. Am. Chem. Soc. 80 (1958) 4817.
[3] M.G.B. Drew, D.M.L. Goodgame, M.A. Hitchman, D. Rogers, Proc. Chem. Soc. (1964) 363.
[4] M.A. Porai-koshits, L.K. Minacheva, J. Struc. Chem. (Engl. Transl.) 5 (1964) 595.
[5] (a) D.M.L. Goodgame, M.A. Hitchman, Inorg. Chem. 3 (1964) 1389;
(b) D.M.L. Goodgame, M.A. Hitchman, Inorg. Chem. 4 (1965) 721;
(c) D.M.L. Goodgame, M.A. Hitchman, Inorg. Chem. 6 (1966) 1303.
[6] (a) R.W. Green, J. Chem. Soc., Chem. Commun. (1969) 1463;
(b) R.W. Green, B. Bell, Aust. J. Chem. 26 (1973) 1663.
[7] A.E. Shvelashvili, L.P. Sarishvili, R.M. Vashaidze, Russ.J. Inorg. Chem. 19 (1974) 307.
[8] M.J. Goldberg, R.E. Marsh, Acta Crystallogr., Sect. B 35 (1979) 960.
[9] A.J. Finney, M.A. Hitchman, C.L. Raston, G.L. Rowbottom, A.H. White, Aust. J. Chem. 34 (1981) 2047, 2069, 2085, 2125, 2141 and 2163.
[10] M.A. Hitchman, G.L. Rowbottom, Coord. Chem. Rev. 42 (1982) 55.
[11] (a) D. Das, I.R. Laskar, A. Ghosh, A. Mondal, K. Okamoto, N. Ray Chaudhuri, J. Chem. Soc., Dalton Trans. (1998) 3979;
(b) I.R. Laskar, G. Mostafa, D. Das, K. Okamoto, N. Ray Chaudhuri, Acta Cryst. C55 (1999) 1994;
(c) I.R. Laskar, A. Ghosh, G. Mostafa, D. Das, A. Mondal, N. Ray Chaudhuri, Polyhedron 19 (2000) 1015;
(d) I.R. Laskar, D. Das, G. Mostafa, T.H. Lu, T.C. Keng, J.C. Wang, A. Ghosh, N. Ray Chaudhuri, New J. Chem. 25 (2001) 764.
[12] A.I. Vogel, A Text Book of Quantitative Inorganic Analysis, fourth ed., Longman, New York, 1978.
[13] B.N. Figgis, J. Lewis, in: J. Lewis, R.C. Wilkins (Eds.), Modern Coordination Chemistry, fourth ed., Interscience, New York, 1960, p. 403.
[14] SMART and SAINT Software Reference Manuals, Version 6.22, Bruker AXS Analytic X-Ray Systems, Inc., Madison, WI, 2000.
[15] G.M. Sheldrick, SADABS, Software for Empirical Absorption Correction, University of Gottingen, Germany, 2000.
[16] G.M. Sheldrick, SHELXS-97, Program for Solution of Crystal Structure, University of Gottingen, Germany, 1997.
[17] G.M. Sheldrick, SHELXL-97, Program for Solution of Crystal Structure, University of Gottingen, Germany, 1997.
[18] K. Nakamoto, Infrared Spectra of Inorganic and Coodination Compounds, Wiley, New York, 1977, p. 223.
[19] A.B.P. Lever, Inorganic Electronic Spectroscopy, second ed., Elsevier, Amsterdam, 1984, p. 507.
[20] A.L. Spek, PLATON, Molecular Geometry Program, University of Utrecht, The Netherlands, 1999.
[21] C.K. Johnson, ORTEP, III Report ORNL – 5138, Oak Ridge National Laboratory, Oak Ridge, TN, USA.

spectrophoto-meter. ^{1}H NMR, ^{13}C NMR and ^{27}Al NMR spectra were recorded in $CDCl_3$ using a 500 MHz Bruker instrument.

All solvents and reagents used in the synthesis were of reagent grade quality. The solvents used for spectroscopic work were purified and distilled prior to use. Pyrrole, benzaldehyde, 4-methoxy benzaldehyde, 3,4-dimethoxy benzaldehyde, sodium sulfate, lithium hydroxide monohydrate, hexamethylenetetramine, trifluoroacetic acid, 3,4,5,6-tetrachloro-1,2-benzoquinone (*p*-chloranil), BF_3 etherate, 2,3-dichloro-5,6-dicyano-1,4-benzoquinone (DDQ), 1,2-bis(2-chloroethoxy)ethane, barium chlorate monohydrate, magnesium nitrate hexahydrate, aluminum nitrate nonahydrate, sodium perchlorate monohydrate, calcium nitrate tetrahydrate, ammonium hexafluorophosphate, dichloromethane, chloroform, methanol, *n*-hexane and acetonitrile were purchased from Merck. Iron (II) chloride tetrahydrate, zinc acetate dihydrate, potassium perchlorate, *N*,*N*-dimethylformamide (DMF) and alumina for chromatography were obtained from Fluka.

2.2. Synthesis of porphyrins and crown ether appended porphyrins

2.2.1. 5,10,15,20-Tetraphenylporphyrin, $TPPH_2$, and 5,10,15,20-tetrakis(3,4-dimethoxyphenyl)porphyrin, $TDMPPH_2$ (1)

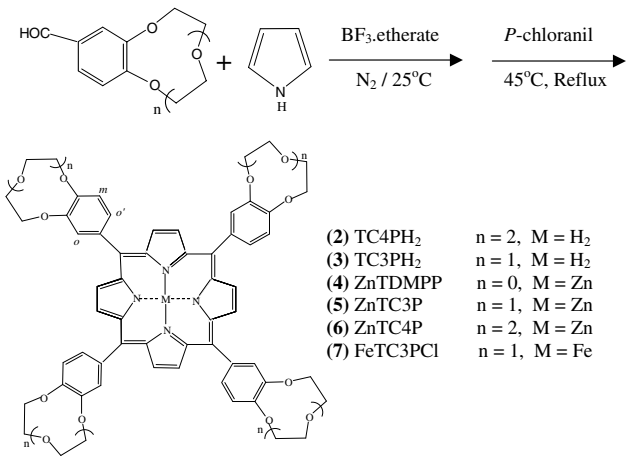
$TPPH_2$ and $TDMPPH_2$ (**1**) were synthesized by Lindsey's method [6] using benzaldehyde and 3,4-dimethoxy benzaldehyde, respectively. The yields were 47% for $TPPH_2$ and 45% for $TDMPPH_2$.

2.2.2. 5,10,15,20-tetrakis(benzo-12-crown-4)porphyrin, $TC4PH_2$ (2), and 5,10,15,20-tetrakis(benzo-9-crown-3)-porphyrin, $TC3PH_2$ (3)

4-Formyl benzo-12-crown-4 and 4-formyl benzo-9-crown-3 were synthesized and purified by literature methods [7]. The compounds (**2**) and (**3**) were synthesized by a modification of Lindsey's method. Correspondingly benzaldehyde (1.5×10^{-2} mol) and pyrrole (1.5×10^{-2} mol) were dissolved in dichloromethane (1 L) and $BF_3 \cdot OEt_3$ (10^{-3} mol) was added to this solution. The mixture was stirred at room temperature for 15 min in the dark and then *p*-chloranil (0.011 mol) was added and refluxed for 1 h. Then the solvent was removed under reduced pressure and the crude material was chromatographed on a basic alumina column eluted with chloroform. The first purple cut, the crown-appended porphyrin, was collected. Further purification was achieved by recrystallization of these compounds in chloroform/methanol solution. The yields were 37% for (**2**) and 35% for (**3**).

2.2.3. Metallation of free base porphyrins

The metallation reactions of (**1**), (**2**) and (**3**) with Zn^{2+} and Fe^{3+} ions were performed using an established procedure [8]. The progress of these reactions was monitored by UV–Vis spectrophotometry and the isolated products were chromatographed on a neutral alumina column to yield 80–85% of (**4**), (**5**), (**6**) and (**7**) (Scheme 1). Compound (**8**), which is an iron μ-oxo dimer of (**7**), was prepared by dissolving 500 mg of compound (**7**) in 50 ml toluene. This was refluxed in the presence of a few pellets of KOH for 2 h. Removal of the solvent gave the crude product, which was loaded onto an alumina column and then eluted with dichloromethane to obtain the pure product.



Scheme 1.

3. Results and discussion

3.1. Synthesis of $TDMPPH_2$ (1), $TC4PH_2$ (2) and $TC3PH_2$ (3)

The above compounds were synthesized according to Lindsey's method [6] in 47–35% yields. The preparation method is shown in Scheme 1. The yields of the crown-appended porphyrins were found to be reduced by around 10% relative to tetraphenylporphyrins. UV–Vis measurement of the soret bands suggests that before chromatography the compounds (**1**), (**2**) and (**3**) were formed in similar yields. Thus relatively significant amounts of crown porphyrins were lost during chromatography. $TDMPPH_2$ (**1**), has a similar structure to (**2**) and (**3**) with regard to substitution in the phenyl rings of the porphyrin macrocycle. So, compound (**1**) can be used in analogy with crown-appended porphyrins, for spectroscopic characterization and chemical investigation. IR spectra of (**2**) and (**3**) have shown new signals at 1250–1290 s, which are absent in (**1**) and were assigned to ν_{c-o} in the crown rings.

3.2. UV–Vis spectral studies

UV–Vis data for compounds (**1**–**8**) have been collected in Table 1. The $TC4PH_2$ (**2**) spectrum resembled

Table 1
UV–Vis spectroscopic data in $CHCl_3$ at room temperature for the porphyrin compounds

Compound	λ_{max} (nm)	
	Soret band (log ε)	Q bands (log ε)
$TPPH_2$	418(5.60)	516(4.27), 550(3.90), 590(3.72), 646(3.53)
(**1**) $TDMPPH_2$	424(5.51)	520(4.38), 556(4.29), 594(4.02), 650(4.03)
(**2**) $TC4PH_2$	423(5.56)	517(4.20), 555(3.98), 592(3.78), 647(3.64)
(**3**) $TC3PH_2$	421(5.41)	516(4.15), 554(3.93), 592(3.77), 647(3.61)
(**4**) ZnTDMPP	430(5.71)	556(4.43), 602(3.95)
(**5**) ZnTC3P	426(5.33)	559(3.99), 597(3.69)
(**6**) ZnTC4P	425	550, 589
(**7**) FeTC3PCl	421	511, 580
(**8**) $(FeTC3P)_2O$	418(5.34)	570(4.32), 620(4.13)

that for $TDMPPH_2$ (**1**), having soret bands at 423 and 424 nm, respectively. The substitution of two mesityl groups on each phenyl ring of the porphyrin macrocycle in (**1**) results in a 6 nm red shift in its soret band in comparison with $TPPH_2$. π-Donation of the meso aryl groups to the porphyrin macrocycle is strengthened by the OCH_3/OCH_2 π-donation and results in red shifts for compounds (**1**) and (**2**) [9]. The lower red shift for compound (**3**) compared to compound (**4**) may indicate less efficient conjugation of the lone pair electrons of the two oxygen atoms that are directly attached to the phenyl rings, and therefore less effective π-donation to the porphyrin macrocycle [10]. This lower red shift in (**3**) might be interpreted by the lesser electron-donating ability of the nine-membered crown ring as compared to (**1**) and (**4**). This could be the result of the restricted orientation of attached oxygen atoms to the phenyl rings in (**3**) that results from the rigid nine-membered crown ring cavity [11].

UV–Vis spectroscopy is a strong tool for following the metallation of the porphyrins. Generally, both the position and number of bands would change upon metallation. The disappearance of four Q-bands in the free base porphyrin and the appearance of two new Q-bands in the metalloprphyrins [12] confirm preparations of the metallated products (**4**–**8**).

3.3. NMR spectral studies

^1H NMR spectra of compounds (**1**) and (**3**) are shown in trace A and B of Fig. 1. The eight multiplets

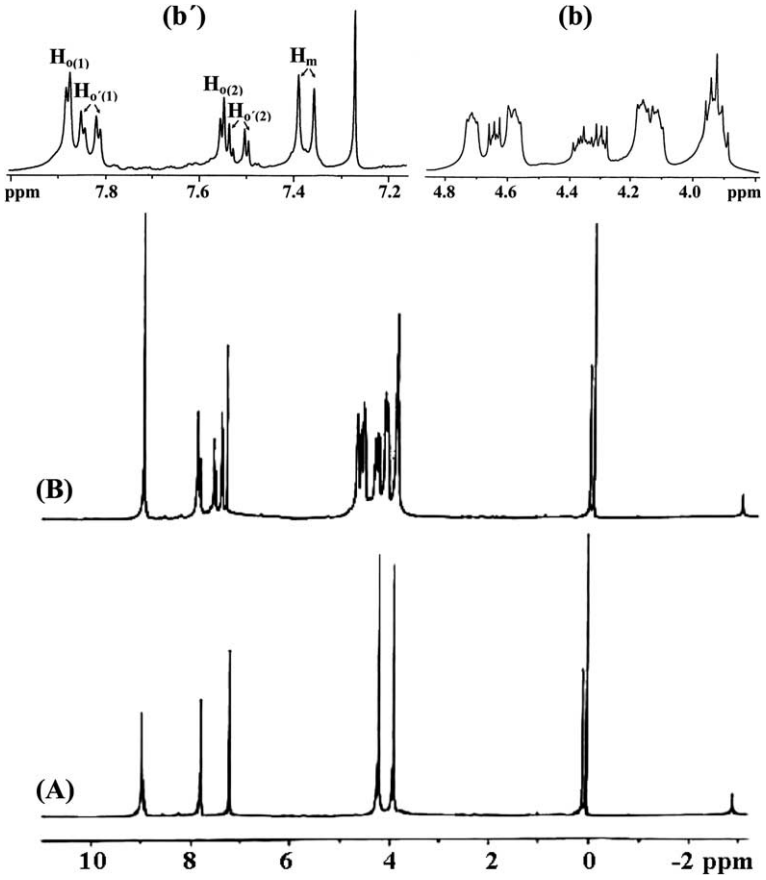
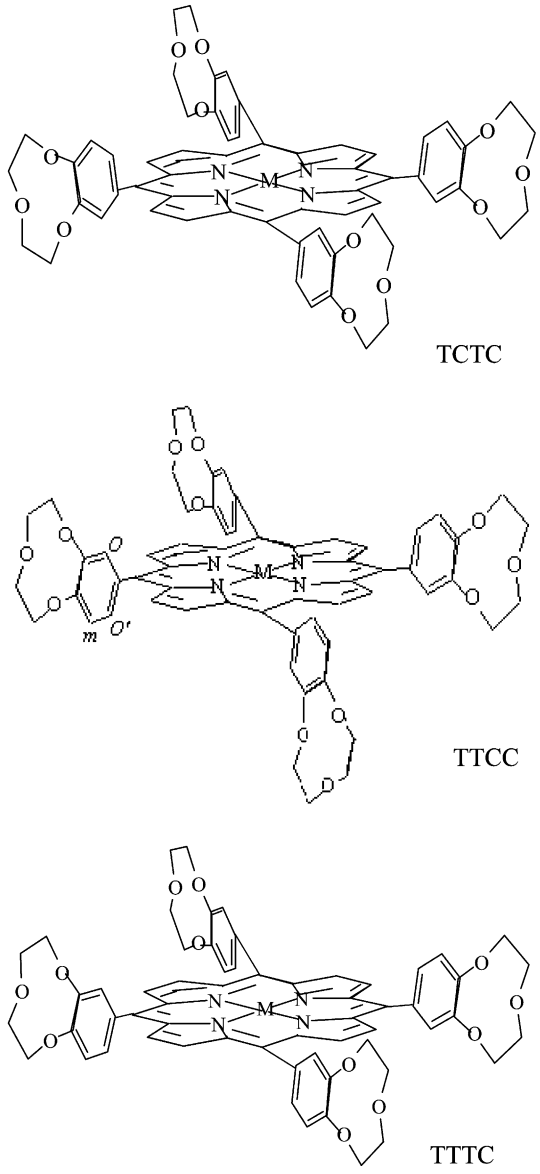


Fig. 1. 500 MHz ^1H NMR spectra of $TDMPPH_2$ (A) and $TC3PH_2$ (B) in $CDCl_3$ at room temperature. The expanded 3.8–4.8 ppm (b) and 7.2–8.0 ppm (b′) regions of the $TC3PH_2$ ^1H NMR spectrum.

in the 3.9–4.7 ppm region correspond to the four methylene hydrogen atoms of the crown cavities. The number of peaks and the pattern of the splitting is more complicated to interpret compared to the expected four triplets, and this confirms different structural isomers. A similar pattern has been observed for the ortho hydrogens atoms of the phenyl rings. The aromatic region of the benzo-9-crown-3 moiety in the ^{1}H NMR spectrum in Fig. 1 (b′ trace), clearly shows two sets of d,d and dd peaks with very close *J*-values. $H_{o'}$(**1**) and $H_{o'}$(**2**) correspond to one stereoisomer while H_o(**1**) and H_o(**2**) indicate the existence of a second. A single doublet H_m peak is shared for both isomers. Therefore, the splitting pattern of the benzo-9-crown-3 aromatic hydrogens clearly confirms the existence of two distinct atropoisomers for this compound (Scheme 2).



Scheme 2.

The ^{13}C NMR spectrum of (**3**), Fig. 2, comparing to $TPPH_2$ shows new signals which correspond to crown ether rings carbons. Signals at 148.5 and 150.3 ppm were assigned to phenyl C–O carbons and the signal at 136.7 ppm to the remaining quaternary carbon in the phenyl rings. Porphyrins carbons are spread out from 118–130 ppm, similar to $TPPH_2$, except that the ortho phenyl signals are sharper in the crown substituted porphyrin here. The most interesting signals in the ^{13}C NMR spectrum arise from carbons of the crown ether cavity which are spread out in the 70–75 ppm region. Ideally we would expect to see four different signals due to 4 methylene carbons in the crown ring of compound (**3**), whereas there are two sets of four different signals with an approximate ratio of 1:2. The NMR spectra indicate the presence of 2 of 3 stereoisomers for compound (**3**). Our attempt to separate these isomers failed. However, based on stability and statistics, we assume that these isomers are T–C–T–C (major) and T–T–C–C (minor). Other authors have reported only the T–C–T–C isomer with larger size crown-appended porphyrins [13].

The ^{1}H NMR of the Zn complex (**5**) compared to (**4**) is presented in Table 2. The same pattern of NMR signals is seen for both (**4**) and (**5**) as expected, and confirms the metallation of (**5**). Details of ^{1}H NMR data for compounds (**1**–**8**) are presented in Table 2. The ^{1}H NMR spectrum of FeTC3PCl (**7**), is presented in trace a of Fig. 3. The pattern of the ^{1}H NMR signals is similar to TPPFeCl [14]. The pyrrole hydrogen signals at 80 ppm at 25 °C in $CDCl_3$ confirm the high-spin iron (III) species. The

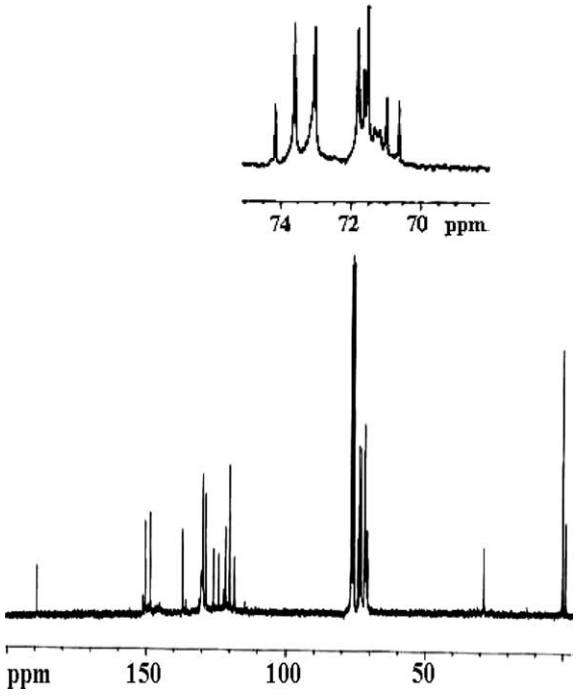


Fig. 2. 125 MHz ^{13}C NMR spectrum of $TC3PH_2$ in $CDCl_3$ at room temperature.

Table 2
^{1}H NMR spectroscopic data in $CHCl_3$ at room temperature for the porphyrin compounds

Compound	δ (ppm)					
	$H_{pyrrole}$	$H_{o,o'}$	H_m	H_{OMe}	H_{crown}	H_N
(**1**) $TDMPPH_2$	8.93 (s, 8H)	7.81 (s, 4H), 7.79 (d, 4H)	7.28 (d, 4H)	4.12, 3.80 (d, 24H)		−2.71 (s, 2H)
(**2**) $TC4PH_2$	8.89 (s, 8H)	[7.84 (d, 4H), 7.78 (dd, 4H)]$_1$ [7.56 (m, 4H)]$_2$	7.33 (d, 4H)		4.49–3.65 (m, 48H)	−2.81 (s, 2H)
(**3**) $TC3PH_2$	8.94 (s, 8H)	[7.87 (d, 4H), 7.83 (dd, 4H)]$_1$ [5.56 (d, 2H), 7.52 (dd, 2H)]$_2$	7.37 (d, 4H)		4.73–3.90 (m, 32H)	−2.80 (s, 2H)
(**4**) ZnTDMPP	9.01 (s, 8H)	7.78 (s, 4H), 7.75 (d, 4H)	7.25 (d, 4H)	4.10 (d, 24H)		
(**5**) ZnTC3P	8.83 (s, 8H)	7.53–7.64 (m, 12H)	7.35 (d, 4H)		4.23–3.49 (m, 32H)	
(**6**) ZnTC4P	8.98 (s, 8H)	7.64–7.67 (m, 12H)	7.30 (d, 4H)		4.25–3.65 (m, 48H)	
(**7**) FeTC3PCl	80.1 (s, 8H)	7.20–7.23 (m, 4H)	11.5 (d, 12H)		3.8–5.1 (m, 32H)	
(**8**) $(FeTC3P)_2O$	13.5 (s, 8H)	7.19–7.24 (m, 4H)	11.3 (d, 12H)		3.7–5.0 (m, 32H)	

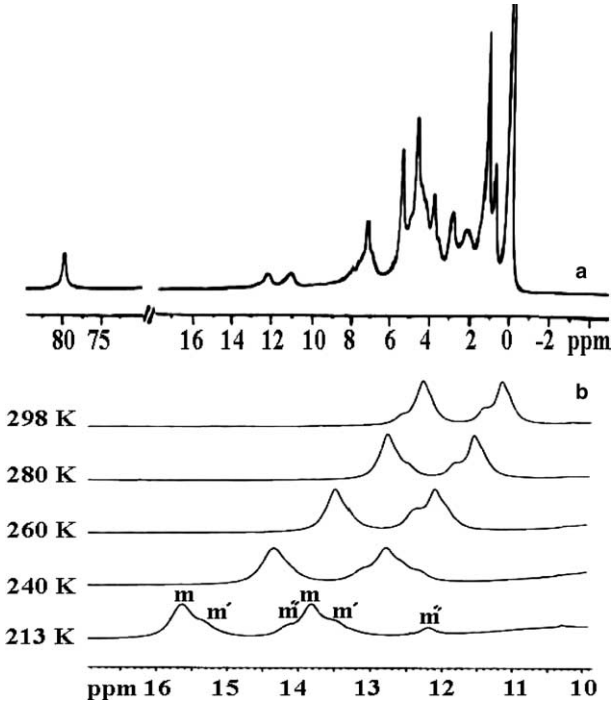
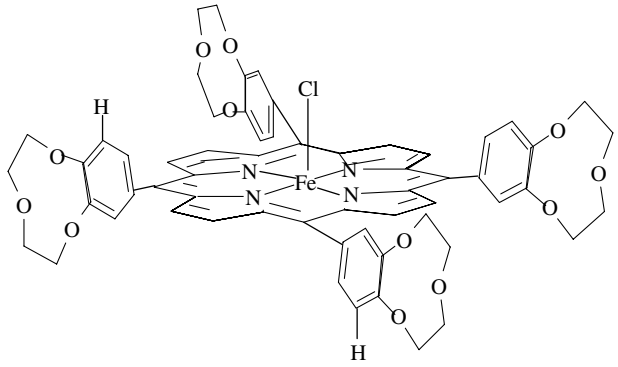


Fig. 3. 500 MHz ^{1}H NMR spectrum of FeTC3PCl (**7**), in $CDCl_3$ at room temperature (a). Variable temperature NMR of the meta position hydrogens indicating three stereoisomers T–T–T–T, T–T–T–C and T–C–T–C (b).

meta-hydrogens on the phenyl rings are usually split [15] to two sets with equal intensities. This confirms that two of the four meta hydrogens are in the same direction as the axial chloro ligand while the other two are on the opposite side, as shown in Scheme 3.

Here two kinds of meta hydrogens (m, m′), seen at ambient temperature, are in accord with the existence of two stereoisomers seen in this compound. Variable temperature studies, shown in trace b of Fig. 3, confirm the existence of a third stereoisomer at 213 K, as a trace compound. However, these stereoisomers, possibly atropoisomers, were seen in the range of 40 to −70 °C and did not show significant dynamic behavior. Any attempt to isolate these isomers was unsuccessful.



Scheme 3. Showing only two of the four meta hydrogens.

3.4. Interaction of metal ions with compounds (2) and (3)

Addition of metal ions Na^+, K^+, NH_4^+, Ca^{2+} and Ba^{2+} to the free base porphyrins (**2**) and (**3**), and to their metalloporphyrins (**5**), (**6**) and (**7**) induced no significant UV–Vis spectral change. However, marked changes were observed when the Al^{3+} ion was added to compound (**2**) or (**3**). Addition of Al^{3+} ions to (**3**) resulted in a significant red shift of the soret band from 421 to 453 nm with isobestic points at 433 and 502 nm. Similar absorption spectral changes and fluorescence intensity changes were observed upon addition of Al^{3+} to (**2**). The discussed spectral changes are consistent with π-acid DDQ or TCNE adduct formation with the porphyrin macrocycle [14], where the macrocycle itself interacts with the acids. The inset b of Fig. 4, confirms that the Al^{3+}/porphyrin (**3**) mole ratio in the resulting complex is about 5 which means that Al^{3+} interacts with 4 crown rings as well as a porphyrin macrocycle here [16]. Similar spectral changes were also observed in the presence of a large excess of the Mg^{2+} cation.

For further investigation of the complexation process, FeTC3PCl and $(FeTC3P)_2O$ were titrated with $Al(NO_3)_3$ under the same conditions as for the free base porphyrins. The results are presented in Fig. 5. Trace b of Fig. 5 shows that the ratio of Al^{3+}/porphyrin in the resulting complex is 4. In controversy with the free base porphyrins, the soret

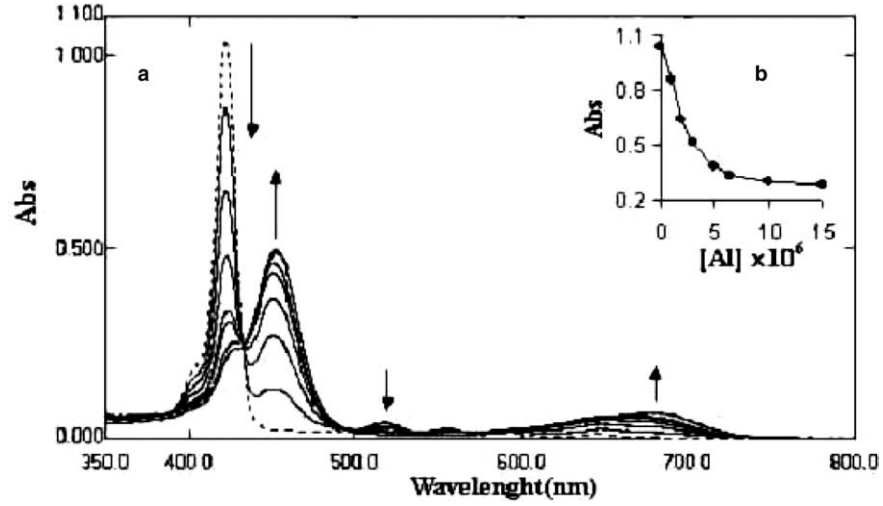


Fig. 4. Absorption spectrum of (**3**) in $CHCl_3$:MeOH (2:1) upon addition of $Al(NO_3)_3$ at room temperature (2.85×10^{-6} M) (a); plot of [metal ion] $\times 10^6$ vs. absorption at room temperature, $\lambda_{max} = 421.5$ nm (b).

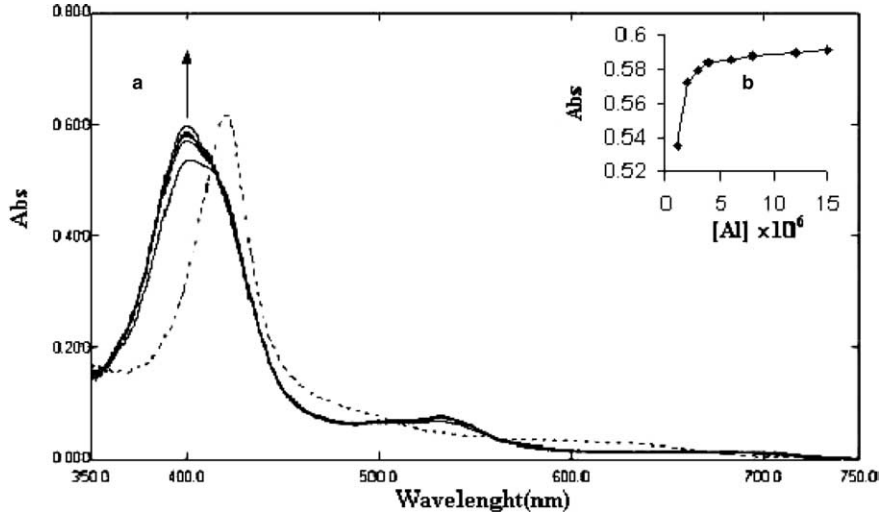


Fig. 5. Absorption spectra of (**7**) in $CHCl_3$:MeOH (2:1) upon addition of $Al(NO_3)_3$ at room temperature (10^{-6} M) (a); plot of [metal ion] $\times 10^6$ vs. absorption at room temperature, $\lambda_{max} = 421.5$ nm (b).

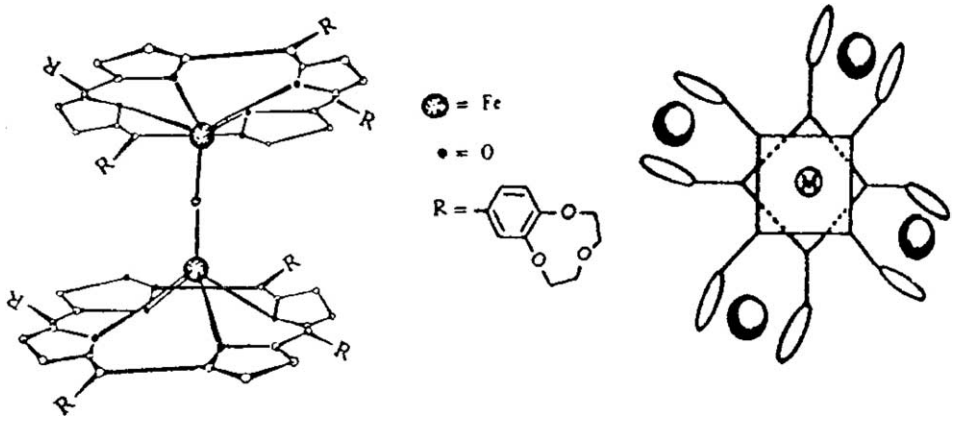


Fig. 6. Proposed structure of the porphyrin dimer induced by Al^{3+}.

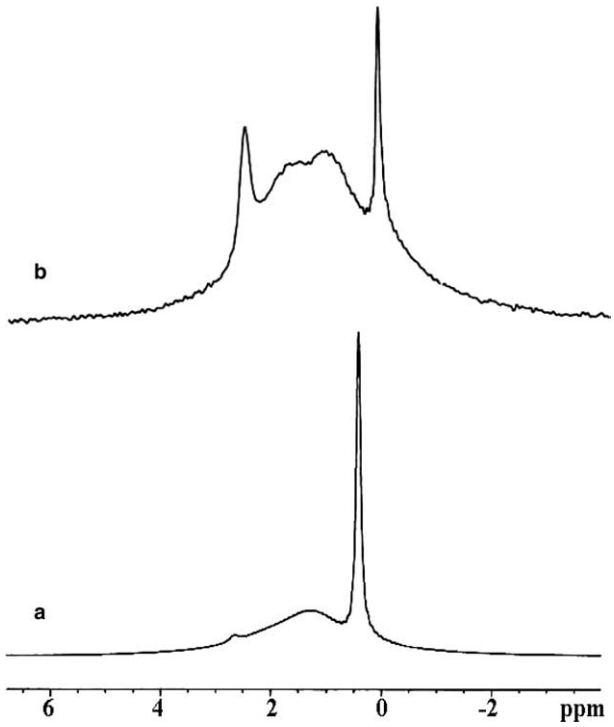


Fig. 7. ^{27}Al NMR spectrum of $Al(NO_3)_3 \cdot 9H_2O$ in $CDCl_3$/MeOH at room temperature (a); TC3PH$_2$ upon addition of $Al(NO_3)_3 \cdot 9H_2O$ (b).

band in these metallated porphyrins shows a blue shift. This kind of blue shift has also been reported for the interaction of metal ions with similar other substituted crown-ether porphyrins [17]. So, we conclude that the Al^{3+} ion could coordinate to the crown cavities as well as the porphyrin core in the free base porphyrins. The proposed structures are presented in Fig. 6.

In addition, the ^{27}Al NMR spectrum of (**3**) upon addition of Al^{3+} under the same conditions was followed to confirm the interaction of Al^{3+} with the crown ether porphyrin. Trace (a) of Fig. 7 shows the ^{27}Al NMR spectrum of $Al(NO_3)_3$ in $CDCl_3$:CD_3OD, 2:1 at 25 °C. Addition of a 10-fold excess of $Al(NO_3)_3$ to compound (**3**) in the same solvent mixture results in the spectral change shown in trace (b) of Fig. 7. The relatively sharp signal at 2.8 ppm could be assigned to the Al^{3+} ion coordinated to the porphyrin macrocycle and a broad signal in the region 1.5–2.5 ppm to the complex formed from the interaction of Al^{3+} species to the crown rings [18].

Acknowledgements

We thank the research and graduate study councils of Shahid Beheshti University for financial support.

References

[1] (a) D.E. Williams, S.E. Hale, R.T. Okita, B.S.S. Masters, J. Biol. Chem. 259 (1984) 14600;
(b) F.P. Guengerich, T.L. Macdonald, Acc. Chem. Res. 17 (1984) 9;
(c) D. Xia, H. Kim, J.Z. Xia, A.M. Kachurin, L. Zhang, L. Yu, J. Deisehhofer, Science 227 (1997) 60;
(d) M.R. Wasielewski, Chem. Rev. 26 (1993) 198;
(e) J.L. Sessler, B. Wang, A. Harriman, J. Am. Chem. Soc. 115 (1993) 10418;
(f) R.E. Fenna, B.W. Matthews, Nature 258 (1975) 573;
(g) P. Jordan, P. Fromme, H.-T. Witt, O. Klukas, W. Saenger, N. Kraub, Nature 411 (2001) 909.
[2] (a) C.A. Hunter, L.D. Sarson, Angew. Chem. Int. Ed. Engl. 33 (1994) 2313;
(b) K. Maruyama, A. Osuka, Pure Appl. Chem. 62 (1990) 1511;
(c) M.D. Ward, Chem. Soc. Rev. 26 (1997) 365;
(d) T. Hayashi, H. Ogoshi, Chem. Soc. Rev. 26 (1997) 355;
(e) J.P. Collman, P.S. Wagenknecht, J.E. Hutchison, Angew. Chem. Int. Ed. Engl. 33 (1994) 1537;
(f) M.J. Gunter, D.C.R. Hockless, M.R. Johnston, B.W. Skelton, A.H. White, J. Am. Chem. Soc. 116 (1994) 4810;
(g) J. Fun, J.A. Whiteford, B. Oleynyuk, M.D. Levin, P.J. Stang, E.B. Fleischer, J. Am. Chem. Soc. 121 (1999) 2741.
[3] (a) X. Chi, A.J. Guerin, R.A. Haycock, C.A. Hunter, L.D. Sarson, J. Chem. Soc., Chem. Commun. (1995) 2567;
(b) J.-M. Lehn, Angew. Chem. Int. Ed. Engl. 27 (1988) 89;
(c) M. Fujita, Chem. Soc. Rev. 27 (1998) 417;
(d) K. Kobayashi, M. Kobayashi, K. Endo, H. Masuda, Y. Aoyama, Chem. Eur. J. 4 (1998) 417;
(e) U. Michelsen, C.A. Hunter, Angew. Chem. Int. Ed. Engl. 39 (2000) 764.
[4] (a) H. Shinmori, H. Furuta, A. Osuka, Tetrahedron Lett. 43 (2002) 4881;
(b) A. Robertson, M. Ikeda, M. Takeuchi, S. Shinkai, Bull. Chem. Soc. Jpn. 74 (2001) 883;
(c) H. Shinmori, A. Osuka, Tetrahedron Lett. 41 (2000) 8527;
(d) T. Yamada, K. Kikawa, S. Shinoda, H. Tsukube, Tetrahedron Lett. 40 (1999) 6967;
(e) H.V. Willigen, T.K. Chandrashekar, J. Am. Chem. Soc. 108 (1986) 709;
(f) V. Thanabal, V. Krishnan, J. Am. Chem. Soc. 104 (1982) 3643;
(g) N. Kobashi, T. Osa, Heterocycles 15 (1981) 675;
(h) A.C. Knipe, J. Chem. Educ. 53 (1976) 618.
[5] L. Michaudet, P. Richard, B. Boitrel, Tetrahedron Lett. 41 (2001) 8289.
[6] J.S. Lindsey, L.C. Seher, H.C. Hsu, A.P.C. Kearney, M.J. Margueretlaz, J. Org. Chem. 52 (1987) 827.
[7] G.W. Buchanan, A.B. Driega, A. Moghimi, C. Bensimon, Can. J. Chem. 71 (1993) 1983.
[8] A.D. Adler, F.R. Longo, F. Kampas, J. Inorg. Nucl. Chem. 32 (1970) 2443.
[9] (a) A. Stone, E.B. Fleischer, J. Am. Chem. Soc. 90 (1968) 2735;
(b) B. Chenge, O.Q. Muro, H.M. Marqus, R. Scheidt, J. Am. Chem. Soc. 119 (1997) 10732.
[10] D. Mohajer, S. Rayati, S. Zakavi, M. Zahedi, N. Safari, H.R. Khavasi, S. Shahbazian, New. J. Chem., in press.
[11] A. Moghimi, M. Faal Rastegar, M. Ghandi, Can. J. Chem. 82 (2004) 1.
[12] J.H. Fuhrhop, K.M. Smith, in: M. Smith (Ed.), Porphyrins and metalloporphyrins, Elsevier, Amsterdam, 1975, p. 279.
[13] V. Thanabal, V. Krishnan, J. Am. Chem. Soc. 13 (1982) 3644.
[14] H. Shinmori, Y. Yasuda, A. Osuka, Eur. J. Org. Chem. (2002) 1197.
[15] G.N. La Mar, F.A. Walker, J. Am. Chem. Soc. 97 (1975) 5103.
[16] J. Mason, Multinuclear NMR, Plenum Press, New York, 1989, p. 259.
[17] (a) D. Mohajer, H. Dehghani, J. Chem. Soc., Perkin Trans. 2 (2000) 199;
(b) D. Mohajer, H. Dehghani, Bull. Chem. Soc. Jpn. 73 (2000) 1477.
[18] H. Shinmori, A. Osuka, Tetrahedron Lett. 41 (2000) 8527.

complexes inhibit DNA biosynthesis at molecular levels through blocking the activity of ribonucleotide diphosphate reductase (RDR), a key enzyme involved in the transformation of DNA to RNA [3]. Another possible mode of action involves binding of complex molecules at the minor groove of the DNA helical structure through intercalation thus preventing the unwinding of DNA [4].

Quinones, as a class of naturally occurring ligands [5], exhibit a wide range of biological activities. It is reported that β-lapachone, a naturally occurring 1,2–naphthoquinone derivative [6], inhibits tumor growth in rats implanted with W-256 carcinoma. Similarly, it is found to be cytotoxic to a variety of human cancer cell lines wherein the mechanistic aspects revealed that these compounds hamper the DNA repair enzymes [7] as well as can induce DNA-TOPO II-mediated cleave of DNA in an ATP-independent manner and these effects may be decisive in the cytotoxicity of these compounds [8]. The cytotoxicity of quinonoidal compounds is mainly through intercalation, inhibition of DNA and RNA, breaking of DNA strands, alteration of cell membrane functions and free radical initiated alkylation [9]. Previously, we have reported [10] that iron (III) and copper (II) complexes of 2-hydroxy-1,4-naphthoquinone-1-thiosemicarbazone inhibit DNA synthesis when evaluated for their in vitro antitumor activity against P-388 Lymphocytic cells. Recently, we have investigated [11] the antitumor properties and mechanisms of transition metal complexes of 1,2-naphthoquinone-thiosemicarbazone against MCF-7 human breast cancer cells as well as their DNA cleavage activities with circular double stranded plasmid DNA pBR-322. In former studies, it was observed that these complexes can only stabilize the single-strand nicked DNA [12] but not double-strand breakage intermediates, while in later case the quantitative conversion was found with super coiled DNA to linearized DNA in the presence of H_2O_2. Moreover, these complexes exerted a substantial effect on topoisomerase II activity. Screening of antiproliferative activities of 9,10-phenanthrenequinone thiosemicarbazone and its metal complexes [13] against the T47D human breast cancer cell line showed that these cytotoxic compounds possess antitumor action via inhibition of steroid binding to the cognitive receptor or by preventing the dimerisation of the estrogen receptor.

In a continuation of our recent efforts in understanding the coordination propensities of thiosemicarbazones, we have investigated the structural and electrochemical features of transition metal complexes with a variety of thiosemicarbazones [14]. The present communication describes the synthesis and structural elucidation of iron (II), iron (III), cobalt (II) and copper (II) complexes of 2-thiosemicarbazido-1,4-naphthoquinone (Fig. 1; NQTSC) involving either thione or thiol coordination.

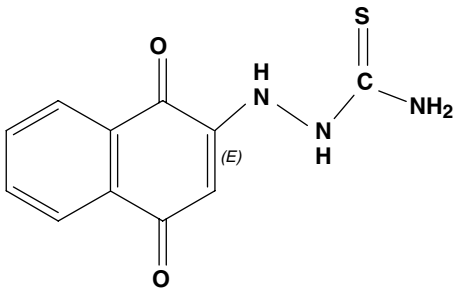


Fig. 1. The 2-Thiosemicarbazido-1,4-naphthoquinone (NQTSC) ligating system.

2. Experimental

All the chemicals used in the present studies were of AnalaR grade, products of Fluka A.G. and were used as received. The solvents were purified by literature methods.

2.1. Synthesis of NQTSC

NQTSC was synthesized according to the procedure described earlier [14d].

2.2. Preparation of complexes

2.2.1. Thionato complexes

0.002 mole of NQTSC was dissolved in 15 ml methanol and the solution was degassed with a N_2 stream for 5 min. 0.001 mole of each of iron (II) chloride tetrahydrate (0.20 g), iron (III) chloride hexahydrate (0.27 g), cobalt (II) chloride hexahydrate (0.24 g) and copper (II) chloride dihydrate (0.17 g) were dissolved in 10 ml of methanol and these solutions were degassed for 5 min with N_2. The metal solutions were added to the ligand solution dropwise under N_2 in a Schlenk assembly with constant stirring. The pH of solution was adjusted to between 3 and 4 using 10% HCl solution in methanol. The reaction mixture was stirred for 1 h after which the organic solvent was stripped off on rotary evaporator under vacuum and the mixture was kept overnight in a refrigerator. The precipitated complexes were filtered, washed with acetone and dried under vacuum over $CaCl_2$. The complexes thus obtained are hereafter referred as:

Iron (II) complex; A-1, iron (III) complex; A-2, cobalt (II) complex; A-3, copper (II) complex; A-4.

2.2.2. Thiolato complexes

The synthesis of these complexes was carried out essentially in a similar manner as described above except that the pH of the reaction mixture was adjusted to ~8 using a 6% methanolic solution of NH_3. The complexes thus obtained are hereafter referred as:

Iron (II) complex; B-1, iron (III) complex; B-2, cobalt (II) complex; B-3, copper (II) complex; B-4.

2.3. Physical measurements

Elemental analyses were carried out using a Hosli-Holland C, H, N analyzer. The magnetic susceptibility measurements between 300 and 16 K were carried out on a Faraday type magnetic balance with a continuous flow of He in a Flow Closed-cycled refrigerator which was calibrated with $Hg[Co(SCN)_4]$. The IR spectra were recorded on a Perkin–Elmer 283-B FTIR spectrometer using KBr discs while the UV–Vis spectral measurements of DMSO solutions were made on a Shimadzu UV-300 spectrophotometer. The X-band ESR spectra at 298 and 77 K were recorded on a Varian 109-ESR spectrophotometer with 100 kHz modulation amplitude. Mössbauer spectra were recorded on a conventional constant acceleration electrochemical drive coupled to a ND-100 multi-channel analyzer operating in the time mode. The isomer shifts were measured against natural α-iron foil. Cyclic voltammetric experiments were performed on a BAS CV-27 assembly equipped with an X–Y recorder. Measurements were made on degassed 10 mM DMSO solutions of the complexes (N_2 bubbled for 15 min prior to measurements) containing 0.1 M tetraethyl ammonium perchlorate as a supporting electrolyte. The working system consisted of Pt–inlay (working), Pt–disc (auxiliary) and Ag/AgCl (reference) electrodes. The Ag/AgCl reference electrode was calibrated with the ferricinium/ferrocene redox couple located at $E_{1/2} = +0.40$ V ($\Delta E_q = 0.06$ V).

3. Results and discussion

Interaction of NQTSC with transition metal salts under two different synthetic conditions yielded red or dark brown colored complexes which are insoluble in common organic solvents such as benzene, chloroform but are soluble in DMF and DMSO. The analytical and conductivity data (Table 1) indicate a $[ML_2]Cl_2$ composition for A-1 to A-4, $[ML_2]$ for B-1, B-3 and B-4 while B-2 has a $[ML_2]Cl$ stoichiometry indicating that complexes A-1 to A-4 probably possess thionato sulfur binding while B-1 to B-4 involve thiolato sulfur coordination.

3.1. Infrared spectra

Thiosemicarbazone ligands, in principle, exhibit thione ↔ thiol tautomerism due to the presence of a thioamide –NH–C=S linkage [1]. The absence of a ν(S–H) absorption near 2570 cm^{-1} with a band around 3140 cm^{-1} from a $\nu(^2N–H)$ stretch for NQTSC signifies that the thione form of the ligand exists in the solid state. The bands at 3260 and 3410 cm^{-1} are attributed to asymmetric and symmetric stretching vibration of the NH_2 functionality [14a] and it is expected that these bands undergo appreciable changes upon complexation with metal ions (Table 2). NQTSC may bind through thione (C=S), thiol (–C–SH) or both as a consequence of tautomerism. In the present studies, all these three possibilities are observed as evidenced from the respective band position of the ν(C=S) vibration. NQTSC exhibits characteristic ν(C=S) bands 1290

Table 1
Analytical data and some physical properties for the complexes

Complex	Analytical data[a]					Λ_M (Ω^{-1} cm^2 mol^{-1})	μ_{RT} (BM)
	C (%)	H (%)	S (%)	Cl (%)	M (%)		
A-1 $[FeC_{22}H_{18}N_6O_4S_2]Cl_2$	42.98 (42.53)	3.08 (2.92)	11.06 (10.32)	10.86 (11.41)	9.62 (8.99)	142.50	3.87
A-2 $[FeC_{22}H_{18}N_6O_4S_2]Cl_2$	40.64 (41.33)	3.09 (3.15)	9.88 (10.03)	11.53 (11.09)	9.14 (8.73)	148.30	4.20
A-3 $[CoC_{22}H_{18}N_6O_4S_2]Cl_2$	42.24 (41.13)	3.51 (3.13)	9.89 (10.03)	10.21 (11.03)	8.95 (9.17)	151.20	D
A-4 $[CuC_{22}H_{18}N_6O_4S_2]Cl_2$	42.71 (42.08)	2.99 (3.24)	9.84 (9.39)	11.02 (10.38)	10.26 (9.30)	146.30	2.14
B-1 $[FeC_{22}H_{16}N_6O_4S_2]$	45.72 (46.49)	3.28 (3.20)	10.87 (11.28)		10.26 (9.82)	1.76	3.76
B-2 $[FeC_{22}H_{16}N_6O_4S_2]Cl$	45.75 (45.25)	2.90 (2.73)	10.68 (10.97)	5.89 (6.06)	9.73 (9.57)	78.60	4.42
B-3 $[CoC_{22}H_{16}N_6O_4S_2]$	45.93 (46.40)	3.58 (3.54)	10.69 (11.26)		11.02 (10.35)	2.04	1.86
B-4 $[CuC_{22}H_{16}N_6O_4S_2]$	46.38 (46.02)	3.34 (3.16)	10.74 (11.17)		10.41 (11.06)	2.61	1.84

[a] Values in the parentheses are the calculated ones.

Table 2
Significant peaks in the IR spectra of NQTSC and its complexes

Assignment[a]	NQTSC	A-1	A-2	A-3	A-4	B-1	B-2	B-3	B-4
$\nu(NH_2)$	3410	3380	3370	3380	3380	3360	3380	3390	3380
	3260	3180	3160	3150	3140	3100	3180	3170	3150
$\nu(^1N–H)$	3370	3280	3270	3280	3280	3260	3280	3290	3280
$\nu(^1C=O)$	1630	1595	1600	1600	1595	1600	1595	1600	1595
$\nu(C=N)$						1565	1570	1575	1570
$\nu(C=S)$	1290	1250	1240	1240	1250	1275	1260	1250	1250
$\nu(N–N)$	1030	1010	1000	1005	1005	1010	1000	1005	1005
$\nu(CN + NN + CS)$	860	830	825	830	830	825	820	825	820
$\nu(M–O)$		525	520	520	510	520	515	510	515
$\nu(M–N)$		455	450	460	470	405	410	410	415
$\nu(M–S)$		335	340	340	340	365	375	350	360

[a] In cm^{-1}.

and 860 cm^{-1} which are red shifted by ~50 and 40 cm^{-1}, respectively, in the spectra of metal complexes [14b]. On the other hand, the $\nu(^1N–H)$ vibration from the same linkage undergoes a downward shift of about 30 cm^{-1} for all the complexes suggesting its coordination while the $\nu(^2N–H)$ vibration disappears suggesting deprotonation of the $^2N–H$ proton thus generating thiolato sulfur which is one of the coordinating centers for B-1 to B-4. In addition, a new band appears around 1580 cm^{-1} due to the formation of the –C=N chromophore as a result of thiol formation. These complexes exhibit characteristic $\nu(M–S)$ vibrations in the region 340–360 cm^{-1}. The quinone carbonyl stretches are observed at two different frequencies. The $\nu(^4C=O)$ band at 1650 cm^{-1} for NQTSC does not show any change after complexation while the other quinone carbonyl absorption $\nu(^1C=O)$ displays a substantial decrease by ~30 cm^{-1} in the spectra of the complexes [11a]. It implies that the ^1C-quinone carbonyl is one of the coordinating centers, that is further confirmed by a new band at about 510 cm^{-1} due to a $\nu(M–O)$ vibration. A downward shift of 50 cm^{-1} for the $\nu(C–N^1)$ vibration from the thiosemicarbazide linkage, along with a characteristic $\nu(M–N)$ stretch at about 440 cm^{-1}, is indicative of hydrazinic nitrogen coordination [15].

3.2. Iron (II) complexes

The dark-red colored iron (II) complexes of NQTSC (A-1 and B-1) exhibit room temperature magnetic moments of 3.87 and 3.76 BM, respectively, which neither correspond to high-spin nor low-spin states. In order to determine the magnetic properties of these complexes, variable temperature magnetic susceptibility measurements were carried out in the range 16–273 K (Fig. 2). It can be seen from the nature of this graph that the magnetic moment remains almost constant throughout the entire temperature range thus ruling out the possibility of a thermal equilibrium between high-spin and low-spin states as well as antiferromagnetically coupled iron

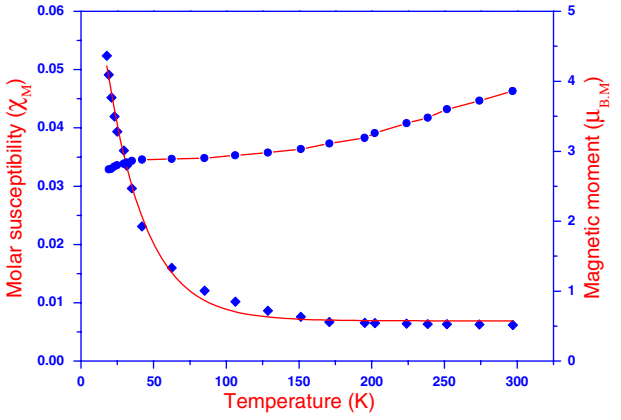


Fig. 2. Temperature dependence of magnetic susceptibility (♦) and effective magnetic moment (●) of A-1.

centers. Careful literature survey revealed that there exists an intermediate spin-state ($S = 1$) for iron (II) complexes wherein it was argued that ligand fields of moderate strength probably control the spin-state as well as impart deviation from octahedral geometry [16]. The susceptibilities for these compounds can be approximated by the Curie–Weiss expression, and the Weiss constant θ was found to be −9 and −12 K for A-1 and B-1, respectively. Moreover, the magnetic measurements in DMSO at 300 K using Evan's method [17] do not reveal any appreciable change in magnetic moment value (3.91 BM) suggesting a similar magnetic behavior both in solution and in the solid state. This observation, together with rather small θ values indicate that these complexes possess an unusual intermediate $S = 1$ ground state.

The molar susceptibilities of the spin-triplet state in a tetragonal (D_{4h}) ligand field [18] is given by the expression

$$\chi_M = (2N\beta^2/3)\{[g_\parallel^2 e^{(-D/kT)}/kT(1 + 2e^{(-D/kT)})] + [g_\perp^2(1 - e^{(-D/kT)}/D(1 + 2e^{(-D/kT)}))]\}, \quad (1)$$

where the terms involved have usual meanings.

In the limit of very low temperatures, this expression can be modified to

$$\chi_M = (4N\beta^2 g_\perp/3D) \text{ when } kT <<<< D. \quad (2)$$

By simulating the susceptibility data utilizing the equation mentioned above, the best fit for the magnetic data can be obtained with $g = 2.74$ and $D = 9.3$ and 10.6 cm^{-1} for A-1 and B-1, respectively. The zero-field splitting values (D) observed for these compounds are considerably lower than those observed for square planar complexes [19], while they are slightly higher than those for octahedral complexes [20]. Small values of D reveal that the intermixing of an excited state with the ground state is minimal and magnetic perturbations are negligible at lower temperatures.

Such behavior is further confirmed by carrying out Mössbauer measurements on these compounds. The zero-field Mössbauer spectra of both the complexes at 298 K exhibit a single quadrupole split doublet (Fig. 3), characteristic of a $S = 1$ ground state [21]. Table 3 summarizes the data on zero-field splitting (D), isomer shift (IS) and quadrupole splitting (EQ) for A-1 and B-1. It can be seen from this table that smaller values of isomer shift signifies the extent of covalent character in the metal-ligand bonding while the lesser values of quadrupole splitting denotes the extent of deviation from idealized geometry. Both these values indicate that there is appreciable covalency in the ironthiosemicarbazone bonding as well as the structure of these complexes being moderately distorted from octahedral geometry. The higher value for B-1 seems to be originating from the difference in the type of sulfur atom bonded to iron (II) center. Moreover, smaller D values suggest negligible mixing of energy states.

The electronic spectra of both the complexes exhibit a prominent peak around 16000 cm^{-1} with a shoulder at about 12300 cm^{-1}. These bands are assigned based on the spectral evidences for mixed ligand complexes of iron (II) with oxalate, maleate, phenanthroline and bipyridine [22]. Although, the exact assignments are not reported for these absorptions, the first band predominantly arises from metal-ligand charge transfer while the second absorption is thought to originate from d–d transitions.

3.3. Iron (III) complexes

Room temperature magnetic moments for A-2 and B-2 neither corresponds to high-spin nor low-spin states (Table 1) and probably suggest that they exhibit either spin-equilibrium behavior or belong to an intermediate $S = 3/2$ spin state. In order to ascertain the exact magnetic properties, variable temperature magnetic susceptibility measurements were carried out in the temperature range 16–300 K (Fig. 4). A plot of temperature vs. magnetization data indicate that they do not fit with a thermally accessible spin-state conversion and clearly reflect the presence of an unusual $S = 3/2$ spin state. Moreover,

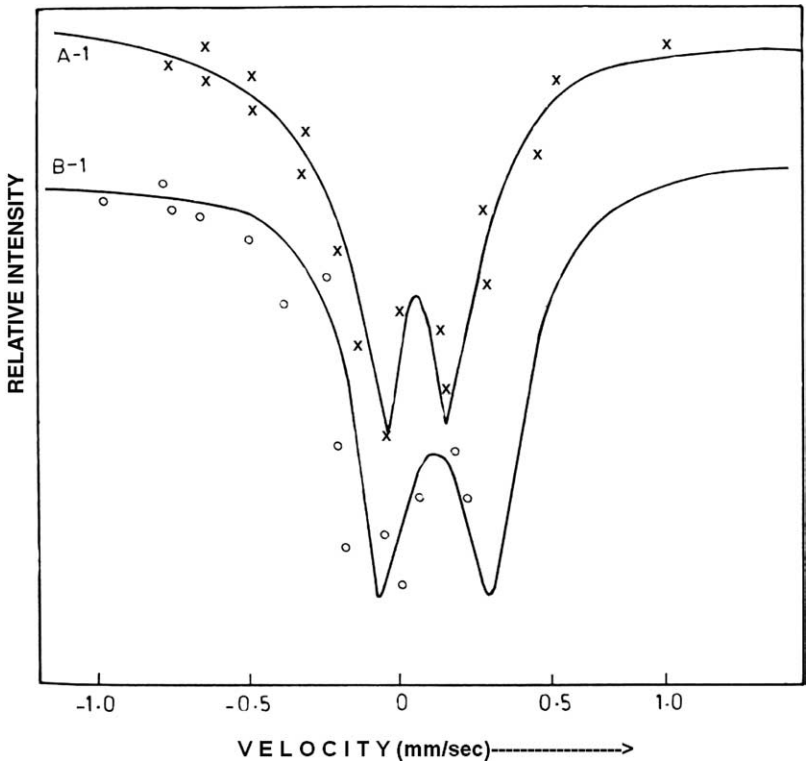


Fig. 3. Mössbauer spectra of A-1 (×) and B-1 (○) at 298 K.

Table 3
Zero-field splitting (D), 'g' values and Mössbauer parameters for iron (II), iron (III) and cobalt (II) complexes of NQTSC

Complex	D, cm^{-1}	g value		IS[a] (δ, mm s^{-1})	QS[a] (ΔE_q mm s^{-1})
		298 K	77 K		
A-1	9.3			0.320	0.32
B-1	10.6			0.330	0.74
A-2	2.16	4.35, 2.014	4.28, 2.18		
B-2	2.43	4.18, 2.11	4.38, 2.107		
B-3		2.15	2.12, 2.003		

[a] Relative to α-iron foil.

at lower temperature, there is no significant drop in magnetic moments, signifying the absence of exchange coupled dimeric iron (III) centers.

The existence of such an intermediate spin-state has been reported for prophyrin [23], dithicarbamate [24] and thiosemicarbazone complexes [1,25]. It is observed that such magnetic behavior originates from either square pyramidal or tetragonal geometries with a weak axial ligand field where the $d_{x^2-y^2}$ orbital lies well above the d_{z^2} orbital in energy and remains unoccupied. Many of these compounds possess magnetic moments in the range 4.2–5.5 BM and this behavior is explained on the basis of quantum admixing of $S = 3/2$ and 5/2 states, presumably through spin–orbit coupling as the energy separation between these states is very small. This feature is recognized with an unusual $g = 4$ signal in the EPR spectrum as well as a drop in the magnetic moment at lower temperatures. Using the crystal field model, Mitra et al. [26] have established that the extent of mixing of the $^6A_1$ with $^4A_2$ state is about 40% for prophyrin complexes. The other justification for the higher magnetic moments is attributed to a large zero-field splitting component leading to unequal population of Kramer's doublets originating from the $S = 3/2$ state, a feature usually found to be associated with prophyrin complexes.

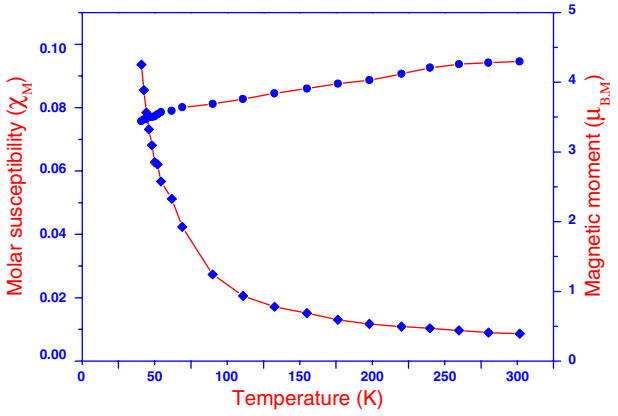


Fig. 4. Temperature dependence of magnetic susceptibility (♦) and effective magnetic moment (●) of B-2.

According to perturbation theory [27], $g_\perp = 4$ and $g_\parallel = 2$ signals are expected when $M_s = \pm 1/2$ doublet is the ground state. ESR spectra of A-2 and B-2 at 298 K can be interpreted in terms of a rhombic pattern exhibiting signals around $g = 2$ (assigned to the $-1/2 \rightarrow +1/2$ transition) and less resolved band at $g = 4$ (Table 3). However, at 77 K (Fig. 5), the former band is found to split as a consequence of rhombic symmetry while there is an enhancement in the intensity of the $g = 4$ signal suggesting a thermal population of the $M_s = -1/2$ state. The zero-field splitting (ZFS) parameter (D) calculated for these two compounds by fitting the experimental ESR data is summarized in Table 3. A positive D value is indicative of $M_s = \pm 1/2$ as the ground state with the first excited state ($M_s = \pm 3/2$) placed at 2D above this level, with the contribution from the E parameter assumed to be zero. A significantly larger value of the ZFS was observed for dithiocarbamate complexes [28] wherein it was argued that at lower temperatures, the population of the $M_s = \pm 3/2$ doublet is negligible with very weak magnetic exchanges.

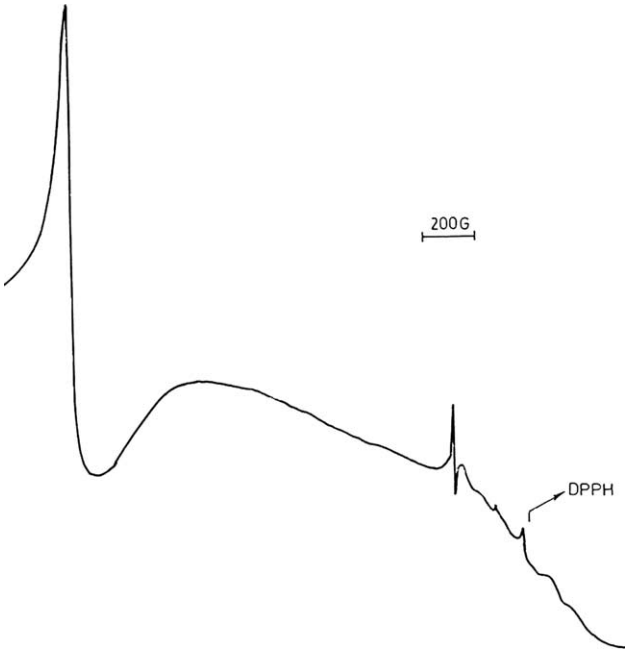


Fig. 5. X-band ESR spectrum of B-2 in DMSO solution at 77 K.

A-2 and B-2 exhibit three electronic transitions in their absorption spectra recorded in DMSO solvent. Out of these absorptions, the first two bands are assigned to $d_{xy} \rightarrow d_{xz}/d_{yz}$ and $d_{xy} \rightarrow d_{z^2}$ transitions while the third band originates from charge-transfer characteristics of metal-thiosemicarbazones [29]. B-2 shows these bands on the higher energy side as compared to A-2, suggesting the weak ligand field for the thione sulfur against the thiol sulfur.

3.4. Cobalt (II) complexes

Although, the interaction of NQTSC with cobalt (II) chloride essentially yields octahedral complexes A-3 and B-3, their magnetic properties are found to be significantly different, with the former complex exhibiting diamagnetism corresponding to a cobalt (III) species while the later compound possesses a low-spin cobalt (II) center with a magnetic moment of 1.86 BM. It has been reported earlier that the interaction of thiosemicarbazones with cobalt (II) yields mixed tautomeric complexes containing both thione and thiol sulfur binding. Such a mixed tautomeric coordination seems to be promoted by trivalent transition metal ions such as Cr(III), Fe(III) and Co(III). We have also observed similar features in cobalt (III) and chromium (III) complexes of pyruvic acid thiosemicarbazone and 2-ketobutyric acid thiosemicarbazone [14a,14b]. Thus, A-3 involves a similar type of binding for NQTSC with both thione and thiol coordination. The supportive evidence for octahedral geometry is obtained from its electronic spectrum wherein three transitions are observed at 13 605, 15 700 and 21 880 cm^{-1} corresponding to $^1A \rightarrow {}^3T_{1g}$, $^1A \rightarrow {}^3T_{2g}$ and $^1A \rightarrow {}^1T_{1g}$ transitions, respectively [30]. The evaluation of ligand field parameters such as $10D_q$ (17 375 cm^{-1}), B (416 cm^{-1}), C (1664 cm^{-1}) and β (0.40) is indicative of a weaker ligand field for NQTSC as compared to other thiosemicarbazone ligands [1] as well as appreciable covalency in the cobalt–ligand bonding.

B-3 exhibits a magnetic moment of 1.86 BM, corresponding to low-spin octahedral cobalt (II) species, which is slightly higher than the spin-only value of 1.73 BM and probably can be explained on the basis of a greater contribution of the orbital angular momentum to the ground state. The ESR spectrum (Table 3) exhibits an axial magnetic symmetry with two principle g values: $g_\perp = 2.12$ and $g_\parallel = 2.003$. The calculation of the spin concentration yields 8.20×10^{20} spins per g, i.e. ≅1 unpaired electron per B-3 molecule [31]. The shift of the $g_\perp$ value towards higher fields indicates the greater strength of the axial bonding as compared to the equatorial ligand field strength [32,33]. The optical spectra of low spin complexes with a ^2D ground term in a D_{4h} crystal field show two characteristic transitions assigned to $^2B_{2g} \rightarrow {}^2A_{1g}$ and $^2B_{2g} \rightarrow {}^2E_g$ with the later band receiving some contribution from charge-transfer features. For B-3, these transitions can be seen at 17 920 and 22 150 cm^{-1}, respectively.

3.5. Copper (II) complexes

The room temperature magnetic moments for A-4 and B-4 are 2.14 and 1.96 BM. The contribution from lower symmetry (D_{2h}) to effective D_{4h} symmetry [34] is found to be 27.17% and 13.30%, respectively. The high value for A-4 probably reflects the weaker thione coordination leading to a larger distortion at the axial position as compared to the thiol binding for B-4. It has been established that six coordinate copper (II) complexes possess elongated tetragonal or rhombic distortions in an octahedral field and display three spin-allowed transitions assigned to $^2B_{1g} \rightarrow {}^2A_{1g}$ (γ_1), $^2B_{1g} \rightarrow {}^2B_{1g}$ (γ_2) and $^2B_{1g} \rightarrow {}^2E_g$ (γ_3) absorptions [30]. However, the first transition usually appears as a shoulder and sometimes overlaps with the later transition (γ_2). A-4 and B-4, exhibit two bands around 17 000 and 23 000 cm^{-1} corresponding to the second and third transitions attributed to $\Delta_\parallel$ and $\Delta_\perp$, respectively (Table 4). The ESR spectra of A-4 and B-4 in the solid state at 298 and 77 K consist of two-principle g values: $g_\parallel = 2.205$ and $g_\perp = 2.054$, consistent with $d_{x^2-y^2}$ ground state in a tetragonal ligand field. However at 300 K, the spectra exhibit four fairly well resolved components originating from −3/2, −1/2, 1/2 and 3/2 transitions ($\Delta M_s = 1$). The signal corresponding to $M_I = -3/2$ clearly splits into five peaks because of superhyperfine coupling with hydrazinic nitrogen

Table 4
ESR spectral data for A-4 and B-4

Magnetic parameter	Complex	
	A-4	B-4
$\Delta_\parallel$[a]	17 390	17 482
$\Delta_\perp$[a]	22 988	22 857
$g_\parallel$	2.205	2.204
$g_\perp$	2.054	2.052
g_0	2.105	2.102
$^{Cu}A_\parallel$[a]	168.5×10^{-4}	159.8×10^{-4}
$^{Cu}A_\perp$[a]	28.1×10^{-4}	25.23×10^{-4}
$^{Cu}A_0$[a]	74.91×10^{-4}	70.08×10^{-4}
$^{N}A_\parallel$[a]	18.51×10^{-4}	17.60×10^{-4}
$^{N}A_\perp$[a]	14.01×10^{-4}	14.04×10^{-4}
$^{N}A_0$[a]	15.50×10^{-4}	15.23×10^{-4}
G	4.66	4.86
$K_\parallel$	0.5501	0.5739
$K_\perp$	0.7088	0.6968
α^2	0.6683	0.6724
α'^2	0.4341	0.4251
β^2	0.8178	0.7996
β'^2	0.9235	0.9266
δ^2	1.0	1.0
δ'^2	0.7750	0.7541

[a] In cm^{-1}.

atoms of bound ligand molecules, with a splitting of about 16*G*. From this spectrum, the isotropic spectrochemical splitting factor (g_0), isotropic hyperfine splitting constant ($^{Cu}A_0$) and isotropic ligand super-hyperfine constant ($^{N}A_0$) are calculated and these are subsequently used in the evaluation of other spectral parameters.

The effective spin-Hamiltonian describing the EPR spectra of copper (II) complexes in tetragonal (D_{4h}) crystal field [35] can be written as:

$$H = \beta[g_{\parallel}H_zS_z + g_{\perp}(H_xS_x + H_yS_y)] + {}^{Cu}A_{\parallel}S_zI_z(\mathrm{Cu}) + {}^{Cu}A_{\perp}[S_xI_x(\mathrm{Cu}) + S_yI_y(\mathrm{Cu})] + [{}^{N}A_{\parallel}S_zI_z(N) + {}^{N}A_{\perp}\{S_xI_x(N) + S_yI_y(N)\}], \quad (3)$$

where the terms involved have their usual meanings.

The low temperature (77 K) DMSO frozen glass EPR spectra (Fig. 6) of these complexes display four line copper hyperfine lines, characteristic of monomeric copper (II) complexes with a $g_{\perp}$ component with well resolved superhyperfine interactions due to two hydrazinic nitrogen atoms of NQTSC. Kivelson and Nieman [36] have pointed out that compounds having $g_{\parallel} \geqslant 2.3$ are ionic in nature while those with $g < 2.3$ are covalent in character. The $g_{\parallel}$ values for A-4 and B-4 reveal appreciable covalency with $d_{x^2-y^2}$ as the ground state. From the low temperature ESR spectra, various bonding parameters such as in-plane σ-bonding, in-plane π-bonding as well as out-of-plane π-bonding are evaluated [14d] in order to understand the nature of the metal–ligand bonding in these complexes (Table 4). The orbital reduction factors, viz. $K_{\parallel}$ and $K_{\perp}$, are calculated using the equations $g_{\parallel} = 2.0023\ \{1-(4K_{\parallel}\lambda/\Delta_{\parallel})\}$ and $g_{\parallel} = 2.0023\ \{1-(K_{\perp}\lambda/\Delta_{\perp})\}$. For pure σ-bonding $K_{\parallel} \cong K_{\perp} \cong 0.77$ while $K_{\parallel} < K_{\perp}$ signifies in-plane π-bonding, with $K_{\parallel} > K_{\perp}$ accounting for out-of-plane π-bonding. Also, $G > 4$ indicates negligible interaction between two copper centers.

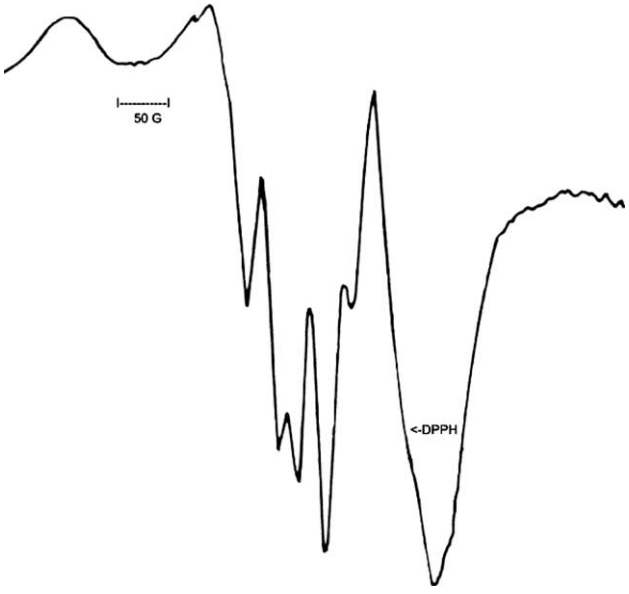


Fig. 6. X-band ESR spectrum of B-4 in DMSO solution at 77 K.

It has been observed [37] that the contribution of the 4s orbital to σ-bonding between metal and ligand donor atom orbitals is predominant in those complexes with α^2 values greater than 0.70. For the present complexes, these values are less than this value, which supports a ground term with purely 3d character. As the ^{14}N tensor is perpendicular to the *z*-axis in D_{4h} symmetry, the superhyperfine splitting along $Cu_{\parallel}$ features corresponds to $^{N}A_{\perp}$ while that on $Cu_{\perp}$, it is found to be equal to $\sqrt{2[(^{N}A_{\parallel})^2 + (^{N}A_{\parallel})^2]^{1/2}}$. There exist relatively sharp features for nitrogen coupling as evidenced from the low temperature spectra of these complexes. The anisotropy observed in the superhyperfine structure suggests that the unpaired electron is delocalized over the ligand orbitals presumably through in-plane σ- and π-bonding as well as out-of-plane π-bonding interactions [38].

The spin-densities in 2s and 2p orbitals of the nitrogen atom can be calculated [39] using the relations $\rho_{2s} = {}^{N}A_0/A_s$ and $\rho_{2p} = {}^{N}A_{\parallel}/A_p$ where A_s (550*G*) and A_p (34.1*G*) are the nitrogen hyperfine splitting parameters when the electron is residing entirely in 2s and 2p orbitals, respectively. Employing these relations, it is observed that there exists appreciable electron density on the nitrogen orbitals accounting for in-plane σ-bonding as well as in-plane π-bonding. Moreover, these values also signify the extent of electron delocalization between metal-ligand bonding. The estimation of such electron densities in 2s and 2p orbitals of the nitrogen atom amounts for a p:s ratio (2.333 and 2.323 for A-4 and B-4) which is in excess of the value expected for the sp^2 hybridization that would indicate a transfer of spin density from metal to ligand through π-bonding interactions. This excess of electron density (ca. 0.33) is obviously donated from copper and corresponds to the net amount of electron density contributed towards σ-bond formation as corroborated by the α^2 parameter. It may be argued that this unpaired electron spends about 33% of its time on donor sites of the coordinated NQTSC ligand and thus attributes for greater covalency as evidenced from the evaluation of the other bonding parameters. Inspection of Table 4 reveals that β^2 and β'^2 values support the appreciable covalency in the metal–ligand bonding, suggesting that the electron density transfers are promoted through low lying vacant π-orbitals on the sulfur atom.

3.6. Electrochemistry

The cyclic voltammetric behavior of NQTSC and its metal complexes is carried out in DMSO solution containing 0.1 M TEAP as the supporting electrolyte and the data is summarized in Table 5. It is well established that quinonoidal compounds exhibit two reversible

Table 5
Cyclic voltammetric data[a] (V) for iron (II), iron (III), cobalt (II) and copper (II) complexes of NQTSC

Compound	E_{pc}[a]	E_{pa}[a]	$E_{1/2}$	% Reversibility (i_{pc}/i_{pa})
A-1	+0.200	+0.330	+0.265	95
A-2	−0.975			
	+0.130	+0.200	+0.175	100
A-3	−0.810	−0.300	−0.555	75
A-4	0.350	−0.250	−0.300	87
	+0.250	+0.350	+0.300	84
B-1	+0.250	+0.375	+0.3125	93
B-2	−0.960			
	+0.250	+0.325	+0.2875	92
B-3	−0.775			
	+0.95			
B-4	−0.600	−0.450	−0.520	71
	+0.175	+0.280	+0.2275	97

[a] At scan rate 0.1 V s^{-1}.

cathodic peaks corresponding to quinone → semiquinone and semiquinone → catechol redox couples [5]. The parent 2-hydroxy-1,4-naphthoquinone (lawsone) exhibits the corresponding reduction peaks at −0.34 and −0.98 V, respectively [11a]. Upon derivatisation with thiosemicarbazide (NQTSC), the former peak is shifted to a more negative potential (−0.55 V) while the second peak is lost with the appearance of a new peak at −1.20 V, assigned to the reduction of the azomethine linkage of the thiosemicarbazide side chain; a behavior usually observed for many thiosemicarbazone ligands.

The voltammetric responses for A-1 and B-1 exhibit an oxidative couple at positive to Ag/AgCl in the range 0.2–0.3 V assigned to the Fe(II)/Fe(III) pair [40]. Quasi-reversibility of this wave is inferred from the peak potential separation $\Delta E_p > 125$ mV as well as the cathodic to anodic current intensity ratio. It can be seen from the data that B-2 is more susceptible to oxidation as compared to A-1, suggesting the effect of the type of sulfur binding. Such a difference stems from the fact that thiolato sulfur induces a more covalent character in Fe–S bonding as compared to thionato sulfur. This can be attributed to the charge accumulation capability of the thione (C=S) linkage against the thiol (C–S) chromophore.

In the DMSO solutions containing TEAP, A-2 and B-2 exhibit nearly identical electrochemical response. The cyclic voltammogram of A-2 (Fig. 7) shows one wave at +0.130 with its counterpart at +0.200 V, attributed to Fe(III)/Fe(II) in the range 0 to +1.0 V. Similar behavior is also displayed by B-2 at a more positive potential. As NQTSC is electrochemically inactive in this potential range, this behavior could be explained on the basis of a metal centered wave originating from reduction of the ferric centers [41]. It seems that the

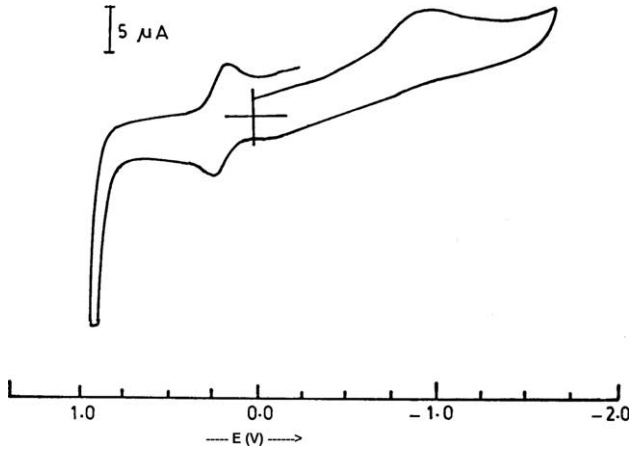


Fig. 7. Cyclic voltammogram for A-2 in DMSO at 0.1 V s^{-1} scan rate.

complex molecule does not experience any structural changes that accompany the reduction process, probably due to the rigidity of the ONS ligating system. The reversible nature of this reduction peak can be ascertained with scan rate dependence studies (Fig. 8), wherein it is observed that the current peak linearly varies with scan rate (γ) in the range 100–700 mV s^{-1} thus indicating a diffusion controlled mechanism, although at higher

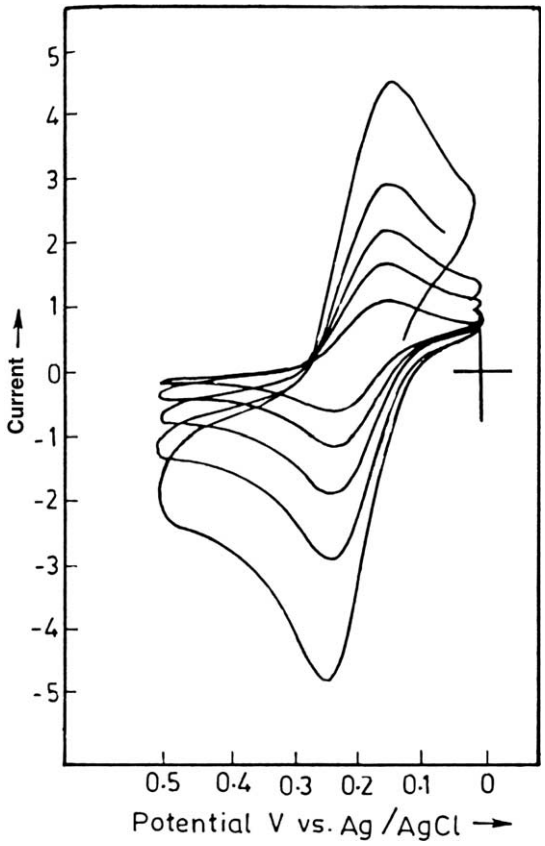


Fig. 8. Scan rate dependence of A-2 at different scan rates ($v = 20$, 50, 100, 200 and 500 V s^{-1}).

scan rates a weak adsorption of the complex at the electrode surface was observed. The peak separation $\Delta E_p = E_p^c - E_p^a$ of about 70 mV was noticed, as expected for a reversible one-electron reduction process [42]. At a slower scan rate, the shape and peak separation was about 70 mV but increased up to 100 mV when the scan rate changed from 100 to 700 mV s^{-1}. The reversible character of this couple was also confirmed by the observation of the cathodic shift of E_p^c of about 30 mV for a fivefold increase in the scan rate. A reduction wave exhibits a linear relationship between scan rate and current function (μA) and the ratio of anodic to cathodic peak current i_p^a/i_p^c is equal to unity suggesting that the iron (II) complex formed in the electro-reduction process is stable within the timescale of the experiment. B-2 exhibits a more positive potential as compared to A-2 indicating the influence of the type of sulfur coordination. On the cathodic scan in the range 0 to −2 V, both these complexes display an irreversible wave around −0.96 V probably originating from reduction of the azomethine linkage.

The cobalt complex of NQTSC (A-3) exhibits a cathodic reduction peak at −0.810 V with its anodic wave at −0.300 V, corresponding to the Co(III)/Co(II) quasi-reversible redox couple [43], having a peak separation of ~0.500 V. It is observed that the anodic peak is broad as against the sharp nature of the cathodic curve, suggesting that the rate of electron transfer is very slow as compared to mass transfer at the electrode surface, as evidenced from negligible deposition of the complex at the electrode surface. On the other hand, B-3 displays somewhat different electrochemical behavior in DMSO solution with the metal-based redox changes occurring at relatively higher potentials. On the cathodic side, the irreversible reduction peak at −0.775 V, assigned to the Co(II)/Co(I) process, undergoes electro-deposition upon the reverse scan thus signifying the formation of an unstable Co(I) complex. Similar behavior is observed when the anodic scans are recorded wherein the irreversible Co(III)/Co(II) couple occurs at +0.95 V indicating that there exists slow electrode to complex electron transfer kinetics and it is likely responsible for the irreversible nature of this peak [44].

The cyclic voltammogram for copper (II) complexes exhibit metal centered electrochemical processes (Fig. 9). Inspection of this figure indicates that the reduction wave (peak A) and it's oxidation counterpart (peak C) are related to the Cu(II)/Cu(I) reduction process in the range 0 to −2 V while on the anodic side (in the range 0 to +2), there exists an oxidation curve (peak E) with its cathodic peak (G). The other peaks are related to either quinone redox forms (peaks B, D and F) or coupled chemical reactions. Some of these species do not exist in the initial scan when the scan directions are reversed and exhibit intensity enhancement only on repetitive scanning.

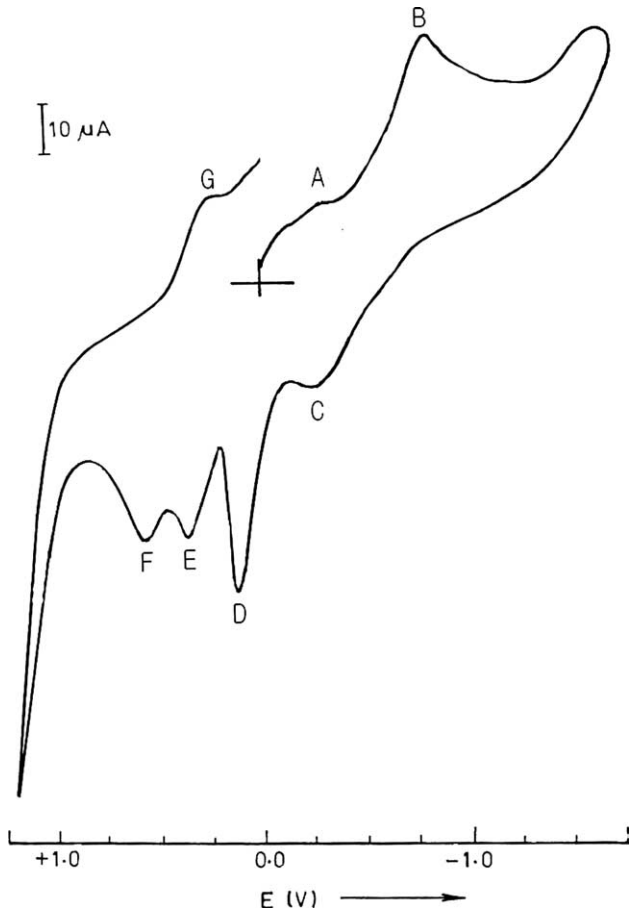


Fig. 9. Cyclic voltammogram of A-4 in DMSO at 0.1 V s^{-1} scan rate.

Analysis of the cyclic voltammetric response of peak A/C indicates that this process originates from a quasi-reversible Cu(II)/Cu(I) redox couple with a peak-to-peak separation (ΔE_p) of about 100 mV and the ratio of i_{pa}/i_{pc} is less than unity. In the absence of either uncompensated solution resistance or anomalous electrode surface effects, the marked departure of ΔE_p from 59 mV can be qualitatively assumed as an index of occurrence of significant geometrical reorganizations accompanying the redox changes [45]. It is expected that the Cu(II)/Cu(I) couple experiences some structural reorganization barrier while undergoing the reduction process. Patterson and Holm [46] have shown that softer ligands tend to favor more positive $E_{1/2}$ values while hard acids give rise to more negative values. The redox potentials observed for the present complexes indicate the moderate character for NQTSC implying that there exists appreciable tetragonal distortion in the structural arrangement of A-4 and B-4, probably due to deformation in the chelate rings of the coordinated thiosemicarbazone.

The cyclic voltammetric behavior of A-4 and B-4 between +1 to 0 V exhibit cathodic response (peak E) in the range 275–405 mV with its counterpart (peak G) in

the range 370–535 mV. This feature corresponds to a quasi-reversible Cu(III)/Cu(II) redox process [47] as indicated by ΔE_p values as well as the non-equivalent current intensities of the cathodic and anodic peaks (% I_{pc}/I_{pa}). The redox process associated with oxidation of Cu(II) to Cu(III) may probably originate due to the presence of the thione/thiol sulfur center and the redox active quinone moiety. Since the quinone ring is planar and the thiosemicarbazide side chain is flexible, the ligand can adopt different conformations so as to fit the smaller sized Cu(III) ion, thus favoring the oxidation process. Moreover, this oxidation step results in the formation of a low-spin d^8 Cu(III) state with preference for a square planar geometry [48]. It is quite likely that this process does not proceed via a change in geometry of the complex in DMSO solution. This fact is clearly reflected in Table 5, indicating that the Cu(III) state can be stabilized at a relatively lower oxidation potential. The redox potentials observed for A-4 and B-4 are significantly lower than those reported earlier for thiosemicarbazone complexes [1] thus reflecting the influence of the electronic features of the redox active quinone moiety.

4. Conclusion

The interaction of NQTSC with iron (II), iron (III), cobalt (II) and copper (II) leads to formation of two different types of complexes containing coordination of thione/thiol or both the tautomers. Ferrous compounds exhibit an unusual spin triplet ground state ($S = 1$) with smaller ZFS values, indicating that NQTSC exerts a moderate ligand field as well as appropriate geometry responsible for fine-tuning of the magnetic properties. Similar behavior is also found to be present for ferric complexes possessing a spin quartet state ($S = 3/2$) thus suggestive of the potential of the thiosemicarbazone ligand for inducing uncharacteristic magnetic behavior. Moreover, there exists a reasonable amount of distortion in the octahedral geometry as a consequence of appreciable mixing of excited states. It is significant to note that the type of sulfur coordination as well as effective symmetry around the metal centers strongly influences the magnetic properties, thus stabilizing abnormal spin-states. Mixed tautomeric complexes are formed with iron (III) and cobalt (III) complexes under acidic conditions suggesting a lower pK_a value for NQTSC. There exists appreciable covalency in the metal-ligand bonding as well as a significant amount of tetragonal distortion in the octahedral geometry as evidenced from the ESR spectral measurements on the copper (II) complexes. The estimation of various bonding parameters indicate that substantial delocalization has occurred within the chelate rings of NQTSC mediated via in-plane π-bonding along with σ-donation, thus resulting in an increased structural stability. Metal-centered processes that are strongly influenced by the nature of sulfur binding dominate the redox behavior of these complexes. In general, thiol coordination seems to favor an oxidation process at lower potentials whereas a thione sulfur substantially manipulates the reduction behavior of these complexes.

References

[1] D.X. West, A.E. Liberta, S.B. Padhye, R.C. Chikate, P.B. Sonawane, A.S. Kumbhar, R.G. Yerande, Coord. Chem. Rev. 123 (1993) 49.
[2] A.G. Quiroga, C.N. Ranninger, Coord. Chem. Rev. 248 (2004) 119.
[3] J. Easmon, G. Purstinger, G. Heinisch, T. Roth, H.H. Fiebig, W. Holzer, W. Jager, M. Jenny, J. Hoffmann, J. Med. Chem. 44 (2001) 2164.
[4] G. Nocentini, Crit. Rev. Oncol. Hematol. 22 (1996) 89.
[5] C.G. Pierpont, Coord. Chem. Rev. 216–217 (2001) 99.
[6] C.J. Li, L.J. Zhang, B.J. Dezubw, C.S. Crumpacker, A.B. Pardee, Proc. Natl. Acad. Sci. USA 90 (1993) 1839.
[7] D.A. Boothman, D.K. Trask, A.B. Pardee, Cancer Res. 49 (1989) 605.
[8] B. Frydman, L.J. Marton, J.S. Sun, Cancer Res. 57 (1997) 620.
[9] (a) H. Kappus, Biochem. Pharmacol. 35 (1986) 1;
(b) T.W. Grant, D.N.R. Rao, R.P. Mason, G.M. Cohen, Chem. Biol. Interact. 65 (1988) 157.
[10] S.B. Padhye, R.C. Chikate, A.S. Kumbhar, J.M. Shallom, M.P. Chitnis, Bio. Metals 5 (1992) 67.
[11] (a) Z. Afrasiabi, E. Sinn, J. Chen, Y. Ma, A.L. Rheingold, L.N. Zakharov, N. Rath, S. Padhye, Inorg. Chim. Acta 357 (2004) 271;
(b) Z. Afrasiabi, E. Sinn, P.P. Kulkarni, V. Ambike, S. Padhye, D. Deobagakar, M. Heron, C. Gabbutt, C.E. Anson, A.K. Powell, Inorg. Chim. Acta 24 (2005) 889.
[12] J. Chen, Y. Huang, G. Liu, Z. Afrasiabi, E. Sinn, S. Padhye, Y. Ma, Tox. Appl. Pharmacol. 197 (2004) 40.
[13] Z. Afrasiabi, E. Sinn, S. Padhye, S. Dutta, S. Padhye, C. Newton, C.E. Anson, A.K. Powell, J. Inorg. Biochem. 95 (2003) 306.
[14] (a) R.C. Chikate, P.B. Sonawane, A.S. Kumbhar, S.B. Padhye, R.J. Butcher, Inorg. Chim. Acta 205 (1993) 59;
(b) P.B. Sonawane, R.C. Chikate, A.S. Kumbhar, S.B. Padhye, R.J. Doedens, Polyhedron 13 (1994) 195;
(c) A. Murugkar, S. Padhye, S. Guha-Roy, U. Wagh, Inorg. Chem. Commun. 2 (1999) 545;
(d) R.C. Chikate, A.R. Belapure, S.B. Padhye, D.X. West, Polyhedron 358 (2005) 2023.
[15] P. Bindu, M.R.P. Kurup, T.R. Satyakeerty, Polyhedron 18 (1999) 321.
[16] E. Konig, B. Kenellakopulos, Chem. Phys. Lett. 12 (1972) 485.
[17] D.F. Evans, J. Chem. Soc. (1959) 2003.
[18] R.L. Carlin, J. Chem. Edn. 43 (1966) 521.
[19] D.P. Riley, J.A. Stone, D.H. Busch, J. Am. Chem. Soc. 99 (1977) 767.
[20] E. Konig, G. Ritter, B. Kenellakopulos, J. Chem. Phys. 58 (1973) 3001.
[21] (a) E. Konig, S. Hufner, E. Steichele, K. Madeja, Z. Naturforschg. A 22 (1967) 1543;
(b) E. Konig, S. Hufner, E. Steichele, K. Madeja, Z. Naturforschg. A 23 (1968) 632.
[22] E. Konig, Coord. Chem. Rev. 3 (1968) 471.
[23] L.A. Yatsunyk, F.A. Walker, Inorg. Chem. 43 (2004) 757.
[24] G.A. Eisman, W.M. Reiff, R.J. Butcher, E. Sinn, Inorg. Chem. 20 (1981) 3484.
[25] Y.K. Bhoon, Polyhedron 5 (1983) 365.

[26] (a) S. Mitra, V.R. Marathe, R. Birdy, Chem. Phys. Lett. 96 (1983) 103;
(b) L.B. Dugad, V.R. Marathe, S. Mitra, Proc. Ind. Acad. Sci.; Chem. Sci. 95 (1985) 189.
[27] R.L. Carlin, Science 227 (1985) 1291.
[28] G.C. DeFotis, B.K. Failon, F.V. Wells, H.H. Wickman, Phys. Rev. B 29 (1984) 3795.
[29] S.K. Jain, B.S. Garg, Y.K. Bhoon, Transition Met. Chem. 11 (1986) 89.
[30] A.B.P. Lever, Inorganic Electronic Spectroscopy, 2nd ed., Elsevier, Amsterdam, 1984.
[31] J. Janczak, R. Kubiak, Inorg. Chim. Acta 342 (2003) 64.
[32] M.C.R. Symons, T. Taiwo, A.M. Sargeson, M.M. Ali, A.S. Tabl, Inorg. Chim. Acta 241 (1996) 5.
[33] S. Iwatsuki, H. Kato, K. Obeyama, S. Funahashi, N. Koshino, K. Kashivabara, T. Suzuki, H.D. Takagi, Inorg. Chem. Commun. 3 (2000) 501.
[34] W.E. Hatfield, Comments Inorg. Chem. 1 (1981) 105.
[35] A.H. Maki, B.R. McGarvey, J. Chem. Phys. 29 (1961) 35.
[36] D. Kivelson, R. Niemen, J. Chem. Phys. 35 (1961) 149.
[37] B.J. Hathaway, Struct. Bond. 14 (1973) 60.
[38] M.J.M. Campbell, A.J. Collis, R. Grzeskowiak, Bioinorg. Chem. 6 (1976) 305.
[39] M.C.R. Symons, Adv. Phys. Org. Chem. 1 (1962) 332.
[40] J. Simaan, S. Poussereau, G. Blondin, J.J. Girerd, D. Defaye, C. Philouze, J. Guilhem, L. Tchertanov, Inorg. Chim. Acta 299 (2000) 221.
[41] H.C. Harrop, P.K. Mascharak, Acc. Chem. Res. 37 (2004) 253.
[42] B. Nigovic, N. Kujundzic, Polyhedron 21 (2002) 1661.
[43] T.C. Higgs, D. Ji, R.S. Czernuszewicz, B.F. Matzanke, V. Schunemann, A.X. Trautwein, M. Helliwell, W. Ramirez, C.J. Carrano, Inorg. Chem. 37 (1998) 2383.
[44] S. Chang, V.V. Karambelkar, R.D. Sommer, A.L. Reingold, D.P. Goldberg, Inorg. Chem. 41 (2002) 239.
[45] A.R. Hendrickson, R.L. Martin, N.M. Rhode, Inorg. Chem. 15 (1976) 2115.
[46] G.S. Patterson, R.H. Holm, J. Bioinorg. Chem. 4 (1975) 1257.
[47] E. Franco, E. Lopez-Torres, M.A. Mendiola, M.T. Sevilla, Polyhedron 19 (2000) 441.
[48] X.H. Bu, X.Ch. Cao, D.L. An, R.H. Zhang, C. Thomas, E. Kimura, J. Chem. Soc., Dalton Trans. (1998) 433.

1. Introduction

In the second half of the last century many aminopolycarboxylate ligands, structurally related to edta (the ethylenediaminetetraacetate ion), have been prepared and used to form hexadentate complexes with transition metal ions [1,2]. One such ligand is the 1,3-propanediamine-*N*,*N*′-diacetate-*N*,*N*′-di-3-propionate ion (1,3-pddadp), Fig. 1(a), having a lengthened diamine and two carboxylate chains with respect to edta. In the reactions between 1,3-pddadp and metal ions with hexadentate coordination of this ligand, theoretically three geometrical isomers are possible: *trans*(O_5), *trans*(O_5O_6) and *trans*(O_6); where O_5 and O_6 refer to the five- and six-membered N–O rings, respectively, Fig. 1(b). The same geometrical isomers are also possible for hexadentate $[M(eddadp)]^{n-}$ (where eddadp is the ethylenediamine-*N*,*N*′-diacetate-*N*,*N*′-di-3-propionate ion) complexes, and for these complexes it was found that six-membered β-alaninate rings serve better for the formation of less-strained G rings, favoring the *trans*(O_5) geometry [2–13]. Contrary to this, all possible isomers of the $[M(1,3\text{-pddadp})]^{n-}$ complex have been reported for Cr(III) [14], but only two isomers (*trans*(O_5O_6) and *trans*(O_6) for Co(III) [15,16] and *trans*(O_5) and *trans*-(O_5O_6) for Rh(III) [17,18] and Ni(II) [19]) have been isolated and characterized. In addition, only one dominant isomer of the same complex (*trans*(O_6)) of Cu(II) [20] has been described. The so far available X-ray data are limited to: *trans*(O_6)-[Cr(1,3-pddadp)]$^-$ [14], *trans* (O_6)-[Co(1,3-pddadp)]$^-$ [16,21], *trans*(O_5)-[Rh(1,3-pddadp)]$^-$ [18], *trans*(O_5O_6)-[Rh(1,3-pddadp)]$^-$ [18], *trans*(O_5)-[Ni(1,3-pddadp)]$^{2-}$ [19] and *trans*(O_6)-[Cu(1,3-pddadp)]$^{2-}$ [20] complexes.

In the reaction of the 1,3-pddadp ligand with Co(III) ion two geometrical isomers (*trans*(O_5O_6) and *trans*(O_6)) of the hexadentate [Co(1,3-pddadp)]$^-$ complex have been obtained, resolved and characterized [15]. The $(+)_{546}$-*trans*(O_5O_6)-[Co(1,3-pddadp)]$^-$ and $(+)_{546}$-*trans*-(O_6)-[Co(1,3-pddadp)]$^-$ enantiomers, with a positive CD peak at the lowest energy in the first spin-allowed d–d absorption band region, were tentatively assigned the *Λ* absolute configuration. The *trans*(O_6) geometry of [Co(1,3-pddadp)]$^-$ has been established in the crystal structure of racemate *trans*(O_6)-K[Co(1,3-pddadp)] · $3H_2O$ [16], as well as in the crystal structure of optically pure compounds: $(-)_{589}$-*trans*(O_6)-$K_{1/2}(H_5O_2)_{1/2}$[Co(1,3-pddadp)] · $2H_2O$ [21] and $(-)_{589}$-*trans*(O_6)-Li[Co(1,3-pddadp)] · $7H_2O$ [21]. The crystallographic studies of Co(III) amine carboxylates have been of particular interest in connection with different kinds of "mysteries" of hydronium ions [21]. Namely, it has been found that minor variations in composition and/or stereochemistry of Co(III) amine carboxylates are sufficient to influence the crystallization of the hydronium ion or the mixed potassium–hydronium salts, as evidenced in the crystal structure of $(-)_{589}$-*trans*(O_6)-$K_{1/2}(H_5O_2)_{1/2}$[Co-(1,3-pddadp)] · $2H_2O$ [21].

The characterization of the *trans*(O_5O_6) geometry of the [Co(1,3-pddadp)]$^-$ complex using crystallographic methods is described here first. In addition, molecular mechanics (MM) calculations were applied for establishing the relative energies of the three geometrical isomers: *trans*(O_5), *trans*(O_5O_6) and *trans*(O_6) of the [Co(1,3-pddadp)]$^-$ complex.

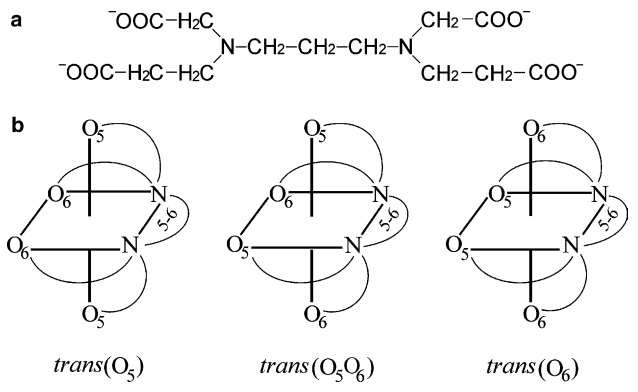


Fig. 1. Formula of the 1,3-pddadp ligand (a); and possible geometrical isomers of the hexadentate $[M(1,3\text{-pddadp})]^{n-}$ and/or $[M(eddadp)]^{n-}$ complex (b); O_5 and O_6 refer to the five- and six-membered N–O rings, respectively.

2. Experimental

The investigated complex *trans*(O_5O_6)-[Co(1,3-pddadp)]$^-$ was prepared according to the previously described procedure [15]. Recrystallization of this complex was accomplished from hot water by adding ethanol and cooling of the solution in a refrigerator.

2.1. Crystallographic data collection and refinement of the structure

For the hexadentate *trans*(O_5O_6)-K[Co(1,3-pddadp)] · $3H_2O$ complex, X-ray analysis was performed on the basis of the reflection intensities measured at 293 K on a KM4CCD kappa-geometry diffractometer [22] using graphite monochromated Mo Kα radiation.

Crystal data: $KCoC_{13}H_{24}N_2O_{11}$ (FW = 482.37), monoclinic, space group $P2/c$, $a = 14.591(3)$, $b = 9.815(2)$, $c = 12.922(3)$ Å, $\beta = 94.06(3)°$, $V = 1845.9(7)$ Å^3, $Z = 4$, $D_{calc} = 1.736$ g cm^{-3}, λ (Mo Kα) = 0.71073 Å, $T = 293$ K, $\mu = 1.218$ mm^{-1}, $F(000) = 1000$.

The structure was solved by direct methods using SHELXS97 [23] and refined by least-squares techniques with SHELXL97 [24] to $R = 0.057$ and $Rw = 0.151$. Anisotropic thermal parameters were employed for the non-hydrogen atoms. The positions of the hydrogen atoms attached to the C-atoms were calculated at standardized distances of 0.96 Å. An attempt to localize water hydro-

gens on subsequent difference Fourier maps was not fully successful. Moreover, one of the hydrogen atoms connected to O4W formed a very short non-bonding contact with its inversion related equivalent (H6W···H6W($2-x$, $-y$, $-z$) 1.21 Å). Therefore, we have assumed the presence of a disordered configuration, with half occupancy of one of the two O4W water hydrogens, but the alternative position of this hydrogen atom could not be determined on the subsequent difference Fourier maps. We were also unable to locate one of the two hydrogen atoms connected to O1W. During the structure determination process it became obvious that this hydrogen must also be disordered, this time over the two sites that are related by a twofold axis. The disorder model for the H-atom positions allowed us to postulate the presence, in the crystal, of statistically distributed, anti-parallel homodromic hydrogen bonded water chains (see Fig. 1S in the supplementary material). All OW–H distances have been standardized to a value of 0.85 Å. The hydrogen atoms were refined using a "riding model" with isotropic temperature factors 30% higher than the isotropic equivalent for the atom to which the H-atom was bonded. A Siemens Stereochemical Workstation was used to prepare the drawings [25].

2.2. Molecular mechanics calculations

Conformational analysis of the three geometrical isomers of the $[Co(1,3\text{-pddadp})]^-$ complex was carried out using the consistent force field (CFF) conformational program [26] with force field parameters particularized earlier [27,28]. The only new parameters are for the cobalt atom and the values are given in Table 1. The conformational energy was calculated from the following equation:

$$E_{\text{total}} = \Sigma E_{\text{b}} + \Sigma E_{\theta} + \Sigma E_{\varphi} + \Sigma E_{\text{nb}} + \Sigma E_{\text{e}}, \quad (1)$$

where the summations are over all energy contributions from bond stretching (E_{b}), angle bending (E_{θ}), torsion angle (E_{φ}), non-bonded (E_{nb}) and electrostatic interactions (E_{e}). The potential functions and parameters constituting the energy terms in Eq. (1) have been described previously [29], and we used essentially the same forms in this study, except the type for the non-bonded potential function. In this work we used the Lennard–Jones '12-6' rather then the Lennard–Jones '9-6' type function and this approach proved to be quite adequate for the present study. With this potential function we recalculated the conformations of the $[Cr(ed3p)(H_2O)]$ (ed3p is the ethylenediamine-*N*,*N*,*N*′-tri-3-propionate) and $[Cr(ed3a)(H_2O)]$ (ed3a is the ethylenediamine-*N*,*N*,*N*′-triacetate) complexes and obtained practically the same results as previously reported [27,28].

The force field is parameterized on the basis of the two different types of carbon atom (sp^3 – (C) and sp^2 – (C′) carbons), two different types of oxygen atom (carbonyl (O′) and coordinated (O) oxygens), one type of hydrogen (H) and of nitrogen (N), as well as the central metal atom (Co). Comprehensive preliminary calculations did not justify the distinction between aliphatic carbons from glycinate, β-alaninate and 1,3-propanediamine chelate rings. All the stable conformers were found by energy minimization of the numerous theoretically possible initial structures having all the permissible conformations of 1,3-propanediamine and β-alaninate rings. By this strategy we believe that we have achieved a comprehensive and reliable spanning of the three geometrical isomers of $[Co(1,3\text{-pddadp})]^-$. The procedure used in the generation of the initial structures is similar to that in our previous paper [27].

Geometry optimizations were carried out using the combination of steepest-descent, Davidon–Fletcher–Powell and Newton–Raphson methods [26]. The steepest-descent and Davidon–Fletcher–Powell methods were

Table 1
Additional CFF parameters for edta-type complexes

Bond stretching	k_r (kcal/mol Å^2)	r_0 (Å)
M–O	500.00	1.910
M–N	500.00	1.895
Angle bending	k_θ (kcal/mol rad^2)	θ_0 (rad)
N–M–N	90.95	1.571
M–O–K	180.01	2.184
Electrostatic	q (esu)	
M	1.118	
van der Waals	ε* (kcal/mol)	r* (Å)
M—N	0.033	4.02
C—M	0.030	4.10
M—O	0.032	3.94
M—Q	0.036	3.94
M—H	0.031	3.70

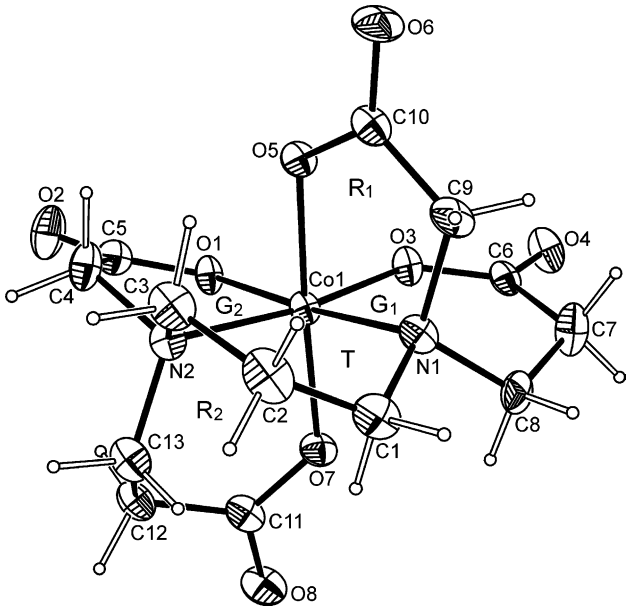


Fig. 2. Molecular structure of the complex anion *trans*(O_5O_6)-$[Co(1,3\text{-pddadp})]^-$ in *trans*(O_5O_6)-$K[Co(1,3\text{-pddadp})] \cdot 3H_2O$.

Table 2
Selected bond distances (Å) and bond angles (°) for *trans*(O_5O_6)-K[Co(1,3-pddadp)] · $3H_2O$

Bond distances	
K1–O4	2.697(3)
K1–O2^{i}	2.832(4)
K1–O2W^{ii}	3.037(5)
K1–O6^{ii}	3.190(4)
K2–O1	2.843(3)
K2–O3	2.796(3)
K2–O5	2.998(3)
K2–O6^{ii}	2.779(3)
Co1–O1	1.925(3)
Co1–O3	1.903(3)
Co1–O5	1.885(3)
Co1–O7	1.908(3)
Co1–N1	1.970(3)
Co1–N2	1.988(3)
Bond angles	
O4–K1–O4^{iii}	135.1 (2)
O4–K1–O2^{i}	134.70(11)
O4–K1–O2^{iv}	85.81(11)
O2^{i}–K1–O2^{iv}	68. 8(2)
O4–K1–O2W^{ii}	67.39(14)
O2^{i}–K1–O2W^{ii}	79.75(13)
O2^{iv}– K1–O2W^{ii}	98.68(11)
O4–K1–O2W^{v}	113.39(12)
O2W^{ii}– K1–O2W^{v}	178.1(2)
O4–K1–O6^{v}	70.98(10)
O2^{i}–K1–O6^{v}	151.15(9)
O2W^{ii}–K1–O6^{v}	128.45(13)
O4–K1–O6^{ii}	77.46(10)
O2^{i}–K1–O6^{ii}	107.29(10)
O2W^{ii}–K1–O6^{ii}	53.24(10)
O6^{v}–K1–O6^{ii}	89.40(13)
O6^{ii}–K2–O6^{v}	107.7(2)
O6^{ii}–K2–O3	78.86(10)
O6^{v}–K2–O3	83.67(10)
O3^{iii}–K2–O3	150.19(13)
O6^{ii}–K2–O1	122.32(9)
O6^{v}–K2–O1	99.78(9)
O3–K2–O1	54.72(8)
O1–K2–O1^{iii}	106.68(12)
O3–K2–O5^{iii}	140.66(8)
O1–K2–O5^{iii}	99.36(9)
O6^{ii}–K2–O5	71.36(9)
O6^{v}–K2–O5	137.06(9)
O3–K2–O5	53.59(8)
O1–K2–O5	54.54(8)
O5^{iii}–K2–O5	139.08(12)
O5–Co1–O3	87.48(13)
O5–Co1–O7	176.21(13)
O3–Co1–O7	88.75(13)
O5–Co1–O1	89.41(12)
O3–Co1–O1	85.25(12)
O7–Co1–O1	90.62(13)
O5–Co1–N1	87.23(14)
O3–Co1–N1	92.22(14)
O7–Co1–N1	92.57(14)
O1–Co1–N1	175.89(14)
O5–Co1–N2	89.01(14)
O3–Co1–N2	169.43(14)
O7–Co1–N2	94.77(14)
O1–Co1–N2	84.75(13)
N1–Co1–N2	97.6(2)

[i] $-x+1, y-1, -z+0.5$.
[ii] $-x+1, -y+1, -z$.
[iii] $-x+1, y, -z+0.5$.
[iv] $x, y-1, z$.
[v] $x, -y+1, z+0.5$.

mostly used, in that order, for initial exploratory searches and minimizations of conformations far from equilibrium. The number of iterations varied widely in the optimization experiments. In particularly difficult cases it was necessary to alternate between these two procedures more than once. To approach true minima Newton–Raphson iterations were always employed. Geometry optimizations were carried out down to an energy rms gradient of $<10^{-6}$ kJ/mol Å.

ORTEP III for Windows [30] was used to depict the energy-minimized structures.

3. Results and discussion

3.1. The crystal structure of the *trans*(O_5O_6)-K[Co(1,3-pddadp)] · $3H_2O$ complex

The ORTEP diagram of the *trans*(O_5O_6)-[Co(1,3-pddadp)]$^{-}$ complex anion is presented in Fig. 2, where the numbering scheme adopted for the respective atoms is also given. Selected bond distances and valence angles are listed in Table 2.

The Co(III) ion is encircled by all of the donating atoms (2N and 4O) of the 1,3-pddadp ligand to form an octahedral geometry. The complex anion [Co(1,3-pddadp)]$^{-}$ represents a *trans*(O_5O_6) isomer with the two (R) rings (glycinate R_1 and β-alaninate R_2) in the *trans* positions and the two (G) rings (β-alaninate G_1 and glycinate G_2) coordinated in the equatorial plane making a 5–6–6 ring system in the G-plane (Fig. 2). The format for describing the various chelate rings formed in these kinds of chelates was credited to Weakliem and Hoard [31]. We have compared the mode and degree of puckering of the chelate rings observed in the presented *trans*(O_5O_6)-[Co(1,3-pddadp)]$^{-}$ complex with those for *trans*(O_6)-[Co(1,3-pddadp)]$^{-}$ complexes [16] having a 5–6–5 combination of the ring members in the G-plane. The results are presented in the form of Table 1S in the supplementary material. In both *trans* (O_5O_6) and *trans*(O_6) complexes of Co(III), the six-membered diamine (T) ring adopts a nearly perfect *twist-boat* conformation. The helicity of the six-membered diamine ring is δ for the enantiomorph presented in Fig. 2 of Λ configuration. The same is observed for

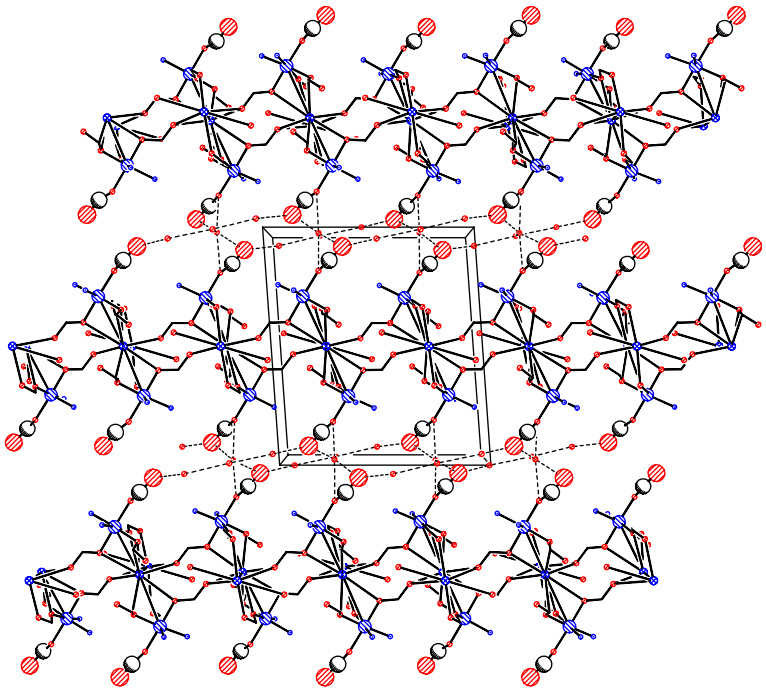


Fig. 3. Packing in the crystal structure of *trans*(O_5O_6)-K[Co(1,3-pddadp)] · $3H_2O$ showing the separation of ionic and water layers. Atoms involved in carbonyl dipolar interactions operating between the layers are marked by substantially bigger circles. H-atoms have been omitted for clarity.

the *trans*(O_6)-[Co(1,3-pddadp)]$^-$ complex of *Λ* configuration. In these two complexes the six-membered β-alaninate rings coordinated in axial positions are very distorted and their distortion from the ideal conformations is so severe that they cannot be uniquely described by the commonly used conventions. Contrary to this, the six-membered β-alaninate ring of equatorial orientation in *trans*(O_5O_6)-[Co(1,3-pddadp)]$^-$ adopts an almost ideal *half-chair* form. The five-membered glycinate rings coordinated in the G-plane display different conformational modes (*envelope* in the *trans*(O_5O_6) Co(III) complex and *twist* in the *trans*(O_6) Co(III) complex), however, the degree of puckering of these rings is nearly the same (20.6–23.6°). In the [Co(1,3-pddadp)]$^-$ complexes of *trans*(O_5O_6) and *trans*(O_6) geometry the six-membered diamine rings (T rings) also exhibit nearly the same degree of ring puckering (the average torsion angle magnitude sums 41.7° and 44.1°, respectively). Similar values for the average torsion angle moduli have been observed in the [Co(1,3-pdta)]$^-$ (41.1°) (where 1,3-pdta is the 1,3-propanediaminetetraacetate ion), [Rh(1,3-pdta)]$^-$ (40.9°) and *trans*(O_5O_6)-[Rh(1,3-pddadp)]$^-$ (42.5°) complexes in which the six-membered diamine rings adopt the same *twist-boat* conformation [18]. The equatorially coordinated glycinates in the *trans*(O_5O_6)-[Co(1,3-pddadp)]$^-$ and *trans*(O_6)-[Co(1,3-pddadp)]$^-$ complexes are highly puckered, while that one coordinated in the axial position in the *trans*(O_5O_6) isomer is nearly *planar*. However, the six-membered β-alaninate rings display nearly the same degree of ring puckering, independent of their axial or equatorial orientation, so they seem to be the less easy to modify with respect to the glycinates. The values of the average torsion angle magnitudes cover a range from 31.8° to 35.7°. Similar behavior of β-alaninate rings has also been observed in the [Rh(1,3-pddadp)]$^-$ complexes of *trans*(O_5) and *trans*-(O_5O_6) geometry [18].

In the crystal structure of *trans*(O_5O_6)-K[Co(1,3-pddadp)] · $3H_2O$, potassium ions (K1 and K2), as well as O1W and O3W water solvent molecules, are settled on a twofold axis of symmetry. K1 is octacoordinated with six carbonyl oxygen atoms (O4, O2^{i}, O6^{ii}, O4^{iii}, O2^{iv} and O6^{v}; symmetry codes: i = $-x+1$, $y-1$, $-z+0.5$; ii = $-x+1$, $-y+1$, $-z$; iii = $-x+1$, y, $-z+0.5$; iv = x, $y-1$, z and v = x, $-y+1$, $z+0.5$) from six different but symmetry-related 1,3-pddadp ligands and with two symmetry-related water molecules O2W^{ii} and O2W^{v}. The coordination polyhedron formed around K1 is distorted in shape and can be described as a square antiprism. K2 is surrounded by eight carboxylate oxygen atoms (O1, O1^{iii}, O3, O3^{iii}, O5, O5^{iii}, O6^{ii} and O6^{v}) from four symmetry-related ligands. The two carbonyl oxygen atoms O6^{ii} and O6^{v} are shared between the K1 and K2 ions. The coordination polyhedron around K2 is midway between bi-capped trigonal prism and bi-capped trigonal antiprism with a twist angle *Φ*[1] [32] of 30.7°.

[1] *Φ* (calculated applying method 1 reported in [32]) is the average value of the three pseudotorsion angles that are measured along the line joining the centroids of two nearly parallel triangular faces of a bi-capped trigonal prism and adopt absolute values in the range 0–60°.

The crystalline *trans*(O_5O_6)-K[Co(1,3-pddadp)] · $3H_2O$ complex is a two-dimensional polymer (Fig. 3). It consists of (1 0 0) layers (see Fig. 2S in the supplementary material) built up of potassium ions, situated on twofold symmetry axes, joined by bridging oxygen atoms (O6 and its symmetrical equivalent) and by bridging carboxylate groups (O3–C6–O4 and its twofold symmetry equivalent along the *b*-axis, and O5–C10–O6 and its centrosymmetric equivalent along the *c*-axis). The construction of the polymeric layer structure formed by the potassium ions and their first coordination sphere is further supported by hydrogen bonds between the O2W water molecule coordinated to K1 and one of the uncoordinated carboxylate oxygens (O2) (Fig. 3). The Co1 octahedra are situated on both sides of the layer formed by cationic polyhedra, and are joined exclusively to K2 polyhedra by sharing one of the triangular faces of the Co1 octahedron. Consequently, the approach of the complex anion by the complex cation takes place from the side of the planar glycinate R_1 ring.

The consecutive ionic layers are separated by layers formed by hydrogen bonded non-coordinated water molecules (O1W and O3W, situated on a twofold axis, and O4W in a general position) and O7–C11–O8 carboxylate groups (Fig. 3). Two of these water molecules (O1W and O4W) have one of the two hydrogen atoms disordered (O1W around a twofold axis, O4W around the centre of symmetry) in a way that allows formation of antiparallel homodromic chains of hydrogen-bonded water molecules, statistically distributed in the crystal, running along the *c*-axis, which are graphically illustrated in Fig. 1S in the supplementary material. Hydrogen bond distances and angles are listed in Table 2S in the supplementary material. Interactions between neighbouring layers formed by the complex molecules include, besides hydrogen bonds, dipolar interactions between antiparallel C11=O8 carbonyl groups around the centre of symmetry (Fig. 3).

3.2. Strain analysis of Co(III)-edta-type chelates

The results of a comparative study of the strain characteristics of a related series of Co(III)-edta-type chelates are given in Table 3. The major contributions to strain were considered to be: (i) the octahedral angles around the Co(III) ion, (ii) the ring angle sums of the various kinds of rings, (iii) the Co–O–C bond angles, and (iv) the bond angles that the chelating nitrogen atom makes with its connectors.

The greatest octahedral distortion has been observed for the $[Co(edta)]^-$ (**7**) [31,33] complex (48°) having a 5–5–5 combination of the ring members in an equatorial plane. Introducing the six-membered β-alaninate ring(s) in the $[Co(edta)]^-$ (**7**) [31,33] system causes a decrease of octahedral strain as evidenced by $\Sigma\Delta(O_h)$ values calculated for the *trans*(O_5)-$[Co(eddadp)]^-$ (**4**) [8] (31°), *trans*(O_5)-$[Co(ed3ap)]^-$ (**5**) [34] (29°) and $[Co(edtp)]^-$ (**6**) [13] (29°) complexes. However, an increase of octahedral strain was observed when some of the glycinate rings in the $[Co(1,3\text{-}pdta)]^-$ (**3**) [35] complex are replaced by six-membered β-alaninate rings, as can be seen from the comparison of $\Sigma\Delta(O_h)$ values for the *trans*(O_5O_6)-$[Co(1,3\text{-}pddadp)]^-$ (**1**) (36°) and *trans*(O_6)-$[Co(1,3\text{-}pddadp)]^-$ (**2**) [16] (38°) complexes with that of $[Co(1,3\text{-}pdta)]^-$ (**3**) [35] (34°). Mostly due to the strain formed by chelation of in-plane glycinate rings, manifested

Table 3
Strain analysis of edta-type chelates of Co(III)[a]

Complexes	Rings in G-plane	$\Sigma\Delta(O_h)$[b]	$\Delta\Sigma$[c]			Δ(Co–O–C)[d]		$\Sigma\Delta$(N)[e]	Ref.
			T (E)	R	G	R	G		
With 1,3-propanediamine (T) ring									
trans(O_5O_6)-$[Co(1,3\text{-}pddadp)]^-$ (**1**)[f]	5–6–6	36	+34	0, +36	−9, +44	+6, +19	+5, +24	18, 14	this work
trans(O_6)-$[Co(1,3\text{-}pddadp)]^-$ (**2**)	5–6–5	38	+28	+33	−11	+17	+4	16	[16]
$[Co(1,3\text{-}pdta)]^-$ (**3**)	5–6–5	34	+36	+1	−12	+7	+5	15	[35]
With ethylenediamine (E) ring									
trans(O_5)-$[Co(eddadp)]^-$ (**4**)	6–5–6	31	−11	−1	+38	+6	+18	13	[8]
trans(O_5)-$[Co(ed3ap)]^-$ (**5**)[f]	5–5–6	29	−11	±1	−13, +44	+4, +5	+5, +19	18, 12	[34]
$[Co(edtp)]^-$ (**6**)	6–5–6	29	−14	+42	+41	+21	+21	18	[13]
$[Co(edta)]^-$ (**7**)	5–5–5	48	−12	−1	−9	+5	+3	18	[31,33]

[a] Abbreviations of ligands: 1,3-pddadp = 1,3-propanediamine-*N*,*N*′-diacetate-*N*,*N*′-di-3-propionate, 1,3-pdta = 1,3-propanediaminetetraacetate, eddadp = ethylenediamine-*N*,*N*′-diacetate-*N*,*N*′-di-3-propionate, ed3ap = ethylenediamine-*N*,*N*,*N*′-triacetate-*N*′-3-propionate, edtp = ethylenediamine-*N*,*N*,*N*′,*N*′-tetra-3-propionate and edta = ethylenediaminetetraacetate.

[b] $\Sigma\Delta(O_h)$ is the sum of the absolute values of the deviations from 90° of the L–Co–L′ bite angles. All values rounded off to the nearest degree.

[c] $\Delta\Sigma$(ring) is the deviation from the ideal of the corresponding chelate rings' bond angle sum. A mean value of the two rings (R or G) is reported for complexes having an approx. C_2 molecular symmetry.

[d] Δ(Co–O–C) (ring) is the mean value of the deviation of the corresponding rings' Co–O–C bond angle from 109.5°.

[e] $\Sigma\Delta$(N) is the sum of the absolute values of the deviations from 109.5° of the six bond angles made by the nitrogen atoms. A mean value for the two nitrogens is reported.

[f] For the complexes (**1**) and (**5**) having C_1 molecular symmetry two values are reported.

in octahedral bond angles, the *trans*(O_6)-[Co(1,3-pddadp)]$^-$ [16] complex with a 5–6–5 ring system in the G-plane is more strained than *trans* (O_5O_6)-[Co(1,3-pddadp)]$^-$ having an in-plane 5–6–6 combination of the ring members. The strain formed around the chelating nitrogen atoms in [Co(1,3-pddadp)]$^-$ complexes of *trans*(O_5O_6) and *trans*(O_6) geometry is practically the same. As expected five-membered chelate rings coordinated in-plane are much more strained than those coordinated in axial positions. Of all the ethylenediamine rings observed in complexes (**4**–**7**), the greatest strain was registered for the ethylenediamine ring in the [Co(edtp)]$^-$ (**6**) [13] complex with the ligand ethylenediamine-*N*,*N*,*N*′,*N*′-tetra-3-propionate, which is able to form only six-membered carboxylato rings. For this ring the deviation from the ideal sum of chelate ring bond angles is −14°. For the analyzed Co(III) chelates the greatest strain among in-plane coordinated glycinates was registered for the glycinate ring in the *trans*(O_5)-[Co(ed3ap)]$^-$ (**5**) complex for which the total deviation sums −13°. The total deviation of six-membered chelate rings is positive and is the greatest for in-plane coordinated β-alaninate rings in the *trans*-(O_5O_6)-[Co(1,3-pddadp)]$^-$ (**1**) and *trans*(O_5)-[Co(ed-3ap)]$^-$ (**5**) complexes (+44°). The in-plane β-alaninate rings of the *trans*(O_5)-[Co(eddadp)]$^-$ (**4**) complex are less strained, favoring the *trans*(O_5) geometry, as expected for [M(eddadp)]$^{n-}$ complexes [2–13]. The two N-geminal β-alaninate rings (R and G) in [Co(edtp)]$^-$ (**6**) show the same positive total deviation of ca. 41°. The bond angles of the M–O–C fragment are expected to be between 109.5° and 120°, depending on the degree of covalency of the M–O bond [13]. These bond angles in the β-alaninate rings are as high as 130°. In general, these values are larger for the G β-alaninate rings than for the R β-alaninate rings and for Co(III) chelates are in the range 18–24° versus 17–21°.

3.3. Molecular mechanics results

The energy minimization and geometry optimization procedure resulted in several stable conformations for each geometrical isomer, *trans*(O_5), *trans*(O_5O_6) and *trans*(O_6), regardless of the initial conformation we started with. The structural parameters for the resulting most stable energy-minimized structures, as well as a comparison with the X-ray structures, are presented in Table 4. Ortep illustrations for each of the resulting structures are shown in Fig. 4.

Calculated energies for *trans*(O_5), *trans*(O_5O_6) and *trans*(O_6) isomers of [Co(1,3-pddadp)]$^-$ show that the *trans*(O_5O_6) isomer represents the most stable one

Table 4
Summary of molecular mechanics results

	X-ray, *trans*(O_6)	X-ray, *trans*(O_5O_6)	*trans*(O_5O_6)	*trans*(O_6)	*trans*(O_5)
Energy terms (kcal/mol)					
E_{total}			39	42	44
E_b			9	9	10
E_θ			29	28	27
E_φ			4	8	7
E_{nb}			24	24	27
E_e			−27	−27	−27
Selected average bond lengths (Å)					
M–N	1.964	1.979	1.977	1.967	1.983
M–O	1.906	1.906	1.904	1.902	1.900
C′–O	1.279	1.288	1.272	1.273	1.272
C_α–C′	1.509	1.500	1.512	1.517	1.515
C_α–C_β	1.506	1.512	1.519	1.522	1.523
C–C	1.529	1.522	1.524	1.536	1.523
N–C_α	1.491	1.494	1.506	1.503	1.508
N–C_β	1.500	1.496	1.502	1.508	1.509
N–C	1.497	1.500	1.495	1.489	1.493
Selected average valence angles (°)					
N–M–O	89.4	89.7	88.7	88.0	87.8
M–O–C′	120.0	123.2	123.7	120.8	122.1
O–C′–C_α	116.9	117.4	118.9	117.9	118.1
C′–C_α–C_β	112.9	115.9	113.7	109.4	111.5
C_α–C_β–N	114.3	115.4	116.5	116.7	117.2
C_α–N–M	103.4	105.5	107.6	105.7	108.0
C_β–N–M	115.3	112.8	112.7	114.4	112.2
N–M–N	98.0	97.6	99.7	100.7	98.8
M–N–C	111.1	110.6	111.1	110.2	111.4
N–C–C	113.7	115.6	116.3	115.0	116.2
C–C–C	117.5	118.0	118.0	118.6	117.6

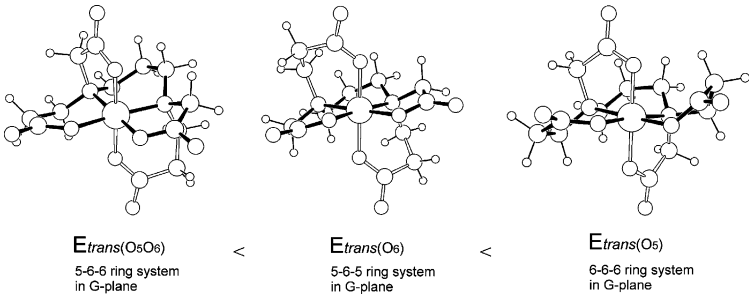


Fig. 4. Ortep illustrations of the energy-minimized structures of the three isomers of $[Co(1,3\text{-pddadp})]^-$.

(Table 4), but the energy differences between isomers are rather small and result mostly form torsional contributions to the total energy. The analysis of the torsional contributions to the total strain shows that in *trans*(O_5) and *trans*(O_6) isomers the strain is pronounced mainly in endocyclic torsions involving M–O and O–C′ bonds in the β-alaninate rings (G and R rings, respectively). In addition, in these β-alaninate rings we also noticed significant deviation from planarity of the coordinated carboxylato moiety, as indicated by the M–O–C′–O′ torsion angles of nearly 160° for all chelate rings considered. In the crystal structure of the *trans*(O_6)-$[Co(1,3\text{-pddadp})]^-$ complex the mean M–O–C′–O′ torsion angle in the axially coordinated β-alaninate rings is 154°. This might be the reason for greater torsional contributions to the total energy in the case of the *trans*(O_5) and *trans*(O_6) isomers.

The geometries of the calculated structures are in good agreement with the corresponding structures for which X-ray data are available (the *trans*(O_5O_6)-$[Co(1,3\text{-pddadp})]^-$ complex presented here and the earlier reported *trans*(O_6)-$[Co(1,3\text{-pddadp})]^-$ [16]). The lowest energy conformer corresponds to the configuration that has been found in the X-ray structure presented in this paper. The total energy of the minimized structures for three geometrical isomers of $[Co(1,3\text{-pddadp})]^-$ increases in the order $E_{total}(trans(O_5O_6)) < E_{total}(trans(O_6)) < E_{total}(trans(O_5))$, Table 4.

4. Concluding remarks

For the ligands having the ethylenediamine fragment and mixed five- and six-membered carboxylate arms (ed3ap [34,36] and eddadp [2–13]) geometrical isomers are possible that differ in the number (0, 1, or 2) of six-membered rings lying in the equatorial plane (G-plane). These ligands generally minimize strain by forming isomers that have six-membered ring(s) in the G-plane [2,13]. In the so far well known reactions of Co(III), [3,4,8] Cr(III), [6,10] Fe(III), [7] Rh(III) [5,9] and Ni(II) [12] with the ligand ethylenediamine-*N*,*N*′-diacetate-*N*,*N*′-di-3-propionate (eddadp) the *trans*(O_5) geometry (Fig. 1(b)) is favored due to the lower steric strain formed by chelation of the two in-plane β-alaninate rings [2,13]. However, in the case of the 1,3-propanediamine-*N*,*N*′-diacetato-*N*,*N*′-di-3-propionato (1,3-pddadp) complex, especially with small metal ions such as Co(III) (0.685 Å), [37] the *trans*(O_5) isomer should be sterically disfavored because of the concentration of all three six-membered rings in the equatorial plane. The 6–6–6 combination of the chelate rings in the girdle plane has been observed in the *trans*(O_5) isomer of the 1,3-pddadp complex containing the Rh(III) ion, with an ionic radius of 0.805 Å [18], but has not been so far obtained for Co(III) [15,16], with an ionic radius of 0.685 Å. Of the two isomers that have been isolated for the $[Co(1,3\text{-pddadp})]^-$ system, i.e., *trans*(O_5O_6) and *trans*(O_6), the lowest energy conformer corresponds to the *trans*(O_5O_6) configuration that has been found in the X-ray structure presented here. In addition, it has also been observed that the *trans*(O_5O_6) isomer of the $[Co(1,3\text{-pddadp})]^-$ complex is slightly more free from octahedral strain with respect to the *trans*(O_6) configuration of the same complex.

Acknowledgments

We thank the Ministry of Science and Environmental Protection of the Republic of Serbia for financial support of the scientific projects No. 1569 and No. 1254.

This work was funded in part by the Polish State Committee for Scientific Research as scientific project No. 4 T09A 185 25 during the years 2003–2006.

Appendix A. Supplementary data

Supplementary data are given in a form of Tables 1S–2S and Figs. 1S–2S. The crystallographic cif files are available from the CCDC, 12 Union Road, Cambridge CB2 1EZ, UK, fax: +44 1223 336 033, e-mail: deposit @ccdc.cam.uk or on the web www: http://www.ccdc.cam.ac.uk) on request, quoting the Deposition No. CCDC 262196. Supplementary data associated with this article can be found, in the online version at doi:10.1016/j.poly.2005.04.035.

References

[1] D.J. Radanović, Coord. Chem. Rev. 54 (1984) 159, and refs. therein.
[2] B.E. Douglas, D.J. Radanović, Coord. Chem. Rev. 128 (1993) 139, and refs. therein.
[3] W. Byers, B.E. Douglas, Inorg. Chem. 11 (1972) 1470.
[4] D.J. Radanović, B.E. Douglas, Inorg. Chem. 14 (1975) 6.
[5] D.J. Radanović, K.D. Gailey, M.I. Djuran, B.E. Douglas, J. Coord. Chem. 10 (1980) 115.
[6] D.J. Radanović, B.E. Douglas, J. Coord. Chem. 4 (1975) 191.
[7] T. Yamamoto, K. Mikata, K. Miyoshi, H. Yoneda, Inorg. Chim. Acta 150 (1988) 237.
[8] T. Mizuta, T. Yamamoto, N. Shibata, K. Miyoshi, Inorg. Chim. Acta 169 (1990) 257.
[9] R. Herak, L.j. Manojlović-Muir, M.I. Djuran, D.J. Radanović, J. Chem. Soc., Dalton Trans. (1985) 861.
[10] F.T. Helm, W.H. Watson, D.J. Radanovic, B.E. Douglas, Inorg. Chem. 16 (1977) 2351.
[11] K. Kanamori, J. Kumada, M. Yamamoto, T. Okayasu, K. Okamoto, Bull. Chem. Soc. Jpn. 68 (1995) 3445.
[12] D.J. Radanović, S. Ianelli, G. Pelosi, Z.D. Matović, S. Tasić-Stojanović, B.E. Douglas, Inorg. Chim. Acta 278 (1998) 66.
[13] M. Parvez, C. Maricondi, D.J. Radanović, M.I. Djuran, B.E. Douglas, Inorg. Chim. Acta 182 (1991) 177.
[14] S. Kaizaki, M. Byakuno, M. Hayashi, J.I. Legg, K. Umakoshi, S. Ooi, Inorg. Chem. 26 (1987) 2395.
[15] D.J. Radanović, S.R. Trifunović, M.S. Cvijović, C. Maricondi, B.E. Douglas, Inorg. Chim. Acta 196 (1992) 161.
[16] M. Parvez, C. Maricondi, D.J. Radanović, S.R. Trifunović, V.D. Miletić, B.E. Douglas, Inorg. Chim. Acta 248 (1996) 89.
[17] D.J. Radanović, M.I. Djuran, T.S. Kostić, B.E. Douglas, Inorg. Chim. Acta 211 (1993) 149.
[18] U. Rychlewska, M.I. Djuran, M.M. Vasojević, D.D. Radanović, V.M. Ristanović, D.J. Radanović, Inorg. Chim. Acta 328 (2002) 218.
[19] Z.D. Matović, S. Ianelli, G. Pelosi, S.K. Janićijević, V.M. Ristanović, G. Ponticelli, D.J. Radanović, Polyhedron 21 (2002) 2667.
[20] D.J. Radanović, B.V. Prelesnik, D.D. Radanović, Z.D. Matović, B.E. Douglas, Inorg. Chim. Acta 262 (1997) 203.
[21] I. Bernal, J. Cetrullo, J. Myrczek, J.S. Ricci Jr., D.J. Radanović, S.R. Trifunović, in: W. Gans, J.C.A. Boyens (Eds.), Intermolecular Interactions, Plenum Press, New York, 1998, p. 155.
[22] Kuma Diffraction KM4CCD Software. Version 1.168, Kuma Diffraction Instruments GmbH, Wrocław, Poland, 1999.
[23] G.M. Sheldrick, Acta Crystallogr., Sect. A 46 (1990) 467.
[24] G.M. Sheldrick, SHELXL97, Program for the Refinement of Crystal Structures, University of Göttingen, Germany, 1997.
[25] Stereochemical Workstation Operation Manual, Release 3.4, Siemens Analytical X-ray Instruments, Inc., Madison, WI, 1989.
[26] S.R. Niketić, K. Rasmussen, The Consistent Force Field: A Documentation, Springer-Verlag, Berlin, Heidelberg, New York, 1977.
[27] S. Grubišić, M. Gruden, S.R. Niketić, N. Sakagami, S. Kaizaki, J. Mol. Struct. 609 (2002) 1.
[28] S. Grubišić, M. Gruden-Pavlović, S.R. Niketić, S. Kaizaki, N. Sakagami, Inorg. Chem. Commun. 6 (2003) 1180.
[29] M. Gruden, S. Grubišić, S.R. Niketić, A.G. Coutsolelos, J. Mol. Struct. 595 (2001) 209.
[30] L.J. Farrugia, J. Appl. Crystallogr. 30 (1997) 565.
[31] H.A. Weakliem, J.L. Hoard, J. Am. Chem. Soc. 81 (1959) 549.
[32] K.R. Dymock, G.J. Palenik, Inorg. Chem. 14 (1975) 1220.
[33] K. Okamoto, T. Tsukihara, J. Hidaka, Y. Shimura, Bull. Chem. Soc. Jpn. 51 (1978) 3534.
[34] D.J. Radanović, V.D. Miletić, T. Ama, H. Kawaguchi, Bull. Chem. Soc. Jpn. 71 (1998) 1605.
[35] R. Nagao, F. Marumo, Y. Saito, Acta Crystallogr., Sect. B 28 (1972) 1852.
[36] (a) D.J. Radanović, M.I. Djuran, T.S. Kostić, C. Maricondi, B.E. Douglas, Inorg. Chim. Acta 207 (1993) 111;
(b) D.J. Radanović, N. Sakagami, V.M. Ristanović, S. Kaizaki, Inorg. Chim. Acta 292 (1999) 16;
(c) D.J. Radanović, T. Ama, D.M. Gurešić, D.M. Ristanović, D.D. Radanović, H. Kawaguchi, Bull. Chem. Soc. Jpn. 73 (2000) 2283.
[37] R.D. Shannon, Acta Crystallogr., Sect. A 32 (1976) 751.

2. Experimental

2.1. Physical measurements

Elemental analyses were performed on a Perkin–Elmer-2400 CHN/O analyzer. Infrared spectra were recorded on a Perkin–Elmer Model 983 spectrophotometer with the sample prepared as KBr pellets. Electronic spectra were recorded on a Hitachi-300 spectrophotometer. The ^{1}H NMR and ^{13}C{^{1}H} NMR spectra were recorded in acetone-d_6 and $CDCl_3$ solvents with TMS as internal standard and recorded on a Bruker ACF-300 (300 MHz) spectrometer, the coupling constants J being given in Hz. Electro-chemical studies (in acetonitrile) were performed with a PARC electrochemistry system as described elsewhere [13]. In cyclic voltametry (CV) the following parameters were used, namely, the scan rate 100 mV s^{-1} and the formal potential $E^0 = 0.5(E_{pa} + E_{pc})$, where E_{pa} and E_{pc} are the anodic and cathodic peak potentials, respectively; and ΔE_p is the peak-to-peak separation.

2.2. Materials and methods

All chemicals used were of reagent grade. All reactions were carried out in distilled and dried solvents. Rhodium chloride and iridium chloride were purchased from Arora Matthey Ltd., and used as received. Pyridine 2-carboxaldehyde (Fluka) was used as received. All liquid aromatic amines were reagent grade and were distilled prior to use, while solid aromatic amines were used as such. The ligands C_5H_4N-2-CH=NC_6H_4-*p*-X (where X = H, CH_3, OCH_3, Cl, NO_2) [14], and the precursor complexes [{(η^5-C_5Me_5)M(μ-Cl)Cl}$_2$] (where M = Rh (**1**) and Ir (**2**)) [15] were prepared by known literature methods. The purification of acetonitrile and the preparation of tetrabutylammonium perchlorate [Bu$^n_4$N][ClO_4], used as solvent and supporting electrolyte, respectively, in the electrochemical experiments, were performed following a literature method [16].

2.3. Synthesis of [(η^5-C_5Me_5)RhCl(C_5H_5N-2-CH=NC_6H_4-p-X)]$^+$ (**3a-e**), (X = H (**3a**), CH_3 (**3b**), OCH_3 (**3c**), Cl (**3d**), NO_2 (**3e**))

The following general procedure was used for the preparation of these five complexes:

Method 1: A mixture of the starting complex [{(η^5-C_5Me_5)Rh(μ-Cl)Cl}$_2$] (**1**) (100 mg, 0.110 mmol), the appropriate Schiff base ligand **2-PP** (0.242 mmol) and NH_4PF_6 (0.242 mmol) was stirred in methanol–acetone (20/10 v/v mixture) for 6 h until the color of the solution changed from red to orange. The solvent was removed in vacuo, the residue dissolved in dichloromethane (5 ml), and the solution filtered to remove ammonium chloride. The orange solution was concentrated to 2 ml, when addition of excess hexane gave the orange-yellow complex, which was separated and dried under vacuum.

Method 2: A mixture of the complex [{(η^5-C_5Me_5)Rh(μ-Cl)Cl}$_2$] (**1**) (100 mg, 0.110 mmol), the ligand **2-PP** (0.242 mmol) and NH_4PF_6 (0.242 mmol) was stirred in methanol (20 ml) for a few hours, whereupon the orange-yellow product separated out. The orange-yellow product was centrifuged, washed with diethyl ether and dried under vacuum.

3a. Yield: 152 mg, (78%). IR (KBr pellets, cm^{-1}): $\nu_{(C=N)}$ 1593 (s), $\nu_{(P-F)}$ 844 (s).

^{1}H NMR ($CDCl_3$ and acetone-d_6, δ): 1.56 (s, 15H, C_5Me_5), 7.32–7.56 (m, 3H, Ph), 7.64 (d, 2H, J_{H-H} = 6.53 Hz, Ph), 8.03–8.55 (m, 3H, py), 8.97 (d, 1H, J_{H-H} = 4.86 Hz, py), 9.24 (s, 1H, imine C–H).

^{13}C NMR (acetone-d_6, δ): 7.60 (CH_3, C_5Me_5), 97.53 (C, C_5Me_5), 122.44, 129.43, 129.79, 131.36 (Ph), 140.34, 148.80, 152.66, 154.04, 155.32 (py), 166.97 (C–H).

Elemental *Anal.* Calc. for $C_{22}H_{25}RhN_2ClPF_6$: C, 43.98; H, 4.19; N, 4.66. Found: C, 43.65; H, 4.02; N, 4.71%.

UV–Vis (acetone): λ_{max} = 359.6 nm.

3b. Yield: 159 mg, (80%). IR (KBr pellets, cm^{-1}): $\nu_{(C=N)}$ 1596 (m), $\nu_{(P-F)}$ 844 (s).

^{1}H NMR ($CDCl_3$ and acetone-d_6, δ): 1.52 (s, 15H, C_5Me_5), 2.44 (s, 3H, CH_3), 7.35 (d, 2H, J_{H-H} = 2.31 Hz), 7.67 (d, 2H, J_{H-H} = 8.22 Hz), 7.83–7.87 (dd, 1H, J_{H-H} = 3.96 Hz), 8.20 (d, 2H, J_{H-H} = 4.22 Hz), 8.57 (d, 1H, J_{H-H} = 2.81 Hz), 8.89 (d, 2H, J_{H-H} = 5.36 Hz).

^{13}C NMR (acetone-d_6, δ): 7.63 (CH_3, C_5Me_5), 18.34 (CH_3), 98.37 (C, C_5Me_5), 112.24, 115.62, 116.96, 122.32 (Ph), 123.37, 126.21, 128.56, 131.34, 145.36 (py), 158.56 (C–H).

Elemental *Anal.* Calc. for $C_{23}H_{27}RhN_2ClPF_6$: C, 44.93; H, 4.42; N, 4.55. Found: C, 45.56; H, 4.38; N, 4.56%.

UV–Vis (acetone): λ_{max} = 344.6 nm.

3c. Yield: 146 mg, (72%). IR (KBr pellets, cm^{-1}): $\nu_{(C=N)}$ 1596 (s), $\nu_{(P-F)}$ 840 (s).

^{1}H NMR (acetone-d_6, δ): 1.55 (s, 15H, C_5Me_5), 3.89 (s, 3H, CH_3), 7.17 (d, 2H, J_{H-H} = 4.55 Hz), 7.79 (d, 2H, J_{H-H} = 4.48 Hz), 7.99 (td, 2H, J_{H-H} = 2.14 Hz, 5.22 Hz), 8.37 (d, 1H, J_{H-H} = 7.36 Hz), 8.66 (d, 1H, J_{H-H} = 2.79 Hz), 9.15 (d, 1H, J_{H-H} = 5.29 Hz).

^{13}C NMR (acetone-d_6, δ): 8.80 (CH_3, C_5Me_5), 56.08 (CH_3), 96.35 (C, C_5Me_5), 115.35, 118.38, 122.46, 124.96 (Ph), 126.24, 127.37, 130.44, 141.27, 153.56 (py), 166.36 (C–H).

Elemental *Anal.* Calc. for $C_{23}H_{27}RhN_2OClPF_6$: C, 43.79; H, 4.31; N, 4.44. Found: C, 43.36; H, 4.36; N, 4.53%.

UV–Vis (acetone): λ_{max} = 363.6 nm.

3d. Yield: 161 mg, (79%). IR (KBr pellets, cm^{-1}): $\nu_{(C=N)}$ 1600 (s), $\nu_{(B-F)}$ 1056 (s).

^{1}H NMR ($CDCl_3$, δ): 1.82 (s, 15H, C_5Me_5), 7.52 (d, 2H, J_{H-H} = 8.68 Hz, Ph), 7.89 (d, 2H, J_{H-H} = 8.64 Hz, Ph), 8.14 (td, 1H, J_{H-H} = 9.04 Hz, 7.68 = Hz, py), 8.24 (d, 2H, J_{H-H} = 7.28 Hz, py), 8.58 (d, 1H, J_{H-H} = 2.76 Hz, imine C–H), 8.74 (d, 1H, J_{H-H} = 5.76 Hz, py).

^{13}C NMR ($CDCl_3$, δ): 8.57 (CH_3, C_5Me_5), 90.17 (C, C_5Me_5), 121.32, 126.26, 130.38, 132.47 (Ph), 135.58, 139.24, 145.31, 149.27, 155.51 (py), 164.73 (C–H).

Elemental *Anal*. Calc. for $C_{22}H_{24}RhN_2Cl_2PF_6$: C, 41.66; H, 3.81; N, 4.41. Found: C, 41.34; H, 3.47; N, 4.26%.

UV–Vis (acetone): λ_{max} = 372.5 nm.

3e. Yield 153 mg, (73%). IR (KBr pellets, cm^{-1}): $\nu_{(C=N)}$ 1593 (s), $\nu_{(NO_2,\,asymmetric)}$ 1527 (s), $\nu_{(NO_2,\,symmetric)}$ 1348 (s), $\nu_{(P-F)}$ 837 (s).

^{1}H NMR (acetone-d_6, δ): 1.47 (s, 15H, C_5Me_5), 8.06 (m, 3H, py), 8.43 (d, 2H, J_{H-H} = 8.63 Hz, Ph), 8.54 (d, 2H, J_{H-H} = 8.91 Hz), 9.07 (d, 1H, J_{H-H} = 2.80 Hz, CH), 9.24 (d, 1H, J_{H-H} = 5.36 Hz, α proton of py).

^{13}C NMR (acetone-d_6, δ): 8.84 (CH_3, C_5Me_5), 90.34 (C, C_5Me_5), 98.46, 106.54, 115.68, 124.55 (Ph), 125.92, 131.16, 131.62, 141.29, 153.57 (py), 169.84 (C–H).

Elemental *Anal*. Calc. for $C_{22}H_{24}RhN_3O_2ClPF_6$: C, 40.92; H, 3.74; N, 6.50. Found: C, 39.48; H, 3.88; N, 6.08%.

UV–Vis (acetone): λ_{max} = 369.4 nm.

*2.4. Synthesis of [(η^5-C_5Me_5)IrCl(C_5H_5N-2-CH=N–C_6H_4-p-X)]$^+$ (**4a-e**), (X = H (**4a**), CH_3 (**4b**), OCH_3 (**4c**), Cl (**4d**), NO_2 (**4e**)*

These complexes were prepared by the same method given in Section 2.3 using [{(η^5-C_5Me_5)Ir(μ-Cl)Cl}$_2$] (**2**) instead of complex [{(η^5-C_5Me_5)Rh(μ-Cl)Cl}$_2$] (**1**).

4a. Yield: 136 mg, (79%). IR (KBr pellets, cm^{-1}): $\nu_{(C=N)}$ 1600 (s), $\nu_{(P-F)}$ 844 (s).

^{1}H NMR (acetone-d_6, δ): 1.55 (s, 15H, C_5Me_5), 7.55–7.61 (m, 3H, Ph), 7.80 (d, 2H, J_{H-H} = 7.95 Hz, Ph), 7.99–8.40 (m, 3H, py), 9.19 (d, 1H, J_{H-H} = 5.05 Hz, α proton of py), 9.35 (s, 1H, CH).

^{13}C NMR (acetone-d_6, δ): 8.51 (CH_3, C_5Me_5), 91.22 (C, C_5Me_5), 123.57, 130.47, 130.90, 131.42 (Ph), 136.32, 138.47, 141.51,153.24, 157.83 (py), 169.43 (imine C–H).

Elemental *Anal*. Calc. for $C_{22}H_{25}IrN_2ClPF_6$: C, 38.29; H, 3.65; N, 4.06. Found: C, 38.47; H, 3.32; N, 4.12%.

UV–Vis (acetone): λ_{max} = 385.7 nm.

4b. Yield: 112 mg, (63%). IR (KBr pellets, cm^{-1}): $\nu_{(C=N)}$ 1633 (s), $\nu_{(P-F)}$ 844 (s).

^{1}H NMR (acetone-d_6, δ): 1.55 (s, 15H, C_5Me_5), 2.47 (s, 3H, CH_3), 7.48 (d, 2H, J_{H-H} = 8.14 Hz, Ph), 7.70 (d, 2H, J_{H-H} = 8.31 Hz, Ph), 8.00–8.03 (m, 1H, py), 8.35–8.40 (m, 2H, py), 8.51 (d 1H, J_{H-H} = 7.39 Hz, imine C–H), 9.18 (d, 1H, J_{H-H} = 5.39 Hz, α proton of py).

^{13}C NMR (acetone-d_6, δ): 8.54 (CH_3, C_5Me_5), 21.16 (CH_3), 91.17 (C, C_5Me_5), 123.49, 128.36, 130.71, 131.26 (Ph), 141.50, 148.23, 152.54, 153.20, 155.21 (py), 166.76 (imine C–H).

Elemental *Anal*. Calc. for $C_{23}H_{27}IrN_2ClPF_6$: C, 39.23; H, 3.86; N, 3.97. Found: C, 40.32; H, 3.83; N, 4.04%.

UV–Vis (acetone): λ_{max} = 385.75 nm.

4c. Yield: 133 mg, (73%). IR (KBr pellets, cm^{-1}): $\nu_{(C=N)}$ 1606 (s), $\nu_{(P-F)}$ 844 (s).

^{1}H NMR (acetone-d_6, δ): 1.57 (s, 15H, C_5Me_5), 3.76 (s, 3H, CH_3), 7.23 (d, 2H, J_{H-H} = 6.23 Hz, Ph), 7.62 (d, 2H, J_{H-H} = 6.23 Hz, Ph), 7.86–8.34 (m, 3H, py), 8.58 (d, 1H, J_{H-H} = 3.06 Hz, α proton of py), 9.23 (1H, J_{H-H} = 4.66 Hz, imine C–H).

^{13}C NMR (acetone-d_6, δ): 7.57 (CH_3, C_5Me_5), 55.15 (CH_3), 90.12 (C, C_5Me_5), 114.35, 114.60, 124.14, 129.43 (Ph), 130.10, 140.45, 148.32, 149.69, 152.15 (py), 166.64 (imine C–H).

Elemental *Anal*. Calc. for $C_{23}H_{27}IrN_2OClPF_6$: C, 38.36; H, 3.77; N, 3.89. Found: C, 38.06; H, 3.46; N, 3.95%.

UV–Vis (acetone): λ_{max} = 368.23 nm.

4d. Yield: 128 mg, (71%). IR (KBr pellets, cm^{-1}): $\nu_{(C=N)}$ 1633 (s), $\nu_{(P-F)}$ 844 (s).

^{1}H NMR (acetone-d_6, δ): 1.56 (s, 15H, C_5Me_5), 7.73 (d, 2H, J_{H-H} = 8.55 Hz, Ph), 7.65 (d, 2H, J_{H-H} = 8.81 Hz, Ph), 8.01–8.06 (m, 3H, py), 8.95 (d, 1H, J_{H-H} = 2.74 Hz, imine C–H), 9.21 (d, 1H, J_{H-H} = 5.39 Hz, α proton-py).

^{13}C NMR (acetone-d_6, δ): 7.57 (CH_3, C_5Me_5), 90.28 (C, C_5Me_5), 124.35, 129.56, 130.12, 130.58 (Ph), 140.56, 142.63, 147.34, 149.52, 152.28 (py), 169.08 (imine C–H).

Elemental *Anal*. Calc. for $C_{22}H_{24}IrN_2Cl_2PF_6$: C, 36.52; H, 3.34; N, 3.87. Found: C, 36.61; H, 3.08; N, 3.66%.

UV–Vis (acetone): λ_{max} = 385.75 nm.

4e. Yield: 132 mg, (72%). IR (KBr pellets, cm^{-1}): $\nu_{(C=N)}$ 1593 (s), $\nu_{(NO_2,\,asymmetric)}$ 1527 (s), $\nu_{(NO_2,\,symmetric)}$ 1348 (s), $\nu_{(P-F)}$ 844 (s).

^{1}H NMR (acetone-d_6, δ): 1.59 (s, 15H, C_5Me_5), 8.05–8.10 (m, 2H, py), 8.41 (d, 2H, J_{H-H} = 1.41 Hz, Ph), 8.54–8.61 (m, 1H, py), 9.26 (d, 1H, J_{H-H} = 5.5 Hz, α proton-py), 9.54 (s, 1H, imine C–H).

^{13}C NMR (acetone-d_6, δ): 8.39 (CH_3, C_5Me_5), 91.25 (C, C_5Me_5), 124.77, 125.91, 131.55, 131.77 (Ph), 141.45, 149.36, 153.20, 154.26, 156.54 (py), 171.26 (imine C–H).

Elemental *Anal*. Calc. for $C_{22}H_{24}IrN_3O_2ClPF_6$: C, 35.94; H, 3.29; N, 5.71. Found: C, 35.76; H, 3.43; N, 5.92%.

UV–Vis (acetone): λ_{max} = 387.13 nm.

3. Crystallographic investigations

Crystals suitable for X-ray diffraction study for compound **3d**[BF_4] were grown by slow diffusion of hexane

into an acetonitrile solution of **3d**[BF_4], and for compound **4e**[PF_6] by slow diffusion of hexane into a dichloromethane solution of **4e**[PF_6]. The orange crystals of compounds **3d**[BF_4] and **4e**[PF_6] were mounted on a Bruker Apex CCD diffractometer in a full reciprocal sphere equipped with a CCD detector, and were used for data collection. X-ray intensity data were collected with graphite monochromated Mo Kα radiation at 293(2) K, with 0.3° ω scan mode and 10 s per frame. The intensity data were corrected for Lorentz and polarization effects. Absorption corrections were done using the SAINT program [17]. A summary of the crystal data, data collection parameters and convergence results is compiled in Table 1. An empirical absorption correction was made by modelling a transmission surface by spherical harmonics employing equivalent reflections with $I > 2\sigma(I)$ (program SADABS) [18]. The structures were solved by direct methods [19]. All the non-hydrogen atoms were refined anisotropically using the full-matrix, least-squares technique on F^2 using the SHELXL-97 software [20]. All the hydrogen atoms were found from difference Fourier synthesis after four cycles of an isotropic refinement and as per the ''riding'' model. Figs. 3 and 4 display the ORTEP [21] representations of the molecules with 50% probability thermal ellipsoids. Refinement converged at final R_1 values of 0.0366 and 0.0313 (for observed data F) for compounds **3d**[BF_4] and **4e**[PF_6], respectively.

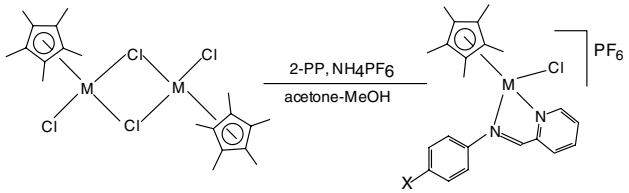
Table 1
Crystal data and structure refinement parameters for complexes **3d**[BF_4] and **4e**[PF_6]

Formula	$C_{22}H_{24}BCl_2F_4N_2Rh$	$C_{22}H_{24}ClF_6IrN_3O_2P$
M_r	577.05	735.06
T (K)	293(2)	293(2)
Wavelength (Å)	0.71073	0.71073
Crystal system	monoclinic	monoclinic
Space group	$P2_1/n$	$P2_1/n$
a (Å)	10.1944(6)	10.4116(6)
b (Å)	11.6110(6)	11.5786(6)
c (Å)	20.4223(11)	21.7809(12)
β (°)	96.334(10)	98.097(10)
V (Å^3)	2402.6(2)	2599.5(2)
Z	4	4
Crystal size (mm^3)	$0.45 \times 0.27 \times 0.25$	$0.15 \times 0.28 \times 0.35$
D_{calc} (g cm^{-3})	1.595	1.878
$F(000)$	1160	1424
θ (°)	2.01–28.30	1.89–28.30
Reflections collected	20524	22158
Independent reflections [R_{int}]	5645 [0.0180]	6119 [0.0285]
Absorption coefficient (mm^{-1})	0.977	5.368
Completeness to θ (°)	28.30	28.30
Data/restraints/parameters	5645/0/255	6119/0/297
Goodness-of-fit on F^2	1.046	1.059
R_1 ($I > 2\sigma(I)$), wR_2	0.0366, 0.1062	0.0313, 0.0812
R_1, R_2 (all data)	0.0410, 0.1100	0.0417, 0.0863
Largest difference in peak and hole (e Å^{-3})	+0.804 and −0.617	+2.159 and −0.616

4. Results and discussion

The dinuclear complexes [{(η^5-C_5Me_5)M(μ-Cl)Cl}$_2$] {M = Rh (**1**) and Ir (**2**)} undergo a bridge cleavage reaction with *N*,*N*′-donor Schiff base ligands (**2-PP**) in methanol to yield cationic complexes **3** and **4** (Scheme 1), respectively. These complexes are isolated as the hexafluorophosphate salts. The orange-yellow complexes are air-stable microcrystalline solids, partially soluble in chloroform, methanol and benzene, soluble in dichloromethane, acetone and insoluble in hexane, petroleum ether and diethyl ether.

The infrared spectra of these complexes show a strong band in the range 1593–1633 cm^{-1} due to the $\nu_{C=N}$ group of the Schiff base ligand, and a strong band in the range 837–844 cm^{-1} due to the ν_{P-F} mode of the PF_6^- group. The complexes **3e** and **4e** exhibit the characteristic bands for ν_{NO_2} (asymmetric stretch at 1527 cm^{-1} and symmetric stretch at 1346 cm^{-1}). The ^{1}H NMR spectral data of these complexes along with their assignments are recorded in the experimental section. In the ^{1}H NMR spectra of these complexes, the methyl group of the pentamethylcyclopentadienyl protons appears as a singlet in the range 1.47–1.82 ppm, which are shifted downfield as compared to that in the precursor complexes. A downfield shift in the position of the Cp* protons might result from the change in electron density on the metal center due to chelation of the Schiff base ligands through their nitrogen atoms. The multiplet observed in the range 7.32–8.61 ppm is due to the phenyl protons of the amine group and the *N*-heterocyclic ring of the ligands (**2-PP**), these resonance values being consistent with the reported values [8]. The ^{13}C {^{1}H} NMR spectra of complexes **3** and **4** exhibit resonances for the methyl carbons of the pentamethylcyclopentadienyl group at around 8.00 ppm and for the ring carbons at around 90.12–98.37 ppm. The resonance observed in the range 158.56–171.26 ppm is assigned to the imine group of the ligand (**2-PP**). The spectra also show resonances in the range 98.46–157.83 ppm for the aromatic carbon of the phenyl group and pyridyl group carbons (see Fig. 1).



M = Rh(1) Ir(2)

2-PP = N-(pyrid-2-ylmethelene)phenylamine

M = Rh; X = H(3a)
CH_3(3b)
OCH_3(3c)
Cl(3d)
NO_2(3e)

M = Ir X = H(4a)
CH_3(4b)
OCH_3(4c)
Cl(4d)
NO_2(4e)

Scheme 1.

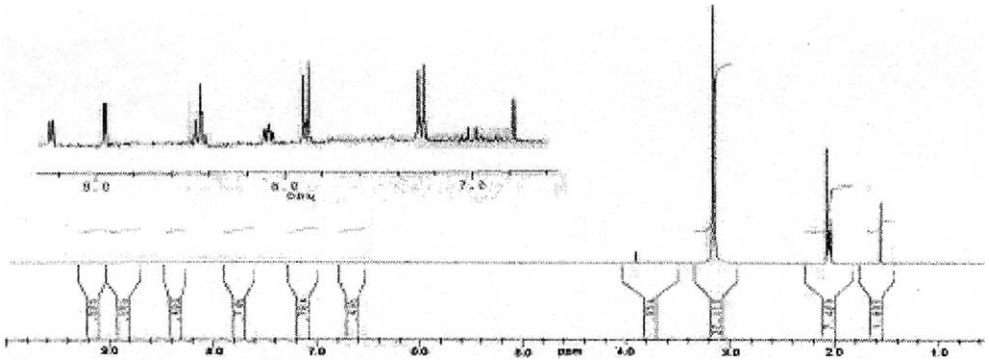


Fig. 1. ^{1}H NMR spectrum of complex $[(\eta^5\text{-}C_5Me_5)RhCl(C_5H_4N\text{-}2\text{-}CH{=}N\text{–}C_6H_4\text{-}p\text{-}OMe)]^+$ (**3c**) in acetone-d_6.

The electronic absorption spectra for rhodium (III) and iridium (III) Schiff base complexes typically contains π–π* and *n*–π* bands in the ultraviolet region The interaction of the filled dπ (t_2g) orbitals on rhodium (III) and iridium (III) with low lying π* orbitals on the Schiff base imine (C=N) ligands should provide a metal-to-ligand charge transfer (MLCT) transition (t_2g-π*) in the electronic spectra of these complexes [22–24] with the transition energy of these bands varying with the nature of the ligands acting as π-acceptors. The electronic spectra of these complexes in acetone exhibit bands in the range of 344–387 nm. This low-energy absorption is assigned to a Rh dπ (or Ir dπ) to ligand π* metal-to-ligand charge transfer (MLCT) transition (see Fig. 2).

Electron transfer properties of the representative compound **3a**[PF_6] are studied in acetonitrile solvent by cyclic voltametry. The first reduction wave of this rhodium (III) complex occurs at around −0.544 V and the corresponding oxidation wave at −0.113 V; it shows a quasi-reversible plot (ΔE = −431 mV). This is assigned to the Rh(III)/Rh(II) couple [Eq. (1)]. The second reduction wave occurs at −1.199 V and the corresponding oxidation wave −0.824 V; this also shows a quasi-reversible plot (ΔE = −375 mV), which is a two-electron transfer Rh(III)/Rh(I) couple. We have also observed here the Rh(III)/Rh(II) and Rh(II)/Rh(I) couple.

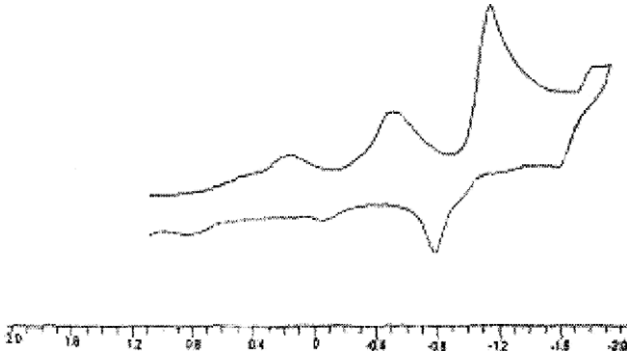


Fig. 2. Cyclic voltammogram of complex $[(\eta^5\text{-}C_5Me_5)RhCl(C_5H_4N\text{-}2\text{-}CH{=}N\text{–}C_6H_5)]^+$ (**3a**) in acetonitrile using a Pt-disk milli electrode at 298 K, SCE reference and TBAP (0.1 M) supporting electrolyte.

$$[(\eta^5 - C_5Me_5)RhCl(2 - PP)]^+ + e^- \leftrightarrows [(\eta^5 - C_5Me_5)RhCl(2 - PP)] \quad (1)$$

In general, ligand effects appear in the Ru(IV/III) and Ru(III/II) redox potentials. Ligand effects on the Ru(III/II) couple are well known, where Ru(III/II) potentials are influenced along with the ligand. Ru(II) is stabilized by the contribution of dπ–π* (L) back bonding in the presence of the ligands. The replacement of a Schiff-base ligand by the strongly electron-donating pentamethylcyclopentadienyl group destabilizes the lower rhodium oxidation states, making reduction more difficult. Indeed, in our observation the reduction potential for the +3/+1 couple of $[Cp^*RhCl(2\text{-}PP)]^+$ falling may arise from the intermediate $[Rh(Cp^*)_2]^+$ and $[Rh(2\text{-}PP)_3]^{3+}$.

5. Molecular structures

Single crystal X-ray structure determinations were carried out for compounds **3d** and **4e** for confirmation of their formulae and structure. The rhodium atom compound **3d** and the iridium atom compound **4e** are coordinated to two nitrogen atoms of the Schiff base (**2-PP**) ligand, one chloride ion and the pentamethylcyclopentadienyl molecule in a η^5-fashion leading to the usual 'three-legged piano stool' structures. The geometry around the metal atom can be regarded as distorted octahedral if the η^5-pentamethylcyclopentadienyl moieties are assumed to occupy three facial-coordinated positions. A summary of the single-crystal X-ray structure analyses is shown in Table 1. Selected bond lengths and bond angles are given in Tables 2 and 3. The ORTEP drawings of compounds **3d** and **4e** are shown in Figs. 3 and 4, respectively.

The tetrafluoroborate salt of complex $[(\eta^5\text{-}C_5Me_5)RhCl(C_5H_4N\text{-}2\text{-}CH{=}N\text{–}C_6H_4\text{-}p\text{-}Cl)]^+$**3d** and hexafluorophosphate salt of complex $[(\eta^5\text{-}C_5Me_5)IrCl(C_5H_4N\text{-}2\text{-}CH{=}N\text{–}C_6H_4\text{-}p\text{-}NO_2)]^+$ **4e** crystallize in the monoclinic space group $P2_1/n$ (Figs. 3 and 4). The two metal-centroid distances are indistinguishable (1.791 Å). The bond distances between the rhodium and iridium metal

Table 2
Selected bond lengths (Å) and bond angles (°) for $[(\eta^5\text{-}C_5Me_5)RhCl(C_5H_4N\text{–}2CH{=}N\text{–}C_6H_4\text{-}p\text{-}Cl)]^+$ (**3d**)

Bond lengths (Å)	
Rh–N	2.123(2)
N–C(21)	1.422(2)
N(32)–C(31)	1.3900
Rh–N(32)	2.0949(11)
N–C	1.271(4)
Rh–C[a]	1.791
Rh–Cl(1)	2.3756(7)
N(32)–C(33)	1.3900
Bond angles (°)	
N(32)–Rh–N	76.17(7)
N(32)–Rh–Cl(1)	85.13(4)
N–Rh–Cl(1)	86.76(6)

[a] Rhodium to centroid of Cp*.

Table 3
Selected bond lengths (Å) and bond angles (°) for $[(\eta^5\text{-}C_5Me_5)IrCl(C_5H_4N\text{-}2\text{-}CH{=}N\text{–}C_6H_4\text{-}p\text{-}NO_2)]^+$ (**4e**)

Bond lengths (Å)	
Ir–N(1)	2.099(4)
N(21)–C(26)	1.3900
N(1)–C(1)	1.285(5)
Ir–C[a]	1.792
Ir–Cl	2.3726(11)
N(21)–C(22)	1.3900
N(2)–O(1)	1.198(8)
Ir–N(21)	2.0862(18)
N(1)–C(31)	1.408(4)
N(2)–O(2)	1.171(8)
Bond angles (°)	
N(21)–Ir–Cl	84.45(8)
N(1)–Ir–Cl	85.17(9)
N(21)–Ir–N(1)	75.98(11)

[a] Iridium to centroid of Cp*.

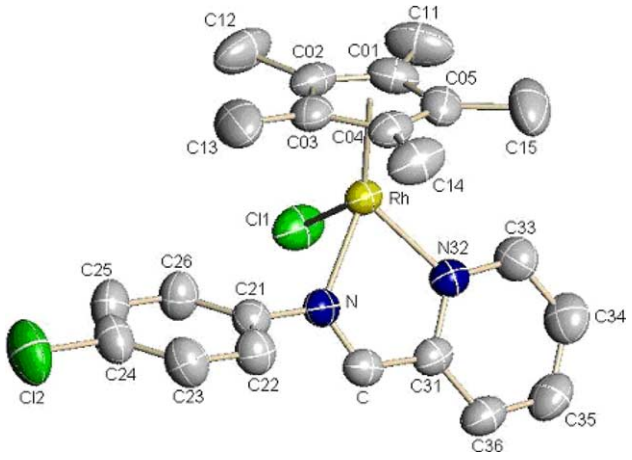


Fig. 3. ORTEP representation of the complex **3d** with 50% probability thermal ellipsoids. Hydrogens and BF_4^- are omitted for clarity.

atoms and the chelated ligand nitrogen atoms are similar to each other (~2.1 Å). There is no significant difference in the C–C bond lengths in the pentamethylcyclopentadienyl ring, all being about 1.42

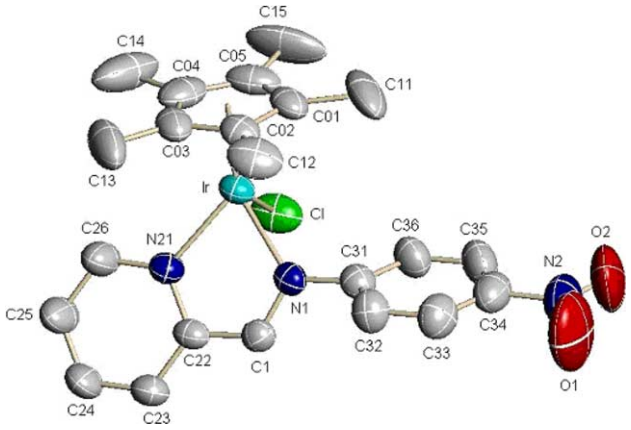


Fig. 4. ORTEP representation of the complex **4e** with 50% probability thermal ellipsoids. Hydrogens and PF_6^- are omitted for clarity.

Å and pointing to π-electron delocalization in the ring. Furthermore, the five membered ring is planar as evident in the nearly equal bond distances between metal atom and the ring carbons. The Rh–Cl and Ir–Cl bond distances are 2.3756(7) and 2.3726(11) Å, respectively, which are closely similar to another related two-coordinated chelating polypyridyl rhodium complex $[Cp^*RhCl(Phterpy)]^+$ (2.3984(1)) [25].

6. Concluding remarks

We have observed interesting phenomena in the case of the pentamethylcyclopentadienyl compounds of **1** and **2**, which distinguish them from the analogous pentamethylcyclopentadienyl or indenyl ruthenium (II) systems, even though these are all isoelectronic. Unlike in the case of the compounds **1** and **2**, the reactions of Schiff bases with the $[(\eta^5\text{-}Cp^*)Ru(PPh_3)_2Cl]$ and $[(\eta^5\text{-ind.})Ru(PPh_3)_2Cl]$ systems yielded complexes without any organic group. In order to obtain similar complexes for these cases, one has to start from the acetonitrile complexes.

Acknowledgements

We thank Professor R.H. Duncan Lyngdoh for his help in preparing the manuscript and Dr. A. Lemtur for helpful discussions in the electrochemistry part.

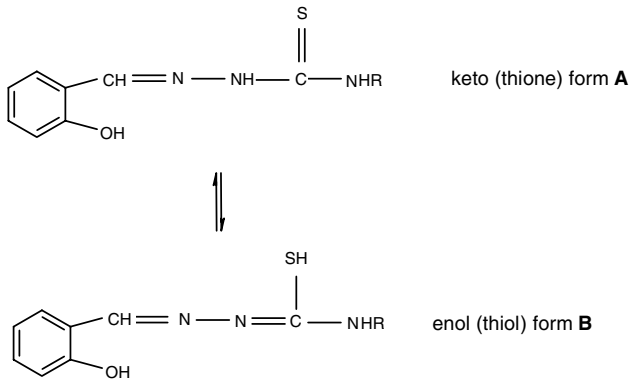
Appendix A. Supplementary data

Crystallographic data (excluding structure factors) for the structures reported in this paper have been deposited with the Cambridge Crystallographic Data Centre as supplementary publication No. CCDC 265789 for complex **3d**[BF_4] and CCDC 265788 for

complex **4e**[PF_6]. Copies of the data can be obtained free of charge on application to CCDC, 12 Union Road, Cambridge CB2 1EZ, UK (fax: Int. code +(44) 1223/336033; e-mail: deposit@ccdc.cam.ac.uk or http://www.ccdc.cam.ac.uk). Supplementary data associated with this article can be found, in the online version at doi:10.1016/j.poly.2005.04.034.

References

[1] H. Brunner, Adv. Organomet. Chem. 18 (1980) 151.
[2] S.G. Davies, Pure Appl. Chem. 60 (1988) 13.
[3] J.W. Faller, M.R. Mazzieri, J.T. Nguyen, P. Parr, M. Tokunaga, Pure Appl. Chem. 66 (1994) 1463.
[4] E.P. Kundig, A. Quettropani, M. Inage, A. Ripa, C. Dupre, A.F.J. Cunningham, B. Bourdin, Pure Appl. Chem. 68 (1996) 97.
[5] R. Noyori, S. Hashiguchi, Acc. Chem. Res. 30 (1997) 97, and references therein.
[6] V.I. Sokolov, Chirality and Optical Activity in Organometallic Compounds, Gordon and Breach, 1990.
[7] G. Consiglio, F. Morandini, Chem. Rev. 87 (1987) 761.
[8] (a) P. Govindaswamy, Y.A. Mozharivskyj, M.R. Kollipara, Polyhedron 23 (2004) 1567;
(b) R. Lalrempuia, M.R. Kollipara, P.J. Carroll, Polyhedron 22 (2003) 605;
(c) S.S. Keisham, Y.A. Mozharivskyj, P.J. Carroll, M.R. Kollipara, J. Organomet. Chem. 689 (2004) 1249.
[9] R. Lalrempuia, P. Govindaswamy, Y.A. Mozharivskyj, M.R. Kollipara, Polyhedron 23 (2004) 1069.
[10] M.R. Kollipara, E.K. Rymmai, Polyhedron 22 (2003) 307.
[11] (a) P. Govindaswamy, Y.A. Mozharivskyj, M.R. Kollipara, J. Organomet. Chem. 689 (2004) 3265;
(b) P. Govindaswamy, H.P. Yennawar, M.R. Kollipara, J. Organomet. Chem. 689 (2004) 3108;
(c) P. Govindaswamy, P.J. Carroll, Y.A. Mozharivskyj, M.R. Kollipara, J. Organomet. Chem. 690 (2005) 885;
(d) P. Govindaswamy, Y.A. Mozharivskyj, M.R. Kollipara, Polyhedron 23 (2004) 3115.
[12] (a) D.L. Davies, J. Fawcett, R. Krafczyk, D.R. Russell, J. Organomet. Chem. 545–546 (1997) 581;
(b) S.K. Mandal, A.R. Chakravarty, Polyhedron 10 (1991) 2483.
[13] S. Pal, T.K. Misra, C. Sinha, A.M.Z. Slawin, J.D. Woolins, Polyhedron 19 (2000) 1925.
[14] (a) R.N. Dominey, B. Hauser, J. Habbard, J. Dunham, Inorg. Chem. 30 (1991) 4754;
(b) E.V. Dose, L.J. Wilson, Inorg. Chem. 17 (1978) 2660.
[15] (a) J.W. Kang, K. Moseley, P.M. Maitlis, J. Am. Chem. Soc. 91 (1969) 5970;
(b) R.G. Ball, W.A.G. Graham, D.M. Heinekey, J.K. Hoyano, A.D. McMaster, B.M. Mattson, S.T. Michel, Inorg. Chem. 29 (1990) 2023;
(c) C. White, A. Yates, P.M. Maitlis, Inorg. Synth. 29 (1992) 228.
[16] P. Byabartta, J. Dinda, P.K. Santra, C. Sinha, K. Panneerselvam, F.-L. Liao, T.-H. Lu, J. Chem. Soc., Dalton Trans. (2001) 2825.
[17] D. Becke, J. Chem. Phys. 98 (1993) 5648.
[18] XRD Single Crystal Software; Bruker Analytical X-ray Systems, Madison, USA, 2002.
[19] G.M. Sheldrick, SHELXS86, Program for Crystal Structure Solution, University of Göttengen, Göttengen, Germany, 1986.
[20] M. Sheldrick, SHELXS97, Program for Crystal Structure Refinement, University of Göttengen, Göttengen, Germany, 1997.
[21] C.K. Johnson, ORTEP – II: A Fortran Thermal Ellipsoid Plot Program for Crystal Structure Illustrations, ORNL – 5138, 1976.
[22] B.K. Ghosh, A. Chakravorty, Coord. Chem. Rev. 95 (1989) 239.
[23] (a) N. Bag, G.K. Lahiri, A. Chakravorty, Inorg. Chem. 31 (1992) 40;
(b) G.K. Lahiri, S. Bhattacharya, S. Goswami, A. Chakravorty, J. Chem. Soc., Dalton Trans. (1990) 561;
(c) G.K. Lahiri, S. Goswami, L.R. Falvello, A. Chakravorty, Inorg. Chem. 26 (1987) 3365;
(d) P. Ghosh, A. Chakravorty, J. Chem. Soc., Dalton Trans. (1985) 361.
[24] (a) T.K. Misra, D. Das, C. Sinha, P.K. Ghosh, C.K. Pal, Inorg. Chem. 37 (1998) 1672;
(b) P. Byabartta, S.K. Jasimuddin, B.K. Ghosh, C. Sinha, A.M.Z. Slawin, J.W. Woollins, New J. Chem. 26 (2002) 1415;
(c) J. Dinda, D. Das, P.K. Santra, C. Sinha, L.R. Falvello, J. Organomet. Chem. 629 (2001) 28;
(d) J. Dinda, S.K. Jasimuddin, G. Mostafa, C.-H. Hung, C. Sinha, Polyhedron 23 (2004) 793;
(e) S. Pal, D. Das, C. Sinha, C.H.L. Kennard, Inorg. Chim. Acta 313 (2001) 21.
[25] H. Aneetha, P.S. Zacharias, B. Srinivas, G.H. Lee, Y. Wang, Polyhedron 18 (1999) 299.



Scheme 1.

decrease of negative charge at the substituted N hydrazinic atom [8].

The thiosemicarbazone ligands can act as tridentate ligands (**A** form) being coordinated through the deprotonated phenolic O, imino N and thiocarbonyl S, or as doubly negatively charged tridentate ligands by losing another proton from the tautomeric mercapto group (**B** form) (Scheme 1) [8].

The biological activity, particularly antitumour activity of this class of compounds is most probably associated with their structures [9–11] as it was found for thiosemicarbazone copper(II) complexes.

2. Experimental

The starting complex $[MoO_2(acac)_2]$ [12], salicylaldehyde and 3-methoxysalicylaldehyde 4-methylthiosemicarbazone were prepared as described in the literature [7]. Acetonitrile was of reagent grade and used as purchased. Methanol was dried over magnesium ethoxide.

C, H and N analyses were provided by the Analytical Services Laboratory of Rudjer Bošković Institute, Zagreb. Molybdenum was determined according to the already known method [13]. Infrared spectra were recorded in KBr with an FTIR 1600 Fourier transform spectrophotometer in the 4500–450 cm^{-1} region. Thermogravimetric analyses were measured on a Mettler TG 50 thermobalance using aluminum crucibles under oxygen atmosphere with a heating rate of 5 °C min^{-1}. For all experiments the temperature ranged from 25 to 600 °C. The results were developed by applying the Mettler STAR^e 6.1. programme.

2.1. Syntheses of molybdenum(VI) complexes: *I, II, 1a, 2a, 2b*

A mixture of $[MoO_2(C_5H_7O_2)_2]$ (0.30 g, 0.92 mmol) and salicylaldehyde 4-methylthiosemicarbazone (0.19 g, 0.92 mmol) for **I** (or 3-methoxysalicylaldehyde 4-methylthiosemicarbazone 0.22 g, 0.92 mmol for **II)** in acetonitrile (40 cm^3) was refluxed for 6 h for **I** and 20 h for **II**, respectively. The brown products **I** or **II** were deposited during refluxing of the reaction mixture and filtered off. The orange crystals **2b** were obtained from the filtrate when it was left at room temperature for two weeks.

(**I**) Yield: 0.23 g, 74.58%. *Anal.* Calc. for $C_9H_9MoN_3O_3S$: C, 32.3; H, 2.7; Mo, 28.6; N, 12.5; S, 9.6. Found: C, 32.0; H, 2.6; Mo, 28.4; N, 12.4; S, 9.8%.

IR (cm^{-1}): 3428(s), 1606(s), 1595(m), 1560(s), 1541(s), 1498(s), 920(vs), 843(s), 806(vs), 765(vs).

(**II**) Yield: 0.20 g, 59.5%. *Anal.* Calc. for $C_{10}H_{11}MoN_3O_4S$: C, 42.7; H, 2.7; Mo, 26.3; N, 11.5; S, 8.8. Found: C, 42.6; H, 2.6; Mo, 26.4; N, 11.4; S, 8.6%.

IR (cm^{-1}): 3409(s), 3342(m), 3309(m), 1568(s), 1545(s), 1273(vs), 923(s), 808(vs).

(**2b**) Yield: 0.01 g, 2.7%. *Anal.* Calc. for $C_{12}H_{16}MoN_4O_5S$: C, 42.4; H, 3.6; Mo, 22.6; N, 13.2; S, 7.6. Found: C, 42.1; H, 3.5; Mo, 22.8; N, 13.1; S, 7.6%.

IR (cm^{-1}): 3376(s), 1593(s), 1565(s), 1525(s), 1412(s), 1259(s), 933(s), 891(vs).

The methanolic solution (15 cm^3) of **I** (0.10 g) or **II** (0.10 g) was refluxed for 4 h and was then evaporated to one-third of its volume. Upon standing at room temperature for few days the orange crystals of **1a** (or **2a**) were obtained and filtered off.

(**1a**) Yield: 0.08 g, 23.7%. *Anal.* Calc. for $C_{10}H_{12}MoN_3O_4S$: C, 32.7; H, 3.3; Mo, 26.1; N, 11.4; S, 8.7. Found: C, 32.8; H, 3.5; Mo, 26.0; N, 11.2; S, 9.0%.

IR (cm^{-1}): 3315(m), 1606(s), 1559(s), 1526(s), 1412(s), 1288(s), 1013(vs), 932(s), 890(vs), 758(vs).

(**2a**) Yield: 0.05 g, 13.8%. *Anal.* Calc. for $C_{11}H_{15}MoN_3O_5S$: C, 42.3; H, 3.6; Mo, 24.2; N, 10.6; S, 8.1. Found: C, 42.5; H, 3.5; Mo, 24.5; N, 10.4; S, 8.4%.

IR (cm^{-1}): 3332(s), 1602(s), 1568(s), 1538(vs), 1467(s), 1438(s), 1293(s), 1258(vs), 934(vs), 889(vs).

2.2. X-ray crystallography

Diffraction intensity data for **1**, **1a**, **2**, **2a** and **2b** were collected by ω-scans on Oxford Diffraction Xcalibur CCD diffractometer with graphite-monochromated Mo Kα radiation ($\lambda = 0.71073$ Å) and reduced using the CRYSALIS software package [14]. Crystal data, experimental conditions and final refinement parameters are summarized in Table 1. The structures were solved using SHELXS97 [15]: the structures of ligands **1** and **2** by direct methods, and the structures of complexes **1a**, **2a** and **2b** by the Patterson method. The refinement procedure by the full-matrix least-squares method based on F^2 against all reflections included anisotropic displacement parameters for all non-hydrogen atoms. All hydrogen atoms were located in the difference Fourier maps. Those with poor geometry were then refined with restraints. Hydrogen atoms in **1** and **2** were refined isotropically except the methyl H atoms in both structures for which only the torsion angles and grouped isotropic temperature

Table 1
Crystallographic data for compounds **1**, **1a**, **2**, **2a** and **2b**

Compound	**1**	**1a**	**2**	**2a**	**2b**
Chemical formula	$C_9H_{11}N_3OS$	$[MoO_2(C_9H_9N_3OS)(CH_3OH)]$	$C_{10}H_{13}N_3O_2S$	$[MoO_2(C_{10}H_{11}N_3O_2S)(CH_3OH)]$	$[MoO_2(C_{10}H_{11}N_3O_2S)(H_2O)] \cdot CH_3CN$
M_r	209.27	367.23	239.29	397.26	424.29
Crystal colour, habit	colourless, plate	orange, needle	colourless, needle	orange, needle	orange-red, prismatic
Crystal size (mm)	$0.12 \times 0.77 \times 0.84$	$0.06 \times 0.07 \times 0.59$	$0.05 \times 0.09 \times 0.34$	$0.10 \times 0.18 \times 0.68$	$0.15 \times 0.18 \times 0.42$
Crystal system	triclinic	orthorhombic	monoclinic	monoclinic	monoclinic
Space group	$P\bar{1}$	$Pna2_1$	$P2_1/c$	$P2_1/n$	$P2_1/c$
Unit cell dimensions					
a (Å)	6.0270(10)	20.635(3)	11.699(2)	21.2125(10)	7.4539(5)
b (Å)	8.5276(11)	7.1710(10)	6.0149(10)	6.9469(4)	16.4922(12)
c (Å)	10.4743(13)	17.832(2)	16.048(3)	21.2189(13)	13.2293(10)
α (°)	75.724(11)	90	90	90	90
β (°)	75.802(13)	90	102.234(18)	108.105(5)	104.995(6)
γ (°)	82.155(12)	90	90	90	90
V (Å^3)	504.12(13)	2638.7(6)	1103.6(3)	2972.0(3)	1570.9(2)
Z	2	8	4	8	4
T (K)	295(2)	295(2)	100(1)	100(1)	100(1)
D_{calc} (g cm^{-3})	1.379	1.849	1.440	1.776	1.794
μ(Mo Kα) (mm^{-1})	0.291	1.165	0.282	1.047	0.998
Absorption correction	multi-scan	analytical	none	analytical	analytical
T_{min}	0.778	0.685		0.622	0.739
T_{max}	0.966	0.947		0.899	0.883
F(0 0 0)	220	1472	504	1600	856
Total data	6721	27744	12946	49514	13686
Unique data	2775	7029	3217	8632	4326
R_{int}	0.0281	0.0422	0.0576	0.0219	0.0157
R_σ	0.0206	0.0521	0.0528	0.0153	0.0128
Observed data [$I > 2\sigma(I)$]	2455	5283	2250	7862	4040
θ_{max} (°)	30.07	30.00	30.06	30.00	29.99
Ranges of h, k, l	−5, 8; −12, 12; −14, 14	−29, 29; −9, 10; −25, 25	−16, 16; −7, 8; −22, 22	−29, 29; −8, 9; −29, 29	−10, 10; −23, 23; −18, 17
Number of parameters	160	348	175	393	227
Flack's parameter x		0.48(3)			
R_1	0.0419	0.0371	0.0622	0.0322	0.0209
wR_2	0.1203	0.0700	0.1688	0.0741	0.0527
S	1.053	0.951	1.009	1.158	1.087
$\Delta\rho_{max}$ (e Å^{-3})	0.26	0.56	0.68	1.51	0.51
$\Delta\rho_{min}$ (e Å^{-3})	−0.38	−0.40	−0.38	−0.58	−0.63

factor were refined while the geometry was kept fixed. In the structures of the complexes, only H atoms refined isotropically were H atoms bound to the oxygen atoms in **2a**, and H atoms attached to C1 and to the heteroatoms in **2b**, while the other H atoms were refined using the riding model. The structure of **1a** was refined as twinned and consisted of two components with opposite polarities. The final BASF coefficient (Flack's parameter *x*) for **1a** was 0.48(3) [16,17]. Refinement was performed using SHELXL97 [18], geometry calculations were done using PLATON [19,20] and PARST [21,22], and the structure drawings were prepared using ORTEP [23].

2.3. NMR spectroscopy

All one- (^{1}H and APT), and gradient-selected two-dimensional (gCOSY, gHSQC and gHMBC) NMR spectra were recorded at ambient temperature on a Bruker Avance DRX500 and Bruker Avance DPX 300 spectrometers equipped with 5 mm inverse detection probe and dual probe, respectively. Sample concentration in DMSO-d_6 was 20 mg ml^{-1}. TMS was used as the internal standard.

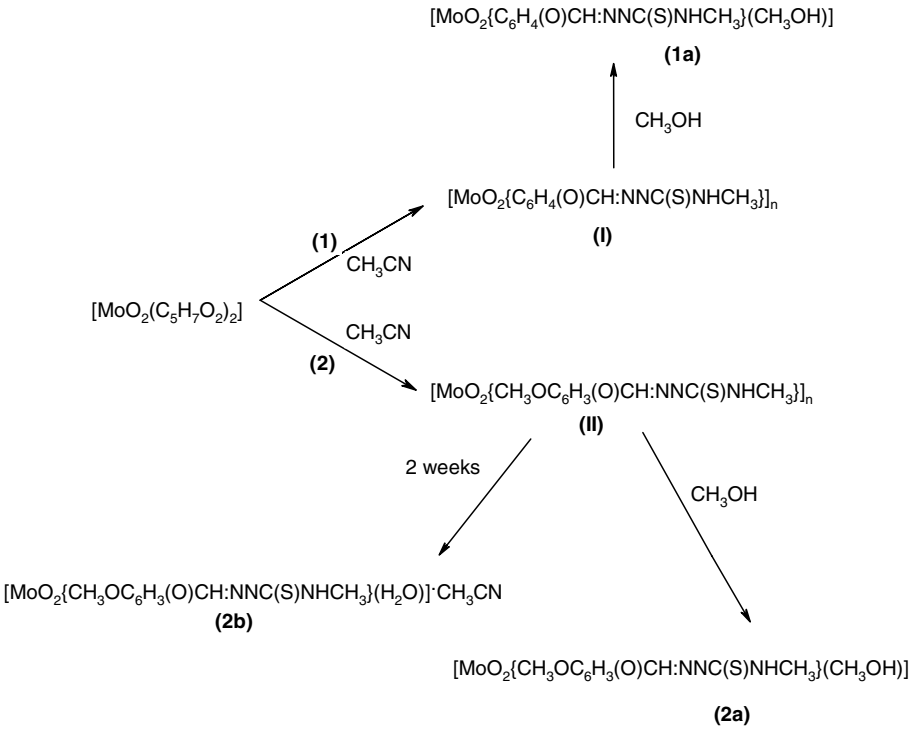
The typical spectral conditions for one-dimensional ^{1}H and ^{13}C (APT) spectra were as follows. The spectra were recorded using 64K data points and spectral widths of 7700 and 32 000 Hz for ^{1}H and ^{13}C experiments, respectively. Digital resolution was 0.12 and 0.48 Hz per point, respectively. The number of scans was 16 for ^{1}H and 500–1000 for APT spectra.

The COSY spectra were recorded under the following conditions: spectral width was 7700 Hz in both dimensions, 2K data points were applied in time domain and 512 increments were collected for each data set with linear prediction and zero filling to 2K. 8 scans were applied for each increment. Digital resolution was 6.50 Hz per point in both dimensions. The gradient selected inverse ^{1}H–^{13}C correlation experiments, gHSQC and gHMBC were recorded using the acquisition matrix of $1K \times 256$ with 16 and 32 scans, respectively, and processed with $2K \times 1K$ transformed matrix. The spectral width was 6600 Hz in f2 dimension and 32 000 Hz in f1 dimension for both experiments. Digital resolution was 3.25 Hz per point and 30.70 Hz per point in f2 and f1, respectively. HMBC spectra were recorded using a low-pass *J*-filter (3.4 s) and a delay for long-range coupling of 65 ms.

3. Results and discussion

3.1. Synthesis of the complexes

As a part of our studies [24–26] on molybdenum complexes with oxygen, sulfur and/or nitrogen donor



(1) $C_6H_4(OH)CH{:}NNC(SH)NHCH_3$ H_2SalTSC-4-Me

(2) $CH_3OC_6H_3(OH)CH{:}NNC(SH)NHCH_3$ H_2VanTSC-4-Me

Scheme 2.

ligands we describe here the syntheses and structures of molybdenum(VI) complexes coordinated by salicylaldehyde or by 3-methoxysalicylaldehyde 4-methylthiosemicarbazone ligand (Scheme 2). The brown polymeric complexes $[MoO_2\{SalTSC\text{-}4\text{-}Me\}]_n$ (**I**) and $[MoO_2\{VanTSC\text{-}4\text{-}Me\}]_n$ (**II**) were obtained by the reaction of $[MoO_2(C_5H_7O_2)_2]$ with a stoichiometric amount of corresponding thiosemicarbazone ligand in acetonitrile.

The monomeric complex $[MoO_2\{VanTSC\text{-}4\text{-}Me\}(H_2O)] \cdot CH_3CN$ (**2b**) was obtained when the filtrate of **II** was left at room temperature for two weeks. In **2b**, the molybdenum atom is additionally coordinated by a water molecule most probably from the atmospheric moisture and stabilized by the solvated acetonitrile molecule. Also, it should be mentioned that such a product was obtained only when the ligand was 3-methoxysalicylaldehyde 4-methylthiosemicarbazone. All attempts to isolate

Table 2
Selected bond distances (Å), angles (°) and torsion angles (°) for **1**, **1a**, **2**, **2a** and **2b**

Compound	**1**	**1a**		**2**	**2a**		**2b**
		A	**B**		**A**	**B**	
Bond distances							
O3–C6	1.3604(17)	1.336(5)	1.340(5)	1.363(3)	1.341(3)	1.342(3)	1.3418(17)
C6–11	1.3997(18)	1.410(6)	1.407(6)	1.395(3)	1.400(3)	1.407(3)	1.4035(19)
C11–C1	1.4501(18)	1.440(5)	1.453(5)	1.461(3)	1.449(3)	1.449(3)	1.4441(19)
C1–N1	1.2861(16)	1.298(5)	1.292(5)	1.287(3)	1.294(3)	1.292(3)	1.2999(18)
N1–N2	1.3763(16)	1.399(4)	1.419(4)	1.370(3)	1.409(2)	1.410(2)	1.3963(16)
N2–C3	1.3501(16)	1.319(6)	1.305(5)	1.363(3)	1.317(3)	1.317(3)	1.3137(18)
C3–S1	1.6833(13)	1.757(4)	1.766(4)	1.695(2)	1.763(2)	1.763(2)	1.7506(13)
C3–N4	1.3236(17)	1.332(5)	1.335(5)	1.326(3)	1.333(3)	1.335(3)	1.3430(17)
N4–C5	1.4484(18)	1.441(6)	1.442(6)	1.457(3)	1.453(3)	1.456(3)	1.4537(18)
Mo1–O1		1.686(3)	1.686(3)		1.7000(14)	1.7002(15)	1.6998(12)
Mo1–O2		1.706(3)	1.712(3)		1.7206(16)	1.7188(14)	1.7172(10)
Mo1–O3		1.927(3)	1.934(3)		1.9322(14)	1.9332(16)	1.9359(10)
Mo1–N1		2.265(3)	2.236(3)		2.2558(18)	2.2554(16)	2.2733(12)
Mo1–S1		2.4120(13)	2.4047(13)		2.4226(5)	2.4206(5)	2.4504(4)
Mo1–O4		2.399(3)	2.400(3)		2.3594(15)	2.3792(15)	2.3081(12)
Bond angles							
N1–C1–C11	122.60(11)	126.2(3)	124.8(3)	120.8(2)	125.0(2)	125.38(19)	126.79(12)
N2–N1–C1	114.94(11)	115.0(3)	113.8(3)	115.07(19)	113.88(17)	114.03(16)	112.95(11)
N1–N2–C3	121.89(11)	111.8(3)	111.4(3)	120.36(19)	112.34(17)	111.99(16)	114.24(11)
N2–C3–N4	117.46(12)	120.5(4)	121.3(4)	116.1(2)	120.5(2)	120.65(19)	118.86(12)
S1–C3–N2	118.54(10)	124.6(3)	124.3(3)	119.29(17)	124.18(16)	124.16(16)	125.37(10)
S1–C3–N4	124.00(10)	114.8(4)	114.4(3)	124.65(18)	115.29(16)	115.16(16)	115.78(10)
C3–N4–C5	123.87(12)	124.4(4)	124.1(4)	124.0(2)	123.22(19)	122.67(18)	122.85(12)
S1–Mo1–O1		96.54(11)	96.68(11)		96.26(6)	96.45(6)	96.19(4)
S1–Mo1–O2		90.33(12)	90.02(12)		91.05(5)	91.40(6)	91.33(4)
S1–Mo1–O3		153.37(9)	153.13(9)		153.82(5)	153.33(4)	154.71(3)
S1–Mo1–O4		83.54(8)	83.25(8)		84.16(4)	84.04(4)	81.38(3)
S1–Mo1–N1		74.71(8)	74.78(9)		74.90(5)	74.69(5)	75.84(3)
O1–Mo1–O2		105.43(16)	105.73(16)		104.92(7)	105.04(7)	105.27(5)
O1–Mo1–O3		98.95(13)	99.18(14)		97.99(7)	98.45(7)	98.66(5)
O1–Mo1–O4		172.34(13)	170.78(13)		172.31(7)	172.70(6)	169.91(4)
O1–Mo1–N1		95.51(13)	94.13(13)		94.79(7)	95.40(7)	92.66(5)
O2–Mo1–O3		106.12(14)	106.23(14)		106.24(7)	105.81(7)	104.25(4)
O2–Mo1–O4		82.23(14)	83.48(14)		82.74(6)	82.21(6)	84.62(5)
O2–Mo1–N1		155.60(14)	156.36(14)		157.02(7)	156.52(7)	159.08(5)
O3–Mo1–O4		78.27(11)	77.68(11)		78.87(6)	78.46(6)	80.43(4)
O3–Mo1–N1		82.32(11)	82.54(12)		82.11(6)	81.98(6)	83.11(4)
O4–Mo1–N1		77.09(10)	76.92(10)		77.88(7)	77.67(7)	77.25(4)
Torsion angles							
O3–C6–C11–C1	−2.53(19)	0.6(6)	2.3(6)	−1.2(3)	−0.4(3)	0.7(3)	1.5(2)
C6–C11–C1–N1	1.4(2)	−11.4(6)	−11.2(7)	−177.3(2)	12.7(3)	−12.9(3)	−5.2(2)
C11–C1–N1–N2	−176.74(11)	176.1(3)	173.8(4)	176.2(2)	−176.5(2)	176.6(2)	175.53(13)
C1–N1–N2–C3	175.50(12)	160.1(3)	158.3(4)	174.3(2)	−159.8(2)	158.0(2)	171.93(12)
N1–N2–C3–S1	−170.08(9)	−3.6(4)	−3.7(5)	175.18(16)	2.3(3)	−2.1(3)	4.69(18)
S1–C3–N4–C5	2.20(19)	−176.8(3)	−176.7(3)	1.7(3)	178.09(16)	−177.67(16)	−172.64(11)

In **1a** and **2a** two crystallographically independent complex molecules are labelled **A** and **B**.

the mononuclear molybdenum(VI) complex coordinated by a water molecule after isolation of complex **I** were unsuccessful even if some water was added to the solution. We believe that the electronic effect of the methoxy group attached to the phenolic ring 3-methoxysalicylaldehyde is responsible for the formation of this aqua complex.

We were also able to isolate monomeric orange crystals of $[MoO_2\{SalTSC\text{-}4\text{-}Me\}(CH_3OH)]$ (**1a**) and $[MoO_2\{VanTSC\text{-}4\text{-}Me\}(CH_3OH)]$ (**2a**) from the methanolic solution of **I** and **II**.

The IR data for thiosemicarbazone ligands are in accordance with the literature data [27]. The IR spectra of the complexes **I** and **II** showed characteristic strong vibrations at 806 and 808 cm^{-1}, respectively, assigned to the bridging Mo–O···Mo group which were absent in the case of mononuclear **1a**, **2a** and **2b** complexes. Also **I** and **II** showed single stretching frequencies at 920 and 923 cm^{-1}, respectively, assigned to ν(Mo=O), while the IR spectra of all three mononuclear complexes with the *cis*-MoO_2 core showed usual doublet at 933 and 891 cm^{-1} in **1a**, 934 and 889 cm^{-1} in **2a** and 932 and 892 cm^{-1} in **2b**.

The thermal analysis data of complexes **1a** and **2a** showed that their ligands decomposed in the range 224–554 °C and 222–512 °C, respectively, while those of complexes **1a**, **2a** and **2b** revealed two main processes:

(1) loss of coordinated methanol, water or acetonitrile within the range 92–141 °C in **1a**, 30–92 °C in **2a**; loss of coordinated water and acetonitrile in one step 30–95 °C in **2b**,
(2) complex decomposition occurring within the range 170–507 °C for **I**, 221–514 °C for **II** and 210–530 °C for **2b**.

3.2. Structural studies

Comparison of the selected bond distances, bond angles and torsion angles of the free ligands **1** and **2** and of their complexes **1a**, **2a** and **2b** is given in Table 2. Hydrogen bonding parameters are listed in Table 3.

3.2.1. Structures of ligands

Figs. 1 and 2 show ORTEP plots of the structures of the free ligand molecules **1** and **2**. Both molecules are found to be in the thioketo tautomeric form with the distances C3–S1 [1.6833(13) in **1** and 1.695(2) in **2**] and N2–C3 [1.3501(16) in **1** and 1.363(3) in **2**] similar to those found in the analogous thiosemicarbazone compounds [8,28–34]. The bond distances (Table 2) suggest electron delocalization throughout the thiosemicarbazone chain. The ligand molecules consist of two nearly planar moieties connected by a single N1–N2 bond: *N*-methylthioureide

Table 3
Hydrogen bonding geometry in structures **1**, **1a**, **2**, **2a** and **2b**

D–H···A	*d*(D–H) (Å)	*d*(H···A) (Å)	*d*(D···A) (Å)	∠(D–H···A) (°)
*Compound **1***				
N2–H2···O3^{i}	0.83(2)	2.50(3)	3.1285(18)	133(2)
O3–H3···N1	0.84(3)	1.92(3)	2.6846(17)	150(2)
N4–H4···N1	0.85(2)	2.33(2)	2.6961(16)	106.5(18)
*Compound **1a***				
N4A–H4A···O2B^{ii}	0.86	2.40	3.243(5)	166
N4B–H4B···O2A^{iii}	0.86	2.15	2.996(5)	169
O4A–H41A···N2B	0.93	1.93	2.819(4)	159
O4B–H41B···N2A^{iv}	0.93	2.01	2.911(4)	162
*Compound **2***				
N2–H2···O3^{v}	0.90(4)	2.13(3)	2.935(3)	148(3)
O3–H3···O5	0.82(4)	2.17(3)	2.631(3)	115(3)
O3–H3···S1^{v}	0.82(4)	2.50(4)	3.1861(19)	141(3)
N4–H4···N1	0.81(3)	2.31(3)	2.639(3)	105(3)
*Compound **2a***				
N4A–H4A···O2B	0.88	2.09	2.892(2)	151
N4B–H4B···O2A^{vi}	0.88	2.08	2.924(2)	160
O4A–H41A···N2A^{vii}	0.75(4)	2.10(4)	2.827(3)	165(3)
O4B–H41B···N2B^{viii}	0.76(3)	2.09(3)	2.851(2)	174(3)
*Compound **2b***				
N4–H4···O2^{ix}	0.80(2)	2.20(2)	2.9287(16)	151.2(18)
O4–H41···N2^{x}	0.81(3)	1.97(3)	2.7761(16)	173(3)
O4–H42···N3	0.80(3)	2.09(2)	2.8742(18)	168(2)

Symmetry codes: i = 1 + *x*, *y*, *z*; ii = 1−*x*, 1−*y*, −1/2 + *z*; iii = 3/2−*x*, 1/2 + *y*, 1/2 + *z*; iv = *x*, 1 + *y*, *z*; v = 2−*x*, 1−*y*, 1−*z*; vi = 1/2 + *x*, 3/2−*y*, 1/2 + *z*; vii = 1/2−*x*, −1/2 + *y*, 1/2−*z*; viii = 1/2−*x*, −1/2 + *y*, 3/2−*z*; ix = *x*, 3/2−*y*, −1/2 + *z*; x = 1−*x*, 1−*y*, −*z*.

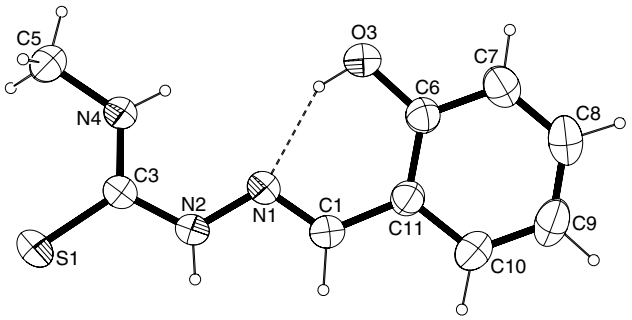


Fig. 1. ORTEP plot of the ligand molecule **1** with the atom labelling scheme. Ellipsoids are drawn at the 50% probability level. The O3–H3···N1 hydrogen bond is denoted by dashed line.

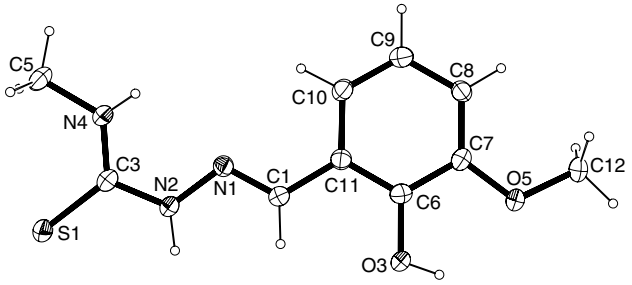


Fig. 2. ORTEP plot of the ligand molecule **2** with the atom labelling scheme. Ellipsoids are drawn at the 50% probability level.

fragment comprising N2, C3, S1, N4 and C5 [mean plane deviation of 0.007(6) Å in **1** and 0.0070(1) Å in **2**] and salicylaldimine fragment comprising N1, C1, C6–C11 and O3 [mean plane deviation of 0.0154(1) Å in **1** and 0.0160(1) Å in **2**]. Dihedral angles between these two planes are 12.54(3)° and 12.27(1)° for **1** and **2**, respectively. The atoms O5 and C12 from the methoxy group in **2**, although rather coplanar with others from the salicylaldimine fragment [mean plane deviation of 0.0237(1) Å], were excluded from the planarity calculations for the sake of comparability.

The striking difference between the molecular structures of the two ligands is the orientation of the phenyl ring moiety. In **1** the *syn* conformation of the C6 atom in respect to the N1 atom [torsion angle C6–C11–C1–N1 = 1.4(2)°] is stabilized by the intramolecular resonance-assisted O3–H3···N1 hydrogen bond, while in **2** the atoms C6 and N1 are *anti* to each other [torsion angle C6–C11–C1–N1 = –177.3(2)°] and O3–H3···O5 and O3–H3···S1 ($2-x$, $1-y$, $1-z$) hydrogen bonds are formed (Table 3). This seems to confirm an already given observation for the structures of the salicylaldehyde thiosemicarbazone derivates [31]: the intramolecular hydrogen bond between the hydroxyl group and the azomethine N atom would not be formed if another potential hydrogen bond acceptor for the hydroxyl H atom is present.

In the crystal structure of **1** molecules are interconnected by the N2–H2···O3 ($1+x$, y, z) hydrogen bonds thus forming chains parallel to the crystallographic *a* axis. In **2** a pair of molecules related by a centre of symmetry dimerize by forming the N2–H2···O3 ($2-x$, $1-y$, $1-z$) and O3–H3···S1 ($2-x$, $1-y$, $1-z$) hydrogen bonds. In both ligand structures there is an intramolecular hydrogen-bond-like contact N4–H4···N1.

3.2.2. Structures of complexes

Complex molecules found in the crystal structures of **1a** and **2a** are shown in Figs. 3 and 4, respectively. The asymmetric unit of structures **1a** and **2a** consists of two crystallographically independent complex molecules denoted as **A** and **B**. In **2b** the complex molecules cocrystallize with molecules of acetonitrile (Fig. 5).

The complex molecules consist of the *cis*-$[MoO_2]^{2+}$ core to which the doubly deprotonated tridentate ligand (**1** in **1a**; **2** in **2a** and **2b**) is meridionally bonded through the S1, N1 and O3 atoms. The sixth site of the distorted octahedral coordination around Mo is occupied either by methanol (in **1a** and **2a**) or water molecules (in **2b**).

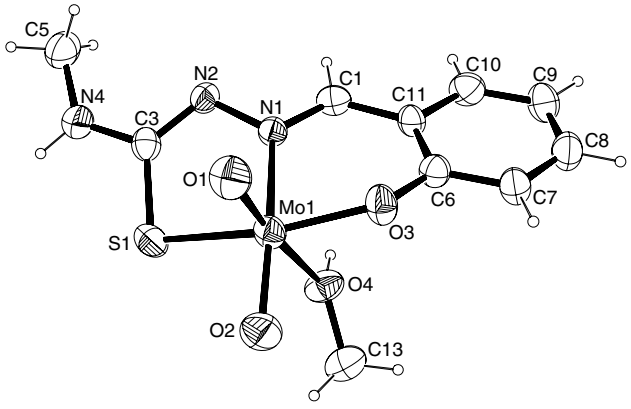


Fig. 3. ORTEP plot of the complex molecule **1aA** with the atom labelling scheme. Ellipsoids are drawn at the 50% probability level.

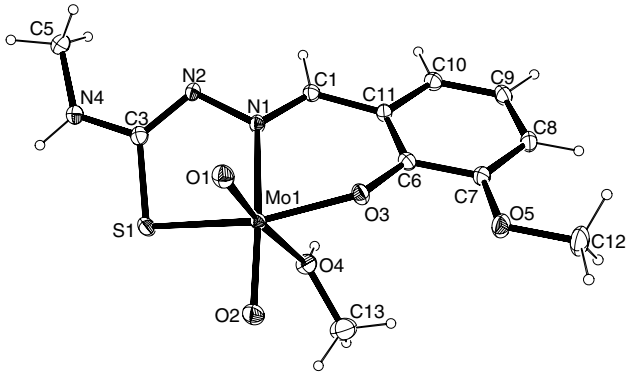


Fig. 4. ORTEP plot of the complex molecule **2aB** with the atom labelling scheme. Ellipsoids are drawn at the 50% probability level.

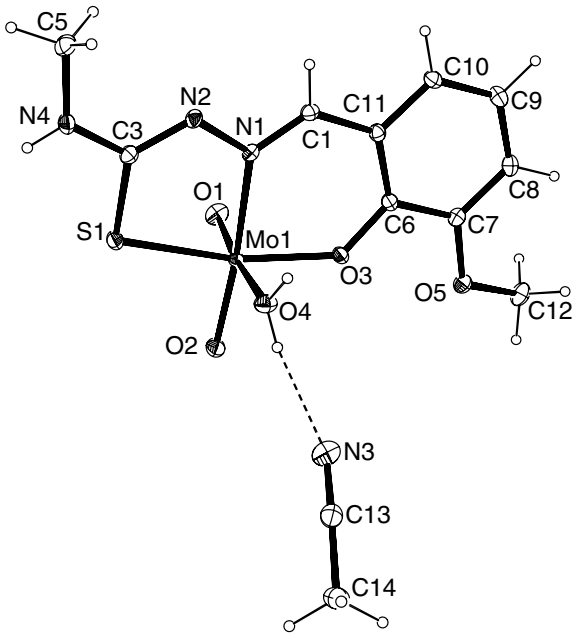


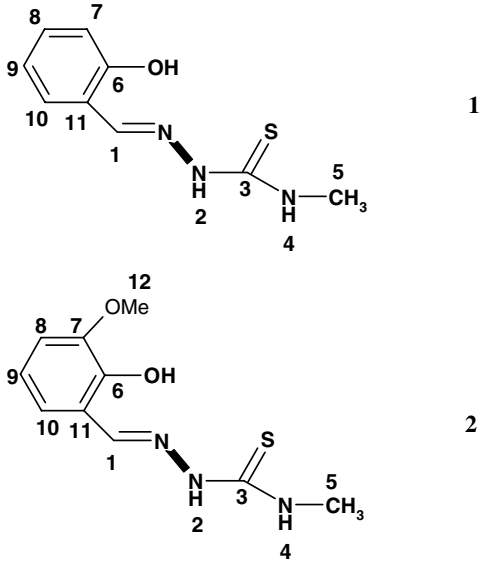
Fig. 5. ORTEP plot of the asymmetric unit of **2b** with the atom labelling scheme. Ellipsoids are drawn at the 50% probability level. The O4–H42···N3 hydrogen bond is represented by dashed line.

In all of the complex compounds, the Mo=O bond lengths [1.686(3)–1.7206(16) Å] and the O=Mo=O bond angles [104.92(7)–105.7(2)°] have values which are usual for *cis*-dioxomolybenum(VI) complexes. Also, the bond distances of Mo1–S1 [2.4047(13)–2.4504(4) Å], Mo1–N1 [2.236(3)–2.2733(12) Å] and Mo1–O3 [1.927(3)–1.9359(10) Å] are similar to those found in other thiosemicarbazonato molybdenum(VI) complexes [35–40]. The bond distances Mo1–O4 [2.359(2)–2.400(3) Å in **1a** and **2a**; 2.308(1) Å in **2b**] are significantly larger compared to the Mo1–O3.

As indicated by the bond distances N2–C3 [1.305(5)–1.319(6) Å] and C3–S1 [1.751(1)–1.766(4) Å], the ligands in the complexes are bonded in their enthiol form, i.e., in the tautomeric form different from that found in the structures of the free ligands (cf. in Table 2). In both bonded ligands, the C5 atom from the *N*-methyl group is *trans* relative to the S1 atom, while in the free ligands it is in the *cis* conformation. In order for ligands **1** and **2** to chelate the $[MoO_2]^{2+}$ moiety through the ONS donor set, as in the studied complexes, rotation of ~180° around the N2–C3 bond is necessary. Additionally for **2**, the phenyl ring moiety has to flip around the C11–C1 bond (Table 2). The 5- and 6-membered chelate rings thus formed (Mo1–N1–N2–C3–S1 and Mo1–O3–C6–C11–C1–N1) are not planar, but are rather puckered. In **1a** and **2a** the 5-membered chelate ring is close to the envelope conformation with Mo1 being the atom most out of the mean plane of the ring [ϕ_2 amounting to −3.5(2)° in the complex molecule **2aB** and 175.4(4)–176.8(2)° in **1a** and **2aA**], while the conformation of the 6-membered ring is nearly a screw-boat with the Mo1 and O3 atoms at the opposite sides of the mean plane of the ring [ϕ_2 amounting to −154.0(4)° in **2aB** and 24.1(4)–27.1(8)° in **1a** and **2aA**; θ amounting to −113.1(4)° in **2aB** and 65.8(8)–66.6(8)° in **1a** and **2aA**] [41,42]. The 5-membered chelate ring in **2b** is nearly planar [mean deviation of 0.0131(9) Å], but with conformation closer to twisted than to the envelope [ϕ_2 = 61(2)°] with C3 and S1 at the opposite sides of the mean plane. The 6-membered chelate ring conformation is almost an envelope with Mo1 being the atom most out of the mean plane of the ring [ϕ_2 = 7.7(3)° and θ = 59.2(3)°] [41,42].

Mean plane deviations for the *N*-methylthioureide [0.015(3) Å and 0.015(4) Å in **1a**; 0.010(2) and 0.012(2) Å in **2a**; 0.032(1) Å in **2b**] and the salicylaldimine [0.026(4) Å and 0.024(4) Å in **1a**; 0.034(2) Å and 0.030(2) Å in **2a**; 0.018(1) Å in **2b**] fragments (defined above for the structures of the ligands) show that in the molecules of the complexes these two fragments retain their planarity. But, in **1a** and **2a** dihedral angles between calculated RMS planes through the fragments [34.00(10)° and 36.64(9)° in **1a**; 35.05(4)° and 36.40(4)° in **2a**] are significantly different from those found in the free ligands. Also, torsion angles C1–N1–N2–C3 differ (Table 2), indicating rotation around the N1–N2 bond upon ligand binding. This is accompanied by the N1–N2 bond lengthening of ~0.02–0.04 Å. In **2b** the dihedral angle between the two fragments [10.74(4)°] and the C1–N1–N2–C3 torsion angle are both similar to those in **2**, but the N1–N2 bond lengthening of ~0.03 Å still occurs upon ligand binding.

In the crystal structure of **1a** two crystallographically independent molecules are bonded into dimers



Scheme 3.

Table 4
^{1}H and ^{13}C chemical shifts (ppm) of the ligands **1** and **2** and their molybdenum(VI) complexes **I** and **II**

Comp. atom	**1**		**I**		**2**		**II**	
	^{1}H	^{13}C	^{1}H	^{13}C	^{1}H	^{13}C	^{1}H	^{13}C
1	8.37	139.09	8.57	152.10	8.39	138.93	8.54	152.37
2	11.47				11.43			
3		177.68				177.67		166.24
4	8.42		7.46		8.41		7.46	
5	3.01	30.96	2.81	31.32	3.00	30.95	2.80	31.62
6		156.46		159.09		146.01		149.19
7	6.87	116.16	6.82	118.44		148.06		149.43
8	7.22	131.09	7.41	133.74	6.96	112.83	7.10	116.21
9	6.83	119.32	6.98	121.26	6.78	119.03	6.92	121.37
10	7.95	126.72	7.60	133.95	7.55	118.17	7.18	125.48
11		120.62		121.61		121.05		122.19
12					3.81	56.02	3.77	56.59
OH	9.87				9.17			

by the O4A–H41A···N2B hydrogen bond. Such dimers are further connected in the infinite chain parallel to *b* axis by the O4B–H41B···N2A (x, $1 + y$, z) hydrogen bonds. Different chains are interlinked together by the hydrogen bonds formed between the amino N4–H4 and terminal oxygen O2 of the neighbouring molecule (Table 3).

Two molecules in the asymmetric unit of **2a** are connected by the N4A–H4A···O2B hydrogen bond. Similarly to **1a**, in the crystal structure of **2a**, there are also intermolecular hydrogen bonds between the amino N4–H4 and terminal oxygen O2 of the neighbouring molecule and between the methanol O4–H41 and the imine N2 from the symmetry equivalent molecule.

One hydrogen atom from the coordinated water molecule in the structure of **2b** participates in the hydrogen bonding with the cocrystallized acetonitrile molecule (Fig. 5), while the other hydrogen atom is part of the hydrogen bond with the imine N2 atom from the molecule related by an inversion centre. The centrosymmetrical dimers formed in this way are further connected by the intermolecular hydrogen bonds between the amino N4–H4 and the terminal oxygen O2 (also observed in **1a** and **2a**).

3.3. NMR spectroscopy

The complete ^{1}H and ^{13}C atom assignments in DMSO-d_6 were made on the basis of the combined use of several one- (^{1}H and APT sequences) and two-dimensional homo- and heteronuclear experiments (COSY, HSQC and HMBC sequences). The proton and carbon chemical shifts of the ligands **1** and **2** (Scheme 3) and complexes **1a** and **2a** are given in Table 4.

The observed chemical shift values are similar to those reported previously for the related thiosemicarbazone ligands and their molybdenum(VI) complexes [40]. In the proton NMR spectra of the free ligands a broad OH signal was observed at 9–10 ppm indicating a participation of this hydroxyl proton in an intramolecular O–H···N1 hydrogen bonds in DMSO, which is in line with our previous results. Carbon chemical shifts and HMBC correlation peaks have confirmed that both ligands exist in the thioketo form in solution, as also found in the solid state. The absence of OH and N2H protons in the proton spectra of **1a** and **2a** corroborates a formation of the complexes with molybdenum. An up-field shift of N4H protons of about 1 ppm (Table 4) is in accordance with this. Slight coordination induced down-field shifts have also been observed for H1 protons. The largest changes in carbon chemical shifts in **1a** and **2a** have been found for carbons at the two interacting sites, C-1 and C-3. The down-field shifts of up to 13.4 ppm for the former and up-field shifts of approximately 11.0 ppm for the latter were observed. The shielding effects at C-3 arised from two contributions, i.e. from a coordination induced-shift and from the formation of an imine C=N bond in the complex instead of a thiocarbonyl C=S bond in the ligand. The carbon atoms at the third interacting site, e.g., C-6 exhibited only moderate chemical shift changes, as already found for the related molybdenum complexes with thiosemicarbazone donors.

4. Supplementary material

CCDC nos. 260969, 260970, 260971, 260972 and 260973 contain the supplementary crystallographic data for compounds **1**, **1a**, **2**, **2a** and **2b**, respectively. These data can be obtained free of charge via www.ccdc.cam.ac.uk/data_request/cif, or by emailing data_request@ccdc.cam.ac.uk, or by contacting The Cambridge Crystallographic Data Centre, 12, Union Road, Cambridge CB2 1EZ, UK, fax: +44 1223 336033.

Acknowledgements

This research was supported by the Ministry of Science and Technology of the Republic of Croatia Grants no. 0119631, 0119632 and 119641.

References

[1] Z. Afrasiabi, E. Sinn, J. Chen, Y. Ma, A.L. Rheingold, L.N. Zakharov, N. Rath, S. Padhye, Inorg. Chim. Acta 357 (2004) 271.
[2] K.H. Thompson, J.H. McNeill, C. Orvig, Chem. Rev. 99 (1999) 2561.
[3] M.A. Ali, S.E. Livingstone, Coord. Chem. Rev. 13 (1974) 101.
[4] D.K. Johnson, T.B. Murphy, N.J. Rose, W.H. Goodwin, L. Pickart, Inorg. Chim. Acta 67 (1982) 159.
[5] K. Srinivasan, S. Perrier, J. Mol. Catal. 36 (1986) 297.
[6] P.K. Bhattacharya, Proc. Ind. Acad. Sci. (Chem. Sci.) 102 (1990) 247.
[7] S. Purohit, A.P. Koley, L.S. Prasad, P.T. Manoharan, S. Ghosh, Inorg. Chem. 28 (1989) 3735.
[8] D. Chatoapadhyay, S.K. Mazumdar, T. Banerjee, S. Gosh, T.C.W. Mak, Acta Crystallogr., Sect. C 44 (1988) 1025.
[9] P. Umapathy, R.P. Budhkar, C.S. Dorai, J. Indian Chem. Soc. 63 (1986) 714.
[10] J. Crim, H. Petering, Cancer Res. 27 (1967) 1278.
[11] G.W. Bushnell, A.Y.M. Tsang, Can. J. Chem. 57 (1979) 603.
[12] J. Chen, J.W. McDonald, W.E. Newton, Inorg. Chem. 15 (1976) 2612.
[13] G.A. Parker, Analytical Chemistry of Molybdenum, Springer-Verlag, New York, 1983.
[14] Oxford Diffraction, Oxford Diffraction Ltd., Xcalibur CCD system, CRYSALIS Software system, Version 1.170, 2003.
[15] G.M. Sheldrick, SHELXS97, Program for the Solution of Crystal Structures, University of Göttingen, Germany, 1997.
[16] H.D. Flack, Acta Crystallogr., Sect. A 39 (1983) 876.
[17] G. Bernardinelli, H.D. Flack, Acta Crystallogr., Sect. A 41 (1985) 500.
[18] G.M. Sheldrick, SHELXL-97, Program for the Refinement of Crystal Structures, University of Göttingen, Germany, 1997.
[19] A.L. Spek, Acta Crystallogr., Sect. A 46 (1990) C34.
[20] A.L. Spek, PLATON, A Multipurpose Crystallographic Tool, Utrecht University, Utrecht, The Netherlands, 1998.
[21] M. Nardelli, Comput. Chem. 7 (1983) 95.
[22] M. Nardelli, J. Appl. Crystallogr. 28 (1995) 659.
[23] L.J. Farrugia, J. Appl. Crystallogr. 30 (1997) 565.
[24] M. Cindrić, N. Strukan, T. Kajfež, G. Giester, B. Kamenar, Z. Anorg. Allg. Chem. 627 (2001) 2604.
[25] M. Cindrić, N. Strukan, V. Vrdoljak, B. Kamenar, Z. Anorg. Allg. Chem. 630 (2004) 585.
[26] M. Cindrić, N. Strukan, T. Kajfež, B. Kamenar, Struct. Chem. 13 (2002) 361.
[27] M. Milanesio, D. Viterbo, R.P. Hernandez, J.D. Rodriguez, J. Ramirez-Ortiz, J. Valdes-Martinez, Inorg. Chim. Acta 306 (2000) 125.
[28] M. Soriano-García, J. Valdés-Martínez, R.A. Toscano, J. Gómez-Lara, M. Villalobos-Peñaloza, Acta Crystallogr., Sect. C 42 (1986) 623.
[29] M. Soriano-García, J. Valdés-Martínez, R.A. Toscano, Acta Crystallogr., Sect. C 44 (1988) 1247.
[30] S.W. Ng, V.G.K. Das, B.W. Skelton, A.H. White, J. Organomet. Chem. 377 (1989) 211.
[31] J. Valdés-Martínez, M. Rubio, R. Cetina Rosado, J. Salcedo-Loaiza, R.A. Toscano, G. Espinosa-Pérez, S. Hernandez-Ortega, K. Ebert, J. Chem. Cryst. 27 (1997) 627.
[32] D.B. Lovejoy, D.R. Richardson, P.V. Bernhardt, Acta Crystallogr., Sect. C 56 (2000) 341.
[33] S. Selvanayagam, M. Yogavel, V. Rajakannan, D. Velmurugan, S.S.S. Raj, H.-K. Fun, Acta Crystallogr., Sect. E 58 (2002) o1336.
[34] P.V. Bernhardt, L.M. Caldwell, D.B. Lovejoy, D. Richardson, Acta Crystallogr., Sect. C 59 (2003) o629.
[35] C. Bustos, O. Burckhardt, R. Schrebler, D. Carrillo, A.M. Arif, A.H. Cowley, C.M. Nunn, Inorg. Chem. 29 (1990) 3996.
[36] A.B. Ilyukhin, V.L. Abramenko, V.S. Sergienko, Koord. Khim. 20 (1994) 653.
[37] G. Argay, A. Kálmán, V.M. Leovac, V.I. Češljević, B. Ribár, J. Coord. Chem. 37 (1996) 165.
[38] S.K. Dutta, D.B. McConville, W.J. Youngs, M. Chaudhury, Inorg. Chem. 36 (1997) 2517.
[39] A. Rana, R. Dinda, P. Sengupta, S. Ghosh, L.R. Falvello, Polyhedron 21 (2002) 1023.
[40] M. Cindrić, V. Vrdoljak, N. Strukan, B. Kamenar, Polyhedron 24 (2005) 369.
[41] D. Cremer, J.A. Pople, J. Am. Chem. Soc. 97 (1975) 1354.
[42] J.C.A. Boeyens, J. Cryst. Mol. Struct. (1978) 317.

homoleptic species had been crystallographically characterized, including $[Zr(OR)_4 \cdot nHOR]_x$ {OR = OCH_2CH_3 (OEt), $n = 0$, $x = 4$ [17]; $OCH(CH_3)_2$ (OPr^i), $n = 1$, $x = 2$ [18,19]} while several mixed alkoxy Zr (and Ti) compounds have been reported [19,20]. Due to this limited supply of useful precursors, it was necessary to develop a new family of similarly ligated species that possessed different structural arrangements. Previously, we have used a series of structurally characterized carboxylic acid (H-ORc, Fig. 1(a)–(e)) modified $Ti(OR)_4$ [OR = OPr^i; $OCH_2C(CH_3)_3$ (ONep)], to generate anatase (TiO_2) films of varied densities [21,22]. Due to our success with the congener system, we followed a similar approach to study ZrO_2 thin films.

The widespread utility of ZrO_2 thin films [1–12] makes it of interest to determine the optimal precursors that will control the densification of the final films. A search of the literature reveals only a few $Zr(OR)_4$ have been crystallographically characterized, including $[Zr_2(\mu_3\text{-OEt})(\mu\text{-OEt})(OEt)_5]_2$ [17] (**1**) [18,19], $[Zr(\mu\text{-}OPr^i)(ONep)_3(H\text{-}ONep)]_2$ [20], Zr(1,2,5,6-di-*O*-isopropylidene-α-D-glucfuranose)$_4$(py)$_2$ [23], and $[(\mu\text{-THME})Zr_2(OPr^i)_5]_2$ [19] (THME = tris(hydroxymethyl)ethane). The dinuclear compounds adopt a standard edge-shared bi-octahedral geometry using two alcohol ligands to complete their geometry.

Several unusual $Zr(OR)_4$ species, derivatized with a variety of H-ORc-modifiers have been reported as: $Zr_6O_2(OPr^n)_{16}(O_2C\text{-}C_{10}H_6O)_2(Pr^iO\text{-}H)_2$, $Zr_{10}O_6(OH)_4(O_2C\text{-}C_6H_4OH)_8(O_2C\text{-}C_6H_4O)_8 \cdot 6H\text{-}OPr$ [24], $[Zr_6(OH)_4O_4(acrylate)_{10}]_2(\mu\text{-acrylate})$ [25], $Zr_6(OH)_4O_4(O_2CR)_{12}(PrOH\text{-}Pr^n)$ (R = Ph, CMe=CH_2) [25], $Zr_6(\mu_3\text{-O})_2(\mu\text{-EtOEt})_6(\mu\text{-}C_3H_2O_2Me)(C_3H_2O_2Me)_4(EtOEt)$ [26], and $Zr_6(\mu_3\text{-O})_2(\mu\text{-OMe})_4(\mu\text{-}C_3H_2O_2Me)_6(C_3H_2O_2Me)_8(EtOEt)_2$ [27]. It is of note that additional ORc-modified mixed metal alkoxide [26,27] and oxo hydroxy [28–30] compounds have also been reported.

From these compounds, it is obvious that a systematic series of ORc-modified $Zr(OR)_4$ compounds was not available to initiate a study on the densification of ZrO_2 thin films. Therefore, it was necessary to synthesize a novel family of ORc-modified $Zr(OR)_4$ precursors that had similar hydrolysis and condensation routes but were structurally varied. These compounds would then be used to generate thin films of ZrO_2 to explore the effects these subtle structural changes had on the density of the final films. The products we isolated, their characterization, and the affect their structures have on the final film densification are presented.

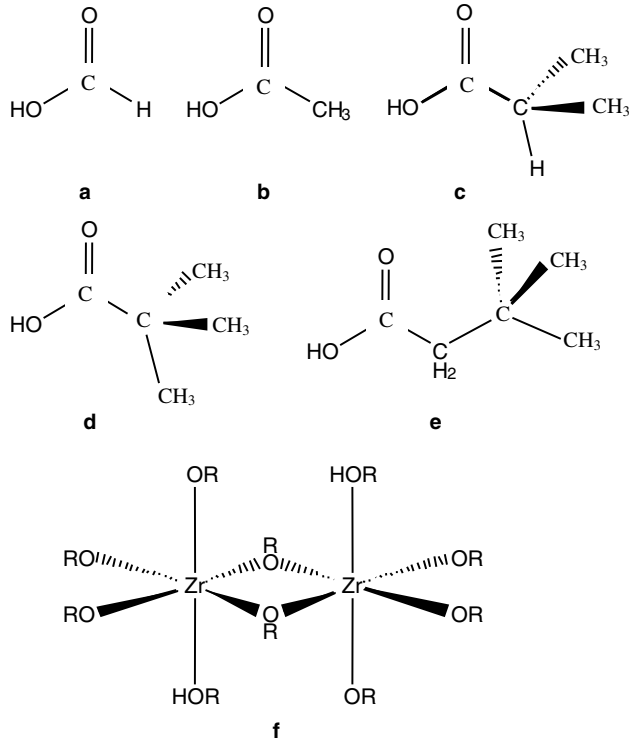


Fig. 1. Schematic representation of the various carboxylic acid (H-ORc) modifiers (a) formic acid (H-O_2CH or H-OFc), (b) acetic acid (H-O_2CH_3 or H-OAc), (c) iso-butyric acid (H-$O_2CH(CH_3)_2$ or H-OPc), (d) trimethyl acetic acid (H-$O_2C(CH_3)_3$ or H-OBc), (e) *t*-butyl acetic acid (H-$O_2CH_2C(CH_3)_3$ or H-ONc), and (f) $[Zr(\mu\text{-OR})(OR)_3H\text{-OR}]_2$ (OR = $OCHMe_2$; **1**).

2. Results and discussion

Since $[Zr(OPr^i)_4 \cdot H\text{-}OPr^i]_2$ (**1**, Fig. 1(f)) was commercially available, we initiated our study by modifying the ligand set of **1** with a series of carboxylic acids (H-ORc), including formic acid (H-O_2CH or H-OFc), acetic acid (H-O_2CCH_3 or H-OAc), isobutyric acid (H-$O_2CCH(CH_3)_2$ or H-OPc), trimethyl acetic aid (H-$O_2CC(CH_3)_3$ or H-OBc), and *t*-butyl acetic acid (H-$O_2CCH_2C(CH_3)_3$ or H-ONc). Schematic representations of the H-ORc structures are shown in Fig. 1(a)–(e). For H-ORc-modified **1** (Fig. 1(f)), the following compounds were characterized as: $Zr_4(\mu_4\text{-O})(\mu\text{-O})(\mu\text{-OFc})_2(\mu\text{-}OPr^i)_4(OPr^i)_6$ (**2**), $Zr_3(\mu_3\text{-O})(\mu\text{-OAc})_3(OAc)_2(\mu\text{-}OPr^i)_2(OPr^i)_3$ (**3**), $[Zr_2(\mu\text{-OPc})_2(\mu\text{-}OPr^i)_2(OPr^i)_4]_2$ (**4**), $Zr_2(\mu\text{-OBc})(\mu\text{-}OPr^i)_2(OPr^i)_5 \cdot (H\text{-}OPr^i)(H\text{-}OPr^i)$ (**5**), and $Zr_2(\mu\text{-ONc})(ONc)(\mu\text{-}OPr^i)_2(OPr^i)_4(H\text{-}OPr^i)$ (**6**). Due to its structural variation in comparison to **1**, we furthered our precursor set by modifying the novel compound $[Zr_3(\mu_3\text{-O})(\mu_3\text{-ONep})(\mu\text{-ONep})_3(ONep)_6]$ (**7**) with the same set of ORc modifiers. These products were identified as: $Zr_3(\mu_z\text{-O})(\mu\text{-OAc})_3(\mu\text{-ONep})_2(ONep)_5$ (**8**), $Zr_5(\mu\text{-O})_3(\mu\text{-OPc})_6(\mu\text{-ONep})_2(ONep)_6$ (**9**), $[Zr(\mu\text{-OPc})(\mu\text{-ONep})(ONep)_2]_2$ (**10**), and $Zr_5(\mu\text{-O})_3(\mu\text{-ONc})_6(\mu\text{-ONep})_2\text{-}(ONep)_6(H\text{-}ONep)1/2(C_7H_8)$ (**11**). This new family (**2**–**11**) of ORc-modified $Zr(OR)_4$ were characterized by a variety of analytical techniques and subsequently used to investigate the structural influences the precursors have on the final densification of ZrO_2 thin films.

2.1. Syntheses of ORc-modified $Zr(OR)_4$

The synthesis of precursors was initiated with the commercially available **1** (Fig. 1(f)) and the appropriate H-ORc (Fig. 1(a)–(e)). After stirring for 12 h, all of the reactions remained clear and were set aside to allow slow evaporation of volatile material. If X-ray quality crystals were not isolated in a short time frame, then the reaction volume was drastically reduced by rotary evaporation and the mixture cooled to −35 °C until crystals formed. Figs. 2–6 show the plots of the solved structures of **2**–**6**, respectively. FTIR spectra of **2**–**6** revealed the standard OPr^i peaks with a notable shift of the C=O stretch of the ORc ligand which is consistent with it being coordinated to a metal center. For **2** and **4**, no OH stretches were observed; however, for **3**, **5**, and **6** a strong broad OH stretch was noted. The resulting powders were very air-sensitive but elemental analyses were found to be consistent with the solid state structure.

Previously, we have reported the synthesis of $[Zr(\mu\text{-}OPr^i)(ONep)_3\cdot(H\text{-}ONep)]_2$ [22]. This compound was initially used in our development of acceptable precursors for production of ZrO_2 thin films; however, the products isolated were identical to those noted for **7** (vide infra).

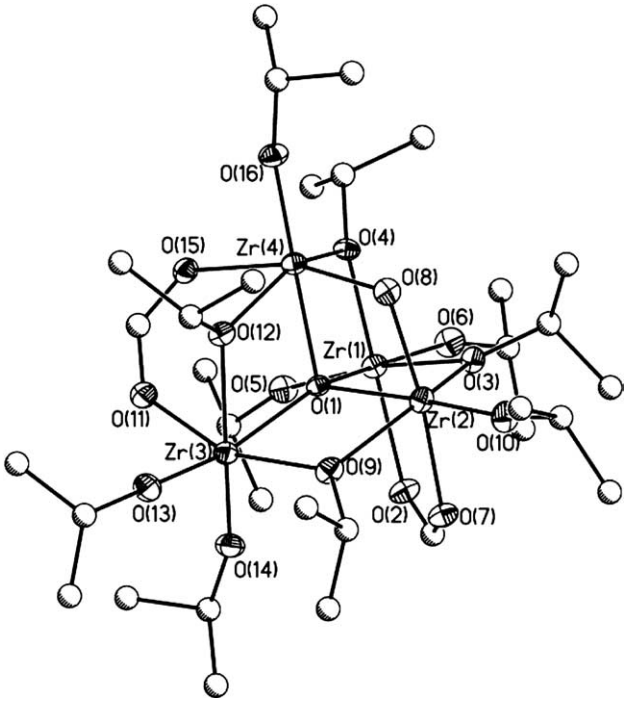


Fig. 2. Structure plot of **2**. Thermal ellipsoids of heavy atoms are drawn at the 30% level, hydrogen atoms are omitted, and carbon atoms are shown as stick and ball for clarity. Selected bond distances (Å): Zr(1)–O(1) 2.178(2); Zr(1)–O(2) 2.234(2); Zr(1)–O(4) 2.154(2); Zr(1)–O(3) 1.932(3); Zr(1)–O(5) 1.914(3); Zr(1)–O(6) 2.180(3). Selected bond angles (°): O(5)–Zr(1)–O(6) 90.82(10); O(5)–Zr(1)–O(4) 100.93(10); O(5)–Zr(1)–O(2) 168.75(10); O(5)–Zr(1)–O(1) 96.22(10); O(5)–Zr(1)–O(3) 100.25(11); O(6)–Zr(1)–O(3) 75.38(7); O(4)–Zr(1)–O(3) 83.70(6); O(2)–Zr(1)–O(3) 88.37(10); O(1)–Zr(1)–O(3) 163.53(10).

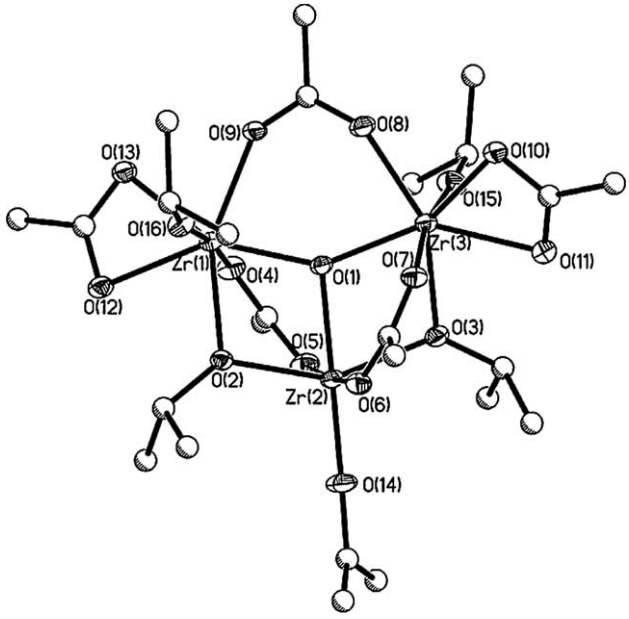


Fig. 3. Structure plot of **3**. Thermal ellipsoids of heavy atoms are drawn at the 30% level, hydrogen atoms are omitted, and carbon atoms are shown as stick and ball for clarity. Selected bond distances (Å): Zr(1)–O(1) 2.078(2); Zr(1)–O(2) 2.185(3); Zr(1)–O(4) 2.254(3); Zr(1)–O(9) 2.212(2); Zr(1)–O(12) 2.295(3); Zr(1)–O(13) 2.265(3); Zr(1)–O(16) 1.891(2); Zr(2)–O(1) 2.102(2): Zr(2)–O(2) 2.095(3); Zr(2)–O(3) 2.098(2); Zr(2)–O(5) 2.162(3); Zr(2)–O(6) 2.145(3); Zr(2)–O(14) 1.926(2). Selected bond angles (°): O(16)–Zr(1)–O(1) 104.93(11); O(16)–Zr(1)–O(2) 91.61(11); O(16)–Zr(1)–O(4) 172.25(11); O(16)–Zr(1)–O(12) 95.56(11); O(16)–Zr(1)–O(9) 91.61(11); O(1)–Zr(1)–O(9) 80.84(9); O(1)–Zr(1)–O(2) 72.24(9); O(1)–Zr(1)–O(4) 81.64(9); O(1)–Zr(1)–O(13) 145.86(10); O(1)–Zr(1)–O(12) 143.12(9); O(14)–Zr(2)–O(5) 91.88(11); O(3)–Zr(2)–O(5) 91.65(10); O(2)–Zr(2)–O(5) 87.22(10); O(1)–Zr(2)–O(5) 87.15(10); O(6)–Zr(2)–O(5) 175.53(10); O(14)–Zr(2)–O(3) 105.92(11); O(14)–Zr(2)–O(2) 105.70(11); O(14)–Zr(2)–O(1) 179.08(11); O(14)–Zr(2)–O(6) 92.59(11).

This is not unexpected since the less sterically hindering OPr^i ligand would be the most susceptible to exchange and hydrolysis, leaving only ONep ligands for structural influences. Therefore, the full series for this precursor was not pursued.

From an in situ generated amide, the ONep derivative of Zr was isolated as **7** (Eq. (1)), an off white powder. This compound was selected for further modification since the trinuclear central core should allow for a wide range of structural variations in comparison to the OPr^i derivatives. The OFc reaction yielded a precipitate that could not be re-dissolved. All of the remaining H-ORc modifications were undertaken using toluene as the solvent with no color changes or precipitates observed. Figs. 7–11 show the plots of structure plots of **7** and the ORc modified species **8**–**11**. The FT-IR spectra of these compounds revealed standard ONep stretches and bends intermixed with stretches that indicated the ORc ligand was coordinated to the Zr metal center. No –OH stretches were observed. The elemental analysis of **8**–**11** proved to be inconsistent with the solid

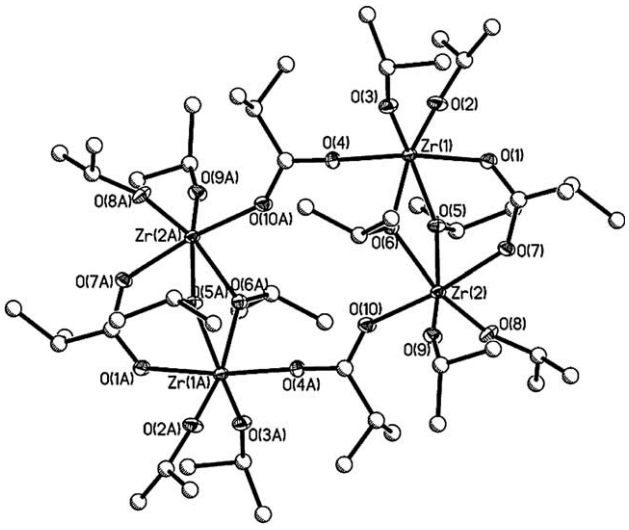


Fig. 4. Structure plot of **4**. Thermal ellipsoids of heavy atoms are drawn at the 30% level, hydrogen atoms are omitted, and carbon atoms are shown as stick and ball for clarity. Selected bond distances (Å): Zr(1)–O(1) 2.173(4); Zr(1)–O(2) 1.933(4); Zr(1)–O(3) 1.932(4); Zr(1)–O(4) 2.109(4); Zr(1)–O(5) 2.181(4); Zr(1)–O(6) 2.181(4). Selected bond angles (°): O(3)–Zr(1)–O(2) 99.31(18); O(3)–Zr(1)–O(4) 96.27(17); O(3)–Zr(1)–O(1) 88.54(16); O(3)–Zr(1)–O(6) 94.15(16); O(2)–Zr(1)–O(5) 95.04(17); O(4)–Zr(1)–O(5) 90.78(15); O(1)–Zr(1)–O(5) 83.14(15); O(6)–Zr(1)–O(5) 70.89(15).

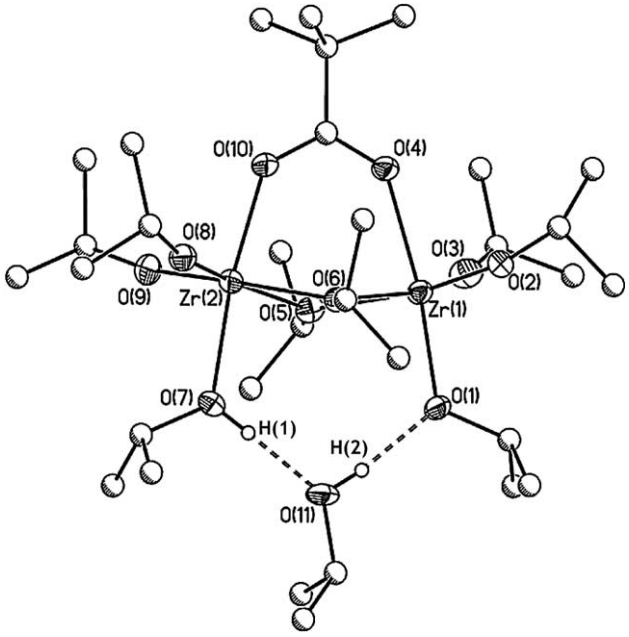


Fig. 5. Structure plot of **5**. Thermal ellipsoids of heavy atoms are drawn at the 30% level, hydrogen atoms are omitted, and carbon atoms are shown as stick and ball for clarity. Selected bond distances (Å): Zr(1)–O(1) 2.058(4); Zr(1)–O(2) 1.946(4); Zr(1)–O(3) 1.941(4); Zr(1)–O(4) 2.263(4); Zr(1)–O(5)2.202(4); Zr(1)–O(6) 2.192(4); O(11)–H(1) 0.8400; O(7)–H(1) 0.845(18); O(1)–H(2) 1.862; O(11)–H(1) 1.740. Selected bond angles (°): O(3)–Zr(1)–O(2) 99.94(11); O(3)–Zr(1)–O(1) 97.09(10); (3)–Zr(1)–O(6) 161.42(10); O(3)–Zr(1)–O(4) 87.21(9); O(3)–Zr(1)–O(4) 87.21(9); O(2)–Zr(1)–O(4) 88.24(9); O(1)–Zr(1)–O(4) 172.62(8); O(6)–Zr(1)–O(4) 82.48(8); O(5)–Zr(1)–O(4) 82.57(8); O(1)–H(2)–O(11) 167.34(2); O(7)–H(1)–O(11) 175.56(3).

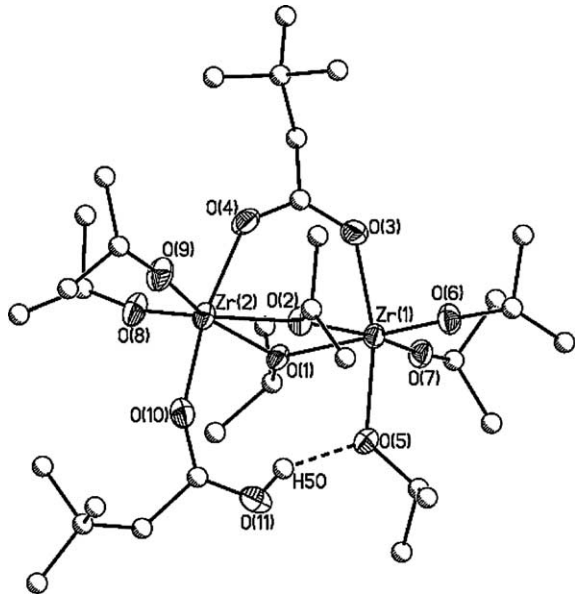


Fig. 6. Structure plot of **6**. Thermal ellipsoids of heavy atoms are drawn at the 30% level, hydrogen atoms are omitted, and carbon atoms are shown as stick and ball for clarity. Selected bond distances (Å): Zr(1)–O(1) 2.151(6); Zr(1)–O(2) 2.162(6); Zr(1)–O(3) 2.155(6); Zr(1)–O(5) 2.195(6); Zr(1)–O(6) 1.924(6); Zr(1)–O(7) 1.921(6); Zr(2)–O(1) 2.176(6); Zr(2)–O(2) 2.192(6); Zr(2)–O(4) 2.183(6); Zr(2)–O(8) 1.925(6); Zr(2)–O(9) 1.926(6); Zr(2)–O(10) 2.074(6). O(11)–H(50) 2.019; O(5)–H(50) 0.85. Selected bond angles (°): O(7)–Zr(1)–O(6) 99.6(3); O(7)–Zr(1)–O(2) 165.2(2); O(7)–Zr(1)–O(1) 92.2(2); O(7)–Zr(1)–O(3) 93.3(3); O(7)–Zr(1)–O(5) 94.3(3); O(8)–Zr(2)–O(2) 165.2(2); O(9)–Zr(2)–O(2) 92.7(3); O(10)–Zr(2)–O(2) 90.4(3); O(1)–Zr(2)–O(2) 71.5(2); O(4)–Zr(2)–O(2) 81.9(2); C(22)–O(11)–H(50) 88.25(6); Zr(1)–O(5)–H(50) 109.25(6).

state structures; however, when a molecule of solvent (i.e., toluene) was included the analyses fell within the acceptable range of error.

$$ZrCl_4 + 4LiNMe_2 \xrightarrow{tol} Zr(NMe_2)_4 \xrightarrow[+4HONep]{-4LiCl} 1/3Zr_3(O)(ONep)_{10} \quad (1)$$

2.2. Single crystal X-ray structures of ORc-modified $Zr(OR)_4$

In order to determine the solid state structures of **2**–**11**, single crystal X-ray analysis were undertaken. The crystal of **2**–**11** were found to be very air sensitive and therefore were handled under inert conditions to minimize exposure to atmospheric conditions while the crystals were being mounted. Discussions concerning the structural aspects of **1**–**11** are detailed below.

2.2.1. Single crystal X-ray structures of OPr^i derivatives

The commercially available **1** is shown in Fig. 1(f) and several reports on its structure are available [18,19]. Each Zr metal center is octahedrally (Oh) bound by two μ-OPr^i, three terminal OPr^i, and one coordinated

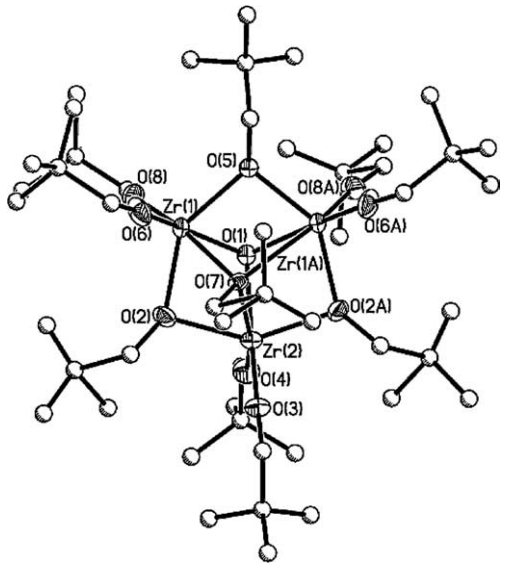


Fig. 7. Structure plot of **7**. Thermal ellipsoids of heavy atoms are drawn at the 30% level, hydrogen atoms are omitted, and carbon atoms are shown as stick and ball for clarity. Selected bond distances (Å): Zr(1)–O(8) 1.903(5); Zr(1)–O(6) 1.925(4); Zr(1)–O(1) 2.082(3); Zr(1)–O(5) 2.164(3); Zr(1)–O(2) 2.167(4); Zr(1)–O(7) 2.196(7); Zr(1)–O(7) 2.742(6);. Selected bond angles (°): O(8)–Zr(1)–O(6) 101.9(3); O(8)–Zr(1)–O(1) 99.0(2); O(8)–Zr(1)–O(5) 105.90(19); O(8)–Zr(1)–O(2) 100.7(2); O(8)–Zr(1)–O(7) 165.2(2); O(6)–Zr(1)–O(7) 89.4(2); O(1)–Zr(1)–O(7) 70.4(2); O(5)–Zr(1)–O(7) 81.6(2); O(2)–Zr(1)–O(7) 67.1(2).

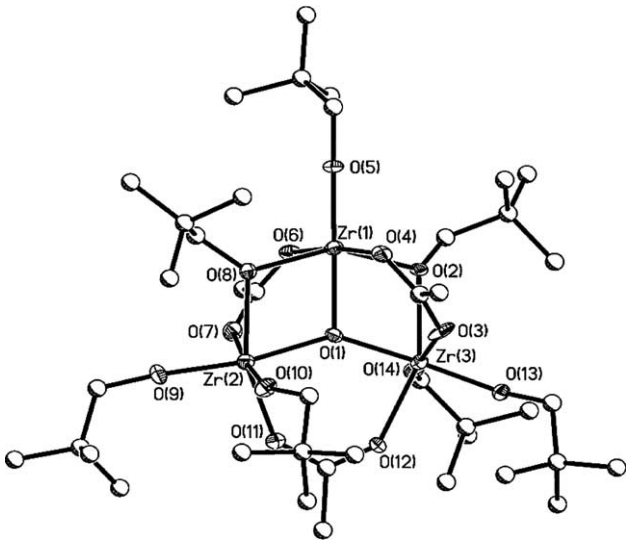


Fig. 8. Structure plot of **8**. Thermal ellipsoids of heavy atoms are drawn at the 30% level, hydrogen atoms are omitted, and carbon atoms are shown as stick and ball for clarity. Selected bond distances (Å): Zr(1)–O(5) 1.919(4); Zr(1)–O(1) 2.063(4); Zr(1)–O(2) 2.125(4); Zr(1)–O(8) 2.130(4); Zr(1)–O(4) 2.141(4); Zr(1)–O(6) 2.141(4). Zr(3)–O(13) 1.916(4); Zr(3)–O(14) 1.948(4); Zr(3)–O(3) 2.058(4); Zr(3)–O(12) 2.176(4); Zr(3)–O(2) 2.204(4); Zr(3)–O(3) 2.291(4). Selected bond angles (°): O(5)–Zr(1)–O(1) 179.45(18); O(5)–Zr(1)–O(2) 104.30(18); O(1)–Zr(1)–O(2) 75.15(16); O(5)–Zr(1)–O(8) 104.75(17); O(1)–Zr(1)–O(8) 75.80(16); O(2)–Zr(1)–O(8) 150.86(16); O(5)–Zr(1)–O(4) 93.02(18); O(1)–Zr(1)–O(4) 86.99(17); O(2)–Zr(1)–O(4) 86.41(17); O(8)–Zr(1)–O(4) 89.78(17); O(5)–Zr(1)–O(6) 94.52(18); O(1)–Zr(1)–O(6) 85.50(17); O(2)–Zr(1)–O(6) 94.28(17); O(8)–Zr(1)–O(6) 85.74(16); O(4)–Zr(1)–O(6) 172.01(17).

H-OPr^i molecule. This molecule is very robust and has been used as a sterically hindering ligand for other metal centers [31–35]. Therefore, it was expected that we would observe structures that possessed multiplets of the dinuclear subunit, substituted with ORc ligands.

The OFc derivative of **1** was isolated as the tetranuclear species **2** (Fig. 2), wherein, the four Zr atoms are tetrahedrally (Td) arranged around a μ_4-O. Another oxide is present as μ-O atom linking two of the four Zr atoms with the remaining ligands asymmetrically arranged around this central core: four μ-OPr^i, six terminal OPr^i, and two μ-OFc ligands. Both OFc ligands bridge two different Zr atoms. This arrangement was unexpected because compound **2** is structurally identical to the OFc derivative of Ti(OPr^i)$_4$ (''Ti-OPr^i/OFc'') described as a face-shared corner-missing cube structure, [Ti$_4$(μ_4-O)(μ-O)(μ-OFc)(μ-OPr^i)$_4$(OPr^i)$_6$] [22]. The basic core structure of **2** appears to have significantly altered the dinuclear starting material **1** but **2** can be thought of as two of the dinuclear species of **1** bound perpendicularly by OFc and O ligands.

By increasing the steric bulk of the ORc ligand from a –H (OFc) to a –CH$_3$ (OAc) group, the nuclearity of the resulting product **3** was reduced to a trinuclear species (Fig. 3). The molecule possesses a C_2 center of symmetry with two Zr atoms adopting a pentagonal bipyramidal (PBP) geometry whereas the unique Zr atom adopted an Oh geometry. The three Zr metal centers surround a μ_3-O with a symmetric distribution of a single μ-OAc, two μ-OPr^i, and a terminal OPr^i for each metal center. The unique Zr metal center bridges to each of the PBP-coordinated Zr metal centers using a μ-OAc ligand. Finishing the PBP coordination of these Zr metal centers is a chelating OAc ligand. Based on the previous reported stability of **1**, it was surprising that the central core was so easily disrupted by HOAc forming a structure similar to ''Ti-ONep/OFc'' complex which generated the highest dense films of TiO$_2$ [22].

For compound **4**, even though the steric bulk of the pendant chain of OPc (CH(CH$_3$)$_2$) is greater than the OAc (CH$_3$), an increase in nuclearity was observed (see Fig. 4) possibly due to the lack of oxo formation. The structure possesses a C_{2h} symmetry where the two sub-moieties are linked by μ-OPc ligands. These smaller units consist of two Zr metal centers bridged by two OPr^i, one μ-OPc ligand, and two terminal OPr^i ligands. This molecule can be thought of as linking two OPc substituted moieties of **1** (multiplet of the subunit). There are no similar Ti based structures known.

Introduction of the most sterically demanding ligand investigated, OBc, led to the isolation of the simple substituted complex **5**, shown in Fig. 5. This molecule consists of two Oh-coordinated Zr atoms bridged by

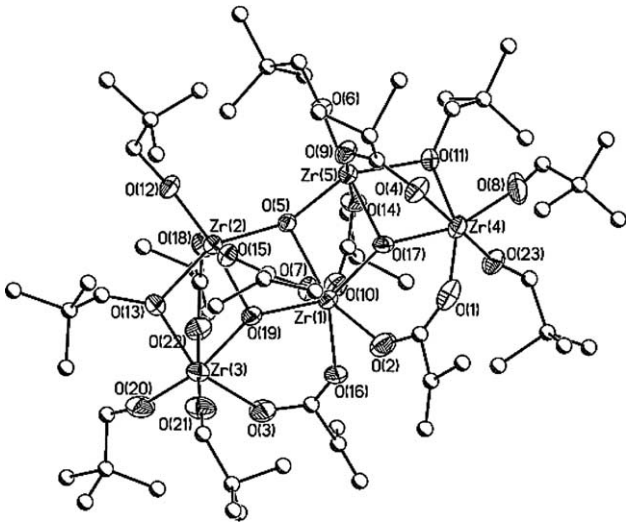


Fig. 9. Structure plot of **9**. Thermal ellipsoids of heavy atoms are drawn at the 30% level, hydrogen atoms are omitted, and carbon atoms are shown as stick and ball for clarity. Selected bond distances (Å): Zr(1)–O(17) 2.020(4); Zr(1)–O(19) 2.033(4); Zr(1)–O(7) 2.180(4); Zr(1)–O(2) 2.182(4); Zr(1)–O(16) 2.183(4); Zr(1)–O(10) 2.191(4); Zr(1)–O(5) 2.273(4). Selected bond angles (°): O(17)–Zr(1)–O(19) 147.13(16); O(17)–Zr(1)–O(7) 92.17(15); O(19)–Zr(1)–O(7) 82.84(15); O(17)–Zr(1)–O(2) 82.56(16); O(19)–Zr(1)–O(2) 126.32(15); O(7)–Zr(1)–O(2) 74.25(17); O(17)–Zr(1)–O(16) 125.397(16); O(19)–Zr(1)–O(16) 82.26(16); O(7)–Zr(1)–O(16) 123.44(16); O(2)–Zr(1)–O(16) 72.01(17); O(17)–Zr(1)–O(10) 82.18(15); O(19)–Zr(1)–O(10) 123.31(17); O(16)–Zr(1)–O(10) 74.17(16); O(17)–Zr(1)–O(5) 73.73(14); O(19)–Zr(1)–O(5) 73.40(14); O(7)–Zr(1)–O(5) 79.94(14); O(2)–Zr(1)–O(5) 144.03(15); O(16)–Zr(1)–O(5) 143.96(15); O(10)–Zr(1)–O(5) 80.27(14).

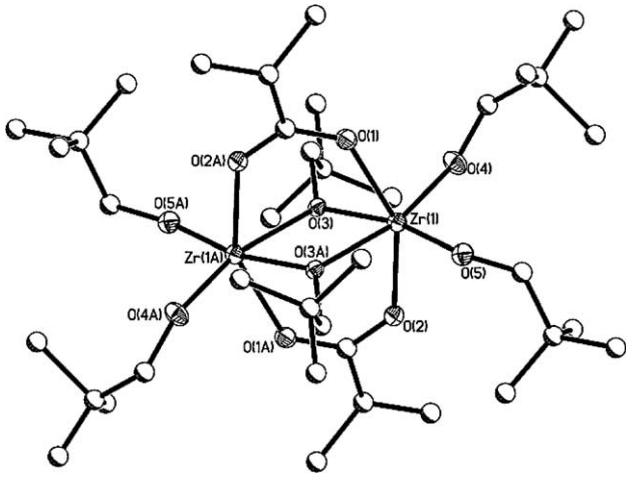


Fig. 10. Structure plot of **10**. Thermal ellipsoids of heavy atoms are drawn at the 30% level, hydrogen atoms are omitted, and carbon atoms are shown as stick and ball for clarity. Selected bond distances (Å): Zr(1)–O(4) 1.909(6); Zr(1)–O(3) 1.939(6); Zr(1)–O(2) 2.163(6); Zr(1)–O(5) 2.182(6); Zr(1)–O(2) 2.184(6); Zr(1)–O(1) 2.201(6). Selected bond angles (°): O(4)–Zr(1)–O(3) 96.3(2); O(4)–Zr(1)–O(2) 168.1(2); O(3)–Zr(1)–O(2) 92.9(2); O(4)–Zr(1)–O(2) 94.4(2); O(3)–Zr(1)–O(2) 165.9(2); O(2)–Zr(1)–O(2) 78.7(2); O(5)–Zr(1)–O(2) 81.4(2); O(4)–Zr(1)–O(1) 107.2(2); O(3)–Zr(1)–O(1) 92.0(2); O(2)–Zr(1)–O(1) 80.8(2); O(5)–Zr(1)–O(14) 150.8(2).

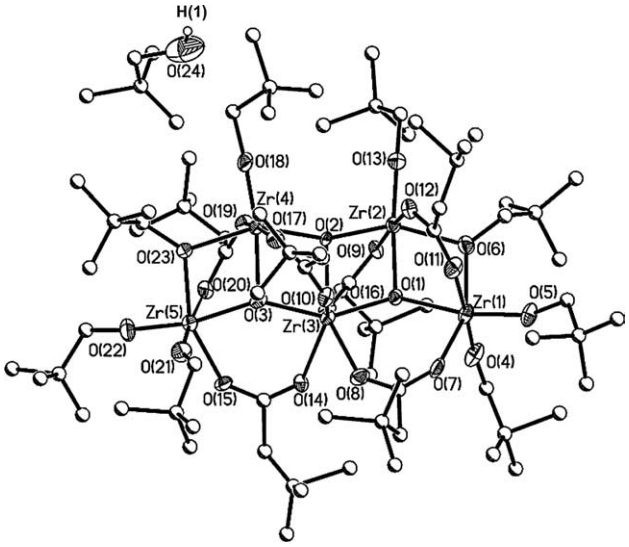


Fig. 11. Structure plot of **11**. Thermal ellipsoids of heavy atoms are drawn at the 30% level, hydrogen atoms are omitted, and carbon atoms are shown as stick and ball for clarity. Selected bond distances (Å): Zr(1)–O(7) 1.914(5); Zr(1)–O(1) 1.950(5); Zr(1)–O(5) 2.101(4); Zr(1)–O(4) 2.136(5); Zr(1)–O(6) 2.174(5); Zr(1)–O(11) 2.272(5). Selected bond angles (°): O(7)–Zr(1)–O(1) 98.6(2); O(7)–Zr(1)–O(5) 97.33(18); O(7)–Zr(1)–O(4) 93.7(2); O(7)–Zr(1)–O(6) 101.24(19); O(7)–Zr(1)–O(11) 177.2(2); O(1)–Zr(1)–O(11) 81.46(19); O(5)–Zr(1)–O(11) 82.87(17); O(4)–Zr(1)–O(11) 83.58(19); O(2)–Zr(1)–O(11) 81.48(18).

two μ-OPr^i and one μ-OBc ligands. The coordination is completed by three OPr^i ligands. Due to charge balance, one of these ligands must be an H-OPr^i with an additional H-OPr^i was also found in the unit cell. From bond distances and angles, it appears that there is H-bonding between the unit cell H-OPr^i, free H-OPr^i, and terminal OPr^i. Compound **6** was dinuclear as well with a similar arrangement with one μ-ONc, one terminal ONc, two μ-OPr^i, four OPr^i, and a bound H-OPr^i. A structure plot of **6** is shown in Fig. 6. The H-OPr^i also appears to be H-bound to the terminal acid. Both **5** and **6** are similar to what was observed for the "Ti-OPr^i/OBc" species [22] and again show retention of the Zr dinuclear subunit.

2.2.2. Single crystal X-ray structures of ONep derivatives

The structure of **7** is a symmetric trinuclear species with μ_3-O and μ_3-ONep ligands (see Fig. 7). The three Zr atoms are bridged by a μ-ONep ligand and the final Oh coordination is filled by terminal ONep ligands. In contrast, for the Ti-ONep system, generated through the same reaction pathway, a halide was retained [36]. The variation in the structure of **7** in comparison to **1** was of interest to further modify with ORc ligands to increase the number of precursors for thin film investigation. Modification with H-OFc, yielded precipitates that could not be re-dissolved and X-ray quality crystals from the H-OBc derivatives could not be isolated in our hands.

Modification of **7** with H-OAc led to the trinuclear species **8** (Fig. 8). The central core of **8** is similar to **7**

with the μ_3-O bridging the three Oh-coordinated Zr metal centers. Two μ-ONep and two μ-OAc ligands bridge to Zr(1) from Zr(2) and Zr(3). The latter metal centers are bridged by a single μ-OAc ligand. Zr(1) finishes its coordination by binding one terminal ONep ligand whereas Zr(2) and Zr(3) possess two terminal ONep ligands. From this structure, the general constructs of **7** were found to be stable with simple OR–ORc exchanges. The constructs of compound **8** are similar to **3** and the "Ti-OPr^i/OFc" complex [22].

For the OPc derivative of **7**, two species were isolated, **9** and **10**. Compound **9** appears to be the major product based on the elemental analysis and numerous single crystal experiments. Compound **9** is a ladder-like structure containing five Zr atoms (see Fig. 9). The molecule contains a C_2 center of symmetry that creates three types of Zr atoms (ratios of 2:1:2). The unique Zr has no terminal ONep ligands but uses four μ-OPc and three μ_3-O ligands to form a PBP geometry around the 7-coordinated Zr atoms. Two Oh-coordinated Zr atoms have one terminal ONep ligand and to μ-OPc, two μ_3-O, and one μ-ONep set of ligands. The final two Zr are Oh bound with two OPc, two terminal ONep, one μ-ONep, and one μ_3-O ligand sets. Compound **9** is unique in the previously identified Group 4 OR-ORc structure types [22] and reveals the disruption of the trinuclear **7**. Another structure was isolated from this reaction mixture, **10** (Fig. 10). This compound is a simple dinuclear species with two μ-ONep, two μ-OPc, and four terminal ONep ligands filling the Oh geometry of the two Zr atoms; however, **10** is similar to the structure noted for the "Ti-ONep/OBc" species [22]. Compound **11** is structurally similar to **9** with ONc ligands replacing the OPc ligands and is shown in Fig. 11.

2.3. Solution behavior of ORc-modified $Zr(OR)_4$ species

Since the precursor will necessarily be dissolved in a solvent prior to spin-cast deposition, it is important, if possible, to understand their solution behavior. To investigate whether the solid state structure were retained in solution, NMR studies were undertaken by dissolving crystals of **2**–**11** in toluene-d_8. The ^{1}H NMR spectra did not reveal a great deal of information concerning the structural aspects of **2**–**6** due to the numerous, overlapping peaks that were present. As previously reported for the Ti system [22], rapid ligand-exchange processes are common for these types of species and would explain the complicated NMR spectra. For each sample resonances were clearly present for OPr^i and the appropriate ORc ligands. In an attempt to further clarify the solution behavior, ^{13}C NMR spectra were obtained for **2**–**6**. The resonances associated with the ORc ligands should yield the most information concerning the solution behavior of these compounds. If the solid state structures are retained in solution, for **2**,**4**, and **6**, a 1:1 ratio of ORc carbon (R-CO_2) resonances should be observed, for **3**, a 2:2:1 ratio and for **5** only one resonance should be observed. For **2**, only one set of broad ^{13}C resonance was noted for the disparate OPr^i ligands and a very weak but broad OFc resonance. The spectrum of **3** also showed numerous broad peaks for the OPr^i peaks but only a single broad OAc resonance. Compounds **4** and **5** did not yield high quality spectra due to the low solubility of these compounds. The spectrum of **6** revealed the presence of two types of ONc ligands and multiple resonances for the OPr^i ligands.

The ONep derivatives (**8**, **9**, and **11**) are expected to yield a 2:1 ratio of ligand resonances (**9** and **11** may also display a 2:2:1 ratio). Again, due to the complexity of the ^{1}H NMR spectrum for each sample, information concerning the nuclearity of these compounds could not be discerned; however, the appropriate ligand resonances for the various samples were noted. From the ^{13}C NMR spectra, only a single resonance for **8** was observed. With rapid ONep ligand exchange the unequivalent ORc ligands could easily become equivalent and therefore a singlet is not unexpected. For **9**, the expected three resonances were noted. In contrast, compound **11** revealed only a single broad resonance for the ONc derivative; however, the alkyl peaks were also broad. These results indicated that a great deal of ligand scrambling is occurring.

Although solution behavior was difficult to establish because of low compound solubility and observed ligand scrambling, we assumed, based on the similarity of structures between the Ti and Zr systems, that similar solution behavior should occur. For the Ti system, ligand scrambling did not alter the general constructs [22] and this concept was applied to the Zr system described here.

2.4. Thin film behavior of ORc-modified $Zr(OR)_4$

It was of interest to determine how the various structural changes of these compounds affected the densification of the final ZrO_2 thin films. For the Ti system, the oxo species appeared to assist in holding the compounds together during hydrolysis and trinuclear species with some oxo ligands present were found to be the best precursors to generate highly dense anatase thin films [22].

Due to the low solubility of the Zr compounds it was difficult to generate solutions that produced films without cracks or large defects. The defects formed during film processing are most likely due to the increased steric hindrance of the ONep ligand preventing controlled cross-linking resulting from exposure to ambient humidity to form the necessary extended Zr–O–Zr network of a film. Instead, upon condensation the limited interaction would cause *closo*-structures to form, negating extended networks causing cracks. This general argument also can be used to explain the poor properties

of all of the ONep derivatives in comparison to the smaller OPr^i species.

Acceptable films were generated from solutions of **3**–**5**. In contrast to the characteristics of the optimal precursors for generation of dense antase films, none of the Zr compounds that made the best films possess oxo moieties but are simply the substituted compounds. From the films that could be analyzed, it was discovered that by increasing the steric bulk of the pendant ORc ligand increased the film thickness which ranged from 2500 to 2700 Å. However, due to the poor quality, additional ligand manipulation will be necessary to fully explore higher density films. In general, it appears that the same trends observed for the anatase system did not apply to the zirconium oxide thin films. This is most likely due to the different hydrolysis rates of the two metal cations. Efforts to improve the solubility of the Zr precursors are underway in order to garner a larger set of useful precursors necessary to adequately explore the densification of zirconium oxide thin films.

3. Summary and conclusions

We have synthesized and characterized a series of ORc-modified $Zr(OR)_4$ species using commercially available **1** and specialty precursor **7**. The molecules of the OPr^i derivatives range from simple substitutions of ORc for OR groups resulting in tetranuclear (**4**) and dinuclear (**5** and **6**) species to partially hydrolyzed trinuclear species (**2** and **3**). For the derivatives of **7**, the majority of species had an oxo group present but this may be a reflection of the starting materials composition. The nuclearity of these species was either tri- (**8**) or pentanuclear (**9** and **11**). Surprisingly, the previously unobserved structure type was found for two acid modifiers in this system. Of these species, three (**3**–**5**) generated acceptable quality films which could be monitored for film thickness and densification. The remainder produced cracked films. For **3**–**5**, the larger pendant ORc chains generated the thickest films.

4. Experimental

All compounds described below were handled with rigorous exclusion of air and water using standard Schlenk line and glove box techniques. All solvents were used as received from Aldrich in sure seal bottles. H-OFc (Aldrich) and H-OAc (Fisher) were dried and freshly distilled, immediately prior to use. The following compounds were stored under argon upon receipt (Aldrich) and used without further purification: H-ONep, H-OPc, H-OBc, H-ONc, **1**, $ZrCl_4$, and $LiNMe_2$. Samples for all analyses were prepared from dried crystalline material.

4.1. Physical measurements

FT-IR data were obtained on a Bruker Vector 22 MIR Spectrometer using KBr pellets under an atmosphere of flowing nitrogen. Elemental analyses were performed on a Perkin–Elmer 2400 CHN-S/O Elemental Analyzer. All NMR samples were handled and stored under an argon atmosphere and re-dissolved in toluene-d_8 at saturated solution concentrations immediately prior to use. All solution spectra were obtained on a Bruker DRX400 spectrometer at 399.8 and 100.1 MHz for ^1H and ^{13}C experiments, respectively. A 5 mm broadband probe was used for all experiments. The ^1H NMR spectra were obtained using a direct single pulse excitation, with a 10 s recycle delay and 8 signal averages. The $^{13}C\{^1H\}$ NMR spectra were obtained using a WALTZ-16 composite pulse ^1H decoupling, a 5 s recycle delay and a $\pi/4$ pulse excitation.

4.2. General synthesis of ORc-modified $Zr(OR)_4$

The appropriate $Zr(OR)_4$ (**1** or **7**) was dissolved in toluene and then added via pipette to a stirring mixture of the desired carboxylic acid (H-ORc, Fig. 1) already dissolved in toluene. After 12 h, the reaction was allowed sit to slowly evaporate the volatile material until crystals formed. If crystals did not form, the reaction mixture was further concentrated by rotary evaporation and then placed into a freezer (−35 °C) until crystals formed. Scale and analytical data are presented for each compound (vide infra).

4.2.1. $Zr_4(O)_2(OFc)_2(OPr^i)_{10}$ (**2**)

Used **1** (0.500 g, 1.29 mmol), H-OFc (0.0590 g, 1.29 mmol) and ~10 mL of toluene. Yield 0.390 g (56.1%). FT-IR (KBr, cm^{-1}) 2969(s), 2931(s), 2864(s,sh), 2626(m), 2364(w), 2345(w), 1590(s), 1463(s), 1375(s), 1338(s,sh), 1167(s), 1051(w,sh), 1018(s), 955(s), 847(s). Elemental *Anal.* Calc. for $Zr_4O_{16}C_{32}H_{72}$: C, 35.66; H, 6.73. Found: C, 35.63; H, 6.36%.

4.2.2. $Zr_3(O)(OAc)_5(OPr^i)_5$ (**3**)

Used **1** (0.500 g, 1.29 mmol), H-OAc (0.0770 g, 1.29 mmol) and ~10 mL of toluene, heated for 10 min until solution went clear. Yield 0.350 g (46.3%). FT-IR (KBr, cm^{-1}) 2969(s), 2932(m), 2863(w), 2625(w), 1548(s), 1450(s), 1375(m), 1363(m,sh), 1337(w), 1168(s), 1049(sh), 1017(s), 947(s), 847(m), 826(m,sh), 653(m), 617(m), 554(s), 461(s). Elemental *Anal.* Calc. for $Zr_3O_{16}C_{25}H_{50}$: C, 34.11; H, 5.72. Found: C, 34.04; H, 5.62%.

4.2.3. $[Zr_2(OPc)_2(OPr^i)_6]_2$ (**4**)

Used **1** (0.500 g, 1.29 mmol), H-OPc (0.113 g, 1.29 mmol) and ~10 mL of toluene, heated for 10 min until solution went clear. Yield 0.370 g (40.4%). FT-IR

(KBr, cm^{-1}) 2970(s), 2932(m), 2868(m), 2624(w), 2367(w), 2345(w), 1578(s), 1561(s,sh), 1510(w), 1476(m), 1439(s), 1375(s), 1362(s,sh), 1338(m), 1301(m), 1262(w), 1169(s), 1099(sh), 1021(s), 1009(sh), 974(m), 847(m), 824(m), 775(w), 654(m), 542(s), 462(s). Elemental *Anal.* Calc. for $Zr_2O_{10}C_{26}H_{56}$: C, 43.91; H, 7.94. Found: C, 44.16; H, 7.61%.

4.2.4. $Zr_2(OBc)(OPr^i)_7(H\text{-}OPr^i)(H\text{-}OPr^i)$ (**5**)

Used **1** (0.500 g, 1.29 mmol), H-OBc (0.132 g, 1.29 mmol) and ~10 mL of toluene. Yield 0.400 g (38.1%). FT-IR (KBr, cm^{-1}) 2969(s), 2930(m), 2865(w), 2625(w), 2346(w), 1583(s,sh), 1561(s), 1509(w), 1485(s), 1460(m,sh), 1431(s), 1407(w,sh), 1374(s), 1361(s), 1339(m), 1229(m), 1171(s), 1023(s), 945(s), 898(w), 847(m), 822(m), 791(w), 601(s), 561(s), 545(s), 461(s), 432(w,sh), 407(m). Elemental *Anal.* Calc. for $C_{32}H_{74}O_{11}Zr_2$: C, 47.02; H, 9.12. Found: C, 46.82; H, 8.87%.

4.2.5. $Zr_2(\mu\text{-}ONc)(H\text{-}ONc)(OPr^i)_7$ (**6**)

Used **1** (0.500 g, 1.29 mmol), H-ONc (0.150 g, 1.29 mmol) and ~10 mL of toluene. Yield 0.430 g (40.2%). FT-IR (KBr, cm^{-1}) 2966(s), 2867(s,sh), 2625(m), 1561(s), 1459(s), 1337(s,sh), 1307(m), 1277(m), 1237(m), 1168(s), 1022(s), 948(s), 847(m), 821(m), 726(m), 628(sh), 548(s), 462(s), 411(s, sh). Elemental *Anal.* Calc. for $Zr_2O_{11}C_{33}H_{72}$: C, 47.91; H, 8.77. Found: C, 47.56; H, 8.43%.

4.2.6. $Zr_3(O)(ONep)_{10}$ (**7**)

$Zr(NMe_2)_4$ was synthesized from the reaction of $ZrCl_4$ (1.00 g, 4.29 mmol) and $LiNMe_2$ (0.876 g, 17.1 mmol) in THF (~8 mL). The precipitate was removed by centrifugation, the soluble fraction dried, extracted with hexanes, and dried by rotary evaporation. The $Zr(NMe_2)_4$ (0.869 g, 3.24 mmol) powder was re-dissolved in toluene (~5 mL), H-ONep (1.28 g, 14.6 mmol) in toluene (~5 mL) was added and the reaction was allowed to stir. After 8 h, the resultant mixture was warmed (~60 °C) for 1 h, allowed to cool to room temperature and all of the volatile material removed in vacuo. The resultant white powder was dissolved in a warmed solution of hexanes and toluene (3:1) and allowed to cool to room temperature. X-ray quality crystals were isolated. Yield 1.06 g (63.8%). FT-IR (KBr, cm^{-1}) 2952(s), 2866(s,sh), 2701(w,sh), 2363(m), 2345(m), 1479(s), 1467(m,sh), 1395(s), 1362(s), 1259(m), 1144(s), 1056(m), 1026(w,sh), 958(w), 901(w), 617(m), 517(m), 455(m). ^1H NMR (400 MHz, toluene-d_8) δ 3.84 (2H, s, $OCH_2C(CH_3)_3$), 1.02, 0.97 (12.8H, s, $OCH_2C(CH_3)_3$). $^{13}C\{^1H\}$ NMR (100.1 MHz, toluene-d_6) δ 77.7 ($OCH_2C(CH_3)_3$), 24.7, ($OCH_2C(CH_3)_3$), 28.1, 27.3 ($OCH_2C(CH_3)_3$). Elemental *Anal.* Calc. for $C_{50}H_{110}O_{11}Zr_3$: C, 51.72; H, 9.54. Found: C, 52.20; H, 9.54%.

4.2.7. $Zr_3(O)(OAc)_3(ONep)_7$ (**8**)

Used **7** (0.500 g, 0.431 mmol), H-OAc (0.0780 g, 0.431 mmol), and ~10 mL of toluene. Yield 0.300 g (64.7%). FT-IR (KBr, cm^{-1}) 2953(s), 2906(w), 2867(s), 2834(s,sh), 2704(w), 2362(w), 2344(w), 1572(s), 1479(s), 1458(s), 1396(s), 1362(s), 1296(w). 1260(w), 1143(s), 1120(s,sh), 1060(m), 1023(s), 994(m), 936(m), 921(m), 751(m), 632(s), 588(m), 538(s), 453(s). Elemental *Anal.* Calc. for $Zr_3O_{14}C_{41}H_{86}$: C, 45.73; H, 8.04. Found: C, 49.73; H, 8.50%.

4.2.8. $Zr_5(O)_3(OPc)_6(ONep)_8$ (**9**)

Used **7** (0.500 g, 0.431 mmol), H-OPc (0.114 g, 0.431 mmol) and ~10 ml of toluene, heated for 10 min until solution went clear. Yield 0.198 g (86.8%). FT-IR (KBr,cm^{-1}) 2953(s), 2868(s), 2796(w), 2701(m), 2362(m), 2344(m), 1562(s), 1523(w,sh), 1476(s), 1431(s), 1395 (w,sh), 1678(w), 1368(m), 1298(s), 1266(w,sh), 1128(s), 1088(w,sh), 1055(w,sh), 1037(m), 1026(m), 1010(s), 964 (w), 935(s), 901(m), 861(m), 840(w), 763(w,sh), 750(m), 623(s), 579(s), 527(s), 456(s). Elemental *Anal.* Calc. for $Zr_5O_{23}C_{64}H_{130}$: C, 44.59; H, 7.60. Found: C, 46.31; H, 7.12%.

4.2.9. $Zr_5(O)_3(ONc)_6(ONep)_8(H\text{-}ONep)1/2(C_7H_8)$ (**11**)

Used **7** (0.500 g, 0.431 mmol), H-ONc (0.150 g, 0.431 mmol) and ~10 mL of toluene. Yield 0.390 g (74.4%). FT-IR (KBr, cm^{-1}) 2955(s), 2907(m), 2870(w), 2719(w), 2370(w), 2345(w), 1708(s), 1612(m,sh), 1571(s), 1528(w,sh), 1459(s), 1414(s), 1367(s), 1307(s), 1276(s), 1235(s), 1198(m), 1145(m), 1047(m), 1035(w,sh), 978(m), 936(w), 910(m), 811(m), 757(m), 726(m), 691(m), 640(s), 593(s), 500(m,sh), 449(m), 411(s). Elemental *Anal.* Calc. for $C_{84.5}H_{170}O_{24}Zr_5$: C, 50.09; H, 8.46 and for solvent free: Calc. for $C_{75}H_{155}O_{23}Zr_5$: C, 47.89; H, 8.30. Found: C, 48.12; H, 8.77%.

4.3. General X-ray crystal structure information [37]

Each crystal was mounted onto a thin glass fiber from a pool of Fluorolube™ and immediately placed under a liquid N_2 boil-off stream, on a Bruker AXS diffractometer. The radiation used was graphite monochromatized Mo Kα radiation ($\lambda = 0.7107$ Å). The lattice parameters were optimized from a least-squares calculation on carefully centered reflections. Lattice determination and data collection were carried out using SMART version 5.054 software. Data reduction was performed using SAINT version 6.01 software. The structure refinement was performed using XSHELL 3.0 software. The data were corrected for absorption using the SADABS program within the SAINT software package.

Each structure was solved using direct methods. This procedure yielded the heavy atoms, along with a number

of the C atoms. Subsequent Fourier synthesis yielded the remaining C atom positions. The crystal structures of metal alkoxides are often plagued by disorder in the pendant chain of the ligand. The different orientations adopted causes larger *R*-values than normally observed for other structures. When possible, the hydrogen atoms were fixed in positions of ideal geometry and refined within the XSHELL software. These idealized hydrogen atoms had their isotropic temperature factors fixed at 1.2 or 1.5 times the equivalent isotropic *U* of the C atoms for which they were bonded. The final refinement of each compound included anisotropic thermal parameters on all non-hydrogen atoms. Additional information concerning the data collection and final structural solutions of **2**–**11** can be found in the supplemental information. Data collection parameters for **2**–**11** are given in Table 1. Descriptions of the problems encountered for the less well behaved structure solutions are described below.

4.3.1. General X-ray crystal structure information for alkoxide ligands of 2–11

Final crystal solutions that contain alkoxides are notorious for positional disorder behavior problems. The carbon atoms of the alkoxide ligands (OPr^i or ONep) of these compounds show significant translational disorder. Attempts were made to model this disorder by distributing the positions of the C over several sites. These attempts proved fruitless as the disorder does not display clearly defined positions for the partial occupied sites. Hence, these attempts were abandoned in favor of one large thermal ellipsoid for many of the OR ligands in these structures. Specific information can be found in the Supplemental information.

4.3.2. Specific X-ray crystal structure information for 5

A coordinated solvent molecule of ($H\text{-}OPr^i$) was observed in the lattice. Hydrogen bond lengths for the solvent were H(7)–O(11) = 1.742 Å and H(11)–O(1) = 1.827 Å. Significant positional disorder was observed for the methyl groups on the OBc ligand. Two possible orientations of the methyl groups were refined resulting in C(12)/C(12′), C(13)/C(13′), and C(14)/C(14′) methyl pairs each with 0.5 site occupancy.

4.3.3. Specific X-ray crystal structure information for 6

Disorder of a terminal methyl group of the ONc led to expected bond deviations and large atomic displacement parameters due to fractional occupancy as well as ill-defined site location resulting from the ligand disorder (the other fraction of the site is found with the C11 terminal methyl).

4.3.4. Specific X-ray crystal structure information for 7

Two disordered hexane solvent molecules were located within the cell and were modeled using the PLATON/SQUEEZE program (ver. 01-11-99). The SQUEEZE

Table 1
Crystal data and structure refinement for **2**–**11**

Compound	**2**	**3**	**4**	**5**	**6**	**7**	**8**	**9**	**10**	**11**
Chemical formula	$C_{32}H_{72}O_{16}Zr_4$	$C_{25}H_{50}O_{16}Zr_3$	$C_{52}H_{112}O_{20}Zr_4$	$C_{32}H_{74}O_{11}Zr_2$	$C_{33}H_{72}O_{11}Zr_2$	$C_{57}H_{124}O_{11}Zr_3$	$C_{41}H_{86}O_{14}Zr_3$	$C_{67.5}H_{130}O_{23}Zr_5$	$C_{38}H_{82}O_{10}\ Zr_2$	$C_{84.5}H_{170}O_{24}Zr_5$
Formula weight	1077.78	880.31	1422.30	817.35	827.35	1259.22	1076.76	1769.85	881.48	2026.31
Temperature (K)	168(2)	168(2)	168(2)	168(2)	168(2)	168(2)	168(2)	168(2)	168(2)	168(2)
Space group	triclinic, $P\bar{1}$	triclinic, $P\bar{1}$	triclinic, $P\bar{1}$	triclinic, $P\bar{1}$	triclinic, $P\bar{1}$	monoclinic $P2_1/m$	monoclinic, $P2_1/n$	triclinic, $P\bar{1}$	triclinic, $P\bar{1}$	triclinic, $P\bar{1}$
a (Å)	13.4398(9)	9.8929(7)	11.208(2)	12.737(3)	9.624(3)	11.8464(17)	23.789(4)	14.316(2)	10.158(12)	15.051(8)
b (Å)	13.4459(9)	10.6117(8)	12.049(2)	12.943(3)	13.527(4)	19.439(3)	9.2954(16)	14.728(2)	10.195(12)	15.642(9)
c (Å)	14.2656(9)	18.7655(13)	14.234(3)	15.756(4)	18.304(5)	16.311(2)	27.339(5)	25.401(4)	11.147(13)	25.761(15)
α (°)	107.2800(10)	80.9980(13)	85.227(3)	76.786(4)	82.945(4)			81.535(3)	86.68(3)	95.090(11)
β (°)	97.8110(10)	75.4050(10)	81.458(3)	86.427(4)	77.997(4)	110.325(3)	115.287(3)	84.447(3)	88.40(2)	93.180(11)
γ (°)	96.6610(10)	84.2320(10)	67.976(3)	61.086(3)	71.463(4)			61.118(3)	84.50(3)	117.329(10)
V (Å^3)	2405.2(3)	1879.1(2)	1761.4(6)	2209.9(9)	2205.7(11)	3522.2(9)	5466.3(16)	4636.3(12)	1153(2)	5335(5)
Z	2	2	1	2	2	2	4	2	1	2
D_{calc} (Mg/m^3)	1.488	1.556	1.341	1.228	1.246	1.187	1.308	1.268	1.276	1.261
μ(Mo Kα) (mm^{-1})	0.899	0.878	0.636	0.517	0.519	0.483	0.614	0.602	0.502	0.533
R_1[a] (%) (all data)	3.58 (5.37)	3.44 (5.10)	5.13 (9.36)	3.96 (4.84)	6.19 (15.33)	7.47 (10.86)	5.89 (12.60)	6.78 (9.85)	7.48 (17.06)	6.44 (14.67)
wR_2[b] (%) (all data)	8.62 (9.72)	7.86 (9.31)	12.12 (13.45)	10.73 (11.61)	14.07 (18.25)	20.27 (22.87)	12.98 (16.77)	15.54 (16.93)	16.01 (20.72)	15.05 (17.93)

[a] $R_1 = \sum||F_o| - |F_c||/\sum|F_o| \times 100$.
[b] $wR_2 = [\sum w(F_o^2 - F_c^2)^2/\sum(w|F_o|^2)^2]^{1/2} \times 100$.

program located the solvent centers at (0.037, 3/3, 0.402) and (−0.030, 1/4, 0.598), with a potential volume of 744.2 Å^3 and electron count of 90 electrons/cell, consistent with two hexane molecules.

4.3.5. Specific X-ray crystal structure information for ***9***

One of the terminal methyl carbon attached to a translationally disordered OPc acid group occupies multiple site locations which leads to spatially disordered C(55) and C(56) methyl carbons. Attempts were made to model this disorder, however a simple disorder model for this ligand was not possible. Partially occupied sites tended to elongate severely and often became non-positive definite. The modeling of the disorder was abandon in favor of the individual C(55) and C(56) carbon sites with abnormally large thermal ellipsoids, with the understanding that these ellipsoids represent the large variability of methyl carbon atoms from molecule to molecule. C(16) possesses a high U_{eq} in comparison to other atoms because it is located on a terminal ONep ligand which has rotational disorder. The apparent rotational disorder displayed on this ligand does not affect all the carbons. In fact the rotation appears to pivot about the central C(17) carbon which allows this carbon to be relatively well defined; all the associated carbon atoms bond to this atom, however tend to displace due to the rotation. O(7) is also bound to a translationally disordered yielding large thermal ellipsoids for the associated carbons while the O7 which is more rigidly bound to the Zr(5) atom remains relatively fixed.

4.3.6. Specific X-ray crystal structure information for ***11***

One ONc ligand (O10, O11) showed rotational disordering of carbon atoms and was modeled by split (0.5 occupancy) methyl C sites C36/C36′ and C38/C38′. Due to the disorder, hydrogen atoms were not refined on these split sites, however 12 hydrogens were added to the contents of the unit cell during the final refinement to properly calculate the crystal data. An H-ONep molecule was located in the unit cell. This molecule is centered at (0.288, 0.307, 0.370). A disordered toluene solvent molecule was observed in the unit cell. The toluene was centered at (0, 1/2, 0). Attempts to model the disordered toluene failed. The solvent electron density was modeled using PLATON/SQUEEZE (ver. 01-11-99), which located a potential solvent volume of 281.4 Å^3 and an electron count of 46 electrons/cell consistent with one toluene molecule.

4.4. Thin film production

Thin films of all new compounds were generated using standard sol–gel spin cast deposition methods [22,38]. The general preparatory route involved generating under an argon atmosphere an ~0.40 M precursor solution with the appropriate compound dissolved in toluene. The solution was then transferred to a syringe, removed from the glovebox and the precursor solution deposited onto a platinized silicon substrate. The wafer was spun at 3000 rpm for 30 s and was then transferred to a hot plate at 300 °C to initiate crystallization. The wafer was removed from the heat after no more color changes were observed (~30 s), the wafer was removed, allowed to cool, and then another layer added. This was repeated so that 3 layers were deposited. The films were then fired in a furnace at 550 °C for one hour under ambient atmosphere. Subsequently, the films were analyzed using standard ellipsometry techniques at three different times during the film making process, (i) preheat, (ii) post hot plate, and (iii) post fire.

Acknowledgments

Sandia is a multiprogram laboratory operated by Sandia Corporation, a Lockheed Martin Company, for the United States Department of Energy's National Nuclear Security Administration under contract DE-AC04-94AL85000. The authors would also like to thank the office of Basic Energy Sciences of the Department of Energy for their support of this work and the technical assistance of Dr. Todd M. Alam (SNL), Dr. Scott D. Bunge (Kent St.), Mr. Kelly P. Peters, and Mr. Jesus J. Gallegos, III.

Appendix A. Supplementary data

Crystallographic data for the structural analyses of **2**–**11** have been deposited with Cambridge Crystallographic Data Center, CCDC Nos. 272310–272319. Copies of this information may be obtained free of charge from The Director, CCDC, 12 Union Road, Cambridge CB2 1EZ, UK (fax: +44 1233 336 033; e-mail: deposit@ccdc.cam.ac.uk or http://www.ccdc.cam.ac.uk). Supplementary data associated with this article can be found, in the online version at doi:10.1016/j.poly. 2005.05.005.

References

[1] H. Yoshida, M.G. Chaskar, Y. Kato, T. Hattori, J. Photochem. Photobiol. A – Chem. 160 (2003) 47.
[2] T. Kimura, Studies Surf. Sci. Cat. 145 (2003) 485.
[3] R.D. Reeleder, B.B. Capell, L.D. Tomlinson, W.J. Hickey, Can. J. Plant Pathol. 25 (2003) 182.
[4] H.K. Yueh, B. Cox, J. Nucl. Mater. 323 (2003) 57.
[5] C. Lomenech, E. Simoni, R. Drot, J.J. Ehrhardt, J. Mielczarski, J. Colloid Interf. Sci. 261 (2003) 221.
[6] S. Pikus, E. Olszewska, S. Kalinowska, J. Appl. Crystallogr. 36 (2003) 749.
[7] J. Ciosek, W. Paszkowicz, P. Pankowski, J. Firak, U. Stanislawek, R. Ostrowski, Proc. Soc. Phot-Optical Instrum. Eng. (SPIE) 5230 (2003) 34.

[8] N. Rana, P. Raghu, E. Shero, F. Shadman, Appl. Surf. Sci. 205 (2003) 160.
[9] P. Raghu, N. Rana, C. Yim, E. Shero, F. Shadman, J. Electrochem. Soc. 150 (2003) F186.
[10] Z.W. Zhao, B.K. Tay, G.Q. Yu, S.P. Lau, J. Phys. Condens. Matter 15 (2003) 7707.
[11] C.D. Chandler, C. Roger, M.J. Hampden-Smith, Chem. Rev. 93 (1993) 1205.
[12] L.G. Hubert-Pfalzgraf, New. J. Chem. 11 (1987) 663.
[13] N.Y. Turova, e.P. Turevskaya, V.G. Kessler, M.L. Yanovskay, The Chemistry of Metal Alkoxides, Kluwer Academic Publishers, Boston, 2002.
[14] D.C. Bradley, Chem. Rev. 89 (1989) 1317.
[15] D.C. Bradley, R.C. Mehrotra, A.P. Rothwell, A. Singh, Alkoxo and Aryloxo Derivatives of Metals, Academic Press, San Diego, 2001.
[16] D.C. Bradley, R.C. Mehrotra, D.P. Gaul, Metal Alkoxides, Academic Press, New York, 1978.
[17] V.W. Day, W.G. Klemperer, M.M. Pafford, Inorg. Chem. 40 (2001) 5738.
[18] B.A. Vaartstra, J.C. Huffman, P.S. Gradeff, L.G. Hubert-Pfalzgraf, J.-C. Daran, S. Parraud, K. Yunlu, K.G. Caulton, Inorg. Chem. 29 (1990) 3126.
[19] T. Boyle, R. Schwartz, R. Doedens, J. Ziller, Inorg. Chem. 34 (1995) 1110.
[20] T.J. Boyle, J.J.I. Gallegos, D.M. Pedrotty, E.R. Mechenbeir, B. Scott, Coord. Chem. 47 (1999) 155.
[21] T.J. Boyle, T.A. Alam, C.J. Tafoya, B.L. Scott, Inorg. Chem. 37 (1998) 5588.
[22] T.J. Boyle, R.P. Tyner, T.A. Alam, B.L. Scott, J.W. Ziller, B.G. Potter, J. Am. Chem. Soc. 121 (1999) 12104.
[23] D.N. Williams, U. Piarulli, C. Floriani, A. Chiesi-Villa, C. Fissoli, J. Chem. Soc., Dalton Trans. (1994) 1243.
[24] G. Kickelbick, U. Schubert, J. Chem. Soc., Dalton Trans. (1999) 1301.
[25] G. Kickelbick, P. Wiede, U. Schubert, Inorg. Chim. Acta 284 (1999) 1.
[26] B. Moraru, S. Gross, G. Kickelbick, G. Rimmel, U. Shubert, Monatsh. Chem. 132 (2001) 993.
[27] L. Ma, D.A. Payne, Chem. Mater. 6 (1994) 875.
[28] G. Kickelbick, U. Schubert, Chem. Ber. 130 (1997) 473.
[29] M.Y. Reza, H. Matsushima, M. Koikawa, M. Nakashima, T. Tokii, Polyhedron 18 (1999) 787.
[30] G. Trimmel, S. Gross, G. Kickelbick, U. Schubert, Appl. Organomet. Chem. 15 (2001) 401.
[31] M. Veith, C. Mathur, S. Mathur, V. Huch, Organometallics 16 (1997) 1292.
[32] W.J. Evans, G.W. Nyce, M.A. Greci, J.W. Ziller, Inorg. Chem. 40 (2001) 6725.
[33] W.J. Evans, M.A. Johnston, J.W. Ziller, Inorg. Chem. 39 (2000) 3421.
[34] W.J. Evans, M.A. Greci, M.A. Johnston, Chem. A – Eur. J. 5 (1999) 3482.
[35] W.J. Evans, M.A. Greci, M.A. Ansari, J. Chem Soc., Dalton Trans. (1997) 4503.
[36] T.J. Boyle, T.M. Alam, E.R. Mechenbeir, B. Scott, J.W. Ziller, Inorg. Chem. 36 (1997) 3293.
[37] The listed versions of SAINT, SMART, XSHELL, XPOW in SHELXTL, and SADABS software from bruker analytical X-ray systems Inc., 6300 Enterprise Lane, Madison, WI 53719 were used in analysis.
[38] T.J. Boyle, US Patent No. 5858451, 1991.

bulky silylamido ligands that can be potentially utilized as ligand-transfer reagents in reactions with CO_2. Although the bulky silylamine ligands $HN(SiMe_3)(R)$ (R = –$SiPh_2{}^tBu$ [36], –$Si(SiMe_3)_3$ [37], –$SiPh_3$ [38a], and adamantyl (ad)) [38b] have been previously prepared, few examples were reported to use their lithium derivatives as transmetallating agents [14,39]. With the exception of the structural characterization of $\{LiN(SiMe_3)[Si(SiMe_3)_3]\}_2$ [37], surprisingly little is known about the spectroscopic and structural details of these key $Li[N(SiMe_3)(SiR_3)]$ species in which nitrogen is bound to both a –$SiMe_3$ group and a significantly sterically crowded –SiR_3 moiety.

We now report the syntheses and structural characterizations of the dimeric lithium amides $\{Li[N(SiMe_3)(SiPh_2{}^tBu)]\}_2$ (**1**) and $\{Li[N(SiMe_3)(SiPh_3)]\}_2$ (**2**). Addition of an excess of coordinating solvents such as thf, py, or hmpa provide monomeric derivatives containing two solvent molecules per complex. These monomeric compounds are extremely soluble in hydrocarbon solvents, allowing the formation of colorless crystals at low temperature. We also describe the synthesis and characterization of $Li\{N(SiMe_3)[Si(SiMe_3)_3]\}(py)_2$ (**7**), prepared directly from the secondary amide and pyridine Finally, in an entirely unexpected reaction, we describe the synthesis of a more complex lithium amide **8** derived from the reaction of in situ generated $Li[N(ad)(SiMe_3)]$ with CaI_2.

2. Experimental

2.1. General considerations

All manipulations were carried out in an Ar-filled glove box or by using standard Schlenk techniques [40]. Anhydrous solvents were purchased from Aldrich or Fisher Scientific Company, after which they were stored in the glove box over 4 Å molecular sieves. Anhydrous CaI_2 and *n*-BuLi (2.5 M in hexane) were purchased from Aldrich. $(Me_3Si)(R)NH$ (R = –$SiPh_2{}^tBu$, –$SiPh_3$, –$Si(SiMe_3)_3$, and adamantyl) were synthesized by literature procedures [36–38]. ^1H and ^{13}C NMR spectra were obtained on a Bruker AMX 250 spectrometer using C_6D_6 as solvent. Infrared spectra were obtained as KBr pellets utilizing a Bruker Vector 22 Model spectrophotometer. Characteristic peaks are listed. It should be noted that the IR spectra are complex, particularly in the fingerprint region between 1500 and 500 cm^{-1}. Elemental analyses for carbon, hydrogen, and nitrogen were measured in sealed volatile sample pans using a Perkin–Elmer series II CHNS/O 2400 analyzer, or performed commercially at Desert Analytics, Tucson, Arizona. Despite the fact that an additional oxidizer (WO_3) was added during the analyses for CHN, in several cases the analyzed carbon content was lower than the calculated value. However, this was not the case with the hydrogen or nitrogen analyses. In none of the duplicate sample preparations sent for analysis did we ever see an elevated carbon content – the carbon content was consistently slightly lower than expected.

2.2. $[LiN(SiMe_3)(SiPh_2{}^tBu)]_2$ (1)

($^tBuPh_2Si$)(Me_3Si)NH (3.28 g, 10.0 mmol) dissolved in 50 mL hexane was cooled to 0 °C in an ice bath and treated with *n*-BuLi (4.0 mL, 10.0 mmol). The solution was stirred overnight at room temperature. The solution was reduced to 30 mL and cooled to −20 °C to yield **1** as colorless crystals (2.86 g, 86%); m.p. 136–138 °C. ^1H NMR (C_6D_6): δ 0.21 (s, 18H, SiMe_3), 1.06 (s, 18H, CMe_3), 7.16 (m, 15H, C_6H_5), 7.57 (m, 4H, C_6H_5). ^{13}C NMR (C_6D_6): δ 6.09 (SiMe_3), 20.55 (CMe$_3$), 29.70 (SiCMe_3), 128.49 (C_6H_5), 129.24 (C_6H_5), 135.84 (C_6H_5), 140.53 (C_6H_5). IR (cm^{-1}): 3376 (w), 3064–2895 (br, m), 1965 (m), 1893 (m), 1811 (m), 1576 (m), 1556 (w). *Anal.* Calc. for $C_{38}H_{56}N_6Si_4Li_2$: C, 68.42; H, 8.46; N, 4.22. Found: C, 68.18; H, 8.82; N, 4.05%.

2.3. $[LiN(SiMe_3)(SiPh_3)]_2$ (2)

Similar to **1**, **2** was synthesized by the treatment of (Ph_3Si)(Me_3Si)NH (3.47 g, 9.98 mmol) with *n*-BuLi (4.0 mL, 10.0 mmol) in 80 mL hexane. After workup as in **1**, cooling to −20 °C yielded **2** as colorless crystals (2.79 g, 79%); m.p. 165–166 °C. ^1H NMR (C_6D_6): δ 0.10 (s, 18H, SiMe_3), 7.15 (m, 24H, C_6H_5), 7.64 (m, 6H, C_6H_5). ^{13}C NMR (C_6D_6): δ 6.55 (SiMe_3), 128.46 (C_6H_5), 129.36 (C_6H_5), 135.88 (C_6H_5), 140.35 (C_6H_5). IR (cm^{-1}): 3339 (w), 3064 (m), 2953 (m), 1954 (m), 1893 (m), 1821 (m), 1472 (s), 1586 (s), 1545 (m). *Anal.* Calc. for $C_{42}H_{48}N_2Si_4Li_2$: C, 71.35; H, 6.84; N, 3.96. Found: C, 71.24; H, 6.97; N, 3.89%.

2.4. $[(^tBuPh_2Si)(Me_3Si)N]Li(thf)_2$ (3)

Compound **1** (0.67 g, 1.00 mmol) was dissolved in 60 mL hexane, and then treated with an excess of thf (0.43 g, 6.0 mmol) at room temperature. The solution was stirred for 1 h, then the solvent was removed under vacuum. The crude product was recrystallized from hexane at −20 °C to give colorless crystals of **3** (0.76 g, 80%); m.p. 100–101 °C. ^1H NMR (C_6D_6): δ 0.41 (s, 9H, SiMe_3), 1.22 (t, 8H, –CH_2–, $^3J_{H-H}$ = 6.5 Hz), 1.46 (s, 9H, CMe_3), 3.20 (t, 8H, –OCH_2–, $^3J_{H-H}$ = 6.5 Hz), 7.20 (m, 8H, C_6H_5), 8.04 (m, 2H, C_6H_5). ^{13}C NMR (C_6D_6): δ 6.76 (SiMe_3), 21.05 (CMe$_3$), 25.16 (–CH$_2$–), 29.26 (CMe_3), 68.19 (–OCH$_2$–), 127.21 (C_6H_5), 127.61 (C_6H_5), 136.17 (C_6H_5), 145.26 (C_6H_5). IR (cm^{-1}): 3370 (m), 2955 (br, s), 1958 (m), 1893 (m), 1822 (m), 1589

(m). *Anal*. Calc. for $C_{27}H_{44}NO_2Si_2Li$: C, 67.88; H, 9.28; N, 2.93. Found: C, 65.96; H, 9.03; N, 3.12%.

2.5. [(^{t}BuPh$_2$Si)(Me$_3$Si)N]Li(py)$_2$ (4)

Compound **4** was obtained by addition of excess py (0.37 g, 4.74 mmol) to a solution of **1** (0.53 g, 0.79 mmol) dissolved in 60 mL hexane. After workup as in **3** the crude product was recrystallized from hexane at −20 °C to form colorless crystals of **4** (0.64 g, 82%); m.p. 114–116 °C. ^{1}H NMR (C_6D_6): δ 0.49 (s, 9H, Si*Me*$_3$), 1.48 (s, 9H, C*Me*$_3$), 6.58 (m, 4H, C_5H_5N), 6.92 (m, 2H, C_5H_5N), 7.17 (m, 8H, C_6H_5), 8.04 (m, 2H, C_6H_5), 8.10 (m, 4H, C_5H_5N). ^{13}C NMR (C_6D_6): δ 7.05 (Si*Me*$_3$), 21.15 (*C*Me$_3$), 29.42 (C*Me*$_3$), 124.19 (C_5H_5N), 127.21 (C_6H_5), 127.61 (C_6H_5), 136.40 (C_6H_5), 137.28 (C_5H_5N), 145.34 (C_6H_5), 149.47 (C_5H_5N). IR (cm^{-1}): 3365 (w), 3068 (m), 2960 (br, m), 1975 (m), 1944 (m), 1903 (m), 1586 (m), 1556 (w). *Anal*. Calc. for $C_{29}H_{38}N_3Si_2Li$: C, 70.83; H, 7.79; N, 8.55. Found: C, 69.85; H, 7.71; N, 8.10%.

2.6. [(^{t}BuPh$_2$Si)(Me$_3$Si)N]Li(hmpa)$_2$ (5)

Complex **5** was obtained by addition of excess hmpa (1.81 g, 10.1 mmol) to a solution of **1** (1.12 g, 1.68 mmol) dissolved in 60 mL hexane. After workup as in **3** the crude product was recrystallized from hexane at −20 °C to form colorless crystals of **5** (1.76 g, 76%); m.p. 118–119 °C. ^{1}H NMR (C_6D_6): δ 0.37 (s, 9H, Si*Me*$_3$), 1.43 (s, 9H, C*Me*$_3$), 2.32 (d, 36H, $^3J_{P-H}$ = 9.45 Hz, (*Me*$_2$N)$_3$PO), 7.30 (m, 8H, C_6H_5), 8.20 (m, 2H, C_6H_5). ^{13}C NMR (C_6D_6): δ 6.66 (Si*Me*$_3$), 21.05 (*C*Me$_3$), 29.75 (C*Me*$_3$), 36.76 ((*Me*$_2$N)$_3$PO), 126.57 (C_6H_5), 126.72 (C_6H_5), 136.95 (C_6H_5), 146.82 (C_6H_5). IR (cm^{-1}): 3222 (m), 2889 (br, s), 2364 (m), 2179 (m). *Anal*. Calc. for $C_{31}H_{64}N_7O_2P_2Si_2Li$: C, 53.81; H, 9.32; N, 14.17. Found: C, 52.62; H, 8.94; N, 14.24%.

2.7. [(Ph$_3$Si)(Me$_3$Si)N]Li(py)$_2$ (6)

Compound **6** was obtained by addition of excess py (0.63 g, 8.0 mmol) to a solution of **2** (0.71 g, 1.0 mmol) dissolved in 50 mL hexane. After workup as in **3** the crude product was recrystallized from hexane at −20 °C to yield colorless crystals of **6** (0.87 g, 85%); m.p. 131–133 °C. ^{1}H NMR (C_6D_6): δ 0.41 (s, 9H, Si*Me*$_3$), 6.49 (m, 4H, C_5H_5N), 6.82 (m, 2H, C_5H_5N), 7.18 (m, 12H, C_6H_5), 7.99 (m, 3H, C_6H_5), 8.06 (m, 4H, C_5H_5N). ^{13}C NMR (C_6D_6): δ 6.64 (Si*Me*$_3$), 124.17 (C_5H_5N), 127.48 (C_6H_5), 127.61 (C_6H_5), 136.16 (C_6H_5), 137.23 (C_5H_5N), 145.38 (C_6H_5), 149.44 (C_5H_5N). IR (cm^{-1}): 3346 (m), 1954 (w), 1883 (w), 1822 (w), 1597 (s), 1556 (w). *Anal*. Calc. for $C_{31}H_{34}N_3Si_2Li$: C, 72.76; H, 6.70; N, 8.21. Found: C, 70.89; H, 7.02; N, 7.90%.

2.8. {[(Me$_3$Si)$_3$Si](Me$_3$Si)N}Li(py)$_2$ (7)

HN(SiMe$_3$)[Si(SiMe$_3$)$_3$] (3.36 g, 10.0 mmol) in 60 mL hexane was treated with *n*-BuLi (4 mL, 10.0 mmol) at room temperature to generate the Li salt. This solution was not isolated but treated directly with an excess of py (3.16 g, 40.0 mmol) for 1 h. The solvents were removed under vacuum and the crude product was recrystallized from hexane at −20 °C to give colorless crystals of **7** (3.95 g, 79%); m.p. 97–98 °C. ^{1}H NMR (C_6D_6): δ 0.66 (s, 9 H, Si*Me*$_3$), 0.75 (s, 27H, (Si(Si*Me*$_3$)$_3$)), 7.14 (m, 4H, C_5H_5N), 7.43 (m, 2H, C_5H_5N), 8.97 (m, 4H, C_5H_5N). ^{13}C NMR (C_6D_6): δ 2.49 (Si(Si*Me*$_3$)$_3$), 6.55 (Si*Me*$_3$), 124.31 (C_5H_5N), 137.31 (C_5H_5N), 150.06 (C_5H_5N). IR (cm^{-1}): 3376 (w), 2947 (br, m), 1900 (m), 2149 (w), 1893 (m), 1472 (s), 1464 (s). *Anal*. Calc. for $C_{22}H_{46}N_3Si_5Li$: C, 52.85; H, 9.27; N, 8.40. Found: C, 51.94; H, 8.60; N, 7.98%.

2.9. [(ad)(SiMe$_3$)N]$_2$Li$_3$(μ_3-I)(thf)$_2$ (8)

[(ad)(Me$_3$Si)N]Li was prepared from (ad)(Me$_3$Si)NH (2.23 g, 9.98 mmol) and *n*-BuLi (4.0 mL, 10.0 mmol), and was then treated with anhydrous CaI_2 (0.92 g, 5.0 mmol) in 50 mL thf. The mixture was stirred overnight and evaporated to dryness. The residue was held under vacuum for 6 h and was extracted with 70 mL hexane, and the extracts were filtered through Celite filter aid. The hexane was removed to yield a crude product (ca. 2.7 g). Recrystallization from a toluene/hexane solution at −20 °C afforded pure **8** as colorless crystals (1.33 g, 55% based on Li); m.p. 122–124 °C. ^{1}H NMR (C_6D_6): δ 0.38 (s, 18 H, Si*Me*$_3$), 1.26 (t, 8H, –C*H*$_2$–, $^3J_{H-H}$ = 6.7 Hz), 1.68 (m, 6H, –C*H*–), 1.95 (m, 12H, –C*H*$_2$–), 2.14 (m, 12H, –C*H*$_2$–), 3.64 (t, 8H, –OC*H*$_2$–, $^3J_{H-H}$ = 6.7 Hz). ^{13}C NMR (C_6D_6): δ 7.15 (Si*Me*$_3$), 25.23 (–*C*H$_2$–), 31.16 (–*C*H$_2$–), 37.03 (–*C*H$_2$–), 51.42 (–*C*H–), 53.06 (N*C*), 69.22 (–O*C*H$_2$–). IR (cm^{-1}): 3335 (w), 1955 (m), 1893 (m), 1822 (m), 1586 (m), 1545 (w). *Anal*. Calc. for $C_{34}H_{62}N_2O_2Si_2ILi_3$: C, 55.58; H, 8.51; N, 3.81. Found: C, 55.20; H, 9.21; N, 3.64%.

2.10. X-ray crystallography

Crystallography data for **1**–**8** are given in Tables 1 and 2. As all of the compounds are extremely air-sensitive the crystals were always handled under inert atmosphere, covered with oil and immediately transferred to the N_2 stream of the diffractometer. Data were collected at 218 K on Bruker P4/CCD (**1**, **3**, **4**, **6**, **8**) and at 100 K on Smart Apex CCD (**2**, **5**, **7**) diffractometers using Mo Kα radiation (λ = 0.71073 Å). Absorption corrections were applied for all data by SADABS. Non-hydrogen atoms in all structures were refined with anisotropic displacement coefficients except the C atoms in the disordered thf molecules

Table 1
Crystallographic data and parameters for complexes **1**–**4**

	1	**2**	**3**	**4**
Empirical formula	$C_{38}H_{56}N_2Si_4Li_2$	$C_{42}H_{48}N_4Si_4Li_2$	$C_{27}H_{44}NO_2Si_2Li$	$C_{29}H_{38}N_3Si_2Li$
F_w	667.09	707.06	477.75	491.74
Crystal size (mm)	$0.30 \times 0.20 \times 0.10$	$0.30 \times 0.25 \times 0.20$	$0.40 \times 0.30 \times 0.20$	$0.25 \times 0.15 \times 0.10$
Crystal System	monoclinic	monoclinic	monoclinic	monoclinic
Space group	$P2_1$	$P2_1/n$	$P2_1/c$	$P2_1/c$
a (Å)	10.1376(6)	11.9435(10)	18.143(6)	17.1016(10)
b (Å)	19.5508(13)	14.2048(12)	8.950(3)	18.3325(10)
c (Å)	10.1784(7)	23.953(2)	18.656(6)	19.9385(11)
α (°)	90	90	90	90
β (°)	97.6920(10)	94.548(2)	101.999(6)	107.5370(10)
γ (°)	90	90	90	90
Volume (Å^3)	1999.2(2)	4050.9(6)	2963.0(16)	5960.5(6)
Z, Z'	2, 1	4, 1	4, 1	8, 2
Calculated density (g/cm^3)	1.108	1.159	1.071	1.096
μ (mm^{-1})	0.176	0.177	0.141	0.139
Measured reflections (R_{int})	14709 (0.0306)	25123 (0.0481)	17962 (0.0272)	43514 (0.0367)
Independent reflections	7939	9172	6709	14103
Absorption correction (T_{min}/T_{max})	SADABS (0.823)	SADABS (0.902)	SADABS (0.903)	SADABS (0.833)
T (K)	218(2)	100(2)	218(2)	218(2)
R_1,[a] $wR2$[b] (all data)	0.0631, 0.1418	0.0901, 0.1648	0.0904, 0.2432	0.0868, 0.1633
R_1,[a] wR_2[b] [$I > 2\sigma(I)$]	0.0587, 0.1391	0.0606, 0.1502	0.0752, 0.2265	0.0622, 0.1505
Goodness-of-fit on F^2	1.157	1.026	1.049	1.121

[a] $R = \sum |F_o| - |F_c| / \sum |F_o|$.
[b] $R(\omega F^2) = \{\sum[\omega(F_o^2 - F_c^2)^2] / \sum[\omega(F_o^2)^2]\}^{1/2}$.

Table 2
Crystallographic data and parameters for complexes **5**–**8**

	5	**6**	**7**	**8**
Empirical formula	$C_{31}H_{64}N_7O_2P_2Si_2Li$	$C_{31}H_{34}N_3Si_2Li$	$C_{22}H_{46}N_3Si_5Li$	$C_{34}H_{62}N_2O_2Si_2ILi_3$
F_w	691.95	511.73	500.01	734.76
Crystal size (mm)	$0.40 \times 0.30 \times 0.20$	$0.35 \times 0.25 \times 0.15$	$0.40 \times 0.30 \times 0.10$	$0.38 \times 0.27 \times 0.20$
Crystal system	monoclinic	triclinic	monoclinic	triclinic
space group	$P2_1/n$	$P\bar{1}$	$P2_1/n$	$P\bar{1}$
a (Å)	12.2807(11)	10.3020(6)	10.5031(17)	12.6654(6)
b (Å)	18.6322(16)	11.3207(7)	18.976(3)	13.5176(7)
c (Å)	18.0884(16)	14.6340(8)	15.795(3)	23.8396(12)
α (°)	90	82.5490(10)	90	78.4000(10)
β (°)	92.0260(10)	73.2910(10)	92.797(3)	87.4770(10)
γ (°)	90	67.4040(10)	90	84.4130(10)
Volume (Å^3)	4136.3(6)	1508.81(15)	3144.5(9)	3977.9(3)
Z, Z'	4, 1	2, 1	4, 1	4, 2
Calculated density (g/cm^3)	1.111	1.126	1.056	1.227
μ (mm^{-1})	0.197	0.140	0.241	0.894
Measured reflections (R_{int})	18520 (0.0309)	11253 (0.0228)	26281 (0.0385)	29060 (0.0205)
Independent reflections	6113	6915	7153	18092
Absorption correction (T_{min}/T_{max})	SADABS (0.736)	SADABS (0.843)	SADABS (0.783)	SADABS (0.808)
T (K)	100(2)	218(2)	100(2)	218(2)
R_1,[a] wR_2[b] (all data)	0.0962, 0.2165	0.0647, 0.1661	0.0627, 0.1401	0.0611, 0.1332
R_1,[a] wR_2[b] [$I > 2\sigma(I)$]	0.0814, 0.2058	0.0521, 0.1509	0.0484, 0.1307	0.0455, 0.1240
Goodness-of-fit on F^2	1.092	1.034	1.052	1.020

[a] $R = \sum |F_o| - |F_c| / \sum |F_o|$.
[b] $R(\omega F^2) = \{\sum[\omega(F_o^2 - F_c^2)^2] / \sum[\omega(F_o^2)^2]\}^{1/2}$.

in **3** and **8** and the disordered NMe_2 groups in **5** that were refined with isotropic thermal parameters. All H atoms were treated as idealized contribution, except the H atoms of the disordered thf molecules in **3** and **5** that were not taken into consideration. The Flack parameter for non-centrosymmetrical structure of **1** is 0.0(1). All software and sources of scattering factors are contained in the SHELXTL (5.10) program package (G. Sheldrick, Bruker XRD, Madison, WI) [41].

3. Results and discussion

3.1. Syntheses and characterization of 1–8

Treatment of either (^{t}BuPh$_2$Si)(Me$_3$Si)NH or (Ph$_3$Si)(Me$_3$Si)NH with 1 equiv of *n*-BuLi in hexane results in high isolated yields of **1** and **2**, respectively. Addition of a multimolar excess of the donor solvents thf, py, or HMPA to **1** afforded the solvated monomeric lithium salts Li[N(SiMe$_3$)(SiPh$_2$^{t}Bu)](L)$_2$ (L = thf (**3**); py (**4**); hmpa (**5**)), while addition of excess py to **2** afforded Li[N(SiMe$_3$)(SiPh$_3$)](py)$_2$ (**6**). Crystals suitable for X-ray diffraction analyses can be obtained via crystallization from their saturated hexane solutions at −20 °C. While all compounds are air- and moisture-sensitive as expected, the dimeric complexes **1** and **2** appear to be more stable than the corresponding monomeric derivatives, whether in solution or the solid state. All the compounds have been well characterized by ^{1}H and ^{13}C NMR spectra and the solid state structures further established by X-ray crystallography.

The ^{1}H and ^{13}C NMR spectra of the new compounds **1**–**6** are straightforward to interpret, and assignments are given in the Experimental. Briefly, the basic backbone structures of the amido ligands are shown to continue in each of these compounds, and **1** and **2** are further marked by the absence of solvent ligands in the NMR spectra. In **3**–**6** the solvent ligands are present, and integrated ratios in the ^{1}H NMR spectra indicate that there are two-coordinated solvent ligands per Li atom. However, the NMR data do not indicate the overall nuclearity of the species **1**–**6**, and so we had to result to X-ray crystallography to determine the solid state structures (vide infra).

The addition of *n*-BuLi to [(Me$_3$Si)$_3$Si](Me$_3$Si)NH in hexane solution afforded {LiN(SiMe$_3$)[Si(SiMe$_3$)$_3$]}$_2$, which had been previously reported by Westerhausen [37]. This dimeric complex was not isolated, but rather the in situ generated compound was treated with excess pyridine to produce the solvated monomeric compound **7**. As above, **7** has been fully characterized by ^{1}H and ^{13}C NMR spectra as well as X-ray diffraction analysis. While NMR indicated retention of the basic backbone structure again there was no indication of the overall nuclearity of **7**. Interestingly, treatment of LiN[(SiMe$_3$)(ad)], generated from the reaction of HN[(SiMe$_3$)(ad)] with *n*-BuLi in thf, with anhydrous CaI$_2$ afforded the unusual lithium amide **8** in moderate yields rather than the expected calcium bis(amide) species. We propose that the initially formed metathesis product LiI combines with unreacted {LiN[(SiMe$_3$)(ad)]} to give **8**, along with undetermined side products containing Ca, amide, and I. While ^{1}H and ^{13}C NMR spectra together could not suggest the structure of **8**, we eventually confirmed this unusual structure by X-ray diffraction analysis. **8** is an extremely air- and moisture sensitive complex that is unstable in thf solutions, but relatively stable when isolated in the solid state.

3.2. Solid state structures of dimeric lithium amides 1 and 2

The X-ray structures of **1** and **2** are shown in Figs. 1 and 2 while selected bond distances and angles are given in Table 3. **1** and **2** are solvent-free dimeric compounds with very similar structures. The core structure consists of an N$_2$Li$_2$ ring. The central (μ_2-N)$_2$Li$_2$ cycle in **1** is not planar; the dihedral angle between the Li(1)–Li(2)–N(1) and Li(1)–Li(2)–N(2) planes is 15.1(4)°. The N(1)–Li(1), N(1)–Li(2), N(2)–Li(1), and N(2)–Li(2) distances in **1** are 2.007(6), 2.021(6), 2.079(6) and 2.065(6) Å, respectively. These values are quite comparable to the related distances in **2**, which are 1.974(5), 2.000(5), 2.003(5), and 2.052(5) Å for the corresponding bonds lengths in **2**. The structure of **1** indicated as well that there are several close interactions of the ligands with the electron-deficient bridging Li atoms. The short Li(1)···C(23), Li(1)···C(24), Li(2)···C(4) and Li(2)···C(5) contacts (all in the 2.40–2.55 Å range) in **1** indicate interactions between lithium and carbon atoms of the ligands, and that the ligands do not serve as simple spectator ligands. Similarly short Li···C distances are also found in [LiN(CH$_2$Ph)]$_3$ and [LiN(SiMe$_2$Ph)]$_2$ where Li π bonding is assumed to occur as well [4,42]. The relative short Li···H distances of ca. 2.20 Å suggest there are some bonding (agostic) type interactions between lithium and the hydrogen atoms on either the Me$_3$Si– or phenyl groups. As was seen in **1**, the phenyl groups in **2** interact with the two lithium cations in a π-bonding fashion [42],

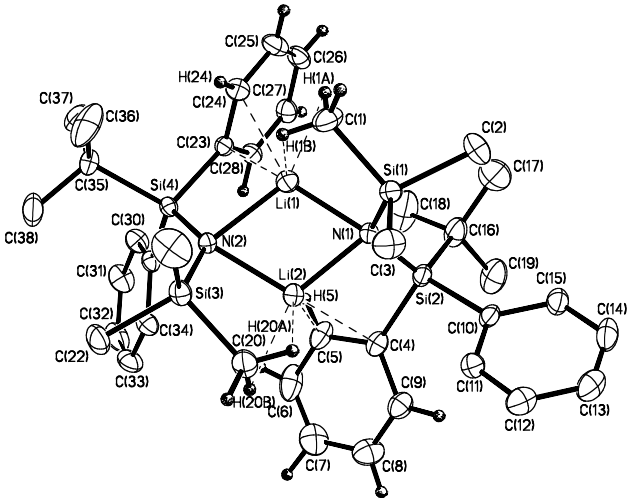


Fig. 1. X-ray structure of **1** (30% ellipsoids). The H atoms of Me and Ph groups involved in coordination to the Li atoms are shown for clarity. The shortest Li···H and Li···C contacts are shown by dashed lines.

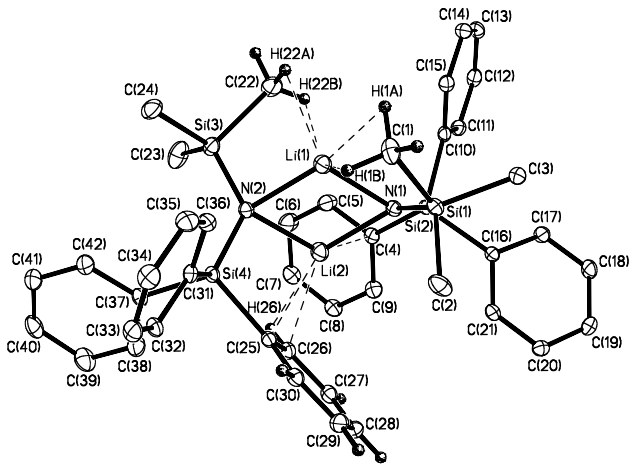


Fig. 2. X-ray structure of **2** (30% ellipsoids). Only the H atoms of Me and Ph groups involved in bonding to the Li atoms are shown for clarity. The shortest Li···H contacts are shown by dashed lines.

Table 3
Selected bond lengths (Å) and angles (°) for **1** and **2**

	1	**2**
Li(1)–N(1)	2.007(6)	1.974(5)
Li(2)–N(1)	2.021(6)	2.000(5)
Li(2)–N(2)	2.065(6)	2.052(5)
Li(1)–N(2)	2.079(6)	2.003(5)
Li(1)···Li(2)	2.343(8)	2.329(7)
Li(1)···C(24)	2.510(6)	
Li(1)···C(23)	2.427(6)	
Li(2)···C(5)	2.411(7)	
Li(2)···C(4)	2.525(6)	
Li(1)···C(22)		2.376(6)
Li(2)···C(25)		2.501(6)
Li(1)···C(1)		2.408(6)
Li(2)···C(26)		2.361(6)
Li(1)–N(1)–Li(2)	71.2(2)	71.8(2)
N(1)–Li(1)–N(2)	108.6(3)	110.4(2)
Li(2)–N(2)–Li(1)	68.9(2)	70.1(2)
N(1)–Li(2)–N(2)	108.6(3)	107.5(2)

as may be seen by the short distances of Li(2)–C(25) (2.501(6) Å) and Li(2)–C(26) (2.361(6) Å). Additionally, the agostic-type interactions between lithium cations and the hydrogen atoms from either the Me_3Si– or phenyl groups can be also found in **2**. The two N–Li–N angles in **1** are the same (108.6(3)°) and similar to the corresponding angles in **2** (110.4(2)°, 107.5(2)°). The acute Li–N–Li angles of 71.2(2)° and 68.9(2)° vary slightly from the corresponding angles in **2**, 71.8(2)° and 70.1(2)°. In the related compound $[LiN(SiMe_3)(SiMe_2Ph)]_2$ this angle is 71.70(12)° [43]. Generally, the N–Li–N angles found in **1** and **2** are greatly smaller than those found in $[LiN(SiMe_3)_2]_3$ (92.00(2)°) [1a], $[LiN(SiMe_3)Ph]_2[N(SiMe_3)\ PhLi]_2$ (77.2(3)°, 77.3(3)°) [43], and $[LiN(SiMe_3)_2]_2$ 80(3)° (measured by electron diffraction) [44].

*3.3. Solid state structures of solvated monomeric lithium amides **3**–**7***

The X-ray structures of **3**–**7** are presented (Figs. 3–7 and Table 4). Compounds **3**, **4**, and **5** utilize the ligand $–N(SiMe_3)(SiPh_2{}^tBu)$ while compounds **6** and **7** derive from the amido ligands $–N(SiMe_3)(SiPh_3)$ and $–N(SiMe_3)[Si(SiMe_3)]$, respectively. The molecular structures of **3**–**7** are quite similar; they are monomeric with three-coordinate lithium cations bound to one ligand nitrogen atom along with two solvent molecules. The Li–N bond lengths in **3**, **4**, and **5** were found to be quite comparable, ranging in length from 1.939(4) to 1.964(6) Å. These values are significantly shorter than the Li–N bond lengths in the dimeric compound **1** (average 2.04 Å.) The Li–O bond lengths in **3** (thf) and **5** (hmpa) differ by 0.054 Å on average. The Li–O bond lengths 1.920(5) and 1.934(5) Å in **3** are comparable to those found in $Li(thf)_2[N(SiPh_3)_2]$ (1.945(4) Å) [32], and slightly longer than those in $Li(thf)_2[N(SiMePh_2)_2]$ 1.907(3) Å [32]. The Li–O bond lengths of **5** (1.865(6) and 1.876(6) Å) are noticeably shorter than those in $[Li(OC_6H_2\text{-}4\text{-}Me\text{-}2,6\text{-}{}^tBu_2(OEt_2))]_2$ 1.961(11) Å [45] and $\{Li[N(SiMe_3)_2](OEt_2)\}_2$ 1.95(2) Å [46], and comparable to that seen in $[\{Li_2(\mu\text{-}[N(SiMe_3)_2])(\mu\text{-TEMPO})\cdot\ 2TEMPO\}^+\{Mg[N(SiMe_3)_2]_3\}^-]$, 1.821(6) Å (TEMPO = 2,2,6,6-tetramethy-1-piperidinyloxy) [47]. It is interesting to note that the O–Li–O angle in **5** is significantly larger by ca. 5.5° than that in **3**. The widened O–Li–O angle in **5** can be attributed to the larger volumetric requirements for the two solvent molecules of hmpa versus the smaller thf.

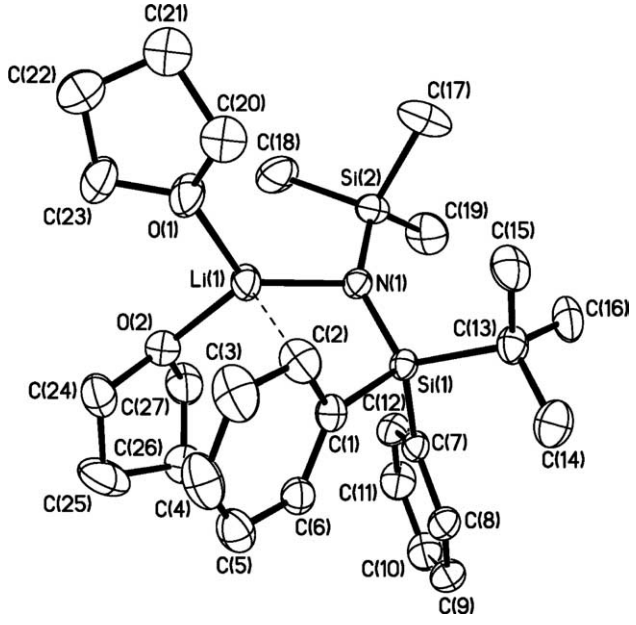


Fig. 3. X-ray structure of **3** (30% ellipsoids). The H atoms are omitted for clarity. The shortest Li···C contact is shown by dashed lines.

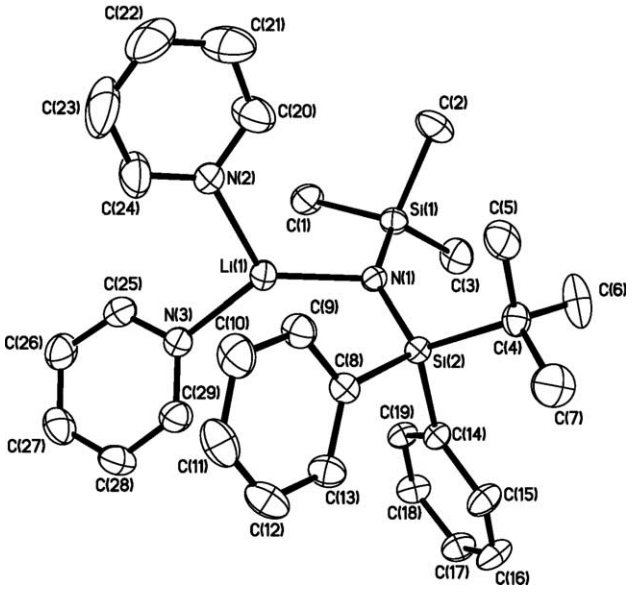


Fig. 4. X-ray structure of **4** (30% ellipsoids). The H atoms are omitted for clarity.

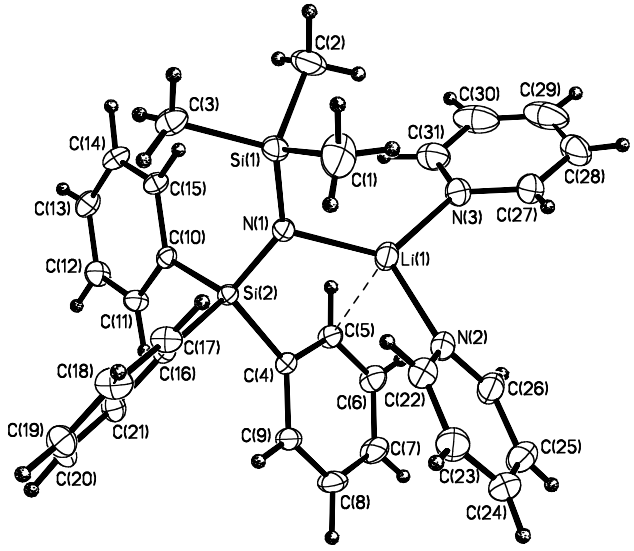


Fig. 6. X-ray structure of **6** (30% ellipsoids). For clarity, only H atoms in the groups involved in coordination to the Li atoms are shown. The shortest Li···C contact is shown by a dashed line.

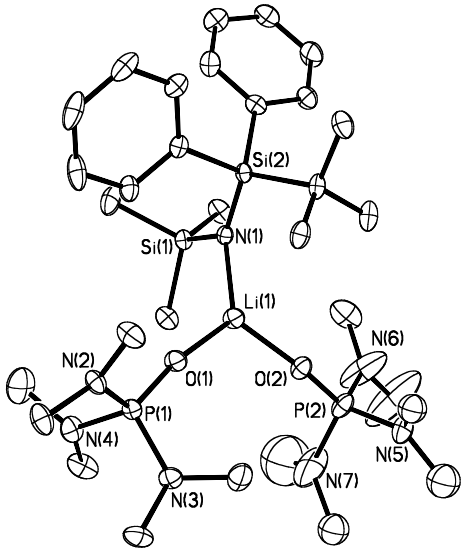


Fig. 5. X-ray structure of **5** (30% ellipsoids). The H atoms are omitted for clarity.

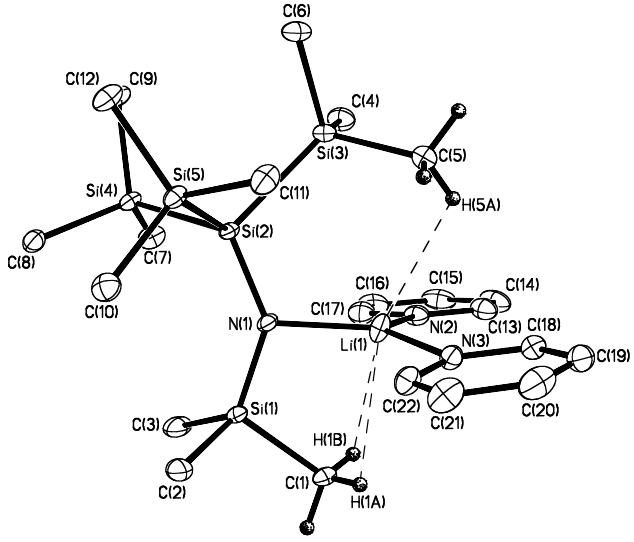


Fig. 7. X-ray structure of **7** (50% ellipsoids). For clarity, only the H atoms of the Me groups involved in coordination to Li are shown. The shortest Li···H contacts are shown by dashed lines.

Compounds **4**, **6**, and **7** all have two molecules of py per Li as the coordinating solvent. There are two symmetrically independent molecules in the crystal structure of **4**. The bond lengths between donating nitrogen atoms and lithium in **4** (2.072(4) (2.072(5)) and 2.038(4) (2.043(4)) Å) are comparable to those in **6** (2.019(4) and 2.043(4) Å), $\{(Li[N(SiMe_3)_2]\cdot py\}_2$ 2.05(1) Å, $\{Mg[N(SiMe_3)_2]_3Li\cdot(py)\}$ 2.083(3) Å, $\{Mg[N(SiMe_3)_2]_2(Bu)Li\cdot py\}$ 2.065(5) Å [48], and they are substantially shorter than those in $\{Li[N(SiMe_3)_2]$ (pmdien)}, 2.265(6) Å, and $[Li[N(SiMe_3)_2])$ $(PhCH_2NMe_2)]_2$, 2.240(4) Å [49]. The N(2)–Li(1)–N(3) angles in the two independent molecules in **4** (106.6(2)° and 113.3(2)°) are comparable with the corresponding angle in **6** (110.8(2)°). Additionally, another interesting feature of the structure of **6** and **3** is the weak molecular interaction that occurs between lithium and a carbon atom in one of the phenyl groups, as judged by the short Li···C distances of 2.779(7) and 2.783(5) Å, respectively in **3** and **6**. The bond length N(1)–Li(1) of 1.930(4) Å in **7** is slightly shorter than is seen in the dimeric complex $[Li\{N[SiMe_3][Si(SiMe_3)_3]\}]_2$ (2.006(7) Å) [37]. Compared with **4** and **6**, compound **7** has the largest N–Li–N angle of 125.6(2)°. Moreover, the short contact distances

Table 4
Selected bond distances (Å) and angles (°) for **3**–**7**

	3	4	5	6	7
Li(1)–N(1)	1.948(5)	1.939(4) (1.933(4))	1.964(6)	1.943(4)	1.930(4)
Li(1)–O(1)	1.920(5)		1.865(6)		
Li(1)–O(2)	1.934(5)		1.876(6)		
Li(1)–N(2)		2.072(4) (2.072(5))		2.019(4)	2.039(4)
Li(1)–N(3)		2.038(4) (2.043(5))		2.043(4)	2.033(4)
Li(1)···C(Ph)	2.779(7)		2.783(5)		
P(1)–N(4)			1.651(3)		
Si(1)–N(1)	1.661(2)	1.672(2) (1.674(2))	1.673(3)	1.667(2)	1.674(2)
Si(2)–N(1)	1.678(2)	1.658(2) (1.657(2))	1.667(3)	1.648(2)	1.694(2)
P(1)–O(1)			1.478(2)		
P(1)–N(2)			1.645(3)		
P(1)–N(3)			1.650(3)		
O(1)–Li(1)–O(2)	105.3(2)		110.6(3)		
O(2)–Li(1)–N(1)	123.6(3)		124.6(3)		
O(1)–Li(1)–N(1)	128.4(3)		124.8(3)		
Si(1)–N(1)–Si(2)	142.2(1)		129.1(2)		
N(1)–Li(1)–N(2)		120.7(2) (118.4(2))		120.4(2)	116.4(2)
N(1)–Li(1)–N(3)		132.1(2) (126.6(2))		126.9(2)	117.8(2)
N(2)–Li(1)–N(3)		106.6(2) (113.3(2))		110.8(2)	125.6(2)
Si(1)–N(1)–Si(2)		138.7(1) (140.4(1))		138.1(1)	139.2(1)
Li(1)–N(1)–Si(1)		108.7(2) (108.5(2))		114.2(1)	104.7(1)
Li(1)–N(1)–Si(2)		111.8(2) (110.2(2))		107.6(1)	115.8(1)

For **4** the values for two independent molecules are given.

(ca. 2.90 Å) between lithium and the hydrogen atoms on the pendant $SiMe_3$ group suggest that the agostic interactions are again present in **7**.

3.4. Solid state structure of trilithium amide **8**

Interestingly, compound **8** was isolated from the reaction of $LiN(SiMe_3)(ad)$ with CaI_2 in thf rather than the anticipated calcium (bis)amide. ^1H and ^{13}C NMR spectra indicated that **8** had both $–SiMe_3$ and adamantyl groups, indicating that the ligand remained intact. However, this information was insufficient to postulate an actual structure for **8**. An X-ray diffraction study (Fig. 8 and Table 5) revealed a structure that was unexpected. X-ray analysis revealed that instead of the Ca amide we were attempting to prepare we had instead produced a dimeric Li amide complexed with LiI and thf solvent. We propose that the Li amide reacts with the CaI_2 to form initially a mixed amido/iodo calcium complex, which is not isolated (Scheme 1). The LiI formed in the metathesis reaction reacts with the starting Li amide, thus generating **8** and unidentified side products. As our

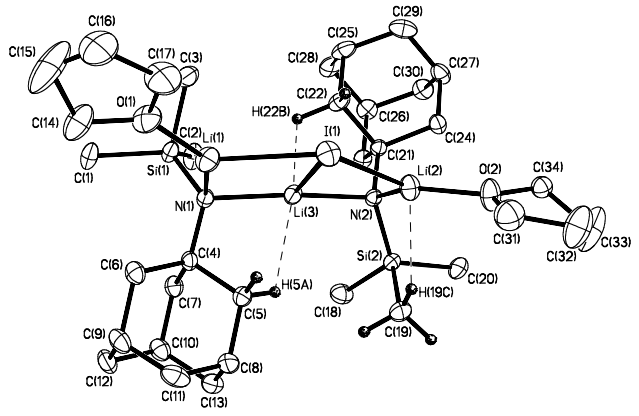
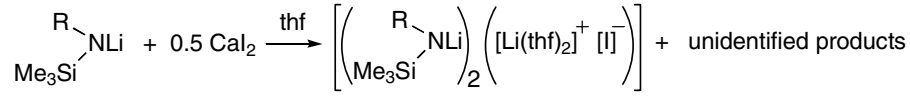


Fig. 8. X-ray structure of **8** (30% ellipsoids). Only H atoms interacting with Li are shown. The shortest Li···H contacts are shown by dashed lines.

Table 5
Selected bond lengths (Å) and angles (°) for **8**

Li(1)–N(1)	1.954(6) (1.968(6))
Li(2)–N(2)	1.963(5) (1.968(6))
Li(3)–N(1)	2.022(5) (2.049(5))
Li(3)–N(2)	2.055(5) (2.046(5))
I(1)–Li(2)	2.736(6) (2.756(5))
I(1)–Li(1)	2.742(6) (2.735(6))
I(1)–Li(3)	3.109(5) (3.126(6))
Li(1)–O(1)	1.894(6) (1.899(6))
Li(2)–O(2)	1.895(6) (1.895(6))
Si(1)–N(1)	1.701(2) (1.699(2))
Si(2)–N(2)	1.695(2) (1.701(2))
Li(2)–I(1)–Li(3)	57.4(1) (57.4(1))
Li(1)–I(1)–Li(3)	58.0(1) (58.0(1))
O(1)–Li(1)–N(1)	136.1(3) (134.8(3))
O(1)–Li(1)–I(1)	112.2(3) (112.6(2))
N(1)–Li(1)–I(1)	111.7(2) (112.5(2))
N(1)–Li(3)–N(2)	165.1(3) (165.4(3))
N(1)–Li(3)–I(1)	96.98(2) (96.8(2))
Li(2)–I(1)–Li(1)	115.5(1) (115.4(2))
N(2)–Li(3)–I(1)	97.9(2) (97.8(2))
N(2)–Li(2)–I(1)	113.7(2) (112.9(2))



R = adamantyl

8

Scheme 1.

ligand/Ca stoichiometry of 2:1 was geared to produce a Ca bis(amide), the side products formed in addition to **8** must contain at least Ca, I, and amide. The structure shows that two four-membered rings containing I, Li, N, and Li atoms are fused via a common Li–I bond, in which the three lithium atoms have a three-coordinate environment. One of the lithium atoms is uniquely bonded to two ligand nitrogen atoms and one iodine atom, and the other two lithium atoms are bonded to one ligand nitrogen atom, one iodine atom, and one thf molecule. In the crystal structure there are two symmetrically independent molecules of **8** with the same structure. Similar structures containing a μ_3-I bonded to lithium atom(s) can be found in $[(thf)_3Li_3(\mu_3\text{-}I)\{Te(N^tBu)_3\}]$ [50], $\{Li(thf)_2[Te_2(N^tBu)_4](\mu_3\text{-}I)[LiI(Te_2(N^tBu)_4)]\}$ [50], and $[(thf)_3Li_3(\mu_3\text{-}I)\{S(N^tBu)_3\}]$ [51]. The two bulky adamantly groups attached to the amide ligands are located on opposite sides of the fused rings and situated as far away from each other as possible. The Li(1)–I(1) and Li(2)–I(1) bond lengths in **8** are almost identical (2.742(6) (2.735(6)) and 2.736(6) (2.756(6)) Å, respectively) but are much shorter than the unique bridging bond length of Li(3)–I(1) bond length of 3.109(5) (3.126(6)) Å. The same situation is also found in the similar structure of $\{[(^nBu)(C(N^tBu)_2)]_2\}Li_3(\mu_3\text{-}I)(thf)_2$, where the bridging Li(3)–I(1) bond length is significantly longer than the two other Li–I bonds [52]. In addition, the longer bond lengths seen in **8** between the two ligand nitrogen atoms and Li(3) (average 2.04(1) Å for both independent molecules) compared to the comparable bond lengths for Li(1)–N(1) or Li(2)–N(2) (average 1.963(9) Å for both independent molecules) indicate that the ligand nitrogen atoms are more weakly bound to the Li(3) atom. Interestingly, this weak bonding can lead to close interactions between Li(3) and the H atoms in the pendant ad or $–SiMe_3$ groups. This can be seen by noting the short distances of Li(3)···H(5A) and Li(3)···H(22B) (ca. 2.90 Å). Additionally, the N(1)–Li(3)–N(2) angle is somewhat distorted from linearity (165.1(3)° (165.4(3)°)), giving a slightly bent T-shape to Li(3).

4. Summary

In summary, we have synthesized dimeric lithium amides **1** and **2** containing bulky ligands, and described the Li···H agostic interactions in the molecules. In **1** and **2**, ligand nitrogen atoms are bridged with two lithium atoms consisting of four-membered N_2Li_2 ring with two-coordinate lithium centers. The monomeric compounds **3**–**6** derived from solvation of **1** and **2** displayed three-coordinate lithium atoms bonded to the nitrogen of one amido ligand and an additional two solvent molecules. Compound **7** has also been shown to be a monomeric three-coordinated lithium derivative, with the electron-deficient lithium atom contributing to agostic type interactions with the H atoms from the $–SiMe_3$ group. Compound **8** provided an unusual structure with two fused four-membered rings via a Li–I bridge. In this molecule one of three lithium atoms is bonded to two ligand nitrogen atoms and the μ_3-bridging iodine atom, while the other two lithium atoms are coordinated to one ligand nitrogen atom, one thf solvent molecule, and the bridging iodine atom. Each lithium atom adopts a three-coordinate geometry. The Li···H agostic interactions were seen between the Li and H atoms on the adamantyl and $SiMe_3$ groups. This work describes a number of structurally characterized silylamido-containing lithium amides that can now be used in various synthetic applications, including our own interests in the synthesis of main group metal amides and their interactions with carbon dioxide [35].

Acknowledgments

We thank the National Science Foundation, Grant No. CHE-0213165 for financial support. Sandia is a multiprogram laboratory operated by Sandia Corporation, a Lockheed Martin Company, for the US Department of Energy's National Nuclear Security Administration under Contract DE-AC04-94-AL85000.

Appendix A. Supplementary data

Crystallographic data for the structural analysis have been deposited with the Cambridge Crystallographic Data Centre, CCDC Nos. 257350–257357 for the compounds **1**–**8**. Copies of this information may be obtained free of charge from The Director, CCDC, 12 Union Road, Cambridge CB2 1EZ, UK (fax: +44 1223 336033; email; deposit@ccdc.cam.ac.uk or www:

http://www.ccdc.cam.ac.uk). Supplementary data associated with this article can be found, in the online version, at doi:10.1016/j.poly.2005.05.006.

References

[1] (a) D. Mootz, A. Zinnius, B. Böttcher, Angew. Chem., Int. Ed. Engl. 8 (1969) 378;
(b) R.D. Rogers, J.L. Atwood, R. Grüning, J. Organomet. Chem. 157 (1978) 229.
[2] K. Gregory, P.V.R. Schleyer, R. Snaith, Adv. Inorg. Chem 37 (1991) 47.
[3] R.E. Mulvey, Chem. Soc. Rev 20 (1991) 167.
[4] D.R. Armstrong, R.E. Mulvey, G.T. Walker, D. Barr, R. Snaith, J. Chem. Soc., Dalton Trans. (1988) 617.
[5] D.R. Armstrong, D.R. Baker, F.J. Craig, R.E. Mulvey, W. Clegg, L. Horsburgh, Polyhedron 15 (1996) 3533.
[6] D. Barr, W. Clegg, R.E. Mulvey, R. Snaith, J. Chem. Soc., Chem. Commun. (1984) 287.
[7] D. Seebach, Angew. Chem., Int. Ed. Engl. 27 (1988) 1624.
[8] P. Beak, A. Basu, D.J. Gallagher, Y.S. Park, S. Thayumanavan, Acc. Chem. Res. 29 (1996) 552.
[9] D. Hoppe, T. Hense, Angew. Chem., Int. Ed. Engl. 36 (1997) 2282.
[10] V. Snieckus, Chem. Rev. 90 (1990) 879.
[11] P.J. Cox, N.S. Simpkins, Tetrahedron: Asymmetry 2 (1991) 1.
[12] P.J. O'Brien, J. Chem. Soc., Perkin Trans. I (1998) 1439.
[13] P.J. O'Brien, J. Chem. Soc., Perkin Trans. I (2001) 95.
[14] M. Westerhausen, J. Greul, H.-D. Hausen, W. Schwarz, Z. Anorg. Allg. Chem. 622 (1996) 1295.
[15] H. Schumann, J. Gottfriedsen, S. Dechert, F. Girgsdies, Z. Anorg. Allg. Chem. 626 (2000) 747.
[16] C. Eaborn, P.B. Hitchcock, J. David Smith, S.E. Sözerli, Organometallics 16 (1997) 5653.
[17] W.S. Rees Jr., D.M. Green, W. Hesse, Polyhedron 11 (1992) 1697.
[18] K.B.P. Ruppa, N. Desmangles, S. Gambarotta, G. Yap, A.L. Rheingold, Inorg. Chem. 36 (1997) 1194.
[19] M. Rahim, N.J. Taylor, S. Xin, S. Collins, Organometallics 17 (1998) 1315.
[20] P.H.M. Budzelaar, A.B. van Oort, A.G. Orpen, Eur. J. Inorg. Chem. 10 (1998) 1485.
[21] V.C. Gibson, P.J. Maddox, C. Newton, C. Redshaw, G.A. Solan, A.J.P. White, D.J. Williams, Chem. Commun. (1998) 1651.
[22] B. Qian, D.L. Ward, M.R. Smith III, Organometallics 17 (1998) 3070.
[23] L. Kakaliou, W.J. Scanlon IV, B. Qian, S.W. Baek, M.R. Smith III, D.H. Morty, Inorg. Chem. 38 (1999) 5964.
[24] (a) P.L. Holland, W.B. Tolman, J. Am. Chem. Soc. 121 (1999) 7270;
(b) P.L. Holland, W.B. Tolman, J. Am. Chem. Soc. 122 (2000) 6331.
[25] C.C. Cui, H.W. Roesky, H.-G. Schmidt, M. Noltemeyer, H. Hao, F. Cimpoesu, Angew. Chem., Int. Ed. Engl. 39 (2000) 4274.
[26] (a) R. Boese, U. Klingebiel, J. Organomet. Chem. 315 (1986) C17;
(b) L. Marcus, U. Klingebiel, L. Lameyer, D. Stalke, Z. Anorg. Allg. Chem. 624 (1998) 1041;
(c) J. Niesmann, U. Klingebiel, C. Ropken, M. Noltemeyer, R. Herbst-Irmer, Main Group Chem. 2 (1998) 297;
(d) D. Stalke, U. Klingebiel, G.M. Sheldrick, Chem. Ber. 121 (1998) 1457;
(e) D. Grosskopf, L. Marcus, U. Klingebiel, M. Noltemeyer, Phosphorus Sulfur Silicon Relat. Elem. 97 (1994) 113.
[27] A.R. Sadique, M.J. Heeg, C.H. Winter, Inorg. Chem. 40 (2001) 6349.
[28] P.J. Bailey, C.M. Dick, S. Fabre, S. Parsons, J. Chem. Soc., Dalton Trans. (2000) 1655.
[29] D. Driess, J. Magull, Z. Anorg. Allg. Chem. 620 (1994) 814.
[30] J. Kim, S.G. Bott, D.M. Hoffman, Inorg. Chem. 37 (1998) 3835.
[31] R.A. Bartlett, P.P. Power, J. Am. Chem. Soc. 109 (1987) 7563.
[32] H. Chen, R.A. Bartlett, H.V.R. Dias, M.M. Olmstead, P.P. Power, J. Am. Chem. Soc. 111 (1989) 4338.
[33] M.F. Lappert, P.P. Power, A.R. Sanger, R.C. Srivastava, Metal and Metalloid Amides, Horwood-Wiley, Chichester, 1980.
[34] R.E. Mulvey, Chem. Soc. Rev. 27 (1998) 339.
[35] (a) Y. Tang, L.N. Zakharov, A.L. Rheingold, R.A. Kemp, Organometallics 23 (2004) 4788;
(b) Y. Tang, W.S. Kassel, L.N. Zakharov, A.L. Rheingold, R.A. Kemp, Inorg. Chem. 44 (2005) 359;
(c) Y. Tang, L.N. Zakharov, A.L. Rheingold, R.A. Kemp, Organometallics 24 (2005) 836;
(d) Y. Tang, W.S. Kassel, L.N. Zakharov, A.L. Rheingold, R.A. Kemp, Inorg. Chim. Acta 358 (2005) 2014.
[36] J.R. Bowser, R.H. Neilson, R.L. Wells, Inorg. Chem. 17 (1978) 1882.
[37] M. Westerhausen, W. Schwarz, Z. Anorg. Allg. Chem. 619 (1993) 1053.
[38] (a) G. Mattogno, A. Monaci, Ric. Sci., Rend., Sez. A 8 (1965) 482;
(b) V.F. Mironov, N.S. Fedotov, Zh. Obshch. Khim. 42 (1972) 166.
[39] (a) R.C. Samuel, R.P. Kashyap, M. Krawiec, W.H. Watson, R.H. Neilson, Inorg. Chem. 41 (2002) 7113;
(b) J.R. Klaehn, R.H. Neilson, Inorg. Chem. 41 (2002) 5859.
[40] D.F. Shriver, The Manipulation of Air-sensitive Compounds, McGraw-Hill, New York, 1986.
[41] (a) G.M. Sheldrick, SADABS (2.01), Bruker/Siemens area detector absorption correction program, Bruker AXS, Madison, WI, 1998;
(b) G.M. Sheldrick, SHELXTL: Program Package for Structure Solution and Refinement, Bruker AXS, Madison, WI, 1997.
[42] M. Veith, A. Koban, K. Fries, P. Spaniol, R. Elsässer, A. Rammo, V. Huch, U. Kleinsteuber, Organometallics 17 (1998) 2612.
[43] F. Antolini, P.B. Hitchcock, M.F. Lappert, P. Merle, Chem. Commun. (2000) 1301.
[44] T. Fjeldberg, P.B. Hitchcock, M.F. Lappert, A.J. Thome, J. Chem. Soc., Chem. Commun. (1984) 822.
[45] B. Cetinkaya, I. Gümrükcü, M.F. Lappert, J.L. Atwood, R. Shakir, J. Am. Chem. Soc. 102 (1980) 2086.
[46] M.F. Lappert, M.J. Slade, A. Singh, J. Am. Chem. Soc. 105 (1983) 302.
[47] G.C. Forbes, A.R. Kennedy, R.E. Mulvey, P.J.A. Rodger, Chem. Commun. (2001) 1400.
[48] G.C. Forbes, A.R. Kennedy, R.E. Mulvey, P.J.A. Rodger, R.B. Rowlings, J. Chem. Soc., Dalton Trans. (2001) 1477.
[49] K.W. Henderson, A.E. Dorigo, Q.-Y. Liu, P.G. Williard, J. Am. Chem. Soc. 119 (1997) 11855.
[50] T. Chivers, M. Parvez, G. Schatte, Inorg. Chem. 40 (2001) 540.
[51] (a) R. Fleischer, D. Stalke, Coord. Chem. Rev. 176 (1998) 431;
(b) R. Fleischer, S. Freitag, D. Stalke, J. Chem. Soc., Dalton Trans. (1998) 193.
[52] T. Chivers, A. Downard, M. Parvez, Inorg. Chem. 38 (1999) 4347.

from sodium. *cis*-$Ru(bpy)_2Cl_2$ was synthesized according to the literature procedures [11].

2.2. Physical characterization

NMR spectra were recorded on a Bruker AVANCE 400 MHz or a Bruker ACP 200 MHz spectrometer using $CDCl_3$ for the free ligands and CD_3CN for the complex with TMS as internal reference. UV–Vis–NIR absorption spectra were recorded using a Shimadzu 3101 PC spectrometer. IR spectra were obtained using a Bruker Vector 22 FT using KBr.

Electrochemical measurements were made with a BAS 50 W using a conventional three electrode cell. Steady-state photoluminescence (PL) spectra were obtained with a Spex Fluorolog that had been calibrated with a standard NIST tungsten–halogen lamp.

2.3. Synthesis

2.3.1. 1,10-Phenanthroline-5-yl-1,2-ferrocenylethanol

0.88 g of 5-methyl-1,10-phenanthroline (4.5 mmol) were dissolved in 20 mL of dry THF. The solution was cooled in a liquid nitrogen–ethanol bath. To the chilled solution 2.5 mL of lithium diisopropylamide, LDA 2.0 M were added. The dark solution formed was stirred for 1 h; the liquid nitrogen–ethanol bath was then changed for an ice-bath and 1.1 g of ferrocene carboxaldehyde (5 mmol) in 15 mL of dry THF were added. The solution was stirred overnight, subsequently quenched with water and extracted four times with chloroform (15 mL). The organic phase was dried with anhydrous sodium sulfate and the solvent eliminated. The solid obtained was purified by alumina chromatography using increasing polarity hexanes–diethyl ether–dichloromethane mixtures as mobile phase. Evaporation of the solvent gave 0.97 g of pure compound with a 52% yield. IR (KBr cm^{-1}) 3226, 1618, 1045, 752, 738, ^1H RMN 400 MHz ($CDCl_3$) 9.18 (1H, dd), 9.15 (1H, dd), 8.41 (1H, dd), 8.16 (1H, dd), 7.6 (3H, m), 4.80 (CH, m), 4.32 (1H, cp, s), 4.22 (5H, cp, s), 4.18 (1H, cp, s), 4.13 (1H, cp, s), 3.46 (CH2, m), 2.3 (OH, s): ^{13}C RMN 150.3, 150.1, 146.1, 135.8, 133.8, 132.9, 128.7, 128.5, 127.6, 123.5, 122.9, 93.8, 70.5, 68.7, 68.6, 68.4, 67.9, 65.1, 41.8.

2.3.2. 5-[(E)-2-ferrocenylvynil]-1,10-phenanthroline (fcvp)

0.5 g of 1,10-phenanthroline-5-yl-1,2-ferrocenylethanol (1.22 mmol) and 0.3 g of pyridinium-*p*-toluene sulfonate (1.22 mmol) in 30 mL of toluene, were refluxed for 6 h. After that period the solvent was eliminated. Water was added to the solid and the resulting mixture was extracted with 4 portions of chloroform (15 mL). The organic phase was dried with anhydrous sodium sulfate and the solvent evaporated under vacuum. The resulting solid was purified by alumina chromatography. 0.40 g of an orange solid were obtained with a 82% yield. IR (KBr, cm^{-1}) 1628, 1597, 1420, 820, 735, ^1H RMN 400 MHz ($CDCl_3$) 9.21 (1H, dd), 9.14 (1H, dd), 8.55 (1H, dd), 8.24 (1H, dd), 7.90 (1H, s), 7.67 (1H, dd), 7.61 (1H,), 7.35 (1H, d), 7.06 (1H, d), 4.57 (2H pt), 4.37 (2H pt), 4.21 (5H s): ^{13}C RMN 150.4, 150.1, 146.7, 146.1, 135.9, 134.9, 132.7, 129.0, 127.7, 123.7, 123.1, 122.5, 121.4, 83.138, 69.9, 69.7, 67.6. *Anal.* Calc. for $C_{24}H_{18}N_2Fe$: C, 73.86; H, 4.65; N, 7.18. Found: C, 72.91; H, 4.77; N, 7.17%.

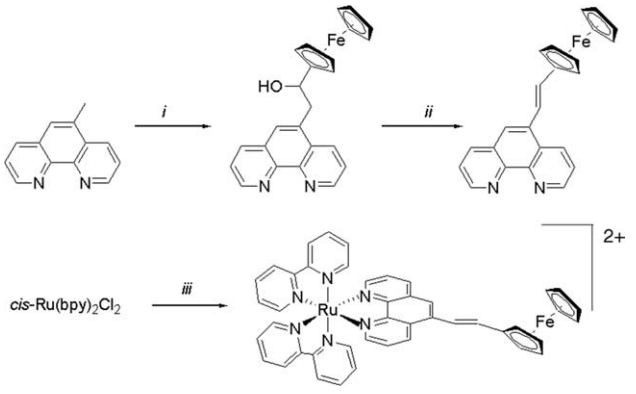
2.3.3. $[Ru(bpy)_2(fcvp)](PF_6)_2$

A solution of fcvp (0.5 mmol) and *cis*-$Ru(bpy)_2Cl_2$ (0.5 mmol) in H_2O/MeOH (1:2) (25 mL) were refluxed for 4 h. The solvent was evaporated until dryness. Water was added and the resulting solution filtered. NH_4PF_6 was added to the aqueous phase to induce the precipitation of the complex. The solid was filtered off and washed with water and ethylic ether. The orange brown solid was dissolved in acetonitrile and precipitated by the addition of a large quantity of ethyl ether. Yield 80% IR (KBr, cm^{-1}) 1630, 1606, 841, ^1H RMN 400 MHz (CD_3CN, ppm) 8.91 (d, 1H), 8.53 (m, 5H), 8.40 (s, 1H), 8.12 (m, 3H), 8.05 (m, 3H), 8.05 (m, 6H), 7.91 (d, 2H), 7.8 (dd, 1H), 7.72 (dd, 1H), 7.56 (m, 2H), 7.48 (m, 3H), 7.35 (d, 1H), 7.26 (m, 2H), 4.80 (s, 2H), 4.51 (s, 2H), 4.29 (s, 5H). *Anal.* Calc. for $C_{42}H_{32}F_{12}FeN_6P_2Ru$: C, 47.25; H, 3.02; N, 7.87. Found: C, 46.92; H, 3.21; N, 7.54%.

3. Results and discussion

3.1. Synthesis

The ligand 5-[(*E*)-2-ferrocenylvinyl]-1,10-phenanthroline, fcvp was synthesized in two steps following the literature methods [12] for similar compounds (Scheme 1). The first step consisted in the lithiation of



Scheme 1. Synthetic route of fcvp ligand: (i) LDA, ferrocene carboxaldehyde; (ii) pyridinium *p*-toluenesulfonate; (iii) EtOH/H_2O, NH_4PF_6.

5-methyl-1,10-phenanthroline with lithium diisopropylamide with the subsequent addition of ferrocene carboxaldehyde to form 2-(1,10-phenanthrolin-5-yl)-1-ferrocenylethanol. The second step was the dehydration of the former ligand with pyridinium *p*-toluenesulfonate to obtain the desired ligand.

The ruthenium complex was synthesized by reaction with *cis*-$Ru(bpy)Cl_2$ and isolated as the hexafluorophosphate salt.

3.2. NMR

The ^1H NMR of the fcvp ligand, Fig. 1 shows a set of seven signals for the phenanthroline ring protons denoting their magnetic inequivalence. The highest displacement in chemical shift, compared to 1,10-phenanthroline, is observed for proton 4 which moves lowfield from 8.20 to 8.58 ppm (see Fig. 1 for numbering). On the other hand, proton 6 moves high field compared to 1,10-phenanthroline.

The AB system in the ethene bridge appears relatively lowfield (7.36 and 7.04 ppm) with a coupling constant, $J_{AB} = 15.4$ Hz which indicates a *trans* geometry [13] for the ligand. The inset in Fig. 1 shows the characteristic pattern of proton signals for the monosubstituted and the unsubstituted cp rings [14].

In the ^1H NMR of the $[Ru(bpy)_2fcvp]^{2+}$ overlap of the bipyridine and fcvp ligand signals are observed. The complete assignation of the ^1H NMR spectrum was made using bidimensional techniques, Fig. 2.

The ligand fcvp maintains the set of 7 signals for the phenanthroline region. The chemical shifts of these signals are quite similar than the free ligand with the sole exception of protons 7 and 1 that move high field due to the diamagnetic currents produced by the bipyridine rings in the pseudooctahedric geometry [15].

As commonly observed for heteroleptic ruthenium complexes of the $[Ru(bpy)_2LL]$ type, two sets of signals were found for the bipyridine rings.

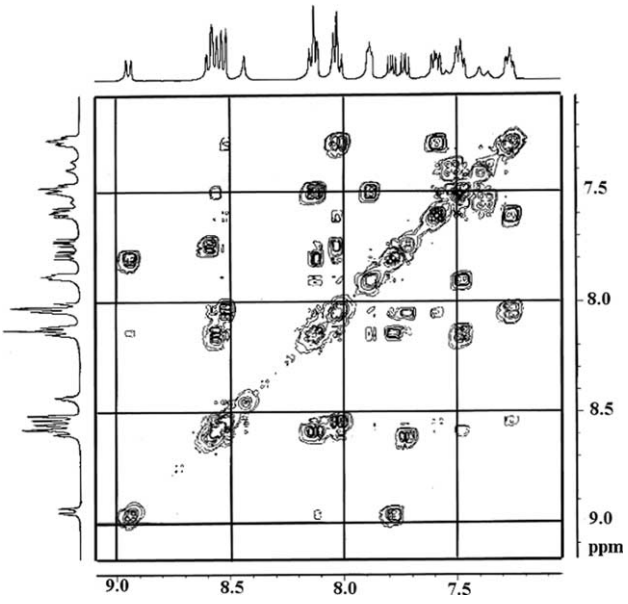


Fig. 2. Aromatic region H–H COSY of the complex $[Ru(bpy)_2(fcvp)](PF_6)_2$ in CD_3CN.

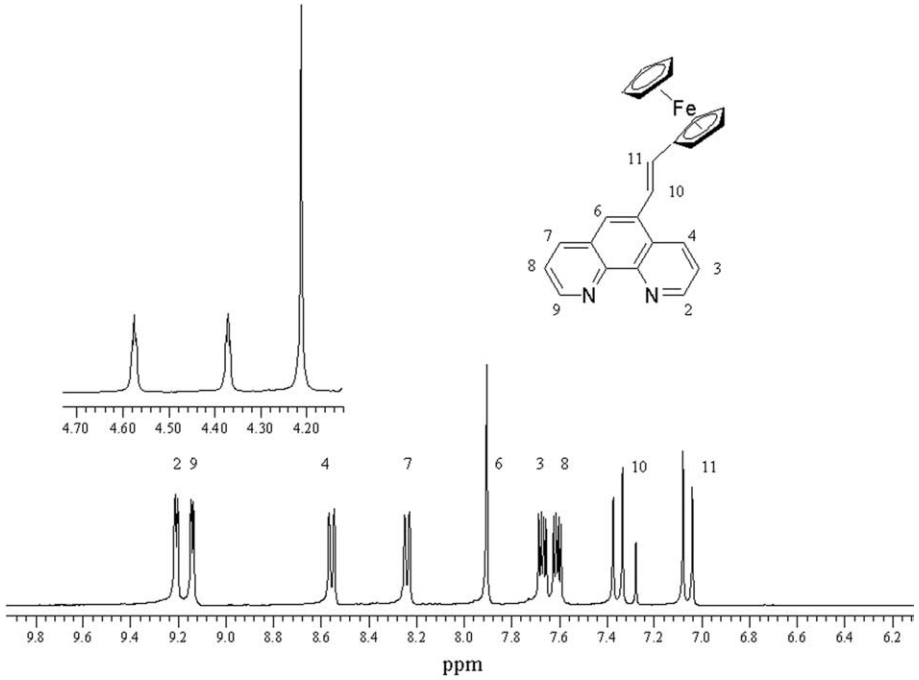


Fig. 1. Aromatic region ^1H NMR spectra of the fcvp ligand in $CDCl_3$. The inset shows the ferrocenyl proton signals.

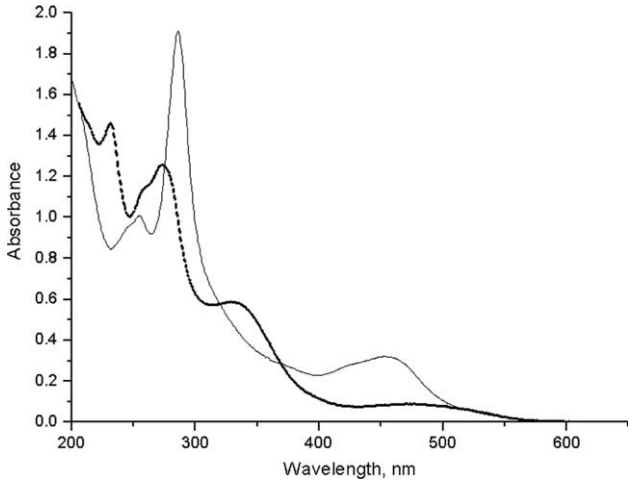


Fig. 3. UV–Vis spectra of fcvp ligand (dotted line) and $[Ru(bpy)_2(fcvp)](PF_6)_2$ complex (solid line) in acetonitrile.

3.3. Electronic spectra

The electronic spectra of the free ligand (Fig. 3) present two low energy absorption bands, which are present in most of the ferrocenyl-acceptor compounds. Barlow et al. [16] proposed a model to explain these absorptions. In this model, the lowest energy band arises from the transition between mainly non-bonding metal orbitals $(d(\pi)^6_{Fc})$ to an empty π^* orbital in the π acceptor, in this case the phenanthroline ring (π^*_{phen}). This transition differs from the reported for ferrocene, since it is more intense and displaced to the red. The second low energy transition is assigned to a transition between the highest occupied cyclopentadienyl cp, orbital and the acceptor region. Nevertheless this absorption band is probably overlapped with $\pi \rightarrow \pi^*$ phenanthroline bands.

In order to obtain information about the structure and orbital energy levels of the fcvp ligand DFT calculations[1] were performed with the GAUSSIAN [17] software package. The optimized geometries show that the phenanthroline and the ferrocenyl unit are not coplanar due to steric repulsions between the protons of the bridge and the phenanthroline ring. The eclipsed conformation of the metallocene was found to be the global minima in agreement with calculations for the ferrocene unit [18].

The LUMO (Fig. 4(b)) corresponds to the π acceptor orbital predicted by the Barlow's model while the HOMO (Fig. 4(a)) and the HOMO − 1 correspond to the metal centered non-bonding orbitals. The highest occupied cp molecular orbital was the HOMO − 6 and not the HOMO − 2 as should be expected. The energy level of this orbital is similar to π orbitals of the phenanthroline ring. This is in agreement with the possible overlap of the second ferrocene to ligand charge transfer band with $\pi \rightarrow \pi^*$ phenanthroline bands.

The visible absorption spectra of the $[Ru(bpy)_2fcvp]^{2+}$ complex (Fig. 3) on the other hand is dominated by $(d(\pi)^6) \rightarrow (d(\pi)^5(\pi)^1)$ MLCT bands characteristic of the polypyridinic ruthenium complexes. The lowest energy ferrocene to ligand charge transfer transition is also observable in the complex and appears as a shoulder on the MLCT band.

3.4. Electrochemistry

The half-wave potentials of the ligand fcvp as well its ruthenium complex are reported in Table 1.The cyclic voltammogram of the fcvp ligand shows a reversible oxidation at 0.55 V versus SCE, assigned to the ferrocenyl moiety. It is shifted to more positive potentials than the corresponding free ferrocene oxidation (0.41 V versus SCE), evidencing, therefore, that the phenanthroline region is behaving as an electron acceptor. In the complex, the reversible couple assigned to the ferrocene unit appears at almost the same potential than in the free fcvp ligand, denoting a poor interaction of the Fe and the Ru centers. Towards more positive potentials, an irreversible oxidation peak was observed at 1.37 V. This peak was assigned to the oxidation of the ruthenium center. This oxidation potential is very close to the one observed for the $[Ru(bpy)_2(phen)]^{2+}$ complex (phen = 1,10-phenanthroline). The current associated to this oxidation is, nevertheless, higher than the expected for a one-electron process, considering the ferrocene oxidation as a reference.

This behavior was observed in similar compounds [19] and could possibly be due to a intermolecular reduction of the Ru^{3+} generated by any other unoxidized ferrocene moieties attached to other surrounding complexes [20].

In order to analyze further, the degree of communication between the metal centers a mixed valence complex was generated in situ by the stoichiometric addition of a cerium salt[2] and the presence of an intervalence transfer band in it investigated. This procedure generates the mixed valence complex $[Ru^{II}(bpy)_2(fcvp^+)]^{3+}$, where ruthenium it is in a formal oxidation state 2+ while iron is in a 3+ formal oxidation state.

The UV–Vis–NIR spectra of the $[Ru(bpy)_2(fcvp)]^{2+}$ complex before and after the addition of the cerium salt it is presented in Fig. 5. The observable changes in the spectra are the bleach of the ferrocene to phenanthroline charge transfer and the merging of a low intensity band at 800 nm. Low intensity intervalence bands in ruthe-

[1] Optimized geometries were obtained using the B3LYP functional with a LANL2DZ basis set. A frequency analysis was also done, showing that all the frequencies were real and positive, indicating that an energy minimum was reached.

[2] Similar results were obtained by oxidation at controlled potential, 0.7 V, in 0.1 M TBAH acetonitrile solution.

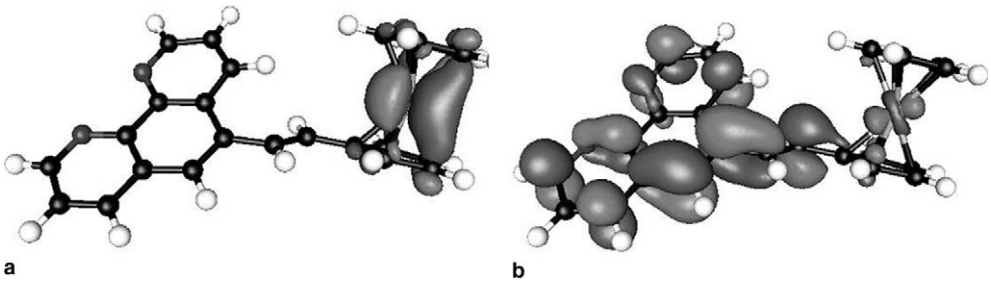


Fig. 4. HOMO (a) and LUMO (b) 0.032 a.u. isosurfaces of the fcvp ligand.

Table 1
$E_{1/2}$ potentials for fcvp ligand and its ruthenium complex in acetonitrile[a]

	$E_{1/2}$ Fc^+/Fc	$E_{1/2}$ $Ru^{III/II}$	$E_{1/2}$ $Ru^{II*/+}$
fcvp	0.55		
$[Ru(bpy)_2(fcvp)]^{2+}$	0.50	1.37	0.80[b]
$[Ru(bpy)_2(phen)]^{2+}$		1.32	0.85[b]

[a] $E_{1/2}$ values vs. the saturated calomel electrode (SCE) in 0.1 M $N(n\text{-}C_4H_9)_4PF_6/CH_3CN$ at room temperature.
[b] Calculated from the E_{00} energy obtained from fits of 77 K emission spectrum [18].

nium ferrocene mixed valence complexes have been reported [21]; nevertheless a band of these characteristics can also be assigned to the oxidized fc+ moiety. The presence of a similar band in the oxidized form of the fcvp free ligand, as well as in related ligands [22], and the general behavior of the complex described in the preceding paragraphs, supports the assignment of the 800 nm band to a transition in the oxidized fc+ moiety, and not to an intervalence transfer band. Therefore, little, if any interaction between the Ru and Fe centers is observed in the $[Ru(bpy)_2(fcvp)]^{2+}$ complex in the ground state.

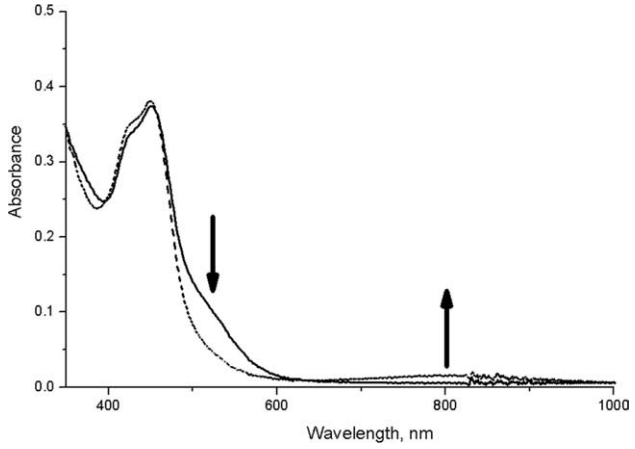


Fig. 5. Vis–NIR spectra of complex $[Ru^{II}(bpy)_2(fc^{II}vp)]^{2+}$ before (solid line) and after (dotted line) the addition of 1 equivalent of Ce^{IV} in acetonitrile.

3.5. Photophysics

In contrast with most of the polypyridinic ruthenium complexes which show photoluminescence at room temperature, no emission was observed for the complex $[Ru(bpy)_2(fcvp)](PF_6)_2$.[3]

There is evidence that in the thermal equilibrated excited state of the $[Ru(bpy)_2(phen)]^{2+}$ complex the electron resides in one of the bipyridine ligands [24]. It can be expected that in the $[Ru(bpy)_2(fcvp)]^{2+}$ complex the bipyridine ligands remain as the acceptor ligand.

It is well know that ferrocene is an effective quencher of the excited triplet state in ruthenium complexes [23].

The absence of emission therefore can be attributed to an intramolecular excited state electron transfer process between ferrocene and ruthenium III which is the formal oxidation state of this metal in the excited state.

Therefore, after excitation an electron from the ruthenium center should be transferred to a bipyridine ligand. The MLCT emissive excited state is then reductively quenched by an electron transfer from the ferrocene moiety to the ruthenium center

$$[Ru^{III}(bpy^-)(bpy)(fcvp^{II})]^* \rightarrow [Ru^{II}(bpy^-)(bpy)(fcvp^{III})]^* (\Delta G^0 \approx -0.3\ \text{eV}) \quad (1)$$

The driving force for this process, Eq. (1), was estimated according to the literature methods [8] from the oxidation potentials of the metal centers and the free energy stored in the excited state, which was assumed to be equal to the parent complex $[Ru(bpy)_2(phen)]^{2+}$. Although the electron transfer process is thermodynamically allowed, and is the most probably quenching route, an energy transfer mechanism for the quenching of the photoluminescence cannot be completely ruled out.

[3] During the photoluminescence experiments some emission was observed but it was assigned to traces of $[Ru(bpy)_3]^{2+}$ complex due to the very low quantum yields and similar lifetimes.

4. Conclusions

The synthesis of a new ferrocenyl donor ligand was achieved in relative good yield. The donor ability of the ferrocene unit was observed by the presence of ferrocene to ligand charge transfer bands.

The bis bypyridine ruthenium complex synthesized with this ligand shows little, if any, interaction between the metal centers in the ground state. The electrochemical results and the properties of the mixed valence complex are in agreement with this behavior.

Nevertheless, the absence of the characteristic emission of Ru-polypyridinic complexes in $[Ru(bpy)_2(fcvp)]^{2+}$ manifests an interaction in the excited state, probably through an electron transfer process. Further photophysical studies are needed to confirm these hypotheses.

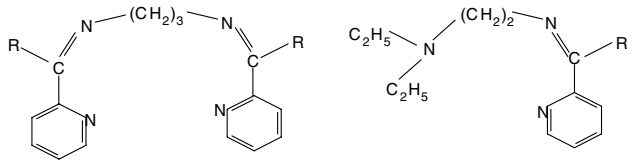
From the solar energy conversion point of view this process could be helpful to achieve a long distance charge separation in the excited state, and therefore avoiding undesired recombination processes.

Acknowledgments

We gratefully acknowledge Professor Gerald Meyer (Johns Hopkins University) for useful discussions and comments. This work was supported by CONICYT (doctoral thesis support grant to A.D.), FONDECYT Lineas Complementarias 890007, and FONDECYT 1020517.

References

[1] L.X. Dai, T. Tu, S.L. Xou, W.P. Deng, X.L. Hou, Acc. Chem. Res. 36 (2003) 659.
[2] T.J. Colacot, Chem. Rev. 103 (2003) 3101.
[3] P.D Beer, P.A. Gale, G.Z. Chen, J. Chem. Soc., Dalton Trans. 12 (1999) 1897.
[4] Edward C. Constable, Angew. Chem. 103 (1991) 418.
[5] S. Marder, J. Sohn, G. Stucky (Eds.), Materials for Nonlinear Optics: Chemical Perspectives, American Chemical Society, Washington, DC, 1991.
[6] D.J. Williams, Angew. Chem., Int. Ed. Engl. 23 (1984) 690.
[7] N.J. Long, Angew. Chem., Int. Ed. Engl. 34 (1995) 21.
[8] K. Kalyanasundaram, Photochemistry of Polypyridine and Porphyryn Complexes, Academic Press, London, 1992.
[9] A. Juris, V. Balzani, F. Barigelletti, S. Campagna, P. Belser, A. von Zelewsky, Coord. Chem. Rev. 84 (1988) 3381.
[10] S. Fery-Forgues, B. Delavaux-Nicot, J. Photochem. Photobiol. A 132 (2000) 137.
[11] B.P. Sullivan, D.J. Salmon, T.J. Meyer, Inorg. Chem. 12 (1978) 3334.
[12] P. Beer, O. Kocian, J. Chem. Soc., Dalton. Trans. (1990) 3283.
[13] F.A. Bovey, Nuclear Magnetic Resonance Spectroscopy, Academic Press, San Diego, 1988.
[14] D. Slocum, C. Ernst, Adv. Organomet. Chem. 10 (1972) 79.
[15] G. Orellana, C. Alvarez, J. Santoro, Inorg. Chem. 27 (1988) 1025.
[16] S. Barlow, H.E. Bunting, C. Ringham, J.C. Green, G.U. Bublitz, S.G. Boxer, J.W. Perry, S.R. Marder, J. Am. Chem. Soc. 121 (1999) 371.
[17] M.J. Frisch, G.W. Trucks, H.B. Schlegel, G.E. Scuseria, M.A. Robb, J.R. Cheeseman, V.G. Zakrzewski, J.A. Montgomery Jr., R.E. Stratmann, J.C. Burant, S. Dapprich, J.M. Millam, A.D. Daniels, K.N. Kudin, M.C. Strain, O. Farkas, J. Tomasi, V. Barone, M. Cossi, R. Cammi, B. Mennucci, C. Pomelli, C. Adamo, S. Clifford, J. Ochterski, G.A. Petersson, P.Y. Ayala, Q. Cui, K. Morokuma, D.K. Malick, A.D. Rabuck, K. Raghavachari, J.B. Foresman, J. Cioslowski, J.V. Ortiz, A.G. Baboul, B.B. Stefanov, G. Liu, A. Liashenko, P. Piskorz, I. Komaromi, R. Gomperts, R.L. Martin, D.J. Fox, T. Keith, M.A. Al-Laham, C.Y. Peng, A. Nanayakkara, C. Gonzalez, M. Challacombe, P.M.W. Gill, B. Johnson, W. Chen, M.W. Wong, J.L. Andres, C. Gonzalez, M. Head-Gordon, E.S. Replogle, J.A. Pople, GAUSSIAN 98, Revision A.7, Gaussian, Inc., Pittsburgh, PA, 1998.
[18] Z. Xu, Y. Xie, W. Feng, H.F. Schaefer III, J. Phys. Chem. A 107 (2003) 2716.
[19] K. Hutchison, J. Morris, T. Nile, J. Walsh, D. Thompson, J. Petersen, J. Schoonover, Inorg. Chem. 38 (1999) 2516.
[20] I. Wyman, T.J. Burchell, K.N. Robertson, T.S. Cameron, M.A.S. Aquino, Organometallics 23 (2004) 5353.
[21] N. Dowling, P. Henry, N. Lewis, H. Taube, Inorg. Chem. 20 (1981) 2345.
[22] A. Delgadillo, B. Loeb (in preparation).
[23] E.J. Lee, M.S. Wrighton, J. Am. Chem. Soc. 113 (1991) 8562.
[24] Y.J. Chang, X. Xu, T. Yabe, S.C. Yu, D.R. Anderson, L.K. Orman, J.B. Hopkins, J. Phys. Chem. 94 (1990) 729.



R = H, pfpd
R = Ph, pbpd

R = H, pfed
R = Ph, pbed

Scheme 1.

different oxidation states. We have successfully isolated six cobalt(II) and six cobalt(III) mononuclear complexes of the types $[Co(L^1)(X)_2]$ (**1a**–**1f**) and $[Co(L^2)(X)_3]$ (**2a**–**2f**) [L^1 = *N*,*N*′-(bis(pyridin-2-yl)formylidene)propane-1,3-diamine (pfpd) or *N*,*N*′-(bis(pyridin-2-yl)benzylidene)propane-1,3-diamine (pbpd); L^2 = (*N*,*N*-diethyl, *N*′-(pyridin-2-yl)formylidene)ethane-1,2-diamine (pfed) or (*N*,*N*-diethyl,*N*′-(pyridin-2-yl)benzylidene)ethane-1,2-diamine (pbed), Scheme 1; X = N_3^-, NCS^- or NCO^-] using one-pot reactions of cobalt(II) salt, L and pseudohalide in 1:1:2 and 1:1:3 molar ratios, respectively, at room temperature in methanol–water solvent mixtures. All the complexes are characterized using microanalytical, spectroscopic, magnetic, electrochemical and other physicochemical results. In two representative cases, $[Co(pfpd)(NCS)_2]$ (**1c**) and $[Co(pbed)(N_3)_3]$ (**2b**), crystal structures have been solved by X-ray diffraction measurements to define the coordination spheres. This paper has addressed the details of syntheses, structures and properties of these new complexes and focused on the stabilization of metal oxidation levels through judicious choice of Schiff base-pseudohalide combinations.

2. Experimental

2.1. Materials

High purity 2-benzoylpyridine (Lancaster, UK), pyridine-2-carboxaldehyde (Lancaster, UK), *N*,*N*-diethylethane-1,2-diamine (SRL, India), propane-1,2-diamine (SRL, India), cobalt nitrate hexahydrate (E. Merck, India), sodium azide (E. Merck, India), ammonium thiocyanate (E. Merck, India), and sodium cyanate (Lancaster, UK) were used as received. Cobalt perchlorate hexahydrate was prepared on treatment of cobalt carbonate (E. Merck, India) with perchloric acid (E. Merck) followed by slow evaporation on a steam bath, filtration through a fine glass-frit and preservation in a desiccator containing concentrated sulphuric acid (E. Merck, India) for subsequent use. Purification of MeCN and preparation of supporting electrolyte ($[Et_4N][ClO_4]$) for electrochemical work were executed following reported method [14]. All other chemicals were of analytical grade and were used without further purification.

Caution! Perchlorate and azide compounds of metal ions are potentially explosive especially in presence of organic ligands. Only a small amount of the materials should be prepared and handled with care.

2.2. Physical measurements

Elemental analyses (carbon, hydrogen and nitrogen) were performed on a Perkin–Elmer 2400 CHNS/O elemental analyzer. IR spectra (KBr discs, 4000–300 cm^{-1}) were recorded using a Jasco FT-IR Model 420 spectrometer. Molar conductances were measured using a Systronics conductivity meter where the cell constant was calibrated with 0.01 M KCl solution and dry MeCN was used as solvent. Room-temperature magnetic susceptibilities of powder samples were done on a PAR 155 vibrating sample magnetometer, with $Hg[Co(SCN)_4]$ as the reference. Diamagnetic corrections were made using Pascal's constants. Ground state absorption and steady-state fluorescence measurements were made with a Jasco Model V-530 UV–Vis spectrophotometer and Hitachi Model F-4010 spectrofluorimeter, respectively. Time-resolved fluorescence measurements were carried out using a time-correlated single photon counting (TCSPC) spectrometer Edinburgh Instruments, Model 199; hydrogen filled coaxial flash lamp with a pulse width of 1.2 ns at FWHM and a Philips XP-2020Q Photomultiplier tube were, respectively, used as the excitation source and for the fluorescence detection. Electrochemical measurements (cyclic voltammetry, CV) were made with a computer controlled EG&G PARC VersaStat Model 270 electrochemical instrument using a platinum disk working electrode as described elsewhere [15]. The solution was IR-compensated and the results were collected at 298 K. The following parameters and relations were used: scan rate (v), 50 mV s^{-1}; formal potential $E^\circ = 0.5(E_{pa} + E_{pc})$ where E_{pa} and E_{pc} are anodic and cathodic peak potentials, respectively; ΔE_p is the peak-to-peak separation. The potentials are referenced to a saturated calomel electrode (SCE) and are uncorrected for junction contributions.

2.3. Preparation of Schiff bases

The Schiff bases pfpd, pbpd, pfed and pbed were prepared following a reported [11a] procedure with a little modification.

2.3.1. *N,N′-(bis(pyridin-2-yl)formylidene)-propane-1,3-diamine (pfpd) and N,N′-(bis(pyridin-2-yl)-benzylidene)propane-1,3-diamine (pbpd)*

Propane-1,3-diamine (0.074 g, 1 mmol) and pyridine-2-carboxaldehyde (0.214 g, 2 mmol) were mixed together and refluxed in dehydrated alcohol (25 cm^3) for 10 h. The yellow solution that resulted was concentrated on

a steam-bath and dried in vacuo over $CaCl_2$ to a yellow solid. Yield: 0.176 g (70%). pbpd was prepared (yield, 74%) using similar procedure except that 2-bezoylpyridine instead of pyridine-2-caboxaldehyde was used. *Anal*. Calc. for $C_{15}H_{16}N_4$ (pfpd): C, 71.4; H, 6.4; N, 22.2. Found: C, 72.0; H, 6.7; N, 22.5%. IR (KBr disc, cm^{-1}): ν(C=N) 1594. UV–Vis (MeCN): λ_{max}, 260 and 392 nm. Found: C, 80.4; H, 5.8; N, 14.2%. *Anal*. Calc. $C_{27}H_{24}N_4$ (pbpd): C, 80.2; H, 6.0; N, 13.9%. IR (KBr disc, cm^{-1}): ν(C=N) 1595. UV–Vis (MeCN): λ_{max}, 260 and 390 nm.

2.3.2. (N,N-diethyl,N′-(pyridin-2-yl)formylidene)-ethane-1,2-diamine (pfed) and (N,N-diethyl,N′-(pyridin-2-yl)benzylidene)-ethane-1,2-diamine (pbed)

The procedure is similar to the synthesis of pfpd/pbpd except that the reaction time is longer. *N*,*N*-diethylethane-1,2-diamine (0.116 g, 1 mmol) and pyridine-2-carboxaldehyde (0.107 g, 1 mmol) were refluxed in dehydrated alcohol (30 cm^3) for 12 h. The yellow solution was processed as above in case of pfpd to yield a semisolid, which was stored in vacuo over $CaCl_2$ for subsequent use. Yield: 0.153 g (75%). Pbed was prepared (yield, 78%) similarly using 2-benzoylpyridine instead of pyridine-2-carboxaldehyde. *Anal*. Calc. for $C_{12}H_{19}N_3$ (pfed): C, 70.2; H, 9.3; N, 20.4. Found: C, 70.4; H, 9.0; N, 20.7%. IR (KBr disc, cm^{-1}): ν(C=N) 1592. UV–Vis (MeCN): λ_{max}, 242 and 370 nm. Found: C, 76.3; H, 8.4; N, 14.6%. *Anal*. Calc. $C_{18}H_{23}N_3$ (pbed): C, 76.8; H, 8.3; N, 14.9%. IR (KBr disc, cm^{-1}): ν(C=N) 1590. UV–Vis (MeCN): λ_{max}, 245 and 372 nm.

2.4. Preparation of the complexes

Mononuclear type 1 complexes were prepared from both nitrate and perchlorate salts of cobalt(II) using 1:1:2 mole ratio of the metal salts, tetradentate blockers (pfpd and pbpd) and pseudohalides (azide, thiocyanate and cyanate). Type 2 compounds were isolated using a 1:1:3 ratio of the cobalt(II) salts, tridentate Schiff bases (pfed and pbed) and the pseudohalides. The typical syntheses with perchlorate salt are described below.

2.4.1. [Co(pfpd)$(N_3)_2$] (**1a**) and [Co(pbpd)$(N_3)_2$] (**1b**)

A methanolic solution (5 cm^3) of faint yellow pfpd (0.126 g, 1 mmol) was added dropwise to a pink Co$(ClO_4)_2 \cdot 6H_2O$ (0.183 g, 1 mmol) solution (5 cm^3) in the same solvent. To this NaN_3 (0.065 g, 2 mmol) in water (5 cm^3) was added slowly. The final red solution was filtered and left for slow evaporation in air at room temperature. After 3–4 days fine red microcrystalline product of **1a** separated out, which was filtered, washed with methanol and dried in vacuo over $CaCl_2$. Yield: 0.138 g (70%). Compound **1b** was prepared (yield, 72%) similarly except that pbpd instead of pfpd was used. *Anal*. Calc. for $C_{15}H_{16}N_{10}Co$ (**1a**): C, 45.58; H, 4.08; N, 35.43. Found: C, 45.72; H, 4.02; N, 35.65%. *Anal*. Calc. for $C_{27}H_{24}N_{10}Co$ (**1b**): C, 59.23; H, 4.42; N, 25.58. Found: C, 59.42; H, 4.45; N, 25.82%.

2.4.2. [Co(pfpd)$(NCS)_2$] (**1c**) and [Co(pbpd)$(NCS)_2$] (**1d**)

These were prepared (yield, 70–75%) using the same reaction condition and reaction stoichiometry as described in **1a/1b** except that NH_4NCS (2 mmol) in water (5 cm^3) instead of NaN_3 was added. The reaction solution was processed as above to result in crystalline **1c/1d**. *Anal*. Calc. for $C_{17}H_{16}N_6S_2Co$ (**1c**): C, 47.77; H, 3.77; N, 19.66. Found: C, 47.68; H, 4.72; N, 19.18%. *Anal*. Calc. for $C_{29}H_{24}N_6S_2Co$ (**1d**): C, 60.09; H, 4.17; N, 14.49. Found: C, 60.35; H, 4.22; N, 14.28.%.

2.4.3. [Co(pfpd)$(NCO)_2$] (**1e**) and [Co(pbpd)$(NCO)_2$] (**1f**)

These were also prepared (yield, 70–75%) using the same procedure as described in **1a/1b** except that NaNCO (2 mmol) in water (5 cm^3) instead of NaN_3 was added. *Anal*. Calc. for $C_{17}H_{16}N_6O_2Co$ (**1e**): C, 51.65; H, 4.08; N, 21.26. Found: C, 51.68; H, 4.10; N, 21.23%. *Anal*. Calc. for $C_{29}H_{24}N_6O_2Co$ (**1f**): C, 63.62; H, 4.42; N, 15.35. Found: C, 63.65; H, 4.40; N, 15.38%.

2.4.4. [Co(pfed)$(N_3)_3$] (**2a**) and [Co(pbed)$(N_3)_3$] (**2b**)

To a methanolic solution (5 cm^3) of Co$(ClO_4)_2 \cdot 6H_2O$ (0.183 g, 1 mmol) were added pfed (0.103 g, 1 mmol) in the same solvent (5 cm^3) and NaN_3 (0.098 g, 3 mmol) in water (5 cm^3). The deep wine red solution was filtered and was kept for slow evaporation. After 7 days **2a** was separated, washed with methanol and dried in vacuo over $CaCl_2$. Yield: 0.146 g (75%). Compound **2b** was prepared (yield, 72%) using a similar procedure as described above except that pbed instead of pfed was used. *Anal*. Calc. for $C_{12}H_{19}N_{12}Co$ (**2a**): C, 36.93; H, 4.91; N, 43.06. Found: C, 36.76; H, 3.84; N, 43.24%. *Anal*. Calc. for $C_{18}H_{23}N_{12}Co$ (**2b**): C, 46.35; H, 4.97; N, 36.04. Found: C, 46.27; H, 4.89; N, 36.22%.

2.4.5. [Co(pfed)$(NCS)_3$] (**2c**) and [Co(pbed)$(NCS)_3$] (**2d**)

These were prepared (yield, 70–72%) using the same reaction condition and reaction stoichiometry as described in **2a/2b** except that NH_4NCS (3 mmol) in water (5 cm^3) instead of NaN_3 was added. The reaction solution was processed as above to result in crystalline **2c/2d**. *Anal*. Calc. for $C_{15}H_{19}N_{12}S_3Co$ (**2c**): C, 34.48; H, 3.66; N, 32.17. Found: C, 34.60; H, 3.58; N, 32.10%. *Anal*. Calc. for $C_{21}H_{23}N_{12}S_3Co$ (**2d**): C, 42.13; H, 3.87; N, 28.08. Found: C, 42.25; H, 3.76; N, 28.25%.

2.4.6. [Co(pfed)(NCO)$_3$] (2e) and [Co(pbed)(NCO)$_3$] (**2f**)

These were also prepared (yield, 70–74%) using the same procedure as described in **2a**/**2b** except that NaNCO (3 mmol) in water (5 cm^3) instead of NaN_3 was added. *Anal*. Calc. for $C_{15}H_{19}N_{12}O_3Co$ (**2e**): C, 37.98; H, 4.04; N, 35.44. Found: C, 37.66; H, 4.07; N, 35.53%. *Anal*. Calc. for $C_{21}H_{23}N_{12}O_3Co$ (**2f**): C, 45.82; H, 4.21; N, 30.54. Found: C, 45.85; H, 4.01; N, 30.71%.

2.5. X-ray crystallographic analysis

Red single crystals of **1c** and dark brown crystals of **2b** suitable for X-ray analyses were obtained by slow evaporation of MeOH–H_2O (2:1) solutions of the reaction mixtures at room temperature (298 K). Diffraction data were measured at 293(2) K on a Siemens SMART CCD diffractometer equipped with a graphite monochromated Mo Kα (λ = 0.71073 Å) radiation. The unit cell parameters were determined by least-squares method using all observed reflections. A summary of the crystallographic data and structure refinement parameters is given in Table 1. Of 12050 and 13562 collected reflections, 4378 and 4956 unique reflections were recorded using ω-scan technique for **1c** and **2b**, respectively. The intensity data were corrected for Lorentzian polarization effects and an empirical absorption correction based on ψ scans was employed [16]. The structures were solved by the heavy atom method using SHELXS-97 [17] and successive difference Fourier syntheses. All non-hydrogen atoms were refined anisotropically. The hydrogen atoms were fixed geometrically and refined using a riding model. In the final difference Fourier map the residual maxima and minima for **1c** and **2b** were 0.268 and −0.241 and 0.501 and −0.346 e Å^{-3}, respectively. All calculations were carried out using SHELXL-97 [18].

3. Results and discussion

3.1. Synthesis and formulation

The hexacoordinated mononuclear complex [Co(pfpd)(NCS)$_2$] (**1c**) was initially formed in aqueous methanolic solution containing a 1:1:1 mixture of $Co(ClO_4)_2 \cdot 6H_2O$, pfpd and NH_4NCS – a reactant ratio expected to yield a dithiocyanato bridged dinuclear species of the composition $[(pfpd)Co^{II}(NCS)_2Co^{II}(pfpd)](ClO_4)_2$. However, microanalyses showed a 1:1:2 ratio of metal, blocking ligand and pseudohalide, and in the IR spectrum, no presence of perchlorate bands was noticed. Reactant ratio corresponding to the product stoichiometry afforded better yield of **1c**. An effort to get dinuclear

Table 1
Crystallographic data of [Co(pfpd)(NCS)$_2$] (**1c**) and [Co(pbed)(N$_3$)$_3$] (**2b**)

Complex	**1c**	**2b**
Empirical formula	$C_{17}H_{16}N_6S_2Co$	$C_{18}H_{23}N_{12}Co$
Formula weight	427.41	466.41
Colour	orange	dark brown
T (K)	293(2)	293(2)
λ (Å)	0.71073	0.71073
Crystal system	monoclinic	monoclinic
Space group	$P2_1/c$	$P2_1/c$
a (Å)	8.3095(5)	7.9753(6)
b (Å)	9.5110(6)	13.4972(11)
c (Å)	24.6886(16)	20.3435(16)
β (°)	98.2490(10)	99.789(2)
V (Å^3)	1931.0(2)	2158.0(3)
Z	4	4
D_{calc} (Mg m^{-3})	1.470	1.436
μ (mm^{-1})	1.118	0.828
F(000)	876	968
Crystal size (mm^3)	0.38 × 0.27 × 0.22	0.40 × 0.15 × 0.10
θ ranges (°)	2.30–27.51	1.82–27.54
$h/k/l$	−10,10/−12,12/−19,31	−9,10/−17,14/−26,16
Reflections collected	12050	13562
Independent reflections (R_{int})	4378 (0.0235)	4956 (0.0310)
Completeness to θ (°)	98.6	99.3
T_{max} and T_{min}	0.9486 and 0.7756	0.9486 and 0.6709
Data/restraints/parameters	4378/0/253	4956/0/282
Goodness-of-fit on F^2	0.788	0.745
Final R indices [$I > 2\sigma(I)$]	R_1 = 0.0308, wR_2 = 0.0578	R_1 = 0.0347, wR_2 = 0.0619
R indices (all data)	R_1 = 0.0647, wR_2 = 0.0634	R_1 = 0.0750, wR_2 = 0.0684
Largest peak and hole (e Å^{-3})	0.268 and −0.241	0.501 and −0.346

species, in which the starting material was changed to $Co(NO_3)_2 \cdot 6H_2O$, and a 1:1:1 molar ratio of the nitrate salt, ligand and pseudohalide followed by addition of extraneous KPF_6 (2 equivalent) produced **1c** with lower yield. Use of a 1:1:2 molar ratio of nitrate salt, Schiff base and azide results in **1c** in good yield. The different syntheses are reproducible. Change of ligands from pfpd to pbpd and the pseudohalides from NCS^- to N_3^- and NCO^- showed similar behaviour and compounds $[Co(pfpd)(N_3)_2]$ (**1a**), $[Co(pbpd)(N_3)_2]$ (**1b**), $[Co(pbpd)(NCS)_2]$ (**1d**), $[Co(pfpd)(NCO)_2]$ (**1e**) and $[Co(pbpd)(NCO)_2]$ (**1f**) were isolated. Changing the tetradentate Schiff bases (L^1 = pfpd or pbpd) to tridentate Schiff bases (L^2 = pfed or pbed) and use of metal perchlorate, organic ligand and pseudohalide in 1:1:1.5 molar ratio – a reactant ratio expected to yield a triazido bridged dinuclear species of the composition $[(L^2)Co^{III}(N_3)_3Co^{III}(L^2)]ClO_4$, resulted mononuclear complexes of the type $[Co(L^2)(X)_3]$ (L = pfed, $X = N_3^-$, **2a**; NCS^-, **2b**; NCO^-, **2c**; L = pbed, $X = N_3^-$, **2d**; NCS^-, **2e**; NCO^-, **2f**). Microanalyses showed a 1:1:3 ratio of metal, blocking ligand and pseudohalide, and once again in the IR spectrum, no presence of perchlorate bands was noticed. Use of required molar ratios of the building units corresponding to formulation of the product afforded better yields of **2**. With a view to getting tribridged dinuclear species, the starting material was changed to $Co(NO_3)_2 \cdot 6H_2O$, and a 1:1:1.5 molar ratio of the nitrate salt, ligand and pseudohalide followed by addition of extraneous KPF_6 (1 equivalent). This also produced **2** but in lower yield. Use of a 1:1:3 molar ratio of nitrate salt, Schiff base and azide results in **2** in good yield. Once again all these syntheses are reproducible.

The complexes **1** and **2** are sufficiently stable in air and in the presence of moisture. Analytical data for all the complexes are consistent with the calculated values. The compounds are soluble in a range of common organic solvents like methanol, acetonitrile, dimethylformamide and dimethylsulphoxide but are insoluble in water. In MeCN they behave as non-electrolytes as are indicated [19] by their very low Λ_M ($\sim$5 Ω^{-1} cm^2 mol^{-1}) values. Room-temperature solid-phase magnetic susceptibility measurements show that type **1** complexes behave as three-electron paramagnets with μ_{eff} value $\sim$3.9 BM whereas type **2** compounds are diamagnetic (singlet ground state with t_{2g}^6 configuration) (Table 2). In the IR spectra, the most striking observation in type **1** complexes is a sharp, single, intense band of the pseudohalides. Compounds **1a** and **1b** show the asymmetric stretch as a strong band at about 2030 cm^{-1}. Compounds **1c** and **1d** exhibit ν_{as}(CN) stretching vibration at about 2100 cm^{-1}. The position of the signal strongly suggests N-coordination of bound isothiocyanate [10]. Compounds **1e** and **1f** display asymmetric cyanate stretching vibration at about 2050 cm^{-1} which is substantially higher than the free ion value [20] and is consistent [21] with N-bonding rather O-bonding. The single band in each case is in line with the presence of *trans*-CoX_2 ($X = N_3^-$, NCS^-, NCO^-) frame in $[Co(L^1)(X)_2]$. Three distinct splittings (vide Table 2) of asymmetric stretching vibrations of the terminal pseudohalides in type **2** compounds are strongly suggestive of the less symmetric *meridional* structure over the more symmetric *facial* arrangement. The ν(C=N) stretching vibrations of the metal bound Schiff bases are seen at around 1590 cm^{-1}. Several bands in the range 2800–3000 cm^{-1} are assigned to the aliphatic ν(CH) stretching vibration of ligand. All other characteristic L vibrations are seen in the 1600–600 cm^{-1} range. X-ray structures of **1c** and **2b** show definite proof of this hypothesis.

The complexes exhibit several absorption bands in MeCN solutions in the 200–900 nm range. The high

Table 2
Some characterization data of the complexes

Compound	IR[a] (cm^{-1}) ν_{as}(X)	UV–Vis[b] λ_{max}, nm (10^{-3} ε M^{-1} cm^{-1})	Λ_M[c] (Ω^{-1} cm^2 mol^{-1})	μ_{eff} (BM)	Co^{III}–Co^{II} E°_{298}, V (ΔE_p, mV)[e]
1a	2025	552 (0.55), 412 (0.73), 384 (12.76)	3	3.88	0.32 (70)
1b	2028	554 (0.54), 415 (0.70), 382 (12.98)	4	3.87	0.33 (70)
1c	2095	555 (0.52), 412 (0.72), 384 (12.78)	3	3.86	0.33 (70)
1d	2098	551 (0.55), 410 (0.75), 382 (13.01)	5	3.85	0.34 (70)
1e	2250	550 (0.56), 413 (0.71), 380 (13.12)	4	3.86	0.31 (70)
1f	2248	556 (0.52), 415 (0.69), 385 (12.68)	5	3.87	0.32 (70)
2a	2002, 2010, 2025	508 (0.68), 404 (0.74), 332 (16.82)	3	[d]	0.36 (70)
2b	2004, 2008, 2026	510 (0.66), 406 (0.71), 330 (16.71)	4	[d]	0.37 (70)
2c	2061, 2077, 2095	512 (0.64), 402 (0.76), 334 (16.23)	5	[d]	0.34 (70)
2d	2060, 2078, 2098	511 (0.63), 402 (0.75), 328 (17.08)	4	[d]	0.36 (70)
2e	2255, 2235, 2218	510 (0.65), 404 (0.73), 332 (16.79)	5	[d]	0.34 (70)
2f	2252, 2233, 2215	512 (0.63), 406 (0.70), 333 (16.74)	4	[d]	0.35 (70)

[a] KBr disc.
[b] In MeCN at 298 K.
[c] In MeCN at 298 K.
[d] Diamagnetic.
[e] Working electrode is platinum.

intensity band below 400 nm is of ligand origin assignable [11b] to intraligand n–π*/π–π* transition. Above this wavelength the transitions are LMCT for cobalt(III) complexes and MLCT type for cobalt(II) members as are evident from their intensity values (Table 2). The bands show systematic blue shift in going from type **1** to type **2** complexes. The spectral pattern supports [22] six-coordinate distorted octahedral symmetry around cobalt centre.

3.2. X-ray crystal structures

3.2.1. Crystal structure of [Co(pfpd)(NCS)$_2$] (**1c**)

An ORTEP view with atom numbering scheme of the mononuclear dithiocyanato complex, **1c**, is shown in Fig. 1. Selected bond lengths and angles relevant to the coordination sphere are listed in Table 3. The cobalt(II) centre is best described as a distorted octahedron with a CoN_6 chromophore. Distortion from the ideal octahedral geometry is due to the asymmetric nature of the bound tetradentate Schiff base and the deviations of the refine angles (90°/180°) formed at the metal centre (Table 3). The coordination includes two pyridine nitrogens [N(3), N(6)], two imine nitrogens [N(4), N(5)] of the Schiff base and two nitrogens [N(1), N(2)] of the terminal thiocyanates. The equatorial positions are occupied with the four nitrogen atoms [N(3), N(4), N(5) and N(6)] of the tetradentate ligand while the nitrogens [N(1), N(2)] of the isothiocyanato groups are placed at the axial positions. The degrees of distortion of the coordination sphere are reflected in the *cisoid* [77.11(7)–113.07(7)°] and the *transoid* angles [169.47(7)–174.59(7)°]. The equatorial Co–N distances are in the range [2.0982(17)–2.1695(18) Å], comparable to the corresponding values in similar systems [1–3]. Axial

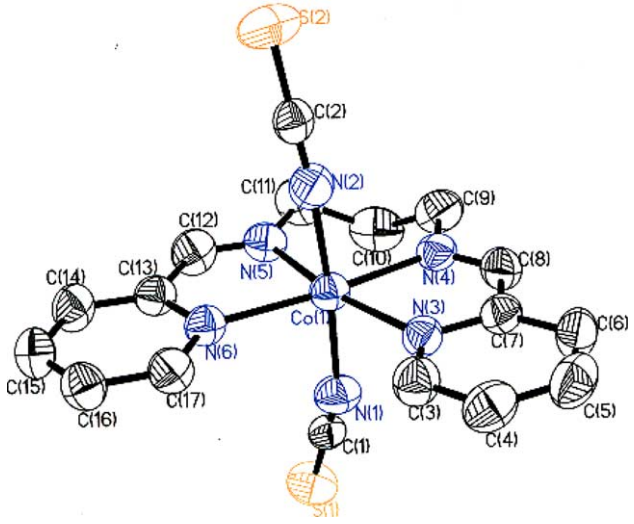


Fig. 1. ORTEP view of [Co(pfpd)(NCS)$_2$] (**1c**) with atom numbering scheme and 40% probability ellipsoids for all non-hydrogen atoms.

Table 3
Selected bond lengths (Å) and bond angles (°) for [Co(pfpd)(NCS)$_2$] (**1c**)

Bond distances (Å)	
Co(1)–N(2)	2.0813(18)
Co(1)–N(1)	2.0844(19)
Co(1)–N(4)	2.0982(17)
Co(1)–N(5)	2.1061(18)
Co(1)–N(6)	2.1591(17)
Co(1)–N(3)	2.1695(18)
S(1)–C(1)	1.621(2)
S(2)–C(2)	1.618(2)
N(1)–C(1)	1.160(1)
N(2)–C(2)	1.152(2)
Bond angles (°)	
N(2)–Co(1)–N(1)	174.59(7)
N(2)–Co(1)–N(4)	93.73(7)
N(1)–Co(1)–N(4)	91.64(7)
N(2)–Co(1)–N(5)	89.91(7)
N(1)–Co(1)–N(5)	90.54(7)
N(4)–Co(1)–N(5)	92.45(8)
N(2)–Co(1)–N(6)	87.27(7)
N(1)–Co(1)–N(6)	87.56(7)
N(4)–Co(1)–N(6)	169.80(8)
N(5)–Co(1)–N(6)	77.40(7)
N(2)–Co(1)–N(3)	89.49(7)
N(1)–Co(1)–N(3)	91.05(7)
N(4)–Co(1)–N(3)	77.11(7)
N(5)–Co(1)–N(3)	169.47(7)
N(6)–Co(1)–N(3)	113.07(7)
C(1)–N(1)–Co(1)	156.96(19)
C(2)–N(2)–Co(1)	170.25(19)
N(1)–C(1)–S(1)	178.7(2)
N(2)–C(2)–S(2)	178.7(2)

Co–N distances [2.0813(18)–2.0844(19) Å] indicate stronger coordination of the anionic isothiocyanate over neutral Schiff base. The *trans* N1–Co1–N2 angle has a value [174.59(7)°] close to the ideal 180.00°. The angles N(6)–Co(1)–N(5), N(5)–Co(1)–N(4) and N(4)–Co(1)–N(3) in the equatorial plane have values 77.40(7)°, 92.45(8)° and 77.11(7)°, respectively, which are much less than the N(3)–Co(1)–N(6) angle [113.07(7)°] where N(3) and N(6) belong to the two ends of the tetradentate Schiff base. Both isothiocyanates are almost linear with the same N–C–S angle 178.7(2)°. N–C [1.152(2)–1.160(2) Å] and C–S [1.618(2)–1.621(2) Å] bond lengths are as expected for N-coordination [12]. The bond lengths and angles pertaining the ligand network are close to expected values [9–11]. The propylenic part [N(5)–C(11)–C(10)–C(9)–N(4)] of the Schiff base is to some extent puckered. The sequestering of cobalt(II) by four hard N donor centres of the tetradentate chelator (pfpd) imparts hardness to the metal centre even in low oxidation state; this influences preferential N-coordination of both the terminal NCS^- ions through electronegative hard N donor centres (Fig. 1) ignoring the other possibilities, viz., both S-coordination and N- plus S-coordinations.

3.2.2. Crystal structure of [Co(pbed)(N_3)$_3$] (**2b**)

An ORTEP diagram of the mononuclear triazido compound **2b**, is displayed in Fig. 2. Selected bond lengths and angles pertaining to the coordination sphere are set in Table 4. The cobalt(III) centre adopts a distorted octahedral coordination sphere with a CoN_6 chromophore. Three nitrogen atoms [N(10), N(11), N(12)] of the tridentate Schiff base in combination with three nitrogen atoms [N(1), N(4), N(7)] of three different azides in a *meridional* alignment complete octahedral coordination of the metal ion. The equatorial positions are occupied by the three nitrogen atoms [N(10), N(11), N(12)] of the tridentate blocker and one nitrogen atom [N(4)] of the terminal azide while other two nitrogen atoms [N(1), N(7)] of the two azides are placed at the axial positions. Distortion from the ideal octahedral geometry is due to the asymmetric nature of the bound tridentate Schiff base and the deviations of the refine angles (90°/180°) formed at the metal centre (Table 4). The degrees of distortion from an ideal octahedral (90°) geometry are reflected in the *cisoid* [87.64(8)–96.69(8)°] and the *transoid* [167.90(7)–177.26(8)°] angles. Azide Co–N distances [1.9451(19)–1.9801(18) Å] indicate stronger coordination of the anionic terminals over those [1.8858(17)–2.0544(18) Å] of neutral Schiff base chelator. The azide terminals are almost linear with N–N–N angles 175.6(2)–177.7(2)°. N(1)–N(2) [1.185(2) Å], N(4)–N(5) [1.198(2) Å] and N(7)–N(8) [1.198(2) Å] distances are longer than the N(2)–N(3) [1.158(2) Å], N(5)–N(6) [1.150(3) Å] and N(8)–N(9) [1.160(2) Å] in usual manner [9–11] reflecting N(1), N(4) and N(7) connection of the pseudohalides. The ethylenic part [N(11)–C(13)–C(14)–N(10)] of the Schiff base is also to some extent puckered (Fig. 2) which has significant effect on variation of equatorial angles.

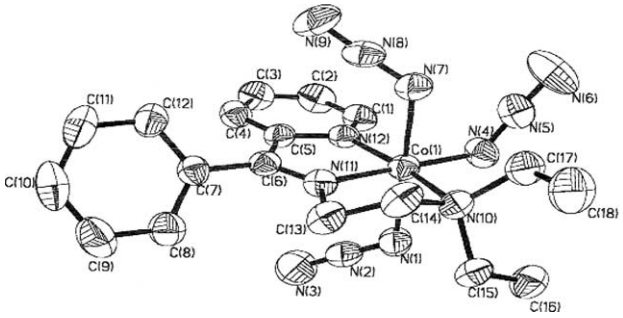


Fig. 2. ORTEP plot of [Co(pbed)(N_3)$_3$] (**2b**) with atom numbering scheme and 40% probability ellipsoids for all non-hydrogen atoms.

Table 4
Selected bond distances (Å) and bond angles (°) for [Co(pbed)(N_3)$_3$] (**2b**)

Bond distances (Å)	
Co(1)–N(1)	1.9801(18)
Co(1)–N(4)	1.9451(19)
Co(1)–N(7)	1.9637(19)
Co(1)–N(10)	2.0544(18)
Co(1)–N(11)	1.8858(17)
Co(1)–N(12)	1.9290(17)
N(1)–N(2)	1.185(2)
N(2)–N(3)	1.158(2)
N(4)–N(5)	1.198(2)
N(5)–N(6)	1.150(3)
N(7)–N(8)	1.198(2)
N(8)–N(9)	1.160(2)
Bond angles (°)	
N(2)–N(1)–Co(1)	119.14(15)
N(5)–N(4)–Co(1)	122.72(16)
N(8)–N(7)–Co(1)	120.11(16)
N(1)–Co(1)–N(10)	94.12(8)
N(4)–Co(1)–N(1)	87.64(8)
N(7)–Co(1)–N(1)	177.26(8)
N(12)–Co(1)–N(1)	88.29(8)
N(11)–Co(1)–N(1)	90.20(8)
N(4)–Co(1)–N(7)	90.67(9)
N(12)–Co(1)–N(10)	167.90(7)
N(4)–Co(1)–N(10)	96.69(8)
N(7)–Co(1)–N(10)	88.22(8)
N(3)–N(2)–N(1)	177.6(2)
N(6)–N(5)–N(4)	175.6(3)
N(9)–N(8)–N(7)	177.7(2)

3.3. Electrochemical properties

The electroactivity of the complexes was examined in MeCN solutions using cyclic voltammetry (CV) at a platinum-working electrode. A representative voltammogram is shown in Fig. 3. The complexes show (Table 2) nearly reversible (ΔE_p = 70–90 mV) oxidative response (for type **1**) and reductive response (for type **2**) presumably due to Co^{III}–Co^{II} couple as is shown in the following reactions:

$$[Co^{III}(L^1)(X)_2]^{1+} + e^- \rightleftharpoons [Co^{II}(L^1)(X)_2] \quad (1)$$

$$[Co^{III}(L^2)(X)_3] + e^- \rightleftharpoons [Co^{II}(L^2)(X)_3]^{1-} \quad (2)$$

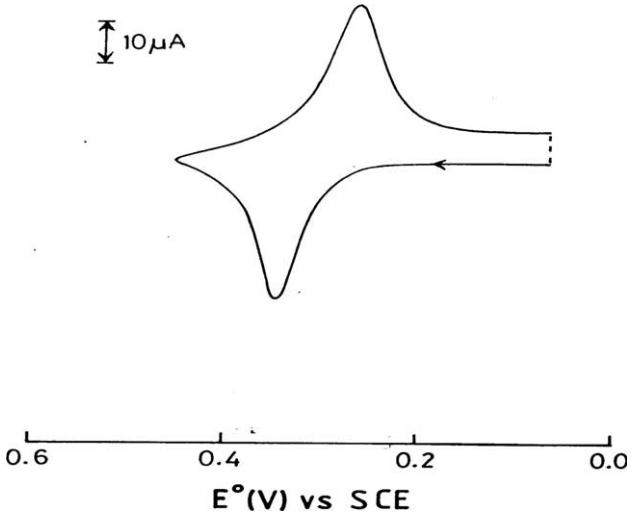


Fig. 3. Cyclic voltammogram of **2b** in MeCN at 298 K.

Table 5
Photophysical data for **1c** and **2b**

Compound	Emission (λ/nm)		Lifetime (ns)
	Fluorescence[a]	Phosphorescence[b]	
1c	478	550	2.33
2b	476	548	2.42

[a] In MeOH at room temperature (298 K).
[b] In MeOH at 77 K.

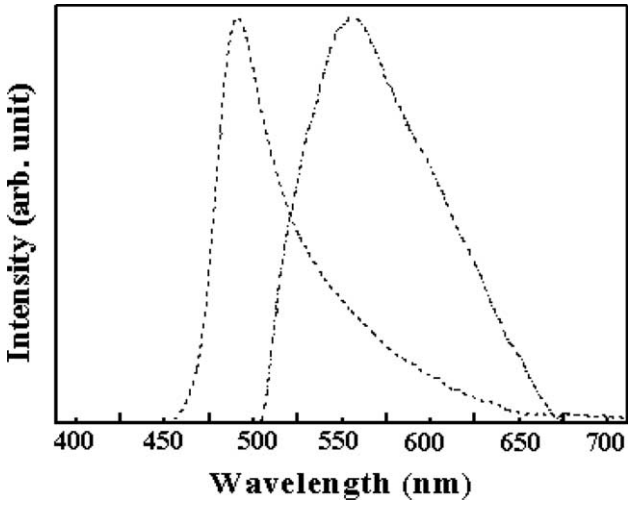


Fig. 4. Fluorescence (- - - - - -) in MeOH solution at 298 K, phosphorescence (·—·—·) in MeOH glass at 77 K of **1c**.

The responses are reproducible with no trace of decomposition after a number of cycles. The formal potentials lie close to ~0.3 V versus SCE. One-electron nature of the couple was verified with cobalt(II)azido complexes of arylazoimidazole ligands [23].

3.4. Luminescence properties

The spectroscopic data of selected complexes in methanol solutions and glasses are listed in Table 5. Compound **1c** shows emission at 478 nm while compound **2b** has a band at 476 nm at 298 K. These are assignable to intraligand $^1(\pi–\pi^*)$ fluorescence. A representative pattern is shown in Fig. 4. The lifetimes for **1c** and **2b** are 2.33 and 2.42 ns, respectively. In glassy solutions (77 K) a red shift is observable (550 nm for **1c** and 548 nm for **2b**) which is presumably due to $^3(\pi–\pi^*)$ phosphorescence [10].

4. Conclusion

We have prepared two different sets of cobalt(II) and cobalt(III) pseudohalide complexes by changing denticities of the Schiff base blockers. Structures of two representative complexes, $[Co(pfpd)(NCS)_2]$ (**1c**) and $[Co(pbed)(N_3)_3]$ (**2b**), are solved by X-ray study. Spectroscopic, electrochemical and other physicochemical properties strongly suggest that the structures **1a**, **1b** and **1d**–**1f** are cognate with **1c**, whereas **2a** and **2c**–**2f** with **2b**. The neutral tetradentate Schiff bases in combination with two monodentate pseudohalide ions satisfy hexacoordination of cobalt(II) as well as its charge; such a combination simultaneously satisfying both coordination number and charge of central ion results in stabilization of +2 oxidation state of the central. Similarly, judicious choice of one tridentate neutral Schiff base ligand and three pseudohalide ions satisfies hexacoordination of the central ion and its +3 oxidation level. This work shows that control of oxidation state of metal ion can be done through judicious choice of ligand matrices so as to satisfy coordination number and charge of metal ions simultaneously. The new complexes are good examples of luminous materials.

5. Supplementary data

Crystallographic data for the structure analysis have been deposited with the Cambridge Crystallographic Data Centre Nos. 210735 for $[Co(pfpd)(NCS)_2]$ (**1c**) and 240924 for $[Co(pbed)(N_3)_3]$ (**2b**). Copies of this information can be obtained free of charge from The Director, CCDC, 12 Union Road, Cambridge CB2 1EZ, UK (fax: +44 1223 336 033; e-mail: deposit@ccdc.cam.ac.uk or www:http://www.ccdc.cam.ac.uk).

Acknowledgements

The authors are grateful to the Department of Science and Technology (DST) and Council of Scientific and Industrial Research (CSIR) New Delhi, India for financial support.

References

[1] F.A. Cotton, G. Willkinson, C.A. Murrilo, M. Bochmann, Advanced Inorganic Chemistry, 6th ed., Wiley, New York, 1999, p. 598.
[2] (a) V.G. Makhankova, O.Y. Vassilyeva, V.N. Kokozay, J. Reedijk, G.A. Vanalbada, J. Jezierska, B.W. Skelton, Eur. J. Inorg. Chem. (2002) 2163;
(b) C. Demunno, F. Cipriani, D. Armentano, M. Julve, J.A. Real, New J. Chem. 25 (2001) 1031.
[3] (a) D.M. Ciurtin, Y.B. Dong, M.D. Smith, T. Barclay, H.C. Zurloye, Inorg. Chem. 40 (2001) 2825;
(b) C.J. Matthews, L.K. Thompson, S.R. Parsons, Z. Xu, D.O. Miller, S.L. Heath, Inorg. Chem. 40 (2001) 4448;
(c) A. Sreekanth, U.L. Kala, C.R. Nayar, M.R.P. Kurup, Polyhedron 23 (2004) 41.
[4] B. Cornils, W.A. Herrmann, R. Schlogl (Eds.), Catalysis from A to Z: A Concise Encyclopedia, Wiley, New York, 2000.

[5] (a) J.R. Farraro, J.M. Williams, Introduction to Synthetic Electrical Conductors, Academic Press, New York, 1987;
(b) G.W. Gokel, A. Mukhopadhyay, Chem. Soc. Rev. 30 (2001) 274.
[6] (a) O. Kahn, Molecular Magnetism, VCH, New York, 1993;
(b) J.S. Miller, M. Drillon (Eds.), Magnetism: Molecules to Materials IV, Wiley–VCH, Weinheim, 2003.
[7] (a) D. Demus, J.W. Goodby, G.W. Gray, H.-W. Spiess, V. Vill (Eds.), Handbook of Liquid Crystals, Wiley–VCH, Weinheim, 1998;
(b) O.R. Evans, W. Lin, Acc. Chem. Res. 35 (2002) 511.
[8] (a) Special Issue on Focus on Self-Assembly, Acc. Chem. Res. 32 (1999) No. 4;
(b) B.J. Holliday, C.A. Mirkin, Angew. Chem. Int. Ed. 40 (2001) 2023.
[9] T.K. Karmakar, S.K. Chandra, J. Ribas, G. Mostafa, T.-H. Lu, B.K. Ghosh, Chem. Commun. (2002) 2364.
[10] D. Bose, J. Banerjee, Sk.H. Rahaman, G. Mostafa, H.-K. Fun, R.D. Bailey Walsh, M.J. Zaworotko, B.K. Ghosh, Polyhedron 23 (2004) 2045.
[11] (a) J. Banerjee, D. Bose, Sk.H. Rahaman, R.D. Bailey Walsh, M.J. Zaworotko, B.K. Ghosh, Indian J. Chem. A 43 (2004) 1119;
(b) Sk.H. Rahaman, R. Ghosh, D. Bose, H.-K. Fun, B.K. Ghosh, Indian J. Chem. A 43 (2004) 1901.
[12] (a) A.M. Golub, H. Kohler, V.V. Skopenko (Eds.), Chemistry of Pseudohalides, Elsevier, Amsterdam, 1986;
(b) J. Ribas, A. Escuer, M. Monfot, R. Vicente, R. Cortes, L. Lezama, T. Rojo, Coord. Chem. Rev. 193 (1999) 102.
[13] (a) V. Alexander, Chem. Rev. 95 (1995) 273;
(b) A.D. Garnovskii, A.L. Nivorozhkin, V.I. Minkin, Coord. Chem. Rev. 126 (1993) 1.
[14] D.T. Sawyer, J.L. RobertsJr. (Eds.), Experimental Electrochemistry for Chemists, Wiley, New York, 2000, p. 167.
[15] D. Bose, H. Rahaman, J. Banerjee, N.K. Mondal, B.K. Ghosh, Indian J. Chem. A 41 (2002) 1374.
[16] G.M. Sheldrick, SHELXL-Plus, Siemens Analytical X-ray Instruments, Inc., Madison, WI, USA, 1990.
[17] G.M. Sheldrick, SHELXS-97: Program for Refinement of Crystal Structures, University of Göttingen, Göttingen, Germany, 1997.
[18] G.M. Sheldrick, SHELXL-97: Program for Refinement of Crystal Structures, University of Göttingen, Göttingen, Germany, 1997.
[19] W.J. Geary, Coord. Chem. Rev. 7 (1971) 81.
[20] K. Nakamoto, Infrared and Raman Spectra of Inorganic and Coordination Compounds, Part B: Application in coordination, Organometalic, and Bioinorganic Chemistry, 5th ed., Wiley, New York, 1997, p. 171.
[21] M.A.S. Goher, F.A. Mautner, J. Chem. Soc., Dalton Trans. (1999) 1923.
[22] A.B.P. Lever, Inorganic Electronic Spectroscopy, 2nd ed., Elsevier, New York, 1984.
[23] U. Ray, B. Chand, G. Mostafa, J. Cheng, T.-H. Lu, C. Sinha, Polyhedron 22 (2003) 2587.

Based on the previous considerations, we are initiating a line of investigation on the coordination chemistry of compounds containing thiazine and 2-aminobenzimidazole rings. In this paper, we report the characterization by elemental analysis, infrared spectra (IR), ultraviolet and visible spectra (UV–Vis), single crystal X-ray diffraction, proton nuclear magnetic resonance (^{1}H NMR) and carbon nuclear magnetic resonance (^{13}C NMR) of *N*-(5,6-dihydro-4H-1,3-thiazin-2-yl)-2-aminobenzimidazole (BzTz). Contrary to what we had thought, the ligand BzTz acts as monodentate through nitrogen atom of benzimidazole ring, the thiazine ring being uncoordinated. Thus, the Cd(II) and Co(II) complexes have been isolated and their characterization has been carried out by means of elemental analysis, IR and X-ray diffraction. The cobalt complex has also been characterized through UV–Vis-NIR diffuse reflectance and magnetic susceptibility measurement, and whereas, in the case of the cadmium complex, through proton nuclear magnetic resonance (^{1}H NMR), carbon nuclear magnetic resonance (^{13}C NMR) and ultraviolet and visible spectra (UV–Vis).

2. Experimental

2.1. Preparation of N-(5,6-dihydro-4H-1,3-thiazin-2-yl)-2-aminobenzimidazole (BzTz)

BzTz was prepared according to the procedure reported by Haugwitz et al. [18]. The resulting oil was flash chromatographed using 2:1 v/v glyme/ether as eluent. Last fraction contained BzTz. The product was recrystallized from glyme. ^{1}H NMR ($CDCl_3$): δ 7.74 (d, J = 8.1 Hz, 1H), 7.34 (d, J = 7.9 Hz, 1H), 7.14 (t, J = 7.6 Hz, 1H), 7.01 (t, J = 7.7 Hz, 1H), 6.45 (s, 2H), 3.90 (t, J = 5.5 Hz, 2H), 3.22 (t, J = 6.0 Hz, 2H), 1.98 (m, 2H); ^{13}C NMR ($CDCl_3$): δ 153.3, 147.9, 142.0, 131.0, 122.8, 119.5, 116.2, 112.2, 46.5, 26.9, 19.1. *Anal.* Calc. for $C_{11}H_{12}N_4S$: C, 56.87; H, 5.21; N, 24.12; S, 13.80. Found: C, 56.72; H, 5.24; N, 23.83; S, 14.05%. UV–Vis (EtOH): λ_{max}, nm; (ε, L mol^{-1} cm^{-1}) 211 (22 693), 242 (21 171), 280 (7034).

2.2. Preparation of [$CoCl_2$(BzTz)$_2$]

This complex was prepared by reacting a methanol solution (1 mL) of $CoCl_2 \cdot 6H_2O$ (102.4 mg, 0.43 mmol) with a methanol solution (15 mL) of BzTz (100 mg, 0.43 mmol), obtaining blue powder which was dissolved in chloroform and by means of liquid-vapour diffusion of ether over this chloroform solution, blue crystals were isolated (110.5 mg, 43.2%). The crystals were filtrated and washed with cold ether and air-dried. *Anal.* Calc. for $C_{22}H_{24}CoN_8S_2Cl_2$: C, 44.45; H, 4.07; N, 18.85; S, 10.79. Found: C, 44.15; H, 4.11; N, 18.65; S, 10.59%.

2.3. Preparation of [$CdCl_2$(BzTz)$_2$]

This complex was prepared by reacting a methanol solution (1 mL) of $CdCl_2 \cdot 2.5H_2O$ (98.3 mg, 0.43 mmol) with a methanol solution (15 mL) of BzTz (100 mg, 0.43 mmol), being obtained colourless crystals after a slow evaporation of the solution at room temperature (125.0 mg, 44.9%). The crystals were filtrated and washed with cold ether and air-dried. ^{1}H NMR ($CDCl_3$): δ 7.76 (s, 2H), 7.75 (d, J = 8.4 Hz, 1H), 7.59 (d, J = 7.6 Hz, 1H), 7.13 (t, J = 7.6 Hz, 1H), 7.03 (t, J = 8.0 Hz, 1H), 3.96 (t, J = 5.6 Hz, 2H), 3.29 (t, J = 6.0 Hz, 2H), 2.05 (m, 2H); ^{13}C NMR ($CDCl_3$): δ 154.5, 147.8, 138.2, 129.4, 124.1, 121.1, 115.4, 112.8, 46.6, 27.2, 19.0. *Anal.* Calc. for $C_{22}H_{24}CdN_8S_2Cl_2$: C, 40.78; H, 3.73; N, 17.30; S, 9.90. Found: C, 40.54; H, 3.87; N, 17.09; S, 9.63%. UV–Vis (EtOH): λ_{max}, nm; (ε, L mol^{-1} cm^{-1}) 208 (65 207), 243 (36 740), 276 (11 507).

2.4. Instrumental procedures

Chemical analyses of carbon, hydrogen, nitrogen and sulfur were performed by microanalytical methods using a Leco CHNS-932 microanalyser. IR spectra were recorded on a Perkin–Elmer FT-IR 1720 spectrophotometer, from KBr pellets in the 4000–370 cm^{-1} range and on a Perkin–Elmer FT-IR 1700X spectrophotometer, from polyethylene pellets in the 500–150 cm^{-1} range. Electronic spectra in solution of ligand and the cadmium complex were measured on a Shimadzu UV-3101 PC using a 10 mm quartz cell. The UV–Vis-NIR reflectance spectra for the cobalt complex in the 200–1800 nm range was registered from a pellet of the sample, using a Shimadzu UV-3101 PC spectrophotometer and $BaSO_4$ as a reference. Magnetic measurement was made at room temperature on a magnetometer with pendulum MANICS DSM8, equipped with helium continuous-flow cryostat and an electromagnetometer DRUSCH EAF 16 UE. Data were corrected for temperature-independent paramagnetism and diamagnetic contributions, which were estimated from the Pascal constants. ^{1}H and ^{13}C NMR spectra were obtained with a Bruker AM 400 instrument at 400 and 100 MHz, respectively, in $CDCl_3$ using Me_4Si as internal standard.

2.5. Crystal structure determinations

Experimental details of crystal structure determinations including crystal data, data collection, structure determination and refinement parameters for BzTz, [$CoCl_2$(BzTz)$_2$] and [$CdCl_2$(BzTz)$_2$] are listed in Table 1. X-ray diffraction measurements were performed at room temperature (298 K) using a Bruker SMART CCD diffractometer equipped with graphite-monochromated Mo Kα radiation (λ = 0.71073 Å) using the ϕ–ω

Table 1
Crystal data, data collection and refinement details for BzTz, $[CoCl_2(BzTz)_2]$ and $[CdCl_2(BzTz)_2]$

	BzTz	$[CoCl_2(BzTz)_2]$	$[CdCl_2(BzTz)_2]$
Crystal shape	prism	prism	prism
Colour	colourless	blue	colourless
Size (mm)	$0.53 \times 0.43 \times 0.31$	$0.50 \times 0.45 \times 0.35$	$0.57 \times 0.37 \times 0.27$
Chemical formula	$C_{11}H_{12}N_4S$	$C_{22}H_{24}Cl_2CoN_8S_2$	$C_{22}H_{24}Cl_2CdN_8S_2$
Formula weight	232.3	594.5	647.9
Crystal system	monoclinic	monoclinic	monoclinic
Space group	*C2/c*	*Cc*	$P2_1/n$
Unit cell dimensions			
a (Å)	26.050(2)	11.565(1)	11.084(1)
b (Å)	7.832(1)	18.111(2)	13.777(1)
c (Å)	11.316(1)	12.657(1)	16.852(1)
β (°)	94.668(2)	104.727(2)	97.271(1)
Cell volume (Å^3)	2301.1(3)	2563.9(4)	2552.6(2)
Z	8	4	4
D_{calc} (g cm^{-3})	1.341	1.540	1.686
μ (mm^{-1})	0.259	1.069	1.258
F(0 0 0)	976	1220	1304
2θ range	5.44–56.54	4.82–51.44	3.84–56.62
Index ranges	$-26 \leqslant h \leqslant 34$, $-9 \leqslant k \leqslant 10$, $-13 \leqslant l \leqslant 15$	$-14 \leqslant h \leqslant 14$, $-22 \leqslant k \leqslant 22$, $-15 \leqslant l \leqslant 9$	$-12 \leqslant h \leqslant 14$, $-17 \leqslant k \leqslant 12$, $-21 \leqslant l \leqslant 19$
Independent reflections	2725	3456	5705
Observed reflections	2032[$F > 4.0\sigma(F)$]	3229 [$F > 4.0\sigma$(F)]	5092 [$F > 4.0\sigma(F)$]
Maximum/minimum transmission	0.924/0.875	0.706/0.617	0.728/0.534
Number of refined parameters	146	326	317
R [$F > 4.0\ \sigma(F)$][a]	0.042	0.044	0.031
wR[$F > 4.0\sigma(F)$][b]	0.103	0.124	0.081
Goodness-of-fit[c]	1.015	1.075	1.022
ρ_{max}, ρ_{min} (e Å^{-3})	0.381/−0.368	1.49/−0.58	0.774/−0.658

[a] $R = \sum\|F_o\|-|F_c\|/\sum|F_o|$.
[b] $R = \{\sum[w(F_o^2 - F_c^2)^2]/\sum[w(F_o^2)^2]\}^{1/2}$.
[c] The goodness-of-fit (GOF) equals $\{\sum[w(F_o^2 - F_c^2)^2]/(N_{rflns} - N_{params})\}^{1/2}$.

scan technique. The first 50 frames were recollected at the end of data collection to monitor for decay. Empirical absorption corrections were applied using program SADABS. The structures were solved by direct methods and subsequent Fourier differences using the WINGX package [19] and refined by full-matrix least-squares on F^2. All non-hydrogen atoms were refined with anisotropic displacement parameters. In the structure of the cobalt complex, only one of the two thiazine shows a dynamic disorder affecting C(3) and C(3A) atoms, being the value of the refined occupancy 0.52(4) for C(3) and 0.48(4) for C(3A). Hydrogen atoms attached to carbon and nitrogen atoms were positioned geometrically, with U_{iso} values derived from U_{eq} values of the corresponding carbon and nitrogen atoms.

3. Results and discussion

3.1. Description of the structures

The single crystal X-ray diffraction analysis revealed that the crystals of BzTz are made up of monoclinic unit cells, each containing eight BzTz. A diagram of the molecular structure and the numbering system used is shown in Fig. 1. Selected bond lengths and angles are listed in Table 2.

In the S–C(1)–N(1)–C(2)–C(3)–C(4) ring, the short endocyclic C=N bond [C(1)–N(1) = 1.264(2) Å] is

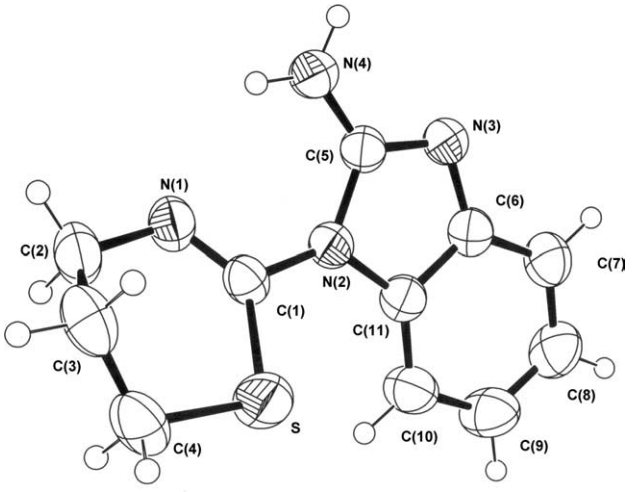


Fig. 1. Crystal structure of BzTz, showing the atom-numbering scheme. The thermal ellipsoids are plotted at the 50% probability level.

Table 2
Selected bond lengths (Å), angles (°) and hydrogen-bond parameters for BzTz

S–C(1)	1.759(2)	S–C(4)	1.807(2)
C(1)–N(1)	1.264(2)	N(1)–C(2)	1.465(2)
N(2)–C(1)	1.421(2)	N(2)–C(11)	1.414(2)
N(3)–C(5)	1.312(2)	N(3)–C(6)	1.387(2)
N(2)–C(5)	1.402(2)	C(5)–N(4)	1.333(2)
C(1)–S–C(4)	101.5(1)	C(1)–N(1)–C(2)	120.2(2)
N(1)–C(1)–S	129.4(1)	N(1)–C(2)–C(3)	114.2(2)
N(1)–C(1)–N(2)	118.3(1)	N(2)–C(1)–S	112.2(1)
N(3)–C(5)–N(2)	112.7(1)	C(1)–N(2)–C(5)	124.8(1)
C(1)–N(2)–C(11)	128.8(1)	C(5)–N(2)–C(11)	105.7(1)

D–H···A	D–H (Å)	H···D (Å)	D···A (Å)	D–H···A (°)
N(4)–H(4B)···N(1)	0.860(2)	2.228(1)	2.818(2)	125.8(1)
N(4)–H(4A)···N(3)[a]	0.860(2)	2.111(1)	2.937(2)	161.0(1)

[a] Equivalent position, $-x, -y-1, -z$.

accompanied by an high N–C–S angle [N(1)–C(1)–S = 129.4(1)°] and a relatively long S^{II}–C(sp^2) bond [S–C(1) = 1.759(2) Å], which is characteristic of a 5,6-dihydro-4H-1,3-thiazine ring [20]. Likewise, the bond distances and angles of the benzimidazole ring system are comparable to those obtained earlier for the free benzimidazole [21].

The thiazine ring shows a conformation near to half-boat with the C(3) atom deviating 0.710 Å above the plane formed by S, C(1), N(1), C(2) and C(4) [maximum least square plane deviation for C(4) = 0.038 Å]. This geometry is proved by the puckering parameters $Q = 0.523$ Å, $\theta = 54.3°$ and $\phi = 178.8°$, calculated according to Cremer and Pople [22]. As was to be expected, the benzimidazole ring system is essentially planar with maximum least square plane deviations for C(10) [0.041 Å].

The crystal structure is stabilized by an hydrogen-bond network in which thiazinic N(1) and benzimidazolinic N(3) nitrogen atoms act as acceptors of hydrogen, whereas nitrogen atom of amino group N(4) acts as donor. A diagram showing this network is given in Fig. 2.

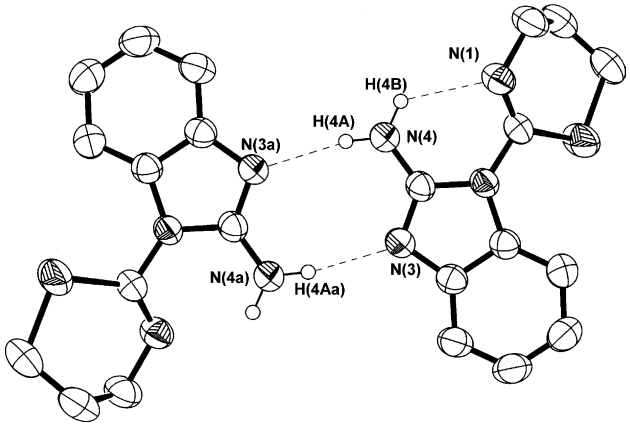


Fig. 2. View of the hydrogen bond network of BzTz.

The structure of $[CoCl_2(BzTz)_2]$ consists of discrete neutral monomeric units in which the environment around the cobalt(II) atom may be described as a distorted tetrahedral geometry. The metallic atom is coordinated by two chlorine atoms [Co–Cl(1) = 2.242(2) Å; Co–Cl(2) = 2.258(2) Å] and two benzimidazole nitrogen atoms from two BzTz ligands [Co–N(3) = 2.022(4) Å; Co–N(7) = 2.019(4) Å]. The overall view and labelling of the atoms of cobalt complex are displayed in Fig. 3. Table 3 lists selected bond lengths, angles and hydrogen-bond parameters.

The Co–Cl bond lengths are similar and comparable to the calculated average value [2.242(27) Å] for 116 tetrahedral cobalt(II) complexes with a chromophore group $CoCl_2N_2$ obtained from CONQUEST software [23] from the Cambridge Structural Database (CSD) [24]. Likewise, the $Co–N_{benzimidazole}$ bond distances are slightly shorter than the mean value [2.082(73) Å] calculated for 7 cobalt(II) complexes collected in CSD. The ligand–metal–ligand bite angles differ from the ideal value of 109.5° varying between 113.3(1)° [Cl(1)–Co–Cl(2)] and 102.6(2)° [N(3)–Co–N(7)].

The thiazine ring S(2)–C(12)–N(5)–C(13)–C(14)–C(15) shows a conformation near to half-boat with the C(14) atom deviating 0.454 Å above the plane formed by S(2), C(12), N(5), C(13) and C(15) [maximum least square plane deviation for C(15) = 0.015 Å]. This geometry is proved by the puckering parameters $Q = 0.338$ Å, $\phi = 245.2°$ and $\theta = 49.7°$ [22].

The other thiazine ring shows two conformations due to disorder. One of them shows an intermediate form between half-chair and half-boat [$Q = 0.373$ Å, $\phi = 260.1°$ and $\theta = 50.5°$] [22], with the C(3) and C(4) atoms deviating 0.395 and −0.156 Å, respectively, from the plane formed by S(1), C(1), N(1) and C(2) [maximum least square plane deviation for C(2) = 0.005 Å]. On the contrary, the second conformation is near to half-boat [$Q = 0.335$ Å, $\phi = 46.8°$ and $\theta = 123.0°$] [22], with the apex at C(3A). This atom is out of the plane

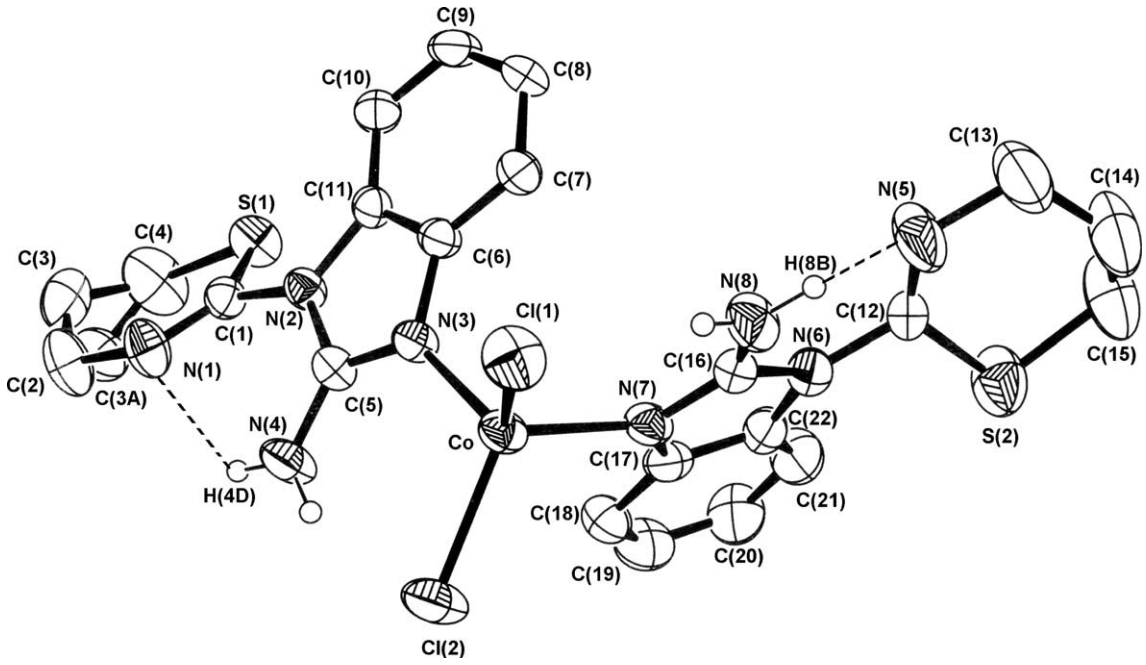


Fig. 3. Molecular structure of $[CoCl_2(BzTz)_2]$, showing the atom-numbering scheme. The thermal ellipsoids are drawn at the 40% probability level. Figure includes a view of the hydrogen bonds.

formed by S(1), C(1), N(1) and C(2) [maximum least square plane deviation for C(4) = 0.092 Å].

Finally, the crystal structure presents an hydrogen-bond network in which the nitrogen atoms of thiazine rings N(1) and N(5) act as acceptors of hydrogen, whereas the nitrogen atoms of amino groups N(4) and N(8) act as donors. A diagram showing this network is given in Fig. 3.

The molecular structure of $[CdCl_2(BzTz)_2]$ with the atomic labelling is shown in Fig. 4. Selected bond

Table 3
Selected bond lengths (Å) and angles (°) and hydrogen-bond parameters for $[CoCl_2(BzTz)_2]$ and $[CdCl_2(BzTz)_2]$

	$[CoCl_2(BzTz)_2]$	$[CdCl_2(BzTz)_2]$
M–Cl(1)	2.242(2)	2.441(1)
M–Cl(2)	2.258(2)	2.411(1)
M–N(3)	2.022(4)	2.265(2)
M–N(7)	2.019(4)	2.233(2)
N(3)–C(5)	1.317(7)	1.326(3)
N(7)–C(16)	1.321(7)	1.332(3)
N(3)–C(6)	1.404(6)	1.398(3)
N(7)–C(17)	1.391(8)	1.397(3)
Cl(1)–M–Cl(2)	113.3(1)	120.6(1)
Cl(1)–M–N(3)	112.2(1)	100.4(1)
Cl(1)–M–N(7)	108.4(2)	117.0(1)
Cl(2)–M–N(3)	108.0(1)	108.6(1)
Cl(2)–M–N(7)	111.8(1)	104.5(1)
N(3)–M–N(7)	102.6(2)	104.3(1)
C(5)–N(3)–C(6)	106.0(4)	105.8(2)
C(16)–N(7)–C(17)	106.0(4)	106.3(2)

D–H···A	D–H (Å)	H···D (Å)	D···A (Å)	D–H···A (°)
[CoCl₂(BzTz)₂]				
N(4)–H(4B)···N(1)	0.860(6)	2.211(6)	2.787(8)	124.1(4)
N(8)–H(8B)···N(5)	0.860(5)	2.168(8)	2.739(10)	124.2(5)
[CdCl₂(BzTz)₂]				
N(4)–H(4A)···Cl(1)	0.860(2)	2.403(1)	3.226(3)	160.3(2)
N(4)–H(4B)···N(1)	0.860(2)	2.194(2)	2.772(3)	124.5(2)
N(8)–H(8B)···N(5)	0.860(2)	2.145(2)	2.728(3)	124.7(2)

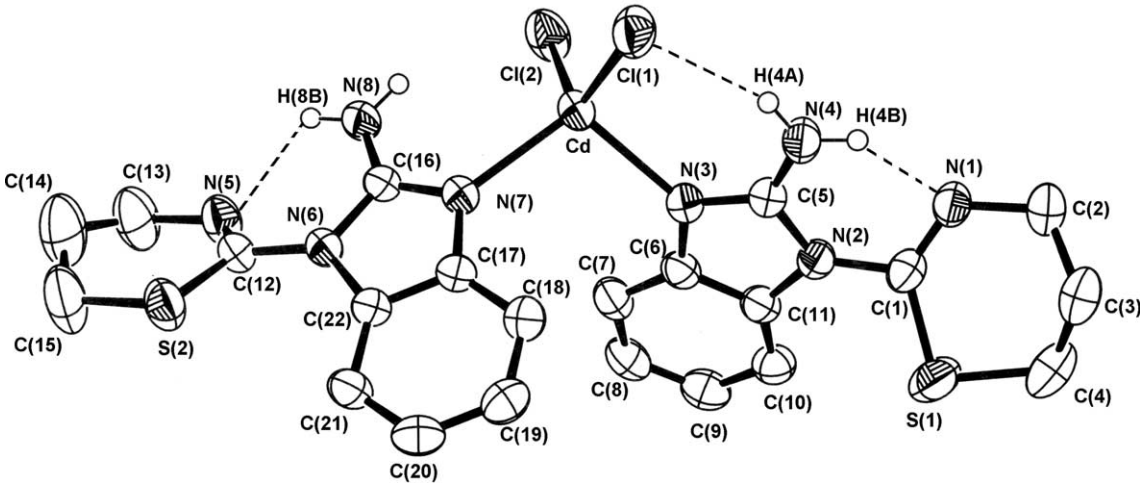


Fig. 4. Molecular structure of $[CdCl_2(BzTz)_2]$, showing the atom-numbering scheme. The thermal ellipsoids are drawn at the 50% probability level. Figure includes a view of the hydrogen bonds.

lengths, angles and hydrogen-bond parameters are given in Table 3.

The cadmium(II) complex is bound to two chlorine atoms [Cd–Cl(1) = 2.441(7) Å; Cd–Cl(2) = 2.414(7) Å] and two benzimidazole nitrogen atoms from two BzTz ligands [Cd–N(3) = 2.265(2) Å; Cd–N(7) = 2.233(2) Å]. The distortion of the tetrahedral environment of the cadmium(II) ion is higher than in cobalt(II) complex, being indicated by the ligand–metal–ligand bite angles that vary between 120.6(1)° [Cl(1)–Cd–N(3)] and 100.4(1)° [Cl(1)–Cd–Cl(1)].

The Cd–Cl distances are comparable to the calculated average value [2.481(69) Å] for 87 four-coordinated cadmium(II) complexes found in CSD. Finally, the Cd–$N_{benzimidazole}$ bond distances are slightly shorter than found in $[Cd(BBP–H)_2]$ [2.331(73) Å] [25].

The values of the puckering parameters for thiazine ring S(1)–C(1)–N(1)–C(2)–C(3)–C(4), calculated according to Cremer and Pople [22], are $Q = 0.500$ Å, $\phi = 262.4°$ and $\theta = 50.1°$, whereas for the other thiazine ring S(2)–C(12)–N(5)–C(13)–C(14)–C(15) are $Q = 0.377$ Å, $\phi = 73.4°$ and $\theta = 128.6°$. These values indicate that the first one shows a conformation near to half-chair with the atoms C(3) and C(4) deviating by 0.498 and −0.246 Å, respectively, above the plane formed by S(1), C(1), N(1) and C(2) [maximum least square plane deviation for N(1) = 0.006 Å]. The second one presents a conformation near to half-boat, with the apex at C(14), deviating 0.502 Å from the plane formed by S(2), C(12), N(5), C(13) and C(15) [maximum least square plane deviation for C(15) = 0.048 Å].

The crystal structure presents an hydrogen-bond network in which chloro ligand Cl(1) and nitrogen atoms N(1) and N(5) act as acceptors of hydrogen, whereas nitrogen atoms of amino groups N(4) and N(8) act as donors. A diagram showing this network is given in Fig. 4.

In benzimidazole system of both complexes, the formation of the metal–$N_{benzimidazole}$ bond results in an increase the N(3)–C(5) [or N(7)–C(16)] and N(3)–C(6) [or N(7)–C(17)] distances with respect to the structure of free BzTz.

Finally, it should be pointed out that BzTz acts in both complexes as a monodentate ligand through nitrogen atom of benzimidazole ring, whereas the thiazine ring and amino group being uncoordinated. This fact could be due to existence of a intramolecular hydrogen bond between amine group and thiazine nitrogen atom in free ligand. This hydrogen bond exists in complexes and avoids coordination through the mentioned nitrogen atoms.

3.2. Physical measurements

The observed molar magnetic susceptibility for $[CoCl_2(BzTz)_2]$ was corrected for diamagnetism and temperature-independent paramagnetism to provide the fully corrected magnetic moment at room temperature ($\mu_{eff} = 4.52$ BM). This value is consistent with an tetrahedral environment around cobalt(II) [3,26–28].

The diffuse reflectance spectrum shows one intense band at 37 037 cm^{-1} (270 nm), which is assigned to transitions $\pi \rightarrow \pi^*$ of the organic ligand corresponding to a displaced B-bond of benzene. Moreover, the spectrum exhibits two main bands that have intensities consistent with spin-allowed d–d transitions. These bands may be assigned as: ν_2 [$^4A_2(F) \rightarrow {}^4T_1(F)$] (7259 cm^{-1}) and ν_3 [$^4A_2(F) \rightarrow {}^4T_1(P)$] (15 873 cm^{-1}) transitions, in an idealized T_d symmetry. It must be pointed out that the ν_2 assignment has been made by calculating the barycenter of three bands (8929, 7102, 5924 cm^{-1}) of approximately equal intensity in the solid-state spectrum [29]. The ligand-field parameters, $10D_q$ and B, were calculated

Table 4
Infrared bands (cm^{-1}) assigned to organic moiety of BzTz, $[CoCl_2(BzTz)_2]$ and $[CdCl_2(BzTz)_2]$

Assignment	BzTz	$[CoCl_2(BzTz)_2]$	$[CdCl_2(BzTz)_2]$
Thiazine			
Ψ_1	1662 (vs)	1636 (vs)	1646 (vs)
Ψ_2	964 (m)	951 (w)	951 (m)
Ψ_3	920 (m)	930 (w)	931 (w)
Ψ_4	878 (m)	882 (m)	882 (m)
Ψ_5	717 (m)		723 (w)
Ψ_6	694 (m)	695 (m)	695 (m)
Ψ_7	669 (m)	672 (w)	
Ψ_8	606 (w)	604 (w)	608 (m)
ϕ_1	501 (m)	505 (m)	503 (m)
ϕ_2	465 (w)	469 (w)	
Benzimidazole			
ν	1622 (vs)	1606 (m)	1605 (s)
	1607 (m)	1592 (s)	1591 (s)
	1498 (w)		
	1462 (vs)	1467 (s)	1467 (vs)
	1402 (s)		1427 (vs)
	1364 (m)		
	1346 (s)	1347 (m)	1348 (m)
	1299 (s)	1294 (m)	1299 (m)
	1258 (m)	1254 (m)	1256 (m)
δ (in p.b.)	1012 (m)	1015 (m)	1015 (m)
	900 (m)	911 (w)	904 (m)
	842 (m)	848 (m)	847 (m)
	646 (m)		
	618 (w)	646 (m)	
	434 (m)	431 (m)	430 (m)
δ (o.p.b.)	568 (w)	587 (w)	582 (w)
τ	559 (w)	558 (m)	563 (m)
Amine group			
$\nu(NH_2)$	3424 (s)	3378 (s)	3367 (s)
	3402 (s)	3295 (s)	3288 (s)
$\delta(NH_2)$	1541 (w)	1542 (w)	1546 (w)
$\omega(NH_2)$	1346 (s)	1347 (m)	1348 (m)
$r(NH_2)$	1012 (m)	1029 (w)	1030 (m)

Abbreviations. (s) strong; (m) medium; (w) weak; (v) very.

using the following known relationships [30] for tetrahedral d^7 complexes:

$$\nu_2[^4A_2(F) \rightarrow {}^4T_1(F)] = 15D_q + (15/2)B - 1/2[(-6D_q + 15B)^2 + 64(D_q)^2]^{1/2},$$

$$\nu_3[^4A_2(F) \rightarrow {}^4T_1(P)] = 15D_q + (15/2)B + 1/2[(-6D_q + 15B)^2 + 64(D_q)^2]^{1/2}.$$

The calculated values of the ligand-field parameters $10D_q = 4225\ cm^{-1}$ and $B = 697\ cm^{-1}$ are in fair agreement with the predicted values for tetrahedral complexes and are consistent with the presence of a chromophore group $[CoN_2Cl_2]$ [3,28,31–33].

The IR spectrum of BzTz in the 4000–370 cm^{-1} region shows the presence of bands due to thiazine ring vibrations at 1662 (Ψ_1), 964 (Ψ_2), 920 (Ψ_3), 878 (Ψ_4), 717 (Ψ_5), 694 (Ψ_6), 669 (Ψ_7), 606 (Ψ_8), 501 (ϕ_1) and 465 (ϕ_2) cm^{-1} [3,4,34,35].

Likewise, the spectrum of the ligand exhibits bands assignable to the benzimidazole ring vibrations at 1622, 1607, 1498, 1462, 1402, 1364, 1346, 1299 and 1258 cm^{-1} for stretching vibrations (ν); at 1012, 900, 842, 646, 618 and 434 cm^{-1} for bending in-plane vibrations (δ in p.b.); at 568 cm^{-1} for bending out-of-plane vibration (δ o.p.b.); and at 559 cm^{-1} for torsion vibration (τ) [36–39].

Moreover, the bands of NH_2 vibration are detected at 3424, 3402 [$\nu(NH_2)$], 1541 [$\delta(NH_2)$], 1346 [$\omega(NH_2)$] and 1012 [$r(NH_2)$] cm^{-1} [40–43]. Finally, band assignable to ν(C–N) vibration is registered at 1078 cm^{-1} [40,44].

In the 4000–370 cm^{-1} region of the IR spectra of $[CoCl_2(BzTz)_2]$ and $[CdCl_2(BzTz)_2]$ complexes the observed bands due to the organic moiety vibrations are shown in Table 4.

As can be observed in Table 4, the bands assignable to stretching vibration of the benzimidazole ring suffer,

in general, a shift to lower frequencies which substantiate the coordination through the benzimidazole nitrogen atom.

The far IR spectra $[CoCl_2(BzTz)_2]$ and $[CdCl_2(BzTz)_2]$ show absorption bands assignable to metal–ligand stretching vibrations. Thus, the Co(II) spectrum shows a bands at 330 and 302 cm^{-1} corresponding to the ν(Co–Cl) vibration [3,28,45–47], whereas, band at 251 cm^{-1} corresponding to the ν(Co–$N_{benzimidazole}$) vibration in accord with literature data for this type of bonds [48]. In the Cd(II) spectrum, the bands at 278 and 249 cm^{-1} could be attributed to the ν(Cd–Cl) vibration [49]. Finally, band at 203 cm^{-1} is tentatively assigned to the (Cd–$N_{benzimidazole}$) vibration, according to the consulted bibliography for cadmium complexes containing imidazole derivative ligands [50,51].

As usual [52], the coordination to the d^{10} Cd(II) ion shifts the ^1H NMR signals of the complex downfield from those of the free ligand ($\Delta\delta \approx 0.0$ to 0.2 ppm). The major downfield shifts of the H-7 (δ 7.34 ppm in BzTz; 7.60 in complex) and NH_2 (δ 6.45 ppm in BzTz; 7.76 in complex) signals are attributable to coordination through the benzimidazole nitrogen atom [25]. The trends in the shifts in carbon-13 spectroscopy are less straightforward. However, in the ^{13}C NMR spectra of cadmium complex the shift of C5 signal (δ 142.0 ppm in BzTz; 138.2 in complex) to higher field is in consonance with coordination through the benzimidazole nitrogen atom. This conclusion is supported by the X-ray diffraction structure of $[CdCl_2(BzTz)_2]$. The chemical shifts of the other carbon atoms in the compound are similar to free ligand.

4. Supplementary material

CCDC 267998, 267999 and 268000 corresponding to BzTz, $[CoCl_2(BzTz)_2]$ and $[CdCl_2(BzTz)_2]$ contain the supplementary crystallographic data for this paper. These data can be obtained free of charge via www.ccdc.cam.ac.uk/conts/retrieving.html (or from the CCDC, 12 Union Road, Cambridge CB2 1EZ, UK; fax: +44 1223 336033; e-mail: deposit@ccdc.cam.ac.uk).

Acknowledgements

We thank the Junta de Extremadura (Consejería de Educación, Ciencia y Tecnología) and the FEDER [Projects 2PR02A098 and 2PR04A011] for financial support. M.A.M.-R. thanks the Spanish Ministerio de Ciencia y Tecnología and E. Viñuelas-Zahínos thanks the Junta de Extremadura (Consejería de Educación, Ciencia y Tecnología) and the FEDER for their Ph.D. fellowships.

References

[1] A.T. Chaviara, P.J. Cox, K.H. Repana, R.M. Papi, K.T. Papazisis, D. Zambouli, A.H. Kortsaris, D.A. Kyriakidis, C.A. Bolos, J. Inorg. Biochem. 98 (2004) 1271.
[2] S. Bräse, C. Gil, K. Knepper, Bioorg. Med. Chem. 10 (2002) 2415.
[3] F.J. Barros-García, A. Bernalte-García, A.M. Lozano-Vila, F. Luna-Giles, E. Viñuelas-Zahínos, Polyhedron 24 (2005) 129.
[4] A. Bernalte-García, F.J. García-Barros, F.J. Higes-Rolando, F. Luna-Giles, R. Pedrero-Marín, J. Inorg. Biochem. 98 (2004) 15.
[5] F.J. Barros-García, A. Bernalte-García, F.J. Higes-Rolando, F. Luna-Giles, R. Pedrero-Marín, Polyhedron 23 (2004) 1453.
[6] H.A. Al-Khamees, S.M. Bayomi, H.A. Kandil, K.E.H. El-Tahir, Eur. J. Med. Chem. 25 (1990) 103.
[7] M. Koketsu, K. Tanaka, Y. Takenaka, C.D. Kwong, H. Ishihara, Eur. J. Pharm. Sci. 15 (2002) 307.
[8] B. Tozkoparan, G. Aktay, E. Yesilada, Il Farmaco 57 (2002) 145.
[9] J.D. Bourzat, C. Cotrel, C. Guyon, Ph. Pitchen, US Patent 4994569, 1991.
[10] R.F. Schinazi, R.A. Floyd, PCT Int. Appl. WO 90 (13) (1991) 296 (Cl. A61K31/54).
[11] R.F. Schinazi, R.A. Floyd, Chem. Abstr. 115 (1991) 105989.
[12] J.F. Gonzales, P.A. Todd, Drugs 34 (1987) 298.
[13] W. Nawrocka, Boll. Chim. Farm. 135 (1996) 18.
[14] W. Nawrocka, B. Stuzba, M.W. Kowalska, H. Liszkiewicz, J. Wietrzyk, A. Nasulewicz, M. Pelczynska, A. Opolski, Il Farmaco 59 (2004) 83.
[15] P. Winstaley, Lancet 352 (1998) 1080.
[16] A. Carpio, J. Neurol. Neurosurg. Ps. 66 (1999) 411.
[17] C.A. Bolos, K.T. Papazisis, A.H. Kortsaris, S. Voyatzi, D. Zambouli, D.A. Kyriakidis, J. Inorg. Biochem. 88 (2002) 25.
[18] R.D. Haugwitz, B.V. Maures, A.J. Martinez, G.A. Jacobs, V.L. Narayanan, Synthesis (1976) 336.
[19] L.J. Farrugia, J. Appl. Cryst. 32 (1999) 837.
[20] G. Argay, A. Kalman, A. Kapor, B. Ribar, Acta Crystallogr., Sect. B 36 (1980) 363.
[21] A. Escande, J.L. Galigne, Acta Crystallogr., Sect. B 30 (1974) 1647.
[22] D. Cremer, J.A. Pople, J. Am. Chem. Soc. 97 (1975) 1354.
[23] F.H. Allen, Acta Crystallogr., Sect. B 58 (2002) 380.
[24] I.J. Bruno, J.C. Cole, P.R. Edington, M. Kessler, C.F. Macrae, P. McCabe, J. Pearson, R. Taylor, Acta Crystallogr., Sect. B 58 (2002) 389.
[25] S. Wang, Y. Cui, R. Tan, Q. Luo, J. Shi, Q. Wu, Polyhedron 13 (1994) 1661.
[26] B.N. Figgis, J. Lewis, Prog. Inorg. Chem. 6 (1964) 37.
[27] R.L. Carlin, Transit. Metal Chem. 1 (1965) 21.
[28] A. Bernalte-García, F.J. García-Barros, F.J. Higes-Rolando, F. Luna-Giles, Polyhedron 20 (2001) 3315.
[29] F.A. Cotton, D.M.L. Goodgame, M. Goodgame, J. Am. Chem. Soc. 83 (1961) 4690.
[30] D.K. Rastogi, K.C. Sharma, S.K. Dua, M.P. Teotia, J. Inorg. Nucl. Chem. 37 (1975) 685.
[31] J.A. Weaver, P. Hambright, P.T. Talbert, E. Kang, A.N. Thorpe, Inorg. Chem. 9 (1970) 268.
[32] Y.J. Weaver, J.A. Weaver, J. Inorg. Nucl. Chem. 37 (1975) 1309.
[33] A.C. Fabretti, G. Peyronel, G.C. Franchini, Inorg. Chim. Acta 35 (1979) 49.
[34] A.I. Meyers, J. Org. Chem. 26 (1961) 218.
[35] A. Pastura, K. Thewalt, J. Prakt. Chem. 38 (1968) 177.
[36] S. Yurdakul, M. Kurt, J. Mol. Struct. 650 (2003) 181.
[37] D.P. Drolet, D.M. Manuta, A.J. Lees, Inorg. Chim. Acta 146 (1988) 173.
[38] E. Sahin, S. Ide, M. Kurt, S. Yurdakul, J. Mol. Struct. 616 (2002) 259.
[39] S. Yurdakul, C. Yilmaz, Vib. Spectrosc. 21 (1999) 127.

[40] A. Bernalte-García, F.J. García-Barros, F.J. Higes-Rolando, A.M. Pizarro-Galán, C. Valenzuela-Calahorro, Thermochim. Acta 339 (1999) 95.
[41] K.C. Patil, J.P. Vital, J. Chem. Soc., Dalton Trans. (1992) 2291.
[42] D.N. Sathayanarayana, D. Nicholls, Spectrochim. Acta 34A (1978) 263.
[43] K.C. Patil, R. Soundararajan, V.R.P. Verneker, Inorg. Chem. 18 (1979) 1969.
[44] R.T. Conley, in: Espectroscopía Infrarroja, Alhambra, Madrid, 1979.
[45] E.J. Duff, M.N. Hughes, K.J. Rutt, J. Chem. Soc. (1969) 2101.
[46] C.E. Taylor, A.E. Underhill, J. Chem. Soc. A (1969) 368.
[47] W.J. Eilbeck, F. Holmes, C.E. Taylor, A.E. Underhill, J. Chem. Soc. A (1969) 1189.
[48] M.J.M. Campbell, D.W. Card, R. Grzeskowiak, M. Goldstein, J. Chem. Soc., Dalton Trans. 15 (1972) 1687.
[49] A. Castiñeiras, R. Carballo, T. Pérez, Polyhedron 20 (2001) 441.
[50] C. Pettinari, F. Marchetti, A. Cingolani, S.I. Troyanov, A. Drozdov, Polyhedron 17 (1998) 1677.
[51] S.H. Tarulli, O.V. Quinzani, E.J. Baran, O.E. Piro, E.E. Castellano, J. Mol. Struct. 656 (2003) 161.
[52] C. Janiak, S. Deblon, H.P. Wu, M.J. Kolm, P. Küflers, H. Piotrowski, P. Mayer, Eur. J. Inorg. Chem. (1999) 1507.

(R = Me **1**, *n*-Bu **2**, $PhCH_2$ **3**, Cy **4**, Ph **5**). The X-ray crystallography data show that the tin atoms of complexes **1**–**5** are all five-coordinated with distorted trigonal bipyramidal geometry. Interestingly, complexes **1**–**4** exhibit 1D polymeric chains through Sn and N intermolecular interactions.

2. Experimental

2.1. Materials and measurements

Trimethyltin chloride, tri-*n*-butyltin chloride, triphenyltin chloride, tricyclohexyltin chloride and 5-phenyl-1,3,4-oxadiazole-2-thiol were commercially available, and they were used without further purification. Tribenzyltin chloride was prepared by a standard method reported in the literature [11]. The melting points were obtained with Kofler micro melting point apparatus and are uncorrected. Infrared-spectra were recorded on a Nicolet-460 spectrophotometer using KBr discs and sodium chloride optics. ^{1}H and ^{13}C NMR spectra were recorded on Varian Mercury Plus 400 spectrometer operating at 400 and 100.6 MHz, respectively. The spectra were acquired at room temperature (298 K) unless otherwise specified; ^{13}C spectra are broadband proton decoupled. The chemical shifts were reported in ppm with respect to the references and were stated relative to external tetramethylsilane (TMS) for ^{1}H and ^{13}C NMR. Elemental analyses were performed with a PE-2400II apparatus.

2.2. Syntheses of the complexes *1*–*5*

The general route of synthesis is shown in the following. The reaction was carried out under nitrogen atmosphere. The 5-phenyl-1,3,4-oxadiazole-2-thiol (1 mmol) was added to the solution of benzene 20 ml with sodium ethoxide (1 mmol), then add R_3SnCl (1 mmol) to the mixture, continuing the reaction for 12 h at 40 °C. After cooling down to the room temperature, the solution was filtered. The solvent of the filtrate was gradually removed by evaporation under vacuum until solid product was obtained. The solid was then recrystallized from dichloromethane-*n*-hexane. Colorless crystal was formed.

2.2.1. $Me_3Sn[S(C_8H_5N_2O)]$ (*1*)

Yield, 70%; m.p. 116–118 °C. *Anal.* Calc. for $C_{11}H_{14}N_2OSSn$: C, 38.74; H, 4.14; N, 8.21. Found: C, 38.65; H, 4.04; N, 8.10%. ^{1}H NMR ($CDCl_3$): δ 7.24–7.83 (m, 5H,C_6H_5–C), 0.76 (s, 9H, Sn–CH_3) ppm. ^{13}C NMR: δ 145.7 (C-1 ligand), 136.6 (C-2), 136.6 (C-2′), 128.4 (C-3), 128.4 (C-3′), 129.5 (C-4), 168.2 (C–S), 168.7 (C–Ph), 8.11 (Me) ppm. IR (KBr, cm^{-1}): ν(C=N) 1584, $\nu(Sn–C)_{as}$ 530, $\nu(Sn–C)_s$ 504, ν(Sn–S) 313, ν(Sn–N) 486.

2.2.2. $(n\text{-}Bu)_3Sn[S(C_8H_5N_2O)]$ (*2*)

Yield, 74%; m.p. 69–72 °C. *Anal.* Calc. for $C_{20}H_{32}N_2OSSn$: C, 51.41; H, 6.90; N, 6.00. Found: C, 51.50; H, 6.70; N, 6.22%. ^{1}H NMR ($CDCl_3$): δ 7.25–7.82 (m, 5H, C_6H_5–C), 0.85–1.68 (s, 27H, Sn–C_4H_9) ppm. ^{13}C NMR: δ 145.6 (C-1 ligand), 136.5 (C-2), 136.5 (C-2′), 128.3 (C-3), 128.3 (C-3′), 129.4 (C-4), 168.3 (C–S), 168.8 (C–Ph), 13.5, 26.3, 27.5, 29.2 (*n*-Bu) ppm. IR (KBr, cm^{-1}): ν(C=N) 1586, $\nu(Sn–C)_{as}$ 528, $\nu(Sn–C)_s$ 502, ν(Sn–S) 315, ν(Sn–N) 485.

2.2.3. $(PhCH_2)_3Sn[S(C_8H_5N_2O)]$ (*3*)

Yield, 76%; m.p. 125–127 °C. *Anal.* Calc. for $C_{29}H_{26}N_2OSSn$: C, 61.18; H, 4.60; N, 4.92. Found: C, 61.05; H, 4.41; N, 4.80%. ^{1}H NMR ($CDCl_3$): δ 7.31–7.47 (m, 5H, C_6H_5–C), 6.91–7.17 (m, 15H, Sn–$CH_2C_6H_5$), 2.76 (s, 6H, Sn–$CH_2C_6H_5$). ^{13}C NMR: δ 145.5 (C-1 ligand), 136.4 (C-2), 136.4 (C-2′), 128.2 (C-3), 128.2 (C-3′), 129.3 (C-4), 168.1 (C–S), 168.6 (C–Ph), 37.4 (CH_2–Ph), 127.5 (*m*-C), 128.7 (*p*-C), 127.6 (*o*-C), 124.5 (*i*-C) ppm. IR (KBr, cm^{-1}): ν(C=N) 1596 $\nu(Sn–C)_{as}$ 460, $\nu(Sn–C)_s$ 437, ν(Sn–S) 308, ν(Sn–N) 484.

2.2.4. $Cy_3Sn[S(C_8H_5N_2O)]$ (*4*)

Yield, 77%; m.p. 120–121 °C. *Anal.* Calc. for $C_{26}H_{38}N_2OSSn$: C, 57.26; H, 7.02; N, 5.14. Found: C, 57.15; H, 7.11; N, 5.05%. ^{1}H NMR ($CDCl_3$): δ 7.21–7.41 (m, 5H, C_6H_5–C), 0.82–1.65 (m, 33H, Sn–C_6H_{33}). ^{13}C NMR: δ 145.3 (C-1 ligand), 136.2 (C-2), 136.2 (C-2′), 128.2 (C-3), 128.2 (C-3′), 129.2 (C-4), 168.3 (C–S), 168.6 (C–Ph), 26.6 (*m*-C), 26.5 (*p*-C), 26.8 (*o*-C), 27.5 (*i*-C) ppm. IR (KBr, cm^{-1}): ν(C=N) 1592, $\nu(Sn–C)_{as}$ 450, $\nu(Sn–C)_s$ 427, ν(Sn–S) 307, ν(Sn–N) 483.

2.2.5. $Ph_3Sn[S(C_8H_5N_2O)]$ (*5*)

Yield, 75%; m.p. 185–187 °C. *Anal.* Calc. for $C_{26}H_{20}N_2OSSn$: C, 59.23; H, 3.82; N, 5.31. Found: C, 59.11; H, 3.71; N, 5.22%. ^{1}H NMR ($CDCl_3$): δ 7.21–7.42 (m, 5H, C_6H_5–C), 7.45–7.76 (m, 15H, Sn–C_6H_5) ppm. ^{13}C NMR: δ 145.2 (C-1 ligand), 136.3 (C-2), 136.3 (C-2′), 128.1 (C-3), 128.1 (C-3′), 129.1 (C-4), 168.0 (C–S), 168.5 (C–Ph), 127.9 (*m*-C), 129.0 (*p*-C), 136.4 (*o*-C), 148.5 (*i*-C) ppm. IR (KBr, cm^{-1}): ν(C=N) 1590, $\nu(Sn–C)_{as}$ 464, $\nu(Sn–C)_s$ 429, ν(Sn–S) 311.

2.3. X-ray crystallographic studies of complexes *1*–*5*

Crystals were mounted in Lindemann capillaries under nitrogen. All X-ray crystallographic data were collected on a Bruker SMART CCD 1000 diffractometer with graphite monochromated Mo Kα radiation (λ = 0.71073 Å) at 298(2) K. A semi-empirical absorption correction was applied to the data. The structure was solved by direct methods using SHELXS-97 and refined against F^2 by full-matrix least squares using SHELXL-97. Hydrogen atoms were placed in calculated

Table 1
Crystal data and structure refinement parameters for complexes **1**–**5**

Complexes	**1**	**2**	**3**	**4**	**5**
Empirical formula	$C_{11}H_{14}N_2OSSn$	$C_{20}H_{32}N_2OSSn$	$C_{29}H_{26}N_2OSSn$	$C_{26}H_{38}N_2OSSn$	$C_{26}H_{20}N_2OSSn$
Formula weight	340.99	467.23	569.27	543.32	527.19
Crystal system	monoclinic	triclinic	orthorhombic	monoclinic	monoclinic
Space group	$P2_1/m$	$P\bar{1}$	$P2_12_12_1$	$P2_1/c$	$P2_1/n$
Unit cell dimensions					
a (Å)	6.891(3)	10.56(1)	6.789(2)	12.603(1)	10.82(4)
b (Å)	7.509(4)	12.55(1)	19.326(6)	12.549(1)	12.97(5)
c (Å)	13.354(7)	18.31(2)	19.896(6)	19.818(1)	16.43(6)
α (°)	90	88.42(1)	90	90.00	90
β (°)	104.723(5)	75.27(1)	90	125.503(4)	101.92
γ (°)	90	87.48(1)	90	90.00	90
V (Å^3)	668.2(6)	2345(5)	2610(1)	2551.5(4)	2257(1)
Z	2	4	4	4	4
D_c (Mg m^{-3})	1.695	1.324	1.449	1.414	1.552
Absorption coefficient (mm^{-1})	2.050	1.188	1.082	1.103	1.245
F(0 0 0)	336	960	1152	1120	1056
Crystal size (mm)	$0.37 \times 0.28 \times 0.21$	$0.48 \times 0.46 \times 0.16$	$0.44 \times 0.25 \times 0.21$	$0.20 \times 0.18 \times 0.13$	$0.48 \times 0.41 \times 0.36$
θ Range (°)	3.06–25.02	1.62–25.03	1.47–25.03	2.298–27.983	2.07–25.05
Reflections collected	2792	11 766	13 718	28 636	10 466
Independent reflections [R_{int}]	1028 [0.0203]	8112 [0.0309]	4571 [0.0294]	5812 [0.0274]	3638 [0.1630]
Data/restraints/parameters	1028/9/100	8112/30/451	4571/0/307	5812/0/0280	3638/0/280
Goodness-of-fit onF^2	1.026	0.997	1.002	1.045	1.008
Final R indices [$I > 2\sigma(I)$]	$R_1 = 0.0503$	$R_1 = 0.0491$	$R_1 = 0.0263$	0.0343	$R_1 = 0.0739$
	$wR_2 = 0.1392$	$wR_2 = 0.1154$	$wR_2 = 0.0526$	0.0858	$wR_2 = 0.1483$
R indices (all data)	$R_1 = 0.0508$	$R_1 = 0.0963$	$R_1 = 0.0312$	0.0410	$R_1 = 0.1120$
	$wR_2 = 0.1400$	$wR_2 = 0.1438$	$wR_2 = 0.0547$	0.0906	$wR_2 = 0.1722$

positions. Crystal data and experimental details of the structure determinations are listed in Table 1.

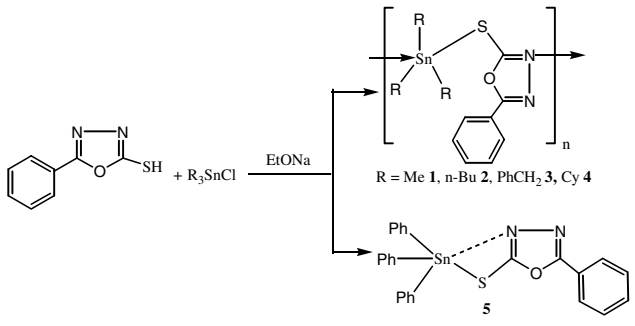
3. Results and discussion

3.1. Syntheses of complexes 1–5

The synthesis procedure is given in Scheme 1.

3.2. IR spectroscopic studies of complexes 1–5

Comparing the IR spectra of the free ligand with complexes **1**–**5**, the band at 2560–2430 cm^{-1}, which appears in the spectra of the free ligand as the ν(S–H) vibration, is absent in those of complexes **1**–**5** thus indicating metal–ligand bond formation through this site. In the far-IR spectra, the absorption about 310 cm^{-1} region for all complexes **1**–**5**, which is absent in the spectrum of the ligand, is assigned to the Sn–S stretching mode of the vibration and all the values are located within the range for Sn–S vibration observed in common organotin derivatives of thiolate (300–400 cm^{-1}) [12,13]. In organotin complexes, the IR spectra can provide useful information concerning the geometry of the SnC_n moiety [14]. In the case of our complexes, for triorganotin(IV) derivatives, two bands were assigned to asymmetric and symmetric Sn–C vibrations. Thus suggesting non-planar SnC_3 fragments for triorganotins. The middle intensity bands observed at about 1600 cm^{-1} in the spectra of all complexes have been assignable to ν(C=N) according to the literatures [15,16], which suggested the coordination of free ligand to these complexes is through sulfur atoms via thiol form.



Scheme 1.

3.3. ^1H and ^{13}C NMR data of complexes 1–5

^{1}H NMR data showed that the signal of the –SH proton in the spectrum of the ligand is absent in all of the complexes, indicating the removal of the –SH proton and the formation of Sn–S bonds. The formation accords well with what the IR data have revealed. Moreover, the ^{1}H NMR spectra show that the chemical shifts of the phenyl group (Sn–C_6H_5) in complex **5**,

7.45–7.76 ppm, and those of methylene connected directly with tin in complex **3**, 2.76 ppm, upfield shift as compared with those of their corresponding precursors. All these data are similar to those cases in literature [17], indicating there may exist novel coordination of the ligand to tin atom for all the five complexes **1**–**5**. In addition, the resonance of the phenyl group connected with the oxadiazole ring (C–C_6H_5) appears at 7.21–7.83 ppm for all complexes **1**–**5**.

The structural changes occurring in ligand upon deprotonation and coordination to the Sn atom should be reflected by the changes in the ^{13}C NMR spectra of our complexes. If the ligand chelate tin through thiolate form, C–S should be further low frequency in the spectra of all complexes compared with those in free ligands. As shown above, the chemical shifts of C–S in complexes **1**–**5** are shifted by 8 ppm to low frequency compared with the free ligand (δ 176.2 ppm), indicating that the ligands involved in these complexes act as thiolate form. All of the above analyses are confirmed by X-ray diffraction.

3.4. Crystal structures of complexes *1*–*5*

The crystal structures and polymeric chains of complexes **1**–**4** are shown in Figs. 1–8, respectively. And the crystal structure and cell packing diagram of complex **5** are shown in Figs. 9 and 10. All H atoms have been omitted for the purpose of clarity. Table 1 lists the crystal data and structure refinement parameters for complexes **1**–**5** and their selected bond lengths and angles are shown in Tables 2–6, respectively.

3.4.1. $Me_3Sn[S(C_8H_5N_2O)]$ (*1*), $(n\text{-}Bu)_3Sn[S(C_8H_5N_2O)]$ (*2*), $(PhCH_2)_3Sn[S(C_8H_5N_2O)]$ (*3*) and $Cy_3Sn[S(C_8H_5N_2O)]$ (*4*)

For complexes **1**–**4**, the X-ray diffraction investigation has shown that they exhibit 1D polymeric chains through intermolecular Sn–N bonds. The central tin atoms in complexes **1**–**4** are all five-coordinate with the *trans*-trigonal–bipyramidal geometry. The methyl carbons in complex **1**, the methylene carbons which are next to tin in complex **2**, the methylene carbons in complex **3** and the –CH– carbons in complex **4** are in equatorial positions and the axial positions are occupied by the sulfur atom and the nitrogen atom of a neighboring molecule, respectively. The sum of equatorial angles are 359.4° (C(10)#1–Sn(1)–C(10) (123.4(5)°), C(10)#1–Sn(1)–C(9) (118.0(3)°) and C(9)–Sn(1)–C(10) (118.0(3)°)), in complex **1**; 359.9° (C(25)–Sn(1)–C(21) (118.7(5)°), C(25)–Sn(1)–C(17) (124.7(6)°) and C(21)–Sn(1)–C(17) (116.5(5)°)), in complex **2**; 358.04° (C(23)–Sn(1)–C(9) (116.42(14)°), C(23)–Sn(1)–C(16) (111.64(14)°) and C(9)–Sn(1)–C(16) (129.98(13)°)), in complex **3**; 359.86° (C(7)–Sn(1)–C(13) (122.50(14)°), C(7)–Sn(1)–C(1) (121.21(12)°) and C(13)–Sn(1)–C(1) (116.15(13)°)), in complex **4**, respectively. They are all

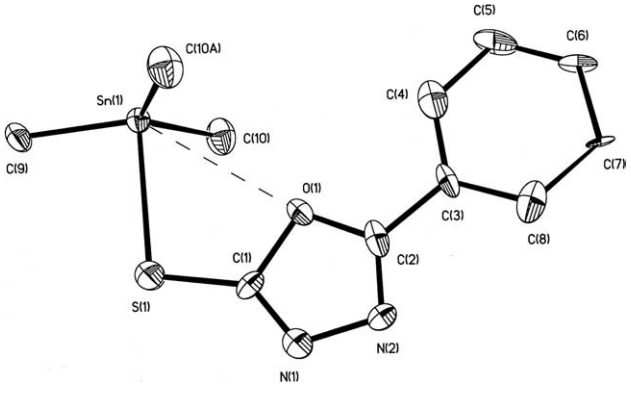


Fig. 1. Molecular structure of the complex **1**.

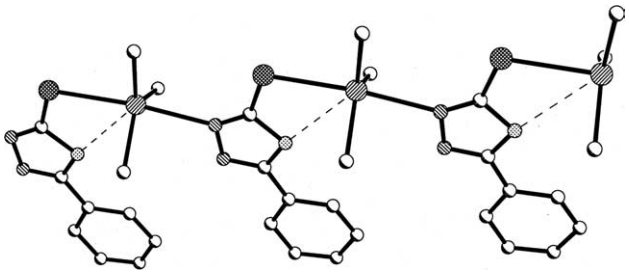


Fig. 2. Perspective view showing the 1D polymeric chain of the complex **1**.

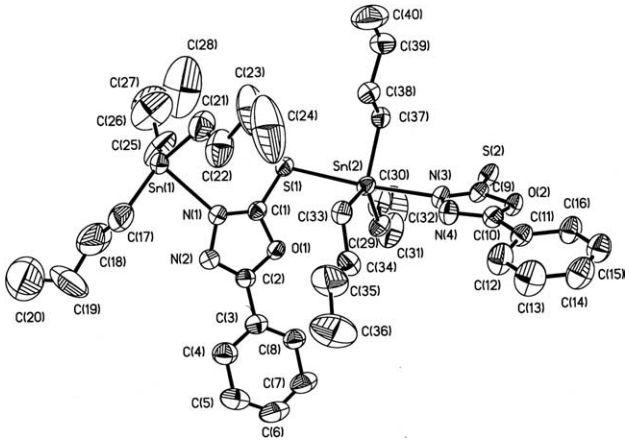


Fig. 3. Molecular structure of the complex **2**.

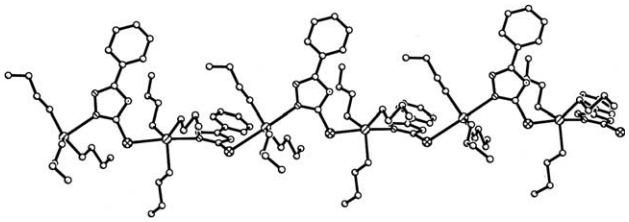


Fig. 4. Perspective view showing the 1D polymeric chain of the complex **2**.

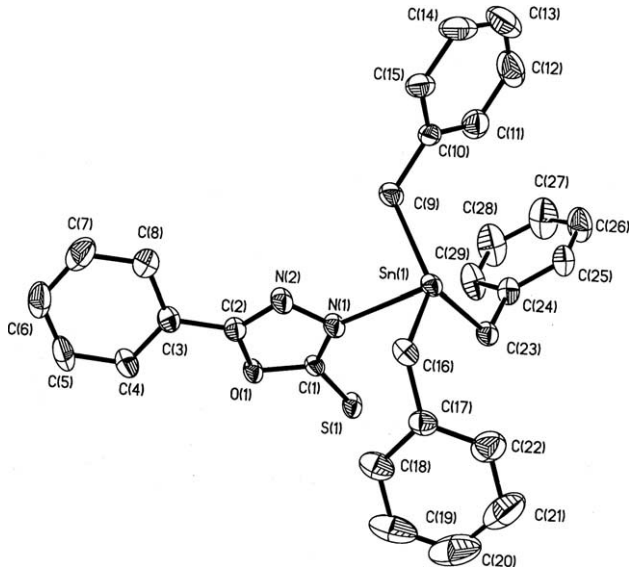


Fig. 5. Molecular structure of the complex **3**.

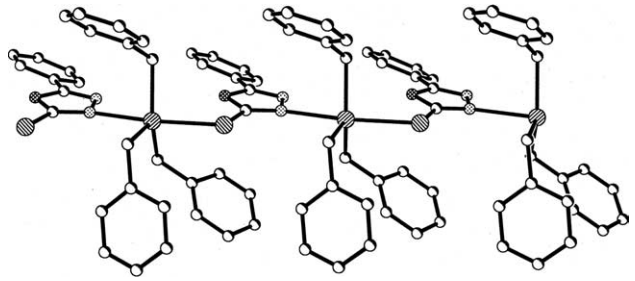


Fig. 6. Perspective view showing the 1D polymeric chain of the complex **3**.

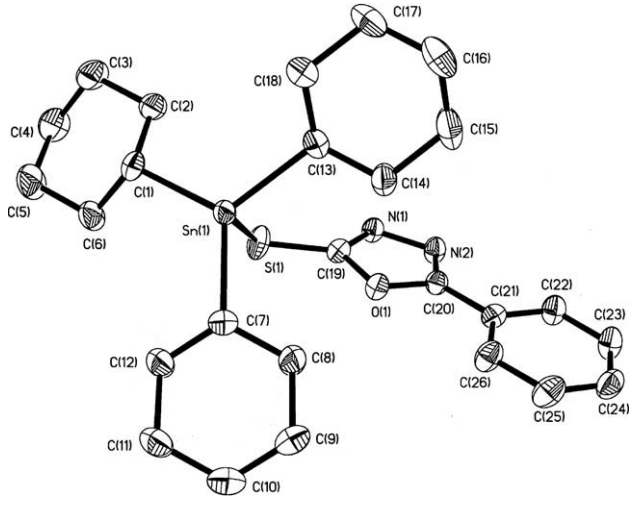


Fig. 7. Molecular structure of the complex **4**.

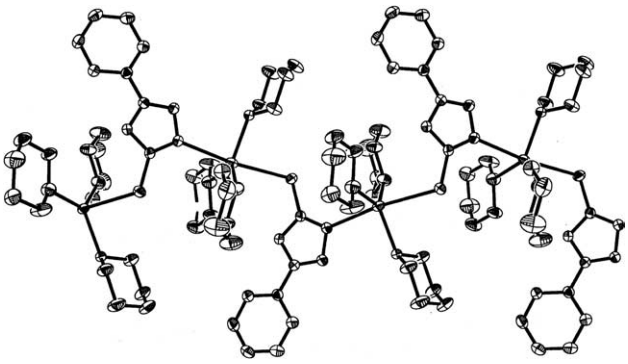


Fig. 8. Perspective view showing the 1D polymeric chain of the complex **4**.

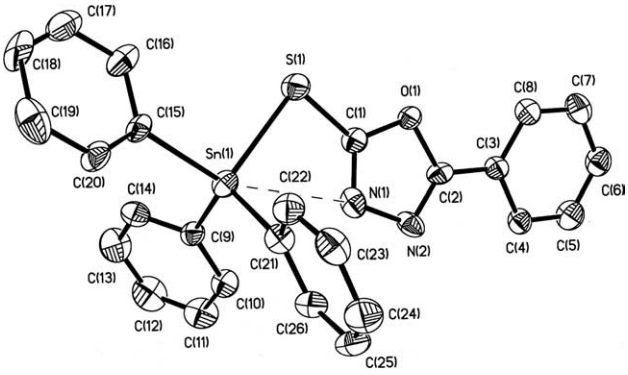


Fig. 9. Molecular structure of the complex **5**.

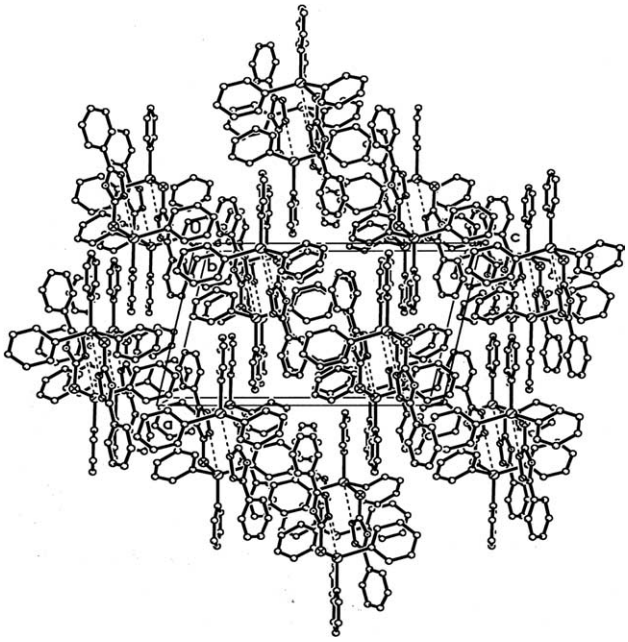


Fig. 10. Packing diagram of complex **5**.

a little less than 360°, indicating that the corresponding atoms are almost in the same plane. But the axial angles are S(1)–Sn(1)–N(1)#2 (173.0(2)°) in complex **1**; N(1)–Sn(1)–S(2)#1 (177.49(15)°) in complex **2**; N(1)–Sn(1)–S(1)#1 (174.51(7)°) in complex **3**; N(1)–Sn(1)–S(1) (172.36(6)°) in complex **4**, respectively, slightly

Table 2
Selected bond lengths (Å) and bond angles (°) for complex **1**

Bond lengths	
Sn(1)–C(10)	2.125(9)
Sn(1)–S(1)	2.713(4)
Sn(1)–C(9)	2.13(1)
Sn(1)···O(1)	3.278(9)
Bond angles	
C(10)#1–Sn(1)–C(10)	123.4(5)
C(9)–Sn(1)–S(1)	91.0(4)
C(10)#1–Sn(1)–C(9)	118.0(3)
N(1)#2–Sn(1)–S(1)	173.0(2)
C(10)–Sn(1)–C(9)	118.0(3)
C(10)#1–Sn(1)–O(1)	70.3(3)
C(10)#1–Sn(1)–N(1)#2	83.6(4)
C(10)–Sn(1)–O(1)	70.3(3)
C(10)–Sn(1)–N(1)#2	83.6(4)
C(9)–Sn(1)–O(1)	143.0(4)
C(9)–Sn(1)–N(1)#2	96.0(4)
N(1)#2–Sn(1)–O(1)	121.0(3)
C(10)#1–Sn(1)–S(1)	93.1(3)
S(1)–Sn(1)–O(1)	52.0(1)
C(10)–Sn(1)–S(1)	93.1(3)

Table 3
Selected bond lengths (Å) and bond angles (°) for complex **2**

Bond lengths	
Sn(1)–C(25)	2.11(1)
Sn(2)–C(37)	2.144(7)
Sn(1)–C(21)	2.11(1)
Sn(2)–N(3)	2.440(6)
Sn(1)–C(17)	2.17(1)
Sn(2)–S(1)	2.773(3)
Sn(1)–N(1)	2.415(6)
Sn(2)···O(1)#1	3.461(3)
Sn(1)–S(2)#1	2.765(3)
Sn(1)···N(2)	3.310(3)
Sn(2)–C(33)	2.131(6)
Sn(2)···N(4)	3.389(3)
Sn(2)–C(29)	2.140(7)
Bond angles	
C(25)–Sn(1)–C(21)	118.7(5)
C(33)–Sn(2)–C(29)	121.4(3)
C(25)–Sn(1)–C(17)	124.7(6)
C(33)–Sn(2)–C(37)	118.0(3)
C(21)–Sn(1)–C(17)	116.5(5)
C(29)–Sn(2)–C(37)	120.4(3)
C(25)–Sn(1)–N(1)	88.4(3)
C(33)–Sn(2)–N(3)	85.8(2)
C(21)–Sn(1)–N(1)	90.9(3)
C(29)–Sn(2)–N(3)	91.7(3)
C(17)–Sn(1)–N(1)	88.5(3)
C(37)–Sn(2)–N(3)	87.9(3)
C(25)–Sn(1)–S(2)#1	89.6(3)
C(33)–Sn(2)–S(1)	93.1(2)
C(21)–Sn(1)–S(2)#1	91.4(3)
C(29)–Sn(2)–S(1)	93.5(2)
C(17)–Sn(1)–S(2)#1	91.5(3)
C(37)–Sn(2)–S(1)	87.8(2)
N(1)–Sn(1)–S(2)#1	177.5(2)
N(3)–Sn(2)–S(1)	174.4(1)

Table 4
Selected bond lengths (Å) and bond angles (°) for complex **3**

Bond lengths	
Sn(1)–C(23)	2.152(3)
Sn(1)–N(1)	2.455(3)
Sn(1)–C(9)	2.166(3)
Sn(1)–S(1)#1	2.657(1)
Bond angles	
C(23)–Sn(1)–C(9)	116.4(1)
C(23)–Sn(1)–S(1)#1	91.01(9)
C(23)–Sn(1)–C(16)	111.6(1)
C(9)–Sn(1)–S(1)#1	99.3(1)
C(9)–Sn(1)–C(16)	130.0(1)
C(16)–Sn(1)–S(1)#1	92.8(1)
C(23)–Sn(1)–N(1)	93.6(1)
N(1)–Sn(1)–S(1)#1	174.51(7)
C(9)–Sn(1)–N(1)	81.2(1)
C(1)–S(1)–Sn(1)#2	98.2(1)
C(16)–Sn(1)–N(1)	82.8(1)

Table 5
Selected bond lengths (Å) and bond angles (°) for complex **4**

Bond lengths	
Sn(1)–C(7)	2.160(3)
Sn(1)–N(1)	2.524(2)
Sn(1)–C(13)	2.163(3)
Sn(1)–S(1)	2.8108(8)
Sn(1)–C(1)	2.173(3)
Bond angles	
C(7)–Sn(1)–C(13)	122.5(1)
C(7)–Sn(1)–S(1)	96.1(1)
C(7)–Sn(1)–C(1)	121.2(1)
C(13)–Sn(1)–S(1)	92.1(1)
C(13)–Sn(1)–C(1)	116.2(1)
C(1)–Sn(1)–S(1)	85.19(8)
C(7)–Sn(1)–N(1)	84.8(1)
N(1)–Sn(1)–S(1)	172.36(6)
C(13)–Sn(1)–N(1)	93.9(1)
C(1)–Sn(1)–N(1)	87.85(9)

Table 6
Selected bond lengths (Å) and bond angles (°) for complex **5**

Bond lengths	
Sn(1)–C(21)	2.105(9)
Sn(1)–S(1)	2.476(8)
Sn(1)–C(9)	2.12(1)
Sn(1)···N(1)	2.90(1)
Sn(1)–C(15)	2.14(1)
S(1)–C(1)	1.71(1)
Bond angles	
C(21)–Sn(1)–C(9)	120.9(4)
C(21)–Sn(1)–N(1)	78.5(3)
C(21)–Sn(1)–C(15)	108.2(3)
C(9)–Sn(1)–N(1)	82.8(3)
C(9)–Sn(1)–C(15)	109.6(3)
C(15)–Sn(1)–N(1)	157.9(3)
C(21)–Sn(1)–S(1)	107.3(3)
S(1)–Sn(1)–N(1)	59.2(2)
C(9)–Sn(1)–S(1)	109.7(2)
C(1)–N(1)–Sn(1)–	83.3(6)
C(15)–Sn(1)–S(1)	98.9(2)
N(2)–N(1)–Sn(1)	169.2(6)

deviating from 180°, thus they are all distorted trigonal–bipyramidal geometry.

All the Sn–S bond lengths Sn(1)–S(1)#1 (2.713(4) Å) for complex **1**; Sn(1)–S(2)#1 (2.765(3) Å) for complex **2**; Sn(1)–S(1)#1 (2.6565(11) Å) for complex **3**; Sn(1)–S(1) (2.8108(8) Å) for complex **4**, are a little longer than the covalent radii of Sn and S (2.42 Å) [18,19], and quite shorter than the van der Waals radii of of Sn and S (4.00 Å) [20]. Concerning Sn–N bond lengths, the values are Sn(1)–N(1)#2 (2.450(12) Å) for complex **1**; Sn(1)–N(1) (2.415(6) Å) for complex **2**; Sn(1)–N(1) (2.455(3) Å) for complex **3**; Sn(1)–N(1) (2.524(2) Å) for complex **4**, respectively. All these lie in the range recorded in the Cambridge Crystallographic Database from 2.27 to 2.58 Å [21b], slightly greater than the sum of the covalent radii of tin and nitrogen atoms (2.15 Å) but considerably less than the van der Waals radii of the two atoms (3.74 Å) [21a].

The intramolecular interaction distances of Sn, N(2)#1 and/or Sn, O(1)#1 are: 3.158 and 3.278(9) Å for complex **1**; 3.310 and 3.583 Å for complex **2**; 3.206 and 3.127 Å for complex **3**; 3.397 Å for complex **4**, respectively. All the bond distances are within the van der Waals radii of Sn and N atoms (3.74 Å) [21a] and Sn and O atoms (3.68 Å) [22a]. But they are much longer than the values recorded in the Cambridge Crystallographic Database (Sn–N 2.27–2.58 Å) [21b] and Sn–O (2.61–3.02 Å) [22b,c], and cannot be regarded as weak coordination bonds.

Further, most Sn–S and Sn–N bond lengths in complexes **1**–**4** are comparable with those in organotin(IV) derivatives from heterocyclic thionates containing a nitrogen atom (or more), such as organotin thiotetrazoles complexes (Sn–S 2.477(4)–2.614(5) Å and Sn–N 2.464(5)–2.810(7) Å) [6,10a]. To some extent, our ligand has some resemblance with thiotetrazoles. Due to the multidentate nature of the oxadiazole and tetrazole ring, both of them have the possibility to act as a fulcrum through which lattice construction is orchestrated in one or more dimensions [23]. And polymeric chains of complexes **1**–**4** in this paper are covalently linked through intermolecular Sn–N bonds, while organotin thiotetrazoles complexes prefer to adopt both covalent bond and all kinds of hydrogen bonding to construct polymeric chain, 2D zigzag sheets and 3D arrays [24].

3.4.2. $Ph_3Sn[S(C_8H_5N_2O)]$ (**5**)

For complex **5**, the central tin atom forms four primary bonds: three to the phenyl groups and one to the sulfur atom. The Sn–S bond length (2.476(8) Å) lies toward the middle of the range reported for triphenyltin heteoarenethiolates (2.405–2.481 Å) [18,19]. This bond length is a little longer than the sum of covalent radii of Sn and S atoms (2.42 Å) [18,19], but is considerably shorter than the sum of van der Waals radii of Sn and S atoms (4.00 Å) [20]. And it is similar to that found in $Ph_3Sn[S(C_7H_5N_4O)]$ (2.4760(17) Å) [9] and $Ph_3Sn(S–C_2SN_2–S)SnPh_3$ (2.467(2) Å) [8]. Besides, there exist intramolecular Sn···N weak interaction, common observed in triphenyltin heteroarenethiolates [25]. The Sn···N bond length (2.896(12) Å) is midway between the sums of the covalent radii and van der Waals radii of tin and nitrogen (2.15–3.74 Å) [21a] and can be regarded as weak coordination bond. Including the Sn···N weak interaction, the geometry at tin in complex **5** becomes distorted *cis*-trigonal–bipyramidal with the axial-tin-axial angle C(15)–Sn(1)–N(1) (157.9(3)°). As a result of the Sn···N weak coordination bond, though the C–Sn–C bond angles are close to the theoretical tetrahedral angle, the C–Sn–S bond angles are more acute or obtuse than it, largest deviations occurring in C(9)–Sn(1)–S(1) 109.7(2)°, C(15)–Sn(1)–S(1) 98.9(2)° and C(21)–Sn(1)–S(1) 107.3(3)°. In the oxadiazole, the C–S bond distance (C(1)–S(1) 1.708(11) Å) lies between the average value of the double C=S bond in thioureas (1.681 Å) and the single C–S bond in the C–S–Me fragment (1.789 Å) [26], suggesting that the C–S bond has some double-bond character in the deprotonated oxadiazole.

4. Conclusions

A series of organotin(IV) complexes based on 5-phenyl-1,3,4-oxadiazole-2-thiol have been synthesized and characterized. Detailed studies on the structures and spectra of these complexes indicate that the stereo-constraints from the R groups of trialkyltin chloride have great influence on the final coordination mode and crystal structures. Methyl, *n*-butyl, benzyl, cyclohexyl have the smaller spatial resistance, consequently, complexes **1**–**4** adopt the same coordination modes and exhibit 1D polymeric chains through Sn and N intermolecular interactions, respectively. But, phenyl has the bigger stereo-constraints and prevents another ligand chelating the central tin atom, so, complex **5** does not form a 1D polymeric chain. Therefore, we conclude that the decrease of stereo-constraints may benefit the coordination of nitrogen atoms.

5. Supplementary material

Crystallographic data (excluding structure factors) for the structure reported in this paper have been deposited with the Cambridge Crystallographic Data Center as supplementary publication nos. CCDC-257756 for **1**, 238959 for **2**, 257755 for **3**, 261920 for **4** and 238958 for **5**. Copies of the data can be obtained free of charge on application to the Director, CCDC, 12 Union Road, Cambridge, CB2 1EZ, UK,

fax: +44 1223 336033, e-mail: deposit@ccdc.cam.ac.uk or http://www.ccdc.cam.ac.uk.

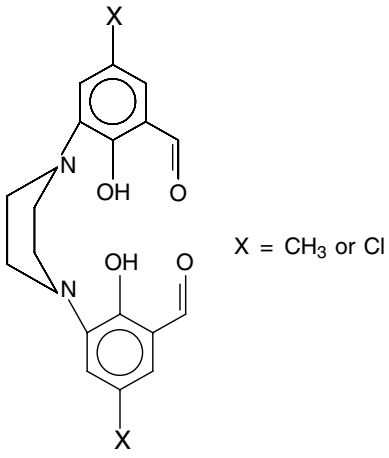
Acknowledgements

We thank the National Natural Science Foundation of China (20271025) and the Natural Science Foundation of Shandong Province for financial support.

References

[1] N. Speziali, B.G. Guimarães, R.M. Silva, P.H. Duarte, S.R. Aguiar, Acta Crystallogr. C50 (1994) 1059.
[2] G.D. Andreeti, G. Bocelli, G. Calestani, P. Sgarabotto, J. Organomet. Chem. 273 (1984) 31.
[3] L. Pellerito, L. Nagy, Coordin. Chem. Rev. 224 (2002) 111.
[4] J.A. Deiters, R.R. Holmes, J. Am. Chem. Soc. 109 (1987) 1686.
[5] K.C. Molloy, S.J. Blunden, R. Hill, J. Chem. Soc., Dalton Trans. (1988) 1259.
[6] S. Bhandari, M.F. Mahon, J.G. Mc Ginley, K.C. Molloy, C.E.E. Roper, J. Chem. Soc., Dalton Trans. (1998) 3425.
[7] C.L. Ma, Q. Jiang, R.F. Zhang, J. Organomet. Chem. 678 (2003) 148.
[8] C.L. Ma, F. Li, Q. Jiang, R.F. Zhang, J. Organomet. Chem. 689 (2004) 96.
[9] C.L. Ma, J.F. Sun, Polyhedron 23 (2004) 1547.
[10] (a) R.J. Deeth, K.C. molloy, M.F. Mahon, S. Whittaker, J. Organomet. Chem. 430 (1992) 25;
(b) O. Jiménez-Sandoval, R. Cea-Olivares, S. Hernández-Ortega, Polyhedron 16 (1997) 4129;
(c) R. Cea-Olivares, O. Jiménez-Sandoval, G. Espinosa-Pérez, C. Silvestru, Polyhedron 13 (1994) 2809;
(d) J. Bravo, M.B. Cordero, J.S. Casas, A. Sánchez, J. Sordo, E.E. Castellano, J. Zukerman-Schpector, J. Organomet. Chem. 482 (1994) 147;
(e) R. Cea-Olivares, O. Jiménez-Sandoval, G. Espinosa-Pérez, C. Silvestru, J. Organomet. Chem. 484 (1994) 33.
[11] K. Sisido, Y. Takeda, Z. Kinugawa, J. Am. Chem. Soc. 83 (1961) 538.
[12] T.A. George, J. Organomet. Chem. 31 (1971) 233.
[13] J.R. May, W.R. Mc Whinnie, R.C. Poller, Spectrochim. Acta A 27 (1971) 969.
[14] R.C. Poller, The Chemistry of Organotin Compounds, Logos Press, London, 1970.
[15] C.L. Ma, Q. Jiang, R.F. Zhang, Can. J. Chem. 81 (2003) 825.
[16] C.L. Ma, Q. Jiang, R.F. Zhang, Appl. Organomet. Chem. 17 (2003) 623.
[17] Y. Ye, Q. Zeng, L.Z. Liu, Synth. Commun. 31 (2001) 2373.
[18] B.D. James, R.J. Magee, W.C. Patalinghug, B.W. Skelton, A.H. White, J. Organomet. Chem. 467 (1994) 51.
[19] J.S. Casas, A. Castineiras, E.G. Martinez, A.S. González, A. Sánchez, J. Sordo, Polyhedron 16 (1997) 795.
[20] V. Vrabel, J. Lokaj, E. Kello, J. Garaj, A.C. Batsanov, Yu.T. Struchkov, Acta Crystallogr., Sect. C 48 (1992) 633.
[21] (a) J.E. Huheey, E.A. Keiter, R.L. Keiter, Principles and Applications of Inorganic Chemistry, 4th ed., Harper Collins, New York, 1993;
(b) F.H. Allen, S.A. Bellard, M.D. Brice, B.A. Cartwright, A. Doubleday, H. Higgs, T. Hummelink, B.G. Hummelink-Peters, O. Kennard, W.D.S. Motherwell, J.R. Rogers, D.G. Watson, Acta Crystallogr., Sect. B 35 (1979) 2331.
[22] (a) A. Bondi, J. Phys. Chem. 68 (1964) 441;
(b) K.C. Molloy, T.G. Purcell, K. Quill, I.W. Nowell, J. Organomet. Chem. 267 (1984) 237;
(c) A.R. Forrester, S.J. Garden, R.A. Howie, J.L. Wardell, J. Chem. Soc., Dalton Trans. (1992) 2615.
[23] (a) A. Goodger, M. Hill, M.F. Mahon, J. McGinley, K.C. Molloy, J. Chem. Soc., Dalton Trans. (1996) 847;
(b) M. Hill, M.F. Mahon, K.C. Molloy, J. Chem. Soc., Dalton Trans. (1996) 1857.
[24] (a) M.F. Mahon, K.C. Molloy, P.C. Waterfield, J. Organomet. Chem. 361 (1989) C5;
(b) M. Hill, M.F. Mahon, J.G. McGinley, K.C. Molloy, J. Chem. Soc., Dalton Trans. (1996) 835.
[25] N.G. Fumanova, Yu.T. Strchkov, E.M. Rokhlina, D.N. Kravtsov, J. Struct. Chem. Engl. Trans. 21 (1980) 766.
[26] F.H. Allen, O. Kennard, D.G. Watson, L. Brammer, A.G. Orpen, R. Taylor, J. Chem. Soc., Perkin Trans. II S1 (1987).

reported several macromonocyclic metal complexes, which are of interest for availing magneto-structural correlations and as useful model for electrochemical studies. Our previous works [26–30] report the magnetic and electrochemical properties of various acyclic and macromonocyclic copper(II), Mn(III) and Ni(II) complexes of the following type of ligand (**I**):



(**I**)

Our recent works [31–33] focused on synthesis and characterization of new macrobicyclic tricompartmental copper(II) complexes containing nitrogen and oxygen donor atoms. Herein we report the interesting chemistry (redox-driven translocation of reduced metal ion) observed in electrochemical studies of synthesized unsymmetrical tricompartmental macrobicyclic nickel(II) complexes and also their catalytic studies. The role of Ni(II) ion in promoting the hydrolysis of phosphate esters [34,35] has been the subject of considerable study and a great deal is now known. The mechanism of 4-nitrophenyl phosphate (NPP) hydrolysis involves the concerted binding of the substrate molecule on one metal centre and the nucleophilic attack of water or hydroxide ion at the other metal centre.

2. Experimental

Elemental analysis was carried out on a Carlo Erba Model 1106 elemental analyzer. ^{1}H NMR spectra were recorded using FX-80-Q Fourier transition NMR spectrometer. Electronic spectral studies were carried out on a Hitachi 320 spectrophotometer in the range 200–800 nm. IR spectra were recorded on a Hitachi 270-50 spectrophotometer on KBr disks in the range 4000–250 cm^{-1}. The mass spectra were obtained on JEOL DX-303 mass spectrometer. The electrospray (ES) mass spectra of the complexes were obtained on a micromass Quatro II triple quadropole mass spectrometer. Molar conductivity was measured by using an Elico model SX 80 conductivity bridge using freshly prepared solution of the complex in CH_3CN. Cyclic Voltammograms were obtained on CHI600A (CHI Instruments Co., USA) electrochemical analyzer using DMF. The measurements were carried out under oxygen free condition by purging nitrogen gas, using a three electrode cell in which glassy carbon electrode was working electrode, saturated Ag/AgCl electrode was reference electrode and platinum wire was used as auxiliary electrode. Glassy carbon electrode surface was pretreated by metallographic polishing with alumina on a velvet cloth (abraded with fine grade of emery paper), followed by ultrasonic cleaning in double distilled water and washing with small amount of highly diluted acid and DMF. Two separate double step chronocoulometry experiments were carried out for the binuclear nickel(II) complexes in the first and second reduction/oxidation potential range under oxygen free condition. The plots have been corrected for background. Ferrocene/Ferrocenium (1+) couple was used as standard and $E_{1/2}$ of the Ferrocene/Ferrocenium (Fc/Fc^+) couple under the experimental condition is 470 mV in DMF and ΔE_p for Fc/Fc^+ is 70 mV. Tetra(*n*-butyl)ammonium perchlorate (TBAP) was used as supporting electrolyte. The kinetic investigation of hydrolysis of 4-nitrophenyl phosphate was carried out spectrophotometrically by choosing the strongest absorbance at 420 nm and monitoring the increase in the absorbance at this wavelength as a function of time. A plot of $\log(A_\infty/A_\infty - A_t)$ versus time was made for each complexes and the rate constant of hydrolysis of 4-nitrophenyl phosphate was calculated. All the kinetic studies were carried out in DMF solvent at room temperature (25 °C).

2.1. Materials

5-Methylsalicyladehyde [36], 3-chloromethyl-5-methylsalicylaldehyde [37] and 3,4:9,10-dibenzo-1,13-diaza-5,9-dioxacycloheptadecane [38,39] were prepared from the literature methods. TBAP used as supporting electrolyte in electrochemical measurement was purchased from Fluka and recrystallised from hot methanol. [*Caution*! TBAP is potentially explosive; hence care should be taken in handling the compound.] DMF and CH_3CN were obtained from E. MERCK.

Methanol was sufficiently added to acetonitrile fractionated at high reflux until the boiling temperature rises from 60 to 80 °C and the distillate became optically clear. Sodium hydride was added and the mixture was refluxed for 15 min and then distilled rapidly.

DMF can be azeotropically distilled with benzene (10% v/v, previously dried over CaH_2) at atmospheric pressure; water and benzene distill at <80 °C. The liquid remaining in the distillation flask was dried further by adding $MgSO_4$. After the flask and its contents were shaken for 1 day, an additional amount of $MgSO_4$

was added and the DMF was distilled at a pressure of 15–20 mmHg.

All other chemicals and solvents were of analytical grade and were used as received without any further purification.

2.2. Synthesis of precursor compound

2.2.1. 3,4:9,10-Dibenzo-1,13[N,N′-bis{(3-formyl-2-hydroxy-5-methyl)benzyl}diaza]-5,9-dioxacycloheptadecane (Precursor compound)

A mixture of 3,4:9,10-dibenzo-1,13-diaza-5,9-dioxacycloheptadecane (1.088 g, 3.2 mmol) and triethylamine (1.32 g, 6.4 mmol) in 30 ml of THF was added slowly to a stirred solution of 3-chloromethyl-5-methylsalicylaldehyde (1.16 g, 6.4 mmol) in 30 ml of THF. After the addition was over the stirring was continued further for one more hour. The whole solution was then refluxed under water bath for 3 h and was allowed to cool on standing at room temperature. Copious water was added to this solution to dissolve any salt obtained. Then the required compound was extracted in organic medium using chloroform. The extraction was repeated for two to three times. A pale yellow compound was obtained on evaporation of solvent at room temperature (25 °C). Light yellow microcrystals were obtained on recrystallization from chloroform. Yield: 1.61 g (79%), m.p.: 81 °C. *Anal.* Calc. data for $C_{39}H_{44}O_6N_2$: C, 73.58; H, 6.91; N, 4.40. Found: C, 73.69; H, 7.08; N, 4.65%. IR data (ν cm^{-1}): 1670 (νC=O, s), 3396 (νOH, br). ^{1}H NMR (δ ppm in $CDCl_3$): 10.0 (s, 2H, CHO protons), 7.2 (m, 12H, aromatic protons), 4.5 (m, 4H, methylene protons attached to oxygen atom), 3.8 (m, 8H, benzylic protons), 3.5 (s, 4H, methylene protons attached to nitrogen atom), 2.3 (s, 6H, CH_3 protons attached to aromatic ring), 2.1 (s, 4H, CH_2 protons attached to alkyl chain. Mass (EI) *m/z*: 636 (m^+).

2.3. Synthesis of macrobicyclic mononuclear nickel(II) complexes

2.3.1. [NiL^1](ClO$_4$)

A methanolic solution (20 ml) of nickel(II)perchlorate hexahydrate (0.694 g, 1.9 mmol) [*Caution*! Nickel(II) perchlorate salt is potentially explosive; hence care should be taken in handling the compound.] was added to the hot solution of precursor compound (1.208 g, 1.9 mmol) in 25 ml of $CHCl_3$ followed by the addition of 1,2-diaminoethane (0.128 g, 1.9 mmol) in 5 ml of methanol. The solution was refluxed on water bath for 24 h. After the reaction was over, the solution was filtered at hot condition and allowed to stand at room temperature. After slow evaporation of the solvent at 25 °C, the orange red compound was obtained, washed with methanol and dried in vacuum. Yield: 1.24 g (76%). *Anal.* Calc. data for $C_{43}H_{50}O_8N_5ClNi$: C, 60.13; H, 5.82; N, 8.15. Found: C, 60.22; H, 5.94; N, 8.21%. Selected IR (KBr): 1624 (s), 1091 (s), 627 (s) cm^{-1}. Conductance (Λ_m/S cm^2 mol^{-1}) in CH_3CN: 155. λ_{max} (nm) (ε/M^{-1} cm^{-1}) in CH_3CN: 599 (177), 364 (13 100), 252 (37 100).

2.3.2. [NiL^2](ClO$_4$)

[NiL^2](ClO$_4$) was synthesized by following the previously described procedure for [NiL^1](ClO$_4$), using 1,3-diaminopropane instead of 1,2-diaminoethane. The compound obtained was orange red. Yield: 1.22 g (73%). *Anal.* Calc. data for $C_{44}H_{52}O_8N_5ClNi$: C, 60.55; H, 5.96; N, 8.02. Found: C, 60.61; H, 6.03; N, 8.15%. Selected IR (KBr): 1625 (s), 1100 (s), 626 (s) cm^{-1}. ^{1}H NMR (δ ppm in CH_3CN): 8.0 (s, 2H, protons in CH=N), 6.6 to 7.1 (m, 12H, aromatic protons), 3.9 (m, 4H, methylene protons attached to oxygen atom), 2.1 (m, 2H, methylene protons attached to CH_2–O), 4.5 (s, 4H, benzylic protons attached to $^+$NH in the amine compartment), 3.6 (s, 4H, benzylic protons attached to N in the amine compartment), 3.2 (s, 2H, methylene protons attached to $^+$NH in the amine compartment), 1.7 (s, 2H, methylene protons attached to $^+$NH–CH_2 in the amine compartment), 1.3 (s, 2H, methylene protons attached to N–CH_2 in the amine compartment), 2.3 (s, 2H, methylene protons attached to N in the amine compartment), 2.3 (s, 6H, aromatic CH_3 protons), 3.4 (s, 4H, CH_2 protons attached to imine nitrogen), 1.6 (s, 2H, CH_2 protons attached to CH_2–N=). ^{13}C NMR (δ ppm in CH_3CN): 163 (s, carbon in CH=N), 118, 124, 128, 130, 133 and 155 (m, aromatic carbons in imine compartment), 114, 120, 123, 126, 129 and 159 (m, aromatic carbons in ether oxygen compartment), 69 (m, 2C, carbons in *C*H_2–O), 31 (m, 1C, carbon in *C*H_2–CH_2–O), 49 (s, 4C, benzylic carbons attached to $^+$NH and N in the amine compartment), 53 (s, 1C, methylene carbon in *C*H_2–$^+$NH and carbon in *C*H_2–N), 24 (s, 1C, methylene carbon in *C*H_2–CH_2–$^+$NH), 28 (s, 1C, methylene carbon in *C*H_2–CH_2–N), 22 (s, 2C, carbons in Ar–*C*H_3), 164 (s, 2C, carbons in Ar–*C*H=N), 34 (s, 2C, carbons in =N–*C*H_2–*C*H_2–N=), 21 (s, 1C, carbon in *C*H_2–CH_2–N=). Conductance (Λ_m/S cm^2 mol^{-1}) in CH_3CN: 139. λ_{max} (nm) (ε/M^{-1} cm^{-1}) in CH_3CN: 610 (168), 376 (15 700), 263 (34 000).

2.3.3. [NiL^3](ClO$_4$)

[NiL^3](ClO$_4$) was synthesized by following the previously described procedure for [NiL^1](ClO$_4$), using 1, 4-diaminobutane instead of 1,2-diaminoethane. The compound obtained was orange red. Yield: 1.34 g (80%). *Anal.* Calc. data for $C_{46}H_{54}O_8N_5ClNi$: C, 62.30; H, 6.09; N, 7.90. Found: C, 62.44; H, 6.20; N, 8.01%. Selected IR (KBr): 1622 (s), 1090 (s), 625 (s) cm^{-1}. Conductance (Λ_m/S cm^2 mol^{-1}) in CH_3CN: 144. λ_{max} (nm) (ε/M^{-1} cm^{-1}) in CH_3CN: 636 (139), 372 (15 900), 258 (30 600).

2.3.4. $[NiL^4](ClO_4)$

$[NiL^4](ClO_4)$ was synthesized by following the previously described procedure for $[NiL^1](ClO_4)$, using *o*-phenylenediamine instead of 1,2-diaminoethane. The compound obtained was orange red. Yield: 1.36 g (79%). *Anal*. Calc. data for $C_{47}H_{50}O_8N_5ClNi$: C, 62.25; H, 5.51; N, 7.72. Found: C, 62.41; H, 5.69; N, 7.86%. Selected IR (KBr): 1620 (s), 1100 (s), 628 (s) cm^{-1}. Conductance (Λ_m/S cm^2 mol^{-1}) in CH_3CN: 158. λ_{max} (nm) (ε/M^{-1} cm^{-1}) in CH_3CN: 632 (150), 401 (15 600), 360 (17 300), 256 (38 700).

2.3.5. $[NiL^5](ClO_4)$

$[NiL^5](ClO_4)$ was synthesized by following the previously described procedure for $[NiL^1](ClO_4)$, using 1,8-diaminonaphthalene instead of 1,2-diaminoethane. The compound obtained was orange red. Yield: 1.43 g (79%). *Anal*. Calc. data for $C_{51}H_{52}O_8N_5ClNi$: C, 64.01; H, 5.43; N, 7.32. Found : C, 64.19; H, 5.58; N, 7.48%. Selected IR (KBr): 1625 (s), 1099 (s), 625 (s) cm^{-1}. Conductance (Λ_m/S cm^2 mol^{-1}) in CH_3CN: 150. λ_{max} (nm) (ε/M^{-1} cm^{-1}) in CH_3CN: 665 (161), 410 (15 600), 370 (16 100), 262 (32 100).

2.4. Synthesis of macrobicyclic binuclear nickel(II) complexes

2.4.1. $[Ni_2L^1](ClO_4)_2$

A methanolic solution (20 ml) of nickel(II)perchlorate hexahydrate (0.694 g, 1.9 mmol) [*Caution*! Nickel(II) perchlorate salt is potentially explosive; hence care should be taken in handling the compound.] was added to the hot solution of PC (1.208 g, 1.9 mmol) in 25 ml of $CHCl_3$ followed by the addition of 1,2-diaminoethane (0.128 g, 1.9 mmol) and triethylamine (0.265 g, 1.9 mmol) in 5 ml of methanol. After 1 h, nickel(II) perchlorate (0.694 g, 1.9 mmol) in 20 ml of methanol was added and the whole reaction mixture was refluxed on water bath for 24 h. After the reaction was over, the reaction mixture was filtered and allowed for standing at room temperature (25 °C). After slow evaporation of the solvent at 25 °C, the orange red compound obtained was washed with methanol and dried in vacuum. Yield: 1.60 g (80%). *Anal*. Calc. data for $C_{45}H_{52}O_{12}N_6Cl_2Ni_2$: C, 51.13; H, 4.92; N, 7.95. Found: C, 51.29; H, 5.08; N, 8.10%. Selected IR (KBr): 1625 (s), 1100 (m), 626 (s) cm^{-1}. Conductance (Λ_m/S cm^2 mol^{-1}) in CH_3CN: 282. λ_{max} (nm) (ε/M^{-1} cm^{-1}) in CH_3CN: 599 (231), 362 (11 900), 255 (38 200). Mass (ES) *m*/*z*: 974 (m^+).

2.4.2. $[Ni_2L^2](ClO_4)_2$

$[Ni_2L^2](ClO_4)_2$ was synthesized by following the previously described procedure for $[Ni_2L^1](ClO_4)_2$, using 1,3-diaminopropane instead of 1,2-diaminoethane. The compound obtained was orange red. Yield: 1.59 g (78%). *Anal*. Calc. data for $C_{46}H_{54}O_{12}N_6Cl_2Ni_2$: C, 51.58; H, 5.04; N, 7.85. Found: C, 51.71; H, 5.16; N, 8.02%. Selected IR (KBr): 1624 (s), 1100 (m), 627 (s) cm^{-1}. Conductance (Λ_m/S cm^2 mol^{-1}) in CH_3CN: 280. λ_{max} (nm) (ε/M^{-1} cm^{-1}) in CH_3CN: 615 (242), 374 (12 850), 265 (32 300).

2.4.3. $[Ni_2L^3](ClO_4)_2$

$[Ni_2L^3](ClO_4)_2$ was synthesized by following the previously described procedure for $[Ni_2L^1](ClO_4)_2$, using 1,4-diaminobutane instead of 1,2-diaminoethane. The compound obtained was orange red. Yield: 1.55 g (75%). *Anal*. Calc. data for $C_{47}H_{56}O_{12}N_6Cl_2Ni_2$: C, 52.02; H, 5.23, N, 7.74. Found: C, 52.21; H, 5.38; N, 7.83%. Selected IR (KBr): 1622 (s), 1098 (m), 628 (s) cm^{-1}. Conductance (Λ_m/S cm^2 mol^{-1}) in CH_3CN: 298. λ_{max} (nm) (ε/M^{-1} cm^{-1}) in CH_3CN: 630 (224), 370 (12 300), 260 (32 500).

2.4.4. $[Ni_2L^4](ClO_4)_2$

$[Ni_2L^4](ClO_4)_2$ was synthesized by following the previously described procedure for $[Ni_2L^1](ClO_4)_2$, using *o*-phenylenediamine instead of 1,2-diaminoethane. The compound obtained was orange red. Yield: 1.58 g (72%). *Anal*. Calc. data for $C_{49}H_{52}O_{12}N_6Cl_2Ni_2$: C, 53.26; H, 4.71, N, 7.60. Found: C, 53.40; H, 4.88; N, 7.74%. Selected IR (KBr): 1620 (s), 1100 (m), 625 (s) cm^{-1}. Conductance (Λ_m/S cm^2 mol^{-1}) in CH_3CN: 310. λ_{max} (nm) (ε/M^{-1} cm^{-1}) in CH_3CN: 620 (265), 410 (14 500), 362 (14 100), 258 (37 200).

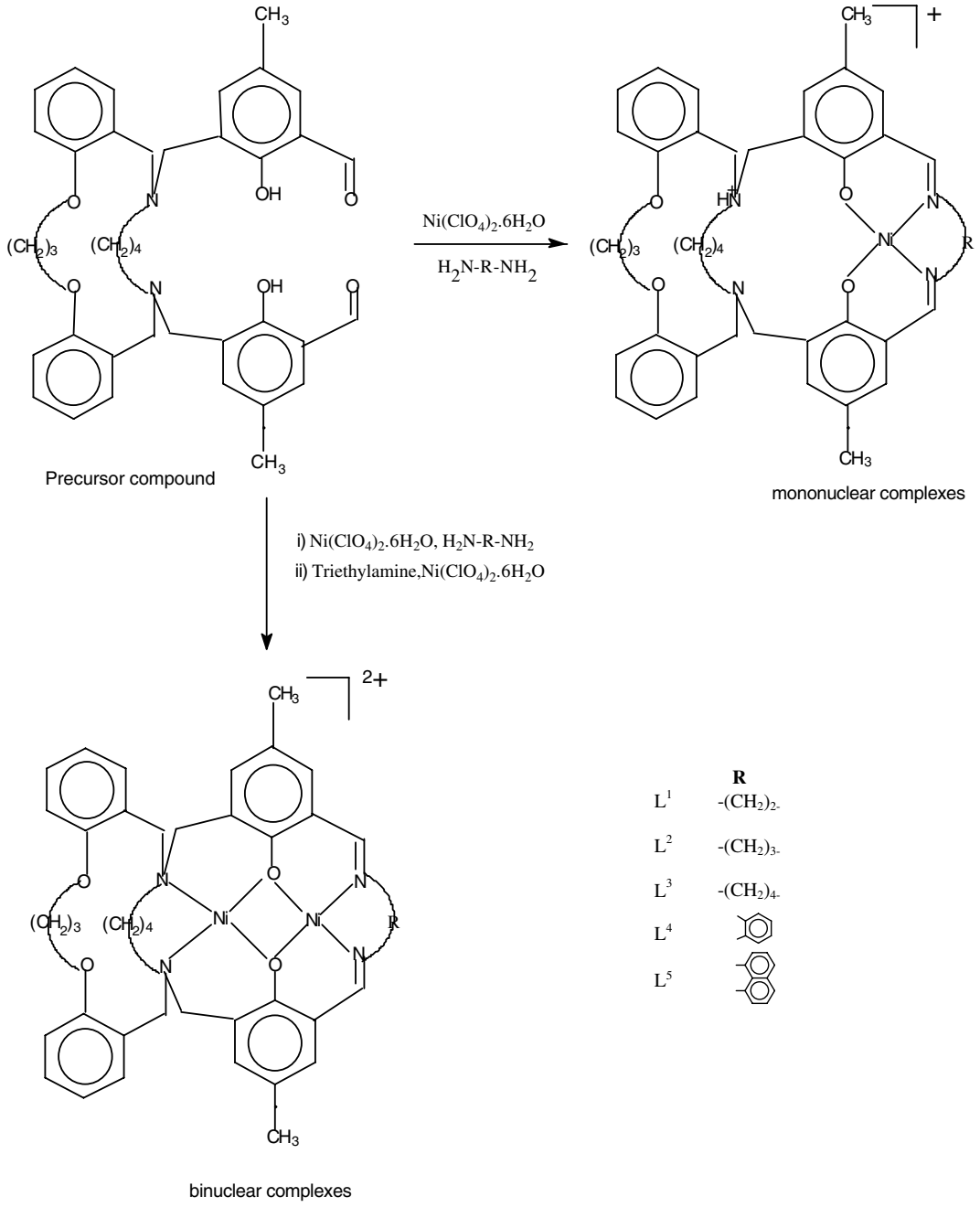
2.4.5. $[Ni_2L^5](ClO_4)_2$

$[Ni_2L^5](ClO_4)_2$ was synthesized by following the previously described procedure for $[Ni_2L^1](ClO_4)_2$, using 1,8-diaminonaphthalene instead of 1,2-diaminoethane. The compound obtained was orange red. Yield: 1.58 g (72%). *Anal*. Calc. data for $C_{53}H_{56}O_{12}N_6Cl_2Ni_2$: C, 55.11; H, 4.68, N, 7.27. Found: C, 55.29; H, 4.84; N, 7.39%. Selected IR (KBr): 1622 (s), 1099 (m), 626 (s) cm^{-1}. Conductance (Λ_m/S cm^2 mol^{-1}) in CH_3CN: 299. λ_{max} (nm) (ε/M^{-1} cm^{-1}) in CH_3CN: 660 (268), 405 (14 700), 371 (16 220), 263 (36 820).

In all cases we could obtain only microcrystals and attempts to obtain the crystals suitable for X-ray analysis were unsuccessful.

3. Results and discussion

Schiff's base condensation of the precursor compounds with diamines in the presence of metal ion by template method results into various macrobicyclic mono and binuclear nickel(II) complexes. Scheme 1 represents the synthetic pathway of mono and binuclear complexes. Our previous studies [31,32] rationalize the crystal structure of another series of similar type of copper(II) complexes Hence, in accordance with this, it is



Scheme 1. Synthesis of macrobicyclic mono and binuclear nickel(II) complexes.

proposed that the geometry around nickel(II) ion is distorted square planar and in the mononuclear complexes, one of the tertiary nitrogen atoms is protonated. Conductivity measurements indicate that mono and binuclear nickel(II) complexes are 1:1 and 1:2 electrolyte type, respectively. Extensive spectral, electrochemical and kinetic studies of the complexes were carried out.

3.1. Spectral studies

The IR spectra of the complexes show ν(C=N) peak [40] at 1620–1625 cm^{-1}. The effective Schiff's base condensation is evidenced by the formation of this new peak and the disappearance of the ν(C=O) peak at 1674 cm^{-1} in the complexes. The peaks appeared near 1100 and 620 cm^{-1} are characteristics of the uncoordinated perchlorate ion. The electronic spectra of the complexes show three main transitions. A weak band observed in the range 599–665 nm is due to d–d transition of the metal ion. On moving from the complexes of ligand L^1 to L^3 and L^4 to L^5, an increase in λ_{max} (red shift) [41] of the d–d transition of Ni(II) ion in the complexes was observed for both mono and binuclear copper(II) complexes. A moderate intensive band observed in the range

360–376 nm is due to ligand to metal charge transfer transition and the strong band observed in the range 252–263 nm is due to intraligand charge transfer transition [42]. Apart from these, additional peaks are observed for the complexes of ligands L^4 to L^5 due to the presence of aromatic ring in the imine nitrogen compartment. All the nickel(II) complexes are diamagnetic [30,43–45] and ESR silent.

3.2. Electrochemistry

The conductivity measurements [46,47] of the complexes in acetonitrile indicate that the mononuclear nickel(II) complexes are of 1:1 (139–158 Λ_m/S cm^2 mol^{-1}) electrolyte type and binuclear nickel(II) complexes are 1:2 (280–310 Λ_m/S cm^2 mol^{-1}) electrolyte type. Electrochemical properties of the complexes reported in the present work were studied by cyclic voltammetry in the potential range 0 to −1.6 V and 0 to +1.6 V in dimethylformamide containing 10^{-1} M tetra(*n*-butyl)-ammonium perchlorate. All the nickel(II) complexes undergo both reduction and oxidation in cathodic and anodic potential, respectively. Since the macrobicyclic complexes of ditopic ligands contain non-equivalent compartments, the translocation process has also been studied electrochemically using redox-driven mechanism.

3.2.1. Chronocoulometry study

Chronocoulometry [48] is an alternative and very useful mode for recording the electrochemical response. This is especially valuable for the study of surface process. The main two components of this technique are single step and double step experiments. The double step experiment is considered to be more versatile and generally in this case two curves are obtained. The first curve is due to the addition of the charge at the electrode and the second curve is obtained due to the reverse process, i.e., the removal of charge from the electrode surface. If the magnitude of slope of both the curves is same then it is said to be reversible and if the magnitude varies it is said to be quasireversible. Hence, in order to examine the nature of the process, two separate double step chronocoulometry experiments were carried out for binuclear nickel(II) complexes both in cathodic and anodic potential. In each experiment, two curves are obtained and from the studies it is inferred that the calculated magnitude of slope of both the curves varies and hence they are said to be quasireversible in nature. Figs. 1 and 2 represent the double step chronocoulometry response of binuclear nickel(II) complex $[Ni_2L^3](ClO_4)_2$ in cathodic and anodic potential, respectively.

3.2.2. Cyclic voltammetry study

3.2.2.1. Reduction at cathode. The cyclic voltammograms for the mononuclear complexes are shown in Fig. 3.

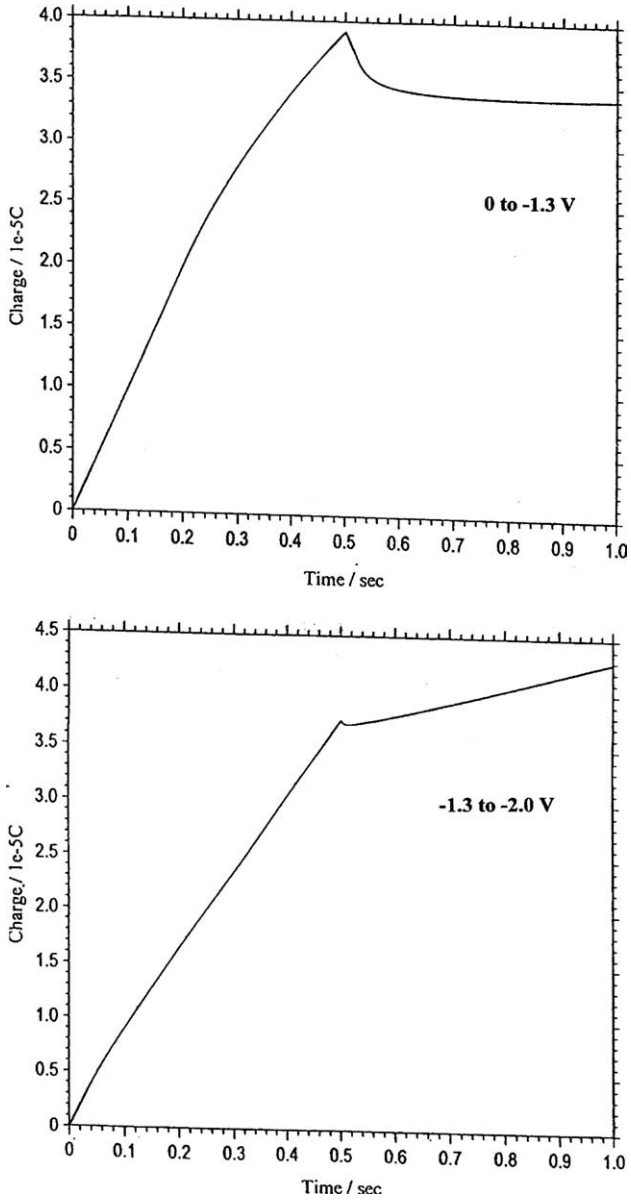


Fig. 1. Double step chronocoulometry response of binuclear complex $[Ni_2L^3](ClO_4)_2$ in reduction process.

Each voltammogram shows one quasireversible reduction wave at negative potential in the range −0.83 to −1.07 V. Controlled potential electrolysis carried out at 100 mV more negative than the reduction wave reveals the consumption of one electron per molecule ($n = 0.94$) and the experiment reports that the couple corresponding to one electron transfer process. Fig. 4 represents the cyclic voltammograms of the binuclear complexes. Binuclear complexes show two quasireversible reduction waves. The first reduction potential ranges from −0.95 to −1.29 V and the second reduction potential falls in the range −1.32 to −1.67 V. Tables 1 and 2 represent the electrochemical data of nickel(II) complexes in cathodic and anodic potential, respectively. Controlled potential electrolysis also carried out

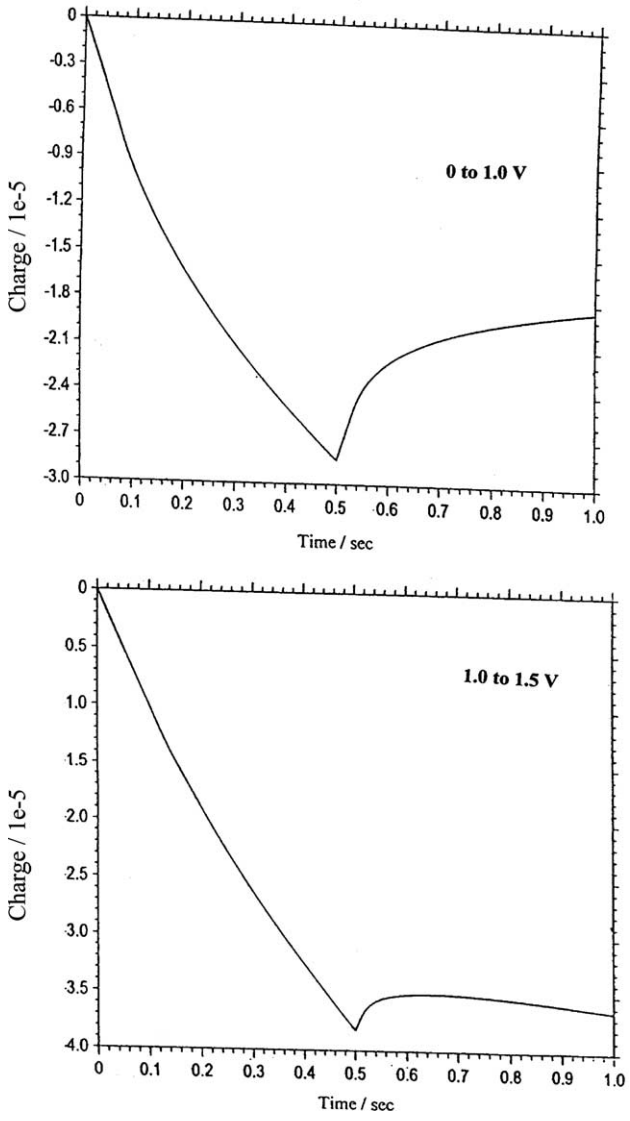


Fig. 2. Double step chronocoulometry response of binuclear complex $[Ni_2L^3](ClO_4)_2$ in oxidation process.

and the experiment reports that the each couple corresponding to one electron transfer process. So, the two redox processes are assigned as follows:

$$Ni^{II}Ni^{II} \rightleftharpoons Ni^{II}Ni^{I} \rightleftharpoons Ni^{I}Ni^{I}$$

The conproportionation constant for the equilibrium

$$Ni^{II}Ni^{II} + Ni^{I}Ni^{I} \overset{K_{con}}{\rightleftharpoons} 2Ni^{II}Ni^{I}$$

was calculated using the relationship $\log K_{con} = \Delta E/0.0591$.

The electrochemical behaviour of the complexes was compared on the basis of macrocyclic ring size. The reduction potential of the mononuclear nickel(II) complexes of ligands L^1 to L^3 and L^4 to L^5 shifts anodically from -0.89 to -0.82 V and from -1.01 to -0.91 V, respectively, as the macrocyclic ring size increases due to the presence of bulky group. This imparts more flexibility to the macrocycle [24,30,49,50] and tries to stabilize nickel(I) complex. In this case, the calculated ΔE values for quasireversible waves are generally larger and this may be due to the occurrence of electrochemical interconversion (translocation) [51] of reduced cation Ni(I) from the rigid imine nitrogen compartment

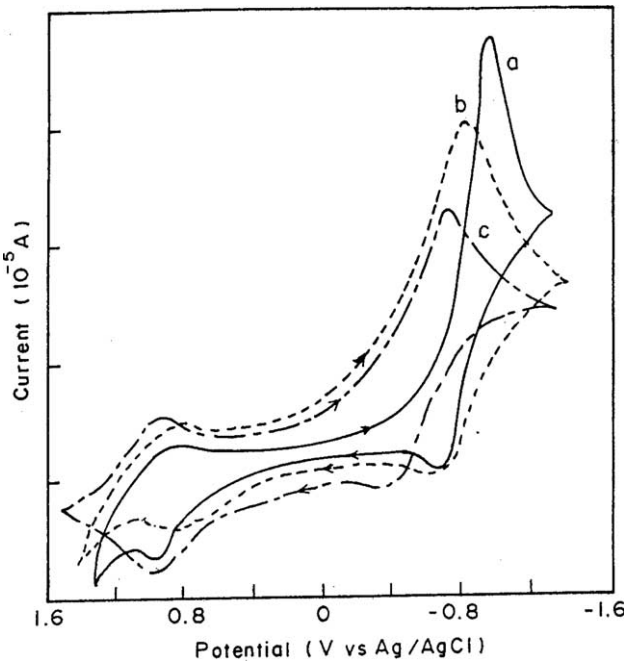


Fig. 3. Cyclic votammograms of the mononuclear nickel(II) complexes (1×10^{-3} M): (a) $[NiL^1](ClO_4)$, (b) $[NiL^2](ClO_4)$, (c) $[NiL^3](ClO_4)$.

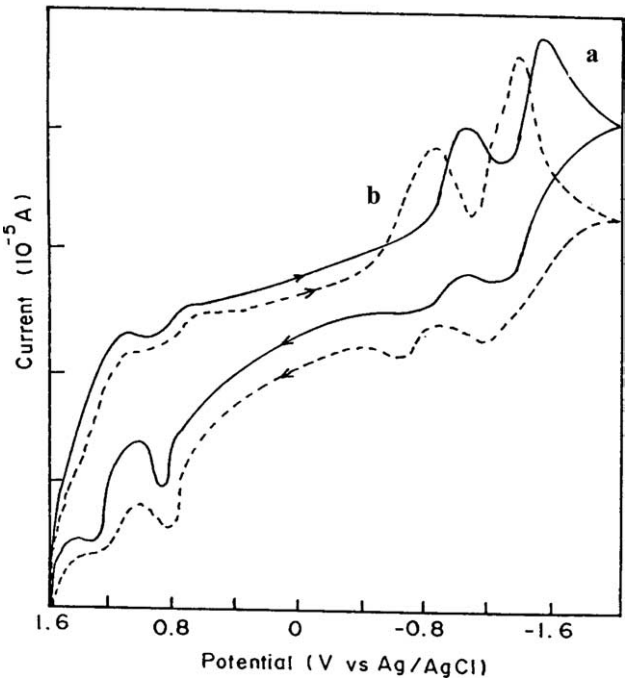


Fig. 4. Cyclic votammograms of the binuclear nickel(II) complexes (1×10^{-3} M): (a) $[Ni_2L^4](ClO_4)_2$, (b) $[Ni_2L^5](ClO_4)_2$.

Table 1
Electrochemical data[a] of mono and binuclear nickel(II) complexes in DMF medium (reduction)

Complexes	E^1_{pc} (V)	E^1_{pa} (V)	$E^1_{1/2}$ (V)	ΔE (mV)	E^2_{pc} (V)	E^2_{pa} (V)	$E^2_{1/2}$ (V)	ΔE (mV)	K_{con}
$[NiL^1](ClO_4)$	−0.89	−0.72	−0.81	170					
$[NiL^2](ClO_4)$	−0.86	−0.70	−0.78	160					
$[NiL^3](ClO_4)$	−0.82	−0.67	−0.75	150					
$[NiL^4](ClO_4)$	−1.01	−0.91	−0.96	100					
$[NiL^5](ClO_4)$	−0.91	−0.81	−0.86	100					
$[Ni_2L^1](ClO_4)_2$	−1.25	−1.08	−1.14	170	−1.64	−1.52	−1.58	120	2.79×10^7
$[Ni_2L^2](ClO_4)_2$	−1.21	−1.05	−1.12	160	−1.45	−1.35	−1.40	100	7.79×10^3
$[Ni_2L^3](ClO_4)_2$	−0.85	−0.73	−0.79	120	−1.22	−1.04	−1.13	180	5.66×10^5
$[Ni_2L^4](ClO_4)_2$	−1.27	−1.08	−1.18	190	−1.38	−1.21	−1.30	170	1.07×10^2
$[Ni_2L^5](ClO_4)_2$	−1.17	−1.08	−1.12	90	−1.29	−1.18	−1.24	110	1.07×10^2

[a] Measured by CV at 25 mV/s. *E* vs. Ag/AgCl conditions: GC working and Ag/AgCl reference electrodes; supporting electrolyte TBAP; concentration of complex 1×10^{-3} M, concentration of TBAP 1×10^{-1} M.

Table 2
Electrochemical data[a] of mono and binuclear nickel(II) complexes in DMF medium (oxidation)

Complexes	E^1_{pa} (V)	E^1_{pc} (V)	$E^1_{1/2}$ (V)	ΔE (mV)	E^2_{pa} (V)	E^2_{pc} (V)	$E^2_{1/2}$ (V)	ΔE (mV)
$[NiL^1](ClO_4)$	0.96	0.85	0.91	110				
$[NiL^2](ClO_4)$	0.88	0.76	0.82	120				
$[NiL^3](ClO_4)$	0.98	0.86	0.92	120				
$[NiL^4](ClO_4)$	0.72	0.59	0.66	130				
$[NiL^5](ClO_4)$	0.80	0.66	0.73	140				
$[Ni_2L^1](ClO_4)_2$	0.93	0.85	0.89	80	1.13	1.01	1.07	120
$[Ni_2L^2](ClO_4)_2$	0.83	0.73	0.78	100	1.07	0.97	1.02	100
$[Ni_2L^3](ClO_4)_2$	0.86	0.75	0.81	110	1.12	1.02	1.07	100
$[Ni_2L^4](ClO_4)_2$	0.91	0.81	0.86	100	1.19	1.08	1.14	110
$[Ni_2L^5](ClO_4)_2$	0.87	0.76	0.82	110	1.17	1.06	1.12	110

[a] Measured by CV at 25 mV/s. *E* vs. Ag/AgCl conditions: GC working and Ag/AgCl reference electrodes; supporting electrolyte TBAP; concentration of complex 1×10^{-3} M, concentration of TBAP 1×10^{-1} M.

(N_2O_2) to flexible tertiary nitrogen compartment (N_2O_2), which favours the tetrahedral geometry. The larger ΔE values indicate that the reduction process is associated with ECE mechanism. The decrease in ΔE value is observed as the chain length between two imine nitrogens increases and this eases the translocation process [31–33,51–54] moving from the complexes of ligands L^1 to L^3 and L^4 to L^5.

As the size of macrocycle is increased, shifting of both first and second reduction potentials towards anodic is observed for the binuclear nickel(II) complexes. For example the complex $[Ni_2L^1](ClO_4)_2$ has $E^1_{pc} = -1.25$ and $E^2_{pc} = -1.64$ V, which is more negative compared to the complex $[Ni_2L^2](ClO_4)_2$ ($E^1_{pc} = -1.21$ and $E^2_{pc} = -1.45$ V) and the same observation is inferred for the complexes of ligand L^{4-5} also. Thus due to the presence of bulky group in the imine nitrogen compartment, the whole macrocyclic ring becomes more flexible and hence undergoes easy reduction. Thus the large size of cavity easily holds the reduced cation and stabilizes the formation of Ni(I) in both the compartment. Concern in the calculation of K_{con} values of binuclear Ni(II) complexes leads to another interesting feature that the variation of K_{con} is random and not uniform as the macrocyclic ring size increases which has no explanation.

From the cyclic voltammetric studies it can be stated that the complexes containing aromatic diimines get reduced at higher negative potential than that of the complexes containing aliphatic diimine, even though it is expected to stabilize Ni(I) more effectively. The reason may be due to the increased stability of the macrocyclic systems due to aromatic and less deviation from planarity.

3.2.2.2. Oxidation at anode. The cyclic voltammograms of nickel(II) complexes obtained at positive potential region ranging from 0 to +1.5 V show one electron transfer waves. The oxidation process is also quasireversible in nature. It is obvious to say that the increase in macrocyclic ring size influences the oxidation potential to less extend only and no uniform variation is observed. Hence, the influence of macrocyclic ring size is unpredictable. The oxidation process can be assigned as follows:

$$Ni^{II}Ni^{II} \rightleftharpoons Ni^{II}Ni^{III} \rightleftharpoons Ni^{III}Ni^{III}$$

3.3. Kinetic studies of hydrolysis of 4-nitrophenylphosphate

The investigation of the kinetic studies of the nickel(II) complexes implies that the complexes act as model for phosphate hydrolase. The kinetics of the hydrolysis of 4-nitrophenyl phosphate was carried out using an equal concentration of the complex catalyst and tetramethylammonium hydroxide (10^{-3} M) and 4-nitrophenyl phosphate (10^{-1} M). The chromophore leaving group 4-nitrophenolate, which is the hydrolysis product of the substrate was monitored at 420 nm. The course of the reaction was followed at 420 nm nearly 45 min at regular time interval. The slope was determined by monitoring the growth of 420 nm band of the product 4-nitrophenolate ion. We have carried out the reaction in the absence of metal complex. No detectable hydrolysis of test substrate was observed when the metal complex was absent. We have also carried out the hydrolysis of 4-nitrophenyl phosphate for various concentration of the metal complex. A linear relationship for rate and the complex concentration obtained for the complex shows a pseudo first order dependence on the complex concentration. This clearly shows that this is truly catalytic.

Plots of $\log(A_\infty/A_\infty - A_t)$ versus time for catalytic activity of the mono and binuclear complexes hydrolysis for 4-nitrophenyl phosphate are obtained and shown in Figs. 5 and 6, respectively. The rate constant values are also reported in Table 3. The first apparent result was that the reactivities of the complexes differ significantly, as the size of macrocycle increases. The binuclear complexes have higher activities than the mononuclear complexes [55–59]. For example the binuclear complexes $[Ni_2L^1](ClO_4)_2$, $[Ni_2L^2](ClO_4)_2$, $[Ni_2L^3](ClO_4)$, $[Ni_2L^4](ClO_4)_2$ and $[Ni_2L^4](ClO_4)_2$ have the rate constant values 1.98×10^{-2}, 3.34×10^{-2}, 4.15×10^{-2}, 1.86×10^{-2} and $2.67\times10^{-2}\,min^{-1}$, respectively, whereas the mononuclear complexes $[NiL^1](ClO_4)$, $[NiL^2](ClO_4)$, $[NiL^3](ClO_4)$, $[NiL^4](ClO_4)$ and $[NiL^5](ClO_4)$ have the rate constant values 1.80×10^{-3}, 2.04×10^{-3}, 2.40×10^{-3}, 1.36×10^{-3} and $1.68\times10^{-3}\,min^{-1}$, respectively. This simply shows that the presence of two metal ions in close proximity enhances the catalytic activity in binuclear complexes than that of mononuclear complexes, which contain single metal ion and hence the rate constant values of binuclear complexes are comparatively high. This is due to the fact that the mononuclear complexes proceed via S_N1 type of reaction mechanism wherein, the external hydroxide ion coordinate to the metal ion, followed by deprotonation of OH and formation of an intermediate with the phosphate group and then cleavage of the bond to form the phenolate anion, along with

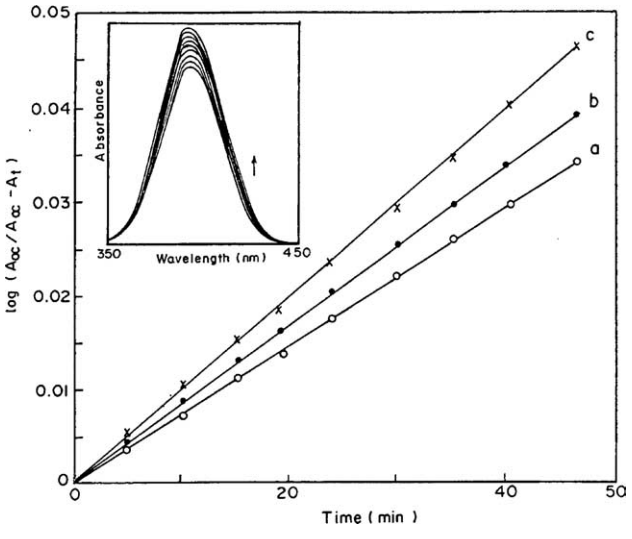


Fig. 5. Catalytic activity of mononuclear nickel(II) complexes for hydrolysis of 4-nitrophenylphosphate: (a) $[NiL^1](ClO_4)$, (b) $[NiL^2](ClO_4)$, (c) $[NiL^3](ClO_4)$.

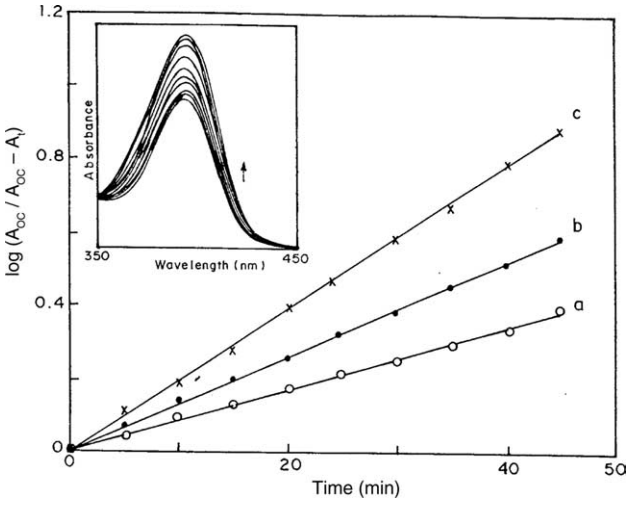


Fig. 6. Catalytic activity of binuclear nickel(II) complexes for hydrolysis of 4-nitrophenylphosphate: (a) $[Ni_2L^1](ClO_4)_2$, (b) $[Ni_2L^2](ClO_4)_2$, (c) $[Ni_2L^3](ClO_4)_2$.

Table 3
Catalytic activity[a] of mono and binuclear nickel(II) complexes for hydrolysis of 4-nitrophenyl phosphate

Complexes	Rate constant (min^{-1})
$[NiL^1](ClO_4)$	1.80×10^{-3}
$[NiL^2](ClO_4)$	2.04×10^{-3}
$[NiL^3](ClO_4)$	2.40×10^{-3}
$[NiL^4](ClO_4)$	1.36×10^{-3}
$[NiL^5](ClO_4)$	1.68×10^{-3}
$[Ni_2L^1](ClO_4)_2$	1.98×10^{-2}
$[Ni_2L^2](ClO_4)_2$	3.34×10^{-2}
$[Ni_2L^3](ClO_4)_2$	4.15×10^{-2}
$[Ni_2L^4](ClO_4)_2$	1.86×10^{-2}
$[Ni_2L^5](ClO_4)_2$	2.67×10^{-2}

[a] Measured spectrophotometrically in DMF medium. Concentration of the complexes and tetramethylammonium hydroxide: 1×10^{-3} M, concentration of 4-nitrophenyl phosphate: 1×10^{-1} M.

hydroxylation of the phosphate group. The binuclear nickel(II) complexes follow a concerted S_N2 type of mechanism where the nucleophile OH^- adds to one of the Ni ions and the phosphate is bound to the other metal ion. Here, bond formation and bond breakage, occur at the same time. The mechanism of the hydrolysis has already been reported [35,60,61]. The catalytic activities of both mono and binuclear complexes are found to increase as the macrocyclic ring size increases due to the intrinsic flexibility. The catalytic activity of the complexes containing aromatic diimines is found to be less than that of the complexes containing aliphatic diimines. This can be explained that the planarity, which is associated with aromatic ring, imparts less catalytic efficiency due to the rigidity of the systems as observed in the case of electrochemical reduction of the complexes.

4. Conclusion

This work involves the synthesis of lateral macrobicyclic compartmental nickel(II) complexes with phenolate bridging atoms. Various macrobicyclic mono and binuclear nickel(II) complexes have been synthesized and their extensive spectral, electrochemical and catalytic studies were carried out with significant modification in the ligand framework. The increase in macrocyclic ring size in the ligand framework influences the reduction (electrochemical) and catalytic properties of the complexes whereas it has no influence on the oxidation (electrochemical) properties of the complexes.

Acknowledgements

The author M.T. gratefully appreciates the financial support received from CSIR and UGC major project sanctioned to M.K., New Delhi.

References

[1] R.J. Butcher, G. Diven, G.R. Erickson, J. Jasinski, G.M. Mockler, R.Y. Pozdniakov, E. Sinn, Inorg. Chim. Acta 239 (1995) 107.
[2] G. Psomas, A.J. Stemmler, C.D. Samara, J.J. Bodwin, M. Schneider, M. Alexiou, J.W. Kampf, D.P. Kessissoglou, V.L. Pecoraro, Inorg. Chem. 40 (2001) 1562.
[3] L.F. Lindoy, The Chemistry of Macrocyclic Ligands Complexes, Cambridge University Press, Cambridge, 1989.
[4] R.M. Izatt, K. Pawalak, J.S. Bradshaw, R.L. Bruening, Chem. Rev. 91 (1991) 1721.
[5] P. Dapporto, V. Fusi, M. Micheloni, P. Palma, P. Paoli, R. Pontellini, Inorg. Chim. Acta 275–276 (1998) 168.
[6] R.R. Fenton, R. Gauci, P.C. Junk, L.F. Lindoy, R.C. Luckay, G.V. Meehan, J.R. Price, P. Turner, G. Wei, J. Chem. Soc., Dalton Trans. (2002) 2185.
[7] A. McAuley, S. Subramanian, Coord. Chem. Rev. 75 (2000) 200.
[8] L.F. Lindoy, Coord. Chem. Rev. 174 (1998) 327.
[9] R.D. Hancock, A.E. Martell, Chem. Rev. 89 (1989) 1875.
[10] R.D. Hancock, J. Chem. Educ. 69 (1992) 615.
[11] P. Diaz, A. Domenech, E.G. Espana, L. Lopez, S.V. Luis, J. Miravet, M. Querol, P. Sole, J. Supramol. Chem. 2 (2002) 107.
[12] D.A. Lawrence, T. Jiang, M. Levett, Chem. Rev. 95 (1995) 2229.
[13] G.R. Desijraju, Angew. Chem., Int. Ed. Engl. 34 (1995) 2311.
[14] C.F.V. Nostrum, R.J.M. Nolbe, J. Chem. Soc., Chem. Commun. (1996) 2385.
[15] W. Huang, S. Gou, D. Hu, S. Chantrapromma, H.-K. Fun, Q. Meng, Inorg. Chem. 41 (2002) 864.
[16] K.K. Nanda, L.K. Thompson, J.N. Bridson, K. Nag, J. Chem. Soc., Chem. Commun. (1994) 1337.
[17] R. Das, K. Nag, Inorg. Chem. 30 (1991) 2831.
[18] S.K. Mandal, L.K. Thompson, M.J. Newlands, A.K. Bisvas, B. Adhikari, K. Nag, Can. J. Chem. 87 (1989) 362.
[19] S.K. Mandal, L.K. Thompson, K. Nag, J.P. Charland, K.J. Gabe, Inorg. Chem. 26 (1987) 1391.
[20] M. Yinemura, Y. Usuki, M. Ohba, H. Okawa, J. Chem. Soc., Dalton Trans. (2000) 3624.
[21] H. Adams, D.E. Fenton, S.R. Haque, S.L. Heath, M. Ohba, H. Okawa, S.E. Spey, J. Chem. Soc., Dalton Trans. (2000) 1849.
[22] M. Yamami, H. Frutachi, Y. Yokohama, H. Okawa, Inorg. Chem. 37 (1998) 6832.
[23] H. Okawa, J. Nishio, M. Ohba, M. Tadokoro, N. Matsumoto, M. Koikawa, S. Kida, D.E. Fenton, Inorg. Chem. 32 (1993) 2949.
[24] H. Okawa, M. Tadokora, T.Y. Aretake, M. Ohba, K. shinda, M. Mitsumi, M. Koikawa, M. Tomono, D.E. Fenton, J. Chem. Soc., Dalton Trans. (1993) 253.
[25] T.Y. Aretake, M. Ohba, h. Sakiyama, M. Todokoro, N. Massumo, H. Okawa, Inorg. Chim. Acta 212 (1993) 183.
[26] S. Karunakaran, M. Kandaswamy, J. Chem. Soc., Dalton Trans. (1994) 1595.
[27] M. Marappan, V. Narayanan, M. Kandaswamy, J. Chem. Soc., Dalton Trans. 3 (1998) 3405.
[28] N. Sengottuvelan, J. Manonmani, M. Kandaswamy, Polyhedron 21 (2002) 2767.
[29] J. Manonmani, R. Thirumurugan, M. Kandaswamy, M. Kuppayee, S. Shanmuga Sundararaj, M.N. Ponnuswamy, G. Shanmugam, H.K. Fun, Polyhedron 19 (2001) 2011.
[30] J. Manonmani, R. Thirumurugan, M. Kandaswamy, V. Narayanan, S.S. Raj, M.N. Ponnuswamy, G. Shanmugam, H.K. Fun, Polyhedron 20 (2001) 3039.
[31] M. Thirumavalavan, P. Akilan, M. Kandaswamy, K. Chinnakali, G. Senthil Kumar, H.K. Fun, Inorg. Chem. 42 (2003) 3308.
[32] M. Thirumavalavan, P. Akilan, M. Kandaswamy, Inorg. Chem. Commun. 5 (2002) 422.
[33] P. Akilan, M. Thirumavalavan, M. Kandaswamy, Polyhedron 22 (2003) 1407.
[34] M.A. Rosh, W.C. Trogelr, Inorg. Chem. 29 (1990) 2409.
[35] D. Volkmer, B. Hommerich, K. Giesar, W. Haase, B. Krebs, Inorg. Chem. 35 (1996) 3792.
[36] J.C. Duff, J. Chem. Soc. (1941) 547.
[37] J.D. Crane, D.E. Fenton, J.M. Latour, A.J. Smith, J. Chem. Soc., Dalton Trans. (1991) 2279.
[38] L.G. Armstrong, L.F. Lindoy, Inorg. Chem. 14 (1975) 1322.
[39] P.G. Grimsley, L.F. Lindoy, H.C. Lip, R.J. Smith, J.T. Baker, Aust. J. Chem. 30 (1977) 2095.
[40] G. Das, R. Shukala, S. Mandal, R. Singh, P.K. Bharadwaj, J.V. Singh, K.U. Whitmire, Inorg. Chem. 36 (1997) 323.
[41] R. Bhalla, M. Helliwell, C.D. Garner, Inorg. Chem. 36 (1997) 2944.
[42] P. Amudha, M. Kandaswamy, L. Govindaswamy, D. Velmurugan, Inorg. Chem. 37 (1998) 4490.
[43] A. Bottcher, H. Elias, E. Jager, H. Langfelderova, M. Mazur, L. Mullor, H. Paulus, P. Pelikan, M. Rudolph, M. Valko, Inorg. Chem. 32 (1993) 4131.

[44] A.B.P. Lever, Inorganic Electronic Spectroscopy, 2nd ed., Elsevier, Amsterdam, 1984.
[45] S. Bhattacharya, T.J.R. Weakley, M. Chudhury, Inorg. Chem. 38 (1999) 633.
[46] W.J. Geary, Coord. Chem. Rev. 7 (1971) 81.
[47] K.R. Adam, G. Andergee, L.F. Lindoy, H.C. Lip, M. Mcpartlin, J.H. Rea, R.J. Smith, P.A. Tasker, Inorg. Chem. 19 (1980) 2956.
[48] A.J. Bard, L.R. Faulkner, Electrochemical Methods: Fundamentals and Applications, John Wiley & Sons, Inc., 1980.
[49] E. Gao, W. Bu, G. Yang, D. Liao, Z. Jiang, S. Yan, G. Wang, J. Chem. Soc., Dalton Trans. (2000) 1431.
[50] P.A. Connick, K.A. Macor, Inorg. Chem. 30 (1991) 4654.
[51] V. Amendola, L. Fabbrizzi, C. Mangano, P. Pallavicini, Acc. Chem. Res. 43 (2001) 488.
[52] J.-P. Collin, C.D. Buchecker, P. Gavina, M.C.J. Molero, J.-P. Sauvage, Acc. Chem. Res. 34 (2001) 477.
[53] C.A. Schalley, K. Beizi, F. Vogtle, Acc. Chem. Res. 34 (2001) 465.
[54] A.N. Shipway, I. Willner, Acc. Chem. Res. 34 (2001) 421.
[55] S. Parimala, S.N. Gita, M. Kandaswamy, Polyhedron 17 (1998) 3445.
[56] K. Moore, G.S. Vigee, Inorg. Chim. Acta 66 (1982) 125.
[57] G.S. Vigee, E.E. Eduok, J. Inorg. Nucl. Chem. 43 (1981) 2171.
[58] N. Oishi, Y. Nishida, K. Ida, Bull. Chem. Soc. Jpn. 53 (1980) 2847.
[59] J. Reim, B. Krebs, J. Chem. Soc., Dalton Trans. (1997) 3793.
[60] S. Parimala, M. Kandaswamy, Inorg. Chem. Commun. 6 (2003) 1252.
[61] N.P. Sadler, C.-C. Chuang, R.M. Milburn, Inorg. Chem. 34 (1995) 402.

2. Experimental

2.1. General comments

All non-hydrolytic procedures were carried out under a nitrogen atmosphere (ultra-high purity) using standard schlenk techniques [30]. Solvents were dried and distilled prior to use [31]. Polymerization grade ethene was further purified by passage through columns of 10 A molecular sieves and MnO. Al(^{i}Bu)$_3$, ^{n}BuLi and $TiCl_4$ were purchased from Aldrich. 2-(3, 4-diphenyl cyclopentadienyl)-4, 6-di-*tert*-butyl phenoxytitanium dichloride (**1**), 2-(3, 4-diphenyl cyclopentadienyl)-6-*tert*-butyl phenoxytitanium dichloride (**2**) [28], and $Ph_3C^+B(C_6F_5)^-$ [32–34] were prepared according to literature procedures. NMR spectra were measured using a Varian Unity-400 or Varian Mercury-300 NMR spectrometer. Hydrolysis reactions were carried out in air using commercial solvents without purification.

2.2. Preparation of {[η^5;η^1-2-(3,4-Ph_2Cp)-4,6-di-^{t}Bu-C_6H_2O]TiCl}$_2$O (**3**)

Complex **1** (100 mg, 0.185 mmol) was dissolved in CH_2Cl_2 (20 mL), the color of the solution changed slowly from red to yellow (Scheme 1). After 24 h, the solvent was removed to leave a yellow solid. Recrystallization from CH_2Cl_2:hexane (1:3) gave pure **3** as orange yellow crystals (88.3 mg, 93.0%). *Anal.* Calc. for $C_{62}H_{64}Cl_2O_3Ti_2$ (1023.81): C, 72.73; H, 6.30. Found: C, 72.67; H, 6.25%. ESI-MS, *m/z*: 927.6 $[M - {}^tBu - 3CH_2 + 2H]^+$, 814.4 $[M - 2{}^tBu - 2Cl - 2CH_2 + 3H]^+$, 701.4 $[M - 2{}^tBu - 2CO - 6CH_2 - 2Cl + 2H]^+$; MALDI-MS, *m/z*: 842.7 $[M - 2CO - 4CH_2 - 2Cl + 2H]$, 422.7 $[ligand]^+$. ^{1}H NMR ($CDCl_3$, 300 MHz; 298 K) δ 6.73–7.58 (m, 24H, Ph), 6.81 (d, $^4J_{H-H} = 3$ Hz, 2H, Cp), 4.49 (d, $^4J_{H-H} = 3$ Hz, 2H, Cp), 1.40 (s, 18H, Ph–^{t}Bu), 1.30 (s, 18H, Ph–^{t}Bu). ^{13}C NMR ($CDCl_3$, 75 MHz; 298 K) δ 171.8, 145.7, 143.8, 134.9, 133.4, 132.8, 131.3, 130.4, 130.3, 129.8, 129.6, 129.5, 128.5, 128.3, 128.2, 128.0, 126.6, 124.0, 122.8, 35.3, 35.1, 32.1, 29.9 ppm.

2.3. Preparation of {[η^5;η^1-2-(3,4-Ph_2Cp)-6-^{t}Bu-C_6H_3O]TiCl}$_2$O (**4**)

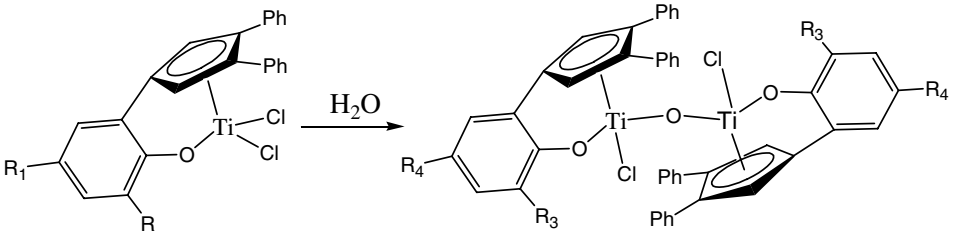
Complex **4** (100 mg, 0.207 mmol) was prepared in the same way as described above for the synthesis of **3** (Scheme 1). Pure **4** (86 mg, 91.2% was obtained as yellow solid); *Anal.* Calc. for $C_{54}H_{48}Cl_2O_3Ti_2$ (911.60): C, 71.15; H, 5.31. Found: C, 71.09; H, 5.27%. ESI-MS, *m/z*: 814.4 $[M - 2Cl - 2CH_2 + 1H]^+$, 701.4 $[M - 2CO - 4CH_2 - 2Cl - 2Me + 2H]^+$; MALDI-MS, *m/z*: 730.8 $[M - 2CO - 4CH_2 - 2Cl + 2H]^+$, 366.7 $[ligand]^+$. ^{1}H NMR ($CDCl_3$, 300 MHz; 298 K) δ 6.77–7.59 (m, 26H, Ph and 2H, Cp), 4.60 (d, $^4J_{H-H} = 3$ Hz, 2H, Cp), 1.29 (s, 18H, Ph–^{t}Bu). ^{13}C NMR ($CDCl_3$, 75 MHz; 298 K) δ 174.0, 143.7, 136.1, 134.4, 132.3, 131.5, 130.4, 130.1, 129.9, 129.8, 129.6, 128.7, 128.4, 128.3, 128.0, 127.0, 126.5, 125.9, 122.3, 35.0, 29.7 ppm.

2.4. X-ray structure determinations of *3*

Single crystals of **3** suitable for X-ray structural analysis were obtained from solution of CH_2Cl_2:hexane (V/V = 1/3). Diffraction data were collected at 293 K on a Bruker SMART-CCD diffractometer (graphite-monochromated Mo Kα-radiation: $\lambda = 0.71073$ Å). Details of the crystal data, data collections, and structure refinements are summarized in Table 1. The structure was solved by direct method [35] and refined by full-matrix least-squares on F^2. All non-hydrogen atoms were refined anisotropically and the hydrogen atoms were included in idealized position. All calculations were performed using the SHELXTL [36] crystallographic software packages.

2.5. Polymerization reactions

A dry 250 mL steel autoclave was charged with 70 mL of toluene, thermostated at desired temperature and saturated with ethene (1.0 bar). The polymerization reaction was started by injection of a mixture of catalyst and Al(^{i}Bu)$_3$ in toluene (5 mL) and a solution of $Ph_3C^+B(C_6F_5)_4^-$ in toluene (5 mL) at the same time.



Scheme 1. Synthetic procedure of complexes **3**–**4**.

Table 1
Crystal data and structural refinements details for **3**

Empirical formula	$C_{31}H_{32}ClO_{1.50}Ti$
Formula weight	511.92
Crystal system	monoclinic
Temperature (K)	293(2)
Wavelength (Å)	0.71073
Space group	*C*2/*c*
a (Å)	24.863(5)
b (Å)	9.902(2)
c (Å)	23.726(6)
β (°)	106.540(5)
Volume (Å^3)	5599(2)
Z	8
D_c (g cm^{-3})	1.215
F(0 0 0)	2152
Absorption coefficient (mm^{-1})	0.423
Scan type	$\omega - 2\theta$
2θ Range (°)	$3.42 \leqslant 2\theta \leqslant 46.56$
Reflections collected	6354
Reflections unique (R_{int})	3983 (0.0381)
Refinement method	full-matrix least-squares on F^2
Data/restraints/parameters	3983/7/312
Goodness-of-fit on F^2	0.917
Final *R* indices [$I > 2\sigma(I)$]	$R1 = 0.0522$, $wR_2 = 0.1155$
R indices (all data)	$R_1 = 0.1047$, $wR_2 = 0.1327$
Largest difference peak and hole (e Å^{-3})	0.355 and −0.281

The vessel was repressurized to needed pressure with ethene immediately and the pressure was kept by continuously feeding monomer. After 30 min, the polymerization was quenched by injecting acidified methanol [HCl (3 M):methanol = 1:1]. The mixture was stirred overnight and the polymer was collected by filtration, washed with water, methanol, and dried in vacuo.

3. Results and discussions

3.1. Synthesis and analysis of complexes 3 and 4

It has been found that complexes **1** and **2** are stable to air and moisture in solid state and can be left in air for several days without obvious change [28]. They also exhibit good thermostability and could be heated to about 200 °C without decomposition. However, complexes **1** and **2** can be easily hydrolyzed in solution to produce corresponding dimeric oxo-bridged complexes **3** and **4**, which can be obtained in high yields by dissolving **1** and **2** in wet solvent, such as CH_2Cl_2, toluene, and hexanes. Similar hydrolysis reaction for titanocene type complexes has been reported previously [37–39]. In some instances, stable polynuclear oxo-bridged species containing dimer, trimer and tetramer had been produced by aerobic oxidation [40] or hydrolysis processes [41–45]. In our case, only the dimeric hydrolytic product **3** or **4** has been obtained and no polynuclear oxo-bridged complex has been observed.

^{1}H and ^{13}C NMR spectra of **3** and **4** are obviously complicated than those of **1** and **2**, which could be attributed to that the dimeric oxo-bridged complexes **3** and **4** both adopt a chiral environment about Ti atom. For this reason, the two phenyl groups on the Cp ring and the two protons of the Cp group of **3** and **4** are inequivalent. As a result, the number of inequivalent C in ^{13}C NMR spectra of **3** and **4** is six more than that of complexes **1** and **2**, respectively. Due to steric repulsion between two units of the molecule, the ^{1}H NMR signal for one of the two protons shifts to high-field ($\delta = 4.49$ ppm for **3**, $\delta = 4.60$ ppm for **4**), while the signal for the other proton does not change very much compared to the Cp protons of complexes **1** and **2** [28] (6.81 ppm for **3**, the signal for **6** is mixed with the signals of the Ph protons). The coupling constant ($^4J_{H-H}$) of the two protons for **3** and **4** are both about 3 Hz.

3.2. Crystal structure of 3

The molecular structure of complex **3** was determined by single crystal diffraction analysis. The ORTEP drawing of the molecular structure is shown in Fig. 1. The selected bond lengths and angles are summarized in Table 2. The molecular structure consists of two {[η^5;η^1-2-(3,4-Ph_2Cp)-4,6-di-^{t}Bu-butyl-C_6H_2O]TiCl} units linked by Ti–O–Ti linkage. Selected bond lengths and angles for one unit will be used in subsequent discussions. The whole molecule adopts a C_2-symmetric structure. The geometry around titanium can be described as pseudo-tetrahedral, which is defined by a substituted cyclopentadienyl ring, a chloride atom, and two oxygen atoms (one is from the oxo-bridge, the other is from the phenoxy). The Cp(cent)–Ti1–O2 angle of 105.9° is slightly smaller than the one in **2**

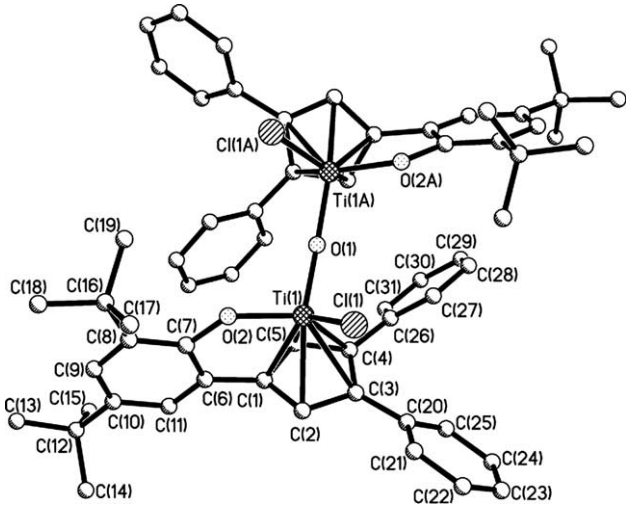


Fig. 1. Structure of complex **3**. (Thermal ellipsoids are drawn at the 30% probability level.)

Table 2
Selected bond lengths and angles for complex **3**

Ti(1)–O(1)	1.8125(9)
Ti(1)–C(1)	2.332 (4)
Ti(1)–C(3)	2.470(4)
Ti(1)–C(5)	2.309(4)
O(2)–C(7)	1.377(4)
C(1)–C(6)	1.473(5)
C(4)–C(26)	1.483(5)
Ti(1)–H(5)	2.861
O(1)–Ti(1)–O(2)	104.16(10)
Cp1(cent)–Ti(1)–O(1)	119.1
Ti(1)–Cp1(cent)–C(1)	87.1
C(1)–C(6)–C(7)	113.7(4)
C(7)–O(2)–Ti(1)	128.9(3)
Ti(1)–O(2)	1.842(3)
Ti(1)–C(2)	2.385(4)
Ti(1)–C(4)	2.396(4)
Ti(1)–Cl(1)	2.2607(15)
Cp(cent)–Ti(1)	2.051
C(3)–C(20)	1.477(6)
Ti(1)–H(2)	2.957
O(2)–Ti(1)–Cl(1)	106.58(10)
O(1)–Ti(1)–Cl(1)	102.48(11)
Cp1(cent)–Ti(1)–O(2)	105.9
C(6)–C(1)–Cp(cent)	169.3
C(6)–C(7)–O(2)	114.5(4)

(106.7°) [28], indicating similar sterically open features for **3** to complexes **1** and **2** as catalyst precursors. The Ti1–C_{ring} (av.) distance of 2.378 Å is slightly longer than the one in **2** 2.362 Å. The distances of Ti1–C2 2.384(5) Å and Ti1–C3 (2.470(4) Å) are longer than the one of Ti1–C5 (2.309(4)) and Ti1–C4 (2.396(4)), respectively, which could be obviously attributed to the sterical repulsion between the bulky ligands on the two Ti atoms. The phenolate plane – Cp plane dihedral angle is 86.0° and the (phenolate)C–C(ring) vector is bent 10.3° from the Cp ring plane. The corresponding data for **2** are 86.5° and 9.4°, reflecting more steric strain in **3** than in **2**. The Ti–O2 bond lengths of 1.842(3) Å is shorter than that in **2** (1.818(4) Å) and the Ti–O–C7 angles of 128.9(3)° is larger than the one in **2** (129.8(4)°), indicating less Ti–O double-bond character in complex **3** [17,46–48].

3.3. Ethene polymerization studies

Complexes **3** and **4** were studied as ethene polymerization catalysts and the results were summarized in Table 3. Upon activation with $Al(^iBu)_3$ and $Ph_3C^+B(C_6F_5)_4^-$, complexes **3** and **4** both show good catalytic activity for ethene polymerization, producing polyethylenes with moderate molecular weights and melting temperatures. The order of the catalytic activity for ethene polymerization under similar conditions (see run 2, 5 on Table 3) is **3** > **4**, which could be attributed to the nature of the substituents on the phenolate. As seen from the structures of complexes **3** and **4**, the electron-donating effect of the ^{t}Bu group at the *para* position of the phenolate would increase the catalytic activity of complex **3**. For both **3** and **4**, the catalytic activity increases with the increase in Al/Ti ratio and reaches the highest catalytic activities with the Al/Ti ratio about 40. Further increasing in the Al/Ti ratio results in decrease in the catalytic activity. Under the same conditions the catalytic activities for ethene polymerization of complexes **3** ($1.8–3.1 \times 10^6$ g polymer/mol Ti) and **4** ($1.3–2.3 \times 10^6$ g polymer/mol Ti) are roughly equal to those of their corresponding dichloride complexes **1** ($1.9–3.2 \times 10^6$ g polymer/mol Ti) and **2** ($1.3–2.0 \times 10^6$ g polymer/mol Ti) [28], which could be explained by that the catalytic active species produced during the polymerization from **1** and **2** should be the same as that produced from **3** and **4**.

4. Conclusions

Two new dimeric oxo-bridged cyclopentadienyloxochlorotitanium(IV) complexes **3** and **4** have been synthesized by hydrolysis of the corresponding dichlorides **1** and **2**. Structures of **3** and **4** have been confirmed by ^{1}H and ^{13}C NMR spectra and X-ray crystallography. When activated with $^iBu_3Al$ and $Ph_3C^+B(C_6F_5)_4^-$, complexes **3** and **4** exhibit reasonable catalytic activity for ethylene polymerization, producing polyethylenes with moderate molecular weights and melting temperatures.

Table 3
Summary of ethene polymerization catalyzed by complexes **3** and **4** (activated by $Ph_3C^+[B(C_6F_5)_4]^-$)[a]

Run	Catalyst	Al:Ti	T (°C)	Amount of polymer (g)	Activity[b]	$M\eta$[c] $\times 10^{-4}$	T_m (°C)[d]
1	**3**	20	80	2.11	2160	4.5	122.7
2	**3**	40	80	3.07	3143	3.9	123.2
3	**3**	60	80	1.78	1822	4.7	124.1
4	**4**	20	80	1.44	1313	5.0	124.3
5	**4**	40	80	2.29	2088	4.3	125.4
6	**4**	60	80	1.31	1194	4.8	126.4

[a] Polymerization conditions: solvent 80 mL of toluene, catalyst 1 mg, B/Ti ratio 1.5, time 30 min, ethene pressure 5 bar.
[b] kg PE (mol Ti)$^{-1}$ h^{-1}.
[c] Measured in decahydro-naphthalene at 135 °C.
[d] Determined by DSC at a heating rate of 10 °C min^{-1}.

5. Supplementary data

^{1}H and ^{13}C NMR spectra for **3** and **4** are available in supplementary data. The Crystallographic data for **3** has been deposited with Cambridge Crystallographic Data Center as supplementary publication number CCDC: 225984. Copies of this information can be obtained free of charge via www.ccdc.cam.ac.uk/conts/retrieving.html (or from the Cambridge Crystallographic Data Centre, 12, Union Road, Cambridge CB2 1EZ, UK; fax: (+44) 1223 336 033; or e-mail deposit@ccdc.cam.ac.uk).

Acknowledgment

This work was supported by the National Natural Science Foundation of China (Nos. 20374023 and 29734143).

References

[1] A.L. McKnight, R.M. Waymouth, Chem. Rev. 98 (1998) 2587.
[2] U. Siemeling, Chem. Rev. 100 (2000) 1495.
[3] J.C. Stevens, F.J. Timmers, D.R. Wilson, G.F. Schmidt, P. N. Nickas, R.K. Rosen, G.W. Knight, S.Y. Lai, Eur. Pat. Appl. EP 416 815 A2, 1991 (Dow).
[4] J.A.M. Canich, Eur. Pat. Appl. EP 420436–Al, 1991 (Exxon).
[5] J.A.M. Canich, G.G. Hlatky, H.W. Turner, PCT Appl. WO 92–00333, 1992 (Exxon).
[6] J.A.M. Canich, U.S. Patent 5, 026, 798, 1991 (Exxon).
[7] J.A.M. Canich, G.F. Licciard, U.S. Patent 5, 057, 475, 1991 (Exxon).
[8] J.A.M. Canich, PCT Int. Appl. WO 96/00244, 1996 (Exxon).
[9] A.K. Hughes, A. Meetsma, J.H. Teuben, Organometallics 12 (1993) 1936.
[10] K.E. du Plooy, U. Moll, S. Wocadol, W. Massa, J. Okuda, Organometallics 14 (1995) 3129.
[11] J. Okuda, S. Verch, T.P. Spaniol, R. Stuermer, Chem. Ber. 129 (1996) 1429.
[12] F. Amor, J. Okuda, J. Organomet. Chem. 520 (1996) 245.
[13] J. Okuda, T. Eberle, T.P. Spaniol, Chem. Ber. 130 (1997) 209.
[14] J.T. Park, S.C. Yoon, B.-J. Bae, W.S. Seo, I.-H. Suh, T.K. Han, J.R. Park, Organometallics 19 (2000) 1269.
[15] M. Dahlmann, J. Schottek, R. Fröhlich, D. Kunz, M. Nissinen, G. Erker, G. Fink, R. Kleinschmidt, J. Chem. Soc., Dalton Trans. (2000) 1881.
[16] J. Okuda, Chem. Ber. 123 (1990) 1649.
[17] Y.X. Chen, C.L. Stern, S. Yang, T.J. Marks, J. Am. Chem. Soc. 118 (1996) 12451.
[18] H.G. Alt, A. Reb, W. Milins, A. Weis, J. Organomet. Chem. 628 (2001) 169.
[19] A. Rau, S. Schmitz, G. Luft, J. Organomet. Chem. 608 (2000) 71.
[20] S.D.R. Christie, K.W. Man, R.J. Whitby, A.M.Z. Slawin, Organometallics 18 (1999) 348.
[21] E.E.C.G. Gielens, J.Y. Tiesnitsch, B. Hessen, J.H. Teuben, Organometallics 17 (1998) 1652.
[22] A.A.H. van der Zeijden, C. Matteis, Organometallics 16 (1997) 2651.
[23] G. Trouve, D.A. Laske, A. Meetsma, J.H. Teuben, J. Organomet. Chem. 511 (1996) 255.
[24] J. Christoffers, R.G. Bergman, Angew. Chem., Int. Ed. Engl. 34 (1995) 2266.
[25] Q. Huang, Y. Qian, G. Li, Y. Tang, Trans. Met. Chem. 15 (1990) 483.
[26] K. Kunz, G. Erker, G. Kehr, R. Fröhlich, H. Jacobsen, H. Berke, O. Blacque, J. Am. Chem. Soc. 124 (2002) 3316.
[27] Y.L. Qian, J.L. Huang, Polyhedron 13 (1994) 1105.
[28] Y.T. Zhang, J.H. Wang, Y. Mu, Z. Shi, C.S. Lü, Y.R. Zhang, L.J. Qiao, S.H. Feng, Organometallics 22 (2003) 3877.
[29] Y.X. Chen, T.J. Marks, Organometallics 16 (1997) 5958.
[30] D.F. Shriver, M.A. Drezdzon, The Manipulation of Air-Sensitive Compounds, second ed., Wiley-Interscience, 1986.
[31] D.D. Perrin, W.L.F. Armarego, D.R. Perrin, The Purification of Laboratory Chemicals, Pergamon, New York, 1980.
[32] A.G. Massey, A.J. Park, J. Org. Chem. 2 (1962) 245.
[33] A.G. Massey, A.J. Park, J. Organomet. Chem. 5 (1966) 218.
[34] J.C.W. Chien, W.M. Tsai, M.D. Rasch, J. Am. Chem. Soc. 113 (1991) 8570.
[35] SHELXTL; PC Siemens Analytical X-ray Instruments: Madison WI, 1993.
[36] G.M. Sheldrick, SHELXTL Structure Determination Programs, Version 5.0; PC Siemens Analytical Systems: Madison, WI, 1994.
[37] J.L. Petersen, Inorg. Chem. 19 (1980) 181.
[38] T. Carofiglio, C. Floriani, A. Sgamellotti, M. Rosi, A.C. Villa, C. Rizzoli, J. Chem. Soc., Dalton trans. (1992) 1081.
[39] U. Thewalt, K. Döppert, J. Organomet. Chem. 320 (1987) 177.
[40] S.A. Giddings, Inorg. Chem. 3 (1964) 684.
[41] P. Corradini, G. Allegra, J. Am. Chem. Soc. 81 (1959) 5510.
[42] U. Thewalt, D. Schomburg, J. Organomet. Chem. 127 (1977) 169.
[43] H. Kopf, S. Grabowski, R. Voigtländer, J. Organomet. Chem. 216 (1981) 185.
[44] J.C. Flores, J.S. Wood, J.C.W. Chien, M.D. Rausch, Organometallics 15 (1996) 4944.
[45] I. Dorado, J.C. Flores, M. Galakhov, P.G. Sal, A. Martin, P. Royo, J. Organomet. Chem. 563 (1998) 7.
[46] J.C. Huffman, K.G. Moloy, J.A. Marsella, K.G. Caulton, J. Am. Chem. Soc. 102 (1980) 3009.
[47] B. Cetinkaya, P.B. Hitchcock, M.F. Lappert, S. Torroni, J.L. Atwood, W.E. Hunter, M.J. Zaworotko, J. Organomet. Chem. 188 (1980) C31.
[48] R. Fandos, A. Meetsma, J.H. Teuben, Organometallics 10 (1991) 59.

nitrogen atmosphere. The mixture was heated at 80 °C under nitrogen atmosphere for 16 h. The reaction mixture was hydrolyzed slowly with 100 ml of degassed ice water and then concentrated NH_4OH was added to become pH 9 and to precipitate $Al(OH)_3$. After filtration, a yellow solid was obtained by adding 20 ml of an aqueous HPF_6. The precipitation was filtered, and dried in vacuo. The dried crude product was treated with 50 ml of CH_2Cl_2. The CH_2Cl_2 solution was filtered and concentrated to 5 ml by evaporation. Then a large amount of ether was added to give yellow microcrystals (*o*-complex: 0.881 g, 20.4%. *m*-complex: 1.02 g, 23.6%. *p*-complex: 0.915 g, 21.2%.). The insoluble product to CH_2Cl_2 was treated with a large amount of acetone until all yellow residue was dissolved and then filtered. The acetone solution was evaporated to give yellow microcrystals (*o*-complex: 3.15 g, 47.6%. *m*-complex: 2.35 g, 35.4%. *p*-complex: 2.11 g, 31.8%.). *Anal*. mononuclear *o*-complex: ^{1}H NMR(δ/ppm, CD_3CN) 5.14(5H), 6.15–6.44(4H), 6.81–8.16(10H). FAB Mass 351 ([CpFe(*o*-terphenyl)]$^+$). Dinuclear *o*-complex: ^{1}H NMR(δ/ppm, CD_3CN) 4.95(10H), 6.04(4H), 6.21(6H), 7.78(2H), 8.00(2H). FAB Mass 617 ([[(CpFe)$_2$(*o*-terphenyl)]$^{2+}$-PF_6^-]$^+$). Mononuclear *m*-complex: ^{1}H NMR(δ/ppm, CD_3CN) 4.88(5H), 6.54–6.83(4H), 7.26–7.91(10H). FAB Mass 351 ([CpFe(*m*-terphenyl)]$^+$). Dinuclear *m*-complex: ^{1}H NMR(δ/ppm, CD_3CN) 4.99(10H), 6.38(2H), 6.47(4H), 6.78(4H), 7.78(1H), 8.04(2H), 8.16(2H). FAB Mass 617 ([[(CpFe)$_2$(*m*-terphenyl)]$^{2+}PF_6^-$]$^+$). Mononuclear *p*-complex: ^{1}H NMR(δ/ppm, CD_3CN) 5.12(5H), 6.83–7.14(4H), 7.61–7.90(10H). FAB Mass 351 ([CpFe(*p*-terphenyl)]$^+$). Dinuclear *p*-complex: ^{1}H NMR(δ/ppm, CD_3CN) 4.98(10H), 6.38(2H), 6.47(4H), 6.74(4H), 8.03 (4H). FAB Mass 617 ([[(CpFe)$_2$(*p*-terphenyl)]$^{2+}PF_6^-$]$^+$).

2.2. X-ray crystal structural analyses

Single crystals for X-ray crystallography of mononuclear and dinuclear *o*-, *m*-, and *p*-terphenyl complexes except for mononuclear *m*-isomer were obtained by the following method. The mononuclear complexes were dissolved in dichloromethane, while the dinuclear complexes were in acetone and then they were put in the hexane atmosphere at −15 °C. After several weeks single crystals for X-ray structural analysis were obtained as yellow column-shape crystals. They were cut so that the longest side was less than 0.5 mm. All measurements were made on Mac Science DIP 2030 imaging plate area detector using graphite-monochromated Mo Kα radiation. The cell parameters and intensities for the reflection were estimated by program package of Mac DENZO [12]. The crystal structures were solved by direct methods and expanded using Fourier techniques. The non-hydrogen atoms were refined anisotropically, while hydrogen atoms were refined isotropically. All calculations were performed with the CrystalStructure crystallographic software packages of Rigaku and Molecular Structure Corporation [13]. Table 1 summarizes crystallographic data and experimental details.

2.3. ^{57}Fe Mössbauer spectroscopic measurements

A ^{57}Co(Rh) source moving in a constant-acceleration mode was used for ^{57}Fe Mössbauer spectroscopic measurements. ^{57}Fe Mössbauer spectra at 78 K were obtained by using a Wissel spectrometer. The ^{57}Fe Mössbauer parameters were obtained by least-squares fitting to Lorentzian peaks. The isomer shift values are referred to metallic iron.

Table 1
Details of crystal structure determinations

	Mononuclear *o*-complex	Dinuclear *o*-complex	Dinuclear *m*-complex	Mononuclear *p*-complex	Dinuclear *p*-complex
Formula	$C_{23}H_{19}FePF_6$	$C_{31}H_{30}Fe_2P_2F_{12}O$	$C_{31}H_{30}Fe_2P_2F_{12}O$	$C_{23}H_{19}FePF_6$	$C_{28}H_{24}Fe_2P_2F_{12}$
Formula weight	496.21	820.2	820.2	496.21	762.12
Crystal system	monoclinic	monoclinic	monoclinic	monoclinic	monoclinic
Space group	$P2_1/n$(#14)	$C2/c$(#15)	$P2_1/c$(#14)	Pn(#7)	$P2_1/n$(#14)
T (K)	296	296	296	296	296
a (Å)	10.7100(4)	26.6550(5)	12.7670(2)	9.8310(3)	10.5720(3)
b (Å)	10.7160(3)	10.4660(2)	16.9570(3)	10.6700(4)	12.9810(4)
c (Å)	19.0790(9)	23.0270(6)	15.1310(3)	10.3780(3)	10.8340(4)
β (°)	102.5260(10)	107.9020(10)	92.9480(10)	105.968(3)	100.9000(10)
V (Å^3)	2187.25(12)	6112.9(2)	3271.38(9)	1046.61(6)	1459.98(7)
Z	4	8	4	2	2
D_{calc}	1.542	1.782	1.665	1.574	1.733
μ	8.39	11.54	10.78	8.56	11.98
R[a]	0.119	0.054	0.078	0.036	0.100
R_w[b]	0.177	0.121	0.095	0.042	0.116

[a] $R = \sum\|F_o| - |F_c\|/\sum|F_o|$.
[b] $R_w = (\sum w(|F_o| - |F_c|)^2/\sum w|F_o|^2)^{1/2}$.

3. Results and discussion

3.1. Syntheses and separations

We have synthesized the present arene complexes by ligand exchange reaction between ferrocene and terphenyl [4]. The reaction products include mononuclear and dinuclear complexes. Total yield changes depending on isomer, which is attributable to the difference in melting point among *o*-(58–59 °C), *m*-(86–87 °C), and *p*-terphenyl(213–216 °C). The mononuclear and dinuclear products were isolated by using the difference in solubility; mononuclear complex is soluble to dichloromethane, while dinuclear complex is not soluble to dichloromethane but soluble to acetone. The difference in solubility is maybe caused by the difference in charge between monocation and dication. The molar ratio of the mononuclear to the dinuclear complex was dependent on the isomer: i.e., 3:7 for *o*-derivative, while 2:3 for *m*- and *p*-derivatives. The trinuclear complex is not obtained, maybe because of large decrease in electron density on the third benzene ring.

3.2. X-ray crystallography

Figs. 1 and 2 show ORTEP drawings for mononuclear *o*- and *p*-terphenyl complex cations, respectively. It can easily be seen that the $FeCp^+$ is introduced to the central benzene ring in both isomers. Figs. 3–5 show ORTEP drawings for dinuclear *o*-, *m*-, and *p*-terphenyl complex cations, respectively. It can also easily be seen that the two $FeCp^+$ are introduced to the terminal benzene rings in all isomers. Figs. 1–5 also reveal that all benzenes are not coplanar. The Cp ring has very anisotropic thermal ellipsoids especially in dinuclear *m*- and *p*-terphenyl complex cations. This suggests the rotation of Cp ring around 5-fold axis.

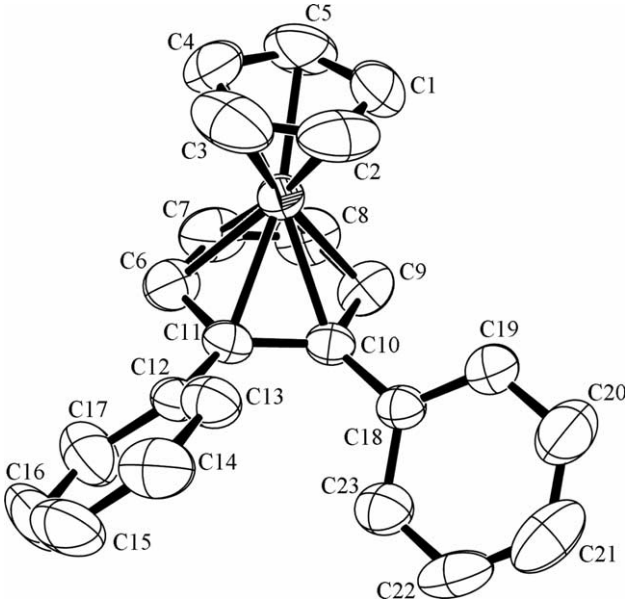


Fig. 1. ORTEP drawing of mononuclear *o*-terphenyl complex cation with 50% probability drawing ellipsoids.

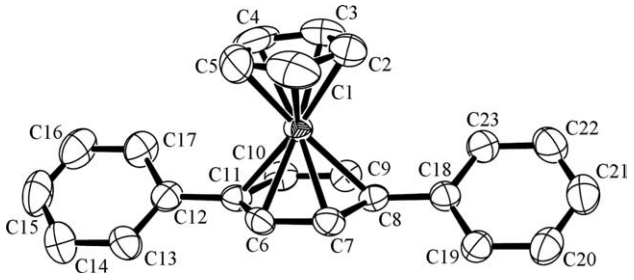


Fig. 2. ORTEP drawing of mononuclear *p*-terphenyl complex cation with 50% probability drawing ellipsoids.

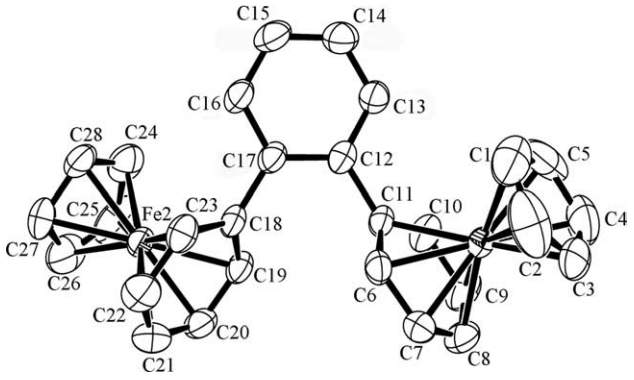


Fig. 3. ORTEP drawing of dinuclear *o*-terphenyl complex cation with 50% probability drawing ellipsoids.

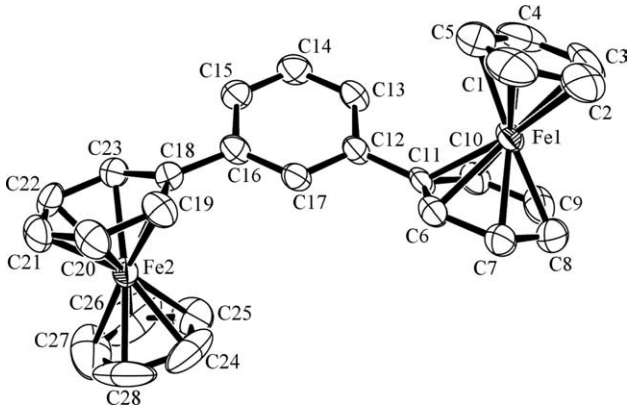


Fig. 4. ORTEP drawing of dinuclear *m*-terphenyl complex cation with 50% probability drawing ellipsoids.

Crystallographic data are listed in Table 1, and selected bond distances and angles are summarized in Table 2. The average C–C distance in the central benzene ring is longer by 0.02–0.03 Å than those of terminal benzene rings in the mononuclear *o*- and *p*-terphenyl complexes. The average C–C distances in the terminal benzene rings are longer by 0.01–0.02 Å than that of central benzene ring in the dinuclear *o*-, *m*-, and *p*-terphenyl

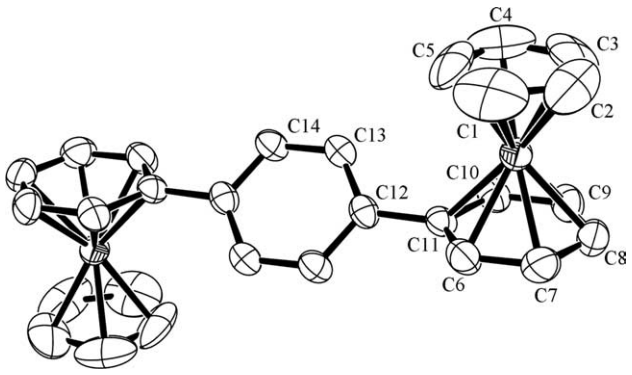


Fig. 5. ORTEP drawing of dinuclear *p*-terphenyl complex cation with 50% probability drawing ellipsoids.

complexes. The change in C–C distance by coordination is more drastic in mononuclear complexes than in dinuclear complexes.

The dihedral angles between the neighboring benzene rings are also summarized in Table 2. There is not significant difference in the angle between mononuclear and dinuclear terphenyl complexes in each isomer. The angles for mononuclear and dinuclear *o*-terphenyl complexes are apparently larger than those of the corresponding mononuclear and dinuclear *m*- and *p*-complexes, suggesting ortho effect. The dihedral angles are 52.61° and 52.02° for mononuclear *o*-complex and 51.18° and 52.51° for dinuclear *o*-complex. This is interesting because these values approach to the average value of those of the metal-free *o*-terphenyl (62.1° and 42.5°) [14]. The difference of dihedral angles in metal-free *o*-terphenyl was explained by the difference in intermolecular interactions in the lattice [14]. We thought that the packing effect around the present *o*-terphenyl complex cations and then the interaction of the cation with its surroundings become more symmetric.

Dinuclear *o*- and *m*-complexes contain acetone molecule as solvent molecule, while dinuclear *p*-complex does not. As a result, two irons are not equivalent for *o*- and *m*-complexes, while equivalent for *p*-complex.

3.3. ^{57}Fe Mössbauer spectroscopy

^{57}Fe Mössbauer spectroscopy was applied to know the electronic state of the present complexes. As the dinuclear *o*-, *m*-terphenyl complexes include solvent molecule, the measurement was done at 78 K by using single crystals. Typical ^{57}Fe Mössbauer spectrum is shown in Fig. 6. A ferrocene-like single doublet is seen. All other complexes also showed the similar single doublet. The ^{57}Fe Mössbauer parameters (isomer shift (IS) and quadrupole splitting (QS)) are summarized in Table 3. The Mössbauer parameters are similar to each other and to [{BenzeneFeCp}$^+$][PF_6^-]. The decrease in QS value of the present arene complexes(1.65–1.75 mm s^{-1})

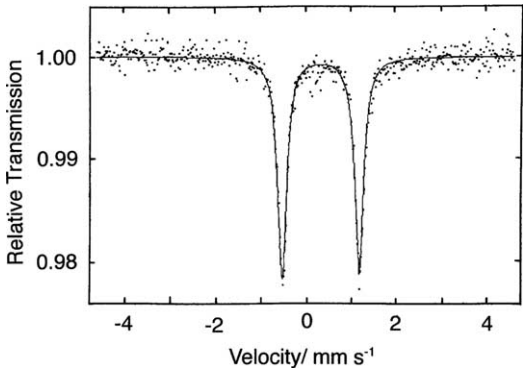


Fig. 6. ^{57}Fe Mössbauer spectrum of dinuclear *o*-terphenyl complex at 78 K.

Table 3
^{57}Fe Mössbauer parameters at 78 K

Sample	IS (mm s^{-1})	QS (mm s^{-1})	Γ (mm s^{-1})
Mononuclear *o*-complex	0.55	1.71	0.33
Dinuclear *o*-complex	0.54	1.75	0.27
Mononuclear *m*-complex	0.53	1.68	0.25
Dinuclear *m*-complex	0.53	1.66	0.29
Mononuclear *p*-complex	0.54	1.65	0.28
Dinuclear *p*-complex	0.54	1.69	0.24

Table 2
Selected bond lengths and angles

	Mononuclear *o*-complex	Dinuclear *o*-complex	Dinuclear *m*-complex	Mononuclear *p*-complex	Dinuclear *p*-complex
Fe–C(Cp) (Å)	2.039(4)	2.036(2)	2.026(3)	2.039(4)	2.042(3)
		2.057(2)	2.053(3)		2.042(3)
Fe–C(arene) (Å)	2.098(3)	2.088(1)	2.086(2)	2.093(2)	2.087(2)
		2.094(1)	2.093(2)		2.087(2)
Fe–F(PF_6) (Å)	5.526	5.335	5.487	5.359	5.319
		5.429	5.582		5.319
Dihedral angle (°)	52.02	51.18	32.52	35.38	38.79
	52.61	52.51	30.92	32.94	38.79
C–C(Cp) (Å)	1.382(5)	1.405(3)	1.403(5)	1.390(4)	1.38(1)
		1.379(4)	1.355(7)		1.38(1)
C–C(terminal) (Å)	1.378(4)	1.410(2)	1.406(3)	1.387(3)	1.405(3)
C–C(central) (Å)	1.407(4)	1.392(2)	1.394(3)	1.416(3)	1.398(3)
C–C(terminal) (Å)	1.386(4)	1.410(2)	1.402(3)	1.385(3)	1.405(3)

compared to ferrocene (2.4 mm s^{-1}) is explained by the interaction of the e_{2g} d orbitals with the ring orbitals [8]. Although the X-ray crystal structural analyses showed that the two iron sites are slightly different in the dinuclear *o*- and *m*-terphenyl complexes, the slight difference in the site does not appear in the Mössbauer spectra. And the difference between the mononuclear and the dinuclear complexes does not significantly appear in the ^{57}Fe Mössbauer spectra. Close inspection, however, reveals that *o*-terphenyl complexes show slightly larger QS value.

4. Conclusion

We succeeded to obtain mononuclear and dinuclear arene complexes of *o*-, *m*-, and *p*-terphenyl and to separate them by using the difference in solubility. We confirmed that $FeCp^+$ was introduced to the central benzene in the mononuclear complexes, while they were introduced to the terminal benzenes in the dinuclear complexes.

Acknowledgments

We thank Dr. T. Oda of Hiroshima University for supporting X-ray structural analysis.

Appendix A. Supplementary data

Crystallographic data for the structural analysis have been deposited at the Cambridge Crystallographic Data Centre, CCDC 249481–249485. Copies of this information may be obtained free of charge from the Director, CCDC, 12 Union Road, Cambridge CB2 1EZ, UK (fax: +44 1223 336033; e-mail: deposit@ccdc.cam.ac.uk or www: http//www.ccdc.cam.ac.uk). Supplementary data associated with this article can be found, in the online version, at doi:10.1016/j.poly.2005.07.002.

References

[1] D.B. Brown, J.T. Wrobleskii, in: D.B. Brown (Ed.), Mixed-Valence Compounds: Theory and Applications in Chemistry, Physics, Geology, and Biology, D. Reidel, Dordrecht, The Netherlands, 1980, pp. 243–270.
[2] D.N. Hendrickson, in: K. Prassides (Ed.), Mixed Valency System: Applications in Chemistry, Physics, and Biology, Kluwer, Dordrecht, The Netherlands, 1991, pp. 67–90.
[3] S. Nakashima, Recent Res. Dev. Pure & Appl. Chem. 2 (1998) 247.
[4] M. Lacoste, H. Rabaa, D. Astruc, N. Ardoin, F. Varret, J. Saillard, A. Beuze, J. Am. Chem. Soc. 112 (1990) 9548.
[5] J.M. Manriquez, M.D. Ward, W.M. Reiff, J.C. Calabrese, N.L. Jones, P.J. Carroll, E.E. Bunel, J.S. Miller, J. Am. Chem. Soc. 117 (1995) 6182.
[6] D. Astruc, Tetrahedron 39 (1983) 4027.
[7] W.H. Morrison Jr., E.L. Ho, D.N. Hendrickson, J. Am. Chem. Soc. 96 (1974) 3603.
[8] W.H. Morrison Jr., E.K. Ho, D.N. Hendrickson, Inorg. Chem. 14 (1975) 500.
[9] M. Maekawa, N. Hashimoto, T. Kuroda-Sowa, Y. Suenaga, M. Munakata, Inorg. Chim. Acta 328 (2002) 254.
[10] M. Miyake, K. Yasuda, T. Kashihara, T. Teranishi, Chem. Lett. (1999) 1037.
[11] S. Nlate, J.-C. Blais, D. Astruc, Inorg. Chim. Acta 357 (2004) 1670.
[12] MacDENZO: D. Gewrth, (with the cooperation of the program authors, Z. Otwinowski and M. Minor), in: The MacDENZO Manual – A Description of the Programs DENZO, XDISPLAYF, and SCALEPACK, Yale University, New Haven, CT, 1995.
[13] CrystalStructure 2.00: Crystal Structural Analysis Package, Rigaku and MSC, 2001.
[14] S. Aikawa, Y. Maruyama, Y. Ohashi, Y. Sasada, Acta Cryst. B 34 (1978) 2901.

early transition metal derivatives [12], but more recent work [13], including this paper, addresses the disparity [14].

Phenoxides are anionic oxygen-donor ligands that often bridge metal centers and typically bind hard metal centers in relatively high oxidation states. In transition metal compounds requiring monodentate phenoxides, one method to prevent bridging by the electron-rich oxygen donors, is to furnish the ligand with bulky substituents at the 2- and 6-positions. Our laboratory has demonstrated an alternative approach, namely that the bridging propensity may be reduced by extensive fluorination of the phenyl ring as in OC_6F_5 (OAr^F) or $OC_6H_3(CF_3)_2$ (OAr′) [13]. This modification is an electronic approach, instead of a steric one, and thus results in metal centers that may still bind to other ligands for catalysis or more complex structure development. All monodentate phenoxide ligands are simple X-type ligands in the MLXZ classification system [15], but their steric and electronic properties differ significantly. Herein we describe four more compounds with monodentate fluoroaryloxides whose simple OC_6H_5 analogs have not been reported in all cases. These compounds serve to develop further comparisons of OPh and OAr^F as ligands as well as increase the number of known and structurally characterized monodentate M–OAr^F and M–OAr′ linkages.

2. Experimental

2.1. General considerations

All studies were carried out at room temperature on a Schlenk line or in a nitrogen- or argon-filled glovebox. For solvents dried in stills, methylene chloride and deuterated methylene chloride were refluxed over CaH_2. THF and hexane were refluxed over potassium and toluene was refluxed over sodium. All solvents were refluxed under nitrogen or argon. Some work was also done with solvents (hexanes, CH_2Cl_2, and toluene) dried in a nitrogen-filled MBraun SPS (solvent purification system) using Al_2O_3. Celite was dried overnight in vacuo while heated to 125 °C with an oil bath. $TlOC_6F_5$ ($TlOAr^F$) and $TlOC_6H_3(CF_3)_2$ (TlOAr′) were prepared according to our previously reported procedures [13]. [(Ph_3P)Au(OPh)] was prepared from [(Ph_3P)AuCl] and KOPh [16]. All other reagents were obtained commercially and were not purified further. NMR spectra were measured on a Varian 300 MHz, Bruker 300 or 400 MHz spectrometer. UV–Vis data were recorded with a Varian Cary 50 spectrometer. ^1H and ^{13}C chemical shifts were referenced to $(CH_3)_4Si$ via the resonance of residual protiosolvent (^1H) or the ^{13}C resonance of the solvent. ^{19}F shifts were referenced to external $CFCl_3$. ^{31}P shifts were referenced to internal $(MeO)_3PO_4$ or external 85% H_3PO_4. Microanalyses were performed by H. Kolbe Microanalytisches Laboratorium, Mülheim an der Ruhr, BRD.

2.2. Synthesis of $[(Ph_3P)_2Ni(OAr^F)_2]$ (**1a**)

In a 25 ml round bottom flask a portion of $TlOAr^F$ (0.3014 g, 0.7780 mmol) was dissolved in ~10 ml CH_2Cl_2. $(PPh_3)_2NiCl_2$ (0.2529 g, 0.3866 mmol) was added to the reaction mixture. The reaction mixture turned a dark red-brown color and a white precipitate also evolved. The reaction was left to stir overnight at room temperature, and was filtered through Celite to remove TlCl. The mixture was concentrated in vacuo and recrystallized from CH_2Cl_2 and hexanes (1:1). Dark brown crystals were collected in 56% yield (0.2039 g). ^1H NMR, (δ, ppm, CD_2Cl_2) 6.780 (t, 6 H, *para*, $^3J = 7.38$ Hz), 7.347 (t, 12H, *ortho*, $^3J = 7.83$ Hz), 7.696 (t, 12H, *meta*, $^3J = 7.38$ Hz). ^{19}F {^1H} NMR, (δ, ppm, CD_2Cl_2) −153.99 (*o*, m), −171.04 (*m*, m), −177.47 (*p*, m). UV–Vis (CH_2Cl_2) [λ_{max}, nm (ε_M, $cm^{-1}\,M^{-1}$)] 456.0 (3698). *Anal.* Calc. for $C_{48}H_{30}O_2F_{10}P_2Ni$: C, 60.73; H, 3.19. Found: C, 60.68; H, 3.21%.

2.3. Synthesis of $[(PPh_3)_2Ni(OAr')_2]$ (**1b**)

In a 25 ml round bottom flask a portion of TlOAr′ (0.3003 g, 0.7744 mmol) was dissolved in ~10 ml CH_2Cl_2. $(PPh_3)_2NiCl_2$ (0.2535 g, 0.3872 mmol) was added to the reaction mixture. The reaction mixture turned a dark red-brown color and a white precipitate also evolved. The reaction was left to stir overnight at room temperature, and was filtered through Celite to remove TlCl. The mixture was concentrated in vacuo and recrystallized from CH_2Cl_2 and hexanes (1:1). Dark brown crystals (0.3629 g) were collected in 90% yield. ^1H NMR, (δ, ppm, CD_2Cl_2) 6.350 (br, 2H, *para*-OAr′), 7.211 (br, 4H, *ortho*-OAr′), 7.260 (t, 12H, *meta*, $^3J = 2.85$ Hz), 7.680 (m, 18H, *ortho* + *para*). ^{19}F {^1H} NMR, (δ, ppm, CD_2Cl_2) −63.27 (CF_3, s). UV–Vis (CH_2Cl_2) [λ_{max}, nm (ε_M, $cm^{-1}\,M^{-1}$)] 446.0 (2905), *Anal.* Calc. for $C_{52}H_{36}O_2F_{12}P_2Ni$: C, 59.97; H, 3.48. Found: C, 59.77; H, 3.41%.

2.4. Synthesis of $[(COD)Pt(OAr^F)_2]$ (**2**)

A portion of $[(COD)_2PtCl_2]$ (151.5 mg, 0.4049 mmol) was dissolved in 5 mL of CH_2Cl_2 and 2 equivalents of $KOAr^F$ (179.9 mg, 0.8098 mmol) in 5 mL of THF were added. The solution immediately turned pale yellow and a white precipitate (presumably KCl) was observed. The solution was allowed to stir overnight and then the precipitate was removed via filtration through Celite. The solution was concentrated to dryness in vacuo, and the crude very pale yellow product was recrystallized from CH_2Cl_2 and hexanes. X-ray quality crystals

were grown from the same mixture. Recrystallized yield 167 mg (61.6%). ^{1}H NMR (δ, ppm, CD_2Cl_2) 2.714 (q, CH_2, 4H, $^3J_{HH} = 8.0$ Hz), 3.262 (m, CH_2, 4H), 5.759 (t, CH, 4H, $^3J_{HH} = 28.8$ Hz). ^{13}C {^{1}H} NMR, (δ, ppm, CD_2Cl_2) 31.29 (s, CH_2), 100.97 (t, CH, $^1J_{CPt} = 76.7$ Hz). ^{19}F {^{1}H} NMR, (δ, ppm, CD_2Cl_2) −158.25 (*o*, d, $^3J_{FF} = 21.2$ Hz), −164.55 (*m*, t, $^3J_{FF} = 21.5$ Hz), −158.25 (*p*, t of t, $^3J_{FF} = 15.2$, 6.2 Hz). UV–Vis (CH_2Cl_2) [λ_{max}, nm (ε_M, $cm^{-1}\,M^{-1}$)] 233 (15200), 280 (8660). *Anal.* Calc. for $C_{20}H_{10}O_2F_{10}Pt$: C, 35.89; H, 1.81; F, 28.38. Found: C, 35.91; H, 1.79; F, 28.42%.

2.5. Synthesis of [(Ph$_3$P)Au(OAr^F)] (3)

A portion of [(Ph_3P)AuCl] (100.0 mg, 0.2021 mmol) was dissolved in 5 mL of CH_2Cl_2. One equivalent of $KOAr^F$ (44.9 mg, 0.2021 mmol) was dissolved in 2 mL of THF and the solutions mixed together. No obvious color changes were observed. After stirring for several hours, the solvents were removed in vacuo and the crude product dissolved in 5 mL of CH_2Cl_2 and filtered through Celite to remove presumed KCl. A saturated solution of the product in CH_2Cl_2 (~1 mL) was prepared and layered with an equal volume of hexanes to yield colorless crystalline material, including crystals suitable for X-ray diffraction. Recrystallized yield 60 mg (46.2%). ^{1}H NMR (δ, ppm, CD_2Cl_2) 7.53 (br, Ph). ^{13}C {^{1}H} NMR, (δ, ppm, CD_2Cl_2) 120.14 (s, *ipso*-OC_6F_5), 128.54 (s, *m*-*C*F), 128.99 (s, *p*-*C*F), 129.41 (s, *o*-*C*F), 129.82 (d, *m*, *C*H, $^1J_{CP} = 12.1$ Hz), 132.63 (d, *p*, *C*H, $^1J_{CP} = 12.1$ Hz), 134.72 (d, *o*, *C*H, $^1J_{CP} = 13.61$ Hz). ^{19}F {^{1}H} NMR, (δ, ppm, CD_2Cl_2) −164.65 (*o*, m,), −168.89 (*m*, m,), −180.10 (*p*, m). ^{31}P (δ, ppm, CD_2Cl_2) 24.61. UV–Vis (CH_2Cl_2) [λ_{max}, nm (ε_M, $cm^{-1}\,M^{-1}$)] 236 (30,200), 268 (4460), 276 (3540). *Anal.* Calc. for $C_{24}H_{15}OF_6PAu$: C, 44.89; H, 2.35; F, 14.79. Found: C, 44.97; H, 2.28; F, 14.67%.

2.6. X-ray crystallography

A summary of crystal data, details of data collections and refinement parameters for all compounds are given in Table 1. X-ray diffraction data were collected using Mo Kα radiation ($\lambda = 0.71073$ Å) on a Bruker SMART APEX CCD (**1a**, **1b**, **2**) and a Siemens P4/CCD (**3**) diffractometers [17]. Space groups were determined through inspection of systematic absences (**1a**, **1b**) and intensity statistics (**2**, **3**). All data were corrected for absorption by SADABS [18] The structures were solved using direct methods or the Patterson function and difference map techniques, and were refined by full-matrix least squares procedures on F^2. All non-hydrogen atoms were refined with anisotropic displacement parameters. The H atoms in **1a** and **2** were found from the F-map and refined with isotropic thermal parameters. In **1b** and **3** the H atoms were treated as idealized contributions. All software and sources of scattering factors are contained in the SHELXTL program package [19].

Table 1
Summary of X-ray crystallographic data

	1a	**1b**	**2**	**3**
Formula	$C_{48}H_{30}F_{10}NiO_2P_2$	$C_{52}H_{36}F_{12}$ NiO_2P_2	$C_{20}H_{12}F_{10}O_2Pt$	$C_{24}H_{15}AuF_5OP$
Formula weight	949.37	1041.46	669.39	642.30
Space group	$P2_1/c$	$P2_1/n$	$P\bar{1}$	$P\bar{1}$
a (Å)	11.4462(8)	10.5517(5)	7.4721(4)	8.9435(7)
b (Å)	15.5033(10)	14.8822(7)	10.2036(6)	10.8180(8)
c (Å)	11.1220(7)	29.7183(13)	13.1568(7)	11.0364(9)
α (°)			71.170(1)	84.628(1)
β (°)	91.699(1)	92.829(1)	80.831(1)	81.113(1)
γ (°)			82.371(1)	89.126(2)
V (Å^3)	1972.8(2)	4661.1(4)	933.73(9)	1050.33(14)
Z,Z'	2, 0.5	4, 1	2, 1	2, 1
Crystal color, habit	brown, plate	brown, block	colorless, block	colorless, block
ρ_{calc} (g cm^{-3})	1.598	1.484	2.381	2.031
μ(Mo Kα) (mm^{-1})	0.663	0.574	7.629	7.138
Temperature (K)	100(2)	120(2)	100(2)	218(2)
Reflections measured	12614	29786	5919	7731
Reflections independent [R_{int}]	4675 [0.0492]	10948 [0.0493]	4110 [0.0156]	4802 [0.0241]
Absorption correction	SADABS	SADABS	SADABS	SADABS
(T_{min}/T_{max})	(0.900)	(0.883)	(0.676)	(0.652)
$R(F)$ (%)[a]	0.0510	0.0650	0.0195	0.0299
$R(wF^2)$ (%)[b]	0.1204	0.1579	0.0483	0.0730

[a] $R = \sum ||F_o| - |F_c|| / \sum |F_o|$.

[b] $R(\omega F^2) = \left\{ \sum[\omega(F_o^2 - F_c^2)^2] / \sum[\omega(F_o^2)^2] \right\}^{1/2}$; $\omega = 1/[\sigma^2(F_o^2) + (aP)^2 + bP]$, $P = [2F_c^2 + \max(F_o, 0)]/3$.

3. Results and discussion

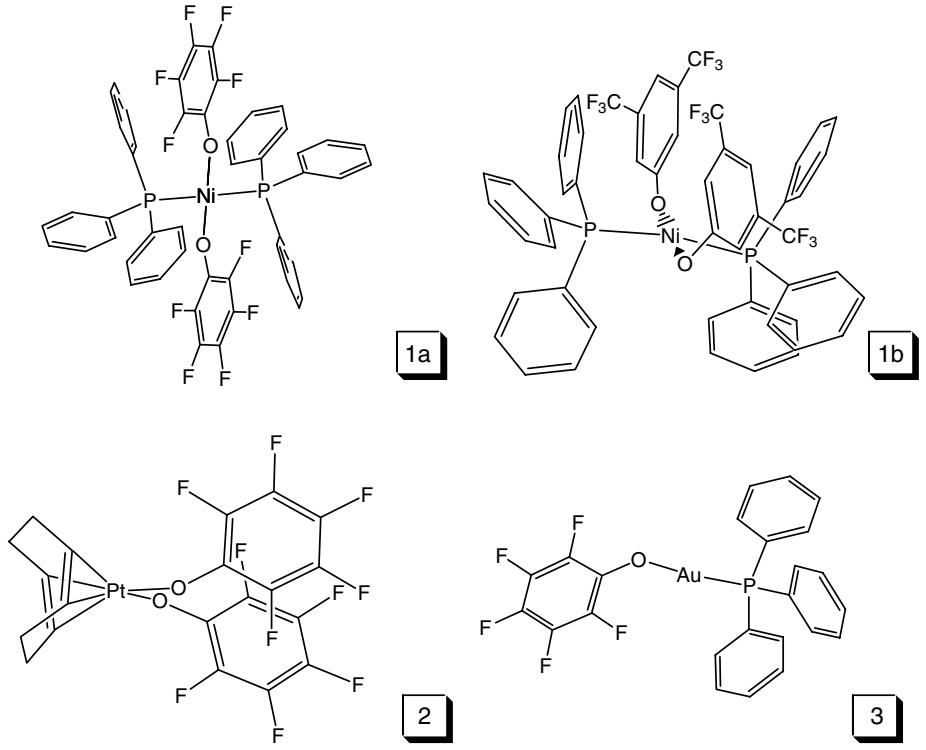
The four compounds whose crystal structures are reported herein are shown in Scheme 1. The compounds add to the library of monodentate fluorinated aryloxide compounds reported by our group [13] and others. Extensive structural and spectroscopic studies of the $[Co(OAr^F)_4]^{2-}$ and $[Cu(OAr^F)_4]^{2-}$ anions in comparison with the well-known $[CoCl_4]^{2-}$ and $[CuCl_4]^{2-}$ anions demonstrated that the pentafluorophenoxide ligand generates a similar but slightly stronger ligand field than Cl^-, consistent with qualitative expectations for the more electronegative oxygen ligand. Attempts to make $[M(OPh)_4]^{2-}$ by analogous routes with perhydro OC_6H_5 led to exclusive formation of $[(PhO)_2M(\mu\text{-}OPh)_2M(OPh)_2]^{2-}$ (M = Co, Cu) [13] anions with bridging phenoxide ligands. These results suggested that highly electronegative substituents on the aryloxide ring reduce the electron density at the metal center and decrease the bridging propensity of the aryloxide oxygen atom. Described herein are further investigations of the late transition metals with these highly fluorinated aryloxide ligands and the effects of reduced electron density on compound stability.

3.1. Synthesis

Successful synthesis of isolable metal–phenoxide compounds results from control of the strongly nucleophilic character of the oxygen donor atom. Many different strategies have been used to prevent polymerization through bridging aryloxides or reduction of the metal center. The most common approach is incorporation of the aryloxide into a chelate ring (e.g., salen, salicylate, quinolate) or a macrocycle (calixarene). Table 2 contains the results of several searches in the Cambridge Structural Database V5.25 (CSD) [20] to put into context the compounds discussed herein. These values represent the crystallographically characterized subset of known compounds and are therefore not an exhaustive survey of all known compounds. They provide a quantitative picture of the relative distribution of different types of compounds in the literature.

3.1.1. Nickel

Nickel aryloxide bonds are typically prepared with chelating ligands, e.g., salen, as shown in Table 2, or additional soft and somewhat π-accepting ligands in the coordination sphere to balance the powerful donation from the aryloxide, with phosphines being the most common. Interestingly, a survey [20] of structurally characterized $[(Ph_3P)_2NiX_2]$ compounds (27 examples) reveals no compounds with strongly Lewis basic X^- ligands (F^-, CH_3^-) or oxygen donor atoms. Instead softer ligands with π-acceptor character and/or sulfur donor atoms are found with such electron rich ligands. Nickel phosphine complexes with hard ligands have more electron donating phosphines as in $[(Me_3P)_2Ni(o\text{-}OC_6H_4\text{-}Cl)_2]$ [21], $[(Me_3P)_2Ni(OPh)(Me)]$ [22], $[(Et_3P)_2Ni(C_5F_4N)(OPh)]$ [23], $[(Me_3P)_2NiMe(OAr^F)]$



Scheme 1.

Table 2
Comparison of structurally characterized[a] nickel, platinum, and gold aryloxide compounds

Category	Aryloxide linkage	Ni	Pt	Au
A	M–OAr	850	76	17
B	A and acyclic OAr	14	9	7
C	M–(μ_2-OAr)–M′	325	4	0
D	P–M–OAr	56	38	10
E	(*O*,*N*)-M–OAr[b]	752	29	9
F	A and D and E	21	5	3
G	A not D or E	63	14	1
H	G and acyclic OAr	3	5	0

[a] Cambridge Structural Database V5.25 [20].
[b] Includes five- and six-membered chelate rings.

Table 3
Selected interatomic distances, bond lengths and angles[a]

Compound	Distances (Å)		Angles (°)	
1a	Ni1–O1	1.852(2)	O1–Ni1–P1	88.88(7)
	Ni1–P1	2.2862(7)	O1–Ni1–P1_3	91.12(7)
	O1–C1	1.334(3)	O1–Ni1–O1	180.00(8)
	P1–C7	1.827(3)	P1–Ni1–P1	180.00(4)
	P1–C13	1.819(3)	Ni1–O1–C1	126.71(19)
	P1–C19	1.822(3)	Ni1–P1–C7	112.12(10)
			Ni1–P1–C13	112.13(10)
			Ni1–P1–C19	117.11(9)
			C7–P1–C13	105.09(12)
			C7–P1–C19	104.21(13)
			C13–P1–C19	105.14(13)
1b	Ni1–O1	1.858(3)	O2–Ni1–O1	178.49(12)
	Ni1–O2	1.856(2)	O1–Ni1–P1	94.50(8)
	Ni1–P1	2.2383(10)	O1–Ni1–P2	86.32(8)
	Ni1–P2	2.2422(10)	O2–Ni1–P1	84.97(8)
	O1–C1	1.281(5)	O2–Ni1–P2	93.94(9)
	O2–C9	1.322(4)	P1–Ni1–P2	169.35(4)
	P1–C17	1.814(4)	Ni1–O1–C1	122.4(2)
	P1–C23	1.827(4)	Ni1–O2–C9	121.0(2)
	P1–C29	1.817(4)	Ni1–P1–C17	111.91(12)
	P2–C35	1.822(4)	Ni1–P1–C23	111.44(12)
	P2–C41	1.815(4)	Ni1–P1–C29	118.04(12)
	P2–C47	1.810(4)	Ni1–P2–C35	111.17(12)
			Ni1–P2–C41	117.50(13)
			Ni1–P2–C47	112.23(12)
2	Pt1–O1	2.014(2)	Pt1–O1–C9	122.63(19)
	Pt1–O2	2.019(2)	Pt1–O2–C15	122.59(19)
	Pt1–C1	2.153(3)	O1–Pt1–O2	94.95(9)
	Pt1–C2	2.141(3)		
	Pt1–C5	2.146(3)		
	Pt1–C6	2.134(3)		
	C1–C2	1.409(5)		
	C5–C6	1.397(5)		
	O1–C9	1.328(4)		
	O2–C15	1.336(3)		
3	Au1–O1	2.028(3)	Au1–O1–C1	128.5(3)
	Au1–P1	2.1978(11)	P1–Au1–O1	172.76(9)
	O1–C1	1.291(6)	Au1–P1–C11	114.78(15)
	P1–C11	1.796(4)	Au1–P1–C21	112.96(14)
	P1–C21	1.802(4)	Au1–P1–C31	109.50(14)
	P1–C31	1.803(4)		

[a] Numbers in parentheses are estimated deviations of the last significant.

[24], $[(Me_3P)_2Ni(OAr)_2]$ [25], and *trans*-$[(Bz_3P)_2NiH(OPh)]\cdot HOPh$ [26]. More rarely nickel–aryloxide linkages are found with other strongly electron donating ligands as observed in $[(Cp^*)(Et_3P)Ni(p\text{-}OC_6H_4Me)]$ [27] and $[(py)_3Ni(2,4,6\text{-}OC_6Cl_3H_2)_2]$ [28]. Nickel–aryloxide linkages have also been prepared with chelating O,P-ligands that possess both hard and soft donor atoms [29–31]. Usually the phenoxide is a monodentate ligand but a few examples of bridging phenoxides have been studied with allyl ligands such as $[Ni(\eta^3\text{-allyl})(\mu_2\text{-OAr})]_2$ in diene polymerization [32–34] and bridging phenoxide compounds have also been stabilized by the multidentate Klaui ligand [35].

The present report addresses the effect of fluorination in comparisons of OAr^F and OAr′ versus OPh and O-*m*-$C_6H_3(CH_3)_2$ complexes. Toward that end only a handful of nickel compounds with fluoroaryloxide ligands have been reported previously including the anion [36] $[Ni_2(C_6F_5)_4(\mu_2\text{-}OAr^F)_2]^{2-}$ and the neutral species $[Ni(\eta^3\text{-allyl})(\mu_2\text{-}OAr^F)]_2$ and $[Ni(\eta^3\text{-allyl})(\mu_2\text{-}OAr')]_2$ which were studied as diene polymerization activators [32]. The polymeric $[Ni(OAr^F)_2]_\infty$ has also been reported [37,38].

Simple reaction of $[(Ph_3P)_2NiCl_2]$ with the appropriate TlOAr reagent yielded compounds **1a** and **1b** as brown crystalline compounds. Under the same conditions, reaction between $[(Ph_3P)_2NiBr_2]$ and TlOAr led to insoluble materials. It has been previously reported that $[(Ph_3P)_2NiCl_2]$ compounds are sensitive to reduction to Ni(I) with strong nucleophiles such as $[NR_2]^-$ and it may be that Ni(II) compounds with less electronegative halides are more susceptible to such reduction under nucleophilic attack [39]. Too strongly basic ligands may lead to Ph_3P dissociation and subsequent decomposition or reduction of Ni(II) to Ni(I) or Ni(0). A similar sensitivity for **1a** and **1b** to that previously observed for $[(Ph_3P)_2NiCl_2]$ in CH_2Cl_2 [40–42] and $CHCl_3$ [43] was noted. Attempts to synthesize these compounds in THF, however, by methods analogous to those described below for CH_2Cl_2 were unsuccessful and led to colorless solutions with orange-brown precipitates. $[(Ph_3P)_2NiCl_2]$ has been isolated in both tetrahedral [44–47] (blue-green) and square-planar [46,48,49] (deep red) forms but no evidence for a tetrahedral form of **1a** or **1b** has been observed. The square planar form of $[(Ph_3P)_2NiCl_2]$ has been characterized only in the presence of CH_2Cl_2 or $ClCH_2CH_2Cl$ whereas crystals of the tetrahedral isomer were prepared from neat ethanol. Some Ni(II) compounds exhibit a tetrahedral form in non-coordinating solvents and an octahedral form in donor solvents such as DMF [50] or DMSO [43] in which solvent molecules are bound in two of six coordination sites. Compounds **1a** and **1b** are infinitely stable in the solid state but the orange-brown CH_2Cl_2 or acetone solutions turn pale-yellow over time, the latter much more rapidly. A time-dependent UV–Vis study of **1b** in CH_2Cl_2 showed only decay of the **1b** absorbances and no new colored species (Supplementary Figure 1).

Attempts to prepare the non-fluorinated analogs of **1a** and **1b** were unsuccessful. Reaction of $[(Ph_3P)_2NiCl_2]$ with either KOPh or TlOPh in THF led to pale yellow or yellow-orange solutions similar to the results of decomposition of **1a**. These results could indicate reduction of Ni to Ni(I) ($[(Ph_3P)_3NiCl]$ is yellow, for example) or Ni(0), but no clean products have been isolated. Reaction of $[(Ph_3P)_2NiCl_2]$ with TlOPh in CH_2Cl_2 led to insoluble orange powders. The insoluble orange powders could be a reduced Ni species or a polymeric Ni(II) compound formed by loss of phosphine. Two equivalents of KO–*m*-$C_6H_3(CH_3)_2$ when reacted with $[(Ph_3P)_2NiCl_2]$ produced copious amounts of an insoluble brown/tan powder and yellow solution. These observations suggest that the formation of Ni–OAr bonds in **1a** and **1b** relies on the electron-withdrawing properties of OAr^F and OAr′ to be stable on a $[(Ph_3P)_2Ni]^{2+}$ center. The formation of **1a** and **1b**, themselves somewhat unstable in solution, is clearly made possible by the fluorination of the aryloxide rings, in the absence of which, soluble Ni(II) compounds are not obtained.

3.1.2. Platinum

Reaction of $[(COD)PtCl_2]$ with two equivalents of $KOAr^F$ in THF cleanly afforded $[(COD)Pt(OAr^F)_2]$ with no sign of Pt metal formation. (Use of thallium reagents was avoided in the platinum and gold chemistry because heterometallic M–Tl species sometimes have resulted instead of thallium halide precipitation [51].) Platinum bis(aryloxide) complexes of the form $[L_2Pt(OAr)_2]$ are relatively rare [52], with mono(aryloxides) $[L_2Pt(OAr)X]$ being more common. Platinum(II) aryloxide compounds summarized in Table 2 follow some of the same trends as Ni(II) species, although there are far fewer of the heavier congener because Pt(II) preferentially binds heavier chalcogenides and this type of compound has been studied more frequently. Consistent with this preference for softer ligands is the much greater fraction of phosphine-bearing compounds for Pt versus Ni. Of the 14 Pt–OAr compounds that have neither a phosphine nor a *O*,*N* chelate ring, only 5 do not have the phenoxide involved in any chelate ring. There are two L_2PtX_2 cases, [(bpy)Pt(OPh)Me] [53] and $[(\eta^3\text{-}Me_2N\text{-}C_6H_4\text{-}CHCH_2)Pt(OAr^F)Cl]$ [54] and one example each of $[L_3PtX]^+$, $[(terpy)Pt(3,4\text{-}OC_6H_3Me_2)]BF_4$, [55] and $[LPtX_3]^-$, $(Et_4N)[Pt(C_6F_5)_2(CO)\{p\text{-}OC_6H_4(NO_2)\}]$ [56], and one Pt(IV) species, $[(bpy)Pt(Me)_2I(OPh)]$ [53].

Conspicuously absent are terminal platinum aryloxides with π-accepting ligands as demonstrated in **2**. The most similar known compound to **2** is the catecholate derivative $[(COD)Pt(O_2C_6H_4)]$ [57]. No report existed of $[(COD)Pt(OPh)_2]$ prior to our work and attempts to make $[(COD)Pt(OPh)_2]$ by a route analogous to **2** led

to black-brown precipitates, suggestive of Pt reduction. These observations suggest that an electron-withdrawing aryloxide such as OAr^F is required to stabilize Pt–OAr linkages in the absence of phosphines or chelates and prevent ligand loss (COD) and subsequent metal reduction. Platinum compounds with OAr^F as a ligand are also exceedingly rare [54,56,58,59].

3.1.3. Gold

Synthesis of $[(Ph_3P)Au(OAr^F)]$ (**3**) was achieved via the straightforward metathesis of $[(Ph_3P)AuCl]$ with $KOAr^F$ at room temperature. No evidence of gold reduction was observed. Compounds with gold(I)–oxygen bonds are relatively fewer in the literature compared to gold(I)–phosphorous or gold(I)–sulfur because of the relative hardness of oxygen ligands and the demonstrated preference of gold for softer chalcogenide ligands [60]. Only a few gold complexes with phenoxide ligands have been reported in the literature [12,61], and the data in Table 2 show only seven crystallographically characterized species with acyclic Au–O–Ar linkages, six containing Au(I) [62–66] and one with Au(III) [67]. Each of these Au(I) examples has a tertiary phosphine *trans* to the aryloxide ligand. The perhydro derivative $[(Ph_3P)Au(OPh)]$ has been reported [16] but not characterized with X-ray diffraction or UV–Vis spectroscopy.

3.2. Structural characterization

There are only six crystallographically characterized compounds [20] with $[P_2NiO_2]$ coordination sphere. Among these, five compounds have chelating ligands and one is an octahedral compound with two bidentate acetylacetonate-type ligands.

The nickel compounds $[(Ph_3P)_2Ni(OAr^F)_2]$ (**1a**) and $[(Ph_3P)_2Ni(OAr')_2]$ (**1b**) both contain square-planar nickel centers with *trans* Ph_3P ligands. Square planar $[(Ph_3P)_2NiX_2]$ complexes are more rare than tetrahedral isomers, but not unknown. The nickel atom in **1a**, shown in Fig. 1, sits on a center of inversion such that one half of the molecule is in the asymmetric unit. Selected distances and angles are listed in Table 3. The Ni–PPh_3 distance is well within the range of other four-coordinate Ni(II)–PPh_3 bond lengths. In a search of the Cambridge structural database (CSD) V5.25 [20], 85 such compounds were found with an average Ni–P bond length of 2.22(5) Å. The angles around Ni (Table 3) are virtually 90/180°. The only crystallographically characterized Ni–OAr^F species both have bridging phenoxide ligands with necessarily longer average Ni–O bond lengths of 1.933 [36] and 2.058(3) [35] Å compared to **1a**.

The structure of **1b**, shown in Fig. 2, is largely similar to that of **1a**. The most noticeable difference is that both phenyl groups are on the same side of the NiO_2P_2 plane, an artifact of crystal packing, whereas in solution free

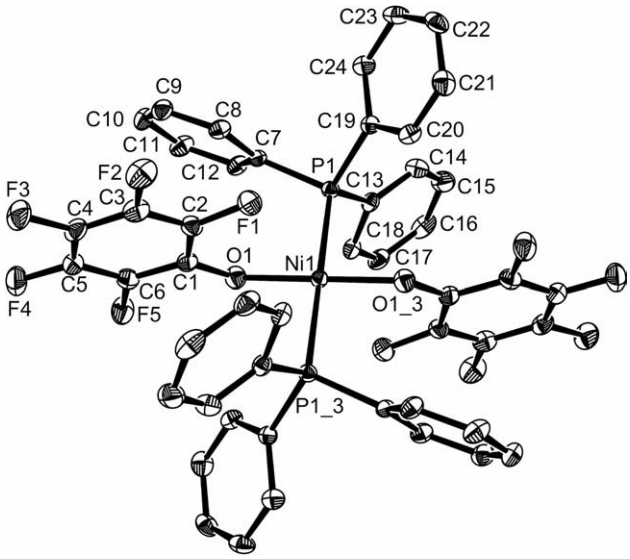


Fig. 1. ORTEP diagram of $[(Ph_3P)_2Ni(OAr^F)_2]$ (**1a**). Hydrogen atoms have been omitted for clarity. Selected distances (Å) and angles (°): Ni1–O1 1.852(2), Ni1–P1 2.2862(7), O1–C1 1.334(3); O1–Ni1–P1, 88.88(7), O1–Ni1–P1_3, 91.12(7), Ni1–O1–C1, 126.71(19). Ellipsoids are shown at the 50% probability level.

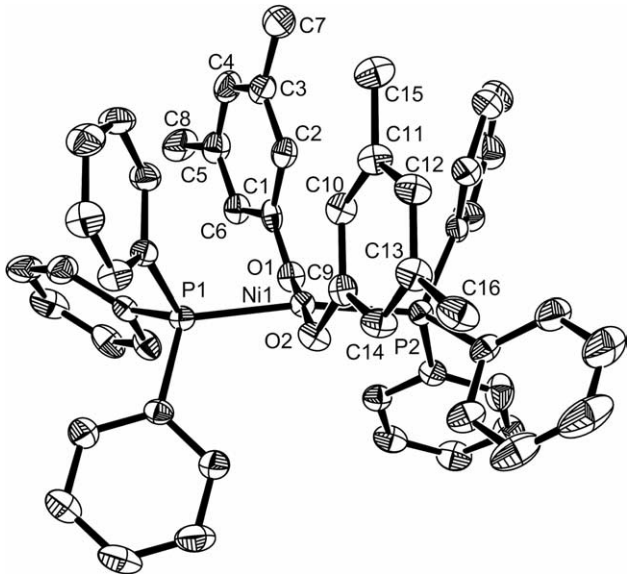


Fig. 2. ORTEP diagram of $[(Ph_3P)_2Ni(OAr')_2]$ (**1b**). Hydrogen and fluorine atoms have been omitted for clarity. Selected distances (Å) and angles (°): Ni1–O1 1.858(3), Ni1–O2 1.856(2), Ni1–P1, 2.2383(10), Ni1–P2, 2.2422(10), O1–C1, 1.281(5), O2–C9, 1.322(4); O2–Ni1–O1, 178.49(12), O1–Ni1–P1, 94.50(8), O1–Ni1–P2, 86.32(8), O2–Ni1–P1, 84.97(8), O2–Ni1–P2, 93.94(9), P1–Ni1–P2, 169.35(4), Ni1–O1–C1, 122.4(2), Ni1–O2–C9, 121.0(2). Ellipsoids are shown at the 50% probability level.

rotation about the C–O bonds is expected. At this writing, except for **1b**, crystallographically characterized OAr′ linkages have been reported only in $[M(OAr')_4]^{2-}$ compounds [13] and the $[(Ar'O)_2H]^-$ anion [68]. Again the distances and angles at the nickel center are within the range of related complexes in the literature.

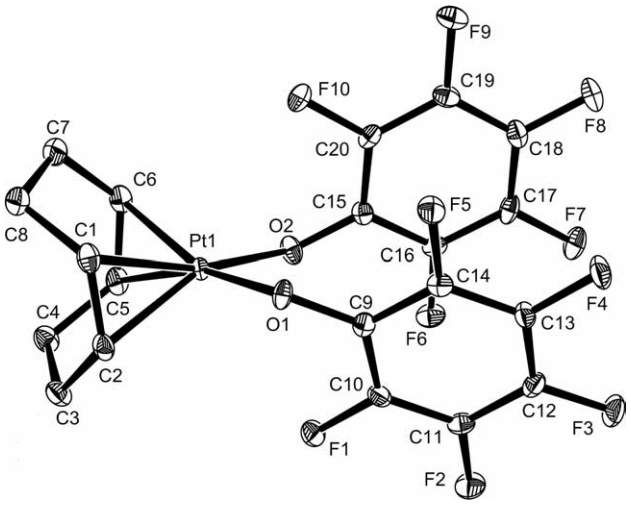


Fig. 3. ORTEP diagram of $[(COD)Pt(OAr^F)_2]$ (**2**). Hydrogen atoms have been omitted for clarity. Selected distances (Å) and angles (°): Pt1–O1 2.014(2), Pt1–O2 2.019(2), Pt1–C1 2.153(3), Pt1–C2 2.141(3), Pt1–C5 2.146(3), Pt1–C6 2.134(3), C1–C2 1.409(5), C5–C6 1.397(5), O1–C9 1.328(4), O2–C15 1.336(3); Pt1–O1–C9 122.63(19), Pt1–O2–C15 122.59(19), O1–Pt1–O2 94.95(9). Ellipsoids are shown at the 50% probability level.

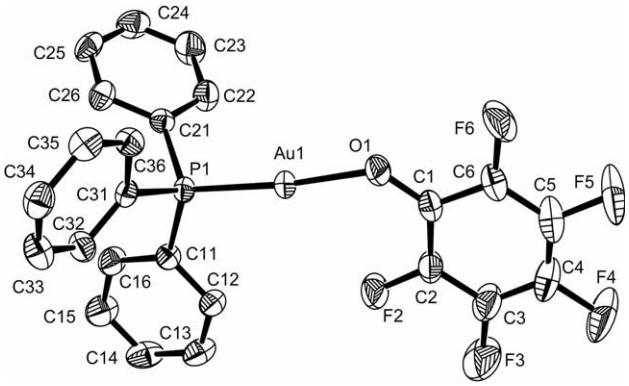


Fig. 4. ORTEP diagram of $[(Ph_3P)Au(OAr^F)]$ (**3**). Hydrogen atoms have been omitted for clarity. Selected distances (Å) and angles (°): Au1–P1, 2.1978(11), Au1–O1 2.028(3), O1–C1 1.291(6); Au1–O1–C1 128.5(3), P1–Au1–O1, 172.76(9). Ellipsoids are shown at the 50% probability level.

The crystal structure of **2** is shown with an ORTEP in Fig. 3, clearly demonstrating that this compound is a member of the L_2MX_2 ligand class [15]. The cyclooctadiene ligand is bound in a η^4-mode with the C=C bonds perpendicular to the PtO_2 plane. A plethora of structurally characterized $[(COD)Pt]^{2+}$ compounds exist, but relatively few with hard oxygen donor ligands, consistent with the soft character of Pt(II) [69,70], and only nine with a $[(COD)Pt(O)_2]$ coordination sphere, according to a CSD search. The most relevant structural comparison is that with [(COD)Pt(catecholate)] in which the doubly-deprotonated catechol ligand forms a five-membered chelate ring with platinum [57]. The Pt–O bonds have lengths (Å) of 1.972 and 1.978 in contrast to the slightly longer average bond length in **2** of 2.017(2). The less basic OC_6F_5 ligand has been shown previously to form slightly longer bonds [13]. The average Pt–C bond lengths (Å) are virtually the same in **2**, 2.144(8), and the catecholate compound, 2.156(12). Slightly shorter Pt–C bonds in **2** are consistent with less donating fluorinated arlyoxide ligands that result in more electron donation by the COD ligand. The coordinated COD bonds in **2** have lengths consistent with double bonds and within the range of 1.37(4) Å in 205 crystallographically characterized [20] $[(COD)Pt]^{2+}$ units. To our knowledge, only one prior report exists of a crystallographically characterized Pt–OAr^F bond, namely that in $[(o\text{-}Me_2NC_6H_4\text{-}CHCH_2)Pt(OAr^F)Cl]$ [54] which has Pt–O and O–C bond lengths of 2.017(5) and 1.341(9) Å, respectively. The former bond is virtually identical with that in **2** and the latter is somewhat longer.

Fig. 4 shows an ORTEP of compound **3** with a simple LMX [15] motif. The geometry at Au is virtually linear, as are the vast majority of Au(I) complexes [69,70]. The gold phenoxide bond is 2.028(3) Å in length and the Au–O–C angle is 128.5(3)°. The parameters are quite similar to those of the five crystallographically characterized Au(I) phenoxide compounds mentioned above that have average Au–O distances of 2.03(1) Å and Au–O–C angles of 126(4)°. The intraligand distances and angles are unexceptional.

3.3. Spectroscopy

The ^1H NMR chemical shifts in **1a** and **1b** are unexceptional. Both phosphine and aryloxide ligands are observed, though the signals decay over several hours. When the solution colors have become pale or colorless, only resonances for Ph_3P are visible in the ^1H and ^{31}P NMR spectra. No ^{31}P NMR signals for coordinated phosphine were observed, perhaps due to some paramagnetic character of the decomposition products. In the ^{19}F NMR spectrum of **1a**, three signals for the *ortho*, *meta*, and *para* fluorine atoms are observed but the $^3J_{FF}$ coupling is not resolved, in contrast to the spectrum of compound **2** (vide infra). A singlet is observed for the CF_3 groups in **1b**. The ^1H, ^{13}C, and ^{19}F NMR spectra of **2** show bound COD and OAr^F ligands and are unexceptional compared to other $[(COD)PtX_2]$ complexes with oxygen-donor ligands in the literature [57,71]. The NMR spectra for **3** are consistent with the solid-state structure shown in Fig. 4 and otherwise unremarkable.

UV–Vis spectra for $[(COD)PtCl_2]$ and **2** are shown in Supplementary Figure 2. Consistent with previous comparisons of Cl^- versus OAr^{F-} as ligands [13], the extinction coefficients increase significantly upon changing halide to aryloxide, but the spectra are largely similar. Increased absorbance above 300 nm is consistent with

the pale yellow color of **2** versus the colorless starting material. UV–Vis spectra for **3** are compared with [(Ph$_3$P)AuOPh] and [(Ph$_3$P)AuCl] in Supplementary Figure 3. Again the aryloxide derivatives absorb with greater intensity than the halide, but no significant shifts of the λ_{max} values are observed, suggesting these transitions do not involve exclusively the X ligand, but are largely π–π* transitions in the phosphine phenyl rings.

4. Summary

The late-transition metal complexes [(Ph$_3$P)$_2$Ni(OAr^F)$_2$] (**1a**), [(Ph$_3$P)$_2$Ni(OAr′)$_2$] (**1b**), and [(COD)Pt(OAr^F)$_2$] (**2**) have been prepared and spectroscopically as well as structurally characterized. The compound [(Ph$_3$P)Au(OAr^F)] (**3**) for which a preliminary synthetic report exists, was also structurally and spectroscopically characterized. These four compounds exemplify the conditions under which electronic modification of aryloxide ligands enables less common metal aryloxide bonds to be formed. For late transition metals that prefer softer, less donating ligands such as phosphorous or sulfur donors, these monodentate aryloxide compounds are unusual species. Among the four compounds, a perhydro analog is known only for [(Ph$_3$P)Au(OAr^F)]. Attempts to make non-fluorinated analogs of the nickel and platinum compounds resulted in metal precipitation, insoluble products, or other evidence of metal reduction instead of complex formation. The balance of electronic effects from anionic X-type ligands and neutral L-type ligands in this study suggests that highly basic aryloxides promote ligand dissociation for weaker L donors, which can lead to metal reduction and complex decomposition.

Acknowledgments

This work was supported by an NSF-CAREER award (CHE-0134817) and the donors of the Petroleum Research Fund administered by the American Chemical Society (PRF #38007-GB3). The Barnard College NMR facility is supported by the National Science Foundation (DUE-9952633). L.H.D. thanks C.C. Cummins for hospitality during a sabbatical when some of these data were collected.

Appendix A. Supplementary data

Supplementary Figures 1–3 with UV–Vis spectra and crystallographic information files for **1a**, **1b**, **2**, and **3** have been deposited with the Cambridge Crystallographic Data Centre, CCDC Nos. 249765, 249766, 249767, and 249768, respectively. Crystallographic data can be obtained free of charge via www.ccdc.cam.ac.uk/data_request/cif, or by emailing data_request@ccdc.cam.ac.uk, or by contacting The Cambridge Crystallographic Data Centre, 12, Union Road, Cambridge CB2 1EZ, UK; fax: +44 1223 336033. Supplementary data associated with this article can be found, in the online version, at doi:10.1016/j.poly.2005.06.012.

References

[1] Q.-Y. He, A.B. Mason, R.C. Woodworth, B.M. Tam, R.T.A. MacGillivray, J.K. Grady, N.D. Chasteen, J. Biol. Chem. 273 (1998) 17018.
[2] K.N. Raymond, E.A. Dertz, S.S. Kim, Proc. Natl. Acad. Sci. USA 100 (2003) 3584.
[3] E.A. Lewis, W.B. Tolman, Chem. Rev. 104 (2004) 1047.
[4] L.M. Mirica, X. Ottenwaelder, T.D.P. Stack, Chem. Rev. 104 (2004) 1013.
[5] D.C. Bradley, R.C. Mehrotra, I.P. Rothwell, A. Singh, Alkoxo and Aryloxo Derivatives of Metals, 2nd ed., Academic Press, New York, 2001, p. 704.
[6] D.M. Roundhill, Prog. Inorg. Chem. 43 (1995) 533.
[7] E.N. Jacobsen, Acc. Chem. Res. 33 (2000) 421.
[8] R.R. Schrock, Polyhedron 14 (1995) 3177.
[9] I.P. Rothwell, Chem. Commun. (1997) 1331.
[10] D.J. Darensbourg, M.W. Holtcamp, G.E. Struck, M.S. Zimmer, S.A. Niezgoda, P. Rainey, J.B. Robertson, J.D. Draper, J.H. Reibenspies, J. Am. Chem. Soc. 121 (1999) 107.
[11] D.J. Darensbourg, J.R. Wildeson, S.J. Lewis, J.C. Yarbrough, J. Am. Chem. Soc. 124 (2002) 7075.
[12] D.C. Bradley, R.C. Mehrotra, I.P. Rothwell, A. Singh, in: Alkoxo and Aryloxo Derivatives of Metals, 2nd ed., Academic Press, New York, 2001, p. 704 (Chapter 6).
[13] M.C. Buzzeo, A.H. Iqbal, C.M. Long, D. Millar, S. Patel, M.A. Pellow, S.A. Saddoughi, A.L. Smenton, J.F.C. Turner, J.D. Wadhawan, R.G. Compton, J.A. Golen, A.L. Rheingold, L.H. Doerrer, Inorg. Chem. (2004) 7709.
[14] J.R. Fulton, A.W. Holland, D.J. Fox, R.G. Bergman, Acc. Chem. Res. 35 (2002) 44.
[15] M.L.H. Green, J. Organomet. Chem. 500 (1995) 127.
[16] S. Komiya, M. Iwata, T. Sone, A. Fukuoka, J. Chem. Soc., Chem. Commun. (1992) 1109.
[17] SMART: Software for the CCD Detector System, 5.626; Bruker AXS: Madison, WI, 2000.
[18] G.M. Sheldrick, SADABS: Area Detector Absorption Correction, University of Göttingen, Göttingen, BRD, 2001.
[19] G.M. Sheldrick, SHELXTL: Program Library for Structure Solution and Molecular Graphics, 5.10, Bruker AXS, Madison, WI, 2000.
[20] F.H. Allen, Acta Crystallogr. B58 (2002) 380.
[21] H.-F. Klein, A. Dal, T. Jung, U. Flörke, H.-J. Haupt, Eur. J. Inorg. Chem. 44 (1998) 2027.
[22] Y.-J. Kim, K. Osakada, A. Takenaka, A. Yamamoto, J. Am. Chem. Soc. 112 (1990) 1096.
[23] T. Braun, S. Parsons, R.N. Perutz, M. Voith, Organometallics 18 (1999) 1710.
[24] H.F. Klein, T. Wiemer, Inorg. Chim. Acta 189 (1991) 267.
[25] H.F. Klein, A. Dal, T. Jung, S. Braun, C. Roehr, U. Floerke, H.J. Haupt, Eur. J. Inorg. Chem. (1998) 621.
[26] A.L. Seligson, R.L. Cowan, W.C. Trogler, Inorg. Chem. 30 (1991) 3371.
[27] P.L. Holland, M.E. Smith, R.A. Andersen, R.G. Bergman, J. Am. Chem. Soc. 119 (1997) 12815.
[28] M.F. Richardson, G. Wulfsberg, R. Marlow, S. Zaghonni, D. McCorkle, K. Shadid, J. Gagliardi Jr., B. Farris, Inorg. Chem. 32 (1993) 1913.

[29] K.R. Dunbar, J.-S. Sun, A. Quillevere, Inorg. Chem. 33 (1994) 3598.
[30] J. Heinicke, A. Dal, H.-F. Klein, O. Hetche, U. Florke, H.-J. Haupt, Z. Naturforsch. Teil B 54 (1999) 1235.
[31] J. Heinicke, M. Koehler, N. Peulecke, W. Keim, J. Catal. 225 (2004) 16.
[32] P.D. Hampton, S. Wu, T.M. Alam, J.P. Claverie, Organometallics 13 (1994) 2066.
[33] J. Campora, M.L. Reyes, T. Hackl, A. Monge, C. Ruiz, Organometallics 19 (2000) 2950.
[34] J. Campora, M.L. Reyes, K. Mereiter, Organometallics 21 (2002) 1014.
[35] D.-q. Ma, S. Hikichi, M. Akita, Y. Moro-oka, Dalton (2000) 1123.
[36] G. Sanchez, F. Ruiz, J.L. Serrano, G. Garcia, G. Lopez, J. Casabo, E. Molins, C. Miravitlles, Anal. Quim. 93 (1997) 49.
[37] R.S. Nyholm, B.R. Hollebone, J. Chem. Soc. A (1971) 332.
[38] S.T. Lin, R.N. Narske, K.J. Klabunde, Organometallics 4 (1985) 571.
[39] D.C. Bradley, M.B. Hursthouse, R.J. Smallwood, A.J. Welch, J. Chem. Soc., Chem. Commun. (1972) 872.
[40] F.A. Cotton, O.D. Faut, D.M.L. Goodgame, J. Am. Chem. Soc. 83 (1961) 344.
[41] L.H. Pignolet, W.D. Horrocks Jr., R.H. Holm, J. Am. Chem. Soc. 92 (1970) 1855.
[42] L. Que Jr., L.H. Pignolet, Inorg. Chem. 12 (1973) 156.
[43] H. Kato, K. Yorita, Y. Kato, Bull. Chem. Soc. Jpn. 52 (1979) 2465.
[44] G. Garton, D.E. Henn, H.M. Powell, L.M. Venanzi, J. Chem. Soc. (1963).
[45] H.J. Bruins Slot, W.K.L. Van Havere, J.H. Noordik, P.T. Beurskens, P. Royo, J. Crystallogr. Spectrosc. Res. 14 (1984) 623.
[46] B. Corain, B. Longato, R. Angeletti, G. Valle, Inorg. Chim. Acta 104 (1985) 15.
[47] L. Brammer, E.D. Stevens, Acta Crystallogr. C C45 (1989) 400.
[48] J. Sletten, J.A. Kovacs, J. Crystallogr. Spectrosc. Res. 23 (1993) 239.
[49] A.S. Batsanov, J.A.K. Howard, Acta Crystallogr. E E57 (2001) m308.
[50] H. Ohtsu, K. Tanaka, Inorg. Chem. 43 (2004) 3024.
[51] T. Devic, P. Batail, M. Fourmigue, N. Avarvari, Inorg. Chem. 43 (2004) 3136.
[52] J. Ni, C.P. Kubiak, Adv. Chem. Ser. 230 (1992) 515.
[53] G.M. Kapteijn, M.D. Meijer, D.M. Grove, N. Veldman, A.L. Spek, G. van Koten, Inorg. Chim. Acta 264 (1997) 211.
[54] M.K. Cooper, N.J. Hair, D.W. Yaniuk, J. Organomet. Chem. 150 (1978) 157.
[55] X. Liu, S.L. Renard, C.A. Kilner, M.A. Halcrow, Inorg. Chem. Commun. 6 (2003) 598.
[56] J. Ruiz, V. Rodriguez, G. Lopez, P.A. Chaloner, P.B. Hitchcock, Organometallics 15 (1996) 1662.
[57] M.-J. Don, K. Yang, S.G. Bott, M.G. Richmond, J. Chem. Crystallogr. 26 (1996) 335.
[58] W. Beck, B. Purucker, E. Strissel, Chem. Ber. 106 (1973) 1781.
[59] M.K. Cooper, D.W. Yaniuk, J. Organomet. Chem. 164 (1979) 211.
[60] J.P.J. Fackler, W.E. vanZyl, B.A. Prihoda, Gold chalcogen chemistry, in: H. Schmidbaur (Ed.), Gold: Progress in Chemistry, Biochemistry and Technology, John Wiley & Sons, New York, 1999, p. 894.
[61] E.G. Perevalova, E.I. Smyslova, K.I. Granberg, Y.T. Struchkov, L.G. Kuz'mina, D.N. Kravtsov, T.I. Voevodskaya, Koord. Khim. 15 (1989) 504.
[62] L.G. Kuz'mina, Y.T. Struchkov, Koord. Khim. 14 (1988) 1262.
[63] A. Kolb, P. Bissinger, H. Schmidbauer, Inorg. Chem. 32 (1993) 5132.
[64] L.G. Kuz'mina, O.Y. Burtseva, N.V. Dvortsova, M.A. Porai-Koshits, E.I. Smyslova, Koord. Khim. 15 (1989) 773.
[65] L.G. Kuz'mina, Y.T. Struchkov, E.I. Smyslova, Koord. Khim. 15 (1989) 368.
[66] L.G. Kuz'mina, N.V. Dvortsova, M.A. Porai-Koshits, E.I. Smyslova, K.I. Grandberg, Metalloorg. Khim. 2 (1989) 1179.
[67] T. Sone, M. Iwata, N. Kasuga, S. Komiya, Chem. Lett. (1991) 1949.
[68] M.C. Buzzeo, L.N. Zakharov, A.L. Rheingold, L.H. Doerrer, J. Mol. Struct. 657 (2003) 19.
[69] A.F. Holleman, E. Wiberg, Inorganic Chemistry, Academic Press, New York, 2001, p. 1884.
[70] F.A. Cotton, G. Wilkinson, C.A. Murillo, M. Bochmann, Advanced Inorganic Chemistry, 6th ed., John Wiley & Sons Inc., New York, 1999.
[71] A. Fukuoka, A. Sato, Ky. Kodama, M. Hirano, S. Komiya, Inorg. Chim. Acta 294 (1999) 266.

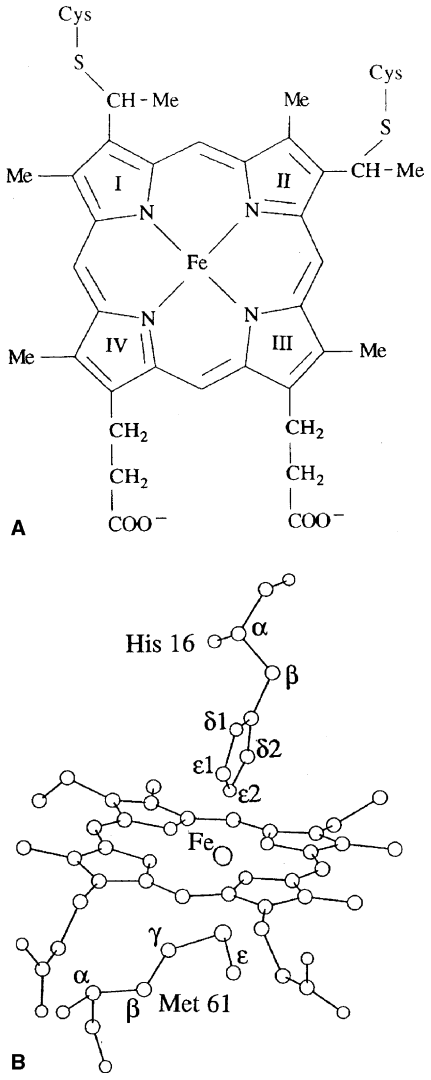


Fig. 1. The heme group of cytochrome *c*-551 from *Pae.* (A) Protoporphyrin IX ring. The nomenclature utilized for a protoporphyrin IX ring is of the IUPAC-IUB. (B) Spatial relationships of the heme group and the axial ligands, His-16 and Met-61.

protoporphyrin IX ring [6–8]. The pK_a value obtained is 6.2 for the oxidized form of the protein [6]. Additionally, data from EPR and electronic spectroscopy studies at pH >9.4 demonstrate the existence of a high spin species brought about by replacement of the iron ligand from the Met-61 thioether sulfur by other weak ligands, probably OH^- [9,10]. At higher pH values (pH >11) the existence of low-spin ferricyt *c*-551 has been proposed [9].

In the last two decades, paramagnetic ^{1}H NMR spectroscopy has been applied to different metalloproteins studies [11–13]. In particular information about coordination characteristics as well as the electronic properties for active sites in solution, by the study of isotropically shifted resonances and relaxation times, can be obtained. A number of previous reports have studied the assignment of heme protons on the oxidized form of the protein by means of heteronuclear multiple quantum coherence [14,15] or 2D ^{1}H NMR paramagnetic spectroscopy [16,17]. The present article reports on further research of the electronic properties and coordination geometry of ferricyt *c*-551 from *Pae* at high pH by using ^{1}H NMR of paramagnetic systems.

2. Experimental

2.1. Materials

All compounds used were analytical grade chemicals and purchased from Sigma and Merck. DEAE-Sephacel and CM-Sephadex (Pharmacia) were used for ion exchange chromatography. Sephadex-G100 (Pharmacia) was used for size-exclusion chromatography. D_2O (99.9%) was obtained from SDS Chemical. The protein was concentrated by using Amicon Model 8200 ultrafiltration cells equipped with PLBC 062 Millipore membranes and an ultrafree-15 centrifugal filter device from Millipore. Sample concentrations for ^{1}H NMR were 3–4 mM in protein dissolved in D_2O or in 95% H_2O/5% D_2O. Because the cyt *c*-551 sample is not totally in the oxidized form, an excess of potassium ferricyanide was added to the sample before the NMR experiments. The measurements were carried out with 20 mM potassium phosphate buffer at various pH values.

2.2. Bacterial growth and protein purification

Cytochrome *c*-551 was extracted from *P. aeruginosa* (CECT110) grown anaerobically at 35 °C in the medium described by Parr et al. [18] and purified in the partially oxidized state as described earlier [18,19]. The Bradford colorimetric assay [20] was used to determine the total amount of protein in the sample. Purified cyt *c*-551 shows a single band in PAGE and an UV–Vis spectral ratio in the reduced form of the protein $(A_{551} - A_{570})/A_{280}$ of 1.13–1.17 [21]. The cyt *c*-551 concentration was measured spectrophotometrically by means of the molar extinction coefficient for the reduced form of the protein $\varepsilon_{551} = 28.3 \times 10^3\ M^{-1}\ cm^{-1}$ [21].

2.3. Physical techniques

The optical spectra in the UV–Vis region were recorded on a Varian Cary 1 or a Shimadzu UV-2401PC recording spectrophotometer using 1 cm path length cuvettes. pH values of solutions were measured with a Crison micropH2000 pH meter provided with a Crison microelectrode. The pD measurements were corrected by the isotope effect.

NMR spectra were recorded on a Varian Unity 400 spectrometer operating at 400 MHz. One-dimensional spectra were recorded in H_2O or D_2O solvents using

the super-WEFT (water-eliminated Fourier transform) multipulse sequence [22] (d_1–180°–τ–90°–acq, where d_1 is the relaxation delay and acq the acquisition time) to eliminate the H_2O or HDO signal. Relaxation delay times of 20–50 ms, τ delay of 80–120 ms and acquisition times of 50–150 ms were used. The spectral widths ranged from 30 to 80 kHz for all experiments. 1D spectra were processed using exponential line-broadening weighting functions as apodization with values of 20–40 Hz. Chemical shifts were referenced to residual solvent protons of D_2O resonating at 4.81 ppm (293 K) relative to TMS. The longitudinal relaxation times of the hyperfine shifted resonances were determined by using the inversion recovery pulse sequence [23] (d_1–180°–τ–90°–acq); seventeen values of τ were selected between 0.5 and 200 ms, (d_1 + acq) values were at least five times the longest expected T_1 value, ranging from 80 to 200 ms, and the number of scans was 5000. The T_1 values were calculated from the inversion-recovery equation. Transverse relaxation times were obtained by measuring the line broadening of the isotropically shifted signals at half-height through the equation $T_2^{-1} = \pi\Delta\nu_{1/2}$.

2D NOESY or EXSY experiments were recorded in the hypercomplex mode [24]. All 2D experiments in H_2O or D_2O were performed with presaturation of the H_2O or HDO residual signal. Ranges of NMR parameters were utilized to overcome the diverse ^1H relaxation time. The mixing time varied from 3 to 40 ms. The parameter ranges are as follows: 1024–2048 number of scans, acquisition times of 40–100 ms, relaxation delays of 20–50 ms, 30–60 kHz spectral widths in both dimensions, 256–512 number of t_1 increments and 512–2048 number of points in the t_2 dimension. In addition, NOESY or EXSY were processed with Fourier-transforming using square sine bell weighting functions shifted 60° or 75° and the number of points used for processing were 1024 or 2048 in both dimensions. At the same time, 2D experiments were base line corrected. NMR data were processed on a SUN Sparc 5 station using the VNMRX 4.3B program.

3. Results and discussion

3.1. ^1H NMR spectrum of ferricyt c-551 at high pH

The ^1H NMR spectrum of ferricyt *c*-551 in H_2O as solvent (pH 8.9, 303 K, 20 mM potassium phosphate) is shown in Fig. 2, bottom. The spectrum shows the same pattern of chemical shifts as the spectrum of the oxidized low-spin ferricyt *c*-551 acquired at pD = 7.2 and described previously [17]. The resolved hyperfine shifted signals of low-spin ferricyt *c*-551 have been assigned to heme group protons as well as to protons of Met-61, which directly coordinates the iron and other residues near the heme group such as Cys-12, Gly-24, Ile-48 and Trp-56 [17].

When the pH is increased from 8.9 to 11.4 for the low-spin ferricyt *c*-551, the hyperfine shifted signals disappear in a slow exchange regime on the NMR timescale and, at the same time, another group of broader signals appears at pH values greater than 10.8 (Fig. 2, top). The ^1H NMR spectrum of ferricyt *c*-551 at pH 11.4 displays, in the downfield region, 10 relatively well resolved hyperfine shifted signals (a′–j′) and six other non-resolved signals (A′–F′). Additionally, in the upfield region, it displays three shifted signals (l′–n′). When the spectrum of ferricyt *c*-551 at pH 11.4 is acquired in D_2O no change is detected. The proton

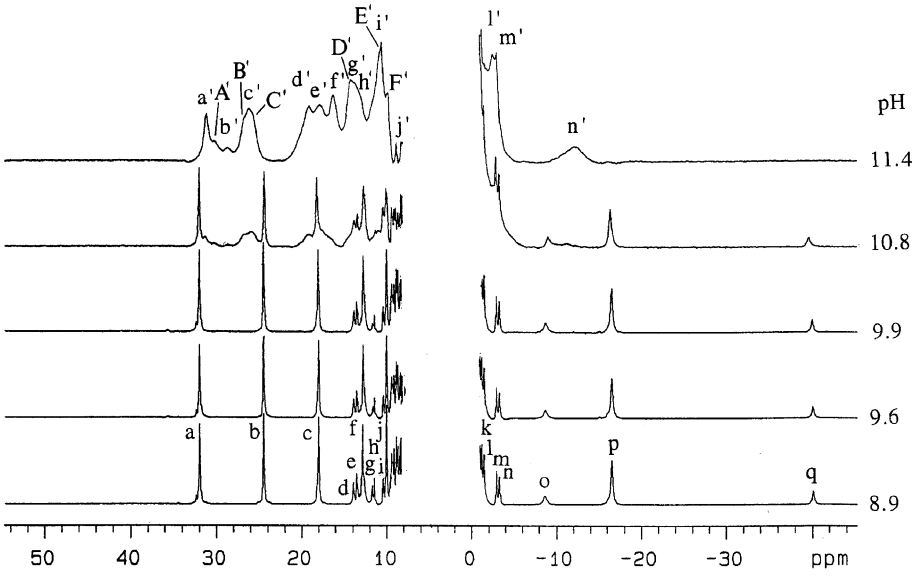


Fig. 2. Proton NMR spectra of ferricyt *c*-551 in H_2O at different pH values (8.9–11.4), 303 K and 3.3 mM protein sample.

longitudinal relaxation time values (T_1) and linewidths at half-height for the hyperfine-shifted resonances are reported in Table 1. The signals have linewidths from about 1000 Hz for signal n′ to ~300–400 Hz for signal a′. The longitudinal relaxation time values are relatively short from 1 ms, in the case of signal n′, to 48 ms for signal f′. The ^{1}H NMR spectra of ferricyt *c*-551 from *Pae* in the oxidized form at high pH, from 9 to 11.4, exhibit a drastic change if compared to the spectrum in acid or neutral media. Thus, the hyperfine shifted signals are broader with decreasing isotropic shift at high field. Additionally, the T_1 values of the low-spin iron(III) hemoprotein are smaller by about approximately 80–100 ms [25], while in the case of specie at high pH the T_1 values are as small as ~1 ms. The T_1 values are somewhat larger than in normal high-spin systems and this has been interpreted as being due to a relatively small zero-field splitting (ZFS) [25]. These results are consistent with the presence of a high-spin d^5 iron(III) in the oxidized forms of the protein. EPR studies [9] are in agreement with this electronic structure and confirm that the high-spin iron(III) cyt *c*-551 species has one soft ligand bound to the heme core. Moreover, Mössbauer spectra of ferricytochrome *c*-551 at high pH could help to confirm the final coordination number. Because the transition between pH 10.8 and 11.4 is steep, no intermediate pH values can be useful to assess the nature of the transition and determine the number of protons involved in the process. At higher pH than 11.4 no changes have been detected in the NMR spectra.

2D saturation transfer experiments were recorded on a sample at pH ~10.8, containing the low-spin species, and on high-spin species of the metalloprotein. In Fig. 3, some exchange cross-peaks are detected between signals outside the diamagnetic region. On the basis of the NMR assignment for low-spin ferricyt *c*-551 [17] the signals labelled c′, d′ and g′ can be assigned to the 12^1, 2^1 and 18^1 methyls, respectively (Fig. 3). Surprisingly, no signals are found in the typical high-spin hemoprotein methyl region, approximately from 50 to 100 ppm. In addition, the existence of exchange connectivities between the signal j and f′ confirms the assignment to 13^{1b}-CH of propionic acid number 13 (see the assignment in Table 1). In spite of very diverse acquisition and processing parameters no more exchange cross-peaks were found. The very short value of T_1 observed for the signal n′ suggests the assignment of the signal to one of the coordinated ligands since this is influenced by the paramagnetic effect of the metallic center with more intensity. Moreover, it is of interest to note that when the experiment was carried out in D_2O the shifted signals are the same as we observed in H_2O, showing the absence of the exchangeable NH proton that corresponds to the coordinated histidine. This is in agreement with the deprotonation of the axial ligand His-16, coordinated to the iron(III) heme group. Consequently, the deprotonated His-16 is more electron-withdrawing and the Fe–N_{His16} bond is shorter and the Fe–S_{Met61} bond is longer, allowing finally the complete decoordination of the ligand Met-61, the iron site remaining as a pentacoordinate system.

Table 1
^{1}H NMR (400 MHz) parameters of the hyperfine-shifted resonances in ferricyt *c*-551 from *Pseudomonas aeruginosa* at pH 11.4 and 303 K

Signal	δ (ppm)	T_1 (ms)	$\Delta\nu_{1/2}$ (Hz)	T_2 (ms)	Assignment
a′	31.2	16.0	350	0.96	
A′[a]	27.9	[b]	[b]	[b]	
b′	28.7	[b]	[b]	[b]	
B′[c]	27.6	[b]	[b]	[b]	
c′	26.2	31.0	[b]	[b]	methyl-12^1
C′[c]	26.4	[b]	[b]	[b]	
d′	19.1	28.6	[b]	[b]	methyl-2^1
e′	17.9	[b]	[b]	[b]	
f′	16.3	48.3	600	0.55	13^{1b}
D′[a]	14.0	[b]	[b]	[b]	
g′	14.2	42.8	[b]	[b]	methyl-18^1
h′	13.8	[b]	[b]	[b]	
E′[d]	10.5	[b]	[b]	[b]	
i′	10.6	25.4	[b]	[b]	
F′[d]	9.6	[b]	[b]	[b]	
j′	8.9	21.6	[b]	[b]	
k′	−0.4	[b]	[b]	[b]	
l′	−2.5	[b]	[b]	[b]	
m′	−2.9	[b]	[b]	[b]	
n′	−12.2	1.2	1075	0.30	

[a] Measured at 323 K.
[b] Overlap prevents measurement of this value.
[c] Measured at 293 K.
[d] Measured at 313 K.

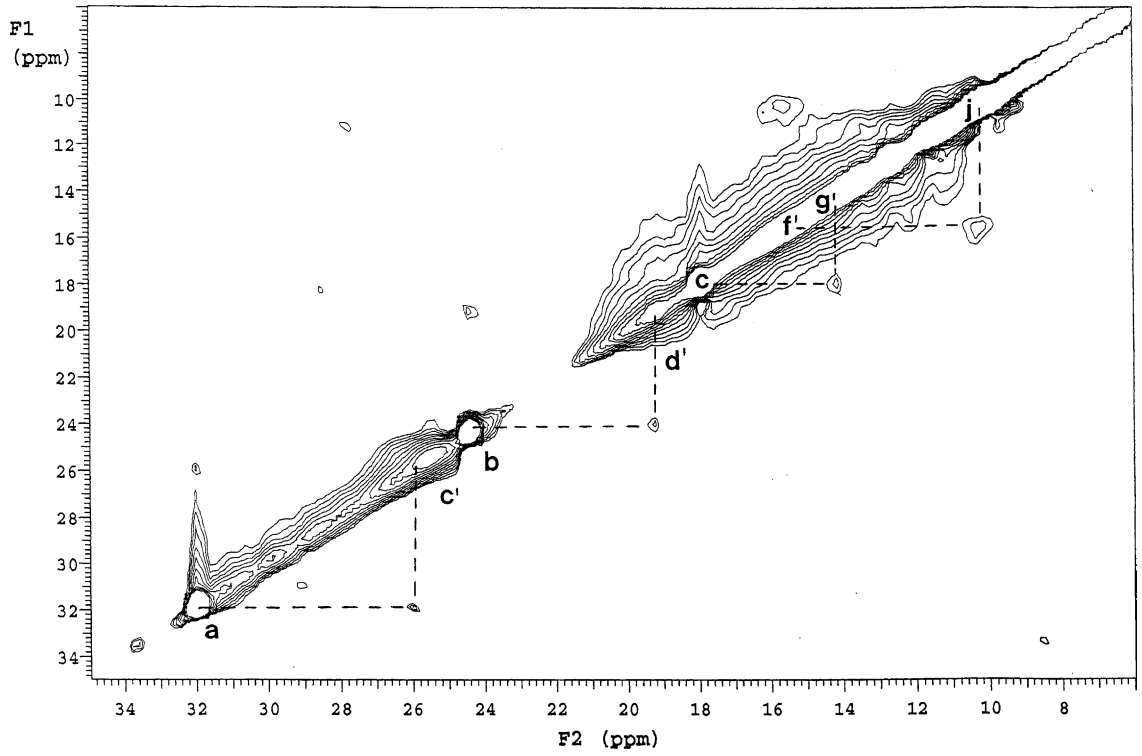


Fig. 3. Portion of 400 MHz EXSY map of ferricyt *c*-551 in H_2O solvent at 303 K and pH 10.8. The sample contained low spin Fe(III) and high-spin Fe(III) forms of the protein. Other conditions are given in the text.

At this point, it is interesting to remark that ferricyt *c*-551 in basic medium (pH 11.4) without exposure to light and in an inert atmosphere is stable for 48–72 h, after which it is progressively altered and the metalloprotein is not stable. In neutral medium certain instability has already been observed for ferricyt *c*-551 [16,26]. This process has been associated with the photoreduction mechanism of the iron(III) and is brought about by free radicals provided by amines or hydroxyl species.

3.2. Temperature dependence of the isotropically shifted signals

Variable temperature ^{1}H NMR spectra of ferricyt *c*-551 at pH 11.4 were registered in the range from 283 to 323 K. The temperature dependence of some non-overlapped isotropically shifted resonances is plotted as a function of $1/T$ (Fig. 4). All isotropically shifted signals follow a Curie behavior whereas the signals a′, h′ and n′ are more temperature dependent with a significant intercept value at infinite temperature, −3.2, −3.0 and −6.1 ppm, respectively. These results are indicative of some pseudocontact contribution to the hyperfine shifted signals, and are compatible with the existence of high-spin iron(III) complexes with the $^6A_1$ ground state ($S = 5/2$). The small dipolar contribution to the shift is due to the presence of a zero-field splitting and that is characteristic of high-spin iron(III) porphyrins

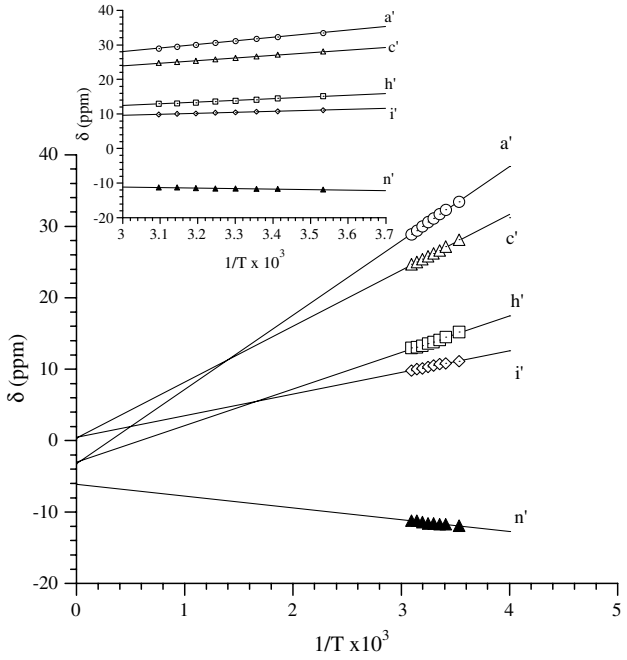


Fig. 4. Temperature dependence of the hyperfine shifted resonances of ferricyt *c*-551 in H_2O at pH 11.4 between 10 and 50 °C. The insert shows a plot with an expanded $1/T$ axis.

[27–30]. At this point, it is interesting to note that while the temperature dependence in the case of low-spin iron(III) cyt *c* is of both the Curie and anti-Curie type

[31–34], we observed only the Curie type. This behavior is characteristic of high-spin iron(III) porphyrins [29,30] and, consequently, of high-spin ferricyt *c*-551. In addition, the temperature dependence of the hyperfine shifted resonances in oxidized cyt *c*-551 at high pH suggests that these differences in the spin state are due to a possible modification in the coordination site of the heme group that is, naturally, responsible for the electronic transfer function of the metalloprotein cyt *c*-551. On the other hand, the protein is not damaged after exposure to 323 K and pH 11.4 because the spectra were reproducible and completely reversible in the temperature range 10–50 °C. In addition, it has been reported that the oxidized form of mesophile *Pae* cyt *c*-551 was thermostable at least up to 70 °C [35,36].

3.3. Comparisons of the spin crossover between ferricyt c-551 from Pae and other ferricytochromes c

Because the cytochromes *c* are relatively small electronic transfer hemoproteins, several research groups have investigated cytochromes *c* in general and, in particular, on the cyt *c*-551 from *Pae*, see for example the references [35,37–42]. Our study of the pH effect in the interval 9–11.5 reveals a drastic change in the protein, with Fe(III) experiencing a change in spin of from $S = 1/2$ to $S = 5/2$ on increasing the pH to 10.8 or above. A decrease in the relaxation times, T_1, and an increase in the linewidth of the new signals accompanies this change, suggesting a change in coordination geometry or at least the decoordination of one axial ligand coordinated to the heme group. Thus, we can think that the Met-61 axial ligand would be replaced with ligands like OH^-. This hypothesis agrees with data from an EPR study reported on cytochrome *c*-551 in the oxidized form with varying pH [9] that presented similar conclusions which refers to the substitution of the Met-61 axial ligand for other weaker ligands near to the group heme. Surprisingly, however, these authors postulate the formation of low-spin cyt *c*-551 at pH values >11 [9].

The change of the axial ligand at alkaline pH for ferricyt *c*-551 not only has been studied by means of EPR techniques, but also electronic [9,10] and IR [43,44] spectroscopy. From the electronic absorption studies for an alkaline solution of *Pae* cyt *c*-551, Li et al. [10] conclude that the Met-61 ligand is replaced by OH^-. Moreover, the RR spectra show that at alkaline pH, the heme iron and methionine sulfur bond is cleaved and replaced by another ligand, for example lysine, but the heme iron to histidine nitrogen bond remains intact. Studies on ferricytochromes *c* from other sources reach similar conclusions [31,32,45,46]. Some differences between them can be exposed. Timkovich and Cork [32] suggest that the methionine ligand is displaced at high pH (pH up to 10) for ferricyt *c*-554 from *Alcaligenes faecalis*. Ferricyt *c*-551 from *Rhodocyclus gelatinosus* exhibits changes in the NMR spectra at pH ~8 that are attributed to a new form of the cytochrome [31]. The alkaline conformational changes of tuna and horse ferricytochromes *c* have been studied by FTIR spectroscopy [45]. The optical spectrum shows a pH dependence in the interval of pH 8–12 and it has been proposed that the ionization of a heme propionate of mitochondrial cyt *c* cause the alkaline transition, and thus a transition from a low-spin iron(III) to high-spin iron(III) electronic state [45]. At the same time, the conformational change triggers the dissociation of the coordinated methionine and its replacement for another hard ligand, perhaps a lysine [45,47]. A similar behavior to the one observed for the ferricyt *c*-551 from *Pae* has been studied in ferricyt *c*-550 from *Thiobacillus versutus* [46,48]. In this case, when the pH increases over 11 for ferricyt *c*-550, a new species is detected, and again a change in the iron(III) coordination has been suggested [46]. This change has been tentatively identified later as a species with a Lys-His^- ligation of the heme iron(III) by means of EPR [48]. The results obtained for *T. versutus* cyt *c*-550 Met100Lys mutant, at pH >11, show the Lys-His^- coordination of the heme iron, that it is similar with those observed for the alkaline form of wild-type cyt *c* [49]. On the other hand, Gadsby and Thomson [50] have reported the assignment of axial ligands of ferric ion in some low-spin cytochromes at high pH by means of near-IR MCD data and EPR spectra. These are horse heart cytochrome c at pD 11.0 with Lys/His as ligands of heme and cytochrome *b*-562 from *Escherichia coli* at pD 10.5 with Met/His^- as ligands of heme.

As mentioned above, the deprotonation of the histidine amino-acid coordinated to the iron of the heme

	12				16				20	
A	Cys	Val*	Ala*	Cys	**His**	Ala*	Ile*	Asp	Thr	Lys
B	Cys	Ala*	Gln	Cys	**His**	Thr	Val*	Glu	Lys	Gly*
C	Cys	Ala*	Gln	Cys	**His**	Thr	Val*	Glu	Asn	Gly*
D	Cys	Lys	Ala*	Cys	**His**	Met*	Val*	Gln	Ala*	Pro*
E	Cys	Leu*	Ala*	Cys	**His**	Gln	Val*	Asp	Lys	Lys

Fig. 5. Portion of the alignment, including the coordinated His, of some mitochondrial and bacterial cytochromes *c*: (A) *Pseudomonas aeruginosa* cyt *c*-551 [51], (B) horse heart cyt *c*-550 [52], (C) skipjack tuna cyt *c*-550,[1] (D) *Thiobacillus versutus* cyt *c*-550 [53], (E) *Rhodocyclus gelatinosus* cyt *c*-551.[1] Amino-acid sequence number refers to *Pae* cyt *c*-551. The asterisks denote the hydrophobic amino-acids.

[1] Swissprot Database.

group at high pH can trigger the decoordination of Met axially bound to iron(III) and consequently the alkaline transition. The observed differences in alkaline conformation change for different ferricytochromes *c* can be related to the hydrophobic amino-acid next to the histidine residue that is coordinated to the iron (Fig. 5). Thus, with an increase in the hydrophobicity, the deprotonation of the coordinated histidine occurs at higher pH and this is in agreement with the fact that the alkaline conformation change is detected at higher pH. It is remarkable that the alkaline conformation change for ferricyt *c*-551 from *Pae* is similar to that reported for ferricyt *c*-550 from *T. versutus* and appears at pH 11–12. At the same time, the hydrophobic environment in these cases is similar and more hydrophobic than that of horse heart, tuna or *Rhodocyclus gelatinosus* ferricyt *c*, see Fig. 5.

4. Conclusions

The ^{1}H NMR spectra of ferricyt *c*-551 in the oxidized form, in basic medium between pH 9 and 11.4, demonstrate a drastic change compared to spectra acquired in acid or neutral medium. The signals broaden and the isotropic shift decreases. Additionally, whereas in the low-spin Fe(III) hemoprotein the longitudinal relaxation times are between 80 and 200 ms, for the high-spin species, the longitudinal relaxation time varied from 1 to 48 ms. On the other hand, the temperature dependence of the hyperfine shift indicates a weak dipolar contribution. These results are consistent with the existence of a paramagnetic center that presents a small magnetic anisotropy. The high-spin iron(III) probably forms a penta or hexacoordinated geometry and an $^6A_1$ ground state with a spin of $S = 5/2$ in which the orbital contribution is very low and the magnetic anisotropy would be negligible. The isotropically shifted resonances present essentially a contact contribution. In our case, the dipolar contribution is practically non-existent as it is observed in the isotropically shifted proton resonances as a function of temperature, which confirms the penta or hexacoordinated geometry expected for a complex of high-spin iron(III). The results show that a change of spin state from low-spin iron(III) to high-spin iron(III) has been produced for a pH of 10.8. This change of spin state is probably associated with deprotonation of the axially coordinated amino-acid, His-16, which would provoke the dissociation of the second axial amino-acid, Met-61.

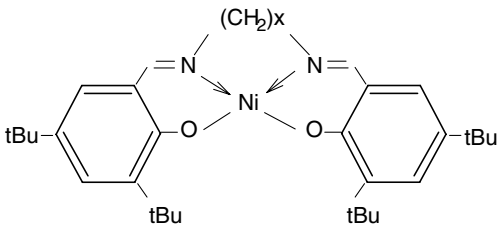
Acknowledgments

This work was supported by the DGICYT, Ministerio de Educación y Cultura, Spain (PB98-1444). The NMR section of SCSIE (University of Valencia) is gratefully acknowledged for the use of NMR facilities. H.R.J. is indebted to María Arbona for assistance and suggestions.

References

[1] G.W. Pettigrew, G.R. Moore, in: A. Rich (Ed.), Cytochromes *c*: Biological Aspects, Springer-Verlag, Berlin, 1987.
[2] R.A. Scott, A.G. Mauk (Eds.), Cytochrome *c*. A Multidisciplinary Approach, University Science Books, Sausalito, CA, 1996.
[3] G.R. Moore, G.W. Pettigrew, Cytochromes *c*: Evolutionary, Structural and Physicochemical Aspects, Springer, Berlin, 1990.
[4] Y. Matsuura, T. Takano, R.E. Dickerson, J. Mol. Biol. 156 (1982) 389.
[5] D.J. Detlefsen, V. Thanabal, V.L. Pecoraro, G. Wagner, Biochemistry 30 (1991) 9040.
[6] G.R. Moore, G.W. Pettigrew, R.C. Pitt, R.J.P. Williams, Biochim. Biophys. Acta 590 (1980) 261.
[7] F.A. Leitch, G.R. Moore, G.W. Pettigrew, Biochemistry 23 (1984) 1831.
[8] M.H. Chau, M.L. Cai, R. Timkovich, Biochemistry 29 (1990) 5076.
[9] Y.H. Chao, R. Bersohn, P. Aisen, Biochemistry 18 (1979) 774.
[10] Y. Li, K. Imaeda, H. Inokuchi, J. Phys. Chem. 98 (1994) 4726.
[11] I. Bertini, C. Luchinat, NMR of Paramagnetic Molecules in Biological Systems, Benjamin Cummings, Menlo Park, CA, 1986.
[12] G.N. La Mar, J.D. Satterlee, J.S. de Ropp, in: K.M. Kadish, K.M. Smith, R. Guilard (Eds.), Nuclear Magnetic Resonance of Hemoproteins, The Porphyrin Handbook, vol. 5, Academic Press, San Diego, CA, 2000, p. 185.
[13] I. Bertini, C. Luchinat, G. Parigi, Solution NMR of Paramagnetic Molecules. Applications to Metallobiomolecules and Models, Elsevier, New York, 2001.
[14] R. Timkovich, Biochemistry 29 (1990) 7773.
[15] R. Timkovich, Inorg. Chem. 30 (1991) 37.
[16] R. Timkovich, M.L. Cai, Biochemistry 32 (1993) 11516.
[17] J.M. Moratal, A. Donaire, J. Salgado, H.R. Jiménez, J. Castells, M. Piccioli, FEBS Lett. 324 (1993) 305.
[18] S.R. Parr, D. Barber, C. Greenwood, B.W. Phillips, J. Melling, Biochem. J. 157 (1976) 423.
[19] R.P. Ambler, M. Wynn, Biochem. J. 131 (1973) 485.
[20] M.M. Bradford, Anal. Biochem. 72 (1976) 248.
[21] T. Horio, T. Higashi, M. Sasagawa, K. Kusai, M. Nakai, K. Okunuki, Biochem. J. 77 (1960) 194.
[22] T. Inubushi, E.D. Becker, J. Magn. Reson. 51 (1983) 128.
[23] R.L. Vold, J.S. Waugh, M.P. Klein, D.E. Phelps, J. Chem. Phys. 48 (1968) 3831.
[24] D.J. States, R.A. Haberkorn, D.J. Ruben, J. Magn. Reson. 48 (1982) 286.
[25] I. Bertini, P. Turano, A.J. Vila, Chem. Rev. 93 (1993) 2833.
[26] C. Bartocci, F. Scandola, A. Ferri, V. Carassiti, J. Am. Chem. Soc. 102 (1980) 7067.
[27] G.N. La Mar, F.A. Walker, in: D. Dolphin (Ed.), Nuclear Magnetic Resonance of Paramagnetic Metalloporphyrins, The Porphyrins, vol. IV, Academic, New York, 1979, p. 61.
[28] R. Guilard, I. Perrot, A. Tabard, P. Richard, C. Lecomte, Y.H. Liu, K.M. Kadish, Inorg. Chem. 30 (1991) 27.
[29] H.R. Jiménez, J.M. Moratal, J. Latorre, M. Momenteau, New J. Chem. 21 (1997) 223.
[30] H.R. Jiménez, J.M. Moratal, B. Loock, New J. Chem. 26 (2002) 323.
[31] L. Banci, I. Bertini, M.T. Cambria, F. Capozzi, A. Dikiy, Eur. J. Biochem. 219 (1994) 663.

[32] R. Timkovich, M.S. Cork, Biochemistry 23 (1984) 851.
[33] H. Santos, D. Turner, Eur. J. Biochem. 206 (1992) 721.
[34] R. Timkovich, M.L. Cai, B.L. Zhang, D.M. Arciero, A.B. Hooper, Eur. J. Biochem. 226 (1994) 159.
[35] J. Hasegawa, H. Shimahara, M. Mizutani, S. Uchiyama, H. Arai, M. Ishii, Y. Kobayashi, S.J. Ferguson, Y. Sambongi, Y. Igarashi, J. Biol. Chem. 274 (1999) 37533.
[36] Y. Yamamoto, N. Terui, N. Tachiiri, K. Minakawa, H. Matsuo, T. Kameda, J. Hasegawa, Y. Sambougi, S. Uchiyama, Y. Kobayashi, Y. Igarashi, J. Am. Chem. Soc. 124 (2002) 11574.
[37] C. Costa, G.R. Moore, Inorg. Chim. Acta 276 (1998) 256.
[38] M.A. Ceruso, A. Grottesi, A. Di Nola, Proteins 50 (2003) 222.
[39] F. Cutruzzola, M. Arese, G. Ranghino, G. Van Pouderoyen, G.W. Canters, M. Brunori, J. Inorg. Biochem. 88 (2002) 353.
[40] R.E.M. Diederix, M. Ubbink, G.W. Canters, Biochemistry 41 (2002) 13067.
[41] B.S. Russell, L. Zhong, M.G. Bigotti, F. Cutruzzola, K.L. Bren, J. Biol. Inorg. Chem. 8 (2003) 156.
[42] M. Brunori, M.G. Bigotti, F. Cutruzzola, S. Gianni, C. Travaglini-Allocatelli, Biophys. Chem. 100 (2003) 409.
[43] W.G. Valance, T.C. Strekas, J. Phys. Chem. 86 (1982) 1804.
[44] T. Kitagawa, Y. Ozaki, J. Teraoka, Y. Kyogoku, T. Yamanaka, Biochim. Biophys. Acta 494 (1977) 100.
[45] P. Tonge, G.R. Moore, C.W. Wharton, Biochem. J. 258 (1989) 599.
[46] A. Lommen, A. Ratsma, N. Bijlsma, G.W. Canters, J.E. Van Wielink, J. Frank, J. Van Beeumen, Eur. J. Biochem. 192 (1990) 653.
[47] P.M.A. Gadsby, J. Peterson, N. Foote, C. Greenwood, A.J. Thomson, Biochem. J. 246 (1987) 43.
[48] M. Ubbink, G.C.M. Warmerdam, A.P. Campos, M. Teixeira, G.W. Canters, FEBS Lett. 351 (1994) 100.
[49] M. Ubbink, A.P. Campos, M. Teixeira, N.I. Hunt, H.A.O. Hill, G.W. Canters, Biochemistry 33 (1994) 10051.
[50] P.M.A. Gadsby, A.J. Thomson, J. Am. Chem. Soc. 112 (1990) 5003.
[51] R.J. Almassy, R.E. Dickerson, Proc. Natl. Acad. Sci. USA 75/6 (1978) 2674.
[52] E. Margoliash, E.L. Smith, G. Kreil, H. Tuppy, Nature 192 (1961) 1121.
[53] M. Ubbink, J. Van Beeumen, G.W. Canters, J. Bacteriol. 174 (1992) 3707.



H_2L_x	$Ni(L_x)$	$(CH_2)_x$
H_2L_1	$Ni(L_1)$	$-(CH_2)_2CH(CH_3)-$
H_2L_2	$Ni(L_2)$	$-(CH_2)_2-$
H_2L_3	$Ni(L_3)$	$-(CH_2)_3-$
H_2L_4	$Ni(L_4)$	$-(CH_2)_4-$
H_2L_5	$Ni(L_5)$	$-(CH_2)_5-$
H_2L_6	$Ni(L_6)$	$-(CH_2)_6-$

Scheme 1.

on the aniline or salicylaldehyde moieties have stimulated their possible antioxidant activity and ability to form stable phenoxyl- or semiquinone type radical complexes on chemical oxidation or reduction [15]. In some cases the complexation of these ligands was accomplished by non-predictable redox-reactions depending on the nature of the ligands, solvents and oxidants [15,16]. The introduction of bulky groups in these ligands influences the redox reactivity and overall catalytic properties of the complexes [2b,15c,16]. In this study, we present the synthesis, spectroscopic and electrochemical behaviour of a new series of *N*,*N*′-polymethylenebis(3,5-di-*tert*-butylsalicylaldiminato)nickel(II) complexes, $Ni(L_x)$, [H_2L_x = *N*,*N*′-bis(3,5-di-*tert*-butylsalicylidene)-polymethylenediamines] (Scheme 1).

2. Experimental

2.1. Preparation of the ligands and the complexes

All the ligands and their Ni(II) complexes were prepared according to the methods in the literature [17–19] and the analyses of the compounds were made by comparing the spectroscopic results with the reported ones [17,20–24].

2.2. Electrochemistry

Voltammetric recordings were made using Volta Lab PGZ 301 Dynamic Voltammetry. A platinum-bead working, platinum-coil counter electrode and saturated calomel reference electrode (SCE) were used for CV measurements. Cyclic voltammograms (CV) were recorded under N_2 gas atmosphere in DMF at room temperature. The concentration of the complexes was 0.001 M in the electrolyte solution, where commercially obtained [*n*-$(C_4H_9)_4N$]BF_4 was used as a supporting electrolyte. The voltage scan rate during the CV measurements was 100 mV/s. Controlled potential electrolysis at the anodic peak potential was carried out with a Ag-wire reference electrode after making a correction between the SCE and the Ag-wire (280 mV for SCE, and the oxidation potential of the ferrocene/ferrocenium couple was found to be 0.84 V versus SCE and 0.56 V versus Ag-wire, in our system). The oxidation process was followed in situ on a Hewlett Packard UV–Vis HP 8453A diode array spectrophotometer. Platinum gauze electrodes were used as the working and the counter electrodes. N_2 gas was bubbled through the electrolysis solution for stirring purposes between the scans.

2.3. Electron paramagnetic resonance spectroscopy (EPR)

The EPR spectrum of the electrochemically generated product, $Ni^{III}(L_x)$, was recorded by using a Varian E12 spectrometer in a quartz EPR cell in liquid nitrogen where diphenylpicrylhydrazyl (DPPH) was used as a reference.

3. Results and discussion

3.1. Voltammetric studies

The electrochemical data for all the Ni(II) complexes obtained in this study are presented in Table 1. The vol-

Table 1
Cyclic voltammetry data (VSR = 100 mV/s) for H_2L_x and $Ni(L_x)$ complexes in DMF

Compound	E_a (V)	E_c (V)	ΔE_p (V)
$Ni(L_1)$	0.90[a], 1.20	1.10[b]	0.062
$Ni(L_2)$	0.84[a], 1.17	1.10[b]	0.059
$Ni(L_3)$	0.74[a], 1.00	0.93[b]	0.058
$Ni(L_4)$	0.68[a], 0.96	0.80[b]	0.062
$Ni(L_5)$	0.84, 1.11		
$Ni(L_6)$	0.83, 1.16		
H_2L_1	0.98		
H_2L_2	1.10		
H_2L_3	1.10		
H_2L_4	1.06		
H_2L_5	1.12		
H_2L_6	1.17		

E_a represents the oxidation peak potential.
E_c represents the reduction peak potential.
ΔE_p represents the difference between the peak potentials of the reversible anodic peaks.
[a] Reversible peak potential.
[b] Dependence on the second oxidation peak potential.

tammograms of all the Ni(II) complexes exhibits two step oxidation processes in DMF at room temperature under N_2 gas atmosphere. As shown in Fig. 1 and Table 1, the first oxidation peak potential of all the Ni(II) complexes, except Ni(L_5) and Ni(L_6), reveals a reversible electron transfer from 0.68 to 0.90 V versus SCE.

A linear dependence, which was observed between i_p and $V^{1/2}$ and between E_p and i_p as the voltage scan rate (V) increased, indicates a diffusion controlled electron exchange reaction. The plot of current function ($i_p/(C \cdot V^{1/2})$ versus Log V gave a straight line parallel to the horizontal axis (Log V) for the first oxidation peak potential, indicating a reversible electrode exchange reaction according to Nicholson–Shain criteria [25]. Furthermore, the ratio i_{pc}/i_{pa} was independent of scan rate and equal to unity for scan rates changing from 100 mV/s to 1 V/s.

The number of electrons transferred at the first oxidation peak was found to be one by using a digital coulometer. Since the integrated area under the second oxidation peak is twice the area under the first anodic peak, a $2e^-$ transfer was assigned for the second anodic peak.

The oxidation potentials (Table 1) are dependent on the diamine bridge, [=N–$(CH)_n$–N=]. More positive potentials are obtained as the methylene-group chain (Scheme 1) decreases from $n = 4$ to 2. It is known that the oxidation potentials of tetradentate N_2O_2 salen type systems are markedly dependent on the imine bridges and the salicylaldehyde moieties. For the metal centered one electron processes, the anodic peak potentials shift to more positive values with electron withdrawing substituents, whereas electron donating groups have the opposite effect [26]. Moreover, an increase in the length of the bridging N–$(CH_2)_n$–N chain ($n = 2$–4) was expected initially to increase the steric strain in the ligand ring [27]. However, for nickel(II), increasing n ($n = 2$–4) leads to an effective weakening of the ligand field strength [24]. A weak ligand field leads to a decrease in the energy levels of the d-orbitals in our complexes. This decrease must be due to an increase in the size of the ligand cavity with the $(CH_2)_{2-4}$ bridge. When the chelate ring size decreases, the in-plane ligand field strength increases [9].

The redox behaviour of Ni(L_5)and Ni(L_6) was different from the other Ni(II) complexes. The voltammograms of these complexes consist of two irreversible oxidation peaks at around 0.84 and 1.11 V for Ni(L_5) and at 0.83 and 1.16 V for Ni(L_6) versus SCE. The geometry of Ni(L_x) ($x = 2$–4) gradually changes from square planar to pseudo-tetrahedral, resulting in a cathodic shift in their redox potentials. These complexes, unlike other complexes containing macrocyclic ligands, afford easier access to mixed donor environments, and the open equatorial ring size of these ligands can accommodate the metal size, which changes upon oxidation/reduction [8,28]. The difference in the electronic absorption spectra and the electrochemical behaviour of Ni(L_5) and Ni(L_6) is most probably related to their structural reorganization as dinuclear complexes (Scheme 2). As shown in Scheme 2, the size of the chelating cavity is smaller than that of other Ni(II) complexes, although the length of methylene bridge increases. The chelate ring geometry of Ni(L_5) and Ni(L_6) can be assumed as similar to that of Ni(L_2). It should be noted that if the oxidation state of Ni(III) in these complexes is less stabilized due to steric hindrance of the bulky ligand structure, the decomposition of the oxidized species can be possible as well. However, the electrochemistry of these complexes have not been studied in detail here.

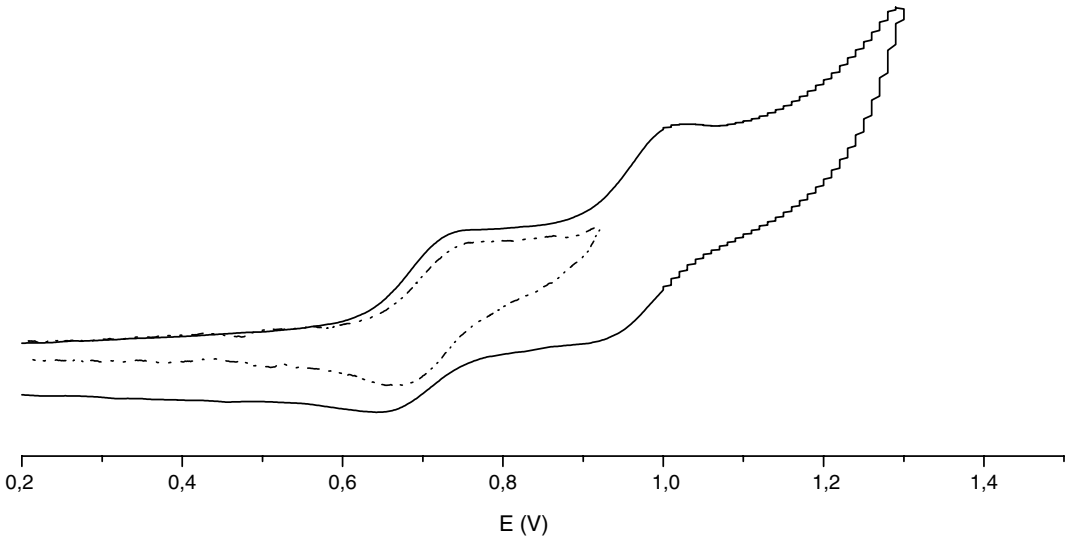
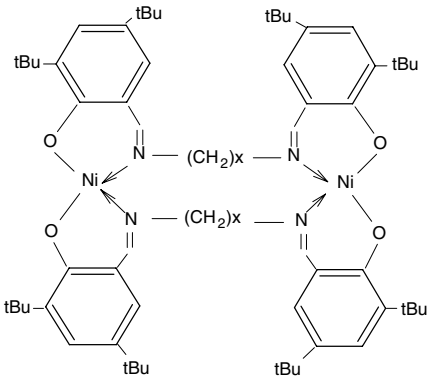


Fig. 1. Cyclic voltammogram of 0.001 M Ni(L_3) in DMF at room temperature vs. SCE (VSR = 100 mV/s).



Scheme 2.

3.2. Electrochemical oxidation of Ni(L_x) complexes

Electrochemical oxidation of Ni(L_3) solution was carried out approximately at 70 mV more positive potential than its first oxidation peak potential (0.74 V) in DMF versus Ag-wire at −10 °C. The changes in the electronic absorption spectrum of the complex were followed in situ by measuring the spectra during the electrolysis every 10-mC interval (Fig. 2(a)). The electronic absorption spectrum of the original complex in DMF contains two absorption bands at 355 and 426 nm in the working range of 265–1100 nm. During the oxidation, the band at 355 nm shifted to 350 nm with an increase in its intensity, while the intensity of the band at 426 nm decreased gradually. A new band at 505 nm formed with two-well defined isosbestic points at 406 and 449 nm, until the end of the $1e^-$ transfer. This process produces a change in color of the electrolyte solution from yellow to pink, implying the formation of a new species.

The EPR spectrum of the electrochemically produced pink product (Fig. 3(a)) at 77 K exhibited three well separated g-values of $g_1(g_x) = 2.24$, $g_2(g_y) = 2.21$ and $g_3(g_z) = 2.014$, indicating rhombic stereochemistry, where g_1 and g_2 refer to the lowest and highest magnetic field g values, respectively [6–12]. A large g-tensor anisotropy ($g_{avr} \gg 2$) and d^7-low spin ($S = 1/2$) electron configuration demonstrates the formation of Ni(III), which has a typical d^7-low spin ($t_2^6e^1$) configuration [6,11]. The observed spectral pattern is consistent with Ni(III) in a tetragonal geometry (g_x, $g_y > g_z$) and $^2A_{1g}$ [$(d_z^2)^1$] ground state, rather than square-planar geometry ($g_z > g_x$, g_y) [29]. No superhyperfine splitting was assignable due to the equatorial nitrogens in any of the three g regions. Addition of excess pyridine to the freshly prepared $[Ni^{III}(L_3)]^+$ solution in DMF resulted in an axial spectrum ($g_x \cong g_y$) with $g_\perp > g_\parallel$ and three-line hyperfine splitting in the $g_\parallel$ component. The g_x and g_y values are approximately equal and are not resolved. The appearance of three lines splitting in the $g_\parallel$ region with $a_\parallel = 8$ G (0.00748 cm^{-1}) suggests a single pyridine molecule bound to the axial positions of the $[Ni^{III}(L_3)]^+$ complex (inset of Fig. 3(a)) [13,14]. These results suggests that the initial $[Ni^{III}(L_3)(DMF)_2]^+$ complex in the presence of pyridine is converted to a tetragonally elongated octahedral monopyridine adduct, $[Ni^{III}(L_3)(DMF)(Py)]^+$ or penta-coordinated $[Ni^{III}(L_3)(Py)]^+$ complex having axially coordinated pyridine in a square pyramidal geometry (C_{4v}). It is known that both these geometries possess the $(d_{xy})^2(d_{z^2})^1$ ground state with the relation g_x, $g_y > g_z \approx 2$ [30].

Consequently, the electrode reaction, which is consistent with the $1e^-$ reversible oxidation process of the Ni(L_3) complex at its first anodic peak potential in DMF, can be proposed as follows:

$$[Ni^{II}(L_3)] \rightleftharpoons [Ni^{III}(L_3)]^+ + e^- \quad (1)$$

$$[Ni^{III}(L_3)]^+ + S \rightarrow [Ni^{III}(L_3)(S)]^+ \quad \text{(where S = solvent)} \quad (2)$$

This process is followed by a decay path of the electrochemically generated Ni(III) species back to the neutral Ni(II) complex. The decay occurs in a few seconds at room temperature. Decay of the Ni(III) species (Fig. 4) that was studied at −10 °C indicates a second order rate law with a rate constant $k = 5.00 \times 10^{-4}$ L/mol s. The previous studies on the decomposition of Ni(III) complexes with macrocyclic ligands [8], reveal that an intramolecular electron transfer mechanism should be operative from the ligand to the Ni(III) center to form radical species. Thus, further reactions following the reversible electron transfer are as follows:

$$[Ni^{III}(L_3)(S)]^+ \rightarrow [Ni^{II}(L_3^{\bullet+})(S)] \quad (3)$$

$$2[Ni^{II}(L_3^{\bullet+})(S)] \rightarrow [Ni^{II}(L_3)(S)] + [Ni^{II}(L_3^{ox})(S)] \quad \text{(slow)}$$

$$\text{(where } L^{ox} = \text{the two electron oxidised ligand)} \quad (4)$$

$$[Ni^{II}(L_3^{ox})(S)] \rightarrow Ni^{II}(solv) + (L_3^{ox}) + S \quad (5)$$

The electronic absorption spectra recorded in situ imply that only half of the original complex was recovered and the other half decomposed to the free ligand and Ni(II) species. The characteristic absorption band of the free ligand (328 nm) could not be observed in the electronic absorption spectrum of the solution after the decay, since the skirt of the highly intense band at 350 nm obscured this region completely. These observations support our proposed mechanism. Studies on the decay kinetics have still to be continued.

The second oxidation peak that appears in the CV of Ni(L_3) was assigned as the stepwise oxidation of the two aromatic rings of the ligand. The electrochemical oxidation of the complex, which was carried out

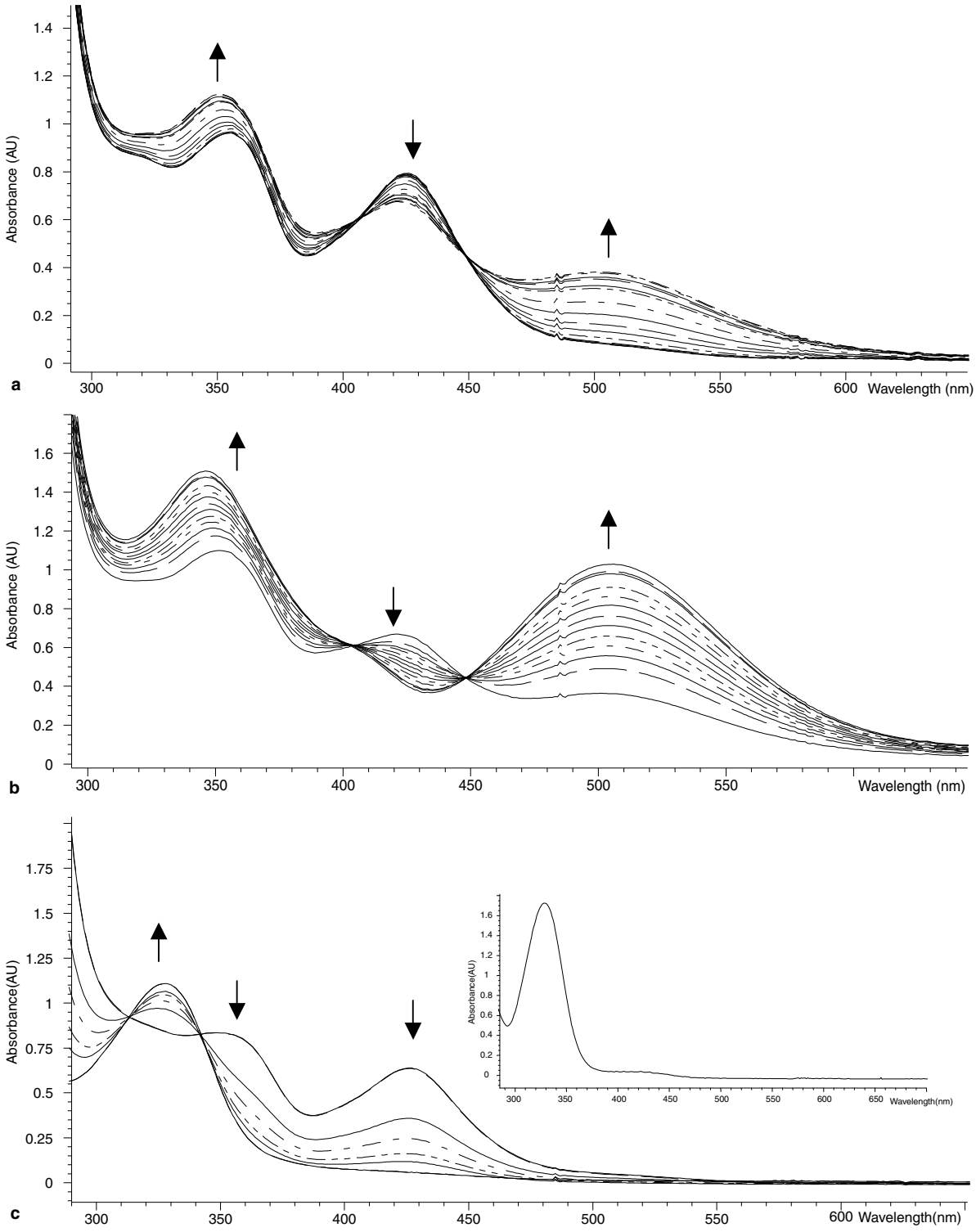


Fig. 2. (a) The changes in the electronic absorption spectrum of 1.2×10^{-3}M Ni(L_3) during the electro-oxidation at its first electrode potential vs Ag-wire. There are 10 mC intervals between the two scans; (b) the spectral changes that are obtained during the electrolysis at the second oxidation peak potential; (c) the spectral changes that are obtained after the third electron transfer; inset: the electronic absorption spectrum of the free H_2L_3 ligand.

at the second anodic peak potential after the one electron transfer, yielded a red product solution with an increase in the intensity of the absorption band at 505 nm. The spectral changes showed two sharp isosbestic points at 406 and 454 nm. While the absorption band at 350 nm shifted to 345 nm with an increase in its intensity, the band at around 416 nm disappeared completely (Fig. 2(b)).

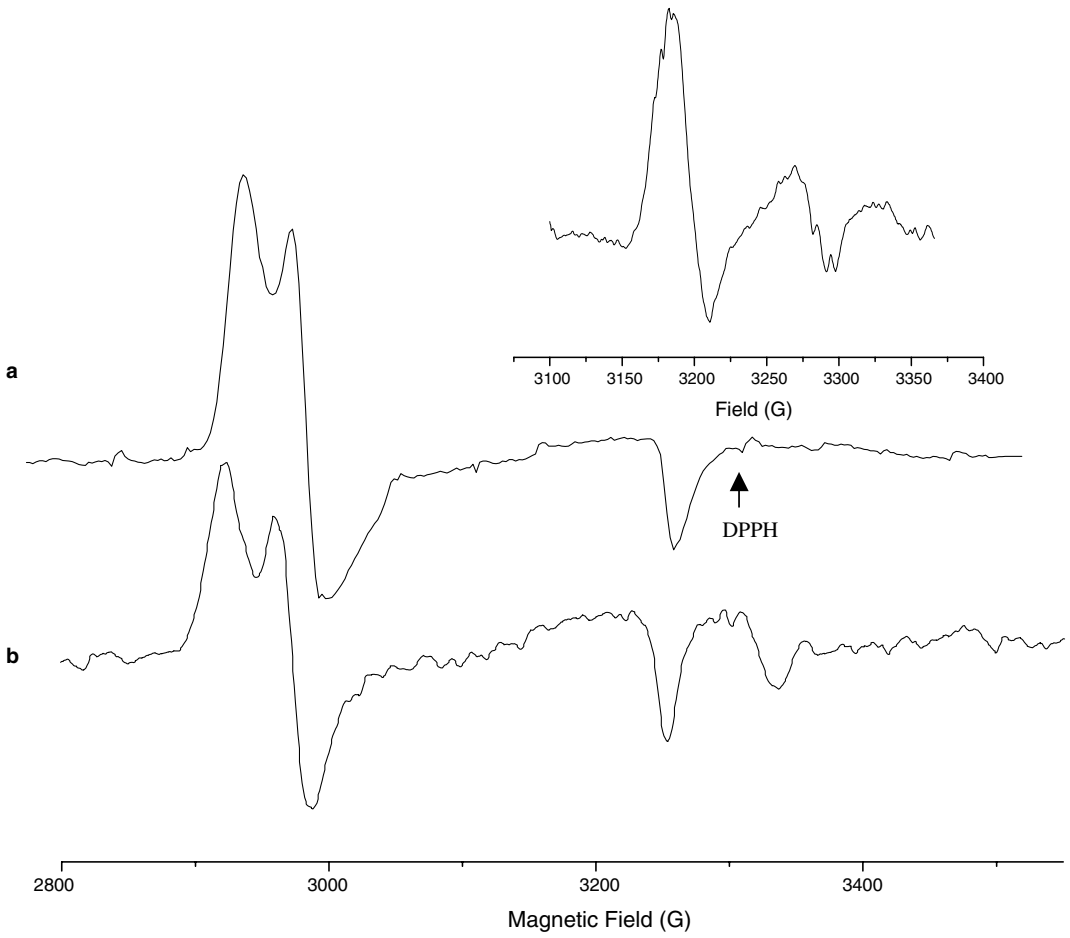


Fig. 3. (a) EPR spectrum of the electrochemically generated Ni(III) species at 77 K; (b) EPR spectrum of the product obtained after the second electron transfer at 77 K; inset: EPR spectrum of the pyridine adduct of the electrochemically generated Ni(III) species at 77 K.

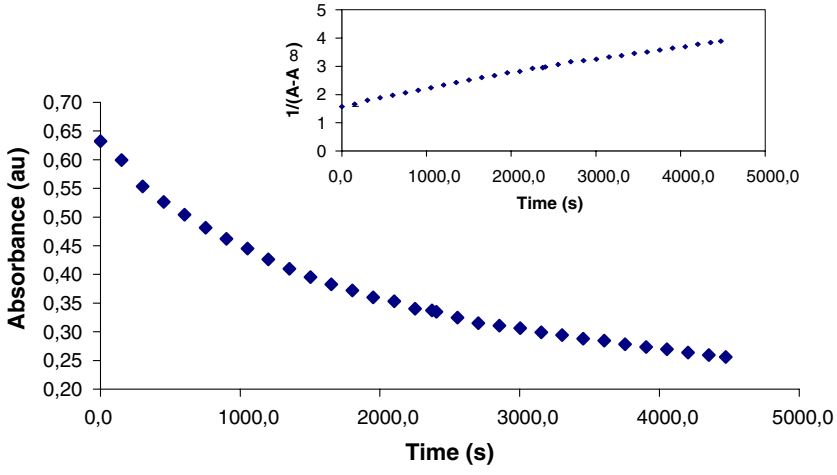


Fig. 4. Time traces for the decay of Ni(III) species at −10 °C in DMF; inset: second order fit for the decay of Ni(III) species.

The EPR spectrum of the electrochemically generated red solution demonstrated the characteristic Ni(III) signals as well as a broad feature at 77 K which can be assigned to a ligand radical species (Fig. 3(b)) by the formation of a coordinated phenoxy-radical structure in the electrolyte solution.

$$[Ni^{III}(L_3)(S)]^+ \rightarrow [Ni^{III}(L_3^{\bullet+})(S)]^+ + e^- \quad (6)$$

When the oxidation process continued at the same electrode potential as the second electron transfer, the electronic spectrum was changed completely. All the bands corresponding to the complex solution disappeared and a new highly intense characteristic band of the ligand at 328 nm was formed (Fig. 2(c)).

The radical ligand species obtained after the one electron transfer at the second oxidation peak potential is stabilised by the *tert*-butyl groups of the aromatic ring. Thus, the decomposition of the complex was not observed on the CV timescale and the reduction peak observed after the second anodic peak is proposed as the reduction of the red product back to the original complex. The observation of no new oxidation or reduction peak formation in the voltammograms after this cathodic electron transfer also supports our assignment.

Similar electrochemical results were obtained for the Ni(L_1), Ni(L_2) and Ni(L_4) complexes. In each case, a red product was obtained at the end of the two-electron transfer process, implying the formation of the same product that was observed in the oxidation of the Ni(L_3) complex.

4. Conclusions

The electrochemical behaviours of Ni(L_x) are different from those reported for analogous salen type Ni(II) complexes with polymethylene bridges. This feature seems to be due to the steric requirements of the *tert*-butyl groups on the 3,3′-positions of the salicylic fragments. The first oxidation peaks in the cyclic voltammograms of Ni(L_1), Ni(L_2), Ni(L_3) and Ni(L_4) complexes appear at 0.90, 0.84, 0.74 and 0.68 V, respectively, versus SCE in DMF. The reversible one electron process corresponds to the oxidation of the metal center, producing Ni(III) species with solvent molecule coordination. EPR spectra taken in liquid nitrogen supported the formation of a penta-coordinated Ni(III) complex as well. The second oxidation peak observed at around 1.0 V for all complexes was assigned as an electron transfer from a ligand based orbital by formation of a coordinated phenoxy radical.

In order to identify the final products of the electrooxidation, electrolysis of the complexes were followed in situ by UV–Vis spectrophotometry. In the case of Ni(L_3), well-defined isosbestic points were observed in the electronic spectrum, implying only one type of electrode reaction. Similar electrochemical results were obtained for Ni(L_1), Ni(L_2) and Ni(L_4).

A comparison of the first oxidation peak potentials suggests that: (i) more positive potentials are obtained as the methylene group chain decreases from 4 to 2, however the steric strain in the ligand ring increases in the reverse order; (ii) the methylene group with a long C-chain in the aliphatic diamine bridge destabilises the complex; (iii) the steric hindrance is effective on the stability of the Ni(II) state; (iv) the donation ability of the N atoms decreases as the hole cavity gets smaller. So, the basicity strength of the ligands can be ordered as $(L_4) > (L_3) > (L_2) > (L_1)$.

References

[1] R. Gammack, Adv. Inorg. Chem. 32 (1988) 297.
[2] (a) J.P. Collin, J.P. Sauvage, Coord. Chem. Rev. 93 (1989) 245;
(b) V.T. Kasumov, S.A. Rzaev, A.A. Medjidov, Kinet. Catal. 32 (1991) 594.
[3] R.H. Holm, G.W. Everett, A. Chakravorty, Prog. Inorg. Chem. 7 (1966) 83.
[4] (a) L.J. Klein, K.S. Alleman, D.G. Peters, J.A. Karty, J.P. Reilly, J. Electroanal. Chem. 481 (2000) 24;
(b) A.A. Isse, A. Cenno, E. Vianello, Electrochim. Acta 47 (1992) 113.
[5] (a) J. Hanss, H.J. Krüger, Angew. Chem. Int. Ed. 37 (1998) 360;
(b) L. Gomes, E. Periera, B. Castro, J. Chem. Soc., Dalton Trans. (2000) 1373, and refs. therein.
[6] L.F. Mehne, B.B. Wayland, Inorg. Chem. 14 (1975) 881.
[7] B. de Castro, C. Freire, Inorg. Chem. 29 (1990) 5113.
[8] C. Freire, B. de Castro, E. Pereira, J. Chem. Soc., Dalton Trans. (1994) 571, and refs. therein.
[9] C. Freire, B. de Castro, Polyhedron 17 (1998) 4227.
[10] C. Freire, B. de Castro, J. Chem. Soc., Dalton Trans. (1998) 1491.
[11] A. Desideri, J.B. Raynor, J. Chem. Soc., Dalton Trans. (1977) 2051.
[12] A. Buttafava, L. Fabbrizzi, A. Perotti, A. Poggi, G. Poli, B. Seghi, Inorg. Chem. 25 (1986) 1456.
[13] H.-J. Krüger, G. Peng, R.H. Holm, Inorg. Chem. 30 (1991) 734.
[14] A. Bencini, L. Fabbrizzi, A. Poggi, Inorg. Chem. 20 (1981) 2544.
[15] (a) A.A. Medjidov, V.T. Kasumov, H.S. Mamedov, Koord. Khim. 7 (1981) 66;
(b) M.K. Guseyinova, A.A. Medjidov, V.T. Kasumov, J. Struct. Chem. 23 (1982) 114;
(c) V.T. Kasumov, A.A. Medjidov, Russ. J. Coord. Chem. 16 (1990) 1355;
(d) V.T. Kasumov, J. Coord. Chem. 52 (2001) 57.
[16] (a) V.T. Kasumov, A.A. Medjidov, R.Z. Rzaev, I.A. Golubeva, Russ. J. Coord. Chem. 19 (1993) 933;
(b) V.T. Kasumov, A.A. Medjidov, Russ. J. Coord. Chem. 21 (1995) 210.
[17] V.T. Kasumov, Ş. Özalp-Yaman, E. Taş, Spectrochim. Acta Part A (2005) (in press).
[18] V.T. Kasumov, A.A. Medjidov, İ.A. Golubeva, O.V. Shubina, R.Z. Rzaev, Russ. J. Coord. Chem. 17 (1991) 1698.
[19] R.G. Konsler, J. Karl, E.N. Jacobsen, Russ. J. Coord. Chem. 120 (1998) 10780.
[20] G.C. Percy, D.A. Thornton, J. Inorg. Nucl. Chem. 34 (1972) 3357.
[21] C. Fraser, B. Bosnich, Inorg. Chem. 33 (1994) 338.
[22] P.W. Alexander, R.J. Sleet, Aust. J. Chem. 23 (1970) 1183.
[23] (a) G. Maki, J. Phys. Chem. 28 (1958) 651;
(b) H. Gary, C.J. Ballhausen, J. Am. Chem. Soc. 85 (1963) 260.
[24] (a) R.H. Holm, J. Am. Chem. Soc. 82 (1960) 5632;
(b) W.C. Hoyt, G.W. Everett, J. Inorg. Chem. 8 (1969) 2013.
[25] R.S. Nicholson, I. Shain, Anal. Chem. 36 (1964) 706.

[26] (a) M.Y. Chavan, T.J. Meade, D.H. Busch, T. Kuwana, Inorg. Chem. 25 (1986) 314;
(b) D.H. Busch, J.C. Olszanski, W.P. Schammel, M. Kojima, N. Herron, L.L. Zimmer, K.A. Holter, J. Mocak, J. Am. Chem. Soc. 103 (1981) 1472.
[27] S.J. Gruber, C.M. Harris, E. Sinn, J. Inorg. Nucl. Chem. 30 (1968) 1805.
[28] E. Pereira, L. Comes, B. de Castro, J. Chem. Soc., Dalton Trans. (1998) 629.
[29] A.G. Lappin, S.K. Murray, D.W. Matgerum, Inorg. Chem. 17 (1978) 1630.
[30] (a) B.J. Hathaway, D.E. Billing, Coord. Chem. Rev. 5 (1970) 143;
(b) Y. Nishida, H. Shimohori, Bull. Chem. Soc. Jpn. 46 (1973) 2406.

presence of azide ions, and isolated a 3:4:2 Cd:(nic$^-$):azide (**1**) and a 1:1:1 Zn:(nic$^-$):azide (**2**) complex.

2. Experimental

2.1. Material and instrumentation

C, H, N elemental analyses were carried out using a Perkin–Elmer analyzer, Cd and Zn were analyzed by a Perkin–Elmer Analyst 300, AAS atomic absorption spectrometer. Infrared spectra were recorded on a Bruker IFS-125 model FT-IR spectrophotometer as KBr pellets. Raman spectra were recorded on a BRUKER IFS 6/s FT-Raman spectrometer with Nd:CYAG laser wavelength (1064 nm) as the light source. ^{1}H NMR and ^{13}C NMR (DMSO-d_6) spectra were recorded on a Jeol JNM-ECA 500 MHz spectrometer. TGA and DTA were carried out on a Shimadzu-50H under a nitrogen flow rate 30 ml/min. Nicotinic acid was purchased from Aldrich Company and other chemicals were of analytical grade quality and used as received.

Caution. Metal azide complexes are potentially explosives. Only a small amount of material should be prepared and handled with caution.

2.2. Synthesis

2.2.1. $[Cd_3(nic)_4(N_3)_2(H_2O)_2]$ (**1**)

To an aqueous solution (20 cm^3) of $3CdSO_4 \cdot 8H_2O$ (0.77 g, 1.0 mmol, 3 mmol in Cd^{2+}) nicotinic acid (0.74 g, 6 mmol) in methanol/water (15 cm^3) was added, followed by dropwise addition of an aqueous solution of NaN_3(0.65 g, 10 mmol) with continuous stirring. The mixture was heated, filtered off, boiled again and the final clear mixture was allowed to cool gradually to room temperature then placed in a refrigerator for several days. Yellow crystals suitable for X-ray measurement were collected, dried in air, with a yield of ~85%. *Anal.* Calc.: C, 30.48; H, 2.13; N, 14.81; Cd, 35.66. Found: C, 30.38; H, 2.23; N, 14.74; Cd, 35.69%. ^{1}H NMR (DMSO-d_6): δ 7.53 (t, 4H), 8.34 (d, 4H), 8.67 (s, 4H), 9.19 (s, 4H); ^{13}C NMR (DMSO-d_6): δ 124.24, 131.22, 138.60, 151.24, 151.72 and 170.82.

Table 1
Crystallographic data and structure refinement for compounds **1** and **2**

	1	**2**
Empirical formula	$C_{24}H_{20}Cd_3N_{10}O_{10}$	$C_6H_4ZnN_4O_2$
Formula weight	945.70	229.50
Temperature (K)	173(2)	173(2)
Wavelength (Å)	0.71073	0.71073
Crystal system	triclinic	orthorhombic
Space group	$P\bar{1}$	$P2_12_12_1$
Unit cell dimensions		
a (Å)	6.7224(1)	5.9585(1)
b (Å)	10.1819(1)	10.4445(1)
c (Å)	11.7912(2)	12.5726(1)
α (°)	75.063(1)	90
α (°)	74.514(1)	90
γ (°)	88.173(1)	90
Volume (Å^3)	750.898(17)	782.437(16)
Z	1	4
D_{calc} (Mg/m^3)	2.091	1.948
Absorption coefficient (mm)$^{-1}$	2.177	3.106
F(000)	458	456
Crystal size (mm^3)	$0.08 \times 0.06 \times 0.04$	$0.42 \times 0.39 \times 0.22$
θ range for data collection (°)	1.86–30.00.	2.54–32.80
Index ranges	$-9 \leqslant h \leqslant 9$, $-14 \leqslant k \leqslant 14$, $-16 \leqslant l \leqslant 15$	$-9 \leqslant h \leqslant 9$, $-15 \leqslant k \leqslant 15$, $-18 \leqslant l \leqslant 19$
Reflections collected	10696	13250
Independent reflections [R_{int}]	4350 [0.0481]	2803 [0.0280]
Absorption correction	multi-scan	multi-scan
Maximum and minimum transmission	0.9180 and 0.8451	0.5482 and 0.3554
Refinement method	full-matrix least-squares on F^2	full-matrix least-squares on F^2
Data/restraints/parameters	4350/2/223	2803/0/122
Goodness-of-fit on F^2	1.028	1.038
Final R indices [$I > 2\sigma(I)$]	$R_1 = 0.0457$, $wR_2 = 0.0952$	$R_1 = 0.0185$, $wR_2 = 0.0495$
R indices (all data)	$R_1 = 0.0732$, $wR_2 = 0.1062$	$R_1 = 0.0188$, $wR_2 = 0.0498$
Largest difference peak and hole (e Å^{-3})	1.348 and −1.373	0.561 and −0.398

Table 2
Selected bond lengths (Å) and bond angles (°) for complex **1**

Cd(1)–N(1)^{i}	2.285(4)
Cd(1)–N(1)	2.285(4)
Cd(1)–O(2B)^{ii}	2.315(3)
Cd(1)–O(2B)^{iii}	2.315(3)
Cd(1)–O(2A)^{iv}	2.330(3)
Cd(1)–O(2A)^{v}	2.330(3)
Cd(2)–O(1B)^{iii}	2.277(3)
Cd(2)–N(1)	2.296(4)
Cd(2)–O(1)	2.304(4)
Cd(2)–O(1A)^{vi}	2.324(3)
Cd(2)–N(1A)	2.348(4)
Cd(2)–N(1B)	2.351(4)
O(1)–H(1)	0.88(2)
O(1)–H(2)	0.88(2)
N(1)–N(2)	1.211(5)
N(2)–N(3)	1.146(5)
N(1)^{i}–Cd(1)–N(1)	180.0
N(1)^{i}–Cd(1)–O(2B)^{ii}	93.35(13)
N(1)–Cd(1)–O(2B)^{ii}	86.65(13)
N(1)^{i}–Cd(1)–O(2B)^{iii}	86.65(13)
N(1)–Cd(1)–O(2B)^{iii}	93.35(13)
O(2B)^{ii}–Cd(1)–O(2B)^{iii}	180.0
N(1)^{i}–Cd(1)–O(2A)^{iv}	91.68(14)
N(1)–Cd(1)–O(2A)^{iv}	88.32(14)
O(2B)^{ii}–Cd(1)–O(2A)^{iv}	86.54(13)
O(2B)^{iii}–Cd(1)–O(2A)^{iv}	93.46(13)
N(1)^{i}–Cd(1)–O(2A)^{v}	88.32(14)
N(1)–Cd(1)–O(2A)^{v}	91.68(14)
O(2B)^{ii}–Cd(1)–O(2A)^{v}	93.46(13)
O(2B)^{iii}–Cd(1)–O(2A)^{v}	86.54(13)
O(2A)^{iv}–Cd(1)–O(2A)^{v}	180.0
O(1B)^{iii}–Cd(2)–N(1)	95.70(13)
O(1B)^{iii}–Cd(2)–O(1)	86.67(13)
N(1)–Cd(2)–O(1)	94.67(14)
O(1B)^{iii}–Cd(2)–O(1A)^{vi}	174.18(12)
N(1)–Cd(2)–O(1A)^{vi}	88.95(13)
O(1)–Cd(2)–O(1A)^{vi}	96.45(12)
O(1B)^{iii}–Cd(2)–N(1A)	89.99(14)
N(1)–Cd(2)–N(1A)	94.25(15)
O(1)–Cd(2)–N(1A)	170.74(14)
O(1A)^{vi}–Cd(2)–N(1A)	86.19(13)
O(1B)^{iii}–Cd(2)–N(1B)	88.47(13)
N(1)–Cd(2)–N(1B)	175.39(13)
O(1)–Cd(2)–N(1B)	87.51(14)
O(1A)^{vi}–Cd(2)–N(1B)	86.76(12)
N(1A)–Cd(2)–N(1B)	83.77(15)
N(2)–N(1)–Cd(1)	123.2(3)
N(2)–N(1)–Cd(2)	118.3(3)
Cd(1)–N(1)–Cd(2)	117.19(16)
N(3)–N(2)–N(1)	179.1(5)

Symmetry transformations used to generate equivalent atoms: (i) $-x,-y,-z$; (ii) $x, y, z-1$; (iii) $-x,-y, -z+1$; (iv) $x, y-1, z$; (v) $-x, -y+1, -z$; (vi) $-x+1, -y+1, -z$; (vii) $x, y+1, z$; (viii) $x, y, z+1$.

2.2.2. [Zn(nic)(N$_3$)] (2)

This complex was prepared by mixing zinc sulfate $ZnSO_4 \cdot 7H_2O$ (0.50 g, 1.74 mmol) in water (30 cm^3) with nicotinic acid (0.43 g, 3.5 mmol) in ethanol/water (20 cm^3). An aqueous solution of NaN_3 (0.65 g, 10 mmol) was added dropwise with continuous stirring. The final mixture was then allowed to stand for several days to yield pale brown crystals of the complex suitable for X-ray diffraction (65% yield). *Anal.* data for the complex $C_6H_4N_4O_4Zn$: Calc.: C, 31.40; H, 1.76; N, 24.41; Zn, 28.48. Found: C, 31.38; H, 1.82; N, 24.56; Zn, 28.53%. ^{1}H NMR (DMSO-d_6): δ 7.57 (t, 1H), 8.58 (d, 1H), 8.64 (d, 1H), 9.08 (s, 1H); ^{13}C NMR (DMSO-d_6): δ 124.78, 131.41, 139.31, 150.69, 151.51 and 169.65.

Table 4
Selected bond lengths (Å) and bond angles (°) for complex **2**

Zn(1)–N(1A)^{i}	2.0325(11)
Zn(1)–N(1)	2.0484(11)
Zn(1)–N(1A)	2.0523(11)
Zn(1)–O(8)^{ii}	2.0651(9)
Zn(1)–O(9)^{iii}	2.1898(10)
O(8)–Zn(1)^{iv}	2.0651(9)
O(9)–Zn(1)^{v}	2.1898(10)
N(1A)–Zn(1)^{vi}	2.0325(11)
N(1A)–N(2A)	1.2205(14)
N(2A)–N(3A)	1.1443(16)
N(1A)^{i}–Zn(1)–N(1)	118.56(4)
N(1A)^{i}–Zn(1)–N(1A)	128.20(3)
N(1)–Zn(1)–N(1A)	112.30(5)
N(1A)^{i}–Zn(1)–O(8)^{ii}	94.37(4)
N(1)–Zn(1)–O(8)^{ii}	94.96(4)
O(8)^{ii}–Zn(1)–O(9)^{iii}	177.82(4)
N(2A)–N(1A)–Zn(1)^{vi}	118.25(9)
N(2A)–N(1A)–Zn(1)	120.79(9)
Zn(1)^{vi}–N(1A)–Zn(1)	111.96(5)
N(3A)–N(2A)–N(1A)	178.08(16)
N(1A)–Zn(1)–O(8)^{ii}	90.33(4)
N(1A)^{i}–Zn(1)–O(9)^{iii}	85.59(4)
N(1)–Zn(1)–O(9)^{iii}	86.96(4)
N(1A)–Zn(1)–O(9)^{iii}	87.99(4)
N(2A)–N(1A)–Zn(1)^{vi}	118.25(9)
N(2A)–N(1A)–Zn(1)	120.79(9)
Zn(1)^{vi}–N(1A)–Zn(1)	111.96(5)
N(3A)–N(2A)–N(1A)	178.08(16)

Symmetry transformations used to generate equivalent atoms: (i) $x-1/2, -y+1/2, -z+1$; (ii) $-x+1/2, -y+1, z+1/2$; (iii) $-x+1, y-1/2, -z+1/2$; (iv) $-x+1/2, -y+1, z-1/2$; (v) $-x+1, y+1/2, -z+1/2$; (vi) $x+1/2, -y+1/2, -z+1$.

Table 3
Hydrogen bonds for $[Cd_3(nic)_4(N_3)_2(H_2O)_2]_n$ (**1**) (Å and °)

D–H···A	*d*(D–H)	*d*(H···A)	*d*(D···A)	∠(DHA)
O(1)–H(1)···O(2A)^{iv}	0.88(2)	1.87(3)	2.727(5)	164(8)
O(1)–H(2)···O(2B)^{ix}	0.88(2)	2.00(2)	2.874(5)	177(8)

Symmetry transformations used to generate equivalent atoms: (i) $-x, -y, -z$; (ii) $x, y, z-1$; (iii) $-x,-y, -z+1$; (iv) $x, y-1, z$; (v) $-x, -y+1, -z$; (vi) $-x+1, -y+1, -z$; (vii) $x, y+1, z$; (viii) $x, y, z+1$; (ix) $-x+1, -y, -z+1$.

2.3. X-ray crystallography

All diffraction data were collected using a Siemens SMART CCD diffractometer with Mo Kα radiation ($\lambda = 0.71073$ Å, graphite monochromator). The crystals were cooled to 173(2) K by a flow of nitrogen gas using the LT-2A device. A full sphere of reciprocal lattices were scanned by 0.3° steps in ω with a crystal-to-detector distance of 3.97 cm. Preliminary orientation matrices were obtained from the first frames using SMART [21].

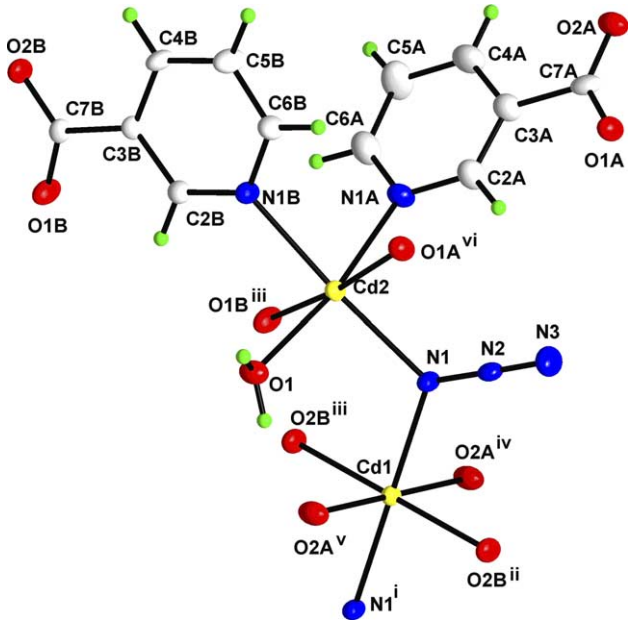


Fig. 1. Numbering scheme of $[Cd_3(nic)_4(N_3)_2\ (H_2O)_2]_n$ complex **1** and atomic displacement ellipsoids draw at the 50% probability level. Note that just a part of the tri-nuclear complex is shown, the rest of it is symmetry dependent. For symmetry codes see Table 3.

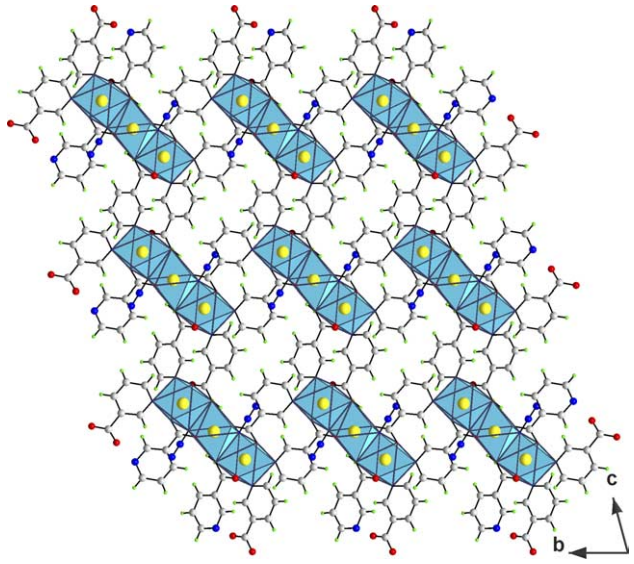


Fig. 2. A 4 × 4 superunit with coordination polyhedra of $[Cd_3(nic)_4(N_3)_2(H_2O)_2]_n$ complex **1**. Projection along the *a*-axis.

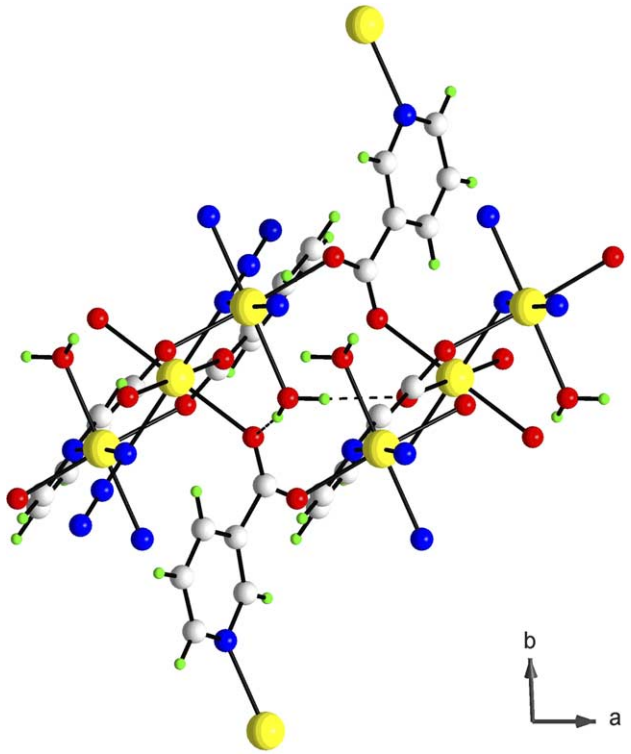


Fig. 3. A projection along the *c*-axis of **1**. Both ligands and hydrogen bonds, with the water molecule as a donor, bridging perpendicularly to the planes of the trinuclear units.

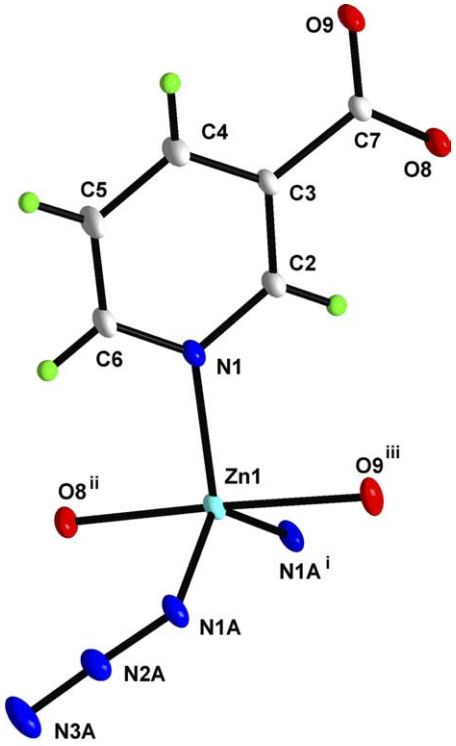


Fig. 4. Numbering scheme of $[Zn(nic)(N_3)_2]_n$ complex **2** and atomic displacement ellipsoids at the 50% probability level.

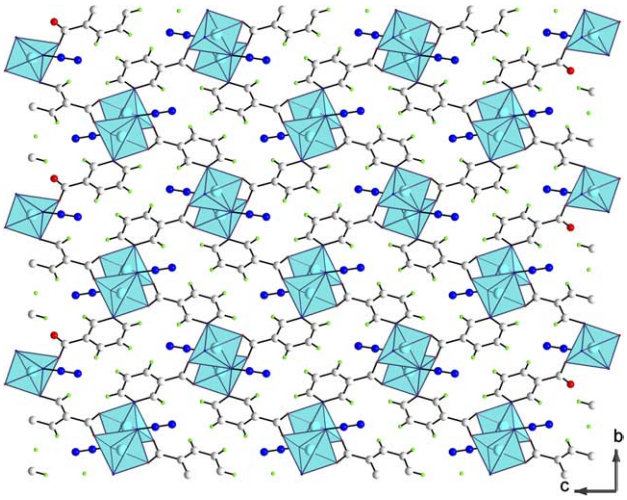


Fig. 5. Projection of the complex **2** structure along the *a*-axis. Coordination polyhedra for Zn atoms are shown.

The collected frames were integrated using the preliminary orientation matrices which were updated every 100 frames. Final cell parameters were obtained by refinement of the positions of reflections with $I > 10\sigma(I)$ after integration of all the frames using SAINT [21]. The data were empirically corrected for absorption and other effects using the SADABS [22] program. The structures were solved by direct methods and refined by full-matrix least squares on all F^2 data using SHELXTL software [23]. The non-H atoms were refined anisotropically, while hydrogen atoms were refined isotropically with use of geometrical restrains. The crystallographic and refinement data are summarized in Table 1. Selected bond distances and bond angles are given in Tables 2 and 4 for complexes **1** and **2**, respectively. Molecular graphics (Figs. 1–5) were prepared using the DIAMOND [24] program Table 3.

3. Results and discussion

The reaction between cadmium(II) and zinc(II) ions and nicotinic acid in the presence of the azide ion afforded 3:4 and 1:1 complexes, respectively. Complexes **1** and **2** are insoluble in non-polar solvents, e.g., benzene, CCl_4, etc. and in polar solvents, e.g., H_2O, MeOH, EtOH, $CHCl_3$, acetone, etc. indicating their polymeric nature. Both complexes are slightly soluble in DMSO. The ^1H NMR spectra of these complexes in DMSO suggest a partial substitution of the azido ligands by DMSO.

3.1. Structures

3.1.1. $[Cd_3(nic)_4(N_3)_2(H_2O)_2]_n$ (1)

X-ray single crystal structure determination reveals that complex **1** has a 3D network structure consisting of a novel linear, trinuclear unit containing three Cd(II) atoms, four nicotinate anions, two azide ions and two aqua molecules as shown in Fig. 1. All the three cadmium atoms are hexa-coordinated in a distorted octahedral environment. The central cadmium atom Cd1 is surrounded by two N atoms of two $\mu_{1,1}$-azido groups at [Cd–N 2.285(4) Å] and four O atoms of four different μ-N,O,O′-nicotinate anions [Cd–O 2.330(3) and 2.315-(3) Å], having a CdN_2O_4 chromophore. Each of the other two Cd atoms (Cd2) is surrounded by two hetero nitrogen atoms of two bridging μ-N,O,O′-tridentate nicotinate anions [Cd–N 2.348(4) and 2.351(4) Å]; one N atom of a bridging ($\mu_{1,1}$-N_3) group [Cd–N 2.296(4) Å] and three O atoms from two bridging carboxylate groups of two different nicotinate anions [Cd–O 2.277(3) and 2.324(3) Å] and one aqua molecule [Cd–O 2.304(4) Å]. Fig. 2 presents a 4×4 superunit with coordination polyhedra of the complex illustrating each nicotinate anion bridging one unit through its hetero nitrogen atom and other units through its carboxylate oxygen, assembling a sheet structure. The water molecule is further H-bonded to a neighboring unit [H···OH, 1.87(3) and 2.00(2) Å], Fig. 3. The Cd–O distances are shorter than those reported in other Cd(II) carboxylate structures, Cd–O 2.502(7) and 2.732(7) Å [25].

3.1.2. $[Zn(nic)(N_3)]_n$ (2)

Complex **2** crystallizes in the non-centrosymmetric space group $P2_12_12_1$, representing a right handed chiral complex from achiral molecules. The atom labelling scheme for complex **2** is shown in Fig. 4. The absolute structure was determined with Flack's parameter [26] being so good (0.001(8)) as to indicate that it has been unequivocally determined. The structure of **2** reveals a Zn(II) to nicotinate anion ratio of 1:1 as predicted from the elemental analysis. In this structure, the zinc atom is located at the center of a trigonal bipyramidal structure. The two axial positions of the trigonal bipyramidal structure are occupied by two oxygen atoms of two carboxylate groups [Zn–O 2.0651(9) and 2.1898(10) Å] from two different nicotinate anions with an O–Zn–O angle of 177.82(4)°. This is different from the bidendate O,O′-nicotinate anion in $[Ln_2(nic)_6(H_2O)_4]$ complexes, in which the two O atoms of the carboxylate group bind the same Ln atom, forming a four membered ring [8]. At the equatorial positions the zinc atom is linked by three nitrogen atoms, one N hetero atom [Zn–N 2.0484(11) Å] of the nicotinate anion and two N atoms of 2 ($\mu_{1,1}$-N_3) groups [Zn–N 2.0325(11) and 2.0523(11) Å]. The nicotinate anion, therefore behaves as a N,O,O′-tridentate bridging ligand, as in complex **1**, giving rise to a 3D structure for complex **2**, Fig. 5. The Zn–N and Zn–O bond lengths fall within the range found for other similar complexes, Zn–N 2.040(8) Å and Zn–O 2.152 Å for [Zn(H-pic)(pic)Cl] [12]. It is also comparable to the bonds in the dimeric Zn_2N_2 unit of the structure of

$[Zn(dpa)(N_3)(NO_3)]_2$ (dpa = 2,2′-dipyridylamine) [Zn–N 2.090(2) and 2.130(2) Å] [27]. The larger $N(1A)^{i}$–Zn(1)–N(1A) bond angle [128.20(3)°] is due to the Zn_2N_2 unit which has a $Zn(1)^{vi}$–N(1A)–Zn(1) bond angle of 111.96(5)°. The reported $[Zn_3(bpy)_3(hip)_2]\cdot 5H_2O$ complex has two different penta coordinated Zn(II) ions in a trigonal bipyramidal geometry with Zn–L (L = O, N) distances in the range of 1.997(9)–2.257(14) Å and bond angles in the equatorial plane in the range of 98.2(5)–142.3(5)° [28]. The bridging azide ion is asymmetric [N(1A)–N(2A) 1.2205(14) Å and N(2A)–N(3A) 1.1443(16) Å] and linear [N(3A)–N(2A)–N(1A) 178.08-(16)°].

3.2. Spectra

The room temperature IR spectra of the crystalline nicotinic acid and the sodium salt of nicotinic acid, and also the IR and Raman spectra of $[Cd_3(nic)_4(N_3)_2(H_2O)_2]_n$ complex **1** and $[Zn(nic)(N_3)]_n$ complex **2**, are given with tentative assignments of the bands in Table 5. In the high energy region complex **1** exhibits a strong broad band around 3400 cm^{-1} corresponding to the water molecules coordinated to the Cd(II) ions bridging the trinuclear units. Hydrogen bonding of the type N···H–O is indicated in the free acid by the presence of broad, medium strong bands near 2450 and 1880 cm^{-1} (IR) [29]. These bands are completely absent in the spectra of the solid complexes **1** and **2**, as well as the corresponding sodium salt [30]. The vibration frequencies of the free nicotinic acid in a KBr pellet at 1715 vs, br, ν(C=O) and 1640 s cm^{-1}, ν_{as}(–COO^-) (IR) [31,32] disappeared in both IR and Raman spectra of the complexes **1** and **2**. Instead the spectra of **1** and **2** show strong peaks around 1609 vs, (IR) and 1612 w cm^{-1} (Raman) and 1617 vs, (IR) and 1610 w cm^{-1} (Raman), respectively. These results indicate that only the nicotinate anions are coordinated to the Cd(II) and Zn(II) ions through their carboxylate oxygen atoms. The bands related to the pyridine ring in the IR spectra of **1** and **2** show systematic shifts in accordance with those found for pyridine complexes [33]. Thus, the nicotinate anions in both complexes **1** and **2** are coordinating via their carboxylate O atoms and the hetero N atoms.

The peaks at 2070 (vs), 1289 (m) cm^{-1} (IR) and 2110 (s), 1294 (vs) cm^{-1} (Raman) for **1** and 2100 (vs), 1292 (m) cm^{-1} (IR) and 2070 (m), 1290 (w) cm^{-1} (Raman) for **2** were assigned as (ν_{as}-N_3) and (ν_s-N_3), respectively. This is in agreement with the asymmetric nature of the bridging ($\mu_{1,1}$-N_3) groups [N(1)–N(2), 1.211(5) and N(2)–N(3), 1.146(5) Å for

Table 5
Selected vibrational frequencies (cm^{-1}) in the IR and Raman spectra of nicotinic acid, sodium nicotinate and complexes **1** and **2**

HNic	NaNic	$[Cd_3(nic)_4(N_3)_2(H_2O)_2]_n$		$[Zn(nic)(N_3)]_n$		Assignments
IR	IR	IR	Raman	IR	Raman	
		3329 s,b	3250 s,b			νOH water
			3064 vs			
2450 m,b						νN···H–O
1880 s,b						
		2070 vs	2110 s	2100 vs	2070 m	ν_{as}-N_3^-
		1289 m	1294 vs	1292 s	1290 w	ν_s-N_3^-
1708 s,b						νC=O st
1645 s	1602 vs	1609 vs	1612 s	1617 vs	1610 w	ν_{as}(–COO^-)
1600 s						
1380 ms	1396 vs	1387 vs	1396 vs	1401 vs	1394 s	ν_s(COO^-)
1330 m			1334 w		1351 w	
700 wm	702 vs	696 s		696 vs	700 w	δ(COO^-)
700 wm		669 m	656 s	654 m	640 s	
1585 sh	1558 vs	1587 vs	1582 s	1591 vs	1590 vs	pyridine ring
1550 m	1483 vs	1562 vs	1571 s	1569 vs	1551 w	vibrations
1484 sh	1466 s	1469 m	1476 w	1467 wm	1474 vw	
1190 m	1194 s	1196 s	1193 m	1194 s	1196 s	
1130 m	1152 s	1156 ms	1134 vs	1163 m	1140 w	
1095 w	1102 s	1119 ms		1113 s	1112 w	
	1089 s	1093 m		1091 s	1089 w	
1035 s	1040 m	1046 s	1034 vs	1056 s	1043 s	
951 m	968 wm	963 vw	965 w	971 w	970 w	
830 m	843 s	841 m	854 s	851 s	849 s	
750 vs	759 vs	758 s		757 vs		
630 ms	638 s	641 m				
	593 s	593 m		599 wm	570 w,b	
500 wm	508 s	538 m		545 m		
390 wm	392 m	425 m	441 w	431 ms	406 w	

Abbreviations. w, weak; m, medium; s, strong; v, very; b, broad; sh, shoulder; st, stretching.

complex **1** and N(1A)–N(2A), 1.2205(14) and N(2A)–N(3A), 1.1443(16) Å for complex **2**].

3.3. Thermal analysis

The TGA and DTA curves for complexes **1** and **2** are given in Fig. 6. As these complexes are expected to be explosives we used small amounts for such thermal analyses, as suggested previously for thermal decomposition measurements of azido compounds. [34] Complex **1** is stable until 180 °C, after which it decomposes (180–230 °C), losing one H_2O molecule (Exp. 1.95%, Theor. 1.91%), followed by the loss of the other H_2O molecule and one N_3 group (Exp. 6.6%, Theor. 6.3%), and then a third stage (305–350 °C), with a weight loss of 4.9%, corresponds to loss of the second N_3 group. These three stages are successive and appear as stages of one step ending at 350 °C. This appears in the DTA curve as a very weak endothermal peak at 241 °C. In the next step (350–440 °C) the weight loss is 38.73%, which corresponds to the loss of three nicotinates, (Theor. 38.69%), the loss of the forth nicotinate molecule starts at 440 °C (Exp. 12.8%, Theor. 12.9%). This last step appears in the DTA curve as two overlapped exotherms at 450 and 458 °C (Fig. 6). The weight of the final residue of 35.6% suggests that some explosion occurred since the residue is found to be CdO, as indicated by X-ray powder diffraction. Accordingly the residue should be 40.6%, which is much higher than the experimental value.

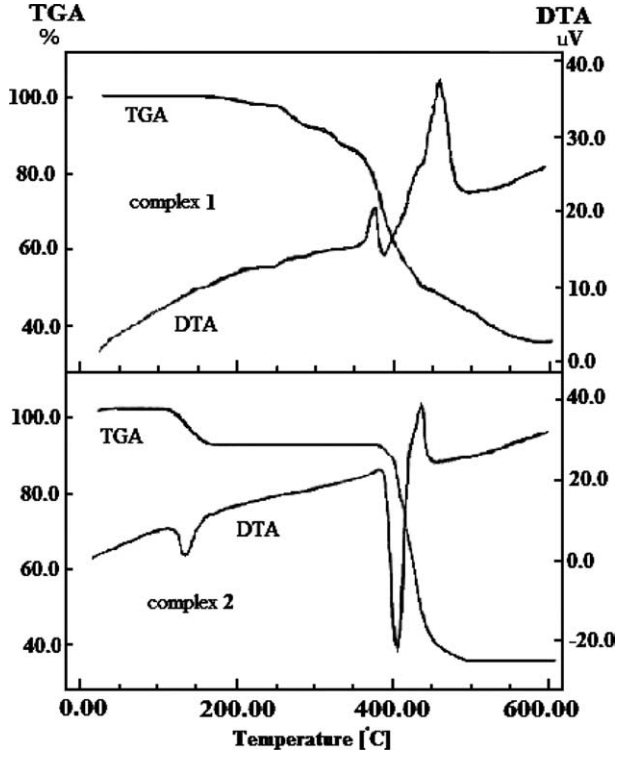


Fig. 6. Thermal behaviour of complexes **1** and **2**.

The TGA curve for complex **2** shows only two steps; the first step starts around 120 °C, followed by a long plateau. The weight loss of 8.9% in this step corresponds to the loss of a half N_3 ion (Theor. 9.1%). This step appears as an endotherm at 135 °C in the DTA curve. The second step starts at 375 °C with a weight loss of 57% suggesting a loss of the other half N_3 ion, CO and pyridine radical (Theor. 55.3%), leaving a ZnO residue of 35% (Theor. 35.6%).

Acknowledgments

This work was supported by the Swedish Research Council through the SIDA-Swedish Research Links Program (Grant No. 348-2002-6879). We are grateful to Prof. Vratislav Langer (Department of Environmental Inorganic Chemistry, Chalmers University of Technology) for his advice, the use of his equipment and computational facilities. Thanks to Prof. Yehia Badr, Cairo University, Egypt for the Raman measurements.

Appendix A. Supplementary data

Supplementary data are available from the CCDC, 12 Union Road, Cambridge CB2 1EZ, UK on request, quoting the deposition numbers: CCDC 258680 and 258681 for **1** and **2**, respectively. Supplementary data associated with this article can be found, in the online version, at doi:10.1016/j.poly.2005.05.026.

References

[1] (a) M.A.S. Goher, M. Dratovsky, Coll, Czech. Chem. Commun. 40 (1975) 26;
(b) M.A.S. Goher, T.C.W. Mak, Inorg. Chim. Acta 127 (1987) L13.
[2] M.A.S. Goher, Bull. Chim. Soc. Fr. (1981) 329.
[3] X. Hao, Y.-G. Wei, Q. Liu, S.-W. Zhang, Acta Crystallogr. C 56 (2000) 296.
[4] A. Anagnostopoulos, M.G.B. Drew, R.A. Walton, J. Chem. Soc., Chem. Commun. 19 (1969) 1241.
[5] J. Hong-Bin, Y. Jie-Hui, X. Ji-Qing, Y. Ling, D. Hong, J. Wei-Jie, W. Tie-Gang, X. Jia-Ning, L. Zeng-Chun, J. Mol. Struct. 23 (2002) 641.
[6] B.C. Marina, D. Paolo, G. Carlo, M. Amos, N. Mario, Gazz. Chim. Ital. 101 (1971) 815.
[7] W.E. Broderick, M.R. Pressprich, U. Geiser, R.D. Willett, J.I. Legg, Inorg. Chem. 25 (1986) 3372.
[8] J.W. Moore, M.D. Glick, W.A. Baker Jr., J. Am. Chem. Soc. 94 (1972) 1856.
[9] F. Gaber, F. Charbonnier, R. Fauer, M. Retit-Ramel, Z. Kristalloger. 209 (1994) 536.
[10] G. Smith, A.N. Reddy, K.A. Byriet, C.H.L. Kennrad, Polyhedron 13 (1994) 2425.
[11] K. Per-Olov, G. Jekabs, F. Mats, S. Fredrik, Polyhedron 20 (2001) 2747.
[12] M.A.S. Goher, M.A.M. Abu-Youssef, F.A. Mautner, Polyhedron 15 (1996) 453.
[13] F.A. Mautner, M.A.M. Abu-Youssef, M.A.S. Goher, Polyhedron 16 (1997) 235.

[14] M.A.S. Goher, F.A. Mautner, M.A.M. Abu-Youssef, A.K. Hafez, A.M.A. Badr, J. Chem. Soc., Dalton Trans. (2002) 3309.
[15] M.A.S. Goher, F.A. Mautner, A.K. Hafez, M.A.M. Abu-Youssef, C. Gspan, A.M.A. Badr, Polyhedron 22 (2003) 975.
[16] F.A. Mautner, C. Gspan, M.A.S. Goher, M.A.M. Abu-Youssef, Monatsh. Chem. 134 (2003) 1311.
[17] M.A.S. Goher, F.A. Mautner, M.A.M. Abu-Youssef, A.K. Hafez, A.M.A. Badr, C. Gspan, Polyhedron 22 (2003) 3137.
[18] F.A. Mautner, C. Gspan, K. Gatterer, M.A.S. Goher, M.A.M. Abu-Youssef, E. Bucher, W. Sitte, Polyhedron 23 (2004) 1217.
[19] M.A.S. Goher, A.K. Hafez, M.A.M. Abu-Youssef, A.M.A. Badr, C. Gspan, F.A. Mautner, Polyhedron 23 (2004) 2349.
[20] F.A. Mantner, G. Gspan, M.A.M. Abu-Youssef, M.A.S. Goher, Monatsh. Chem. 136 (2005) 107.
[21] SMART and SAINT: Area Detector Control and Integration Software, Siemens AXS, Madison, WI, USA, 1995.
[22] G.M. Sheldrick, SADABS Program for Empirical Absorption Correction of Area Detectors (Version 2.03), University of Göttingen, Germany, 2002.
[23] SHELXTL: Structure Determination Programs (Version 6.10), Bruker AXS Inc., Madison, WI, USA, 2001.
[24] K. Brandenburg, DIAMOND: Visual Crystal Structure Information System (Version 2.1e), Crystal Impact GbR, Bonn, Germany, 2001.
[25] Z.-M. Sun, J.-G. Mao, Y.-Q. Sun, H.-Y. Zeng, A. Clearfield, Inorg. Chem. 43 (2004) 336.
[26] H.D. Flack, Acta Crystallogr A 39 (1983) 876.
[27] D. Bose, Sk.H. Rahaman, G. Mostafa, R.D.B. Walsh, M.J. Zaworotko, B.K. Ghosh, Polyhedron 23 (2004) 545.
[28] X.-M. Zhang, J.-S. Chen, K.-Y. Xu, C.-R. Ding, W.-L. She X.-M. Chen, Inorg. Chim. Acta. 357 (2004) 1389.
[29] Y. Ichida, Y. Kuroda, D. Nakamura, M. Kubo, Spectrochim. Acta 28A (1972) 2433.
[30] R.F. Evans, W. Kynaston, J. Chem. Soc. (1962) 1005.
[31] S. Yoshida, M. Asia, Chem. Pharm. Bull. (Japan) 7 (1959) 162.
[32] I. Nakagawa, T. Shimanouchi, Spectrochim. Acta 20 (1964) 429.
[33] N.S. Gill, R.H. Nuttall, D.E. Ecife, R.W.A. Sharp, J. Inorg. Nucl. Chem. 18 (1961) 78.
[34] M.A.S. Goher, Thermochim. Acta 336 (1999) 61.

(0D) units in **1** and **2** self-assemble via O–H···N and N–H···O hydrogen bonds resulting in 2D sheets, which thereby yield 3D supramolecular architectures through π···π and C–H···π interactions. Both complexes behave as luminous materials, which can be correlated to their supramolecular networks.

2. Experimental

2.1. Materials

High purity 2,2′-dipyridylamine (Fluka, Germany), nickel acetate tetrahydrate (E. Merck, India), zinc acetate dihydrate (E. Merck, India) and sodium azide (E. Merck, India) were purchased from the respective concerns and used as received. All other chemicals and solvents were of analytical reagent grade. For electrochemical work the solvent DMF was purified and the supporting electrolyte [*n*-Bu_4N][ClO_4] was prepared following a reported procedure [23].

Caution! Azido compounds of metal ions are potentially explosive. Only a small amount of material should be prepared and handled with care.

2.2. Physical measurement

Elemental analyses (C, H and N) were performed on a Perkin–Elmer 2400 CHNS/O elemental analyzer. IR spectra (KBr pellet, 4000–300 cm^{-1}) were recorded using a Jasco FT-IR Model 420 or Perkin–Elmer RX 1 spectrometer. Molar conductances were measured using a Systronics conductivity meter where the cell constant was calibrated with 0.01(M) KCl solution and DMF was used as solvent. Ground state absorption and steady-state fluorescence measurements were made with a Jasco Model V-530 UV–Vis spectrophotometer and Hitachi Model F-4010 spectrofluorimeter, respectively. Time-resolved fluorescence measurements were carried out using a time-correlated single photon counting (TCSPC) spectrometer Edinburgh Instruments, Model 199; a hydrogen filled coaxial flash lamp with a pulse width of 1.2 ns at FWHM and a Philips XP-2020Q Photomultiplier tube were, respectively, used as the excitation source and the fluorescence detector. Room-temperature solid phase magnetic susceptibility was measured at 25 °C with a PAR 155 vibrating sample magnetometer using Hg[$Co(SCN)_4$] as the reference. Diamagnetic corrections were made using Pascal's constants. Thermal analysis (TG-DTA) was carried out using a Shimadzu DT-30 thermal analyzer under N_2. Cyclic voltammetry (CV) experiments were carried out (in DMF solution) with the use of a computer controlled EG&G PARC VersaStat Model 270 electrochemical instrument at a platinum disk working electrode as described elsewhere [24].

2.3. Preparation of the complexes

Complex **1** was obtained from both the metal nitrate and acetate using a 1:2:2 mole ratio of the metal salt, dpa and azide. However, for the preparation of **2**, zinc acetate was required; use of zinc nitrate always led to the complex [$Zn(dpa)(N_3)_2$] [13a].

2.3.1. $[Ni(dpa)_2(N_3)_2]\cdot H_2O$ (**1**)

The synthesis with nickel acetate is described. dpa (0.11 g, 0.648 mmol) in acetonitrile (5 cm^3) was added slowly to a $Ni(OAc)_2\cdot 4H_2O$ (0.08 g, 0.343 mmol) solution (10 cm^3) in the same solvent. NaN_3 (0.042 g, 0.648 mmol) in water (5 cm^3) was added dropwise to it. After filtration through a fine glass frit, the supernatant blue solution was kept in air for slow evaporation. After a week blue crystals of **1** were deposited, which were separated by filtration and dried in vacuo over silica gel indicator. Yield: 0.129 g (75%). *Anal*. Calc. for $C_{20}H_{20}N_{12}ONi$ (**1**): C, 47.74; H, 4.01; N, 33.40. Found: C, 47.52; H, 3.92; N, 33.14%. IR (KBr, cm^{-1}): *ν*(N–H) 3300; *ν*(N=N=N) 2060, 2038; *ν*(C=N) 1590. UV–Vis (*λ*, nm): 315, 590 (sh) and 956 (sh). μ_{eff}: 2.92 BM. Λ_M (DMF, Ω^{-1} cm^2 mol^{-1}): 5. E° (DMF): 1.22 V.

2.3.2. $[Zn(dpa)_2(N_3)_2]\cdot H_2O$ (**2**)

An acetonitrile solution (5 cm^3) of dpa (0.11 g, 0.628 mmol) was added to a solution of $Zn(OAc)_2\,.\,2H_2O$ (0.10 g, 0.324 mmol) in the same solvent (10 cm^3) followed by NaN_3 (0.043 g, 0.656 mmol) in water (5 cm^3). The mixture was filtered and the supernatant liquid was kept in air for slow evaporation. After a few days **2** was separated, washed with toluene and dried in vacuo over silica gel indicator. Yield: 0.218 g (70%). *Anal*. Calc. for $C_{20}H_{20}N_{12}OZn$ (**2**): C, 47.12; H, 3.95; N, 32.97. Found: C, 47.18; H, 3.90; N, 32.85%. IR (KBr, cm^{-1}): *ν*(N–H) 3300 (br); *ν*(N=N=N) 2062, 2038; *ν*(C=N) 1590. Λ_M (DMF, Ω^{-1} cm^2 mol^{-1}): 5. UV–Vis (*λ*, nm): 255, 315.

2.4. X-ray diffraction study

Single crystals of the title complexes **1** and **2** were obtained by slow evaporation of 3:1 MeCN–H_2O solutions of the reaction mixtures. Diffraction data were collected on a Siemens SMART diffractometer equipped with a graphite monochromator and Mo Kα ($\lambda = 0.71073$ Å) radiation. The intensity data were corrected for Lorentz and polarisation effects and *φ* and *ω* scan absorption correction was employed using the SAINT [25] and SADABS [26] programs for the complexes. The structures were solved by the Patterson syntheses using SHELXS-97 [27] and followed by successive Fourier and difference Fourier syntheses. Full-matrix least-squares refinements on F^2 were carried out using SHELXL-97 [28]. The hydrogen atoms were fixed geomet-

rically and refined using a riding model. All non-hydrogen atoms were anisotropically refined. The water hydrogens were first located from the difference maps and then were constrained to ride on the carrier oxygen atom with U_{iso} values also constrained to $1.2U_{eq}$ of the carrier atom for refinement. In the final difference Fourier map the residual maxima and minima were 0.33 and −0.38 e Å^{-3} for **1**, 0.30 and −0.44 e Å^{-3} for **2**, respectively. All calculations were carried out using PLATON-99 [29] and ORTEP-32 [30]. The crystal data, data collection parameters and the results of analyses of **1** and **2** can be found in Table 1.

3. Results and discussion

3.1. Synthesis and formulation

Hexacoordinated mononuclear blue compound **1** was obtained as a crystalline product through the single-pot reaction of a 1:2:2 mole ratio of the metal acetate/nitrate, organic blocker and the pseudohalide in an aqueous acetonitrile solution. The use of the nitrate salt in the case of zinc leads to the tetracoordinated $[Zn(dpa)(N_3)_2]$ species, which is in conformity with earlier reports of Bose et al. [13a]. However, with the use of zinc(II) acetate, hexacoordinated colourless **2** was obtained in good yield. The complexes were characterized using microanalytical, spectroscopic, magnetic and physicochemical results. The air stable moisture insensitive products are insoluble in common solvents like water, methanol, ethanol, dichloromethane and acetonitrile, but are moderately soluble in dimethylformamide and dimethylsulfoxide on warming. In DMF solutions they show non-electrolytic behaviour [31] as is evident from low Λ_M values. Room temperature solid phase magnetic measurements show that **1** is a two-electron paramagnet with a moment close to the spin only value, whereas **2** behaves as a diamagnet. In the IR spectra, **1** and **2** display two characteristic azido stretches, which is in conformity with a mutual *cis* alignment of the two terminal pseudihalides [32]. Complexes **1** and **2** show superposable IR spectra, with a slight frequency shift particularly at $\nu(N_3)$. Reflectance spectra [**1**: λ, 315, 592, 956 nm; **2**: λ, 255, 315 nm] in nujol and electronic spectra in DMF solutions are akin in each complex reflecting a similar gross geometric structure and electronic structure in the solid state and in solution [33]. Thermal study (TG-DTA) reveals a weight loss of 3.46% and 3.54% at 60–80 °C, corresponding to loss of one crystalline water molecule in **1** and **2**, respectively. In the CV, a quasi-reversible (ΔE_p = 170 mV) oxidative response due to the Ni^{III}/Ni^{II} couple is observable in **1**. The formal potential lies close to ca. 1.2 V versus SCE. The one-electron nature of the couple was verified with comparison to a standard sample [34]. Compound **2** was found to be electro-inactive as expected for a d^{10}-ion.

Table 1
Crystal data and structure refinement parameters for **1** and **2**

Compound	**1**	**2**
Empirical formula	$C_{20}H_{20}N_{12}ONi$	$C_{20}H_{20}N_{12}OZn$
Formula weight	503.19	509.85
T (K)	293	293(2)
λ (Å)	0.71073	0.71073
Crystal system	triclinic	triclinic
Space group	$P\bar{1}$	$P\bar{1}$
a (Å)	7.6596(5)	7.7566(2)
b (Å)	9.2868(6)	9.3592(5)
c (Å)	16.7376(11)	16.6611(8)
α (°)	79.441(10)	79.254(1)
β (°)	84.071(10)	84.062(1)
γ (°)	69.743(10)	69.552(1)
V (Å^3)	1097.02(12)	1112.47(8)
Z	2	2
D_{calc} (Mg m^{-3})	1.523	1.522
μ (mm^{-1})	0.926	1.145
$F(000)$	520	524
Crystal size (mm^3)	0.15 × 0.18 × 0.23	0.36 × 0.29 × 0.26
θ Ranges (°)	1.2–28.3	2.35–28.28
$h/k/l$	−10, 9/−12, 12/−22, 21	−10, 9/−12, 12/−22, 21
Reflections collected	11 579	7109
Independent reflections (R_{int})	5182 (0.035)	5238 (0.0158)
T_{max} and T_{min}	0.969 and 0.864	0.7550 and 0.6833
Data/restraints/parameters	5182/0/387	5238/0/387
Goodness-of-fit on F^2	1.13	1.118
Final R indices [$I > 2\sigma(I)$]	R_1 = 0.0531, wR_2 = 0.1017	R_1 = 0.0374, wR_2 = 0.0791
Largest peak and hole (e Å^{-3})	0.969 and 0.864	0.304 and −0.438

3.2. X-ray structures

The structural analyses show that **1** and **2** are isomorphous and consist of mononuclear (0D) units which are further engaged in cooperative intermolecular hydrogen bondings and π···π and C–H···π interactions among themselves to result in a 3D supramolecular continuum. The ORTEP diagram with the atom numbering scheme of the mononuclear units in **1** and **2** are shown in Figs. 1 and 2, respectively. The perspective view of the 1D chain through O–H···N hydrogen bonds leading to a 1D sheet, the 2D sheet formed by interwoven O–H···N and N–H···O hydrogen bonds, and the 3D continuum formed by face-to-face π···π and edge-to-face C–H···π interactions in one case, **1**, are given in Figs. 3–5, respectively. Selected bond distances and bond angles relevant to the metal coordination spheres in **1** and **2** are given in Table 2. The significant hydrogen bonding, π···π and C–H···π interaction parameters are set in Table 3.

The coordination polyhedron around both metal centres in **1** and **2** is best described as a distorted octahedron with a MN_6 chromophore. The coordination includes two chelated tailored diimines (–N=C–NH–C=N–) ligated by four pyridine N atoms (N1, N3, N4, N6) and two terminal azide N atoms (N7, N10). Three pyridine nitrogens (N1, N4, N6) of two different dpa units and

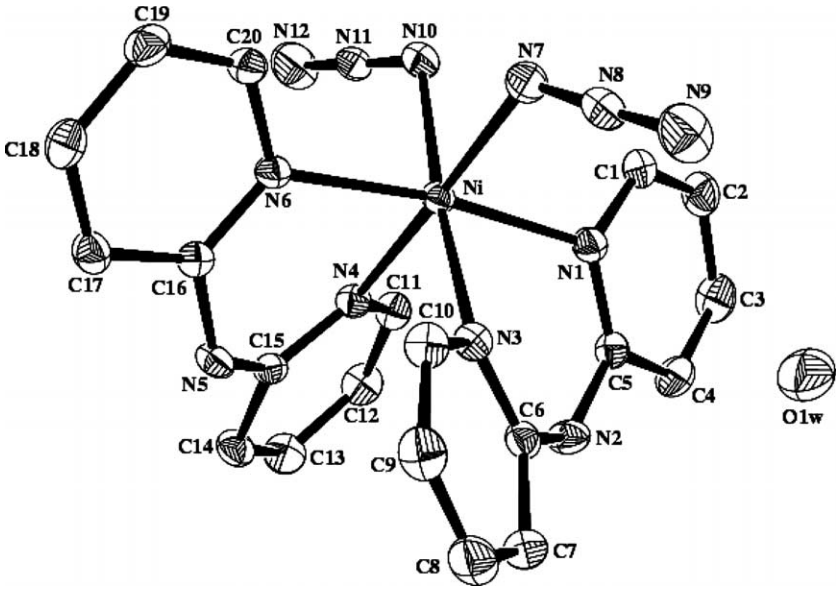


Fig. 1. ORTEP representation of $[Ni(dpa)_2(N_3)_2]\cdot H_2O$ (**1**) with the atom labelling scheme and 40% probability ellipsoids for all non-hydrogen atoms.

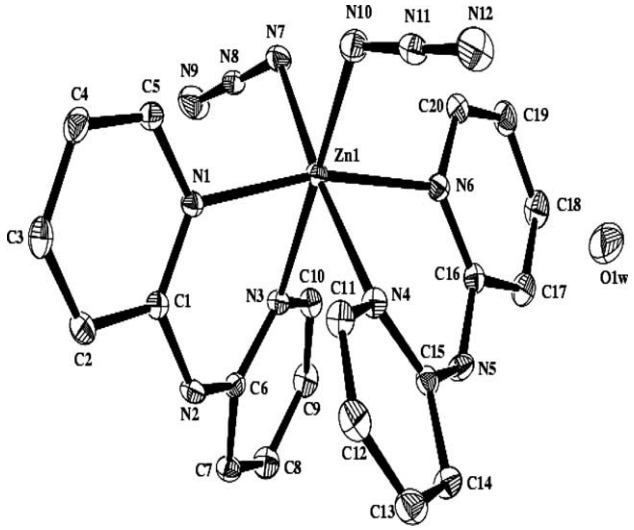


Fig. 2. ORTEP diagram of $[Zn(dpa)_2(N_3)_2]\cdot H_2O$ (**2**) with the atom labelling scheme and 40% probability ellipsoids for all non-hydrogen atoms.

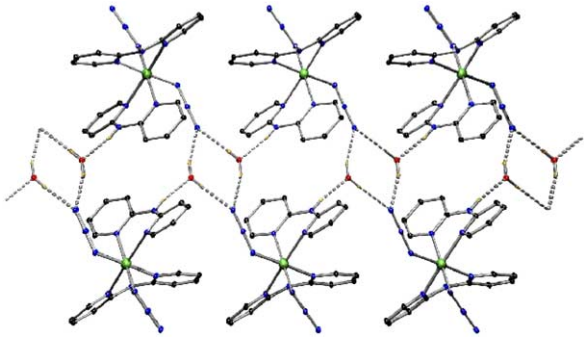


Fig. 3. View of the cyclic $R_2^4(8)$ formed by the water donor in **1**.

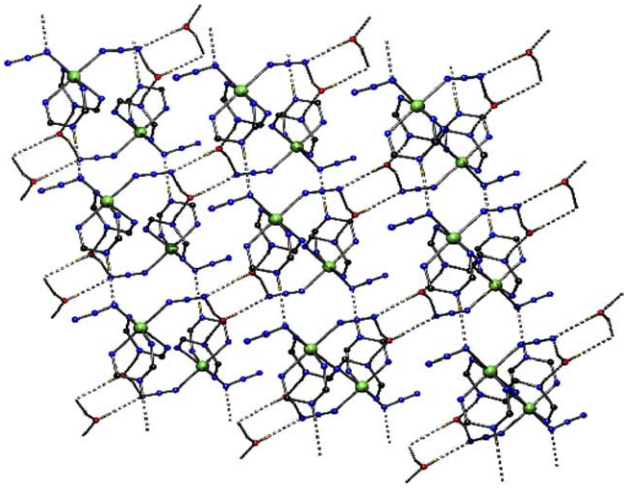


Fig. 4. View of the 2D sheet built by the monomeric units of **1** through hydrogen bonding (for clarity the pyridine part of the dpa ligand has been omitted).

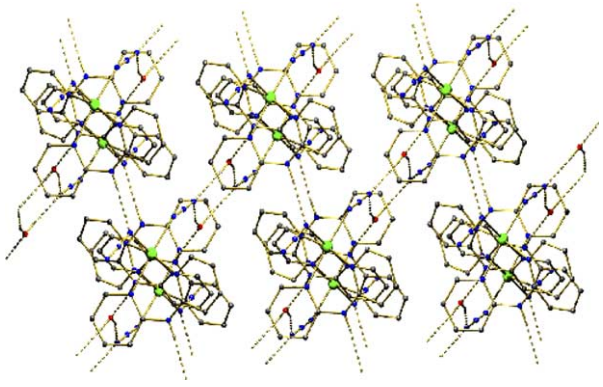


Fig. 5. 3D supramolecular network in **1** using weak interactions (hydrogen bonding, π stacking and C–H···π interactions).

one nitrogen (N7) of the pendant azido group define the equatorial plane around the metal(II) centre. The *trans* axial sites are occupied by one nitrogen (N3) from the remaining pyridine ring of a dpa unit and one nitrogen (N10) from the other pendant azido ligand (Figs. 1 and 2). The basal nitrogen atoms are planar with a rms deviation of 0.0425 and 0.059 Å, in **1** and **2**, respectively. The maximum deviation of any equatorial atom (N3) from the mean plane around nickel(II) in **1** and around zinc(II) in **2** are 0.045(2) and 0.064(2) Å, respectively. Deviations of nickel(II) and zinc(II) from the mean plane towards the azido nitrogen (N10) are about 0.048(1) and 0.127 (1) Å, respectively.

Table 2
Selected bond distances (Å) and bond angles (°) for **1** and **2**

Compound **1**		Compound **2**	
Bond distances (Å)			
Ni(1)–N(1)	2.109(2)	Zn(1)–N(1)	2.1490(17)
Ni(1)–N(3)	2.121(2)	Zn(1)–N(3)	2.2107(17)
Ni(1)–N(4)	2.105(2)	Zn(1)–N(4)	2.2423(18)
Ni(1)–N(6)	2.085(2)	Zn(1)–N(6)	2.1864(18)
Ni(1)–N(7)	2.124(3)	Zn(1)–N(7)	2.1149(19)
Ni(1)–N(10)	2.109(3)	Zn(1)–N(10)	2.147(2)
Bond angles (°)			
N(7)–Ni(1)–N(10)	87.29(10)	N(7)–Zn(1)–N(10)	89.79(8)
N(1)–Ni(1)–N(3)	83.86(9)	N(1)–Zn(1)–N(3)	81.30(6)
N(1)–Ni(1)–N(4)	90.21(9)	N(1)–Zn(1)–N(4)	89.70(7)
N(1)–Ni(1)–N(6)	172.15(9)	N(1)–Zn(1)–N(6)	166.12(6)
N(1)–Ni(1)–N(7)	91.83(10)	N(1)–Zn(1)–N(7)	95.61(7)
N(1)–Ni(1)–N(10)	93.12(9)	N(1)–Zn(1)–N(10)	95.39(7)
N(3)–Ni(1)–N(4)	91.17(9)	N(3)–Zn(1)–N(4)	88.52(7)
N(3)–Ni(1)–N(6)	91.32(9)	N(3)–Zn(1)–N(6)	88.71(7)
N(3)–Ni(1)–N(7)	88.69(10)	N(3)–Zn(1)–N(7)	93.77(7)
N(3)–Ni(1)–N(10)	174.90(10)	N(3)–Zn(1)–N(10)	175.35(8)
N(4)–Ni(1)–N(6)	83.67(9)	N(4)–Zn(1)–N(6)	80.38(7)
N(4)–Ni(1)–N(7)	177.92(10)	N(4)–Zn(1)–N(7)	174.48(7)
N(4)–Ni(1)–N(10)	92.96(9)	N(4)–Zn(1)–N(10)	88.20(8)
N(6)–Ni(1)–N(7)	94.26(9)	N(6)–Zn(1)–N(7)	94.63(7)
N(6)–Ni(1)–N(10)	92.10(9)	N(6)–Zn(1)–N(10)	93.98(8)

All the six Ni–N bond lengths in **1** lie within a close range [2.085(2)–2.124(3) Å] and are consistent with the corresponding values of nickel(II)–N systems [20,21] and in **2** there are lengthened Zn–N bonds [2.1149(19) –2.2423(18) Å] which are consistent with the corresponding values of Zn(II)–N systems [19]. In both compounds the azido ligands are linear and mutually in a *cis* alignment. The dpa bites [N1–Ni–N3 83.86(9)°, N4–Ni–N6 83.67(9)° in **1** and N1–Zn1–N3 81.30(6)°, N4–Zn1–N6 80.38(7)° in **2**] are similar. In **1** the ranges of the *cisoid* and the *transoid* angles are 83.67(9)–94.26(9)° and 172.15(9)–177.92(10)°, respectively, and those in complex **2** are 80.38(7)–95.61(7)° and 166.12(6)–175.35(8)°, respectively, which reflect the degrees of distortion from the ideal octahedral geometry (Table 2). The dpa ligands are not planar as reflected by the dihedral angles between the planar pyridine rings (N1, C1 → C5 and N3, C6 → C10; N4, C11 → C15 and N6, C16 → C20) which are 21.9(2)°, 28.1(2)° for **1** and 25.6(1)° 18.2(1)° for **2**.

Table 3
H–bond donor/acceptor scheme (Å, °)

Compound	D–H···A	D–H	H···A	D···A	∠D–H···A
1	N2–H2N···O1W[a]	0.81(3)	2.06(3)	2.863(4)	170(3)
2	N5–H1N5···O1W[i]	0.78(3)	2.09(3)	2.864(3)	171(3)
1	O1W–H1W1···N9	0.86(5)	2.05(5)	2.878(5)	162(4)
2	O1W–H1W1···N12[ii]	0.77(3)	2.16(3)	2.925(4)	173(3)
1	O1W–H2W1···N9[b]	0.71(6)	2.23(6)	2.938(5)	175(6)
2	O1W–H1W1···N12[ii]	0.77(3)	2.16(3)	2.925(4)	173(3)
1	N5–H5N···N10[c]	0.79(4)	2.32(4)	3.107(4)	176(4)
2	N2–H1N2···N7[iii]	0.82(3)	2.28(3)	3.091(3)	174(3)

Symmetry code: a: $2-x, 2-y, -z$; b: $1+x, y, z$; c: $1-x, 3-y, -z$; i: $-x, 1-y, -1-z$; ii: $1+x, y, z$; iii: $1-x, -y, -1-z$.

C–H···π Interactions bond donor/acceptor scheme (Å, °)

Compound	D–H···A	D–H	H···Cg	X···Cg	∠X–H···Cg
1	C10–H10···Cg6	0.93(3)	3.00(3)	3.589(4)	123(2)
2	C10–H10···Cg6	0.97(3)	2.84(3)	3.447(3)	121(2)
1	C11–H11···Cg3	0.93(3)	2.79(3)	3.408(3)	125(2)
2	C11–H11···Cg3	0.93(3)	3.06(3)	3.634(3)	122(2)

π–π Interactions (face-to-face) (°, Å)

Compound	Cg–Cg	Cg–Cg distance	Dihedral angle(*i*,*j*)	Perpendicular distance between baricentres(*i*,*j*)
1	Cg6–Cg6[a]	3.809(1)	0.03	3.504

The packing diagram of **1** in the *ab*-plane exhibits a 2D supramolecular architecture arising from two types of hydrogen bondings (Figs. 3 and 4). The solvent water molecule (O1W) and amine nitrogen atoms (N2, N5) play a vital role in the formation of the 2D sheet. Four neighbouring mononuclear units are held together through hydrogen bondings between the donor water molecule and azide acceptor [O1W···N9 2.878(5) Å, ∠O1W–H1W1···N9 162(4)°; O1W···N9 2.938(5) Å, ∠O1W–H2W1···N9 175(6)°]. The O–H···N bonds generate a cyclic motif $R_2^4(8)$ in Etter's graph notation [35]. This, in turn, results in a 1D chain (Fig. 3). These 1D chains are connected through hydrogen bonding between the amine nitrogen donors (N2, N5) and the water and azido nitrogen (N10) acceptors [N2···O1W 2.863(4) Å, ∠N2–H2N···O1W 170(3)°; N5···N10 3.107(4) Å, ∠N5–H5N···O1W 176(4)°]. These two types of hydrogen bondings are interwoven and facilitate the formation of a 2D supramolecular sheet in the *ab*-plane (Fig. 4). The same overall average N···O distance (2.89 Å) between hydrogen-bonded groups is indicative of the presence of moderate directional hydrogen bonding, which may be used in crystal engineering. The pyridyl planes (N6–C16–C17–C18–C19–C20) from adjacent sheets form face-to-face π···π and intramolecular C–H···π interactions, resulting in a 3D continuum (Fig. 5). The dihedral angle between the pyridyl rings is 0.0° and the perpendicular distance between the baricenters of these planes is about 3.521 Å. In each sheet, the Ni···Ni separation between the nearest neighbours is 7.66 Å.

3.3. Luminescence spectra

The spectroscopic data are listed in Table 4. The emission energy of **1** and **2** in DMF solutions at 298 K is almost same ($\lambda_{max} \approx 350$ nm) and is assignable to intraligand fluorescence [19,20]. The lifetimes of the fluorescence of **1** and **2** are 2.62 and 2.60 ns, respectively. In glassy solutions (DMF at 77 K) both fluoresce and $^3(\pi-\pi^*)$ phosphorescence is observed at 425 nm. In the solid state they show a distinct emission band at 374 nm, differing from their fluorescence spectra in DMF.

Table 4
Luminescence data for **1** and **2**

Sample	Absorption (λ/nm)	Emission (λ/nm)			Lifetime (ns)
		Fluorescence	Phosphorescence	Solid state	
dpa	314	349	425	366	2.58
1	315	350	425	374	2.62
2	315	352	425	374	2.60

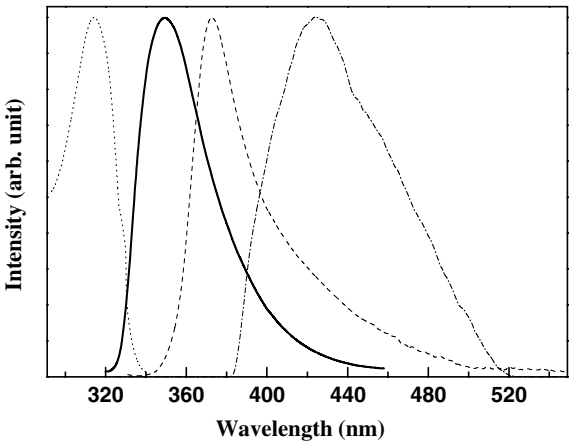


Fig. 6. Emission spectra of **1**: UV in DMF solution at 298 K (·····), fluorescence (——), phosphorescence in DMF glassy solution (- – – -), solid state at 298 K (- - - - - -).

This emission is expected to be due to excimer formation arising from the π···π aromatic stacking in the solid state and due to the similar strength of π···π stacking in both the complexes (Fig. 6).

4. Conclusion

We have shown that dpa can be used towards crystal design in combination with azide terminals leading to 3D network structures through cooperative forces from 0D building blocks. An emphasis has been made to show how the use of such non-covalent forces may be effectively harnessed to synthesize non-molecular solids of varied architectures [4a,13a]. The long-range structural motif ensures further study of dpa in combination with different pseudohalides like thiocyanate, cyanate, selenocyanate and carboxylates such as acetate around different 3d and 4d metal ions. The preparation of these compounds illustrates a potentially versatile approach to the construction of uncharged inorganic organic hybrid luminous materials.

5. Supplementary data

Crystallographic data (excluding structure factors) for the structures reported in this paper have been deposited with the Cambridge Crystallographic Data Centre as supplementary publication Nos. CCDC 202628 (**1**) and 239455 (**2**). Copies of this information can be obtained, free of charge, from The Director, CCDC, 12 Union Road, Cambridge CB2 1EZ, UK (fax: +44 1223 336033; e-mail: deposit@ccdc.cam.ac.uk or www: http://www.ccdc.cam.ac.uk).

Acknowledgements

Financial support from the Department of Science and Technology (DST) and the Council of Scientific and Industrial Research (CSIR), New Delhi, India is gratefully acknowledged.

References

[1] (a) J.M. Lehn, Supramolecular Chemistry, VCH, Weinheim, 1995; (b) J.W. Steed, J.L. Atwood, Supramolecular Chemistry, Wiley, New York, 2000; (c) B. Moulton, M.J. Zaworotko, Chem. Rev. 101 (2001) 1629.
[2] (a) M.J. Zaworotko, Chem. Commun. (2001) 1; (b) H. Zhang, X. Wang, K. Zhang, B.K. Teo, Coord. Chem. Rev. 183 (1999) 157.
[3] J.K.A. Howard, F.H. Allen, Implications of Molecular and Materials Structure for New Technologies, Kluwer, Dordrecht, 1999.
[4] (a) D. Bose, J. Banerjee, Sk.H. Rahaman, G. Mostafa, H.-K. Fun, R.D. Bailey Walsh, M.J. Zaworotko, B.K. Ghosh, Polyhedron 23 (2004) 2045; (b) T. Steiner, Angew. Chem. Int. Ed. 41 (2002) 48; (c) G.R. Desiraju, Acc. Chem. Res. 35 (2002) 565.
[5] (a) C. Janiak, J. Chem. Soc., Dalton Trans. (2000) 3885; (b) M.J. Zaworotko, Chem. Commun. (2002) 199; (c) L. Pan, N.W. Zheng, N.W. Wu, X.Y. Huang, J. Coord. Chem. 41 (1999) 551; (d) C.A. Hunter, Chem. Soc. Rev. 23 (1994) 101.
[6] (a) S.V. Lindeman, D. Kosynkin, J.K. Kochi, J. Am. Chem. Soc. 120 (1998) 6431; (b) C.D. Abernethy, C.L.B. Macdonald, J.A.C. Clyburne, A.H. Cowley, Chem. Commun. (2001) 61; (c) L. Rong-Guang, T. Zhu, X. Sai-Feng, Z. Quin-Jiang, W.G. Jackson, W. Zhan-Bing, L. La-Sheng, Polyhedron 22 (2003) 3467.
[7] G.W. Gokel, A. Mukhopadhyay, Chem. Soc. Rev. 30 (2001) 274.
[8] (a) S.R. Marder, in: D.W. Bruce, D. O'Hare (Eds.), Metal Containing Materials for Nonlinear Optics in Inorganic Materials, 2nd ed., Wiley, Chichester, 1996, pp. 121–169; (b) O.R. Evans, W. Lin, Acc. Chem. Res. 35 (2002) 511.
[9] (a) J.S. Miller, M. Drillon (Eds.), Magnetism: Molecules to Materials IV, Wiley–VCH, Weinheim, 2003; (b) O. Kahn, Molecular Magnetism, VCH, New York, 1993.
[10] B. Cornils, W.A. Herrmann, R. Schlogl (Eds.), Catalysis from A to Z: A Concise Encyclopedia, Wiley, New York, 2000.
[11] M. Kondo, T. Yoshitomi, K. Seki, M. Matsuzaka, S. Kitagawa, Angew. Chem., Int. Ed. Engl. 36 (1997) 1725.
[12] (a) T.K. Karmakar, S.K. Chandra, J. Ribas, G. Mostafa, T.-H. Lu, B.K. Ghosh, Chem. Commun. (2002) 2364; (b) J. Ribas, M. Monfort, B.K. Ghosh, R. Cortes, X. Solans, M. Font-Bardia, Inorg. Chem. 35 (1996) 864.
[13] (a) D. Bose, Sk.H. Rahaman, G. Mostafa, R.D. Bailey Walsh, M.J. Zaworotko, B.K. Ghosh, Polyhedron 23 (2004) 545; (b) D. Bose, G. Mostafa, H.-K. Fun, B.K. Ghosh, Polyhedron 24 (2005) 747.
[14] P. Comba, T.W. Hambley, Molecular Modelling of Inorganic and Coordination Compounds, 2nd ed., VCH, Weinheim, 2001.
[15] A. Camus, N. Marsich, A.M.M. Lanfredi, F. Ugozzoli, C. Massera, Inorg. Chim. Acta 309 (2000) 1.
[16] (a) F.A. Cotton, L.M. Daniels, G.T. Jordan IV, C.A. Murillo, J. Am. Chem. Soc. 119 (1997) 10377; (b) K.-Y. Ho, W.-Y. Yu, K.-K. Cheung, C.-M. Che, Chem. Commun. (1998) 2101.

[17] (a) E.-C. Yang, M.-C. Cheng, M.-S. Tsai, S.-M. Peng, J. Chem. Soc., Chem. Commun. (1994) 2377;
(b) M. Villanueva, J.L. Mesa, M.K. Urtiaga, R. Cortés, L. Lezama, M.I. Arriortua, T. Rojo, Eur. J. Inorg. Chem. (2001) 1581.
[18] L.-P. Wu, P. Field, T. Morrissey, C. Murphy, P. Nagle, B. Hathaway, C. Simmons, P. Thornton, J. Chem. Soc., Dalton Trans. (1990) 3835.
[19] (a) W. Liu, A. Hassan, S. Wang, Organometallics 16 (1997) 4257;
(b) K.-Y. Ho, W.-Y. Yu, K.-K. Cheung, C.-M. Che, J. Chem. Soc., Dalton Trans. (1999) 1581.
[20] (a) D.-Z. Niu, B.-W. Sun, Z.-S. Lu, Z.-M. Wang, C.-H. Yan, Acta Crystallogr., Sect. E 57 (2001) m58;
(b) J. Ribas, M. Monfort, B.K. Ghosh, X. Solans, M. Font-Bardia, Polyhedron 15 (1996) 1091.
[21] (a) A. Escuer, R. Vicente, J. Ribas, X. Solans, Inorg. Chem. 34 (1995) 1793;
(b) M. Monfort, I. Resino, J. Ribas, X. Solans, M. Font-Bardia, P. Rabu, M. Drillon, Inorg. Chem. 29 (2000) 2572.
[22] J. Ribas, A. Escuer, M. Monfort, R. Vicente, R. Cortes, L. Lezama, T. Rojo, Coord. Chem. Rev. 193 (1999) 1027.
[23] D.T. Sawyer, J.L. Roberts Jr., Experimental Electrochemistry for Chemists, Wiley, New York, 1974, p. 167.
[24] D. Bose, H. Rahaman, J. Banerjee, N.K. Mondal, B.K. Ghosh, Indian J. Chem. A 41 (2002) 1374.
[25] G.M. Sheldrick, SAINT Ver. 5, Siemens Analytical X-ray Instrument, Inc., Madison, WI, 1995.
[26] SADABS v2.02: Area-Detector Absorption Correction, Siemens Industrial Automation, Inc., Madison, WI, 1996.
[27] G.M. Sheldrick, Acta Crystallogr., Sect. A 46 (1990) 467.
[28] G.M. Sheldrick, SHELXL-97: Program for Refinement of Crystal Structures, University of Göttingen, Göttingen, Germany, 1997.
[29] A.L. Spek, PLATON: Molecular Geometry Program, University of Utrecht, The Netherlands, 1999.
[30] L.J. Farrugia, J. Appl. Crystallogr. 30 (1997) 565.
[31] W.J. Geary, Coord. Chem. Rev. 7 (1971) 81.
[32] K. Nakamoto, Infrared and Raman Spectra of Inorganic and Coordination Compounds, 5th ed., Wiley, New York, 1997.
[33] A.B.P. Lever, Inorganic Electronic Spectroscopy, 2nd ed., Elsevier, New York, 1984.
[34] J. Dinda, U. Ray, G. Mostafa, T.-H. Lu, A. Usman, I.A. Razak, S. Chantrapromma, H.-K. Fun, C. Sinha, Polyhedron 22 (2003) 247.
[35] M.C. Etter, J. Phys. Chem. (1991) 4601.

and structural characterization of several $M^{II}{}_2$- $[M^{IV}(CN)_8]\cdot nH_2O$ [13h–13n] ($2 \leqslant n \leqslant 9$) and amine-functionalized networks been described [13b,14]; analogues containing $Cu^{II}/Mo(CN)_8{}^{n-}$ and $Co^{II/III}/\ W(CN)_8{}^{n-}$ units are reported to exhibit reversible photo-induced magnetization changes and we anticipate that incorporation of such bistable materials into electronic circuitry may ultimately afford molecule-based nanoscale switchable devices [13a,13b,13l–13n,15].

While we experienced limited success in crystallizing octacyanometalate networks via hydrothermal and slow diffusion methods, we began to explore the utility of amine ligands to direct and limit the number of cyano linkages formed between transition metal centers. Bidentate amines such as ethylenediamine (en) and 1,3-propanediamine (tn), find extensive use in the preparation of so-called "expanded Prussian blue solids" [16], but surprisingly few octacyanometalate derivatives are known [14a–14g,15,17]; octacyanometalate clusters containing these amines are also relatively rare [18].

In the present contribution, we describe the synthesis, structural, spectroscopic, and magnetic characterization of three unusual amine-expanded octacyanometalate(IV) networks that crystallize from aqueous mixtures of amines, octacyanometalate, and divalent transition metal salts.

2. Experimental

2.1. General considerations

All operations were conducted in the dark. Solvents were distilled under dinitrogen from CaH_2 (acetonitrile), Mg turnings (methanol), or sodium–benzophenone (diethyl ether). Deionized water, ammonium hydroxide (Malinkrodt), and $CuCl_2\cdot 2H_2O$ (Baker) were used as received. The preparation of $K_4[Mo(CN)_8]\cdot 2H_2O$ [19,20], $K_4[W(CN)_8]\cdot 2H_2O$ [21], and $Ni(OTs)_2$ [22] are described elsewhere while $Cs_3[Mo(CN)_8]\cdot 4H_2O$ [13o,21,23] and $[Ni(tn)_3][OTs]_2$ [22] were prepared via modifications to previously described procedures. The IR spectra were recorded as Nujol mulls between KBr plates on a Mattson Galaxy 5200 FTIR instrument. Room-temperature magnetic susceptibility measurements were conducted on a Johnson–Matthey Magnetic Susceptibility Balance. Variable temperature magnetic measurements were conducted on Quantum Design MPMS or MPMS2 SQUID magnetometers located at the Frederick Seitz Materials Characterization Laboratory at the University of Illinois at Urbana-Champaign. Photomagnetic studies were conducted using a Quantum Design Fiber Optic Sample Holder (FOSH) using infrared filtered white, red (Meade #23A), or blue (Meade #80A) light from a Dolan Jenner Fiber-Lite source. Diamagnetic corrections were estimated using Pascal's constants [24]: $\chi_{dia} = -200.32\times 10^{-6}\ cm^3\ mol^{-1}$ for **1**, $-458.32\times 10^{-6}\ cm^3\ mol^{-1}$ for **2**, $-464.32\times 10^{-6}\ cm^3\ mol^{-1}$ for **3**, and $-848.92\times 10^{-6}\ cm^3\ mol^{-1}$ for **4**. Microanalyses were performed by the University of Illinois Microanalytical Laboratory.

2.2. Preparation of complexes and networks

2.2.1. $[Ni^{II}(tn)_3][OTs]_2$ (**1**)

An aqueous (20 mL) solution of $Ni(OTs)_2$ (3.57 g, 7.02 mmol) was prepared by heating (100 °C) and 1,3-propanediamine (3.0 mL, 35.9 mmol) was added affording a purple suspension. The mixture was filtered and the filtrate was concentrated (10 mL) by heating to boiling. The concentrated mixture was allowed to stand at −20 °C for 2 h and then warm to room temperature. The purple crystals were isolated by suction filtration and were washed with EtOH (2×10 mL), Et_2O (10 mL), and dried under vacuum at room temperature for 2 h. Yield: 2.99 g (71.7%). *Anal.* Calc. for $C_{23}H_{45}N_6NiS_2O_{6.5}$: C, 43.48; H, 7.64; N, 13.21. Found: C, 43.52; H, 7.08; N, 12.94%. IR (nujol, cm^{-1}): 3477 (s, br), 3306 (vs), 3269 (vs), 3182 (vs), 2227 (w), 2133 (w), 1912 (w), 1611 (vs), 1494 (m), 1402 (m), 1261 (s), 1197 (vs), 1182 (vs), 1123 (vs), 1107 (vs, sh), 1075 (s, sh), 1064 (s, sh), 1033 (vs), 1011 (vs), 946 (vs), 904 (m), 856 (w), 840 (w), 815 (s), 803 (w, sh), 773 (w), 710 (m), 685 (vs), 662 (s, sh), 614 (m), 567 (vs), 521 (w), 479 (w), 451 (w). μ_{eff} (μ_B) Calc.: 2.83. μ_{eff} (μ_B) Found: 2.93.

2.2.2. $\{[trans\text{-}Ni^{II}(tn)_2(OH_2)][trans\text{-}Ni^{II}(tn)_2][(\mu\text{-}NC)_3Mo^{IV}(CN)_5]\cdot 6H_2O\}$ (**2**)

A hot methanol (40 mL) solution of $Ni(OTs)_2$ (1.54 g, 1.57 mmol) was treated with 1,3-propanediamine (2.64 mL, 3.56 mmol) and was allowed to cool to room temperature. Additional MeOH (85 mL) was added and addition of $K_4[Mo(CN)_8]\cdot 2H_2O$ (0.95 g, 1.91 mmol) in water (7 mL) afforded brown crystals within 1 h; the slow deposition of crystals ceased after four weeks at room temperature. The brown needles were isolated by suction filtration and washed with water (10 mL), EtOH (10 mL), Et_2O (3×10 mL), and dried under vacuum at room temperature overnight. Yield: 0.305 g (49.1%). *Anal.* Calc. for $C_{18}H_{46}N_{18}Ni_2O_7Mo$: C, 30.07; H, 7.09; N, 28.07. Found: C, 30.51; H, 6.01; N, 27.66%. IR (nujol, cm^{-1}): 3633 (vs), 3547 (s), 3326 (vs), 3292 (vs), 3271 (vs), 3257 (vs), 3168 (s), 2154 (s), 2142 (s), 2129 (vs), 2120 (vs). 2109 (vs), 2077 (m), 1673 (m), 1609 (s), 1592 (s), 1402 (m), 1330 (w), 1310 (w), 1279 (m), 1196 (s), 1158 (m), 1131 (vs), 1086 (m), 1067 (m), 1050 (m), 1019 (s), 1003 (vs), 905 (s), 879 (w), 647 (s), 615 (s), 469 (m). μ_{eff} (μ_B) Calc.: 4.0. μ_{eff} (μ_B) Found: 4.53.

2.2.3. {[trans-$Ni^{II}(tn)_2(OH_2)$][trans-$Ni^{II}(tn)_2$]-[(μ-NC)$_3W^{IV}(CN)_5$]·$6H_2O$} (3)

An aqueous (25 mL) solution of **1** (0.72 g, 1.14 mmol) was treated with aqueous (10 mL) $K_4[W(CN)_8]\cdot 2H_2O$ (0.70 g, 1.19 mmol) and the resulting brown solution was allowed to stand; brown needles began to deposit within 1 h and ceased after 24 h. The brown needles were isolated by suction filtration and washed with water (2×10 mL), MeOH (2×10 mL), Et_2O (2×10 mL), and dried under vacuum at room temperature overnight. Yield: 0.24 g (47.9%). *Anal.* Calc. for $C_{18}H_{46}N_{18}Ni_2O_7W$: C, 24.30; H, 5.51; N, 28.34. Found: C, 27.29; H, 5.31; N, 25.01%. IR (nujol, cm^{-1}): 3625 (vs), 3540 (vs), 3340 (vs), 3290 (vs), 3255 (vs), 3167 (vs), 2153 (s), 2140 (s, sh), 2128 (vs, sh), 2115 (vs), 2103 (vs), 2076 (s, sh), 2061 (vs), 1677 (m), 1659 (m), 1612 (s), 1591 (vs), 1401 (m), 1332 (m), 1280 (s), 1259 (m), 1196 (m), 1160 (s), 1128 (vs), 1084 (s), 1067 (s), 1050 (m), 1017 (s), 1001 (s), 903 (s), 879 (m), 674 (m), 649 (m), 614 (m), 476 (m). μ_{eff} (μ_B) Calc.: 4.0. μ_{eff} (μ_B) Found: 4.41.

2.2.4. $Cs_4[Cu^{II}(OH_2)_4]_2[Cu^{II}(NH_3)]_4[Mo^{IV}(CN)_8]_4\cdot 2H_2O$ (4)

Treatment of a concentrated ammonia (30 mL) solution of $CuCl_2\cdot 2H_2O$ (0.33 g, 1.94 mmol) with $Cs_3[Mo(CN)_8]$ (0.89 g, 1.16 mmol) in ammonia (30 mL) afforded a brown solution that was allowed to stand for 2 weeks. The iridescent copper plates that deposited were isolated by suction filtration and washed with water (3×10 mL), EtOH (3×5 mL), and Et_2O (3×10 mL). The crystals were dried under vacuum at room temperature overnight. Yield: 0.72 g (96.0%). *Anal.* Calc. for $C_{32}H_{40}N_{44}O_2Cs_4Cu_6Mo_4$: C, 15.33; H, 1.29; N, 20.12. Found: C, 15.74; H, 1.22; N, 21.75%. IR (nujol, cm^{-1}): 3350 (vs, br), 2952 (vs), 2922 (vs), 2856 (vs), 2172 (vs, sh), 2158 (vs), 2145 (vs, sh), 2125 (vs), 2109 (vs, sh), 2084 (vs, sh), 1683 (m, sh), 1660 (s, sh), 1613 (vs), 1462 (vs), 1455 (vs), 1377 (vs), 1262 (vs), 1250 (vs), 1241 (vs), 1169 (w), 1155 (w), 1097 (m), 1073 (m), 1038 (m), 919 (w), 887 (w), 843 (m), 810 (m), 719 (vs), 705 (vs), 664 (s), 605 (w), 590 (w), 566 (w), 548 (m), 532 (m), 520 (s), 467 (vs), 462 (vs), 426 (vs), 414 (vs), 403 (vs). μ_{eff} (μ_B) Calc.: 4.24. μ_{eff} (μ_B) Found: 4.34.

2.3. Structure determinations and refinements

Crystals of **2** and **3** were grown from aqueous $[Ni(tn)_3][OTs]_2$ or $Ni(OTs)_2$/1,3-propanediamine mixtures treated with either $K_4Mo(CN)_8\cdot 2H_2O$ (**2**) or $K_4W(CN)_8\cdot 2H_2O$ (**3**). Crystals of **4** were grown from aqueous ammonia solutions of $CuCl_2\cdot 4H_2O$ and $Cs_3Mo(CN)_8$. X-ray diffraction data were collected at 90.0(2) K on a Nonius kappaCCD diffractometer from irregular shaped crystals mounted in Paratone-N oil on glass fibers. Initial cell parameters were obtained (DENZO) [25] from ten 1° frames and were refined via a least-squares scheme using all data-collection frames (SCALEPACK) [26]. Lorentz/polarization corrections were applied during data reduction. The structures were solved by direct methods (SHELXS97) [26] and completed

Table 1
Crystallographic data for {[*trans*-$Ni^{II}(tn)_2(OH_2)$][*trans*-$Ni^{II}(tn)_2$][(μ-NC)$_2Mo^{IV}(CN)_6$]·$6H_2O$}$_\infty$ (**2**), {[*trans*-$Ni^{II}(tn)_2(OH_2)$][*trans*-$Ni^{II}(tn)_2$]-[(μ-NC)$_2W^{IV}(CN)_6$]·$6H_2O$} (**3**), and $Cs_4[Cu^{II}(OH_2)_4]_2[Cu^{II}(NH_3)]_4[Mo^{IV}(CN)_8]_4\cdot 2H_2O$ (**4**)

Compound	(**2**)	(**3**)	(**4**)
Chemical formula	$C_{20}H_{53}MoN_{16}Ni_2O_{6.5}$	$C_{20}H_{53}N_{16}Ni_2O_{6.5}W$	$C_{32}H_{32}Cs_4Cu_6Mo_4N_{36}O_{18}$
Formula weight	835.14	923.05	2505.49
Temperature (K)	90.0(2)	90.0(2)	90.0(2)
λ (Å)	0.71073	0.71073	0.71073
Crystal size (mm)	$0.22\times 0.22\times 0.10$	$0.30\times 0.20\times 0.05$	$0.60\times 0.15\times 0.01$
Space group	triclinic	triclinic	monoclinic
Crystal system	$P\bar{1}$	$P\bar{1}$	$C2/m$
a (Å)	10.05000(10)	10.05000(10)	11.0247(9)
b (Å)	11.2870(2)	11.27600(10)	10.3382(8)
c (Å)	16.8840(3)	16.8740(2)	15.6133(13)
α (°)	105.6820(7)	105.7020(4)	90
β (°)	101.0440(7)	101.0610(4)	90.543
γ (°)	92.3270(7)	92.3430(5)	90
V (Å^3)	1801.12(5)	1797.93(3)	1779.5(2)
ρ (g cm^{-3})	1.540	1.705	2.252
Z	2	2	2
μ (mm^{-1})	1.436	4.286	4.523
Final R indices [$I>2\sigma(I)$][a]	$R_1=0.0303$	$R_1=0.0185$	$R_1=0.0332$
	$wR_2=0.0681$	$wR_2=0.0421$	$wR_2=0.0645$
R indices (for all data)	$R_1=0.0407$	$R_1=0.0212$	$R_1=0.0495$
	$wR_2=0.0743$	$wR_2=0.0427$	$wR_2=0.0702$

[a] $R=\Sigma||F_o|-|F_o||\Sigma|F_o|$. $R_w=[(\Sigma w(|F_o|F_c|)^2/\Sigma wF_o^2)]^{1/2}$.

by difference Fourier methods (SHELXL97) [26]. Refinement was performed against F^2 by weighted full-matrix least-squares (SHELXL97) [26] and empirical absorption corrections (either SCALEPACK [25] or SADABS [26]) were applied. Hydrogen atoms were found in difference maps and subsequently placed at calculated positions using suitable riding models with isotropic displacement parameters derived from their carrier atoms. Non-hydrogen atoms were refined with anisotropic displacement parameters. Atomic scattering factors were taken from the International Tables for Crystallography vol. C [27]. Crystal data, relevant details of the structure determinations, and selected geometrical parameters are provided in Tables 1–3.

3. Results and discussion

3.1. Synthesis and spectroscopic characterization

We have previously described that a series of bi- and trimetallic clusters and salts, rather than networks, are obtained when aqueous $[M^{II}(en)_3][OTs]_2$($OTs^- = p$-toluenesulfonate) is treated with $M(CN)_8^{n-}$ ($M = Mo^{IV,V}$, $W^{IV,V}$). We rationalized that substitution of ethylenediamine (en) for 1,3-propanediamine (tn), would afford kinetically labile $Ni^{II}(tn)_3^{2+}$ ions that undergo dissociative tn loss, forming reactive *cis*-$Ni^{II}(tn)_2(OH_2)_2^{2+}$ intermediates, and a series of amine-expanded octacyanometalate networks of $[Ni^{II}(tn)_2]_2[M^{IV}(CN)_8] \cdot nH_2O$ and $[Ni^{II}(tn)_2]_3[M^{V}(CN)_8]_2 \cdot nH_2O$ stoichiometry. Indeed, treatment of either aqueous mixtures of nickel(II) tosylate and 1,3-propanediamine or $[Ni^{II}(tn)_3][OTs]_2$ with $M(CN)_8^{n-}$ ($M = Mo^{IV,V}$, $W^{IV,V}$) affords isostructural one-dimensional networks of {[*trans*-$Ni^{II}(tn)_2(OH_2)$][*trans*-$Ni^{II}(tn)_2$][(μ-NC)$_3M^{IV}(CN)_5$] · $6H_2O$}.(M^{IV} = Mo, **2**; W, **3**) stoichiometry.

Rationalizing that bidentate amines may hinder the formation of two- and three-dimensional networks, we reasoned that unidentate donors such as ammonia may facilitate greater network dimensionality. However, attempts to prepare two-dimensional copper(II) substituted analogues described by Meske and co-workers consistently met with failure [14f]. Treatment of copper(II) chloride dihydrate with cesium octacyanomolybdate(V) in aqueous ammonia unexpectedly affords a three-dimensional network of $Cs_4[Cu^{II}(OH_2)_4]_2[Cu^{II}(NH_3)]_4[Mo^{IV}(CN)_8]_4 \cdot 2H_2O$ stoichiometry, via $Mo^{V}(CN)_8^{3-}$ reduction; such behavior has been previously reported [28,29].

The infrared spectra of **2**–**4** suggest that bridging and terminal cyano ligands are present and the cyano stretching absorptions (ν_{CN}) range from 2061 to 2172 cm^{-1}. The highest energy ν_{CN} absorptions are found for the Cu^{II} derivative, consistent with the formation of M^{II}–NC–M^{IV} units and depopulation of the cyanide 5σ orbital; increasing π-backbonding progressing from Cu^{II} to Ni^{II} compensates this effect and progressively lowers the ν_{CN} absorption energies from 2172 to 2153 cm^{-1} for **4** and **2**, respectively [30]. These ν_{CN} absorptions are shifted to higher energies relative to those found for $K_4Mo(CN)_8 \cdot 2H_2O$ (2126, 2012,

Table 2
Selected bond distances (Å) for {[*trans*-$Ni^{II}(tn)_2(OH_2)$][*trans*-$Ni^{II}(tn)_2$][(μ-NC)$_2Mo^{IV}(CN)_6$] · $6H_2O$}$_\infty$ (**2**), {[*trans*-$Ni^{II}(tn)_2(OH_2)$][*trans*-$Ni^{II}(tn)_2$][(μ-NC)$_2W^{IV}(CN)_6$] · $6H_2O$}$_\infty$ (**3**), and $Cs_4[Cu^{II}(OH_2)_4]_2[Cu^{II}(NH_3)]_4[Mo^{IV}(CN)_8]_4 \cdot 2H_2O$ (**4**)

(**2**)		(**3**)		(**4**)	
Mo(1)–C(1)	2.149(3)	W(1)–C(1)	2.160(2)	Mo–C(1)	2.152(12)
Mo(1)–C(2)	2.156(3)	W(1)–C(2)	2.157(2)	Mo–C(2)	2.170(12)
Mo(1)–C(3)	2.158(3)	W(1)–C(3)	2.165(2)	Mo–C(3)	2.161(11)
Mo(1)–C(4)	2.159(3)	W(1)–C(4)	2.156(2)	Mo–C(4)	2.147(14)
Mo(1)–C(5)	2.168(3)	W(1)–C(5)	2.165(2)	Mo–C(5)	2.184(16)
Mo(1)–C(6)	2.173(3)	W(1)–C(6)	2.157(2)	Mo–C(5B)	2.148(16)
Mo(1)–C(7)	2.162(3)	W(1)–C(7)	2.162(2)	Mo–C(6)	2.153(8)
Mo(1)–C(8)	2.158(3)	W(1)–C(8)	2.177(2)	Mo–C(6A)	2.153(8)
C(1)–N(1)	1.150(4)	C(1)–N(1)	1.148(3)	C(1)–N(1)	1.165(13)
C(2)–N(2)	1.150(4)	C(2)–N(2)	1.145(3)	Cu(1)–N(1)	2.257(10)
Ni(1)–N(1)	2.040(2)	Ni(2)–N(2)	2.0384(18)	Cu(1)–N(2A)	2.005(9)
Ni(1)–N(9)	2.102(2)	Ni(2)–N(13)	2.0998(18)	Cu(1)–N(3A)	2.575(10)
Ni(1)–N(10)	2.137(2)	Ni(2)–N(14)	2.1384(18)	Cu(1)–N(6A)	2.028(6)
Ni(1)–N(11)	2.088(2)	Ni(2)–N(15)	2.0875(18)	Cu(1)–N(6B)	2.028(6)
Ni(1)–N(12)	2.115(2)	Ni(2)–N(16)	2.1158(18)	Cu(1)–N(7)	1.985(8)
Ni(1)–O(1)	2.191(2)	Ni(2)–O(1)	2.1904(15)	Cu(2)–N(4)	2.477(11)
Ni(2)–N(2)	2.069(2)	Ni(1)–N(5A)	2.093(3)	Cu(2)–O(8)	2.03(3)
Ni(2)–N(3A)	2.091(3)	Ni(1)–N(1)	2.0715(18)	Cu(2)–O(9)	2.043(11)
Ni(2)–N(13)	2.135(2)	Ni(1)–N(9)	2.1401(18)		
Ni(2)–N(14)	2.104(3)	Ni(1)–N(10)	2.1041(19)		
Ni(2)–N(15)	2.120(2)	Ni(1)–N(11)	2.1155(18)		
Ni(2)–N(16)	2.133(2)	Ni(1)–N(12)	2.1394(18)		

Table 3
Selected bond angles (°) for $\{[trans\text{-}Ni^{II}(tn)_2(OH_2)][trans\text{-}Ni^{II}(tn)_2][(\mu\text{-}NC)_2Mo^{IV}(CN)_6]\cdot 6H_2O\}_\infty$ (**2**), $\{[trans\text{-}Ni^{II}(tn)_2(OH_2)][trans\text{-}Ni^{II}(tn)_2][(\mu\text{-}NC)_2W^{IV}(CN)_6]\cdot 6H_2O\}_\infty$ (**3**), and $Cs_4[Cu^{II}(OH_2)_4]_2[Cu^{II}(NH_3)]_4[Mo^{IV}(CN)_8]_4\cdot 2H_2O$ (**4**)

(**2**)		(**3**)		(**4**)	
C(1)–Mo(1)–C(2)	123.58(10)	C(1)–W(1)–C(2)	123.41(8)	C(1)–Mo–C(2)	72.6(4)
C(1)–Mo(1)–C(3)	73.46(10)	C(1)–W(1)–C(3)	71.30(7)	C(1)–Mo–C(3)	145.0(4)
C(1)–Mo(1)–C(4)	77.31(10)	C(1)–W(1)–C(4)	71.45(8)	C(1)–Mo–C(4)	146.2(4)
C(1)–Mo(1)–C(5)	143.58(10)	C(1)–W(1)–C(5)	135.99(8)	C(1)–Mo–C(5)	87.9(5)
C(1)–Mo(1)–C(6)	131.50(10)	C(1)–W(1)–C(6)	144.96(8)	C(1)–Mo–C(5B)	73.8(5)
C(1)–Mo(1)–C(7)	69.42(10)	C(1)–W(1)–C(7)	80.96(7)	C(1)–Mo–C(6)	88.8(2)
C(1)–Mo(1)–C(8)	77.13(10)	C(1)–W(1)–C(8)	74.63(8)	C(1)–Mo–C(6A)	88.8(2)
Mo(1)–C(1)–N(1)	177.7(2)	W(1)–C(1)–N(1)	171.26(18)	C(2)–Mo–C(3)	72.3(4)
Mo(1)–C(2)–N(2)	171.0(2)	W(1)–C(2)–N(2)	177.28(18)	C(2)–Mo–C(6)	73.43(19)
Ni(1)–N(1)–C(1)	174.0(2)	Ni(2)–N(2)–C(2)	174.36(18)	C(3)–Mo–C(6)	81.4(2)
Ni(2)–N(2)–C(2)	149.5(2)	Ni(1)–N(1)–C(1)	148.91(16)	Mo–C(1)–N(1)	174.7(9)
N(1)–Ni(1)–O(1)	177.41(9)	N(2)–Ni(2)–O(1)	177.25(7)	Mo–C(2)–N(2)	178.3(9)
N(1)–Ni(1)–N(9)	91.61(9)	N(1)–Ni(1)–N(9)	92.42(7)	Mo–C(6)–N(6)	174.6(7)
N(1)–Ni(1)–N(10)	90.62(9)	N(1)–Ni(1)–N(10)	91.35(7)	N(1)–Cu(1)–N(2B)	91.9(3)
N(1)–Ni(1)–N(11)	91.49(9)	N(1)–Ni(1)–N(11)	93.33(7)	N(1)–Cu(1)–N(6B)	90.61(17)
N(1)–Ni(1)–N(12)	93.30(10)	N(1)–Ni(1)–N(12)	88.86(7)	N(1)–Cu(1)–N(7)	94.6(3)
N(9)–Ni(1)-N1(10)	89.34(9)	N(9)–Ni(1)–N(10)	89.07(7)	N2B-Cu(1)–N(7)	173.3(3)
N(9)–Ni(1)–N(11)	176.89(10)	N(9)–Ni(1)–N(11)	174.18(7)	C(1)–N(1)–Cu(1)	170.2(8)
N(9)–Ni(1)–N(12)	91.15(10)	N(9)–Ni(1)–N(12)	88.86(7)	C(6)–N(6)–Cu(1)	161.4(6)
N(10)–Ni(1)–N(12)	176.03(9)	N(10)–Ni(1)–N(12)	177.92(8)	C(2B)–N(2B)–Cu(1)	170.7(8)
N(2)–Ni(2)–N(3A)	176.49(9)	N(2)–Ni(2)–N(5A)	176.54(7)	O(8)–Cu(2)–O(9)	90.4(5)
N(2)–Ni(2)–N(13)	92.06(9)	N(2)–Ni(2)–N(13)	91.65(7)	C(4)–N(4)–Cu(2)	138.8(10)
N(2)–Ni(2)–N(14)	91.41(10)	N(2)–Ni(2)–N(14)	90.54(7)	N(4)–Cu(2)–O(8)	86.0(2)
N(2)–Ni(2)–N(15)	93.57(10)	N(2)–Ni(2)–N(15)	91.41(7)	N(4)–Cu(2)–O(8A)	94.0(2)
N(2)–Ni(2)–N(16)	88.85(9)	N(2)–Ni(2)–N(16)	93.28(7)	N(4)–Cu(2)–O(9)	61.7(2)
N(13)–Ni(2)–N(14)	91.41(10)	N(13)–Ni(2)–N(14)	89.44(7)	N(4)–Cu(2)–O(9A)	118.3(2)
N(13)–Ni(2)–N(16)	88.74(10)	N(13)–Ni(2)–N(16)	91.02(7)	N(4)–Cu(2)–N(4B)	180.0
N(14)–Ni(2)–N(15)	91.28(10)	N1(14)–Ni(2)–N(15)	90.66(7)		

2060 cm^{-1}) and $K_4W(CN)_8\cdot 2H_2O$ (2125, 2095, 2056 cm^{-1}) [31], and are comparable to those exhibited by a variety of networks containing copper(II) and nickel(II) centers [14]. Unfortunately, the infrared characterization of $[M^{II}(NH_3)_4]_2[Mo^{IV}(CN)_8]\cdot 2H_2O$ (M^{II} = Co, Ni) lattices have not been reported [13f].

Generally, $M^{IV}(CN)_8^{4-}$ compounds exhibit cyano stretching absorptions that range from 2060 to 2160 (ionic) and 2085 to 2141 cm^{-1} (cyanide-bridged) [17,18,31–33]. The ν_{CN} absorptions of bridging cyanides are often found at higher energies than terminal ones, but this assumption is only applicable to compounds derived from bridged metal centers that do not function as donor–acceptor pairs. If kinematic effects, or the mechanical restraint of cyanide motion in M–CN–M′ units, are operative between the cyanide-bridged donor and acceptor centers, the ν_{CN} absorptions are expected to move to higher energies [30,34]. If however, increased π-backbonding compensates the kinematic effect by decreasing the C–N bond order, then red-shifted ν_{CN} absorptions that scale as a function of the donor–acceptor charge-transfer absorption oscillator strength, will be observed [30,34]. Assuming that π-backbonding effects are minor, we tentatively assign the bridging and terminal cyano stretching absorptions as those near 2140 and 2080 cm^{-1}, respectively.

3.2. Crystallographic studies

Crystals of **2** and **3** are in the $P\bar{1}$ space group and crystallize as one-dimensional chains of $\{[trans\text{-}Ni^{II}(tn)_2(OH_2)][trans\text{-}Ni^{II}(tn)_2][(\mu\text{-}NC)_3M^{IV}(CN)_5]\cdot 6H_2O\}$. stoichiometry (Table 1). The winding 1-D chains are composed of $[trans\text{-}(\mu\text{-}CN)Ni^{II}(tn)_2(\mu\text{-}NC)M^{IV}(CN)_6]$. ($M^{IV}$ = Mo, **2**; W, **3**) linkages with appended *trans*-Ni-$(tn)_2(OH_2)$ units that propagate parallel to the crystallographic *a* direction (Figs. 1 and 2). These "T-shaped chains" pack via inversion centers around a channel of lattice water molecules that are hydrogen bonded to adjacent cyanide, ammine, and aquo ligands along the crystallographic *c* direction. Coordination networks containing similar chain-like species have recently been reported by Kahn et al. we postulate that **2** and **3** are the efflorescent crystals described by Gao et al. [14e,15e].

Extensive interchain hydrogen bonding interactions are present between lattice water, aquo ligands, and terminal cyanides in **2** and **3**. The nearest neighbor contacts for **2** range from 2.685(5) (O(2WA)···O(3WA)) to 2.869(5) Å (N(6DD)···O(1WA)) while those for **3** range from 2.792(4) (O(1A)···O(1WB)) to 3.060(4) Å (O(5WC)···O(6WA)). Additional hydrogen bonding interactions (ca. 3.0–3.1 Å) are also present between lattice waters and coordinated tn and aquo ligands.

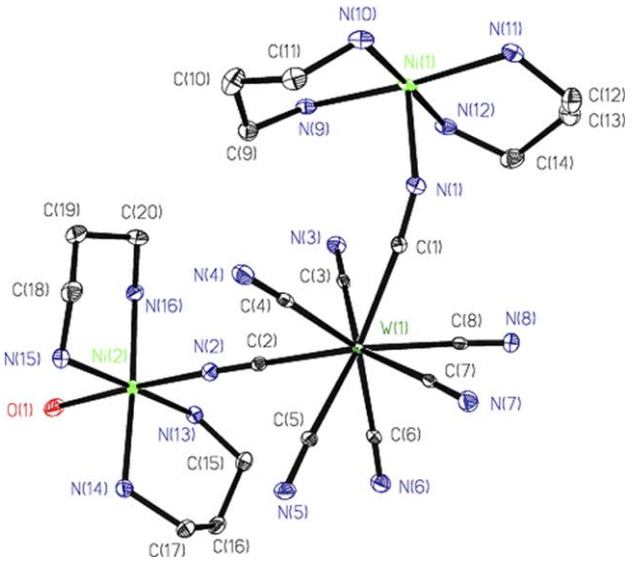


Fig. 1. X-ray structure of asymmetric unit of **3**. Hydrogen atoms are omitted for clarity and ellipsoids are at the 50% probability level.

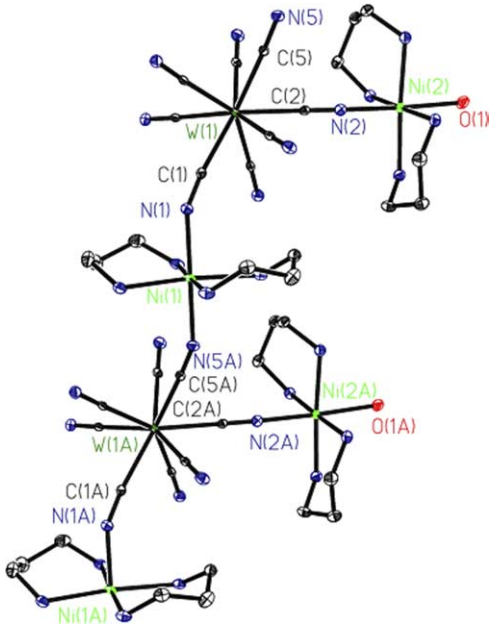


Fig. 2. X-ray structure of **3**. Hydrogen atoms and lattice water are omitted for clarity and all ellipsoids are at the 50% level.

Each three-connected $M^{IV}(CN)_8^{4-}$ center adopts a distorted square antiprismatic geometry and forms cyanide linkages to adjacent *trans*-$Ni^{II}(tn)_2(\mu\text{-}NC)_2$ and *trans*-(μ-CN) $Ni^{II}(tn)_2(OH_2)$ units. The average M^{IV}–C bond distances are 2.160(3) and 2.162(2) Å, while the C–M^{IV}–C bond angles range from 69.42(10)° to 143.58(10)° and 71.30(7)° to 144.96(8)°, for **2** and **3**, respectively (Tables 2 and 3). Cyanide nitrogen atoms N_1, N_2, and N_3 form μ-CN linkages to adjacent $Ni^{II}(tn)_2$ and $Ni^{II}(tn)_2(OH_2)$ fragments, whose M^{IV}–C bond distances range from 2.149(3) to 2.173(3) and 2.157(2) to 2.177(2) Å, for **2** and **3**, respectively. These M^{IV}–C and M^{II}–N bond distances are comparable to previously reported values.

The one-dimensional chain backbones are comprised of *trans*-$Ni^{II}(tn)_2(\mu\text{-}NC)_2$ units connected via cyanide linkages to each octacyanometalate(IV) center. The Ni–N_{tn} bond distances within each fragment range from 2.088(2) to 2.137(2) and 2.040(2) to 2.0384(18) Å while the Ni–$N_{cyanide}$ bond distances are nearly identical, ranging from 2.069(2) to 2.091(3) and 2.072(4) to 2.093(5) Å for **2** and **3**, respectively. For **2** and **3**, the nickel(II)–nitrile N–Ni(1)–N bond angles are nearly linear, 176.5(3)° and 176.5(3)° while the N_{tn}–Ni–$N_{cyanide}$ bond angles are nearly 90° (Tables 2 and 3).

Appended to each chain via a single bridging cyanide are *trans*-(μ-CN)$Ni^{II}(tn)_2(OH_2)$ units. These fragments exhibit slightly longer Ni–$N_{cyanide}$ and Ni–N_{tn} bond distances in comparison to the *trans*-$Ni^{II}(tn)_2(\mu\text{-}NC)_2$ fragments, with Ni–$N_{cyanide}$ bond distances of 2.040(2) and 2.0384(18) Å, and Ni–N_{tn} bond distances ranging from 2.088(2) to 2.137(2) and 2.0875(18) to 2.1384(18) Å, for **2** and **3**, respectively (Table 2). The Ni(1)–N(1)–C(1) and O(1)–Ni(1)–N(1) bond angles are described in Table 3.

Crystals of **4** are in the monoclinic *C*2/*m* space group (Table 1) and consist of anionic two-dimensional sheets containing an infinite array of distorted $\{Cs[(H_3N)Cu^{II}(\mu\text{-}NC)_5Mo^{IV}(CN)_3]_4\}_n^{3n-}$ box-like units (Fig. 3). The copper(II) and molybdenum(IV) centers reside in alternate corners of each box and are connected via μ-CN linkages, forming anionic

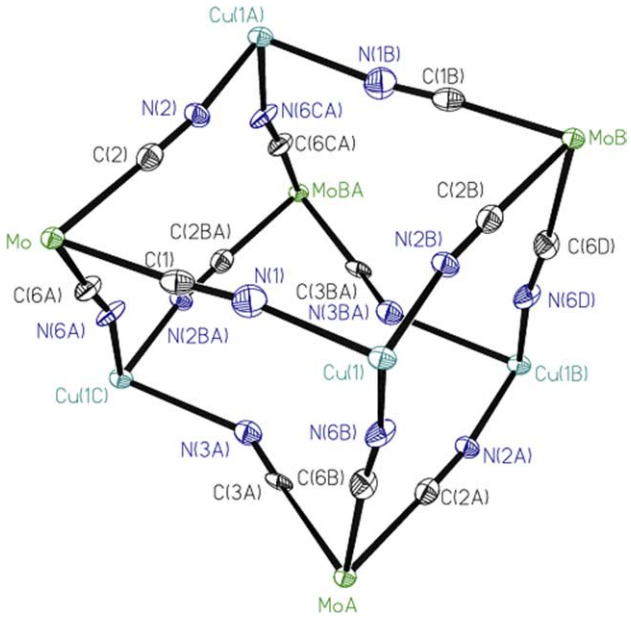


Fig. 3. X-ray structure of **4** showing distorted square portion of anionic 2-D sheet. Ellipsoids are at the 50% probability level and ammonia ligands, hydrogen atoms, cesium cations, and selected cyanides are eliminated for clarity.

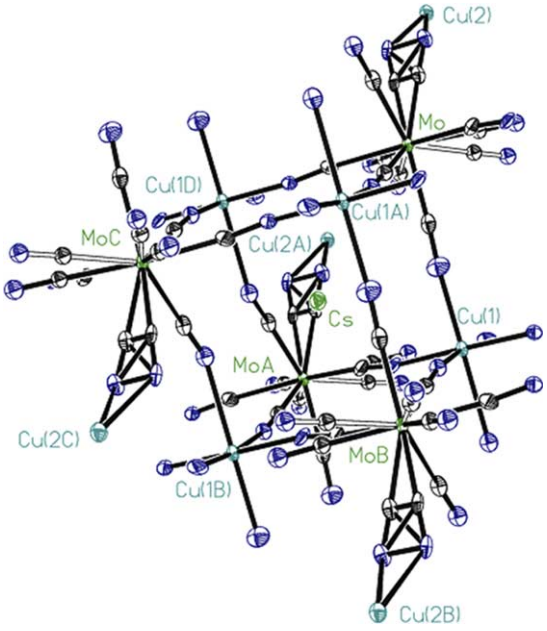


Fig. 4. X-ray structure of **4** showing distorted square portion of anionic 2-D sheet. Ellipsoids are at the 50% probability level and selected cyanide carbon and all aqua and hydrogen atoms are eliminated for clarity. Only nitrogen atoms (dark blue), carbon (black), copper (pale blue), and molybdenum (green). (For interpretation of the references to colour in this figure legend, the reader is referred to the web version of this article.)

$\{Cs[(H_3N)Cu^{II}(\mu\text{-}NC)_5Mo^{IV}(CN)_3]_4\}_n^{4n-}$ slabs (Fig. 4). The parallel slabs are connected via disordered cyanides to *trans*-$Cu^{II}(OH_2)_4(\mu\text{-}NC)_2$ units that also exhibit canting along the Jahn–Teller N–Cu–N bond axis (Fig. 5). Overall, **4** adopts an unusual and complicated three-dimensional structure of $Cs_4[Cu^{II}(OH_2)_4]_2[Cu^{II}(NH_3)]_4$-$[Mo^{IV}(CN)_8]_4 \cdot 2H_2O$ stoichiometry (Fig. 6).

For **4**, the average Mo–C bond lengths of the $Mo^{IV}(\mu\text{-}CN)_6(CN)_2^{4-}$ centers range from 2.152(12) to 2.184(16) Å (Table 2). The cyanides linked to adjacent Cu^{II} centers range from 2.152(12) (Mo–C(1)) to 2.170(12) (Mo–C(2)) while those connected to Cu^{II} centers external to the sheet range from 2.147(12) (Mo–C(4)) to 2.184(16) (Mo–C(5)). The longest Mo–C bonds are found for terminal cyanides (2.184(16) Å) while cyanides *trans*- to the ammine in $(H_3N)Cu(\mu\text{-}NC)_5$ are comparatively shorter (2.170(12) Å); the *cis*-cyanides range from 2.152(12) to 2.161(11) Å (Table 2). Overall, the $Mo^{IV}(CN)_8^{4-}$ centers exhibit Mo–C–N bond angles ranging from 72.6(5)° to 146.2(5)° and adopt a distorted square anitprismatic coordination geometry (Table 3).

The Cu–N bond distances for the highly distorted $(H_3N)Cu(\mu\text{-}NC)_5^{3-}$ units range from 1.985(8) to 2.575(9) Å for **4**. Tetragonal elongation along N(1)–Cu(1)–N(3A) bond vector in each $(H_3N)Cu(\mu\text{-}NC)_5$ fragment affords comparatively longer Cu–N bond distances, 2.257(9) (N_1–Cu_1) and 2.575(9) Å (N_{3A}–Cu_1), relative to either the Cu_1–NH_3 (1.985(8) Å, Cu_1–N_7),

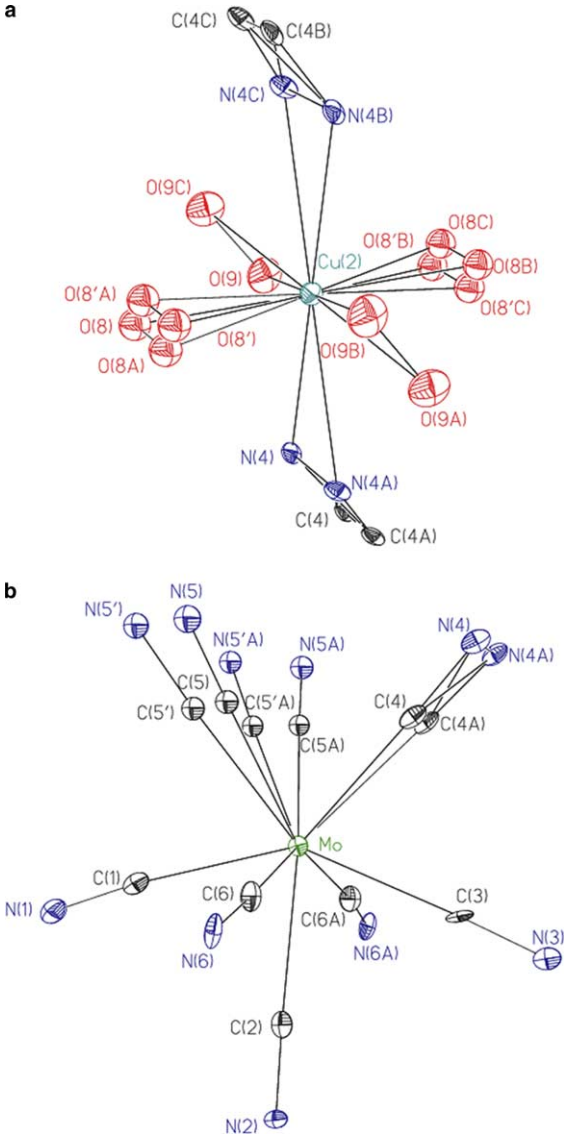


Fig. 5. X-ray structure of interlayer-bridged copper (a) and intralayer molybdenum centers (b) in **4**. Ellipsoids are at the 20% level.

or remaining cyanide linkages (ca. 2.020(10) Å ; Table 2). The N–Cu_1–N bond angles range from 90.61(17)° to 94.6(3)° (Table 3) and we conclude that the Jahn–Teller axis lies along the N(1)–Cu(1)–N(3A) bond vector.

In comparison, the *trans*-$Cu(OH_2)_4(\mu\text{-}NC)_2$ fragments connecting each sheet clearly show that the Jahn–Teller axis lies along the N(4)–Cu(2)–N(4A) vector. Rather long Cu–N bond distances (2.477(11) Å) are found between the copper and disordered cyanides with average Cu–O values of 2.04(3) Å. The copper atoms occupy crystallographically equivalent positions where the cyano and aquo ligands are disordered via canting (26.5°) along the Jahn–Teller axis (Fig. 5). Overall, incorporation of Jahn–Teller distorted copper(II) ions into **4** affords a rather complicated, unusual, and highly distorted three-dimensional structure (Fig. 6).

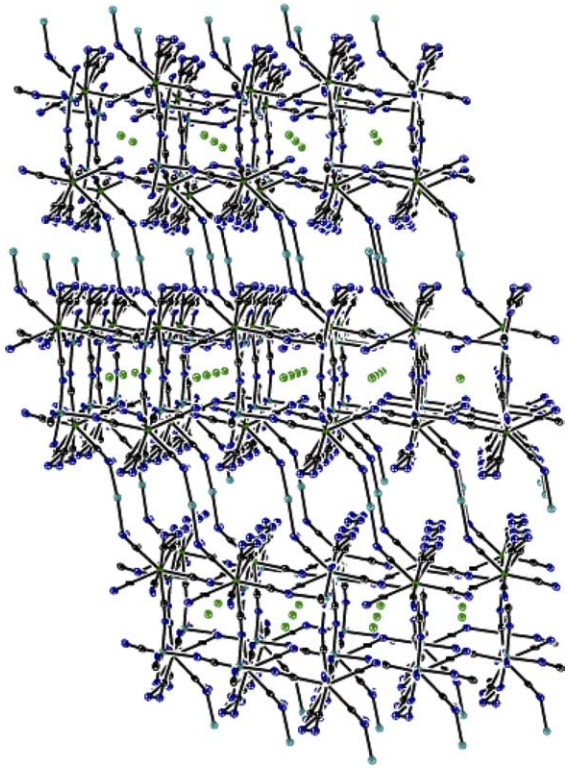


Fig. 6. X-ray structure of **4** showing connectivity of anionic 2-D sheets (center) via *trans*-(μ-CN)Cu(OH_2)$_4$(μ-NC) linkages down the *b* axis. Ellipsoids are at the 50% level and only carbon (black), cesium (green), copper (pale blue), nitrogen (blue), and molybdenum (dark green) are shown for clarity. (For interpretation of the references to colour in this figure legend, the reader is referred to the web version of this article.)

3.3. Magnetic studies

Given that each lattice contains diamagnetic centers, we did not initiate extensive magnetic studies. The room temperature effective magnetic moments (μ_{eff}) of **2**–**4** using crushed crystals indicate that the $M^{IV}(CN)_8^{4-}$ (M^{IV} = Mo, W) centers are diamagnetic and that the paramagnetism of each network is due to the divalent transition metal centers (Ni, Cu) present. The calculated μ_{eff} values expected, assuming that $g = 2$, for a 2:1 ratio of paramagnetic (M^{II}) and diamagnetic (M^{IV}) centers is 4.0 μ_B for **2** and **3**; a 6:4 ratio of Cu^{II} to Mo^{IV} centers would afford a value of 4.24 μ_B for **4**. The experimental values are close to those expected and are 4.53, 4.41, and 4.34 μ_B for **2**–**4**, respectively. Assuming that spin-orbit coupling effects are operative, then the calculated *g* values are 2.27, 2.21, and 2.05 for the Ni^{II} and Cu^{II} centers in **2**–**4**, respectively [24,35,36].

4. Conclusions

In summary, a series of one- and three-dimensional octacyanometalate(IV) networks containing 1,3-propanediamine and ammine ligands have been synthesized and characterized via structural and magnetic methods. The distorted square antiprismatic $M^{IV}(CN)_8^{4-}$ centers are diamagnetic and the paramagnetism of each network originates from the Ni^{II} and Cu^{II} centers present. The photomagnetic properties of each network will be reported in a subsequent manuscript.

5. Supplementary material

CCDC numbers 263402–263404 contain the supplementary crystallographic data for this paper. These data may be obtained free of charge from The Director, CCDC, 12 Union Road, Cambridge, CB2 1EZ, UK, fax: +44 1223 366 033, e-mail: deposit@ccdc.ac.uk or via www.ccdc.cam.ac.uk/data_request/cif.

Acknowledgements

Acknowledgment is made to the Donors of the American Chemical Society Petroleum Research Fund (PRF-38388-G3), the National Science Foundation Research Experience for Undergraduates (CHE-0097668), and the University of Kentucky Summer Faculty Research Fellowship programs for partial financial support. S.M.H. is also grateful for access to the Frederick Seitz Materials Research Laboratory magnetometer facility at the University of Illinois at Urbana-Champaign.

References

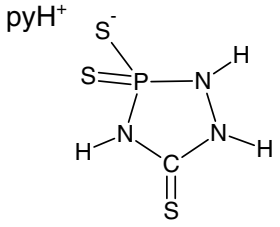
[1] J.M. Manriquez, G.T. Yee, R.S. McLean, A.J. Epstein, J.S. Miller, Science 252 (1991) 1415.
[2] S. Ferlay, T. Mallah, R. Ouahès, P. Veillet, M. Verdaguer, Nature 378 (1995) 701.
[3] W.R. Entley, G.S. Girolami, Science 268 (1995) 397.
[4] K.R. Dunbar, R.A. Heintz, Prog. Inorg. Chem. 45 (1997) 283.
[5] M. Verdaguer, A. Bleuzen, V. Marvaud, J. Vaissermann, M. Seuleiman, C. Desplanches, A. Scuiller, C. Train, R. Garde, G. Gelly, C. Lomenech, I. Rosenman, P. Veillet, C. Cartier, F. Villain, Coord. Chem. Rev. 190–192 (1999) 1023.
[6] S.M. Holmes, G.S. Girolami, J. Am. Chem. Soc. 121 (1999) 5593.
[7] Ø. Hatlevik, W.E. Buschmann, J. Zhang, J.L. Manson, J.S. Miller, Adv. Mater. 11 (1999) 914.
[8] J.J. Sokol, A.G. Hee, J.R. Long, J. Am. Chem. Soc. 124 (2002) 7656.
[9] H.J. Choi, J.J. Sokol, J.R. Long, Inorg. Chem. 43 (2004) 1606.
[10] C.P. Berlinguette, D. Vaughn, C. Cañada-Vilalta, J.R. Galán-Mascarós, K.R. Dunbar, Angew. Chem. Int. Ed. 42 (2003) 1523.
[11] (a) K.R. Dunbar, E.J. Schelter, A.V. Palii, S.M. Ostrovsky, V.Y. Mirovitskii, J.M. Hudson, M.A. Omary, S.I. Klokishner, B.S. Tsukerblat, J. Phys. Chem. A 107 (2003) 11102;
(b) E.J. Schelter, A.V. Prosvirin, W.M. Reiff, K.R. Dunbar, Angew. Chem. Int. Ed. 43 (2004) 4912;
(c) E.J. Schelter, A.V. Prosvirin, K.R. Dunbar, J. Am. Chem. Soc. 126 (2004) 15004;
(d) S. Wang, J.-J. Zuo, H.-C. Zhou, H.J. Choi, Y. Ke, J.R. Long, X.-Z. You, Angew. Chem. Int. Ed. 43 (2004) 5940;

(e) D. Li, S. Parkin, G. Wang, G.T. Yee, S.M. Holmes, Inorg. Chem. 44 (2005) 5903.
[12] (a) Z.J. Zhong, H. Seino, Y. Mizobe, M. Hidai, A. Fujishima, S. Ohkoshi, K. Hashimoto, J. Am. Chem. Soc. 122 (2000) 2952;
(b) J. Larionova, M. Gross, H.A. Pilkington, H. Stoeckli-Evans, H.U. Güdel, S. Decurtins, Angew. Chem. Int. Ed. 39 (2000) 1605;
(c) F. Bonadio, M. Gross, H. Stoeckli-Evans, S. Decurtins, Inorg. Chem. 41 (2002) 5891;
(d) M. Pilkington, S. Decurtins, Chimia 54 (2000) 563.
[13] (a) O. Sato, Acc. Chem. Res. 36 (2003) 692;
(b) Y. Arimoto, S. Ohkoshi, Z.J. Zhong, H. Seino, Y. Mizobe, K. Hashimoto, J. Am. Chem. Soc. 125 (2003) 9240;
(c) T. Yokoyama, K. Okamoto, T. Ohta, S.-I. Ohkoshi, K. Hashimoto, Phys. Rev. 65B (2001) 1;
(d) S.-I. Ohkoshi, K. Hashimoto, J. Am. Chem. Soc. 121 (1999) 10591;
(e) O. Sato, T. Iyoda, A. Fujishima, K. Hashimoto, Science 272 (1996) 704;
(f) O. Sato, Y. Einaga, T. Iyoda, A. Fujishima, K. Hashimoto, Inorg. Chem. 38 (1999) 4405;
(g) N. Shimamoto, S.-I. Ohkoshi, O. Sato, K. Hashimoto, Inorg. Chem. 41 (2002) 678;
(h) A. Bleuzen, C. Lomenech, V. Escax, F. Villain, F. Varret, C. Cartier dit Moulin, M. Verdaguer, J. Am. Chem. Soc. 122 (2000) 6648;
(i) C. Cartier dit Moulin, F. Villain, A. Bleuzen, M. Arrio, P. Sainctavit, C. Lomenech, V. Escax, F. Baudelet, E. Dartyge, M. Verdaguer, J. Am. Chem. Soc. 122 (2000) 6653;
(j) S.-I. Ohkoshi, S. Yorozu, O. Sato, T. Iyoda, A. Fujishima, K. Hashimoto, Appl. Phys. Lett. 70 (1997) 1040;
(k) S.-I. Ohkoshi, Y. Einaga, A. Fujishima, K. Hashimoto, J. Electroanal. Chem. 473 (1999) 245;
(l) S.-I. Ohkoshi, M. Mizuno, G. Hung, K. Hashimoto, J. Phys. Chem. 40 (2000) 9365;
(m) Z.-Z. Gu, O. Sato, T. Iyoda, K. Hashimoto, A. Fujishima, J. Phys. Chem. 100 (1996) 18289;
(n) Z.-Z. Gu, O. Sato, T. Iyoda, K. Hashimoto, A. Fujishima, Chem. Mater. 9 (1997) 1092;
(o) S.-I. Ohkoshi, K. Hashimoto, J. Photochem. Photobiol. C: Photochem. Rev. 2 (2001) 71;
(p) S.-I. Ohkoshi, N. Machida, Z.J. Zhong, K. Hasimoto, Synth. Met. 122 (2001) 523;
(q) G. Rombaut, M. Verelst, S. Golhen, L. Ouahab, C. Mathonière, O. Kahn, Inorg. Chem. 40 (2001) 1151.
[14] (a) D. Li, L. Zheng, X. Wang, J. Huang, S. Gao, W. Tang, Chem. Mater. 15 (2003) 2094;
(b) D. Li, T. Okamura, W. Sun, N. Ueyama, W. Tang, Cryst. Struct. Commun. C58 (2002) m280;
(c) D. Li, D. Yang, S. Li, W. Tang, Inorg. Chem. Commun. 5 (2002) 791;
(d) R. Podgajny, Y. Dromzée, K. Kruczała, B. Sieklucka, Polyhedron 20 (2001) 685;
(e) F. Chang, H.-L. Sun, H.-Z. Kou, S. Gao, Inorg. Chem. Commun. 5 (2002) 660;
(f) W. Meske, D.Z. Babel, Anorg. Allg. Chem. 625 (1999) 51;
(g) G.F. McKnight, G.P. Haight, Inorg. Chem. 12 (1973) 3007;
(h) W.U. Malik, S.I. Ali, Bull. Chem. Soc. Jpn. (1961) 1306;
(i) W.U. Malik, S.I. Ali, Bull. Chem. Soc. Jpn. (1961) 1310;
(j) W.R. Bucknall, W. Wardlaw, J. Chem. Soc. (1927) 2981;
(k) J.M. Herrera, D. Armentano, G. de Munno, F. Lloret, M. Julve, M. Verdaguer, New J. Chem. 27 (2003) 128;
(l) J.M. Herrera, A. Bleuzen, Y. Dromzée, M. Julve, F. Lloret, M. Verdaguer, Inorg. Chem. 42 (2003) 7052;
(m) S. Willemin, J. Larionova, R. Clérac, B. Donnadieu, B. Henner, X.F. Le Goff, C. Guérin, Eur. J. Inorg. Chem. (2003) 1866.
[15] (a) A.K. Sra, G. Rombaut, F. Lahitête, S. Golhen, L. Ouahab, C. Mathonière, J.V. Yakhmi, O. Kahn, New J. Chem. 24 (2000) 871;
(b) R. Billing, A.J. Vogler, J. Photochem. Photobiol. A: Chem. 103 (1997) 239;
(c) S.I. Ali, K. Majid, Thermochim. Acta 317 (1998) 141;
(d) A.K. Sra, M. Andruh, O. Kahn, S. Golhen, L. Ouahab, J.V. Yakhmi, Angew. Chem. Int. Ed. 38 (1999) 2606;
(e) G. Rombaut, S. Golhen, L. Ouahab, C. Mathonière, O. Kahn, J. Chem. Soc., Dalton Trans. (2000) 3609.
[16] (a) A. Yuan, J. Zou, B. Li, Z. Zha, C. Duan, Y. Liu, Z. Xu, S. Keizer, Chem. Commun. (2000) 1297;
(b) M. Ohba, N. Fukita, H. kawa, Dalton Trans. (1997) 1733;
(c) H.-Z. Kou, W. Bu, D. Liao, Z. Jiang, S. Yan, Y. Fan, G. Wang, Dalton Trans. (1998) 4161;
(d) M. Ohba, N. Usuki, N. Fukita, H. Kawa, Inorg. Chem. 37 (1998) 3349;
(e) N. Fukita, M. Ohba, H. kawa, K. Matsuda, H. Iwamura, Inorg. Chem. 37 (1998) 842;
(f) S. Zhang, D. Fu, W. Sun, Z. Hu, K. Yu, W. Tang, Inorg. Chem. 39 (2000) 1142;
(g) N. Usuki, M. Yamada, M. Ohba, H. kawa, J. Solid State Chem. 159 (2001) 328;
(h) M. Ohba, H. kawa, N. Fukita, Y. Mashimoto, J. Am. Chem. Soc. 119 (1997) 1011;
(i) F. Thétiot, S. Triki, J.S. Pala, New J. Chem. 26 (2002) 196;
(j) H.-Z. Kou, J.-K. Tang, D.-Z. Liao, S. Gao, P. Cheng, Z.-H. Jiang, S.-P. Yan, G.-L. Wang, B. Chansou, J. Tuchagues, Inorg. Chem. 40 (2001) 4839.
[17] B. Sieklucka, J. Szklarzewicz, T.J. Kemp, W. Errington, Inorg. Chem. 39 (2000) 5156.
[18] (a) R. Kania, K. Lewinski, B. Sieklucka, Dalton Trans. (2003) 1033;
(b) J.M. Herrera, V. Marvaud, M. Verdaguer, J. Marrot, M. Kalisz, C. Mathonière, Angew. Chem. Int. Ed. 43 (2004) 5467;
(c) J.R. Withers, C. Ruschmann, P. Bojang, S. Parkin, S.M. Holmes, Inorg. Chem. 44 (2005) 532.
[19] J.G. Leipoldt, L.D. Bok, P.J. Cilliers, Z. Anorg. Allg. Chem. 409 (1974) 343.
[20] N.H. Furman, C.O. Miller, P.G. Arvan, L.F. Audrieth, Inorg. Synth. 3 (1950) 160.
[21] L.D. Bok, J.G. Leipoldt, S.S. Basson, Z. Anorg. Allg. Chem. 415 (1975) 81.
[22] S.M. Holmes, S.G. McKinley, G.S. Girolami, P.S. Szalay, K.R. Dunbar, Inorg. Synth. 33 (2002) 91.
[23] B. Saha, M. Hung, D.M. Stanbury, Inorg. Chem. 41 (2002) 5538.
[24] (a) R.L. Carlin, Magnetochemistry, Springer-Verlag, New York, 1986;
(b) O. Kahn, Molecular Magnetism, VCH, New York, 1993;
(c) E.A. Boudreaux, N. Cressy, H.F. Hameka, L.N. Mulay, Theory and Applications of Molecular Diamagnetism, Wiley, New York, 1976.
[25] Z. Otwinowski, W. Minor, Methods Enzymol. 276 (1997) 307.
[26] (a) G.M. Sheldrick, SADABS – An Empirical Absorption Correction Program, Bruker Analytical X-Ray Systems, Madison, Wisconsin, 1996;
(b) G.M. Sheldrick, SHELX-97. Programs for Crystal Structure Solution and Refinement, University of Gottingen, Germany, 1997.
[27] International Tables for Crystallography, vol. C, Kluwer Academic Publishers, Dordrecht, The Netherlands, 1992.
[28] (a) M. Bogdanov, R. Grybos, A. Samotus, K. Bogolitsyn, Transit. Met. Chem., Dordrecht 18 (1993) 59;
(b) C.R. Dennis, S.S. Basson, J.G. Leipoldt, Polyhedron 2 (1983) 1357;
(c) D. Li, S. Gao, L. Zheng, K. Yu, W. Tang, New. J. Chem. 26 (2002) 1190;

(d) A. Marchaj, A. Plesinski, Z. Stasicka, Rocz. Chem. 50 (1976) 1239.
[29] (a) W.L. Waltz, A.W. Adamson, P.D. Fleischauer, J. Am. Chem. Soc. 89 (1967) 3923;
(b) K.R. Butter, T.J. Kemp, B. Sieklucka, A. Samotus Soc., J. Chem. Soc., Dalton Trans. (1986) 1217;
(c) S. Zofia, B. Hanna, Rocz. Chem. 48 (1974) 389;
(d) S.I. Zofia, Rocz. Chem. 47 (1973) 1993;
(e) G.W. Gray, J.T. Spence, Inorg. Chem. 10 (1971) 2751.
[30] K. Nakamoto, Infrared and Raman Spectra of Inorganic and Coordination Compounds, 5th ed., Wiley, New York, 1997, Part B, pp. 54–58 and 105–116.
[31] (a) T.V. Long, G.A. Vernon, J. Am. Chem. Soc. 93 (1971) 1919;
(b) K.O. Hartman, F.A. Miller, Spectrochim. Acta 24A (1968) 669;
(c) E.G. Brame, F.A. Johnson, E.M. Larsen, V.W. Meloche, J. Inorg. Nucl. Chem. 2 (1958) 99.
[32] (a) Y. Arimoto, S. Ohkoshi, Z.J. Zhong, H. Seino, Y. Mizobe, K. Hashimoto, Chem. Lett. (2002) 832;
(b) Y. Song, S. Ohkoshi, Y. Arimoto, H. Seino, Y. Mizobe, K. Hashimoto, Inorg. Chem. 42 (2003) 1848;
(c) Y. Arimoto, S.-I. Ohkoshi, Z.J. Zhong, H. Seino, Y. Mizobe, K. Hashimoto, J. Am. Chem. Soc. 125 (2003) 9240;
(d) Z.J. Zhong, H. Seino, Y. Mizobe, M. Hidai, M. Verdaguer, S.-I. Ohkoshi, K. Hashimoto, Inorg. Chem. 39 (2000) 5095;
(e) T. Korzeniak, R. Podgajny, N.W. Alcock, K. Lewiński, M. Bałanda, T. Wasiutyński, B. Sieklucka, Polyhedron 22 (2003) 2183;
(f) D. Li, S. Gao, L. Zheng, W. Tang, J. Chem. Soc., Dalton Trans. (2002) 2805;
(g) J.M. Herrera, A. Bleuzen, Y. Dromzee, M. Julve, F. Lloret, M. Verdaguer, Inorg. Chem. 42 (2003) 7052;
(h) D. Li, L. Zheng, Y. Zhang, S. Gao, W. Tang, Inorg. Chem. 42 (2003) 8203;
(i) D. Li, S. Gao, L. Zheng, W. Sun, T. Okamura, N. Ueyama, W. Tang, New J. Chem. 26 (2002) 485.
[33] T. Kashiwagi, S.-I. Ohkoshi, H. Seino, Y. Mizobe, K. Hashimoto, J. Am. Chem. Soc. 126 (2004) 5024.
[34] (a) C.A. Bignozzi, R. Argazzi, J.R. Schoonover, K.C. Gordon, R.B. Dyer, F. Scandola, Inorg. Chem. 31 (1992) 5260;
(b) M.A. Watzky, J.F. Endicott, X. Song, Y. Lei, A. Mccatangay, Inorg. Chem. 35 (1996) 3463;
(c) K.F. Purcell, S.M. Yeh, J.S. Eck, Inorg. Chem. 16 (1977) 1708;
(d) M.Y. Darensbourg, H.L.C. Barros, Inorg. Chem. 18 (1979) 3286;
(e) M.J. Scott, R.H. Holm, J. Am. Chem. Soc. 116 (1994) 11357;
(f) H. Vahrenkamp, A. Geiss, G.N. Richardson Soc., J. Chem. Soc., Dalton Trans. (1997) 3643;
(g) B.S. Lim, R.H. Holm, Inorg. Chem. 37 (1998) 4898;
(h) G.N. Richardson, U. Brand, H. Vahrenkamp, Inorg. Chem. 38 (1999) 3070;
(i) A. Geiss, H. Vahrenkamp, Eur. J. Inorg. Chem. (1999) 1793;
(j) A. Geiss, H. Vahrenkamp, Inorg. Chem. 39 (2000) 4029;
(k) R. Podgajny, C. Desplanches, B. Sieklucka,B., R. Sessoli, V. Villar, C. Paulsen, W. Wernsdorfer, Y. Dromzée, M. Verdaguer, Inorg. Chem. 41 (2002) 1323;
(l) C.A. Bignozzi, F. Scand ola, Inorg. Chem. 23 (1984) 1540;
(m) K.F. Purcell, J. Am. Chem. Soc. 89 (1967) 247;
(n) K.F. Purcell, Inorg. Chem. 89 (1967) 6139.
[35] (a) W.K. Robinson, S.A. Friedberg, Phys. Rev. 117 (1960) 402;
(b) J.L. Manson, C.R. Kmety, Q.-Z. Huang, J.W. Lynn, G.M. Bendele, S. Pagola, P.W. Stephens, L.M. Liable-Sands, A.L. Rheingold, A.J. Epstein, J.S. Miller, Chem. Mater. 10 (1998) 2252;
(c) L.G. Beauvais, J.R. Long, J. Am. Chem. Soc. 124 (2002) 12096.
[36] (a) M.-U. Haque, C.N. Caughlan, K. Emerson, Inorg. Chem. 9 (1970) 2421;
(b) J.E. Enemark, M.S. Quinby, L.L. Reed, M.J. Steuck, K.K. Walthers, Inorg. Chem. 9 (1970) 2397;
(c) M. Murmoo, C.M. Kepert, New J. Chem. 22 (1998) 1515;
(d) J.L. Manson, A.M. Arif, J.S. Miller, J. Mater. Chem. 9 (1999) 979.

The composition of heterocyclic products was dependent on a number of factors. If triethylamine was present (as an acceptor of released HCl), the four-membered heterocyclic compounds of diazadiphosphetidine type with P–N–P–N rings were formed, while the compounds with five-membered P–N–N–C–S heterocycles were obtained in the reactions that were carried out in an absence of the HCl acceptor. It is worth to mention the molecular structure of the reaction product for its unusual structure where a three-coordinate positively charged carbon atom is present in the heterocycle. This positive charge is compensated by a negative charge on the exocyclic sulfur atoms.

A planar heterocyclic compound with the five membered P–N–C–N–N cycle, pyridinium salt of 3-sulfido-3,5-dithioxo-1,2,4,3λ^5-triazaphospholidine, was the product of the reaction between **I** and non-subsituted thiosemicarbazide [10] carried out in acetonitrile in the presence of pyridine.



This article deals with the study of reactions of chlorodithiophosphoric acid pyridiniumbetaine **I** (py · PS_2Cl) with 4-methyl- and 4-ethylthiosemicarbazide that can be considered potential four-functional nucleophiles. The formation of new heterocyclic compounds was expected.

2. Experimental

All reactions were performed under dry nitrogen in anhydrous solvents using conventional Schlenk techniques with the exception of preparations of thiosemicarbazide derivatives. All chemicals were used as supplied (Aldrich, Lachema). Solvents were dried by standard methods and were distilled prior to their use [11]. Chlorodithiophosphoric acid pyridiniumbetaine (**I**) [12] and thiosemicarbazide derivatives [13] were prepared according to the known procedures. The ^{31}P NMR spectra were measured in acetonitrile or pyridine using a Bruker AVANCE DRX 300 instrument and were referenced to H_3PO_4 (85%). The IR spectra were recorded in Nujol mulls on a Bruker IFS 28 spectrometer. The Raman spectra of solid samples were collected in Raman capillaries on a Bruker Equinox X55/S instrument (see Table 1).

Diffraction data were collected on a KUMA KM-4 κ-axis diffractometer equipped with CCD detector with graphite-monochromated Mo Kα radiation ($\lambda = 0.71073$ Å). Because of the small absorption coefficients the absorption correction was neglected. All the structures were solved by direct methods and refined by full-matrix least-squares methods using anisotropic thermal parameters for the non-hydrogen atoms. The hydrogen atoms on N1 and N2 were refined isotropically; all other hydrogens were placed in calculated idealized positions and refined as riding. The software packages used were: XCALIBUR CCD system [14] for the data collection/reduction, and SHELXTL [15] for the structure solution, refinement, and drawing preparation (thermal ellipsoids are drawn at the 50% probability level). Lattice parameters and other crystallographic data for **II** and **III** are given in Table 2, selected bond lengths and angles in Table 3, and hydrogen bonding parameters in Table 4. The molecular structures are drawn in Figs. 1 and 2.

2.1. Reaction of py · PS_2Cl (*I*) with thiosemicarbazide derivatives

The solution of **I** was prepared in acetonitrile. Pyridine and the solid thiosemicarbazide derivative were added to obtain a 1:1:1 molar ratio of components (Table 1). The reaction mixture was stirred on a magnetic stirrer at ambient temperature for 48 h. The extent of the reaction was followed by ^{31}P NMR spectroscopy. A white solid product was precipitated in the course of the reaction. It was filtered off by a Schlenk frit and dried under vacuum. Further portions of the product were obtained after partially concentrating the filtrates.

2.2. Pyridinium salt of 4-methyl-3-sulfido-3, 5-dithioxo-1,2,4,3λ^5-triazaphospholidine (*II*)

White powder, yield: 93% (with respect to **I**). ^{31}P NMR (acetonitrile): δ 112.8 ppm, quartet, ^3J[P–H] = 8.63 Hz. IR: 3211 w, 3125 m, 3092 m, 3061 m, 3042 m, 2725 m, 1633 m, 1603 m, 1523 s, 1478 vs, 1457 vs, 1351 m, 1273

Table 1
Amounts of starting compounds and solvents used in the reactions

Product	4-Alkyl-thiosemicarbazide			py · PS_2Cl (g)	Acetonitrile (ml)	Pyridine (ml)	Yield (%)
		(g)	(mmol)				
II	methyl	0.50	4.76	0.997	40	0.39	93
III	ethyl	0.50	4.19	0.879	40	0.34	92

Table 2
Basic crystallographic data and refinement parameters for compounds **II** and **III**

	II	**III**
Empirical formula	$[C_2H_5N_3PS_3]Cl \cdot 2C_5H_6N$	$[C_3H_7N_3PS_3]Cl \cdot 2C_5H_6N$
Formula weight	393.91	407.93
Temperature (K)	120(2)	120(2)
Crystal system	monoclinic	triclinic
Space group	$P2_1/c$	$P\bar{1}$
a (Å)	14.040(3)	9.177(2)
b (Å)	7.028(1)	10.439(3)
c (Å)	18.536(4)	11.030(3)
α (°)	90	108.67(2)
β (°)	102.99(3)	95.33(2)
γ (°)	90	103.10(2)
Volume (Å^3)	1784.8(6)	959.2(4)
Z	4	2
Calculated density (Mg/m^3)	1.466	0.975
μ (mm^{-1})	0.657	0.587
Crystal size (mm)	$0.50 \times 0.40 \times 0.40$	$0.50 \times 0.50 \times 0.30$
θ Range (°)	3.26–25.00	3.14–25.00
Number of reflections	10 535	6105
Independent data	3140	3277
Final R indices $[I > 2\sigma(I)]$	0.0384, 0.0911	0.0314, 0.0842
Final R indices [all data]	0.0411, 0.0926	0.0348, 0.0876
$\Delta\rho_{max}/\Delta\rho_{min}$ (e Å^{-3})	0.617 and −0.682	0.724 and −0.792

s, 1189 m, 1112 m, 1054 s, 903 m, 831 m, 761m, 749 s, 718 s, 675 vs, 607 m, 586 m, 517 s. RA: 83 vs, 93 vs, 192 m, 352 w, 397 m, 401 m, 515 w, 583 s, 609 m, 636 m, 827 w, 1005 vs,

Table 3
Selected bond lengths (Å) and angles (°) for compounds **II** and **III**

	II	**III**
P(1)–S(1)	1.956(1)	1.959(1)
P(1)–S(2)	1.958(1)	1.968(1)
P(1)–N(1)	1.707(2)	1.711(2)
P(1)–N(3)	1.741(2)	1.738(2)
N(1)–N(2)	1.424(3)	1.433(2)
N(2)–C(1)	1.356(3)	1.362(3)
C(1)–N(3)	1.352(3)	1.348(3)
C(1)–S(3)	1.683(2)	1.686(2)
N(3)–C(2)	1.458(3)	1.469(3)
S(1)–P(1)–S(2)	118.5(1)	118.7(1)
S(1)–P(1)–N(1)	112.1(1)	111.2(1)
S(1)–P(1)–N(3)	113.1(1)	111.8(1)
S(2)–P(1)–N(1)	112.1(1)	111.8(1)
S(2)–P(1)–N(3)	107.6(1)	109.6(1)
N(3)–P(1)–N(1)	89.9(1)	90.1(1)
P(1)–N(1)–N(2)	107.5(1)	108.8(1)
N(1)–N(2)–C(1)	114.6(2)	114.1(2)
N(2)–C(1)–S(3)	122.7(2)	122.7(2)
N(3)–C(1)–S(3)	126.3(2)	125.8(2)
C(1)–N(3)–C(2)	122.7(2)	123.4(2)
P(1)–N(3)–C(2)	122.7(2)	123.3(1)
P(1)–N(3)–C(1)	111.0(2)	112.7(1)

Table 4
Hydrogen bonding parameters (Å, °) for compounds **II** and **III**

D–H···A	D–H	H···A	D···A	D–H···A
II				
N(21)–H(21A)···S(3)[a]	0.88	2.40	3.247(2)	160.9
N(11)–H(11A)···Cl(1)[b]	0.88	2.20	3.063(2)	165.4
N(2)–H(2N)···Cl(1)[c]	0.80(3)	2.45(3)	3.247(2)	177(2)
N(1)–H(1N)···Cl(1)[d]	0.78(3)	2.72(3)	3.353(2)	140(2)
III				
N(2)–H(2N)···Cl(1)	0.86(2)	2.35(2)	3.191(2)	166(2)
N(1)–H(1N)···Cl(1)[a]	0.78(2)	2.56(2)	3.311(2)	163(2)
N(21)–H(21A)···Cl(1)[b]	0.88	2.19	3.072(2)	175.7
N(11)–H(11A)···S(3)	0.88	2.51	3.260(2)	143.5
N(11)–H(11A)···Cl(1)	0.88	2.98	3.451(2)	115.5

Symmetry transformations used to generate equivalent atoms (**II**): [a] $-x+1, -y, -z+2$; [b] $x, y+1, z$; [c] $x, -y-1/2, z+1/2$; [d] $-x+1, y+1/2, -z+3/2$.
Symmetry transformations used to generate equivalent atoms (**III**): [a] $-x, -y+1, -z+1$; [b] $x-1, y, z$.

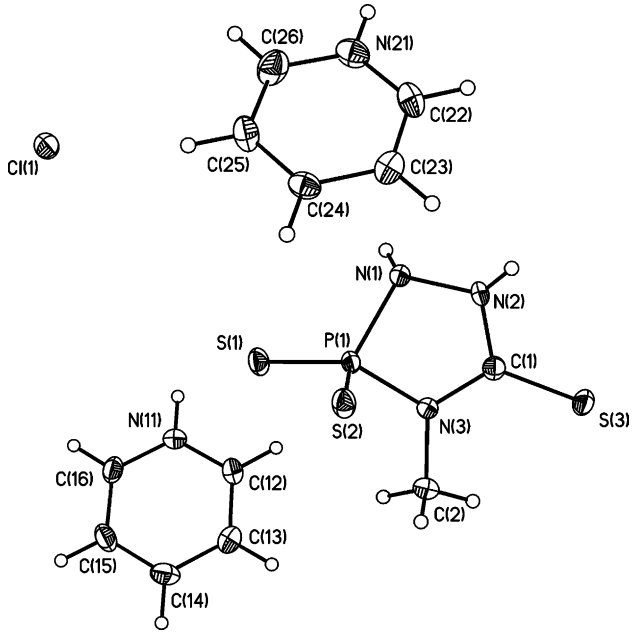


Fig. 1. The ORTEP drawing of **II**, showing the atom numbering scheme.

1024 m, 1054 w, 1187 m, 1195 m, 1632 w, 3025 w, 3069 m, 3083 m.

*2.3. Pyridinium salt of 4-ethyl-3-sulfido-3, 5-dithioxo-1,2,4,3λ^5-triazaphospholidine (**III**)*

White powder, yield: 92% (with respect to **I**). ^{31}P NMR (acetonitrile): δ 111.0 ppm, triplet, ^3J[P–H] = 11.1 Hz. IR: 3231 w, 3207 w, 3152 m, 3128 m, 3096 m, 3082 m, 3057 m, 3039 m, 3024 m, 3004 m, 2739 m, 1632 m, 1606 m, 1532 s, 1485 s, 1457 vs, 1448 vs, 1378 s, 1339 m, 1315 m, 1252 m, 1178 m, 1161 m,

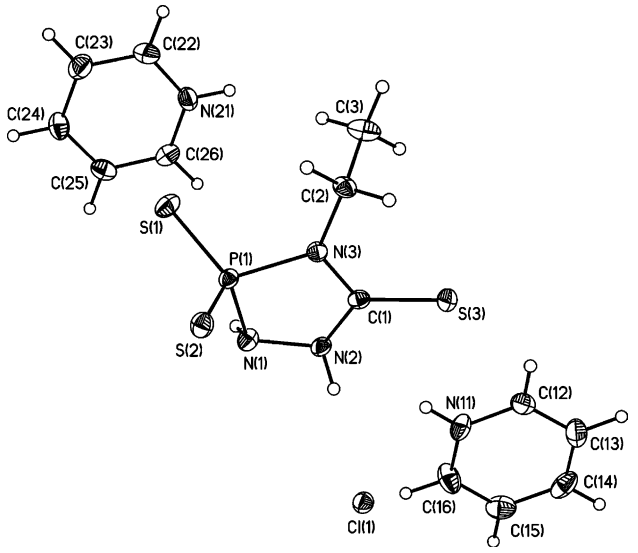


Fig. 2. The ORTEP drawing of **III**, showing the atom numbering scheme.

1125 m, 1044 m, 911 m, 846 w, 770 m, 746 s, 725 s, 714 s, 681 vs, 674 vs, 609 m, 592 m, 513 m, 438 w. RA: 84 vs, 95 vs, 221 m, 350 w, 397 s, 512 m, 588 m, 609 m, 637 m, 849 w, 1005 vs, 1026 m, 1157 w, 1192 m, 1458 w, 1633 w, 2932 m, 2958 w, 3069 m, 3083 m.

3. Discussion

The formation of the heterocyclic compounds **II** and **III** in the course of reactions between **I** and monosubstituted thiosemicarbazide derivatives (R = methyl, ethyl) is described in Eq. (1). Asimilar mechanism was found when the reaction of **I** with non-substituted thiosemicarbazide was studied [10]. The ^{31}P NMR spectra of products **II** and **III** were very simple. Only one signal was observed, which was split to the corresponding multiplet by the coupling between phosphorus and hydrogen nuclei of the organic moiety. No further interactions between phosphorus and nitrogen atoms or N–H protons were observed in the NMR spectra.

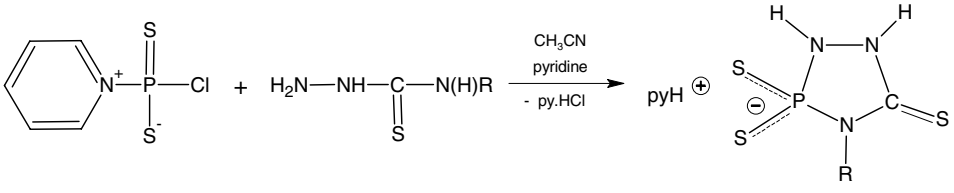
Many absorption bands above 3000 cm^{-1} were present in the IR spectra of **II** and **III**. These signals belong to the C–H bonds in the pyridinium cation. The bands above 3200 cm^{-1} can be ascribed to the N–H vibrations. Deformation vibrations of **N**–H groups (nitrogen atoms are present in the P–N–C–**N**–**N** cycle) were found at 1523 and 1532 cm^{-1} for **II** and **III**. In both cases the bands at 749 and 718 cm^{-1} (compound **II**) and 746 and 714 cm^{-1} (compound **III**) belong to P–S vibrations (ν_s, ν_{as}) in PS_2 groups, signals at 1480 cm^{-1} (1478 cm^{-1} for **II**, 1485 cm^{-1} for **III**) correspond to deformation vibrations of methyl groups.

Molecular structures of **II** and **III** were definitely confirmed by the X-ray diffraction analysis (Figs. 1 and 2). Single crystals of **II** and **III** were grown from concentrated acetonitrile solutions at room temperature over a few days. Pyridinium chloride (a by-product) was found in the crystal lattice in both cases.

The crystals of **II** are monoclinic (space group $P2_1/c$), **III** crystallizes as triclinic (space group $P\bar{1}$). Nevertheless, the molecular structures of **II** and **III** are very similar and can be compared to the structure of 3-sulfido-3,5-dithioxo-1,2,4,3λ^5-triazaphospholidine pyridinium salt **IV** [10], containing an analogous non-substituted P–N–C–N–N cycle. The five-membered rings in compounds **II**–**IV** show different degree of deviation from planarity. The ring in **IV** is the most planar (the r.m.s. deviation from the P(1)–N(1)–N(2)–C(1)–N(3) plane is 0.0400 Å), the five-membered rings of **II** and **III** are remarkably more distorted (r.m.s. deviations 0.1126 Å for **II** and 0.0795 Å for **III**).

The presence of pyridinium chloride in the crystal lattices of both **II** and **III** results in two kinds of intermolecular interactions (Figs. 3 and 4). First, the hydrogen bonding between the hydrogen atoms of N–H groups and chlorine atoms, and second, the interaction of exocyclic S(3) atom with hydrogen atom of the pyridinium cation. The hydrogen bonding parameters are summarized in Table 4.

The substitution in the position 4 led to changes in bond lengths and angles when compared with the non-substituted P–N–C–N–N cycle in **IV** [10]. With the



R= methyl (**II**)
R= ethyl (**III**)
R= H (**IV**), ref [10]

(1)

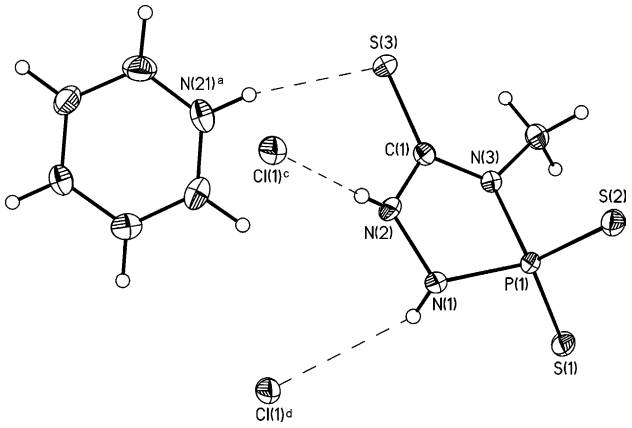


Fig. 3. H-bonding in the crystal structure of **II**. For symmetry transformations see Table 4.

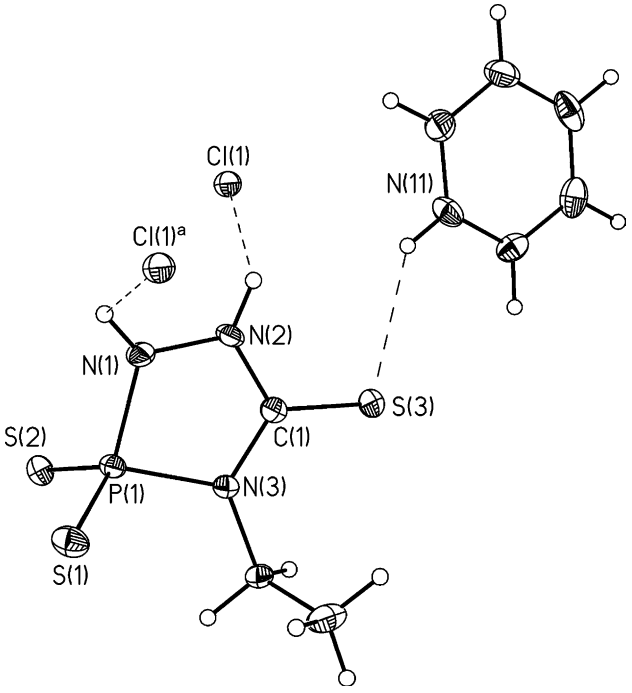


Fig. 4. H-bonding in the crystal structure of **III**. For symmetry transformations see Table 4.

exception of the N(3)–C(1) bonding distance, the elongation of practically all bonds was observed. Especially the extension of P(1)–N(3) from 1.699(2) Å in **IV** to 1.741(2) Å in **II**, and 1.738(2) Å in **III**, respectively, can be considered very significant. Two bond angles are contracted in the substituted cycles, namely P(1)–N(3)–C(1) (115.2(1)° in **IV**), and P(1)–N(1)–N(2) (110.1(1)° in **IV**). All other internal bond angles are slightly greater. As a result of the above mentioned changes, the size of the substituted rings increased.

The C(1)–S(3) lengths are practically identical in both **II** and **III**. The value of this parameter argues for a double bond character of this interaction (C=S 1.676 Å [10], 1.697 Å [16], 1.66–1.68 Å [17]). The lengths of both P–S bonds in **II** are very similar, which is in agreement with our conception of the delocalization of the negative charge. However, the P–S bond lengths in **III** differ slightly more (about 0.01 Å). Thus we can say that the negative charge is more localized on the S(2) atom, which is accordingly more distant from the phosphorus. No intermolecular interactions between the sulfur atoms bonded to phosphorus and hydrogens of pyridinium cation were observed.

To conclude, we have prepared and structurally characterized two anionic heterocyclic rings. We have found that the substitution in the rings is accompanied by variations in the internal bonding parameters as well as in the overall conformation of the cycles. However, because of the numerous intermolecular contacts in the solid phase, it is very uncertain to attribute the deformations within the cycles exclusively to the influence of the substituents. The preparation of the crystals without strongly interacting by-products (pyridinium chloride) or theoretical calculations on our derivatives would be helpful in better understanding of bonding in these interesting main-group heterocycles.

4. Supplementary material

Crystallographic data for the structural analysis have been deposited with the Cambridge Crystallographic Data Centre. Copies are available from The Director, CCDC, 12 Union Road, Cambridge CB2 1EZ, UK, fax: +44 1223 336 033, e-mail: deposit@ccdc.cam.ac.uk, or on the web http://www.ccdc.cam.ac.uk on request, quoting CCDC Nos. 261275 and 261276 for compounds **II** and **III**.

Acknowledgements

This work was supported by the FRVŠ Grant No. 576/2004, Ministry of Education, Czech Republic. We are grateful to Pavel Pazdera for valuable discussion.

References

[1] Ch. Donath, M. Meisel, K.-H. Jost, K.K. Palkina, S.I. Maksimova, N.T. Tchibiskova, Z. Naturforsch. 41b (1986) 1201.
[2] Ch. Donath, B. Wallis, M. Meisel, P. Liebnitz, Z. Anorg. Allg. Chem. 576 (1989) 33.
[3] G. Ohms, J. Zessin, Z. Žák, Phosphorus, Sulfur Silicon 113 (1996) 107.
[4] Ch. Donath, M. Meisel, Z. Anorg. Allg. Chem. 549 (1987) 46.
[5] M. Meisel, Ch. Donath, Phosphorus Sulfur 18 (1983) 159.
[6] M. Meisel, Dissertation, Berlin, 1986.
[7] V. Novoměstská, J. Marek, J. Příhoda, Polyhedron 18 (1999) 2723.
[8] M. Meisel, Ch. Donath, Phosphorus, Sulfur Silicon 64 (1992) 63.

[9] M. Janča, M. Nečas, Z. Žák, J. Příhoda, Polyhedron 20 (2001) 2823.
[10] M. Janča, Dissertation, Masaryk University Brno, 2002.
[11] D.D. Perrin, W.L.F. Armarego, Purification of Laboratory Chemicals, Pergamon Press, Oxford, 1988.
[12] M. Meisel, H. Grunze, Z. Anorg. Allg. Chem. 360 (1968) 277.
[13] K.A. Jensen, U. Anthoni, B. Kägi, Ch. Larsen, C.T. Pedersen, Acta Chem. Scand. 22 (1968) 1.
[14] Oxford Diffraction Ltd., XCALIBUR CCD System, CrysAlis Software System, Version 1.168. Oxford, England, 2001.
[15] Bruker, SHELXTL, Version 5.10, Bruker AXS Inc., Madison, WI, USA, 1997.
[16] E.J. Valente, J.D. Zubkowsky, A. Jabalameli, S. Mazhari, R. Venkatraman, R.H. Sullivan, J. Chem. Crystallogr. 28 (1998) 27.
[17] A.J.C. Wilson (Ed.), International Tables for X-ray Crystallography, vol. C, Kluwer Academic, Dordrecht, 1995, p. 685.

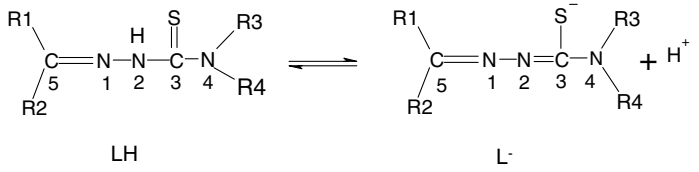


Fig. 1. Protonated and deprotonated forms of the thiosemicarbazone ligands.

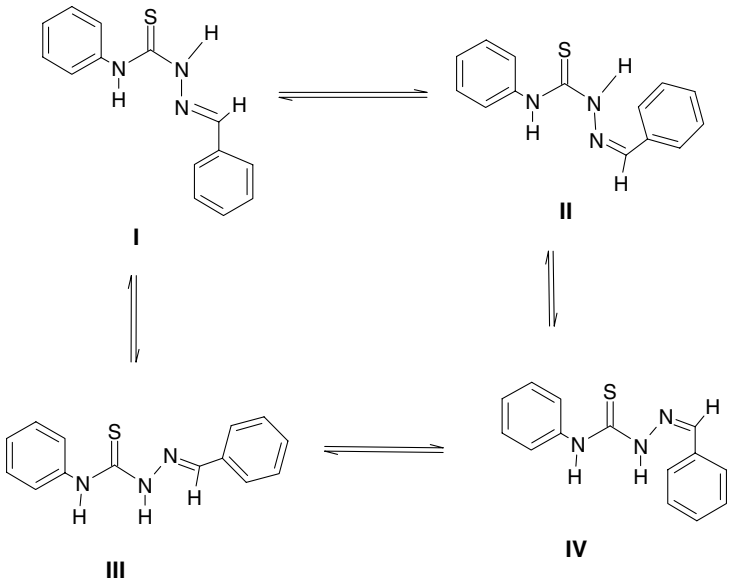


Fig. 2. Planar conformations of benzaldehyde 4-(phenyl)-thiosemicarbazone.

found that the thiosemicarbazonate(1^-) moiety is coordinated to dimethyl thallium(III) as a N,S chelating ligand, forming either a four-membered or a five-membered chelate ring depending on the substituent on the N(4) atom. The four-membered chelate ring was also observed [4–6] for organometallic derivatives of group 13 elements (Al, Ga and In), for Pd as well as another dimethyl thallium(III) complex. Bhattacharya et al. [2] tried to rationalize the formation of the four-membered chelate ring in terms of the known crystal structures [7] of benzaldehyde thiosemicarbazone and the corresponding ruthenium(II) and osmium(II) complexes. They argued that in the solid state the benzaldehyde thiosemicarbazone exists in form I (Fig. 2). Deprotonation of the N(2)–H proton can easily lead to the formation of a four-membered chelate ring. However, formation of a five-membered chelate ring requires rotation of 180° about the C(3)–N(2) bond to give form III.

Bhattacharya et al. also showed that formation of the five-membered chelate ring by form III results in a steric interaction between the ortho hydrogen of the phenyl ring of the benzaldehyde moiety with the metal atom, as well as between the two thiosemicarbazone moieties. Accordingly they reported that it is this steric factor which is responsible for the stabilization of the relatively uncommon four-membered chelate ring in these complexes compared to the more usual five-membered chelate rings. In this communication, we will examine this hypothesis more closely both from the viewpoint of available experimental results as well as quantum chemical calculations. Quantum chemical calculations of ruthenium complexes are quite popular today as they help to better understand the observed structural and experimental data. The most common methodologies adapted are DFT [8–11], INDO/S [11,12] and PM3 [9,13].

2. Experimental

2.1. Materials

Commercial ruthenium trichloride ($RuCl_3 \cdot xH_2O$), purchased from Arora Matthey (Kolkata, India), was processed by repeated evaporation to dryness with conc. HCl. $Ru(PPh_3)_3Cl_2$ was prepared by the published procedure [14]. The ligand, 4-(phenyl)thiosemicarbazone of benzaldehyde (BzTscHbz),was prepared by a modification of the published procedure [15]. Acetonitrile used for spectroscopic and electrochemical studies was purified according to a reported method [16]. Tetraethylam-

monium perchlorate (TEAP), used for the electrochemical work, was prepared as reported in the literature [17]. All other chemicals are of analytical grade and were used without further purification.

2.2. Physical measurements

Elemental analyses were performed on a Perkin–Elmer 240 C,H,N analyzer. UV–Vis spectra were recorded using a JASCO 7850 spectrophotometer. Magnetic susceptibilities were measured with a PAR Model 155 vibrating sample magnetometer with $Hg[Co(SCN)_4]$ as the calibrant. ^{1}H NMR spectra were recorded on a Bruker AVANCE DPX 300 MHz spectrometer using $Si(CH_3)_4$ as internal standard. Cyclic voltammetry was carried out using a PAR Versastat instrument driven by E-chem software. A three-electrode configuration with Pt working and auxiliary electrodes, Ag/AgCl reference electrode and TEAP as supporting electrolyte was used. The potentials were calibrated against the ferrocene/ferrocenium couple.

2.3. Synthesis of the complexes

Safety note! Perchlorate salts of organic and metallo-organic species are potentially explosive, and although we have not encountered any problems in our work, nevertheless they should be handled with care.

2.3.1. Synthesis of cis-$[Ru(PPh_3)_2(BzTscbz)_2]$ (**1a**), $[Ru_2(PPh_3)_2(BzTscbz)_4]$ (**1b**)

To a 30 ml methanolic solution of BzTscHbz (128 mg, 0.5 mmol), Et_3N (50 mg, 0.5 mol) was added, followed by the addition of solid $[Ru(PPh_3)_3Cl_2]$ (240 mg, 0.25 mmol). After 3 h of reflux, a shining yellow precipitate was collected by filtration and washed thoroughly with cold methanol. Recrystallization of the product from 1:1 dichloromethane–hexane solution in nitrogen atmosphere leads to two types of crystals, golden yellow (**1a**) and red (**1b**). The products were separated mechanically under a microscope. Yield: **1a**, 170 mg (60%), **1b**, 52 mg (12.5%). *Anal*. Calc. for $RuC_{64}H_{54}N_6S_2P_2$ (**1a**): C, 67.78; H, 4.76; N, 7.41% Found: C, 67.81; H, 4.80; N, 7.42%; electronic spectra (dichloromethane solution, λ_{max}/nm, ε/L mol^{-1} cm^{-1}) 431[a] (6178), 340 (20758), 265[a] (43247), 227 (78586), ([a]shoulder); ^{1}H NMR ($CDCl_3$, 300 MHz), δ 9.06 (s, 2H), 8.01 (s, 2H), 7.41–7.38 (m, 4H), 7.36–7.30 (m, 12H), 7.28–7.21 (m, 14H), 7.17–7.12 (t, 8H, $J = 7.1$ Hz), 7.05–6.96 (m, 12H); Cyclic voltammetric data[b]: ($E_{1/2}$ in V (ΔE_p in mV)) Ru^{II}/Ru^{III}, 0.51 (107); Ru^{III}/Ru^{IV}, 1.25 (238); ([b]in CH_2Cl_2, 50 mV s^{-1} scan rate). *Anal*. Calc. for $Ru_2C_{92}H_{78}N_{12}S_4P_2$ (**1b**): C, 63.37; H, 4.47; N, 9.64% Found: C, 63.43; H, 4.51; N, 9.61%; electronic spectra (dichloromethane solution) 418[a] (8576), 340[a] (19113), 260[a] (41168), 228 (80866) ([a]shoulder); ^{1}H NMR ($CDCl_3$, 300 MHz), δ 8.39 (s, 2H), 8.27 (d, 2H, $J = 6.9$ Hz), 7.81 (d, 2H, $J = 12.0$ Hz), 7.60 (d, 2H, 7.4 Hz), 7.26–7.20 (m, 14H), 7.09–6.94 (m, 24H), 6.92–6.79 (m, 24H), 6.69–6.67 (d, 8H, $J = 7.7$ Hz).

2.3.2. Synthesis of $[Ru(PPh_3)_2(BzTscHbz)_2](ClO_4)_2$ (**2**)

To a 30 ml hot methanolic solution of the ligand BzTscHbz (128 mg, 0.5 mmol), solid $[Ru(PPh_3)_3Cl_2]$ (240 mg, 0.25 mmol) was added. The mixture was then refluxed for 3 h. The resulting orange yellow solution was concentrated to about 10 ml in a rotary evaporator; a 2 ml aqueous saturated solution of $NaClO_4$ was then added. The resulting precipitate was collected by filtration, washed with water and then dried over fused $CaCl_2$. Recrystallization of the crude product from 1:1 dichloromethane–hexane solution gave the analytically pure compound; yield 190 mg (57%). *Anal*. Calc. for $RuC_{64}H_{56}N_6S_2P_2Cl_2O_8$: C, 57.57; H, 4.19; N, 6.29% Found: C, 57.73; H, 4.21; N, 6.31%; electronic spectra (dichloromethane solution, λ_{max}/nm, ε/L mol^{-1} cm^{-1}) 400[a](3946), 337[a](9866), 252(45387), ([a]shoulder); ^{1}H NMR ($CDCl_3$, 300 MHz), δ 8.97 (s, 2H), 7.83 (s, 4H), 7.68–7.61 (m, 8H), 7.52–7.43 (m, 12H), 7.32–7.16 (m, 30H). Differential pulse voltammetric data[b]: ($E_{1/2}$ in V) Ru^{II}/Ru^{III}, 0.86; Ru^{III}/Ru^{IV}, 1.28 ([b]in CH_2Cl_2, 20 mV s^{-1} scan rate).

2.4. Computation

The total energy (E_{tot}) of the ligands and energy barriers (E_b) for transformation between the conformers depicted in Fig. 2 were calculated by PM3 [18], as well as DFT [19] methods. The PM3 calculations were carried out on the MM^+ optimized structure of the molecules using CIS involving 10 occupied and 10 unoccupied orbitals. A window based HYPERCHEM program [20] was used for both MM^+ and PM3 calculations and the default parameters of the program were adapted. The energy barriers for rotation around C(5)=N(1) and N(2)–C(3) bonds were calculated by changing the appropriate torsion angles between 0° and 180° and calculating the E_{tot} at each step and taking the difference of E_{tot} between its maximum value and that for a torsion angle of 0°. The DFT calculations on the ligand were carried out using the GAUSSIAN-98 program [21] and B3LYP/6-31+G* methodology, whereas for the calculations on the model transition metal complexes the ADF program [22] was used. For all elements the ZORA approximation was used together with the default TZP basis sets using a small core. In addition Vosko, Wilk and Nusair's local exchange correlation potential was used [23] together with Becke's non-local exchange [24] and Perdew's correlation corrections [25]. With GAUSSIAN-98 and ADF

programs, geometry optimization was carried out using the default criteria for convergence.

2.5. X-ray crystallography

Single crystals of the complex *cis*-$[Ru(PPh_3)_2(BzTscbz)_2]$ (**1a**) were grown by slow evaporation from a dichloromethane–hexane solution of the complex in nitrogen atmosphere. Data were measured with Mo Kα radiation using the MAR research Image Plate System The crystal was positioned at 70 mm from the Image Plate. 100 frames were measured at 2° intervals with a counting time of 2 min. Data analysis was carried out with the XDS program [26] to provide 10413 independent reflections. The structure was solved using direct methods with the SHELX-86 program [27]. Non-hydrogen atoms were refined with anisotropic thermal parameters. The hydrogen atoms bonded to carbon were included in geometric positions and given thermal parameters equivalent to 1.2 times those of the atom to which they were attached. An empirical absorption correction was applied using DIFABS [28]. The structure was refined on F^2 using SHELXL [29] to R_1 0.1105, wR_2 0.1645 for 4179 reflections with $I > 2\sigma(I)$. The high R-value was due to the poor quality of the crystals, which led to mis-shapen spots in the diffraction pattern. Crystal data for **1a** appear in Table 1.

Table 1
Crystallographic data for **1a**

Empirical formula	$C_{64}H_{54}N_6S_2P_2Ru$
Formula weight	1134.26
T (K)	293(2)
λ (Å)	0.71073
Crystal system	monoclinic
Space group	$P2_1/n$
Unit cell dimensions	
a (Å)	13.063(15)
b (Å)	28.870(30)
c (Å)	15.412(17)
α (°)	90
β (°)	98.23(10)
γ (°)	90
V (Å^3)	5752.5(109)
Z	4
D_{calc} (g/cm^3)	1.310
Absorption coefficient (mm^{-1})	0.446
$F(000)$	2344
Crystal size (mm^3)	$0.25 \times 0.25 \times 0.3$
θ Range for data collection (°)	1.51–25.93
Index ranges	$-15 \leqslant h \leqslant 15$, $-35 \leqslant k \leqslant 24$, $-18 \leqslant l \leqslant 18$
Reflections collected	23900
Independent reflections (R_{int})	10413 (0.1173)
Absorption correction	semi-empirical from equivalent reflections
Refinement method	full-matrix least-squares on F^2
Data/restraints/parameters	10403/3/677
Goodness-of-fit on F^2	1.265
Final R indices [$I > 2\sigma(I)$]	$R_1 = 0.1105$, $wR_2 = 0.1224$
R indices (all data)	$R_1 = 0.2634$, $wR_2 = 0.1650$
Largest difference in peak and hole (e Å^{-3})	0.404 and −0.573

3. Results and discussion

3.1. Synthesis and characterization

Reaction of $Ru(PPh_3)_3Cl_2$ with BzTscHbz in refluxing methanol in the presence of Et_3N results in the precipitation of a yellow product. On recrystallization from a dichloromethane-hexane mixture in nitrogen atmosphere two types of crystals were obtained. The major product was golden yellow needles, which was formulated as *cis*-$[Ru(PPh_3)_2(BzTscbz)_2]$ (**1a**) and the other product was some red rhombic crystals formulated as $[Ru_2(PPh_3)_2(BzTscbz)_4]$ (**1b**). $[Ru(PPh_3)_2(BzTscHbz)_2](ClO_4)_2$ (**2**) was obtained using a similar procedure as above, except Et_3N was not added during the reaction and the compound was precipitated by addition of 2ml of saturated methanolic solution of $NaClO_4$. Elemental analyses and spectroscopic data for the complexes are consistent with the proposed formulations. In the NMR spectra, the two C–H protons of the coordinated thiosemicarbazones of **1a** and **2** appear at δ 9.06 and 8.97, respectively, as a broad singlet, whereas the four C–H protons of the four ligands of **1b** appear at δ 8.39 and 8.27. The signals at δ 8.01, 7.83 may be due to the N–H protons of **1a** and **2**, respectively. The two doublets at δ 7.81 and 7.60 for **1b** may be assigned as N–H protons. All other protons appear in the aromatic region as multiplets and overlapping signals.

Room temperature magnetic moment measurement indicates all the complexes are diamagnetic; hence ruthenium is in the +2 oxidation state. Complex **2** behaves as a 1:2 electrolyte in MeCN solution ($\Lambda_M = 230\ \Omega^{-1}\ cm^2\ mol^{-1}$), indicating the thiosemicarbazone ligands act as neutral N–S donors in this complex. The products **1a** and **1b** were separated mechanically under a microscope and X-ray crystal structures of both were determined.

3.2. Description of the crystal structures for (*1a*) and (*1b*)

The selected bond distances and bond angles for *cis*-$[Ru(PPh_3)_2(BzTscbz)_2]$ (**1a**) are summarized in Table 2. In the compound *cis*-$[Ru(PPh_3)_2(BzTscbz)_2]$ (**1a**) the coordination geometry of Ru(II) is similar to that observed earlier [2], where two P atoms as well as two nitrogen atoms are cis to each other, while the sulfur atoms are trans to each other (Fig. 3).

The average bond distances are Ru–P, 2.314 Å; Ru–S, 2.439 Å; Ru–N, 2.140 Å and the bite angle for the four-membered chelate ring is 65.20°. This may be compared with the values reported [30] (average Ru–P,

Table 2
Bond distances (Å) and bond angles (°) of **1a**

Ru1–N83	2.116(9)
Ru1–N73	2.164(9)
Ru1–P2	2.308(3)
Ru1–P1	2.320(3)
Ru1–S71	2.437(3)
Ru1–S81	2.441(3)
N83–Ru1–N73	80.5(3)
N83–Ru1–P2	91.3(2)
N73–Ru1–P2	164.3(2)
N83–Ru1–P1	168.4(2)
N73–Ru1–P1	92.3(2)
P2–Ru1–P1	97.76(12)
N83–Ru1–S71	99.9(2)
N73–Ru1–S71	65.5(2)
P2–Ru1–S71	103.25(11)
P1–Ru1–S71	85.14(11)
N83–Ru1–S81	65.4(2)
N73–Ru1–S81	98.4(2)
P2–Ru1–S81	90.13(11)
P1–Ru1–S81	107.13(11)
S71-Ru1–S81	160.65(11)

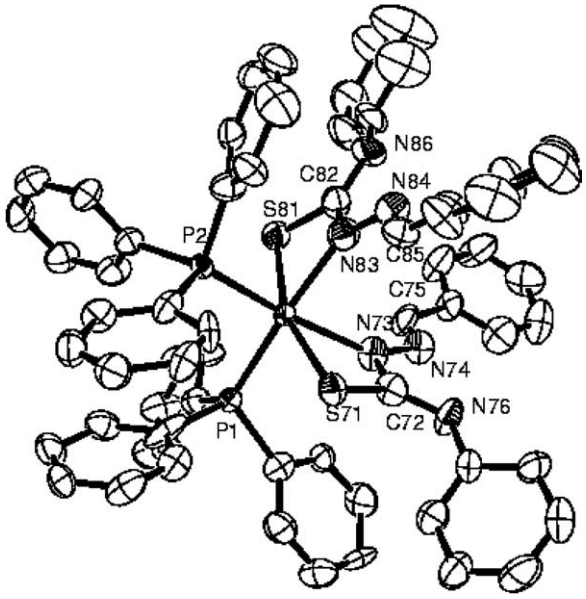


Fig. 3. ORTEP diagram and atom numbering scheme for *cis*-$[Ru(PPh_3)_2(BzTscbz)_2]$ (**1a**). Hydrogen atoms are omitted for clarity. Thermal ellipsoids are at 25% probability.

2.382 Å; Ru–S, 2.368 Å; Ru–N, 2.145 Å, bite angle for the five-membered chelate is 81.65°) for *cis*-$[Ru(PPh_3)(CyTscHPy)_2](ClO_4)_2$ (**3**) (where for CyTscPy $R_1 = H$, $R_2 = Py$, $R_3 = H$, $R_4 =$ cyclohexyl in Fig. 1), which has identical donor atoms (*cis*-P_2, *cis*-N_2, *trans*-S_2) to those reported here but the two thiosemicarbazone moieties are in the protonated form and coordinate in a more conventional way forming five-membered chelate rings. Normally, the anionic chelates are expected to have shorter bond lengths than the corresponding neutral variety. However, in this case the Ru–P bonds are shorter in **1a** than in **3**, while the Ru–S distances are longer in **1a**, clearly indicating that the Ru–S bond in the four-membered chelate ring is much weaker compared to that in the five-membered ring.

The lack of good crystal quality of **1b** resulted in poor refinement of the structure to an R_1 value of 0.25 so that no detailed comment on the dimensions can be made. [Crystal data, **1b**, $Ru_2C_{92}H_{78}N_{12}S_4P_2$, triclinic, $Z = 4$, $a = 16.042(17)$ Å, $b = 16.471(19)$ Å, $c = 18.238(19)$ Å, $\alpha = 76.63(1)°$, $\beta = 76.39(1)°$, $\gamma = 66.36(1)°$, $V = 4448.1$ Å^3, $D_{calc} = 1.302$ g cm^{-3}]. However, the atoms in the structure could be located well enough to show that there are two independent centrosymmetric dimers in the unit cell in which the two Ru(II) centers are bridged by two thiolato sulfur atoms. Each Ru(II) center is coordinated by one PPh_3 and two thiosemicarbazonate moieties, of which one thiosemicarbazonate forms a four-membered chelate ring while the other one forms a five-membered chelate ring, and it is the thiolato group belonging to the later variety which is responsible for bridging the Ru(II) centers (Fig. 4).

3.3. Probable structure of *2*

We have also synthesized the complex $[Ru(PPh_3)_2(BzTscHbz)_2](ClO_4)_2$ (**2**) containing the non-deprotonated thiosemicarbazone ligand. Although we have not been able to get a single crystal of the compound, the similarities of electronic spectra and the E^0[Ru(III)/Ru(II)] values of this complex with those reported by Ghosh et al. [30] suggest that it has a similar structure to one of their complexes, i.e., *cis*-P_2, *trans*-S_2, *cis*-N_2, where the thiosemicarbazone is coordinated as a five-membered chelating N,S donor. This is further corroborated by the fact that the addition of a dilute solution of a base such as Et_3N to a solution of **2** in dichloromethane or acetonitrile does not generate the spectra of **1a**.

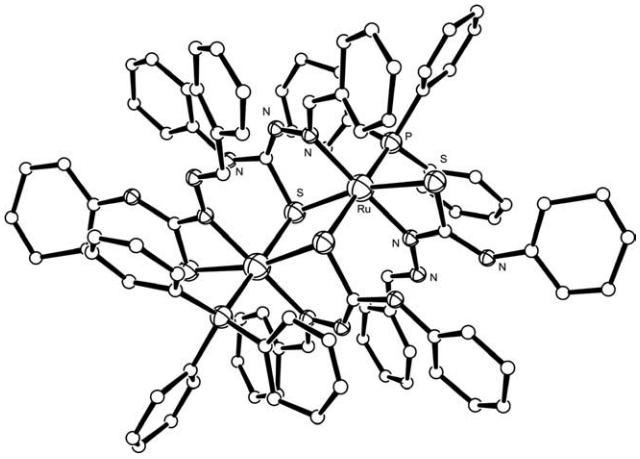


Fig. 4. X-ray structure of centrosymmetric $[Ru_2(PPh_3)_2(BzTscbz)_4]$ (**1b**). Hydrogen atoms are omitted for clarity.

Similarly, addition of dilute acid to a dichloromethane solution of **1a** does not generate the spectra of **2**. If the thiosemicarbazone is coordinated to both **1a** and **2** in a similar manner, then rapid interconversion between them is expected due to acid or base addition, which is not the case here. It may also be noted that so far in all the structurally characterized thiosemicarbazone complexes, when it is found to form a four-membered chelate ring, it is always present in the deprotonated form. Thus, on the basis of the above discussion, it is logical to conclude in **2** that thiosemicarbazone is present as a five-membered chelate ring.

3.4. Relative stability of four-membered versus five-membered chelate rings

In the light of the above results, we can reassess the possible binding modes of thiosemicarbazones in general and benzaldehyde thiosemicarbazone in particular. Benzaldehyde thiosemicarbazone can exist in the four conformations depicted in Fig. 2. Some important results of the quantum chemical calculations on these conformers are summarized in Table 3. It may be noted from the table that although the E_{tot} values for each conformer substantially differ between the two methods of calculations, the relative stabilities of the conformers as well as the E_{b1} value (see below) given by the semi-empirical PM3 method and more accurate DFT method are quite similar. In the solid state BzTscHbz exists in form I as revealed by the crystal structure determination [7]. When it coordinates in this form it has to undergo deprotonation of N(2)H followed by four-membered chelate ring formation. Form II can also participate in a similar four-membered chelate ring formation. However, conversion of form I to form II requires crossing of an energy barrier of ~45 kcal mol^{-1} (E_{b1}), without any benefit of additional bond energy; rather the phenyl ring will undergo steric repulsion with the rings of the tri(phenyl) phosphine and thus this form has not been found to coordinate.

Table 3
The E_{tot}^{rel} values for the different conformers of BzTscHbz

Conformer	Method of calculation	E_{tot}^{rel} (kcal mol^{-1})
I	PM3	0.0
	DFT	0.0
II	PM3	−0.40
	DFT	3.58
III	PM3	10.85
	DFT	11.02
IV	PM3	11.67
	DFT	15.59

E_{tot}^{rel} is the E_{tot} values of different conformers relative to conformer I, whose E_{tot} value is −58295.40 (PM3)/−692628.45 (DFT).

From these energies, the barriers for rotation about the C(5)=N(1) (E_{b1}) and N(2)–C(3) (E_{b2}) bonds can be calculated as 48.0, 15.5 kcal mol^{-1}, respectively, with PM3 and 45.6 and 31.3 kcal mol^{-1}, respectively, with DFT methods.

Forming a five-membered chelate ring requires either form III or form IV. However, it was shown by Bhattachyarya et al. [2] that coordination in form III results in severe steric strain. So like form II, form III has never been found to be coordinated in metal complexes. Thus, formation of a five-membered chelated complex requires form IV and crossing of an energy barrier of 45–50 kcal mol^{-1}, equivalent to the energy of a chemical bond, which is readily available in a chemical reaction like the present one where a psuedo-five coordinated Ru(II) is converted to a six coordinated species and deprotonations take place (considering the crystal field stabilization energy (CFSE) of Ru^{II} ~ 350 kcal mol^{-1}, solvation energy of a proton in MeOH ~ 180 kcal mol^{-1} and proton affinity of Et_3N ~ 230 kcal mol^{-1}). The benefit of stronger bond formation should lead to the coordination by form IV, in preference to form I, i.e., the metal complex containing the five-membered chelate ring with form IV should be thermodynamically more stable compared to one containing the four-membered chelate ring with form I. This is particularly so as form I is only ~16 kcal mol^{-1} more stable than form IV according to the DFT calculations. The structure determination of two Ni(II) complexes [31] containing (4-fluoro)benzldehyde thiosemicarbazonate(−1) and (4-*N*,*N*-dimethylamino)benzaldehyde S-benzyl dithiocarbazate(−1) as well as the Ru(II) complex of the more sterically encumbered ligand pyridine-2-aldehyde(4-cyclohexyl) thiosemicarbazone, all containing the five-membered chelate ring, bears testimony to the above hypothesis.

3.5. DFT calculations

We have also carried out DFT calculations on Ru complexes with these types of ligands using the ADF program. We first used two model complexes with less bulky ligands, namely $Ru(MeTscMe)_2(PMe_3)_2$, where MeTscMe is the 4-(methyl)thiosemicarbazone of acetaldehyde and $Ru(BzTscbz)_2(PMe_3)_2$. We then performed calculations on $Ru(BzTscbz)_2(PPh_3)_2$ as well. All models were constrained in C_2 symmetry and their geometry refined to convergence. The crystal structure of $Ru(BzTscbz)_2(PPh_3)_2$ has a structure only slightly distorted from C_2 symmetry. The results of the ADF calculations are given in Table 4.

From the results it is clear that five-membered chelate containing metal complexes are always thermodynamically more stable than the corresponding four-membered chelate containing complexes, even when the steric bulk of the axial phosphines are increased from PMe_3 to PPh_3. Indeed it is clear that steric effects of

Table 4
Results of DFT calculations on some thiosemicarbazone complexes

Complex	E^1_{tot} (kcal mol^{-1})	E^2_{tot} (kcal mol^{-1})	ΔE_{tot}	Ru–N (Å)		Ru–S (Å)	
				Four-membered	Five-membered	Four-membered	Five-membered
trans-[Ru(MeTscMe)$_2$(PMe$_3$)$_2$]	−7425.02	−7450.74	25.72	2.140	2.117	2.396	2.337
trans-[Ru(BzTscbz)$_2$(PMe$_3$)$_2$]	−12140.55	−12157.87	17.32	2.122	2.111	2.386	2.331
trans-[Ru(BzTscbz)$_2$(PPh$_3$)$_2$]	−19139.66	−19171.09	31.43	2.129	2.088	2.372	2.341

$\Delta E_{tot} = E^1_{tot} - E^2_{tot}$ (E^1_{tot} and E^2_{tot} corresponds to four-membered and five-membered chelated complexes, respectively).

Table 5
The frontier orbitals in the 5- and 4-chelation mode of *trans*-[Ru(BzTscbz)$_2$(PPh$_3$)$_2$]

	Energy (a.u.)	Percentage of atomic orbital coefficients
4-Chelation mode		
LUMO	−0.095649	no metal contribution
HOMO	−0.159906	31.6 Ru d_{xy}, 14.4 S p_y, 5.1 S p_z
HOMO − 1	−0.166758	50.6 Ru d_{xz}, 12.7 S p_x, 5.0 S p_z
HOMO − 2	−0.170253	20.1 Ru d_{z^2}, 17.7 d_{xy}, 9.8 S p_y
HOMO − 3	−0.175612	no metal contribution
5-Chelation mode		
LUMO	−0.085458	no metal contribution
HOMO	−0.156133	20.3 Ru d_{xy}, 18.85 S p_y, 16.0 Ru $d_{x^2-y^2}$
HOMO − 1	−0.161880	35.5 Ru d_{xz}, 17.07 S p_x, 8.9 S p_z, 8.0 Ru d_{z^2}
HOMO − 2	−0.176128	20.5 Ru d_{z^2}, 12.0 $d_{x^2-y^2}$, 9.40 S p_y
HOMO − 3	−0.181913	no metal contribution

the bulky phenyl rings compared to those of the methyl groups do not favour one type of chelation over another. It would appear that the electronic effects are of paramount importance.

The bond lengths shown in Table 4 indicate that the Ru–S and Ru–N bond lengths are significantly shorter in the five-membered chelation mode for all three complexes. Details of the frontier orbitals in the 5 and 4 chelation mode of *trans*-[Ru(BzTscbz)$_2$(PPh$_3$)$_2$] are given in Table 5.

As is apparent from the pattern of frontier orbitals there are very few differences between the 4 and 5 chelation modes. The HOMO–LUMO gaps are 0.064257 and 0.070675 a.u., respectively, so the gap is slightly larger for the 5 chelation mode. However, the contribution of the atoms to the HOMO orbitals are very similar with the top three having major contributions only from the metal and sulfur atoms. However, HOMO − 3 and the LUMO both are orbitals, which do not include the metal atom in any way.

4. Conclusion

The quantum chemical calculations on the metal complexes discussed above as well as the crystal structure data of the vast majority of structurally characterized thiosemicarbazone complexes clearly suggest that for the thiosemicarbazone complexes, five-membered chelate rings are thermodynamically more stable than the four-membered chelate rings, as is intuitively expected. In fact by suitable substitution on the N(4), and/or on the C atom attached to N(1) one can get either the five-membered chelate or both the four- and five-membered chelates as shown in this work as well as in the works of Casas and Ghosh et al. [3,30]. Casas and co-workers [32] have also demonstrated that even when R_2 is a bulky substituent such as ferrocenyl, both five- and four-membered chelate complexes can be isolated. Similarly in [PbPh$_2$(EtGTSC)$_2$] (where HEtGTSC = thiosemicarbazone of ethylglyoxalate), one arm of the thiosemicarbazone moiety forms a four-membered chelate ring whereas the other thiosemicarbazone arm forms a five-membered chelate ring [33]. They concluded that although the five-membered chelate ring may be more stable, the four-membered ring retains the N(4)–H···N(1) hydrogen bond that is present in the free ligand. Thus, a small difference in weak interactions or in the steric requirement of the packing may decide the actual coordination mode.

Acknowledgements

D.M. and S.N. acknowledge CSIR and UGC, respectively, for their fellowships. S.K.C. acknowledges AICTE and UGC, New Delhi for financial support. We thank EPSRC (UK) and the University of Reading for funds for the Image Plate System.

Appendix A. Supplementary data

The structure of **1a** has been deposited with the Cambridge Crystallographic Data Centre and the deposition number is 248342. Copies of this information may be obtained free of charge from The Director, CCDC, 12 Union Road, Cambridge CB2 1EZ, UK (fax: +44 1223 336 033; e-mail: deposit@ccdc.cam.ac.uk or http://www.ccdc.cam.ac.uk). Supplementary data associated with this article can be found, in the online version, at doi:10.1016/j.poly.2005.05.018.

References

[1] (a) M.J.M. Campbell, Coord. Chem. Rev. 15 (1975) 297;
(b) D.X. West, S.B. Padhye, P.B. Sonawane, Struct. Bonding (Berlin) 76 (1991) 1;
(c) J.S. Casas, M.S. Garcia-Tasenda, J. Sordo, Coord. Chem. Rev. 209 (2000) 197.

[2] (a) F. Basuli, S.-M. Peng, S. Bhattacharya, Inorg. Chem. 36 (1997) 5645;
(b) F. Basuli, M. Ruf, C.G. Pierpont, S. Bhattacharya, Inorg. Chem. 37 (1998) 6113;
(c) F. Basuli, S.-M. Peng, S. Bhattacharya, Inorg. Chem. 39 (2000) 1120.

[3] J.S. Casas, V. Castaño, M.C. Cifuentes, A. Sánchez, J. Sordo, Polyhedron 21 (2000) 1651.

[4] (a) C. Paek, S.O. Kong, J. Ko, P.J. Carroll, Organometallics 16 (1997) 1503;
(b) C. Paek, S.O. Kong, J. Ko, P.J. Carroll, Organometallics 16 (1997) 2110;
(c) C. Paek, S.O. Kong, J. Ko, P.J. Carroll, Organometallics 16 (1997) 4755;
(d) C. Paek, S.O. Kong, J. Ko, P.J. Carroll, Organometallics 16 (1997) 5522.

[5] A. Castiñeiras, E. Bermejo, D.X. West, A.K. El-Sawaf, J.K. Swearingen, Polyhedron 17 (1998) 2751.

[6] J.S. Casas, E.E. Castellano, A. Macías, Rodríguez-Argüelles, A. Sánchez, J. Sordo, J. Chem. Soc., Dalton Trans. (1993) 1293.

[7] (a) H.K. Fun, K. Sivakumar, B.C. Yip, Y.P. Tian, C.Y. Duan, Z.L. Lu, X.Z. You, Acta Cryatallogr., Sect. C 51 (1995) 2080;
(b) D. Chattopadhyay, S.K. Mazumdar, T. Banerjee, S. Ghosh, T.C.W. Mak, Acta Cryatallogr., Sect. C 44 (1988) 1025.

[8] J. Otsuki, N. Omokawa, K. Yoshiba, I. Yoshikawa, T. Akasaka, T. Suenobu, T. Takido, K. Araki, S. Fukuzumi, Inorg. Chem. 42 (2003) 3057.

[9] M. Cheng, W.B. Euler, Inorg. Chem. 42 (2003) 5384.

[10] J. Chang, S. Plummer, E.S.F. Berman, D. Striplin, D. Blanch, Inorg. Chem. 43 (2004) 1735.

[11] S.I. Gorelsky, A.B.P. Lever, J. Organomet. Chem. 635 (2001) 187.

[12] A.B.P. Lever, S.I. Gorelsky, Coord. Chem. Rev. 208 (2000) 153.

[13] A.C. Benniston, G. Chapman, A. Harriman, M. Mchrabi, C.A. Sams, Inorg. Chem. 43 (2004) 4227.

[14] T.A. Stephenson, G. Wilkinson, J. Inorg. Nucl. Chem. 28 (1966) 945.

[15] (a) S.K. Chattopadhyay, S. Ghosh, Inorg. Chim. Acta 131 (1987) 15;
(b) S.K. Chattopadhyay, S. Ghosh, Inorg. Chim. Acta 163 (1989) 245.

[16] D.T. Sawyer, A. Sobkowiak, J.L. Roberts Jr., Electrochemistry for Chemists, 2nd ed., Wiley, New York, 1995, p. 333.

[17] D.T. Sawyer, A. Sobkowiak, J.L. Roberts Jr., Electrochemistry for Chemists, 2nd ed., Wiley, New York, 1995, p. 336.

[18] (a) J.J.P. Stewart, J. Comput. Chem. 12 (1991) 320;
(b) J.J.P. Stewart et al. QCPE# 50.

[19] J.B. Foresman, Æ. Frisch, in: Exploring Chemistry with Electronic Structure Methods, 2nd ed., Gaussian Inc., Pittsburgh, PA, 1996.

[20] HYPERCHEM for Windows, Release 7.01, Hypercube Inc., 115 NW 4th Street, Gainesville, FL 32601, USA.

[21] J. Frisch, G.W. Trucks, H.B. Schlegel, G.E. Scuseria, M.A. Robb, J.R. Cheeseman, V.G. Zakrzewski, J.A. Montgomery, R.E. Stratmann, J.C. Burant, S. Dapprich, J.M. Millam, A.D. Daniels, K.N. Kudin, M.C. Strain, O. Farkas, J. Thomasi, V. Barone, M. Cossi, R. Cammi, B. Mennucci, C. Pomelli, C. Adamo, S. Clifford, J. Ochterski, G.A. Petersson, P.Y. Ayala, Q. Cui, K. Morokuma, D.K. Malick, A.D. Rabuck, K. Raghavachari, J.B. Foresman, J. Cioslowski, J.V. Ortiz, B.B. Stefanov, G. Liu, A. Liashenko, P. Piskorz, I. Komaromi, R. Gomperts, R.L. Martin, D.J. Fox, T. Keith, M.A. Al-Laham, C.Y. Peng, A. Nanayakkara, C. Gonzalez, M. Challacombe, P.M.W. Gill, B. Johnson, W. Chen, M.W. Wong, J.L. Andres, M. Head-Gordon, E.S. Replogle, J.A. Pople, Gaussian Inc., Pittsburgh, PA, 1998.

[22] E.J. Baerends, A. Berces, C. Bo, P.M. Boerrigter, L. Cavallo, L. Deng, R.M. Dickson, D.E. Ellis, L. Fan, T.H. Fisher, C. Fonseca-Guerra, S.J.A. van Gisbergen, J.A. Groeneveld, O.V. Gritsenko, F.E. Harris, D. van Hoek, P.H. Jacobson, G. van Kessel, F. Kootstra, E. van Lenthe, V.E. Osinga, P.H.T. Philipson, D. Post, C.C. Pye, W. Ravenek, P. Ros, P.R.T. Schipper, G. Schreckenback, J.G. Snijders, M. Sola, D. Swerhone, G. te Velde, P. Vernooijs, L. Versluis, O. Visser, E. van Wezenbeek, G. Wiesenekker, S.K. Wolff, T. Woo, T. Ziegler, Theoretical Chemistry, SCM Inc., Vrije Universiteit, Amsterdam, The Netherlands, 2000.

[23] S.H. Vosko, L. Wilk, M. Nusair, Can. J. Phys. 58 (1980) 1200.

[24] A.D. Becke, J. Chem. Phys. 88 (1988) 1053.

[25] (a) J.P. Perdew, Phys. Rev. B33 (1986) 8822;
(b) J.P. Perdew, Phys. Rev. B 34 (1986) 7406.

[26] W. Kabsh, J. Appl. Crystallogr. 21 (1988) 916.

[27] G.M. Sheldrick, Acta Crystallogr., Sect. A 46 (1990) 467.

[28] N. Walker, D. Stuart, Acta Crystallogr., Sect. A 39 (1983) 158.

[29] G.M. Sheldrick, Program for Crystal Structure Refinement, University of Göttingen, Göttingen, Germany, 1998.

[30] P. Sengupta, R. Dinda, S. Ghosh, W.S. Sheldrick, Polyhedron 22 (2003) 447.

[31] (a) Y.P. Tian, C.Y. Duan, Z.L. Lu, X.Z. You, H.K. Fun, S. Kandasamy, Polyhedron 15 (1996) 2263;
(b) M.B. Ferrari, S. Capacchi, G. Reffo, G. Pelosi, P. Tarasconi, R. Albertini, S. Pinelli, P. Lunghi, J. Inorg. Biochem. 81 (2000) 89.

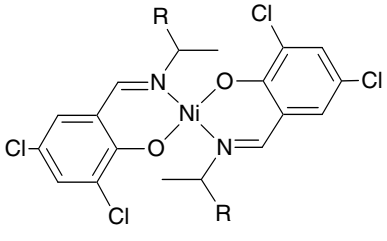
[32] J.S. Casas, M.V. Castiño, M.C. Cifuentes, A. Sánchez, J. Sordo, Polyhedron 21 (2002) 1651.

[33] J.S. Casas, E.E. Castellano, J. Ellena, M.S. G-Tasende, A. Sánchez, J. Sordo, Á T-Varela, Inorg. Chem. Commun. 7 (2004) 1109.

advantage that photoisomerization can be induced by light irradiation at room temperature [10].

Conventionally, it has been well known that a series of certain Schiff base complexes, namely bis(*N*-alkyl-salicylideneimine)copper (II) or nickel (II), exhibit flexible structural changes of coordination environment from square planar to tetrahedral depending on various conditions [11]. For the Ni(II) complexes, both square planar [12–14] and tetrahedral [15–17] complexes have been obtained by steric and/or electronic requirements of the ligands. Furthermore, these complexes also exhibit structural isomerization caused by a thermally induced structural phase transition [18,19] and paramagnetism when they are dissolved in inert organic solvents [20–22]. Many aspects of the stereochemistry of Cu(II) complexes are similar to that of Ni(II) complexes. Very recently, light promoted trimerization at room temperature has been reported for a certain Schiff base Cu(II) complex [23]. Unfortunately, we could not observed photo-responsive properties of some square planar bis-(*N*-alkyl-salicylideneimine)copper (II) complexes [24–26] as well as compressed tetrahedral chiral ones [27,28] solely in the solid state at room temperature. However, various excellent merits will be provided by organic/inorganic hybrid self-assembling systems which consist of photochromic organic compounds and Schiff base complexes; for example applications for spin crossover systems, tunable homogeneous molecular catalysts, and molecular recognition based on chirality and so on. No such supramolecular systems have been reported to date.

Herein, we describe the crystal structures and electronic properties of two new Ni(II) complexes incorporating 3,5-dichloro-substituted Schiff base ligands (Scheme 1). We have also investigated flexible structural changes by steric and/or electronic natures of their ligands, external conditions such as a thermally induced structural phase transition, and negative solvatochromism. Furthermore, we have attempted to construct a supramolecular solvatochromism system by using a photochromic solute, 4-hydroxyazobenzene. After UV light irradiation, we have successfully detected a slight conformational change of the chiral ligands by means of absorption and CD spectra for the first time.



1 : R = C_6H_5

2 : R = CH_3

Scheme 1. Molecular structures of the nickel complexes, **1** and **2**.

2. Experimental

2.1. Materials

Chemicals of the highest commercial grade available (Aldrich and Wako) were used as received without further purification.

2.2. Physical measurements

Elemental analyses (C, H, N) were carried out on an Elementar Vario EL analyzer at Keio University. Infrared spectra were recorded using Nujol mulls on a BIORAD FTS-60A spectrophotometer in the range 4000–400 cm^{-1} at 298 K. Thermal analysis was performed on a SHIMADZU DSC-60 differential scanning calorimeter (DSC), where the heating rate was 10 K min^{-1} in the range 313–673 K. Diffuse reflectance spectra were measured on a JASCO V-560 spectrophotometer equipped with an integrating sphere in the range 850–220 nm at 298 K. Absorption spectra were measured on a JASCO V-560 spectrophotometer in the range 900–200 nm at 298 K. Circular dichroism (CD) spectra were measured on a JASCO J-720WI spectropolarimeter in the range 900–200 nm at 298 K. Magnetic susceptibility was measured with a Sherwood Scientific magnetic susceptibility balance at 298 K. Magnetic data were corrected for the magnetization of diamagnetic contributions, which were estimated from Pascal constants. The magnetic properties were investigated with a Quantum Design MPMS-5S superconducting quantum interference device magnetometer (SQUID) at an applied field 5000 Oe in a temperature range 2–300 K. XPS were recorded on a JEOL JPS-9000MC spectrometer at 298 K. ESR spectra were measured using a JEOL JES-RE3X X band ESR spectrometer at 298 K. Semi-empirical molecular orbital calculations were performed with the program ZINDO in a CAChe software package based on the crystal structures determined.

2.3. Synthesis of bis(*N*-*R*-1-phenylethyl-3,5-dichloro-salicydenaminato)nickel (II) (**1**)

Treatment of 3,5-dichlorosalicylaldehyde (1.91 g, 10.0 mmol), *R*-1-phenylethylamine (1.33 g, 11.0 mmol) and nickel (II) acetate tetrahydrate (1.24 g, 5.00 mmol) in methanol (150 mL) at 318 K for 3 h gave rise to deep green crude precipitates. Recrystallization from an acetone solution at 298 K over a period of several days yielded brown prismatic single crystals (**1**) suitable for X-ray crystallography. *Anal.* Calc. for $C_{30}H_{24}N_2Cl_4$-

NiO_2: C, 56.04; H, 3.45; N, 4.36. Found: C, 55.75; H, 3.18; N, 4.27%. IR (KBr): 1616 cm^{-1} (C=N), 442 cm^{-1} (Ni–N), 420 cm^{-1} (Ni–O). M.p. 580 K (decomposition). $\mu_{eff}/\mu_{B.M.} = 2.98$ at 298 K. XPS Ni2p$_{3/2}$ 831 eV.

2.4. Synthesis of bis(N-2-propyl-3,5-dichlorosalicydenaminato)nickel (II) (2)

Treatment of 3,5-dichlorosalicylaldehyde (1.91 g, 10.0 mmol), 2-propylamine (1.24 g, 21.0 mmol) and nickel (II) acetate tetrahydrate (1.24 g, 5.00 mmol) in methanol (150 mL) at 318 K for 3 h gave rise to deep green crude precipitates. Recrystallization from an acetone solution at 298 K over a period of several days yielded green prismatic single crystals (**2**) suitable for X-ray crystallography. *Anal.* Calc. for $C_{20}H_{20}N_2Cl_4NiO_2$: C, 46.12; H, 3.87; N, 5.38. Found: C, 46.08; H, 4.03; N, 5.36%. IR (KBr): 1620 cm^{-1} (C=N), 446 cm^{-1} (Ni–N), 419 cm^{-1} (Ni–O). M.p. 587 K (decomposition). $\mu_{eff}/\mu_{B.M.} = 0$ (diamagnetic) at 298 K. XPS Ni2p$_{3/2}$ 832 eV.

2.5. X-ray crystallography

Intensity data were collected on a Rigaku AFC-7R four-circle diffractometer. The structures were solved by direct methods using SIR92 [29] and expanded by Fourier techniques. The structures were refined on F^2 anisotropically for non-hydrogen atoms by full-matrix least-squares methods with SHLEXL97 [30] on the teXsan program package [31]. Empirical absorption corrections were applied based on ψ scans; scaled transmission factors for **1** and **2** were 0.719–0.797 and 0.613–0.660, respectively. No significant decay in the intensity of three standard reflections was observed throughout the data collection. The hydrogen atoms were located at geometrically calculated positions, C–H = 0.950 Å, and refined isotropically. All the non-hydrogen atoms were refined anisotropically. Crystallographic data for **1** and **2** are summarized in Table 1.

3. Results and discussion

3.1. Crystal structure of 1

The molecular structure of **1** is depicted in Fig. 1. Selected bond lengths and angles are given in Table 2. The molecule of **1** possess a C_2 axis passing through the central nickel atom, and the absolute configuration was found to be $\Lambda(R,R)$ for the single crystal examined. The complex **1** affords a compressed tetrahedral [NiN_2O_2] coordination geometry taking an umbrella conformation. In contrast to analogous Cu(II) complexes [28,32], the phenyl moieties of the ligands are faced to the inside of the molecule. The bond angles

Table 1
Crystallographic data for **1** and **2**

	1	**2**
Formula	$C_{30}H_{24}Cl_4N_2NiO_2$	$C_{20}H_{20}Cl_4N_2NiO_2$
Molecular weight	645.00	520.87
Crystal system	monoclinic	monoclinic
Space group	$C2$ (no. 5)	$P2_1/a$ (no. 14)
a (Å)	13.934(3)	8.465(2)
b (Å)	10.929(3)	16.605(3)
c (Å)	10.091(2)	8.036(2)
β (°)	117.44(1)	102.81(2)
V (Å^3)	1363.8(6)	1101.4(4)
Z	2	2
D_{calc} (g cm^{-3})	1.571	1.571
$F(000)$	660	532
μ(mm^{-1})	1.136	1.385
Crystal size (mm)	0.30 × 0.30 × 0.20	0.70 × 0.30 × 0.30
Temperature (K)	297	297
θ_{min}, θ_{max} (°)	5.10, 27.50	5.05, 27.50
Wavelength (Mo Kα)	0.71073	0.71073
Total reflections	1652	2953
Unique reflections	1591	2530
Observed reflections ($I > 2\sigma(I)$)	1374	1949
Number of refined parameters	177	134
R[a], R_w[b], S	0.0235, 0.0842, 0.744	0.0600, 0.1844, 1.071
Flack parameter	0.00(2)	
Minimum and maximum residual Densities (e Å^{-3})	−0.20, 0.18	−1.12, 0.99

[a] $R = \sum||F_o| - |F_c||/\sum|F_o|$.
[b] $R_w = (\sum w(|F_o|-|F_c|)^2/\sum w|F_o|^2)^{1/2}$, $w = 1/(\sigma^2(F_o) + (0.1P)^2)$ for **1**, and $w = 1/(\sigma^2(F_o) + (0.1322P)^2 + 0.2552P)$ for **2**, where $P = (F_o^2 + 2|F_c^2|)/3$.

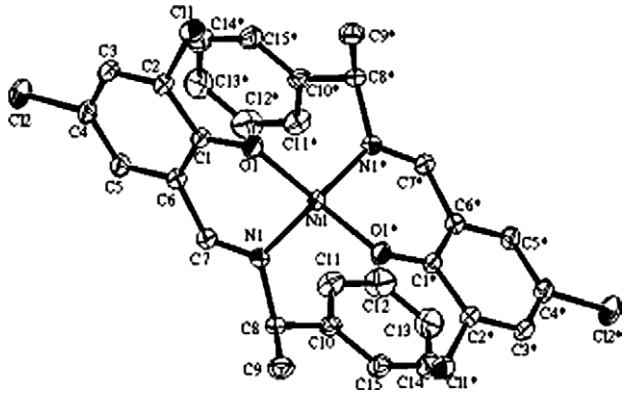


Fig. 1. The molecular structure of **1** showing the atom labelling scheme. Displacement ellipsoids are drawn at the 30% probability level. H atoms are omitted for clarity. Atoms marked with *'s are expanded by the symmetry operation $(-x-2, y, -z-2)$.

Table 2
Selected geometric parameters (Å, °) for **1**

Ni1–N1	2.013(3)
O1–C1	1.299(4)
N1–C8	1.490(4)
C2–Cl1	1.745(4)
Ni1–O1	1.905(2)
N1–C7	1.275(5)
C6–C7	1. 456(4)
C4–Cl2	1.734(4)
N1–Ni1–O1	92.8(1)
N1–Ni1–N1*	116.3(2)
Ni1–N1–C7	121.3(2)
Ni1–O1–C1	126.1(2)
N1–Ni1–O1*	107.5(1)
O1–Ni1–O1*	141.4(2)
Ni1–N1–C8	122.8(2)
N1–C7–C6	127.8(3)

Atoms marked with *'s are expanded by the symmetry operation $(-x-2, y, -z-2)$.

are N1–Ni1–O1 = 92.8(1)°, N1–Ni1–O1* = 107.5(1)°, N1–Ni1–N1* = 116.3(2)° and O1–Ni1–O1* = 141.4(2)°. The dihedral angles between the C1/O1/Ni1/N1/C7/C6 plane and C1*/O1*/Ni1/N1*/C7*/C6* plane is 100.0(1)°, in other words the deviation of the interplanar angle from 90° is 10.0(1)°, showing significant non-coplanarity of the $[NiN_2O_2]$ plane and the six-membered chelate ring. The bond distances are Ni1–N1 = 2.013(3) Å and Ni1–O1 = 1.905(2) Å, which are comparable with analogous tetrahedrally distorted Ni(II) complexes incorporating Schiff base ligands [15–17], and appreciably longer than those of the square planar complexes [12–14]. Comparing analogous tetrahedrally distorted complexes [24], the present imine double bond distance of N1=C7 = 1.275(5) Å suggests that the σ coordination bonds are weak in dπ–pπ interaction. In the crystals, there are no remarkable intermolecular hydrogen bonds and π–π interactions within van der Waals radii [33]. Thus, the crystal packing may be dominated by non-covalent and weak van der Waals forces. The molecular arrangement shows one-dimensional chains along the crystallographic *a* axis.

3.2. Crystal structure of **2**

The molecular structure of **2** is depicted in Fig. 2. Selected bond lengths and angles are given in Table 3. Complex **2** affords a square planar *trans*-$[NiN_2O_2]$ coordination geometry, whose central Ni(II) atom lies on the center of symmetry. Similar to analogous Cu(II) complexes [34], steric effects of the 2-propyl moieties and electron withdrawing by Cl-substituents lead to this square planar coordination environment. Indeed, no structural features indicating steric repulsion due to the 2-propyl moieties can be observed for **2**. The

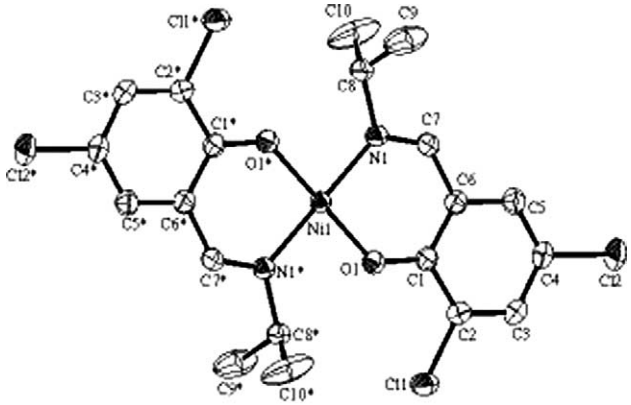


Fig. 2. The molecular structure of **2** showing the atom labelling scheme. Displacement ellipsoids are drawn at the 30% probability level. H atoms are omitted for clarity. Atoms marked with *'s are expanded by the symmetry operation $(2-x, -y, -z)$.

Table 3
Selected geometric parameters (Å, °) for **2**

Ni1–N1	1.949(3)
O1–C1	1.293(5)
N1–C8	1.499(5)
C2–Cl1	1.734(4)
Ni1–O1	1.834(3)
N1–C7	1.275(5)
C6–C7	1.432(5)
C4–Cl2	1.750(5)
N1–Ni1–O1	92.4(1)
N1–Ni1–N1*	180.0
Ni1–N1–C7	124.0(3)
Ni1–O1–C1	131.4(2)
N1–Ni1–O1*	87.6(1)
O1–Ni1–O1*	180.0
Ni1–N1–C8	121.0(3)
N1–C7–C6	128.3(4)

Atoms marked with *'s are expanded by the symmetry operation $(2-x, -y, -z)$.

cis-N1–Ni1–O1 and *cis*-N1–Ni1–O1* bond angles are 92.4(1)° and 87.6(1)°, respectively. The bond distances are Ni1–N1 = 1.949(3) Å and Ni1–O1 = 1.834(3) Å, which are comparable with analogous square planar Ni(II) complexes such as **1**. The imine double bond distance N1=C7 = 1.275(5) Å of **2** is identical to that of **1**, which suggests that the electronic effects on the imine double bonds are more important than the geometric factors in the case of **1** and **2** [35]. In the crystals, there are no remarkable intermolecular hydrogen bonds and π–π interactions. The anti-parallel orientation of the molecular planes is found along the crystallographic *c* axis.

3.3. Calculations

Selected results of semi-empirical calculations (ZINDO) [36,37] are summarized in Table 4. Single point calculations of the heat of formation of the crystal structures determined are 315.5 and 255.4 kJ mol^{-1} for **1** and **2**, respectively.The dipole moments of the overall molecules **1** and **2** were evaluated to be 1.76 and 0.07 Debye, respectively. The very small value of **2** is ascribed to planarity and high symmetry of the molecules. On the other hand, the larger dipole moment of **1** is induced by distortion of the overall molecular structure containing Cl-substituents in the ligands.

The formal charges on the coordinating O and N atoms of the bidentate ligands and Ni(II) ions have been calculated and the net atomic charges thus obtained have been averaged. The formal charges on the Ni(II) ions are 0.813 and 0.792 for **1** and **2**, respectively, which indicates that the more tetrahedrally distorted coordination environment prevents charge distribution through coordination bonds. In contrast to the Ni(II) ions, considerable differences are not observed for the N and O atom. The averaged formal charges on the N atoms are −0.647 and −0.628, and the O atoms are −0.357 and −0.354 for **1** and **2**, respectively. Hence, we cannot discuss charge transfer bands based on these calculated formal charges on the coordinating N and O atoms for **1** and **2** at present. Indeed, the correlation between the average negative charge of the coordinating N and O atoms and the peaks of the electronic spectra may not be simple, because electronic spectra consist of several types of transitions. The calculation estimates that the predominant peak of the lowest component of π–π transitions is 32600 and 32300 cm^{-1} for **1** and **2**, respectively.

3.4. IR and electronic spectra and magnetic properties in the solid state

In the IR spectra of **1** and **2**, the imine C=N vibrations are observed at 1616 and 1620 cm^{-1}, respectively. Moreover, the Ni–N vibrations are found at 442 and 446 cm^{-1} and the Ni–O vibrations are found at 420 and 419 cm^{-1} for **1** and **2**, respectively. These peaks are in agreement with related complexes regardless of the degree of distortion of the coordination environment. In contrast to some other examples [11], the IR spectra are not sensitive to distortion of the coordination environment for the present complexes.

As shown in the diffuse reflectance electronic spectra (Fig. 3), the ligand field transition band(s) measured with the diffuse reflectance technique at 298 K are found at 13600 and 17100 cm^{-1} for **1** and 15500 cm^{-1} for **2**. These values are consistent with a common ligand field transition for tetrahedrally distorted planar or square planar [NiN_2O_2] chromophores, respectively. In addition, continuous broad bands over 24000 and 32000 cm^{-1} can be assigned to LMCT bands and π–π* transitions, respectively. The features of the d–d bands suggest that distortion of the coordination environment from square planar (**2**) to compressed tetrahedral (**1**) results in the spin state of the ground state, $S = 0$ or $S = 1$, respectively [38].

A polycrystalline sample of the square planar complex **2** exhibits diamagnetism at 298 K. On the other

Table 4
Summary of the results of ZINDO calculations for **1** and **2**

	1	**2**
Heat of formation (kJ mol^{-1})	315.5	255.4
Dipole moment (Debye)	1.76	0.07
HOMO–LUMO gap (eV)	7.406	7.466
Formal charge Ni	0.813	0.792
N	−0.647	−0.628
O	−0.357	−0.354
Predominant components of π–π* transitions (cm^{-1})	32600 (HOMO → LUMO) 40500 (HOMO − 6 → LUMO) 44600 (HOMO → LUMO + 4) 51200 (HOMO − 6 → LUMO + 4)	32300 (HOMO − 2 → LUMO + 1) 43700 (HOMO − 6 → LUMO) 48300 (HOMO − 4 → LUMO + 1)

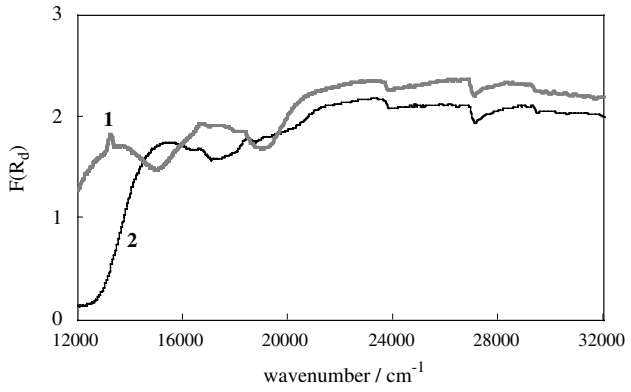


Fig. 3. Diffuse reflectance electronic spectra at 298 K for **1** and **2**.

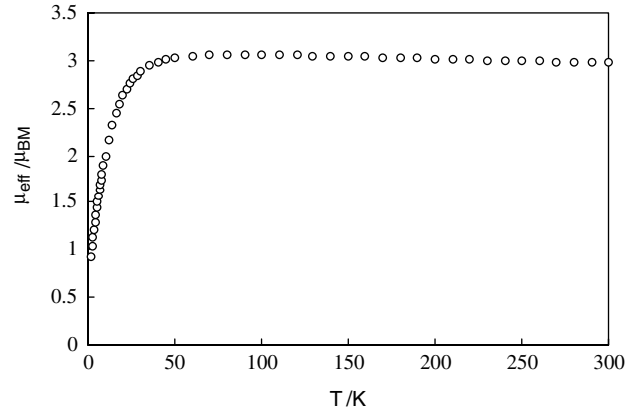


Fig. 4. Temperature dependence of effective magnetic moment (μ_{eff}) for **1**.

hand, magnetic measurement of compressed tetrahedral **1** reveals that mononuclear **1** obeys the Curie–Weiss law at low temperatures above ca. 20 K, because the effective magnetic moment stays almost temperature-independent. Fig. 4 shows the effective magnetic moment of polycrystalline samples in a range 2–300 K. The data were analyzed by the Curie–Weiss equation [$\chi_M = C/(T-\theta)$], giving a negative Weiss temperature (θ) of $-10.0(1)$ K with $C = 1.19(1)$ cm^3 K mol^{-1}. The effective magnetic moment (μ_{eff}) value of 2.98 B.M. at 298 K is slightly larger than the theoretical spin-only value of 2.83 B.M. for the $S = 1$ systems. The fact that the μ_{eff} value decreases to a small positive constant (0.924 B.M at 2 K) suggests that the ground state has a negative zero-field splitting parameter (D) with Kramers doublet, $|S,M_S\rangle = |1,+1\rangle$ or $|1,-1\rangle$ [39].

3.5. Thermally induced structural phase transition

It is well known that the related Ni(II) or Cu(II) complexes incorporating Schiff base ligands exhibit a thermally induced structural phase transition [11,18,19]. On heating from room temperature, square planar or compressed tetrahedral complexes turn into tetrahedral ones generally. The DSC curves of heating show an endothermic peak at 456 and 453 K for **1** and **2**, respectively. In analogy with related complexes, the structural phase transition may be ascribed to a transformation from a low temperature phase (compressed tetrahedral) into a high temperature phase (closer to tetrahedral). In addition, the structural phase transition seems to be irreversible. Further heating of the complexes results in decomposition at 580 and 587 K for **1** and **2**, respectively. However, such a structural phase transition could not be induced by light irradiation of any wavelength, though a certain Schiff base ligand itself exhibits both thermochromism and photochromism [40,41].

3.6. Absorption spectra in various solvents

A summary of the absorption spectra in several solvents and some physical properties of the solvents employed are given in Table 5. The general appearance of the solution and solid electronic spectra are considerably different from each other, and the absorption spectrum of **1** is quite similar to that of **2**, which suggests that the coordination geometries are different in solution (closer to tetrahedral) to that in the solid (compressed tetrahedral for **1** or square planar for **2**). The weak band at around 16000 cm^{-1} is assigned to d–d transitions. According to a discussion based on group theory [42] (approximately, in D_{2h} symmetry), ligand field bands consist of a spin-forbidden transition $^1A_g \rightarrow {}^3B_{1g}$ related to $d_{xy} \rightarrow d_{x^2-y^2}$ orbital excitation at around 12000 cm^{-1}, a spin-allowed $^1A_g \rightarrow {}^1B_{1g}$ transition related to $d_{xy} \rightarrow d_{x^2-y^2}$ orbital excitation at around 16000 cm^{-1}, and a $^1A_g \rightarrow {}^1B_{3g}$ d–d transition related to $d_{yz} \rightarrow d_{x^2-y^2}$ orbital excitation overlapped with a $^1A_g \rightarrow {}^1B_{2g}$ charge transition band around 20000 cm^{-1}. On the other hand, the strong band at around 30000 cm^{-1} is assigned to π–π* excitations due to imine groups. The absorption bands in the UV region would be ascribed to $^1A_g \rightarrow {}^1B_{2g}$ at around 24000 cm^{-1}, $^1A_g \rightarrow {}^1B_{3u}$,$^1B_{2u}$ at around 28000 cm^{-1} and $^1A_g \rightarrow {}^1B_{3u}$ at around 30000 cm^{-1}. The last one is ascribed to the electric-dipole allowed exciton coupling mode due to imine π–π* transitions.

In the CD spectrum of **1** in chloroform solution, positive and negative weak peaks in the d–d region are observed at 18200 and 20400 cm^{-1}, respectively. While positive strong peaks are observed at 23000, 24700, 26600 and 30800 cm^{-1}, which are assigned to π–π* transitions. The CD spectral pattern corresponds to the $\Lambda(R,R)$ absolute configuration of **1** determined in the solid state. However, as far as we know, there have not been reported CD data for analogous complexes incorporating identical ligands [28,43]. Thus, we could not discuss the spectral features involving their intensity at present.

Table 5
Maximum absorbance wavenumbers of d–d and π–π bands of **1** and **2** in various solutions, 0.01 mM at 25 °C

Solvents	Acetone	Methanol	Chloroform
μ (Debye)	3.11	2.97	1.11
ε	20.700	32.630	4.806
n_D^{20}	1.356	1.326	1.444
$(n^2-1)/(2n^2+1)$	0.179314	0.167888	0.209880
$(\varepsilon-1)(\varepsilon+2)-(n^2-1)/(n^2+2)$	0.649349	0.711608	0.293582
d–d peaks (cm^{-1})			
1	16500	16300	15900
2	16500	16300	16100
π–π* peaks (cm^{-1})			
1	31500	25500	29400
2	31700	25600	29400

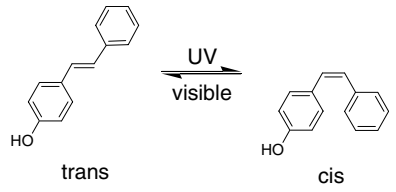
The values of the dipole moment μ, dielectric constant ε, refractive index n_D^{20}.

Furthermore, the predominant d–d and π–π* peaks are sensitive to the polarity of the solvents, which is well known for the related Ni(II) and Cu(II) complexes [44,45]. The peaks of both the d–d band and the π–π* band shift to higher energies in solvents of increasing polarity. This significant negative solvatochromic behavior is in accordance with the interaction of the dipole moment of the solute complexes and the surrounding solvent. According to the theory of dielectric polarization, negative solvatochromism is expected for transitions from a state with a high dipole moment to a state with a smaller one. It suggests that short-range interactions between the dipole moment of the solute and the solvent can induce structural changes of the solute complexes in accordance with the alignment of the transition moment for ground and excited states of a certain transition [46].

3.7. Towards solvatochromism induced by a photochromic solute

In this way, we have also attempted to tune solvatochromism of the complex by means of a doping photochromic solute in solution. At first, we have confirmed that neither precipitates nor a solution of **1** solely exhibit any spectral changes by light irradiation. Next, we prepared a 0.01 mM chloroform solution of **1** containing equimolar 4-hydroxyazobenzene (4HAZ). It is well known that irradiation of UV and visible light results in reversible photoisomerization of 4HAZ to *cis* and *trans* forms (Scheme 2) in solution. The dipole moment of the *cis* and *trans* forms could be evaluated by the ZINDO method to be ca. 3 and almost 0 Debye, respectively. It should be noted that 4HAZ is hardly expected to coordinate to this four-coordinated Ni(II) complex to generate a six-coordinated Ni(II) complex in solution.

As shown in Fig. 5, the absorption spectrum shows a weak peak at around 23000 cm^{-1} and strong peak at 29000 cm^{-1}. The latter is attributed to overlap of **1** and very intense π–π* bands of 4HAZ. The corresponding ESR spectrum resonance occurs at $g = 2.11$, which is comparable to the values for **2** and 4HAZ as well as any analogous Schiff base Ni(II) complexes. This result does



Scheme 2. Photoisomerization of 4-hydroxyazobenzene (4HAZ).

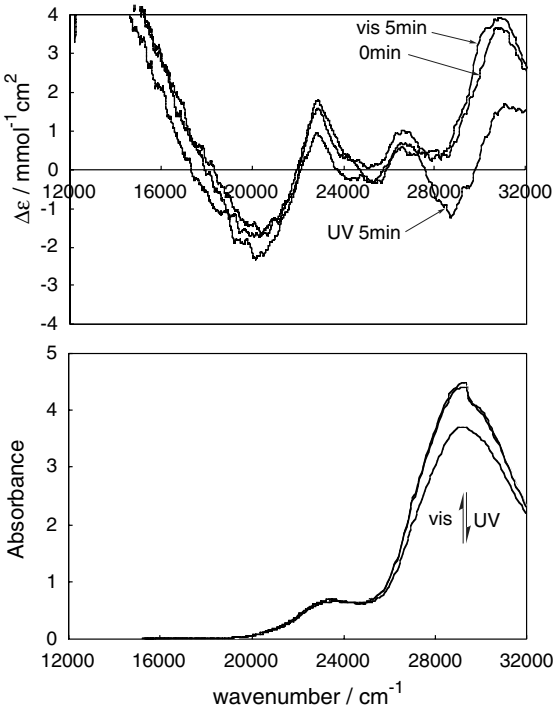


Fig. 5. Absorption spectra (below) and CD spectra (above) of 0.01 mM of **1** and 4HAZ at 298 K before and after UV or visible light irradiation for 5 min.

not suggest the appearance of radical or (de)protonated species nor other supramolecular structures such as a helix involving 4HAZ and **1** in solution. UV or visible light irradiation for 5 min resulted in a reversible decrease or increase of the intensity of the peak at 29 000 cm^{-1}. The corresponding CD spectrum (Fig. 5) exhibits a negative peak of the d–d band at 20 000 cm^{-1} and positive peaks of the π–π* bands at 23 000, 27 000 and 31 000 cm^{-1} in the initial state. Slight spectral changes could be observed after visible light irradiation for 5 min, a decrease of the intensities at 23 000 and 31 000 cm^{-1}, and the appearance of a negative peak at 29 000 cm^{-1} could be observed after UV light irradiation for 5 min. However, **2** and 4HAZ did not exhibit such changes of the absorption spectrum. This fact suggests that π–π interaction between the phenyl moieties of both complex (**1**) and 4HAZ solute is important for the photo-induced spectral change of **1** and 4HAZ.

In general, the rotatory strength between ground (0) and excited (a) states, R_{0a}, is given by Eq. (1) [45]

$$R_{0a} = \mathrm{Im}\langle 0 \mid \mathbf{P} \mid a\rangle\langle a \mid \mathbf{M} \mid 0\rangle = c\,|\mathbf{P}||\mathbf{M}|\cos(\mathbf{P},\mathbf{M}), \quad (1)$$

where **P**, **M** and (**P, M**) denote electric and magnetic dipole operators and the angles between them. According to the experimental results, the geometrically possible range of the angle (**P**, **M**), and dynamic equilibria of the related Ni(II) complexes in solutions [47], the spectral change of the CD spectra in the π–π* region can be attributed to a slight conformational change of the pendant phenyl moieties in the chiral ligands of **1** through short-range dipole–dipole and/or π–π interactions. However, the coordination environment and *Λ*(*R*,*R*) absolute configuration [48] or spin state [49] are conserved still within such a slight change of dipole moment, only 3 Debye. The magnitude is sufficiently smaller than the differences in dipole moment of the several solvents investigated.

4. Concluding remarks

The syntheses, structures, thermodynamical and electronic properties have been reported for two new Ni(II) complexes. These flexible complexes can easily vary their coordination geometries by introduction of steric and electronic substitutents, structural phase transition by heating, and dissolving in various solvents. The absorption spectra in various solvents also exhibit solvatochromism by the polarity of various organic solvents in accordance with the relationship between molecular structures and dipole moment, similar to conventional analogous complexes. In addition, we have firstly attempted *solvatochromism induced by a photochromic solute*, which results in only slight conformational changes of the chiral ligands. This new approach based on supramolecular photochemistry has the possibility of designing optical-magnetic switching materials, nanoscaled molecular machines and tuning homogeneous (chiral) catalysts of transition metal complexes [50] without photochromic groups in their ligands [4]. Detailed and extended studies for analogous systems are underway now.

5. Supplementary material

Crystallographic data for the structural analyses have been deposited with the Cambridge Crystallographic Data Centre, CCDC with deposition numbers 263944 and 263945 for **1** and **2**, respectively. Copies of this information can be obtained from The Cambridge Crystallographic Data Centre, 12 Union Road, Cambridge CB2 1EZ, UK (fax: +44-1223-336033; e-mail: deposit@ccdc.cam.ac.uk or www: http://www.ccdc.cam.ac.uk).

Acknowledgments

This work was supported by Grant-in-Aid for the 21st Century COE program 'KEIO Life Conjugate Chemistry' from the Ministry of Education, Culture, Sports, Science and Technology, Japan. The authors thank Professor Yohru Yamada and Dr. Taketo Ikeno (Keio University) for the use of the DSC apparatus, Professor Hidenari Inoue (Keio University) for the use of the CD spectrometer, and Professor Katsuya Inoue (Institute for Molecular Scicence) for the use of the SQUID instrument.

References

[1] O. Sato, Acc. Chem. Rev. 36 (2003) 692.
[2] O. Sato, S. Hayami, Y. Einaga, Z.-Z. Gu, Bull. Chem. Soc. Jpn. 76 (2003) 443.
[3] S. Kume, M. Kurihara, H. Nishihara, Chem. Commun. (2001) 1656.
[4] D. Pucci, A. Bellusci, A. Crispini, M. Ghedini, M. La Deda, Inorg. Chim. Acta 357 (2004) 495.
[5] P. Gutlich, Y. Garcia, H.A. Goodwin, Chem. Soc. Rev. 29 (2000) 419.
[6] P. Gutlich, Y. Garcia, T. Woike, Coord. Chem. Rev. 219–221 (2001) 839.
[7] O. Sato, T. Iyoda, A. Fujishima, K. Hashimoto, Science 272 (1996) 704.
[8] T. Murahashi, Y. Higuchi, T. Katoh, H. Kurosawa, J. Am. Chem. Soc. 124 (2002) 14288.
[9] K. Takahashi, R. Nakajima, Z.-Z. Gu, H. Yoshiki, A. Fujishima, O. Sato, Chem. Commun. (2002) 1578.
[10] R. Mikami, M. Taguchi, K. Yamada, K. Suzuki, O. Sato, Y. Einaga, Angew. Chem., Int. Ed. 43 (2004) 6135.
[11] S. Yamada, Coord. Chem. Rev. 190–192 (1999) 537.
[12] R.L. Braun, E.C. Lingagelter, Acta Crystallogr. 21 (1966) 546.

[13] K. Ravikumar, S.S. Rajan, V. Rajaram, S.K. Ramalingam, S. Natarajin, Z. Krist. 175 (1986) 117.
[14] V. Manriquez, J. Vargas, J. Costamagna, H.G. von Schnering, K. Peters, Acta Crystallogr., Part C 46 (1990) 772.
[15] M.R. Fox, E.C. Lingafelter, P.L. Orioli, L. Sacconi, Nature 197 (1963) 1104.
[16] M.R. Fox, L. Orioli, L. Sacconi, Acta Crystallogr. 17 (1964) 1159.
[17] R.L. Braun, E.C. Lingagelter, Acta Crystallogr. 22 (1967) 780.
[18] N. Arai, M. Sorai, S. Seki, Bull. Chem. Soc. Jpn. 45 (1972) 2398.
[19] T. Ashida, S. Iwata, T. Yamane, M. Kakudo, A. Takeuchi, S. Yamada, Bull. Chem. Soc. Jpn. 49 (1976) 3502.
[20] J.B. Willis, D.P. Mellor, J. Am. Chem. Soc. 69 (1947) 1237.
[21] L. Sacconi, P. Paoletti, M. Ciampolini, J. Am. Chem. Soc. 85 (1963) 411.
[22] H. Hoss, H. Elias, Inorg. Chem. 32 (1993) 317.
[23] M.K. Saha, I. Bernal, F.R. Fronczek, Chem. Commun. (2004) 84.
[24] T. Akitsu, Y. Einaga, Acta Crystallogr., Part E 60 (2004) m436.
[25] T. Akitsu, Y. Einaga, Acta Crystallogr., Part E 60 (2004) m1552.
[26] T. Akitsu, Y. Einaga, Acta Crystallogr., Part E 60 (2004) m1555.
[27] T. Akitsu, Y. Einaga, Acta Crystallogr., Part E 60 (2004) m1602.
[28] T. Akitsu, Y. Einaga, Acta Crystallogr., Part C 60 (2004) m640.
[29] A. Altomare, G. Cascarano, C. Giacovazzo, A. Guagliardi, M.C. Brurla, G. Polidori, M. Camalli, J. Appl. Cryst. 27 (1994) 435.
[30] G.M. Sheldrick, SHELXL97, Program for the Refinement of Crystal Structures, University of Göttingen, Göttingen, Germany, 1997.
[31] Molecular Structure Corporation. TEXSAN. Version 1.11., MSC, 9009 New Trails Drive, The Woodlands, TX 77381-5209, USA, 2001.
[32] G.-P. Li, Q.-C. Yang, Y.-Q. Tang, Y.-D. Guan, Z.-H. Shang, Acta Chim. Sinica 45 (1987) 421.
[33] A. Bondi, J. Phys. Chem. 68 (1964) 441.
[34] P.L. Orioli, L. Sacconi, J. Am. Chem. Soc. 88 (1966) 277.
[35] P.C. Chia, D.P. Freyberg, G.M. Mockler, E. Sinn, Inorg. Chem. 16 (1977) 254.
[36] M.C. Zerner, G.H. Lowe, R.F. Kirchner, U.T. Mueller-Westerhoff, J. Am. Chem. Soc. 102 (1980) 589.
[37] J.D. Head, M.C. Zerner, Chem. Phys. Lett. 131 (1986) 359.
[38] W.C. Hoyt, G.W. Everett Jr., Inorg. Chem. 8 (1969) 2013.
[39] R. Boca, Coord. Chem. Rev. 248 (2004) 757.
[40] E. Hadjoudis, I.M. Mavridis, Chem. Soc. Rev. 33 (2004) 579.
[41] T. Akitsu, Y. Takeuchi, Y. Einaga, Acta Crystallogr., Part C 60 (2004) o801.
[42] B. Bosnich, J. Am. Chem. Soc. 90 (1968) 627.
[43] C. Evans, D. Luneau, J. Chem. Soc., Dalton Trans. (2002) 83.
[44] H. Okawa, M. Nakamura, S. Kida, Inorg. Chim. Acta 120 (1986) 185.
[45] Y. Nishida, S. Kida, Bull. Chem. Soc. Jpn. 43 (1970) 3814.
[46] I. Veroni, A. Rontoyianni, C.A. Mitsopoulou, J. Chem. Soc., Dalton Trans. (2003) 255.
[47] R.E. Ernst, M.J. O'Connor, R.H. Holm, J. Am. Chem. Soc. 89 (1969) 6104.
[48] J.J. Jodry, R. Frantz, J. Lacour, Inorg. Chem. 43 (2004) 3329.
[49] T. Nakabayashi, T. Ishida, T. Nogami, Inorg. Chem. Commun. 7 (2004) 1221.
[50] M. Kettunen, A.S. Abu-Surrah, H.M. Abdel-Halim, T. Repo, M. Leskela, M. Laine, I. Mutikainen, M. Ahlgren, Polyhedron 23 (2004) 1649.

Table 1
Equilibrium constants ($\log\beta_{pqr}(\sigma)$, at 25 °C and I = 3.0 mol dm^{-3} $NaClO_4$)[a], analytical composition of solutions used and fractions of the total phosphorus concentration

$\log\beta_{011}$ −1.89(1)	$\log\beta_{002}$ 0.0(2)	$\log\beta_{012}$ −1.44(5)	$\log\beta_{111}$ 0.13(3)	$\log\beta_{122}$ 1.04(2)		$\log\beta_{352}$ −0.81(1)	$\log\beta_{363}$ 0.23(2)	$\log\beta_{383}$ −6.11(1)		$\log\beta_{364}$ 2.62(4)	$\log\beta_{385}$ 0.98(2)		$\log\beta_{361}$ 9.60(2)
Solution	C_P	C_M	$-\log[H^+]$	P_{001}	P_{011}	P_{002}	P_{012}	P_{111}	P_{122}	P_{352}	P_{363}	P_{364}	P_{385}
1	0.010	0.010	1.49	0.41	0.16			0.12	0.26		0.01	0.01	
2	0.010	0.010	1.96	0.17	0.19			0.10	0.24	0.06	0.12	0.08	0.03
3	0.010	0.050	1.59	0.11	0.06			0.24	0.17	0.23	0.13	0.06	
4	0.010	0.100	1.00	0.31	0.04			0.40	0.20	0.03	0.01	0.01	
5	0.010	0.100	2.00	0.01	0.01			0.08	0.01	0.83	0.07		
6	0.030	0.050	2.13	0.02	0.03			0.05	0.05	0.42	0.35	0.06	0.02
7	0.040	0.060	1.93	0.03	0.03			0.06	0.08	0.29	0.34	0.14	0.03
8	0.050	0.050	1.45	0.13	0.05			0.10	0.30	0.04	0.09	0.25	0.04
9	0.070	0.050	2.15	0.04	0.07			0.02	0.12	0.04	0.19	0.21	0.31
10	0.100	0.020	1.40	0.44	0.14	0.04	0.04	0.02	0.29			0.02	0.02
11	0.100	0.050	0.97	0.36	0.04	0.02	0.01	0.07	0.40			0.08	0.01
12	0.100	0.050	1.00	0.35	0.05	0.02	0.01	0.07	0.40		0.01	0.08	0.01
13	0.100	0.050	1.40	0.21	0.07	0.02	0.01	0.04	0.38		0.02	0.19	0.07
14	0.100	0.050	1.80	0.13	0.10		0.01	0.02	0.26		0.03	0.18	0.26
15	0.100	0.050	2.16	0.07	0.13			0.01	0.15		0.04	0.11	0.47
16	0.100	0.100	1.50	0.06	0.02			0.07	0.20	0.06	0.16	0.37	0.06
17	0.100	0.200	2.00					0.02	0.01	0.68	0.24	0.03	
18	0.050		1.70	0.55	0.36	0.04	0.07						
19	0.050		2.15	0.32	0.61	0.01	0.06						
20	0.050		4.05		1.00								

Phosphorus fractions lower than 0.01 are omitted.

[a] Ref. [5]. The possible formation the hydroxo species $AlOH^{2+}$, $Al_2(OH)_2^{4+}$ and $Al_3(OH)_4^{5+}$ was considered, adding to the model the values $\log\beta_{101} = -4.55$, $\log\beta_{202} = -7.6$ and $\log\beta_{304} = -13.4$, calculated from the literature [8]. The equilibrium concentration of these species was found to be negligible in all solutions used.

which the NMR spectra were recorded were significantly different from those of the potentiometric investigation. We have therefore obtained new NMR data under the same conditions as were used in the EMF study and have made semi-quantitative assignments of the NMR peaks. We have previously reported the results of a similar investigation of NMR data with regard to phosphato complexes of beryllium(II) [6].

2. Notation

Reagents: Al^{3+}, H_2O and H_3PO_4

Equilibria: $pAl^{3+} + qH_2O + rH_3PO_4 \rightleftarrows Al_pH_{-q}(H_3PO_4)_r^{3p-q} + qH^+$,
$\beta_{p,q,r}(p,q,r)^{3p-q} = Al_pH_{-q}(H_3PO_4)_r^{3p-q}$

C_M: total concentration (mol dm^{-3}) of aluminium

C_P: total concentration (mol dm^{-3}) of phosphate

P_{pqr}: concentration of phosphorus in the species $(p,q,r)^{3p-q}$ as a fraction of the total phosphorus concentration, $P_{pqr} = r[Al_pH_{-q}(H_3PO_4)_r^{3p-q}]/C_P$

I_X: area under peak(s) X as a fraction of the total peak area. X may represent a single peak or the sum of many peaks

δ_{pqr}: chemical shift (ppm) of the peak originating from the species $(p,q,r)^{3p-q}$

δ_X: chemical shift (ppm) of peak X

3. Experimental

3.1. Chemicals and analysis

Test solutions were prepared with analytical grade commercial products and analysed as described in the potentiometric work [5]. The composition of each solution used in this study is given in Table 1.

3.2. NMR measurements

$^{31}P\{^1H\}$ NMR spectra were recorded at 121.42 MHz using a Varian VXR 300 Spectrometer. The probe temperature was 25 ± 1 °C. The field-frequency stabilisation was established by means of a coaxial capillary tube filled with D_2O. All ^{31}P chemical shifts are reported in ppm toward higher frequency with respect to external reference consisting of 85% commercial H_3PO_4. The chemical shifts therefore refer to the dimer $(H_3PO_4)_2$, which, according to Wertz and Cook [7], is the predominant species present in 85% phosphoric acid. No corrections were made for differences in bulk susceptibilities.

4. Results

Observed ^{31}P NMR spectra are shown in Fig. 1. On the basis of the shape of the spectral bands, it can

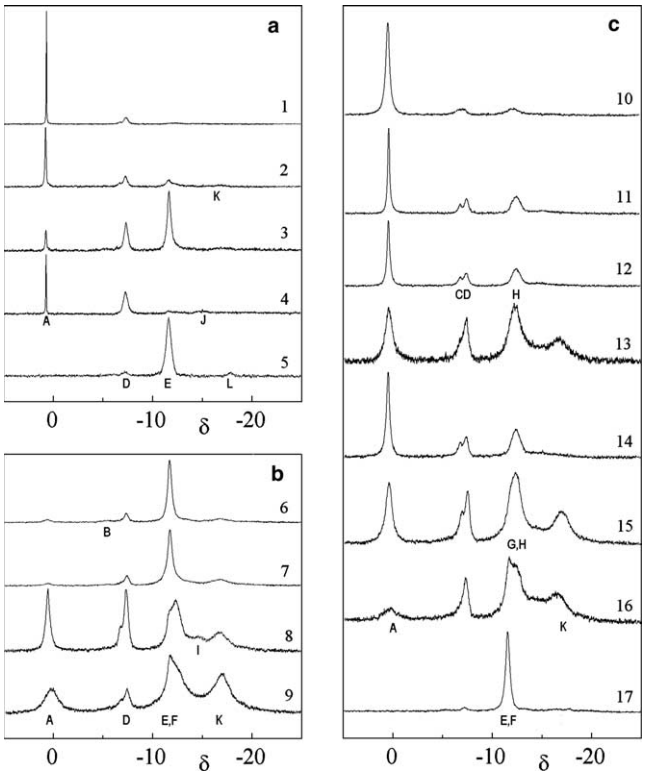


Fig. 1. ^{31}P NMR spectra at 25 °C of solutions 1–17 (Table 1). (a) $C_P = 0.01$ mol dm^{-3}, (b) $0.03 \leqslant C_P \leqslant 0.07$ mol dm^{-3}, and (c) $C_P = 0.1$ mol dm^{-3}. Capital letters refer to assignments in Table 2.

generally assumed that there is slow exchange, on the NMR time scale, at the aluminium centre. This implies that each phosphorus atom in a complex should give rise to a signal whose area, as a fraction of the total area, is equal to the concentration of phosphorus in the complex as a fraction of the total phosphorus concentration. Fractional phosphorus concentrations, calculated using equilibrium constants determined in the potentiometric investigation [5], are shown in Table 1. The assignment was based on the principle that the fractional area of each peak should be equal to the sum of the fractional concentrations of the species contributing to the peak. Observed chemical shifts are given in Table 2.

The species $(361)^{3+}$ and $(383)^{+}$ never attain a phosphorus content of more than 1% of the total. The signals for these species was not sought in the spectra.

4.1. Peak A: fast proton exchange

The chemical shift of peak A is dependent on [H$^+$], due to fast proton exchange. Its value is the mol-fraction-weighted average of the chemical shifts of all the species contributing to the peak, as expressed as in Eq. (1). To a first approximation peak A may be assigned to the species (001)

Table 2
Peaks in ^{31}P NMR spectra

Peak	δ (ppm)	Assignment
A	0.3–0.9	H_3PO_4–$H_2PO_4^-$, in part $Al_3H_{-6}(H_3PO_4)_4^{3+}$, $Al_3H_{-8}(H_3PO_4)_5^{+}$
B	−5.4	not assigned
C	−6.80 ± 0.04	$Al(H_2PO_4)_2^{+}$
D	−7.37 ± 0.06	$AlH_2PO_4^{2+}$, $Al(H_2PO_4)_2^{+}$
E	−11.52 ± 0.04	$Al_3H_{-5}(H_3PO_4)_2^{4+}$
F	−11.68 ± 0.03	$Al_3H_{-6}(H_3PO_4)_3^{3+}$
G	−12.20	$Al_3H_{-8}(H_3PO_4)_5^{+}$
H	−12.44 ± 0.05	$Al(H_2PO_4)_2^{+}$
I	−13.8	not assigned
J	−15.10	not assigned
K	−16.3 to −17.0	$Al_3H_{-6}(H_3PO_4)_4^{3+}$
L	−17.76 to −17.94	not assigned

$$\delta_A = \frac{\sum P_{pqr}\delta_{pqr}}{\sum P_{pqr}} \quad (1)$$

(H_3PO_4) and $(011)^-$ ($H_2PO_4^-$). Peak integrals agree to within 10% or better with the sum $P_{001} + P_{011}$. Furthermore, the plot δ_A versus $P_{011}/(P_{001} + P_{011})$ (Fig. 2) indicates that the majority of the points falls on the straight line fitting the data of solutions 18, 19 and 20 (circles) in which aluminium(III) was absent. Points well away from the straight line indicate that other species are in fast exchange. For example, in solutions 18–20 some of phosphorus is present in form of dimers (002) ($H_6(PO_4)_2$) and $(012)^-$ ($H_5(PO_4)_2^-$. To explain the shift of A in absence of aluminium(III) we postulated that $\delta_{002} = 0$ ppm, since the reference solution of aqueous 85% phosphoric acid contains practically only $H_6(PO_4)_2$, and, furthermore, that $\delta_{011} = 0.91 \pm 0.01$ ppm as it results from the chemical shift observed for solution 20 where more than 99% of phosphorus is given by $H_2PO_4^-$. On account of these δ_{002} and δ_{011} values, we calculated from data of solutions 18 and 19 $\delta_{001} = 0.63 \pm 0.03$ ppm and $\delta_{012} = 0.37 \pm 0.15$ ppm. The error limits were estimated by error propagation from the error on δ_{011}.

Solutions 7, 9, 14, 15 and 16 have δ_A values well off the straight line. It is noteworthy that the signals are

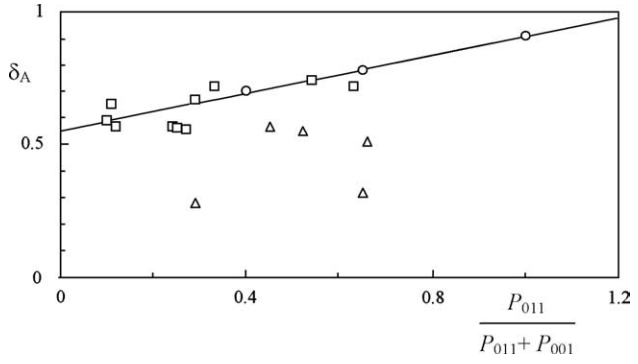


Fig. 2. Chemical shifts of peak A, δ_A, as a function of $P_{011}/(P_{001} + P_{011})$. Circles refer to solutions 18, 19 and 20; triangles to solutions 7, 9, 14, 15 and 16; squares to remaining solutions in Table 1. The straight line represents equation: $0.57 + 0.34P_{011}/(P_{001} + P_{011})$.

broad whereas peaks whose shifts fall near the straight line are sharp. Probably, peak A broadens due to a dynamic process involving free and metal coordinated phosphate groups present in species other than H_3PO_4 and $H_2PO_4^-$. In the mentioned solutions, there is an abundant percentage of the species $(364)^{3+}$ and $(385)^{+}$. We suggest that in these complexes there are loosely bound phosphate groups which can exchange rapidly with free H_3PO_4 and $H_2PO_4^-$. The $(364)^{3+}$ species may result from the addition of H_3PO_4 to $(363)^{3+}$ either through replacement of water molecules in the coordination sphere of the metal to produce a form symbolised as ζ-$(364)^{3+}$ or through association by hydrogen bonds with coordinated water and phosphate groups to give a complex which we denote as ε-$(364)^{3+}$ form. The ε-$(364)^{3+}$ form would contribute to A with a fraction of phosphorus $P_\varepsilon = 1/4P_{364}(1 + K_{\varepsilon\zeta})^{-1}$, where $K_{\varepsilon\zeta}$ is the equilibrium constant for ε-$(364)^{3+} \rightleftarrows \zeta$-$(364)^{3+}$. The ζ form would resonate in a different region of the spectrum. Similarly, $(385)^{+}$ should be an equilibrium mixture of a η-$(385)^{+}$ form, in which two phosphate are hydrogen bonded to coordinated phosphate groups and water, and of a θ-$(385)^{+}$ form with groups directly coordinated by the metal. Therefore, indicating with $K_{\eta\theta}$ the constant for η-$(385)^{+} \rightleftarrows \theta$-$(385)^{+}$ one has the fraction of phosphorus contributing to A, i.e., $P_\eta = (2/5)P_{385}$-$(1 + K_{\eta\theta})^{-1}$. According to these definitions the intensity of peak A and its shift can be expressed as (2) and (3). The sum $P_{001} + P_{011} + P_{002} + P_{012}$

$$I_A = P_{001} + P_{011} + P_{002} + P_{012} + \frac{P_{364}}{4(1+K_{\varepsilon\zeta})} + \frac{2P_{385}}{5(1+K_{\eta\theta})}, \tag{2}$$

$$\delta_A = \frac{\delta_{001}P_{001} + \delta_{011}P_{011} + \delta_{012}P_{012} + \frac{P_{364}\delta_\varepsilon}{4(1+K_{\varepsilon\zeta})} + \frac{2P_{385}\delta_\eta}{5(1+K_{\eta\theta})}}{I_A}, \tag{3}$$

accounts for more than 90% of I_A. Thus, the terms relative to species $(364)^{3+}$ and $(385)^{+}$ contribute negligibly to I_A within experimental error. It is sufficient that $K_{\varepsilon\zeta}$ and $K_{\eta\theta}$ have values just superior to unity to make the last two terms on the right-hand side of Eq. (2) less than 10% of I_A. On the contrary, the influence of quantities in Eq. (3) corresponding to species $(364)^{3+}$ and $(385)^{+}$ may be significant primarily due to the magnifying effect of δ_ε and δ_η. Assuming that $I_A \approx P_{001} + P_{011} + P_{002} + P_{012}$ the most probable $\delta'_\varepsilon = \delta_\varepsilon(1 + K_{\varepsilon\zeta})^{-1}$ and $\delta'_\eta = \delta_\eta(1 + K_{\eta\theta})^{-1}$ were calculated by a standard least squares procedure in which $\delta_{001} = 0.63$ ppm, $\delta_{011} = 0.91$ ppm, $\delta_{012} = 0.37$ ppm and $\delta_{002} = 0$ as established above, were kept constant. This treatment led to $\delta'_\varepsilon = -0.30 \pm 0.05$, $\delta'_\eta = -0.30 \pm 0.05$ and $\sigma(\delta_A) = 0.05$ ppm. The results of the δ_A data analysis can be visualized by plotting the values, cleaned from the contributions of the metal complexes, versus $P_{011}/(P_{001} + P_{011})$. As Fig. 3 shows, the fitting between these values, ${}^*\delta_A$ in Eq. (4), and the straight line drown with $\delta_{001} = 0.63$ ppm and

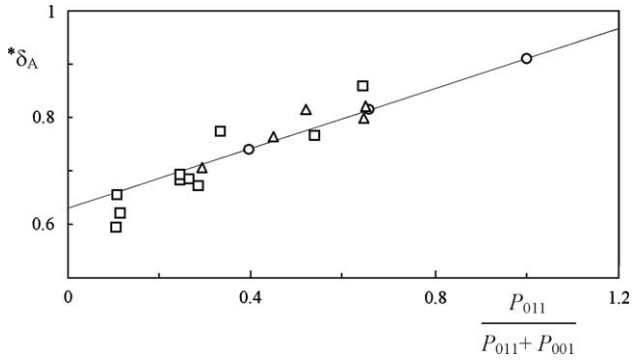


Fig. 3. ${}^*\delta_A$, Eq. (4), as a function of $P_{011}/(P_{001} + P_{011})$. The straight line represents equation $0.63 + 0.28P_{011}/(P_{001} + P_{011})$.

$$^*\delta_A = \frac{I_A\delta_A - 0.37P_{012} + 0.30 \cdot 0.25P_{364} + 0.30 \cdot 0.40P_{385}}{P_{001} + P_{011}} = \delta_{001} + \frac{(\delta_{011} - \delta_{001})P_{011}}{P_{001} + P_{011}} \tag{4}$$

$\delta_{011} - \delta_{001} = 0.28$ ppm is satisfactory. The standard deviation from the linear dependence amounts to 0.03 ppm.

4.2. Peaks C, D and H: complexes mononuclear in Al

On the basis of the potentiometric model [5], the main aluminium complex present in solutions 10, 11 and 12 has the composition $(122)^{+}$ $(Al(H_2PO_4)_2^{+})$. In the spectra of these solutions three peaks are observed: C −6.71, D −7.42 and H −12.48 ppm. Peaks C and D are partly overlapped in the spectra of solution 10. Therefore, the complex with general composition $(122)^{+}$ should be an equilibrium mixture of isomers. The global area of the three peaks, $I_C + I_D + I_H$, in spectra relative to solutions 10, 11 and 12 matches P_{122} within 0.08. Furthermore, the distribution of the phosphorus in the various signals follows approximately the expressions $(I_C + I_D)/P_{122} \approx 0.4$ and $I_H/P_{122} \approx 0.6$, so that $I_H/(I_C + P_D) \approx 1.5$. In a few cases, as for instance solution 4, $I_H/(I_C + I_D)$ is much lower than 1.5 indicating the presence of a complex differing from $(122)^{+}$ but resonating in the vicinity of peak D. Probably the new complex is $AlH_2PO_4^{2+}$, since, for data relative to solution 4, one has $P_{111} = 0.40$ which is close to $I_D = 0.47$. Therefore, the intensity of peaks C and D are explained within the limits of experimental error by assuming $I_C + I_D = P_{111} + 0.4P_{122}$. The results of evaluations, given in Table 3, show the good agreement between measured and expected signal intensity. From the residuals between measured and calculated peak area, a standard deviation of 0.05 was estimated. It proved convenient for further analysis to separate peaks C and D from spectra giving distinct but in part overlapping bands.

Table 3
Resolution of peaks C and D

Solution	$I_C + I_D$	$P_{111} + 0.40P_{122}$	I_C	$I_C/(I_C + I_D - P_{111})$
1	0.31	0.22	0.09 ± 0.02	$0.4_7 \pm 0.1$
2	0.24	0.20	0.05 ± 0.01	$0.3_6 \pm 0.1$
4	0.47	0.48		
8	0.20	0.22		
9	0.11_5	0.06	0.03 ± 0.02	0.3 ± 0.2
10	0.11	0.14		
11	0.23	0.23	0.09 ± 0.01	0.56 ± 0.06
12	0.18	0.23	0.07 ± 0.01	$0.6_3 \pm 0.1$
13	0.16	0.19		
14	0.18	0.12	0.08/0.01	0.50 ± 0.06
15	0.14	0.07	0.06 ± 0.03	$0.4_6 \pm 0.2$
16	0.16	0.14		

We postulated no overlapping in the outsides of the bands so that the area of the left-hand side of C is due only to the species originating that signal. The areas were computed with the old honoured method of counting squares beneath the curve. From the results presented in Table 3 we estimate that $I_C/P_{122} = 0.2 \pm 0.1$, therefore, C originates from 20% of the total phosphorus in the $(122)^+$ species. Furthermore, as reported in Table 3, the ratio $I_C/(I_C + I_D - P_{111}) = 0.5$ within the limits of estimated uncertainty corroborates the hypothesis that peak D stems from 20% of P_{122}. In conclusion peaks C, H and part of D are likely attributable to isomers of $Al(H_2PO_4)_2^+$, whereas part of D originates from $AlH_2PO_4^{3+}$. Peak C and the part of D arising from $(122)^+$ have comparable intensity. Therefore, they might stem from the same complex having not equivalent P atoms.

4.3. Peaks E, F, G and K: complexes trinuclear in Al

Peak E is observed as an intense signal at −11.52 ppm in spectra obtained from solution 5. The species $(352)^{4+}$ predominates in this solution, making the assignment straightforward.

With solutions 6 and 7 peak F is observed, close to peak E. The $(363)^{3+}$ complex has a relatively high concentration in these solutions. The fractional intensity of peak F is equal, within experimental error, to the sum $P_{363} + P_{352}$, as shown in Table 4. It was concluded that peak F is due to $(363)^{3+}$ with a significant contribution from $(352)^{4+}$.

Peak G at −12.20 ppm partly overlaps peak H. The latter was assigned to 60% $(122)^+$. Table 5 shows that the peak area is in reasonable agreement with $P_{385} + 0.60P_{122}$. It seems therefore reasonable to assign peak G to the species $(385)^+$.

Table 4
Comparison of the fraction of phosphorus in the species $(363)^{3+}$ and $(352)^{4+}$ with the area of NMR peak E

Solution	I_F	$P_{363} + P_{352}$
6	0.72	0.77
7	0.66	0.63
17	0.80	0.92

Table 5
Comparison of the fraction of phosphorus in the species $(385)^+$ and $(122)^+$ with the area of NMR peak G

Solution	I_G	$P_{385} + 0.60P_{122}$
8	0.39	0.43
14	0.41	0.42
15	0.44	0.56

Table 6
Comparison of the fraction of phosphorus in the species $(364)^{3+}$ with the area of NMR peak K

Solution	I_K	P_{364}
2	0.09	0.08
6	0.13	0.06
7	0.23	0.14
8	0.17	0.25
9	0.24	0.21
12	0.09	0.08
13	0.18	0.19
14	0.14	0.18
15	0.19	0.11
16	0.35	0.37

Peak K was observed in several spectra as a broad band in the region from −16.3 to −17.0 ppm. The fractional intensity of the signal is in modest agreement with the phosphorus percentage in the $(364)^{3+}$ complex, as shown in Table 6. This peak was therefore assigned to the species $(364)^{3+}$.

4.4. Unassigned peaks

Peak B was only found in solution 6 as a weak broad signal at −5.4 ppm. It does not appear to correlate with any species identified in the potentiometric investigation [5]. Peaks I, J and L have been observed as weak broad signals. They appear only in spectra obtained from solutions whose Al and P concentration falls outside the range explored during the potentiometric study so may correspond to species not detectable in that study [5].

5. Discussion

The most important conclusion of the present investigation is that NMR spectroscopy can be used to support a complicated equilibrium model derived from potentiometric data by correlating fractional NMR peak intensities with fractional concentrations calculated with the equilibrium model. In a system with slow exchange, such as the one studied here, the use of NMR data as independent source of information to derive a chemical model would be possible only with a spectrometer of very high resolution and sensitivity.

Potentiometry is a powerful tool for the determination of stability constants, but it only provides so-called macro-constants. NMR spectrometry, on the other hand, can provide information on micro-species, that is, species having the same stoichiometry or isomers in common parlance. In Scheme 1, we show some of the possible isomers of the ion $Al(H_2PO_4)_2^+$. There are possibilities of *cis*/*trans* isomerism and *monodentate* or *bidentate* phosphate binding. Three peaks, C, D and H, have been assigned to this complex.

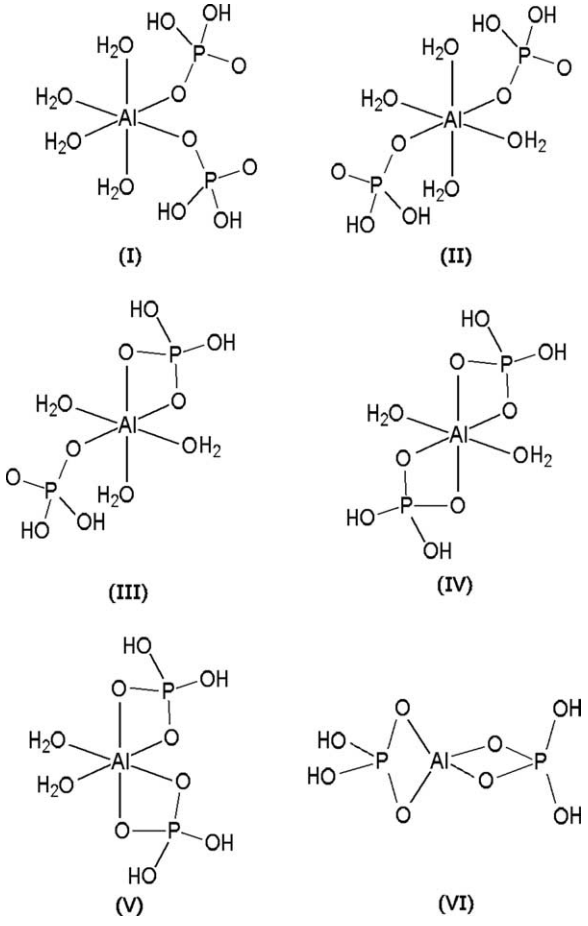
We believe that the forms (I) and (II) are less likely to be present because for the reaction $AlH_2PO_4^{2+} + H_3PO_4 \rightleftarrows Al(H_2PO_4)_2^+ + H^+$, $\log K = 0.91$, is higher than $\log\beta_{111}$ (0.13). This means that the disproportion $2AlH_2PO_4^{2+} \rightleftarrows Al(H_2PO_4)_2^+ + Al^{3+}$ is favoured. The extra stabilization of $Al(H_2PO_4)_2^+$ against $AlH_2PO_4^{2+}$ is consistent with the formation of chelate rings in (III) to (VI) and/or with coordination changes from the octahedral (I) to (V) to the tetrahedral (VI). Then two hypotheses can be formulated: (i) the presence of (III) with inequivalent phosphorus nuclei gives rise to C and D of equal intensity, consequently, only one of (IV) to (VI) is sufficient to explain the resonance H; (ii) if (III) is absent the three peaks are due to (IV), (V) and (VI).

It is the more likely that hypothesis (i) is correct as peak D has a contribution from $AlH_2PO_4^{2+}$ which most probably contains a monodentate phosphate group. Thus peak C may derive from a bidentate dihydrogenphosphate group. There is a remarkable difference between the chemical shifts of C and D on the one hand and H on the other. This could well be because H corresponds to the tetrahedral structure (VI) while all the other monomeric complexes are octahedral.

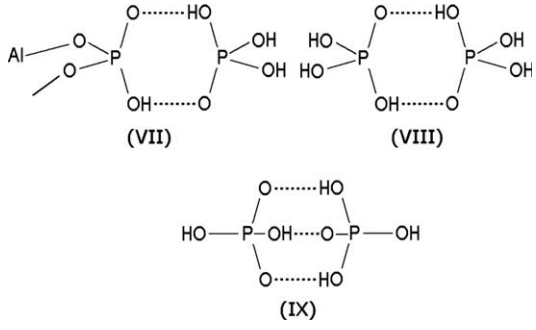
Peaks G and K, assigned to $(385)^+$ and $(364)^{3+}$, are apparently inert on the NMR time-scale, but both species appear to be involved in the fast proton exchange which causes the chemical shift of peak A to vary with $-\log[H^+]$. This suggests the presence in their structures of loosely bound phosphate groups. In the section devoted to peak A the isomers ε-$(364)^{3+}$, ζ-$(364)^{3+}$, η-$(385)^+$ and θ-$(385)^+$ were assumed to explain the anomalies in the shift of A. The ε-$(364)^{3+}$ and η-$(38)^+$ forms could contain in their molecule fragments as (VII) in Scheme 2, in which phosphate groups are bound through hydrogen bonds to groups coordinated by the metal. This hypothesis is consistent with the tendency [9] of phosphoric acid and its conjugate bases to dimerise to form (VIII), (IX) and similar species. Structural data in solution for (VIII) were obtained by Wertz and Cook [7].

5.1. Comparison with previous NMR results

The ^{31}P chemical shifts observed by various authors under different experimental conditions are summarised in Fig. 4. The more numerous signals found by Wilson et al. [4] might be due, in spite of higher temperature, to lower phosphate concentration. In fact, Akitt et al. [1], noticed that ^{31}P resonances tend to coalesce at increasing phosphoric acid concentration. Thus, a progressive sharpening of the peaks occurs as the phosphate concentration is reduced. The plethora of peaks in our spectra may be due fact that the solutions were relatively dilute (≤0.1 M).



Scheme 1.



Scheme 2.

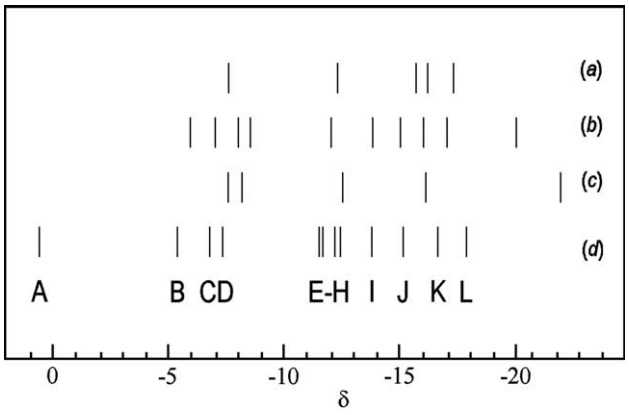


Fig. 4. Comparison of the ^{31}P chemical shift (δ/ppm) reported in the literature and those observed in the present study. (a) Ref. [1]: $T = -15$ °C, $0.4 \leqslant C_P \leqslant 10$ mol dm^{-3}; (b) Ref. [4]: $T = -5$ °C, $C_P = 0.2$ mol dm^{-3}; (c) Ref. [2]: $T = -15$ °C, $0.5 \leqslant C_P \leqslant 6$ mol dm^{-3}; (d) this work: $T = 25$ °C, $0.01 \leqslant C_P \leqslant 0.10$ mol dm^{-3}. Capital letters refer to assignments in Table 3.

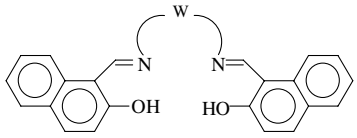
The findings of Akitt et al. [1] are in good agreement with those of Rudolph and Steger [2]. These workers used almost identical experimental conditions. Their spectra are less well resolved than those of Wilson et al. [4]. There is substantial agreement between our data and that of Wilson and co-workers. The chemical shifts shown in Fig. 4 probably equate to B, C, D, G, I, J and K in Table 2, with the exception of shifts at −8.5 and −20 ppm. Different experimental conditions probably account for the presence of E and F in our spectra only, and the signals at −8.5 ppm (the forth from the left) and −20 ppm (the most upfield one) in the spectra of Wilson and co-workers [4].

Acknowledgements

We thank Dr. Peter Gans for helpful discussion. Financial support by the Italian Ministero dell'Istruzione, dell'Università e della Ricerca (COFIN 2002) and the University of Firenze is gratefully acknowledged.

References

[1] J.W. Akitt, N.N. Greenwood, G.D. Lester, J. Chem. Soc. (A) (1971) 2450.
[2] W. Rudolph, W.E. Steger, Z. Phys. Chem. (Munich) 176 (1992) 185.
[3] S.J. Karlik, G.A. Elgavish, R.P. Pillai, G.L. Eichhorn, J. Magn. Reson. 49 (1982) 164.
[4] M.A. Wilson, P.J. Collin, J.W. Akitt, Anal. Chem. 61 (1989) 1253.
[5] L. Ciavatta, M. Iuliano, Ann. Chim. (Rome) 86 (1996) 1.
[6] L. Ciavatta, M. Iuliano, R. Porto, P. Innocenti, A. Vacca, Polyhedron 19 (2000) 1043.
[7] D.L. Wertz, G.A. Cook, J. Solution Chem. 14 (1985) 41.
[8] C.F. Baes Jr., R.E. Mesmer, The Hydrolysis of Cations, Wiley, New York, 1976, p. 121.
[9] L. Ciavatta, M. Iuliano, R. Porto, E. Vasca, Polyhedron 10 (1991) 2587.



Where W = - $(CH_2)_2$ - H_2L1 = H_2 – Naphen
- $(CH(CH_3)CH_2)$ - H_2L2 = H_2 – Naphpn
- $(CH_2\text{-}CH_2\text{-}CH_2)$ - H_2L3 = H_2 – Naphprn
- (C_6H_4) - H_2L4 = H_2 – Naphoph

Scheme 1. Structure of the tetradentate Schiff bases.

the chemistry of ruthenium bi- or polypyridyl complexes, the luminescent chemistry of ruthenium(II) complexes containing Schiff bases is not well developed. Furthermore, metal complexes of ruthenium containing triphenylphosphine or arsine, nitrogen and oxygen donor ligands are found to be effective catalysts for oxidation [13,14]. In particular, the selective oxidation of alcohols into carbonyl compounds by metal complexes is well documented in the literature [15–17]. Sharpless et al. [18] carried out a yield oriented study of oxidation of cholesterol, geranial, etc., catalyzed by ruthenium complexes in the presence of *N*-methylmorpholine-*N*-oxide (NMO) and *N*-*N*-dimethylaniline-*N*-oxide, and only a very few reports are available on the oxidation chemistry using NMO as co-oxidant.

In view of the rich photophysical and catalytic properties of organometallic ruthenium complexes, the introduction of Schiff bases with a 2N2O donor set to ruthenium(II) carbonyl complexes containing triphenylphosphine/triphenylarsine and heterocyclic bases has been carried out. As an extension of our preliminary communication [19–21] and to provide further insight on the catalytic and emission behaviors, an extensive series of ruthenium(II) carbonyl complexes containing tetradentate Schiff bases have been synthesized and characterized. Further, the redox and luminescent properties are also reported along with the catalytic activity of ruthenium(II) complexes towards oxidation of primary and secondary alcohols. The tetradentate Schiff bases were derived from condensation of 2-hydroxy-1-naphthaldehyde with the appropriate diamines. The following Schiff bases were used to prepare the new ruthenium(II) complexes shown in Scheme 1.

2. Experimental

2.1. Material and physical measurements

The Schiff bases were prepared in 80–90% yield by condensation of two mole equivalents of 2-hydroxy-1-naphthaldehyde and one mole equivalent of the corresponding diamine by following the reported procedure [22]. All the reagents used were chemically pure or analytical reagent grade. Solvents were purified and dried according to standard procedures. $RuCl_3 \cdot 3H_2O$ was purchased from Loba chemie pvt Ltd. Bombay, India and was used without further purification. [RuHCl(CO)$(PPh_3)_3$] [23], [RuHCl(CO)$(PPh_3)_2$ (B)] [24] (where B = py (or) pip) and [RuHCl(CO)$(AsPh_3)_3$] [25] were prepared by reported literature methods.

The analysis of carbon, hydrogen and nitrogen were performed on a Carlo Erba 1160 and a model 240 Perkin–Elmer CHN analyzer at the Central Drug Research Institute, Lucknow, India. IR spectra were recorded in KBR pellets in the 4000–200 cm^{-1} region in a Jasco 400 plus spectrophotometer. Electronic spectra were recorded in CH_2Cl_2 solution with a Cary 300 Bio UV–Vis Varian spectrophotometer in the range of 800–200 nm. ^1H NMR spectra were recorded on a Bruker 400 MHz instrument using TMS as an internal reference. Emission intensity measurements were carried out by using a Jasco FP-6500 spectrofluorimeter with 5 nm exit slit. Cyclic voltammetric measurements were carried out on a Bio Analytical System (BAS) model CV-50W electrochemical analyzer using acetonitrile as solvent. Melting points were recorded with a Boetius micro-heating table and are uncorrected. The catalytic yields were determined using HP 6890 series GC-FID with a DP-5 column of 30 m length, 0.32 mm diameter and 0.25 μm film thickness.

2.2. Synthesis of Ru(II) carbonyl Schiff base complexes

All the new complexes were prepared by the following general procedure. To a solution of [RuHCl(CO)-$(EPh_3)_2$ (B)] (where E = P; B = PPh_3, py (or) pip) and [RuHCl(CO)$(AsPh_3)_3$] (100 mg; 0.10–0.13 mmol) in benzene the appropriate Schiff base (39–53 mg; 0.10–0.13 mmol) was added and heated under reflux for 5 h. The resulting solution was concentrated to ca. 3 cm^3 and cooled. Light petroleum (60–80 °C) (5 cm^3) was then added whereupon the complex separated out. The solid was filtered off, washed and recrystallized from CH_2Cl_2/light petroleum ether mixture and dried in vacuo. The purity of the compounds were checked by TLC (yield: 65–70%).

2.3. Catalytic oxidation

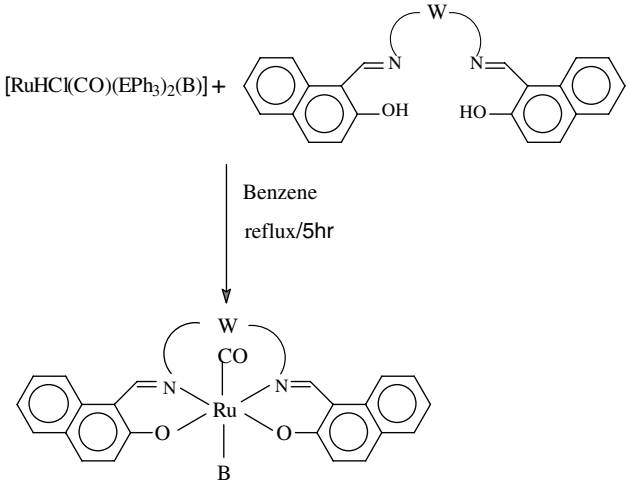
Catalytic oxidation of primary alcohols to the corresponding aldehydes and secondary alcohols to ketones by ruthenium(II) carbonyl complexes was studied in the presence of NMO as co-oxidant. A typical reaction using the complex [Ru(CO)(PPh_3)(L1)] as a catalyst, and primary or secondary alcohol as substrates at a 1:100 molar ratio is described as follows. A solution of ruthenium complex **1** (0.01 mmol) in 20 $cm^3CH_2Cl_2$ was added to the solution of substrate (1 mmol) and

NMO (3 mmol). The solution mixture was refluxed for 3 h and the solvent was then evaporated from the mother liquor under reduced pressure. The residue was then extracted with pet. ether (60–80 °C) (20 cm^3) and was analyzed by GC. The oxidation products are known and are commercially available, and were identified by GC co-injection with authentic commercial samples.

3. Results and discussions

Complexes of the general formula [Ru(CO)(B)(L)]- (where B = PPh_3, $AsPh_3$, py (or) pip; L = dibasic tetradentate Schiff bases) were synthesized by the reactions of [RuHCl(CO)(PPh_3)$_3$], [RuHCl(CO)(PPh_3)$_2$(py)], [RuHCl(CO)(PPh_3)$_2$(pip)] (or) [RuHCl(CO)($AsPh_3$)$_3$] with the respective tetradentate Schiff bases in a 1:1 molar ratio in benzene as shown in Scheme 2.

The analytical data for the new complexes agree well with the proposed molecular formula (Table 1). In all the reactions it has been observed that the Schiff bases behave as dibasic tetradentate ligands by substituting for the chloride ion, hydride ion and two triphenylphosphine/arsine ligands from each mole of the starting complexes to form the mononuclear complexes. These observations do indicate a more labile nature of the Ru–P bond compared to the Ru–N bond of the heterocyclic nitrogen bases in these complexes. The difference in the strength of Ru–P/As and R–N bonds may be explained as being due to the better σ donating ability of the nitrogen bases compared to that of triphenylphosphine/arsine. The Schiff base ruthenium(II) complexes are highly colored, stable to air and light, and soluble in chloroform, methylene chloride, benzene, DMF and DMSO.



Scheme 2. Formation of Ru(II) carbonyl Schiff base complexes (where E = P; B = PPh_3, py or pip; E = As, B = $AsPh_3$ W = –$(CH_2)_2$–, –$(CH_2)_3$–, –$(CH(CH_3)CH_2)$–, –(C_6H_4)–).

3.1. Spectroscopic characterization

The important IR absorption bands for the synthesized complexes are shown in (Table 2). The observed bands may be classified into those originating from the ligands and those arising from the bonds formed between Ru(II) and the coordinating sites. The free Schiff base ligands showed a strong band in the region 1628–1640 cm^{-1}, which is characteristic of the azomethine (>C=N) group [19]. Coordination of the Schiff bases to the metal through the nitrogen atom is expected to reduce the electron density in the azomethine link and lower the $\gamma_{C=N}$ absorption frequency. The band due to $\gamma_{C=N}$ is shifted to lower frequencies and appears around 1615–1625 cm^{-1}, indicating coordination of the azomethine nitrogen to the ruthenium metal [26]. A strong band observed at 1310–1330 cm^{-1} in the free Schiff bases has been assigned to phenolic C–O stretching. On complexation this band is shifted to a higher frequency range 1321–1360 cm^{-1}, indicating coordination through the phenolic oxygen. This has been further supported by the disappearance of the broad γ_{OH} band around 3395–3410 cm^{-1} in the complexes, indicating deprotonation of the phenolic proton prior to coordination [27]. The coordination of the azomethine nitrogen and phenolic oxygen are further supported by the appearance of two bands at 510–540 and 400–460 cm^{-1} due to γ_{M-O} [27] and γ_{M-N} [28], respectively. The spectra of all the complexes are dominated by a sharp band between 1925 and 1950 cm^{-1} due to a terminal $\gamma_{C\equiv O}$ group. In addition, other characteristic bands due to PPh_3 and $AsPh_3$ are also present around 1435 cm^{-1} in the spectra of all the Schiff base complexes. A medium intensity band is observed in the 1020 cm^{-1} region, characteristic of the coordinated pyridine or piperidine [28].

The ^{1}H NMR spectra of all the complexes were recorded to confirm the binding of the Schiff base to the ruthenium ion (Table 3). The spectra of all the complexes showed a singlet in the region δ 8.90–9.54 ppm, which has been assigned to the azomethine proton (>C=N). The position of the azomethine signal in the complexes is downfield in comparison with that of the free ligands, suggesting deshielding of the azomethine proton due to its coordination to ruthenium through the azomethine nitrogen. Multiplets are observed around δ 6.45–8.50 ppm in all the complexes and have been assigned to the aromatic protons of triphenylphosphine, triphenylarsine, pyridine and naphthalene Schiff base ligands [29]. Two methylene protons appear as one triplet in the region δ 3.53–3.83 ppm in **1**, **5**, **9** and **13**. For the complexes **3**, **7**, **11** and **15**, the signal for the methylene protons appear as one triplet and one quintet in the region 3.65–3.85 ppm and δ 2.17–2.44 ppm, respectively [30]. A broad singlet appears in the region δ 1.2–1.4 ppm for the methylene protons

Table 1
Physico-chemical and analytical data of Ru(II) carbonyl Schiff base complexes

S. No.	Complex	Formula	Colour	M.p. (°C)	Found (calculated) (%)		
					C	H	N
1	[Ru(CO)(PPh_3)(L1)]	$C_{43}H_{33}N_2O_3PRu$	Green	202	67.95(68.12)	3.97(4.39)	3.47(3.70)
2	[Ru(CO)(PPh_3)(L2)]	$C_{44}H_{35}N_2O_3PRu$	Green	185	69.90(70.30)	1.87(2.02)	3.53(3.72)
3	[Ru(CO)(PPh_3)(L3)]	$C_{44}H_{35}N_2O_3PRu$	Green	164	69.98(70.30)	2.45(2.02)	3.87(3.72)
4	[Ru(CO)(PPh_3)(L4)]	$C_{47}H_{33}N_2O_3PRu$	Brown	215	71.10(71.30)	3.87(4.20)	1.54(1.77)
5	[Ru(CO)(py)(L1)]	$C_{30}H_{23}N_3O_3Ru$	Green	235	62.47(62.70)	3.90(4.20)	7.02(7.37)
6	[Ru(CO)(py)(L2)]	$C_{31}H_{25}N_3O_3Ru$	Green	195	63.01(63.26)	3.89(4.28)	6.98(7.14)
7	[Ru(CO)(py)(L3)]	$C_{31}H_{25}N_3O_3Ru$	Green	157	62.94(63.26)	4.03(4.28)	7.34(7.14)
8	[Ru(CO)(py)(L4)]	$C_{34}H_{24}N_3O_3Ru$	Brown	216	65.74(65.48)	3.57(3.88)	6.42(6.74)
9	[Ru(CO)(pip)(L1)]	$C_{30}H_{28}N_3O_3Ru$	Green	217	61.84(62.16)	4.55(4.89)	7.57(7.25)
10	[Ru(CO)(pip)(L2)]	$C_{31}H_{30}N_3O_3Ru$	Green	182	60.42(60.70)	4.87(5.12)	7.29(7.07)
11	[Ru(CO)(pip)(L3)]	$C_{31}H_{30}N_3O_3Ru$	Green	150	60.51(60.70)	4.95(5.12)	6.87(7.07)
12	[Ru(CO)(pip)(L4)]	$C_{34}H_{34}N_3O_3Ru$	Brown	185	64.46(64.96)	4.26(4.65)	6.28(6.68)
13	[Ru(CO)($AsPh_3$)(L1)]	$C_{43}H_{33}N_2O_3AsRu$	Green	182	64.65(64.42)	3.89(4.15)	3.05(3.49)
14	[Ru(CO)($AsPh_3$)(L2)]	$C_{44}H_{35}N_2O_3AsRu$	Green	164	64.38(64.78)	4.45(4.33)	2.07(1.72)
15	[Ru(CO)($AsPh_3$)(L3)]	$C_{44}H_{35}N_2O_3AsRu$	Green	162	64.47(64.78)	4.04(4.33)	1.53(1.72)
16	[Ru(CO)($AsPh_3$)(L4)]	$C_{47}H_{33}N_2O_3AsRu$	Brown	152	66.62(66.43)	3.71(3.91)	3.12(3.30)

Table 2
Important IR, electronic spectral data[e] and fluorescence data[e,f] of the Ru(II) carbonyl Schiff base complexes

Complex	$\gamma_{C=N}$ (cm^{-1})	γ_{C-O} (cm^{-1})	$\gamma_{C\equiv O}$ (cm^{-1})	λ_{max} (nm) (ε) ($dm^3\ mol^{-1}\ cm^{-1}$)	Fluorescence data λ_{max} (nm)
1	1617	1351	1934	751(515)[a], 415(16688)[b], 324(27680)[d], 281(39040)[c]	474
2	1620	1338	1931	718(166)[a], 409(14170)[b], 332(26190)[d], 280(34830)[c]	474
3	1617	1360	1933	680(112)[a], 419(9880)[b], 331(19010)[d], 263(38940)[c]	499
4	1617	1321	1935	673(227)[a], 487(15000)[b], 341(21890)[d], 271(39040)[c]	552
5	1615	1349	1936	429(13820)[b], 335(14080)[d], 291(17510)[c]	471
6	1617	1339	1933	671(210)[a], 436(37480)[b], 342(41730)[d], 283(55390)[c]	516
7	1625	1335	1935	658(107)[a], 413(37690)[b], 344(41880)[d], 281(43130)[c]	
8	1619	1321	1942	779(118)[a], 454(10630)[b], 329(20200)[d], 270(36900)[c]	534
9	1616	1327	1941	589(248)[a], 406(909)[b], 325(16890)[d], 287(21120)[c]	466
10	1617	1358	1937	718(276)[a], 426(35860)[b], 343(40840)[d], 297(49310)[c]	490
11	1617	1360	1931	716(212)[a], 408(13670)[b], 334(29390)[d], 270(37790)[c]	502
12	1617	1325	1950	485(6210)[b], 335(11510)[d], 269(31360)[c]	542
13	1616	1321	1925	669(148)[a], 419(4280)[b], 318(11190)[d], 269(23680)[c]	
14	1617	1321	1918	691(196)[a], 439(14250)[b], 334(20340)[d], 272(38080)[c]	
15	1617	1338	1924	688(606)[a], 428(35520)[b], 344(40090)[d], 290(49940)[c]	478
16	1625	1321	1947	457(5720)[b], 336(8560)[d], 270(30100)[c]	527

[a] $^1A_{1g} \rightarrow {}^1T_{1g}$.
[b] Charge transfer.
[c] π–π^*.
[d] n–π^*.
[e] Solvent – dichloromethane.
[f] Excitation at the higher wavelength absorption peak.

and another singlet in the region δ 10.10–10.30 ppm for the NH protons in **9**, **11** and **12**. A sharp singlet observed for the OH protons of all the ligands in the region δ 14.0 ppm disappeared in all the complexes. A representative spectrum of the complex [Ru(CO)(PPh_3)(L4)] is shown in Fig. 1.

The electronic absorption spectra of all the complexes in dichloromethane showed three to four bands in the region 263–779 nm. All the Schiff base ruthenium complexes are diamagnetic, indicating the presence of ruthenium in the +2 oxidation state. The ground state of ruthenium(II) in an octahedral environment is $^1A_{1g}$, arising from the t_{2g}^6 configuration, and the excited states corresponding to the $t_{2g}^5e_g^1$ configuration are $^3T_{1g}$, $^3T_{2g}$, $^1T_{1g}$ and $^1T_{2g}$. Hence, four bands corresponding to the transitions $^1A_{1g} \rightarrow {}^3T_{1g}$, $^1A_{1g} \rightarrow {}^3T_{2g}$, $^1A_{1g} \rightarrow {}^1T_{1g}$ and $^1A_{1g} \rightarrow {}^1T_{2g}$ are possible in order of the increasing energy.

The bands around 779–589 nm and 485–406 nm are assigned to $^1A_{1g} \rightarrow {}^1T_{1g}$ [20,31] and charge transfer (CT) transitions respectively are listed in Table 2. The charge transfer bands observed in all the complexes due to M $\rightarrow$ L transitions are possible in the visible region [31–33]. Moreover, the presence of carbonyl, triphenylphospine/arsine and heterocyclic bases as ligands, which are capable of producing strong ligand field e_g^*

Table 3
^{1}H NMR data of Ru(II) carbonyl Schiff base complexes

Complex	^{1}H NMR data (ppm)
1	6.80–8.10(Ar, m), 8.9(CH=N, s), 3.73(N–$(CH_2)_2$, t)
3	6.95–8.10(Ar, m), 9.15(CH=N, s), 3.85(CH_2, t), 2.34(CH_2, q)
4	6.85–8.15(Ar, m), 9.34(CH=N, s).
5	6.75–8.15(Ar, m), 8.85(CH=N, s), 3.83(N–$(CH_2)_2$, t).
7	6.84–8.1(Ar, m), 9.25(CH=N, s), 3.83(CH_2, t), 2.17(CH_2, q)
8	6.81–8.30(Ar, m), 9.42(CH=N, s).
9	6.90–7.90(Ar, m), 9.34(CH=N, s), 3.65(N–$(CH_2)_2$, t), 1.24(CH_2, s), 10.13(NH, s).
11	6.70–8.10(Ar, m), 9.3(CH=N, s), 3.84(CH_2, t), 2.30(CH_2, q), 1.40(CH_2, s), 10.30(NH, s)
12	6.57–8.40(Ar, m), 9.14(CH=N, s), 1.35(CH_2, s), 10.1(NH, s)
13	6.70–8.35(Ar, m), 9.15(CH=N, s), 3.53(N–$(CH_2)_2$, t)
15	6.95–8.45(Ar, m), 9.21(CH=N, s), 3.65(CH_2, t), 2.44(CH_2, q)
16	6.45–8.32(Ar, m), 9.0(CH=N, s)

levels place these levels relatively high in energy. Therefore, the lowest charge bands due to excitation of an electron from the metal t_{2g} level to an unfilled molecular orbital derived from the π* level of the ligands should appear in the relatively high energy region compared to those due to $t_{2g} \rightarrow e_g^*$ transitions [32–34]. The other high intensity bands in the 344–269 nm region were characterized by ligand-centered (LC) bands and have been designated as π–π* and *n*–π* transitions for the electrons localized on the azomethine group of the Schiff bases [33]. The pattern of the electronic spectra of all the complexes indicated the presence of an octahedral environment around the ruthenium(II) ion, similar to that of other ruthenium(II) octahedral complexes [21].

Emission properties of the ruthenium(II) Schiff base complexes were examined in dichloromethane solution at room temperature, and excitation and emission maxima are listed in Table 2. In the present series, the excitation of all the complexes was made at their charge transfer bands and the emission maxima of the complexes have experienced a positive shift of the order of 50–90 nm. The emission maxima fall in the range 471–552 nm and a representative spectrum is shown in Fig. 2. The observed CT luminescence in these complexes may be due to the presence of di-imine functions. It is likely that the emission originates from the lowest energy metal to ligand charge transfer (MLCT) state, probably derived from the excitation involving a $d\pi(Ru) \rightarrow \pi^*$ (di-imine) MLCT transition, and similar MLCT transitions are observed in ruthenium(II) bipyridyl complexes [34,35]. The slightly lower MLCT transition energy is probably due to the chelate ring of the complexes. In the complexes **4**, **8**, **12** and **16** it is observed that an increase in the rigidity of the ligand results in an increase in the emission maxima. If increased rigidity of the complexes is solely responsible for potential emission changes then it would be expected that this is because of the ligands present in the complexes [36].

3.2. Electrochemistry of the complexes

The redox properties of all the complexes were investigated in acetonitrile solution by cyclic voltammetry and the redox potentials are expressed with reference to Ag/AgCl. The cyclic voltammograms of all the complexes (1×10^{-3}) display one quasi-reversible oxidation with $E_{1/2}$ values 0.76–1.04 V and one irreversible reduction, with respect to the SCE. In general, the changes in oxidation and reduction potential are probably due to the relative stabilization of the ruthenium(II) state over ruthenium(III) by a combination of σ and π effects exhibited by the ligand. A representative voltammogram of [Ru(CO)($AsPh_3$)(L4)] is shown in Fig. 3 and voltammetric data are presented in Table 4. The oxidation observed is quasi-reversible in nature, characterized by a rather

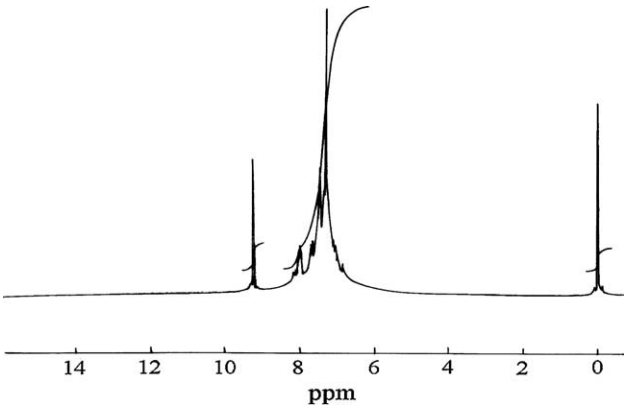


Fig. 1. ^{1}H NMR spectrum of [Ru(CO)(PPh_3)(L4)].

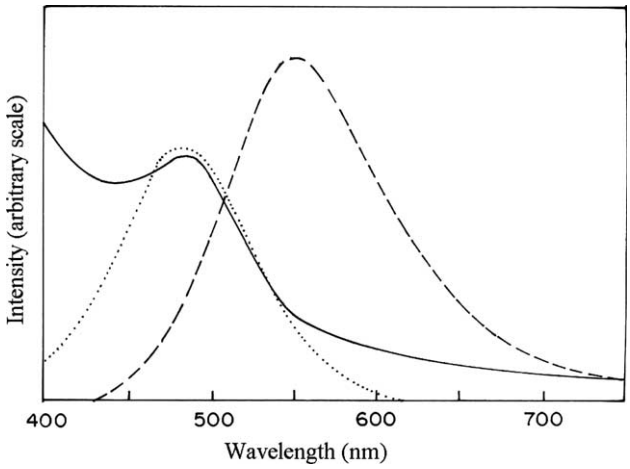


Fig. 2. Absorption (—), fluorescence (– – –) and excitation (· · ·) spectra of [Ru (CO)(pip)(L4)] in dichloromethane.

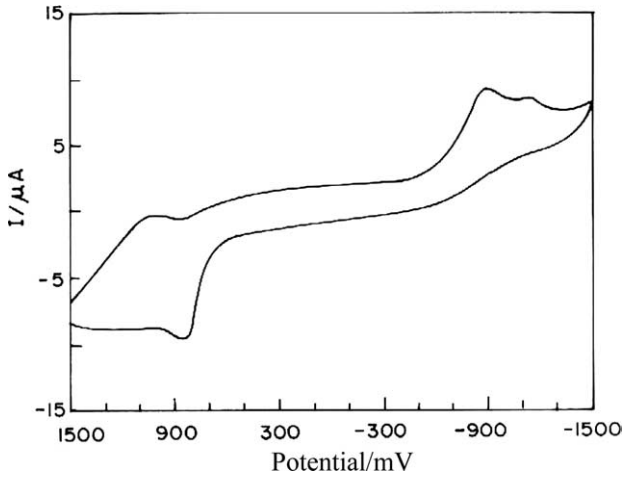


Fig. 3. Cyclic voltammogram of [Ru(CO)($AsPh_3$)(L4)].

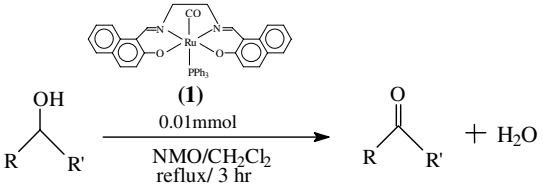
large peak-to-peak separation (ΔE_p) of 110–220 mV and the cathodic peak current (i_{pc}) is less than the anodic peak current(i_{pa}). The one electron nature of this oxidation has been verified by comparing its current height (i_{pa}) with that of the standard ferrocene–ferrocenium couple under identical experimental conditions [37].

The reason for the irreversibility observed for reductive response of all the complexes may be due to a short lived reduced state of the metal ion [38] or due to oxidative degradation of the ligands [39]. The reduction potential of Ru(II) complexes are affected by chelate rings of the ligands and it is observed that the reduction potential of complexes with a larger chelate ring is more than that of complexes with a smaller chelate ring. Further, an irreversible ligand based reduction peak is observed in the range −0.96 to −1.18 V, which corresponds to reduction of the azomethine(−C=N) moiety of the Schiff base ligands, and the reduction occurred at more negative values.

It has also been observed from the electrochemical data that there is not much variation in the redox potential due to triphenylphosphine, triphenylarsine, pyridine or piperidine [21]. Hence, it is inferred from the electrochemical data that the present ligand system is ideally suitable for stabilizing the higher oxidation state of ruthenium.

3.3. Catalytic activity of the complexes

Catalytic oxidation of primary alcohols and secondary alcohols by the synthesized ruthenium(II) carbonyl Schiff base complex [Ru(CO)(PPh_3)(L1)] was carried out in CH_2Cl_2 in the presence of NMO, and the by product water was removed by using molecular sieves. Complex **1** oxidizes primary alcohols to the corresponding aldehydes and secondary alcohols to ketones with high yield and the results are listed in Table 5 (entries 1–8). The aldehydes or ketones formed after 3 h of refluxing were determined by GC and there was no detectable oxidation in the absence of ruthenium complex.



R,R'=alkyl (or) aryl (or) H

Table 4
Cyclic voltammetry data of Ru(II) carbonyl Schiff base complexes

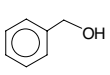
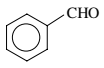
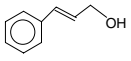
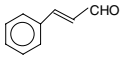
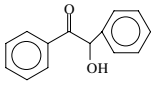
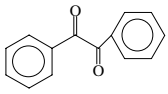
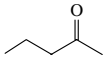
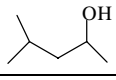
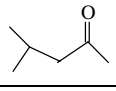
Complex	Metal based oxidation					Ligand based reduction
	Ru^{III}/Ru^{II}				Ru^{II}/Ru^{I}	
	E_{pa}(V)	E_{pc}(V)	ΔE_p(mV)	$E_{1/2}$(V)	E_{pc}(V)	E_{pc}(V)
1	0.90	0.70	200	0.80	−0.95	
2	0.88	0.71	170	0.80	−0.70	−0.98
3	0.86	0.69	170	0.76	−0.73	−0.96
4	0.83	0.70	130	0.77	−0.88	−1.18
5	0.86	1.02	160	0.94	−0.91	
6	1.06	0.93	130	1.00	−0.86	
7	0.89	0.70	190	0.80	−0.83	−1.01
8	0.86	0.96	100	0.91	−0.79	−1.12
9	0.85	0.97	120	0.91	−0.94	
10	0.89	0.67	220	0.78	−0.85	−0.98
11	0.96	0.76	200	0.86	−0.77	−1.06
12	0.85	0.98	130	0.92	−0.70	−0.97
13	0.96	1.07	110	1.01	−0.94	
14	1.09	0.98	110	1.04	−0.85	−1.02
15	0.90	1.08	180	0.99	−0.79	−0.97
16	0.87	1.01	140	0.94	−0.88	−1.11

Supporting electrolyte: NBu_4ClO_4 (0.005 M); complex: 0.001 M; solvent: CH_3CN; $\Delta E_p = E_{pa} - E_{pc}$ where E_{pa} and E_{pc} are anodic and cathodic potentials, respectively; $E_{1/2} = 0.5(E_{pa} + E_{pc})$; scan rate: 100 mV s^{-1}.

Results of the present investigation suggest that the complexes are able to react efficiently with NMO to yield a high valent ruthenium-oxo species [2,40] capable of oxygen atom transfer to alcohols. This was further supported by spectral changes that occur by addition of NMO to a dichloromethane solution of the ruthenium(II) complexes. The appearance of a peak at 390 nm is attributed to the formation of Ru^{IV}=O species, which is in conformity with other oxo ruthenium(IV) complexes [2,41,42]. Further support in favor of the formation of such species was identified from the IR spectrum of the solid mass (obtained by evaporation of the resultant solution to dryness), which showed a band at 860 cm^{-1}, characteristic of Ru^{IV}=O species [2,40,41].

The oxidation of benzylalcohol to benzaldehyde resulted in 89% conversion. Unsaturated cinnamylalcohol was oxidized to cinannamaldehyde with 95% conversion, without cleavage of carbon–carbon double bonds. This is an important characteristic of the ruthenium/NMO system. Further, the complex effectively catalyzes the oxidation of aliphatic alcohols such as butane-2-ol, methylpropylcarbinol and isobutylmethylcarbinol to the corresponding ketones with high conversions. In the case of benzoin the oxidation product was isolated and characterized by melting point, IR and ^{1}H NMR. Moreover, the complex efficiently catalyzes the oxidation of five and six membered cyclic alcohols to the corresponding ketones with conversions of 99% and 92%, respectively. This reaction provides a new environmentally friendly route to the conversion of alcoholic functions to carbonyl group and water is the only by product during the course of the reaction. It has been observed that complex **1** has a better catalytic efficiency in the case of oxidation of primary and secondary alcohols when compared to an earlier report [42–44] on similar ruthenium complexes as catalysts in the presence of NMO/*t*-BuOOH. Hence, it is relevant from the cyclic voltammetric data that the oxidation effected by catalysts is likely to occur via higher ruthenium oxidation states, which are easily accessible through chemical oxidation with co-oxidants like NMO, *t*-BuOOH, PhIO etc. [42].

Table 5
Catalytic oxidation of alcohols to the corresponding aldehydes and ketones with complex **1** in the presence of NMO

Entry	Substrate	Product	Conversion (%)[b]	Turnover[c]
1			89	89
2			95	95
3			99	99
4			92.2	92.2
5			46[a]	46
6			88	88
7			99	99
8			99	99

Substrate (1 mmol); NMO (3 mmol); complex (0.01 mmol): solvent dichloromethane.

[a] Isolated yield, characterized by melting point, ^{1}H NMR and IR.

[b] Yield determined by GC and comparing with the analyses of authentic samples.

[c] Moles of product per mole of catalyst.

4. Conclusion

A new family of ruthenium(II) carbonyl complexes containing tetradentate Schiff bases were synthesized and characterized. These complexes are found to have luminescent properties and attempts will be made for further investigation on this study. The oxidation of alcohols to carbonyl compounds has been studied with NMO in the presence of catalyst **1** and high yields were obtained.

Acknowledgment

We express sincere thanks to the Sophisticated Instrument Facility, Indian Institute of Science, Bangalore for providing the NMR facility.

References

[1] F.A. Cotton, G. Wilkinson, Advanced Inorganic Chemistry, 4th ed., Interscience, New York, 1980 (Chapter 22-F).
[2] M.M.T. Khan, Ch. Sreelatha, S.A. Mirza, G. Ramachandraiah, S.H.R. Abdi, Inorg. Chim. Acta 154 (1988) 103.
[3] B. De Clercq, F. Verpoort, Macromolecules 35 (2002) 8943.
[4] T. Opstal, F. Verpoort, Synletters 6 (2002) 935.
[5] T. Opstal, F. Verpoort, Angew. Chem., Int. Ed. 42 (2003) 2876.
[6] (a) L. De cola, P. Elser, Coord. Chem. Rev. 177 (1998) 301; (b) T.E. keyes, B. Evrard, J.G. Vos, C. Brady, J.J. McGarvey, P. Yayaweera, J. Chem. Soc., Dalton Trans. (2004) 2341.
[7] V. Balzani, F. Bolletta, M.T. Gandolfi, Top. Curr. Chem. 75 (1978) 1.
[8] K. Kalyanasundaram, Coord. Chem. Rev. 46 (1982) 85.
[9] A. Juris, V. Balzani, F. Barigelletti, S. Campagna, P. Belser, A. Von Zelewsky, Coord. Chem. Rev. 84 (1988) 85.

[10] E.M. Kober, J. Carper, R.S. Lumpkin, T.J. Meyar, J. Phys. Chem. 90 (1986) 3722.
[11] V.W.W. Yam, B.W.K. Chu, C.C. Ko, K.K. Cheung, J. Chem. Soc., Dalton Trans. (2001) 1911.
[12] H. Wolpher, O. Johansson, M. Abrahamson, M. Kritikos, L. Sun, B. Akermark, Inorg. Chem. Commun. 7 (2004) 337.
[13] R.S. Sdrawn, M. Zamakani, J.C. Coho, J. Am. Chem. Soc. 108 (1986) 3510.
[14] R.I. Kureshy, N.H. Khan, S.H.R. Abdi, S.T. Patel, P. Iyer, J. Mol. Catal. 150 (1999) 175.
[15] S.K. Maiti, K.M. Abdul Malik, R. Bhattacharyya, Inorg. Chem. Commun. 7 (2004) 823.
[16] R.A. Sheldon, J.K. Kochi, Metal-Catalyzed Oxidation of Organic Compounds, Academic Press, New York, 1981.
[17] G.J. Brink, I.W.C.E. Arends, R.A. Sheldon, Science 287 (2000) 1636.
[18] K.B. Sharpless, K. Akashi, K. Oshima, Tetrahedron Lett. 29 (1976) 2503.
[19] R. Ramesh, S. Maheswaran, J. Inorg. Biochem. 96 (2003) 457.
[20] R. Ramesh, M. Sivagamasundari, Synth. React. Inorg. Met-Org. Chem. 33 (2003) 899.
[21] K. Naresh Kumar, R. Ramesh, Spectrochim. Acta A 60 (2004) 2913.
[22] B. Furniss, A.J. Hannaford, P.W.G. Smith, A.R. Tachell, Vogel's Textbook of Practical Organic Chemistry, 5th edn. 1982.
[23] N. Ahmed, J.J. Lewison, S.D. Robinson, M.F. Uttley, Inorg. Synth. 15 (1974) 48.
[24] S. Gopinathan, I.R. Unny, S.S. Deshpande, C. Gobinathan, Ind. J. Chem. 25A (1986) 1015.
[25] R.A Sanchez-pelgado, W.Y. Lee, S.R. Choi, Y. Cho, M.J. Jun, Trans. Met. Chem. 16 (1991) 241.
[26] S.A. Ali, A.A. Soliman, M.M. Aboaly, R.M. Ramadan, J. Coord. Chem. 55 (2002) 1161.
[27] R.C. Maurya, P. Patel, S. Rajput, Synth. React. Inorg. Met-org. Chem. 23 (2003) 817.
[28] K. Nakamoto, Infrared and Raman Spectra of Inorganic and Coordination Compounds, Wiley-Interscience, New York, 1971.
[29] J.R. Dyer, Application of Absoption Spectroscopy of Organic Compounds, Prentice-Hall, New Jersy, 1978.
[30] B.G. Jeong, C.P. Rim, H.N. Chae, K.H. Chjo, K.C. Nam, Y.K. Choi, Bull. Korean Chem. Soc. 17 (1996) 688.
[31] K. Natarajan, R.K. Poddar, C. Agarwala, J. Inorg. Nucl. Chem. 39 (1977) 431.
[32] A.B.P. Lever, A.B.P. Lever, Inorganic Electronic Spectroscopy, 2nd ed., Elsevier, New York, 1984.
[33] K. Chichak, U. Jacquenard, N.R. Branda, Eur. J. Inorg. Chem. (2002) 357.
[34] V.W.W. Yam, B.W.K. Chu, C.C. Ko, K.K. Cheung, J. Chem. Soc., Dalton Trans. (2001) 1911, and references there in.
[35] B.K. Panda, K.G. Ghosh, S. Chattoppadhyay, A. Chkravoty, J. Organomet. Chem. 674 (2003) 107, and references there in.
[36] T. Duff, A. Grubing, J.C. Thaomas, J.G. Vos, Polyhedron 22 (2003) 775.
[37] S. Dutta, S.M. Peng, S. Bhattacharya, J. Chem. Soc., Dalton Trans. (2000) 4623.
[38] A.M. Bond, R. Colton, D.R. Mann, Inorg. Chem. 29 (1990) 4665.
[39] A. Basu, T.G. Kasan, N.Y. Sapre, Inorg. Chem. 27 (1988) 4639.
[40] W.H. Leung, C.M. Che, Inorg. Chem. 28 (1989) 4619.
[41] A.S. Goldstein, R.S. Drago, J. Chem. Soc., Chem. Commun. (1991) 21.
[42] A.M. El-Hendawy, A.H. Alkubaisi, A.E. Kourashy, M.M. Shanab, Polyhedron 12 (1993) 2343.
[43] D. Chattergee, A. Mitra, B.C. Roy, J. Mol. Catal. A: Chem. 161 (2000) 17.
[44] M.S. El- Shahawi, A.F. Shoair, Spectrochim. Acta, Part A 60 (2004) 121.

The studies show dependence of these reactions on the starting material, N-donor ligand, solvent and temperature. Although the factors determining the formation of the $Re_2O_3^{4+}$ complexes have not been formalised, water seems to be a source of the bridging oxo group. No intermediates have been isolated in the syntheses mentioned above, but the formation of intermediate hydroxo-species seems to be crucial [1–22].

These findings prompted us to explore the reactions of $[ReOBr_3(OAsPh_3)(Asph_3)]$ with pyrazine (pyz) and pyridazine (pyd) in acetone at room temperature. Two dinuclear complexes, $[\{ReOBr_2(pyz)_2\}_2(\mu\text{-}O)]$ with a linear O═Re–O–Re═O backbone (**1**) and $[\{ReOBr_2\}_2(\mu\text{-}O)(\mu\text{-}pyd)_2]$ with a bent $Re_2O_3^{4+}$ core (**2**), have been isolated. Here, we report the syntheses, crystal and molecular structures, spectroscopic investigations and the density functional theory (DFT) calculations for the complexes **1** and **2**.

Only a few calculations concerning the nature of the bonding could be found in the literature for transition metal oxocomplexes. Dunitz and Orgel [25] were the first who based on crystal-field considerations presented a molecular orbital energy ordering for the Ru–O–Ru core in $[Ru_2OCl_{10}]^{4-}$ and explained the unusual features of the complex – diamagnetism, short Ru–O bond length and the linear geometry of the Ru–O–Ru group. Since then many authors used the Dunitz and Orgel molecular orbital diagram to discuss the $[Cl_5M\text{–}O\text{–}MCl_5]^{n-}$ anions with linear and bent bridges (M = Ru(IV), Os(IV), Re(IV), Re(III), W(IV)) [26–32]. The ab initio calculations were done for the $[Cl_5Ru\text{–}O\text{–}RuCl_5]^{4-}$ anion with the GAMESS and EXTEN-97 programs [33]. Currently, density functional theory (DFT) is commonly used to examine the electronic structure of transition metal complexes. It meets with the requirements of being accurate, easy to use and fast enough to allow the study of relatively large molecules of transition metal complexes [34–37]. Therefore, we have chosen this tool for performing a study of the electronic structure of $[\{ReOBr_2(pyz)_2\}_2(\mu\text{-}O)]$ (**1**) with a linear Re_2O_3 core and $[\{ReOBr_2\}_2(\mu\text{-}O)(\mu\text{-}pyd)_2]$ (**2**) with a bent Re_2O_3 unit. In order to obtain additional information about binding in the complexes **1** and **2**, we have applied NBO analysis.

The time-dependent DFT method (TDDFT) has been applied to calculate the spin-allowed singlet-singlet electronic transitions of complexes **1** and **2**, and the UV–Vis spectra of these compounds have been discussed on this basis.

2. Experimental

2.1. General procedure

All manipulations and reactions were carried out open to the atmosphere. All solvents were of reagent grade and were used as received. Ammonium perrhenate, triphenylarsine, pyrazine and pyridazine were purchased from Aldrich and used as received. The $[ReOBr_3(AsPh_3)(OAsPh_3)]$ complex was prepared according to the literature method [38].

Infrared spectra were recorded on a Nicolet Magna 560 spectrophotometer in the spectral range 4000–400 cm^{-1} with the samples in the form of potassium bromide pellets. Electronic spectra were measured on a spectrophotometer Lab Alliance UV-VIS 8500 in the range 800–200 nm in deoxygenated CH_2Cl_2 solution for **1** and dmso for **2**. Elemental analyses (C H N) were performed on a Perkin–Elmer CHN-2400 analyzer.

2.2. Preparation of $[\{ReOBr_2(pyz)_2\}_2(\mu\text{-}O)]$ (1)

$[ReOBr_3(AsPh_3)(OAsPh_3)]$ (O.5g, 0.47 mmol) was suspended in a solution of pyrazine (0.1g, 1.25 mmol) in acetone (60 ml) and the reaction mixture was stirred for 24 h. Diethyl ether (100 ml) was added and green precipitate of **1** was filtered. The crystals suitable for X-ray investigation were obtained by slow diffusion of diethyl ether into an acetone solution of **1**. (Yield 65%).

IR of **1** (KBr, cm^{-1}) 3084 (w), 3049 (w), 2979 (w), 1714 (s), 1590 (m), 1423 (s), 1361 (m), 1229 (m), 1163 (m), 1124 (m), 1062 (m), 973 (m), 810 (m) 709 (s), 674 (vs), 531 (w), 472 (m).

Anal. Calc. for $C_{19}H_{22}N_8Br_4O_4Re_2$ (**1**): C, 20.40; H, 1.98; N, 10.02. Found: C, 20.50; H, 2.08; N, 10.12%.

2.3. Preparation of $[\{ReOBr_2\}_2(\mu\text{-}O)(\mu\text{-}pyd)_2]$ (2)

A procedure similar to that for **1** was used with $[ReOBr_3(AsPh_3)(OAsPh_3)]$ (O.5g, 0.47 mmol) and pyridazine (0.1g, 1.25 mmol). Dark green crystals of **2** were collected in 60% yield, and crystals suitable for X-ray structure determination were obtained by slow diffusion of diethyl ether into an acetone solution of **2**.

IR of **2** (KBr, cm^{-1}) 3094 (m), 3063 (m), 3002 (w), 1700 (s), 1581 (m), 1450 (s), 1417 (s), 1366 (m), 1307 (s), 1227 (m), 1075 (m), 1001 (m) 957 (s), 780 (s), 757(s), 742 (s), 682 (vs), 534 (w), 503 (m), 444 (m).

Anal. Calc. for $C_{11}H_{14}N_4Br_4O_4Re_2$ (**2**): C, 13.79; H, 1.47; N, 5.85. Found: C, 13.92; H, 1.58; N, 5.94%.

2.4. Crystal structure determination and refinement

The X-ray intensity data of **1** and **2** were collected on a KM-4-CCD automatic diffractometer equipped with CCD detector. 20 and 48 s exposure times were used respectively and reflections were collected up to $\theta = 25.11°$. The unit cell parameters were determined from least-squares refinement of the setting angles of 3138 and 7270 strongest reflections respectively for **1** and **2**. Details concerning crystal data and refinement are given in Table 1. Lorentz, polarization and numerical

Table 1
Crystal data and structure refinement for the complexes $\mathbf{1}\cdot CH_3COCH_3$ and $\mathbf{2}\cdot CH_3COCH_3$

Complex	$\mathbf{1}\cdot CH_3COCH_3$	$\mathbf{2}\cdot CH_3COCH_3$
Empirical formula	$C_{19}H_{22}Br_4N_8O_4Re_2$	$C_{11}H_{14}Br_4N_4O_4Re_2$
Formula weight	1118.49	958.30
T (K)	293(2)	293(2)
λ (Å)	0.71073	0.71073
Crystal system	triclinic	monoclinic
Space group	$P\bar{1}$	$P2_1/n$
Unit cell dimensions		
a (Å)	9.6336(11)	9.3336(6)
b (Å)	10.3554(8)	14.3871(13)
c (Å)	15.7435(15)	15.9623(11)
α (°)	105.163(7)	
β (°)	95.910(8)	92.618(6)
γ (°)	15.7435(15)	
V (Å^3)	1467.7(2)	2141.2(3)
Z	2	4
D_{calc} (Mg/m^3)	2.531	2.973
Absorption coefficient (mm^{-1})	13.725	18.782
$F(000)$	1028	1720
Crystal size (mm)	$0.36\times0.14\times0.04$	$0.30\times0.21\times0.00$
θ Range for data collection (°)	3.10–25.10	2.94–25.11
Index ranges	$-11\leqslant h\leqslant 11$, $-12\leqslant k\leqslant 12$, $-18\leqslant l\leqslant 18$	$-11\leqslant h\leqslant 11$, $0\leqslant k\leqslant 17$, $0\leqslant l\leqslant 19$
Reflections collected	14387	3812
Independent reflections	5231	3812
Completeness to 2θ (%)	99.8	95.6
Maximum and minimum transmission	0.6030 and 0.0827	0.9634 and 0.0696
Data/restraints/parameters	5231/0/336	3812/0/228
Goodness-of-fit on F^2	1.029	0.990
Final R indices [$I>2\sigma(I)$]	$R_1=0.0604$, $wR_2=0.1515$	$R_1=0.0574$, $wR_2=0.1497$
R indices (all data)	$R_1=0.0790$, $wR_2=0.1641$	$R_1=0.0824$, $wR_2=0.1639$
Largest difference in peak and hole (e Å^{-3})	3.515 and −2.216	1.686 and −2.973

absorption corrections [39] were applied. The structures were solved by the Patterson method and subsequently completed by difference Fourier recycling. All the non-hydrogen atoms were refined anisotropically using the full-matrix least-squares technique. The hydrogen atoms bonded to the aromatic atoms were treated as ''riding'' on their parent carbon atoms and assigned isotropic temperature factors equal to 1.2 times the value of the equivalent temperature factor of the parent atom. The methyl groups were allowed to rotate about their local threefold axis. SHELXS-97 [40], SHELXL-97 [41] and SHELXTL [42] programs were used for all the calculations. Atomic scattering factors were those incorporated in the computer programs.

3. Computational details

The GAUSSIAN-03 program [43] was used in the calculations. The geometry optimization was carried out with the DFT method with the use of B3LYP functional [44,45]. The electronic spectrum was calculated with the TDDFT method [46]. The LANL2DZ basis set [47] with additional d (with exponent $\alpha=0.3811$) and f (with exponent $\alpha=2.033$) functions was used on the rhenium, 6-31G(d) on the bromine, nitrogen and carbon atoms and 6-31G basis on the hydrogen atoms in the calculations.

Natural bond orbital (NBO) calculations were performed with the NBO code [48] included in GAUSSIAN-03.

4. Results and discussion

4.1. Preparation

Treatment of the $[ReOBr_3(AsPh_3)(OAsPh_3)]$ complex with an excess of pyrazine (pyz) in acetone at ambient temperature leads to the $[\{ReOBr_2(pyz)_2\}_2(\mu\text{-}O)]$ complex (**1**) with a nearly linear O═Re–O–Re═O moiety and four terminal pyz ligands, whereas the reaction of $[ReOBr_3(AsPh_3)(OAsPh_3)]$ with pyridazine (pyd) affords $[\{ReOBr_2\}_2(\mu\text{-}O)(\mu\text{-}pyd)_2]$ (**2**) with a bent Re_2O_3 unit and two Re centers linked through two bridging pyridazine molecules and an oxo group.

The formation of the above mentioned dinuclear complexes doubtlessly involves water and intermediate hydroxo-species [1–22]. Both the reactions have been carried out in air and without special drying of acetone, so that some water has been present in the reaction

systems. Different positions of the nitrogen atoms in the rings of pyrazine and pyridazine can explain the formation of the different (with terminal or bridging N-donor ligands) dinuclear oxo complexes in the reaction with the oxo complex.

4.2. Infrared data

The IR spectra of **1** and **2** show sharp bands at 973 and 957 cm^{-1} assignable to the symmetric Re=O stretch. The strong bands at 674 for **1** and 682 cm^{-1} for **2** result from overlapping of the antisymmetric Re–O–Re stretching modes with the aromatic ring out-of-plane deformation vibrations. In comparison with the $[(ReCl_5)_2(\mu\text{-}O)]^{4-}$ complex with an antisymmetric ν_{as}(Re–O–Re) stretching mode in the range 850–855 cm^{-1}[49], a significant reduction in the frequency of ν_{as}(Re–O–Re) is observed for compounds **1** and **2**. It is a consequence of the electron-withdrawing effect of the terminal Re=O groups causing a relative weakening of the bridging Re–O bonds.

4.3. Crystal structure

Both the complexes crystallise as solvates **1** · CH_3COCH_3 and **2** · CH_3COCH_3, respectively. The accurate cell parameters and crystal data for **1** · CH_3COCH_3 and **2** · CH_3COCH_3 are given in Table 1. The acetone molecules from the crystallization are not bonded to any other atom, with the exception of some rather weak hydrogen bonds. The weak intra- and intermolecular hydrogen bonds [50,51] of **1** · CH_3COCH_3 and **2** · $CH_3COCH_3$are presented in Table 2.

Table 2
Hydrogen bonds for **1** · CH_3COCH_3 and **2** · CH_3COCH_3

D	A	H···A	D···A	D—H···A
Complex 1				
C(4)	Br(1)	2.91	3.400(15)	113.9
C(9)	Br(1)	2.78	3.660(12)	158.3
C(13)	Br(2)	2.91	3.819(15)	165.0
C(8)	Br(3)	2.78	3.679(15)	163.3
C(1)	Br(4)	2.80	3.680(14)	158.8
C(16)	O(2)	2.49	2.905(18)	107.3
C(2)	N(4)#1	2.55	3.42(2)	156.6
C(4)	N(8)#2	2.52	3.27(2)	137.7
C(11)	Br(1)#3	2.92	3.627(15)	133.9
Complex 2				
C(4)	O(1)	2.57	2.93(2)	103.1
C(1)	O(2)	2.49	2.88(2)	105.1
C(3)	O(3)#4	2.35	3.23(2)	156.7
C(5)	Br(1)#5	2.89	3.68(2)	142.8
C(99)	O(1)#6	2.59	3.52(3)	164.0

Symmetry codes: #1: $1-x, -y, -z$; #2: $2-x, 1-y, 1-z$; #3: $-1+x, y, z$; #4: $x+0.5, y+0.5, -z+0.5$; #5: $x+1, y, z$; #6: $-x+1, -y+1, -z$.

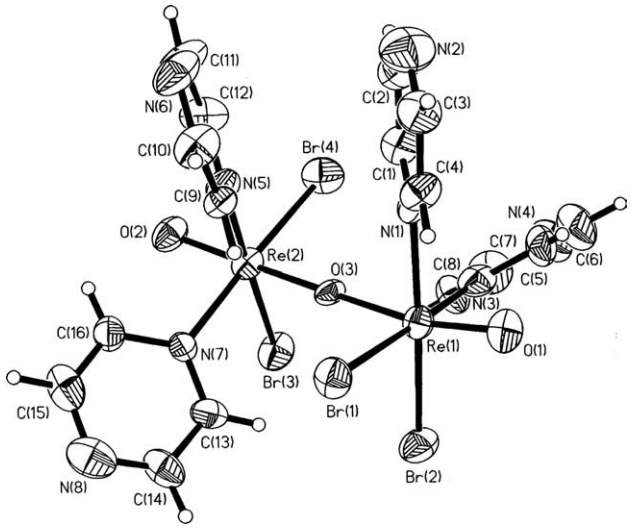


Fig. 1. The molecular structure of **1**.

The molecular structure of **1** is shown in Fig. 1. The structure presents a nearly linear O=Re–O–Re=O unit with the rhenium atoms in a pseudo-octahedral coordination environment, slightly displaced from the N_2Br_2 mean plane towards the terminal oxo ligand. The halves of the dimer are rotated about the Re–O–Re fragment away from an eclipsed conformation: thus one nitrogen ligand on each Re atom is stacked with the corresponding one on the second Re. These pyrazine molecules are determined as stacking ligands (L_s), while the others N-donors are designated as terminal ones (L_t). The selected pseudo-torsion angles describing the relative arrangement of the respecting substituents for **1** are collected in Table 3. This arrangement avoids short contacts between the L_t ligands in different halves of the dimer and allows some stacking to take place between the L_s ligands.

The structure of **2** reveals the presence of two rhenium(V) centers linked through two bridging pyridazine molecues and an oxo group (Fig. 2). Due to the geometric constraints of the two bridging N-donor ligands the $\{Re_2O_3\}$ core in **2** is bent with a Re–O–Re angle equal to 128.3(6)°.

The most important bond lengths and angles for compounds **1** and **2** are reported in Tables 3 and 4, respectively. The departure from the ideal octahedron in **1** is mainly attributed to the electronic repulsion of the short Re=O bond. For complex **2** the bridging N–N ligands introduce some additional strain.

The Re–N, Re–$O_{terminal}$ and Re–$O_{bridging}$ bond lengths in **1** and **2** agree well with the comparable values found in rhenium compounds with a O=Re–O–Re=O framework [1–22]. The Re–$O_{terminal}$ bond lengths, mean 1.698 and 1.675 Å for **1** and **2** respectively, correspond to the values reported for mononuclear mono-oxo d^2 rhenium complexes with an average

Table 3
The experimental and optimized bond lengths [Å] and angles [°] for **1**

	Experimental	Optimized
Bond lengths (Å)		
Re(1)–O(1)	1.696(9)	1.689
Re(1)–O(3)	1.919(7)	1.944
Re(1)–N(1)	2.188(10)	2.239
Re(1)–N(3)	2.168(14)	2.189
Re(1)–Br(1)	2.5259(15)	2.609
Re(1)–Br(2)	2.4952(15)	2.553
Re(2)–O(2)	1.700(9)	1.689
Re(2)–O(3)	1.940(7)	1.944
Re(2)–N(5)	2.174(11)	2.240
Re(2)–N(7)	2.162(10)	2.186
Re(2)–Br(3)	2.4975(14)	2.550
Re(2)–Br(4)	2.5246(17)	2.609
Bond angles (°)		
O(1)–Re(1)–O(3)	168.3(4)	165.4
O(1)–Re(1)–N(3)	88.7(5)	87.3
O(1)–Re(1)–N(1)	85.2(4)	83.0
O(3)–Re(1)–N(3)	85.8(4)	86.7
O(3)–Re(1)–N(1)	84.5(3)	83.8
N(3)–Re(1)–N(1)	91.4(4)	90.7
O(1)–Re(1)–Br(2)	97.9(3)	99.0
O(3)–Re(1)–Br(2)	92.3(2)	94.1
N(1)–Re(1)–Br(2)	176.7(3)	177.5
N(3)–Re(1)–Br(2)	87.4(3)	87.8
O(1)–Re(1)–Br(1)	95.2(4)	94.8
O(3)–Re(1)–Br(1)	90.6(3)	91.3
N(1)–Re(1)–Br(1)	90.0(3)	89.8
N(3)–Re(1)–Br(1)	175.9(3)	177.9
Br(2)–Re(1)–Br(1)	90.90(6)	91.6
O(2)–Re(2)–O(3)	167.5(4)	165.1
O(2)–Re(2)–N(7)	88.1(4)	87.4
O(3)–Re(2)–N(7)	86.4(4)	86.7
O(2)–Re(2)–N(5)	85.3(4)	82.9
O(3)–Re(2)–N(5)	83.4(3)	83.6
N(7)–Re(2)–N(5)	88.5(4)	90.8
O(2)–Re(2)–Br(3)	98.2(3)	99.3
O(3)–Re(2)–Br(3)	92.8(2)	94.1
N(7)–Re(2)–Br(3)	88.6(3)	87.4
N(5)–Re(2)–Br(3)	175.4(3)	177.1
O(2)–Re(2)–Br(4)	94.8(4)	94.8
O(3)–Re(2)–Br(4)	90.8(2)	91.2
N(7)–Re(2)–Br(4)	177.1(3)	177.7
N(5)–Re(2)–Br(4)	91.9(3)	90.1
Br(3)–Re(2)–Br(4)	90.76(6)	91.7
Re(1)–O(3)–Re(2)	178.6(5)	176.4
Pseudo-torsion angles (°)		
N(1)–Re(1)···Re(2)–N(5)	−25.6(4)	
N(1)–Re(1)···Re(2)–N(7)	−114.4(4)	
N(3)–Re(1)···Re(2)–N(5)	−117.4(4)	
N(3)–Re(1)···Re(2)–N(7)		
Br(1)–Re(1)···Re(2)–Br(3)	−112.9(1)	
Br(1)–Re(1)···Re(2)–Br(4)	156.3(1)	
Br(2)–Re(1)···Re(2)–Br(3)	−22.0(1)	
Br(2)–Re(1)···Re(2)–Br(4)	−112.8(1)	
O(1)–Re(1)···Re(2)–O(2)	−82(2)	

Re–$O_{terminal}$ distance of 1.691Å [52]. The Re–$O_{terminal}$ bonds of **1** and **2** appear therefore to be normal triple bonds. The Re–$O_{bridging}$ bond distances of 1.929 and

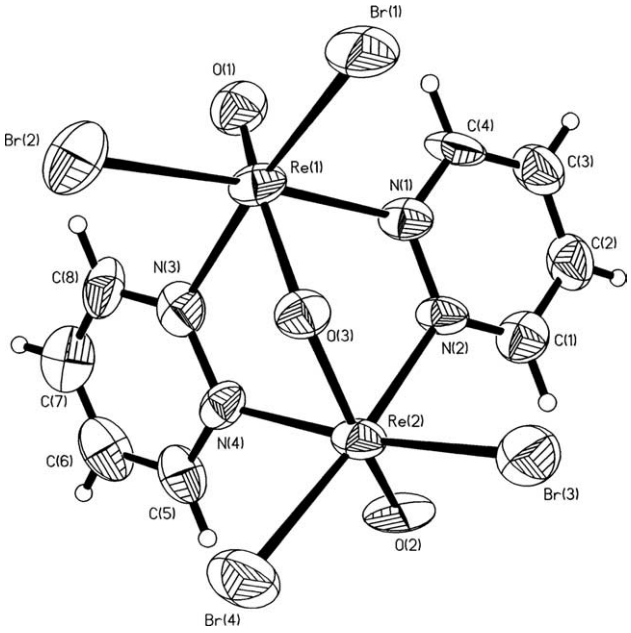


Fig. 2. The molecular structure of **2**.

1.898 Å for **1** and **2** suggest that a small amount of overlap also occurs between the d_{xz} and d_{yz} rhenium orbitals and the suitable p orbitals of the bridging oxygen. An ideal single Re–O bond length, predicted by the use of Pauling's covalent radius for oxygen and Cotton and Lippard's value for the octahedral covalent radius of rhenium(V), should be ca. 2.04 Å [53].

4.4. NBO analysis

Table 5 presents the occupancies and hybridization of the calculated natural bond orbitals (NBOs) between the rhenium and the oxo ligands for the complexes **1** and **2**. Table 6 shows the occupancies and atomic orbital compositions of the lone pairs (LP) of the oxo ligands, as well as the character of the acceptor orbital and stabilization energies (ΔE_{ij}) for the corresponding donor-acceptor interactions for **1** and **2**. The interactions between 'filled' (donor) Lewis-type NBOs and 'empty' (acceptor) non-Lewis NBOs lead to loss of occupancy from the localized NBOs of the idealized Lewis structure into the empty non-Lewis orbitals, and they are referred to as 'delocalization' corrections to the zeroth-order natural Lewis structure. The stabilization energy ΔE_{ij} (kcal/mol) associated with delocalization is estimated by the second–order perturbative as

$$\Delta E_{ij} = q_i(F(i,j)^2)/(\varepsilon_j - \varepsilon_i),$$

where q_i is the donor orbital occupancy, ε_i, ε_j are diagonal elements (orbital energies) and $F(i,j)$ is the off-diagonal NBO Fock matrix element [54].

Table 4
The experimental and optimized bond lengths (Å) and angles (°) for **2**

	Experimental	Optimized
Bond lengths (Å)		
Re(1)–O(1)	1.665(14)	1.697
Re(1)–O(3)	1.911(11)	1.908
Re(1)–N(1)	2.167(14)	2.229
Re(1)–N(3)	2.212(15)	2.229
Re(1)–Br(1)	2.488(2)	2.528
Re(1)–Br(2)	2.484(2)	2.528
Re(2)–O(2)	1.685(11)	1.697
Re(2)–O(3)	1.885(11)	1.908
Re(2)–N(2)	2.179(12)	2.229
Re(2)–N(4)	2.139(14)	2.229
Re(2)–Br(3)	2.484(2)	2.528
Re(2)–Br(4)	2.493(2)	2.528
Bond angles (°)		
O(1)–Re(1)–O(3)	158.5(5)	154.4
O(1)–Re(1)–N(1)	85.5(6)	85.4
O(1)–Re(1)–N(3)	89.0(6)	85.4
O(3)–Re(1)–N(1)	78.5(5)	77.1
O(3)–Re(1)–N(3)	77.5(5)	77.1
N(1)–Re(1)–N(3)	91.9(5)	92.3
O(1)–Re(1)–Br(2)	101.6(5)	100.8
O(3)–Re(1)–Br(2)	94.6(3)	96.8
N(1)–Re(1)–Br(2)	172.9(4)	173.8
N(3)–Re(1)–Br(2)	88.0(3)	87.5
O(1)–Re(1)–Br(1)	100.9(5)	100.8
O(3)–Re(1)–Br(1)	92.7(3)	96.8
N(1)–Re(1)–Br(1)	87.7(4)	87.5
N(3)–Re(1)–Br(1)	170.0(4)	173.8
Br(2)–Re(1)–Br(1)	91.17(8)	92.1
O(2)–Re(2)–O(3)	159.8(6)	154.4
O(2)–Re(2)–N(4)	88.8(6)	85.4
O(3)–Re(2)–N(4)	78.3(5)	77.1
O(2)–Re(2)–N(2)	85.6(6)	85.3
O(3)–Re(2)–N(2)	79.2(5)	77.0
N(4)–Re(2)–N(2)	91.2(6)	92.3
O(2)–Re(2)–Br(3)	100.1(5)	100.8
O(3)–Re(2)–Br(3)	92.4(4)	96.8
N(2)–Re(2)–Br(3)	86.8(4)	87.5
N(4)–Re(2)–Br(3)	170.7(4)	173.8
O(2)–Re(2)–Br(4)	101.2(5)	100.8
O(3)–Re(2)–Br(4)	94.0(3)	96.9
N(2)–Re(2)–Br(4)	173.1(3)	173.8
N(4)–Re(2)–Br(4)	88.5(4)	87.5
Br(3)–Re(2)–Br(4)	92.35(8)	92.1
Re(2)–O(3)–Re(1)	128.3(6)	130.4

Table 5
The occupancies and hybridization of the calculated natural bond orbitals (NBOs) between the rhenium and the oxo ligands for **1** and **2**

BD[a]	Occupancy	Hybridization of NBO
*Complex **1***		
Re(1)–O(1)	1.990	$0.571(d)_{Re} + 0.821(p)_O$
Re(1)–O(1)	1.991	$0.568(d)_{Re} + 0.823(p)_O$
Re(2)–O(2)	1.990	$0.571(d)_{Re} + 0.821(p)_O$
Re(2)–O(2)	1.991	$0.567(d)_{Re} + 0.823(p)_O$
Re(1)–O(1)[b]	0.291	$0.821(d)_{Re} - 0.571(p)_O$
Re(1)–O(1)[b]	0.279	$0.823(d)_{Re} - 0.568(p)_O$
Re(2)–O(2)[b]	0.290	$0.821(d)_{Re} - 0.571(p)_O$
Re(2)–O(2)[b]	0.279	$0.823(d)_{Re} - 0.567(p)_O$
*Complex **2***		
Re(1)–O(1)	1.993	$0.559(d)_{Re} + 0.830(p)_O$
Re(1)–O(1)	1.984	$0.572(d)_{Re} + 0.820(p)_O$
Re(2)–O(2)	1.926	$0.529(d)_{Re} + 0.849(p)_O$
Re(2)–O(2)	1.984	$0.572(d)_{Re} + 0.820(p)_O$
Re(2)–O(3)	1.786	$0.391(sd^{3.87})_{Re} + 0.921(sp^{3.30})_O$
Re(1)–O(1)[b]	0.298	$0.830(d)_{Re} - 0.559(p)_O$
Re(1)–O(1)[b]	0.336	$0.820(d)_{Re} - 0.572(p)_O$
Re(2)–O(2)[b]	0.270	$0.849(d)_{Re} - 0.529(p)_O$
Re(2)–O(2)[b]	0.336	$0.820(d)_{Re} - 0.572(p)_O$
Re(2)–O(3)[b]	0.499	$0.391(sp^{3.30})_O - 0.921(sd^{3.87})_{Re}$

[a] BD denotes 2-center bond.
[b] Denotes antibond NBO.

For each Re atom of **1** and **2**, two natural Re–O_t bond orbitals were detected. They are all polarized towards the oxygen atom (ca. 68%), and the p oxygen orbitals and d rhenium orbitals are involved in the Re–O_t bond formation. The atomic orbital compositions of the detected Re–O_t bond orbitals (Table 5) indicate their π character. The non-detected $\sigma_{Re–Ot}$ bonds have character of predominantly Coulomb-type interactions between the central ion and ligands [55]. Each terminal oxo ligand of **1** and **2** has two lone pairs, and the electron density from one of them (for each atom) is strongly delocalized into non-Lewis rhenium orbitals (Table 6). In complex **1**, the bridging oxygen ligand has four lone pairs (LP) and the Re–O_b bonds were not detected indicating predominant Coulomb-type Re–ligand interactions. The LP orbitals of σ symmetry of the bridging oxo ligand interact with the empty d and sd Re orbitals, whereas LP orbitals of π symmetry interact with $\pi^*_{Re–O(t)}$ orbitals. In both cases significant loss of occupancy from LP orbitals of bridging oxo ligand can be noticed.

In complex **2**, one Re–O_b bond orbital was detected and consequently the bridging oxo ligand has three LP orbitals. The detected Re(1)–O(3) bond is strongly polarized towards the bridging oxygen atom (ca. 85%), and the s and p oxygen orbitals and s and d rhenium orbitals take part the bond formation. The non-detected Re(1)–O(3) bond has predominantly ionic character. A larger loss of occupancy can be noticed from the lone pair orbitals of π symmetry interacting with $\pi^*_{Re–O(t)}$ orbitals.

4.5. Geometry optimisation

The optimised geometric parameters of **1** and **2** are gathered in Tables 3 and 4, respectively. A good agreement with the experimental values can be noticed for the Re–O and Re–N bond lengths. Larger differences between calculated and experimental bond lengths are seen for Re–Br distances, the maximum deviations for

Table 6
Stabilization energies associated with delocalisation from the lone pair orbitals of the oxo ligands for **1** and **2**

Donor orbital	Occupancy of donor orbital	Acceptor orbital	ΔE_{ij} (kcal/mol)
Complex ***1***			
$(sp^{0.56})_{O(1)}$	1.960	$d_{Re(1)}$	11.2
		$(sd^{0.28})_{Re(1)}$	31.9
$(sp^{2.03})_{O(1)}$	1.617	$d_{Re(1)}$	111.1
		$(sd^{0.28})_{Re(1)}$	168.9
$(sp^{0.56})_{O(2)}$	1.960	$d_{Re(2)}$	11.2
		$(sd^{0.28})_{Re(2)}$	31.8
$(sp^{2.04})_{O(2)}$	1.618	$d_{Re(2)}$	110.9
		$(sd^{0.28})_{Re(2)}$	168.3
$s_{O(3)}$	1.766	$d_{Re(1)}$	31.1
		$(sd^{0.28})_{Re(1)}$	64.7
		$d_{Re(2)}$	28.9
		$(sd^{0.28})_{Re(2)}$	59.6
$p_{O(3)}$	1.758	$d_{Re(1)}$	26.6
		$(sd^{0.28})_{Re(1)}$	30.5
		$d_{Re(2)}$	37.2
		$(sd^{0.28})_{Re(2)}$	42.1
$p_{O(3)}$	1.653	$0.821(d)_{Re(1)}$–$0.571(p)_{O(1)}$	27.1
		$0.821(d)_{Re(2)}$–$0.571(p)_{O(2)}$	25.5
$p_{O(3)}$	1.642	$0.823(d)_{Re(1)}$–$0.568(p)_{O(1)}$	23.6
		$0.823(d)_{Re(2)}$–$0.567(p)_{O(2)}$	22.2
Complex ***2***			
$(sp^{0.50})_{O(1)}$	1.962	$(sd^{1.00})_{Re(1)}$	31.4
$(sp^{2.98})_{O(1)}$	1.638	$(sd^{1.00})_{Re(1)}$	205.9
$(sp^{0.50})_{O(2)}$	1.962	$0.391(sp^{3.30})_{O(3)}$-$0.921(sd^{3.87})_{Re(2)}$	13.6
$(sp^{2.99})_{O(2)}$	1.638	$0.391(sp^{3.30})_{O(3)}$-$0.921(sd^{3.87})_{Re(2)}$	136.8
		$0.849(d)_{Re(2)}$–$0.529(p)_{O(2)}$	25.4
$(sp^{0.30})_{O(3)}$	1.824	$(sd^{1.00})_{Re(1)}$	62.8
		$0.849(d)_{Re(2)}$–$0.529(p)_{O(2)}$	18.8
$p_{O(3)}$	1.718	$(sd^{1.00})_{Re(1)}$ $0.391(sp^{3.30})_{O(3)}$-	66.4
		$0.921(sd^{3.87})_{Re(2)}$	35.8
		$0.849(d)_{Re(2)}$–$0.529(p)_{O(2)}$	19.1
$p_{O(3)}$	1.610	$0.820(d)_{Re(2)}$–$0.572(p)_{O(2)}$	44.4

Re–Br bond lengths are equal to 0.08 and 0.044 Å for **1** and **2**, respectively.

4.6. Charge distribution

Table 7 presents the atomic charges from the natural population analysis (NPA) for complexes **1** and **2**. The calculated charges on the rhenium atoms are considerably lower than the formal charge of +5. The population of the d_{xy}, d_{xz}, d_{yz}, $d_{x^2-y^2}$ and d_{z^2} orbitals of the central atoms in **1** and **2** is as follows: complex **1** – Re(1): 0.964, 0.861, 1.569, 0.920 and 1.067; Re(2): 0.972, 0.860, 1.562, 0.916 and 1,070; complex **2** – Re(1) and Re(2): 0.881, 1.118, 0.968, 1.381 and 1.069. This is a result of significant charge donation from oxo ligands, bromine ions and N-heterocyle molecules. The Re centers of **2** are less positive in comparison with the metal ions of **1**. In both complexes **1** and **2**, considerable differences in the values of charges are observed for the terminal and bridging oxo ligands–less negative are the terminal oxo ligands, which indicates the higher electron density delocalization from the terminal ligands towards the rhenium centers and corresponds to differences in the Re–O_t and Re–O_b bonds lengths. The higher charge donation from the terminal oxo ligands can be noticed for the linear complex, whereas the bridging oxo ligand is less negative in the complex **2**.

4.7. Electronic structure

The energy and character of the selected MOs for **1** and **2** are presented in Table 8. The rhenium atoms in

Table 7
Atomic charges from the natural population analysis (NPA) for **1** and **2**

Atom	**1**	**2**
Re(1)	1.16	1.12
Re(2)	1.16	1.12
O(1)	−0.46	−0.51
O(2)	−0.46	−0.51
O(3)	−0.82	−0.75
N(1)	−0.45	−0.23
N(2)	−0.40	−0.23
N(3)	−0.45	−0.23
N(4)	−0.40	−0.23
N(5)	−0.45	
N(6)	−0.40	
N(7)	−0.45	
N(8)	−0.40	
Br(1)	−0.39	−0.28
Br(2)	−0.30	−0.28
Br(3)	−0.30	−0.28
Br(4)	−0.39	−0.28

both **1** and **2** possess the d^2 configuration, the two highest MOs of these compounds are of d type with antibonding contributions from p_π bromine orbitals. The remaining eight d-type orbitals of rhenium are found among unoccuppied MOs. In the case of **1**, the d_{xz} and d_{yz} rhenium orbitals make the largest contribution into the LUMO, LUMO + 1, LUMO + 6 and LUMO + 7 orbitals, and they bear antibonding character towards the oxygen atoms. The participation of the d_{xz} and d_{yz} orbitals in the other molecular orbitals of **1** do not reach 10%. In complex **2** the d_{xz} and d_{yz} rhenium orbitals are dispersed among a larger number of the molecular orbitals. The significant participations of the d_{xz} and d_{yz} orbitals are shown in LUMO, LUMO + 1, LUMO + 2, LUMO + 3, LUMO + 6 and LUMO + 7. In all of them the d_{xz} and d_{yz} orbitals bear antibonding character towards the oxygen atoms. The π orbitals of the pyridazine rings also contribute to the LUMO, LUMO + 1, LUMO + 2 orbitals. Figs. 3 and 4 present the energy and contours of the occupied and unoccupied molecular orbitals with the largest contributions of d rhenium orbitals for **1** and **2**, respectively. As it can be seen from Figs. 3 and 4, each molecular orbital is a plus or minus combination of the symmetry equivalent d orbitals of the two rhenium atoms.

4.8. Electronic spectra

The experimental and calculated electronic spectra of **1** and **2** are presented in Figs. 5 and 6, respectively. Each calculated transition in Figs. 5(b) and 6(b) was represented by a gaussian function with the height equal to the oscillator strength and the width equal to 0.04.

The investigated complexes are of large size and the number of basis functions is equal to 590 and 406 for **1** and **2**, respectively. Eighty electron transitions calculated by the TDDFT method do not comprise all the experimental absorption bands. The UV–Vis spectra of **1** and **2** were calculated to ~280 nm, so the shortest wavelength experimental bands cannot be assigned to the calculated transitions. However, considering that the solution spectra of pyrazine and pyridazine exhibit

Table 8
The energy and character of selected occupied and virtual MOs for **1** and **2**

MO	**1**		**2**	
	E (eV)	Character	*E* (eV)	Character
LUMO + 11	−1.462	$d_{x^2-y^2}$–σ_{Br}–σ_N	0.607	d_{z^2}–σ_O–σ_N–σ_{Br}
LUMO + 10	−1.505	$d_{x^2-y^2}$–σ_{Br}–σ_N	−0.251	d_{z^2}–σ_O–σ_N–σ_{Br}
LUMO + 9	−1.719	π(pyz)	−1.185	$d_{x^2-y^2}$–σ_{Br}–σ_N
LUMO + 8	−1.746	π(pyz)	−1.567	$d_{x^2-y^2}$–σ_{Br}–σ_N
LUMO + 7	−2.046	d_{xz}(Re)–$p_\pi(O_t)$–$p_\pi(O_b)$	−1.633	d_{xz}(Re)–$p_\pi(O_t)$–$p_\pi(O_b)$
LUMO + 6	−2.164	d_{yz}(Re)–$p_\pi(O_t)$–$p_\pi(O_b)$	−2.044	d_{yz}(Re)–$p_\pi(O_t)$–$p_\pi(O_b)$
LUMO + 5	−2.403	π(pyz)	−2.478	π(pyd)
LUMO + 4	−2.485	π(pyz)	−2.527	π(pyd), d_{yz}(Re)–$p_\pi(O_t)$–$p_\pi(O_b)$
LUMO + 3	−2.729	π(pyz)	−2.784	d_{xz}(Re)–$p_\pi(O_t)$
LUMO + 2	−2.870	π(pyz)	−3.166	d_{yz}(Re)–$p_\pi(O_t)$, π(pyd)
LUMO + 1	−3.403	d_{yz}(Re)–$p_\pi(O_t)$	−3.314	π(pyd), d_{xz}(Re)–$p_\pi(O_t)$
LUMO	−3.475	d_{xz}(Re)–$p_\pi(O_t)$	−3.710	π(pyd), d_{yz}(Re)–$p_\pi(O_t)$
HOMO	−6.169	d_{xy}(Re)–p_π(Br)	−5.938	d_{xy}(Re)–p_π(Br)–$p_\pi(O_b)$
HOMO − 1	−6.279	d_{xy}(Re)–p_π(Br)	−6.088	d_{xy}(Re)–p_π(Br)
HOMO − 2	−6.866	p_π(Br)	−6.706	p_π(Br)
HOMO − 3	−6.943	p_π(Br)	−6.768	p_π(Br)
HOMO − 4	−7.093	p_π(Br); $p_\pi(O_t)$	−6.973	p_π(Br); $p_\pi(O_b)$
HOMO − 5	−7.223	p_π(Br); $p_\pi(O_t)$; $p_\pi(O_b)$	−7.058	p_π(Br); $p_\pi(O_t)$
HOMO − 6	−7.230	p_π(Br); $p_\pi(O_t)$; $p_\pi(O_b)$	−7.259	p_π(Br); $p_\pi(O_b)$
HOMO − 7	−7.377	p_π(Br); $p_\pi(O_t)$; $p_\pi(O_b)$	−7.285	p_π(Br); $p_\pi(O_t)$
HOMO − 8	−7.846	σ(Br); σ(N), $p_\pi(O_t)$	−8.082	p_π(Br); $p_\pi(O_t)$; $p_\pi(O_b)$

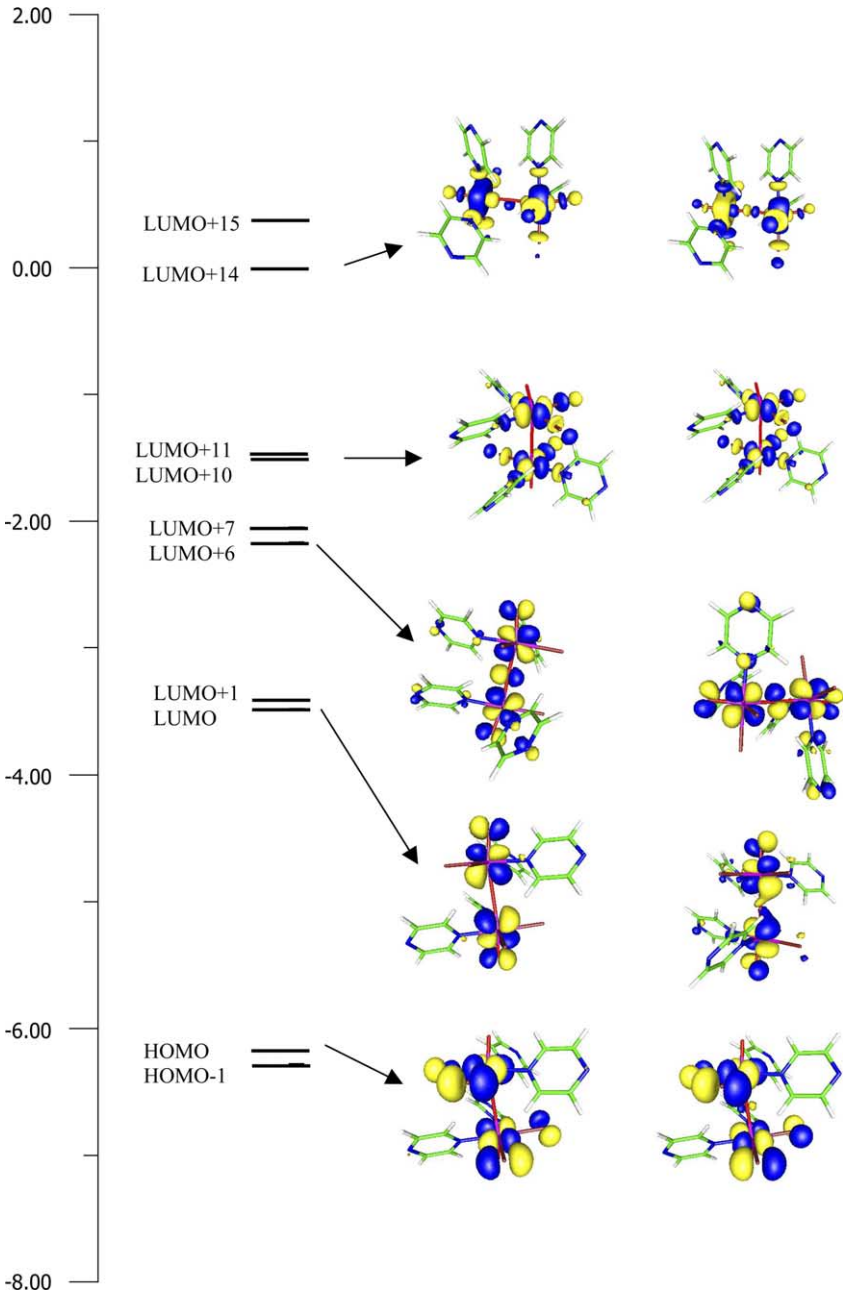


Fig. 3. The energy (eV), character and contours of the occupied and unoccupied molecular orbitals of **1** with the largest contributions of the d rhenium orbitals.

intense absorption bands in the 260–200 nm region, some additional intraligand and interligand transitions are expected to be found at higher energies in the calculations for these complexes.

4.9. *[{ReOBr$_2$(pyz)$_2$}$_2$(μ-O)] (**1**)*

The longest wavelength experimental band at 675.4 nm is attributed to the transitions of d → d character with small oscillator strengths calculated in the range 785–700 nm.

The absorption band at 486.2 nm is assigned to the electronic transitions of MLCT d → π^*_{pyz} character calculated in the range 447–418 nm.

The next experimental band at 389.6 nm corresponds to the electronic transitions calculated between 415 and 380 nm. These transitions are mainly of LMCT (π(Br)/π(O) → d) character.

The transitions calculated between 365 and 290 nm are ascribed to the experimental band at 331.4 nm. They are of LLCT (π(Br)/π(O) → π*(pyz)) and MLCT d → π^*_{pyz} and LMCT (σ(Br)/σ(N) → d) character.

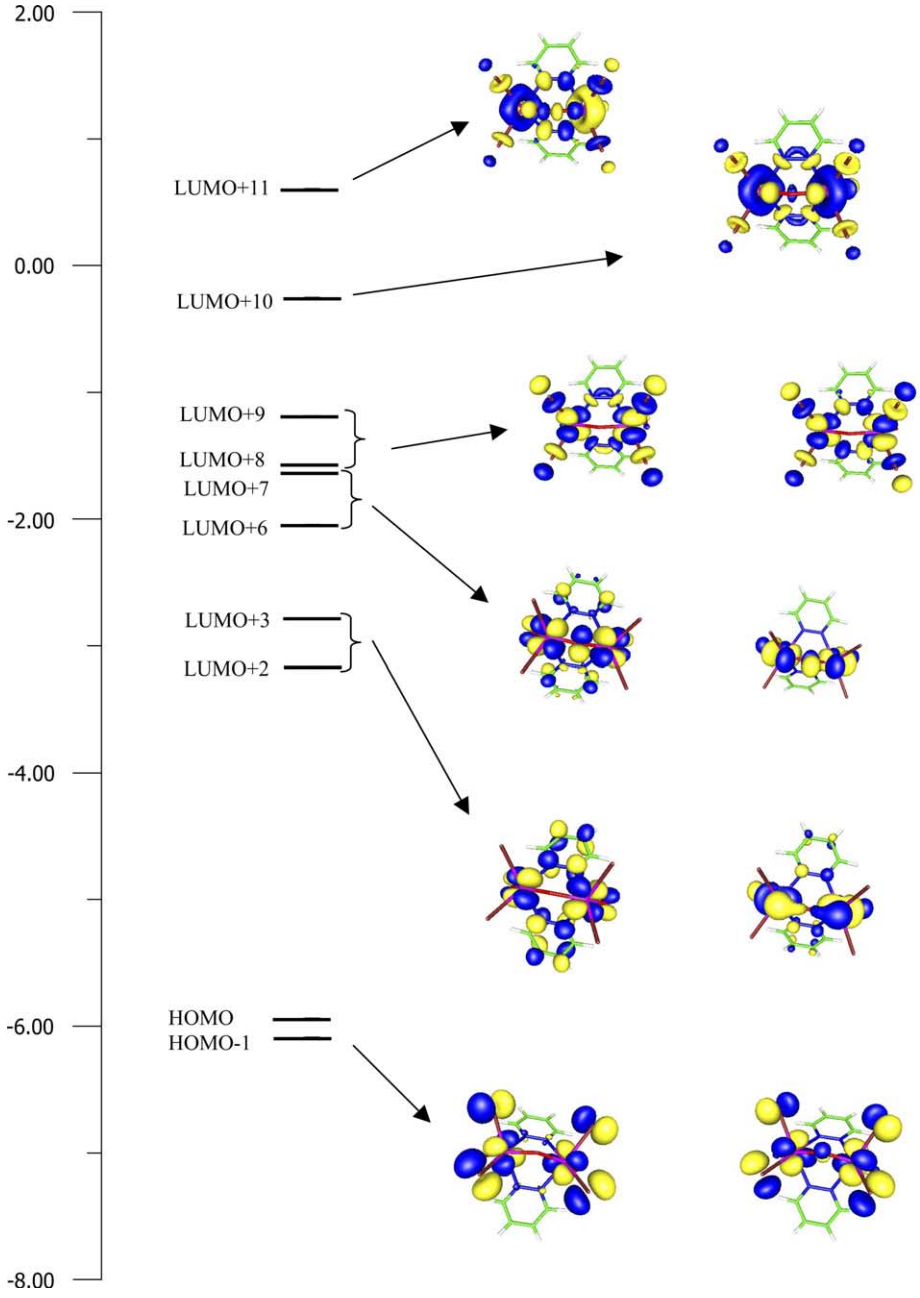
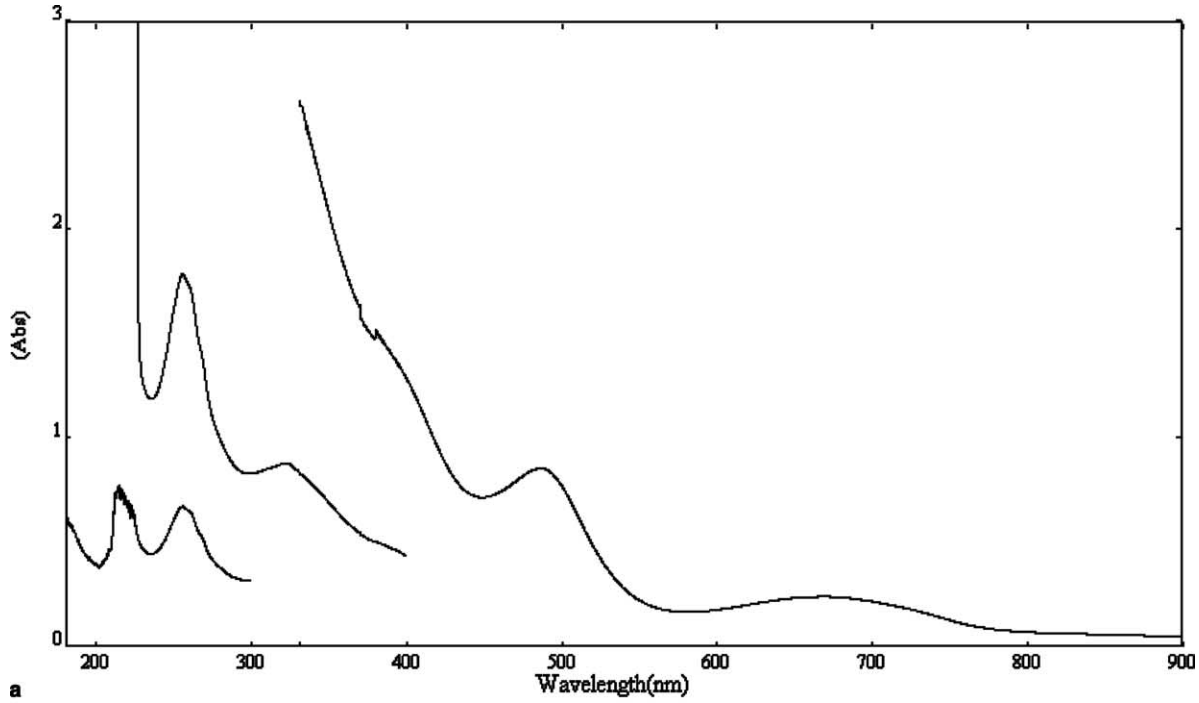


Fig. 4. The energy (eV), character and contours of the occupied and unoccupied molecular orbitals of **2** with the largest contributions of the d rhenium orbitals.

*4.10. [{$ReOBr_2$}$_2$(μ-O)(μ-pyd)$_2$] (**2**)*

The longest wavelength experimental band of complex **2** is very broad and asymmetrical. It spreads from 850 nm to 555 nm and its maximum lies at 675 nm. Similar to complex **1** this band corresponds mainly to the transitions from HOMO and HOMO − 1 to LUMO and LUMO + 1 orbitals. However, due to a significant participation of π* orbitals of the pyridazine ligands in the LUMO and LUMO + 1 orbitals, the character of the electronic transitions corresponding to the band is ascribed as d → d/π*(pyd). This experimental band is more intense in comparison with complex **1** and the calculated oscillator strengths for transitions in this region are considerably higher for complex **2**.

The absorption band at 430.0 nm is assigned to the electronic transitions calculated in the range 520–370 nm. These transitions are π(Br)/π(O) → d/π*(pyd), π(Br) → d/π*(pyd), d → π*(pyd) and d → d in origin.



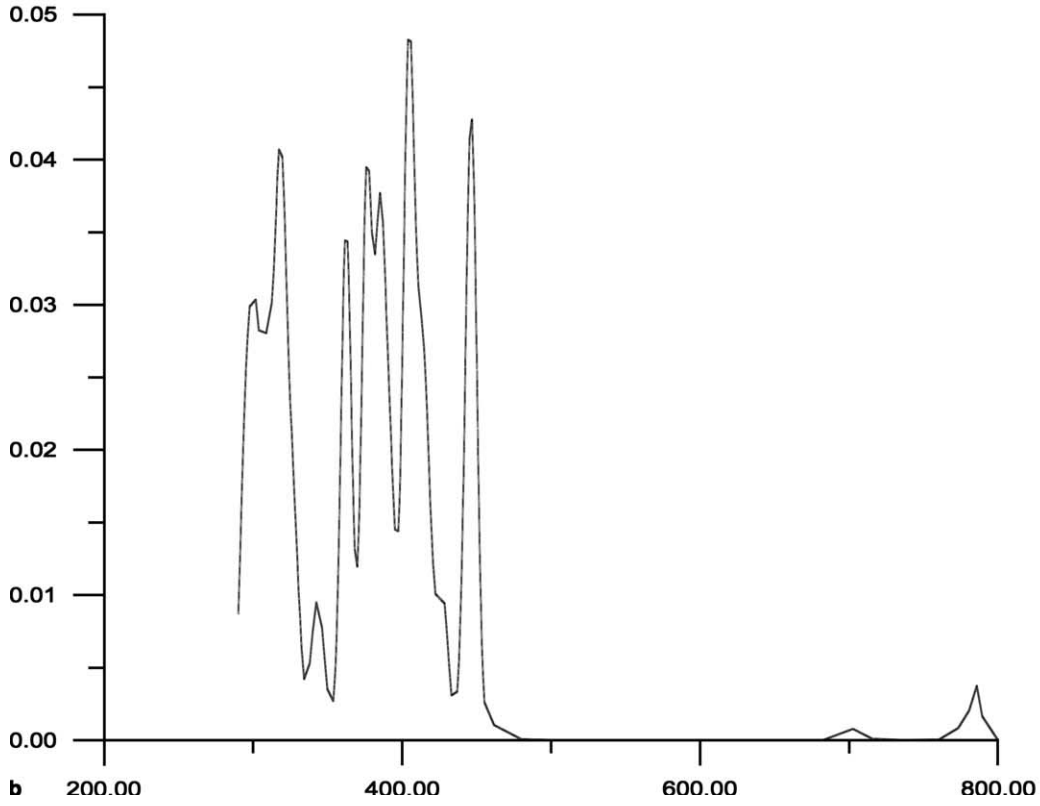


Fig. 5. The experimental (a) and calculated (b) electronic absorption spectrum of **1**.

The experimental bands at 331.2 and 273.2 nm correspond mainly to the transitions of LMCT ($\pi(Br)/\pi(O) \rightarrow d$) and LLCT ($\pi(Br)/\pi(O) \rightarrow \pi^*(pyd)$) character.

Generally, the $\pi(Br)/\pi(O) \rightarrow d$ transitions of the complex with a bent $Re_2O_3^{4+}$ unit are shifted to higher energy in comparison with that one containing a linear O═Re–O–Re═O backbone.

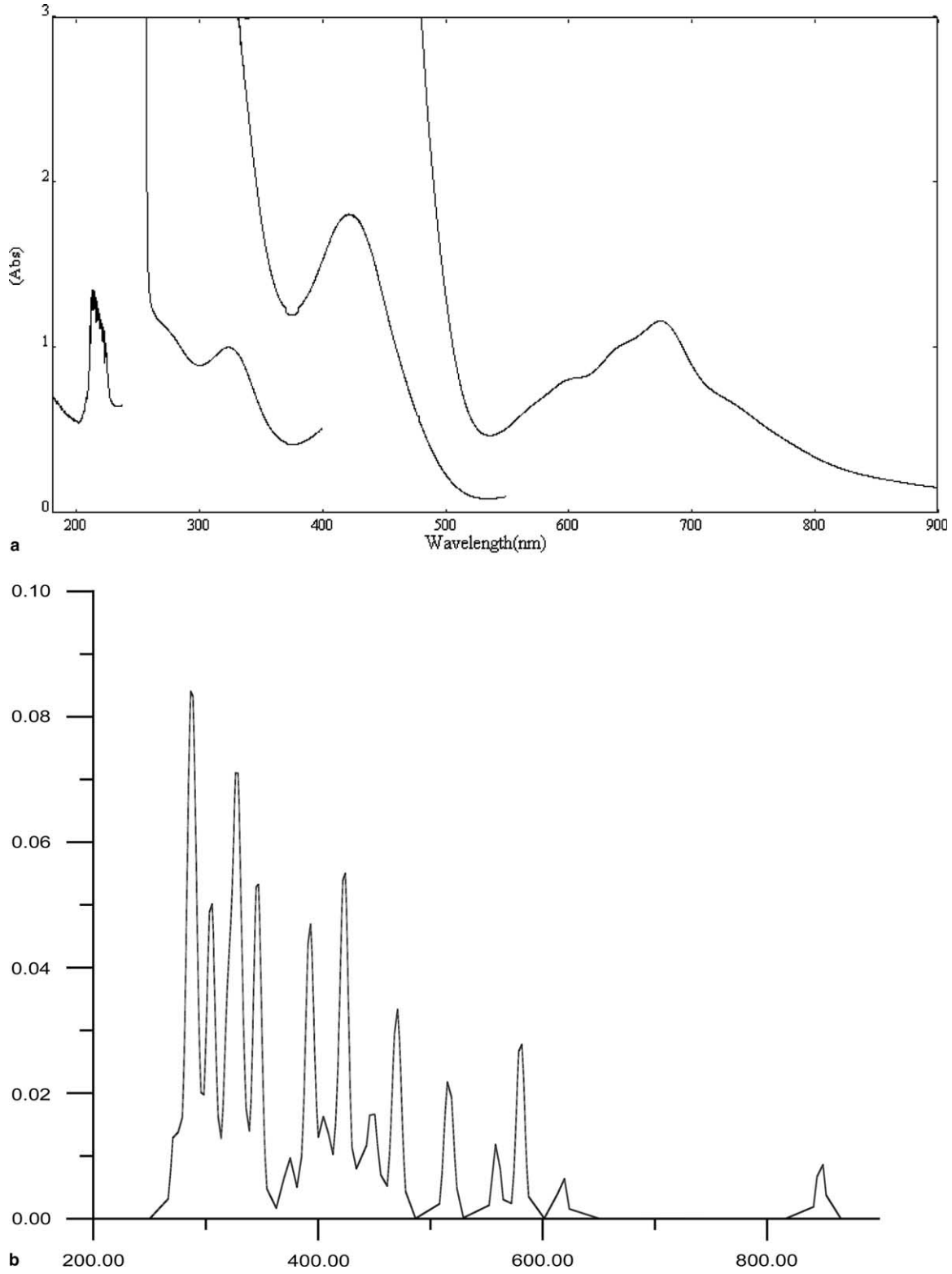


Fig. 6. The experimental (a) and calculated (b) electronic absorption spectrum of **2**.

5. Conclusions

The DFT calculations performed for two rhenium oxo complexes with linear (**1**) and bent (**2**) structures show that the investigated complexes have the rhenium atoms in a d^2 electronic configuration. The bending of the Re_2O_3 unit in **2** is a consequence of steric congestion introduced by two coordinated pyridazine bridging

ligands. For both complexes, NBO analysis confirms the presence of a triple bond between the rhenium atoms and terminal oxo ligands. The Re–O_b bonds have character of predominant Coulomb-type Re–ligand interactions, and a significant loss of occupancy from the LP orbitals of the bridging oxo ligand can be noticed for both **1** and **2**. The considerable differences in values of charges observed for the terminal and bridging oxo ligands also indicates the higher electron density delocalization from the terminal ligands towards the rhenium centers and corresponds to differences in the Re–O_t and Re–O_b bonds lengths.

6. Supplementary data

Supplementary data are available from the CCDC, 12 Union Road, Cambridge CB2 1EZ, UK on request, quoting the depositions numbers: 264637 for $C_{19}H_{22}Br_4N_8O_4Re_2$ and 264638 for $C_{11}H_{14}Br_4N_4O_4Re_2$.

Acknowledgements

The Gaussian03 calculations were carried out in the Wrocław Centre for Networking and Supercomputing, WCSS, Wrocław, Poland under calculational Grant No. 51/96.

The crystallographic part was financed by funds allocated by the Ministry of Scientific Research and Information Technology to the Institute of General and Ecological Chemistry, Technical University of Łódź.

References

[1] K.P. Maresca, D.J. Rose, J. Zubieta, Inorg. Chim. Acta 260 (1997) 83.
[2] F.E. Hahn, L. Imhof, T. Lügger, Inorg. Chim. Acta 269 (1998) 347.
[3] S. Fortin, A.L. Beauchamp, Inorg. Chim. Acta 279 (1998) 159.
[4] G. Battistuzzi, A.B. Corradi, D. Dallari, M. Saladini, R. Battistuzzi, Polyhedron 18 (1999) 57.
[5] S. Bélanger, A.L. Beauchamp, Acta Crystallogr., Sect. C 55 (1999) 517.
[6] E. Alessio, E. Zangrando, E. Iengo, M. Macchi, P.A. Marzilli, L.G. Marzilli, Inorg. Chem. 39 (2000) 294.
[7] S. Fortin, A.L. Beauchamp, Inorg. Chem. 39 (2000) 4886.
[8] H. Kooijman, K.J.C. van Bommel, W. Verboom, D.N. Reinhoudt, J. Kroon, A.L. Spek, Acta Crystallogr., Sect. C 56 (2000) 749.
[9] W.-T. Huang, J.-M. Lo, H.-H. Yao, F.-L. Liao, Acta Crystallogr., Sect. C 56 (2000) 172.
[10] L. Hansen, Y.D. Lampeka, S.P. Gavrish, X. Xu, A.T. Taylor, L.G. Marzilli, Inorg. Chem. 39 (2000) 5859.
[11] K.J.C. van Bommel, W. Verboom, R. Hulst, H. Kooijman, A.L. Spek, D.N. Reinhoudt, Inorg. Chem. 39 (2000) 4099.
[12] E. Iengo, E. Zangrando, S. Mestroni, G. Fronzoni, M. Stener, E. Alessio, J. Chem. Soc., Dalton Trans. (2001) 1338.
[13] H.-F. Lang, P.E. Fanwick, R.A. Walton, Inorg. Chim. Acta 322 (2001) 17.
[14] A. Lazzaro, G. Vertuani, P. Bergamini, N. Mantovani, A. Marchi, L. Marvelli, R. Rossi, V. Berolasi, V. Ferretti, J. Chem. Soc., Dalton Trans. (2002) 2843.
[15] L.J. Morris, A.J. Downs, J.C. Green, T.M. Greene, S.J. Teat, S. Parsons, J. Chem. Soc., Dalton Trans. (2002) 3142.
[16] Ch. Tessier, F.D. Rochon, A.L. Beauchamp, Inorg. Chem. 41 (2002) 6527.
[17] H. Sugimoto, T. Takahira, T. Yoshimura, M. Shiro, M. Yamasaki, H. Miyake, K. Umakoshi, Y. Sasaki, Inorg. Chim. Acta 337 (2002) 203.
[18] T.I.A. Gerber, E. Hosten, Z.R. Tshentu, P. Mayer, E. Pérex-Carreño, S. Garcia-Granda, J.G.H. du Preez, J. Coord. Chem. 56 (2003) 1063.
[19] G. Patsis, I. Pirmettis, Ch. Tsoukalas, M. Pelecanou, C.P. Raptopoulou, A. Terzis, M. Papadopoulos, E. Chiotellis, Inorg. Chim. Acta 342 (2003) 272.
[20] B. Machura, J.O. Dzięgielewski, S. Michalik, R. Kruszynski, T.J. Bartczak, J. Kusz, Transition Met. Chem. 28 (2003) 939.
[21] B. Machura, J.O. Dzięgielewski, R. Kruszynski, T.J. Bartczak, Polyhedron 22 (2003) 2869.
[22] B. Machura, J.O. Dzięgielewski, R. Kruszynski, T.J. Bartczak, J. Kusz, Inorg. Chim. Acta 357 (2004) 1011.
[23] S. Trofimenko, Chem. Rev. 72 (1972) 497.
[24] S. Trofimenko, Inorg. Chem. 34 (1986) 115.
[25] J.D. Dunitz, L.E. Orgel, J. Chem. Soc. (1953) 2594.
[26] J. San Filipo Jr., P.J. Fagan, F.J. Di Salvo, Inorg. Chem. 16 (1977) 1016.
[27] R.J.H. Clark, M.L. Franks, P.C. Turtle, J. Am. Chem. Soc. 99 (1977) 2473.
[28] J.R. Campell, R.J.H. Clark, J. Chem. Soc., Faraday Trans. II 76 (1980) 1103.
[29] D. Appleby, R.I. Crisp, P.B. Hitchcock, C.L. Hussey, T.A. Ryan, J.R. Sanders, K.R. Seddon, J.E. Turp, J.A. Zora, J. Chem. Soc., Chem. Commun. 1 (1986) 483.
[30] J.R. Campell, R.J.H. Clark, Mol. Phys. 36 (1978) 1133.
[31] T.R. Weaver, T.J. Meyer, S.A. Adeyemi, G.M. Brown, R.P. Eckberg, W.E. Hatfield, E.C. Johnson, R.W. Murray, D. Untereker, J. Am. Chem. Soc. 28 (1975) 3039.
[32] R. Scheneider, T. Weyhermüller, K. Wieghardt, Inorg. Chem. 32 (1993) 4925.
[33] L.W. Paes, R.B. Faria, J.O. Machuca-Herrera, S. de P. Machado, Inorg. Chim. Acta 321 (2001) 22.
[34] T. Ziegler, Chem. Rev. 91 (1991) 651.
[35] W. Kohn, A.D. Becke, R.G. Parr, J. Phys. Chem. 100 (1996) 12974.
[36] M.E. Casida, C. Jamorski, K.C. Casida, D.R. Salahub, J. Chem. Phys. 108 (1998) 4439.
[37] S.I. Gorelsky, A.B.P. Lever, J. Organomet. Chem. 635 (2001) 187.
[38] J.O. Dzięgielewski, B. Machura, T.J. Bartczak, J. Kusz, J. Warczewski, J. Coord. Chem. 55 (2002) 1315.
[39] STOE & Cie, X-RED. Version 1.18. STOE & Cie GmbH, Darmstadt, Germany, 1999.
[40] G.M. Sheldrick, Acta Crystallogr., Sect. A 46 (1990) 467.
[41] G.M. Sheldrick, SHELXL97: Program for the Solution and Refinement of Crystal Structures, University of Göttingen, Göttingen, Germany, 1997.
[42] G.M. Sheldrick, SHELXTL: release 4.1 for Siemens Crystallographic Research Systems, 1990.
[43] M.J. Frisch, G.W. Trucks, H.B. Schlegel, G.E. Scuseria, M.A. Robb, J.R. Cheeseman, J.A. Montgomery Jr., T. Vreven, K.N. Kudin, J.C. Burant, J.M. Millam, S.S. Iyengar, J. Tomasi, V. Barone, B. Mennucci, M. Cossi, G. Scalmani, N. Rega, G.A. Petersson, H. Nakatsuji, M. Hada, M. Ehara, K. Toyota, R. Fukuda, J. Hasegawa, M. Ishida, T. Nakajima, Y. Honda, O. Kitao, H. Nakai, M. Klene, X. Li, J.E. Knox, H.P. Hratchian, J.B.

Cross, C. Adamo, J. Jaramillo, R. Gomperts, R.E. Stratmann, O. Yazyev, A.J. Austin, R. Cammi, C. Pomelli, J.W. Ochterski, P.Y. Ayala, K. Morokuma, G.A. Voth, P. Salvador, J.J. Dannenberg, V.G. Zakrzewski, S. Dapprich, A.D. Daniels, M.C. Strain, O. Farkas, D.K. Malick, A.D. Rabuck, K. Raghavachari, J.B. Foresman, J.V. Ortiz, Q. Cui, A.G. Baboul, S. Clifford, J. Cioslowski, B.B. Stefanov, G. Liu, A. Liashenko, P. Piskorz, I. Komaromi, R.L. Martin, D.J. Fox, T. Keith, M.A. Al-Laham, C.Y. Peng, A. Nanayakkara, M. Challacombe, P.M.W. Gill, B. Johnson, W. Chen, M.W. Wong, C. Gonzalez, J.A. Pople, GAUSSIAN-03: Revision B.03, Gaussian, Inc., Pittsburgh, PA, 2003.

[44] A.D. Becke, J. Chem. Phys. 98 (1993) 5648.

[45] C. Lee, W. Yang, R.G. Parr, Phys. Rev. B 37 (1988) 785.

[46] M.E. Casida, in: J.M. Seminario (Ed.), Recent Developments and Applications in Modern Density Functional Theory, Theoretical and Computational Chemistry, vol. 4, Elsevier, Amsterdam, 1996.

[47] P.J. Hay, W.R. Wadt, J. Chem. Phys. 82 (1985) 299.

[48] E.D. Glendening, A.E. Reed, J.E. Carpenter, F. Weinhold, NBO (version 3.1).

[49] W.P. Griffith, T.D. Wickins, J. Chem. Soc. A (1967) 675.

[50] G.A. Jeffrey, W. Saenger, Hydrogen Bonding in Biological Structures, Springer, Berlin, 1994.

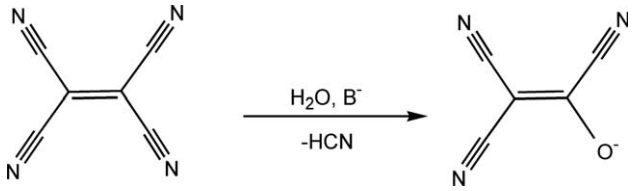
[51] G.R. Desiraju, T. Steiner, The Weak Hydrogen Bond in Structural Chemistry and Biology, Oxford University Press, Oxford, 1999.

[52] J.M. Mayer, Inorg. Chem. 27 (1988) 3899.

[53] S.R. Flechter, A.C. Skapski, J. Chem. Soc., Dalton Trans. (1972) 1073.

[54] A.E. Reed, L.A. Curtiss, F. Weinhold, Chem. Rev. 88 (1988) 899.

[55] M.L. Kuznestov, A.J.L. Pombeiro, J. Chem. Soc., Dalton Trans. (2003) 738.



Scheme 1. Hydrolysis reaction of tetracyanoethylene to produce the tricyanoethenolate ligand.

This consideration notwithstanding, there are examples of compounds in which one of the nitrile N atoms are coordinated rather than the O atom [7]. It has also been noted in several instances that the anion is outer-sphere rather than being coordinated to metal centers [4a,4c].

In this paper, we report two new Fe(II) and Co(II) compounds in which the tricyanoethenolate ligand coordinates via two of its three nitrile N atoms which leads to the formation of two-dimensional sheets. Since the study of this derivative of TCNE as a bridging ligand for magnetic materials has not been explored very well, we undertook measurements of the magnetic properties of the layered materials. The results indicate that the metal spins are essentially isolated paramagnets with no evidence of coupling through the tricyanoethenolate bridging ligand.

2. Experimental

2.1. Materials and methods

The tetracyanoethylene (TCNE) ligand was obtained from TCI and purified by sublimation before use. The starting materials $Fe_4Cl_8(THF)_6$ and $Co_4Cl_8(THF)_6$ were prepared according to the literature procedures [8]. All operations were carried out under a N_2 atmosphere using standard Schlenk line techniques. Solvents were distilled prior to use from the appropriate drying agents.

2.2. Synthesis

2.2.1. $\{Fe(C_5N_3O)_2(CH_3CN)_2\}_\infty$ (1)

A mixture of $Fe_4Cl_8(THF)_6$ (0.094 g, 0.10 mmol), TCNE (0.104 g, 0.80 mmol) in acetonitrile (20 mL) was stirred for three days at room temperature to yield a green solution and a tan precipitate. The precipitate was removed by filtration and the filtrate was layered with diethyl ether to yield colorless, diffraction quality crystals in ~13% yield based on the Fe content in the starting material.

2.2.2. $\{Co(C_5N_3O)_2(C_4H_4O)_2\}_\infty$ (2)

A mixture of $Co_4Cl_8(THF)_6$ (0.095 g, 0.10 mmol), TCNE (0.104 g, 0.80 mmol) in tetrahydrofuran (25 mL) was refluxed for two days yielding a light blue solution and a blue precipitate. The precipitate was removed by filtration and the filtrate was layered with hexane to yield large, yellow, X-ray quality crystals in ~5% yield based on the Co content in the starting material.

2.3. X-ray crystallography

Single crystal X-ray intensities were collected on a Bruker SMART CCD area detector diffractometer at 110(2) K for **1** and at 173(2) K for **2**. The frames were integrated with the Bruker SAINT software package [9]. The data were corrected for absorption using SADABS [10] and the structures solved (by direct methods) and refined using X-SEED [11], a graphical interface to the SHELX [12]. Electron density syntheses indicated that the TCNE ion had undergone a decomposition reaction, where one of the nitrile groups had been lost and replaced by an O^- group. At this stage, we were not sure that the atom labeled O1 was an O atom because the C–O bond was shorter and the C–C bond shorter than normal, and an O^- group would seem to be the preferred site for binding to metal cations. The data for (**1**) were used to explore the effect of interchanging O and N atoms for the atom labeled O1 and to establish its identity as oxygen. Refinement as an O atom led to lower values for R_1 (0.028 instead of 0.035 for (**1**)), lower residual electron densities (0.25, −0.22 e Å^3 instead 0.57 and −0.27 for (**1**)) and displacement parameters. Further evidence that this atom is correctly assigned as O was obtained by analyzing the hydrogen bonds accepted by this atom. This atom accepts two hydrogen bonds with an approximate H···O···H angle of 95°. The C–O and central C–C distances (1.218(2) and 1.423(2) Å for **1**) are similar to those of other ethanolate complexes

Table 1
Crystallographic data and structural refinement parameters for compounds $[Fe(C_5N_3O)_2(CH_3CN)_2]$ (**1**) and $[Co(C_5N_3O)_2(C_4H_4O)_2]$ (**2**)

	(**1**)	(**2**)
Chemical formula	$C_7H_3N_4FeO$	$C_9H_8N_3CoO_2$
a (Å)	7.9970(16)	9.875(2)
b (Å)	8.9870(18)	11.268(2)
c (Å)	11.758(2)	9.7207(19)
α (°)	90	90
β (°)	102.06(3)	108.75(3)
γ (°)	90	90
V (Å^3)	826.4(3)	1024.2(4)
Z	2	2
Formula weight	214.98	249.11
Space group	$P2_1n$	$P2_1c$
T (K)	110(2)	110(2)
λ (Å)	0.71073	0.71073
D_{calc} (g cm^{-3})	1.5033	0.808
μ (cm^{-1})	0.891	0.828
R (F_o)[a]	0.0287	0.0520
R_w (F_o^2)[b]	0.0621[c]	0.1231[c]
GOF on F^2	0.953	1.1012

[a] $R(F)_o = \sum[(F_o - F_o)]/\sum(F_o)$.
[b] $R_w(F_o^2) = \{\sum[w(F_o^2 - F_c^2)^2]/\sum[w(F_o^2)^2]\}^{1/2}$.
[c] $w = 1/[\sigma^2(F_o^2) + (0.0904P)^2]$ where $P = (F_o^2 + 2F_c^2)/3$.

Table 2
Selected bond distances (Å) for compound **1**

Fe–N(2)	2.1389(15)
Fe–N(1)	2.1419(16)
Fe–N(3)	2.1589(14)
O(1)–C(6)	1.218(2)
C(1)–N(1)	1.151(2)
C(1)–C(5)	1.405(2)
C(3)–N(3)	1.151(2)
C(3)–C(5)	1.415(2)
C(6)–C(5)	1.421(2)
C(6)–C(4)	1.496(2)
C(2)–N(2)	1.137(2)
C(2)–C(7)	1.451(2)
N(4)–C(4)	1.139(2)

[4,6,7]. Crystal parameters and basic information pertaining to data collection and refinement for both structures are summarized in Table 1. Relevant bonding distances and angles are listed in Tables 2–5.

Table 3
Selected angles (°) for compound **1**

N2–Fe1–N2	180
N2–Fe1–N1	86.58(6)
N1–Fe1–N1	180.00(7)
N2–Fe1–N3	89.50(5)
N1–Fe1–N3	86.96(5)
N2–Fe1–N3	90.50(5)
N1–C1–C5	178.25(16)
N3–C3–C5	177.52(17)
C1–N1–Fe1	163.55(13)
C3–N3–Fe1	158.71(13)
O1–C6–C5	127.24(15)
O1–C6–C4	118.44(15)
C5–C6–C4	114.32(14)
N2–C2–C7	179.28(18)
C1–C5–C3	118.03(14)
C1–C5–C6	121.56(14)
C3–C5–C6	120.09(15)
N4–C4–C6	178.05(18)
C2–N2–Fe1	169.94(13)

Table 4
Selected bond distances (Å) for compound **2**

Co–N(1)	2.071(3)
Co–O(2)	2.084(2)
Co–N(2)	2.126(3)
C(1)–N(1)	1.154(4)
O(2)–C(6)	1.447(4)
O(2)–C(9)	1.462(4)
C(1)–C(4)	1.401(4)
C(4)–C(2)	1.418(4)
C(4)–C(5)	1.423(4)
O(1)–C(5)	1.216(4)
N(2)–C(2)	1.141(4)
N(3)–C(3)	1.150(4)
C(3)–C(5)	1.483(4)
C(9)–C(8)	1.492(5)

Table 5
Selected angles (°) for compound **2**

N1–Co1–O2	88.76(10)
O2–Co1–O2	180.00(3)
N1–Co1–N2	87.38(9)
O2–Co1–N2	89.56(10)
C1–N1–Co1	174.5(3)
C6–O2–Co1	124.7(2)
C6–O2–C9	109.4(3)
C9–O2–Co1	125.6(2)
N1–C1–C4	179.7(3)
C1–C4–C2	117.4(3)
C1–C4–C5	122.2(3)
C2–C4–C5	120.4(3)
C2–N2–Co1	162.0(2)
N3–C3–C5	176.3(4)
O1–C5–C4	127.2(3)
O1–C5–C3	119.6(3)
O2–C9–C8	106.9(3)
O2–C6–C7	106.8(4)
C6–C7–C8	106.7(4)

2.4. Physical measurements

Infrared spectra were measured as Nujol mulls between KBr plates on a Nicolet 740 FT-IR spectrometer. Magnetic susceptibility and magnetization measurements were carried out with a Quantum Design SQUID magnetometer MPMS-XL. DC magnetic measurements were performed with an applied field of 1000 G in the 2–300 K temperature range. The data were corrected for diamagnetic contributions by use of Pascal's constants [13].

3. Results and discussion

3.1. Synthesis and infrared spectra

The reactions of $Fe_4Cl_8(THF)_6$ and $Co_4Cl_8(THF)_6$ with TCNE lead to the formation of crystals of the polymers $\{Fe(C_5N_3O)_2(CH_3CN)_2\}_\infty$ and $\{Fe(C_5N_3O)_2(C_4H_4O)_2\}_\infty$. The exact mechanism of the presence of $[OC(CN)C(CN)_2]^-$ in the products can been ascertained from their IR spectra based on a comparison to the known compounds listed [4a]. The broad and intense bands at 1591 cm^{-1} for (**1**) and 1601 cm^{-1} for (**2**) are due to the C=O stretching vibration [4a], whereas the features at 2240 and 2211 cm^{-1} for (**1**) and 2244 and 2211 cm^{-1} for (**2**) can be attributed to CN stretches.

3.2. Descriptions of the structures

The structures of the title compounds consist of infinite, two-dimensional sheets of $[Fe(C_5N_3O)_2(CH_3CN)_2]$ and $[Co(C_5N_3O)_2(C_4H_4O)_2]$ units with Miller indices [1 0 1] in **1** and [1 0 0] in **2** (Figs. 1 and 3). Both compounds crystallize in the space group $P2_1/n$ with the metal atoms on inversion centers. The 1,2,2-tricyanoe-

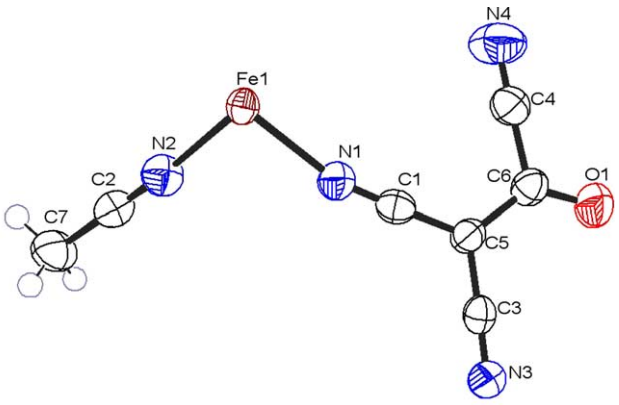


Fig. 1. Thermal ellipsoid plot of the asymmetric unit in$\{Fe(C_5N_3O)_2(CH_3CN)_2\}_\infty$ (**1**) drawn at the 50% probability level.

thenolate ion is bidentate and binds to the metal atoms via two of its three CN groups and not the O atom. The ligands are bound to the Co and Fe ions head-on, i.e., the coordinating CN groups are attached to the same C atom of the central C–C bond (see Fig. 2). Acetonitrile (in **1**) and tetrahydrofuran (in **2**) molecules are coordinated to Fe and Co atoms in the axial positions. The Fe and Co atoms are in nearly ideal octahedral coordination environments. The two independent Fe–N bonds in **1** are slightly different (2.139(2) and 2.142(2) Å). The independent Co–N and Co–O bonds in **2** are also slightly different (2.072(3) and 2.085(3) Å). The C–O bond distances (1.218(2) Å in **1** and 1.226(4) Å in **2**) are shorter than C–O single bond distances, and the C–C distances between atoms C4 and C5 (1.421(2) Å in **1** and 1.423(4) Å) in **2** are also much shorter than C–C single bond distances. The low basicity of the O atom can be attributed delocalization of negative charge. The partial negative charge on this O atom is stabilized since this O in involved in weak hydrogen bonds from methyl hydrogen atoms of coordinated acetonitrile solvent molecules in **1** and from $-CH_2-$ groups of coordinated tetrahydrofuran solvent molecules in **2** (Figs. 3 and 4).

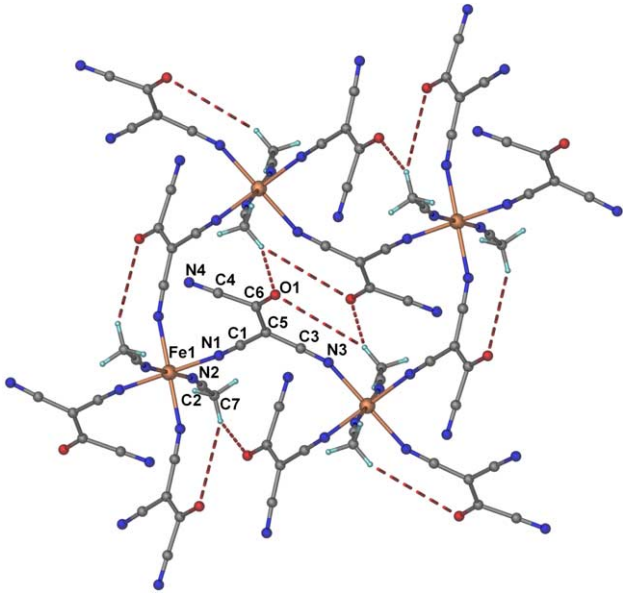


Fig. 2. Packing diagram of compound **1** illustrating the O interactions to methyl hydrogen atoms of coordinated acetonitrile solvent molecules in **1**.

3.3. Magnetic properties of compounds *1* and *2*

Magnetic susceptibility measurements of complexes **1** and **2** were performed on crushed crystals of the compounds. Random crystals from the batches were selected from the samples used for the SQUID and subjected to unit cell determinations. These results are shown in Fig. 5.

The value of χT at 300 K is 3.8 emu mol^{-1} K for compound **1**, which is in good agreement with the expected value for isolated high spin Fe(II) ions ($S = 2$ and $g = 2.25$) in a magnetically dilute sample. The χT

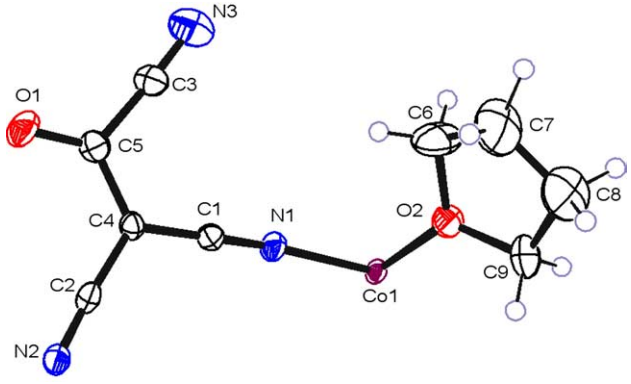


Fig. 3. Thermal ellipsoid plot of the asymmetric unit in $\{Co(C_5N_5O)_2(C_4H_4O)_2\}_\infty$ (**2**) drawn at the 50% probability level.

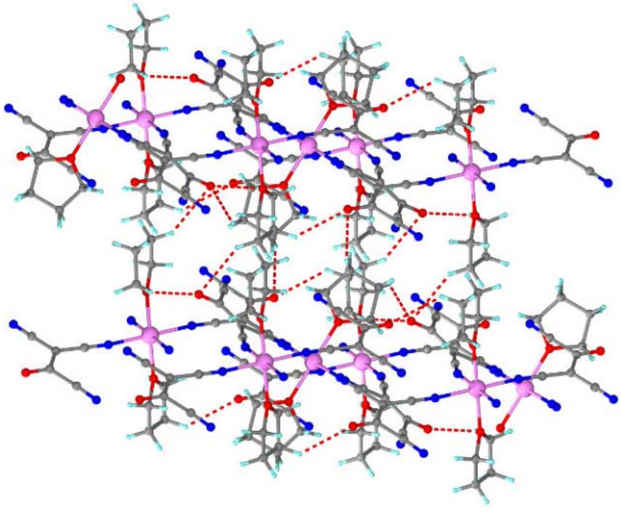


Fig. 4. Packing diagram of compound **2** illustrating the O interactions to hydrogen atoms of coordinated THF solvent molecules in **2**.

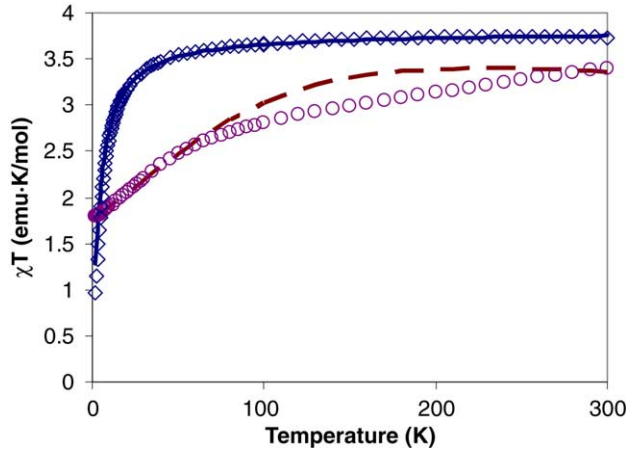


Fig. 5. Plots of $\chi_m T$ vs. T for $[Fe(C_5N_3O)_2(CH_3CN)_2]_\infty$ (**1**) (blue diamond) and $[\{Co(C_5N_3O)_2(C_4H_4O)_2\}_\infty]$ (**2**) (purple circles). The solid line is a fit of the data for (**1**) to the Curie–Weiss law and the dashed line corresponds to the best fit obtained with Eq. (1) for (**2**).

value continuously decreases from room temperature and reaches a value of 1 emu mol^{-1} K at 1.8 K. The temperature dependence of $1/\chi$ between 300 and 2 K approximates Curie–Weiss behavior with $C = 3.8$ emu mol^{-1} K and $\theta = -3.9$ K. The negative sign of the Curie–Weiss constant may indicate antiferromagnetic interactions or zero-field splitting effects.

The value of χT at 300 K is 3.4 emu mol^{-1} K for compound **2**, which is in good agreement with the expected value for isolated high spin Co(II) ions with an orbital contribution ($S = 3/2$ and $g = 2.8$) in a magnetically dilute sample. The χT value continuously decreases from room temperature and reaches a value of 1.8 emu mol^{-1} K at 1.8 K. The temperature dependence of $1/\chi$ between 300 and 50 K approximates Curie–Weiss behavior with $C = 3.8$ emu mol^{-1} K and $\theta = -40$ K. The negative Curie–Weiss constant indicates a dominant spin–orbit coupling effects for Co(II) ion.

The ground state for high-spin octahedral Co(II) is a $^4T_{1g}$, which is subject to unquenched spin–orbit coupling. The Hamiltonian for spin–orbit coupling is written as: $H = -\lambda LS$. The χT expression for a mononuclear Co(II) complex in an octahedral environment is provided in Eq. (1) [11].

$$\chi_{Co}T = \frac{\frac{7(3-A)^2x}{5} + \frac{12(2+A)^2}{25A} + \left\{\frac{2(11-2A)^2x}{45} + \frac{176(2+A)^2}{675A}\right\}x\exp\left(\frac{-5Ax}{2}\right) + \left\{\frac{(5+A)^2x}{9} - \frac{20(2+A)^2}{27A}\right\}\exp(-4Ax)}{\frac{8x}{3}\left\{3 + 2\exp\left(\frac{-5Ax}{2}\right) + \exp(-4Ax)\right\}}. \quad (1)$$

In this equation, $x = \lambda/k_BT$, (λ is the spin–orbit coupling parameter which is -170 cm^{-1} for the free ion) and A is a measure of the crystal field strength due to the inter-electronic repulsions (1.5 for a weak field, 1.0 for a strong field and 1.32 for a free ion). Using Eq. (1), we obtained a fit for the magnetic susceptibility data in the temperature range of 2–300 K with parameters $\lambda = -110$ cm^{-1}, and $A = 1.5$. The fitting is indicative of the usual problems associated with the anisotropy of the Co(II) ion. In both cases, there is no indication that the bridging ligand facilitates superexchange interactions between the metal ions whose closest separations in the compounds are 7.805 Å (Fe···Fe) and 7.441 Å (Co···Co).

4. Conclusions

In this study, two new coordination polymers $\{Fe(C_5N_3O)_2(CH_3CN)_2\}_\infty$ (**1**) and $\{Co(C_5N_3O)_2(C_4H_4O)_2\}_\infty$ (**2**) have been prepared and their structures and magnetic properties have been determined. The two complexes represent rare examples in which the tricyanoethenolate ligand coordinates via two of its three nitrile N atoms which leads to the formation of two-dimensional sheets. Although delocalization of negative charge on the tricyanoethenolate ligand may be expected to facilitate on magnetic exchange interactions, magnetic susceptibility measurements of compounds **1** and **2** indicate that the metal spins are essentially isolated paramagnets with little or no coupling being evident.

5. Supplementary material

Crystallographic data for the structural analyses have been deposited with Cambridge Crystallographic Data Center, CCDC Nos. 267178 and 267179 for compounds **1** and **2**, respectively. Copies of this information may be obtained free from the Director, CCDC, 12 Union Road, Cambridge CB2 1EW, UK (fax: +44 1223 336 033; e-mail: deposit@ccdc.cam.ac.uk or www: http://www.ccdc.com.ac.uk).

Acknowledgments

Kim R. Dunbar gratefully acknowledges the National Science Foundation for support from Nanoscale Science and Engineering Grant (NIRT: DMR-0103455), the Telecommunication and Informatics Task Force (TITF 2001-3) at Texas A&M University, DOE-DE-FG03-02ER45999 and the National Science

Foundation for an Equipment grant to purchase the SQUID magnetometer (NSF-9974899).

References

[1] (a) A. Caneschi, D. Gatteschi, R. Sessoli, Inorg. Chem. 20 (1993) 4612;
(b) A. Caneschi, D. Gatteschi, A. Lelirzin, J. Mater. Chem. 4 (1994) 319;
(c) D. Luneau, P. Rey, Mol. Cryst. Liq. Cryst. Sci. Technol., Sect. A 273 (1995) 81;
(d) A. Caneschi, D. Gatteschi, R. Sessoli, Mol. Cryst. Liq. Cryst. Sci. Technol., Sect. A 278 (1996) 177.

[2] (a) K.I. Pokhodnya, N. Petersen, J.S. Miller, Inorg. Chem. 41 (2002) 1996;
(b) D.K. Rittenberg, J.S. Miller, Inorg. Chem. 38 (1999) 4838;
(c) J. Zhang, J. Ensling, V. Ksenofontov, P. Gütlich, A.J. Epstein, J.S. Miller, Angew. Chem. Int. Ed. 37 (1998) 657;
(d) J.M. Manriquez, G.T. Yee, R.S. McClean, A.J. Epstein, J.S. Miller, Science 252 (1991) 1415;
(e) D.K. Rittenberg, A.M. Arif, J.S. Miller, J. Chem. Soc. Dalton Trans. (2000) 3939;
(f) J.S. Miller, A.J. Epstein, Chem. Commun. (1998) 1319;
(g) J.S. Miller, J.C. Calabrese, H. Rommelmann, S.R. Chittipeddi, J.H. Zhang, W.M. Reiff, A.J. Epstein, J. Am. Chem. Soc. 109 (1987) 769;
(h) R.D. Jones, D.A. Summerville, F. Basolo, J. Am. Chem. Soc. 100 (1978) 4416;
(i) J.S. Miller, J.C. Calabrese, R.S. Mclean, A.J. Epstein, Adv. Mater. 4 (1992) 498;
(j) S. Mikami, K. Sugiura, T. Maruta, Y. Maeda, M. Ohba, N. Usuki, H. Okawa, T. Akutagawa, S. Nisihara, T. Nakamura, K. Iwasaki, N. Miyazaki, S. Hino, E. Asato, J.S. Miller, Y. Sakata, J. Chem. Soc., Dalton Trans. (2001) 448.

[3] (a) R.C. Thompson, V.K. Gujral, H.J. Wagner, C.F. Schwerdtfeger, Phys. Stat. Sol. 53 (1979) 181;
(b) R.C. Thompson, Y. Hoyano, C.F. Schwerdtfeger, Solid State Commun. 23 (1977) 633;
(c) K.R. Dunbar, Angew Chem. 35 (1996) 1659;
(d) H. Zhao, R.A. Heintz, R.D. Rogers, K.R. Dunbar, J. Am. Chem. Soc. 118 (1996) 12844;
(e) H. Zhao, R.A. Heintz, X. Ouyang, K.R. Dunbar, C.F. Campana, R.D. Rogers, Chem. Mater. 11 (1999) 736;
(f) R. Clérac, S. O'Kane, J. Cowen, X. Ouyang, R. Heintz, H. Zhao, M.J. Bazile Jr., K.R. Dunbar, Chem. Mater. 15 (15) (2003) 1840;
(g) H. Zhao, M.J. Bazile, J.R. Galán-Mascarós, K.R. Dunbar, Angew. Chem. Int. Ed. 42 (2003) 1015;
(h) S.L. Bartley, M.J. Bazile Jr., R. Clérac, H. Zhao, X. Ouyang, K.R. Dunbar, J. Chem. Soc. Dalton Trans. (2003) 2937;
(i) E.B. Vickers, T.D. Selby, M.S. Thorum, M.L. Taliaferro, J.S. Miller, Inorg. Chem. 43 (2004) 6414.

[4] (a) E.J. Brandon, G.P.A. Yap, A.L. Rheingold, A. Arif, J.S. Miller, Inorg. Chim. Acta 240 (1995) 515;
(b) O.W. Webster, W. Mahler, R.E. Benson, J. Am. Chem. Soc. (1962) 3678;
(c) V. Jacob, S. Mann, G. Huttner, O. Walter, L. Zsolnai, E. Kaifer, P. Rutsch, P. Kircher, E. Bill, Eur. J. Inorg. Chem. (2001) 2625.

[5] F. Conan, B. LeGall, J.-M. Kerbaol, S.L. Stang, J. Sala-Pala, Y.L. Mest, J. Bacsa, X. Ouyang, K.R. Dunbar, C.F. Campana, Inorg. Chem. 43 (2004) 3673.

[6] C.C. Fuller, R.A. Jacobson, Inorg. Chim. Acta 48 (1981) 191.

[7] R.A. Jacobson, W.P. Jensen, Inorg. Chim. Acta 52 (1981) 219.

[8] H. Zhao, R. Clérac, J.S. Sun, X. Ouyang, J.M. Clemente-Juan, C.J. Gómez-Garíca, E. Coronado, K.R. Dunbar, J. Solid State Chem. 159 (2001) 281.

[9] Bruker, SAINT-PLUS. Version 6.35A. Bruker AXS Inc., Madison, Wisconsin, USA, 2002.

[10] Bruker, SADABS. Version 2.05. Bruker AXS Inc., Madison, Wisconsin, USA, 2003.

[11] L.J. Barbour, J. Supramol. Chem. 1 (2001) 189.

[12] G.M. Sheldrick, SHELX, Programs for Solving and Refining Crystal Structures, University of Göttingen, Germany, 1997.

[13] E.A. Boudreaux, L.N. Mulay (Eds.), Theory and Applications of Molecular Paramagnetism, Wiley, New York, 1976.

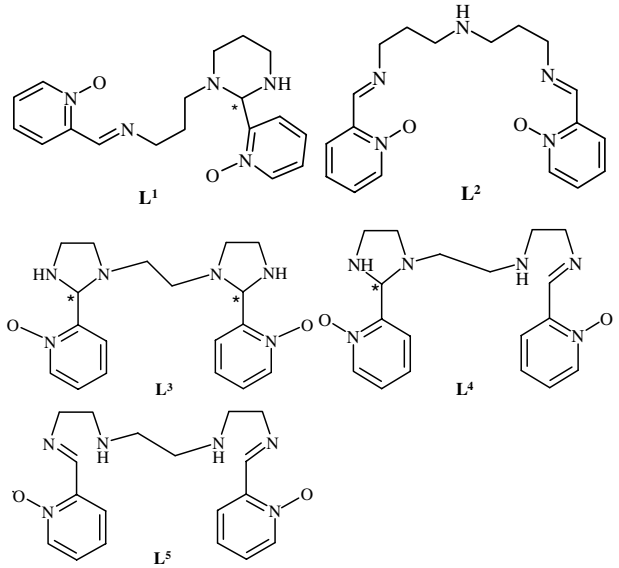


Fig. 1. Two isomers of the condensation product of 2-pyridinecarboxaldehyde N-oxide with dipropylenetriamine ($\mathbf{L^1}$ and $\mathbf{L^2}$) and three isomers of the condensation product of 2-pyridinecarboxaldehyde N-oxide with triethylenetetramine ($\mathbf{L^3}$, $\mathbf{L^4}$ and $\mathbf{L^5}$). *, chiral centre.

of four different complexes of Cu(II), Zn(II) and Fe(III) were reported with all possible isomers $\mathbf{L^3}$, $\mathbf{L^4}$ and $\mathbf{L^5}$ (Fig. 1) of the ligand as condensation product of 2-pyridinecarboxaldehyde N-oxide with triethylenetetramine [6]. In addition, liberation of one pyridine N-oxide fragment is possible during complexation [7] as shown in the system of 2-pyridinecarboxaldehyde N-oxide/diethylenetriamine in excess of copper (II) cations.

In this work, we present the structure of the copper (II) complex with the isomer $\mathbf{L^2}$. The solvatochromism and isomerisation of the ligand from $\mathbf{L^1}$ to $\mathbf{L^2}$ during complexation on copper were also studied in situ by electronic spectra as well as the solvatochromism and isomerisation of the ligand from $\mathbf{L^3}$ to $\mathbf{L^4}$ during complexation on copper in situ.

2. Experimental

Ligand preparation: Preparation of the ligands $\mathbf{L^1}$ and $\mathbf{L^3}$ and their detailed characterisation by ^{1}H and ^{13}C NMR and IR spectra is given elsewhere [1].

Complex preparation: All starting compounds and solvents were used as commercial products (copper perchlorate, acetonitrile, Fluka; ethanol, methanol, DMSO, Mikrochem) of analytical grade without any purification. 2-pyridinecarboxaldehyde-N-oxide was prepared according to the literature [8].

*$[Cu(L^2)](ClO_4)_2$ – complex (**1**)*: A solution of 0.185 g (0.5 mmol) of $Cu(ClO_4)_2 \cdot 6H_2O$ in ethanol (5 cm^3) was slowly added to a solution of 0.171 g (0.5 mmol) of the ligand $\mathbf{L^1}$ in ethanol (15 cm^3) under stirring at room temperature. A green solid immediately precipitated. The additional ethanol (30 cm^3) was added and the mixture was boiled for 30 min. Then the mixture was let to cool spontaneously under stirring for 3 h. The green product was filtered off, washed with ether and air-dried. Yield 0.159 g (53%), m.p. explosive decomposition above 200 °C. *Anal.* Calc. for $C_{18}H_{23}N_5O_{10}Cl_2Cu$ (M = 603.86): C, 35.8; H, 3.84; N, 11.6. Found: C, 35.4; H, 3.42; N, 11.4%. Soluble in acetone, alcohols, DMSO, pyridine, acetonitrile; insoluble in diethylether.

Single crystals of **1** for X-ray analysis were prepared by isothermal recrystallisation from acetonitrile.

*$[CuL^4(ClO_4)](ClO_4)$ – Method 1, complex (**2**)*: Preparation of this complex from the methanolic solutions and its detailed characterisation is given elsewhere [6].

*Method 2, complex **2a***: A solution of 0.185 g (0.5 mmol) of $Cu(ClO_4)_2 \cdot 6H_2O$ in dimethylformamide (3 cm^3) was slowly added to a solution of 0.178 g (0.5 mmol) of the ligand $\mathbf{L^3}$ in dimethylformamide (15 cm^3) under stirring at room temperature. A violet solution was formed. Chloroform (100 cm^3) was slowly added under stirring to precipitate a violet solid product that was filtered off, washed with chloroform and air-dried. Yield 0.186 g (62%).

*Method 3, complex **2b***: A solution of 0.185 g (0.5 mmol) of $Cu(ClO_4)_2 \cdot 6H_2O$ in DMSO (1.5 cm^3) was slowly added to a solution of 0.178 g (0.5 mmol) of the ligand $\mathbf{L^3}$ in DMSO (7.5 cm^3) under stirring at room temperature. A violet solution was formed. Then ether (60 cm^3) was slowly added under stirring to precipitate violet solid product that was filtered off, washed with ether and air-dried. Yield 0.254 g (86%).

*Method 4, complex **2c***: 0.185 g (0.5 mmol) of solid $Cu(ClO_4)_2 \cdot 6H_2O$ and 0.178 g (0.5 mmol) of the solid ligand $\mathbf{L^3}$ were stirred in DMSO (5 cm^3) at room temperature for 1 h. The formed dark violet solution was let to spontaneously evaporate one week. Then a dark violet polycrystalline solid was separated.

Caution! Heating of concentrated solutions of perchlorates can cause an explosion.

Physical measurements: Elemental (C, H, N) analyses were carried out by a commercial Automatic Elemental Analyzer Flash EA 1112 CHNS-O/MAS 200 (Thermo Finnigan).

*Crystal data of complex **1***: A suitable single crystal was mounted on a SMART diffractometer (Bruker-AXS) with a CCD area detector. Graphite-monochromated Mo Kα radiation ($\lambda = 0.71073$ Å) was used for all measurements. The crystal-to-detector distance was 4.40 cm. A hemisphere of data was collected by a combination of three sets of exposures at 294 K. Each set had a different ϕ angle for the crystal, and each exposure took 20 s and covered 0.3° in ω. The data were corrected for polarization and Lorentz effects, and an empirical absorption correction (SADABS) was applied [9]. The cell dimensions were refined with all unique reflections.

Structure determination. The structures were solved by direct methods (SHELXS-86) [10a]. Refinement was carried out with the full-matrix least-squares method based on F^2 (SHELXL-97) [10b] with anisotropic thermal parameters for all non-hydrogen atoms. Hydrogen atoms were inserted only at non-disordered atoms (see below) in calculated positions and refined riding with the corresponding atom. Due to a disorder in the alkyl chains the C atoms C11, C12, and C14 were refined in two independent positions each with occupancy of 0.5. No H atoms were added at the disordered and adjacent C atoms. The oxygen atoms of the two perchlorate anions were also disordered and were refined each in two positions with occupancy of 0.5 for the O30, O31, O32 and O33 and with an occupancy ratio of 0.8:0.2 for O40, O41, O42 and O43.

X-ray powder pattern of **1** was collected on Stoe Stadi P transmission diffractometer equipped with a curved Ge (1 1 1) monochromator placed in the primary beam and a linear PSD. In order to achieve a better resolution Mo Kα radiation was used. The measured range of 2θ was 3–50° at room temperature.

The X-band EPR spectra of polycrystalline powdered samples **1** and **2** were recorded on a Bruker EMX spectrometer equipped with a variable temperature unit. Line positions were measured accurately using internal field markers generated by an NMR gauss-meter, while the microwave frequency was measured by a microwave frequency counter. 100 kHz magnetic field modulation (peak-to-peak amplitude ≈3 G) was used.

The EPR spectra were simulated on an IBM compatible computer using either program QPOW [11] developed by R.L. Belford (University of Illinois, Urbana) or commercially available program SIMFONIA [12].

IR spectra of the complexes were measured on PU 9800 FTIR (Philips) spectrometer in the nujol suspension at room temperature in the range 4000–400 cm^{-1} with the resolution of 1 cm^{-1} using a mirror velocity of 2.0 mm s^{-1}.

Electron spectra were measured on Specord M 400 (Carl Zeiss) in the range of 350–900 nm in different solutions at room temperature in 1 cm cell. Electron spectra were measured by two methods: In the first case (Method 1) the measured spectra were of solutions prepared by dissolution of the complexes **1** and **2** in different solvents. The solvents and concentrations are summarised in Table 1.

In the second case (Method 2) solutions of the ligand and copper perchlorate were mixed directly in measuring cell and inserted into spectrometer. These operations had to be made as fast as possible. The solvents and concentrations are summarised in Table 1.

Table 1
Solvents and concentrations for ES investigation of the complexes **1** and **2** by dissolution (Method 1) and by preparation "in situ" (Method 2)

Solvent	Concentration (mmol dm^{-3})			
	Complex **1**		Complex **2**	
	Method 1	Method 2	Method 1	Method 2
Methanol	1.5	3.07	1.5	3.07
Acetonitrile	6.0	4.00	6.0	
Water	6.0	5.60	6.0	5.60
DMSO	6.0	2.26	6.0	2.26
DMF	6.0	2.40	6.0	2.4
Pyridine	6.0	6.0		
Ethylenediamine	6.0		6.0	
Nitromethane	2.1		2.5	

3. Results and discussion

The structure of ***1***: The structure of the complex **1** (crystal data is shown in Table 2) consists of $[CuL^2]^+$ cations and ClO_4^- anions. The copper atom reveals a trigonal bipyramidal coordination by three nitrogen atoms and two oxygens of the two pyridine N-oxide groups of the ligand. Both imine nitrogen atoms (N(9) and N(17)) occupy the axial position while the equatorial plane is formed by the remaining amine nitrogen (N(13)) and by both oxygen atoms from the pyridine N-oxide groups (O(1) and O(25)). The axial N–Cu–N angle of the trigonal pyramid is with 176.60(12)° only slightly distorted and the equatorial plane is also nearly perfect with a maximum deviation of the Cu atom 0.019 Å out of this plane. However the equatorial angles are distorted, while two of them are smaller than the expected 120° (O(1)–Cu(1)–N(13): 115.08(14)°; N(13)–

Table 2
Crystal data and structure refinement for **1**

Empirical formula	$C_{18}H_{23}N_5O_{10}Cl_2Cu$
M (g mol^{-1})	603.86
Colour	dark green
Crystal system	monoclinic
Space group	$P2(1)/n$
a (Å)	6.459(2)
b (Å)	20.419(7)
c (Å)	18.047(6)
α (°)	90
β (°)	90.485(7)
γ (°)	90
V ($Å^3$)	2380.1(14)
T (K)	294(2)
Z	4
ρ_{calc} (Mg/m^3)	1.654
Crystal size (mm)	$0.58 \times 0.22 \times 0.14$
μ (mm^{-1})	1.206
hkl ranges	−8,8; −26,27; −24,19
No. of data collected	16366
Independent reflections (R_{int})	5901 (0.0298)
Data, restraints, parameters	5901,0,424
R (F)[$I > 2\sigma(I)$]	5.20%
R_w (F^2) (all data)	15.85%
Goodness-of-fit on F^2	1.033
Largest peak and hole (e $Å^{-3}$)	0.859, −0.775

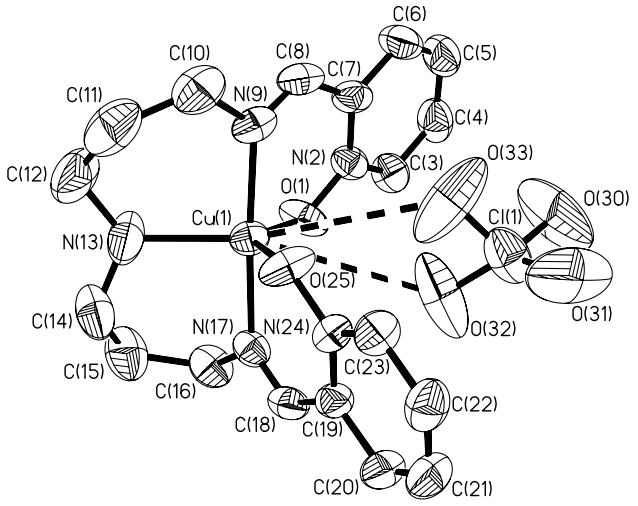


Fig. 2. ORTEP view of $[CuL^2](ClO_4)^+$ fragment (hydrogen atoms are excluded for clarity, thermal ellipsoids of 50% probability level).

Cu(1)–O(25): 110.95(14)°) one is substantially larger (O(1)–Cu(1)–O(25): 133.92(12)°). In the formed gap of the coordination polyhedron a very weak interaction with the oxygen atoms of a perchlorate groups were found (Cu(1)–O(32): 3.442(1) Å and at Cu(1)–O(33): 3.495(1) Å) (Fig. 2). These distances are too long even for a semi-coordination description of this interaction, which is different from those of our previous works [6,7] where the ligands were coordinated to the central metal atom through all donor atoms and the coordination sphere was completed by oxygen atom from perchlorate group at longer distance (2.689, 2.819 Å, respectively) forming distorted octahedra with coordination 4 + 1 + 1.

The double bonds within Schiff-bases are as short as N(17)–C(18) = 1.264(4) Å and C(8)–N(9) = 1.266(5) Å. These distances are almost the same as those in the previously described compounds [6,7]. Selected bond lengths and angles are presented in Table 3.

Table 3
Selected bond lengths (Å) and angles (°) for **1**

Bond length (Å)		Bond angles (°)	
Cu(1)–N(17)	1.953(3)	N(17)–Cu(1)–N(9)	176.60(12)
Cu(1)–N(13)	2.100(3)	N(17)–Cu(1)–O(1)	88.82(10)
Cu(1)–N(9)	1.953(3)	N(9)–Cu(1)–O(1)	89.49(11)
Cu(1)–O(25)	2.021(2)	N(17)–Cu(1)–O(25)	88.97(10)
Cu(1)–O(1)	2.010(2)	N(9)–Cu(1)–O(25)	90.07(10)
N(17)–C(18)	1.264(4)	O(1)–Cu(1)–O(25)	133.92(12)
C(8)–N(9)	1.266(5)	N(17)–Cu(1)–N(13)	90.31(13)
O(1)–N(2)	1.326(3)	N(9)–Cu(1)–N(13)	93.08(14)
N(24)–O(25)	1.327(3)	O(1)–Cu(1)–N(13)	115.08(14)
Cu(1)–O(32)	3.442(1)	O(25)–Cu(1)–N(13)	110.95(14)
Cu(1)–O(33)	3.495(1)		

Because of a disorder of the C-atoms of the alkyl chain C(11), C(12), and C(14) no hydrogen atoms were added at the disordered and adjacent carbon atoms. Consequently, no hydrogen atom was found for N(13) even though it is highly expected, because there is no reason for N(13) to be imine nitrogen instead of amine one. Furthermore, if N(13) would be an imine nitrogen then the ligand would have a negative charge and there is no indication in the structure for a possible compensation. The packing of the structure in the unit cell is shown in Fig. 3.

*X-ray powder patterns of **1***: In order to check whether a powdered sample of **1** is the same compound as solved from single crystals the powder pattern was recorded. Powder diffraction pattern of **1** was successfully indexed by Stoe WINXPOW 1.2 program using Louër's routine [13,14] using the first 21 diffraction lines. Obtained ' 90.70°) are close to the cell parameters from single crystal. Thus it was concluded that the complex **1** has the identical structure as powder (prepared by fast precipitation

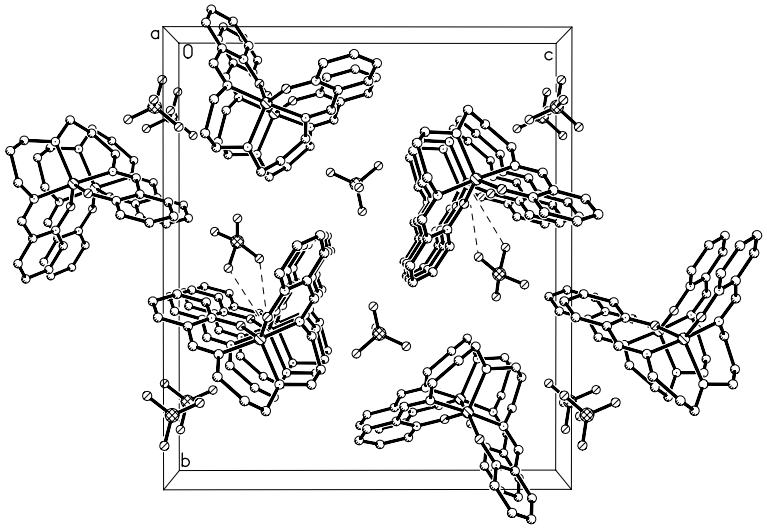


Fig. 3. The packing of the structure in the unit cell.

from ethanol) and single crystal (slowly grown from acetonitrile solution).

EPR spectra of the complexes: The EPR spectrum of **1** measured in polycrystalline form is shown in Fig. 4. The EPR data , $g_\perp = 2.241$ and $g_\parallel = 1.998$, are typical for the copper (II) complexes in distorted trigonal-bipyramidal (TBP) crystal field symmetry (exhibiting d_{z^2} ground state), in agreement with the conclusions from X-ray measurements. The EPR spectrum of **2** (Fig. 4) exhibits also d_{z^2} ground electronic state of the copper (II) ion, however with shifted perpendicular band towards higher magnetic field. Computer simulation of the EPR spectrum of **2** provided following EPR data: $g_\perp = 2.139$ and $g_\parallel = 2.065$.

In the case of the compressed configuration of the coordination polyhedron of $[CuL^2]^{2+}$ (or $[CuL^2(ClO_4)]^{+}$) fragment, the perpendicular and parallel components of the axially symmetrical *g*-tensor can be described, in the crystal field theory approximation, by the equations

$$g_\perp = 2.0023 + 6\lambda/\Delta E(a_1' \rightarrow e''), \quad g_\parallel = 2.0023 \tag{1}$$

where λ is the spin–orbital interaction constant of the Cu(II) ion. From Eq. (1) is clear that for a compressed TBP structure computer simulation provides $g_\perp > g_\parallel \sim 2.0023$. The relation $g_\perp > g_\parallel \sim 2.0023$ holds for the EPR spectra of both compounds under study.

In the elongated TBP configuration of the Cu(II) ion, the ground electronic state is the doubly degenerated e' state. According to the Jahn-Teller theorem [15], this orbital degeneracy of the ground state must be removed. Thus, any distortion leads to a new electronic state, either $d_{x^2-y^2}$ or d_{xy}. The compressed TBP configuration for **1** points to the ground electronic state of the copper. This is consistent with the parameters of the EPR spectra obtained, which satisfy the relation $g_\perp > g_\parallel \sim 2.0023$. Generally, five coordinated complexes can adopt either trigonal–bipyramidal geometry (TBP, D_{3h}), or square–pyramidal geometry (SP, C_{4v}), or intermediate geometry (C_{2v} symmetry). The X-ray data for the complex **1** revealed, that the chromophore $\{CuN_3O_2\}$ of this complex adopts slightly distorted trigonal bi-pyramid geometry, thus based also on EPR data, no exact point group symmetry was assigned to the complex **1** (see also below).

In our previous paper [7], we studied copper complexes with the Schiff base mono- and bis-condensation products of 2-pyridinecarboxaldehyde-N-oxide with diethylenetriamine (triamine of ethylene bridges). From the point of view of EPR spectroscopy all of these complexes exhibit $d_{x^2-y^2}$ ground state of copper (II). On the contrary, copper complexes of 2-pyridinecarboxaldehyde N-oxide with triamine of propylene bridges (complex **1**) or tetramine of ethylene bridges (complex **2**), presented in this work, exhibit relatively rare, d_{z^2} ground electronic state of copper.

Infrared spectra of 1: According to infrared spectra, we can suggest the presence of some structural segments. Valence vibrations of N–H of the secondary cyclic amines can be observed in the range of 3380–3205 cm^{-1}. The range of valence vibrations of N–H of secondary aliphatic amines is quite narrow around 3330 cm^{-1} [16]. According to infrared spectra, the form $\mathbf{L^1}$ in the pure ligand is expected. The characteristic IR vibrations of the ligand $\mathbf{L^1}$ are the following: $\nu_{\nu(N-H)} = 3260\ cm^{-1}$ (strong), $\nu_{\delta(N-H)} = 1566\ cm^{-1}$ (weak), $\nu_{\nu(N-O)} = 1234\ cm^{-1}$ (strong), $\nu_{\delta(C=N)} = 1634\ cm^{-1}$ (strong).

The characteristic IR vibrations of the complex **1** are the following: $\nu_{\nu(N-H)} = 3252\ cm^{-1}$ (medium), $\nu_{\delta(N-H)} = 1563\ cm^{-1}$ (medium), $\nu_{\nu(N-O)} = 1203\ cm^{-1}$ (strong), $\nu_{\nu(C=N)} = 1658\ cm^{-1}$ (strong), $\nu_3(ClO_4) = 1087\ cm^{-1}$

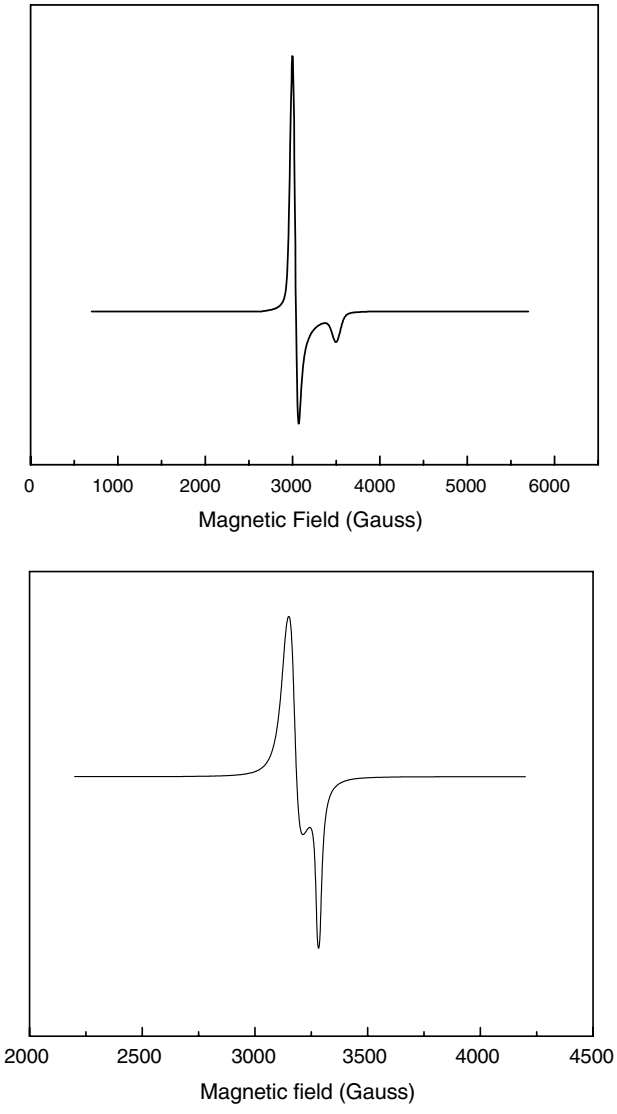


Fig. 4. The EPR spectrum of **1** and **2** in polycrystalline form.

(strong, broad), $v_4(ClO_4) = 622\ cm^{-1}$ (strong), vibrations at 432 cm^{-1} (weak) and 455 cm^{-1} (weak) (and expected below 400 cm^{-1}; out of our measuring limit) can be attributed to M–O and M–N, vibrations.

Generally, after coordination the position of some vibrations would change. Thus in the case of the complexes it is difficult to distinguish between different isomers based only on N–H vibrations. The position of $v_{\nu(N-H)} = 3252\ cm^{-1}$ is far from the range for secondary aliphatic amines and thus the formation of secondary cyclic amines would be expected in contradiction to the structure determination.

As can be seen, the positions of valence C=N vibration of the imino- group in the complex **1** has shifted to higher energies and the valence N–O vibration has shifted to lower energies in comparison with the pure ligand. Both vibrations are sensitive to the coordination of the ligand to metal atom. The relatively high wave number of C=N vibration was also observed in other copper complexes [6,7,17]. It is probably due to coordination properties of the ligand.

Vibrations v_3 of perchlorate groups are relatively broad with gentle structure. This indicates observed distortion of perchlorate groups. The presence of hydrogen bonding network cannot be excluded as well.

IR spectra of the complexes ***2***, ***2a–c***: (Detailed assignment of vibrations of the complex **2** is given elsewhere [6]. The presence of two N–H valence vibrations in the powdered samples indicates the presence of both secondary cyclic and secondary aliphatic amine groups. Thus the powdered sample is the same as in the single crystal.) These complexes were prepared in order to obtain the copper complexes with the ligand in a different isomeric form. However, the IR spectra of all four complexes are perfectly identical without any contribution from solvents. One could expect that in the case of DMF or DMSO the ligand in the isomeric form $\mathbf{L^3}$ should be present as was observed in the zinc complex [6]. It was explained that the donor number of DMSO is so strong that it occupies two coordination places of zinc atom and the ligand remaining four ones, thus forming the isomer $\mathbf{L^3}$ instead of $\mathbf{L^5}$ when the complex was prepared from methanol. Furthermore the high hardness of the central atom M (which serves for a measure of the Lewis acidity), may lead to a preference for the [ML^5] complex with the hexadentate ligand $\mathbf{L^5}$. Thus, the presence of the ligand in the form $\mathbf{L^4}$ in the copper complex prepared from DMSO seems to be in contradiction with expectation. We may try an explanation by the rule "similar likes similar". If zinc is a very strong (hard) acid (in terms of Pearson's theory) it will attract a strong base like DMSO. The copper is a soft (or middle) acid and does not prefer to interact with strong bases like DMSO. The result is the formation of the same copper complexes from different solvents. The isomeric form $\mathbf{L^4}$ is then the result of the competition between acidity of a central atom and acidity of the –C=N– site [6]. Methanol, on the other hand, is more acidic than basic and it will therefore not interact with the copper atom and instead the oxygen atom from perchlorate will do.

Electron spectra: For the d^9 complexes the free-atom ground ^2D term splits to the ^2E_g and $^2T_{2g}$ terms in the octahedral symmetry (or to $^2T_2$ and ^2E terms in tetrahedral symmetry). Here only one transition could be observed. These terms may undergo further splitting to A, B and eventually E type terms by lowering the symmetry. The final number of terms and their order thus depends on the degree of distortion. For D_{4h} and D_{3d} symmetries one should expect three transitions and in all other lower symmetries four transitions should be observed. But the energy levels may lie too close to each other so that two different transitions will not be observed separately. Taking into consideration the nature of the ligand it should be clear that all formed complexes probably will have highly asymmetric coordination spheres. Moreover, d–d transitions are forbidden by selection rules and thus they are very weak and difficult or impossible to observe.

Electron spectra of the complex ***1***: The electron spectra of the complex **1** in different solutions (see Section 2 – Method 1) are shown in Fig. 5. In fact the d–d transitions were observed in the range of 470–640 nm. Based on the arguments given above we are not able to estimate the coordination sphere of the copper centres based on electron spectra alone. From structural results the coordination polyhedron does not exhibit any symmetry (C_1).

Two separated bands can be observed in all spectra, except ethylenediamine solution. Generally, the band at higher energies (lower wave lengths) is only present as shoulders and bands at lower energies are observed either as real band with maximum or as shoulder as well. In ethylenediamine solution only one band was observed

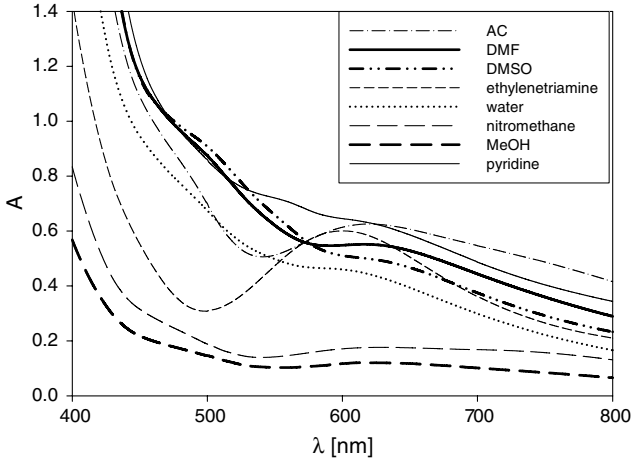


Fig. 5. Electron spectra of the complex **1** in different solvents.

because the complex may decompose. The data are summarized in Table 4.

Relatively vivid solvatochromic effect was observed. The directly observed bands both λ^1_{max} and λ^2_{max} were correlated with solvent properties. The parameters like acceptor number, donor number [18], dielectric constants and dipole momentum were investigated. But, no reasonable dependence was observed. As the solvents used are chemically fairly different we classified them into four groups with similar properties (DMF and DMSO; AC and nitromethane; water and methanol; ethylenediamine and pyridine). Similar trends can be found in all investigated parameters; acceptor number, donor number, dielectric constant and dipole momentum correlations.

Also electron spectra "in situ" in different solutions were measured (see Section 2 – Method 2). "In situ" means a period of less then 30 s between the replacing of the mixed solutions into the spectrometer and launching the measurement. The zero on the time axis in the following figures denotes the starting time. The complexation reactions start 20–30 s earlier.

In the case of water (Fig. 6), methanol (Fig. 7) and DMSO logarithmic shape of the absorbance dependency on time for observed λ_{max} was found. During this time probably isomerisation reaction of the ligand from the form $\mathbf{L^1}$ to $\mathbf{L^2}$ takes place.

In the case of AC and DMF solutions completely different shape of absorbance dependence on time was found (Fig. 8). Gradual decrease of the absorbance was observed. If we assign this evolution also to the isomerisation reaction the mechanism in AC and DMF solutions is different from that in water, methanol and DMSO solutions.

Electron spectra of the complex **2**: The electron spectra of the complex **2** in different solutions (see Section 2 – Method 1) are shown in Fig. 9. In fact the d–d transitions were observed in the range of 500–620 nm. No symmetry of the coordination polyhedron can be expected as in the complex **1**.

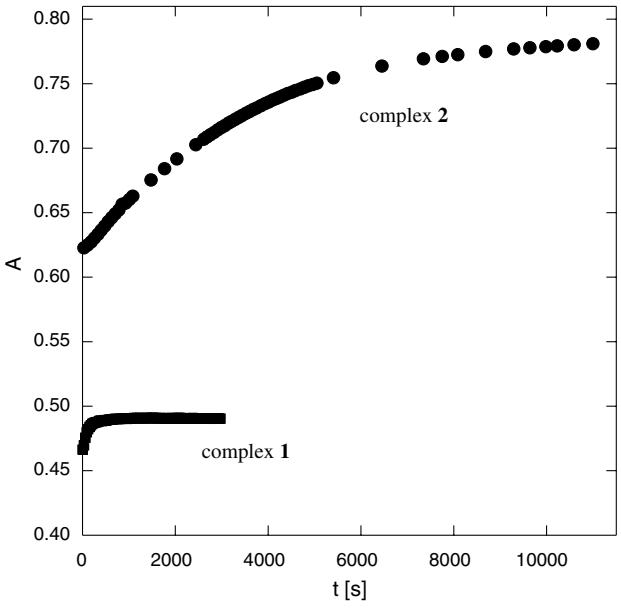


Fig. 6. Time dependence of absorbance in water "in situ" solution at $\lambda^1_{max} = 590$ for **1** and at $\lambda^1_{max} = 576$/nm for **2**.

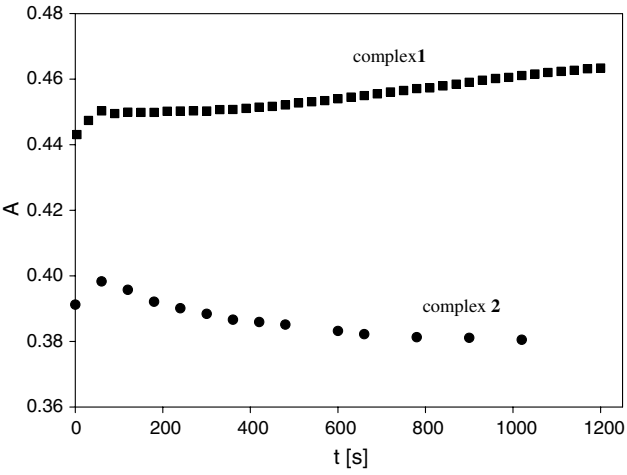


Fig. 7. Time dependence of absorbance in methanol "in situ" solution at $\lambda^1_{max} = 620$ for **1** and at $\lambda^1_{max} = 562$ for **2**.

Table 4
Solvents and values of λ_{max} of d–d transitions of the complexes **1** and **2**

Solvent	Complex **1**		Complex **2**		
	λ^1_{max} [nm]	λ^2_{max} [nm]	λ^1_{max} (λ^1_{calc}) [nm]	λ^2_{max} (λ^2_{calc}) [nm]	R
Water	590	479	576 (603)	–(542)	0.9999
DMSO	613	488	560 (599)	510 sh (518)	0.9991
DMF	615	489	557 (585)	510 sh (502)	0.9995
Acetonitrile	620	475	578 (591)	500 (488)	0.9987
Nitromethane	633	476	592 (589)	505 (484)	0.9987
Methanol	620	474	562 (612)	–(524)	0.9988
Ethylenediamine	600		606		
Pyridine	602	545	616		

In brackets are the values of λ obtained by deconvolution of the bands into two peaks, R is discrepancy factor.
sh, shoulder.

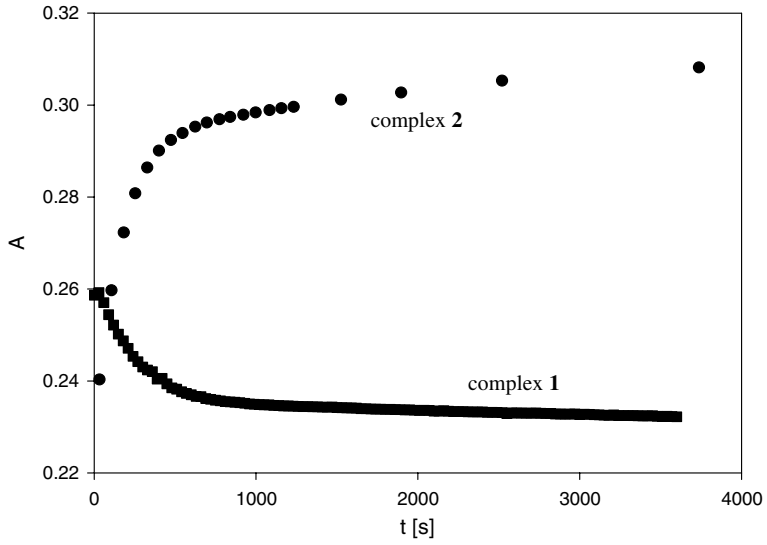


Fig. 8. Time dependence of absorbance in DMF "in situ" solution at $\lambda^1_{max} = 615$ for **1** and at $\lambda^1_{max} = 557$ nm for **2**.

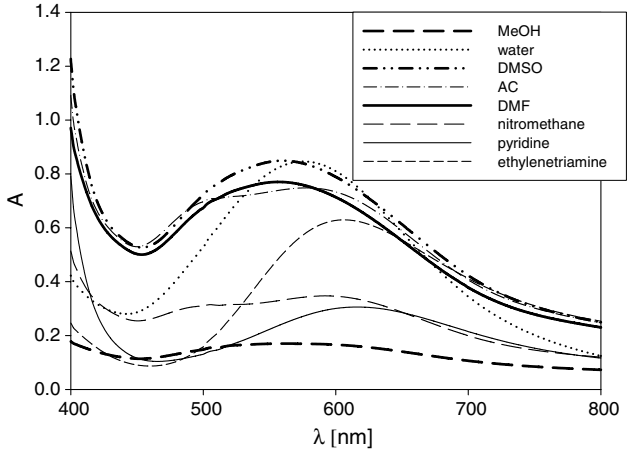


Fig. 9. Electron spectra of the complex **2** in different solvents.

In nitromethane and acetonitrile two well-separated bands are observed. In water, methanol, DMSO and DMF only one band seems to be present. It implies to the idea that these one-band spectra are probably composed from two badly resolved bands. Consequently, the deconvolution method was used to obtain two bands positions. The data are summarized in Table 4 together with bands obtained by direct observation of the spectra.

In the case of pyridine and ethylenediamine the situation is quite different. The bands are centred at considerably lower energies (higher wave lengths). Further, the complexes can decompose in these solvents to form $[Cu(en)_3]^{2+}$ and $[Cu(py)_6]^{2+}$ complex cations with higher symmetry, thus the deconvolution was omitted. The decomposition of the complex **2** can be supported by the observation when complex $Cu_2(DAP)Cl_4 \cdot 2H_2O$ (DAP = condensation product of 2-pyridinecarboxaldehyde N-oxide with diethylenetriamine) [7] was recrystallised from pyridine providing the complex $[CuCl_2(py)_2]$. The presence of only one band in the ethylenediamine solution in the complex **1** at very similar position as in the complex **2** supports the decomposition of both complexes.

We can conclude that solvatochromic effect was observed, similarly as in the complex **1**. We tried to find a similar correlation between solvents properties and the position of the transition bands maxima. Two different analyses were performed. In the first case the directly observed bands λ^1_{max} were correlated with solvent properties, in the second case both bands obtained from deconvolution calculations were correlated. We obtained similar results as in the complex **1**. No apparent dependence was observed, for the same reasons as above. However, when the observed band maxima λ^1_{max} and the λ^1_{calc} were used for correlation, we could conclude that the similar solvents were placed to each other. Again four groups of solvents can be suggested (DMF and DMSO; AC and nitromethane; water and methanol; ethylenediamine and pyridine). Similar trends can be found in all investigated parameters; acceptor number, donor number, dielectric constant and dipole momentum correlations.

With the comparison of the complex **1** the two bands are closer to each other. It means that energy difference between these two sets of transitions is lower in the case of the complex **2**.

Also electron spectra "in situ" in different solutions were measured (see Section 2 – Method 2). In water (Fig. 6), DMF (Fig. 8) and DMSO logarithmic shape of the absorbance dependency on time for observed λ_{max} was found. During this time probably an isomerisation reaction of the ligand from the form $\mathbf{L^3}$ to $\mathbf{L^4}$ takes place. In the case of water, the maximum of the absorbance seems not to be reached after two hours. This

may be due to a decomposition of the ligand in water. The isothermal recrystallisation of the complex **2** from water led to the $[Cu(pyc)_2]\cdot 2H_2O$ complex (pycH = pyridine-2-carboxylic acid) [19].

In methanolic solution completely different shape, gradual decrease of absorbance dependence on time, was found (Fig. 7). If we assign this evolution also to the isomerisation reaction then the mechanism in methanol solutions is different than in water, DMF and DMSO solutions.

The time evolution of absorbances of the complexes **1** and **2** for DMSO and water solutions exhibits logarithm dependence. Surprisingly, the absorbance evolutions of the complexes **1** and **2** are opposite to each other in the DMF solutions (exponential for **1** and logarithm for **2**) and methanol (logarithm for **1** and exponential for **2**) as well.

4. Conclusions

By single crystal analysis the structure of the complex **1** was solved. In the structure, the ligand exists in the form of aliphatic polyamine containing two Schiff bases in contrary to the free form of the ligand with one pyrimidine ring and one Schiff base. No hydrogen bonds were identified.

X-ray powder analysis demonstrated identical structures for fast precipitated and slowly crystallised forms of the complex **1**.

By EPR spectra measured in polycrystalline form it was concluded distorted trigonal-bipyramidal (TBP) geometry for the complex **1** and d_{x^2} ground electronic state of copper (II) for both complexes **1** and **2**.

IR spectra confirmed the identity of fast precipitated and slowly crystallised forms of the complex **2**. Preparation of the complexes in different solvents and by template method result in the formation of the complexes with the same isomer form of the ligand.

By ES spectra vivid solvatochromic effect was observed for both complexes **1** and **2**. It was suggested that similar solvents cause similar equilibrium in the system. From time dependent measurement of absorbances it can be suggested that at least two different ways of isomerisation of the ligand during complexation exist.

5. Supplementary material

Crystallographic data for the structural analysis have been deposited with the Cambridge Crystallographic Data Centre, CCDC No. 265970 for **1**. Copies of this information may be obtained free of charge from The Director, CCDC, 12 Union Road, Cambridge, CB2 1EZ, UK (fax: 44 1223 336 033; e-mail: deposit@ccdc.cam.ac.uk or www: http://www.ccdc.cam.ac.uk).

Acknowledgements

The authors greatly acknowledge to the Slovak APVT project 20-005204, to the MWFZ and Forschungsfond of the University Mainz and the DFG (SPP 1137; RE 1627/1-2), and to the Alexander von Humboldt Foundation for financial support.

References

[1] M. Boča, D. Valigura, W. Linert, Tetrahedron 56 (2000) 441.
[2] M.G.B. Drew, J. Nelson, S.M. Nelson, J. Chem. Soc., Dalton Trans. (1981) 1678.
[3] S.M. Nelson, F.S. Esho, M.G.B. Drew, P. Bird, J. Chem. Soc., Chem. Commun. (1979) 1035.
[4] M.G.B. Drew, J. Nelson, S.M. Nelson, J. Chem. Soc., Dalton Trans. (1981) 1691.
[5] R.H. Petty, E.V. Dose, M.F. Tweedle, L.J. Wilson, Inorg. Chem. 17 (1978) 1064.
[6] M. Boča, P. Baran, R. Boca, H. Fuess, G. Kickelbick, W. Linert, F. Renz, I. Svoboda, Inorg. Chem. 39 (2000) 3205.
[7] M. Boča, M. Valko, G. Kickelbick, M. Ďurík, W. Linert, Inorg. Chim. Acta 349 (2003) 111.
[8] D. Jerchel, I. Heider, H. Wagner, Annalen 153 (1958) 613.
[9] G.M. Sheldrick, SADABS. Empirical Absorption Corrections Program, University of Göttingen, Göttingen, Germany, 1997.
[10] (a) G.M. Sheldrick, SHRLXS-86. Program for the Solution of Crystal Structures, University of Göttingen, Göttingen, Germany, 1986;
(b) G.M. Sheldrick, SHELXL-93. Program for Crystal Structure Determination, University of Göttingen, Göttingen, Germany, 1986.
[11] (a) Program QPOW, R.L. Belford, M.J. Nilges, Computer simulation of powder spectra, EPR Symposium, in: 21st Rocky Mountain Conference, Denver, Colorado, 1979;
(b) M.J. Nilges, Ph.D. Thesis, University of Illinois, Urbana, IL;
(c) J.B. Cornelius, J. Me Cracken, R.B. Clarkson, R.L. Belford, J. Peisach, J. Phys. Chem. 94 (1990) 6977.
[12] Program SIMFONIA, Bruker, shareware, Madison, WI, 1996.
[13] D. Louër, M. Louër, J. Appl. Cryst. 5 (1972) 271.
[14] A. Boultif, D. Louër, J. Appl. Cryst. 24 (1991) 987.
[15] R. Boca, M. Breza, P. Pelikan, Struct. Bond. 71 (1989) 57.
[16] M. Horák, D. Papoušek, Infračervená spektroskopia a sruktura molekul [Infrared spectroscopy and the structure of molecules, in Czech], Academia Praha, 1976.
[17] M. Kwiatkowski, E. Kwiatkowski, A. Olechnowicz, G. Bandoli, A. Dolmela, Inorg. Chim. Acta 201 (1992) 177.
[18] (a) V. Gutmann, The Donor–Acceptor Approach to Molecular Interactions, Plenum Press, New York, 1978;
(b) V. Gutmann, E. Hennge, Anorganische Chemie, fifth ed., VCH, Weinheim, 1990, p. 203;
(c) W. Linert, R.F. Jameson, G. Bauer, A. Taha, J. Coord. Chem. 42 (1997) 211.
[19] (a) A. Takenaka, H. Utsumi, T. Yamamoto, A. Furusaki, I. Nitta, J. Chem. Soc. Jpn., Pure Chem. 91 (1970) 928;
(b) R. Faure, H. Loiseleur, G. Thomas-David, Acta Crystallogr., Sect. B 29 (1973) 1890.

synthesis of asymmetrically dibridged dicopper(II) complexes using *p*-hydroxycinnamic acid as the carboxylate. The Schiff base H_3L with two acetylacetoneimine moieties is similar to H_3L' that has two salicylaldimine groups. Herein, we report the synthesis, crystal structure and the magnetic properties of the complexes $[Cu_2L(O_2C{-}CH{=}CH{-}C_6H_4\text{-}p\text{-}OH)(MeOH)]\cdot MeOH$ (**1**·MeOH) and $[Cu_2L(O_2C{-}CH{=}CH{-}C_6H_4\text{-}p\text{-}OH)]\cdot H_2O$ (**2**·H_2O). The significant observation of this study is the crystal structures of the complexes showing formation of different types of supramolecular structures. The complex **2**·H_2O forms a helical structure through intermolecular hydrogen bonding interactions involving only the carboxylate ligands. The lattice water is non-covalently bound to the Schiff base of the dinuclear unit and does not take part in the supramolecular structure formation.

2. Experimental

2.1. Materials and measurements

All reagents and chemicals were purchased from commercial sources and used as received. The solvents were purified following reported procedures [13]. The Schiff base *N*,*N*′-1,3-diyl-bis(acetylacetoneimine)propan-2-ol (H_3L) and the dicopper(II) precursor complex, $[Cu_2L(O_2CMe)]$ were prepared by literature methods [14]. The elemental analysis was done using a Thermo Finnigan FLASH EA 1112 CHN analyzer. The electronic and infrared spectral data were obtained from Lambda 55 and Perkin–Elmer Spectrum One FT-IR spectrometers, respectively. Variable temperature magnetic susceptibility data for the polycrystalline samples were obtained in the temperature range 18–300 K using a Model 300 Lewis-coil-force magnetometer of George Associates Inc. (Berkeley, USA) make equipped with a Cahn balance and a closed cycle cryostat (Air products). $Hg[Co(NCS)_4]$ was used as a standard. Experimental susceptibility data were corrected for diamagnetic contributions and temperature independent paramagnetism ($N_\alpha = 60\times10^{-6}$ cm^3 M^{-1} per copper). The molar magnetic susceptibilities were fitted to the modified Bleany–Bowers expression by means of a least-squares computer program [15,16]. The Hamiltonian and susceptibility equation used are: $\hat{\boldsymbol{H}} = -2J(\hat{\boldsymbol{S}}_1\cdot\hat{\boldsymbol{S}}_2)$ ($\boldsymbol{S}_1 = \boldsymbol{S}_2 = 1/2$ for a d^9–d^9 dicopper(II) core) and $\chi_{Cu} = [Ng^2\beta^2/k(T-\theta)][3+\exp(-2J/k(T-\theta))]^{-1}(1-\rho) + (Ng_1^2\beta^2/4kT)\rho + N_\alpha$, where ρ is the fraction of monomeric impurity and $2J$ is the singlet–triplet separation energy. The magnetic moments were calculated in μ_B unit. TGA measurements were made using a Mettler Toledo Star thermal analyzer.

2.2. Preparation of $[Cu_2L(O_2C{-}CH{=}CH{-}C_6H_4\text{-}p\text{-}OH)(MeOH)]$ (**1**)

Complex $[Cu_2L(O_2CMe)]$ (0.15 g, 0.33 mmol) in MeOH (10 mL) was reacted with the sodium salt of *p*-hydroxycinnamic acid, prepared in situ by reacting the carboxylic acid (0.056 g, 0.33 mmol) with NaOH (0.013 g, 0.33 mmol) in methanol (5 mL), and the reaction mixture was refluxed for 30 min, followed by cooling to an ambient temperature. The solution was filtered and the filtrate on slow evaporation gave the green product in ~70% yield. Single crystals of composition **1**·MeOH, suitable for X-ray diffraction, were obtained from the mother liquor. *Anal.* Calc. for $C_{23}H_{30}N_2O_7Cu_2$ (**1**): C, 48.24; H, 5.10; N, 4.89. Found: C, 48.02; H, 5.24; N, 5.13%. Electronic spectral data in DMSO [λ_{max}, nm (ε, M^{-1} cm^{-1})]: 632 (350), 315 (126000), 290 (109000). FT-IR (KBr phase), cm^{-1}: 3400br, 2920w, 1612s, 1508s, 1400s, 1272s, 1169m, 1013m, 942m, 833m, 701m (br, broad; s, strong; m, medium; w, weak). Magnetic moment (μ_{eff}) per copper in the dimeric unit: 1.63 μ_B at 300 K; 0.17 μ_B at 18 K; $2J = -160$ cm^{-1} from the theoretical fitting with $g = 2.13$, $\rho = 0.004$, $g_1 = 2.2$, $R = 8.5\times10^{-3}$.

2.3. Preparation of $[Cu_2L(O_2C{-}CH{=}CH{-}C_6H_4\text{-}p\text{-}OH)]$ (**2**)

The dimeric precursor $[Cu_2L(O_2CMe)]$ (0.22 g, 0.49 mmol) in 1-propanol (20 mL) was reacted with the sodium salt of *p*-hydroxycinnamic acid, prepared in situ by reacting the carboxylic acid (0.082 g, 0.49 mmol) with NaOH (0.019 g, 0.47 mmol) in 1-propanol (10 mL) and the reaction mixture was refluxed for 30 min, followed by cooling to room temperature. The solution was filtered and the filtrate on slow evaporation gave the green product in ~65% yield. *Anal.* Calc. for $C_{22}H_{28}N_2O_7Cu_2$ (**2**): C, 47.22; H, 5.04; N, 5.00. Found: C, 47.29; H, 5.08; N, 5.12%. Electronic spectral data in DMSO [λ_{max}, nm (ε, M^{-1} cm^{-1})]: 630 (320), 315 (132000), 285 (100000). FT-IR (KBr phase, cm^{-1}): 3510br, 3001w, 1640s, 1606s, 1550s, 1514s, 1397s, 1281s, 1250s, 1162s, 1015m, 986m, 831s, 761m, 712m. Magnetic moment (μ_{eff}) per copper: 1.67 μ_B at 300 K; 0.17 μ_B at 18 K; $2J = -132$ cm^{-1} from the theoretical fitting with $g = 2.07$, $\rho = 0.005$, $g_1 = 2.14$, $R = 2.8\times10^{-2}$. Single crystals of **2**·H_2O were obtained on slow evaporation of the mother liquor in the presence of a trace quantity of water.

2.4. X-ray crystallographic studies

Single crystals of the complexes $[Cu_2L(O_2C{-}CH{=}CH{-}C_6H_4\text{-}p\text{-}OH)(MeOH)]\cdot MeOH$ (**1**·MeOH) and $[Cu_2L(O_2C{-}CH{=}CH{-}C_6H_4\text{-}p\text{-}OH)]\cdot H_2O$ (**2**·H_2O) of the respective sizes $0.49\times0.21\times0.13$ and

$0.26 \times 0.18 \times 0.11$ mm^3 were mounted on glass fibers with epoxy cement. All geometric and intensity data were collected using a Bruker SMART APEX CCD diffractometer having a fine focus 1.75 kW sealed tube Mo Kα X-ray source with increasing ω (width of 0.3° per frame) at a scan speed of 5 s/frame for **1**·MeOH and 12 s/frame for **2**·H_2O. A total of 20 555 reflections were collected for **1** in the range $1.47 \leqslant \theta \leqslant 27.18°$ of which 4356 reflections with $I \geqslant 2\sigma(I)$ were used for structure solution using 361 parameters. For **2**·H_2O, a total of 16 283 reflections were collected in the range $2.0 \leqslant \theta \leqslant 24.71°$, of which 3457 reflections with $I \geqslant 2\sigma(I)$ were used for structure solution using 310 parameters. The hydrogen atoms attached to the carbon atoms, except two methanol molecules in **1**·MeOH, were fixed in their calculated positions and refined using a riding model for both the structures. The hydrogen atoms of the copper-bound and lattice methanol molecules were located in the difference Fourier maps and were refined isotropically. In both the structures, the hydrogen atom of the *p*-hydroxy group was located in the difference Fourier map and was refined isotropically. The hydrogen atoms of the lattice water in **2**·H_2O were also located from the difference Fourier map and blocked after refining for the last few cycles to lower the shift/e.s.d. values. All the non-hydrogen atoms in the structures were refined anisotropically. The structure solution and refinement were made using the SHELX system of programs [17]. The perspective views of the molecules were obtained by ORTEP [18]. Selected crystallographic data are given in Table 1.

Table 1
Crystallographic data for [$Cu_2L(O_2C{-}CH{=}CH{-}C_6H_4$-*p*-OH)(MeOH)]·MeOH (**1**·MeOH) and [$Cu_2L(O_2C{-}CH{=}CH{-}C_6H_4$-*p*-OH)]·$H_2O$ (**2**·H_2O)

	1·MeOH	**2**·H_2O
Empirical formula	$C_{24}H_{34}N_2O_8Cu_2$	$C_{22}H_{28}N_2O_7Cu_2$
Crystal size (mm)	$0.25 \times 0.19 \times 0.09$	$0.25 \times 0.17 \times 0.11$
Crystal morphology	cuboid	cuboid
Crystal system	monoclinic	monoclinic
Space group	$P2_1/n$	$P2_1/n$
Formula weight	605.61	559.54
Unit cell dimensions		
a (Å)	8.684(13)	10.472(4)
b (Å)	11.316(17)	9.236(4)
c (Å)	27.91(4)	25.156(9)
$\alpha = \gamma$ (°)	90	90
β (°)	95.98(3)	100.484(6)
V (Å^3)	2728(7)	2392.6(16)
Z	4	4
$d_{calc.}$ (g cm^{-3})	1.47	1.55
μ(Mo) (mm^{-1})	1.61	1.82
F(000)	1256	1152
λ(Mo Kα) (Å)	0.71073	0.71073
T (K)	293(2)	293(2)
Reflections collected	20 555	16 283
Independent reflections	5575	4074
Observed reflections, [$I > 2\sigma(I)$]	4356	3457
Parameters	361	310
Goodness of fit on F^2	1.020	1.182
R (observed data) [R (all data)]	0.050 [0.068]	0.043 [0.052]
R_w (observed data) [R_w(all data)]	0.1114 [0.1189]	0.1011 [0.1051]
Largest difference peak and hole (e Å^{-3})	0.583 and −0.447	0.737 and −0.527
Weight factor: $w = 1/[\sigma^2(F_o^2) + (AP)^2 + BP]$	$A = 0.0524$, $B = 1.5669$	$A = 0.0446$, $B = 2.1385$

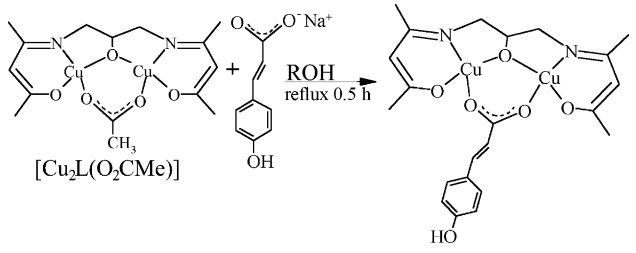
3. Results and discussion

3.1. Synthesis and general aspects

Dicopper(II) complexes **1** and **2** are prepared in good yield by substituting the acetate of the precursor complex [$Cu_2L(O_2CMe)$] having a pentadentate trianionic Schiff base *N*,*N*′-(2-hydroxypropane-1,3-diyl)bis-(acetylacetoneimine) (H_3L) by the carboxylate ligand, HO-*p*-$C_6H_4{-}CH{=}CH{-}CO_2^-$ in methanol or propanol solvent. We have prepared the complex from two different solvents with an objective to isolate supramolecular host structures stabilized by different lattice guest molecules (Scheme 1). The choice of propanol as a reaction medium is to isolate a complex with lattice water molecule(s) as propanol is less likely to support a supramolecular structure by hydrogen bonding interactions. The complexes are characterized from the analytical and spectral data. They are crystallized as [$Cu_2L(O_2C{-}CH{=}CH{-}C_6H_4$-*p*-OH)(MeOH)]·MeOH (**1**·MeOH) and [$Cu_2L(O_2C{-}CH{=}CH{-}C_6H_4$-*p*-OH)]·$H_2O$ (**2**·H_2O) and are structurally characterized by single crystal X-ray crystallography. The complexes are soluble in polar organic solvents and display a d–d band in the electronic spectra at ~630 nm in DMSO.

3.2. Crystal structures

Both the complexes crystallize in the centrosymmetric monoclinic space group $P2_1/n$ with four dicopper units in the unit cell, having alternating chains of opposite helical chirality in the crystal. Selected bond distance and bond angle data are given in Table 2. The crystal structure of **1**·MeOH shows the presence of a dicopper(II) complex with a (μ-alkoxo)(μ-carboxylate)-dicopper(II) core in which the Cu(1) atom has a square



Scheme 1. Synthetic scheme for the complexes **1** and **2**.

Table 2
Selected bond distances (Å) and angles (°) in **1**·MeOH and **2**·H_2O

	1·MeOH	**2**·H_2O
Cu(1)···Cu(2)	3.504(4)	3.500(1)
Cu(1)–O(1)	1.918(3)	1.900(3)
Cu(1)–O(2)	1.925(3)	1.900(3)
Cu(1)–O(5)	1.946(3)	1.922(3)
Cu(1)–N(1)	1.923(3)	1.920(3)
Cu(2)–O(2)	1.931(3)	1.922(3)
Cu(2)–O(3)	1.930(4)	1.904(3)
Cu(2)–O(4)	1.973(3)	1.957(3)
Cu(2)–O(7)	2.339(4)	
Cu(2)–N(2)	1.961(3)	1.933(3)
Cu(1)–O(2)–Cu(2)	130.6(1)	132.8(1)
O(1)–Cu(1)–O(2)	177.4(1)	175.5(1)
O(1)–Cu(1)–O(5)	85.3(1)	84.9(1)
O(1)–Cu(1)–N(1)	95.0(2)	94.4(1)
O(2)–Cu(1)–O(5)	94.9(1)	95.3(1)
O(2)–Cu(1)–N(1)	84.8(2)	85.7(1)
O(5)–Cu(1)–N(1)	178.0(1)	175.1(1)
O(2)–Cu(2)–O(3)	169.1(1)	178.5(1)
O(2)–Cu(2)–O(4)	93.1(1)	93.9(1)
O(2)–Cu(2)–N(2)	85.2(1)	84.6(1)
O(2)–Cu(2)–O(7)	93.4(1)	
O(3)–Cu(2)–O(4)	87.1(1)	87.2(1)
O(3)–Cu(2)–O(7)	97.4(1)	
O(3)–Cu(2)–N(2)	92.4(1)	94.2(1)
O(4)–Cu(2)–O(7)	88.2(2)	
O(4)–Cu(2)–N(2)	168.8(1)	178.3(1)
O(7)–Cu(2)–N(2)	103.0(2)	

planar $CuNO_3$ coordination geometry and the Cu(2) atom has a square pyramidal (4 + 1) coordination geometry, giving a Cu···Cu distance of 3.504(1) Å (Fig. 1). The Schiff base ligand displays a pentadentate mode of coordination with the alkoxo oxygen atom bridging the copper centers. The Cu(2) atom is bonded to a methanol ligand at the elongated axial site. The basal planes at the metal centers are nearly coplanar, forming an angle of 10.1(1)°. The —CH=CHC_6H_4— moiety of the *p*-hydroxycinnamate in **1**·MeOH is nearly planar giving an angle of 7.3(3)° between the planes having the $^-$OOC—CH=CH— group and the aromatic C_6H_4 ring. The cinnamate ligand forms an angle of 5.1(1)° with the coordination plane of the $\{Cu_2L\}^+$ moiety. The complex self assembles into a supramolecular structure through hydrogen bonding interactions (Fig. 2). There are two types of intermolecular hydrogen bonding interactions observed in this crystal structure. The copper-bound methanol ligand is involved in the hydrogen bonding interactions with the terminal Schiff base oxygen forming a non-covalently bound "tetrameric" unit [Fig. 2(a); O(7)···O(1)#1, 2.969(5) Å; O(7)–H(25)··· O(1)#1, 162.0°; #1: $-x+1, -y+1, -z+2$]. The other hydrogen-bonding network forms a supramolecular structure involving the lattice methanol molecule, the pendant hydroxy group of the carboxylate and the terminal oxygen atom of the Schiff base (Fig. 2(b)). The O(6)···O(8) and O(8)···O(3)#2 distances are 2.709(6) and 2.812(6) Å, respectively (#2: $-x+1/2+1, -y+1/2, -z+1/2+1$). The hydrogen bonds are nearly linear as evidenced from the O(6)–H(6)···O(8) and O(8)–H(26)···O(3)#2 angles of 167.5° and 163.8°, respectively.

The crystal structure of **2**·H_2O has a (μ-alkoxo)(μ-carboxylate)dicopper(II) core formed by the pentadentate Schiff base (L) and the bridging carboxylate. The copper centers have a square planar $CuNO_3$

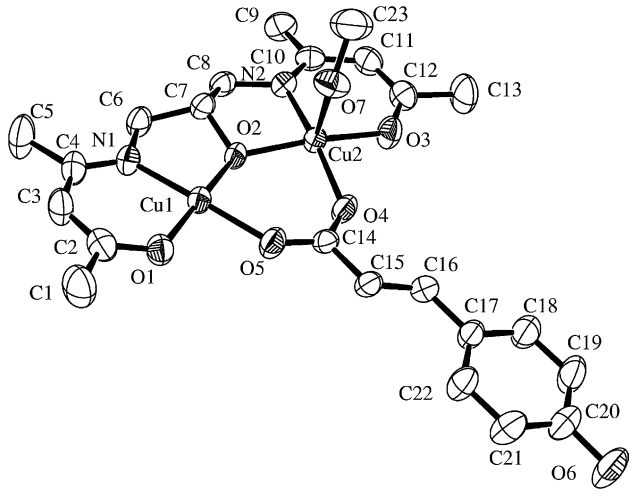


Fig. 1. ORTEP view of the complex [$Cu_2L(O_2C$—CH=CH—C_6H_4-*p*-OH)(MeOH)]·MeOH (**1**·MeOH).

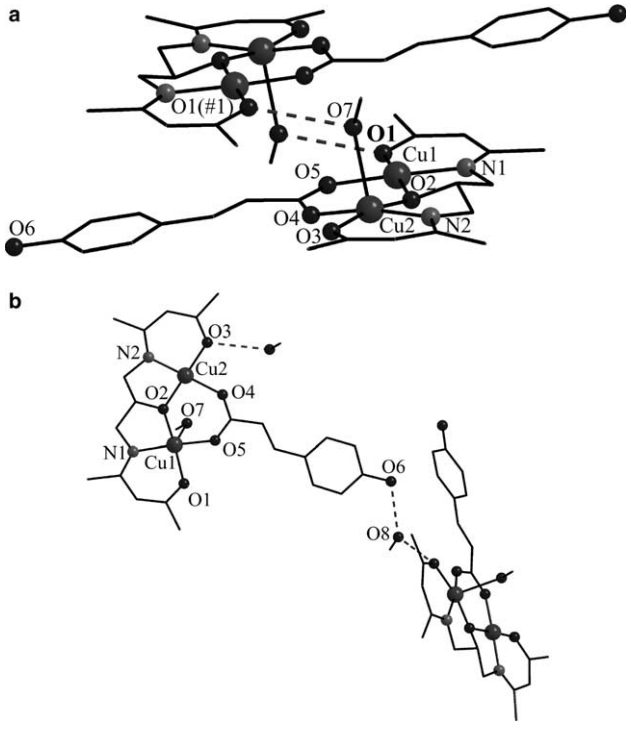


Fig. 2. (a) The hydrogen bonding interactions involving the copper-bound methanol ligand and the terminal oxygen atom of the Schiff base in **1**·MeOH. (b) The hydrogen bonding interactions involving the *p*-hydroxy group of the carboxylate, lattice methanol and the oxygen atom of the Schiff base in **1**·MeOH.

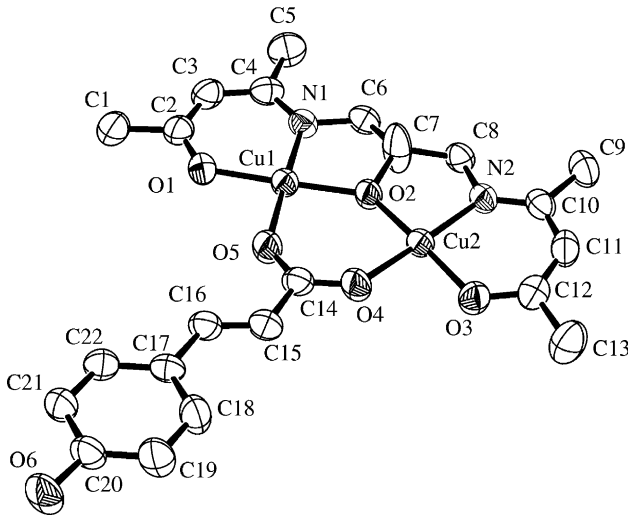


Fig. 3. ORTEP view of the complex in $[Cu_2L(O_2C{-}CH{=}CH{-}C_6H_4\text{-}p\text{-}OH)]\cdot H_2O$ ($\mathbf{2}\cdot H_2O$).

coordination geometry, giving a Cu···Cu distance of 3.501(1) Å (Fig. 3). The basal planes at the copper(II) centers are nearly coplanar, forming an angle of 5.2(1)°. The $-CH{=}CHC_6H_4-$ moiety of the *p*-hydroxycinnamate is nearly planar giving an angle of 4.2(3)° between the $-CH{=}CH-$ group and the aromatic C_6H_4 ring. The cinnamate ligand forms an angle of 5.8(1)° with the coordination plane of the $\{Cu_2L\}^+$ moiety. This is in contrast to its analogous complex $[Cu_2L'(O_2C{-}CH{=}CH{-}C_6H_4\text{-}p\text{-}OH)]\cdot 2H_2O$, having the Schiff base *N*,*N*′-(2-hydroxypropane-1,3-diyl)bis(salicylaldimine) (H_3L'), forming an angle of ~30° between the plane of $\{Cu_2L'\}$ and the *p*-hydroxycinnamate ligand. The essentially planar structure in $\mathbf{2}\cdot 2H_2O$ could be due to the absence of any steric rigidity in comparison to H_3L' that has two salicylaldimine moieties. Complex $\mathbf{2}\cdot H_2O$ self assembles in a unique way to form a helical supramolecular structure through bifurcated hydrogen bonding interactions involving the *p*-hydroxy group of the carboxylate and the terminal oxygen atom O(1) of the Schiff base and one oxygen atom of the bridging carboxylate O(5) [Fig. 4; O(6)···O(1)#1, 2.899(4) Å, O(6)–H(6)··· O(1)#1, 144.7°; O(6)··· O(5)#1, 2.975(4) Å, O(6)–H(6)···O(5)#1, 144.9°; #1: $-x+1/2+1, +y+1/2, -z+1/2+1$]. This is in contrast to the helical structure of its H_3L' analog that involves the *p*-hydroxy group of the carboxylate and the phenoxo atom of the Schiff base (L′) in the hydrogen bonding interactions. The O(7) lattice water molecule in $\mathbf{2}\cdot H_2O$ is hydrogen bonded to the terminal oxygen atom O(3) of the Schiff base belonging to the binuclear complex [O(7)···O(3), 2.902(6) Å; O(7)–H(7B)···O(3), 178.9°]. The lattice water in $\mathbf{2}\cdot H_2O$ does not take part in the helical structure formation but could be partially responsible for the overall planarity of the carboxylate and the $\{Cu_2L\}^+$ moieties.

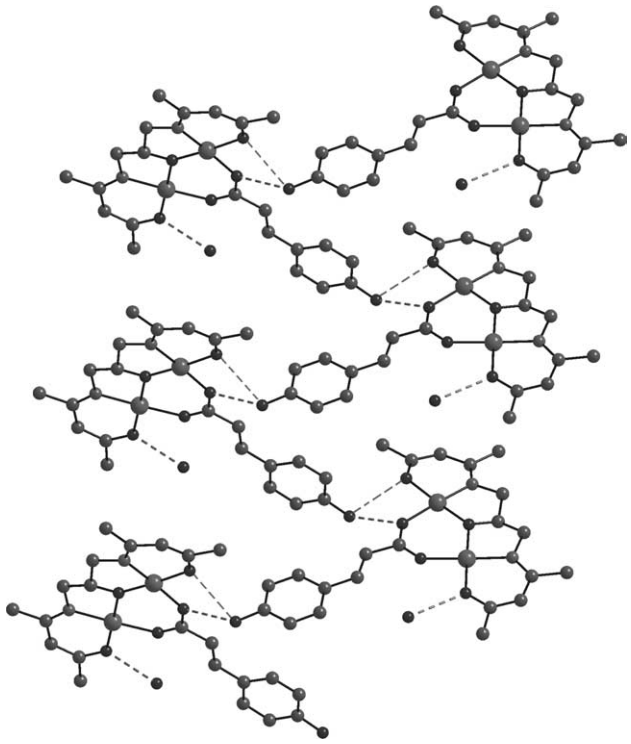


Fig. 4. Perspective view of the self-assembled helical supramolecular structure of $\mathbf{2}\cdot H_2O$. The bifurcated hydrogen bond is shown (---).

3.3. Magnetic properties

The variable-temperature magnetic susceptibility data for the complexes in the temperature range 300–18 K show an antiferromagnetic (AF) behavior of the complexes (Fig. 5). The magnetic moment values (per copper) of ~1.7 μ_B at 300 K and ~0.2 μ_B at 18 K indicate significant AF spin–spin coupling in the asymmetrically dibridged dicopper(II) core. The theoretical fittings of the magnetic susceptibility data, obtained by using the modified Bleaney–Bowers expression, gave the sin-

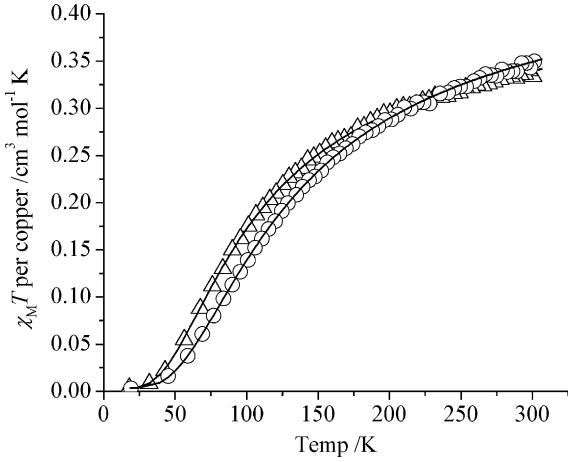


Fig. 5. $\chi_M T$ vs. T plots for the complexes **1** and **2**. The solid lines show the theoretical fit to the experimental data (△, **1**; ○, **2**).

glet–triplet energy separation ($2J$) value of $-160\ cm^{-1}$ for **1** and $-132\ cm^{-1}$ for **2**, with the singlet as the ground state [16]. Complexes **1** and **2** belong to the class of asymmetrically dibridged dicopper(II) complexes in which the nature and magnitude of the intramolecular magnetic exchange interactions in the $\{Cu_2(\mu\text{-}OR)(\mu\text{-}O_2CR)\}$ core primarily depend upon the Cu–O–Cu angle [14,19–28]. The lower magnitude of the $2J$ value, even with a large Cu–O–Cu angle of ~130°, is attributed to the counter-complimentary nature of overlap of the magnetic orbitals and is directly proportional to the energy separation of the symmetric and antisymmetric combinations of magnetic orbitals. It is interesting to note that complex **1** with a lower Cu–O–Cu angle of 130.6(1)° has greater AF interaction than complex **2** that has a Cu–O–Cu angle of 132.7(1)°. The difference could be due to stronger Cu–O (carboxylate) bonds in **2** than in **1**. Complexes **1** and **2** differ considerably in their supramolecular structures due to the involvement of the oxygen atoms in the non-covalent interactions. They also differ in the core structure where **1** has four and five coordinate copper centers, while the copper atoms in **2** have a four coordinate geometry. Again, the average Cu–O distance in the $\mu\text{-}O_2CR$ bridge of **1**·MeOH is 1.96 Å and the same for **2**·H_2O is 1.94 Å. The coordinating planes having copper atoms Cu(1) and Cu(2) have a dihedral angle of 9.54(7)° in **1**·MeOH and 5.14(6)° for **2**·H_2O. The observation of higher overall counter-complimentary effect in **2** in comparison to **1** could be due to the structural variations involving the carboxylate bridge and the supramolecular helices.

3.4. Thermogravimetric studies

Complex **1**·MeOH shows a weight loss of 4.1% in the temperature range of 50–115 °C, which is lower than the calculated percentage of 5.3% for the lattice methanol (Fig. 6). The discrepancy could be due to the labile nature of the lattice methanol at room temperature. Further, it is noticed that the copper bound methanol is not released in this temperature range, possibly due to the participation of the copper-bound methanol in the non-covalent "tetrameric" structure formation. We have observed a weight loss of ~40% above 225 °C. This could be due to the degradation of the complex above this temperature. Complex **2**·H_2O shows the TGA graph with a weight loss of 3.0% in the temperature range of 110–140 °C, which is in accordance of the theoretical value of 3.22% (Fig. 6). A further weight loss of ~46% is observed above 240 °C due to possible degradation of the complex.

In summary, two new asymmetrically dibridged dicopper(II) complexes with a pentadentate Schiff base and *p*-hydroxycinnamate are prepared and structurally characterized by X-ray crystallography. The complexes form helical supramolecular structures involving hydrogen bonding interactions. The crystal structure of the complex with a lattice water molecule differs considerably from its analogous structure having the Schiff base *N*,*N*′-1,3-diyl-bis(salicylaldiminato)propan-2-ol (H_3L'). The angle between the plane of $\{Cu_2L\}$ with the carboxylate plane in **2**·H_2O is ~6°, while the angle involving $\{Cu_2L'\}$ and the carboxylate in the reported structure is ~30° [11]. The helix formation in **2**·H_2O involves the bridging and pendant *p*-hydroxy group oxygen atoms of the carboxylate through hydrogen bonding interactions along with the terminal oxygen atom of the Schiff base. Its analogous complex having the H_3L' ligand forms a helix of a different structure [11,12]. The present work shows the significant effect of the pentadentate Schiff base in the self-assembly process of supramolecular helix formation with different structural conformations.

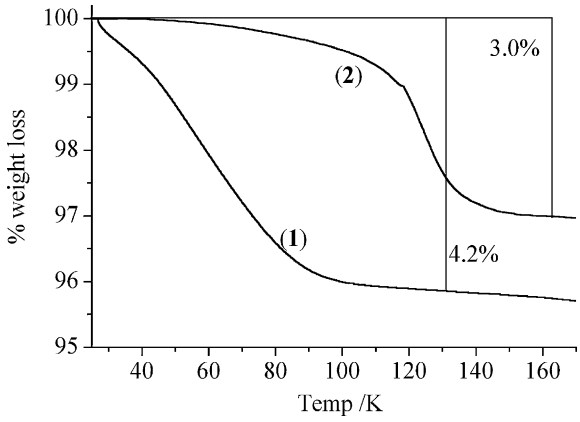


Fig. 6. Thermogravimetric plots of (a) **1**·MeOH and (b) **2**·H_2O showing weight loss of the sample with increasing temperature.

Acknowledgements

We thank the Department of Science and Technology, Government of India, for the financial support and for the CCD X-ray diffractometer facility. S.G. thanks CSIR for a fellowship.

Appendix A. Supplementary data

Crystallographic data for the structural analysis of **1**·MeOH and **2**·H_2O have been deposited with the Cambridge Crystallographic Data Center, CCDC Nos. 267777 and 267778. Copies of this information may be obtained free of charge from The Director, CCDC, 12 Union Road, Cambridge, CB2 1EZ, UK (fax: +44-1223-366-033; e-mail: deposit@ccdc.ac.uk or www: http://www.ccdc.cam.ac.uk). Supplementary data associated with this article can be found, in the online version, at doi:10.1016/j.poly.2005.05.015.

References

[1] J.M. Lehn, Supramolecular Chemistry, VCH, Weinheim, 1995.
[2] M. Albrecht, Chem. Rev. 101 (2001) 3457.
[3] C. Piguet, G. Bernardinelli, G. Hopfgartner, Chem. Rev. 97 (1997) 2005.
[4] M.J. Hannon, L.J. Childs, Supraml. Chem. 16 (2004) 7.
[5] B. Sreenivasulu, J.J. Vittal, Angew. Chem., Int. Ed. 43 (2004) 5769.
[6] O. Mamula, A. von Zelewsky, T. Bark, G. Bernardinelli, Angew. Chem., Int. Ed. 38 (1999) 2945.
[7] G. Baum, E.C. Constable, D. Fenske, C.E. Housecroft, T. Kulke, Chem. Eur. J. 5 (1999) 1862.
[8] M.J. Hannon, C.L. Painting, N.W. Alcock, Chem. Commun. (1999) 2023.
[9] C. Kaes, M.W. Hosseini, C.E.F. Rickard, B.W. Skelton, A.H. White, Angew. Chem., Int. Ed. 110 (1998) 970.
[10] D.A. McMorran, P.J. Steel, Angew. Chem., Int. Ed. 37 (1998) 329.
[11] A. Mukherjee, M.K. Saha, M. Nethaji, A.R. Chakravarty, Chem. Commun. (2004) 716.
[12] A. Mukherjee, M.K. Saha, M. Nethaji, A.R. Chakravarty, New J. Chem. 29 (2005) 596.
[13] D.D. Perin, W.L.F. Armarego, D.R. Perrin, Purification of Laboratory Chemicals, Pergamon Press, Oxford, 1980.
[14] Y. Nishida, S. Kida, J. Chem. Soc., Dalton Trans. (1986) 2633.
[15] O. Kahn, Molecular Magnetism, VCH, Weinheim, 1993.
[16] B. Bleaney, K.D. Bowers, Proc. R. Soc. London, A 214 (1952) 451.
[17] G.M. Sheldrick, SHELX 97, Programs for Crystal Structure Solution and Refinement, University of Göttingen, Göttingen, Germany, 1997.
[18] M.N. Burnett, C.K. Johnson, ORTEP-III, Report ORNL-6895, Oak Ridge National Laboratory, Oak Ridge, TN, 1996.
[19] K. Geetha, M. Nethaji, N.Y. Vasanthacharya, A.R. Chakravarty, J. Coord. Chem. 47 (1999) 77.
[20] P.J. Hey, J.C. Thibeault, R.H. Hoffmann, J. Am. Chem. Soc. 97 (1975) 4884.
[21] W. Mazurek, B.J. Kennedy, K.S. Murray, M.J. O'Connor, J.R. Rodgers, M.R. Snow, A.G. Wedd, P.R. Zwack, Inorg. Chem. 24 (1985) 3258.
[22] Y. Nishida, M. Takeuchi, K. Takahashi, S. Kida, Chem. Lett. (1982) 1815.
[23] Y. Nishida, M. Takeuchi, K. Takahashi, S. Kida, Chem. Lett. (1985) 631.
[24] Y. Nishida, M. Takeuchi, K. Takahashi, S. Kida, Chem. Lett. (1983) 1815.
[25] M. Mikurriya, K. Minowa, R. Nukada, Bull. Chem. Soc. Jpn. 75 (2002) 2595.
[26] T. Kawata, S. Ohba, Y. Nishida, T. Tokii, Acta Crystallogr. C 49 (1993) 2070.
[27] W.M. Davis, D.H. Busch, Acta Crystallogr. C 43 (1987) 639.
[28] T. Kawata, M. Yamanaka, S. Ohba, Y. Nishida, M. Nagamatsu, T. Tokii, M. Kato, O.W. Steward, Bull. Chem. Soc. Jpn. 65 (1992) 2739.

2. Experimental

2.1. Synthesis

2.1.1. Boc–Gly–ΔPhe–Gly–Gly–ΔPhe Gly–OMe, Boc–Gly–ΔAla–Gly–Gly–ΔAla–Gly–OMe

TEA (0.029 ml, 0.21 mmol) was added to a solution of Boc–Gly–ΔPhe–Gly (0.038 g, 0.1 mmol), Gly–ΔPhe–Gly–OMe*TFAOH (0.041 g, 0.1 mmol) or Boc–Gly–ΔAla–Gly (0.030 g, 0.1 mmol), Gly–ΔAla–Gly–OMe*TFAOH (0.033 g, 0.1 mmol) in 3 ml ACN and stirred for 15 min. Then TBTU (0.043 g, 0.105 mmol) was added. The reaction was carried out for 24 h at room temperature. ACN was removed under reduced pressure. The resulting oil was dissolved in 20 ml EtOAc and washed successively with 1 M HCl (4 × 2 ml), saturated potassium bicarbonate (4 × 2 ml) and brine 2 ml. The organic layer was dried over $MgSO_4$, and then the drying agent was removed by filtration. The product was crystallized from EtOAc–MeOH (40:1 v/v)/hexane.

Yield: 0.063 g (97%), tt = 188–191 °C (*E*)(*E*); 0.062 g (96%), tt = 145–147 °C (*Z*)(*Z*); 0.032 g (65%), tt = 141.5–143.5 °C ΔAla–ΔAla.

Elemental *Anal*. Calc. for $C_{32}H_{38}N_6O_9$ (650.676): C, 59.06; H, 5.89; N, 12.92. Found: C, 59.26; H, 5.80; N, 13.03%.

Elemental *Anal*. Calc. for $C_{20}H_{30}N_6O_9$ (498.492): C, 49.19; H, 6.07; N, 16.86. Found: C, 49.40; H, 6.17; N, 16.65%.

HPLC column Alltech Alltima, C-18 5 micrometer, 150 × 4.6 mm. A – H_2O; B – ACN, A:B = 40:60 flow rate 1 ml/min, purity 97.9%.

2.1.2. Boc–Gly–ΔPhe–Gly–ΔPhe–Ala–OMe

TEA (0.014 ml, 0.1 mmol) was added to a solution of Boc–Gly–ΔPhe (0.032 g, 0.1 mmol), Gly–ΔPhe–Ala–OMe*TFAOH (0.042 g, 0.1 mmol) in 0.5 ml THF and stirred for 15 min. Then DMT-MM (0.028 g, 0.1 mmol) was added. The reaction was carried out for 6 h at room temperature. The precipitate was filtered out and then filtrate was evaporated to an oil. The resulting oil was dissolved in 20 ml EtOAc and washed successively with 1 M HCl (4 × 3 ml), saturated potassium bicarbonate (4 × 3 ml) and brine 3 ml. The organic layer was dried with $MgSO_4$ and then the drying agent was removed by filtration. The product was crystallized from *i*-PrOH/hexane. Yield 0.057 g (94%), tt = 194 °C decomp.

Elemental *Anal*. Calc. for $C_{31}H_{37}N_5O_8$ (607.662): C, 61.27; H, 6.14; N, 11.52. Found: C, 61.09; H, 5.99; N, 11.70%.

HPLC column Alltech Alltima, C-18 5 micrometer, 150 × 4.6 mm. A – H_2O; B – ACN, A:B = 40:60 flow rate 1 ml/min, purity 98%.

2.1.3. Deprotection –OMe

Sodium hydroxide 1 M (0.125 ml) was added to a solution of the peptides (0.1 mmol) in 0.6 ml methanol and the reaction mixture was stirred at room temperature for 1 h. Then the reaction mixture was acidified by 1 M hydrochloric acid to pH 3, finally brine 5 ml was added and the product extracted with EtOAc (5 × 3 ml). The collected organic layer was washed with hydrochloric acid 0.5 M (2 × 3 ml) and brine (2 × 3 ml). The organic layer was dried over $MgSO_4$ (1 h only). The drying agent was removed by filtration. The products were crystallized from EtOAc–MeOH (4:1 v/v)/hexane.

Yield: 0.054 g (85%), tt = 198 °C – decomp. (*E*)(*E*); 0.056 g (88%), tt = 180–184 °C – decomp. (*Z*)(*Z*).

Elemental *Anal*. Calc. for $C_{31}H_{36}N_6O_9$ (636.66): C, 58.43; H, 5.70; N, 13.20. Found: C, 58.27; H, 5.80; N, 13.34%.

HPLC column Alltech Alltima, C-18 5 micrometer, 150 × 4.6 mm. A – H_2O; B – ACN, A:B = 40:60 flow rate 1 ml/min, purity 98.5%.

2.1.4. B–G–ΔA–G–G–ΔA–G–OH

Precipitated by hexane, yield 0.043 g (88%).

Elemental *Anal*. Calc. for $C_{19}H_{28}N_6O_9$ (484.465): C, 47.10; H, 5.82; N, 17.35. Found: C, 47.33; H, 5.92; N, 17.23%.

2.1.5. B–G–ΔPhe–G–ΔPhe–A–OH

The product was crystallized from EtOAc–MeOH (4:1 v/v)/hexane, yield 0.059 g (99%), tt = 204 °C decomp.

Elemental *Anal*. Calc. for $C_{30}H_{35}N_5O_8$: C, 60.70; H, 5.94; N, 11.80. Found: C, 60.88; H, 5.88; N, 11.99%.

HPLC column Alltech Alltima, C-18, 5 micrometer, 150 × 4.6 mm. A – H_2O; B – ACN, A:B = 40:60 flow rate 1 ml/min, purity 98.8%.

2.1.6. Boc-deprotection

The Boc-protected dehydro-peptides 0.1 mmol were dissolved in 0.5 ml dichloromethane, 1 ml anhydrous trifluoroacetic acid and 0.1 ml aniosole and stirred at room temperature for 20 min. Then dichloromethane was added and the volatile components of the reaction mixture were purified by adding 10 ml diethyl ether followed by evaporation. This procedure was repeated three times. The resulting trifluoroacetates peptides were dissolved in 3 ml isopropanol and the products were precipitated by hexane.

Yield: G–ΔPhe–G–G–ΔPhe–G*TFAOH 0.0514 g (79%) (*E*)(*E*), 0.052 g (80%) (*Z*)(*Z*).

Elemental *Anal*. Calc. for $C_{28}H_{29}N_6O_9F_3$ (650.567): C, 51.69; H, 4.49; N, 12.92. Found: C, 51.77; H, 4.56; N, 13.00%.

Yield: G–ΔA–G–G–ΔA–G*TFAOH 0.038 g (75%).

Elemental *Anal*. Calc. for $C_{16}H_{21}N_6O_9F_3$ (498.372): C, 38.56; H, 4.25; N, 16.86. Found: C, 38.69; H, 4.45; N, 16.68%.

Yield: G–ΔPhe–G–ΔPhe–A*TFAOH 0.060 g (99%).

Elemental *Anal*. Calc. for $C_{27}H_{28}N_5O_8F_3$ (607.542): C, 53.38; H, 4.64; N, 11.53. Found: C, 53.49; H, 4.78; N 11.42%.

2.2. Potentiometric studies

The stability constants for the proton and Cu(II) complexes were calculated from titration curves carried out at 25 °C. Alkali was added from a 0.250 ml micrometer syringe, which was calibrated by weight titrations of standard materials. The metal ion concentration was 1×10^{-3} M and the metal-to-ligand ratios were 1:1. The pH-metric titrations were performed in 0.1 M KNO_3 on a MOLSPIN pH-meter system using a Russell CMAW 711 semi micro combined electrode calibrated in hydrogen ion concentration using HNO_3, and three titrations were performed for each system. A SUPERQUAD [9] computer program was used for stability constant calculations. Standard deviations quoted were computed by SUPERQUAD and refer to random errors only. They are, however, a good indication of the importance of a particular species in the equilibrium.

2.3. Spectroscopic studies

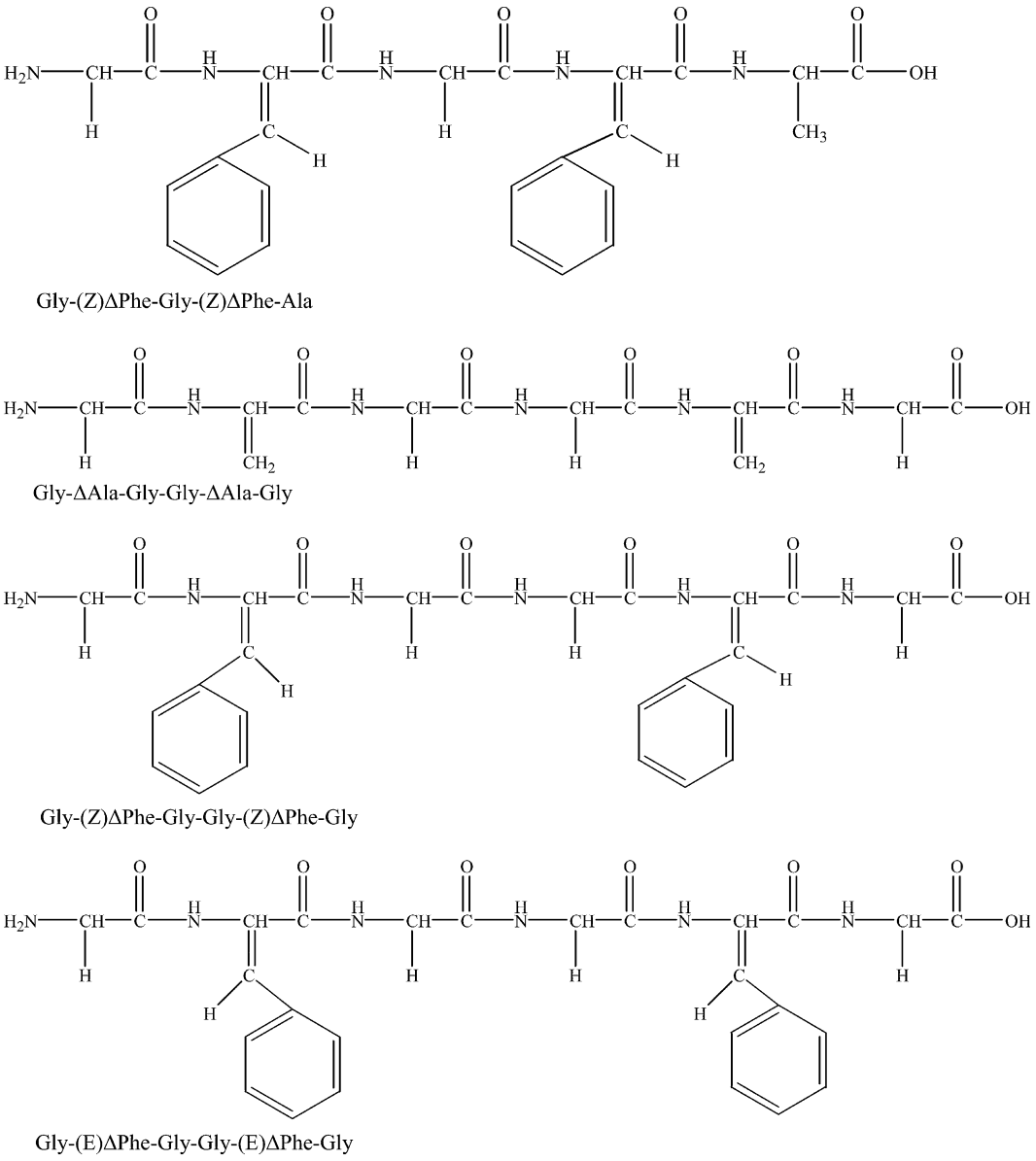
Absorption spectra were recorded on a Perkin Elmer Lambda Bio-20 spectrophotometer, circular dichroism (CD) spectra on a JASCO J 715 spectropolarimeter in the 850–200 nm range and electron paramagnetic resonance (EPR) spectra on a Bruker ESP 300E spectrometer at X-band frequency (9.4 GHz) at 120 K. The metal concentration in these measurements were adjusted to 1×10^{-3} M and the metal-to-ligand rations were 1:1. The spectroscopic parameters were obtained at the maximum concentration of the particular species.

3. Results and discussion

The stability constants for the proton and Cu^{2+} complexes are given in Table 1. All ligands (Scheme 1) have two protonation constants [$\log K(NH_2)$ and $\log K(COO^-)$] assigned to amino and carboxyl groups. The protonation constants of amino groups as well as those of carboxyl groups are similar for all the studied ligands. In comparison to pentaGly, insertion of the dehydro-amino acid residue into the peptide sequence makes the proton from the amino group more acidic; the value of $\log K(NH_2)$ for dehydro-peptides is lower than for pentaGlycine (Table 1). The protonation constant for the carboxyl group is similar for the studied ligands as well as for pentaGlycine.

Table 1
Stability constants for copper(II) complexes of bis-dehydro-peptides at 25 °C, $I = 0.10$ M (KNO_3)

	Gly–(*Z*)ΔPhe–Gly–(*Z*)ΔPhe–Ala	Gly–(*Z*)ΔPhe–Gly–(*Z*)ΔPhe–Gly [7]	Gly–(*Z*)ΔPhe–Gly–Gly–(*Z*)ΔPhe–Gly	Gly–(*E*)ΔPhe–Gly–Gly–(*E*)ΔPhe–Gly	Gly–(*E*)ΔPhe–Gly–(*E*)ΔPhe–Gly [7]	Gly–ΔAla–Gly–Gly–ΔAla–Gly	Gly–Gly–Gly–Gly–Gly [11]
HL	7.47 ± 0.01	7.57	7.47 ± 0.02	7.39 ± 0.02	7.56	7.57 ± 0.02	7.86
H_2L	10.87 ± 0.0	10.19	10.85 ± 0.03	10.92 ± 0.03	11.11	10.90 ± 0.03	11.25
$\log K(NH_2)$	7.47	7.57	7.47	7.39	7.56	7.57	7.86
$\log K(COO^-)$	3.40	2.62	3.38	3.53	3.55	3.33	3.39
CuL		4.96		4.55 ± 0.06	4.42	5.64 ± 0.06	5.32
CuH_1L	0.40 ± 0.01	0.71	0.91 ± 0.01	−0.15 ± 0.01	−0.41	1.21 ± 0.02	−0.68
CuH_2L	−5.48 ± 0.02	−5.92	−6.09 ± 0.02	−6.24 ± 0.01	−7.06	−4.64 ± 0.02	−7.58
CuH_3L	−11.55 ± 0.01	−11.68	−13.98 ± 0.02	−13.26 ± 0.01	−13.51	−11.92 ± 0.03	−15.62
CuH_4L	−21.17 ± 0.04	−21.09	−24.10 ± 0.03	−22.19 ± 0.01	−23.37	−21.05 ± 0.04	
$\log K_1^{amide}$		4.25		4.70	4.83	4.43	6.00
$\log K_2^{amide}$	5.88	6.63	7.00	6.09	6.65	5.85	6.90
$\log K_3^{amide}$	6.07	5.76	7.89	7.02	6.45	7.28	8.04
$\log K_4$	9.62	9.41	10.12	8.93	9.86	9.13	



Scheme 1.

Coordination of Cu^{+2} ions starts at the nitrogen of the amino group and then the oxygen of the adjacent carbonyl group, except for ligands having two (*Z*)ΔPhe residues. In the latter case the $CuH_{-1}L$ complex is formed as the first main species (Table 1). When the pH increases, the $CuH_{-2}L$ complex is formed by all ligands. The EPR parameters for all the ligands, as well as UV–Vis spectra for the (*E*)Phe(*E*)Phe isomer and ligands with two ΔAla residues (Table 2), suggest three nitrogen atoms bound to the metal ion. This complex is formed by coordination of a second amide nitrogen and the binding mode for this complex is $\{NH_2, 2 \cdot N^-\}$. With a further the pH increase, the studied ligands form complexes losing the proton from the next amide bond [10] (Table 1) and the $CuH_{-3}L$ complex with a $\{NH_2, 3 \cdot N^-\}$ binding mode is formed. The spectroscopic parameters (Table 2) confirm that four nitrogen atoms are coordinated to copper ion.

The final complex formed at high pH is $CuH_{-4}L$. The spectroscopic parameters for the $CuH_{-4}L$ complex are the same as for $CuH_{-3}L$. It supports four nitrogen coordination to the Cu^{2+} ion. The CD spectra of the chiral pentapeptide (Scheme 1) obtained from $CuH_{-3}L$ and $CuH_{-4}L$ complexes are very similar to each other (Table 2), suggesting that the formation of the latter complex could derive from the partial hydrolysis of the former species.

Figs. 1 and 2 show a competition between the binding of the Cu^{+2} ion by hexapeptide and chiral pentapeptide with two the (*Z*)ΔPhe residues. Below pH 6 hexapeptide

Table 2
Absorption, CD and EPR parameters for copper(II) complexes with bis-dehydro-peptides

Ligand	Species	λ/nm	ε/dm^3 mol^{-1} cm^{-1}	$A_\parallel$/G	$g_\parallel$	λ/nm	$\Delta\varepsilon$/dm^3 mol^{-1} cm^{-1}
Gly–(*Z*)ΔPhe–Gly–(*Z*)ΔPhe–Ala	$CuH_{-1}L$	644.5	63	179	2.261	217	−0.802
						274.5[b]	+1.402
						324[c]	−0.412
						692[d]	−0.045
	$CuH_{-2}L$	[a]		186	2.256	280[b]	+0.565
						356[c]	+0.080
						506[d]	+0.067
						683.5[d]	−0.0214
	$CuH_{-3}L$	507	329	202	2.176	220.5	+0.786
						258.5[b]	−1.398
						329.5[c]	+0.898
						495.5[d]	+0.1894
	$CuH_{-4}L$	507	329	202	2.176	220.5	+0.866
						258.5[b]	−1.336
						326[c]	+0.406
						496[d]	+0.189
Gly–(*Z*)ΔPhe–Gly–Gly–(*Z*)ΔPhe–Gly	$CuH_{-1}L$	616	109	176	2.257		
	$CuH_{-2}L$	[a]		183	2.240		
	$CuH_{-3}L$	510	234	205	2.186		
Gly–(*E*)ΔPhe–Gly–Gly–(*E*)ΔPhe–Gly	$CuH_{-1}L$	666	91	173	2.260		
	$CuH_{-2}L$	582	149	179	2.254		
	$CuH_{-3}L$	210	280	210	2.170		
Gly–ΔAla–Gly–Gly–ΔAla–Gly	$CuH_{-1}L$	625	83	174	2.318		
	$CuH_{-2}L$	582	104	177	2.220		
	$CuH_{-3}L$	510.5	162	206	2.161		

[a] Unresolved broad shoulder around 510 nm.
[b] $NH_2 \rightarrow Cu^{2+}$ charge transfer transition.
[c] $N^-_{amide} \rightarrow Cu^{2+}$ charge transfer transition.
[d] d–d transition.

forms a more stable complex $CuH_{-1}L$ (Figs. 1 and 2), while above pH 6 the pentapeptide is more efficient (Fig. 2). It could derive from the closer vicinity of the (*Z*)ΔPhe residues in the pentapeptide ligand and formation of the more stable $CuH_{-3}L$ complex with the $\{NH_2, 3 \cdot N^-\}$ binding mode.

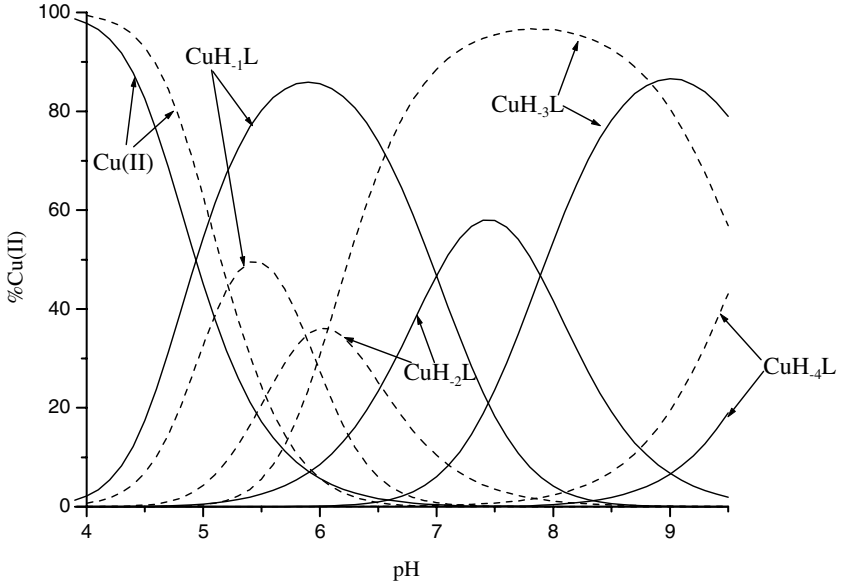


Fig. 1. Species distribution curves for Cu(II)–Gly–(*Z*)ΔPhe–Gly–Gly–(*Z*)ΔPhe–Gly (solid line) and Cu(II)–Gly–(*Z*)ΔPhe–Gly–(*Z*)ΔPhe–Ala (dashed line) complexes at 25 °C and $I = 0.1$ mol dm^{-3} KNO_3. Metal concentration 1×10^{-3} mol dm^{-3}. Ligand to metal ratio 1:1.

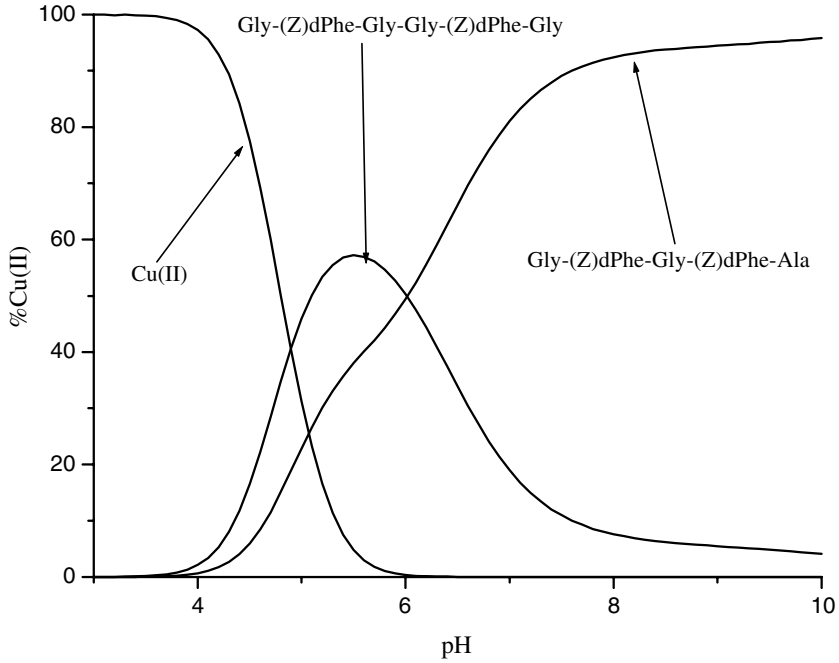


Fig. 2. Competition diagrams for Cu(II)–Gly–(*Z*)ΔPhe–Gly–Gly–(*Z*)ΔPhe–Gly and Gly–Gly–(*Z*)ΔPhe–Gly–(*Z*)ΔPhe–Ala in binding of Cu(II) ions as a function of pH for 1:1:1 (ligand 1:metal:ligand 2) molar ratio and metal concentration 1×10^{-3} mol dm^{-3}.

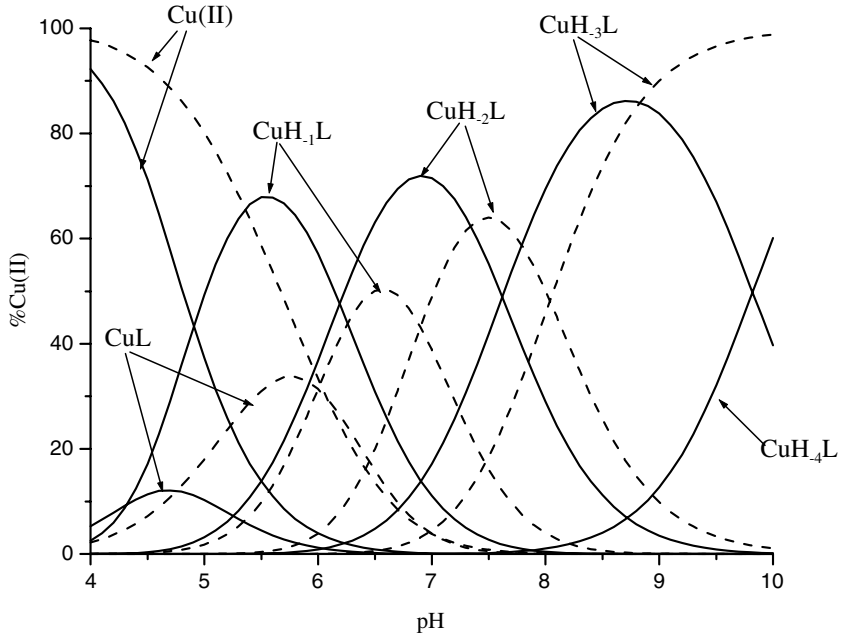


Fig. 3. Species distribution curves for Cu(II)–Gly–ΔAla–Gly–Gly–ΔAla–Gly (solid line) and Cu(II)–pentaglycine (dashed line) complexes at 25 °C and $I = 0.1$ mol dm^{-3} KNO_3. Metal concentration 1×10^{-3} mol dm^{-3}. Ligand to metal ratio 1:1.

As it shows in Fig. 3, the insertion of two dehydroamino acid residues into the peptide sequence makes the ligand distinctly more effective in metal ion binding when compared to the pentaglycine. Interestingly, at physiological pH both ligands form $CuH_{-2}L$ complexes with a $\{NH_2, 2 \cdot N^-\}$ binding mode (Fig. 3).

A comparison of the binding ability of (*Z*)ΔPhe(*Z*)-ΔPhe and (*E*)ΔPhe(*E*)ΔPhe is given in Fig. 4. The competition diagram for both ligands is shown in Fig. 5. The former ligand binds Cu^{2+} more effectively below pH 7. Up to this pH value the (*Z*,*Z*) isomer forms a very stable $CuH_{-1}L$ complex, while above pH 7 the isomer

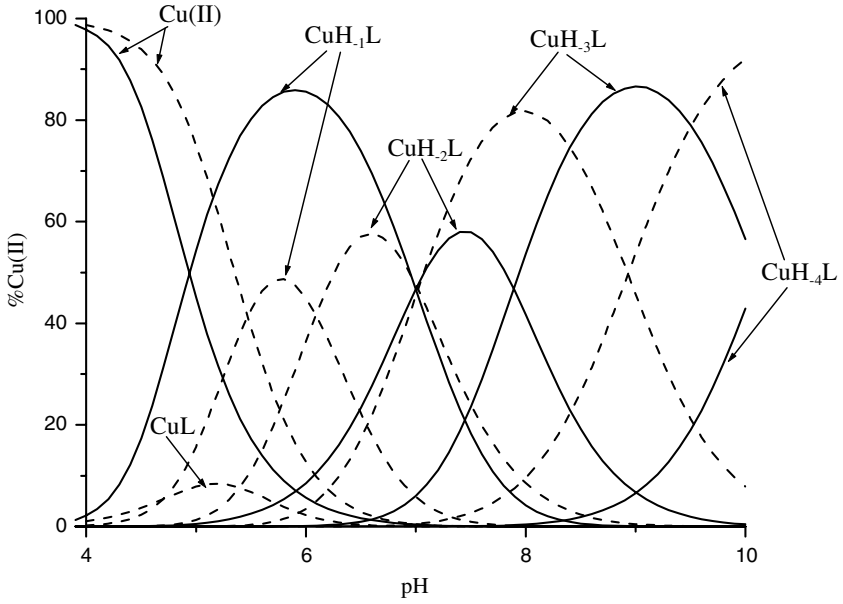


Fig. 4. Species distribution curves for Cu(II)–Gly–(*Z*)ΔPhe–Gly–Gly–(*Z*)ΔPhe–Gly (solid line) and Cu(II)–Gly–(*E*)ΔPhe–Gly–Gly–(*E*)ΔPhe–Gly (dashed line) complexes at 25 °C and $I = 0.1$ mol dm^{-3} KNO_3. Metal concentration 1×10^{-3} mol dm^{-3}. Ligand to metal ratio 1:1.

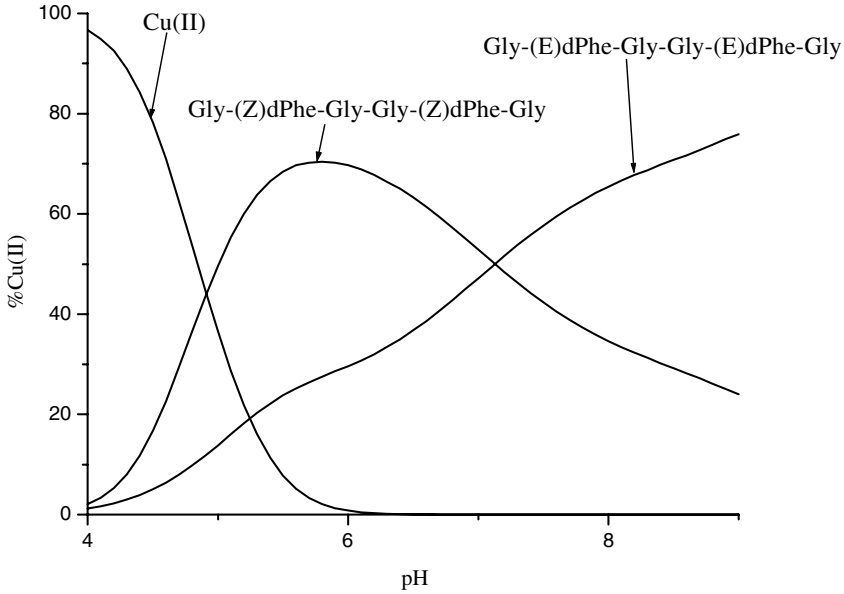


Fig. 5. Competition diagrams for Cu(II)–Gly–(*Z*)ΔPhe–Gly–Gly–(*Z*)ΔPhe–Gly and Gly–Gly–(*E*)ΔPhe–Gly–Gly–(*E*)ΔPhe–Gly in binding of Cu(II) ions as a function of pH for 1:1:1 (ligand 1:metal:ligand 2) molar ratio and metal concentration 1×10^{-3} mol dm^{-3}.

E, which forms the $CuH_{-3}L$ species easier, is more effective (Figs. 4 and 5). In the $CuH_{-1}L$ complex, the metal ion is coordinated to a nitrogen from an amino group and an amide nitrogen from the first dehydro-residue. A greater influence of the double bond on the amide nitrogen is observed in the (*Z*) residue than in the (*E*) residue [8]. It makes the $CuH_{-1}L$ complex more stable for the (*Z*,*Z*) isomer. The dehydro-residue in position 5 has no impact on metal ion binding. For this reason the formation of the $CuH_{-3}L$ complex is independent of the dehydro-amino acid residue. The higher stability of the $CuH_{-3}L$ complex for the (*E*,*E*) isomer may be caused by steric reasons.

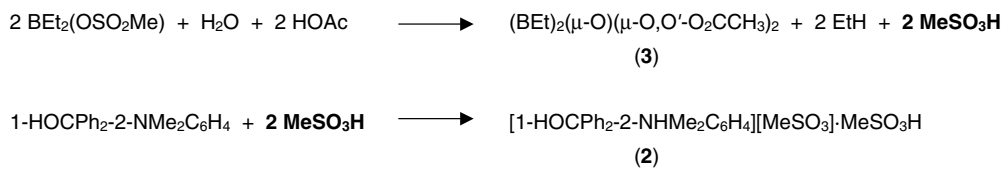
4. Conclusions

The data discussed above indicates that the bis-dehydro-hexapeptides binds metal ions with similar efficiency as bis-dehydro-pentapeptides and are much more effective than pentaglycine. The dehydro-amino acid residue at position 5 in the bis-dehydro-hexapeptides

has insignificant impact on the efficiency of Cu^{+2} binding as well as on coordination of the third amide nitrogen. The increase of the distance between two dehydro-amino acid residues has no significant influence on the coordination of the metal ion to the second dehydro-amino group.

References

[1] M.P. Waalkes, S. Rehm, Fundam. Appl. Toxicol. 23 (1994) 21.
[2] G. Jung, Angew. Chem., Int. Ed. Engl. 30 (1991) 1051.
[3] L. Smełka, Z. Kubica, B. Rzeszotarska, H. Kozłowski, Pol. J. Chem. 67 (1993) 1355.
[4] M. Jeżowska-Bojczuk, H. Kozłowski, I. Sovago, Z. Kubica, B. Rzeszotarska, L. Smełka, Polyhedron 10 (1991) 2331.
[5] M. Jeżowska-Bojczuk, K. Varnagy, I. Sovago, G. Pietrzynski, M. Dyba, Z. Kubica, B. Rzeszotarska, L. Smełka, H. Kozlowski, J. Chem. Soc., Dalton Trans. (1996) 3265.
[6] J. Brasuń, L. Chruściński, E. Chruścińska, M. Makowski, H. Kozłowski, J. Świątek-Kozłowska, New J. Chem. (2000) 893.
[7] J. Świątek-Kozłowska, J. Brasuń, M. Łuczkowski, M. Makowski, J. Inorg. Biochem. 90 (2002) 106.
[8] J. Brasuń, M. Makowski, S. Ołdziej, J. Świątek-Kozlowska, J. Inorg. Biochem. 98 (2004) 1391.
[9] P. Gans, A. Sabatini, A. Vacca, J. Chem. Soc., Dalton Trans. (1985) 1196.
[10] H. Sigel, R.B. Martin, Chem. Rev. 82 (1982) 385.
[11] F.H. Allen, R. Kennar, R. Taylor, Acc. Chem. Res. 16 (1983) 146.



Scheme 1. Proposed mechanism for the formation of **2** and **3**.

H_2O (from glacial acetic acid) and HOAc react with $BEt_2(OSO_2Me)$ to give compound **3**, ethane and methylsulfonic acid. The last-named then reacts with the organic compound 1-$HOCPh_2$-2-$NMe_2C_6H_4$ to afford the ammonium methylsulfonate **2**. Correspondingly, compound **2** was also obtained from **1** and methylsulfonic acid. Compound **3** was previously prepared by the reaction of triethylboroxin with acetic acid anhydride and structurally characterized [8].

2.2. Spectroscopic properties

In the ^1H NMR spectrum of **2**, the $N(CH_3)_2$ protons give rise to one singlet at 2.78 ppm and one singlet for the Me protons of $MeSO_3$ and $MeSO_3H$ at 2.95 ppm. The NH and OH protons are not observed, while the proton of the methylsulfonic acid (S–OH) is observed as a broad signal at ca. 12.1 ppm. In the ^{13}C NMR spectrum of **2**, the $N(CH_3)_2$ carbon atoms appear as one singlet at 47.7 ppm, while the $MeSO_3$ and $MeSO_3H$ carbon atoms are observed as one singlet at 40.0 ppm. The ^{13}C NMR signal for the C–O carbon atom appears at 84.5 ppm.

2.3. Molecular structure of 2

In **2** (Fig. 1), the three components [1-$HOCPh_2$-2-$NHMe_2C_6H_4$]$^+$, $[MeSO_3]^-$ and $MeSO_3H$ are associated via two intermolecular hydrogen bonds [11] between the cation [1-$HOCPh_2$-2-$NHMe_2C_6H_4$]$^+$ and the $MeSO_3^-$ anion [O(1)–H(1O)···O(4): O(1)–H(1O) 0.78(2), H(1O)···O(4) 1.98(2), O(1)···O(4) 2.752(2) Å, O(1)–H(1O)···O(4) 166(2)°], and between the $MeSO_3^-$ anion and a neutral sulfonic acid molecule, $MeSO_3H$ [O(5)–H(5O)···O(2): O(5)–H(5O) 0.96(3), H(5O)···O(2) 1.53(3), O(5)···O(2) 2.483(2) Å, O(5)–H(5O)···O(2) 174(3)°]. This type of hydrogen bonding in acid salts of general formula $M^+X^- \cdot HX$ (with $X = MeSO_3$ in the present case) can be classified as a Type B structure (with crystallographically non-equivalent anion X and neutral molecule HX) according to Speakman [12]. The structure of a related *p*-toluenesulfonic acid/*p*-toluenesulfonate salt, (3*S*,4*S*)-3-methoxy-4-methylammoniopyrrolidine *p*-toluenesulfonic acid *p*-toluenesulfonate was reported, where the main interest was, however, in the determination of the absolute configuration of the ammonium cation rather than hydrogen bonding. Thus, no details concerning O···O or O···N distances were reported [13].

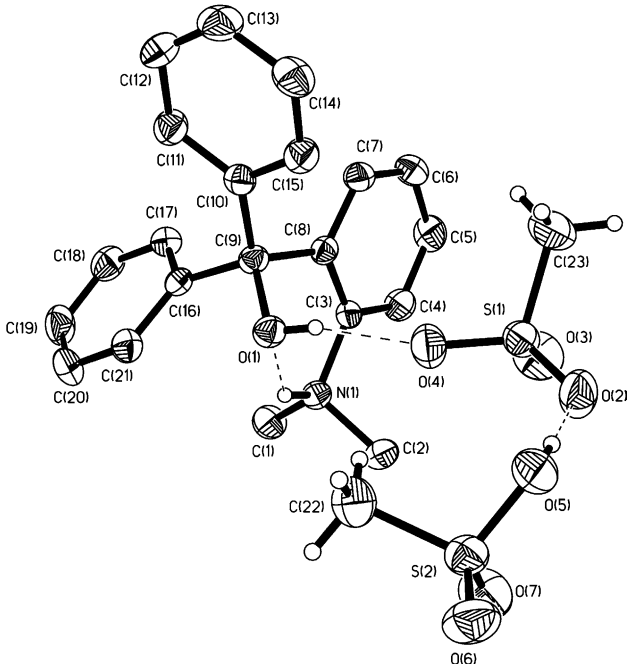


Fig. 1. Molecular structure of **2** (ORTEP, 50% probability, SHELXTL PLUS; XP [15], hydrogen atoms of Ph and NMe_2 groups omitted for clarity).

In **2**, additionally an intramolecular N(1)–H···O(1) hydrogen bond [N(1)–H 0.90(2), H···O(1) 1.99(2), N(1)···O(1) 2.738(2) Å, N(1)–H···O(1) 139(2)°] is observed in the cation [1-$HOCPh_2$-2-$NHMe_2C_6H_4$]$^+$. The intramolecular N(1)–H···O(1) hydrogen bond is weaker than the intramolecular O(1)–H···N(1) hydrogen bond in the related organic compound **1** [O(1)–H(1) 0.95(2), H(1)···N(1) 1.82(2), O(1)···N(1) 2.659(2) Å, O(1)–H(1)···N(1) 146(2)°] [10]. The bond lengths and angles of **2** not discussed above are normal and in agreement with those observed for the corresponding organic ligand **1** [10].

3. Experimental

3.1. General

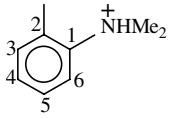
All experiments were carried out under purified dry nitrogen. Solvents were dried and freshly distilled under

nitrogen. The NMR spectra were recorded in $CDCl_3$ with an AVANCE DRX 400 spectrometer (Bruker): ^1H (400.1 MHz) and ^{13}C NMR spectra (100.6 MHz) with tetramethylsilane as external standard. Infrared spectra were recorded with a Perkin–Elmer System 2000 FT-IR spectrometer between 4000 and 400 cm^{-1} using KBr disks. Elemental analyses were determined with a VARIO EL (Heraeus). Melting points (Gallenkamp) are uncorrected. 1-$HOCPh_2$-2-$NMe_2C_6H_4$ [10] and $BEt_2(OSO_2CH_3)$ [5] were prepared according to the literature methods.

*[1-$HOCPh_2$-2-$NHMe_2C_6H_4$][$MeSO_3$] · $MeSO_3H$ (**2**) and ($BEt)_2(\mu$-$O)(\mu$-O,O'-$O_2CCH_3)_2$ (**3**)* Refluxing 1-$HOCPh_2$-2-$NMe_2C_6H_4$ (**1**; 0.5 g, 1.65 mmol) with BEt_2-(OSO_2CH_3) (0.3 g, 1.65 mmol) in the presence of acetic acid (1.4 g, 23.33 mmol) in 150 ml toluene for 2 h afforded a red oily residue. After removal of the solvent in vacuum at r.t. the red oily residue was separated by column chromatography (70/230 mesh silica gel/hexane), whereby two products were obtained. The first product was recrystallized from diethyl ether at 20 °C to give colorless crystals of **2** in 20% yield (0.16 g). M.p. 129–132 °C. The second product **3** was obtained as colorless crystals from toluene at −30 °C. The NMR data are in agreement with those reported in the literature [8].

*[1-$HOCPh_2$-2-$NHMe_2C_6H_4$][$MeSO_3$] · $MeSO_3H$ (**2**)* was independently prepared from **1** and $MeSO_3H$. $MeSO_3H$ (0.317 g, 3 mmol) was added very slowly to a solution of **1** (0.50 g, 1.6 mmol) in 10 ml THF. White crystals of **2** formed at room temperature overnight. Yield: 0.47 g (57%). M.p. 127 °C.

Spectroscopic data of **2** obtained as described above and as described here are identical.



Phenyl ring numbering scheme

^1H NMR (δ/ppm): 2.78 (s, 6H, $N(CH_3)_2$), 2.95 (s, 6H, $MeSO_3$ and $MeSO_3H$), 6.82–7.52 (m, 14H, C_6H_4 and C_6H_5), ca. 12.1 (s, 1H, S–OH); OH and NH not observed. ^{13}C NMR (δ/ppm): 40.0 (s, $MeSO_3$ and $MeSO_3H$), 47.7 (s, $N(CH_3)_2$), 84.5 (s, C–O), 121.7 (s, C6 in C_6H_4), 128.8 (s, C4 in C_6H_4), 129.2 (s, C3 in C_6H_4), 129.3 (s, C5 in C_6H_4), 130.0 (s, *p*-C in C_6H_5), 130.9 (s, *o*-C in C_6H_5), 131.9 (s, *m*-C in C_6H_5), 139.4 (s, C2 in C_6H_4), 142.8 (s, C1 in C_6H_4), 144.2 (s, *ipso*-C in C_6H_5). IR (KBr): 3283 br, 3068 w, 2965 m, 2935 m, 1658 m, 1596 s, 1496 vs, 1473 vs, 1448 vs, 1426 vs, 1340 vs, 1281 vs, 1233 vs, 1172 vs, 1132 vs, 1089 vs, 1034 s, 1008 vs, 971 s, 885 s, 768 vs, 742 vs, 706 vs, 639 vs, 582 m, 545 vs, 503 vs, 467 vs cm^{-1}. *Anal.* Calc. for $C_{23}H_{29}NO_7S_2$: C, 55.74; H, 5.90; S, 12.94. Found: C, 54.8; H, 6.09; S, 12.8%.

Table 1
Crystal data and structure refinement for **2**

	2
Formula	$C_{23}H_{29}NO_7S_2$
M_r	495.59
T (K)	213(2)
Crystal system	monoclinic
Space group	$P2_1/n$
a (Å)	15.7169(9)
b (Å)	8.3135(5)
c (Å)	18.688(1)
α (°)	90
β (°)	103.548(1)
γ (°)	90
V (Å^3)	2373.8(2)
Z	4
ρ_{calcd} (Mg m^{-3})	1.387
$F(000)$	1048
Absorption coefficient (mm^{-1})	0.269
Number of reflections collected	13151
Number of independent reflections	4676
R_{int}	0.0279
Number of parameters	405
R_1 ($I>2\sigma(I)$)	0.0323
wR_2 (all data)	0.0890
$(\Delta/\rho)_{min}$ (e Å^{-3})	0.235
$(\Delta/\rho)_{max}$ (e Å^{-3})	−0.359

4. X-ray crystallographic study

Crystallographic data are given in Table 1. Data [λ (Mo Kα) = 0.71073 Å] were collected with a Siemens CCD (SMART) diffractometer. All observed reflections were used for determination of the unit cell parameters. Empirical absorption correction with SADABS [14]. The structure was solved by direct methods (SHELXTL PLUS [15]). H atoms located by difference maps and refined isotropically.

Acknowledgments

We thank Mrs. A. Scholz and Dr. P. Lönnecke, University of Leipzig, for the independent synthesis of **2** from **1** and $MeSO_3H$.

Appendix A. Supplementary data

Crystallographic data for the structural analysis have been deposited with the Cambridge Crystallographic Data Centre, CCDC No. 264739 for **2**. These data can be obtained from Cambridge Crystallographic Data Centre, 12, Union Road, Cambridge CB2 1EZ, UK, fax: (internat.) +44 1223 336 033, e-mail: deposit@ccdc.cam.ac.uk or on the web http://www.ccdc.cam.ac.uk. Supplementary data associated with this article can be found, in the online version at doi:10.1016/j.poly.2005.06.002.

References

[1] (a) R. Schlengermann, J. Sieler, S. Jelonek, E. Hey-Hawkins, Chem. Commun. (1997) 197;
(b) R. Schlengermann, J. Sieler, E. Hey-Hawkins, Main Group Chem. 2 (1997) 141.

[2] H.T. Al-Masri, J. Sieler, S. Blaurock, P. Lönnecke, P.C. Junk, E. Hey-Hawkins, Z. Anorg. Allg. Chem. 631 (2005) 518.

[3] H.T. Al-Masri, J. Sieler, P.C. Junk, K. Domasevitch, E. Hey-Hawkins, J. Organomet. Chem. 690 (2005) 469.

[4] H.T. Al-Masri, J. Sieler, P. Lönnecke, P.C. Junk, E. Hey-Hawkins, Inorg. Chem. 43 (2004) 7162.

[5] R. Papp, F.B. Somoza Jr., J. Sieler, S. Blaurock, E. Hey-Hawkins, J. Organomet. Chem. 582 (1999) 127.

[6] S. Trofimenko, J. Am. Chem. Soc. 91 (1969) 2139.

[7] S. Trofimenko, Inorg. Chem. 8 (1969) 1714.

[8] R. Köster, A. Sporzynski, W. Schussler, D. Blaser, R. Boese, Chem. Ber. 127 (1994) 1191.

[9] J. Kronawitter, H. Nöth, Chem. Ber. 105 (1972) 2423.

[10] H.T. Al-Masri, J. Sieler, P. Lönnecke, S. Blaurock, K. Domasevitch, E. Hey-Hawkins, Tetrahedron 60 (2004) 333.

[11] W.C. Hamilton, J.A. Ibers, Hydrogen Bonding in Solids, W.A. Benjamin, New York, 1968.

[12] J.C. Speakman, Struct. Bond. 12 (1972) 141.

[13] Y. Tsuzuki, K. Chiba, K. Mizuno, K. Tomita, K. Suzuki, Tetrahedron: Asymm. 12 (2001) 2989.

[14] G.M. Sheldrick, SADABS – a Program for Empirical Absorption Correction, Göttingen, 1998.

[15] SHELXTL PLUS, Siemens Analyt. X-ray Inst. Inc., 1990, XS, Program for Crystal Structure Solution; XL, Program for Crystal Structure Determination; XP, Interactive Molecular Graphics.

directly to cobalt cations to form porous layers. A different type of SbS_2^- chain is found in $(CH_3NH_3)_2Sb_2S_4$ [15], where $Sb_2S_4^{2-}$ units, each consisting of a pair of edge-sharing SbS_3 trigonal pyramids, are linked by secondary Sb···S interactions to generate an infinite chain.

Although it is believed that simple thioantimonate ions play a fundamental role in the crystallisation of new structure types under solvothermal conditions, it is rare to observe such species totally isolated in the solid products of these reactions. The few known examples include the SbS_3^{3-} anion, found isolated in M_3SbS_3 (M = Cu, Ag, Tl) [16–18], and the Sb(V)-containing SbS_4^{3-} tetrahedron in $Cr(en)_3SbS_4$ [19]. The more complex $Sb_4S_8^{4-}$ heteroring is found isolated in $[Ni(C_4H_{13}N_3)_2]_2Sb_4S_8$ [20] and $[Ni(C_3H_{10}N_2)_3]_2Sb_4S_8 \cdot 2H_2O$ [21], whilst discrete $Sb_3S_6^{3-}$ units have been identified in $[Ni(C_4H_{13}N_3)_2]_3(Sb_3S_6)_2$ [22]. Although a number of compounds have been formulated with the Sb_2S_5 stoichiometry, they do not contain discrete $Sb_2S_5^{4-}$ ions. For example, in $Ca_2Sb_2S_5$ [23], isolated SbS_3^{3-} and $Sb_2S_4^{2-}$ units coexist, whilst in compounds $Mn_2(L)Sb_2S_5$ (L = methylamine [24], ethylenediamine [25] and 1,3-diaminopropane [26]), the antimony–sulfide unit is incorporated with manganese into heterocubane-like moieties, linkage of which generates infinite rod-like structural units. In addition, in the compounds $[M(C_6H_8N_4)]_2Sb_2S_5$ (M = Co, Mn) [27], $Sb_2S_5^{4-}$ behaves as a ligand by coordinating to two $[M(tren)]^{2+}$ complexes via sulfur.

The present work is concerned with the $Sb_2S_5^{4-}$ anion, of which there is only one known example of a discrete ion; namely, $Sr_2Sb_2S_5 \cdot 15H_2O$ [28]. Although $Ba_2As_2Q_5$ (Q = S, Se) [29] has analogous stoichiometry, this structure contains isolated AsQ_3^{3-} and $As(Q)_2Q_2$ units rather than $As_2Q_5^{4-}$ anions. Here, we describe the synthesis and characterisation of a new templated antimony sulfide, $[Fe(en)_3]_2Sb_2S_5 \cdot 0.55H_2O$ (**1**), which represents the first example of a material in which isolated $Sb_2S_5^{4-}$ anions crystallise with complex transition-metal cations. Furthermore, we demonstrate that a relatively modest rise of 25 K in the preparation temperature causes these $Sb_2S_5^{4-}$ units to polymerise to generate infinite SbS_2^- chains in the compound $[Fe(en)_3]_2Sb_4S_8$ (**2**), providing support for the view that relatively simple molecular units play a key role in crystallisation from the complex heterogeneous mixtures that constitute a solvothermal reaction.

2. Experimental

2.1. Synthesis and characterisation

The compounds $[Fe(en)_3]_2Sb_2S_5 \cdot 0.55H_2O$ (**1**) and $[Fe(en)_3]_2Sb_4S_8$ (**2**) were prepared under solvothermal conditions in a Teflon-lined stainless steel autoclave with an inner volume of 23 ml. For **1**, Sb_2S_3 (0.679 g, 2 mmol), $FeCl_2 \cdot 4H_2O$ (0.296 g, 1.5 mmol), S (0.160 g, 5 mmol) and 5 ml ethylenediamine (en, Aldrich, 99%), with approximate molar composition Sb:Fe:S:en of 4:1.5:11:75, were thoroughly mixed, heated at 413 K for 4 days and cooled to room temperature at a cooling rate of 20 K h^{-1}. The solid product was filtered, washed in ethylenediamine and dried in air at room temperature. The product consisted of yellow plates, identified by single-crystal X-ray diffraction as $Fe(en)_3Sb_4S_7$ [7], darker yellow "golf ball" like crystals of **1** as a minor phase, together with an unidentified black polycrystalline powder. CHN analysis of a handpicked sample of **1**: *Anal.* Calc. for $[Fe(en)_3]_2Sb_2S_5 \cdot 0.55H_2O$: C, 16.28; H, 5.58; N, 18.99. Found: C, 16.29; H, 5.61; N, 18.45%. For **2**, the composition of the reagents was identical to that used for **1**, but the mixture was heated for 4 days at 438 K. The cooling regime and product washing were as above. The product consisted of orange crystals of **2** along with an unidentified black polycrystalline powder. CHN analysis of a handpicked sample of **2**: *Anal.* Calc. for $[Fe(en)_3]_2Sb_4S_8$: C, 11.89; H, 3.98; N, 13.82. Found: C, 11.74; H, 4.06; N, 13.64%.

Magnetic susceptibility measurements were performed using a Quantum Design MPMS2 SQUID susceptometer. About 2 mg of hand-picked crystals of each of the title compounds were loaded into a gelatine capsule at room temperature and data were collected over the temperature range ($5 \leqslant T/K \leqslant 300$) after cooling in the measuring field of 1000 G. Data were corrected for the diamagnetism of the gelatine capsule and for intrinsic core diamagnetism.

2.2. Crystal structure determination

Single-crystal X-ray diffraction data for **1** were collected at room temperature using a Nonius Kappa CCD diffractometer with graphite monochromated Mo Kα radiation ($\lambda = 0.71073$ Å). Data were processed using the DENZO and SCALEPACK programs [30]. Corresponding intensity data for **2** were collected at 100 K using a Bruker Nonius X8 Apex diffractometer also using Mo Kα radiation ($\lambda = 0.71073$ Å) and data were processed using the APEX-2 software [31]. The structures were solved by direct methods using the program SIR-92 [32], which located all Fe, Sb and S atoms. Subsequent Fourier calculations and least-square refinements on *F* were carried out using the CRYSTALS program suite [33]. The C and N atoms of the amine were located in difference Fourier maps for **1** and **2**, together with the oxygen atom of a water molecule for **1**. Hydrogen atoms were placed geometrically on the C and N atoms after each cycle of refinement in each case. In the final cycles, positional and anisotropic thermal parameters for all non-hydrogen atoms were refined, together with the occupancy factor of the oxygen atom, for which a value

Table 1
Crystallographic data for $[Fe(en)_3]_2Sb_2S_5 \cdot 0.55H_2O$ (**1**) and $[Fe(en)_3]_2Sb_4S_8$ (**2**)

Complex	1	2
Formula	$[FeC_6N_6H_{24}]_2$ $Sb_2S_5(H_2O)_{0.55}$	$[FeC_6N_6H_{24}]_2$ Sb_4S_8
M_r	886.086	1215.82
Crystal system	orthorhombic	monoclinic
Crystal habit	yellow block	orange plate
Crystal dimensions (mm)	$0.1 \times 0.1 \times 0.1$	$0.05 \times 0.16 \times 0.16$
Space group	$Pca2_1$	$P2_1/c$
T (K)	293(3)	100(3)
a (Å)	15.8835(3)	21.017(4)
b (Å)	17.9586(3)	14.557(3)
c (Å)	11.4942(4)	12.445(3)
β (°)	90	100.42(3)
V (Å^3)	3278.67	3744.7
Z	4	4
μ (cm^{-1})	2.843	4.072
ρ_{calc} (g cm^{-3})	1.793	2.156
Measured data	10427	155055
Unique data	7451	12049
Observed data ($I \geqslant 3\sigma(I)$)	4939	4348
R_{int}	0.024	0.048
Residual electron density (minimum, maximum) (e Å^{-3})	−0.84, 1.27	−0.83, 0.84
Number of parameters refined	310	343
$R(F)$	0.0407	0.0237
$wR(F)$	0.0446	0.0235

of 0.55(3) was obtained. The crystal of **1** is an inversion twin with refined Flack parameter 0.53(6). Crystallographic and refinement details are given in Table 1. Crystallographic data for structures reported in this paper have been deposited with the Cambridge Crystallographic Data Centre.

3. Results and discussion

The local coordination and atom labelling scheme of the $Sb_2S_5^{4-}$ anion and distinct $[Fe(en)_3]^{2+}$ cations found in $[Fe(en)_3]_2Sb_2S_5 \cdot 0.55H_2O$ (**1**) are depicted in Fig. 1. Selected bond lengths, angles and valence sums are presented in Table 2. Magnetic susceptibility data for **1** clearly indicate paramagnetism (Fig. 2(a)). However, a plot of reciprocal susceptibility as a function of temperature exhibits pronounced curvature below 200 K. Above this temperature, the plot is sufficiently linear to enable fitting of a Curie–Weiss expression, yielding a Curie constant of 7.1(1) cm^3 K mol^{-1} and Weiss constant of $\theta = -115.6(4)$ K. This corresponds to an effective magnetic moment per iron atom of 5.34 μ_B, which is somewhat higher than the spin-only value of 4.89 μ_B calculated for octahedral *hs*-Fe^{2+}. This enhancement of the spin-only moment is typical for *hs*-Fe^{2+} and is associated with the orbital contribution arising from the $^5T_{2g}$ ground state of the ion. The orbital degeneracy of this ground state, leading to a temperature-dependent

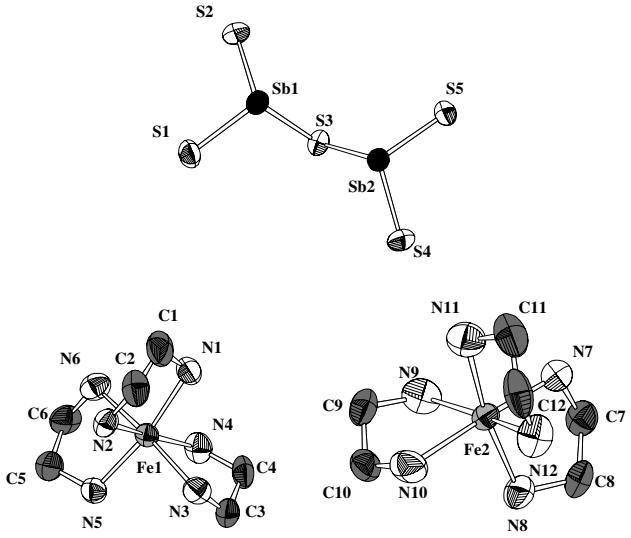


Fig. 1. Local coordination of the anionic and cationic components of $[Fe(en)_3]_2Sb_2S_5 \cdot 0.55H_2O$ (**1**), showing the atom labelling scheme and thermal ellipsoids at 50% probability The two crystallographically distinct iron complexes possess different conformations.

effective magnetic moment, may also be responsible for the marked curvature of the plot of reciprocal susceptibility as a function of temperature and for an unrealistic Weiss constant, which in a magnetically dilute system such as this is essentially an empirical parameter and not an indicator of exchange interactions.

The crystal structure of **1** consists of isolated $Sb_2S_5^{4-}$ anions, constructed from two SbS_3^{3-} trigonal pyramids sharing a common vertex, together with two crystallographically distinct iron cations complexed by ethylenediamine ligands. In the anionic part of the structure, the bridging Sb–S distances are 2.503(2) and 2.481(2) Å, whilst the terminal Sb–S bonds are significantly shorter, ranging between 2.371(2) and 2.378(3) Å. The S–Sb–S angles lie in the range 101.05(8)–103.52(8)°. These distances and angles are in good agreement with those of the $Sb_2S_5^{4-}$ unit in $Sr_2Sb_2S_5 \cdot 15H_2O$ [28]. Bond valence sums [34] for **1** are consistent with a formal oxidation state of +3 for each antimony atom (Table 2). The Fe–N distances in the two $[Fe(en)_3]^{2+}$ cations range from 2.162(8) to 2.249(8) Å with (*cis*) N–Fe–N angles lying between 78.6(3)° and 96.1(4)°, comparing well with values previously reported for Fe(II)–ethylenediamine complexes [35]. All Fe(1) complexes have the Λ(δδδ) conformation, whilst those containing Fe(2) are Δ(λλλ).

The isolated $Sb_2S_5^{4-}$ ions are arranged in sheets which lie in the *bc*-plane, with the Sb(1)–Sb(2) axis inclined at ca. 50° to this plane (Fig. 3). Within these sheets, the molecular anions lie in rows parallel to the [0 0 1] direction, with an alternation of the direction of the molecular axis between successive rows in the [0 1 0] direction. The sheets are non-planar and contain depressions in which the $[Fe(en)_3]^{2+}$ cations are located. These mixed anion–cation sheets are stacked along the

Table 2
Selected bond lengths (Å), angles (°) and bond valences (v.u.) for the $Sb_2S_5^{4-}$ anion in $[Fe(en)_3]_2Sb_2S_5 \cdot 0.55H_2O$ (**1**)

		v^a
Sb(1)–S(1)	2.371(2)	1.24
Sb(1)–S(2)	2.373(2)	1.23
Sb(1)–S(3)	2.503(2)	0.87
		3.34
Sb(2)–S(3)	2.481(2)	0.92
Sb(2)–S(4)	2.378(2)	1.21
Sb(2)–S(5)	2.371(2)	1.24
		3.37
S(1)–Sb(1)–S(2)	103.52(8)	
S(1)–Sb(1)–S(3)	101.05(8)	
S(2)–Sb(1)–S(3)	101.23(8)	
S(3)–Sb(2)–S(4)	101.67(8)	
S(3)–Sb(2)–S(5)	102.92(8)	
S(4)–Sb(2)–S(5)	102.78(9)	
Sb(1)–S(3)–Sb(2)	96.62(6)	

[a] Bond valences and their sums calculated using parameters from [34].

[1 0 0] direction, such that neighbouring sheets are displaced by $c/2$ with respect to each other (Fig. 4). A network of hydrogen bonds links molecules within the layers and in neighbouring layers. The nitrogen atoms of the ethylenediamine ligands of both Fe(1) and Fe(2) are all within hydrogen-bonding distance to the sulfur atoms of the $Sb_2S_5^{4-}$ anions (N···S = 3.41–3.79 Å). In addition, N(1) also forms a hydrogen bond to O(1) of the water molecule (N(1)···O(1) = 3.16 Å).

The structure differs from that of $Sr_2Sb_2S_5 \cdot 15H_2O$, the only other reported example of a material containing isolated $Sb_2S_5^{4-}$ anions [28]. In $Sr_2Sb_2S_5 \cdot 15H_2O$, a unit cell translation of molecular anions along [1 0 0] generates rows of ions, with neighbouring rows along [0 1 0] being displaced by $(\frac{1}{2}\,0\,0)$. This packing produces almost planar anionic layers parallel to the *ab*-plane that are interleaved with layers of hydrated strontium cations (Fig. 5). This contrasts with the rippled layers of $[Fe(en)_3]_2Sb_2S_5 \cdot 0.55H_2O$, in which layers contain both cations and anions. The plane containing the Sb–S–Sb linkage of the $Sb_2S_5^{4-}$ unit is approximately parallel to the crystallographic *ab*-plane, whereas in $[Fe(en)_3]_2Sb_2S_5 \cdot 0.55H_2O$, the analogous molecular plane is directed at ca. 60° to the plane in which the anions and cations are located. Compounds $[M(en)_3]_2Sb_2Se_5$ (M = Fe [35] and Mn [36]), containing the selenium analogue of $Sb_2S_5^{4-}$ described here, have been reported to crystallise in the space groups *Pbca* and $P2_1/n$, respectively, indicating different packing arrangements to that of the thioantimonate. The molecular anion in the iron-containing antimony–selenide was also found to be disordered over two symmetry-related positions [36].

The local coordination and atom labelling scheme of **2** is depicted in Fig. 6. Significant bond lengths and angles are presented in Table 3. Reciprocal magnetic susceptibility data for **2** also exhibit curvature (Fig. 2(b)), although this is less pronounced than for **1**. Fitting a Curie–Weiss expression to the high-temperature data (>200 K), produces a Curie constant of 6.1(1) cm^3 K mol^{-1} and a Weiss constant of $\theta = -20.5(4)$ K. The former corresponds to an effective magnetic moment of 4.94(5) μ_B per Fe atom, consistent with the presence of octahedral *hs*-Fe^{2+}. Bond-valence sums [34] indicate a formal oxidation state of +3 for each antimony atom (Table 3).

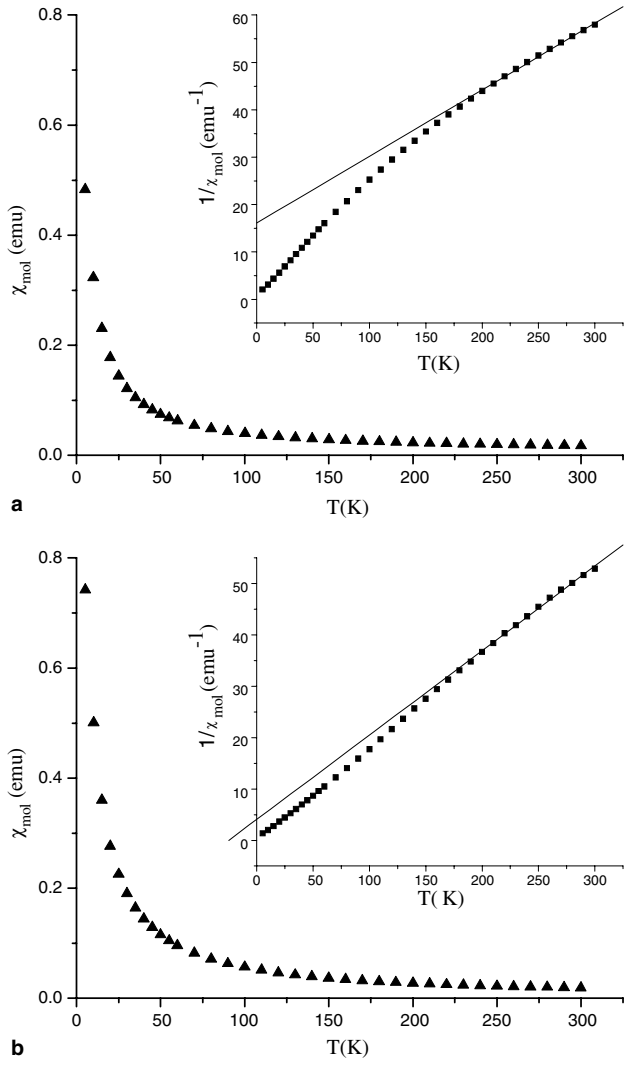


Fig. 2. Field-cooled magnetic susceptibility data and inverse susceptibility data (inset) for (a) $[Fe(en)_3]_2Sb_2S_5 \cdot 0.55H_2O$ and (b) $[Fe(en)_3]_2Sb_4S_8$. The solid line shows the fit to the Curie–Weiss expression above 200 K.

The crystal structure of $[Fe(en)_3]_2Sb_4S_8$ (**2**) is very similar to those of $[M(en)_3]_2Sb_4S_8$ (M = Co, Ni) [7], consistent with the suggestion, based on comparison of unit cell parameters, that all three materials are isostructural. Compound **2** contains SbS_2^- chains directed along [0 0 1] (Fig. 7). The SbS_2^- chains may be considered as a polymeric version of the $Sb_2S_5^{4-}$ dimeric units

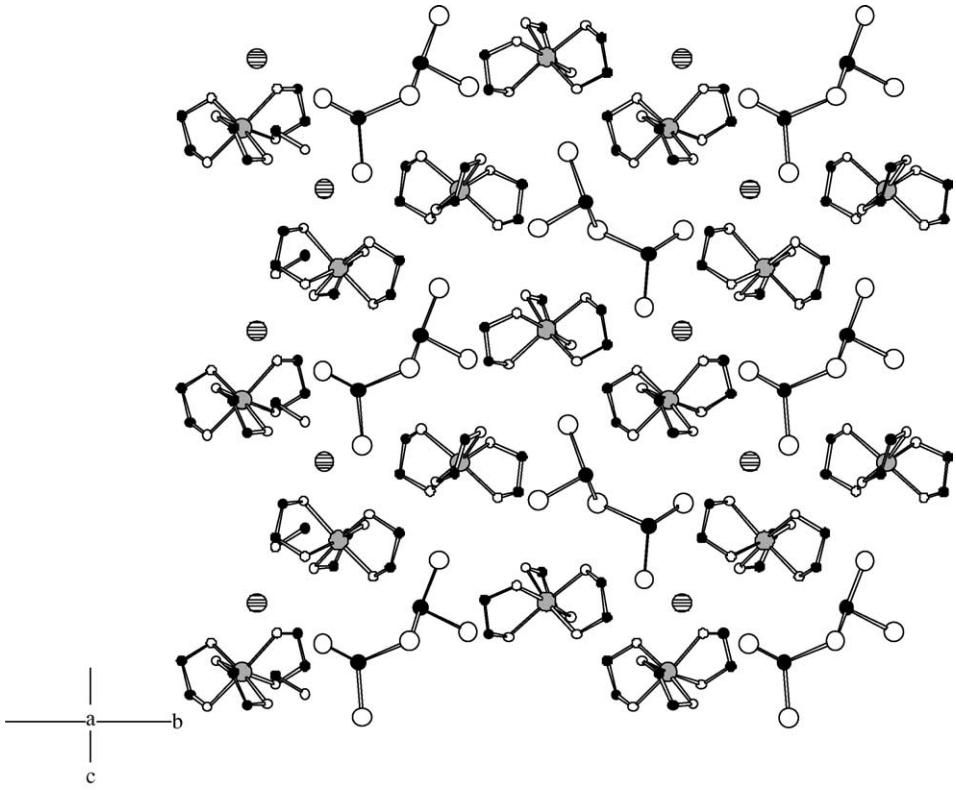


Fig. 3. View along [1 0 0] of one layer of $Sb_2S_5^{4-}$ anions and $Fe(en)_3^{2+}$ cationic complexes in **1**. *Key*: antimony, large solid circles; sulfur, large open circles; iron, large shaded circles; carbon, small solid circles; nitrogen, small open circles; oxygen, large hashed circles.

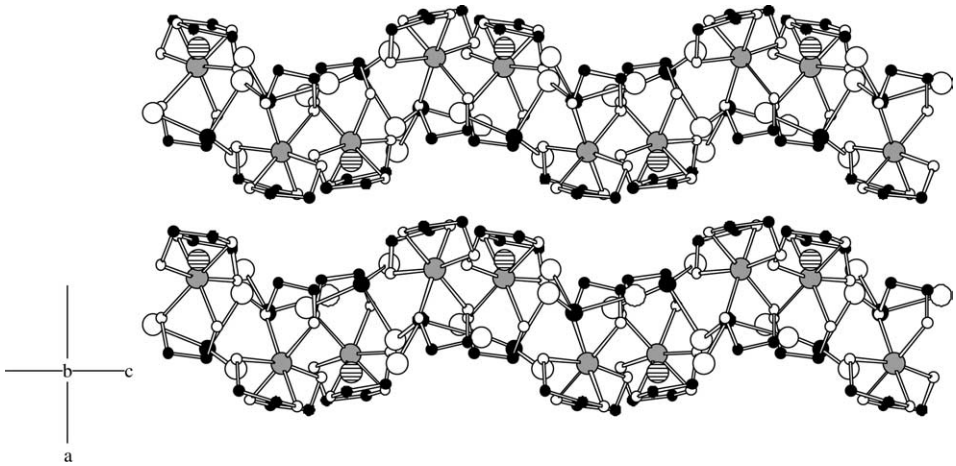


Fig. 4. View along [0 1 0] of the stacking of the layers of $Sb_2S_5^{4-}$ anions and $Fe(en)_3^{2+}$ cationic complexes in $[Fe(en)_3]_2Sb_2S_5 \cdot 0.55H_2O$ (**1**). *Key* as for Fig. 3.

found in **1**, in which vertex linking of SbS_3^{3-} trigonal pyramids is extended into infinite chains. There are two crystallographically distinct SbS_2^- chains, in which the bridging Sb–S bond distances range from 2.458(2) to 2.484(2) Å. The terminal Sb–S distances are slightly shorter and lie in the range 2.317(2)–2.364(2) Å. S–Sb–S angles range from 99.95(5)° to 100.15(5)°, which are typical for pyramidal SbS_3 units. Unusually for this class of material, there is only one longer Sb···S interaction (Sb(3)···S(8′) = 3.62 Å) within the sum of the van der Waals' radii of antimony and sulfur (ca. 3.8 Å), which corresponds to a very weak intrachain Sb···S secondary interaction in one of the anionic chains. The SbS_2^- chains are essentially isolated, as

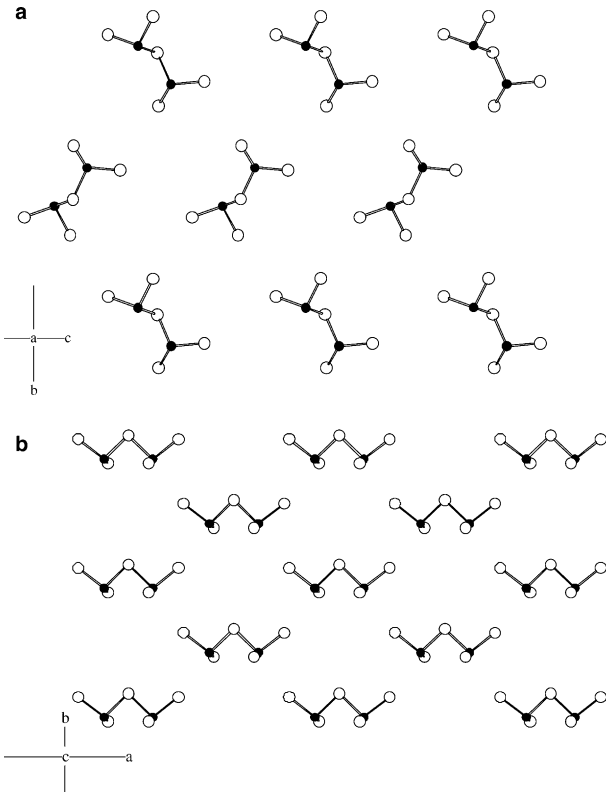


Fig. 5. Comparison of the arrangements of the $Sb_2S_5^{4-}$ anions in a single layer of (a) $[Fe(en)_3]_2Sb_2S_5 \cdot 0.55H_2O$ and (b) $SrSb_2S_5 \cdot 0.15H_2O$ [28]. For clarity, the $Fe(en)_3^{2+}$ cations are omitted from the former. *Key* as for Fig. 3.

each is surrounded by discrete $Fe(en)_3^{2+}$ complexes in both the [1 0 0] and [0 1 0] directions. There are two crystallographically distinct iron cations, in which. the Fe–N distances range from 2.184(4) to 2.241(5) Å, while

Table 3
Selected bond lengths (Å), angles (°) and bond valences (v.u.) for the $Sb_4S_8^{4-}$ anion in $[Fe(en)_3]_2Sb_4S_8$ (**2**)

		v[a]
Sb(1)–S(1)	2.4885(15)	0.90
Sb(1)–S(2)	2.4584(17)	0.98
Sb(1)–S(3)	2.3464(16)	1.32
		3.20
Sb(2)–S(1)	2.4779(17)	0.92
Sb(2)–S(2)	2.4596(14)	0.97
Sb(2)–S(4)	2.3170(17)	1.43
		3.32
Sb(3)–S(5)	2.4699(15)	0.95
Sb(3)–S(6)	2.4529(16)	0.99
Sb(3)–S(7)	2.3643(15)	1.26
		3.20
Sb(4)–S(5)	2.4843(16)	0.91
Sb(4)–S(6)[i]	2.4560(14)	0.98
Sb(4)–S(8)	2.3360(16)	1.36
		3.25
S(1)–Sb(1)–S(2)	94.72(6)	
S(1)–Sb(1)–S(3)	100.28(5)	
S(2)–Sb(1)–S(3)	100.60(6)	
S(1)–Sb(2)–S(2)[i]	98.83(5)	
S(1)–Sb(2)–S(4)	99.03(6)	
S(2)[i]–Sb(2)–S(4)	101.38(6)	
S(5)–Sb(3)–S(6)	98.45(6)	
S(5)–Sb(3)–S(7)	99.84(5)	
S(6)–Sb(3)–S(7)	97.93(6)	
S(5)–Sb(4)–S(6)[i]	100.15(5)	
S(5)–Sb(4)–S(8)	97.47(6)	
S(6)[i]–Sb(4)–S(8)	99.37(5)	
Sb(1)–S(1)–Sb(2)	95.01(6)	
Sb(1)–S(2)–Sb(2)[ii]	101.96(6)	
Sb(3)–S(5)–Sb(4)	96.69(6)	
Sb(3)–S(6)–Sb(4)[ii]	99.95(5)	

[a] Bond valences and their sums calculated using parameters from [34].
[i] x, $3/2 - y$, $z - 1/2$.
[ii] x, $3/2 - y$, $z + 1/2$.

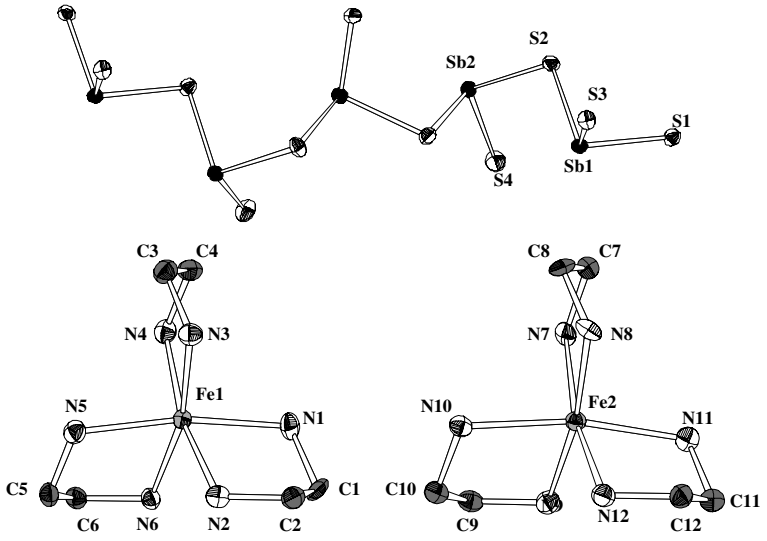


Fig. 6. Local coordination of the anions and cations in $[Fe(en)_3]_2Sb_4S_8$ (**2**) showing the atom labelling scheme and thermal ellipsoids at 50% probability (**2**). The second SbS_2^- chain containing Sb(3), Sb(4) and S(5)–S(8) has essentially the same atomic arrangement as the one shown. For each of the crystallographically distinct iron complexes, only one of the two conformations is shown.

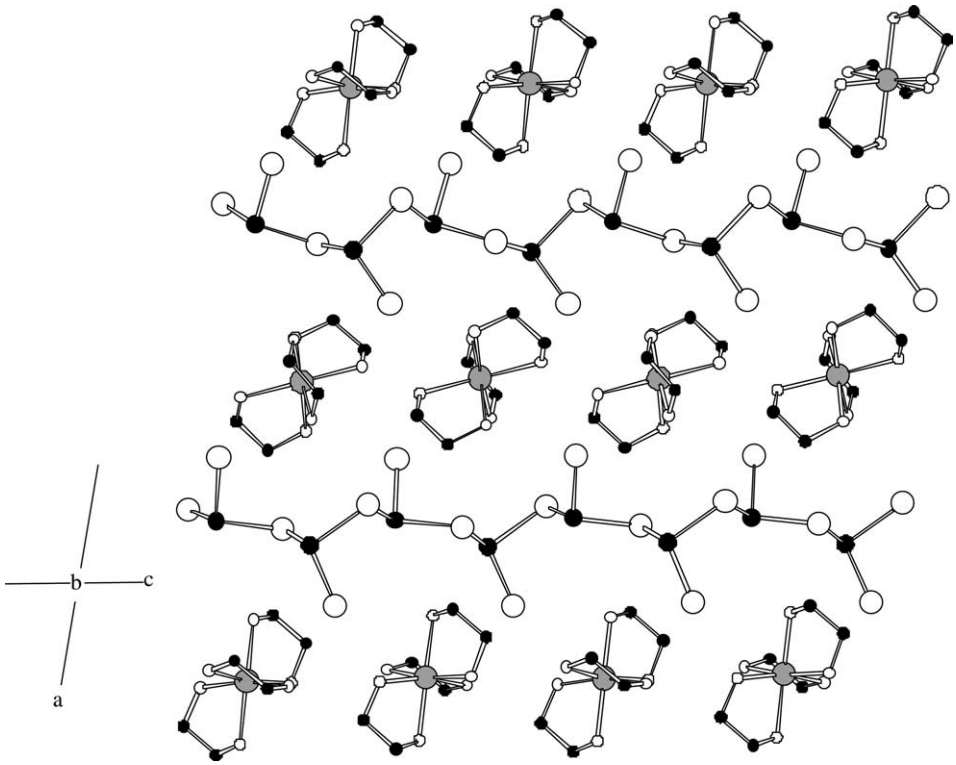


Fig. 7. View along [0 1 0] of the arrangement of SbS_2^- chains and $Fe(en)_3^{2+}$ cations in $[Fe(en)_3]_2Sb_4S_8$ (**2**). *Key* as for Fig. 3.

(*cis*) N–Fe–N angles lie between 78.9(2)° and 97.8(2)°. These are similar to the bond lengths and angles of the $[Fe(en)_3]^{2+}$ cations in $[Fe(en)_3]_2Sb_2S_5 \cdot 0.55H_2O$ (Table 2). Chains of Fe(1) or Fe(2) cations are directed along the *c*-axis, with neighbouring cations being related by the *c*-glide plane, thereby generating an alternating arrangement of complexes with Δ(λλλ) and Λ(δδδ) conformations, similar to that observed in $[Co(en)_3]Sb_2S_4$ [7]. Sulfur–nitrogen distances in the range of 3.32–3.50 Å, suggest an extensive network of hydrogen bonds between anions and cations.

In conclusion, we have succeeded in synthesising, in the presence of ethylenediamine, the new compound $[Fe(en)_3]_2Sb_2S_5 \cdot 0.55H_2O$ (**1**), which provides the first example of a thioantimonate(III) templated by a cationic transition-metal complex to contain discrete $Sb_2S_5^{4-}$ anions. This result is in marked contrast with previous reactions carried out in ethylenediamine, which usually generate $Sb_4S_7^{2-}$ chains. The isolation of the $Sb_2S_5^{4-}$ anion provides support for the growing belief that synthesis of thioantimonates under solvothermal conditions proceeds via relatively simple molecular building blocks. Further support for this view is provided by our observation that a relatively modest increase in reaction temperature produces, from the same reaction mixture, a product, $[Fe(en)_3]_2Sb_4S_8$ (**2**), in which the thioantimonate network may be considered to arise from the polymerisation of $Sb_2S_5^{4-}$ units to form infinite SbS_2^- chains.

4. Supplementary material

CCDC-245806 (**1**) and CCDC-245807 (**2**) contain the supplementary crystallographic data for this paper. These data can be obtained free of charge from The Director, CCDC, 12 Union Road, Cambridge, CB2 1EZ, UK (fax: +44 1223 336 033; e-mail: deposit@ccdc.cam.ac.uk or at www.ccdc.cam.ac.uk/conts/retrieving.html).

Acknowledgements

The authors acknowledge financial support for this work from the UK EPSRC and thank Dr A.R. Cowley, University of Oxford, for assistance in the collection of single-crystal X-ray diffraction data. A.M.C. also thanks The Leverhulme Trust for a Research Fellowship.

References

[1] R.L. Bedard, S.T. Wilson, L.D. Vail, J.M. Bennett, E.M. Flanigen, in: P.A. Jacobs, R.A. van Santen (Eds.), Zeolites: Facts, Figures, Future, Elsevier, Amsterdam, 1989.
[2] J. Li, Z. Chen, R.J. Wang, D.M. Proserpio, Coord. Chem. Rev. 190–192 (1999) 707.
[3] T. Jiang, A. Lough, G.A. Ozin, R.L. Bedard, R. Broach, J. Mater. Chem. 8 (1998) 721.
[4] W.S. Sheldrick, M. Wachold, Coord. Chem. Rev. 176 (1998) 211.
[5] J.B. Parise, Y. Ko, Chem. Mater. 4 (1992) 1446.

[6] W. Bensch, M. Schur, Z. Naturforsch. B 52 (1997) 405.
[7] H.O. Stephan, M.G. Kanatzidis, Inorg. Chem. 36 (1997) 6050.
[8] K. Tan, Y. Ko, J.B. Parise, J.H. Park, A. Darovsky, Chem. Mater. 8 (1996) 2510.
[9] K. Tan, Y. Ko, J.B. Parise, Acta Crystallogr., Sect. C 50 (1994) 1439.
[10] X.Q. Wang, Eur. J. Solid State Inorg. Chem. 32 (1995) 303.
[11] A.V. Powell, S. Boissière, A.M. Chippindale, Chem. Mater. 12 (2000) 182.
[12] P.T. Wood, G.L. Schimek, J.W. Kolis, Chem. Mater. 8 (1996) 721.
[13] P. Lemoine, D. Carre, F. Robert, Acta Crystallogr., Sect. C 47 (1991) 938.
[14] H.O. Stephan, M.G. Kanatzidis, J. Am. Chem. Soc. 118 (1996) 12226.
[15] M. Schur, A. Gruhl, C. Näther, I. Jeß, W. Bensch, Z. Naturforsch. B 54 (1999) 1524.
[16] A. Pfitzner, Z. Kristallogr. 213 (1998) 228.
[17] K.A. Schönau, S.A.T. Redfern, J. Appl. Phys. 92 (2002) 7415.
[18] N. Rey, J.C. Jumas, J. Olivier-Fourcade, E. Philippot, Acta Crystallogr., Sect. C 40 (1984) 1655.
[19] M. Schur, H. Rijnberk, C. Näther, W. Bensch, Polyhedron 18 (1999) 101.
[20] W. Bensch, C. Näther, R. Stähler, Chem. Commun. (2001) 477.
[21] L. Engelke, W. Bensch, Acta Crystallogr., Sect. E 59 (2003) m378.
[22] R. Kiebach, F. Studt, C. Näther, W. Bensch, Eur. J. Inorg. Chem. (2004) 2553.
[23] G. Cordier, H. Schäfer, Rev. Chim. Miner. 18 (1981) 218.
[24] M. Schur, C. Näther, W. Bensch, Z. Naturforsch. B 56 (2001) 79.
[25] M. Schur, W. Bensch, Z. Naturforsch. B 57 (2002) 1.
[26] W. Bensch, M. Schur, Eur. J. Solid State Inorg. Chem. 33 (1996) 1149.
[27] M. Schäfer, C. Näther, N. Lehnert, W. Bensch, Inorg. Chem. 43 (2004) 2914.
[28] G. Cordier, H. Schäfer, C. Schwidetzky, Rev. Chim. Miner. 22 (1985) 722.
[29] G. Cordier, C. Schwidetzky, H. Schäfer, Rev. Chim. Miner. 22 (1985) 93.
[30] Z. Otinowski, DENZO, Department of Molecular Biophysics and Biochemistry, Yale University, New Haven, CT, 1993.
[31] APEX-2 Software, Bruker-AXS, Madison, WI, USA, 2004.
[32] A. Altomare, G. Cascarano, C. Giacovazzo, A. Guangliardi, M. Burla, G. Polidori, M. Camalli, J. Appl. Crystallogr., Sect. A 27 (1994) 435.
[33] D.J. Watkin, C.K. Prout, J.R. Carruthers, P.W. Betteridge, CRYSTALS, Issue 10, Chemical Crystallography Laboratory, University of Oxford, Oxford, 1996.
[34] N.E. Brese, M. O'Keeffe, Acta Crystallogr., Sect. B 47 (1991) 192.
[35] Z. Chen, R. Wang, X. Huang, J. Li, Acta Crystallogr., Sect. C 56 (2000) 1100.
[36] C. Näther, F. Wendland, W. Bensch, Acta Crystallogr., Sect. E 59 (2003) m119.

$Na_2SiO_3 \cdot 9H_2O$, 99% $Na_2WO_4 \cdot 2H_2O$, 99% $Na_2MoO_4 \cdot 2H_2O$, 99% 1,4-dioxane, 99.5% KCl, and 35–37% hydrochloric acid (Wako). Infrared absorption spectra were recorded as a KBr pellet on a JASCO FT/IR-460 spectrometer.

2.2. Preparation

0.73 g (3 mmol) of $Na_2MoO_4 \cdot 2H_2O$ was dissolved in 7 mL water, followed by the addition of 10 mL of 12 M HCl and 10 mL of 1,4-dioxane. To this solution, 2.45 g (1 mmol) of $Na_9SiW_9O_{34}H \cdot 23H_2O$ [15] and 1.49 g (20 mmol) of KCl in 10 mL water were added. Yellow plate crystals of the title compound precipitated after a day.

2.3. Crystal structure determination

$K_4[A\text{-}\beta\text{-}SiMo_3W_9O_{40}] \cdot 9H_2O$ (formula weight 2929.10) crystallizes in orthorhombic, space group *Pnma* (no. 62) with $a = 20.4174(12)$ Å, $b = 15.3906(5)$ Å, $c = 12.9537(9)$ Å, $Z = 4$. A crystal with the dimension of $0.12 \times 0.12 \times 0.04$ mm was mounted on a Rigaku RAXIS RAPID imaging plate diffractometer with a rotating anode X-ray generator (Mo Kα radiation, $\lambda = 0.71069$ Å). Diffraction images were collected by the oscillation method at 93 K. A total of 33 507 reflections were indexed and integrated using PROCESS-AUTO [16], of which 4670 were unique ($R_{int} = 0.0704$). The effect of absorption was corrected by the numerical method [17] based on the crystal shape measured using a CCD camera [18]. The structure was solved by the direct method using SHELXS-97 [19] and refined by the full-matrix least-squares method on F^2 using SHELXL-97 [20]. The final agreement factors are $R_1 = 0.0348$ for 4483 reflections with $F_o^2 > 2\sigma(F_o^2)$ and $wR_2 = 0.0771$ for all reflections.

3. Results and discussion

The title compound, $K_4[A\text{-}\beta\text{-}SiMo_3W_9O_{40}] \cdot 9H_2O$, crystallized in the isomorphous structure with $K_4[\beta\text{-}SiW_{12}O_{40}] \cdot 9H_2O$ [21] and $K_4[\beta_1\text{-}SiMoW_{11}O_{40}] \cdot 9H_2O$ [11]. The $[A\text{-}\beta\text{-}SiMo_3W_9O_{40}]^{4-}$ anion exhibits the β-isomer [22] of the Keggin [8] structure and the arrangement of its nine W atoms conform to the A-type β-XM_9 geometry [23]. The anion consists of three MoW_2O_{13} units of edge-sharing one MoO_6 and two WO_6 octahedra and one W_3O_{13} unit of edge-sharing three WO_6 octahedra. The W_3O_{13} unit is rotated by 60° with respect to the α-Keggin structure. The three Mo atoms occupy the three metal positions at the opposite side of the β-junction, which is the same arrangement with the A-β-$[PMo_3W_9O_{40}]^{3-}$ anion in A-β-$[N(CH_3)_4]_3[PMo_3W_9O_{40}]$ [13] and A-β-$[N(C_4H_9)_4]_3[PMo_3W_9O_{40}]$ [14] and is rationally expected from the structure of the precursor, $Na_9SiW_9O_{34}H \cdot 23H_2O$ [24]. The $[A\text{-}\beta\text{-}SiMo_3W_9O_{40}]^{4-}$ anion is located on the crystallographic mirror plane and thus the half of the anion is crystallographically independent. Fig. 1 illustrates the structure of the anion and the geometrical parameters are summarized in Table 1. Oxygen atoms are numbered as follows: O1–O7 for the terminal O atoms, O8–O14 for the μ_2-O atoms at the linkage of corner-shared octahedra, O15–O21 for the μ_2-O atoms at the linkage of edge-shared octahedra and O22–O24 for the μ_4-O atoms bridging three Mo/W atoms and the central Si atom.

In the $[A\text{-}\beta\text{-}SiMo_3W_9O_{40}]^{4-}$ anion, the distances of the terminal W–O bonds [1.705–1.713 Å, average 1.709 Å] are longer by ca. 0.03 Å than those of the terminal Mo–O bonds [1.668 and 1.678 Å]. The distances to the μ_4-O atoms (O22–O24) that are *trans* to the terminal W/Mo–O bonds are in turn ca. 0.04 Å shorter for the W atoms [2.325–2.376 Å, average 2.338 Å] than for the Mo atoms [2.379 and 2.381 Å]. As for the doubly bridging oxygen atoms (O8–O21), no distinct differences are observed: 1.878–1.965 Å [average 1.919 Å] for Mo–μ_2-O and 1.891–1.954 Å [average 1.919 Å] for W–μ_2-O. The Mo···W distances for the edge-shared octahedra (those within the same MoW_2O_{13} units) are 3.351–3.384 Å [average 3.362 Å], which is slightly longer than the W···W distances for the edge-shared octahedra [3.301–3.346 Å, average 3.323 Å]. The W···W and W···Mo distances between two $(MoW)_3O_{13}$ units seem to be more strongly affected by the geometrical distortion upon forming the β-isomer [25] than the substitu-

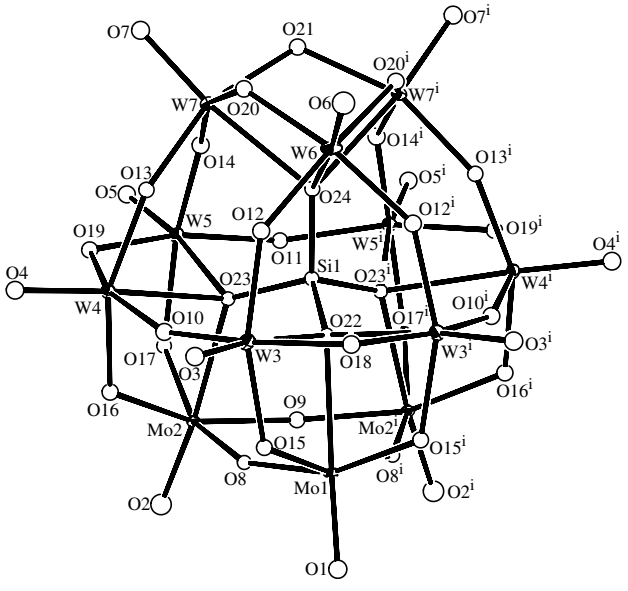


Fig. 1. An ORTEP [28] view of the $[A\text{-}\beta\text{-}SiMo_3W_9O_{40}]^{4-}$ anion. Thermal ellipsoids are scaled to enclose 50% probability levels. [Symmetry code: (i) x, $1/2 - y$, z.]

Table 1
Selected interatomic distances (Å) for $K_4[A\text{-}\beta\text{-}SiMo_3W_9O_{40}]\cdot 9H_2O$

Si–O distances			
Si1–O24	1.628 (9)	Si1–O23	1.628 (6)
Si1–O22	1.632 (9)		
Mo–O distances			
Mo1–O1	1.668 (9)	Mo1–O8	1.878 (6)
Mo1–O15	1.965 (6)	Mo1–O22	2.379 (9)
Mo2–O2	1.678 (7)	Mo2–O17	1.905 (6)
Mo2–O9	1.910 (2)	Mo2–O16	1.914 (6)
Mo2–O8	1.936 (6)	Mo2–O23	2.381 (6)
W–O distances			
W3–O3	1.708 (6)	W3–O10	1.891 (6)
W3–O15	1.916 (6)	W3–O12	1.923 (6)
W3–O18	1.924 (5)	W3–O22	2.326 (6)
W4–O4	1.713 (7)	W4–O19	1.903 (6)
W4–O13	1.916 (6)	W4–O16	1.929 (6)
W4–O10	1.932 (6)	W4–O23	2.330 (6)
W5–O5	1.705 (6)	W5–O14	1.892 (6)
W5–O11	1.900 (2)	W5–O19	1.925 (6)
W5–O17	1.954 (6)	W5–O23	2.325 (6)
W6–O6	1.709 (10)	W6–O12	1.909 (6)
W6–O20	1.944 (6)	W6–O24	2.376 (9)
W7–O7	1.708 (6)	W7–O20	1.894 (6)
W7–O13	1.907 (6)	W7–O21	1.922 (4)
W7–O14	1.953 (6)	W7–O24	2.334 (6)
M···M distances for the edge-shared octahedra			
Mo1···W3	3.3843 (10)	Mo2···W4	3.3505 (8)
Mo2···W5	3.3525 (8)	W3···W3^{i}	3.3136 (7)
W4···W5	3.3011 (5)	W6···W7	3.3464 (6)
W7···W7^{i}	3.3325 (7)		
M···M distances for the corner shared octahedra			
Mo1···Mo2	3.6965 (11)	Mo2···Mo2^{i}	3.7287 (14)
W3···W4	3.7492 (5)	W5···W5^{i}	3.7101 (7)
W3···W6	3.6564 (6)	W4···W7	3.6568 (5)
W5···W7	3.6601 (6)		

Symmetry code: (i) x, $1/2 - y$, z.

Table 2
Comparison of the infrared absorption data between $K_4[A\text{-}\beta\text{-}SiMo_3W_9O_{40}]\cdot 9H_2O$ and $K_4[\beta\text{-}SiW_{12}O_{40}]\cdot 9H_2O$

Compound	ν (cm^{-1})	Ref.
$K_4[A\text{-}\beta\text{-}SiMo_3W_9O_{40}]\cdot 9H_2O$	1011(w), 979(s), 912(vs), 860(vw), 788(vs), 546(w), 520(m)	this work
$K_4[\beta\text{-}SiW_{12}O_{40}]\cdot 9H_2O$	1018(w), 984(s), 917(vs), 865(vw), 791(vs), 550(sh), 530(m), 510(sh)	[26]

tion with Mo: W···W distances at the β junction [3.656–3.660 Å, average 3.658 Å] are shorter than the other W···W and W···Mo distances [3.697–3.749 Å, average 3.721 Å].

The infrared absorption spectroscopic data of $K_4[A\text{-}\beta\text{-}SiMo_3W_9O_{40}]\cdot 9H_2O$ are listed in Table 2 together with those for $K_4[\beta\text{-}SiW_{12}O_{40}]\cdot 9H_2O$ cited from [26]. For the α-isomers, Rocchiccioli-Deltcheff et al. [27] reported that the vibrational frequencies for the terminal M–O stretching modes are lower for the molybdates than for the tungstates. The same tendency can be retrieved from the data of the β-isomers [26]. The shifts in the wavenumbers by changing from $K_4[\beta\text{-}SiW_{12}O_{40}]\cdot 9H_2O$ to $K_4[A\text{-}\beta\text{-}SiMo_3W_9O_{40}]\cdot 9H_2O$ are approximately 20–40% of those by changing from $[(n\text{-}C_4H_9)_4N]_4[\beta\text{-}SiW_{12}O_{40}]$ to $[(n\text{-}C_4H_9)_4N]_4[\beta\text{-}SiMo_{12}O_{40}]$ and from $[(n\text{-}C_4H_9)_4N]_4[\beta\text{-}GeW_{12}O_{40}]$ to $[(n\text{-}C_4H_9)_4N]_4[\beta\text{-}GeMo_{12}O_{40}]\cdot xH_2O$, reflecting the partial substitution of W with Mo.

4. Supplementary material

Crystallographic data for $K_4[A\text{-}\beta\text{-}SiMo_3W_9O_{40}]\cdot 9H_2O$ have been deposited with the Fachinformationszentrum Karlsruhe, CSD-No. 415281.

Acknowledgments

T.O. thanks CREST (Core Research for Evolutional Science and Technology), the Japanese Science and Technology Agency (JST) and the Japanese Society for the Promotion of Science (Grant-in-Aid for Scientific Research No. 15550047) for partial funding for this research.

References

[1] M.T. Pope, Heteropoly and Isopoy Oxometalates, Springer, Berlin, 1983.
[2] C.L. Hill (Ed.), Thematic Issue on Polyoxometalates, Chem. Rev. 98 (1998) 1.
[3] T. Yamase, T. Ozeki, H. Sakamoto, S. Nishiya, A. Yamamoto, Bull. Chem. Soc. Jpn. 66 (1993) 103.
[4] Y. Lin, T.J.R. Weakley, B. Rapko, R.G. Finke, Inorg. Chem. 32 (1993) 5095.
[5] Y. Sakai, K. Yoza, C.N. Kato, K. Nomiya, J. Chem. Soc., Dalton Trans. (2003) 3581.
[6] W.G. Klemperer, A. Yagasaki, Chem. Lett. (1989) 2041.
[7] M. Pohl, Y. Lin, T.J.R. Weakley, K. Nomiya, M. Kaneko, H. Weiner, R.G. Finke, Inorg. Chem. 34 (1995) 767.
[8] J.F. Keggin, Nature 131 (1933) 908.
[9] I. Kawafune, H. Tamura, G. Matsubayashi, Bull. Chem. Soc. Jpn. 70 (1997) 2455.
[10] K. Nomiya, T. Hasegawa, R. Noguchi, K. Nomura, M. Takahashi, H. Yokoyama, Chem. Lett. (2001) 1278.
[11] F. Robert, A. Tézé, G. Hervé, Y. Jeannin, Acta Crystallogr., Sect. B 36 (1980) 11.
[12] A. Leclaire, M.M. Borel, J. Chardon, B. Raveau, Mater. Res. Bull. 30 (1995) 1075.
[13] I. Kawafune, G. Matsubayashi, Chem. Lett. (1992) 1869.
[14] I. Kawafune, G. Matsubayashi, Bull. Chem. Soc. Jpn. 67 (1994) 694.
[15] A. Tézé, G. Hervé, Inorg. Synth. 27 (1990) 85.
[16] Rigaku Corporation, PROCESS-AUTO. Automatic Data Acquisition and Processing Package for Imaging Plate Diffractometer, Tokyo, Japan, 1998.
[17] T. Higashi, Numabs – Numerical Absorption Correction, Rigaku Corporation, Tokyo, Japan, 1999.
[18] T. Higashi, Shape – Program to obtain Crystal Shape using CCD camera, Rigaku Corporation, Tokyo, Japan, 1999.
[19] G.M. Sheldrick, Acta Crystallogr., Sect. A 46 (1990) 467.
[20] G.M. Sheldrick, SHELXL-97, Program for the Crystal Structure Refinement, University of Göttingen, Göttingen, Germany, 1997.
[21] K.Y. Matsumoto, A. Kobayashi, Y. Sasaki, Bull. Chem. Soc. Jpn. 48 (1975) 3146.
[22] L.C.W. Baker, J.S. Figgis, J. Am. Chem. Soc. 92 (1970) 3794.
[23] G. Hervé, A. Tézé, Inorg. Chem. 16 (1977) 2115.
[24] F. Robert, A. Tézé, Acta Crystallogr., Sect. B 37 (1981) 318.
[25] W.A. Neiwert, J.J. Cowan, K.I. Hardcastle, C.L. Hill, I.A. Weinstock, Inorg. Chem. 41 (2002) 6950.
[26] C. Rocchiccioli-Deltcheff, M. Fournier, R. Franck, R. Thouvenot, Inorg. Chem. 22 (1983) 207.
[27] C. Rocchiccioli-Deltcheff, R. Thouvenot, R. Franck, Spectrochim. Acta, Part A 32 (1976) 587.
[28] M.N. Burnett, C.K. Johnson, ORTEP-III, ORNL-6895, Oak Ridge National Laboratory, Oak Ridge, TN, 1996.

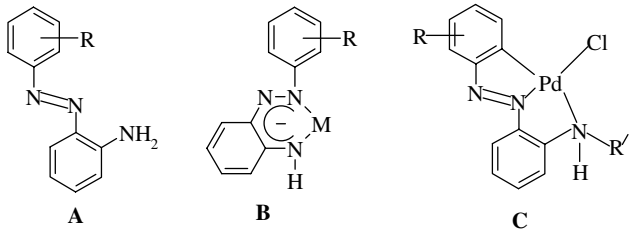


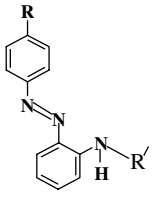
Chart 1.

structure of one of the complexes has been determined to confirm the molecular structure. Weak unsupported dimers have been recognized in the crystal lattice.

2. Results and discussion

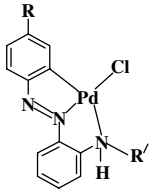
2.1. Syntheses

The orange coloured 2-arylazo-1*N*-alkyl aniline, **1a**–**11a** (Chart 2) ligands were prepared by refluxing 2-(arylazo) anilines with the appropriate alkyl halide in ethanol or DMF in the presence of potassium carbonate (Scheme 1). The product formations were monitored on a TLC plate. Eleven ligands were prepared by modifying R′ and R as given in Chart 2. The R′ substituents were chosen on the basis of increasing chain length (H_3C–, H_5C_2–, $H_{17}C_8$–,) and varying the probable binding sites (CH_2=CH–CH_2–, 2-$MeOC_6H_4CH_2$–, $C_6H_5CH_2$–, EtO_2CCH_2–). Reaction of **1a**–**11a** with sodium tetrachloropalladate in methanol at room temperature afforded brown coloured complexes of composition **1b**–**11b** (Scheme 1) as shown in (Chart 1). The orthopalladated complexes are formed upon substitution of the *ortho* aryl proton from the azobenzene fragment of the ligand precursors **1a**–**11a**. Eleven orthopalladated complexes were prepared, where the binding modes (C,N,N) of the ligands were identical (^{1}H NMR and X-ray, see below), unlike 2-(arylazo) aniline [6]. One of the important observations is the coordination of the secondary amino nitrogen without dissociating the proton. In the case of other azoamine ligands, the secondary amino groups bind the metals only when the amino proton gets dissociated [7]. Thus the complexes, **1b**–**11b**, are the first family of orthopalladated azoamine molecules. The formation of a metal–carbon bond has been presumed to occur as a result of prior binding with a suitable hetero donor atom fulfilling the electronic criteria and appropriate geometry about the metal with respect to the *ortho* carbon atom.



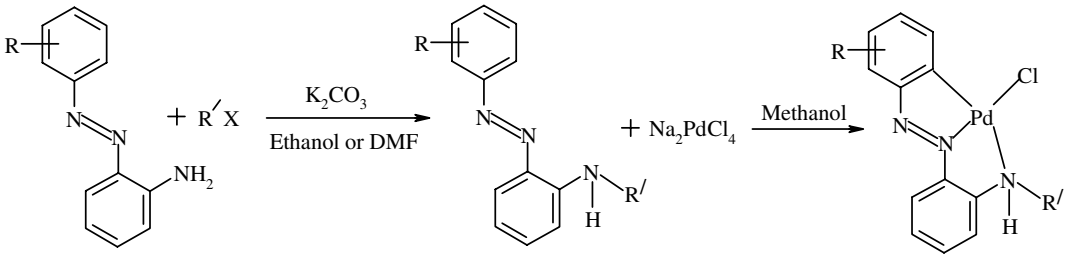
Ligand

Ligand	R	R′	Complex
1a	H	CH_3	**1b**
2a	CH_3	CH_3	**2b**
3a	H	C_2H_5	**3b**
4a	CH_3	C_2H_5	**4b**
5a	CH_3	C_8H_{17}	**5b**
6a	CH_3	CH_2CHCH_2	**6b**
7a	CH_3	2-$MeOC_6H_4CH_2$	**7b**
8a	H	CH_2Ph	**8b**
9a	CH_3	CH_2Ph	**9b**
10a	Cl	CH_2Ph	**10b**
11a	CH_3	$CH_2CO_2C_2H_5$	**11b**



Complex

Chart 2.



Scheme 1.

2.2. Characterisation

The ligands, **1a**–**11a**, and the corresponding orthopalladated complexes, **1b**–**11b**, exhibit characteristic UV–Vis spectra. Representative spectra for **9a** and **9b** have been shown in Fig. 1. It is interesting to observe that the UV–Vis spectra of all the brown orthopalladated complexes are similar, with a low energy split band in the range 490–470 nm and a structured band within the range 410–360 nm. The spectral data for all the ligands and complexes are collected in Table 1.

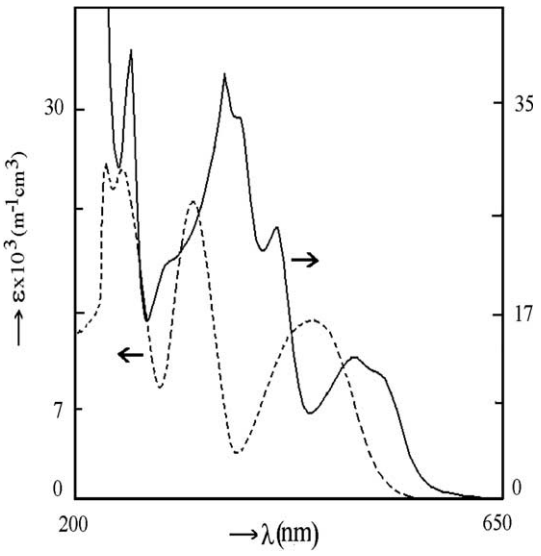


Fig. 1. UV–Vis spectra of **9a** (---) and **9b** (—). The arrows indicate scales of the corresponding spectra.

The ligands, **1a**–**11a**, displayed a ν_{N-H} absorption as a single band in the range of 3488–3413 cm^{-1}, whereas for the complexes **1b**–**11b**, the ν_{N-H} band appeared within the range 3283–3071 cm^{-1} in the IR spectra. The $\nu_{N=N}$ band (1518–1506 cm^{-1}) of all the ligands shifted to lower frequency (1394–1383 cm^{-1}) in the complexes, consistent with coordination of the azo nitrogen. The ν_{Pd-Cl} absorption of the palladium complexes was observed in the range 296–288 cm^{-1}. The spectral data for all the ligands and complexes are collected in Table 1.

The ^1H NMR spectra of all the ligands and complexes were recorded. The spectra are consistent with the composition and structure. However, to avoid unnecessary inclusion, we have tabulated only the data for the complexes in Table 2. The ^1H NMR data of the ligands are given in Table 3.

Some important features of the ^1H NMR spectra that occur upon palladation are as follows: (i) The N–H resonance of the ligands (δ 9.58–8.60) is shifted to upfield (δ 8.12–6.38) in the complexes; (ii) The aromatic proton count of the complexes is one less than that of the ligands indicating orthometallation. Further, the complexes where R is Me display a singlet within the range (δ 7.29–6.61) in the aromatic region, consistent with the orthometallation. (iii) The equivalent methylene protons

Table 1
UV–Vis[a] and IR[b] spectral data

Compound	λ_{max}/nm (ε/M^{-1} cm^{-1})	ν/cm^{-1}		
		ν_{N-H}	$\nu_{N=N}$	ν_{Pd-Cl}
1a	450 (9500), 315 (18050), 250 (23840), 230 (21500)	3426	1517	
1b	490 (6300), 400 (14600), 370 (27700), 360 (28750), 248 (25540), 230 (29600)	3238	1391	293
2a	450 (31400), 325 (53950), 250 (51620), 230 (56100)	3427	1517	
2b	490 (16100), 410 (29700), 370 (42900), 360 (44500), 260 (42800), 230(51300)	3236	1386	294
3a	460 (9800), 320 (16000), 250 (16700), 230 (17500)	3414	1514	
3b	490 (6500), 410 (15300), 370 (29830), 360 (30700), 250 (27050), 230 (38100)	3225	1388	296
4a	460 (13500), 325 (20900), 250 (20200), 230 (22000)	3413	1514	
4b	490 (8800), 410 (16850), 370 (24650), 360 (25500), 260 (23820), 230 (28800)	3229	1383	294
5a	465 (27300), 315 (40300), 250 (59300), 230 (60800)	3417	1514	
5b	490 (13150), 410 (24900), 375 (36550), 360 (37300), 260 (36500), 230 (47650)	3099	1391	290
6a	455 (18700), 320 (30650), 245 (35300), 230 (38200)	3420	1513	
6b	490 (12400), 410 (23500), 375 (33900), 360 (35000), 260 (34400), 230 (44200)	3097	1394	290
7a	450 (8450), 320 (25400), 270 (31600), 230 (57200)	3420	1510	
7b	490 (6500), 410 (12700), 375 (18200), 360 (18000), 260 (20300), 230 (33400)	3283	1387	289
8a	460 (6500), 315 (17600), 230(16600)	3421	1506	
8b	490 (2050), 406 (4800), 375 (8600), 360 (9100), 250 (8560), 230 (12000)	3231	1384	289
9a	450 (12270), 325 (20503), 250 (22770), 230 (23000)	3415	1510	
9b	490 (11400), 410 (21811), 375 (30500), 360 (34200), 260 (36500)	3205	1393	293
10a	450 (8614), 320 (14570), 250 (17000), 230 (16700)	3421	1508	
10b	480 (5237), 415 (11734), 375 (11800), 360 (16000), 260 (14200), 230 (23250)	3219	1386	290
11a	430 (29600), 320 (52000), 245 (48050), 230 (50600)	3488	1518	
11b	490 (7500), 410 (14000), 370 (20200), 360 (20600), 260 (20000), 230 (25600)	3071	1390	296

[a] In dichloromethane.
[b] KBr disc.

Table 2
^{1}H NMR spectra of the complexes, **1b**–**11b**

Compound	δ[a] (X, *n*H)[b]			
	Aromatic protons	Non-aromatic protons	R (CH_3)	N–H
1b[d]	6.72(t, 1H), 6.87(d, 1H), 7.01(t, 1H), 7.22(t, 1H), 7.44(d, 1H), 7.52(m, 3H)	3.16(d, 3H)		6.38(b, 1H)
2b[d]	6.65(s, 1H), 6.80(d, 1H), 7.16(t, 1H), 7.37(d, 1H), 7.45(d, 1H), 7.49(t, 1H), 7.55(d, 1H)	3.14(d, 3H)	2.00(s, 3H)	6.47(s, 1H)
3b[d]	6.71(t, 1H), 6.85(d, 1H), 6.99(t, 1H), 7.15–7.22(m, 1H), 7.42(d, 1H), 7.53(d, 2H), 7.58(d, 1H)	1.25(t, 3H), 3.52(m, 1H), 3.65(m, 1H)		6.69(s, 1H)
4b[d]	6.68(s, 1H), 6.81(d, 1H), 7.16(t, 1H), 7.40(d, 1H), 7.47(d, 1H), 7.52(m, 2H)	1.24(t, 3H), 3.53(m, 1H), 3.65(m, 1H)	2.03(s, 3H)	6.73(b, 1H)
5b[d]	6.61(s, 1H), 6.78(d, 1H), 7.11(t, 1H), 7.33(d, 1H), 7.44(d, 1H), 7.48(t, 1H), 7.52(d, 1H)	0.81(t, 3H), 1.16–1.40(m, 12H), 3.40(b, 1H), 3.54(b, 1H),	1.99(s, 3H)	6.82(s, 1H)
6b[d]	6.81(m, 2H), 7.15(t, 1H), 7.38(d, 1H), 7.46(d, 1H), 7.48(t, 1H), 7.54(d, 1H)	4.05(b, 1H), 4.24(b, 1H), 5.08(d, 1H), 5.14(d, 1H), 6.13–6.19(m, 1H)	2.02(s, 3H)	6.68(s, 1H)
7b[d]	6.78(s, 1H), 6.81–6.86(m, 3H), 6.89(d, 1H), 7.10(t, 1H), 7.21(t, 1H), 7.27–7.32(m, 2H), 7.44(d, 1H), 7.50(d, 1H)	3.91(s, 3H), 4.17(b, 1H), 5.14(b, 1H)	2.10(s, 3H)	6.65(t, 1H)
8b[c]	7.15–7.29(m, 5H), 7.44(t, 2H), 7.54(t, 3H), 7.74(t, 2H), 7.91(t, 1H)	4.51(s, 2H)		7.93(s, 1H)
9b[c]	7.02(d, 1H), 7.09–7.13(m, 3H), 7.29(s, 1H), 7.36(d, 1H), 7.53(d, 2H), 7.61(t, 1H), 7.68(d, 1H), 7.74(d, 1H), 7.80(s, 1H)	4.52(s, 2H)	2.30(s, 3H)	7.93(s, 1H)
10b[c]	7.16(t, 3H), 7.31(d, 1H), 7.41(t, 2H), 7.52(t, 2H), 7.69(t, 1H), 7.78(d, 1H), 7.84(d, 2H)	4.54(s, 2H)		8.12(s, 1H)
11b[d]	6.82(s, 1H), 6.83(d, 1H), 7.23(t, 1H), 7.45–7.51(m, 3H) 7.55(d, 1H)	1.22(t, 3H), 4.20(m, 2H), 4.22(d, 1H), 4.40(d, 1H)	2.06(s, 3H)	6.73(b, 1H)

[a] In ppm.
[b] X = multiplicity (m = multiplet, s = singlet, d = doublet, t = triplet, b = broad), *n* = proton count.
[c] In DMSO-d_6.
[d] In $CDCl_3$.

(N–CH_2–) of R′ in the ligands become inequivalent in the complexes (excepting R′ = CH_2Ph), diagnostic for binding of the amino nitrogen. All of these features have been shown in Fig. 2, in representative spectra for **6a** and **6b**. (iv) The N–H proton resonance of the metal complexes vanishes upon shaking with D_2O, confirming its non-dissociation upon coordination.

2.3. X-ray structure

The suitable crystals of **9b** were grown by slow diffusion of hexane into a dichloromethane solution. The crystals are triclinic and the space group is $P\bar{1}$. A perspective view with the atom numbering scheme is given in Fig. 3. Selected bond distances and angles are collected in Table 4.

The asymmetric unit of **9b** contains two molecules, which are held as a weak dimer with a non-covalent Pd···Pd interaction. The geometry and bond parameters are similar in the two molecules. The molecular structure of each monomer molecule exhibits a distorted square planar geometry about the palladium, where the anionic ligand (**9a**)$^-$ binds the metal in a tridentate (C,N,N) fashion. A chloride ligand completes the tetracoordination about Pd(II). The Pd–Cl and Pd–N(azo) distances (2.312(2) and 1.943(4) Å, respectively), are within the normal range [7b]. The Pd–C bond length (1.986(5) Å) is also matched well with the Pd–C lengths

Table 3
^{1}H NMR spectra of the ligands, **1a**–**11a**

Compound	δ[a] (X, *n*H)[b]			
	Aromatic protons	Non-aromatic protons	*p*-CH_3	N–H
1a[c]	6.72–6.80(m, 2H), 7.20–7.54(m, 9H), 7.79(d, 2H), 7.81(d, 1H)	4.54(s, 2H)		9.24(s, 1H)
2a[c]	6.74–6.84(m, 2H), 7.22–7.39(m, 8H), 7.68(d, 2H), 7.84(d, 1H)	4.54(s, 2H)	2.41(s, 3H)	9.20(s, 1H)
3a[c]	6.87(t, 2H), 7.22–7.44(m, 8H), 7.72(d, 2H), 7.84(d, 1H)	4.54(s, 2H)		9.58(s, 1H)
4a[c]	6.77–6.84(m, 2H), 7.25–7.52(m, 4H), 7.80–7.87(m, 3H)	3.01(s, 3H)		8.60(s, 1H)
5a[c]	6.77(t, 2H), 7.29(t, 4H), 7.81(d, 2H), 8.10(d, 1H)	2.99(s, 3H)	2.46(s, 3H)	8.60(s, 1H)
6a[c]	6.76(t, 2H), 7.34–7.56(m, 4H), 7.77–7.94(m, 3H)	3.33–3.35(m, 2H), 1.37(t, 3H)		8.80(s, 1H)
7a[c]	6.77–6.87(m, 2H), 7.23–7.31(m, 3H), 7.75(d, 2H) 7.82(d, 1H)	3.30–3.40(m, 2H), 1.38(t, 3H)	2.43(s, 3H)	8.70(s, 1H)
8a[c]	6.74–6.79(m, 2H), 7.23–7.30(m, 3H), 7.71(d, 2H), 7.83(d, 1H)	3.94(s, 2H), 5.22(d, 1H), 5.35(d, 1H), 5.97–6.01(m, 1H),	2.41(s, 3H)	8.72(s, 1H)
9a[c]	6.79(t, 1H), 6.86(d, 2H), 6.94(t, 2H), 7.17(t, 1H), 7.18(t, 1H), 7.21(m, 3H), 7.38(d, 1H), 7.70(d, 1H)	3.79(s, 3H), 4.55(s, 2H)	2.43(s, 3H)	9.04(s, 1H)
10a[c]	6.73–6.78(m, 2H), 7.24–7.30(m, 3H), 7.70(d, 2H), 7.82(d, 1H)	3.27(d, 2H), 1.69–1.75(m, 2H) 1.44–1.50(m, 2H), 1.25–1.39(m, 8H), 0.88(t, 3H)	2.41(s, 3H)	8.85(s, 1H)
11a[c]	6.63(d, 1H), 6.86(t, 1H), 7.28(m, 3H), 7.81–7.90(m, 3H)	1.25–1.36(m, 3H), 4.08(s, 2H), 4.28–4.32(m, 2H)	2.42(s, 3H)	8.93(b, 1H)

[a] In ppm.
[b] X = multiplicity (m = multiplet, s = singlet, d = doublet, t = triplet, b = broad), *n* = proton count.
[c] In $CDCl_3$.

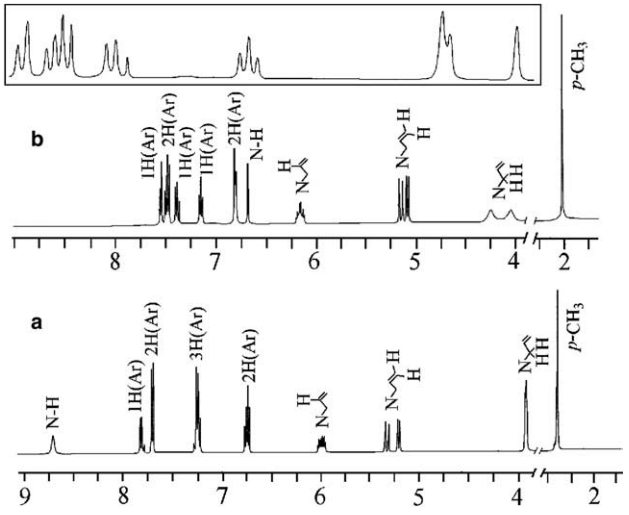


Fig. 2. The ^{1}H NMR spectra of (a) **6a** and (b) **6b** in $CDCl_3$, where *n* of *n*H(Ar) stands for the proton count. The expansion of the aromatic region (δ 6.81–7.54) of **6b** has been shown in the inset.

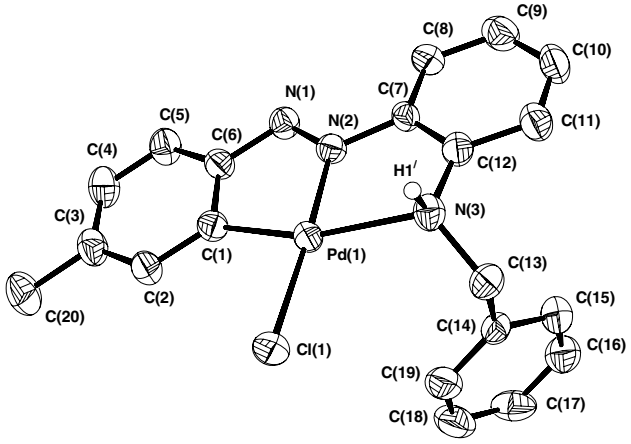


Fig. 3. Perspective view of **9b** with the atom numbering scheme. Hydrogen atoms excepting on N3 are omitted for clarity.

in other orthopalladated azo benzene complexes [8]. The Pd–N(amine) bond length (2.194(1) Å) is much longer than the Pd–N(azo) distance, presumably as a consequence of the stronger *trans* influence of the aryl carbon [9]. The N(3)–Pd–C(1) (161.17(19)°) and N(2)–Pd–Cl (177.06(13)°) bond angles deviate a little from linearity. The chelate ring bite angles are also considerably smaller [N(2)–Pd–N(3), 81.75(17)°; N(2)–Pd–C(1), 79.5(2)°] than the ideal values (90°) of a square geometry, although the atoms within the coordination sphere lie on a plane (mean deviation 0.01 Å). In fact the whole molecule, excepting the benzyl group, is planar (mean deviation 0.05 Å).

Table 4
Selected bond distances (Å) and angles (°) for **9b**

Pd(1)–C(1)	1.986(1)
Pd(1)–N(2)	1.942(1)
Pd(1)–N(3)	2.194(1)
Pd(1)–Cl(1)	2.312(2)
N(1)–C(6)	1.399(1)
N(1)–N(2)	1.266(1)
N(2)–C(7)	1.431(1)
C(7)–C(12)	1.391(1)
C(1)–C(6)	1.413(1)
N(3)–C(12)	1.465(1)
N(2)–Pd(1)–C(1)	79.5(2)
N(2)–Pd(1)–N(3)	81.7(2)
C(1)–Pd(1)–N(3)	161.1(2)
N(2)–Pd(1)–Cl(1)	177.0(1)
C(1)–Pd(1)–Cl(1)	97.9(2)
N(3)–Pd(1)–Cl(1)	100.7(1)
C(12)–N(3)–Pd(1)	106.2(3)

The dimer contained in the asymmetric unit, is held in a staggered conformation (dihedral angle is 60°) with three non-bonding inter-monomeric interactions, Pd···Pd, 3.301 Å; N(amine)···Cl, 3.256 Å and N(amine)···Pd, 3.635 Å. The dimeric unit with the non-bonding interactions is shown in Fig. 4.

However, in the packing of the molecule, no infinite stacking has been observed, where the discrete dimers are arranged in a regular pattern in the crystal lattice. A partial packing diagram has been shown in Fig. 5.

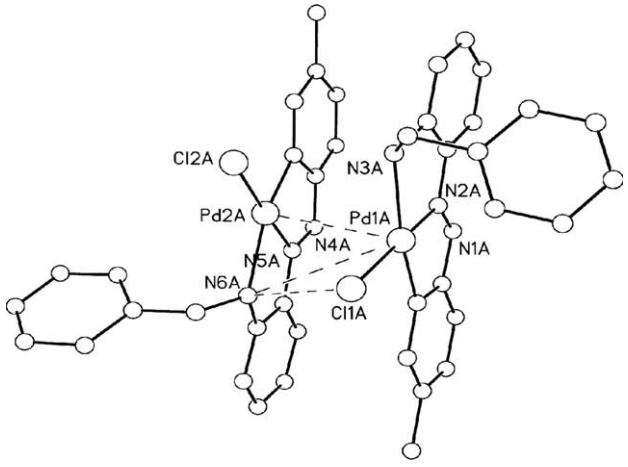


Fig. 4. A view of the dimeric unit of **9b**. The broken lines indicate the weak interactions.

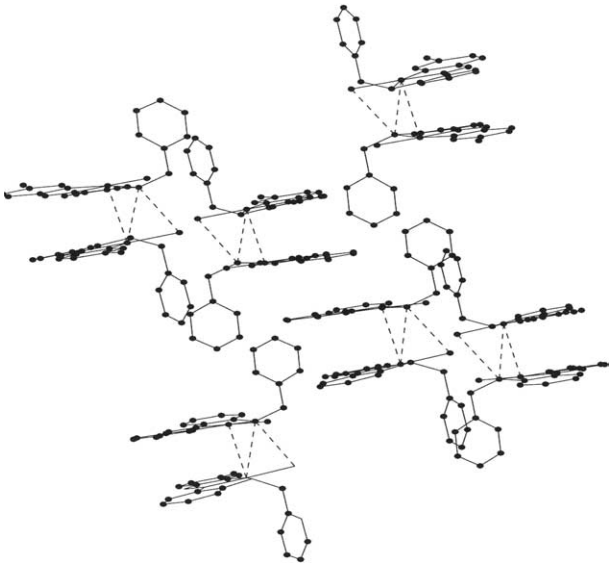


Fig. 5. Partial packing diagram of complex **9b** along the *c*-axis.

3. Experimental

3.1. Materials

The solvents used in the reactions were of reagent grade obtained from E. Merck, Kolkata, India, and were purified and dried by reported procedures [6]. The 2-(arylazo) anilines were prepared according to a reported procedure [6]. Palladium chloride, benzyl chloride, methyl iodide, ethyl bromide and potassium carbonate were purchased from E. Merck, Kolkata, India. Allyl chloride, ethyl chloroacetate, *n*-bromooctane and *o*-cresol were purchased from SRL, Mumbay, India. Disodium tetrachloropalladate was prepared by a reported procedure [6].

3.2. Syntheses of ligands

3.2.1. *1a* and *2a*

To prepare the ligands **1a** and **2a**, methyl iodide (0.095 cm^3, 1.52 mmol) was refluxed for 2 h with 2-(phenylazo) aniline (0.3 g, 1.52 mmol) and 2-(*p*-tolylazo) aniline (0.32 g, 1.52 mmol), respectively, in 30 cm^3 ethanol in the presence of 1 g of K_2CO_3. From the orange solid mass that was obtained after evaporation of ethanol, the ligands **1a** and **2a** were isolated by column chromatography on silica gel (60–120 mesh). The eluent was petroleum ether. Upon evaporation of the solvent, the orange-red semi-solid of pure ligand was obtained. Yield: **1a**, 65%; **2a**, 70%. *Anal*. Calc. for $C_{13}H_{13}N_3$, **1a**: C, 73.93; H, 6.16; N, 19.90. Found: C, 73.90; H, 6.10; N, 19.85%. Calc. for $C_{14}H_{15}N_3$, **2a**: C, 74.66; H, 6.66; N, 18.66. Found: C, 74.61; H, 6.68; N, 18.62%.

3.2.2. *3a* and *4a*

The ligands **3a** and **4a** were prepared following the same procedure as described in the case of **1a** and **2a** using ethyl bromide (0.114 cm^3, 1.52 mmol) in place of methyl iodide. The refluxing time was 4 h. Yield **3a**, 50%; **4a**, 65%. *Anal*. Calc. for $C_{14}H_{15}N_3$, **3a**: C, 74.66; H, 6.66; N, 18.66. Found: C, 74.63; H, 6.65; N, 17.05%. *Anal*. Calc. for $C_{15}H_{17}N_3$, **4a**: C, 75.31; H, 7.11; N, 17.57. Found: C, 75.27; H, 7.10; N, 17.53%.

3.2.3. *5a, 6a and 7a*

5a, **6a** and **7a** were prepared by refluxing 2-(*p*-tolylazo) aniline (0.32 g, 1.52 mmol) with *n*-bromooctane (0.264 cm^3, 1.52 mmol), allyl chloride (0.125 cm^3, 1.52 mmol) and 2-bromomethyl anisole (0.305 g, 1.52 mmol), respectively, in 30 cm^3 ethanol in the presence of 1 g of $K_2CO_3$for 4 h. The ligands were purified by the same procedure as described above. Yield: **5a**, 65%; **6a**, 65%; **7a**, 65%. *Anal.* Calc. for $C_{21}H_{29}N_3$, **5a**: C, 78.01; H, 8.97; N, 13.00. Found: C, 78.00; H, 8.91; N, 13.07%. *Anal*. Calc. for $C_{16}H_{17}N_3$, **6a**: C, 76.49; H, 6.77; N, 16.73. Found: C, 76.45; H, 6.75; N, 16.75%. *Anal*. Calc. for $C_{21}H_{21}N_3O$, **7a**: C, 76.13; H, 6.34; N, 12.69. Found: C, 76.10; H, 6.30; N, 12.70%.

3.2.4. *8a, 9a and 10a*

8a, **9a** and **10a** ligands were prepared by refluxing benzyl chloride (0.193 cm^3, 1.52 mmol) with 2-(phenylazo) aniline (0.3 g, 1.52 mmol), 2-(*p*-tolylazo) aniline (0.32 g, 1.52 mmol) and 2-(*p*-chlorophenylazo) aniline (0.352 g, 1.52 mmol), respectively, in 30 cm^3 ethanol and 1 g of K_2CO_3 for 4 h. The ligands were purified by the same procedure as described above. Yield: **8a**, 50%; **9a**, 65%; **10a**, 50%. *Anal*. Calc. for $C_{19}H_{17}N_3$, **8a**: C, 79.44; H, 5.97; N, 14.63. Found: C, 79.70; H, 6.10; N, 14.55%. *Anal*. Calc. for $C_{20}H_{19}N_3$, **9a**: C, 79.69; H, 6.36; N, 13.95. Found: C, 79.70; H, 6.40; N, 13.97%. *Anal*. Calc. for $C_{19}H_{16}N_3Cl$, **10a**: C, 70.90; H, 5.00; N, 13.00. Found: C, 70.70; H, 5.30; N, 13.40%.

3.2.5. *11a*

2-(*p*-Tolylazo) aniline (0.32 g, 1.52 mmol) was mixed with ethyl chloroacetate (0.185 cm^3, 1.52 mmol) in 30 cm^3 DMF. 1 g of K_2CO_3 was added to this mixture and which was then refluxed for 4 h. From the orange solid mass that was obtained after evaporation of DMF, the ligand **11a** was isolated by column chromatography on silica gel (60–120 mesh). The eluent was petroleum ether. Upon evaporation of solvent the orange-red semi-solid of pure ligand was obtained. Yield: 65%. *Anal.* Calc. for $C_{17}H_{19}N_3O_2$, **11a**: C, 68.68; H, 6.39; N, 14.14. Found: C, 68.65; H, 6.40; N, 14.10%.

3.3. Syntheses of complexes

3.3.1. *1b*

A solution of **1a** (0.110 g, 0.52 mmol) in 10 cm^3 methanol was added to a solution of Na_2PdCl_4 (0.150 g, 0.52 mmol) in 5 cm^3 methanol. The mixture was stirred for 8 h. The dark solid precipitate was separated by filtration and purified by column chromatography using silica gel (60–120 mesh). The eluent was toluene-acetonitrile mixed solvent (90/10 v/v) and upon evaporation of the solvent, dark red solid **1b** was obtained. Yield: 55%. *Anal*. Calc. for $C_{13}H_{12}N_3PdCl$: C, 44.32; H, 3.40; N, 11.93. Found: C, 44.29; H, 3.35; N, 11.40%.

3.3.2. *2b–11b*

The complexes **2b**–**11b** were prepared following a similar procedure as described in the case of **1b**, but the durations of the reactions were different. These are 8 h for **2b**–**4b**, 6 h for **5b**, 7 h for **6b**, 15 h for **7b**, 5 h for **8b**–**10b** and 15 h for **11b**.

Yield: **2b**, 60%; **3b**, 40%; **4b**, 60%; **5b**, 60%; **6b**, 50%; **7b**, 45%; **8b**, 60%; **9b**, 70%; **10b**, 30%; **11b**, 30%. *Anal*. Calc. for $C_{14}H_{14}N_3PdCl$, **2b**: C, 45.91; H, 3.82; N, 11.47. Found: C, 45.90; H, 3.85; N, 11.95%. *Anal*. Calc. for $C_{14}H_{14}N_3PdCl$, **3b**: C, 45.91; H, 3.82; N, 11.47. Found: C, 45.87; H, 3.80; N, 11.45%. *Anal*. Calc. for $C_{15}H_{16}N_3PdCl$, **4b**: C, 47.37; H, 4.21; N, 11.05. Found: C, 47.35; H, 4.15; N, 11.00%. *Anal*. Calc. for $C_{21}H_{28}N_3PdCl$, **5b**: C, 54.31; H, 6.03; N, 9.05. Found: C, 54.35; H, 6.07; N; 9.00%. *Anal*. Calc. for $C_{16}H_{16}N_3PdCl$, **6b**: C, 48.98; H, 4.08; N, 10.71. Found: C, 48.95; H, 4.05; N, 10.70%. *Anal*. Calc. for $C_{21}H_{20}N_3OPdCl$, **7b**: C, 53.39; H, 4.23; N, 8.89. Found: C, 53.40; H, 4.25; N, 8.85%. *Anal*. Calc. for $C_{19}H_{16}N_3PdCl$, **8b**: C, 53.28; H, 3.77; N, 9.80. Found: C, 53.50; H, 4.00; N, 9.70%. *Anal*. Calc. for $C_{20}H_{18}N_3PdCl$, **9b**: C, 54.27; H, 4.07; N, 9.49. Found: C, 54.30; H, 4.10; N, 9.51%. *Anal*. Calc. for $C_{19}H_{15}N_3PdCl_2$, **10b**: C, 49.30; H, 3.27; N, 9.00. Found: C, 49.70; H, 3.40; N, 9.31%. *Anal*. Calc. for $C_{17}H_{18}N_3O_2PdCl$, **11b**: C, 46.58; H, 4.11; N, 9.59. Found: C, 46.55; H, 4.05; N, 9.56%.

3.4. Physical measurements

Microanalyses (C,H,N) were performed using a Perkin–Elmer 240C elemental analyzer. Infrared spectra were recorded on a Perkin–Elmer L120-00A FT-IR spectrometer with the samples prepared in KBr pellets. Electronic spectra were recorded on a Shimadzu UV-2401 PC spectrophotometer. ^1H NMR spectra were obtained on Brucker AC-200, Brucker Avance DPX 300, Brucker Avance DPX 400 and Brucker Avance RPX 500 NMR spectrometers in $CDCl_3$, DMSO-d_6, D_2O using TMS as the internal standard.

3.5. Crystallography

Data of **9b** was collected by the ω-scan technique on a Nicolet R3m/v diffractometer with Mo Kα radiation monochromated by a graphite crystal. The structure solution was done by direct methods with the SHELXS-97 program. Full-matrix least-squares refinements were performed using the SHELX-97 program (PC version). All non-hydrogen atoms were refined anisotropically using reflections $I > 2\sigma(I)$. Hydrogen atoms were included at calculated positions. The crystal data and data collection parameters are listed in Table 5.

Table 5
Crystallographic data for **9b**

Chemical formula	$C_{20}H_{18}ClN_3Pd$
Formula weight	442.22
Space group	$P\bar{1}$
Crystal system	triclinic
a (Å)	10.802(5)
b (Å)	13.159(5)
c (Å)	14.397(8)
α (°)	102.17(3)
β (°)	110.25(4)
γ (°)	98.65(4)
λ (Å)	0.71073
V (Å^3)	1820.2(15)
Z	4
Temperature (K)	293(2)
ρ_{cald} (Mg/m^3)	1.614
μ (mm^{-1})	1.173
$F(000)$	888
R(all data)	$R_1 = 0.0730$, $wR_2 = 0.1080$
Unique reflections/$[I > 2\sigma(I)]$	6770/6400 [$R_{int} = 0.0277$]
R_1[a]/GOF[b]	0.0419/1.065
wR_2[c] $[I > 2\sigma(I)]$	0.0969

[a] Observation criterion: $I > 2\sigma(I)$. $R_1 = \sum \|F_o| - |F_o\| / \sum |F_o|$.
[b] GOF $= [\sum [w(F_o^2 - F_c^2)^2]/(n-p)]^{1/2}$.
[c] $wR_2 = [\sum [w(F_o^2 - F_c^2)^2] / \sum [w(F_o^2)^2]]^{1/2}$, where $w = 1/\sigma^2(F_o^2) + (aP)^2 + bP$, $P = (F_o^2 + 2F_c^2)/3$.

4. Supplementary data

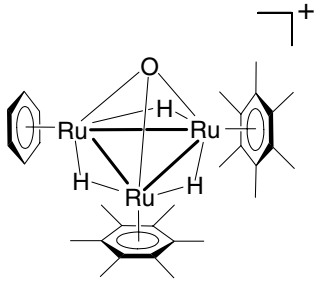
Crystallographic data for the structural analysis have been deposited with the Cambridge Crystallographic Data Centre, CCDC Reference Number 212758. Copies of this information may be obtained free from the Director, CCDC, 12 Union Road, Cambridge CB2 1EW, UK (fax: +44 1223 336 033; e-mail: deposit@ccdc.cam.ac.uk or www: http://www.ccdc.com.ac.uk).

Acknowledgements

We are thankful to the DST (New Delhi) for funding and fellowship to JP under the DST-SERC Project. The necessary laboratory and infrastructural facilities are provided by the Dept. of Chemistry, University of Kalyani. We acknowledge the National facility (X-ray diffractometer) at RSIC, IIT Madras for X-ray studies. We are thankful to Dr. G. Saha (Chembiotek). The support of DST under the FIST Program to the Department of Chemistry, University of Kalyani is acknowledged.

References

[1] (a) W.D. Jones, Acc. Chem. Res. 36 (2003) 140, and references therein;
(b) R.H. Crabtree, Chem. Rev. 95 (1995) 987;
(c) W.D. Jones, Activation of C–H bonds: stoichiometric reactions and catalytic reactions "Topics in Organometallic Chemistry". Activation of unreactive bonds and organic synthesis, Springer, Berlin, 1999 (Chapter 2).
[2] (a) H. Rau, in: H. Dürr, H. Bouas-Laurent (Eds.), In Studies in Organic Chemistry 40: Photochromism, Molecules and Systems, Elsevier, Amsterdam, 1990, p. 165;
(b) K. Janus, J. Sworakowski, J. Phys. Chem. B. 109 (2005) 93;
(c) S. Kume, M. Kurihara, H. Nishihara, Chem. Commun. (2001) 1656;
(d) C. Ruslim, K. Ichimura, J. Mater. Chem. (2000) 2704.
[3] (a) U. Ray, D. Banerjee, G. Mostafa, T.H. Lu, C. Sinha, New J. Chem. 28 (2004) 1437;
(b) S. Kar, B. Pradhan, R.K. Sinha, T. Kundu, P. Kodgire, K.K. Rao, V.G. Puranic, G.K. Lahiri, J. Chem. Soc., Dalton Trans. (2004) 1752;
(c) A. Sanyal, P. Banerjee, G.H. Lee, S.M. Peng, C.H. Hung, S. Goswami, Inorg. Chem. 43 (2004) 7456.
[4] (a) S. Kurihara, S. Nomiyama, T. Nonaka, Chem. Mater. 13 (2001) 1992;
(b) K. Inoue, H. Takeuchi, S. Konaka, J. Phys. Chem. A 105 (2001) 6711;
(c) T. Yamamoto, A. Ohashi, S. Yoneyama, M. Hasegawa, O. Tsutsumi, A. Kanazawa, T. Shiono, T. Ikeda, J. Phys. Chem. B 105 (2001) 2308.
[5] (a) C. Ruslim, K. Ichimura, J. Mater. Chem. (2000) 2704;
(b) S. Kume, M. Kurihara, H. Nishihara, Chem. Commun. (2001) 1656;
(c) B. Mondal, M.G. Walawalkar, G.K. Lahiri, J. Chem. Soc., Dalton Trans. (2000) 4209;
(d) B. Mondal, S. Chakraborty, P. Munshi, M.G. Walawalkar, G.K. Lahiri, J. Chem. Soc., Dalton Trans. (2000) 2327;
(e) C. Cojocariu, P. Rochon, J. Mater. Chem. (2004) 2909.
[6] (a) N. Maiti, S. Pal, S. Chattopadhyay, Inorg. Chem. 40 (2001) 2204;
(b) N. Maiti, B.K. Dirghangi, S. Chattopadhyay, Polyhedron 22 (2003) 3109;
(c) N. Maiti, S. Chattopadhyay, Indian. J. Chem. 42A (2003) 2327.
[7] (a) C. Das, S.-M. Peng, G.-H. Lee, S. Goswami, New J. Chem. 26 (2002) 222;
(b) K.K. Kamar, S. Das, C.-H. Hung, A. Castineiras, M.D. Kuzmin, C. Rillo, J. Bartolome, S. Goswami, Inorg. Chem. 42 (2003) 5367.
[8] (a) S. Chattopadhyay, C. Sinha, A. Basu, A. Chakravorty, J. Organomet. Chem. 414 (1991) 421;
(b) S. Chattopadhyay, C. Sinha, A. Basu, A. Chakravorty, Organometallics. 10 (1991) 1135, and references therein.
[9] A.H. Velders, H. Kooijman, A.L. Spek, J.G. Haasnoot, D. de Vos, J. Reedijk, Inorg. Chem. 39 (2000) 2966.



1

However, for *benzene* hydrogenation catalysis derived from organometallic precatalysts the true nature of the catalytic species has remained a debatable point (''is it homogeneous or heterogeneous catalysis?'') [4]. In the case of the putative homogeneous $[(C_8H_{17})_3Me][RhCl_4]$ ion pair catalyst [5], Finke and co-workers [6] were able to demonstrate that rhodium(0) nanoclusters are the true catalysts (''soluble analogs of heterogeneous catalysts''). Benzene and other arene hydrogenation catalysts have been reviewed recently by Finke [7] and by Dyson [8], and the question of the true nature of the catalytic species in arene hydrogenation catalysis beginning with soluble metal complexes has been critically addressed by Finke et al. [9].

Prior to addressing the ''is it homogeneous or heterogeneous catalysis?'' question for benzene hydrogenation beginning with [**1**][BF_4] [9,10], it proved necessary to develop an improved synthesis for the quantities of **1** that were required, since it is difficult to obtain pure [**1**][BF_4] by crystallization according to the original procedure [1]. In addition, we decided to study the redox properties and the ligand exchange processes of this cluster in detail. It is these topics that are the focus of the present paper.

Elsewhere we report our collaborative kinetic studies of the benzene hydrogenation catalyzed by **1**, transmission electron microscopy studies of the reaction mixture and high-pressure in situ NMR measurements of the reaction of **1** with H_2 in D_2O, results which rule out **1** as the true catalyst. Instead, Ru(0) nanoparticles formed in small quantities from **1** under hydrogen pressure are implicated as the true catalytically active species [11]. The development of an improved synthesis of **1** was crucial to those as well as future studies of **1**, a synthesis which is reported as part of what follows.

2. Results and discussion

2.1. Improved synthesis of $[H_3Ru_3(C_6H_6)(C_6Me_6)_2(O)][BF_4]$ ([1][BF_4])

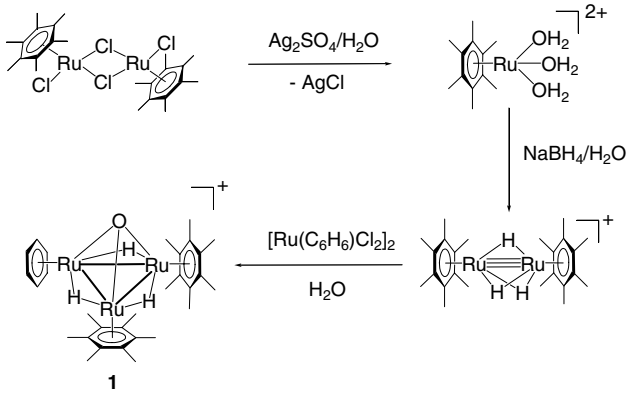
The well-known mononuclear triaqua complex $[Ru(C_6H_6)(H_2O)_3]^{2+}$ [12], formed in situ from the chloro-bridged precursor $[Ru(C_6H_6)Cl_2]_2$ [13] in aqueous solution, reacts with the electron-deficient dinuclear trihydrido complex $[H_3Ru_2(C_6Me_6)_2]^+$ [14] to give the trinuclear cluster cation $[H_3Ru_3(C_6H_6)(C_6Me_6)_2(O)]^+$ (**1**), isolated as tetrafluoroborate salt. Herein, we report an improved synthesis and purification of [**1**][BF_4] based on chromatographic methods. The steps of the synthesis are summarised in Scheme 1.

Key modifications of the original procedure are: (i) the slow (dropwise) addition of the aqueous $NaBH_4$ solution via an oxygen-free cannula with cooling to 10 °C in order to avoid foaming; and (ii) purification of the [**1**][BF_4] precipitate by preparative thin-layer chromatography on silica-gel using a dichloromethane–acetone mixture (2:1) as eluant to remove $NaBF_4$, by-products and other contaminats. The details are given in Section 4.

2.2. Aerobic oxidation of $[H_3Ru_3(C_6H_6)(C_6Me_6)_2(O)]^+$ (1) to $[H_2Ru_3(C_6H_6)(C_6Me_6)_2(O)(OH)]^+$ (2)

Exposure of an aqueous solution of [**1**][BF_4] to air gives the oxidised cluster $[H_2Ru_3(C_6H_6)(C_6Me_6)_2(O)(OH)]^+$ (**2**), although **1** is not noticeably air-sensitive in its solid form. This reaction is best carried out in aqueous solution under atmospheric pressure of air, the complete conversion of **1** into **2** taking about 4 days. An NMR study of the conversion of **1** into **2**, carried out at 27 °C in D_2O solution with approximately 10 equivalents of O_2 (with respect to **1**), shows no indication of any detectable intermediary species. On the other hand, under hydrogen pressure (60 bars) at 110 °C, **2** converts back quantitatively into **1** within 2 h (see Fig. 1).

The reversible transformation of **1** into **2** in aqueous solution suggests interesting redox properties of these clusters. Hence, these were studied by electrochemical methods as detailed in the next section.



1

Scheme 1.

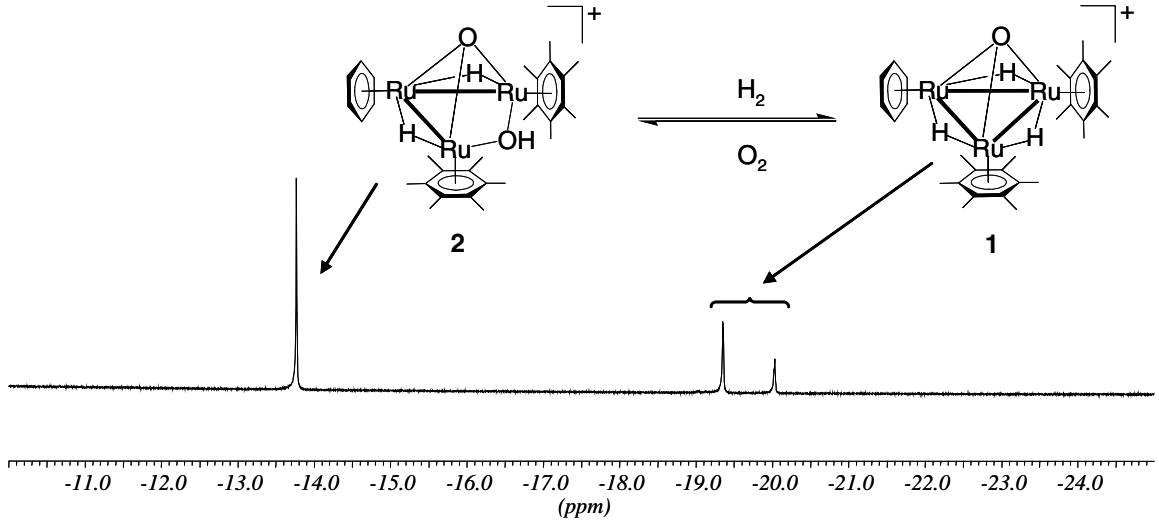


Fig. 1. Conversion of **2** into **1** with molecular hydrogen and the conversion of **1** back into **2** with 0.5 equivalent of molecular oxygen. The ^{1}H NMR spectrum shows a D_2O solution of both **1** and **2**. (The enlargement reveals the hydride signal of **2** being a singlet at $\delta = -13.77$ ppm, while the hydride signals of **1** show the expected multiplicities [$\delta = -19.35$ ppm (doublet) and $\delta = -20.03$ ppm (triplet)] in a 2:1 integral ratio).

2.3. Electrochemical properties of $[H_3Ru_3(C_6H_6)(C_6Me_6)_2(O)]^+$ (1) and $[H_2Ru_3(C_6H_6)(C_6Me_6)_2(O)(OH)]^+$ (2)

Cyclic voltammetry (scan rate 0.1 V s^{-1}) of **1** (Fig. 2) in a deoxygenated solution of acetonitrile shows, in the potential range 0 to +1.5 V versus SCE, three successive anodic peaks ($E_{pa_1} = +0.52$ V versus SCE; $E_{pa_2} = +0.90$ V versus SCE; $E_{pa_3} = +1.29$ V versus SCE). Only the first one corresponds to a chemically and electrochemically reversible system ($E_{pa_1} = +0.52$ V versus SCE; $E_{pc_1} = +0.45$ V versus SCE). The same behaviour was observed at a glassy carbon or a platinum electrode using either 0.1 M $LiClO_4$ or 0.1 M $BuNClO_4$ containing H_2O (10%), as electrolyte.

Complex **2** in acetonitrile is irreversibly oxidised at a potential (+0.46 V versus SCE) close to **1** (Fig. 3). Consequently, the anodic oxidation of **1** cannot give **2** as final product. Other ill-defined irreversible waves are observed at higher potential. Moreover, **1** and **2** are not reduced in the potential range 0 to −2 V versus SCE.

Bulk electrolysis at a working potential corresponding to the plateau of the first anodic wave (+0.6 V versus SCE) of **1** and **2** in deoxygenated acetonitrile both involve about 2–3 F per mol. Electrolysis of **1** was monitored by voltammetry at a platinum rotating disc

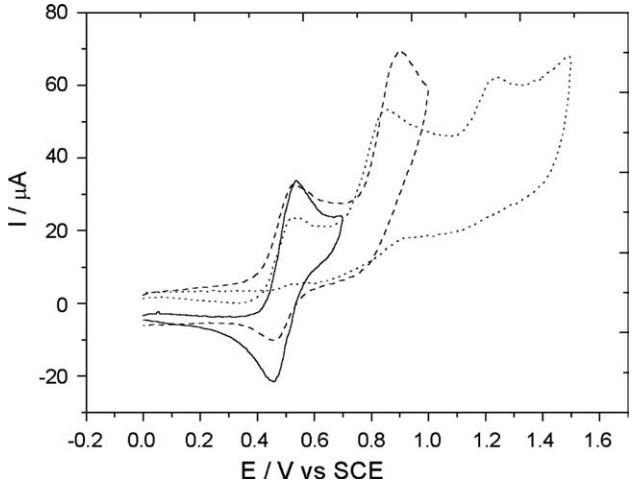


Fig. 2. Cyclic voltammetry of a saturated solution of $[H_3Ru_3(C_6H_6)(C_6Me_6)_2(O)][BF_4]$ in acetonitrile +0.1 M Bu_4NClO_4 at a glassy carbon electrode, by varying the potential from 0 V_{SCE} to 0.7 V_{SCE} (——), 1 V_{SCE} (----) and 1.5 V_{SCE} (···). Scan rate: 0.1 V s^{-1}.

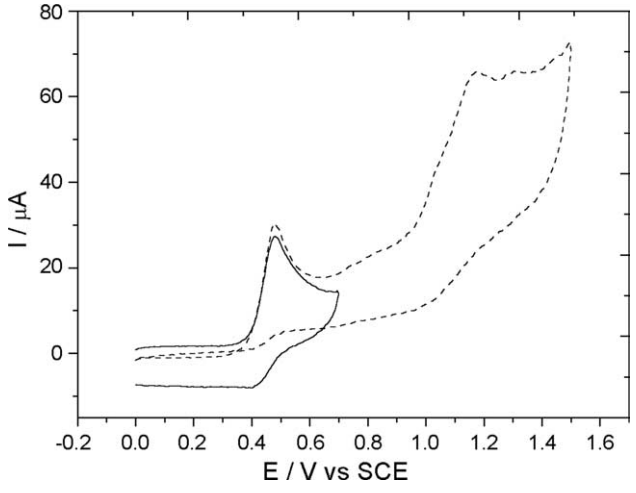


Fig. 3. Cyclic voltammetry of a saturated solution of $[H_2Ru_3(C_6H_6)(C_6Me_6)_2(O)(OH)][BF_4]$ (3×10^{-3} mol L^{-1}) in acetonitrile +0.1 M Bu_4NClO_4 at a glassy carbon electrode, by varying the potential from 0 V_{SCE} to 0.7 V_{SCE} (—) and 1.5 V_{SCE} (----). Scan rate: 0.1 V s^{-1}.

electrode. The first anodic wave ($E_{1/2} = +0.48$ V versus SCE) decreased during electrolysis without the appearance of the expected reversible cathodic wave observed by cyclic voltammetry of **1**. A transient cathodic wave ($E_{1/2} = -0.03$ V versus SCE) which totally disappeared at the end of electrolysis was observed.

Thus, under the time scale of a macroscale electrolysis, the product resulting from the anodic oxidation of **1** is not stable enough to be isolated. After work up, $[(C_6Me_6)_2Ru_2(OH)_3]^+$ was identified from the mixture of decomposition products. After electrolysis of **2**, $[(C_6Me_6)_2Ru_2(OH)_3]^+$ was also identified from the mixture of isolated products by electrospray mass spectrometry of the acetone extract.

In summary, the redox behaviour of **1** and **2** is more complicated than it appears from the reversible aerobic oxidation of **1**–**2** in aqueous solution: under electrochemical conditions and in the absence of H^+, **1** and **2** surprisingly do not interconvert.

2.4. Ligand exchange studies

The catalytic activity of **1** for the hydrogenation of arenes evokes the question whether or not the arene and/or hydrido ligands in **1** are involved in the catalytic process. This is why we studied ligand exchange reactions of **1** with arenes, with molecular hydrogen and with water.

Previously we observed that the hydrogenation of hexadeutero-benzene, C_6D_6, catalysed by $[H_3Ru_3(C_6H_6)(C_6Me_6)_2(O)]^+$ (**1**) under biphasic conditions (catalyst/substrate ratio 1:1000, 110 °C, 60 bar) yields the expected 1,2,3,4,5,6-hexadeuterocyclohexane, while cluster **1** still contains one C_6H_6 and two C_6Me_6 ligands (and no coordinated C_6D_6) after the catalytic reaction, according to NMR and MS data [15]. It was of interest, therefore, to study the exchange reactions of **1** with other arenes: in the case of toluene hydrogenation (catalyst/substrate ratio 1:1000, 110 °C, 60 bar), exchange of the benzene ligand for a toluene molecule is indeed observed. While the ^1H NMR spectrum of the organometallic residue of the aqueous phase dissolved in D_2O showed only the expected signals of **1**, the electrospray mass spectrum of the organometallic residue revealed a small amount of the toluene-exchanged cluster $[H_3Ru_3(C_6H_5Me)(C_6Me_6)_2(O)]^+$ (**3**). Given that this cluster is not visible in the NMR spectrum, we estimate its presence to less than 5%. The same exchange (less than 5%) takes place by heating a mixture of toluene with an aqueous solution of **1** (1000:1) for 2 h to 110 °C without hydrogen pressure. However, in all cases the extent of the arene exchange in **1** is <5%.

High-pressure in situ NMR measurements of the reaction of **1** with D_2 in D_2O and of the deuterated derivative $[D_3Ru_3(C_6H_6)(C_6Me_6)_2(O)]^+$ (**1a**) with H_2 in H_2O were performed in order to study the possible H/D and D/H exchange reactions affecting hydrido and deuterido ligands, respectively (Eqs. (1) and (2)).

$$\underset{\mathbf{1}}{[H_3Ru_3(C_6H_6)(C_6Me_6)_2(O)]^+} \xrightarrow[D_2O]{D_2} \underset{\mathbf{1a}}{[D_3Ru_3(C_6H_6)(C_6Me_6)_2(O)]^+} \quad (1)$$

$$\underset{\mathbf{1a}}{[D_3Ru_3(C_6H_6)(C_6Me_6)_2(O)]^+} \xrightarrow[H_2O]{H_2} \underset{\mathbf{1}}{[H_3Ru_3(C_6H_6)(C_6Me_6)_2(O)]^+} \quad (2)$$

Under a pressure of 50 bar of D_2 (or H_2, respectively) we observed complete H/D exchange according to Eqs. (1) and (2) at 90 °C over a period of 6 h (Fig. 4). The exchange reaction does not take place at temperatures below 80 °C, however. As shown in Fig. 4, partially deuterated derivatives $[H_2DRu_3(C_6H_6)(C_6Me_6)_2(O)]^+$ and $[HD_2Ru_3(C_6H_6)(C_6Me_6)_2(O)]^+$ are not observed, at least not in concentrations detectable by NMR.

Hydrogen (or deuterium) pressure is required for the H/D exchange process: an NMR study of **1** in D_2O without D_2 (or **1a** in H_2O without H_2) reveals that the hydride signals of the cluster remain unchanged even

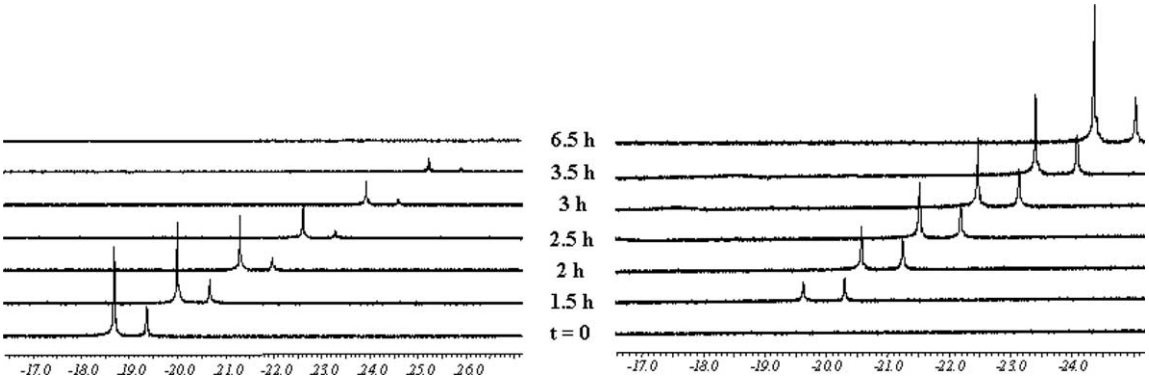


Fig. 4. NMR spectra showing H/D exchange reaction affecting hydrido ligands in **1** (on the left) and D/H exchange reaction affecting deuterido ligands in **1a** at 90 °C under 50 bar of D_2 in D_2O and 50 bar of H_2 in H_2O, respectively.

at 90 °C over a period of 24 h. That is, there is no exchange of the hydrido ligands in **1** with water even at 90 °C.

3. Summary

In conclusion, an improved preparation resulting in 51% of pure [**1**][BF_4] (185 mg scale) has been reported. We have also surveyed the electrochemistry and H/D and arene exchange reactions of [**1**][BF_4]. The results show that while [**1**][BF_4] is a novel composition and structure organometallic complex, it is quite stable and relatively unreactive. These findings are consistent with our conclusions elsewhere that trace $Ru(0)_n$ nanoclusters are the true benzene hydrogenation catalyst derived from [**1**][BF_4] and not this otherwise interesting organometallic complex itself.

4. Experimental

4.1. Syntheses

General remarks: All manipulations were carried out in an inert argon atmosphere using standard Schlenk techniques unless stated otherwise. Filtrations were carried out using a Mülheim apparatus. Doubly distilled water was degassed and saturated with argon prior to use. Organic solvents used for chromatography were distilled under argon prior to use. Silica-gel G used for preparative thin-layer (20 × 20 cm) chromatography was purchased from Macherey-Nagel GmbH. NMR spectra were recorded using a Bruker 400 MHz spectrometer. Electrospray mass spectra were obtained in positive-ion mode using a LCQ Finnigan mass spectrometer. Deuterated NMR solvents were purchased from Cambridge Isotope Laboratories, Inc. The starting dinuclear complexes $[Ru(C_6Me_6)Cl_2]_2$ [16] and $[Ru(C_6H_6)Cl_2]_2$ [13] were prepared according to published methods.

4.1.1. Improved preparation of $[H_3Ru_3(C_6H_6)(C_6Me_6)_2(O)][BF_4]$ ([1][BF_4])

In a 250 mL brown-glass Schlenk tube, 300 mg (0.449 mmol) of $[Ru(C_6Me_6)Cl_2]_2$ were mixed with a solution of 282 mg (0.904 mmol) of Ag_2SO_4 in 30 mL of water. The suspension was stirred at room temperature until the orange solid has completely dissolved to give a yellow solution of $[Ru(C_6Me_6)(H_2O)_3]^{2+}$ (around one hour). The white precipitate of AgCl formed was removed from the aqueous solution by filtration through filter pulp. The resulting clear yellow filtrate was cooled in an ice-bath for 30 min. In a separate 50 mL Schlenk tube, 75 mg (1.974 mmol) of $NaBH_4$ were dissolved in 15 mL of water at room temperature. After stirring for 5 min, the $NaBH_4$ solution was transferred very slowly through a cannula into the ice-bath-cooled $[Ru(C_6Me_6)(H_2O)_3][SO_4]$ solution. The colour of the solution changed to black, due to the formation of $[H_3Ru_2(C_6Me_6)_2]^+$. The resulting solution was immediately filtered through filter pulp under argon to remove unsoluble black particles. To the dark solution containing $[H_3Ru_2(C_6Me_6)_2]^+$, solid $[Ru(C_6H_6)Cl_2]_2$ (210 mg, 0.420 mmol) was added. The mixture was stirred at room temperature, until the orange solid had completely dissolved. Then, the solution was transferred under argon into a 300 mL closed Schlenk pressure tube and stirred under argon pressure (two atmospheres) at 60 °C for 3 days.

During this time, the colour of the solution changed from black to red. After cooling to room temperature, the red solution containing **1** was filtered through filter pulp. Then a large excess of solid $NaBF_4$ was added to the filtrate to precipitate [**1**][BF_4]. After stirring for one hour at room temperature, the red precipitate was centrifuged in air (1500 rpm, 10 min), the aqueous solution was removed from the centrifuge tube with a glass pipette. The red solid was dissolved in CH_2Cl_2 and again filtered through filter pulp to eliminate excess $NaBF_4$. Then the methylene chloride solution was concentrated to 15 mL in vacuo. The resulting solution was subjected to preparative thin-layer chromatography on silica-gel using CH_2Cl_2/acetone (2/1) as eluant. The pure [**1**][BF_4] was extracted from the main red band with acetone. Evaporation of acetone under vacuum gave 185 mg (51%) of [**1**][BF_4] as a red powder.

Spectroscopic data for **1**: ^{1}H NMR (400 MHz, acetone-d_6): $\delta = -19.93$ (t, 1H, $^2J = 3.84$ Hz, Ru-*H*), −19.08 (d, 2H, $^2J = 3.84$ Hz, Ru-*H*), 2.31 (s, 36H, $C_6(CH_3)_6$), 5.70 (s, 6H, C_6H_6). $^{13}C\{^1H\}$ (50 MHz, acetone-d_6): $\delta = 17.48$, 71.45, 95.06. MS (ESI positive mode, in acetone): *m*/*z*: 726 $[M + 2H]^+$.

4.1.2. Preparation of $[H_3Ru_3(C_6H_6)(C_6Me_6)_2(O)(OH)][BF_4]$ ([2][BF_4])

In a Schlenk pressure tube, a red solution of 50 mg (0.062 mmol) of [**1**][BF_4] in 80 mL of water were heated at 50 °C under about 3 bars of air during 3 days. The resulting orange-yellow solution was filtered through filter pulp, and then the water was removed by evaporation under reduced pressure. The residue was dissolved in 5 mL of CH_2Cl_2 and subjected to preparative thin-layer chromatography on silica-gel using CH_2Cl_2/acetone (2/1) as eluant. The pure [**2**][BF_4] was extracted from the main orange band with acetone. Evaporation of acetone under vacuum gave 20 mg (39%) of [**2**][BF_4] as an orange powder.

Spectroscopic data for **2**: ^{1}H NMR (400 MHz, acetone-d_6): $\delta = -13.67$ (s, 2H, Ru-*H*), 2.15 (s, 36H, $C_6(CH_3)_6$), 5.82 (s, 6H, C_6H_6). MS (ESI positive mode, in acetone): *m*/*z*: 742 $[M + H]^+$.

4.1.3. Preparation of $[D_3Ru_3(C_6H_6)(C_6Me_6)_2(O)][BF_4]$ ($[\mathbf{1a}][BF_4]$)

The deuterated derivative [**1a**][BF_4] was prepared and purified according to the same procedure as [**1**][BF_4], water being replaced by heavy water and $NaBH_4$ being replaced by $NaBD_4$. However, the yield is significantly lower (less than 20%).

Spectroscopic data for **1a**: ^{1}H NMR (400 MHz, acetone-d_6): $\delta = 2.31$ (s, 36H, $C_6(CH_3)_6$), 5.70 (s, 6H, C_6H_6). $^{13}C\{^1H\}$ (50 MHz, acetone-d_6): $\delta = 17.48$, 71.45, 95.06. MS (ESI positive mode, in acetone): m/z: 728 $[M + H]^+$.

4.2. Electrochemical studies

Conventional electrochemical equipment was used for cyclic voltammetry and voltammetry at a rotating disc electrode (EG&G Princeton applied Research Model 362 scanning potentiostat with an XY recorder or a power Lab/4SP, Scope version 3.6.10, ADInstrument). For both cyclic voltammetry or voltammetry at a rotating disc electrode ($\omega = 2000$ rpm), the working electrode was a disc of glassy carbon (3 mm diameter) or platinum (1 mm diameter). All potentials referred to the saturated calomel electrode (SCE) and were not corrected for the ohmic drop. The $E_{1/2}$ and ΔE_p of ferrocene in our cell were + 0.40 V versus SCE and 0.08 V versus SCE, respectively.

Controlled potential electrolyses were performed in a divided cell [17] equipped with a planar platinum electrode (4 cm diameter). The coulometric measurements were determined with a current integrator Tacussel IG5. Electrolyses under continuous bubbling of nitrogen generally involve 3×10^{-5}–8×10^{-5} mol of substance **1** or **2** in 50 mL of non-dried CH_3CN containing 0.2 M $LiClO_4$ as electrolyte. After electrolysis of **1** and **2**, water (50 mL) was added to the electrolysed solution. Acetonitrile was removed in vacuo before adding an aqueous solution of HBF_4. The resulting solution was extracted twice with CH_2Cl_2 which was dried over magnesium sulfate and evaporated in vacuo. The resultant red solid was washed with diethyl ether.

4.3. Ligand exchange studies

4.3.1. Arene exchange study

In a 300 mL closed Schlenk pressure tube was stirred a mixture of an aqueous solution of [**1**][BF_4] (10 mg, 1.23×10^{-5} mol, 10 mL) with toluene (1.32 mL, 12.3 mmol) for 2 h at 110 °C. After cooling, the toluene was removed by decanting and extraction with 5 mL of diethyl ether followed by evaporation of the aqueous solution to dryness under reduce pressure. The red residue was analysed by ^{1}H NMR spectroscopy and by mass spectrometry.

4.3.2. Hydride exchange studies (high-pressure NMR experiments)

All H–D or D–H exchange experiments were carried out under oxygen-free conditions using glove box and Schlenk techniques. D_2O (99.9%) was purchased from Cambridge Isotope Laboratories, whereas D_2 was purchased from Linde. Experiments under pressure were carried out in a 10 mm medium pressure sapphire NMR-tube [18] under 5 MPa of H_2 or D_2 pressure. Spectra were collected on a Bruker DRX 400 MHz instrument, the integrals were calculated using the WIN-NMR program and the ^{1}H chemical shifts were referenced to 3-trimethylsilyl-1-propanesulfonic acid Na salt (TSPSANa), external standard.

The exchange reactions were carried out at 363 K temperature, using **1a** or **1** under 50 bars of H_2 or D_2 pressure in solvent H_2O or D_2O, respectively. The time delays between spectra are 10 min in case of D–H exchange and 20 min in case of H–D exchange. In case of D–H exchange, the measurements were carried out in sweep off mode and use a water suppression pulse sequence (1-3-3-1) because of lack of lock and the presence of the large H_2O signal [19].

Acknowledgements

Financial support from NSF Switzerland 200020-105132 (to G.S.F.) and 200020-105335/1 (to G.L.) is gratefully acknowledged as is financial support from NSF (US) #CHE-0314678 (to R.G.F.).

References

[1] M. Faure, M. Jahncke, A. Neels, H. Stœckli-Evans, G. Süss-Fink, Polyhedron 18 (1999) 2679.
[2] G. Süss-Fink, M. Faure, T.R. Ward, Angew. Chem. 114 (2002) 105.
[3] G. Süss-Fink, M. Faure, T.R. Ward, Angew. Chem. Int. Ed. 41 (2002) 99.
[4] Y. Lin, R.G. Finke, Inorg. Chem. 33 (1994) 4891.
[5] (a) K.R. Januszkiewicz, H. Alper, Organometallics 2 (1983) 1055; (b) J. Blum, I. Amer, K.P.C. Vollhardt, H. Schwarz, G. Hoehne, J. Org. Chem. 52 (1987) 2804.
[6] K.S. Weddle, J.D. Aiken III, R.G. Finke, J. Am. Chem. Soc. 120 (1998) 5653.
[7] J.A. Widegren, R.G. Finke, J. Mol. Catal. A: Chem. 191 (2003) 187.
[8] P.J. Dyson, Dalton Trans. (2003) 2964.
[9] J.A. Widegren, R.G. Finke, J. Mol. Catal. A: Chem. 198 (2003) 317.
[10] J.A. Widegren, M.A. Bennett, R.G. Finke, J. Am. Chem. Soc. 125 (2003) 10301.
[11] C.M. Hagen, L. Vieille-Petit, G. Laurenczy, G. Süss-Fink, R.G. Finke, Organometallics 24 (2005) 1819.
[12] M. Stebler-Röthlisberger, W. Hummel, P.A. Pittet, H.-B. Bürgi, A. Ludi, A.E. Merbach, Inorg. Chem. 27 (1988) 1358.
[13] M.A. Bennett, A.K. Smith, J. Chem. Soc. Dalton 2 (1974) 233.
[14] (a) M.A. Bennett, J.P. Ennett, K.I. Gell, J. Organomet. Chem. 233 (1982) C17;

(b) M.A. Bennett, J.P. Ennett, Inorg. Chim. Acta 198–200 (1992) 583;
(c) M. Jahncke, G. Meister, G. Rheinwald, H. Stoeckli-Evans, G. Süss-Fink, Organometallics 16 (1997) 1137.
[15] G. Süss-Fink, B. Therrien, L. Vieille-Petit, M. Tschan, V.B. Romakh, T.R. Ward, M. Dadras, G. Laurenczy, J. Organomet. Chem. 689 (2004) 1362.
[16] M.A. Bennett, T.-N. Huang, T.W. Matheson, A.K. Smith, Inorg. Synth. 21 (1982) 74.
[17] G. Jacob, C. Moinet, Bull. Soc. Chim. Fr. (1983) 291.
[18] G. Laurenczy, F. Joó, L. Nádasdi, Inorg. Chem. 39 (2000) 5083.
[19] G. Kovács, L. Nádasdi, G. Laurenczy, F. Joó, Green Chemistry 5 (2003) 213.

even though the apda ligand was bonded in a tetradentate fashion. Yet another study showed that apda can also act as a tridentate ligand with the pronated β-alaninato arm opened in the formation of [Co(dien)(Hapda)]ClO_4 [11]. This obvious versatility leaves the possibility to synthesise and characterise complexes with very interesting bonding modes and kinetic behaviour.

Furthermore, the strain experienced by the bonded glycinate arms of these tripod type ligands make for very interesting study. According to Weakliem et al. [12] unstrained glycinate rings should be planar with the sum of the endocyclic angles in the ring equal to 538.4°. The reasons for the strain on these rings have been of interest. It was suggested earlier that it could be due to a combined effect of hydrogen bonding and van der Waals forces and the angular strain on the co-ordinated nitrogen atom of the tripod ligand. It was also shown that the presence of large cationic species do not increase the strain to a visible degree [8]. Furthermore, it is peculiar that the in-plane *R* rings experience the least strain in all the complexes studied.

Thirdly, very little work has been done on the subject of ^1H NMR spectroscopy of cobalt(III)-tripod type ligand complexes. A recent study showed how ^1H NMR can be used effectively to determine the conformation of cobalt(III)-nta complexes [8]. The crystallographic study of [Co(apda)$(H_2O)_2$] did not include ^1H NMR spectroscopy data [9].

This paper deals with the synthesis and molecular and crystal structure of $[Co(H_2O)_6] \cdot [Co(Hapda)_2]_2 \cdot H_2O$ as well as the influence of pH on solutions of $[Co(Hapda)_2]_2^{2-}$. The aim of the present work is to study the co-ordination modes of the apda ligand and to provide more information for the identification of Co(III)-tripod type ligands by ^1H NMR. The strain in the glycinato rings of the apda ligand is also discussed.

2. Experimental

2.1. Synthesis of N-(2-carboxyethyl)iminodiacetic acid (apda)

N-(2-carboxyethyl)iminodiacetic acid (apda) was synthesised according to a method obtained from Niclós-Gutiérrez [10]. Chloroacetic acid (10.84 g, 115 mmol) was neutralized by adding potassium hydroxide (6.42 g, 118.5 mmol) in a N_2 atmosphere over a period of 20 min at 5 °C. β-alanin (5.00 g, 56 mmol), neutralized with potassium hydroxide (3.14 g, 56 mmol), was added to the chloroacetic acid solution. The solution was refluxed in a water bath for 5 h under N_2, while adding potassium hydroxide (6.42 g, 115 mmol) over the first 30 min of heating (ca. 90 °C). The solution was cooled to room temperature and the pH was adjusted to ~6.5 with hydrochloric acid (6 M). The solution was concentrated under vacuum (60 °C) until potassium hydroxide crystals separated out. The resulting solution was then cooled to room temperature and the potassium hydroxide crystals were filtered off. The pH was adjusted to 2.5 with the aid of hydrochloric acid (6 M) and the solution was allowed to stand overnight, while the N-(2-carboxyethyl)iminodiacetic acid (apda) precipitated. The precipitate was filtered off and re-crystallized from water (60 °C).

(apda): yield 67%. Important infrared data (KBr, cm^{-1}): *ν*(COOH) 1706 (s). ^1H NMR (D_2O, ppm) *δ*: 3.08 (s, 2H), 3.61 (d, 2H), 3.78 (s, 2H), 4.17 (d, 2H).

2.2. Synthesis of $[Co(apda)(H_2O)_2] \cdot H_2O$

[Co(apda)$(H_2O)_2$] was prepared similar to the method described by Tsuchiya and co-workers [1]. $CoCl_2 \cdot 6H_2O$ (5.7 g, 24.3 mmol) was added to a 25 cm^3 solution containing apda (5 g, 24.3 mmol) and $KHCO_3$ (5 g, 50 mmol). The mixture was heated on a water bath for about 1 h. The solution was then placed on an ice bath and H_2O_2 (1 cm^3, 30%) was added after which it was stirred for 30 min. The pH of the resultant solution was adjusted to 3 with $HClO_4$ (6 M) and stirred for another 2 h. Ethanol (200 cm^3) was added to the mixture until precipitation occurred. The precipitate was re-dissolved in the minimum amount of water. Purple crystals separated out after 24 h.

[Co(apda)$(H_2O)_2$]: yield 44%. Important infrared data (KBr, cm^{-1}): *ν*(COOH) 1670 (s), 1580 (m). ^1H NMR (D_2O, ppm) *δ*: 2.57 (d, 1H), 2.80 (m, 2H), 3.47 (m, 2H), 3.78 (d, 1H), 3.97 (d, 1H), 4.18 (d, 1H). UV–Vis (λ_{max} (nm) (ε, M^{-1} cm^{-1})): 209.9 (1.48×10^4), 240.0 (1.29×10^4), 400.0 (1.07×10^2), 559.9 (1.63×10^2).

2.3. Synthesis of $[Co(H_2O)_6][Co(Hapda)_2]_2 \cdot H_2O$

$CoCl_2 \cdot 6H_2O$ (5.7 g, 24.3 mmol) was added to a 25 cm^3 solution containing apda (5 g, 24.3 mmol) and $KHCO_3$ (5 g, 50 mmol). The mixture was heated on a water bath for about 1 h, placed on an ice bath and H_2O_2 (1 cm^3, 30%) was added. After stirring for approximately 20 min, the pH of the mixture was adjusted to 2. This was stirred at room temperature for 24 h. Ethanol (200 cm^3) was added to the mixture and the complex precipitated. The precipitate was washed with ice water and then re-dissolved in warm water, ca. 60 °C after which pink crystals, suitable for X-ray crystallography, separated out (10 h).

$[Co(H_2O)_6][Co(Hapda)_2]_2 \cdot H_2O$: yield 12%. Important infrared data (KBr, cm^{-1}): *ν*(COOH) 1705(m),

1597(s). UV–Vis (λ_{max} (nm) (ε, M^{-1} cm^{-1})): 230.0 (3.59×10^4); 375.0 (1.68×10^2), 540.0 (1.96×10^2).

2.4. Synthesis of $Na[Co(Hapda)_2] \cdot xH_2O$

An ion-exchange column was filled with sufficient strong-base anion-exchange resin to give a 20 cm column. The column was washed with NH_3 (6 M, 50 cm^3) followed by water (100 cm^3) and HCl (2 M, 100 cm^3). $[Co(H_2O)_6][Co(Hapda)_2]_2 \cdot H_2O$ (3.00 g, 2.7 mmol) was introduced into the column to separate the anionic species $[Co(Hapda)_2]^{3-}$ from the cationic counter ion, $[Co(H_2O)_6]^{2+}$. The column was washed with water (200 cm^3) and the $Na[Co(Hapda)_2] \cdot xH_2O$ was eluted with NaCl (2 M, 150 cm^3). The solution was evaporated until a pink precipitate was formed. The precipitate was filtered and washed with ice cold water (50 cm^3). The precipitate was re-crystallised from hot water (ca. 60 °C). Unfortunately the crystals obtained were not suitable for X-ray diffraction data collection.

$Na[Co(Hapda)_2] \cdot xH_2O$: Important infrared data (KBr, cm^{-1}): ν(COOH) 1702(s), 1609(m). ^1H NMR (D_2O, ppm) δ: 2.77 (t, 4H), 3.59 (d, 4H), 3.74 (t, 4H), 4.18 (d, 4H). UV–Vis (λ_{max} (nm) (ε, M^{-1} cm^{-1})): 230.0 (1.50×10^4), 365.1 (8.4×10^1), 515.0 (5.6×10^1).

2.5. X-ray data collection, solution of the structure and refinement

Intensity data were collected on a Bruker SMART 1K CCD area detector diffractometer with graphite monochromated Mo Kα radiation (50 kV, 30 mA). The collection method involved ω-scans of width 0.3°. Data reduction was carried out using the program SAINT+ [13] and absorption corrections were made using the program SADABS [14].

The crystal structure was solved by direct methods using SHELXTL [15]. Non-hydrogen atoms were first refined isotropically followed by anisotropic refinement by full matrix least-squares calculations based on F^2 using SHELXTL. With the exception of hydrogen atoms involved in hydrogen bonding, all hydrogen atoms were first located in the difference map then positioned geometrically and allowed to ride on their respective parent atoms. Hydrogen atoms involved in hydrogen bonding were placed from the difference map, restrained to reasonable O–H distances using DFIX and refined isotropically. Diagrams and publication material were generated using SHELXTL and DIAMOND [16]. A summary of the crystal data, experimental details and refinement results is given in Table 1.

2.6. Spectroscopic studies

Routine IR spectra were recorded on a Digilab FTS2000 FT-IR spectrometer. UV–Vis spectra were recorded on a Cary spectrophotometer. ^1H NMR spectra were recorded on a 300 MHz Bruker spectrometer.

Table 1
Crystal data and structure refinement for $[Co(H_2O)_6][Co(Hapda)_2]_2 \cdot H_2O$

Empirical formula	$C_{28}H_{52}Co_3N_4O_{32}$
Formula weight	1133.53
Temperature (K)	293(2)
Wavelength (Å)	0.71073
Crystal system	triclinic
Space group	$P\bar{1}$
Unit cell dimensions	
a (Å)	9.2498(14)
b (Å)	10.5353(16)
c (Å)	12.3433(19)
α (°)	114.141(3)
β (°)	93.068(3)
γ (°)	104.260(3)
Volume (Å^3)	1047.5(3)
Z	1
Density (calculated) (Mg/m^3)	1.797
Absorption coefficient (mm^{-1})	1.289
F(0 0 0)	585
Crystal size (mm)	$0.36 \times 0.14 \times 0.10$
Theta range for data collection (°)	1.84–26.00
Index ranges	$-11 \leqslant h \leqslant 11$, $-12 \leqslant k \leqslant 12$, $-15 \leqslant l \leqslant 12$
Reflections collected	6279
Independent reflections	4079 [R_{int} = 0.0228]
Completeness to theta = 26.00°	99.0%
Absorption correction	semi-empirical from equivalents
Maximum and minimum transmission	0.8819 and 0.6540
Refinement method	full-matrix least-squares on F^2
Data/restraints/parameters	4079/10/348
Goodness-of-fit on $F2$	1.012
Final R indices [$I > 2\sigma(I)$]	R_1 = 0.0366, wR_2 = 0.0754
R indices (all data)	R_1 = 0.0555, wR_2 = 0.0816
Largest difference peak and hole (e Å^{-3})	0.311 and −0.480

3. Results and discussion

3.1. Description of the structure

Bond distances and angles between selected non-hydrogen atoms are given in Table 2. Hydrogen bonding interactions are represented in Table 3. Relevant torsion angles, endocyclic angles of the glycinato rings and the calculated distances of Co and N from the CCOO planes are given in Table 4. The numbering scheme for one of the anionic units is shown in the perspective drawing in Fig. 1.

The compound consists of two anionic cobalt(III)-Hapda units and one $[Co(H_2O)_6]^{2+}$ unit [Co(2)] which acts as a counter ion. Hapda acts as a tridentate ligand in both units, the propionate arm being open in both cases. This imply that the Co(III) centres are surrounded by four oxygen atoms and two nitrogen atoms.

Table 2
Selected bond distances (Å) and angles for the anionic units, $[Co(Hapda)_2]^-$

Bond distance (Å)	
Co(1)–O(3)	1.880(2)
Co(1)–O(1)	1.880(2)
Co(1)–N(1)	1.976(2)
N(1)–C(4)	1.494(3)
N(1)–C(2)	1.495(3)
N(1)–C(7)	1.501(3)
O(2)–C(1)	1.246(3)
O(4)–C(3)	1.235(3)
O(6)–C(5)	1.207(3)
Co(1′)–O(1′)	1.879(2)
Co(1′)–O(3′)	1.900(2)
Co(1′)–N(1′)	1.973(2)
Bond angle (°)	
O(3)–Co(1)–O(1)	90.54(9)
O(3)–Co(1)–N(1)	87.84(9)
O(1)–Co(1)–N(1)	87.88(9)
O(1′)–Co(1′)–O(3′)	89.67(9)
O(3′)–Co(1′)–N(1′)	85.07(9)
O(1′)–Co(1′)–N(1′)	88.32(9)
C(4)–N(1)–C(2)	112.5(2)
C(4)–N(1)–C(7)	110.3(2)
C(2)–N(1)–C(7)	110.1(2)
C(4′)–N(1′)–C(2′)	110.6(2)
C(4′)–N(1′)–C(7′)	110.8(2)
C(7′)–N(1′)–C(2′)	111.8(2)

Table 3
Hydrogen bonds for $[Co(H_2O)_6][Co(Hapda)_2]_2 \cdot H_2O$ (Å and °)

D–H···A	*d*(D–H)	*d*(H···A)	*d*(D···A)	∠(DHA)
O(5)–H(5)···O(2′)	0.84(3)	1.91(3)	2.752(3)	175(4)
O(5′)–H(5′)···O(2)	0.85(3)	1.78(3)	2.621(3)	173(4)
O(5′)–H(5′)···O(1)	0.85(3)	2.64(4)	3.211(3)	126(3)
O(7)–H(7E)···O(4′)	0.82(1)	1.88(3)	2.693(3)	169(4)
O(7)–H(7F)···O(2)	0.81(3)	2.08(4)	2.844(3)	157(4)
O(8)–H(8A)···O(6)	0.82(3)	2.01(2)	2.771(3)	155(4)
O(8)–H(8B)···O(10)	0.82(4)	1.94(4)	2.757(4)	175(5)
O(9)–H(9A)···O(6)	0.82(3)	2.34(3)	2.973(4)	135(4)
O(9)–H(9B)···O(4)	0.82(3)	1.98(3)	2.789(3)	173(4)
O(10)–H(10A)···O(6′)	0.82(3)	2.11(3)	2.914(4)	169(5)
O(10)–H(10B)···O(6′)	0.83(4)	2.26(3)	2.928(4)	138(4)

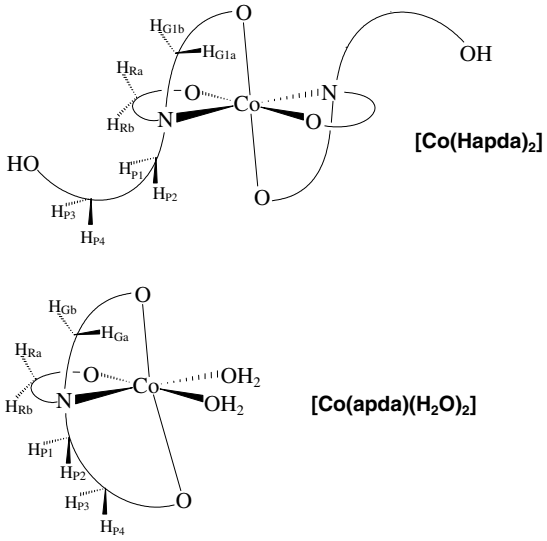


Fig. 1. Sketch of different Co-apda complexes, illustrating relevant H atoms in ^1H NMR spectroscopy.

The octahedral cation, $[Co(H_2O)_6]^{2+}$, is slightly distorted, but centro-symmetric, with the atom Co(2) at the inversion centre. The Co–O distances vary between 2.051(2) and 2.115(2) Å and the right angles between 86.97(11)° and 93.03(11)°. This compares very well with several different crystal structures with $[Co(H_2O)_6]^{2+}$ as counter ion [17–19].

Close inspection indicates that the two cobalt(III) units are not similar in terms of octahedral distortion around the metal centre. Unit A has a very slightly distorted octahedron around the cobalt(III) centre with the O–Co–O, O–Co–N and N–Co–N bonding angles ranging between 87.84(9)° and 92.16(9)°. The O–Co–O, O–Co–N and N–Co–N bonding angles in unit B however, vary between 85.07(9)° and 94.93(9)°. The Co–nitrogen bonding distances vary between 1.973(2) and 1.976(2) Å, while the Co–oxygen distances vary between 1.8794(19) and 1.9005(19) Å for both A and B. The rest of the N–C, C–C and C–O bond distances of the apda

Table 4
Endocyclic angles, distances of N and Co from the CCOO planes and torsion angles for both anionic units, $[Co(Hapda)_2]^-$, A and B

	Anionic unit A		Anionic unit B	
	G	*R*	*G*	*R*
Endocyclic angles (°)	536.52	537.77	527.77	539.33
N distance from CCOO[a] plane (Å)	−0.346(5)	0.155(5)	0.562(5)	0.124(5)
Co distance from CCOO plane (Å)	−0.037(4)	−0.157(4)	−0.059(4)	0.225(4)
Torsion angles (°)				
N–Co–O–C	−7.9(2)	10.5(2)	18.6(2)	6.9(2)
Co–O–C–C	−2.3(3)	−4.0(3)	−1.1(3)	−9.1(3)
N–C–C–O	15.5(4)	−7.7(4)	−24.4(3)	6.6(4)
Co–N–C–C	−19.4(3)	14.3(3)	35.3(3)	−1.0(3)
O–Co–N–C	15.0(2)	−13.3(2)	−29.5(2)	−2.7(2)

[a] Two carbon atoms, one carboxylate oxygen and a metal bonded oxygen.

ligand are all considered normal and agree well with those found for $[Co(apda)(H_2O)_2]$ and other similar tripod type ligands like nta (nta = nitrilotriacetic acid) [4,9,20].

The sums of the endocyclic angles of the rings in the two cobalt(III) units are 536.52° and 540.47° for A and 539.33° and 527.77° for B. This information is very interesting since it seems that the glycinate rings in A has almost zero strain according to Weakliem and Hoard [12], while the *G* ring in B is quite severely strained. Both the glycinate rings in [Co(dien)(Hapda)]-ClO_4 were almost planar, indicating almost zero strain [11].

The nitrogen tetrahedra of A and B are both slightly distorted but are the same within experimental error. C–N–C angles for A vary between 110.1(2)° and 112.5(2)° compared to 110.6(2) to 111.8(2) for B.

The angular strain around the nitrogen atom of Hapda can be demonstrated by the non-planarity of the *G* rings, see Table 4. Deviations of N from the CCOO planes vary between 0.155(5) and 0.346(5) Å for anionic unit A and 0.124(5) and 0.562(5) Å for anionic unit B. Similarly the out-of-plane distances for cobalt were calculated to be between 0.037(4) and 0.157(4) Å for anionic unit A and between 0.059(4) and 0.225(4) Å for anionic unit B. The deviation of N from the planes decrease in the order $G > R$ for both anionic units, while the deviation of Co from the planes increase in the order $G > R$ for both anionic units. The main reason for this is possibly that the nitrogen atom is more displaced from the CCOO plane (0.346(5) and 0.562(5) Å) in the *G* rings of anionic unit A and B, respectively. This forces the Co atom into the *G* plane and out of the *R* plane (Co distance from *R* plane in anionic unit A and B is surprisingly long, 0.157(4) and 0.225(4) Å, respectively).

From the above discussion, it is obvious that A and B differ only in terms of the strain experienced by the glycinato rings of the apda ligand. All the other bonding information seems to be the same within experimental error. The only reasonable explanation then could only be that these rings experience different external pushing/pulling effects due to intermolecular hydrogen bonding and other van der Waals interactions.

3.2. Spectral properties

The IR spectrum obtained for $[Co(H_2O)_6][Co(Hapda)_2]_2 \cdot H_2O$ shows stretching frequencies at 1705 and 1597 cm^{-1}. These values point towards the presence of both coordinated and uncoordinated carboxylate groups [21] as expected. The observed COO-stretching for $Na[Co(Hapda)_2] \cdot xH_2O$ at 1702 and 1609 cm^{-1} compares very well with that of $[Co(H_2O)_6][Co(Hapda)_2]_2 \cdot H_2O$. In the case of $[Co(apda)(H_2O)_2]$, the spectrum shows frequencies at 1670 and 1580 cm^{-1}, which is consistent with the spectrum obtained by Gladkikh et al. for this complex [9] and which points to coordinated COO groups.

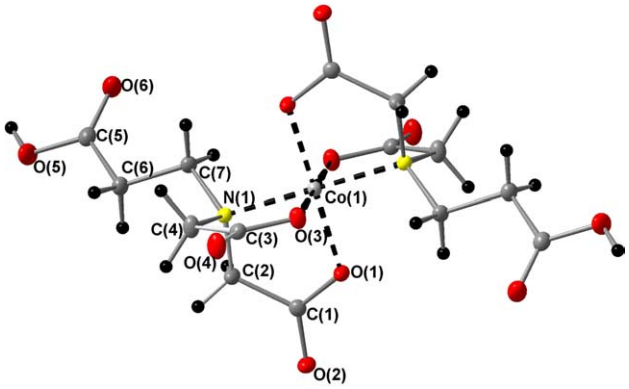


Fig. 2. Perspective drawing of anionic Unit A.

Usable ^1H NMR spectra of $[Co(H_2O)_6][Co(Hapda)_2]_2 \cdot H_2O$ could not be obtained due to paramagnetic interference from the Co(II) counter ion. Spectra of $[Co(apda)(H_2O)_2]$ and $Na[Co(Hapda)_2] \cdot xH_2O$ are represented in Figs. 3 and 4. The spectrum of $[Co(apda)(H_2O)_2]$ indicates that all the protons are non-equivalent as expected. The glycinate *G* ring protons (H_{Ga} and H_{Gb} in Fig. 2) and *R* ring protons (H_{Ra} and H_{Rb}) all experience a different chemical environment and are therefore non-equivalent. This result in three distinctive doublets with an AB pattern with centers between 3.6 and 4.5 ppm and a fourth doublet in the 3.5 ppm region (see Fig. 3). The multiplet at 3.5 ppm and the other downfield peaks are assigned to the β-alaninato ring protons, which are all non-equivalent. This is confirmed with the spectrum of the free ligand, which shows two triplets between 2.5 and 3.5 ppm (4 β-alaninato protons) and the singlet observed between 3.5 and 4 ppm (glycinate protons).

The spectrum of $[Co_2(Hapda)_2]^-$ is somewhat simpler in that two distinctive triplets are observed at ~2.8 and 3.8 ppm, indicating that the β-alaninato arm is opened.

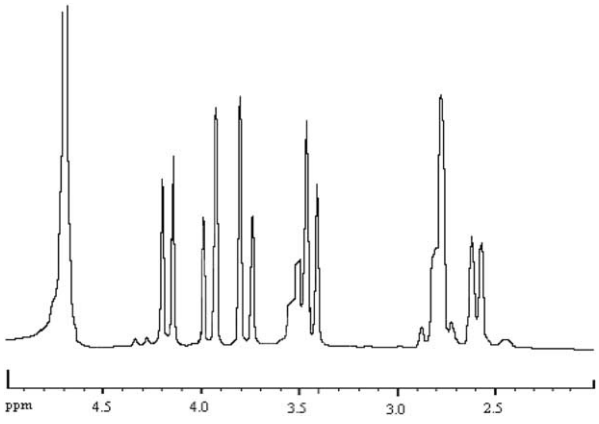


Fig. 3. ^1H NMR spectrum of $[Co(apda)(H_2O)_2]$.

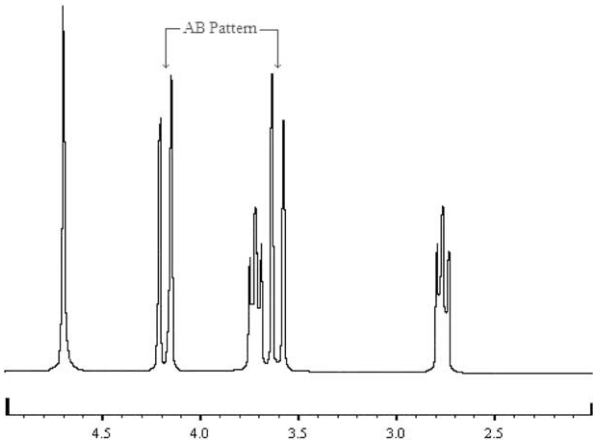


Fig. 4. ^{1}H NMR spectrum of $Na[Co(Hapda)_2] \cdot xH_2O$.

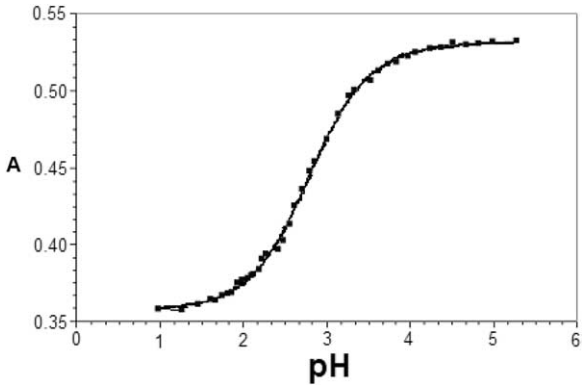


Fig. 5. Plot of Abs. (λ = 348 nm) vs. pH for $[Co(apda)_2]^{3-}$ (4.5×10^{-3} M), 25 °C, μ = 1.0 M ($NaClO_4$).

The disappearance of the singlet observed for the free ligand and the appearance of two doublets with an AB pattern at ~3.6 and 4.2 ppm, both integrating for four protons, indicate that the glycinate protons keep some equivalency. If all the protons were non-equivalent one would have expected four doublets integrating for one proton each. In this case, H_{Ga} is equivalent with H_{Rb}, while H_{Gb} and H_{Ra} are equivalent. These observations for $Na[Co(Hapda)_2] \cdot xH_2O$ are consistent with the structural data reported for $[Co(H_2O)_6][Co(Hapda)_2]_2 \cdot H_2O$. This fact together with the i.r. and UV–Vis data suggests that the anionic unit, $[Co_2(Hapda)_2]^-$, is the same for both these complexes.

3.3. pH dependance of $[Co(Hapda)_2]^-$

The pH of solutions upon dissolving crystals of $Na[Co(Hapda)_2] \cdot xH_2O$ is ca. 5.5. The UV–Vis spectrum shows an immediate decrease in absorption at both the absorption maximum at 515 nm and the shoulder at 365 nm upon lowering the pH from ~5.5 to 2. The pH was adjusted to 5.5 again (KOH, 1 M) and the spectrum recorded. This resulted in the immediate increase in absorption at 515 and 365 nm to its original position, indicating a reversible process.

In another experiment the pH of a solution of $Na[Co(Hapda)_2] \cdot xH_2O$ was adjusted to 1 and kept over time. No change in the absorption spectrum was observed indicating that solutions of $[Co(Hapda)_2]^-$ is stable at pH 1 for several hours.

It was also observed that the final UV–Vis spectra at pH 2 is similar to the spectra obtained from the reaction solutions from which the crystals of $[Co(H_2O)_6][Co(Hapda)_2]_2 \cdot H_2O$ were obtained, indicating that the final product at pH ~ 2 is $[Co(Hapda)_2]^-$. An initial potentiometric titration revealed that the mole ratio of H^+-ions:complex ion is 2:1 between pH 6 and 2. This diprotic behaviour of $[Co(Hapda)_2]^-$ is illustrated in Eqs. (1) and (2).

$$[Co(Hapda)_2]^- \overset{K_{a_1}}{\rightleftharpoons} [Co(Hapda)(apda)]^{2-} + H^+ \quad (1)$$

$$[Co(Hapda)(apda)]^{2-} \overset{K_{a_2}}{\rightleftharpoons} [Co(apda)_2]^{3-} + H^+ \quad (2)$$

The acid dissociation constants of $[Co(Hapda)_2]^-$ and $[Co(Hapda)(apda)]^{2-}$, K_{a_1} and K_{a_2}, were spectrophotometrically determined at λ = 348 nm at 25 °C by adjusting the pH of a $[Co(apda)_2]^{3-}$ solution from pH 5.28 to 0.98 (4.5×10^{-3} M) with HCl (1 M) and immediately measuring the absorbance. The spectrophotometric data were fitted to Eq. (3) (solid line in Fig. 5) and the values for pK_{a_1} and pK_{a_2} were determined as 2.6(1) and 2.8(1), respectively.

$$A_{tot} = \frac{A_a + A_h(K_{a_1}/[H^+]) + A_0(K_{a_1}K_{a_2}/[H^+]^2)}{K_{a_1}/[H^+] + (K_{a_1}K_{a_2}/[H^+]^2)}. \quad (3)$$

In Eq. (3), A_{tot} is the absorbance at a specific $[H^+]$, A_a = absorbance of the H_2A species, A_0 = absorbance of A^{2-}, A_h = absorbance of the HA^- species and K_{a_1} and K_{a_2} the acid dissociation constants.

The values for K_{a_1} and K_{a_2} are very close. This is to be expected since the chemical environments of $[Co(Hapda)_2]^-$ and $[Co(Hapda)(apda)]^{2-}$ are very similar.

4. Conclusion

In summary, a novel Co(III) complex, $[Co(H_2O)_6][Co(Hapda)_2]_2 \cdot H_2O$, has been synthesised and structurally characterised. The X-ray crystallographic data points to the fact that the strain in glycinato rings of Co(III) complexes with tripod type ligands could be attributed to packing effects.

The value of ^{1}H NMR as an identification tool for these complexes has been highlighted with the spectra of the title complex and $[Co(apda)(H_2O)_2]$. The difference in chemical environment of bonded and unbonded arms of tripod ligands like apda, enables the scientist to

determine whether tri- or tetradentate bonding has occurred.

5. Supplementary material

Crystallographic data reported in this paper have been deposited with the CCDC, No. 244 034. Copies of this information may be obtained free of charge from the Director, CCDC, 12 Union Road, Cambridge CB2 1EZ, UK (fax: +44 1223 336033; e-mail: deposit@ccdc.cam.ac.uk) and www.ccdc.cam.ac.uk/conts/retrieving.html.

Acknowledgements

We thank the research fund of the University of the Free State for their strong support.

References

[1] R. Tsuchiya, A. Uehara, E. Kyuno, Bull. Chem. Soc. Japan 42 (1968) 1886.
[2] H.G. Visser, J.G. Leipoldt, W. Purcell, D. Mostert, Polyhedron 13 (1994) 1051.
[3] H.G. Visser, W. Purcell, S.S. Basson, Q. Claassen, Polyhedron 16 (1997) 2851.
[4] H.G. Visser, W. Purcell, S.S. Basson, Polyhedron 18 (1999) 2795.
[5] H.G. Visser, W. Purcell, S.S. Basson, Polyhedron 20 (2001) 185.
[6] F. Almazan, E. Garcia-Espana, M. Mollar, F. Lloret, M. Julve, J.J. Faus, J. Chem. Soc., Dalton Trans. (1990) 2565.
[7] H.G. Visser, W. Purcell, S.S. Basson, Transition Met. Chem. 26 (2001) 175.
[8] H.G. Visser, W. Purcell, S.S. Basson, Transition Met. Chem. 28 (2003) 235.
[9] O.P. Gladkikh, A.L. Poznyak, T.N. Polynova, M.A. Porai-Koshits, Russ. J. Inorg. Chem. 42 (1997) 1346.
[10] J.M. Gonzalez Perez, J. Niclós-Gutiérrez, N. Dung, B. Viossat, A. Busnot, M. Winterberger, Inorg. Chim. 184 (1991) 243.
[11] A.E. Obodovskaya, L.M. Shkol'nikova, A.L. Poznyak, Zhurnal Neorganicheskoi Khimii 37 (1992) 594.
[12] H.A. Weakliem, J.L. Hoard, J. Am. Chem. Soc. 81 (1959) 549.
[13] Bruker, SAINT+. Version 6.02 (includes XPREP and SADABS), Bruker AXS INC., Madison, WI, 1999.
[14] G.M. Sheldrick, SADABS, Version 2.03, University of Gottingen, Germany, 1996.
[15] Bruker, SHELXTL. Version 5.1 (includes XS, XL, XP, XSHELL), Bruker AXS INC., Madison, WI, 1999.
[16] K. Brandenburg, M. Berndt, Visual Crystal Structure Information System, Version 2.1, Germany, 1998.
[17] G.M. Bancroft, M.J. Mays, B.E. Prater, J. Chem. Soc., Chem. Commun. (1968) 1575.
[18] G.M. Bancroft, E.T. Libbey, J. Chem. Soc., Dalton Trans. (1973) 2103.
[19] J.E Barcley, A. Hills, D.L. Hughes, G.J. Leigh, J. Chem. Soc., Dalton Trans. (1988) 2871.
[20] S.H. Whitlow, Acta Crystallogr., Sect. B 28 (1972) 1914.
[21] K. Nakamoto, Infrared Spectra of Inorganic and Coordination Compounds, Wiley, New York, 1963.

those of the penicillin group. Cephalosporins interfere with the synthesis of the bacterial cell wall and consequently, act as bactericides [10]. With epidemic strains of bacteria often being resistant to several antibiotics, and the growing problem worldwide of Gram-negative antimicrobial resistance, cephalosporins, rather than penicillin, constitute the essential tool with which to face this problem [11,12].

Considerable attention has been paid recently to the synthesis and characterization of siderophore analogues. Siderophores are low-molecular-weight organic ligands (0.5–1.5 kDa) with high affinity and specificity for iron. Under iron-limiting conditions, siderophores are excreted by cyanobacteria and heterotrophic bacteria [13–15]. Due to their attributes, this type of compound has been investigated for clinical use in the detoxification of certain metals [16]. Among them, there have been characterized siderophores containing thiazine rings, such as the desferrithiocin analogue DL-2-(3-hydroxypyridin-2-yl)-4H-5,6-dihydro-1,3-thiazine-4-carboxylic acid [17]. Unfortunately, many of these substances cannot be crystallized as single crystals of appropriate size and quality for conventional single-crystal diffractometry. For such cases, therefore, the structure has to be determined by powder diffractometry, which is very far from being routine.

The method followed in this study to resolve the crystal structure of the title compound can be categorized as one of the so-called 'direct-space methods' [18]. Here, a structural model of the compound is first elaborated and then optimized by molecular modelling without reference to the experimental XRD pattern. Subsequently, these molecules are placed arbitrarily within the unit cell previously determined from the diffraction data. The position of the molecules is then modified by global optimization techniques (typically Monte Carlo methods, genetic algorithms, or grid search methods) with the objective of finding the best agreement between the theoretical and experimental XRD patterns (the comparison between both patterns is quantified in terms of the *R*-factors). Finally, the best model of the crystal structure is refined using the Rietveld method.

This is the methodological framework of the present study, which determines the crystal structure of the title zinc(II) coordination compound from powder diffraction data. Because of the challenge represented by the alternative to the conventional single-crystal diffractometry and the biological reasons mentioned above, we report the characterization by elemental analysis, infrared (IR) spectroscopy, and X-ray powder diffractometry of the zinc(II) complex [$ZnCl_2$(TdTz)] [TdTz = 2-(3,4-dichlorophenyl)imino-N-(2-thiazin-2-yl)thiazolidine]. In addition, we report the crystal structure of the TdTz ligand determined by X-ray single-crystal diffractometry.

2. Experimental

2.1. Preparation of 2-(3,4-dichlorophenyl)imino-N-(2-thiazin-2-yl)thiazolidine (TdTz)

The synthesis of the TdTz ligand was performed according to the procedure reported elsewhere [19], and was recrystallized from ethanol 96% (1.5 g; 53%).

2.2. Preparation of [$ZnCl_2$(TdTz)]

The [$ZnCl_2$(TdTz)] complex was isolated from an ethanol–water solution of $ZnCl_2$ (39.4 mg, 0.3 mmol) that was added to an ethanol–water solution of TdTz (100 mg, 0.3 mmol). The resulting solution was allowed to evaporate slowly at room temperature. After a few days, colourless crystals were isolated from the solution (83 mg, 60%). The crystals were first separated by filtration, then washed with cold ether and finally air-dried. *Anal*. Calc. for $C_{13}H_{13}Cl_4ZnN_3S_2$: C, 32.36; H, 2.71; N, 8.71; S, 13.29. Found: C, 32.74; H, 2.85; N, 8.83; S, 13.19%.

2.3. Instrumental procedures

Chemical analyses of carbon, hydrogen, nitrogen, and sulfur were performed by microanalytical methods using a Leco CHNS-932 microanalyser. IR spectra were recorded on a Perkin–Elmer FT-IR 1720 spectrophotometer from KBr pellets for the 4000–370 cm^{-1} range, and on a Perkin–Elmer FT-IR 1700X spectrophotometer from polyethylene pellets for the 500–150 cm^{-1} range.

2.4. Crystal structure determinations

Crystals of the TdTz ligand with the appropriate size and quality for X-ray single-crystal diffractometry were isolated and used for the structural analysis. Unfortunately, this was not possible for the [$ZnCl_2$(TdTz)] complex, and therefore its crystal structure was determined by X-ray powder diffractometry. The crystals resulting from the synthesis of the [$ZnCl_2$(TdTz)] complex were highly elongated needles (aspect ratio of about 20) with lengths ranging from 100 to 800 μm (see Fig. 1). To avoid texture effects in the XRD pattern, these crystals were ground to a fine powder consisting of equiaxed particles (aspect ratio of about 1.1) with sizes ranging from 0.5 to 5 μm (see Fig. 2).

The experimental details of the crystal structure determination, including crystal data, data collection, structure determination, and refinement are listed in Table 1 for the ligand. X-ray single-crystal diffraction measurements were performed using a Bruker SMART CCD diffractometer. The first fifty frames were collected at the completion of data recording to monitor

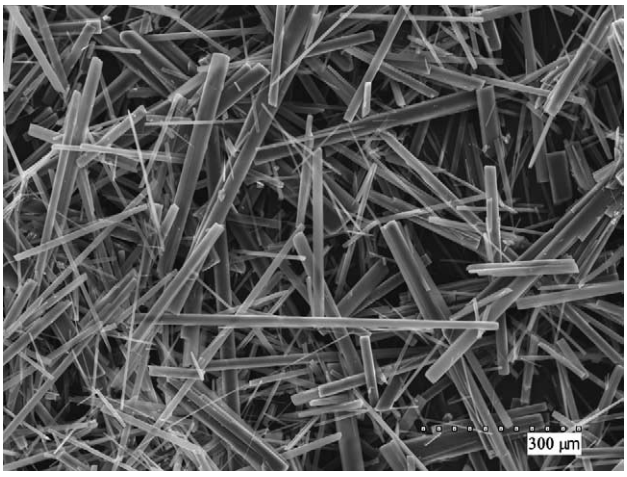


Fig. 1. Scanning electron microscopy image of the [$ZnCl_2$(TdTz)] complex crystals in the as-synthesized condition.

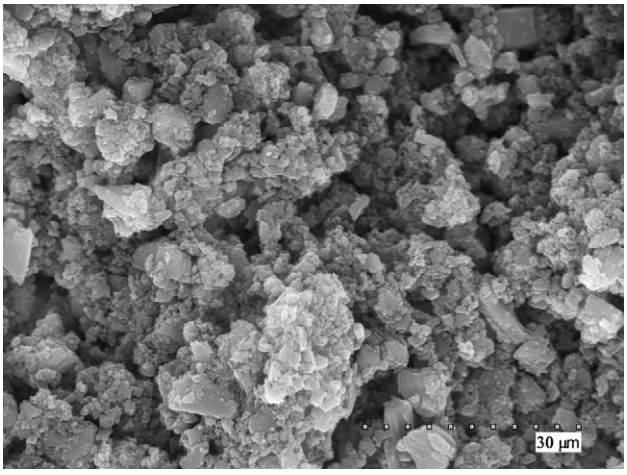


Fig. 2. Scanning electron microscopy image of the powder particles obtained after milling the [$ZnCl_2$(TdTz)] complex crystals.

for decay. Absorption corrections were applied using the program SADABS. The crystal structure was solved by means of direct methods and subsequent Fourier differences using the WINGX package [20], followed by a full-matrix least-squares refinement. The H atoms attached to the C atoms were positioned geometrically with the U_{iso} values derived from the U_{eq} values of the corresponding C atom. In the structure of ligand, C(3) and C(4) are disordered at two sites and refined with occupancy of two alternate orientations constrained to unity. The EADP restraints were applied to the disordered atoms to achieve convergence during least-squares refinement. The refined occupancy factor was 0.62 for orientation named A and 0.38 for orientation named B.

The XRD pattern for the structural determination of the complex was obtained via conventional powder diffractometry. Table 2 gives the experimental and set-up conditions used. Sample preparation included spreading the fine powder onto the holder (about 3 mm thick) and pressing slightly with a glass slide to ensure a flat surface.

Table 1
Details of the crystal data, data collection, and refinement for the [TdTz] ligand

Crystal shape	prism
Colour	colourless
Size (mm)	$0.47 \times 0.39 \times 0.35$
Chemical formula	$C_{13}H_{13}Cl_2N_3S_2$
Formula weight	346.30
Crystal system	monoclinic
Space group	C_12_1
Unit cell dimensions	
a (Å)	25.997(4)
b (Å)	7.895(1)
c (Å)	7.357(1)
β (°)	99.26(1)
Cell volume (Å^3)	1490.4(4)
Z	4
T (K)	298(2)
D_{calc} (g cm^{-3})	1.543
μ (mm^{-1})	0.708
F(0 0 0)	712
Diffractometer	bruker SMART CCD
Radiation	Mo Kα (λ = 0.71073 Å)
Collection method	ϕ–ω
2θ range	3.2–56.5
Index ranges	$-34 \leqslant h \leqslant 23$, $-10 \leqslant k \leqslant 9$, $-9 \leqslant l \leqslant 9$
Independent reflections	3018
Observed reflections	2472 [$F > 4.0\sigma(F)$]
Absorption correction	empirical
Max/min transmission	0.732/0.790
No. of refined parameters	182
R [$I > 2\sigma(I)$][a]	0.0474
wR [$I > 2\sigma(I)$][b]	0.1353
GOF[c]	1.062
ρ_{max}, ρ_{min} (e Å^{-3})	0.435, −0.327

[a] $R = \sum ||F_o| - |F_c|| / \sum |F_o|$.

[b] $R = \left\{ \sum \left[w\left(F_o^2 - F_c^2\right)^2 \right] / \sum \left[w\left(F_o^2\right)^2 \right] \right\}^{1/2}$.

[c] The goodness-of-fit (GOF) equals $\left\{ \sum \left[w\left(F_o^2 - F_c^2\right)^2 \right] / \left(N_{rf\,\mathrm{ln}s} - N_{\mathrm{params}}\right) \right\}^{1/2}$.

Table 2
Details of the data collection, structure solution, and refinement for the [$ZnCl_2$(TdTz)] complex

2θ range (°)	5–90
Step scan increment (°), counting time (s)	0.02, 20
Program used for structure solution	FOX [47]
Structure refinement	FULLPROF [44,45]
Number of reflections	2045
Number of atoms (H excluded)	23
Number of global parameters refined	47
Number of profile parameters refined	10
Number of structural parameters refined	74
R_{wp}, R_p, χ_r^2	0.093, 0.071, 6.23

Diffractometer: D5000 Siemens; Radiation: Cu Kα, graphite monochromator.

3. Results and discussion

3.1. Description of the crystal structure of the organic ligand (TdTz)

The X-ray single-crystal study of the TdTz ligand showed that the crystals are made up of monoclinic unit cells, each one containing four TdTz molecules. Fig. 3 is a diagram of the molecular structure with the atomic labelling. Selected bond lengths and angles are given in Table 3.

In the S(1)–C(1)–N(1)–C(2)–C(3)–C(4) ring, the short endocyclic C=N bond [C(1)–N(1) = 1.259(3) Å] is accompanied by a high S–C–N angle [S(1)–C(1)–N(1) = 127.3(2)°] and a relatively large S^{II}-C(sp^2) bond [S(1)–C(1) = 1.762(2) Å]. This is characteristic of a thiazine ring, as was deduced from comparison with 24 compounds containing a thiazine ring in their structure, obtained by the CONQUEST software [21] from the Cambridge Structural Database (CSD) [22] [mean values: C(1)–N(1) = 1.276 Å; S(1)–C(1)–N(1) = 128.5°; S(1)–C(1) = 1.751 Å]. In contrast, the S(2)–C(5)–N(2)–C(6)–C(7) ring shows a smaller S–C–N angle [S(2)–C(5)–N(2) = 111.2(2)°] and a short exocyclic C=N bond [C(5)–N(3) = 1.261(3) Å], which are indicative of an imino-thiazolidine form [23]. It is known that the imino tautomers can exist as two geometrical isomers, *syn* (*Z*) and *anti* (*E*), although in this crystal only *Z* isomers were observed.

The thiazolidine ring is essentially planar, with maximum mean-plane deviation for C(6) (0.037 Å). Due to the disorder found in C(3) and C(4), discussion of the thiazine ring conformation is pointless.

The crystal structure presents a static disorder affecting the Cl atom linked to the aromatic ring in position 3, due to an alternation of the Cl(1A)–H10 and Cl(1B)–H12 pairs with occupancy degrees of 48% and 52%, respectively.

The least-squares plane of the imino-thiazolidine moiety is practically coplanar to the best plane of the thiazine (8.2°) and is rotated 89.3° with respect to the least-squares plane of the 3,4-dichlorophenyl ring.

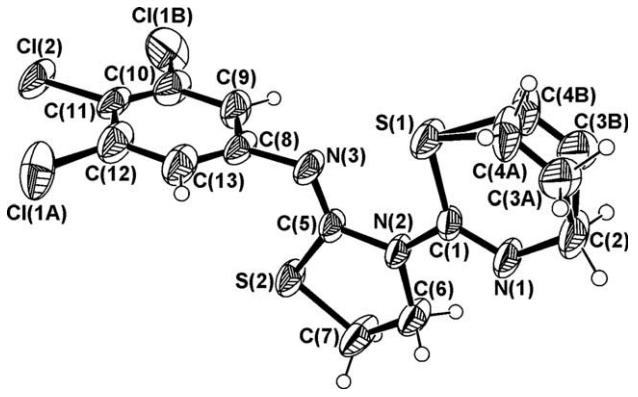


Fig. 3. Molecular structure of the [TdTz] ligand, showing the atom numbering scheme. The thermal ellipsoids are drawn at the 40% level.

Table 3
Selected bond lengths (Å) and bond angles (°) for the [TdTz] ligand

S(2)–C(5)	1.755(2)	S(2)–C(7)	1.786(3)
S(1)–C(1)	1.762(2)	S(1)–C(4A)	1.859(10)
S(1)–C(4B)	1.890(16)	N(2)–C(5)	1.386(3)
N(2)–C(1)	1.403(3)	C(5)–N(3)	1.261(3)
C(8)–N(3)	1.421(3)	C(1)–N(1)	1.259(3)
C(5)–S(2)–C(7)	93.1(1)	C(5)–N(2)–C(6)	115.1(2)
C(5)–N(2)–C(1)	127.0(2)	C(1)–N(2)–C(6)	117.7(2)
C(9)–C(8)–C(13)	119.1(2)	N(3)–C(8)–C(9)	117.0(8)
S(2)–C(5)–N(3)	124.6(2)	S(2)–C(5)–N(2)	111.2(2)
C(8)–N(3)–C(5)	119.2(2)	N(2)–C(5)–N(3)	123.9(2)
C(1)–N(1)–C(2)	124.1(2)	S(1)–C(1)–N(1)	127.3(2)
N(2)–C(1)–N(1)	115.9(2)	C(1)–S(1)–C(4A)	97.9(3)
C(1)–S(1)–C(4B)	97.7(5)		

3.2. Spectroscopic study

The IR spectrum of the TdTz organic-ligand has been described elsewhere [19]. The IR spectrum of the complex [$ZnCl_2$(TdTz)] shows bands assignable to: the thiazine ring vibrations at 1545 (Ψ_1), 1006 (Ψ_2), 943 (Ψ_3), 838 (Ψ_4), 757 and 748 (Ψ_5), 721 (Ψ_6), 628 (Ψ_7), 589 (Ψ_8), and 538 cm^{-1} (ϕ_1) [25–27]; the thiazolidine ring vibrations at 1030 (νn_1), 914 (νn_2), 893 (νn_3), 696 (νn_4), 671 (νn_5), and 475 cm^{-1} (δn_2) [28,29]; and the 3,4-dichlorophenyl ring vibrations at 1588 (8b), 1463 (19b), 1373 (19a), 1251 (14), and 1119 (1) cm^{-1} [25]. Other relevant bands are observed at 1613 [ν(C=N)$_{imine}$], 1357 [ν(C–N)], and 1064 cm^{-1} [ν(C–Cl)$_{ortho}$] [30,31].

Comparison of the strong ν(C=N)$_{imine}$ absorption of the complex (1613 cm^{-1}) to that of the uncoordinated imine function of the ligand (1631 cm^{-1}) shows the former to be significantly shifted to a lower wavenumber. The same is the case with the in-plane stretching vibration corresponding to ν(C=N) skeletal vibration of the heterocyclic ring (Ψ_1 of the complex: 1545 cm^{-1}), which is also shifted towards lower wavenumbers compared to the free ligand (1604 cm^{-1}). One may hence deduce coordination via the imino nitrogens of the ligand [32–35].

The far IR spectrum of this complex shows the presence of three bands due to the metal–ligand stretching vibrations at 330, 304, and 218 cm^{-1}. Of these, the band at 330 cm^{-1} may include the ν(Zn–N_{imino}) vibration [32–34,36] and one ν(Zn–Cl) vibration [37,38], whereas the band at 304 cm^{-1} is assigned to the other ν(Zn–Cl) vibration [37,38]. Finally, the band at 218 cm^{-1} is assignable to ν(Zn–$N_{thiazine}$), in good agreement with the literature data for several complexes containing thiazoline or thiazine derivative ligands [19,38–40].

The results of this study together with the elemental analysis allow one to deduce a tetra-coordinated geometry for the complex.

3.3. Structural determination of the complex

The sequence used in the determination of the structure from the XRD pattern was: data reduction and indexing, molecular modelling, use of direct-space methods with a 'Monte–Carlo/parallel tempering' search algorithm, and finally Rietveld refinement [18].

3.3.1. Data reduction and indexing

The peak positions were identified using a derivative-based algorithm that is implemented in CELREF [41]. The XRD pattern was then indexed in the monoclinic system using the CRYSFIRE software package [42]; the best solution was obtained with the *TREOR90* indexer, and had a de Wolff figure-of-merit of $M(20) = 39.5$. By analyzing the XRD data with CHECKCELL [43] we obtained $a = 10.640(1)$ Å, $b = 9.019(1)$ Å, $c = 20.435(2)$ Å, $\beta = 108.35(1)°$, and $V = 1861(4)$ Å^3, whereas the space group was unambiguously found to be $P12_1/c1$. From this space group, we deduced the existence within the monoclinic unit cell of four molecules of $C_{13}H_{13}Zn_1N_3S_2Cl_4$. This result is in clear agreement with the experimental density of 1.72(1) Mg m^{-3} determined by the Archimedes method.

In this first stage, we also performed the Le Bail fit implemented as an option in the FULLPROF program [44,45], which will be used later for the final Rietveld refinement. The Le Bail fit, which makes no reference to any structure model, had a threefold objective: (1) to assess the goodness of the space group and the choice of cell; (2) to estimate the shape and width of the Bragg reflections, and the instrumental shifts; and (3) to evaluate the error not associated with the structure model. The *R*-factors obtained were $R_{wp} = 0.058$ and $R_p = 0.045$.

3.3.2. Molecular modelling

A first approximation to the molecular structure inside the crystal was obtained by molecular optimization using semi-empirical methods, since the compounds bonded by the weak van der Waals–London interaction (and perhaps hydrogen bonds) remain almost unmodified when switching from the isolated molecules to the crystalline states. We used the AM1, PM3, MNDO, and MNDO/d force fields included in the HYPERCHEM software package [46], with the starting model built from IR-spectroscopy data and the ligand structure determined by single-crystal diffractometry. The best optimization was obtained with MNDO/d (binding energy $E_b = -3530$ kcal mol^{-1}), with a conclusive difference in E_b of 12 kcal mol^{-1} with respect to the second-best optimized model.

3.3.3. Monte Carlo methods

The crystal structure was determined by Monte Carlo methods, using the 'parallel tempering' algorithm implemented in the FOX software package [47]. The structure was described in the Z-matrix formalism, which is especially useful for organic molecules of relative complexity [48,49]. In this formalism the geometry of the molecules is described by the bond distances, the bond angles, and the dihedral angles between the different atoms [50]. From the optimized molecular structure, the corresponding Fenske–Hall Z-matrix was built using the BABEL program [51], with the heavy Zn atom as pivot. In a first step we treated the molecule as a rigid body, and only refined the six translational and rotational degrees of freedom. After 800 000 movements, the weighted residual was $R_{wp} = 0.169$. To check for "uniqueness", this step was repeated several times using different random starting positions for the Zn pivot and molecule orientations. In the next step we relaxed the constraints on the Z-matrix parameters, and, after 450 000 additional movements, the weighted residual decreased to $R_{wp} = 0.148$. The Z-matrix coordinates were next converted to crystallographic coordinates for the Rietveld refinement.

3.3.4. Rietveld refinement

According to the Le Bail criterion [52], the final refinement of the structures determined from powder diffractometry must be performed using the Rietveld method [53]. We used the FULLPROF program implemented in the WINPLOTR software package [44,45], and refined the following items: background (cubic spline interpolation), scale factor, instrumental shifts, cell parameters, atomic positions (excluding the H atoms, which were rigidly linked to their bonding atoms), and Debye–Waller atomic thermal parameters, as well as the shape, width, and asymmetry of the Bragg reflections assumed to have pseudo-Voigtian form. The Rietveld refinement was initialized using the profile and instrumental parameters obtained previously with the Le Bail fit. In a first step the molecule was treated as rigid body, and then the atomic coordinates were refined applying restrains on bond lengths and angles. The final residuals were $\chi^2_r = 6.23$, $R_{wp} = 0.093$, $R_p = 0.071$, and $R_F = 0.106$, and the refined cell parameters were $a = 10.612(6)$ Å, $b = 9.006(5)$ Å, $c = 20.385(9)$ Å, and $\beta = 108.364(3)°$. Comparison of this R_{wp} value with that obtained from the Le Bail fit showed that the error associated with the structural model was small – 3.5% – thereby confirming the validity of the crystal structure. The plotted output from the Rietveld analysis is shown in Fig. 4. Table 4 gives the most representative crystallographic parameters. Fig. 5 shows a representation of the refined crystal structure.

3.4. Description of the structure of [$ZnCl_2$(*TdTz*)]

We discuss next the crystal structure of the zinc(II) complex, although our interpretation should be treated with caution since the crystallographic data were

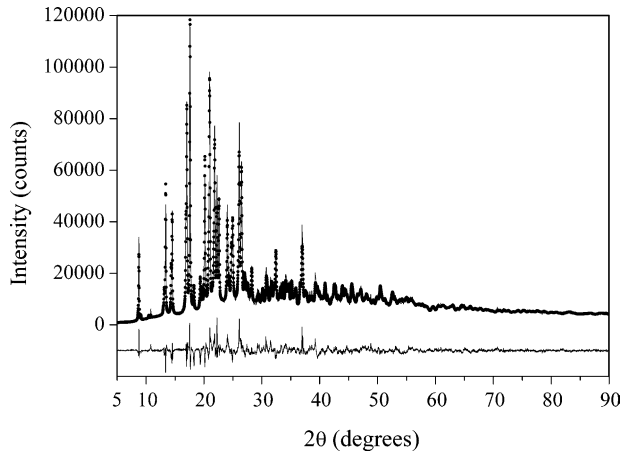


Fig. 4. Plot output from the Rietveld analysis of the X-ray diffraction pattern corresponding to the [$ZnCl_2$(TdTz)] complex. Points are the experimental X-ray diffraction data; the solid line is the calculated pattern; the residuals are plotted at the bottom.

Table 4
Main crystallographic data for the [$ZnCl_2$(TdTz)] complex obtained by X-ray powder diffractometry

Chemical formula	$C_{13}H_{13}Cl_4ZnN_3S_2$
Space group	P_12_1/c_1
Cell parameters	
a (Å)	10.612(6)
b (Å)	9.006(5)
c (Å)	20.385(9)
β (°)	108.364(3)

Coordinates

Atoms	*x*	*y*	*z*
Zn	0.6065(3)	0.1874(4)	0.6625(1)
N1	0.7536(3)	0.3477(5)	0.7328(2)
N2	0.6383(3)	0.5777(4)	0.6539(2)
N3	0.4548(3)	0.3555(4)	0.6075(1)
C1	0.7571(3)	0.4993(5)	0.7154(2)
C2	0.8748(3)	0.2788(6)	0.7834(2)
C3	0.9780(3)	0.3775(6)	0.8302(2)
C4	0.9268(3)	0.5120(6)	0.8445(2)
C5	0.5027(3)	0.5118(4)	0.6091(1)
C6	0.6685(4)	0.6949(4)	0.6189(2)
C7	0.5347(4)	0.7733(4)	0.5911(2)
C8	0.3397(3)	0.3248(4)	0.5949(1)
C9	0.2432(3)	0.4000(6)	0.6172(3)
C10	0.1074(3)	0.3663(6)	0.5855(2)
C11	0.0681(3)	0.2596(6)	0.5317(2)
C12	0.1653(3)	0.1863(6)	0.5094(3)
C13	0.3004(2)	0.2185(5)	0.5410(2)
S1	0.8462(4)	0.6279(5)	0.7687(2)
S2	0.4039(4)	0.6439(4)	0.5681(1)
Cl1	0.6982(3)	0.0772(4)	0.5952(2)
Cl2	0.5440(3)	0.0355(4)	0.7272(1)
Cl3	−0.0092(3)	0.4577(8)	0.6138(3)
Cl4	−0.0973(3)	0.2166(7)	0.4923(2)

determined from powder diffractometry. Selected bond lengths and angles of the complex are listed in Table 5, and the molecular structure is shown in Fig. 6.

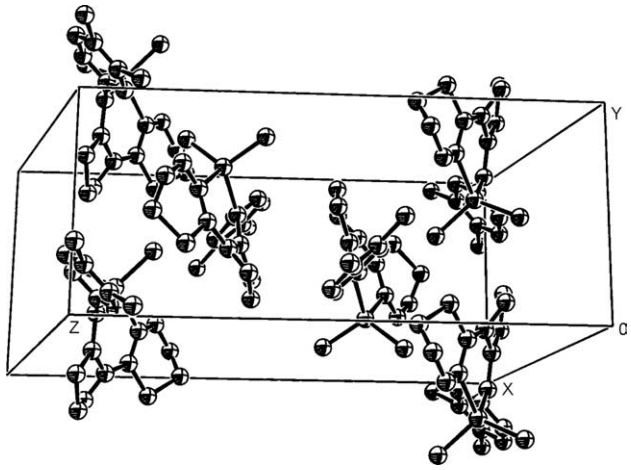


Fig. 5. Representation of the crystal structure of the [$ZnCl_2$(TdTz)] complex after refinement using the Rietveld method.

Table 5
Selected bond lengths (Å) and bond angles (°) for the [$ZnCl_2$(TdTz)] complex

Zn–Cl(1)	2.158(5)	Zn–Cl(2)	2.145(4)
Zn–N(1)	2.273(5)	Zn–N(3)	2.237(4)
C(1)–N(1)	1.414(6)	N(2)–C(5)	1.558(4)
N(2)–C(1)	1.632(5)	C(8)–N(3)	1.199(4)
C(5)–N(3)	1.493(5)		
Cl(1)–Zn–Cl(2)	112.7(3)	Cl(1)–Zn–N(3)	113.0(3)
Cl(2)–Zn–N(3)	115.3(3)	Cl(1)–Zn–N(1)	109.6(3)
Cl(2)–Zn–N(1)	107.5(3)	N(3)–Zn–N(1)	97.4(2)
C(5)–N(2)–C(1)	129.2(3)	Zn–N(3)–C(5)	116.1(3)
Zn–N(3)–C(8)	118.4(4)	C(5)–N(3)–C(8)	122.6(5)
Zn–N(1)–C(1)	121.5(4)	C(1)–N(1)–C(2)	119.0(5)
N(2)–C(1)–N(1)	122.4(5)	N(3)–C(5)–N(2)	128.1(4)

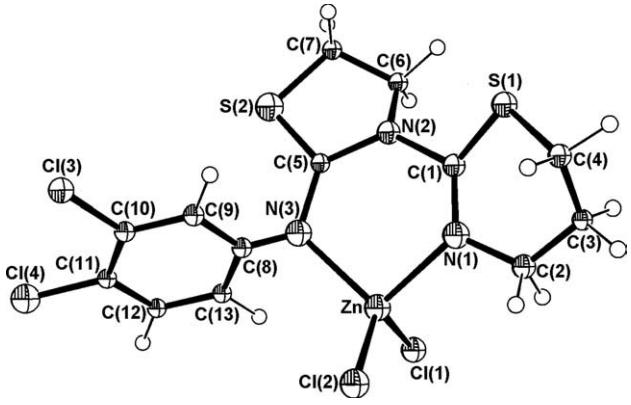


Fig. 6. Molecular structure of the [$ZnCl_2$(TdTz)] complex, showing the atom numbering scheme. The thermal ellipsoids are drawn at the 50% level.

The crystal's structure is a monoclinic lattice with four complex molecules per unit cell. The zinc(II) is bound to two chlorine atoms [Zn–Cl(1) = 2.158(5) Å; Zn–Cl(2) = 2.145(4) Å], one thiazine nitrogen [Zn–N(1) = 2.273(5) Å], and one imino nitrogen [Zn–N(3) = 2.237(4) Å] in a distorted tetrahedral geometry.

The [$ZnCl_2$(TdTz)] complex is the first compound with a 1,3-thiazine linked to zinc(II) that has been characterized structurally. The Zn–Cl bond lengths are slightly shorter than the average value [2.225(30) Å] calculated for 161 tetrahedral zinc(II) complexes with a chromophore group $ZnCl_2N_2$ found in a survey using the CSD. The $Zn–N_{imino}$ bond distance is comparable to the mean value [2.037(26) Å] calculated from the 62 crystal structures with chromophore group $ZnCl_2N_2$ and imino nitrogen contained in the CSD.

The ligand–metal–ligand bite angles differ from the ideal value of 109.5°, varying between 115.3(3)° [N(3)–Zn–Cl(2)] and 97.4(2)° [N(3)–Zn–N(1)].

The six-membered chelate ring Zn–N(1)–C(1)–N(2)–C(5)–N(3) [$Q = 0.324$ Å; $\theta = 60.9°$; $\phi = 1.6°$] [24] has a near to half-boat conformation, with the Zn atom deviating 0.532 Å from the plane formed by N(1)–C(1)–N(2)–C(5)–N(3) [the maximum mean-plane deviation for N(2) is 0.025 Å]. The puckering parameters calculated for the thiazine ring S(1)–C(1)–N(1)–C(2)–C(3)–C(4) [$Q = 0.547$ Å; $\theta = 73.5°$; $\phi = 288.1°$] indicate a near to twist-boat conformation according to Cremer and Pople [24]. Finally, the thiazolidine ring S(2)–C(5)–N(2)–C(6)–C(7) has a near to half-chair conformation, with the N(2) and C(6) atoms deviating 0.270 and 0.337 Å from the plane formed by S(2), C(5), and C(7), respectively.

As can be observed, the organic moiety in this complex preserves the imino-thiazolidine form detected in the TdTz ligand. The main difference is due to the different degree of rotation of the thiazine ring around the C(1)–N(2) bond, which permits electron donation through N(1) [torsion angles: S(1)–C(1)–N(2)–C(6) = 48.9° in the complex; −178.7° in the TdTz]. Similarly, there has been a rotation of the 3,4-dichlorophenyl ring around the C(8)–N(3) bond [torsion angles: C(9)–C(8)–N(3)–C(5) = −39.8° in the complex; −95.4° in the TdTz]. These two findings may be explainable in terms of crystal packing effects.

4. Supplementary material

CCDC 268601, corresponding to [TdTz], and CCDC 268602, to [$ZnCl_2$(TdTz)], contain the supplementary crystallographic data for this paper. These data can be obtained free of charge via www.ccdc.cam.ac.uk/conts/retrieving.html (or from the CCDC, 12 Union Road, Cambridge CB2 1EZ, UK; fax: +44 1223 336033; e-mail: deposit@ccdc.cam.ac.uk).

Acknowledgements

The authors thank the Junta de Extremadura (Consejería de Educación, Ciencia y Tecnología) and the FEDER [Project 2PR02A098] and [Project 2PR04A011] for financial support.

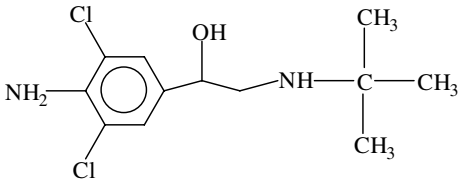
References

[1] A.J. Lucke, J.D.A. Tyndall, Y. Singh, D.P. Fairlie, J. Mol. Graphics Modell. 21 (2003) 341.
[2] J.D. Bourzat, C. Cotrel, C. Guyon, Pitchen, Ph. US Patent 4994569, 1991.
[3] A. Dozal, H. Keyzer, H.K. Kim, W.W. Wang, Int. J. Antimicrobial Agents 14 (2000) 261.
[4] D. Bozsing, P. Sohar, G. Gigler, G. Kovacs, Eur. J. Med. Chem. 31 (1996) 663.
[5] B. Tozkoparan, G. Aktay, E. Yesilada, Il Farmaco 15 (2002) 145.
[6] I.A. Shehata, H.I. Elsubbagh, A.M. Abdelal, M.A. Elsherbeny, A.A. Alobaid, Med. Chem. Res. 6 (1996) 148.
[7] R.F. Schinazi, R.A. Floyd, PCT Int. Appl. WO 90 13,296 (Cl. A61K31/54) (1991) Chem. Abstr. 115 (1991) 105989.
[8] M. Koketsu, K. Tanaka, Y. Takenaka, C.D. Kwong, H. Ishihara, Eur. J. Pharm. Sci. 15 (2002) 307.
[9] C.A. Bolos, K.T. Papazisis, A.H. Kortsaris, S. Voyatzi, D. Zambouli, D.A. Kyziakidis, J. Inorg. Biochem. 88 (2002) 25.
[10] A. Korolkovas, J.H. Burckhalter in: Compendio Esencial de Química Farmacéutica, Reverte, Barcelona, 1978.
[11] H. Wang, M. Chen, Diagnostic Microbiol. Infectious Dis. 51 (2005) 201.
[12] A. Carbonne, T. Naas, K. Blanckaert, C. Couzigou, C. Cattoen, J.-L. Chagnon, P. Nordmann, P. Astagneau, J. Hospital Infect. 60 (2005) 14.
[13] J.B. Neilands, J. Biol. Chem. 270 (1995) 26723.
[14] P.D. Tortell, M.T. Maldonado, J. Granger, N.M. Price, FEMS Microbiol. Ecol. 29 (1999) 1.
[15] S.W. Wilhelm, C.G. Trick, Limnol. Oceanogr. 39 (1994) 1979.
[16] K. Langemann, D. Heineke, S. Rupprecht, K.N. Raymond, Inorg. Chem. 35 (1996) 5663.
[17] R.J. Bergeron, C.Z. Liu, J.S. Mcmanis, M.X.B. Xia, S.E. Algee, J. Wiegand, J. Med. Chem. 37 (1994) 1411.
[18] L.M. González-Méndez, PhD Thesis, Department of Physics, University of Extremadura, Spain, 2002.
[19] F.J. Barros-García, A. Bernalte-García, A.M. Lozano-Vila, F. Luna-Giles, E. Viñuelas-Zahínos, Polyhedron 24 (2005) 129.
[20] L.J. Farrugia, J. Appl. Cryst. 32 (1999) 837.
[21] F.H. Allen, Acta Cryst. B58 (2002) 380.
[22] I.J. Bruno, J.C. Cole, P.R. Edington, M. Kessler, C.F. Macrae, P. McCabe, J. Pearson, R. Taylor, Acta Cryst. B58 (2002) 389.
[23] G. Argay, A. Kálmán, D. Lazar, B. Ribár, G. Tóth, Acta Crystallogr., Sect. B 33 (1977) 99.
[24] D. Cremer, J.A. Pople, J. Am. Chem. Soc. 97 (1975) 1354.
[25] A. Bernalte García, F.J. García Barros, F.J. Higes Rolando, F. Luna Giles, R. Pedrero Marín, J. Inorg. Biochem. 98 (2004) 15.
[26] A.I. Meyers, J. Org. Chem. 26 (1961) 218.
[27] A. Pastura, K. Thewalt, J. Prakt. Chem. 38 (1968) 177.
[28] M. Guiliano, G. Mille, J. Choteau, J. Mol. Struct. 50 (1978) 233.
[29] M. Guiliano, G. Mille, T. Avignon, J. Chouteau, J. Raman Spectrosc. 7 (1978) 214.
[30] R.T. Conley, in: Espectroscopía Infrarroja, Alhambra, Madrid, 1979.
[31] E. Pretsch, T. Clerc, J. Seibl, W. Simon, in: Tablas para la determinación estructural por métodos espectroscópicos, Springer-Verlag Ibérica, Barcelona, 2000.
[32] M. Shakir, S.P. Varkey, F. Firdaus, P.S. Hameed, Polyhedron 13 (1994) 2319.
[33] B. Singh, R.N. Singh, R.C. Aggarwal, Polyhedron 4 (1985) 401.
[34] M.M. Mostafa, M.A. Khattab, K.M. Ibrahim, Polyhedron 2 (1983) 583.

[35] J. Nelson, S. Martin Nelson, W.D. Perry, J. Chem. Soc., Dalton Trans. (1976) 1282.
[36] N.K. Singh, S. Agrawal, R.C. Aggarwal, Polyhedron 3 (1984) 1271.
[37] Y.J. Weaver, J.A. Weaver, J. Inorg. Nucl. Chem. 37 (1975) 1309.
[38] J.A. Weaver, P. Hambright, P.T. Talbert, E. Kang, A.N. Thorpe, Inorg. Chem. 9 (1970) 268.
[39] A. Bernalte García, F.J. García Barros, F.J. Higes Rolando, F. Luna Giles, Polyhedron 20 (2001) 3315.
[40] A.C. Fabretti, G. Peyronel, G.C. Franchini, Inorg. Chim. Acta 35 (1979) 49.
[41] U.D. Altermatt, I.D. Brown, Acta Cryst. A43 (1987) 125.
[42] R. Shiley, CRYSFIRE: a powder indexing suite. Collaborative computational project, number 14 (CCP14), School of Human Sciences, University of Surrey, UK, 1999.
[43] J. Laugier, B. Bochu, CHECKCELL: a software performing automatic cell/space group determination. Collaborative computational project, number 14 (CCP14), Laboratory of Materials and Physics Engineering, School of Physics, University of Grenoble, France, 2000.
[44] J. Rodríguez-Carvajal, FULLPROF: a program for Rietveld refinement and pattern matching analysis. In abstract of the satellite meeting on powder diffraction of the XV congress of the International Union of Crystallography, Toulouse, France, 1990.
[45] T. Roisel, J. Rodríguez-Carvajal, Mater. Sci. Forum 118 (2001) 378.
[46] HYPERCHEM. Release 5. Standalone Version. Computational Chemistry, Hypercube Inc., Publication HC50-00-03-00, October 1996, ISBN 1-896164-17-X.
[47] V. Favre-Nicolin, R. Cerný, FOX: a program for ab initio structure solution from powder diffraction data. Laboratory of Crystallography, University of Geneva, Switzerland, 2000.
[48] L.M. González-Méndez, F.L. Cumbrera, M.C. García-Cuesta, F. Sánchez-Bajo, A.L. Ortiz, F.J. Higes-Rolando, F. Luna-Giles, Mater. Lett. 58 (2004) 672.
[49] M.C. García-cuesta, A.M. Lozano, J.J. Meléndez-Martínez, F. Luna-Giles, A.L. Ortiz, L.M. González-Méndez, F.L. Cumbrera, J. Appl. Cryst. 37 (2004) 993.
[50] V. Favre-Nicolin, R. Cerný, J. Appl. Cryst. 35 (2002) 734.
[51] P. Walters, M. Stahl, BABEL: a program for the interconversion of file formats used in molecular modelling. Department of Chemistry, University of Arizona, USA, 1994.
[52] A. Le Bail, In the Structure Determination from Powder Diffraction Forum, http://www.cristal.org/sdpd/, 2002.
[53] R.A. Young, The Rietveld Method, Oxford University Press, Oxford, UK, 1993.

a chemical point of view these medications represent aminoalcohols, forming stable chelate mono- and binuclear complexes with copper(II), which have been thoroughly examined and characterized [4–6,9–11]. In some cases we were able to prove directly that the corresponding copper complexes are more active and have longer biological effects compared to the pure non-coordinated drugs [11,12].

Developing further the above ideas, it seemed challenging to study other aminoalcohols that have been used as medicines for treatment of different diseases and to try to clarify the following major topics: do they also form complexes with copper; are their compositions and structures analogous to those of the β-blocker complexes and finally – what is the biological effect of their copper complexes compared to the pure non-complexed drugs. The medication selected for the present study was the β_2-adrenergetic agonist Clenbuterol: 4-amino-α-(*t*-butylaminomethyl)-3,5-dichlorobenzyl alcohol hydrochloride, used in the clinical practice as a bronchodilator in the treatment of bronchial asthma, as bronchorelaxant and tokolytic agent in a series of other respiratory diseases. Due to its influence on the heart and respiratory rates it is used also as a doping agent.



HL

Although formally an aminoalcohol, Clenbuterol differs from the β-blockers by two features: (i) the aminoalcohol chain is directly attached to the phenyl ring and not through an oxygen atom as in the β-blockers; (ii) there is a second donor group ($-NH_2$) in the phenyl ring of HL capable of coordination, although it is sterically hindered by the two adjacent chlorine atoms. These differences in the ligand structure could change the complexation of copper, its homeostasis and hence – the effect of the drug.

Even the first preliminary experiments have shown that the aminoalcohol HL forms two types of complexes, depending mainly on the molar metal-to-ligand ratio and the solvent used as a reaction medium. With an excess of the ligand (M:HL = 1:10), in the presence of NaOH (HL·HCl:NaOH = 1:2) and in methanolic solution, the mononuclear violet complex **2** was obtained, while with comparable amounts of the reagents (M:HL = 1:1) and in a mixed solvent of higher polarity (CH_3OH + DMSO), 50% v/v, the binuclear green complex **1** was formed.

2. Experimental

2.1. Materials and synthesis

The aminoalcohol Clenbuterol, HL·HCl was supplied by Sopharma, Bulgaria, and used without any further purification. $CuCl_2 \cdot 2H_2O$ and NaOH were obtained from Riedel E. de Haën AG, CH_3OH from Fluka and DMSO from Merck. All reagents and solvents used were of analytical grade.

The binuclear complex **1** was obtained at ambient temperature when a 0.025 M solution of the ligand in DMSO (0.0784 g HL·HCl in 10 cm^3 DMSO) was mixed with 0.025 M $CuCl_2$ (0.0426 g $CuCl_2 \cdot 2H_2O$ in 10 cm^3 DMSO). Dropwise addition of 0.025 M NaOH (0.0200 g NaOH in 20 cm^3 CH_3OH) to the latter solution resulted in a green coloration, the molar ratio of the reagents being Cu:HL·HCl:NaOH = 1:1:2. Green prismatic crystals began to form and precipitate after one day at room temperature. The crystals were filtered, washed with 5 cm^3 of the DMSO + CH_3OH mixed solvent and dried over P_2O_5. Yield 40%; Chemical analysis: Calc. for $Cu_2L_2Cl_2 \cdot 4DMSO$: C, 36.16; H, 5.50; N, 5.27; Cl, 20.01; Cu, 11.96. Found: C, 35.88; H, 5.37; N, 5.38; Cl, 19.79; Cu, 11.42%. Melting point 157 °C.

The mononuclear complex **2** was obtained from a MeOH solution in the presence of a large excess of the ligand. A methanolic 0.025 M solution of HL·HCl (0.0784 g in 10 cm^3 MeOH) was mixed with 0.025 M $CuCl_2 \cdot 2H_2O$ (0.0043 g in 1.0 cm^3 MeOH) at a molar ratio Cu:HL·HCl = 1:10, followed by dropwise addition of 0.025 M NaOH in MeOH; HL·HCl:NaOH = 1:2. The above procedures led to a blue-violet coloration and violet crystals precipitated after 2 days at room temperature. They were filtered, washed with 5 cm^3 MeOH and dried over P_2O_5 (yield ca 21%). Calc. for $CuL_2 \cdot 2CH_3OH$: C, 45.92; H, 6.23; N, 8.24; Cl, 20.85; Cu, 9.34. Found: C, 46.32; H, 5.89; N, 8.59; Cl, 21.58; Cu, 8.92%. Melting point 111 °C.

2.2. Instrumentation and analysis

Electronic spectra were obtained on a Specord UV–Vis (Carl-Zeiss, Jena) instrument. IR spectra were recorded in the range 4000–400 cm^{-1} on a Specord-75 IR spectrometer, and in the range 500–75 cm^{-1} on a Bruker 113 V instrument in polyethylene. Thermogravimetric analyses were performed using a Perkin–Elmer TGS-2 instrument. The EPR spectra in the X-band were obtained with an ERS 220/Q instrument, using Mn/ZnS standard. Magnetic susceptibilities were measured between 2 and 300 K in a magnetic field of 1 kOe using a commercial SQUID magnetometer (Quantum Design MPMS-XL) with sensitivity in the range of 10^{-7} emu. The data were corrected for the diamagnetic response of the sample holder and for the diamagnetic contribu-

tion from the sample (Pascal's constants). Elemental analyses were performed according to classical methods: C, H were determined as CO_2 and H_2O, N through the Dumas' method, chlorine by titration with $Hg(NO_3)_2$ after wet digestion of the sample. Copper was determined by atomic absorption after wet digestion of the sample.

For the structure determinations a rod-shaped green crystal, $0.20 \times 0.06 \times 0.05$ mm in size, of compound **1** and a rod-shaped violet crystal, $0.24 \times 0.05 \times 0.06$ mm in size, of compound **2** were selected and mounted on a SIEMENS SMART X-ray diffractometer with a 1 K CCD area detector. Data sets were collected at room temperature using graphite monochromatized Mo Kα radiation ($\lambda = 0.71073$ Å). Hemispheres of data (1271 frames each at 5 cm detector distance) were collected using a narrow-frame method with scan widths of 0.30° in ω and an exposure time of 30 s/frame. The first 50 frames were measured again at the end of each data collection to monitor instrument and crystal stability. The data were integrated using the Siemens SAINT program [16]. The program SADABS was used for the absorption corrections [17]. Both structures were solved by direct methods and refined by full matrix least-squares techniques with the SHELX 97 software package [18]. Initially all non-hydrogen atoms were found from the Fourier maps. For compound **1** the hydrogen atoms have been added to the refinement model and their thermal parameters refined isotropically. Supplementary calculations when the hydrogen atoms were added and refined as riding models by using the appropriate AFIX commands resulted in a less satisfactory model not included in this manuscript [18]. The refinement of compound **2** has been carried out introducing all hydrogen atoms as riding models [18]. The main crystallographic details for complexes **1** and **2** are summarized in Table 1.

3. Results and discussion

3.1. Binuclear $Cu_2L_2Cl_2 \cdot 4DMSO$ complex *1*

3.1.1. X-ray data and crystal structure

The experimental data revealed that the green complex **1** has a binuclear structure with a general formula of $Cu_2L_2Cl_2 \cdot 4DMSO$. In the structure all atoms occupy general (2i: x, y, z) positions. The asymmetric unit of the title compound consists of one copper and one Cl atom, one ligand and two DMSO molecules, i.e., one half of the complex and solvent molecules (Fig. 1). Each copper atom is coordinated by one terminal chlorine, one nitrogen and two oxygen atoms

Table 1
Crystal data and structure refinement for $Cu_2L_2Cl_2 \cdot 4DMSO$ (**1**) and $CuL_2 \cdot 2CH_3OH$ (**2**)

	Complex **2**	Complex **1**
Empirical formula	$C_{26}H_{44}CuCl_4N_4O_4$	$C_{32}H_{58}C_{16}Cu_2N_4O_6S_4$
Formula weight	682.02	1062.84
Temperature (K)	293(2)	293(2)
Wavelength (Å)	0.71073	0.71073
Crystal system, space group	triclinic, $P\bar{1}$ (#2)	triclinic, $P\bar{1}$ (#2)
Unit cell dimensions		
a (Å)	9.284(4)	8.8110(6)
b (Å)	9.769(4)	10.9536(7)
c (Å)	9.984(4)	12.7832(8)
α (°)	99.675(8)	93.0840(10)
β (°)	110.372(7)	102.4080(10)
γ (°)	105.211(8)	104.4110(10)
Z, volume (Å^3)	1784.7(5)	11,159.48(13)
Calculated density (g/cm^3)	1.443	1.522
Absorption coefficient (mm^{-1})	1.074	1.486
F(000)	357	550
Crystal size (mm)	$0.24 \times 0.05 \times 0.06$	$0.20 \times 0.06 \times 0.05$
θ Range for data collection (°)	2.26–26.00	1.64–23.99
Limiting indices	$-10 \leqslant h \leqslant 10$, $-10 \leqslant k \leqslant 10$, $-10 \leqslant l \leqslant 10$	$-10 \leqslant h \leqslant 10$, $-12 \leqslant k \leqslant 12$, $-14 \leqslant l \leqslant 14$
Reflections collected/unique [R_{int}]	4925/2177 [0.0369]	8609/3626 [0.0278]
Refinement method	full-matrix least-squares on F^2	full-matrix least-squares on F^2
Data/parameters	2177/206	3626/361
Goodness-of-fit on F^2	1.091	1.062
Final R indices [$I > 2\sigma(I)$]	[a] $R_1 = 0.0523$, $wR_2 = 0.1273$	[a] $R_1 = 0.0358$, $wR_2 = 0.0959$
R indices (all data)	$R_1 = 0.0676$, [b] $wR_2 = 0.1338$	$R_1 = 0.0446$, [c] $wR_2 = 0.1006$
Large differential peak and hole (e A^{-3})	0.566 and −0.468	0.239 and −0.380

[a] $R_1 = \sum||F_o| - F_c|/\sum|F_o|$ (based on reflections with $I > 2\sigma(I)$).
[b] $wR_2 = [\sum w(|F_o| - |F_c|)^2/\sum w|F_o|2]^{1/2}$; $w = 1/[\sigma^2(F_o^2) + (0.0702)^2 + 1.01P]$.
[c] $wR_2 = [\sum(w|F_o| - |F_c|)^2/\sum w|F_o|2]^{1/2}$; $w = 1/[\sigma^2(F_o^2) + (0.0657P)^2]$, $P = [\max(F_o^2, 0) + 2F_c^2]/3$ (all data).

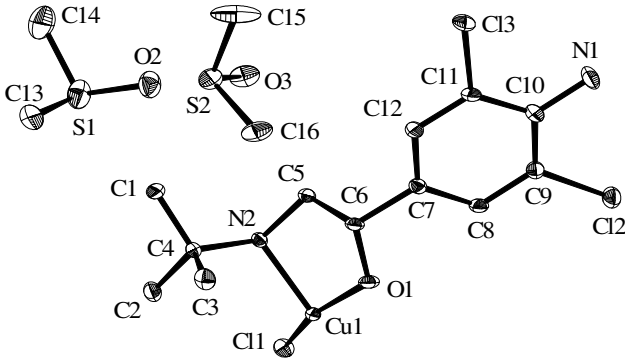


Fig. 1. Asymmetric unit, 50% thermal ellipsoids and labelling scheme of the binuclear complex **1**.

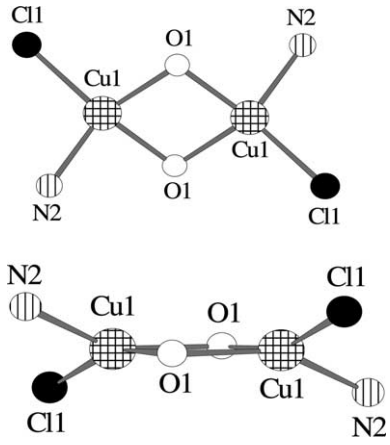


Fig. 2. Copper coordination of the binuclear complex **1**.

of two different ligand molecules (Fig. 2). Both oxygen atoms are connected to two adjacent copper atoms and thus act as bridges between them. The Cu_2O_2 structural core represents a flat rhomboid (distorted plain square) with Cu–O distances of 1.914(1) and 1.926(1) Å and O–Cu–O angles of 78.09(7)° (Table 2). The nitrogen and chlorine atoms completing the copper coordination reside out of the Cu_2O_2 plane at angles of 16.77(6)° and 17.02(6)°, respectively (Fig. 2, Table 2), the corresponding Cu–N and Cu–Cl distances being essentially the same as found in other similar complexes [12].

Each molecule of the binuclear complex participates also in the formation of H-bonds with four molecules of DMSO, two of them bonded with hydrogen atoms of the coordinated NH functions and two with the uncoordinated free NH_2 groups of the ligands (Fig. 3). Due to the different length of the two type H-bonds (N1–H13 = 0.86(1) Å, H13···O2 = 2.13(2) Å, N2–H1 = 0.80(1) Å and H1···O3 = 2.16(2) Å, Table 2), they differ in their bond-strength, confirmed also by the corresponding thermogravimetric data (see below).

The overall structure of complex **1** could be described as a layered one consisting of slabs of $Cu_2L_2Cl_2$ molecules oriented parallel to the *ab* plane, separated by double layers of solvent DMSO molecules (Fig. 4).

Table 2
Selected bond lengths (Å) and angles (°) for the binuclear complex **1**

Cu(1)–O(1)#1	1.914(1)
Cu(1)–O(1)#2	1.926(1)
Cu(1)–N(2)#3	1.994(2)
Cu(1)–Cl(1)	2.2249(6)
Cu(1)–Cu(1)#3	2.9827(5)
N(1)–H(13)	0.86(1)
O(2)···H(13)H-bond	2.13(2)
N(2)–H(1)	0.80(1)
O(3)···H(1)H-bond	2.16(2)
O(1)#1–Cu(1)–O(1)#2	78.09(7)
O(1)#1–Cu(1)–N(2)#3	85.15(6)
O(1)#2–Cu(1)–N(2)#3	149.01(6)
O(1)#1–Cu(1)–Cl(1)	158.52(4)
O(1)#2–Cu(1)–Cl(1)	100.66(4)
N(2)#3–Cu(1)–Cl(1)	104.26(5)
Cl(1)–Cu(1)–O(1)–O(1)	16.77(7)
N(2)–Cu(1)–O(1)–O(1)	17.02(8)

Symmetry transformations used to generate equivalent atoms. #1: $-x+1, -y, -z+1$; #2: $x+1, y, z$; #3: $-x+2, -y, -z+1$; #4: $x-1, y, z$.

3.1.2. Thermogravimetric data

The thermogravimetric (TG) study revealed that in the temperature range 110–195 °C the mass of the complex diminished by 29.1%, equivalent to the release of four molecules of DMSO. The relatively low temperature for the beginning of the process could be related to the fact that DMSO is not directly coordinated to copper(II) but is incorporated in the crystal lattice by hydrogen bond formation.

The process of the DMSO removal proceeds in two stages. The first one that takes place at 110–165 °C is obviously due to the loss of the two DMSO molecules bound by weaker H-bonds with the hydrogens from the NH-functions (O3···H1, $r = 2.16(2)$ Å), while the last two DMSO molecules are associated with the hydrogens of the NH_2 group (O2···H13, $r = 2.13(2)$ Å) and are lost at higher temperatures (165–195 °C).

3.1.3. EPR and magnetochemical data

The intramolecular distance between the two copper(II) centres needs special attention, as it determines to a great extent the magnetochemical and EPR behaviour of the complex. In both frozen solution and solid samples at 77 K the green binuclear complex **1** is EPR silent and does not show any signals, a fact that correlates well with the short Cu–Cu distance of about 2.98 Å (Table 1). Evidently, the close vicinity and the proper orientation of the corresponding overlapping orbitals lead to a significant antiferromagnetic exchange interaction and to quenching of the signal.

These conclusions are in accordance with the magnetochemical data as well. As can be seen in Fig. 5, the

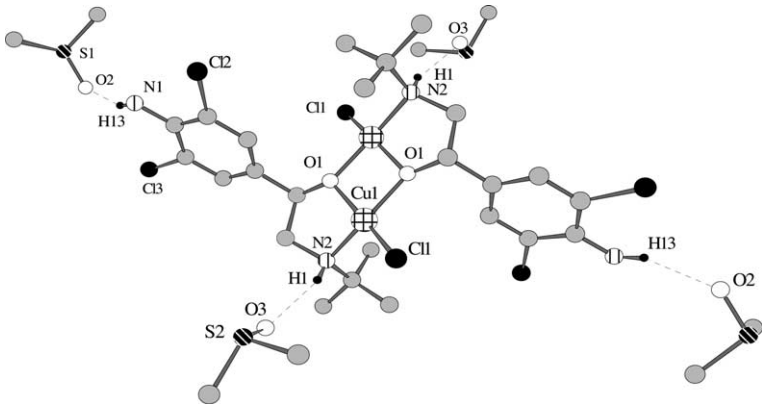


Fig. 3. Connectivity and H-bonding in $Cu_2L_2Cl_2 \cdot 4DMSO$.

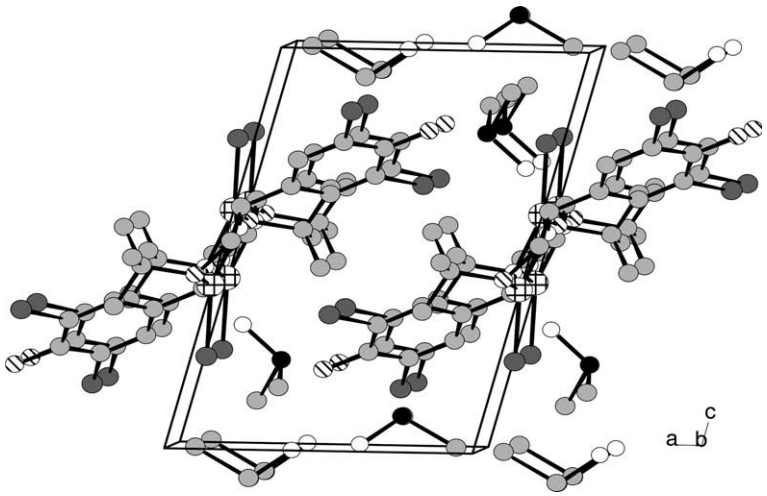


Fig. 4. Unit cell and 3-D packing of the binuclear complex **1**. The copper, nitrogen, chlorine, sulfur, carbon and oxygen atoms are shown as cross-hatched, hatched, dark-grey, black, grey and open circles, respectively, hydrogen atoms are omitted for clarity.

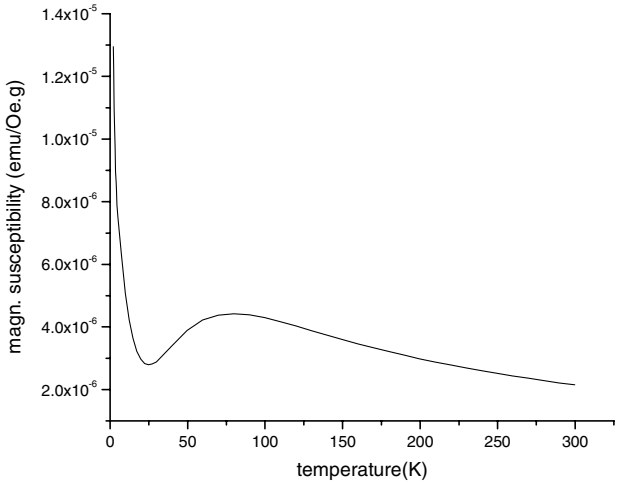


Fig. 5. Magnetic susceptibility vs. T for the binuclear complex **1**, measured at 1 kOe applied field.

magnetic susceptibility versus temperature curve has a complicated character with a maximum at T_N 80 K and an exponential course at lower temperatures. This later increase is signalling a paramagnetic contribution to the susceptibility at very low temperatures. At 125–300 K the Curie–Weiss law is followed with a large correlation coefficient of $R = 0.9993$. The effective magnetic moment calculated from the experimental data is 2.71 BM (the Weiss constant $C_m = 0.92$). Note that subtraction of the low-temperature paramagnetic component has negligible effect on both, the value of the effective magnetic moment and T_N. The absolute value of the paramagnetic asymptotic temperature, $\theta_N \approx -80$ K, is close to T_N suggesting that a paramagnetic-antiferromagnetic transition takes place at 80 K. The experimentally found magnetic moment is close to the theoretical one, which for a crystal field of $\Delta = 3000$ cm^{-1} is 2.65 BM [19–21]. Obviously, at temperatures over 125 K the antiferromagnetic interactions vanish and the Cu(II) centres show their paramagnetic character.

3.1.4. Electronic spectra

The binuclear complex **1** shows absorption bands at 750 and 380 nm in the mixed MeOH + DMSO solvent

described above. The first relatively weak band was assigned to a d–d transition in a near square-planar copper(II) structure, while the second more intense one at 380 nm ($\varepsilon \approx 460\,l\,mol^{-1}\,cm^{-1}$) was attributed to a charge-transfer transition O → Cu. The last band is typical for copper(II) polynuclear complexes with bridging oxygen atoms of the type Cu–O–Cu [22–24].

3.1.5. IR spectra

The pure ligand HL·HCl shows absorption bands at 3400, 3355, 3320–3120 cm^{-1} within the range 3500–3000 cm^{-1}, which are assigned to the stretching vibrations of hydroxyl, imino and aminogroups engaged in H-bonding of the intra- and intermolecular type [25]. This assignment is also supported by the fact that the coordination with Cu(II) leads to a pronounced decrease of the absorbance in the 2800–2300 cm^{-1} range due to the formation of H-bonds. Complex **1** shows only three bands at 3420, 3330 and 3180 cm^{-1}, ascribed to $\nu_{as}(NH_2)$, $\nu_{sym}(NH_2)$ and ν(NH). The reduction of the number of bands in this range after complexation could be related to deprotonation of the hydroxyl group and hence to the disappearance of the ν(OH) stretching vibration. At the same time three new bands in the far IR-spectrum appear at 490, 382 and 254 cm^{-1}, assigned to ν(Cu–N), ν(Cu–O) and ν(Cu–Cl), respectively [25]. Another broad and intensive band appears at 1030 cm^{-1} attributed to the stretching vibration ν(S=O) of the SO-group from the DMSO molecules [25].

3.2. Mononuclear $CuL_2 \cdot 2CH_3OH$ complex 2

3.2.1. X-ray data and crystal structure

The X-ray analysis and structure refinement showed that the violet compound **2** is a mononuclear complex with a square-planar structure and a general formula of $CuL_2 \cdot 2CH_3OH$. In the structure the copper atoms are located on an inversion centre and occupy one crystallographically independent special position (1c: 0, 1/2, 0), while all other atoms occupy general (2i: x, y, z) positions. The asymmetric unit of the complex consists of one copper atom, one ligand molecule, coordinated through its oxygen and nitrogen atoms, and one CH_3OH molecule, i.e., one half of the complex and solvent molecules (Fig. 6). The CuO_2N_2 core has a nearly square-planar structure with O–Cu–O and N–Cu–N angles of 180° (Fig. 7, Table 3). The Cu–O and Cu–N distances (Table 3) are in good agreement with those for other aminoalcohol complexes of Cu(II) [7,12]. The methanol molecules included in the overall structure are not directly coordinated to Cu(II) but form hydrogen bonds of the type $CH_3OH\cdots O$ with the oxygen atom of the ligand (Fig. 8) with O2–H15 and H15···O1 distances of 0.778(2) and 1.870(2) Å, respectively.

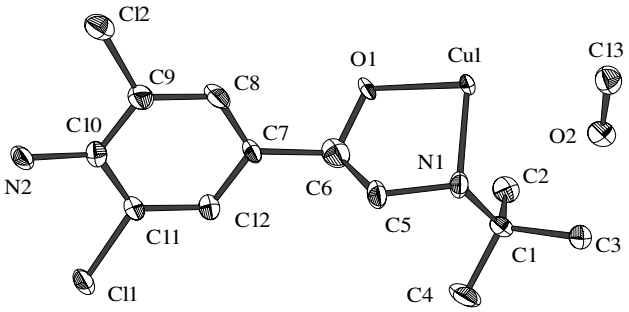


Fig. 6. Asymmetric unit, numbering scheme and thermal ellipsoids (50%) of the mononuclear complex **2**.

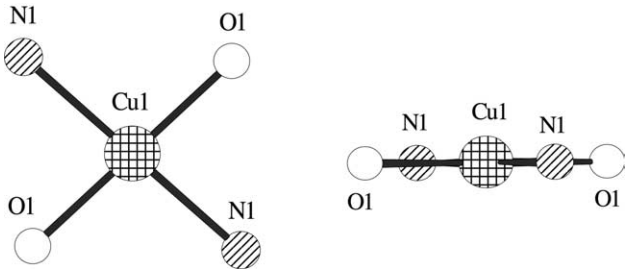


Fig. 7. Copper coordination of the mononuclear complex **2**.

Table 3
Selected bond lengths (Å) and angles (°) for the mononuclear complex **2**

Cu(1)–O(1)	1.898(2)
Cu(1)–N(1)#1	2.043(3)
Cu(1)–O(1)#1	1.898(2)
Cu(1)–N(1)	2.043(3)
O(1)···H(15)H-bond	1.870(2)
O(1)–Cu(1)–O(1)#1	180.0
O(1)#1–Cu(1)–N(1)#1	85.61(10)
O(1)–Cu(1)–N(1)	85.61(10)
O(1)#1–Cu(1)–N(1)	94.39(10)
O(1)–Cu(1)–N(1)#1	94.39(10)
N(1)–Cu(1)–N(1)#1	180.0

Symmetry transformations used to generate equivalent atoms. #1: $-x$, $-y+1$, $-z$; #2: $x-1$, y, z; #3: $x+1$, y, z.

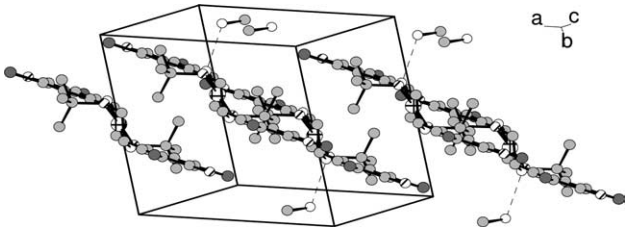


Fig. 8. Unit cell, 3-D packing and H-bonds in $CuL_2 \cdot 2CH_3OH$. The copper, nitrogen, chlorine, carbon and oxygen atoms are shown as cross-hatched, hatched, dark-grey, grey and open circles, respectively, hydrogen atoms are omitted for clarity.

3.2.2. Electronic, IR and EPR spectra

The electronic spectrum of the mononuclear complex **2** in methanol shows one broad asymmetric absorption band at 580 nm ($\varepsilon \approx 200\ l\ mol^{-1}\ cm^{-1}$) assigned to the d–d transition in a distorted tetragonal structure of the Cu(II) complex, where copper is bound with oxygen and nitrogen donor atoms.

The IR spectrum of **2** shows five bands in the 3470–3100 cm^{-1} range, assigned to the stretching vibrations of NH_2 and NH, shifted as a result of the coordination to Cu(II), and of (OH) from CH_3OH. In addition two new bands in the far IR spectrum appeared at 490 and 396 cm^{-1}, ascribed to ν(Cu–N) and ν(Cu–O), respectively [25]. The strong absorbance of the free ligand in the 2800–2300 cm^{-1} range is reduced in intensity due to the ligand coordination and the H-bond rupture caused by it.

The X-band EPR spectra of the complex, both in the solid phase and in frozen solutions (77 K), are typical for mononuclear paramagnetic Cu(II) complexes. The EPR parameters $g_{\|} = 2.245$, $g_{\perp} = 2.022$, $A = 160$ G and the relation $g_{\|} > g_{\perp}$ show that the unpaired d-electron of Cu(II) occupies predominately the $d_{x^2-y^2}$-orbital. Thus the formation of a strongly distorted (practically a square-planar) complex was confirmed again. The frozen solution spectra reveal also an unresolved SHFS from ^{14}N in the perpendicular magnetic field, due to the coordination of the NH-function to Cu(II). The same solution shows an isotropic signal with $g_{iso} = 2.120$ and $A_{iso} = 68$ G at 293 K. The experimental EPR data correlate well with those reported for similar copper(II) complexes [12].

4. Conclusions

Clenbuterol forms two complexes with copper(II) – the binuclear $Cu_2L_2Cl_2 \cdot 4DMSO$ and the mononuclear $CuL_2 \cdot 2CH_3OH$, acting as a bidentate chelate forming ligand with its imino and deprotonated hydroxyl functions. In both complexes copper has a slightly distorted square-planar coordination. In complex **1** the two copper atoms are linked together through oxygen atom bridges from two ligand molecules. Thus the coordination sphere around each of the two Cu centres includes two oxygen, one nitrogen and one terminal Cl atom. In complex **2** Cu(II) is coordinated with two oxygen and two nitrogen atoms from two ligand molecules.

The relatively short distance between the two copper atoms in **1** is responsible for a strong antiferromagnetic exchange interaction, that determines its interesting magnetic properties – a complete quenching of the EPR signals and a specific temperature dependence of the magnetic susceptibility. As for complex **2**, it shows the typical behaviour of a normal paramagnetic Cu(II) complex.

In the solid phase, solvent molecules (4DMSO or $2CH_3OH$ per molecule of the complex) are also incorporated in the crystal lattice, linked through H-bonds with the ligand. There is a marked difference, however, between the bonding of the two solvents. In **1** the DMSO molecules with their S=O groups serve as H-atom acceptors, the hydrogen atoms of the bond coming from NH and NH_2 of the ligand, while in **2** the H-atom acceptor is the oxygen of the deprotonated ligand, the H-atom donor being the OH function of CH_3OH.

5. Supplementary information

Full crystallographic details have been deposited in *cif*-format with the Cambridge Crystallographic Data Centre, CCDC 268587 for **1** and 268588 for **2**. Copies of this information can be obtained free of charge from the Director, CCDC, 12 Union Road, Cambridge, CB2 1EZ, UK, fax: +44 1223 336 033, e-mail: deposit@ccdc.cam.ac.uk, Web: http://www.ccdc.cam.ac.uk/conts/retrieving/html.

Acknowledgements

The authors greatly acknowledge the financial support provided by the National Research Fund of Bulgaria. They also thank Dr. R. Stoyanova from the Institute of General and Inorganic Chemistry, Bulgarian Academy of Sciences, for some of the EPR data.

References

[1] P.R. Bontchev, H. Kadum, G. Gochev, B. Evtimova, J. Macicek, Ch. Nachev, Polyhedron 11 (1992) 1973.
[2] P.R. Bontchev, G. Gochev, B. Evtimova, H. Kadum, Ch. Nachev, J. Inorg. Biochem. 46 (1992) 23.
[3] P.R. Bontchev, B. Ivanova, K. Koicheva, in: Proceedings of the 5th International Symposium on Applied Inorganic and Bioinorganic Chemistry, Corfu, Greece, 1999, p. 138.
[4] P.R. Bontchev, H. Kadum, B. Evtimova, Ch. Nachev, E. Zhecheva, D. Mehandjiev, D. Ivanov, J. Inorg. Biochem. 48 (1992) 153.
[5] P.R. Bontchev, I.N. Pantcheva, B. Ivanova, D.R. Mehandjiev, Bulg. Chem. Commun. 31 (1999) 59.
[6] P.R. Bontchev, I.N. Pantcheva, G. Gochev, D.R. Mehandjiev, D.S. Ivanov, Transition Met. Chem. 25 (2000) 196.
[7] P.R. Bontchev, B.B. Ivanova, R.P. Bontchev, D.R. Mehandjiev, D.S. Ivanov, Polyhedron 19 (2000) 1843.
[8] P.R. Bontchev, B.B. Ivanova, R.P. Bontchev, D. Mehandjiev, Polyhedron 20 (2001) 231.
[9] P.R. Bontchev, I.N. Pantcheva, T. Todorov, D.R. Mehandjiev, N.S. Savov, J. Inorg. Biochem. 83 (2001) 25.
[10] P.R. Bontchev, B.B. Ivanova, R.P. Bontchev, D. Mehandjiev, J. Coord. Chem. 54 (2001) 117.
[11] P.R. Bontchev, I.N. Pantcheva, R.P. Bontchev, D.S. Ivanov, N. Danchev, BioMetals 15 (2002) 79.

[12] P.R. Bontchev, I.N. Pantcheva, Transition Met. Chem. 27 (2002) 1.
[13] P.R. Bontchev, D.R. Mehandjiev, B.B. Ivanova, R.P. Bontchev, Transition Met. Chem. 28 (2003) 745.
[14] P.R. Bontchev, B.B. Ivanova, D.R. Mehandjiev, Bulg. Chem. Commun. 35 (2003) 21.
[15] P.R. Bontchev, Ch. Nachev, B. Evtimova, N.D. Yordanov, E. Zhecheva, D. Mehandjiev, in: Proceedings of the 12th International Conference on Coordination Chemistry, Smolenice, Slovakia, 1989, p. 47.
[16] Siemens Analytical X-ray Instruments; SAINT, Version 4.05, Madison, WI, USA, 1995.
[17] G.M. Sheldrick, Program SADABS, University of Göttingen, 1995.
[18] G.M. Sheldrick, SHELX 97 (Includes SHELXS 97, SHELXL97, CIFTAB) – Programs for Crystal Structure Analysis (Release 97-2). Institut für Anorganische Chemie der Universität, Tammanstrasse 4, D-3400 Göttingen, Germany, 1998.
[19] R. Boča, Theoretical Foundations of Molecular Magnetism, Elsevier, Amsterdam, 1999.
[20] E.A. Bondreaux, L.N. Mulay, Theory and Applications of Molecular Paramagnetism, Wiley, New York, 1976.
[21] O. Kahn, Molecular Magnetism, Wiley, Chichester, UK, 1994.
[22] T. Lindgren, R. Sillanpaeae, T. Nortia, K. Pihladja, Inorg. Chim. Acta 73 (1983) 153.
[23] G.A. van Albada, M.T. Lakin, N. Veldman, A.L. Spek, J. Reedijk, Inorg. Chem. 34 (1995) 4910.
[24] G.A. van Albada, W.J.J. Smeets, A.L. Spek, J. Reedijk, Inorg. Chim. Acta 260 (1997) 151.
[25] K. Nakamoto, Infrared and Raman Spectra of Inorganic and Coordination Compounds, 5th ed., Wiley, New York, Toronto, 1997.

For example, the mononuclear complex [Co(L-cys-*N*,*S*)$_3$] shows only the Δ isomer due to the large energy gap between the Δ and Λ diastereomers [8,9]. For trinuclear Co(III) complexes with L-cys-*N*,*S* and D-pen-*N*,*S* ligands, interesting synthetic behavior was observed [10–14], that is, the selectivities sometimes show a difference between L-cys-*N*,*S* and D-pen-*N*,*S* ligands, because of the structural effect of the two methyl groups on the carbon atom next to the sulfur atom in the D-pen-*N*,*S* ligand [10,11]. However, the L-cys-*N*,*S* and D-pen-*N*,*S* complexes are not good models for aet polynuclear complexes by virtue of the carboxyl group, which greatly influences the stereoselectivity of polynuclear structures by forming intermolecular hydrogen bonds [12–14]. On the other hand, the reaction using optically active *R*-1,2-propanediamine (*R*-pn) gave optically active metal centers, e.g., the configuration of [Co(*R*-pn)$_3$]$^{3+}$ is mainly a Δ configuration [15,16]. It has been reported that the polynuclear complexes ΔΔ-[M{Co(aet)$_2$(*R*-pn)}$_2$]$^{4+}$ (M = Ni^{II}, Pd^{II}, Pt^{II}) and Δ-[M(bpy){Co(aet)$_2$(*R*-pn)}]$^{3+}$ (M = Pd^{II}, Pt^{II}), have been stereoselectively obtained with an optically active ligand *R*-pn [17–20]. In these complexes, all *R*-pn chelate rings take a λ conformation because the methyl groups of *R*-pn take equatorial configurations. Therefore, introduction of chirality by a methyl group on the carbon atom next to the sulfur atom can play a role in not only stereochemical and electrochemical effects for thiolato sulfur atoms, but also stereoselective formation of S-bridged polynuclear complexes.

Recently, we have reported the aggregation of polynuclear structures using the *racemic* penicillaminate ligand. The reaction of [Co(D-pen-*N*,*O*,*S*)(L-pen-*N*,*O*,*S*)]$^-$ with $HgCl_2$ did not give [Hg{Co(D-pen-*N*,*O*,*S*)(L-pen-*N*,*O*,*S*)}$_2$] but [Hg{Co(D-pen-*N*,*O*,*S*)$_2$}{Co(L-pen-*N*,*O*,*S*)$_2$}], accompanied by ligand-exchange on the mononuclear Co^{III} units [21]. Based on these observations, we designed 1-amino-2-propanethiolate (1-Meaet) as an aet derivative, which has a methyl group on the carbon atom next to the bridging sulfur atom. The methyl group does not form intramolecular hydrogen bonds and behaves as a small optically active center, distinct from the carboxylate group in L-cys-*N*,*S*, D-pen-*N*,*S* and L-pen-*N*,*S*. Therefore, the 1-Meaet ligand is expected to affect the stereoselective formation of S-bridged polynuclear complexes. In the [M(1-Meaet)$_3$] type unit, however, too many isomers were possible due to the Δ,Λ isomer and *R*,*S* configurations. Accordingly, it is convenient that the Ni(II) ion is used to construct polynuclear structures because of the simple geometry of the mononuclear unit [Ni(1-Meaet)$_2$] and substitution activity of the Ni(II) ion.

In this work, the structural and spectroscopic behaviors of mononuclear and polynuclear Ni(II) complexes with aet and the 1-Meaet ligand were investigated. First, the spectroscopic properties of the mononuclear complexes [Ni(aet)$_2$] and [Ni(1-Meaet)$_2$] are discussed. It is important to know the properties of the mononuclear units deeply when the structural and chemical properties of the polynuclear structures are approached. Moreover, the environment around the sulfur atom in the complexes is known at ease without difficult structural analysis, when the spectroscopic behavior of the sulfur compounds is ascertained [22–29]. Further, the synthesis and characterization of trinuclear complexes [Ni{Ni(1-Meaet)$_2$}$_2$]$^{2+}$, hexanuclear complexes [Pd$_2$-{M(1-Meaet)$_2$}$_4$]$^{4+}$ (M = Ni^{II}, Pd^{II}), and dinuclear complexes [Pt(bpy){Ni(1-Meaet)$_2$(L)}]$^{2+}$ (L = (H$_2$O)$_2$, bpy) are reported. The structures of [Pd$_2${Ni$_{0.6}$Pd$_{0.4}$-(1-Meaet)$_2$}$_4$]$^{4+}$ and [Pt(bpy){Ni(1-Meaet)$_2$(bpy)}]$^{2+}$ were determined by X-ray diffraction. Spectral properties are discussed for all complexes. Furthermore, ligand optical selectivity for each complex was observed and these complexes are compared with the corresponding aet complexes [30–33].

2. Experimental

2.1. Materials

The complexes [Ni(aet)$_2$] (**1a**) [34], [Ni{Ni(aet)$_2$}$_2$]$^{2+}$ (**2a**) [30], [Pd$_2${Ni(aet)$_2$}$_4$]$^{4+}$ (**3a**) [31], [Pt(bpy){Ni(aet)$_2$-(H$_2$O)$_2$}]$^{2+}$ (**4a**) [33], [Pt(bpy){Ni(aet)$_2$(bpy)}]$^{2+}$ (**5a**) [33] and [PtCl$_2$(bpy)] [35,36] were prepared by procedures similar to those in the literatures. The reagents were purchased from Tokyo Kasei Kogyo Co., Ltd., Wako Pure Chemical Ind., Ltd., Kanto Chemical Co., Inc. and Aldrich Chemical Co., Inc. All the chemicals were of reagent grade and were used without further purification.

2.2. Synthesis of the ligand

The ligand was prepared by modified methods of the literature [37,38].

2.2.1. 1-Amino-2-propylsulfate

A mixture of 1-amino-2-propanol (75.1 g, 1.0 mol) and carbon tetrachloride (400 cm^3) was cooled in a salt–ice bath. Chlorosulfonic acid (116.5 g, 1.0 mol) was added slowly to the cooled mixture. The reaction mixture was kept for 1 d and carbon tetrachloride was removed with vacuo. The crude solid was crushed with methanol (500 cm^3) and isolated by filtration. A pure white powder of 1-amino-2-propylsulfate was obtained by recrystallization from water/methanol. Yield: 63.2 g (41%). Calc. for $NH_2CH_2CH(CH_3)OSO_3H = C_3H_9NO_4S$: C, 23.22; H, 5.85; N, 9.03. Found: C, 23.35; H, 5.66; N, 9.15%. ^{1}H NMR in D_2O (δ (ppm) from DSS): 1.40 (3H, d, $J = 6.5$ Hz, CC*H*$_3$), 3.12 (1H, dd, $J = 8.8$ and 13.7 Hz, NC*H*$_2$), 3.27 (1H, dd, $J = 2.9$ and 13.7 Hz, NC*H*$_2$), 4.72 (1H, m, OC*H*).

2.2.2. 5-Methyl-2-thiazolidinethione

To a suspension containing 1-amino-2-propylsulfate (135 g, 0.87 mol) and carbon disulfide (79.5 g, 1.05 mol) in 50% ethanol (500 cm^3) was added NaOH (80 g, 2.0 mol) in water (200 cm^3) slowly in a salt–ice bath. After refluxing the reaction mixture for 40 min, ethanol was removed by evaporation. White crystals of 5-methyl-2-thiazolidinethione were obtained by recrystallization from water. Yield: 63.3 g (48%). Calc. for $NHCH_2CH(CH_3)SCS = C_4H_7NS_2$: C, 36.06; H, 5.30; N, 10.51. Found: C, 35.72; H, 5.37; N, 10.22%. ^1H NMR in D_2O (δ (ppm) from DSS): 1.43 (3H, d, $J = 6.5$ Hz, CCH_3), 3.71 (1H, dd, $J = 4.1$ and 11.3 Hz, NCH_2), 4.10 (1H, m, SC*H*), 4.13 (1H, dd, $J = 7.1$ and 11.3 Hz, NCH_2).

2.2.3. 1-Amino-2-propanethiol hydrochloride (1-MeaetH·HCl)

A suspension of 5-methyl-2-thiazolidinethione (19.8 g, 0.15 mol) in 6 M HCl (100 cm^3) was refluxed for 1 week. After evaporation to an oil, a white precipitate of 1-MeaetH·HCl was obtained by addition of a large amount of ethanol. Yield: 13.2 g (50%). Calc. for $NH_2CH_2CH(CH_3)SH\cdot HCl\cdot 0.75(H_2O) = C_3H_{11.5}ClNO_{0.75}S$: C, 25.53; H, 8.21; N, 9.92. Found: C, 26.07; H, 8.00; N, 9.90%. ^1H NMR in D_2O (δ (ppm) from DSS): 1.41 (3H, d, $J = 6.9$ Hz, CCH_3), 2.99 (1H, dd, $J = 8.9$ and 12.8 Hz, NCH_2), 3.16 (1H, m, SC*H*), 3.25 (1H, dd, $J = 5.1$ and 12.9 Hz, NCH_2).

2.3. Synthesis of the complexes

2.3.1. [Ni(1-Meaet)$_2$] (**1b**)

A solution containing 1-MeaetH·HCl (10.2 g, 0.080 mol) and NaOH (6.4 g, 0.16 mol) in water (100 cm^3) was added dropwise to a solution containing $NiCl_2\cdot 6H_2O$ (9.51 g, 0.040 mol) in water (100 cm^3). The mixture was stirred at 95 °C for 10 min. After cooling to room temperature, the resulting green precipitate was collected by filtration and washed with a large amount of water and methanol. Yield: 9.96 g (83%). Calc. for $[Ni(1\text{-}Meaet)_2] = C_6H_{16}N_2NiS_2$: C, 30.15; H, 6.75; N, 11.72. Found: C, 30.16; H, 6.61; N, 11.68%.

2.3.2. [Ni{Ni(1-Meaet)$_2$}$_2$]Cl$_2$ (**2b**Cl$_2$)

A solution containing $NiCl_2\cdot 6H_2O$ (2.4 g, 10 mmol) in ethanol (50 cm^3) was added dropwise to a suspension containing [Ni(1-Meaet)$_2$] (0.48 g, 2.0 mmol) in ethanol (30 cm^3). The mixed solution was stirred at room temperature for 1 h. The resulting brown powder was collected by filtration and washed with ethanol. Yield: 0.27 g (44%). Calc. for $[Ni\{Ni(1\text{-}Meaet)_2\}_2]Cl_2 = C_{12}H_{32}Cl_2N_4Ni_3S_4$: C, 23.72; H, 5.31; N, 9.22. Found: C, 23.62; H, 5.44; N, 9.09%.

2.3.3. [Pd$_2${Ni$_{0.6}$Pd$_{0.4}$(1-Meaet)$_2$}$_4$]Br$_4$ (**3b**Br$_4$)

To a green suspension containing [Ni(1-Meaet)$_2$] (0.71 g, 2.4 mmol) in water (50 cm^3) was added $Na_2[PdCl_4]$ (0.35 g, 1.2 mmol). The mixture was stirred at 40 °C for 2 h, which gave a deep red solution. After the mixture was allowed to stand at room temperature for 1 h, the [Ni(1-Meaet)$_2$] was filtered out. Addition of sat. NaBr aq. (20 cm^3) gave deep red crystals, which were washed with small amount of methanol–ethanol (1:1). One of the crystals was used for X-ray structural analysis. Yield: 0.41 g (43%). Pd:Ni = 3.66:2.34 (ICP analysis). Calc. for $[Pd_2\{Ni_{0.6}Pd_{0.4}(1\text{-}Meaet)_2\}_4]Br_4\cdot H_2O = C_{24}H_{66}Br_4N_8Ni_{2.4}OPd_{3.6}S_8$: C, 18.21; H, 4.20; N, 7.08. Found: C, 18.25; H, 4.34; N, 7.07%.

2.3.4. [Pt(bpy){Ni(1-Meaet)$_2$(H$_2$O)$_2$}](NO$_3$)$_2$ (**4b**(NO$_3$)$_2$)

To a suspension containing [$PtCl_2$(bpy)] (0.51 g, 1.2 mmol) in water (25 cm^3) was added [Ni(1-Meaet)$_2$] (0.36 g, 1.2 mmol). The mixture was stirred at 40 °C for 1 h, whereupon the mixture became a yellow-brown solution. After filtering off the unreacted materials, to the yellow-brown filtrate was added a saturated $NaNO_3$ solution (30 cm^3). The mixture was allowed to stand at room temperature for 3 d and the resulting yellow-brown crystals were collected by filtration. Yield: 0.55 g (61%). Calc. for [Pt(bpy){Ni(1-Meaet)$_2$(H$_2$O)$_2$}](NO$_3$)$_2$ = $C_{16}H_{28}N_6NiO_8PtS_2$: C, 25.61; H, 3.76; N, 11.20. Found: C, 25.56; H, 3.66; N, 11.51%.

2.3.5. [Pt(bpy){Ni(1-Meaet)$_2$(bpy)}](NO$_3$)$_2$ (**5b**(NO$_3$)$_2$)

To a solution containing [Pt(bpy){Ni(1-Meaet)$_2$(H$_2$O)$_2$}](NO$_3$)$_2$ (0.15 g, 0.2 mmol) in water (30 cm^3) was added 2,2′-bipyridine (0.030 g, 0.1 mmol). The mixture was stirred at 50 °C for 10 min, whereupon the color of the solution changed from yellow-brown to red-brown. To the solution was added a small amount of a saturated $NaNO_3$ solution, followed by standing at room temperature for 3 d. The resulting microcrystals were collected by filtration. One of the crystals was used for X-ray structural analysis. Yield: 0.11 g (59%). Calc. for [Pt(bpy){Ni(1-Meaet)$_2$(bpy)}](NO$_3$)$_2$·2H$_2$O = $C_{26}H_{32}N_8NiO_8PtS_2$: C, 34.60; H, 3.57; N, 12.42. Found: C, 34.88; H, 3.79; N, 12.45%.

2.4. Measurements

The elemental analysis (C, H, and N) was performed by the Research Facility Center for Science and Technology or the Department of Chemistry in the University of Tsukuba. The concentrations of the metal ions in the complexes were determined with a NIPPON Jarell-Ash ICPA-575 spectrophotometer. The UV/Vis absorption spectra were recorded with a JASCO V-570 spectrophotometer and solid state diffuse

reflectance (DR) spectra were recorded with the JASCO V-570 spectrophotometer equipped with an integrating sphere apparatus (JASCO ISN-470) using powder samples diluted with MgO. The IR and far-IR spectra were recorded with a JASCO FT/IR-550 spectrometer using KBr disks in the range 4600–400 cm^{-1} and Nujol mulls between polyethylene plates in the range 650–50 cm^{-1}. The Raman spectra were obtained on a JASCO RFT-200 laser Raman spectrophotometer using KBr disks with excitation by a YAG laser line (1064 nm). The ^{1}H and ^{13}C NMR spectra were recorded with a BRUKER AM-600 or AM-500 NMR spectrometer in D_2O and sodium 4,4-dimethyl-4-silapentane-1-sulfonate (DSS) was used as an internal reference. The sulfur K-edge XAS measurement was carried out in the fluorescence mode at the beamline BL-9A of the Photon Factory, High Energy Accelerator Research Organization (KEK-PF) using synchrotron radiation at 2.5 GeV with an average current of 400 mA. X-rays were monochromatized with a Si(1 1 1) double crystal monochromator and higher orders were reduced with a pair of Ni-coated flat mirrors [39,40]. The energy of the peaks of $Na_2S_2O_3 \cdot H_2O$ was assumed as 2472.02 eV. All the measurements were carried out at room temperature.

2.5. X-ray structure determination

Single crystal X-ray data collections were performed on a Rigaku R-AXIS RAPID (**3b**$Br_4 \cdot 4H_2O$) or a Rigaku Mercury CCD (**5b**$(NO_3)_2$) area detector with graphite-monochromatized Mo Kα (0.71069 Å) radiation. The intensity data were collected up to 55° at 296 K. The crystal data and experimental parameters are listed in Table 1. The positions of most non-hydrogen atoms were determined by a direct method (SIR-92 [41]) and some remaining atom positions were found by successive difference Fourier techniques (DIRDIF-99) [42]. The structures were refined by full-matrix least-square techniques using anisotropic thermal parameters for non-hydrogen atoms. In **3b**$Br_4 \cdot 4H_2O$, the mixed Ni/Pd sites (0.6Ni + 0.4Pd) atoms (M1 and M2) were refined as Ni atoms with a site occupancy factor of 1.277, according to the reported method [31], and no hydrogen atoms were included in the refinement. In **5b**$(NO_3)_2$, the disordered C16 and C27 atoms were refined with a site occupancy factor 0.5, and all hydrogen atoms except those connect to disordered carbon atoms were included in the refinement but restrained to ride on the atoms (C–H = N–H = 0.95 Å, $U(H) = 1.2U(C, N)$). The calculations were performed using the CrystalStructure crystallographic software package [43].

3. Results and discussion

3.1. Synthesis and properties of the ligand

1-MeaetH·HCl was prepared by modified methods of the literature [37,38]. There was a very simple description

Table 1
Crystallographic data for $[Pd_2\{Ni_{0.6}Pd_{0.4}(1\text{-Meaet})_2\}_4]Br_4 \cdot 4H_2O$ (**3b**$Br_4 \cdot 4H_2O$) and $[Pt(bpy)\{Ni(1\text{-Meaet})_2(bpy)\}](NO_3)_2$ (**5b**$(NO_3)_2$)

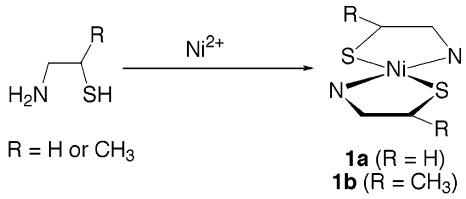
	3b$Br_4 \cdot 4H_2O$	**5b**$(NO_3)_2$
Empirical formula	$C_{24}H_{72}Br_4N_8Ni_{2.4}O_4Pd_{3.6}S_8$	$C_{26}H_{32}N_8NiO_6PtS_2$
Formula weight	1636.90	870.50
Crystal color, habit	orange, platelet	red, prism
Crystal dimensions (nm)	$0.10 \times 0.10 \times 0.20$	$0.45 \times 0.30 \times 0.20$
Crystal system	triclinic	monoclinic
Space group	$P\bar{1}$ (No. 2)	$P2_1/a$ (No. 14)
a (Å)	11.5581(6)	10.172(6)
b (Å)	13.0131(7)	23.878(13)
c (Å)	19.767(1)	13.665(8)
α (°)	82.379(2)	
β (°)	78.316(4)	112.448(7)
γ (°)	70.597(2)	
Volume ($Å^3$)	2739.2(3)	3067.5(31)
Z	2	4
D_{calc} ($g\,cm^{-3}$)	1.984	1.885
μ (cm^{-1})	52.32	53.42
Reflections collected	23 339	49 960
Reflections unique	12 004	7144
R_{int}	0.094	0.069
Reflections used ($I>2\sigma(I)$)	5386	5647
Parameters	505	431
R[a]	0.086	0.059
R_w[b]	0.087	0.094
Goodness of fit	1.000	1.001

[a] $R = \sum||F_o| - |F_c||/\sum|F_o|$.
[b] $R_w = [\sum w(|F_o| - |F_c|)^2/\sum wF_o^2]^{1/2}$, $w = 1/(0.0001F_o^2 + 3\sigma F_o^2 + 0.5)$ for **3b**$Br_4 \cdot 4H_2O$ and $1/(0.005F_o^2 + \sigma F_o^2)$ for **5b**$(NO_3)_2$.

with an aminothiol series in the literature, therefore the synthesis of 1-MeaetH·HCl was examined and was improved in detail. This ligand was obtained by a three step reaction (Scheme 1), and the compounds of each step and the desired ligand were characterized by elemental analysis and ^{1}H NMR spectra. The first step reaction is violent, even when the reaction was carried out on a salt–ice bath, to give 1-amino-2-propylsulfate. Elevation of the reaction temperature accelerates side reactions. The second step reaction gave 5-methyl-2-thiazolidinethione with ring formation reaction of 1-amino-2-propylsulfate and carbon disulfide. The third step reaction in 6 M HCl aqueous solution is a ring opening reaction giving 1-MeaetH·HCl. This ligand is soluble in water and less soluble to general organic solvents, and can be purified by washing with an organic solvent to remove 5-methyl-2-thiazolidinethione.

3.2. Synthesis and spectrochemical properties of the mononuclear complexes

The mononuclear complex [Ni(1-Meaet)$_2$] (**1b**) was prepared by a modified method of the corresponding aet complex [Ni(aet)$_2$] (**1a**), which involved the reaction of the 1-Meaet ligand with the Ni(II) ion in basic aqueous solution (Scheme 2). These neutral complexes **1a** and **1b** are not soluble in general solvents, but are soluble in acidic water following protonation on the sulfur atoms of coordinated thiolato group.

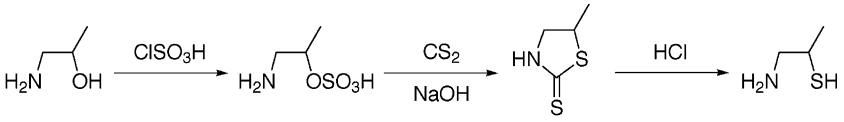


Scheme 2.

Table 2
Spectrochemical data of mononuclear complexes

	1a	1b	
DR (10^3 cm^{-1})	16.6	16.6	
	21.4	21.3	
	26.6	26.1	
	31.8	32.9	
	41.2	40.5	
Far-IR (cm^{-1})	545m	557s	ν(M–N)
	478w	491m	in-plane skeletal deformation
	378vs	419s	ν(M–S)
	334vs	391vs	σ(N–M–S)
		329m	
	292s	293vs	ring pucker
		277m	
	167m	170w	
	153s	142vs	σ(M–S–C)
	156w	121w	
		125w	
		115w	
Raman (cm^{-1})	514m	524m	ν(M–N)
	453s	455m	
		426m	
	328m	364s	ν(M–S)
	274w	278w	
	258m		
	235s	219vs	ring pucker
XAS (eV)	2470.3	2470.2	1s-antibonding(S–M)
	2472.2	2472.2	1s-σ*(S–C)

It is well known that the bonding relation of metal ion and donor atoms is reflected in the vibration spectra of the far-IR region about 600–100 cm^{-1}. By comparing with the Raman spectral data, the far-IR spectrum is more accurately attributed. The far-IR and Raman spectra are shown in Fig. 1. These data were assigned by a comparison to the spectra of complexes containing aet and related compounds [44–47] (Table 2). In general, the metal–amino stretching band is weaker than the metal–thiolato stretching band, which is discussed well in the literature [45–48]. The Ni–S stretching band of **1b** was observed at a higher region than that of **1a**, whereas the Ni–N band of **1b** was observed at a very similar region to that of **1a**. Namely, the Ni–S bands were influenced in the far-IR and Raman spectra by the methyl group on the carbon atom next to the sulfur atom. In addition, the far-IR and Raman spectra show complementary bands to each other, showing a *trans*(*S*)-N_2S_2 geometry.



Scheme 1.

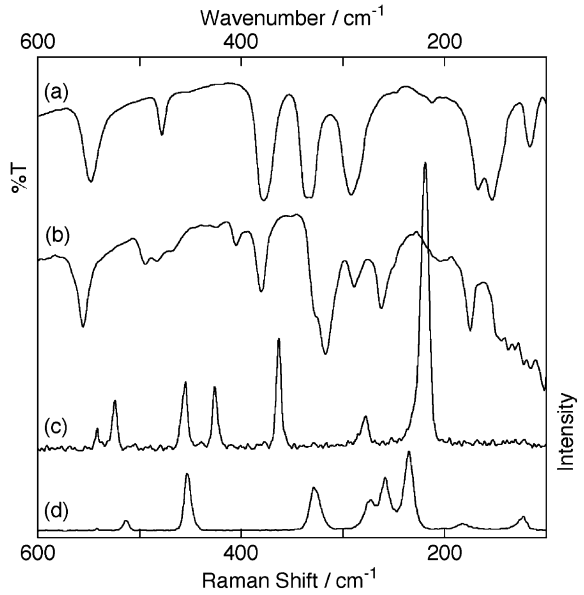


Fig. 1. Far-IR spectra of $[Ni(aet)_2]$ (**1a**) (a) and $[Ni(1\text{-}Meaet)_2]$ (**1b**) (b); Raman spectra of **1b** (c) and **1a** (d).

The sulfur atom has four X-ray absorption bands at ca. 2472, 229, 165 and 164 eV which derive from $1S_{1/2}$, $2S_{1/2}$, $2P_{1/2}$ and $2P_{3/2}$, respectively [22]. In the mononuclear complexes, the sulfur atoms have bonding only to carbon and metal ions. Recently, the analysis of the X-ray absorption spectrum of the ligand has paid attention to the relationship between the coordinated atom and metal ion. It is reported that the ligand K-edge spectra involve the nature of the electron transition from the 1s to np orbital [22–29]. The energy changes for the 3p orbital of the sulfur atom due to the effect of metal ion, and the transition energy from 1s to 3p also changes. In **1a** and **1b** there are two absorption bands at 2470 and 2472 eV in agreement with each other (Table 2). The band at 2470.3 eV in **1a** is shifted to 2470.6 eV in the isomeric metal complex $[Pd(aet)_2]$, regardless that the band at 2472.2 eV in **1a** is observed in same region in $[Pd(aet)_2]$ [49]. Consequently, the shifted band seems to be assigned to the transition from the S 1s orbital to the antibonding orbital of the S–M bond, and the unshifted band was assigned to the transition from the S 1s orbital to the σ* orbital of S–C bond.

3.3. Synthesis and spectrochemical properties of linear-type trinuclear complexes

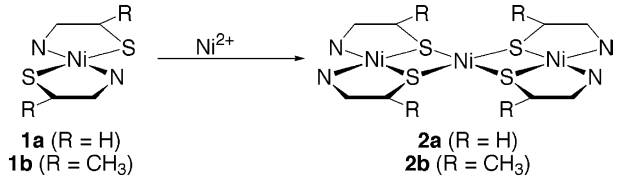
The reaction of $[Ni(1\text{-}Meaet)_2]$ (**1b**) with $NiCl_2\cdot 6H_2O$ in ethanol gave the S-bridged trinuclear complex, $[Ni\{Ni(1\text{-}Meaet)_2\}_2]Cl_2$ (**2b**Cl_2), which was not obtained in aqueous solution, different from the corresponding aet complex, $[Ni\{Ni(aet)_2\}_2]Cl_2$ (**2a**Cl_2) (Scheme 3). **2b** is soluble in water and methanol, but it easily decomposes to Ni(II) ion and ligand, and cannot be recrystallized conveniently. Namely, **2b** cannot retain its structure in a donating solvent such as water. This reflects the lower coordination ability of 1-Meaet compared to aet. Accordingly, all the measurements were carried out in the solid state.

The IR spectral pattern of **2b**Cl_2 shows more broadening than that of **2a**Cl_2 (Fig. S2), similar to those of the corresponding mononuclear complexes **1b** and **1a**. This behavior may depend on the existence of the diastereomers of **2b**Cl_2. In the far-IR spectra, the same phenomenon was observed (Fig. S3). On the other hand, DR spectral data of **2b**Cl_2, summarized in Table 3, exhibit some DR bands which are in good agreement with those of **2a**Cl_2. Consequently, **2b**Cl_2 is in agreement for a trinuclear alignment on the metal center like **2a**Cl_2 [30], although some diastereomers in **2b**Cl_2 differ from the aet derivative **2a**Cl_2.

3.4. Synthesis, structure and spectrochemical properties of pinwheel-like hexanuclear complexes

Syntheses of the complex $[Pd_2\{Ni_{0.6}Pd_{0.4}(1\text{-}Meaet)_2\}_4]^{4+}$ (**3b**) was achieved by the reaction of the mononuclear complex $[Ni(1\text{-}Meaet)_2]$ (**1b**) with 0.5 M equivalents $Na_2[PdCl_4]$ in water under moderate conditions (Scheme 4), in accord with the preparation of $[Pd_2\{Ni(aet)_2\}_4]^{4+}$ (**3a**) [31]. The partial substitution of the Ni(II) ion by the Pd(II) ion occurred during the reaction of **3b**. The ratio of metal ions was determined by ICP analysis. In contrast, no metal substitutions were observed for the corresponding aet complex **3a** [31]. From these facts, the coordination bonds of the Ni(II) and sulfur atoms for **3b** are weaker than those of **3a**. In the formation of **2b**, a similar synthetic behavior was observed.

X-ray structural analysis of **3b**$Br_4\cdot 4H_2O$ showed the presence of two crystallographically independent complex

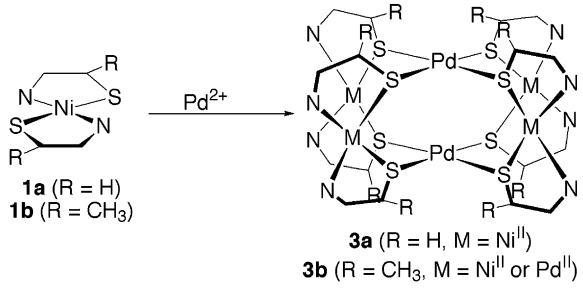


Scheme 3.

Table 3
Diffuse reflectance spectral data of the trinuclear complexes

	2aCl_2	**2b**Cl_2
DR (10^3 cm^{-1})	16.7	17.4
	19.9	19.8sh[a]
	23.5	23.5
	31.8	31.8

[a] sh denotes a shoulder.



Scheme 4.

cations, bromide anions and water molecules. A perspective drawing of one of the two complex cations of **3b** is shown in Fig. 2. The selected bond distances and angles are listed in Table 4. The structures of the two complex cations resemble each other well. The ICP analysis for **3b** gave a value of Ni:Pd = 2.4:3.6. Therefore, it was assigned that **3b** consists of four square-planar *cis*(*S*)-[M(1-Meaet)$_2$] (M = 0.6Ni + 0.4Pd) units and two central Pd atoms. Two S atoms in each of the four *cis*(*S*)-[M(1-Meaet)$_2$] units bind to two Pd atoms such that each Pd atom is situated in a square-planar environment. As a result, four S atoms in each PdS_4 plane are required to have the same absolute configuration, completing a pinwheel-like S-bridged hexanuclear structure with C_{4h} symmetry similar to **3a** [31]. The angles around the Pd atom are approximately 90°, which suggest substantially an ideal square-planar structure. The angles around the M (0.6Ni + 0.4Pd) atom also suggest a square-planar configuration. This structure is in agreement with that of **3a**. The Pd···Pd distances of **3b** (average 3.073(3) Å) are intermediate between **3a** (3.0240(7) Å) and $[Pd_2\{Pd(aet)_2\}_4]^{4+}$ (3.1886(6) Å) [31]. Considering the chirality due to the asymmetric carbon atom of the 1-Meaet ligand in the *cis*(*S*)-[M(1-Meaet)$_2$] unit, three isomers, *RR*, *RS* and *SS*, are possible. In the solid state structure, the complex cation exhibits the *RS* isomer with high selectively. When four square-planar *cis*(*S*)-[M(1-Meaet)$_2$] units coordinate to

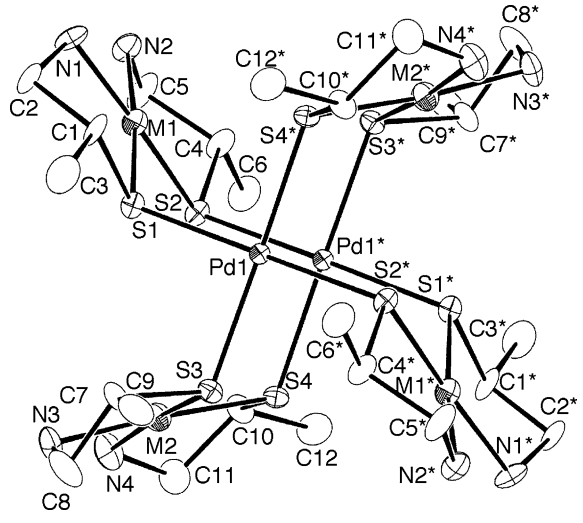


Fig. 2. X-ray structure of molecule A of $[Pd_2\{Ni_{0.6}Pd_{0.4}\text{-}(1\text{-Meaet})_2\}_4]^{4+}$ (**3b**).

Table 4
Selected bond distances (Å) and angles (°) for $[Pd_2\{Ni_{0.6}Pd_{0.4}\text{-}(1\text{-Meaet})_2\}_4]Br_4\cdot 4H_2O$ (**3b**$Br_4\cdot 4H_2O$)

Molecule A	
Pd1–S1	2.341(7)
Pd1–S2[i]	2.346(7)
Pd1–S3	2.349(7)
Pd1–S4[i]	2.341(7)
M1[a]–S1	2.175(7)
M1[a]–S2	2.175(7)
M2[a]–S3	2.196(6)
M2[a]–S4	2.185(9)
M1[a]–N1	1.99(2)
M1[a]–N2	1.94(2)
M2[a]–N3	1.98(3)
M2[a]–N4	2.01(2)
Pd1···Pd1[i]	3.070(3)
S1–Pd1–S3	89.6(2)
S1–Pd1–S4[i]	90.0(3)
S2[i]–Pd1–S3	91.1(3)
S2[i]–Pd1–S4[i]	89.1(3)
S1–M1[a]–S2	93.6(3)
N1–M1[a]–N2	88.0(9)
S1–M1[a]–N1	89.2(6)
S2–M1[a]–N2	89.0(7)
S3–M2[a]–S4	91.9(3)
N3–M2[a]–N4	89(1)
S3–M2[a]–N3	88.8(6)
S4–M2[a]–N4	89.1(9)
Molecule B	
Pd2–S5	2.340(7)
Pd2–S6[ii]	2.345(7)
Pd2–S7	2.339(6)
Pd2–S8[ii]	2.360(6)
M3[a]–S5	2.176(7)
M3[a]–S6	2.189(7)
M4[a]–S7	2.200(6)
M4[a]–S8	2.191(9)
M3[a]–N5	1.99(2)
M3[a]–N6	2.00(2)
M4[a]–N7	1.99(3)
M4[a]–N8	1.97(2)
Pd2···Pd2[ii]	3.076(3)
S5–Pd2–S7	89.0(2)
S5–Pd2–S8[ii]	91.2(3)
S6[ii]–Pd2–S7	90.4(3)
S6[ii]–Pd2–S8[ii]	89.3(3)
S5–M3[a]–S6	93.0(3)
N5–M3[a]–N6	90(1)
S5–M3[a]–N5	88.7(7)
S6–M3[a]–N6	87.8(7)
S7–M4[a]–S8	92.2(3)
N7–M4[a]–N8	90(1)
S7–M4[a]–N7	89.2(6)
S8–M4[a]–N8	88.2(8)

[a] M = $Ni_{0.6}Pd_{0.4}$. *Symmetry codes.* (i) $1-x, -y, -z$; (ii) $-x, 1-y, 1-z$.

two square-planar Pd(II) ions by the pinwheel-like structure, a δλ conformation of two 1-Meaet chelate rings is required. Since the *R* configuration for a λ conformation and the *S* configuration for a δ conformation are more stable, it seems that in the polynuclear structures a configuration with the lowest steric hindrance is attained in spite of the existence of many diastereomers in the mononuclear complex **1b**.

The IR spectra of **3b** suggest the stereoselective formation of a hexanuclear geometry in Fig. S4. The IR spectral patterns are relatively sharp in **3b**Br_4, unlike the Ni(II) mononuclear complex **1b** and trinuclear complex **2b**. A small broad pattern for **3b**Br_4 compared to that for **3a**Br_4 derives from the mixed metal mononuclear units.

The ^1H and ^{13}C NMR spectra of **3b** showed complicated signals and the chemical shifts could not be assigned clearly (Fig. 3 and Table 5). This may be attributed to the fact that many metal substituted isomers coexist for this complex in solution. In the case of the corresponding aet complex, **3a**, the ^1H NMR spectrum showed simple signals for CH_2 and the ^{13}C NMR spectrum showed only two sharp signals for carbons neighbouring to S and N [31]. On the other hand, the absorption spectra in the UV/Vis region of **3a** and **3b** in water exhibit characteristic bands as illustrated in Fig. 4. Their data are summarized in Table 5. The absorption intensity in the region 15–50 × 10^3 cm^{-1} for **3b** was smaller than that for **3a** because the Ni ratio of **3b** is smaller than that of **3a**. Thus, the partial metal substitution of the mononuclear unit was clearly observed in the NMR and UV/Vis spectra.

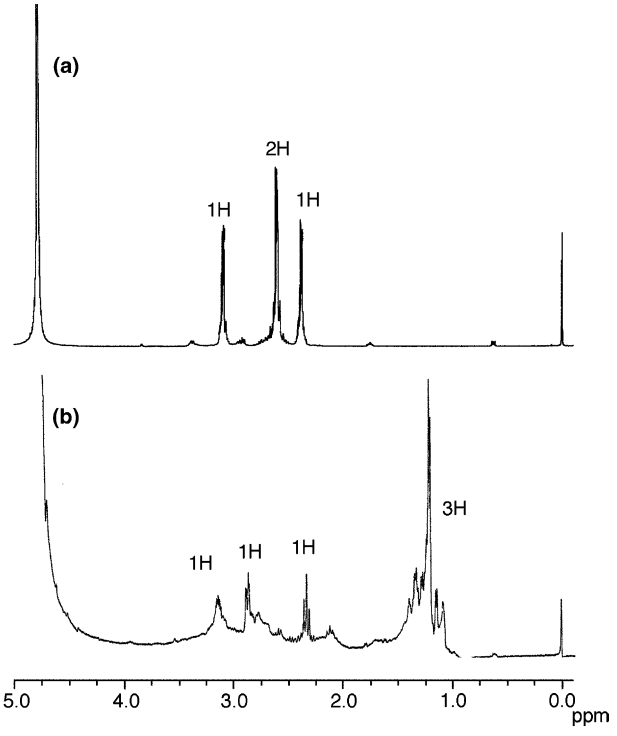


Fig. 3. ^1H NMR spectra of $[Pd_2\{Ni(aet)_2\}_4]^{4+}$ (**3a**) (a) and $[Pd_2\{Ni_{0.6}Pd_{0.4}(1\text{-Meaet})_2\}_4]^{4+}$ (**3b**) (b).

3.5. Synthesis, structure and spectrochemical properties of heteroleptic dinuclear complexes

The dinuclear complexes $[Pt(bpy)\{Ni(1\text{-Meaet})_2(H_2O)_2\}]^{2+}$ (**4b**) and $[Pt(bpy)\{Ni(1\text{-Meaet})_2(bpy)\}]^{2+}$ (**5b**) were prepared using 1-MeaetH·HCl by the same methods as those for $[Pt(bpy)\{Ni(aet)_2(H_2O)_2\}]^{2+}$ (**4a**) and $[Pt(bpy)\{Ni(aet)_2(bpy)\}]^{2+}$ (**5a**) (Scheme 5). The reaction of $[Ni(1\text{-Meaet})_2]$ (**1b**) with $[PtCl_2(bpy)]$ in water at 40 °C gave the heterodinuclear complex **4b**. Two chloride ligands, which are replaced easily by other ligands, are coordinated in $[PtCl_2(bpy)]$. Therefore, the heterodinuclear geometry of **4b** was controlled by the substitution reaction to the metalloligand **1b**. The coordinated water molecules were further replaced by a bpy ligand, and gave the dinuclear complex **5b**. Addition of nitrate ion to the reaction mixture gave single crystals, whereas the presence of the bromide ion caused the dissociation of the bpy ligand.

The X-ray structural analysis for **5b**$(NO_3)_2$ revealed the presence of a discrete divalent hetero-ligand complex cation and two nitrate anions. A perspective drawing of the complex cation is given in Fig. 5. Selected bond distances and angles are listed in Table 6. The complex cation contains one Ni atom and one Pt atom to form the dinuclear complex. The Ni atom in **5b** is surrounded by two 1-Meaet ligands and one bpy ligand, having an approximately octahedral geometry. The Pt atom has a square planar geometry, which has been coordinated by two bridged S atoms from the Ni(II) mononuclear unit and two N atoms from bpy. There is pseudo C_2 symmetry on the Pt–Ni axis. The Pt···Ni distance in **5b** is similar to that in **5a** (3.4987(8) Å) [32,33]. The Ni–S (average 2.446(3) Å), Pt–S (average 2.308(3) Å) distances, and related bonding are very similar to those of **5a**. The introduction of the methyl group has no effect on the bond distances and angles. Considering the absolute configurations (Δ and Λ) of the *cis*(*S*)-[Ni(1-Meaet)$_2$(bpy)] unit and the chirality due to the asymmetric carbon atoms (*R* and *S*) of the 1-Meaet ligand, three isomers Δ_{RR}/Λ_{SS}, Δ_{RS}/Λ_{RS} and Δ_{SS}/Λ_{RR} are possible. In the crystal, the complex cation exists as a mixed crystal of Δ_{RR}/Λ_{SS} and Δ_{RS}/Λ_{RS} isomers. The representative Λ isomer is indicated in Fig. 5. The PdS_4 plane and the NiS_2N_2 plane with δλ conformation in **3b** are bent, whereas the PtS_2N_2 plane and the NiS_2N_2 equatorial plane in **5b** are essentially coplanar. Therefore, when the Λ unit coordinates to the square-planar Pt(II) ion, the δδ conformation of two 1-Meaet chelate rings is required. Although the *SS* configuration for the δδ conformation is the most stable, a secondary stable *RS* configuration is also formed due to incomplete stereo-

Table 5
Spectroscopic data of the hexanuclear complexes

	3a	3b
^{1}H NMR (ppm)	2.38 (1H, d, $J = 7.5$ Hz, SCH_2)	1.0–1.5 (3H, m, CCH_3)
	2.60 (2H, m, SCH_2 and NCH_2)	2.2–2.4 (1H, m, SCH)
	3.10 (1H, d, $J = 6.8$ Hz, NCH_2)	2.7–2.9 (1H, m, NCH_2)
		3.0–3.2 (1H, m, NCH_2)
^{13}C NMR (ppm)	37.53 (SCH_2)	19.60 (CCH_3)[a]
	49.55 (NCH_2)	49.12 (SCH_2)[a]
		54.86 (NCH)[a]
Absorbance maximum, 10^3 cm^{-1} (log ε)	10.78 (0.73)	10.51 (0.71)
	21.6 (3.76)sh[b]	20.26 (2.73)
	25.58 (4.10)	27.51 (3.51)
	33.56 (4.53)	33.28 (3.90)
	37.45 (4.68)	39.0 (4.20)sh[b]
	43.61 (4.75)	42.46 (4.28)

[a] Main signals.
[b] sh denotes a shoulder.

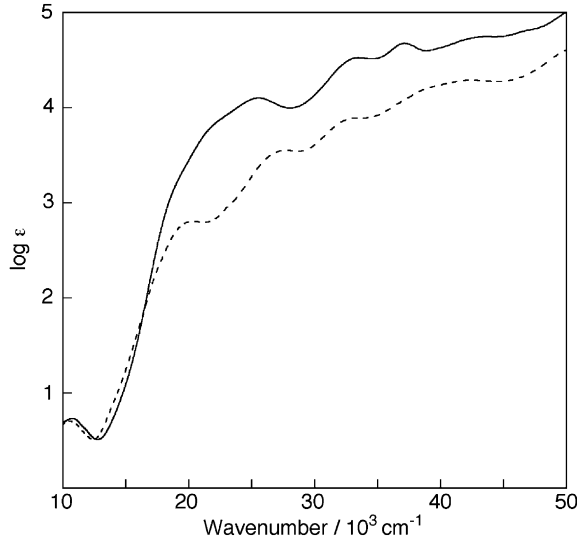


Fig. 4. Absorption spectra of $[Pd_2\{Ni(aet)_2\}_4]^{4+}$ (**3a**) (—) and $[Pd_2\{Ni_{0.6}Pd_{0.4}(1\text{-Meaet})_2\}_4]^{4+}$ (**3b**) (---).

selectivity. Consequently, the ΛΔ unit contains at least one *S* (or *R*) isomer of two 1-Meaet ligands.

In the IR spectra, the spectral patterns of **4b**$(NO_3)_2$ and **5b**$(NO_3)_2$ are similar to those of **4a**$(NO_3)_2$ and **5a**$(NO_3)_2$, respectively (Fig. S5). Strong stretching bands were observed at ca. 1350 cm^{-1}, which suggested the

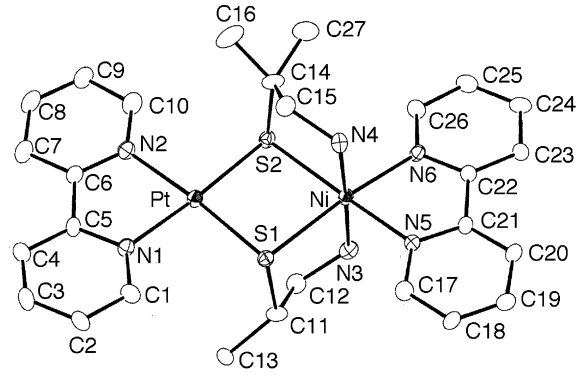
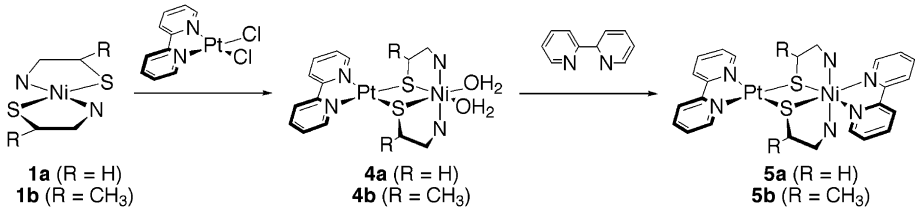


Fig. 5. X-ray structure of Λ isomer of $[Pt(bpy)\{Ni(1\text{-Meaet})_2(bpy)\}]^{2+}$ (**5b**). The disordered C16 and C27 atoms were refined with a site occupancy factor 0.5.

existence of free nitrate ion. These spectral patterns of 1-Meaet complexes are relatively sharp, which indicate that only a few isomers are in the complex as discussed in the structural section.

As illustrated in Fig. 6, the absorption spectra of **4b** and **5b**, and those of the corresponding aet complexes in water exhibit characteristic bands in the region 15–50×10^3 cm^{-1}. Their data are summarized in Table 7. Both 1-Meaet dinuclear complexes exhibit weak absorption bands at about 11.5 and 17.5×10^3 cm^{-1}. Similar absorption bands were also observed for aet dinuclear complexes and related Ni(II) mononuclear complexes,



Scheme 5.

Table 6
Selected bond distances (Å) and angles (°) for [Pt(bpy){Ni(1-Meaet)$_2$(bpy)}](NO$_3$)$_2$ (**5b**(NO$_3$)$_2$)

Pt–S1	2.305(3)	Pt–S2	2.310(2)
Pt–N1	2.085(7)	Pt–N2	2.09(1)
Ni–S1	2.456(2)	Ni–S2	2.435(3)
Ni–N3	2.117(9)	Ni–N4	2.127(9)
Ni–N5	2.079(9)	Ni–N6	2.101(7)
Pt···Ni	3.528(1)		
S1–Pt–S2	87.15(9)	N1–Pt–N2	79.4(3)
S1–Pt–N1	96.7(3)	S2–Pt–N2	96.8(2)
S1–Ni–S2	81.16(9)	N5–Ni–N6	78.1(3)
S1–Ni–N3	85.6(2)	S2–Ni–N4	85.1(3)
Pt–S1–Ni	95.58(9)	Pt–S2–Ni	96.05(9)

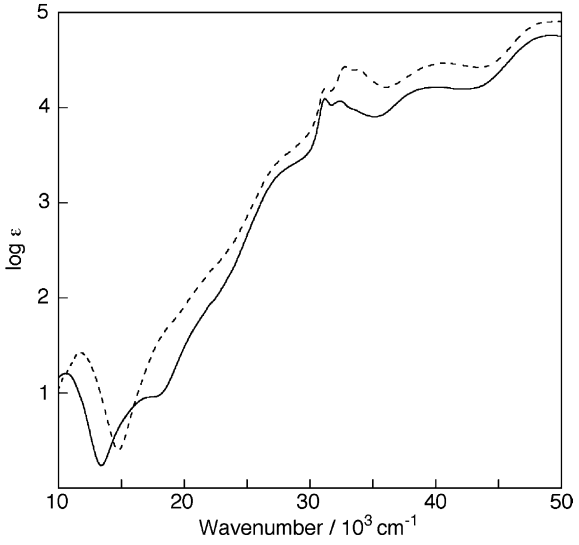


Fig. 6. Absorption spectra of [Pt(bpy){Ni(1-Meaet)$_2$(H$_2$O)$_2$}]$^{2+}$ (**4b**) (—) and [Pt(bpy){Ni(1-Meaet)$_2$(bpy)$_2$}]$^{2+}$ (**5b**) (---).

in which the bands have been assigned as spin-allowed d–d transitions, $^3A_{2g} \rightarrow {}^3T_{2g}$ and $^3A_{2g} \rightarrow {}^1T_{2g}$, respectively, from the lower energy side [50–53]. Further, characteristic intense bands in the region 30–35 × 10^3 cm^{-1} were observed, which are assigned to the π system in the ligand. Comparing the spectral pattern of **4b** and **5b**, the absorption intensity of **4b** ($\varepsilon = 11\,800$ mol^{-1} dm^3 cm^{-1}) is about half that of **5b** ($\varepsilon = 26\,900$ mol^{-1} dm^3 cm^1), depending on the number of bpy ligands as reported earlier for the corresponding aet complexes [33].

4. Summary

In this work, the structures and spectrochemical properties of nickel(II) complexes have been discussed. The 1-Meaet ligand, which has a chiral center on the carbon next to the coordinated sulfur atom, was newly used. The spectroscopic behavior of the mononuclear complexes [Ni(aet)$_2$] and [Ni(1-Meaet)$_2$] was discussed in detail using DR, IR, far-IR, Raman and sulfur K-edge X-ray absorption spectra. The spectrochemical properties of mononuclear complexes are very important and useful for the investigation of S-bridged polynuclear complexes. Further, the 1-Meaet ligand was used for the synthesis of polynuclear complexes. By the introduction of the methyl group, the nucleophilicity of the coordinated sulfur atom seems to be lower considering the instability of the solution state of [Ni{Ni(1-Meaet)$_2$}$_2$]$^{2+}$ (**2b**) and the metal displacement behavior of [Pd$_2${Ni$_{0.6}$Pd$_{0.4}$(1-Meaet)$_2$}$_4$]$^{4+}$ (**3b**). It is difficult to observe the *R*,*S* and δ,λ selectivity of the *racemic* ligand without X-ray crystal structures. The crystal structure of **3b** consists only of the [M(*R*-1-Meaet)(*S*-1-Meaet)] (M = 0.6Ni + 0.4Pd) unit with a δλ conformation, which assembled without steric hindrance. This indicates that not only conformation but also configuration of the 1-Meaet ligand are selected perfectly in the bent S-bridged structure. On the other hand, the crystal structure of [Pt(bpy){Ni(1-Meaet)$_2$-(bpy)}]$^{2+}$ (**5b**) consists of Δ_{RR}/Λ_{SS} and Δ_{RS}/Λ_{RS}-[Ni(1-Meaet)$_2$(bpy)] units with λλ/δδ conformation. This suggests that the configuration of the ligand shows weak selectivity although the conformation of the ligand is selected in the planar S-bridged structure. Thus, the ligand selectivity on polynuclearization is very closely related to the structures of polynuclear complexes with substitution active metal ions.

Table 7
Absorption spectral data of the dinuclear complexes

	4a	**4b**	**5a**	**5b**
Absorbance maximum, 10^3 cm^{-1} (log ε)	10.64 (1.22)	10.66 (1.21)	10.7 (1.20)sh[a]	10.5 (1.18)sh[a]
	17.3 (0.97)sh[a]	17.0 (0.96)sh[a]	11.79 (1.41)	11.75 (1.43)
	28.7 (3.48)sh[a]	28.3 (3.30)sh[a]	28.3 (3.55)sh[a]	27.2 (1.43)sh[a]
	31.30 (4.16)	31.22 (4.10)	31.29 (4.23)	31.25 (4.21)
	32.53 (4.12)	32.44 (4.07)	32.84 (4.45)	32.79 (4.43)
	33.7 (4.03)sh[a]	33.6 (3.98)sh[a]	33.86 (4.42)	34.0 (4.40)sh[a]
	40.24 (4.29)	40.16 (4.22)	40.60 (4.50)	40.65 (4.47)

[a] sh denotes a shoulder.

Acknowledgments

This work was supported by Grants-in-Aid for Scientific Research and the 21st Century COE (Center of Excellence) Program, ''Promotion of Creative Interdisciplinary Materials Science for Novel Functions'' under the Ministry of Education, Culture, Sports, Science and Technology, Japan.

Appendix A. Supplementary data

CCDC-266782 for **3b**$Br_4 \cdot 4H_2O$ and CCDC-266783 for **5b**$(NO_3)_2$ contain the supplementary crystallographic data for this paper. These data can be obtained free of charge at www.ccdc.cam.ac.uk/conts/retrieving.html [or from the Cambridge Crystallographic Data Center, 12 Union Road, Cambridge CB2 1EZ, UK; fax: +44 1223 336 033; e-mail: deposit@ccdc.cam.ac.uk]. Supplementary data (Figs. S1–S5) associated with this article can be found, in the online version at, doi:10.1016/j.poly.2005.05.023.

References

[1] T. Konno, Bull. Chem. Soc. Jpn. 77 (2004) 627, and references therein.
[2] K. Okamoto, C. Sasaki, Y. Yamada, T. Konno, Bull. Chem. Soc. Jpn. 72 (1999) 1685, and references therein.
[3] G.R. Brubaker, B.E. Douglas, Inorg. Chem. 6 (1967) 1562.
[4] S. Miyanowaki, T. Konno, K. Okamoto, J. Hidaka, Bull. Chem. Soc. Jpn. 61 (1988) 2987.
[5] T. Konno, S. Aizawa, K. Okamoto, J. Hidaka, Bull. Chem. Soc. Jpn. 63 (1990) 792.
[6] T. Konno, K. Nakamura, K. Okamoto, J. Hidaka, Bull. Chem. Soc. Jpn. 66 (1993) 2582.
[7] Y. Miyashita, N. Sakagami, Y. Yamada, T. Konno, J. Hidaka, K. Okamoto, Bull. Chem. Soc. Jpn. 71 (1998) 661.
[8] R.D. Gillard, R. Maskill, J. Chem. Soc., Chem. Commun. (1968) 160.
[9] M. Kita, K. Yamanari, Y. Shimura, Bull. Chem. Soc. Jpn. 55 (1982) 2873.
[10] K. Okamoto, T. Yonemura, T. Konno, J. Hidaka, Bull. Chem. Soc. Jpn. 65 (1992) 794.
[11] T. Yonemura, Z.-P. Bai, K. Okamoto, T. Ama, H. Kawaguchi, T. Yasui, J. Hidaka, J. Chem. Soc., Dalton Trans. (1999) 2151.
[12] T. Konno, S. Aizawa, K. Okamoto, J. Hidaka, Chem. Lett. (1985) 1017.
[13] K. Okamoto, S. Aizawa, T. Konno, H. Einaga, J. Hidaka, Bull. Chem. Soc. Jpn. 59 (1998) 175.
[14] Y. Miyashita, H. Yoshida, T. Sato, Y. Yamada, K. Fujisawa, K. Okamoto, Bull. Chem. Soc. Jpn. 76 (2003) 1191.
[15] S.E. Harnung, S.A.M. Kallesoe, C.E. Schaeffer, Phys. Inorg. Chem. 28 (1974) 385.
[16] M. Kojima, Y. Yoshikawa, K. Yamasaki, Inorg. Nucl. Chem. Lett. 9 (1973) 689.
[17] Y. Yamada, Y. Maeda, Y. Miyashita, K. Fujisawa, T. Konno, K. Okamoto, Bull. Chem. Soc. Jpn. 73 (2000) 1219.
[18] Y. Yamada, Y. Maeda, T. Konno, K. Fujisawa, K. Okamoto, Bull. Chem. Soc. Jpn. 73 (2000) 1831.
[19] Y. Yamada, Y. Miyashita, K. Fujisawa, K. Okamoto, Bull. Chem. Soc. Jpn. 75 (1998) 1151.
[20] Y. Yamada, M. Uchida, M. Fujita, Y. Miyashita, K. Okamoto, Polyhedron 22 (2003) 1507.
[21] Y. Yamada, A. Hirano, M. Fujita, N. Amir, Y. Miyashita, K. Okamoto, Inorg. Chem. Acta 358 (2005) 667.
[22] E.I. Solomon, B. Hedman, K.O. Hodgson, A. Dey, R.K. Szilagyi, Coord. Chem. Rev. 249 (2005) 97.
[23] S.D. George, L. Basumallick, R.K. Szilagy, D.W. Randall, M.G. Hill, A.M. Nersissian, J.S. Valentine, B. Hedman, K.O. Hodgson, E.I. Solomon, J. Am. Chem. Soc. 125 (2003) 11314.
[24] R.K. Szilagy, B.S. Lim, T. Glaser, R.H. Holm, B. Hedman, K.O. Hodgson, E.I. Solomon, J. Am. Chem. Soc. 125 (2003) 9158.
[25] S.D. George, M. Metz, R.K. Szilagy, H. Wang, S.P. Cramer, Y. Lu, W.B. Tolman, B. Hedman, K.O. Hodgson, E.I. Solomon, J. Am. Chem. Soc. 123 (2001) 5757.
[26] L. Basumallick, D.W. Randall, M.G. Hill, A.M. Nersissian, J.S. Valentine, B. Hedman, K.O. Hodgson, E.I. Solomon, J. Am. Chem. Soc. 125 (2003) 11314.
[27] D.W. Randall, S.D. George, B. Hedman, K.O. Hodgson, K. Fujisawa, E.I. Solomon, J. Am. Chem. Soc. 122 (2000) 11629.
[28] I.J. Pickering, R.C. Prince, T. Divers, G.N. George, FEBS Lett. 441 (1998) 11.
[29] S.E. Shadle, J.E. Penner-Hahn, H.J. Schugar, B. Hedman, K.O. Hodgson, E.I. Solomon, J. Am. Chem. Soc. 115 (1993) 767.
[30] C.H. Wei, L.F. Dahl, Inorg. Chem. 9 (1970) 1878.
[31] T. Konno, K. Yonenobu, J. Hidaka, K. Okamoto, Inorg. Chem. 33 (1994) 861.
[32] T. Konno, Y. Yoshinari, K. Okamoto, Chem. Lett. (1995) 989.
[33] K. Okamoto, Y. Yoshinari, Y. Yamada, N. Sakagami, T. Konno, Bull. Chem. Soc. Jpn. 71 (1998) 1363.
[34] D.C. Jicha, D.H. Busch, Inorg. Chem. 1 (1962) 872.
[35] N. Baidya, D. Ndreu, M. Olmstead, K. Mascharak, Inorg. Chem. 30 (1991) 2448.
[36] R.H. Herber, M. Croft, M.J. Coyer, B. Bilash, A. Sahiner, Inorg. Chem. 33 (1994) 2422.
[37] S.D. Turk, R.P. Louthan, C.R. Bresson, J. Org. Chem. 27 (1962) 2846.
[38] T.C. Owen, J. Chem. Soc. (C) (1967) 1373.
[39] M. Nomura, A. Koyama, J. Synchrotron Rad. 6 (1999) 182.
[40] M. Nomura, A. Koyama, Nucl. Instrum. Meth. Phys. Res. A 467–468 (2001) 733.
[41] A. Altomare, G. Cascarano, C. Giacovazzo, A. Guagliardi, M. Burla, G. Polidori, M. Camalli, J. Appl. Crystallogr. 27 (1994) 435.
[42] P.T. Beurskens, G. Admiraal, G. Beurskens, W.P. Bosman, R. de Gelder, R. Israel, J.M.M. Smits, The DIRDIF-99 Program System, Technical Report for the Crystallography Laboratory, University of Nijmegen, The Netherlands, 1999.
[43] Crystal Structure Analysis Package, Version 3.5.1, Rigaku and Rigaku/MSC, The Woodlands, TX, 2000–2003.
[44] K. Kanamori, K. Kawai, Bull. Chem. Soc. Jpn. 53 (1980) 2520.
[45] J. Suades, X. Solans, M. Font-Altaba, Polyhedron 3 (1984) 1227.
[46] C.W. Schlaepfer, K. Nakamoto, Inorg. Chim. Acta 6 (1972) 177.
[47] U.A. Jayasooriya, D.B. Powell, Spectrosc. Lett. 6 (1973) 763.
[48] U.A. Jayasooriya, D.B. Powell, Spectrochim. Acta 30A (1974) 553.
[49] M. Fujita, Ph.D. Thesis, University of Tsukuba, Japan, 2005.
[50] G. Wilkinson, R.D. Gillard, J.A. McCleverty, Comprehensive Coordination Chemistry, vol. 5, 1st ed., Pergamon Press, Oxford, England, 1987.
[51] R.A. Pakmer, T.S. Piper, Inorg. Chem. 5 (1966) 864.
[52] C. Furlani, G. Mattogno, A. Monaci, F. Tarli, Inorg. Chim. Acta 4 (1970) 187.
[53] S. Bunel, L. Gil, E. Moraga, H. Bobadilla, Inorg. Chim. Acta 4 (1970) 415.

2. Experimental

2.1. Materials and syntheses

All chemicals and solvents used in this work were of AR grade.

Caution!! Although no problems were encountered in this study, transition metal perchlorate is potentially explosive and should be handled with proper precautions.

The ligand *N*,*N*-dimethyl-*N*′-(pyrid-2-ylmethyl)-ethylenediamine (L) was synthesized according to the published procedure [10]. IR spectra were recorded as KBr discs on a Shimadzu IR-408 infrared spectrophotometer in the 4000–600 cm^{-1} region. The ultraviolet, visible, and near IR spectra were measured on a Hitachi UV-330 UV–Vis–NIR spectrophotometer using water as the solvent. Elemental analyses (C, H, N) were performed on a Perkin–Elmer 240C analyser. Magnetic susceptibility measurements of crystalline samples were carried out in the temperature range 2–300 K on a Maglab system 2000 magnetometer.

2.1.1. $[Ni_2L_2(\mu\text{-}SCN)_2(SCN)_2]\cdot 2H_2O$ (**1**)

To a methanol solution of $NiCl_2\cdot 6H_2O$ (1 mmol) and L (1 mmol) was added a concentrated aqueous solution of NH_4SCN (0.5 mmol). The resulting mixture was stirred for 4 h and then filtered. The blue single crystals suitable for X-ray analysis were obtained by slow evaporation of the filtrate. Yield: 66.06 mg (71%). *Anal.* for $C_{24}H_{38}N_{10}Ni_2O_2S_4$: Found. C, 38.7; H, 5.2; N, 18.8%. Calc. C, 38.7; H, 5.2; N, 18.8%. Selected IR data (KBr, ν cm^{-1}): 2110, 1600, 1009, 765. UV–Vis–NIR (λ_{max}, nm) (ε, $dm^3\,mol^{-1}\,cm^{-1}$) (H_2O): 986 (23.03), 586 (15.28), 362 (39.98).

2.1.2. $[Ni_2L_2(\mu_{1,1}\text{-}N_3)_2(N_3)_2]\cdot CH_3OH$ (**2**)

NaN_3 (0.5 mmol) in 10 ml of 5:1 (V:V) methanol–water solution was added to a methanol solution (10 ml) containing 1 mmol of $NiCl_2\cdot 6H_2O$ and 1 mmol of ligand L. The mixture was stirred for 4 h and then filtered. The blue single crystals were obtained by slow evaporation of the filtrate. Yield: 54.47 mg (68%). *Anal.* for $C_{21}H_{38}N_{18}Ni_2O$: Found. C, 37.4; H, 5.6; N, 37.3%. Calc. C, 37.3, H, 5.7, N, 37.3%. Selected IR data (KBr, ν cm^{-1}): 2040, 1600, 1470, 1430, 1100, 1020, 770. UV–Vis–NIR (λ_{max}, nm) (ε, $dm^3\,mol^{-1}\,cm^{-1}$) (H_2O): 992 (20.81), 594 (15.13), 365 (30.43).

2.1.3. $[Ni_2L_2(H_2O)_2(\mu_2\text{-}C_2O_4)]\cdot 2ClO_4$ (**3**)

$Ni(ClO_4)_2\cdot 6H_2O$ (1 mmol) was added to a methanol solution (5 ml) of the Ligand L (1 mmol). The mixture was stirred for 1 h and a concentrated aqueous solution of $K_2C_2O_4\cdot 6H_2O$ (1 mmol) was added slowly. The resulting solution was stirred for another 2 h and then filtered. The blue single crystals suitable for X-ray analysis were obtained by slow evaporation of the filtrate. Yield: 303.58 mg (76%). *Anal.* for $C_{24}H_{38}N_{10}Ni_2O_2S_4$: Found. C, 33.1; H, 4.7; N, 10.6%. Calc. C, 33.1; H, 4.8; N, 10.5%. Selected IR data (KBr, ν cm^{-1}):, 1651, 1600, 1471, 1444, 1313, 1121, 1108, 1091, 799, 626. UV–Vis–NIR (λ_{max}, nm) (ε, $dm^3\,mol^{-1}\,cm^{-1}$) (H_2O): 986 (12.79), 586 (13.19), 360 (22.13).

2.2. X-ray data collection and crystal structure determination

Single crystal X-ray diffraction studies were performed on a Bruker Smart 1000 CCD diffractometer with Mo Kα radiation ($\lambda = 0.71073$ Å). The structures were solved by direct methods and semi-emperical absorption corrections were applied. The non-hydrogen atoms were located by direct phase determination and full-matrix least-squares refinement on F^2, while the hydrogen atoms for non-water protons were treated using the riding mode. Further details of the structural analyses are summarized in Table 1. All calculations were carried out using SHELXS-97 [11], SHELXL-97 [12] programs.

3. Results and discussion

3.1. Spectroscopic characterization

The IR spectra of binuclear species **1**–**3** show medium bands at ca. 1600 cm^{-1}, which were assigned to the ν(pyridyl) stretching. The ν(CN) stretching frequency of **1** was found at 2110 cm^{-1}, and the $\nu(N_3^-)$ stretching frequency of **2** at 2040 cm^{-1}. In the IR spectrum of **3** bonds at 1651, 799, and 1300–1400 cm^{-1} are attributed to ν(COO), δ(COO) and ν_s(COO), respectively, demonstrating the coordination of the oxalate group. The solution electronic spectra in water exhibit three major transitions at 360–365, 586–594, and 986–992 nm at 298 K, which is tentatively attributed to the electronic transitions $^3A_{2g} \rightarrow {}^3T_{1g}(P)$, $^3A_{2g} \rightarrow {}^3T_{1g}$, and $^3A_{2g} \rightarrow {}^3T_{2g}$. This spectrum is d-d charge-transfer bands in the octahedron Ni(II) surrounding [13].

3.2. Description of the structure

The structures of **1**, **2** and **3** with atom numbering are shown in Figs. 1–3, respectively. The selected bond distances and angles of **1**, **2** and **3** are listed in Table 2.

The X-ray diffraction of **1** reveals a neutral centrosymmetric binuclear entity $[Ni_2L_2(\mu\text{-}SCN)_2(SCN)_2]$ (Fig. 1) together with two crystallization water molecules. In the dimeric unit, two Ni(II) atoms are bridged by two thiocyanate ligands in an end-to-end fashion with the Ni···Ni separation of 5.750 Å. One S atom and one N atom from two different bridging thiocyanate

Table 1
Crystallographic data for **1**, **2** and **3**

Compound	**1**	**2**	**3**
Formula	$C_{24}H_{38}N_{10}Ni_2O_2S_4$	$C_{21}H_{38}N_{18}Ni_2O$	$C_{11}H_{19}ClN_3NiO_7$
Formula weight	744.30	676.11	399.45
T (K)	273(2)	293(2)	293(2)
Crystal system	orthorhombic	triclinic	monoclinic
Space group	*Pbca*	$P\bar{1}$	$P2_1/n$
Unit cell dimensions			
a (Å)	9.408(3)	10.469(5)	9.252(3)
b (Å)	15.251(5)	11.255(5)	17.454(7)
c (Å)	24.185(8)	15.405(7)	10.505(4)
α (°)	90	103.185(7)	90
β (°)	90	100.543(7)	101.350(6)
γ (°)	90	109.965(7)	90
Z	4	2	4
μ (mm^{-1})	1.363	1.230	1.364
$F(0\,0\,0)$	1552	708	828
Reflections collected/unique [R_{int}]	13465/3062 [0.0513]	5812/5382 [0.0171]	7668/3295 [0.0513]
Data/restraints/parameters	3062/0/192	5382/0/379	3295/4/220
Final R indices	$R_1 = 0.0542$	$R_1 = 0.0411$	$R_1 = 0.0659$
$[I > 2\sigma(I)]$	$wR_2 = 0.1200$	$wR_2 = 0.1002$	$wR_2 = 0.1353$
R indices (all data)	$R_1 = 0.0828$	$R_1 = 0.0705$	$R_1 = 0.1204$
	$wR_2 = 0.1334$	$wR_2 = 0.1112$	$wR_2 = 0.1549$

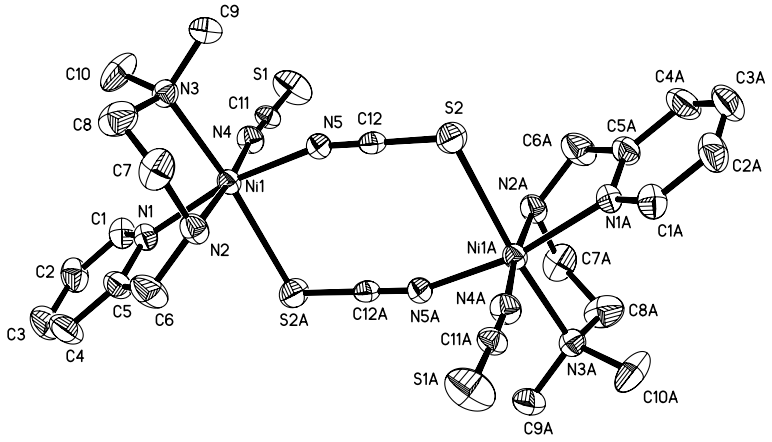


Fig. 1. View of complex **1** showing the numbering scheme. Themal ellipsoids were drawn with 30% probability. (Hydrogen atoms and water molecules are omitted for clarity.)

ligands, one N atom from a terminal SCN^- and three N atoms from one tridentate ligand L coordinate to the Ni(II) atom to complete a distorted octahedral coordination geometry. The Ni–N bond lengths are in the range of 2.030–2.158 Å, in which the bond length of Ni1–N3 (tertiary amine) is the longest. The Ni–S distance is 2.635 Å, which is similar to that reported for thiocyanate bridging nickel complexes [2,14–16]. The Ni–S–C and Ni–N–C angles for bridging SCN^- groups are 102.7 and 162.4°, respectively. In comparison, the Ni–N–C angles for terminal SCN^- groups are 173.2°. The dihedral angle formed by the mean-plane $(NCS)_2$ and the N–Ni–S plane is 13.4°.

There are two independent dinuclear [Ni–Ni] units and two disordered methanol molecules in **2** (Fig. 2). Each Ni(II) atom is coordinated by three N atoms from one tridentate ligand L, one N atom from one terminal azido ligand, and two N atoms from two azido bridging ligands. The two azido ligands link two Ni(II) atoms in an end-on form resulting in the Ni···Ni separation of 3.395 and 3.333 Å for molecules 1 and 2, respectively. It is noteworthy that the longest Ni–N bond is the Ni–N (tertiary amine) bond for molecule 1, while it is the Ni–N (bridging azido ligand) bond for molecule 2. All of the Ni–N (bridging azido) bonds in both molecules rang from 2.142(3) to 2.200(3) Å, which are close to the values reported in other end-on azido Ni(II) complexes [2,17]. The Ni–N–Ni angles are 103.3 and 100.3 for molecules 1 and 2, respectively.

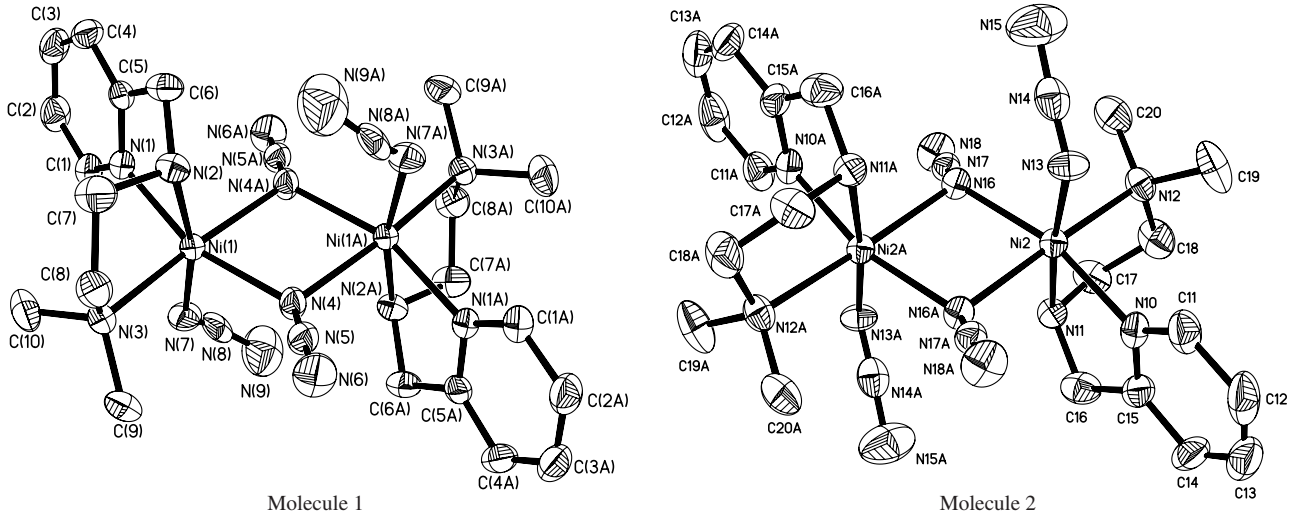


Fig. 2. View of the two independent molecules in complex **2** showing the numbering scheme.

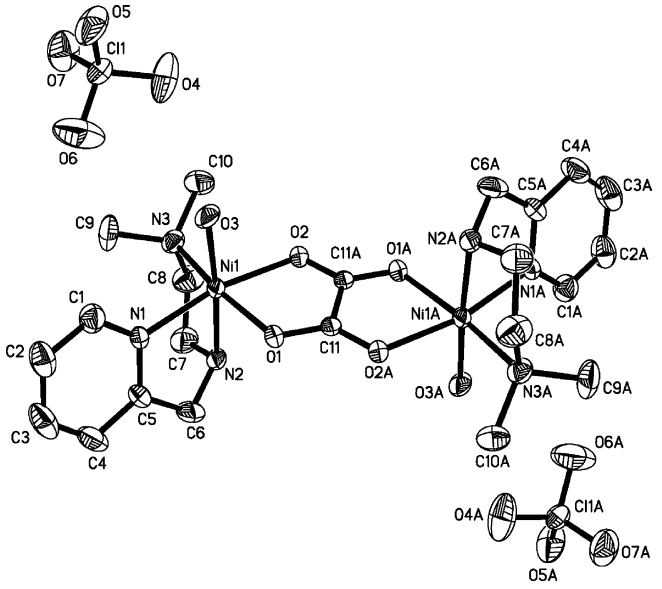


Fig. 3. View of complex **3** showing the numbering scheme (the methanol molecule is omitted for clarity).

As shown in Fig. 3, the structure of **3** contains one $[Ni_2L_2(H_2O)_2(\mu_2\text{-}C_2O_4)]^{2+}$ and two ClO_4^- anions. The dinuclear unit consists of two $[Ni(II)LH_2O]^{2+}$ subunits bridged by a bis-bidentate oxalate dianion. Each Ni(II) atom has a distorted octahedral coordination geometry, completed by three N atoms from the tridentate ligand L, two O atoms from the oxalate dianion, and one water O atom. The Ni–N bond lengths vary from 2.060(4) to 2.147(5) Å, close to those in **1** and **2**. The Ni···Ni separation (5.390 Å) is comparable well to that in the reported dinuclear oxalato-bridged complexes [18–22]. In the oxalate dianion, the C–O bond lengths are 1.249(6) and 1.255(6) Å and the C–C bond length is 1.537(11) Å. The $C_2O_4^{2-}$ ion is planar (maximum deviation, 0.0020 Å), while the two Ni(II) atoms deviate by 0.0847 Å from the plane. The bite angle formed by the Ni(II) atom and the two O atoms of oxalate ligand is 80.6° which is typical for oxalato-bridged binuclear complex [8,9,22,23].

3.3. Magnetic properties

The magnetic behavior of the dinuclear Ni(II) complexes could be interpreted using isotropic spin Hamiltonian $H = -2JS_1S_2$, where $S_1 = S_2 = 1$ and J is the exchange integral. The experimental data have been fitted to the expression [24]

$$\chi_M = \frac{2Ng^2\beta^2}{k(T-\theta)}\left[\frac{5+\exp(-4J/kT)}{5+3\exp(-4J/kT)+\exp(-6J/kT)}\right]. \quad (1)$$

Table 2
Selected bonds distances (Å) and angles (°) for **1**, **2** and **3**

Complex ***1***					
Bond lengths (Å)					
Ni(1)–N(5)	2.030(4)	Ni(1)–N(2)	2.088(4)	Ni(1)–S(2A)	2.635(2)
Ni(1)–N(4)	2.033(4)	Ni(1)–N(3)	2.158(4)	Ni(1)–N(1)	2.080(4)
Bond angles (°)					
N(5)–Ni(1)–N(4)	94.0(2)	N(1)–Ni(1)–N(2)	80.4 (2)	N(1)–Ni(1)–N(3)	93.8(2)
N(5)–Ni(1)–N(1)	167.4(2)	N(5)–Ni(1)–N(3)	94.3(2)	N(2)–Ni(1)–N(3)	83.9(2)
N(4)–Ni(1)–N(1)	95.2(2)	N(4)–Ni(1)–N(3)	93.2(2)	N(5)–Ni(1)–S(2A)	89.5(1)
N(5)–Ni(1)–N(2)	90. 8(2)	N(2)–Ni(1)–S(2A)	92.0(1)	N(4)–Ni(1)–S(2A)	90.6(1)
N(4)–Ni(1)–N(2)	174.6(2)	N(3)–Ni(1)–S(2A)	174.4(1)	N(1)–Ni(1)–S(2A)	81.8(1)
Complex ***2***					
Bond lengths (Å)					
Ni(1)–N(2)	2.117(3)	Ni(1)–N(4A)	2.174(3)	Ni(2)–N(13)	2.131(3)
Ni(1)–N(1)	2.132(3)	Ni(1)–N(3)	2.188(3)	Ni(2)–N(16)	2.142(3)
Ni(1)–N(4)	2.155(3)	Ni(2)–N(10)	2.113(3)	Ni(2)–N(16A)	2.200(3)
Ni(1)–N(7)	2.170(5)	Ni(2)–N(11)	2.117(3)	Ni(2)–N(12)	2.217(3)
Bond angles (°)					
N(2)–Ni(1)–N(1)	78.0(1)	N(2)–Ni(1)–N(3)	83.2(1)	N(13)–Ni(2)–N(16)	93.1(1)
N(2)–Ni(1)–N(4)	94.0(1)	N(1)–Ni(1)–N(3)	98.8(1)	N(10)–Ni(2)–N(16B)	87.2(1)
N(1)–Ni(1)–N(4)	161.7(1)	N(4)–Ni(1)–N(3)	96.6(1)	N(11)–Ni(2)–N(16B)	91.5(1)
N(2)–Ni(1)–N(7)	167.3(2)	N(7)–Ni(1)–N(3)	89.5(17)	N(13)–Ni(2)–N(16B)	92.0(1)
N(1)–Ni(1)–N(7)	93.0(2)	N(4)#1–Ni(1)–N(3)	172.5(1)	N(16)–Ni(2)–N(16B)	79.7(1)
N(4)–Ni(1)–N(7)	97.2(2)	N(10)–Ni(2)–N(11)	81.1(1)	N(10)–Ni(2)–N(12)	92.9(1)
N(2)–Ni(1)–N(4A)	93.9(1)	N(10)–Ni(2)–N(13)	94.3(1)	N(11)–Ni(2)–N(12)	82.9(1)
N(1)–Ni(1)–N(4A)	87.3(1)	N(11)–Ni(2)–N(13)	174.2(1)	N(13)–Ni(2)–N(12)	93.7(1)
N(4)–Ni(1)–N(4A)	76.7(1)	N(10)–Ni(2)–N(16)	165.2(1)	N(16)–Ni(2)–N(12)	99.4(1)
N(7)–Ni(1)–N(4A)	94.5(2)	N(11)–Ni(2)–N(16)	92.2(1)	N(16)#2–Ni(2)–N(12)	174.3(1)
Complex ***3***					
Bond lengths (Å)					
Ni(1)–N(1)	2.060(4)	Ni(1)–N(2)	2.071(5)	Ni(1)–O(1)	2.087(4)
Ni(1)–O(2)	2.066(4)	Ni(1)–O(3)	2.086(4)	Ni(1)–N(3)	2.147(5)
Bond angles (°)					
N(1)–Ni(1)–O(2)	168.1(2)	N(2)–Ni(1)–O(3)	173.8(2)	N(1)–Ni(1)–N(3)	98.8(2)
N(1)–Ni(1)–N(2)	80.2(2)	N(1)–Ni(1)–O(1)	89.4(2)	O(2)–Ni(1)–N(3)	90.8(2)
O(2)–Ni(1)–N(2)	93.7(2)	O(2)–Ni(1)–O(1)	80.6(1)	N(2)–Ni(1)–N(3)	84.9(2)
N(1)–Ni(1)–O(3)	93.6(2)	N(2)–Ni(1)–O(1)	92.0(2)	O(3)–Ni(1)–N(3)	96.9(2)
O(2)–Ni(1)–O(3)	92.3(2)	O(3)–Ni(1)–O(1)	87.2(2)	O(1)–Ni(1)–N(3)	170.6(2)

Symmetry transformations used to generate the equivalent atoms: complex **1**, A: $-x$, $-y+1$, $-z+1$; complex **2**, A: $-x+1$, $-y+1$, $-z$; B: $-x$, $-y+1$, $-z+1$.

The magnetic behavior of **1** is shown in Fig. 4 by plotting χ_M and μ_{eff} vs. T. The μ_{eff} at room temperature is $4.10\mu_B$ which is slightly larger than the expected value for two uncoupled $S=1$ canters (the theoretical value with $g=2$, $\mu_{eff}=4.0\mu_B$). As the temperature is lowed, μ_{eff} increases to $4.76\mu_B$ at 7 K, and then decreases to $4.73\mu_B$ at 5 K. A least-squares fit of the data to the equation yields the values of $J=3.90\ cm^{-1}$, $g=2.03$, $\theta=0.3$, $R=4.0\times10^{-3}$. This is indicative of the presence of ferromagnetic interactions in **1**. The decrease of μ_{eff} from $4.76\mu_B$ at 7 K to $4.73\mu_B$ at 5 K may be due to intermolecular interactions or (and) single-ion zero-field splitting.

In according to the Goodenough–Kanamori rules [24], the ferromagnetism in the idealized structures with the idealized angles of Ni–N–C and Ni–S–C (180° and 90°) can be explained in terms of $e_g\|\sigma\perp\pi\|e'_g$ pathways. With these idealized angles, the overlap is zero and the orthogonality of the orbitals creates the possibility of ferromagnetism. Hendrickson [25] assumes that for a symmetric bridging situation, the antiferromagnetic coupling is enhanced. In **1**, the angles of Ni–N–C and Ni–S–C are 102.67° and 162.4°, respectively, which show less pronounced rectangular geometry. Thus it has a smaller J value of ca. 3.9 cm^{-1}. The J value is lower than the values (6.3 and 8.8 cm^{-1}) for dinuclear thiocyanato and selenocyanato derivatives with the angles of Ni–S–C/Ni–Se–C (96.2° and 97.4°) and Ni–N–C (166.7° and 169.1°) [2,26]. On the other hand, the observed value corresponds well with the value of 4.3–4.9 cm^{-1} found for the dinuclear thiocyanato Ni(II) complexex with the angles of Ni–S–C (100.0–100.7°) and Ni–N–C (159.0–167.0°) [26–28].

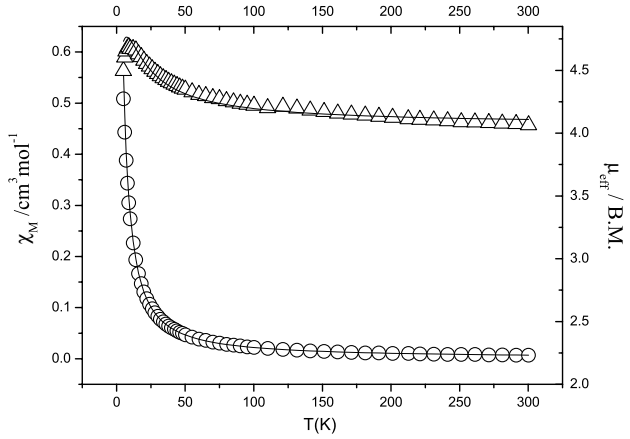


Fig. 4. A plot for complex **1** of temperature dependence of χ_M (○) vs. T and μ_{eff} (△) vs. T. The solid lines are theoretical fits based on Eq. (1).

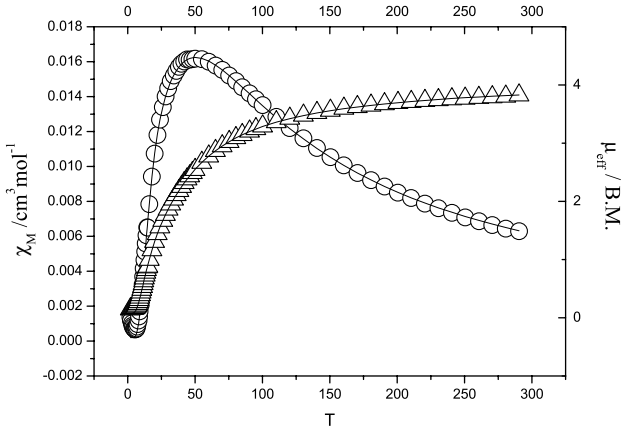


Fig. 6. A plot for complex **3** of temperature dependence of χ_M (○) vs. T and μ_{eff} (△) vs. T. The solid lines are theoretical fits based on Eq. (1).

The magnetic susceptibility measurement of **2** is plotted in Fig. 5. At 300 K, the μ_{eff} value is 4.08 μ_B, which compares well to the theoretical value of 4.0 μ_B. When the temperature is lowered, μ_{eff} rises smoothly to reach a maximum of 4.30μ_B at 28 K and then decreases down to a value of 3.87μ_B at 5 K. The best fit of the data to Eq. (1) in the high-temperature region 28–300 K yields magnetic parameters of $g = 2.03$, $J = 1.91\ cm^{-1}$, and $R = 1.8 \times 10^{-4}$. The result is consistence with the ferromagnetic coupling for dibridged azido Ni(II) in $\mu_{1,1}$ fashion [2,17].

The magnetic behavior of **3** is shown in Fig. 6. At 300 K the μ_{eff} value is 3.83μ_B, which is slightly smaller than the theoretical value. When the temperature is lowered, μ_{eff} decreases smoothly. A least-squares fit of the data to the Eq. (1) yields the values of $J = -17.1\ cm^{-1}$, $g = 2.00$, $R = 6.7 \times 10^{-4}$. The exchange integrals J found for **3** shows that the ferromagnetic coupling is the extent of overlap between the magnetic orbitals of the paramagnetic nickel ions and the μ-oxalato bridging ligand. For Ni(II) complexes in octahedral geometry, the unpaired electron resides in a $d_{x^2-y^2}$ type orbital, which is aligned to allow overlap with the oxalate σ-orbitals. For **3**, the observed J value of $-17.1\ cm^{-1}$ is in agreement with the antiferromagnetic interaction ($J = -11.25$ to $-39.0\ cm^{-1}$) observed in other oxalato-bridged Ni(II) complexes [8,9,17].

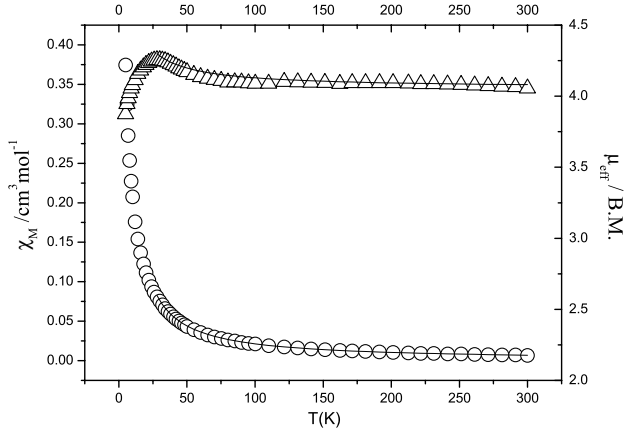


Fig. 5. A plot for complex **2** of temperature dependence of χ_M (○) vs. T and μ_{eff} (△) vs. T. The solid lines are theoretical fits based on Eq. (1).

4. Supplementary data

Data Centre as Supplementary Publication No. CCDC 263465 for complex **1**, 263466 for complex **2**, and 263467 for complex **3**. Copies of the data can be obtained free of charge on Application to CCDC, 12 Union Road, Cambridge CB2 1EZ, UK (fax (internet): +44 1223/336 033; e-mail: deposit@ccdc.cam.ac.uk).

Acknowledgments

This work was supported by the National Natural Science Foundation of China (No. 20331020) and the Science Foundation of Guangxi of China (0342025).

References

[1] P.J. Koningsbruggen, M.W. Gluth, V. Ksenofontov, D. Walcher, D. Schollmeyer, G. Levchenko, P. Gütlich, Inorg. Chim. Acta 273 (1998) 54.
[2] M. Monfort, J. Ribas, X. Solans, Inorg. Chem. 33 (1994) 4271.
[3] H. Zhang, Z. Wang, K. Zhang, B.K. Teo, Coord. Chem. Rev. 183 (1999) 157.
[4] J. Ribas, A. Escuer, M. Monfort, R. Vicente, R. Cortés, L. Lezama, T. Rojo, Coord. Chem. Rev. 193–195 (1999) 1027.
[5] S. Youngme, G.A. Albada, N. Chaichit, P. Gunnasoot, P. Kongsaeree, I. Mutikainen, O. Roubeau, J. Reedijk, U. Turpeinen, Inorg. Chim. Acta 353 (2003) 119.

[6] P. Orioli, B. Bruni, M.D. Vaira, L. Messori, F. Piccioli, Inorg. Chem. 41 (2002) 4312.
[7] H.D. Bian, W. Gu, J.Y. Xu, F. Bian, S.P. Yan, D.Z. Liao, Z.H. Jiang, P. Cheng, Inorg. Chem. 42 (2003) 4265.
[8] A. Escuer, R. Vicente, M.S.E. Fallah, J. Jaud, Inorg. Chim. Acta 232 (1995) 151.
[9] F. Březina, Z. Smékal, Z. Trávníček, Z. Šindelář, R. Pastorek, J. Marek, Polyhedron 16 (1997) 1331.
[10] H.D. Bian, J.Y. Xu, W. Gu, S.P. Yan, D.Z. Liao, Z.H. Jiang, P. Cheng, Inorg. Chem. Commun. 3 (2003) 573.
[11] G.M. Sheldrick, SHELXS-97, Program for the Solution of Crystal Structures, University of Göttingen, Germany, 1990.
[12] G.M. Sheldrick, SHELXL-97, Program for the Refinement of Crystal Structures, University of Göttingen, Germany, 1997.
[13] M. Schröeder, in: R.B. King (Ed.), Encyclopedia of Inorgnic Chemistry: Nickel: Inorgnic and Coordination Compounds, vol. 5, Wiley, New York, 1994, pp. 2392–2412, references cited therein.
[14] R. Vicente, A. Escuer, J. Ribas, X. Solans, J. Chem. Soc., Dalton Trans. (1994) 259.
[15] A. Mondal, C. Pariya, N.R. Chaudhuri, N.P. Nayak, A.K. Mukherjee, A. Ghosh, Polyhedron 16 (1997) 39.
[16] B. Żurowska, J. Mroziński, M. Julve, F. Lloret, A. Maslejova, W. Sawka-Dobrowolska, Inorg. Chem. 41 (2002) 1771.
[17] S.K. Dey, N. Mondal, M.S.E. Fallah, R. Vicente, A. Escuer, X. Solans, M. Font-Bardia, T. Matsushita, V. Gramlich, S. Mitra, Inorg. Chem. 43 (2004) 2427.
[18] M.F. Charlot, M. Verdaguer, Y. Journaux, P. de Loth, J.P. Daudey, Inorg. Chem. 23 (1984) 3804.
[19] M. Julve, M. Verdaguer, A. Gleizes, M. Philoche-Levisalles, O. Kahn, Inorg. Chem. 23 (1984) 3808.
[20] M. Julve, M. Verdaguer, O. Kahn, A. Gleizes, M.P. Levisalles, Inorg. Chem. 22 (1983) 258.
[21] M. Julve, J. Faus,, M. Verdaguer, A. Gleizes, J. Am. Chem. Soc. 106 (1984) 8306.
[22] B. Bag, N. Mondal, S. Mitra, V. Gramlich, J. Ribas, M.S.E. Fallah, Polyhedron 20 (2001) 2113.
[23] M. Bröring, S. Prikhodovski, C.D. Brandt, Inorg. Chim. Acta 357 (2004) 1733.
[24] A.P. Ginsberg, R.L. Martin, R.W. Brookes, R.C. Sherwood, Inorg. Chem. 11 (1972) 2884.
[25] M.D. Duggan, D.N. Hendrickson, Inorg. Chem. 13 (1974) 2929.
[26] R. Vicente, A. Escuer, J. Ribas, X. Solans, M. Font-Bardfa, Inorg. Chem. 32 (1993) 6117.
[27] T. Rojo, R. Cortés, L. Lezama, M.L. Arriotua, K. Urtiaga, G. Vilenueve, J. Chem. Soc. Dalton Trans. (1991) 1779.
[28] A.E. Shvelashvili, M.A. Porai-Koshity, S.S. Antsyshkins, J. Struct. Chem. (Engl. Transl.) 10 (1969) 552.

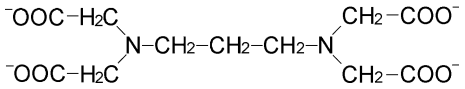


Fig. 1. Formula of ligand 1,3-propanediaminetetraacetate ion.

Recently, with aim to investigate the stereochemical properties of 1,3-pdta complexes with spherically symmetric metal ions of different size we have prepared homometallic $[Mg(H_2O)_6][Mg(1,3\text{-pdta})]\cdot 2H_2O$ and $[Ca(H_2O)_3Ca(1,3\text{-pdta})(H_2O)]\cdot 2H_2O$ complexes, and their crystal structures were determined by X-ray crystallography [8]. While the crystals of $[Mg(H_2O)_6]$-$[Mg(1,3\text{-pdta})]\cdot 2H_2O$ [8] complex appeared isomorphic with those of other $[M(H_2O)_6][M'(1,3\text{-pdta})]\cdot 2H_2O$ (M(II),M′(II) = Mg,Cu [5a]; Mn,Cu [5b]; Mg,Ni [6]; Mg,Co [7]; and Co,Co [7]) complexes, in the case of $[Ca(H_2O)_3Ca(1,3\text{-pdta})(H_2O)]\cdot 2H_2O$ [8] complex we have obtained the coordination number higher than six. Moreover, in the solid state $[Ca(H_2O)_3Ca(1,3\text{-pdta})$-$(H_2O)]\cdot 2H_2O$ [8] displayed substantially different packing pattern than that observed for the $[M(H_2O)_6]$ $[M'(1,3\text{-pdta})]\cdot 2H_2O$ series.

This work is a continuation of our study concerned with the structural characteristics of 1,3-pdta complexes containing different metal(II) ions. We report here the syntheses and characterization of hexadentate $[Mg(H_2O)_6][Zn(1,3\text{-pdta})]\cdot 2H_2O$ (**1**), $[Zn(H_2O)_6][Zn$-$(1,3\text{-pdta})]\cdot 2H_2O$ (**2**) and $[Mg(H_2O)_6][Cd(1,3\text{-pdta})$-$(H_2O)]\cdot 2H_2O$ (**3**) complexes. The structures of **1**, **2** and **3** were studied by single-crystal X-ray crystallography. IR, ^{1}H NMR and ^{13}C NMR spectral data for **1**, **2** and **3** have also been reported here.

2. Experimental

2.1. Compounds preparation

All commercially obtained reagent-grade chemicals were used without further purification. The preparation of barium (1,3-propanediaminetetraacetato)barium(II) dihydrate, $Ba[Ba(1,3\text{-pdta})]\cdot 2H_2O$, has been reported elsewhere [5a,15].

2.1.1. Preparation of hexaaquamagnesium (1,3-propanediaminetetraacetato)zincate(II) dihydrate, $[Mg(H_2O)_6][Zn(1,3\text{-pdta})]\cdot 2H_2O$ (1)

$ZnSO_4\cdot 7H_2O$ (2.87 g; 0.01 mol) was dissolved in 25 cm^3 of distilled water at 60 °C. To this solution, solid $Ba[Ba(1,3\text{-pdta})]\cdot 2H_2O$ (6.13 g; 0.01 mol) was added and the reaction mixture was heated (60 °C) with stirring for 30 min. Then, $MgSO_4\cdot 6H_2O$ (2.28 g; 0.01 mol) was added and stirring was continued for 30 min. The precipitated barium sulphate was filtered out. To the obtained filtrate 5–6 cm^3 of ethanol was added and the solution was left to stand in a refrigerator overnight. The colourless crystals of $[Mg(H_2O)_6][Zn(1,3\text{-pdta})]\cdot 2H_2O$ (**1**), were collected, washed with ethanol, and air-dried. The yield was 1.25 g (23%). *Anal.* Calc. for $[Mg(H_2O)_6][Zn(1,3\text{-pdta})]\cdot 2H_2O$ (**1**), $MgZnC_{11}H_{30}N_2O_{16}$ (FW = 536.05): C, 24.65; H, 5.64; N, 5.23. Found: C, 24.28; H, 5.80; N, 5.45%. Selected IR frequencies (KBr, cm^{-1}): ν_{asym}(COO–Zn) 1610, ν_{sym} (COO–Zn) 1414. ^{1}H NMR (200 MHz, D_2O): δ 3.29 (AB pattern, 4CH$_2$(gly), δ_A 3.41, δ_B 3.18, $J_{AB} = 16.65$ Hz), 2.98 (t, 2CH$_2$(1,3-pd)), 1.65 (m, CH$_2$(1,3-pd)). ^{13}C NMR (200 MHz, D_2O): δ 181.33 (4COO$^-$), 64.51 (4CH$_2$(gly)), 61.71 (2CH$_2$(1,3-pd)), 25.74 (CH$_2$(1,3-pd)).

2.1.2. Preparation of hexaaquazinc (1,3-propanediaminetetraacetato)zincate(II) dihydrate, $[Zn(H_2O)_6][Zn(1,3\text{-pdta})]\cdot 2H_2O$ (2)

$ZnSO_4\cdot 7H_2O$ (5.75 g; 0.02 mol) was dissolved in 25 cm^3 of distilled water at 60 °C. To this solution, solid $Ba[Ba(1,3\text{-pdta})]\cdot 2H_2O$ (6.13 g; 0.01 mol) was added and the reaction mixture was heated (60 °C) with stirring for 1 h. The precipitated barium sulphate was filtered out. To the obtained filtrate 5–6 cm^3 of ethanol was added and the solution was left to stand in a refrigerator overnight. The colourless crystals of $[Zn(H_2O)_6][Zn(1,3\text{-pdta})]\cdot 2H_2O$ (**2**) were collected, washed with ethanol, and air-dried. The yield was 4.50 g (78%). The crystalline $[Zn(H_2O)_6][Zn(1,3\text{-pdta})]\cdot 2H_2O$ (**2**) was also obtained from the reaction mixture containing $Ba[Ba$-$(1,3\text{-pdta})]\cdot 2H_2O$ (6.13 g; 0.01 mol), $3CdSO_4\cdot 8H_2O$ (2.56 g; 0.003 mol) and $ZnSO_4\cdot 7H_2O$ (2.87 g; 0.01 mol), as evidenced by X-ray crystallography. *Anal.* Calc. for $[Zn(H_2O)_6][Zn(1,3\text{-pdta})]\cdot 2H_2O$ (**2**), $Zn_2C_{11}H_{30}N_2O_{16}$ (FW = 577.11): C, 22.89; H, 5.24; N, 4.85. Found: C, 22.17; H, 5.03; N, 4.67%. Selected IR frequencies (KBr, cm^{-1}): ν_{asym}(COO–Zn) 1599, ν_{sym} (COO–Zn) 1404. ^{1}H NMR (200 MHz, D_2O): δ 3.32 (AB pattern, 4CH$_2$(gly), δ_A 3.43, δ_B 3.21, $J_{AB} = 16.69$ Hz), 2.99 (t, 2CH$_2$(1,3-pd)), 1.67 (m, CH$_2$(1,3-pd)). ^{13}C NMR (200 MHz, D_2O): δ 181.38 (4COO$^-$), 64.47 (4CH$_2$(gly)), 61.76 (2CH$_2$(1,3-pd)), 25.76 (CH$_2$(1,3-pd)).

2.1.3. Preparation of hexaaquamagnesium (aqua)(1,3-propanediaminetetraacetato)cadmate(II) dihydrate, $[Mg(H_2O)_6][Cd(1,3\text{-pdta})(H_2O)]\cdot 2H_2O$ (3)

$3CdSO_4\cdot 8H_2O$ (2.56 g; 0.003 mol) was dissolved in 25 cm^3 of distilled water at 60 °C. To this solution, solid $Ba[Ba(1,3\text{-pdta})]\cdot 2H_2O$ (6.13 g; 0.01 mol) was added and the reaction mixture was heated (60 °C) with stirring for 30 min. Then, $MgSO_4\cdot 6H_2O$ (2.28 g; 0.01 mol) was added and stirring was continued for 30 min. The precipitated $BaSO_4$ was filtered out. To the obtained filtrate 5–6 cm^3 of ethanol was added and the solution was left to stand in a refrigerator overnight. The colourless crystals of $[Mg(H_2O)_6][Cd(1,3\text{-pdta})(H_2O)]\cdot 2H_2O$ (**3**), were collected, washed with ethanol, and air-dried. The yield

was 4.10 g (68%). *Anal.* Calc. for $[Mg(H_2O)_6][Cd(1,3\text{-}pdta)(H_2O)]\cdot 2H_2O$ (**3**), $MgCdC_{11}H_{32}N_2O_{17}$ (FW = 601.10): C, 21.98; H, 5.37; N, 4.66. Found: C, 22.16; H, 5.37; N, 4.67%. Selected IR frequencies (KBr, cm^{-1}): ν_{asym}(COO–Cd) 1600, ν_{sym}(COO–Cd) 1410. ^1H NMR (200 MHz, D_2O): δ 3.12 (AB pattern, $4CH_2$(gly), δ_A 3.22, δ_B 3.03, $J_{AB} = 16.26$ Hz), 2.79 (t, $2CH_2$(1,3-pd)), 1.83 (m, CH_2(1,3-pd)); ^{13}C NMR (200 MHz, D_2O): δ 180.69, 180.58 ($4COO^-$), 62.87 ($4CH_2$(gly)), 61.86 ($2CH_2$(1,3-pd)), 25.10 (CH_2(1,3-pd)).

2.2. Physical measurements

The IR spectra in the solid state were recorded on a Perkin–Elmer Spectrum One FT-IR Spectrometer using KBr pellets. ^1H NMR and ^{13}C NMR spectra of D_2O solutions containing 3-trimethylsilylpropane-1-sulfonate (TSP) as internal reference were recorded with a Varian Gemini 200 MHz spectrometer. Elemental microanalyses for carbon, hydrogen, and nitrogen were done by the Department of Chemistry, University of Belgrade, Serbia.

2.3. Crystallographic data collection and refinement of the structures

The crystal data for **1**, **2** and **3** and the parameters of data collection are summarized in Table 1. The intensity data were measured with a KM4CCD kappa-geometry diffractometer [16] using graphite monochromated Mo Kα radiation ($\lambda = 0.71073$ Å) at 130 K for **1** and **2**, and 293 K for **3**. The structures were solved by direct methods using SHELXS-97 [17] and refined by least-squares techniques with SHELXL-97 [18]. The intensity data were corrected for Lp effects as well as for absorption in the case of **1**, **2** and **3** and for extinction in the case of **3**. Anisotropic thermal parameters were employed for the non-hydrogen atoms. The positions of H-atoms attached to the C-atoms were calculated at standardized distances of 0.96 Å, and refined in a so-called "riding model" with the atomic displacement parameters 30% higher than the displacement parameters for the atoms to which they are bonded. All of the water hydrogen atoms were located from subsequent difference Fourier maps

Table 1
Crystal data summary for complexes **1**, **2** and **3**

Compound	**1**	**2**	**3**
Formula	$MgZnC_{11}H_{30}N_2O_{16}$	$Zn_2C_{11}H_{30}N_2O_{16}$	$MgCdC_{11}H_{32}N_2O_{17}$
Formula weight	536.05	577.11	601.10
T (K)	130	130	293
Wavelength Mo Kα (Å)	0.71073	0.71073	0.71073
Crystal system	orthorhombic	orthorhombic	orthorhombic
Space group	*Pnna*	*Pnna*	*Pbcn*
a (Å)	13.234(3)	13.235(3)	11.884(2)
b (Å)	11.651(2)	11.669(2)	9.727(2)
c (Å)	13.775(3)	13.754(3)	19.622(4)
V (Å^3)	2124.0(8)	2124.2(8)	2268.2(8)
Z	4	4	4
D_{calc} (g cm^{-3})	1.676	1.805	1.760
μ (mm^{-1})	1.267	2.340	1.073
$F(000)$	1120	1192	1232
Crystal size (mm)	$0.50\times0.30\times0.30$	$0.25\times0.20\times0.20$	$0.30\times0.30\times0.30$
θ Range (°)	4.10–27.10	3.77–26.02	3.41–26.06
Index ranges	$-16\leqslant h\leqslant 16$, $-13\leqslant k\leqslant 14$, $-17\leqslant l\leqslant 15$	$-16\leqslant h\leqslant 16$, $-6\leqslant k\leqslant 14$, $-16\leqslant l\leqslant 16$	$-9\leqslant h\leqslant 14$, $-11\leqslant k\leqslant 12$, $-24\leqslant l\leqslant 24$
T_{min} and T_{max}	0.715 and 1.000	0.848 and 1.000	0.837 and 1.000
Number of reflections measured	25216	16895	17906
Number of independent reflections	2339	2098	2234
Number of observed reflections [$I > 2\sigma(I)$]	2046	1740	1896
Number of parameters	175	172	190
Refinement method	full-matrix least squares F^2		
$S(F^2)$	1.104	1.032	1.110
R [$I > 2\sigma(I)$]	0.0233	0.0250	0.0211
wR	0.0600	0.0550	0.0559
Weighting scheme	$w = 1/[\sigma^2(F_o)^2 + (0.0342P)^2 + 0.2015P]$ where $P = (F_o^2 + 2F_c^2)/3$	$w = 1/[\sigma^2(F_o)^2 + (0.0275P)^2]$ where $P = (F_o^2 + 2F_c^2)/3$	$w = 1/[\sigma^2(F_o)^2 + (0.0321P)^2 + 0.3855P]$ where $P = (F_o^2 + 2F_c^2)/3$
Extinction correction			SHELXL
Extinction coefficient			0.0045(4)
ρ_{max} and ρ_{min} (e Å^{-3})	0.268 and −0.492	0.313 and −0.390	0.422 and −0.549

and refined isotropically except for the O5W solvent water hydrogen in **2** which was also refined as riding. In the crystal structure of **3**, carbon atom C2, as well as hydrogen atoms attached to C1 are disordered and were refined with occupation number 0.5. A Siemens Stereochemical Workstation was used to prepare drawings [19].

3. Results and discussion

3.1. Crystallization of divalent metal ions with 1,3-propanediaminetetraacetato ligand

Numerous attempts to obtain crystalline Co(II) complexes with 1,3-pdta ligand (1,3-pdta = 1,3-propanediaminetetraacetate ion) and alkaline metals as counter ions have not been successful. The crystalline product obtained from aqueous solutions containing a combination of either Na^+ and Co^{2+} or Li^+ and Co^{2+} cations and 1,3-propanediaminetetraacetate ion contained solely the hexadentate $[Co(H_2O)_6][Co(1,3\text{-pdta})]\cdot 2H_2O$ complex. We have recently reported the crystal structure of this complex and of the isomorphic Co(II) complex with Mg(II) as counter cation which have been prepared using the same facile method for the preparation of M(II)-1,3-pdta complexes as described previously [7].

Analogously, we have witnessed frequent occurrence of only one type of crystals obtained from the aqueous solutions containing 1,3-propanediaminetetraacetate ion and Mg^{2+}, Zn^{2+} and Cd^{2+} cations. From the solution containing Zn^{2+} and Cd^{2+} cations we have obtained as the solely crystalline product the $[Zn(H_2O)_6][Zn(1,3\text{-pdta})]\cdot 2H_2O$ (**2**) complex, isomorphic with the other complexes of $[M(H_2O)_6][M'(1,3\text{-pdta})]\cdot 2H_2O$ type [5–8], instead of the expected ZnCd(1,3-pdta) complex. Combination of Mg^{2+} and Zn^{2+} ions has lead to the $[Mg(H_2O)_6][Zn(1,3\text{-pdta})]\cdot 2H_2O$ (**1**) complex, again isomorphic with the complexes mentioned above. However, using Cd^{2+} ion in combination with Mg^{2+}, we were able to obtain seven-coordinate $[Mg(H_2O)_6][Cd(1,3\text{-pdta})(H_2O)]\cdot 2H_2O$ (**3**) complex, different from those of $[M(H_2O)_6][M'(1,3\text{-pdta})]\cdot 2H_2O$ type [5–8], but isomorphic with the $[Mg(H_2O)_6][Mn(edta)(H_2O)]\cdot 2H_2O$ [20] analogue. The complexes of coordination number (CN) higher than six with 1,3-pdta ligand are very rare, and so far only one such complex, i.e., $[Ca(H_2O)_3Ca(1,3\text{-pdta})(H_2O)]\cdot 2H_2O$ [8] (CN = 8), has been prepared and characterized. Presented in this paper, the $[Mg(H_2O)_6][Cd(1,3\text{-pdta})(H_2O)]\cdot 2H_2O$ (**3**), having the CN equal to 7, constitutes the second case. Complex **3** is also the first example of the transition metal complex with 1,3-pdta ligand that possesses the CN higher than 6.

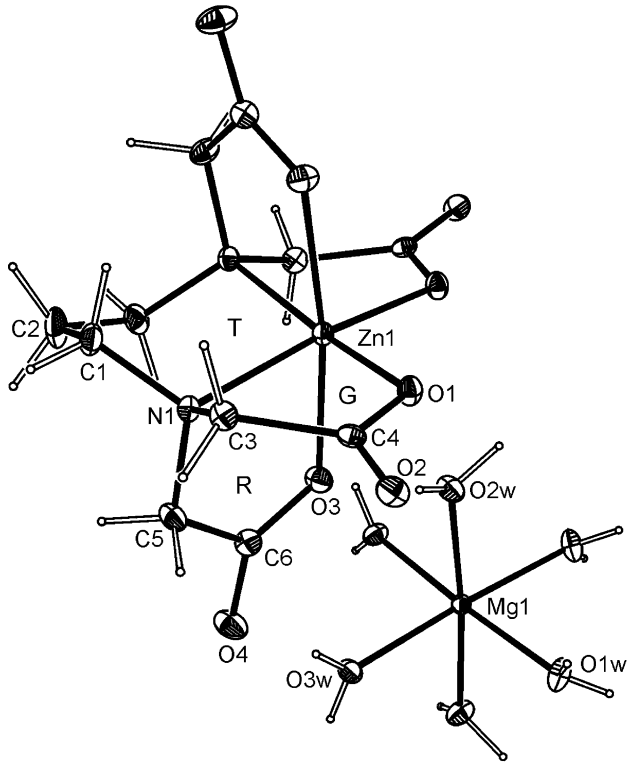


Fig. 2. The ORTEP drawing of the $[Zn(1,3\text{-pdta})]^{2-}$ and $[Mg(H_2O)_6]^{2+}$ octahedra. Generation of the second half of the complex anion and cation requires the symmetry operations $x, -y-0.5, -z+0.5$ and $x, -y-1.5, -z+0.5$, respectively. Thermal ellipsoids are drawn at the 40% probability level.

3.2. The crystal structures of $[Mg(H_2O)_6][Zn(1,3\text{-pdta})]\cdot 2H_2O$ (1) and $[Zn(H_2O)_6][Zn(1,3\text{-pdta})]\cdot 2H_2O$ (2) complexes

The crystals of **1** and **2** are isomorphic with those of $[M(H_2O)_6][M'(1,3\text{-pdta})]\cdot 2H_2O$ type complexes [5–8]. An ORTEP drawing of the $[Mg(H_2O)_6][Zn(1,3\text{-pdta})]\cdot 2H_2O$ (**1**), is depicted in Fig. 2, where the numbering scheme adopted for the respective atoms is also given. Metal–ligand bond lengths and valence angles around metal ions are listed in Table 2.

The structural units of **1** and **2** consist of discrete $[Zn(1,3\text{-pdta})]^{2-}$ and $[M^{II}(H_2O)_6]^{2+}$ [M(II) = Mg (**1**) or Zn (**2**)] octahedra, and two water solvent molecules all of which lie on a twofold axis of symmetry. The highest symmetry (C_2) axis of the complex anion passes through the Zn and C2 atoms and bisects the N1–Zn1–N1[a] bond angle ([a]stands for the symmetry operation $x, -y-0.5, -z+0.5$) making the two out-of-plane glycinate rings (R rings), as well as the two in-plane glycinate rings (G rings), identical. The R rings are almost flat, while the G-rings are much more puckered and are halfway between an *envelope* and *twist* conformations. The conformation of the six-membered 1,3-propanediamine ring (T ring) is *twist-boat*. The mean deviation from octahe-

Table 2
Bond distances (Å) and valence angles (°) with e.s.d.'s about metal ions in complexes **1**, **2** and **3**[A]

Complexes **1** and **2**		Complex **3**	
Zn1–N1	2.155(2)	Cd1–N1	2.442(1)
Zn1–O1	2.036(1)	Cd1–O1	2.547(1)
Zn1–O3	2.149(3)	Cd1–O3	2.273(1)
		Cd1–O1W	2.252(2)
N1–Zn1–N1[a]	94.83(10)	O1–Cd1–O1W	71.68(3)
O1–Zn1–O1[a]	101.4(3)	O1–Cd1–O1[c]	143.36(6)
O1–Zn1–N1	82.67(9)	O1W–Cd1–O3	98.58(4)
O1–Zn1–N1[a]	170.07(3)	O3–Cd1–O1[c]	83.81(5)
O1–Zn1–O3[a]	90.61(1)	N1–Cd1–O1[c]	146.54(4)
O3–Zn1–N1[a]	94.6(1)	O1–Cd1–O3	101.63(5)
O1–Zn1–O3	94.47(5)	O1W–Cd1–N1	134.54(3)
O3–Zn1–N1	79.99(2)	O3–Cd1–O3[c]	162.84(7)
O3–Zn1–O3[a]	171.99(11)	N1–Cd1–O3[c]	94.73(5)
		O1–Cd1–N1	66.84(4)
		O3–Cd1–N1	73.03(5)
		N1–Cd1–N1[c]	90.93(7)
Mg1–O1W/Zn2–O1W	2.069(1)/2.089(2)	Mg1–O2W	2.052(1)
Mg1–O2W/Zn2–O2W	2.046(1)/2.066(2)	Mg1–O3W	2.077(2)
Mg1–O3W/Zn2–O3W	2.068(1)/2.091(2)	Mg1–O4W	2.083(2)
O1W–Mg1–O1W[b]/O1W–Zn2–O1W[b]	88.48(7)/89.24(11)	O2W–Mg1–O3W	89.93(6)
O1W–Mg1–O3W[b]/O1W–Zn2–O3W[b]	176.97(5)/177.16(7)	O2W–Mg1–O3W[d]	90.07(6)
O1W–Mg1–O3W/O1W–Zn2–O3W	88.60(5)/88.00(7)	O4W–Mg1–O2W[d]	90.90(7)
O3W–Mg1–O3W[b]/O3W–Zn2–O3W[b]	94.33(6)/94.76(10)	O2W–Mg1–O4W	89.10(7)
O1W–Mg1–O2W/O1W–Zn2–O2W	91.58(5)/92.81(7)	O3W–Mg1–O3W[d]	180.0
O2W–Mg1–O3W/O2W–Zn2–O3W	89.16(5)/89.22(8)	O4W–Mg1–O3W[d]	92.70(7)
O1W–Mg1–O2W[b]/O1W–Zn2–O2W[b]	91.72(5)/91.60(8)	O2W–Mg1–O2W[d]	180.00(8)
O2W–Mg1–O3W[b]/O2W–Zn2–O3W[b]	87.71(5)/86.59(7)	O3W–Mg1–O4W	87.30(7)
O2W–Mg1–O2W[b]/O2W–Zn2–O2W[b]	175.40(7)/173.81(11)	O4W–Mg1–O4W[d]	180.00(13)

Symmetry codes: a: $x, -y-0.5, -z+0.5$; b: $x, -y-1.5, -z+0.5$; c: $-x+1, y, -z+1.5$; and d: $-x+1, -y+1, -z+2$.
[A] The average values of metal–ligand bond distances and valence angles for $[Zn(1,3\text{-pdta})]^{2-}$ units are given.

dral angles (ΔO_h) for $[Zn(1,3\text{-pdta})]^{2-}$on average equals to 5.85°, which indicates a nearly regular octahedral geometry of the complex anion.

Table 3 lists bond lengths to the metal(II) atoms in octahedral $[M(H_2O)_6][M'(1,3\text{-pdta})]\cdot 2H_2O$ (M(II), M′(II) = Mg,Cu [5a]; Mn,Cu [5b]; Mg,Ni [6]; Mg,Co [7]; Co,Co [7] and Mg,Mg [8]) complexes and the mean deviation from octahedral angles (av. ΔO_h). Among the complexes listed, $[Ni(1,3\text{-pdta})]^{2-}$ [6] in which the Ni–N and Ni–O_R bonds are equal in length, is the closest to the ideal octahedral geometry. On the contrary, in the $[Mg(1,3\text{-pdta})]^{2-}$ [8] complex, which is the most distorted, the Mg–N bond lengths are significantly longer than the corresponding Mg–O bonds, in line with the observation that for edta-like complexes of predominantly electrostatic binding metal ions the interactions of such metals with amine nitrogens are relatively weak. As can be seen from Table 3, influence of charge

Table 3
Geometry around divalent metal ions in a series of isomorphic crystals of the $[M(H_2O)_6][M'(1,3\text{-pdta})]\cdot 2H_2O$ type complexes

M/M′	M′–N (Å)	M′–O_G (Å)[a]	M′–O_R (Å)[a]	Average ΔO_h (°)	Reference
Mg(II)/Mg(II)	2.199	2.015	2.087	7.4	[8]
Mg(II)/Co(II)[b]	2.142	2.054	2.110	5.9	[7]
Co(II)/Co(II)[b]	2.143	2.055	2.112	5.9	[7]
Mg(II)/Zn(II)[b]	2.156	2.037	2.146	5.9	this work
Zn(II)/Zn(II)[b]	2.153	2.035	2.152	5.8	this work
Mg(II)/Cu(II)	2.047	1.974	2.272	5.4	[5a]
Mn(II)/Cu(II)	2.049	1.974	2.285	5.3	[5b]
Mg(II)/Ni(II)	2.073	2.027	2.078	5.2	[6]

[a] M–O_G is the mean in-plane bond length; M–O_R is the mean out-of-plane bond length.
[b] Low-temperature data.

compensating cations on the distortion of $[M(1,3\text{-pdta})]^{2-}$ complexes is not significant (compare $[M^{II}(H_2O)_6][Cu(1,3\text{-pdta})]\cdot 2H_2O$ (M(II) = Mg [5a] and Mn [5b]) and $[M^{II}(H_2O)_6][Zn(1,3\text{-pdta})]\cdot 2H_2O$ [M(II) = Mg (**1**) and Zn (**2**)] complexes). However, compared with similar complexes of Co(III) [1] and Rh(III) [2] with the same 1,3-pdta ligand for which ΔO_h values sum 2.8° and 4.7°, respectively, all complexes listed in Table 3 display greater degree of octahedral distortion. Moreover, the out-of-plane *trans* O–M–O bond angles in $[M(1,3\text{-pdta})]^{2-}$ (M(II) = Cu [5], Ni [6], Co [7], Mg [8] and Zn) are much more bent than the corresponding ones in $[Co(1,3\text{-pdta})]^{-}$ and $[Rh(1,3\text{-pdta})]^{-}$ complexes. For the $[M(1,3\text{-pdta})]^{2-}$ (M(II) = Cu [5], Ni [6], Co [7], Mg [8] and Zn) complexes these *trans* bond angles are in the range 168.4–175.1°, while in $[Co(1,3\text{-pdta})]^{-}$ and $[Rh(1,3\text{-pdta})]^{-}$ complexes they are almost linear (180°). This is to be expected owing to the fact that virtually all Co(III) complexes, being low-spin, produce particularly high crystal field stabilization energy (CFSE) and this effect is expected to be even more marked in the case of heavier element (Rh(III)).

Similar to other crystal structures of divalent metal ions with 1,3-pdta ligand, the discrete $[Zn(1,3\text{-pdta})]^{2-}$ and $[M^{II}(H_2O)_6]^{2+}$ octahedra [M(II) = Mg for **1** and Zn for **2**] alternate in the crystal in such a way that each complex anion is surrounded by six complex cations situated at the corners of a distorted octahedron and vice versa. As a result, not only the first but also the second metal coordination sphere displays nearly octahedral geometry. Such an alternating arrangement of the cationic and anionic species might indicate nearly spherical charge distribution on each of the complex units, which is consistent with their first coordination sphere being close to a regular octahedron.

The packing in the structure is determined by an extended network of relatively strong hydrogen bonds predominantly involving water molecules [coordinated to M (M = Mg(II) for **1** and Zn(II) for **2**) or two water solvent molecules] and carboxylate oxygens. The two-coordination octahedra are connected via hydrogen bonds in three dimensions.

3.3. The crystal structure of $[Mg(H_2O)_6]$-$[Cd(1,3\text{-pdta})(H_2O)]\cdot 2H_2O$ (**3**) complex

An ORTEP drawing of the $[Mg(H_2O)_6][Cd(1,3\text{-pdta})(H_2O)]\cdot 2H_2O$ (**3**) complex, is depicted in Fig. 3, where the numbering scheme adopted for the respective atoms is also given. Metal–ligand bond lengths and valence angles around metal ions are listed in Table 2.

The structural unit of **3** consists of discrete complex ions: $[Cd(1,3\text{-pdta})(H_2O)]^{2-}$ and $[Mg(H_2O)_6]^{2+}$ which are situated on twofold axis of symmetry and inversion centre, respectively, and two symmetry related water solvent molecules (O5W and O5W^{d}, where the symmetry code d: $-x+1, -y+1, -z+2$). The highest symmetry (C_2) axis of the complex anion passes through the Cd1 and O1W atoms making the two out-of-plane glycinate rings (R rings), as well as the two in-plane glycinate rings (G rings), identical. The central carbon atom (C2) of the six-membered 1,3-propanediamine ring and hydrogen atoms attached to C1 are statistically distributed about the twofold symmetry axis. The Cd1 has

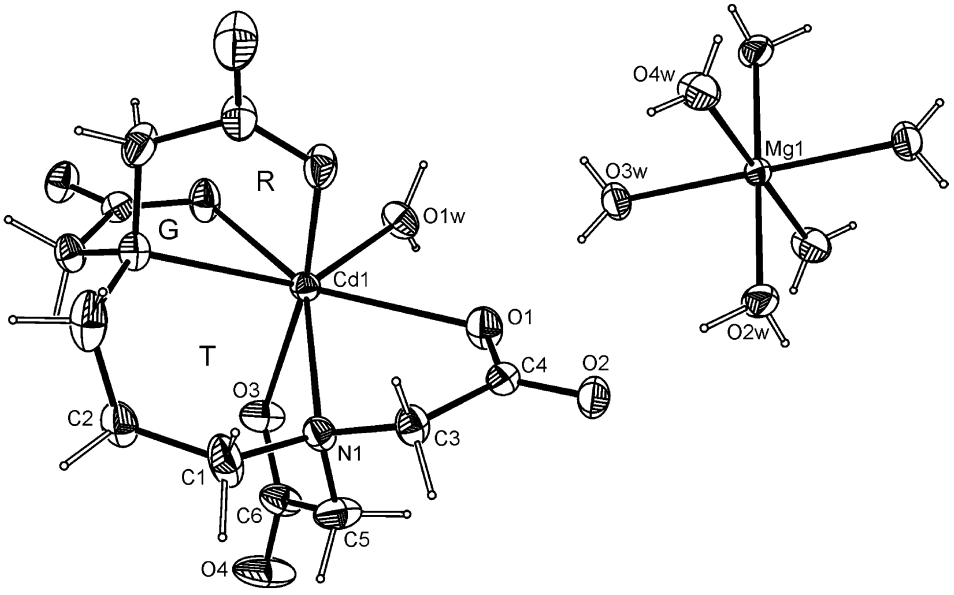


Fig. 3. The ORTEP drawing of the $[Cd(1,3\text{-pdta})(H_2O)]^{2-}$ and $[Mg(H_2O)_6]^{2+}$ polyhedra. Generation of the second half of the complex anion and cation requires the symmetry operations $-x+1, y, -z+1.5$ and $-x+1, -y+1, -z+2$, respectively. Thermal ellipsoids are drawn at the 40% probability level.

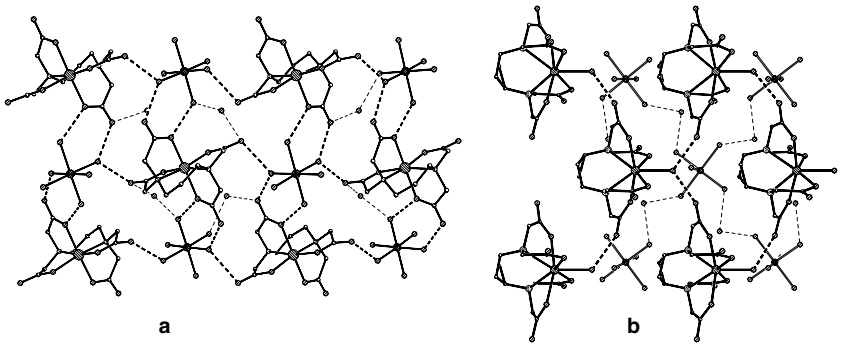


Fig. 4. (a) View of the (1 0 0) layer shows $[Zn(1,3\text{-pdta})]^{2-}$ and $[Mg(H_2O)_6]^{2+}$ polyhedra, present in **1**, connected by hydrogen bonds that propagate throughout the entire crystal. (b) View along [0 0 1] shows alternating layers of $[Cd(1,3\text{-pdta})(H_2O)]^{2-}$ anions (full lines) and $[Mg(H_2O)_6]^{2+}$ cations (open lines), present in **3**. Hydrogen bonds between crystalline and coordinated water molecules, and between water molecules and carboxylate oxygens operate within and between the cationic and anionic layers.

sevenfold coordination: with hexadentate 1,3-pdta ligand and one water molecule O1W. The coordination polyhedron formed around Cd1 is distorted pentagonal bipyramid (PB) with in-plane *cis* bond angles in the range 66.84–90.93°, and with very bent out-of-plane *trans* bond angle (O3–Cd1–O3^c) of 162.84°. Among in-plane *cis* bond angles, O1–Cd1–O1W is the closest to the value of 72° expected for ideal PB structure, while the largest deviation is observed for diamine bite angle (N1–Cd1–N1^c) which sums 90.93°. Conformations of the chelate rings are found to be *envelope* for the glycinates and almost ideal *sofa* for the six-membered diamine ring, while almost perfect twist-boat conformation was present in **1** and **2**. The Mg1 ion is coordinated with six water molecules and forms almost an ideal octahedral structure.

Packing in the crystal structure of $[Mg(H_2O)_6]$-$[Cd(1,3\text{-pdta})(H_2O)]\cdot 2H_2O$ (**3**) complex differs from that of $[M(H_2O)_6][M'(1,3\text{-pdta})]\cdot 2H_2O$ type (M(II), M′(II) = Mg,Cu [5a]; Mn,Cu [5b]; Mg,Ni [6]; Mg,Co [7]; Co,Co [7]; Mg,Mg [8]; Mg,Zn (**1**) and Zn,Zn (**2**)) complexes. While in the above mentioned isomorphic crystals an alternating cation/anion arrangement propagates throughout the entire crystal (Fig. 4(a)), in **3** the cationic and anionic species are separated into the alternating cationic and anionic layers propagating along [0 0 1] (Fig. 4(b)). Anionic layers are polar and loosely packed, thus allowing for static disorder within the 1,3-pdta ring (vide supra). The complex anions self-assemble within the layer by means of hydrogen bonds between a water molecule coordinated to Cd (O1W) and two O4 carboxylate oxygens belonging to two molecules related to each other by a unit translation along x. Hydrogen bonds within cationic layers involve both crystalline (O5W) and coordinated (to Mg) water molecules (O2W and O4W). Apart from electrostatic interactions, the cationic and anionic layers are joined together via water/carboxylate type of hydrogen bonds. Except for crystalline water molecule, which displays dual hydrogen bond functionality, all coordinated water molecules act solely as hydrogen bond donors to all carboxylate oxygens acting as acceptors.

4. Conclusion

The present study and previous investigations have shown how the change in length of the methylene chain in the amino fragment of the edta-type ligand and the type of the charge compensating cations influence the mode of crystallization of edta-type complexes. The results can be summarized as follows: (1) 1,3-pdta ligand under the hexadentate coordination favours the formation of octahedral complexes with metal(II) ions with ionic radii of about 0.8–0.9 Å. (2) Complexes of this type form isomorphic crystals in which the charge compensating cations are the divalent cations in a form of aqua ions. (3) For metal ions with ionic radii exceeding 0.9 Å, the CN equal to 7, with 1,3-pdta ligand acting as hexadentate, is to be expected.

5. Supplementary data

Supplementary data are available from the CCDC, 12 Union Road, Cambridge CB2 1EZ, UK (fax: +44 1223 336 033; e-mail: deposit@ccdc.cam.uk or www: http://www.ccdc.cam.ac.uk) on request, quoting the deposition numbers CCDC 260104, 260105 and 260106 for complexes **1**, **2** and **3**, respectively.

Acknowledgements

The authors D.D.R. and M.I.D. are grateful to the Ministry of Science and Environmental Protection of the Republic of Serbia for the financial support (Projects Nos. 1569 and 1254).

This work was partially financed during the years 2003–2006 by the Polish State Committee for Scientific Research as a scientific Project No. 4 T09A 185 25.

References

[1] R. Nagao, F. Marumo, Y. Saito, Acta Crystallogr., Sect. B 28 (1972) 1852.
[2] R. Herak, G. Srdanov, M.I. Djuran, D.J. Radanović, M. Bruvo, Inorg. Chim. Acta 83 (1984) 55.
[3] (a) T. Yamamoto, K. Mikata, K. Miyoshi, H. Yoneda, Inorg. Chim. Acta 150 (1988) 237;
(b) K. Okamoto, K. Kanamori, J. Hidaka, Acta Crystallogr., Sect. C 46 (1990) 1640;
(c) H.P. Bommeli, G. Anderegg, W. Petter, Z. Kristallogr. 174 (1986) 23.
[4] J.C. Robles, Y. Matsuzaka, S. Inomata, M. Shimoi, W. Mori, H. Ogino, Inorg. Chem. 32 (1993) 13.
[5] (a) U. Rychlewska, D.D. Radanović, V.S. Jevtović, D.J. Radanović, Polyhedron 19 (2000) 1;
(b) M. Hernandez-Padilla, E. Chinea, S. Dominguez, A. Mederos, M.C. Munoz, F. Lloret, Polyhedron 19 (2000) 1175.
[6] D.J. Radanović, T. Ama, H. Kawaguchi, N.S. Drašković, D.M. Ristanović, S. Janićijević, Bull. Chem. Soc. Jpn. 74 (2001) 701.
[7] D.D. Radanović, U. Rychlewska, M.I. Djuran, N.S. Drašković, M.M. Vasojević, I.M. Hodžić, D.J. Radanović, Polyhedron 22 (2003) 2745.
[8] D.D. Radanović, U. Rychlewska, M.I. Djuran, B. Warżajtis, N.S. Drašković, D.M. Gurešić, Polyhedron 23 (2004) 2183.
[9] H.A. Weakliem, J.L. Hoard, J. Am. Chem. Soc. 81 (1959) 549.
[10] N.V. Novozhilova, T.N. Polynova, M.A. Porai-Koshits, N.I. Pechurova, L.I. Martynenko, A. Khadi, Zh. Strukt. Khim. 14 (1973) 745.
[11] X. Solans, M. Font-Altaba, J. Oliva, J. Herrera, Acta Crystallogr., Sect. C 39 (1983) 435.
[12] E. Coronado, M. Drillon, A. Fuertes, D. Beltran, A. Mosset, J. Galy, J. Am. Chem. Soc. 108 (1986) 900.
[13] E.F.K. McCandlish, T.K. Michael, J.A. Neal, E.C. Lingafelter, N.J. Rose, Inorg. Chem. 17 (1978) 1383.
[14] F.H. Allen, O. Kennard, Chem. Des. Autom. News 8 (1993) 1, p. 31.
[15] J.A. Weyh, R.E. Hamm, Inorg. Chem. 7 (1968) 2431.
[16] Kuma Diffraction KM4CCD Software. Version 1.168. Kuma Diffraction Instruments GmbH, Wrocław, Poland, 1999.
[17] G.M. Sheldrick, Acta Crystallogr., Sect. A 46 (1990) 467.
[18] G.M. Sheldrick, SHELXL-97: Program for the Refinement of Crystal Structures, University of Göttingen, Göttingen, Germany, 1997.
[19] Stereochemical Workstation Operation Manual, Release 3.4. Siemens Analytical X-ray Instruments, Inc., Madison, WI, 1989.
[20] X. Solans, S. Gali, M. Font-Altaba, J. Oliva, J. Herrera, Afinidad 45 (1988) 243.

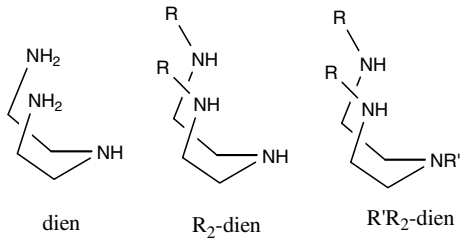


Fig. 1. Diethylenetriamine and derivatives (R or R′ = alkyl, aryl, silyl or a combination).

Ar_2-dien-supported metal halide complexes. Notably, the cobalt-containing examples exhibit, on activation with methylaluminoxane (MAO), some activity for the oligomerisation of ethylene [9]. In this article we are concerned with derivatising the central amine in Ar_2-dien with an alkyl group or with a potential donor group, 2-pyridylmethyl (2-picolyl), and examining the resultant coordination chemistry with divalent iron and cobalt halide precursors.

2. Results and discussion

2.1. Synthesis of the ligands

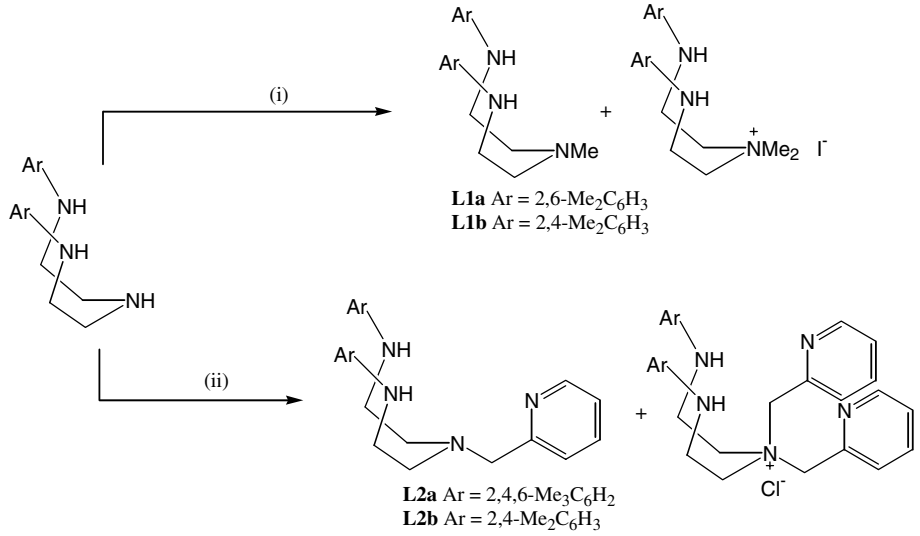
The ligands, $(ArHNCH_2CH_2)_2NMe$ (Ar = 2,6-$Me_2C_6H_3$ **L1a**, 2,4-$Me_2C_6H_3$ **L1b**), could be prepared in modest yield by treating $(ArHNCH_2CH_2)_2NH$ with MeI under conditions established by Schrock et al. for the preparation of $(MesHNCH_2CH_2)_2NMe$ [7a]. However, we have found this approach for the synthesis of **L1a** and **L1b** to be hampered by the ready formation of ammonium salts of the type $((ArHNCH_2CH_2)_2NMe_2)I^-$ (Scheme 1).

To circumvent this problem, we have employed a palladium catalysed N-C(aryl) coupling reaction of *N*-methyldiethylenetriamine (prepared from *N*-methyldiethanolamine [10]) with two equivalents of the corresponding aryl bromide using experimental conditions established by Buchwald and Hartwig [11]. Following work-up **L1a** and **L1b** could be isolated as the sole product in high yield (Scheme 2).

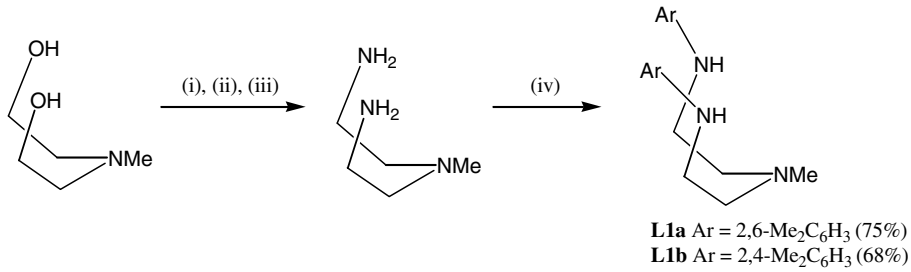
The picolyl-substituted ligands, $(ArHNCH_2CH_2)_2\{(2\text{-}C_5H_4N)CH_2\}N$ (Ar = 2,4,6-$Me_3C_6H_2$ **L2a** [12], 2,4-$Me_2C_6H_3$ **L2b**) could be prepared in modest yield from $(ArHNCH_2CH_2)_2NH$ (Ar = 2,4,6-$Me_3C_6H_2$, 2,4-$Me_2C_6H_3$) by treating them with 2-picolyl chloride hydrochloride in acetonitrile at 55 °C in the presence of potassium carbonate (Scheme 1). Following purification on an alumina column, **L2a** and **L2b** could be isolated as yellow oils. All the new ligands have been characterised by IR, ^1H and ^{13}C NMR spectroscopy, mass spectrometry (see Section 4).

2.2. Synthesis of the complexes

The reaction of **L1a** and **L1b** with $CoCl_2$ in *n*-butanol at elevated temperatures gave complexes $[\{(ArHNCH_2CH_2)_2NMe\}CoCl_2]$ (Ar = 2,6-$Me_2C_6H_3$ **1a**, 2,4-$Me_2C_6H_3$ **1b**) in high yield (Scheme 3), respectively. The corresponding reactions of **L1** with $FeCl_2$ in *n*-butanol at elevated temperature or with $FeCl_2(THF)_{1.5}$ in tetrahydrofuran at ambient temperature gave only unreacted starting materials. Complexes **1a** and **1b** have been characterised by FAB mass spectrometry, infrared spectroscopy, magnetic susceptibility and by elemental analysis (see Table 1). In addition, a crystal of **1a** has been the subject of a single crystal X-ray diffraction study.

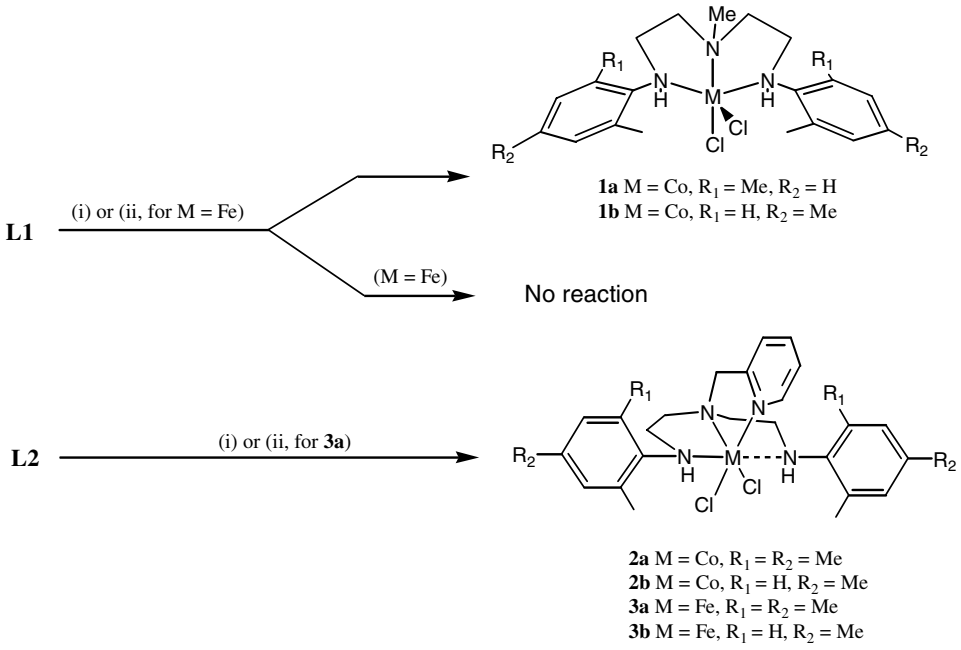


Scheme 1. Reagents and conditions: (i) K_2CO_3, 0 °C, MeI; (ii) K_2CO_3, 55 °C, $C_5H_4NCH_2Cl \cdot HCl$.



L1a Ar = 2,6-$Me_2C_6H_3$ (75%)
L1b Ar = 2,4-$Me_2C_6H_3$ (68%)

Scheme 2. Reagents and conditions: (i) Phthalimide, heat [10]; (ii) H^+; (iii) NaOH; (iv) Ar–Br, $Pd_2(dba)_3$ (0.5 mol%), *rac*-BINAP, $NaOBu^t$, toluene, heat.



1a M = Co, R_1 = Me, R_2 = H
1b M = Co, R_1 = H, R_2 = Me

2a M = Co, $R_1 = R_2$ = Me
2b M = Co, R_1 = H, R_2 = Me
3a M = Fe, $R_1 = R_2$ = Me
3b M = Fe, R_1 = H, R_2 = Me

Scheme 3. Reagents and conditions: (i) MCl_2, *n*-BuOH, heat; (ii) $FeCl_2(THF)_{1.5}$, THF, room temperature.

Table 1
Spectroscopic and analytical data for the new complexes **1–3**

Compound	μ_{eff}(BM)[a]	ν(N–H) (cm^{-1})[b]	FAB mass spectrum	Microanalysis (%)[c]		
				C	H	N
1a	3.90	3286w	454 $[M]^+$, 419 $[M - Cl]^+$	55.65 (55.39)	7.02 (6.86)	9.11 (9.23)
1b	4.01	3257w	454 $[M]^+$, 419 $[M - Cl]^+$			
2a	3.80	3245w	524 $[M - Cl]^+$	60.13 (60.00)	6.94 (6.76)	10.14 (10.00)
2b	4.10	3190w	496 $[M - Cl]^+$	58.59 (58.65)	6.11 (6.39)	10.30 (10.53)
3a	4.88	3209w	521 $[M - Cl]^+$	60.11 (60.34)	6.79 (6.87)	10.09 (10.05)
3b	5.11	3233w	493 $[M - Cl]^+$	59.12 (58.98)	6.51 (6.43)	10.81 (10.59)

[a] Recorded on an Evans Balance at room temperature.
[b] Recorded on a Perkin–Elmer Spectrum One FT-IR spectrometer on solid samples.
[c] Calculated values are shown in parentheses.

Dark blue crystals of **1a** suitable for the X-ray determination were grown by layering an acetonitrile solution of the complex with hexane at ambient temperature. A view of **1a** is shown in Fig. 2; selected bond distances and angles are listed in Table 2. The structure consists of a cobalt centre surrounded by a tridentate

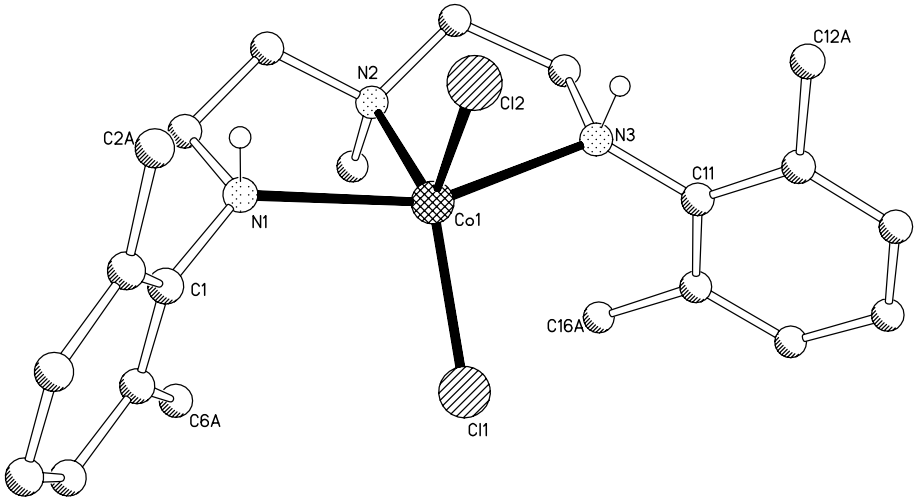


Fig. 2. Molecular structure of **1a** including the atom numbering scheme. All hydrogen atoms except for H1 and H3 have been omitted for clarity.

Table 2
Selected bond distances (Å) and angles (°) for **1a**

Bond lengths	
Co(1)–N(1)	2.274(4)
Co(1)–N(2)	2.088(3)
Co(1)–N(3)	2.289(4)
Co(1)–Cl(1)	2.2472(16)
Co(1)–Cl(2)	2.3136(15)
Bond angles	
N(1)–Co(1)–N(2)	80.24(13)
N(1)–Co(1)–N(3)	156.94(12)
N(2)–Co(1)–N(3)	80.49(12)
N(1)–Co(1)–Cl(1)	100.49(10)
N(2)–Co(1)–Cl(1)	132.81(10)
N(3)–Co(1)–Cl(1)	101.88(9)
N(1)–Co(1)–Cl(2)	87.09(10)
N(2)–Co(1)–Cl(2)	108.46(10)
N(3)–Co(1)–Cl(2)	87.10(9)
Cl(1)–Co(1)–Cl(2)	118.72(6)

N,*N*,*N*-chelate and two terminal chloride ligands. The geometry at the cobalt(II) centre may be best described as distorted trigonal bipyramidal with the equatorial plane defined by N(2), Cl(1) and Cl(2) [N(2)–Co(1)–Cl(1) 132.81(10)°, N(2)–Co(1)–Cl(2) 108.46(10)°] and the axial sites by N(1) and N(3) [N(1)–Co(1)–N(3) 156.94(12)°]. The *N*,*N*,*N*-chelate is bound in a *meridional* configuration and contains two five-membered chelate rings, the bite angle for each being 80.24(13)° [N(1)–Co(1)–N(2)] and 80.49(12)° [N(2)–Co(1)–N(3)]. The *ortho*-methyl groups of the *N*-aryl substituents are positioned above and below the plane defined by N(1)–N(2)–N(3)–Co(1) [max. deviation from plane: Co(1) 0.170 Å] with C2A and C12A pointing in a similar direction to Cl(2). There is a difference in the Co–N bond lengths with the central Co–N being shorter than the terminal Co–N bond lengths [Co(1)–N(2) 2.088(3) Å versus Co(1)–N(1) 2.274(4) Å, Co(1)–N(3) 2.289(4) Å]. The two Co–Cl bond distances are asymmetric with Co–Cl(2) being ca. 0.07 Å longer than Co–Cl(1). The Cl(1)–Co(1)–Cl(2) bond angle of 118.72(6)° falls in the mid-range for those found in related five-coordinate cobalt(II) dichloride complexes [9,13]. Complex **1a** has two chiral centres at N(1) and N(3) and crystallises with the relative configuration being distinct. The structural features of **1a** closely resemble those observed for the related complexes [{$(ArNHCH_2CH_2)_2$-NH}$CoCl_2$] (Ar = 2,6-$Me_2C_6H_3$, 2,4, 6-$Me_3C_6H_2$) [9].

The FAB mass spectrometric data for **1a** and **1b** reveal molecular ions peaks along with fragmentation peaks corresponding to the loss of chloride ions; no peaks are evident for dimeric species. In their IR spectra, the υ(N–H) absorption band is seen at ca. 3270 cm^{-1} and is ca. 100 cm^{-1} lower in wavenumber than in the free-ligands (**L1a** and **L1b**). The room temperature magnetic susceptibility measurements (Evans Balance) for **1a** and **1b** afforded magnetic moments of ca. 3.95 BM, characteristic of high spin cobalt(II) configurations ($S = 3/2$) containing three unpaired electrons. Attempts to acquire assignable paramagnetically shifted ^1H NMR spectra in acetonitrile-d_3 at room temperature proved unsuccessful.

It is uncertain as to why a stable complex (under the conditions employed) containing **L1** cannot be isolated with iron chloride. It is noteworthy that we have also been similarly unsuccessful in isolating iron complexes with the non-methylated counterpart of **L1**, $(ArHNCH_2CH_2)_2NH$ [9]. Replacement of one $ArHNCH_2CH_2$ arm in $(ArHNCH_2CH_2)_2NH$ with a picolyl group has, however, afforded isolable complexes with iron chloride [14]. It would appear that the π-acceptor capability of the pyridyl donor plays a key role in complex stability.

Interaction of **L2a** or **L2b** with MCl_2 in *n*-butanol at elevated temperatures gave complexes [{$ArNHCH_2$-

$CH_2\}_2\{(2\text{-}C_5H_4N)CH_2\}NMCl_2]$ (M = Co, Ar = 2,4,6-$Me_3C_6H_2$ **2a**, 2,4-$Me_2C_6H_3$ **2b**; M = Fe, Ar = 2,4,6-$Me_3C_6H_2$ **3a**, 2,4-$Me_2C_6H_3$ **3b**) in good yield. Complexes **3a** and **3b** can also be prepared from the reaction of $FeCl_2(THF)_{1.5}$ with **L2** in tetrahydrofuran at room temperature (Scheme 1). Complexes **2** and **3** have been characterised by FAB mass spectrometry, infrared spectroscopy, magnetic susceptibility and by elemental analysis (see Table 1). In addition, crystals of **2a** · CH_2Cl_2 and **3a** · MeCN have been the subject of a single crystal X-ray diffraction study.

Pale blue crystals of **2a** · CH_2Cl_2 and golden crystals of **3a** · MeCN suitable for X-ray determinations were grown by layering dichloromethane and acetonitrile solutions of the complexes with hexane at ambient temperature, respectively. The molecular structures of **2a** and **3a** are essentially the same and only **3a** will be discussed in any detail. A view of **3a** is shown in Fig. 3; selected bond distances and angles for both complexes are listed in Table 3.

Table 3
Selected bond distances (Å) and angles (°) for **2a** · CH_2Cl_2 and **3a** · MeCN

	2a · CH_2Cl_2 (M = Co)	**3a** · MeCN (M = Fe)
Bond lengths		
M(1)–N(1)	2.217(2)	2.248(4)
M(1)–N(2)	2.117(2)	2.165(5)
M(1)–N(3)	2.202(2)	2.319(4)
M(1) ··· N(4)	2.795(2)	2.597(4)
M(1)–Cl(1)	2.3219(8)	2.3215(17)
M(1)–Cl(2)	2.4238(8)	2.480(2)
Bond angles		
N(1)–M(1)–N(2)	78.38(9)	77.89(18)
N(1)–M(1)–N(3)	80.45(8)	78.13(15)
N(2)–M(1)–N(3)	109.98(8)	104.89(16)
N(1)–M(1)–Cl(1)	172.95(6)	170.73(13)
N(2)–M(1)–Cl(1)	94.59(6)	93.23(14)
N(3)–M(1)–Cl(1)	101.65(7)	101.90(12)
N(1)–M(1)–Cl(2)	91.70(6)	92.44(13)
N(2)–M(1)–Cl(2)	160.27(6)	166.94(14)
N(3)–M(1)–Cl(2)	84.71(6)	81.31(12)
Cl(1)–M(1)–Cl(2)	95.19(3)	96.73(6)

The structure of **3a** consists of a single iron centre bound by an *N*,*N*,*N*,*N*-chelate and two monodentate chloride ligands to form a geometry that can be best described as a distorted octahedral. The pyridyl donor [N(2)] is *trans* to Cl(2) and the tertiary amine N(1) is *trans* to Cl(1) leaving the mesityl-substituted amines located mutually *trans*. There is considerable variation in the Fe–N bond lengths with the distance to the pyridyl donor being the shortest [Fe(1)–N(2) 2.165(5) Å] followed by the distance to the tertiary amine [Fe(1)–N(1) 2.248(4) Å]. Despite the same substitution pattern on N(3) and N(4), the Fe–N(4) [2.597(4) Å] bond distance is significantly longer than that for Fe–N(3) [2.319(4) Å] and ca. 0.3 Å longer than that found for the corresponding distance in related ferrous complexes [9,14]. Indeed in **2a** this asymmetry is even more dramatic [Co(1)–N(4) 2.795(2) Å vs. Co(1)–N(3) 2.202(2) Å] to the point where a weak interaction offers a more suitable description. The origin of the elongation of the M(1)–N(4) distance is likely to be steric; the pyridyl donor, due to geometry constraints within the ligand framework, is inclined more towards one aryl-amine than the other with the result than an *ortho*-methyl group [C(28)] hinders efficient coordination of N(4). Unfortunately, single crystals of **2b** and **3b**, which lack one *o*-Me group per aryl ring, could not be grown in order to demonstrate this steric effect. Notably, in $[\{(ArNHCH_2CH_2)\{(2\text{-}C_5H_4N)CH_2\}_2N\}FeCl_2]$ (Ar = 2,4-$Me_2C_6H_3$, 2,6-$Me_3C_6H_2$) effective coordination of the aryl-amine arm occurs for the 2,4-Me_2Ph derivative but not for the 2,6-Me_2Ph derivative [14]. The two Fe–Cl bond distances are asymmetric with Fe–Cl(2) being ca. 0.16 Å longer than Fe–Cl(1), presumably as a consequence of the *trans*-coordinated pyridyl group.

The IR spectra of **2a** and **3a** both show broad υ(NH) absorption bands at ca. 3200 cm^{-1} which, in comparison with the free ligand **L1a**, are shifted to

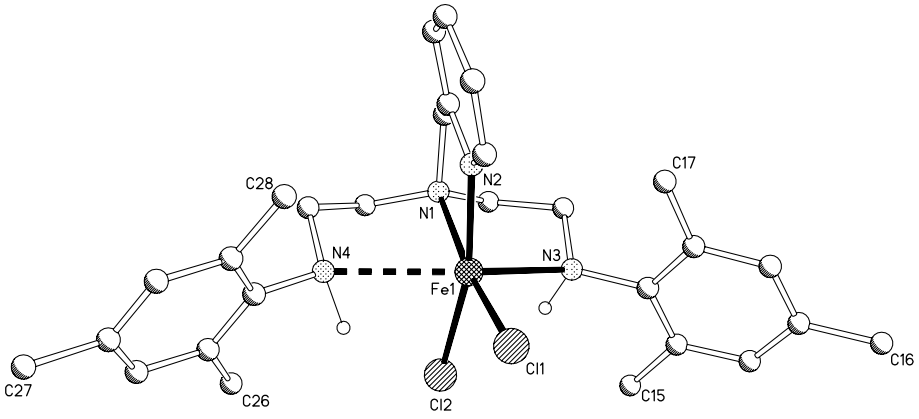


Fig. 3. Molecular structure of **3a** including the atom numbering scheme. All hydrogen atoms except for H3 and H4 have been omitted for clarity.

lower wavenumber by ca. 100 cm^{-1} (Table 1). Similar shifts in wavenumber are observed for **2b** and **3b**. The room temperature magnetic susceptibility measurements for **2** and **3** indicate high spin behaviour with the iron(II) complexes (**2**) displaying magnetic moments of ca. 5.0 BM (consistent with four unpaired electrons) and ca. 3.9 BM for the cobalt(II) complexes (consistent with three unpaired electrons).

Solution state studies performed on complexes **2a** and **3a** in acetonitrile-d_3 at room temperature support their paramagnetic nature with broad shifted ^{1}H NMR spectra in the range of −10.0 to 130.0 ppm (see Section 4). Interpretation of the paramagnetic ^{1}H NMR spectra can be achieved by comparison of chemical shifts and relaxation times (T_1) to related metal(II) complexes such as $[\{(ArNHCH_2CH_2\}\{(C_5H_4N)CH_2\}NH\}MCl_2]$ (M = Fe, Co) [9] and to previously reported polypyridyl metal(II) systems [15–17].

For **2a** the protons of the coordinated pyridyl arm display characteristic chemical shifts and relaxation times [H_α, $\delta = 97.0$; $H_\beta/H_{\beta'}$, $\delta = 50.3/46.8$ ($T_1 = 10.1$ and 16.4 ms); H_γ, $\delta = 0.3$ ($T_1 = 31.0$ ms)]. The methylene protons are not observed, possibly as a consequence of the significant broadening of the spectrum. The aromatic region can be assigned as: Ar–H_m at $\delta = 9.3$ ($T_1 = 39.4$ ms), ArMe_p at $\delta = 11.5$ ($T_1 = 135$ ms) and Ar-Me_o at $\delta = -4.8$ ($T_1 = 2.8$ ms). For **3a** the H_α of the coordinated pyridyl arm is shifted downfield the most at $\delta = 128.6$, whilst $H_{\beta/\beta'}$ appear as sharp signals at $\delta = 53.6$ and 52.1 ($T_1 = 13.1$ and 11.1 ms) and H_γ is the most upfield at $\delta = 18.2$ ($T_1 = 42.3$ ms). The methylene protons are exceedingly broad and shifted downfield at $\delta \approx 115$ and 35. The aromatic region can be assigned as: ArMe_p at $\delta = 13.3$ ($T_1 = 40.5$ ms), Ar–H_m at $\delta = 12.0$ ($T_1 = 150$ ms) and ArMe_o at $\delta = 8.7$ ($T_1 = 3.1$ ms).

It is noteworthy that, despite the inequivalence of the aryl-amine arms in **2a** and **3a** in the solid state, their behaviour in solution at ambient temperature reveals signals (albeit rather broad) consistent with one type of aryl group environment. Scheme 4 illustrates a series of equilibria that could account for the apparent C_2 symmetry in solution.

Complexes **1a** and **1b**, on activation with MAO (300 eq.; conditions, 1 bar ethylene, room temperature, in toluene), are modest catalysts for the oligomerisation of ethylene, (ca. 45 g mmol/h/bar) giving a broad range of linear and branched products including α-olefins, internal olefins, vinylidenes and trisubstituted olefins. In contrast, **2** and **3** show scarcely any activity; it would seem likely that the additional nitrogen donor in the supporting ligand makes the metal centre too electron rich.

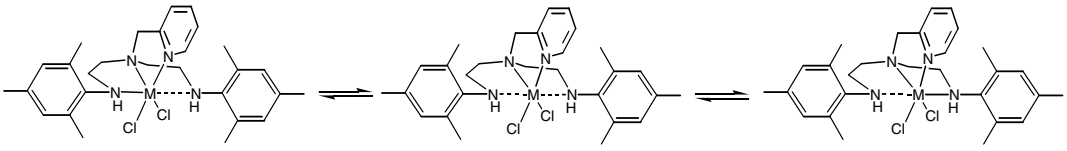
3. Conclusions

In conclusion, a series of new aryl-substituted dien ligands (**L1** and **L2**) containing a central tertiary amine have been prepared and fully characterised. Tetradentate coordination is possible for **L2** in iron(II) and cobalt(II) complexes; the effect of steric bulk on efficient coordination is apparent. Coordination of **L1** as a tridentate ligand has only been observed in cobalt(II) halide complexes. The **L1**-supported cobalt systems show some activity as precatalysts for ethylene oligomerisation.

4. Experimental

4.1. General

All reactions were carried out under an atmosphere of dry, oxygen-free nitrogen, using standard Schlenk techniques or in a nitrogen purged glove box. Solvents were distilled under nitrogen from appropriate drying agents and degassed prior to use [18]. The infrared spectra were recorded as Nujol mulls between 0.5 mm NaCl plates or on a Perkin–Elmer 1600 series or in the solid state using a Perkin–Elmer spectrum one FT-IR spectrometer The ES and the FAB mass spectra were recorded using a micromass Quattra LC mass spectrometer and a Kratos Concept spectrometer with methanol or NBA as the matrix respectively. ^{1}H and ^{13}C NMR spectra were recorded on a Bruker ARX spectrometer (250 or 300 MHz); chemical shifts (ppm) are referred to the residual protic solvent peaks; relaxation times (T_1) are in seconds. Magnetic susceptibility studies were performed using an Evans Balance (Johnson Matthey) at room temperature. The magnetic moment was calculated following standard methods [19] and corrections for underlying diamagnetism were applied to data [20]. Elemental analyses were performed at the Department of Chemistry, University of North London by Dr S. Boyer.



Scheme 4. Possible interconversion occurring in solution for **2a** or **3a**.

The reagents, 2-picolyl chloride hydrochloride, sodium *t*-butoxide, the aryl halides and the metal dichlorides were purchased from Aldrich Chemical Co. and used without further purification. *rac*-BINAP was purchased from Strem Chemical Co. The compounds, $Pd_2(dba)_3$ [21], $(H_2NCH_2CH_2)_2NMe$ [10], $FeCl_2(THF)_{1.5}$ [22] and $(ArNHCH_2CH_2)_2NH$ (Ar = 2,4,6-$Me_3C_6H_2$ [3], 2,4-$Me_2C_6H_3$ [23]) were prepared according to previously reported procedures. All other chemicals were obtained commercially and used without further purification.

4.2. Synthesis of *L1*

(a) **L1a**, Ar = 2,6-$Me_2C_6H_3$: An oven-dried Schlenk flask equipped with a magnetic stir bar was evacuated and backfilled with nitrogen. The flask was charged with $(H_2NCH_2CH_2)_2NMe$ (1.20 g, 10.3 mmol), 2-bromo-*m*-xylene (2.74 ml, 3.81 g, 20.6 mmol), $Pd_2(dba)_3$ (0.047 g, 0.052 mmol, 0.005 eq.), *rac*-BINAP (0.096 g, 0.155 mmol, 0.015 eq.), $NaOBu^t$ (2.97 g, 30.9 mmol) and toluene (40 ml). The reaction mixture was heated at reflux and stirred for a period of 4 days. After cooling to room temperature, the solvent was removed under reduced pressure to afford an oily residue. The residue was dissolved in diethyl ether (30 ml) and washed with water (3×30 ml) and saturated NaCl solution (3×30 ml). The organic layer was separated and dried over $MgSO_4$. The solvent was removed under reduced pressure and the residue left under vacuum at 50 °C for 24 h to give [{(2,6-$Me_2C_6H_3$)$HNCH_2CH_2$}$_2$NMe] (**L1a**) as a viscous oil. Yield: 75% (2.50 g, 7.73 mmol). Compound **L1a**: ES mass spectrum, *m*/*z* 326 ($M^+ + H$). IR (cm^{-1}): 3357 (NH, medium). NMR ($CDCl_3$, 293 K): ^1H NMR, δ 6.90 (d, 4H, ^3J(HH) 7.2, Ar-H_m), 6.74 (t, 2H, Ar-H_p), 3.03 (t, 4H, ^3J(HH) 6.0, CH_2), 2.55 (t, 4H, CH_2), 2.21 (s, 12H, Me_o) and 2.19 (s, 3H, N–Me). ^{13}C (^1H composite pulse decoupled), δ 146.9 (s, C, Ar), 129.3 (s, C, Ar), 129.2 (s, C, Ar), 121.8 (s, C, Ar), 58.7 (s, CH_2), 46.1 (s, CH_2), 41.7 (s, N–Me) and 19.1 (s, Me_o).

(b) **L1b**, Ar = 2,4-$Me_2C_6H_3$: Using the same procedure and molar quantities of reagents as above in 4.2(a) employing 4-bromo-*m*-xylene (2.78 cm^3, 3.81 g, 20.6 mmol) as the aryl bromide, [{(2,4-$Me_2C_6H_3$)-$HNCH_2CH_2$}$_2$NMe] (**L1b**) was isolated as a viscous red oil. Yield: 68% (2.27 g, 6.97 mmol). Compound **L1b**: ES mass spectrum, *m*/*z* 326 ($M^+ + H$). IR (cm^{-1}): 3347 (NH, medium). NMR ($CDCl_3$, 293 K): ^1H NMR, δ 6.82 (m, 4H, Ar–H), 6.45 (d, 2H, ^3J(HH) 8.1, Ar–H), 3.20 (t, 4H, ^3J(HH) 6.0, CH_2), 2.71 (t, 4H, CH_2), 2.14 (s, 6H, Me_o), 2.05 (s, 6H, Me_p) and 2.10 (s, 3H, N–Me). ^{13}C (^1H composite pulse decoupled), δ 144.6 (s, C, Ar), 131.3 (s, C, Ar), 127.7 (s, C, Ar), 126.4 (s, Ar), 122.8 (s, C, Ar), 110.5 (s, C, Ar), 48.7 (s, CH_2), 44.2 (s, CH_2), 41.8 (s, N-Me), 20.7 (s, Me_p) and 17.9 (s, Me_o).

4.3. Synthesis of *L2*

(a) **L2a**, Ar = 2,4,6-$Me_3C_6H_2$: An oven dried Schlenk flask was charged with [{(2,4,6-$Me_3C_6H_2$)-$HNCH_2CH_2$}$_2$NH] (0.50 g, 1.54 mmol), 2-picolyl chloride hydrochloride (0.380 g, 2.31 mmol), K_2CO_3 (0.457 g, 4.62 mmol) and acetonitrile (40 ml). The reaction mixture was heated to 55 °C and stirred for a period of three days. After cooling to room temperature, the solution was filtered and the solvent removed under reduced pressure to afford an oily residue. The residue was dissolved in diethyl ether (30 ml) and washed with water (3×30 ml). The organic phases were combined and concentrated on a rotary evaporator to give a brown oil. The crude product was purified via alumina column chromatography employing ethyl acetate and hexane (1:4) as the eluting solvents to give {(2,4,6-$Me_3C_6H_2$)$NHCH_2$-CH_2}$_2${(2-C_5H_4N)CH_2}N (**L2a**) as a yellow oil. Yield: 31% (0.202 g, 0.48 mmol). Compound **L2a**: ES mass spectrum: *m*/*z* 431 $[M + H]^+$. IR (cm^{-1}): 3356 (N–H, medium), 1590 (C = $N_{pyridine}$). NMR ($CDCl_3$, 293 K): ^1H NMR, δ 8.45 (dd, 1H, ^3J(HH) 5.0, ^4J(HH) 1.0, PyC*H*), 7.55 (dt, 1H, ^3J(HH) 7.0, ^4J(HH) 1.8, PyC*H*), 7.39 (d, 1H, ^3J(HH) 7.9, PyC*H*), 7.07 (m, 1H, PyC*H*), 6.70 (s, 4H, ArC*H*), 3.80 (s, 2H, PyCH_2), 3.22 (br s, 2H, N–*H*), 3.0 (t, 4H, CH_2), 2.74 (t, 4H, ^3J(HH) 6.0, CH_2) and 2.13 (s, 18H, *Me*). ^{13}C NMR (^1H composite pulse decoupled): δ 159.4 (s, C, Py), 149.2 (s, C, Py), 143.7 (s, C, Ar), 136.4 (s, C, Py), 130.9 (s, C, Ar), 129.4 (s, C, Ar), 129.3 (s, C, Ar), 123.0 (s, C, Py), 122.1 (s, C, Py), 60.5 (s, Py*C*H_2), 55.1 (s, *C*H_2), 46.1 (s, *C*H_2), 20.6 (s, Me_p) and 18.5 (s, Me_o).

(b) **L2b**, Ar = 2,4-$Me_2C_6H_3$: Using the same procedure and molar quantities of reagents as above in 4.3(a) employing [{(2,4-$Me_2C_6H_3$)$HNCH_2CH_2$}$_2$NH] (0.49 g, 1.54 mmol), 2-picolyl chloride hydrochloride 0.380 g, 2.31 mmol), K_2CO_3 (0.457 g, 4.62 mmol) gave {(2,4-$Me_3C_6H_3$)$NHCH_2CH_2$}$_2${(2-C_5H_4N)CH_2}-N (**L2b**) as a yellow oil. Yield: 29% (0.184 g, 0.47 mmol). Compound **L2b**: ES mass spectrum: *m*/*z* 403 $[M + H]^+$. IR (cm^{-1}): 3371 (N–H, medium). NMR ($CDCl_3$, 293 K):^1H NMR, δ 8.61 (dd, 1H, ^3J(HH) 5.8, ^4J(HH) 1.1, PyC*H*), 7.51 (dt, 1H, ^3J(HH) 7.0, ^4J(HH) 1.8, PyC*H*), 7.46 (d, 1H,^3J(HH) 7.9, PyC*H*), 7.05 (m, 1H, PyC*H*), 6.90 (m, 4H, Ar–H), 6.45 (d, 2H, ^3J(HH) 8.1, Ar–H), 3.86 (s, 2H, PyCH_2), 3.55 (m, 4H, CH_2), 3.20 (m, 4H, CH_2), 2.12 (s, 6H, Me_p) and 2.00 (s, 6H, Me_o). ^{13}C NMR (^1H composite pulse decoupled), δ 160.2 (s, C, Py), 149.5 (s, C, Py), 143.9 (s, C, Ar), 136.4 (s, C, Py), 131.3 (s, C, Ar), 127.7 (s, C, Ar), 126.4 (s, C, Ar), 122.8 (s, C, Ar), 122.5 (s, C, Py), 122.3 (s, C, Py), 110.5 (s, C, Ar), 59.9 (s, Py*C*H_2), 48.7 (s, *C*H_2), 44.2 (s, *C*H_2), 20.7 (s, Me_p) and 17.9 (s, Me_o).

4.4. Synthesis of (1)

(a) **1a**, Ar = 2,6-$Me_2C_6H_3$: An oven-dried Schlenk flask equipped with a magnetic stir bar was evacuated and backfilled with nitrogen. The flask was charged with $CoCl_2$ (0.040 g, 0.32 mmol) in *n*-BuOH (5 ml) at 90 °C and a solution of **L1a** (0.105 g, 0.32 mmol) in *n*-BuOH was introduced to form a green solution. After being stirred at 90 °C for 1 h, the reaction was allowed to cool to room temperature. The reaction mixture was concentrated and hexane added to induce precipitation of the product. The suspension was stirred overnight, filtered, washed with hexane (2 × 30 ml) and dried under reduced pressure to give [{((2,6-$Me_2C_6H_3$)$NHCH_2CH_2$)}$_2$N-Me}$CoCl_2$] (**1a**) as a pale blue solid. Layering of an acetonitrile solution of **1a** with hexane gave **1a** as pale blue crystals suitable for a single crystal X-ray structure determination. Yield: 75% (0.110 g, 0.24 mmol).

(b) **1b**, Ar = 2,4-$Me_2C_6H_3$: Using the same procedure and molar quantities of reagents as above in 4.4(a) employing **L1b** (0.104 g, 0.32 mmol) and $CoCl_2$ (0.042 g, 0.32 mmol), gave [{((2,4-$Me_2C_6H_3$)$NHCH_2CH_2$)}$_2$NMe $CoCl_2$] (**1b**) as a pale blue solid. Yield: 71% (0.103 g, 0.23 mmol).

4.5. Synthesis of (2)

(a) **2a**, Ar = 2,4,6-$Me_3C_6H_2$: An oven-dried Schlenk flask equipped with a magnetic stir bar was evacuated and backfilled with nitrogen. The flask was charged with $CoCl_2$ (0.020 g, 0.15 mmol) in *n*-BuOH (5 ml) and the reaction stirred at 90 °C until dissolution. **L2a** (0.065 g, 0.15 mmol) in *n*-BuOH (2 ml) was added and the reaction mixture stirred at 90 °C for 20 min. Following concentration of the reaction mixture hexane was added to induce precipitation of the product. The suspension was stirred overnight, filtered, washed with hexane (2 × 30 ml) and dried under reduced pressure to afford [{(2,4,6-$Me_2C_6H_2$)-$NHCH_2CH_2$)}$_2${(2- C_5H_4N)CH_2}N}$CoCl_2$] (**2a**) as a pale blue solid. Layering of a acetonitrile solution of **2a** with hexane gave pale blue crystals suitable for a single crystal X-ray diffraction study. Yield: 81% (0.068 g, 0.12 mmol). ^{1}H NMR (acetonitrile-d_3, 293 K): δ 97.0 (H_α), 50.3 (10.1 ms, H_β or $H_{\beta'}$), 46.8 (16.4 ms, H_β or $H_{\beta'}$), 11.5 (135 ms, $ArMe_p$), 9.3 (39.4 ms, Ar–H_m), 0.31 (31.0 ms, H_γ) and −4.8 (2.8 ms, $ArMe_o$).

(b) **2b**, Ar = 2,4-$Me_2C_6H_3$: Using the same procedure and molar quantities of reagents as above in 4.5(a) employing **L2b** (0.061 g, 0.15 mmol) and $CoCl_2$ (0.020 g, 0.15 mmol), gave [{(2,4-$Me_2C_6H_3$)-$NHCH_2$-CH_2)}$_2${(2-C_5H_4N)CH_2}N}$CoCl_2$] (**2b**) as a pale blue solid. Yield: 65% (0.052 g, 0.10 mmol).

4.6. Synthesis of (3)

(a) **3a**, Ar = 2,4,6-$Me_2C_6H_2$: An oven-dried Schlenk flask equipped with a magnetic stir bar was evacuated and backfilled with nitrogen. The flask was charged with $FeCl_2(THF)_{1.5}$ (0.108 g, 0.47 mmol) in THF (10 ml) and a solution of **L2a** (0.200 g, 0.47 mmol) in THF (5 ml) was introduced to form a yellow solution. After being stirred at room temperature for 24 h, the reaction mixture was concentrated and hexane added to induce precipitation of the product. The suspension was stirred overnight, filtered, washed with hexane (2 × 30 ml) and dried under reduced pressure to give [{(2,4,6-$Me_2C_6H_2$)$NHCH_2CH_2$)}$_2${(2-C_5H_4N)CH_2}N}$FeCl_2$] (**3a**) as a pale yellow solid. Layering of an acetonitrile solution of **3a** with hexane gave **3a** as golden crystals suitable for a single crystal X-ray structure determination. Yield: 80% (0.212 g, 0.38 mmol). ^{1}H NMR (acetonitrile-d_3, 293 K): δ 128.6 (H_α), 115.0 (very broad, CH_2), 53.6 (13.1 ms, H_β or $H_{\beta'}$), 52.1 (11.1 ms, H_β or $H_{\beta'}$), 35.0 (very broad, CH_2), 18.2 (42.3 ms, H_γ) 13.3 (40.5 ms, Ar–Me_p), 12.0 (150.0 ms, Ar–H_m), and 8.7 (3.1 ms, $ArMe_o$).

(b) **3b**, Ar = 2,4-$Me_2C_6H_3$: An oven-dried Schlenk flask equipped with a magnetic stir bar was evacuated and backfilled with nitrogen. The flask was charged with $FeCl_2$ (0.019 g, 0.15 mmol) in *n*-BuOH (5 ml) and the reaction stirred at 90 °C until dissolution. **L2b** (0.063 g, 0.15 mmol) in *n*-BuOH (2 ml) was added and the reaction mixture stirred at 90 °C for 20 min. Following concentration of the reaction mixture hexane was added to induce precipitation of the product. The suspension was stirred overnight, filtered, washed with hexane (2 × 30 ml) and dried under reduced pressure to afford [{(2,4-$Me_2C_6H_3$)$NHCH_2CH_2$)}$_2${(2-C_5H_4N)-CH_2}N}$FeCl_2$] (**2a**) as a pale yellow solid. Yield: 65% (0.053 g, 0.10 mmol).

4.7. Ethylene oligomerisation

The precatalyst (**1**–**3**) (0.01 mmol) was added to a Schlenk tube, dissolved or suspended in toluene (40 ml) and MAO (4.0 mmol, 400 equiv.) introduced. The tube was purged with ethylene and the contents stirred under 1 bar ethylene at room temperature for the duration of the test. After 0.5 h the test was terminated by the addition of dilute aqueous hydrogen chloride. The organic phase was separated, analysed by GC and then the solvent removed by distillation and the residue analysed by NMR spectroscopy.

4.8. Crystallography

Data for **1a** and **3a** were collected on a Bruker P4 diffractometer while that for **2a** on a Bruker APEX 2000 CCD diffractometer. Details of data collection, refinement and crystal data are listed in Table 4. The data were corrected for Lorentz and polarisation effects and empirical absorption corrections applied. Structure solution by Patterson methods and structure refinement on F^2 employed SHELXTL version 6.10 [24,25]. Hydrogen

Table 4
Crystallographic and data processing parameters for complexes **1a**, **2a** and **3a**

Complex	**1a**	**2a**	**3a**
Formula	$C_{21}H_{31}Cl_2CoN_3$	$C_{28}H_{38}Cl_2CoN_4 \cdot CH_2Cl_2$	$C_{28}H_{38}Cl_2FeN_4 \cdot CH_3CN$
M	455.32	645.38	596.41
Crystal size (mm)	$0.52 \times 0.33 \times 0.14$	$0.11 \times 0.18 \times 0.32$	$0.15 \times 0.03 \times 0.03$
Temperature (K)	200(2)	150(2)	120(2)
Crystal system	monoclinic	triclinic	triclinic
Space group	$P2(1)/c$	$P\bar{1}$	$P\bar{1}$
Lattice parameters			
a (Å)	12.727(8)	7.3225(12)	7.4106(15)
b (Å)	13.796(8)	15.150(3)	15.244(3)
c (Å)	13.816(8)	15.669(3)	15.311(3)
α (°)	90	114.669(3)	115.74(3)
β (°)	112.66(4)	99.627(3)	97.86(3)
γ (°)	90	97.162(3)	99.89(3)
U (Å^3)	2239(2)	1520.2(4)	1490.7(5)
Z	4	2	2
D_c (Mg m^{-3})	1.351	1.410	1.333
$F(000)$	956	674	632
μ(Mo Kα) (mm^{-1})	1.016	0.942	0.713
Reflections collected	4814	9555	10326
Independent reflections	4377	4362	5606
R_{int}	0.0489	0.0241	0.1691
Parameters/restraints	249/0	349/0	343/0
Final R indices			
$I > 2\sigma(I)$	$R_1 = 0.0555$, $wR_2 = 0.1220$	$R_1 = 0.0318$, $wR_2 = 0.0746$	$R_1 = 0.0607$, $wR_2 = 0.0945$
All data	$R_1 = 0.0906$, $wR_2 = 0.1399$	$R_1 = 0.0463$, $wR_2 = 0.0789$	$R_1 = 0.2275$, $wR_2 = 0.1298$
Goodness of fit on F^2 (all data)	1.019	0.961	0.870

Data in common: graphite-monochromated Mo Kα radiation, $\lambda = 0.71073$ Å; $R_1 = \sum\|F_o| - |F_c\|/\sum|F_o|$, $wR_2 = [\sum w(F_o^2 - F_c^2)^2/\sum w(F_o^2)^2]^{1/2}$, $w^{-1} = [\sigma^2(F_o)^2 + (aP)^2], P = [\max(F_o^2, 0) + 2(F_c^2)]/3$, where a is a constant adjusted by the program; goodness of fit $= [\sum(F_o^2 - F_c^2)2/(n-p)]^{1/2}$ where n is the number of reflections and p the number of parameters.

atoms were included in calculated positions (C–H = 0.96 Å) riding on the bonded atom with isotropic displacement parameters set to 1.5 U_{eq}(C) for methyl H atoms and 1.2 U_{eq}(C) for all other H atoms. All non-H atoms were refined with anisotropic displacement parameters.

5. Supplementary data

Crystallographic data for the structural analyses have been deposited with the Cambridge Crystallographic Data Centre, CCDC nos. 269720-269722. Copies of the information may be obtained free of charge from The Director, CCDC, 12 Union Road, Cambridge, CB2 1EZ (fax: +44 1223 336033; e-mail deposit@ccdc.cam.ac.uk or at www.ccdc.cam.ac.uk).

Acknowledgements

We thank the EPSRC (to CJD), ExxonMobil (to CJD) and the Nuffield Foundation for an Undergraduate Summer Bursary (to SJH) for financial assistance. Financial and equipment support from the Department of Chemistry at the University of Leicester and the Royal Society are gratefully acknowledged. Johnson Matthey PLC are thanked for their loan of palladium chloride.

References

[1] (a) N. Emig, R. Réau, H. Krautscheid, D. Fenske, G. Bertrand, J. Am. Chem. Soc. 118 (1996) 5822;
(b) N. Emig, H. Nguyen, H. Krautscheid, R. Réau, J.B. Cazaux, G. Bertrand, Organometallics 17 (1998) 3599.
[2] F.G.N. Cloke, P.B. Hitchcock, J.B. Love, J. Chem. Soc., Dalton Trans. (1995) 25.
[3] L.-C. Lang, R.R. Schrock, W.M. Davis, D.H. McConville, J. Am. Chem. Soc. 121 (1999) 5797.
[4] (a) G.K.B. Clentsmith, V.M.E. Bates, P.B. Hitchcock, F.G.N. Cloke, J. Am. Chem. Soc. 121 (1999) 10444;
(b) G.P. Clancy, H.C.S. Clark, G.K.B. Clentsmith, F.G.N. Cloke, P.B. Hitchcock, J. Chem. Soc., Dalton Trans. (1999) 3345;
(c) J.B. Love, H.C.S. Clark, F.G.N. Cloke, J.C. Green, P.B. Hitchcock, J. Am. Chem. Soc. 121 (1999) 6843;
(d) P.E. Collier, S.M. Pugh, H.S.C. Clark, J.B. Love, A.J. Blake, F.G.N. Cloke, P. Mountford, Inorg. Chem. 39 (2000) 2001;
(e) B.D. Ward, S.R. Dubberley, A. Maisse-Francois, L.H. Gade, P. Mountford, J. Chem. Soc., Dalton Trans. (2002) 4649;
(f) K. Feghali, D.J. Harding, D. Reardon, S. Gambarotta, G. Yap, Q. Wang, Organometallics 21 (2002) 968;

(g) R.R. Schrock, S.W. Seidel, N.C. Mosch-Zanetti, K.-Y. Suih, M.B. O'Donoghue, W.M. Davis, W.K. Reiff, J. Am. Chem. Soc. 119 (1997) 11876.
[5] A. Dumistrescu, B. Martin-Vaca, H. Gornitzka, J.-B. Cazaux, D. Bourissou, G. Bertrand, Eur. J. Inorg. Chem. (2002) 1948.
[6] G.R. Giesbrecht, A. Shafir, J. Arnold, Chem. Commun. (2000) 2315.
[7] (a) R.R. Schrock, A.L. Casado, J.T. Goodman, L.-C. Liang, P.J. Bonitatebus Jr., W.M. Davis, Organometallics 19 (2000) 5325;
(b) R.R. Schrock, P.J. Bonitatebus Jr., Y. Schrodi, Organometallics 20 (2001) 1056;
(c) Y. Schrodi, R.R. Schrock, P.J. Bonitatebus Jr., Organometallics 20 (2001) 3560;
(d) F.V. Cochran, R.R. Schrock, Organometallics 20 (2001) 2127;
(e) J.P. Araujo, D.K. Wicht, P.J. Bonitatebus Jr., R.R. Schrock, Organometallics 20 (2001) 5682;
(f) R.R. Schrock, P.J. Bonitatebus Jr., X. Schrodi, Organometallics 20 (2001) 1056;
(g) F.V. Cochran, P.J. Bonitatebus Jr., R.R. Schrock, Organometallics 19 (2000) 2414.
[8] (a) M.E.G. Skinner, P. Mountford, J. Chem. Soc., Dalton Trans. (2002) 1694;
(b) M.E.G. Skinner, B.R. Tyrell, B.D. Ward, P. Mountford, J. Organomet. Chem. 647 (2002) 145;
(c) M.E.G. Skinner, Y. Li, P. Mountford, Inorg. Chem. 41 (2002) 1110;
(d) M.E.G. Skinner, D.A. Cowlig, P. Mountford, Chem. Commun. (2000) 1167.
[9] R. Cowdell, C.J. Davies, S.J. Hilton, J.-D. Maréchal, G.A. Solan, O. Thomas, J. Fawcett, Dalton Trans. (2004) 3231.
[10] G. Riggio, W.H. Hopff, A.A. Hofmann, P.G. Waser, Helv. Chim. Acta 63 (1980) 488.
[11] (a) J.P. Wolfe, S. Wagsaw, S.L. Buchwald, J. Am. Chem. Soc. 118 (1996) 7215;
(b) F. Paul, J. Patt, J.F. Hartwig, J. Am. Chem. Soc. 116 (1994) 5969.
[12] For an alternative synthetic route see, F. Bonnet, A.C. Hillier, A. Collins, S.R. Dubberley, P. Mountford, Dalton Trans. (2005) 421.
[13] Cl–Co–Cl range 101.8–134.4°: see for example,
(a) G.J.P. Britovsek, M. Bruce, V.C. Gibson, B.S. Kimberley, P.J. Maddox, S. Mastroianni, S.J. McTavish, C. Redshaw, G.A. Solan, S. Strömberg, A.J.P. White, D.J. Williams, J. Am. Chem. Soc. 121 (1999) 8728;
(b) B.L. Small, M. Brookhart, J. Am. Chem. Soc. 120 (1998) 7143;
(c) B.L. Small, M. Brookhart, A.M.A. Bennett, J. Am. Chem. Soc. 120 (1998) 4049;
(d) T.M. Kooistra, K.F.W. Hekking, Q. Knijnenburg, B. de Bruin, P.H.M. Budzelaar, R. de Gelder, J.M.M. Smits, A.W. Gal, Eur. J. Inorg. Chem. (2003) 648;
(e) N. di Vaira, P.L. Orioli, Inorg. Chem. 8 (1969) 2729;
(f) Z. Dori, R. Eisenberg, H.B. Gray, Inorg. Chem. 6 (1967) 483;
(g) M. Gerloch, J. Chem. Soc. A (1966) 1317;
(h) S.J. Shieh, C.-C. Chou, G.H. Lee, C.-C. Wang, S.M. Peng, Angew. Chem. Int. Ed. Engl. 36 (1997) 56;
(i) S.-C. Sheu, M.-J. Tien, M.-C. Cheng, T.-I. Ho, S.M. Peng, Y.-C. Lin, J. Chem. Soc., Dalton Trans. (1995) 3503.
[14] C.J. Davies, J. Fawcett, R. Shutt, G.A. Solan, Dalton Trans. (2005) in press.
[15] Y. Zang, J. Kim, Y. Dong, E.C. Wilkinson, E.H. Appelman, L. Que Jr., J. Am. Chem. Soc. 119 (1997) 4197.
[16] A. Diebold, K.S. Hagen, Inorg. Chem. 37 (1998) 215.
[17] D. Mandon, A. Machkour, S. Goetz, R. Welter, Inorg. Chem. 41 (2002) 5364.
[18] W.L.F. Armarego, D.D. Perrin, Purification of Laboratory Chemicals, 4th ed., Butterworth Heinemann, London, 1996.
[19] F.E. Mabbs, D.J. Machin, Magnetism and Transition Metal Complexes, Chapman and Hall, London, 1973.
[20] (a) C.J. O'Connor, Prog. Inorg. Chem. 29 (1982) 203;
(b) R.C. Weast (Ed.), Handbook of Chemistry and Physics, 70th ed., CRC Press, Boca Raton, FL, 1990, p. E134.
[21] T. Ukai, H. Kawazura, Y. Ishii, J.J. Bonnett, J.A. Ibers, J. Organomet. Chem. 65 (1974) 253.
[22] D. Astruc, J.R. Morow, Bull. Chem. Soc. Fr. 129 (1992) 319.
[23] C.J. Davies, G.A. Solan, unpublished results.
[24] G.M. Sheldrick, SHELXS-97, Program for Crystal Structure Solution, University of Göttingen, Germany, 1993.
[25] G.M. Sheldrick, SHELXL-97, Program for Crystal Structure Refinement, University of Göttingen, Germany, 1993.

2. Experimental

2.1. Materials and physical measurements

(−)-Menthyl acrylate and triphenyltin hydride were prepared according to the respective reported methods [19,20]. The other chemicals were of reagent grade and were used without further purification. Carbon and hydrogen analyses were obtained using a Perkin–Elmer 2400 Series II elemental analyzer. Melting points were measured on an X-4 microscopic melting point apparatus. Optical activities were determined by using Wzz-3 digital auto-polarimeter. IR spectra were recorded on a Nicolet 470 FT-IR spectrophotometer using KBr discs in the range 4000–400 cm^{-1}. ^1H and ^{13}C NMR spectral data were collected using a Bruker Avance DMX500 FT-NMR spectrometer with $CDCl_3$ as solvent and TMS as internal standard. ^{119}Sn NMR spectra were recorded in $CDCl_3$ on a Varian Mercury Vx300 spectrometer using Me_4Sn as an internal reference.

2.2. Synthesis of [2-((−)-menthoxycarbonyl)ethyl]-triphenyltin (*1*)

Triphenyltin hydride (8.78 g, 25 mmol), (−)-menthyl acrylate (6.31 g, 30 mmol) and azodiisobutyronitrile (AIBN) (0.1 g) were dissolved in 150 mL of dry tetrahydrofuran (THF) under a nitrogen atmosphere. The mixture was stirred for 12 h under reflux, and the solvent was evaporated off. The residue was recrystallized from ethanol to yield 9.02 g of **1** as a white crystalline solid. Yield 64%, m.p. 105–106 °C, $[\alpha]_D^{20}$ −21.7° (c, 0.59, CH_2Cl_2). *Anal*. Calc. for $C_{31}H_{38}O_2Sn$: C, 66.33; H, 6.82. Found: C, 66.26; H, 6.73%. IR (KBr): 1720 (vs, C=O) cm^{-1}. ^1H NMR (500 MHz, $CDCl_3$) δ : 0.68 (d, J = 7.1 Hz, 3H, CH_3), 0.83 (d, J = 7.0 Hz, 3H, CH_3), 0.85 (d, J = 7.0 Hz, 3H, CH_3), 0.76–1.78 (m, 9H, Men), 1.66 (t, J = 7.5 Hz, $^2J(^{119/117}Sn–^1H)$ = 56/53 Hz, 2H, CH_2Sn), 2.68 (t, J = 7.5 Hz, $^3J(^{119}Sn–^1H)$ = 65 Hz, 2H, $COCH_2$), 4.60 (dt, J_{ae} = 4.4 Hz, J_{aa} = 11.0 Hz, 1H, CHO), 7.35–7.37 (m, 9H, *p*-H and *m*-H), 7.54–7.57 (m, 6H, $^3J(^{119}Sn–^1H)$ = 45 Hz, *o*-H). ^{13}C NMR (125 MHz, $CDCl_3$) δ: 16.32, 20.76, 22.00, 23.38, 26.19, 31.27, 34.21, 40.67, 46.89, 74.29 (Men), 5.57 ($^1J(^{119/117}Sn–^{13}C)$ = 402/382 Hz, CH_2Sn), 31.02 ($^2J(^{119}Sn–^{13}C)$ = 21 Hz, CH_2CO), 174.47 (C=O), 128.45 ($^3J(^{119}Sn–^{13}C)$ = 49 Hz, *m*-C), 128.84 ($^4J(^{119}Sn–^{13}C)$ = 11 Hz, *p*-C), 137.09 ($^2J(^{119}Sn–^{13}C)$ = 36 Hz, *o*-C), 138.82 ($J(^{119/117}Sn–^{13}C)$ = 503/481 Hz, *i*-C). ^{119}Sn NMR (111.9 MHz, $CDCl_3$) δ: −100.2.

2.3. Synthesis of [2-((−)-menthoxycarbonyl)ethyl]-diphenyltin chloride (*2*)

A solution of iodonium chloride (0.81 g, 5 mmol) in chloroform (50 mL) was slowly added dropwise with stirring to a solution of **1** (2.81 g, 5 mmol) in chloroform (50 mL) at −5 °C. The colour of iodonium chloride disappeared immediately. The resulting colourless solution was allowed to warm to room temperature and stirred for 1 h. The solvent was evaporated off at reduced pressure. Prolonged pumping to remove iodobenzene obtained an oily product, which was further purified by column chromatography on silica gel with ether/petroleum ether (30–60°) (1/9) as eluant. Yield 1.93 g (74%), $[\alpha]_D^{20}$ −40.2° (c, 0.27, CH_2Cl_2). *Anal*. Calc. for $C_{25}H_{33}ClO_2Sn$: C, 57.78; H, 6.40. Found: C, 57.49; H, 6.33%. IR (film): 1667 (vs, C=O) cm^{-1}. ^1H NMR (500 MHz, $CDCl_3$) δ: 0.66 (d, J = 6.9 Hz, 3H, CH_3), 0.85 (d, J = 6.9 Hz, 3H, CH_3), 0.90 (d, J = 6.9 Hz, 3H, CH_3), 0.82–1.88 (m, 9H, Men), 1.75 (t, J = 7.5 Hz, $^2J(^{119/117}Sn–^1H)$ = 78/75 Hz, 2H, CH_2Sn), 2.82 (t, J = 7.5 Hz, $^3J(^{119}Sn–^1H)$ = 101 Hz, 2H, $COCH_2$), 4.83 (dt, J_{ae} = 4.3 Hz, J_{aa} = 11.1 Hz, 1H, CHO), 7.33–7.41 (m, 6H, *p*-H and *m*-H), 7.79–7.84 (m, 4H, $^3J(^{119}Sn–^1H)$ = 62 Hz, *o*-H). ^{13}C NMR (125 MHz, $CDCl_3$) δ: 16.30, 20.75, 22.01, 23.33, 26.18, 31.25, 34.20, 40.65, 46.87, 78.66 (Men), 14.96 ($^1J(^{119/117}Sn–^{13}C)$ = 550/524 Hz, CH_2Sn), 30.33 ($^2J(^{119}Sn–^{13}C)$ = 37 Hz, CH_2CO), 180.04 (C=O), 128.50 ($^3J(^{119}Sn–^{13}C)$ = 66.2 Hz, *m*-C), 129.43 ($^4J(^{119}Sn–^{13}C)$ = 15 Hz, *p*-C), 136.36 ($^2J(^{119}Sn–^{13}C)$ = 49.6 Hz, *o*-C), 139.92 (*i*-C). ^{119}Sn NMR (111.9 MHz, $CDCl_3$) δ: −74.6.

2.4. Synthesis of [2-((−)-menthoxycarbonyl)ethyl]-phenyltin dichloride (*3*)

This compound was prepared in a manner analogous to that of **2**, using **1** (1.40 g, 2.5 mmol) and iodonium chloride (0.81 g, 5 mmol) in chloroform (100 mL) at room temperature. After removal of all volatiles in vacuo, the remaining solid was crystallized from hexane–chloroform (1:1, v/v). Yield 61%, m.p. 117–118 °C, $[\alpha]_D^{20}$ −50.2° (c, 0.52, CH_2Cl_2). *Anal*. Calc. for $C_{19}H_{28}Cl_2O_2Sn$: C, 47.74; H, 5.90. Found: C, 47.76; H, 5.83%. IR (KBr): 1649 (vs, C=O) cm^{-1}. ^1H NMR (500 MHz, $CDCl_3$), δ: 0.75 (d, J = 6.9 Hz, 3H, CH_3), 0.89 (d, J = 7.0 Hz, 3H, CH_3), 0.92 (d, J = 6.5 Hz, 3H, CH_3), 0.87–2.00 (m, 9H, Men), 1.96 (t, J = 7.5 Hz, 2H, $^2J(^{119/117}Sn–^1H)$ = 85/82 Hz, CH_2Sn), 2.93 (t, J = 7.7 Hz, $^3J(^{119/117}Sn–^1H)$ = 135/129 Hz, 2H, $COCH_2$), 4.91 (dt, J_{aa} = 10.9 Hz, J_{ae} = 4.5 Hz, 1H, CHO), 7.45–7.49 (m, 3H, *p*-H and *m*-H), 7.91–7.92 (m, 2H, $^3J(^{119}Sn–^1H)$ = 86 Hz, *o*-H). ^{13}C NMR (125 MHz, $CDCl_3$) δ: 16.50, 20.86, 22.11, 23.44, 26.52, 31.55, 34.08, 40.70, 47.11, 79.43 (Men), 20.09 ($^1J(^{119/117}Sn–^{13}C)$ = 664/624 Hz, CH_2Sn), 29.23 ($^2J(^{119}Sn–^{13}C)$ = 50 Hz, CH_2CO), 180.56 ($^2J(^{119}Sn–^{13}C)$ = 70.2 Hz, C=O), 129.18 ($^3J(^{119}Sn–^{13}C)$ = 90 Hz, *m*-C), 131.01 ($^4J(^{119}Sn–^{13}C)$ = 18 Hz, *p*-C), 135.71 ($^2J(^{119}Sn–^{13}C)$ = 63.4 Hz, *o*-C), 141.23 (*i*-C). ^{119}Sn NMR (111.9 MHz, $CDCl_3$) δ: −56.3.

2.5. Synthesis of 2-((−)-menthoxycarbonyl)ethyltin-trichloride (4)

This compound was prepared according to a similar method for $MeOCOCH_2CH_2SnCl_3$ [1]: $SnCl_2$ (4.75 g, 25 mmol) and (−)-menthyl acrylate (5.25 g, 25 mmol) in 100 mL of dichloromethane were placed in a 250 mL three-neck flask equipped with a reflux condenser, a mechanical stirrer and a gas inlet tube. Through the stirred suspension was bubbled anhydrous hydrogen chloride at room temperature until a homogeneous solution was obtained. After removal of solvent at reduced pressure, the remaining solid was recrystallized from hexane–chloroform (3:1, v/v) to give colorless crystals (8.37 g). Yield 77%, m.p. 115–116 °C, $[\alpha]_D^{20}$ −62.1° (c, 0.51, CH_2Cl_2). *Anal.* Calc. for $C_{13}H_{23}Cl_3O_2Sn$: C, 35.78; H, 5.31. Found: C, 35.75; H, 5.23%. IR (KBr): 1645 (vs, C=O) cm^{-1}. ^1H NMR (500 MHz, $CDCl_3$), δ: 0.77 (d, $J = 7.0$ Hz, 3H, CH_3), 0.91 (d, $J = 7.0$ Hz, 3H, CH_3), 0.93 (d, $J = 6.6$ Hz, 3H, CH_3), 0.87–2.01 (m, 9H, Men), 2.20 (t, $J = 7.6$ Hz, $^2J(^{119/117}Sn–^1H) = 109/105$ Hz, 2H, CH_2Sn), 2.91 (t, $J = 7.6$ Hz, $^3J(^{119/117}Sn–^1H) = 198/184$ Hz, 2H, $COCH_2$), 4.97 (dt, $J_{aa} = 10.9$ Hz, $J_{ae} = 4.5$ Hz, 1H, CHO), ^{13}C NMR (125 MHz, $CDCl_3$), δ: 16.45, 20.85, 22.06, 23.37, 26.60, 31.50, 33.99, 40.48, 47.09, 81.27 (Men), 24.18 ($^1J(^{119/117}Sn–^{13}C) = 833/796$ Hz, CH_2Sn), 28.24 ($^2J(^{119}Sn–^{13}C) = 67$ Hz, CH_2CO), 180.64 ($^2J(^{119}Sn–^{13}C) = 140$ Hz, C=O). ^{119}Sn NMR (111.9 MHz, $CDCl_3$) δ: −116.6.

2.6. Synthesis of the dietherate of dimeric 2-((−)-menthoxycarbonyl)ethyltin dichloride hydroxide (5 · 2(C2H5)2O)

A solution of compound **4** (0.44 g, 1 mmol) in diethyl ether (50 mL) with a little added water was stirred for 2 h at room temperature. The solution was evaporated slowly at room temperature and crystals containing two molecular ethers as crystalline solvent, $\mathbf{5} \cdot 2(C_2H_5)_2O$, were obtained in 78% yield. M.p. 88–89 °C, $[\alpha]_D^{20}$ −54.6° (c, 0.09, dioxane). *Anal.* Calc. for $C_{26}H_{48}Cl_4O_6Sn_2 \cdot 2(C_2H_5)_2O$: C, 41.49; H, 6.96. Found: C, 41.17; H, 6.72%. IR (KBr): 3420 (s, OH), 1642 (vs, C=O) cm^{-1}.

2.7. Crystal structure determination of compounds 1, 3, 4 and 5 · 2(C2H5)2O

The colorless single crystals were obtained from chloroform–hexane (1:2, v/v) for **1**, **3** and **4**, and from ether for $\mathbf{5} \cdot 2(C_2H_5)_2O$ by slow evaporation. The intensity data for crystals of the compounds were measured at 295(2) K on a Bruker P4 four-circle diffractometer or a Bruker Smart Apex area-detector fitted with graphite monochromatized Mo Kα radiation (0.71073 Å) using the omega scan technique. The structures were solved by direct methods [21] and refined by a full-matrix least squares procedure based on F^2 using the SHELXL-97 [22]. The non-hydrogen atoms were refined anisotropically, and hydrogen atoms were placed at calculated positions and

Table 1
Crystallographic data and structure refinements for **1** and **3**–**5**

Compound	**1**	**3**	**4**	**5** · $2C_4H_{10}O$
Empirical formula	$C_{31}H_{38}O_2Sn$	$C_{19}H_{28}Cl_2O_2Sn$	$C_{13}H_{23}Cl_3O_2Sn$	$C_{26}H_{48}Cl_4O_6Sn_2 \cdot 2C_4H_{10}O$
Formula weight	561.30	478.02	436.35	984.10
Crystal system	monoclinic	orthorhombic	orthorhombic	monoclinic
Space group	$P2_1$	$P2_12_12_1$	$P2_12_12_1$	$P2_1$
a (Å)	10.5371(6)	8.424(2)	6.8876(8)	9.9185(4)
b (Å)	9.5647(6)	12.109(3)	10.2258(8)	24.240(1)
c (Å)	14.2019(8)	21.187(5)	25.954(4)	10.5218(5)
β (°)	96.551(1)	90	90	110.886(1)
Volume (Å^3)	1422.0(1)	2161.2(9)	1828.0(4)	2363.5(2)
Z	2	4	4	2
D_c (g cm^{-3})	1.311	1.469	1.586	1.383
μ (mm^{-1})	0.992	1.438	1.832	1.322
θ_{max} (°)	27.50	27.49	25.00	27.50
Crystal size (mm)	0.25 × 0.22 × 0.11	0.25 × 0.22 × 0.11	0.24 × 0.19 × 0.17	0.32 × 0.22 × 0.17
Dataset	$-13 \leqslant h \leqslant 10$	$-10 \leqslant h \leqslant 10$	$-8 \leqslant h \leqslant 1$	$-12 \leqslant h \leqslant 12$
	$-11 \leqslant k \leqslant 12$	$-15 \leqslant k \leqslant 15$	$-1 \leqslant k \leqslant 12$	$-31 \leqslant k \leqslant 31$
	$-18 \leqslant l \leqslant 18$	$-23 \leqslant l \leqslant 27$	$-30 \leqslant l \leqslant 1$	$-13 \leqslant l \leqslant 13$
Total data	8792	13410	2552	20494
Unique data (R_{int})	5626 (0.022)	4859 (0.039)	2350 (0.016)	10486 (0.046)
Observed data [$I > 2\sigma(I)$]	5228	3769	1864	8872
Flack x	0.01(2)	−0.01(3)	−0.17(6)	−0.040(17)
Goodness-of-fit on F^2	1.015	0.993	1.173	0.985
Final R indices [$I > 2\sigma(I)$]	$R = 0.0284$	$R = 0.0390$	$R = 0.0370$	$R = 0.0410$
	$R_w = 0.0645$	$wR = 0.0708$	$wR = 0.0894$	$wR = 0.0833$
R indices (all data)	$R = 0.0311$	$R = 0.0576$	$R = 0.0549$	$R = 0.0489$
	$R_w = 0.0659$	$wR = 0.0768$	$wR = 0.1211$	$wR = 0.0868$
ρ_{max}, ρ_{min} (e Å^{-3})	−0.312, 0.465	−0.294, 0.558	0.731, −0.657	0.685, −0.530

were included in the refinement in the riding-model approximation. The absolute configurations of the compounds were confirmed by the X-ray study [23]. The crystallographic parameters and refinements are summarized in Table 1.

3. Results and discussion

3.1. Synthesis

Compound **1** was synthesized by hydrostannation [24] of (−)-menthyl acrylate with triphenyltin hydride using AIBN as a catalyst in THF. The reaction of **1** with iodonium chloride in 1:1 and 1:2 molar ratios yielded the corresponding chloride **2** and dichloride **3**, respectively. The hydrolysis of compound **4**, obtained from the reaction of (−)-menthyl acrylate with $SnCl_2$/HCl in dichloromethane, afforded compound **5**, isolated as a diethetate ($\mathbf{5}\cdot 2(C_2H_5)_2O$). The equations are as follows:

$$CH_2{=}CHCO_2Men + Ph_3SnH \rightarrow \underset{\mathbf{1}}{1\ MenOCOCH_2CH_2SnPh_3}$$

$$\mathbf{1} + n\mathrm{ICl} \rightarrow MenOCOCH_2CH_2SnCl_nPh_{3-n} + n\mathrm{PhI} \quad n=1,\mathbf{2};\ n=2,\mathbf{3}$$

$$CH_2{=}CHCO_2Men + SnCl_2 + HCl \rightarrow \underset{\mathbf{4}}{MenOCOCH_2CH_2SnCl_3}$$

$$2\,\mathbf{4} + 2H_2O + 2(C_2H_5)_2O \rightarrow \underset{\mathbf{5}\cdot 2(C_2H_5)_2O}{[MenOCOCH_2CH_2SnCl_2(OH)]_2\cdot 2(C_2H_5)_2O} + 2\,HCl$$

Compound **2** is an oily product and other compounds are colorless crystalline solids with sharp melting points. Compounds **1**–**4** are soluble in general organic solvents, whilst compound $\mathbf{5}\cdot 2(C_2H_5)_2O$ is only slightly soluble in dichloromethane, methanol and acetone.

3.2. IR spectroscopy

Among the stretching modes, the carbonyl band ν(C=O) in the 1640–1740 cm^{-1} region is known to depend on the nature of coordination of the carbonyl oxygen to metal [5,25]. The ν(C=O) band of **1** (1720 cm^{-1}) is in the same region as that of the free esters (~1730 cm^{-1}), whereas the bands of compounds $\mathbf{2}$–$\mathbf{5}\cdot 2(C_2H_5)_2O$ exhibit a remarkable red shift and appear in the range of 1642–1667 cm^{-1}. These results clearly indicate that the carbonyl is coordinated to the tin atom in compounds $\mathbf{2}$–$\mathbf{5}\cdot 2(C_2H_5)_2O$ and is not in **1** [5,20]. From **1** to $\mathbf{5}\cdot 2(C_2H_5)_2O$, with the increasing of Lewis acidity of the tin center, the stretching vibrations of the carbonyl generally shift to lower wavenumber, from 1720 to 1642 cm^{-1}. The fact that there is almost no variation of the carbonyl frequency between the pure compound and a solution of dichloromethane for $\mathbf{2}$–$\mathbf{5}\cdot 2(C_2H_5)_2O$ indicates the C=O → Sn coordination is intramolecular coordination [5,25].

3.3. NMR spectroscopy

The ^1H and ^{13}C resonance assignments and coupling constants obtained for compounds **1**–**4** are given in the experimental details. The NMR data of compound **5** were not determined due to the small solubility in $CDCl_3$ and CD_3COCD_3. The assignments of ^1H and ^{13}C of CH_2Sn in compounds **1**–**4**, $MenOCOCH_2CH_2SnCl_nPh_{3-n}$ (n = 0–3), were made from the lower $^2J(^{119}Sn{-}^1H)$ (56–109 Hz) and $^2J(^{119}Sn{-}^{13}C)$ (21–67 Hz) couplings compared with the corresponding $^3J(^{119}Sn{-}^1H)$ (65–198 Hz) and $^1J(^{119}Sn{-}^{13}C)$ (402–833 Hz) couplings, respectively. The δ (^1H and ^{13}C) values of CH_2Sn and the coupling constants ^2J(Sn–H) and ^1J(Sn–C) increase consecutively in the sequence $\mathbf{1} < \mathbf{2} < \mathbf{3} < \mathbf{4}$, which is consistent with the increasing of electron withdrawing ability of $SnCl_nPh_{3-n}$ (n = 0–3) in $MenOCOCH_2CH_2SnCl_nPh_{3-n}$. The NMR data also support the presence of carbonyl oxygen to tin coordination in compounds **2**–**4**. The δ values of the CHO proton of menthoxyl in **2**–**4** show a downfield shift ($\Delta\delta$ = ~0.3) compared with that in **1** and the ^{13}C δ values of CHO and C=O in **2**–**4** are deshielded by $\Delta\delta$ = ~5 and $\Delta\delta$ = ~6, respectively, relative to those of **1** because the coordination of carbonyl to tin (CHOC=O → Sn) causes the deshielding of CHOCO. The stepwise increasing of chemical shift (^1H and ^{13}C) of CHOCO from **1** to **4** indicates that the intramolecular interactions between the C=O and Sn strengthen in the order $\mathbf{1} < \mathbf{2} < \mathbf{3} < \mathbf{4}$. The ^{119} Sn chemical shifts depend on the number and nature of the groups coordinated with tin central atom. The ^{119}Sn chemical shift of compounds **1**–**4** is −100.2, −74.6, −56.3 and −116.6, respectively, in agreement with that found in four-coordinated $MeOCOCH_2CH_2SnPh_3$ (−99.8) [26] and five-coordinated $MeOCOCH_2CH_2SnCl_3$ (−115.0) [27].

3.4. Molecular structures of *1*, *3*, *4* and $\mathbf{5}\cdot 2(C_2H_5)_2O$

The molecular structures of **1**, **3**, **4** and $\mathbf{5}\cdot 2(C_2H_5)_2O$ are shown in Figs. 1–4 respectively, and selected interatomic parameters are given in Tables 2–5. The coordination geometry of the tin atom in compound **1** is a distorted tetrahedral geometry with the range of angles around tin being 105.5(1)–113.1(1)°. The Sn(1)···O(1) separation (3.342(4) Å) is shorter than the sum of Van der Waals radii of tin and oxygen (3.73 Å) [28] and much larger than the sum of the covalent radii (2.07 Å) [28], indicating there is a weak interaction between O(1) and Sn(1). Thus, the O(1) atom exerts a steric influence and contributes to the distortion of the

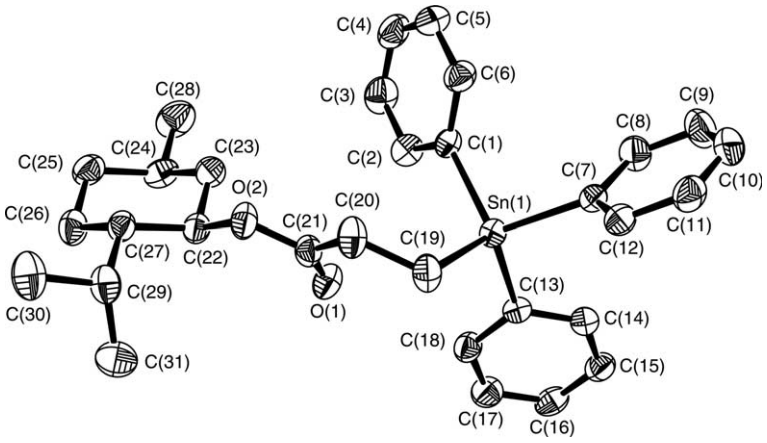


Fig. 1. Molecular structure of compound **1**.

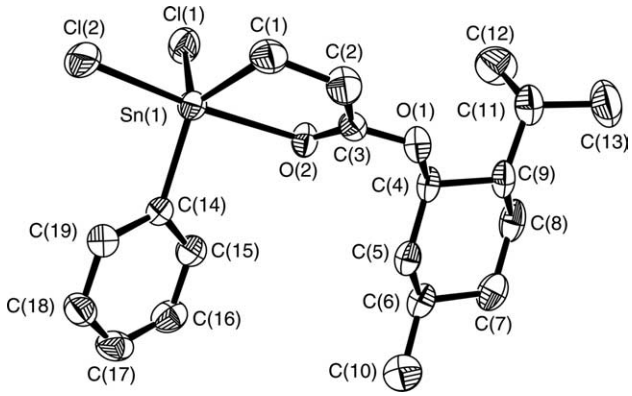


Fig. 2. Molecular structure of compound **3**.

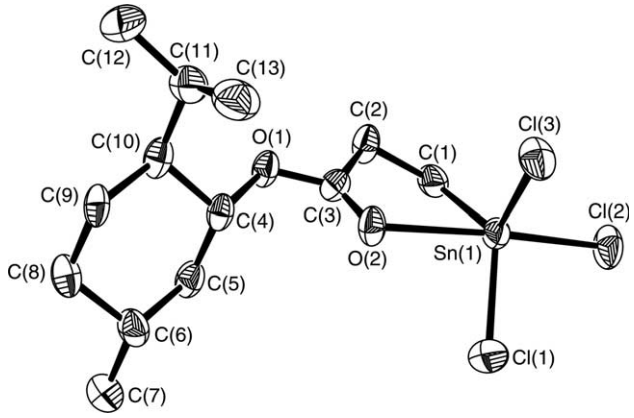


Fig. 3. Molecular structure of compound **4**.

geometry at the tin atom. The closest non-hydrogen intermolecular contact in the lattice of **1** is C(24)$\cdots$O(2)^{i} (3.632(1) Å) (symmetry code i: $-x+2$, $y-1/2$, $-z+2$), indicating the compound is a discrete molecule with no close intermolecular contacts.

The Sn atom in **3** is five coordinated and possesses a distorted trigonal bipyramid geometry with the trigonal plane defined by C(1), C(14) and Cl(1) atoms and the axial positions occupied by the Cl(2) and O(2) atoms, with the Cl(2)–Sn(1)–O(2) angle being 172.87(8)°. The three bond angles on the trigonal plane are in the range 110.4(1)–132.3(2)°. The Sn(1)–O(2) distance of 2.424(3) Å is in the range of a normal Sn–O coordination bond length [9,13], clearly indicating significant bonding interactions between the Sn atom and O(1) atom of the carbonyl group. The formation of the five-membered chelate ring causes a small contraction of the O(2)–C(3)–C(2) angle (122.9(4)°) in **3** compared with that (126.0(3)°) of **1**. The axial Sn(1)–Cl(2) (2.397(1) Å) is longer than the equatorial Sn(1)–Cl(1) (2.343(1) Å).

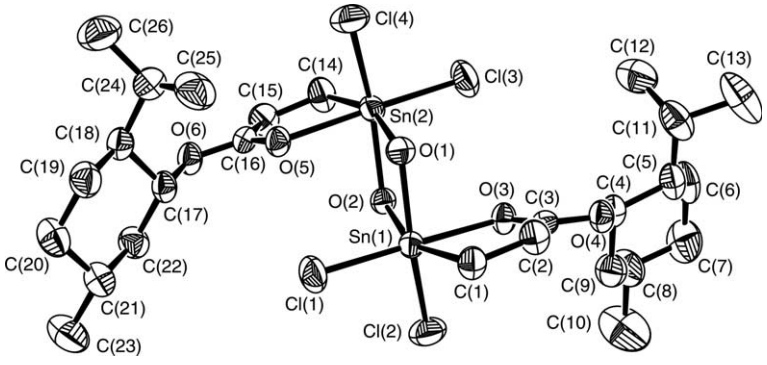


Fig. 4. Molecular structure of compound **5** in **5** $\cdot$ $2C_4H_{10}O$.

Table 2
Selected bond lengths (Å) and bond angles (°) for **1**

Sn(1)···O(1)	3.342(4)
Sn(1)–C(1)	2.144(3)
Sn(1)–C(7)	2.134(3)
Sn(1)–C(13)	2.139(3)
Sn(1)–C(19)	2.137(3)
O(1)–C(21)	1.182(6)
O(2)–C(21)	1.336(4)
C(1)–Sn(1)–C(7)	105.5(1)
C(1)–Sn(1)–C(13)	112.3(1)
C(1)–Sn(1)–C(19)	111.3(1)
C(7)–Sn(1)–C(13)	105.8(1)
C(7)–Sn(1)–C(19)	108.3(1)
C(13)–Sn(1)–C(19)	113.1(1)

Table 3
Selected bond lengths (Å) and bond angles (°) for **3**

Sn(1)–O(2)	2.424(3)
Sn(1)–C(1)	2.129(5)
Sn(1)–C(14)	2.123(4)
Sn(1)–Cl(1)	2.343(1)
Sn(1)–Cl(2)	2.397(1)
O(2)–C(3)	1.217(5)
O(1)–C(3)	1.305(5)
C(14)–Sn(1)–C(1)	132.3(2)
C(14)–Sn(1)–Cl(1)	110.4(1)
C(1)–Sn(1)–Cl(1)	111.6(2)
C(14)–Sn(1)–Cl(2)	98.1(1)
C(1)–Sn(1)–Cl(2)	97.7(1)
Cl(1)–Sn(1)–Cl(2)	97.74(5)
C(14)–Sn(1)–O(2)	87.5(1)
C(1)–Sn(1)–O(2)	75.3(2)
Cl(1)–Sn(1)–O(2)	84.30(8)
Cl(2)–Sn(1)–O(2)	172.87(8)
C(3)–O(1)–C(4)	117.4(3)
C(3)–O(2)–Sn(1)	110.6(2)

Table 4
Selected bond lengths (Å) and bond angles (°) for **4**

Sn(1)–O(2)	2.397(7)
Sn(1)–C(1)	2.12(1)
Sn(1)–Cl(1)	2.301(4)
Sn(1)–Cl(2)	2.371(3)
Sn(1)–Cl(3)	2.304(3)
O(2)–C(3)	1.21(1)
O(1)–C(3)	1.30(1)
Cl(1)–Sn(1)–Cl(2)	95.6(1)
Cl(1)–Sn(1)–Cl(3)	108.4(1)
Cl(1)–Sn(1)–O(2)	82.7(2)
Cl(1)–Sn(1)–C(1)	128.0(3)
Cl(2)–Sn(1)–Cl(3)	99.5(1)
Cl(2)–Sn(1)–O(2)	173.9(2)
Cl(2)–Sn(1)–C(1)	101.9(3)
Cl(3)–Sn(1)–O(2)	86.6(2)
Cl(3)–Sn(1)–C(1)	116.2(3)
O(2)–Sn(1)–C(1)	74.9(3)
C(3)–O(1)–C(4)	118.1(8)
C(3)–O(2)–Sn(1)	110.9(6)

Table 5
Selected bond lengths (Å) and bond angles (°) for **5**

Sn(1)–O(1)	2.122(3)
Sn(1)–O(2)	2.023(3)
Sn(1)–O(3)	2.317(3)
Sn(1)–C(1)	2.128(4)
Sn(1)–Cl(1)	2.375(1)
Sn(1)–Cl(2)	2.411(2)
O(3)–C(3)	1.226(5)
O(4)–C(3)	1.302(5)
Sn(2)–O(2)	2.148(3)
Sn(2)–O(1)	2.022(3)
Sn(2)–O(5)	2.321(3)
Sn(2)–C(14)	2.126(5)
Sn(2)–Cl(3)	2.374(2)
Sn(2)–Cl(4)	2.418(2)
O(5)–C(16)	1.233(5)
O(6)–C(16)	1.311(5)
O(1)–Sn(1)–O(2)	70.3(1)
O(2)–Sn(1)–C(1)	155.3(2)
O(1)–Sn(1)–C(1)	94.4(1)
O(2)–Sn(1)–O(3)	82.1(1)
O(1)–Sn(1)–O(3)	86.2(1)
C(1)–Sn(1)–O(3)	77.4(2)
O(2)–Sn(1)–Cl(1)	97.4(1)
O(1)–Sn(1)–Cl(1)	95.1(1)
C(1)–Sn(1)–Cl(1)	103.4(1)
O(3)–Sn(1)–Cl(1)	178.4(1)
O(2)–Sn(1)–Cl(2)	89.9(1)
O(1)–Sn(1)–Cl(2)	158.3(1)
C(1)–Sn(1)–Cl(2)	100.8(2)
O(3)–Sn(1)–Cl(2)	82.3(1)
Cl(1)–Sn(1)–Cl(2)	96.24(8)
Sn(2)–O(1)–Sn(1)	110.5(1)
C(3)–O(3)–Sn(1)	111.3(3)
C(3)–O(4)–C(4)	117.8(3)
O(1)–Sn(2)–O(2)	69.8(1)
O(1)–Sn(2)–C(14)	157.6(2)
O(2)–Sn(2)–C(14)	94.5(2)
O(2)–Sn(2)–O(5)	81.0(1)
O(1)–Sn(2)–O(5)	84.1(1)
C(14)–Sn(2)–O(5)	77.5(2)
O(1)–Sn(2)–Cl(3)	97.6(1)
O(2)–Sn(2)–Cl(3)	97.1(1)
C(14)–Sn(2)–Cl(3)	100.2(2)
O(5)–Sn(2)–Cl(3)	176.9(1)
O(1)–Sn(2)–Cl(4)	89.5(1)
O(2)–Sn(2)–Cl(4)	156.3(1)
C(14)–Sn(2)–Cl(4)	101.7(2)
O(5)–Sn(2)–Cl(4)	85.7(1)
Cl(3)–Sn(2)–Cl(4)	96.95(8)
Sn(1)–O(2)–Sn(2)	109.4(1)
C(16)–O(5)–Sn(2)	111.0(3)
C(16)–O(6)–C(17)	120.0(3)

The geometry around the tin atom in compound **4** is a distorted trigonal bipyramid with C(1), Cl(1) and Cl(3) in the equatorial positions and Cl(2) and O(2) in the axial positions through intramolecular carbonyl oxygen to tin coordination. The three bond angles on the trigonal plane are in the range 108.4(1)–128.0(3)°, and the Cl(2)–Sn(1)–O(2) angle is 173.9(2)°. The distortion may be caused partly by the small bite angle of O(2)–Sn(1)–C(1) (74.9(3)°) with the concomitant expansion of

Cl(2)–Sn(1)–C(1) (101.9(3)°). The intramolecular Sn(1)–O(2) bond (2.397(7) Å) in **4** is slightly longer than that found in $MeOCOCH_2CH_2SnCl_3$ (2.347(5) Å) [2] and *c*-$C_6H_{11}OCOCH_2CH_2SnCl_3$ (2.362(3) Å) [4]. The axial Sn(1)–Cl(2) (2.371(3) Å) is longer than the equatorial Sn(1)–Cl(1) (2.301(4) Å) and Sn(1)–Cl(3) (2.304(3) Å), which is consistent with $MeOCOCH_2CH_2SnCl_3$ [2] and *c*-$C_6H_{11}OCOCH_2CH_2SnCl_3$ [4]. The unit acts as a chelating ligand by utilizing the carbonyl oxygen as an additional donor center.

Compound **5** in **5** · $2(C_2H_5)_2O$ exists as a non-centrosymmetrically six-coordinated dimer with bridging hydroxyl groups. Each tin atom is coordinated by two chloride atoms occupying mutually *cis* positions and a carbon and a carbonyl oxygen from the chelating $COCH_2CH_2$ moiety. The remaining positions in the distorted octahedral coordination geometry about each tin atom are occupied by two μ_2-hydroxide groups. The major distortions in the tin atom geometries may be traced to the acute angles induced by the Sn_2O_2 ring (O(1)–Sn(1)–O(2) 70.3(1)°, O(1)–Sn(2)–O(2) 69.8(1)°) and five-membered chelate CSnO ring (C(1)–Sn(1)–O(3) 77.4(2)°, C(14)–Sn(2)–O(5) 77.5(2)°). The Sn–O distances within the four-membered rings are not symmetrical, with the bond *trans* to a carbon atom being shorter (Sn(1)–O(2) 2.023(3) Å, Sn(2)–O(1) 2.022(3) Å) than that *trans* to a chlorine atom (Sn(1)–O(1) 2.122(3) Å, Sn(2)–O(2) 2.148(3) Å), which are comparable with those found in [*n*-$BuSn(OH)Cl_2(H_2O)]_2$ [29], [*i*-$PrSn(OH)Cl_2(H_2O)]_2$ [30], [$EtSn(OH)Cl_2(H_2O)]_2$ [31] and $[(H_2O)(OH)Cl_2Sn(CH_2)_3SnCl_2(OH)(H_2O)]_n$ [32]. The Sn–O distances in the five-membered chelate rings are Sn(1)–O(3) 2.317(3) Å and Sn(2)–O(5) 2.321(3) Å, which are shorter than that of the six-coordinated $EtOCOCH_2CH_2SnCl_3 \cdot OSBu_2$ [10]. The two Sn–Cl distances around each tin center are significantly different, which is similar to those of [*n*-$BuSn(OH)Cl_2(H_2O)]_2$ [29], [*i*-$PrSn(OH)Cl_2(H_2O)]_2$ [30], [$EtSn(OH)Cl_2(H_2O)]_2$ [31] and $[(H_2O)(OH)Cl_2Sn(CH_2)_3SnCl_2(OH)(H_2O)]_n$ [32]. There is intermolecular hydrogen bonding in the lattices (Fig. 5). The diethyl ether molecule is hydrogen bonded to the oxygen of the Sn_2O_2 ring. For O(1)–H(1)···O(8)^{i}, H(1)···O(8)^{i} is 1.98 Å, O(1)···O(8)^{i} is 2.78 Å and O(1)–H(1)···O(8)^{i} 160.8°(symmetry code i: $1-x$, $-1/2+y$, $1-z$). For O(2)–H(2)···O(7)^{ii}, H(2)···O(7)^{ii} is 1.90 Å, O(2)···O(7)^{ii} is 2.73 Å and O(2)–H(2)···O(7)^{ii} is 176.8° (symmetry code ii: x, y, $-1+z$).

From **1** to **5** · $2(C_2H_5)_2O$, the stepwise shortening of the distances between the carbonyl O and Sn (from 3.342(4) to 2.317(3) Å) indicates an increasing degree of O–Sn donor–acceptor interaction, which is consistent with the increasing Lewis acidity of the central tin atom.

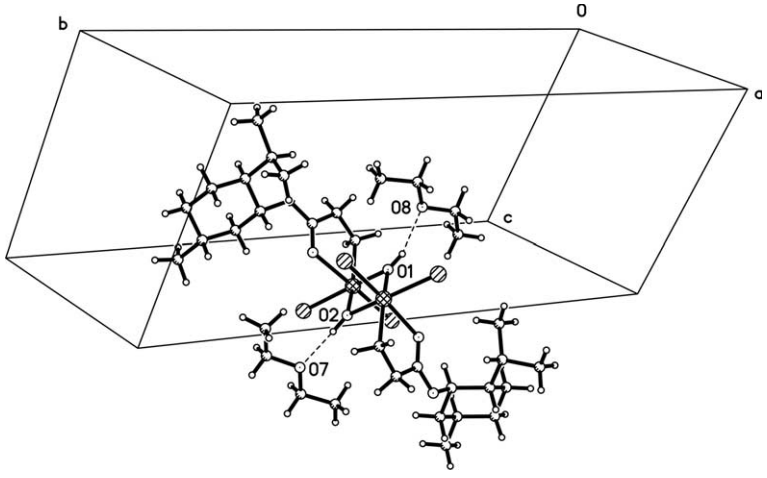


Fig. 5. Hydrogen-bonding interactions between **5** and ether in **5** · $2(C_2H_5)_2O$.

Table 6
Torsion angles (°) for the chelating rings in **3**, **4** and **5** · $2C_4H_{10}O$

Torsion angles	**3**	**4**	Torsion angles	**5** · $2C_4H_{10}O$
Sn(1)–C(1)–C(2)–C(3)	16.1(6)	−32.9(10)	Sn(1)–C(1)–C(2)–C(3)	−17.8(6)
Sn(1)–O(2)–C(3)–C(2)	−5.9(5)	−4.2(13)	Sn(1)–O(3)–C(3)–C(2)	−6.1(5)
C(3)–O(2)–Sn(1)–C(1)	11.1(3)	−11.6(7)	C(3)–O(3)–Sn(1)–C(1)	−3.3(3)
O(2)–Sn(1)–C(1)–C(2)	−13.7(4)	3.6(7)	O(3)–Sn(1)–C(1)–C(2)	11.1(4)
			Sn(2)–C(14)–C(15)–C(16)	10.8(7)
			Sn(2)–O(5)–C(16)–C(15)	−0.6(6)
			C(16)–O(5)–Sn(2)–C(14)	5.1(3)
			O(5)–Sn(2)–C(14)–C(15)	−8.2(5)

The slight forcing of the O–Sn coordination (C=O → Sn and HO → Sn) leads to a shift toward octahedral in the tetrahedron–trigonal bipyramid–octahedron path. The five-membered chelate ring formed by intramolecular carbonyl to tin bonding exhibits a near envelope conformation in **3**–**5** · $2(C_2H_5)_2O$ (see Table 6). The distance of the C=O bond in **3** (1.217(5) Å), **4** (1.21(1) Å) and **5** (1.226(5) and 1.233(5) Å) is significant longer when compared with **1** (1.182(6) Å), which is caused by the transfer of electron density from C=O to tin in **3**–**5** · $2(C_2H_5)_2O$.

4. Supplementary material

Crystallographic data for the structures reported in this paper have been deposited with the Cambridge Crystallographic Data Centre, CCDC Nos. 269744 for **1**, 269745 for **3**, 214281 for **4**, and 269746 for **5** · $2(C_2H_5)_2O$. Copies of this information may be obtained free of charge from The Director, CCDC, 12 Union Road, Cambridge, CB2 1EZ, UK, fax: +44 1223 336 033, e-mail: deposit@ccdc.cam.ac.uk or http://www.ccdc.cam.ac.uk.

Acknowledgments

We thank the Natural Science Foundation of Shandong Province and Qufu Normal University for financial support.

References

[1] R.E. Hutton, J.W. Burley, V. Oakes, J. Organomet. Chem. 156 (1978) 369.
[2] P.G. Harrison, T.J. King, M.A. Healy, J. Organomet. Chem. 182 (1979) 17.
[3] R.A. Howie, E.S. Paterson, J.L. Wardell, J.W. Burley, J. Organomet. Chem. 304 (1986) 301.
[4] L. Tian, Z. Zhou, B. Zhao, W. Yu, P. Yang, Synth. React. Inorg. Met.-Org. Chem. 30 (2000) 1363.
[5] D. Maughan, J.L. Wardell, J.W. Burley, J. Organomet. Chem. 212 (1981) 59.
[6] O.S. Jung, J.H. Jeong, Y.S. Sohn, Polyhedron 8 (1989) 1413.
[7] O.S. Jung, J.H. Jeong, Y.S. Sohn, J. Organomet. Chem. 399 (1990) 235.
[8] R. Balasubramanian, Z.H. Chohan, S.M.S.V. Doidge-Harrison, R.A. Howie, J.L. Wardell, Polyhedron 16 (1997) 4283.
[9] H. Buchanan, R.A. Howie, A. Khan, G.M. Spencer, J.L. Wardell, J. Chem. Soc., Dalton Trans. (1996) 541.
[10] L. Tian, Z. Zhou, B. Zhao, W. Yu, Polyhedron 17 (1998) 1275.
[11] L. Tian, Z. Zhou, Q. Yu, X. Liu, Synth. React. Inorg. Met.-Org. Chem. 33 (2003) 259.
[12] B.F. Milne, R.P. Pereira, A.M. Rocco, J.M.S. Skakle, A.J. Travis, J.L. Wardell, Appl. Organometal. Chem. 19 (2005) 363.
[13] P. Harston, R.A. Howie, G.P. McQuillan, J.L. Wardell, E. Zanetti, S.M.S.V. Doidge-Harrison, N.S. Stewart, P.J. Cox, Polyhedron 10 (1991) 1085.
[14] D. Dakternieks, K. Dunn, D.J. Henry, C.H. Schiesser, E.R.T. Tiekink, Organometallics 18 (1999) 3342.
[15] D. Dakternieks, K. Dunn, C.H. Schiesser, E.R.T. Tiekink, J. Organomet. Chem. 605 (2000) 209.
[16] D. Dakternieks, K. Dunn, C.H. Schiesser, E.R.T. Tiekink, J. Chem. Soc., Dalton Trans. (2000) 3693.
[17] D. Mandolesi, L.C. Koll, A.B. Chopa, J.C. Podesta, J. Organomet. Chem. 555 (1998) 209.
[18] M.B. Faraoni, A.D. Ayala, V. Vetere, M.L. Casella, O.A. Ferretti, J.C. Podesta, Appl. Organomet. Chem. 19 (2005) 465.
[19] C.S. Marvel, R.L. Frank, J. Am. Chem. Soc. 64 (1942) 1675.
[20] H.D. Kuivila, O.F. Beumel, J. Am. Chem. Soc. 83 (1961) 1246.
[21] G.M. Sheldrick, SHELX 97, Program for Crystal Structure Solution, University of Göttingen, Germany, 1997.
[22] G.M. Sheldrick, SHELXL-97, Program for the Crystal Structure Refinement, University of Göttingen, Germany, 1997.
[23] H.D. Flack, Acta Crystallogr., Sect. A 39 (1983) 876.
[24] E. Nakamura, Y. imanishi, D. Machii, J. Org. Chem. 59 (1994) 8178.
[25] E.S. Paterson, J.L. Wardell, J.W. Burley, J. Organomet. Chem. 273 (1984) 313.
[26] H.J. Buchanan, P.J. Cox, J.L. Wardell, Main Group Metal Chem. 21 (1998) 751.
[27] R. Willem, M. Biesemans, P. Jaumier, B. Jousseaume, J. Organomet. Chem. 572 (1999) 233.
[28] S. Hu, C. Zhou, Q. Cai, Acta Phys. Chim. Sin. 19 (2003) 1073.
[29] R.R. Holmes, S. Shafieezad, V. Chandrasekhar, J.M. Holmes, R.O. Day, J. Am. Chem. Soc. 110 (1988) 1174.
[30] H. Puff, H. Reuter, J. Organomet. Chem. 364 (1989) 57.
[31] C. Lecompte, J. Protas, M. Devaud, Acta Crystallogr., Sect. B 32 (1976) 923.
[32] B. Zobel, A. Duthie, D. Dakternieks, E.R.T. Tiekink, Organometallics 20 (2001) 2820.

Since the first report of ferromagnetism in a molecule-based material, the charge-transfer salt $[Fe(Cp^*)_2]$ TCNE (TCNE = tetracyanoethylene), in 1986, [5,6] similar charge transfer salts with different transition metal bisdithiolene anions have been studied. These salts show different types of structures and a variety of magnetic behaviours, becoming model systems for the study of magnetic interactions in molecular solids [7].

The sulfur rich dithiolate ligands have been extensively explored in this context because the S–S interactions improve both the magnitude and dimensionality of the solid state interactions. Much less effort has been devoted to other extended dithiolene π-ligands containing different heteroatoms like N and O. However, it was recently demonstrated with pyrazinediselenate [8,9] and pyrazinedithiolate [10] Cu complexes that N atoms in these type of ligands can act as an extra coordinating site providing an additional degree of freedom in the crystal engineering of these solids. These pyrazine type complexes were also used as anions in the preparation of an unusual type of charge transfer salt with a unique type of transitions [11–13]. Therefore there is substantial interest in studying similar complexes based on N containing dithiolene ligands such as 2,3-dicyano-5,6-dimercaptopyrazyne (dcdmp), which has been a lot less explored. The monoanionic Ni complex with this ligand $Ni(dcdmp)_2^-$ [14] was reported initially almost 10 years ago and more recently we reported the Au analogue [15], which has already been used to prepare charge transfer salts with TTF type donors [16].

Pursuing an effort to explore complexes of this ligand with other metals, and the possible use of these complexes as building blocks in novel molecular materials, we report in this paper the synthesis and characterization of the $Cu(dcdmp)_2$ complex, in both monoanionic and dianionic forms, and we describe a salt of this Cu^{II} complex with decamethylferrocenium displaying a large anisotropic paramagnetic behaviour but with no ordering down to 2 K.

2. Experimental

2.1. Synthesis

3: Tetrabutylammonium salt of copper (II) bis-2,3-dicyano-5,6-dimercaptopyrazyne, $[n\text{-}Bu_4N]_2Cu(dcdmp)_2$: to a suspension of sodium sulfate monohydrate (241 mg, 1×10^{-3} mol) in acetone (40 ml) was added, under stirring, a solution of 5,6-dichloro-2,3-dicyanopyrazine (100 mg, 5.02×10^{-4} mol) in acetone (10 ml). The formed red solution was filtered and added to a solution of copper chloride (43 mg, 2.51×10^{-4} mol) in acetone (2 ml), turning to an orange-brown mixture. The inorganic precipitate was removed and the liquor added to 1 ml of a solution of tetrabutylammonium bromide (162 mg, 5.02×10^{-4} mol) in acetone, giving rise to a brown-red solution. The stirring was maintained in all steps until no visible modification was observed. This solution was then filtered and slow evaporation of the solvent was allowed. The brown-gold solid obtained was filtered and recrystallised in acetone to afford plate shape crystals suitable for X-ray diffraction measurements. Yield: 22% (52.5 mg); Mp: 213–215 °C; IR (KBr): $\tilde{\nu}=440$ (m), 744 (s, C–S), 987 (s), 897 (m), 1525–1222 (m, s, pyrazine ring), 2220 (s, C≡N), 2427 (w, –N=C–), 2871–2958 (s, C–H aliphat) cm^{-1}. UV–Vis (CH_3CN): $\lambda_{max}=1724$ nm. *Anal.* Calc. for CHNS ($C_{44}H_{72}N_{10}S_4Cu$): C, 56.64; H, 7.77; N, 15.01; S, 13.75. Found: C, 56.43; H, 8.06; N, 15.31; S, 13.51%.

4: Tetrabutylammonium salt of copper (III) bis-2,3-dicyano-5,6-dimercaptopyrazyne, $n\text{-}Bu_4NCu(dcdmp)_2$: to a solution of **3** (310 mg, 3.3×10^{-4} mol) in acetone (150 ml) was added, under stirring, an acetone solution (50 ml) of I_2 (360 g, 1.4×10^{-3} mol). The stirring was maintained for 1 h with no visible alterations of the color and then ~80% of the solvent was slowly evaporated, under nitrogen, over 3 days. After filtering, and washing with cold acetone, brown needle shape crystals suitable for X-ray measurements were obtained. Yield: 77% (176 mg); Mp: 260–262 °C. IR (KBr): $\tilde{\nu}=429$ (w), 733 (w, C–S), 1450–1177 (m, s, pyrazine ring), 2231 (m, C≡N), 2360 (m, –N=C–), 2964–2874 (s, C–H aliphat) cm^{-1}. UV–Vis (CH_3CN): $\lambda_{max}=1729$ nm. *Anal.* Calc. for CHNS ($C_{28}H_{36}N_9S_4Cu$): C, 48.71; H, 5.26; N, 18.26; S, 18.57. Found: C, 49.17; H, 4.22; N, 18.53; S, 18.81%.

5: Decamethylferrocinium salt of copper (II) bis-2,3-dicyano-5,6-dimercaptopyrazyne, $[Fe(Cp^*)_2]_2[Cu(dcdmp)_2]$: Two saturated solutions of $(n\text{-}Bu4N)_2[Cu(dcdmp)_2]$ (50 mg, 5.36×10^{-5} mol) and $Fe(Cp^*)_2BF_4$ (44 mg, 1.0×10^{-4} mol) in acetonitrile (<20 ml) were added together under stirring. Almost immediately a crystalline yellow-gold precipitate appeared. The best needle shape crystals, suitable for X-ray measurements, were obtained by recrystallisation in acetonitrile, followed by slow evaporation of the solvent. Yield 70%. *Anal.* Calc. for CHNS ($C_{52}H_{60}N_8S_4CuFe$): C, 56.75; H, 5.49; N, 10.18; S, 11.65. Found: C, 57.28; H, 4.56; N, 10.21; S, 11.58%.

2.2. X-ray structure determination

The data collection for compound **3** was performed at room temperature on an Enraf–Nonius CAD4 diffractometer, equipped with graphite monochromatised Mo Kα radiation ($\lambda=0.71073$ Å), in the $\omega-2\theta$ scan mode. A semi-empirical absorption correction was applied based on ψ-scans ($T_{max}=0.9999$, $T_{min}=0.8953$). For compound **5** the data were collected at 100(2) K on a Bruker AXS SMART APEX CCD detector diffractometer using graphite-monochromatised Mo Kα radia-

Table 1
Crystallographic data for compounds $(n\text{-}Bu_4)_2[Cu(dcdmp)_2]$ and $[Fe(Cp^*)_2]_2[Cu(dcdmp)_2]$

	$(n\text{-}Bu_4)_2[Cu(dcdmp)_2]$	$Fe(Cp^*)_2]_2$-$[Cu(dcdmp)_2]$
Formula	$C_{44}H_{72}CuN_{10}S_4$	$C_{52}H_{60}CuFe_2N_8S_4$
Formula weight	932.90	1100.56
T [K]	293 (2)	100 (2)
Crystal system	triclinic	monoclinic
Space group	$P\bar{1}$	$C2/c$
a (Å)	9.9512(6)	15.8911(14)
b (Å)	10.5407(12)	10.5133(7)
c (Å)	13.2211(11)	30.264(3)
α (°)	69.756(9)	
β (°)	88.112(6)	91.105(2)
γ (°)	79.658(7)	
Volume (Å^3)	1279.4(2)	5055.3(7)
Z, D_{calc} (Mg/m^3)	1, 1.211	4, 1.446
μ (mm^{-1})	0.630	1.193
$F(000)$	499	2292
Crystal color/shape	brown plate	yellow needle
Crystal size (mm)	$0.5 \times 0.4 \times 0.1$	$0.2 \times 0.1 \times 0.08$
θ Range (°)	2.09–27.01	2.32–33.20
Index range (h,k,l)	−12/0, −13/13, −16/16	−24/12, −15/15, −43/42
Reflections collected	5850	20164
Unique reflections [R_{int}]	5528 [0.0623]	8278 [0.0622]
Refined parameters	268	313
Goodness-of-fit	0.867	0.898
R_1 [$I > 2\sigma(I)$]	0.0795	0.0525
wR_2	0.1143	0.0850
$\Delta\rho_{max,\,min}$ (e Å^{-3})	0.263, −0.276	0.578, −0.539

tion ($\lambda = 0.71073$ Å) in the ϕ and ω scans. No absorption correction was applied.

The structures were solved by direct methods using SIR97 [17] and refined by full-matrix least-squares methods using the program SHELXL97 [18] and the WINGX software package [19]. All non-hydrogen atoms were refined anisotropically. Hydrogen atoms were placed in idealised positions and allowed to refine riding on the parent C atom. Molecular graphics were prepared using ORTEP 3 [20] and SCHAKAL-97 [21]. Crystal data and structure refinement are summarised in Table 1.

2.3. Magnetic properties

Magnetic measurements were performed using either a longitudinal Faraday system (Oxford Instruments) with a 7 T superconducting magnet for static measurements in the range 2–300 K or a Maglab 2000 system (Oxford Instruments) for magnetisation and AC-susceptibility under fields up to 12 T and down to 1.5 K. The Faraday system was used with a magnetic field of 5 T and forward and reverse gradient fields of 1 T/m. A polycrystalline sample (10–15 mg) was placed inside a previously calibrated thin wall Teflon bucket. The force was measured with a microbalance (Sartorius S3D-V). The Maglab 2000 system was used for magnetisation measurements of similar polycrystalline samples at different magnetic fields using an extraction technique and for AC susceptibility measurements using an AC field of 1 Oersted. Magnetization data were corrected for contributions due to the sample holder and core diamagnetism, estimated from tabulated Pascal constants as -5.9734×10^{-4} and -3.8744×10^{-4} emu-mol^{-1} for **3** and **5**, respectively.

EPR spectra at room temperature were obtained with an X-Band Bruker ESP 300E spectrometer equipped with a microwave bridge ER041XK, a rectangular cavity operating in T102 mode and a Field controller ER 032M system. The modulation amplitude was kept well below the line width and the microwave power well below saturation.

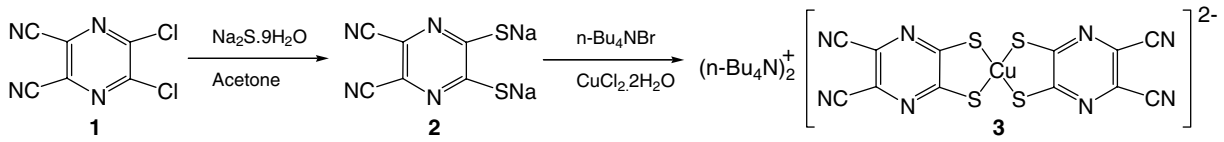
3. Results and discussion

3.1. Synthesis

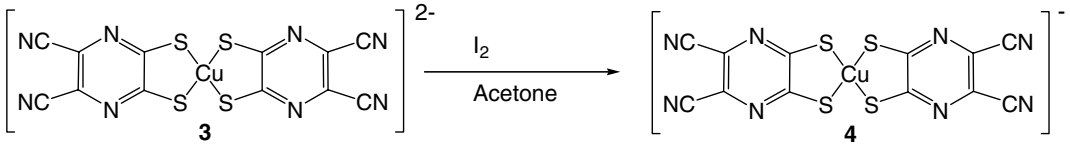
The synthesis of the copper complex **3** was performed following a standard procedure used for the preparation of dithiolates from dichlorides (Scheme 1), similar to that used to prepare the Ni and Au analogues [14]. The dithiolate ligand (**2**) in solution was obtained from the corresponding chloride salt (**1**) by treatment with Na_2S in acetone. This ligand, without intermediate isolation, was successively reacted with copper chloride and n-Bu_4NBr, also in acetone solutions, followed by slow evaporation of the solvent under an inert atmosphere, to give the copper (II) complex (**3**) that was obtained as gold-brown plate shaped crystals (Scheme 1). The elemental analysis is consistent with a 2:1 stoichiometry, as confirmed by the X-ray crystal structure determination.

Upon oxidation of **3**, with iodine, the corresponding copper (III) complex, **4**, was obtained as gold-brown needle shaped crystals (Scheme 2).

Cyclic voltammetry of **3** in acetonitrile shows a pair of reversible redox waves at 0.206 V vs. Ag/AgCl, ascribed to the couple $[Cu(dcdmp)_2]^-/[Cu(dcdmp)_2]^{2-}$, with no other processes visible in the range up to 1.0 V. These results should be compared with those obtained in Cu complexes with related ligands, namely $Cu(pdt)_2$ (−0.33 V vs. Ag/AgCl) [10] and $Cu(dcbdt)_2$, where dcbdt = dicyano benzene dithiolate (−0.07 V vs. $Ag/AgNO_3$) [22]. As expected, the two cyano groups in the dcdmp ligand make the oxidation more difficult than in the pdt complex and stabilize the dianion, which was readily oxidised to the monoanion by air exposure in the case of $Cu(pdt)_2$. The occurrence of just one reversible redox process in $Cu(dcdmp)_2$ points out to a not so significantly extended ligand contribution to the frontier orbitals of this complex, the oxidation being essentially Cu and S4 centered, as with $Cu(pdt)_2$ [10]. This contrasts with $Cu(dcbdt)_2$ where around 1 V there are additional oxidation processes associated with the formation of partially oxidised species [22] (see Fig. 1).



Scheme 1.



Scheme 2.

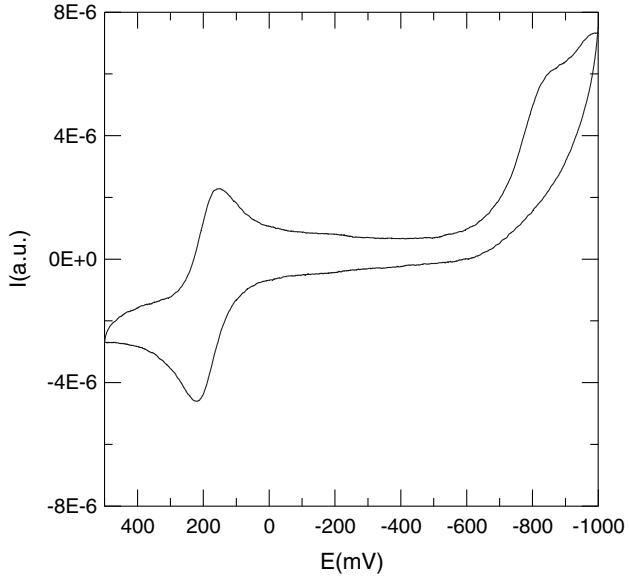


Fig. 1. Cyclic voltammetry of $(n\text{-}Bu_4N)_2[Cu(dcdmp)_2]$ in acetonitrile.

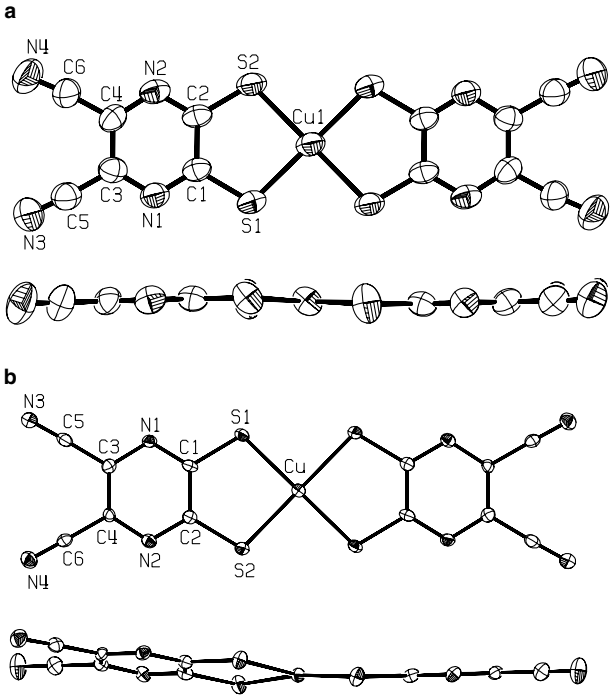


Fig. 2. ORTEP views with thermal ellipsoids at 50% probability and atomic numbering scheme of $Cu(dcdmp)^{2-}$ in **3** (a) and in **5** (b).

3.2. Structural characterisation

The crystal quality made it possible to solve the crystal structures of compounds **3** and **5**. Although the crystal quality of **4** was not sufficient to accurately refine the crystal structure, the final agreement factors were $R_1 = 0.126$ and $wR_2 = 0.283$, the unit cell parameters obtained ($a = 35.281(4)$ Å, $b = 9.501(1)$ Å, $c = 21.885(2)$ Å and $\beta = 109.842(9)°$, monoclinic space group $C2_1/c$), clearly indicate that this Cu compound is isostructural with the corresponding gold analogue [15].

As expected, in both **3** and **5** the $Cu(dcdmp)_2^{2-}$ anion presents a square planar coordination geometry (Fig. 2). However, while in **3** the anion is essentially planar with only a slight chair type distortion (the atomic deviations from the average molecular plane are less than 0.09 Å, see Fig. 2) in complex **5** there is a small but significant important tetrahedral distortion of the coordinating sulfur atoms. These distortions are certainly due to the several C–H···S hydrogen bonds formed between S1 and the Cp* ring of the cations as discussed in more detail below. These interactions twist the two ligands towards opposite directions, where the S2 atom does not interact with any neighbouring atom. Therefore, the non-planarity of the $[Cu(dcdmp)_2]^{2-}$ anion, in **5**, is denoted by a dihedral angle between the average plane of the two ligands of 13.14°.

The Cu–S bond lengths in the anions are 2.2398(14) and 2.2821(13) Å, in complex **3** and 2.2418(7) and 2.2888(7) Å in **5**. Although all these values lie in the typical range of Cu^{II} complexes it is worth referring that in both compounds two Cu–S bond lengths are on the upper side of this range while the other two are close

to the opposite limit. In both complexes, within experimental uncertainty, the dcdmp ligands are identical, presenting a geometry also very close to that found in the corresponding Ni and Au analogues [15] (see Table 2). The $Fe(Cp^*)_2$ units adopt the most common geometry of the metallocenium cations [5,23].

The tetrabutylammonium salt **3**, crystallises in the triclinic system, space group $P\bar{1}$, $Z = 1$, with unit cell parameters $a = 9.9512(6)$ Å, $b = 10.541(1)$ Å, $c = 13.221(1)$ Å, $\alpha = 69.756(9)°$, $\beta = 88.112(6)°$ and $\gamma = 79.658(7)°$. The unit cell contains one independent $[Cu(dcdmp)_2]^{2-}$ anion, with the metal located at an inversion centre, and one independent tetrabutylammonium cation. The crystal structure can be seen as well segregated layers (a, $b - c$) of cations and anions, alternating along $b + c$. There are no short contacts between species of the same layer and the only significant interactions observed are hydrogen bonds, both of C–H···N and C–H···S types, between cations and anions in neighbouring layers. All the sulfur and the terminal nitrogen atoms of the anion species are involved in these interactions (Fig. 3, Table 3).

Salt **5** crystallises in the monoclinic system, space group $C2/c$, $Z = 4$, with unit cell parameters $a = 15.891(1)$ Å, $b = 10.5133(7)$ Å, $c = 30.264(3)$ Å and $\beta = 91.105(2)°$. The unit cell contains two independent $Fe(Cp^*)_2$ cations and one independent $[Cu(dcdmp)_2]^{2-}$ complex, with the Cu atom at an inversion center. Its crystal structure consists of columns along b of alternated dianions and side-by-side pairs of cations, $\ldots A^{2-}(D^+D^+)A^{2-}(D^+D^+)\ldots$ The unit cell contains four columns which are parallel to each other but arranged out-of-registry. This structural motive belongs to the so called type IV structure according to the classification scheme of metalloceniun bisdithiolene salts proposed by Gama and Duarte [7]. However, among this type IV structures, **5** is a rare case where the dithiolate is in the dianionic state, previously observed only for the $Cu(mnt)_2^{2-}$ analogue [24]. All other examples of type IV structure previously known are based on monoanionic dithiolate complexes, with an extra anion in the structure to balance the charge. The main difference in the structure of **5** relative to that of $[Fe(Cp^*)_2]_2$-$Cu(mnt)_2$ is the orientation of the $Fe(Cp^*)_2$ cations that are rotated with the Cp* plane almost 90° relative to the mnt ligand, while in this $Cu(dcdmp)_2$ salt the Cp* planes are almost parallel to the ligands (Fig. 4).

In the crystal structure of **5** the anions are well isolated from each other with no direct contacts. Each anion has short contacts with 10 different close neighbouring $[Fe(Cp^*)_2]^+$ cations, all being hydrogen bonds of different types (see Table 4 and Figs. 5 and 6). Along the column, with cations I–IV, the observed interactions are of the C–H···S and C–H···C type. The contacts with the four cations placed closer at the ends of the long axis of the anions (VI, VII, IX, X) are of C–H···N type, while the interactions with the other two cations closer to the centre of the anion (V, VIII) are exclusively of the C–H···S type. The only significant cation–cation short contact is between the pairs positioned side-by-side in the same column (I and II, III and IV), which present an H···H contact.

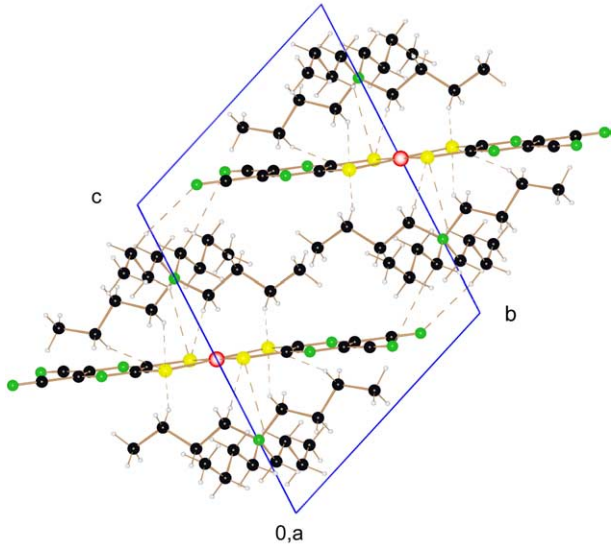


Fig. 3. Crystal structure of **3**: view along a.

Table 2
Selected bond lengths (Å) for $[Cu(dcdmp)_2]^{2-}$ in **3** and **5**

	3	**5**
Cu–S1	2.2389(14)	2.2418(7)
Cu–S2	2.2821(13)	2.2888(7)
S1–C1	1.723(5)	1.715(3)
S2–C2	1.706(5)	1.719(3)
C1–C2	1.458(6)	1.455(3)
C3–C4	1.406(6)	1.388(3)
C1–N1	1.332(5)	1.336(3)
C2–N2	1.322(6)	1.339(3)
C3–N1	1.331(6)	1.350(3)
C4–N2	1.348(6)	1.340(3)
C3–C5	1.445(7)	1.452(4)
C4–C6	1.426(7)	1.447(4)
C5–N3	1.128(6)	1.140(3)
C6–N4	1.149(6)	1.147(3)

Table 3
Hydrogen bonds in the crystal structure **3**

	d (Å)	Angle (°)
C33–H33a···S1	2.847(1)	159.4
C31–H31a···S1	2.993(1)	152.5
C23–H23a···S1	2.983(2)	158.9
C21–H21b···S2	2.967(2)	177.2
C42–H42a···S2	2.980(2)	133.2
C43–H43a···N3	2.739(6)	156.5
C11–H11a···N4	2.651(6)	165.4

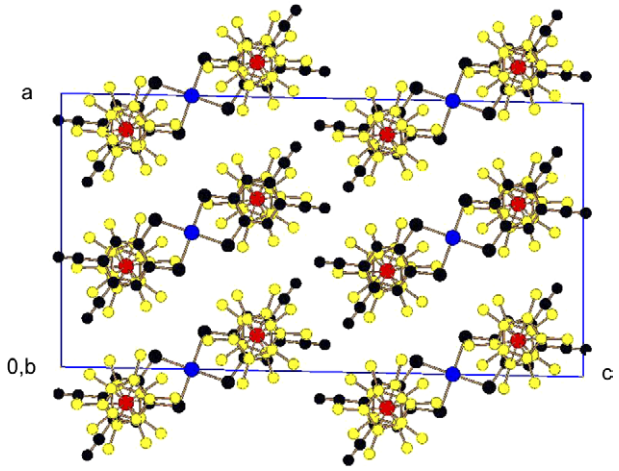


Fig. 4. Crystal structure of **5**: view along *b*.

Table 4
Hydrogen bonds and short contacts in the crystal structure **5**

	d (Å)	Angle (°)
C19–H19c···S1	2.900(1)	160.57
C18–H18b···S1	2.841(1)	169.4
C17–H17b···S1	2.935(1)	170.5
C27–H27c···S1	2.826(1)	145.9
C29–H29a···N3	2.734(3)	119.9
C28–H28c···N4	2.662(2)	154.4
C29–H29b···N4	2.718(2)	156.2
H26b···H26b	2.331(2)	

Probably due to these interactions, the cations axes in these pairs are not exactly parallel to each other and the dihedral angle between the average planes of the two molecules is close to 3°. In each metallocenium the Cp* rings are not exactly parallel, making a dihedral angle of (1.4°) a distortion related with the asymmetry of the hydrogen bonds in the two rings. Apart from this slight deviation between the two Cp* rings of each cation, their planes are almost parallel to the dcdmp ligands, being well centered over the pyrazine ring. However the average distance between the pyrazine and the Cp* rings (3.576 Å) do not denote a very significant π–π interaction, probably due to the size of the methyl groups that prevent a closer interaction between these rings. The shorter distances between these rings are denoted by the distances N2···C13 (3.419 Å) and C2···C14 (3.500 Å), exceeding only by 5 and 3%, respectively, the sum of the Van der Waals radii. As mentioned above the more significant short contacts between these units are the previously referred hydrogen bonds, which probably also preclude the development of a more significant π–π interaction.

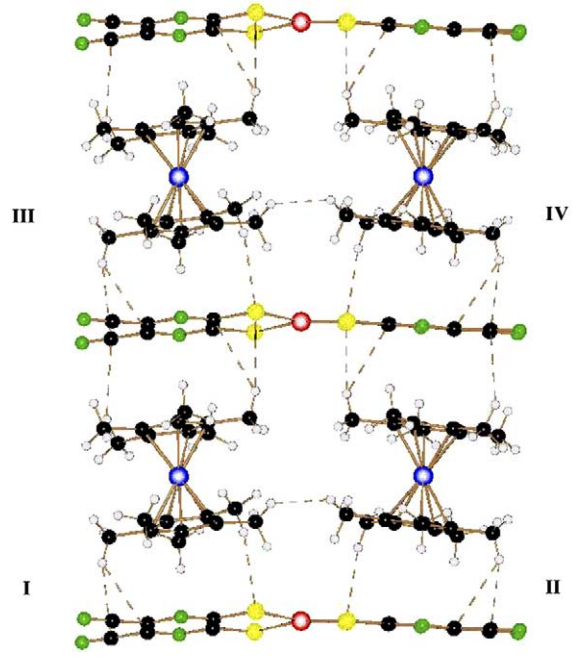


Fig. 5. Partial view of one $\ldots D^+D^+A^-D^+D^+A^- \ldots$ chain in the crystal structure of **5**.

3.3. Magnetic characterisation

As expected for Cu(III) in a square planar coordination geometry, **4** is diamagnetic while **3**, a the Cu(II) complex that is a d^9 species, is paramagnetic. This is confirmed by EPR and magnetisation measurements. Single crystal EPR data for **3** shows, at room temperature, a single line between 34 and 82 G wide and *g* values of 2.024 and 2.040. At room temperature the effective magnetic moment, μ_{eff}, of 1.70 μ_B, is very close to the value of 1.76 μ_B predicted for independent $S = 1/2$ spins with $\langle g_{Cu} \rangle = 2.03$. As shown in Fig. 7, μ_{eff} shows a slight increase upon cooling, until ca. 15 K where a maximum of 1.75 μ_B is observed and it decreases for lower temperatures. The analysis of the crystal structure suggests that the magnetic interactions in **3** must be very weak, as the anionic radicals are isolated by the diamagnetic TBA^+ cations. This is in good agreement with the magnetization isothermal obtained at 1.7 K (see Fig. 8), which follows closely the calculated Brillouin function, with the experimental values only slightly inferior to the calculated ones, as expected for a system of spins with a very weak AFM coupling. At high applied magnetic fields the magnetization saturates at a value of 1.0149 $N\mu_B$, in good agreement with the calculated value of $M_S = gS = 1.015\ N\mu_B$.

In the case of **5**, the magnetic measurements are expected to show paramagnetic contributions both from the acceptors, $[Cu(dcdmp)_2]^{2-}$, and the donors, $[Fe(Cp^*)_2]^+$. The paramagnetic susceptibility of this compound does not follows a Curie–Weiss behaviour, instead the effective magnetic moment shows a maximum at ca. 70 K, as shown in Fig. 7, concerning the measurements obtained with a compressed pellet. At room temperature $\mu_{eff} = 3.56\ \mu_B$, a value lower than

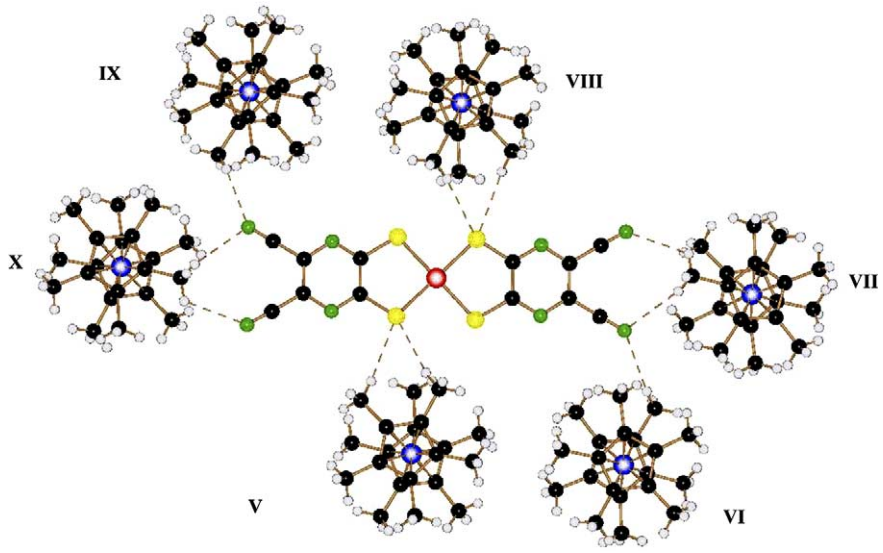


Fig. 6. Partial view along b of the crystal structure of **5** showing the interactions between one anion and the cations in neighbouring chains.

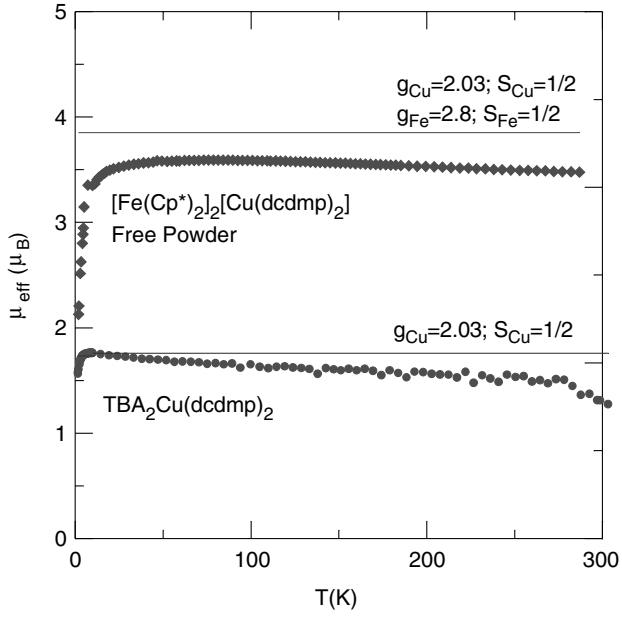


Fig. 7. Effective magnetic moment, μ_{eff}, of **3** (circles) and **5** (squares), as a function of temperature at 5 and 2 T, respectively.

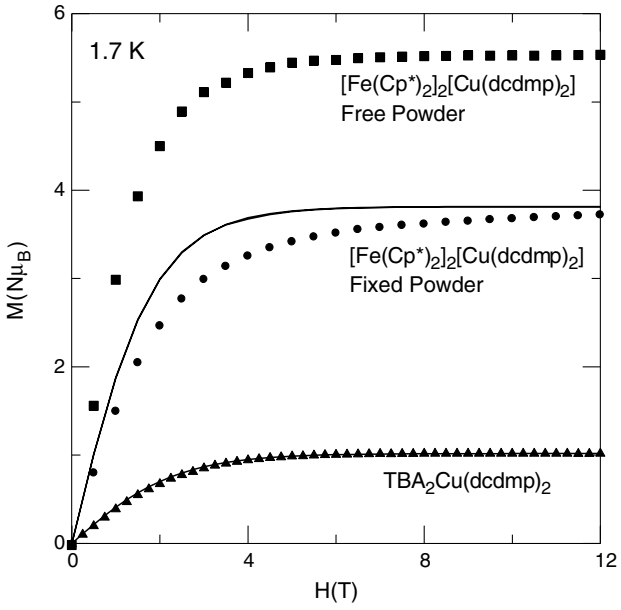


Fig. 8. Isothermal magnetisation at 1.7 K of **3** (triangles) and **5**, as fixed (circles) and free (squares) powder samples.

the calculated one, 3.854 μ_B, for a spin system with $S_A = 1/2$ and $S_D = 1/2$ and $\langle g_A \rangle = 2.03$ and $\langle g_D \rangle = 2.8$ [5]. This difference can be attributed to an AFM coupling between the donors and the acceptors. It should be noted that the magnetisation measurements (effective magnetic moment) give significantly different results for a fixed powder (in a compressed pellet) and in a polycrystalline sample with powder free to rotate. This is ascribed to a large anisotropy due to the g factor anisotropy of the donor, $[Fe(Cp^*)_2]^+$, with $g_{\parallel} = 4.4$ and $g_{\perp} = 1.4$ [5].

The unusual temperature dependence of μ_{eff}, namely the increase of μ_{eff} from room temperature down to 70 K, can be ascribed to a ferrimagnetic (FIM) like behaviour induced by an AFM intrachain DA coupling, which could lead to a spin arrangement in the DDAD-DA chains as $\cdots\uparrow\uparrow\downarrow\uparrow\uparrow\downarrow\cdots$, with $S_D = S_A = 1/2$. This effect is expected to be further enhanced by the fact that g_D ($\sim$2.8) is considerably larger than g_A ($\sim$2). At low temperatures, the antiferromagnetic nature of the dominant interactions is also confirmed by the isothermal magnetization curves, as shown in Fig. 8 for measurements

obtained at 1.7 K. The experimental magnetisation values are lower than those predicted by the Brillouin function. At high fields the magnetization approaches 3.75 $N\mu_B$, in good agreement with the calculated value for the saturation magnetization $M_S = g_A S_A + 2g_D S_D = 3.815\ N\mu_B$. AC magnetic susceptibility measurements show no sign of magnetic ordering down to 1.5 K. This absence of magnetic order is consistent with the fact that the intrachain DA magnetic interactions are not expected to be very strong and the interchain interactions are expected to be weak.

4. Conclusion

The $Cu(dcdmp)_2$ complex was prepared in both dianionic and monoanionic states as air stable compounds. The $[Fe(Cp^*)_2]_2[Cu(dcdmp)_2]$ salt, in spite of a structure favourable for ferrimagnetic behaviour, does not shows any magnetic ordering down to 1.7 K. The magnetic properties show, however, a large anisotropy, ascribed to the *g*-factor anisotropy of the $Fe(Cp^*)_2^+$ cations.

5. Supplementary material

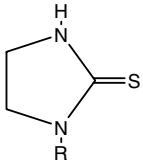
Crystallographic data (excluding structure factors) for the structures reported in this paper have been deposited with the Cambridge Crystallographic Data Centre. The deposition numbers are CCDC-269571 and CCDC-269572 for compounds **3** and **5**, respectively. Copies of the data can be obtained free of charge upon application to the director of CCDC, 12 Union Road, Cambridge CB2 1EZ, UK [fax: +441223/336/033, e-mail deposit@ccdc.cam.ac.uk].

Acknowledgement

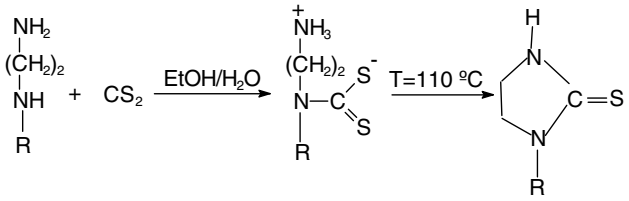
This work was partially supported by FCT-Portugal (Contract POCTI/QUI/45108/2002).

References

[1] (a) J.A. McCleverty, Prog. Inorg. Chem 10 (1968) 29;
(b) U.T. Muller-Westerhoff, B. Vance, G. Wilkinson, R.D. Gillard, J.A. McCleverty (Eds.), Comprehensive Coordination Chemistry, Pergamon, Oxford, 1987;
(c) L. Alcácer, H. Novais, in: J.S. Miller (Ed.), Extended Linear Chain Compounds, vol. 3, Plenum Press, New York, 1983, p. 319;
(d) N. Robertson, L. Cronin, Coord. Chem. Rev. 227 (2002) 93;
(e) K.D. Karlin, E.I. Tiefel (Eds.), Progress in Inorganic Chemistry, Dithiolene Chemistry: Synthesis, Properties, and Applications, vol. 52, Wiley, 2004.
[2] (a) M. Ahamad, A.E. Underhill, J. Chem. Soc., Chem. Commun. (1981) 67;
(b) M.M. Ahmad, D.J. Turner, A.E. Underhill, C.S. Jacobsen, K. Mortensen, K. Carneiro, Phys. Rev. B 29 (1984) 4796.
[3] P. Cassoux, L. Valade, in: D.W. Bruce, D. O'Hare (Eds.), Inorganic Materials, second ed., Willey, Chichester, 1996, p. 1.
[4] P. Cassoux, J.S. Miller, in: L.V. Interrante, M.J. Hampden-Smith (Eds.), Chemistry of Advanced Materials, Willey-VCH, New York, 1998, p. 19.
[5] J.S. Miller, J.C. Calabrese, H. Rommelmann, S.R. Chittipeddi, J.H. Zhang, W.M. Reiff, A.J. Epstein, J. Am. Chem. Soc. 109 (1987) 769.
[6] S. Chittipedi, K.R. Cromack, J.S. Miller, A.J. Epstein, Phys. Rev. Lett. 58 (1987) 2695.
[7] V. Gama, M.T. Duarte, in: Joel S. Miller, Marc Drillon (Eds.), Magnetism Molecules to Materials V, Wiley-VCH, New York, 2005, pp. 1–40.
[8] X. Ribas, J. Dias, J. Morgado, K. Wurst, M. Almeida, J. Veciana, C. Rovira, Cryst. Eng. Commun. 93 (2002) 4.
[9] X. Ribas, J.C. Dias, J. Morgado, K. Wurst, I.C. Santos, M. Almeida, J. Vidal-Gancedo, J. Veciana, C. Rovira, Inorg. Chem. 43 (2004) 3631.
[10] X. Ribas, J.C. Dias, J. Morgado, K. Wurst, E. Molins, E. Ruiz, M. Almeida, J. Veciana, C. Rovira, Chem. Eur. J. 10 (2004) 1691.
[11] E.B. Lopeses, J.C. Dias, J.P. Seiça, I.C. Santos, J. Morgado, R.T. Henriques, M. Almeida, X. Ribas, K. Wurst, J. Veciana, C. Rovira, P. Foury-Leylekian, J. Phys. IV 114 (2004) 537.
[12] J.C. Dias, J. Morgado, H. Alves, E.B. Lopes, I.C. Santos, M.T. Duarte, R.T. Henriques, M. Almeida, X. Ribas, C. Rovira, J. Veciana, Polyhedron 22 (2003) 2447.
[13] J.C. Dias, X. Ribas, J. Morgado, J.P. Seiça, E.B. Lopes, I.C. Santos, R.T. Henriques, M. Almeida, K. Wurst, P. Foury-Leylekian, E. Canadell, J. Vidal-Gancedo, Jaume Veciana, C. Rovira, J. Mater. Chem. (2005) in press, doi:10.1039/b505724h.
[14] M. Tomura, S. Tanaka, Y. Yamashita, Synth. Metals 24 (1994) 197.
[15] D. Belo, I.C. Santos, M. Almeida, Polyhedron 23 (2004) 1351.
[16] D. Belo, J. Morgado, E.B. Lopes, I.C. Santos, V. Gama, R.T. Henriques, M. Almeida, Synth. Metals 102 (1999) 1751.
[17] A. Altomare, M.C. Burla, M. Camalli, G. Cascarano, G. Giacovazzo, A. Guagliardi, A.G.G. Moliterni, G. Polidori, R. Spagna, J. Appl. Cryst. 32 (1999) 115.
[18] G.M. Sheldrick, SHELXL97, A Program for Crystal Structure Refinement, University of Göttingen, Germany, 1997.
[19] L.J. Ferrugia, J. Appl. Cryst. 32 (1999) 837.
[20] L.J. Ferrugia, J. Appl. Cryst. 30 (1997) 565.
[21] E. Keller, SCHAKAL-97 A Computer Program for the Representation of Molecular and Crystallographic Models, Kristallographisches Institut der Universität Freiburg i., Br., Germany, 1997.
[22] H. Alves, D. Simão, I.C. Santos, V. Gama, R.T. Henriques, H. Novais, M. Almeida, Eur. J. Inorg. Chem. (2004) 1318.
[23] J.S. Miller, J.C. Calabrese, A.J. Epstein, Inorg. Chem. 28 (1989) 4230.
[24] M. Fettouhi, L. Ouahab, M. Agiwara, E. Codjovi, O. Kahn, H. Constant-Machado, F. Varret, Inorg. Chem. 34 (1995) 4152.



Scheme 1. R = CH_3, Et, Propyl, ^{i}Propyl.



Scheme 2.

synthesis of metal complexes with heterocyclic thiones [5]. In addition to other advantages, the fact that the same metal can be used as the starting material avoids the presence in solution of other anionic species that are competitors for the ligand under investigation. This situation means that the nature of the compounds obtained can differ from those prepared using more traditional methods. In a similar way to other heterocyclic thiones, such as pyridine-2-thione or pyrimidine-2-thione, these ligands can show a large degree of versatility in their coordination forms, yielding complexes with unusual geometries, variable nuclearity and great structural diversity. Moreover, there is experimental evidence that the nature and location of the substituent in the heterocyclic ring is important in determining the structure of metal-heterocyclic thionate complexes and, for this reason, we decided to study the influence of the nature of different substituents in the N-heterocyclic ring (Scheme 1) on the structure of the corresponding complexes [5]. The structural and spectral characterization of these complexes is also included in this report.

2. Experimental

2.1. General considerations

Copper and silver (Aldrich) were used as plates (ca. 2×2 cm). 1-Methylethylenediamine, 1-ethylethylenediamine, 1-isopropylethylenediamine, 1-propylethylenediamine and carbon disulfide (Aldrich) were used as supplied.

Elemental analysis was performed using a Carlo-Erba EA microanalyser. IR spectra were recorded as KBr mulls on a Bruker IFS-66V spectrophotometer. ^{1}H and ^{13}C NMR spectra were recorded on a Bruker AMX 300 MHz instrument using $CDCl_3$ as solvent. Chemical shifts were recorded against TMS as the internal standard. The mass spectra (FAB) were recorded on a Micromass Autospec spectrometer, with 3-nitrobenzyl alcohol as the matrix.

2.2. Preparation of ligands

The ligands were synthesized by reaction of the appropriately substituted R-ethylenediamine and carbon disulfide in methanol–water using slight modifications of the standard literature procedure [18] (see Scheme 2).

Details are given for a representative example.

2.2.1. 1-Propylimidazolidine-2-thione (1-PrImSH)

Carbon disulfide (0.6 ml, 9.95 mmol) was added dropwise to a cooled (ice bath) solution of 1-propylethylenediamine (3.64 g, 35.7 mmol) in ethanol (9 ml) and water (9 ml). A white precipitate was formed. The reaction mixture was heated at 60 °C and a further quantity of carbon disulfide (3 ml, 49.7 mmol) was added. The precipitate initially dissolved but shortly after a large amount of white solid precipitated out. The reaction mixture was heated under reflux (110 °C) for 1 h and conc. HCl (0.5 ml) was added. The mixture was heated under reflux for a further 10 h. The reaction mixture was cooled and stored in a freezer. The resulting precipitate was filtered off and washed with cold acetone to give the desired ligand (2.78 g, 53.6%). *Anal.* Calc. for $C_6H_{12}N_2S$: C, 49.9; H, 8.4; N, 19.4; S, 22.2. Found: C, 49.8; H, 8.1; N, 19.3; S, 22.0%. IR (KBr, cm^{-1}): 3192 s, br, 2950 m, 2920 m, 2860 m, 1497 vs, br, 1465 s, 1450 s, 1375 m, 1315 s, 1300 s, 1270 s, 1230 vs, 1180 w, 1130 m, 1120 m, 1080 w, 1030 w, 960 m, 890 w, 800 vw, 670 m, 612 m, 510 m, 340 w, 290 vw. ^{1}H NMR ($CDCl_3$, ppm): 6.57 (s, 1H, NH); 3.44–3.68 (m, 8H, H4, H5 and CH_2), 0.88 (t, 3H, CH_3). ^{13}C NMR ($CDCl_3$, ppm): 183.6 (C2), 48.3 (C5), 41.8 (C4), 48.8 (N-*CH_2), 20.8 (*CH_2–CH_3), 11.5 (CH_3).

2.2.2. 1-Ethylimidazolidine-2-thione (1-EtImSH)

1-Ethylethylenediamine (2.53 g, 28.7 mmol) and CS_2 (2.55 ml, 42.2 mmol) gave the corresponding ligand (2.58 g, 70.9%). *Anal.* Calc. for $C_5H_{10}N_2S$: C, 46.1; H, 7.7; N, 21.5; S, 24.6. Found: C, 45.9; H, 7.9; N, 21.0; S, 23.9%. IR (KBr, cm^{-1}): 3180 s, br, 2950 w, 2860 w, 1495 vs, 1470 s, 1455 m, 1440 m, 1370 m, 1350 m, 1320 s, 1275 s, 1250 vs, 1190 w, 1130 m, 1100 w, 1070 w, 1030 w, 940 m, 790 m, 765 m, 625 s, 610 s, 510 s, 440 w, 360 m, 280 w. ^{1}H NMR ($CDCl_3$, ppm): 6.29 (s, 1H, NH); 3.51–3.59 (m, 6H, H4, H5, N–CH_2); 3.70 (t, 2H, C*H_2–CH_3), 1.15 (t, 3H, CH_3). ^{13}C NMR ($CDCl_3$, ppm): 183.3 (C2), 48.3 (C5), 42.0 (C4), 41.7 (*CH_2–CH_3), 12.5 (CH_3).

2.2.3. 1-Methylimidazolidine-2-thione (1-MeImSH)

1-Methylethylethylenediamine (3.8 g, 51 mmol) and CS_2 (4.03 ml, 76 mmol) of CS_2 gave the corresponding

ligand (2.87 g, 48.5%). *Anal.* Calc. for $C_4H_8N_2S$: C, 41.3; H, 7.7; N, 24.1; S, 27.6. Found: C, 41.1; H, 6.7; N, 23.8; S, 26.5%. IR (KBr, cm^{-1}): 3190 s, br, 2930 w, 2860 w, 1515 s, 1500 vs, 1470 m, 1435 m, 1395 m, 1180 m, 1290 s, br, 1230 m, 1195 m, 1105 s, 1030 w, 955 m, 668 m, 635 w, 610 m, 511 s, 395 vw, 280 m. ^{1}H NMR ($CDCl_3$, ppm): 6.49 (s, 1H, NH); 3.49–3.69 (m, 4H, H4, H5); 3.07 (s, 3H, CH_3). ^{13}C NMR ($CDCl_3$, ppm): 184.1 (C2), 51.5 (C5), 41.6 (C4), 34.6 (CH_3).

2.2.4. 1-isopropylimidazolidine-2-thione (1-^{i}PrImSH)

The diamine (9.13 g, 91.3 mmol) and CS_2 (9.22 ml, 127.6 mmol) gave the corresponding ligand (6.94 g, 52.3%). *Anal*. Calc. for $C_6H_{12}N_2S$: C, 49.9; H, 8.4; N, 19.4; S, 22.2. Found: C, 49.7; H, 8.2; N, 19.2; S, 22.3%. IR (KBr, cm^{-1}): 3280 vs, 2960 s, 2920 w, 2860 m, 1505 vs, 1490 s, 1460 s, 1440 s, 1365 m, 1330 m, 1260 s, br, 1205 w, 1190 w, 1160 m, 1125 m, 1060 s, 960 s, 740 w, 670 m, 620 m, 605 s, 520 m, 490 m, 425 w, 376 w. ^{1}H NMR ($CDCl_3$, ppm): 6.17 (s, 1H, NH): 3.51–3.63 (m, 4H, H4, H5); 4.77 (m, 1 H, CH), 1.16 (d, 6H, CH_3). ^{13}C NMR ($CDCl_3$, ppm): 182.7 (C2), 43.2 (C5), 41.9 (C4), 47.2 (CH–Pr), 19.8 (CH_3).

2.3. Electrochemical synthesis

The electrochemical method used in the synthesis of the complexes was similar to that described earlier [19]. The anode consisted of metal foil suspended from a platinum wire and the cathode was a platinum wire. The ligand was dissolved in acetonitrile and a small amount of tetramethylammonium perchlorate was added to the solution as an electrolyte carrier. Applied voltages of 10–15 V allowed sufficient current flow for smooth dissolution of the metal. Nitrogen was bubbled through the solution during electrolysis to provide an inert atmosphere and also to stir the reaction mixture. Under these conditions the cell can be summarised as $M_{(+)}$/CH_3CN + 1-RImSH/$Pt_{(-)}$. M = Cu, Ag.

2.3.1. [Cu(1-MeImS)]

Electrochemical oxidation of a copper anode in a solution of 1-MeImSH (0.190 g, 1.65 mmol) in acetonitrile (40 ml) at 20 V and 10 mA for 4 h caused 95 mg of copper to be dissolved, $E_f = 1.0$ mol F^{-1}. During the electrolysis process, hydrogen was evolved at the cathode and at the end of the reaction an insoluble crystalline solid was observed at the bottom of the vessel. The solid was filtered off, washed with acetonitrile and ether, and dried under vacuum. *Anal.* Calc. for $C_4H_7CuN_2S$: C, 26.9; H, 3.9; N, 15.7; S, 17.9%. Found: C, 27.0; H, 3.8; N, 15.5; S, 17.5%. IR (KBr, cm^{-1}): 2910 m, 2850 m, 1515 vs, 1470 m, 1450 m, 1420 m, 1380 s, 1300 vs, 1270 vs, 1180 w, 1100 vs, 1005 w, 980 vw, 950 m, 630 s, 480 m, 420 vw, 315 vw.

2.3.2. [Cu(1-EtImS)]

1-EtImSH (0.190 g, 1.47 mmol) in acetonitrile (40 ml); 21 V; 10 mA; 2 h; 50 mg of copper dissolved, $E_f = 1.1$ mol F^{-1}. *Anal.* Calc. for $C_5H_9CuN_2S$: C, 31.2; H, 4.7; N, 14.5; S, 16.6. Found: C, 31.2; H, 5.1; N, 14.2; S, 16.1%. IR (KBr, cm^{-1}): 2950 m, 2910 m, 2850 m, 1515 vs, 1470 w, 1445 m, 1430 m, 1395 s, 1370 w, 1350 m, 1290 m, 1240 vs, br, 1180 m, 1115 s, 1080 w, 1065 w, 1015 m, 985 vw, 950 w, 936 w, 780 w, 620 m, 480 m, 315 vw. ^{1}H NMR ($CDCl_3$, ppm): 3.45–3.47 (m, 6H, H4, H5, CH_2); 1.14 (t, 3H, CH_3). FAB (*m*/*z*): $[Cu_4(1\text{-EtImS})_3]^+$ 642, $[Cu_3(1\text{-EtImS})_2]^+$ 447, $[Cu_2(1\text{-EtImS})_2]^+$ 382, $[Cu_2(1\text{-EtImS})_2\text{–}CH_3]^+$ 367, $[Cu_2(1\text{-EtImS})_2\text{-Et}]^+$ 323, $[Cu(1\text{-EtImS})]^+$ 191, $[1\text{-EtImS}]^+$ 129. Crystals suitable for X-ray studies were obtained directly from the cell.

2.3.3. [Cu(1-PrImS)]

1-PrImSH (0.190 g, 1.30 mmol) in acetonitrile (50 ml); 16 V, 10 mA, 3.5 h; 84 mg of copper dissolved, $E_f = 1.0$. *Anal.* Calc. for $C_6H_{11}CuN_2S$: C, 34.8; H, 5.4; N, 13.5; S, 15.5. Found: C, 34.9; H, 5.5; N, 13.5; S, 16.1%. IR (KBr, cm^{-1}): 2950 m, 2910 w, 2850 w, 1510 s, 1450, m, 1390 s, 1340 w, 1290 s, 1270 m, 1235 m, 1210 s, 1175 w, 1115 s, 1020 w, 960 vw, 860 vw, 670 w, 625 m, 470 m. ^{1}H NMR ($CDCl_3$, ppm): 3.35–3.52 (m, 4H, H4, H5, N–CH_2); 1.55 (m, 2H, C*H_2–CH_3), 0.91 (t, 3H, CH_3). FAB (*m*/*z*): $[Cu_4(1\text{-PrImS})_4]^+$ 826, $[Cu_4(1\text{-PrImS})_3]^+$ 683, $[Cu_3(1\text{-PrImS})_3]^+$ 620, $[Cu_2(1\text{-PrImS})_3]^+$ 559, $[Cu_3(1\text{-PrImS})_2]^+$ 477, $[Cu_2(1\text{-PrImS})_2]^+$ 413, $[Cu_2(1\text{-PrImS})]^+$ 267, $[Cu(1\text{-PrImS})]^+$ 207, $[1\text{-PrImS}]^+$ 143. Crystals suitable for X-ray studies were obtained directly from the cell.

2.3.4. [Cu(1-^{i}PrImS)]

1-^{i}PrImSH (0.193 g, 1.30 mmol) in acetonitrile (40 ml), 25 V, 10 mA, 3.5 h, 85 mg of metal dissolved, $E_f = 1.0$. *Anal.* Calc. for $C_6H_{11}CuN_2S$: C, 34.8; H, 5.4; N, 13.5; S, 15.5. Found: C, 34.8; H, 5.6; N, 13.5; S, 14.8%. IR (KBr, cm^{-1}): 2960 m, 2920 w, 2860 w, 1510 vs, 1445 m, 1390 s, 1355 m, 1330 w, 1290 s, 1245 s, br, 1200 m, 1180 w, 1165 w, 1115 m, 1055 s, 1015 w, 960 w, 635 m, 610 s, 525 m, 475 m, 430 m. ^{1}H NMR ($CDCl_3$, ppm): 3.37–3.50 (m, 4H, H4, H5); 4.46 (s, H, CH), 1.14 (s, 6H, CH_3).

2.3.5. [Ag(1-MeImS)]

Electrochemical oxidation of a silver anode in a solution of 1-MeImSH (0.190 g, 1.65 mmol) in acetonitrile (40 ml) at 23 V and 10 mA for 4 h caused 161 mg of silver to be dissolved, $E_f = 1.0$ mol F^{-1}. During the electrolysis process, hydrogen was evolved at the cathode and at the end of the reaction needles of a crystalline solid was observed at the bottom of the vessel. The solid was filtered off, washed with acetonitrile and ether, and dried under vacuum. *Anal.* Calc. for $C_4H_7AgN_2S$:

C, 21.5; H, 3.2; N, 12.6; S, 14.4. Found: C, 21.5; H, 3.2; N, 11.9; S, 14.4%. IR (KBr, cm^{-1}): 2900 w, 2840 w, 1500s, 1470 w, 1440 w, 1410 w, 1380 m, 1295 s, 1265 s, 1180 w, 1100 vs, 1000 w, 950 m, 630 m, 490 m, 420 w, 330 w.

2.3.6. [Ag(1-EtImS)]

1-EtImSH (0.190 g, 1.47 mmol) in acetonitrile (40 ml); 26 V; 10 mA; 3.5 h; 148 mg of silver dissolved, $E_f = 1.1$ mol F^{-1}. *Anal.* Calc. for $C_5H_9AgN_2S$: C, 25.3; H, 3.8; N, 11.8; S, 13.5. Found: C, 25.3; H, 3.8; N, 11.2; S, 13.4%. IR (KBr, cm^{-1}): 2960 m, 2910 m, 2850 m, 1500 vs, br, 1440 w, 1380 m, 1340 w, 1290 m, 1230 vs, br, 1115 s, 1070 m, 1020 w, 990 vw, 950 w, 790 w, 625 m, 500 m, 340 w. ^{1}H NMR ($CDCl_3$, ppm): 3.48–3.68 (m, 4H, H4, H5); 3.75 (t, 2H, CH_2), 1.16 (t, 3H, CH_3). FAB (*m/z*): $[Ag_4(1\text{-EtImS})_5\text{-}CH_3]^+$ 1063, $[Ag(1\text{-EtImS})_3]^+$ 711, $[Ag_2(1\text{-EtImS})_2]^+$ 474, $[Ag(1\text{-EtImS})_2]^+$ 367, $[Ag(1\text{-EtImS})]^+$ 237.

2.3.7. [Ag(1-PrImS)]

1-PrImSH (0.190 g, 1.30 mmol) in acetonitrile (50 ml); 25 V, 10 mA, 3.5 h; 146 mg of silver dissolved, $E_f = 1.0$ mol F^{-1}. *Anal.* Calc. for $C_6H_{11}AgN_2S$: C, 28.7; H, 4.4; N, 11.2; S, 12.8. Found: C, 28.0; H, 4.7; N, 10.5; S, 12.2%. IR (KBr, cm^{-1}): 2940 m, 2910 m, 2855 m, 1515 vs, 1550 m, 1395 m, 1370 w, 1290 m, 1270 m, 1240 m, 1205 s, 1115 s, 1005 m, 955 m, 890 w, 740 w, 625 m, 480 m, 440 w. ^{1}H NMR ($CDCl_3$, ppm): 3.34–3.68 (m, 4H, H4, H5); 3.72 (t, 2H, N-CH_2), 1.57 (m, 2H, C*H_2–CH_3), 0.91 (t, 3H, CH_3). FAB (*m/z*): $[Ag_4(1\text{-PrImS})_3]^+$ 861, $[Ag_3(1\text{-PrImS})_3]^+$ 754, $[Ag_2(1\text{-PrImS})_3]^+$ 647, $[Ag_3(1\text{-PrImS})_2]^+$ 609, $[Ag_2(1\text{-PrImS})_2]^+$ 502, $[Ag(1\text{-PrImS})_2]^+$ 395, $Ag_2(1\text{-PrImS})]^+$ 358, $[Ag(1\text{-PrImS})]^+$ 251, $[(1\text{-PrImS})]^+$ 143. Crystals suitable for X-ray studies were obtained directly from the cell.

2.3.8. [Ag(1-^{i}PrImS)]

1-^{i}PrImSH (0.193 g, 1.30 mmol) in acetonitrile (40 ml), 21 V, 10 mA, 2.5 h, 100 mg of silver dissolved, $E_f = 0.99$ mol F^{-1}. *Anal.* Calc. $C_6H_{11}AgN_2S$: C, 28.7; H, 4.4; N, 11.2; S, 12.8. Found: C, 28.7; H, 4.2; N, 11.0; S, 12.6%. IR (KBr, cm^{-1}): 2960 m, 2920 m, 2860 m, 1500 vs, br, 1440 m, 1390 s, 1360 m, 1295 s, 1250 vs, 1200 m, 1115 m, 1045 s, 1005 m, 960 m, 635 vw, 610 m, 525 m, 475 m, 425 w. ^{1}H NMR ($CDCl_3$, ppm): 3.51–3.89 (m, 4H, H4, H5); 4.60 (s, H, CH); 1.06 (s, 6H, CH_3). ^{13}C NMR ($CDCl_3$, ppm): 180.4 (C2), 43.5(C5), 42.4(C4), 47.4 (*CH-Pr), 19.9 (^{i}Pr). FAB (*m/z*): $[Ag_4(1\text{-}^i\text{PrImS})_4{}^+\text{-}CH_3]$ 986, $[Ag_4(1\text{-}^i\text{PrImS})_3]^+$ 860, $[Ag_3(1\text{-}^i\text{PrImS})_3]^+$ 753, $[Ag_2(1\text{-}^i\text{PrImS})_3]^+$ 649, $[Ag_3(1\text{-}^i\text{PrImS})_2]^+$ 609, $[Ag_2(1\text{-}^i\text{PrImS})_2]^+$ 503, $[Ag(1\text{-}^i\text{PrImS})_2]^+$ 395, $[Ag(1\text{-}^i\text{PrImS})]^+$ 251, $[1\text{-}^i\text{PrImS}]^+$ 143. Crystals suitable for X-ray studies were obtained directly from the cell.

2.4. X-ray crystallographic studies

Intensity data sets for all compounds were collected with the use of a Smart-CCD-1000 Bruker diffractometer (Mo Kα radiation, $\lambda = 0.71073$ Å) equipped with a grafite monochromator. All crystals were measured at 293 K. The ω scan technique was employed to measure intensities in all crystals. No decomposition of the crystals occurred during data collection. The intensities of all data sets were corrected for Lorentz and polarization effects. Absorption effects were corrected using the program SADABS [20]. The crystal structures of all compounds were solved by direct methods. Crystallographic programs used for structure solution and refinement were those of SHELX-97 [21]. Atomic scattering factors and anomalous-dispersion corrections for all atoms were taken from International Tables for X-ray Crystallography [22]. Missing atoms were located in the difference Fourier map and included in subsequent refinement cycles. The structures were refined by full-matrix least-squares refinement on F^2. Hydrogen atoms were placed geometrically with C–H distances of 0.96–0.97 Å and refined using a riding model with U_{iso} constrained at 1.2 (for non-methyl groups) and 1.5 (for methyl groups) times U_{eq} of the carrier C atom. For all structures non-hydrogen atoms were anisotropically refined, and in the last cycles of refinement a weighting scheme was used, where weights are calculated from the following formula $w = 1/[\sigma^2(F_o^2) + (aP)^2 + bP]$, where $P = (F_o^2 + 2F_c^2)/3$.

Due to the use of room-temperature data, the N-side chains of all compounds display high thermal disorder, specially the propyl groups of compound **3** and the isopropyl groups of compound **4**. Attempts to explain the disorder considering split positions affected convergence and were disregarded.

Table 1 summarizes pertinent details of the data collections and structure refinements, while Tables 2–5 lists important geometrical data for all compounds. Ortep3 [23] drawings with the numbering scheme used are shown in Figs. 1, 2, 5 and 6.

3. Results and discussion

The anodic oxidation of copper or silver in an electrochemical cell containing an acetonitrile solution of the ligand 1-RImSH gives complexes of formula [M(1-RImS)], in which M is Cu or Ag and 1-RImS represents the anionic form of the ligand.

The compounds are sparingly soluble in acetonitrile and they are therefore obtained directly from the cell as crystalline solids. In some cases the quality of the crystals obtained is suitable for X-ray diffraction studies. The complexes are partially soluble in various chlorinated solvents such as chloroform and

Table 1
Summary of crystal data and structure refinement

Identification code	[Cu(1-EtImS)] (**1**)	[Cu(1-PrImS)] (**2**)	[Ag(1-PrImS)] (**3**)	[Ag(1^{i}PrImS)] (**4**)
Empirical formula	$C_{10}H_{18}N_4S_2Cu_2$	$C_{12}H_{22}N_4S_2Cu_2$	$C_{36}H_{66}N_{12}S_6Ag_6$	$C_{36}H_{66}N_{12}S_6Ag_6$
Formula weight	385.48	413.54	1506.59	1506.59
Temperature (K)	293(2)	293(2)	293(2)	293(2)
Wavelength (Å)	0.71073	0.71073	0.71073	0.71073
Crystal system, space group	monoclinic, $C2/c$	monclinic, $C2/c$	triclinic, $P\bar{1}$	triclinic, $P\bar{1}$
Unit cell dimensions				
a (Å)	16.9794(4)	19.7292(2)	11.406(2)	11.4205(6)
b (Å)	11.8535(2)	11.9893(2)	13.986(3)	14.8021(8)
c (Å)	14.5482(3)	14.6157(2)	16.795(3)	16.5182(9)
α (°)	90	90	89.820(19)	90.941(1)
β (°)	104.124(1)	105.580(1)	84.156(11)	94.220(1)
γ (°)	90	90	81.466(16)	99.527(1)
Volume (Å^3)	2839.53(10)	3330.16(8)	2635.6(9)	2745.2(3)
Z, Calculated density (Mg/m^3)	8, 1.803	8, 1.650	2, 1.898 3	2, 1.823
Absorption coefficient (mm^{-1})	3.276	2.800	2.462	2.364
$F(000)$	1568	1696	1488	1488
Crystal size (mm)	$0.15\times0.10\times0.05$	$0.40\times0.30\times0.25$	$0.20\times0.15\times0.10$	$0.25\times0.15\times0.10$
θ Range for data collection (°)	2.12–28.33	2.01–28.30	1.22–23.25	1.24–23.25
Limiting indices	$-22\leqslant h\leqslant 21$	$-26\leqslant h\leqslant 26$	$-10\leqslant h\leqslant 12$	$-12\leqslant h\leqslant 12$
	$-11\leqslant k\leqslant 15$	$-15\leqslant k\leqslant 8$	$-15\leqslant k\leqslant 14$	$-10\leqslant k\leqslant 16$
	$-18\leqslant l\leqslant 19$	$-19\leqslant l\leqslant 19$	$-18\leqslant l\leqslant 17$	$-18\leqslant l\leqslant 18$
Reflections collected/unique [R_{int}]	9228/3487 [0.0539]	11 908/4114 [0.0358]	12 206/7465 [0.0627]	12 325/7775 [0.0670]
Completeness to θ max (%)	98.7	99.3	98.4	98.5
Data/restraints/parameters	3487/0/165	4114/0/183	7465/84/541	7775/0/541
Goodness-of-fit on F^2	1.039	1.022	0.857	1.001
Final R indices [$I>2\sigma(I)$]	$R_1=0.0517$	$R_1=0.0383$	$R_1=0.0469$	$R_1=0.0734$
	$wR_2=0.0964$	$wR_2=0.0838$	$wR_2=0.0878$	$wR_2=0.1522$
R indices (all data)	$R_1=0.1071$	$R_1=0.0683$	$R_1=0.1018$	$R_1=0.1289$
	$wR_2=0.1160$	$wR_2=0.0954$	$wR_2=0.1037$	$wR_2=0.1710$
Largest different peak and hole (e Å^{-3})	0.685 and −0.629	0.795 and −0.375	0.830 and −0.921	1.398 and −1.516

Table 2
Selected bond lengths [Å] and angles [°] for [Cu(1-EtImS)] (**1**)

Cu(1)–N(1)	1.982(4)	Cu(1)–S(2)#1	2.2488(14)
Cu(1)–S(1)#1	2.3132(16)	Cu(2)–N(3)	1.980(4)
Cu(2)–S(1)	2.2572(14)	Cu(2)–S(2)#1	2.3408(15)
S(1)–C(1)	1.759(5)	S(2)–C(6)	1.770(5)
N(1)–Cu(1)–S(2)#1	120.61(13)	N(1)–Cu(1)–S(1)#1	112.72(5)
S(2)*–Cu(1)–S(1)#1	126.59(5)	N(3)–Cu(2)–S(2)#1	111.93(12)
N(3)–Cu(2)–S(1)	119.78(12)	S(1)–Cu(2)–S(2)#1	128.19(5)

*Hydrogen bonds parameters for (**1**) (Å and °)*

D–H···A	d(D–H)	d(H···A)	d(D···A)	∠(DHA)
C7–H7a···S1#2	0.97	2.967	3.793	143.70
C7–H7a···Cg[a]	0.97	2.932	3.659	132.60
C10–H10c···S2#5	0.96	3.062	3.766	131.40
C10–H10b···Cg[b]	0.96	3.057	3.609	118.11

#1 = $-x$, y, $-z+1/2$.
Cg stand centroid of the double bond (a) C6#2=N3S#2; (b) C1#4=N1#4. Symmetry code: #2 = $-x$, $-y+1$, $-z+1$; #4 = $x-1/2$, $y+1/2$, z;

dichloromethane, which allows solution studies using techniques such as NMR spectroscopy; the low solubility of the compound in which R = Me precluded this type of study.

The electrochemical efficiency value – defined by the relationship between the number of moles of metal dissolved per mole of charge circulated through the cell – was around 1 mol F^{-1} in all cases. This fact, along with the evolution of hydrogen gas at the cathode, is consistent with the following reaction mechanism:

$$\text{Cathode}: \text{1-RImSH} + 1e^- \rightarrow 1/2H_2 + \text{1-RImS}^-$$

$$\text{Anode}: \text{1-RImS}^- + M \rightarrow [M(\text{1-RImS})] + 1e^-$$

M = Cu, Ag

Table 3
Selected bond lengths [Å] and angles [°] for [Cu(1-PrImS)] (**2**)

Cu(1)–N(1)	1.974(2)	Cu(1)–S(2)	2.2564(10)
Cu(1)–S(1)#1	2.3238(10)	Cu(2)–N(3)	1.978(3)
Cu(2)–S(1)#1	2.2472(9)	Cu(2)–S(2)#1	2.3074(10)
S(1)–C(1)	1.756(3)	S(2)–C(7)	1.752(3)
N(1)–Cu(1)–S(2)	118.71(8)	N(1)–Cu(1)–S(1)#1	112.94(8)
S(2)–Cu(1)–S(1)#1	128.21(3)	N(3)–Cu(2)–S(1)#1	120.37(9)
N(3)–Cu(2)–S(2)#1	113.98(9)	S(1)*–Cu(2)–S(2)#1	125.57(3)

*Hydrogen bonds parameters for (**2**) (Å and °)*

D–H···A	*d*(D–H)	*d*(H···A)	*d*(D···A)	∠(DHA)
C3–H3b···S2#2	0.97	3.022	3.787	136.69
C3–H3b···Cg[a]	0.97	2.836	3.595	135.71
C6–H6b···S1#5	0.96	3.012	3.734	133.06
C6–H6c···Cg[b]	0.96	2.817	3.646	145.17

#1 = $-x+1$, y, $-z+1/2$.
Cg stand centroid of the double bond (a) C1#2 = N1S#2; (b) C7#4 = N3#4. Symmetry codes: #2 = $-x+1$, $-y$, $-z$; #4 = $x+1/2$, $y-1/2$, z; #5 = $-x+3/2$, $y-1/2$, $-z-1/2$.

Table 4
Selected bond lengths [Å] and angles [°] for [Ag(1-PrImS)] (**3**)

Ag(1)–N(1)	2.235(7)	Ag(1)–S(2)	2.489(3)
Ag(1)–S(3)	2.497(3)	Ag(2)–N(3)	2.198(11)
Ag(2)–S(3)#1	2.484(3)	Ag(2)–S(1)	2.498(2)
Ag(3)–N(5)	2.221(8)	Ag(3)–S(2)#1	2.465(3)
Ag(3)–S(1)	2.521(3)	S(1)–C(1)	1.741(10)
S(2)–C(7)	1.742(11)	S(2)–Ag(3)#1	2.465(3)
S(3)–C(13)	1.754(9)	S(3)–Ag(2)#1	2.484(3)
Ag(4)–N(7)	2.255(8)	Ag(4)–S(5)	2.497(2)
Ag(4)–S(6)	2.503(3)	Ag(5)–N(9)	2.216(8)
Ag(5)–S(6)#2	2.469(2)	Ag(5)–S(4)	2.519(2)
Ag(6)–N(11)	2.231(8)	Ag(6)–S(5)#2	2.464(2)
Ag(6)–S(4)	2.542(3)	S(4)–C(19)	1.752(9)
S(5)–C(25)	1.755(12)	S(5)–Ag(6)#2	2.464(2)
S(6)–C(31)	1.740(9)	S(6)–Ag(5)#2	2.469(2)
N(1)–Ag(1)–S(2)	113.9(2)	N(1)–Ag(1)–S(3)	111.7(2)
S(2)–Ag(1)–S(3)	127.64(9)	N(3)–Ag(2)–S(3)#1	120.5(2)
N(3)–Ag(2)–S(1)	115.1(2)	S(3)#1–Ag(2)–S(1)	116.97(9)
N(5)–Ag(3)–S(2)#1	130.3(2)	N(5)–Ag(3)–S(1)	107.1(2)
S(2)#1–Ag(3)–S(1)	118.04(9)	N(9)–Ag(5)–S(6)#2	131.1(2)
N(9)–Ag(5)–S(4)	107.6(2)	S(6)#2–Ag(5)–S(4)	115.73(8)
N(11)–Ag(6)–S(5)#2	133.7(2)	N(11)–Ag(6)–S(4)	107.3(2)
S(5)#2–Ag(6)–S(4)	115.21(10)		

*Hydrogen bonds parameters for (**3**) (Å and °)*

D–H···A	*d*(D–H)	*d*(H···A)	*d*(D···A)	∠(DHA)
C15#3–H15b#3···N4	0.97	3.049	3.696	125.33
C15#3–H15a#3···Cg[a]	0.97	3.175	3.715	116.85
C30#2–H30c#2···N12#5	0.97	3.111	3.785	128.61
C26#2–H26b#2···Cg[b]	0.97	4.108	4.379	99.83
C27#2–H27a#2···Cg[c]	0.96	3.781	4.353	120.45

Symmetry transformations used to generate equivalent atoms: #1 $-x,-y+1,-z$ #2 $-x,-y,-z+1$.
Cg stand centroid of the double bond (a) C7=N3; (b) C25#3=N9#3, (c) C31#5=N11#5. Symmetry code: #2 = $-x$, $-y$, $-z+1$; #3 = $x-1$, y, z; #5 = $-x-1$, $-y$, $-z+1$.

Attempts were made to obtain mixed complexes that would incorporate an additional ligand in the coordination sphere of the metal. Depending on the nature of the metal ion in question, different phosphines were used as coligands and these were either monodentate (triphenylphosphine) or bidentate [bis(diphenylphosphino)methane (dppm) or 1,2-bis(diphenylphosphine)ethane (dppe)]. The addition of these new ligands to the electrochemical cell gave rise to complexes whose analytical data are consistent with the formula [M(RImS)], meaning that the

Table 5
Selected bond lengths [Å] and angles [°] for [Ag(1-^{i}PrImS)] (**4**)

Ag(1)–N(1)	2.234(11)	Ag(1)–S(2)	2.496(4)
Ag(1)–S(3)	2.504(4)	Ag(2)–N(3)	2.225(12)
Ag(2)–S(3)#1	2.481(4)	Ag(2)–S(1)	2.510(4)
Ag(3)–N(5)	2.218(11)	Ag(3)–S(2)#1	2.470(4)
Ag(3)–S(1)	2.525(4)	S(1)–C(1)	1.752(14)
S(2)–C(7)	1.757(14)	S(2)–Ag(3)#1	2.470(4)
S(3)–C(13)	1.747(16)	S(3)–Ag(2)#1	2.481(4)
Ag(4)–N(7)	2.232(12)	Ag(4)–S(5)	2.489(4)
Ag(4)–S(6)	2.490(4)	Ag(5)–N(9)	2.250(12)
Ag(5)–S(6)#2	2.474(3)	Ag(5)–S(4)	2.521(4)
Ag(6)–N(11)	2.214(12)	Ag(6)–S(5)#2	2.459(4)
Ag(6)–S(4)	2.526(4)	S(4)–C(19)	1.749(15)
S(5)–C(25)	1.738(17)	S(5)–Ag(6)#2	2.459(4)
S(6)–C(31)	1.757(14)	S(6)–Ag(5)#2	2.474(3)
N(1)–Ag(1)–S(2)	113.9(3)	N(1)–Ag(1)–S(3)	111.6(3)
S(2)–Ag(1)–S(3)	127.48(12)	N(3)–Ag(2)–S(3)#1	125.6(3)
N(3)–Ag(2)–S(1)	111.5(4)	S(3)#1–Ag(2)–S(1)	116.45(13)
N(5)–Ag(3)–S(2)#1	130.9(3)	N(5)–Ag(3)–S(1)	106.7(3)
S(2)#1–Ag(3)–S(1)	117.58(12)	N(7)–Ag(4)–S(5)	115.1(3)
N(7)–Ag(4)–S(6)	114.6(3)	S(5)–Ag(4)–S(6)	123.66(13)
N(9)–Ag(5)–S(6)#2	128.3(3)	N(9)–Ag(5)–S(4)	109.5(3)
S(6)#2–Ag(5)–S(4)	116.64(14)	N(11)–Ag(6)–S(5)#2	127.2(3)
N(11)–Ag(6)–S(4)	111.3(3)	S(5)#2–Ag(6)–S(4)	115.86(13)

*Hydrogen bonds parameters for (**4**) (A and °)*

D–H···A	*d*(D–H)	*d*(H···A)	*d*(D···A)	∠(DHA)
C15#3–H15b#3···N4	0.97	3.174	3.884	131.40
C15#3–H15a#3···Cg[a]	0.97	3.164	3.646	112.37
C30#2–H30c#2···N12#5	0.96	3.043	4.000	174.43
C26#2–H26b#2···Cg[b]	0.97	2.904	3.737	144.67
C27#2–H27a#2···Cg[c]	0.97	2.943	3.670	132.66

Symmetry transformations used to generate equivalent atoms: #1 $-x+2,-y,-z$ #2 $-x+2,-y+1,-z-1$.
Cg stand centroid of the double bond (a) C7=N3; (b) C25#3=N9#3. Symmetry codes: #2 = $-x+2$, $-y+1$, $-z-1$; #3 = $x+1$, y, z; #5 = $-x+3$, $-y+1$, $-z-1$.

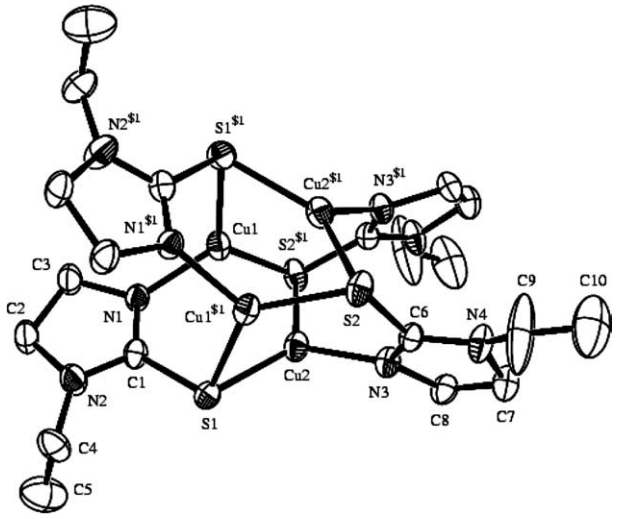


Fig. 1. ORTEP drawing of the molecular structure of [Cu(1-EtImS)] (**1**) showing 40% probability ellipsoids.

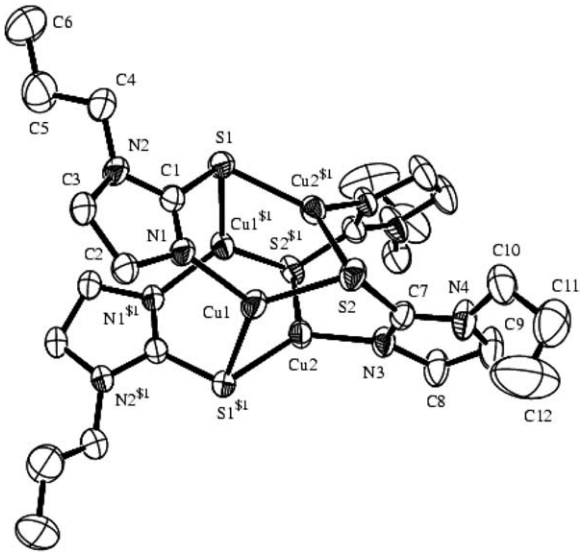


Fig. 2. ORTEP drawing of the molecular structure of [Cu(1-PrImS)] (**2**) showing 40% probability ellipsoids.

phosphine ligand was not incorporated within the coordination sphere. The lack of solubility of these species and their rapid precipitation from the reaction solution could impede the incorporation of the phosphine. For this reason, attempts were made to react the complexes, which had previously been obtained electrochemically, with the appropriate phosphine under reflux in a suitable

solvent. Unfortunately, this approach did not give the desired results. This behavior is in marked contrast to that observed when similar reactions are carried out on silver and copper complexes of pyridine and pyrimidine-2-thionates, which give rise to dinuclear compounds with stoichiometries such as $[Cu_2(6\text{-}^t\text{BuM}E_2\text{SipyS})_2(\text{dppm})_2]$ [24], $[Cu_2(3\text{-M}E_3\text{SipyS})_2(\text{dppe})_3]$ [25], or $[Ag_2\{4,6\text{-(Ph, Me)pymS}\}_2(\text{dppe})_2]$ [26].

The IR spectra of the complexes confirm the presence of the ligands coordinated to the metal. The band attributable to ν(N–H), which appears at 3200–3180 cm^{-1} in the free ligands, is absent in the spectra of the complexes – indicating that in the complexes the ligands are in the deprotonated form. This situation is confirmed by the disappearance of the Δ(N–H) bending band, which in the free ligands is observed in the range 600–670 cm^{-1}. In addition, the ν(C–S) bands of the free ligands, which appear between 520 and 510 cm^{-1}, are shifted to lower wavenumbers in the complexes (500 and 475 cm^{-1}) with respect to the free ligands. This shift is consistent with a decrease in the order of the (C–S) bond due to coordination with the metal.

The ^{1}H NMR spectra of the complexes do not contain a signal for the NH proton, which in the free ligands appears in the range 6.0–6.5 ppm, and this is the result of deprotonation of the ligand. The spectra of the different complexes show signals for all of the ring protons and these appear in the range 3.3–3.7 ppm. Signals due to the R groups appear at higher field in the complexes than in the ligands.

The ^{13}C NMR spectrum could only be recorded for $[Ag(1\text{-}^i\text{PrImS})]_6$ due to the low solubility of the other compounds. However, this spectrum shows all of the expected signals and the main change observed is the shift in the C_2 signal, which is at higher field than that in the free ligand. This is probably due to the reduction in the order of the C–S bond [27]. This finding again provides evidence that the thionato form of the ligand predominates in the complex.

The FAB spectrum of [Cu(1-PrImS)] shows a peak at m/z 826, due to the molecular ion of the tetrameric species $[Cu_4(1\text{-PrImS})_4]^+$, with the appropriate isotope distribution, a peak at m/z 683, corresponding to $[Cu_4(1\text{-PrImS})_3]^+$, which is formed by the loss of one ligand from the tetrameric species, along with other peaks at m/z 620, 477, 413, and 267 corresponding to different fragments of the tetrameric compound, $[Cu_3(1\text{-PrImS})_3]^+$, $[Cu_3(1\text{-PrImS})_2]^+$, $[Cu_2(1\text{-PrImS})_2]^+$ and $[Cu_2(1\text{-PrImS})]^+$, respectively. In the case of $[Cu_4(1\text{-EtImS})_4]$, the FAB spectrum does not show the molecular ion peak but does show a peak associated with $[Cu(1\text{-EtImS})]^+$ at $m/z = 191$ as well as peaks due to the fragments $[Cu_4(1\text{-EtImS})_3]^+$, $[Cu_3(1\text{-EtImS})_2]^+$ and $[Cu_2(1\text{-EtImS})_2]^+$, at $m/z = 642$, 447 and 382, respectively.

The FAB mass spectra of the silver complexes [Ag(1-PrImS)] and $[Ag(1\text{-}^i\text{PrImS})]$ do not show molecular ion peaks, $[Ag_6(1\text{-RImS})_6]$, but do contain peaks that can be assigned to fragments of these molecular ions. For example, the spectrum of $[Ag_6(1\text{-}^i\text{PrImS})_6]$ contains a peak corresponding to the tetrameric species with the loss of a methyl group, $[Ag_4(1\text{-}^i\text{PrImS})_4\text{-CH}_3]$ at $m/z = 989$. In both cases peaks are also observed at $m/z = 860$, 753, 609, 502, 395 and 251, and these can be assigned to the fragments $[Ag_4(1\text{-RImS})_3]^+$, $[Ag_4(1\text{-RImS})_3]^+$, $[Ag_3(1\text{-RImS})_2]^+$, $[Ag_2(1\text{-RImS})_2]^+$, $[Ag(1\text{-RImS})_2]^+$ and $[Ag(1\text{-RImS})]^+$, respectively. As in the copper complexes, the peak clusters have the appropriate isotope distribution.

The complexes [Cu(1-EtImS)] (**1**), [Cu(1-PrImS)] (**2**), [Ag(1-PrImS)] (**3**) and $[Ag(1\text{-}^i\text{PrImS})]$ (**4**) were studied by X-ray diffraction.

3.1. Crystal and molecular structures of [Cu(1-EtImS)] (1) and [Cu(1-PrImS)] (2)

The structures of **1** and **2** are shown in Figs. 1 and 2, respectively. Crystallographic data are shown in Tables 1–3 along with bond distances and angles.

The two compounds are isostructural, with four molecules per unit cell. The compounds consist of neutral tetrameric units formed by four copper atoms and four *N*-alkyl-2-mercaptoimidazolidine ligands, which are related in a pairwise manner by a two-fold rotation axis. In this arrangement the four imidazolidine rings in each unit (which are essentially planar) are disposed in two groups that are practically perpendicular to one another. The copper atoms are arranged in a distorted tetrahedral disposition; the Cu–Cu distances are in the range 2.6288(9)–2.9908(13) Å in **1** and 2.6338(6)–3.0219(8) Å in **2**. These distances are longer than those found in the elemental copper itself (2.40 Å) [28] and are not consistent with the existence of interactions between the metal centers. Each ligand is bonded to three copper centers – two through a sulfur atom that acts as a bridge and the other through the nitrogen atom. In this way the ligand is located above the center of each of the four faces of the tetrahedron formed by the metal atoms, acting as a μ^2-N,S(η^2-S; η^1-N) triple bridge and a five-electron donor. The environment of each of the metal atoms is distorted trigonal $[CuS_2N]$ with each of the donor atoms belonging to a different ligand. The angles around the metal (see Tables 2 and 3) are clearly different and are far from the theoretical value of 120° expected for a regular geometry. On the other hand, the metal atom is slightly out of the plane that contains the three donor atoms, with distances to these planes in the range 0.03–0.05 Å.

The bond distances between the bridging sulfur and the two metal centers are slightly different to those between the metal and fully bonded sulfur. This gives rise

to a situation where there is an asymmetric bridge, with distances between 2.2472(9) and 2.2572(14) Å for the shortest and 2.3074(10) and 2.3408(15) Å for the longest distance. However, it should be noted that none of these distances are significantly different to the average Cu–S bond distances [29–31] found in other complexes with heterocyclic thiones – with a trigonal geometry around each metal center. The Cu–N distances, average value of 1.981(4) Å for **1** and 1.976(3) Å for **2**, are also similar to those found in the complexes mentioned above; e.g., that found in the copper complex with the ligand 1-methylimidazol-2-thione [32], which has an average Cu–N distance of 1.985(3) Å. The S–C bond distances, which have average values of 1.765(5) Å for **1** and 1.754(3) Å for **2**, are very similar to those found in other complexes with heterocyclic thiones in which the ligand is coordinated to the metal in its thiolate form [33].

The crystal packing of **1**, see Figs. 3 and 4, shows that each unit interacts with other units through non-classic hydrogen bonds. One of the hydrogens on C7 in each of the imidazolidine ligands L2 (N3, N4, C6–C10) is involved in a bifurcated intermolecular hydrogen bond (Fig. 3) [34]; one of the interactions is of the C–H···S type [35,36] and the other is C–H···π [37–39] with the double bond C6#2═N3#2 belonging to a ligand that is equivalent by symmetry. These interactions are established along the crystallographic *c* axis. For symmetry reasons, carbon atom C7#1 of the ligand L2#1 forms the same interaction with another neighboring complex molecule and these are also along the *c* axis (see Fig. 3).

It can be seen from Fig. 4 that, besides the interactions discussed above, one of the hydrogen atoms of the methyl group (C10) in each of the imidazolidine ligands involved in the aforementioned interactions also establishes an intermolecular C–H···S hydrogen-bonding interaction. Another of the hydrogen atoms from the same methyl group forms a C–H···π interaction

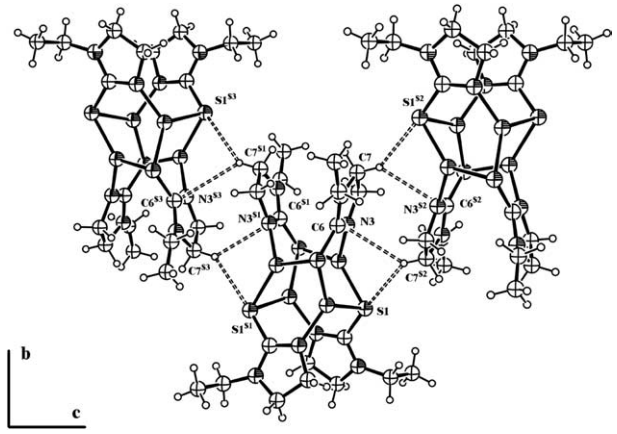


Fig. 3. The crystal packing of **1**, viewed along the *a* axis. Dashed lines show the C–H···π and the C–H···S interactions. [Symmetry codes: #1 = $-x$, y, $-z+1/2$; #2 = $-x$, $-y+1$, $-z+1$; #3 = x, $-y+1$, $z-1/2$.]

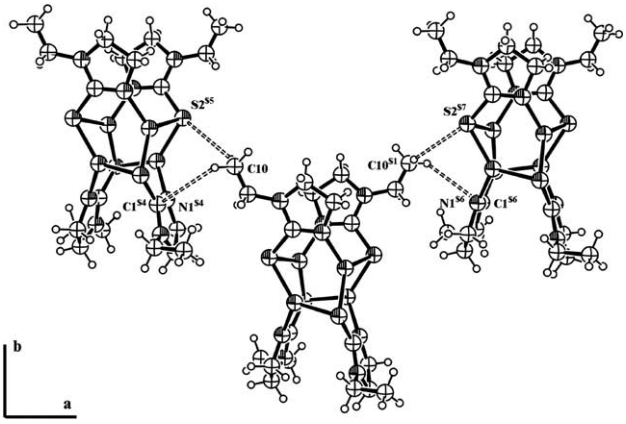


Fig. 4. The crystal packing of **1**, viewed along the *c* axis. Dashed lines show the C–H···π and the C–H···S interactions. [Symmetry codes: #1 = $-x, y, -z+1/2$; #4 = $x-1/2, y+1/2, z$; #5 = $-x-1/2, y+1/2, -z+1/2$; #6 = $-x+1/2, y+1/2, -z+1/2$; #7 = $x+1/2, y+1/2, z$.]

with the double bond C1#4═N1#4 belonging to a non-equivalent ligand from a neighboring tetrameric unit. These interactions are established along the crystallographic *a* axis, i.e., perpendicular to the interactions discussed above. In a similar way, the carbon atom C10#1 from the equivalent ligand L2#2 in the same tetramer also forms the same interactions along the *a* axis, as can be seen in Fig. 4.

The crystal packing of compound **2** [Cu(1-PrImS)] also shows these types of interactions along the *c* and *a* axes. In this case, however, the interactions involve the methyl group on the *N*-propyl unit rather than the ethyl group as in **1**. Given that the propyl is larger than the ethyl group and that the interactions in which they are involved are directed along the *a* axis, the tetrameric units along this axis are separated by a greater distance in complex **2** than in **1**. This situation is reflected in the crystal cell parameters of the two compounds (Table 1), which are very similar apart from the *a* parameter [16.9794(4) Å in compound **1** and 19.7292(2) Å in compound **2**].

3.2. Crystal and molecular structure of [Ag(1-PrImS)] (**3**) and [Ag(1-^{i}PrImS)] (**4**)

The crystal structures of compounds **3** and **4** are shown in Figs. 3 and 4, respectively. Crystallographic data and bond distances and angles are given in Tables 1, 4 and 5, respectively.

The two complexes are isostructural and both consist of hexameric units with the six silver atoms located at the vertices of a highly distorted octahedron. The unit cell contains two different complex molecules and each of these has a center of symmetry located at the center of the Ag_6S_6 unit. The differences between the two units for each of the complexes arise due to the disposition of

the *N*-alkyl chain (propyl for **3** and isopropyl for **4**) (see Figs. 5 and 6).

The distances between the silver atoms are in the range 2.9508–3.3335 Å and, although the shortest values are not significantly different to those found in metallic silver (2.88 Å) [40], the absence of interactions between the metal centers can be deduced.

Each of the thiolate ligands is bonded to three different metal centers, which define one of the faces of the octahedron. These ligands are bound through their nitrogen and sulfur atoms, with the sulfur acting as a bridge between two metals in a μ^2-N,S(η^2-S; η^1-N) five-electron donor system. On the other hand, each silver atom is bonded to the sulfur atoms from two ligands and the nitrogen atom of a third ligand. The geometry is distorted trigonal [AgS_2N] and the silver atoms are markedly displaced from the plane containing the donor atoms, with out-of-plane distances of between 0.3864 and 0.2945 Å.

The Ag–S [2.459(4)–2.542(3) Å] and Ag–N [2.198(11)–2.255(8) Å] bond distances are very similar to those found in other silver complexes with heterocyclic thione derivatives with a trigonal geometry around the metal center [31,41]. The average S–C bond distances are 1.747 Å for **3** and 1.750 Å for **4**, and these indicate that the ligand is coordinated to the metal in the thiolate form [33].

An alternative way to describe this structure is to consider it as a *paddlewheel* whose center consists of the two Ag_6S_6 rings and the six paddles are the ligand fragments that act as bridges between the two Ag_6S_6 rings. The paddles are not arranged in a uniform way around the wheel, as shown by the angles between each pair of imidazolidine ligands. This arrangement means that in each hexamer there are two larger 'holes' and within these 'holes' the weak interactions between hexamers arise that determine the crystal packing. The crystal packing arrangements in compounds **3** and **4** involve weak interactions between one unit and another that is equivalent by symmetry. Interactions do not occur between non-equivalent units.

It can be seen in Fig. 7 that one of the hydrogen atoms on C15 is involved in a C–H···N hydrogen bond [42,43] and the other hydrogen forms a C–H···π interaction with the C7=N3 double bond belonging to a symmetry equivalent ligand of a unit 1 neighbor. For symmetry reasons, the equivalent carbon C15#1 is involved in the same type of interactions and this situation causes these units to pack parallel to the crystallographic *a* axis, as can be seen in Fig. 7.

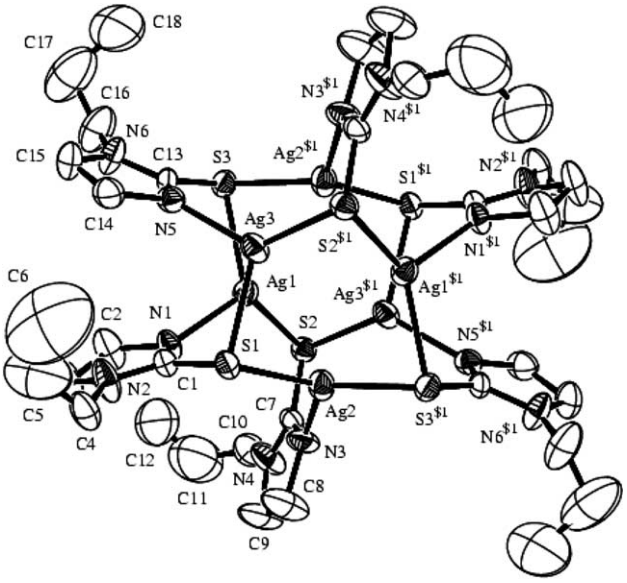


Fig. 5. ORTEP drawing of the molecular structure of [Ag(1-PrImS)] (**3**) showing 30% probability ellipsoids.

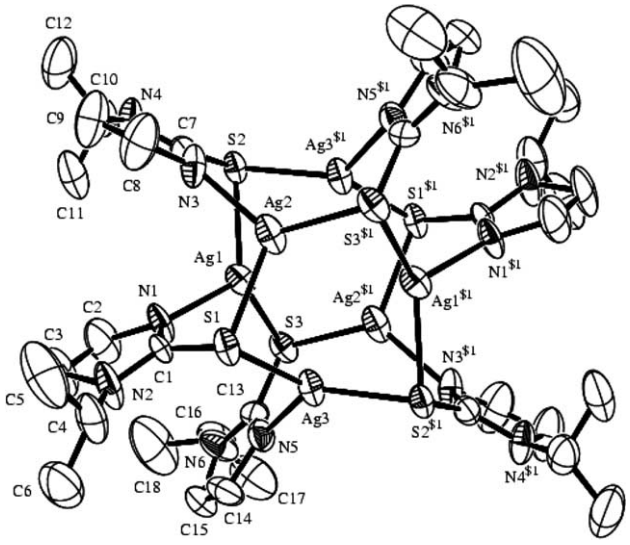


Fig. 6. ORTEP drawing of the molecular structure of [Ag(1-^{i}PrImS)] (**4**) showing 40% probability ellipsoids.

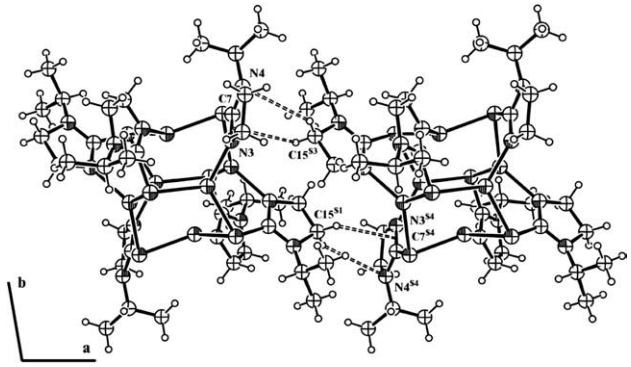


Fig. 7. Interaction between units 1 in the crystal packing of **4**, viewed along the *c* axis. Dashed lines show the C–H···π and the C–H···N interactions. [Symmetry codes: #1 = $-x+2$, $-y$, $-z$; #3 = $x+1$, y, z; #4 = $-x+3$, $-y$, $-z$.]

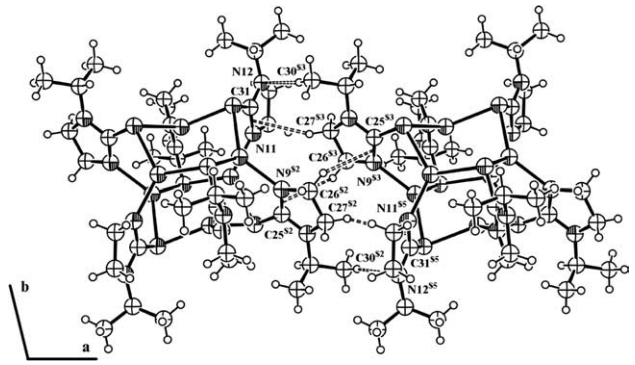


Fig. 8. Interaction between units 2 in the crystal packing of **4**, viewed along the *c* axis. Dashed lines show the C–H···π and the C–H···N interactions. [Symmetry codes: #2 = $-x+2$, $-y+1$, $-z+1$; #3 = $x+1$, y, z; #5 = $-x+3$, $-y+1$, $-z+1$.]

The interactions between units 2 in compound **4** are represented in Fig. 8. The different dispositions of the *N*-alkyl chains in compounds **3** and **4** do not have a significant impact on the packing arrangement, although a slight change in the distances between neighboring hexamers is evident. These differences are also apparent in the interaction parameters and give rise to other new interactions. As shown in Fig. 8, the significant interactions are C–H···π between a hydrogen on C27 and the C31=N11 double bond of a hexameric unit 2 neighbor (analogous to the interaction between C15 and C7=N3 for units 1) and the interaction between a hydrogen on C26 and the C25=N9 double bond of a unit 2 neighbor (analogous to the interactions between C14 and C13=N5 for units 1 – although in this case the distance was to long to be considered). The different disposition of the N-^{i}propyl chain in compound **4** means that the C–H···N interaction in units 1 between a carbon in the imidazolidine ring (C15) and the *N*-alkyl nitrogen (N4) is, in this case, established between a hydrogen of a methyl of the ^{i}propyl group (C30) and the *N*-alkyl nitrogen (denoted in unit 2 as N12).

In a similar way to the arrangement for units 1, the equivalent carbons C26#2, C27#2 and C30#2 are involved in the same types of interaction for symmetry reasons. This causes units 2 to pack parallel to the crystallographic *a* axis, as shown in Fig. 8.

4. Supplementary material

Crystallographic data for the structures reported in this paper have been deposited at the Cambridge Crystallographic Data Centre as supplementary publication numbers CCDC-270945-270948 for (**1**)–(**4**). Copies of the data can be obtained free of charge on application to CCDC, 12 Union Road, Cambridge CB2 1EZ, UK (fax: (internat.) +44-1223/336-033; e-mail: deposit@ccdc.cam.ac.uk).

Acknowledgments

We thank the Ministerio de Educación y Cultura of Spain (BQU2002-01819) and the Xunta de Galicia (PGIDT00PXI20305PR) for financial support.

References

[1] B. Krebs, G. Henkel, Angew. Chem. Int. Ed. Engl. 30 (1991) 769.
[2] W.H. Armstrong, in: L. QueJr. (Ed.), Metal Clusters in Proteins, ACS, 1988, p. 1.
[3] R.H. Holm, E.I. Solomon, Chem. Rev. (1996) 96.
[4] M. Bochmann, Chem. Vapor Depos. 2 (1996) 85.
[5] J.A. García-Vázquez, J. Romero, A. Sousa, Coord. Chem. Rev. 193–195 (1999) 691–745.
[6] P.D. Akivos, Coord. Chem. Rev. 181–210 (2001) 213.
[7] L.P. Battaglia, A.B. Corradi, M. Nardelli, Croat. Chim. Acta 57 (1984) 5215.
[8] E.R. Atkinson, D.J. Gardiner, A.R.W. Jackson, E.S. Raper, Inorg. Chim. Acta 98 (1985) 35.
[9] J.R. Creighton, D.J. Gardiner, A.C. Gorvin, C. Gutteridge, A.R.W. Jackson, E.S. Raper, P.M.A. Sherwood, Inorg. Chim. Acta 103 (1985) 195.
[10] E.S. Raper, J.R. Creighton, J.D. Wilson, W. Clegg, A. Milne, Inorg. Chim. Acta 155 (1989) 77.
[11] E.S. Raper, J.R. Creighton, J.D. Wilson, W. Clegg, A. Milne, Inorg. Chim. Acta 155 (1989) 85.
[12] E. Raper, J.D. Wilson, W. Clegg, Inorg. Chim. Acta 194 (1992) 51.
[13] S. Ramaprabhu, E.A.C. Lucken, G. Bernardinelli, J. Chem. Soc., Dalton Trans. 1185 (1993).
[14] S. Ramaprabhu, E.A.C. Lucken, G. Bernardinelli, J. Chem. Soc., Dalton Trans. 115 (1995).
[15] A.A. Isab, S. Ahmad, M. Arab, Polyhedron 21 (2002) 1267.
[16] A.A. Isab, Transit. Met. Chem. 17 (1992) 374.
[17] F.B. Stocker, D. Britton, V.G. Young, Inorg. Chem. 39 (2000) 3479.
[18] C.F.H. Allen, C.O. Eden, J. Van Allen, Organic Synthesis, Coll. Vol. III, Wiley, New York, 1959, p. 394, 1959.
[19] D.G. Tuck, Pure Appl. Chem. 51 (1979) 2005.
[20] G.M. Sheldrick, SADABS: Program for absorption correction using area detector data, University of Göttingen, Germany, 1996.
[21] SHELX-97 [Includes SHELXS-97, SHELXL-97, CIFTAB] – Programs for Crystal Structure Analysis (Release 97-2). G.M. Sheldrick, Institüt für Anorganische Chemie der Universität, Tammanstrasse 4, D-3400 Göttingen, Germany, 1998.
[22] International tables vol. C – A.J.C. Wilson (Ed.), International Tables for Crystallography, Kluwer Academic Publishers, Dordrecht, The Netherlands, 1995.
[23] ORTEP3 for Windows – L.J. Farrugia, J. Appl. Cryst. 30 (1997) 565.
[24] P. Pérez-Lourido, J. Romero, J.A. García-Vázquez, M.L. Louro, A. Sousa, J. Zubieta, Inorg. Chim. Acta 271 (1998) 1.
[25] R. Castro, J. Romero, J.A. García-Vázquez, A. Sousa, Y.D. Yanng, J. Zubieta, Inorg. Chim. Acta 345 (1996) 119.
[26] A. Rodríguez, Tésis Doctoral, Universidad de Santiago de Compostela, Spain, 2002.
[27] J.-M. Bret, P. Castan, G. Commenges, J.-P. Laurent, Polyhedron 2 (1983) 901.
[28] F.A. Cotton, G. Wilkinson, C.A. Murillo, M. Bochmann, Advances Inorganic Chemistry, sixth ed., Wiley, New York, 1999, p. 861.
[29] S. Kitagawa, M. Munakata, H. Shimono, S. Matsuyama, H. Masuda, J. Chem. Soc. Dalton Trans. (1990) 2105.

[30] R. Castro, M.L. Durán, J.A. García-Vázquez, J. Romero, A. Sousa, E.E. Castellano, J. Chem. Soc. Dalton Trans. (1992) 2559.
[31] E. Block, M. Gernon, H. Kang, J. Zubieta, Angew. Chem. Int. Ed. Engl. 27 (1988) 1342.
[32] E.S. Raper, J.R. Creighton, W. Clegg, Inorg. Chim. Acta 183 (1991) 179.
[33] J.A. García-Vázquez, J. Romero, A. Sousa-Pedrares, M. Louro, A. Sousa, J. Zubieta, J. Chem. Soc., Dalton Trans. (2000) 559, and references therein.
[34] T. Steiner, Angew. Chem. Int. Ed. Engl. 41 (2002) 48.
[35] Q.B. Song, Y.Z. Li, Y.M. Liang, Y.X. Ma, Acta Cryst. E 59 (2003) m861.
[36] D.M. Hatch, W.F. Wacholtz, J.T. Mague, Acta Cryst. C59 (2003) m452.
[37] C. Janiak, T.G. Scharmann, Polyhedron 22 (2003) 1123.
[38] S. Venkatraman, V.G. Anand, V. PrabhuRaja, H. Rath, J. Sankar, T.K. Chandrashekar, W. Teng, K. Ruhlandt, Chem. Commun. (2002) 1660.
[39] G. Mehta, G. Vanessa, K. Islam, K. Venkatesan, Acta Cryst. C 60 (2004) 90.
[40] N.N. Greenwood, A. Earnshaw, Chemistry of the Elements, Pergamon, Oxford, UK, 1989, p. 1368.
[41] P. Pérez Lourido, J.A. García-Vázquez, J. Romero, M. Louro, A. Sousa, Q. Chem, Y. Chang, J. Zubieta, J. Chem. Soc., Dalton Trans. (1996) 2047.
[42] F. Tuna, J. Hamblin, G. Clarkson, W. Errington, N.W. Alcock, M.J. Hannon, Chem. Eur. J. 8 (2002) 4957.
[43] M. Mazik, D. Bläser, R. Boese, Tetrahedron 57 (2001) 5791.

compound (−)-DIOP, construct higher nuclearity linked clusters and potential asymmetric hydrogenation catalysts, Herein, we report the synthesis and characterization of four new Ru–Co mixed-metal linked tetrahedral clusters, $[(\mu_3\text{-E})RuCo_2(CO)_8]_2$((−)-DIOP) (E = Se, **1**; S, **2**), $[(\mu_3\text{-E})RuCoMo(CO)_7(CpC(O)CH_3)]_2$((−)-DIOP) (E = Se, **3**, S, **4**) and a mono-tetrahedral cluster $[(\mu_3\text{-Se})RuCoMo(CO)_6(CpC(O)CH_3)$((−)-DIOP)] (**5**), which was obtained by the reaction of **1** with $Na[Mo(CO)_3(\eta^5\text{-}C_5H_4C(O)CH_3)]$ at 60 °C. The structure of cluster **1** has been determined by single-crystal X-ray diffraction. All clusters were characterized by C, H elemental analysis, IR and ^{1}H NMR spectroscopy. To further confirm the structures of these cluster products, the clusters **1**, **2**, **4**, **5** also were characterized by ^{31}P NMR spectroscopy.

2. Experimental

2.1. General details

All preparative work was carried out under an atmosphere of pure nitrogen by using standard Schlenk or vacuum-line techniques. Solvents were carefully dried: *n*-hexane, petroleum ether (60–90 °C) and THF were dried and deoxygenated by distillation from sodium benzophenone ketyl, and dichloromethane was distilled from calcium hydride. Chromatographic separations were carried out using silica gel columns (160–200 mesh) of varying length. Thin-layer chromatography (TLC) was performed on commercial Merck plates coated with a 0.20 mm layer of silica gel.

Infrared spectra were recorded in NaCl cells on a Bruker 120 HR FT-IR spectrophotometer. Absorptions are designated in cm^{-1} relative to an internal laser standard. Spectra of compounds in the solid state were recorded as pressed KBr discs. NMR spectra were measured on a Bruker AM-400 MHz spectrometer in chloroform-d_1 solvent. All ^{1}H NMR chemical shifts are relative to tetramethylsilane. ^{31}P NMR positive chemical shifts are downfield from 85% H_3PO_4 as external reference. Elemental analyses (C, H) were performed on a Carlo-Erba 1106 type analyzer.

$(\mu_3\text{-E})RuCo_2(CO)_9$ (E = S, Se) [24], $[(\mu_3\text{-E})RuCoMo(CO)_8(CpC(O)CH_3)]$ (E = S, Se) [25,26], $Na[Mo(CO)_3(\eta^5\text{-}C_5H_4COCH_3)]$ [27] were prepared according to literature method with little modification and (−)-DIOP was commercial sample.

2.2. Synthesis of cluster *1* and *2*

To a solution of $(\mu_3\text{-Se})RuCo_2(CO)_9$ (166 mg, 0.30 mmol) in 20 ml of *n*-hexane at room temperature was added dropwise a solution of (−)-DIOP (75 mg, 0.15 mmol) in 5 ml of CH_2Cl_2 under nitrogen. The mixture was stirred at room temperature for 2 h. During the stirring the color of the solution gradually changed from brown-red to black-red and monitoring by TLC showed the disappearance of the starting material. After hexane was removed, the residue was extracted by a small amount of CH_2Cl_2 and transferred to the top of a 2.5×40 cm silica gel chromatography column. Elution with CH_2Cl_2:petroleum ether (1:3) afforded the major brown-red band. Condensing the solvent and crystallization at −20 °C gave black crystals $[(\mu_3\text{-Se})RuCo_2(CO)_8]_2$((−)-DIOP) (**1**) (210 mg, 90.8%, based on (−)-DIOP). *Anal*. Calc. for $[C_{47}H_{32}O_{18}Se_2P_2Co_4Ru_2]$: C, 36.60; H, 2.09. Found: C, 36.67; H, 2.02%. IR (KBr disc): *ν*(Ar–H) 3054w; *ν*(CO) 2084s, 2051vs, 2011vs, 1964s, 1872m cm^{-1}; ^{1}H NMR: *δ* 7.64–7.12 (m, 20H, $4C_6H_5$), 3.93–3.83 (d, 2H, 2CH), 2.62–2.37 (m, 4H, $2CH_2$), 1.27 (s, 6H, $2CH_3$). ^{31}P NMR: *δ* 53.21 (s, PCo), 52.04 (s, PCo).

The preparation procedure for cluster **2** was similar to that of cluster **1**.

$[(\mu_3\text{-S})RuCo_2(CO)_8]_2$((−)-DIOP) (**2**) (195 mg, 89.7%. based on (−)-DIOP). *Anal*. Calc. for $[C_{47}H_{32}O_{18}S_2P_2Co_4Ru_2]$: C, 38.97; H, 2.23. Found: C, 39.12; H, 2.35%. IR (cm^{-1}): *ν*(Ar–H) 3058w; *ν*(CO) 2085(s), 2047(vs), 2012(vs), 1881(m). ^{1}H NMR: *δ* 7.67–7.38 (m, 20H, $4C_6H_5$), 3.97–3.81 (m, 2H, 2CH), 2.68–2.37 (m, 4H, $2CH_2$), 1.28 (s, 6H, $2CH_3$).^{31}P NMR: *δ* 50.46 (s, PCo), 48.83 (s, PCo).

2.3. Synthesis of cluster *3* and *4*

$(\mu_3\text{-Se})RuCoMo(CO)_8(CpC(O)CH_3)$ (200 mg, 0.30 m mol) reacted with (−)-DIOP (75 mg, 0.15 mmol) in 25 ml of CH_2Cl_2:*n*-hexane (1:1) at room temperature for 6 h with stirring. Removal of the solvent under reduced pressure and the residue was purified by chromatography on silica gel using THF/petroleum ether (2:5) as an eluent and gave the major black-red band $[(\mu_3\text{-Se})RuCoMo(CO)_7(CpC(O)CH_3)]_2$((−)-DIOP) (**3**) (116 mg, 43.6%, based on (−)-DIOP). *Anal*. Calc. for $[C_{59}H_{46}O_{18}Se_2P_2Co_2Mo_2Ru_2]$: C, 39.93; H, 2.61. Found: C, 40.12; H, 2.58%. IR (cm^{-1}): *ν*(Ar–H) 3056w; *ν*(CO) 2066s, 1997vs, 1964vs, 1887m, 1801m; *ν*(C=O) 1680m. ^{1}H NMR: *δ* 7.61–6.98 (m, 20H, $4C_6H_5$), 5.83–5.00 (m, 8H, $2C_5H_4$), 3.75–3.58 (m, 2H, 2CH), 2.58–2.15 (m, 10H, $2CH_2$, $2CH_3$), 1.25 (s, 6H, $2CH_3$).

In the same manner, the cluster **4** was prepared.

$[(\mu_3\text{-S})RuCoMo(CO)_7(CpC(O)CH_3)]_2$((−)-DIOP) (**4**) (128 mg, 50.8%, based on (−)-DIOP). *Anal*. Calc. for $[C_{59}H_{46}O_{18}S_2P_2Co_2Mo_2Ru_2]$: C, 42.16; H, 2.76. Found: C, 42.37; H, 2.86%. IR (cm^{-1}): *ν*(Ar–H) 3056w; *ν*(CO) 2068s, 2000vs, 1969vs, 1936m, 1867m,; *ν*(C=O) 1679m, 1634. ^{1}H NMR: *δ* 7.64–6.98 (m, 20H, $4C_6H_5$), 5.94–4.89 (m, 8H, $2C_5H_4$), 3.91 (s, 2H, 2CH), 2.66–2.17 (m, 10H, $2CH_2$, $2CH_3$), 1.25 (s, 6H, $2CH_3$). ^{31}P NMR: *δ* 49.45 (s, PCo), 48.37 (s, PCo).

2.4. Reaction of 1 with Na[Mo(CO)$_3$-(η^5-C$_5$H$_4$CO CH$_3$)]

$Mo(CO)_6$ (64 mg, 0.24 mmol) was added to a solution of $Na(C_5H_4COCH_3)$ (32 mg, 0.24 mmol) in 25 ml of THF. The mixture was refluxed for 15 h and cooled to room temperature. Then 154 mg (0.1 mmol) of cluster **1** was added and the mixture was stirred at 60 °C for another 1 h. The solvent was removed in vacuo, the residue was extracted by a small amount of CH_2Cl_2 and the extract was subjected to a 2.5×40 cm silica gel column chromatography. CH_2Cl_2:petroleum ether (5:2) eluted a known cluster complex (μ_3-Se)RuCoMo(CO)$_8$(CpC(O)CH$_3$) and a black-red band [(μ_3-Se)RuCoMo(CO)$_6$(CpC(O)CH$_3$)((−)-DIOP)] (**5**) (96 mg, 43.2%, based on **1**). *Anal*. Calc. for [$C_{44}H_{39}O_9SeP_2CoMoRu$]: C, 47.49; H, 3.54. Found: C, 47.56; H, 3.37%. IR (cm^{-1}): *v*(Ar–H) 3056w; *v*(CO) 2072s, 2033s 2005vs, 1945s, 1890m; *v*(C═O) 1684m. ^{1}H NMR: δ 7.38–6.98 (s, br, 20H, 4C$_6$H$_5$), 5.89–5.47 (m, 4H, C$_5$H$_4$), 3.78–3.66 (s, 2H, 2CH), 2.53–2.19 (m, 7H, 2CH$_2$, CH$_3$), 1.25 (s, 6H, 2CH$_3$). ^{31}P NMR: δ 52.38 (s, PCo), 38.83 (s, PRu).

2.5. Crystal data of cluster 1

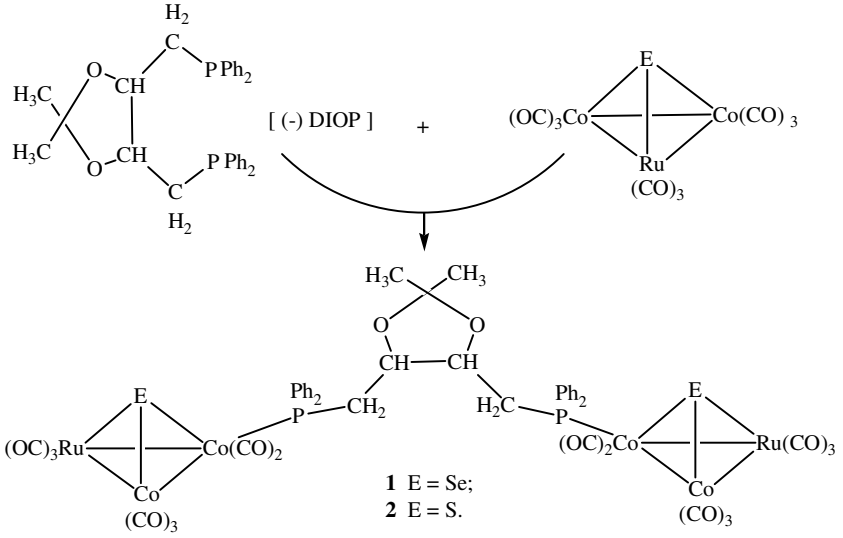
Suitable crystals of cluster **1** were obtained from *n*-hexane/CH_2Cl_2 at −20 °C. The crystals were mounted on a glass fiber. Preliminary examination and data collection were performed with Mo Kα radiation (λ = 0.71073 Å) on a Bruker CCD APEX diffractometer equipped with graphite monochromator for cluster **1**. The empirical absorption corrections were applied using the SADABS [28] program. The structures were solved by direct methods and expanded using Fourier techniques and all non-hydrogen atoms were refined anisotropically by full-matrix least-squares on F^2 using the SHELXL-97 [29] crystallographic program package. Hydrogen atoms were added according to geometrical method. It should be note that the cluster **1** possesses a chiral structure as result of the absolute structure parameter, i.e. flack factor (−0.01(2)) and extinction coefficient (0.0031(3)) [30].

3. Results and discussion

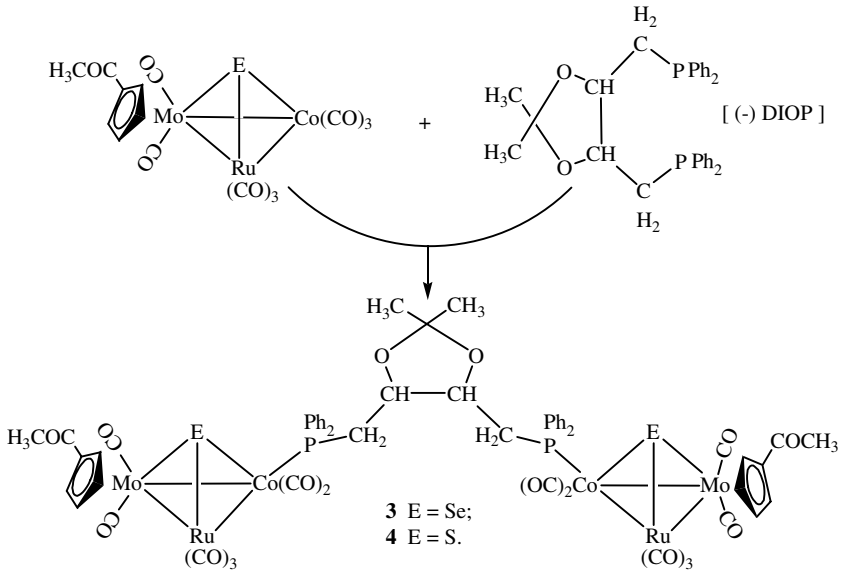
3.1. Synthesis of clusters 1–4

The reactions described in this work are summarized in Schemes 1 and 2. In order to investigate the metallosite selectivity in carbonyl substitution of Ru–Co heteronuclear tetrahedral cluster derivatives and construct higher nuclearity linked clusters and potential asymmetric hydrogenation catalysts, we treated the cluster [(μ_3-E)RuCo$_2$(CO)$_9$] (E = Se, S) and [(μ_3-E)RuCoMo(CpC(O)CH$_3$)(CO)$_8$] (E = Se, S) in *n*-hexane or THF with diphosphine compound (−)-DIOP in 1:1 and 2:1 molar ratio at room temperature and obtained four new linked tetrahedral cluster derivatives [(μ_3-E)RuCo$_2$(CO)$_8$]$_2$((−)-DIOP) (E = Se, **1**; S, **2**), [(μ_3-E)RuCoMo(CO)$_7$(CpC(O)CH$_3$)]$_2$((−)-DIOP) (E = Se, **3**; S, **4**) as the major products, respectively.

During the substituted reactions, the color of solution changed from brown-red to black-red. The Ru–Co–Co cluster reacts readily with (−)-DIOP, but the Ru–Co–Mo cluster reacts hard under the conditions and the yields of **3** and **4** are much lower than that of **1** and **2**. This may be due to the presence of the CpC(O)CH$_3$ group increasing the electron density on the metals in the clusters [(μ_3-E)RuCoM(CO)$_8$(CpC(O)CH$_3$)] (E = Se, S), which would make the CO ligand substituted difficulty by (−)-DIOP at room temperature. These new



Scheme 1.



Scheme 2.

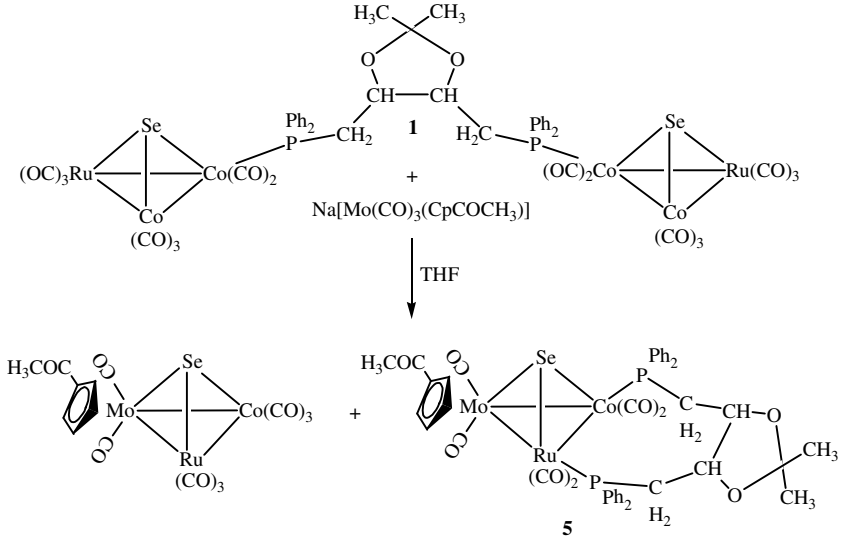
cluster complexes **1**–**4** are stable in air in solid state and soluble in common organic solvents.

3.2. Reaction of cluster *1* with $Na[Mo(CO)_3(\eta^5\text{-}C_5H_4COCH_3)]$

To learn more about the metallic exchange reaction in the linked tetrahedral carbonyl cluster, the reaction of the cluster **1** with $Na[Mo(CO)_3(\eta^5\text{-}C_5H_4COCH_3)]$ in 1:1 molar ratio was checked in THF at 60 °C. During the reaction, the (−)-DIOP bridge of cluster **1** broke to give a known metallic exchange product $(\mu_3\text{-Se})RuCoMo(CO)_8(CpC(O)CH_3)$ [23] and a new (−)-DIOP substituted tetrahedral cluster $[(\mu_3\text{-Se})RuCoMo(CO)_6(CpC(O)CH_3)((-)\text{-DIOP})]$ (**5**) (see Scheme 3). Unfortunately, we did not get the analogous $[(\mu_3\text{-Se})RuCo_2(CO)_7((-)\text{-DIOP})]$ cluster and other linked metallic exchange products. It is likely that the metallic exchange reaction and the broken course of (−)-DIOP bridge are simultaneous under this condition. Further studies on the metallic exchange reactions of the linked mixed-metal clusters are currently underway.

3.3. Characterization of clusters *1*–*5*

The IR spectra of all clusters show a weak absorption band around 3056 cm^{-1} and intense absorption bands in the range 2084–1801 cm^{-1}, characteristic of the benzene



Scheme 3.

rings of (−)-DIOP and the terminal carbonyl and semi-bridging carbonyl ligand, respectively. Comparing the IR spectra of **1** and **5** with that of the parent cluster [(μ_3-Se)RuCo$_2$(CO)$_9$], it can be seen that the highest value of terminal CO stretching frequencies shift from 2101 cm^{-1} [24] toward the lower value 2084 cm^{-1} (**1**), further to the value 2072 cm^{-1}(**5**), resulting from the carbonyl ligands are replaced, step-by-step, by two PPh_2 groups in the tetrahedral unit of the cluster **1** and **5**, respectively. This is consistent with our knowledge that the PPh_2 group behaves as a stronger σ-donor and a weaker π-acceptor, when compared to the CO ligand, increasing the electron density on the metals in the clusters. It should be noted that in the IR spectra of **3** and **4**, besides the terminal and semi-bridging carbonyl absorption bands, there are absorption bands at 1680 cm^{-1}, which are characteristic of acetyl bonded to the cyclopentadienyl ring.

The ^{1}H NMR spectra of all of clusters **1**–**5** are consistent with the (−)-DIOP substituted cluster structure and show the presence of hydrogen atoms in their corresponding organic groups. The signals at about δ 7.67–6.98 are caused by the protons of phenyl ring in the ^{1}H NMR spectra of clusters **1**–**5**. The signals at 3.97–3.58 reveal the protons of the CH group of the (−)-DIOP and the signals at δ 2.68–2.15 which can be assigned to methylene protons (CH_2) of the (−)-DIOP and the protons of methyl bonded to cyclopentadienyl ring. For the protons of the methyl of the (−)-DIOP, the ^{1}H NMR spectra of clusters **1**–**5** exhibit a singlet around δ 1.25, respectively. In addition, the signals at 5.94–4.89 also reveal the presence of the protons of the cyclopentadienyl moiety in the ^{1}H NMR spectra of clusters **3**–**5**.

Table 1
Crystal data and structure refinement for clusters **1**

Empirical formula	$C_{47}H_{32}O_{18}Se_2P_2Co_4Ru_2$
Formula weight	1542.45
Temperature (K)	293(2)
Radiation (Mo Kα) (Å)	0.71073
Crystal system	orthorhombic
Space group	$P2_12_12_1$
a (Å)	9.625(3)
B (Å)	20.13(7)
C (Å)	28.14(1)
β (°)	90
V (Å^3)	5453(3)
Z	4
$D_{calc.}$ (g/cm^3)	1.879
Absorption coefficient (mm^{-1})	3.191
F(0 0 0)	3008
Scan type	ϕ–ω
θ_{max} (°)	38.19
Number of observations [$I > 2\sigma(I)$]	9576
Number of variables	680
R[a]	0.0850
R_w[b]	0.1692
Absolute structure parameter	−0.01(2)
Extinction coefficient	0.0031(3)
Largest difference peak and hole (e Å^{-3})	1.694 and −0.906

[a] $R = \sum |F_o| - |F_c| / \sum |F_o|$.
[b] $R_w = [\sum \omega(|F_o| - |F_c|)^2 / \sum \omega F_o^2]^{1/2}$.

The ^{31}P NMR spectrum of cluster **1** is consistent with the structure established by X-ray analysis. Thus the two singlets observed at δ 53.21 and 52.04 are assigned to terminal P atoms (labeled P1 and P2, respectively, in Fig. 1). The ^{31}P NMR spectra of clusters **2** and **4** are similar to that of cluster **1** and show two singlets at the range δ 50.46–48.37, respectively, assigned to the P atoms bonded to Co atoms. For the cluster **5**, the signals

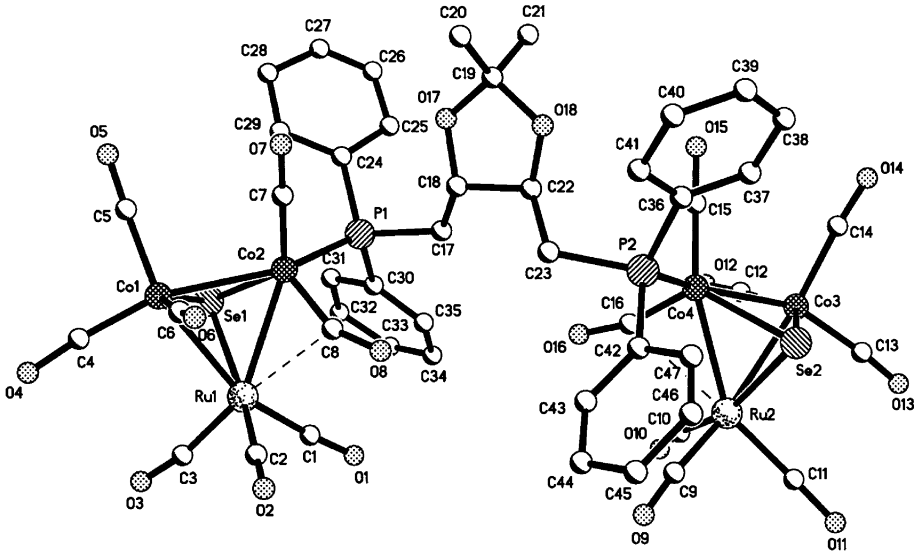


Fig. 1. The molecular structure of the cluster **1** (hydrogen atoms are omitted for clarity). Thermal ellipsoids are drawn at the 30% probability level.

Table 2
Selected bond lengths (Å) and angles (°) for cluster **1**

Ru(1)–C(3)	1.85(2)	Ru(2)–Co(4)	2.66(3)	Co(3)–Se(2)	2.32(3)
Ru(1)–C(1)	1.86(3)	Co(1)–C(4)	1.75(2)	Co(3)–Co(4)	2.54(3)
Ru(1)–C(2)	1.90(3)	Co(1)–C(6)	1.76(2)	Co(4)–C(16)	1.72(2)
Ru(1)–Se(1)	2.44(3)	Co(1)–C(5)	1.78(3)	Co(4)–C(15)	1.72(2)
Ru(1)–C(8)	2.45(2)	Co(1)–Se(1)	2.30(3)	Co(4)–P(2)	2.19(5)
Ru(1)–Co(2)	2.64(3)	Co(1)–Co(2)	2.53(3)	Co(4)–Se(2)	2.30(3)
Ru(1)–Co(1)	2.65(3)	Co(2)–C(8)	1.72(2)	P(1)–C(24)	1.78(2)
Ru(2)–C(10)	1.85(3)	Co(2)–C(7)	1.73(3)	P(1)–C(17)	1.79(2)
Ru(2)–C(11)	1.86(2)	Co(2)–P(1)	2.19(5)	P(1)–C(30)	1.86(2)
Ru(2)–C(9)	1.88(2)	Co(2)–Se(1)	2.29(3)	P(2)–C(36)	1.82(2)
Ru(2)–Se(2)	2.43(3)	Co(3)–C(12)	1.74(3)	P(2)–C(23)	1.82(2)
Ru(2)–C(16)	2.61(2)	Co(3)–C(13)	1.79(2)	P(2)–C(42)	1.84(2)
Ru(2)–Co(3)	2.64(3)	Co(3)–C(14)	1.82(2)		
Se(1)–Ru(1)–Co(2)	53.50(8)	P(1)–Co(2)–Co(1)	150.0(2)	P(2)–Co(4)–Ru(2)	119.0(2)
Se(1)–Ru(1)–Co(1)	53.55(8)	Se(1)–Co(2)–Co(1)	56.68(9)	Se(2)–Co(4)–Ru(2)	58.18(9)
Co(2)–Ru(1)–Co(1)	57.27(9)	P(1)–Co(2)–Ru(1)	119.1(2)	Co(3)–Co(4)–Ru(2)	61.05(8)
Se(2)–Ru(2)–Co(3)	54.17(8)	Se(1)–Co(2)–Ru(1)	58.82(9)	Co(2)–Se(1)–Co(1)	66.98(1)
Se(2)–Ru(2)–Co(4)	53.45(8)	Co(1)–Co(2)–Ru(1)	61.63(9)	Co(2)–Se(1)–Ru(1)	67.68(1)
Co(3)–Ru(2)–Co(4)	57.16(8)	Se(2)–Co(3)–Ru(2)	58.29(8)	Co(1)–Se(1)–Ru(1)	67.94(1)
Se(1)–Co(1)–Co(2)	56.34(9)	Co(4)–Co(3)–Ru(2)	61.80(9)	Co(4)–Se(2)–Co(3)	66.65(1)
Se(1)–Co(1)–Ru(1)	58.51(9)	P(2)–Co(4)–Se(2)	99.19(2)	Co(4)–Se(2)–Ru(2)	68.37(9)
Co(2)–Co(1)–Ru(1)	61.10(9)	P(2)–Co(4)–Co(3)	153.6(2)	Co(3)–Se(2)–Ru(2)	67.54(9)
P(1)–Co(2)–Se(1)	96.62(2)	Se(2)–Co(4)–Co(3)	57.02(9)	Se(2)–Co(3)–Co(4)	56.32(9)

observed at δ 52.38 and δ 38.83 are assigned to the P atoms bonded to Co atom and Ru atom, respectively. It is similar to that described by P. Braunstein [22].

On the basis of the above described for **5**, we propose its structure as the following form: [(μ_3-Se)RuCoMo-$(CO)_6$($CpC(O)CH_3$)((−)-DIOP)] in which the $Mo(CO)_2$-($CpC(O)CH_3$) unit substituted the $Co(CO)_3$ fragment of the $SeRuCo_2$ core forming a chiral tetrahedral cluster and one phosphorus atom of the (−)-DIOP bonded to Co atom, another coordinated to Ru atom not to Mo atom.

3.4. Crystal structure of cluster *1*

The crystal structure of cluster **1** was determined by X-ray structural analyses. Crystal data and experimental details for **1** are collected in Table 1. Table 2 gives the selected bond lengths and angles. An ORTEP drawing of **1** with numbering is shown in Fig. 1.

As seen in Fig. 1, the structure of cluster **1** contains two slightly distorted tetrahedral cores $SeRuCo_2$, which are connected via (−)-DIOP as a bridging unit. The phosphorus atoms of (−)-DIOP ligand substituted one carbonyl of one of two cobalt atoms of each $SeRuCo_2$ core, respectively, and the average bond distance between the cobalt atom and phosphorus atom is 2.187 Å. So, both $SeRuCo_2$ cores can be looked as chiral units resulting from the different coordination environments of the two cobalt atoms in each tetrahedral framework, to our knowledge. Additionally, the μ_3-Se ligand may be viewed as a 4-electron donor, with the result that each $SeRuCo_2$ core contains a total of 48 electrons and is electronically saturated. This may be the reason that the kind of cluster can present stably in the air in solid state. It is worthy to note that the carbonyls of C(8)–O(8) and C(16)–O(16) attached to Co(2) and Co(4) atoms belong to semi-bridging, due to its asymmetric parameter $\alpha = (d_2 - d_1)/d_1 = 0.42, 0.52$, respectively, fall in the range of α value defined for semi-bridging carbonyl's by Curtis [31]. The coexistence of both terminal and semi-bridging carbonyls are in good agreement with the IR spectrum showing several strong absorption bands from 2084 to 1872 cm^{-1} of cluster **1**.

According to the crystal structure of cluster **1** and that of above described, it can be suggested that during the reactions of SeRuCoM (M = Co, Mo) heteronuclear tetrahedral cluster with (−)-DIOP, the metallosite selectivity in carbonyl substitution of Ru, Co and Mo follows as the series of Co > Ru > Mo.

4. Supplementary material

Crystallographic data for the structural analysis have been deposited with the Cambridge Crystallographic Data Center, CCDC No. 261513 for cluster **1**. Copies of this information may be obtained free of charge from The Director, CCDC, 12 Union Road, Cambridge CB2 1EZ, UK (fax: +44-1223-336033; e-mail: deposit@ccdc.cam.ac.uk or www: http://www.ccdc.cam.ac.uk).

Acknowledgments

We are grateful to the National Science Foundation of China for the financial support of this work. We

thank Dr. Yan-Long Gu for donation of the sample of (−)-DIOP.

References

[1] G. Schmid, Clusters and Colloids: From Theory to Applications, VCH, Weinheim, 1994.
[2] L.J. de Jongh, Physics and Chemistry of Metal Cluster Compounds, Kluwer, Dordrecht, 1994.
[3] M.P. Cifuentes, M.G. Humphrey, J.E. McGrady, P.J. Smith R., Stranger, K.S. Murray, B. Moubaraki, J. Am. Chem. Soc. 119 (1997) 2647.
[4] N.T. Lucas, J.P. Blitz, S. Petrie, R. Stranger, M.G. Humphrey, G.A. Heath, V. Otieno-Alego, J. Am. Chem. Soc. 124 (2002) 5139.
[5] R.D. Adams, F.A. Cotton, Catalysis by Di- and Polynuclear Metal Cluster Complexes, Wiley-VCH, New York, 1998.
[6] P. Braunstein, L.A. Oro, P.R. Raithby, in: P. Braunstein, L.A. Oro, P.R. Raithby (Eds.), Metal Clusters in Chemistry, vol. 2, Wiley-VCH, Weinheim, Germany, 1999.
[7] M.J. Overett, R.O. Hill, J.R. Moss, Coord. Chem. Rev. 206–207 (2000) 581.
[8] B.C. Gates, J. Mol. Catal. A: Chem. 163 (2000) 55.
[9] H. Paul, S. Bhaduri, G.K. Lahiri, Organometallics 22 (15) (2003) 3019.
[10] H. Nagashima, C. Itonaga, J. Yasuhara, Y. Motoyama, K. Matsubara, Organometallics 23 (24) (2004) 5779.
[11] W. Levason, in: F.R. Hartley (Ed.), The Chemistry of Organophosphorus Compounds, vol. 1, Wiley, New York, 1990 (Chapter 15).
[12] C.C. Borg-Breen, M.T. Bautista, C.K. Schauer, P.S. White, J. Am. Chem. Soc. 122 (2000) 3952.
[13] C. Babij, C.S. Browning, D.H. Farrar, I.O. Koshevoy, I.S. Podkorytov, A.J. Poe, S.P. Tunik, J. Am. Chem. Soc. 124 (2002) 8922.
[14] R.D. Adams, B. Captain, W. Fu, M.B. Hall, J. Manson, M.K. Smith, C.E. Webster, J. Am. Chem. Soc. 126 (2004) 5253.
[15] M.G. Richmond, J.K. Kochi, Organometallics 6 (1987) 254.
[16] (a) J.-D. Chen, F.A. Cotton, L.R. Falvello, J. Am. Chem. Soc. 112 (1990) 1076;
(b) J.-D. Chen, F.A. Cotton, J. Am. Chem. Soc. 113 (1991) 2509.
[17] N.C. Zanetti, F. Spindler, J. Spencer, A. Togni, G. Rihs, Organometallics 15 (1996) 860.
[18] B. Wu, W.-J. Zhang, S.-Y. Yu, X.-T. Wu, J. Chem. Soc., Dalton Trans. (1997) 1795.
[19] Y.-Y. Yan, T.V. RajanBabu, Org. Lett. 2 (26) (2000) 4137.
[20] L. Viau, R. Chauvin, J. Organomet. Chem. 654 (2002) 180.
[21] A.J. Edwards, S.R. Mack, M.J. Mays, C.-Y. Mo, P.R. Raithby, M.-A. Rennie, J. Organomet. Chem. 519 (1996) 243.
[22] P. Braunstein, C. Graiff, C. Massera, G. Predieri, J. Rosé, A. Tiripicchio, Inorg. Chem. 41 (6) (2002) 1372.
[23] A. Choualeb, P. Braunstein, J. Rosé, R. Welter, Inorg. Chem. 43 (1) (2004) 57.
[24] E. Roland, H. Vahrenkamp, Chem. Ber. 117 (1984) 1039.
[25] Y.H. Zhang, J.C. Yuan, W.J. Lao, Y.Q. Yin, J. Organomet. Chem. 628 (2001) 123.
[26] E.R. Ding, S.M. Liu, Z.Y. Zhao, Y.Q. Yin, et al., Polyhedron 16 (1997) 2387.
[27] W.R. Hart, H. Dong, D. Rausch, J. Organomet. Chem. 282 (1985) 111.
[28] G.M. Sheldrick, SADABS, Program for Empirical Absorption Correction of Area Detector Data, University of Gottingen, Germany, 1996.
[29] G.M. Sheldrick, SHELXL-97, Program for Crystal Structure Refinement, University of Gottingen, Germany, 1997.
[30] H.D. Flack, Acta Crystallogr., Sect. A 39 (1983) 876.
[31] The asymmetric parameter α is defined as $\alpha = (d_2 - d_1)/d_1$, where d_1 and d_2 are the short and long distances of M–C(O), respectively. If $0.1 \leqq \alpha \leqq 0.6$, a semibridging carbonyl is designated according to Curtis' suggestion. M.D. Curtis, K.R. Han, W.M. Butler, Inorg. Chem. 19 (1980) 2096.

Available online at www.sciencedirect.com
SCIENCE DIRECT®
Polyhedron 24 (2005) 2063–2064
POLYHEDRON
www.elsevier.com/locate/poly

Preface

The IX International Conference on Molecule-based Magnets (ICMM 2004) was held from October 4 to 8, 2004 at the International Conference Hall in Tsukuba, Japan. There were more than 400 participants, including 130 participants from 18 countries other than Japan. The organizers are indebted to all the participants for the great success of the Conference, which was brought about by their extremely active participation. The organizers are also happy to hear that approximately 150 excellent papers are appearing in this special issue of *Polyhedron* published by Elsevier as the Proceedings of ICMM 2004.

The research area of the conference, so-called 'molecular magnetism', originated from the discovery of high spin molecules and organic ferromagnets. Since then, this research field has expanded rapidly by absorbing many related fields. As a result, photo-magnets, ferromagnetic transition metal complexes, single-molecule magnets, etc. have been discovered in the last decade or so, and the ICMM conferences have been the most important occasions to report the hottest results in the field.

Topics covered by the ICMM meetings have changed drastically in recent years. Their interest has leaped from the stage of searching for molecular magnets with high T_c to a new stage of developing dynamic spin systems where molecular spins play an essential role. Researchers have also been aiming to create a new frontier by amalgamating molecular spins with nano-spins and/or bio-spins. In order to cover these new trends, the ICMM 2004 organizers arranged new sessions on nano-spins and bio-spins; in these sessions, spin-electronics using spin-polarized molecules, and spin-imaging techniques using novel spin-labels, etc., were discussed as hot topics.

Let us briefly revisit the main topics of the Conference. On the first day, R.C. Haddon gave a plenary lecture on the design and physical properties of phenalenyl radicals and their charge transfer complexes. S. Tarucha addressed the basis and application of quantum dots made of semiconductors in his plenary lecture. Nine lectures followed the plenary talks, including the design and preparation of new phenalenyl radicals, and the development of batteries using radical polymers. There was also a pioneering report on Mössbauer spectroscopic exploration of soils and rocks on Mars. In the evening there were six lectures in the bio-spin session: detailed studies of in vivo ESR spectroscopy using spin-labeled molecules, a high magnetic field effect on supramolecular systems, including living tissues, and bio-mineralization of ferrites in bacteria. Novel directions of self-assembling spin molecules were discussed involving spin molecules carrying a nucleic acid unit.

On the second day, the plenary lecture of G. Christou was presented on single-molecule magnets and exchange-bias tunneling of two interacting clusters. He also powerfully addressed some future aspects of single-molecule magnetism. In the quantum spin session that followed there were 12 lectures, including novel quantum-spin phenomena based on organic–inorganic hybrid magnets, and the extensive current research on single-chain magnets. Fine results obtained from a new tool, such as micro-SQUID, were also presented. The first multi-functional session started in the evening, focusing on properties of conducting magnets, and results involving spin-valve systems were also presented there.

On the third day, the multi-functional session continued with 14 excellent lectures on cooperative effects and related new topics exhibited by spin-crossover complexes. The topics of the second multi-functional spin session concentrated on opto-magnetic functions. Chiral-magnets and photo-magnets were the main topics in this session.

On the morning of the final day, M.E. Welland gave a plenary lecture on the characteristic domain patterns and the applications of nano-magnets. Thereafter, new directions of photo-active spins systems were discussed, such as a photo-induced phase transition of organic radical crystals, photo-switching using the photo-chromic spin-coupler, and spin-alignment in the photo-excited states of π-radicals.

Poster sessions were presented in the evening of the first and second Conference days. It is to be stressed that 346 excellent posters were presented in a hot atmosphere. It should also be mentioned that "demo-presentations" were held as a new program in ICMM 2004. Spectacular demo-experiments to show the beauty of molecular magnetism were performed. This program was greeted with great applause, and enthusiastic support was given to continue the program in the next ICMM Conference in Vancouver.

0277-5387/$ - see front matter © 2005 Published by Elsevier Ltd.
doi:10.1016/S0277-5387(05)00666-2

All throughout the Conference, presentations on manipulating spin systems arising from quantum effects of molecular spins drew much attention from the participants. They are convinced that this field has grown up as a big interdisciplinary field between physics, chemistry, biology, and theoretical science. It may be said that ICMM 2004 has succeeded in manifesting a new horizon of "molecular magnetism".

Finally, the organizers hope that this special issue of *Polyhedron* will recall the enthusiasm exhibited by the participants in ICMM 2004, and at the same time will provide a guide for your future work.

Organizers of ICMM 2004, Tsukuba
Tadashi Sugawara
Department of Basic Science, Graduate School of Arts & Science, The University of Tokyo, Tokyo, Japan

Hiroki Oshio
Department of Chemistry, University of Tsukuba, Tsukuba, Japan

Kunio Awaga
Department of Chemistry, Graduate School of Science, Nagoya University, Nagoya, Japan

and the most studied to date due to its large spin ($S = 10$) and high symmetry (S_4). The Mn_{12} family also possesses the largest blocking temperature ($T_B \sim 3$ K) against magnetization relaxation of any SMM. Only recently has a detailed understanding emerged concerning the symmetry breaking responsible for the QTM in $Mn_{12}Ac$ [68–70]. Hence, $Mn_{12}Ac$ and the Mn_{12} family remain an attractive and productive area for further research area.

One of our goals over the last several years has been to develop an arsenal of methods for modifying the Mn_{12} family of SMMs in a variety of controllable and useful ways. In these molecules, the central inorganic Mn/O core is contained within a shell of organic ligands, and one goal has therefore been the modification of this organic periphery (shell) via ligand substitution reactions. Among other things, this would allow us to tune the solubility, redox and magnetic properties of the molecules. Another objective has been to obtain Mn_{12} complexes in different oxidation states to investigate the influence of the electron count on various properties of the molecules. A further but more subtle way of modifying the molecules is to grow the crystals from various solvents, which can lead to variations in the space group and precise solvent content of the crystals, and this in turn leads to variations in the local site-symmetry and environment around the molecule. While the latter variation might be predicted to lead to insignificant changes to the properties of the molecule, in fact we have found these changes to lead to surprisingly large effects. All the above controlled modifications will be summarized in more detail in this paper, and these have greatly advanced our knowledge and understanding of the properties of these Mn_{12} SMMs.

In addition to modifying known types of SMMs, we have also continued to seek new synthetic methods to new structural types of high-nuclearity Mn clusters that might have interesting structural and/or magnetic properties, and that might be new SMMs. We shall also describe a number of new results along these lines. For example, the use of MeOH in some reactions has led to the synthesis of new clusters of nuclearities Mn_{12} [71], Mn_{16} [61], and Mn_{84} [67], and all of these have been discovered to be new SMMs. In addition, recent work with polydentate chelates containing alcohol groups has yielded a new Mn_{12} cluster with an interesting loop structure, which is also a new SMM. All these will be described in this report.

2. Modification of single-molecule magnets

2.1. Carboxylate substitution

Several procedures have been developed to replace the $MeCO_2^-$ ligands of $Mn_{12}Ac$ with almost any other type of carboxylate group, leading to increased solubility in organic solvents and greatly altered redox properties [41,72]. Methods have also been developed to obtain Mn_{12} complexes containing more than one type of peripheral bridging ligand (the four H_2O ligands are terminal). One such strategy involves the site-specific replacement of some of the bound carboxylates to give either: (i) mixed-carboxylate complexes of formula $[Mn_{12}O_{12}(O_2CR)_8(O_2CR')_8(H_2O)_4]$ [73] or (ii) mixed organic–inorganic ligation in the complex $[Mn_{12}O_{12}(O_2CR)_{12}(NO_3)_4(H_2O)_4]$, which contains bridging NO_3^- groups and is thus the first Mn_{12} complex to contain non-organic bridging ligands [34]. Subsequently, we showed that it is also possible to site-specifically substitute half the carboxylate groups with: (i) benzenesulfonate ($PhSO_3^-$) groups to give $[Mn_{12}O_{12}(O_2CMe)_8(O_3SPh)_8(H_2O)_4]$ [33] with the $PhSO_3^-$ groups occupying axial positions on the Mn_{12} cluster or (ii) with diphenylphosphinate ($Ph_2PO_2^-$) groups to give $[Mn_{12}O_{12}(O_2CMe)_8(O_2PPh_2)_8(H_2O)_4]$ with both axial and equatorial $Ph_2PO_2^-$ groups [30]. One such transformation is summarized as an example in Eq. (1), for the $PhSO_3H$ reaction.

$$[Mn_{12}O_{12}(O_2CMe)_{16}(H_2O)_4] + 8PhSO_3H \rightarrow [Mn_{12}O_{12}(O_2CMe)_8(O_3SPh)_8(H_2O)_4] + 8MeCO_2H \quad (1)$$

Considerable insight has been obtained from these chemical modifications on the Mn_{12} SMM, leading to much new magnetostructural knowledge and information on this important family of SMMs.

2.2. Reduced Mn_{12} complexes

The feasibility of chemically reducing a Mn_{12} SMM was initially established by the observation of quasi-reversible oxidation and reduction processes in the cyclic voltammograms. The oxidation processes are at rather high potentials, but the reduction processes are much more accessible, and it was therefore decided to initially seek isolation of one-electron reduced species. For this purpose, the reducing agent chosen was I^- because of its sufficient, yet mild reducing strength, its ready availability as a variety of salts of organic cations, and the high solubility of many of the latter in organic solvents. Indeed, chemical reduction of the $[Mn_{12}O_{12}(O_2CR)_{16}(H_2O)_4]$ complexes with C^+I^- (C^+ is NR_4^+, PPh_4^+, etc.) in MeCN or CH_2Cl_2 was found to provide a convenient route to the corresponding salts of the $[Mn_{12}]^-$ anions in good (>50%) yield. The C^+I^- reagent provides the required cation, and the only byproduct is elemental I_2, which is easy to remove (Eq. (2)).

$$[Mn_{12}O_{12}(O_2CR)_{16}(H_2O)_4] + I^- \rightarrow [Mn_{12}O_{12}(O_2CR)_{16}(H_2O)_4]^- + \tfrac{1}{2}I_2 \quad (2)$$

It has been proven by X-ray crystallography that the added electron is localized on an outer (originally Mn^{III}) ion rather than an inner (cubane) Mn^{IV} ion, producing a trapped-valence $Mn^{II}Mn_7^{III}Mn_4^{IV}$ anion. These $[Mn_{12}]^-$ compounds have a half-integer ground state spin of $S = 19/2$ in almost all the cases studied [41–43], with $S = 21/2$ occasionally being reported [45]. In addition, they retain the SMM properties of the neutral Mn_{12} species, and are of particular interest for studying QTM in half-integer spin species; QTM is not allowed in such complexes in the absence of an applied field.

The carboxylate substitution reactions mentioned above have allowed the incorporation onto the Mn_{12} core of carboxylate groups containing strongly electron-withdrawing substituents (e.g., $CHCl_2CO_2^-$ groups), and these raise the reduction potentials to the point that the second reduction is also within the capability of our reductant of choice, iodide I^-. Thus, clean, two-electron reduction to $[Mn_{12}]^{2-}$ salts has consequently also been successfully accomplished (Eq. (3)) [46–49].

$$[Mn_{12}O_{12}(O_2CR)_{16}(H_2O)_4] + 2I^- \rightarrow [Mn_{12}O_{12}(O_2CR)_{16}(H_2O)_4]^{2-} + I_2 \quad (3)$$

As for the $[Mn_{12}]^-$ anion, the extra electrons in $[Mn_{12}]^-$ are localized on outer (originally Mn^{III}) ions rather than on inner (cubane) Mn^{IV} ions, producing a trapped-valence $Mn_2^{II}Mn_6^{III}Mn_4^{IV}$ anion. In contrast to the $[Mn_{12}]^-$ salts, the ground state spin is again an integer $S = 10$ for two-electron reduced species. In addition, they retain the SMM properties of the neutral Mn_{12} species and $[Mn_{12}]^-$ species. In fact, a detailed examination of the magnetic properties of the $[Mn_{12}]^z$ ($z = 0$, $1-$, $2-$) series has shown that although they are all SMMs, they show a decreasing effective barrier to magnetization relaxation (U_{eff}), which is primarily due to the decreasing magnitude of the axial anisotropy parameter $|D|$ as the Mn^{III} content of the clusters decreases; Jahn-Teller distorted Mn^{III} ions are the main source of anisotropy in the Mn_{12} molecules. All three Mn_{12} oxidation states display resonant QTM, and this work thus provides useful comparisons of QTM in half-integer versus integer spin systems, as well as of quantum phase interference.

2.3. High-symmetry Mn_{12} complexes

Among all Mn_{12} complexes to date, Mn_{12}Ac has become the most widely studied SMM, not only because it

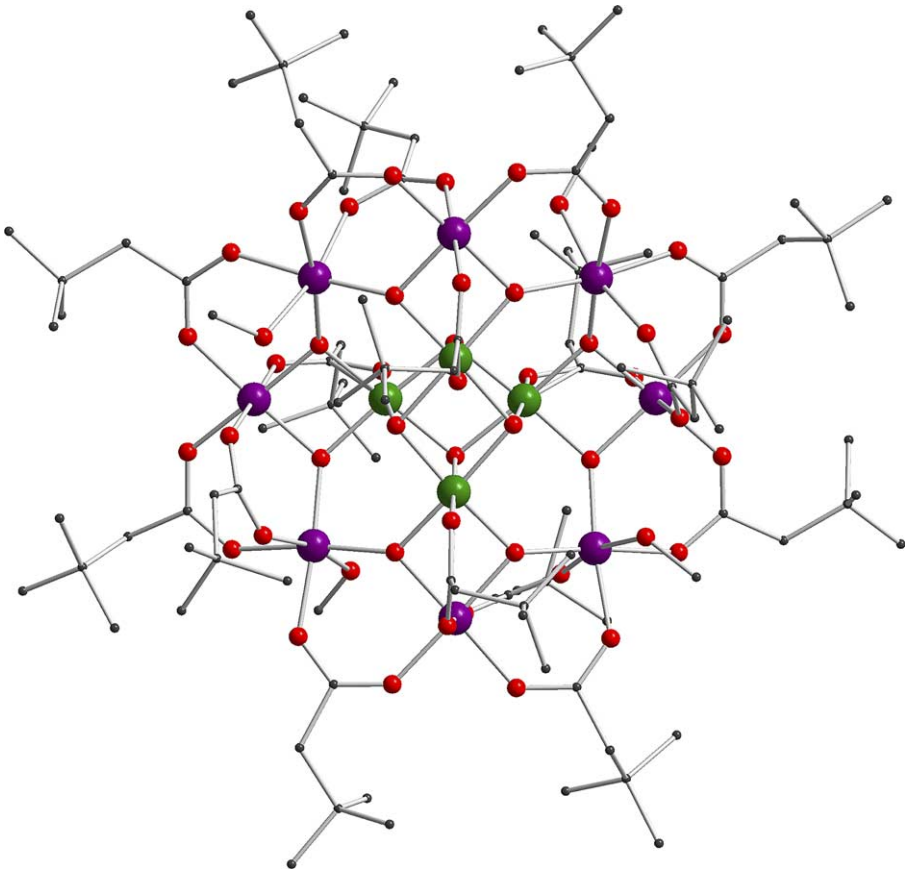


Fig. 1. The structure of $[Mn_{12}O_{12}(O_2CCH_2{}^tBu)_{16}(MeOH)_4]$, excluding hydrogen atoms. Color code: green, Mn^{IV}; purple, Mn^{III}; red, O; gray, C.

was the first to be recognized as an SMM but also because of its high spin of $S = 10$ and its high molecular symmetry (S_4). These factors contribute to the largest blocking temperature ($T_B \sim 3$ K) against magnetization relaxation of any known SMM. Recently, an improved understanding has emerged concerning the symmetry breaking responsible for the QTM in $Mn_{12}Ac$ [68–70]. Disorder associated with the acetic acid solvent leads to discrete local environments, resulting in a significant fraction of the molecules (>50%) possessing twofold symmetry with a rhombic crystal-field parameter $E \sim 0.01$ cm^{-1} [69]. In effect, the $Mn_{12}Ac$ complex is a mixture of species with different site symmetries, only some of which are truly axial, and it is clear that it is therefore *not* an ideal Mn_{12} for detailed study using models that assume axial symmetry in the spin Hamiltonians. We have thus been exploring the synthesis and study of other Mn_{12} complexes with true axial symmetry in order to finally obtain the real properties of axially symmetric Mn_{12} SMMs.

In 2001, the high symmetry (space group $I4_1/a$) $[Mn_{12}O_{12}(O_2CCH_2Br)_{16}(H_2O)_4] \cdot 4CH_2Cl_2$ ($Mn_{12}BrAc$) complex was reported by An et al. [26]. This was prepared using our ligand substitution reaction with bromoacetic acid. This complex is overall similar to $Mn_{12}Ac$ in its structure and magnetic properties, except

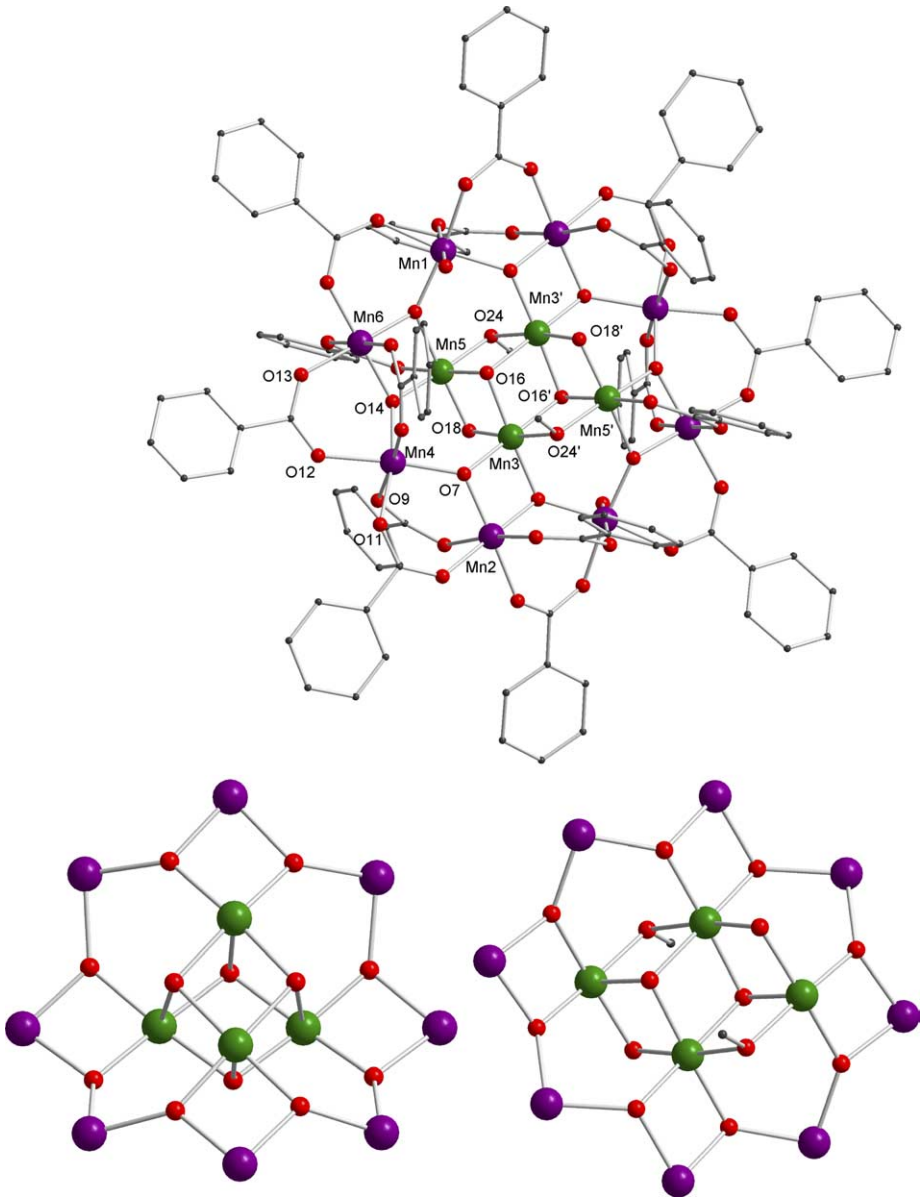


Fig. 2. The structure of the anion of $[Mn_{12}O_{12}(OMe)_2(O_2CPh)_{16}(H_2O)_2]$, excluding hydrogen atoms. Color code: green, Mn^{IV}; purple, Mn^{III}; red, O; gray, C. Bottom: Comparison of the cores of "normal" $[Mn_{12}]$ (left) and the anion of "flat" $[Mn_{12}]$ (bottom).

that it is much 'cleaner,' not being composed of a mixture of species with very different environments. We have recently investigated the properties of this complex in depth using micro-SQUID, high-frequency EPR and ^{55}Mn NMR techniques, in all cases using single crystals. All measurements reveal far superior quality data than for Mn_{12}Ac [74,75]. Given this improvement, we have also sought other high-symmetry Mn_{12} complexes, and have recently prepared $[Mn_{12}O_{12}(O_2CCH_2{}^tBu)_{16}(MeOH)_4]\cdot MeOH$, ($Mn_{12}{}^tBuAc$), (Fig. 1), which crystallizes in the high-symmetry space group $I\bar{4}$ [76]. In $Mn_{12}{}^tBuAc$, there is only one MeOH solvent molecule of crystallization, which sits on an S_4 symmetry axis and does not perturb the magnetic properties of this complex. Furthermore, the large bulky ^{t}BuAc groups more efficiently separate the clusters from their neighbors, minimizing inter-cluster interactions. Preliminary magnetic studies reveal the characteristic behavior of the Mn_{12} family. However, the data are remarkably clean and allow deeper insights into the fine details of the physical properties of Mn_{12} SMMs than has proven possible in the past.

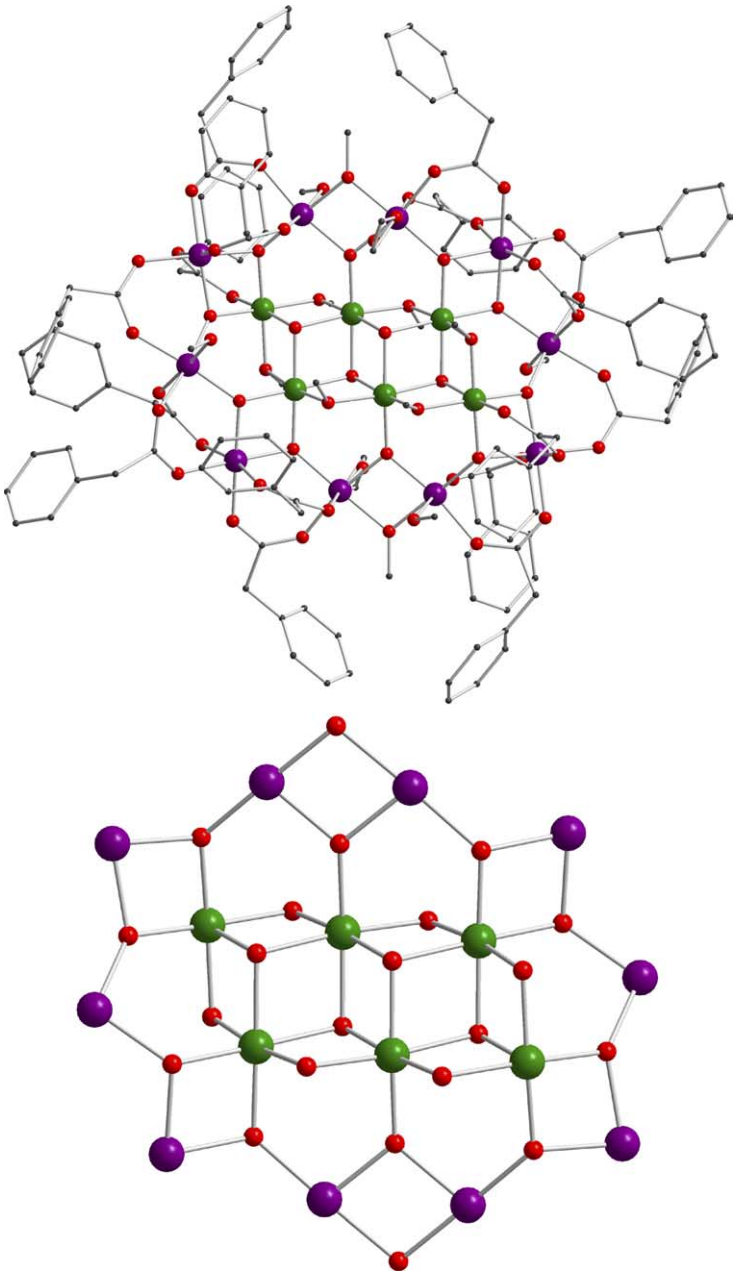


Fig. 3. The structure of $[Mn_{16}O_{16}(OMe)_6(O_2CCH_2Ph)_{16}(MeOH)_6]$ and its planar central core (bottom). Hydrogen atoms have been omitted for clarity. Color code: green, Mn^{IV}; purple, Mn^{III}; red, O; gray, C.

3. Some new procedures to SMMs

3.1. Reductive aggregation

The standard synthesis of $Mn_{12}Ac$ consists of the comproportionation reaction between $Mn(O_2CMe)_2 \cdot 4H_2O$ and $KMnO_4$ in 60% aqueous acetic acid. This is a convenient procedure involving oxidation of Mn^{II} ions and concomitant reduction of Mn^{VII} ions, producing a product at the $8Mn^{III}$, $4Mn^{IV}$ oxidation level. The Mn^{II}:Mn^{VII} reaction ratio can readily be varied, as can other reaction conditions and the presence of other reagents such as chelates. Various complexes, including mixed-valent Mn^{IV}/Mn^{III} [4–9,24–49,51–53] and Mn^{III}/Mn^{II} [7,8] species, can thus be obtained. As part of our general search of new synthetic methods to Mn_x clusters, a new procedure was developed in which the Mn^{II} source was omitted and MeOH was used as both the reducing agent for Mn^{VII} and as a potential source of MeO^- bridging ligands, in the presence also of excess carboxylic acid to prevent formation of manganese oxides and/or hydroxides. The procedure, which we have termed 'reductive aggregation,' proved its worth with the synthesis of $(N^nBu_4)_2[Mn_{12}O_{12}(OMe)_2(O_2CPh)_{16}(H_2O)_2]$ (Fig. 2) when benzoic acid was employed [71]; this is a new cluster type and SMM not available, at least to date, by any other route. It has since been possible to isolate two different analogues of this new structural type of Mn_{12} complex, $[Mn_{12}O_{10}(OMe)_3(OH)^-(O_2CC_6H_3F_2)_{16}(MeOH)_2] \cdot 4MeOH$ and $[Mn_{12}O_{10}(OMe)_4(O_2C^tBu)_{16}(MeOH)_2]$. These complexes all have significant structural similarity with $[Mn_{12}O_{12}(O_2CR)_{16}(H_2O)_4]$, all comprising a non-planar Mn_8^{III} ring around a central Mn_4^{IV} unit, but the central core of the new type of Mn_{12} cluster now contains alkoxide bridges. In effect, the central $[Mn_4O_4]$ cubane

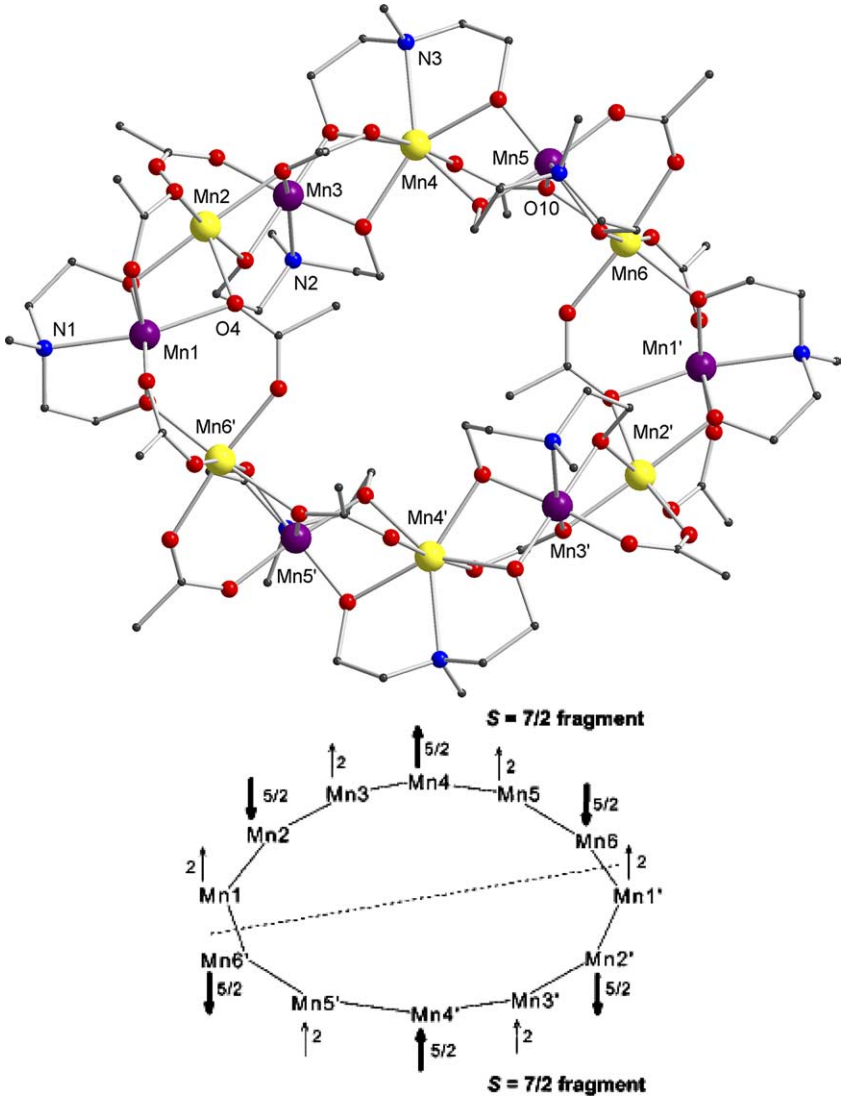


Fig. 4. The structure of $[Mn_{12}(O_2CMe)_{14}(mda)_8]$, excluding hydrogen atoms. Color code: yellow, Mn^{II}; purple, Mn^{III}; red, O; blue, N; gray, C. Bottom: Depiction of the spin alignments in the $S = 7$ ground state of the Mn_{12} loop as predicted by the DFT calculations.

of normal Mn_{12} complexes has been flattened, with the four central Mn^{IV} ions now forming a planar Mn_4 rhombus, i.e., the central core unit is a defect dicubane rather than a cubane (Fig. 2, bottom). In addition, the number of alkoxide bridges in the central core differs for all three of the new type of Mn_{12} clusters, ranging from two for the benzoate cluster, three for the difluorobenzoate cluster, and four for the pivalate cluster. Hence, these complexes represent the progressive replacement of oxide-bridges by alkoxide ones within the central core of $[Mn_{12}O_{12}(O_2CR)_{16}(H_2O)_4]$. In spite of their difference in the structure of the central core compared with normal Mn_{12} SMMs, the new types of Mn_{12} complexes still retain a significant barrier to magnetization relaxation, and they are thus SMMs, exhibiting hysteresis loops at low temperatures.

The new reductive aggregation procedure to Mn_x clusters has been subjected to further investigation by the use of various carboxylic acids. It was subsequently found that the reaction of phenylacetic acid, chloroacetic acid and bromoacetic acid with $N^nBu_4MnO_4$ in MeOH did not give further examples of the new Mn_{12} type of complex mentioned above, but instead a family of $[Mn_{16}O_{16}(OMe)_6(O_2CR)_{16}(MeOH)_6]$ complexes was obtained. These are similar but not identical to the Mn_{16} complex reported by Murray and co-workers [60]. The reductive aggregation reactions are clearly very complicated, and the reaction solutions likely contain a complicated mixture of several species in equilibrium, with factors such as relative solubility, lattice energies, crystallization kinetics and others determining the identity of the isolated product. One (or more) of these factors is undoubtedly the reason that changing the

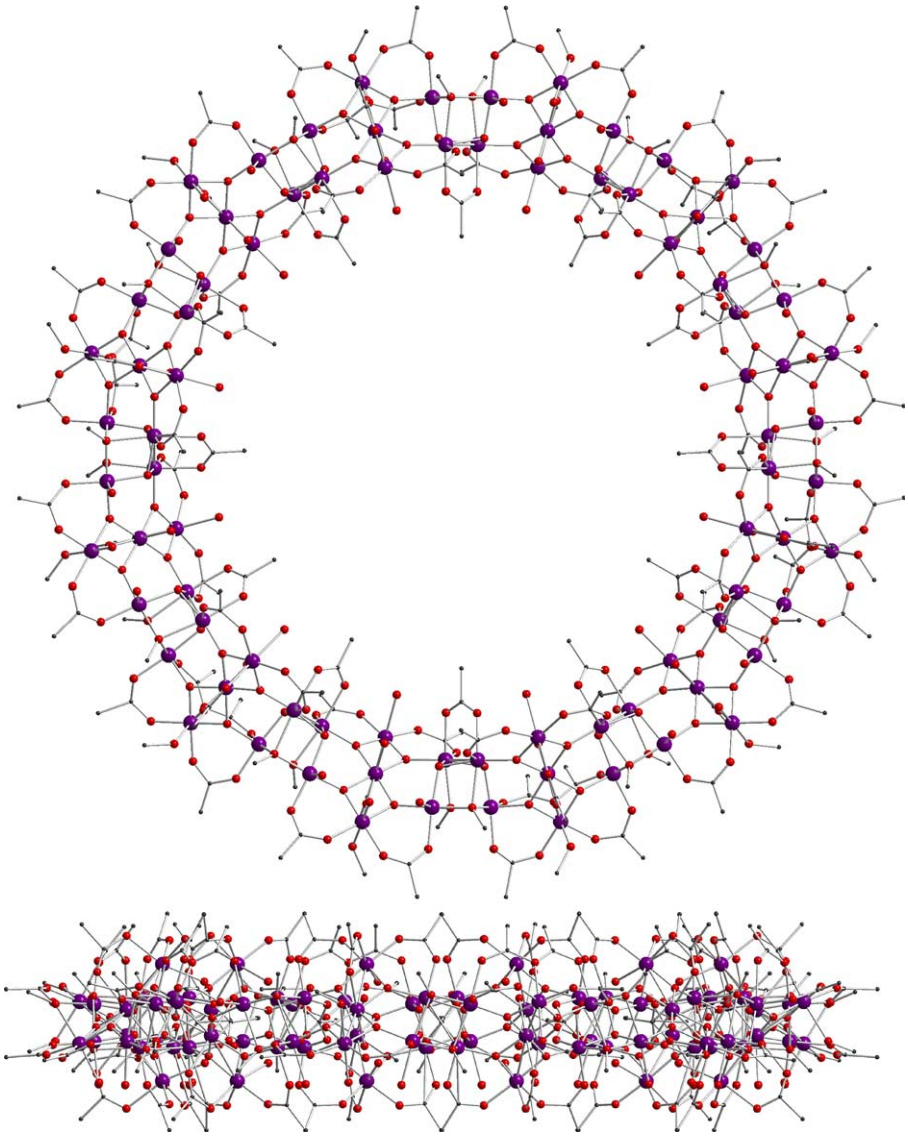


Fig. 5. The structure of the Mn_{84} torus, excluding hydrogen atoms. Bottom: Side-view of the molecule emphasizing its planarity.

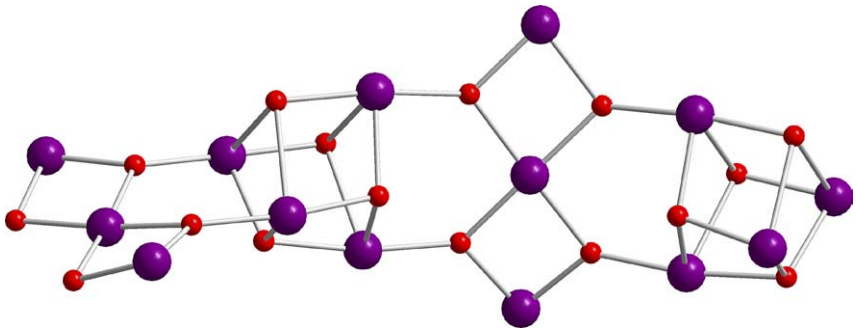


Fig. 6. The repeating [Mn_{14}] unit that represents the contents of the asymmetric unit; for clarity, carbon atoms and hydrogen atoms have been omitted.

carboxylic acid used from benzoic acid to the ones mentioned causes a major change in the isolated product from a Mn_{12} species to a Mn_{16} one. Furthermore, the three carboxylic acids employed are all derivatives of acetic acid, and it is thus interesting that when acetic acid itself was used, the product was the previously reported $[Mn_{84}O_{72}(O_2CMe)_{78}(OMe)_{24}(MeOH)_{12}(H_2O)_{42}(OH)_6]$ [67]. This contrasts with the fact that it was the acetate cluster $[Mn_{16}O_{16}(OMe)_6(O_2CMe)_{16}(MeOH)_3(H_2O)_3]$ that was obtained by Murray and co-workers [60] from the comproportionation reaction of $Mn(NO_3)_2$and $N^nBu_4MnO_4$ in excess MeOH; Murray's compound is essentially isostructural with the above Mn_{16} clusters, except for the terminal H_2O molecules replacing three of the MeOH molecules.

The phenylacetate Mn_{16} cluster (Fig. 3) has a roughly planar core comprising six Mn^{IV} and 10 Mn^{III} ions bridged by 14 μ_3-O^{2-}, two μ-O^{2-}, six μ-MeO^- and 16 μ-$PhCH_2CO_2^-$ groups (Fig. 3, bottom). The six Mn^{IV} ions are located within a central $[Mn_6^{IV}(\mu_3\text{-}O)_4(\mu\text{-}O)_2(\mu\text{-}MeO)_4]^{8+}$ core, with the six Mn^{IV} ions planar and the bridging O atoms above and below this plane, reminiscent of the planar CdI_2-type sheet structure. Encapsulating the central core is a non-planar ring of 10 Mn^{III} atoms to which it is connected by 10 μ_3-O^{2-} ions in the plane of the molecule and two μ-$PhCH_2CO_2^-$ groups one above and one below the plane. Thus, a useful description is as a small piece of a Mn oxide mineral held within a non-planar ring of Mn^{III} ions. The remaining 14 μ-$PhCH_2CO_2^-$ ligands, two μ-MeO^- groups (bridging Mn1 and Mn7a, and their symmetry equivalents) and six terminal MeOH molecules provide the peripheral ligation of the complete complex.

The Mn_{16} complexes have $S = 2$ ground states, and single-crystal magnetization versus DC field scans down to 0.04 K for the phenylacetate Mn_{16} cluster show hysteresis loops at <1 K, confirming SMM behaviour. No clear steps characteristic of QTM were observed in the hysteresis loops. Hence, although this compound has a small ground state, the near-parallel alignment of the Mn^{III} Jahn-Teller elongation axes provides sufficient molecular anisotropy to result in a small barrier to magnetization relaxation and hysteresis loops at very low temperatures.

3.2. Reactions with N-methyl-diethanolamine

Recently, we have been exploring the products from reactions employing alcohol-based ligands such as *N*-methyldiethanolamine ($mdaH_2$) to complement our previous work with the less flexible 2-hydroxymethylpyridine (hmpH) and pyridine-2,6-bis(dimethanol)

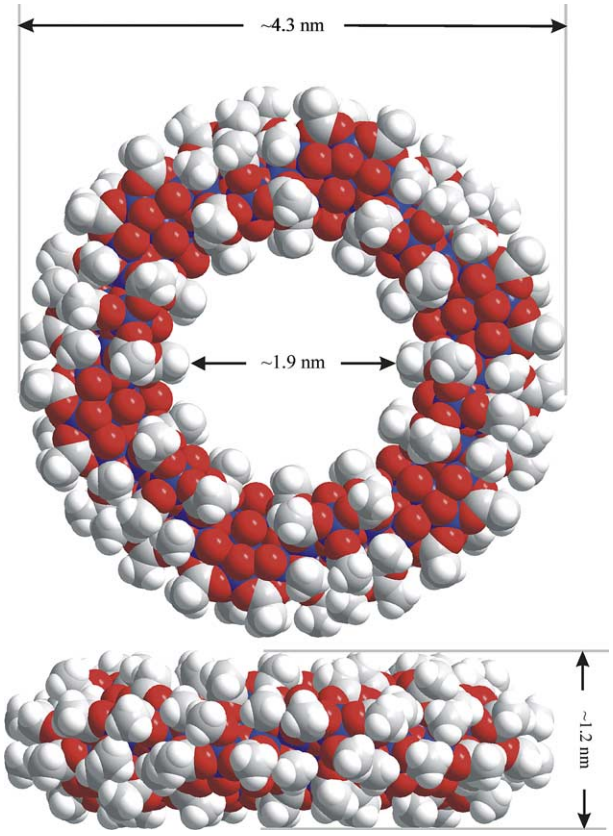


Fig. 7. Space-filling representations (including hydrogen atoms) from viewpoints perpendicular (top) and parallel (bottom) to the plane of the torus, showing the dimensions of the molecule and its central hole.

($pdmH_2$). With this reagent, we have isolated mixed-valent $[Mn_{12}(O_2CMe)_{14}(mda)_8]$ ($Mn_6^{II}Mn_6^{III}$), whose structure consists of a centrosymmetric Mn_{12} loop with a chair conformation (Fig. 4). All the manganese centers are six-coordinate except Mn^{II} ions Mn4 and Mn4′, which have a very distorted pentagonal-bipyramidal coordination sphere. Six mda^{2-} ligands each chelate a Mn^{III} ion, and the two alkoxide O atoms bridge to the adjacent Mn^{II} ions. The other two mda^{2-} groups chelate Mn^{II} ions and bridge by their alkoxide O atoms to Mn^{III} ions. As a result, the mda^{2-} groups alternate between being axial and equatorial with respect to the plane of the Mn_{12} loop. Each Mn_2 pair is additionally bridged by an acetate group in its familiar η^1,η^1,μ(*syn*, *syn*) binding mode on the outside of the loop, whereas the final two acetate groups bridge in a rarer η^1,η^2,μ^3 mode on the inside of the loop. This Mn_{12} loop complex has also been reported by others [57]. The complex has a relatively large ground-state spin value of $S = 7$: this is unusually intermediate in magnitude for a single-stranded Mn_6^{II}, Mn_6^{III} loop complex: antiferromagnetic or ferromagnetic Mn^{II}/Mn^{III} exchange interactions would be expected to give $S = 3$ or 27 ground states, respectively, so it is clear that there must be both types of interaction within this low-symmetry complex. To probe this further, we have carried out DFT calculations [77–81], and found both ferro- and antiferromagnetic interactions to be present, with all the J values being very weak, in the range $4.0 > J > -4.6$ cm^{-1}. This range is fully consistent with values for $Mn^{II}Mn^{III}$ exchange parameters, which are always weak and either side of zero, depending on the bridges [82]. Within the uncertainty of the DFT calculation, the Mn1–Mn6′ and Mn1′–Mn6 interactions are calculated to be 0.0 cm^{-1}: in fact, they are almost certainly either very weakly positive or negative. Since the spin of each half of the molecule is calculated to be $S = 7/2$, positive Mn1–Mn6′ and Mn1′–Mn6 interactions would give a ground-state spin of $S = 0$ while negative Mn1–Mn6′ and Mn1′–Mn6 interactions give $S = 7$ for the complete molecule (Fig. 4, bottom). On the basis of the magnetization data that clearly rule out an $S = 0$ ground state, we conclude that the ground state is $S = 7$, resulting from the spin alignments in (Fig. 4, bottom), in complete agreement with the magnetization studies.

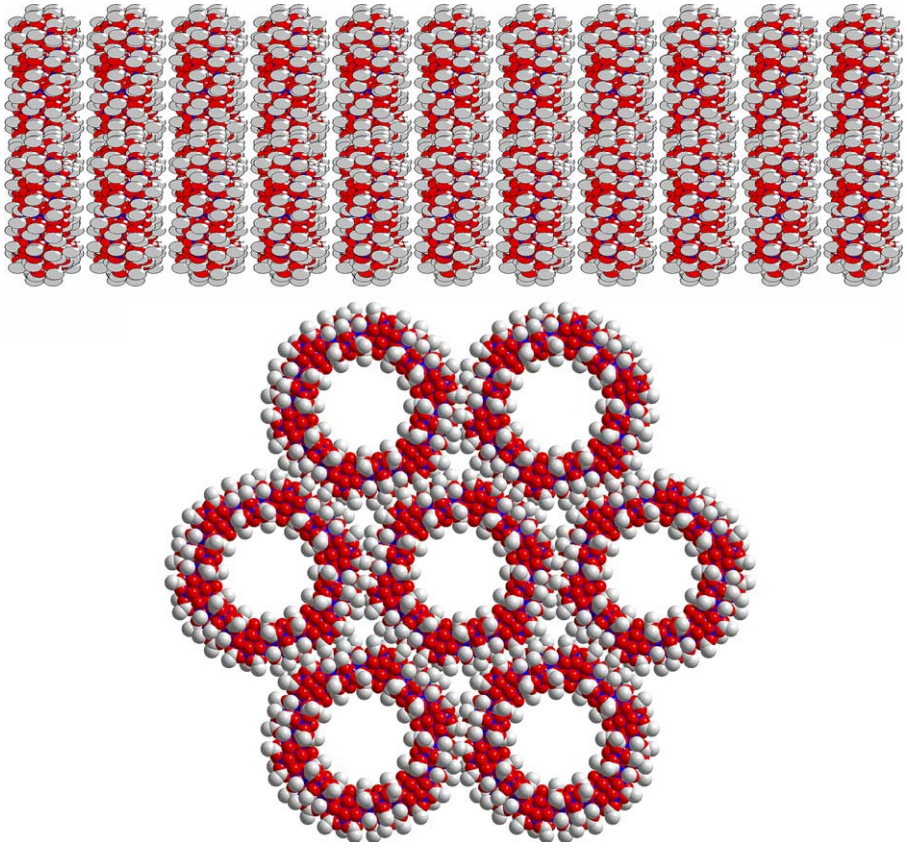


Fig. 8. Top: Ordered arrangement of Mn_{84} molecules (excluding hydrogen atoms) into two adjacent supramolecular nanotubes viewed perpendicular to the propagation axis; this view emphasizes the exact registry of molecules in adjacent tubes and thus the sheet-like structure formed. Bottom: A view along the propagation axes of seven tubes showing the hexagonal packing of neighbors within a single sheet of molecules (excluding hydrogen atoms).

3.3. Methanolysis routes to a Mn_{84} torus

We have long sought to synthesize SMMs of very large dimensions (by molecular standards) to probe whether products from the molecular (or bottom-up) approach to nanoscale magnetic materials can reach the size regime of the traditional (or top-down) approach. As part of these efforts, we have obtained $[Mn_{84}O_{72}(O_2CMe)_{78}(OMe)_{24}(MeOH)_{12}(H_2O)_{42}(OH)_6]$ (Mn_{84}) from the reaction of $Mn_{12}Ac$ with $N^nBu_4MnO_4$ in MeOH. The structure (Fig. 5) comprises a giant Mn_{84} torus with a >4 nm diameter composed of alternating near-linear $[Mn_3O_4]$ and cubic $[Mn_4]$ subunits (Fig. 6). All the Mn ions are Mn^{III}. The Mn_{84} complex exhibits hysteresis and QTM and is thus the largest SMM prepared to date. A better appreciation of the structure and the size of the molecule is provided by the space-filling plots of Fig. 7, which show that the torus has a diameter of about 4.3 nm and a thickness of about 1.2 nm, with a central hole of diameter 1.9 nm. The Mn_{84} molecules order within the crystal in an aesthetically pleasing manner, giving nanotubular stacks parallel to the crystal c axis and to their neighbors (Fig. 8). This yields a hexagonal close packing analogous to densely packed straws in a box. The crystalline structure of Mn_{84} thus displays extensive cylindrical channel formation along one dimension. Molecules in neighboring chains are exactly adjacent (Fig. 8), and thus the structure may be alternatively described as consisting of graphite-like Mn_{84} sheets lying on top of each other with perfect registry.

4. Conclusions

The field of single-molecule magnets, or molecular nanomagnets, continues to grow and branch out in several directions. We have tried in this short review to emphasize the importance of obtaining synthetic control over obtained species, so that they can be modified in desirable ways. This thus allows expansion of a particular structural type into a family of related species that are invaluable in probing the various factors that affect the observed magnetic properties. We have also tried to emphasize the variety of species that can be obtained in Mn chemistry, which continues to be the richest source of SMMs, as the number of synthetic methods continues to increase.

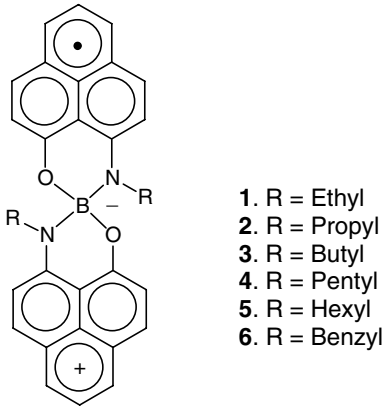
Acknowledgment

The work described herein was supported by the National Science Foundation.

References

[1] R. Sessoli, D. Gatteschi, A. Caneschi, M.A. Novak, Nature 365 (1993) 141.
[2] R. Sessoli, H.-L. Ysai, A.R. Schake, S. Wang, J.B. Vincent, K. Folting, D. Gatteschi, G. Christou, D.N. Hendrickson, J. Am. Chem. Soc. 115 (1993) 1804.
[3] S.M. Aubin, N.R. Gilley, L. Pardi, J. Krzystek, M.W. Wemple, L.C. Brunel, M.B. Marple, G. Christou, D.N. Hendrickson, J. Am. Chem. Soc. 120 (1998) 4991.
[4] S.M. Aubin, M.W. Wemple, D.M. Adams, H.-L. Tsai, G. Christou, D.N. Hendrickson, J. Am. Chem. Soc. 118 (1996) 7746.
[5] E.K. Brechin, J. Yoo, J.C. Huffman, D.N. Hendrickson, G. Christou, Chem. Commun. (1999) 783.
[6] J. Yoo, E.K. Brechin, A. Yamaguchi, M. Nakano, J.C. Huffman, A.L. Maniero, L.C. Brunel, K. Awaga, H. Ishimoto, G. Christou, D.N. Hendrickson, Inorg. Chem. 39 (2000) 3615.
[7] J. Yoo, A. Yamaguchi, M. Nakano, J. Krzystek, W.E. Streib, L.-C. Brunel, H. Ishimoto, G. Christou, D.N. Hendrickson, Inorg. Chem. 40 (2001) 4604.
[8] E. Yang, N. Harden, W. Wernsdorfer, L. Zakharov, E.K. Brechin, A.L. Rheingold, G. Christou, D.N. Hendrickson, Polyhedron 22 (2003) 1857.
[9] L.M. Wittick, K.S. Murray, B. Moubaraki, S.R. Batten, L. Spiccia, K.J. Berry, J. Chem. Soc., Dalton Trans. (2004) 1003.
[10] A.K. Powell, S.L. Heath, D. Gatteschi, L. Pardi, R. Sessoli, G. Spina, F. Del Giallo, F. Pieralli, J. Am. Chem. Soc. 117 (1995) 2491.
[11] D. Gatteschi, R. Sessoli, A. Cornia, Chem. Commun. (2000) 725.
[12] H. Oshio, N. Hoshino, T. Ito, J. Am. Chem. Soc. 122 (2000) 12602.
[13] C. Cadiou, M. Murrie, C. Paulsen, V. Villar, W. Wernsdorfer, R.E.P. Winpenny, Chem. Commun. (2001) 2666.
[14] S.T. Ochsenbein, M. Murrie, E. Rusanov, H. Stoeckli-Evans, C. Sekine, H. Güdel, Inorg. Chem. 41 (2002) 4604.
[15] J.J. Sokol, A.G. Hee, J.R. Long, J. Am. Chem. Soc. 124 (2002) 7656.
[16] A.K. Boudalis, B. Donnadieu, V. Nastopoulos, J.M. Clemente-Juan, A. Mari, Y. Sanakis, J.P. Tuchagues, S.P. Perlepes, Angew. Chem. Int. Ed. 43 (2004) 2266.
[17] S. Osa, T. Kido, N. Matsumoto, N. Re, A. Pochaba, J.J. Mrozinski, J. Am. Chem. Soc. 126 (2004) 420.
[18] M. Murrie, S.J. Teat, H. Stoeckli-Evans, H.U. Güdel, Angew. Chem. Int. Ed. 42 (2003) 4653.
[19] G.W. Powell, H.N. Lancashire, E.K. Brechin, D. Collison, S.L. Heath, T. Mallah, W. Wernsdorfer, Angew. Chem. Int. Ed. 43 (2004) 5772.
[20] C. Benelli, J. Cano, Y. Journaux, R. Sessoli, G.A. Solan, R.E.P. Winpenny, Inorg. Chem. 40 (2001) 188.
[21] A.L. Barra, A. Caneschi, A. Cornia, F. Fabrizi de Biani, D. Gatteschi, C. Sangregorio, R. Sessoli, L. Sorace, J. Am. Chem. Soc. 121 (1999) 5302.
[22] M. Nakano, L.N. Zakharov, R.D. Sommer, A.L. Rheingold, M. Ledezma-Gairaud, G. Christou, J. Appl. Phys. 91 (1991) 7382.
[23] Z. Sun, C.M. Grant, S.L. Castro, D.N. Hendrickson, G. Christou, Chem. Commun. (1998) 721.
[24] T. Lis, Acta Crystallogr., Sect. B 36 (1980) 2042.
[25] Z. Sun, D. Ruiz, E. Rumberger, C.D. Incarvito, K. Folting, A.L. Rheingold, G. Christou, D.N. Hendrickson, Inorg. Chem. 37 (1998) 4758.
[26] J. An, Z. Chen, X. Zhang, H.G. Raubenheimer, C. Esterhuysen, S. Gao, G. Xian Xu, J. Chem. Soc., Dalton Trans. (2001) 3352.
[27] M. Soler, W. Wernsdorfer, Z. Sun, J.C. Huffman, D.N. Hendrickson, G. Christou, Chem. Commun. (2003) 2672.

[28] H. Zhao, C.P. Berlinguette, J. Basca, A.V. Prosvirin, J.K. Bera, S.E. Tichy, E.J. Schelter, K.R. Dunbar, Inorg. Chem. 43 (2004) 1359.
[29] S.M. Aubin, Z. Sun, H.J. Eppley, E.M. Rumberger, I.A. Guzei, K. Folting, P.K. Gantzel, A.L. Rheingold, G. Christou, D.N. Hendrickson, Inorg. Chem. 40 (2001) 2127.
[30] C. Boskovic, M. Pink, J.C. Huffman, D.N. Hendrickson, G. Christou, J. Am. Chem. Soc. 123 (2001) 9914.
[31] J.T. Brockman, K.A. Abboud, D.N. Hendrickson, G. Christou, Polyhedron 22 (2003) 1765.
[32] A.R. Schake, H.-L. Tsai, N. de Vries, R.J. Webb, K. Folting, D.N. Hendrickson, G. Christou, J. Chem. Soc., Chem. Commun. (1992) 181.
[33] N.E. Chakov, W. Wernsdorfer, K.A. Abboud, D.N. Hendrickson, G. Christou, J. Chem. Soc., Dalton Trans. 11 (2003) 2243.
[34] P. Artus, C. Boskovic, J. Yoo, W.E. Streib, L.-C. Brunel, D.N. Hendrickson, G. Christou, Inorg. Chem. 40 (2001) 4199.
[35] N.C. Chakov, K.A. Abboud, L.N. Zahkarov, A.L. Rheingold, D.N. Hendrickson, G. Christou, Polyhedron 22 (2003) 1759.
[36] T. Kuroda-Sowa, S. Fukuda, S. Miyoshi, M. Maekawa, M. Munakata, H. Miyasaka, M. Yamashita, Chem. Lett. 31 (2002) 682.
[37] G.-Q. Bian, T. Kuroda-Sowa, H. Konaka, M. Hatano, M. Maekawa, M. Munakata, H. Miyasaka, M. Yamashita, Inorg. Chem. 43 (2004) 4790.
[38] T. Kuroda-Sowa, T. Handa, M. Maekawa, M. Munakata, H. Miyasaka, M. Yamashita, Chem. Lett. 33 (2004) 540.
[39] G.-Q. Bian, T. Kuroda-Sowa, N. Gunjima, M. Maekawa, M. Munakata, Inorg. Chem. Commun. 8 (2005) 208.
[40] M. Pacchioni, A. Cornia, A.C. Fabretti, L. Zobbi, D. Bonacchi, A. Caneschi, G. Chastanet, D. Gatteschi, R. Sessoli, Chem. Commun. (2004) 2604.
[41] H.J. Eppley, H.-L. Tsai, N. de Vries, K. Folting, G. Christou, D.N. Hendrickson, J. Am. Chem. Soc. 117 (1995) 301.
[42] S.M.J. Aubin, Z. Sun, L. Pardi, J. Krzystek, K. Folting, L.-C. Brunel, A.L. Rheingold, G. Christou, D.N. Hendrickson, Inorg. Chem. 38 (1999) 5329.
[43] M. Soler, S.K. Chandra, D. Ruiz, E.R. Davidson, D.N. Hendrickson, G. Christou, Chem. Commun. (2000) 2417.
[44] T. Kuroda-Sowa, T. Nogami, H. Konaka, M. Maekawa, M. Munakata, H. Miyasaka, M. Yamashita, Polyhedron 22 (2003) 1795.
[45] T. Kuroda-Sowa, M. Lam, A.L. Rheingold, C. Frommen, W.M. Reiff, M. Nakano, J. Yoo, A.L. Maniero, L.C. Brunel, G. Christou, D.N. Hendrickson, Inorg. Chem. 40 (2001) 6469.
[46] M. Soler, W. Wernsdorfer, K.A. Abboud, J.C. Huffman, E.R. Davidson, D.N. Hendrickson, G. Christou, J. Am. Chem. Soc. 125 (2003) 3576.
[47] M. Soler, W. Wernsdorfer, K.A. Abboud, D.N. Hendrickson, G. Christou, Polyhedron 22 (2003) 1777.
[48] R. Basler, A. Sieber, G. Chaboussant, H.U. Gudel, N.E. Chakov, M. Soler, G. Christou, A. Desmedt, R. Lechner, Inorg. Chem. 44 (2005) 649.
[49] E. Coronado, A. Forment-Aliaga, A. Gaita-Ari, C. Giménez-Saiz, F.M. Romero, W. Wernsdorfer, Angew. Chem. Int. Ed. 43 (2004) 6152.
[50] H. Miyasaka, R. Clérac, W. Wernsdorfer, L. Lecren, C. Bonhomme, K. Sugiura, M.A. Yamashita, Angew. Chem. Int. Ed. 43 (2004) 2801.
[51] H. Andres, R. Basler, H.-U. Güdel, G. Aromí, G. Christou, H. Büttner, B. Rufflé, J. Am. Chem. Soc. 122 (2000) 12469.
[52] S. Hill, R.S. Edwards, N. Aliaga-Alcalde, G. Christou, Science 302 (2003) 1015.
[53] W. Wernsdorfer, N. Aliaga-Alcalde, D.N. Hendrickson, G. Christou, Nature 416 (2002) 406.
[54] C.J. Milios, C.P. Raptopoulou, A. Terzis, F. Lloret, R. Vicente, S.P. Perlepes, A. Escuer, Angew. Chem. Int. Ed. 43 (2003) 210.
[55] M. Murugesu, W. Wernsdorfer, K.A. Abboud, G. Christou, Angew. Chem. Int. Ed. 44 (2005) 892.
[56] E.K. Brechin, M. Soler, J. Davidson, D.N. Hendrickson, S. Parsons, G. Christou, Chem. Commun. (2002) 2252.
[57] E.M. Rumberger, L.N. Zakharov, A.L. Rheingold, D.N. Hendrickson, Inorg. Chem. 43 (2004) 6531.
[58] D. Foguet-Albiol, T.A. O'Brien, W. Wernsdorfer, B. Moulton, M.J. Zaworotko, K.A. Abboud, G. Christou, Angew. Chem. Int. Ed. 44 (2005) 897.
[59] C. Boskovic, E.K. Brechin, W.E. Streib, K. Folting, J.C. Bollinger, D.N. Hendrickson, G. Christou, J. Am. Chem. Soc. 124 (2002) 3725.
[60] D.J. Price, S.R. Batten, B. Moubaraki, K.S. Murray, Chem. Commun. (2002) 762.
[61] P. King, W. Wernsdorfer, K.A. Abboud, G. Christou, Inorg. Chem. 43 (2004) 7315.
[62] M. Murugesu, J. Raftery, W. Wernsdorfer, G. Christou, E.K. Brechin, Inorg. Chem. 43 (2004) 4203.
[63] M. Murugesu, M. Habrych, W. Wernsdorfer, K.A. Abboud, G. Christou, J. Am. Chem. Soc. 126 (2004) 4766.
[64] L.F. Jones, G. Rajaraman, J. Brockman, M. Murugesu, E.C. Sanudo, J. Raftery, S.J. Teat, W. Wernsdorfer, G. Christou, E.K. Brechin, D. Collison, Chem. Eur. J. 10 (2004) 5180.
[65] M. Soler, E. Rumberger, K. Folting, D.N. Hendrickson, G. Christou, Polyhedron 20 (2001) 1365.
[66] M. Soler, W. Wernsdorfer, K. Folting, M. Pink, G. Christou, J. Am. Chem. Soc. 126 (2004) 2156.
[67] A.J. Tassiopoulos, A. Vinslave, W. Wernsdorfer, K.A. Abboud, G. Christou, Angew. Chem. Int. Ed. 43 (2004) 2117.
[68] A. Cornia, R. Sessoli, L. Sorace, D. Gatteschi, A.L. Barra, C. Daiguebonne, Phys. Rev. Lett. 89 (2002) 257201.
[69] S. Hill, R.S. Edwards, S.I. Jones, J.M. North, N.S. Dalal, Phys. Rev. Lett. 90 (2003) 217204.
[70] E. del Barco, A.D. Kent, E.M. Rumberger, D.N. Hendrickson, G. Christou, Phys. Rev. Lett. 91 (2003) 047203.
[71] A.J. Tasiopoulos, W. Wernsdorfer, K.A. Abboud, G. Christou, Angew. Chem. Int. Ed. 43 (2004) 6338.
[72] M. Soler, S.K. Chandra, D. Ruiz, E.R. Davidson, D.N. Hendrickson, G. Christou, Chem. Commun. (1998) 803.
[73] M. Soler, P. Artus, K. Folting, J.C. Huffman, D.N. Hendrickson, G. Christou, Inorg. Chem. 40 (2001) 4902.
[74] A.G. Harter, N.E. Chakov, B. Roberts, R. Achey, A. Reyes, P. Kuhns, G. Christou, N.S. Dalal, Inorg. Chem. 44 (2005) 2122.
[75] E. del Barco, A.D. Kent, S. Hill, J.M. North, N.S. Dalal, E.M. Rumberger, D.N. Hendrickson, N. Chakov, G. Christou, arXiv/cond-mat/0404390 (2004).
[76] S. Hill, N. Anderson, A. Wilson, S. Takahashi, K. Petukhov, N. Chakov, M. Murugesu, J.M. North, N.S Dalal, G. Christou, Polyhedron (2005) in press.
[77] J. Cano, P. Alemany, S. Alvarez, M. Verdaguer, E. Ruiz, Chem. Eur. J. 4 (1998) 476.
[78] E. Ruiz, J. Cano, S. Alvarez, P. Alemany, J. Am. Chem. Soc. 120 (1998) 11122.
[79] E. Ruiz, J. Cano, S. Alvarez, P. Alemany, J. Comput. Chem. 20 (1999) 1391.
[80] E. Ruiz, A. Rodriguez-Fortea, J. Cano, S. Alvarez, J. Comput. Chem. 24 (2003) 982.
[81] R. Carrasco, J. Cano, T. Mallah, L.F. Jones, D. Collison, E.K. Brechin, Inorg. Chem. 43 (2004) 5410.
[82] L. Que, A.E. True, Prog. Inorg. Chem. 38 (1990) 97.



Scheme 1.

than that of the propyl (**2**) and pentyl (**4**) radicals [6,7] (see Scheme 1).

In the present paper, we report the synthesis, redox properties and solid state structures of hexacoordinated germanium ($\mathbf{7}^{+}\mathbf{TFPB}^{-}$) and silicon ($\mathbf{8}^{+}\mathbf{TFPB}^{-}$) cations containing three phenalenyl (PLY) units; such octahedral silicon and germanium complexes with 9-oxophenalenone ligands are not well known.

2. Results and discussion

2.1. Synthesis

The synthetic procedure for the preparation of $\mathbf{7}^{+}\mathbf{TFPB}^{-}$ and $\mathbf{8}^{+}\mathbf{TFPB}^{-}$ are shown in Scheme 2. A toluene solution of 9-hydroxyphenalenone was treated with $GeCl_4$ and $SiCl_4$ to obtain the corresponding chloride salts which were used as such for the next reaction without further purification. The chloride salts are quite insoluble in most common organic solvent but are sparingly soluble in dichloromethane. The anion exchange reactions were performed in dry dichloromethane at

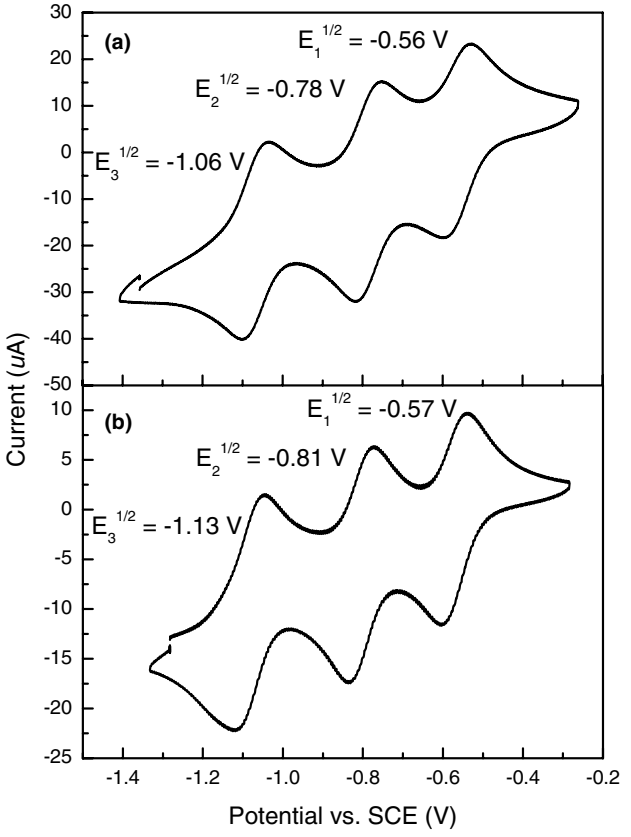
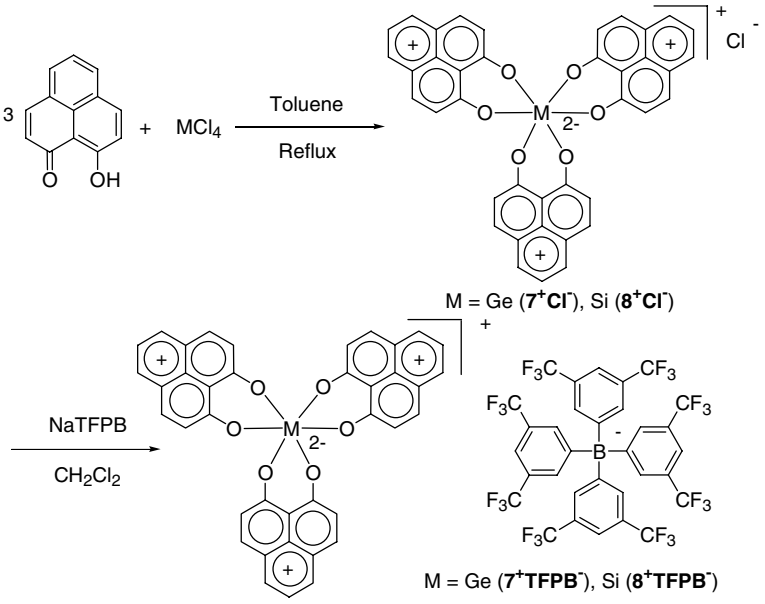
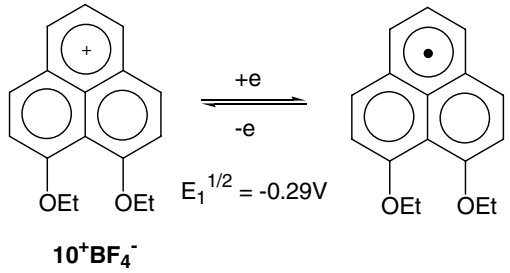


Fig. 1. Cyclic voltammetry of: (a) $\mathbf{7}^{+}\mathbf{TFPB}^{-}$ and (b) $\mathbf{8}^{+}\mathbf{TFPB}^{-}$ in acetonitrile, reference to SCE via internal ferrocene (not shown).



Scheme 2.

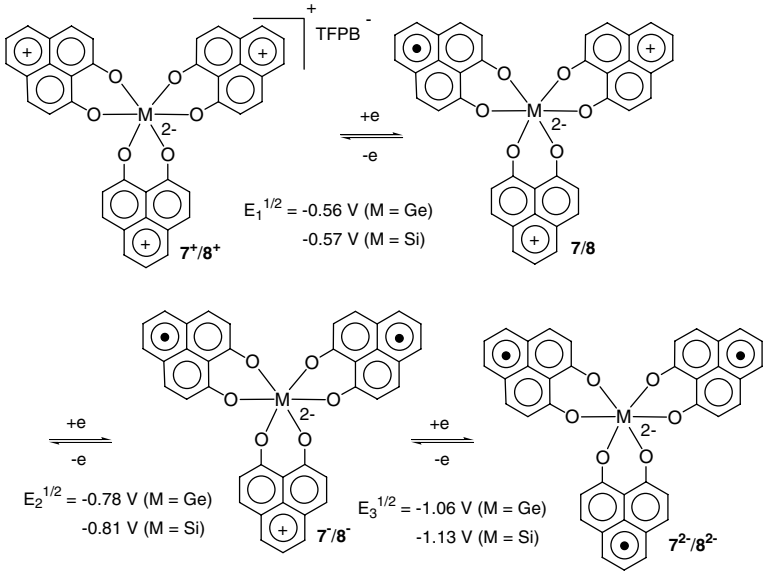
room temperature. Addition of solid sodium tetrakis[3,5-bis(trifluoromethyl)phenyl]borate (NaTFPB) leads to dissolution of the cations due to the formation of the TFPB salt. The excess chloride salt and the NaCl formed during the reaction were separated by filtration. Compound $\mathbf{7}^{+}\mathbf{TFPB}^{-}$ and $\mathbf{8}^{+}\mathbf{TFPB}^{-}$ were found to be stable in the solid state and in solution at room temperature.



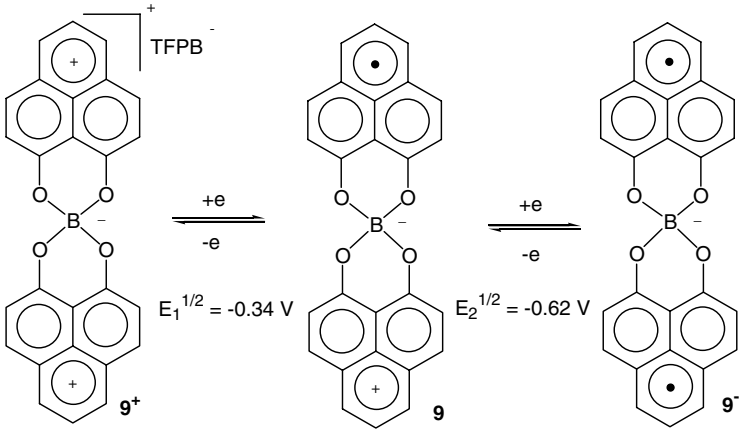
Scheme 5.

2.2. Electrochemistry

The cyclic voltammetry of $\mathbf{7}^{+}\mathbf{TFPB}^{-}$ and $\mathbf{8}^{+}\mathbf{TFPB}^{-}$ exhibit three reversible redox waves at $E_1^{1/2} = -0.56$ V, $E_2^{1/2} = -0.78$ V, $E_3^{1/2} = -1.06$ V and $E_1^{1/2} = -0.57$ V, $E_2^{1/2} = -0.81$ V and $E_3^{1/2} = -1.13$ V versus SCE (Fig. 1) corresponding to the successive reduction to radical, anion and dianion of the phenalenyl moiety (Scheme 3). The relative ease of reduction of these complexes follows the electronegativities of the central atoms: Ge, 2.02; Si, 1.74. The potentials may be compared to the reduction potentials observed for $\mathbf{9}^{+}$: $E_1^{1/2} = -0.34$ V and $E_2^{1/2} = -0.62$ V (Scheme 4), and $\mathbf{10}^{+}$: $E_1^{1/2} = -0.29$ V versus SCE (Scheme 5). The ease of the first reduction of these compounds follows the order: $\mathbf{10}^{+} > \mathbf{9}^{+} > \mathbf{7}^{+}$ and $\mathbf{8}^{+}$, which is in the sequence of 1,



Scheme 3.



Scheme 4.

2 and 3 phenalenyl units per molecule. This sequence may be understood by considering the degree of charge that is localized in a single phenalenyl ring in the complexes – clearly one PLY ring bears most of the charge density in the salt $\mathbf{10}^+$, and along this series it is apparent that any given PLY unit will bear a lower positive charge in the salt as the number of the PLY units increases and, therefore, the first electron transfer will become progressively more difficult. This is in agreement with the bond length data for the salts $\mathbf{7}^+$, $\mathbf{8}^+$ and the beryllium compound, [8] shown in Table 3 where it may be seen that the C1–O1 and C9–O2 bond lengths are 1.302, 1.296, 1.287 and 1.300, 1.308, 1.290 Å, respectively. The bond length should be a sensitive indicator of the degree of charge separation in the complexes with longer bond lengths associated with a greater degree of charge separation. A six-coordinated silicon (IV) complex with a tripodal phenalenyl-based hexadentate ligand was recently shown to undergo three reductions at potentials of −0.97, −1.19 and −1.43 V versus SCE [9], due to reduction to the radical, anion and dianion. This compound is more difficult to reduce than $\mathbf{7}^+\mathbf{TFPB}^-$ and $\mathbf{8}^+\mathbf{TFPB}^-$, because of the presence of nitrogen in the coordination sphere of silicon.

The disproportionation potential of $\mathbf{7}^+$ and $\mathbf{8}^+$, $\Delta E_{2-1} = E_2^{1/2} - E_1^{1/2} = -0.22$ and -0.24 V versus SCE, are considerably lower in magnitude than the values found for the boron compounds previously reported [3–5]. Table 1 lists the results of the cyclic voltammetry experiments carried out on salts $\mathbf{1}^+$, $\mathbf{2}^+$, $\mathbf{3}^+$, $\mathbf{4}^+$, $\mathbf{5}^+$, $\mathbf{6}^+$ (with BPh_4^- as the counterion) together with the new compounds. The small ΔE_{2-1} value seen in $\mathbf{7}^+$ and $\mathbf{8}^+$ can be explained in terms of the reduction in the electron repulsion by the delocalization of the charge over the three PLY sites. The ΔE_{2-1} value largely determines the on-site Coulomb correlation energy (U) in the solid state and is well established as an important discriminator for organic metals [10,11]. The three reduction waves in the cyclic voltammogram indicate that it is possible to introduce one electron into each of the PLY ring (Scheme 3).

Table 1
Half-wave potentials[a] and the disproportionation potentials of various tetraphenylborate and TFPB salts

Cation	$E_1^{1/2}$	$E_2^{1/2}$	$E_3^{1/2}$	ΔE_{2-1}	References
$\mathbf{7}^+\mathbf{TFPB}^-$	−0.56	−0.78	−1.06	−0.22	this work
$\mathbf{8}^+\mathbf{TFPB}^-$	−0.57	−0.81	−1.13	−0.24	this work
$\mathbf{1}^+$	−0.75	−1.10		−0.35	[5]
$\mathbf{2}^+$	−0.75	−1.10		−0.35	[6]
$\mathbf{3}^+$	−0.73	−1.09		−0.36	[5]
$\mathbf{4}^+$	−0.74	−1.11		−0.37	[7]
$\mathbf{5}^+$	−0.74	−1.11		−0.37	[3]
$\mathbf{6}^+$	−0.68	−1.02		−0.34	[4]

[a] In acetonitrile, referenced to SCE (saturated calomel electrode) via internal reference ferrocene.

2.3. Crystallography

Single crystals of $\mathbf{7}^+\mathbf{TFPB}^-$ and $\mathbf{8}^+\mathbf{TFPB}^-$ were grown from diethyl ether and hexane solution at room temperature and studied by single crystal X-ray diffraction. Crystallization of $\mathbf{7}^+\mathbf{TFPB}^-$ and $\mathbf{8}^+\mathbf{TFPB}^-$ gave needle like crystals of diethyl ether solvates, which belong to the triclinic space group $P\bar{1}$, with two molecules per unit cell. Table 2 provides crystal data of compound $\mathbf{7}^+\mathbf{TFPB}^-$ and $\mathbf{8}^+\mathbf{TFPB}^-$. An ORTEP plot of the molecular structure of $\mathbf{7}^+\mathbf{TFPB}^-$ and $\mathbf{8}^+\mathbf{TFPB}^-$ are shown in Fig. 2.

The molecular geometry around germanium and silicon are approximately octahedral, consisting of three bidentate chelating PLY ligands. The plane of the three PLY rings in $\mathbf{7}^+\mathbf{TFPB}^-$ reveal some distortion from the ideal octahedral symmetry; their dihedral angles are 84°

Table 2
Crystal data for $\mathbf{7}^+\mathbf{TFPB}^-$ and $\mathbf{8}^+\mathbf{TFPB}^-$

Compound	$\mathbf{7}^+\mathbf{TFPB}^-$	$\mathbf{8}^+\mathbf{TFPB}^-$
Formula	$C_{71}H_{33}BF_{24}GeO_6\cdot[C_4H_{10}O]_{2.5}$	$C_{71}H_{33}BF_{24}SiO_6[C_4H_{10}O]_{2.5}$
Crystal system	triclinic	triclinic
Formula weight	1706.67	1662.17
Unit cell dimensions		
a (Å)	12.2965(16)	12.297(2)
b (Å)	17.104(2)	17.124(3)
c (Å)	18.536(2)	17.124(3)
α (°)	75.645(3)	75.762(3)
β (°)	82.109(3)	82.337(4)
γ (°)	74.879(2)	74.869(3)
V (Å)	3635.0(8)	3636.0(11)
Space group	$P\bar{1}$	$P\bar{1}$
Z	2	2
Temperature (K)	223(2)	233(2)
μ (mm^{-1})	0.543	0.154
Data/restrain/parameter	14 870/1082/1227	14 864/631/1323
Final R indices [$I > 2\sigma(I)$]	$R_1 = 0.0543$, $wR_2 = 0.1489$	$R_1 = 0.0589$, $wR_2 = 0.1557$
R indices (all data)	$R_1 = 0.0758$, $wR_2 = 0.1676$	$R_1 = 0.0949$, $wR_2 = 0.1873$

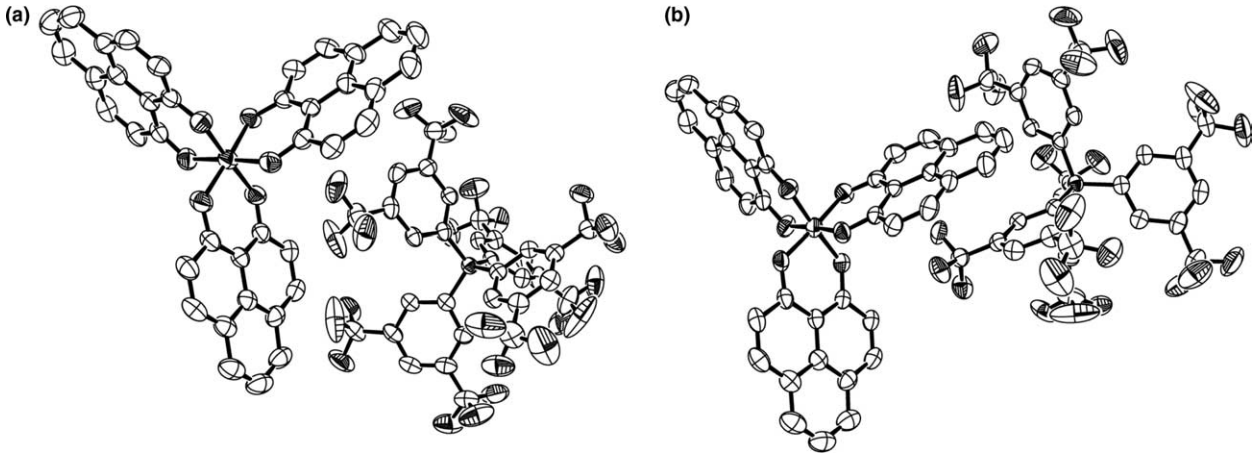


Fig. 2. ORTEP diagram of the molecular structure of: (a) $7^{+}TFPB^{-}$ and (b) $8^{+}TFPB^{-}$.

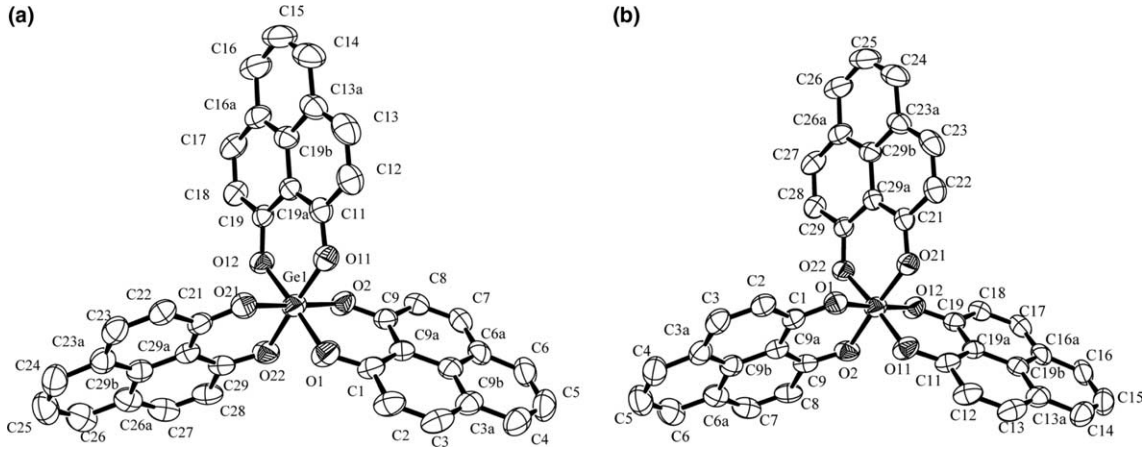


Fig. 3. ORTEP diagram of the molecular structure of: (a) $7^{+}TFPB^{-}$ and (b) $8^{+}TFPB^{-}$ (only the cation part) and the numbering of the atoms.

(C_1–C_{9b}, C_{11}–C_{19b}), 80.5° (C_{11}–C_{19b}, C_{21}–C_{29b}) and 102.9° (C_{21}–C_{29b}, C_1–C_{9b}) (see Fig. 3), rather than 90° as expected in ideal octahedral symmetry. The corresponding dihedral angles for the silicon compound are 83.8°, 80.1° and 102.8°. The dihedral angles are different from that observed in the *cis*-hexacoordinate (tropolonato)$_2$ $SiPh_2$ (an α-diketonate compound) in which the angle of the two tropolonate chelating planes is 81.1° [12]. The structure distorts so that the metal atom deviates from the chelate-ring plane, and this has been noted in studies of several acetylacetonato complexes and is ascribed to the packing forces in the crystals [13]. The comparison of the bond lengths in Table 3 indicates that there is a considerable amount of charge separation in the cationic complexes of germanium and silicon as reflected by the C–O bond lengths in these compounds.

The structure of the counter anion (TFPB) also deviates from the ideal tetrahedral geometry and this is probably due to the presence of bulky substituents (CF_3) on the phenyl ring. In the crystal structure of $7^{+}TFPB^{-}$ four out of eight CF_3 groups in the counter anion show disorder. In compound $8^{+}TFPB^{-}$ all the CF_3 groups were refined as disordered CF_3.

In the molecular structure of the salt ($7^{+}TFPB^{-}$), each cation is involved in π–π interactions with two neighbouring molecules and thus these cations form chains in the solid state (Fig. 4). The chain formation

Table 3
Comparison of bond length (in Å) among Be, Ge and Si complexes

Bond type	$[PLY(O,O)]_2Be$	$7^{+}TFPB^{-}$	$8^{+}TFPB^{-}$
O1–C1	1.287(2)	1.302(4)	1.296(4)
O2–C9	1.290(2)	1.300(4)	1.308(4)
C1–C2	1.427(3)	1.419(4)	1.428(4)
C1–C9a	1.421(2)	1.412(4)	1.417(4)
C2–C3	1.345(3)	1.349(5)	1.351(5)
C3–C3a	1.422(3)	1.424(5)	1.430(5)
C3a–C9b	1.422(2)	1.408(4)	1.421(4)
C3a–C4	1.397(2)	1.402(5)	1.396(5)
C4–C5	1.375(3)	1.383(6)	1.372(6)
C5–C6	1.384(3)	1.370(6)	1.380(6)
C6–C6a	1.400(2)	1.404(5)	1.406(5)
C6a–C9b	1.408(2)	1.414(4)	1.421(4)
C6a–C7	1.423(2)	1.415(5)	1.421(5)
C7–C8	1.349(2)	1.356(5)	1.351(5)
C8–C9	1.430(2)	1.423(4)	1.426(4)
C9–C9a	1.426(2)	1.418(4)	1.414(4)
C9a–C9b	1.424(2)	1.430(4)	1.418(4)

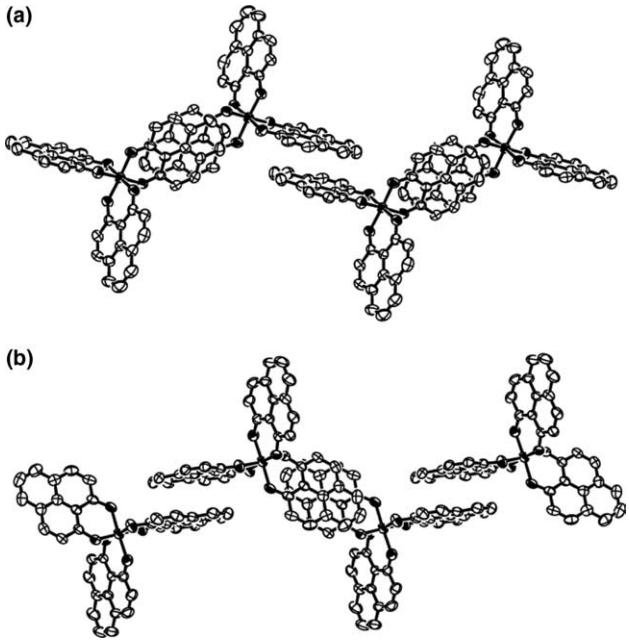


Fig. 4. Packing diagram of the cations (7^+) in the lattice, showing the overlap between four of the neighbouring cations: (a) and (b) are perpendicular views of each of the two sets of phenalenyl units.

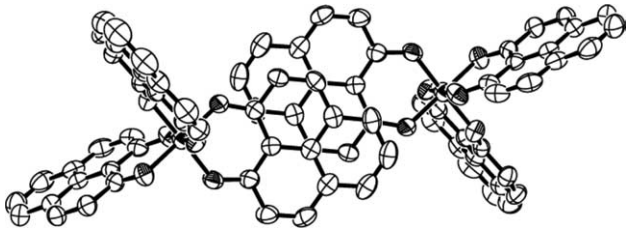


Fig. 5. Overlap between a pair of cations 7^+.

occurs along the *Z*-direction of the unit cell. Out of the three two PLY are involved in π-dimer chain formation. But the C–C distances of the PLY carbon with the nearest neighbour are not identical. There are two sets of C–C distances are shown in the Fig. 6. The shortest C–C distance observed is 3.274 Å for compound $\mathbf{7^+TFPB^-}$ and 3.297 Å for compound $\mathbf{8^+TFPB^-}$. The projection of cation 7^+ (Fig. 5) demonstrates the almost perfect superposition of some of the carbon atoms in the π-dimers. A similar packing pattern was observed for cation 8^+ which are not shown in the figure.

3. Experimental

3.1. Materials and methods

All manipulations were carried out under an atmosphere of argon using standard Schlenk techniques. Solvents were dried and distilled according to the standard procedures. Toluene was distilled from sodium benzophenone ketyl immediately before use. Dichloromethane was distilled from anhydrous CaH_2 before use. Germanium tetrachloride and silicon tetrachloride (Aldrich) were all commercial products and were used as received. 9-Hydroxyphenalenone and sodium tetrakis[3,5-bis(trifluoromethyl)phenyl]borate (NaTFPB) were synthesized according to literature procedures [14,15]. Melting points are uncorrected. Infrared spectra were recorded on a Nicolet Nexus 670 FT-IR spectrometer (at 2 cm^{-1} resolution). ^1H NMR spectra were run on a Varian Inova 300 MHz NMR spectrometer. Elemental analysis were performed by Microanalysis Laboratory (School of Chemical Science, University of Illinois, Urbana, IL).

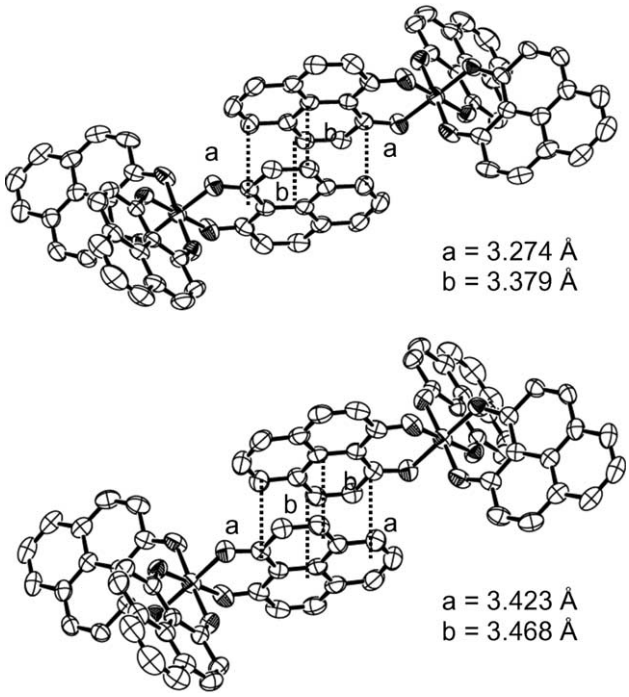


Fig. 6. The closest distances between a pair of cations 7^+.

3.2. Preparation of 7^+Cl^-

9-Hydroxyphenalenone (1.96 g, 10 mmol) in anhydrous toluene (50 mL) was treated with germanium tetrachloride (0.71 g, 3.3 mmol) under argon and the mixture was refluxed for 12 h. The yellow solid was isolated by filtration (1.5 g, 32%). Melting point: Compound does not melt till 380 °C. ^1H NMR (CD_3OD); δ 8.28 (d, 6H), 8.18 (d, 6H), 7.69 (t, 3H), 7.18 (d, 6H). IR (ATR, 4000–600 cm^{-1}): 3002 (w), 2986 (w), 1622 (m), 1570 (s), 1496 (s), 1467 (w), 1429 (w), 1353 (w), 1335 (w), 1322 (w), 1273 (s), 1238 (m), 1181 (w), 1142 (w), 1129 (w), 982 (w), 851 (s), 763 (s), 750 (s), 701 (w), 682 (w).

3.3. Preparation of 7^+TFPB^-

A mixture of $\mathbf{7^+Cl^-}$ (1.02 g, 1.47 mmol) and NaTFPB (1.15 g, 1.30 mmol) was added to 100 mL of dry

CH_2Cl_2. The mixture was stirred for 3 h until all yellow solids went into the solution and a white solid had precipitated. The yellow solution was filtered and the solvent was evaporated to give a brownish-yellow solid. Crystallization from ether–hexane (10:1) gave yellow needles. Yield: 1.85 g (93%); m.p. 98 °C. ^{1}H NMR ($CDCl_3$): δ 8.36 (d, 6H), 8.28 (d, 6H), 7.79 (t, 3H), 7.72 (br, 8H), 7.48 (br, 4H), 7.28 (d, 6H). IR (ATR, 4000–600 cm^{-1}): 3050 (w), 3028 (w), 1627 (w), 1618 (w), 1568 (m), 1496 (m), 1470 (w), 1434 (w), 1354 (w), 1336 (w), 1273 (s), 1241 (m), 1122 (s), 987 (w), 854 (w), 759 (w), 712 (w). *Anal*. Calc. for $C_{71}H_{33}BO_6GeF_{24}$: C, 56.05; H, 2.19; B, 0.71; Ge, 4.77. Found: C, 57.80; H, 2.71; B, 0.69; Ge, 4.39%.

3.4. Preparation of 8^+Cl^-

9-Hydroxyphenalenone (2.4 g, 12.2 mmol) was dissolved in 50 mL of dry toluene followed by addition of $SiCl_4$ (4 mL, 4 mmol) in dichloromethane. The reaction mixture was refluxed for 8 h. The yellow solid was isolated by filtration (3.0 g, 86%). When a melting point determination was attempted, the salt turned brown (~290 °C). ^{1}H NMR (CD_3OD): δ 8.60 (d, 6H), 8.48 (d, 6H), 7.91 (t, 3H), 7.26 (d, 6H). IR (ATR, 4000–600 cm^{-1}): 3004 (w), 2987 (w), 1621 (w), 1571 (w), 1501 (w), 1343 (w), 1274 (m), 1256 (m), 1144 (w), 1125 (w), 993 (w), 852 (w), 764 (s), 749 (s), 652 (m), 641 (s).

3.5. Preparation of 8^+TFPB^-

Synthesis of $\mathbf{8^+TFPB^-}$ is exactly the same as the preparation of $\mathbf{7^+TFPB^-}$. Yield: 1.8 g (88%); m.p. 84 °C. ^{1}H NMR ($CDCl_3$); δ 8.37 (d, 6H), 8.26 (d, 6H), 7.78 (t, 3H), 7.70 (br, 8H), 7.45 (br, 4H), 7.24 (d, 6H). IR (ATR, 4000–600 cm^{-1}): 3004 (w), 2987 (w), 1621 (w), 1576 (m), 1504 (m), 1349 (m), 1275 (s), 1240 (w), 1119 (s), 993 (w), 851 (m), 764 (m), 751 (m). *Anal*. Calc. for $C_{71}H_{33}BO_6SiF_{24}$: C, 57.74; H, 2.24. Found: C, 57.95; H, 2.11%.

3.6. X-ray crystallography

Data were collected on a Bruker SMART 1000 platform-CCD X-ray diffractometer system (Mo radiation, $\lambda = 0.71073$ Å, 50 kV/40 mA power) at 223 K. The orange crystal gave a triclinic unit cell (space group $P\bar{1}$, $z = 2$), with unit cell parameters $a = 12.2965(16)$ Å, $b = 17.104(2)$ Å, $c = 18.536(2)$ Å, $\alpha = 75.645(3)°$, $\beta = 82.109(3)°$, $\gamma = 74.879(2)°$ and $V = 3635.0(8)$ Å^3 for compound $\mathbf{7^+TFPB^-}$ and $a = 12.297(2)$ Å, $b = 17.124(3)$ Å, $c = 18.505(3)$ Å, $\alpha = 75.762(3)°$, $\beta = 82.337(4)°$, $\gamma = 74.869(3)°$ and $V = 3636.0(11)$ Å^3 for compound $\mathbf{8^+TFPB^-}$. The structure ($\mathbf{7^+TFPB^-}$) was refined with 14870 reflections, yielding $R[I > 2\sigma(I)]$, $R_1 = 0.0543$, $wR_2 = 0.1489$, and R indices for all data $R_1 = 0.0758$ and $wR_2 = 0.1676$ (Table 2). The structure of $\mathbf{8^+TFPB^-}$ was refined with 14864 reflections, yielding $R[I > 2\sigma(I)]$, $R_1 = 0.0589$, $wR_2 = 0.1557$, and R indices for all data $R_1 = 0.0949$, and $wR_2 = 0.1873$ (Table 2). Full details, including bond lengths and bond angles, are given in the supporting Information.

3.7. Cyclic voltammetry

Cyclic Voltammetry was performed using a PINE Bipotentiostat, model AFCC1BP1, with scan rates 50–100 mV s^{-1} on solutions (<10^{-3} M) of $\mathbf{7^+TFPB^-}$ and $\mathbf{8^+TFPB^-}$ in CH_3CN (dried by distillation from P_2O_5 and CaH_2) containing 0.1 M tetra-*n*-butylammonium hexafluorophosphate as supporting electrolyte. Potentials were scanned with respect to the quasi-reference electrode in a single compartment cell fitted with Pt electrodes and referenced to the Fc/Fc^+ couple of ferrocene at 0.38 V versus SCE [16]. The $E_{pa} - E_{pc}$ separation of the reversible couples was within 10% of that of the Fc/Fc^+ couple.

4. Summary and conclusions

In summary, two new cationic tris-(9-oxophenalenone) germanium (IV) and silicon (IV) of $\mathbf{7^+}$ and $\mathbf{8^+}$ have been synthesized in high yield and high purity. Cyclic voltammetry indicated these complexes could be easily reduced to its corresponding radical. The hexacoordinated geometry was determined by single crystal X-ray diffraction analysis in the solid state. Molecular structure also shows a π–π interaction between the two neighboring PLY plane and a one-dimensional chain like structure in the solid state.

5. Supplementary material

Crystallographic data have been deposited at the Cambridge Crystallographic Data Center, CCDC Reference Nos. 265567 ($\mathbf{7^+TFPB^-}$) and 265568 ($\mathbf{8^+TFPB^-}$). Copies of this information may be obtained free of charge from the Director, CCDC, 12 Union Road, Cambridge, CB2 IEZ, UK (fax: +44 1223 336033; e-mail: deposit@ccdc.cam.ac.uk or http://www.ccdc. cam.ac.uk).

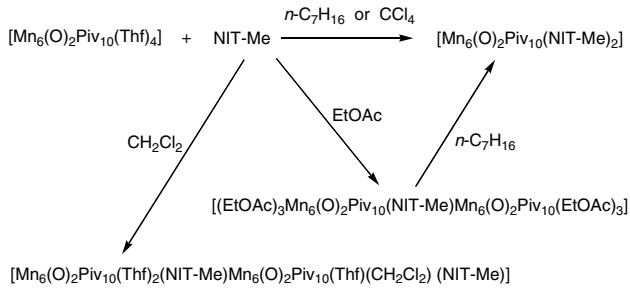
Acknowledgement

This work was supported by the Office of Basic Energy Sciences, Department of Energy, under Grant Nos. DE-FG03-01ER45879.

References

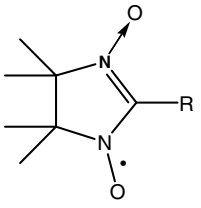
[1] R.C. Haddon, Aust. J. Chem. 28 (1975) 2343.
[2] R.T. Oakley, Can. J. Chem. 71 (1993) 1775.

[3] X. Chi, M.E. Itkis, B.O. Patrick, T.M. Barclay, R.W. Reed, R.T. Oakley, A.W. Cordes, R.C. Haddon, J. Am. Chem. Soc. 121 (1999) 10395.
[4] S.K. Pal, M.E. Itkis, R.W. Reed, R.T. Oakley, A.W. Cordes, F.S. Tham, T. Siegrist, R.C. Haddon, J. Am. Chem. Soc. 126 (2004) 1478.
[5] X. Chi, M.E. Itkis, K. Kirschbaum, A.A. Pinkerton, R.T. Oakley, A.W. Cordes, R.C. Haddon, J. Am. Chem. Soc. 123 (2001) 4041.
[6] X. Chi, M.E. Itkis, R.W. Reed, R.T. Oakley, A.W. Cordes, R.C. Haddon, J. Phys. Chem. B 106 (2002) 8278.
[7] X. Chi, M.E. Itkis, F.S. Tham, R.T. Oakley, A.W. Cordes, R.C. Haddon, Int. J. Quantum Chem. 95 (2003) 853.
[8] R.C. Haddon, S.V. Chichester, J.H. Marshall, Tetrahedron 42 (1986) 6293.
[9] S. Samanta, M.E. Itkis, R.W. Reed, R.T. Oakley, F.S. Tham, R.C. Haddon, Synthetic Met. (2004), submitted.
[10] A.F. Garito, A.J. Heeger, Acc. Chem. Res. 7 (1974) 232.
[11] J.B. Torrance, Acc. Chem. Res. 12 (1979) 79.
[12] M. Kira, L. Zhang, C. Kabuto, H. Sakurai, Chem. Lett. 8 (1995) 659.
[13] T. Ito, K. Toriumi, F.B. Ueno, K. Saito, Acta Cryst. B 36 (1980) 2998.
[14] R.C. Haddon, F. Wudl, M.L. Kaplan, J.H. Marshall, R.E. Cais, F.B. Bramwell, J. Am. Chem. Soc. 100 (1978) 7629.
[15] R.S. Bahr, P. Boudjouk, J. Org. Chem. 57 (1992) 5545.
[16] R.T. Boere, K.H. Moock, M. Parvez, Z. Anorg. Allg. Chem. 620 (1994) 1589.



Scheme 1.

$(H_2O)]$, $[Mn_6(O)_2Piv_{10}(NIT\text{-}p\text{-}Py)_4]$, $[Mn_6(O)_2\ Piv_{10}(NIT\text{-}p\text{-}Py)_4]\cdot\ 0.5C_7H_{16}$, $[Mn_6(O)_2Piv_{10}(NIT\text{-}p\text{-}Py)_2(H_2O)]$, $[Mn_6(O)_2Piv_{10}(NIT\text{-}n\text{-}Bu\text{-}Pz)_2(HPiv)_2]$, and $[Mn_6(O)_2Piv_{10}(NIT\text{-}n\text{-}Bu\text{-}Pz)(Thf)(H_2O)]\cdot C_6H_{14}$, analyzing the factors that hinder bridging coordination of NIT-R when $R \neq CH_3$.



NIT-R, R = H, Me, Et, *p*-Py, *n*-Bu-Pz

2. Experimental

2.1. Synthesis

All the solvents were commercially available and used as received. The $[Mn_6(O)_2Piv_{10}(Thf)_4]\cdot Thf$ and $[(EtOAc)_3Mn_6(O)_2Piv_{10}(NIT\text{-}Me)Mn_6(O)_2Piv_{10}(EtOAc)_3]$ clusters were prepared by using the method described elsewhere [1]. Nitronyl nitroxides 4,4,5,5-tetramethyl-4,5-dihydro-1*H*-imidazolyl-3-oxide-1-oxyl (NIT-H), 2,4,4,5,5-pentamethyl-4,5-dihydro-1*H*-imidazolyl-3-oxide-1-oxyl (NIT-Me), 4,4,5,5-tetramethyl-2-ethyl-4,5-dihydro-1*H*-imidazolyl-3-oxide-1-oxyl (NIT-Et), 4,4,5,5-tetramethyl-2-(pyridine-4′-yl)-4,5-dihydro-1*H*-imidazolyl-3-oxide-1-oxyl (NIT-*p*-Py), and 4,4,5,5-tetramethyl-2-(1′-*n*-butyl-pyrazole-4′-yl)-4,5-dihydro-1*H*-imidazolyl-3-oxide-1-oxyl (NIT-*n*-Bu-Pz) were prepared by the procedure of [2].

2.1.1. $[Mn_6(O)_2Piv_{10}(NIT\text{-}H)_4]\cdot 0.5CH_2Cl_2$

$[Mn_6(O)_2Piv_{10}(Thf)_4]\cdot Thf$ (0.1 g, 0.029 mmol) was dissolved while stirring in CH_2Cl_2 (4 ml). The resulting solution was carefully dropped through a glass filter to a solution of NIT-H (0.036 g, 0.230 mmol) in CH_2Cl_2 (2 ml) in such a way as to let the drops go down the wall of the flask. Then heptane (5 ml) was carefully added in the same manner without stirring. After storing the reaction mixture at 4 °C for a few days, dark red crystals formed which decomposed in air, losing the CH_2Cl_2 crystallization molecules. Yield 58%. *Anal.* Calc. for $Mn_6C_{78}H_{142}N_8O_{30}$: C, 46.8; H, 7.2; N, 5.6; (for the unsolvated product). Found: C, 47.1; H, 7.3; N, 5.1%. $[Mn_6(O)_2Piv_{10}(NIT\text{-}H)_4]\cdot 0.5CH_2Cl_2$ is formed in a $CH_2Cl_2/n\text{-}C_7H_{16}$ or $CH_2Cl_2/n\text{-}C_6H_{14}$ mixture with a reagent ratio of $[Mn_6(O)_2Piv_{10}(Thf)_4]\cdot Thf$/NIT-H of 1/8 or 1/16; it is also formed in the reaction of $[(EtOAc)_3Mn_6(O)_2Piv_{10}(NIT\text{-}Me)Mn_6(O)_2Piv_{10}(EtOAc)_3]$ or $[(EtOAc)_3Mn_6(O)_2Piv_{10}(Ac\text{–}Ac)Mn_6(O)_2Piv_{10}(EtOAc)_3]$ (see Section 2.1.4) with NIT-H in a $CH_2Cl_2/n\text{-}C_7H_{16}$ mixture.

2.1.2. $[Mn_6(O)_2Piv_{10}(NIT\text{-}Et)_3\ HPiv]\cdot 0.5C_7H_{16}$

This compound was prepared as described above. The reaction mixture was allowed to stay for a few days at room temperature to give crimson crystals. Yield 60%. *Anal.* Calc. for $Mn_6C_{82}H_{151}N_6O_{30}$: C, 48.5; H, 7.5; N, 4.1%. Found: C, 49.2; H, 7.6; N, 4.5%. $[Mn_6(O)_2Piv_{10}(NIT\text{-}Et)_3HPiv]\cdot 0.5C_7H_{16}$ formed when the reaction was conducted in CH_2Cl_2 or heptane. A mixture of these solvents provided optimum conditions for growth of quality crystals. Varying the initial reagent ratio $[Mn_6(O)_2Piv_{10}(Thf)_4]\cdot Thf$/NIT-Et (1:8, 1:16, 1:40) did not affect the composition of the final product.

2.1.3. $[Mn_6(O)_2Piv_{10}(NIT\text{-}Et)_4]$

$[(EtOAc)_3Mn_6(O)_2Piv_{10}(NIT\text{-}Me)Mn_6(O)_2Piv_{10}(EtOAc)_3]$ (0.05 g, 0.015 mmol) was dissolved with stirring in CH_2Cl_2 (4 ml). The resulting solution was carefully dropped through a glass filter to a solution of NIT-Et (0.032 g, 0.172 mmol) in CH_2Cl_2 (1 ml) in such a way that the drops were let down the wall of the flask. Then heptane (5 ml) was carefully added in the same manner without stirring. After storing the solution at room temperature for a few days, crystals of two types formed: crimson plates of $[Mn_6(O)_2Piv_{10}(NIT\text{-}Et)_3HPiv]\cdot 0.5C_7H_{16}$ and dark red bulky crystals of $[Mn_6(O)_2Piv_{10}(NIT\text{-}Et)_4]$. The crystals were filtered off, washed with cold heptane, dried in air, and mechanically separated. Yield 0.030 g (50% based on the total mass of the product). The same product mixture was obtained by varying the starting reagent ratio from 1/12 to 1/24 or by using $[(EtOAc)_3Mn_6(O)_2Piv_{10}(Ac\text{–}Ac)Mn_6(O)_2Piv_{10}(EtOAc)_3]$ as the starting reagent (see Section 2.1.4). *Anal.* Calc. for $Mn_6C_{86}H_{158}N_8O_{30}$: C, 48.8; H, 7.9; N, 4.6. Found: C, 48.9; H, 7.5; N, 5.3%.

2.1.4. $[(EtOAc)_3Mn_6(O)_2Piv_{10}(Ac\text{–}Ac)Mn_6(O)_2Piv_{10}(EtOAc)_3]$

$[Mn_6(O)_2Piv_{10}(Thf)_4]\cdot Thf$ (0.05 g, 0.029 mmol) was dissolved with stirring and heating to 50 °C in EtOAc (4 ml). The resulting solution was kept for a few days

at room temperature. This gave plate-like tawny crystals, which gradually decomposed in air, losing ethyl acetate molecules. Yield 50%. *Anal.* Calc. for $Mn_{12}C_{104}H_{186}O_{46}$: C, 44.1; H, 6.6. Found: C, 43.7; H, 6.7%. The same compound is formed in the presence of NIT-R, where R = H, Et.

2.1.5. $[Mn_6(O)_2Piv_{10}(Me_2CO)_2(H_2O)]$

$[Mn_6(O)_2Piv_{10}(Thf)_4]\cdot Thf$ C (0.05 g, 0.029 mmol) was dissolved with stirring and heating to 50 °C in acetone (10 ml). The resulting solution was added to the solution of NIT-Et (0.011 g, 0.059 mmol) in acetone (1 ml). After storing the solution for a few days at room temperature, brown plate-like crystals formed. They were filtered off and dried in air. Yield 57%. *Anal.* Calc. for $Mn_6C_{56}H_{104}O_{25}$: C, 44.6; H, 7.0. Found: C, 44.9; H 6.8%. The same compound is formed if the solution contains NIT-Me or NIT-H.

2.1.6. $[Mn_6(O)_2Piv_{10}(NIT\text{-}p\text{-}Py)_4]$ and $[Mn_6(O)_2Piv_{10}(NIT\text{-}p\text{-}Py)_4]\cdot 0.5C_7H_{16}$

The synthetic procedure for $[Mn_6(O)_2Piv_{10}(NIT\text{-}p\text{-}Py)_4]$ is identical to the one described in Section 2.1.1. After storing the reaction mixture for a few days at room temperature, the dark gray crystals were filtered off, washed with cold heptane, and dried in air. Yield 83%. *Anal.* Calc. for $Mn_6C_{98}H_{154}N_{12}O_{30}$: C, 51.0; H, 6.7; N, 7.3. Found: C, 51.8; H, 7.2; N, 7.0%. Using $[(EtOAc)_3Mn_6(O)_2Piv_{10}(NIT\text{-}Me)Mn_6(O)_2Piv_{10}(EtOAc)_3]$ as the starting compound in an analogous procedure leads to a crystalline product containing solvated heptane molecules. Yield 95%. *Anal.* Calc. for $Mn_{12}C_{203}H_{324}N_{24}O_{60}$: C, 51.7; H, 6.9; N, 7.1. Found: C, 51.1; H, 6.7; N, 7.4%.

2.1.7. $[Mn_6(O)_2Piv_{10}(NIT\text{-}p\text{-}Py)_2(H_2O)]$

The synthetic procedure is similar to the one described in Section 2.1.5. As the starting cluster one uses $[Mn_6(O)_2Piv_{10}(Thf)_4]\cdot Thf$ or $[(EtOAc)_3Mn_6(O)_2Piv_{10}(NIT\text{-}Me)Mn_6(O)_2Piv_{10}(EtOAc)_3]$. The procedure is not sensitive to the initial cluster/nitroxide ratio. Yield 84%. *Anal.* Calc. for $Mn_6C_{74}H_{124}N_6O_{27}$: C, 47.7; H, 6.7; N, 4.5. Found: C, 47.7; H, 6.8; N, 4.1%.

2.1.8. $[Mn_6(O)_2Piv_{10}(NIT\text{-}n\text{-}Bu\text{-}Pz)_2(HPiv)_2]$ and $[Mn_6(O)_2Piv_{10}(NIT\text{-}n\text{-}Bu\text{-}Pz)(Thf)(H_2O)]\cdot C_6H_{14}$

A sample of $[Mn_6(O)_2Piv_{10}(Thf)_4]\cdot Thf$ (0.1 g, 0.055 mmol) was dissolved with stirring and heating to 50 °C in hexane (10 ml). The resulting solution was filtered, and a solution of *n*-Bu-Pz (0.008–0.032 g, 0.028–0.11 mmol) in hexane (3 ml) was added to it. Storing the solution for 3 days at room temperature resulted in a conglomerate of hardly isolable $[Mn_6(O)2\text{-}Piv_{10}(NIT\text{-}n\text{-}Bu\text{-}Pz)_2(HPiv)_2]$ and $[Mn_6(O)_2Piv_{10}(NIT\text{-}n\text{-}Bu\text{-}Pz)(Thf)(H_2O)]\cdot C_6H_{14}$ crystals and starting $[Mn_6(O)_2Piv_{10}(Thf)_4]\cdot Thf$ crystals. The mixture occasionally contained $[Mn_6(O)_2Piv_{10}(NIT\text{-}n\text{-}Bu\text{-}Pz)_2\text{-}(HPiv)_2]$ or $[Mn_6(O)_2Piv_{10}(NIT\text{-}n\text{-}Bu\text{-}Pz)(Thf)(H_2O)]\cdot C_6H_{14}$ single crystals, which were selected for an X-ray diffraction study.

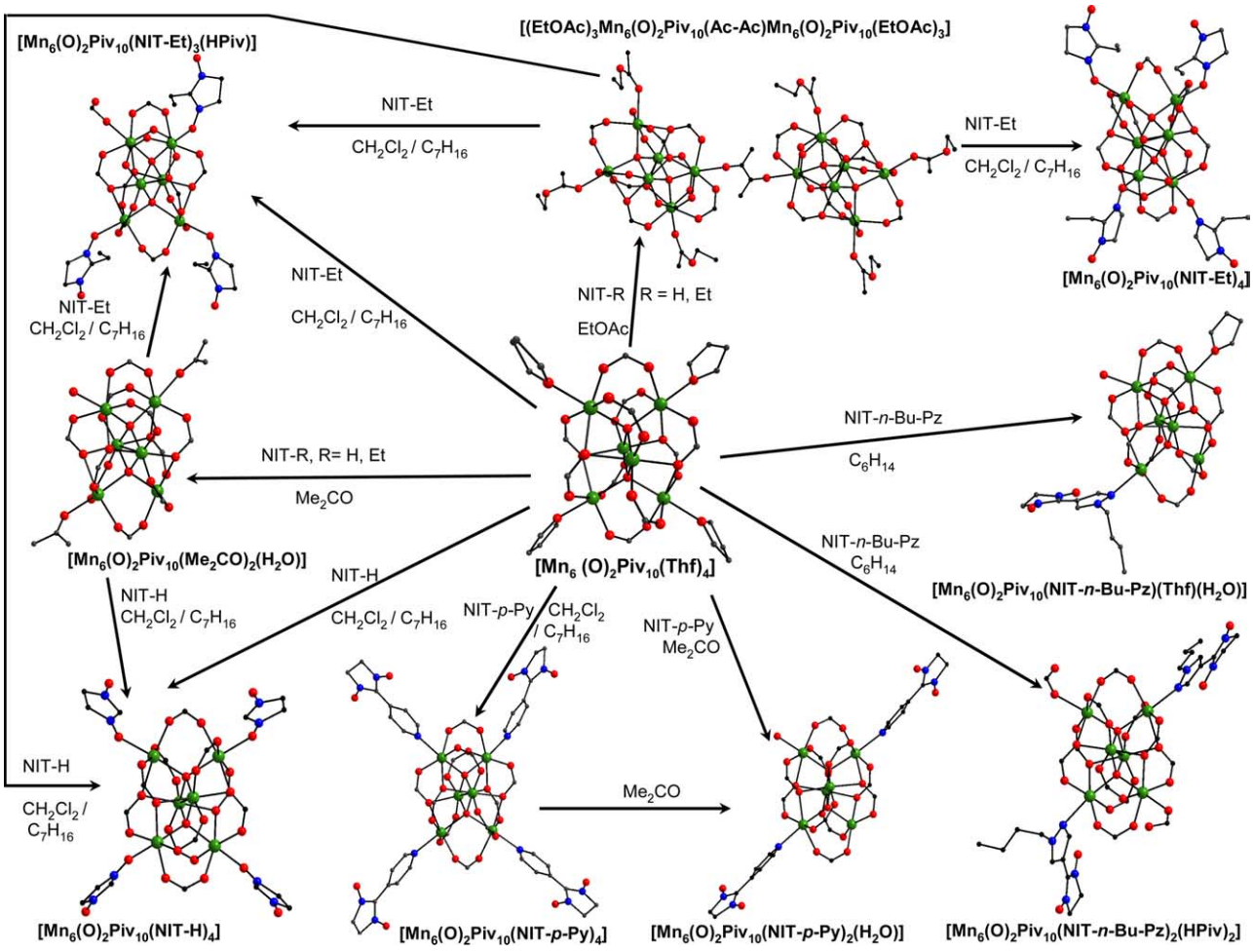
2.2. X-ray crystallography and magnetic measurements

The single crystal diffraction data were collected on a SMART APEX CCD (Bruker AXS) automatic diffractometer (Mo radiation, an absorption correction applied using the Bruker SADABS program, version 2.03). The structures were solved by direct methods. The full-matrix least-squares refinement was carried out anisotropically for non-hydrogen atoms. The H atoms were mostly generated theoretically. The methyl H atoms were refined isotropically as rigid groups. All structure solution and refinement calculations were performed with SHELX-97 and Bruker SHELXTL Version 6.12. All magnetic measurements were carried out on an MPMS-5S SQUID magnetometer (Quantum Design) in the temperature range of 1.9–300 K. Molar magnetic susceptibility was calculated using corrections for the diamagnetism of the compounds. The effective magnetic moment was calculated as $\mu_{eff} = (8\chi T)^{1/2}$.

3. Results and discussion

3.1. Synthesis of compounds

As shown in [1], NIT-Me reacts with $[Mn_6(O)_2\text{-}Piv_{10}(Thf)_4]\cdot Thf$, forming a 1D polymer $[Mn_6(O)_2\text{-}Piv_{10}(Thf)_2(NIT\text{-}Me)Mn_6(O)_2Piv_{10}(Thf)(CH_2Cl_2)(NIT\text{-}Me)]$ when the reaction is conducted in CH_2Cl_2; a 3D polymer $[Mn_6(O)_2Piv_{10}(NIT\text{-}Me)_2]$ is generated in hexane or heptane, and dumbbel-like $[(EtOAc)_3Mn_6(O)_2\text{-}Piv_{10}(NIT\text{-}Me)Mn_6(O)_2Piv_{10}(EtOAc)_3]$ molecules are produced in ethyl acetate. The solvent used proved to be the critical factor governing the formation of a particular compound, while the initial reagent ratio $[Mn_6(O)_2Piv_{10}]$/NIT-Me was inessential to the composition of the product mixture. It is important that in all $[Mn_6(O)_2Piv_{10}]$ compounds, the fragments were linked by NIT-Me bridging molecules. Using the synthetic approaches reported in [1], we tried to expand the scope of heterospin compounds based on the $[Mn_6(O)_2Piv_{10}]$ polymetallic unit and NIT-R, where R = H, Et, *p*-Py, *n*-Bu-Pz. It appeared, however, that replacement of NIT-Me even by its close analogs NIT-H and NIT-Et leads to absolutely different products, where nitroxide performs only the monodentate function. Without going into details of synthesis (represented together with interconversions in Schemes 2 and 3), we discuss the key points.



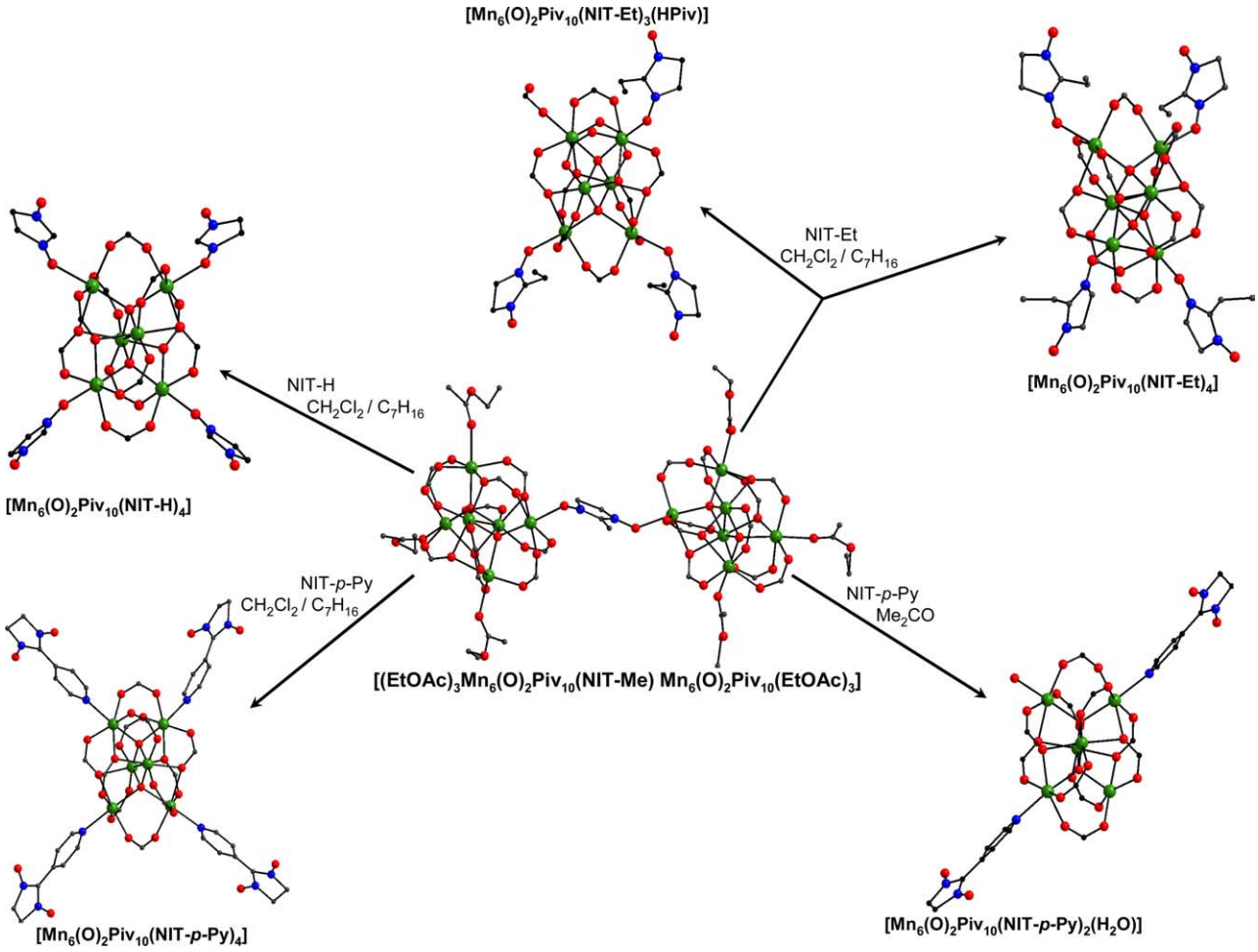
Scheme 2.

3.1.1. Starting polymetallic matrix

Along with the $[Mn_6(O)_2Piv_{10}(Thf)_4]$ hexanuclear polymetallic matrix, we also used the 12-nuclear $[(EtOAc)_3Mn_6(O)_2Piv_{10}(NIT\text{-}Me)Mn_6(O)_2Piv_{10}(EtOAc)_3]$ as the starting component. As can be seen by comparing Schemes 2 and 3, the reaction of $[Mn_6(O)_2Piv_{10}(Thf)_4]\cdot Thf$ or $[(EtOAc)_3Mn_6(O)_2Piv_{10}(NIT\text{-}Me)Mn_6(O)_2Piv_{10}(EtOAc)_3]$ with NIT-R gave almost the same products. Minor discrepancies were observed in two cases. First, the reaction of $[Mn_6(O)_2Piv_{10}(Thf)_4]\cdot Thf$ with NIT-*p*-Py always gave $[Mn_6(O)_2Piv_{10}(NIT\text{-}p\text{-}Py)_4]$ crystals, while the reaction of $[(EtOAc)_3Mn_6(O)_2Piv_{10}(NIT\text{-}Me)Mn_6(O)_2Piv_{10}(EtOAc)_3]$ with NIT-*p*-Py in the solid state reproducibly formed the solvate of this complex, $[Mn_6(O)_2Piv_{10}(NIT\text{-}p\text{-}Py)_4]\cdot 0.5C_7H_{16}$. Second, the interaction of NIT-Et with $[Mn_6(O)_2Piv_{10}(Thf)_4]\cdot Thf$ led to the formation of only $[Mn_6(O)_2Piv_{10}(NIT\text{-}Et)_3HPiv]\cdot 0.5C_7H_{16}$; the reaction with $[(EtOAc)_3Mn_6(O)_2Piv_{10}(NIT\text{-}Me)Mn_6(O)_2Piv_{10}(EtOAc)_3]$ resulted in a mixture of $[Mn_6(O)_2Piv_{10}(NIT\text{-}Et)_3HPiv]\cdot 0.5C_7H_{16}$ and $[Mn_6(O)_2Piv_{10}(NIT\text{-}Et)_4]$ crystals, which were separated mechanically.

3.1.2. Reactions of the polynuclear compounds with the solvent

It is common knowledge that polynuclear carboxylates exhibit activity in transformations of organic substrates, including organic solvents used in the synthesis. We encountered transformation of solvent molecules in only one case, namely, when investigating the products of the reaction of $[Mn_6(O)_2Piv_{10}(Thf)_4]\cdot Thf$ with NIT-H or NIT-Et in ethyl acetate (EtOAc). From the reaction mixture we always isolated the 12-nuclear crystalline product $[(EtOAc)_3Mn_6(O)_2Piv_{10}(Ac\text{–}Ac)Mn_6(O)_2Piv_{10}(EtOAc)_3]$ containing the bridging diacetyl molecule (Scheme 2). The nitroxide remained in solution and had no pronounced effect on the process. The same product crystallized with the same yield from the reaction mixture under similar conditions when $[Mn_6(O)_2Piv_{10}(Thf)_4]\cdot Thf$ was simply dissolved in EtOAc. It should be noted that NIT-Me and NIT-R (R = H, Et) differ substantially in their chemical behavior. As indicated in Scheme 1, NIT-Me reacts with $[Mn_6(O)_2Piv_{10}(Thf)_4]\cdot Thf$. The reaction also forms a 12-nuclear compound, $[(EtOAc)_3Mn_6(O)_2Piv_{10}(NIT\text{-}Me)Mn_6(O)_2Piv_{10}(EtOAc)_3]$, but the



Scheme 3.

bridging function in it is performed by the nitroxide molecule. This large discrepancy in the chemical behavior of NIT-Me and NIT-R (R = H, Et) deserves special attention, and we will further return to this discussion.

3.1.3. Stereochemical lability of the $[Mn_6(O)_2Piv_{10}]$ fragment

It was noted [1] that the solvent used was a critical factor determining the formation of a particular compound during the reaction of $[Mn_6(O)_2Piv_{10}(Thf)_4] \cdot Thf$ with NIT-Me (Scheme 1). The solvent effect was still more significant when we tried to use acetone. After $[Mn_6(O)_2Piv_{10}(Thf)_4] \cdot Thf$ was mixed with NIT-R (R = H, Me or Et), $[Mn_6(O)_2Piv_{10}(Me_2CO)_2(H_2O)]$ was the only product that crystallized from the solution (Scheme 2). The same product separated from an acetone solution without a nitroxide addition. Thus nitronyl nitroxides bearing no additional donor fragments cannot compete with acetone molecules in an acetone solution for the coordination sites of the $[Mn_6(O)_2Piv_{10}]$ polymetallic fragment. This prompted us to employ NIT-*p*-Py and NIT-*n*-Bu-Pz as more powerful donors. Indeed, $[Mn_6(O)_2Piv_{10}(Thf)_4] \cdot Thf$ or $[(EtOAc)_3Mn_6(O)_2Piv_{10}(NIT\text{-}Me)Mn_6(O)_2Piv_{10}(EtOAc)_3]$ react vigorously with NIT-*p*-Py in acetone. The $[Mn_6(O)_2Piv_{10}(NIT\text{-}p\text{-}Py)_2(H_2O)]$ product, which formed at any reagent ratio (Schemes 2 and 3), topologically corresponds almost exactly with $[Mn_6(O)_2Piv_{10}(Me_2CO)_2(H_2O)]$ molecules. The $[Mn_6(O)_2Piv_{10}]$ fragment is considerably distorted so that one of the terminal Mn(II) atoms is drawn into the polynuclear framework, losing its ligand-coordinating ability. The other three terminal Mn(II) atoms coordinate the water molecule (all syntheses were performed in open apparatuses, without taking any precautions to keep out air moisture) and the two *trans* NIT-*p*-Py or Me_2CO molecules. Stated differently, the distorted $[Mn_6(O)_2Piv_{10}]$ fragment of $[Mn_6(O)_2Piv_{10}(Me_2CO)_2(H_2O)]$ is completely preserved when NIT-*p*-Py molecules are substituted for acetone molecules. The same fragment is present in the structure of $Mn_6(O)_2Piv_{10}(NIT\text{-}n\text{-}Bu\text{-}Pz)(Thf)(H_2O)] \cdot 0.5C_6H_{14}$ (Scheme 2), which (as noted in Section 2) was isolated as single crystals.

3.2. Structural data

In $[Mn_6(O)_2Piv_{10}(NIT\text{-}H)_4]$, $[Mn_6(O)_2Piv_{10}(NIT\text{-}Et)_3HPiv] \cdot 0.5C_7H_{16}$, $[Mn_6(O)_2Piv_{10}(NIT\text{-}Et)_4]$, $[(EtOAc)_3Mn_6(O)_2Piv_{10}(Ac\text{–}Ac)Mn_6(O)_2Piv_{10}(EtOAc)_3]$, $[Mn_6(O)_2Piv_{10}(NIT\text{-}p\text{-}Py)_4]$, and $[Mn_6(O)_2Piv_{10}(NIT\text{-}n\text{-}Bu\text{-}Pz)_2(HPiv)_2]$ molecules, $[Mn^{II}_4Mn^{III}_2(O)_2(Piv)_{10}]$ is the nucleus (Fig. 1). As in other derivatives of this polymetallic nucleus [3], in these molecules the distance between the internal Mn^{III} ions (Mn1–Mn2 2.800–2.845 Å) is much shorter than the distances to the terminal Mn(3-6) atoms (3.067–3.248 Å) and the Mn3–Mn4 and Mn5–Mn6 distances, which are longer than 3.5 Å (Table 1). The Mn1 and Mn2 atoms are common to the two oxo-centered $[Mn_4O]$ tetrahedra (Fig. 1). In the tetrahedra, the Mn–O distances to the internal Mn(1–2) atoms (1.863–1.934 Å) are much shorter than the analogous distances to the terminal Mn(3–6) atoms (2.085–2.221 Å). Importantly, the Mn3–Mn4 and Mn5–Mn6 edges are not parallel; they form an angle of ~24°, which favors a 3-D diamond-like structure. An example of a compound with this structure is found in [1]. All compounds under study have molecular structures. Each (internal) Mn atom is surrounded by a distorted octahedron formed by four O atoms of the bridging Piv ligands and two μ_4-O atoms, lying inside the $[Mn_4O]$ tetrahedra. For terminal Mn atoms, however, only five of six vertices are occupied by the O atoms of the bridging pivalates and the μ_4-O atoms. The other coordination sites of the four terminal Mn atoms are occupied by the O atoms of the monodentate NIT-R, EtOAc, and Ac–Ac ligands or by the N atoms of NIT-*p*-Py and NIT-*n*-Bu-Pz. Table 1 lists selected bond lengths.

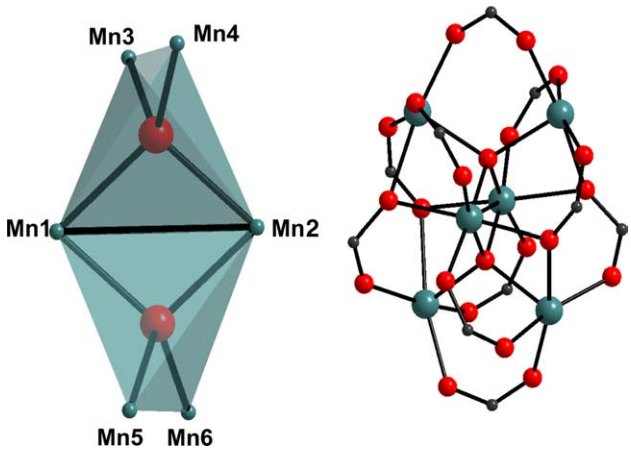


Fig. 1. Two edge-sharing $\{Mn_4O\}$ tetrahedra and the symmetrical $\{Mn_6(O)_2(Piv)_{10}\}$ fragment.

In $[Mn_6(O)_2Piv_{10}(Me_2CO)_2(H_2O)]$, $[Mn_6(O)_2Piv_{10}(NIT\text{-}p\text{-}Py)_2(H_2O)]$ and $[Mn_6(O)_2Piv_{10}(NIT\text{-}n\text{-}Bu\text{-}Pz)(Thf)(H_2O)] \cdot C_6H_{14}$, the terminal Mn atom that faces the atom having H_2O in its environment is surrounded by a square pyramid. The $[Mn_6O_2(piv)_{10}]$ nucleus is distorted, the distortion being especially pronounced

Table 1
Selected bond lengths (Å)

Compound	Mn–Mn	Mn–Mn	Mn–O_L	Mn–N_L
$[Mn_6(O)_2Piv_{10}(NIT\text{-}H)_4] \cdot 0.5CH_2Cl_2$	2.834(1)	3.147(1) 3.156(1)	2.259(4) 2.221(5)	
$[Mn_6(O)_2Piv_{10}(NIT\text{-}Et)_3(HPiv)] \cdot 0.5C_7H_{16}$	2.8064(9)	3.130(1)–3.2092(9)	2.205(3) 2.268(3) 2.291(3) 2.385(5) (HPiv)	
$[Mn_6(O)_2Piv_{10}(NIT\text{-}Et)_4]$	2.804(2)	3.163(1) 3.176(1)	2.275(6) 2.221(6)	
$[(EtOAc)_3Mn_6(O)_2Piv_{10}(Ac\text{–}Ac)Mn_6(O)_2Piv_{10}(EtOAc)_3]$	2.823(1)	3.108(1)–3.169(1)	2.259(4) 2.257(4) 2.280(4) 2.554(4) (Ac–Ac)	
$[Mn_6(O)_2Piv_{10}(Me_2CO)_2(H_2O)]$	2.841(1)	3.114(1) 3.205(1) 3.212(1) 3.115(1)	2.246(5) 2.344(7) 2.478(10) (O1w)	
$[Mn_6(O)_2Piv_{10}(NIT\text{-}p\text{-}Py)_4]$	2.811(1)	3.1863(5)		2.346(3)
$[Mn_6(O)_2Piv_{10}(NIT\text{-}p\text{-}Py)_4] \cdot 0.5C_7H_{16}$	2.845(2)	3.230(3)–3.257(3)		2.401(7) 2.355(7) 2.417(7) 2.371(6)
$[Mn_6(O)_2Piv_{10}(NIT\text{-}p\text{-}Py)_2(H_2O)]$	2.821(2)	3.209(2) 3.214(2) 3.067(3) 3.182(2)	2.225(8) (H_2O)	2.331(11) 2.380(10)
$[Mn_6(O)_2Piv_{10}(HPiv)_2(NIT\text{-}n\text{-}Bu\text{-}Pz)_2]$	2.800(2)	3.127(2)–3.195(2)	2.313(9) (HPiv) 2.255(7) (HPiv)	2.541(8) 2.336(9)
$[Mn_6(O)_2Piv_{10}(NIT\text{-}n\text{-}Bu\text{-}Pz)(Thf)(H_2O)] \cdot C_6H_{14}$	2.829(1)	3.228(1) 3.248(1) 3.085(1) 3.179(1) 3.380(1)	2.324(6) (H_2O) 2.290(6) (Thf)	2.396(7)

for $[Mn_6(O)_2Piv_{10}(NIT\text{-}n\text{-}Bu\text{-}Pz)(Thf)(H_2O)] \cdot C_6H_{14}$, in which all three terminal monodentate ligands are different (Table 1).

Structural data obtained in this work provide a clue to the understanding of differences in the chemical behavior of NIT-R (R = H, Me, Et). Recall that replacement of NIT-Me even by its closest analogs NIT-H or NIT-Et leads to absolutely different products where the nitroxide performs only the monodentate function (Sections 3.1 and 3.1.2).

It appeared that NIT-Et cannot perform the bridging function for steric reasons. This can readily be verified if the structure of the $[(EtOAc)_3Mn_6(O)_2Piv_{10}(NIT\text{-}Me)Mn_6(O)_2Piv_{10}(EtOAc)_3]$ molecule is represented by a space-filling model (Fig. 2(a)). A transition from NIT-Me to NIT-Et is only possible at a sacrifice of the bridging function because otherwise there is no space for the ethyl fragment. Substitution of the CH_3 groups by the C_2H_5 groups leads to an inadmissible overlap between the methyl fragment of the ethyl group and the trimethyl acetate groups of the polymetallic nucleus (Fig. 2(b)). Therefore, bridging coordination of nitronyl nitroxide is impossible with bulkier alkyl groups R in NIT-R. In other words, in compounds based on the $[Mn_6(O)_2Piv_{10}]$ unit, the bridging type of coordination is possible for NIT-Me or NIT-H alone when we are concerned with the group of nitronyl nitroxides under discussion. However, the arrangement of NIT-H molecules in the isolated $[Mn_6(O)_2Piv_{10}(NIT\text{-}H)_4] \cdot 0.5CH_2Cl_2$ was radically different from that in compounds with NIT-Me (or NIT-Et). In the polynuclear complexes of $[Mn_6(O)_2Piv_{10}]$ with NIT-Me or NIT-Et, the torsion angle between the plane of the C, N, and O atoms of the ·O–N–C=N → O nitronyl nitroxide fragment and the plane of the N, O, and Mn atoms (Fig. 3) varies from 54.8° to 106.9° for all compounds under study. This kind of nitroxide coordination minimizes steric hindrance to the trimethyl acetate groups (Fig. 2(a)), placing the groups one after another. In $[Mn_6(O)_2Piv_{10}(NIT\text{-}H)_4] \cdot 0.5CH_2Cl_2$, the ·O–N–C=N → O fragment is almost perpendicular to the equatorial plane of the Mn octahedron. The MnONC torsion angle (marked by triangles in Fig. 3) is up to 5.7°. With this type of radical orientation, the bridging function of NIT-H can hardly be realized because the two $[Mn_6O_2(piv)_{10}]$ fragments should be in strictly opposite positions (i.e., in an eclipsed conformation), inevitably leading to an overlap between the trimethyl acetate groups. This situation is illustrated by Fig. 4. The space-filling model includes two $[Mn_6(O)_2Piv_{10}(NIT\text{-}H)_4]$ molecules. Their mutual orientation is such that each molecule faces the NIT-H oxygen atom (denoted by O_L in the figure) on the periphery of the other molecule to form a bridge of two terminal NIT-H molecules by the counter-motion of the molecules. It can readily be verified that the methyl groups of the trimethyl acetate groups will simply overlap each other. It is difficult to explain this specific orientation of NIT-H molecules relative to the $[Mn_6O_2(piv)_{10}]$ unit, hindering the bridging type of nitroxide coordination and hence the generation of highly dimensional structures. This may be the consequence of the electronic effects because the inductive

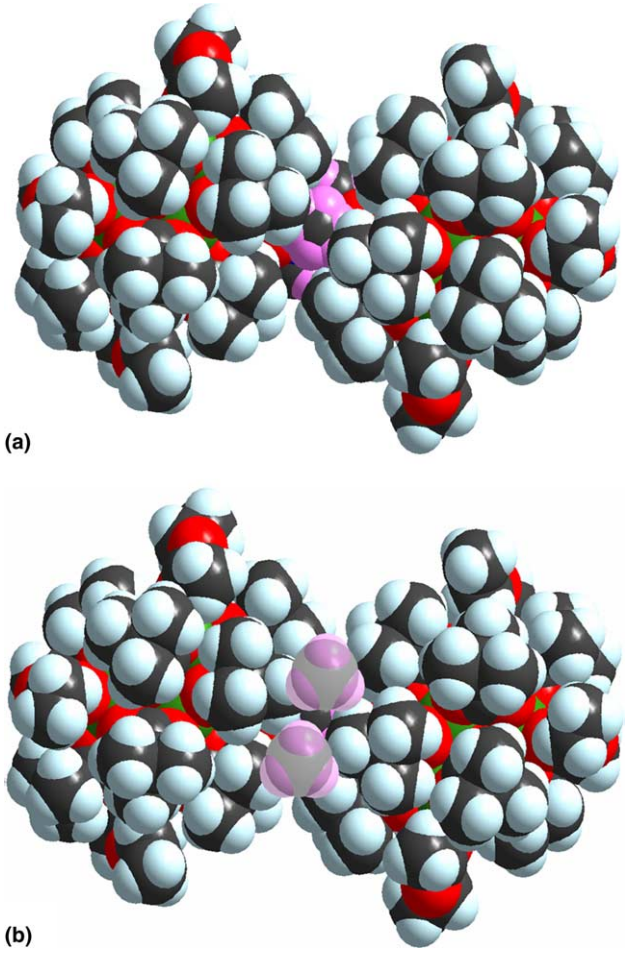


Fig. 2. Space-filling view of the $[(EtOAc)_3Mn_6(O)_2Piv_{10}(NIT\text{-}Me)\text{-}Mn_6(O)_2Piv_{10}(EtOAc)_3]$ molecule (a), showing the unacceptable overlap between the methyl group and the trimethyl acetate fragment in the case of NIT-Et (b).

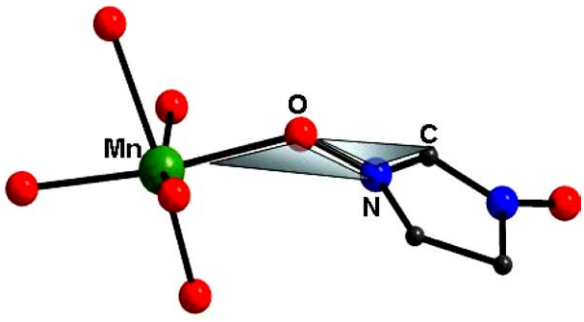


Fig. 3. Torsion angle (triangles) between the plane of the C, N, and O atoms of the ·O–N–C=N → O fragment and the plane of N, O, and Mn atoms.

effect of the H atom differs substantially from that of the CH_3 group. Moreover, the donor ability of the O atoms of the nitronyl nitroxide fragment of NIT-H is much weaker than that of NIT-Me.

Thus the bridging function of the nitronyl nitroxide fragment between the $[Mn_6O_2(piv)_{10}]$ units was realized for NIT-Me but not for NIT-H and NIT-Et. To obtain highly dimensional structures with bridging NIT-R ($R = C_nH_{2n+1}$, $n > 1$) it is reasonable to employ polymetallic nuclei whose carboxylate ligands contain less bulky substituents compared to $-C(CH_3)_3$ to provide high solubility of the polymetallic nucleus in organic solvents.

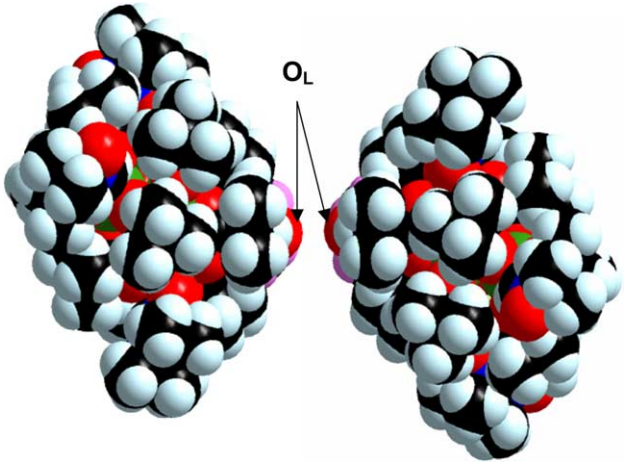


Fig. 4. $[Mn_6(O)_2Piv_{10}(NIT\text{-}H)_4]$ fragments facing each other by their NIT-H molecules, the arrangement that permits linkage into a bridge by the counter-motion.

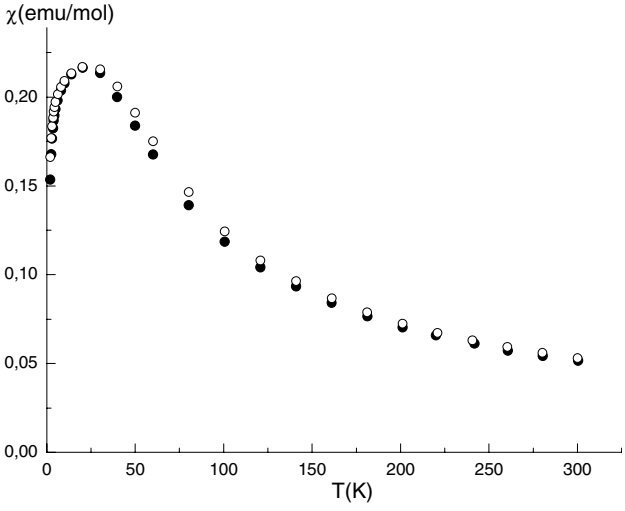


Fig. 5. Temperature dependences of magnetic susceptibility (χ) for $[Mn_6(O)_2Piv_{10}(Me_2CO)_2(H_2O)]$ (●) and $[(EtOAc)_3Mn_6(O)_2Piv_{10}(Ac\text{–}Ac)Mn_6(O)_2Piv_{10}(EtOAc)_3]$ (○).

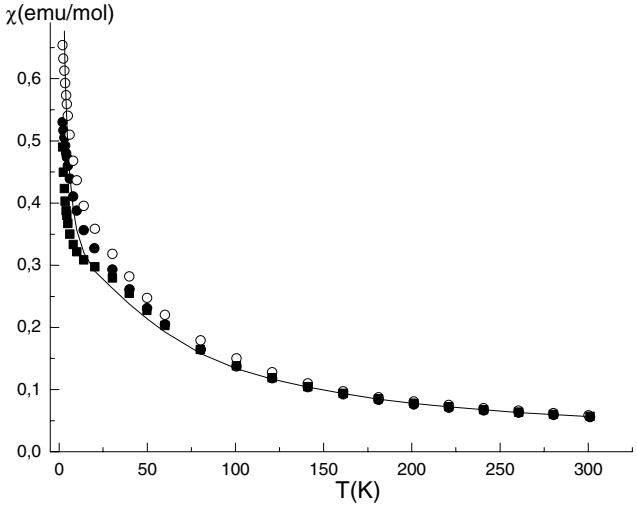


Fig. 6. Temperature dependences of magnetic susceptibility (χ) for $[Mn_6(O)_2Piv_{10}(NIT\text{-}p\text{-}Py)_4]$ (●), $[Mn_6(O)_2Piv_{10}(NIT\text{-}p\text{-}Py)_4] \cdot 0.5C_6H_{14}$ (○), and $[Mn_6(O)_2Piv_{10}(NIT\text{-}p\text{-}Py)_2(H_2O)] \cdot C_6H_{14}$ (■).

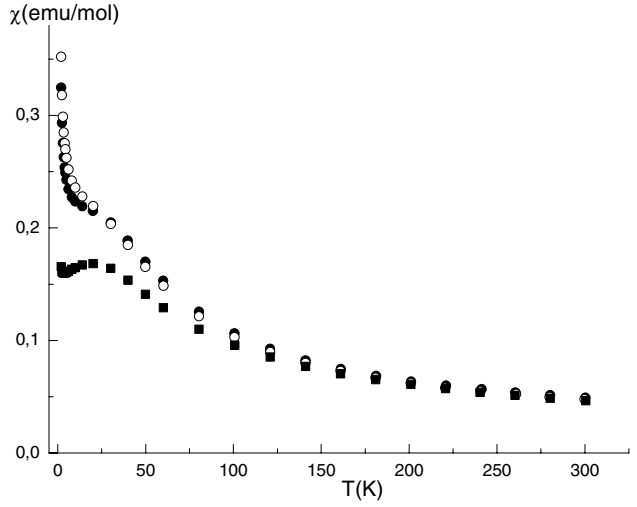


Fig. 7. Temperature dependences of magnetic susceptibility (χ) for $[Mn_6Piv_{10}(O)_2(NIT\text{-}Et)_4]$ (●), $[Mn_6(O)_2Piv_{10}(NIT\text{-}Et)_3HPiv] \cdot 0.5C_7H_{16}$ (○) and $[Mn_6(O)_2Piv_{10}(NIT\text{-}H)_4]0.5CH_2Cl_2$ (■).

3.3. Magnetic properties

The magnetic properties of the compounds are illustrated by the temperature dependence of the molar magnetic susceptibility (Figs. 5–8). For $[Mn_6(O)_2Piv_{10}(Me_2CO)_2(H_2O)]$ and $[(EtOAc)_3Mn_6(O)_2Piv_{10}(Ac\text{–}Ac)Mn_6(O)_2Piv_{10}(EtOAc)_3]$, having no paramagnetic ligands (Fig. 5), the $\chi(T)$ curve shows a broad maximum, which points to antiferromagnetic interaction in $[Mn_6(O)_2Piv_{10}]$ exchange clusters. Above the temperature of the maximum, the curve obeys the Curie–Weiss law with the constants listed in Table 2. The magnetic properties of hexanuclear carboxylates of $[Mn_6(O)_2(RCOO)_{10}(L)_4]$ type, where L is a monodentate

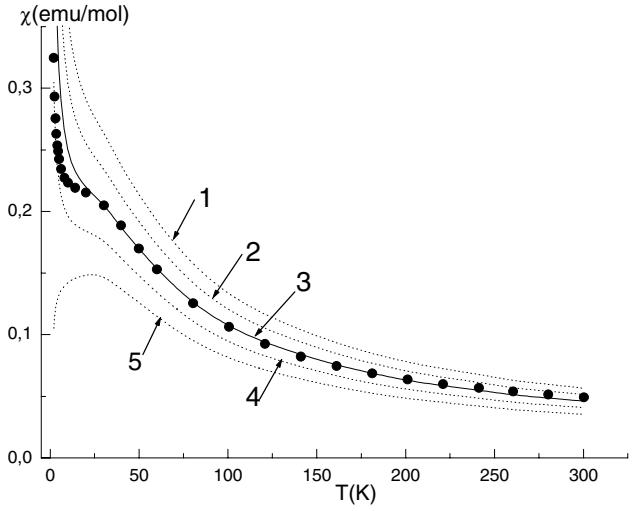


Fig. 8. Experimental temperature dependence of magnetic susceptibility (χ) for $[Mn_6Piv_{10}(O)_2(NIT\text{-}Et)_4]$ (•) and theoretical curves for different cases described in the text.

diamagnetic ligand (Py, EtOH, CH_3CN) exhibiting spin frustration, are well documented [4]. Based on the results of these studies, one would expect that at high temperatures the effective magnetic moment (μ_{ef}) of $[Mn_6(O)_2Piv_{10}(Me_2CO)_2(H_2O)]$ and $[(EtOAc)_3Mn_6(O)_2Piv_{10}(Ac\text{–}Ac)Mn_6(O)_2Piv_{10}(EtOAc)_3]$ will tend to the theoretical values of 12.0 and 17.1μ_B, respectively. It was assumed that in the $[Mn_6(O)_2Piv_{10}]$ cluster unit, the moments of the two internal Mn(III) ions lying at very short distances of ~2.8 Å fully compensate each other as a result of a strong antiferromagnetic interaction [3c,4a,4b]. Indeed, the experimental values of μ_{eff} for these compounds tend to approach these values at 300 K (Table 2).

It is assumed that there is a strong antiferromagnetic exchange between the internal Mn(III) ions, leading to complete spin coupling between the two ions. Then the magnetic moments of the complexes (including complexes with nitroxides) are evaluated by the formula $\mu_{calc}{}^2 = 4(\mu_{MnII})^2 + n_R(\mu_R)2$, where μ_{MnII} is the magnetic moment of the high-spin Mn(II) ion, μ_R is the magnetic moment of the nitroxide, and n_R is the number of radicals in the molecule. Fig. 6 presents data for $[Mn_6(O)_2Piv_{10}(NIT\text{-}p\text{-}Py)_4]$, $[Mn_6(O)_2Piv_{10}(NIT\text{-}p\text{-}Py)_4]\cdot 0.5C_6H_{14}$, and $[Mn_6(O)_2Piv_{10}(NIT\text{-}p\text{-}Py)_2(H_2O)]\cdot C_6H_{14}$, in which the nitronyl nitroxide fragment is not coordinated and is far from the $[Mn_6(O)_2Piv_{10}]$ unit (Schemes 2 and 3). The $\chi(T)$ curves contain a kink in the region of the maximum for clusters having no radicals (Fig. 5). To evaluate the coupling between the odd electrons of the terminal Mn(II) atoms and the radicals, we use the curve (solid line in Fig. 6) obtained as the sum of the magnetic susceptibility of the hexanuclear $[Mn_6(O)_2Piv_{10}(Me_2CO)_2(H_2O)]$ cluster and four independent susceptibilities of NIT-*p*-Py: $\chi_{clust\,+\,4R} = \chi_{clust} + 4(0.375/T)$. As can be seen from Fig. 6, the dependence thus obtained (solid line) reproduces the experimental data well, indicating that there is weak exchange between the Mn(II) ions and the nitroxides via the pyridine ring. Good agreement between the experimental and calculated effective magnetic moments also follows from Table 2.

The most interesting results were obtained for $[Mn_6Piv_{10}(O)_2(NIT\text{-}Et)_4]$, $[Mn_6(O)_2Piv_{10}(NIT\text{-}Et)_3HPiv]\cdot 0.5C_7H_{16}$, and $[Mn_6(O)_2Piv_{10}(NIT\text{-}H)_4]\cdot 0.5CH_2Cl_2$. As the magnetic properties of these compounds are similar (Fig. 7), the $\chi(T)$ dependence is discussed for $[Mn_6Piv_{10}(O)_2(NIT\text{-}Et)_4]$ alone (Fig. 8). Fig. 8 shows five calculated curves for cases when (1) the terminal Mn(II) ions do not interact with all coordinated nitroxides (dotted curve 1); (2) the spin of one of the nitroxides is completely coupled to one of the electrons of the coordinating Mn(II) ion (dotted curve 2); (3) the spins of two nitroxides are completely coupled to the electrons of two Mn(II) ions (solid line 3); (4) the spins of the three nitroxides are completely coupled to the electrons of the three Mn(II) ions (dotted curve 4); and (5) the spin of each of the four coordinated nitroxides cancels the moment of one of the five odd electrons on each of the four terminal Mn(II) ions (dotted curve 5). As can be seen in Fig. 8, solid line 3 is the only curve that reproduces the experimental data well. In the low-temperature range, it slightly deflects from the experimental values due to the neglect of weak inter- and intramolecular interactions. If these interactions are taken into account by Weiss constant −3.5 K, then in the low-temperature region we also achieve good agreement with the experimental data. Thus analysis of the $\chi(T)$ dependence for

Table 2
Magnetic characteristics of the compounds

Compound	C (emu K mol^{-1})	$-\theta$ (K)	$\mu_{eff} = \sqrt{8C}/\mu_B$	μ_{calc}/μ_B
$[Mn_6(O)_2Piv_{10}(NIT\text{-}H)_4]\cdot 0.5CH_2Cl_2$	17.76	88	11.9	12.3
$[Mn_6(O)_2Piv_{10}(NIT\text{-}Et)_3HPiv]\cdot 0.5C_7H_{16}$	17.29	72	11.8	12.2
$[Mn_6Piv_{10}(O)_2(NIT\text{-}Et)_4]$	17.87	73	12.0	12.3
$[Mn_6(O)_2Piv_{10}(Me_2CO)_2(H_2O)]$	17.97	48	12.0	11.8
$[(EtOAc)_3Mn_6(O)_2Piv_{10}(Ac\text{–}Ac)Mn_6(O)_2Piv_{10}(EtOAc)_3]$	36.47	42	17.1	16.7
$[Mn_6(O)_2Piv_{10}(NIT\text{-}p\text{-}Py)_4]$	18.56	37	12.2	12.3
$[Mn_6(O)_2Piv_{10}(NIT\text{-}p\text{-}Py)_4]\cdot 0.5C_6H_{14}$	19.06	30	12.4	12.3
$[Mn_6(O)_2Piv_{10}(NIT\text{-}p\text{-}Py)_2(H_2O)]\cdot C_6H_{14}$	19.16	41	12.4	12.1

$[Mn_6Piv_{10}(O)_2(NIT\text{-}Et)_4]$ unambiguously showed that the odd electrons of the two coordinated NIT-Et are completely coupled to one of the electrons of the two coordinating Mn(II) ions, while the odd electrons of the other two coordinated NIT-Et interact very weakly with the odd electrons of the other two Mn(II) ions. The results of structural analysis indicated that the magnetic data completely correlate with structural data for the compound. Indeed, in $[Mn_6Piv_{10}(O)_2(NIT\text{-}Et)_4]$, the $Mn–O_{NO}$ distances of two nitroxides are much shorter than those of the other two (2.221 and 2.275 Å, Table 1). As would be expected, extension of the $Mn–O_{NO}$ bond by ~0.055 Å drastically weakens exchange interactions in {Mn–'O–N<} exchange clusters. The strong antiferromagnetic interactions between the odd electrons of Mn(II) and the nitroxides lying at short distances (~2.2 Å) lead to larger values of θ for $[Mn_6Piv_{10}(O)_2(NIT\text{-}Et)_4]$, $[Mn_6(O)_2Piv_{10}(NIT\text{-}Et)_3HPiv] \cdot 0.5C_7H_{16}$, and $[Mn_6(O)_2Piv_{10}(NIT\text{-}H)_4] \cdot 0.5CH_2Cl_2$ compared to other compounds under study (Table 2).

4. Supplementary material

Crystal data for the structural analysis for $[Mn_6(O)_2Piv_{10}(NIT\text{-}H)_4] \cdot 0.5CH_2Cl_2$, $[Mn_6(O)_2Piv_{10}(NIT\text{-}Et)_3HPiv] \cdot 0.5C_7H_{16}$, $[Mn_6(O)_2Piv_{10}(NIT\text{-}Et)_4]$, $[(EtOAc)_3Mn_6(O)_2Piv_{10}(Ac–Ac)Mn_6(O)_2Piv_{10}(EtOAc)_3]$, $[Mn_6(O)_2Piv_{10}(Me_2CO)_2(H_2O)]$, $[Mn_6(O)_2Piv_{10}(NIT\text{-}p\text{-}Py)_4]$, $[Mn_6(O)_2Piv_{10}(NIT\text{-}p\text{-}Py)_4] \cdot 0.5C_7H_{16}$, $[Mn_6(O)_2Piv_{10}(NIT\text{-}p\text{-}Py)_2(H_2O)]$, $[Mn_6(O)_2Piv_{10}(NIT\text{-}n\text{-}Bu\text{-}Pz)_2(HPiv)_2]$, and $[Mn_6(O)_2Piv_{10}(NIT\text{-}n\text{-}Bu\text{-}Pz)(Thf)\ (H_2O)] \cdot C_6H_{14}$ have been deposited with the Cambridge Crystallographic Data Center, CCDC Nos. 250482, 250483, 250487-250493, and 250752. Copies of this information may be obtained free of charge from the Director, CCDC, 12 Union Road, Cambridge, CB21EZ, UK (fax: +44 1223 336 033, e-mail: deposit@ccdc. cam.ac.uk, or on the web http://www.ccdc.cam.ac.uk).

Acknowledgements

Research funded in part by US Civilian Research and Development Foundation (grants NO-008-X1, Y2-C-08-01), RFBR (grants 03-03-32518, 04-03-08002, 05-03-32095, 05-03-32305), RAS and SB RAS grants.

References

[1] V. Ovcharenko, E. Fursova, G. Romanenko, V. Ikorskii, Inorg. Chem. 43 (2004) 3332.
[2] (a) E.F. Ullman, J.H. Osiecki, D.G.B. Boocock, R. Darcy, J. Am. Chem. Soc. 94 (1972) 7049;
(b) E.F. Ullman, L. Call, J.H. Osiecki, J. Org. Chem. 35 (1970) 3623;
(c) V.I. Ovcharenko, S.V. Fokin, I.V. Korobkov, P. Rey, Russ. Chem. Bull. 48 (1999) 1519 (Engl. Transl.);
(d) V.I. Ovcharenko, S.V. Fokin, G.V. Romanenko, V.N. Ikorskii, E.V. Tretyakov, S.F. Vasilevsky, R.Z. Sagdeev, Mol. Phys. 100 (2002) 1107.
[3] (a) M. Murrie, S. Parsons, R.E.P. Winpenny, J. Chem. Soc., Dalton Trans. (1998) 1423;
(b) K. Koehler, H.W. Roesky, M. Noltemeyer, H.-G. Schmidt, C. Freire-Erdbruegger, G.M. Sheldrick, Chem. Ber. 126 (1993) 921;
(c) A.R.E. Baikie, A.J. Howes, M.B. Hursthouse, A.B. Quick, P. Thornton, J. Chem. Soc., Chem. Commun. (1986) 1587;
(d) N.V. Gerbeleu, A.S. Batsanov, G.A. Timko, Yu.T. Struchkov, K.M. Indrichan, G.A. Popovich, Dokl. Akad. Nauk SSSR (Russ.) (Proc. Natl. Acad. Sci. USSR) 294 (1987) 878.
[4] (a) S. Wang, H.-L. Tsai, W.E. Streib, G. Christou, D.N. Hendrickson, J. Chem. Soc., Chem. Commun. (1992) 677;
(b) A.R. Schake, J.B. Vincent, Q. Li, P.D.W. Boyd, K. Folting, J.C. Huffman, D.N. Hendrickson, G. Christou, Inorg. Chem. 28 (1989) 1915;
(c) D.N. Hendrickson, G. Christou, E.A. Schmitt, E. Libby, J.S. Bashkin, S. Wang, H.-L. Tsai, J.B. Vincent, P.D.W. Boyd, J.C. Huffman, K. Folting, Q. Li, W.E. Streib, J. Am. Chem. Soc. 114 (1992) 2455.

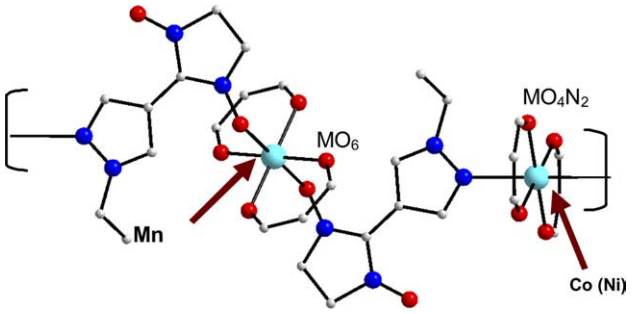


Fig. 1. Polymer chain with a 'head-to-head' motif in $Cu(hfac)_2L^{Et}$.

Mn and Co (or Ni) for M because Mn is suitable to replace the Cu atoms in the CuO_6 coordination units of $Cu(hfac)_2L^{Et}$ polymer chains, while Co (or Ni) conveniently replaces the Cu atoms in the CuO_4N_2 units (Fig. 1). We succeeded in synthesizing solid solutions, whose structure and magnetic properties are described here along with their synthesis.

2. Experimental

2.1. Synthesis

All the solvents were commercially available and used as received. Nitronyl nitroxide 4,4,5,5-tetramethyl-2-(1′-ethyl-pyrazole-4′-yl)-4,5-dihydro-1*H*-imidazolyl-3-oxide-1-oxyl (L^{Et}) and $Cu(hfac)_2L^{Et}$ were prepared by the procedure of [6].

2.1.1. $Mn(hfac)_2L^{Et}$

A sample of $Mn(hfac)_2 \cdot 2H_2O$ (101 mg, 20 mmol) was dissolved in diethyl ether (3 ml). The solution was added through a filter to a solution of L^{Et} (50 mg, 20 mmol) in diethyl ether (2 ml). Hexane (15 ml) was added to the resulting mixture, and the mixture was allowed to stay in an open flask at 5 °C for 1 or 2 days. After approximately one half of the mother solution had evaporated, the greenish blue crystals were filtered off, washed with hexane, and dried in air. The complex is readily soluble in diethyl ether, THF, and acetone, but practically insoluble in benzene and saturated hydrocarbons. Yield 83%. *Anal.* Calc. for $MnC_{22}H_{21}N_4O_6F_{12}$: C, 36.7; H, 2.9; N, 7.8; F, 31.7. Found: C, 36.7; H, 2.8; N, 7.4; F, 31.2%.

2.1.2. $Ni(hfac)_2L^{Et}$ and $Co(hfac)_2L^{Et}$

The complexes were prepared by a similar procedure using THF instead of diethyl ether and heptane instead of hexane. The complexes separated as conglomerates of finely disperse, dark indigo blue crystals. They are well soluble in acetone, sparingly soluble in THF, and practically insoluble in benzene and saturated hydrocarbons. Yield 80–85%. *Anal.* Calc. for $NiC_{22}H_{21}N_4O_6F_{12}$: C, 36.5; H, 2.9; N, 7.8; F, 31.5. Found: C, 36.8; H, 2.9; N, 7.7; F, 31.4%. *Anal.* Calc. for $CoC_{22}H_{21}N_4O_6F_{12}$: C, 36.5; H, 2.9; N, 7.7; F, 31.5%. Found: C, 36.3; H, 3.0; N, 7.4; F, 31.3.%. $Co(hfac)_2L^{Et}$ single crystals were obtained as follows. $Co(hfac)_2 \cdot 2H_2O$ (101 mg, 20 mmol) and L^{Et} (50 mg, 20 mmol) were dissolved in acetone (5 ml), and hexane (10 ml) was added. The reaction mixture was heated to boiling while intermittently shaking the flask. Thin plates of dark indigo blue crystals formed after a while in the hot solution. The crystals were filtered off and washed with hexane. Yield 30%.

2.1.3. $Mn_xCu_{1-x}(hfac)_2L^{Et}$

A mixture of $Cu(hfac)_2L^{Et}$ and $Mn(hfac)_2L^{Et}$ or $Cu(hfac)_2$ and $Mn(hfac)_2$ with L^{Et}, in which the mole fraction $x = \nu_{Mn}/(\nu_{Mn} + \nu_{Cu})$ was varied from 0.10 to 0.45 (the total mass of the sample was 150 ± 1 mg), was dissolved in a mixture of acetone (2 ml) and CH_2Cl_2 (4 ml). Then hexane (8 ml) was added. The resulting solutions were allowed to slowly evaporate at 5 °C. After 5 days, the crystals of $Mn_xCu_{1-x}(hfac)_2L^{Et}$ solid solutions were filtered off, washed with hexane, dried in air, and used for magnetic measurements and XRD analysis. Yields were 50–70%.

2.1.4. $Co_xCu_{1-x}(hfac)_2L^{Et}$

A mixture of $Cu(hfac)_2L^{Et}$ and $Co(hfac)_2L^{Et}$ or $Cu(hfac)_2$ and $Co(hfac)_2$ with L^{Et}, in which the mole fraction $x = \nu_{Co}/(\nu_{Co} + \nu_{Cu})$ was varied from 0.02 to 0.12 (the total mass of the sample was 150 ± 1 mg), was dissolved in acetone (2 ml). Then hexane (10 ml) was added. The resulting solutions were allowed to slowly evaporate at 5 °C. After 3 or 4 days, the crystals of $Co_xCu_{1-x}(hfac)_2L^{Et}$ solid solutions were filtered off, washed with hexane, dried in air, and used for magnetic measurements and XRD analysis. Yields were 45–70%.

2.1.5. $Ni_xCu_{1-x}(hfac)_2L^{Et}$

A mixture of $Cu(hfac)_2L^{Et}$ and $Ni(hfac)_2L^{Et}$ or $Cu(hfac)_2$ and $Ni(hfac)_2$ with L^{Et}, where the mole fraction $x = \nu_{Ni}/(\nu_{Ni} + \nu_{Cu})$ was varied from 0.02 to 0.12 (the total mass of the sample was 150 ± 1 mg), was dissolved in a mixture of acetone (1.5 ml) and CH_2Cl_2 (2 ml). Then hexane (10 ml) was added. The resulting solutions were allowed to slowly evaporate at 5 °C. After 4 or 5 days, the crystals of $Ni_xCu_{1-x}(hfac)_2L^{Et}$ solid solutions were filtered off, washed with hexane, dried in air, and used for magnetic measurements and XRD analysis. Yields were 45–75%.

2.2. Metal determination

Samples of $Mn_xCu_{1-x}(hfac)_2L^{Et}$, $Co_xCu_{1-x}(hfac)_2L^{Et}$, and $Ni_xCu_{1-x}(hfac)_2L^{Et}$ solid solutions were dissolved in ethanol. Metal determination for these mixed-metal samples was carried out by the atomic

Table 1
Cu–O_L and Cu–N bond lengths (Å) in $Cu(hfac)_2L^{Et}$ at different temperatures

T (K)	295	241	229	221	218	215	208	180	115
Cu–O_L	2.237(4)	2.183(2)	2.175(2)	2.176(5)	2.242(2)	2.250(2)	2.260(1)	2.260(3)	2.281(3)
Cu–N	2.375(5)	2.326(2)	2.306(2)	2.246(5)	2.133(2)	2.113(2)	2.096(2)	2.079(4)	2.055(4)

Table 2
M–O_L and M–N bond lengths (Å) in $Mn(hfac)_2L^{Et}$ and $Co(hfac)_2L^{Et}$ at different temperatures

Compound	$Mn(hfac)_2L^{Et}$			$Co(hfac)_2L^{Et}$		
T (K)	295	200	115	240	180	120
M–O_L	2.156(2)	2.143(2)	2.140(1)	2.075(3)	2.060(4)	2.052(6)
M–N	2.299(2)	2.281(3)	2.276(2)	2.174(4)	2.167(4)	2.177(8)

Table 3
Variation of M–O_L and M–N (Å) bond lengths in $Mn_xCu_{1-x}(hfac)_2L^{Et}$ (T = 295 K)

x	0.00	0.15	0.22	0.41	0.46	0.57	0.79	1.00
M–O_L	2.237(4)	2.221(4)	2.184(2)	2.189(3)	2.173(4)	2.157(3)	2.161(4)	2.156(2)
M–N	2.375(5)	2.372(5)	2.372(3)	2.378(3)	2.374(4)	2.364(3)	2.320(5)	2.299(2)

absorption technique (with atomization in air-acetylene flame on a Hitachi Z-8000 atomic absorption spectrophotometer) using the calibrating curves preliminarily obtained for ethanolic solutions of $Cu(hfac)_2L^{Et}$ and $M(hfac)_2L^{Et}$ with known concentrations of M and Cu.

2.3. X-ray crystallography

The intensity data for the single crystals of the compounds were collected on a SMART APEX (Bruker AXS) automatic diffractometer using the standard procedure (Mo radiation). The structures were solved by direct methods and refined by the full-matrix least-squares procedure anisotropically for non-hydrogen atoms and isotropically for hydrogens. The H atoms were located in difference electron density syntheses. All calculations were fulfilled with the SHELXTL program package. The crystal data are given in Tables 6–8.

2.4. Magnetic measurements

All measurements were carried out on an MPMS-5S SQUID magnetometer (Quantum Design) in the temperature range 2–300 K and on Faraday balance in the temperature range 77–300 K with a magnetic field of up to 5 kOe. Molar magnetic susceptibility was calculated using diamagnetic corrections for the complexes.

3. Results and discussion

Investigation of the dynamics of CuO_6 and CuO_4N_2 coordination units in the region of the phase transition of the $Cu(hfac)_2L^{Et}$ single crystal indicated that the Cu–O_L and Cu–N distances in the crystallographically independent centrosymmetric CuO_6 and CuO_4N_2 units are shortened when the temperature decreases from

Table 4
Variation of M–O_L and M–N (Å) bond lengths in $Co_xCu_{1-x}(hfac)_2L^{Et}$ (T = 295 K)

x	0.00	0.04	0.08	0.11	0.15	0.16	0.20	1.00
M–O_L	2.237(4)	2.236(3)	2.236(3)	2.231(3)	2.232(4)	2.223(5)	2.232(3)	2.071(5)
M–N	2.375(5)	2.359(4)	2.347(4)	2.328(4)	2.316(4)	2.317(6)	2.282(3)	2.180(6)

Table 5
M–O_L and M–N (Å) bond lengths in $M_xCu_{1-x}(hfac)_2L^{Et}$ at different temperatures

	$Mn_{0.22}Cu_{0.78}(hfac)_2L^{Et}$					$Ni_{0.08}Cu_{0.92}(hfac)_2L^{Et}$		
T (K)	110	140	180	220	295	200	220	240
M–O_L	2.159(4)	2.140(4)	2.152(4)	2.162(4)	2.185(2)	2.245(2)	2.223(2)	2.222(3)
M–N	2.315(5)	2.289(5)	2.308(5)	2.326(5)	2.375(2)	2.104(2)	2.148(3)	2.245(4)

Table 6
Crystal data for $Cu(hfac)_2L^{Et}$, $Mn(hfac)_2L^{Et}$ and $Co(hfac)_2L^{Et}$

Compound	$Cu(hfac)_2L^{Et}$						$Mn(hfac)_2L^{Et}$			$Co(hfac)_2L^{Et}$		
Space group, Z	$C2/c$, 8						$C2/c$, 8			$C2/c$, 8		
T (K)	208	215	218	221	229	241	115	200	295	120	180	240
a (Å)	29.552(6)	29.567(6)	29.660(6)	29.811(8)	30.098(6)	30.189(6)	29.7819(19)	29.851(2)	30.026(7)	29.431(13)	29.475(8)	29.582(7)
b (Å)	9.512(2)	9.491(2)	9.490(2)	9.407(2)	9.457(2)	9.471(2)	9.5055(6)	9.6120(6)	9.799(2)	9.387(4)	9.481(3)	9.565(3)
c (Å)	24.428(5)	24.460(5)	24.520(5)	24.659(7)	24.923(5)	24.991(5)	24.6333(15)	24.6773(16)	24.771(8)	24.548(12)	24.564(6)	24.609(6)
β (°)	121.48(3)	121.62(3)	121.91(3)	123.169(9)	123.75(3)	123.90(3)	123.8910(10)	123.7750(10)	123.49(2)	123.782(7)	123.566(4)	123.302(5)
V (Å^3)	5856(2)	5845(2)	5859(2)	5789(3)	5899(2)	5931(2)	5788.7(6)	5885.6(7)	6078(3)	5637(5)	5720(3)	5820(3)
$D_{calc.}$ (g cm^{-3})	1.654	1.657	1.653	1.673	1.642	1.633	1.653	1.626	1.574	1.707	1.682	1.653
μ (mm^{-1})	0.866	0.867	0.865	0.876	0.859	0.855	0.577	0.568	0.550	0.733	0.723	0.710
θ (°)	1.62–28.25	1.77–28.30	1.62–28.26	1.74–28.48	1.63–28.26	1.63–28.31	1.99–23.26	1.99–23.28	1.97–25.00	1.75–23.32	1.75–23.31	1.65–23.35
I_{hkl} (meas/uniq)	17339/6865	17156/6870	17119/6880	16760/6820	17379/6940	17447/6972	12187/4162	12375/4237	5470/5359	7410/3864	11468/4113	11549/4128
R_{int}	0.0232	0.292	0.0400	0.2886	0.0232	0.0214	0.0200	0.0210	0.0284	0.0778	0.0605	0.0776
Goodness-of-fit	1.050	0.781	1.026	1.399	1.006	1.097	0.643	1.084	1.018	0.643	1.067	0.995
R_1 ($I_{hkl} > 2\sigma_I$)	0.0408	0.0423	0.0448	0.1088	0.0425	0.0445	0.0318	0.0478	0.0543	0.0987	0.0687	0.0619
wR_2	0.1075	0.1144	0.1129	0.2663	0.1055	0.1163	0.0780	0.1420	0.1496	0.2091	0.1603	0.1589
R_1 (all data)	0.0483	0.0505	0.0542	0.1324	0.0533	0.0556	0.0348	0.0524	0.0665	0.1458	0.0931	0.0774
wR_2	0.1157	0.1247	0.1232	0.2806	0.1155	0.1264	0.0811	0.1464	0.1614	0.2281	0.1728	0.1704

Table 7
Crystal data for solid solutions $Mn_xCu_{1-x}(hfac)_2L^{Et}$ and $Co_xCu_{1-x}(hfac)_2L^{Et}$ ($T = 295$ K)

Compound	$Mn_xCu_{1-x}(hfac)_2L^{Et}$							$Co_xCu_{1-x}(hfac)_2L^{Et}$					
Space group, Z	$C2/c$, 8							$C2/c$, 8					
x	0.15	0.22	0.27	0.41	0.46	0.57	0.79	0.04	0.08	0.11	0.15	0.16	0.19
a (Å)	30.451(8)	30.357(3)	30.400(3)	30.342(3)	30.307(4)	30.242(3)	30.104(3)	30.496(2)	30.431(2)	30.383(2)	30.343(3)	30.344(5)	30.242(3)
b (Å)	9.531(3)	9.5645(8)	9.5813(10)	9.5947(10)	9.5832(13)	9.6117(8)	9.6724(10)	9.5559(7)	9.5502(6)	9.5555(7)	9.5455(11)	9.5799(16)	9.5761(8)
c (Å) Å	25.203(7)	25.182(2)	25.215(3)	25.202(2)	25.188(3)	25.122(2)	24.948(3)	25.1771(19)	25.1171(17)	25.0755(19)	25.037(3)	25.056(4)	24.978(2)
β (°)	124.050(5)	124.197(1)	124.194(2)	124.208(2)	124.183(2)	124.108(1)	123.835(2)	123.849(2)	123.753(1)	123.569(2)	123.585(2)	123.442(3)	123.152(1)
V (Å^3)	6060(3)	6047.4(9)	6074.9(11)	6067.6(10)	6051.6(14)	6046.4(9)	6034.1(11)	6093.5(8)	6069.2(7)	6065.8(8)	6041.2(12)	6077.7(18)	6056.0(9)
$D_{calc.}$ (g cm^{-3})	1.591	1.591	1.584	1.583	1.587	1.587	1.587	1.583	1.588	1.589	1.595	1.586	1.591
μ (mm^{-1})	0.730	0.675	0.677	0.642	0.645	0.621	0.5756	0.738	0.718	0.719	0.721	0.717	0.720
θ (°)	2.28–23.31	2.28–23.39	2.27–23.28	1.95–23.29	1.70–23.30	2.27–23.31	1.63–23.29	1.95–23.25	1.95–23.29	1.61–23.26	1.61–23.31	1.61–23.31	1.95–23.29
I_{hkl} (meas/uniq)	12436/4341	12592/4339	12681/4362	12480/4366	12749/4364	12539/4346	12340/4310	12828/4357	12821/4361	12742/4352	12667/4352	12564/4378	12688/4368
R_{int}	0.1283	0.0521	0.0695	0.0849	0.0961	0.0608	0.0694	0.0973	0.0683	0.0636	0.0797	0.1163	0.0872
Goodness-of-fit	0.963	1.145	0.898	1.012	0.845	1.054	1.037	0.695	0.613	0.687	0.701	0.868	0.677
R_1 ($I_{hkl} > 2\sigma_I$)	0.0678	0.0468	0.0491	0.0678	0.0584	0.0564	0.0841	0.043	0.0392	0.0424	0.0449	0.0703	0.0417
wR_2	0.1272	0.0987	0.1162	0.1474	0.1273	0.1341	0.1897	0.1057	0.0871	0.0985	0.1010	0.1411	0.0982
R_1 (all data)	0.1199	0.0608	0.0627	0.0984	0.1034	0.0727	0.1412	0.0790	0.0882	0.0843	0.1017	0.1473	0.0684
wR_2	0.1364	0.1030	0.1240	0.1602	0.1484	0.1465	0.2183	0.1253	0.1116	0.1193	0.1316	0.1735	0.1143

Table 8
Crystal data for $Mn_{0.22}Cu_{0.78}(hfac)_2L^{Et}$ and $Ni_{0.08}Cu_{0.92}(hfac)_2L^{Et}$

Compound	$Mn_{0.22}Cu_{0.78}(hfac)_2L^{Et}$				$Ni_{0.08}Cu_{0.92}(hfac)_2L^{Et}$		
Space group, Z	$C2/c$, 8				$C2/c$, 8		
T (K)	110	140	180	220	200	220	240
a (Å)	30.189(7)	29.887(6)	30.068(5)	30.247(6)	29.567(3)	29.707(2)	30.244(5)
b (Å)	9.554(2)	9.4884(18)	9.5939(17)	9.695(2)	9.4951(8)	9.4853(7)	9.5735(15)
c (Å)	24.986(6)	24.726(5)	24.875(5)	25.032(5)	24.457(2)	24.564(2)	25.011(4)
β (°)	123.936(3)	123.936(3)	123.891(3)	123.833(3)	121.583(2)	122.088(2)	122.941(3)
V (Å^3)	5979(2)	5817(2)	5956.6(19)	6097(2)	5849.2(9)	5864.3(8)	6077.5(16)
D_{calc} (g cm^{-3})	1.615	1.660	1.622	1.584	1.655	1.650	1.593
μ (mm^{-1})	0.783	0.806	0.787	0.769	0.860	0.858	0.828
θ (°)	1.63–23.33	1.64–23.28	1.63–23.28	1.71–23.30	1.62–23.28	1.62–23.28	1.72–23.29
I_{hkl} (meas/uniq)	12171/4253	12069/4149	12335/4256	12556/4356	12261/4219	12405/4225	12460/4359
R_{int}	0.0706	0.0641	0.0766	0.0893	0.0585	0.0831	0.0903
Goodness-of-fit	0.842	0.842	0.862	1.018	0.980	0.862	0.966
R_1 ($I_{hkl} > 2\sigma_I$)	0.0654	0.0637	0.0661	0.0742	0.0394	0.0456	0.0560
wR_2	0.1641	0.1596	0.1647	0.1895	0.0820	0.0946	0.1135
R_1 (all data)	0.0913	0.0878	0.0971	0.1126	0.0549	0.0618	0.0864
wR_2	0.1802	0.1796	0.1941	0.2073	0.0876	0.1004	0.1251

295 to 221 K (Table 1). As the temperature decreases further from 218 to 115 K, the Cu–N distances are shortened from 2.133(2) to 2.055(4) Å, while the Cu–O_L distances are lengthened from 2.242(2) to 2.281(3) Å. The changes in the Cu–O_L and Cu–N distances are generally nonlinear, the maximum of the derivatives $\partial d_{Cu-OL}/\partial T$ and $\partial d_{Cu-N}/\partial T$ lying in the temperature range adjacent to 220 K (Fig. 2), i.e., in the region of the magnetic anomaly.

According to XRD data, $Mn(hfac)_2L^{Et}$ and $Co(hfac)_2L^{Et}$ proved to be isostructural with $Cu(hfac)_2L^{Et}$. Like $Cu(hfac)_2L^{Et}$, they have a polymer chain structure with a "head-to-head" motif of the chain, resulting from bridging coordination of L^{Et} via the imine N atom of the pyrazole ring and one of the O atoms of the nitronyl nitroxide fragment (Fig. 1). The chain has centrosymmetric coordination units of two types – MO_6 and MO_4N_2. While in the Cu(II) complex the Cu(II) Jahn-Teller ions are surrounded by a square bipyramid, in the Mn(II) and Co(II) complexes the coordination polyhedron is nearly isometric. The M–O_L distances in MO_6 coordination units (at room temperature) are 2.075(3)–2.156(2) Å (Table 2), and the M–N distances in MO_4N_2 units are 2.174(4)–2.299(2) Å; the M–O_{hfac} distance to the O atom of the hexafluoroacetylacetonate ligand is ~2.1 Å. In the Mn(II) and Co(II) complexes, the M–O_L and M–N distances change insignificantly at reduced temperatures. When solid $Mn(hfac)_2L^{Et}$ and $Co(hfac)_2L^{Et}$ are cooled, the MO_6 and MO_4N_2 units are uniformly compressed, with M–O_L and M–N distances decreasing by no more than 0.025 Å (Table 2). We failed to grow X-ray quality $Ni(hfac)_2L^{Et}$ single crystals. According to X-ray powder diffraction patterns, $Ni(hfac)_2L^{Et}$ is isostructural with $Co(hfac)_2L^{Et}$.

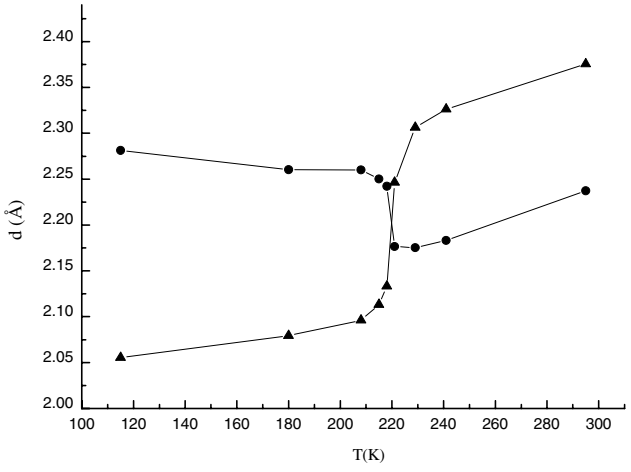


Fig. 2. Variation of Cu–O_L (●) and Cu–N (▲) bond lengths in CuO_6 and CuO_4N_2 coordination units, respectively.

The dependences $\mu_{eff}(T)$ for $M(hfac)_2L^{Et}$ (M = Mn, Co, Ni) are very similar. Fig. 3 shows the experimental dependence $\mu_{eff}(T)$ and the theoretical curve for $Mn(hfac)_2L^{Et}$ as an example. The theoretical curve corresponds to the optimal parameters $g_M = 2.0$, $J/k = -110$ K, $J'z/k = -0.017$ K of the spin Hamiltonian $\hat{H} = -2J(\hat{s}_{NO}\hat{s}_M + \hat{s}_M\hat{s}_{NO}) - \beta(2g_M\hat{s}M + 2g_{NO}\hat{s}_{NO})H - 2J'z\hat{S}\langle\hat{S}\rangle$ that includes spin coupling in the exchange cluster, Zeeman interaction, and weak interchain and intercluster interactions. Due to the strong antiferromagnetic interactions in $\gtrdot$N–·O–Mn^{2+}–O·–N$\lessdot$ exchange clusters, the spins of the coordinated $\gtrdot$N–·O groups are completely coupled to the two spins of Mn^{2+} at $T < 140$ K. Below this temperature, magnetic susceptibility has contributions only from the residual moments of these exchange clusters ($s = 3/2$) and the moments of the Mn^{2+} ions located in MnO_4N_2 coordination units ($s = 5/2$). Therefore, the dependence $\mu_{eff}(T)$ calculated for the $\{Mn(hfac)_2L^{Et}\}$ fragment tends to the theoretical

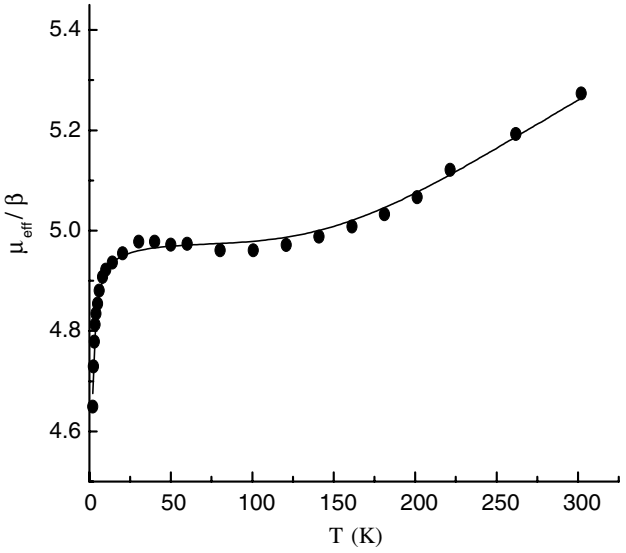


Fig. 3. Dependence $\mu_{eff}(T)$ for $Mn(hfac)_2L^{Et}$.

value of $\mu = \sqrt{0.5 \times 15 + 0.5 \times 35} = 5\beta$. Further decrease in μ_{eff} at $T < 10$ is explained by the weak interchain and intercluster interactions.

For solid $Mn(hfac)_2L^{Et}$, $Co(hfac)_2L^{Et}$, and $Ni(hfac)_2L^{Et}$, the $\mu_{eff}(T)$ curves did not show any anomalies; the character of the curves suggests that there are strong antiferromagnetic exchange interactions in $\gtrdot$N–·O–M(II)–O·–N$\lessdot$ exchange clusters. For $Cu(hfac)_2L^{Et}$, however, the $\mu_{eff}(T)$ curve showed that at 220 K μ_{eff} increased dramatically, and antiferromagnetic exchange interactions changed to ferromagnetic (Fig. 5(a), $x = 0$). At room temperature the value of μ_{eff} is close to the theoretical value of 2.45β for a system of almost uncoupled spins of Cu(II) and nitroxide as calculated for the $\{Cu(hfac)_2L^{Et}\}$ fragment. When the complex is cooled from room temperature to ~225 K, the value of μ_{eff} gradually decreases to $\sim 2.4\beta$ because in the temperature range 225–300 K, antiferromagnetic interactions dominate in the $\gtrdot$N–·O–Cu(II)–O·–N$\lessdot$ exchange clusters of $Cu(hfac)_2L^{Et}$ in view of the short Cu–O_L axial distance (2.237 Å) in the octahedral CuO_6 units [6,8]. Below the transition temperature, the Cu–O_L distances are lengthened (Table 1), and ferromagnetic interactions start to dominate in $\gtrdot$N–·O–Cu(II)–O·–N$\lessdot$ exchange clusters so that μ_{eff} increases until the temperature has reached ~25 K. A detailed description of this unusual spin transition and evaluation of exchange integrals for the high- ($J/k = -121$ K) and low-temperature regions ($J/k = 41.7$ K) are given elsewhere [6,8]. Below this temperature, μ_{eff} quickly decreases because of antiferromagnetic intermolecular exchange interactions.

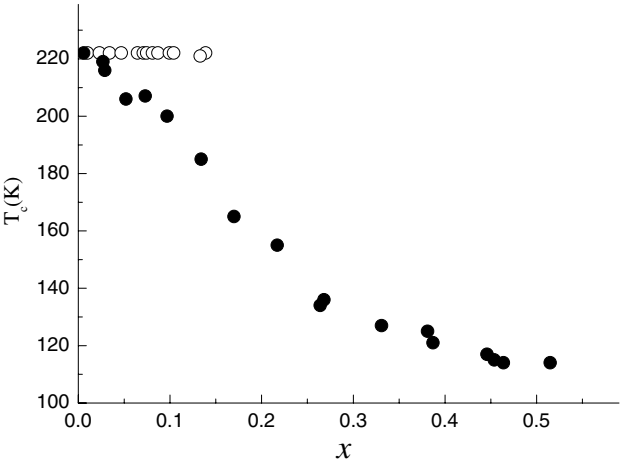


Fig. 4. Dependence of the transition temperature on the composition of $Mn_xCu_{1-x}(hfac)_2L^{Et}$ (●) and $Ni_xCu_{1-x}(hfac)_2L^{Et}$ (○) solid solutions.

The isostructural character of $M(hfac)_2L^{Et}$, where M = Cu, Mn, Co, Ni, is a favorable factor for the formation of $M_xCu_{1-x}(hfac)_2L^{Et}$ solid solutions. Note that $Mn_xCu_{1-x}(hfac)_2L^{Et}$ solid solutions obtained as described in Experimental generally separated as perfect single crystals irrespective of the mole fraction $x = \nu_M/(\nu_M + \nu_{Cu})$ of the second metal in the starting reaction mixture. The quality of $Co_xCu_{1-x}(hfac)_2L^{Et}$ and $Ni_xCu_{1-x}(hfac)_2L^{Et}$ crystals deteriorated markedly when x increased to 0.5. Also note that all solid solution crystals grew in kinetic but not thermodynamic equilibrium conditions because they formed in the course of gradual evaporation of the solvent from the mother solution. Nevertheless, when repeated in similar conditions for systems with different total samples of the starting compounds and different solvent mixtures, experiments gave well reproducible results.

As mentioned above, when choosing the second metal (M) we assumed that Mn will replace Cu atoms in the CuO_6 units of $Cu(hfac)_2L^{Et}$ polymer chains, while Co (or Ni) will substitute Cu atoms in the CuO_4N_2 units (Fig. 1). X-ray diffraction analysis for $M_xCu_{1-x}(hfac)_2L^{Et}$ confirmed this assumption. Tables 3 and 4 illustrate how M–O_L and M–N bond lengths change in series of $M_xCu_{1-x}(hfac)_2L^{Et}$ solid solutions. For $Mn_xCu_{1-x}(hfac)_2L^{Et}$ solid solutions, the M–O_L distances of the MO_6 units decrease when the mole fraction of Mn increases, while the M–N distances of the MO_4N_2 units remain the same as in pure $Cu(hfac)_2L^{Et}$ (2.375 Å). The reverse is true for $Co_xCu_{1-x}(hfac)_2L^{Et}$. As the mole fraction of Co increases, the M–N distances of the MO_4N_2 units are gradually shortened due to the incorporation of Co(II) ions. In the MO_6 units, the M–O_L bond lengths remain unchanged.

The magnetic properties of the solid solutions also change differently when a second metal is incorporated in different coordination units. In $Mn_xCu_{1-x}(hfac)_2L^{Et}$ solid solutions, the transition temperature decreases monotonously from 220 to 115 K when x increases from 0 to ~0.5. When $x > 0.5$, the transition is completely suppressed by the incorporated manganese (Fig. 4).

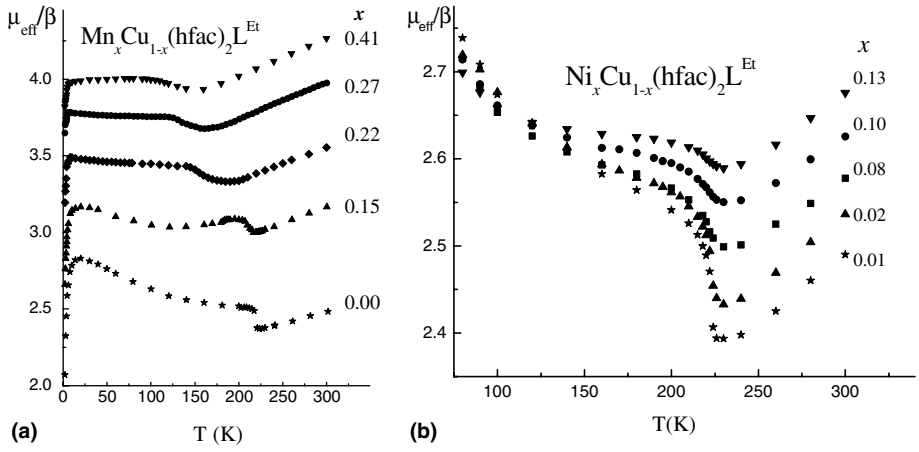


Fig. 5. Dependences $\mu_{eff}(T, x)$ for $Mn_xCu_{1-x}(hfac)_2L^{Et}$ (a) and $Ni_xCu_{1-x}(hfac)_2L^{Et}$ (b).

For $Ni_xCu_{1-x}(hfac)_2L^{Et}$, substitution of Cu(II) ions does not affect the transition temperature until x becomes ~0.2 (Fig. 4), but in the range $0.20 < x < 0.25$, the transition is suppressed.

Fig. 5 shows selected experimental dependences $\mu_{eff}(T)$ for mixed-metal solid solutions with different values of x. As Cu(II) ions are replaced by Mn(II) ions in the series of $Mn_xCu_{1-x}(hfac)_2L^{Et}$ solid solutions, the transition occurs at lower temperatures and becomes more diffuse (Fig. 5(a)). That is, incorporation of Mn in the chains leads to increased "rigidity" of MO_6 units and of the crystal in general. Therefore, more profound cooling is needed to achieve a transition through rearrangement of the remaining CuO_6 coordination units containing $\gtrdot$N–˙O–Cu(II)–O˙–N$\lessdot$ exchange clusters. This is supported, for example, by crystal structure investigations of the $Mn_{0.22}Cu_{0.78}(hfac)_2L^{Et}$ solid solution at different temperatures. It appeared that the M-O_L distances in the MO_6 polyhedra increase only at $T < 140$ K (Table 5). Therefore, cooling the crystal to low temperatures is needed to achieve rearrangement of the remaining CuO_6 coordination units containing $\gtrdot$N–˙O–Cu(II)–O˙–N$\lessdot$ exchange clusters. This completely agrees with magnetochemical experimental data (Fig. 5). When $x = 0.41$ (Fig. 5(a)), i.e., in situations when the MO_6 units are completely occupied by manganese, the transition is barely visible; μ_{eff} does not increase with decreasing temperature because this behavior of $\mu_{eff}(T)$ is not inherent in $Mn(hfac)_2L^{Et}$ (Fig. 3).

For $Ni_xCu_{1-x}(hfac)_2L^{Et}$ and $Co_xCu_{1-x}(hfac)_2L^{Et}$ solutions, the dependence $\mu_{eff}(T)$ behaves differently when x increases than it does in the same case for $Mn_xCu_{1-x}(hfac)_2L^{Et}$. For $Ni_xCu_{1-x}(hfac)_2L^{Et}$ (as well as $Co_xCu_{1-x}(hfac)_2L^{Et}$) solutions with low values of $x = 0.15$, the transition temperature does not change (Figs. 4 and 5(b)), but at higher values of x, the transition is suppressed. Unlike Mn ions, Ni (or Co) ions enter the MO_4N_2 units without changing the CuO_6 units, whose dynamics is just responsible for the magnetic effect. On the other hand, because of the similarity between the ionic radii of Ni(II) (or Co(II)) and Cu(II), minor additions of Ni(II) (or Co(II)) to the MO_4N_2 units ($x = 0.15$) do not markedly perturb the structure of $Cu(hfac)_2L^{Et}$ in general, and the temperature of the magnetic anomaly remains unaltered. However, at certain critical values of $x > 0.2$, the Ni(II) (or Co(II)) ions, not possessing the Jahn-Teller nature, start to hinder the shortening of M–N distances in the MO_4N_2 units, thereby indirectly violating the dynamics of CuO_6 coordination units. This is supported by the observed lengthening of Cu–O_L distances in $\gtrdot$N–˙O–Cu(II)–O˙–N$\lessdot$ exchange clusters with concomitant pronounced shortening of M–N distances in the MO_4N_2 units of $Ni_{0.08}Cu_{0.92}(hfac)_2L^{Et}$ (Table 5). When the motion of NiO_4N_2 (or CoO_4N_2) units is no longer possible ($x > 0.2$), the dynamics of the CuO_6 units responsible for the magnetic anomaly is also suppressed. For $x < 0.2$, however, the character of the structural motions of CuO_6 and MO_4N_2 units in the region of the phase transition does not change.

Thus we have synthesized new compounds, $M_xCu_{1-x}(hfac)_2L^{Et}$, from the class of heterospin systems liable to undergo thermally induced spin transitions. By varying the metal and the value of x one can alter the temperature of the magnetic anomaly and its character.

4. Supplementary material

Crystal data for structural analysis of the investigated compounds have been deposited with the Cambridge Crystallographic Data Centre, CCDC Nos. 250780–250810. Copies of this information may be obtained free of charge from The Director, CCDC,

12 Union Road, Cambridge, CB2 1EZ, UK (fax: +44-1233-336033; e-mail: deposit@ccdc.cam.ac.uk or www: http://www.ccdc.cam.ak.uk).

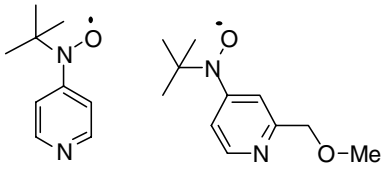
Acknowledgements

Research was funded by RFBR (03-03-32518, 02-03-33112, 04-03-08002), CRDF (NO-008-Xl, Y1-C-08-03), Russian Science Support Foundation, NSh (2298.2003.3) RAS and SB RAS Grants.

References

[1] A. Caneschi, D. Gatteschi, P. Rey, Prog. Inorg. Chem. 39 (1991) 331.
[2] A. Caneschi, P. Chiesi, L. David, F. Ferraro, D. Gatteschi, R. Sessoli, Inorg. Chem. 32 (1993) 1445.
[3] F. Lanfranc de Panthou, E. Belorizky, R. Calemczuk, D. Luneau, C. Marcenat, E. Ressouche, P. Turek, P. Rey, J. Am. Chem. Soc. 117 (1995) 11247.
[4] F. Lanfranc de Panthou, D. Luneau, R. Musin, L. Öhrström, A. Grand, P. Turek, P. Rey, Inorg. Chem. 35 (1996) 3484.
[5] F. Iwahory, K. Inoue, H. Iwamura, Mol. Cryst. Liq. Cryst. 334 (1999) 533.
[6] V.I. Ovcharenko, S.V. Fokin, G.V. Romanenko, Yu.G. Shvedenkov, V.N. Ikorskii, E.V. Tretyakov, S.F. Vasilevsky, Russ. J. Struct. Chem. 43 (2002) 153.
[7] V.I. Ovcharenko, S.V. Fokin, G.V. Romanenko, V.N. Ikorskii, E.V. Tretyakov, S.F. Vasilevsky, R.Z. Sagdeev, Mol. Phys. 100 (2002) 1107.
[8] P. Rey, V.I. Ovcharenko, in: J.S. Miller, M. Drillon (Eds.), Magnetism: Molecules to Materials IV, Wiley-VCH, 2003, p. 41.
[9] V.I. Ovcharenko, K.Yu. Maryunina, S.V. Fokin, E.V. Tretyakov, G.V. Romanenko, V.N. Ikorskii, Russ. Chem. Bull., Int. Ed. 11 (2004) 2305.

$M(NO_3)_2$, M = Mn^{II}, **1**; Co^{II}, **2**; Ni^{II}, **3**; Cu^{II}, **4**, with **4NOPy-OMe** and their magnetic properties were investigated by X-ray structure analysis and SQUID magneto/susceptometry, respectively.



4NOPy **4NOPy-OMe**

2. Experimental

2.1. General

Melting points were recorded with a MEL-TEMP heating block and were uncorrected. Elemental analysis was performed in the analytical center of Kyushu University.

2.2. X-ray crystal and molecular structure analyses

Crystallographic data and experimental details for the complexes **1**–**4** are summarized in Table 1. The selected suitable single crystals were glued on a glass fiber by epoxy resin. All the X-ray data were collected on a Rigaku Raxis-Rapid diffractometer with graphite monochromated Mo Kα radiation ($\lambda = 0.71069$ Å). Reflections were collected at 123 ± 1 K for complex **1** and **2**, and 296 ± 1 K for **3** and **4**, respectively. The structures were solved by direct methods (SIR92) [6] and expanded using Fourier techniques (DIRDIF94) [7]. The refinements were converged using the full-matrix least-squares method of Crystal Structure software package [8] to give space group as *Pbcn*, for the complexes. All non-hydrogen atoms were refined anisotropically. Hydrogen atoms were found by standard method or from differential electron map and refined isotropically.

2.3. Measurements and analyses of magnetic properties

Magnetic susceptibility data were obtained on Quantum Design MPMS2 and MPMS5S SQUID susceptometer and corrected for the magnetization of the sample holder and capsule. The diamagnetic contributions to the samples were estimated from Pascal's constants [9].

2.4. Preparation

Pyridine ligand, **4NOPy-OMe**, was prepared by the procedure reported in the literature [4]. The solution of **4NOPy-OMe** in ether (ca. 0.05 M) was used for the complexation with metal ion immediately after the preparation without further purification. Hydrated metal nitrate was used as received.

2.4.1. $Mn(NO_3)_2$(**4NOPy-OMe**)$_2$ (**1**)

To a solution of $Mn(NO_3)_2 \cdot (H_2O)_6$ (141 mg, 0.49 mmol) in acetonitrile (30 ml) was added **4NOPy-OMe** ethereal solution (1.05 mmol). The mixture was evaporated to 10 ml and filtered. On the red solution of the filtrate in test tube, ether was load slowly and carefully without disturb. After keeping in a refrigerator for several days, orange prism single crystal was collected by filtration. Yield: 36 mg (12.3%), m.p., 145–8 °C (decomp.). *Anal.* Calc. for $MnC_{22}H_{34}N_6O_{10}$: C, 44.23; H, 5.74; N, 14.07. Found: C, 44.01; H, 5.78; N, 13.94%.

Table 1
Crystallographic data of **1**–**4**

	1	**2**	**3**	**4**
Formula	$MnC_{22}H_{34}N_6O_{10}$	$CoC_{22}H_{34}N_6O_{10}$	$NiC_{22}H_{34}N_6O_{10}$	$CuC_{22}H_{34}N_6O_{10}$
MW	597.48	601.48	601.24	606.09
Crystal system	orthorhombic	orthorhombic	orthorhombic	orthorhombic
Space group	*Pbcn* #60	*Pbcn* #60	*Pbcn* #60	*Pbcn* #60
a (Å)	10.3455(8)	10.372(9)	10.072(3)	10.5253(9)
b (Å)	11.2999(9)	11.282(9)	11.666(5)	11.1371(9)
c (Å)	24.159(2)	23.65(2)	24.36(1)	24.148(2)
V (Å^3)	2824.3(4)	2767(4)	2862(1)	2830.7(4)
Z	4	4	4	4
Temperature (K)	123	123	296	296
Crystal habit	prism	chip	chip	block
Color	orange	dark orange	pale brownish green	brownish green
Dimension	$0.5 \times 0.5 \times 0.1$	$0.45 \times 0.25 \times 0.10$	$0.18 \times 0.15 \times 0.03$	$0.35 \times 0.25 \times 0.08$
$D_{calc.}$	1.405	1.443	1.395	1.422
R, *Rw*	0.038, 0.090	0.073, 0.136	0.044, 0.042	0.079, 0.158
Goodness-of-fit	1.298	1.532	0.798	0.905
No. of observations	2237	1249	695	2605
No. of variables	194	194	194	221

2.4.2. $Co(NO_3)_2$(**4NOPy-OMe**)$_2$ (**2**)

To a solution of $Co(NO_3)_2 \cdot (H_2O)_6$ (52 mg, 0.18 mmol) in acetonitrile (2 ml), **4NOPy-OMe** (0.4 mmol) in ether (20 ml) was added. The mixture was kept at −30 °C for several days. Dark orange cubic crystals appeared and were filtered off. Yield: 26 mg (24.2%), m.p. 147–52 °C (decomp.). *Anal*. Calc. for $CoC_{22}H_{34}N_6O_{10}$: C, 43.93; H, 5.70; N, 13.97. Found: C, 43.63; H, 5.72; N, 14.01%.

2.4.3. $Ni(NO_3)_2$(**4NOPy-OMe**)$_2$ (**3**)

On a solution of $Ni(NO_3)_2 \cdot (H_2O)_6$ (65 mg, 0.22 mmol) in acetonitrile (2 ml), ethereal solution of **4NOPy-OMe** (10 ml, 0.5 mmol) was loaded slowly. The mixture was kept untouched in refrigerator for one day. Pale brownish green scale crystal appeared and the solvent was removed by a pipette carefully. The remained single crystal was washed by ether and dried under the atmosphere. Yield: 14 mg (11.0%). m.p. 152–8 °C (decomp.). *Anal*. Calc. for $NiC_{22}H_{34}N_6O_{10}$, C, 43.95; H, 5.70; N, 13.98. Found: C, 43.91; H, 5.66; N, 13.63%.

2.4.4. $Cu(NO_3)_2$(**4NOPy-OMe**)$_2$ (**4**)

The copper complex **4** was prepared by the procedure similar to the one for the nickel complex **3** using $Cu(NO_3)_2 \cdot (H_2O)_3$ in place with $Ni(NO_3)_2 \cdot (H_2O)_6$. Brownish green scale crystal was collected by filtration. Yield: 35 mg (31.7%). m.p. 155–61 °C (decomp.). *Anal*. Calc. for $CuC_{22}H_{34}N_6O_{10}$: C, 43.60; H, 5.65; N, 13.87. Found: C, 43.33; H, 5.62; N, 13.86%.

3. Results and discussion

3.1. X-ray crystal and molecular structures

The single crystals for the complexes, **1**–**4** were isolated successfully and were stable under the atmosphere condition.

Four complexes, **1**–**4** are isostructural with space group *Pbcn* (#60) and $Z = 4$. Each complex has a C_2 axis through metal ion and the coordination geometry is a distorted octahedral. The metal ion is surrounded by two methoxy oxygen atoms, two pyridine nitrogen atoms, and two (or four) nitrate oxygen atoms in which the first ligands, and the second and third ones coordinate in *trans*- and *cis*-configurations, respectively. In the complexes **4**, large disorders of the coordination of nitrates are observed. ORTEP drawing of the molecular structure for the cobalt complex **2** is shown in Fig. 1.

The bond lengths of M–N(pyridine) are 2.258 Å (Mn–N), 2.075 Å (Co–N), 2.061 Å (Ni–N) and 2.021 Å (Cu–N), respectively. The bond lengths of M–O2 (methoxy); 2.381, 2.208, 2.117 and 2.464 Å for **1**–**4**, respectively, are long, compared with the ones for M–N(pyridine), indicating that methoxy oxygen atoms

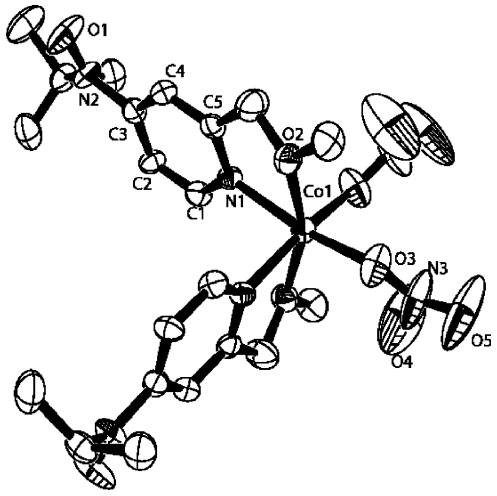


Fig. 1. ORTEP drawing of the molecular structures for **2** showing 50% probabilities ellipsoids, hydrogen atoms are omitted for clarity.

coordinate to metal ions weakly. In four complexes, the bond angles of O2–M–O2′, which are the longest bond axes, are strongly distorted; 147.01°, 160.89°, 157.97°, and 163.78° for **1**, **2**, **3** and **4**, respectively. The dihedral angles between radical moiety (defined as the plane O1N2C3) and pyridine plane (defined as the plane C1C3C5) are found to be 15.21°, 15.07°, 18.54°, and 14.46° for **1**, **2**, **3** and **4**, respectively. From these small dihedral angles, the significant magnetic exchange coupling between the metal ion and aminoxyl centers would be expected to take place in the complexes. Selected bond lengths, bond angles, and dihedral angles are given in Table 2. In crystal packing for four complexes, no short contacts within 4 Å between neighboring molecules were observed.

3.2. Magnetic properties of $M(NO_3)_2$ (**4NOPy-OMe**)$_2$, *M = Mn, **1**; Co, **2**; Ni, **3**; Cu, **4***

The pulverized crystals of all complexes were used as the samples. Temperature dependences of the molar

Table 2
Selected bond lengths (Å), bond angle (°), and dihedral angle (°)

	1	**2**	**3**	**4**
Bond lengths				
M–N1	2.258(2)	2.075(6)	2.061(9)	2.021(3)
M–O2	2.381(1)	2.208(6)	2.117(7)	2.464(3)
M–O(nitrate)	2.27(1)	2.023(8)	2.062(8)	2.04(1)
	2.40(3)			2.73(2)
	2.44(1)			2.83(1)
	2.21(2)			
O1–N2	1.280(2)	1.29(1)	1.25(2)	1.269(6)
N2–C3	1.405(3)	1.39(1)	1.40(2)	1.408(6)
Bond angle				
O1–N2–C3	116.5(2)	116.5(8)	119(1)	116.0(4)
Dihedral angle				
O1N2C3/C1C3C5	15.206	15.072	18.540	14.461

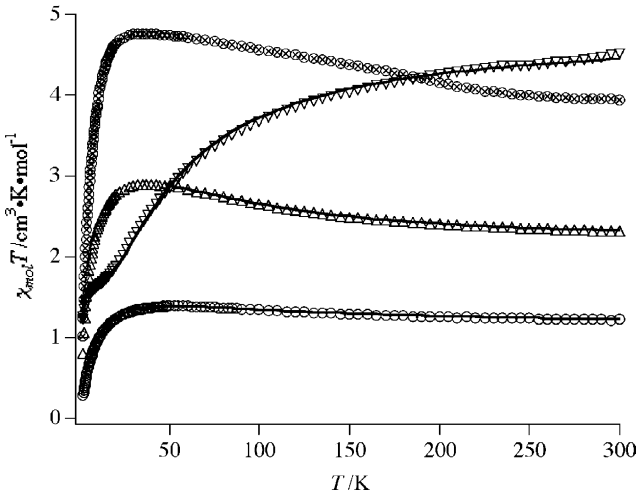


Fig. 2. Temperature dependence of molar susceptibilities as expressed by $\chi_{mol}T$ vs. T plots for complex **1** (▽), **2** (⊗), **3** (△), **4** (○). The solid curves are theoretical ones as described in the text.

paramagnetic susceptibilities χ_{mol} for all complexes were measured at the constant field of 5 kOe in the temperature range of 2–300 K. The $\chi_{mol}T$ versus T plot for four complexes is shown in Fig. 2.

3.2.1. $Mn(NO_3)_2$(*4NOPy-OMe*)$_2$ (*1*)

As the temperature was lowered, the $\chi_{mol}T$ value gradually decreased, reaching a plateau of 1.75 $cm^3\,K\,mol^{-1}$ at ca. 10 K, and then abruptly decreased (1.14 $cm^3\,K\,mol^{-1}$ at 2 K). The $\chi_{mol}T$ value of complex **1** at 300 K was 4.35 $cm^3\,K\,mol^{-1}$, which was slightly smaller than the theoretical one ($\chi_{mol}T = 5.13$ $cm^3\,K\,mol^{-1}$) calculated for isolated two radicals ($S = 1/2$) and Mn(II) ion ($S = 5/2$). Observed thermal profile of $\chi_{mol}T$ values is a typical antiferromagnetic behavior, indicating that the magnetic coupling between aminoxyl radicals and Mn(II) ion through pyridine rings is antiferromagnetic. The abrupt decrease below 10 K might be due to the intermolecular antiferromagnetic interaction. The $\chi_{mol}T$ versus T plot for the complex **1** was analyzed quantitatively based on a triangle three spin model, S_1–S_{Mn}–S_2; $H = -2J(S_{Mn}S_1 + S_{Mn}S_2)$. Equation (1) [10] for three spins with $S_1 = S_2 = 1/2$ and $S_{Mn} = 5/2$ was fitted to the experimental data by means of a least-squares method,

$$\chi_{mol}T = \frac{Ng^2\beta^2T}{4k_B(T-\theta)}\,\frac{85\exp(5J/k_BT) + 35\exp(-2J/k_BT) + 10\exp(-7J/k_BT) + 35}{4\exp(5J/k_BT) + 3\exp(-2J/k_BT) + 2\exp(-7J/k_BT) + 3}. \quad (1)$$

All the symbols have their usual meaning. The best fitting parameters were $J = -13.4 \pm 0.1$ K, $g = 1.940 \pm 0.002$, $\theta = -0.78 \pm 0.02$ K. The signs of J and θ values indicate that both intra- and intermolecular magnetic interactions are antiferromagnetic. The theoretical curve is represented by a solid line in Fig. 2.

3.2.2. $Co(NO_3)_2$(*4NOPy-OMe*)$_2$ (*2*)

When the temperature decreased, the $\chi_{mol}T$ values for the complex **2** gradually increased, reached a round maximum of 4.761 $cm^3\,K\,mol^{-1}$ at 35 K and then decrease rapidly to 1.01 $cm^3\,K\,mol^{-1}$ at 2 K. The $\chi_{mol}T$ value of 3.94 $cm^3\,K\,mol^{-1}$ at 300 K is larger than the spin-only one (2.63) for isolated two radicals ($S = 1/2$) and cobalt ion ($S = 3/2$). The difference could be interpreted as the contribution of spin-orbit coupling of cobalt ion, which is often observed in octahedral coordinated cobalt ion with $^4T_{1g}$ ground state [9]. The increase of $\chi_{mol}T$ values between 35 and 300 K strongly suggest the ferromagnetic interaction between aminoxyl radicals and the cobalt ion. The decrease below 20 K is due to the intermolecular antiferromagnetic interaction and/or the effect of zero-field splitting of cobalt ion.

3.2.3. $Ni(NO_3)_2$(*4NOPy-OMe*)$_2$ (*3*)

As temperature is lowered from 300 to 2 K, the $\chi_{mol}T$ values for the complex **3** increased, reached a round maximum of 2.90 $cm^3\,K\,mol^{-1}$ at 38 K, and then steeply decreased. The $\chi_{mol}T$ value of 2.32 $cm^3\,K\,mol^{-1}$ at 300 K is larger than spin only one (1.75 $cm^3\,K\,mol^{-1}$) with isolated two radicals ($S = 1/2$) and a nickel ion ($S = 2/2$). The thermal behavior of $\chi_{mol}T$ values in the temperature range of 300–38 K indicate that the aminoxyl radicals interact with the nickel ion ferromagnetically to form a high-spin species with $S = 4/2$. The rapid decrease of $\chi_{mol}T$ value below 30 K might be due to the intermolecular antiferromagnetic interaction and/or the effect of zero-field splitting of nickel ion.

Considering that the orbital contribution of nickel ion is insignificant at high temperature, the $\chi_{mol}T$ versus T plot for the complex **3** was analyzed quantitatively based on a triangle three spin model, S_1–S_{Ni}–S_2; $H = -2J(S_{Mn}S_1 + S_{Mn}S_2)$. Equation (2) for three spins with $S_1 = S_2 = 1/2$ and $S_{Ni} = 2/2$ was fitted to the experimental data between 50 and 300 K by means of a least-squares method [10],

$$\chi_{mol}T = \frac{2Ng^2\beta^2T}{k_B(T-\theta)}\left[\frac{5\exp(4J/k_BT) + 1 + \exp(2J/k_BT)}{5\exp(4J/k_BT) + 3 + \exp(-2J/k_BT) + 3\exp(2J/k_BT)} + N\alpha\right]. \quad (2)$$

All symbols have their usual meaning and $N\alpha$ is temperature independent paramagnetism. The best fitting parameters were $J/k_B = 48.7 \pm 2.1$ K, $g = 2.07 \pm 0.02$, $\theta = -2.82 \pm 0.41$ K and $N\alpha = 473 \times 10^{-6}$. The signs of J and θ values indicate that intra- and intermolecular magnetic interactions are ferro- and antiferromagnetic, respectively. The theoretical curve is represented by a solid line in Fig. 2.

3.2.4. $Cu(NO_3)_2$(*4NOPy-OMe*)$_2$ (*4*)

With cooling the temperature, the $\chi_{mol}T$ values for the complex **4** gradually increased, reached the round maximum ($\chi_{mol}T$ values of 1.39 $cm^3\,K\,mol^{-1}$ at 53 K), and then decreases sharply below 30 K. The $\chi_{mol}T$ values of 1.22 $cm^3\,K\,mol^{-1}$ at 300 K is consistent with the spin-only one (1.13) calculated with two isolated aminoxyl radicals ($S = 1/2$) and a copper ion ($S = 1/2$). This thermal profile of $\chi_{mol}T$ values suggests that the intra- and intermolecular interactions in this complex are ferro- and antiferromagnetic respectively. The $\chi_{mol}T$ versus T plot for the complex **4** was analyzed quantitatively based on a linear three spin model, S_1–S_{Cu}–S_2; $H = -2J(S_{Cu}S_1 + S_{Cu}S_2)$. Equation (3) for three spins with $S_1 = S_2 = S_{Cu} = 1/2$ was fitted to the experimental data by means of a least-squares method [11],

$$\chi_{mol}T = \frac{Ng^2\beta^2T}{3k_B(T-\theta)}\,\frac{60\exp(3J/k_BT) + 6\exp(2J/k_BT) + 6}{16\exp(3J/k_BT) + 8\exp(2J/k_BT) + 8}. \quad (3)$$

All symbols have their usual meaning. The best fit gives $J/k_B = 57.0 \pm 1.2$ K, $g = 2.002 \pm 0.002$, and $\theta = -9.8 \pm 0.07$ K. The theoretical curve is represented by a solid line in Fig. 2.

4. Conclusion

Four complexes of $M(NO_3)_2$, M = Mn^{II}, **1**; Co^{II}, **2**; Ni^{II}, **3**; and Cu^{II}, **4**, coordinated with **4NOPy-OMe** were prepared and their molecular structures were revealed by an X-ray crystal structure analysis. Their magnetic properties were investigated by SQUID magneto/susceptometry. Temperature dependence of $\chi_{mol}T$ values indicated that the exchange coupling between metal ion and aminoxyl radicals was antiferromagnetic for Mn ion and were ferromagnetic for Co, Ni, and Cu ions. By the fitting experiments based on the spin Hamiltonian, $H = -2J(S_1S_M + S_MS_2)$, the exchange coupling parameters, J/k_B, were estimated to be -13.4 ± 0.1, 48.7 ± 2.1, and 57.0 ± 1.2 K for the complex **1**, **3**, and **4**, respectively. Interestingly, the magnitude of J/k_B values in the complex **1**, **3** and **4** are comparable with those for the corresponding $M(hfac)_2$(**4NOPy**)$_2$, hfac = hexafluoroacetylacetonato, reported in literatures [11,12].

The bidentate ligand, **4NOPy-OMe**, is found to form the 1:2 complexes with various metal ions and to interact magnetically with metal ion. Therefore, the anisotropic metal ion coordinated with **4NOPy-OMe** is expected to form a low dimensional magnetic complex having a structural anisotropy through the intermolecular magnetic interaction. Research work along this line is in progress.

5. Supplementary material

Full crystallographic data (CCDC Nos. 250534, 250690, 250691 and 250692 for complex **1**, **4**, **2** and **3** have been deposited at the Cambridge Crystallographic Database Center and are available on request from the Director, CCDC, 12 Union Road, Cambridge, CB2 1EZ, UK (Fax: +44-1223-336-033; E-mail: deposit@ccdc.cam.ac.uk or http://www.ccdc.cam.ac.uk).

Acknowledgements

This work was supported by a Grant-in-Aid for Scientific Research (A)(2)(No. 14204071) and a Grant-in-Aid for Scientific Research on Priority Areas "Application of Molecular Spin" (No. 15087205) from the Ministry of Education, Science, Sports and Technology (MEXT), Japan. A part of this work was supported by "Nanotechnology Support Project" of the Ministry of Education, Culture, Sports, Science and Technology (MEXT), Japan.

References

[1] D. Gatteschi, R. Sessoli, Angew. Chem., Int. Ed. 42 (2003) 268.
[2] S. Karasawa, G. Zhou, H. Morikawa, N. Koga, J. Am. Chem. Soc. 125 (2003) 13676.
[3] S. Kanegawa, S. Karasawa, M. Nakano, N. Koga, Chem. Commun. 1750 (2004).
[4] Z. Zhu, S. Karasawa, N. Koga, to be submitted.
[5] Z. Zhu, S. Karasawa, N. Koga, unpublished result.
[6] SIR92: A. Altomare, G. Cascarano, C. Giacovazzo, A. Guagliardi, M. Burla, G. Polidori, M. Camalli, J. Appl. Cryst. 27 (1994) 435.
[7] DIRDIF99: P.T. Beurskens, G. Admiraal, G. Beurskens, W.P. Bosman, R. de Gelder, R. Israel, J.M.M. Smits, The DIRDIF-99 Program System, Technical Report of the Crystallography Laboratory, University of Nijmegen, The Netherlands. 1994.
[8] CrystalStructure 3.5.1: Crystal Structure Analysis Package, Rigaku and Rigaku/MSC (2000–2003), 9009 New Trails Dr., The Woodlands, TX 77381, USA.

[9] O. Kahn, Molecular Magnetism, VCH Publishers, Weinheim, 1993.
[10] N. Fukita, M. Ohba, T. Shiga, H. Okawa, Y. Ajiro, J. Chem. Soc., Dalton trans. 64 (2001).
[11] Y. Ishimaru, M. Kitano, M. Kumada, N. Koga, H. Iwamura, Inorg. Chem. 37 (1998) 2273.
[12] M. Kitano, Y. Ishimaru, K. Inoue, N. Koga, H. Iwamura, Inorg. Chem. 33 (1994) 6012.

molecules are sometimes hard to give complexes. This result prompts us to prepare diradical-ion salts and complexes to obtain compounds composed of mono- and di-radicals. In this paper, we present magnetic behavior of two diradical cation salts of (2,6-PYBNN)$^{\bullet}$ and a diradical anion salt of (2,4-POBNN)$^{\bullet}$ by investigating temperature dependence of magnetic susceptibility and magnetization isotherms at low temperatures.

2. Experimental

The diradicals, of which molecular structures are shown in Fig. 1, were prepared according to the procedures reported [4] and purified through column chromatography. The diradical cation salt (2,6-PYBNN)$^{\bullet+}Cl^{-}$ was prepared by the reaction between the neutral diradical (2,6-PYBNN)$^{\bullet}$ in a dichloromethane solution and hydrogen chloride diluted in an aqueous solution, while the diradical cation salt $(2,6\text{-PYBNN})^{\bullet+}BF_4^{-}$ was obtained by the reaction of the diradical in dichloromethane with tetrafluoroboric acid dissolved in methanol. The diradical anion salt $(C_4H_9)_4N^{+}$(2,4-POBNN)$^{\bullet-}$ was prepared by dissolving the neutral diradical (2,4-POBNN)$^{\bullet}$ directly into a methanol solution of tetrabutylammonium hydroxide. The molecular structures of these diradical ion salts are also shown in Fig. 1. The magnetization isotherms up to 7 T and magnetic susceptibility over the temperature range from 1.8 to 300 K was measured by using two Quantum Design MPMSXL7 SQUID (superconducting quantum interference device) magnetometers. The contribution of the diamagnetism to the susceptibility was subtracted by extrapolating the temperature dependence of susceptibility to high temperatures, at which the Curie–Weiss law is applicable.

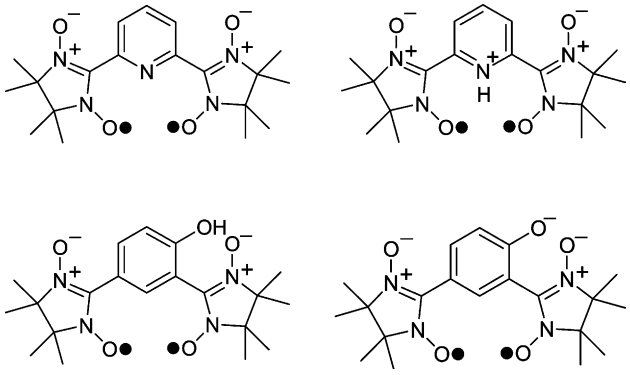


Fig. 1. The molecular structures of the diradicals (2,6-PYBNN)$^{\bullet}$ (top left) and (2,4-POBNN)$^{\bullet}$ (bottom left), the diradical ion (2,6-PYBNN)$^{\bullet+}$ (top right), and the diradical anion (2,4-POBNN)$^{\bullet-}$ (bottom right).

3. Results and discussion

Fig. 2 shows the temperature dependence of the product of paramagnetic susceptibility χ_p and temperature T of the diradical cation salts (2,6-PYBNN)$^{\bullet+}Cl^{-}$ (represented by open circles) and $(2,6\text{-PYBNN})^{\bullet+}BF_4^{-}$ (open triangles) together with that of neutral diradical (2,6-PYBNN)$^{\bullet}$ (crosses). As shown in Fig. 2, the product, χ_pT, of (2,6-PYBNN)$^{\bullet}$ decreases monotonously upon lowering the temperature down to about 20 K. However, a plateau is observed below 20 K. This magnetic behavior is already interpreted [5] successfully in terms of the four-spin linear tetramer model [6] with the intramolecular FM interaction $J/k = +10$ K and intermolecular AFM interaction $J'/k = -57$ K, where J and J' is respectively the intra- and inter-molecular exchange coupling constants and k is the Boltzmann constant.

In $(2,6\text{-PYBNN})^{\bullet+}BF_4^{-}$, χ_pT decreases monotonously down to 1.8 K as shown in Fig. 2. This behavior is interpreted by considering the interacting triplet molecule model by using the following equation [7]

$$\chi_pT = (2Ng^2\mu_B^2/k)\{3 + \exp[2J/(kT)]\}^{-1}[T/(T-\theta)], \quad (1)$$

where N is the number of molecules, g the g factor, μ_B the Bohr magneton and θ the Weiss constant. By fitting the experimental data to Eq. (1), $J/k = +9.0$ K and $\theta = -15.5$ K are obtained as represented by the solid line for open triangles in Fig. 2. The intramolecular coupling constant $J/k = +9.0$ K is FM and close to $J/k = +10$ K obtained for (2,6-PYBNN)$^{\bullet}$, which is the precursory neutral diradical of the salt. In contrast, the intermolecular interaction J'/k is reduced from -57 to -15.5 K, which is derived from the Weiss constant θ by using the relation for $S = 1/2$ spins based on the molecular mean-field theory [8]

$$J'/k = 2\theta/z, \quad (2)$$

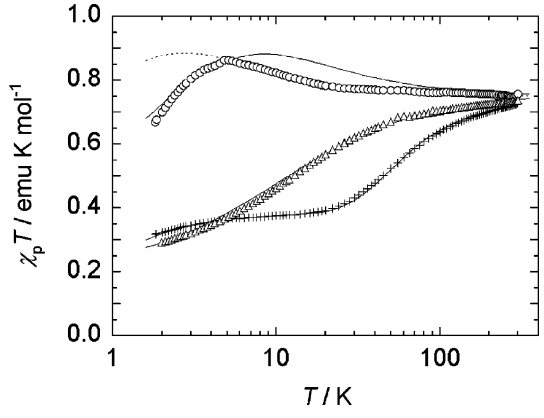


Fig. 2. Temperature dependence of χ_pT of (2,6-PYBNN)$^{\bullet+}Cl^{-}$, $(2,6\text{-PYBNN})^{\bullet+}BF_4^{-}$ and (2,6-PYBNN)$^{\bullet}$ are shown by the open circles, open triangles and crosses, respectively. Theoretical fitting for each compound by using Eq. (1) (see the text) is represented by a solid or dashed line.

where z is the number of neighboring molecules interacting with each other and assumed to be 2 in this case, although the crystal structure of (2,6-PYBNN)$^{\bullet+}BF_4^-$ is not known yet. If z is more than 2, J'/k would be further reduced. The results mentioned above suggest that the intermolecular magnetic interaction is considerably reduced in the diradical cation salt due probably to the presence of counter anions in the solid, whereas the intramolecular magnetic interaction is not so much affected in the salt because of its molecular origin.

A most remarkable change in magnetism occurs in the diradical salt (2,6-PYBNN)$^{\bullet+}Cl^-$. As shown in Fig. 2, χ_pT increases monotonously down to 4.5 K. At 4.5 K, however, χ_pT decreases to some extent suddenly and below 4.5 K decreases monotonically down to 1.8 K, which is the lowest temperature examined by us. This behavior indicates that a magnetic phase transition occurs around 4.5 K in (2,6-PYBNN)$^{\bullet+}Cl^-$. The temperature dependences of χ_pT of both high- and low-temperature (HT and LT) phases are interpreted by considering the interacting triplet molecule model discussed above. From the best fits of the experimental data to Eq. (1), J/k = +9.0 K and θ = −0.75 K for the LT phase and J/k = +3.0 K and θ = −0.24 K for the HT phase are obtained as represented by the solid and dashed lines, respectively, for the open circles in Fig. 2. The intramolecular FM interaction J/k = +9.0 K obtained for the LT phase is close to that observed in (2,6-PYBNN)$^{\bullet}$. The intermolecular AFM interaction, however, is significantly reduced in (2,6-PYBNN)$^{\bullet+}Cl^-$. The value of θ = −0.75 K is only less than 1/50 of that observed in (2,6-PYBNN)$^{\bullet}$. The large reduction of intermolecular AFM interaction might be due to the increase of intermolecular distances by incorporating the Cl^- anion into the solid. Both the intramolecular FM interaction and intermolecular AFM interaction are further reduced in the HT phase. To discuss further, however, it is indispensable to know crystal structures of both phases and nature of the phase transition.

The intramolecular FM interaction of (2,6-PYBNN)$^{\bullet}$ becomes explicit in the diradical salt (2,6-PYBNN)$^{\bullet+}Cl^-$ because of the strong reduction of the intermolecular AFM interaction, which hides the contribution of the intramolecular FM interaction coexisted. A clear evidence for the FM interaction is obtained in the temperature dependence of magnetic susceptibility exhibiting increase of χ_pT with the decrease of temperature as shown in Fig. 2. Another evidence for the intramolecular FM interaction is observed in the magnetization isotherms of (2,6-PYBNN)$^{\bullet+}Cl^-$ at temperatures below 10 K. Fig. 3 shows the magnetization isotherms of (2,6-PYBNN)$^{\bullet+}Cl^-$ at 1.85 (represented by open circles), 2.8 (closed circles), 4.5 (open triangles) and 10 K (close triangles). The magnetization isotherm at 1.85 K follows the Brillouin-function curve for S = 1/2 represented by the dashed line in Fig. 3. However, the magnetization

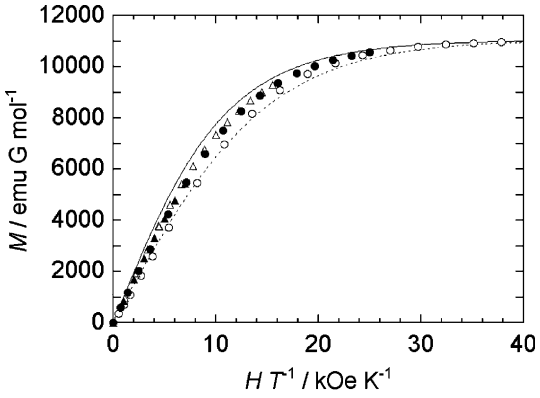


Fig. 3. Magnetization isotherms of (2,6-PYBNN)$^{\bullet+}Cl^-$ at 1.85, 2.8, 4.5 and 10 K are shown by the open circles, closed circles, open triangles and closed triangles, respectively. Theoretical curves based on the Brillouin function for S = 1/2 and 1 are represented by dashed and solid lines, respectively.

isotherm at 2.8 K deviates from the S = 1/2 line and tends to follow the Brillouin-function curve for S = 1 represented by the solid line in Fig. 3. The magnetization isotherm at 4.5 K, just below the phase transition temperature, is more close to the S = 1 line, while that at 10 K becomes to be near the S = 1/2 line again. The magnetization isotherms following the S = 1 line are clear evidence for the existence of triplet state, i.e., the intramolecular FM interaction in (2,6-PYBNN)$^{\bullet+}Cl^-$. In contrast, the magnetization isotherms of (2,6-PYBNN)$^{\bullet}$ follow the S = 1/2 line at any low temperatures [9].

In summary, the intramolecular FM interaction of the diradical (2,6-PYBNN)$^{\bullet}$ is maintained when it forms diradical cation salts. This result suggests us that molecular complexes combined (2,6-PYBNN)$^{\bullet}$ with monoradicals would give magnetic systems, in which two spin centers with different spin multiplicities are incorporated.

Fig. 4 shows the temperature dependence of χ_pT of the diradical anion salt $(C_4H_9)N^+$(2,4-POBNN)$^{\bullet-}$ (represented by open circles) together with that of (2,4-POBNN)$^{\bullet}$ (crosses). The diradical anion salt shows low and almost constant χ_pT values below 100 K, while the values increase steeply with increasing temperature above 100 K. The temperature dependence of χ_pT of $(C_4H_9)_4N^+$(2,4-POBNN)$^{\bullet-}$ at temperatures higher than 100 K is interpreted in terms of thermally excited triplet state by using Eq. (1) with J'/k = −515 K and θ = 0 K as represented by the solid line for the open circles in Fig. 4. A very strong intermolecular AFM interaction of J'/k = −850 K, which is beyond that observed in our diradical anion salt, have recently been reported for the aminoxyl diradical, biphenyl-3,5-diylbis(*t*-butyl nitroxide) [10]. The deviation towards higher values observed around 60 K appears to be a contribution of paramagnetic susceptibility due to adsorbed dioxygen onto the sample, since the magnitude of the deviation varies sample to sample and the temperature dependence of the deviating

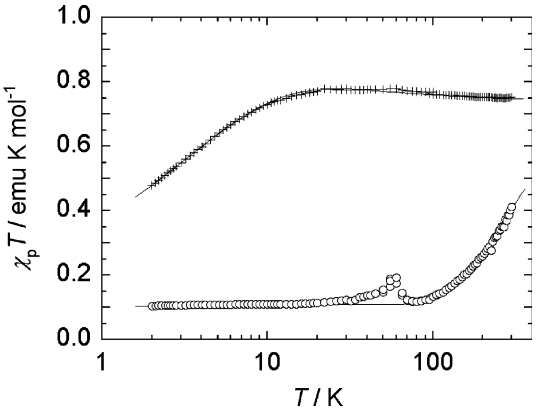


Fig. 4. Temperature dependence of $\chi_p T$ of $(C_4H_9)N^+(2,4\text{-POBNN})^{\bullet\bullet-}$ and (2,4-POBNN)•• are shown by open circles and crosses, respectively. Theoretical fitting for each compound with Eq. (1) (see the text) is represented by a solid line.

portion follows approximately that observed in dioxygen solid [11]. The strong intermolecular AFM interaction hides the intramolecular FM interaction observed in the precursor neutral diradical (2,4-POBNN)••.

As was reported [12], the temperature dependence of (2,4-POBNN)•• is explained in terms of the interacting triplet molecule model by using Eq. (1) with the intramolecular FM interaction $J/k = +15$ K and the intermolecular AFM interaction $\theta = -3.3$ K as shown by the solid line for the crosses in Fig. 4. The intramolecular FM interaction observed in (2,4-POBNN)•• suggests that this diradical would also be a promising candidate for preparing purely organic ferrimagnets. Unfortunately, however, it is unclear from the results obtained for the diradical anion salt shown here that the diradical anion $(2,4\text{-POBNN})^{\bullet\bullet-}$ maintains the intramolecular FM interactions or not, because the very strong intermolecular AFM interaction conceals the FM interaction coexist.

4. Conclusion

In conclusion, we have suggested that the diradical ion salts of (2,6-PYBNN)•• are promising candidates of molecular components to yield purely organic ferrimagnets, since the intramolecular FM interactions could be maintained when (2,6-PYBNN)•• forms diradical cation salts and complexes as shown here. It was hard to conclude whether the intramolecular FM interaction is maintained or not in the diradical anion salts of (2,4-POBNN)•• because of strong intermolecular AFM interaction hides the FM contribution. To confirm these results and to acquire further insight into the magnetism in diradical ion compounds, preparations and magnetic studies of molecular complexes consisting of these diradical ions and organic monoradical counter-ions are currently in progress.

Acknowledgments

This work was in part carried out using facilities of the Institute for Solid State Physics, the University of Tokyo. One of the authors (T.S.) is grateful to Professor H. Mori for using the SQUID magnetometer.

References

[1] K. Itoh, M. Kinoshita (Eds.), Molecular Magnetism – New Magnetic Materials, Kodansha Ltd/Gordon and Breach Science Publishers, Tokyo/Amsterdam, 2000.
[2] D.B. Amabilino, J. Veciana, in: J.S. Miller, M. Drillon (Eds.), Magnetism: Molecules to Materials II, Wiley-VCH, Weinheim, 2001, p. 1.
[3] The papers published in Polyhedron, 20 (2001) and 22 (2003).
[4] E.F. Ullman, J.H. Osiecki, D.G.B. Boocock, R. Darcy, J. Am. Chem. Soc. 94 (1972) 7049.
[5] T. Sugano, M. Tamura, M. Kinoshita, Synth. Met. 55–57 (1993) 3305.
[6] G.V. Rubenacker, J.E. Drumheller, K. Emerson, R.D. Willett, J. Magn. Magn. Mater. 54–57 (1986) 1483.
[7] B. Bleaney, K.D. Bowers, Proc. Roy. Soc. A 214 (1952) 451.
[8] C. Domb, A.R. Miedema, Prog. Low Temp. Phys. 4 (1964) 296.
[9] T. Sugano, unpublished results.
[10] G. Kurokawa, T. Ishida, T. Nogami, Chem. Phys. Lett. 392 (2004) 74.
[11] E. Kanda, T. Haseda, A. Otsubo, Physica 20 (1954) 131.
[12] S. Hase, D. Shiomi, K. Sato, T. Takui, J. Mater. Chem. 11 (2001) 756.

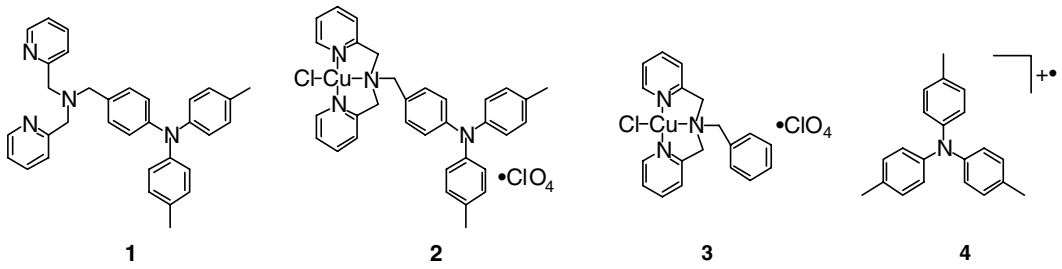


Fig. 1. Structures of compounds **1**–**4**.

mixed-valence molecular systems [3]. To our knowledge, however, no study was reported for TAA cation radical–metal ion correlation systems.

As part of our work on functionalized mono- and oligomeric TAAs, we have been studying various TAA derivatives with a 4-pyridyl group as a metal coordination site. These compounds give relatively stable cation radicals, but their association constants toward metal complexes, such as zinc tetraphenylporphyrin, are not sufficiently large to allow various spectroscopic measurements. Many studies have been devoted to the chemistry of copper complexes of ligands with bis(2-picolyl)amine moieties as biomimetic models of copper proteins [4]. The coordination site is known to react with various metal ions to give complexes with large stability constants. In view of the potential relevance to biological metal sites with a nearby radical center, we here report on a tridentate ligand, 4,4′-dimethyl-4″-[*N*,*N*′-bis(2-pyridylmethyl)aminomethyl]-triphenylamine (**1**) and its copper complex **2** (Fig. 1). The complex **2** is expected to give a novel complex species with a stable pendent radical upon one electron oxidation.

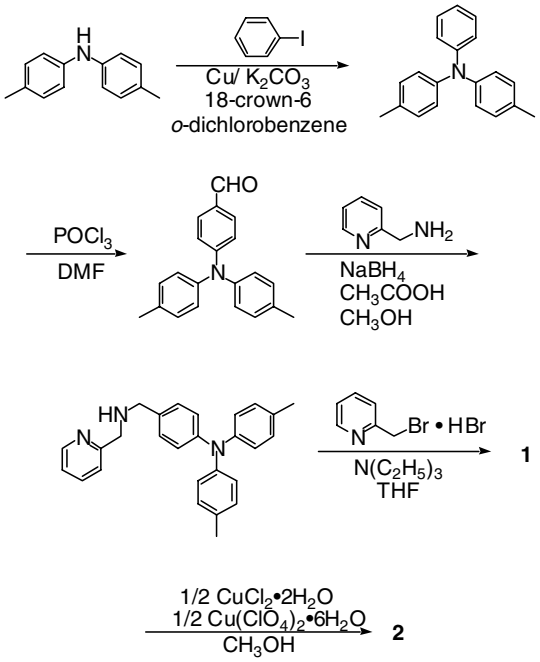


Fig. 2. Synthetic route of **1** and **2.**

2. Experimental

Synthetic detail will be reported elsewhere. All new compounds were fully characterized by spectroscopic methods or elemental analysis. Data only for **1** and **2** are given below.

1;^{1}H NMR ($CDCl_3$); δ 2.30 (s, 6H), 3.65 (s, 2H), 3.83 (s, 4H), 6.92–7.29 (m, 14H) 7.56–7.67 (m, 4H), 8.50 (d, 2H, J = 5.1 Hz).

2; Blue crystal, *Anal*. Calc. for $C_{33}H_{32}N_4CuCl_2O_4$: C, 58.24; N, 4.72; H, 8.03. Found: C, 58.02; N, 4.72; H, 8.02%.

3. Results and discussion

3.1. Synthesis of the ligand and the Cu(II) complex

The ligand, 4,4′-dimethyl-4″-[*N*,*N*′-bis(2-pyridylmethyl)aminomethyl]triphenyl-amine, was synthesized as shown in Fig. 2. Ullmann coupling reaction of di-*p*-tolylamine with iodobenzene gave 4,4′-dimethyltriphenylamine in 29% yield. This compound in turn was transformed into 4-formyl-4′,4″-dimethyltriphenylamine by the reaction with phosphoryl chloride. The formylation occurred specifically and successfully at the *para* position of triarylamine. Treatment of 4-formyl-4′,4″-dimethyltriphenylamine with 2-picolylamine and sodium borohydride gave the secondary amine, 4,4′-dimethyl-4″-[*N*-(2-pyridylmethyl)aminomethyl]triphenylamine. This compound then was reacted with 2-(bromomethyl)pyridine hydrobromide under a basic condition to give the target compound, **1**, in excellent isolated yield (72%). The corresponding copper complex **2** was prepared by reacting **1** with copper (II) chloride/copper (II) perchrorate.

3.2. UV/Vis spectrum and cyclic voltammetry measurements

In order to examine the spectroscopic properties of the ligand and the metal complexes, UV/Vis spectrum

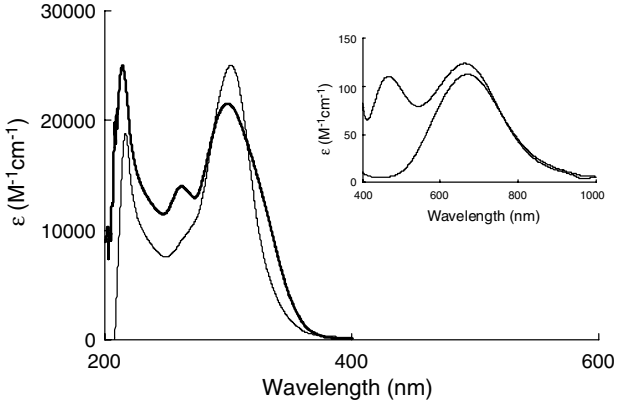


Fig. 3. UV/Vis spectra of **1** (plain), **2** (bold) in *n*-butyronitrile. Inset: UV/Vis spectra (bold), **3** (plain) in *n*-butyronitrile (expanded around 700 nm).

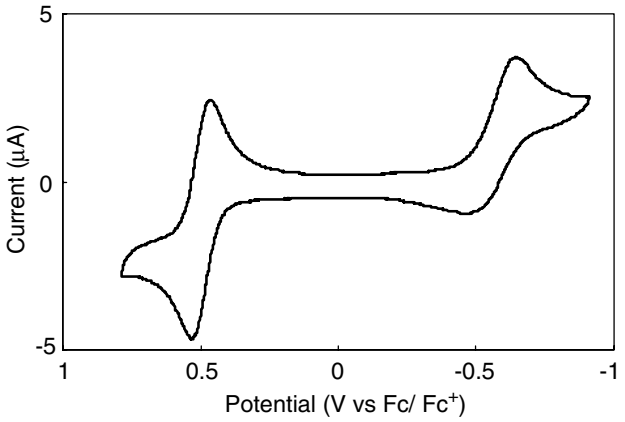


Fig. 4. The cyclic voltammogram of **2** in *n*-butyronitrile.

measurements were examined. The spectrum of those compounds are shown in Fig. 3. In *n*-butyronitrile solution, the ligand and the copper complex exhibited a strong absorption around 300 nm, respectively, which is characteristic for triarylamine chromophores [5]. In addition, the copper complex exhibited two weak absorptions at 468 nm ($\varepsilon = 110\ M^{-1}\ cm^{-1}$) and 666 nm ($\varepsilon = 124\ M^{-1}\ cm^{-1}$). The latter can be assigned to the d–d transition of the copper (II) ion. As no peak was observed around 468 nm for copper *N*,*N*-bis(2-pyridylmethyl)aminomethylbenzene (**3**), which has no triarylamino group, the absorption at 468 nm for the copper complex would indicate some interaction between the triarylamino group and the copper (II) ion.

3.3. Cyclic voltammetric measurements

Electrochemical behavior of the copper complex was studied by cyclic voltammetry in *n*-butyronitrile at ambient temperature. Upon sweeping anodically, ligand **1** showed one set of reversible redox waves ($E^0 = 0.464$ V versus Fc/Fc^+), which can be assigned to the one electron oxidation process ($TAA/TAA^{+\cdot}$). Besides the oxidation peak, an irreversible shoulder oxidation peak ($E_{ox} = 0.414$ V versus Fc/Fc^+) was also observed, which can be assigned to the one electron oxidation of the bis(2-picolylamino)aminomethylbenzene site. Upon sweeping anodically, copper complex **2** exhibited reversible redox waves ($E^0 = 0.475$ V versus Fc/Fc^+) as shown in Fig. 4, which can be similarly assigned to the one electron oxidation process of the TAA unit. No significant difference in the redox potential of the TAA moiety was observed between the ligand and the complex. A shoulder peak observed for **1** was not shown due to the complexation of the bis(2-picolylamino)amino group with Cu(II) ion. On the other hand, upon sweeping cathodically, one set of quasi-reversible redox waves ($E^0 = -0.630$ V versus Fc/Fc^+) was observed. Upon repeating sweeps several times in potential ranging from 1.0 to – 1.0 (V versus Fc/Fc^+), no decrease in the current peak intensity was observed, indicating the three possible species (Cu(I)-TAA, Cu(II)-TAA and Cu(II)-TAA^+) are stable in terms of the time scale of cyclic voltammetry.

3.4. ESR measurements

The magnetic properties of **2** and its oxidized species were examined by ESR measurements in acetonitrile/propionitrile (1:1) at 77 K. Tri(*p*-tolyl)amine cation radical (**4**) and (**3**) were also examined under the same conditions for comparison (Fig. 5). Compound **2** gave

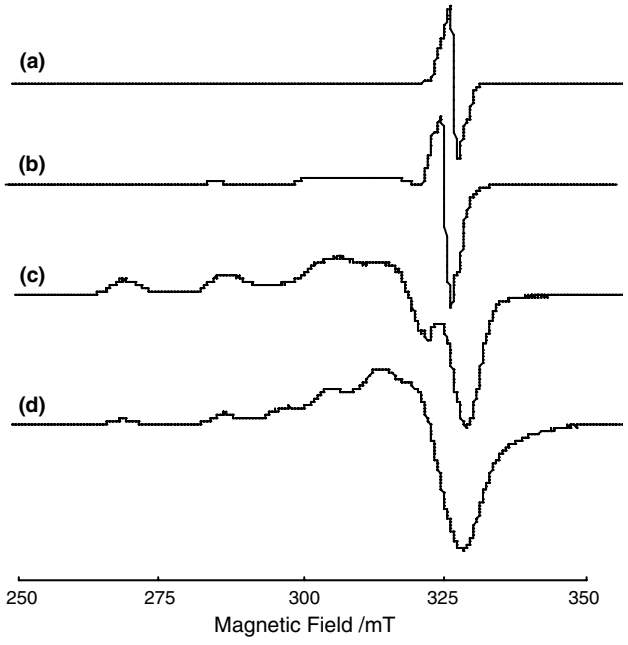


Fig. 5. ESR spectra of (a) **4**, (b) the 1:1 mixture of **3** and **4**, (c) **2** and (d) the 1:1 mixture of **2** and CAN in CH_3CN/C_2H_5CN (1:1) at 77 K.

an ESR hyperfine absorption shown in Fig. 5(c), which is characteristic of copper bis(2-picolyl)amine complexes. Upon addition of one equivalent of cerium ammonium nitrate (CAN), the color of the solution immediately changed from light blue to deep purple, which revealed the generation of the TAA cation radical chromophore. The ESR spectrum of the oxidized species is shown in Fig. 5(d). Obviously, the spectrum is different from that of the 1:1 mixture of **3** and **4** (Fig. 5(b)), which can be assigned to the sum of the spectrum of each species, suggesting the occurrence of intramolecular magnetic interaction between Cu(II) and the TAA radical. [1]

The detailed analysis of the spectrum is now in progress to identify spin multiplicities and magnetic parameters by invoking pulse-ESR based 2D electron spin transient nutation spectrsoscopy.

4. Conclusions

A novel ligand having a redox active triarylamine group and a coordinating group was designed and synthesized. The corresponding copper complex was also successfully prepared. The cyclic voltammetric study revealed that the copper complex gave a novel complex species with a pendent radical, Cu(II)-TAA$^{+\cdot}$. The ESR study of the Cu(II)-TAA$^{+\cdot}$ species suggested intramolecular spin–spin coupling. Preparation of various metal complexes, such as Co(II) and Fe(II) complexes, of this ligand, and molecular design and organic synthesis of novel π-extended ligands are under way.

[1] The degree of an intramolecular interaction through a methylene unit is controversial. However, the hyperconjugation effect of the methylene unit in **2** would be large enough to be operative as the intramolecular interaction between the metal and cation radical unit.

References

[1] (a) E.T. Seo, R.F. Nelson, J.M. Fritsch, L.S. Marcoux, D.W. Leedy, R.N. Adams, J. Am. Chem. Soc. 88 (1966) 3498;
(b) R.F. Nelson, R.N. Adams, J. Am. Chem. Soc. 90 (1968) 3925.
[2] (a) K. Itoh, M. Kinoshita (Eds.), Molecular Magnetism, New Magnetic Materials, Gordon & Breach Inc., Amsterdam, 2000 (Kodansha as copublisher, Tokyo);
(b) P.M. Lahti (Ed.), Magnetic Properties of Organic Materials, Marcel Dekker Inc., New York, 1999, and references therein;
(c) K. Sato, M. Yano, M. Furuichi, D. Shiomi, K. Abe, T. Takui, K. Itoh, A. Higuchi, K. Katuma, Y. Shirota, J. Am. Chem. Soc. 119 (1997) 6607;
(d) M. Yano, K. Sato, D. Shiomi, A. Ichimura, K. Abe, T. Takui, K. Itoh, Tetrahedron Lett. 37 (1996) 9207;
(e) K.R. Stickley, S.C. Blackstock, J. Am. Chem. Soc. 116 (1994) 11576;
(f) K.R. Stickley, S.C. Blackstock, Tetrahedron Lett. 36 (1995) 1585;
(g) K.R. Stickley, T.D. Selby, S.C. Blackstock, J. Org. Chem. 62 (1994) 448;
(h) T.D. Selby, S.C. Blackstock, J. Am. Chem Soc. 62 (1997) 448;
(i) A. Ito, H. Ino, K. Tanaka, K. Kanemoto, T. Kato, J. Org. Chem. 67 (2002) 491;
(j) M. Yano, Y. Ishida, K. Aoyama, M. Tatsumi, K. Sato, D. Shiomi, A. Ichimura, T. Takui, Synth. Met. 137 (2003) 1275;
(k) M. Yano, Y. Ishida, M. Tatsumi, K. Sato, D. Shiomi, M. Oyama, T. Takui, J. Phys. Chem. Solids. 65 (2004) 733.
[3] (a) J. Bonvoisin, J.P. Launay, M.V. Auweraer, F.C.D. Schryver, J. Phys. Chem. 98 (1994) 5052;
(b) J. Bonvoisin, J.P. Launay, W. Verbouwe, M.V. Auweraer, F.C.D. Schryver, J. Phys. Chem. 100 (1996) 17079;
(c) C. Lambert, G. Nöll, J. Am. Chem. Soc. 121 (1999) 8434;
(d) C. Lambert, G. Nöll, Angew. Chem. Int. Ed. Engl. 37 (1998) 2107.
[4] L.M. Mirica, X. Ottenwaelder, T.D.P. Stack, Chem. Rev. 104 (2004) 1013.
[5] (a) F.A. Neugebauer, S. Bamberger, W.R. Groh, Chem. Ber. 108 (1975) 2406;
(b) W. Schmidt, E. Steckhan, Chem. Ber. 113 (1980) 577.

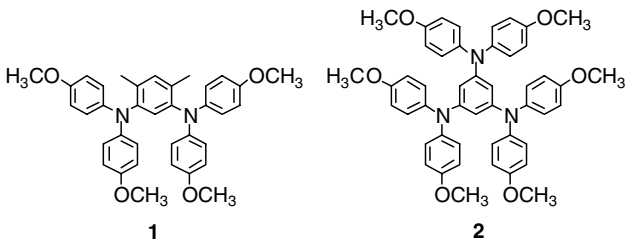


Fig. 1. Structures of *N*,*N*,*N*′,*N*′-tetrakis(4-anisyl)-4,6-dimethyl-1,3-phenylenediamine (**1**) and *N*,*N*,*N*′,*N*′,*N*″,*N*″-hexakis(4-anisyl)-1,3,5-phenylenetriamine (**2**).

Monomeric triarylamines with various substituents at their *para* positions are widely known to give extremely stable monocation radicals upon chemical or electrochemical oxidation [3]. However, as previously pointed out by Stickley et al. [2f], the stability of monomeric cation radical is not always a sufficient indicator of the stability of the corresponding oligocationic states of extended oligoarylamines.

As part of our work, we have recently designed and synthesized a series of tetraaryl-*m*-phenylenediamines having various substituents varying in electronic nature at their peripheral rings [2j]. The electron transfer stopped-flow (ETSF) method revealed that the stability of the monocationic states does not depend on the electronic nature of the substituent. On the other hand, the stability of the dicationic state strongly depends on the electronic nature of the substituent. Especially, the compound with methoxy groups, strong electron-donating groups, gave very stable dication $\mathbf{1}^{2+}$, which did not decay over 1 min. In contrast, the compound with electron-withdrawing chloro groups gave very unstable dication, which disappeared completely less than 5 s. These results suggest that introduction of electron-donating groups, which can raise the HOMO energy level, is effective to stabilize the corresponding dicationic states.

Very recently, Ito et al. [2h] reported that highly brominated *meta*-connected oligoarylamines (**3**, **4**) shown in Fig. 2 gave the stable corresponding dicationic states in solution, which exhibited ground states triplets. The report surprised us. These compounds have many electron-withdrawing bromo groups, which would lower the HOMO energy levels significantly, leading to the thermodynamically unstable mono- and oligocationic states. In the systems, bromine atoms on **3** and **4** seem to play an unknown important role to stabilize the dicationic states.

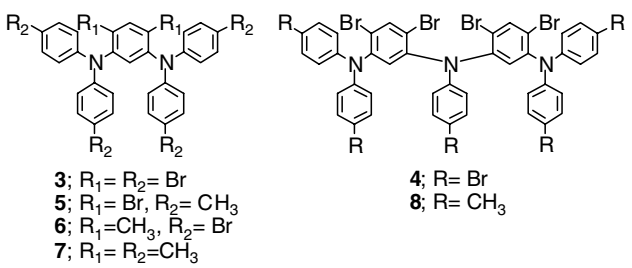


Fig. 2. Structures of tertaaryl-*m*-phenylenediamines (**3**, **5**, **6**, **7**) and 3,3′-bis(diphenylamino)triphenylamines (**4**, **8**).

In this study, we designed and synthesized three types of bromo substituted tetraaryl-*m*-phenylenediamines and examined the stabilities of the corresponding mono- and dicationic states by using the ETSF method, and elucidated the role of bromo groups in the system. Furthermore, based on the principles obtained for the diamines, we also designed and successfully synthesized a one-dimensional triamine, 3,3′-bis(diphenylamino)triphenylamine, which is expected to give a ground-state quartet upon three-electron oxidation.

2. Experimental

2.1. Synthesis of *N,N,N′,N′*-tetrakis(p-bromophenyl)-4,6-dibromo-1,3-phenylenediamine (*3*)

A mixture of 0.2 g (4.84×10^{-4} mol) of *N*,*N*,*N*′,*N*′-tetraphenyl-1,3-phenylenediamine, 1.39 g (4.36×10^{-3} mol) of pyridinium hydrobromide perbromide in 6 ml of benzene/ethanol (1:1) was heated under reflux for 90 min. The resulting solution was washed with aqueous sodium thiosulfate, extracted with ethyl acetate, and dried over sodium sulfate. The solvent was distilled off under reduced pressure. The obtained crude crystals were recrystallized from ethanol to give gray crystals (0.49 g, yield 87%). ^{1}H NMR ($CDCl_3$); δ 6.76 (d, 8H, J = 8.4 Hz), 7.32 (d, 8H, J = 8.4 Hz), 6.97 (s, 1H), 7.89 (s, 1H)

Compounds **5**, **6** and **8** were also synthesized and purified by the similar method described above.

Compound **5**: purple crystal (yield 92%), ^{1}H NMR ($CDCl_3$); δ 2,27 (s, 12H), 6.81 (d, 8H, J = 8.5 Hz), 7.00 (d, 8H, J = 8.5 Hz), 7.02 (s, 1H), 7.25 (s, 1H), compound **6**: colorless crystal (yield 98%), ^{1}H NMR ($CDCl_3$); δ 1.97 (s, 6H), 6.77 (d, 8H, J = 8.9 Hz), 6.82 (s, 1H), 7.11 (s, 1H), 7.27 (d, 8H, J = 8.9 Hz). Compound **8**: colorless crystal (yield 78.3%), ^{1}H NMR ($CDCl_3$); δ 2,21 (s, 15H), 6.59–6.97 (m, 20H), 7.21 (s 1H), 7.34 (s, 1H), 7.64 (s, 1H), 7.70 (s, 1H).

3. Results and discussion

3.1. Molecular design and organic synthesis

The brominated diamine **3** has two types of bromo atoms. In order to examine which bromo atom makes larger contribution towards the stabilization of the dication $\mathbf{3}^{2+}$, we designed two types of bromo-substituted

derivatives **5** and **6**. The former has two bromine atoms on the central ring, and the latter has four bromine atoms on the peripheral rings. Bromination of the corresponding diamines with an excess amount of pyridinium hydrobromide perbromide gave **5** and **6** in 92% and 98% isolated yield, respectively. Similarly, the compound **3** was also synthesized for comparison (yield 87%).

3.2. Cyclic voltammetry measurements

For all compounds, **3**, **5** and **6**, cyclic voltammetry in *n*-butyronitrile at ambient temperature revealed two chemically reversible one-electron transfers, indicating stable mono- and dications in solution. Reflecting the electronic nature of the substituents, a derivative with more bromo groups shifted more anodically (**3**; $E_1^0 = 0.824$ V, $E_2^0 = 0.940$ V; **5**; $E_1^0 = 0.574$ V, $E_2^0 = 0.708$ V; **6**; $E_1^0 = 0.647$ V, $E_2^0 = 0.813$ V versus Fc/Fc^+).

3.3. Electron transfer stopped-flow method

The detail of the ETSF method was described previously [4,5]. The ETSF measurements were carried out in dehydrated acetonitrile (AN) as a solvent at ambient temperature. In this study, tris(2,4-dibromophenyl)amine cation radical ($TDBPA^{+\cdot}$)[1] was employed. Compound **3**, upon mixing with one equivalent of $TDBPA^{+\cdot}$, exhibited an absorption peak at 758 nm, and no decrease in the peak intensity was observed over 1 min, indicating the very stable monocation (Fig. 3). The molar absorptivity (ε) of $\mathbf{3}^{+\cdot}$ was determined to be 2.49×10^4 M^{-1} cm^{-1} at 758 nm. Under the same condition, compounds **5** and **6** also gave very stable monocations, respectively ($\mathbf{5}^{+\cdot}$: $\lambda_{max} = 738$ nm, $\varepsilon = 2.55 \times 10^4$ M^{-1} cm^{-1}; $\mathbf{6}^{+\cdot}$: $\lambda_{max} = 698$ nm, $\varepsilon = 2.54 \times 10^4$ M^{-1} cm^{-1}). These results indicate that the number of bromine atom and position of substituents are not important factors to govern the stability of the mono cationic state.

On the other hand, compound **3**, upon mixing with two equivalents of $TDBPA^{+\cdot}$, exhibited an absorption peak of the dication $\mathbf{3}^{2+}$ at 770 nm, red shifted by 12 nm than that of $\mathbf{3}^{+}$. The ε value for $\mathbf{3}^{2+}$ was about two times that of $\mathbf{3}^{+}$, being characteristic of tetraaryl-*m*-phenylenediamine systems. Surprisingly, despite expecting the thermodynamic unstability for $\mathbf{3}^{2+}$, the dication $\mathbf{3}^{2+}$ was more stable. No significant decrease in the peak intensity was observed over 1 min (Fig. 4). Similarly, compound **5** gave stable dication $\mathbf{5}^{2+}$ ($\lambda_{max} = 748$ nm, $\varepsilon = 5.78 \times 10^4$ M^{-1} cm^{-1}). However, compound **6** gave very unstable dication $\mathbf{6}^{2+}$ ($\lambda_{max} = 738$ nm, $\varepsilon = 5.59 \times 10^4$ M^{-1} cm^{-1}), which disappeared completely within 4 s. Judging from the redox potentials

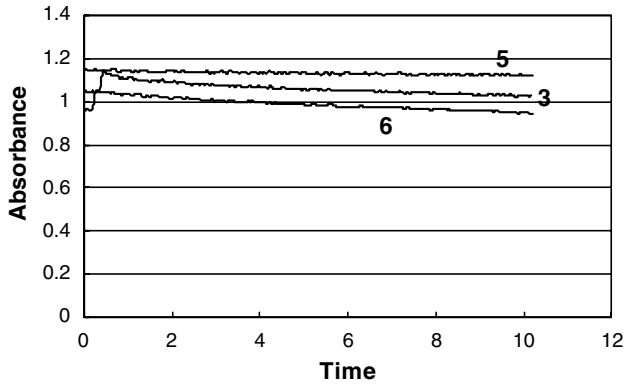


Fig. 3. Time profiles in the absorbance maximum observed after mixing an AN solution of 0.10 mM $TDBPA^{+\cdot}$ with an AN solution of 0.10 mM **3**, **5** and **6**.

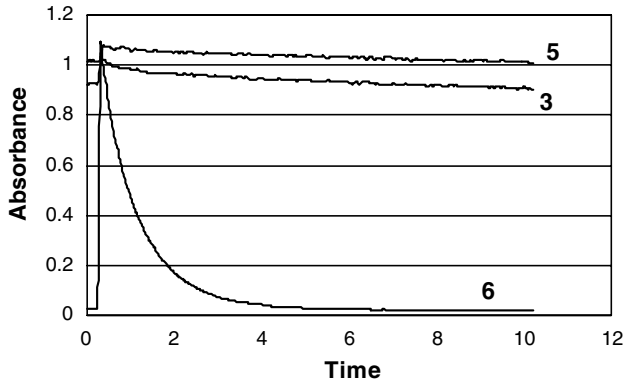


Fig. 4. Time profiles in the absorbance maximum observed after mixing an AN solution of 0.10 mM $TDBPA^{+\cdot}$ with an AN solution of 0.05 mM **3**, **5** and **6**.

for **3**, **5** and **6**, dication $\mathbf{6}^{2+}$ would be thermodynamically the most stable species, being inconsistent with the results of the ETSF measurements. Previously, we examined the stability of dication $\mathbf{7}^{2+}$, which has six methyl groups on both the central and the peripheral rings [2j]: CV measurements showed two reversible couples ($E_1^0 = 0.391$ V, $E_2^0 = 0.593$ V versus Fc/Fc^+).

Nevertheless, the dication $\mathbf{7}^{2+}$ decomposed gradually under the same ETSF measurement condition. Considering the relationship between the molecular structures and the stabilities of the corresponding dications, compounds **6** and **7**, which have methyl groups on the central ring, gave the unstable dications, while compounds **3** and **5** with bromo groups on the central ring gave the stable dications. In the previous study, we demonstrated that the introduction of methyl groups into the central ring of non-substituted tetraphenyl-*m*-phenylenediamine remarkably improves the stabilities of the mono- and dicationic states [2e]. However, the present study revealed that the bromo group on the central ring can be a better protecting unit to prolong the life time of the dication. The mechanism of the

[1] TDBPA was synthesized by WAKO Pure Chemicals Ltd. after receiving our special order. See also [5].

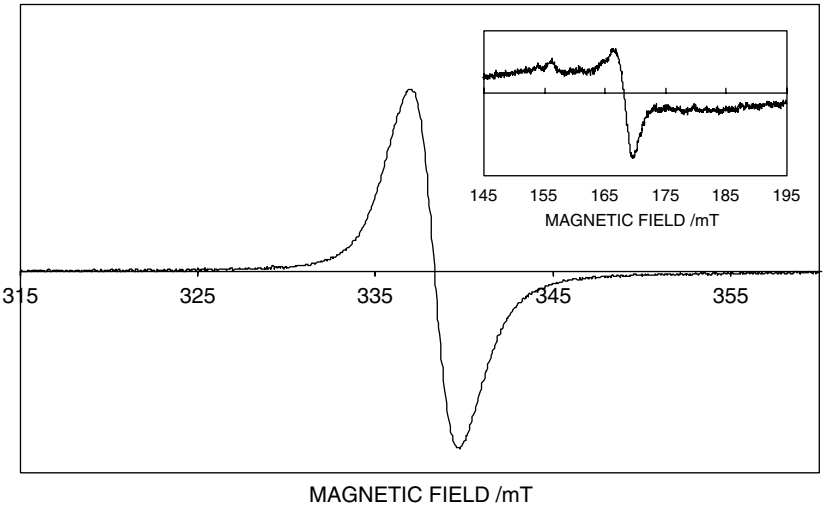


Fig. 5. ESR spectrum of the randomly oriented **8** oxidized by two equivalents of $SbCl_5$ observed at 5 K in an allowed ESR transition region (inset: in the $\Delta M_s = \pm 2$ region). The microwave frequency was 9.48078 GHz.

stabilization is not fully clear yet; the introduction of the bromo group might suppress decomposition reactions, such as intramolecular hydrogen abstraction.

Then, we have extended this work to include the study of 3,3′-bis(diarylamino)triphenylamine, which is a suitable synthetic target as a model precursor for one-dimensional positively charged high-spin systems. Previously, Ito et al. [2h] reported the highly brominated derivative **4**, which gave stable dication upon two-electron oxidation. However, they failed to detect the trication with polybromo substitutions. With this result in mind, we designed and synthesized compound **8**, which has only four bromo groups on the two central rings. The compound **8** is expected to give more thermodynamically stable mono- and oligocations than those of **4**. The CV measurement of **8** showed the generation of both stable dication $\mathbf{8}^{2+}$ and moderately stable trication $\mathbf{8}^{3+}$ at ambient temperature ($E_1^0 = 0.605$ V (2e transfer), $E_2^0 = 1.07$ V (1e transfer) versus Fc/Fc^+).

ETSF examination of **8** revealed that the mono-, di- and tricationic states give a broad absorption around 730 nm, respectively ($\mathbf{8}^{+}$: $\lambda_{max} = 732$ nm, $\varepsilon = 2.06 \times 10^4$ M^{-1} cm^{-1}; $\mathbf{8}^{2+}$: $\lambda_{max} = 732$ nm, $\varepsilon = 4.30 \times 10^4$ M^{-1} cm^{-1}; $\mathbf{8}^{3+}$: $\lambda_{max} = 736$ nm, $\varepsilon = 6.07 \times 10^4$ M^{-1} cm^{-1}). The ratio of ε formonocation:dication:trication of **8** was nearly 1:2:3, as expected. The quantum chemistry-based rationale for this expectation will be given elsewhere.

3.4. ESR measurements

In order to examine the electronic structures of $\mathbf{8}^{2+}$ and $\mathbf{8}^{3+}$, particularly top identify the spin multiplicity in the ground state, ESR measurements of chemically oxidized **8** were carried out at liquid-helium temperature. Upon addition of two equivalents of $SbCl_5$ into CH_2Cl_2 solution of **8**, the color of the solution immediately turned blue, indicating the generation of oxidized species. The continuous-wave ESR spectrum of the randomly oriented oxidized species at 5 K is shown in Fig. 5. There appeared a broad line in an allowed ESR transition region. Furthermore, a weak forbidden transition was also observed in the $\Delta M_s = \pm 2$ region, clearly indicating the presence of spin-triplet species (Fig. 5). No signal was observed in the $\Delta M_s = \pm 3$ region. The temperature dependence of the signal intensities in the $\Delta M_s = \pm 2$ region showed that the dicationic state $\mathbf{8}^{3+}$ is spin-triplet in the ground state.

On the other hand, upon addition of three equivalents of $SbCl_5$, the color of solution of **8** similarly turned blue immediately, however, followed by rapid discoloration to red in a few seconds, suggesting the occurrence of rapid decomposition reaction of $\mathbf{8}^{3+}$.

4. Conclusions

In order to elucidate the role of bromo groups on the stabilization of the oligocationic species reported by Ito et al., we have systematically designed and synthesized three types of brominated tetraaryl-*m*-phenylenediamines, **3**, **5** and **6**. Cyclic voltammetry and ETSF measurements have revealed that the bromo groups, over methyl groups, on the central aromatic ring can stabilize the dicationic states effectively. These results serve for establishing guidelines for molecular designing of charged high-spin molecular systems in a more sophisticated way.

Furthermore, based on the knowledge, tetra-brominated 3,3′-bis(diarylamino)triphenylamine (**8**) was synthesized, which gave a moderately stable tricationic state. This is the first report on detection of a one-dimensional oligoarylamine-based tricationic state. Conventional continuous-wave ESR study of chemically oxidized **8** showed that the dication $\mathbf{8}^{2+}$ is spin-triplet in

the ground state. The tricationic $\mathbf{8}^{3+}$ was not stable enough in a time scale for the conventional ESR sampling. Further stabilization of $\mathbf{8}^{3+}$ by chemical modification is underway.

References

[1] K. Itoh, M. Kinoshita (Eds.), Molecular Magnetism: New Magnetic Materials, Gordon & Breach/Kodansha, Amsterdam/Tokyo, 2000.
[2] (a) P.M. Lahti (Ed.), Magnetic Properties of Organic Materials, Marcel Dekker, New York, 1999 (Chapter 9) and references therein;
(b) K. Sato, M. Yano, M. Furuichi, D. Shiomi, K. Abe, T. Takui, K. Itoh, A. Higuchi, K. Katuma, Y. Shirota, J. Am. Chem. Soc. 119 (1997) 6607;
(c) M. Yano, K. Sato, D. Shiomi, A. Ichimura, K. Abe, T. Takui, K. Itoh, Tetrahedron Lett. 37 (1996) 9207;
(d) K.R. Stickley, S.C. Blackstock, J. Am. Chem. Soc. 116 (1994) 11576;
(e) K.R. Stickley, S.C. Blackstock, Tetrahedron Lett. 36 (1995) 1585;
(f) K.R. Stickley, T.D. Selby, S.C. Blackstock, J. Org. Chem. 62 (1994) 448;
(g) T.D. Selby, S.C. Blackstock, J. Am. Chem Soc. 62 (1997) 448;
(h) A. Ito, H. Ino, K. Tanaka, K. Kanemoto, T. Kato, J. Org. Chem. 67 (2002) 491;
(i) M. Yano, Y. Ishida, K. Aoyama, M. Tatsumi, K. Sato, D. Shiomi, A. Ichimura, T. Takui, Synth. Met. 137 (2003) 1275;
(j) M. Yano, Y. Ishida, M. Tatsumi, K. Sato, D. Shiomi, M. Oyama, T. Takui, J. Phys. Chem. Solids 65 (2004) 733.
[3] (a) E.T. Seo, R.F. Nelson, J.M. Fritsch, L.S. Marcoux, D.W. Leedy, R.N. Adams, J. Am. Chem. Soc. 88 (1966) 3498;
(b) R.F. Nelson, R.N. Adams, J. Am. Chem. Soc. 90 (1968) 3925.
[4] M. Oyama, T. Higuchi, S. Okazaki, J. Chem. Soc., Perkin Trans. 2 (2001) 1287.
[5] M. Oyama, J. Matsui, H. Park, Chem. Commun. (2002) 604.

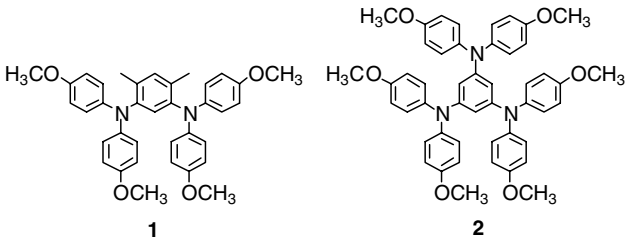


Fig. 1. Structures of *N*,*N*,*N*′,*N*′-tetrakis(*p*-anisyl)-4,6-dimethyl-1,3-phenylenediamine (**1**) and *N*,*N*,*N*′,*N*′,*N*″,*N*″-hexakis(*p*-anisyl)-1,3,5-phenylenetriamine (**2**).

cursors. For example, poly(aryl)carbenes of particular π-electron networks, well known high-spin molecules, can usually survive only at low temperature, and their precursors, polydiazo derivatives, are thermally and photochemically unstable except several cases. On the other hand, we have shown that the structural modification of tetraphenyl-*m*-phenylenediamine by suitable substituents is quite effective in stabilizing the dicationic states, which are stable even at ambient temperature [2c,2j].

Those oligoarylamines described above have no functional group available for further extension of their π-electron network, preventing us from utilizing them in organic syntheses. So, we attempted to design and synthesize functionalized tetraaryl-*m*-phenylenediamines. Generally, aryl halides are widely used as convenient compounds in conventional and modern organometallic syntheses. Until now, numerous organic syntheses using aryl halides have been reported. Among them, Sonogashira coupling [3] is an attractive and powerful method for syntheses of acetylene bridged compounds in excellent yields. In fact, the coupling has been utilized in many laboratories for syntheses of natural and artificial molecules. In this study, we propose two types of iodinated tetraaryl-1,3-phenylenediamines (**3** and **4**) as "synthons" for molecular devices and supramolecular systems. Furthermore, using Sonogashira coupling, the compounds can be transformed into highly extended tetraaryl-*m*-phenylenediamines.

2. Results and discussion

2.1. Molecular designs and syntheses of target molecules

As target molecules, we chose *N*,*N*,*N*′,*N*′-tetrakis(4-iodophenyl)-4,6-dimethyl-1,3-phenylenediamine (**3**) and *N*-(4-iodophenyl)-*N*,*N*′,*N*′-tris(4-methylphenyl)-4,6-dimethyl-1,3-phenylenediamine (**4**). In the compounds, the reactive iodo groups are introduced at the *para*-positions of the peripheral aryl ring, and in the middle part of the molecules, the 4,6-positions of the central aryl ring are capped with methyl groups, which can enhance the stabilities of the mono- and dicationic states of tetraaryl-*m*-phenylenediamines. The synthetic routes of **3** and **4** are shown in Fig. 2.

Synthesis of **3**: 5-Nitro-2,4-xylidine was reduced with tin dichloride/hydrochloric acid in ethanol to give 4,6-dimethyl-1,3-phenylenediamine (**5**), which was reacted with iodobenzene under Ullmann coupling condition [4] to give *N*,*N*,*N*′,*N*′-tetraphenyl-4,6-dimethyl-1,3-phenylenediamine (**6**) (yield 56% for the two steps). This compound was iodinated with potassium iodide/potassium iodate in acetic acid to give **3**, which was purified by column chromatography ($CHCl_3$/*n*-hexane = 1/3) in 93% isolated yield.

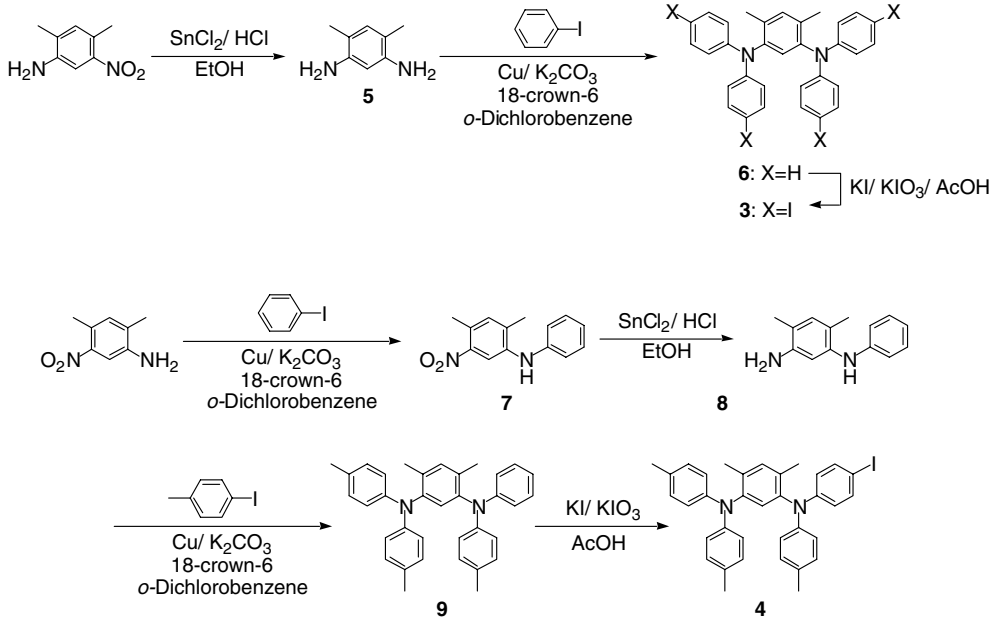


Fig. 2. Synthetic routes for **3** and **4**.

3: ^{1}H NMR δ 1.97 (s 6H), 6.65 (d, 8H, J = 8.91 Hz), 6.82 (s, 1H), 7.10 (s, 1H), 7.38 (d, 8H, J = 8.91 Hz).

Synthesis of **4**: 5-Nitro-2,4-xylidine was reacted with iodobenzene to give *N*-diphenyl-5-nitro-2,4-xylidine (**7**) in 35% isolated yield. Stoichiometrically, only one equivalent of iodobenzene is required to obtain **7**, however, the best result was obtained when 5-nitro-2,4-xylidine was reacted with iodobenzene in the ratio of 1:2 under reflux for 7 h. Prolonged reaction time gave the undesired di-substituted compound, *N*,*N*-diphenyl-5-nitro-2,4-xylidine, predominantly. The compound **7** was quantitatively reduced with tin dichloride/hydrochloric acid in ethanol to give *N*-phenyl-4,6-dimethyl-1,3-phenylenediamine (**8**), which was reacted with an excess amount of *p*-iodotoluene under Ullmann coupling reaction to give *N*,*N*′,*N*′-tris(4-methylphenyl)-*N*-phenyl-4,6-dimethyl-1,3-phenylenediamine (**9**), in 49% isolated yield. Compound **9** was iodinated with potassium iodide/ potassium iodate in acetic acid to give **4**, which was purified by column chromatography ($CHCl_3$/*n*-hexane = 1/5) in quantitative yield.

4: ^{1}H NMR δ 1.97 (s, 3H), 1.99 (s, 3H), 2.25 (s, 6H), 2.31 (s, 3H), 6.62 (d, 2H, J = 8.90 Hz), 6.80 (d, 4H, J = 8.40 Hz), 6.87 (d, 2H, J = 8.90 Hz), 6.89 (d, 2H, J = 8.90 Hz), 6.90 (s, 1H), 7.00 (d, 4H, J = 8.40 Hz), 7.06 (s, 1H), 7.37 (d, 2H, J = 8.90 Hz).

2.2. π-Extension using Sonogashira coupling

In order to examine the reactivity of **3** and **4**, various acetylene compounds were coupled with them under Sonogashira coupling condition [3a] to obtaine π-extended tetraaryl-*m*-phenylenediamines (**10a**–**e** and **11a**–**d**) shown in Fig. 3. The synthetic procedure of **10a** is described below.

Compound **3** was mixed with a catalytic amount of copper iodide, dichlorobis (triphenylphosphine) palladium (II) and six equivalents of trimethylsilylacetylene, and stirred under argon atmosphere for 12 h at ambient temperature. The obtained crude oil was purified by column chromatography ($CHCl_3$/*n*-hexane = 1/1) in 98% yield. Compounds **10c**–**e** and **11a, c**–**d** were also prepared in a similar manner. Compounds **10b** and **11b** were prepared by desilylation of **10a** and **11a** in the presence of potassium carbonate in methanol/THF in quantitative yield. The NMR spectra of these molecules are consistent with their assigned structures.

2.3. UV/Vis spectroscopic and cyclic voltammetry measurements

Compounds **3** exhibited a broad absorption band around 300 nm in chloroform, which is characteristic of triarylamine chromophores. Comparing with the UV/Vis spectrum of **1**, no significant difference was observed between **1** and **3**, indicating their similar electronic structures. Also compound **4** exhibited a similar absorption band (λ_{max} = 301 nm). Upon cyclic voltammetry in *n*-butyronitrile with 0.1 M Bu4NPF6 as a supporting electrolyte, Compounds **3** and **4** showed two sets of reversible redox couples (**3**: $E_1^0 = 679$ mV, $E_2^0 = 854$ mV versus Fc/Fc^+, **4**: $E_1^0 = 428$ mV, $E_2^0 = 678$ mV versus Fc/Fc^+), respectively. These results indicate that **3** and **4** yield the stable mono- and dications upon consecutive oxidation.

The UV/Vis spectra of **10a–e** in chloroform exhibited a broad absorption maximum around 375 nm, which are remarkably red-shifted in comparison with that of **1**. On the other hand, the UV/Vis spectra of **11a–d** in chloroform exhibited an absorption maximum around 300 nm. Besides the absorption peak, another absorption was observed around 360 nm. The spectra of **10e** and **11d** are shown in Fig. 4 as representative cases. A preliminary study revealed that **10a–d** and

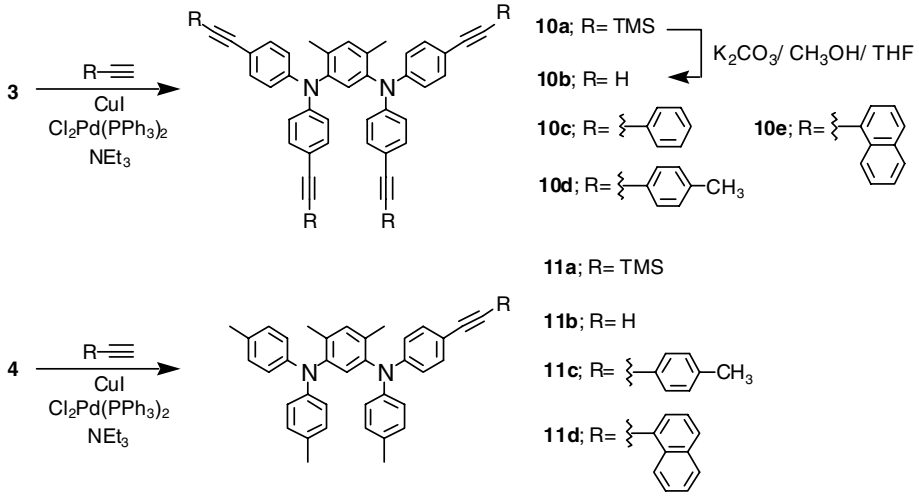


Fig. 3. Synthetic routes for **10a–e** and **11a–d**.

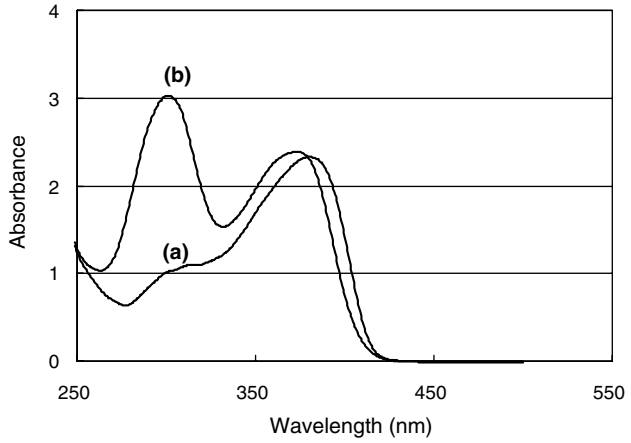


Fig. 4. Absorption spectra of: (a) **10e**, (b) **11d** in chloroform.

11c–**11d** exhibit fluorescent emission upon irradiation of ultraviolet light.

Compounds **10a** showed well resolved two sets of reversible redox couples ($E_1^0 = 608$ mV, $E_2^0 = 753$ mV versus Fc/Fc$^+$), however, compounds **10b** showed the first oxidation wave at 550 (versus Fc/Fc$^+$), followed by two oxidation peaks upon further sweeping, and no reduction wave was observed, indicating that monocation radical **10b**$^{+\cdot}$ is unstable. Similarly, compounds **10c**–**e** showed similar complicated voltammograms, suggesting the generation of unstable monocation radicals.

Compound **11a** showed two sets of reversible redox couples ($E_1^0 = 430$ mV, $E_2^0 = 660$ mV versus Fc/Fc$^+$), while compound **11b** showed the first reversible redox couple and the second quasi-reversible redox couple ($E_1^0 = 434$ mV, $E_2^0 = 678$ mV versus Fc/Fc$^+$). Similarly, compounds **11c**–**d** gave stable monocation radical and fairly unstable dication, respectively (**11c**: $E_1^0 = 429$ mV, $E_2^0 = 612$ mV, **11d**: $E_1^0 = 430$ mV, $E_2^0 = 617$ mV versus Fc/Fc$^+$).

2.4. Electron transfer stopped-flow method measurements

As a novel method to observe the absorption spectra of short-lived cation radicals in solution, one of the authors (M.O.) has proposed electron transfer stopped-flow (ETSF) method [5,6]. Using this technique, the absorption spectra of aromatic amine cation radicals were successfully detected, and the kinetic processes were analyzed. The ETSF measurements were carried out in dehydrated acetonitrile (AN) as a solvent at ambient temperature. Depending on the oxidation potential of each compound, tris(4-bromophenyl)amine cation radical (TBPA$^{+\cdot}$) or tris(2,4-dibromophenyl)amine cation radical (TDBPA$^{+\cdot}$), more powerful oxidizing reagents, are employed.[1] The formal potential of TDBPA$^{+\cdot}$/TDBPA couple is 1.06 V versus Fc/Fc$^+$, which is 0.44 V positive to that of TBPA$^{+\cdot}$/TBPA couple. In this study, TDBPA$^{+\cdot}$ was employed.

Compound **10a**, upon mixing with one equivalent of TDBPA$^{+\cdot}$, exhibited a broad absorption peak at 816 nm (Fig. 5), and any significant decrease in the peak intensity was not observed over 1 min. Compared with the spectrum of **1**$^{+\cdot}$ [2j], the λ_{max} of **10a**$^{+\cdot}$ is extremely red shifted by 131 nm, indicating the occurrence of effective π-network extension. The molar absorptivity (ε) of **10a**$^{+\cdot}$ was determined to be 2.19×10^4 M^{-1} cm^{-1} at 816 nm. Similarly, mixing with two equivalent of TDBPA$^{+\cdot}$, **10a** showed an absorption peak at 842 nm ($\varepsilon = 4.41 \times 10^4$ M^{-1} cm^{-1}), which was slightly reduced over 10 s.

On the other hand, upon mixing with one equivalent of TDBPA$^{+\cdot}$, compound **10b**, TMS deprotected compounds, exhibited a weak absorption peak at 710 nm ($\varepsilon = 1.05 \times 10^4$ M^{-1} cm^{-1}) (Fig. 5), any significant decrease in the peak intensity was not observed over 1 min. It seems that the peak is derived from monocation radical **10a**$^{+\cdot}$. No significant difference in electronic structure between **10a**$^{+\cdot}$ and **10b**$^{+\cdot}$ would be expected. However, compared with the spectrum of **10a**$^{+\cdot}$, λ_{max} of **10b** upon one electron oxidation is much red shifted, and the intensity of the peak at 710 nm is about one-fourth of that of **10a**$^{+\cdot}$ at 816 nm. Moreover, no spectrum change was observed by changing the substrate/oxidizing reagent concentration ratio. On the basis of the results described above, we concluded that the lifetime of **10b**$^{+\cdot}$ is too short to be determined even by the ETSF method, and that the species observed is not **10b**$^{+\cdot}$ but other stable species produced by follow-up reactions. Decomposition process is not clear yet, but an AM1 calculation suggested that both compounds **10a** and **10b** have large electron densities at the terminal acetylene carbon atoms. Bulky trimethylsilyl substituent in **10a** would protect the site effectively, suppressing

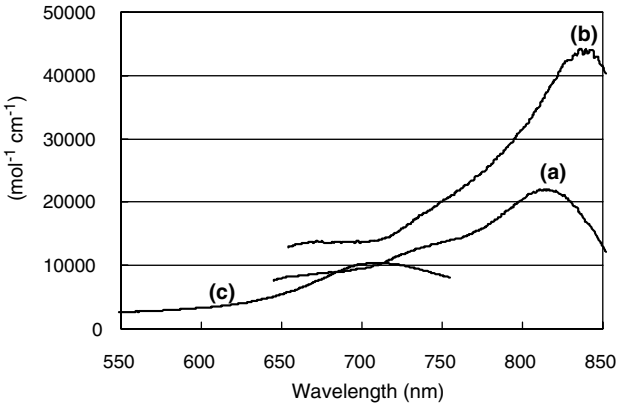


Fig. 5. Absorption spectra observed after mixing of an AN solution of 0.10 mM TDBPA$^{+\cdot}$ with an AN solution of: (a) 0.10 mM of **10a**; (b) 0.05 mM of **10a**; (c) 0.10 mM of **11a**.

[1] TDBPA was synthesized by WAKO Pure Chemicals Ltd. after receiving our special order. See also Ref. [5].

follow-up reactions. Similar to **10b**, both compounds **10c** and **10d** gave very unstable monocation radicals. The ETSF measurements for **11a–d** are now underway.

As ETSF measurements revealed that **10a** gives the corresponding mono- and dicationic states, we tried to carry out ESR measurements of the species. We selected $SbCl_5$ as an oxidant, which is widely used for electron oxidation of various organic compounds. Upon addition of two equivalents of $SbCl_5$ into a CH_2Cl_2 solution of **10a**, the color of the solution immediately turned blue, however, followed by rapid discoloration to red in less than a few seconds at ambient temperature. Any dominant fine-structure spectra attributable to the short-lived high-spin entities in solution could not be identified at glassy solvents at low temperature: Only trace from the short-lived triplet species or monocationic ones was detected by conventional continuous wave ESR spectroscopy. This indicated the occurrence of rapid follow-up reactions in solution at ambient temperature. Surprisingly, addition of one equivalent of $SbCl_5$ gave a similar result. These results indicate that both the mono- and dicationic states are very unstable under the condition. Other oxidants such as cerium ammonium nitrate (CAN)/AN were met with failure. Resolution of these difficulties is the target of future work, exploring alternative oxidants.

3. Summary

In conclusion, we have designed and successfully synthesized iodinated tetraaryl-1,3-phenylenediamines (**3** and **4**). In designing novel molecular devices and supramolecular systems, these compounds will serve as intriguing building blocks, which are expected to exhibit triplet ground states upon two electron oxidation. Starting from **3** and **4**, highly π-extended tetraaryl-1,3-phenylenediamines (**10a–e**, **11a–d**) have been synthesized in excellent yields by Sonogashira coupling. The ETSF measurements showed that only **10a** gives the stable dication, probably due to steric protection. Unfortunately, **10b–e** gave very short-lived monocation radicals. We are currently exploring effective aryl groups that can protect the acetylene site. Molecular designs and syntheses of novel photochemically or electrochemically active derivatives coupled with **3** or **4** are also in progress.

References

[1] K. Itoh, M. Kinoshita (Eds.), Molecular Magnetism, New Magnetic Materials, Gordon & Breach, Inc., Amsterdam (Kodansha as copublisher, Tokyo), 2000.
[2] (a) P.M. Lahti (Ed.), Magnetic Properties of Organic Materials, Marcel Dekker, Inc., New York, 1999, Chapter 9 and references therein;
(b) K. Sato, M. Yano, M. Furuichi, D. Shiomi, K. Abe, T. Takui, K. Itoh, A. Higuchi, K. Katuma, Y. Shirota, J. Am. Chem. Soc. 119 (1997) 6607;
(c) M. Yano, K. Sato, D. Shiomi, A. Ichimura, K. Abe, T. Takui, K. Itoh, Tetrahedron Lett. 37 (1996) 9207;
(d) K.R. Stickley, S.C. Blackstock, J. Am. Chem. Soc. 116 (1994) 11576;
(e) K.R. Stickley, S.C. Blackstock, Tetrahedron Lett. 36 (1995) 1585;
(f) K.R. Stickley, T.D. Selby, S.C. Blackstock, J. Org. Chem. 62 (1994) 448;
(g) T.D. Selby, S.C. Blackstock, J. Am. Chem. Soc. 62 (1997) 448;
(h) A. Ito, H. Ino, K. Tanaka, K. Kanemoto, T. Kato, J. Org. Chem. 67 (2002) 491;
(i) M. Yano, Y. Ishida, K. Aoyama, M. Tatsumi, K. Sato, D. Shiomi, A. Ichimura, T. Takui, Synthetic Met. 137 (2003) 1275;
(j) M. Yano, Y. Ishida, M. Tatsumi, K. Sato, D. Shiomi, M. Oyama, T. Takui, J. Phys. Chem. Solids 65 (2004) 733.
[3] (a) K. Sonogashira, Y. Tohda, N. Hagihara, Tetrahedron Lett. 50 (1975) 4467;
(b) S. Huang, J.M. Tour, Tetrahedron Lett. 40 (1999) 3347;
(c) M. Eredelyi, A. Gogoll, J. Org. Chem. 66 (2001) 10.
[4] S. Gauthier, J.M. Frechet, Synthesis (1987) 383.
[5] M. Oyama, T. Higuchi, S. Okazaki, J. Chem. Soc., Perkin Trans. 2 (2001) 1287.
[6] M. Oyama, J. Matsui, H. Park, Chem. Commun. (2002) 604.

Table 1
Crystallographic data of PPh_4 and NMe_4 salts

Compound	(PPh_4)(**N1**) · acetonitrile	(NMe_4)(**N2**)	(PPh_4)(**N3**) · acetonitrile	(PPh_4)(**M1**) · acetone	(PPh_4)(**M3**) · acetone	(PPh_4)(**O1**) $(benzene)_{0.5}$	(PPh_4)(**O2**) · diethylether	(PPh_4)(**O3**)
Formula	$C_{42}H_{45}N_3O_5PS$	$C_{20}H_{34}N_3O_5S$	$C_{42}H_{45}N_3O_5PS$	$C_{44}H_{50}N_2O_6PS$	$C_{44}H_{50}N_2O_6PS$	$C_{43}H_{44}NO_6PS$	$C_{44}H_{51}NO_7PS$	$C_{40}H_{41}NO_6PS$
F_W	734.87	428.57	734.87	765.92	765.92	733.86	768.92	694.81
Cell setting	triclinic	triclinic	triclinic	monoclinic	triclinic	triclinic	triclinic	triclinic
Space group	$P\bar{1}$	$P\bar{1}$	$P\bar{1}$	$P2_1/c$	$P\bar{1}$	$P\bar{1}$	$P\bar{1}$	$P\bar{1}$
Diffractometer	Rigaku AFC5R	Rigaku AFC5R	Rigaku AFC5R	Rigaku AFC5R	Rigaku AFC5R	Rigaku AFC5R	Rigaku AFC5R	Quantum CCD
Unit cell dimensions								
a (Å)	13.891(3)	11.534(6)	12.911(3)	17.906(3)	18.593(4)	13.705(3)	12.474(3)	10.913(2)
b (Å)	13.926(2)	13.365(2)	13.746(4)	12.290(4)	21.31(1)	13.972(3)	17.234(5)	12.325(3)
c (Å)	12.231(2)	7.983(3)	11.760(3)	19.819(3)	10.946(3)	12.273(2)	10.865(4)	14.724(1)
α (°)	106.23(1)	106.14(2)	104.66(2)	90.0	93.08(3)	106.98(2)	108.38(3)	91.945(2)
β (°)	113.66(1)	98.23(4)	110.54(2)	109.31(1)	92.38(2)	113.78(1)	110.66(2)	102.389(1)
γ (°)	100.69(1)	91.42(3)	81.59(2)	90.0	106.76(3)	100.10(2)	94.28(3)	111.810(1)
V (Å^3)	1957.9(8)	1167.2(8)	1886.9(9)	4116(2)	4140(3)	1938(1)	2028(2)	1781.7(6)
Z	2	2	2	4	4	2	2	2
T (K)	298	298	298	299	296	298	301	298
μ (mm^{-1})	0.1709	0.1720	0.1774	0.1664	0.1654	0.1731	0.1702	0.184
Crystal size (mm)	$0.5 \times 0.4 \times 0.25$	$0.5 \times 0.1 \times 0.1$	$0.5 \times 0.45 \times 0.3$	$0.45 \times 0.4 \times 0.25$	$0.3 \times 0.3 \times 0.08$	$0.4 \times 0.3 \times 0.15$	$0.5 \times 0.5 \times 0.2$	$0.2 \times 0.2 \times 0.1$
θ_{max} (°)	55.0	55.0	55.0	55.0	55.0	55.0	55.0	55.0
Data total	9295	5746	9031	10224	19585	9272	9883	15302
Data unique	8927	5364	8646	9917	19062	8903	9321	7175
Data used	4082 ($I > 2\sigma I$)	1642 ($I > 2\sigma I$)	4896 ($I > 2\sigma I$)	2550 ($I > 3\sigma I$)	3901 ($I > 3\sigma I$)	3813 ($I > 2\sigma I$)	3839 ($I > 2\sigma I$)	3042 ($I > 5\sigma I$)
Absorption method	ψ scans	ψ scans	ψ scans	ψ scans	ψ scans	ψ scans	ψ scans	empirical
T_{min}/T_{max}	0.953/1.000	0.923/1.000	0.977/1.000	0.968/1.000	0.927/1.000	0.974/1.000	0.895/1.000	0.544/1.741
R_{int}	0.0280	0.0590	0.1209	0.3528	0.0969	0.0335	0.0720	0.097
Parameters	469	262	469	458	973	454	487	442
R	0.061	0.069	0.061	0.090	0.069	0.058	0.061	0.064
R_w	0.062	0.047	0.065	0.090	0.057	0.038	0.060	0.044
Goodness-of-fit (S)	1.690	1.830	1.820	3.340	1263	1.730	1.830	1.188
$\Delta\rho_{max}$ (e$^-$/Å^3)	0.263	0.295	0.457	0.826	0.34	0. 338	0.313	0.31
$\Delta\rho_{min}$ (e$^-$/Å^3)	−0.317	−0.274	−0.430	−0.412	−0.34	−0.418	−0.293	−0.32

2. Experimental

The anions TEMPO–NHCO–(*o*-, *m*-, *p*-)$C_6H_4SO_3^-$ (**N1**, **N2**, **N3**), TEMPO–N(CH_3)CO–(*o*-, *p*-)$C_6H_4SO_3^-$ (**M1**, **M3**), and TEMPO–OCO–(*o*-, *m*-, *p*-)$C_6H_4SO_3^-$ (**O1**, **O2**, **O3**) were prepared by the condensation reaction of HOOC–(*o*-, *m*-, *p*-)$C_6H_4SO_3^-$ with TEMPO–NH_2, TEMPO–N(CH_3)H, and TEMPO–OH, respectively, in the presence of dicyclohexylcarbodiimide (DCC) and dimethylaminopyridine (DMAP) in 30 mL of CH_2Cl_2 at room temperature with stirring over a few days. Metathesis with $PPh_4 \cdot Br$ gave their PPh_4 salts (yields: 40, 59, 16, 26, 8, 25, and 6% for the **N1**, **N3**, **M1**, **M3**, **O1**, **O2**, and **O3** salts, respectively), as orange crystals. $PPh_4 \cdot$ **N2** was obtained as an orange tar and metathesis with $N(CH_3)_4 \cdot Cl$ yielded the crystalline product (20% yield). Their TTF salts were prepared by metathesis of $(TTF)_3(BF_4)_2$ and their organic cation salts in CH_3CN or a mixture of CH_3CN and CH_3OH. The BEDT-TTF salt of **M1** was obtained by electrocrystallization in PhCl with BEDT-TTF and $PPh_4 \cdot$ **M1**. All materials were identified by X-ray analysis. Single crystal X-ray diffraction data were collected using a Quantum CCD area detector on a Rigaku AFC-7R diffractometer or Rigaku AFC-5R 4-circle diffractometer at room temperature. The Mo Kα radiation was used for all crystals. All calculations were performed by teXsan for Windows version 1.06 and CRYSTALS version 12. Electrical resistivity measurements were carried out by the conventional four probe method. Magnetic susceptibility measurements of polycrystalline samples from 2 to 300 K were measured with a Quantum Design MPMS5SH magnetometer.

3. Results and discussion

3.1. PPh_4 and $N(CH_3)_4$ salts

The crystal data of seven tetraphenylphosphonium and one tetramethylammonium salts are listed in Table 1.

The amido, *N*-methylamido, and ester (–NHCO–, –N(CH_3)CO–, and –OCO–) bonds of all anions apart from **M1** have *trans* conformation. **M1** only has *cis* conformation. For example, molecular structures of **N3**, **M1**, and **O2** of their PPh_4 salts are shown in Fig. 1. There are no magnetically important short contacts between the TEMPO moieties for all salts because the anions are surrounded by the relatively large organic cations and/or the incorporated solvent molecules. The results indicate that magnetic interactions are unlikely. Indeed the **N1**, **N2**, **N3**, **M1**, **M3**, **O1**, **O2**, and **O3** salts show Curie–Weiss behaviours with C (emu K mol^{-1})/θ (K) = 0.369/−0.17, 0.376/−0.31, 0.334/0.25, 0.360/−0.03, 0.377/−1.91, 0.362/−0.18, 0.329/−0.16, and 0.354/0.00, respectively. In addition, the incorporated diethylether of the **O2** salt is so heavily disordered that the hydrogen atoms on the solvent were not included in the refinement procedure. The other incorporated molecules also have large thermal ellipsoids, suggesting dynamic disorder.

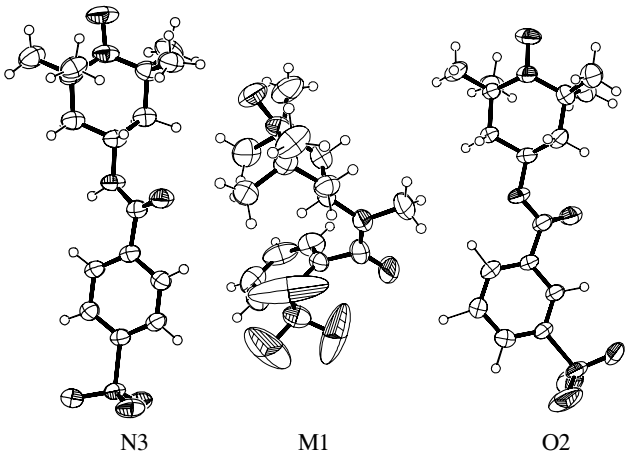


Fig. 1. Molecular structures of **N3**, **M1**, and **O2** in their PPh_4 salts.

3.2. TTF salts

The crystal data of five TTF salts together with a BEDT-TTF salt are shown in Table 2. Now we focus on the TTF salts. In the five salts, each TTF is a monocation and forms a face-to-face dimer, indicating the formation of a spin singlet. Thus, the TTF dimers in all salts are non-magnetic. There are many S···S interactions between both TTF cations of the dimers. On the other hand, there is no or one short S···S contact between dimers for all TTF salts, indicating a poor conduction pathway, and low electrical conductivities for all salts. Actually, the electrical resistivity of more than 10^6 Ω cm are observed for all TTF salts.

The **N2**, **O1**, and **O3** salts have a centrosymmetric TEMPO···TTF···TTF···TEMPO unit, in which the two TTF molecules form a face-to-face dimer which interacts with the TEMPO parts, as shown in Fig. 2. Many short S···S contacts between both TTFs and one or two short contacts between an S or C atom of TTF and the spin centre O atom of TEMPO are observed. However, no direct interactions between the TEMPO parts are observed. Therefore, the magnetic interaction between TEMPO parts via the intraunit route is likely. Their temperature-dependent magnetic susceptibilities are explained, however, by an ordinary Curie–Weiss model with C = 0.379, 0.365, and 0.361 emu K mol^{-1} and θ = +0.06, −0.17, and +0.07 K for the **N2**, **O1**, and **O3** salts, respectively. The small Weiss constants ($\ll$1 K) indicate that there are little magnetic interactions between the two TEMPO moieties

Table 2
Crystallographic data of TTF and BEDT-TTF (ET) salts

Compound	(TTF)(**N2**) · acetonitrile	(TTF)(**N3**) · 0.33H_2O	(TTF)(**M3**) · H_2O	(TTF)(**O1**) (acetonitrile)$_{0.5}$	(TTF)(**O3**)	$(ET)_3$(**M1**)$_2$ · 8H_2O
Formula	$C_{24}H_{29}N_3O_5S_5$	$C_{22}H_{26.67}N_2O_{5.33}S_5$	$C_{23}H_{30}N_2O_6S_5$	$C_{23}H_{26.5}N_{1.5}O_6S_5$	$C_{22}H_{25}NO_6S_5$	$C_{64}H_{88}N_4O_{18}S_{26}$
F_W	599.81	564.79	590.80	580.27	559.74	2034.98
Cell setting	monoclinic	monoclinic	monoclinic	monoclinic	triclinic	monoclinic
Space group	$P2_1/c$	$P2_1/n$	$P2_1/c$	$C2/c$	$P\bar{1}$	$P2_1/a$
Diffractometer	Rigaku AFC5R	Rigaku AFC5R	Rigaku AFC5R	Rigaku AFC5R	Rigaku AFC5R	Quantum CCD
Unit cell dimensions						
a (Å)	15.700(5)	8.100(4)	7.763(4)	21.635(3)	11.541(4)	11.780(2)
b (Å)	7.733(5)	29.754(4)	37.60(1)	15.694(5)	18.472(5)	12.345(2)
c (Å)	23.040(5)	10.670(4)	10.813(4)	16.010(4)	6.413(2)	30.142(2)
α (°)	90.0	90.0	90.0	90.0	96.05(2)	90.0
β (°)	98.91(2)	91.57(3)	108.82(3)	91.37(2)	96.59(2)	96.631(3)
γ (°)	90.0	90.0	90.0	90.0	107.53(2)	90.0
V (Å^3)	2764(2)	2571(2)	2987(2)	5435(2)	1280.9(7)	4353.9(9)
Z	4	4	4	8	2	2
T (K)	299	293	293	303	299	293
μ (mm^{-1})	0.4594	0.489	0.4252	0.4657	0.4905	0.7018
Crystal size (mm)	$0.5 \times 0.15 \times 0.15$	$0.5 \times 0.17 \times 0.15$	$0.5 \times 0.15 \times 0.05$	$0.5 \times 0.5 \times 0.18$	$0.5 \times 0.25 \times 0.15$	$0.2 \times 0.2 \times 0.001$
θ_{max} (°)	55.0	55.0	55.0	55.0	55.0	55.0
Data total	7050	6040	7476	6709	6181	22846
Data unique	6810	5908	6986	6483	5885	8243
Data used	2955 ($I > 2\sigma(I)$)	3564 ($I > 2\sigma(I)$)	1142 ($I > 3\sigma(I)$)	4396 ($I > \sigma(I)$)	4425 ($I > 3\sigma(I)$)	2343 ($I > 3\sigma(I)$)
Absorption method	ψ scans	ψ scans	ψ scans	ψ scans	ψ scans	empirical
T_{min}/T_{max}	0.970/1.000	0.982/1.000	0.598/1.000	0.876/1.000	0.944/1.000	0.263/3.143
R_{int}	0.0632	0.0296	0.1937	0.0110	0.0103	0.3960
Parameters	354	347	325	322	373	505
R	0.056	0.060	0.072	0.057	0.032	0.199
R_w	0.056	0.066	0.075	0.036	0.039	0.196
Goodness-of-fit (S)	1.700	1.048	1.850	1.840	1.780	3.670
$\Delta\rho_{max}$ (e$^-$/Å^3)	0.449	0.56	0.539	0.284	0.331	1.327
$\Delta\rho_{min}$ (e$^-$/Å^3)	−0.493	−0.65	−0.461	−0.369	−0.257	−1.392

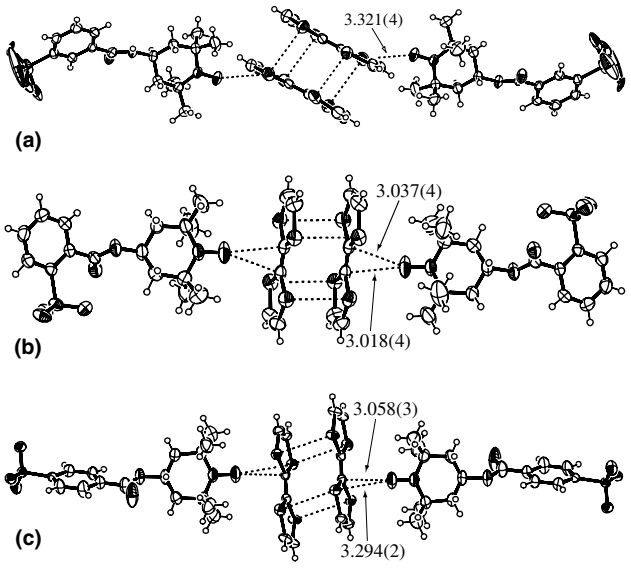


Fig. 2. Structures of the TEMPO···TTF···TTF···TEMPO units in (a) (TTF)(**N2**) · CH_3CN, (b) (TTF)(**O1**) · $0.5CH_3CN$, and (c) (TTF)(**O3**). Dashed lines indicates short S···S (<3.70 Å), S···O (<3.35 Å), and O···C (<3.25 Å) contacts.

via the TTF dimer in the TEMPO···TTF···TTF···TEMPO unit.

The **N3** and **M3** salts do not have any interactions between TEMPO and TTF but have an interaction between TEMPOs. The networks of the TEMPO moieties in the **N3** salt are shown in Fig. 3. The O atom of the spin centre of TEMPO interacts with both an ethylene group and the amino group of the nearest TEMPO to form a 1-D magnetic network along the *n* axis. According to McConnell's theory, both contacts can mediate a ferromagnetic interaction [25]. Actually, the magnetic behaviour is explained by the 1-D ferromagnetic Heisenberg model with $C = 0.331$ emu K mol^{-1} and $\theta = 0.16$ K. In addition, there is positional disorder of three sulfonate O atoms, and each atom refined over two possible positions. The elongated displacement ellipsoids of the O atoms suggest rotational disorder of the $-SO_3$ group.

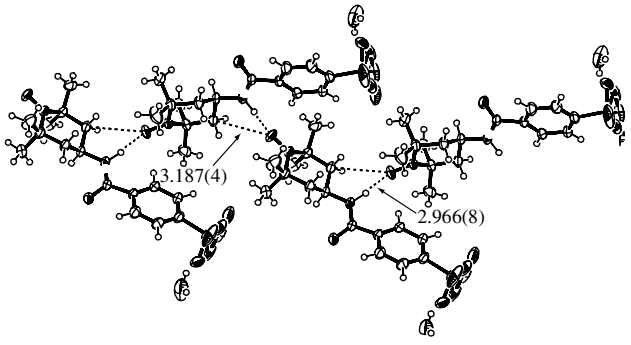


Fig. 3. TEMPO–TEMPO interactions in (TTF)(**N3**) · $0.33H_2O$.

The crystal structure of the **M3** salt is shown in Fig. 4. There are one TTF cation, one **M3** anion, and one water molecule in the asymmetric unit. The TTF cations form dimers which stack along the *a* axis to form a 1-D column, though the interdimer interaction is weak. There are many short S···O contacts between S atoms of TTF and O atoms of both sulfonate and amido as shown in Fig. 4. A magnetically important interaction between the TTF S atoms and the TEMPO O atom was not observed. However, a magnetically important interaction, a short contact (labeled A in Fig. 4) between the O atom of TEMPO and a methylene group of the adjacent TEMPO moiety was observed. Through the interactions, the anions form a 1-D magnetic chain along the *a* axis (see Fig. 4). According to the McConnell's theory, the contact can mediate the ferromagnetic interaction [25]. The distance of the contact of 3.37(2) Å, however, is slightly larger than their van der Waals distance (3.35 Å), suggesting that the interaction is weak. This crystallographic information suggests that the salt is a weak 1-D ferromagnet. However, the magnetic susceptibility data does not obey a 1-D ferromagnetic nor antiferromagnetic Heisenberg model but obeys a Curie–Weiss model with $C = 0.376$ emu K mol^{-1} and $\theta = -7.75$ K. The relatively large negative Weiss constant indicates that there are relatively large magnetic interactions. We have tried to deduce if this occurs through space. The shortest O···O distance of 5.407(2) Å is, however, somewhat longer for the large Weiss constant. Interactions between TTF and **M3** (see Fig. 4) may play some role. In addition, the anion has *cis* conformation in the TTF salt, though it has *trans* conformation in the starting material, (PPh_4)(**M3**) · CH_3CN as mentioned in the Section 3.1.

3.3. BEDT-TTF salt

So far, we have obtained only one BEDT-TTF salt, α-(BEDT-TTF)$_3$(**M1**)$_2$ · $8H_2O$. The crystal structure is shown in Fig. 5.

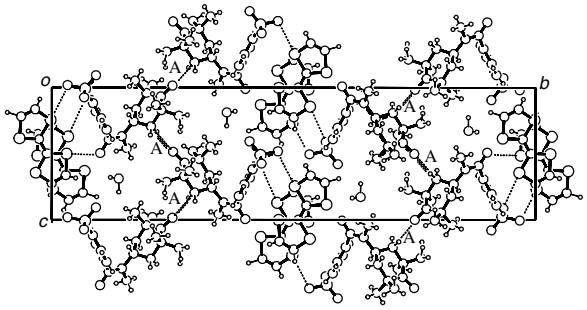


Fig. 4. Projection of the crystal structure of (TTF)(**M3**) · H_2O down the *a* axis. Thinner dashed lines indicate short S···O contacts (<3.35 Å) and thicker dashed lines labeled A indicate short O···C contact of 3.37(2) Å between the TEMPO parts.

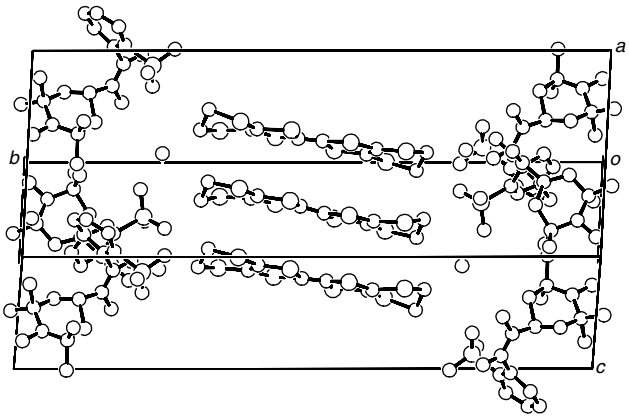


Fig. 5. Crystal structure of α-(BEDT-TTF)$_3$(**M1**)$_2 \cdot 8H_2O$.

In the asymmetric unit, there are one and a half donors, one anion, and four water molecules. The donor forms a trimer about a centre of symmetry. It stacks along the *a* axis and the stacks interact with each other, giving an α-type 2-D conducting sheet (Fig. 6). The formal charge of +2 on each BEDT-TTF trimer is calculated, so that each trimer has two spins which form a spin singlet, suggesting that the trimer is non-magnetic and the salt is a band insulator. Actually, the salt shows semiconductive behaviour with a room temperature electrical resistivity of $1.6 \times 10^3\ \Omega$ cm and an activation energy of 0.95 eV.

Neither the interaction between the BEDT-TTF cation and the TEMPO moiety nor the interaction between the TEMPO parts is observed. Thus, any magnetic interactions are unlikely. Nevertheless, a Curie–Weiss behaviour with a relatively large Weiss constant (C = 0.281 emu K mol^{-1} and $\theta = -3.64$ K) was observed. In addition, the observed shortest O···O distance of 5.908(2) Å suggests that through-space interaction between the TEMPO parts is also unlikely. The CT interaction between TEMPO and BEDT-TTF may play some part in the magnetic interaction.

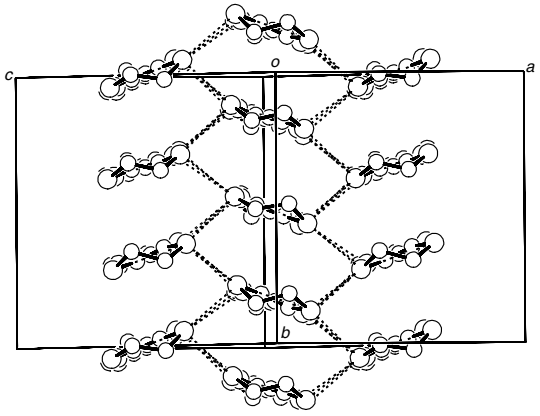


Fig. 6. Donor packing arrangement of α-(BEDT-TTF)$_3$(**M1**)$_2 \cdot 8H_2O$. Dashed lines indicate short S···S contacts less than 3.7 Å.

4. Conclusion

We have found new TTF- and BEDT-TTF-based CT salts that include a genuine organic magnetic anion, TEMPO–A–CO–(*o*-, *m*-, *p*-)$C_6H_4SO_3^-$(A = NH, NCH_3, O). The (TTF)(TEMPO–NHCO–*m*-$C_6H_4SO_3$ (**N2**)) · CH_3CN, (TTF)(TEMPO–OCO–*o*-$C_6H_4SO_3$ (**O1**)) · $0.5CH_3CN$, and (TTF)(TEMPO–OCO–*p*-$C_6H_4SO_3$ (**O3**)) salts contain the TEMPO···TTF··· TTF···TEMPO unit. Both spin centre O atoms of TEMPO interact via TTF face-to-face dimer through short S···O contacts. However, the Weiss constants of their salts are much less than 1 K, indicating little magnetic interaction. On the other hand, the (TTF)(TEMPO–NCH_3CO–*p*-$C_6H_4SO_3$ (**M3**)) · H_2O and (BEDT-TTF)$_3$(TEMPO–NCH_3CO–*o*-$C_6H_4SO_3$ (**M1**))$_2 \cdot 8H_2O$ salts have no crystallographically significant short contacts that can mediate magnetic interactions between the TEMPO spin centres, but have relatively large Weiss constants. Further investigation to establish the origin of magnetic interactions is now in progress.

5. Supplementary material

Full crystallographic data (CCDC 255996 for (PPh_4)(**N1**) · CH_3CN, CCDC 255997 for (NMe_4)(**N2**), CCDC 255998 for (PPh_4)(**N3**) · CH_3CN, CCDC 255999 for (PPh_4)(**M1**) · CH_3COCH_3, CCDC 256000 for (PPh_4)(**M3**) · CH_3COCH_3, CCDC 256001 for (PPh_4)(**O1**) · $0.5C_6H_6$, CCDC 256002 for (PPh_4)(**O2**) · $C_2H_5OC_2H_5$, CCDC 256003 for (PPh_4)(**O3**), CCDC 256004 for (TTF)(**N2**) · CH_3CN, CCDC 256005 for (TTF)(**N3**) · $0.33H_2O$, CCDC 256006 for (TTF)(**M3**) · H_2O, CCDC 256007 for (TTF)(**O1**) · $0.5CH_3CN$, CCDC 256008 for (TTF)(**O3**), and CCDC 256009 for (ET)$_3$(**M1**)$_2 \cdot 8H_2O$) have been deposited at the Cambridge Crystallographic Database Centre and are available on request from the Director CCDC, 12 Union Road, Cambridge, CB21EZ, UK (Fax: +44-1223-336-033; Email: deposit@ccdc.cam.ac.uk or http://www.ccdc.cam.ac.uk).

Acknowledgements

We thank Dr. Scott. S. Turner of Exeter University, UK for helpful discussion. This work has been supported by a Grant-in-Aid for Scientific Research (No. 14740330) from Japan Society for the Promotion of Science.

References

[1] M. Kurmoo, A.W. Graham, P. Day, S.J. Coles, M.B. Hursthouse, J.L. Caulfield, J. Singleton, F.L. Pratt, W. Hayes, L. Ducasse, P. Guionneau, J. Am. Chem. Soc. 117 (1995) 12209.

[2] E. Coronado, J.R. Galán-Mascarós, C.J. Gómez-García, V. Laukhin, Nature 408 (2000) 447.
[3] T. Ishiguro, K. Yamaji, G. Saito, Organic Superconductors, Springer-Verlag, Berlin-Heidelberg, 1998.
[4] H. Kobayashi, A. Kobayashi, P. Cassoux, Chem. Soc. Rev. 29 (2000) 325.
[5] S. Uji, H. Shinagawa, T. Terashima, T. Yakabe, Y. Terai, M. Tokumoto, A. Kobayashi, H. Tanaka, H. Kobayashi, Nature 410 (2001) 908.
[6] T. Sugano, T. Fukasawa, M. Kinoshita, Synth. Met. 41–43 (1991) 3281.
[7] H. Fujiwara, H. Kobayashi, Chem. Commun. (1999) 2417.
[8] H. Fujiwara, E. Fujiwara, H. Kobayashi, Chem. Lett. (2002) 1048.
[9] H. Fujiwara, H.-J. Lee, H. Kobayashi, E. Fujiwara, A. Kobayashi, Chem. Lett. 32 (2003) 482.
[10] J. Nakazaki, M.M. Matsushita, A. Izuoka, T. Sugawara, Tetrahedron Lett. 40 (1999) 5027.
[11] J. Nakazaki, Y. Ishikawa, A. Izuoka, T. Sugawara, Y. Kawada, Chem. Phys. Lett. 319 (2000) 385.
[12] T. Sugimoto, S. Yamaga, M. Nakai, K. Ohmori, M. Tsujii, H. Nakatsuji, H. Hosoito, Chem. Lett. (1993) 1361.
[13] K.A. Hutchison, G. Srdanov, R. Menon, J.-C.P. Gabriel, B. Knight, F. Wudl, J. Am. Chem. Soc. 118 (1996) 13081.
[14] S. Nakatsuji, H. Anzai, J. Mater. Chem. 7 (1997) 2161.
[15] Y. Nakamura, N. Koga, H. Iwamura, Chem. Lett. (1991) 69.
[16] K. Mukai, S. Jinno, Y. Shimobe, N. Azuma, Y. Hosokoshi, K. Inoue, M. Taniguchi, Y. Misaki, K. Tanaka, Polyhedron 20 (2001) 1537.
[17] S. Aonuma, H. Casellas, C. Faulmann, B. Garreau de Bonneval, I. Malfant, P. Cassoux, P.G. Lacroix, Y. Hosokoshi, K. Inoue, J. Mater. Chem. 11 (2001) 337.
[18] G. Harada, T. Jin, A. Izuoka, M.M. Matsushita, T. Sugawara, Tetrahedron Lett. 44 (2003) 4415.
[19] E. Fujiwara, A. Kobayashi, H. Fujiwara, T. Sugimoto, H. Kobayashi, Chem. Lett. 33 (2004) 964.
[20] H. Akutsu, J. Yamada, S. Nakatsuji, Chem. Lett. (2001) 208.
[21] H. Akutsu, J. Yamada, S. Nakatsuji, Synth. Met. 120 (2001) 871.
[22] H. Akutsu, J. Yamada, S. Nakatsuji, Acta Crystallogr., Sect. C 59 (2003) o433.
[23] H. Akutsu, J. Yamada, S. Nakatsuji, Acta Crystallogr., Sect. E 59 (2003) o1441.
[24] H. Akutsu, J. Yamada, S. Nakatsuji, Chem. Lett. 32 (2003) 1118.
[25] H.M. McConnell, J. Chem. Phys. 39 (1963) 1910.

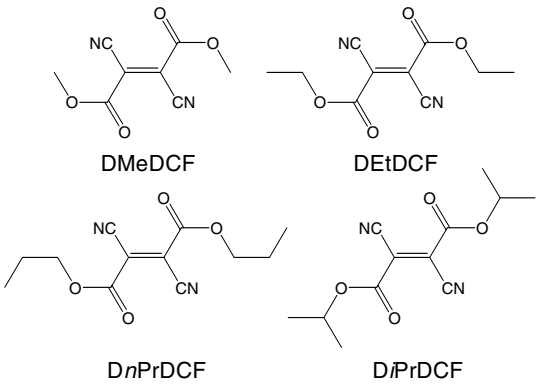


Fig. 1. One-electron acceptors discussed in this paper.

below 5.4 K [4]. The structure of both of these compounds can be characterized as pseudo-one-dimensional stacks with ferromagnetic interactions within the stack (as indicated by a positive θ value) but with interstack interactions that appears to change sign as the result of adding two methylene groups to the acceptor in going from DMeDCF to DEtDCF. At the time of those publications, due to a lack of a crystal structure for the diethyl homolog, we speculated that the change in magnetic properties was solely the result of the added bulk leading to an increasing the separation between stacks, an idea that we here show was not entirely correct.

To investigate this family of compounds further and to help to more firmly establish a structure–property relationship, two yet more bulky acceptors, di-*n*-propyl dicyanofumarate (D*n*PrDCF) and di-isopropyl dicyanofumarate (D*i*PrDCF) (Fig. 1) and their corresponding decamethylchromocene CT salts were prepared by adapting previously published methods [5]. Single crystal X-ray diffraction analysis of these compounds and comparison to the dimethyl and diethyl homologs has revealed a clear correlation between molecular packing and magnetic properties. The corresponding manganese analogs have also been prepared and, assuming these have the same structure as the chromium compounds, similarly clear patterns relating structure and behavior are apparent.

2. Experimental

2.1. General considerations

Preparations of air-sensitive compounds were carried out in a nitrogen-filled vacuum atmospheres glove box and by using standard Schlenk techniques. Decamethylchromocene and decamethylmanganocene were purchased from Strem Chemicals. All other reagents were purchased from Aldrich or Alfa. Reagents were used as received except as noted below. Dichloromethane was distilled from P_2O_5. Diethyl ether was distilled from Na/benzophenone. All solvents were degassed with glove box N_2 prior to use. Di-*n*-propyl dicyanofumarate and di-isopropyl dicyanofumarate were synthesized by adaptation of the previously published route [5]. Elemental analyses were performed by Desert Analytics, Tucson, AZ.

2.2. Magnetic measurements

All the magnetic measurements were performed on a 7 T Quantum Design MPMS SQUID magnetometer. Measurements of magnetization as a function of temperature were performed from 1.8 to 300 K and in a 1000 G applied field. Powder samples were cooled in zero applied field and measured upon warming. Samples were prepared as previously described [6]. The amplitude of the oscillating magnetic field used for ac susceptibility measurements was 3.5 Oe with zero dc bias field and at frequencies of 1, 10, 100, and 1000 Hz. Diamagnetic corrections were applied based on Pascal's constants for χT and χ^{-1} versus T plots but no corrections were applied to the M versus H or ac data. Magnetic measurements were performed on partially or fully desolvated materials except for one ac susceptibility experiment performed on $[CrCp^*_2][DiPrDCF] \cdot 2CH_2Cl_2$ in the presence of excess mother liquor.

2.3. X-ray crystallography

Dark Red plates ($0.12 \times 0.12 \times 0.055$ mm^3) of $[CrCp^*_2]$-[D*i*PrDCF], **4** were crystallized from dichloromethane by slow diffusion of pentane at room temperature in the glovebox. The chosen crystal was mounted on a nylon CryoLoop™ (Hampton Research) with Krytox® Oil (DuPont) and centered on the goniometer of an Oxford Diffraction Xcalibur2™ diffractometer equipped with a Sapphire 2™ CCD detector. The data collection routine, unit cell refinement, and data processing were carried out with the program CrysAlis [7]. The Laue symmetry was consistent with the triclinic space group $P\bar{1}$. The structure was solved by direct methods using Sir92 [8] via the WinGX [9] graphical user interface. The structure was refined using the SHELXTL NT program package [10]. The asymmetric unit of the structure comprises 0.5 crystallographically independent $[CrCp^*_2][DiPrDCF]$ formula unit and one CH_2Cl_2 solvate. The final refinement model involved anisotropic displacement parameters for non-hydrogen atoms and a riding model for all hydrogen atoms. The program package SHELXTL NT was used for molecular graphics generation [8].

2.4. Decamethylchromocenium di-n-propyl dicyanofumarate $[CrCp^*_2][DnPrDCF]$ (3)

Decamethylchromocene (55 mg, 1.7×10^{-4} mol) was dissolved in 2 ml of CH_2Cl_2. To this solution was added a solution of di-*n*-propyldicyanofumarate (40 mg,

1.6×10^{-4} mol) in 2 ml of CH_2Cl_2. Immediately, the color of the solution turned from yellow to brown. After the solution had stirred for 0.5 h at room temperature, 12 ml of diethyl ether was slowly added to precipitate an air-sensitive, brown solid. This solid was filtered, washed with diethyl ether, and dried in vacuo. Yield: 44 mg (48%). *Anal.* Calc. for $[CrCp^*_2][DnPrDCF] \cdot 2CH_2Cl_2$, $C_{33}H_{46}N_2O_4Cl_2Cr$: C, 60.27; H, 7.05; N, 4.26. Found: C, 59.46; H, 7.31; N, 4.23%.

2.5. Decamethylchromocenium di-isopropyl dicyanofumarate [$CrCp^*_2$][DiPrDCF] (4)

This salt was synthesized using the same procedure as above starting with di-isopropyl dicyanofumarate. Yield: 27 mg (29%). *Anal.* Calc. for $[CrCp^*_2][DiPrDCF] \cdot 2CH_2Cl_2$, $C_{33}H_{46}N_2O_4Cl_2Cr$: C, 60.27; H, 7.05; N, 4.26. Found: C, 59.82; H, 7.42; N, 4.41%.

2.6. Decamethylmanganocenium di-n-propyl dicyanofumarate [$MnCp^*_2$][DnPrDCF] (5)

Under nitrogen, decamethylmanganocene (51 mg, 1.6×10^{-4} mol) was dissolved in 2 ml of CH_2Cl_2, and the solution was cooled to −77 °C using a dry ice/acetone bath. To this solution was added a solution of di-*n*-propyl dicyanofumarate (37 mg, 1.5×10^{-4} mol) in 3 ml CH_2Cl_2. The solution turned from yellow to brown after addition of a few drops. After the solution had stirred for 0.5 h at −77 °C, 12 ml of diethyl ether was slowly added to precipitate a greenish brown solid. This solid was collected on a pre-cooled glass frit by vacuum filtration and washed with diethyl ether. The solid was dried in vacuo at low temperature for 2 h, then 0.5 h at room temperature. Yield: 72 mg (88%). *Anal.* Calc. for $[MnCp^*_2][DnPrDCF] \cdot 0.05CH_2Cl_2$, $C_{32.05}H_{44.1}N_2O_4Cl_{0.1}Mn$: C, 66.38; H, 7.66; N, 4.83. Found: C, 65.72; H, 7.92; N, 4.83%.

2.7. Decamethylmanganocenium di-isopropyl dicyanofumarate [$MnCp^*_2$][DiPrDCF] (6)

This salt was synthesized using the same procedure as above, starting with di-isopropyl dicyanofumarate. Yield: 65 mg (79%). *Anal.* Calc. for $[MnCp^*_2][DiPrDCF] \cdot 0.05CH_2Cl_2$, $C_{32.05}H_{44.1}N_2O_4Cl_{0.1}Mn$: C, 66.38; H, 7.66; N, 4.83. Found: C, 66.85; H, 7.45; N, 4.71%.

3. Results and discussion

3.1. Structures

Compounds **3** and **4** have been prepared by adapting previously published procedures and their properties are quite reminiscent of compound **2**. All three compounds crystallize as dichloromethane solvates with two solvent molecules and one CT salt formula unit in the unit cell. The structure of **2** was previously published and the structure of **4** is shown in Fig. 2 and the parameters given in Table 1. Compound **3** does not crystallize as well, but a low resolution structure solution reveals the symmetry and parameters of the unit cell as well as the packing motif. The isomorphous structures of **2**–**4** are comprised of pseudo-one-dimensional stacks of alternating donors and acceptors. One of the methyl groups of each isopropyl group in **4** is pointed in the direction of the metallocene and that increases the distance between the donor and acceptor within a stack slightly, due to a steric interaction. The *n*-propyl of **3**, like the ethyl compound of **2**, and the methyl compound of **1** (which crystallizes in the orthorhombic space group *Pnma*) are essentially planar (Figs. 2 and 3). Together, **1**–**4** form a homologous series.

The principal differences between the structures of **1** and **2**–**4** are that:

(1) Whereas for **1**, the metallocene is exactly above the middle of the inversion center of the acceptor, in **2**–**4** there is a slight offset of approximately 0.6 ± 0.2 Å, with a greater shift for isopropyl and essentially equivalent smaller shifts for Et and *n*-Pr.
(2) In the structures of **2**–**4**, the donors and acceptors are offset slightly in the direction of the stacking axis, so that they form a stepped structure.
(3) The methyl groups on the metallocene are eclipsed for **1**, but staggered for **2**–**4**.
(4) **2**–**4** are all dichloromethane solvates, whereas **1** is unsolvated.
(5) Perhaps most importantly, when viewed down the stacking axis, the donors in **1** form a zig-zag chain, whereas for **2**–**4**, they form linear chains. The effect of this and the presence of solvent molecules is a

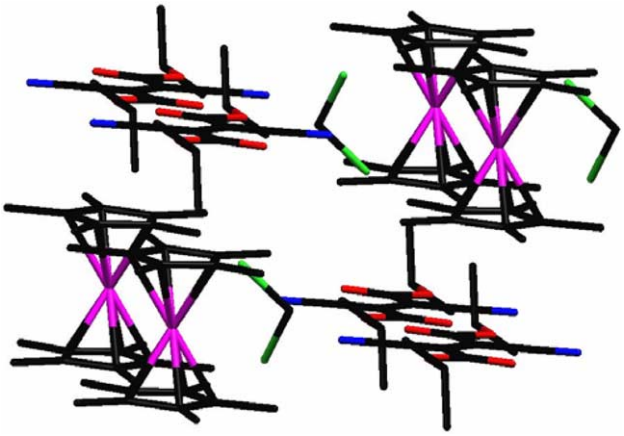


Fig. 2. Packing diagram of $[CrCp^*_2][DiPrDCF] \cdot 2CH_2Cl_2$ (not all solvent molecules shown).

Table 1
Crystal data and structure refinement for $[CrCp^*_2][DiPrDCF] \cdot 2CH_2Cl_2$

Empirical formula	$[C_{20}H_{30}Cr][C_{12}H_{14}N_2O_4] \cdot 2CH_2Cl_2$
Formula weight	742.54
Temperature (K)	100(2)
Wavelength (Å)	0.71073
Crystal system	triclinic
Space group	$P\bar{1}$
Unit cell dimensions	
a (Å)	9.7212(19)
b (Å)	9.7292(14)
c (Å)	11.5723(16)
α (°)	80.760(12)
β (°)	68.779(15)
γ (°)	66.333(16)
Volume (Å^3)	934.3(3)
Z	1
D_{calc} (Mg/m^3)	1.320
Absorption coefficient (mm^{-1})	0.630
F (0 0 0)	390
Crystal size (mm)	$0.120 \times 0.119 \times 0.055$
Theta range for data collection (°)	2.64–25.05
Index ranges	$-11 \leqslant h \leqslant 11$, $-11 \leqslant k \leqslant 11$, $-13 \leqslant l \leqslant 13$
Reflections collected	6573
Independent reflections	3316 [R_{int} = 0.0322]
Completeness to theta = 25.05° (%)	99.8
Absorption correction	none
Refinement method	full-matrix least-squares on F^2
Data/restraints/parameters	3316/0/212
Goodness-of-fit on F^2	1.032
Final R indices [$I > 2\sigma(I)$]	R_1 = 0.0452, wR_2 = 0.1038
R indices (all data)	R_1 = 0.0799, wR_2 = 0.1360
Largest differential peak and hole (e Å^{-3})	0.703 and −0.563

much greater distance between donors perpendicular to this axis as shown in Figs. 4 and 5 (9.103 Å versus 11.572 Å).

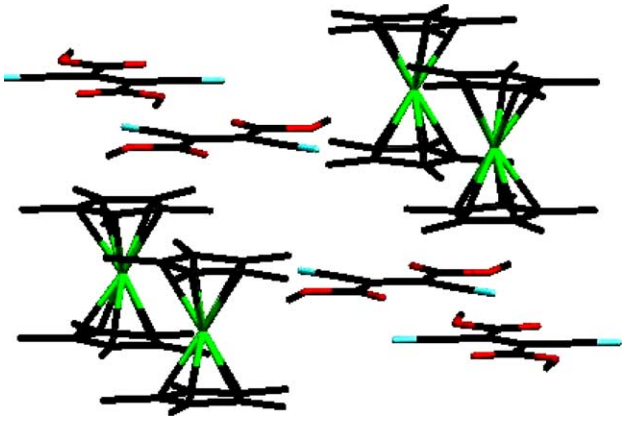


Fig. 3. Packing diagram of $[CrCp^*_2][DMeDCF]$.

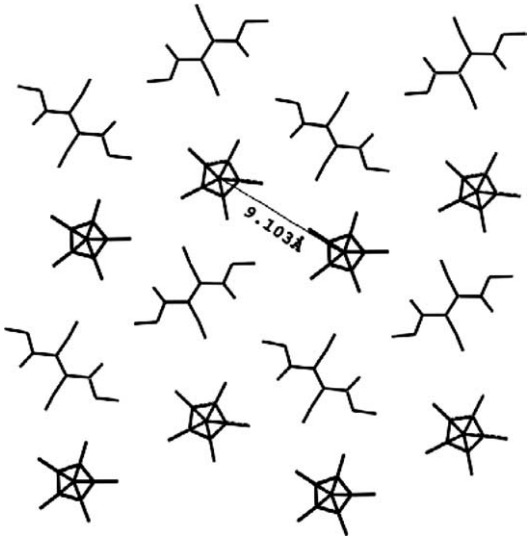


Fig. 4. View down the stacking axis of $[CrCp^*_2][DMeDCF]$ showing the zig-zag chains of donors and acceptors.

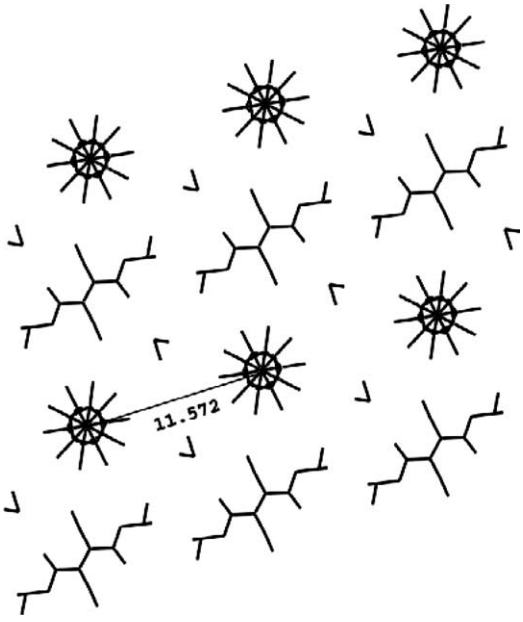


Fig. 5. View down the stacking axis of $[CrCp^*_2][DiPrDCF] \cdot 2CH_2Cl_2$ showing the straight chains of donors and acceptors and the solvent of crystallization.

3.2. Magnetic properties

Previously, we have identified that ferromagnetic $[CrCp^*_2][DMeDCF]$ crystallizes in the space group, *Pnma*, and we assume that the manganese analog, $[MnCp^*_2][DMeDCF]$, also has this structure. The unit cell, which is orthorhombic (Fig. 3), has four formula units in the unit cell arranged as four mixed stacks of donors and acceptors in two adjacent pairs, with one pair shifted with respect to the other stack by one-half repeat unit. Similar patterns have been observed for

ferromagnetic [$FeCp^*_2$][TCNE] which crystallizes in *C*2/*c*, a monoclinic space group with eight formula units in the unit cell [11]. However, what we observe here is that when we move to higher homologs of the dialkyl dicyanofumarate family, we crystallize in the lower triclinic symmetry and we observe a change to antiferromagnetic (metamagnetic) order. As described below, this behavior is seen for compounds **2**–**4**.

3.3. Decamethylchromocenium salts

Measurements of χT versus temperature, χ^{-1} versus temperature, magnetization versus applied field at 1.8 K and ac susceptibility at 1 Hz (Figs. 6–11) reveal that **3** (*n*-propyl) and **4** (isopropyl) are metamagnets with $T_N = 4.6$ and 3.9 K, respectively. The compounds obey the Curie–Weiss law with $\theta = 28$ and 19 K, respectively. Metamagnetism is indicated by frequency-independent peaks in χ' and no non-zero χ'' in each plot. The critical field, above which the magnetization switches from antiferromagnetic to ferromagnetic-like, for each of these two compounds is very small, consistent with the lack of single ion anisotropy for Cr^{3+}, which in this geometry, has a ^4A ground state. The saturation magnetization for each compound approaches 22 340 emu-G/mol expected for four unpaired spins with $g = 2.0$. The previously reported behavior of **2** is also that of a metamagnet with $T_N = 5.4$ K and similar other magnetic properties. These data are consistent with the observed isomorphous structures with the possibility of a weak trend toward lower ordering temperatures with the bulkier di-isopropyl dicyanofumarate ligand.

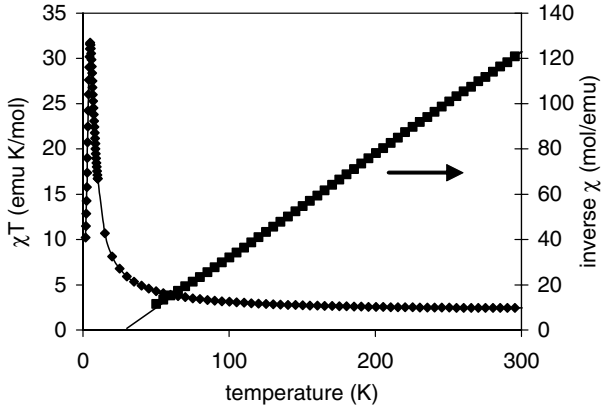


Fig. 6. χT vs. T (◆) and χ^{-1} vs. T (■) for [$CrCp^*_2$][D*n*PrDCF].

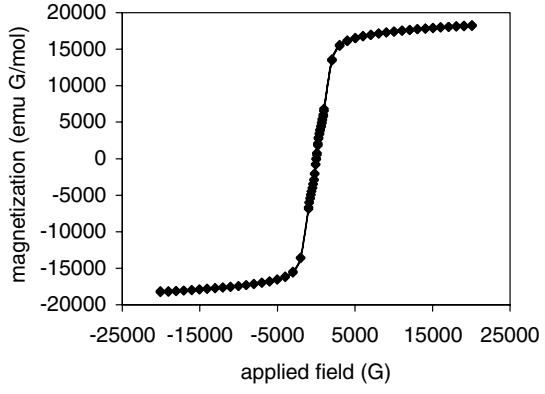


Fig. 7. M vs. H for [$CrCp^*_2$][D*n*PrDCF] at 1.8 K.

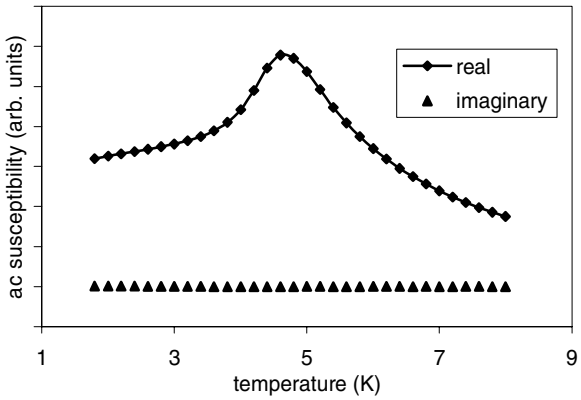


Fig. 8. Ac susceptibility for [$CrCp^*_2$][D*n*PrDCF].

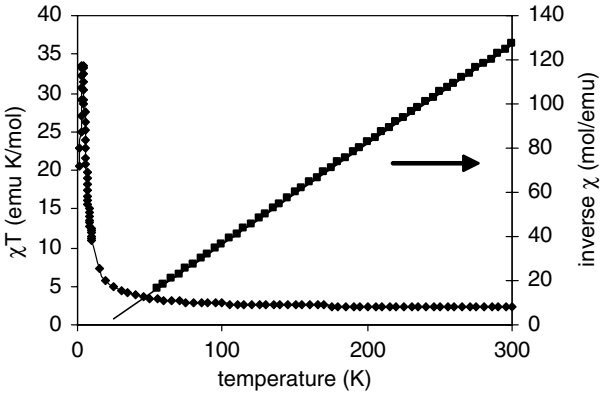


Fig. 9. χT vs. T (◆) and χ^{-1} vs. T (■) for [$CrCp^*_2$][D*i*PrDCF].

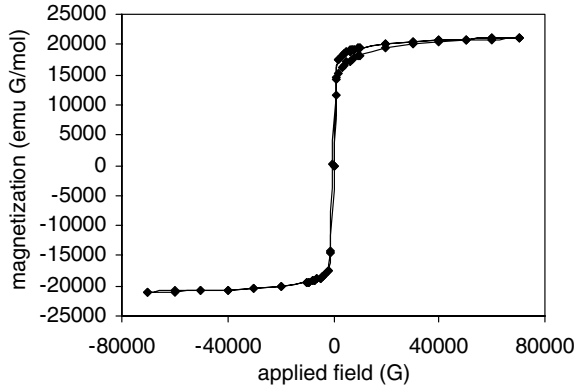


Fig. 10. M vs. H for [$CrCp^*_2$][D*i*PrDCF] at 1.8 K.

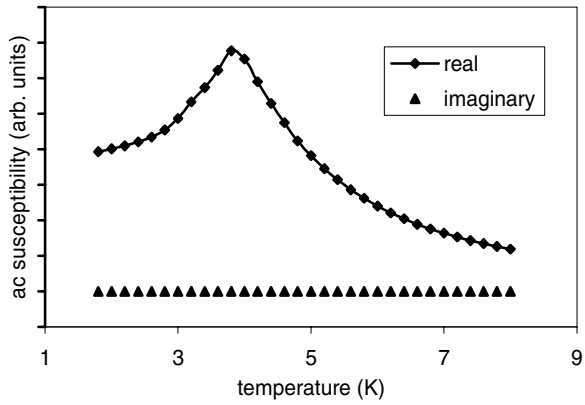


Fig. 11. Ac susceptibility for $[CrCp^*_2][DiPrDCF]$.

Because both of the samples described above are partially desolvated, the ac susceptibility of a fully solvated sample was determined. Fig. 12 illustrates the frequency-independent ac susceptibility of $[CrCp^*_2][DiPrDCF]\cdot 2CH_2Cl_2$, which required that the data be collected in the presence of excess dichloromethane mother liquor. As can be seen, the solvated sample is still a metamagnet, although there is a slight lowering of T_N and sharpening of the peak in χ' relative to the data from the partially desolvated compound. This is consistent with preservation of the single crystal structure with its solvent of crystallization intact, which causes the stacks to be further apart but also makes the interstack separation (and interaction) more uniform.

3.4. Decamethylmanganocenium salts

Compounds **5** and **6**, the manganese analogs of **3** and **4**, respectively, have also been prepared. These compounds have not been successfully crystallized because they are not stable in solution except at very low temperatures as has been seen previously for the dimethyl and diethyl esters. In fact, under the synthesis conditions, the materials are almost completely desolvated, as indicated by elemental analysis results. As a result, the crystallinity is destroyed and no X-ray powder diffraction is observed, although the compounds do exhibit reproducible magnetic properties (vide infra).

The plots of χT versus temperature and χ^{-1} versus temperature for **5** and **6** (Figs. 13 and 16, respectively)

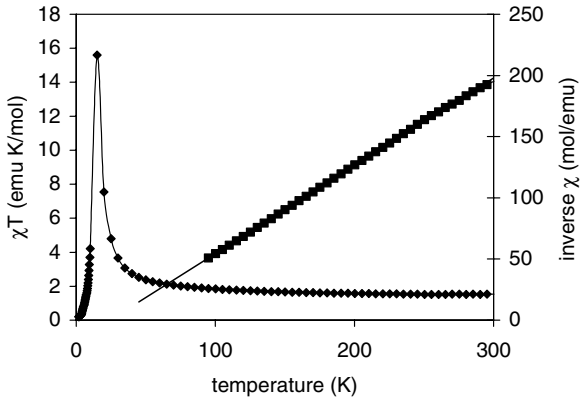


Fig. 13. χT vs. T (◆) and χ^{-1} vs. T (■) for $[MnCp^*_2][DnPrDCF]$.

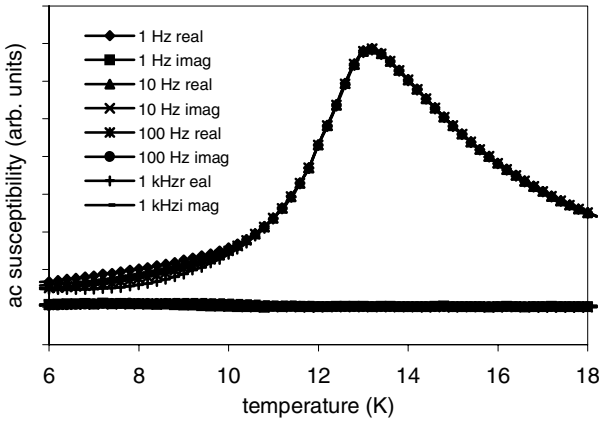


Fig. 14. Ac susceptibility for $[MnCp^*_2][DnPrDCF]$.

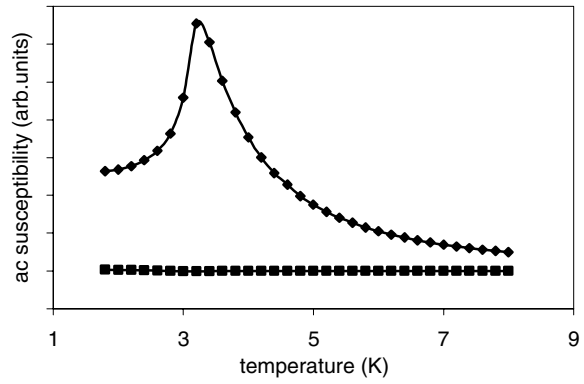


Fig. 12. Ac susceptibility for $[CrCp^*_2][DiPrDCF]\cdot 2CH_2Cl_2$.

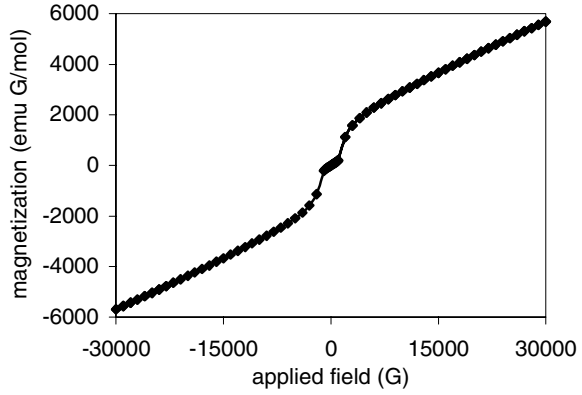


Fig. 15. M vs. H for $[MnCp^*_2][DnPrDCF]$ at 13 K.

suggest dominant ferromagnetic coupling, with $\theta = 24$ and 7.3 K, respectively. But the more revealing data are the ac susceptibility and the magnetization versus applied field (M versus H) plots. Figs. 14 and 17 show the ac susceptibility data for **5** and **6** which in each case is characterized by what appears to be a frequency independent antiferromagnetic phase transition followed at lower temperature by a frequency dependent region indicative of a glassy magnetic state. We have previously speculated that the glassy region is due to additional antiferromagnetic interstack interactions that become significant as the temperature is lowered.

M versus H data (Figs. 15 and 18, respectively), collected at a temperature just below the peak in χ' as determined from the ac data for each compound, exhibit the characteristic shape of a metamagnet. Well below these temperatures (Figs. 19 and 20), at 1.8 K, in the glassy state, however, a wide hystersis loop opens up, just as seen previously for $[MnCp^*_2][DEtDCF]$ (**8**). For **5**, at 1.8 K, the coercive field is 1.3 T and the remanance is 5500 emu-G/mol whereas for **6**, the coercive field is 1.3 T and the remanance is 8000 emu-G/mol. In neither case does the magnetization in 7 T applied field approach even close to the expected value for co-linear spins, indicating some canting of the manganese moments.

In contrast, $[MnCp^*_2][DMeDCF]$ (**7**), is a ferromagnet with $T_c = 10$ K, paralleling exactly the behavior observed in the chromium family.

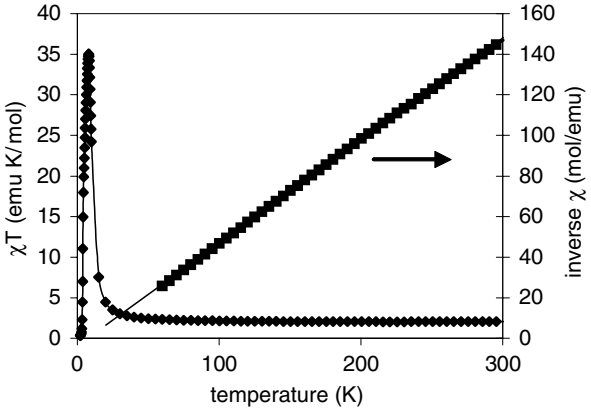


Fig. 16. χT vs. T (◆) and χ^{-1} vs. T (■) for $[MnCp^*_2][DiPrDCF]$.

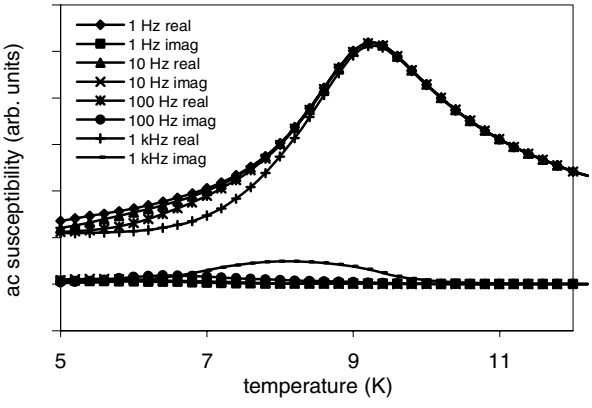


Fig. 17. Ac susceptibility for $[MnCp^*_2][DiPrDCF]$.

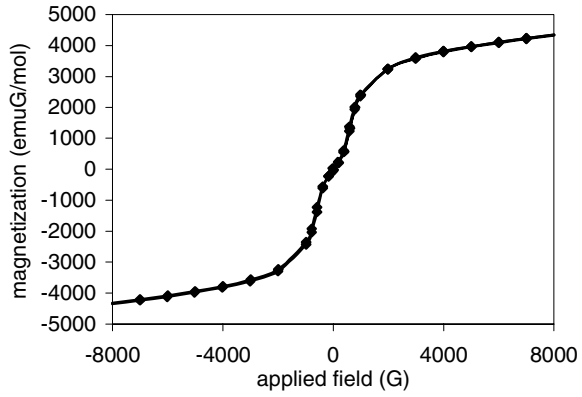


Fig. 18. M vs. H for $[MnCp^*_2][DiPrDCF]$ at 9 K.

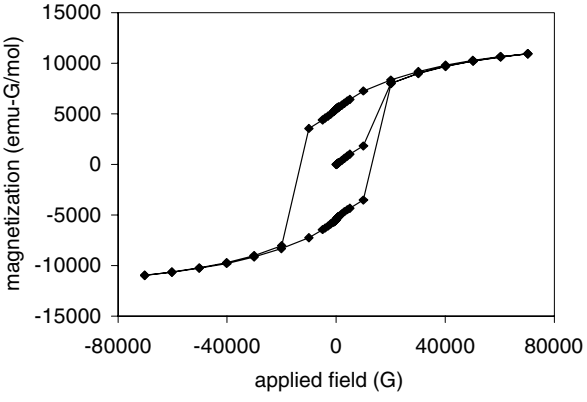


Fig. 19. M vs. H at 1.8 K for $[MnCp^*_2][DnPrDCF]$.

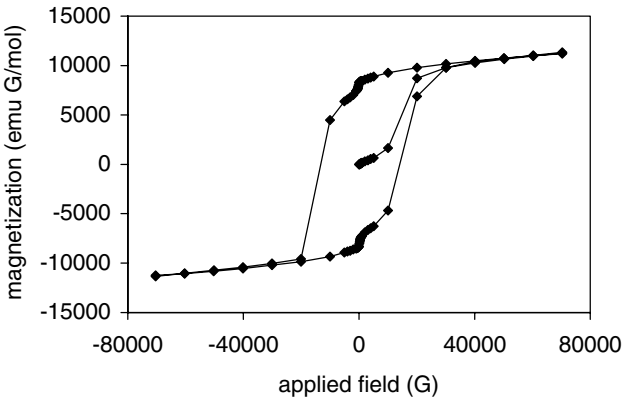


Fig. 20. M vs. H at 1.8 K for $[MnCp^*_2][DiPrDCF]$.

Table 2
Magnetic and structural data for all compounds in this paper

$[CrCp^*_2][DMeDCF]$	FM, 5.7 K	*Pnma*	$[MnCp^*_2][DMeDCF]$	FM, 10 K
$[CrCp^*_2][DEtDCF]$	MM, 5.4 K	$P\bar{1}$	$[MnCp^*_2][DEtDCF]$	MM, 12 K
$[CrCp^*_2][DiPrDCF]$	MM, 3.9 K	$P\bar{1}$	$[MnCp^*_2][DiPrDCF]$	MM, 9.3 K
$[CrCp^*_2][DnPrDCF]$	MM, 4.6 K	$P\bar{1}$	$[MnCp^*_2][DnPrDCF]$	MM, 13.4 K

The manganese structures are assumed to be the same as their chromium analogs. $P\bar{1}$ structures listed are for solvated crystals.

4. Summary

Decamethylmetallocene-based CT salts are excellent examples of pseudo-one-dimensional materials exhibiting magnetic long range order that must arise solely from through-space interactions because the solids feature only non-covalent interactions between the spin centers. As such, they are excellent platforms on which to base experiments that seek to understand how order is achieved by systematic variation of the building blocks. In this paper, we have established that there is a correlation between crystal packing and three-dimensional magnetic order as summarized in Table 2.

Furthermore, in both the decamethylchromocene and decamethylmanganocene families, the sterically more demanding di-isopropyl dicyanofumarate enforces greater intrastack separation, which results in lower θ values and ordering temperatures. It should be noted that single crystals are solvated, whereas most of the magnetic measurements were performed on partially or fully desolvated powders. However, one ac experiment was performed in the presence of excess solvent and the behavior is qualitatively similar, with the difference being a sharpening in the peak in χ' and slight lowering of temperature at which the peak occurs. This is consistent with the expectation of greater interstack separation and greater interstack uniformity in the crystalline materials.

Although our previous supposition that the switch from ferromagnetism to metamagnetism results from simply separating the stacks to a greater extent was not entirely correct, we now have a more complete and satisfying picture in which the change in magnetic behavior is brought about by a change in crystal packing. However, the details of how the specific intrastack and interstack interactions give rise to magnetic order remain to be determined.

Acknowledgments

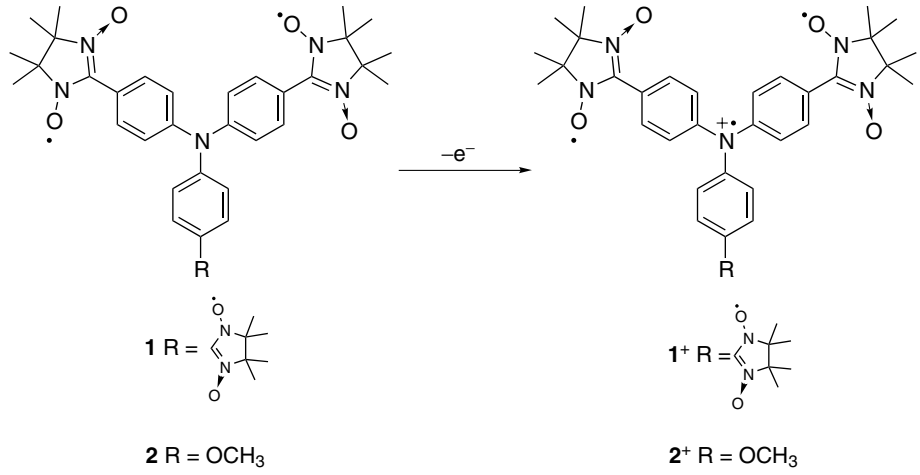
We thank the NSF (Grant CHE-0131128) for funding the purchase of the Oxford Diffraction Xcalibur2 single crystal diffractometer and (Grant CHE-023488) for partially funding the purchase of the SQUID magnetometer. We thank the CCDC for use of the Mercury program for visualizing crystal structures.

Appendix A. Supplementary data

X-ray crystallographic details (in CIF format) for $[CrCp^*_2][DiPrDCF] \cdot 2CH_2Cl_2$. Unit cell parameters for **2**–**4**. Supplementary data associated with this article can be found, in the online version, at doi:10.1016/j.poly.2005.03.030.

References

[1] J.A. Crisp, M.B. Meredith, T.P. Hanusa, G. Wang, W.W. Brennessel, G.T. Yee, Inorg. Chem. 44 (2005) 172–174.
[2] G. Wang, C. Slebodnick, R.J. Butcher, M.C. Tam, T.D. Crawford, G.T. Yee, J. Am. Chem. Soc. 126 (2004) 16890–16895.
[3] B.B. Kaul, R.D. Sommer, B.C. Noll, G.T. Yee, Inorg. Chem. 39 (2000) 865–868.
[4] B.B. Kaul, R.D. Sommer, B.C. Noll, G.T. Yee, J. Solid State Chem. 159 (2001) 420–427.
[5] C.J. Ireland, K. Jones, J.S. Pizey, S. Johnson, Synth. Commun. 3 (1976) 185–191.
[6] S.P. Sellers, B.J. Korte, J.P. Fitzgerald, W.M. Reiff, G.T. Yee, J. Am. Chem. Soc. 120 (1998) 4662–4670.
[7] CrysAlis v1.171, Oxford Diffraction, Wroclaw, Poland, 2004.
[8] A. Altomare, G. Cascarano, C. Giacovazzo, A. Guagliardi, J. Appl. Cryst. 26 (1993) 343–350.
[9] L.J. Farrugia, J. Appl. Cryst. 32 (1999) 837–838.
[10] G.M. Sheldrick, SHELXTL NT Ver. 6.12, Bruker Analytical X-ray Systems Inc., Madison, WI, 2001.
[11] J.S. Miller, J.C. Calabrese, H. Rommelmann, S.R. Chittipeddi, J.H. Zhang, W.M. Reiff, A.J. Epstein, J. Am. Chem. Soc. 109 (1987) 769–781.



Scheme 1.

(δ77.0 ppm) for ^{13}C NMR. IR spectra were recorded using KBr disks on a JASCO FT/IR-460Plus spectrometer. ESR spectra were recorded on a JEOL JES-SRE2X or a JEOL JES-TE200 spectrometer, and a Mn^{2+}/MnO solid solution was used as a reference for the determination of g values and hyperfine coupling constants. Magnetic susceptibilities of the powder samples were measured by a Quantum Design MPMS-5S system. The raw data were corrected for both the magnetization of sample holder alone and the diamagnetic contribution of the sample itself. The estimation of the diamagnetic contribution was done by using Pascal's constants. Elemental analyses were performed by Center for Organic Elemental Microanalysis, Kyoto University. Toluene and *n*-butyronitrile were distilled from CaH_2 under an argon atmosphere, acetonitrile was dried over molecular sieves 3A, and benzonitrile was dried through alumina (ICN, Alumina N, Akt. I) column with bubbling of argon, just before use. All the other purchased reagents and solvents were used without further purification. Column chromatography was performed using silica gel (Kanto Chemical Co., Inc., Silica gel 60N, spherical neutral).

2.2. Tris(4-formylphenyl)amine (7)

7 was prepared by the modified method of literature procedure [15]. To a solution of imidazole (2.50 g, 36.0 mmol) in acetonitrile (30 mL) was added dropwise trifluoroacetic anhydride (16.00 g, 75.4 mmol) under an argon atmosphere. The mixture was refluxed for 1 h, and then cooled by removal of the oil bath. Triphenylamine (2.50 g, 9.99 mmol) was added to the mixture, and then the reaction mixture was refluxed for 20 h. After cooling to room temperature, the reaction mixture was treated with ice to give a green precipitate, which was filtrated and washed with water. The precipitate was dissolved in CH_2Cl_2, washed with saturated aqueous $NaHCO_3$, and dried over $MgSO_4$, and the solvent was removed under reduced pressure to afford a greenish yellow solid (9.77 g), which was used for the next step without further purification.

To a suspension of this crude product (9.77 g) in acetonitrile (200 mL) was added a dilute hydrochloric acid (20 mL of conc. hydrochloric acid and 100 mL of water) under an argon atmosphere. The mixture was refluxed for 4 h, and extracted with Et_2O after cooling and neutralization with saturated aqueous Na_2CO_3 at 0 °C. The organic layer was dried over $MgSO_4$, and the solvent was removed under reduced pressure. The residue was chromatographed on silica gel (CH_2Cl_2:*n*-hexane = 3:1 as eluent), and washed with hot ethyl acetate and *n*-hexane to afford **7** (2.12 g, 64 %) as a yellow solid: IR(KBr) 2805, 2729, 1697 cm^{-1}; ^1H NMR (400 MHz, $CDCl_3$) δ 9.94 (s, 3H), 7.84 (d, J = 8.7 Hz, 6H), 7.25 (d, J = 8.7 Hz, 6H); ^{13}C NMR (100 MHz, $CDCl_3$) δ 190.3, 151.1, 132.5, 131.4, 124.5. *Anal.* Calc. for $C_{21}H_{15}NO_3$: C, 76.58; H, 4.59; N, 4.25; O, 14.57. Found: C, 76.30; H, 4.50; N, 4.14; O, 14.54%.

2.3. Tris[4-(1-oxyl-3-oxide-4,4,5,5-tetramethylimidazolin-2-yl)phenyl]amine (1)

A reaction flask equipped with a Soxhlet apparatus filled with molecular sieves 4A was charged with **7** (0.65 g, 1.98 mg), 2,3-bis(hydroxyamino)-2,3-dimethyl butane (1.41 g, 9.51 mmol) and 2,3-bis(hydroxyamino)-2,3-dimethylbutane sulfate (0.47 g, 1.90 mmol) in methanol (150 mL), and refluxed for 18 h under an argon atmosphere. The reaction mixture was concentrated by evaporation, and the resulting precipitate was collected and washed with cold methanol to afford a yellowish white solid (0.64 g). The further purification was not performed.

To a solution of the product (0.64 g) in dichloromethane (36 mL) and methanol (3.6 mL) was added a

solution of $NaIO_4$ (0.48 g, 2.24 mmol) in water (3.6 mL). The mixture was stirred for 30 min in the open air. The organic layer was separated, dried over $MgSO_4$ and the solvent was removed under reduced pressure. The residue was chromatographed on silica gel (ethyl acetate:*n*-hexane = 4:1 as eluent), concentrated by evacuation of solvent, and washed with the mixed solvent (CH_2Cl_2:*n*-hexane = 1:9) to afford **1** (30.8 mg, 2%) as a blue solid: ESR (toluene) 13 lines, $g = 2.007$, $|a_N| = 2.5$ G.

2.4. N,N-diphenyl-4-methoxyphenylamine (4)

4 was prepared by the modified method of literature procedure [16]. A mixture of 4-iodoanisole (7.65 g, 32.7 mmol), diphenylamine (5.53 g, 32.7 mmol), CuI (0.15 g, 0.79 mmol) and KO*t*-Bu (11.0 g, 98.0 mmol) in toluene (120 mL) was refluxed under argon atmosphere for 1 day. After cooling to room temperature, the solvent was evaporated. Water and CH_2Cl_2 was added to the residue, and the organic layer was separated, dried over $MgSO_4$ and evaporated. The residue was chromatographed on silica gel (ethyl acetate:CH_2Cl_2:*n*-hexane = 1:9:30) to afford **4** (4.27 g, 47%) as a yellow solid: ^{1}H NMR (400 MHz, $CDCl_3$) δ 7.19 (dd, $J = 8.5$, 7.3 Hz, 4H), 7.06 (d, $J = 9.0$ Hz, 2H), 7.02 (dd, $J = 7.3$, 1.2 Hz, 4H), 6.93 (tt, $J = 7.3$, 1.2 Hz, 2H), 6.83 (d, $J = 9.0$ Hz, 2H), 3.79 (s, 3H); ^{13}C NMR (100 MHz, $CDCl_3$) δ 156.0, 148.1, 140.7, 129.0, 127.2, 122.8, 121.8, 114.7, 55.5. *Anal*. Calc. for $C_{19}H_{17}NO$: C, 82.88; H, 6.22; N, 5.09; O, 5.81. Found: C, 82.82; H, 6.08; N, 5.07; O, 5.66%.

2.5. N,N-Bis(4-formylphenyl)-4-methoxyphenylamine (8)

8 was prepared by the similar method of literature procedure [15]. To a solution of imidazole (2.72 g, 40.0 mmol) in acetonitrile (80 mL) was added dropwise trifluoroacetic anhydride (16.80 g, 80.0 mmol) under an argon atmosphere. The mixture was refluxed for 30 min, and then cooled by removal of the oil bath. **4** (4.27 g, 15.5 mmol) was added to the mixture, and then the reaction mixture was refluxed for 1 day. After cooling to room temperature, the reaction mixture was treated with ice to give a green precipitate, which was filtrated and washed with water.

The precipitate was suspended in acetonitrile (200 mL) and a dilute hydrochloric acid (36 mL of conc. hydrochloric acid and 144 mL of water) under an argon atmosphere. The mixture was refluxed for 4 h, and extracted with Et_2O after cooling and neutralization with saturated aqueous K_2CO_3 at 0 °C. The organic layer was dried over $MgSO_4$, and the solvent was removed under reduced pressure. The residue was chromatographed on silica gel (ethyl acetate:*n*-hexane = 1:4 as eluent) to afford **8** (2.89 g, 56%) as a yellow solid: IR(KBr) 2835, 2739, 1686, 1040 cm^{-1}; ^{1}H NMR (400 MHz, $CDCl_3$) δ 9.87 (s, 2H), 7.75 (d, $J = 8.3$ Hz, 4H), 7.16 (d, $J = 8.3$ Hz, 4H), 7.11 (d, $J = 8.3$ Hz, 2H), 6.94 (d, $J = 8.3$ Hz, 2H), 3.84 (s, 3H); ^{13}C NMR (100 MHz, $CDCl_3$) δ 190.3, 158.0, 152.0, 138.0, 131.2, 130.8, 128.8, 122.0, 115.4, 55.6. *Anal.* Calc. for $C_{21}H_{17}NO_3$: C, 76.12; H, 5.17; N, 4.23; O, 14.49. Found: C, 75.98; H, 5.31; N, 4.26; O, 14.60%.

2.6. N,N-Bis[4-(1-oxyl-3-oxide-4,4,5,5-tetramethyl imidazolin-2-yl)phenyl]-4-methoxyphenylamine (2)

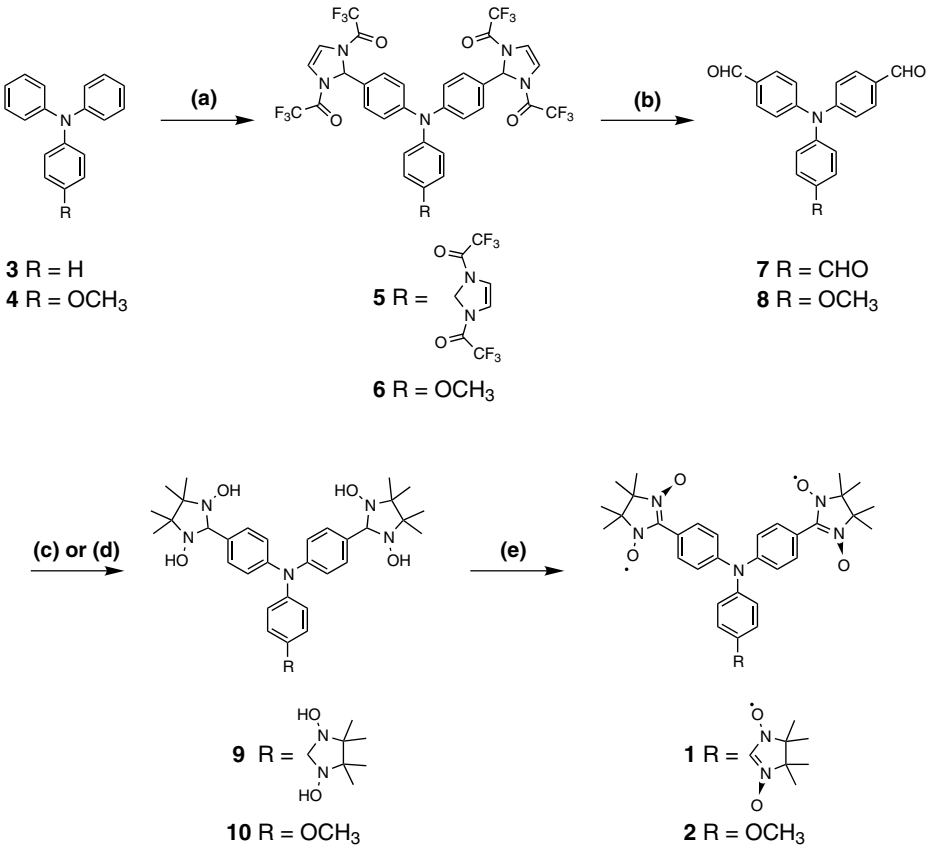
A reaction flask equipped with a Soxhlet apparatus filled with molecular sieves 4A was charged with 2,3-bis(hydroxyamino)-2,3-dimethylbutane sulfate (1.30 g, 5.28 mmol) and K_2CO_3 (2.42 g, 17.5 mmol) in methanol (150 mL). To the mixture was added **8** (0.58 g, 1.75 mmol) under an argon atmosphere, and refluxed for 1 day. The reaction mixture was filtered, and the organic layer was separated after adding CH_2Cl_2 and water, dried over $MgSO_4$, and the solvent was removed under reduced pressure to afford a yellow solid (0.85 g).

To a solution of the product in dichloromethane (58 mL) and methanol (5.8 mL) was added a solution of $NaIO_4$ (0.29 g, 1.35 mmol) in water (5.8 mL). The mixture was stirred for 1 h in the open air. The organic layer was separated, dried over $MgSO_4$ and the solvent was removed under reduced pressure. The residue was chromatographed on silica gel (ethyl acetate:*n*-hexane = 3:1 as eluent) to afford **2** (50 mg, 5%) as a blue solid: ESR (toluene) nine lines, $g = 2.007$, $|a_N| = 3.7$ G.

3. Results and discussion

3.1. Synthesis

To synthesize our target molecules **1** and **2** according to the Ullman's method [17], trialdehyde **7** and dialdehyde **8** become key compounds. However, the usual Vilsmeier-Haack formylation of triphenylamine produces **7** in very low yield in spite of using the vigorous reaction conditions [18]. Therefore, we attempted to synthesize **7** and **8** by another method [15]. The synthetic routes of **1** and **2** were summarized in Scheme 2. First of all, imidazole was reacted with trifluoroacetic anhydride to generate the electrophilic *N*,*N*′-bis(trifluoroacetyl)imidazolium ion. The generated imidazolium ion was treated with the corresponding triphenylamines **3** and **4** to afford tris- and bisadduct **5** and **6**. These adducts were readily hydrolyzed to give **7** and **8** under the acidic condition. The resulting aldehydes were condensed with 2,3-bis(hydroxyamino)-2,3-dimethylbutane to give the corresponding hydroxylamine **9** and **10**. Finally, **1** and



Scheme 2. Reagents and conditions: (a) imidazole, trifluoroacetic anhydride, CH_3CN; (b) HCl aq, acetonitrile; (c) 2,3-bis(hydroxyamino)-2,3-dimethylbutane, 2,3-bis(hydroxyamino)-2,3-dimethylbutane sulfate, CH_3OH; (d) 2,3-bis(hydroxyamino)-2,3-dimethylbutane sulfate, K_2CO_3, CH_3OH; (e) $NaIO_4$, H_2O, CH_2Cl_2, CH_3OH.

2 were obtained by the oxidation of hydroxylamine with sodium periodate.

3.2. Electrochemical property

The electrochemical properties for **1** and **2** were investigated by the cyclic voltammetry in benzonitrile at 25 °C. The oxidation potentials versus ferrocene/ferrocenium are summarized together with their related compounds in Table 1, and the cyclic voltammogram of **2** is shown in Fig. 1. Judging from the oxidation potentials and the current ratio of the reference compounds, 2-phenyl-4,4,5,5-tetramethylimidazoline-1-oxyl-3-oxide (**11**), triphenylamine (**12**) and 4-methoxytriphenylamine (**13**), the first oxidation process of **1** can be ascribed to the simultaneous three-electron oxidation of the corresponding three nitronyl nitroxide moieties, while the first and second oxidation processes of **2** to stepwise one-electron oxidations of the two nitroxide moieties.

Table 1
Redox potentials (V) of **1**, **2** and their related compounds[a]

	E_1	E_2	E_3
1	+0.30[b]		
2	+0.26	+0.34	+0.80
11	+0.32		
12	+0.51[c]		
13	+0.38		

[a] 0.1 M n-Bu_4BF_4 in PhCN, potential vs. Fc/Fc^+, Pt electrode, 25 °C, scan rate 100 mV s^{-1}.
[b] Quasi-three-electron transfer.
[c] Irreversible oxidation process represented by anodic peak potential.

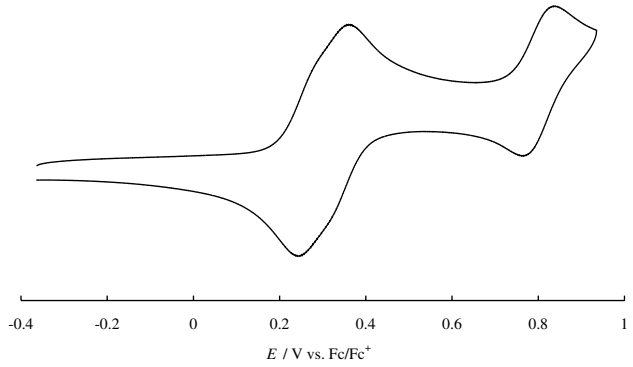


Fig. 1. Cyclic voltammogram of **2** in benzonitrile containing 0.1 M n-Bu_4BF_4 on a platinum electrode.

On the other hand, the oxidation process for the triphenylamine moiety of **1** was not observed in the range of potential window, whereas the potential value +0.80 V of **2** was due to the oxidation of triphenylamine moiety. This is probably because **1** has a considerable amount of positive charges after oxidation of the three nitronyl nitroxide moieties and, hence, the triphenylamine moiety becomes no longer oxidizable, as compared with **2**. The oxidation potential for the triphenylamine moiety of **2** increases by 0.42 V compared with **13** owing to such a charging effect of the oxidized nitronyl nitroxide moieties.

3.3. Magnetic property

Magnetic measurements of triradical **1** and diradical **2** were carried out on a SQUID susceptometer from 300 to 2 K. The temperature dependences of the molar magnetic susceptibilities (χ_m) of the microcrystalline samples were measured at a constant field of 500 G. The plot of $\chi_m T$ versus T for **1** and **2** are shown in Fig. 2.

The $\chi_m T$ value of **1** at 300 K was close to the theoretical one of 1.125 emu K mol^{-1} for isolated three spins of 1/2. On lowering the temperature, the $\chi_m T$ value decreased gradually and reached 0.28 emu K mol^{-1} at 2 K, indicating the antiferromagnetic interaction between radical spins.

The magnetic interaction in a nonsymmetrical triangular three spin system [13,14,19,20] can be described by the spin Hamiltonian (Eq. (1)), where J_{ij} is the exchange coupling constant between $\boldsymbol{S}_i$ and $\boldsymbol{S}_j$. In this case, the $\chi_m T$ is expressed by Eq. (2) as a function of Δ_1 and Δ_2 defined by Eqs. (3) and (4), which are the energy differences between the two spin doublet states and the one between the spin doublet state and the spin quartet state, where f is the purity factor for the sample, N_A the Avogadro number, g the g-factor, k_B the Boltzmann constant, μ_B the Bohr magneton, and θ the Weiss constant. Herein, we assumed the same g value for the three multiplets and, furthermore, the value was fixed $g = 2$ in the fitting procedure for simplicity.

$$H = -2(J_{12}\boldsymbol{S}_1\boldsymbol{S}_2 + J_{23}\boldsymbol{S}_2\boldsymbol{S}_3 + J_{31}\boldsymbol{S}_3\boldsymbol{S}_1), \tag{1}$$

$$\chi_m T = f\frac{N_A g^2 \mu_B^2}{4k_B}\frac{1+\exp(-\Delta_1/k_B T)+10\exp(-\Delta_2/k_B T)}{1+\exp(-\Delta_1/k_B T)+2\exp(-\Delta_2/k_B T)} \times \frac{T}{(T-\theta)}, \tag{2}$$

$$\Delta_1 = 2(J_{12}^2 + J_{23}^2 + J_{31}^2 - J_{12}J_{23} - J_{23}J_{31} - J_{31}J_{12})^{1/2}, \tag{3}$$

$$\Delta_2 = \Delta_1/2 - (J_{12} + J_{23} + J_{31}). \tag{4}$$

Since the crystal structure of **1** is not unknown to date, we carried out the least-squares fitting procedure by assuming the equilateral triangle for three spins, where $J = J_{12} = J_{23} = J_{31}$ and $\Delta_1 = 0$ gives Eq. (5). The best fit to the data was $f = 0.998 \pm 0.001$, $J/k_B = -3.93 \pm 0.06$ K and $\theta = -0.62 \pm 0.05$ K, roughly indicating the quartet state was above the doubly degenerate doublet states by ca. $3J/k_B = 12$ K. It was revealed that the intramolecular antiferromagnetic interaction of **1** was much smaller than that of tris[4-(*N*-oxy-*N*-*tert*-butylamino)phenyl]amine in the case of assuming the equilateral triangle model ($J/k_B = -135 \pm 3$ K) [13,14].

$$\chi_m T = f\frac{N_A g^2 \mu_B^2}{4k_B}\frac{1+5\exp(3J/k_B T)}{1+\exp(3J/k_B T)}\frac{T}{(T-\theta)}. \tag{5}$$

The $\chi_m T$ value of **2** at 300 K was relatively smaller than the theoretical one of 0.75 emu K mol^{-1} for isolated two spins of 1/2. Considering the $\chi_m T$ value of 0.64 emu K mol^{-1} in the wide temperature range, it seems to be not due to the antiferromagnetic interaction but to the experimental errors on weighing a sample or to the purity of a sample. As the temperature was lowered, the $\chi_m T$ value decreased gradually and reached 0.18 emu K mol^{-1} at 2 K, indicating the antiferromagnetic interaction between radical spins. The observed data were analyzed by the modified Bleaney–Bowers [21] equation for singlet–triplet model (Eq. (6)) to give the best fit parameters: $f = 0.8665 \pm 0.0006$, $J/k_B = -1.85 \pm 0.03$ K and $\theta = -1.21 \pm 0.04$ K.

$$\chi_m T = f\frac{2N_A g^2 \mu_B^2}{k_B}\frac{1}{3+\exp(-2J/k_B T)}\frac{T}{(T-\theta)}. \tag{6}$$

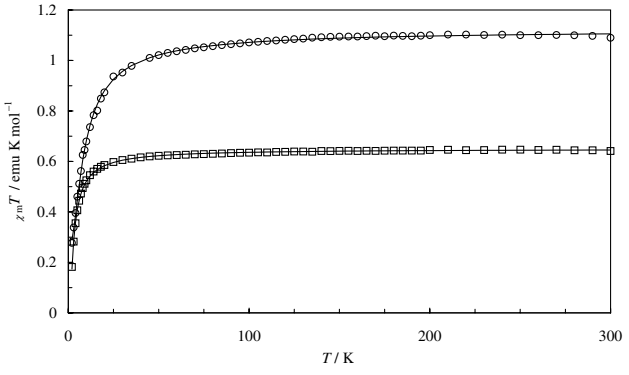


Fig. 2. Temperature dependence of $\chi_m T$ of **1** (○) and **2** (□) under a field of 500 G. The solid line represents the best theoretical fit to the data (see text).

3.4. ESR spectroscopy

The ESR spectrum in toluene at room temperature showed a 13-line pattern centered at $g = 2.007$ with a hyperfine coupling constant $|a_N| = 2.5$ G due to six equivalent nitrogen atoms for **1**, and a 9-line pattern ($g = 2.007$, $|a_N| = 3.7$ G) due to four equivalent nitrogen

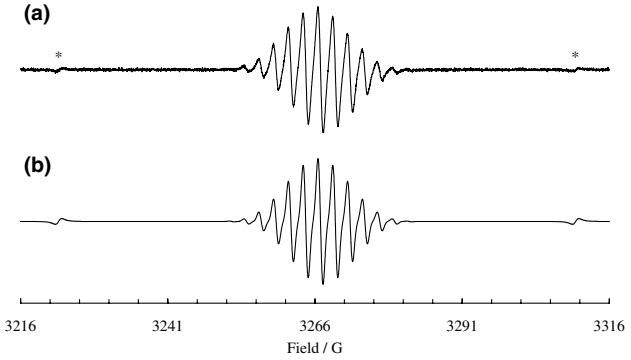


Fig. 3. ESR spectrum of **1** in toluene (5×10^{-5} M) at room temperature (a) and its simulation (b) ($|a_N| = 2.5$ G, $\Delta H_{pp} = 0.86$ G). The asterisks in the spectrum show the signals due to the Mn^{2+} standard.

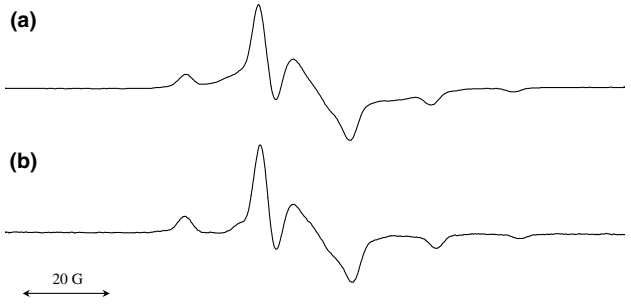


Fig. 4. ESR spectra of (a) **2** oxidized with tris(4-bromophenyl)aminium hexachloroantimonate and (b) monoradical **11** in frozen *n*-butyronitrile solution at 123 K.

atoms for **2**. For instance, the solution ESR spectrum of **1** is shown in Fig. 3. The hyperfine coupling constants of **1** and **2** were estimated to one third and a half of the hyperfine coupling constant ($|a_N| = 7.4$ G) of monoradical **11**, respectively. This indicates that the exchange interactions between radical spins in triradical **1** and diradical **2** are larger than the hyperfine interaction.

After treated with tris(4-bromophenyl)aminium hexachloroantimonate as an oxidizing agent, **1** and **2** in frozen *n*-butyronitrile at 123 K did not show the fine-structured spectra attributed to spin-quintet or quartet species. Instead of the fine-structured spectra, the observed spectra were similar to that of mono nitronyl nitroxide **11**, as shown in Fig. 4. This is consistent with the electrochemical result that the nitronyl nitroxide moieties of **1** and **2** are oxidized more easily than the triphenylamine moieties.

4. Summary

The syntheses of triradical **1** and diradical **2** having the triphenylamine skeleton were succeeded, and it is found that their neutral radicals in the solid states showed weak antiferromagnetic interactions between radical spins. However, the electrochemical and ESR measurements showed the nitronyl nitroxide moieties had the lower oxidation potentials than the core triphenylamine moieties even in the case of electron-donating methoxy-group-substitution (**2**). Therefore, in order to generate triphenylaminium cation radical and, furthermore, enhance the intramolecular ferromagnetic interaction, it is necessary to introduce more electron-donating substituent, e.g. *N*,*N*-dimethylamino group, to lower the oxidation potential. Actually, 4-*N*,*N*-dimethylaminotriphenylamine exhibits the first oxidation potential of −0.05 V. The syntheses of novel triphenylamine derivatives with nitroxide radicals are currently being undertaken, and their results will be reported in the future.

Acknowledgments

The present work was supported by Grant-in-Aids for Scientific Research from Japan Society for the Promotion of Science (JSPS) and by CREST (Core Research for Evolutional Science and Technology) of Japan Science and Technology Agency (JST).

References

[1] V. Balzani, M. Venturi, A. Credi, Molecular Devices and Machines, Wiley–VCH, Weinheim, 2003.
[2] J. Park, A.N. Pasupathy, J.I. Goldsmith, C. Chang, Y. Yaish, J.R. Petta, M. Rinkoski, J.P. Sethna, H.D. Abruna, P.L. McEuen, D.C. Ralph, Nature 417 (2002) 722.
[3] W. Liang, M.P. Shores, M. Bockrath, J.R. Long, H. Park, Nature 417 (2002) 725.
[4] S. Kubatkin, A. Danilov, M. Hjort, J. Cornil, J.-L. Brédas, N. Stuhr-Hanson, P. Hedegård, T. Bjørnholm, Nature 425 (2003) 698.
[5] S. Rajca, A. Rajca, J. Am. Chem. Soc. 117 (1995) 9172.
[6] A. Ito, H. Ino, Y. Matsui, Y. Hirao, K. Tanaka, J. Phys. Chem. A 108 (2004) 5715.
[7] Y. Morita, S. Nishida, J. Kawai, K. Fukui, S. Nakazawa, K. Sato, D. Shiomi, T. Takui, K. Nakasuji, Org. Lett. 4 (2002) 1985.
[8] (a) K. Matsuda, M. Irie, J. Am. Chem. Soc. 122 (2000) 7195; (b) K. Matsuda, M. Irie, J. Am. Chem. Soc. 122 (2000) 8309.
[9] Y. Shirota, J. Mater. Chem. 10 (2000) 1.
[10] A.R. Forrester, J.M. Hay, R.H. Thomson, Organic Chemistry of Stable Free Radicals, Academic Press, New York, 1968.
[11] C. Lambert, W. Gaschler, E. Schmälzlin, K. Meerholz, C. Bräuchle, J. Chem. Soc., Perkin Trans. 2 (3) (1999) 577.
[12] T. Itoh, K. Matsuda, H. Iwamura, Angew. Chem., Int. Ed. 38 (1999) 1791.
[13] T. Itoh, K. Matsuda, H. Iwamura, K. Hori, J. Am. Chem. Soc. 122 (2000) 2567.
[14] T. Itoh, K. Matsuda, H. Iwamura, K. Hori, J. Solid State Chem. 159 (2001) 428.
[15] H. Oelschläger, H.J. Peters, Arch. Pharm. (Weinheim) 320 (1987) 379.
[16] A.A. Kelkar, N.M. Patil, R.V. Chaudhari, Tetrahedron Lett. 43 (2002) 7143.

[17] E.F. Ullman, J.H. Osiecki, D.G.B. Boocock, R. Darcy, J. Am. Chem. Soc. 94 (1972) 7049.
[18] G. Lai, X.R. Bu, J. Santos, E.A. Mintz, Synlett (1997) 1275.
[19] O. Kahn, Molecular Magnetism, VCH, New York, 1993.
[20] A. Bencini, C. Benelli, A. Dei, D. Gatteschi, Inorg. Chem. 24 (1985) 695.
[21] B. Bleaney, K.D. Bowers, Proc. R. Soc. London A214 (1952) 451.

of acetonitrile (dehydrated) under argon atmosphere in a water- and oxygen-free grove-box. The suspension was heated to 80 °C for 130 h in an airtight glass container. Then the suspension was filtrated, and washing the residual with 100 ml of acetonitrile (dehydrated), 100 ml of ethanol (dehydrated) and 100 ml of dichloromethane gave anhydrous CoC_2 as beige powder. It is noted that, according to the ICP analysis, anhydrous CoC_2 contains ca. 35% of CaC_2 as raw material. Consequently, the results of the magnetism shown later are obtained by dividing the measured value by 0.65. Hydrous CoC_2 for magnetic measurement was obtained by exposing anhydrous CoC_2 to air (25 °C, humidity 70%). Though hydrous CoC_2 can also be formed by water-exposure in short time, slow water absorption in air atmosphere allow us to measure the magnetism of the intermediate state between hydrous and anhydrous. For the powder X-ray diffraction (XRD) measurement, hydrous CoC_2 was prepared by washing the air-exposed (2 days) sample with water to remove $Ca(OH)_2$. We confirmed that the peak position and width of CoC_2 are not changed by water exposure, while the peaks of CaC_2 and $Ca(OH)_2$ disappear after washing with water.

XRD pattern of hydrous CoC_2 was measured with *Mac science* MXP^{3}VA Powder X-ray Diffractometer at 293 K, using Cu Kα radiation (λ = 1.5418 Å). That of anhydrous CoC_2 encapsulated in glass tube (0.03ϕ) was carried out at the beam line 1A of the Photon Factory in KEK, using synchrotron radiation (λ = 0.9988 Å). Magnetic susceptibilities were measured by using *Quantum-Design* MPMS-XL SQUID magnetometer for powder sample embedded in epoxy resin to keep CoC_2 nanoparticles from rotating.

3. Results and discussion

Before analyzing the crystal structure, it is necessary to guess the rough structural model of CoC_2. According to the crystal structures of the related materials CaC_2 [5] and MgC_2 [6], it is suggested that Co^{2+} dications and C_2^{2-} dianions are stacked alternately like as NaCl-type structure. In addition, XRD pattern of CoC_2 approximately depends only on the arrangement of Co^{2+} dication due to its larger scattering factor than that of C_2^{2-}. The observed XRD pattern of anhydrous CoC_2 contaminated with CaC_2 is shown in Fig. 1. The observed pattern is well fitted by the two calculated patterns; one is CaC_2 based on the reported structure [5], and the other is the fcc-arrangement of Co^{2+} sublattices with the lattice constants $a = b = c = 4.82$ Å. The isotropic structure of Co^{2+} dications indicates the static or dynamic orientation disorder of C_2^{2-} like as CaC_2 IV [5], or else the lattice is distorted and the symmetry becomes low such as tetragonal or orthorhombic where the diffraction peaks split. The structural model of anhydrous

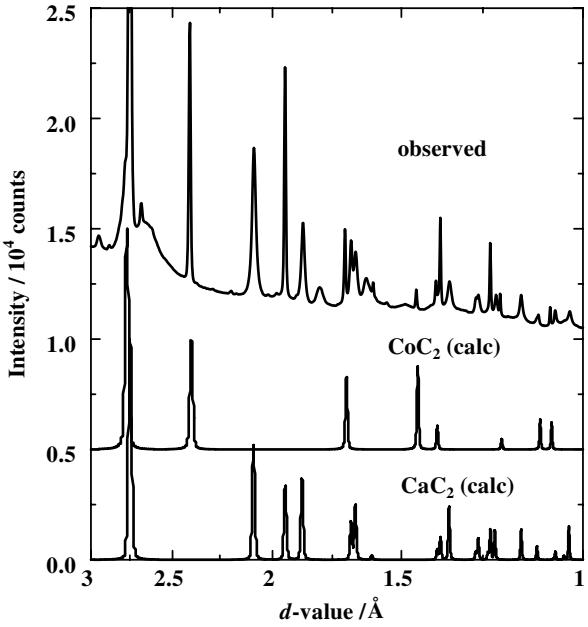


Fig. 1. The observed XRD patterns of anhydrous CoC_2 measured with synchrotron radiation (λ = 0.9988 Å) and the calculated patterns of anhydrous CoC_2 and CaC_2 (raw material). The observed pattern and calculated pattern of anhydrous CoC_2 are vertically shifted by 0.75 and 0.5×10^4, respectively, for clarify. In the calculation of the pattern of anhydrous CoC_2, the body-centered lattice of Co^{2+} sublattice was assumed and the lattice parameters are decided as the calculated pattern reproduces the observed one.

CoC_2 is shown in Fig. 2(b), where only a part of the unit cell is shown to compare with the structure of the hydrous CoC_2 discussed later. Incidentally, the peaks of CoC_2 are fairly sharp, from which the crystallite size D of CoC_2 is estimated as $D > 45$ nm by using Scherrer formula [7].

The air-exposure changes the peak position and width drastically as shown in Fig. 2(a). The observed XRD pattern of hydrous CoC_2 shows good agreement with that expected from the EXAFS result suggesting the MgC_2-type structure.[2] Contrary to anhydrous CoC_2, C_2^{2-} dianions are ordered in hydrous CoC_2 and the Co^{2+} dications forms body-centered tetragonal lattice as shown in Fig. 2(c). In the structure, Co^{2+} dications and C_2^{2-} dianions form alternate chains elongated parallel to the c-axis, which shrinks through air-exposure, while the a- and b-axes related to the inter-chain directions are expanded by the absorbed water. Judging from the crystal structures, intra-chain Co^{2+}–C_2^{2-}–Co^{2+} exchange interaction becomes stronger in hydrous phase due to the shorter Co^{2+}–C_2^{2-} distance and orientation ordering of C_2^{2-}, while the inter-chain interaction becomes weaker due to the longer inter-chain distances. The structural change cut the CoC_2

[2] The structural analysis based on the EXAFS results will be submitted to another journal by K. Kosugi.

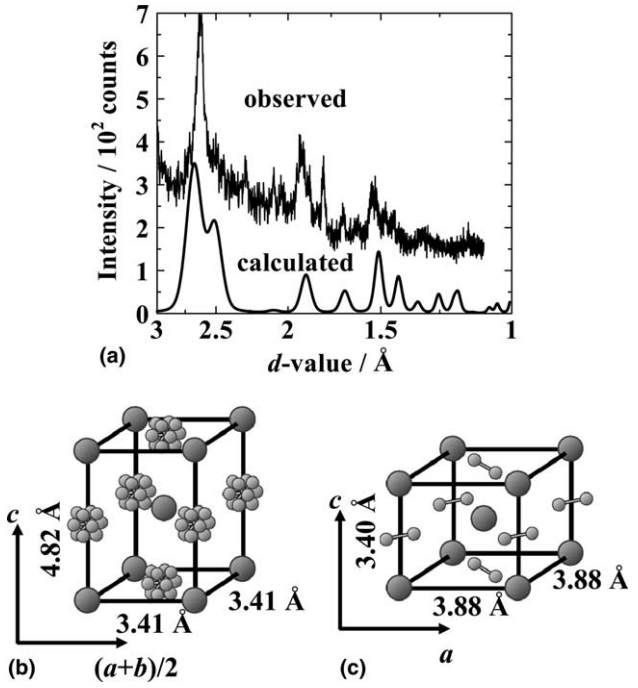


Fig. 2. (a) The observed and the calculated XRD pattern of hydrous CoC_2. The calculation is based on the structure shown in Fig. 2(c), which is consistent with the EXAFS result. (b, c) The expected crystal structures and lattice constants of anhydrous (b) and hydrous (c) CoC_2 based on the observed XRD pattern.

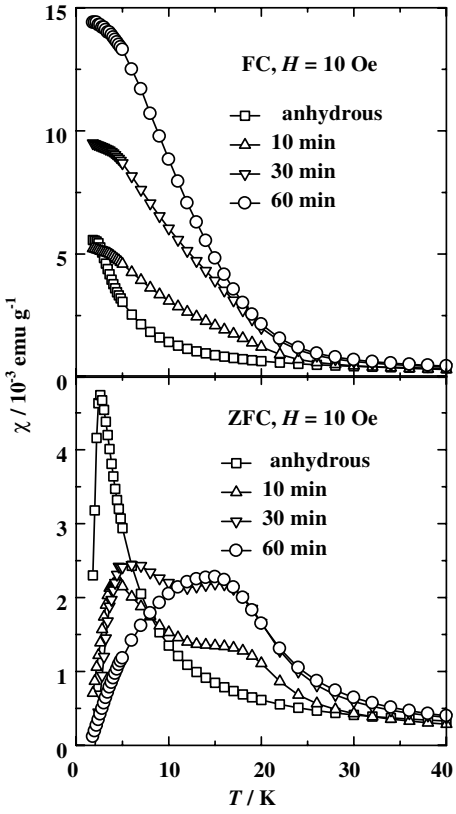


Fig. 3. Field-cooled in 10 Oe (top) and zero-field-cooled (bottom) magnetic susceptibilities of anhydrous, 10, 30 and 60 min air-exposed CoC_2 measured with the external field $H = 10$ Oe.

particle into many small structural domains having the crystallite size $D \sim 10$ nm, resulting in the broad peak widths of the hydrous CoC_2.

As mentioned in the discussion about the XRD results, it is expected that the magnetism of CoC_2 is also changed owing to the change of the inter- and intra-chain interaction by water absorption. The field-cooled (FC, $H = 10$ Oe) and zero-field-cooled (ZFC) magnetic susceptibility of anhydrous, 10, 30 and 60 min air-exposed CoC_2 are shown in Fig. 3. In the anhydrous phase, χ obeys the Curie–Weiss law in the high temperature range above ca. 70 K with Curie constant $C = 1.1$ emu K/mol and antiferromagnetic (AF) Weiss temperature $\Theta = -10$ K, the former of which is obviously larger than the value of Co^{2+} dication ($C = 0.375$), suggesting the short-range strong ferromagnetic (FM) interaction. The paramagnetic behavior despite the strong FM interaction indicates the smallness of the ferromagnetic domains. Below 2.5 K, the anhydrous CoC_2 shows ferromagnetism as discussed in later, but the FM part is only less than 8%. When CoC_2 is exposed to air, the Curie constant increases from 1.1 to 2.8 emu K/mol as the exposure time increases from 0 to 60 min suggesting the extension of the FM domains, while Θ changes from -10 to -3 K suggesting the weakening of the AF interaction between FM domains. The enhance of the ferromagnetism is also clearly seen in the FC and ZFC susceptibility. The FC susceptibility at low temperature increases monotonously as the air-exposure time increases. At the same time, the intension of the FM character raises the peak position of the ZFC susceptibility. Especially, the two peaks of 10 and 30 min air-exposed samples are originated from the coexistence of the low-T_C ferromagnet and high-T_C ferromagnet. Fig. 4 shows the magnetization curves of CoC_2. Anhydrous phase shows only a small hysteresis loop with coercive force $H_C = 120$ Oe and small remanent magnetization $M_{REM} = 0.75$ emu/g. According to the fact that the absorbed water causes the ferromagnetism, the small amount of FM part of anhydrous CoC_2 was probably brought about by the residual water in epoxy resin. In consequence of the expansion of the FM domains, H_C and M_{REM} increase monotonously from 120 to 900 Oe and 0.75 to 2.7 emu/g, respectively, as the air-exposure time increases.

In the following, the mechanism of the water-induced ferromagnetism is discussed. The possible configurations of C_2^{2-} dianions are classified into three types; that is, Co^{2+}–Co^{2+} direction and the molecular axis of C_2^{2-} are perpendicular, parallel or neither as shown in Fig. 5(a) (I), (II) and (III), respectively. In the paramagnetic anhydrous phase, the configuration of C_2^{2-} dianions is the mixture of the three possible configurations because

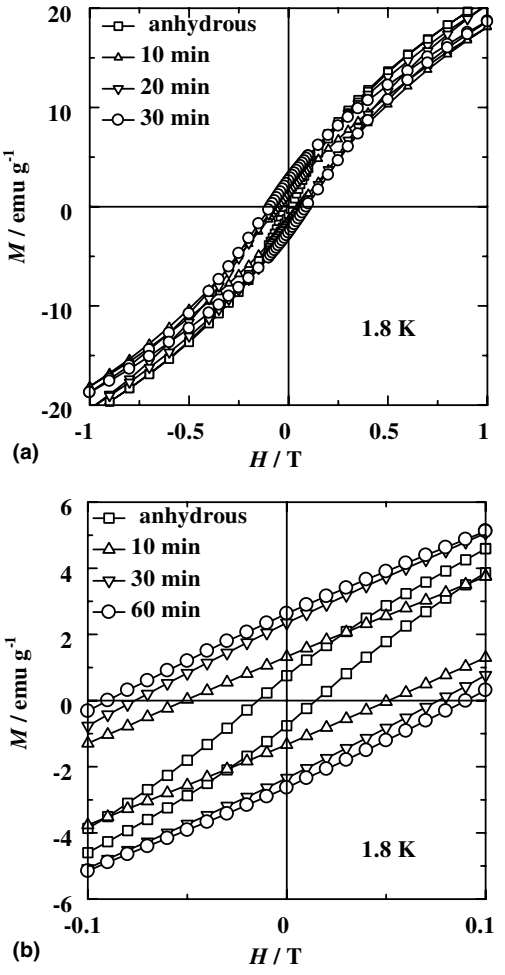


Fig. 4. (a) Magnetization curves of anhydrous, 10, 30 and 60 min air-exposed CoC_2 at 1.8 K. (b) The enlargement of the magnetization curves near the origin.

of the orientation disorder of C_2^{2-} dianions. On the other hand, only the perpendicular configuration is allowed in the hydrous phase where the ferromagnetism is observed. Judging from these facts, it is concluded that the perpendicular configuration brings about the FM interaction between Co^{2+} dications, while the other two configurations causes only the very weak FM or AF interaction. Here, we summarize the experimental findings on the this interaction model. In anhydrous CoC_2, strong FM and weak FM/AF interactions are mixed, resulting in the small FM domains as shown in Fig. 5(b). The small FM domains have the larger Curie constant than that of a single Co^{2+} dication, but the smallness of the FM domains keeps CoC_2 superparamagnet. After the air/water exposure, the orientation of C_2^{2-} dianions are aligned by absorbed water, where the many spins of Co^{2+} dications are connected ferromagnetically as shown in Fig. 5(b). The larger FM domain shows larger Curie constant, high-Curie temperature and large hysteresis loop as observed.

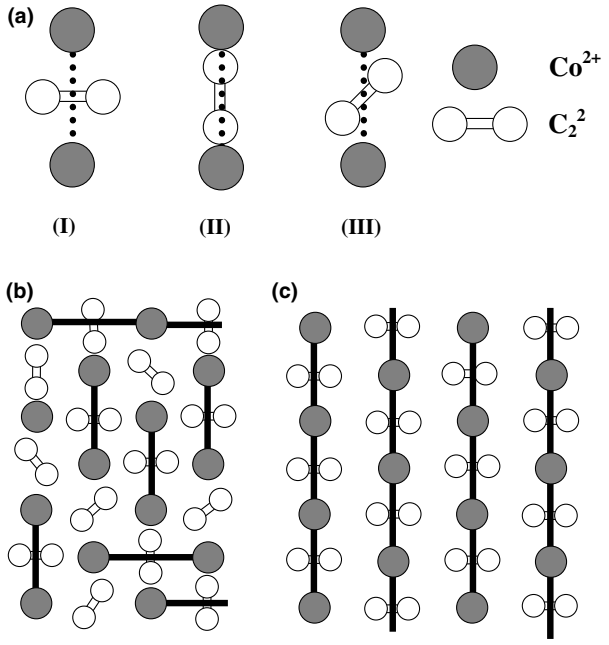


Fig. 5. (a) The three possible configurations of C_2^{2-} dianions; perpendicular (I), parallel (II) and intermediate (III). (b) The magnetic structural model of anhydrous CoC_2. The ferromagnetic domains are cut into the small parts by the disorder of C_2^{2-} dianions. The bold lines in (b) and (c) indicates the FM interaction caused by the perpendicular configuration of C_2^{2-} dianions. (c) The magnetic structural model of hydrous CoC_2. The order of C_2^{2-} dianions caused by the absorbed water brings about the long one dimensional ferromagnetic domains, resulting in the ferromagnetism.

4. Summary

As-prepared anhydrous CoC_2 nanoparticle having a large structural domain is characterized by the orientation disorder of C_2^{2-} dianions. The disorder brings about the mixture of the strong FM and weak FM/AFM interactions, resulting in the small FM domains and superparamagnetism. The nanoparticle promptly absorbs the water in air-atmosphere, bringing about the orientation ordering of C_2^{2-} dianions and the lattice expansion in *a*- and *b*-axes. Though the anisotropic structural expansion cut the nanoparticles into small structural domains, the structural change aligns the strong FM interactions one dimensionally, resulting in the larger FM domains which shows ferromagnetism. In conclusion, CoC_2 is the first molecule-based magnet showing the water-induced ferromagnetism owing to the flexibility of the orientation of C_2^{2-} dianions.

References

[1] J.M. Manriquez, G.T. Yee, R.S. McLean, A.J. Epstein, J.S. Miller, Science 252 (1991) 1415.
[2] S. Ferlay, T. Mallah, R. Ouahes, P. Veillet, Nature 378 (1995) 701.
[3] N. Nishi, K. Kosugi, K. Hino, T. Yokoyama, E. Okunishi, Chem. Phys. Lett. 369 (2003) 198.

[4] N. Nishi, K. Kosugi, K. Hino, T. Yokoyama, Eur. Phys. J. D 24 (2003) 97.
[5] M. Knapp, U. Ruschewitz, Chem. Eur. J. 7 (2001) 874.
[6] P. Karen, A. Kjekshus, Q. Huang, V.L. Karen, J. Alloy Compd. 282 (1999) 72.
[7] P. Scherrer, Gött. Nachr. 2 (1918) 98.

magnetic systems; that is, two-dimensional magnetic layers where the exchange interaction, J, in one dimension is different from the exchange in the second dimension, J'. Rectangular systems allow for the study of magnetic behavior between one- and two-dimensions. If we define J' as the smaller of the two exchange constants, then the ratio J'/J can vary from 0 (a linear chain, one-dimensional) to 1 (a square lattice, two-dimensional). The Cu(pyrazine)Cl_2 model system provides an exceptional opportunity since a family of compounds can be prepared using substituted pyrazines. By varying the structure of the pyrazine, one can change the value of J_{pz} (through the pyrazine moiety) while maintaining a relatively constant value of J_X (through the bihalide bridge). The bihalide bridge can also be varied by substituting bromide for chloride. This will give a series of compounds with different values of J'/J, potentially ranging from near zero to near one. Here we report the preparation and magnetic susceptibility behavior of (2,5-dmpz)copper(II) chloride (**1**), and (2,6-dmpz)$_2$copper(II) chloride (**2**) [2,5-dmpz = 2,5-dimethylpyrazine; 2,6-dmpz = 2,6-dimethylpyrazine].

2. Experimental

Reagents were purchased from Aldrich or Aesar Chemical and used without further purification. Infrared spectra were recorded on a Paragon 500 Spectrophotometer and referenced to polystyrene. The composition of **1** and **2** was confirmed by combustion analysis (Marine Science Institute, University of California, Santa Barbara, CA 93106).

2.1. (2,5-Dmpz)copper(II) chloride (*1*)

A solution of $CuCl_2$ (1.34 g, 10 mmol) in 50 ml of methanol was added to a solution of 2,5-dmpz (1.08 g, 10 mmol) in 50 ml of methanol. The solution was stirred at room temperature for an hour and the resulting slurry filtered to give a green powder, 0.76 g (31%). The filtrate was left to evaporate slowly at room temperature, yielding green needles suitable for X-ray diffraction. CHN for $C_{12}H_{16}N_4Cl_2Cu$ Calc.: C, 29.71; H, 3.32; N, 11.55. Found: C, 29.61; H, 3.45; N, 11.29%. IR (KCl) – ν 3129w, 3038m, 2946w, 1506s, 1375m, 1347m, 1161m, 1089m, 1134w, 990w, 882m cm^{-1}.

2.2. (2,6-Dmpz)$_2$ copper(II) chloride (*2*)

A solution of $CuCl_2$ (1.34 g, 10 mmol) in 50 ml of methanol was added to a solution of 2,6-dmpz (1.08 g, 10 mmol) in 50 ml of methanol. The solution was stirred at room temperature for an hour and the resulting slurry filtered to give a light blue powder, 0.63 g (40%). The filtrate was left to evaporate slowly at room temperature, but only additional powder was obtained. CHN for $C_{12}H_{16}N_4Cl_2Cu$ Calc.: C, 41.09; H, 4.60; N, 15.97. Found: C, 40.78; H, 4.72; N, 15.46%. IR (KCl) – ν 3079w, 2965w, 2928w, 1534m, 1427m, 1378m, 1256m, 1167s, 1023m, 947w, 866m, 731m, 497m cm^{-1}.

2.3. X-ray data collection and refinement for *1*

$C_6H_8Cl_2CuN_2$; Crystal system, monoclinic; space group, $P2_1/c$; $Z = 2$; unit cell dimensions: a = 6.7493(13) Å, b = 10.667(2) Å, c = 6.3102(13) Å; β = 106.81(3) μ = 3.058 mm^{-1}; θ range = 3.69–30.05°; Total reflections collected = 5458 [1239 independent; R_{int} = 0.0386]; completeness to θ = 30.05°, 97%. Crystals of compound **1** were removed from the flask and covered with a layer of hydrocarbon oil. A green needle-shaped crystal, 0.40 mm × 0.09 mm × 0.05 mm, was selected and attached to a glass fiber. Data for **1** were collected at 293(2) K using a Bruker/Siemens SMART APEX instrument (Mo Kα radiation, λ = 0.71073 Å) equipped with a Cryocool NeverIce low temperature device. Data were measured using omega scans of 0.3° per frame for 5 s, and a full sphere of data was collected. A total of 2132 frames were collected with a final resolution of 0.77 Å. The first 50 frames were recollected at the end of data collection to monitor for decay. Cell parameters were retrieved using SMART [10] software and refined using SAINTPLUS [11] on all observed reflections. Data reduction and correction for Lp and decay were performed using the SAINTPLUS software. Absorption corrections were applied using SADABS [12]. The structure was solved by direct methods and refined by least squares method on F^2 using the SHELXTL program package [13]. The structure was solved in the space group $P2(1)/c$ (# 14) by analysis of systematic absences. Non-hydrogen atoms were refined anisotropically. No decomposition was observed during data collection. Hydrogen atoms were place in calculated positions and refined as a riding model with fixed isotropic U's. Full-matrix least-squares refinement on F^2 for 1239 data and 52 parameters gave final R indices of R_1 = 0.0375, wR_2 = 0.0984 [$I > 2\sigma(I)$ and R_1 = 0.0465, wR_2 = 0.1036 (all data). Largest final difference peak and hole were 0.53 and −0.54 e$^-$/Å^3. Complete crystallographic data are available (see Supplementary Material). Selected bond distances and angles are given in Table 1.

2.4. Magnetic studies

The magnetic susceptibility of polycrystalline samples of **1** and **2** were studied in a field of 1000 Oe using a Quantum Design MPMS-XL SQUID Magnetometer. Corrections were made for the temperature independent magnetism of the Cu(II) ion ($\chi_{TIP} = 60 \times 10^{-6}$ emu/mol) and for the diamagnetic contributions calculated from Pascal's constants.

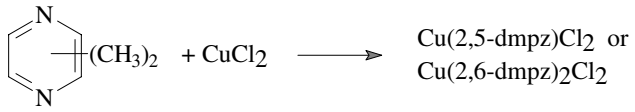
Table 1
Bond lengths [Å] and angles [°] for **1**

Cu–N	2.004(2)	N–Cu–ClA	89.68(7)
Cu–Cl	2.2334(8)	N–Cu–Cl	90.32(7)
N–C(2)	1.335(3)	C(1)–N–Cu	122.74(18)
N–C(1)	1.339(3)	C(2)–N–Cu	118.11(17)
C(3)–C(1)	1.498(4)	C(2)–N–C(1)	119.1(2)
C(1)–C(2)#1	1.390(3)	N–C(2)–C(1)#1	122.0(2)
		N–C(1)–C(2)#1	118.9(2)
		N–C(1)–C(3)	119.4(2)
		C(2)#1–C(1)–C(3)	121.7(2)

Symmetry transformations used to generate equivalent atoms: A, $-x$, $-y$, $-z$; #1, $-x+1$, $-y$, $-z$.

3. Results and discussion

Reaction of copper(II) chloride with the corresponding dimethylpyrazine in aqueous solution gave Cu(2,5-dmpz)Cl_2 (**1**), or Cu(2,6-dmpz)$_2Cl_2$ (**2**);



(2,5-dmpz) or
(2,6-dmpz)

Single crystals of **1**, suitable for X-ray diffraction, were grown by slow evaporation. Relevant bond lengths and angles are given in Table 1. The molecular unit and a portion of one chain are shown in Fig. 1.

The structure of **1** consists of alternating copper(II) ions and 2,5-dmpz ligands forming chains parallel to the *a*-axis. The Cu(II) ions sit on a crystallographic inversion center and are nearly square planar. The pyrazine rings are canted approximately 80° from the Cu coordination plane. The pyrazine rings themselves show typical bond lengths and angles.

The Cu–N bond [2.004(2) Å] is somewhat short when compared to other Cu(II) 2,5-dmpz complexes such as the acetonitrile adduct of the current complex, Cu(2,5-dmpz)$Cl_2 \cdot CH_3CN$ (2.07 Å) [14] and Cu_2(2,5-dmpz)$[N(CN)_2]_4$ (2.06 Å) [15] and is intermediate in length compared to Cu(I) 2,5-dmpz complexes such as Cu(2,5-dmpz)Cl (1.985 Å) [14], Cu(2,5-dmpz)$_2(PF_6)$ (2.13 Å]) [16] and Cu_2(2,5-dmpz)$_3(BF_4)_2$ (1.97 and 2.08 Å) [16]. The Cu–Cl bond [2.2334(8) Å] is significantly shorter than that in the Cu(I) analog (2.41 Å) [14] and slightly shorter than is observed in the acetonitrile adduct (2.26 Å) [14].

The chains pack in the crystal to form a diamond pattern (see Fig. 2) with short chlorine–chlorine contacts (3.93 Å). The corresponding Cu–Cl···Cl angles are 80.1° and 166.0° and the Cu–Cl···Cl–Cu torsion angle is 104.5°. The potential for through-space contacts between halide ions to provide a significant magnetic superexchange pathway has been well documented, with chloride ions providing weaker exchange than bromide ions [17]. Each Cl ion is in close contact with two additional Cl ions from neighboring chains via identical pathways, generating a two-dimensional superexchange network perpendicular to the pyrazine bridged chains.

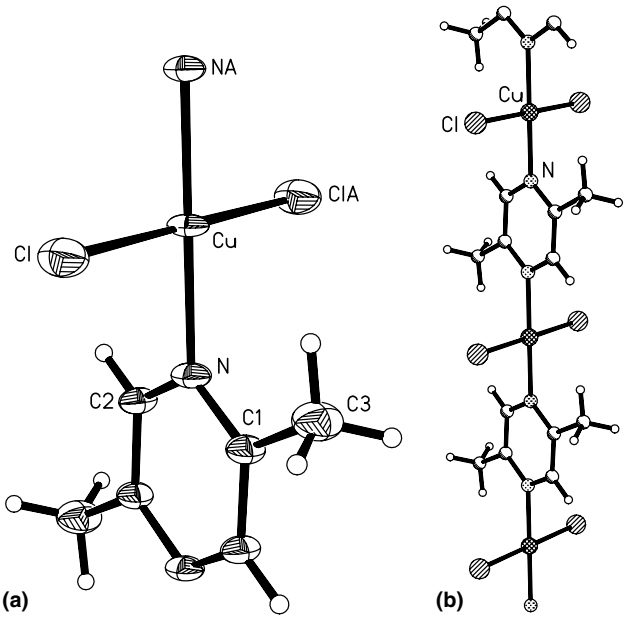


Fig. 1. (a) A plot of the molecular unit of **1** showing 50% probability ellipsoids. Only those atoms in the asymmetric unit and Cu coordination sphere are labeled. H-atoms were placed geometrically and are shown as spheres of arbitrary size. (b) A portion of the chain structure of **1**.

3.1. Magnetic susceptibility results

We use the 2*J* form of the Heisenberg Hamiltonian

$$H = -2J \sum S_i \cdot S_{I+1},$$

where a negative value of *J* corresponds to antiferromagnetic interactions. Susceptibility data were collected for **1** (Fig. 3) and **2** (Fig. 4) from 1.8 to 325 K on powder samples.

The magnetic susceptibility of **1** increases with decreasing temperature reaching a maximum near 10 K and then begins to decrease slowly until near 5 K where there is an abrupt change in slope, signifying a possible phase transition. At high temperatures the χT product approaches 0.41, typical of Cu(II) complexes. Similarly, susceptibility data for **2** show an increase in value at lower temperatures, reaching a local maximum near 13 K and then continuing to rise, suggesting the presence of a paramagnetic impurity in the sample. The χT product nears 0.42 at high temperatures, again in good agreement with expected values.

The discontinuity near 5 K in the susceptibility data for **1** (Fig. 3(a)) suggests the presence of a phase

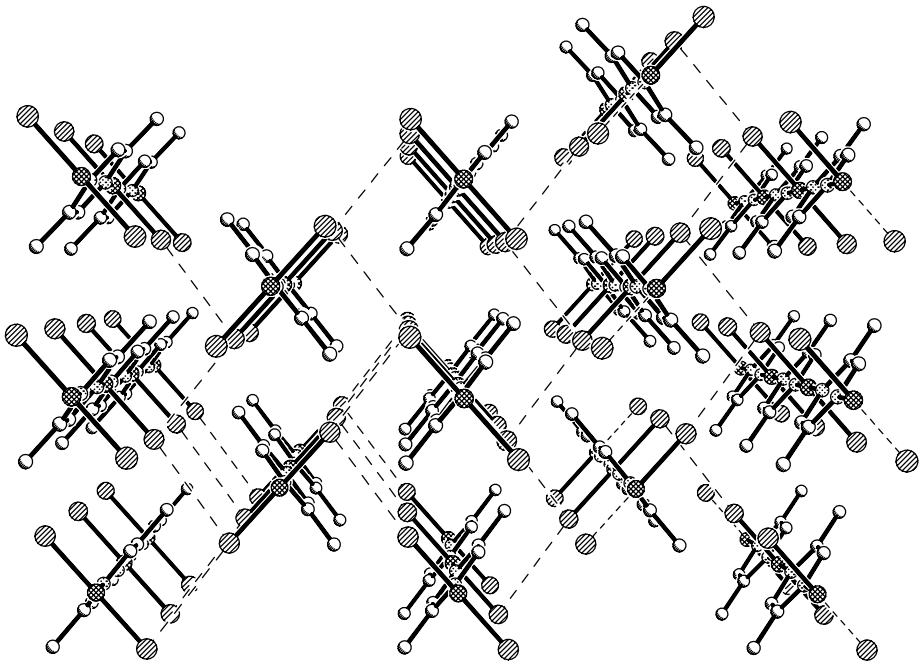


Fig. 2. Packing diagram of **1** viewed parallel to the *a*-axis showing the short intermolecular Cl···Cl contacts (dotted lines).

transition in the sample. Examination of the crystal structure shows two possible superexchange pathways, one via the bridging 2,5-dmpz ligands, linking the Cu(II) ion into chains (Fig. 1(b)) and a second via close non-bonding contacts between the halide ions (double halide exchange), linking the chains into a three-dimensional network (Fig. 2). Pyrazine and substituted pyrazines are well known to provide a superexchange pathway in the range $-5 < 2J < -25$ [1,5–7] while the double halide exchange for chlorides is generally small, but can be as high as 27 K [17a,17e,18]. No theoretical model exists at present for an antiferromagnetic three-dimensional system with two exchange values (J for a chain and J' for the interaction between the chains), so the susceptibility data were fit to the expression for the molar susceptibility χ_{mol} of the $S = 1/2$ Heisenberg antiferromagnetic linear chain [19], both with and without a mean-field correction [20] and over several different temperature ranges above 5 K (see Table 2). The best fit to the data is shown in Fig. 5(a).

It is clear that the available models to analyze the data for **1** are inadequate from the variability of both

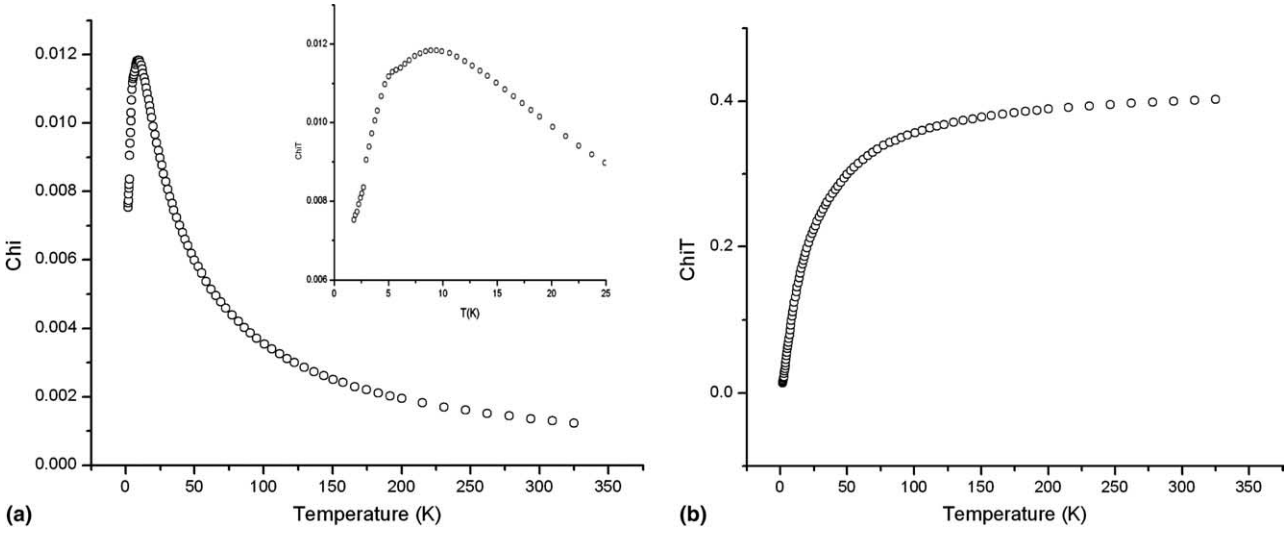


Fig. 3. (a) Magnetic susceptibility as a function of temperature for **1**. The inset is an expansion of the region from 0 to 25 K showing the apparent phase transition near 5 K. (b) The product χT as a function of temperature for **1**.

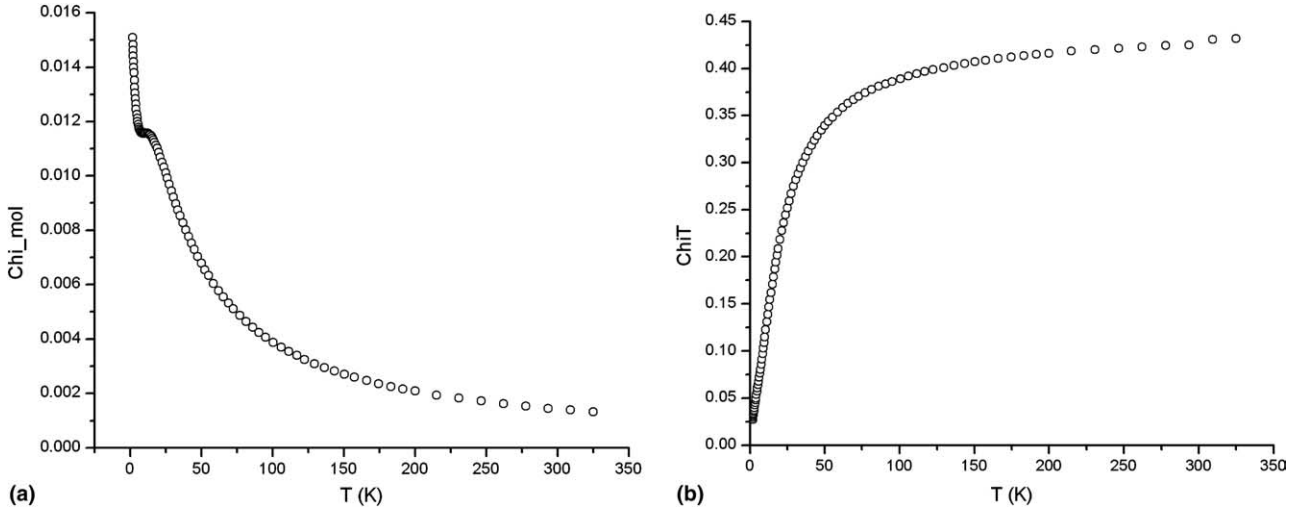


Fig. 4. (a) Magnetic susceptibility as a function of temperature for **2**. (b) The product χT as a function of temperature for **2**.

Table 2
Fitting parameters for the molar susceptibility as a function of temperature for **1** over various temperature ranges

Model[a]	Temp. range (K)	C	$2J$ (K)	$2J'$ (K)
1D	50–325	0.418	−29.4(1)	
1D	30–325	0.408	−26.5(3)	
1D	18–325	0.390	−22.9(3)	
3D	50–325	0.452	−23.7(5)	−2.15(17)
3D	30–325	0.432	−15.7(6)	−4.8(2)
3D	18–325	0.437	−10.2(5)	−6.5(2)
3D	10–325	0.425	−23.7(5)	−2.15(2)
3D	5–325	0.423	−13.5(1)	−4.8(1)

[a] 1D = uniform chain, 3D = uniform chain with mean field correction for four nearest neighbors.

the Curie constant (C) and the values for the exchange constant within (J) and between (J') the pyrazine-bridged chains as the temperature range of the fit is varied. The structure indicates that there should be significant interactions between the chains, so the linear chain model is inappropriate, but at the same time, the mean-field correction is only valid when the interaction between the changes is only a small fraction of the interaction within the chains. Our estimates for the values of the two exchange interactions are $2J = -20(5)$ K and $2J' = -4(2)$ K. More precise values will require the development of an appropriate analytical model.

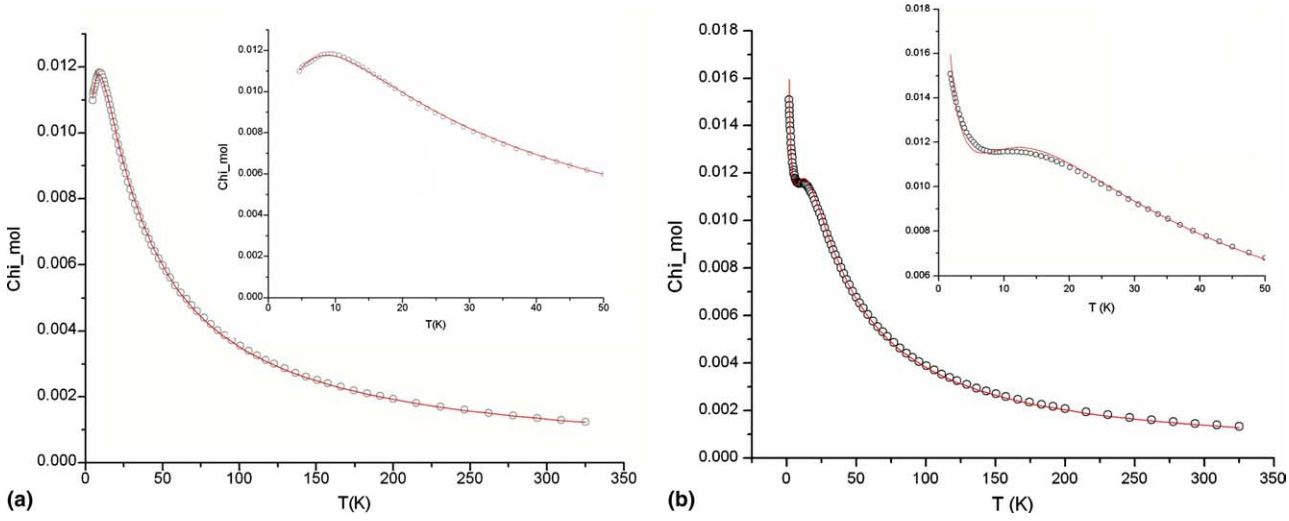


Fig. 5. (a) Theoretical fit (solid line) to the magnetic susceptibility (○) as a function of temperature for **1**. The inset is an expansion of the region from 0 to 50 K. See text for detail of the fitting procedure. (b) Theoretical fit of a uniform chain model (solid line) to the magnetic susceptibility (○) as a function of temperature for **2**. The inset is an expansion of the region from 0 to 50 K.

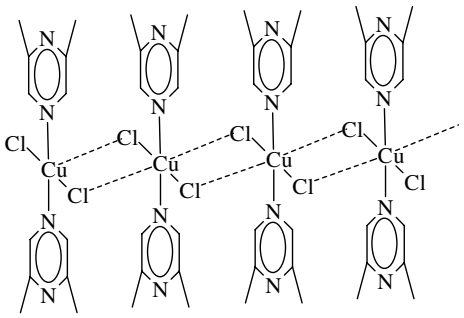


Fig. 6. Proposed structure of compound **2**.

The magnetic behavior of the 2,6-dmpz complex **2** is straightforward (Fig. 4). Although we attempted the preparation of the corresponding mono(2,6-dmpz) complex, bridged by the pyrazine ligand, combustion analysis and magnetic data indicated that the correct formula of the complex is $Cu(2,6\text{-dmpz})_2Cl_2$. The structure of the molecule is, therefore, most likely that of a bihalide bridged chain (see Fig. 6) as has been observed previously for $Cu(py)_2Cl_2$ and related substituted pyridine complexes [9]. It is most likely that the 2,6-dmpz molecules are coordinated through the nitrogen remote from the methyl groups to reduce steric hindrance about the metal center. Although there are complexes where the 2,6-dmpz ligand is known to bridge [21], all reported structures to date show bonding to the distal nitrogen [22]. The magnetic data were therefore fit to a uniform Heisenberg chain model (Fig. 5(b)) [19]. The data converged at values of $C = 0.415(3)$ and $2J = 22.7(2)$ K, allowing for a 3.33(5)% paramagnetic impurity.

4. Conclusions

The ability of pyrazines to provide an effective superexchange pathway has been further demonstrated in compound **1**. In addition, the structure provides an excellent opportunity for further study of the crossover from one-dimensional to three-dimensional behavior. The magnetic data show that the superexchange through double chloride bridge is substantial compared to the exchange through the pyrazine and the symmetry of the packing requires that the exchange is identical for each chain to four nearest neighbors. Future work in this area will require development of an appropriate theoretical model, but we hope that the existence of a model compound to test such a theory will make the problem attractive. Finally, the differing steric requirements of the different substitution patterns on the pyrazine ring are shown in compound **2**, where the desired 2,6-dmpz-bridged complex did not form, in favor of the less sterically demanding chloride-bridged chain. The fact that the corresponding $CuBr_2$ complex, $Cu(2,6\text{-dmpz})Br_2$ exists as pyrazine-bridged chains [23] demonstrate that small changes in the coordination environment can make substantial changes in the structure of the complex.

5. Supplementary material

Crystallographic data have been deposited with the CCDC (12 Union Rd., Cambridge, CB21EZ, UK, fax: +44-1233-336033; e-mail: deposit@ccdc.cam.ac.uk or www: http://www.ccdc.cam.ac.uk) and are available on request quoting the deposition number 250636.

Acknowledgements

The MPMS-XL SQUID magnetometer was purchased with the assistance of funds from the National Science Foundation – IMR-0314773. The Bruker (Siemens) SMART APEX diffraction facility was established at the University of Idaho with the assistance of the NSF-EPSCoR program and the M.J. Murdock Charitable Trust, Vancouver, WA, USA. Technical assistance from Miss Qing Xu is gratefully acknowledged.

References

[1] D.N. Hendrickson, in: R.D. Willett, D. Gatteschi, O. Kahn (Eds.), Magneto-Structural Correlations in Exchange Coupled Systems, Reidel Publishers, Dordrecht, 1985, p. 555.
[2] A. Santoro, A.D. Mighell, C.W. Reimann, Acta Crystallogr., Sect. B 26 (1970) 979.
[3] (a) J.F. Villa, W.E. Hatfield, J. Am. Chem. Soc. 93 (1971) 4081; (b) D.B. Losee, H.W. Richardson, W.E. Hatfield, J. Chem. Phys. 59 (1973) 3600.
[4] G. Mennenga, L.J. De Jongh, W.J. Huiskamp, J. Reedjik, J. Magn. Magn. Mater. 44 (1984) 89.
[5] W.W. Richardson, W.E. Hatfield, J. Am. Chem. Soc. 98 (1976) 835.
[6] S. Amaral, W.E. Jensen, C.P. Landee, M.M. Turnbull, F.M. Woodward, Polyhedron 20 (2001) 1317.
[7] C.P. Landee, M.M. Turnbull, Mol. Cryst. Liq. Cryst. 335 (1999) 193.
[8] Th. Fetzer, A. Lentz, T. Debaerdemaeker, Z. Naturforsch. B 44 (1989) 553.
[9] (a) V. Kupcik, S. Durovic, Czech. J. Phys. 10 (1960) 182; (b) M. Laing, G. Carr, J. Chem. Soc. A (1971) 1141; (c) W.E. Marsh, E.J. Valente, D.J. Hodgson, Inorg. Chim. Acta 51 (1981) 49; (d) W. Zhang, J.R. Jeitler, M.M. Turnbull, C.P. Landee, M.-y. Wei, R.D. Willett, Inorg. Chim. Acta 256 (1997) 183; (e) B. Morosin, Acta Crystallogr., Sect. B 31 (1975) 632.
[10] SMART: v.5.626, Bruker Molecular Analysis Research Tool, Bruker AXS, Madison, WI, 2002.
[11] SAINTPLUS: v. 6.22, Data Reduction and Correction Program, Bruker AXS, Madison, WI, 2001.
[12] G.M. Sheldrick, SADABS: V.2.01, An Empirical Absorption Correction Program, Bruker AXS Inc., Madison, WI, 2001.
[13] G.M. Sheldrick, SHELXTL: V. 6.10, Structure Determination Software Suite, Bruker AXS Inc., Madison, WI, 2001.
[14] C. Nather, J. Greve, I. Jess, Solid State Sci. 4 (2002) 813.

[15] W.-F. Yeung, S. Gao, W.-T. Wong, T.-C. Lau, New J. Chem. 26 (2002) 523.
[16] T. Otieno, S.J. Rettig, R.C. Thompson, J. Trotter, Inorg. Chem. 32 (1993) 1607.
[17] (a) K. Halvorson, R.D. Willett, Acta Crystallogr., Sect. C 44 (1988) 2071;
(b) B.R. Patyel, B.L. Scott, R.D. Willett, Phys. Rev. B 41 (1990) 1657;
(c) F.M. Woodward, C.P. Landee, J. Giantsidis, M.M. Turnbull, C. Richardson, Inorg. Chim. Acta 324 (2001) 324;
(d) B.C. Watson, V.N. Kotov, M.W. Meisel, D.W. Hall, G.E. Granroth, W.T. Montfrooij, S.E. Nagler, D.A. Jensen, R. Backov, M.A. Petruska, G.E. Fanucci, D.R. Talham, Phys. Rev. Lett. 86 (2001) 5168;
(e) F.M. Woodward, A.S. Albrecht, C.M. Wynn, C.P. Landee, M.M. Turnbull, Phys. Rev. B 65 (2002) 144412.
[18] G.S. Long, M. Wei, R.D. Willett, Inorg. Chem. 36 (1997) 3102.
[19] J.C. Bonner, M.E. Fisher, Phys. Rev. 135 (1964) A640.
[20] J.N. McElearney, D.B. Losee, S. Merchant, R.L. Carlin, Phys. Rev. B 7 (1973) 3314.
[21] (a) L. Brammer, M.D. Burgard, M.D. Eddleston, C.S. Rodger, N.P. Rath, H. Adams, Cryst. Eng. Commun. 4 (2002) 239;
(b) D.J. Chesnut, D. Plewak, J. Zubieta, J. Chem. Soc., Dalton Trans. (2001) 2567;
(c) S. Kitagawa, S. Kawata, M. Kondo, Y. Nozaka, M. Munadata, Bull. Chem. Soc. Jpn. 66 (1993) 3387.
[22] (a) C. Lopez, S. Alvarez, X. Solans, M. Font-Altaba, Inorg. Chem. 25 (1986) 2962;
(b) C. Lopez, S. Alvarez, X. Solans, M. Font-Altaba, Inorg. Chim. Acta 121 (1986) 71;
(c) S. Amaral, M.M. Turnbull, J. Chem. Cryst. 32 (2002) 11.
[23] F.F. Awwadi, C.P. Landee, M.M. Turnbull, B. Twamley, B.M. Wells, unpublished results.

Found: C, 36.1; N, 10.3; H, 1.77%. *Anal.* Calc. for $C_{41}H_{23.5}N_{10.5}F_2S_8Pt_2$ (**2**): C, 36.5; N, 10.9; H, 1.76. Found: C, 36.2; N, 10.7; H, 1.79%.

2.2. X-ray crystallography

The diffraction data were collected at 298 K on a Rigaku R-AXIS RAPID IP area detector for **2**. Structures were solved by direct methods and refined by the full-matrix least-square method on F^2 using SHELXL-97 program [7]. All non-hydrogen atoms were treated anisotropically and the hydrogen atoms were introduced at calculated positions. Crystal data for **2**: $C_{41}H_{23.5}N_{10.5}F_2S_8Pt_2$, $T = 298(2)$ K, space group $P\bar{1}$, $a = 11.1571(4)$ Å, $b = 11.2031(5)$ Å, $c = 21.3037(10)$ Å, $\alpha = 98.115(3)°$, $\beta = 94.016(2)°$, $\gamma = 114.643(2)°$, $V = 2371.37(18)$ Å^3, $Z = 2$, $\rho_{calc} = 1.888$ g cm^{-3}; 33 467 measured ($3.00° \leqslant \theta \leqslant 27.48°$), 10 764 ($R_{int} = 0.1155$) unique, 7758 observed ($I > 2.00\sigma(I)$). Lorentz polarization absorption corrections ($\mu = 6.296$ mm^{-1}), 291 parameters. R_1(on F^2) = 0.1099, wR_2(on F^2) = 0.2708, residual electron density: 3.91 (closed to S(4)) and −3.01 (closed to Pt(1)) e Å^{-3}.

2.3. Magnetic susceptibility measurements

Magnetic susceptibility of polycrystalline sample was measured in 2–350 K using a Quantum Design MPMS XL superconducting quantum interference device (SQUID) magnetometer.

2.4. Molecular orbital calculations

The spin dimer analyses for the neighboring $[Pt(mnt)_2]^-$ anions were performed within the tight-binding approximation using extended Hückel molecular orbital calculations [8]. The SOMO of $[Pt(mnt)_2]^-$ anion was used as the basis functions, the extended Hückel parameters for Slater-type atomic orbitals were taken from [9].

3. Results and discussion

3.1. Structural descriptions

*Stacking structure of $[Pt(mnt)_2]^-$ anions in **1** [6].* The asymmetric unit contains three crystallographically independent $[Pt(mnt)_2]^-$ anions, the S–Pt–S chelate angles and Pt–S bond lengths in them are in agreement with those reported $[Pt(mnt)_2]^-$ compounds [10]. The molecular planes, defined by coordination S atoms, of containing Pt(1) and Pt(2) are nearly parallel to each other with a dihedron of 1.21°, while the molecular plane including Pt(3) is approximately perpendicular to that including Pt(1) and Pt(2) (the dihedral angle between the entries of Pt(3) and Pt(2) is 85.3°). Symmetry-generated anions containing Pt(1) and Pt(2) stack into columns along *b*-axis, and the inter-planar separations between adjacent anions within a column are alternately 3.540 Å between anions containing Pt(1) and Pt(2) and 3.634 Å between anions containing Pt(1) and Pt(1) $(1 - x, -y, 1 - z)$. Symmetry-generated anions containing Pt(3) dimerize, the separation between planes in a dimer is 3.488 Å. These dimers connect the anionic columns into 2D anionic networks, via S···S interactions, in *ab* plane (Fig. 1).

*Crystal structure of **2**.* Compound **2** crystallizes in $P\bar{1}$ space group with two couples of $[Pt(mnt)_2]^-$ and 1-(4′-fluorobenzyl)pyridinium, and one half solvent molecule, MeCN, in an asymmetric unit. The molecular structures both cations and anions in **2** are similar to, but the stack structures are different from **1**. Two crystallographically independent anions are almost parallel to each other, the dihedral angle between mean molecular planes, defined by coordination S atoms, is only 1.7°. The distortion from planarity of anion is observed in both Pt(1) and Pt(2) entries owing to CN groups being departure from the mean molecular plane, the terminal N atoms of CN are away the mean plane from 0.09 to 0.28 Å in Pt(1) entry, while 0.31–0.41 Å in Pt(2) entry. As shown in Fig. 2(a), the anions are stacked face-to-face along *ab* direction to form a fourfold anionic subunit. In each subunit, the stack is regular, two types of independent Pt···Pt distances are 3.552 Å between Pt(1) and Pt(2), 4.373 Å between Pt(2) and Pt(2) $(1 - x, 2 - y, 2 - z)$, respectively, and corresponding inter-planar separations alternate as 3.569 and 4.883 Å. The neighboring fourfold anionic subunits form a 2D anionic layer, which is approximately perpendicular to [1 1 1] axis, via weakly lateral S···S interactions (The S···S separations are in the range of 3.515–3.854 Å).

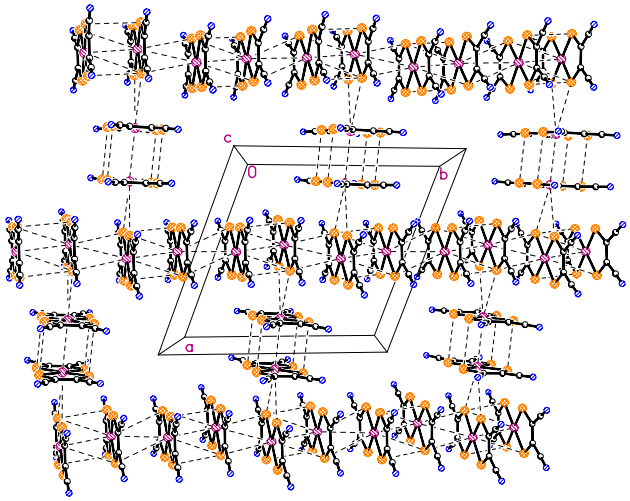


Fig. 1. 2D anionic networks in *ab* plane, projected along *c*-axis in **1**.

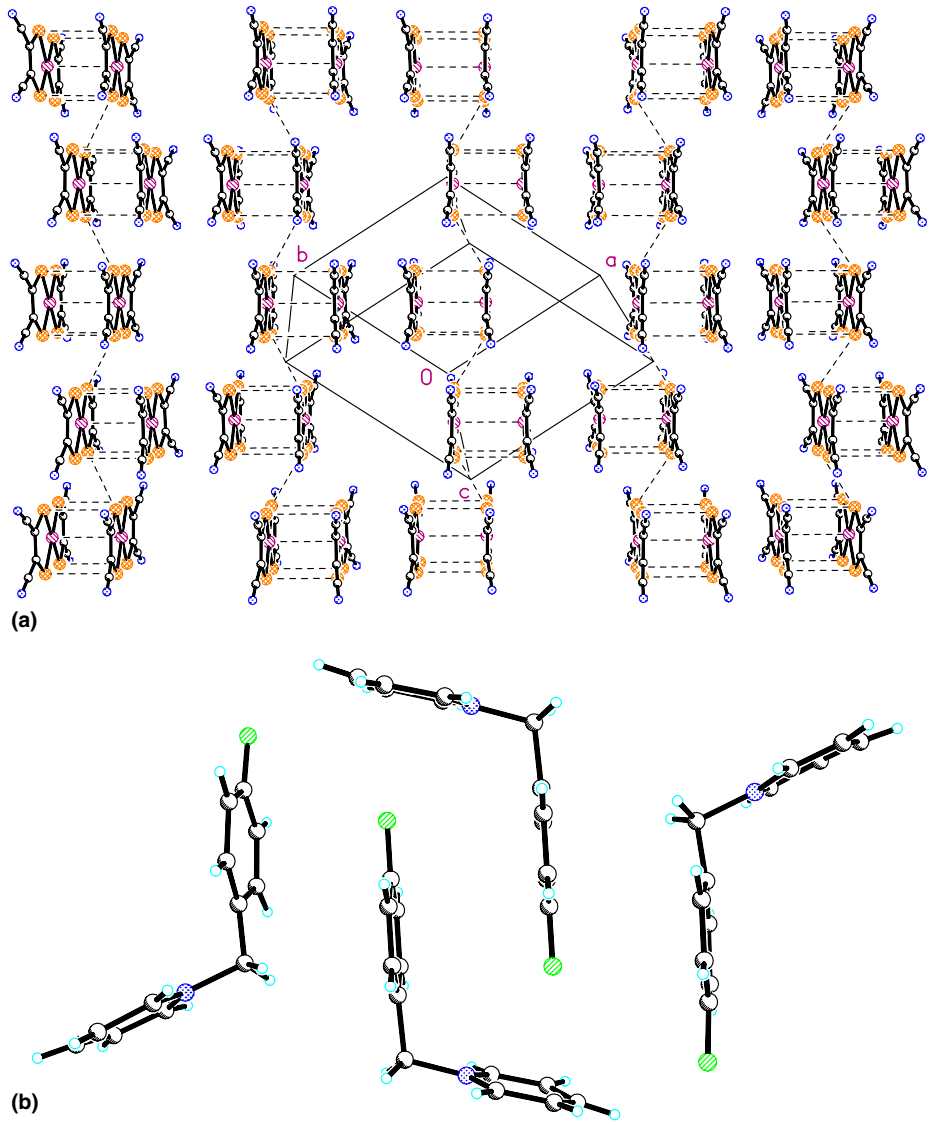


Fig. 2. (a) 2D anionic layer projected along the direction of [1 1 1] axis and (b) a cationic subunit in **2**.

Two crystallographic independent cations also stack into a fourfold subunit in a fashion of F(1)···F(2)···F(2)···F(1) (Fig. 2(b)). Two neighboring benzene rings, containing F(1) and F(2), are nearly parallel to each other with a small dihedral angle of 8.3°, the inter-planar space is 3.57 Å for the overlap pairs of F(1)···F(2) and 3.65 Å of F(2)···F(2). No any significant π···π stack interaction is observed in the cationic fourfold subunit. The anionic layers are completely separated by the intermediate cations.

3.2. Magnetic properties

The plots of $\chi_m(T)$–T both **1** and **2** are displayed in Fig. 3, and their magnetic behaviors exhibit the character with antiferromagnetically coupled interactions between nearest neighboring spins.

For an AFM coupling domination system, the magnetic exchange constant between two spins can be described as

$$J_{AF} \propto -(2t)^2/U_{eff}, \quad (1)$$

where U_{eff} is the effective on-site Coulomb repulsion and nearly constant for a defined magnetic solid, t is transfer integral between the spin sites and proportional to the overlap integral of the interaction magnetic orbitals [11]. For a sake of simplification, t is defined as $-10S$ eV (S is overlap integral). The anionic intermolecular interaction schemes are illustrated in Fig. 4, and the calculations for the transfer integral were performed within a tight-binding approximation using extended Hückel molecular orbital method, and the results indicate that relative stronger AFM interactions involve in two spin dimers, Pt(1) and Pt(2), Pt(3) and Pt(3)

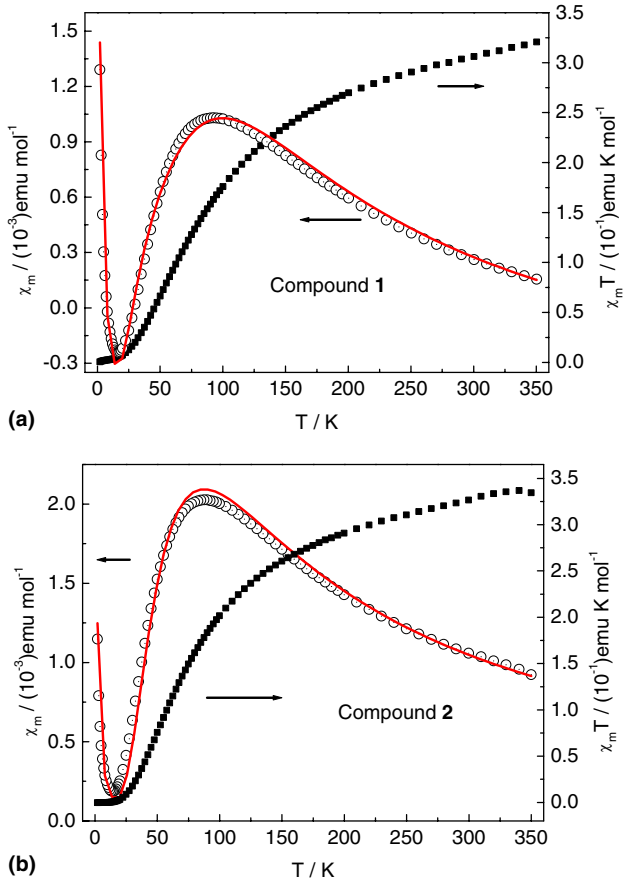


Fig. 3. Plots of χ_m vs. T in **1** (a) and **2** (b), open circles: experimental data and solid lines: theoretic calculations (plots of $\chi_m T$ reproduced after subtracting C and $\chi_0 T$).

$(2-x, 1-y, 1-z)$ in **1**. These qualitative analyses suggest two types of magnetic exchange schemes, an AFM alternating chain with $s = 1/2$ and a spin dimer of $s = 1/2$, can be considered in **1**, thus, we try to fit magnetic susceptibility to the formula:

$$\chi_m = (2/3)\chi_{chain} + (1/3)\chi_{dimer} + C/T + \chi_0 \quad (2)$$

and

$$\chi_{chain} = \frac{Ng^2\mu_B^2}{k_B T} \cdot \frac{A + BX^{-1} + CX^{-2}}{1 + DX^{-1} + EX^{-2} + FX^{-3}}, \quad (3)$$

$$\chi_{dimer} = \frac{Ng^2\mu_B^2}{k_B T} \cdot (3 + \exp(\Delta/k_B T)^{-1}), \quad (4)$$

where Eq. (3) is deduced from spin Hamiltonian $H = -2J\sum_{i=1}^{n/2}[\hat{S}_{2i} \cdot \hat{S}_{2i-1} + \alpha\hat{S}_{2i} \cdot \hat{S}_{2i+1}]$, $X = k_B T/|J|$, $J(<0)$ is coupled constant, α represents an alternating parameter, and A–F are a set of parameters depended on α [12]. Eq. (4) is based on spin Hamiltonian $H = -2J\hat{S}_1 \cdot \hat{S}_2$, in which $\Delta(=2|J|)$ is the energy gap between singlet and triplet state. C/T and χ_0 show the contributions of the magnetic impurity and the sum of diamagnetic and van Vleck paramagnetic parts, respectively. The best fit gives rise to $|J|/k_B = 107.6$ K, $\alpha = 0.012$; $\Delta/k_B = 93.9$ K, $C = 0.0036$ emu K mol^{-1} and $\chi_0 = -7.7 \times 10^{-4}$ emu mol^{-1} with g of 2.0 fixed.

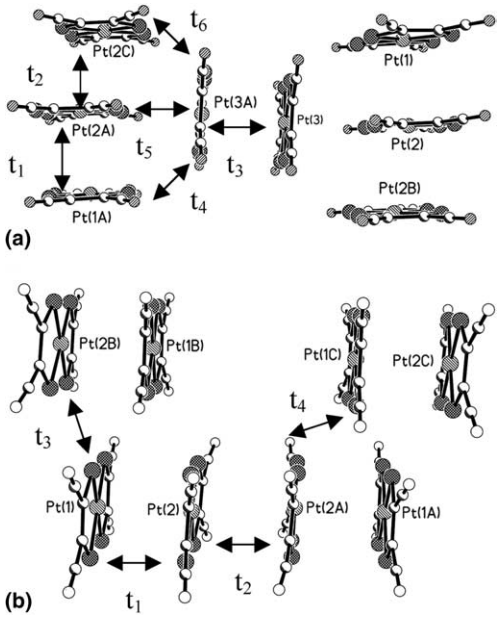


Fig. 4. Intermolecular interaction schemes and transfer integrals in **1** (a, $t_1 = 2.04 \times 10^{-1}$, $t_2 = 3.17 \times 10^{-2}$, $t_3 = 3.71 \times 10^{-1}$, $t_4 = -2.39 \times 10^{-3}$, $t_5 = -5.38 \times 10^{-3}$ and $t_6 = 1.51 \times 10^{-2}$ eV) and **2** (b, $t_1 = -3.14 \times 10^{-1}$, $t_2 = -3.56 \times 10^{-2}$, $t_3 = -9.99 \times 10^{-3}$ and $t_4 = -1.05 \times 10^{-2}$ eV).

Based on the analyses both crystal structural and t values of **2**, approximately, an anionic fourfold subunit is treated as two isolated dimers, and the coupled interactions between dimers are further dealt with molecular field theory [13], thereby χ_m is expressed below

$$\chi_m = \frac{\chi_{dimer}}{[1 - (zJ'/Ng^2\mu_B^2)\chi_{dimer}]} + \frac{C}{T} + \chi_0, \quad (5)$$

the data of χ_m in 2–350 K were simulated by using Eq. (5) to yield the parameters $\Delta/k_B = 141.7$ K, $zJ'/k_B = -2.6$ K, $C = 2.7 \times 10^{-3}$ emu K mol^{-1} and $\chi_0 = -4.0 \times 10^{-5}$ emu mol^{-1} with g factor of 2.0 fixed. The temperature dependence of $\chi_m T$ for **1** and **2** are reproduced by subtracting the sums of C and $\chi_0 T$ and illustrated in Fig. 3.

4. Conclusions

In conclusion, we have presented the structural and magnetic characterizations for two compounds based on [1-(4′-fluorobenzyl)pyridinium][Pt(mnt)$_2$]. Polymorphism is caused from the solvent molecule, MeCN, incorporating into lattice. The anionic stacking patterns in both compounds are distinct difference. The regular stacking columns formed by anions are connected by the anionic dimers to further construct into 2D anionic networks in **1**, while the fourfold anionic subunit develop into anionic layers via lateral S···S interactions in **2**. Two

compounds exhibit magnetic behaviors, with AFM coupled interaction domination, and their magnetic exchange schemes were built on the analyses both crystal structural analyses and extended Hückel molecular orbital calculations. The magnetic property was well explained by an alternating AFM Heisenberg chain with an isolated AFM coupling dimer for **1**, and a spin dimer system with $s = 1/2$ for **2**. The magnetic coupled parameters gained from best fit for both compounds are, on the whole, in agreement with the results of theoretic analyses based on Hückel molecular orbital calculations.

Acknowledgments

The authors thank Professor Ichimura for use of the SQUID magnetometer. Dr. X.M. Ren, a JSPS postdoctoral follow (ID No. P03271), thank Japan Society for the Promotion of Science for financial support.

Appendix A. Supplementary data

Crystallographic data for **2** (excluding structure factors) for the structures reported in this paper have been deposited with the Cambridge Crystallographic Data Center as supplementary publications (CCDC-249471). Copies of the data can be obtained free of charge on application to CCDC, 12 Union Road, Cambridge CB21EZ, UK (fax: +44 1223 336 033; e-mail: deposit@ccdc.cam.ac.uk). Supplementary data associated with this article can be found, in the online version, at doi:10.1016/j.poly.2005.03.034.

References

[1] (a) T. Lorenz, M. Hofmann, M. Grüninger, A. Freimuth, G.S. Uhrig, M. Dumm, M. Dressel, Nature 418 (2002) 614;
(b) M.E. Itkis, X. Chi, A.W. Cordes, R.C. Haddon, Science 296 (2002) 1443;
(c) E. Laukhina, J. Vidal-Gancedo, V. Laukhin, J. Veciana, L. Chuev, V. Tkacheva, K. Wurst, C. Rovira, J. Am. Chem. Soc. 125 (2003) 3948;
(d) J.S. Miller, Angew. Chem. Int. Ed. 42 (2003) 27;
(e) W. Fujita, K. Awaga, Science 286 (1999) 261;
(f) S. Tarutani, J.-I. Yamaura, K. Takahashi, R. Kato, Solid State Commun. 123 (2002) 251;
(g) T. Nakamura, J. Phys. Soc. Jpn. 72 (2003) 213;
(h) A.T. Coomber, D. Beljonne, R.H. Friend, J.L. Brédas, A. Charlton, N. Robertson, A.E. Underhill, M. Kurmoo, P. Day, Nature 380 (1996) 144;
(i) I.D. Parker, R.H. Friend, P.I. Clemenson, A.E. Underhill, Nature 324 (1986) 547.
[2] X.M. Ren, H. Okudera, R.K. Kremer, Y. Song, C. He, Q.J. Meng, P.H. Wu, Inorg. Chem. 43 (2004) 2569.
[3] X.M. Ren, Q.J. Meng, Y. Song, C.S. Lu, C.J. Hu, X.Y. Chen, Z.L. Xue, Inorg. Chem. 41 (2002) 5931.
[4] J.L. Xie, X.M. Ren, Y. Song, W.W. Zhang, W.L. Liu, C. He, Q.J. Meng, Chem. Commun. (2002) 2346.
[5] J.L. Xie, X.M. Ren, C. He, Z.M. Gao, Y. Song, Q.J. Meng, R.K. Kremer, Chem. Phys. Lett. 369 (2003) 41.
[6] X.M. Ren, J.L. Xie, Q.J. Meng, Acta Crystallogr. E59 (2003) m855.
[7] G.M. Sheldrick, SHELXL-97, Program for the Refinement of Crystal Structure, University of Göttingen, Germany, 1997.
[8] (a) R. Hoffmann, J. Chem. Phys. 39 (1963) 1397;
(b) T. Mori, A. Kobayashi, Y. Sasaki, H. Kobayashi, G. Saito, H. Inokuchi, Bull. Chem. Soc. Jpn. 57 (1984) 627, The program for the transfer integrals calculations is freely available from: http://www.op.titech.ac.jp/lab/mori/data.html .
[9] (a) K.A. Joergensen, R. Hoffmann, J. Am. Chem. Soc. 108 (1986) 1867;
(b) R.H. Summerville, R. Hoffmann, J. Am. Chem. Soc. 98 (1976) 7240;
(c) R. Hoffmann, J.M. Howell, A.R. Rossi, J. Am. Chem. Soc. 98 (1976) 2484;
(d) M.M.L. Chen, R. Hoffmann, J. Am. Chem. Soc. 98 (1976) 1467.
[10] A.E. Pullen, C. Faulmann, K.I. Pokhodnya, P. Cassoux, M. Tokumoto, Inorg. Chem. 37 (1998) 6714.
[11] M.-H. Whangbo, H.-J. Koo, D. Dai, J. Solid, State Chem. 176 (2003) 417 (references therein).
[12] J.W. Hall, W.E. Marsh, R.R. Weller, W.E. Hatfield, Inorg. Chem. 20 (1981) 1033.
[13] C.J. O'Connor, Prog. Inorg. Chem. 29 (1982) 203.

effects, that is with pairs of *cis*-$[Fe(NCX)_2(N)_4]$ chromophores, joined by ligand-to-solvate H-bonding, within unique pseudo-dimeric crystalline species **1** to **3**. Ligand–solvate H-bonding has previously been reported in mononuclear Fe(II) system [1,8–10], thus yielding information on cooperativity between mononuclear SCO centres, but has not, to our knowledge, been observed within a dimeric system. Preliminary aspects of parts of this work have recently been communicated [11]. Variation of the reaction conditions used to make **1**–**3** has led to formation of a family of covalently bridged dinuclear species $[Fe_2(\mu\text{-pypz})_2(pypzH)_2(NCX)_2]2H_2O$, X = S, Se, BH_3, displaying unique one-step high-spin (HS–HS) to low-spin (LS–LS) transitions. These are described separately [12].

2. Experimental

Elemental analyses (C, H, N) were carried out by Campbell Microanalytical Laboratory, University of Otago, Dunedin, New Zealand. IR spectra were recorded on a Perkin–Elmer 1600 Series Fourier Transform Spectrophotometer. Samples were prepared as KBr discs. Commercially available solvents and chemicals were used without further purification. The ligand 2-(1H-pyrazol-3-yl)-pyridine (pypzH) was prepared according to a known procedure [13].

2.1. Synthesis

2.1.1. $\{[Fe(pypzH)_2(NCS)_2]_2(\mu\text{-}OH_2)(H_2O)_2\}\cdot H_2O\cdot MeOH$ (**1**)

To a methanolic solution (15 mL) of $[Fe(H_2O)_6](ClO_4)_2$ (153 mg, 0.42 mmol) (and a pinch of ascorbic acid) was added a solution of KNCS (82 mg, 0.84 mmol) in the same solvent (15 mL), under nitrogen. The mixture was stirred for 15 min then filtered (to remove $KClO_4$) via a cannula into a Schlenk flask containing a solution of pypzH (120 mg, 0.84 mmol) in methanol. Water (5 mL) was added and the solution stirred for 1 h at room temperature, then left to slowly evaporate under nitrogen. The first batch of yellow block-like crystals grew within two days and were filtered off and dried in air. X-ray structural analyses was performed on a single block-like crystal. Infrared spectrum (KBr disk, cm^{-1}): 3417br, 3232sh, 2084s, 1606m, 1567w, 1510w, 1459w, 1432m, 1364w, 1291w, 1250w, 1199w, 1156w, 1091w, 1061w, 1011w, 968w, 927w, 772s, 707w, 636w, 470w, 412w.

2.1.2. $\{[Fe(pypzH)_2(NCSe)_2]_2(\mu\text{-}OH_2)(H_2O)_2\}\cdot H_2O\cdot MeOH$ (**2a**, **2b**)

The complex was made using the same method but substituting the KNCS with KNCSe (122 mg, 0.84 mmol). Ambient temperature (**2b**; 298 K) and nitrogen stream (**2a**; 123 K) X-ray structural analysis was performed on a single-block like crystal. Infrared spectrum (KBr disk, cm^{-1}): 3417br, 3232sh, 2056s, 1606m, 1567w, 1510w, 1459w, 1432m, 1364w, 1291w, 1250w, 1199w, 1156w, 1091w, 1061w, 1011w, 968w, 927w, 772s, 707w, 636w, 470w, 412w.

2.1.3. $\{[Fe(pyimH)_2(NCS)_2]_2(\mu\text{-}MeOH)_2\}\cdot 2MeOH$ (**3**)

To a methanolic solution (15 mL) of $[Fe(H_2O)_6](ClO_4)_2$ (153.12 mg, 0.422 mmol) (and a pinch of ascorbic acid) was added to a solution of KNCS (82 mg, 0.844 mmol) in the same solvent (35 mL). The mixture was stirred for 15 min, filtered to remove the $KClO_4$ precipitate then transferred using a cannula into another Schlenk flask containing a solution of pyimH (120 mg, 0.844 mmol) in methanol. Water (15 mL) was added and the solution stirred for 1 h at room temperature, then left to slowly evaporate under N_2. X-ray structural analysis was performed on an orange/red single crystal. Infrared spectrum (KBr disk, cm^{-1}): 3551sh, 3415br, 2070s, 1701w, 1638sh, 1616m, 1543w, 1473m, 1384w, 1292w, 1150w, 1106w, 962w, 788w, 701w, 621w, 473w.

2.1.4. $\{[Fe(pypzH)_2(NCS)_2](\mu\text{-}OH_2)\}_n$ (**4**)

Only one single crystal of the pseudo-chain **4** was obtained. This was a side product from the recrystallisation of $[Fe(pypzH)(NCS)_2]_2(\mu\text{-bpym})$ [14] using methanol/water (1:1) as a solvent (where bpym is 2,2′-bipyrimidine). Thus, far the pseudo-chain **4** has not been remade by a direct route. The μ-bpym complex is made as follows. To a methanolic solution (15 mL) of $[Fe(H_2O)_6](ClO_4)_2$ (153.12 mg, 0.422 mmol) (and a pinch of ascorbic acid) was added a solution of KNCS (82 mg, 0.844 mmol) in the same solvent (15 mL). The mixture was stirred for 15 min and was filtered to remove the $KClO_4$ precipitated, before addition to a Schlenk flask containing a solution of pypzH (61 mg, 0.422 mmol) in methanol. This solution was stirred for 10 min then a methanolic solution (10 mL) of bpym (33.4 mg, 0.211 mmol) was added dropwise. After stirring (90 min) and warming (60 °C) the precipitate was filtered then washed with Et_2O (3 × 30 mL) and dried in air (yield 0.12 g, 36%). Infrared spectrum (KBr disk, cm^{-1}): 3411br, 2057s, 1638sh, 1606m, 1571m, 1431m, 1406m, 1364w, 1292w, 1215w, 1090w, 1016w, 966w, 927w, 825w, 760m, 710w, 614w, 481w, 406w. Microanalysis: Found: C, 40.14; H, 2.54; N, 23.4%. Calculated for $C_{28}H_{20}N_{14}S_4Fe_2$: C, 42.4; H, 2.5; N, 24.7%.

2.1.5. $[Fe(pypzH)_2(NCS)_2]H_2O$ (**5**)

The complex **5** was prepared as a side product in the preparation of **1**. Following this procedure, the first crop of yellow block-like crystals of **1** grew within two days, and were filtered off. The remaining filtrate was allowed to evaporate for a further week affording crystals of the

monomeric species $[Fe(pypzH)_2(NCS)_2]H_2O$ (**5**). Infrared spectrum (KBr disk, cm^{-1}): 3419br, 2083s, 1607m, 1510w, 1459w, 1324w, 1091m, 968w, 772m, 638m, 472w.

2.2. X-ray crystallographic studies

Table 1 contains the crystallographic data and details for all the structural determinations. All X-ray crystallographic measurements were performed at 123(2) K (except for **2b**, 298(2) K) using a Nonius Kappa CCD diffractometer, fitted with a Mo Kα radiation source and graphite monochromator ($\lambda = 0.71073$). DENZO-SMN [15] was used for data integration and SCALEPACK [15] corrected data for Lorentz-polarisation effects. Direct methods (SHELXS-97) [16] and successive Fourier difference methods with refinement of full-matrix least-squares on F^2_{obs} (SHELXL-97) [16] afforded structural solutions. All non-hydrogen atoms were refined using anisotropic thermal parameters. Hydrogen atoms of coordinated H_2O groups were located in the difference maps and allowed to refine freely with the remaining hydrogen atoms assigned to geometrically idealised positions.

2.3. Magnetic studies

Magnetic measurements were carried out on a Quantum Design MPMS 5 SQUID magnetometer calibrated by us of a standard palladium sample (Quantum Design) of accurately known magnetisation or by use of magnetochemical calibrants such as $CuSO_4 \cdot 5H_2O$. Susceptibility versus temperature studies in the linear portion of the magnetisation versus field curve was made using a field of 1 T. Powdered samples were contained in calibrated gelatine capsules held at the centre of a drinking straw fixed to the end of the sample rod.

3. Results and discussion

3.1. Synthesis and characterization

The *N*,*N*-chelating ligands employed are 2-(1H-pyrazol-3-yl)-pyridine (pypzH) and 2-(1H-imidazol-2-yl)-pyridine (pyimH). The pseudo-dimer $\{cis\text{-}[Fe(pypzH)_2(NCS)_2]_2(\mu\text{-}OH_2)(H_2O)_2\} \cdot H_2O \cdot MeOH$ (**1**), where μ implies H-bonding bridging, was prepared under nitrogen by mixing two equivalents of methanolic pypzH to a methanolic solution of $Fe(NCS)_2$ created in situ from the reaction of $[Fe(H_2O)_6](ClO_4)_2$ and KNCS using a pinch of ascorbic acid to prevent formation of Fe(III), a common approach employed in all Fe(II) preparations. Water was added to the solution and the mixture was stirred, then left to slowly evaporate under nitrogen. Yellow block-like crystals of **1** grew within two days. During the preparation of **1**, slow evaporation of the solution led to crystals of **1**, but after two days, additional yellow crystals of the monomeric compound *cis*-$[Fe(pypzH)_2(NCS)_2]H_2O$ (**5**) were obtained.

$\{cis\text{-}[Fe(pypzH)_2(NCSe)_2]_2(\mu\text{-}OH_2)(H_2O)_2\} \cdot H_2O \cdot MeOH$ (**2a**, **2b**) was prepared in the same way as **1** but employing KNCSe in place of KNCS to generate, in situ, the $Fe(NCSe)_2$ used to generate **2a**/**2b** as yellow block-like crystals. The related, pseudo-dimer of $\{cis\text{-}[Fe(pyimH)_2(NCS)_2]_2(\mu\text{-}MeOH)_2\} \cdot 2MeOH$ (**3**) was prepared in a similar way to the pypzH complexes **1** and **2a**, **2b** via use of a methanolic pyimH solution responsible for generating a methanolate bridged complex in place of the previously described water bridges. Large orange/red block like crystals of the pseudo-dimer **3** formed after a period of four days. One crystal was obtained from re-crystallisation of a dinuclear bipyrimidine bridged complex $[Fe(pypzH)(NCS)_2]_2(\mu\text{-bpym})$ [14] and this showed a novel water-bridged chain formulation $\{cis\text{-}[Fe(pypzH)_2(NCS)_2](\mu\text{-}OH_2)\}_n$ (**4**). Attempts to remake **4** in bulk have given the pseudo-dimer **1** or the monomer **5**. Thus, simply by changing the methanol-to-water ratio in the pypzH/NCS^- reactions, different crystalline products were isolated. In contrast, when the selenocyanate analogue was prepared, only the water-bridged dimer was obtained.

3.2. Description of structures

Compounds **1**, **2a**, **2b** proved to be isostructural and the structure determination of the latter, at 123 K, is illustrated in Fig. 1. Fe–N bond lengths are given in Table 2. The bidentate pypzH ligands occupy four-coordination sites with two *cis*-coordinated anionic ligands of NCSe completing the Fe coordination sphere.

It is interesting to note that the unsymmetrical ligand pypzH presents the pyridyl groups [N(5) and N(8)] in a *cis* orientation with each pyridyl group being *trans* to the anionic NCX ligand. Conversely, if the pypzH ligand offers a pyridyl group *trans* to a pyrazolyl group, with the remaining pyrazolyl and pyridyl groups *trans* to the anionic NCX ligands this is the configuration in the isomeric mononuclear complex *cis*-$[Fe(pypzH)_2(NCS)_2]\text{-}H_2O$ (**5**), described below.

The atoms H(4) and H(7) in **2a** were located in the difference map and refined freely with respective H-bond lengths of 1.946 Å [O(2)H(4)] and 2.052 Å [O(3)H(7)]. Furthermore, the N(7)H(7)–O(3)–H(7′)N(7′) H-bonding is clearly evident with an H(7)–O(3)–H(7′) angle of 72.1°. Each half of the dimer is structurally equivalent with the O(3) atom at half occupancy in the asymmetric unit. The structure was also solved at 298 K, viz. **2b**. As expected, the thermal parameters of the atoms were greater at room temperature compared to 123 K. The average Fe–N distance in **2a** at 123 K is 2.098 Å, but this average increased to 2.163 Å at 298 K. Interestingly, the average Fe^{II} to N-donor distance of 2.161 Å in **1** at

Table 1
Crystallographic data for compounds **1**–**5**

Compound	{[Fe(pypzH)$_2$(NCS)$_2$](μ-OH$_2$)-(H$_2$O)$_2$} · H$_2$O · MeOH (**1**)	{[Fe(pypzH)$_2$(NCSe)$_2$]-(μ-OH$_2$)(H$_2$O)$_2$} · H$_2$O · MeOH (**2a**)	{[Fe(pypzH)$_2$(NCSe)$_2$](μ-OH$_2$)-(H$_2$O)$_2$} · H$_2$O · MeOH (**2b**)	{[Fe(pyimH)$_2$(NCS)$_2$]$_2$-(μ-MeOH)$_2$} · 2MeOH (**3**)	{[Fe(pypzH)$_2$(NCS)$_2$]-(μ-OH$_2$)}$_n$ (**4**)	[Fe(pypzH)$_2$(NCS)$_2$]-H$_2$O (**5**)
Formula	$C_{37}H_{31}Fe_2N_{16}O_5S_4$	$C_{37}H_{31}Fe_2N_{16}O_5Se_4$	$C_{37}H_{31}Fe_2N_{16}O_5Se_4$	$C_{20}H_{22}FeN_8O_2S_2$	$C_{18}H_{16}FeN_8OS_2$	$C_{18}H_{14}FeN_8OS_2$
Crystal size (mm)	0.47 × 0.30 × 0.25	0.30 × 0.25 × 0.25	0.38 × 0.33 × 0.13	0.17 × 0.13 × 0.10	0.15 × 0.13 × 0.05	0.30 × 0.30 × 0.20
Crystal colour, habit	yellow, irregular block	yellow, irregular block	yellow, irregular block	red, irregular block	orange, irregular block	yellow, irregular block
Molecular weight	1019.72	1207.32	1207.32	526.43	480.36	478.34
Crystal system	orthorhombic	orthorhombic	orthorhombic	triclinic	monoclinic	monoclinic
Space group (No.)	*Pbcn* (#60)	*Pbcn* (#60)	*Pbcn* (#60)	$P\bar{1}$ (#2)	*C*2/*c* (#15)	$P2_1/n$ (#14)
a (Å)	24.5079(5)	24.5737(1)	24.9532(1)	8.9146(2)	29.3905(13)	11.8214(2)
b (Å)	10.0420(2)	10.1799(3)	10.12794(3)	9.4051(2)	8.432(4)	15.4912(2)
c (Å)	20.7582(3)	20.9183(4)	21.0857(4)	15.9883(4)	18.8557(9)	12.0250(2)
α (°)	90	90	90	96.054(1)	90	90
β (°)	90	90	90	105.662(1)	111.017(2)	99.261(1)
γ (°)	90	90	90	105.696(1)	90	90
V (Å^3)	5108.8(2)	5232.9(2)	5408.6(2)	1219.34(5)	4362(2)	2173.41(6)
Z	4	4	4	2	2	4
T (K)	123(2)	123(2)	298(2)	123(2)	123(2)	123(2)
D_{calc} (g cm^{-3})	1.326	1.532	1.483	1.434	1.463	1.462
μ (Mo Kα) (cm^{-1})	7.85	33.89	32.79	8.23	9.10	9.13
Data collected	62342	62805	68895	19434	20301	23691
Unique data (R_{int})	6295 (0.1278)	6466 (0.1169)	6481 (0.1741)	5905 (0.1098)	5197 (0.890)	5329 (0.0853)
Observed data [$I > 2\sigma(I)$]	3001	3650	2172	3609	2667	3038
Final R_1, wR_2 [$I > 2\sigma(I)$]	0.0729, 0.2129	0.0764, 0.2207	0.0916, 0.2272	0.0853, 0.2130	0.0562, 0.0988	0.0584, 0.1543
R_1, wR_2 (all data)	0.1667, 0.2574	0.1414, 0.2549	0.2570, 0.3089	0.1292, 0.2391	0.1546, 0.1166	0.1201, 0.1753
Goodness-of-fit, *S*	0.990	1.042	0.930	1.018	1.015	1.060
Largest (smallest) difference peak (e Å^{-3})	1.293 (−0.581)	1.614 (−1.890)	0.748 (−1.098)	0.922 (−0.869)	0.683 (−0.588)	1.074 (−0.630)

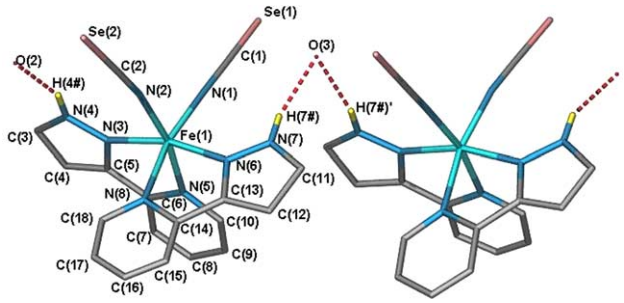


Fig. 1. Molecular structure of {*cis*-[Fe(pypzH)$_2$(NCSe)$_2$]$_2$(μ-OH$_2$)-(H$_2$O)$_2$} · H$_2$O · MeOH (**2a**) at 123 K. Lattice H$_2$O and MeOH are omitted for clarity.

Table 2
Selected bond lengths (Å) for complexes **2a** and **2b**

	123 K (**2a**)	298 K (**2b**)
Fe(1)–N(1)	2.037(6)	2.100(8)
Fe(1)–N(2)	2.067(7)	2.097(8)
Fe(1)–N(3)	2.104(5)	2.172(6)
Fe(1)–N(5)	2.146(5)	2.220(7)
Fe(1)–N(6)	2.093(5)	2.176(7)
Fe(1)–N(8)	2.140(5)	2.210(7)

123 K was the same as that in the room temperature structure of **2**. Both structures have typical high spin (HS) Fe^{II}–N distances whereas the selenocyanate structure at 123 K has an average Fe–N distance of 2.098 Å. A difference of 0.0635 Å is observed between 298 and 123 K. For a complete spin transition, from HS to LS,

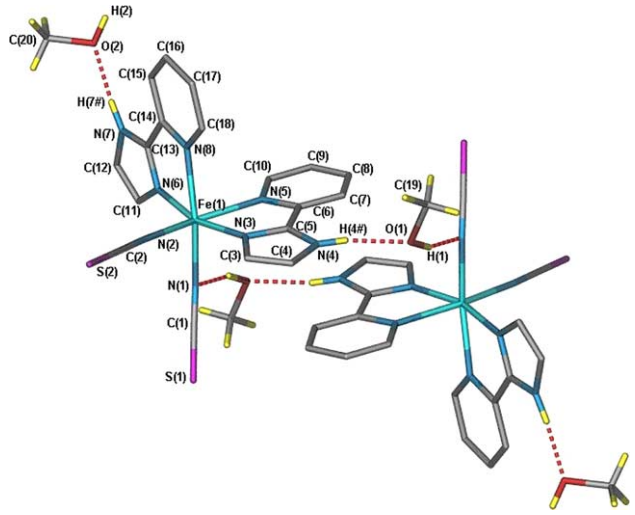


Fig. 2. Molecular structure of the dimer {*cis*-[Fe(pyimH)$_2$(NCS)$_2$]$_2$-(μ-MeOH)$_2$(MeOH)$_2$} (**3**) at 123 K.

the Fe–N bond distance typically decreases by ~0.2 Å [6]. In complex **2**, at 123 K, only about 25% of the HS Fe^{II} centres have undergone a spin-crossover and so only a small decrease in the Fe–N bond length is anticipated, as observed. This structural contraction is further evident from the reduction in the associated unit cell volumes, by 3.1%. Bond angle variations are observed between 298 and 123 K leading to a more regular shape of the [FeN$_6$] core at the lower temperature.

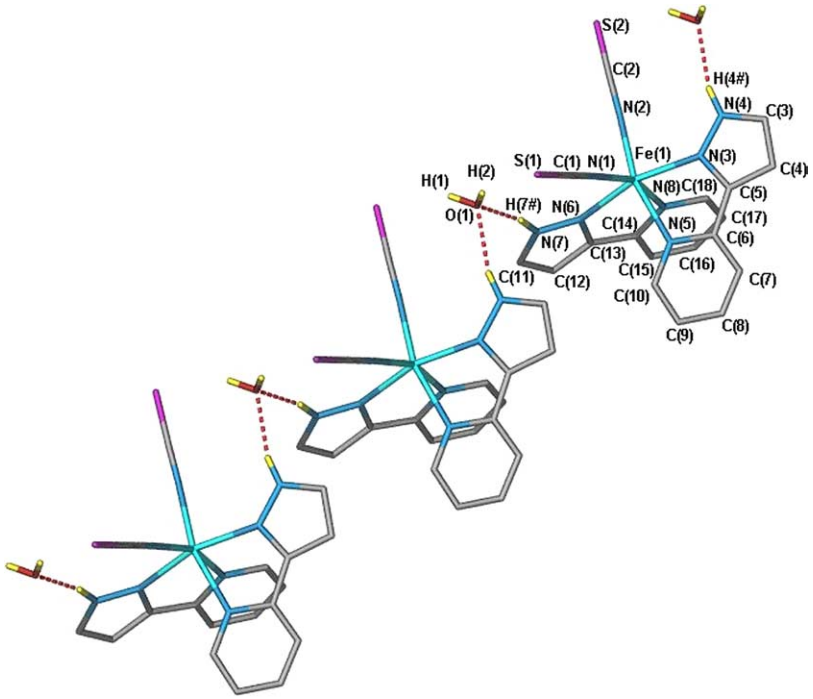


Fig. 3. Chain-like structure of {*cis*-[Fe(pypzH)$_2$(NCS)$_2$](μ-OH$_2$)}$_n$ (**4**) at 123 K.

Compound **3** is also pseudo-dimeric and is bridged by two methanol molecules which are structurally equivalent and H-bonded to the imidazole NH(4) of the molecule, via O(1), and to the thiocyanate N(1) of the other molecule, via H(1) (see Fig. 2). These distances are O(1)–H(4) = 1.94 Å and H(1)–N(1) = 2.09 Å. The overall structure of the dimer is different to that in the pypzH compounds. The bent coordination of the NCS in **3** (C–N–Fe = 149.2°) is unusual and is further evidence for the H-bonding of the MeOH.

The average Fe–N bond length at 123 K in complex **3** is 2.17 Å, comparable to that in the HS pseudo-dimer $\{cis\text{-}[Fe(pypzH)_2(NCS)_2]_2(\mu\text{-}OH_2)\}2H_2O$ (**1**).

In the chain species **4**, water bridging occurs via H-bonding to NH groups of pyrazole rings in neighbouring *cis*-$[Fe(NCS)_2(pypzH)_2]$ molecules. This can be seen in the crystal structure shown in Fig. 3. The packing of the chains is shown in Fig. 4.

The structure of monomer **5** is shown in Fig. 5 and now the pyrazole N(3) is *trans* to pyridine N(8). Only one of the pyrazole NH groups is involved in H-bonding to a single terminal water. The H(4)–O(1) distance is 2.02 Å The average Fe–N distance in the monomer is 2.16 Å, which is a typical Fe–N distance for a HS Fe(II) complex.

The compounds **1**–**5** containing H-bonded ligand contacts raised the significant question of how important H-bonded interactions involving solvate and ligand might be in the SCO behaviour of crystalline Fe^{II} species, be they mono-, bi- or polynuclear. H-bonding "supramolecular" effects have been noted through their influence on ligand field strength and on cooperativity in

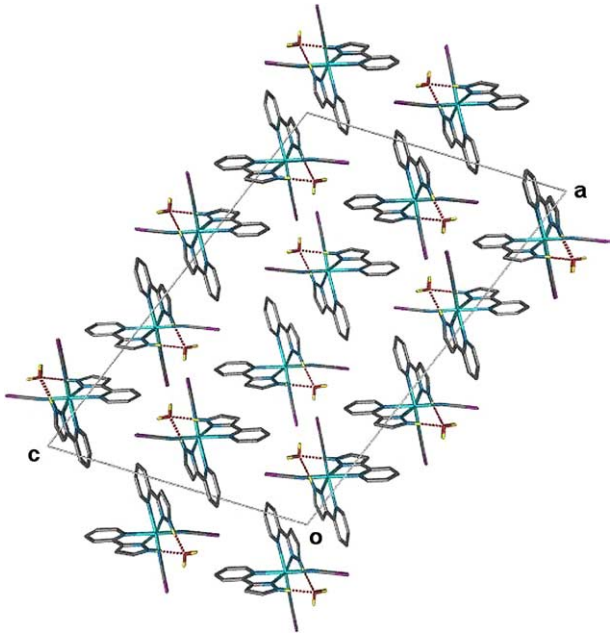


Fig. 4. Packing arrangement of chains of $\{cis\text{-}[Fe(pypzH)_2(NCS)_2]\text{-}(\mu\text{-}OH_2)\}_n$ (**4**) as viewed down the *b*-axis.

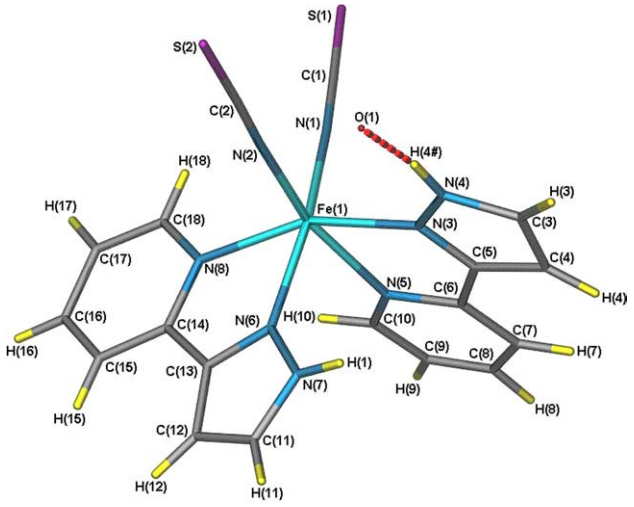


Fig. 5. Molecular structure of the monomer *cis*-$[Fe(pypzH)_2(NCS)_2]H_2O$ (**5**) at 123 K.

mononuclear species [1,4,8,17]. A microporous framework system has also recently been shown to display SCO on those Fe(II) sites which are involved in EtOH···SCN–Fe H-bonding interactions [7]. When the guest EtOH molecules are desorbed the system is high-spin at all temperatures.

3.3. Magnetic properties

Magnetic data show that complex **1** remains HS–HS in the range 4–300 K, μ_{eff} (per Fe) being constant at 5.0 μ_B (χT = 3.125 $cm^3\ mol^{-1}$ K at 300 K) between 300 and 50 K, then decreases to 2.5 μ_B at 2 K because of ligand field and zero-field splitting of the $^5T_{2g}$ derived state (Fig. 6). Any antiferromagnetic exchange coupling contributions, via the ligand–water H-bonding pathways is very weak. Conversely, the NCSe complex **2**, which has a stronger ligand field around each Fe, shows a very gradual 'half' SCO transition corresponding to changes

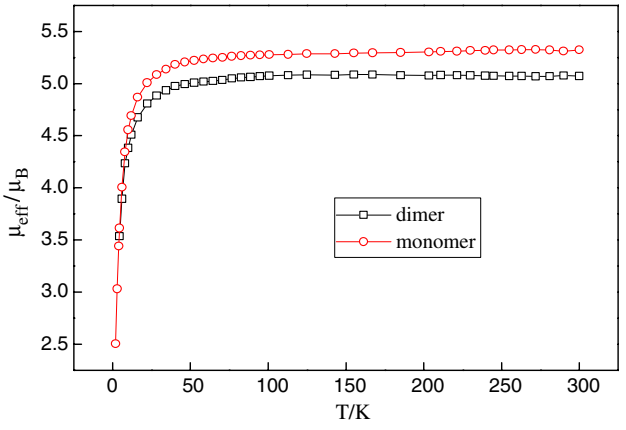


Fig. 6. Magnetic moments, per Fe, of dimeric $\{cis\text{-}[Fe(pypzH)_2(NCS)_2]_2(\mu\text{-}OH_2)(H_2O)_2\} \cdot H_2O \cdot MeOH$ (**1**) and mononuclear *cis*-$[Fe(pypzH)_2(NCS)_2]H_2O$ (**5**) in the range 2–300 K.

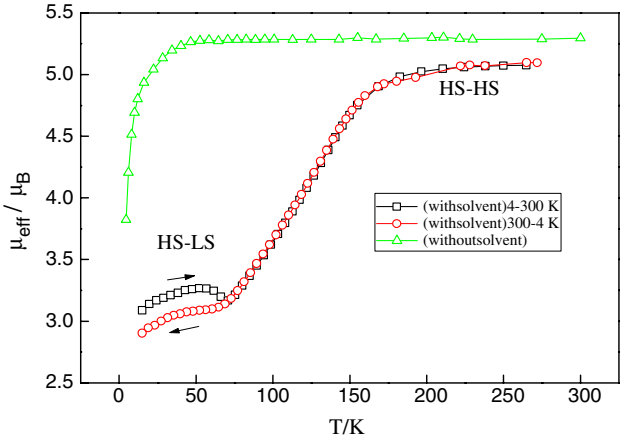


Fig. 7. Magnetic moments, per Fe, of {*cis*-[Fe(pypzH)$_2$(NCSe)$_2$]$_2$-(μ-OH$_2$)(H$_2$O)$_2$} · H$_2$O · MeOH (**2**) plotted as a function of temperature, with and without solvate molecules.

between HS–HS to HS–LS microstates, with no hysteresis, and centred at $T_c \sim 125$ K (Fig. 7). The different values of μ_{eff} observed, on heating and cooling in the range 4–70 K, are due to thermal quenching and consequent trapping of some HS–HS state into the HS–LS state.

The pyimH compound **3** remained in the HS–HS state over the range 4–300 K as seen in the plot of μ_{eff} versus temperature which is very similar to those of **1** and **5**. The observation that complex **2** produces a half SCO transition to yield the HS–LS micro-state below ~70 K, rather than giving a full transition to the LS–LS state, is similar to that observed for the covalently bridged complex [Fe(bpym)(NCSe)$_2$]$_2$(μ-bpym), investigated by Real [6] and for which an absence of thermal hysteresis was also noted. In that case, the stabilisation of a HS–LS state was attributed to intramolecular anti-cooperative interactions, perhaps in conjunction with weak exchange coupling across the bpym bridge. Some other members of the μ-bpym series showed a two-step full SCO, attributed to the cooperativity between dinuclear molecules [6].

Interestingly, when **2** was desolvated by heating, in vacuo, at 80 °C it showed no SCO, but displayed HS–HS magnetic behaviour in the range 2–300 K (Fig. 7). The rapid decrease in μ_{eff} below 50 K was, again, due to zero field splitting effects. Any nearest neighbour exchange coupling is very weak. The H-bonded water bridging is therefore crucial for spin-crossover transitions to occur in the parent complex **2**, not only for modulating the ligand field strength at the Fe(II) centres, but also for providing a new mode of intra-dimer cooperativity, albeit weakly, as judged by the gradual SCO and lack of hysteresis. The H-bonded water molecules shown in Fig. 1 do not H-bond to any neighbouring dimers. The other water and methanol solvate molecules, not shown in Fig. 1, are neither H-bonded to each other or to the dimers. Thus, any inter-dimer cooperativity will be very weak and we believe the intra-dimer contribution is dominant.

The structural equivalence of each Fe chromophore within the dimeric unit in **2**, at 123 K, a temperature above the [HS–LS] plateau, is similar to the equivalence in the two-step μ-bpym system [6]. This contrasts with the trapped HS and LS sites observed within the dinuclear moiety of a recent triazole bridged [HS–LS] example [18]. There are no crystallographic phase transitions occurring in any of these dimeric or dinuclear examples and it is therefore difficult, at this stage, to assign a role, if any, for the H-bonding bridges in stabilizing the HS–LS state in complex **2**.

It can be seen in Fig. 6 that the mononuclear complex *cis*-[Fe(pypzH)$_2$(NCS)$_2$]H$_2$O (**5**) remains HS in the range 4–300 K, μ_{eff} being constant at 5.3 μ_B between 300 and 50 K, then decreasing to 2.5 μ_B at 2 K due to zero-field splitting of the $^5T_{2g}$ derived ground state. The pseudo-dimer {*cis*-[Fe(pypzH)$_2$(NCS)$_2$]$_2$(μ-OH$_2$)(H$_2$O)$_2$} · H$_2$O · MeOH (**1**) behaves similarly. However, bis-chelated monomers such as *cis*-[Fe(2,2′-bipy)$_2$(NCS)$_2$] do show SCO behaviour [1,8] and thus the pypzH ligand produces a weaker ligand field than 2,2′-bipy, probably modulated by the H-bonded water group in **5**.

4. Summary

In this paper, we have described the first example of a family of pseudo-dimeric iron(II) complexes in which {ligand–water–ligand} hydrogen-bonding bridges the two iron centres. The spin-state of the compounds depend upon the X group in the NCX$^-$ co-ligand, the X = Se derivative displaying an incomplete (half) spin-crossover leading to a HS–LS ground state. The X = S derivatives remain HS–HS at all temperatures as does the desolvated X = Se compound. Cooperativity effects are very weak and probably intra-dimer in origin.

5. Supplementary material

Crystallographic data for the structural analysis have been deposited with the Cambridge Crystallographic Data Centre, CCDC Nos. 206921, 206922, 206923, 256928, 256929, 256930. Copies of this information may be obtained free of charge from the Director, CCDC, 12 Union Road, Cambridge CB2 1EZ, UK (fax: +44 1223 336 033; e-mail: deposit@ccdc.cam.ac.uk or http://www.ccdc.cam.ac.uk).

Acknowledgements

This work was supported by Discovery and International Linkage Grants from the Australian Research

Council. B.A.L. and K.S.M. thank Professor Hans Toftlund for valuable discussions, and hospitality, in the University of Southen Denmark, Odense, during which stay the paper was written.

References

[1] P. Gütlich, Y. Garcia, H.A. Goodwin, Chem. Soc. Rev. 29 (2000) 419.
[2] O. Kahn, Nature 21 (1999) 399.
[3] P. Gütlich, A. Hauser, H. Spiering, Angew. Chem. Int. Ed. 33 (1994) 2024.
[4] P. Gütlich, H.A. Goodwin (Eds.), Three Volumes of Topics in Current Chemistry, Springer, Berlin, 2004.
[5] O. Kahn, E. Codjovi, Y. Garcia, P.J. van Koningsbruggen, R. Lapouyadi, L. Sommer, ACS Symp. Ser. 644 (1996) 298.
[6] J.A. Real, in: J.P. Sauvage (Ed.), Bistability in Iron (II) Spin-crossover Systems, Wiley, New York, 1999, pp. 51–93 (Chapter 2).
[7] G.J. Halder, C.J. Kepert, B. Moubaraki, K.S. Murray, J.D. Cashion, Science 298 (2002) 1762.
[8] P. Gütlich, Struct. Bond. 44 (1981) 83.
[9] K.H. Sugiyarto, K. Weitzner, D.C. Craig, H.A. Goodwin, Aust. J. Chem. 50 (1997) 869.
[10] W. Vreugdenhil, J.H. van Diemen, R.A.G. de Graaff, J.G. Haasnoot, J. Reedijk, A.M. van der Kraan, O. Kahn, J. Zarembowitch, Polyhedron 9 (1990) 2971.
[11] K.S. Murray, C.J. Kepert, Top. Curr. Chem. 233 (2004) 195.
[12] B.A. Leita, B. Moubaraki, K.S. Murray, J.P. Smith, J.D. Cashion, Chem. Commun. (2004) 156.
[13] A.J. Amoroso, A.M.C. Thompson, J.C. Jeffery, P.L. Jones, J.A. McCleverty, M.D. Ward, Chem. Commun. (1994) 2751.
[14] S.R. Batten, J. Bjernemose, P. Jensen, B.A. Leita, K.S. Murray, B. Moubaraki, J.P. Smith, H. Toftlund, Dalton Trans. (2004) 3370.
[15] Z. Otwinowski, W. Minor, Methods Enzymol. 276 (1996) 307.
[16] G.M. Sheldrick, SHELX-97: Programs for Crystal Structure Solutions and Refinement, University of Göttingen, Göttingen, Germany, 1997.
[17] D. Chernyshov, M. Hastettler, K.W. Törnroos, H.-B. Bürgi, Angew. Chem. Int. Ed. 42 (2003) 3825.
[18] M.H. Klingele, B. Moubaraki, J.D. Cashion, K.S. Murray, S. Brooker (2005) 987.

the ferromagnetism in α-TDAE-C_{60} and that the transition temperature could be governed by the Hubbard-type negative exchange interaction $\propto -t^2/U$ which depends on the orientation and partially cancels out the direct one. Here, t is the transfer integral and U the on-site Coulomb repulsion energy. This model requires special orientational ordering between the neighboring C_{60} molecules in one-dimensional chain along c-axis [8]. On the other hand, Kawamoto and co-workers [9,10] proposed the importance of the higher order exchange interaction between the neighboring Jahn–Teller orbitals perpendicular to each other, which is successful to reproduce the hydrostatic pressure dependence of the critical temperature [3].

In this report, the uniaxial strain was applied along b-and c-axis to investigate what kind of interaction dominates the ferromagnetism in α-TDAE-C_{60}, which helps to select the models applicable to this system. Since the present study is limited only to a single example for each applied direction, a full report will appear elsewhere.

2. Experimental

Single crystals are prepared with a diffusion technique [4]. Crystallographic axes are determined with X-ray analysis. An epoxy cylinder containing an aligned single crystal put in a coil is set in the Cu–Be clamp-type pressure cell. Magnitude of uniaxial strain is represented by a corresponding pressure applied to a zirconia piston with 6 mm ϕ. A resonance shift of ESR signal is measured at frequencies around 100 MHz [11], which is caused by a demagnetization field due to spontaneous magnetization. It is important to use the low resonance field of several tens of gauss, which does not produce a significant influence on the ferromagnetic transition.

3. Results and discussion

The transition temperature T_C is shown as functions of pressure applied along b- and c-axis together with hydrostatic pressure in Fig. 1, demonstrating anisotropic magnetic interactions. Characteristic features are summarized as follows. (1) The hydrostatic pressure suppresses T_C quadratically, $\propto 1\text{-}P^2$, which can be reproduced well with the orbital ordering model based on the intermolecular cooperative Jahn–Teller distortion (ICJT model) [3,9]. (2) The b-axis strain enhances T_C up to 17.5 K under 4 kbar of the applied pressure. (3) The c-axis strain strongly suppresses the ferromagnetism; 12 K in the minor part and 10 K for the main part of the sample under 1 kbar of the pressure. Interestingly, the b-axis strain also produces a fraction of the sample

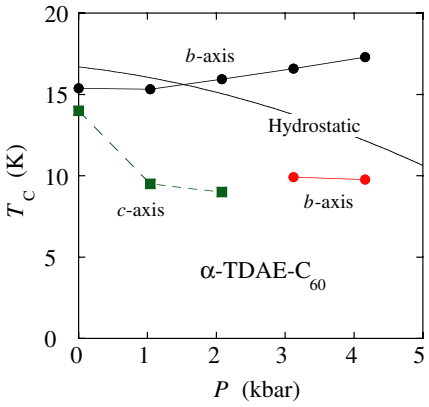


Fig. 1. T_C variations caused by uniaxial strain along b-axis [12] and c-axis, together with by hydrostatic pressure [3].

with the low T_C of about 10 K. The presence of the sub-phase with $T_C \approx 10$ K would relate to a freezing of the flipping between the Jahn–Teller distortion axes around 10 K [13].

To unveil the origin of these pressure dependences of T_C, let me discuss the ICJT mechanism of the high transition temperature. The main reason why the hydrostatic pressure suppresses T_C is a rapid increase of the negative exchange interaction $J \propto -t^2/U$ with pressure, which has been suppressed at ambient pressure because of the cancellation caused by the antiferro-orbital ordered structure with the Jahn–Teller orbitals of the p-like symmetry [3,9]. The important point of this model is such a cancellation of the antiferromagnetic interaction, giving rise to the much less antiferromagnetic than the ferromagnetic interactions coming from the fourth-order perturbation of t. The pressure deteriorates the cancellation, resulting in the suppression of T_C.

The b-axis strain dependence in Fig. 1 requires not only to preserve the cancellation, but also to enhance the ferromagnetic interaction, which can be expected from the increased transfer integrals between neighboring orbitals by pressure. In contrast, the result of the c-axis strain suggests its critical role in strongly disturbing the growth of the cooperative Jahn–Teller distortion, giving rise to the rapid suppression of T_C demonstrated in Fig. 1.

What a structural model do these results meet? There are at least two ways to realize the antiferro-orbital ordered structure, as demonstrated in Fig. 2; (I) the axes of rugby ball structure for the Jahn–Teller distorted C_{60}'s are alternately arranged (parallel and perpendicular) along the c-axis, 1D chain of C_{60}'s, and (II) it aligns always perpendicular to the c-axis and partially fulfills the antiferro-orbital structure in the a–b plane with different a and b lattice constants. The former structure, (I) is preferred from the reasons that the b-axis strain never disturbs the antiferro-orbital ordering in the case (I) and that in the case (II) the b-axis strain directly spoils the

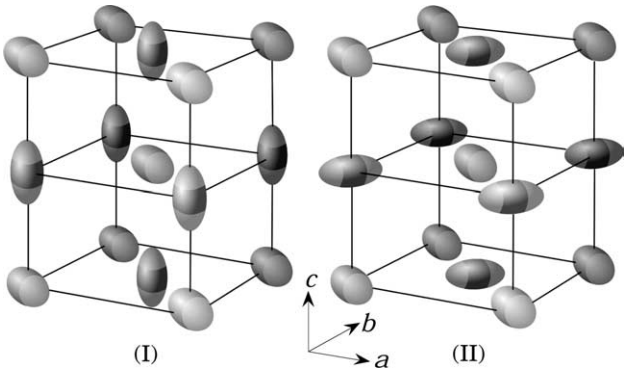


Fig. 2. Two possible antiferro-orbital ordered structures fulfill the requirement by the intermolecular cooperative Jahn–Teller distortion model for the ferromagnetism of TDAE-C_{60}. For simplicity TDAE's are omitted. The angle β of the monoclinic structure is 93.4°.

symmetry required for the cancellation of the antiferromagnetic interaction. This should be consistent with the *c*-axis strain case, too. By virtue of the soft van der Waals coupling, the pressure as small as 1 kbar can easily produce the strain of the order of 0.01 Å between C_{60}'s along *c*-axis, comparable with the expected Jahn–Teller distortion [9]. This suggests that the *c*-axis strain prevents from forming the structure (I) with $T_C = 16$ K, but forces to attain the structure (II) with the lower T_C than the structure (I). Note the possibility of the structure (II) to have $T_C \approx 10$ K corresponding to the second phase in Fig. 1. Therefore, if it were confirmed that the result with the *c*-axis strain was reproducible, and not an artifact caused by a sample degradation suspected because of the somewhat lower T_C than 16 K, the ICJT model would be well consistent with the present uniaxial strain results. Further study and analysis will appear elsewhere.

Acknowledgments

This work was carried out as Joint Project of Japan–Slovenia Research Cooperative Program supported by Japan Society for the Promotion of Science (JSPS). This work is partly supported also by Grant-in-Aid for Scientific Research on the Priority Areas "Molecular conductors", 16038215 by the Ministry of Education, Culture, Sports, Science and Technology of Japan.

References

[1] P.-M. Allemand, K.C. Khemani, A. Koch, F. Wudl, K. Holczer, S. Donovan, G. Gruner, J.D. Thompson, Science 253 (1991) 301.
[2] D. Arcon, R. Blinc, P. Cevc, A. Omerzu, Phys. Rev. B 59 (1999) 5247.
[3] K. Mizoguchi, M. Machino, H. Sakamoto, T. Kawamoto, M. Tokumoto, A. Omerzu, D. Mihailovic, Phys. Rev. B 63 (2001) 040417(R)1.
[4] R. Blinc, K. Pokhodnia, P. Cevc, D. Arcon, A. Omerzu, D. Mihailovic, P. Venturini, L. Golic, Z. Trontelj, J. Luznik, Z. Jeglicic, J. Pirnat, Phys. Rev. Lett. 76 (1996) 523.
[5] A. Mrzel, P. Cevc, A. Omerzu, D. Mihailovic, Phys. Rev. B 53 (1996) R2922.
[6] R. Blinc, P. Cevc, D. Arcon, A. Omerzu, M. Mehring, S. Knorr, A. Grupp, A.-L. Barra, G. Chouteau, Phys. Rev. B 58 (1998) 14416.
[7] T. Sato, T. Saito, T. Yamabe, K. Tanaka, H. Kobayashi, Phys. Rev. B 55 (1997) 11052.
[8] B. Narymbetov, A. Omerzu, V.V. Kabanov, M. Tokumoto, H. Kobayashi, D. Mihailovic, Nature 407 (2000) 883.
[9] T. Kawamoto, M. Tokumoto, H. Sakamoto, K. Mizoguchi, J. Phys. Soc. Jpn. 70 (2001) 1892.
[10] T. Kawamoto, Solid State Commun. 101 (1997) 231.
[11] K. Mizoguchi, Jpn. J. Appl. Phys. 34 (1995) 1.
[12] K. Mizoguchi, M. Takei, M. Machino, H. Sakamoto, M. Tokumoto, T. Kawamoto, A. Omerzu, D. Mihailovic, J. Mag. Mag. Mat. 272 (2004) E215.
[13] P. Jeglic, R. Blinc, T. Apih, A. Omerzu, D. Arcon, Phys. Rev. B 68 (2003) 184422.

2-cyano-4,4,5,5-tetramethyl-4,5-dihydro-1*H*-imidazole-1-oxyl-3-oxide (**3**) [2,3] and 2,3-bis(hydroxylamino)-2,3-dimethylbutane [4,5] were described previously.

2.2. Syntheses of compounds

*Potassium salt of 4,4,5,5-tetramethyl-4,5-dihydro-1H-imidazole-1-oxyl-3-oxide-2-carboxylic acid (K(**1**)).*

Procedure 1. A mixture of nitrile **3** (182 mg, 1.0 mmol), KOH (57 mg, 1 mmol), and water (2 ml) was stirred in a round bottom flask (10 ml) for 1 h on an ice bath. Then the flask was connected to a vacuum pump via a liquid nitrogen trap, and water was distilled at a pressure of <1 Torr. The residue was ground with acetone (5 ml), and the solution containing only *4,4,5,5-tetramethyl-4,5-dihydro-1H-imidazole-1-oxyl-3-oxide* (TLC) was decanted. This procedure was repeated three or four times until acetone ceased to color. Yield: 230 mg (96%); violet powder soluble in MeOH, insoluble in acetone and ether. IR (KBr): $\tilde{\nu}$ (cm^{-1}) 540, 669, 731, 784, 893, 1141, 1168, 1207, 1312, 1368, 1535, 1665, 2991, 3425br. *Anal.* Calc. for $C_8H_{12}KN_2O_4\cdot 3H_2O$: C, 32.8; H, 6.2; N, 9.6. Found: C, 33.0; H, 4.6; N, 9.4%.

Stirring a solution of K(**1**) (0.10 g, 0.42 mmol) in EtOH (5 ml) for 24 h gave NN-H (36 mg, 55%).

A mixture of K(**1**) (0.48 g, 2.01 mmol) and I_2 (0.51 g, 1.99 mmol) in DMF (4 ml) was stirred for 1 h. The solvent was removed and the residue was chromatographed on a SiO_2 column ($CHCl_3$ – eluent), giving NN-I (0.31 g, 54%).

Procedure 2. To a stirred solution of glyoxylic acid monohydrate (0.92 g, 1.0 mmol) in water (5 ml) was added K_2CO_3 (1.38 g, 1.0 mmol). Then 2,3-bis(hydroxylamino)-2,3-dimethylbutane (1.48 g, 1.0 mmol) was added. The reaction mixture was stirred until it thickened and allowed to stay in a refrigerator for 1 day. Then water (3 ml) was added to the reaction mixture. The mixture was stirred, and the precipitate was transferred on a filter, squashed, and dried in vacuum. Yield: 1.78 g (74%); white crystals of the *potassium salt of 1,3-dihydroxy-4,4,5,5-tetramethyl-imidazolidine-2-carboxylic acid (**4**)*. IR (KBr): $\tilde{\nu}$ (cm^{-1}) 541, 577, 658, 699, 814, 850, 916, 977, 994, 1019, 1114, 1164, 1299, 1372, 1508, 1616, 2979, 3214br, 3508. *Anal.* Calc. for $C_8H_{15}KN_2O_4\cdot 2H_2O$: C, 34.5; H, 6.7; N, 10.1. Found: C, 34.5; H, 6.6; N, 10.7%.

To a solution of **4** (0.24 g, 1.0 mmol) in water (5 ml) was added PbO_2 (0.81 g, 3.4 mmol). The reaction mixture was stirred for 1.5 h at room temperature and filtered. The product was isolated from the mother solution as was done in procedure 1. Yield: 0.21 g (88%).

*Lithium salt of 4,4,5,5-tetramethyl-1-oxyl-4,5-dihydro-1H-imidazole-2-carboxylic acid (Li(**2**)).* A mixture of nitrile **6** (330 mg, 1.99 mmol), $LiOH\cdot H_2O$ (84 mg, 2.0 mmol), and water (4 ml) was stirred in a round bottom flask (10 ml) for 14 h at room temperature. Water was distilled off at a pressure of <1 Torr. The residue was ground with acetone (5 ml) and then recrystallized from a mixture of MeOH with *i*-PrOH. Yield of Li(**2**) is 368 mg (97%); very thin, coalesced bronze plates. IR (KBr): $\tilde{\nu}$ (cm^{-1}) 568, 587, 618, 764, 804, 895, 1135, 1218, 1248, 1371, 1395, 1451, 1548, 1674, 2934, 2969, 3434br. *Anal.* Calc. for $C_8H_{12}LiN_2O_3$: C, 50.3; H, 6.3; N, 14.7. Found: C, 50.2; H, 6.3; N, 14.4%.

*Potassium salt of 4,4,5,5-tetramethyl-1-oxyl-4,5-dihydro-1H-imidazole-2-carboxylic acid (K(**2**))* was prepared by the reaction of **6** (240 mg, 1.45 mmol) with a solution of KOH (81 mg, 1.45 mmol) in water (2 ml) by a procedure similar to the one used for **Li(2)**. Yield: 95%; bronze plates; the crystals darken above 230 °C, while at 240 °C they acquire a green hue, and decompose above 255 °C with gas evolution. IR (KBr): $\tilde{\nu}$ (cm^{-1}) 563, 594, 756, 796, 808, 882, 1146, 1211, 1234, 1360, 1439, 1482, 1540, 1657, 2936, 2980, 3421br. *Anal.* Calc. for $C_8H_{12}KN_2O_3$: C, 43.0; H, 5.4; N, 12.6. Found: C, 43.0; H, 5.4; N, 12.4%.

*Tetra-n-butyl ammonium salt of 4,4,5,5-tetramethyl-1-oxyl-4,5-dihydro-1H-imidazole-2-carboxylic acid ((n-Bu)$_4$N(**2**))* was prepared by the reaction of **6** (230 mg, 1.39 mmol) with 40% water solution of $(n\text{-Bu})_4NOH$ (0.90 mg, 1.39 mmol) in water (2 ml). After water had been removed, the yield was 510 mg (86%); red–orange oil. IR (KBr): $\tilde{\nu}$ (cm^{-1}) 755, 888, 1029, 1061, 1107, 1146, 1198, 1235, 1362, 1377, 1434, 1488, 1637, 2875, 2962, 3454br. *Anal.* Calc. for $C_{24}H_{48}N_3O_3\cdot 0.5H_2O$: C, 66.1; H, 11.3; N, 9.6. Found: C, 66.0; H, 11.9; N, 7.9%.

*Cu(**2**)$_2$(CH$_3$OH)$_2$.* A solution of $Cu(OAc)_2\cdot H_2O$ (0.0447 g, 0.22 mmol) in MeOH (20 ml) was slowly added to the solution of K(**2**) (0.1000 g, 0.45 mmol) in MeOH (10 ml). The reaction mixture was kept at room temperature for 1 h. The resulting dark green prismatic crystals were filtered off, washed with MeOH, and dried in air. Yield: 48%. *Anal.* Calc. for $C_{18}H_{32}N_4O_8Cu$: C, 43.6; H, 6.5; N, 11.3. Found: C, 43.2; H, 6.2; N, 11.5%.

*Ni(**2**)$_2$(H$_2$O)$_2$ and Co (**2**)$_2$(CH$_3$OH)$_2$* were synthesized by a similar procedure. *Ni(**2**)$_2$(H$_2$O)$_2$* are coalesced greenish brown crystals. Yield: 82%. *Anal.* Calc. for $C_{16}H_{28}N_4O_8Ni$: C, 41.5; H, 6.1; N, 12.1. Found: C, 41.5; H, 6.3; N, 11.9%. *Co(**2**)$_2$(CH$_3$OH)$_2$* are coalesced bronze crystals. Yield: 79%. *Anal.* Calc. for $C_{18}H_{32}N_4O_8Co$: C, 44.0; H, 6.6; N, 11.4. Found: C, 43.8; H, 6.4; N, 11.4%.

*Cu(**2**)$_2$.* Benzene (5 ml) was poured into $Cu(\mathbf{2})_2(CH_3OH)_2$ (0.0500 g, 0.10 mmol). The mixture was allowed to stay for 1 h at 50 °C. The resulting tawny powder was filtered off, washed with benzene, and dried in air. Yield: 95%. *Anal.* Calc. for $C_{16}H_{24}N_4O_6Cu$: C, 44.5; H, 5.6; N, 13.0. Found: C, 44.6; H, 5.6; N, 12.6%.

*Cu(**2**)$_2$(H$_2$O)$_2$.* A solution of $Cu(OAc)_2\cdot H_2O$ (0.0224 g, 0.11 mmol) in EtOH (20 ml) was slowly added at room temperature to the solution of K(**2**) (0.0500 g,

0.22 mmol) in EtOH (10 ml). After 1 h, a green precipitate formed, which was filtered off, washed with ethanol, and dried in air. Yield: 60%. *Anal.* Calc. for $C_{16}H_{28}N_4O_8Cu$: C, 41.1; H, 6.0; N, 12.0. Found: C, 40.8; H, 5.6; N, 11.7%.

*Ni(**2**)$_2$(dipy)·H$_2$O*. A solution of K(**2**) (0.0500 g, 0.22 mmol) and 4,4′-dipyridyl (0.0175 g, 0.11 mmol) in MeOH (5 ml) was slowly added to the solution of $Ni(OAc)_2·4H_2O$ (0.0279 g, 0.11 mmol) in MeOH (5 ml). The green precipitate was filtered off, washed with MeOH, and dried in air. Yield: 60%. *Anal.* Calc. for $C_{26}H_{34}N_6O_7Ni$: C, 51.9; H, 5.7; N, 14.0. Found: C, 52.1; H, 5.3; N, 13.8%.

*Ni(**2**)$_2$(py)$_2$*. A solution of K(**2**) (0.0500 g, 0.22 mmol) and pyridine (0.1 ml) in MeOH (5 ml) was added to the solution of $Ni(OAc)_2·4H_2O$ (0.0279 g, 0.11 mmol) in MeOH (5 ml). The solvent was slowly evaporated to ~2 ml in an air current. The green prismatic crystals were filtered off, washed with *i*-PrOH, and dried in air. Yield: 40%. *Anal.* Calc. for $C_{26}H_{34}N_6O_6Ni$: C, 53.4; H, 5.9; N, 14.4. Found: C, 53.1; H, 5.8; N, 14.2%.

Table 1
Crystallographic data and experimental details

Compound	$Cu(2)_2(CH_3OH)_2$	$Ni(2)_2(Py)_2$	K(**2**)
Crystal system	triclinic	monoclinic	triclinic
Unit cell dimensions			
a (Å)	7.366(1)	18.607(2)	6.98(2)
b (Å)	8.489(1)	13.6082(15)	7.03(2)
c (Å)	9.601(2)	25.201(3)	11.93(4)
α (°)	83.105(3)		98.18(6)
β (°)	73.605(3)	110.743(2)	90.10(6)
γ (°)	83.369(3)		118.59(5)
V, Å^3	569.6(2)	5967.6(11)	507(3)
Space group	$P\bar{1}$	*C*2/*c*	$P\bar{1}$
Z, D_c (g/cm^3)	2, 1.446	8, 1.303	2, 1.462
μ (mm^{-1})	1.009	0.697	0.507
θ (°)	2.22–23.30	1.90–23.40	3.34–23.70
I_{hkl} (coll/unique)	2479/1629	12793/4332	2040/1428
R_{int}	0.0490	0.0698	0.2019
I_{hkl}/N	1629/207	3237/489	1104/141
Goodness-of-fit	0.953	0.834	1.114
R_1 ($I_{hkl} > 2\sigma_I$)	0.0364	0.0541	0.1398
wR_2	0.0769	0.1320	0.3927
R_1 (all data)	0.0464	0.0734	0.1661
wR_2	0.0805	0.1450	0.4066

2.2.1. X-ray structure analysis

The data were collected on SMART APEX CCD (Bruker AXS) automatic diffractometer at ambient temperature using the standard procedure (Mo radiation). Several H atoms were localized in difference electron density syntheses; the others were generated theoretically. All structure solution and refinement calculations were carried out with SHELX97 software. The crystallographic data and experimental details are given in Table 1; selected bond lengths and angles are given in Table 2.

2.2.2. Magnetic measurements

The magnetochemical experiment was run on an MPMS-5S (“Quantum Design”) SQUID magnetometer

Table 2
Selected bond lengths and angles (Å, °) for $Cu(2)_2(CH_3OH)_2$, $Ni(2)_2Py_2$, and K(**2**)

Cu–O(2)	1.970(2)	Ni–O(2)	2.036(3)	K–O(4A)	2.680(9)
		Ni–O(5)	2.039(3)	K–O(3A)	2.766(9)
				K–O(4B)	2.780(10)
				K–O(2B)	2.852(10)
				K–O(3)	2.917(11)
				K–O(2A)	2.933(10)
Cu–N(1)	1.981(2)	Ni–N(1)	2.107(3)	K–N(1A)	2.917(10)
		Ni–N(3)	2.113(3)	K–N(1)	2.991(11)
Cu–O(1A)	2.410(3)	Ni–N(1A)	2.107(3)	K–K′	3.486(13)
		Ni–N(1B)	2.096(3)	K–K″	3.493(13)
N(1)–C(3)	1.284(3)	N(1)–C(7)	1.284(5)	N(1)–C(7)	1.275(10)
			1.282(5)		
N(2)–C(3)	1.368(3)	N(2)–C(7)	1.377(5)	N(2)–C(7)	1.393(11)
			1.373(5)		
N(2)–O(1)	1.263(3)	N(2)–O(2)	1.256(4)	N(2)–O(2)	1.292(10)
			1.257(4)		
C(3)–C(4)	1.514(4)	C(7)–C(8)	1.518(6)	C(7)–C(8)	1.542(12)
			1.513(5)		
C(4)–O(2)	1.261(3)	C(8)–O(2)	1.261(5)	C(8)–O(2)	1.226(10)
			1.265(5)		
C(4)–O(3)	1.221(3)	C(8)–O(3)	1.215(5)	C(8)–O(3)	1.225(9)
			1.212(5)		
O(1A)–C(1A)	1.331(6)				
C(4)–O(2)–Cu	115.9(2)	C(8)–O(2)–Ni	118.3(3)		
			118.0(2)		

at temperatures from 2 to 300 K in a homogeneous external magnetic field of up to 49.5 kOe. The molar magnetic susceptibility χ was calculated using Pascal's additive scheme including diamagnetic corrections and taking into account temperature-independent paramagnetism of Cu(II) and Ni(II) ions, which were taken to be 60×10^{-6} and 190×10^{-6} cm^3/mol, respectively. For the paramagnetic region, the effective magnetic moment was calculated by the formula $\mu_{\text{eff}} = [(3k/N_A\beta^2)\chi T]^{1/2} \approx (8\chi T)^{1/2}$, where k is Boltzmann's constant, N_A is the Avogadro number, and β is the Bohr magneton. The magnetic phase transition temperature was determined as the extremum of the derivative of magnetic susceptibility with respect to temperature $\partial\chi/\partial T$.

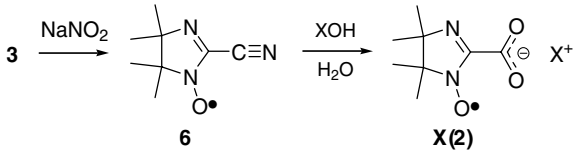
3. Results and discussion

3.1. Syntheses and Properties of NN-COOK (K(1)) and IN-COOM (X(2), X = Li$^+$, K$^+$, (n-Bu)$_4$N$^+$)

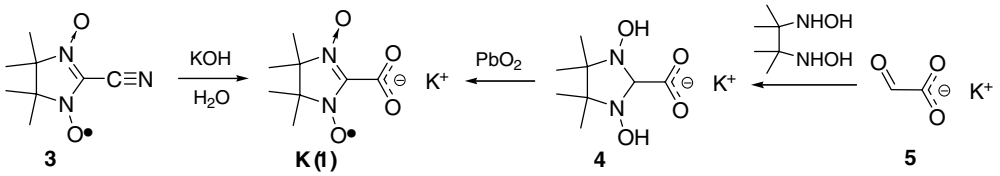
Previously, attempts were made to synthesize the NN-COOH acid or its salts. Thus the NN-COOMe ether was subjected to alkaline hydrolysis [1]. An EPR spectroscopic study revealed that the resulting solution contained the NN-COO$^-$ anion, which was stable in an alkaline solution at 0 °C, but was quickly decarboxylated into NN-H by acidifying or using elevated temperatures. An attempt to synthesize NN-COOH by oxidation of 1,3-dihydroxy-4,4,5,5-tetramethylimidazolidin-2-yl-carboxylic acid with $NaIO_4$ led to nitroxide NN-H as the sole product [6]. These data gave strong evidence that NN-COOH and its salts are liable to undergo spontaneous decarboxylation in solution, which makes it difficult to isolate them from the reaction mixture. This difficulty was overcome to a certain extent by Weiss et al. [7], who treated a THF solution of NN-H with LDA and then carboxylated NN-Li with CO_2. However, this reaction is performed in rather stringent conditions, giving only the lithium salt of **1**. We found that the potassium salt K(**1**) can be obtained in mild conditions by hydrolysis of paramagnetic nitrile **3** in the presence of an equimolar amount of KOH (Scheme 1). This reaction is well reproducible and readily controllable because the greenish blue crystals of the starting **3** are gradually dissolved in the course of the reaction to give a dark violet solution. Subsequent treatment of the reaction mixture as described in Section 2 leads to high yields of K(**1**).

K(**1**) is a dark violet powder insoluble in benzene, ether, and acetone and readily soluble in water, MeOH, EtOH, and DMF. Prolonged (for 1 day or more) storage of a solution of K(**1**) in any polar solvent leads to gradual decarboxylation of the salt, giving mainly NN-H (in up to 55% yields). Treatment of a DMF solution of K(**1**) with I_2 forms NN-I in >50% yield. Note that K(**1**) is also obtainable by condensation of aldehyde **5** with 2,3-bis(hydroxylamino)-2,3-dimethylbutane and further oxidation of **4** with PbO_2 (Scheme 1). The physicochemical characteristics of the thus synthesized K(**1**) are identical with the characteristics of the samples synthesized by alkaline hydrolysis of **1**. At room temperature μ_{eff} is 1.72 BM, which is close to the theoretical value of 1.73 BM for uncoupled $s = 1/2$ spins with a g-factor of 2. At reduced temperature the $\mu_{\text{eff}}(T)$ curve decays, indicating that antiferromagnetic intermolecular exchange interactions are dominant (Fig. 2).

The instability of **1** is due to the weak C–C bond between the carboxyl group and the imidazoline ring, both of which are electron acceptors. Taking into account the circumstance that increasing of electron density on carbon atom in α-position to carboxylic group prevents eliminating of carbon dioxide [8], we suggested less aptitude for decarboxylation of carboxylate **2**. This prompted us to synthesize **2**. This reduction product of **1** was expected to show less aptitude for decarboxylation. Compound X(**2**), where X = Li$^+$, K$^+$, (*n*-Bu)$_4$N$^+$, was synthesized by hydrolysis of paramagnetic nitrile **6** in the presence of an equimolar quantity of the corresponding base XOH (X = Li$^+$, K$^+$, (*n*-Bu)$_4$N$^+$). In the course of the reaction, the orange crystals of nitrile **6**, preliminarily obtained by reduction of **3**, gradually dissolved to form a bright red solution (Scheme 2), from which X(**2**) was isolated after removal of water.



Scheme 2.



Scheme 1.

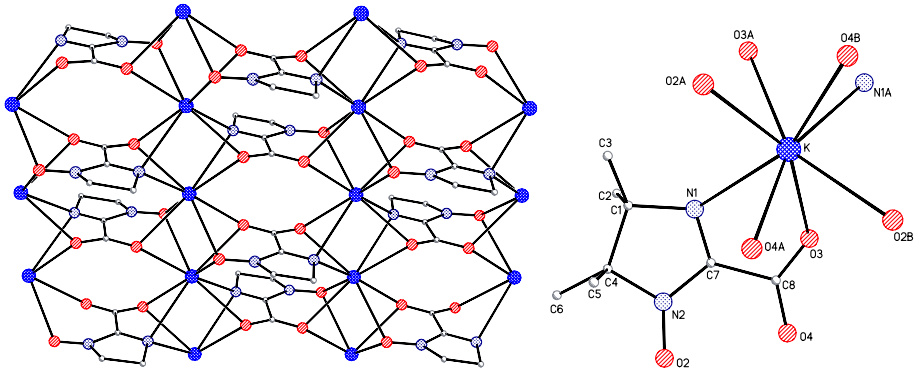


Fig. 1. Fragment of a polymer layer and atomic numbering for K(**2**).

Li(**2**) and K(**2**) are bronze platelike crystals insoluble in benzene, ether, acetone, and 2-propanol, but readily soluble in water, MeOH, EtOH, and DMF. (*n*-Bu)$_4$N(**2**) is a red oil soluble in benzene and CH_2Cl_2. After Li(**2**), K(**2**), and (*n*-Bu)$_4$N(**2**) solutions had been stored at ~0 °C for a few days, TLC did not reveal any decomposition products. A solution of K(**2**) in C_2H_5OH can even withstand boiling. This proves that **2** is much more stable than **1**.

After crystallization from a MeOH–*i*-PrOH mixture, Li(**2**) and K(**2**) were isolated as very thin coalescing bronze plates. For K(**2**) it was possible to perform an X-ray diffraction study and to define its structure. Solid K(**2**) is built from a kind of polymeric layers (Fig. 1). Inside the layer, the K atom is surrounded by a nearly square antiprism, whose bases are bent relative to each other at an angle of ~35°. The K–O distances vary from 2.680(9) to 2.933(10) Å; K–N distances, from 2.917(10) to 2.991(11) Å. The shortest K–K distance in the layer is 3.49(1) Å. The K–K interlayer distances are much longer (at least 11 Å). With this setting, each fragment of **2** is surrounded by four K atoms, and each K atom is surrounded by four fragments of **2**. The distances between the paramagnetic centers in solid K(**2**) are long enough. Therefore, μ_{eff} of this compound is close to 1.73 BM and remains virtually unaltered even at very low temperatures. Unfortunately, numerous attempts to separate quality crystals from conglomerates of Li(**2**) plates failed. For this reason, we failed to investigate the structure of Li(**2**) and to judge the structure of exchange clusters responsible for the ferromagnetic exchange interactions in solid Li(**2**) (Fig. 2).

3.2. Synthesis and structures of coordination compounds

Reaction of K(**1**) with transition metal salts confirmed that **1** is liable to decarboxylation. Addition of transition metal salts to an aqueous solution of K(**1**) merely accelerated the process. After K(**1**) had reacted with $CuCl_2$, the reaction mixture contained small amounts of single crystals, which were shown by X-ray diffraction analysis to be the known NN–NN biradical.

As might be expected, **2** proved to be much more stable in reactions with transition metal salts. The interaction of transition metals with **2**, however, has a number of specific features. If, for example, a solution of a paramagnetic metal salt is added very slowly (for 2 or 3 h or more) to an alcoholic solution of K(**2**), then most of **2** decomposes, preventing one from isolating the desired product. If, however, the solutions of K(**2**) and a transition metal salt are mixed rapidly, the complex also quickly separates as a solid. The product is obtained as a very fine precipitate. Quality single crystals cannot be prepared by further recrystallization of these finely disperse products because they decompose on heating. Single crystals were grown directly from the reaction mixture for Cu(**2**)$_2$(CH$_3$OH)$_2$ and Ni(**2**)$_2$(py)$_2$ complexes alone. A solution of a transition metal salt was carefully dropped for 15–30 min into a solution of K(**2**). The reaction mixture was then allowed to stay at room temperature for 50–70 min from the moment of the start of the

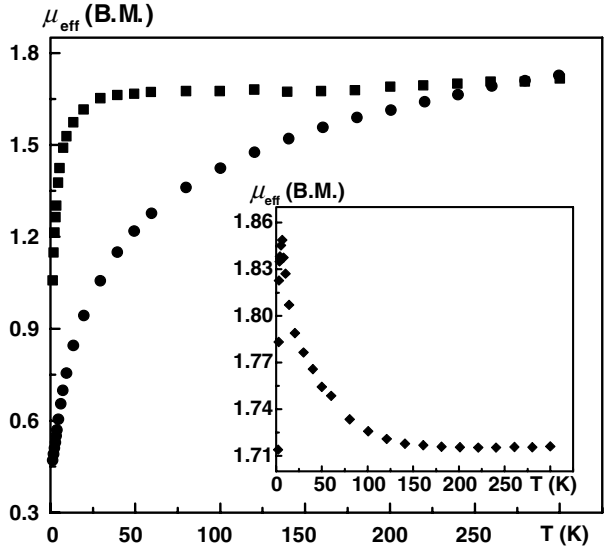


Fig. 2. Dependences $\mu_{eff}(T)$ for K(**1**) (●), K(**2**) (■), and Li(**2**) (inset).

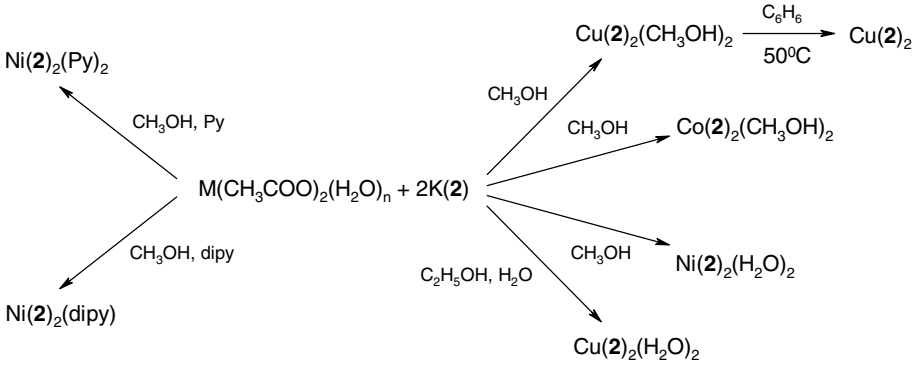
addition, whereupon the crystals were quickly filtered off. If storage in the mother solution is prolonged, the crystals gradually vanish, transforming into soluble decomposition products. Numerous attempts to prepare $Ni(\mathbf{2})_2(H_2O)_2$, $Co(\mathbf{2})_2(CH_3OH)_2$, $Cu(\mathbf{2})_2(H_2O)_2$, and $Ni(\mathbf{2})_2(dipy)\cdot H_2O$ complexes as single crystals by this procedure failed. Stirring $Cu(\mathbf{2})_2(CH_3OH)_2$ crystals in warm (50 °C) benzene yielded finely disperse $Cu(\mathbf{2})_2$ powder. The reactions leading to complexes with **2** are represented below as Scheme 3.

In solid $Cu(\mathbf{2})_2(CH_3OH)_2$, the centrosymmetric square environment of the Cu atom consists of the imine N atoms of the imidazoline ring and the O atoms of the carboxylate groups of the two bidentate molecules **2**; it is completed to a distorted octahedron by the O atoms of the two CH_3OH molecules. The Cu–N, Cu–O, and Cu–O_{OH} distances are 1.981(2), 1.970(2), and 2.410(3) Å, respectively (Fig. 3). The $\{Cu(\mathbf{2})_2(CH_3OH)_2\}$ fragments are combined into chains through H-bonds, which form OH groups of the coordinated alcohol molecules and the O atoms of the paramagnetic ligands not coordinated by the metal atom (Fig. 4). The $O_{OH}\cdots O_{C=O}$ and $O_{OH}\cdots O_{NO}$ distances are 2.845(4) and 2.970(4) Å, respectively.

Solid $Ni(\mathbf{2})_2Py_2$ has a molecular structure. The Ni atom (Table 2) is surrounded by an almost regular octahedron with *cis*-arrangement of the ligands (Fig. 5). In $Ni(\mathbf{2})_2Py_2$, as well as in $Cu(\mathbf{2})_2(CH_3OH)_2$, the N–O distances are 1.256(4)–1.263(3) Å, which are the typical distances of nitroxides. The five-membered chelate rings are nearly planar. The angle between the planes of the atoms of the carboxyl group and the atoms of the CN_2 fragment of the heterocycle is up to 8.

3.3. Magnetic properties

At room temperature, μ_{eff} is 3.55–3.58 BM for Cu(II) complexes and 4.41–4.48 BM for Ni(II) complexes; for $Co(\mathbf{2})_2(CH_3OH)_2$, μ_{eff} (300 K) = 5.71 BM. The observed values of μ_{eff} (300 K) are much higher than the theoretical limits for uncoupled spins of metals and the two nitroxides, which is due to the high efficiency of ferromagnetic exchange channels inside the $\{M(\mathbf{2})_2\}$ bischelate fragments, where M = Cu(II), Ni(II), Co(II). For



Scheme 3.

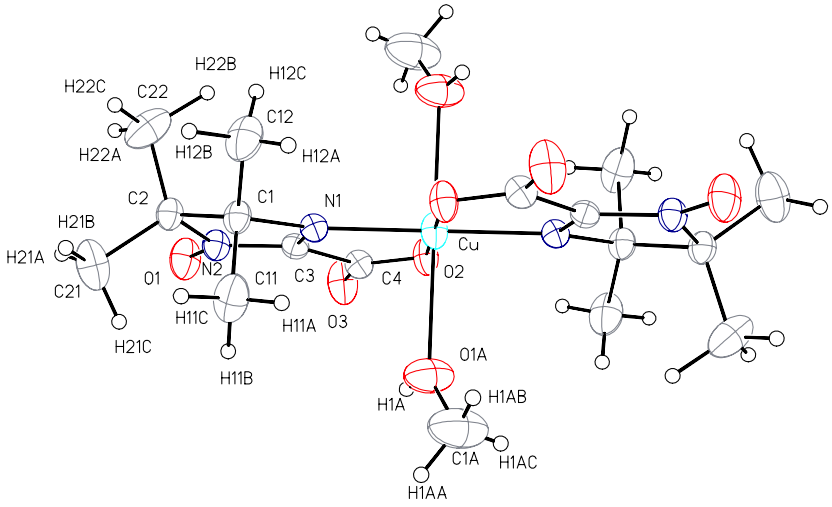


Fig. 3. Structure of $Cu(\mathbf{2})_2(CH_3OH)_2$ and numbering scheme.

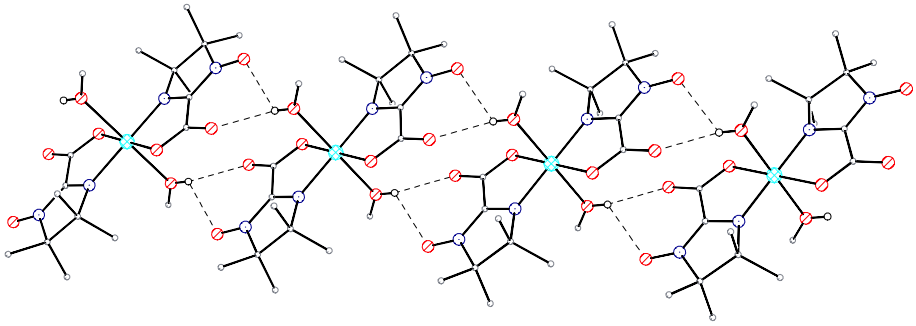


Fig. 4. Chain in the structure of $Cu(\mathbf{2})_2(CH_3OH)_2$.

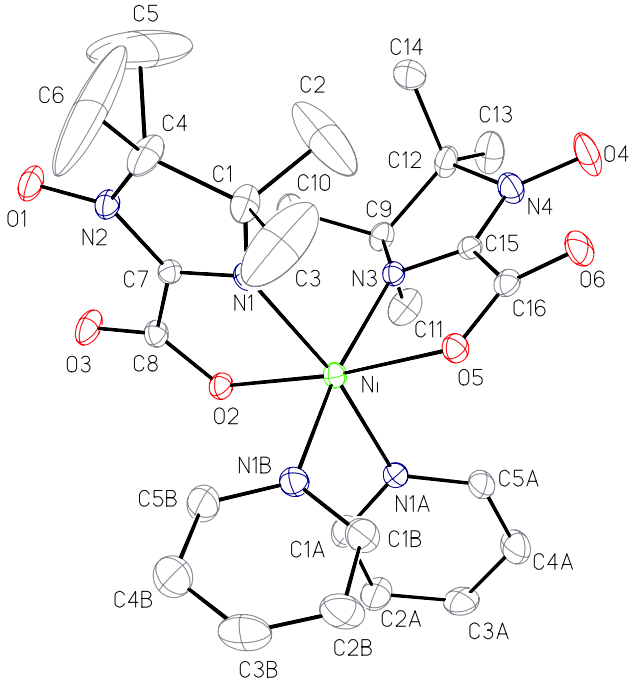


Fig. 5. Structure of $Ni(\mathbf{2})_2Py_2$ and numbering scheme.

$Co(\mathbf{2})_2(CH_3OH)_2$ the low-lying excited levels of Co(II) also make a significant contribution to μ_{eff} (300 K), which is also typical for the octahedral complexes of Co(II) [9] (Figs. 6 and 7). At low temperatures, the $\chi(T)$ functional dependence for $Cu(\mathbf{2})_2(CH_3OH)_2$, $Cu(\mathbf{2})_2(H_2O)_2$, $Ni(\mathbf{2})_2(py)_2$, $Ni(\mathbf{2})_2(H_2O)_2$, and $Co(\mathbf{2})_2(CH_3OH)_2$ shows maxima at 2.2, 2.1, 8, 4, and 3 K, respectively, suggesting that magnetic chains are formed in these solids. The fundamental exchange channels that form the magnetic chain structure are strong ferromagnetic exchange interactions inside $\{M(\mathbf{2})_2\}$ bischelate fragments and weaker antiferromagnetic interactions between $M(\mathbf{2})_2$ bischelates. We evaluated the effective g factors of the metal (g), as well as the exchange parameters inside (J) and between (J_c) the bischelate fragments within the framework of the alternant chain model [10] using the isotropic spin Hamiltonian (Table 3). The corresponding theoretical dependences are presented by solid lines in Figs. 6 and 7.

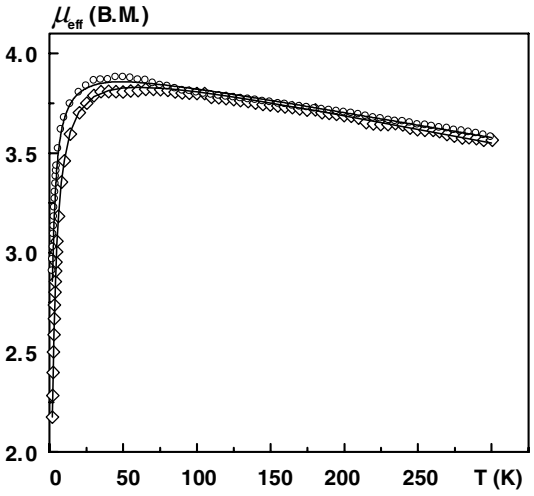


Fig. 6. Dependences $\mu_{eff}(T)$ for $Cu(\mathbf{2})_2(CH_3OH)_2$ (◇) and $Cu(\mathbf{2})_2(H_2O)_2$ (○). Solid lines are theoretical approximation.

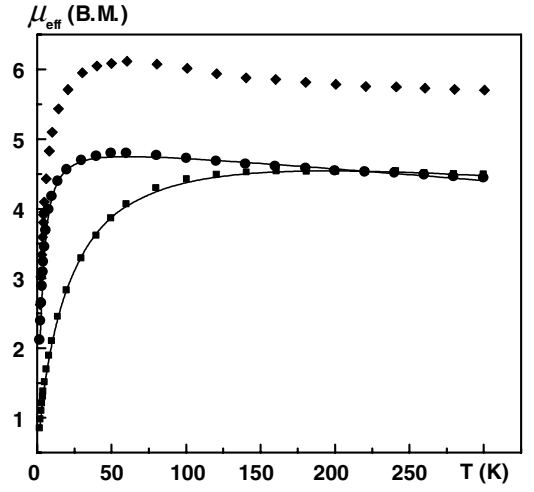


Fig. 7. Dependences $\mu_{eff}(T)$ for $Ni(\mathbf{2})_2(py)_2$ (■), $Ni(\mathbf{2})_2(H_2O)_2$ (●) and $Co(\mathbf{2})_2(CH_3OH)_2$ (◆). Solid lines are theoretical approximation.

For $Cu(\mathbf{2})_2$ at room temperature, μ_{eff} is close to the theoretical limit of 3 BM for three $s = 1/2$ uncoupled spins ($g = 2$). At reduced temperatures, the $\mu_{eff}(T)$ curve

decays, indicating that the antiferromagnetic exchange interactions are dominant. Below 16 K, Cu(**2**)$_2$ is transferred to a magnetically ordered state. Fig. 8 shows zero field cooling magnetization curves ($\sigma(T)$ measured in a magnetic field of 50 Oe during heating and subsequent cooling, and the retentivity curve. From the $\sigma(T)$ dependences obtained it follows that the ordering temperature for the complex is of the order of 16.6 K. The fundamental magnetization curve measured at 2 K (Fig. 9) is linear up to 10 kOe. In stronger magnetic fields, the (σH) curve smoothly departs from linearity, reaching 1650 G cm^3 mol^{-1} at 49.5 kOe. A hysteresis with a loop width of 1050 Oe has been recorded during magnetization reversal for the sample (Fig. 9). The ensuing spontaneous magnetic moment is (σ_s) is 23 G cm^3 mol^{-1}. Note that a hysteresis is observed only for magnetic fields varying from −6 to 6 kOe. Beyond this range, the lines and the reverse σH curves coincide within the limits of the experimental error. Hence, it follows that the *Cu(**2**)$_2$* complex is an antiferromagnet with weak ferromagnetic properties.

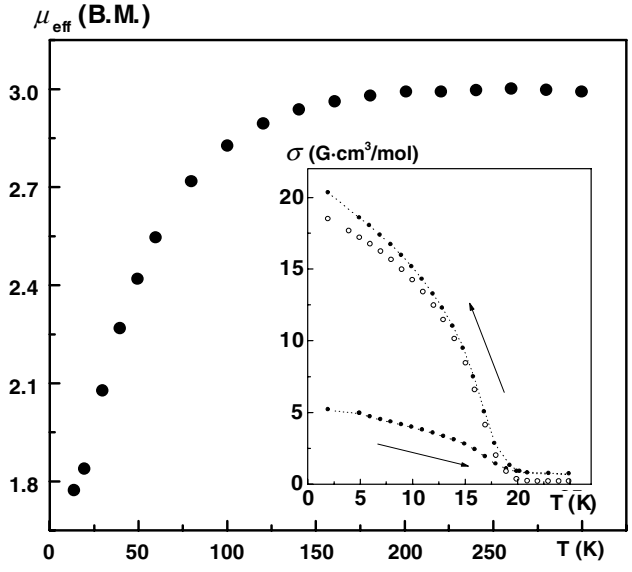


Fig. 8. $\mu_{eff}(T)$ curve in the paramagnetic region for *Cu(**2**)$_2$*. Zero field cooling $\sigma(T)$ curves (•) and residual magnetization curve (○) in the transition area (insert) for *Cu(**2**)$_2$*.

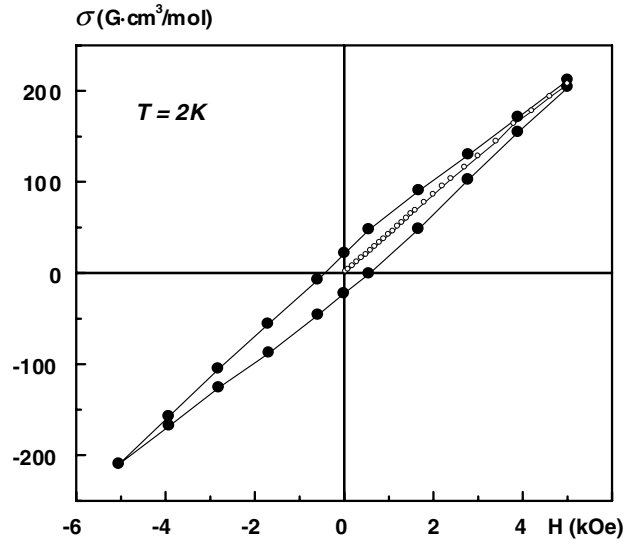


Fig. 9. Main magnetization curve (○) and hysteresis loop (•) for *Cu(**2**)$_2$*.

For Ni(**2**)$_2$(bipy), the magnetic behavior above 5 K (Fig. 10) is similar to the magnetic behavior of *Cu(**2**)$_2$(CH$_3$OH)$_2$*, *Cu(**2**)$_2$(H$_2$O)$_2$*, *Ni(**2**)$_2$(py)$_2$*, *Ni(**2**)$_2$(H$_2$O)$_2$*, or *Co(**2**)$_2$(CH$_3$OH)$_2$*. The calculated exchange parameters are presented in Table 3. Below 5 K, Ni(**2**)$_2$(bipy), like Cu(**2**)$_2$, is a weak ferromagnet with $T_N = 4.6$ K and spontaneous magnetization $\sigma_s = 90$ G cm^3 mol^{-1}. Magnetization reversal for the sample in magnetic fields from −6 to 6 kOe follows the hysteresis curve (Fig. 11) with a loop width of 1680 Oe.

Thus we succeeded in developing an effective procedure for the synthesis of the potassium salt K(**1**). X(**2**) were found to be much more stable, due to which we isolated a series of heterospin complexes with **2**. These compounds are characterized by rather strong ferromagnetic intramolecular exchange interactions. For Cu(**2**)$_2$

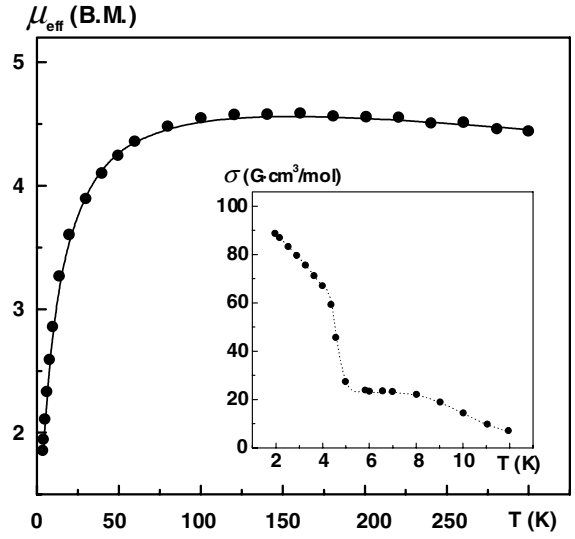


Fig. 10. $\mu_{eff}(T)$ curve in the paramagnetic region (solid line is theoretical approximation) and residual magnetization curve in the transition area (inset) for *Ni(**2**)$_2$(bipy)*.

Table 3
Exchange parameters for chain polymeric compounds

Compound	g	J (cm^{-1})	J_c (cm^{-1})	σ
*Cu(**2**)$_2$(CH$_3$OH)$_2$*	2.13	175	−0.51	0.00017
*Cu(**2**)$_2$(H$_2$O)$_2$*	2.10	186	−0.14	0.00031
*Ni(**2**)$_2$(py)$_2$*	2.20	114	−5.78	0.00107
*Ni(**2**)$_2$(H$_2$O)$_2$*	2.15	89	−1.65	0.00195
*Ni(**2**)$_2$(bipy)*	2.17	127	−2.54	0.00051

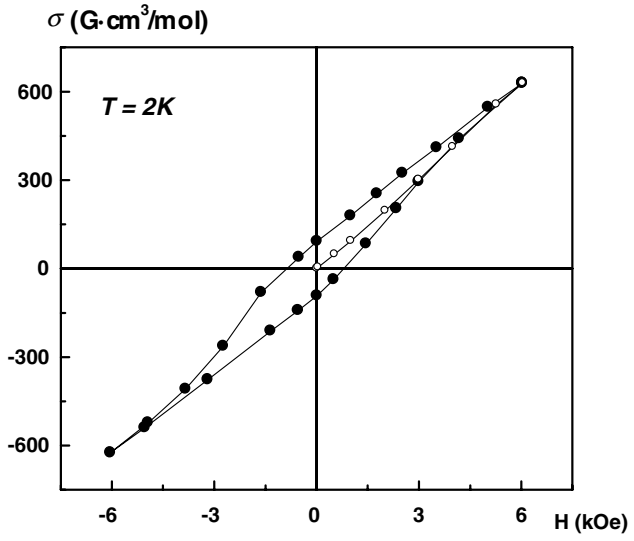


Fig. 11. Main magnetization curve (○) and hysteresis loop (●) for *Ni(**2**)$_2$(bipy)*.

and Ni(**2**)$_2$(bipy), cooperative magnetic ordering effects have also been recorded.

Supplementary materials

Crystal data for the structural analysis of investigated compounds have been deposited with the Cambridge Crystallographic Data Centre, CCDC Nos., and 250022 (K(**2**)), 250023 (Cu(**2**)$_2$(CH$_3$OH)$_2$), 250024 (Ni(**2**)$_2$Py$_2$). Copies of this information may be obtained free of charge from The Director, CCDC, 12 Union Road, Cambridge CB2 1EZ, UK (fax: +44-1233-336033; e-mail: deposit@ccdc.cam.ac.uk or www: http://www.ccdc.cam.ak.uk).

Acknowledgement

This work was supported by RFBR (03-03-32518 and 02-03-33112), BRHE (NO-008-X1, Y1-C-08-03, and Y1-C-08-12), Russian science-support fund, RAS, and SB RAS Grants.

References

[1] D.G.B. Boocock, R. Darcy, E.F. Ullman, J. Am. Chem. Soc. 90 (1968) 5945.
[2] D.G.B. Boocock, E.F. Ullman, J. Am. Chem. Soc. 90 (1968) 6873.
[3] O.V. Koreneva, G.V. Romanenko, V.N. Ikorsky, S.V. Fokin, V.I. Ovcharenko, Russ. J. Struct. Chem. 42 (2001) 977.
[4] V.I. Ovcharenko, S.V. Fokin, P. Rey, Mol. Cryst. Liq. Cryst. 334 (1999) 109.
[5] V.I. Ovcharenko, S.V. Fokin, I.V. Korobkov, P. Rey, Russ. Chem. Bull. 48 (1999) 1519.
[6] C. Bätz, P. Amann, H.-J. Deiseroth, L. Dulog, Liebigs Ann. Chem. (1994) 739.
[7] R. Weiss, N. Kraut, F. Hampel, J. Organomet. Chem. 617–618 (2001) 473.
[8] Weygand-Hilgetag, Organisch-Chemische Experimentierkunst, Johann Ambrosius Barth–Verlag, Leipzig, 1964.
[9] Yu.V. Rakitin, Interpretation of the EPR Spectra of Coordination Compounds, Nauka, Moscow, 1993 (in Russian).
[10] A.B. Gelman, V.N. Ikorskii, Zh. Strukt. Khim. 30 (1989) 81, Chem. Abstr. 111: 223878.

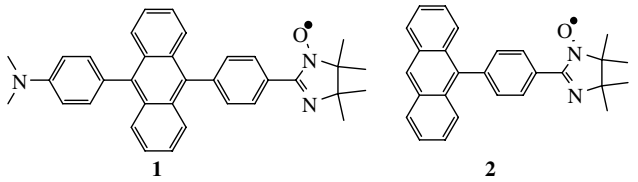


Fig. 1. Molecule studied in this work, **1** and previously reported stable radical, **2** with the excited quartet high-spin state.

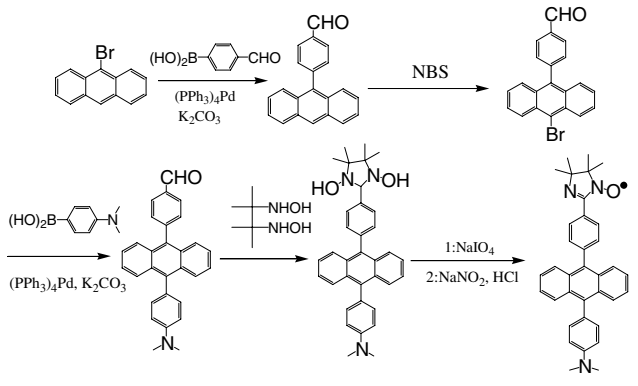
clarify the energy relaxation from the excited high-spin state to the ground state and the photo-induced electron transfer process from the excited state. As a basic study to develop their systems to the functional materials, the charge-transfer complexes based on the stable radicals with the photo-excited high-spin states are important research targets in order to clarify the photo-induced electron transfer from the high-spin excited states.

In this paper, we report the design, synthesis and electronic state of a π-conjugated stable iminonitroxide radical, **1**, electron donor property of which is expected to be improved than that of **2** [1,2] by attaching dimethylamino group. The molecular structures of **1** and **2** are shown in Fig. 1. The electronic and magnetic properties on the ground state were studied by CV, UV–Vis absorption spectra, and ESR. Molecular orbital calculation was also carried out. The spin alignment on the photo-excited state was investigated by a time-resolved ESR (TRESR) experiment. In addition, we also report two CT complexes which are synthesized using **1** as an electron donor.

2. Experimental

2.1. Synthesis of stable radical *1*

2,3-Bis(hydroxyamino)-2,3-dimethylbutane was prepared according to the literature method [13]. Other reagents were used as purchased. Column chromatography was performed on alumina (Merk Aluminum Oxide 60). **1** was synthesized according to Scheme 1. Sample was purified by the column chromatography on toluene.



Scheme 1.

Repeating re-crystalizations from EtOH/toluene gave **1** as red powder: m.p. > 300 °C (Found: C, 81.96; H, 6.67; N, 8.10 requires: C, 82.00; H, 6.68; N, 8.20).

2.2. Preparation of CT complexes

2.2.1. 1-TCNQ

The CT complex was prepared under argon in acetonitrile by the reaction of **1** with TCNQ. In order to accelerate the formation of the complex, the solution was refluxed for 6 h. The residue (excess amount of **1**) was filtered and the solution was evaporated and the precipitate was recrystallized from dichloromethane.

2.2.2. 1-BQF_4

The CT complex was prepared under argon in dichloroethane by mixing **1** with an excess amount of tetrafluoro-1,4-benzoquinone. The mixture was degassed in vacuum and cooled at −20 °C for a few days. The precipitate was filtrated and washed carefully. The dark green powder was purified by removing the contamination of tetrafluoro-1,4-benzoquinone in the precipitate using sublimation method.

The results of the elemental analyses were not sufficient in these complexes. Further improvement of the syntheses and purifications are in progress. Therefore, only the results of the optical absorption and TRESR will be reported and their magnetic properties will be not presented in this paper.

2.3. Measurements

Oxidation potential of **1** was measured by the CV method using a Hokuto Dennko HSV-100 and UV–Vis absorption spectra were obtained with a Hitachi U-3000. Conventional ESR spectra were observed with a JEOL TE300 X-band ESR spectrometer. The ab initio molecular orbital calculations were carried out based on the density functional theory (DFT) using GAUSSIAN 98 [14]. In the ab initio calculations, the STO 6-31G basis sets and UHF Becke 3LYP (UBecke 3LYP) hybrid method were employed. The photo-excited states were investigated by time-resolved ESR (TRESR) method. The detail of our TRESR setup was described in our previous paper [2]. The temperature in the ESR and TRESR measurements was controlled using an Oxford ESR 910 cold He gas flow system.

3. Results and discussion

The oxidation potential value of **1** in acetonitrile solution was 0.44 V on ferrocene which value was ca. 0.35 V smaller than **2**. The optical absorption band assigned to $\pi^* \leftarrow \pi$ transition arising from anthracene moiety was also shifted to longer wavelength. The calculated orbital

energies and molecular orbitals of **1** and **2**, shown in Fig. 2, were consistent with these experimental results. The energy location of π-HOMO of **1** becomes about 0.6 eV higher than that of **2**. These results show that the location of π-HOMO of **1** becomes higher in energy than that of **2** as the result of the attachment of dimethylamino group at the proper position.

The photo-excited state and the photo-induced spin alignment in **1** were investigated by TRESR experiments. Typical TRESR spectrum of **1** observed at 30 K in 2-MTHF glass matrix is shown in Fig. 3 together with the spectral simulation. The simulation was carried out using the eigenfield [15]/exact-diagonalization hybrid method [16] reported previously by taking the dynamic electron spin polarization under zero-magnetic field into account. The spectrum shows well resolved fine-structure splitting. The spectral simulation revealed that the observed TRESR spectrum of **1** has been unambiguously assigned as an excited quartet ($S = 3/2$) spin state (Q). The g value and fine-structure parameters for the quartet state have been determined to be $g(Q) = 2.0043$, $D(Q) = 0.0235\ \mathrm{cm}^{-1}$, $E(Q) = 0.0\ \mathrm{cm}^{-1}$.

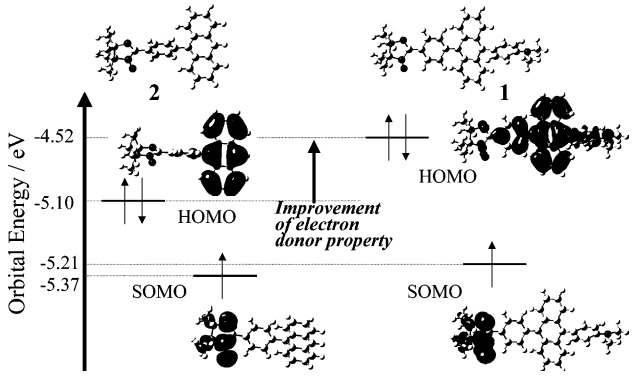


Fig. 2. Orbital energies and molecular orbitals of **1** and **2**.

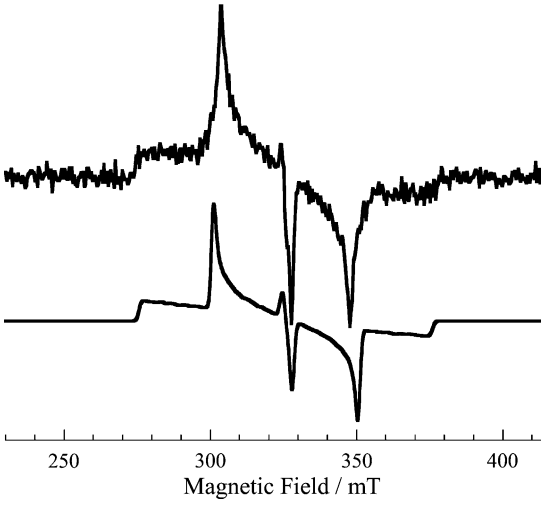


Fig. 3. Typical TRESR spectrum observed at 0.8 μs after LASER excitation.

The magnitude of the fine-structure parameter, D, clearly shows that the observed high-spin excited states are constructed from the ππ* excited metastable triplet state of anthracene and the doublet spin of the dangling radical. The D value of **1** was very close to that of **2** [2]. The characteristic property of the molecule **2** with the excited high-spin state is maintained in **1** and only the property of the electron donor is improved by attaching the dimethylamino group.

Fig. 4 shows the diffuse-reflection absorption spectra of **1**, TCNQ and **1**-TCNQ charge-transfer complex. CT band was clearly observed in **1**-TCNQ. A similar CT complex (1-BQF_4) was also obtained between **1** and BQF_4. A strong Charge-Transfer band was also observed in this case. These results show that **1** can be certainly available as the electron donor for a series of the electron acceptors which one can purchased commercially. The TRESR measurement for **1**-TCNQ gave an absorptive signal shown in Fig. 5. This spectrum was observed in the polar rigid glass matrix (acetonitrile:butylnitrile:

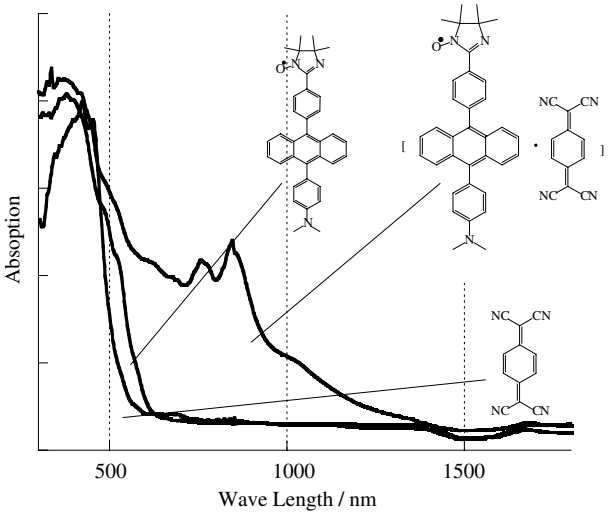


Fig. 4. Diffuse-reflective spectra of **1**, TCNQ and **1**-TCNQ.

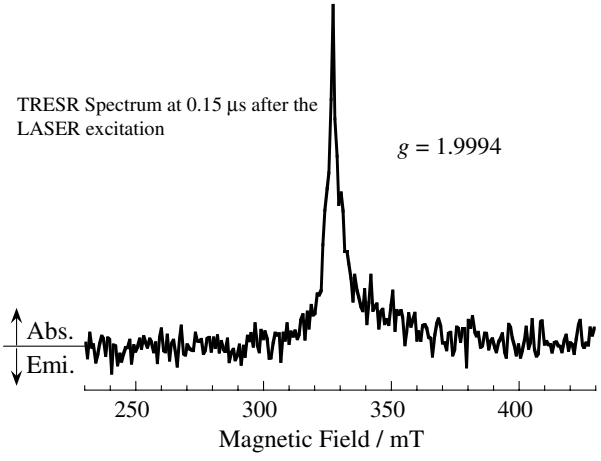


Fig. 5. Typical TRESR of **1**-TCNQ CT Complex.

dichloromethane = 1:1:1 mixed solvent). There is a possibility that this signal comes from the photo-induced electron transfer from the excited quartet high-spin state of 1 to the electron acceptor of TCNQ. However, more careful experiments including the experiments by the photo-excitaion of CT band and the combination studies with optical spectra are necessary to identify the origin of this signal. These studies are going in progress.

4. Conclusions

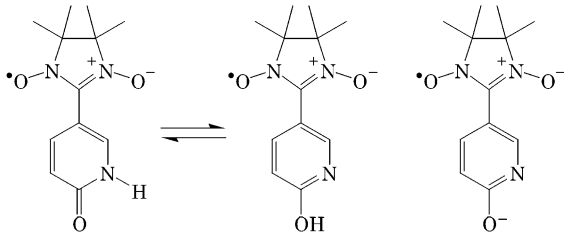
1 was designed based on the ab initio MO calculation and synthesized as the stable radical which electron donor property was improved compared with **2** previously reported. It is confirmed that **1** has the photo-excited high-spin quartet ($S = 3/2$) state as well as **2** by the TRESR experiment. Two CT complexes were synthesized using **1** as an electron donor. A TRESR signal was observed for **1**-TCNQ CT complex which may be arising from the photo-induced electron transfer from the quartet excited state of **1** to the TCNQ acceptor.

Acknowledgements

This work was supported by the Grant-in-Aid for Scientific Research on the general (Nos. 13440211 and 16350079) and Priority Area "Application of Molecular Spins" (Area No. 769, Proposal No. 15087208) from the Ministry of Education, Culture, Sports, Science and Technology, Japan.

References

[1] Y. Teki, S. Miyamoto, K. Iimura, M. Nakatsuji, Y. Miura, J. Am. Chem. Soc. 122 (2000) 984.
[2] Y. Teki, S. Miyamoto, M. Nakatsuji, Y. Miura, J. Am. Chem. Soc. 123 (2000) 294.
[3] Y. Teki, M. Nakatsuji, Y. Miura, Mol. Phys. 100 (2002) 1385.
[4] Y. Teki, M. Nakatsuji, Y. Miura, Int. J. Mod. Phys. B 15 (2001) 4029.
[5] Y. Teki, Polyhedron 20 (2001) 1163.
[6] Y. Teki, M. Kimura, S. Narimatsu, K. Ohara, K. Mukai, Bull. Chem. Soc. Jpn. 77 (2004) 95.
[7] Y. Teki, S. Nakajima, Chem. Lett. 33 (2004) 1500.
[8] (a) C. Corvaja, M. Maggini, M. Prato, G. Scorrano, M. Venzin, J. Am. Chem. Soc. 117 (1995) 8857;
(b) N. Mizouchi, Y. Ohba, S. Yamauchi, J. Chem. Phys. 101 (1997) 5966.
[9] (a) K. Ishii, J. Fujiwara, Y. Ohba, S. Yamauchi, J. Am. Chem. Soc. 118 (1996) 13079;
(b) K. Ishii, J. Fujisawa, A. Adachi, S. Yamauchi, N. Kobayashi, J. Am. Chem. Soc. 120 (1998) 3152.
[10] P. Ceroni, F. Conti, C. Corvaja, M. Maggini, F. Paolucci, S. Roffia, G. Scorrano, A. Toffoletti, J. Phys. Chem. A 104 (2000) 156.
[11] (a) N. Mizouchi, Y. Ohba, S. Yamauchi, J. Phys. Chem. 103 (1999) 7749;
(b) F. Conti, C. Corvaja, A. Toffoletti, N. Mizouchi, Y. Ohba, S. Yamauchi, M. Maggini, J. Phys. Chem. 104 (2000) 4962;
(c) J. Fujiwara, Y. Iwasaki, Y. Ohba, S. Yamauchi, N. Koga, S. Karasawa, M. Fuhs, K. Möbius, S. Weber, Appl. Magn. Reson. 21 (2001) 483.
[12] K. Ishii, Y. Hirose, N. Kobayashi, J. Phys. Chem 103 (1999) 1986.
[13] C. Hirel, K.E. Vostrikova, J. Pecaut, V.I. Ovcharenko, P. Rey, Chem. Eur. J. 7 (2001) 2007.
[14] The DFT calculation was carried out using GAUSSIAN 98, Revision A.11, Gaussian, Inc., Pittsburgh PA, 1998.
[15] G.G. Belford, R.L. Belford, J.F. Burkhalter, J. Magn. Reson. 11 (1973) 251.
[16] Y. Teki, I. Fujita, T. Takui, T. Kinoshita, K. Itoh, J. Am. Chem. Soc. 116 (1994) 11499, In the spectral simulation of the TRESR spectra, the calculation of ESP has been added as a subroutine to the computer program. More detailed procedures of the spectral simulation for high-spin organic molecules are similar to those described in our previous paper for the perturbation approach: Y. Teki, T. Takui, H. Yagi, K. Itoh, and H. Iwamura, J. Chem. Phys. 83 (1985) 539.



Scheme 1.

2. Experimental

2.1. General

The ligand, 5-(4′,4′,5′,5′-tetramethylimidazoline-3′-oxide-1′-oxyl)-2(1*H*)-pyridone, was prepared from corresponding aldehyde precursors according to standard procedures [11,12]. The UV–Vis spectra for DMF solutions were recorded on a JASCO V570 UV/Vis/NIR spectrophotometer. Infrared spectra were recorded on a JASCO FT-IR 230 spectrometer using KBr pellets in the 4000–400 cm^{-1} range. Elemental analyses were performed using a Yanagimoto MT-3 C–H–N coder. ESR spectra were measured on a JEOL JES-TE100 spectrometer (X-band microwave unit). The magnetic susceptibilities were measured with a Quantum Design MPMS-2 SQUID susceptometer in the temperature range of 2–300 K at a constant field of 1 T. Diamagnetic corrections for the samples were determined from Pascal's constants and the literature values.

The X-ray data were collected using Mo Kα radiation on a CCD diffractometer (SMART APEX; Bruker Analytik, GmbH). The structures were solved by direct methods (SIR92 [13]) and refinement converged using full-matrix least squares of the CRYSTALSTRUCTURE [14] program. All non-hydrogen atoms were refined anisotropically. Most of the hydrogen atoms were placed at ideal positions using a rigid model. The tetramethylethylene group in one of the nitronyl nitroxide moieties in **1** was disordered over two sites with occupancy of 1:1; no hydrogens were attached to these methyl carbons. The hydroxyl hydrogen in **2** was located from the Fourier map and refined isotropically. Crystallographic data of **1** and **2** are listed in Table 1, and selected bond lengths and angles are shown in Table 2.

2.2. Preparation of [Cu_2(**L**)$_4$(DMF)$_2$] (**1**)

Sodium methoxide (30 mg, 0.55 mmol) was added to a methanol solution (5 ml) of **HL** (136 mg, 0.54 mmol) cooled in an ice bath. After stirring for 1 h, copper(II) nitrate trihydrate (65 mg, 0.27 mmol) dissolved in methanol (5 ml) was added dropwise. The reaction mixture was stirred overnight at room temperature to obtain light blue powders. The precipitate was dissolved in DMF, and slow evaporation of the solution afforded dark blue plate crystals of [Cu_2(**L**)$_4$(DMF)$_2$] over several weeks, yield 52 mg (30.4%). ESR in DMF solution: a_N = 0.77 mT (2N) at g = 2.007; IR (KBr): ν_{max}/cm^{-1} 1659s, 1611s, 1559m, 1507m, 1394m, 1368m, 1336m, 1133m, 871w, 830, 474w, 437w; λ_{max}/nm (ε/M^{-1} cm^{-1}) (DMF) 286 (36 000), 362 (19 500), 615 (3300). *Anal.* Calc. for $C_{54}H_{74}N_{14}O_{14}Cu_2$: C, 50.69; H, 5.78; N, 15.35. Found: C, 51.06; H, 5.87; N, 15.44%.

Table 1
Crystallographic data **1** and **2**

	1	**2**
Formula	$C_{54}H_{74}N_{14}O_{14}Cu_2$	$C_{24}H_{32}Cl_2N_6O_6Pd$
Formula weight	1270.74	677.86
Crystal system	monoclinic	monoclinic
Space group	$P2_1/n$ (No. 14)	$C2/c$ (No. 15)
a (Å)	10.988(2)	21.809(2)
b (Å)	27.253(3)	10.9736(9)
c (Å)	10.6839(13)	12.0466(10)
β (°)	109.596(6)	101.233(1)
V (Å^3)	3012.0(6)	2827.8(4)
Z	1	4
D_{calc} (g cm^{-3})	1.267	1.592
T (K)	90	153
μ (cm^{-1})	4.33	8.95
Final R[a]	0.080	0.038
Final Rw[b]	0.210	0.105
Goodness-of-fit	1.01	1.00

[a] $R = \sum\|\|F_o\| - |F_c\|\|/\sum|F_o|$.
[b] $R_w = [\sum w(F_o^2 - F_c^2)^2/\sum w(F_o^2)^2]^{1/2}$.

Table 2
Selected bond lengths (Å), bond angles (°), and torsion angles (°) for **1** and **2**

1			
Cu–Cu[a]	2.602(1)	Cu–N(1)	2.022(5)
Cu–N(4)	2.006(6)	Cu–O(1)[a]	1.969(5)
Cu–O(4)[a]	1.968(5)	Cu–O(7)	2.187(4)
Cl–O(1)	1.270(6)	C(13)–O(4)	1.297(6)
N(1)–Cu–N(4)	86.8(2)	N(1)–Cu–O(1)[a]	170.2(2)
N(1)–Cu–O(4)[a]	92.8(2)	O(1)[a]–Cu–N(4)	89.0(2)
O(1)[a]–Cu–O(4)[a]	90.1(2)	N(4)–Cu–O(4)[a]	171.4(2)
Cu[a]–O(1)–C(1)	127.3(4)	Cu[a]–O(4)–C(13)	127.4(4)
N(2)–C(6)–C(4)–C(3)	20.3(14)	N(6)–C(18)–C(16)–C(17)	37.2(14)
2			
Pd–Cl(1)	2.324(1)	Pd–Cl(2)	2.276(1)
Pd–N(1)	2.019(3)	O(3)–C(4)	1.332(4)
N(1)–C(4)	1.349(4)	N(1)–C(5)	1.341(4)
Cl(1)–Pd–Cl(2)	180	Cl(1)–Pd–N(1)	90
Pd–N(1)–C(4)	121.4(2)	C(4)–N(1)–C(5)	119.8(3)
Cl(1)–Pd–N(1)–C(4)	91.0(8)	O(2)–N(3)–C(6)–C(1)	1.9(5)

[a] Symmetry operators: $-x + 1/2$, $y + 1/2$, $-z + 1/2$.

2.3. Preparation of trans-[$PdCl_2$(**HL**)$_2$] (**2**)

To a solution of 18-crown-6 ether (84.7 mg, 0.32 mmol) in 2 ml of dichloromethane:methanol (1:1 v/v) solution

was added potassium tetrachloropalladate(II) (26.1 mg, 0.080 mmol). After stirring for 10 min, a methanol solution (2 ml) of **HL** (40.1 mg, 0.16 mmol) was added dropwise. Slow evaporation of the solution afforded deep blue needle crystals of *trans*-[$PdCl_2$(**HL**)$_2$] in a week, yield 41.7 mg (77%). ESR in DMF solution: $a_N = 0.78$ mT (2N) at $g = 2.008$; IR (KBr): ν_{max}/cm^{-1} 1655s, 1613s, 1425m, 1386m, 1371s, 1307m, 1216m, 1134s, 834m, and 543m; λ_{max}/nm ($\varepsilon/M^{-1}\,cm^{-1}$) (DMF) 289 (35 000), 312sh (21 500), 365 (10 400), 620 (1460), 672 (1200). *Anal.* Calc. for $C_{24}H_{32}Cl_2N_2O_6Pd$: C, 42.52; H, 4.76; N, 12.40. Found: C, 41.76; H, 4.89; N, 11.63%.

3. Results and discussion

3.1. Preparation and crystal structures

Complexes **1** and **2** were prepared by reactions of deprotonated $\mathbf{L}^-$ with copper(II) nitrate and **HL** with potassium tetrachloropalladate(II), respectively. Complex **1** was found to be a dinuclear paddle-wheel copper complex with deprotonated pyridonate ligands, while **2** was a mononuclear palladium complex with neutral ligands. We also attempted preparation of dinuclear palladium(II) complexes with $\mathbf{L}^-$, but crystalline materials were unobtainable for the reaction.

The structure of **1** in the crystal is shown in Fig. 1. The copper atoms are penta-coordinated to form a square-pyramidal coordination geometry. Four pyridonate ligands are coordinated to the copper atoms as bridging ligands in the equatorial planes and two DMF molecules are ligated at axial positions. This complex has a crystallographic inversion center, and orientation of the four pyridonate ligands confers approximate C_{2h} symmetry upon the complex. The Cu–Cu distance of 2.602(1) Å is slightly longer than those for typical dinuclear copper(II) complexes [2b]. Within the ligands, the pyridonate plane and the nitronyl nitroxide plane are twisted by 20.3° and 37.0° for the two crystallographically independent ligands. The radical moieties are intermolecularly well-separated from each other: the shortest intermolecular distance between the neighboring nitronyl nitroxide groups is 4.29 Å.

Fig. 2(a) shows the molecular structure of **2** in the crystal. The complex has a centrosymmetric structure; the palladium ion is located on the inversion center and coordinated with two **HL** ligands and two chlorine atoms in *trans* positions, exhibiting a square planar coordination geometry. Interestingly, the ligand is in a 2-hydroxypyridine form, in which the nitrogen atoms are coordinated to the metal ion and the phenolic group is hydrogen-bonded to the chlorine atom of the adjacent unit. The hydroxypyridine ring of the ligand is almost perpendicular to the coordination plane of the palladium ion, with the dihedral angle of 91.1(2)°. The dihedral angle between the nitronyl nitroxide plane and the hydroxypyridine ring is 20.7(5)°. Fig. 2(b) shows the packing diagram of the complex. One chlorine atom

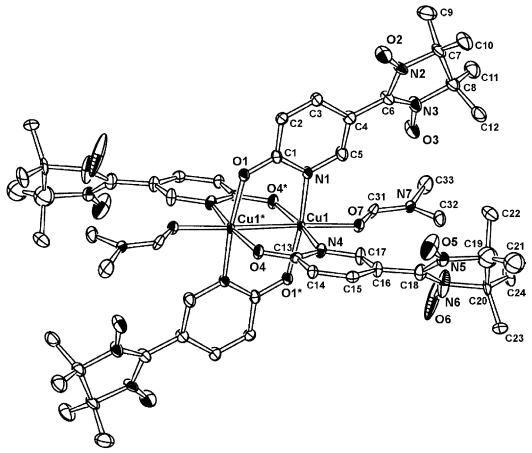


Fig. 1. ORTEP [20] drawing of the molecular structure of **1** showing 50% probability ellipsoids. One of the dimethylethylene groups of the nitronyl nitroxide is disordered over two sites. For clarity, only one moiety is shown.

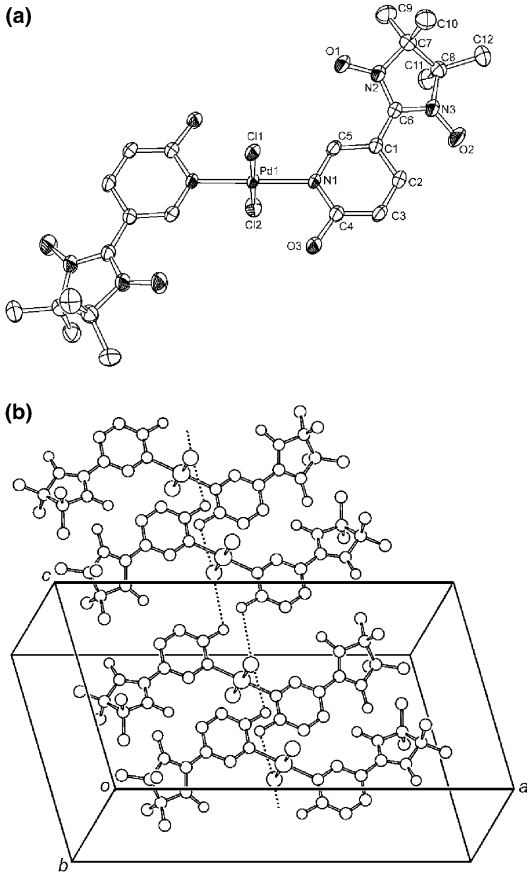


Fig. 2. (a) ORTEP drawing of the molecular structure of **2**, showing 50% probability ellipsoids. (b) Packing diagram of **2**. Hydrogen atoms are omitted for clarity. The dashed lines represents the hydrogen bond along the *c*-axis (O–H···Cl: 3.11 Å).

[Cl(1)] of the complex is hydrogen-bonded by the phenolic groups of two neighboring molecules (–O–H···Cl···H–O–) to form a double-chain hydrogen-bonded network along the *c*-axis, whereas the other chlorine atom Cl(2) is free. The hydrogen-bond distance (O–H···Cl: 3.11 Å) is comparable to those observed in NH···Cl type hydrogen bonds (3.10–3.15 Å) [15]. Several short intermolecular distances exist between the neighboring NO-groups, which are ca. 3.9–4.0 Å.

It has been reported that mononuclear palladium(II) or platinum(II) complexes with pyridone analogues or nucleobases ligands bind metal ions upon deprotonation, producing dinuclear and polynuclear metal complexes [16]. We found that the addition of barium hydroxide to **2** in water exhibit a slight broadening of the ESR spectra, without decomposition, possibly indicating the barium ion binding. Such a radical complex as **2**, bearing additional coordination sites, will be potentially useful for chemical sensing purposes, and useful as a building block for polynuclear metal complexes with radical ligands.

3.2. Magnetic properties

Magnetic susceptibility data for **1** and **2** are shown in Fig. 3 in the form of a χT versus T plot. The room temperature value of χT for **1**, 1.88 emu K mol^{-1}, is markedly smaller than the expected value for an uncorrelated six $S = 1/2$ spin system (2.25 emu K mol^{-1}). The lower value of χT results from the cancellation of the moderately strong antiferromagnetic interaction between the dimeric copper atoms. The χT values decrease steadily with decreasing temperature, then drop rapidly below 10 K. The magnetic susceptibility data were analyzed on the basis of a model consisting of the singlet–triplet term ($\boldsymbol{H} = -2J_{ST}\boldsymbol{S}_a \cdot \boldsymbol{S}_b$) for the dinuclear copper unit and the Curie–Weiss term for the radical spins (Eq. (1)). In that equation, J_{ST} is the exchange coupling of the intramolecular Cu–Cu interaction, n (=4) is the number of organic radicals per dimer, and θ is the intermolecular interaction [16]. The best result was obtained with the parameters $g_{Cu} = 2.2$, $g_{rad} = 2.0$ (fixed), $J_{ST}/k_B = -235$ K, and $\theta = -2.2$ K.

$$\chi = \frac{2Ng_{Cu}^2\mu_B^2}{k_BT[3+\exp(-2J_{ST}/k_BT)]} + n\left[\frac{2Ng_{rad}^2\mu_B^2S(S+1)}{3k_B(T-\theta)}\right] \quad (1)$$

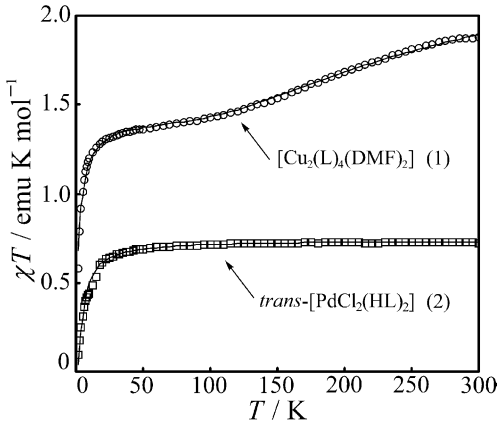


Fig. 3. Plots of χT vs. T for crystalline samples of **1** and **2**. The solid curve corresponds to the data that were fit using the parameters given in the text.

Density functional theory (DFT) calculations of the optimized, i.e., planar, geometry of **L** reveal a small spin density delocalized on the phenolic oxygen, which may engender a metal–radical exchange interaction. However, the magnetic behavior of **1** was analyzed without assuming any such magnetic interactions between the ligands and the metal ions; the interactions are too small to be determined precisely, if at all. This situation is similar to those found in dinuclear copper(II) acetates involving nitroxide pendants [17].

On the other hand, the χT value for **2** at room temperature, 0.74 emu K mol^{-1}, is close to the theoretical one calculated for two $S = 1/2$ non-interacting spins. The χT value showed a rapid decrease below ca. 20 K, suggesting the presence of a marked antiferromagnetic interaction. The magnetic susceptibility was analyzed on the basis of a singlet–triplet model. The parameters of best fit were $g = 1.99$, $J/k_B = -2.78$ K, and $\theta = -2.79$ K. Antiferromagnetic intramolecular interaction may be explained by superexchange through the metal ion; as demonstrated crystallographically, the coordination plane around the metal ion and the hydroxypyridine moiety of the ligand are almost perpendicular to each other, thereby causing the overlap of the 2pπ orbital of the nitrogen atom of the ligand and the d_{xy} orbital of the metal ion [18]. This can be the antiferromagnetic interaction pathway, but the interaction magnitude is small because of the small spin density on the nitrogen.

Previously, we reported the preparation and magnetic properties of a mononuclear platinum(II) complex with pyridyl nitronyl nitroxide radicals, *trans*-[Pt(NH$_3$)$_2$(NITpPy)$_2$](NO$_3$)$_2$ [19]. This complex, which is structurally relevant to **2**, exhibits a Curie–Weiss-like magnetic behavior with only a small antiferromagnetic interaction ($\theta = -1.4$ K). However, **2** exhibited a larger antiferromagnetic interaction that is considered to be intramolecular, as shown above, despite the identical configuration of metal–radical interactions. This is ascribable to the larger spin density on the nitrogen atom of **HL** than that of NITpPy as well as the difference of metal species.

4. Concluding remarks

This study demonstrated that the pyridone-based radical **HL** is useful as a ligand for metal complexes carrying radical moieties. In particular, the dinuclear

complex **1** represents a fundamental polynuclear complex with the open-shell pyridonate ligand. Furthermore, a mononuclear complex like **2** is potentially useful for stepwise construction of polynuclear complexes. Application of the pyridone chemistry to molecular magnetism may allow access to multifunctional compounds of further interest. In addition, construction of complexes involving larger numbers of metals with open-shell pyridone ligands is progressing in our laboratory.

5. Supplementary materials

Crystallographic data for structural analysis have been deposited with the Cambridge Crystallographic Data Centre, CCDC Nos. 191965 and 250331, respectively, for compounds **1** and **2**. Copies of this information may be obtained from the Director, CCDC, 12 Union Road, Cambridge, CB2 1EZ, UK (fax: +44 1133 336033; e-mail: deposit@ccdc.cam.ac.uk or http://www.ccdc.cam.ac.uk).

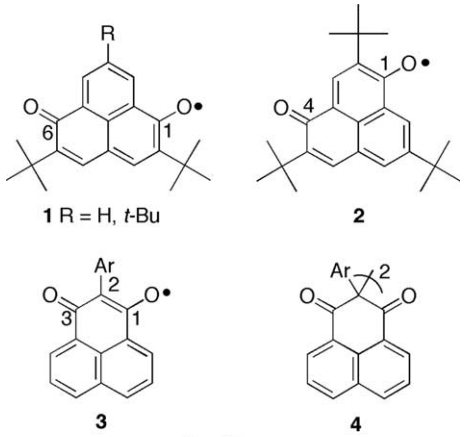
Acknowledgments

This work was supported financially by a Grant-in-Aid for Scientific Research (No. 12740387) from JSPS. We thank PRESTO, JST for the loan of experimental equipment. We thank Dr. Ryo Horikoshi for elemental analyses. This work was carried out under the Visiting Researcher's Program of the Institute for Solid State Physics, the University of Tokyo.

References

[1] R.E.P. Winpenny, J. Chem. Soc., Dalton Trans. (2002) 1 (references cited therein).
[2] (a) F.A. Cotton, R.A. Walton, Multiple Bonds between Metal Atoms, second ed., Clarendon Press, Oxford, 1993;
(b) J.M. Rawson, R.E.P. Winpenny, Coord. Chem. Rev. 139 (1995) 313.
[3] B. Lippert, Coord. Chem. Rev. 182 (1999) 263.
[4] L.S. Hollis, S.J. Lippard, Inorg. Chem. 22 (1983) 2600.
[5] H. Andres, R. Basler, A.J. Blake, C. Cadiou, G. Chaboussant, C.M. Grant, H.-U. Güdel, M. Murrie, S. Parsons, C. Paulsen, F. Semadini, V. Villar, W. Wernsdorfer, R.E.P. Winpenny, Chem. Eur. J. 8 (2002) 4867.
[6] (a) J.S. Miller, M. Drillon (Eds.), Magnetism: Molecules to Materials II, Wiley-VCH, Weinheim, 2001;
(b) E. Coronado, P. Delhaes, D. Gatteschi, J.S. Miller (Eds.), Molecular Magnetism: from Molecular Assemblies to the Devices, Kluwer Academic, Dordrecht, 1996.
[7] (a) T.M. Barclay, R.G. Hicks, M.T. Lemaire, L.K. Thompson, Z. Xu, Chem. Commun. (2002) 1688;
(b) D.J.R. Brook, S. Fornell, J.E. Stevens, B. Noll, T.H. Koch, W. Eisfeld, Inorg. Chem. 39 (2000) 562;
(c) T.M. Barclay, R.G. Hicks, M.T. Lemaire, L.K. Thompson, Chem. Commun. (2000) 2141.
[8] (a) A. Caneschi, F. Ferraro, D. Gatteschi, P. Rey, R. Sessoli, Inorg. Chem. 29 (1990) 1756;
(b) M. Fettouhi, M. Khaled, A. Waheed, S. Golhen, L. Ouahab, J.-P Sutter, O. Kahn, Inorg. Chem. 38 (1999) 3967;
(c) H. Oshio, T. Ito, Cood. Chem. Rev. 198 (2000) 329;
(d) G. Francese, F.M. Romero, A. Neels, H. Stoeckli-Evans, S. Decurtins, Inorg. Chem. 39 (2000) 2087;
(e) K.E. Vostrikova, D. Luneau, W. Wernsdorfer, P. Rey, M. Verdaguer, J. Am. Chem. Soc. 122 (2000) 718;
(f) A. Caneschi, D. Gatteschi, N. Lalioti, C. Sangregorio, R. Sessoli, G. Venturi, A. Vindigni, A. Rettori, M.G. Pini, M.A. Novak, Angew. Chem. Int. Ed. 40 (2001) 1760;
(g) L.M. Field, P.M. Lahti, F. Palacio, Chem. Commun. (2002) 636;
(h) A. Marvilliers, Y. Pei, J.C. Boquera, K.E. Vostrikova, C. Paulsen, E. Rivière, J.-P. Audièra, T. Mallah, Chem. Commun. (1999) 1951.
[9] (a) D. Maspoch, D. Ruiz-Molina, K. Wurst, C. Rovira, J. Veciana, Chem. Commun. (2002) 2958;
(b) R.E.D. Sesto, A.M. Arif, J.S. Miller, Inorg. Chem. 39 (2000) 4894.
[10] (a) T. Mochida, M. Ueda, C. Aoki, H. Mori, Inorg. Chim. Acta 335 (2002) 151;
(b) M. Ueda, T. Mochida, Inorg. Chim. Acta 353C (2003) 306;
(c) T. Mochida, M. Ueda, H. Moriyama, Mol. Cryst. Liq. Cryst. 342 (2000) 91.
[11] M. Ueda, T. Mochida, S. Furukawa, H. Suzuki, H. Moriyama, H. Mori, Mol. Cryst. Liq. Cryst. 379 (2002) 153.
[12] (a) E.F. Ullman, J.H. Osiecki, D.G.B. Boocock, R. Darcy, J. Am. Chem. Soc. 94 (1972) 7049;
(b) F.A. Neugebauer, H. Fischer, R. Siegel, C. Krieger, Chem. Ber. 116 (1983) 3461.
[13] CrystalStructure 3.6.0: Crystal Structure Analysis Package, Rigaku and Rigaku/MSC (2000–2004).
[14] SIR92: A. Altomare, G. Cascarano, C. Giacovazzo, A. Guagliardi, M. Burla, G. Polidori, M. Camalli, J. Appl. Crystallogr. 27 (1994) 435.
[15] E.C. Constable, A.C. King, C.A. Palmer, P.R. Raithby, Inorg. Chim. Acta 184 (1991) 43.
[16] (a) M. Mizutani, S. Miwa, N. Fukushima, Y. Funahashi, T. Ozawa, K. Jitsukawa, H. Masuda, Inorg. Chim. Acta 339 (2002) 543;
(b) B. Lippert, Coord. Chem. Rev. 200–202 (2000) 487.
[17] (a) U. Schatzschneider, T. Weyhermüller, E. Rentschler, Inorg. Chim. Acta 337 (2002) 122;
(b) M. Mikuriya, H. Azuma, J. Sun, D. Yoshioka, M. Handa, Chem. Lett. (2002) 608.
[18] H. Oshio, T. Ito, in: H. Sasabe (Ed.), Hyper-structured Molecules II: Chemistry, Physics, and Applications, Gordon & Breach, Chennai, 2000 (Chapter 8).
[19] M. Ueda, T. Mochida, M. Itou, N. Asanagi, H. Mori, Inorg. Chim. Acta 348C (2003) 123.
[20] ORTEP-3 for Windows: L.J. Farrugia, J. Appl. Crystallogr. 30 (1997) 565.

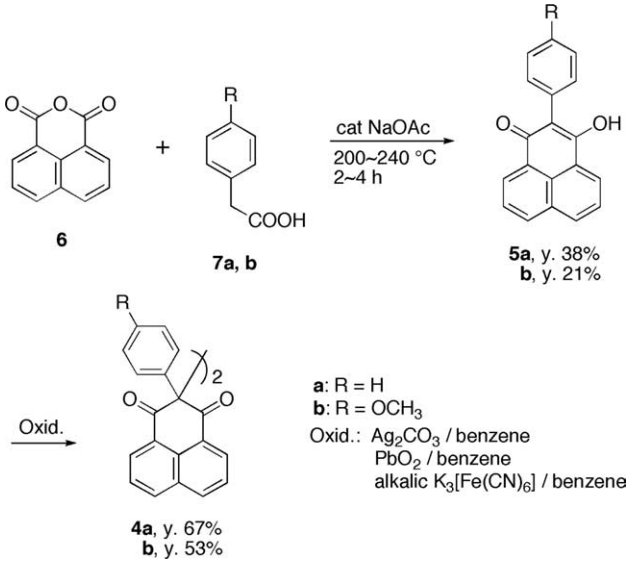
carbon–carbon bond formation at 2-positions [4g]. ESR studies on **3a**, **b** generated by thermal bond cleavage of the dimer **4a**, **b** in a solution state revealed that π-spin density dominantly exists at 2-position and two oxygen atoms, although an appreciable amount of π-spin density is delocalized into 2-aryl groups. In this paper, we discuss a degree of π-spin density delocalization on the phenalenyl skeletons of **3a**–**c** in terms of the dimer structure of **4b** determined by X-ray crystal structure analysis and by variable temperature ^{1}H NMR studies as well as density functional theory calculations of radicals **3a**–**c**.



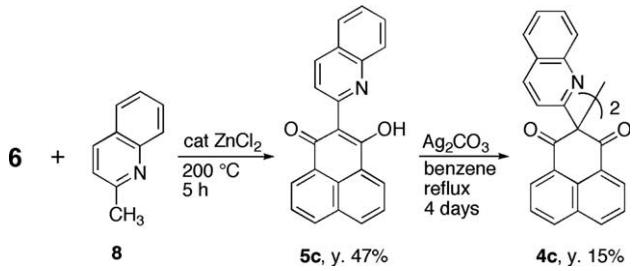
2. Results and discussion

2.1. Synthesis of dimeric compounds *4a*–*c* from 2-aryl-3-hydroxyphenalenone derivatives

2-Aryl-3-hydroxyphenalenone derivatives **5a**, **b** [7] and **5c** [7b] were respectively prepared in 38%, 21% and 47% yields by the condensation reaction of 1,8-naphthalic anhydride **6** with phenylacetic acid derivatives **7a**, **b** and 2-methylquinoline **8** by the same procedure described in the literature (Schemes 1 and 2). Treatment of **5a**, **b** with an excess amount of oxidants such as PbO_2, Ag_2CO_3 and $K_3[Fe(CN)_6]$–KOH aqueous solution in benzene gave corresponding dimers **4a** [8], **4b** in 67% and 53% yields, respectively. Oxidation of **5c** with an excess amount of Ag_2CO_3 in benzene at 80 °C also gave a dimeric compound **4c** in 15% yield. The structures of **4a**–**c** were determined unambiguously by ^{1}H and ^{13}C NMR, IR, mass spectra and elemental analyses.



Scheme 1.



Scheme 2.

2.2. X-ray crystal structure analysis of *4b*

Single crystals of the dimeric compound **4b** suitable for X-ray crystallographic analysis were obtained by recrystallization from benzene–hexane solution at 4 °C.[1] The crystal contains two benzene molecule as crystal solvent per one **4b** molecule. ORTEP drawing of **4b** shows that a carbon–carbon bond is formed between the 2-positions, which agrees with the results of NMR measurements (vide infra) (Fig. 1). The central C2–C2′ distance (1.579 Å) is longer than the average value of C(sp^3)–C(sp^3) distance (1.53 Å) [9].

[1] Crystal data for **4b**·$(C_6H_6)_2$: $C_{52}H_{38}O_6$, M_r = 758.87, crystal dimensions $0.60 \times 0.60 \times 0.20$ mm^3, monoclinic, space group *C*2/*c* (no. 15), a = 19.010(1), b = 10.2227(7), c = 21.139(2) Å, β = 102.507(1)°, V = 4010.3(5) Å^3, Z = 4, $\rho_{calc.}$ = 1.257 g cm^{-3}, μ = 0.81 cm^{-1}, $2\theta_{max}$ = 55.0°, λ(Mo Kα) = 0.71070 Å, ω scan mode, T = 200 K, 27 129 reflections, of which 4578 were unique and 2557 were included in the refinement [$I > 3.0\sigma(I)$], data corrected for Lorentzian and polarization effects; solution by direct methods (SIR92) and refinement on $|F^2|$ by full-matrix least-squares procedures, 262 parameters, the non-H atoms were refined anisotropically, H atoms were included but not refined, final values R_1 = 0.047, wR_2 = 0.113, GOF = 1.54, maximum positive and negative peaks in ΔF map were ρ_{max} = 0.24 e Å^{-3} and ρ_{min} = −0.21 e Å^{-3}. CCDC-258206 contains the supplementary crystallographic data for this paper. These data can be obtained free of charge via www.ccdc.cam.ac.uk/conts/retrieving.html (or from the Cambridge Crystallographic Data Centre, 12, Union Road, Cambridge CB21EZ, UK; fax: +44 1223 336 033; or deposit@ccdc.cam.ac.uk).

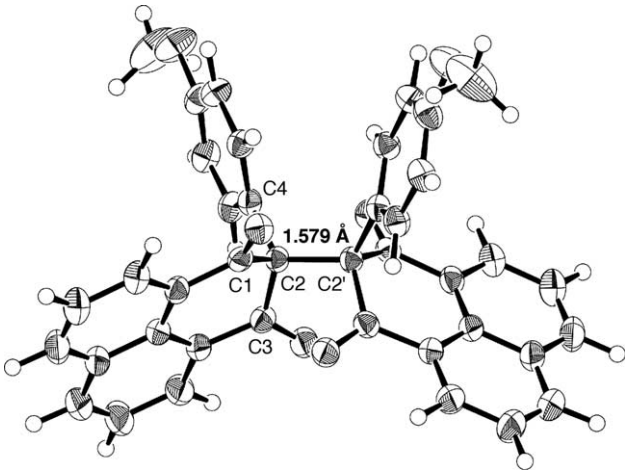


Fig. 1. ORTEP drawing of **4b** · $2C_6H_6$, showing representative atom numbering and bond length.

2.3. Variable temperature ^1H NMR of *4b*

The ^1H NMR spectra in $CDCl_3$ and DMSO-d_6 solutions of **4b** exhibit significant lineshape change in the wide temperature range of −43 to +119 °C, reflecting the occurrence of two types of rate processes (Fig. 2).

The spectrum in $CDCl_3$ at −43 °C, the lowest temperature examined, affords ABCD-type and ABC-DEF-type signals for the aromatic protons of the *p*-methoxyphenyl and the naphthalene moieties, respectively, indicating that two edges of the *p*-methoxyphenyl group as well as those of the naphthalene moiety are magnetically nonequivalent (Figs. 2(a) and (c)). These features show that the compound **4b** adopts in solution a similar conformation as observed in the crystalline state by X-ray crystallography and that internal rotation of both the central C2–C2′ bond and the *p*-methoxyphenyl–C(sp^3) bond is restricted on the NMR timescale.

Upon elevating the temperature, the *p*-methoxyphenyl proton signals broaden and coalesce around room temperature reflecting the increase in the rotation rates of the *p*-methoxyphenyl group. Lineshape analysis [10] of the signals at nine temperatures between −13 and 55 °C in $CDCl_3$ afforded the rate constants of the process at each temperature and the least-square analysis of the Eyring plots gave the following kinetic parameters: $\Delta H^{\ddagger} = 13.3 \pm 0.3$ kcal mol^{-1}, $\Delta S^{\ddagger} = -2.4 \pm 0.9$ cal mol^{-1} K^{-1}, $\Delta G^{\ddagger}(300\ \mathrm{K}) = 14.0$ kcal mol^{-1} (Fig. 2(b)).

At higher temperatures broadening and coalescence of the proton signals due to the naphthalene moiety take place reflecting the occurrence of the interconversion between a chiral conformation due to the central C2–C2′ bond and its enantiomer (Fig. 2(c)). Lineshape analysis of the signals at five temperatures between 83 and 119 °C in DMSO-d_6 and the least-square analysis of the Eyring plots gave the following kinetic parameters: $\Delta H^{\ddagger} = 20.2 \pm 0.6$ kcal mol^{-1}, $\Delta S^{\ddagger} = 2.1 \pm 1.5$ cal mol^{-1} K^{-1}, $\Delta G^{\ddagger}(300\ \mathrm{K}) = 19.6$ kcal mol^{-1} (Fig. 2(d)).

The results of these NMR studies demonstrate that the dimer **4b** possesses a sterically hindered structure.

2.4. DFT calculations of spin density distributions of 3-oxophenalenoxyl derivatives *3a–c*

Spin density distributions of the neutral radicals **3a–c** were calculated by GAUSSIAN 03 at the UBLYP/6-31G(d,p) level of theory (Fig. 3). In **3a** and **3b**, spin

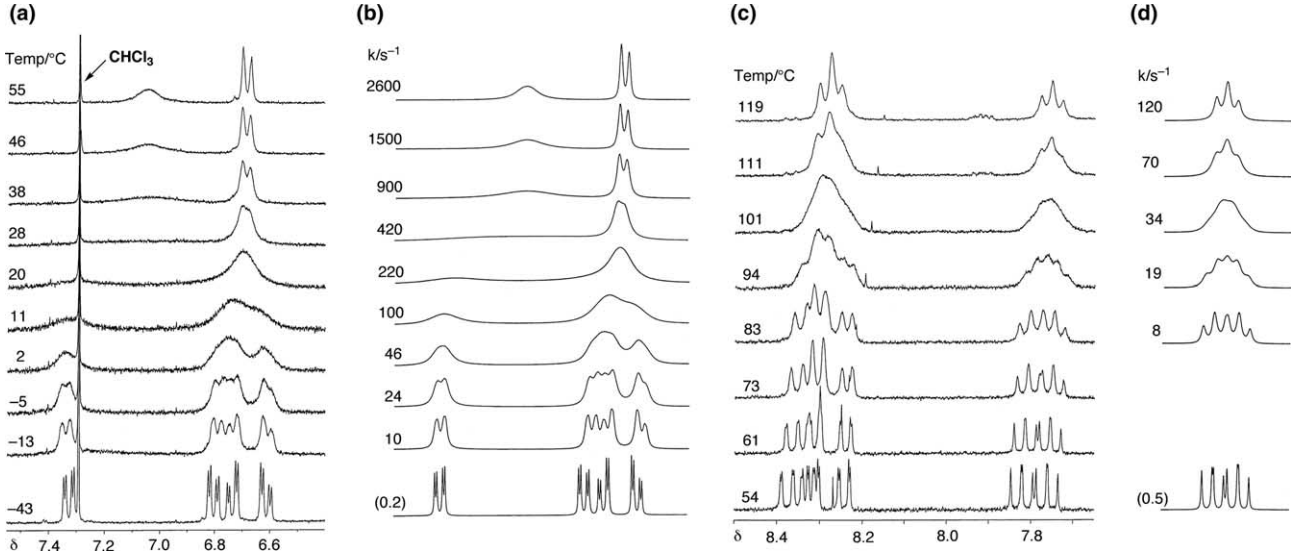


Fig. 2. (a) The observed ^1H NMR spectra in a $CDCl_3$ solution of the *p*-methoxyphenyl region and (c) in a DMSO-d_6 solution of the naphthalene region; (b) and (d) calculated spectra with the best-fit rate constants.

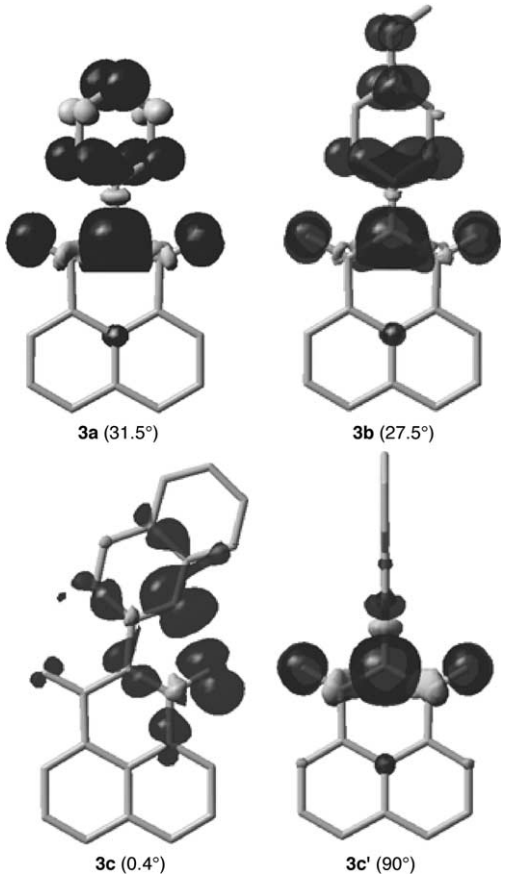


Fig. 3. Spin density distributions for 3-oxophenalenoxyl derivatives with 2-phenyl (**3a**), 2-(*p*-methoxyphenyl) (**3b**) and 2-quinolyl (**3c** and **c′**) calculated at UBLYP/6-31G(d,p) level. Values in parentheses are the torsion angles between aryl moieties and 3-oxophenalenoxyl moieties. Black and gray colors denote positive and negative spin densities, respectively.

densities are dominantly distributed on 2-position, two oxygen atoms and 2-aryl groups, and π-spin delocalization into the whole phenalenyl skeleton is small. These results were in agreement with our previous ESR studies [4g]. In 2-quinolyl derivative **3c**, the calculated spin density distribution shows remarkable difference according to the torsion angle between the quinolyl moiety and 3-oxophenalenoxyl moiety (Fig. 3. **3c**, **3c′**).[2]

3. Conclusion

We synthesized the dimeric compounds **4a**–**c** of 2-aryl-3-oxophenalenoxyl derivatives **3a**–**c** by a carbon–carbon bond formation at 2-positions. The X-ray crystal structure analysis and the variable temperature ^{1}H NMR studies revealed that sterically hindered structure of dimer **4b**. DFT calculations of the radicals **3a**–**c** indicate that π-spin densities dominantly exist at 2-position and the oxygen atoms, although an appreciable amount of them is delocalized into the 2-aryl moieties. These results indicate that the lower stability of 2-aryl-3-oxophenalenoxyl than 4- and 6-oxophenalenoxyl derivatives is ascribable to the smaller spin delocalization into the whole phenalenyl skeleton than that of 6- and 4-oxophenalenoxyl radicals. These studies provide important design criteria for the stable neutral radicals based on phenalenyl system, contributing to the realization of new magnetic materials.

[2] The difference between total energies of two optimized geometries **3c** and **3c′** calculated at UBLYP/6-31G(d,p) level of theory is only 5.98 kcal mol^{-1}.

4. Experimental

4.1. General

4.1.1. General

^{1}H NMR spectra were recorded at 270 and 300 MHz with $CDCl_3$ or DMSO-d_6 as solvent and Me_4Si or residual solvent as an internal standard. Infrared spectra were recorded using KBr plates. 3-nitrobenzyl alcohol was used as matrix for FAB-MS spectra. Elemental analyses were performed at Graduate School of Science in Osaka University and Institute for Molecular Science in Okazaki National Research Institute. X-ray data of **4b** were collected on Rigaku/MSC Mercury CCD with graphite monochromated Mo Kα (λ = 0.71070 Å) radiation at −78 °C. Silica gel 60 (100–200 mesh) was used for column chromatography. Benzene was dried over CaH_2 and distilled under argon prior to use. 2-Phenyl-3-hydroxyphenalenone (**5a**) [7], 2-(*p*-methoxyphenyl)-3-hydroxyphenalenone (**5b**) [7], 2-quinolyl-3-hydroxyphenalenone (**5c**) [7b] and active PbO_2 [11] were prepared and purified by the same procedure described in the literatures.

4.1.2. Typical oxidation procedure

2-Phenyl-3-hydroxyphenalenone (**5a**) (33.5 mg, 123 μmol) was dissolved with benzene (50 mL) under argon atmosphere. To this solution was added an excess amount of PbO_2 and stirred at room temperature under argon atmosphere overnight. The reaction mixture was filtered. The resulting filtrates were concentrated under reduced pressure, and then subjected to silica gel column chromatography.

4.1.3. 2,2-Bis(2-phenyl-2,3-dihydro-3-oxophenalendione) (4a)

Colorless powder; ^{1}H NMR ($CDCl_3$, −50 °C) δ 8.43 (dd, J = 7.3 and 1.1 Hz, 2), 8.41 (dd, J = 7.3 and 1.1 Hz, 2), 8.18 (dd, J = 8.3 and 1.1 Hz, 2), 8.12 (dd, J = 8.3 and 1.1 Hz, 2), 7.72 (dd, J = 8.3 and 7.3 Hz, 2), 7.66 (dd, J = 8.3 and 7.3 Hz, 2), 7.43 (m, 2), 7.28 (m, 4), 7.14 (m, 2), 6.84 (m, 2); ^{13}C NMR (CD_2Cl_2, rt) δ 199.31

(C), 191.70 (C), 134.59 (CH), 134.01 (CH), 132.88 (C), 132.45 (C), 130.17 (CH), 129.63 (C), 129.41 (C), 129.27 (CH), 128.66 (CH), 128.30 (C), 128.23 (CH), 127.37 (CH), 127.10 (CH), 126.99 (CH), 76.84 (C); IR (KBr) 1695, 1668, 1622, 1579, 1493 cm^{-1}; FD-MS *m/z* 543 (M^+ + H, 100%). *Anal*. Calc. for $C_{38}H_{22}O_4 \cdot 2C_6H_6$: C, 85.94; H, 4.90; N, 0.00. Found: C, 85.84; H, 5.06; N, 0.00.

4.1.4. 2,2-Bis(2-(4-methoxyphenyl)-2,3-dihydro-3-oxophenalendione) ***(4b)***

Colorless powder; ^1H NMR ($CDCl_3$, −50 °C) δ 8.46 (dd, J = 7.2 and 1.1 Hz, 2), 8.39 (dd, J = 7.2 and 1.1 Hz, 2), 8.19 (dd, J = 8.2 and 1.1 Hz, 2), 8.14 (dd, J = 8.2 and 1.1 Hz, 2), 7.72 (dd, J = 8.2 and 7.2 Hz, 2), 7.68 (dd, J = 8.2 and 7.2 Hz, 2), 7.33 (dd, J = 8.8 and 2.6 Hz, 2), 6.81 (dd, J = 8.8 and 2.9 Hz, 2), 6.74 (dd, J = 9.0 and 2.6 Hz, 2), 6.62 (dd, J = 9.0 and 2.9 Hz, 2), 3.74 (s, 6); ^{13}C NMR ($CDCl_3$, 30 °C) δ 199.26 (C), 191.62 (C), 159.24 (C), 133.98 (CH), 133.40 (CH), 133.15 (CH), 132.52 (C), 130.05 (CH), 129.47 (C), 129.24 (C), 128.76 (CH), 128.16 (C), 126.70 (CH), 126.43 (CH), 123.49 (C), 112.60 (CH), 75.61 (C), 54.98 (CH_3); IR (KBr) 1697, 1667 cm^{-1}; FD-MS *m/z* 603 (M^+ + H, 100%). *Anal*. Calc. for $C_{40}H_{26}O_4 \cdot 2C_6H_6$: C, 82.30; H, 5.05; N, 0.00. Found: C, 82.14; H, 5.23; N, 0.00.

4.1.5. 2,2-Bis(2-quinolyl-2,3-dihydro-3-oxophenalendione) ***(4c)***

Colorless powder; ^1H NMR ($CDCl_3$, rt) δ 8.52 (dd, J = 7.3 and 1.0 Hz, 2), 8.35 (dd, J = 7.3 and 1.0 Hz, 2), 8.08–7.97 (m, 3), 7.87 (d, J = 6.5 Hz, 1), 7.73–7.65 (m, 2), 7.59–7.52 (m, 2), 7.47–7.42 (m, 2); ^{13}C NMR ($CDCl_3$, rt) δ 198.45 (C), 191.41 (C), 155.49 (C), 147.17 (C), 134.86 (CH), 133.96 (CH), 133.49 (CH), 132.68 (C), 129.95 (CH), 129.92 (CH), 129.14 (CH), 128.95 (CH), 127.49 (C), 127.26 (CH), 126.83 (CH), 126.52 (CH), 126.23 (CH), 123.09 (CH); IR (KBr) 1652 cm^{-1}; HRMS-FAB (*m/z*). *Anal*. Calc. for $C_{44}H_{25}O_4N_2$ (M^+ + H): 645.17893. Found: 645.17893.

4.1.6. Valiable temperature NMR

Variable temperature NMR experiments were performed on a Bruker ARX-300 spectrometer operating at 300 MHz. Temperatures were calibrated with a methanol sample or an ethylene glycol sample and are reliable to ±1 °C. Total lineshape analysis was performed by visual matching of experimental spectra with theoretical ones computed on an NEC PC9821Xs personal computer equipped with a Mutoh PP-210 plotter using the DNMR3K program, a modified version of the DNMR3 program [9] converted for use on a personal computer by Dr. Hiroshi Kihara. Temperature dependence of chemical shift differences and T_2 values were properly taken into account.

Acknowledgments

This work was partially supported by PRESTO-JST, Grant-in-Aid for Scientific Research on Priority Areas "Application of Molecular Spins" (Area No. 769) from Ministry of Education, Culture, Sports, Science, and Technology, Japan, and 21COE program "Creation of Integrated EcoChemistry of Osaka University".

References

[1] For recent overview of molecule-based magnetic materials, see, e.g.;
(a) K. Itoh, M. Kinoshita (Eds.), Molecular Magnetism, Kodansha, and Gordon and Breach Science Publishers, Tokyo, 2000;
(b) P.M. Lahti (Ed.), Magnetic properties of organic materials, Marcel Dekker, New York, 1999;
(c) O. Kahn (Ed.), Mol. Cryst. Liq. Cryst. 334 (1999) 1–712, 335 (1999) 1–706;
(d) K. Itoh, J.S. Miller, T. Takui (Eds.), Mol. Cryst. Liq. Cryst. 305 (1997) 1–586, 306 (1997) 1–520.

[2] K. Goto, T. Kubo, K. Yamamoto, K. Nakasuji, K. Sato, D. Shiomi, T. Takui, M. Kubota, T. Kobayashi, K. Yakushi, J. Ouyang, J. Am. Chem. Soc. 121 (1999) 1619.

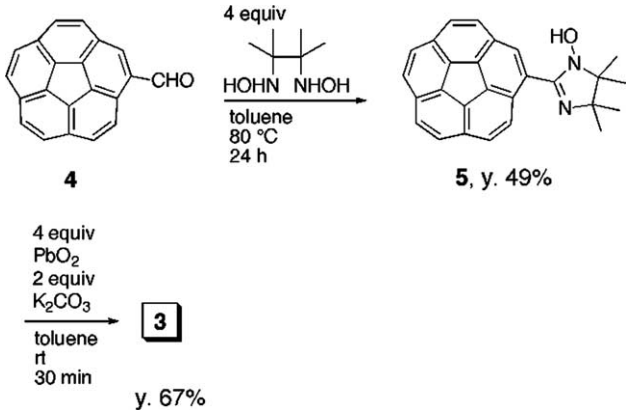
[3] (a) Y. Morita, T. Aoki, K. Fukui, S. Nakazawa, K. Tamaki, S. Suzuki, A. Fuyuhiro, K. Yamamoto, K. Sato, D. Shiomi, A. Naito, T. Takui, K. Nakasuji, Angew. Chem. Int. Ed. 41 (2002) 1793;
(b) Y. Morita, K. Fukui, S. Suzuki, T. Aoki, S. Nakazawa, K. Tamaki, A. Fuyuhiro, K. Yamamoto, K. Sato, D. Shiomi, A. Naito, T. Takui, K. Nakasuji, Polyhedron 22 (2003) 2199;
(c) Y. Morita, S. Suzuki, K. Fukui, S. Nakazawa, K. Sato, D. Shiomi, T. Takui, K. Nakasuji, Polyhedron 22 (2003) 2215;
(d) Y. Morita, S. Suzuki, J. Kawai, S. Nishida, K. Fukui, S. Nakazawa, K. Sato, D. Shiomi, T. Takui, K. Nakasuji, Synth. Met. 137 (2003) 1209.

[4] 6-Oxophenalenoxyl derivatives,
(a) Y. Morita, T. Ohba, N. Haneda, S. Maki, J. Kawai, K. Hatanaka, K. Sato, D. Shiomi, T. Takui, K. Nakasuji, J. Am. Chem. Soc. 122 (2000) 4825;
(b) Y. Morita, J. Kawai, N. Haneda, S. Nishida, K. Fukui, S. Nakazawa, K. Sato, D. Shiomi, T. Takui, T. Kawakami, K. Yamaguchi, K. Nakasuji, Tetrahedron Lett. 42 (2001) 7991;
(c) Y. Morita, S. Maki, K. Fukui, T. Ohba, J. Kawai, K. Sato, D. Shiomi, T. Takui, K. Nakasuji, Org. Lett. 3 (2001) 3099;
(d) Y. Morita, J. Kawai, S. Nishida, N. Haneda, K. Fukui, K. Sato, D. Shiomi, T. Takui, K. Nakasuji, Synth. Met. 137 (2003) 1217;
(e) Y. Morita, S. Nishida, N. Oguchi, J. Kawai, K. Fukui, S. Nakazawa, K. Sato, D. Shiomi, T. Takui, K. Nakasuji, Synth. Met. 137 (2003) 1207;
4-Oxophenalenoxyl derivative,
(f) Y. Morita, J. Kawai, K. Fukui, S. Nakazawa, K. Sato, D. Shiomi, T. Takui, K. Nakasuji, Org. Lett. 5 (2003) 3289;
3-Oxophenalenoxyl derivatives,
(g) K. Hatanaka, Y. Morita, T. Ohba, K. Yamaguchi, T. Takui, M. Kinoshita, K. Nakasuji, Tetrahedron Lett. 37 (1996) 873.

[5] Y. Morita, J. Kawai, S. Nishida, K. Fukui, S. Nakazawa, K. Sato, D. Shiomi, T. Takui, K. Nakasuji, Polyhedron 22 (2003) 2205.

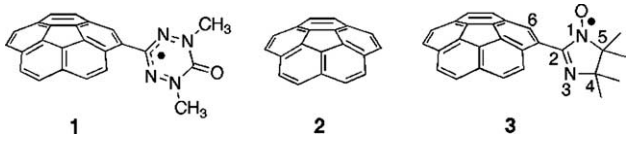
[6] (a) Y. Morita, S. Nishida, J. Kawai, K. Fukui, S. Nakazawa, K. Sato, D. Shiomi, T. Takui, K. Nakasuji, Org. Lett. 4 (2002) 1985;
(b) Y. Morita, S. Nishida, J. Kawai, K. Fukui, S. Nakazawa, K. Sato, D. Shiomi, T. Takui, K. Nakasuji, Polyhedron 22 (2003) 2209.

[7] (a) N.R. Ayyangar, S.V. Joshi, A.G. Lugade, Indian J. Chem. Sect. B 20B (1981) 1043;
(b) W.I. Awad, O.M. Aly, J. Org. Chem. 25 (1960) 1872.
[8] The dimer structure of **4a** was previously characterized by only IR spectrum and elemental analysis, see: I. Meirovics, G. Vanags, Latv. PSR Zinat. Akad. Vestis, Kim. Ser. (1965) 579.
[9] M.B. Smith, J. March, March's Advanced Organic Chemistry Reaction, Mechanisms, and Structure, fifth ed., John Wiley & Sons, New York, 2001, p. 18.
[10] D.A. Kleier, G. Binsch, QCPE Program No. 165.
[11] (a) R. Kuhn, I. Hammer, Chem. Ber. 83 (1950) 413;
(b) W.K. Wilmarth, N. Schwartz, J. Am. Chem. Soc. 77 (1955) 4543.



Scheme 1.

an iminonitroxide derivative **3** with corannulene. In this study, we have shown the π-spin delocalization onto the curved surface π-system of corannulene moiety in terms of ESR/ENDOR/TRIPLE, UV–Vis measurements and density functional theory (DFT) calculations.



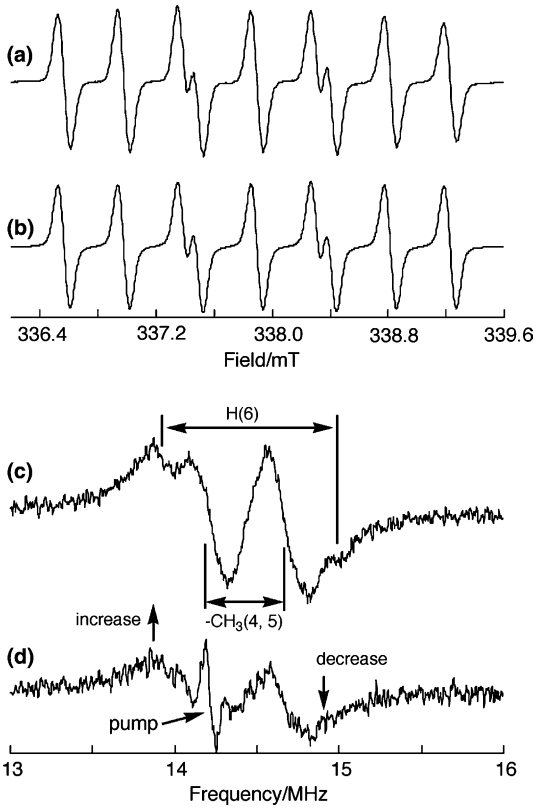


Fig. 1. (a) Observed hyperfine ESR spectrum at 290 K (microwave frequency: 9.493725 GHz) and (b) the corresponding simulated spectrum, (c) ENDOR and (d) TRIPLE (pump frequency: 14.2 MHz) spectra at 270 K for **3** in toluene (3.4×10^{-4} M).

2. Results and discussion

*2.1. Synthesis of iminonitroxide derivative **3** with corannulene*

Radical **3** was synthesized from formylcorannulene **4**[1] in two steps (Scheme 1). The radical precursor **5** was prepared by condensation of **4** with 2,3-bis(hydroxyamino)-2,3-dimethylbutane in toluene at 80 °C. Oxidation of **5** with active PbO_2 in the presence of K_2CO_3 in toluene gave the neutral radical **3** as a vivid red powder. In the solid state, most of the radical **3** remains unchanged in air for a long period of time. The radical is also stable in a toluene solution in the presence of air for a few weeks, indicating that **3** possesses a higher stability than the oxoverdazyl derivative **1** [7].

*2.2. ESR/ENDOR/TRIPLE measurements of the radical **3***

ESR spectrum of radical **3** in degassed toluene solution (3.4×10^{-4} M) at 290 K shows hyperfine splitting arising mainly from the nitrogen atoms of the iminonitroxide moiety (Fig. 1(a)). ENDOR spectroscopy (Fig. 1(c)) at 270 K shows two pairs of splittings attributed to methyl protons on the iminonitroxide and methyne proton on the corannulene skeleton. The relative signs of the hyperfine coupling constants (hfccs) of the two types of protons were determined by TRIPLE spectroscopy (Fig. 1(d)). The spectral simulation (Fig. 1(b)) was satisfactory on the basis of the set of hfccs due to protons obtained by ENDOR spectroscopy and due to two nitrogen atoms. The protons and nitrogens of **3** were assigned in terms of the spin density distribution calculated by the DFT method using the optimized structure[2] [8] (Fig. 2(b) and Table 1). Both the experiment and theoretical calculation show that the degree of π-spin delocalization on the 6-position of **3** from the radical substituent is smaller than that on the corresponding position of the oxoverdazyl derivative **1** [7].

[1] Synthesis of formylcorannulene **4** was carried out by standard procedure; see [7].

[2] In calculation, the spin density at 6-position of **3** is highly affected by the torsion angle between the corannulene moiety and the iminonitroxide moiety. The torsion angle is 10° in the optimized structure calculated at UB3LYP/6-31G level of theory.

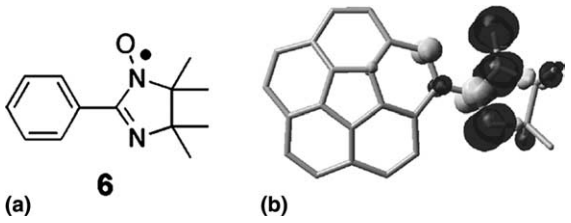


Fig. 2. (a) Molecular structure of **6** and (b) spin density distribution of **3** calculated at UB3LYP/6-31G(d)//UB3LYP/6-31G level. Black and gray colors denote positive and negative spin densities, respectively.

Table 1
Observed and calculated hfccs of proton and nitrogens, and observed *g*-value for **3**

a/mT				*g*-value
$-CH_3$(4, 5)	H(6)	N(1)	N(3)	
−0.011[a]	+0.037[a]	±0.902[b]	±0.413[b]	2.0063
−0.009[c,d]	+0.126[c]	+0.986[c]	+0.667[c]	

[a] The hfccs and the relative signs were determined by ENDOR/TRIPLE spectra in a toluene solution at 270 K.
[b] The hfccs were determined by ESR spectrum in a toluene solution at 290 K and spectral simulation.
[c] These hfccs were calculated for **3** at UB3LYP/6-31G(d)//UB3LYP/6-31G level of theory.
[d] The hfcc of methyl protons were averaged value.

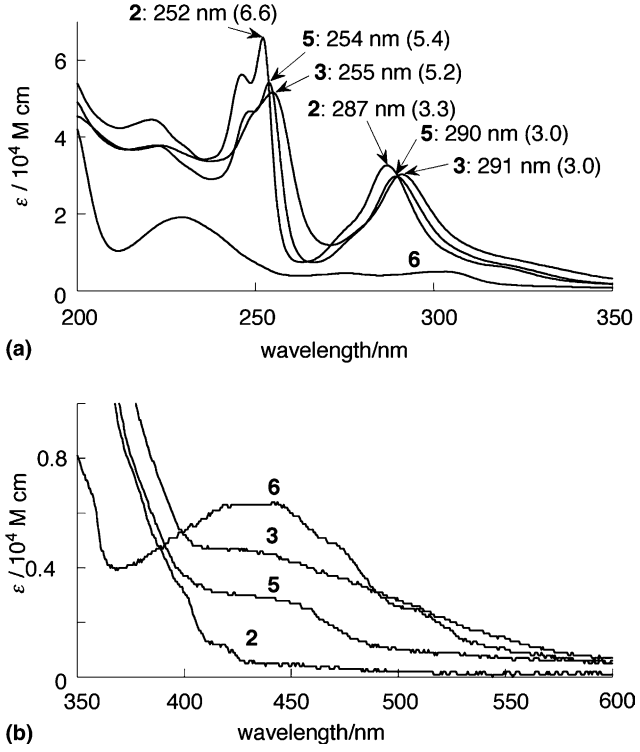


Fig. 3. UV–Vis spectra of **2**, **3**, **5** and **6** in CH_3CN solution (1.0×10^{-5} M). (a) 200–350 nm region and (b) 350–600 nm region. The values in the parentheses of (a) are $\varepsilon/10^4$. The ordinate scale of (b) is magnified seven times than that of (a).

2.3. UV–Vis spectra for 2, 3, 5 and 6

In order to obtain further information on the π-conjugation between the corannulene moiety and the iminonitroxide moiety, we have measured UV–Vis spectra for **2** [9], **3**, **5** and **6** [10] in CH_3CN at room temperature (1.0×10^{-5} M, Fig. 3). The absorption attributed to the iminonitroxide moiety of **3** was observed as a broad band between 400 and 550 nm (Fig. 3(b)). The absorption due to the corannulene moiety of **3** (255 and 291 nm) is broadened compared with **2** and **5**, which shows a similar behavior to the oxoverdazyl derivative **1** [7]. Because the peak maxima for **3** (255 and 291 nm) shift by only 1–4 nm relative to the corresponding peaks for **2** (252 and 287 nm) in the region of 220–350 nm (Fig. 3(a)), it has turned out that the π-conjugation between the corannulene moiety and the iminonitroxide moiety of **3** is weak in the ground state.

3. Conclusion

We have designed and synthesized the iminonitroxide derivative **3** with corannulene as a novel bowl-shaped neutral radical having high stability in air. Our ESR/ENDOR/TRIPLE measurements and DFT calculations have shown that most of the π-spin density is localized on the iminonitroxide moiety, and π-spin delocalization onto the corannulene moiety is smaller than that of the oxoverdazyl derivative **1**. These results are in accord with the UV–Vis spectra, indicating that the π-conjugation between the corannulene moiety and the iminonitroxide moiety of **3** is weak in the ground state.

We believe that high stability of **3** serves as a model to elucidate intermolecular spin–spin interaction in the solid state and investigation of intramolecular spin alignment of the iminonitroxide moiety with a photoexcited triplet state of the corannulene moiety [11,12]. In order to realize a strong intermolecular spin–spin interactions on curved surface π-system in the ground state, design and synthesis of a new bowl-shaped stable neutral radical with a large π-spin delocalization onto the corannulene moiety are now in progress [13].

4. Experimental

4.1. General

^{1}H NMR spectra were recorded at 270 MHz with $CDCl_3$ as solvent and Me_4Si or residual solvent as an internal standard. Infrared spectra were recorded using KBr plates. UV–Vis spectra were recorded in CH_3CN solutions. EI-MS spectra were recorded at 70 eV. Melting points were measured with a hot-stage apparatus and are uncorrected. The liquid-phase ESR, ENDOR,

and TRIPLE spectra were recorded on Bruker ESR/ENDOR spectrometers ESP300/350. R_f values on TLC were recorded on E. Merck precoated (0.25 mm) silica gel 60 F_{254} plates. The plates were sprayed with a solution of 10% phosphomolybdic acid in 95% EtOH and then heated until the spots became clearly visible. Silica gel 60 (100–200 mesh) was used for column chromatography. Toluene was dried over CaH_2 and distilled under argon prior to use. Active PbO_2 [14] was prepared and purified by the same procedure described in the literature. Formylcorannulene **4** [7] and phenyl substituted iminonitroxide derivative **6** [15] were synthesized from corannulene **2** [16] and 2-phenyl-4,4,5,5-tetramethyl-4,5-dihydro-*1H*-imidazol-1-oxyl-3-oxide (phenyl substituted nitronyl nitroxide) [17] according to the literature procedures, respectively. All reactions requiring anhydrous conditions were conducted under argon atmosphere.

4.2. Synthesis of radical precursor 5

Formylcorannulene **5** (160 mg, 0.58 mmol) was placed in a 100-mL Shlenk tube and dissolved with toluene (16 mL) under argon atmosphere. To the mixture was added 2,3-bis(hydroxylamine)-2,3-dimethylbutane (341 mg, 2.30 mmol) and stirred at 80 °C for 24 h. The reaction mixture was cooled to room temperature, and the resulting solid was filtered. The filtrate was poured into 0.1 M pH 7 phosphate buffer and extracted with ethyl acetate (20 mL × 3). The organic extracts were combined and washed with water (50 mL × 2). The organic layer was separated and dried over Na_2SO_4, then filtered and concentrated under reduced pressure, to give crude product as a strong reddish yellow solid. The residue was subjected to silica gel column chromatography with hexane and ethyl acetate (2:1), ethyl acetate and ethyl acetate and EtOH (1:1) as eluant, to give **5** (49%, 111 mg) as a pale yellow powder. M.p. 203–204 °C (dec); TLC R_f 0.54 (ethyl acetate); ^{1}H NMR (500 MHz, $CDCl_3$) δ 1.22 (s, 1), 1.22 (s, 1), 1.31(s, 6), 4.70 (br s, 1), 7.75–7.84 (m, 7), 8.21 (s, 1), 8.22 (s, 1); IR (KBr) 3126, 2973, 2855 cm^{-1}; UV (CH_3CN) λ_{max}, nm (ε): 222 (3.8×10^4), 254 (5.4×10^4), 290 (3.0×10^4); EI-MS, *m/z* 390 (M^+, 2%), 374 (M^+–O, 6%), 276 (M^+–$C_6H_{11}NO$, 38%).

4.3. Synthesis of iminonitroxide derivative 3

A radical precursor **5** (20 mg, 0.05 mmol) was placed in a 20-mL Shlenk tube and dissolved with toluene (6 mL) under argon atmosphere. To the mixture were added potassium carbonate (17 mg, 0.12 mmol) and active PbO_2 (49 mg, 0.21 mmol) and stirred at room temperature for 30 min. The resulting solid was filtered through the celite column. The filtrate was concentrated in vacuo. The residue was subjected to silica gel column chromatography with hexane ~5:1 mixture of hexane and ethyl acetate as eluant, to give **3** (67%, 13.3 mg) as a vivid red powder. M.p. 161–162 °C (dec); TLC R_f 0.43 (hexane/ethyl acetate = 2:1); IR (KBr) 2974 cm^{-1}; UV (CH_3CN) λ_{max}, nm (ε): 224 (3.8×10^4), 255 (5.2×10^4), 291(3.0×10^4); EI-MS, *m/z* 390 ($M^+ + H$, 3%), 389 (M^+, 2%).

Acknowledgments

This work was partially supported by PRESTO-JST, Grant-in-Aid for Scientific Research on Priority Areas "Application of Molecular Spins" (Area No. 769) from Ministry of Education, Culture, Sports, Science, and Technology, Japan, and 21COE program "Creation of Integrated EcoChemistry of Osaka University".

References

[1] For recent overview of molecule-based magnetic materials, see, e.g.:
(a) K. Itoh, M. Kinoshita (Eds.), Molecular Magnetism, Kodansha, and Gordon and Breach Science Publishers, Tokyo, 2000;
(b) P.M. Lahti (Ed.), Magnetic Properties of Organic Materials, Marcel Dekker, New York, 1999;
(c) O. Kahn (Ed.), Mol. Cryst. Liq. Cryst. 334/335 (1999) 1-706–1-712;
(d) K. Itoh, J.S. Miller, T. Takui (Eds.), Mol. Cryst. Liq. Cryst. 305/306 (1997) 1-520–1-586, 1–586.

[2] P.J. Krusic, E. Wasserman, P.N. Keizer, J.R. Morton, K.F. Preston, Science 254 (1991) 1183.

[3] See also overview of radicals based on fullerenes, see: B. Tumanskii, O. Kalina (Eds.), Radical Reactions of Fullerenes and Their Derivatives, Kluwer Academic Publishers, Dortrecht, 2001, pp. 1–192.

[4] K. Goto, T. Kubo, K. Yamamoto, K. Nakasuji, K. Sato, D. Shiomi, T. Takui, M. Kubota, T. Kobayashi, K. Yakushi, J. Ouyang, J. Am. Chem. Soc. 121 (1999) 1619.

[5] (a) Y. Morita, T. Aoki, K. Fukui, S. Nakazawa, K. Tamaki, S. Suzuki, A. Fuyuhiro, K. Yamamoto, K. Sato, D. Shiomi, A. Naito, T. Takui, K. Nakasuji, Angew. Chem. Int. Ed. 41 (2002) 1793;
(b) Y. Morita, K. Fukui, S. Suzuki, T. Aoki, S. Nakazawa, K. Tamaki, A. Fuyuhiro, K. Yamamoto, K. Sato, D. Shiomi, A. Naito, T. Takui, K. Nakasuji, Polyhedron 22 (2003) 2199;
(c) Y. Morita, S. Suzuki, K. Fukui, S. Nakazawa, K. Sato, D. Shiomi, T. Takui, K. Nakasuji, Polyhedron 22 (2003) 2215;
(d) Y. Morita, S. Suzuki, J. Kawai, S. Nishida, K. Fukui, S. Nakazawa, K. Sato, D. Shiomi, T. Takui, K. Nakasuji, Synth. Met. 137 (2003) 1209.

[6] Oxophenalenoxyl systems possess following three topological isomers: 6-Oxophenalenoxyl derivatives
(a) Y. Morita, T. Ohba, N. Haneda, S. Maki, J. Kawai, K. Hatanaka, K. Sato, D. Shiomi, T. Takui, K. Nakasuji, J. Am. Chem. Soc. 122 (2000) 4825;
(b) Y. Morita, J. Kawai, N. Haneda, S. Nishida, K. Fukui, S. Nakazawa, K. Sato, D. Shiomi, T. Takui, T. Kawakami, K. Yamaguchi, K. Nakasuji, Tetrahedron Lett. 42 (2001) 7991;
(c) Y. Morita, S. Maki, K. Fukui, T. Ohba, J. Kawai, K. Sato, D. Shiomi, T. Takui, K. Nakasuji, Org. Lett. 3 (2001) 3099;
(d) Y. Morita, J. Kawai, S. Nishida, N. Haneda, K. Fukui, K. Sato, D. Shiomi, T. Takui, K. Nakasuji, Synth. Met. 137 (2003) 1217;

(e) Y. Morita, S. Nishida, N. Oguchi, J. Kawai, K. Fukui, S. Nakazawa, K. Sato, D. Shiomi, T. Takui, K. Nakasuji, Synth. Met. 137 (2003) 1207, 4-oxophenalenoxyl derivative;
(f) Y. Morita, J. Kawai, K. Fukui, S. Nakazawa, K. Sato, D. Shiomi, T. Takui, K. Nakasuji, Org. Lett. 5 (2003) 3289, 3-oxophenalenoxyl derivatives;
(g) K. Hatanaka, Y. Morita, T. Ohba, K. Yamaguchi, T. Takui, M. Kinoshita, K. Nakasuji, Tetrahedron Lett. 37 (1996) 873;
(h) Y. Morita, S. Nishida, K. Fukui, K. Hatanaka, T. Ohba, K. Sato, D. Shiomi, T. Takui, G. Yamamoto, K. Nakasuji, Polyhedron, submitted for publication.

[7] Y. Morita, S. Nishida, T. Kobayashi, K. Fukui, K. Sato, D. Shiomi, T. Takui, K. Nakasuji, Org. Lett. 6 (2004) 1397.

[8] M.J. Frisch, G.W. Trucks, H.B. Schlegel, G.E. Scuseria, M.A. Robb, J.R. Cheeseman, J.A. Montgomery Jr., T. Vreven, K.N. Kudin, J.C. Burant, J.M. Millam, S.S. Iyengar, J. Tomasi, V. Barone, B. Mennucci, M. Cossi, G. Scalmani, N. Rega, G.A. Petersson, H. Nakatsuji, M. Hada, M. Ehara, K. Toyota, R. Fukuda, J. Hasegawa, M. Ishida, T. Nakajima, Y. Honda, O. Kitao, H. Nakai, M. Klene, X. Li, J.E. Knox, H.P. Hratchian, J.B. Cross, V. Bakken, C. Adamo, J. Jaramillo, R. Gomperts, R.E. Stratmann, O. Yazyev, A.J. Austin, R. Cammi, C. Pomelli, J.W. Ochterski, P.Y. Ayala, K. Morokuma, G.A. Voth, P. Salvador, J.J. Dannenberg, V.G. Zakrzewski, S. Dapprich, A.D. Daniels, M.C. Strain, O. Farkas, D.K. Malick, A.D. Rabuck, K. Raghavachari, J.B. Foresman, J.V. Ortiz, Q. Cui, A.G. Baboul, S. Clifford, J. Cioslowski, B.B. Stefanov, G. Liu, A. Liashenko, P. Piskorz, I. Komaromi, R.L. Martin, D.J. Fox, T. Keith, M.A. Al-Laham, C.Y. Peng, A. Nanayakkara, M. Challacombe, P.M.W. Gill, B. Johnson, W. Chen, M.W. Wong, C. Gonzalez, J.A. Pople, Gaussian 03, Revision C.02, Gaussian Inc., Wallingford, CT, 2004.

[9] (a) W.E. Barth, R.G. Lawton, J. Am. Chem. Soc. 88 (1966) 380;
(b) T.J. Seiders, E.L. Elliott, G.H. Grube, J.S. Siegel, J. Am. Chem. Soc. 121 (1999) 7804;
(c) G.H. Grube, E.L. Elliott, R.J. Steffens, C.S. Jones, K.K. Baldridge, J.S. Siegel, Org. Lett. 5 (2003) 713.

[10] For UV–Vis spectra of the phenyl substituted iminonitroxide derivative **6**, see: E.F. Ullman, L. Call, J.H. Osiecki, J. Org. Chem. 35 (1970) 3623.

[11] Intramolecular spin alignment between a stable radical and the metastable excited triplet state has been observed; see: Y. Teki, S. Miyamoto, M. Nakatsuji, Y. Miura, J. Am. Chem. Soc. 123 (2001) 294, and references therein.

[12] For studies on fluorescence and phosphorescence of corannulene, see:
(a) F.B. Bramwell, J. Gendell, J. Chem. Phys. 52 (1970) 5656;
(b) J.F. Verdieck, W.A. Jankowski, in: E.C. Lim (Ed.), Molecular Luminescence: International Conference, W.A. Benjamin Inc., New York, 1969, pp. 829–836;
(c) Refs. [9b,9c].

[13] K. Fukui, Y. Morita, S. Nishida, T. Kobayashi, K. Sato, D. Shiomi, T. Takui, K. Nakasuji, Polyhedron, in press.

[14] (a) R. Kuhn, I. Hammer, Chem. Ber. 83 (1950) 413;
(b) W.K. Wilmarth, N. Schwartz, J. Am. Chem. Soc. 77 (1955) 4543.

[15] T. Kálai, J. Jekö, Z. Szabó, L. Párkányi, K. Hideg, Synthesis 9 (1997) 1049.

[16] Corannulene **2** was prepared according to the following references with some modifications:
(a) A. Sygula, P.W. Rabideau, J. Am. Chem. Soc. 122 (2000) 6323;
(b) G. Xu, A. Sygula, Z. Marcinow, P.W. Rabideau, Tetrahedron Lett. 41 (2000) 9931;
(c) Ref. [9b].

[17] J.H. Osiecki, E.F. Ullman, J. Am. Chem. Soc. 90 (1968) 1078.

2. Experimental

2.1. Compounds preparation

All chemicals and solvents were used as received. All preparations and manipulation were performed under aerobic conditions. $[Mn_{12}O_{12}(O_2CCH_3)_{16}(H_2O)_4]\cdot 2HO_2C_2H_3\cdot 4H_2O$ (**3**) $\cdot 2HO_2C_2H_3\cdot 4H_2O$ was prepared as literature [25].

2.1.1. $[Mn_{12}O_{12}(O_2CCF_2Cl)_{16}(H_2O)_4]\cdot 4H_2O$ (**1**) $\cdot 4H_2O$

A slurry of complex $\mathbf{3}\cdot 2HO_2C_2H_3\cdot 4H_2O$ (1.005 g, 0.538 mmol) in CH_2Cl_2 (30 mL) was treated with an excess of the HO_2CCF_2Cl (2.106 g, 16.142 mmol). The mixture was stirred for 12 h and filtered to remove any undissolved solid. The resulting filtrate was layered with hexanes (80 mL), stored and left undisturbed overnight. The resultant black crystals were collected by filtration, dissolved in CH_2Cl_2 (30 mL) and the solution was treated with a further amount of HO_2CCF_2Cl and stirred for 12 h. Hexanes (80 mL) was added and the solution was left undisturbed overnight. The black crystals were collected by filtration, dissolved in CH_2Cl_2 (30 mL). The solution was layered with hexanes (80 mL), stored at room temperature for several days and afforded suitable crystals for the X-ray crystal structure analysis. The resultant black crystals were collected by filtration, washed copiously with hexanes and dried in vacuo. The overall yield of **1** was ~80%. Elemental *Anal.* Calc. for $[Mn_{12}O_{12}(O_2CCF_2Cl)_{16}(H_2O)_4]$ (**1**), $C_{32}H_8Cl_{16}F_{32}Mn_{12}O_{48}$: C, 12.83; H, 0.27. Found: C, 12.82; H, 0.32%.

2.1.2. $[PPh_4][Mn_{12}O_{12}(O_2CCF_2Cl)_{16}(H_2O)_4]\cdot 2H_2O\cdot CH_2Cl_2$ (**2**) $\cdot 2H_2O\cdot CH_2Cl_2$

To a stirred dark brown solution of complex $\mathbf{1}\cdot 4H_2O$ (0.992 g, 0.324 mmol) in CH_2Cl_2 (30 mL) was added solid PPh_4I (0.151 g, 0.324 mmol) and stirred for 30 min. The solution was concentrated to remove I_2 and CH_2Cl_2 by evaporation. When almost all the CH_2Cl_2 had been removed, more CH_2Cl_2 (15 mL) was added and removed by evaporation. The addition and removal of CH_2Cl_2 were repeated until no purple color of I_2. The resulting solid was dissolved in CH_2Cl_2/hexanes (30 mL/30 mL) and filtered to remove any undissolved solid. The solution was layered with hexanes (80 mL), stored at room temperature for several days and afforded suitable crystals for the X-ray crystal structure analysis. The resultant black crystals were collected by filtration, washed copiously with hexanes and dried in vacuo. The overall yield of **2** was ~70%. Elemental *Anal.* Calc. for $[PPh_4]$ $[Mn_{12}O_{12}(O_2CCF_2Cl)_{16}(H_2O)_4]$ (**2**), $C_{56}H_{28}Cl_{16}F_{32}Mn_{12}O_{48}P$: C, 20.17; H, 0.84. Found: C, 20.15; H, 0.93%.

2.2. X-ray structure analysis

Crystal data of complex $\mathbf{1}\cdot 4H_2O$: $C_{32}H_{16}Cl_{16}F_{32}Mn_{12}O_{52}$, $M = 3066.93$, black block, crystal dimensions $0.40\times 0.22\times 0.16$ mm, tetragonal, space group $I\bar{4}$, $a = b = 18.6838(1)$ Å, $c = 13.3829(5)$ Å, $V = 4671.76(8)$ Å^3, $Z = 2$, $D_{cal} = 2.180$ Mg/m^3, $F(000) = 2968$, μ(Mo Kα) = 2.175 mm^{-1}. Determination of cell constants and data collections were carried out on an Siemens SMART CCD diffractometer using an ω scan mode in the range $1.54° \leqslant \theta \leqslant 27.50°$ with graphite monochromated Mo Kα radiation ($\lambda = 0.71073$ Å) at 150(1) K. A total of 5338 unique reflections were collected. Data were corrected for absorption effects (SADABS). The structure was solved using the direct method in SHELXS86 [26]. Some disorder problems were observed. Some $-CF_2Cl$ groups showed disorder of their Cl and F atoms (Cl13, Cl14, F5, F6 and F7) in two positions, each was 50% occupation. The final refinement with all non-hydrogen atoms anisotropic except disorder Cl and F atoms by full-matrix least-squares on F^2 (SHELXL93 [27]). Refinement converged at $R_1 = 0.0587$ and $wR_2 = 0.1638$ for 4797 unique data [$I > 2\sigma(I)$], goodness-of-fit = 1.184, where $R_1 = \Sigma\|F_o| - |F_c\|/\Sigma|F_o|$; $wR_2 = \{\Sigma[w(F_o^2 - F_c^2)^2]/\Sigma[w(F_o^2)^2]\}^{1/2}$, and weight scheme $w = 1/[\sigma^2(F_o^2) + (0.0945P)^2 + 15.599P]$, where $P = (F_o^2 + 2F_c^2)/3$. Maximum and minimum peaks in the final difference map were 1.216 and −0.807 e Å^{-3}.

Crystal data of complex $\mathbf{2}\cdot 2H_2O\cdot CH_2Cl_2$: $C_{57}H_{34}Cl_{18}F_{32}Mn_{12}O_{50}P$, $M = 3455.19$, black plate, crystal dimensions $0.25\times 0.25\times 0.10$ mm, monoclinic, space group $P2_1/c$, $a = 18.6623(7)$ Å, $b = 13.3626(5)$ Å, $c = 45.4482(17)$ Å, $\beta = 97.204(2)°$, $V = 11244.3(7)$ Å^3, $Z = 4$, $D_{cal} = 2.041$ Mg/m^3, $F(000) = 6740$, μ(Mo Kα) = 1.878 mm^{-1}. Determination of cell constants and data collections were carried out on a Bruker SMART CCD diffractometer fitted with a CCD-type area detector and a full sphere of data was collected by using graphite monochromated Mo Kα radiation ($\lambda = 0.71073$ Å) at 150(1) K. Data were corrected by semi-empirical from equivalents (multi-scan). Total of 83 487 ($0.90° \leqslant \theta \leqslant 27.50°$) reflections were collected, which yielded 25526 ($R_{int} = 0.0567$) independent reflections. The structure was solved using the direct method in SHELXS97 [26]. Some disorder problems were observed. Seven $-CF_2Cl$ groups showed disorder of their Cl and F atoms (Cl4, F7, F8, Cl5, F9, F10, Cl6, F11, F12, Cl7, F12, F13, Cl11, F21, F22, Cl12, F23, F24, Cl16, F31 and F32) in two positions, each was 50% occupation. The final refinement with all non-hydrogen atoms anisotropic except disorder Cl, F and CH_2Cl_2 atoms by full-matrix least-squares on F^2 (SHELXL97 [27]). Refinement converged at $R_1 = 0.1023$ and $wR_2 = 0.2545$ for 15 591 unique data [$I > 2\sigma(I)$], goodness-of-fit = 1.068, where $R_1 = \Sigma\|F_o| - |F_c\|/\Sigma|F_o|$; $wR_2 = \{\Sigma[w(F_o^2 - F_c^2)^2]/\Sigma[w(F_o^2)^2]\}^{1/2}$, and weight

Table 1
Crystallographic data for complexes **1** and **2**

	1	**2**
Formula	$C_{32}H_{16}Cl_{16}F_{32}Mn_{12}O_{52}$	$C_{57}H_{34}Cl_{18}F_{32}Mn_{12}O_{50}P$
Formula weight (g mol^{-1})	3066.93	3455.19
Space group	$I\bar{4}$	$P2_1/c$
a (Å)	18.6838(1)	18.6623(7)
b (Å)	18.6838(1)	13.3626(5)
c (Å)	13.3829(5)	45.4482 (17)
β (°)		97.204(2)
V (Å^3)	4671.76(8)	11244.3(7)
Z	2	4
T (K)	150(1)	150(1)
Radiation	Mo Kα	Mo Kα
$D_{calc.}$ (g/cm^3)	2.180	2.041
μ (mm^{-1})	2.175	1.878
R_1[a]	0.0587	0.1023
$wR^{b,c}$	0.1638	0.2545

[a] $R_1 = \Sigma\|F_o| - |F_c\|/\Sigma|F_o|$.
[b] $I > 2\sigma(I)$.
[c] $wR_2 = \{\Sigma[w(F_o^2 - F_c^2)^2]/\sum[w(F_o^2)^2\}$, $w = 1/[\sigma^2(F_o^2) + (aP)^2 + bP]$, where $P = (F_o^2 + 2F_c^2)/3$.

scheme $w = 1/[\sigma^2(F_o^2) + (0.1174P^2 + 133.0159P)]$ where $P = (F_o^2 + 2F_c^2)/3$. Maximum and minimum peaks in the final difference map were 1.819 and -1.779 e Å^{-3}. Data collection parameters for complexes **1** and **2** are listed in Table 1.

2.3. Magnetic measurements

Direct current (DC) magnetic susceptibility, magnetization hysteresis and magnetization relaxation decay data were measured by an MPMS-7 Quantum Design SQUID magnetometer equipped with a 7.0 T magnet. Variable-temperature DC magnetic susceptibility data of complexes **1** and **2** were collected for polycrystalline samples in an applied field of 1.0 kG, and in the temperature range 2.00–310.0 K. The samples were embedded in eicosane wax to prevent any torquing of the polycrystalline in the magnetic field. Pascal's constants were used to estimate the diamagnetic corrections for each complex and were subtracted from the experimental molar susceptibility data to give the molar susceptibility [28]. For magnetization hysteresis loop measurements, a polycrystalline of complex **1** was suspended in eicosane at 313 K, oriented in a 7.0 T field and then the eicosane matrix was cooled to room temperature. This gives a waxy cube with the crystals aligned with their easy axes of magnetization parallel. The oriented polycrystalline sample of complex **1** was saturated in a field of +3.0 T then swept down to −3.0 T, and cycled back to +3.0 T at different temperatures between 1.8 and 2.8 K by the reciprocating sample option (RSO) measurement. The data were collected in 200 G decrement/increment step in each hysteresis loop. The magnetization relaxation decay data for oriented polycrystalline sample of complex **1** were collected the magnetization versus time after the applied field turned to zero from 3.0 T between 1.8 and 2.8 K. Alternating current (AC) susceptibility measurements were carried out on a Quantum Design PPMS-9 magnetometer equipped with a 9.0 T magnet and were capable of achieving temperatures 1.8–400 K. AC susceptibility data of complexes **1** and **2** were collected for powdered, microcrystalline samples in an AC field of 1.0 Oe, oscillating in the 250–10 000 Hz range.

3. Results and discussion

3.1. Crystal structure of $[Mn_{12}O_{12}(O_2CCF_2Cl)_{16}(H_2O)_4]\cdot 4H_2O$ (**1**) $\cdot 4H_2O$ and $[PPh_4][Mn_{12}O_{12}(O_2CCF_2Cl)_{16}(H_2O)_4]\cdot 2H_2O\cdot CH_2Cl_2$ (**2**) $\cdot 2H_2O\cdot CH_2Cl_2$

The structure of the complex **1** is shown in Fig. 1, and selected bond distances are listed in Table 2. The structure of complex **1** is quite similar in many respects to the previously characterized [Mn_{12}] complexes [14,16,25]. In addition to one-forth of the Mn_{12} complex, the asymmetric unit was found to contain one H_2O solvate molecules. Some –CF_2Cl groups showed disorder of their Cl and F atoms (Cl13, Cl14, F5, F6 and F7) in two positions, each was 50% occupation. Complex **1** is in $\bar{4}$ symmetry which possesses a [$Mn_{12}(\mu_3\text{-}O)_{12}$] core having a central $[Mn_4^{IV}O_4]^{8+}$ cubane held within a non-planar ring of eight Mn^{III} ions by eight μ_3-O^{2-} ions. The eight Mn^{III} ions separate into two groups of four Mn^{III} ions each. In

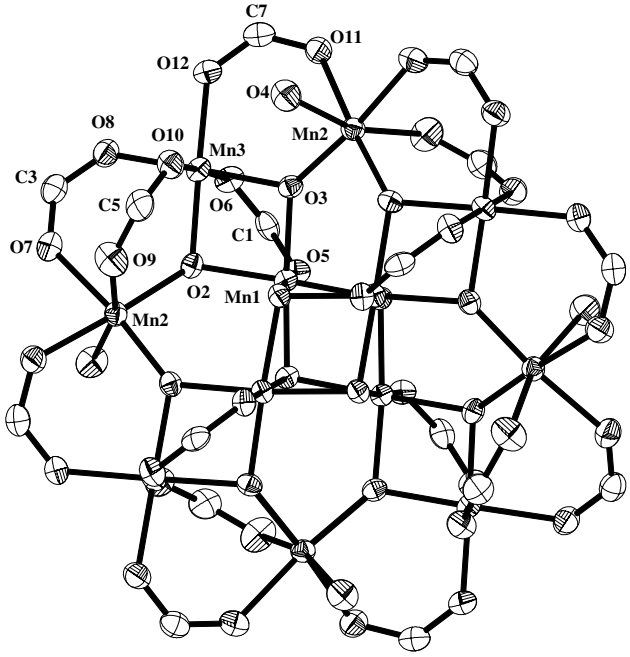


Fig. 1. The X-ray structure of complex **1**. The –CF_2Cl groups of the ligands, and H_2O solvate molecules are omitted for clarity.

Table 2
Selected bond distances (Å) for $[Mn_{12}O_{12}(O_2CCF_2Cl)_{16}(H_2O)_4]\cdot 4H_2O$ (**1**) $\cdot 4H_2O$

Mn(1)–O(3)	1.877(4)
Mn(1)–O(1B)	1.893(5)
Mn(1)–O(1)	1.915(4)
Mn(1)–Mn(3)	2.7912(13)
Mn(1)–Mn(1B)	2.817(2)
Mn(1)–O(2)	1.882(4)
Mn(1)–O(5)	1.919(4)
Mn(1)–O(1A)	1.931(4)
Mn(1)–Mn(1C)	2.817(2)
Mn(1)–Mn(1A)	2.964(2)
Mn(2)–O(3)	1.881(4)
Mn(2)–O(11)	1.991(5)
Mn(2)–O(4)	2.145(5)
Mn(2)–O(2B)	1.917(4)
Mn(2)–O(7B)	1.982(5)
Mn(2)–O(9B)	2.149(5)
Mn(3)–O(3)	1.896(4)
Mn(3)–O(12)	1.937(5)
Mn(3)–O(6)	2.201(5)
Mn(3)–O(2)	1.901(4)
Mn(3)–O(8)	1.951(5)
Mn(3)–O(10)	2.203(5)

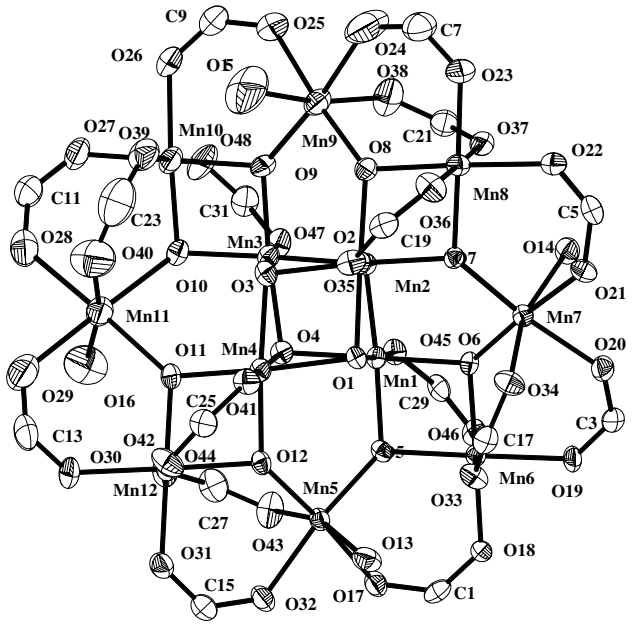


Fig. 2. The X-ray structure of complex **2**. The $-CF_2Cl$ groups of the ligands, PPh_4 ion, and CH_2Cl_2 and H_2O solvate molecules are omitted for clarity.

the first group, each Mn^{III} (Mn3) ion is coordinated to single Mn^{IV} (Mn1) ion via two oxide bridges, while in the second group each Mn^{III} (Mn2) ion is coordinated to two Mn^{IV} (Mn1) via two oxide bridges. Peripheral ligation of complex **1** is proved by 16 η^2-μ_2-carboxylate groups and four H_2O ligands. Complex **1** has one H_2O ligand on each Mn^{III} (Mn2) ion in one set of 4 Mn^{III} ions, which are bonded to two Mn^{IV} ions via two μ_3-O^{2-} ions. The four H_2O ligands of complex **1** are arranged in an alternating up, down, up, down arrangement (1:1:1:1 arrangement), which is quite similar to Mn_{12} acetate complex **3**. The Mn–O bond distances make it clear that all of the atoms in the central cubane are Mn^{IV} ions, while the ring consists of eight Mn^{III} ions. These assignments supported by the marked Jahn–Teller (JT) elongation of the axial Mn^{III}–O bonds (2.144–2.203 AA), which are on average 0.24 Å longer than the analogous equatorial Mn–O bonds (1.881–1.990 Å). The JT distortion in complex **1** appears the mode of an axial elongation of two *trans* bonds and the JT axes are all axially disposed roughly perpendicular to the $Mn_{12}O_{12}$ disk-like core. Consequently, there is a near parallel alignment of the eight Mn^{III} JT axes, which is the origin of the significant magnetic anisotropy that greatly influences the observed magnetic relaxation properties.

An ORTEP plot of complex **2** is shown in Fig. 2, and selected bond distances are given in Table 3. At 150 K, the complex **2** crystallizes in the monoclinic $P2_1/c$ space group with the asymmetric unit consisting of one Mn_{12} molecule, one counter ion PPh_4, two H_2O and one CH_2Cl_2 solvated of crystallization. The anion Mn_{12} moiety is similar to the usual $[Mn_{12}]^-$ complex except that the number and coordination position of water [5,10,14,29,30]. The central cubane $[Mn_4^{IV}O_4]^{7+}$ structure possesses four M^{IV} ions and four μ_3-O^{2-} ions which is held within a non-planar ring of eight Mn^{III}/Mn^{II} ions by eight μ_3-O^{2-} ions. The Mn–O bond distances (1.826–1.967 Å) make it clear that all of Mn atoms in the central cubane are Mn^{IV} ions. These assignments of Mn^{III} ions were supported by the marked Jahn–Teller elongation of the axial Mn–O bonds (2.110–2.235 Å), which are on average 0.247 Å longer than the equatorial Mn–O bonds (1.858–2.043 Å). Fro Mn(11) atom, the equatorial Mn–O bond lengths show a pronounced elongation (2.063–2.135 Å) relative to the equatorial Mn^{III}–O bonds (1.858–2.043 Å). Clearly, the Mn(11) is a Mn^{II} ion, and it does not exhibit a Jahn–Teller distortion as seen for all the Mn^{III} ions in complex **2**. The complex **2** is a valence-tapped $Mn^{II}Mn_7^{III}Mn_4^{IV}$ compound. Peripheral ligation of complex **2** is proved by 16 η^2-μ_3-carboxylate groups and four H_2O ligands. Complex **2** also has a 1:1:1:1 arrangement of H_2O ligands, and the reduction of complex **1** the extra electron is added to Mn(11) without changing the H_2O coordination environment.

In the previous paper on the one-electron reduced Mn_{12} complexes, $[PPh_4][Mn_{12}O_{12}(O_2CEt)_{16}(H_2O)_4]$, $[PPh_4][Mn_{12}O_{12}(O_2CH_2Cl)_{16}(H_2O)_3]$, $[Co(C_5Me_5)_2]$ $[Mn_{12}O_{12}(O_2CC_6F_5)_{16}(H_2O)_4]$, and $[PPh_4][Mn_{12}O_{12}(O_2CC_4H_3\ S)_{16}(H_2O)_2]$, the reduction site was assigned to one of Mn^{III} ions on the basis of the bond valence sum analysis [5,14,29,30]. A bond valence sums is an empirical

Table 3
Selected bond distances (Å) for $[PPh_4][Mn_{12}O_{12}(O_2CCF_2Cl)_{16}(H_2O)_4]\cdot 2H_2O\cdot CH_2Cl_2$ (**2**) $\cdot 2H_2O\cdot CH_2Cl_2$

Mn(1)–O(1)	1.880(5)
Mn(1)–O(5)	1.884(6)
Mn(1)–O(2)	1.903(6)
Mn(1)–O(6)	1.906(5)
Mn(1)–O(4)	1.915(6)
Mn(1)–O(45)	1.935(6)
Mn(1)–Mn(2)	2.7925(17)
Mn(1)–Mn(6)	2.8015(17)
Mn(1)–Mn(4)	2.8124(17)
Mn(1)–Mn(3)	2.9718(17)
Mn(2)–O(2)	1.882(5)
Mn(2)–O(7)	1.887(5)
Mn(2)–O(8)	1.891(6)
Mn(2)–O(1)	1.919(6)
Mn(2)–O(3)	1.919(6)
Mn(2)–O(35)	1.932(6)
Mn(2)–Mn(8)	2.8051(18)
Mn(2)–Mn(3)	2.8309(18)
Mn(2)–Mn(4)	2.9704(17)
Mn(3)–O(10)	1.826(6)
Mn(3)–O(9)	1.853(6)
Mn(3)–O(3)	1.895(6)
Mn(3)–O(47)	1.946(6)
Mn(3)–O(4)	1.951(6)
Mn(3)–O(2)	1.967(6)
Mn(3)–Mn(10)	2.7612(19)
Mn(3)–Mn(4)	2.8531(18)
Mn(4)–O(11)	1.836(6)
Mn(4)–O(12)	1.893(6)
Mn(4)–O(4)	1.897(6)
Mn(4)–O(41)	1.942(6)
Mn(4)–O(1)	1.952(5)
Mn(4)–O(3)	1.952(6)
Mn(4)–Mn(12)	2.7657(18)
Mn(5)–O(5)	1.876(5)
Mn(5)–O(12)	1.892(6)
Mn(5)–O(32)	1.972(6)
Mn(5)–O(17)	1.994(6)
Mn(5)–O(13)	2.150(6)
Mn(5)–O(43)	2.153(7)
Mn(6)–O(6)	1.883(6)
Mn(6)–O(5)	1.888(5)
Mn(6)–O(19)	1.948(6)
Mn(6)–O(18)	1.958(6)
Mn(6)–O(46)	2.186(6)
Mn(6)–O(33)	2.212(6)
Mn(7)–O(7)	1.869(6)
Mn(7)–O(6)	1.898(6)
Mn(7)–O(20)	1.961(6)
Mn(7)–O(21)	1.997(6)
Mn(7)–O(34)	2.159(6)
Mn(7)–O(14)	2.167(6)
Mn(8)–O(8)	1.879(6)
Mn(8)–O(7)	1.890(6)
Mn(8)–O(23)	1.955(7)
Mn(8)–O(22)	1.966(6)
Mn(8)–O(36)	2.195(7)
Mn(8)–O(37)	2.207(7)
Mn(9)–O(8)	1.920(6)
Mn(9)–O(9)	1.921(6)
Mn(9)–O(25)	1.999(8)
Mn(9)–O(24)	2.044(10)
Mn(9)–O(38)	2.109(7)
Mn(9)–O(15)	2.162(10)
Mn(10)–O(10)	1.866(6)
Mn(10)–O(9)	1.893(6)
Mn(10)–O(27)	1.963(7)
Mn(10)–O(26)	1.983(8)
Mn(10)–O(39)	2.185(8)
Mn(10)–O(48)	2.197(7)
Mn(11)–O(11)	2.063(6)
Mn(11)–O(10)	2.103(6)
Mn(11)–O(28)	2.133(9)
Mn(11)–O(40)	2.134(10)
Mn(11)–O(29)	2.147(9)
Mn(11)–O(16)	2.178(9)
Mn(12)–O(1)	1.858(6)
Mn(12)–O(12)	1.905(5)
Mn(12)–O(30)	1.948(6)
Mn(12)–O(31)	1.958(6)
Mn(12)–O(42)	2.180(7)
Mn(12)–O(44)	2.235(6)

value, based on crystallographically determined metal–ligand bond distances, which may be used to calculate the oxidation state of a metal [31]. Bond valence sums(s) are calculated using Eq. (1)

$$S = \exp\left[\frac{r_0 - r}{B}\right], \tag{1}$$

where r is the observed bond length, and r_0 and B are empirically determined parameters. Values for r, are tabulated for Mn^{n+} ($n = 2, 3, 4$).

On the basis of the valence bond sum analysis for complexes **1** and **2** are listed in Table 4. The assignment of +4 oxidation state for Mn(1) and +3 oxidation states for Mn(2) and Mn(3) is reasonable for complex **1**. It is also reasonable to assign the four Mn ions in the central cubane framework [Mn(1)–Mn(4)] as having a +4 oxidation state and the remainder of the Mn ions, except for the Mn(11), as having a +3 oxidation state for

Table 4
Bond valance sums for each Mn atom in complexes **1** $\cdot 4H_2O$ and **2** $\cdot 2H_2O\cdot CH_2Cl_2$[a]

Atom	**1** $\cdot 4H_2O$			**2** $\cdot 2H_2O\cdot CH_2Cl_2$		
	Mn^{II}	Mn^{III}	Mn^{IV}	Mn^{II}	Mn^{III}	Mn^{IV}
Mn(1)	4.429	4.084	*4.008*	4.417	4.072	3.996
Mn(2)	3.430	*3.162*	3.103	4.407	4.064	3.988
Mn(3)	3.468	*3.198*	3.138	4.427	4.082	4.005
Mn(4)				4.343	4.005	3.930
Mn(5)				3.491	*3.219*	3.159
Mn(6)				3.497	*3.225*	3.164
Mn(7)				3.486	*3.215*	3.155
Mn(8)				3.468	*3.198*	3.138
Mn(9)				3.268	*3.013*	2.957
Mn(10)				3.471	*3.200*	3.140
Mn(11)				*2.430*	2.241	2.199
Mn(12)				3.508	*3.235*	3.174

[a] The calculation of a bond valence sums was carried our for each Mn atom, assuming that a Mn atom is either Mn^{II}, Mn^{III}, or Mn^{IV}.

complex **2**. The bond sum value for the Mn(11) ion is closer to 2, indicating a +2 oxidation state. The extra electron is tapped at the Mn(11) ion to form the valence-tapped of $Mn^{II}Mn_7^{III}Mn_4^{IV}$ state in complex **2**. The reduction at a Mn^{III} ion not at a central Mn^{IV} ion is similar to previous results.

3.2. Magnetochemistry

The DC magnetization of **1** and **2** were measured from 2 to 300 K at 1.0 kOe and results are shown in Fig. 3. For complex **1** the value of $\chi_M T$ slowly decreases from 18.3 cm^3 K mol^{-1} at 300.1 K to 16.6 cm^3 K mol^{-1} at 180.1 K, and then increases, reaching a maximum of 47.8 cm^3 K mol^{-1} at 8.0 K, finally decreases to 30.2 cm^3 K mol^{-1} at 2.0 K. The large $\chi_M T$ maximum at low temperature is consistent with $S = 10$ if the g-value equals to 1.86. The data for the one-electron reduced complex **2** show similar temperature dependence; the value of $\chi_M T$ slowly decreases from 20.9 cm^3 K mol^{-1} at 300.1 K to 18.5 cm^3 K mol^{-1} at 170.1 K, and then increases, reaching a maximum of 52.0 cm^3 K mol^{-1} at 7.0 K, finally decreases to 43.1 cm^3 K mol^{-1} at 2.0 K. The large $\chi_M T$ maximum at low temperature is consistent with $S = 21/2$ if the g-value equals to 1.86.

AC magnetic susceptibility studies are an excellent way to detect the slow relaxation of magnetization characteristic of a SMM, which cannot reverse its direction of magnetic moment fast enough to keep in phase with the applied oscillating field while the temperature is lower than its block temperature. The AC susceptibility was obtained for complex **1** in a 1.0 Oe AC field at frequencies (ν) of 250, 500, 750, 1000, 2500, 7500 and 10 000 Hz with a DC field of zero. In Fig. 4(a) are shown

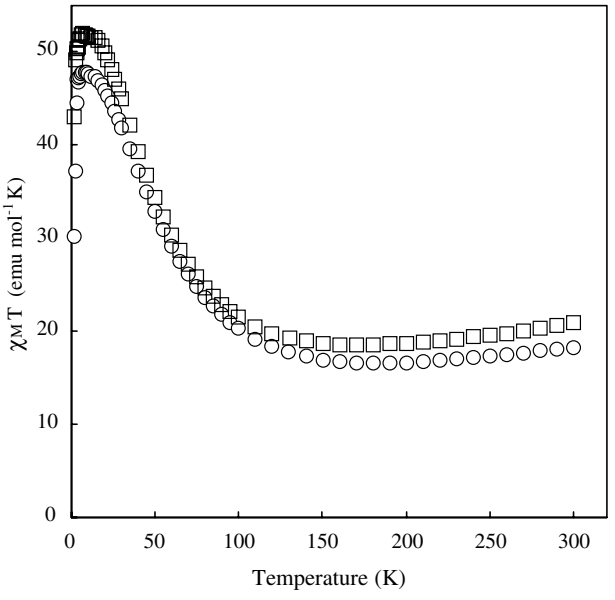


Fig. 3. Plots of $\chi_M T$ vs. temperature for complexes **1** (○) and **2** (□) in an DC field of 1.0 kOe.

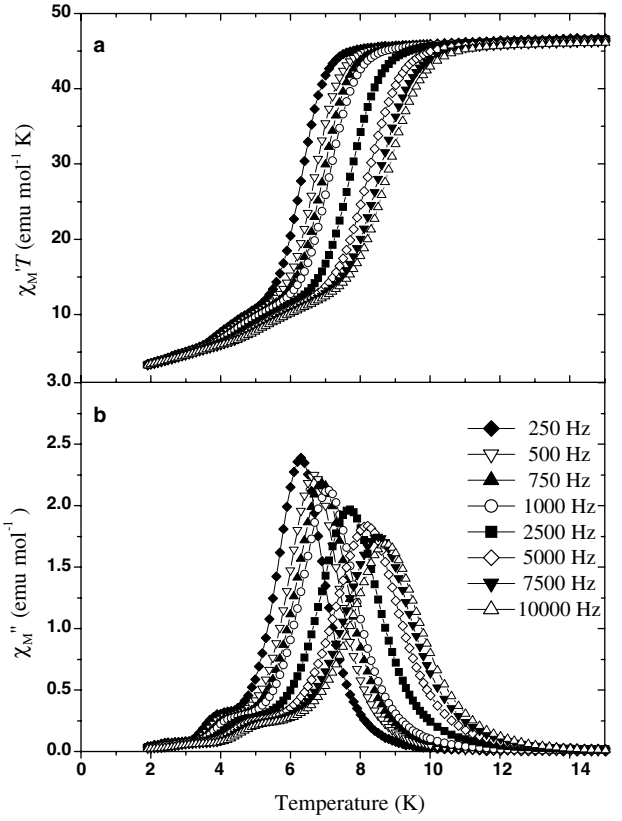


Fig. 4. (a) Plots of $\chi'_M T$ vs. temperature and (b) plots of $\chi''_M T$ vs. temperature for complex **1** in an AC field of 1.0 Oe oscillating at eight different frequencies.

the plots of $\chi' T$ versus temperature, where χ' is the real component of the AC magnetic susceptibility. There is a relatively constant value of $\chi' T \cong 46.5$ cm^3 K mol^{-1} in the 10–15 K range, and this corresponds to the $\chi' T$ value expected for a complex with an $S = 10$ ground state ($g = 1.84$), which showed fairly good agreement to those obtained from DC susceptibility measurement. Also, there are systematic frequency dependence and a "two-step" decrease below 10 K. The decrease in $\chi' T$ is attributable to a relaxation process, thus there are two different regions of relaxation; one in the 5.0–11.0 K range and one in the 3.0–6.5 K range, which are corresponding to the high-temperature (HT) and the low temperature (LT) phases, respectively. These two relaxation processes are also shown in Fig. 4(b), the plots of the out-of-phase χ''AC susceptibility versus temperature, which show predominantly a peak in the 6.3–8.8 K range with a smaller peak in the 3.9–5.1 K range. These two magnetization relaxation processes in Mn_{12} complexes have been elucidated by a Jahn–Teller isomerism [11,15,17,32].

The anisotropy energy barrier U can be calculated by the Arrhenius law, which on the basis the plots of the natural logarithm of the relaxation time τ, when $\tau = 1/(2\pi\nu)$, versus the inverses of the χ'' maximum temper-

ature T_p, which was evaluated from Gauss equation [3]. The anisotropy energy barrier U and pre-exponential factor τ_0, which is the characteristic time of the system, can be estimated by the following equation:

$$\tau = \tau_0 \exp\left[\frac{U}{k_B T_p}\right]. \quad (2)$$

Therefore, by fitting T_p obtained from Fig. 4(b) for different frequency ν, $\tau_0 = 1.33 \times 10^{-9}$ s and $U/k_B = 82.7$ K were obtained for 6.3–8.8 K range, and $\tau_0 = 5.2 \times 10^{-10}$ s and $U/k_B = 56.4$ K were obtained for 3.9–5.1 K. The energy barrier $U/k_B = 82.7$ K is the highest among the Mn_{12} family [17]. For complex **1**, the Jahn–Teller isomerism and/or solvated effect does not been observed any enhancement in AC out-of phase in the low temperature range by drying the sample.

The AC susceptibilities are obtained for complex **2**, in Fig. 5(a) are shown the plots of $\chi'T$ versus temperature. There is a relatively constant value of $\chi'T \cong 53.3\ cm^3\ K\ mol^{-1}$ in the 7–15 K range, and this corresponds to the $\chi'T$ value expected for a complex with an $S = 21/2$ ground state ($g = 1.88$), fairly good agreement to those obtained from DC susceptibility measurement. The decrease in $\chi'T$ is attributable to a relaxation process in the 4.0–9.0 K range. In Fig. 5(b), the plots of the out-of-phase χ'' AC susceptibility versus temperature, which show only a peak in the 4.5–6.4 K range. From the Arrhenius law Eq. (2), the $\tau_0 = 5.93 \times 10^{-10}$ s and $U/k_B = 64.8$ K were obtained for complex **2**. The energy barrier of complex **2** is comparable to those of anionic $[Mn_{12}]^-$ SMMs [29]. For complex **2**, the Jahn–Teller isomerism and/or solvated effect does been observed the enhancement in AC out-of phase in the low temperature range by drying the sample. In Figs. 6(a) and (b) are shown the out-of phase χ'' AC components of complex **2** for drying sample after one day and on week, respectively. These two relaxation processes are also shown in Fig. 6(a), the plots of the out-of-phase χ'' AC susceptibility versus temperature, which show predominantly a peak in the 4.4–5.9 K range with a shoulder peak around 3.0 K. As seen in Fig. 6(b), the lower temperature range relaxation process becomes predominantly after the sample was dried after one week. From the Arrhenius law Eq. (2), the $\tau_0 = 4.26 \times 10^{-9}$ s and $U/k_B = 32.4$ K were obtained for complex **2** in the lower temperature relaxation. The Arrhenius plots for complexes **1** and **2** are shown in Fig. 7. The anisotropy energy barrier U and pre-exponential factor τ_0 are determined from the Arrhenius plots as shown in Table 5. One electron reduction anion

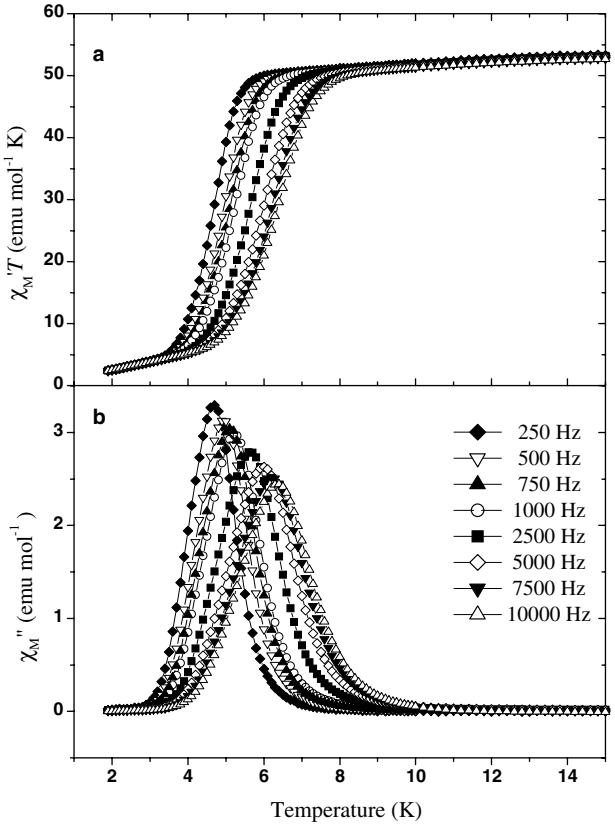


Fig. 5. (a) Plots of $\chi'_M T$ vs. temperature and (b) plots of $\chi''_M T$ vs. temperature for complex **2** in an AC field of 1.0 Oe oscillating at eight different frequencies.

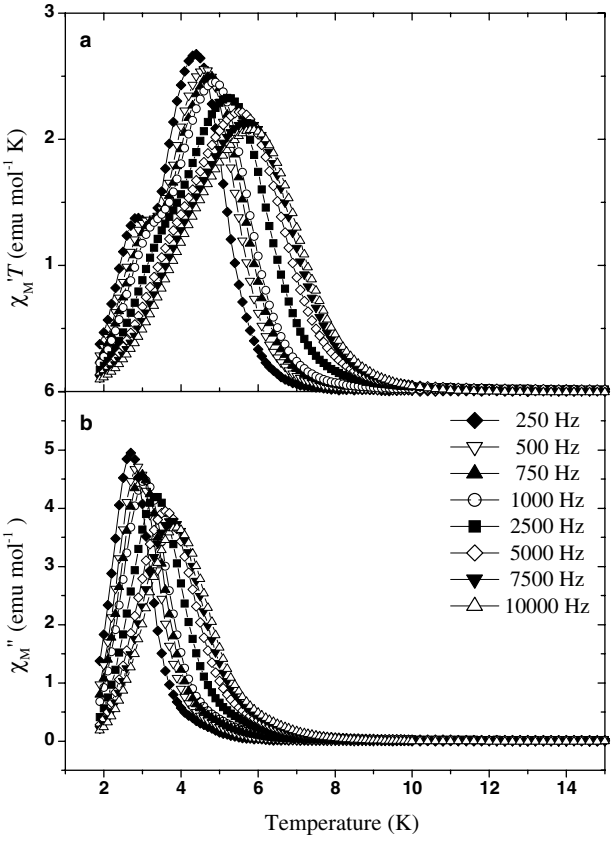


Fig. 6. (a) Plots $\chi''_M T$ vs. temperature for complex **2** after drying one day sample and (b) plots χ''_M vs. temperature for complex **2** after drying one week sample in an AC field of 1.0 Oe oscillating at eight different frequencies.

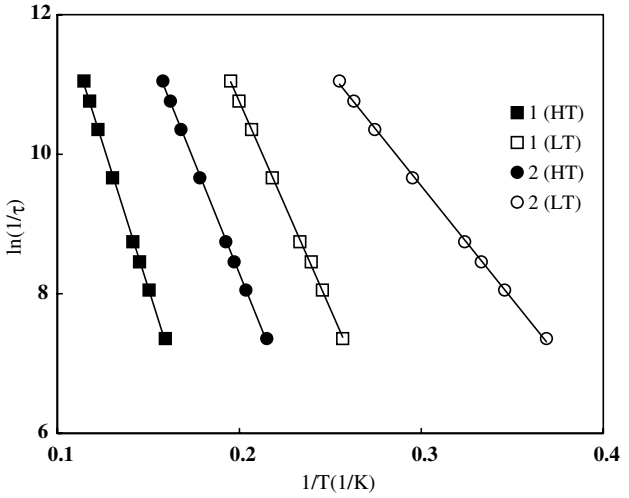


Fig. 7. Plots of the natural logarithm of the inverse of the magnetization relaxation time $\ln(1/\tau)$ vs. the inverse of the absolute temperature of $\chi''_M T$ peak for the HT (■) and LT (□) phase of complex **1** and the HT (●) and LT (○) phase of complex **2**. The solid lines represent least-square fits of the data to the Arrhenius equation.

Table 5
The anisotropy energy barrier U and pre-exponential factor τ_0 are determined from Arrhenius plots for complexes **1** and **2**

Complex	Phase	τ_0 (s)	U (K)
1	HT	1.33×10^{-9}	82.7
1	LT	5.2×10^{-10}	56.4
2	HT	5.93×10^{-10}	64.8
2	LT	4.26×10^{-9}	32.4

$[Mn_{12}]^-$ has smaller energy barrier than that of neutral $[Mn_{12}]$, which has also observed for other Mn_{12} complexes [12,18].

The data of hysteresis loops and the first derivative of the hysteresis plots at eight temperatures for complex **1** are shown in Fig. 8(a) and (b), respectively. Steps are clearly seen on these hysteresis loops, as was reported for complex **3** [6]. The value of H_n, which is correspond to resonant tunneling between quantum spin states in 1.8–2.8 K, are summarized in Fig. 9. As the field is decreased from +3.0 T, the first step is seen at zero field, followed by steps around −0.505, −0.969, −1.504, −1.943 and −2.390 T. The spacing between the steps in the hysteresis loops is given as $\Delta H = -D/g\mu_B$, where g is the gyromagnetic factor and μ_B is the Bohr magneton. The parameter D is the magnitude of axial zero-field splitting ($|D|S_Z^2$). From Fig. 9, we calculate the average step size to be $\Delta H = 0.479$ T, $D = 0.644$ K and the anisotropy energy barrier $U = 64.4$ K, which is similar to the value $\Delta H = 0.44$ T obtained for **3**. However, the anisotropy energy $U = 64.4$ K calculated from the hysteresis loops is smaller than $U = 82.7$ K from high temperature range in AC susceptibilities, and greater than $U = 56.4$ K from low temperature range in AC susceptibilities.

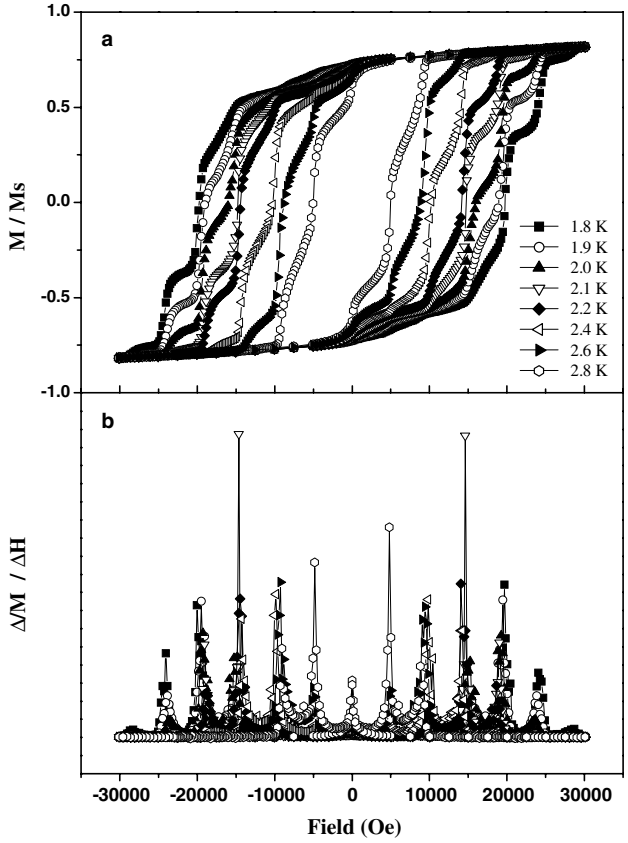


Fig. 8. (a) The plot shows the magnetization hysteresis loops for complex **1** oriented in an eicosane wax matrix at eight different temperatures. (b) The plot is shown a plot of the first derivative of magnetization hysteresis loops.

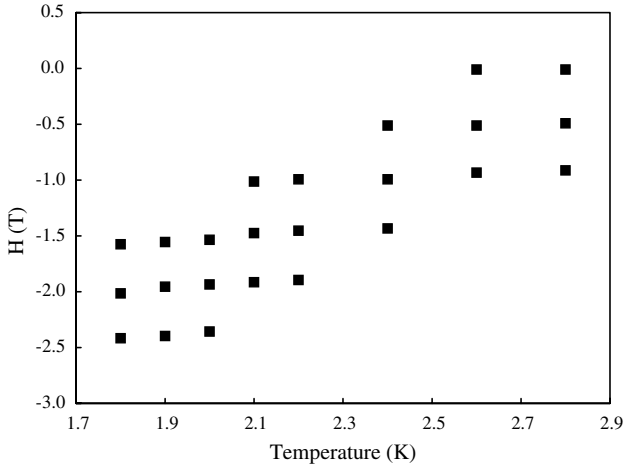


Fig. 9. Field H_n for which is correspond to resonant tunneling between quantum spin states, are plotted vs. temperature for complex **1**.

The magnetization decay experiments for complex **1** were carried out in zero DC field in temperature range of 1.8–2.8 K, as shown in Fig. 10(a). The decay data collected at each temperature are reasonable fit by a single-exponential decay equation (3). M_0 is the initial magnetization, t is the average relaxation time, and B is

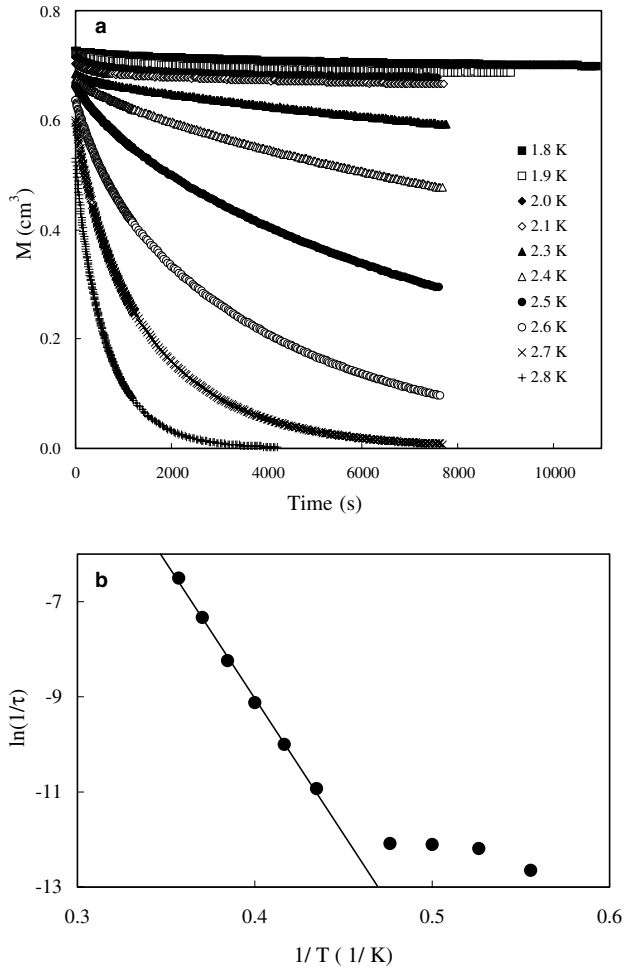


Fig. 10. (a) Magnetization decay plots in zero DC field. (b) Plot of natural logarithm of inverse decay rate ($1/\tau$) vs. inverse of temperature in the temperature range of 1.8–2.8 K for complex **1**.

the width of the distribution. When $B = 1$ the relaxation as a function of time follows a single-exponential decay.

$$M = M_0 \exp\left[-\left(\frac{t}{\tau}\right)^B\right]. \quad (3)$$

The relaxation times obtained using a single-exponential decay are summarized in Table 6. The Arrhenius plot of the natural logarithm of the relaxation rate $1/\tau$ versus 1/T is shown in Fig. 10(b). Least-square fitting of data to Arrhenius equation gives the anisotropy energy barrier $U = 57.0$ K, which is close to the value from the LT AC data.

Table 6
Relaxation fitting parameter M_0 and τ resulting from a single-exponential decay

Temperature (K)	M_0	τ (s)
1.8	0.72	3.12×10^5
1.9	0.71	1.97×10^5
2.0	0.70	1.81×10^5
2.1	0.69	1.77×10^5
2.3	0.67	5.59×10^4
2.4	0.66	2.21×10^4
2.5	0.64	9.15×10^3
2.6	0.59	3.80×10^3
2.7	0.57	1.53×10^3
2.8	0.51	6.68×10^2

4. Conclusion

We have synthesized two Mn_{12} complexes, which showed SMM behavior on AC susceptibility. From the AC and DC magnetic data, complexes **1** and **2** have an $S = 10$ and $S = 21/2$ ground state, respectively. For complex **1**, the anisotropy energy are $U(\mathrm{LT}) = 82.7$ K and $U(\mathrm{LT}) = 56.4$ K obtained from AC out-of-phase singles. For complex **2**, the anisotropy energy are $U(\mathrm{HT}) = 64.8$ K and $U(\mathrm{LT}) = 32.4$ K obtained from AC out-of-phase singles. The step-like hysteresis loops complex **1** show quantum tunneling behavior and the step $\Delta H = 0.479$ T yielded $D = 0.644$ K and $U = 64.4$ K. The magnetization decay data of complex **1**, gave the anisotropy energy barrier $U = 57.0$ K, which is close to the value from the LT AC data.

5. Supplementary material

Crystallographic data for the structural analysis have been deposited with the Cambridge Crystallographic Data Centre under CCDCs 245023 and 245024 for complexes **1** and **2**, respectively. These data can be obtained from the CCDC, 12 Union Road, Cambridge CB2 1EZ, UK, fax: +44 1223 336033, e-mail: deposit@ccdc.cam.ac.uk.

Acknowledgment

We thank the National Science Council of the Republic of China (NSC-92-2113-M-006-011) for support.

References

[1] D. Gatteschi, R. Sessoli, Angew. Chem., Int. Ed. 42 (2003) 43.
[2] G. Christou, D. Gatteschi, D.N. Hendrickson, R. Sessoli, MRS Bull. 25 (2000) 66.
[3] R. Sessoli, D. Gatteschi, A. Caneschi, M.A. Novak, Nature 365 (1993) 141.
[4] R. Sessoli, H.-L. Tsai, A.R. Schake, S. Wang, J.B. Vincent, K. Folting, D. Gatteschi, G. Christou, D.N. Hendrickson, J. Am. Chem. Soc. 115 (1993) 1804.
[5] H.J. Eppley, H.-L. Tsai, N. de Vries, K. Folting, G. Christou, D.N. Hendrickson, J. Am. Chem. Soc. 117 (1995) 301.
[6] L. Thomas, F. Lionti, R. Ballou, D. Gatteschi, R. Sessoli, B. Barbara, Nature 383 (1996) 145.
[7] S.M.J. Aubin, S. Spagna, H.J. Eppley, R.E. Sager, G. Christou, D.N. Hendrickson, Chem. Commun. (1998) 803.

[8] D. Ruiz, Z. Sun, B. Albela, K. Folting, J. Ribas, G. Christou, D.N. Hendrickson, Angew. Chem., Int. Ed. Engl. 37 (1998) 300.
[9] Z. Sun, D. Ruiz, E. Rumberger, C.D. Incarvito, K. Folting, A.L. Rheingold, G. Christou, D.N. Hendrickson, Inorg. Chem. 37 (1998) 4758.
[10] S.M.J. Aubin, Z. Sun, L. Pardi, J. Krzystek, K. Folting, L.-C. Brunel, A.L. Rheingold, G. Christou, D.N. Hendrickson, Inorg. Chem. 38 (1999) 5329.
[11] Z. Sun, D. Ruiz, N.R. Dilley, M. Soler, J. Ribas, K. Folting, M.B. Maple, G.. Christou, D.N. Hendrickson, Chem. Commun. (1999) 1973.
[12] M. Soler, S.K. Chandra, D. Ruiz, E.R. Davidson, D.N. Hendrickson, G. Christou, Chem. Commun. (2000) 2417.
[13] J. An, Z.-D. Chen, J. Bian, J.-T. Chen, S.-X. Wang, S. Gao, G.-X. Xu, Inorg. Chim. Acta 299 (2000) 28.
[14] H.-L. Tsai, T.-Y. Jwo, G.-H. Lee, Y. Wang, Chem. Lett. (2000) 346.
[15] S.M.J. Aubin, Z. Sun, H.J. Eppley, E.M. Rumberger, I.A. Guzei, K. Folting, P.K. Gantzel, A.L. Rheingold, G. Christou, D.N. Hendrickson, Inorg. Chem. 40 (2001) 2127.
[16] H.-L. Tsai', D.-M. Chen, C.-I. Yang, T.-Y. Jwo, C.-S. Wur, G.-H. Lee, Y. Wang, Inorg. Chem. Commun. 4 (2001) 511.
[17] M. Soler, W. Wernsdorfer, Z. Sun, J.C. Huffman, D.N. Hendrickson, G. Christou, Chem. Commun. (2003) 2672.
[18] M. Soler, W. Wernsdorfer, K.A. Abboud, J.C. Huffman, E.R. Davidson, D.N. Hendrickson, G. Christou, J. Am. Chem. Soc. 125 (2003) 3576.
[19] H.-L. Tsai, C.-R. Chang, T.-Y. Jwo, B.-K. Wang, T.-C. Cheng, J. Appl. Phys. 95 (2004) 6888.
[20] H. Zhao, C.P. Berlinguette, J. Bacsa, A.V. Prosvirin, J.K. Bera, S.E. Tichy, E.J. Schelter, K.R. Dunbar, Inorg. Chem. 43 (2004) 1359.
[21] G.Q. Bian, T. Kuroda-Sowa, H. Konaka, M. Hatano, M. Maekawa, M. Munakata, H. Miyasaka, M. Yamashita, Inorg. Chem. 43 (2004) 4790.
[22] D. Gatteschi, A. Caneschi, L. Pardi, R. Sessoli, Science 265 (1994) 1054.
[23] J. Villain, F. Hartman-Boutron, R. Sessoli, A. Rettori, Europhys. Lett. 27 (1994) 159.
[24] D. Loss, D.P. Divincenzo, G. Grinstein, D.D. Awschalom, J.F. Symth, Physica B 189 (1993) 189.
[25] T. Lis, Acta Crystallogr., Sect. B 36 (1980) 2042.
[26] G.M. Sheldrick, Acta Crystallogr. A46 (1990) 467.
[27] G.M. Sheldrick, SHELXL97, a Program for the Refinement of Crystal Structures, University of Göttingen, Germany, 1997.
[28] E.A. Boudreaux, in: E.A. Boudreaux, L.N. Mulay (Eds.), Theory and Application of Molecular Paramagnetism, Wiley, New York, 1976, pp. 491–496.
[29] T. Kuroda-Sowa, M. Lam, A.L. Rheingold, C. Frommen, W.M. Reiff, M. Nakano, J. Yoo, A.L. Maniero, L.-C. Brunel, G. Christou, D.N. Hendrickson, Inorg. Chem. 40 (2001) 6469.
[30] T. Kuroda-Sowa, T. Nogami, H. Konaka, M. Maekawa, M. Munakata, H. Miyasaka, M. Yamashita, Polyhedron 22 (2003) 1795.
[31] I.D. Brown, D. Altermatt, Acta Crystallogr., Sect. B 41 (1985) 244.
[32] D.A. Garanin, E.M. Chudnovsky, Phys. Rev. B B65 (2002) 094424.

An oxygen-rich ligand 2,6-bis(hydroxymethyl)-4-methylphenol (H_3L), containing two benzyl alcohol and a phenol groups, has been utilized in a variety of high-nuclearity complexes [20,21]. Although the structure of H_2L^- is similar to pyridine dimethanol ($pdmH_2^-$), the central phenolate of H_2L^- could coordinate as bridge and terminal ligand in contrast to the pyridine of $pdmH_2^-$ which is only as terminal coordination. This coordination ability of H_3L would provide diversity of structures. Here, we present the syntheses of two Mn_4 complexes with 2,6-bis(hydroxymethyl)-4-methylphenol ligand and the magnetic data of both complexes show that they are SMMs with an $S = 9$ ground state.

2. Experimental

2.1. Synthesis

All solvents and reagents were used as received, and no purification of chemical was needed. All reactions were performed under aerobic conditions.

2.1.1. $[Mn_4(HL)_4(MeOH)_4Cl_2]$ (1)

$MnCl_2 \cdot 4H_2O$ (280 mg, 1.42 mmol) and H_3L (170 mg, 1.03 mmol) were dissolved in methanol (12 ml), followed by addition 1 ml of 1 M NaOH in methanol. The solution was stirred 30 min then filtered. The filtrate was layered by Et_2O and the resulting solution slowly gave well-formed brown crystals. Crystals were collected by filtration, washed with MeOH and Et_2O then dried in air. The yield was 12% (55 mg); IR data (KBr disk, cm^{-1}): 3356vs br, 2920s, 2854s, 1637m, 1474vs, 1251s, 1227s, 1161m, 1127m, 994m, 864m, 815s, 623s, 580m, 562m, 546m, 475m. *Anal*. Calc. for $Mn_4C_{40}H_{56}Cl_2O_{16}$: C, 44.3; H, 5.2. Found: C, 42.2, H, 5.2%. The crystallographic sample was maintained in contact with mother liquor to avoid solvent loss and was identified as $\mathbf{1} \cdot 2Et_2O$.

2.1.2. $[Mn_4(HL)_4(MeOH)_4Br_2]$ (2)

Complex **2** was synthesized by the reaction of $MnBr_2 \cdot 4H_2O$ and H_3L analogous to that employed for complex **1**. The yield was 24%; IR data (KBr disk, cm^{-1}): 3340vs br, 2920s, 2854s, 1637m, 1476vs, 1248s, 1230s, 1160m, 1129m, 990m, 863m, 815s, 622s, 583m, 561m, 543m, 473m. *Anal*. Calc. for $Mn_4C_{40}H_{56}Br_2O_{16}$: C, 40.9; H, 4.8. Found: C, 39.2, H, 4.7%. The crystallographic sample was maintained in contact with mother liquor to avoid solvent loss and was identified as $\mathbf{2} \cdot 2Et_2O$.

2.2. Physical measurements

Variable temperature DC magnetic susceptibility measurements were collected on powder samples of complexes **1** and **2**, restrained in eicosane to prevent torquing, on a Quantum Design MPMS SQUID susceptometer equipped with a 7.0 tesla magnet and operating in the range of 1.7–300.0 K. Variable temperature AC magnetic susceptibility measurements were carried out on a Quantum Design PPMS-9 magnetometer equipped with a 9.0 tesla magnet and operating in the range of 2.0–300 K. Diamagnetic corrections were estimated from Pascal's constants [22] and subtracted from the experimental susceptibility data to obtain the molar paramagnetic susceptibility of the compounds.

3. Results and discussion

3.1. Synthesis

The 2,6-bis(hydroxymethyl)-4-methylphenol (H_3L) ligand has been little explored as a chelating ligand in coordination chemistry, although it has been observed in doubly-deprotonated (HL^{2-}) and act as a tridentate ligand [21]. Treatment of H_3L, $MnX_2 \cdot 4H_2O$ and NaOH in a 3:2:2 molar ratios in methanol gave a red-brown color solution. This solution was layered by Et_2O to form brown crystals, which were identified as $[Mn_4(HL)_4(MeOH)_4X_2]$.

3.2. Description of structures

Labeled ORTEP plots of $\mathbf{1} \cdot 2Et_2O$ and $\mathbf{2} \cdot 2Et_2O$ are shown in Figs. 1 and 2, respectively. Complexes **1** and **2** crystallize in the monoclinic space group C_2/c and crystallographic information of both complexes is given in Table 1. The asymmetric unit of complex **1** contains one half molecule and one Et_2O solvent, while complex **2** comprises a complete Mn_4 cluster and two solvated Et_2O. Disregarding the difference in halide bridges, the complexes **1** and **2** are essentially isostructural. The planar diamond core of the clusters is a mixed-valence $Mn^{II}_2Mn^{III}_2$ dicubane held together by two μ_3-O and four μ_2-O. The peripheral ligations are composed of two halide anions, four MeOH and four H_2L^{2-} ligands, of which two types of bonding are observed. One type of H_2L^{2-} ligands is tridentate with a μ_3-OBz bridging, a μ_2-OPh bridging and a BzOH terminally coordinated, in which the bridging oxygens are deprotonated while the terminal coordinated oxygen is protonated. The other type of H_2L^{2-} is bidentate, possessing a deprotonated μ_2-OBz, a deprotonated OPh terminally coordinated and an uncoordinated HOBz. Two terminal Cl^- and four terminal MeOH ligands complete the coordination environment of complex **1**, while complex **2** contains two Br^- ions. In both complexes, all Mn ions are distorted octahedral geometries; oxidation states of Mn are assigned on the basis of bond valence sum calculations (Table 2) [23] and the presence of a Jahn–Teller

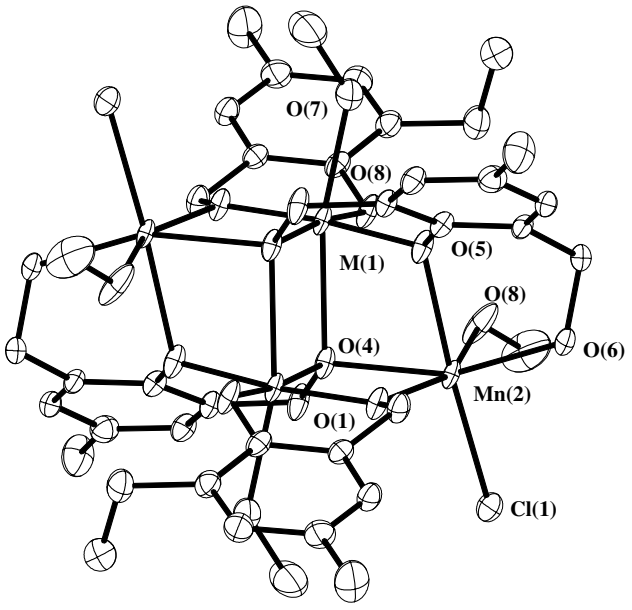


Fig. 1. Crystallographic structure of $[Mn_4(HL)_4(MeOH)_4Cl_2]\cdot 2Et_2O$ (**1**). Thermal ellipsoids at the 50% probability level. The H atoms and solvated molecules have been omitted for clarity.

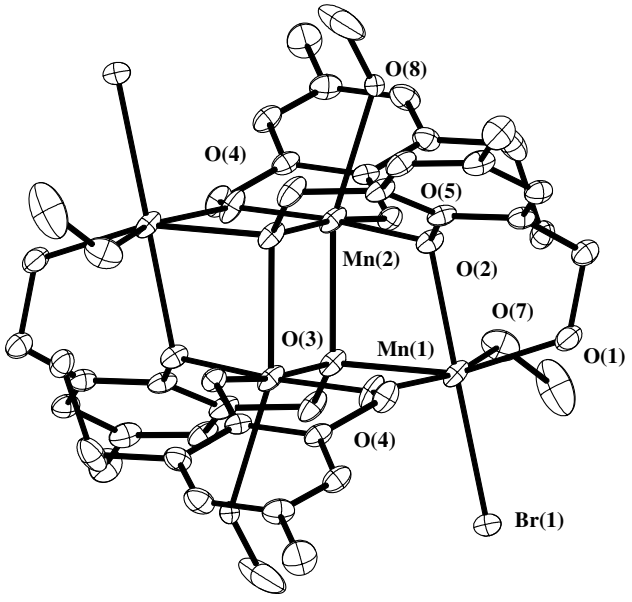


Fig. 2. Crystallographic structure of $[Mn_4(HL)_4(MeOH)_4Br_2]\cdot 2Et_2O$ (**2**). Thermal ellipsoids at the 30% probability level. The H atoms and solvated molecules have been omitted for clarity.

elongation. In complex **2** the O(6), O(6′), O(8) and O(8′) are disorder with 50% occupancy.

3.2.1. $[Mn_4(HL)_4(MeOH)_4Cl_2]$ (**1**)

The asymmetric unit of complex **1** contains one half of the cluster, and a diethyl ether molecule. Mn(2) ions display longer Mn–ligand distances (average 2.24 Å) compared with those for Mn(1) (average 2.01 Å), where Mn(1) shows an elongation of the O(4)–Mn(1)–O(7)

Table 1
Crystallographic data for complexes **1** and **2**

	1 · $2Et_2O$	**2** · $2Et_2O$
Formula	$C_{48}H_{76}Cl_2Mn_4O_{18}$	$C_{48}H_{76}Br_2Mn_4O_{18}$
Formula weight	1231.74	1320.67
Temperature (K)	150(1)	150(1)
Crystal system	monoclinic	monoclinic
Space group	*C*2/*c*	*C*2/*c*
a (Å)	26.0945(19)	25.8145(3)
b (Å)	11.4999(8)	11.6734(2)
c (Å)	21.2188(16)	21.3956(3)
β (°)	121.050(1)	230.1277(6)
V (Å^3)	5455.1(7)	5576.42(14)
Z	4	4
D_{calc} (g cm^{-3})	1.500	1.573
μ(Mo K) (mm^{-1})	2.144	2.386
F(000)	2568	2712
Crystal dimensions (mm)	$0.35\times0.18\times0.12$	$0.35\times 0.18\times0.18$
Reflections measured	21482	30044
Independent reflections	6259	63990
R_{int}	0.0423	0.0424
Goodness-of-fit on F^2	1.206	1.074
R^a (R_w)^b ($I>2\sigma(I)$)	0.0645 (0.1483)	0.0483 (0.1221)
R (R_w) (all data)	0.0730 (0.1525)	0.0726 (0.1452)
Maximum residual peak (e Å^{-3})	1.026	1.384
Minimum residual peak (e Å^{-3})	−0.808	−1.401

[a] $R=(\sum||F_o|-|F_c||)/\sum|F_o|$.
[b] $R_w=[\sum w(|F_o|-|F_c|)^2/\sum w|F_o|^2]^{1/2}$.

Table 2
Bond valence sums of Mn atoms in complexes **1**

	Complex **1**		Complex **2**	
	Mn(1)	Mn(2)	Mn(1)	Mn(2)
Mn(II)	3.4777	*2.1359*	*2.0015*	3.3949
Mn(III)	*3.2069*	1.9695	1.8457	*3.1305*
Mn(IV)	3.1468	1.9326	1.8111	3.0718

Jahn–Teller distortion These axial Mn(1)–O(4) [2.410(3) Å] and Mn(1)–O(7) [2.212(3) Å] distances are distinctly longer than the equatorial bond lengths [1.868(2)–1.928(2) Å]. Therefore the Mn(1) and Mn(2) ions are assigned as Mn^{III} and Mn^{II}, respectively, which are consistent with the results of BVS calculation.

Two types of intermolecular interactions in the form of hydrogen bond are noticeable. One is the typical type of H-bond of O···H–O, involving the uncoordinated O of the HOBz from HL^{2-} and the O atom from the terminal MeOH ligand [O(3)···O(7′) 2.744 Å] as well as the uncoordinated O atom of the HOBz from the HL^{2-} ligand of a neighboring cluster [O(7)···O(7′) 2.713 Å]. The other one is Mn–Cl···H–O type, involving the terminal Cl atom and O atom of terminal protonated HOBz from HL^{2-} of a neighboring cluster [Cl(1)···O(6′) 3.032 Å]. These H-bond interactions effectively mediate a 2D structure network (Fig. 3).

3.2.2. $[Mn_4(HL)_4(MeOH)_4Br_2]$ (**2**)

The asymmetric unit of complex **2** contains one cluster, and two diethyl ether molecules. Mn(1) ions display

longer Mn–ligand distances (average 2.26 Å) compared with those for Mn(2) (average 2.03 Å), while Mn(2) shows an a elongation of the O(3)–Mn(2)–O(7) Jahn–Teller distortion. Thus axial Mn(2)–O(3) [2.376(3) Å] and Mn(1)–O(7) [2.184(6) Å] are distinctly longer than the equatorial bond lengths [1.870(3)–1.931(2) Å]. Consequently the Mn(1) and Mn(2) ions are assigned as Mn^{II} and Mn^{III}, respectively, which are consistent with the results of BVS calculation.

The intermolecular hydrogen bonding interactions in complex **2** are similar to those in complex **1,** involving the uncoordinated O(6) with 50% occupancy of the HOBz from HL^{2-} and the O(8) with 50% occupancy from the terminal MeOH ligand [O(6)···O(8) 2.920(8) Å] as well as the O(8) of a neighboring cluster [O(6)···O(8A) 2.823(7) Å]. The weak M–Br···H–O bonding interaction involves the terminal Br atom and O atom of the terminal protonated HOBz from HL^{2-} of a neighboring cluster [Br(1)···O(1) 3.212(2) Å]. These interactions link the clusters forming a 2D network (Fig. 4).

3.3. DC magnetic susceptibilities and magnetization

The variable temperature DC magnetic susceptibilities were collected for microcrystalline samples of compounds **1** and **2** in the temperature range of 2–300 K at a magnetic field of 1000 G. The experimental $\chi_M T$ versus temperature plots are depicted in Figs. 5 and 6 for complexes **1** and **2**, respectively. For complex **1**, the value of $\chi_M T$ is 16.82 emu K mol^{-1} at 300 K, which is larger than the spin-only value of a $Mn^{II}{}_2Mn^{III}{}_2$ core (12.50 emu K mol^{-1}) indicating the ferromagnetic interactions within the cluster. As the temperature decreases the value of $\chi_M T$ increases steadily and reaches a maximum of 39.87 emu K mol^{-1} at 14 K, then drops sharply upon further decreasing the temperatures. The magnetic susceptibility of complex **2** displays a very similar behavior of complex **1**, with values of 17.55 emu K mol^{-1} at 300 K and 39.52 emu K mol^{-1} at 16 K. The maximum values of $\chi_M T$ at 14–16 K are corresponding to a high-spin $S = 9$ ground state with $g = 1.93$ and 1.92 for complexes **1** and **2**, respectively. The sharp reduction of $\chi_M T$ below 12 K is likely due to the zero-field splitting and Zeeman effects of the high-spin ground state. The parallel magnetic behaviors of tetranuclear manganese complexes have been reported [17].

In order to characterize the coupling interactions within the cluster, the magnetic susceptibility data were fit to the appropriate theoretical expression, which was driven by the van Vleck equation. Only two dominate exchange pathways are considered in this tetranuclear manganese complex (Fig. 7), and the spin Hamiltonian is given in Eq. (1). The equivalent spin Hamiltonian in Eq. (2) is obtained by applying the Kambe coupling approach Eq. (3). The $\chi_M T$ versus temperature for both complexes were least-squares fit to the van Vleck equation, which includes the eigenvalue expression in Eq. (4).

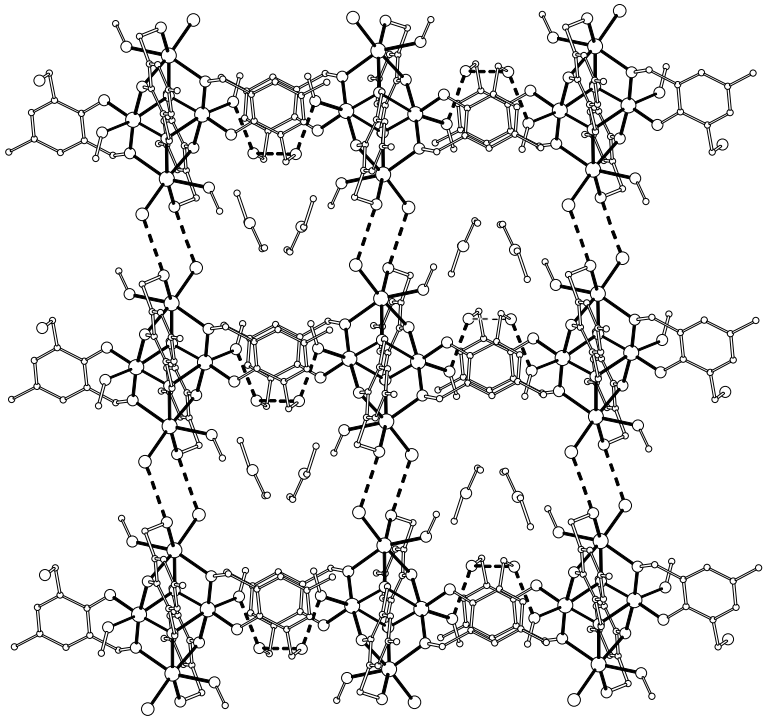


Fig. 3. The hydrogen bonding interactions (dashed line) between adjacent clusters forming a 2D network for complex **1**.

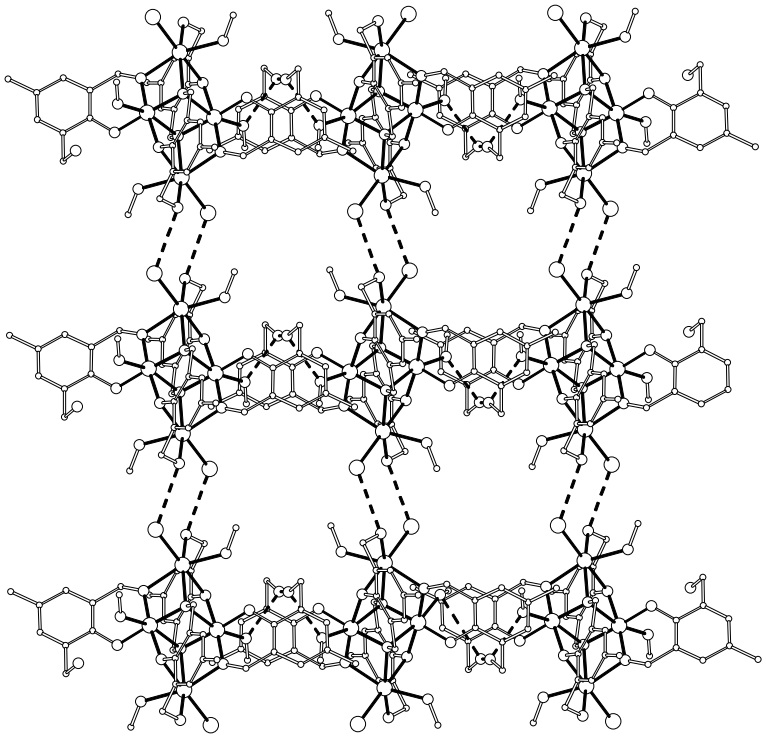


Fig. 4. The hydrogen bonding interactions (dashed line) between adjacent clusters forming a 2D network for complex **2**.

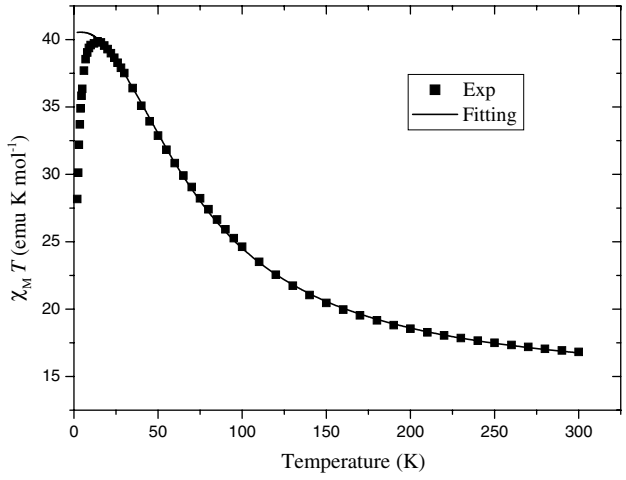


Fig. 5. Plot of $\chi_M T$ vs. temperature for a powder sample of complex **1**. The solid line represents a least-squares fit of the data in the region 16–300 K to the van Vleck equation.

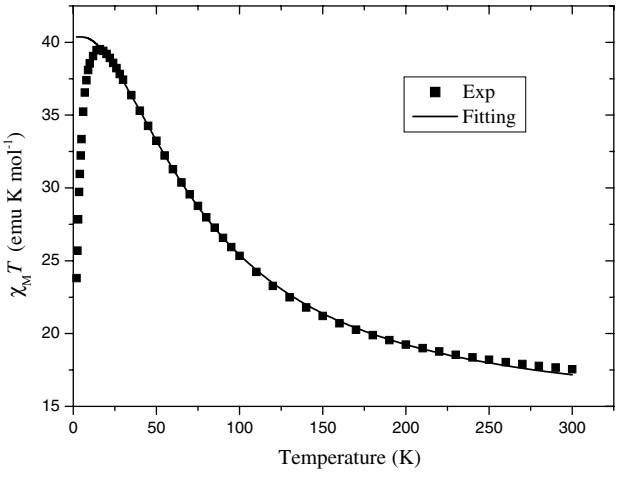


Fig. 6. Plot of $\chi_M T$ vs. temperature for a powder sample of complex **2**. The solid line represents a least-squares fit of the data in the region 14–300 K to the van Vleck equation.

$$H = -2J_{wb}(S_1S_2 + S_1S_4 + S_3S_2 + S_3S_4) - 2J_{bb}(S_1S_3), \quad (1)$$

$$H = -J_{wb}(\hat{S}_T^2 - \hat{S}_A^2 - \widehat{S}_B^2) - J_{bb}(\hat{S}_A^2 - \widehat{S}_1^2 - \widehat{S}_3^2), \quad (2)$$

where

$$\hat{S}_A = \widehat{S}_1 + \widehat{S}_3, \quad \hat{S}_B = \widehat{S}_2 + \widehat{S}_4 \quad \text{and} \quad \hat{S}_T = \widehat{S}_A + \widehat{S}_B. \quad (3)$$

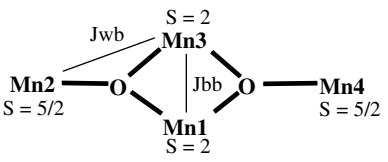


Fig. 7. Diagram showing the definition of atom number and magnetic exchange parameters for the complexes **1** and **2** studied.

The Kambe equivalent operator method gives the eigenvalue expression in Eq. (4).

$$E(S_T) = -J_{wb}[S_T(S_T+1) - S_A(S_A+1) - S_B(S_B+1)] - J_{bb}[(S_A(S_A+1)]. \quad (4)$$

With two $S = 2$ and two $S = 5/2$ interacting ions there are a total of 110 possible states with S_T, the total spin of Mn_4 cluster, ranging from 0 to 9. The data below 14 K for **1** and 16 K for **2** were omitted in the fitting, because zero-field splitting and Zeeman effects are likely to have an effect on the susceptibilities in this temperature range. The results of fitting the experimental data are shown as solid lines in Figs. 5 and 6, with final parameters being $g = 1.89$, $J_{wb} = 3.42\ cm^{-1}$, $J_{bb} = 7.71\ cm^{-1}$ for complex **1**; $g = 1.89$, $J_{wb} = 3.25\ cm^{-1}$, $J_{bb} = 12.46\ cm^{-1}$ for complex **2**, and the temperature independent paramagnetism (TIP) fixed at 600×10^{-6} emu mol^{-1}. It is clear that both molecules are ferromagnetically coupled to give an $S = 9$ ground state. However, the magnitude of the exchange interaction of J_{bb} for complex **2** is almost twice for complex **1**. There is no obvious structural correlation with the exchange coupling interactions, since both complexes are almost isostructural. This kind of phenomenon has been observed also in $[Mn_4(O_2CMe)_2(pdmH)_6](ClO_4)_2 \cdot 2.5H_2O$ [17] and $[Mn_4(hmp)_6Br_2(H_2O)_2]Br_2 \cdot 4H_2O$ [18]. The ground state of complex **1** and **2** are further confirmed by magnetization measurements at 2.0 K up to a 70.0 kG field. In Fig. 8, the $M/N\beta$ values of compounds **1** and **2** are saturated to 17.79 and 18.00, respectively, which corresponds to an $S = 9$ ground state and its saturated magnetization should be $M/N\beta = 2S = 18$.

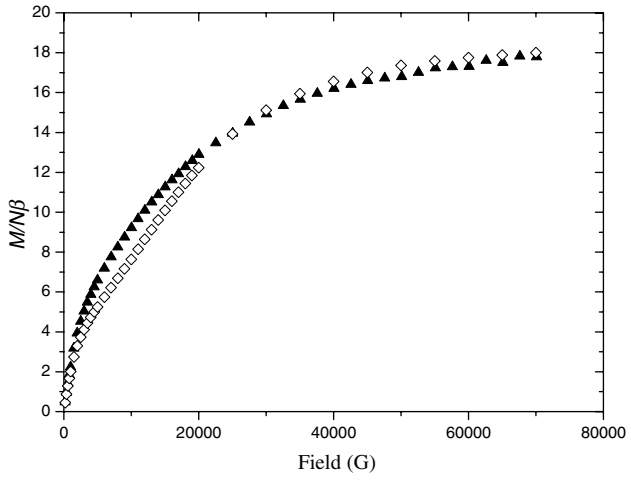


Fig. 8. Isothermal (2 K) field dependence of magnetization of **1** (▲) and **2** (◇).

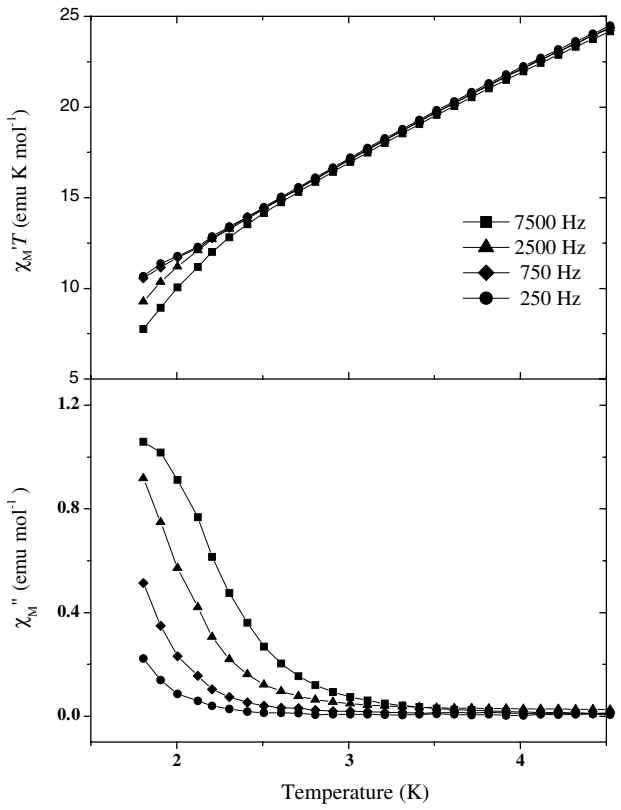


Fig. 9. Plot of $\chi'_M T$ (top) and χ''_M (bottom) vs. temperature for a powder sample of complex **1** in a 1.0 G AC field.

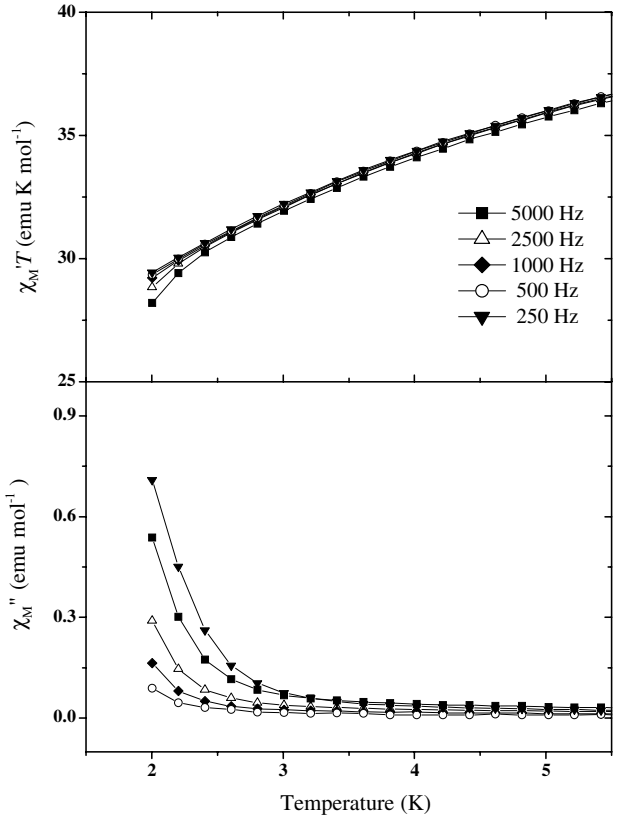


Fig. 10. Plot of $\chi'_M T$ (top) and χ''_M (bottom) vs. temperature for a powder sample of complex **2** in a 1.0 G AC field.

3.4. AC magnetic susceptibilities

Evidence of complexes **1** and **2** function as SMMs was obtained by AC magnetic susceptibility measurements. Being a SMM, it must possess both a large spin ground state and negative zero-field splitting to give rise to an energy barrier between the spin-up and spin-down states. Therefore, if an oscillating magnetic field is applied at low temperature, a reduction in the in-phase ($\chi'_M T$) signal and a corresponding increase in the out-of-phase (χ''_M) signal are seen. The sluggish relaxation of magnetization is due to the energy barrier larger than the thermal energy at low temperature. The AC magnetic susceptibility of powder polycrystalline samples of complexes **1** and **2** were studied in 2.0–10 K range with a 1.0 G AC field oscillating in the range of 250–7500 Hz. Plots of $\chi'_M T$ and χ''_M versus T are given for complexes **1** and **2** in Figs. 9 and 10, respectively. At temperature below 3 K there are significant increases of out-of-phase signals accompanied by collapses of the in-phase signals. The frequency dependence of the AC signals suggests that compounds **1** and **2** are SMMs.

4. Supplementary material

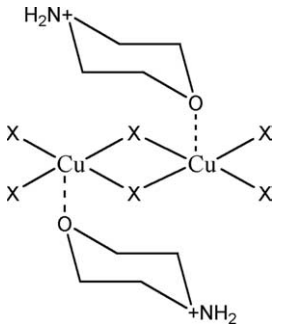
Crystallographic data for the structural analysis have been deposited with the Cambridge Crystallographic Data Centre under CCDC Nos. 251047 and 251048 for compounds **1** and **2**, respectively. Copies of this information may be obtained free of charge from The Director, CCDC, 12 Union Road, Cambridge, CB2 1EZ, UK, fax: +44 1223 366 033, e-mail: deposit@ccdc.ac.uk or on the web www: http://www.ccdc.cam.ac.uk.

Acknowledgment

We thank the National Science Council of the Republic of China (NSC-93-2113-M-006-016) for support.

References

[1] D. Gatteschi, R. Sessoli, Angew. Chem. Int. Ed. 42 (2003) 268 (and references therein).
[2] A.J. Tasiopoulos, A. Vinslava, W. Wernsdorfer, K.A. Abboud, G. Christou, Angew. Chem. Int. Ed. 43 (2004) 2117.
[3] R. Sessoli, H.-L. Tsai, A.R. Schake, S. Wang, J.B. Vincent, K. Folting, D. Gatteschi, G. Christou, D.N. Hendrickson, J. Am. Chem. Soc. 115 (1993) 1804.
[4] R. Sessoli, D. Gatteschi, A. Caneschi, M.A. Novak, Nature 365 (1993) 141.
[5] D. Gatteschi, A. Caneschi, L. Pardi, R. Sessoli, Science 265 (1994) 1054.
[6] (a) H.J. Eppley, H.-L. Tsai, N. de Vries, K. Folting, J. Ribas, G. Christou, D.N. Hendrickson, J. Am. Chem. Soc. 117 (1995) 301; (b) D. Ruiz, Z. Sun, B. Albela, K. Folting, G. Christou, D.N. Hendrickson, Angew. Chem. Int. Ed. 37 (1998) 300; (c) Z. Sun, D. Ruiz, E. Rumberger, C.D. Incarvito, K. Folting, A.L. Rheingold, G. Christou, D.N. Hendrickson, Inorg. Chem. 37 (1998) 4758.
[7] H.-L. Tsai, D.-M. Chen, C.-I. Yang, T.-Y. Jwo, C.-S. Wur, G.-H. Lee, Y. Wang, Inorg. Chem. Commun. 4 (2001) 511.
[8] S.M.J. Aubin, Z. Sun, L. Pardi, J. Krzystek, K. Folting, L.-C. Brunel, A.L. Rheingold, G. Christou, D.N. Hendrickson, Inorg. Chem. 38 (1999) 5329.
[9] H.-L. Tsai, T.-Y. Jwo, G.-H. Lee, Y. Wang, Chem. Lett. (2000) 346.
[10] M. Soler, W. Wernsdorfer, K.A. Abboud, J.C. Huffman, E.R. Davidson, D.N. Hendrickson, G. Christou, J. Am. Chem. Soc. 125 (2003) 3576.
[11] M. Murugesu, M. Habrych, W. Wernsdorfer, K.A. Abboud, G. Christou, J. Am. Chem. Soc. 126 (2004) 4766.
[12] H. Miyasaka, R. Clérac, W. Wernsdorfer, L. Lecren, C. Bonhomme, K. Sugiura, M. Yamashita, Angew. Chem. Int. Ed. 43 (2004) 2801.
[13] M. Soler, W. Wernsdorfer, K. Folting, M. Pink, G. Christou, J. Am. Chem. Soc. 126 (2004) 2156.
[14] (a) J. Villain, F. Hartman-Boutron, R. Sessoli, A. Rettori, Europhys. Lett. 27 (1994) 159; (b) A.K. Boudalis, B. Donnadieu, V. Nastopoulos, J.M. Clemente-Juan, A. Mari, Y. Sanakis, J.-P. Tuchagues, S.P. Perlepes, Angew. Chem. Int. Ed. 43 (2004) 2266; (c) H. Oshio, N. Hoshino, T. Ito, M. Nakano, J. Am. Chem. Soc. 126 (2004) 8805.
[15] S.L. Castro, Z. Sun, C.M. Grant, J.C. Bollinger, D.N. Hendrickson, G. Christou, J. Am. Chem. Soc. 120 (1998) 2365.
[16] C. Cadiou, M. Murrie, C. Paulsen, V. Villar, W. Wernsdorfer, R.E.P. Winpenny, Chem. Commun. (2001) 2666.
[17] E.K. Brechin, J. Yoo, M. Nakano, J.C. Huffman, D.N. Hendrickson, G. Christou, Chem. Commun. (1999) 783.
[18] J. Yoo, E.K. Brechin, A. Yamaguchi, M. Nakano, J.C. Huffman, A.L. Maniero, L.-C. Brunel, K. Awaga, H. Ishimoto, G. Christou, D.N. Hendrickson, Inorg. Chem. 39 (2000) 3615.
[19] L.M. Wittick, K.S. Murray, B. Moubaraki, S.R. Batten, L. Spiccia, K.J. Berry, Dalton Trans. (2004) 1003.
[20] A. Rammal, F. Brisach, M. Henry, J. Am. Chem. Soc. 123 (2001) 5612.
[21] (a) T. Glaser, T. Lügger, Inorg. Chim. Acta 337 (2002) 103; (b) T. Glaser, T. Lügger, R.-D. Hoffmann, Eur. J. Inorg. Chem. (2004) 2356.
[22] E.A. Boudreaux, in: E.A. Boudreaux, L.N. Mulay (Eds.), Theory and Application of Molecular Paramagnetism, Wiley, New York, 1976.
[23] W. Liu, H.H. Thorp, Inorg. Chem. 32 (1993) 4102.



Scheme 1.

lead to the development of a series of spin 1/2 ladder systems [5].

Magneto-structural studies in dimeric $A_2Cu_2X_6$ compounds have been researched extensively in the past [6]. These compounds generally form stacks or chains of $Cu_2X_6^{2-}$ dimers based on the formation of two or one semi-coordinate bonds between adjacent dimers. The discussion of exchange pathways in these studies has focused on the through-bond pathways, i.e., intradimer and intrachain/stack interactions. Unfortunately, the discussion of the role of the close halogen–halogen (2H) contacts within these dimer structures has generally been ignored [7]. However, recently, two neutron scattering studies in $A_2Cu_2Cl_6$ salts have shown that the 2H pathways are stronger than the intrachain/stack interactions [8]. Since this is true in chloride salts, it is expected that the 2H pathway will play an even more significant role in bromide salts.

In this paper, we reexamine the structural and magnetic behavior in the $(MOR)_2Cu_2X_6$ compounds [9], where MOR denotes the morpholinium cation. The extended stack or chain structure is not assumed by these compounds since an oxygen atom on the morpholinium cations occupies one of the semi-coordination sites on each copper atom in the dimeric species, blocking the second semi-coordinate site (Scheme 1). Instead, N–H···X hydrogen bonds force short X···X contacts between dimers, forming non-bonded magnetic exchange pathways so that the compounds behave as alternating AFM chains. In this study, the structural and magnetic properties of both the $(MOR)_2Cu_2Cl_6$ and $(MOR)_2Cu_2Br_6$ end members are reexamined and the extension to a series of mixed $(MOR)_2Cu_2Cl_xBr_{6-x}$ compounds is reported.

2. Experimental

2.1. Synthesis

2.1.1. *(Morpholinium)$_2$Cu$_2$Cl$_6$, (MOR)$_2$Cu$_2$Cl$_6$ (**1**)*

Morpholinium hydrochloride (0.494 g, 4 mmol) and copper chloride dihydrate (0.682 g, 4 mmol) was added to a mixture of 5 mL conc. hydrochloric acid, 5 mL 2-propanol, and 5 mL water. The acidic solution was allowed to stir for 10 min. The red, pleochroic, nearly opaque crystals were collected after several days of evaporation, washed with 2-propanol, and allowed to dry.

2.1.2. *(Morpholinium)$_2$Cu$_2$Br$_6$, (MOR)$_2$Cu$_2$Br$_6$ (**9**)*

Morpholinium hydrobromide (0.672 g, 4 mmol) and copper bromide (0.893 g, 4 mmol) was added to a mixture of 5 mL conc. hydrobromic acid, 5 mL 2-propanol, and 5 mL water. The acidic solution was allowed to stir for 10 min. The violet, pleochroic, nearly opaque crystals were collected after several days of evaporation, washed with 2-propanol, and allowed to dry.

2.1.3. *(Morpholinium)$_2$Cu$_2$Cl$_{6-x}$Br$_x$, (MOR)$_2$Cu$_2$Cl$_{6-x}$Br$_x$ (**2**–**8**)*

The compounds were synthesized by combining the appropriate ratio of morpholinium hydrochloride/morpholinium hydrobromide (4 mmol total) salts and $CuCl_2 \cdot 2H_2O/CuBr_2$ (4 mmol total). This was added to a mixture of the appropriate ratio of conc. hydrochloric/hydrobromic acid (5 mL total), 5 mL 2-propanol, and 5 mL water. The acidic solution was allowed to stir for 10 min. The red-violet, pleochroic, nearly opaque crystals were collected after several days of evaporation, washed with 2-propanol, and allowed to dry. Yields of 25–50% were obtained, depending upon the amount of solvent that was allowed to evaporate.

2.2. X-ray crystallography

Crystals were attached to a glass fiber using glue. Datasets were collected at 293(2) K using a Bruker/Siemens SMART 1K instrument (Mo Kα radiation, $\lambda = 0.71073$ Å). Data were measured using omega scans of 0.3° per frame for 30 s, and a half sphere of data was collected. The first 50 frames were recollected at the end of data collection to monitor for decay. Cell parameters were retrieved using SMART [10] software and refined using SAINTPLUS [11] on all observed reflections. Data reduction and correction for Lp and decay were performed using the SAINTPLUS software. Absorption corrections were applied using SADABS [12]. The structures were solved by direct methods and refined by least squares method on F^2 using the SHELXTL program package [13]. No decomposition was observed during data collection. Structure refinements were straightforward in both cases and no disorder was observed. Data collection parameters are given in Table 1 and significant bond distances and angles given in Table 2. Fig. 1 illustrates the contents of the asymmetric units of both salts, augmented to show the coordination geometry of the Cu(II) ions. Further details are provided in the Supporting Information.

Table 1
Crystallographic data for $(MOR)_2Cu_2Cl_6$ and $(MOR)_2Cu_2Br_6$

Crystal	$(MOR)_2Cu_2Cl_6$	$(MOR)_2Cu_2Br_6$
Formula	$C_8H_{20}N_2O_2Cu_2Cl_6$	$C_8H_{20}N_2O_2Cu_2Br_6$
Formula weight	516.067	782.775
Diffractometer	SMART	SMART
D_{calc} (Mg/m^3)	1.918	2.670
T (K)	296	296
Crystal system	triclinic	monoclinic
Space group	$P\bar{1}$	$P2_1/c$
a (Å)	7.408(7)	14.148(6)
b (Å)	10.458(10)	10.814(4)
c (Å)	11.933(12)	14.298(6)
α (°)	82.26(2)	90.00
β (°)	88.35(2)	117.108(7)
γ (°)	77.22(2).	90.00
V (Å^3)	893.3(15)	1947.1(13)
Independent reflections	3527	4457
R_{int}	0.0431	0.0415
Z	2	4
Goodness-of-fit	1.013	1.030
R_1[a] $[I > 2\sigma]$	0.0529	0.0415
wR_2[b] $[I > 2\sigma]$	0.0897	0.1172
μ (mm^{-1})	3.277	14.497
Trans. range	0.411–0.880	0.078–0.254

[a] $R_1 = \sum|F_o| - |F_c|/\sum|F_o|$.
[b] $wR_2 = \{\sum[w(F_o^2 - F_c^2)^2]/\sum[w(F_o^2)^2]\}^{1/2}$.

The mixed halide salts all crystallize with the monoclinic $(MOR)_2Cu_2Br_6$ structure. Crystallographic data were collected on samples from seven different preparations (Samples **2**–**8**). The fractional occupancy for each of the six halide sites was varied independently. Consistent results were obtained between two refinement procedures: the first where the Cl and Br were constrained to be in the same location for each site; the second where the Cl and Br atoms were allowed to have different coordinates. The former process gave significantly lower R values, despite fewer variables, so it is those results that are reported here. In addition, that process defines a unique average X···X distance for correlation with the magnetic data. Refinement information is available in the Supplementary Data. The fractions of Cl and Br found from the refinements correlates well the observed unit cell volumes, as seen in Fig. 2 and the fractional occupancies of each site are plotted in Fig. 3.

2.3. Magnetic measurements

The susceptibility studies were done on crushed single crystal samples using a Quantum Design MPMS-XL SQUID Magnetometer. The magnetization of each sample was first determined at 1.8 K in fields between 0 and 5 T. The magnetization was linear with field up to at least 1 T for each compound. No hysteresis was detected for any of the compounds. For the determination of the molar magnetic susceptibility, χ_M, the magnetic moment of the compound in a field of 1000 Oe (0.1 T) was determined as a function of temperature between 1.8 and

Table 2
Pertinent intradimer bond distances and angles in $(MOR)_2Cu_2Cl_6$ and $(MOR)_2Cu_2Br_6$

$(MOR)_2Cu_2Cl_6$

Atoms	*Distance*
Cl(1)–Cu(1)	2.245(2)
Cl(2)–Cu(1)	2.255(2)
Cl(3)–Cu(1)	2.302(2)
Cl(3)–Cu(1)i	2.302(2)
Cl(4)–Cu(2)j	2.295(2)
Cl(4)–Cu(2)	2.302(2)
Cl(5)–Cu(2)	2.247(2)
Cl(6)–Cu(2)	2.251(2)
Cu(1)–Cl(3)i	2.302(2)
Cu(1)–O(1)	2.405(4)
Cu(2)–Cl(4)j	2.295(2)
Cu(2)–O(2)	2.405(4)

Atoms	*Angle*
Cl(1)–Cu(1)–Cl(2)	92.04(9)
Cl(1)–Cu(1)–Cl(3)	91.33(10)
Cl(2)–Cu(1)–Cl(3)	169.79(6)
Cl(1)–Cu(1)–Cl(3)i	172.18(6)
Cl(2)–Cu(1)–Cl(3)i	91.26(10)
Cl(3)–Cu(1)–Cl(3)i	84.25(10)
Cl(1)–Cu(1)–O(1)	89.33(12)
Cl(2)–Cu(1)–O(1)	91.35(12)
Cl(3)–Cu(1)–O(1)	98.33(12)
Cl(3)i–Cu(1)–O(1)	97.67(12)
Cl(5)–Cu(2)–Cl(6)	93.32(9)
Cl(5)–Cu(2)–Cl(4)j	171.60(6)
Cl(6)–Cu(2)–Cl(4)j	91.32(10)
Cl(5)–Cu(2)–Cl(4)	91.13(9)
Cl(6)–Cu(2)–Cl(4)	169.03(6)
Cl(4)j–Cu(2)–Cl(4)	83.11(10)
Cl(5)–Cu(2)–O(2)	89.84(12)
Cl(6)–Cu(2)–O(2)	89.91(12)
Cl(4)j–Cu(2)–O(2)	97.16(12)
Cl(4)–Cu(2)–O(2)	100.13(12)
Cu(1)–Cl(3)–Cu(1)i	95.75(10)
Cu(2)–Cl(4)–Cu(2)	96.89(9)

$(MOR)_2Cu_2Br_6$

Atoms	*Distance*
Cu(2)–Br(5)	2.367(1)
Cu(2)–Br(6)	2.397(1)
Cu(2)–Br(4)	2.412(1)
Cu(2)–O(7)	2.431(4)
Cu(2)–Br(3)	2.447(1)
Cu(1)–Br(1)	2.375(1)
Cu(1)–Br(2)	2.388(1)
Cu(1)–Br(4)	2.412(1)
Cu(1)–O(1)	2.419(4)
Cu(1)–Br(3)	2.444(1)

Atoms	*Angles*
Br(5)–Cu(2)–Br(6)	93.78(4)
Br(5)–Cu(2)–Br(4)	170.31(4)
Br(6)–Cu(2)–Br(4)	89.94(4)
Br(5)–Cu(2)–O(7)	89.84(11)
Br(6)–Cu(2)–O(7)	90.91(11)
Br(4)–Cu(2)–O(7)	99.05(11)
Br(5)–Cu(2)–Br(3)	90.53(4)
Br(6)–Cu(2)–Br(3)	170.45(4)
Br(4)–Cu(2)–Br(3)	84.51(4)
O(7)–Cu(2)–Br(3)	97.62(11)

Table 2 (*continued*)

$(MOR)_2Cu_2Cl_6$	
Atoms	*Angles*
Br(1)–Cu(1)–Br(2)	93.39(4)
Br(1)–Cu(1)–Br(4)	170.26(4)
Br(2)–Cu(1)–Br(4)	89.85(4)
Br(1)–Cu(1)–O(1)	91.14(11)
Br(2)–Cu(1)–O(1)	90.43(11)
Br(4)–Cu(1)–O(1)	98.02(11)
Br(1)–Cu(1)–Br(3)	90.94(4)
Br(2)–Cu(1)–Br(3)	170.69(4)
Br(4)–Cu(1)–Br(3)	84.59(4)
O(1)–Cu(1)–Br(3)	97.73(11)
Cu(1)–Br(3)–Cu(2)	94.57(4)
Cu(1)–Br(4)–Cu(2)	96.30(4)

i = $-x+1$, $-y$, $-z$; j = $-x+2$, $-y+1$, $-z+1$.

325 K. Corrections for the small diamagnetic contribution of the sample holder were applied. Corrections to the molar susceptibility have been made for the temperature independent magnetization of the Cu(II) ion (60×10^{-6} emu/mol) and the diamagnetic contribution as calculated from Pascal's constants.

3. Structural properties

3.1. Crystal structures of the pure compounds

The crystal structures of the triclinic $(MOR)_2Cu_2Cl_6$ and the monoclinic $(MOR)_2Cu_2Br_6$ compounds are built up in nearly identical manners, although the resultant symmetries are different. The basic building blocks are the nearly planar bibridged $Cu_2X_6^{2-}$ anions. One morpholinium cation forms a semi-coordinate bond to each copper ion via the oxygen atom of the cation, with the two morpholinium cations arranged in a *trans* configuration in each dimer (Fig. 1). In the triclinic chloride compound, two independent, but nearly identical, centrosymmetric dimers exist, while only a single non-centrosymmetric dimer exists in the monoclinic bromide

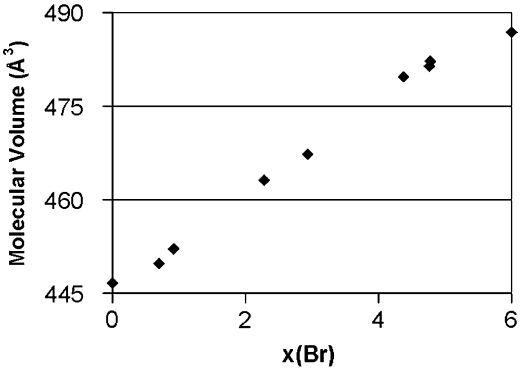


Fig. 2. Plot of molecular volume vs. composition.

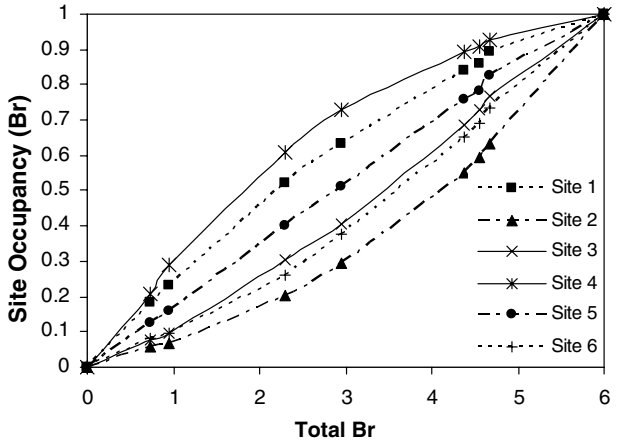


Fig. 3. Plot of site occupancy vs. total Br content for the $(MOR)_2Cu_2Cl_{6-x}Br_x$ salts.

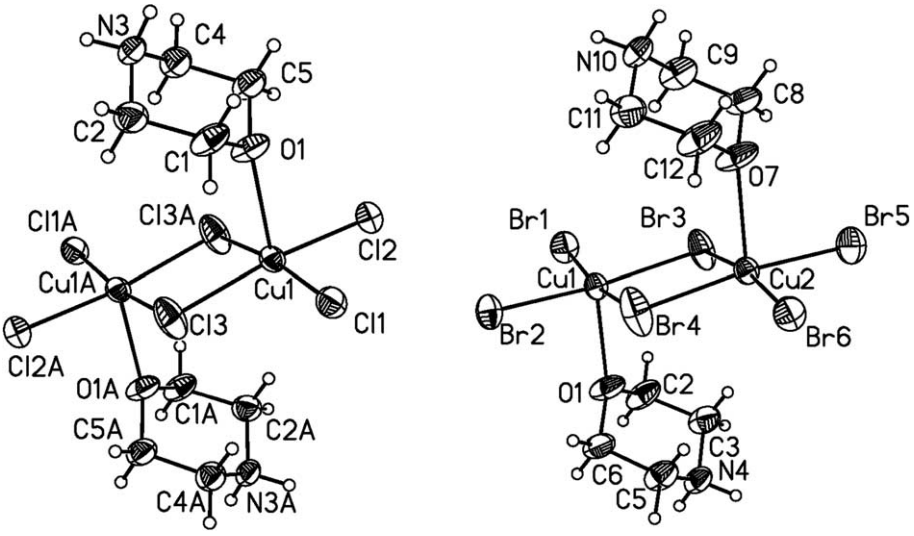


Fig. 1. Illustration of the dimer species in $(MOR)_2Cu_2X_6$. Left: one of the two independent dimers in the chloride salt. Right: the dimer in the bromide salt. Ellipsoids shown at 50%.

Table 3
Mean X···X distances and magnetic parameters for the $(MOR)_2Cu_2Cl_{6-x}Br_x$ salts

Compound	1	2	3	4	5	6	7	8	9
x (Br)	0	0.70	0.92	2.28	2.94	4.38	4.76	4.78	6
X1···X5	3.962[a]	3.997	4.005	4.042	4.043	4.063	4.063	4.067	4.057
X2···X6	3.985[b]	3.923	3.929	3.948	3.945	3.966	3.968	3.971	3.976
J/k (K)	−41.6(1)	∼−40[c]	[d]	−52.8(6)	−62.3(2)	−94.6(4)	−96.8(3)	−98.6(4)	−141.5(5)
J'/k (K)	−18(1)	∼−20[c]		−39(1)	−40(1)	−50(4)	−54(2)	−53(2)	−59(2)
% Defects	0.2			18	4.0	1.7	0.3	0.4	4.5

[a] The Cl1···Cl2 pathway (see Fig. 5).
[b] The Cl5···Cl6 pathway (see Fig. 5).
[c] No fitting possible due to the presence of Cu(II) impurity.
[d] Magnetic measurements not made.

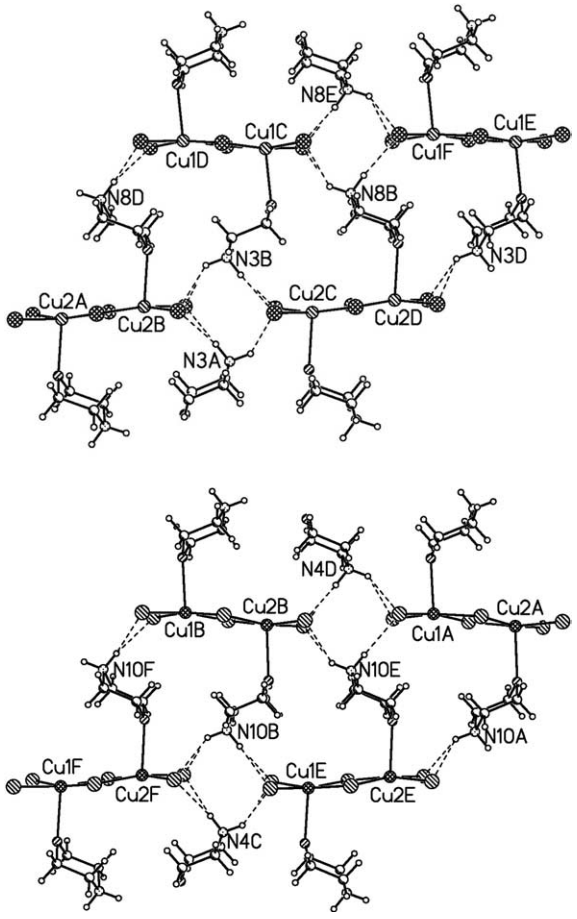


Fig. 4. The layer structures in the $(MOR)_2Cu_2X_6$ salts. N–H···X symbols shown as dashed lines. Top: the layer composed of two independent dimers in the triclinic chloride salt. Bottom: the layer in the monoclinic bromide salt.

salt. The coordination of the morpholinium cation imposes an elongated square pyramidal geometry on each copper ion. Thus the copper halide portion of the dimers is not strictly planar, but the central Cu_2X_2 linkages make angles of 11.0–12.7° with the terminal CuX_2 planes.

The $(MOR)_2Cu_2X_6$ species are assembled into layer structures via N–H···X synthons, as shown in Fig. 4

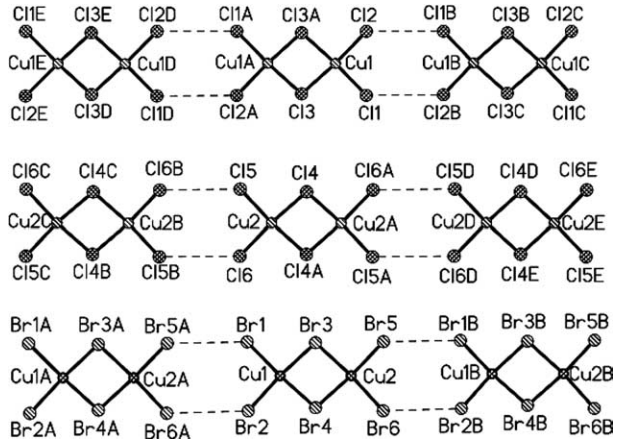


Fig. 5. Illustration of the magnetic chains in the $(MOR)_2Cu_2X_6$ salts. Top and middle: chains 1 and 2 in the chloride salt. Bottom: chain in the bromide salt.

for $(MOR)_2Cu_2Cl_6$ and $(MOR)_2Cu_2Br_6$. As is clear from the two illustrations, the two layers are isostructural, with identical geometrical arrangements, despite the differences in symmetry. The two protons on a given NH_2^+ group form bifurcated hydrogen bonds to the terminal halide ions on adjacent dimers, forcing close X···X contacts between the terminal pairs of halide ions. The N–H···Cl distances range from 3.244 to 3.391 Å while the N–H···Br distances show a slightly greater spread from 3.337 to 3.566 Å. The X···X contacts between dimers define alternating magnetic chains via alternating intradimer and 2H exchange pathways, as are illustrated in Fig. 5. These X···X distance are 3.962 and 3.985 Å for the two crystallographically independent chains in the chloride salt and 3.976 and 4.057 Å for the two independent distances in the pathway of identical chains in the bromide salt. These non-bonded contacts are of importance magnetically, and will be discussed in detail later in the paper.

Adjacent layers are held together weakly by C–H···X interactions. In the chloride salt, adjacent layers are translationally equivalent, while adjacent layers in the bromide salt are related by centers of inversion. The presence of only these weak non-traditional hydrogen

bonds between layers explains the very waxy nature of crystals of these compounds.

3.2. Structural analysis of the $(MOR)_2Cu_2Cl_{6-x}Br_x$ salts ($x > 2$)

The structural analyses for compounds **4**–**8** show that the substitution of Cl for Br in the structure is not random, but the Cl ions occupy certain sites preferentially, as documented in Table 3 and Fig. 3. The pattern of Cl substitution for Br in the Br structure appears to be dictated by the X···X contacts between dimers. The X2···X6 contact is typically ~0.07–0.10 Å shorter than the X1···X5 distance. Thus the smaller Cl atoms preferentially occupy the X2 and X6 positions. Intradimer X···X contacts then dictate that the chloride ions preferentially occupy the X3 position over the X4 position.

The interdimer X···X contacts show a general gradual decrease in distance as the Cl fraction increases. However, the average total decrease (Fig. 6) for these contacts is ~0.07 Å, significantly less than the decrease in van der Waals radii. Thus these X···X contact distances are largely determined by the packing and hydrogen bonding capabilities of the morpholinium cations.

3.3. Structural analysis of the $(MOR)_2Cu_2Cl_{6-x}Br_x$ salts ($x < 1$)

For the two mixed samples with the lowest Br content (**2** and **3**), a large residual peak (~3 e $Å^{-3}$) was found approximately halfway between the terminal halide ions on adjacent dimers. This additional residual was modeled as a Cu atom with partial occupancy. This lowered the *R* values by over 1%. The subsequent difference map showed two additional residuals near X5 and X6, in sites expected from disorder of the halide ions induced by the impurity. The partial occupancies of the copper impurity and the disordered sites were 5.7% for the $x = 0.92\%$ and 7.3% for $x = 0.70$ samples, respectively. Thus, the amount of copper ion impurity appears to increase as the chloride ion fraction increases. As seen in Fig. 7, the Cu impurity sits approximately halfway between adjacent dimers, with Cu–X distances of ~2.25–2.5 Å, but closer to Cu1 than to Cu2. N atoms from two morpholine moieties sit above and below, with Cu–N4 ~ 1.9 and Cu–N10 ~ 2.4 Å. This is a reasonable geometry for an axially compressed copper chloride coordination sphere – very unusual but not unknown as an impurity. To coordinate to the Cu, these two ammonium groups would each have to lose a proton, creating neutral morpholine species. This loss would offset the +2 charge on the Cu impurity. The inclusion of the copper ion impurity may explain why the Cl and Br structures are different. The Br structure can probably only accommodate a small percentage Cu impurity before it breaks down. The presence of this impurity may partially account for the greater shortening of the X···X contacts in these two salts as compared to the salts with higher Br content.

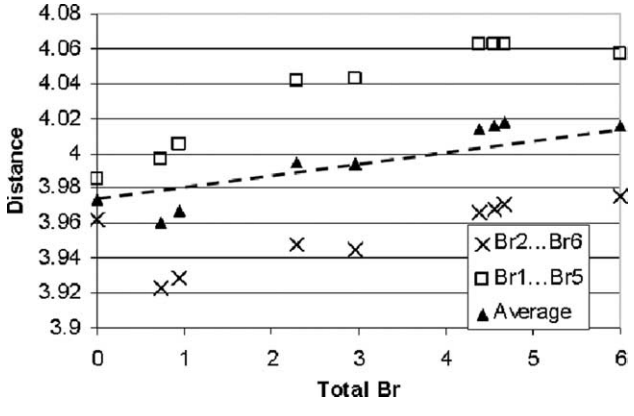


Fig. 6. Plot of halide···halide distances vs. total Br content. x denotes the X1···X5 distances, □ denotes X2···X6 the distances (see Fig. 3 for atom labels). Solid triangles are the average X···X distances for each structure. For the pure chloride salt, the two data points represent the Cl···Cl distances between the dimers in the two crystallographically different chains.

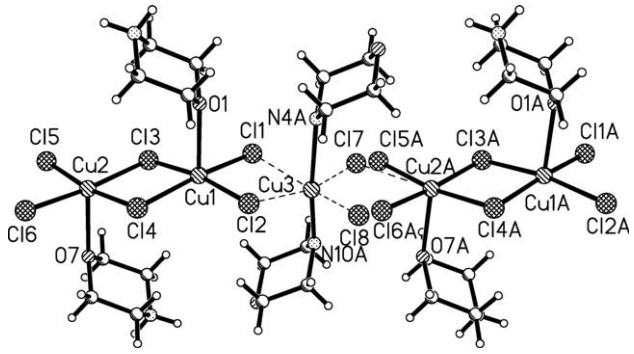


Fig. 7. Illustration of the site of the Cu impurity site in the low bromide content salts. Two pairs of disordered halide sites (label Cl5A/Cl7 and Cl6A/Cl8) induced by the Cu impurity are also shown.

4. Magnetic properties

4.1. Magnetic properties of the pure compounds

As described above, the structures of both the chloride and bromide salts contain isolated $(MOR)_2Cu_2X_6$ molecules that are hydrogen bonded into layer structures. Magnetically, these layers are expected to be well isolated from each other since the only close contacts are C–H···X interactions. Within the layers, the only possible significant exchange pathways between dimers are 2H X···X contacts between adjacent dimers that link these units together into a magnetic chain with alternating exchange pathways: the intradimer coupling, J_d, and the halide···halide coupling, J_{2H}.

Both the chloride and bromide salts exhibit dominant antiferromagnetic behavior as demonstrated by the continuously decreasing value of $\chi_M T$ versus T as the temperature is decreased. The results are in agreement with the experimental values reported earlier [9], with χ_{max} occurring at substantially higher temperature for the bromide salt than the chloride salt. Given the structural characteristics discussed above, the magnetic behavior of both salts was modeled as alternating antiferromagnetic chains (AAFM) with exchange constants J_1 and J_2, characterized by the Hamiltonian $H = -2J_1\sum[s_i \cdot s_{i+1} + \alpha s_{i+1} \cdot s_{i+2}]$ with $0 < \alpha < 1$ and $J_2 = \alpha J_1$. The data was fit with high temperature series expansions for χ_{AAFM} available in the literature [14], with a correction for the paramagnetic 'impurity' that is observed at very low temperatures, according to the equation $\chi_{dimer} = 2(1-f)\chi_{AAFM} + 2f(C/T)$, where f is the mole fraction impurity and C is the Curie constant for a spin 1/2 species. As with many other copper halide systems, the paramagnetic impurity is assumed to be intrinsic, due to defects in the crystal, rather than due to the presence of an impurity compound. The resulting fits are shown in Fig. 8 and the parameters given in Table 3. For the chloride salt, it is found that $J_1/k = -41.6(1)$ K and $J_2/k = -18(1)$ K, while the bromide salt has $J_1/k = -141.5(5)$ K and $J_2/k = -59(2)$ K. The fact that the exchange coupling in the bromide salt is substantially stronger than in the chloride analog, despite the very similar structures, is consistent with the previous report and with the general trend observed in isostructural copper halide dimers [6d].

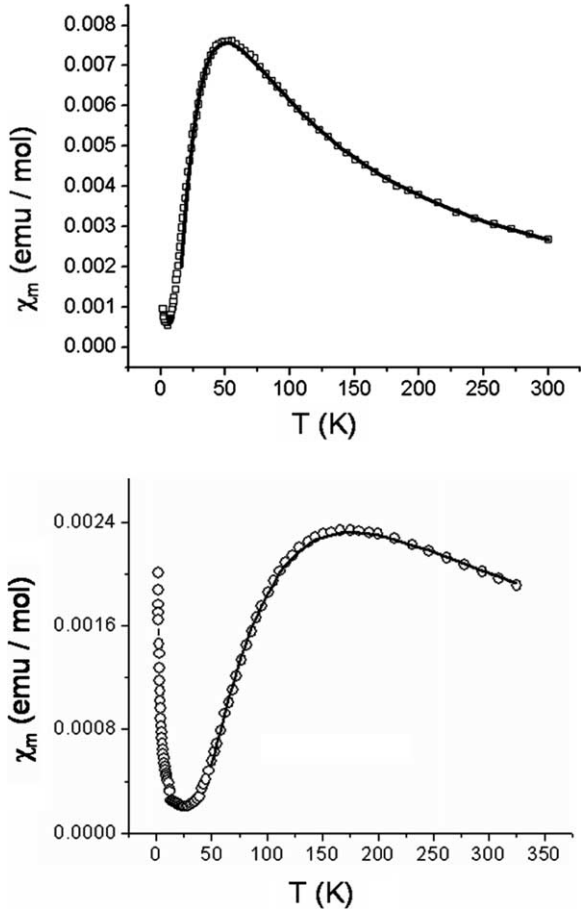


Fig. 8. Plot of χ_M vs. T for $(MOR)_2Cu_2Cl_6$ (top) and $(MOR)_2Cu_2Br$ (bottom). Solid lines are calculated fits to the AAFM model with parameters given in text.

4.2. Magnetic properties of the $(MOR)_2Cu_2Cl_{6-x}Br_x$ salts ($x > 2$)

These compounds all assume the monoclinic $(MOR)_2Cu_2Br_6$ structure with a non-statistical distribution of halide ions. Qualitatively, the magnetic behavior of these salts is similar to that of the pure compounds, with the temperature at which χ_{max} occurs increasing monotonically as the fraction of bromide ion in the salts increases. Since the distribution of halide ion is disordered (although not completely random), these systems are, in principle, examples of spin 1/2 system random chains with dimerization. For such Random Exchange in Heisenberg Antiferromagnetic Chain (REHAC) systems, the behavior $\chi \sim T^{-\gamma}$ is predicted at low temperature, with γ varying continuously. However, for this to be observed, the width of the distribution of exchange parameters must be greater than twice the value of the average exchange coupling [15]. This is not the case here. Thus, the data was analyzed in the same manner as the pure salts, modeled as an AAFM chain with a paramagnetic impurity. The percent impurity increased as the fraction of chloride ion increased, probably because of the presence of interstitial Cu^{2+} impurity ions as observed for samples **2** and **3**. The results are summarized in Table 3 and in Fig. 9. It is seen that J_1/k increases nearly linearly with the bromide content, to a maximum value near 130 K. Also it is noteworthy that one of J values remains nearly constant at $J/k \sim 40$–50 K.

4.3. Magnetic properties of the $(MOR)_2Cu_2Cl_{6-x}Br_x$ salt ($x = 0.70$)

The magnetic behavior of the mixed chloro/bromo salt with $x = 0.70$ exhibits dominant AFM coupling

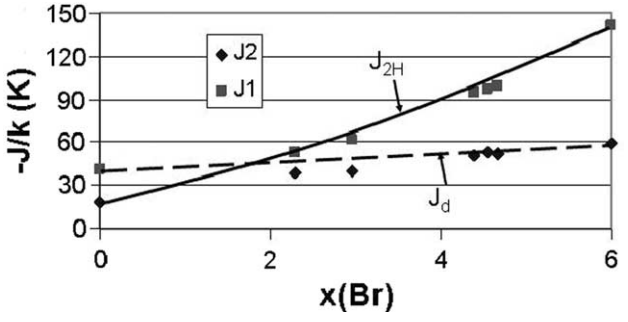


Fig. 9. Plot of the exchange constants for the alternating AFM chains.

at high temperatures, just as all of the other salts. However, at very low temperatures, the behavior is very different. Instead of the $\chi_M T$ approaching zero as T approaches zero (neglecting the paramagnetic impurity contribution seen in all the samples), in this case the $\chi_M T$ value begins to diverge at low temperature. As seen in Fig. 10 the $\chi_M T$ versus T plot begins to diverge below $T = 12$ K. This indicates the presence of a FM interaction that becomes apparent at these low temperatures. Attempts to fit the high T data to the alternating chain model were inconclusive, but good fits could be obtained with $J_1/k = -38 \pm 5$ K and $J_2/k = -20 \pm 5$ K.

This low temperature behavior is extremely unusual. It cannot be due to REHAC-type behavior, since χT will be a decreasing quantity as the temperature is lowered. Thus, to explain the low temperature FM behavior, we examine the structure of the compounds with $x < 1$. As documented in the description of their crystal structure analysis, these compounds contain a copper(II) impurity ion with an associated disorder of the halide ions in the structure. This copper impurity is not located symmetrically between adjacent dimers, but is closer to one dimer than the other. Thus, when the impurity is present, there will be two additional exchange pathways, J'_1 and J'_2, linking the impurity to the neighboring dimers. Three cases can exist: (a) J'_1 and J'_2 are both FM; (b) J'_1 and J'_2 are both AFM; (c) one is FM and one AFM. These three cases are illustrated in Scheme 2, where the spins of the copper ions in the dimers are denoted by the solid arrows and the impurity spins are denoted by the dashed arrows. The ground state alternating AFM spin arrangement in a chain without impurity is shown in the top row. The next two rows show the effect on the spin arrangement when J'_1 and J'_2 have the same sign, FM and AFM, respectively. In these two cases, the presence of the impurity spin reverses the spin arrangement in the adjacent section of the chain. This forces the next impurity spin to be aligned antiparallel to the previous one. Thus, these two cases will lead to an AFM ground state. The last line shows the spin arrangements when J'_1 and J'_2 have alternating sites. Now the spin arrangement on adjacent sections is preserved and each impurity spin has the same orientation as the previous one. Thus this will yield a ferrimagnetic ground state, in agreement with the observed magnetic behavior.

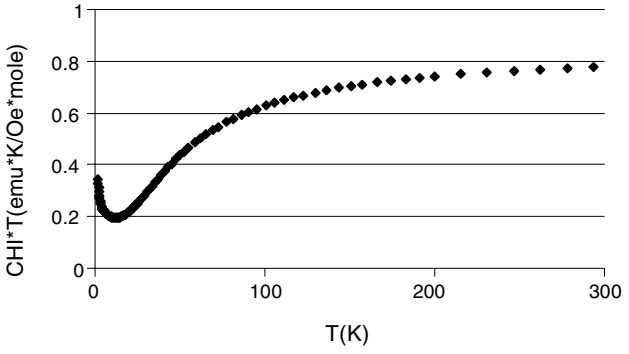
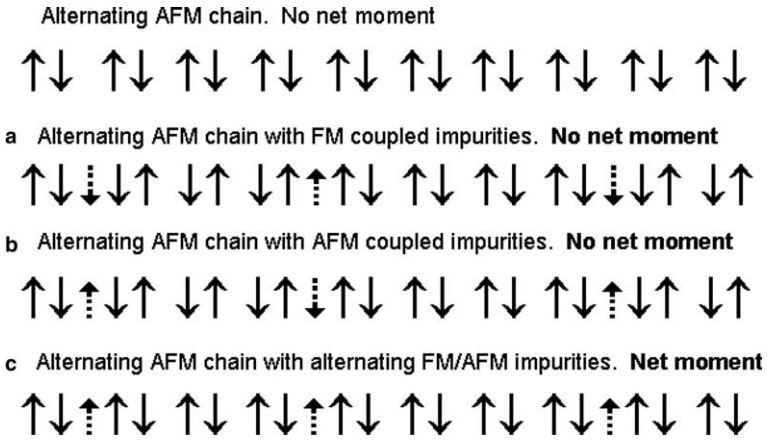


Fig. 10. Plot of $\chi_M T$ vs. T for $(MOR)_2Cu_2Cl_{6-x}Br_x$ $(x = 0.70)$, showing the effect of the weak ferromagnetism induced by the presence of Cu(II) impurities between dimers in the chains.

5. Discussion

The correlation of the structural and magnetic properties in the system reported here clearly shows the presence of two distinct magnetic exchange pathways. The only two possible pathways are the intradimer coupling, J_d, and the halide···halide coupling, J_{2H}. Unfortunately, the thermodynamic measurement of the magnetic susceptibility does not allow a definitive assignment correlation between the magnetic exchange parameters, J_1 and J_2, and the structural pathways, J_d and J_{2H}. Nevertheless, qualitative arguments can be made to support the assignments made in Fig. 9.



Scheme 2.

First, for the pure chloride system, the neutron scattering studies on $KCuCl_3$ and $(piperazinium)_2Cu_2Cl_6$, where the Cl···Cl distances are similar to those in the morpholinium salt, show that J_{2H} is less than J_d. Thus, the value of $J_1/k = 41.6$ K is assigned to J_d, while the $J_2/k = 18$ K value is assigned to J_{2H}. This value of J_d is 50% larger than that observed in $KCuCl_3$. However, the J_d value for the isostructural Tl(I) salt is 25% larger. Thus, the value of J_d appears to be quite sensitive to the environment of the dimer. In particular, with a $4 + 1$ coordination in $(MOR)_2Cu_2Cl_6$ as contrasted to $4 + 2$ in $KCuCl_3$, the basal Cu–Cl distances are shortened in the morpholinium salt, which should lead to more delocalization and stronger AFM coupling.

It has been observed in studies of the 2H exchange in the diammonium layer perovskite salts and in salts containing the distorted tetrahedral CuX_4^{2-} anions that the 2H exchange coupling is typically 5–7 times larger for bromide salts than the corresponding chloride salts when the X···X distances are the same [1–4]. Fig. 5 shows that the X···X distances increase only slightly when the chloride ligand is replaced by bromide. Thus, for the $(MOR)_2Cu_2Cl_{6-x}Br_x$ salts with $2 < x \leqslant 6$, the larger exchange constant, J_1, is clearly associated with J_{2H}.

Another important observation is that the distribution of halide ions is not totally random in the mixed Cl/Br salts. Rather, the chloride ions preferentially occupy the most sterically crowded sites. In these compounds, these are the X2 and X6 sites, where the shortest X···X contacts occur. Thus, J_{2H} should not be expected to vary linearly with the fraction of bromide, x, in the samples, since that is the average occupancy over all sites. Rather J_{2H} should be expected to initially increase at a somewhat slower rate, since the bromide occupancies in the X2 and X6 sites is less than the average occupancy. This is qualitatively represented by the solid line in Fig. 9.

In summary, this study has further elucidated the crucial role of the 2H exchange pathways in the determination of the magnetic behavior of copper halide dimers. The specific contribution of this study is the conclusion that the 2H pathway can become the dominant exchange pathway in the bromide dimers. Thus, discussions of the interpretation of the magnetic behavior of copper halide dimer systems must take this pathway into consideration. In particular, the explanation for the magnetic behavior of the mixed chloro/bromo $[(CH_3)_2CHNH_3]_2Cu_2Cl_{6-x}Br_x$ salts must involve contributions from the 2H exchange pathways. In these compounds, semi-coordinate Cu···X link the dimers into structural chains [16]. However, X···X contacts between chains provide for exchange pathways that define a two-dimensional magnetic lattice. Both pure end members appear to behave as one-dimensional magnetic systems [17]. However, an ordered magnetic phase appears at low temperature in the mixed halide salts [17]. Given the trends in the intradimer and 2H exchange observed in this study, a reasonable rationale can be put forward for the behavior in the $[(CH_3)_2CHNH_3]_2Cu_2Cl_{6-x}Br_x$ system. In the pure chloride salt, the magnetic and structural systems may be identical, that is, the exchange coupling within (J_d) and between (J_c) dimers are the dominant factors. In contrast, the 2H exchange pathway will be much enhanced in the pure bromide salt, so that the magnetic system no longer coincides with the structural chain, but rather consists of the dimer exchange (J_d) and the 2H pathway (J_{2H}). In the mixed halide systems, there could then be a regime where all three exchange pathways have comparable magnitude, giving rise to a two-dimensional magnetic system that can order at low temperatures.

Acknowledgements

Work supported in part by ACS-PRF 34779-CA. The SQUID Magnetometer was purchased by Clark University with the assistance of the National Science Foundation through grant IMR-0314773.

Appendix A. Supplementary data

Crystallographic data for the structures reported here have been deposited with the Cambridge Crystallographic Data Center as Supplementary Publication Nos. CCDC 255598–255607. Copies of this information may be obtained free of charge from: The Director, CCDC, 12 Union Road, Cambridge, CB2 1EZ, UK, fax: +44 1223 336 033, e-mail: deposit@ccdc.cam.ac.uk or on the web http://www.ccdc.cam.ac.uk. Supplementary data associated with this article can be found, in the online version, at doi:10.1016/j.poly.2005.03.121.

References

[1] K. Halvorson, R.D. Willett, Acta Crystallogr. C44 (1988) 2071.
[2] (a) L.O. Snively, G. Tuthill, J.E. Drumheller, Phys. Rev. B 24 (1981) 5349;
(b) R. Block, L. Jansen, Phys. Rev. B 26 (1982) 148.
[3] P. Straatman, R. Block, L. Jenson, Phys. Rev. B 29 (1984) 1415.
[4] (a) F.M. Woodward, A.S. Albrecht, C.M. Wynn, C.P. Landee, M.M. Turnbull, Phys. Rev. B 65 (2002) 144412-1-13;
(b) F.M. Woodward, C.P. Landee, J. Giantsidis, M.M. Turnbull, C. Richardson, Inorg. Chimi. Acta 324 (2001) 324.
[5] (a) B.R. Patyal, B. Scott, R.D. Willett, Phys. Rev. B 41 (1990) 1657;
(b) B.C. Watson, V.N. Kotov, M.W. Meisel, D.W. Hall, G.E. Granoth, W.T. Montfrooij, S.E. Nagler, D.A. Jensen, R. Backov, M.A. Petruska, G.E. Fanucci, D.R. Talham, Phys. Rev. Lett. 86 (2001) 5168;
(c) C.P. Landee, M.M. Turnbull, C. Galeriu, J. Giantsidis, F.M. Woodward, Phys. Rev. B, Rapid Commun. 63 (2001) 100402R;

(d) M.M. Turnbull, C. Galeriu, J. Giantsidis, C.P. Landee, Mol. Cryst. Liq. Cryst. 376 (2002) 469;
(e) R.D. Willett, C. Galeriu, C.P. Landee, M.M. Turnbull, B. Twamley, Inorg. Chem. 43 (2004) 3804.

[6] (a) R.D. Willett, Inorg. Chem. 25 (1986) 1918;
(b) R.D. Willett, T. Grigereit, K.E. Halvorson, B. Scott, Proc. Indian Acad. Sci. 98 (1987) 147;
(c) B. Scott, R.D. Willett, J. Appl. Phys. 61 (1987) 3289;
(d) B. Scott, R.D. Willett, Inorg. Chim. Acta. 141 (1988) 193;
(e) T. Grigereit, J.E. Drumheller, B. Scott, G. Pon, R.D. Willett, J. Magn. Magn. Mat. 104-107 (1992) 198l.

[7] (a) H. Manaka, I. Yamada, K. Yamaguchi, J. Phys. Soc. Jpn. 63 (1997) 564;
(b) H. Manaka, I. Yamada, M. Hagiwara, M. Tokunaga, Phys. Rev. B 63 (2001) 144428;
(c) H. Manaka, I. Yamada, Z. Honda, H. Katori, K. Katsumata, J. Phys. Soc. Jpn. 67 (1998) 3913;
(d) H. Manaka, I. Yamada, N.V. Musunikow, T. Goto, J. Phys. Soc. Jpn. 69 (2001) 675;
(e) H. Manaka, I. Yamada, H. Katori, Phys. Rev. B 63 (2001) 104408.

[8] (a) M.B. Stone, I. Zaliznyak, D.H. Reich, C. Broholm, Phys. Rev. B 64 (2001) 144405;
(b) N. Cavadini, G. Heigold, W. Henggelert, A. Furrer, H.-U. Güdel, J. Phys.: Condens. Matter 12 (2000) 5463.

[9] B. Scott, U. Geiser, B. Patyal, R.D. Willett, C.P. Landee, R.E. Greeney, T. Manfredini, G.C. Pellacani, A. Bonamartini-Corradi, L.P. Battaglia, Inorg. Chem. 27 (1988) 2454.

[10] Bruker, SHELXTL (including XPREP, XCIF, XL, XP, XS) Version 6.10, Bruker AXS Inc., Madison, WI, USA, 2001.

[11] Bruker, SMART Version 5.626, Bruker AXS Inc., Madison, WI, USA, 1996.

[12] Bruker, SAINTPLUS Version 6.22, Bruker AXS Inc., Madison, WI, USA, 1996.

[13] Bruker, SADABS Version 2.03, Bruker AXS Inc., Madison, WI, USA, 1996.

[14] D.C. Johnston, R.K. Dremer, M. Troyer, X. Wang, A. Klümper, S.L. Bud'ko, A.F. Panchula, P.C. Canfield, Phys. Rev. B 61 (2000) 9558.

[15] S. Todo, K. Kato, H. Takayama, in: D.P. Landau, H.-B. Schüttler (Eds.), Computer Simulation Studies in Condensed Matter Physics XI, Springer Verlag, Heidelber, Berlin, 1998.

[16] (a) S.A. Roberts, D.R. Bloomquist, R.D. Willett, H.W. Dodgen, J. Am. Chem. Soc. 103 (1981) 2603;
(b) D.R. Bloomquist, R.D. Willett, J. Am. Chem. Soc. 103 (1981) 2615;
(c) S. O'Brien, R.M. Gaura, C.P. Landee, B.L. Ramakrishna, R.D. Willett, Inorg. Chim. Acta 141 (1987) 83;
(d) L.W. ter Haar, W.E. Hatfield, Inorg. Chem. 24 (1985) 1022.

[17] (a) H. Manaka, I. Yamada, H.A. Katori, Phys. Rev. B 63 (2001) 104408;
(b) H. Manaka, I. Yamada, H.A. Katori, J. Magn. Magn. Mat. 226–230 (2001) 412;
(c) H. Manaka, I. Yamada, H. Mitamura, T. Goto, Phys. Rev. B 66 (2002) 064402-1.

In this paper, we present structural and magnetic results for a metallo-organic system, $(NBu_4)Ni(mnt)_2$, that exhibits a bistable spin-Peierls-type transition with a very high transition temperature, $T_{tr} = 172$ K. Two NBu_4^+ salts of Ni(mnt) are known: the triclinic $(NBu_4)_2$-$Ni(mnt)_2$, with Ni in the +2 oxidation state [4] and the monoclinic $(NBu_4)Ni(mnt)_2$, with a +3 oxidation state. [5]. The latter contains uniform segregated stacks of $(NBu_4)^+$ cations and $Ni(mnt)_2^-$ anions. Here we report on the properties of the monoclinic form. In that form, the high temperature phase already shows structural dimerization, but the magnetic interactions within that dimerized chain are nearly uniform. Thus it is structurally predisposed to form a spin-Peierls-like dimerized state. This fact, plus the presence of the large bulky cation that provides a softness to the lattice, allows the spin dimerization to occur at a much higher temperature than normally observed for such systems.

2. Experimental

2.1. Synthesis

The compound was prepared according to standard literature procedures [6].

2.2. Crystallography

Data were collected at 293(2) and 84(2) K using a Bruker/Siemens SMART APEX instrument (Mo Kα radiation, $\lambda = 0.71073$ Å) equipped with a Cryocool NeverIce low temperature device. Data were measured using omega scans of 0.3° per frame for 20 s, and a full sphere of data was collected. A total of 2132 frames were collected with a final resolution of 0.83 Å. The first 50 frames were recollected at the end of data collection to monitor for decay. Cell parameters were retrieved using SMART [7] software and refined using SAINTPLUS [8] on all observed reflections. Data reduction and correction for Lp and decay were performed using the SAINTPLUS software. Absorption corrections were applied using SADABS [9]. The structure was solved by direct methods and refined by least squares method on F^2 using the SHELXTL [10] program package. The structures of both phases were solved in the space group $C2/c$ by analysis of systematic absences. All atoms were refined anisotropically. No decomposition was observed during data collection. Details of the data collection and refinement are given in Table 1. Further details are provided in the Supporting Information.

2.3. Magnetic measurements

Variable temperature susceptibility measurements were carried out on $(NBu_4)Ni(mnt)_2$ in the temperature range 2–300 K at a magnetic field of 0.1 T on a ground polycrystalline sample with a SQUID magnetometer (Quantum Design MPMS-XL-5). Different sweeping rates were used to determine the possible influence of the cooling and warming rates in the transition temperatures. The susceptibility data were corrected for the diamagnetic contributions of the sample as deduced by using Pascal's constant tables. The thermal variation of the heat capacity, in the 200–150 K range, was measured on several single crystals of the title compound (with a total mass of 0.8116 mg) in a Quantum Design Physical Properties Measurement System (PPMS-9). At each temperature the heat capacity was measured with 1% heating pulses and 5–10 averaged repetitions per point. The lattice heat capacity was subtracted by using a polynomial fit of the points above and below the peaks.

Table 1
Crystal data and structure refinement for $(NBu_4)Ni(mnt)_2$

Formula weight	581.53	581.53
T (K)	293(2)	84(2)
λ (Å)	0.71073	0.71073
Crystal system	monoclinic	monoclinic
Space group	$C2/c$	$C2/c$
Unit cell dimensions		
a (Å)	30.860(3)	31.073(3)
b (Å)	13.804(2)	13.928(1)
c (Å)	15.678(2)	14.414(1)
β (Å)	115.642(3)	115.037(2)
V (Å^3)	6020.8(11)	5652.1(9)
Z	8	8
ρ_{calc} (Mg/m^3)	1.283	1.367
μ (mm^{-1})	0.943	1.004
$F(000)$	2456	2456
Total/independent reflections	30295/5432	40053/8059
R_{int}	0.0627	0.062
Maximum/minimum transmission	0.9544/0.76520.	0.8805/0.7874
Goodness-of-fit on F^2	1.035	1.018
Final R indices [$I > 2\sigma(I)$]	$R_1 = 0.0517$, $wR_2 = 0.1114$	$R_1 = 0.0442$, $wR_2 = 0.1101$
R indices (all data)	$R_1 = 0.0818$, $wR_2 = 0.1246$	$R_1 = 0.0679$, $wR_2 = 0.1000$

$R_1 = \sum||F_o| - |F_c||/\sum|F_o|$.
$wR_2 = (\sum w||F_o|^2 - |F_c|^2|/\sum w|F_o|^2)^{1/2}$.

3. Results

3.1. Crystal structure description

The room temperature crystal structure of the monoclinic phase was verified [6] and the low temperature structure determined at 84 K. At both temperatures, the crystals are monoclinic, space group $C2/c$, with eight formula units per unit cell. Both phases contain segregated stacks of planar $Ni(mnt)_2^-$ anions separated by bulky NBu_4^+ cations. Significant atomic displacements are observed between the two phases and the effect of these shifts is reflected in the magnetic behavior of this system. The room and low temperature molecular units

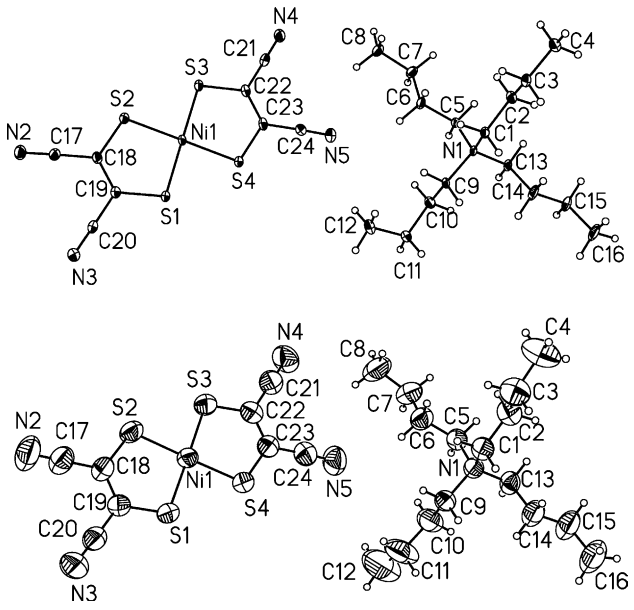


Fig. 1. Illustration of asymmetric unit: top–low temperature phase; bottom–high temperature phase. Thermal ellipsoids shown at the 50% probability level.

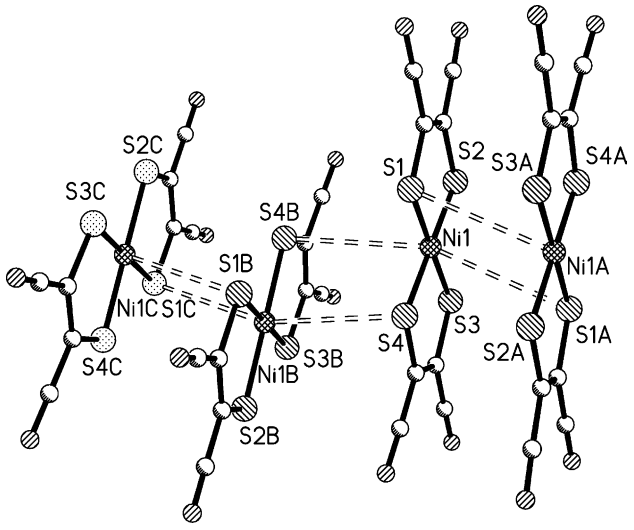


Fig. 2. Illustration of the stacking of the $Ni(mnt)_2^-$ anions. 84 K: Ni1···S1A = 3.648 Å, Ni1···S4B = 3.594 Å. Room T: Ni1···S1A = 3.717 Å, Ni1···S4B = 3.716 Å.

are illustrated in Fig. 1. Clearly evident in the figure for the low temperature phase is the presence of a *gauche* conformation of one arm (the C9–C12 arm). This is the conformation observed in the structure of the triclinic form. However, in the room temperature phase, all four of the butyl arms of the cation appear to have the sterically favorable all-*trans* conformation. However, also observable in the high temperature phase are the much larger thermal ellipsoids on all atoms of both the cation and anion, particularly in the C9–C12 arm. These larger thermal ellipsoids are anticipated when disorder is present, and thus it is concluded that the C12 methyl group is disordered between the *gauche* and the more energetically favorable *trans* conformation in the room temperature structure. The fact that there is no change in the space group, coupled with the observation of disorder of the C12 methyl group in the high temperature structure, implies that this represents an order–disorder transition. Associated with the disorder of the butyl arm of the cation are shifts in the stacking of the $Ni(mnt)_2^-$ anions, as discussed in the following paragraph.

In both phases, the salient feature of the structures is the existence of non-uniform stacks of the planar $Ni(mnt)_2^-$ anions, as shown in Fig. 2. The anions in these stacks are linked by long ($\geqslant$3.6 Å) Ni···S interactions. Pairs of anions, containing the Ni atoms Ni1 and Ni1A in Fig. 2, are related by centers of inversion. Adjacent pairs are generated by twofold rotation operations, generating the pair of anions containing Ni1B and Ni1C. In the room temperature phase, the two independent Ni···S distances within and between the centrosymmetric pairs are accidentally equal (Ni1···S1A = 3.717 Å, Ni1···S4B = 3.716 Å). However, in the low temperature phase, shifts in the positions of the anions have shortened these two distances to different extents, with Ni1···S1A = 3.648 Å and Ni1···S4B = 3.594 Å. The interplanar spacing between the centrosymmetric pair of anions decreases by 0.2 Å between the room temperature and 84 K structures (3.645 versus 3.462 Å. A second part of this structural change is a shift of the relative orientation of the adjacent pairs of anions. For the centro-

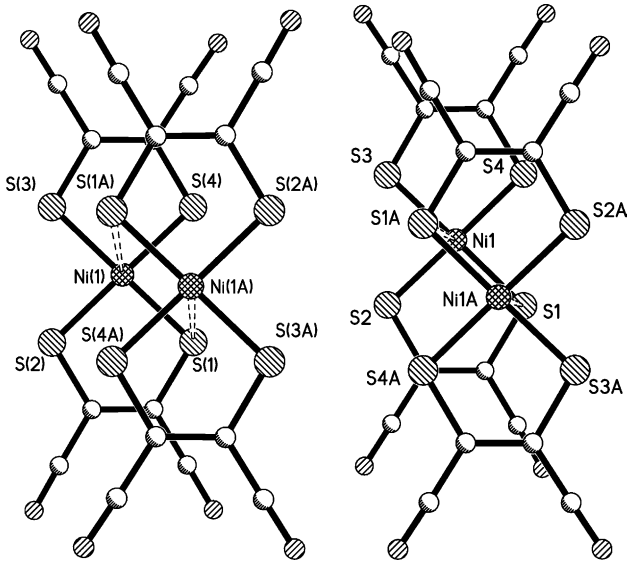


Fig. 3. Illustration of the two anions related by the center of inversion. Left: 84 K: Ni1···S1A = 3.648 Å, angle between NiS_4 plane and (Ni1–S1A) = 70.8°, distance between anion planes = 3.462 Å. Right: Room T: Ni1···S1A = 3.717 Å, angle between NiS_4 plane and (Ni1–S1A) = 80.6°, distance been anion planes = 3.645 Å. The plane of each anion is rotated by 9.1° between the room temperature and 84 K phases.

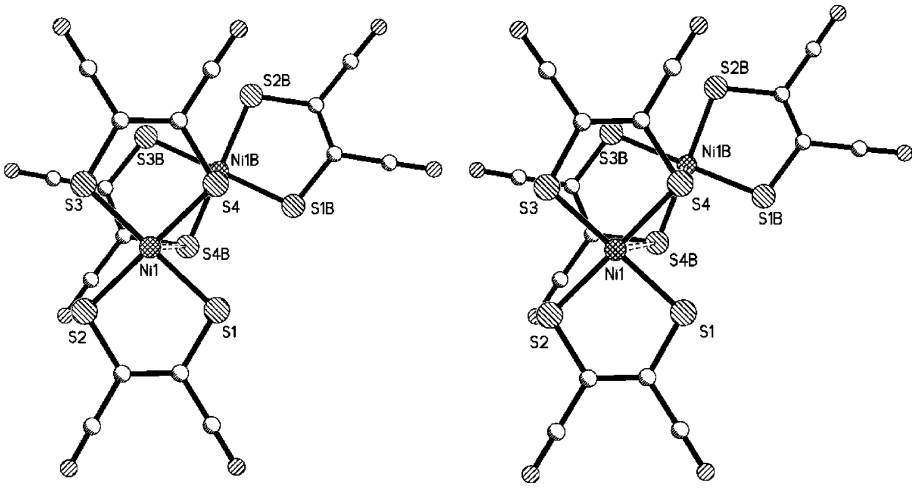


Fig. 4. View of the two anions related by 2-fold rotation axes. Left: 84 K. Ni1–S4B = 3.594 Å, dihedral angle between NiS_4 planes = 7.8°, angle between the mean plane of the anion and Ni1–S4B direction = 77.4°, distance between centroids of the overlapping NiS_2N_2 chelate rings = 3.786 Å. Right: Room T. Ni1–S4B = 3.716 Å, dihedral angle between NiS_4 planes = 15.3°, angle between the mean plane of anion and the Ni1–S4B direction = 76.1°, distance between centroids of the overlapping NiS_2N_2 chelate rings = 3.836 Å.

symmetric pair (Fig. 3), the planes of the anions are parallel by symmetry, but there is a substantial translation (~1 Å) of the two anions relative to each other. In the low temperature phase, the two sulfur atoms (S1 and S4) on one dimer are located approximately above (or below) the centroids of the NiS_2C_2 chelate rings on the adjacent anion. In the room temperature phase, sulfur atom S1 now is located nearly directly over the Ni atom in the adjacent anion. In addition, the planes of the anions are rotated by 9.1° about the *b* direction.

The situation for the pair of anions related by a two-fold symmetry operation is significantly different. For this pair, the molecular planes of the two anions are not required to be parallel by symmetry. Seen in projection (Fig. 4), there seems to be little change in the relative orientation. The two anions are somewhat closer together at 84 K than at room temperature, as measured by the distances between the centroids of the two overlapping NiS_2C_2 chelate rings, 3.836 versus 3.786 Å. This contraction of 0.06 Å is substantially less than the 0.20 Å decrease between the centrosymmetric pair. In addition, there is a 7.5° increase in the dihedral angle between the NiS_4 planes on the two anions.

The distances and angles within the $Ni(mnt)_2^-$ anion are consistent with other compounds containing this anion.

3.2. Magnetic properties

Fig. 5 shows a plot of $\chi_M T$ versus T for $(NBu_4)Ni(mnt)_2$ while Fig. 6 gives a plot of χ_M versus T, with an inset showing details of the temperature regime near the phase transition. For $T > 175$ K, the $\chi_M T$ plot exhibits its typical antiferromagnetic behavior. Upon cooling, a rapid drop in $\chi_M T$ (and in χ_M) occurs at 172 K, followed

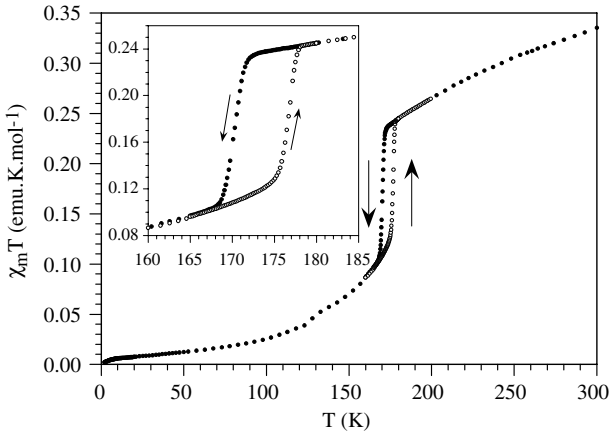


Fig. 5. Plot of χ_{mT} vs. T. Black circles: cooling scan, white circles: warming scan. Inset: the transition temperature region.

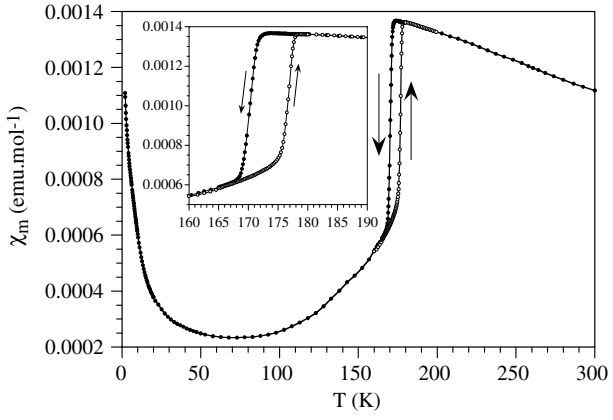


Fig. 6. Illustration of the hysteresis in the magnetic response. Black circles. cooling scan, white circles: warming scan. Inset: the transition temperature region.

by a slow decrease in χ_M in the regime 60–170 K. Below 60 K, a typical paramagnetic tail due to defects in the stacks is observed. Upon heating, the data reproduce the cooling data up to 168 K. The data indicates that the sample continues in the low temperature phase until 175 K, where a rapid rise in χ_M occurs until it merges with the cooling data at ca. 178 K. The derivative of both curves show peaks at 170.5 and 176.9 K, giving a hysteresis of ca. 6.5 K in the transition. Measurements around the transition at different cooling and warming rates indicate that the transition temperatures do not vary significantly (less than 1 K) with the cooling and warming rates in the range 0.5–5.0 K min^{-1}.

A comparison of Figs. 5 and 6 shows that, while the value of $\chi_M T$ decreases in both phases with decreasing temperature, the susceptibility does not drop to zero at the transition temperature. Rather, it drops by about 60%, and then gradually decreases towards zero. This indicates that the magnetic effects of the dimerization do not lead to the formation of an $S = 0$ ground state for the $Ni(mnt)_2^-$ stacks. Rather, there is an alternation in the exchange parameters, albeit with substantially stronger exchange coupling than in the high temperature phase. The behavior of the low temperature phase is consistent with that expected for a system of alternating antiferromagnetic spin 1/2 chains.

Fig. 7 shows the heat capacity results in the region of the phase transition. Although the data present some noise due to the small amount of sample used in the measurements (less than 1 mg) it can be clearly seen that there is a peak at ca. 168–169 K in the cooling scan and ca. 175–176 K in the warming one. Both peaks indicate the temperature of the spin-Peierls-like transition in the cooling and warming scans and are in very good agreement with the transition temperatures, as well as the hysteresis of ca. 7 K, observed in the in the SQUID measurements. The heat capacity measurements data are also different in the cooling and warming scans in the range 177–167 K (178–168 K in the SQUID measurements).

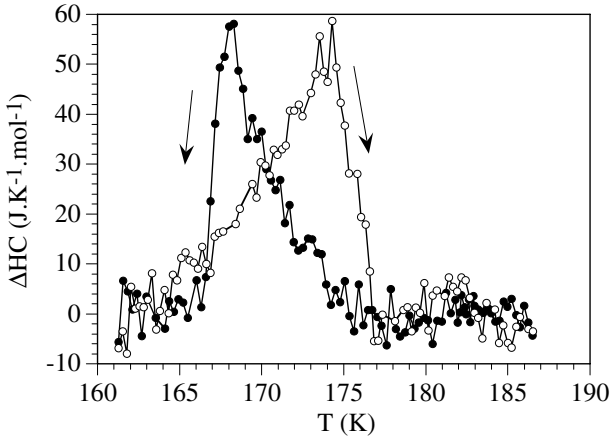


Fig. 7. Plot of the corrected heat capacity data obtained in the cooling (black points) and warming (white points) scans.

4. Discussion

The study of compounds containing $M(mnt)_2^{n-}$ species continues to be actively pursued [11]. A survey of the Cambridge Crystallographic Data Base revealed over 40 structures containing the $Ni(mnt)_2^-$ anion. These structures are very varied: mixed A:D stacks [12], uniform [5,13] and dimerized [14] segregated stacks, isolated dimers [12a,15] and isolated monomers [16]. In the vast majority of the structures, the long axes of the $Ni(mnt)_2^-$ anions have the same orientation. No systematic trends are observable in the distances between adjacent cations or the relative lateral displacement of adjacent cations. However, in one salt, the long axes of adjacent ions in the stacks are rotated by approximately 90°, similar to the arrangement seen for the adjacent pair of anions shown in Fig. 4.

Associated with these variations in structure is a corresponding variation in magnetic interactions. While most show dominant antiferromagnetic interactions [17], examples where the compounds are diamagnetic [18], exhibit ferromagnetic coupling within the chains [19], or undergo magnetic ordering at low temperature [20] have been reported. A number of salts have been reported that undergo dimerization type transitions [19b,21]. Perhaps the most fascinating is [1-(4′-fluorobenzyl)pyridinium]$Ni(mnt)_2$, where the compound undergoes a phase transition at 93 K, exhibiting ferromagnetic coupling above that temperature and becoming diamagnetic below that temperature [19b]. This magnetic behavior at the phase transition is presumed to be due to a dimerization process similar to that reported here. A $Pt(mnt)_2^-$ salt exhibits a rapid drop in the susceptibility at 247 K, although the drop appears to occur over a much larger temperature range than observed in this study [21a]. Crystallographic studies confirm the dimerization of the chain below the phase transition temperature. No hysteretic behavior in the transition is reported. However, the gradual decrease in susceptibility at temperatures below the phase transition is similar to that observed in our study.

It is the observation of hysteresis that makes the $(NBu_4)Ni(mnt)_2$ compound unique, since no other of the $ANi(mnt)_2$ compounds studied have shown the bistable regime associated with a structural and magnetic response at the phase transition. Since the crystal structure of both the room temperature phase and the 84 K phase have the same space group and lattice, with disorder observed in the high temperature phase, this implies that the phase transition is of the order–disorder type. This is supported by the nature of the heat capacity anomaly. The observation of hysteresis in the structural and magnetic properties at the phase transition indicates that the process is likely driven by the order–disorder behavior of the NBu_4^+ cations, and not by the spin dimerization process.

5. Supporting material available

Crystallographic data for the structures reported here have been deposited with the Cambridge Crystallographic Data Center as Supplementary Publication Nos. CCDC-252683 and CCDC-252684 for the room temperature and 84 K structure determinations, respectively. Copies of this information may be obtained free of charge from: The Director, CCDC, 12 Union Road, Cambridge, CB2 1EZ, UK (fax: +44 1223 336 033; e-mail: deposit@ccdc.cam.ac.uk or www:http//www.ccdc.cam.ac.uk).

Acknowledgement

Work supported in part by ACS-PRF 34779-CA and by the Spanish project MAT2001-3507. R.D.W. thanks the University of Valencia for a visitors grant.

References

[1] (a) J.W. Bray, H.R. Hart, L.V. Interrante, I.S. Jacobs, J.S. Kasper, G.D. Watkins, S.H. Wee, J.C. Bonner, Phys. Rev. Lett. 35 (1975) 744;
(b) I.S. Jacobs, J.W. Bray, H.R. Hart, L.V. Interrante, J.S. Kasper, G.D. Watkins, D.E. Prober, J.C. Bonner, Phys. Rev. B 14 (1976) 3036;
(c) S.D. Obertelli, R.H. Friend, D.R. Talham, M. Kurmoo, P. Day, J. Phys.: Condens. Matter 1 (1989) 5671;
(d) I.D. Parker, R.H. Friend, M. Kurmoo, P. Day, J. Phys.: Condens. Matter 1 (1989) 5681;
(e) M. Kurmoo, M.A. Green, P. Day, C. Bellitto, G. Staulo, F.L. Pratt, W. Hayes, Synth. Met. 55–57 (1993) 2380;
(f) L. Ducasse, C. Coulon, D. Chasseau, R. Yagbasan, J.M. Fabre, A.K. Gouasmia, Synth. Met. 27 (1988) B543;
(g) Q. Liu, S. Ravy, J.P. Pouget, C. Coulon, C. Bourbonnais, Synth. Met. 55–57 (1993) 1840.

[2] (a) M. Hase, I. Terasaki, K. Uchinokura, Phys. Rev. Lett. 70 (1993) 3651;
(b) J.P. Boucher, L.P. Regnault, J. Phys. I 6 (1996) 1939;
(c) A. Meetsma, J.L. de Boer, A. Damascelli, J. Jegoudez, A. Revcolevschi, T. Palstra, Acta Cryst. C 54 (1998) 1558;
(d) M. Weiden, R. Hauptmann, C. Geibel, F. Steglich, M. Fischer, P. Lemmens, G. Guntherodt, Z. Phys. B 103 (1997) 1;
(e) V.A. Pashchenko, A. Sulpice, F. Mila, P. Millet, A. Stepanov, P. Wyder, Eur. Phys. J. B 21 (2001) 473.

[3] W. Fujita, K. Awaga, Science 286 (1999) 261.

[4] T. Mochida, S. Suzuki, H. Moriyama, H. Terao, T. Sugawara, Acta Crystallogr. C 56 (2000) 1183.

[5] A. Kobayashi, Y. Sasaki, Bull. Chem. Soc. Jpn. 50 (1977) 2650.

[6] A. Davidson, R.H. Holm, Inorg. Synth. 10 (1971) 8.

[7] SMART: v.5.626, Bruker Molecular Analysis Research Tool, Bruker AXS, Madison, WI, 2002

[8] SAINTPLUS: v. 6.45, Data Reduction and Correction Program, Bruker AXS, Madison, WI, 2001

[9] SADABS: v.2.01, an empirical absorption correction program, G.M. Sheldrick, Bruker AXS Inc., Madison, WI, 2001

[10] SHELXTL: v. 6.10, Structure Determination Software Suite, G.M. Sheldrick, Bruker AXS Inc., Madison, WI, 2001

[11] (a) See, for example: H. Nakajima, M. Katsuhara, M. Ashizawa, T. Kawamoto, T. Mori, Inorg. Chem. 43 (2004) 6075;
(b) H. Alves, D. Simão, I.C. Santos, V. Gama, R.T. Henriques, H. Novais, M. Almeida, Eur. J. Inorg. Chem. (2004) 1318;
(c) X.-M. Ren, J.-L. Xie, Y.-Z. Li, Q.-J. Meng, Acta Crystallogr. E 59 (2003) m1115;
(d) D. Simão, H. Alves, D. Belo, S. Rabaça, E.B. Lopex, I.C. Santos, V. Gama, T. Duarte, R.T. Henriques, H. Novais, M. Almeida, Eur. J. Inorg. Chem. (2001) 3119.

[12] (a) See, for example S. Zurcher, J. Petrig, M. Perseghini, V. Gramlich, M. Worl, D. von Arx, A. Togni, Helv. Chim. Acta 82 (1999) 1324;
(b) K. Brunn, H. Endres, J. Weiss, Z. Naturforsch. B: Chem. Sci. 42 (1987) 1222.

[13] (a) X. Ren, Q. Meng, Y. Song, C. Lu, C. Hu, Inorg. Chem. 41 (2002) 5686;
(b) E. Ribera, C. Rovira, J. Veciana, J. Tarres, E. Canadell, R. Rousseau, E. Molina, M. Mas, J.-P. Schoeffel, J.-P. Pouget, J. Morgado, R.T. Henriques, M. Almeida, Chem.-Eur. J. 5 (1999) 2025;
(c) J. Xie, X. Ren, W. Zhang, Y. Li, C. Ni, Z. Ni, Q. Meng, Y. Yao, J. Coord. Chem. 56 (2003) 1367;
(d) H. Zhang, X.-M. Ren, H.-l. Xie, y.-H. Li, Q.-J. Meng, Acta Crystallogr. E 60 (2004) m960.

[14] (a) C. Mahadevan, M. Seshasayee, B. Burthy, P. Kuppusamy, P.T. Manoharan, Acta Crystallogr. C 39 (1983) 1335;
(b) A. Kobayashi, Y. Sasaki, Bull. Chem. Soc. Jpn. 50 (1977) 2650;
(c) N. Robertson, S. Roehrs, T. Akutagawa, T. Nakamura, A.E. Underhill, J. Chem. Res. (S) (1999) 54.

[15] X. Ren, C. Lu, P. Wu, Q. Meng, J. Chem. Cryst. 31 (2001) 173.

[16] (a) X. Ren, C. Lu, y. Liu, H. Zhu, H. Li, C. Hu, Q. Meng, Transit. Metal Chem. 26 (2001) 136;
(b) B.L. Ramakrishna, P.T. Manoharan, Inorg. Chem. 22 (1983) 2113.

[17] (a) P. Kuppusamy, P.T. Manoharan, Proc. Indian Acad. Sci. (Chem. Sci.) 98 (1987) 115;
(b) B.L. Ramakrishna, J. Appl. Phys. 84 (1988) 5941.

[18] X. Ren, C. Lu, Y. Liu, H. Zhu, H. Li, C. Hu, Q. Meng, Transit. Metal Chem. 26 (2001) 136.

[19] (a) J. Nishijo, E. Ogura, J. Yamaura, A. Miyazaki, T. Enoke, T. Takano, Y. Kuwatani, M. Iyoda, Synt. Metals 133–134 (2003) 539;
(b) J. Xie, X. Ren, Y. Song, W. Zhang, W. Liu, C. He, Q. Meng, Chem. Commun. (2002) 2346;
(c) Y. Chen, G. Liu, H. Xu, H. Zhou, X. Ren, Russ. J. Coord. Chem. 29 (2003) 251;
(d) H. Nakajima, M. Katsuhara, M. Ashizawa, T. Kawamoto, T. Mori, Inorg. Chem. 43 (2004) 6075.

[20] (a) N. Robertson, C. Bergemann, H. Becker, P. Agarwal, S.T. Julian, R.H. Friend, N.J. Hatton, A.E. Underhill, A. Kobayashi, J. Mater. Chem. 9 (1999) 1713;
(b) J. Xie, X. Ren, S. Gao, W. Zhang, Y. Li, C. Lu, C. Ni, W. Liu, Q. Meng, Y. Yao, Eur. J. Inorg. Chem. (2003) 2393;
(c) H. Nakajima, M. Katsuhara, M. Ashizawa, T. Kawamoto, T. Mori, Inorg. Chem. 43 (2004) 6075;
(d) J. Xie, X. Ren, C. He, Y. Song, Q. Meng, R.K. Kremer, Y. Yao, Chem. Phys. Lett. 369 (2003) 41;
(e) A.T. Coomber, d. Beijonne, R.H. Friend, J.L. Bredas, A. Charlton, N. Robertson, A.E. Underhill, M. Kurmoo, P. Day, Nature 380 (1996) 144;
(f) X. Ren, Y. Chen, C. He, S. Gao, J. Chem. Soc., Dalton Trans. (2002) 3915.

[21] (a) A.E. Pullen, C. Faulmann, K.I. Pokhadnya, P. Cassoux, M. Tokumoto, Inorg. Chem. 37 (1998) 6714;
(b) C.-L. Ni, D.-B. Dang, Y.-Z. Li, Z.-R. Yuan, Z.-P. Ni, Z.-F. Tian, Q.-J. Meng, Inorg. Chem. Commun. 7 (2004) 1034;
(c) X.M. Ren, Q.J. Meng, Y. Song, C.L. Lu, C.J. Hu, X.Y. Chen, Z.L. Xue, Inorg. Chem. 41 (2002) 5931;
(d) X.M. Ren, Q.J. Meng, Y. Song, C.S. Lu, C.J. Hu, Inorg. Chem. 41 (2002) 5686.

is an example of a difficult molecule; (iv) [Mn(III)-Cu(II)(Br-sap)$_2$Cl(MeOH)]: it is a small SMM [11]. We suggest the applicable region of the method from these results.

2. Calculation of ZFS parameters

Spin–orbit Hamiltonian is as the form

$$\hat{U} = \frac{1}{i}\sum_{j=1}^{N} \hat{\mathbf{V}}(\mathbf{r}_j)\cdot\hat{\mathbf{S}}_j, \quad \hat{\mathbf{V}}(\mathbf{r}) \equiv -\frac{1}{2c^2}\nabla\times\mathbf{E}(\mathbf{r}), \tag{2}$$

where $\hat{\mathbf{S}}_j$ is a spin operator of a jth electron and $\mathbf{E}(\mathbf{r})$ is the electronic field of the nuclei. The second-order perturbation energy of SOC (SOPT2 energy) from spin-polarized DFT (UDFT) wavefunction Ψ_0 is

$$E^{\mathrm{SOPT2}} = \sum_{\sigma,\tau}^{\alpha,\beta}\sum_{a}^{\sigma\mathrm{occ}}\sum_{s}^{\tau\mathrm{vir}} \frac{\langle\Psi_0|\hat{U}|\Psi_{a\sigma}^{s\tau}\rangle\langle\Psi_{a\sigma}^{s\tau}|\hat{U}|\Psi_0\rangle}{E_0 - E_{a\sigma}^{s\tau}} = \sum_{\sigma,\tau}^{\alpha,\beta}\sum_{p,q}^{\mathrm{x,y,z}}\sum_{s}^{\tau\mathrm{vir}} M_{pq}^{\sigma\tau}S_p^{\sigma\tau}S_q^{\tau\sigma}, \tag{3}$$

$$M_{pq}^{\sigma\tau} = \sum_{a}^{\sigma\mathrm{occ}}\sum_{s}^{\tau\mathrm{vir}} \frac{\langle\psi_a^{\sigma}|\hat{V}_p|\psi_s^{\tau}\rangle\langle\psi_s^{\tau}|\hat{V}_q|\psi_a^{\sigma}\rangle}{\varepsilon_s^{\tau} - \varepsilon_a^{\sigma}}, \tag{4}$$

$$S_p^{\sigma\tau} = \langle\sigma|\hat{S}_p|\tau\rangle \quad (\sigma,\tau = \alpha \text{ or } \beta), \tag{5}$$

where $|\Psi_{a\sigma}^{s\tau}\rangle$ and $E_{a\sigma}^{s\tau}$ are a 1-electron excited configuration (from subscript to superscript) and the energy, respectively, and $|\psi_a^{\sigma}\rangle$ and ε_a^{σ} are an ath σ-spin orbital and the orbital energy, respectively. This energy depends on the direction of the spin quantization axis. The spin matrix $\mathbf{S}_p$ is transformed under the rotation of the spin quantization axis as

$$\mathbf{S}'_p = \mathbf{R}\mathbf{S}_p\mathbf{R}^{\dagger}, \tag{6}$$

$$\mathbf{R} = \begin{pmatrix} e^{i\gamma}\cos\theta/2 & e^{i(\gamma-\phi)}\sin\theta/2 \\ -e^{-i(\gamma-\phi)}\sin\theta/2 & e^{-i\gamma}\cos\theta/2 \end{pmatrix}. \tag{7}$$

The expectation value of the spin operator is also transformed as

$$\langle\hat{\mathbf{S}}'\rangle = \frac{1}{2}\Delta N(\sin\theta\cos\phi, \sin\theta\sin\phi, \cos\theta), \tag{8}$$

where $\Delta N = 2\langle\hat{S}_z\rangle$. The SOPT2 energy is

$$E^{\mathrm{SOPT2}} = \langle\hat{\mathbf{S}}'\rangle^{\mathrm{T}}\mathbf{D}\langle\hat{\mathbf{S}}'\rangle, \tag{9}$$

where $\mathbf{D}$ is the ZFS tensor, which can be calculated as

$$\mathbf{D} \equiv \frac{1}{\Delta N^2}\begin{pmatrix} N_x + N'_y + N'_z & N_{xy} + N'_{xy} & N_{zx} + N'_{zx} \\ N_{xy} + N'_{xy} & N'_x + N_y + N'_z & N_{yz} + N'_{yz} \\ N_{zx} + N'_{zx} & N_{yz} + N'_{yz} & N'_x + N'_y + N_z \end{pmatrix}, \tag{10}$$

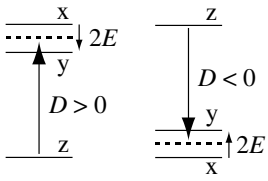


Fig. 1. The energy diagram of the magnetic anisotropy energies when the spin is on $\mathbf{u}_x$, $\mathbf{u}_y$, and $\mathbf{u}_z$ axis.

$$N_{pq} \equiv M_{pq}^{\alpha\alpha} + M_{pq}^{\beta\beta},\ N'_{pq} \equiv M_{pq}^{\alpha\beta} + M_{pq}^{\beta\alpha},\ N_p \equiv N_{pp},\ N'_p \equiv N'_{\mathrm{pp}}. \tag{11}$$

The ZFS tensor is diagonalized, when the spin of the system is in a particular direction.

$$E^{\mathrm{SOPT2}} = d_{xx}\langle\hat{S}''_x\rangle^2 + d_{yy}\langle\hat{S}''_y\rangle^2 + d_{zz}\langle\hat{S}''_z\rangle^2, \tag{12}$$

$$\mathbf{D} = \mathbf{U}\mathbf{d}\mathbf{U}^{\dagger},\ \langle\hat{\mathbf{S}}'\rangle = \mathbf{U}^{\dagger}\langle\hat{\mathbf{S}}'\rangle. \tag{13}$$

The diagonal elements are ordered as $|d_{zz} - d_{yy}| > |d_{yy} - d_{xx}|$ and $d_{yy} \in [d_{xx}, d_{zz}]$ (Fig. 1). The ZFS parameters, D and E, and the principal axis $\mathbf{a}$ are

$$D = d_{zz} - \frac{d_{xx} + d_{yy}}{2}, \quad E = \frac{d_{xx} - d_{yy}}{2}, \tag{14}$$

$$\mathbf{a} = \mathbf{u}_z, \quad \mathbf{U} = (\mathbf{u}_x\ \mathbf{u}_y\ \mathbf{u}_z). \tag{15}$$

The sign of E is not essential, since $\mathbf{u}_x$ and $\mathbf{u}_y$ can be swapped. Therefore, we ignore the sign of E in the present article.

3. Calculation and discussion

3.1. Triplet benzene and naphthalene

Triplet benzene and naphthalene are an example of organic radicals which has very little SOC contribution to D. It was shown that the SOC contribution to ZFS of aromatic hydrocarbons vanishes in view of the CNDO/S CI approximation [12]. This method can describe phosphorescent radiative lifetime for these molecules [9,10]. In the INDO CI method, the SOC contribution to the ZFS parameters of triplet benzene and naphthalene was estimated to be less than 0.01% of the experimental values.

We calculated triplet benzene and naphthalene and the SOC contribution to the D values with UHF, USVWN, UBLYP and UB3LYP [13] and cc-pVDZ basis set [14]. Each geometry is optimized with the method and the basis set. The results are shown in Table 1. All the results are very small, about 0.1% of the experimental values 0.1593 and 0.1003 cm^{-1}. Though these results are larger than the *semiempirical* CI results, they reproduce the fact that the SOC contribution is very small.

Table 1
The list of the estimated D values in cm^{-1}

Method	Benzene	Naphthalene	Carbene	Silylene	Oxygen	SMM
UHF	-2.14×10^{-4}	4.43×10^{-4}	0.00537	0.0774	0.198	0.039
USVWN	2.17×10^{-4}	-1.41×10^{-4}	0.04877	4.3369	2.066	
UBLYP	-1.50×10^{-4}	0.83×10^{-4}	0.04608	8.2780	1.780	−1.290
UB3LYP	-0.98×10^{-4}	1.16×10^{-4}	0.02219	0.4605	0.747	−0.589
UPW91						−1.204
References	$\|D\| \sim 10^{-5}$ [a]	$\|D\| \sim 10^{-5}$ [a]	0.023[b]	1–3[b]	2.3145[c]	−1.81[d]

[a] INDO CI results [9,10].
[b] CISDTQ/cc-pVDZ results [4].
[c] CASSCF(12,10)/aug-cc-pCVTZ result [5].
[d] Experimental value [11].

3.2. Triplet carbene and triplet silylene

Triplet carbene and triplet silylene are examples of simple biradicals. It seems carbene and silylene are similar, but the spin multiplicities of the ground states are different; the ground state of the carbene is triplet and that of the silylene is singlet. According to the CASSCF/D95** study [4], the multiplicity of the ground state is changed at a particular bond angle. In case of carbene, the triplet state is stable. The equilibrium bond angle is 134.0°. The singlet state is stable in the region which bond angle is less than about 93°. In case of silylene, the singlet state is stable. The equilibrium bond angle is 118.4° on the level of large basis set CEPA calculations. However, the singlet and triplet states are degenerated at 113.0°, which is very close to the equilibrium bond angle.

The SOC contribution of these biradicals to D is drastically changed with the bond angle. In the CISDTQ/cc-pVDZ study [4], D is positive at the larger bond angle than the degeneration bond angle and negative at the smaller bond angle than it. The closer the bond angle is to the degeneration point, the larger the magnitude of D is, and D diverges at the degeneration point. In carbene, since the equilibrium geometry is quite far from the degeneration point, the SOC contribution to D is small as 0.023 cm^{-1}. In triplet silylene, however, since the equilibrium geometry is near the degeneration point, the SOC contribution to D is very large as 1–3 cm^{-1}. The SOC contribution to E is very small in both cases.

We performed UHF, USVWN, UBLYP and UB3LYP calculations with aug-cc-pVDZ basis sets to predict the SOC contribution to D at the equilibrium geometry. Each equilibrium geometry is optimized by the method and basis set. The results are shown in Table 1. In carbene, the DFT results are close to the CISDTQ result. The UHF method tends to underestimate D. The basis set dependency is small in all the methods. In triplet silylene, however, the UB3LYP result is quite different from the CISDTQ result. The result is caused by the fact that the equilibrium bond angle is far from the degeneration point in the UB3LYP method.

3.3. Triplet molecular oxygen

Triplet molecular oxygen is an example of a difficult system. In molecular oxygen, E is exactly equal to zero, since oxygen is a uniaxial molecule. The cheep methods failed to estimate the SOC contribution to D. In high-precision CASSCF(12,10)/aug-cc-pCVTZ study, the SOC contribution to D is 2.3145 cm^{-1} [5]. This study is in good agreement with the experiment.

We performed UHF, USVWN, UBLYP, UB3LYP calculations with aug-cc-pCVTZ basis set to calculate the SOC contribution to D of molecular oxygen. The results are shown in Table 1. The pure DFT results are very close to the CASSCF result, but the UHF and UB3LYP results are underestimated also in this case.

We also calculated the bond length dependency of D with UBLYP/aug-cc-pVDZ. In the CASSCF method, D monotonically increases as the bond is lengthened. In the UBLYP result, however, D negatively diverges at a bond length. Over the length, D jumps to positive infinity and decreases.

4. Small SMM

At last, we calculated a small SMM. Since SMMs are metal complexes, SOC mainly contributes to ZFS. Therefore, the computational results of the method of the present work can be directly compared with the experimental values. Pederson et al. calculated several SMMs, but they did not use the hybrid DFT methods. We also examined the validity of the hybrid DFT methods to SMM calculations.

We calculated [Mn(III)Cu(II)(Br-sap)$_2$Cl(MeOH)], which is a small SMM synthesized by Oshio et al. [11]. The spin multiplicity of the SMM is 5/2 and the D value is -1.81 cm^{-1}. We employed UHF, UBLYP, UPW91, and UB3LYP methods with Huzinaga's MIDI basis sets for metal atoms and 6-31G basis sets for the other atoms.

The geometry obtained by X-ray structure analysis was used. The results are shown in Table 1. The results of the UBLYP and UPW91 methods are close to the

experimental value. Also in this case, UB3LYP underestimates the D value. We suggest that the reason is that the energy gap, which is the denominator of Eq. (4), of the hybrid DFT methods tends to be wider than pure DFT methods.

5. Concluding remarks

We applied the Pederson's method to calculate the ZFS parameters to some radicals. The pure DFT results tended to be in good agreement with the results of the high-precision CI or MCSCF methods in the equilibrium region. However, the UB3LYP method, a hybrid DFT method, tends to underestimate D values in some cases. Though the pure DFT methods also failed out of the equilibrium region, this is practically acceptable for computation of D values.

Acknowledgments

This study was performed through a Grand-in-Aid for Scientific Research (No. 14204061) from Ministry of Education, Culture, Sports, Science and Technology.

References

[1] Bernd A. Hess, Robert J. Buenker, Chem. Phys. 71 (1982) 79.
[2] Josef Michl, J. Am. Chem. Soc. 118 (1996) 3568.
[3] Zdenek Havlas, Josef Michl, Theochem 398–399 (1997) 281.
[4] Zdenek Havlas, John W. Downing, Josef Michl, J. Phys. Chem. 102 (1998) 5681.
[5] O. Vahtras, O. Loboda, B. Minaev, H. Ågren, K. Ruud, Chem. Phys. 279 (2002) 133.
[6] O. Loboda, B. Minaev, O. Vahtras, B. Schimmelpfennig, H. Ågren, K. Ruud, D. Jonsson, Chem. Phys. 286 (2003) 127.
[7] M.R. Pederson, S.N. Khanna, Phys. Rev. B 60 (1999) 9566.
[8] Jens Kortus, Mark R. Pederson, Tunna Baruah, N. Bernstein, C.S. Hellberg, Polyhedron 22 (2003) 1871.
[9] B.F. Minaev, Izv. Vyssh. Uchebn. Zaved. Fiz. 5 (1971) 93.
[10] B.F. Minaev, Izv. Vyssh. Uchebn. Zaved. Fiz. 8 (1971) 118.
[11] Hiroki Oshio, Masayuki Nihei, Ayano Yoshida, Hiroyuki Nojiri, Motohiro Nakano, Akira Yamaguchi, Yoshitomo Karaki, Hidehiko Ishimoto, Chem. Eur. J. 11 (2005) 843.
[12] J. Del Bene, H.H. Jaffe, J. Chem. Phys. 48 (1968) 1807.
[13] Axel D. Becke, J. Chem. Phys. 98 (1993) 5648.
[14] T.H. Dunning Jr., J. Chem. Phys. 53 (1970) 2823.

namely $[Cu(2,3\text{-pydc})_2]_x[Mn(H_2O)_6]_x \cdot 2xH_2O$ (**3**) [3]. Unlike the situation in **1** and **2**, in **3** there is no coordinative link between the copper and manganese centers. While the copper ions are bridged in chains by the ligands in **3**, the manganese ions are present in the crystal lattice as isolated $Mn(H_2O)_6^{2+}$ entities in this compound [3]. The structures of both **1** and **2**, reported here in detail, reveal extended arrays of regularly alternating, coordinatively linked, paramagnetic centers of different spin ($S = 1/2$ and 5/2), a classical set-up for ferrimagnetism [4]. With this in mind in particular, we carefully examined the magnetic properties of these systems as well as the magnetic properties of two thermally condensed forms, $Cu(2,4\text{-pydc})_2Mn \cdot H_2O$ (**1d**) and $Cu(2,5\text{-pydc})_2Mn \cdot H_2O$ (**2d**).

2. Experimental

2.1. Syntheses

2,4-Pyridinedicarboxylic acid monohydrate and 2,5-pyridinedicarboxylic acid were used as supplied (Aldrich). Solutions of 0.10 M $Cu(NO_3)_2 \cdot 3H_2O$ (Baker) and 0.10 M $Mn(ClO_4)_2 \cdot 6H_2O$ (Alfa) were prepared in-house. 0.10 M NaOH (Fisher) was diluted according to package directions. Water was deionized in-house.

$[Cu(2,4\text{-pydc})_2Mn(H_2O)_4]_x$ (**1**) was prepared by dissolving 2,4-pydc$H_2 \cdot H_2O$ (1.0 mmol, 0.185 g) in H_2O and NaOH (2.0 mmol, 20 ml × 0.10 M) to a final volume of 100 ml. $Cu(NO_3)_2$ and $Mn(ClO_4)_2$ (each 0.5 mmol, 5.0 ml × 0.10 M) were combined and then added to the proligand solution. The reaction mixture turned bright blue. After sitting for several weeks at room temperature, the mixture was filtered to recover small blue crystals suitable for single-crystal X-ray studies. *Anal.* Calc. for $CuMnC_{14}N_2H_8O_9$: C, 36.0; H, 1.7; N, 6.0. Found: C, 35.8; H, 1.9; N, 5.9%.

$[Cu(2,5\text{-pydc})_2Mn(H_2O)_2]_x \cdot 4xH_2O$ (**2**) was prepared as above substituting 1.0 mmol (0.167g) 2,5-pydcH_2 in place of the 1.0 mmol 2,4-pydc$H_2 \cdot H_2O$. In this case small blue crystals suitable for single-crystal X-ray studies formed after only a few days and these were removed by filtration. *Anal.* Calc. for $CuMnC_{14}H_6N_2O_8 \cdot H_2O$: C, 36.0; H, 1.7; N, 6.0. Found: C, 35.7; H, 1.6; N, 6.0%.

$Cu(2,4\text{-pydc})_2Mn \cdot H_2O$ (**1d**) was prepared by heating a finely ground sample of **1** to 190 °C under dynamic vacuum for seven days to yield a dark blue powder. *Anal.* Calc. for $CuMnC_{14}N_2H_8O_9$: C, 36.0; H, 1.7; N, 6.0. Found: C, 35.8; H, 1.9; N, 5.9%.

$Cu(2,5\text{-pydc})_2Mn \cdot H_2O$ (**2d**) was prepared as above from a finely ground sample of **2**. Compound **2d** is also a dark blue powder. *Anal.* Calc. for $CuMnC_{14}H_6N_2O_8 \cdot H_2O$: C, 36.0; H, 1.7; N, 6.0. Found: C, 35.7; H, 1.6; N, 6.0%.

2.2. Physical measurements

All elemental analyses were performed on finely powdered samples. TGA data were recorded on a TA 51 thermogravimetric analyzer at a 10 °C/min ramp under a 100 cc/min stream of nitrogen. Magnetic susceptibilities were measured using a Quantum Design (MPMS) SQUID magnetometer. The sample holder and details regarding the use of the equipment have been described elsewhere [5]. Magnetic susceptibilities were corrected for background signal of the sample holder. Corrections for the diamagnetism of all atoms [6] came to -221×10^{-6} for **1**, -185×10^{-6} for **1d**, -245×10^{-6} for **2**, and -185×10^{-6} for **2d**. All magnetic measurements were done on finely powdered samples, and the data are reported here on a per mole copper basis. X-ray studies were performed on single crystals mounted on glass fibers. All measurements were made on a Rigaku/ASDC CCD area detector with graphite-monochromated Mo Kα radiation. The positions of hydrogen atoms bonded to carbon were calculated, while those bonded to oxygen were located by electron density.

3. Results and discussion

3.1. $[Cu(2,4\text{-pydc})_2Mn(H_2O)_4]_x$ (1)

Compound **1** was prepared by a one-step synthesis similar to that developed for **3** [3] and recovered as royal blue crystals suitable for single-crystal X-ray studies. TGA studies show **1** to be thermally robust, with no loss of mass until 205 °C, at which temperature a mass equivalent to four water molecules is lost (calc. 14%, obs. 15%). No further loss of mass is observed until 346 °C, at which temperature the compound decomposes.

Structurally, single-crystal X-ray studies show that **1** is a sheet polymer (see Fig. 1 for repeat unit, Fig. 2 for a portion of the sheet, Table 1 for crystallographic data and Table 2 for selected bond lengths and angles). As in the previously reported structure of **3** [3] the copper(II) centers in **1** are linked into chains. Each copper(II) center in **1** has a tetragonally distorted pseudo-octahedral coordination sphere with the equatorial plane occupied by two rotationally equivalent 2,4-pydc^{2-} moieties binding via the ring nitrogen and one 2-carboxyl oxygen, with respective bond lengths of 1.967(2) and 1.936(1) Å (as compared to the Cu–N and Cu–O1 bond lengths of 1.942(2) and 1.962(1) Å, respectively, for **3**). The axial positions are occupied by long bonds (2.664(2) Å, compared to 2.693(1) Å for **3**) to one oxygen of the 4-carboxyl group on adjacent repeat units, resulting in a double bridge linking the copper centers into a chain similar to that observed in the structure of **3** (Fig. 2). The 4-carboxyl in **1** twists at an

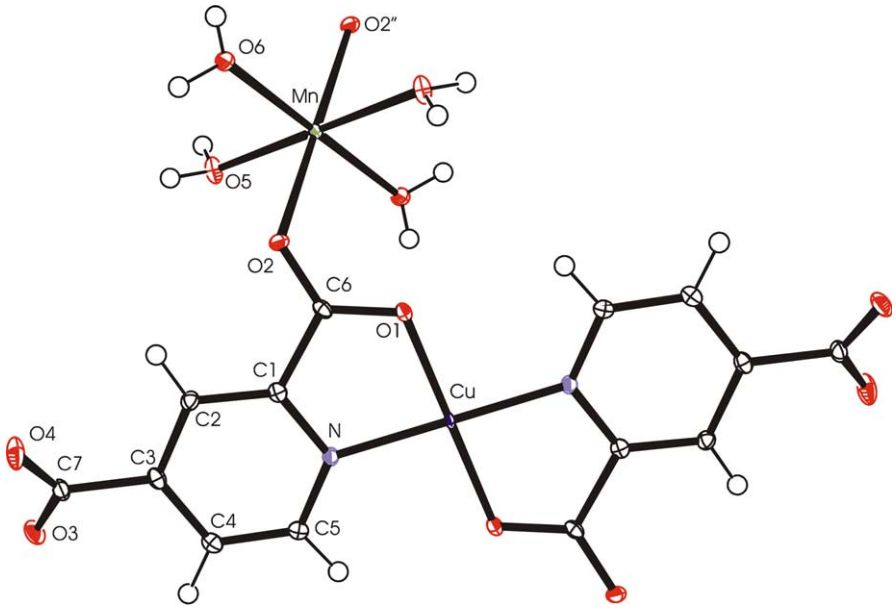


Fig. 1. Repeat unit of **1** with atom numbering scheme.

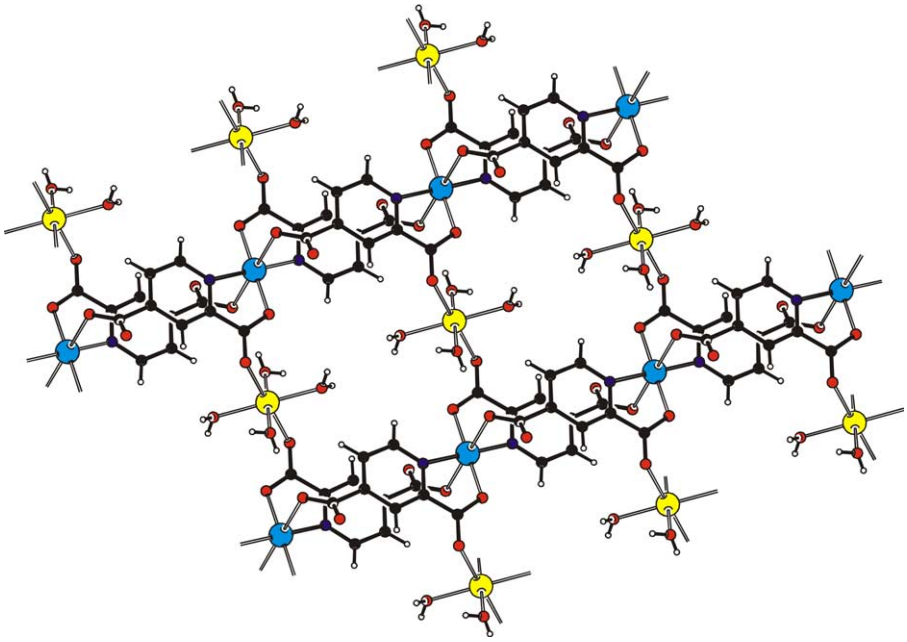


Fig. 2. Polymetallic sheet structure of **1**.

angle of 41.8(1)° to the ring to facilitate this bond; in **3** the 3-carboxyl twists at an angle of 77.3(2)°. As in **3**, the copper(II) chain structure of **1** is further stabilized by a π–π stacking interaction between the pyridine rings forming the double bridge (Table 3). Unlike **3**, however, the copper(II) chains of **1** are linked via covalent bonds into polymetallic sheets through the manganese(II) coordination spheres (Fig. 2), in a structure similar to that of the previously reported compound $[Cu(2,3\text{-pydc})_2Na_2(H_2O)_8]_x$, where copper(II) chains are linked into polymetallic sheets via $Na_2(H_2O)_8^{2+}$ ions [3]. Each manganese(II) center in **1** is ligated by four water molecules in two rotationally equivalent pairs, with the remaining two positions of the pseudo-octahedral coordination sphere filled by bonds to the second 2-carboxyl oxygen atoms of 2,4-$pydc^{2-}$ moieties in adjacent polymetallic chains. The Mn–O distances (2.158(2) and 2.197(2) Å for Mn–O5 and Mn–O6, 2.174(1) Å for Mn–O2) all fall within the range of Mn–O distances observed in the $Mn(H_2O)_6^{2+}$ ion in **3** [3]. This connectivity means that **1** is a sheet polymer consisting of copper(II) chains doubly bridged by 2,4-$pydc^{2-}$ ligands in one

Table 1
Crystallographic data for **1**

Empirical formula	$C_{14}H_{14}N_2O_{12}MnCu$
Formula weight	520.75
Crystal system	triclinic
Space group	*P*1 (#2)
a (Å)	7.4676(8)
b (Å)	7.801(1)
c (Å)	7.987(1)
V (Å^3)	425.5(1)
α (°)	112.290(6)
β (°)	97.285(5)
γ (°)	91.012(3)
Z	1
ρ_{calc} (g cm^{-3})	2.032
μ (Mo Kα) (cm^{-1})	20.68
Crystal size (mm)	0.30 × 0.20 × 0.20
T (K)	173
$R(F)$[a]	0.041
$R_w(F^2)$[b]	0.060
Number of parameters	155
Refinement	F^2

[a] $R(F) = \sum||F_o| - |F_c||/\sum|F_o|$.
[b] $R(F^2) = (\sum(F_o^2 - F_c^2)^2/\sum(F_o^2)^2)^{1/2}$.

Table 2
Selected bond lengths (Å) and angles (°) for **1**

Bond lengths	
Cu–N	1.967(2)
Cu–O1	1.936(1)
Cu–O3	2.664(2)
Mn–O2	2.174(1)
Mn–O5	2.158(2)
Mn–O6	2.197(2)
Bond angles	
O1–Cu–N	84.16(6)
O1–Cu–O3	93.90
O1–Cu–O1′	180.0
O2–Mn–O5	82.59(6)
O2–Mn–O6	83.97(6)
O2–Mn–O2″	180.0
Torsion angles	
Pyridine–O1–C6–O2	10.6(1)
Pyridine–O3–C7–O4	41.8(1)

Table 3
π–π Stacking parameters for **1**

Centroid–centroid distance (Å)	3.393(1)
Ring plane–ring plane distance (Å)	3.348
Ring plane–ring plane angle (°)	0.00
Centroid–centroid to ring normal angle (°)	9.35

direction, and chains of alternating copper(II) and manganese(II) bridged by carboxyl groups in the second dimension. The sheets are stabilized by both π–π stacking interactions and hydrogen bonding between the water hydrogens and nearby carboxyl oxygens (Table 4). Additional hydrogen bonds between adjacent sheets (Table 5) further stabilize the extended structure.

Table 4
Intrasheet hydrogen-bonding interactions for **1**

D–H···A	D–A (Å)	D–H···A (°)
O6–H7···O3	2.837(2)	163(3)

Table 5
Intersheet hydrogen-bonding interactions for **1**

D–H···A	D–A (Å)	D–H···A (°)
O5–H4···O4	2.664(2)	173(3)
O5–H5···O4	2.822(2)	153(3)
O6–H6···O3	2.800(3)	163(3)

DC magnetic susceptibility measurements for **1** were made from 300 to 2 K at an applied field of 10 000 G and from 100 to 2 K at 500 G. The observed increase in moment on decreasing temperature (Fig. 3) indicates ferromagnetic exchange. The data obtained at 10 000 G show the moment to pass through a maximum at 4 K, decreasing in value at lower temperatures. That this effect is likely the result of magnetic saturation at high applied fields is indicated by its absence in the lower field data, and also by the results shown in Fig. 4. Plots of magnetization versus applied field are shown in Fig. 4 for four different temperatures. These data clearly show the magnetization to saturate at high fields and low temperatures. That there is no long-range magnetic ordering in this system above 2K was indicated by AC susceptibility data taken from 50 to 1.8 K at an applied AC field of 1.0 G and frequencies of 10, 100, and 1000 Hz. This study showed no maxima in either χ' or χ''. This result was confirmed by identical zero-field cooled and field-cooled magnetization plots measured from 25 to 2 K and by the absence of magnetic hysteresis when the magnetization was measured at 1.8 K by sweeping the field between +2000 and −2000 G. The magnetization plots of Fig. 4 reveal that at 2.5 K the highest magnetization measured is 35 920 cm^3 G mol^{-1} at an applied field of 55 000 G. This value compares favorably with the saturation magnetization value of 34 070 cm^3 G mol^{-1} calculated [7] for a ferromagnetically coupled $S = 1/2 + S = 5/2$ system (assuming $g = 2.2$ and 2.0, respectively). Ferrimagnetic coupling is clearly ruled out by the fact that the calculated saturation magnetization for a $S = 5/2 - S = 1/2$ system is 21 780 cm^3 G mol^{-1}, significantly below the measured magnetization value.

It is somewhat unexpected that **1** proved to exhibit ferromagnetic behavior. The herringbone-type copper(II) chains seen in **1** were previously reported [3] to be weakly antiferromagnetic, suggesting that the Cu–Cu interaction is not dominating the magnetic behavior of **1**, instead that it is Cu–Mn coupling that dominates. Anti-parallel coupling between the $S = 1/2$ and the $S = 5/2$ centers would have generated the anticipated ferrimagnetic behavior for this system, whereas the observed coupling is clearly ferromagnetic. Adding

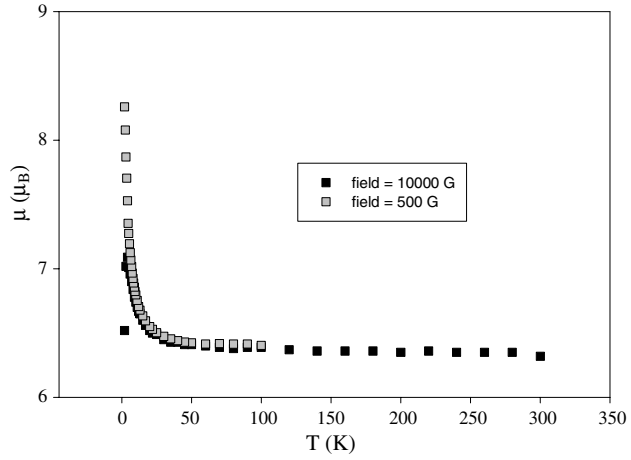


Fig. 3. Magnetic moment plots at 10 000 and 500 G for **1**.

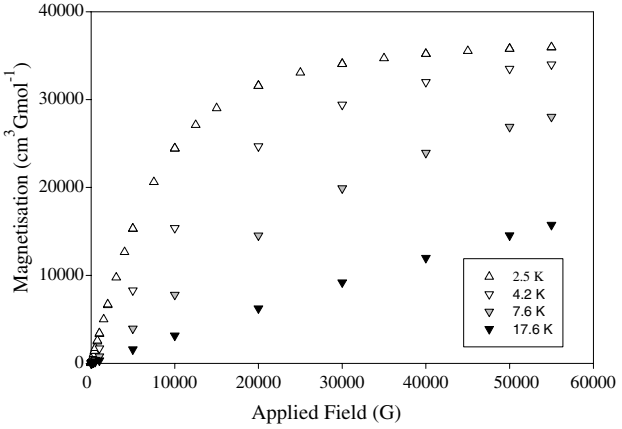


Fig. 4. Magnetization vs. field plots for **1**.

to the unexpected nature of these results is the fact that earlier studies by others on similar O–C–O bridged Cu/Mn systems have shown negligibly small interactions [8].

Heating a bulk sample of **1** at 190 °C under dynamic vacuum produces $Cu(2,4\text{-pydc})_2Mn \cdot H_2O$ (**1d**). DC magnetic susceptibility measurements were made on **1d** in an applied field of 10 000 G. The magnetic properties of **1d** are in sharp contrast to those of the parent compound **1**. The magnetic moment of **1d** decreases as *T* decreases, indicating antiferromagnetic behavior (Fig. 5). Attempts to model the data assuming a linear chain antiferromagnetic model for copper(II) coupled with a zero field splitting model for manganese(II) failed to produce an acceptable fit. It is likely that more complex exchange pathways are extant in this system. It seems reasonable to assume that the structure of **1d** retains the copper(II) chains observed in **1**, and that the changes to the structure are chiefly in the manganese(II) chromophore, which loses three ligating water molecules. An examination of the hydrogen-bonding interactions of the water molecules ligating manganese(II) in **1** shows that the 4-carboxyl oxygens on adjacent sheets are relatively near the manganese(II) ion, and suggests that the coordination sphere of manganese(II) in **1d** is filled by bonds to these atoms, resulting in O–C–O bridges between manganese(II) and copper(II) ions on adjacent polymetallic sheets. This adds another dimension to the connectivity in this "condensed form" of **1**, a connectivity which leads to overall antiferromagnetic behavior. Further speculation on the nature of the magnetic coupling in **1d** is not warranted in the absence of a definitive X-ray determined structure.

3.2. $[Cu(2,5\text{-pydc})_2Mn(H_2O)_2]_x \cdot 4xH_2O$ (2)

A one-pot synthetic approach, similar to that used to prepare **1**, gave compound **2** as dark blue crystals suitable for single-crystal X-ray studies. Thermogravimetric studies show **2** to be moderately thermally robust; it is stable up to 90 °C, at which temperature it loses a mass equivalent to two water molecules (calc. 6%, obs. 7%). A mass equivalent to the remaining four water molecules (calc. 13%, obs. 13%) is lost at 175 °C, and the dehydrated compound is then stable to 340 °C, at which temperature it decomposes. Heating a portion of **2** in a drying pistol at 190 °C yields the stable compound $Cu(2,5\text{-pydc})_2Mn \cdot H_2O$ (**2d**).

The structure of **2** consists of copper(II) ions and manganese(II) ions in pseudo-octahedral coordination spheres linked via the $2,5\text{-pydc}^{2-}$ ligands into a sheet polymer (see Fig. 6 for repeat unit, Fig. 7 for a portion of the sheet, Table 6 for crystallographic data and Table 7 for selected bond lengths and angles). Locally, each copper is chelated by two symmetrically equivalent $2,5\text{-pydc}^{2-}$ ligands via the ring nitrogen and one 2-carboxyl oxygen (Fig. 7). The axial positions of the pseudo-octahedral copper(II) coordination sphere are filled by long bonds to the second 2-carboxyl oxygens of the $2,5\text{-pydc}^{2-}$ moieties in adjacent repeat units, forming a double-O–C–O-bridged copper chain (Fig. 7). The manganese(II) ions are ligated in the equatorial plane by the 5-carboxyl oxygens of $2,5\text{-pydc}^{2-}$ ligands bound to copper(II), with each manganese(II) ion linked to two adjacent repeat units along two adjacent copper(II) chains, such that the manganese(II) ions are linked by double-O–C–O-bridges into chains and the separate copper and manganese chains are cross-linked by double ligand bridges to form an overall extended sheet structure (Fig. 7). The axial positions of the manganese(II) chromophores are filled by two ligated water molecules; the remaining four water molecules occupy crystal lattice positions. Both ligated and lattice water molecules participate in an extensive three-dimensional hydrogen-bonding network reinforcing the structure of the sheets and linking adjacent sheets (Table 8). Adjacent sheets are also linked by π–π stacking interactions, albeit weak ones (Table 9).

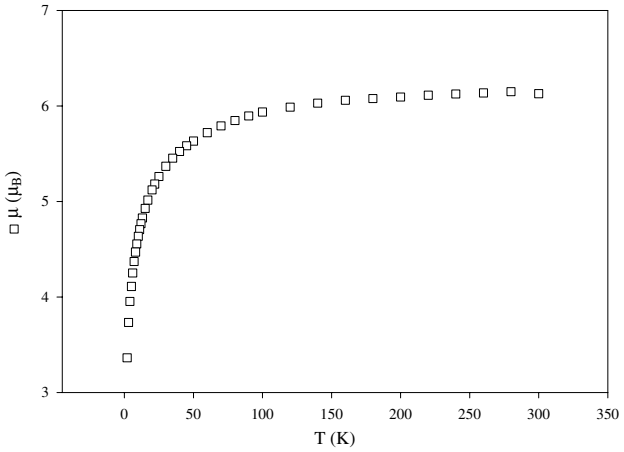


Fig. 5. Magnetic moment plot for **1d**.

DC magnetic susceptibility measurements were made on **2** from 300 to 2 K at 10000 G. The magnetic moment data (Fig. 8) show a regular decrease in value with decreasing temperature indicative of overall antiferromagnetic coupling. To model the magnetic properties, we made the initial simplifying assumption that magnetic coupling between Cu^{2+} and Mn^{2+} centers via the N–C_3–O ligand pathway is weak enough to be ignored. With this assumption, the overall model becomes one in which models for independent copper(II) and manganese(II) chains are simply added. The only justification for this approach comes with its ultimate success. To model the copper(II) chains in **2**, we considered that they have a bridging structure similar to that of $[Cu(2,4\text{-pydcH})_2]_x \cdot 2xCH_3OH$ [9]. This compound is weakly antiferromagnetic and its susceptibility data have been successfully modeled with the Weng model for copper(II) linear chains using the Hiller coefficients for $S = 1/2$ [10] and the parameters $J = -0.073(3)$ cm^{-1} and $g = 2.217(1)$, and a TIP correction of 0.000017(4) cm^3 mol^{-1}. These parameters were used with the Weng model to model the copper(II) chains within the polymetallic structure of **2**. No suitable structural model was found for the manganese(II) chains, so the magnetic data for **2** were initially modeled by adding the chosen model for the

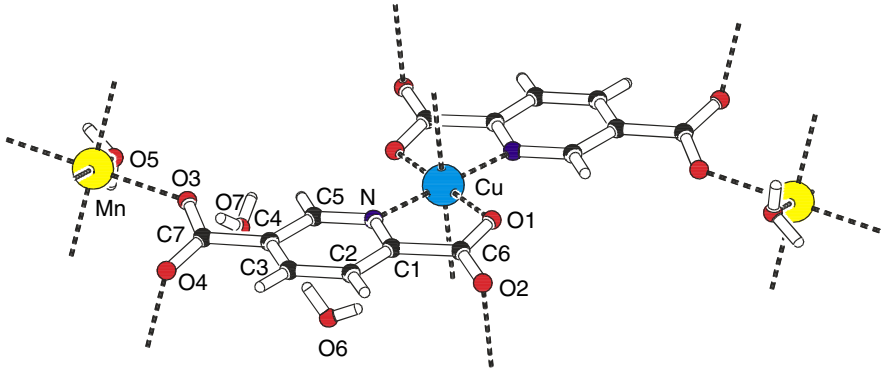


Fig. 6. Repeat unit of **2** with atom numbering scheme.

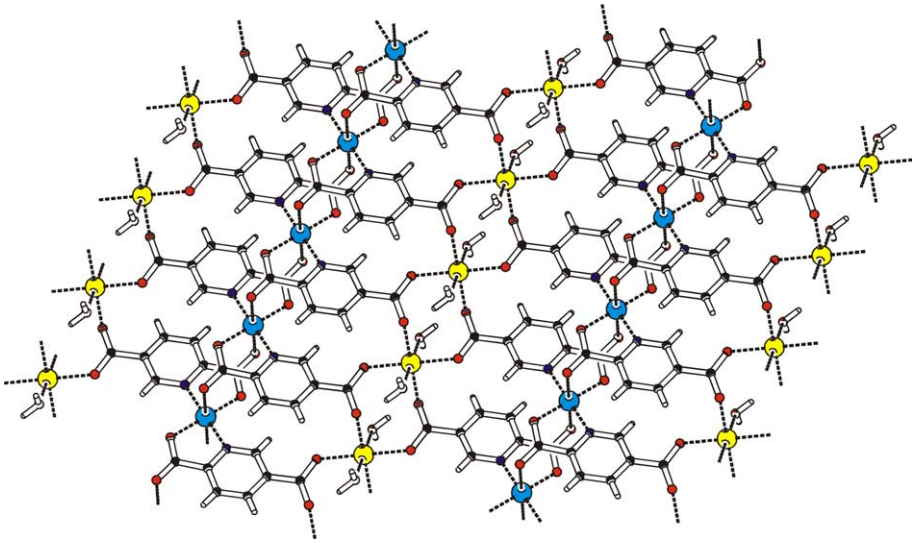


Fig. 7. Polymetallic sheet structure of **2**.

Table 6
Crystallographic data for **2**

Empirical formula	$C_{14}H_{18}N_2O_{14}CuMn$
Formula weight	556.78
Crystal system	triclinic
Space group	*P*1 (#2)
a (Å)	4.7572(5)
b (Å)	7.4134(8)
c (Å)	13.3909(2)
V (Å^3)	469.0(1)
α (°)	81.59(1)
β (°)	81.00(1)
γ (°)	77.03(1)
Z	1
ρ_{calc} (g cm^{-3})	1.971
μ (Mo Kα) (cm^{-1})	18.91
Crystal size (mm)	0.15 × 0.07 × 0.04
T (K)	173
$R(F)$[a]	0.047
$R_w(F^2)$[b]	0.100
Number of parameters	175
Refinement	F^2

[a] $R(F) = \sum||F_o| - |F_c||/\sum|F_o|$.
[b] $R(F^2) = (\sum(F_o^2 - F_c^2)^2/\sum(F_o^2)^2)^{1/2}$.

Table 7
Selected bond lengths (Å) and angles (°) for **2**

Bond lengths	
Cu–N	1.966(2)
Cu–O1	1.940(2)
Cu–O2′	2.673(2)
Mn–O3	2.217(2)
Mn–O4″	2.180(2)
Mn–O5	2.188(2)
Bond angles	
O1–Cu–N	84.50(8)
O1–Cu-O2′	86.86(6)
O3–Mn–O4″	86.93/93.07(6)
O3–Mn–O5	90.68(7)
Torsion angles	
Pyridine–O1–C6–O2	9.7(3)
Pyridine–O3–C7–O4	13.7(3)

Table 8
Hydrogen-bonding parameters for **2**

D–H···A	D–A (Å)	D–H···A (°)
O5–H5a···O7	2.796(3)	166(5)
O5–H5b···O4	2.873(3)	156(4)
O6–H6a···O2	2.855(3)	167(4)
O6–H6b···O7	2.804(3)	160(9)
O7–H7a···O6	2.769(3)	178(4)
O7–H7b···O3	2.953(3)	156(4)

copper(II) chains to the zero-field splitting model for magnetically dilute manganese(II). The attempt at fitting the data with this combined model was not successful, suggesting that coupling between the manganese(II) centers cannot be ignored. The data were then fit with the model for the copper(II) chain added to the Weng model

Table 9
π–π Stacking parameters for **2**

Centroid–centroid distance (Å)	5.105(2)
Ring plane–ring plane distance (Å)	3.098
Ring plane–ring plane angle (°)	0.02
Centroid–centroid to ring normal angle (°)	52.63

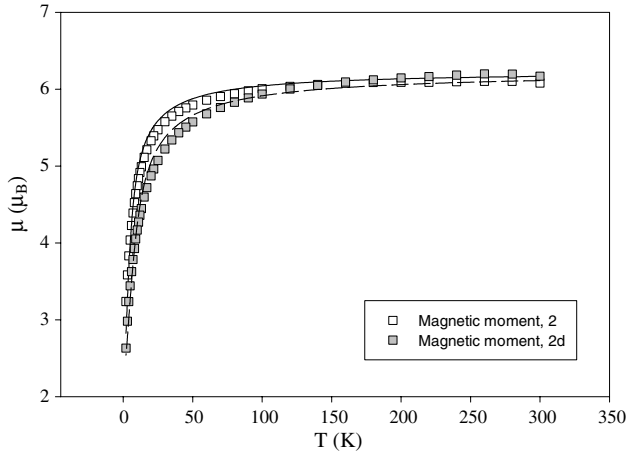


Fig. 8. Magnetic moment plots of **2** and **2d**. Lines were calculated from theory as described in the text.

for manganese(II) chains utilizing the Hiller coefficients for $S = 5/2$ and fixing g(Mn) at 2.00. J(Mn) was employed as the variable parameter. The goodness of fit was measured by the least squares fitting function, F:

$$F = \sqrt{\frac{1}{n}\sum_{1}^{n}\left(\frac{\chi_i^{calc} - \chi_i^{obs}}{\chi_i^{obs}}\right)^2}. \quad (1)$$

This time the fit, shown in Fig. 8, was reasonable ($F = 0.03$), with the parameter J(Mn) = −0.32(1) cm^{-1}. In summary, the magnetic data for **2** are reasonably well explained by weak coupling along each of the separate O–C–O bridged metal chains (J(Cu) = −0.073(3) cm^{-1} and J(Mn) = −0.32(1) cm^{-1}) with no significant Mn–Cu interactions between these chains.

In order to monitor the effect of thermal dehydration on the magnetic properties of **2**, magnetic data were collected for Cu(2,5-pydc)$_2$Mn · H$_2$O (**2d**). Data were taken from 300 to 2 K at a field of 10 000 G. The magnetic moment data for **2d** (Fig. 8) are very similar to those for **2**, the most noticeable difference being a slightly more pronounced decrease in moment with temperature for **2d** suggesting stronger antiferromagnetic coupling in this material. In order to analyze these data, certain assumptions were made about the structure of **2d**. The five water molecules removed from **2** by thermal treatment were assumed to be four lattice water molecules plus one of the two waters ligating manganese(II). The loss of these water molecules therefore would affect the

coordination environment of the manganese centers with the potential to affect the strength of the Mn–Mn exchange interactions, but would not be expected to significantly affect the copper(II) chain structure, or its capacity for mediating magnetic exchange. The structural model used for **2** was therefore assumed to also be valid for **2d**. Accordingly, the data were fit to the same equation used for **2**, the summed Weng models for copper(II) and manganese(II) with the fixed parameters as before and J(Mn) as the only variable parameter. The fit was successful ($F = 0.01$) with the variable parameter J(Mn) found to be $-0.55(1)$ cm^{-1}. This value is 23 standard deviations higher than that found for **2**, indicating that the loss of lattice and ligated water did increase the strength of antiferromagnetic exchange along the Mn–Mn chains in the material.

4. Summary and conclusions

This work has demonstrated the potential of 2,4-pydc^{2-} and 2,5-pydc^{2-} to bridge different kinds of metals, in this case copper(II) and manganese(II), and form extended arrays in which the metals exhibit a regular alternation. These ligands chelate via nitrogen and one 2-carboxyl oxygen to the "softer" metal of two and utilize one or more of the other carboxyl oxygen atoms to bridge to the "harder" metal. Analyses of the magnetic properties of **1** and **2** reveal that the N–C_4–O and N–C_3–O coordinative links between metals, involving the ring N and a 4- or 5-carboxyl oxygen, provide relatively weak pathways for magnetic exchange. More pronounced coupling appears associated with the O–C–O links in these systems. The result is ferromagnetic coupling between the copper and manganese centers in **1** and weak antiferromagnetic coupling within each of the copper and manganese chains in **2** with no measurable coupling between the two different metals in this latter compound.

On thermal dehydration, **1** forms a material **1d** in which the overall exchange is antiferromagnetic. This dramatic change from the overall ferromagnetism of the parent compound is likely caused by structural changes on dehydration opening up an additional pathway for antiferromagnetic exchange in the material. In contrast, the magnetic properties of **2** are little altered on dehydration indicating only marginal differences between the structures of **2** and **2d** such that the dominant antiferromagnetic pathways extant in **2** remain in **2d**.

Finally, it should be noted that in spite of the presence of regularly alternating $S = 1/2$ and $S = 5/2$ centers in both **1** and **2**, and presumed to be present in **1d** and **2d**, none of these systems gave evidence for ferrimagnetic behavior.

5. Supplementary material

Crystallographic data for the structural analyses have been deposited with the Cambridge Crystallographic Centre, CCDC No. 251776 for compound **1** and 251777 for compound **2**. Copies of this information may be obtained free of charge from the Director, CCDC, 12 Union Road, Cambridge, CB2 1EZ, UK (fax: +44 1223 336 033; e-mail: deposit@ccdc.cam.ac.uk or www. http://www.ccdc.cam.ac.uk).

Acknowledgments

R.C.T. and A.S. acknowledge the financial support of the Natural Sciences and Engineering Research Council of Canada. Elemental analyses were performed at UBC by M. Lakha.

References

[1] S. Lee, D.M. Shin, Y.K. Chung, Chem. Eur. J. 10 (2004) 3158.
[2] L. Mao, S.J. Rettig, R.C. Thompson, J. Trotter, S. Xia, Can. J. Chem. 74 (1996) 433.
[3] B.O. Patrick, C.L. Stevens, A. Storr, R.C. Thompson, Polyhedron 22 (2003) 3025.
[4] O. Kahn, Molecular Magnetism, VCH, New York, 1993.
[5] M.K. Ehlert, S.J. Rettig, A. Storr, R.C. Thompson, J. Trotter, Can. J. Chem. 67 (1989) 1970.
[6] E. Konig, Magnetic Properties of Coordination and Organometallic Transition Metal Compounds, vol. 2, Springer, Berlin, 1966.
[7] R.L. Carlin, Magnetochemistry, Springer, Berlin, 1986.
[8] O. Kahn, Adv. Inorg. Chem. 43 (1995) 179.
[9] B.O. Patrick, C.L. Stevens, A. Storr, R.C. Thompson, unpublished results.
[10] W. Hiller, J. Strable, A. Datz, M. Hanack, W.E. Hatfield, L.W. ter Haar, P. Gutlich, J. Am. Chem. Soc. 106 (1984) 329.

Besides this general approach, our proposing approach is due to the expansion of spin units into a metal cluster building block. Recently, Ovcharenko et al. [21] have reported a two-dimensional compound derived from the assembly of a Mn_6 cluster, $[Mn_6O_2(t\text{-}BuCO_2)_{10}(THF)_4]\cdot THF$ (**1**) that possesses an $S_T = 0$ spin ground state itself, with a nitronyl nitroxide unit of 2,4,4,5,5-pentamethyl-4,5-dihydro-1*H*-imidazolyl-3-oxide-1-oxyl [22]. Interestingly, this material underwent a long-range order with $T_c = 3.5$ K. This fact indicates that the significant magnetic-coupling between Mn_6 and radical spin enables to create a new spin ground state.

Our first attempt to connect the Mn_6 cluster has been carried out by employing 4,4′-bipyridine linker to confirm stability of the core structure of Mn_6 subunit in a network skeleton [23]. Both results of Ovcharenko's one and ours proved that this type of Mn_6 clusters was potentially candidate as a building block for creating new molecular frameworks and assembled magnetic materials. Herein, we present a new discrete cluster of the Mn_6 cluster attaching two nitronyl nitroxide groups: $[Mn_6O_2(t\text{-}BuCO_2)_{10}(H_2O)(NNPy)_2]$ (**2**) (NNPy = 2-(*p*-pyridyl)-4,4,5,5-tetramethylimidazoline-1-oxyl-3-oxide). Synthesis, structure, and magnetic properties of **2** are described.

2. Experimental

All chemicals employed syntheses were of reagent grade. Benzene and *n*-hexane were distilled over Na/benzophenone ketyl and freshly distilled prior to use. All manipulations were performed under nitrogen atmosphere with standard Schlenk-tube techniques. The precursors of $[Mn_6O_2(t\text{-}BuCO_2)_{10}(THF)_4]\cdot THF$ (**1**) [21] and 2-(*p*-pyridyl)-4,4,5,5-tetramethylimidazoline-1-oxyl-3-oxide (NNPy) [24] were prepared by methods of the literatures, respectively.

2.1. Preparation of $[Mn_6O_2(t\text{-}BuCO_2)_{10}(H_2O)(NNPy)_2]$ (2)

A 10 ml of benzene solution containing compound **1** (52 mg, 0.03 mmol) was refluxed for 2 h and then cooled to room temperature. To a resulting brown solution was added a solid of NNPy (28 mg, 0.12 mmol), and stirred for an hour. The dark-blue solution was filtered and the filtrate was layered with *n*-hexane (20 ml) in a narrow glass tube. Dark-blue crystals of **2** were obtained after two days. Yield: 42 mg, 75%. Selected IR (KBr, cm^{-1}): *v* 2958(s), 1693(w), 1583(s), 1483(s), 1456(m), 1417(s), 1373(s), 1319(s), 1228(s), 1164(m), 1136(m), 1074(m), 1029(w), 1008(m), 937(w), 893(m), 831(m), 786(m), 613(s), 557(m). *Anal.* Calc. for $C_{74}H_{124}O_{27}N_6Mn_6$: C, 47.80; H, 6.72; N, 4.52. Found: C, 48.12; H, 6.52; N, 4.25%.

2.2. Physical measurements

An infrared spectrum was recorded on KBr pellet with a Shimadzu FT-IR-8600 spectrophotometer. Elemental analysis (C, H, N) was performed at Elemental Analysis Laboratory, Department of Chemistry, Tokyo Metropolitan University. The ESR spectra were recorded on a polycrystalline sample enclosed in a quartz tube at X-band frequency operating 8.96–8.97 GHz with a JEOL spectrometer (ES-TE200/BU). Magnetic susceptibility measurements were conducted by a Quantum Design SQUID magnetometer (MPMS-XL). The sample was put into a gelatin capsule and restrained using Nujol. The obtained data were corrected for the underlying diamagnetic susceptibility using Pascal's constants [25].

2.3. X-ray structure determination

Crystal data for **2** were collected on a Rigaku AFC7R diffractometer with graphite monochromated Mo Kα radiation and a rotating anode generator. The intensities were corrected for Lorentz and polarization effects. The structure was solved by a direct method (SIR-97) [26] and expanded using Fourier techniques. Non-hydrogen atoms were refined anisotropically, besides some carbon atoms on nitronyl nitroxide moiety. Hydrogen atoms were refined using the riding model. The final cycle of full-matrix least-squares refinement on F^2 was based on 10 567 observed reflections and 1085 variable parameters and converged (largest parameter shift was 0.00 times its esd) with unweighted and weighted agreement factors. The crystal data and collection parameters for **2** are summarized in Table 1.

3. Results and discussion

3.1. Structural description

A labeled ORTEP plot of **2** is depicted in Fig. 1(a). Selected interatomic distances and angles are listed in Table 2. Complex **2** crystallizes in the acentric triclinic space group *P*1 (No. 1). Complex **2** consists of a $[Mn_6O_2]^{10+}$ core and two NNPy moieties. Note that the $[Mn_6O_2]^{10+}$ core of the parent cluster **1** is preserved in **2**; the $[Mn_6O_2]^{10+}$ core is composed of six Mn ions positioned at vertices of edge-shared double-tetrahedron with two μ_4-O^{2-} ions at the center of each tetrahedron as shown in Fig. 1(b). The valence of six Mn ions is assigned to be trivalent and divalent, respectively, for two inner Mn ions (Mn(1), Mn(2)) occupying the edge-shared positions and four outer Mn ions (Mn(3), Mn(4), Mn(5), Mn(6)) situating the outer vertices. The coordination geometry around the inner Mn^{III} ions, Mn(1) and Mn(2), has an elongated octahedral

Table 1
Crystallographic data for **2**

Formula	$C_{74}H_{112}O_{27}N_6Mn_6$
Formula weight	1847.35
Crystal system	triclinic
Space group	*P*1 (No. 1)
a (Å)	13.768(3)
b (Å)	15.259(2)
c (Å)	13.200(3)
α (°)	111.09(1)
β (°)	117.43(1)
γ (°)	92.97(2)
V (Å^{-3})	2215.9(7)
T (°C)	−170(1)
Z	1
D_{calc} (g cm^{-3})	1.393
F(000)	976.00
λ (Å)	0.71069
μ (Mo Kα) (cm^{-1})	9.04
Data measured, unique (R_{int})	21 136, 10 565 (0.122)
Number of observations [$I > 2.00\sigma(I)$]	10 567
Number of variables	1085
Goodness-of-fit indicator	1.034
R_1[a] [$I > 2.00\sigma(I)$]	0.049
R_1, wR_2[b] (all data)	0.061, 0.126

[a] $R_1 = \sum||F_o| - |F_c||/\sum|F_o|$.
[b] $wR_2 = [\sum(\omega(F_o^2 - F_c^2)^2)/\sum\omega(F_o^2)^2]^{1/2}$.

environment, where six positions are occupied by oxygen atoms of four pivalate bridging groups and two μ_4-O^{2-} ions. The bond distance corresponding to the elongated axes are found to be Mn(1)–O(3) = 2.308(4) Å, Mn(1)–O(5) = 2.208(4) Å, Mn(2)–O(11) = 2.243(4) Å, Mn(2)–O(13) = 2.183(4) Å, longer than those for the equatrial plane, Mn(1)–O(1,2,7,9) (average 1.916 Å) and Mn(2)–O(1,2,15,17) (average 1.927 Å), demonstrating the Jahn-Teller distortion typically observed for an octahedral high-spin d^4 ion. Among the four outer Mn^{II} ions, Mn(3) and Mn(5) ions that are present in *trans* position of the cluster have a distorted octahedral environment surrounded by five oxygen atoms arisen from four pivalate bridges [Mn(3)–O(3,8,12,19) (average 2.186 Å), Mn(5)–O(5,10,14,22) (average 2.192 Å)] and a μ_4-O^{2-} bridge [Mn(3)–O(1) = 2.175(5) Å, Mn(5)–O(2) = 2.194(5) Å], and one nitrogen atom of pyridine-N of NNPy molecule [Mn(3)–N(1) = 2.351(7) Å, Mn(5)–N(4) = 2.309(7) Å] (vide infra). Mn(4) also has a similar octahedral geometry, except capping of water molecule instead of NNPy, surrounded by six oxygen atoms from pivalate bridges [Mn(4)–O(6,13,16,20) (average 2.180 Å)], a μ_4-O^2 bridge [Mn(4)–O(1) = 2.186(4) Å] and a water molecule [Mn(4)–O(23) = 2.219(4) Å]. While, only Mn(6) is square-pyramidal five-coordinated with five oxygen atoms from pivalate bridges [Mn(6)–O(4,11,18,21) (average 2.140 Å)] and a μ_4-O^{2-} bridge [Mn(6)–O(2) = 2.063(3) Å].

Two NNPy ligands are coordinating to Mn(3) and Mn(5), respectively, in pyridine-N coordination mode to form a linear array of [(NNPy)–Mn_6–(PyNN)]. In each NNPy moiety, the dihedral angle between ON–C_{py}–NO moiety and pyridyl ring is 19.935° and 21.818°, respectively, for ones for Mn(3) and Mn(5). A packing diagram of **2** is depicted in Fig. 2. The closest

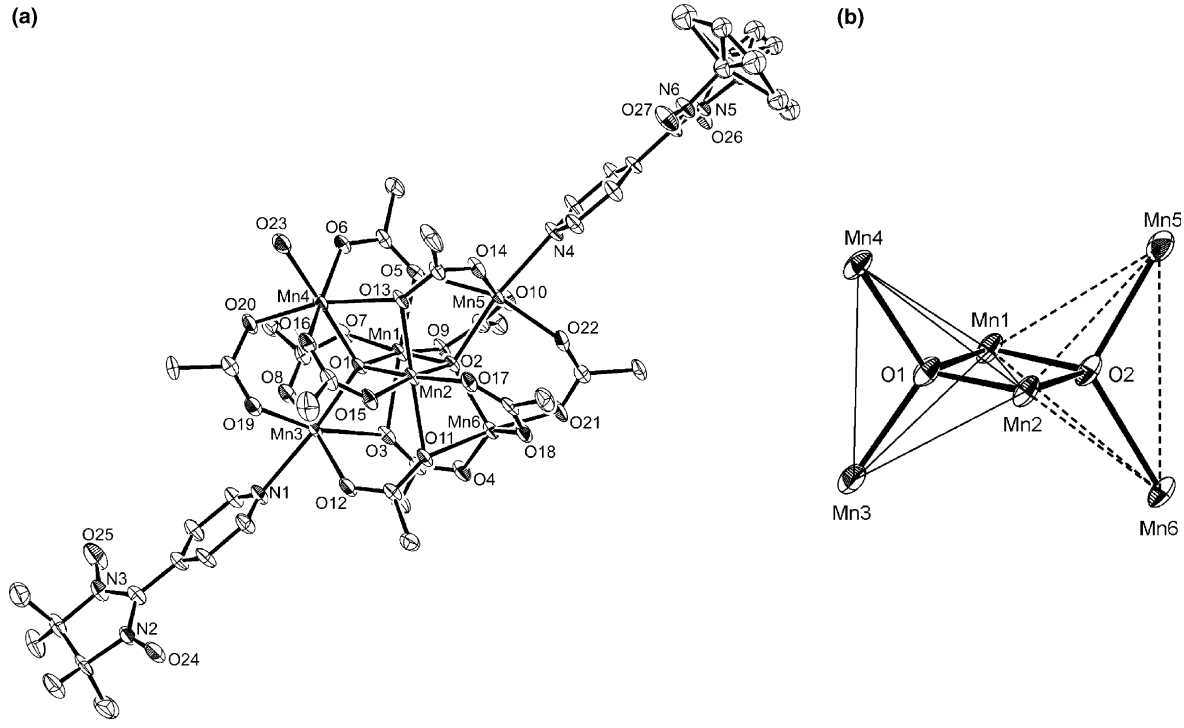


Fig. 1. ORTEP drawing of molecular structure (a) and Mn_6 skeleton (b) of **2** with the atom numbering scheme showing 50% probability ellipsoids. Hydrogen atoms are omitted for clarity.

Table 2
Selected bond lengths (Å) and angles (°) for **2** with the estimated standard deviations in parentheses

Mn(1)–O(1)	1.890(6)	Mn(1)–O(2)	1.878(6)	Mn(1)–O(3)	2.308(4)
Mn(1)–O(5)	2.208(4)	Mn(1)–O(7)	1.939(6)	Mn(1)–O(9)	1.957(7)
Mn(2)–O(1)	1.887(6)	Mn(2)–O(2)	1.898(6)	Mn(2)–O(11)	2.243(4)
Mn(2)–O(13)	2.183(4)	Mn(2)–O(15)	1.957(7)	Mn(2)–O(17)	1.964(6)
Mn(3)–O(1)	2.175(5)	Mn(3)–O(3)	2.382(5)	Mn(3)–O(8)	2.127(7)
Mn(3)–O(12)	2.128(6)	Mn(3)–O(19)	2.107(5)	Mn(3)–N(1)	2.351(7)
Mn(4)–O(1)	2.186(4)	Mn(4)–O(6)	2.101(7)	Mn(4)–O(13)	2.357(5)
Mn(4)–O(16)	2.139(7)	Mn(4)–O(20)	2.121(6)	Mn(4)–O(23)	2.219(4)
Mn(5)–O(2)	2.194(5)	Mn(5)–O(5)	2.355(5)	Mn(5)–O(10)	2.139(7)
Mn(5)–O(14)	2.124(6)	Mn(5)–O(22)	2.151(4)	Mn(5)–N(4)	2.309(7)
Mn(6)–O(2)	2.063(3)	Mn(6)–O(4)	2.079(6)	Mn(6)–O(11)	2.280(6)
Mn(6)–O(18)	2.111(7)	Mn(6)–O(21)	2.088(6)		
O(1)–Mn(1)–O(2)	83.7(2)	O(1)–Mn(1)–O(3)	84.7(2)	O(1)–Mn(1)–O(5)	99.2(2)
O(1)–Mn(1)–O(7)	94.6(2)	O(1)–Mn(1)–O(9)	171.3(2)	O(2)–Mn(1)–O(3)	95.3(2)
O(2)–Mn(1)–O(5)	84.4(2)	O(2)–Mn(1)–O(7)	173.8(2)	O(2)–Mn(1)–O(9)	94.8(2)
O(3)–Mn(1)–O(5)	176.0(2)	O(3)–Mn(1)–O(7)	90.4(2)	O(3)–Mn(1)–O(9)	86.9(2)
O(5)–Mn(1)–O(7)	90.1(2)	O(5)–Mn(1)–O(9)	89.1(2)	O(7)–Mn(1)–O(9)	87.8(3)
O(1)–Mn(2)–O(2)	83.2(2)	O(1)–Mn(2)–O(11)	97.3(2)	O(1)–Mn(2)–O(13)	86.5(2)
O(1)–Mn(2)–O(15)	95.5(3)	O(1)–Mn(2)–O(17)	174.7(2)	O(2)–Mn(2)–O(13)	98.1(2)
O(2)–Mn(2)–O(11)	85.2(2)	O(2)–Mn(2)–O(17)	93.5(2)	O(2)–Mn(2)–O(15)	172.0(2)
O(11)–Mn(2)–O(13)	175.2(3)	O(11)–Mn(2)–O(15)	87.1(2)	O(11)–Mn(2)–O(17)	86.6(2)
O(13)–Mn(2)–O(17)	89.8(2)	O(13)–Mn(2)–O(15)	89.7(2)	O(15)–Mn(2)–O(17)	88.3(3)
O(1)–Mn(3)–O(3)	77.1(2)	O(1)–Mn(3)–O(8)	94.4(2)	O(1)–Mn(3)–O(12)	100.1(2)
O(1)–Mn(3)–O(19)	92.0(2)	O(1)–Mn(3)–N(1)	173.2(2)	O(3)–Mn(3)–O(8)	80.4(2)
O(3)–Mn(3)–O(12)	86.3(2)	O(3)–Mn(3)–O(19)	166.4(2)	O(3)–Mn(3)–N(1)	109.6(2)
O(8)–Mn(3)–O(12)	157.6(2)	O(8)–Mn(3)–O(19)	92.3(2)	O(8)–Mn(3)–N(1)	86.1(3)
O(12)–Mn(3)–O(19)	103.9(2)	O(12)–Mn(3)–N(1)	81.5(2)	O(19)–Mn(3)–N(1)	81.2(2)
O(1)–Mn(4)–O(6)	101.1(2)	O(1)–Mn(4)–O(13)	75.9(2)	O(1)–Mn(4)–O(16)	91.8(2)
O(1)–Mn(4)–O(20)	93.7(2)	O(1)–Mn(4)–O(23)	172.3(3)	O(6)–Mn(4)–O(13)	87.8(2)
O(6)–Mn(4)–O(16)	159.5(2)	O(6)–Mn(4)–O(20)	103.4(3)	O(6)–Mn(4)–O(23)	85.8(2)
O(13)–Mn(4)–O(16)	79.8(2)	O(13)–Mn(4)–O(20)	166.1(2)	O(13)–Mn(4)–O(23)	101.1(2)
O(16)–Mn(4)–O(20)	91.5(2)	O(16)–Mn(4)–O(23)	80.7(2)	O(20)–Mn(4)–O(23)	88.0(2)
O(2)–Mn(5)–O(5)	74.4(2)	O(2)–Mn(5)–O(10)	94.6(2)	O(2)–Mn(5)–O(14)	96.1(2)
O(2)–Mn(5)–O(22)	87.8(2)	O(2)–Mn(5)–N(4)	169.3(2)	O(5)–Mn(5)–O(10)	81.0(2)
O(5)–Mn(5)–O(14)	86.7(2)	O(5)–Mn(5)–O(22)	159.3(2)	O(5)–Mn(5)–N(4)	116.0(2)
O(10)–Mn(5)–O(14)	161.0(2)	O(10)–Mn(5)–O(22)	90.0(2)	O(10)–Mn(5)–N(4)	89.8(3)
O(14)–Mn(5)–O(22)	106.1(2)	O(14)–Mn(5)–N(4)	82.5(2)	O(22)–Mn(5)–N(4)	82.4(2)
O(2)–Mn(6)–O(4)	109.2(2)	O(2)–Mn(6)–O(11)	80.6(2)	O(2)–Mn(6)–O(18)	99.4(2)
O(2)–Mn(6)–O(21)	105.3(2)	O(4)–Mn(6)–O(11)	87.6(2)	O(4)–Mn(6)–O(18)	146.5(2)
O(4)–Mn(6)–O(21)	98.3(3)	O(11)–Mn(6)–O(18)	80.0(2)	O(11)–Mn(6)–O(21)	169.6(3)
O(18)–Mn(6)–O(21)	90.4(3)	Mn(1)–O(1)–Mn(3)	103.3(2)	Mn(1)–O(1)–Mn(4)	116.5(2)
Mn(1)–O(2)–Mn(5)	103.4(2)	Mn(1)–O(2)–Mn(6)	117.8(3)	Mn(1)–O(3)–Mn(3)	85.8(1)
Mn(1)–O(5)–Mn(5)	89.1(1)	Mn(2)–O(1)–Mn(1)	96.5(2)	Mn(2)–O(1)–Mn(3)	118.8(2)
Mn(2)–O(1)–Mn(4)	102.2(2)	Mn(2)–O(2)–Mn(1)	96.6(2)	Mn(2)–O(2)–Mn(5)	120.2(2)
Mn(2)–O(2)–Mn(6)	101.7(3)	Mn(2)–O(11)–Mn(6)	85.6(2)	Mn(2)–O(13)–Mn(4)	88.7(2)
Mn(3)–O(1)–Mn(4)	118.1(2)	Mn(5)–O(2)–Mn(6)	116.2(2)		

inter-cluster Mn···Mn distance is 10.289(1) Å in Mn(3)···Mn(5). The shortest contact between adjacent nitronyl nitroxide moieties is found to be 3.423(6) Å in O(25)···O(27).

3.2. Magnetic properties

DC magnetic measurements were carried out on a Nujol-restrained polycrystalline sample of **2** at 1 kOe in the temperature range of 1.81 to 300 K. The temperature dependence of the magnetic susceptibility χ and χT product is shown in Fig. 3. The $1/\chi_M$ versus T plot roughly obeys the Curie–Weiss law in the high-temperature region with $C = 17.6$ emu K mol^{-1} and $\theta = -36$ K. The Curie constant is smaller than the expected value, 24.3 emu K mol^{-1}, for a magnetically-diluted spin system of ($2Mn^{III}$, $4Mn^{II}$, 2radical) = ($S = 2 \times 2$, $5/2 \times 4$, $1/2 \times 2$) as $g = 2.00$. The value of negative Weiss constant is very similar to that observed in **1** ($\theta = -33$ K), indicating that antiferromagnetic coupling among Mn_6 ions is dominant. As noted in structural description, NNPy is coordinating to Mn^{II} ion in pyridine-N coordination mode. Therefore, the magnetic interaction between nitronyl nitroxide radical and Mn^{II} ion mediated by pyridine moiety is expected to be very weak [27].

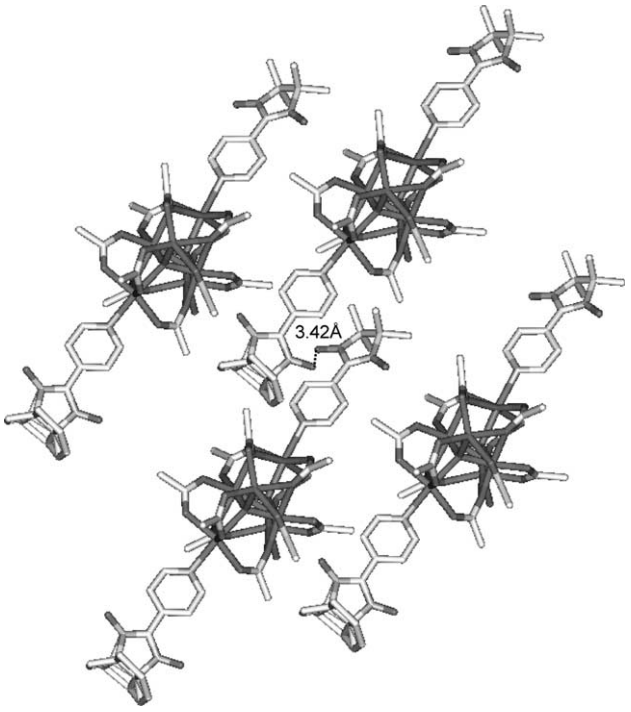


Fig. 2. Packing diagram of **2**.

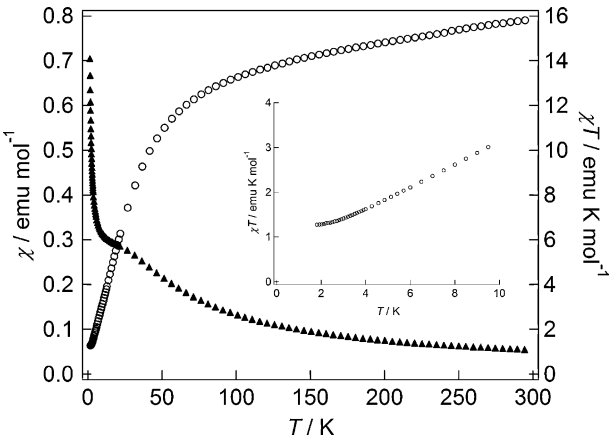


Fig. 3. The temperature dependence of magnetic susceptibility χ_M (close-triangle) and $\chi_M T$ products (open-circle) of **2** measured at 1 kOe. The inset shows $\chi_M T$ products in the low temperature region.

The $\chi_M T$ value of 15.85 emu K mol^{-1} at 300 K is smaller than the spin-only value of 24.25 emu K mol^{-1} ($g = 2.00$). Upon cooling temperature, the value of $\chi_M T$ decreases gradually to 11.00 emu K mol^{-1} at 50 K and more rapidly to 1.27 emu K mol^{-1} at 1.81 K. The whole feature of $\chi_M T$ versus T seems to be very similar to that in **1** (antiferromagnetic coupling among Mn_6 cluster). However, χ_M versus T behavior at low temperatures well expresses the magnetic system of **2**; the χ_M gradually increases from 300 to ca. 20 K, at which shows a kink (peak), then increases abruptly at low temperatures (Fig. 3). The increase of χ_M at lower temperatures indicates the presence of paramagnetic nitronyl nitroxide radicals. Actually, the susceptibility of **1** and a derivative $[Mn_6O_2(PhCO_2)_{10}(py)_2(MeCN)_2] \cdot 2MeCN$ continuously decreases below a broad peak at ca. 20 K [28]. For **2**, the magnetic contribution can be considered as following three possibilities; (i) intra-cluster antiferromagnetic contribution, i.e., magnetic coupling among Mn_6 ions, (ii) interaction between the radical and Mn^{II} ion via pyridine moiety, and (iii) inter-molecule interaction, probably via the O···O contact of adjacent nitronyl nitroxide moieties. The (i) should be the main contributor compared to others $J(Mn^{III}\cdots Mn^{III})/k_B = -60$ K, $J(Mn^{III}\cdots Mn^{II})/k_B = -1.2$ K, $J(Mn^{II}\cdots Mn^{II})/k_B = -3.5$ K for $[Mn_6O_2(PhCO_2)_{10}(py)_2(MeCN)_2] \cdot 2MeCN$ [28]. As mentioned above, the contribution (ii) could be very small as expected from previous reports [27,29–31]. The fact that the spin density on the nitrogen atom of the pyridine ring in NNPy is negligibly

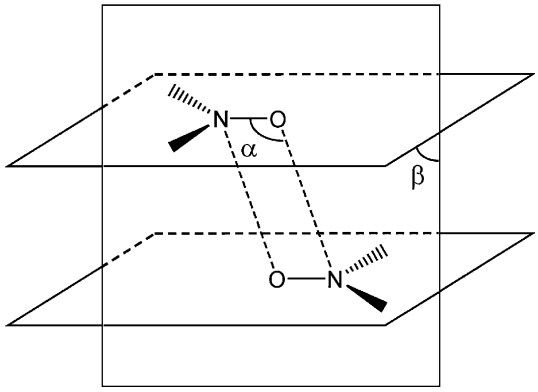


Fig. 4. The definition of the geometrical parameters α and β associating with intermolecular interaction on nitronyl nitroxide molecules.

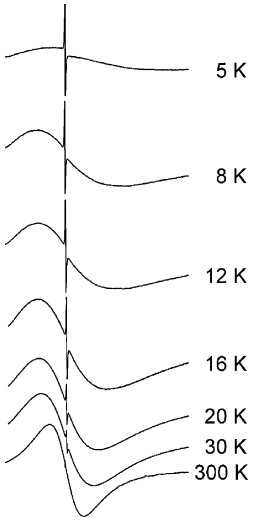


Fig. 5. The temperature dependence of ESR signals measured on a polycrystalline sample of **2** in the range of 300–5 K.

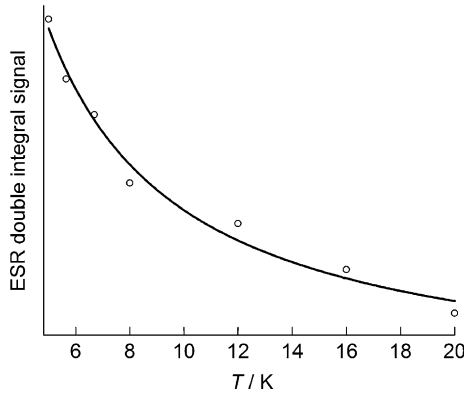


Fig. 6. The variation of double integral of the ESR signal as a function of temperature.

small supports our speculation [31]. Compared to (ii), the contribution of (iii) may be not negligible because of considerable short O···O separation with 3.42 Å of nitronyl nitroxide moieties in **2**. The magnitude of exchange interaction between aminoxyl units depends on their proximity and on the relative orientation of their π*-orbital where the unpaired electron is located. A good estimation for the latter is provided by the geometrical parameters α and β defined in Fig. 4 [32]. For **2**, the relevant parameters for two adjacent NO groups, the N···O distance of 3.46 Å, $\alpha = 143°$, $\beta = 65°$, are indicative of close, but more importantly, a significant decrease of α and β which significantly deviates from 90°, respectively. Consequently, the π*-orbitals are tilted and their overlap could be small. On that account, a weak exchange interaction is anticipated for (iii). Consequently, the nitronyl nitroxide radical acts as if an isolated paramagnetic unit in **2**, consistent with the observation of increase of χ_M below 20 K.

3.3. ESR measurement

The X-band electron spin resonance (ESR) spectra were measured on a polycrystalline sample of **2** at several temperatures in the range of 300–5 K (Fig. 5). ESR signal at 300 K shows a broad single line centered at $g = 1.98$ with peak to peak line width $\Delta H_{pp} = 106.58$ mT. This broad signal is observed in the entire temperature range measured, although the intensity slightly weakens with lowering temperature. This broad signal would be contributed from Mn_6 cluster subunit (metal origin). Below 30 K, a sharp signal is clearly detected at $g = 2.00$ and becomes observable with decreasing temperatures. This is indeed attributable to free radical species (nitronyl nitroxide radical) as suggested from χ_M behavior at low temperatures. The plots of the double integral for the $g = 2.00$ signal versus T display the profile of a paramagnetic species according to the Curie–Weiss law, in agreement with the susceptibility results (see Fig. 6) [33]. Thus, the increase of χ_M below 20 K is assigned to the contribution of nitronyl nitroxide radical as if a free radical. These magnetic results show that the magnetic interaction between the radical of NNPy moiety and Mn^{II} ion (i.e., Mn_6 cluster) is very small compare to the intra-cluster exchange interactions.

4. Conclusion

The assembly reaction of hexanuclear manganese cluster $[Mn_6O_2(t\text{-}BuCO_2)_{10}(THF)_4]\cdot THF$ (**1**) and pyridyl-substituted nitronyl nitroxide radical (NNPy) yielded a hetero-spin complex $[Mn_6O_2(t\text{-}BuCO_2)_{10}(H_2O)(NNPy)_2]$ (**2**) in which the parent cluster core was preserved. The data of temperature dependence of the magnetic susceptibility and ESR clarified the magnetic distribution in **2**; the Mn_6 cluster moiety and NNPy moiety act independently as paramagnetic magnetic centers, producing an $S_T = 0$ spin state for the former and an isolated $S = 1/2$ for the latter.

5. Supplementary material

Crystallographic data (excluding structure factors) for structure reported in this paper have been deposited at the Cambridge Data Centre as supplementary publication No. CCDC-254882 for **2**. This data can be obtained free of charge via www.ccdc.cam.ac.uk/conts/retrieving.html (or from the Cambridge Crystallographic Data Center, 12 Union Road, Cambridge CB2 1EZ, UK; fax: +44 1223 336 033; or e-mail: deposit@ccdc.cam.ac.uk).

Acknowledgements

This work was financially supported by PRESTO (H.M.) and CREST (M.Y.) projects, Japan Science and Technology Agency (JST), and in part by a Grant-in-Aid for Scientific Research from the Ministry of Education, Culture, Sports, Science, and Technology, Japan.

References

[1] R. Sessoli, D. Gatteshi, A. Caneschi, M.A. Novak, Nature 365 (1993) 141.
[2] E.M. Chudnovsky, Science 274 (1996) 938.
[3] L. Thomas, F. Lionti, R. Ballou, D. Gatteschi, R. Sessoli, B. Barbara, Nature 383 (1996) 145.
[4] T. Lis, Acta Crystallogr., Sect. B 36 (1980) 2042.
[5] M. Soler, W. Wernsdorfer, K.A. Abboud, J.C. Huffman, E.R. Davidson, D.N. Hendrickson, G. Christou, J. Am. Chem. Soc. 125 (2003) 3576.
[6] C. Boskovic, M. Pink, J.C. Huffman, D.N. Hendrickson, G. Christou, J. Am. Chem. Soc. 123 (2001) 9914.

[7] H.J. Eppley, H.-L. Tsai, N. de Vries, K. Folting, G. Christou, D.N. Hendrickson, J. Am. Chem. Soc. 117 (1995) 301.
[8] R. Sessoli, H.-L. Tsai, A.R. Schake, S. Wang, J.B. Vincent, K. Folting, D. Gatteschi, G. Christou, D.N. Hendrickson, J. Am. Chem. Soc. 115 (1993) 1804.
[9] A. Caneschi, D. Gatteschi, R. Sessoli, J. Am. Chem. Soc. 113 (1991) 5873.
[10] G.-Q. Bian, T. Kuroda-Sowa, H. Konaka, M. Hatano, M. Maekawa, M. Munakata, H. Miyasaka, M. Yamashita, Inorg. Chem. 43 (2004) 4790.
[11] H. Zhao, C.P. Berlinguette, J. Bacsa, A.V. Prosvirin, J.K. Bera, S.E. Tichy, E.J. Schelter, K.R. Dunbar, Inorg. Chem. 43 (2004) 1359.
[12] A. Forment-Aliaga, E. Coronado, M. Feliz, A. Gaita-Arino, R. Llusar, F.M. Romero, Inorg. Chem. 42 (2003) 8019.
[13] T. Kuroda-Sowa, M. Lam, A.L. Rheingold, C. Frommen, W.M. Reiff, M. Nakano, J. Yoo, A.L. Maniero, L.-C. Brunel, G. Christou, D.N. Hendrickson, Inorg. Chem. 40 (2001) 6469.
[14] M. Soler, P. Artus, K. Folting, J.C. Huffman, D.N. Hendrickson, G. Christou, Inorg. Chem. 40 (2001) 4902.
[15] P. Artus, C. Boskovic, J. Yoo, W.E. Streib, L.-C. Brunel, D.N. Hendrickson, G. Christou, Inorg. Chem. 40 (2001) 4199.
[16] S.M.J. Aubin, Z. Sun, H.J. Eppley, E.M. Rumberger, I.A. Guzei, K. Folting, P.K. Gantzel, A.L. Rheingold, G. Christou, D.N. Hendrickson, Inorg. Chem. 40 (2001) 2127.
[17] S.M.J. Aubin, Z. Sun, L. Pardi, J. Krzystek, K. Folting, L.-C. Brunel, A.L. Rheingold, G. Christou, D.N. Hendrickson, Inorg. Chem. 38 (1999) 5329.
[18] Z. Sun, D. Ruiz, E. Rumberger, C.D. Incarvito, K. Folting, A.L. Rheingold, G. Christou, D.N. Hendrickson, Inorg. Chem. 37 (1998) 4758.
[19] H. Andres, R. Basler, H.-U. Güdel, G. Aromí, G. Christou, H. Büttner, B. Rufflé, J. Am. Chem. Soc. 122 (2000) 12469.
[20] M. Murugesu, M. Habrych, W. Wernsdorfer, K.A. Abboud, G. Christou, J. Am. Chem. Soc. 126 (2004) 4766.
[21] M. Murrie, S. Parsons, R.E.P. Winpenny, J. Chem. Soc., Dalton Trans. (1998) 1423.
[22] V. Ovcharenko, E. Fursova, G. Romanenko, V. Ikorskii, Inorg. Chem. 43 (2004) 3332.
[23] K. Nakata, H. Miyasaka, K. Sugimoto, T. Ishii, K. Sugiura, M. Yamashita, Chem. Lett. (2002) 658.
[24] E.F. Ullman, J.H. Osiecki, D.G.B. Boocock, R. Darcy, J. Am. Chem. Soc. 94 (1972) 7049.
[25] O. Kahn, Molecular Magnetism, VCH, New York, 1993.
[26] A. Altomare, M. Burla, M. Camalli, G. Cascarano, C. Giacovazzo, A. Guagliardi, A. Moliterni, G. Polidori, R. Spagna, J. Appl. Crystallogr. 32 (1999) 115.
[27] I. Dasna, S. Golhen, L. Ouahab, O. Peña, J. Guillevic, M. Fettouhi, J. Chem. Soc., Dalton Trans. (2000) 129.
[28] A.R. Schake, J.B. Vincent, Q. Li, P.D.W. Boyd, K. Folting, J.C. Huffman, D.N. Hendrickson, G. Christou, Inorg. Chem. 28 (1989) 1915.
[29] M. Fettouhi, M. Khaled, A. Waheed, S. Golhen, L. Ouahab, J.-P. Sutter, O. Kahn, Inorg. Chem. 38 (1999) 3967.
[30] L. Li, D. Liao, Z. Jiang, S. Yan, Inorg. Chem. 41 (2002) 421.
[31] A. Caneschi, F. Ferraro, D. Gatteschi, P. Rey, R. Sessoli, Inorg. Chem. 29 (1990) 4217.
[32] M. Fettouhi, B.E. Ali, A.M. El-Ghanam, S. Golhen, L. Ouahab, N. Daro, J.-P. Sutter, Inorg. Chem. 41 (2002) 3705.
[33] F. Bentiss, M. Lagrenée, O. Mentré, P. Conflant, H. Vezin, J. Pierre Wignacourt, E.M. Holt, Inorg. Chem. 43 (2004) 1865.

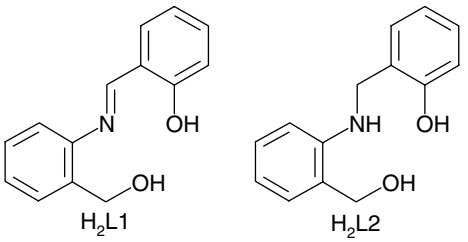


Chart 1.

2. Experimental

2.1. Preparation

All ordinary reagents and solvents were purchased and used as received, unless otherwise noted. Methanol was purified by distillation over magnesium turnings. Dichloromethane was dehydrated with CaH_2 and distilled before using. The ligand H_2L1 [9] and H_2L2 [10] were obtained by the literature methods.

2.1.1. *[Ni4Cl2(L1)2(HL1)2] (1)*

A solution of nickel(II) chloride hexahydrate (0.238 g, 1.0 mmol) and H_2L1 (0.227 g, 1.0 mmol) in methanol (15 cm^3) was stirred for 1 h at room temperature. The solution was evaporated to dryness under reduced pressure. The green residue was extracted by dichloromethane (5 $cm^3 \times 3$). The green microcrystals were obtained after 1 day. Recrystallization from dichloromethane–toluene (1:1 v/v) solution formed deep green crystals suitable for X-ray crystallography. $[Ni_4Cl_2(L1)_2(HL1)_2]$ (**1**); Yield: 15%. *Anal*. Calc. for $C_{56}H_{46}Cl_2N_4Ni_4O_8$: C, 55.65; H, 3.84; N, 4.64; Ni, 19.42. Found: C, 55.61; H, 3.84; N, 4.62; Ni, 18.7%.

2.1.2. *[Mn2Ni2Cl2(L1)4(H2O)2] (2)*

Manganese(II) chloride tetrahydrate (0.198 g, 1.0 mmol) and H_2L1 (0.227 g, 1.0 mmol) were dissolved in methanol (10 cm^3) and a solution of triethylamine (0.5 mmol) in methanol (5 cm^3) was added, and the mixture was stirred for 30 min. To the resulted solution was added a solution of nickel(II) chloride hexahydrate (0.238 g, 1.0 mmol) in methanol (5 cm^3) with stirring. The solution was evaporated to dryness under reduced pressure. The brown residue was extracted by dichloromethane (5 $cm^3 \times 3$). The oak brown microcrystals were obtained after 1 day. Recrystallization from dichloromethane–toluene (1:1 v/v) solution formed brown crystals suitable for X-ray crystallography. $[Mn_2Ni_2Cl_2(L1)_4(H_2O)_2]$ (**2**) $\cdot 2CH_2Cl_2 \cdot H_2O$; Yield: 42%. *Anal*. Calc. for $C_{58}H_{54}Cl_6Mn_2N_4Ni_2O_{11}$: C, 48.95; H, 3.82; N, 3.94; Mn, 7.72; Ni, 8.25. Found: C, 48.98; H, 3.31; N, 3.92; Mn, 7.91; Ni, 8.83%.

2.1.3. *[Ni4(L2)4(CH3OH)2] (3)*

A solution of nickel(II) chloride anhydrous (0.130 g, 1.0 mmol), H_2L2 (0.229 g, 1.0 mmol), and potassium *t*-butoxide (0.152 g, 2.0 mmol) in methanol (15 cm^3) was stirred for 1 h under nitrogen atmosphere. The solution was evaporated to dryness under reduced pressure. The residue was dissolved in dichloromethane, and the solution was filtered to remove insoluble materials. To the filtrate was added 5 cm^3 of methanol and allowed to stand. After a few weeks, the bright green crystals were obtained and collected by suction filtration. $[Ni_4(L2)_4(CH_3OH)_2]$ (**3**) $\cdot CH_2Cl_2 \cdot 2CH_3OH \cdot H_2O$; Yield: 66%. *Anal*. Calc. for $C_{61}H_{72}Cl_2N_4Ni_4O_{13}$: C, 53.29; H, 5.28; N, 4.07; Ni, 17.08. Found: C, 52.59; H, 4.85; N, 4.26; Ni, 17.63%.

2.2. Physical measurements

Elemental analyses for C, H and N were obtained at the Elemental Analysis Service Center, Kyushu University. Analyses of nickel and manganese were made on a Perkin Elmer AAnalyst 100 atomic absorption/flame emission spectrophotometer. Infrared spectra were recorded on a Perkin Elmer Spectrum 2000 FT-IR Spectrometer on KBr disks at the Instrumental Analysis Center, Saga University. The magnetic susceptibilities in the temperature range 2–300 K were measured on a Quantum Design MPMS XL SQUID susceptmeter under an applied magnetic field of 500 G. The susceptibilities were corrected for the diamagnetism of the constituent atoms using Pascal's constant [11]. The effective magnetic moments were calculated from the equation, $\mu_{eff} = [8\chi_M T^{1/2}]$ where χ_M is the molecular magnetic susceptibility.

2.3. X-ray crystallography

The diffraction data were measured on a Rigaku AFC5S automated four-circle diffractometer. The data were collected using the ω–2θ scan technique to a maximum 2θ value of 55°. Crystal data and data collection parameters: **1** $\cdot 4CH_2Cl_2$, $C_{30}H_{27}Cl_5N_2Ni_2O_4$, M = 774.22, triclinic, a = 11.563(3) Å, b = 11.834(4) Å, c = 12.449(3) Å, α = 108.31(2)°, β = 90.92(2)°, γ = 92.64(2)°, V = 1614.7(8) $Å^3$, space group $P\bar{1}$(#2), Z = 2, D_{calc} = 1.592 g/cm^3, T = 298 ± 1 K, F_{000} = 788.00, μ(Mo Kα) = 16.17 cm^{-1}, 5922 reflections observed, No. of variables = 390, final value for $R(I > 2\sigma(I))$ = 0.052/R_w(All reflections) = 0.172. **2** $\cdot 2CH_2Cl_2$, $C_{29}H_{26}Cl_3N_2NiMnO_5$, M = 702.53, triclinic, a = 9.207(2) Å, b = 11.495(3) Å, c = 15.060(5) Å, α = 68.26(3)°, β = 89.27(2)°, γ = 83.87(2)°, V = 1471.4(7) $Å^3$, space group $P\bar{1}$(#2), Z = 2, D_{calc} = 1.586 g/cm^3, T = 298 ± 1 K, F_{000} = 716.00, μ(Mo Kα) = 13.83 cm^{-1}, 6732 reflections observed, No. of variables = 371, final value for $R(I > 2\sigma(I))$ = 0.056/R_w(All reflections) = 0.179. **3** $\cdot CH_2Cl_2 \cdot 2CH_3OH$, $C_{61}H_{70}Cl_2N_4Ni_4O_{12}$, M = 1356.95, triclinic, a = 13.10(1) Å, b = 14.411(5) Å, c = 17.047(4) Å,

$\alpha = 81.05(6)°$, $\beta = 85.17(3)°$, $\gamma = 72.31(5)°$, $V = 3025(3)$ Å^3, space group $P\bar{1}(\#2)$, $Z = 2$, $D_{calc} = 1.490$ g/cm^3, $T = 298 \pm 1$ K, $F_{000} = 1412.00$, μ(Mo Kα) = 13.78 cm^{-1}, 13977 reflections observed, No. of variables = 759, final value for $R(I > 2\sigma(I)) = 0.088$/$R_w$(All reflections) = 0.276.

The structures were solved by direct methods and expanded using Fourier techniques [12,13]. The non-hydrogen atoms were refined anisotropically. All hydrogen atoms were located on the calculated positions and refined isotropically. The final cycle of full-matrix least-squares refinement on F was based on observed reflections and variable parameters and converged with unweighted and weighted agreement factors of R and Rw. All calculations were performed using the CrystalStructure [14] crystallographic software package of Molecular Structure Corporation.

3. Results and discussion

Analytical data of **1**–**3** gave 1:1 ratio of a metal and a ligand. The free H_2L1 ligand shows ν(C=N) vibrations at 1615 cm^{-1}, which shift to 1607–1609 cm^{-1} in **1** and **2**. Complex **3** shows ν(N–H) and ν(C–N) vibrations at 3055 and 1297 cm^{-1}, respectively.

3.1. Crystal structures

3.1.1. $[Ni_4Cl_2(L1)_2(HL1)_2]$ (**1**) · $4CH_2Cl_2$

The structure of **1** is illustrated in Fig. 1. The complex has a tetranuclear structure with an inversion center. The four nickel atoms are located at the four corners of a defective double-cubane core and bridged by each two μ_3-alkoxo, μ-phenoxo, and μ-chloro bridges. There are two types of deprotonated ligand anions ($L1^{2-}$ and $HL1^-$) in the complex. The dianionic ligands, $L1^{2-}$, give μ_3-alkoxo bridge by deprotonated O1 atom, and form bis-μ-alkoxo dinuclear $[Ni(L1)]_2$ unit at the center of the double-cubane core. The O3 atom of monoanionic ligand, $HL1^-$, is protonated and coordinates to Ni2 without bridging. The Ni···Ni distances of Ni1···Ni2, Ni1···Ni2*, Ni1···Ni1*, and Ni2···Ni2* pairs are 3.0671(8), 3.1172(9), 3.1790(7), and 5.3049(9) Å, respectively. Coordination geometries about Ni1 and Ni2 are described as an octahedron and a square pyramid, respectively, but each geometry is significantly distorted due to a longer Ni–Cl bond. The basal-plane of Ni1 is comprised of N1, O1, O2, and O1* and the axial axis is regarded as O4–Ni1–Cl1* direction. In the same way, O1, O3, O4, and N1 atoms define the basal-plane of Ni2, and Cl1 atom locates the apical position. The effect of the longer Ni–Cl bonds lead to large distortion of the double-cubane core compare with that observed for $[Cu(L1)]_4$ [8].

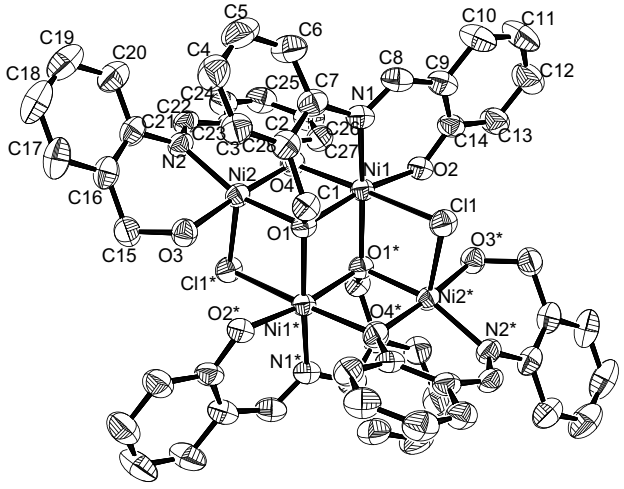


Fig. 1. An ORTEP view of **1** with the atom-numbering scheme. Selected distances (Å) and angles (°): Ni1–O1 2.043(3), Ni1–O2 1.980(3), Ni1–O4 2.090(3), Ni1–N1 2.016(4), Ni1–O1* 2.069(3), Ni1–Cl1* 2.589(1), Ni2–O1 2.009(3), Ni2–O3 2.068(3), Ni2–O4 1.967(3), Ni2–N2 1.986(4), Ni2–Cl1 2.330(1), Ni1···Ni2 3.0671(8), Ni1···Ni1* 3.1790(7), Ni1···Ni2* 3.1172(9), Ni2···Ni2* 5.3049(9); Ni1–O1–Ni2 98.4(1), Ni1–O4–Ni2 98.2(2), Ni1–O1–Ni1* 101.3(1), O1–Ni1–O1* 78.7(1), Ni1–O1*–Ni2* 99.7(1), Ni1–Cl1*–Ni2* 78.46(4), O1–Ni1–O4 79.8(1), O3–Ni2–Cl1 94.74(9).

3.1.2. $[Mn_2Ni_2Cl_2(L1)_4(H_2O)_2]$ (**2**) · $2CH_2Cl_2$

The structure of **2** comprised of a tetranuclear defective double-cubane core (Fig. 2). The asymmetric unit consists of one Ni^{II}, Mn^{III}, Cl^-, water molecule, and two $L1^{2-}$ anions. The two Ni^{II} and two Mn^{III} ions are located at the four corners of a defective double-cubane core and bridged by each two μ_3-alkoxo, μ-alkoxo, and μ-phenoxo bridges. Each Mn^{III} is positioned in both edges of double-cubane and each Ni^{II} resides in central position. Coordination geometries about Ni1 and Mn1

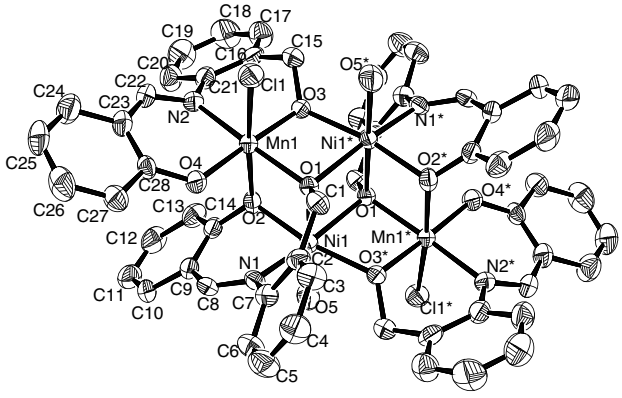


Fig. 2. An ORTEP view of **2** with the atom-numbering scheme. Selected distances (Å) and angles (°): Ni1–O1 2.026(4), Ni1–O3 2.068(3), Ni1–O3* 2.142(4), Ni1–O4 2.010(4), Ni1–O5 2.128(4), Ni1–N2 2.018(5), Mn1–Cl1 2.587(2), Mn1–O1 1.876(4), Mn1–O2 1.861(4), Mn1–O3 1.997(4), Mn1–O4 2.246(4), Mn1–N1 2.039(5), Ni1··· Mn1 3.096(1), Ni1···Ni1* 3.1311(9), Ni1···Mn1* 3.082(1), Mn1···Mn1* 5.326(1); Ni1–O1*–Mn1* 104.3(2), Ni1–O3*–Mn1* 96.2(2), Ni1–O3–Ni1* 96.1(2), O3–Ni1–O3* 83.9(1), Ni1–O3–Mn1 99.4(2), Ni1–O4–Mn1 93.2(2), O1–Mn1–O3 82.9(1), O3–Ni1–O4 85.8(2).

are described as octahedral geometries. The basal-plane of Ni1 is comprised of N1, O2, O1*, and O3*, and axial sites are occupied by O1 and water molecule (O5). Similarly, O1, O3, O4, and N2 atoms define the basal-plane of Mn1, and axial sites are occupied by O2 and chloride anion (Cl1). The Mn1–Cl1 [2.586(2) Å] and Mn1–O4 [2.247(4) Å] distances are elongated relative to the equatorial bond distances [1.862(4)–2.037(6) Å] owing to the Jahn–Teller effect. The M···M distances of Ni1···Mn1, Ni1···Mn1*, Ni1···Ni1*, and Mn1···Mn1* pairs are 3.096(1), 3.082(1), 3.1311(9), and 5.326(1) Å, respectively. The adjacent M···M distances are similar and bond angles around metal ions are close to orthogonal. As a result, the complex **1** has rather fine double-cubane structure compare with **1**, $[Cu(L1)]_4$, and other reported double-cubane complexes [15–18]. Most of tridentate ligands act as meridional forms in both mononuclear and polynuclear complexes [19,20]. In present case, the ligand $L1^{2-}$ coordinating to Ni1 is held as a facial form. This is the first example of structurally characterized facial coordination of $L1^{2-}$.

3.1.3. $[Ni_4(L2)_4(CH_3OH)_2]$ (**3**) · CH_2Cl_2 · $2CH_3OH$

Complex **3** is unstable under open atmosphere. The coordinating ligands $(L2)^{2-}$ in **3** are easily oxidized to $(L1)^{2-}$ as same as the reported complex $[Cu(L2)]_4$. Only a thin crystal of **3** was found to be applicable for X-ray analysis. Though the bond lengths and angles are insufficient for detailed structural discussion, the X-ray analytical results of **3** clearly reveal the geometry around the metal ions and tetranuclear core. A perspective drawing is given in Fig. 3. The complex has a cubane-like Ni_4 core structure. The structure is fundamentally regarded as a dimer-of-dimers structure composed by alkoxo-bridged dinickel units. However, coordination-planes of *ONO*-tridentate ligands in the dimmer unit are not occupied in same plane. The Ni···Ni distances for bis-μ-alkoxo units (3.112(2)–3.124(2) Å) are slightly longer than the other Ni···Ni distances (2.961(2)–3.114(2) Å). It is indicated that the symmetry of cubane-core for **3** is remarkably distorted. Coordination geometry of Ni1 and Ni3 is octahedral by the coordination of a methanol. On the other hand, the geometry of Ni2 and Ni4 is regarded as square-pyramid. The axial positions for Ni2 and Ni4 are covered by phenyl ring from the L2 ligand coordinating to Ni1 and Ni3, respectively. It is supposed that these unusual structural features are caused by sp^3 character of benzyl-C and amine-N atoms [10].

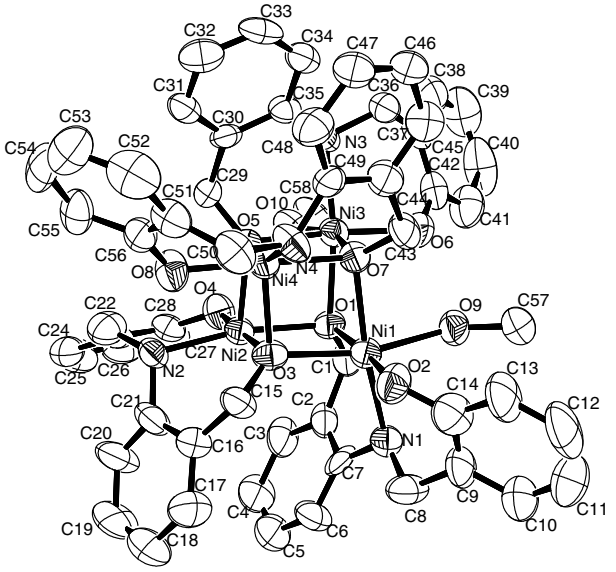


Fig. 3. An ORTEP view of **3** with the atom-numbering scheme. Selected distances (Å) and angles (°): Ni1–O1 2.028(8), Ni1–O2 1.98(1), Ni1–O3 2.089(7), Ni1–O7 2.103(6), Ni1–O9 2.189(7), Ni1–N1 2.138(9), Ni2–O1 2.035(7), Ni2–O3 2.038(9), Ni2–O4 1.94(1), Ni2–O5 2.026(6), Ni2–N2 2.029(8), Ni3–O1 2.060(6), Ni3–O5 2.027(6), Ni3–O6 1.946(8), Ni3–O7 2.103(8), Ni3–O10 2.20(1), Ni3–N3 2.111(8), Ni4–O3 2.059(7), Ni4–O5 2.031(8), Ni4–O7 2.027(6), Ni4–O8 1.954(8), Ni4–N4 2.04(1), Ni1···Ni2 3.124(2), Ni1···Ni3 3.114(2), Ni1···Ni4 3.087(2), Ni2···Ni3 3.016(2), Ni2···Ni4 2.961(2), Ni3···Ni4 3.112(2); Ni1–O1–Ni2 100.5(3), Ni1–O1–Ni3 99.2(3), Ni1–O3–Ni2 98.4(3), Ni1–O3–Ni4 96.2(3), Ni1–O7–Ni3 95.6(3), Ni1–O7–Ni4 96.7(2), Ni2–O1–Ni3 94.9(3), Ni2–O3–Ni4 92.6(3), Ni2–O5–Ni3 96.2(3), Ni2–O5–Ni4 93.8(3), Ni3–O5–Ni4 100.2(3), Ni3–O7–Ni4 97.8(3).

3.2. Magnetic properties

Tetranuclear Ni^{II} complexes **1** and **3** decompose easily even the solid state. Complex **1** change to dinuclear $[Ni(L1)]_2$ unit and mononuclear species and **3** change to Shiff base complex. Therefore, reliable temperature dependence data were not able to obtained. The effective magnetic moments of **1** and **3** are 2.79 and 3.21 B.M./Ni at room temperature. The obtained moments correspond to common values for mononuclear octahedral Ni^{II}-complexes. Judging from structural and magnetic data of $[Cu(L1)]_4$ and $[Cu(L2)]_4$, it is expected that magnetic interactions in **1** and **3** are fairly weak [10].

The $\chi_M T$ versus temperature plots for **2** (per $Ni^{II}_2Mn^{III}_2$) were shown in Fig. 4. The $\chi_M T$ values gradually increased with lowering temperature and reach to a nearly constant value ($\sim$22 $cm^3\,mol^{-1}\,K$) at 4 K. The calculated magnetic moment of 13.2 μ_B at 4 K suggests $S = 6$ spin state which corresponds to the sum of spins for two Ni^{II} ($S = 1$) and two Mn^{III} ($S = 2$) ions. This behavior indicates the presence of ferromagnetic interaction between metal ions in double-cubane core. The experimental data were interpreted by a least squares fit employing the Kambe's method [21] where only two dominant pathways are considered (Chart 2).

The Hamiltonian is written as

$$\hat{H} = -J_{\mathrm{NiMn}}(\hat{S}_{\mathrm{T}}^2 - 2\hat{S}_{\mathrm{A}}^2 - \hat{S}_{\mathrm{B}}^2) - J_{\mathrm{NiNi}}(\hat{S}_{\mathrm{A}}^2 - \hat{S}_1^2 - \hat{S}_3^2), \quad (1)$$

where

$$\hat{S}_{\mathrm{A}} = \hat{S}_1 + \hat{S}_3,\ \hat{S}_{\mathrm{B}} = \hat{S}_2 + \hat{S}_4 \quad \text{and} \quad \hat{S}_{\mathrm{T}} = \hat{S}_{\mathrm{A}} + \hat{S}_{\mathrm{B}}. \quad (2)$$

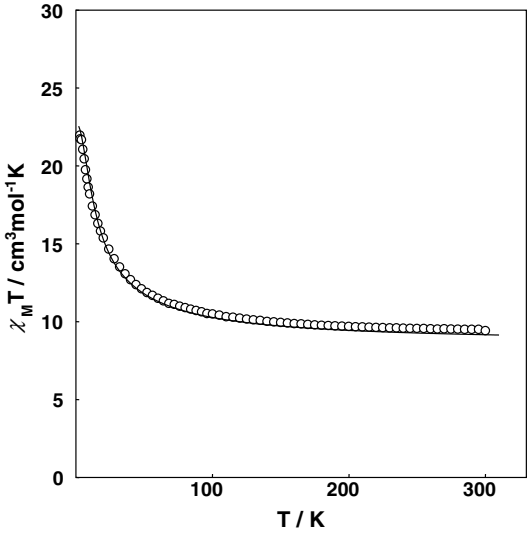


Fig. 4. Plots of $\chi_M T$ vs. T for **2**. The solid line represents a least squares fit of the data as described in the text.

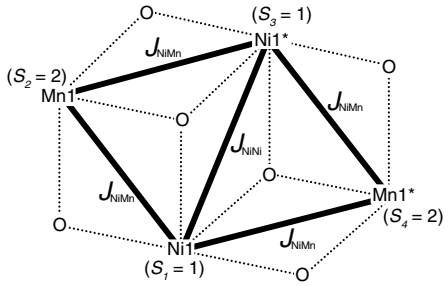


Chart 2.

The Kambe's equivalent operator approach gives the expression in Eq. (3)

$$E(S_T) = -J_{NiMn}[S_T(S_T+1) - S_A(S_A+1) - S_B(S_B+1)] - 2J_{NiNi}[S_A(S_A+1)]. \quad (3)$$

The results of fitting the experimental data are drawn as solid line. The obtained fitting parameters are $g = 2.08$, $J_{NiMn} = 1.5\ cm^{-1}$, $J_{NiNi} = 20\ cm^{-1}$. It is clearly demonstrated that **2** is ferromagnetically coupled between Ni^{II}–Mn^{III}, Ni^{II}–Ni^{II} centers to give the $S = 6$ ground state. The double-cubane structure of $[Cu(L1)]_4$ which shows antiferromagnetic coupling between Cu ions is fairly distorted to triclinic form. As compared this, structural distortion of **2** is quite smaller and metal ions are arranged at nearly ideal positions. The perpendicular arrangement of magnetic orbitals led to the results of the dominant ferromagnetic interactions J_{NiMn} and J_{NiNi} in **2**.

4. Conclusion

Tetranuclear complexes **1**–**3** have been synthesized by the reaction of metal sources with *ONO*-tridentate ligand H_2L1 or H_2L2. Complexes **1**–**3** have been characterized by X-ray crystal structure analyses. The structure analyses reveal that complexes **1** and **2** have a unique defective double-cubane core connected by μ_3-alkoxo bridges and **3** forms cubane core comprised by dimmer-of-dimmers of bis-μ-alkoxo units. The magnetic interactions in **2** are interpreted as ferromagnetic due to the orthogonality of the magnetic orbitals in $Ni^{II}_2Mn^{III}_2$ core.

Acknowledgments

This work was supported by Grants-in-Aid for Science Research (C) (No. 15510092) and Grants-in-Aid for Encouragement of Young Scientists (No. 13740380) from the Ministry of Education, Science, Sports and Culture of Japan.

Appendix A. Supplementary data

Crystallographic data have been deposited at the CCDC. These data can be obtained free of charge via www.ccdc.cam.ac.uk/conts/retrieving.html (or from the CCDC, 12 Union Road, Cambridge CB2 1EZ, UK, fax: +44 1223 336033, e-mail: deposit@ccdc.cam.ac.uk) CCDC reference numbers 265366–265368. Supplementary data associated with this article can be found, in the online version at doi:10.1016/j.poly.2005.03.084.

References

[1] M. Nihei, N. Hoshino, T. Ito, H. Oshio, Polyhedron 22 (2003) 2359.
[2] X.S. Tan, Y. Fujii, R. Nukada, M. Mikuriya, Y. Nakano, J. Chem. Soc., Dalton Trans. (1999) 2415.
[3] K.B. Nolan, A.A. Soudi, Inorg. Chim. Acta 230 (1995) 209.
[4] M. Koikawa, H. Yamashita, T. Tokii, Inorg. Chem. Commun. 6 (2003) 157.
[5] E.-C. Yang, N. harden, W. Wernsdorfer, L. Zakharov, E.K. Brechin, A.L. Rheingold, G. Christou, D.N. Hendrickson, Polyhedron 22 (2003) 1857.
[6] A. Syamal, K.S. Kale, Indian J. Chem., Sect. A 19A (1980) 225.
[7] A. Syamal, K.S. Kale, Indian J. Chem., Sect. A 19A (1980) 488.
[8] M. Koikawa, H. Yamashita, T. Tokii, Inorg. Chim. Acta 357 (2004) 2635.
[9] B. Jezowska-Trzebiatowska, J. Lisowski, A. Vogt, P. Chmielewski, Polyhedron 7 (1988) 337.
[10] H. Yamashita, M. Koikawa, T. Tokii, Mol. Cryst. Liq. Cryst. Sci. Technol., Sect. A 342 (2000) 63.
[11] Landolt-Brnstein, Neue Series II/11, Springer-Verlag, Berlin, 1981.
[12] SIR92: A. Altomare, G. Cascarano, C. Giacovazzo, A. Guagliardi, M. Burla, G. Polidori, M. Camalli, J. Appl. Crystallogr. 27 (1994) 435.
[13] DIRDIF99: P.T. Beurskens, G. Admiraal, G. Beurskens, W.P. Bosman, R. de Gelder, R. Israel, and J.M.M. Smits, The DIRDIF-99

program system, Technical Report of the Crystallography Laboratory, University of Nijmegen, The Netherlands, 1999.
[14] CrystalStructure 3.6: Crystal Structure Analysis Package, Rigaku and MSC, 2004.
[15] L. Hui, Z.J. Zhuang, C. Wei, Y. Xiao-Zeng, J. Chem. Soc., Dalton Trans. (1997) 463.
[16] L. Zhang, L.-F. Tang, Z.-H. Wang, M. Du, M. Julve, F. Lloret, J.-T. Wang, Inorg. Chem. 40 (2001) 3619.
[17] M. Yonemura, H. Okawa, M. Ohba, D.E. Fenton, L.K. Thompson, Chem. Commun. (2000) 817.
[18] Y. Nakamura, M. Yonemura, K. Arimura, N. Usuki, M. Ohba, H. Okawa, Inorg. Chem. 40 (2001) 3739.
[19] W.E. Hatfield, G.W. Inman Jr., Inorg. Chem. 8 (1969) 1376.
[20] T. Tokii, Y. Muto, M. Kato, K. Imai, H.B. Jonassen, J. Inorg. Nucl. Chem. 34 (1972) 3377.
[21] K. Kambe, J. Phys. Soc. Jpn. 5 (1950) 48.

energy caused by the addition of an extra electron, amounts to 60 meV, which is larger than the thermal energy k_BT, e.g., 20 meV at 300 K. Such a small nanaoparticle must operate as a single electron transistor, if a tunnel barrier of the nanoparticle is larger than ca. $h/e^2 = 26\ k\Omega$. Such a nano-particle is expected to work as a single electron transistor. Therefore, it would be extremely interesting to connect these nanoparticles in a networked manner through the conducting molecular wires.

Recently we succeeded in preparing a network structure of gold nanoparticles with average diameter of 4 nm, being connected with molecular wires of oligothiophene 3*mer*, 9*mer*, or 15*mer*, and found that the network as a whole operates as a semiconductor with small activation energies of around 20 meV. Moreover, the contribution of electron tunneling becomes predominant at lower temperatures. The above results prompted us to make a network structure composed of gold nanoparticles and spin-polarized molecular wire. A unique point in this network is that a local spin resides on a π-conjugated molecular wire, whereas conduction electrons hop over or tunnel through gold nanoparticles in the network. We have prepared a pyrrole-based spin-polarized donor with two thienyl groups at α,α′-positions of the central pyrrole ring [8–11]. This wire is expected to interconnect the gold nanoparticle and also chemisorb to gold electrodes through thiol groups introduced at both terminals of the wire, operating as a spin-valve [12,13].

2. Results and discussion

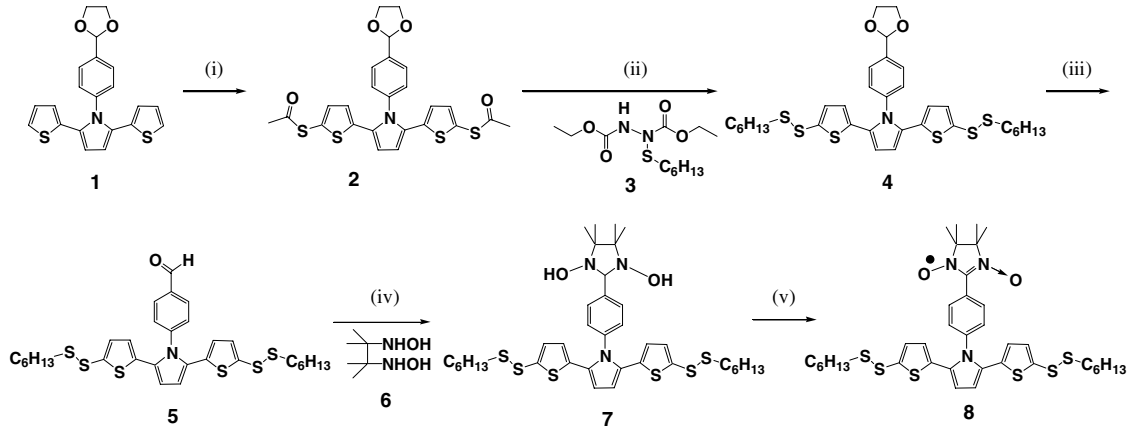
2.1. Preparation of spin-polarized molecular wire

We prepared a spin-polarized molecular wire made of pyrrole-based spin-polarized core, carrying oligothiophens as a molecular wire (**1**). Synthetic route of the spin-polarized molecular wire is shown here (Scheme 1). One problem here is that when the acetylthio group of the radical ligand is deprotected, the generated thiolate kills the radical. Since it is known that this radical disulfide derivative safely chemisorbs on the gold surface, the new precursor, which has hetero-disulfide units at both ends, was synthesized [14]. The designed novel precursor, having disulfide group at both ends, is expected to form a network structure by interconnecting gold nanoparticles. Synthesis of spin-polarized molecular wire (**8**), having disulfide groups at both ends, was performed according to this reaction scheme. This acetal derivative (**4**), which is a precursor of the radical ligand, can also be utilized as a reference compound which does not have an unpaired electron.

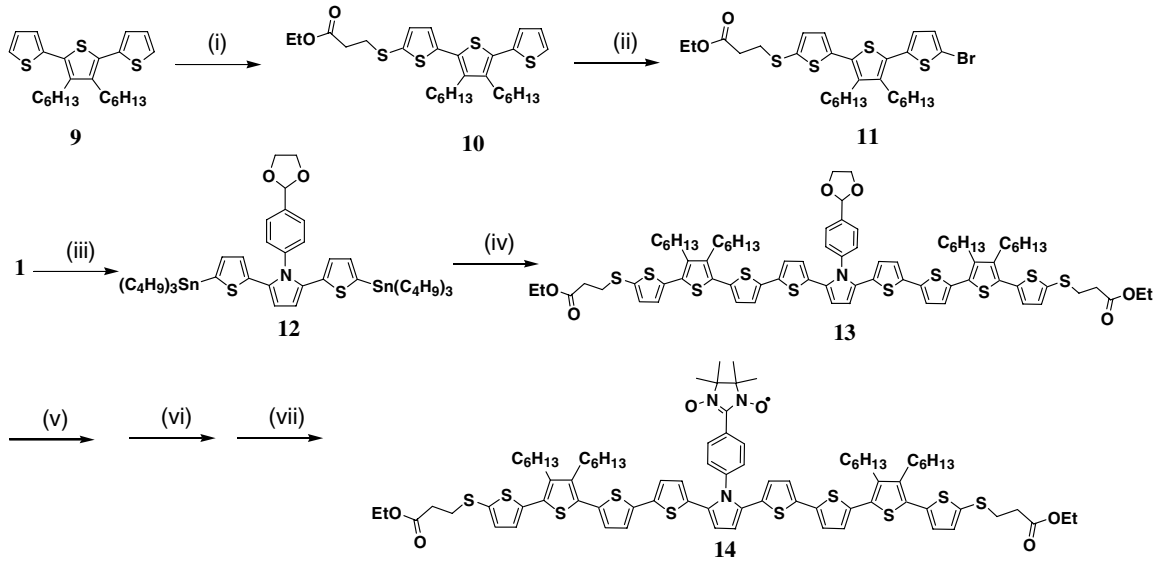
As an perspective along this line, a longer spin-polarized wire with a thiophene–pyrrole hybrid nanomer was also prepared. Preparative rout of an elongated spin-polarized wire made of the hybrid nonamer was shown in Scheme 2. Terthiophene derivative with long alkyl chains and a protected-thiol group was prepared and it was brominated at the α-position (**11**). Then, the brominated trimer was coupled with a hybrid trimer with stanylated thienyl groups (**12**) at both ends to afford a precursor of the spin-polarized molecular wire (**14**) [9,11].

2.2. Preparation of the network structure of gold nanoparticles connected with spin-polarized molecular wire

Preparation of the network structure of gold nanoparticles connected with spin-polarized molecular wire is practically the same as the oligothiophene network [15–17]. Namely, dip the interdigitated electrodes with a gap of 100 μm in a solution of the molecular wire (0.31 mM) for 30 min, and then add a solution of surfac-



Scheme 1. Synthetic scheme of the preparation of thiophene–pyrrole hybrid oligomer type spin-polarized wire with terminal site. Reagents and conditions; (i) (1) *n*-BuLi, THF, −78 to −50 °C, 1 h; (2) S, THF, −50 °C, 3 h; (3) AcCl, THF, −50 °C to r.t., 3 h, 60 %. (ii) (1) aq. NH_3, THF, r.t., 1 h; (2) *N*-hexanesulfenyldicarboxylate (**3**), THF, 53%; (iii) *p*-TsOH · H_2O, acetone, benzene, r.t. 6 h, quant. (iv) (**6**),(**6**) · H_2SO_4, MeOH, benzene, 8 h; (v) PbO_2, K_2CO_3, benzene, r.t., 30 min 80%.



Scheme 2. Synthetic scheme of the preparation of spin-polarized long wire. Reagents and conditions: (i) (1) LDA, THF, −78 to −50 °C, 1 h; (2) S, THF, −50 °C, 3 h; (3) $Br(CH_2)_2CO_2Et$, THF, −20 °C to r.t., 3 h, 40%. (ii) NBS, DMF, r.t., 12 h, 65%. (iii) (1) LDA, THF, −78 °C to −50 °C, 2 h; (2) *n*-Bu_3SnCl, THF, −78 °C to r.t., 3 h, 80%. (iv) (**11**), $Pd(PPh_3)_4$, toluene, 90 °C, 36 h, 40%. (v) *p*-TsOH · H_2O, $CHCl_3$, acetone, r.t. 6 h, quant. (vi) (**6**),(**6**) · H_2SO_4, MeOH, benzene, 8 h. (vii) PbO_2, K_2CO_3, benzene, r.t., 30 min 70%.

tant-stabilized gold nanoparticles (11.25 mM) and leave the mixture standing for 12 h. The resulted sample was washed with toluene and dried (Fig. 1). Since we use electrodes with a gap of 100 μm, it requires at least 1.8×10^4 nanoparticles to link the electrodes.

3. Characterization of network structure of gold nanoparticles connected with spin-polarized molecular wire

These are FE-SEM images of the networked structure of gold nanoparticles with the average diameter of 4 nm, connected by spin-carrying molecular wires on interdigitated electrodes with a gap of 100 μm (Fig. 2). As you see, the network structure covers over the electrodes. When an expanded image of the wire was examined it is to be noticed that the diameter of a granule is as large as 100 nm, which means that gold nanoparticle are assembled to form a cluster, and the clusters are interconnected to form a network.

In order to confirm this interpretation, a sample for the TEM measurement was prepared on a copper-grid (mesh) by drying a droplet out of a mixture of 1 ml of a toluene solution of the spin-polarized molecular wire (0.31 mM) and 1 ml of a toluene solution of TOAB-stabilized nanoparticles (11.25 mM). When the expanded image of the granule was examined it was found that it consisted of gold nanoparticles with the average diameter of 4 nm and that the gold nanoparticles in the granule were separated with each other by about 2 nm. The image is consistent with the network structure of gold nanoparticles connected by molecular wires with a length of 1.6 nm (see Fig. 3).

This a schematic picture to show how the network structure of gold nanoprticles are self-constructed in a hierarchical way. First, a gold atom obtained by the reduction of an aurate ion self-assembles to form a

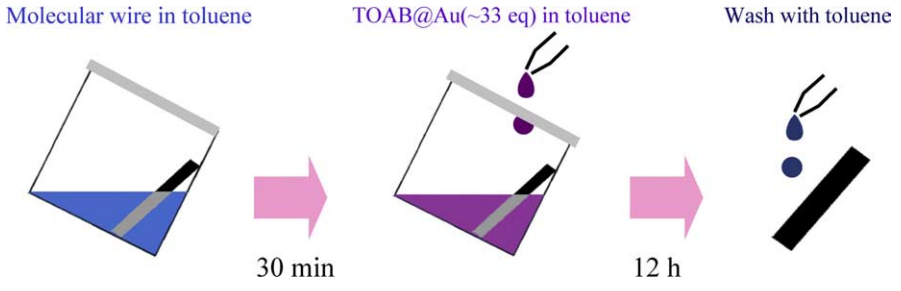


Fig. 1. Preparation of the network structure of gold nanoparticles connected with spin-polarized molecular wire.

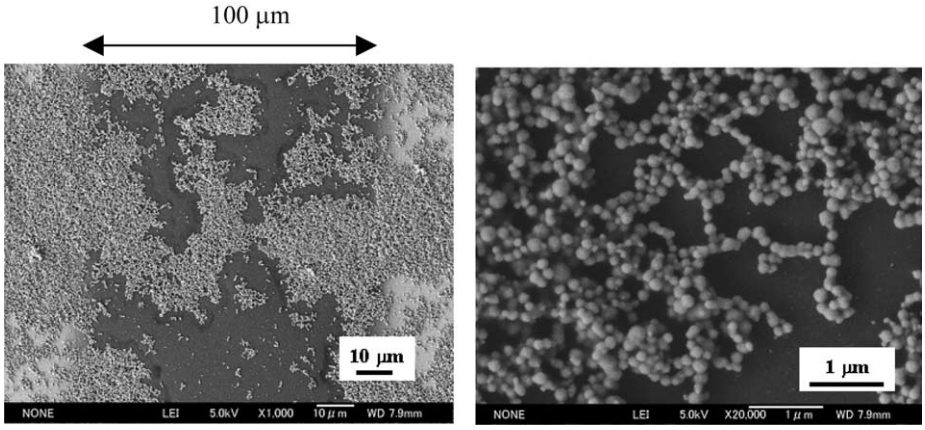


Fig. 2. FE-SEM image of networked gold nanoparticles with spin-polarized molecular wire. Right: a magnified view of network.

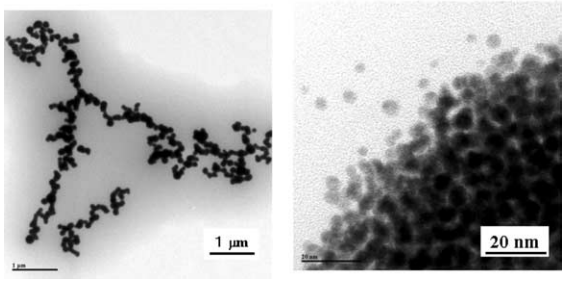


Fig. 3. TEM micrograph for a sample of networked structure cast on carbon-coated Cu-grid. Right: a magnified view of the indicated cluster.

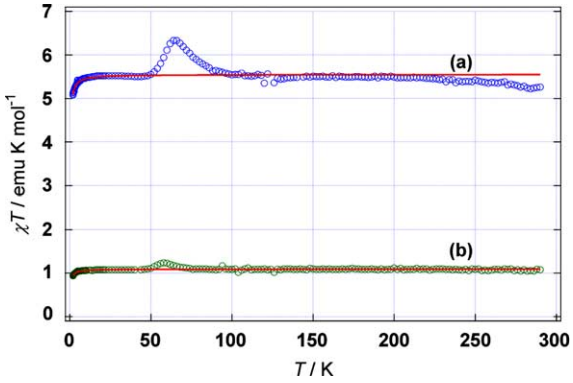


Fig. 4. Magnetic susceptibility of networked structure: (a) spin-polarized wires; (b) spinless wires.

nanoparticle with the average size of 4 nm; the nanoparticles is stabilized as this size by surfactants, such as tetraoctylammonium bromide. Then, nanoparticles are connected with molecular wires to form a cluster, the size of which is as large as 100 nm [18,19]. Finally clusters are further connected with molecular wires to end up with the network structure.

In order to confirm that gold nanoparticle were connected with "radical wires", temperature dependence of the magnetic susceptibility of the network was measured by means of a SQUID apparatus. These are the xT versus temperature plots of networks connected with spin-polarized wires and spinless wires (Fig. 4).

The horizontal plot indicates that radicals on the molecular wires behave paramagnetically, and the Curie constant evaluated from the intercept suggests that about 15 spins are on a nanoparticle in average. The result is consistent with the value estimated by the elemental analysis (C, 4.38%; H, 0.64%; N, 0.28%; ash, 91.3%. indicates that @Au1750:wire:*n*-hexanethiol:TOAB = 1:17:17:22). Since one wire is shared with two particles, at least 30 wires are coated on one nanoparticle. The plot below is derived from the network made of spinless wires. The Curie constant estimated from the plot suggests that one spin per nanoparticle exists in average. Since there are about 1750 gold atoms in one gold nanoparticle with the size of 4 nm, this paramagnetic spin is presumably due to the impurity spin locating at a defect inside of or more probably on the surface of the nanoparticle [20–22].

3.1. Conducting property of network of gold nanoparticles

Temperature dependence of the conductance of three types of the network structures was measured using interdigitated electrodes with a gap of 100 μm: the network connected with spinless molecular wires, spin-polarized molecular wires, and also alkanedithiol wires (σ-network) (see Fig. 5).

Wire	*E*a(H)	*E*a(L)
1,10-Decane-dithiol	21 meV	
Spinless molecular wire	10 meV 300–56 K	3 meV 18–9 K
Spin-polarized molecular wire	15 meV 300–70 K	5.2 meV 22–9 K

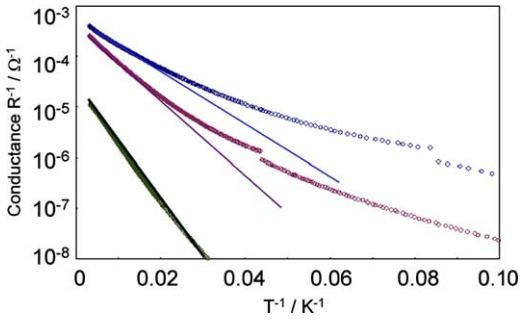


Fig. 5. Temperature dependence of conductance of three types of networked structure. From the top spinless molecular wire, spin-polarized molecular wire, and 1,10-decanedithiol wire.

There are three important characteristics. First, the conductance of these π-networks is much large than that of the σ-network. Second, while the plot for the σ-network shows a straight line, those of π-networks are deviated from the straight line at lower temperatures than 50 K. Third, the conductance of the network connected with the spinless wire is larger than that of the spin-polarized one. The activation energies of these networks are also listed here. The values are in accord with the observed tendency of the conductance of each network.

The non-linear temperature dependence of π-type networks may be interpreted in terms of the variable range hoping mechanism. Besides, the contribution of the electron tunneling through molecular wires to the whole transportation becomes more important at lower temperatures [15–17].

Fig. 6 is a schematic figure depicting the energy levels of frontier orbitals of σ-type wire, π-typle wire and those of the spin-polarized wire near the Fermi level of a gold particle. Among them, the electronic structure of the radical wire is spin-polarized. This means that frontier orbital should be SOMO (β) in the UHF description, provided that the singly occupying electron is α. Under such a circumstance, the tunneling current is expected to be spin polarized to β. Therefore, it is extremely interesting to measure the tunneling current, paying an attention to the effect of application of an external magnetic field.

3.2. Application of external magnetic field on the spin-polarized network

In order to examine the external magnetic field on the networked gold nanoparticle connected with spin-polarized wires, the conductance of the network was

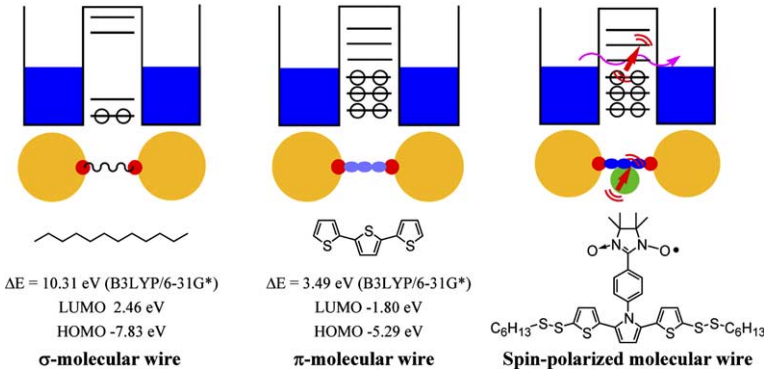


Fig. 6. Energy levels of frontier orbitals of σ-type wire, π-typle wire and the spin-polarized wire. Fermi level of gold is −5.1 eV.

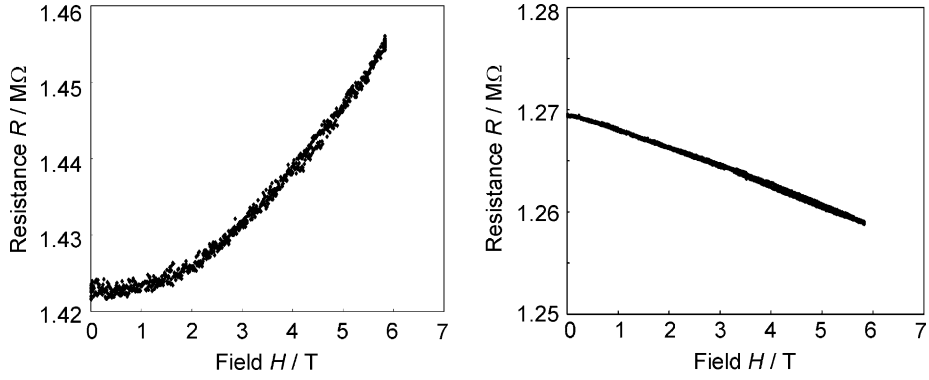


Fig. 7. Magneto resistance of networked gold nanoparticles with spinless molecular wire (left) and spin-polarized molecular wires (right) at 4.2 K.

measured using electrodes with a gap of 2 μm. The preparative method is practically the same as the previous one. It is estimated that 2 μm electrodes can be connected with at least about 360 nanoparticles.

The effect of an external magnetic field on the resistance of the network was examined by applying the field to the parallel direction in reference to the wires so that the Lorentz force does not operate. It was fond that the network made of spinless wires exhibited a small positive magneto resistance at 4 K under the external magnetic field in the range of 0–6 T. To the contrast, the magnetic field effect on the spin-polarized wires exhibited a negative magneto-resistance (Fig. 7). It means that the resistance of the wire decreases under the external magnetic field presumably because the fluctuation of the spins on the molecular wires is suppressed by the external magnetic field. Incidentally, the voltage to detect the conductance is 0.1 V. This voltage corresponds to the voltage to give a flat region in the *I–V* curve shown in the previous *I–V* plot.

4. Summary

Although the detail of the mechanism of electron transportation of the networked gold nanoparticles connected with molecular wires at cryogenic temperatures and of the magneto-resistance effect on the networks have not been fully understood yet, this is the first example that the negative magneto resistance was observed in an organic–inorganic nano-composite in which a local spin is located on the organic molecular wire. The network composed of such a small quantum dots connected with molecular wires in a three-dimensional manner should exhibit exotic non-linear conducting behaviors, including the Coulomb blockade, a memory effect caused by a recoding electric pulse, etc. and give rise to a fundamental results to molecule-based spinelectronic devices.

References

[1] Y. Ishikawa, T. Miyamoto, A. Yoshida, Y. Kawada, J. Nakazaki, A. Izuoka, T. Sugawara, Tetrahedron Lett. 40 (1999) 8819.
[2] John Fink, Christopher J. Kiely, Donald Bethell, David J. Schiffrin, Chem. Mater. 10 (1998) 922.
[3] M. Brust, M. Walker, D. Bethell, D.J. Schiffrin, R.J. Whyman, Chem. Soc. Chem. Commun. (1994) 801.
[4] K.-H. Su, Q.-H. Wei, X. Zhang, J.J. Mock, D.R. Smith, S. Schultz, Nano Lett. 3 (2003) 1087.
[5] P. Nordlander, C. Oubre, E. Prodan, K. Li, M.I. Stockman, Nano Lett. 4 (2004) 899.
[6] Jiwoong Park, Abhay N. Pasupathy, Jonas I. Goldsmith, Connie Chang, Yuval Yaish, Jason R. Petta, Marie Rinkoski, James P. Sethna, Héctor D. Abruña, Paul L. McEuen, Daniel C. Ralph, Nature 417 (2002) 725.
[7] Bernadette M. Quinn, Kyö sti Kontturi, J. Am. Chem. Soc. 126 (2004) 7168.
[8] H. Sakurai, A. Izuoka, T. Sugawara, J. Am. Chem. Soc. 122 (2000) 9723.
[9] J. Nakazaki, I. Chung, R. Watanabe, T. Ishitsuka, Y. Kawada, M.M. Matsushita, T. Sugawara, Internet Electron. J. Mol. Des. 2 (2003) 112.
[10] J. Nakazaki, M.M. Matsushita, A. Izuoka, T. Sugawara, Mol. Cryst. Liq. Cryst. 306 (1997) 81.
[11] J. Nakazaki, T. Sugawara, et al., J. Mater. Chem. 13 (2003) 1011.
[12] G.A. Prinz, Science 282 (1998) 1660.
[13] G. Harada, T. Sugawara, et al., Chem. Lett. (2002) 1030.
[14] T. Mukaiyama et al., TL 56 (1968) 5907.
[15] Francis P. Zamborini, Laura E. Smart, Michael C. Leopold, Royce W. Murray, Anal. Chim. Acta 496 (2003) 3.
[16] R.W. Murray et al., J. Am. Chem. Soc. 122 (2000) 11465.
[17] T. Ogawa, K. Kobayashi, G. Masuda, T. Takase, S. Maeda, Thin Solid Films 393 (2001) 374.
[18] Mathew M. Maye, Jin Luo, I-Im S. Lim, Li Han, Nancy N. Kariuki, Daniel Rabinovich, Tianbo Liu, Chuan-Jian Zhong, J. Am. Chem. Soc. 125 (2003) 9906.
[19] Mathew M. Maye, Sandra C. Chun, Li Han, Daniel Rabinovich, Chuan-Jian Zhong, J. Am. Chem. Soc. 124 (2002) 4958.
[20] T. Teranishi, H. Hori, M. Miyake, J. Chem. Phys. B 101 (1997) 5774.
[21] H. Hori et al., Phys. Lett. A 263 (1999) 406.
[22] W.H. Li et al., Phys. Rev. Lett. 89 (2002) 135504.

data on polycrystalline sample were collected in 2–300 K using a MagLab system 2000 magnetometer.

2.2. Syntheses of $[NO_2BzPy][Ni(dmit)_2]$ (1) and $[BrBzPy][Ni(dmit)_2]$ (2)

1 and **2** were prepared according to the procedure described in [7], elemental *Anal.* Calc. for $C_{18}H_{11}N_2NiO_2S_{10}$: C, 32.4; H, 1.66; N, 4.20. Found: C, 31.9; H, 1.70; N, 4.18% for **1**, and *Anal.* Calc. for $C_{18}H_{11}BrNNiS_{10}$: C, 30.9; H, 1.58; N, 2.00. Found: C, 30.7; H, 1.68; N, 1.96% for **2**.

The single crystals suitable for X-ray analysis were obtained by dispersing Et_2O into MeCN solution of **1** for one week.

2.3. X-ray crystallography

Diffraction data of **1** was collected at 293 K on a CAD4 with Mo Kα radiation. The structure of **1** was solved by direct method and refined on F^2 by full-matrix least-squares method using the SHELXTL program package [8]. All non-hydrogen atoms were refined anisotropically. Hydrogen atoms were placed in their calculated positions and refined following the riding model. Crystal data for **1**: $C_{18}H_{11}N_2NiO_2S_{10}$, $M = 666.60$, triclinic, space group $P\bar{1}$, $a = 9.3500(19)$ Å, $b = 11.780(2)$ Å, $c = 11.860(2)$ Å, $\alpha = 80.16(3)°$, $\beta = 89.52(3)°$, $\gamma = 76.04(3)°$, $V = 1248.3(4)$ Å^3, $Z = 2$, $D_{calc} = 1.773$ g cm^{-3}, $\mu = 1.635$ mm^{-1}, final R, $R_w = 0.0450$, 0.1034. 3601 observed

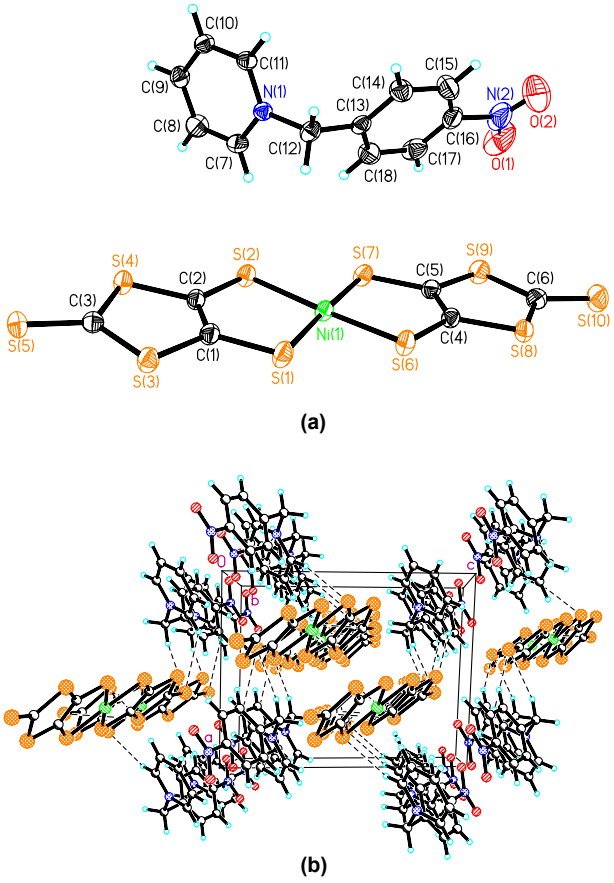


Fig. 1. (a) ORTEP drawing of **1** with 30% possibility ellipsoids and (b) the packing structure projected along *c*-axis.

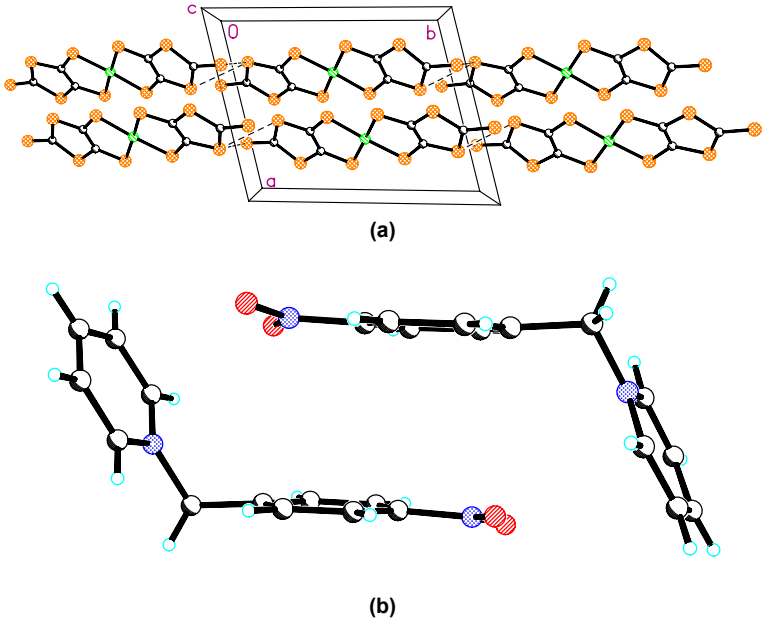


Fig. 2. (a) Spin ladder (the direction of ladder leg is parallel to *b*-axis) (b) dimer of cation in **1**.

reflections [$I > 2\sigma(I)$] out of 4370 unique (R_{int} = 0.0154), GOF = 0.984.

3. Results and discussion

3.1. Descriptions of crystal structures

3.1.1. $[NO_2BzPy][Ni(dmit)_2]$ (1)

The ORTEP view of **1** in an asymmetric unit and the packing structure projected along *c*-axis are shown in Fig. 1(a) and (b). The bond lengths and angles in $[Ni(dmit)_2]^-$ anionic moiety are in good agreement with the reported compounds [1d]. The bond lengths in $[NO_2BzPy]^+$ moiety are close to the values in $[NO_2BzPy][Ni(mnt)_2]$ [4], and the dihedral angles between aromatic rings and the reference plane, C(13)/C(12)/N(1), are 67.0° for benzene ring, 88.2° for pyridine ring, respectively.

Two neighboring anions, which molecular planes are approximately perpendicular to *a*-axis, stack plane-to-plane with each other to form a dimer, the inter-planar distance (the anionic molecular plane is defined by coordination S atoms) is 3.72 Å, the nearest S···S contacts are 3.69 Å between S(3) and S(10)^i, 3.74 Å between S(2) and S(8)^i (symmetry code: i = 1 − *x*, 1 − *y*, 1 − *z*).

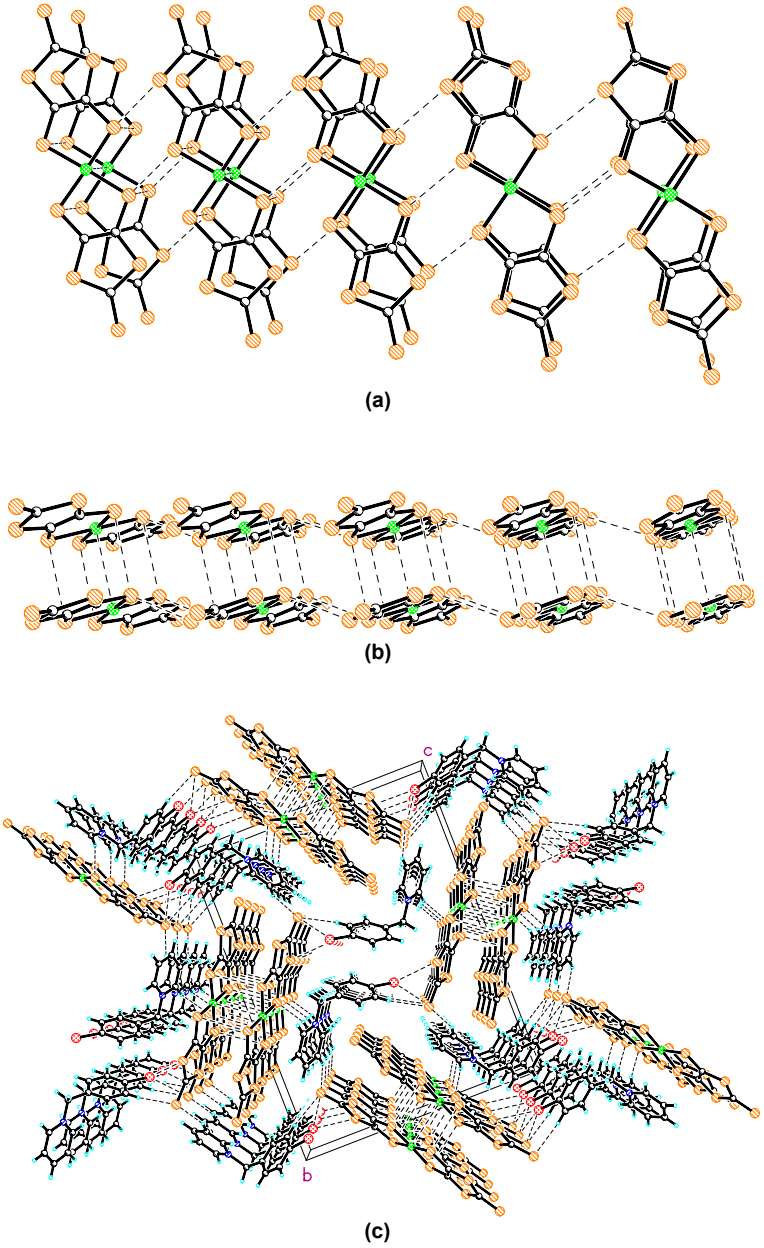


Fig. 3. (a) and (b) Spin ladder of $[Ni(dmit)_2]^-$ anions viewed along different directions (c) molecular packing diagram projected along *a*-axis in **2**.

This dimer develops further into two-leg ladder via terminal S···S interactions along *b*-axis [the shorter S···S separations are S(10)···S(4)^{j} = 3.52 Å, S(8)···S(4)^{j} = 3.38 Å, S(8)···S(5)^{j} = 3.69 Å (symmetry code: j = x, 1 + y, z)] (cf. Fig. 2(a)). Two neighboring $[NO_2BzPy]^+$ cations dimerize in a fashion of a chair-like conformation as illustration in Fig. 2(b). These distances of center-to-center between two benzene rings is 4.50 Å and the inter-planar separation is 3.59 Å, they are so larger that there is no any significant π···π stacking interaction between them. The anionic two-leg ladder is embraced by cationic dimers (Fig. 1(b)) with a van de Waals interactions.

3.1.2. [BrBzPy][Ni(dmit)$_2$] (2) [7]

Compound **2** crystallizes in *P*2(1)/*c* space group, an asymmetric unit contains a couple of anion and cation. The bond parameters in anion moiety are very similar to that in **1**, and those in $[BrBzPy]^+$ moiety are closed to the values in [BrBzPy][Ni(mnt)$_2$] [4]. Compared with **1**, the molecular geometry of $[BrBzPy]^+$ exhibits distinct difference from $[NO_2BzPy]^+$. The dihedral angles between aromatic rings and the reference plane, C(13)/C(12)/N(1), are 106.3° for benzene ring, 160.5° for pyridine ring, which are departures far from 90°. Two adjacent anions are eclipsed to overlap as a dimer as in **1**, whereas the correspondence inter-atomic separations and inter-planar distance are much less than that in **1** [Ni(1)···Ni(1)^{i} of 3.51 Å, S(1)···S(10)^{i} of 3.57 Å, S(5)···S(6)^{i} of 3.49 Å (symmetry code: i = $-x$, 1 − y, $-z$) and the inter-plane distance of 3.49 Å]. The lateral S···S interactions between neighboring anionic dimers lead them to form a two-leg ladder (Fig. 3(a)). Two-leg ladders are held together by intermediate cations via non-normal C–H···S H-bonding interactions to construct into 3D network (Fig. 3(b)) [7].

3.2. Magnetic properties

The temperature dependences of magnetic susceptibility for **1** and **2** are shown in Figs. 4 and 5. With respect to **1**, χ_m increases slowly as temperature goes down, and drops sharply below ~110 K to reveal a magnetic transition, the transition temperature is determined as 100.3 K in plot of $d(\chi_m T)/dT$ versus T (inset of Fig. 4). Above 110 K, AFM exchange interaction between neighboring spins dominates. Below 110 K, χ_m drops exponentially as temperature decreases to illustrate there is a spin energy gap in low-temperature phase. A paramagnetic Curie tail in low temperature region is attributed to the magnetic impurities of uncoupled spins. Based on crystal structural analysis, we try to fit magnetic susceptibility data in high-temperature phase by the exchange model, an isolated spin dimer of $s = 1/2$ or a spin ladder in high temperature limit, but all efforts fail.

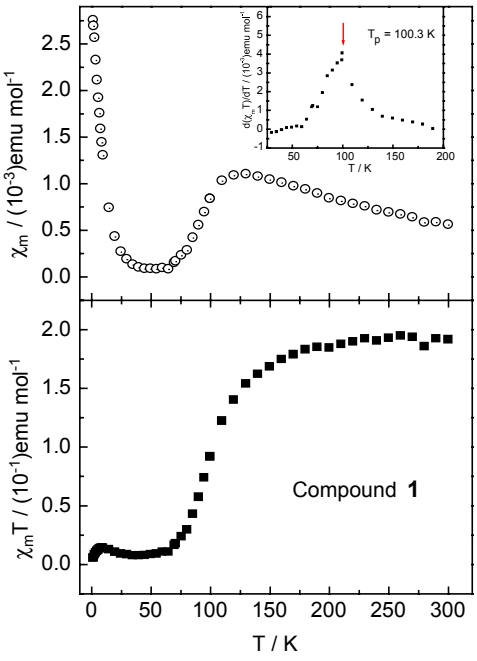


Fig. 4. Plots of $\chi_m - T$ and $\chi_m T - T$ of **1** ($T_{sp} \approx 100.3$ K).

The magnetic susceptibility of **2** increases as temperature deceases, and reaches a maximum with $\chi_m = 6.73 \times 10^{-3}$ emu mol^{-1} at 16.5 K, and then abruptly drops to indicate the character of antiferromagnetic

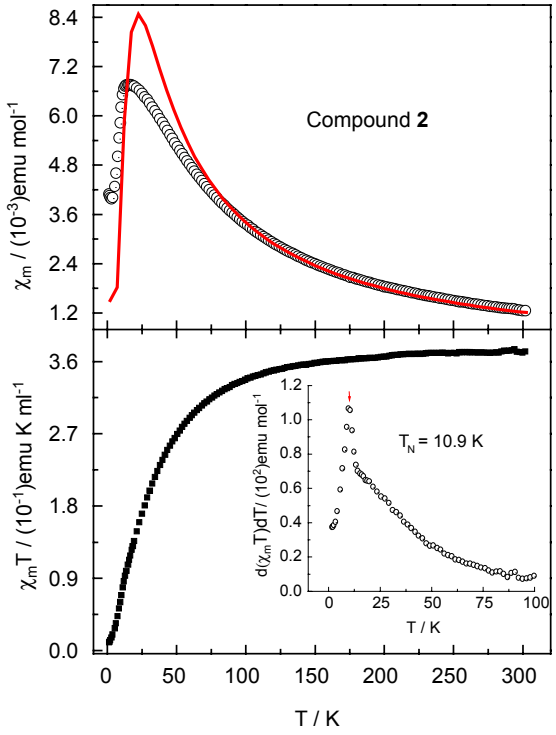


Fig. 5. $\chi_m - T$ and $\chi_m T - T$ of **2** as a function of T ($T_N \approx 10.9$ K), open circle (χ_m): experiment data; solid line (χ_m): theoretically reproduced with the fit parameters.

ordering. Theoretically, the long-range magnetic ordering cannot occur in a 1D magnetic system, as for **2**, the weak H-bonding interactions to connect spin ladders and cations into 3D network were observed, which provide the possible magnetic exchange paths between spin ladders to lead to long-range magnetic ordering [5b,9]. The χ_m value of 4.07×10^{-3} emu mol^{-1} at 2 K is somewhat less than 2/3 the value at the temperature at which it is a maximum. T_N is estimated as 10.9 K corresponding to the peak temperature in plot of $d(\chi_m T)/dT - T$ (inset of Fig. 4). From the viewpoint of structure, the magnetic coupled interaction is much larger within a dimer than between dimers, the formula of χ_m, thereby, in paramagnetic phase can be expressed below:

$$\chi_m = \frac{\chi_{dimer}}{[1 - (zJ'/Ng_2\beta^2)\chi_{dimer}]} + \frac{C}{T} + \chi_0 \quad (1)$$

and

$$\chi_{dimer} = \frac{Ng^2\mu_B^2}{k_B T} \cdot (3 + \exp(\Delta/k_B T))^{-1} \quad (2)$$

in Eq. (1), the first term is a contribution from a dimer of $s = 1/2$ based on spin Hamiltonian $H = -2J\hat{S}_1 \cdot \hat{S}_2$, in which Δ (=2|J|) is the energy gap between singlet and triplet spin state, and the coupled interaction between neighboring dimers is further treated using molecular field theory [10]. C/T and χ_0 show the contribution from the magnetic impurity and the sum of diamagnetic and possible van Vleck paramagnetic parts, respectively. The best fit magnetic susceptibility above 45 K to Eq. (1) gives rise to $\Delta/k_B = 36.1$ K, $zJ = -0.91$ K, $C = 3.2 \times 10^{-3}$ emu K mol^{-1} and $\chi_0 = -4.0 \times 10^{-6}$ emu mol^{-1} with g of 2.0 fixed.

4. Conclusion and remarks

Summarily, we have represented the crystal structural and magnetic susceptibility characterization for two compounds consisting of $[Ni(dmit)_2]^-$ and benzylpyridinium derivative. The anions in two compounds stack into dimers, and these dimers further construct into two-leg ladders via terminal S···S interactions in **1**, and by lateral S···S interactions in **2**. The two-leg ladders are held together by cations through weak H-bonding interactions of C–H···S in **2**, while only weak van de Waals interactions are present in **1**. The $\chi_m(T)$ in 2–300 K indicated that AFM exchange interactions dominate both **1** and **2**. A spin-Peierls-like transition occurs in **1** at ~ 100 K. An AFM ordering below ~ 11 K was found in **2**, and its magnetic behavior in paramagnetic phase can be demonstrated as a spin dimer of $s = 1/2$. In order to clarify the nature of the peculiar magnetic transition in **1** and AFM ordering in **2**, further structural determination in low-temperature phase and DSC/C_p measurements around the transition temperature for **1**, and AC magnetic susceptibility measurement for **2** are in progress.

Acknowledgement

This project was financially supported from the National Natural Science Foundation of China (Grant Nos. 20171001 and 20371002).

Appendix A. Supplementary data

Crystallographic data (excluding structure factors) for the structures reported in this paper have been deposited with the Cambridge Crystallographic Data Center as supplementary publications (CCDC-250087 of **1**). Copies of the data can be obtained free of charge on application to CCDC, 12 Union Road, Cambridge CB21EZ, UK (fax: +44 1223 336 033; e-mail: deposit@ccdc.cam.ac.uk) or on the web http://www.ccdc.cam.ac.uk). Supplementary data associated with this article can be found, in the online version at doi:10.1016/j.poly.2005.03.082.

References

[1] (a) J.L. Xie, X.M. Ren, Y. Song, W.W. Zhang, W.L. Liu, C. He, Q.J. Meng, Chem. Commun. 2346 (2002);
(b) A.T. Coomber, D. Beljonne, R.H. Friend, J.L. Brédas, A. Charlton, N. Robertson, A.E. Underhill, M. Kurmoo, P. Day, Nature 380 (1996) 144;
(c) I.D. Parker, R.H. Friend, P.I. Clemenson, A.E. Underhill, Nature 324 (1986) 547;
(d) T. Autagawa, T. Hasegawa, T. Nakamura, T. Inabe, J. Am. Chem. Soc. 124 (2002) 8903.
[2] X.M. Ren, C.S. Lu, Y.J. Liu, H.Z. Zhu, H.F. Li, C.J. Hu, Q.J. Meng, Trans. Met. Chem. 26 (2001) 136.
[3] X.M. Ren, H. Okudera, R.K. Kremer, Y. Song, H. Cheng, Q.J. Meng, P.H. Wu, Inorg. Chem. 43 (2004) 2569.
[4] X.M. Ren, Q.M. Meng, Y. Song, C.S. Lu, C.J. Hu, Inorg. Chem. 41 (2002) 5686.
[5] (a) J.L. Xie, X.M. Ren, C. He, Z.M. Gao, Y. Song, Q.J. Meng, R.K. Kremer, Chem. Phys. Lett. 369 (2003) 41;
(b) J.L. Xie, X.M. Ren, Y. Song, Y. Zou, Q.J. Meng, J. Chem. Soc., Dalton Trans. 2868 (2002);
(c) J.L. Xie, X.M. Ren, S. Gao, W.W. Zhang, Y.Z. Li, C.S. Lu, C.L. Ni, W.L. Liu, Q.J. Meng, Y.G. Yao, Eur. J. Inorg. Chem. 2393 (2003).
[6] X.M. Ren, H. Okudera, J.L. Xie, Q.J. Meng, J. Mol. Struct. 733 (2005) 119.
[7] W.J. Tong, L. Liu, Q.J. Meng, Y.Z. Li, Acta Cryst. E 58 (2002) m724.
[8] G.M. Sheldrick, SHELXTL, Structure Determination Software programs, Version 5.10. Bruker Analytical X-ray Systems Inc., Madison, WI, USA, 1997.
[9] X.M. Ren, Y.C. Chen, C. He, S. Gao, J. C. S. Dalton Trans. 3915 (2002).
[10] C.J. O'Connor, Prog. Inorg. Chem. 29 (1982) 203.

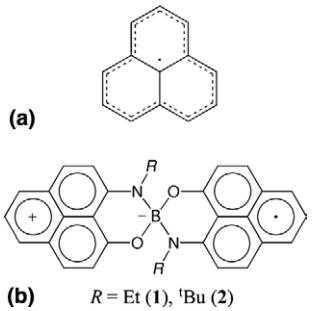


Fig. 1. Molecular structures of phenalenyl (a) and spiro-biphenalenyls (b).

over phenomena in the solids of these spiro-biphenalenyl. Our group have already reported papers for the electronic structures of phenalenyl dimeric pair [7,8]. In the present work, then, the electronic structures of dimeric pairs of **1** are studied in terms of quantum chemistry to examine the mechanism of the change in its magnetism. The structures of the dimeric pairs are derived from the X-ray crystallographic analysis of **1** at each temperature. The dimeric pairs are separated into two groups: π-dimers and not-π-dimers groups. First, the effective exchange integral of the Heisenberg model is calculated by the UHDFT (spin-polarized Kohn–Sham hybrid-density-functional theory) method for the π-dimers and not-π-dimers of **1**. This will show the variation of magnetic interactions within the dimeric pairs when temperature increases. Next, in order to understand electronic structures of the dimeric pairs, the natural orbital (NO) analysis is carried out based on the results of the UHDFT calculations. Investigation of the electronic structure of these radicals in terms of ab initio MO is of important in designing novel organic functional compounds.

2. Computations

2.1. Models

Spiro-biphenalenyl that is an organic neutral radical contain two phenalenyls binding with the spiro junction, the centre of which is a boron atom. The π-electrons on the two phenalenyls can conjugate through the spiro junction. It is said that spiro-biphenalenyls might not be just neutral but zwitter-ion type neutral radicals. In the crystal, spiro-biphenalenyls form π-dimers that consist of their enantiomers. It is interesting that all the nearest contacts of these π-dimers are almost equal or slightly larger than van der Waals radius of carbon.

The structures of π-dimers of **1** at 20, 100, 173 and 298 K have been based on its X-ray crystallographic data from Cambridge Structural Data-base (CSD) [9]. Those are denoted by **20π**, **100π**, **173π** and **298π** in turn (see Fig. 2). The π-orbitals on the phenalenyl moieties in the π-dimers overlap at most of the atoms where major robes place. The intermolecular magnetic interaction then should be antiferromagnetic. The intermolecular distance varies from 3.16 to 3.35 Å with the increase of temperature. Effect of temperature to electronic states was studied by using structures at each temperature, because quantum chemical calculations cannot treat temperature explicitly. The structures of the dimeric pairs (not-π-dimers) of **1** at 100 and 173 K, shown in Fig. 2, were also derived from CSD. They are labeled by **100-1**, **100-2**, **173-1** and **173-2**. These dimeric pairs consist of a molecule nearest to a π-dimer and one half of the π-dimer. The intermolecular magnetic interactions are predicted to be none or weak ferromagnetic since most of the π-orbitals are perpendicular one another.

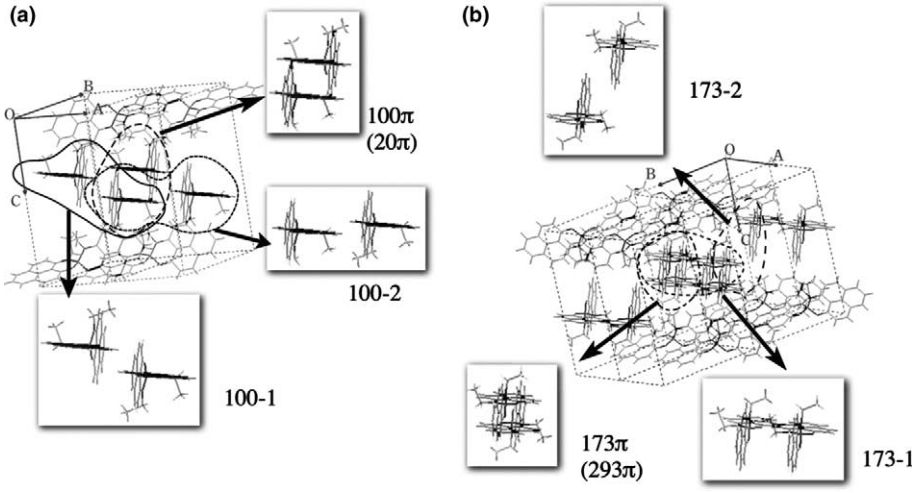


Fig. 2. Structures of π-dimers and not-π-dimers of **1**: (a) LT and (b) HT.

2.2. Methods

The Kohn–Sham hybrid-DFT [10] has been employed to elucidate electronic structures of **1**. It is obvious that this system has the spin-polarization since these dimeric pairs have the closest contacts longer than van der Waals radii of carbon atom at each temperature. In this case, the unrestricted wave functions can descript the electronic correlation better than the restricted ones do. Therefore, the UHDFT can investigate electronic structures of these dimeric pairs. Becke's three-parameter exchange [11] and Lee, Yang, Parr's correlation functionals [12] have been chosen for these compounds, since they are expected to produce feasible solutions judging from the results of our former studies [13]. Actually, UB3LYP/6-31G* has been employed.

3. Theoretical background

3.1. Effective exchange integral and AP

As widely known, the Heisenberg model is sufficient in understanding magnetic interaction between spins. The spin-Hamiltonian is defined as

$$H = \sum_{\langle ij \rangle} -2J_{ij}\mathbf{s}_i \cdot \mathbf{s}_j, \tag{1}$$

where $\mathbf{s}_i$ is a spin at ith radical site and $\langle ij \rangle$ means the summation is taken over the pairs of radical sites in the whole of system. A radical site is regarded as a source of spin-1/2 in this paper. The coefficent J_{ij} is the effective exchange integral between the radical sites i and j. The physical meaning is the energy difference between the singlet spin-state and the triplet spin-state. Negative J_{ij} means the antiferromagnetic interaction is dominant in the ground state, while positive J_{ij} the ferromagnetic interaction dominates the ground state. In most of molecular systems, the spin reduces to its z-component only. The transfer integral of the Hubbard model, denoted by t_{ij}, is related to J_{ij} for the Mott–Hubbard insulators as $J = -2t^2/U$, where $t_{ij} = t_{ji} = t$, $J_{ij} = J_{ji} = J$ and U (>0) is the on-site Coulomb repulsive potential. The U can be regarded as a kind of the difference between ionization potential and electron affinity. If J is large and negative, then t is also large, which means the electrons are delocalized between the pair rather than onto each molecule.

We face to the broken-symmetry (BS) problem in calculating by the unrestricted approach such as UHDFT, namely, eigenvalues of S^2 are not equal to the exact ones of the spin-states. The effective exchange integrals, however, have been evaluated approximately by a spin-projection called AP [14]. For two spin-sites,

$$J^{\mathrm{AP}} = -\frac{E^3 - E^{1(\mathrm{BS})}}{\langle S^2 \rangle^3 - \langle S^2 \rangle^{1(\mathrm{BS})}}, \tag{2}$$

where E is the total energy, $\langle S^2 \rangle$ represents eigenvalues of S^2 and the superscripts indicate spin multiplicities. Eq. (2) holds at any distance between the two spin sites.

3.2. Natural orbital analysis

Even though the unrestricted method describes the electron correlation better than the restricted one, the resultant orbitals are often different from familiar MOs, called the symmetry-adapted (SA) MOs. In order to obtain the SA MO picture from the BS solutions, the NO analysis has been carried out. The NOs are defined to diagonalize the spin-traced (or charge) density matrix [15,16] as

$$\rho(\mathbf{r}, \mathbf{r}') = \sum_i n_i \eta_i(\mathbf{r}) \eta_i(\mathbf{r}'), \tag{3}$$

where n_i (in [0,2]) denotes the occupation number of the i^{th} NO, η_i, which is an SA MO called UNO. The BS magnetic orbitals for up- and down spins (denoted by + and −, respectively) are expressed by

$$\chi^{\pm}(\mathbf{x}) = \cos\theta\eta_{\mathrm{b}}(\mathbf{r}) \pm \sin\theta\eta_{\mathrm{a}}(\mathbf{r}), \tag{4}$$

where η_{b} and η_{a} represent bonding and anti-bonding UNOs, respectively. The orbital overlap integral between the magnetic orbitals, denoted by $S^{\mathrm{mg}} = \langle \chi^+ | \chi^- \rangle$, rewrites the occupation numbers of bonding and anti-bonding UNO as

$$n_{\mathrm{b}} = 1 + S^{\mathrm{mg}} \quad \text{and} \quad n_{\mathrm{a}} = 1 - S^{\mathrm{mg}}. \tag{5}$$

Then the effective bond order is derived by

$$b^{\mathrm{eff}} = \frac{n_{\mathrm{b}} - n_{\mathrm{a}}}{2} (= S^{\mathrm{mg}}). \tag{6}$$

These indices are efficient to investigate natures of chemical bonding in terms of quantum chemistry.

4. Results and discussion

4.1. *J*s of π-dimers

As summarized in Table 1, the effective exchange integrals of **20π** and **100π** have been −447 and −444 cm^{-1} for LT, while **173π** and **293π** −133 and −126 cm^{-1} for HT, respectively. This means that the intermolecular antiferromagnetic interaction reduces to be about 30% in the amplitude by the transition when temperature increases. The magnetic interaction was evaluated to be antiferromagnetic at these ranges of temperature, although the experiment showed paramagnetism for **1** at HT. This result seems inconsistent with each other, whereas it can be understood as follows. The Average of the singlet-triplet energy gap ($-2J$) was about 890 cm^{-1} at LT, which is much larger than the energy of temperature 20 and 100 K (equal to 14 and 70 cm^{-1}, respectively). At HT, however, $-2J$ was

Table 1
Physical parameters and occupation numbers calculated for π-dimers

Model	D (Å)	J (cm^{-1})	ΔE^{h-l} (eV)	n_b	n_a	b^{eff}
20π	3.16	−477.3	0.741	1.623	0.376	0.623
100π	3.18	−443.8	0.740	1.606	0.394	0.606
173π	3.31	−133.5	0.771	1.352	0.648	0.352
293π	3.35	−126.3	0.774	1.342	0.658	0.342

calculated to be 260 cm^{-1}, which becomes closer to temperature 173 and 293 K (120 and 204 cm^{-1}, respectively). Hence, it is concluded that temperature-dependent paramagnetism may be a factor in the mechanism of the magnetism change within π-dimers.

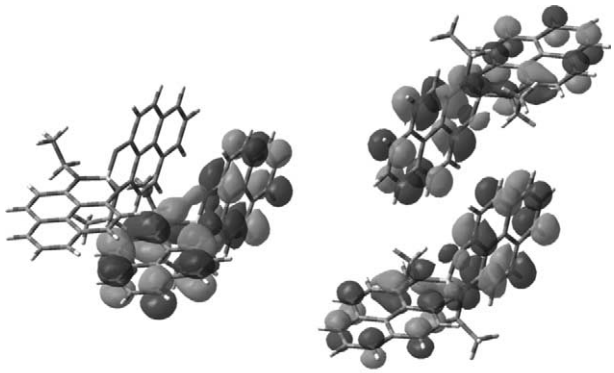
The HOMO–LUMO gap ΔE^{h-l} has been evaluated to be about 0.74 eV for LT structures while 0.77 eV for HT, which grown approximately by 0.03 eV after the transition than before. This implies that the π-dimer becomes less conductive when temperature increases, which reproduces the experimental results. The difference in ΔE^{h-l} for LT and HT will increase when a larger number of molecules are considered in the calculation.

4.2. Js of not-π-dimers

Table 2 lists J-values for the not-π-dimers of **1** at 100 and 173 K. The magnetic interactions of them have been almost none for the structure at 100 K, which suggests that no interaction exist between the radical pair. Those for 173 K, however, have been very weak ferromagnetic for **173-2** and **173-1** has had rather strong ferromagnetic interaction of $J = 130$ cm^{-1}. This difference in J is due to spatial arrangement of the molecules of the not-π-dimers. As shown in Fig. 3, the phenalenyl parts of each molecule are separate from each other for all not-π-dimers except for **173-1**. The spin-density on each molecule has no relation to one another. On the contrary, the phenalenyl parts of each molecule orientate perpendicularly for **173-1**. The orbital-overlap effect vanishes and only the exchange potential effect remains at the structure, which leads strong ferromagnetic interaction [17]. This indicates where that the magnetic interactions cancel out as a whole and **1** becomes paramagnetic, considering that J of **173-1** is close to that of **173π**.

Table 2
Effective exchange integrals for not-π-dimers

Model	J (cm^{-1})
100-1	0.2
100-2	0.2
173-1	130.1
173-2	5.8



173-1 **173-2**

Fig. 3. Molecular orbitals for not-π-dimers of **1**.

4.3. Electron transfer in *1*

The ground state of **1** can be approximately formulated by the linear combination of two zwitter-ionic states as

$$\Psi_0 = c_R\psi_R + c_L\psi_L, \quad (7)$$
$$\Psi_0 : \{\mathrm{PhnlBPhnl}\}^{\bullet}, \quad \psi_R : \mathrm{Phnl}^{+}\mathrm{B}^{-}\mathrm{Phnl}^{\bullet},$$
$$\psi_L : \mathrm{Phnl}^{\bullet}\mathrm{B}^{-}\mathrm{Phnl}^{+}$$

where Phnl and B denote the phenalenyl part and the spiro junction, respectively. If $c_R = c_L$, then the unpaired electron transfer through the molecule without barriers. In this case, c_R is either larger or smaller than c_L because of the molecular geometry, which makes the intramolecular electron transfer harder. Though it is impossible to determine directly the difference between c_R and c_L, the difference may be estimated from ΔE_{loc}, the energy gap between E_0 and E_R (or E_L), where E_0 and E_R (or E_L) are the total energies of Ψ_0 and $\Psi_R \sim \psi_R$ (or $\Psi_L \sim \psi_L$), respectively. The UB3LYP/6-31G* calculated ΔE_{loc} to be 0.196 eV for 100 K and 0.278 eV for 173 K, indicating that the intramolecular electron transfer becomes unlikely to occur with the increase of temperature.

From the examination of the structures of **1** at each temperature, it is found that major geometrical change in the molecule has occurred at the spiro junction. Length of the bond connecting a phenalenyl group has been shorter at LT than at HT in the half side of the spiro junction. It seems that electronic states of one phenalenyl part in the molecule became more stable than

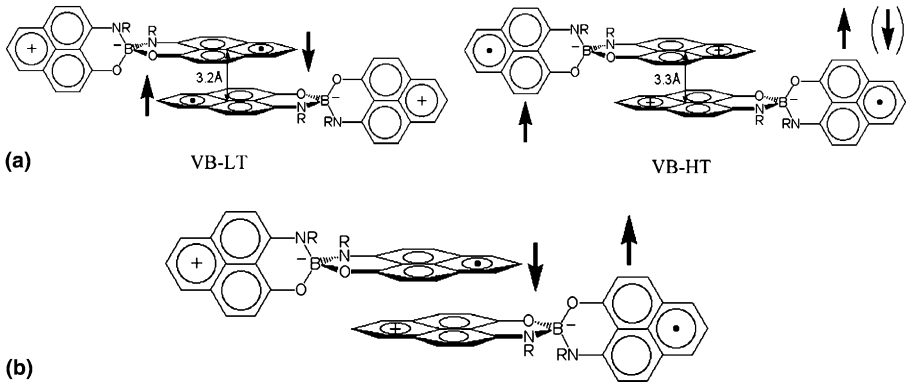


Fig. 4. Haddon's illustration in the valence bond (VB) picture (The down arrow in the round brackets was added by the authors): the VB mechanism and (b) A proposed VB structure for intermediate temperature in this work.

the other because of the geometrical variation. The difference of stability in the electronic state controls intermolecular electron transfer.

A remarkable study has already been reported by Kertesz and the co-workers for the change in conductivity of spiro-biphenalenyls [18]. They performed ab initio band structure calculation with plain-waves for them to reveals the conduction mechanism. In the MO view of us, the intramolecular electronic transfer may arise from the change in length of the spiro junction as described above. From our result it is found that intermolecular electronic transfer can take place for the π-dimers, considering that their effective exchange integrals at LT were rather negatively large. On the other hand, effective exchange integrals at LT for not-π-dimers were almost none, which indicates electrons hardly migrate over these molecular pairs. It is concluded that electrons can transfer through the π-dimer columns in **1** and **2**, although the determination of their conduction paths involves further investigations.

4.4. Electronic structures analyzed by natural orbitals

Haddon and his collaborators have proposed a mechanism for the bistability of spiro-biphenalenyls as shown in Fig. 4 (a). At LT limit, the unpaired electrons lie on the phenalenyl parts closely facing each other at a distance of about 3.2 Å, making a spin pair. This is a diamagnetic π-dimer that has strong antiferromagnetic interaction. At HT limit, the intermolecular distance increases and becomes near 3.3 Å. The unpaired electrons then reside in the outer phenalenyl units, interacting more weakly, which is a paramagnetic π-dimer. This mechanism is called the valence bond (VB) mechanism here.

Shown in Fig. 5 are relevant UNOs for **100π** and **173π**. Compared with the VB-LT, robes of UNO for **100π** are delocalized over the dimers. This can be interpreted as follows. In the VB-LT, the dots on the inter-phenalenyl parts represent a bond between the molecules, while in terms of UNO the bonding is

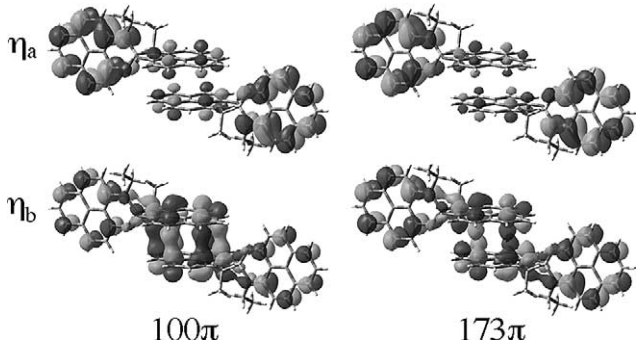


Fig. 5. Bonding and anti-bonding natural orbitals for π-dimers of **1** at 100 (left) and at 173 K (right). Contour value: 0.020.

expressed by connecting robes between the inter-phenaleyl parts. Indeed, the bond is not full since electron correlation mixes an anti-binding electron configuration into that of bonding. As seen in the rightmost column of Table 1, the effective bond orders for these π-dimers have been 0.7 and 0.6 at LT, though those for a full bond have been exact unity. Considering UNOs for **173π**, it is found that the VB-HT suggests the bond almost vanishing at HT. Their effective bond orders are about 0.3 at HT, which means the bond is weakened. It seems that the VB mechanism shows, in a word, binding molecules at LT and separate radicals at HT. If this variation in the bond is represented only by dots, the dots should be placed on the outer-phenalenyl parts. Above results show that both our MO picture and the VB mechanism describe the same fact essentially. The VB structure in Fig. 5-2 is proposed to express the electronic structure of spiro-biphanalenyls at intermediate temperature rather than the VB-HT.

5. Conclusion

Electronic structure and physical parameters have been evaluated for diethyl-substituted spiro-biphanenyl,

a multifunctional organic neutral radical, in order to inquire into a mechanism of the change in their magnetism and conduction. Intermolecular magnetic interaction was examined in terms of the effective exchange integral of the Heisenberg model for dimeric pairs of diethyl-substituted spiro-biphenalenyl. Variation of the magnetic interaction with respect to temperature have been evaluated based on their x-ray crystallographic structures at several temperature points in quantum chemical ways. The results have reproduced the experiments of spiro-biphenalenyl and given us some interesting information of their electronic structures. The intermolecular effective exchange integrals have been negative but reduced to be thirty percent in the magnitude between 100 and 173 K for the π-dimers. They have been almost none from 100 to 173 K except for one pair and the remaining pair had ferromagnetic interaction. Hence, it is concluded that the change in their magnetism is understood by temperature and the formation of a ferromagnetic dimer-pair at 173 K. Moreover, it is found that our natural orbital analysis for the electronic structure of diethyl-substituted spiro-biphenelenyl is equivalent to Haddon's valence bond explanation intrinsically.

For the mechanism of their conductions, ab initio MO results can illustrate it as follows. The conducting electrons go from a phenalenyl part to the other phenalenyl part in the molecule through the spiro linkage. They then transfer to the next molecule that is a half of the π-dimer. The result implied that a conduction path is the π-dimer column.

Acknowledgments

All the single-point energy calculations were performed by GAUSSIAN 98 program packages [19]. Fruitful discussions with the members in Nakasuji Lab. at Osaka University are sincerely appreciated. This work has been supported by Grants-in-aid for Scientific Research on Priority Areas (# 14204061 and 15750120) from the Ministry of Education, Culture, Sports, Science and Technology, Japan. T.T. has also been supported by a Grant-in-aid for JSPS Fellows.

References

[1] K. Goto, T. Kubo, K. Yamamoto, K. Nakasuji, K. Sato, D. Shiomi, T. Takui, M. Kubota, T. Kobayashi, K. Yakusi, J. Ouyang, J. Am. Chem. Soc. 121 (1999) 1619.
[2] Y. Morita, T. Aoki, K. Fukui, S. Nakazawa, K. Tamaki, S. Suzuki, A. Fuyuhiro, K. Yamamoto, K. Sato, D. Shiomi, A. Naito, T. Takui, K. Nakasuji, Angew. Chem., Int. Ed. 41 (2002) 1793.
[3] R.C. Haddon, Nature 256 (1975) 394.
[4] X. Chi, M.E. Itkis, K. Kirschbaum, A.A. Pinkerton, R.T. Oakley, A.W. Cordes, R.C. Haddon, J. Am. Chem. Soc. 123 (2001) 4041.
[5] M.E. Itkis, X. Chi, A.W. Cordes, R.C. Haddon, Science 296 (2002) 1443.
[6] X. Chi, F.S. Tham, A.W. Cordes, M.E. Itkis, R.C. Haddon, Synth. Metals 133–134 (2003) 3671.
[7] Y. Takano, T. Taniguchi, H. Isobe, Y.T. Kubo, Morita, K. Yamamoto, K. Nakasuji, T. Takui, K. Yamaguchi, J. Am. Chem. Soc. 124 (2002) 11122.
[8] Y. Takano, T. Taniguchi, H. Isobe, Y.T. Kubo, Morita, K. Yamamoto, K. Nakasuji, T. Takui, K. Yamaguchi, Chem. Phys. Lett. 358 (2002) 17.
[9] F.H. Allen, O. Kennard, Chem. Des. Automation News 8 (1) (1993) 31–37.
[10] R.G. Parr, W. Young, Density-functional Theory of Atoms and Molecules, Springer, Berlin, 1996.
[11] D. Becke, J. Am. Chem. Soc. 98 (1993) 5648.
[12] C. Lee, W. Yang, R.G. Parr, Phys. Rev. B 37 (1988) 785.
[13] T. Kawakami, T. Taniguchi, Y. Kitagawa, Y. Takano, H. Nagao, K. Yamaguchi, Mol. Phys. 100 (2002) 2641.
[14] K. Yamaguchi, Y. Takahara, T. Fueno, Appl. Quant. Chem. (1986) 155.
[15] J.E. Harriman, J. Chem. Phys. 40 (1964) 2827.
[16] P. Pulay, T.P. Hamilton, J. Am. Chem. Soc. 88 (1988) 4926.
[17] K. Yamaguchi, M. Okumura, K. Takada, S. Yamanaka, Int. J. Quant. Chem. Symp. 27 (1993) 501.
[18] J. Huang, M. Ketesz, J. Am. Chem. Soc. 125 (2003) 13334.
[19] M.J. Frisch, G.W. Trucks, H.B. Schlegel, G.E. Scuseria, M.A. Robb, J.R. Cheeseman, V.G. Zakrzewski, J.A. Montgomery Jr., R.E. Stratmann, J.C. Burant, S. Dapprich, J.M. Millam, A.D. Daniels, K.N. Kudin, M.C. Strain, O. Farkas, J. Tomasi, V. Barone, M. Cossi, R. Cammi, B. Mennucci, C. Pomelli, C. Adamo, S. Clifford, J. Ochterski, G.A. Petersson, P.Y. Ayala, Q. Cui, K. Morokuma, D.K. Malick, A.D. Rabuck, K. Raghavachari, J.B. Foresman, J. Cioslowski, J.V. Ortiz, B.B. Stefanov, G. Liu, A. Liashenko, P. Piskorz, I. Komaromi, R. Gomperts, R.L. Martin, D.J. Fox, T. Keith, M.A. Al-Laham, C.Y. Peng, A. Nanayakkara, C. Gonzalez, M. Challacombe, P.M.W. Gill, B. Johnson, W. Chen, M.W. Wong, J.L. Andres, C. Gonzalez, M. Head-Gordon, E.S. Replogle, J.A. Pople, GAUSSIAN 98, Revision A.11.6, Gaussian Inc., Pittsburgh, PA, 1998.

[4,5]. The origin of the exchange interactions in such compounds has been studied and correlated to the Ni–O–Ni angle within the cubane [6]. In addition to the high spin number, many tetra-nickel cubane molecules also have high molecular symmetry. These characteristics make such molecules great candidates for detailed studies of the origin of zero-field splitting (zfs) and the mechanism for fast magnetization relaxation [7].

Recently, we found a series of Ni_4 cubane metal complexes, with hmp^- (mono-anion of 2-hydroxymethylpyridine) as the bridging ligand, having four-fold pseudo rotation (S_4) symmetry [8,9]. Here, we present data for this series of Ni_4 SMMs. Preliminary results of micro-SQUID magnetometry and high-frequency electron paramagnetic resonance (HFEPR) measurements on single crystals are presented to characterize these Ni_4 SMMs. Fast tunneling of the magnetization is observed in the hysteresis loops. To explore the reasons for the fast tunneling, as well as the origin of the zfs of the molecule, we set out to determine the zfs parameters of the individual Ni^{II} ions by doping small amounts of Ni^{II} into a Zn_4 cubane molecule matrix. Due to the observation of splitting of the peaks in the HFEPR spectra of one of these Ni_4 cubane complexes, heat capacity measurements and low temperature X-ray diffraction studies were also carried out to probe the possible cause of the splitting features.

2. Experimental

2.1. Syntheses

Crystalline samples of complexes **1**, **2**, and **3** ($[Ni(hmp)(ROH)Cl]_4$, R = methyl for **1**, ethyl for **2**, 3,3-dimethyl-1-butyl for **3**) were prepared as previously reported [8,9].

2.2. Physical measurements

High frequency (40–200 GHz) single crystal EPR measurements were carried out using a millimeter-wave vector network analyzer and a high sensitivity cavity perturbation technique; this instrumentation is described elsewhere [10]. Tunneling studies were performed by magnetization measurements on a single crystal using an array of micro-SQUIDs as described in the literature [11]. Specific heat at constant pressure (C_p) measurements at zero-field were made using a quantum design physical properties measurement system (QD PPMS) employing a relaxation method [12]. The platform was calibrated by use of a copper standard.

3. Results and discussion

3.1. Description of structures

In this paper, data are presented for the series of $[Ni(hmp)(ROH)Cl]_4$ complexes, where R stands for the Me, Et, or 3,3-dimethyl-1-butyl groups. An example drawing of the structure of the Ni_4 cubane molecule is shown in Fig. 1. The common feature of the structure of the Ni_4 cubane molecule is that the molecular core consists of four Ni^{II} cations occupying the alternating corners of a distorted cube with oxygen atoms on the other four corners. The four Ni^{II} ($S = 1$) ions ferromagnetically couple through the bridging oxygen atoms to give a $S = 4$ ground state. The structure of the Ni_4 cube is such that the molecule has S_4 site symmetry. As in the case for Mn_{12}, this four-fold symmetry can impose a uniaxial zfs D term, while the transverse E term should be equal to zero on symmetry grounds [13].

3.2. Magnetization hysteresis loops

Previously, we reported [8,9] that this series of complexes shows magnetization hysteresis loops. When the R groups on the alcoholic ligand are small, such as methyl or ethyl, weak intermolecular magnetic exchange interactions are present, leading to an exchange bias of the hysteresis loops, where the first step feature in the loops is significantly shifted from zero field. However, the intermolecular interactions can be turned off by introducing a more bulky aliphatic chain on the alcoholic ligands. Fig. 2 shows the magnetization hysteresis loop for complex **3**. It can be seen that the first magnetization tunneling step occurs essentially at zero field. Another important feature to note is that the rate of this quantum tunneling is very fast compared to other known SMMs such as the Mn_{12} and Mn_4 complexes.

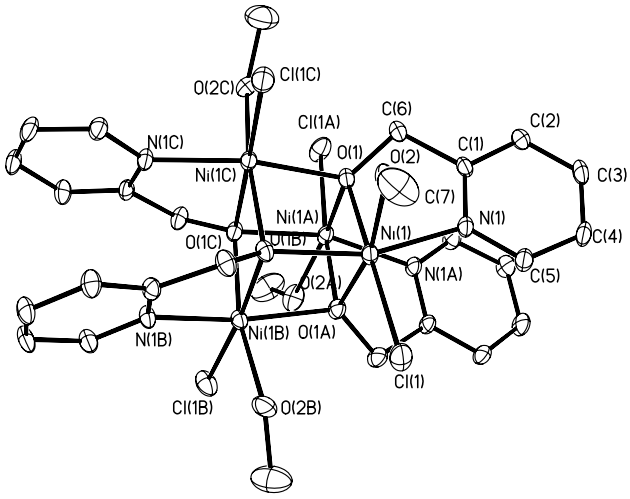


Fig. 1. ORTEP representation of $[Ni(hmp)(MeOH)Cl]_4$ showing 50% probability ellipsoids.

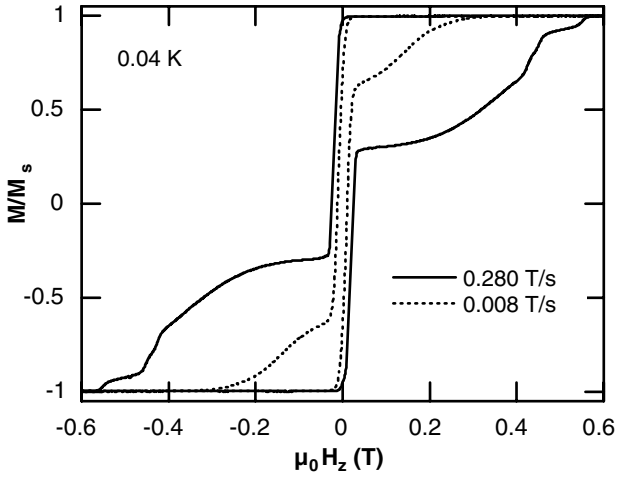


Fig. 2. Magnetization (M) of a single crystal of [Ni(hmp)(dmb)Cl]$_4$ (plotted as a fraction of the maximum value of M_s, the saturation magnetization) versus applied magnetic field ($\mu_0 H$). The magnetic field is parallel to the easy axis. The magnetization loops were obtained at 0.040 K at two different scan rates.

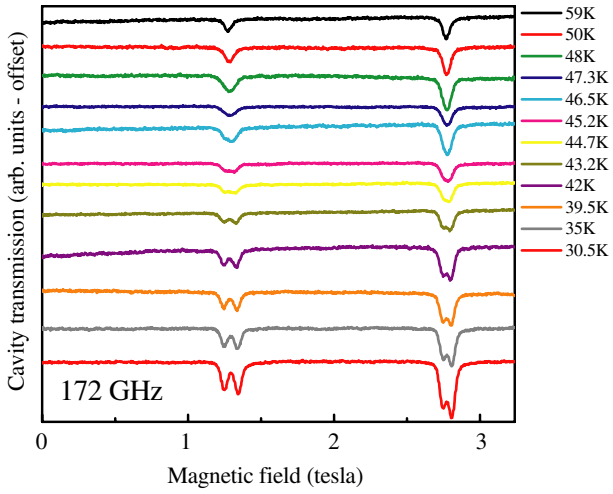


Fig. 3. Variable temperature HFEPR spectra obtained at 172 GHz for a single crystal of [Ni(hmp)(dmb)Cl]$_4$. The magnetic field is oriented parallel to the easy axis of magnetization of the crystal.

To explore the origin of this fast tunneling, a series of HFEPR experiments were performed on complex **3**.

3.3. High-frequency EPR data for the Ni_4 cubane molecule

Single-crystal HFEPR data were collected for complex **3**. The results of a preliminary analysis of these data reveal that these Ni_4 complexes have a $S = 4$ ground state and that the axial zero-field splitting parameter D is negative [8,9]. Due to the molecular S_4 symmetry, it is required that the rhombic zfs E term be zero. Therefore, the fast tunneling of magnetization can be the result of fourth order transverse zero-field interactions, namely the B_4^4 term [14]. The final effective spin Hamiltonian will thus be:

$$\hat{H} = g_z \mu_B \hat{B}_z \cdot \hat{S}_z + D\hat{S}_z^2 + B_4^0 \hat{O}_4^0 + B_4^4 \hat{O}_4^4. \quad (1)$$

The HFEPR spectra confirm the absence of the E term and a significant B_4^4 term for the molecule. In addition to the discovery of a large B_4^4 term, some interesting features have also been observed in the low temperature HFEPR spectra. Fig. 3 presents a few low temperature spectra. As the temperature is reduced from 60 to 30 K, fine structure resonances are observed to split into two features. The low temperature (12 K) X-ray structure confirmed that there are disordered ligand carbon atoms. It is likely that there is a dynamic ligand conformation at high temperatures that becomes frozen into a static disorder below about 50 K.

3.4. Heat capacity measurements

To find the origin of the HFEPR peak splitting observed for Ni_4 cubane complex **3** that occurs around 45 K, heat capacity measurements were performed on complex **3** in the temperature range 2–100 K. It can be seen from Fig. 4 that a peak shows up in the heat-capacity versus temperature plot. This peak indicates there is an order–disorder phase transition at 47 K. The fact that the peak in heat capacity occurs at the same temperature as the peak splitting in the HFEPR spectra further confirms that it is due to a static ligand disorder. Further analysis of the heat capacity data is in progress.

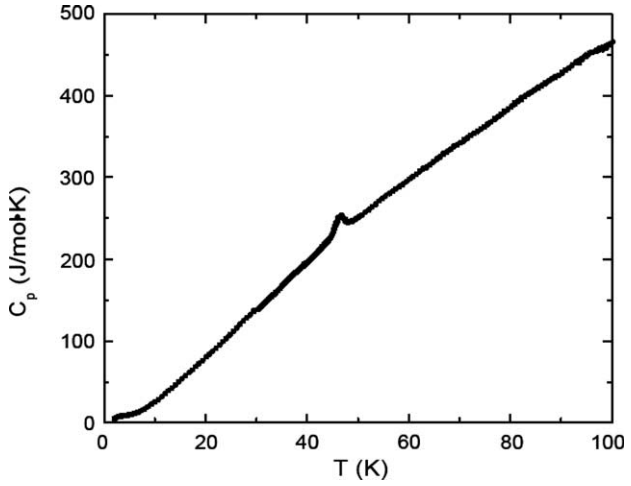


Fig. 4. Heat capacity at constant pressure versus temperature for a polycrystalline sample of complex **3**.

3.5. HFEPR of Ni^{II} doped [Zn(hmp)(dmb)Cl]$_4$ complex

Single-crystal data were collected to determine the zfs parameters of individual Ni^{II} ions in the cubane metal cluster. With the knowledge of the single-ion zfs parameters we may understand the fast tunneling, and the relationship between single-ion and molecular zfs parameters. We have chosen an analog of complex **3**,

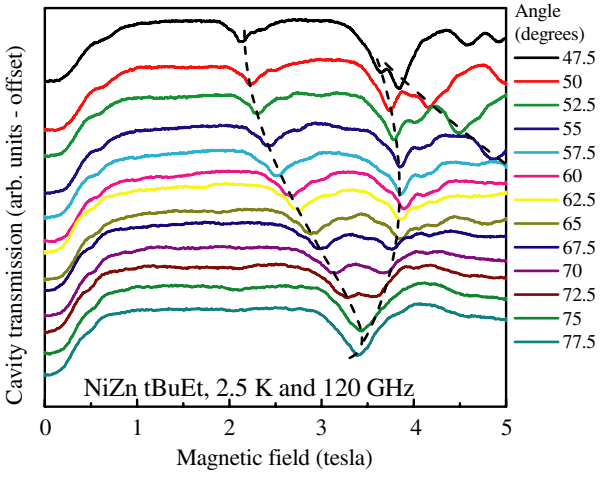


Fig. 5. Angle-dependent HFEPR spectra obtained at 120 GHz for a single crystal of a Ni^{II} doped $[Zn(hmp)(dmb)Cl]_4$ sample.

the Ni^{II} doped Zn_4 cubane molecule, as the candidate to study the zfs of individual Ni^{II} ions. The fact that there is only one symmetry independent molecule in the crystal lattice makes it easier to interpret the spectra. Furthermore, complex **3** contains no solvent in its structure, which could distort the EPR spectra.

The zfs parameters of the individual Ni^{II} ion were found by rotating the applied magnetic field about different crystallographic planes. Fig. 5 illustrates some of the angle-dependent HFEPR spectra for this sample. The angle-dependence, as well as frequency-dependent studies of the spectra, provide access to the zfs parameters for the Ni^{II} ion, $D_i = -5.27\ cm^{-1}$ and $E_i = -1.2\ cm^{-1}$. The z-axis of the individual Ni^{II} ions was also found to be tilted 15° away from the molecular easy axis. The Ni_4 molecular D term that is calculated from the single ion zfs parameters above is $D = -0.69\ cm^{-1}$, which is quite close to the experimental value found for the undoped Ni_4 complex ($D = -0.594\ cm^{-1}$ [8,9]). The tilt of the easy axis and significant E term for individual Ni^{II} ions also provides a possible explanation for the fast quantum tunneling of magnetization in this Ni_4 complex. Detailed analysis of these data will be presented elsewhere [14,15].

4. Conclusion

A series of molecules with the composition $[Ni(hmp)(ROH)Cl]_4$, where R = CH_3 for complex **1**, R = Et for complex **2** and R = 3,3-dimethyl-1-butyl for complex **3**, have been shown to be SMMs. Complex **3** shows no exchange bias in its magnetization hysteresis loop, with a clear step feature at zero magnetic field. The fast QTM process in complex **3** is likely the result of a significant B_4^4 term, and the tilting of the single Ni^{II} ion zfs tensor. Small structure changes cause the splitting of the HFEPR fine-structure resonances as confirmed by heat capacity data.

Acknowledgements

This work was supported by the National Science Foundation (DMR0103290, DMR0239481 and CHE0414155) and by Research Corporation.

References

[1] J.R. Friedman, M.P. Sarachik, J. Tejada, J. Maciejewski, R. Ziolo, J. Appl. Phys. 79 (1996) 6031.
[2] J.R. Friedman, M.P. Sarachik, J. Tejada, R. Ziolo, Phys. Rev. Lett. 76 (1996) 3830.
[3] G. Christou, D. Gatteschi, D.N. Hendrickson, R. Sessoli, MRS Bull. 25 (2000) 66.
[4] M.. Moragues-Canovas, M. Helliwell, L. Ricard, E. Riviere, W. Wernsdorfer, E. Brechin, T. Mallah, Eur. J. Inorg. Chem. 11 (2004) 2219.
[5] M. Nakano, G.E. Matsubayashi, T. Muramatsu, T.C. Kobayashi, K. Amaya, J. Yoo, G. Christou, D.N. Hendrickson, Mol. Cryst. Liq. Cryst. 376 (2002) 405.
[6] M.A. Halcrow, J.S. Sun, J.C. Huffman, G. Christou, Inorg. Chem. 34 (1995) 4167.
[7] D. Gatteschi, L. Sorace, J. Solid State Chem. 159 (2001) 253.
[8] E.C. Yang, W. Wernsdorfer, S. Hill, R.S. Edwards, M. Nakano, S. Maccagnano, L.N. Zakharov, A.L. Rheingold, G. Christou, D.N. Hendrickson, Polyhedron 22 (2003) 1727.
[9] Also R.S. Edwards, S. Maccagnano, E.-C. Yang, S. Hill, W. Wernsdorfer, D. Hendrickson, G. Christou, J. Appl. Phys. 93 (2003) 7807.
[10] M. Mola, S. Hill, P. Goy, M. Gross, Rev. Sci. Inst. 71 (2000) 186.
[11] W. Wernsdorfer, Adv. Chem. Phys. 118 (2001) 99.
[12] G.M. Schmiedeshoff, N.A. Fortune, J.S. Brooks, G.R. Stewart, Rev. Sci. Inst. 58 (1987) 1743.
[13] A. Cornia, R. Sessoli, L. Sorace, D. Gatteschi, A.L. Barra, C. Daiguebonne, Phys. Rev. Lett. 89 (2002) 25, 257201-1.
[14] C. Kirman, J. Lawrence, S. Hill, E.-C. Yang, D.N. Hendrickson, J. Appl. Phys. (2005), in press.
[15] E.-C. Yang, C. Kirman, J. Lawrence, L.N. Zacharov, A. Rheingold, S. Hill, D.N. Hendrickson, Inorg. Chem. (2005), in press.

breaking responsible for the QMT in Mn_{12}-Ac [6–10]. Disorder associated with the acetic acid solvent leads to discrete local environments, resulting in a significant fraction of the molecules (>50%) possessing twofold symmetry with a rhombic crystal-field parameter $E \sim 0.01\ cm^{-1}$ (or $ED \sim 0.02$, where D is the uniaxial crystal-field parameter [7]).

Here, we present accurate angle-resolved high-frequency electron paramagnetic resonance (HFEPR) data collected for single-crystal samples of deuterated and undeuterated Mn_{12}-Ac. The spectra reveal multiple fine structures associated with the various Mn_{12} species in different local environments. Each of the fine structures exhibits a distinct dependence on the applied field orientation, thereby highlighting the discrete nature of the disorder, as well as suggesting that some of the Mn_{12}-Ac variants have their easy axes significantly tilted with respect to the global symmetry direction in the crystal [9]. We then compare these data with spectra obtained for two recently discovered high-symmetry (S_4) analogs of Mn_{12}-Ac, differing only in their ligand and solvent structures. The new complexes are $[Mn_{12}O_{12}(O_2CCH_2Br)_{16}(H_2O)_4]\cdot 4CH_2Cl_2$ [11–13] and $[Mn_{12}O_{12}(O_2CCH_2Bu^t)_{16}(CH_3OH)_4]\cdot CH_3OH$, abbreviated Mn_{12}-BrAc and Mn_{12}-*t*BuAc, respectively. None of the highly reproducible fine-structures seen in the Mn_{12}-Ac samples are found for the new Mn_{12} complexes, thus confirming the idea that the solvent structure significantly influences the QMT dynamics in Mn_{12}-Ac. Indeed, the HFEPR spectra for Mn_{12}-BrAc and Mn_{12}-*t*BuAc provide spectacular resolution, allowing for unique spectroscopic insights into high-symmetry giant spin SMMs.

2. Experimental

Single-crystal HFEPR measurements were carried out using a millimeter-wave vector network analyzer (MVNA) in combination with a cavity perturbation technique which we have described elsewhere [14]. In order to enable in situ two-axis rotation of the sample relative to the applied magnetic field, we employed a split-pair magnet with a 7 T horizontal field and a vertical access, together with a unique cylindrical cavity in which the sample may be rotated about a second orthogonal axis (this cavity is described in [15]). Single-axis rotation measurements were also performed in a 17 T axial superconducting magnet using the rotating cavity [15]. In both setups, the sample temperature was controlled using helium flow cryostats and calibrated Cernox™ resistance sensors. Mn_{12}-Ac samples were prepared separately by two groups according to the usual methods [5]: deuterated d-Mn_{12}-Ac samples were prepared at Florida State University and removed from their mother liquor prior to transportation to the University of Florida; h-Mn_{12}-Ac samples were prepared at the University of Florida and stored in their mother liquor right up until the time of the experiments. Mn_{12}-BrAc crystals were prepared by a ligand substitution procedure involving the treatment of Mn_{12}-Ac with an excess of $BrCH_2CO_2H$ [11–13]. Mn_{12}-*t*BuAc crystals were prepared via a method similar to the one in [16], albeit that CH_3OH solvent was used in the present case, thereby yielding the high symmetry complex (full details will be presented elsewhere [17]). With the exception of the d-Mn_{12}-Ac samples, all other crystals were handled identically with a view to avoiding solvent loss from the structure; the needle shaped single-crystals ($\sim 1.5 \times 0.4 \times 0.4\ mm^3$) were removed directly from their mother liquor and protected with grease before cooling under 1 atm of helium gas.

3. Results and discussion

3.1. Mn_{12}-Ac: in-plane field rotations

Fig. 1 displays experimental microwave absorption obtained for different field orientations within the hard (*xy*-) plane of a deuterated sample of Mn_{12}-Ac (i.e., d-Mn_{12}-Ac); the temperature is 15 K and the frequency is 51.3 GHz in every case. The peaks correspond to EPR. The data were obtained at 7.5° intervals, and the azimuthal angle ϕ represents the field orientation relative to one of the flat edges of the square cross-section

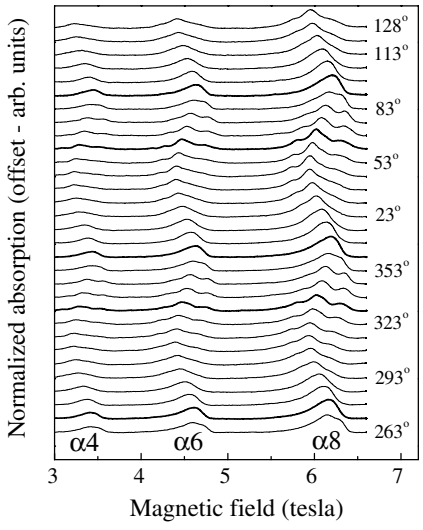


Fig. 1. Microwave absorption obtained for different field orientations within the hard (*xy*-) plane of a deuterated d-Mn_{12}-Ac sample; the temperature was 15 K and the frequency was 51.3 GHz in every case. The peaks in absorption correspond to EPR. The data were obtained at 7.5° intervals, where the angle ϕ refers to the field orientation relative to one of the flat edges of the square cross-section of the sample. The resonances have been labeled according to the scheme described in [9]. The bold traces correspond to field orientations approximately parallel to the hard axes of the $\hat{O}_2^2$ (3 peaks) and $\hat{O}_4^4$ (single peak) tensors.

of the sample. The resonances have been labeled according to the scheme described in [9]. For fields applied approximately parallel to the hard plane, only α-resonances are observed (β-resonances appear for field rotation away from the hard plane – see Figs. 3 and 4 below). The highest field peak, α8, corresponds to an excitation between levels which evolve from the $m_z = \pm 9$ zero-field doublet. The transition from the ground state (α10) is not observed within the available field range for these experiments; at 51 GHz, its expected position is at ~9 T. For a discussion of the resonance labeling scheme, as well as detailed explanations of the temperature, frequency, field and field orientation dependence of the EPR spectra for Mn_{12}-Ac, refer to [9].

Immediately apparent from the Fig. 1 is a fourfold variation in the positions of each band of resonances (α8, α6, etc.). Note that each peak exhibits fine structures (high- and low-field shoulders), which also depend on the field orientation ϕ; these fine structures are related to the disorder in the crystal, as discussed further below. The fourfold shifts are caused by the intrinsic fourth-order operator, $\hat{O}_4^4$, in the spin Hamiltonian [6–10], as has previously been established for h-Mn_{12}-Ac [7]. Fig. 2 shows a grayscale contour plot of the data in Fig. 1, i.e., absorption intensity versus magnetic field strength and the azimuthal angle ϕ. This figure can be compared directly with Fig. 1 of [7], which displays the same data for h-Mn_{12}-Ac. Superimposed on the absorption maxima are two kinds of fit to the ϕ-dependence of each peak. The solid lines were obtained simply by fitting the positions of the peaks obtained from Fig. 1: the central peaks were fit to pure sine functions having fourfold periodicity; meanwhile, the high- and low-field shoulders were fit with superpositions of phase-shifted sine functions having fourfold and twofold periodicities. The fits represented by horizontal bars were obtained by exact diagonalization of the Hamiltonian matrix and are described further below.

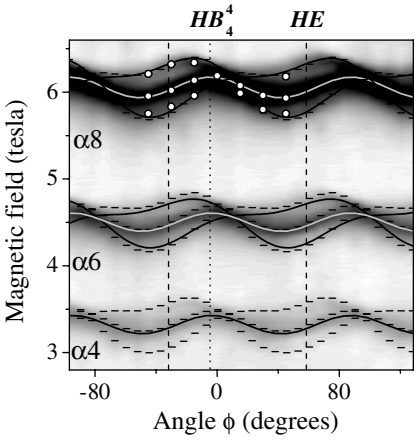


Fig. 2. Grayscale contour plot of the absorption intensity for d-Mn_{12}-Ac (see Fig. 1), vs. magnetic field strength and the azimuthal angle ϕ; the darker shades correspond to stronger absorption. Superimposed on the absorption maxima are fits to the ϕ-dependence of the central positions of each peak deduced from Fig. 1 (solid gray and black curves). The horizontal bars represent best fits to the peak positions based on exact diagonalization of the Hamiltonian matrix; the obtained Hamiltonian parameters are given in the main text. The open circles represent peak positions obtained for h-Mn_{12}-Ac at the same frequency and temperature (see Figs. 3 and 4). The approximate orientations of the hard axes corresponding to the $\hat{O}_2^2$ (*HE*, dashed lines) and $\hat{O}_4^4$ (HB_4^4, dotted line) tensors are indicated at the top of the figure.

We now briefly discuss the origin of the twofold contribution to the positions of the shoulders, which are very apparent in the ranges $\phi = 300$–$330°$ and $\phi = 30$–$60°$ in Fig. 1; a more in-depth discussion can be found in [7–10]. The high- and low-field shoulders are due to the $n = 1$ and $n = 3$ Mn_{12}-Ac hydrogen-bonding variants in Cornia's solvent disorder model [6]. These variants, which comprise 50% of the total molecules, are thought to possess a significant rhombic anisotropy due to the reduced symmetry of the surrounding hydrogen bonded acetic acid solvent molecules. The second-order operator, $\hat{O}_2^2$, associated with the rhombic distortion gives rise to the two-fold behavior, as was clearly demonstrated by del Barco et al. [8]. It is important to recognize that the disorder is discrete, since the acetic acid can only bond at four positions on the Mn_{12} molecule. Thus, one expects only two hard directions (HE_A and HE_B [9]) associated with the $n = 1$ and $n = 3$ low symmetry variants, which are separated by 90°. In HFEPR, the $\hat{O}_2^2$ operator causes shifts in the peak positions. When the applied field is parallel to one of the hard axes, it is obviously perpendicular to the other, which causes shifts in the HFEPR intensity to both the low- and high-field sides of the central peaks, i.e., the shoulders. When the field is applied in between these two directions, the EPR intensity due to the low-symmetry variants collapses into the central portion of the peak, hence the disappearance of the shoulders every 90° (see Figs. 1 and 2). In actual fact, this apparent fourfold behavior reflects the twofold nature of the rhombic distortion caused by the hydrogen bonding acetic acid molecules, with the EPR intensity for a given variant shifting from the low (high) to the high (low) field side of the main peak every 90°, i.e., the periodicity is actually 180°. This twofold behavior is then superimposed on the intrinsic fourfold periodicity, as can be seen from the curves in Fig. 2.

As we have previously reported, there is an offset (phase shift) between the fourfold modulation of the central peak positions, and the twofold pattern associated with the shoulders; the hard directions associated with the $\hat{O}_2^2$ and $\hat{O}_4^4$ operators are indicated, respectively, by dashed and dotted lines in Fig. 2. In fact, this is was one of the more important points discussed originally in [7], which has recently been backed up by theoretical calculations [18]. From the fits in Fig. 2, this offset is found to be $27 \pm 2°$, which is in good agreement with earlier studies of

h-Mn_{12}-Ac [7]. From the maxima and minima in the peak position shifts induced by the $\hat{O}_4^4$ operator, we estimate that the hard and medium directions associated with this intrinsic zero-field-splitting interaction are oriented at $-4.5° \pm 5°$ [$+(i \times 90°)$, where i = integer] and $40.5° \pm 5°$ [$+(i \times 90°)$], respectively, relative to the square edges of a typical single-crystal sample. Once again, this agrees with previous studies of h-Mn_{12}-Ac.

In order to make quantitative comparisons between the disorder-induced effects in h-Mn_{12}-Ac and d-Mn_{12}-Ac, we performed a single fit to the data in Fig. 2 via exact diagonalization of the Hamiltonian matrix [6–10]. This fit is represented by the horizontal bars in Fig. 2. Our procedure obviously takes into account the misalignments of the $\hat{O}_2^2$ and $\hat{O}_4^4$ tensors, as described in [10]. Thus, the employed Hamiltonian is subtly different from the standard form used by most spectroscopists [19–21], which may explain slight differences in the obtained Hamiltonian parameters. We start out by assuming accepted values for the zero-field parameters D and B_4^0 ($D = -0.455\ \mathrm{cm}^{-1}$ and $B_4^0 = -2 \times 10^{-5}\ \mathrm{cm}^{-1}$), which were verified independently from easy axis measurements. The only free parameters in the fit were then the E and B_4^4 coefficients (corresponding to the $\hat{O}_2^2$ and $\hat{O}_4^4$ tensors), for which we obtained the values $\pm 0.014(2)$ and $\pm 3.2(5) \times 10^{-5}\ \mathrm{cm}^{-1}$, respectively. The B_4^4 value is in precise agreement with that found for h-Mn_{12}-Ac [7]. However, the E value is significantly larger than the one obtained in earlier experiments (40% larger than the upper bound quoted in [7]). We attribute some of this difference to the modified Hamiltonian used in our more recent fits, which takes into account the misalignments of the $\hat{O}_2^2$ and $\hat{O}_4^4$ tensors. However, much of the difference appears to be real.

The larger E-value found from the present study is somewhat surprising. However, as will be seen below, more recent measurements on a fresh h-Mn_{12}-Ac sample are in excellent agreement with the value of $0.014(2)\ \mathrm{cm}^{-1}$. Thus, the difference is likely related to sample quality and/or solvent loss. A tell-tale sign of the higher sample quality is the observation of both high- and low-field shoulders on the main EPR peaks. In contrast, only high-field shoulders were seen in the earlier experiments on h-Mn_{12}-Ac. In fact, the absence of a low-field shoulder is discussed at some length in [9], where it is shown that this peak is unresolved from the broad low-field tail associated with the central portion of the peak. The reason for the asymmetry between the high and low-field shoulder is related to easy axis tilting caused by the solvent disorder (see below). Although both shoulders are seen in the present study, a clear asymmetry can be seen from the data in Fig. 1.

We suspect that the samples used in the earlier experiments may have suffered significant solvent loss, either upon cooling from room temperature under high vacuum, or simply as a result of being stored in air for more than 1 year prior to the measurements. Indeed, variations in the D-strain measured in different Mn_{12}-Ac samples has previously been reported by us [22]. Increased D-strain leads to broader EPR linewidths, thus probably explaining why the shoulders are clearly resolved in the present investigation, but not in [7]. Without two well resolved shoulders, it is likely that the E-strain was under-estimated in [7]. Based on experience working with SMMs containing considerably more volatile solvents, we have recently developed sample handling procedures which minimize solvent loss, e.g., encapsulating samples in oil prior to cooling under atmospheric helium gas. The differences between the present measurements and those reported in [7,9] highlight the importance of sample handling. Indeed, it is likely that Mn_{12}-Ac samples prepared by different groups, and studied by different techniques, exhibit significant differences in their solvent content, resulting in subtly different conclusions concerning the quantum dynamics. For this reason, it is advantageous to prepare Mn_{12} SMMs which do not exhibit such a dramatic dependence on solvent content, as is the case for two newer complexes discussed at the end of this article.

3.2. Mn_{12}-Ac: out-of-plane field rotations

We now consider the angle-dependence of the HFEPR spectra for out-of-plane field rotations. The experimental spectra in Fig. 3 were obtained for a fresh sample of h-Mn_{12}-Ac at a frequency of 51.7 GHz and a temperature of 15 K. Data were taken at 0.3° intervals in the polar angle θ, i.e., the field orientation is measured relative to the global easy axis of the crystal. The thick curve corresponds to field alignment within the hard

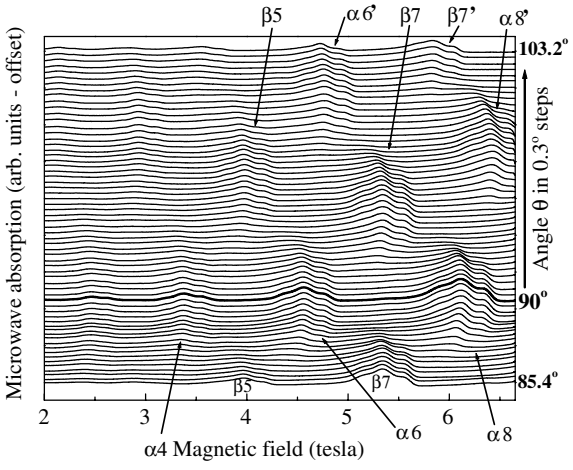


Fig. 3. Microwave absorption spectra obtained for out-of-plane (θ) rotations for a single crystal of h-Mn_{12}-Ac. The plane of rotation corresponds to the azimuthal angle $\phi \approx -15°$. In every case, the temperature is 15 K, the frequency is 51.7 GHz, and the traces are offset for clarity. The resonances are labeled according to the scheme developed in [9].

plane (to within 0.15°). The resonances have again been labeled according to the scheme developed in [9]. Using the two-axis rotation capability, this experiment was repeated for seven different planes of rotation, separated by $\Delta\phi = 15°$ (ϕ is the azimuthal angle). The grayscale contour plots in Fig. 4 display these data for five of the seven rotation planes. The peaks centered at $\theta = 90°$ correspond to α8 (at ~6 T) and α6 (at ~4.5 T); β7 is seen between about $\theta = 93°$ and 98°; β7 is then followed in order of increasing angle by α8′, α6′ and β7′. The data in Fig. 3 correspond to the $\phi = -15°$ orientation (middle trace in Fig. 4), which is approximately in between the hard axis of $\hat{O}_4^4$ and one of the hard $\hat{O}_2^2$ directions. The positions of the peaks and shoulders corresponding to the α8 resonances in Fig. 4 have been added to Fig. 2 for comparison with the measurements on the deuterated Mn_{12}-Ac crystal. As can be seen, the data for the dueterated and undeuterated complexes are in excellent agreement. Indeed, we estimate precisely the same E and B_4^4 values for the two complexes ($\pm 0.014(2)$ and $\pm 3.2(5) \times 10^{-5}$ cm^{-1}, respectively).

Fig. 5(a) displays a simulation of the out-of-plane angle-dependence of the EPR spectra for Mn_{12}-Ac, without disorder, i.e., no E-strain. The simulation was generated using the software package SIM [23], and with the Hamiltonian parameters quoted in the previous section (with $E = 0$); the frequency is 51.5 GHz and the temperature is 15 K. As can be seen from this simulation, there should be no angle overlap in intensity between neighboring α and β transitions; we note that adding a realistic E term does not affect the widths of the gaps between the α and β absorption bands in Fig. 5(a). In contrast, the data in Figs. 3 and 4 exhibit significant overlap of the α and β resonances. More importantly, the degree of overlap depends on the plane of rotation, i.e., the azimuthal angle ϕ. Note that the black contours represent 33% of the maximum absorption, while the white contours correspond to 66%. The reason for the overlapping of the α and β intensity has been discussed at great length in [9], and is attributed to a tilting of the easy axes of the low-symmetry Cornia variants away from the global crystallographic c-direction. The resulting distribution of easy axis directions leads to a smearing of the θ-dependence of the spectra, thereby accounting not only for the α and β overlap, but also for the lack of any curvature to the bands of absorption (compare, e.g., the simulations in Fig. 5(a) with the data in Fig. 4).

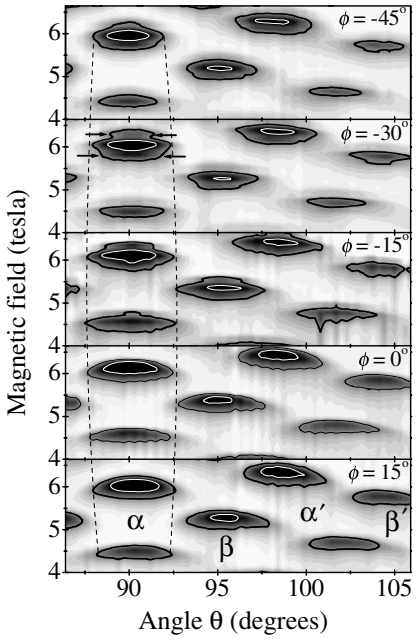


Fig. 4. Grayscale contour maps corresponding to out-of-plane (θ) HFEPR field rotation measurements for five different planes of rotation (indicated in the figures). The darker regions represent stronger EPR absorption. The data are plotted in this manner for direct comparison with subsequent simulations, and data obtained for other Mn_{12} complexes. The $\phi = -15°$ plot (middle panel) corresponds to the data in Fig. 3. The 66% and 33% of maximum absorption (corresponding to the peak of α8) contour lines are emphasized by light gray and black lines, respectively. The ϕ-dependent overlap of the α and β resonances suggests discrete easy-axis tilting; this behavior has been emphasized by the vertical dashed curves and the arrows in the $\phi = -30°$ panel. See main text, Fig. 5(b) and [9] for explanation.

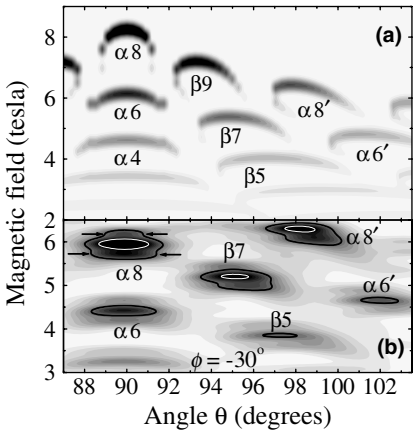


Fig. 5. (a) A simulation of the out-of-plane (θ) angle-dependence of the EPR spectra for d- and h-Mn_{12}-Ac, without disorder ($E = 0$). The simulation was generated using the software package SIM [23], and with the Hamiltonian parameters quoted in the main text; the frequency is 51.5 GHz and the temperature is 15 K. In contrast to the experimental spectra in Fig. 4, there is no angle overlap in intensity between neighboring α and β transitions. (b) A simulation of the $\phi = -30°$ data in Fig. 4. This simulation was generated by adding spectra corresponding to the 3 main species in Cornia's solvent disorder model [6]. The 66% and 33% of maximum absorption (corresponding to the peak of α8) contour lines are emphasized by light gray and black lines, respectively. The low-symmetry $n = 1$ and 3 variants contribute to the high- and low-field shoulders (see main text and Fig. 4). The flattening of the absorption bands (relative to Fig. 5(a)), and the angular overlap of the α and β resonances, is reproduced by convoluting the individual contributions to the spectrum with a Gaussian function with a half width of 1.3°. The arrows illustrate the different widths of the high- and low-field shoulders (see also 2nd panel of Figs. 4 and 6).

It was argued in [9] that the tilting directions associated with the $n = 1$ and $n = 3$ Cornia variants [6] are confined to orthogonal planes defined by the symmetry of the associated rhombic distortion (the $\hat{O}_2^2$ operator). The present study confirms this assertion. The profile of the absorption intensity, as a function of the angle θ (for a fixed field), can be fit reasonably well with a Gaussian function, as shown in Fig. 6 for the α8 peaks and shoulders corresponding to the data in Fig. 3. The full-width-at-half-maximum (FWHM) of the high-field shoulder ($\Delta\theta_H = 2.1°$) is almost 1° less than that of the low-field shoulder ($\Delta\theta_L = 3.0°$), in agreement with previously published results [9]. The reason for this asymmetry is connected with the fact that the molecules contributing to the high-field shoulder are tilted in a plane perpendicular to the field rotation plane, whereas those contributing to the low-field shoulder are tilted in a plane parallel to the rotation plane (see Fig. 6 of [9]). Thus, the full tilt distribution projects onto the field rotation plane for the low-field shoulder, but not for the high-field shoulder. Unfortunately, one cannot independently measure the widths of the shoulders (Δ_H and $\Delta\theta_L$) as one rotates far away from the azimuthal (ϕ) directions of maximum splitting (i.e., the hard $\hat{O}_2^2$ directions, *HE*), because the shoulders merge into the central peak. However, there is a tendency for the width of the high-field shoulder to increase as one rotates away from *HE* (the FWHM is 2.4° for $\phi = -45°$).

The vertical dashed lines in Fig. 4 illustrate the behavior of the 33% width of the central part of the α8 peak ($\Delta\theta_C$). Interestingly, $\Delta\theta_C$ exhibits a clear dependence on ϕ, suggesting that even the Cornia variants which do not possess a significant E term ($n = 0$, 2 and 4 [6]) are tilted. What is more, the maximum $\Delta\theta_C$ occurs fairly close to $\phi = 0°$, corresponding to the hard $\hat{O}_4^4$ direction. This suggests that the magnetic axes of these molecules may be tilted along or near to these orientations. We note that the $n = 2$ cis variants in Cornia's model, which comprise 25% of the molecules, are expected to exhibit significant tilting (~0.4° [6]), but no appreciable E-term.

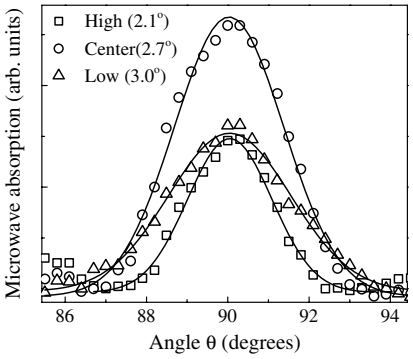


Fig. 6. Gaussian fits (solid curves) to the out-of-plane (θ) angle dependence of the HFEPR absorption intensity corresponding to the central peak (○), and the high (□) and low field (△) shoulders on the α8 resonance in Fig. 3. The FWHM of the three portions of the α8 resonance are indicated in brackets in the figure.

Based on the information in Fig. 6, one can deduce that FWHM of the tilt distribution for the $n = 1$ and $n = 3$ Cornia variants is *at least* 1°, i.e., that the half-width of the distribution is *at least* 0.5°. This is consistent with our previous studies, where it was shown that one could detect molecules in the tails of the distribution which were tilted by as much as 1.7°. In fact, the 0.5° value deduced above represents the magnitude of the solvent-disorder-induced tilting over and above any random tilting (the latter would not exhibit ϕ-dependence). Thus, the true half-width of the tilt distribution associated with the $n = 1$ and $n = 3$ Cornia variants should be larger than this value and, therefore, significantly larger than the value predicted by Cornia et al. (~0.3°) [6].

In order to estimate the actual amount of tilting, we have simulated the out-of-plane angle dependence for the $\phi = -30°$ plane of rotation (Fig. 5(b)), which corresponds approximately to the hard direction of the $\hat{O}_2^2$ tensor. The simulation was generated by adding spectra corresponding to the 3 main species in Cornia's solvent disorder model. We assume that 50% of the molecules possess no E term (the $n = 0$, 2 and 4 variants [6]), so that they contribute to the central portions of the EPR absorption bands. Of the remaining 50% (the $n = 1$ and 3 variants [6]), half possess an E value of $+0.014(2)\ cm^{-1}$, and the other half an E value of $-0.014(2)\ cm^{-1}$ (a change in the sign of E is equivalent to a 90° rotation of the hard and medium directions). These molecules contribute to the high- and low-field shoulders (see Fig. 3). The flattening of the absorption bands (relative to Fig. 5(a)), and the angular overlap of the and β resonances, is then reproduced by convoluting the individual contributions to the spectrum with a Gaussian function, $\exp[-(\theta - 90°)^2/2\sigma^2]$. The FWHM ($w \sim 2.35\sigma$) of the distribution used in Fig. 5(b) is 2.6°, i.e., a half width of 1.3°. Overall agreement with the experimental spectrum in Fig. 4(b) is very good, particularly concerning the widths of the high- and low-field shoulders (as indicated by arrows). We note also that, contrary to recent claims, this value *is* consistent with magnetic studies [24], as discussed at length in [9].

3.3. Mn_{12}-BrAc and Mn_{12}-tBuAc

We conclude this article by presenting data for the two recently discovered analogs of Mn_{12}-Ac: Mn_{12}-BrAc and Mn_{12}-*t*BuAc. The motivation for comparing these compounds is to investigate the influence of the solvent structure on the properties of the Mn_{12} core, which is virtually identical for the three complexes. Fig. 7 displays experimental spectra obtained for out-of-plane (θ-) rotations for Mn_{12}-BrAc, while Fig. 8 presents the same data in grayscale. Figs. 9 and 10 display

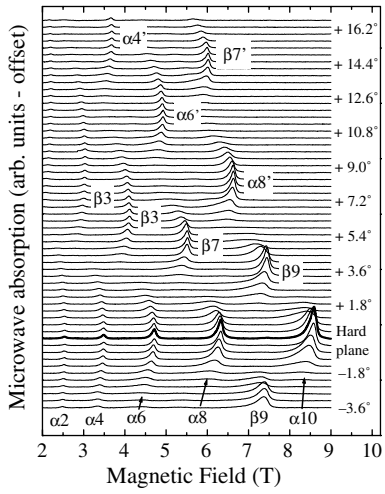


Fig. 7. Microwave absorption spectra obtained for out-of-plane (θ) rotations for a single crystal of Mn_{12}-BrAc. The angle step is 0.36°. In every case, the temperature is 15 K, the frequency is 51.5 GHz, and the traces are offset for clarity. The resonances are labeled according to the scheme developed in [9].

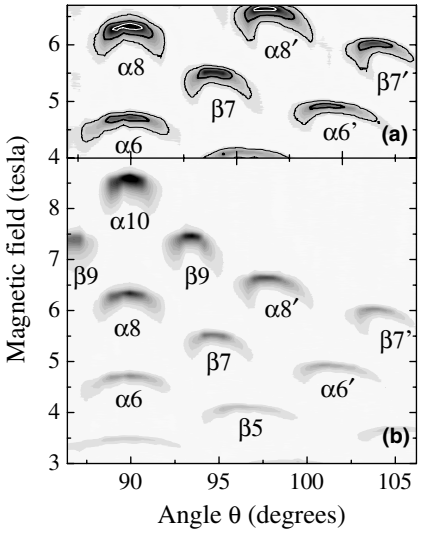


Fig. 8. Grayscale contour maps corresponding to the data in Fig. 7. The darker regions represent stronger EPR absorption. In order to aid comparisons with Fig. 4, (a) depicts an expanded region of the full angle dependence in (b). Contour lines corresponding to 66% (light gray), 33% (thick black) and 15% (thin black) of the maximum absorption (of the α8 peak) are superimposed on the absorption bands to aid the discussion in the main text.

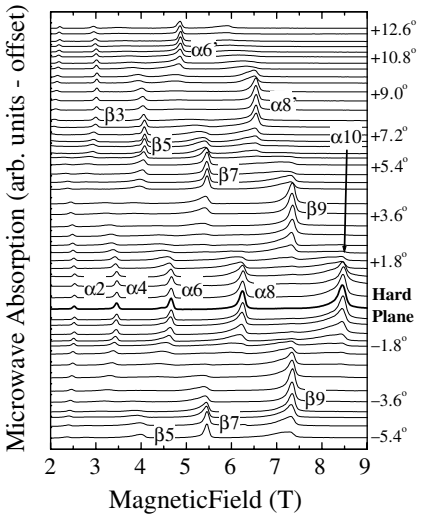


Fig. 9. Microwave absorption spectra obtained for out-of-plane (θ) rotations for a single crystal of Mn_{12}-*t*BuAc. The angle step is 0.36°. In every case, the temperature is 15 K, the frequency is 51.5 GHz, and the traces are offset for clarity. The resonances are labeled according to the scheme developed in [9].

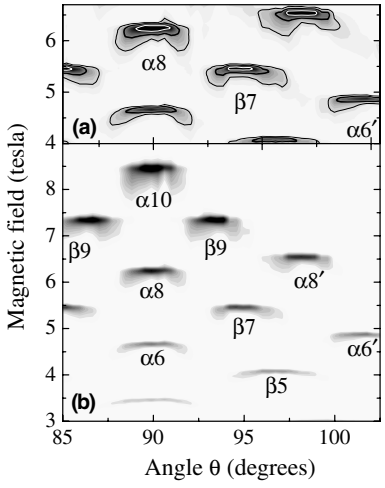


Fig. 10. Grayscale contour maps corresponding to the data in Fig. 9. The darker regions represent stronger EPR absorption. In order to aid comparisons with Fig. 4, (a) depicts an expanded region of the full angle dependence in (b). Contour lines corresponding to 66% (light gray), 33% (thick black) and 15% (thin black) of the maximum absorption (of the α8 peak) are superimposed on the absorption bands to aid the discussion in the main text.

the same measurements for the Mn_{12}-*t*BuAc complex. The frequency was 51.5 GHz and the temperature was 15 K for both sets of measurements. It is immediately apparent that the EPR peaks for the BrAc and *t*BuAc complexes are considerably sharper than those obtained for Mn_{12}-Ac. Furthermore, the fine structures (high- and low-field shoulders) are not seen for either of the newer complexes, irrespective of the choice of rotation plane (i.e., the ϕ angle). This strongly suggests that the complexities of the EPR spectra for Mn_{12}-Ac are strongly influenced by the hydrogen bonding acetic acid solvent. Given the corresponding *E*-strain associated with the low-symmetry species in Cornia's model [6], one can thus assume that the QMT dynamics in Mn_{12}-Ac are significantly affected by extrinsic factors related to the disorder. In contrast, the solvents in the BrAc and *t*BuAc structures do not hydrogen bond to the Mn_{12} core. Furthermore, the possibility for positional and/or orientational solvent disorder does not exist in

the way that it does for Mn_{12}-Ac (Cornia model [6]). In particular, the BrAc complex contains a full compliment of four symmetric CH_2Cl_2 solvents per formula unit. Meanwhile, the lone MeOH solvent associated with the Mn_{12}-*t*BuAc complex resides far from the Mn_{12} core, and is shared equally among four unit cells. Furthermore, crystals of the *t*BuAc complex do not contain any faster relaxing Mn_{12} species, as is known to be the case for Mn_{12}-Ac and even Mn_{12}-BrAc. The absence of complexity in the HFEPR spectra of Mn_{12}-BrAc and Mn_{12}-*t*BuAc suggests that detailed investigations of these compounds may reveal even more information concerning the quantum dynamics of large spins, e.g., a Berry phase associated with the $\hat{O}_4^4$ operator [25].

The linewidths are considerably narrower for the two newer complexes, as compared to the Mn_{12}-Ac. In fact, the $\theta = 90°$ line shape for the Mn_{12}-*t*BuAc complex fits somewhat better to a Lorentzian function than to a Gaussian, suggesting that the linewidth may be close to the intrinsic lifetime broadened limit (width $\approx$0.1 T, implying $\tau \approx 0.4$ ns). Furthermore, the linewidths are almost m_s independent. However, there are vestiges of evidence for inhomogeneous broadening mechanisms (g, D, and E strain), such as the asymmetric lineshapes for the Mn_{12}-BrAc complex, and a small, but measurable m_s dependence of the linewidths for both complexes. Determining the source of any inhomogeneous broadening will require extensive easy-axis measurements as a function of frequency, field (m_s) and temperature. Such an undertaking will represent the subject of a future paper.

Further comparison between the grayscale plots for the three complexes leads one to believe that there are essentially no measurable tilts for the BrAc and *t*BuAc complexes. Not only are there well defined gaps between the and β series' of resonances, in overall agreement with Fig. 5(a), there are also clear evidences for curvature at the edges of each absorption band. This has been emphasized by the 15% contour lines in Figs. 8 and 10. Simulations show that even a modest amount of easy axis tilting dramatically suppresses the curvature seen in the grayscale plots. This curvature is associated with level repulsion, or level mixing. In the high-field limit, the 21 states associated with $S = 10$ may be described in a basis in which the spin projection quantum number m_s refers to the projection of S onto the applied magnetic field axis. Furthermore, each m_s state is essentially pure in this high-field limit. Consequently, rotating the field should not produce dramatic shifts in the EPR peak positions, because the Zeeman term ($g\mu_B \boldsymbol{B} \cdot \hat{\boldsymbol{S}}$) represents the dominant interaction in the Hamiltonian, i.e., the magnitude of the Zeeman interaction does not change upon rotating the field if the spin is free to rotate with the field. However, in the intermediate regime (Zeeman interaction comparable to crystal field), tilting the magnetic field results in a complex interplay between the axial and transverse terms in the spin Hamiltonian, i.e., the transverse Zeeman interaction ($g\mu_B B\hat{S}_x$) may dominate when the field is exactly in the hard plane, whereas tilting of the field results in an out-of-plane magnetic field component which rapidly ($\alpha \sin\theta$) amplifies the axial ($\hat{S}_z$ containing) terms. This interplay results in strong level mixing of states (described in either an $\hat{S}_x$ or and $\hat{S}_z$ basis), and to a non-linear dependence of the resonance positions on the magnetic field strength, leading to the curvature seen in the edges of the absorption bands in Figs. 8 and 10. Therefore, these measurements constitute evidence for coherent superposition states, albeit involving fairly complex admixtures of the simple zero-field $S = 10$ basis states.

The spin Hamiltonian parameters for Mn_{12}-BrAc are very similar to those of Mn_{12}-Ac, and have been published previously by us [13]. Fig. 11 displays fits to single-crystal HFEPR data obtained with the magnetic field applied both parallel [Fig. 11(a)] and perpendicular [Fig. 11(b) and (c)] to the easy axis of the Mn_{12}-*t*BuAc complex. The frequencies used in these experiments span from 50 to 350 GHz. The fits in Fig. 11(a) and (b), together with hard-plane rotation experiments in Fig. 11(c), provide three separate constraints on the spin Hamiltonian

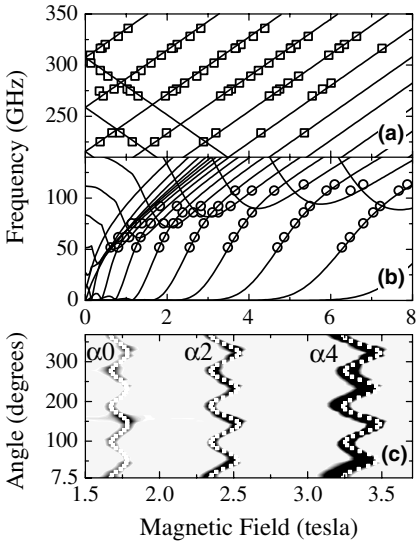


Fig. 11. (a) Fits to the frequency dependence of HFEPR peak positions obtained with the field applied precisely along the easy axis (to within ±0.5°) of a Mn_{12}-*t*BuAc single crystal; the temperature was 15 K for these measurements. Fits for this orientation constrain parameters corresponding to operators in the spin Hamiltonian that commute with $\hat{S}_z$, i.e., D, B_4^0 and g_z. (b) Fits to the frequency dependence of HFEPR peak positions obtained with the field applied precisely within the hard plane (to within ± 0.18°); the temperature was also 15 K for these measurements. Fits for this orientation constrain the transverse Landé factors, g_x and g_y. (c) Fits (white squares) to the fourfold peak-position shifts (dark shaded regions) for field rotations approximately within the hard plane of the sample. Fits for this orientation constrain the transverse term B_4^4, with no dependence on any of the other parameters in the spin Hamiltonian. All fits involved exact diagonalization of the Hamiltonian matrix, and ignored terms with twofold symmetry.

parameters, for which we obtain the following values: $D = -0.462(2)\ \mathrm{cm}^{-1}$, $B_4^0 = -2.5(2) \times 10^{-5}\ \mathrm{cm}^{-1}$, $B_4^4 = \pm 4.3(2) \times 10^{-5}\ \mathrm{cm}^{-1}$, $g_z = 2$, and $g_x = g_y = 1.94$. In contrast to the data for Mn_{12}-Ac, the data in Fig. 11(c) are restricted to lower fields. The reason has to do with the fact that the molecules are so well aligned that it is virtually impossible to rotate precisely in the hard plane. Thus, the high-field peaks exhibit a strong twofold distortion associated with the mis-alignment between the field rotation plane and the hard plane. Even for a 0.5° mis-alignment, the effect is dramatic for α10, α8 and α6. Because of the easy axis tilts in Mn_{12}-Ac, the data in Fig. 2 are relatively insensitive to minor mis-alignments of the rotation plane. However, the *t*BuAc complex is less forgiving. Nevertheless, the fits in Fig. 11 are sufficient for determining B_4^4.

4. Summary and conclusions

We use angle-resolved HFEPR spectroscopy to asses the influence of the solvent structure on the quantum properties of several high-symmetry Mn_{12} single-molecule magnets, including the most widely studied Mn_{12}-Ac. In spite of over 10 years of research, a clear picture has only recently emerged concerning the symmetry breaking responsible for the QMT in Mn_{12}-Ac [6–10]. Disorder associated with the acetic acid solvent leads to discrete local environments, resulting in a significant fraction of the molecules (>50%) possessing twofold symmetry with a rhombic zero-field-splitting term $E = \pm 0.014(2)\ \mathrm{cm}^{-1}$. Differences in the E values deduced from the present measurements and those reported in [7,9] highlight the importance of sample handling. Indeed, it is likely that Mn_{12}-Ac samples prepared by different groups, and studied by different techniques, exhibit significant differences in their solvent content (particularly powder samples), resulting in subtly different conclusions concerning the quantum dynamics. For this reason, it is advantageous to prepare Mn_{12} SMMs which do not exhibit such a dramatic dependence on solvent content. Indeed, we go on to show that all of the unusual solvent-induced anomalies reported for Mn_{12}-Ac are absent in the HFEPR spectra for two related high-symmetry Mn_{12} complexes, Mn_{12}-BrAc and Mn_{12}-*t*BuAc. The absence of complexity in the HFEPR spectra of the BrAc and *t*BuAc Mn_{12} complexes suggests that detailed investigations of these compounds may reveal even more information concerning the quantum dynamics of large spins, e.g., a Berry phase associated with the $\hat{O}_4^4$ operator [25].

Acknowledgments

We thank David Hendrickson and Wolfgang Wernsdorfer for stimulating discussion. Funding is provided by the National Science Foundation (DMR0103290, DMR0239481 and CHE0414155) and by Research Corporation.

References

[1] See, e.g., Molecule-based magnets, Joel S. Miller, Arthur J. Epstein (Eds.), MRS Bull. 25 (11) (2000) 21.
[2] D. Gatteschi, R. Sessoli, Angew. Chem. 42 (2003) 268.
[3] J.R. Friedman, M.P. Sarachik, J. Tejada, R. Ziolo, Phys. Rev. Lett. 76 (1996) 3830.
[4] L. Thomas, F. Lionti, R. Ballou, D. Gatteschi, R. Sessoli, B. Barbara, Nature 383 (1996) 145.
[5] T. Lis, Acta Crystallogr., Sect. B: Struct. Crystallogr. Cryst. Chem. 36 (1980) 2042.
[6] A. Cornia, R. Sessoli, L. Sorace, D. Gatteschi, A.L. Barra, C. Daiguebonne, Phys. Rev. Lett. 89 (2002) 257201.
[7] S. Hill, R.S. Edwards, S.I. Jones, J.M. North, N.S. Dalal, Phys. Rev. Lett. 90 (2003) 217204.
[8] E. del Barco, A.D. Kent, E.M. Rumberger, D.N. Hendrickson, G. Christou, Phys. Rev. Lett. 91 (2003) 047203.
[9] S. Takahashi, R.S. Edwards, J.M. North, S. Hill, N.S. Dalal, Phys. Rev. B 70 (2004) 094429.
[10] E. del Barco, A.D. Kent, S. Hill, J.M. North, N.S. Dalal, E.M. Rumberger, D.N. Hendrickson, N. Chakov, G. Christou, arXiv/cond-mat/0404390 (2004).
[11] J. An, Z.-D. Chen, X.-X. Zhang, H.G. Raubenheimer, C. Esterhuysen, S. Gao, G.-X. Xu, J. Chem. Soc., Dalton Trans. 22 (2001) 3352.
[12] H.-L. Tsai, D.-M. Chen, C.-I. Yang, T.-Y. Jwo, C.-S. Wur, G.-H. Lee, Y. Wang, Inorg. Chem. Commun. 4 (2001) 511.
[13] K. Petukhov, S. Hill, N.E. Chakov, K.A. Abboud, G. Christou, Phys. Rev. B 70 (2004) 054426.
[14] M. Mola, S. Hill, P. Goy, M. Gross, Rev. Sci. Inst. 71 (2000) 186.
[15] S. Takahashi, S. Hill, Rev. Sci. Inst. 76 (2005) 023114.
[16] M. Soler, W. Wernsdorfer, Z. Sun, J.C. Huffman, D.N. Hendrickson, G. Christou, Chem. Commun. 2003 (2003) 2672.
[17] M. Murugesu et al. (in preparation).
[18] Kyungwha Park, Tunna Baruah, Noam Bernstein, Mark R. Pederson, Phys. Rev. B 69 (2004) 144426.
[19] A.L. Barra, D. Gatteschi, R. Sessoli, Phys. Rev. B 56 (1997) 8192.
[20] S. Hill, J.A.A.J. Perenboom, N.S. Dalal, T. Hathaway, T. Stalcup, J.S. Brooks, Phys. Rev. Lett. 80 (1998) 2453.
[21] R. Bircher, G. Chaboussant, A. Sieber, H.U. Güdel, H. Mutka, Phys. Rev. B 70 (2004) 212413.
[22] S. Hill, S. Maccagnano, K. Park, R.M. Achey, J.M. North, N.S. Dalal, Phys. Rev. B 65 (2002) 224410.
[23] C.J.H. Jacobsen, E. Pedersen, J. Villadsen, H. Weihe, Inorg. Chem. 32 (1993) 1216.
[24] W. Wernsdorfer, N.E. Chakov, G. Christou, Phys. Rev. B 70 (2004) 132413.
[25] E. Keçecioglu, A. Garg, Phys. Rev. B 67 (2003) 054406.

orbitals on adjacent octahedra are constrained to be nearly orthogonal, leading to ferromagnetic coupling within each layer [8]. The intralayer exchange coupling is strongly correlated with the long semi-coordinate Cu···X bond distance, decreasing monotonically as the distance increases [9]. Also, since this semi-coordinate distance can vary in length from 2.8 Å to more than 3.3 Å, more complex cations can be incorporated into the Cu(II) perovskite structures. While the intralayer coupling is invariably ferromagnetic and relatively strong, the interlayer coupling is normally very weak and antiferromagnetic, although a few instances of ferromagnetic interlayer couplings are known [10].

An analogous series of layer perovskite structures can be formed with α,ω-diammonium dications, with the general formula $(NH_3RNH_3)MX_4$ [11]. Now the dications hydrogen bond between adjacent halometallate layers, tying the layers together and providing three dimensional stability to the crystalline lattice. These dications force adjacent layers into an eclipsed configuration and, as the hydrocarbon chains shorten, the X···X distances between layers decrease to the point where significant exchange coupling can occur in the magnetic systems [12]. However, with *N*,*N*′-substituted α,ω-diammonium cations, the layer perovskite structure can no longer be formed, since the $R_nNH_{4-n}^+$ groups (n = 2, 3 or 4) cannot be accommodated in the cavities formed by the non-bridging halide ions.

In this paper, we examine the structure and properties of two members of the copper halide layer perovskite family formed when the organic cation is a mono *N*-alkyl substituted ethylenediammonium dication. The cations involved are *N*-methylethylenediammonium (henceforth $MEDA^{2+}$) and *N*-ethylethylenediammonium (henceforth $EEDA^{2+}$). The compounds have the stoichiometric formulas $(REDA)_2CuCl_6$ (R = Me, Et), but are more appropriately formulated as $[(REDA)Cl]_2CuCl_4$, since two of the chloride ions are not coordinated to the Cu(II) ions but are hydrogen bonded to the dications.

2. Experimental

2.1. Preparation

The compounds are conveniently prepared by dissolution of a 2:1 mole ratio of the appropriate *N*-alkylethylenediamine:$CuCl_2 \cdot 2H_2O$ in a hot ethanol solution acidified with concentrated hydrochloric acid. Thin yellow crystals form after slow evaporation of the cooled solution.

2.2. X-ray studies

Crystals were attached to a glass fiber using glue. Datasets were collected at 293(2) K using a Bruker/Siemens SMART 1K instrument (Mo Kα radiation, λ = 0.71073 Å). Data were measured using ω scans of 0.3° per frame for 30 s, and a half sphere of data was collected. The first 50 frames were recollected at the end of data collection to monitor for decay. Cell parameters were retrieved using SMART [13] software and refined using SAINTPLUS [14] on all observed reflections. Data reduction and correction for Lp and decay were performed using the SAINTPLUS software. Absorption corrections were applied using SADABS [15]. The structures were solved by direct methods and refined by least squares method on F^2 using the SHELXTL program package [16]. No decomposition was observed during data collection. Structure refinements were straightforward in both cases and no disorder was observed. Data collection parameters are given in Table 1 and significant bond distances and angles given in Table 2. Fig. 1 illustrates the contents of the asymmetric units of both salts, augmented to show the coordination geometry of the Cu(II) ions. Further details are provided in the Supporting Information.

2.3. Magnetic measurements

Variable temperature susceptibility measurements were carried out in the temperature range 2–300 K with an applied magnetic field of 0.1 T on ground polycrystalline samples with a SQUID magnetometer (Quantum Design MPMS-XL-5). The susceptibility data were corrected for the diamagnetic contributions of the sample

Table 1
Data collection and refinement parameters

Compound	$[(MEDA)Cl]_2CuCl_4$	$[(EEDA)Cl]_2CuCl_4$
Formula	$C_6H_{24}C_{16}CuN_4$	$C_8H_{28}C_{16}CuN_4$
Formula weight	428.53	456.58
T (K)	293(2)	293(2)
λ (Å)	0.71073	0.71073
Crystal system	monoclinic	monoclinic
Space group	$C2/c$	$P2_1/c$
Unit cell dimensions		
a (Å)	33.632(7)	18.690(4)
b (Å)	7.3283(15)	7.3444(15)
c (Å)	7.1442(14)	7.1350(14)
β (°)	92.08(3)	100.58(3)
V (Å^3)	1759.7(6)	962.7(3)
Z	4	2
ρ_{calc} (Mg/m^3)	1.618	1.575
μ (mm^{-1})	2.139	1.960
F(000)	876	470
Reflections total/unique	10789/2024	8837/1683
R_{int}	0.0445	0.0563
Goodness-of-fit	1.062	1.129
R_1 [$I > 2\sigma(I)$]	0.0470	0.0417
wR_2 [$I > 2\sigma(I)$]	0.1081	0.0901
Largest residual (e Å^{-3})	0.806	0.746

$R_1 = \sum||F_o| - |F_c||/\sum|F_o|$.
$wR_2 = (\sum w||F_o^2| - |F_c^2||/\sum w|F_o^2|)^{1/2}$.

Table 2
Selected bond distances and angles

$[(MEDA)Cl]_2CuCl_4$		$[(EEDA)Cl]_2CuCl_4$	
Atoms	Distance (Å)	Atoms	Distance (Å)
Cu–Cl(1)	2.2832(10)	Cu–Cl(1)	2.2827(8)
Cu–Cl(2)	2.3069(11)	Cu–Cl(2)	2.3045(10)
Cu–Cl(1)^{i}	2.8783(10)	Cu–Cl(1)^{iv}	2.8764(9)
Atoms	Angle(°)	Atoms	Angle(°)
Cl(1)^{ii}–Cu–Cl(2)	89.85(4)	Cl(1)^{v}–Cu–Cl(2)	90.09(4)
Cl(1)–Cu–Cl(1)^{i}	91.75(2)	Cl(1)–Cu–Cl(1)^{iv}	91.55(2)
Cl(2)–Cu–Cl(1)i	92.37(4)	Cl(2)–Cu–Cl(1)^{iv}	87.64(3)
Cu–Cl(1)–Cu^{iii}	165.32(5)	Cu–Cl(1)–Cu^{vi}	165.28(4)

Symmetry transformations used to generate equivalent atoms: ^{i} $-x$, $y+1/2$, $-z+1/2$, ^{ii} $-x$, $-y+1$, $-z$, ^{iii} $-x$, $y-1/2$, $-z+1/2$, ^{iv} $-x+1/2$, $y-1/2$, $-z+1/2$, ^{v} $-x+1/2$, $-y+3/2$, $-z$, ^{vi} $-x+1/2$, $y+1/2$, $-z+1/2$.

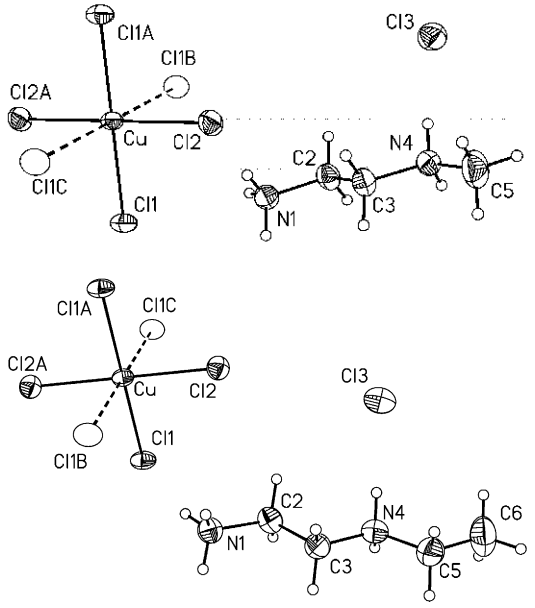


Fig. 1. Illustration of the augmented asymmetric units for the $[(MEDA)Cl]_2CuCl_4$ (top) and $[(EEDA)Cl]_2CuCl_4$ (bottom) salts. Thermal ellipsoids shown at 50% probability level.

as deduced by using Pascal's constant tables. Isothermal magnetization and hysteresis measurements were made at different temperatures, after zero field cooling, between 0 and 5 T. Variable temperature AC susceptibility were performed in the SQUID magnetometer with an alternating field of 0.395 mT at different frequencies (between 1 and 332 Hz) in the temperature range 1.8–15 K.

2.4. EPR measurements

EPR spectra were recorded on a Varian E-3 EPR spectrometer on powdered and single crystals at room temperature and 78 K.

3. Structure description

The basic structures consist of $(CuCl_4^{2-})_n$ perovskite layers sheathed by $[(REDA)^{2+}Cl^{-}]$ moieties. Both structures crystallize in monoclinic space groups, $P2_1/c$ for the MEDA salt and $C2/c$ for the EEDA salt. Despite the difference in space groups, the internal structure of the individual layers is identical in the two salts. Adjacent layers, which lie in the bc planes, are equivalent by translation in both cases. The inorganic framework, consisting of corner-shared tetragonally elongated $CuCl_6$ octahedra (Fig. 2), shows the prototypic layer structure of the $(RNH_3)_2MX_4$ perovskite salts. The short Cu–Cl bonds in the coordination sphere average 2.295 and 2.299 Å for the MEDA and EEDA salts respectively, while the longer semi-coordinate distances are 2.884(1) and 2.878(1) Å. As is always observed in the halocuprate perovskites, the semi-coordinate bonds are arranged in an antiferrodistortive fashion and lie nearly in the plane of the perovskite sheets. Hence the corner sharing linkages involve one short and one longer Cu–Cl bond. The bridging Cu–Cl···Cl angles are nonlinear, with values of 165.3° for both compounds, yielding the typical corrugated sheet structure, as seen in Fig. 2. This puckering of the layers is induced by the hydrogen bonding from the organic cations, as discussed below.

The sheathing of the perovskites layers by the $[(REDA)^{2+}Cl^{-}]$ moieties is stabilized via hydrogen bonding of the $-NH_3^{+}$ groups to the chloride ions in the inorganic framework. The hydrogen bonding scheme can be designated as bt^2, where b denotes an N–H···Cl bond to a bridging chloride ion and t denotes one to a terminal bond. This arrangement forces the cations to lie in planes running approximately parallel to [0 1 1] and [0 1 −1], assuming an antiferrodistortive arrangement reflective of the antiferrodistortive arrangement of the semi-coordinate bonds. The N–Cl distances range from 3.214 to 3.350 Å, with the shortest bonds being to the bridging chloride ions, while the N–H···Cl angles are in the range 160.6–166.4°, with the EEDA salt exhibiting slightly larger ranges than the MEDA salt. The hydrogen bonding is staggered on either side of a given layer, leading to the typical 'washboard' distortion of the layers, as seen in Fig. 2.

To achieve electroneutrality, lattice chloride ions are incorporated into the structure via N–H···Cl hydrogen bonds with the secondary ammonium ion, as also shown in Fig. 2. Each $-NH_2^{+}$ group hydrogen bonds to two lattice chloride ions, forming zigzag hydrogen bonded chains that run parallel to the c axis. These hydrogen bonding distances range from 3.083 to 3.123 Å, while the angles range from 169.5° to 177.4°, with the EEDA salt again showing the larger variations. The hydrogen bonding distances to the layer halide ions are 0.1–0.2 Å longer than those to the lattice chloride ions, indicating

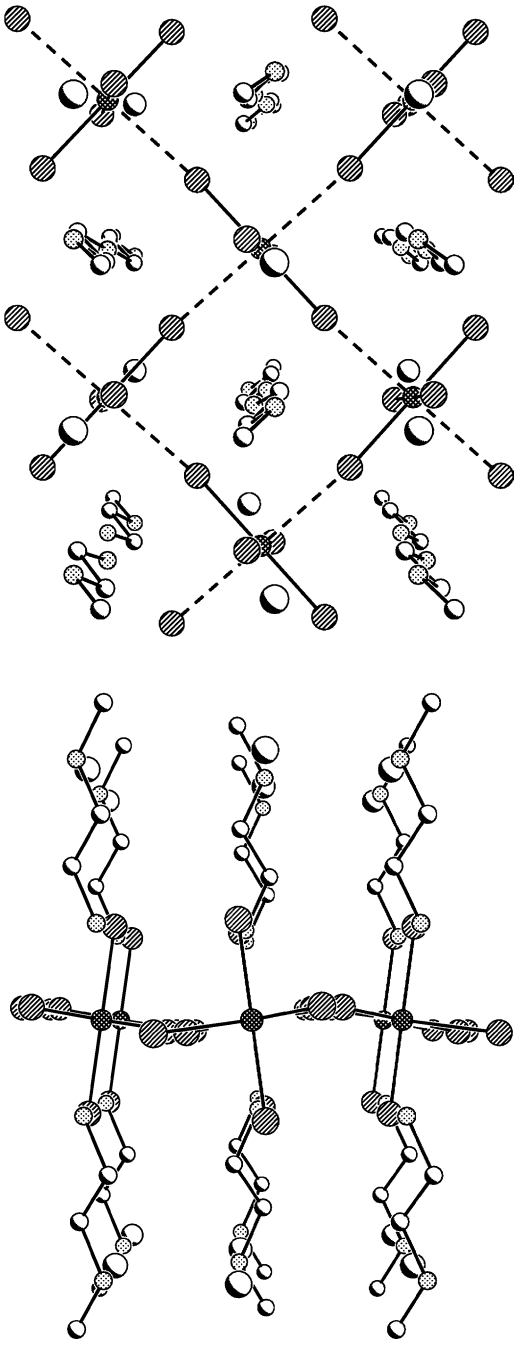


Fig. 2. Illustration of sheathed layer in $[(MEDA)Cl]_2CuCl_4$. Top: top view from (100) direction. Bottom: side view from (001) direction. Lattice chloride ions shown as large highlighted open circles, coordinated chloride ions shown as lined circle.

that the hydrogen bonding cavities in the perovskite layers are somewhat larger than optimal for the hydrogen bonding. In fact, the size of the cavities is more dictated by the packing requirements of the *R* groups than by the hydrogen bonding requirements.

In both compounds, steric repulsions between the terminal methyl groups on adjacent layers forces the layers to be arranged in a staggered conformation. However, this staggered conformation is obtained in a different manner in the two cases. In the MEDA salt, this is achieved by a translation of 1/2 unit cell parallel to the *b*-axis, while in the EEDA salt, this translation is parallel to the *c*-axis.

4. Magnetic results

The magnetic properties of the two salts are essentially indistinguishable from each other, consistent with the identical layer structures of the two salts. Both salts exhibit ferromagnetic coupling, as indicated by the rapid rise in the $\chi_m T$ values as the temperature is lowered. This is illustrated in Fig. 3, for the MEDA salt. The turnover in the value of $\chi_m T$ at low temperature is caused by saturation effects, and is not due to the effects of weak antiferromagnetic coupling, since no maximum is observed in the χ_m as the temperature is lowered to 2 K, as demonstrated in Fig. 4. Fitting of the high temperature data

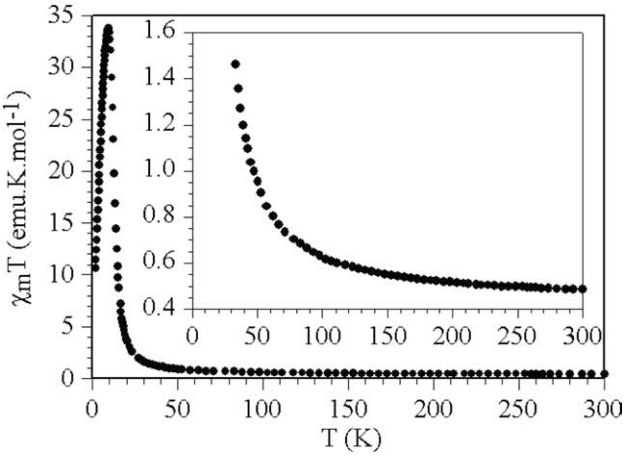


Fig. 3. Thermal variation of the $\chi_m T$ product for the MEDA salt. Inset: the high temperature region.

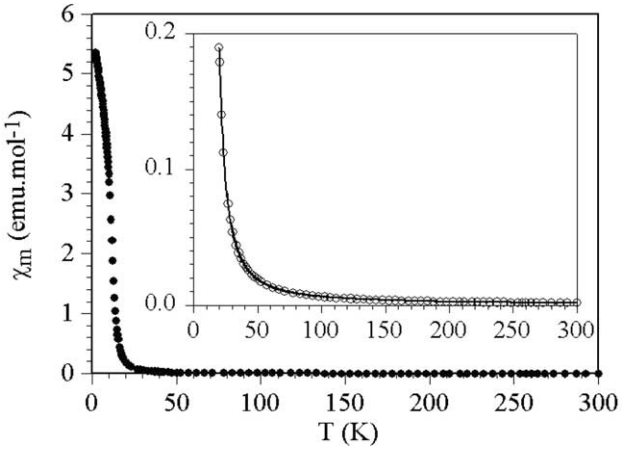


Fig. 4. Thermal variation of the molar magnetic susceptibility, χ_m, for the MEDA salt. Inset: the high temperature region. Solid line is the best fit to the model (see text).

($T > 20$ K, inset in Fig. 4), to the high temperature series expansion for a spin 1/2 two-dimensional ferromagnetic square lattice [17] yields values of $J/k = 19.29(1)$ K with $C = 0.4377(8)$ emu K mol^{-1} for the MEDA salt and $J/k = 19.0(4)$ K with $C = 0.412(1)$ emu K mol^{-1} for the EEDA salt, respectively.

Both salts show a sharp increase in the thermal variation of χ_m below approximately 9 K (Fig. 4), suggesting the presence of a ferromagnetic ordering. To confirm this long range ordering, we have performed ac susceptibility measurements. These measurements show a frequency independent peak in the in-phase signal (χ'_m) at approximately 9.0 K and an out-of-phase (χ''_m) signal in the *ac* susceptibility below that temperature, as shown in Fig. 5 for the EEDA salt. Additional proof is provided by the isothermal magnetizations at $T = 2$ K for both compounds, that show the presence of a rapid saturation at low fields (<0.1 T) with a value close to 1.0 μ_B, as expected for a $S = 1/2$ system (Fig. 6). These data also show the presence of a hysteresis loop for each compound with a coercive field of approximately 1 mT and a remnant magnetization of 0.17 μ_B for the MEDA salt and 0.12 μ_B for the EEDA salt (inset, Fig. 6).

The powder EPR spectrum of both salts consists of a single asymmetric absorption at room temperature, that sharpens to a typical axial spectrum at 78 K with $g = 2.17$ and $g = 2.05$. Single crystal measurements at room temperature gave an essentially axial spectrum with $g = 2.172$ and $g = 2.050$. These results are consistent with the results on previous systems studied [9]. These g values correspond to a Curie constant of 0.410, in good agreement with that found for the EEDA salt, but somewhat lower than that observed for the MEDA salt.

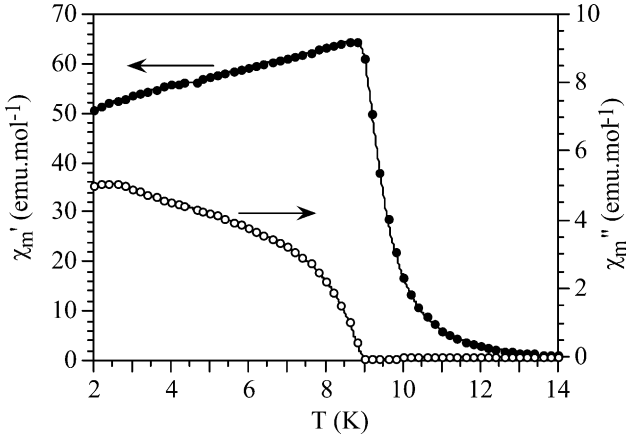


Fig. 5. Thermal variation of the in phase (χ'_m, filled symbols, left scale) and out of phase (χ''_m, empty symbols, right scale) molar AC susceptibility for the MEDA salt with an oscillating magnetic field of 0.395 mT at 10 Hz.

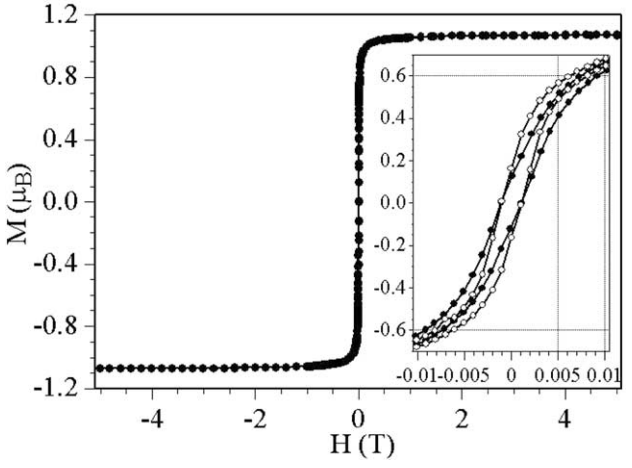


Fig. 6. Hysteresis loop of the EEDA salt at 2 K. Inset: the low field region of the hysteresis loops of the EEDA (filled symbols) and MEDA (empty symbols) salts at 2 K.

5. Discussion

Structurally, a significant feature of this structure is the orientation and relative rigidity of the organoammonium sheaths as a consequence of the presence of the lattice chloride ions. In the simple alkylammonium salts, the R groups typically contain a gauche conformation about one of the first C–C bonds in the alkyl chain and are frequently disordered. In contrast, the existence of strong hydrogen bonding between the secondary ammonium groups and the lattice chloride ions lock the *R*EDA groups into an all-*trans* configuration and provides rigidity to the sheaths. Similar behavior is observed in the $[NH_3(C_2H_4NH_2)_nC_2H_4NH_3 \cdot n\mathrm{Cl}]CuCl_4$ salts ($n = 1$, 2) [18]. Here, again, lattice chloride ions are incorporated into the structure to achieve charge neutrality. In fact, the structures of the $[(MEDA)Cl]_2CuCl_4$ salt can be naively envisioned as being derived from the $[NH_3(C_2H_4NH_2)_2C_2H_4NH_3 \cdot 2\mathrm{Cl}]CuCl_4$ salt by cleavage of the central C–C bond. However, now, due to the steric repulsions of the terminal methyl groups, adjacent layers are in a staggered configuration. As a consequence of the similarities in the structure of the organic sheaths in these two classes of layer perovskites that contain lattice chloride ions, the internal structure of the perovskite layers are virtually identical.

Magnetically, the high temperature data are quite consistent with the results of other copper chloride layer perovskite systems. The correlation of J with the semi-coordinate bond length is obeyed very well [9]. The values of $J/k \sim 19$ K corresponds very well, for example, with that for $[NH_3(C_2H_4NH_2)_2C_2H_4NH_3 \cdot 2\mathrm{Cl}]CuCl_4$, where a value of 19.4 K is observed [18b]. The ordering temperatures of 9.0 K are at the low end of the observed ranges for T_c, but again are in agreement with the values reported for $[NH_3(C_2H_4NH_2)_2C_2H_4NH_3 \cdot 2\mathrm{Cl}]CuCl_4$. That low value of T_c was attributed to the very small

amount of anisotropy present in the ferromagnetic exchange coupling. The nearly axial symmetry of the EPR g values observed for the *R*EDA salts suggests that the same argument holds for these systems.

The observation of the hysteresis loops for the two compounds clearly indicate the presence of ferromagnetic coupling between layers. This is only the second report of such observations, although ferromagnetic coupling between layers has been inferred in several other salts [10].

6. Supporting information

Crystallographic data for the structures reported here have been deposited with the Cambridge Crystallographic Data Center as Supplementary Publication Nos. CCDC-252685 and CCDC-252687 for the MEDA and EEDA compounds, respectively. Copies of this information may be obtained free of charge from: The Director, CCDC, 12 Union Road, Cambridge, CB2 1EZ, UK (fax: +44 1223 336 033; e-mail: deposit@ccdc.cam.ac.uk or www: http//www.ccdc.cam.ac.uk).

Acknowledgments

Work supported in part by ACS-PRF 34779-AC5 and by the Spanish project MAT2001-3507. R.D.W. thanks the University of Valencia for a visitors grant.

References

[1] D.B Mitzi, Prog. Inorg. Chem. 48 (1999) 1, and references therein.
[2] H.A. Groenendijk, A.J. van Duyneveldt, R.D. Willett, Physica B 98 (1979) 53.
[3] C. Bellitto, P. Day, T.E. Wood, J. Chem. Soc., Dalton Trans. (1986) 847.
[4] (a) D.B. Mitzi, K. Liang, J. Solid State Chem. 134 (1997) 376;
(b) D.B. Mitzi, C.A. Feild, W.T.A. Harrison, A.M. Guloy, Nature 369 (1994) 467;
(c) D.B. Mitzi, J. Chem. Soc., Dalton Trans. (2001) 1;
(d) D.B. Mitzi, P. Brock, Inorg. Chem. 40 (2001) 2096;
(e) C.R. Kagan, D.B. Mitzi, C.D. Dimitrakopoulos, Science 286 (1999) 945;
(f) D.B. Mitzi, C.A. Feild, Z. Schlesinger, R.B. Laibowitz, J. Solid State Chem. 114 (1995) 159.
[5] (a) E.R. Peterson, R.D. Willett, J. Chem. Phys. 56 (1972) 1879;
(b) R.D. Willett, E.F. Riedel, Chem. Phys. 8 (1975) 112.
[6] (a) P. Zhou, J.E. Drumheller, B. Patyal, R.D. Willett, Phys. Rev. B 45 (1992) 12365;
(b) G.S. Long, M. Wei, R.D. Willett, Inorg. Chem. 30 (1997) 3102;
(c) C.P. Landee, K.E. Halvorson, R.D. Willett, J. Appl. Phys. 61 (1987) 3295;
(d) R.D. Willett, Acta Crystallogr. C 46 (1990) 565;
(e) T. Sekine, T. Okuno, K. Awaga, Mol. Cryst. Liq. Cryst. Sci. Technol. Sect. A 279 (1996) 65.
[7] F. Barendrecht, H. Schenck, Physica (Utrecht) 49 (1970) 465.
[8] See L.J. de Jongh, A. Miedema, Adv. Phys. 23 (1974) 1.
[9] R.D. Willett, H. Place, M. Middleton, J. Am. Chem. Soc. 110 (1988) 8639.
[10] (a) J.J.M. Steiger, G. Frikkee, L.J. de Jongh, W.D. Huiskamp, Physica B 123 (1984) 24;
(b) L.J. de Jongh, M.D. Amstel, A.R. Miedema, Physica 58 (1972) 227;
(c) T. Sekine, T. Okuno, K. Awaga, Inorg. Chem. 37 (1998) 2129.
[11] K. Halvorson, R.D. Willett, Acta Crystallogr. C 44 (1988) 207, and references therein.
[12] (a) L.O. Snively, D.N. Haines, K. Emerson, J.E. Drumheller, Phys. Rev. B 26 (1982) 5245;
(b) L.O. Snively, P.L. Seifert, K. Emerson, J.E. Drumheller, Phys. Rev. B 20 (1979) 2101;
(c) L.O. Snively, G.K. Tuthill, J.E. Drumheller, Phys. Rev. B 24 (1981) 5349.
[13] SMART: Bruker Molecular Analysis Research Tool, v.5.059. Bruker AXS, Madison, WI, 1997–1998.
[14] SAINTPLUS: Data Reduction and Correction Program. Bruker AXS, Madison, WI, 1999.
[15] G.M. Sheldrick, SADABS V.2.01: an Empirical Absorption Correction Program, Bruker AXS Inc., Madison, WI, 1999.
[16] G.M. Sheldrick, SHELXTL: Version 5.10, Structure Determination Software Suite, Bruker AXS Inc., Madison, WI, 1998.
[17] G.A. Baker, H.E. Gilbert, J. Eve, G.S. Rushbrooke, Phys. Lett. A 25 (1967) 207.
[18] (a) D.W. Phelps, D.B. Losee, W.E. Hatfield, D. Hodgson, J. Inorg. Chem. 15 (1976) 3147;
(b) G.L. Ferguson, B. Zaslow, Acta Crystallogr. B 27 (1971) 849;
(c) T.J. Greenhough, M.F.C. Ladd, Acta Crystallogr. B 33 (1977) 1266.

systems, we have designed, synthesized the novel π-conjugated stable radical or biradicals, **1**–**8** shown in Fig. 1 and characterized their spin alignments [1–7]. The knowledge of photo-induced spin alignment on the excited states will give the guiding principles designing photo-induced/switching magnetic spin systems and the photo-control of the molecular magnetism. These studies will open the new strategy for the photomagnetic devices based on the organic materials.

Intramolecular spin alignment and exchange interaction through π-conjugation are quite important in the field of the molecular magnetism [10]. However, most studies are limited to ground state systems. Although radical (R) and excited-triplet (T) pairs in solution have been extensively investigated by TRESR technique, the direct detections of the excited high-spin states ($S \geqslant 3/2$) arising from the radical–triplet pair are still limited in the solid phase. The first direct TRESR detection of an excited quartet state of a radical–triplet pair was reported for a fullerene–mononitroxide radical system in solution [11] and for a tetraphenyl-porphilinatozinc (II) (ZnTPP) coordinated by *p*-pyridyl nitronylnitroxide (nitpy) system in a solid phase [12]. For homologous systems [13–15], excited high-spin states have been so far reported. However, in these systems, a stable radical couples weakly with the excited triplet chromophore through sigma bonds or coordination, in which the spin exchange interactions are small in magnitude. We reported the first observation of excited quartet ($S = 3/2$) and quintet ($S = 2$) states in purely organic π-conjugated spin systems [1–7], which are generated by a spin alignment through π-conjugation between dangling stable radicals ($S = 1/2$) and the excited triplet ($S = 1$) state of aromatic hydrocarbons. The π-conjugation leads to the strong exchange coupling between the triplet photo-excited state of the aromatic hydrocarbons and the dangling radicals. In the biradical systems, **5**–**8**, the stable radicals couple strongly through the spin coupler by π-conjugation making the robust spin alignment possible.

π-Conjugated spin systems have the following advantages in view point of the material science and molecular magnetism: (1) π-Conjugation leads to the strong exchange coupling which is one of the important conditions for the balk magnetism at finite temperature. (2) One can well design and synthesize the proper spin systems with the desired spin states using the well-established fine-synthetic chemistry. (3) An enhanced intersystem crossing (ISC) mechanism arising from the attachment of the radical species is available [2,6]. This leads to open a way of the direct ESR detection of the silent photo-excited states with little ISC to the triplet state. Actually, since phenyl or diphenylanthracene has very low efficiency of the ISC toward the triplet state, the triplet states can be not directly detected by TRESR. However, by attaching the radical species through π-conjugation, the excited high-spin states arising from the triplet state of phenyl or diphenylanthracene and the doublet state of radical were detected by TRESR as shown later. The photo-induced intra-molecular spin

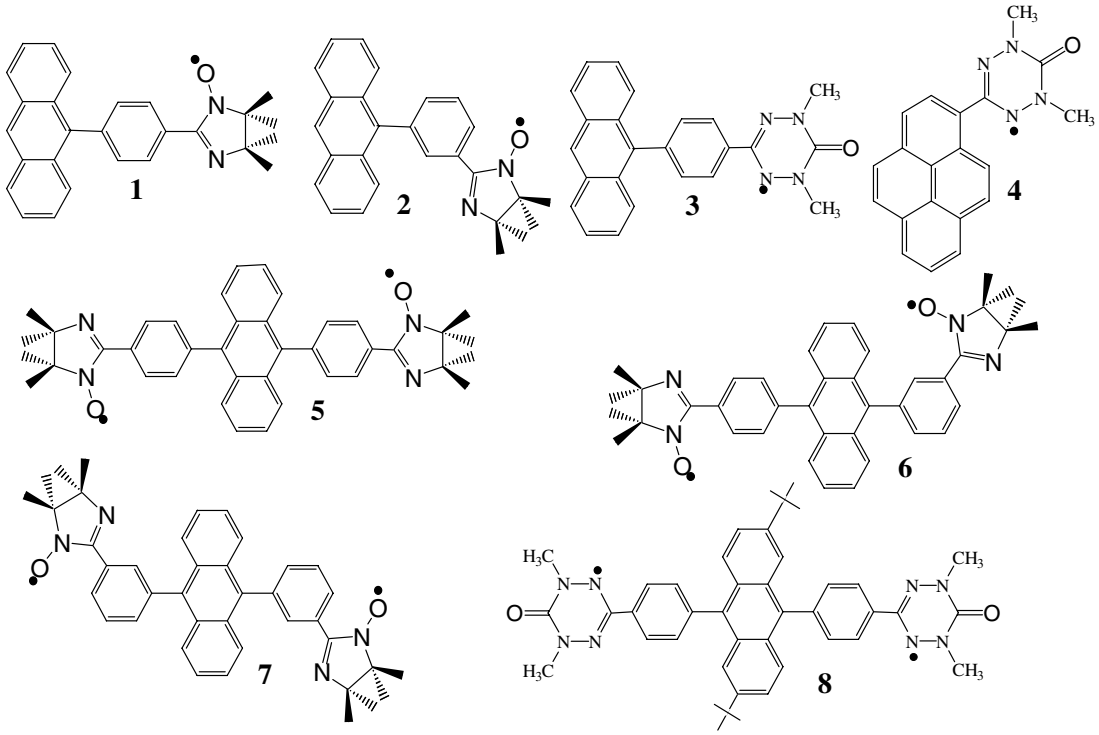


Fig. 1. π-Conjugated organic spin systems in which the photo-excited states were investigated.

alignment through π-conjugation is one of the key processes for the photo-control of the molecular magnetism.

2. Experimental

2.1. Materials

Typical synthetic procedures of monoradical and biradical are shown in Schemes 1 and 2, respectively. 2,3-Bis(hydroxyamino)-2,3-dimethyl-butane was prepared according to the literature method [16]. Other reagents were used as purchased.

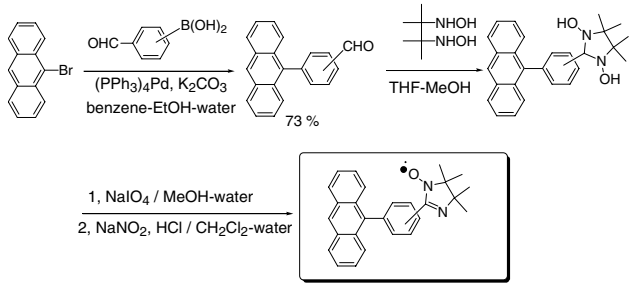
2.2. TRESR measurements and simulation

The photo-excited states were examined by TRESR. A conventional X-band ESR spectrometer (JEOL TE300) was used in the measurements of TRESR spectra without field modulation. Excitation was carried out at 355 nm light using Nd:YAG pulse laser (Continuum Surelite II-10, pulse width <7 ns). The typical laser power used in the experiments was ca. 2–5 mJ. EPA, 2-MTHF, or isopentane–diethylether mixed glass matrix was used for the TRESR experiments. The measurements were carried out at 30–40 K. The typical microwave power was ca. 10 mW.

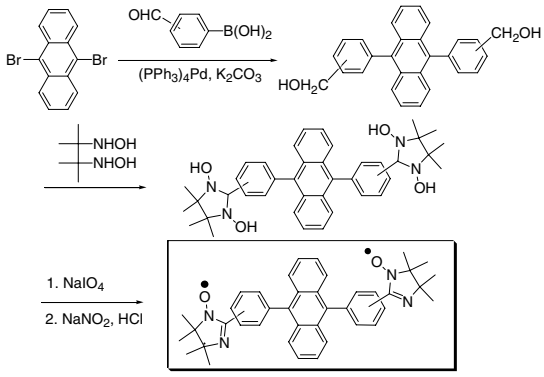
The spectral simulation was carried out by the eigenfield/exact-diagonalization hybrid method [16,17], taking dynamic electron spin polarization (ESP) into account [2]. The effective-exchange interaction between the triplet state of the aromatic hydrocarbon moiety and the dangling radicals is undoubtedly much larger than the Zeeman and fine-structure interactions in the π-conjugated systems. We have, therefore, used the following ordinary spin Hamiltonian of a pure spin state given in Eq. (1) (negligible quantum mixing of the different spin states) for the analysis:

$$H'_{\text{spin}} = \beta_e \boldsymbol{H}.\boldsymbol{g}.S + \boldsymbol{S}.\boldsymbol{D}.\boldsymbol{S}. \tag{1}$$

The resonance field $B_{Ms \leftrightarrow Ms+1}(\theta,\phi)$ for each transition was directly calculated by solving the following eigenfield equation [17]:



Scheme 1. Typical synthetic procedures of monoradical.



Scheme 2. Typical synthetic procedures of biradicals.

$$\boldsymbol{A}\cdot\boldsymbol{Z} = \boldsymbol{B}\boldsymbol{C}\cdot\boldsymbol{Z}, \tag{2}$$

where $\boldsymbol{A}$ and $\boldsymbol{C}$ are given by the following superoperators:

$$\boldsymbol{A} = \omega\boldsymbol{E}\otimes\boldsymbol{E} - \boldsymbol{F}\otimes\boldsymbol{E} + \boldsymbol{E}\otimes\boldsymbol{F} \tag{3}$$

and

$$\boldsymbol{C} = \boldsymbol{G}\otimes\boldsymbol{E} - \boldsymbol{E}\otimes\boldsymbol{G}^{*}. \tag{4}$$

Here, $\boldsymbol{E}$ is a unit matrix and ω is the given microwave frequency. The operators $\boldsymbol{G}$ and $\boldsymbol{F}$ are the field dependent and independent parts of the spin Hamiltonian (1), respectively. By solving the eigenfield equation (Eq. (2)), the resonance field B is obtained. The transition probabilities $I(\theta,\phi,\varphi)$ were evaluated by numerically diagonalization of the spin Hamiltonian matrix at the calculated resonance eigenfield [18,19]. Since the resonance field is independent of the third Euler angle, φ, the above procedure practically saves the computing time for the simulation. The line-shape function of the TRESR spectrum in the glass matrix is given by

$$g(B) = N\sum\int \mathrm{d}\varphi \int \mathrm{d}\phi \int \mathrm{d}\theta \sin\theta P_{Ms\leftrightarrow Ms+1}(\theta,\phi) \times I(\theta,\phi,\varphi) f[B - B_{Ms\leftrightarrow Ms+1}(\theta,\phi)]. \tag{5}$$

In the simulation, the dynamic electron polarization (ESP), $P_{Ms\leftrightarrow Ms+1}(\theta,\phi)$, on each spin sublevel in zero magnetic field was given as parameters. Thus, the relative populations of the Ms sublevels was taken into account as parameters. The simulation was carried out using a program written by the author on a personal computer. The details of the simulation procedures for the high-spin TRESR spectra were described in our previous paper [2].

3. Results and discussion

3.1. Photo-excited quartet high-spin states

Typical TRESR spectrum of **1** is shown in Fig. 2(a) [1,2]. The observed TRESR spectrum with well resolved

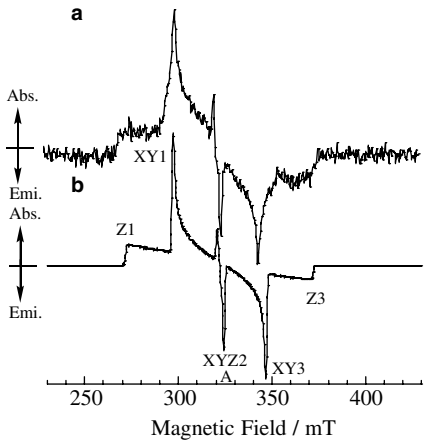


Fig. 2. Typical TRESR spectra of **1** at 30 K in EPA rigid glass matrix. (a) The observed spectrum of **1** at 0.8 μs after laser excitation. (b) The simulated spectrum of the excited quartet state.

fine structure splitting has been unambiguously analyzed to be a excited quartet ($S = 3/2$) state (Q) by the spectral simulation shown in Fig. 2(b). The determined g value, fine-structure parameters, and relative populations of the Ms sublevels are listed in Table 1. Similar excited quartet states were observed for **3** [5] and **4** [6]. The typical TRESR spectrum observed for the pyrene–verdazyl radical, **4**, is also shown in Fig. 3.

In these quartet systems the triplet state of the aromatic hydrocarbon moiety couples with the doublet state of the dangling stable radical by the spin-exchange interaction. In such a exchange-coupled system the wavefunction of the whole molecule $|\Psi(S,M)\rangle$ is approximately given by the direct product of the wavefunctions of the two isolated moieties, $|\mathrm{T}(S^{\mathrm{A}},m_{\mathrm{A}})\rangle$ and $|\mathrm{R}(S^{\mathrm{B}},m_{\mathrm{B}})\rangle$, as

$$|\Psi(S,M)\rangle = \sum C(S^{\mathrm{A}}S^{\mathrm{B}}S;m_{\mathrm{A}}m_{\mathrm{B}}M)|\mathrm{T}(S^{\mathrm{A}},m_{\mathrm{A}})\rangle| \times \mathrm{R}(S^{\mathrm{B}},m_{\mathrm{B}})\rangle, \quad \text{for } S^{\mathrm{A}}=1 \text{ and } S^{\mathrm{B}}=1/2, \quad (6)$$

where $C(S^{\mathrm{A}}S^{\mathrm{B}}S;\, m_{\mathrm{A}}m_{\mathrm{B}}M)$ is the Clebsch–Gordan coefficient. The radical–triplet pair has one quartet and one doublet states. The g and D values for the quartet state (Q) are given by the following relationship [20]:

$$\boldsymbol{g}(\mathrm{Q}) = (2/3)\boldsymbol{g}(\mathrm{T}) + (1/3)\boldsymbol{g}(\mathrm{R}) \quad (7)$$

and

$$\boldsymbol{D}(\mathrm{Q}) = (1/3)\{\boldsymbol{D}(\mathrm{T}) + \boldsymbol{D}(\mathrm{RT})\}. \quad (8)$$

Here, $\boldsymbol{D}(\mathrm{T})$ is the D tensor of the excited triplet moiety, $\boldsymbol{D}(\mathrm{RT})$ is the dipolar interaction between the dangling radical spin and the triplet moiety. Using these equations g and D values were calculated as shown in Table 1. The experimentally determined g, D and E values for the excited quartet state are in excellent agreement with the calculations.

3.2. Excited spin states of the π-topological isomers of *1*

In the ground state π-topology plays very important role in the spin alignment of the alternant hydrocarbons. Spin polarization effect governs the spin alignment and the spin multiplicity of the ground state depends drastically on the π-topology. In order to test the role of the π-topology on the spin alignment in the photo-excited state, TRESR experiments were performed for **2** [2], which is the π-topological isomers of **1**. In contrast to the result of **1**, no TRESR signal attributable to the high-spin excited state was observed for **2** and only a very weak absorptive signal due to the doublet state was observed as shown in Fig. 4. This agrees with the π-topological rule, indicating that the lowest excited state of **2** is a low-spin doublet ($S = 1/2$) spin state and the sign of the intramolecular exchange between the dangling radical spin and the excited triplet spin of the anthracene moiety is antiferromagnetic according to the spin polarization pathway through the dangling phenyl group. This finding shows that the sign of the intramolecular exchange interaction and the spin multiplicity of the lowest photo-excited spin state change drastically depending on the topological nature of π-electron network. Thus, the π-topological rule of the spin polarization established for the ground states of the aromatic hydrocarbons also plays an important role in the spin alignment on the photo-excited states.

Table 1
Spin Hamiltonian parameters (S, g, D and E), relative populations of the Ms sub levels of the zero-field eigenfunctions, and the estimated D values

Molecule	S	g	D (cm^{-1})	$\lvert E\rvert$ (cm^{-1})	Relative population	g_{est}	D_{est} (cm^{-1})	Ref.
1	3/2	2.0043	0.0235	0.0	$P'_{\pm3/2}=0.0,\ P'_{\pm1/2}=0.5$	2.0040	0.0256	[1,2]
3	3/2	2.0040	0.0230	0.0	$P'_{\pm3/2}=0.0,\ P'_{\pm1/2}=0.5$	2.0032	0.0248	[3,5]
4	3/2	2.0035	0.0290	0.0090	$P'_{\pm3/2}=0.0,\ P'_{\pm1/2}=0.5$	2.0033	0.0310	[6]
5	2	2.0043	0.0130	0.0	$P'_{\pm2}=0.0,\ P'_{\pm1}=0.35,\ P'_{0}=0.30$	2.0045	0.0137	[1,2]
6	1	2.0045	0.0360	0.0	$P_X=P_Y=0.0,\ P_Z=1.0$	2.0045		[7]
	2	2.0035	0.0125	0.0	$P'_{\pm2}=0.0,\ P'_{\pm1}=0.0,\ P'_{0}=1.0$	2.0050	0.0120	
8	2	2.0035	0.0128	0.0	$P'_{\pm2}=0.0,\ P'_{\pm1}=0.37,\ P_{0}=0.26$	2.0035	0.0130	[5]

Here, $P_{Ms'}$ is the relative population of the spin sublevels in zero magnetic field, which magnetic quantum number corresponds to the value, Ms, in the high field limit.

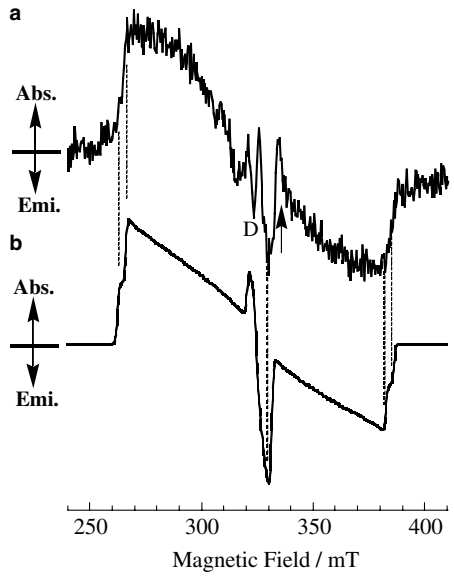


Fig. 3. Typical TRESR spectrum of pyrene–verdazyl radical, **4**.

3.3. Photo-induced spin alignment in diphenylanthracene-bis(radical) systems

In order to clarify the photo-induced spin alignment using the photo-excited molecular field, we investigated the photo-excited spin states of diphenyanthracene-bis(radical) systems which are illustrated in Fig. 5. In this spin system, the diphenylanthracene spin coupler between two dangling stable radical moieties becomes the photo-excited triplet state with two unpaired electrons upon the photo-excitation. Two dangling radicals are interacted with each other through the triplet spin coupler. The total spin Hamiltonian of the four spin system is given by

$$\begin{aligned}\boldsymbol{H}_{\text{spin}} =& \boldsymbol{H}_{\text{ex}} + \beta_e \boldsymbol{H}\cdot\boldsymbol{g}^{\text{T}}\cdot\boldsymbol{S}^{\text{T}} + \beta_e \boldsymbol{H}\cdot\boldsymbol{g}^{\text{R}_1}\cdot\boldsymbol{S}^{\text{R}_1} \\ &+ \beta_e \boldsymbol{H}\cdot\boldsymbol{g}^{\text{R}_2}\cdot\boldsymbol{S}^{\text{R}_2} + \boldsymbol{S}^{\text{T}}\cdot\boldsymbol{D}(\text{T})\cdot\boldsymbol{S}^{\text{T}} \\ &+ \boldsymbol{S}^{\text{R}_1}\cdot\boldsymbol{D}(R_1\text{T})\cdot\boldsymbol{S}^{\text{T}} + \boldsymbol{S}^{\text{R}_2}\cdot\boldsymbol{D}(R_2\text{T})\cdot\boldsymbol{S}^{\text{T}}, \qquad (9)\end{aligned}$$

$$\boldsymbol{H}_{\text{ex}} = -2J_1\boldsymbol{S}^{\text{R}_1}\cdot\boldsymbol{S}^{\text{T}} - 2J_2\boldsymbol{S}^{\text{T}}\cdot\boldsymbol{S}^{\text{R}_2}. \qquad (10)$$

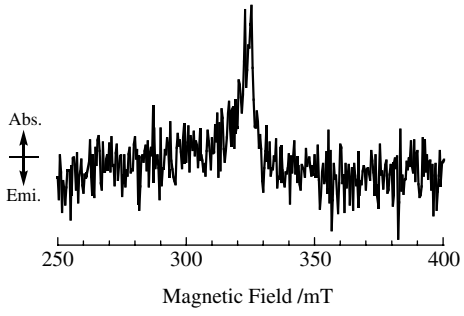


Fig. 4. Typical TRESR spectrum of **2** at 30 K in EPA rigid glass matrix.

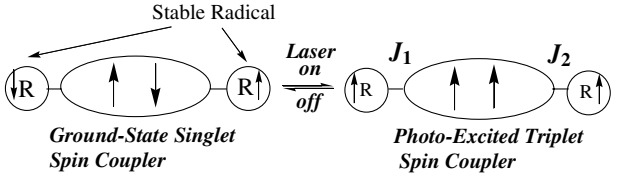


Fig. 5. Photo-induced intramolecular spin alignment.

Here, we omitted the dipolar interactions between two radicals moieties. The π-conjugated spin systems, the exchange interaction is much larger than other interactions in Eq. (9). The energies of each spin state in zero magnetic field were obtained to zero-th order by diagonalizing H_{ex}. The expectation values of the fine-structure terms of each spin states were calculated by using the eigenfunctions. There are two kinds of the triplet states (T_1 and T_2), one quintet state (Qu) and one singlet state (S). The energy versus J_2/J_1 diagram for each spin states are shown in Fig. 6 [7]. The fine-structure terms (D) of each spin states are related to the fine-structure tensor (D(T)) of the triplet state of anthracene by a reduction factor (f) ($D = f\cdot D$(T)). The reduction factor of each spin states are shown in Fig. 7 [7]. In this calculation, we omitted $D(R_1\text{T})$ and $D(R_2\text{T})$ in Eq. (10), because D(T) is much larger than them. As already shown in Sections 3.1 and 3.2, *para*-joint configuration between the iminonitroxide radical and the triplet excited state of the anthracene moiety leads to the ferromagnetic coupling and *meta*-joint configuration is antiferromagnetic coupling between them. Therefore, *para*-joint biradical **5** is expected to have a quintet state ($S = 2$) as the lowest photo-excited state and *meta*-joint biradical **7** has a singlet state ($S = 0$). An interesting lowest photo-excited triplet state arising from four unpaired electrons will be realized in **6** by the antiferromagnetic spin exchange coupling of the two dangling radical spins through the photo-excited triplet spin coupler (diphenylanthracene moiety). In order to prove this prediction, TRESR experiments were carried out for the π-topological isomers, **5**–**8** as shown later.

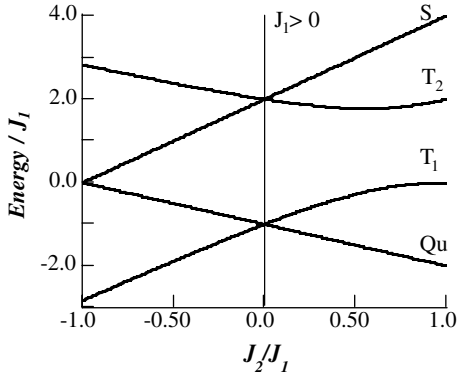


Fig. 6. Energy vs. J_2/J_1 diagram.

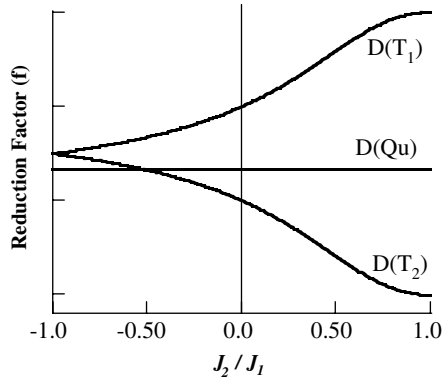


Fig. 7. J_2/J_1 Dependence of the reduction factor.

3.3.1. Photo-excited quintet high-spin states

Typical TRESR spectrum of the photo-excited quintet ($S = 2$) state (Qu) of the biradical system, **5** [1,2], is given in Fig. 8 together with the spectral simulation. The spin Hamiltonian parameters are also listed in Table 1. Similar excited quintet state was observed for a verdazyl biradical, **8** [5]. All the determined spin Hamiltonian parameters and relative population of the *Ms* sublevels of these excited high-spin states are summarized in Table 1.

According to a similar manner described in the case of the quartet state, the *g*, *D* and *E* values of the quintet state (Qu) have been estimated using the following equations, which are listed in Table 1:

$$\boldsymbol{g}(\mathrm{Qu}) = \{2\boldsymbol{g}(\mathrm{T}) + \boldsymbol{g}(\mathrm{R_1}) + \boldsymbol{g}(\mathrm{R_2})\}/4 \tag{11}$$

and

$$\boldsymbol{D}(\mathrm{Qu}) = (1/6)(\boldsymbol{D}(\mathrm{T}) + \boldsymbol{D}(\mathrm{R_1T}) + \boldsymbol{D}(\mathrm{R_2T}) + \boldsymbol{D}(\mathrm{R_1R_2})). \tag{12}$$

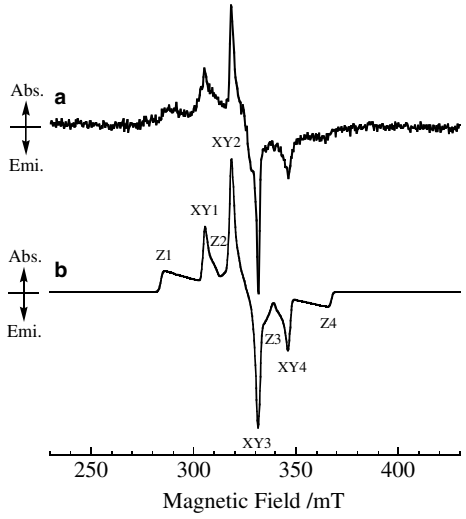


Fig. 8. Typical TRESR spectra of **5** at 30 K in 2-MTHF rigid glass matrix. (a) The observed spectrum of **5** at 0.8 μs after laser excitation. (b) The simulated spectrum of the excited quintet state.

Here, $\boldsymbol{D}(\mathrm{R_1R_2})$ is the dipolar interaction between the two radical spins. This was actually neglected in the estimation because of the small magnitude. The estimated values of the fine-structure parameters are quite well in agreement with the observed values, showing that the observed quintet state is a high-spin species originated from the triplet spin coupler and two dangling radicals.

The direct observations of the excited quintet states show that the photoinduced intramolecular spin alignment is realized between the excited triplet state ($S = 1$) of the diphenylanthracene moiety and the doublet spins ($S = 1/2$) of the dangling radicals as illustrated in Fig. 9. In Qu the photo-induced intramolecular ferromagnetic spin alignment between two dangling radicals is achieved through the photo-excited triplet ($S = 1$) spin coupler of the diphenylanthracene moiety [1,2].

3.3.2. Excited spin states and photo-induced spin alignment of π-topological isomers of 5

In order to test the role of the π-topology on the spin alignment in the photo-excited state, TRESR experiments were performed for **6** [7] and **7** [2], which are the π-topological isomers of **5**. A drastic change in the TRESR spectrum was observed for **6** and **7**. No TRESR signal for the excited spin state was observed in **7**, indicating that the lowest excited state is a low-spin singlet ($S = 0$) spin state, which is ESR silent. Therefore, the intramolecular spin exchange between two dangling radical spins and the excited triplet spin of the spin coupler is antiferromagnetic, similar to the case of **2**.

For the molecule **6**, TRESR signals arising from the lowest triplet photo-excited state (T_1) and the low-lying quintet spin state (Qu) closely above the triplet state were observed as shown in Fig. 10 [7]. The spin-Hamiltonian parameters for both spin states are also listed in Table 1. The magnitude of *D* of the triplet state is ca. 50% of that of anthracene. The unique triplet state has an interesting electronic structure, which *D* value is reduced by the antiferromagnetic spin alignment between two radical spins through the excited spin coupler. This small *D* value is characteristic nature of the unique triplet state, which is constructed from four unpaired electrons and explained well theoretically as already shown in Fig. 7 [7]. From the ratio $D(T_1)/D(Qu)$, determined in this experiment, the ratio of the exchange interactions, can be estimated that $J_2/J_1 = -0.05$. The sign and magnitude of the exchange coupling between the radical moiety and the triplet spin coupler is proportional to the product of the spin densities at linking positions. The sign of the spin densities of the spin coupler linked by two radical moieties is opposite and the spin density for R_2 is expected to be small. Therefore, the small negative value of J_2/J_1 is reasonable. The quintet state is located very closely above the triplet state in this case. The co-existence of the triplet and the quintet signals in the spectrum is well understood from the nearly

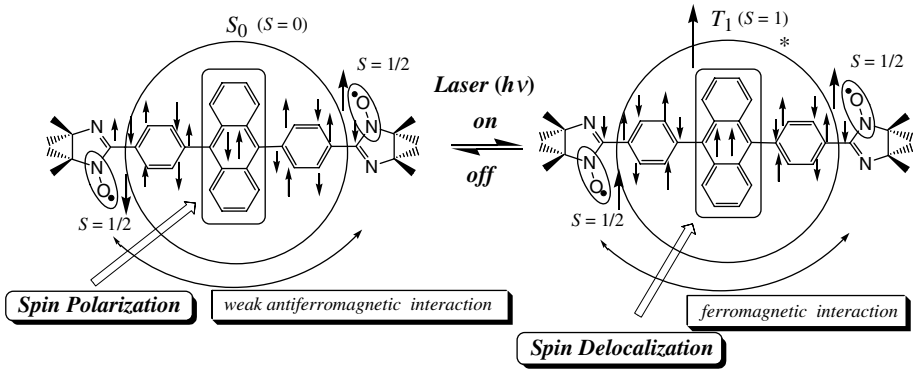


Fig. 9. Photo-induced intramolecular spin alignment and sign inversion of the effective exchange between two dangling radical spins.

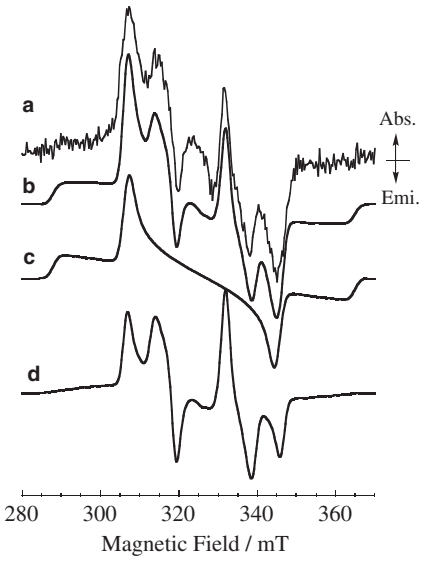


Fig. 10. Typical TRESR spectrum of **6**. (a) Observed spectrum at 0.5 μs after the laser excitation at 30 K in the glass matrix. (b) Simulated spectrum (super-imposed T_1 and Qu). (c) Simulation of T_1. (d) Simulation of Qu.

degenerated energy locations as predicted for the small negative J_2/J_1 value in Fig. 6 [7].

These findings agree with the spin prediction shown in Fig. 6. Thus, the two dangling radical spins can be manipulated through the photo-excited triplet spin coupler (diphenylanthracene moiety) by the photo-excitation. The π-topological rule of the photo-induced spin alignment is established on the excited states based on these findings.

3.4. Physical picture of photoinduced intra-molecular spin alignment in viewpoint of spin density distribution

In order to obtain the physical picture of the photo-induced intramolecular spin alignment, the ab initio molecular orbital calculations were carried out based on the density functional theory (DFT) using GAUSSIAN 98 [21]. In these calculations, an unrestricted Hartree–Fock method (Ubecke 3LYP/6-31G) was employed in order to clarify the role of the spin polarization effect.

Fig. 11 shows the calculated total spin densities on the atomic sites in the excited quartet state of **1** [4]. The mechanism of the spin alignment was clarified based on the spin distribution. In the excited quartet state the spin density distribution of the anthracene moiety is nearly symmetrical as shown in Fig. 11. The almost two net unpaired spins exist on the anthracene moiety and the remained one unpaired spin exists on the dangling radical. This shows that the excited quartet state is generated by the one-electron transition from the β-HOMO (π) to the α-LUMO (π*). These results are consistent with our experimental results, in which the magnitude of the observed fine-structure splitting has been well interpreted as the exchange coupled system constructed from the ππ* excited triplet state of anthracene and the dangling radicals. In the anthracene moiety, positive spin densities overcome the negative spin densities. This spin distribution shows that spin delocalization overcomes the spin polarization effect within the anthracene moiety. In contrast, the alternating sign of the spin density is realized on the dangling phenyl groups as shown in Fig. 11. This sign alternation of the spin densities shows that the spin polarization mechanism overcomes the spin delocalization within the dangling phenyl groups even in the excited state. Thus, through the spin polarization pathway in the dangling phenyl group, the unpaired spin on the dangling radical

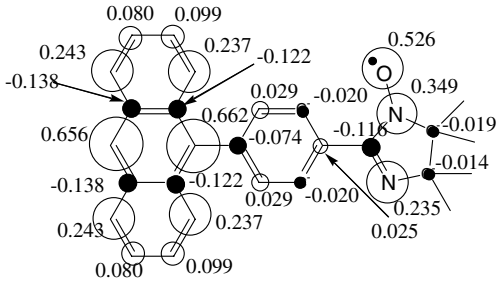


Fig. 11. The spin density distribution in the excited quartet state of **1**.

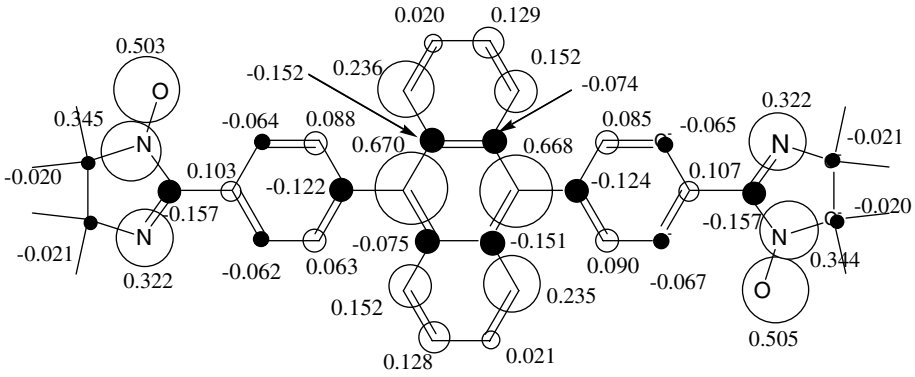


Fig. 12. Spin density distribution in the excited quintet state of **5**.

couples ferromagnetically to the excited triplet spins delocalized on the anthracene moiety, leading to the excited quartet high-spin state.

The calculated spin distribution of the excited quintet state of **5** [4] is shown in Fig. 12. The spin delocalization and spin polarization effects similar to the case of **1** occurred in the quintet state. The large positive spin densities at the 9 and 10 positions of the anthracene moiety are realized by the spin delocalization. Each dangling radical spin ($S = 1/2$) couples ferromagnetically to the large positive spin of the excited triplet spins on the anthracene moiety, through the spin polarization pathway in the phenyl groups. This mechanism leads to the ferromagnetic exchange between excited triplet state and two radical spins in **5**. As the results, the sign of the effective spin coupling of the two dangling radicals in **5** can be changed from antiferromagnetic to ferromagnetic as illustrated in Fig. 9 by the exchange coupling through the excited triplet moiety generated by the photo-excitation. Similar results were obtained for the quintet states of **8**.

3.5. Potential developments toward functional materials using photo-excited high-spin organic systems

The observations of the high-spin photo-excited states mean that the intersystem crossing (ISC) from low-spin state to high-spin states occurs efficiently. As previously reported in our paper [2,6], this effective ISC are generated by the attachment of radical species. The enhanced ISC mechanism is concerned with the π-conjugation between the pπ orbital of radical moiety and aromatic hydrocarbon moiety. The enhanced ISC to the high-spin photo-excited states will open a new channel to relax from the high-spin photo-excited state toward the ground/low-lying high-spin states. Moreover, since the high-spin photo-excited states have fairly long life-time (10–20 μs at 77 K), the energy

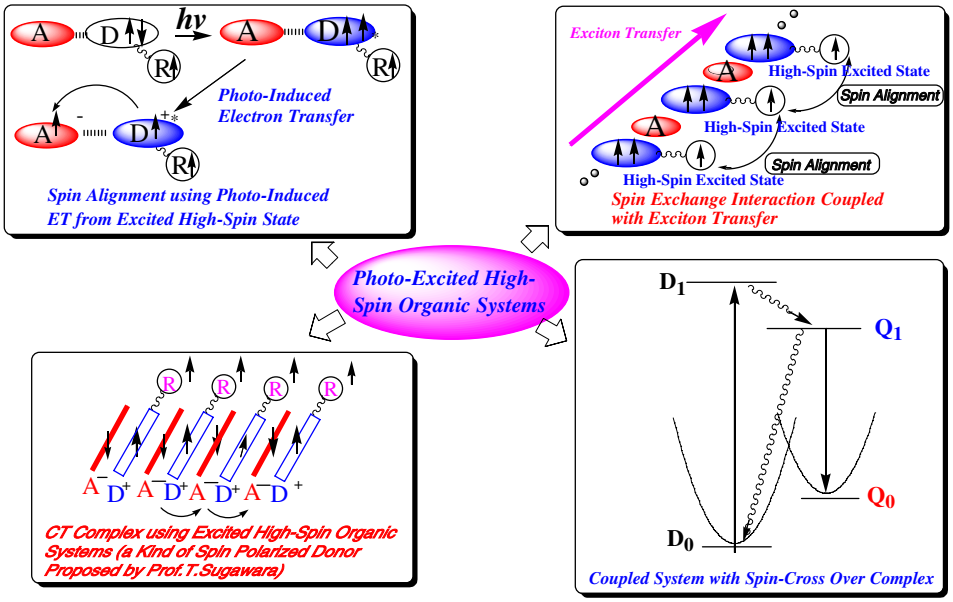


Fig. 13. Potential developments toward functionality materials using the π-conjugated organic spin system with photo-excited high-spin states.

transfer and the photo-induced electron transfer processes will be expected from such high-spin photo-excited states. These processes also channel a new pathway using the photo-excited state toward the new functionality materials.

There are some potential developments of the photo-excited high-spin organic systems toward the functionality materials shown in Fig. 13. In order to realize such functionality materials, it is necessary to develop the systems to superstructure materials. One of the ways is to make the charge-transfer complexes using the excited high-spin organic spin systems as the electron donor and to use the photo-induced electron transfer from the donor to the acceptor. In the intramolecular donor-acceptor linked systems using the photo-excited high-spin molecule are also potential candidates. Moreover, the cation of the photo-excited high-spin system is expected to have interesting electronic structure, in which the triplet state becomes the electronic ground state. Therefore, this system is a kind of the spin-polarized donor proposed by Sugawara et al. [22].

Since the photo-excited high-spin state has fairly long life-time, the exciton transfer is possible to occur in their crystals. The intermolecular photo-induced spin alignment of the dangling radical spins may be achieved by the exciton transfer. The combination with the metal complex will be one of the potential developments. It is special interest in the construction of the spin cross-over complex using the photo-excited high-spin organic molecules as their ligands. In the case, the photo-excitation of the ligand leads to open the new pathway to relax the high-spin ground state of the whole system. There will be also other potential applications of the π-conjugated organic spin systems with the photo-excited high-spin states.

4. Summary

The spin alignment in the photo-excited states of the purely organic π-conjugated spin systems and their topological isomers are reviewed. In the photo-excited states the photo-induced spin alignment is investigated by TRESR experiments and ab initio MO calculations. Role of the spin delocalization and the spin polarization effects are revealed in the spin alignment on the photo-excited states. The photo-induced spin alignment was achieved through the photo-excited triplet spin coupler. π-Topology plays very important role on the spin alignment on the photo-excited states as well as the ground states. One of the key processes for the photo-control of the organic molecular magnetism is established. The guiding principle designing the photo-excited high-spin system and the role of π-topology are clarified. Some ideas of the potential developments toward the functionality materials utilizing the π-conjugated organic spin systems with the photo-excited high-spin states are also proposed.

Acknowledgements

I express my gratitude to all collaborators to the work described here. A particular thank to Prof. Y. Miura for the syntheses of some anthracene derivatives. This work was supported by PRESTO of the Japan Science and Technology Corporation and the Grant-in-Aid for Scientific Research on the general (No. 13440211, 16350079) and Priority Area "Application of Molecular Spins" (Area No. 769, Proposal No. 15087208) from the Ministry of Education, Culture, Sports, Science and Technology, Japan.

References

[1] Y. Teki, S. Miyamoto, K. Iimura, M. Nakatsuji, Y. Miura, J. Am. Chem. Soc. 122 (2000) 984.
[2] Y. Teki, S. Miyamoto, M. Nakatsuji, Y. Miura, J. Am. Chem. Soc. 123 (2001) 294.
[3] Y. Teki, M. Nakatsuji, Y. Miura, Int. J. Mod. Phys. B 15 (2001) 4029.
[4] Y. Teki, Polyhedron 20 (2001) 1163.
[5] Y. Teki, M. Nakatsuji, Y. Miura, Mol. Phys. 100 (2002) 1385.
[6] Y. Teki, M. Kimura, S. Narimatsu, K. Ohara, K. Mukai, Bull. Chem. Soc. Jpn. 77 (2004) 95.
[7] Y. Teki, S. Nakajima, Chem. Lett. 33 (2004) 1500.
[8] K. Itoh, Pure Appl. Chem. 50 (1978) 1251.
[9] Y. Teki, K. Itoh, in: P.M. Lahti (Ed.), Magnetic Properties of Organic Materials, Marcel-Dekker, 1999, p. 237, and references cited therein.
[10] Most recent overviews of the molecule-based magnetism. See: G. Christou (Ed.), Polyhedron 22 (2002) 1725, Proceedings of the VIIIth International Conference on Molecule-based Magnets.
[11] (a) C. Corvaja, M. Maggini, M. Prato, G. Scorrano, M. Venzin, J. Am. Chem. Soc. 117 (1995) 8857;
(b) N. Mizouchi, Y. Ohba, S. Yamauchi, J. Chem. Phys. 101 (1997) 5966.
[12] (a) K. Ishii, J. Fujiwara, Y. Ohba, S. Yamauchi, J. Am. Chem. Soc. 118 (1996) 13079;
(b) K. Ishii, J. Fujisawa, A. Adachi, S. Yamauchi, N. Kobayashi, J. Am. Chem. Soc. 120 (1998) 3152.
[13] P. Ceroni, F. Conti, C. Corvaja, M. Maggini, F. Paolucci, S. Roffia, G. Scorrano, A. Toffoletti, J. Phys. Chem. A 104 (2000) 156.
[14] (a) N. Mizouchi, Y. Ohba, S. Yamauchi, J. Phys. Chem. 103 (1999) 7749;
(b) F. Conti, C. Corvaja, A. Toffoletti, N. Mizouchi, Y. Ohba, S. Yamauchi, M. Maggini, J. Phys. Chem. 104 (2000) 4962;
(c) J. Fujiwara, Y. Iwasaki, Y. Ohba, S. Yamauchi, N. Koga, S. Karasawa, M. Fuhs, K. Möbius, S. Weber, Appl. Magn. Reson. 21 (2001) 483.
[15] K. Ishii, Y. Hirose, N. Kobayashi, J. Phys. Chem. 103 (1999) 1986.
[16] (a) M. Lamchen, T.W. Mittag, J. Chem. Soc. C 2 (1966) 300;
(b) C. Hirel, K.E. Vostrikova, J. Pecaut, V.I. Ovcharenko, P. Rey, Chem. Eur. J. 7 (2001) 2007.

[17] G.G. Belford, R.L. Belford, J.F. Burkhalter, J. Magn. Reson. 11 (1973) 251.
[18] Y. Teki, I. Fujita, T. Takui, T. Kinoshita, K. Itoh, J. Am. Chem. Soc. 116 (1994) 11499.
[19] In the spectral simulation of the TRESR spectra, the calculation of ESP has been added as a subroutine to the computer program. More detailed procedures of the spectral simulation for high-spin organic molecules are similar to those described in our previous paper for the perturbation approach: Y. Teki T. Takui, H. Yagi, K. Itoh, H. Iwamura, J. Chem. Phys. 83 (1985) 539.
[20] A. Bencini, D. Gatteschi, EPR of Exchange Coupled Systems, Springer-Verlag, Berlin, 1990.
[21] The DFT calculation was carried out using GAUSSIAN 98, Revision A.11, Gaussian, Inc., Pittsburgh, PA, 1998.
[22] T. Sugawara, Mol. Cryst. Liq. Cryst. 334 (1999) 257.

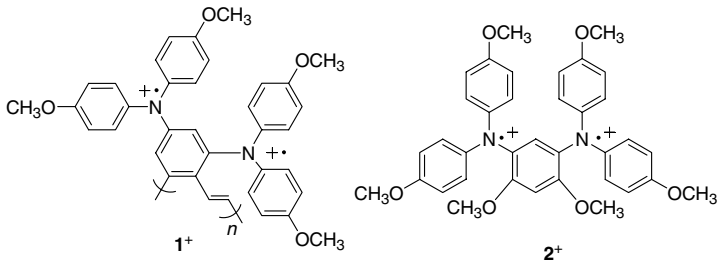
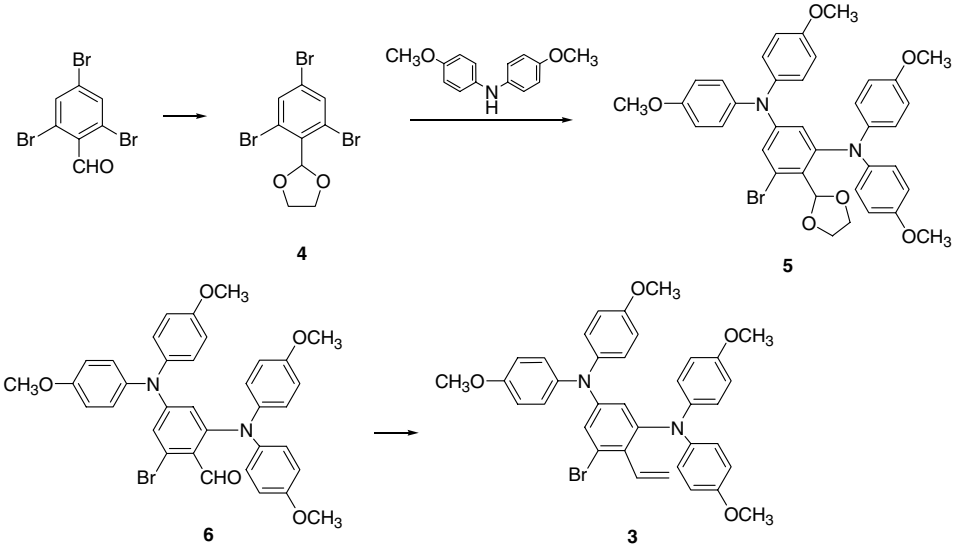


Chart 1.

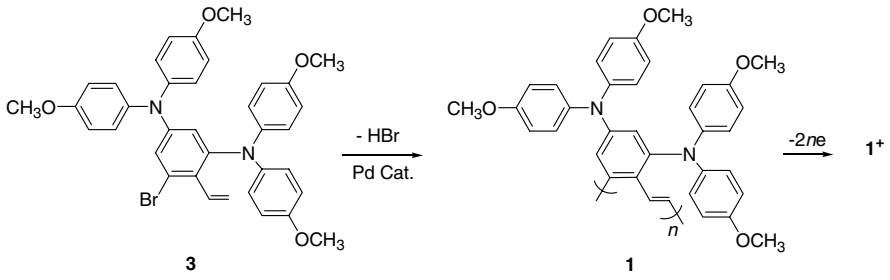
alignment among the pendant unpaired electrons by synthesizing poly(1,2-phenylenevinylene)s that are 4-substituted with stable diphenylaminium cation radicals [6]. The poly(1,2-phenylenevinylene) backbone is characterized as being relatively coplanar with an extended π-conjugation even after the introduction of the pendant radical group. Poly(4-diphenylaminium-1,2-phenylenevinylene) showed the spin quantum number of $S = (4 - 5)/2$ even at room temperature, because the triphenylaminium cation radical has both an excellent chemical stability and an efficient delocalized spin density into the aryl groups [7]. Beside these linear polyradicals, another synthetic approach focuses on the π-conjugated polymer bearing two pendant radicals in one monomer unit. Although these polyradicals are one-dimensional linear π-conjugated polymers, the spin coupling of the neighboring radical units is a ladder-liked connection, which can enhance the interaction between the neighboring (and even remote) pendant radicals [8]. In previous papers, a very strong ferromagnetic interaction was reported in the *m*-phenylene-coupled bis- and tris-phenylaminiums, realizing their triplet and quartet state [9]. This suggests that *m*-phenylene acts as a strong ferromagnetic coupler in an extended polyradical bearing a triplet biradical. In this study, we have synthesized poly[4,6-bis(bis(4-methoxyphenyl)aminium)-1,2-phenylenevinylene] $\mathbf{1}^+$ which has both a very strong ferromagnetic coupling through the *m*-phenylene unit and a moderately strong ferromagnetic coupling through the poly(1,2-phenylenevinylene) unit (see Chart 1).

2. Results and discussion

A head-to-tail linkage structure of the substituted radical group is essential for the non-Kekulé and non-disjoint or the following magnetic study. This was established through the polycondensation via the Heck reaction of the 4,6-disubstituted-2-bromostyrene derivative. 4,6-Bis(bis(4-methoxyphenyl)amino)-2-bromostyrene was synthesized as the monomer for the polycondensation. After the formyl group of 2,4,6-tribromobenzaldehyde was protected by the 1,3-dioxolane group, the palladium-catalyzed amination of **4** with *N,N*,-bis(4-methoxyphenyl)amine followed by deprotection yielded **6** (Scheme 1). The formyl group of **6** was converted to a vinyl group via the



Scheme 1.



Scheme 2.

Wittig reaction to afford the bromostyrene derivative **3** as the monomer.

The bromostyrene monomer **3** was polycondensed through the Heck reaction using the catalyst of palladium and tri(*o*-tolyl)phosphine in the presence of triethylamine and lithium chloride as a base and a source of chloride ion, respectively, in a DMF solution at 70 °C for 72 h (Scheme 2). This polymerization condition was selected for the selective *β*-arylation of the vinyl group with the aryl bromide in order to avoid the formation of chemical defects [6b]. The obtained polymer **1** was soluble in common solvents such as methylene chloride, chloroform, tetrahydrofuran, toluene, and DMF. The number average molecular weight and molecular weight distribution of **1** measured by GPC using polystyrene standards was 2.0×10^3 (1.2). The chloroform solution of the brownish yellow polymer **1** showed two UV/Vis absorption maxima at 301 and 432 nm, with molar absorption coefficient of $\varepsilon = 2 \times 10^4$ and $1 \times 10^4\ M^{-1}\ cm^{-1}$, respectively. They are ascribed to the triarylamine moiety (λ_{max} = ca. 300 nm) and the *trans*-stilbene moiety. The visible absorption was extended to 506 nm for **1**, in comparison with that of poly(1,2-phenylenevinylene) (ca. 430 nm). The solution of **1** exhibited a strong photoluminescence. The λ_{em} for **1** was 504 nm in the chloroform solution (λ_{ex} = 312 nm) and was bathochromically shifted in comparison with that of the model amine **2** (400 nm). The bathochromic shift of λ_{em} for **1** corresponds to the UV absorption edge of **1**, suggesting a developed π-conjugation for **1**.

Cyclic voltammetry of the polymer **1** and model amine **2** in the methylene chloride solution with tetrabutylammonium tetrafluoroborate as the electrolyte gave reversible waves which were repeatedly recorded in the potential sweeps of, e.g., 50 times at room temperature (Fig. 1). This voltammogram result means that the triarylamine groups are electrochemically oxidized to the aminium cationic radicals and reduced to the amines without any subsequent chemical side reactions, such as dimerization, to form a benzidine and a disproportionation. The cyclic voltammogram of **2** showed two waves ascribed to two amine sites ($E_p^{1/2}$ = 885 and 1083 mV). The cyclic voltammogram of **1** showed broader waves than that of **2**, which could be explained by the delocalization effect of the formed aminium cationic radical in the π-conjugation of the polymer.

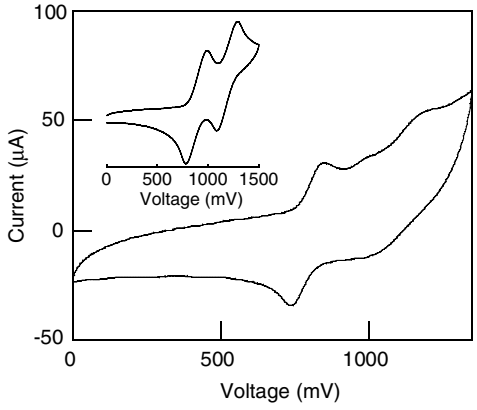


Fig. 1. Cyclic voltammogram of **1** in the methylene chloride solution at a sweep rate of 200 mV/s. Inset: cyclic voltammogram of **2**.

The triaryl aminium cationic radical salts, $\mathbf{1}^+$ and $\mathbf{2}^+$, were prepared by oxidizing the corresponding triaryl amines **1** and **2** with $NOPF_6$ or $SbCl_5$ [10,11]. The oxidation of **2** using $NOPF_6$ resulted in the spin concentration of 0.48 spin/amine unit, which showed a three-line ESR spectrum ascribed to the mono-aminium radical. On the other hand, the oxidation of **2** using $SbCl_5$ produced a spin concentration of 0.90 spin/amine unit and unimodal ESR spectrum, indicating the generation of the di-aminium radical. By considering the oxidation potential of **1**, $SbCl_5$ was selected as the oxidizing reagent of **1**. The color of the methylene chloride solution of **1** turned from pale yellow to deep blue,[1] which is characteristic of triphenylaminium cation radicals [12]. A deep blue-colored powder of $\mathbf{1}^+$ was obtained, of which the spin concentration was estimated to be 0.80 spin/monomer amine unit.[2] The half-life (τ) of the aminium cation

[1] The concentrated methylene chloride solution of $SbCl_5$ was added dropwise to the dilute methylene chloride solution of the amine polymer **1** to provide a high yield upon the aminium cationic radical formation. The $SbCl_6^-$ salt of $\mathbf{1}^+$ was isolated as a blue powder by pouring the methylene chloride solution of $\mathbf{1}^+$ oxidized with $SbCl_5$ into diethyl ether.

[2] Measured by the ESR signal intensity.

radical $\mathbf{1}^+$ in the powder state was 10 days at room temperature, which showed an excellent chemical stability.

The ESR spectrum of $\mathbf{1}^+$ with a low spin concentration gave a three-line signal at $g = 2.0034$ and changed to a strong unimodal signal with the increasing spin concentration, indicating a local high-spin concentration along the polymer backbone (see Inset of Fig. 2). The frozen glass of $\mathbf{1}^+$ gave a $\Delta M_s = \pm 2$ (half field and forbidden) transition at 160 mT which is assigned to a triplet species. The temperature-dependent ESR experiment of $\mathbf{1}^+$ gave a linear relation for the doubly integrated ESR intensity of the $\Delta M_s = \pm 2$ signal as a function of the reciprocal temperature ($1/T$) at higher temperature (>10 K), which was consistent with Curie's law (Fig. 2). However, the plots substantially deviated upward from the linearity observed in the lower temperature region (<10 K). This upward deviation suggests a ferromagnetic interaction between the triplet species.

The $SbCl_6^-$ salt of $\mathbf{1}^+$ was isolated in the presence of poly(styrenesulfonate tetrabutylammonium) as a diamagnetic diluent. This isolated sample of $\mathbf{1}^+$ was subjected to static magnetic susceptibility (χ) and magnetization (M) measurements using a SQUID magnetometer. χ was normalized to the χ_{mol} values with the radical concentration in the sample determined by the saturation magnetization (M_s) of M versus the magnetic field (H) plots. The normalized plots of magnetization (M/M_{sat}) for the diluted $\mathbf{1}^+$ are close to the Brillouin curves for 5/2, indicating a high-spin ground state for $\mathbf{1}^+$. The $\chi_{mol}T$ plots leveled off in the temperature range from 20 to 100 K (see Inset of Fig. 3). The flat $\chi_{mol}T$ plots means that the multiplet ground state for $\mathbf{1}^+$ is significantly large and that $\mathbf{1}^+$ is a paramagnetic molecule with an average $S = (4.5)/2$. These results concluded that a ferromagnetic and intramolecular spin-alignment is realized between the unpaired electrons of the polyaminium cationic radicals. Taking into account both the molecular weight or DP and the spin concentration of $\mathbf{1}^+$, all radical spins in each polymer chain are considered to be aligned. S is expected to proportionally increase with the DP of the poly(aminium cationic radical) $\mathbf{1}^+$.

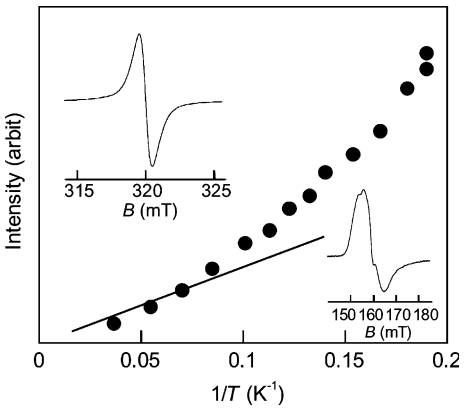


Fig. 2. Temperature dependency of the ESR signal intensity of the $\Delta M_s = \pm 2$ transition of $\mathbf{1}^+$ with 0.80 spins/unit in methylene chloride. The solid line is a least-square fitting to Curie's law (Intensity = C/T). Inset: ESR spectra of the $\mathbf{1}^+$ at room temperature, and the $\Delta M_s \pm 2$ spectrum of $\mathbf{1}^+$ in methylene chloride at 5.0 K.

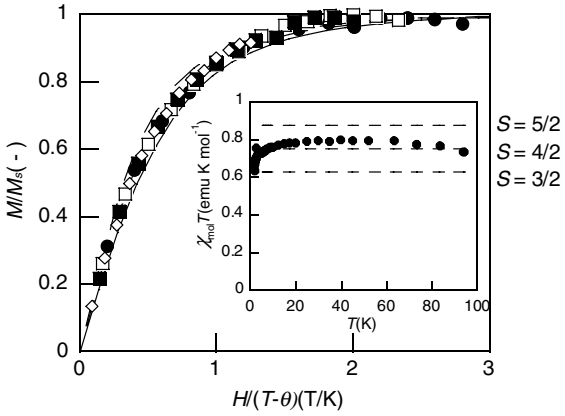


Fig. 3. Normalized plots of magnetization (M/M_s) vs. the ratio of the magnetic field and temperature ($H/(T-\theta)$) for the diluted $\mathbf{1}^+$ (DP = 3.3) with spin concentration = 0.73 spin/amine unit at 1.8 (○), 2.0 (●), 2.5 (□), 3.0 (■), and 5.0 (◇) K and theoretical Brillouin curves corresponding to the $S = 4/2$, 5/2, and 6/2 ($\theta = -0.5$ K). Inset: $\chi_{mol}T$ vs. T plots for the diluted sample of $\mathbf{1}^+$.

2.1. Materials

2,4,6-Tribromobenzaldehyde and 1,5-dibromo-2,4-dimethoxybenzene were prepared according to the literature [13,14]. The other reagents were used as received. The solvents were purified in the usual manners.

2.2. 1,5-Bis[N,N-bis(4-methoxyphenyl)amino]-2,4-dimethoxybenzene (2)

1,5-Dibromo-2,4-dimethoxybenzene (300 mg, 1.01 mmol), 4-methoxy-phenylamine (249 mg, 2.02 mmol) and 1-chloro-4-methoxy-benzene (302 mg, 2.12 mmol) were dissolved in toluene (8.1 ml). Sodium *tert*-butoxide (544 mg, 5.66 mmol), tris(dibenzylideneacetone)dipalladium (27.7 mg, 30.3 μmol), and P(*t*-Bu)$_2$-*o*-biphenyl (36.1 mg, 12.1 μmol) were added, and then the mixture was heated at 80 °C for 24 h. The reaction mixture was neutralized with 1 N aqueous ammonia, and extracted with chloroform. The organic layer was washed with brine, and evaporated to give the crude product, which was purified by HPLC to afford 221 mg of **2**: yield 36%. ^{1}H NMR (500 MHz, $CDCl_3$; ppm) δ 6.97 (s, 1H), 6.87–6.70 (m, 16H), 6.55 (s, 1H), 3.73 (s, 12H), 3.59 (s, 6H); ^{13}C NMR (500 MHz, $CDCl_3$; ppm) δ 154.5, 154.2, 141.8, 131.0, 129.8, 122.2, 114.2, 100.5, 56.4, 55.5. IR (KBr pellet, cm^{-1}) 1239 (ν_{C-O-C}), 1179 (ν_{C-N}), 1036 (ν_{C-O-C}); MS (EI) *m/e* 592, Calc. for $C_{36}H_{36}N_2O_6$: 592.7. *Anal.* Calc. for $C_{36}H_{36}N_2O_6$: C, 73.0; H, 6.1; N, 4.7. Found: C, 72.8; H, 6.0; N, 4.5%.

2.3. 4,6-Bis[N,N-bis(4-methoxyphenyl)amino]-2-bromobenzaldehyde (6)

The mixture of 2,4,6-tribromobenzaldehyde (900 mg, 2.63 mmol), 1,2-ethanediol (1.63 g, 26.3 mmol), benzene (5 ml), and *p*-toluenesulfonic acid monohydrate (2.50 mg, 0.0131 mmol) was refluxed until almost the theoretical amount of water was collected in the trap (ca. 6 h). The reaction mixture was then extracted with chloroform. The organic layer was dried over anhydrous sodium sulfate and evaporated. The crude product was purified using a silica gel column with a hexane eluent to give 2-(2,4,6-tribromophenyl)-1,3-dioxane (**4**) as a white solid (869 mg): yield 86%; m.p. 113 °C; ^{1}H NMR (500 MHz, $CDCl_3$; ppm) 7.74 (s, 1H), 6.32 (s, 1H), 4.31 (t, $J = 3.5$ Hz, 2H), 4.08 (t $J = 3.5$ Hz, 2H); ^{13}C NMR (500 MHz, $CDCl_3$; ppm) δ 206.8, 135.9, 131.9, 125.2, 123.9, 65.9. IR (KBr pellet, cm^{-1}) 940 (ν_{C-O-C}) cm^{-1}; MS (EI) *m/e* 383, 385, 387, 389 Calc. for $C_9H_7Br_3O_2$: 383.8.

4 (55.2 mg, 0.143 mmol) and bis-(4-methoxyphenyl)amine (65.4 mg, 0.285 mmol) were dissolved in toluene (2.2 ml). Sodium *tert*-butoxide (41.1 mg, 0.428 mmol), tris(dibenzylideneacetone)dipalladium (3.92 mg, 4.28 μmol), and (*S*)-(−)-2,2′-bis(diphenylphosphino)-1,1-binaphthyl (4.44 mg, 7.13 μmol) were added, and then mixture was heated at 100 °C for 40 h. The reaction mixture was neutralized with 1 N aqueous ammonia, and extracted with chloroform. The organic layer was washed with brine, and then evaporated to give the crude product, which was purified using a silica gel column with hexane/ethyl acetate (3/1) and HPLC to afford 23.4 mg of **5**: yield 24%. ^{1}H NMR (500 MHz, $CDCl_3$; ppm) δ 9.73–6.95 (m, 18H), 6.10 (s, 1H), 4.10–3.77 (m, 4H), 3.73 (s, 12H); ^{13}C NMR (500 MHz, $CDCl_3$; ppm) δ 156.4, 154.6, 150.7, 142.6, 142.1, 139.2, 126.8, 123.9, 123.3, 123.1, 122.6, 119.8, 114.5, 100.9, 65.3, 55.5, 55.4. IR (KBr pellet, cm^{-1}) 1180 (ν_{C-N}), 960 (ν_{C-O-C}); MS (EI) *m/e* 682, 684 Calc. for $C_{37}H_{35}N_2BrO_6$: 683.6. *Anal*. Calc. for $C_{37}H_{35}N_2BrO_6$: C, 65.0; H, 5.2; N, 4.1; Br, 11.7. Found: C, 64.9; H, 5.3; N, 4.1; Br, 11.8%.

5 (56.1 mg, 82.1 mmol) was dissolved in a mixture of acetone (28 ml) and water (0.90 ml) containing *p*-toluenesulfonic acid (4.68 mg, 24.6 mmol) and refluxed for 3 h. After evaporation, the mixture was extracted with ether. The organic layer was successively washed with aqueous sodium hydrogencarbonate and aqueous saturated sodium chloride and then evaporated. The crude product was purified using a silica gel column with hexane/ethyl acetate (3/1) to give **6** as an orange solid (38.3 mg): yield 73%. ^{1}H NMR (500 MHz, $CDCl_3$; ppm) δ 9.96 (s, 1H), 7.00–6.31 (m, 18H), 3.78 (s, 6H), 3.76 (s, 6H); ^{13}C NMR (500 MHz, $CDCl_3$; ppm) δ 188.2, 157.4, 155.4, 153.1, 142.1, 137.9, 127.7, 126.4, 125.0, 124.5, 119.7, 118.2, 115.4, 114.9, 114.6, 55.5, 55.4. IR (KBr pellet, cm^{-1}) 1680 ($\nu_{C=O}$); MS (EI) *m/e* 638, 640 Calc. for $C_{35}H_{31}N_2BrO_5$: 639.5. *Anal*. Calc. for $C_{35}H_{31}N_2BrO_5$: C, 65.7; H, 4.9; N, 4.4; Br, 12.5. Found: C, 65.9; H, 4.8; N, 4.5; Br, 12.3%.

2.4. 4-[N,N-bis(4-methoxyphenyl)amino]-2-bromostyrene (3)

To 3 ml of a dry THF solution of triphenylmethylphosphonium bromide (139 mg, 0.389 mmol), a 0.161 ml hexane solution of *n*-butyllithium (0.258 mmol) and a dry 0.25 ml THF solution of **6** (83.0 mg, 0.129 mmol) were dropwise added, and stirred at room temperature for 1 h. After evaporation, the crude product was extracted with diethyl ether, washed with brine, dried over anhydrous sodium sulfate, evaporated, and purified with a silica gel column with a hexane/ethyl acetate (20/1) to give 71.5 mg of **3** as a yellow solid: yield 85%. ^{1}H NMR (500 MHz, $CDCl_3$; ppm) δ 6.97–6.59 (m, 18H), 6.32 (dd, $J = 12$, 18 Hz, 1H), 5.51 (d, $J = 18$ Hz, 1H), 5.12 (d, $J = 12$ Hz, 1H), 3.77 (s, 6H), 3.76 (s, 6H); ^{13}C NMR (500 MHz, $CDCl_3$; ppm) δ 156.2, 154.6, 148.8, 147.4, 141.4, 139.7, 132.5, 129.3, 127. 3, 125.3, 123.3, 120.4, 120.0, 118.3, 114.8, 114.3, 55.5, 55.4. IR (KBr pellet, cm^{-1}) 1589 ($\nu_{C=C}$); MS (EI) *m/e*, 636, 638 Calc. for $C_{36}H_{33}N_2BrO_4$: 637.6. *Anal*. Calc. for $C_{36}H_{33}N_2BrO_4$: C, 67.8; H, 5.2; N, 4.4; Br, 12.5. Found: C, 67.6; H, 5.1; N, 4.5; Br, 12.3%.

2.5. Polymerization

The polymerization was carried out by modifying the procedure described in previous papers [6b]. Palladium acetate (1.40 mg, 6.24 μmol), tris(*o*-tolylphosphine) (7.58 mg, 24.9 μmol), triethylamine (104 μl), and lithium chloride (132 mg, 3.12 mmol) were added to the monomer **3** (397 mg, 623 μmol) solution of DMF (1.24 ml), and the mixture was then heated for 3 days to obtain a high molecular weight polymer. The polymerization mixture was poured into methanol, and the precipitated polymer powder was purified by reprecipitation twice from chloroform into the mixture of methanol/benzene (3/7) to afford the **1** polymer (119 mg). The number average molecular weight and molecular weight distribution of **1** measured by GPC (polystyrene gel column, eluent THF, polystyrene calibration) was 2.0×10^3 (1.2).

2.6. Magnetic measurements

The $SbCl_6^-$ salt of $\mathbf{1}^+$ was dissolved in the methylene chloride solution of poly(styrenesulfonate tetrabutylammonium), and then the solvent was thoroughly removed to give the isolated sample. The isolated sample was transferred to a diamagnetic plastic capsule after oxidation. The magnetization and static magnetic susceptibility were measured using a Quantum Design MPMS-7 SQUID magnetometer. The magnetization was

measured from 0.1 to 7 T at 1.8, 2.0, 2.5, 3.0, and 5.0 K. The static magnetic susceptibility was measured from 1.8 to 100 K in a 0.5 T field. The ferromagnetic magnetization ascribed to the impurities was determined by the Honda-Owen plots to be very low (<1 ppm) and subtracted from the overall magnetization. The diamagnetic susceptibility of the diluent and capsule was estimated by the Curie plots of magnetic susceptibility. The corrected magnetization data was fitted to Brillouin functions using the self-consistent version of the mean field approximation [3b].

2.7. Measurements

Cyclic voltammetry was carried out using a BAS 100B/W electrochemical analyzer in a CH_2Cl_2 solution with 0.1 M $(C_4H_9)_4NBF_4$ as the supporting electrolyte. A platinum working electrode and commercial Ag/AgCl electrode as the reference were used. The ESR spectra were taken using a JEOL JES-2XG ESR spectrometer with 100-kHz field modulation. The IR, NMR, mass, and UV spectra were measured using JASCO FT/IR-410, JEOL NMR 500 Λ, Shimazu GC-MS 17A, and JASCO V-550 spectrometers, respectively.

Acknowledgments

This work was partially supported by Grants-in-Aid for the COE Research Programs "Practical Nano-Chemistry" and "Molecular Nano-Engineering" from MEXT, Japan.

References

[1] (a) P.M. Lahti, Magnetic properties of organic materials, Marcel Dekker, New York, 1999;
(b) K. Itoh, M. Kinoshita, Molecular Magnetism: New Magnetic Materials, Kohdansha and Gordon & Breach, Tokyo and Amsterdam, 2000;
(c) J. Veciana, π-Electron magnetism from molecules to magnetic materials, Springer, Berlin, 2001;
(d) J.S. Miller, M. Drillon, Magnetism: molecules to materials III, Wiley–VCH, Weinheim, 2002.
[2] W.T. Borden, E.R. Davidson, J. Am. Chem. Soc. 99 (1977) 4587.
[3] (a) H. Iwamura, N. Koga, Acc. Chem. Res. 26 (1993) 346;
(b) A. Rajca, Chem. Rev. 94 (1994) 871;
(c) H. Nishide, Adv. Mater. 7 (1995) 937;
(d) A. Rajca, Chem. Eur. J. 8 (2002) 4834.
[4] A. Rajca, J. Wongsriratanakul, Science 294 (2001) 1503.
[5] (a) H. Nishide, T. Kaneko, T. Nii, K. Katoh, E. Tsuchida, P.M. Lahti, J. Am. Chem. Soc. 118 (1996) 9695;
(b) H. Nishide, T. Kaneko, S. Toriu, Y. Kuzumaki, E. Tsuchida, Bull. Chem. Soc. Jpn. 69 (1996) 499.
[6] (a) M. Takahashi, T. Nakazawa, E. Tsuchida, H. Nishide, Macromolecules 32 (1999) 6383;
(b) H. Murata, M. Takahashi, K. Namba, N. Takahashi, H. Nishide, J. Org. Chem. 69 (2004) 631.
[7] (a) R.I. Walter, J. Am. Chem. Soc. 77 (1955) 5999;
(b) E.T. Seo, R.F. Nelson, J.M. Fitsch, L.S. Marcoux, D.W. Leedy, R.N. Adams, J. Am. Chem. Soc. 88 (1966) 3498;
(c) L. Hagopian, K. Günyer, R.I. Walter, J. Phys. Chem. 71 (1967) 2290;
(d) S. Sasaki, M. Iyoda, Chem. Lett. (1995) 1011.
[8] (a) T. Kaneko, T. Makino, H. Miyaji, M. Teraguchi, T. Aoki, M. Miyasaka, H. Nishide, J. Am. Chem. Soc. 125 (2003) 3554;
(b) H. Nishide, M. Miyasaka, R. Doi, T. Araki, Macromolecules 35 (2002) 690.
[9] (a) K. Yoshizawa, A. Chano, A. Ito, K. Tanaka, T. Yamabe, H. Fujita, J. Yamauchi, Chem. Lett. (1992) 369;
(b) K. Yoshizawa, A. Chano, A. Ito, K. Tanaka, T. Yamabe, H. Fujita, J. Yamauchi, M. Shiro, J. Am. Chem. Soc. 114 (1992) 5994;
(c) K.R. Stickley, S.C. Blackstock, J. Am. Chem. Soc. 116 (1994) 11576;
(d) K.R. Stickley, S.C. Blackstock, Tetrahedron Lett. 36 (1995) 1585;
(e) M. Yano, M. Furuichi, K. Sato, D. Shiomi, A. Ichimura, K. Abe, T. Takui, K. Itoh, Synth. Met. 85 (1997) 1665;
(f) K. Sato, M. Yano, M. Furuichi, D. Shiomi, T. Takui, K. Abe, K. Itoh, A. Highchi, K. Katsuma, Y. Shirota, J. Am. Chem. Soc. 119 (1997) 6607;
(g) A. Ito, H. Ino, K. Tanaka, K. Kanemoto, T. Kato, J. Org. Chem. 67 (2002) 491.
[10] N.G. Connelly, W.E. Geiger, Chem. Rev. 96 (1996) 877.
[11] J.K. Kochi, Acc. Chem. Res. 25 (1992) 39.
[12] (a) F.A. Neugebauer, S. Bamberger, W.R. Groh, Chem. Ber. 108 (1975) 2406;
(b) W. Schemit, E. Steckhan, Chem. Ber. 113 (1980) 577.
[13] S. Luliński, J. Serwatowski, J. Org. Chem. 68 (2003) 5384.
[14] P. Bovicelli, E. Mincione, R. Antonioletti, R. Bernini, M. Colombari, Synthetic Commun. 31 (2001) 2955.

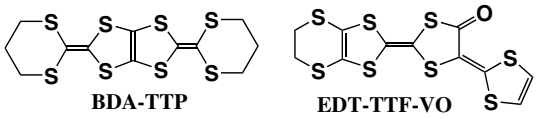


Fig. 1. Molecular structures.

undergoes a metal–insulator (M–I) transition at $T_{MI} = 113$ K, followed by an antiferromagnetic order of the anion spins at $T_N = 8.5$ K. This M–I transition is suppressed under pressure, and a superconducting phase appears above 4.5 kbar. When magnetic field is applied perpendicular to the conducting plane, an abrupt decrease of the resistance is observed at 6 T after the superconductivity is destroyed below 1 T. Though antiferromagnetic order under pressure has not been verified, this resistance anomaly is probably related to the magnetic order. Thus the magnetic order coexists with the superconducting phase.

Another interesting πd-compound is (EDT-TTF-VO)$_2$- $FeBr_4$ (EDT-TTF-VO: ethylenedithiotetrathiafulvalenoquione-1,3-dithiolenethide, Fig. 1) [12,13]. Though the donor is a bent molecule, the $FeBr_4$ salt is fairly conducting, and only weakly semiconducting below the broad resistance minimum around 170 K. The magnetic susceptibility follows the Curie–Weiss law with an antiferromagnetic Weiss constant $\theta = -3.9$ K at high temperatures. Below the minimum of χT at 15 K, χT shows a rapid ferrimagnetic increase. The magnetization saturates to 4.6 μ_B/Fe at 0.4 K, though the hysteresis is not clearly observed. The specific heat indicates a magnetic transition at 1 K. Thus this is the first ferrimagnetic system based on an inorganic anion like $FeBr_4$ (the anion is not a coordination compound). In addition, the π-electron is moderately conducting even at the temperature of the magnetic transition.

The third compound $(BEDT\text{-}TTF)_3(MnCl_4)_2$ has extraordinarily large πd-interactions to the donors incorporated in the anion layer. This compound is important because this is a parent compound of a recently found charge doped system $(BEDT\text{-}TTF)_3(CoCl_4^{2-})_{2-x}(GaCl_4^{-})_x$ [14].

This paper describes estimation of J in these compounds, emphasizing what is different in these compounds from the previous πd-systems.

2. Method of calculation

Transfer integrals of molecular conductors t are estimated from intermolecular overlap of molecular orbitals S (HOMO for donors), by using the relation $t = ES$, where E is the energy level of HOMO (usually −10 eV) [15]. We have used the extended Hückel method to calculate the HOMO, because we like to use the Slater-type atomic orbitals. The same method is applied to calculate the transfers between the donor molecule and the anion ($t_{\pi d}$), and those between the anions (t_d). From this, we can estimate the magnetic interactions J like $J = -2\Sigma t^2/n\Delta$ [7]. Because the $FeCl_4$ anion has five d-like orbitals (Fig. 2), we have to take the sum of the squares t^2 for each d-orbital, and divide the sum by the number of the combinations n. The d-like orbital spreads to Cl to some extent, and the overlap of the Cl orbital with the sulfur orbital of the donor gives rise to finite t. The Coulomb repulsion U, usually appearing in the denominator, is replaced by the difference of the energy levels between the donor HOMO and the d-orbitals, $\Delta = 1$ eV, because Δ is smaller than U of the d-orbital [16]. This calculation method only takes account of the negative (antiferromagnetic) potential exchange, and neglects the positive (ferromagnetic) kinetic exchange. This is somewhat justified by the low symmetry of these πd-systems, and orthogonal orbitals are less probable. The latter contribution is considered in more elaborate calculations [17–19].

To compare the calculated J with the experimentally obtained values, the mean-field theory is useful as the starting point. When the π-electron is localized, the mean-field theory of πd-systems is equivalent to that of ferrimagnets [7], and the Néel temperature T_N is given by

$$2T_N = C_d a_d + C_\pi a_\pi + \sqrt{(C_d a_d - C_\pi a_\pi)^2 + 4C_d C_\pi a_{\pi d}^2}, \quad (1)$$

where C_d and C_π are the Curie constants, and $a_d = 2J_d/N(g\mu_B)^2$ is the molecular field coefficient. When the π-electron is itinerant, this is replaced by

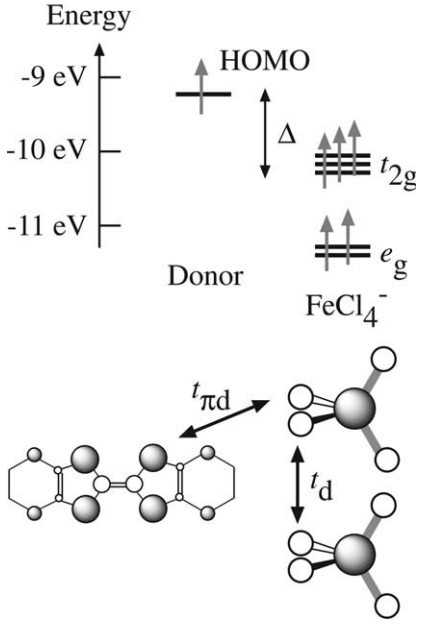


Fig. 2. Energy levels of a TTF-type donor and $FeCl_4$.

$$k_B T_N = 2/3S(S+1)[J_d + \chi_q J_{\pi d}^2]. \quad (2)$$

Then T_N is afforded by the sum of the direct anion–anion interaction (J_d) and the indirect interaction through the π-electron (the second term). If the staggered susceptibility χ_q is approximated by the density of states, and is roughly inverse of the band width W, the second term is approximately $J_{\pi d}^2/W$. Consequently this term is much smaller than $J_{\pi d}$ itself.

3. (BDA-TTP)$_2$FeCl$_4$

As shown in Fig. 3, this compound has a β-type donor arrangement. There are two crystallographically independent donor molecules, which will be hereafter designated as A and B. Then owing to the inversion symmetry (space group $P2_1/a$), a unit cell contains four donor molecules in a conducting layer. One $FeCl_4$ unit is crystallographically independent, and is approximately located on the a glide plane at $y = 1/4$. The anion is translated by this a glide plane to make a linear chain connected by the dd-interaction I along the a axis. This dd-interaction I is calculated to be fairly large (Table 1). There are several πd-interactions 1–5. All these interactions start from a single anion molecule; the interactions 3 and 4 go to the next donor sheet. Then the mean-field sum of $J_{\pi d}$ is given by the sum of all these πd-interactions. On the other hand, the mean-field sum of J_d is $2J_I$, because two equivalent interactions I start from an anion molecule (coordination number of $FeCl_4$ is 2).

We cannot directly compare J_d and $J_{\pi d}$, because we have to multiply different factors $3S(S+1)/2$ coming from the Curie constants. Fig. 4 is a comparison of these values with the BETS salts. If the π-electron is entirely itinerant, the contribution of $J_{\pi d}$ to T_N is very small, because such contribution is given by $J_{\pi d}^2/W$. Then T_N is practically given by J_d multiplied by $3S(S+1)/2$, which is plotted in the right scale of Fig. 4. Accordingly κ-(BETS)$_2$FeBr$_4$ and κ-(BETS)$_2$FeCl$_4$ respectively afford $T_N = 2.5$ and <1 K. In the same way, T_N of (BDA-TTP)$_2$FeCl$_4$ is expected to be 5 K. This agrees with the experiment because the reported $T_N = 8.5$ K corresponds to the maximum of χ, and χ starts to be anisotropic below about 5 K [10,11].

Table 1
Overlap integrals (S) and J values of (BDA-TTP)$_2$FeCl$_4$

Interaction		$S \times 10^{-3}$	$-J/k_B$ (K)
dd	I	2.15	0.43
πd	1 B	1.27	0.75
	2 B	0.68	0.21
	3 A	0.76	0.27
	4 A	0.53	0.13
	5 A	0.48	0.11

Donor A on (0.23, 0.03, 0.92), donor B on (0.72, 0.03, 0.67), and Fe on (0.89, 0.25, 0.38).
$J_d = 2J_I = 0.86$ K and $J_{\pi d} = J_1 + J_2 + J_3 + J_4 + J_5 = 1.49$ K.

The value $J_{\pi d}$ gives the center field of the field-induced superconductivity H_{sc} [7,9], which is shown in the upper scale of Fig. 4. The calculated $J_{\pi d}$ in λ-(BETS)$_2$FeCl$_4$ and κ-(BETS)$_2$FeBr$_4$ affords 36 and 15 T, respectively. Likewise, H_{sc} of the present compound is estimated to be 2 T, which is smaller than H_{c2}, and the field-induced phase is expected to be within the usual superconducting phase. This estimation is, however, based on the ambient-pressure structure, and under pressure in which the superconductivity appears actually, $t_{\pi d}$ and accordingly $J_{\pi d}$ are expected to be considerably enhanced.

In summary, (BDA-TTP)$_2$FeCl$_4$ is a system with large J_d and small $J_{\pi d}$ in comparison with the BETS systems. The small $J_{\pi d}$ is related to the molecular structure where the terminals of the BDA-TTP molecule are capped with inert trimethylene groups. The small $J_{\pi d}$ is also supported by the nearly identical phase diagram to the $GaCl_4$ salt, together with the absence of the splitting of the Shubnikov-de Haas oscillation [10,11].

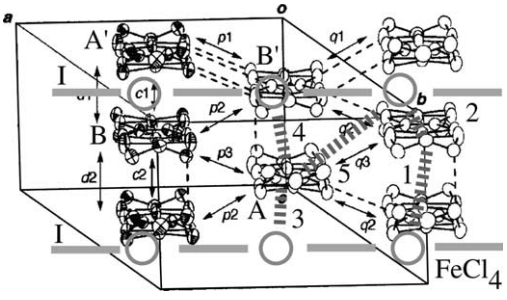


Fig. 3. Crystal structure and intermolecular interactions in (BDA-TTP)$_2$FeCl$_4$.

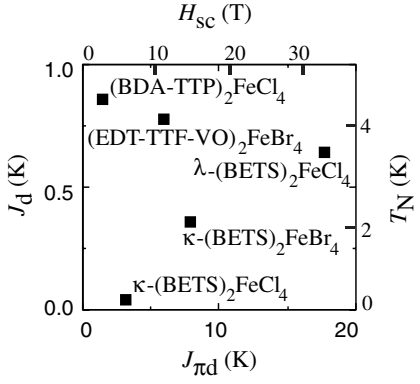


Fig. 4. Calculated J_d and $J_{\pi d}$ values of the present compounds compared with the BETS salts. In the right scale, J_d is converted to T_N according to Eq. (1), and in the upper scale $J_{\pi d}$ is converted to the center field of the field induced superconducting phase.

4. (EDT-TTF-VO)$_2$FeBr$_4$

This compound belongs to a noncentrosymmetric space group, $P1$. The unit cell contains one $FeBr_4$ anion, and two crystallographically independent donor molecules, A and B (Fig. 5). It is characteristic that all C=O bonds are directed in the same direction, so that this crystal is potentially ferroelectric. The HOMO of the donor has the same symmetry as the HOMO of the usual TTF, where the coefficients of all sulfur atoms have the same sign. The calculated interactions are listed in Table 2. The dd-interaction runs along the a (II) and b (I) axes (Fig. 5(a)), and form a square lattice. Then the dd-interactions favor alternating antiferromagnetic spin alignment. The πd-interactions are, however, much larger than the dd-interactions (Table 2); the mean-field sum of $J_{\pi d}$ is 6.04 K, and this is much larger than that of $J_d = 0.78$ K. In particular, the same donor bridges more than two anions; for example the interactions A2 and A3 are large, and bridge the anions 2 and 3. This makes a sharp contrast to the BETS salts, in which only one πd-interaction is overwhelmingly large, and a donor is closely connected with a particular anion [7].

When the π-electron is itinerant, the π-electron makes a very small contribution (of $J_{\pi d}^2/W$) to the magnetic order, leading to an antiferromagnetic order dominated by the dd-interaction, as in the BETS salts. However, when the π-electron is localized, the πd-interaction $J_{\pi d}$ works directly to result in ferrimagnetic order, as observed in some mixed-stack charge-transfer salts. The present compound is intermediate of these two extremes. When the Curie constant is multiplied, J_d and $J_{\pi d}$ give 4.55 and 10.3 K, respectively. The former value is comparable to the high-temperature Weiss temperature, −3.9 K. However, the latter value is larger, and the system prefers ferrimagnetic order if the π-electron is localized.

Table 2
Overlap integrals (S) and J values of (EDT-TTF-VO)$_2$FeBr$_4$ at 298 K

Interaction		$S \times 10^{-3}$	$-J/k_B$ (K)
dd	I//b	0.69	0.04
	II//a	1.94	0.35
πd	A2 [0 1 0]	1.84	1.57
	A3 [1 0 0]	2.05	1.95
	A4 [1 1 0]	0.17	0.01
	A5 [1 0 1]	0.50	0.12
	A6 [1 1 1]	0.26	0.03
	B1 [0 0 0]	0.53	0.13
	B3 [1 0 0]	0.18	0.02
	B5 [1 0 1]	2.18	2.21

Fe on the origin, A on (−0.12, 0.45, 0.62), and B on (−0.14, 0.07, 0.39). $J_d = 2J_I + 2J_{II} = 0.78$ K and $J_{\pi d} = J_{A2} + J_{A3} + J_{A4} + J_{A5} + J_{A6} + J_{B1} + J_{B3} + J_{B5} = 6.04$ K.

To investigate the origin of ferromagnetism, we have calculated the J values based on the low-temperature crystal structure (Fig. 6) [20]. The intra-stack ππ-overlap as well as $J_{\pi d}$ tends to increase at low temperatures, whereas the inter-stack ππ-overlap and J_d remain practically unchanged. It is worth noting that the calculated HOMO levels of the two independent donor molecules, A and B, differ at low temperatures, indicating that charge separation like $A^{1/2-\delta}B^{1/2+\delta}$ occurs at low temperatures. This is probably the origin of the low-temperature semiconducting state. The difference of the energy levels (ΔE), however, drops again at the lowest measured temperature (6.5 K). This suggests a new kind of structural change or rearrangement of the charge at this temperature.

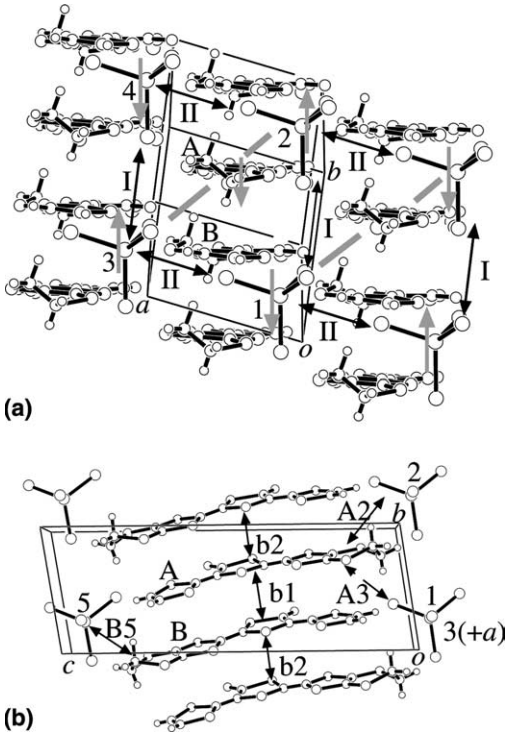


Fig. 5. Crystal structure and intermolecular interactions in (EDT-TTF-VO)$_2$FeBr$_4$.

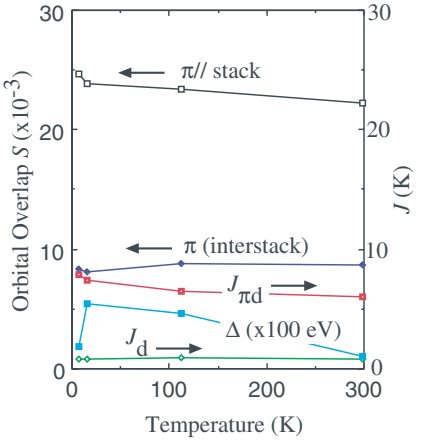


Fig. 6. Temperature dependence of the π-overlap integrals, J_d and $J_{\pi d}$ in (EDT-TTF-VO)$_2$FeBr$_4$. ΔE is the difference of HOMO energy levels.

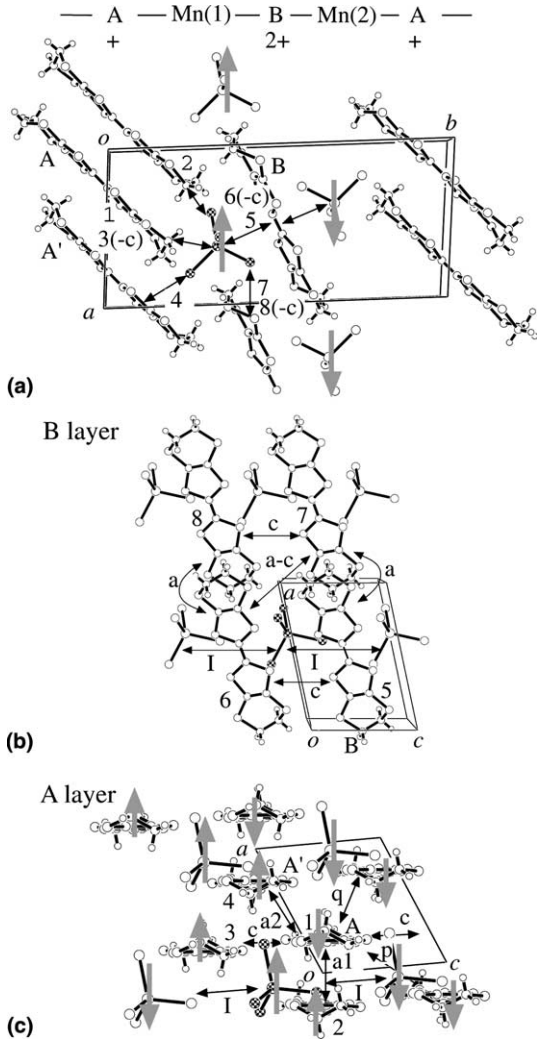


Fig. 7. Intermolecular interactions in $(BEDT\text{-}TTF)_3(MnCl_4)_2$. Nos. 1–8 are πd-interactions from the shaded anion to the numbered donor molecules (Table 3).

In summary, this compound is characterized by larger $J_{\pi d}$ than J_d. The bridging network of $J_{\pi d}$ as well as the practically localized π-electron owing to the charge separation is responsible to the ferrimagnetic order. Dimerization of the present compound is, however, very weak [17–19], and we can hardly determine the phase of the spin wave.

5. $(BEDT\text{-}TTF)_3(MnCl_4)_2$

As shown in Fig. 7(a), $(BEDT\text{-}TTF)_3(MnCl_4)_2$ is composed of the usual donor layer A with β′-structure, and the anion layer including a donor molecule B [21]. The donor charge is distributed as $A_2^{+}B^{2+}$; the B molecule neutralizes the large $MnCl_4^{2-}$ charge. Calculated overlap integrals S and magnetic interactions J are listed in Table 3. There is no ππ-interaction between the A and B molecules, and this compound is regarded as a double layer structure like A–Mn–B–Mn–. πd-interactions from the anion to the A molecules (1–4) are relatively small (the mean-field sum 3.33 K is comparable to 3.12 K in κ-$(BETS)_2FeCl_4$), but πd-interactions to the B molecules (5–8) are large (the mean-field sum 14.14 K is comparable to 17.74 K in λ-$(BETS)_2FeCl_4$ [7]). This is reasonable because the B molecules are incorporated in the anion layer. Since the B^{2+} molecule has no spin, the two large πd-interactions 5 and 6 are expected to mediate "superexchange" interaction, leading to antiferromagnetic coupling of the Mn(1) and Mn(2) anions bridged by the B molecule (Fig. 7(a)). By contrast, the A^{+} donors have spins, and result in antiferromagnetic alignment as shown in Fig. 7(c), particularly on account of the large a1 and a2 ππ-interactions [21]. Then the πd-interaction 1 determines the spin alignment of the anions in the *ac* plane.

The dd-interaction I running along *c* is small; this is one-tenth of dd-interactions in λ-$(BETS)_2FeCl_4$ but comparable to κ-$(BETS)_2FeCl_4$ [7]. This contributes 0.30 K to the Néel and Weiss temperatures (Fig. 4). If the π-electrons on the molecules A are regarded as entirely localized, the large a1 and a2 ππ-interactions give rise to very high Néel temperature, but this is not likely.

Table 3
Overlap integrals (S) and J values of $(BEDT\text{-}TTF)_3(MnCl_4)_2$

		$S\times10^{-3}$	$-J/k_B$ (K)			$S\times10^{-3}$	$-J/k_B$ (K)
πd				ππ			
1	A (0, 0, 0)	2.23	2.31	A	a1	27.1	1704
2	A′ (−1, 0, 0)	0.76	0.27		a2	14.0	455
3	A (0, 0, −1)	0.13	0.01		c	6.1	86
4	A′ (0, 0, 0)	1.26	0.74		p	4.9	56
5	B (0, 0, 0)	3.37	5.27		q	−4.3	43
6	B (0, 0, −1)	4.24	8.34	B	a	−1.0	2.3
7	B (1, 0, 0)	0.79	0.29		c	−5.7	75.4
8	B (1, 0, −1)	0.72	0.24		a–c	−0.2	0.1
dd							
I	(0, 0, 1)	0.526	0.0257				

Mn on (0.62, 0.33, −0.02), A on (0.17, −0.03, 0.12), and B on (0.5, 0.5, 0.5).
$J_{\pi d}(A) = J_1 + J_2 + J_3 + J_4 = 3.33$ K and $J_{\pi d}(B) = J_5 + J_6 + J_7 + J_8 = 14.14$ K.

Then according to the itinerant π-electron approximation (Eq. (2)), the πd-interactions contribute 3.56 K to the Weiss temperature. However, the B molecules do not work in the same way, because the B molecules do not have spins. The A molecules only make 0.13 K contribution. The resulting small Weiss temperature (0.43 K) is consistent with the observation [22]. This is an extraordinary πd-system where the πd-interaction is very large, but the dd-interaction is very small.

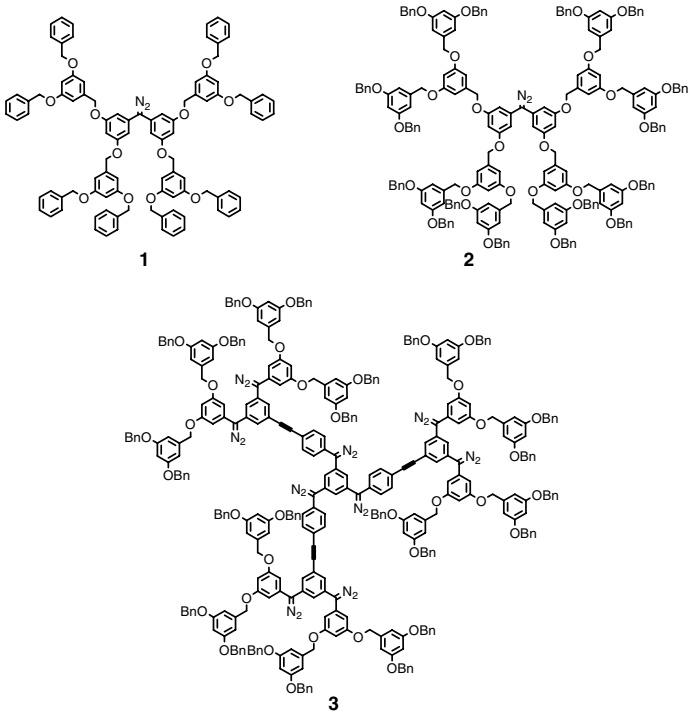
Recently band-filling control has been reported for the isostructural $(BEDT\text{-}TTF)_3(CoCl_4^{2-})_{2-x}(GaCl_4^{-})_x$ [14]. If the excess electron is doped on the A layer, the magnetic property will not change basically. However, if the excess electron is incorporated in the B layer, this may significantly increase the magnetic interaction owing to the large πd-interactions to the B molecules. This probably happens in a ferrimagnetic compound $(BEDT\text{-}TTF)_3(CoCl_4^{2-})_{1.20}(FeCl_4^{-})_{0.80}$ [23].

Acknowledgements

We are grateful for the financial support from a Grant-in-Aid for Scientific Research on Priority Areas of Molecular Conductors (No. 15073211) from the Ministry of Education, Science, Sports, and Culture, Japan, and a Grant for Basic Science Research Project from the Sumitomo Foundation.

References

[1] H. Kobayashi, A. Kobayashi, P. Cassoux, Chem. Soc. Rev. 29 (2000) 325.
[2] T. Enoki, J. Yamaura, A. Miyazaki, Bull. Chem. Soc. Jpn. 70 (1997) 2005.
[3] L. Brossard, R. Clerac, C. Coulon, M. Tokumoto, T. Ziman, D.K. Petrov, V.N. Laukhin, M.J. Naughton, A. Audouard, F. Goze, A. Kobayashi, H. Kobayashi, P. Cassoux, Eur. Phys. J. B 1 (1998) 439.
[4] S. Uji, H. Shinagawa, T. Terashima, T. Yakabe, Y. Terai, M. Tokumoto, A. Kobayashi, H. Tanaka, H. Kobayashi, Nature 410 (2001) 908.
[5] H. Fujiwara, E. Ojima, Y. Nakazawa, B.Z. Narymbetov, K. Kato, H. Kobayashi, A. Kobayashi, M. Tokumoto, P. Cassoux, J. Am. Chem. Soc. 123 (2001) 306.
[6] E. Ojima, H. Fujiwara, K. Kato, H. Kobayashi, H. Tanaka, A. Kobayashi, M. Tokumoto, P. Cassoux, J. Am. Chem. Soc. 121 (1999) 5581.
[7] T. Mori, M. Katsuhara, J. Phys. Soc. Jpn. 71 (2002) 826.
[8] T. Mori, J. Solid State Chem. 168 (2002) 433.
[9] V. Jaccarino, M. Peter, Phys. Rev. Lett. 9 (1962) 290.
[10] J. Yamada, T. Toita, H. Akutsu, S. Nakatsuji, H. Nishikawa, I. Ikemoto, K. Kikuchi, Chem. Commun. (2001) 2538.
[11] E.S. Choi, D. Graf, J.S. Brooks, J. Yamada, H. Akutsu, K. Kikuchi, M. Tokumoto, Phys. Rev. B 70 (2004) 024517.
[12] T. Matsumoto, T. Kominami, K. Ueda, T. Sugimoto, T. Tada, S. Noguchi, H. Yoshino, K. Murata, M. Shiro, E. Negishi, N. Toyota, S. Enodo, K. Takahashi, Inorg. Chem. 41 (2002) 4763.
[13] T. Matsumoto, T. Sugimoto, H.A. Katori, S. Noguchi, T. Ishida, Inorg. Chem. 43 (2004) 3780.
[14] H. Mori, M. Kamiya, M. Haemori, H. Suzuki, S. Tanaka, Y. Nishio, K. Kajita, H. Moriyama, J. Am. Chem. Soc. 124 (2002) 1251.
[15] T. Mori, Bull. Chem. Soc. Jpn. 71 (1998) 2509.
[16] J. Zaanen, G.A. Sawatzky, Can. J. Phys. 65 (1987) 1262.
[17] K. Yamaguchi et al., Polyhedron 22 (2003) 2077.
[18] K. Yamaguchi et al., Chem. Phys. Lett. 207 (1993) 1.
[19] K. Yamaguchi et al., Chem. Phys. Lett. 219 (1993) 36.
[20] H. Fujiwara, et al., private communication.
[21] T. Mori, H. Inokuchi, Bull. Chem. Soc. Jpn. 61 (1988) 591.
[22] T. Mori, P. Wang, K. Imaeda, T. Enoki, H. Inokuchi, Synth. Met. 27 (1988) A451.
[23] H. Mori, M. Suto, H. Suzuki, Y. Nishio, K. Kajita, J. Phys. IV France 114 (2004) 467.



Scheme 1. Molecular structure of dendritic diazo compounds.

Preparations of the target compounds are summarized in Scheme 2. Benzophenone derivatives corresponding to **1** and **2** were prepared by reaction of tetrahydroxybenzophenone with commercially available dendritic benzylbromide derivatives. Nonaketone compound corresponding to **3** was prepared by Sonogashira coupling of an ethynyl derivative substituted by dendritic benzyl ether units with a triiodotriketone compound. Target diazo compounds were prepared by reaction of ketone derivatives with anhydrous hydrazine and hydrazine hydrochloride and following oxidation with manganese dioxide.

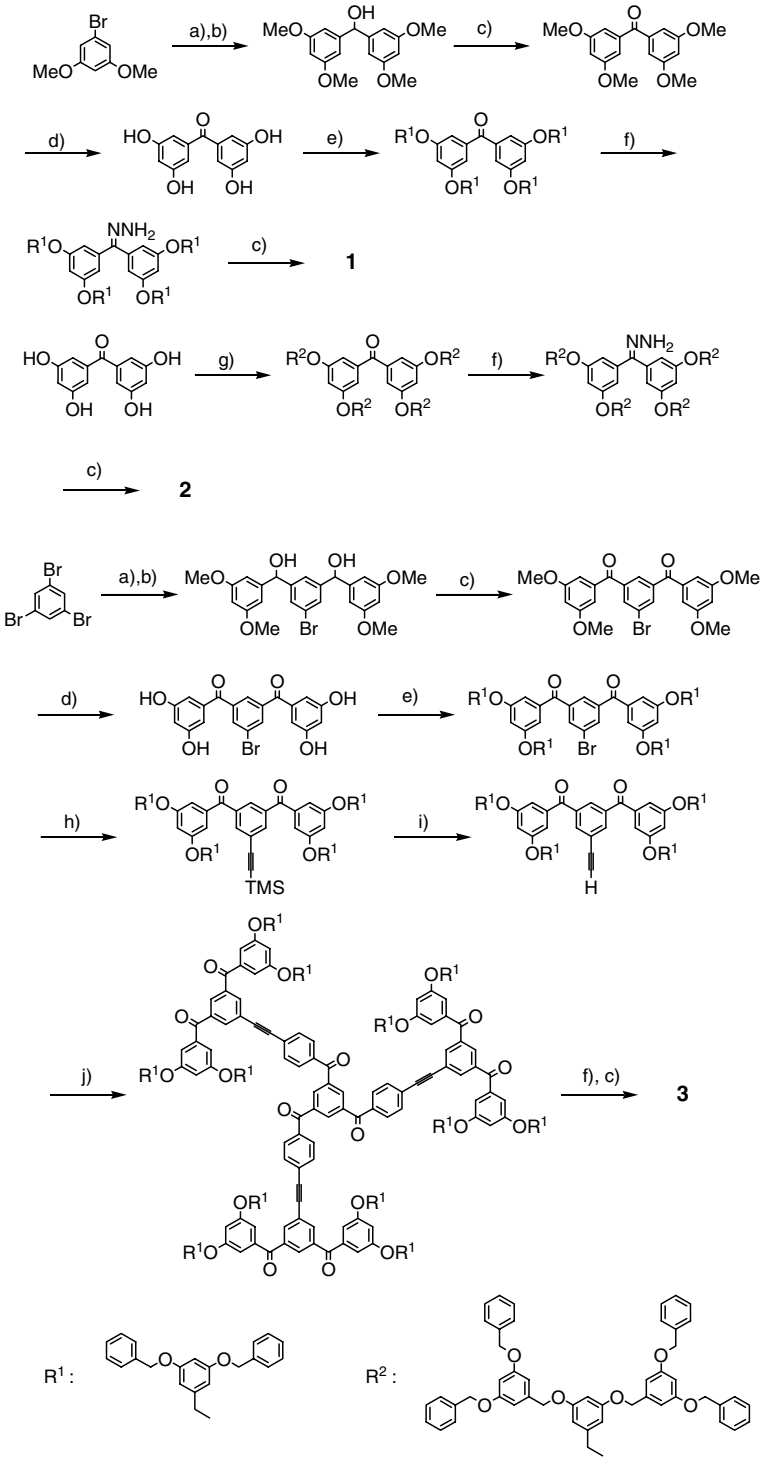
Clear amorphous films of the diazo compounds were easily obtained by evaporation of sample solutions in dichloromethane upon SQUID cells. Prepared films were introduced into SQUID cavity and photolized by an Ar ion laser (514 nm) through a silicate fiber under 15 K. Before irradiation, the samples exhibited negative magnetization due to the diamagnetic diazo compound. As photolysis proceeded, magnetization value got increased and reached plateau within 15 h.[1] Curve fitting of field dependences of magnetization to the Brillouin function provided average spin multiplicity S_{ave} as 0.86 and 0.90 for **1** and **2**, respectively, those are very close to expected value for magnetically isolated triplet carbene. Fig. 1 shows χT versus T plots after irradiation of **1** and **2**. χT values for both of **1** and **2** were almost constant at low temperature range (2 K $\sim$ 10 K), indicating that intermolecular spin interaction were very weak. These two results clearly exhibited that spin centers, i.e., diphenylcarbene parts of **1** and **2** are magnetically isolated from surrounding molecules each other by steric hindrance of the peripheral bulk substituents even in neat films.

In the same way, field dependences of magnetization on early stage of irradiation (2 min) and after irradiation (480 min) of **3** were shown in Fig. 2(a). Curve fitting of both data to the simple Brillouin function provided S_{ave} as 4.4 for early stage of irradiation and 3.1 for after irradiation with poor reproducibility.

When the experimental data were compared to the fitting curves, the systems seemed to be mixture of fast-saturated components and slow-saturated ones. Indeed, by using a model of mixture of two components having high S value and low one,[2] the observed data could be fitted with good agreement as shown in Fig. 2(a).

[1] The irradiation time required to photolize sample films and photolysis degrees of diazo groups depended on the film thickness and laser power. Photolysis degrees of measured samples were determined as 60% for **1**, 30% for **2**, and 30% for **3** based on saturated magnetization value at 2 K and 5 T. Because of the antiferromagnetic interaction of **3** at 2 K, photolysis of **3** should be much more than calculated value, but could not be determined properly.

[2] The fitting function was expressed by linear-combination of two Brillouin functions.



Scheme 2. Preparation of target compounds **1**–**3**: Reagents and conditions: (a) *n*-buthyllithium, diethyl ether, −78 °C; (b) 3,5-dimethoxybenzaldehyde, diethyl ether, −78 °C; (c) MnO_2, dichloromethane, r.t.; (d) BBr_3, dichloromethane, 0 °C; (e) 3,5-bis(benzyloxy)benzylbromide, K_2CO_3, acetone, reflux; (f) NH_2NH_2, NH_2NH_2HCl, dimethylsulfoxide, 90 °C; (g) 3,5-bis{3′,5′-bis(benzyloxy)benzyloxy}benzylbromide, K_2CO_3, acetone, reflux; (h) trimethylsilylacetylene, $Pd(PPh_3)_2Cl_2$, CuI, tetrahydrofuran, triethylamine, 40 °C; (i) K_2CO_3, dichloromethane, methanol, r.t.; (j) 1,3,5-tris(4′-iodobenzoyl)benzene, $Pd(PPh_3)_2Cl_2$, CuI, tetrahydrofuran, triethylamine, r.t.

A χT versus T plot after irradiation of **3** was again shown in Fig. 2(b). As the temperature was lowered from 10 K down to 2 K, χT value decreased gradually. These two results proposed that as the irradiation time prolonged and density of photolized molecules increased, amount of components interacting antiferromagnetically

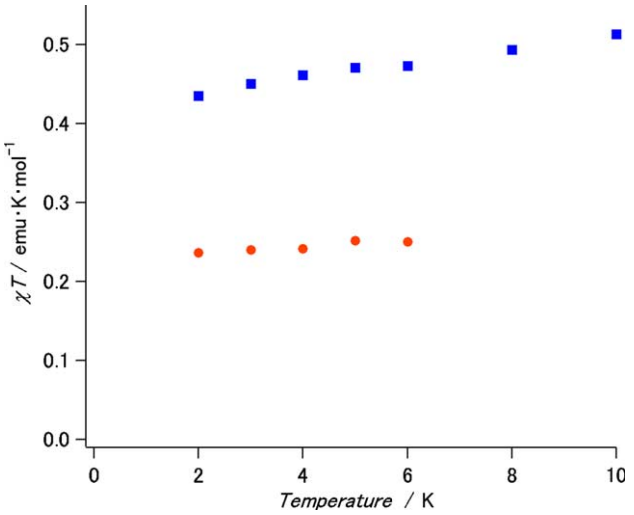


Fig. 1. Temperature dependences of χT value after irradiation of monodiazo compounds **1** (■) and **2** (●).

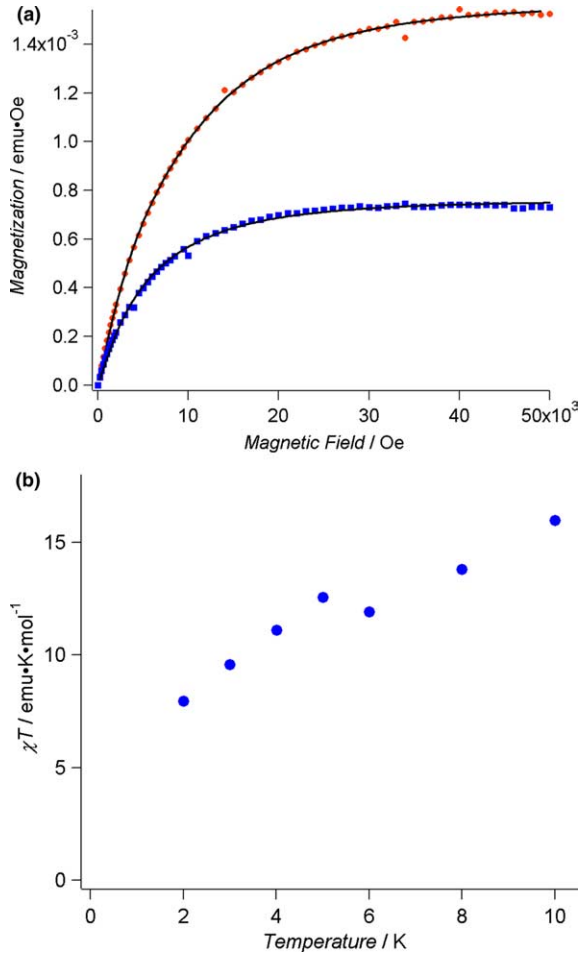


Fig. 2. (a) Field dependences of magnetization of **3** after irradiation for 2 min (■) and for 480 min (●). Solid lines show the fitting curve to two component model with S1 = 9 (N1 = 2.1×10^{15}), S2 = 2.6 (N2 = 8.3×10^{15}) for early stage and S1 = 9 (N1 = 2.9×10^{15}), S2 = 1.8 (N2 = 3.3×10^{16}) for after irradiation. (b) Temperature dependence of χT value after irradiation of nonadiazo compound **3**.

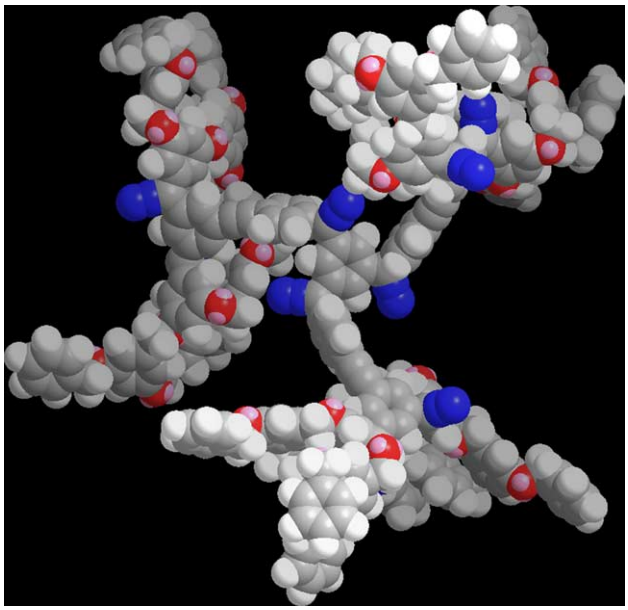


Fig. 3. One of the pseudo-stable structures of **3** obtained by MM2 calculation.

with neighboring molecules got increased, while components of large S value still remained.

Fig. 3 depicts a result of MM2 calculation for **3**, that exhibited the diazo groups (i.e., spin centers after irradiation) were sterically hindered considerably by the bulk peripheral groups, while apertures still found between branches and a few diazo groups were located on surface of the molecule.

Peripheral dendrons of larger generation such as in compound **2** will provide a more effective isolation of spin centers.

Acknowledgments

This work was supported by a Grant-in-Aid for Scientific Research (A)(2)(No. 14204071) and a Grant-in-Aid for Scientific Research on Priority Areas "Application of Molecular Spin" (No. 15087205) from the Ministry of Education, Science, Sports and Technology (MEXT), Japan. A part of this work was supported by "Nanotechnology Support Project" of the Ministry of Education, Science, Sports and Technology (MEXT), Japan.

References

[1] (a) M. Kinoshita, P. Turek, M. Tamura, K. Nozawa, D. Shiomi, Y. Nakazawa, M. Ishikawa, M. Tskahashi, K. Awaga, T. Inabe, Y. Maruyama, Chem. Lett. (1991) 1225;
(b) J.S. Miller, A.J. Epstein, W.M. Reiff, Science 240 (1988) 40.
[2] R. Skomski, J. Phys-Condens. Mater. 15 (2003) R841.
[3] (a) O. Kahn, Curr. Opin. Solid State & Mater. Sci. 1 (1996) 547;

(b) Y. Garcia, V. Niel, M.C. Munoz, J.A. Real, Top. Curr. Chem. 233 (2004) 229.
[4] (a) T. Akita, Y. Mazaki, K. Kobayashi, J. Chem. Soc., Chem. Commun. (1995) 1861;
(b) T. Akita, K. Kobayashi, Adv. Mater. 9 (1997) 346;
(c) J. Cirujeda, E. Hernandezgasio, C. Rovira, J.L. Stanger, P. Turek, J. Veciana, J. Mater. Chem. 5 (1995) 243;
(d) J.C. Noveron, M.S. Lah, R.E. Del Sesto, A.M. Arif, J.S. Miller, P.J. Stang, J. Am. Chem. Soc. 124 (2002) 6613.
[5] (a) A. Rajca, J. Wongsriratanakul, S. Rajca, R. Cerny, Angew. Chem. Int. Ed. 37 (1998) 1229;
(b) T. Akita, N. Koga, Polyhedron 20 (2001) 1475;
(c) S. Karasawa, G. Zhou, H. Morikawa, N. Koga, J. Am. Chem. Soc. 125 (2003) 13676.
[6] K. Tanaka, M. Kozaki, D. Shiomi, K. Sato, T. Takui, K. Okada, Polyhedron 22 (2003) 1803.
[7] D. Marsitzky, R. Vestberg, P. Blainey, B.T. Tang, C.J. Hawker, K.R. Carter, J. Am. Chem. Soc. 123 (2001) 6965.

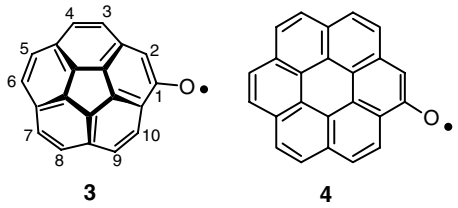
As the first example of stable neutral radicals definitely conjugated with a curved π-network, we have recently synthesized and isolated a new oxoverdazyl radical **2** conjugated with corannulene (**1**) [9]. Optical and ESR spectroscopies revealed a small but measurable spin delocalization onto the curved surface of corannulene. To gain more insight into the spin structure on the curved surface, we have carried out a systematic study on a variety of neutral radicals conjugated with the curved π-network of corannulene in terms of density functional theory (DFT) calculations.

2. Calculation method

All the calculations were carried out using the program GAUSSIAN03 [10]. Each structure was fully optimized by hybrid DFT calculations at the UB3LYP/6-31G level of theory [11] with no symmetry constraints. One-point calculations were implemented at the UB3LYP/6-31G(d) level for the optimized structures. Frequencies were calculated to verify energy minima for the optimized conformations.

3. Results and discussion

Our primary interest concerns the uniqueness of the spin density distribution spread over the curved surface structure of corannulene. To grasp this physical picture, we focused on a model system, corannulenoxyl (**3**), which is expected to show a significant spin delocalization from oxygen atom into corannulene. A DFT calculation for **3** showed that a large amount of spin density is actually delocalized over the corannulene moiety as shown in Fig. 1(a). The spin transmission from the radical substituent to the corannulene moiety exhibited a deflected nature on the curved surface, giving rise to spin-rich and spin-poor regions within the molecule (Fig. 1(a)). The largest positive spin density on the corannulene moiety occurred at the peripheral carbon atom of the 2-position (+0.538). This site agrees with the carbon site of the radical **2** where the hyperfine coupling of its neighboring proton was enough large to be detected in the ESR/ENDOR spectra [9]. On the other hand, the spin densities on the opposite side of the molecule are negligibly small in magnitude, namely, −0.002 for the 7-position and −0.008 for the 8-position. Spin polarization effect was robust enough to induce positive and negative spin densities alternately on the large part of the molecule, except for the above-mentioned region with negligibly small spin densities.



3 **4**

To confirm whether or not the unbalanced spin distribution of **3** is an inherent character of this class of curved π-radicals, we calculated a spin density distribution of coronenoxyl (**4**) which has a flat surface π-conjugated structure. It turned out that the spin densities of **4** are spread over the whole molecule rather evenly (Fig. 1(b)), in contrast with the uneven distribution of **3**. The comparison demonstrated that there is a marked difference between the planar and non-planar π-spin structures.

At this stage, we have two possible explanations for the occurrence of the unbalanced spin distribution of **3**, that is, it may be caused by either structural effect or topological effect. The former effect is associated with the non-planarity or curvature of the π-conjugation structure. As a planar π-radical undergoes distortion to have a non-planar geometry, there will be possibility that its spin density distribution can, more or less, be modulated. The latter effect arises from the connectivity of atoms in a molecule. The corannulenoxyl (**3**) has a five-membered ring in the molecular center, which forms a non-alternant π-conjugation network. Such π-connectivity might cause the unbalanced spin distribution, regardless of the structural deformation. Our preliminary study on the bowl-to-bowl inversion phenomenon for **3** showed that the unbalanced spin distribution is maintained even at the transition state having the planar geometry on the way from one bowl-shaped structure to the other. This indicates that the nature of spin distribution of **3** is governed by the molecular topological effect. The subtle contribution from the structural effect also needs to be assessed in detail.

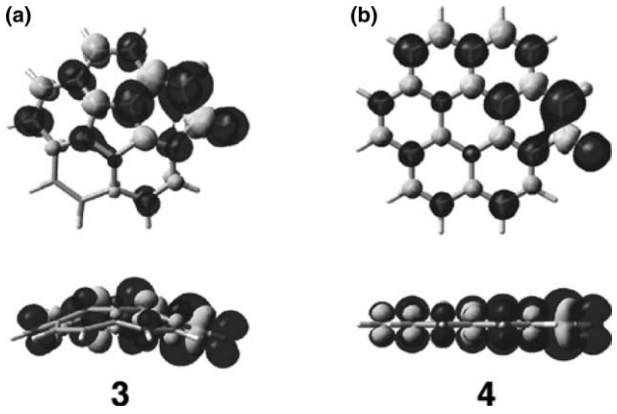


Fig. 1. Spin density distributions of (a) corannulenoxyl (**3**) and (b) coronenoxyl (**4**) calculated by density functional theory at the UB3LYP/6-31G(d)//UB3LYP/6-31G level of theory. Black and gray colors denote positive and negative spin densities, respectively.

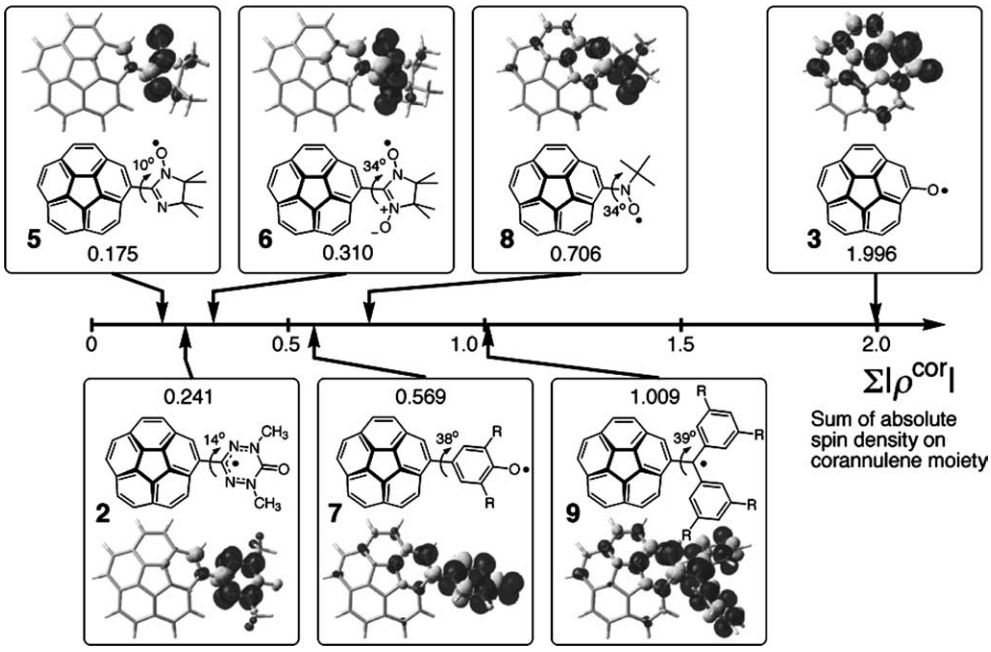


Fig. 2. Spin density distributions for a series of corannulene derivatives with various radical substituents (**2**, **3**, and **5**–**9** where R = H). Numerals plotted on the horizontal axis denote sums of absolute spin density on the corannulene moiety ($\Sigma|\rho^{cor}|$). Calculations were carried out at the UB3LYP/6-31G(d)//UB3LYP/6-31G level of theory. Black and gray colors denote positive and negative spin densities, respectively.

Although the corannulenoxyl (**3**) serves as a good model for evaluating the curved-surface π-spin structure, the radical is predicted to have a lesser kinetic stability because of the large spin densities on the corannulene. The exposed spin densities to the outer space are subject to possible σ-dimerization or unfavorable chemical reactions which yield non-magnetic materials. Synthesis and isolation of such reactive species will require further stabilization on the corannulene moiety such as steric protections as demonstrated in, for example, phenalenyl [12], diazaphenalenyl [13], oxophenalenoxyls [14], and triangulene [15].

Another alternative approach to realize stable and spin-delocalized curved π-systems is to introduce other stable radicals into corannulene. For the molecular design based on this approach, we carried out geometry optimizations and spin density calculations for a series of corannulene derivatives with various radical substituents (**5**–**9** as shown in Fig. 2). Unlike **3**, these derivatives have at least two metastable geometries with respect to the rotational motion of the radical moiety. Thus, we carefully determined the most stable geometry with a global energy minimum for the each derivative.

Fig. 2 summarizes the result of the DFT calculations. The each optimized structure has a non-zero dihedral angle (10–39°) between the radical moiety and the six-membered ring of the corannulene moiety. The dihedral angle may result from a subtle balance between the minimum steric repulsion among the neighboring protons and the maximum resonance stabilization between the two moieties. We evaluated these radicals by putting them in the increasing order of spin-delocalization into the corannulene, using a sum of absolute spin density on the corannulene moiety ($\Sigma|\rho^{cor}|$) (Fig. 2). The iminonitroxide (**5**) [16], oxoverdazyl (**2**), and nitronyl nitroxide derivatives (**6**) are categorized as relatively localized spin systems, while the phenoxyl (**7**), *tert*-butyl nitroxide (**8**), and diphenylmethyl derivatives (**9**) show intermediate spin delocalizations onto the curved surface of corannulene. As described above, corannulenoxyl (**3**) serves as the most spin-delocalized system of all. In spite of the difference in the magnitude of spin delocalization, all these systems showed the unbalanced nature in their spin distributions mentioned above. This trend of the spin delocalization partly supports our previous experiment on **2**, which demonstrated that the radical **2** has a relatively localized character but higher chemical stability in spite of no stabilization given for the corannulene moiety. If the chemical stability of **7**–**9** are enough high to be isolated, these radicals are expected to serve as suitable models to investigate not only the curved-surface π-spin structures in more detail but also magnetic interactions between the curved-surface π-electrons in the crystalline state.

4. Summary

On the basis of our previous experimental study on an oxoverdazyl radical directly conjugated with corannulene, we have carried out DFT calculations for a series of neutral organic π-radicals conjugated with

corannulene. It turned out that the unpaired electron spin is transmitted from the radical substituent into the corannulene moiety, forming an uneven spin distribution on the curved surface. The magnitude of spin delocalization into the corannulene moiety significantly varies, depending on the radical employed. From the experimental viewpoint, it will be of particular interest to study not only the stability and spin structures of largely delocalized systems, but also intermolecular magnetic interactions between the curved surface π-electrons in the crystalline state. Syntheses of these new radical species are in progress.

Acknowledgements

This work was partially supported by PRESTO-JST, Grant-in-Aid for Scientific Research on Priority Areas "Application of Molecular Spins" (Area No. 769) from Ministry of Education, Culture, Sports, Science, and Technology, Japan, and 21COE program "Creation of Integrated EcoChemistry of Osaka University".

References

[1] (a) M. Gomberg, J. Am. Chem. Soc. 22 (1900) 757;
(b) M. Gomberg, Chem. Ber. 33 (1900) 3150.

[2] (a) A.R. Forrester, J.M. Hay, R.H. Thomson, Organic chemistry of stable free radicals, Academic Press, New York, 1968;
(b) E.G. Rozantsev, Free nitroxyl radicals, Plenum Press, New York, 1970;
(c) H.G. Aurich, in: S. Patai, Z. Rappoport (Eds.), Nitrones, Nitronates and Nitroxides, Wiley, New York, 1989 (Chapter 4);
(d) L.B. Volodarsky, V.A. Reznikov, V.I. Ovcharenko, Synthetic chemistry of stable nitroxides, CRC Press, Boca Raton, FL, 1994;
(e) Z.V. Todres, Organic ion radicals, Marcel Dekker, New York, 2004.

[3] (a) M. Tamura, Y. Nakazawa, D. Shiomi, K. Nozawa, Y. Hosokoshi, M. Ishikawa, M. Takahashi, M. Kinoshita, Chem. Phys. Lett. 186 (1991) 401;
(b) Y. Nakazawa, M. Tamura, N. Shirakawa, D. Shiomi, M. Takahashi, M. Kinoshita, M. Ishikawa, Phys. Rev. B 46 (1992) 8906.

[4] (a) K. Itoh, M. Kinoshita (Eds.), Molecular Magnetism, Gordon & Breach, Kodansha, Tokyo, 2000;
(b) P.M. Lahti (Ed.), Magnetic properties of organic materials, Marcel Dekker, New York, 1999.

[5] B. Tumanskii, O. Kalina, Radical Reaction of Fullerenes and Their Derivatives, Kluwer Academic Publishers, Dordrecht, 2001.

[6] M. Yoshida, F. Sultana, N. Uchiyama, T. Yamada, M. Iyoda, Tetrahedron Lett. 40 (1999) 735, and references cited therein.

[7] F. Fülöp, A. Rockenbauer, F. Simon, S. Pekker, L. Korecz, S. Garaj, A. Janossy, Chem. Phys. Lett. 334 (2001) 233, and references cited therein.

[8] (a) C. Corvaja, M. Maggini, M. Prato, G. Scorrano, M. Venzin, J. Am. Chem. Soc. 117 (1995) 8857;
(b) I.A. Nuretdinov, V.P. Gubskaya, V.V. Yanilkin, V.I. Morozov, V.V. Zverev, A.V. Il'yasov, G.M. Fazleeva, N.V. Nastapova, D.V. Il'matova, Russ. Chem. Bull. 50 (2001) 607.

[9] Y. Morita, S. Nishida, T. Kobayashi, K. Fukui, K. Sato, D. Shiomi, T. Takui, K. Nakasuji, Org. Lett. 6 (2004) 1397.

[10] M.J. Frisch, G.W. Trucks, H.B. Schlegel, G.E. Scuseria, M.A. Robb, J.R. Cheeseman, J.A. Montgomery Jr., T. Vreven, K.N. Kudin, J.C. Burant, J.M. Millam, S.S. Iyengar, J. Tomasi, V. Barone, B. Mennucci, M. Cossi, G. Scalmani, N. Rega, G.A. Petersson, H. Nakatsuji, M. Hada, M. Ehara, K. Toyota, R. Fukuda, J. Hasegawa, M. Ishida, T. Nakajima, Y. Honda, O. Kitao, H. Nakai, M. Klene, X. Li, J.E. Knox, H.P. Hratchian, J.B. Cross, C. Adamo, J. Jaramillo, R. Gomperts, R.E. Stratmann, O. Yazyev, A.J. Austin, R. Cammi, C. Pomelli, J.W. Ochterski, P.Y. Ayala, K. Morokuma, G.A. Voth, P. Salvador, J.J. Dannenberg, V.G. Zakrzewski, S. Dapprich, A.D. Daniels, M.C. Strain, O. Farkas, D.K. Malick, A.D. Rabuck, K. Raghavachari, J.B. Foresman, J.V. Ortiz, Q. Cui, A.G. Baboul, S. Clifford, J. Cioslowski, B.B. Stefanov, G. Liu, A. Liashenko, P. Piskorz, I. Komaromi, R.L. Martin, D.J. Fox, T. Keith, M.A. Al-Laham, C.Y. Peng, A. Nanayakkara, M. Challacombe, P.M.W. Gill, B. Johnson, W. Chen, M.W. Wong, C. Gonzalez, J.A. Pople, GAUSSIAN03, Revision C.02, Gaussian, Inc., Pittsburgh, PA, 2003.

[11] (a) A.D. Becke, Phys. Rev. A 38 (1988) 3098;
(b) C. Lee, W. Yang, R.G. Parr, Phys. Rev. B 37 (1988) 785;
(c) A.D. Becke, J. Chem. Phys. 98 (1993) 5648.

[12] K. Goto, T. Kubo, K. Yamamoto, K. Nakasuji, K. Sato, D. Shiomi, T. Takui, M. Kubota, T. Kobayashi, K. Yakushi, J. Ouyang, J. Am. Chem. Soc. 121 (1999) 1619.

[13] Y. Morita, T. Aoki, K. Fukui, S. Nakazawa, K. Tamaki, S. Suzuki, A. Fuyuhiro, K. Yamamoto, K. Sato, D. Shiomi, A. Naito, T. Takui, K. Nakasuji, Angew. Chem. Int. Ed. 41 (2002) 1793.

[14] (a) Y. Morita, T. Ohba, N. Haneda, S. Maki, J. Kawai, K. Hatanaka, K. Sato, D. Shiomi, T. Takui, K. Nakasuji, J. Am. Chem. Soc. 122 (2000) 4825;
(b) Y. Morita, J. Kawai, K. Fukui, S. Nakazawa, K. Sato, D. Shiomi, T. Takui, K. Nakasuji, Org. Lett. 5 (2003) 3289.

[15] J. Inoue, K. Fukui, T. Kubo, S. Nakazawa, K. Sato, D. Shiomi, Y. Morita, K. Yamamoto, T. Takui, K. Nakasuji, J. Am. Chem. Soc. 123 (2001) 12702.

[16] For an experimental study on a corannulene derivative conjugated with iminonitroxide, see: S. Nishida, Y. Morita, T. Kobayashi, K. Fukui, A. Ueda, K. Sato, D. Shiomi, T. Takui, K. Nakasuji, Polyhedron 24 (2005) 2200.

of the electronic state of Au nanocluster by the electron or hole doping might also have an effect on the magnetic interaction of the hybrid material that is composed of Au cluster and organic spin molecules. In order to examine this hole/electron doping effect, ab initio calculations for the Au_3 and Au_{13}-nitroxide hybrid model systems were examined. Implications of the computational results were discussed in relation to rational design of tunable molecular magnets.

2. Calculation method and models

2.1. Calculation method

All the computations were performed by GAUSSIAN-98 and GAUSSIAN-03 program packages [13]. Unrestricted hybrid DFT (UB3LYP) calculation was used for the model systems computations using D95** basis set for C, N, O, and H and the LANL2DZ basis set for Au.

The low spin state and high spin state (LS–HS) energy gap of the systems has been experimentally determined. The LS–HS energy gap of the system can be also calculated by the spin-polarized DFT energies [14,15].

In the case of organic radical molecules, the spin polarization and the spin delocalization of the π electrons are the dominant factors to determine the spin alignment between the localized radical spins while the spin polarization of the conduction electrons are also the important factor for the spin alignment in the case of metal clusters. This is so called RKKY mechanism.

2.2. Calculated models

In the real system, π-radical thiols that are one of phenyl sulfide derivatives (SPN-hex) were chemisorbed onto Au nanoparticles whose mean diameter was about 4 nm. Thus the obtained hybrid system was named SPN-hex@Au. The schematic diagram of this real model was shown in Fig. 1. From the detail analyses, it was found that the representative chemical formula was presented as Au_{1750} $(SPN\text{-}hex)_{125}$, It would be difficult to examine this real system using the ab initio method with current computer resources. However, because our interest is focused on the effects of electron/hole doping of the metal-organic hybrid system, a smaller model system is feasible for the elucidation of this subject. Hence the small model system shown in Fig. 2 was adopted. In the model system, the wire like Au_3 cluster and cubooctahedral Au_{13} cluster were used instead of a large Au cluster and SPN-hex was also modified to phenyl sulfide with simple nitronyl nitroxide group as shown in Fig. 2. The geometry of the organic spin molecule was based on the geometry of NPNN molecule.

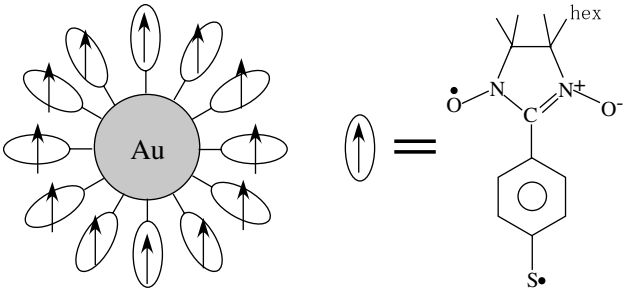


Fig. 1. The schematic diagram of SPN-hex@Au system.

3. Results and discussion

3.1. Au_3 model system

The Au_3 model system was composed of Au_3 cluster and radical fragments. The schematic diagram of this was depicted in Figs. 1 and 2. To begin with, $(SPN\text{-}hex)_2$ was decomposed into two isolated SPN-hex molecules on the surface of Au cluster in the process of the SPN-hex adsorption onto the surface of Au cluster. The S–S bond of $(SPN\text{-}hex)_2$ was cleaved in this process. Therefore, SPN-hex monomer has two radicals. One is

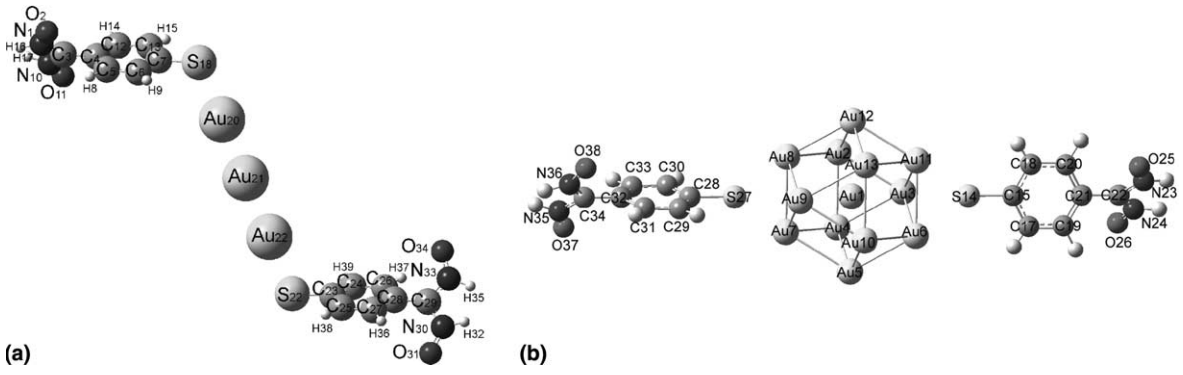


Fig. 2. The illustration of the Au-organic spin molecule hybrid model system: (a) Au_3 model system and (b) Au_{13} model system.

the nitroxide radical and the other was lone pair electron on S atom. The ab initio calculations showed that the ground state of isolated Au_3 cluster was a double state and that of the isolated organic radical fragment was a triplet state. The spin densities of these were shown in Table 2. (Note that only the spin densities of the heavy atoms are summarized in this table.) The neutral Au_3 type model cluster which was composed of the above mentioned fragments was examined. The obtained results were also shown in Table 1. As a doublet state was the ground state of this model system, it was found the low spin state was the ground state of the neutral one. The spin angular moments of the model systems were shown in Table 2. In this table, the spin densities of the heavy atoms were only summarized. In the case of the neutral Au_3 model system, the antiparallel spin moments were presented on the S atoms and nitroxide groups. This result suggests that the hetero-junction between Au cluster and the stable organic spin molecules has an effect on the spin alignment of the Au_3 model system.

With hole doping, it was found that the high spin state became the ground state. The calculated spin density showed that the spin polarization of the Au site was enhanced although the spin densities on the organic radical molecules were greatly decreased. Especially, it was found that the spin densities of the nitroxide groups and S atoms were extremely changed. Therefore, this suggests that the spin polarization for Au_3 and S atom sites of the small Au_3 model system was induced by the hole doping.

To understand the electronic state of the cationic hybrid model system, natural orbital (NO) analysis was carried out for the triplet state of the hole doped (cationic) hybrid model system. There are two natural orbitals whose occupation numbers are 1.0. The first NO is localized on the nitronyl nitroxide group and the second is localized on the region of Au cluster and S atoms. The schematic diagrams are shown in Fig. 3. From this

Table 1
Total energies and total spin angular momenta of the Au_3 model hybrid systems

Charge	Spin state	Energy (h)	S**[2]	ΔE(HS-LS) (h)
Neutral[a]	Doublet	−2263.19954534	1.8986	
	Quintet	−2263.17122532	4.8929	0.02832
Cation[a]	Singlet	−2262.93828722	1.4348	
	Triplet	−2262.93878147	2.2495	−0.00049

[a] UB3LYP/LANL2DZ for Au and D95** for the others is used.

Table 2
Spin densities for the neutral and cationic hybrid model systems

	Au_3	Radical flagment	Neutral	Cation
N1		0.250	0.207	0.105
O2		0.407	0.350	0.022
C3		−0.242	−0.183	−0.112
C4		0.163	0.020	0.071
C5		−0.089	−0.017	−0.043
C6		0.129	0.002	0.065
C7		−0.086	−0.005	−0.040
N10		0.250	0.195	0.161
O11		0.407	0.288	0.394
C12		−0.089	−0.017	−0.042
C13		0.129	0.004	0.060
S18		0.801	−0.296	0.346
Au19	0.621		−0.024	−0.194
Au20	−0.242		−0.010	0.443
Au21	0.621		−0.024	−0.194
S22			−0.296	0.346
C23			−0.005	−0.040
C24			0.004	0.060
C25			0.002	0.065
C26			−0.017	−0.042
C27			−0.017	−0.043
C28			0.020	0.071
C29			−0.183	−0.112
N30			0.207	0.105
O31			0.350	0.022
N33			0.195	0.161
O34			0.288	0.394

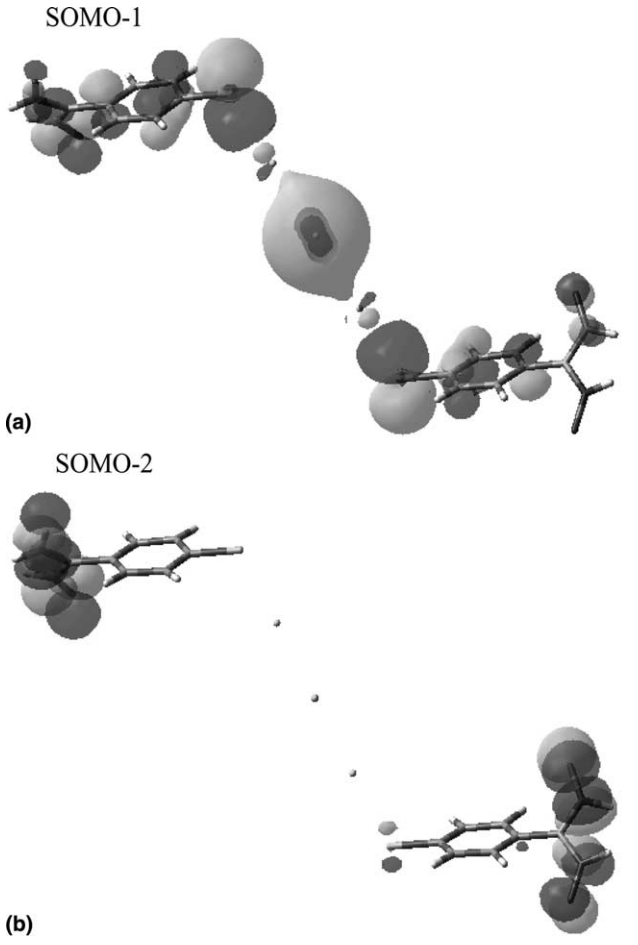


Fig. 3. The natural orbital of the two SOMO for the Au_3 model system.

analysis, it was found that the high spin ground state of the cationic model was formed by the correlation between the radical spin of nitronyl nitroxide and the induced spin by hole doping on the Au cluster site. These results showed that the cationic ground state was not obtained by simple electron extraction from SOMO, meaning that the orbital reorganization occurred due to the hole doping. Therefore, it could be concluded that the correlation between the delocalized Au electrons and the localized spin moment on the organic spin molecule through the medium of the spin polarization is important.

Table 3
Total energies and total spin angular momenta for the Au_{13} model hybrid systems

Charge	Spin state	Energy (h)	S**[2]	ΔE(HS-LS) (h)
Neutral[a]	Doublet	−3618.24033122	1.9168	
	Quartet	−3618.24046763	3.8866	−0.00014
Aniona	Singlet	−3618.37812982	1.1806	
	Quintet	−3618.35688872	6.1350	0.02124
Cationa	Singlet	−3618.00058858	1.6295	
	Quintet	−3617.99725988	6.1277	0.00333

[a] UB3LYP/LANL2DZ for Au and D95** for the others is used.

3.2. Au_{13} model system

The Au_{13} model system was composed of Au_{13} cluster and radical fragments. The calculation results suggested that the ground state of isolated Au_{13} cluster was a double state. Mulliken analysis of the isolated Au_{13} cluster showed that the all the surface Au atoms had the negative charge population (ca. −0.5) and had positive spin densities whose net population was about 1. In the next, Au_{13} hybrid model cluster was also examined. The obtained results were shown in Table 3. The ground state of the neutral cluster was a quintet state. Therefore, it was found that the high spin state was the ground state of this neutral model system. The spin densities of the model systems were shown in Fig. 4. In this figure, the spin densities for each state were depicted. In the case of the quintet state of the neutral Au_{13} hybrid model system, the same sign of the spin moments were presented on two nitroxide groups and the surface Au atoms in Au_{13} cluster, while the spin densities of the hetero-junction sites between Au_{13} cluster and S atoms in organic radical molecules had small spin moments with same sign. This result suggests that the spin delocalization was occurred at the hetero-junction sites.

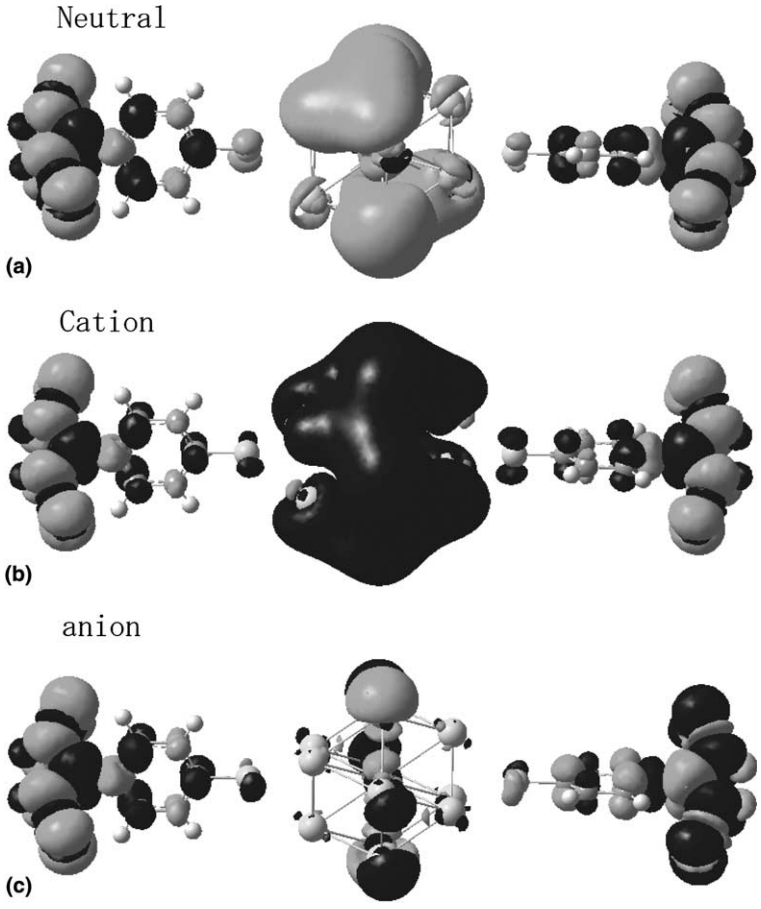


Fig. 4. The schematic diagram of the spin densities for (a) neutral, (b) cationic, and (c) anionic Au_{13} hybrid model systems.

In order to understand the electronic state of this hybrid model system, NO analyses were carried out for the quartet state of the neutral hybrid model system. There are three natural orbital whose occupation numbers are 1.0. The two NOs are localized on the nitroxide groups and the last one is localized on the region of Au cluster and S atoms. These schematic diagrams are shown in Fig. 5. From this analysis, it was found that the magnetic interaction between Au_{13} cluster and nitroxide radicals were the principal cause.

An electron doping into this Au_{13} model system was also examined. The calculated results showed that the low spin state was the ground state and the obtained ground state was a singlet state. The charge density analysis showed that the doped electron was mainly localized on Au cluster site as the total charge on Au_{13} cluster was about -0.64. The spin moment analysis which was depicted in Fig. 4 showed that the spin moments of Au cluster site were greatly decreased as the summation of spin moments in Au_{13} cluster was -0.0014. On the other hand, the two large spin moments were localized on the two nitroxide sites. Therefore, it could be concluded that the spin crossover was occurred by the electron doping into Au_{13}.

In the case of a hole doping, it was also found that the low spin state became the ground state. In this model, the obtained result showed that the doped hole was mainly located on Au_{13} site because the total charge on Au_{13} was about 0.58. On the other hand, the tendency of the spin density analysis was similar to that of Au_3 model system as the calculated spin density showed that the spin polarization of Au site was enhanced although the spin density on organic radical molecule was slightly decreased. Therefore, it could be concluded that the spin crossover was also induced by a hole doping to Au_{13} model system.

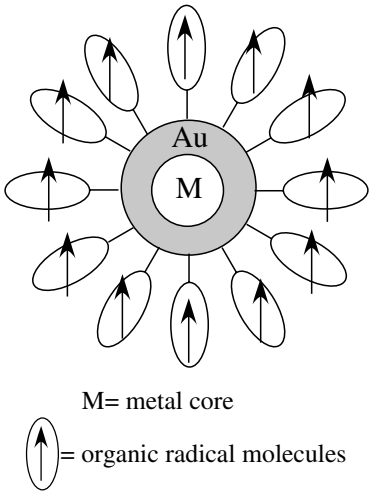


Fig. 6. Possible models of egg shell type nanoorganic metallic hybrid spin cluster system.

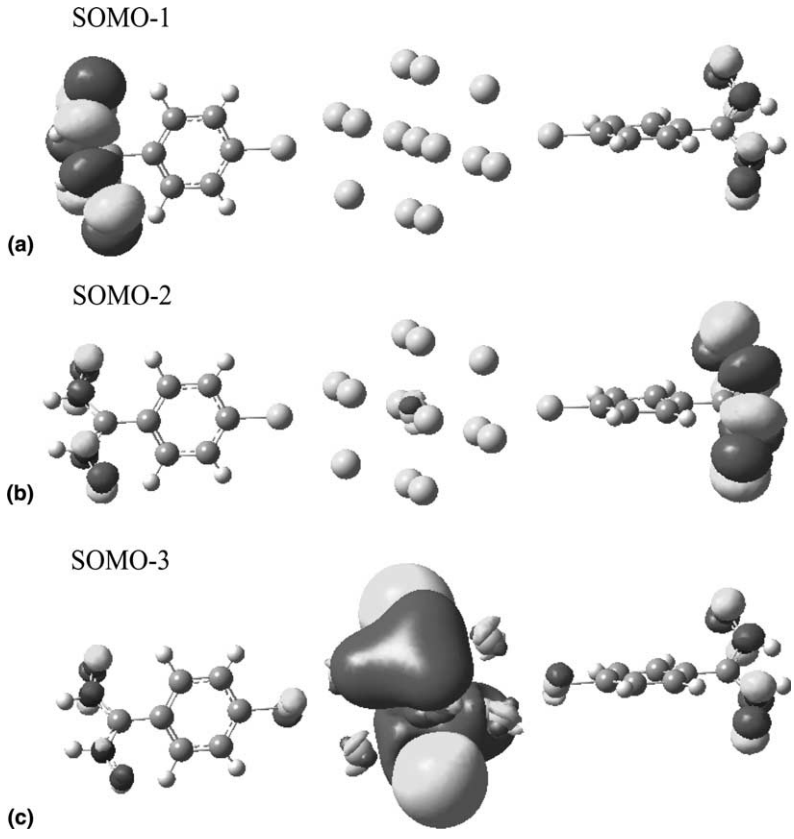


Fig. 5. The natural orbital of the three SOMO for the Au_{13} model system.

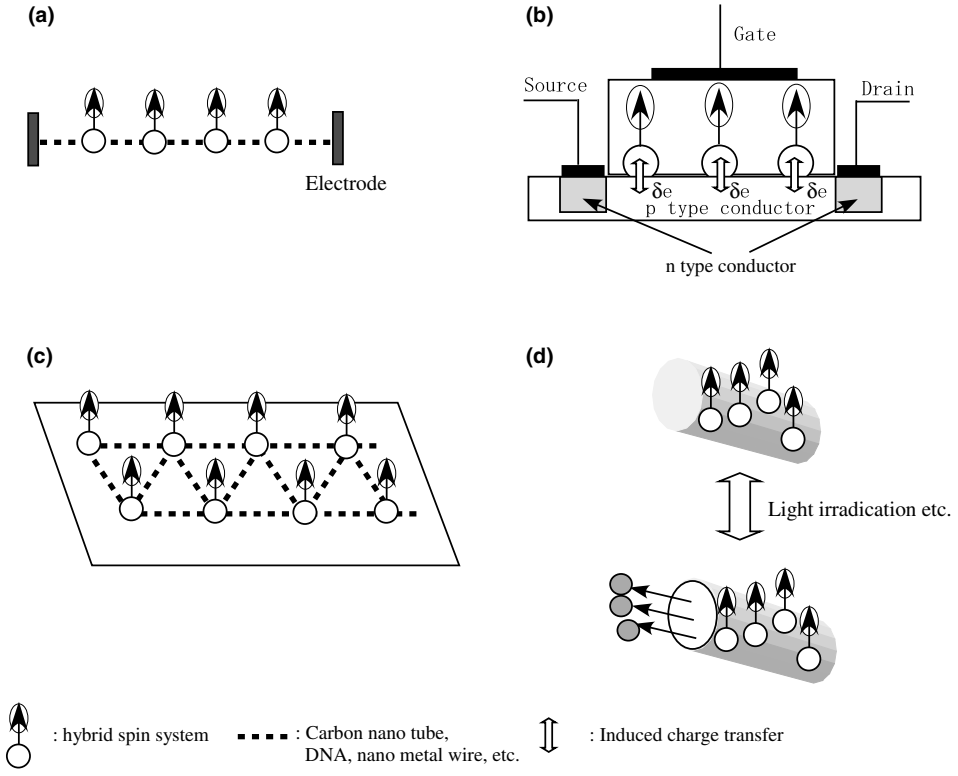


Fig. 7. Possible models of (a) one-dimensional organometallic hybrid spin cluster with conductor network, (b) the cross-section of the nanospin system that is composed of the hybrid nanospin materials, (c) superconductor model by two-dimensional triangular ladder structure and (d) drug delivering system.

3.3. Rational design of tunable molecular magnets

These results suggested that the correlation between the delocalized Au electrons and the localized spin moment on the organic spin molecule through the medium of the spin polarization is important and the electron/hole doping into Au-organic spin molecule hybrid system could change the magnetic interaction of the ground state. On the analogy of these results, the other metal cluster, like Pt, Pd, Ir, Ag, Cu, and organic spin molecule hybrid system would also have unique and controllable magnetic interactions by hole/electron doping. However, the decomposition of the hybrid spin structure might be occurred as some of the above mentioned metals are easily oxidized. To prevent this problem, the egg shell type metal cluster hybrid system whose metal cluster is composed of the metal core and the inert Au outer shell might be promising. The schematic diagram of this model system was illustrated in Fig. 6.

The organic metal hybrid system with nanosize conductor, such as carbon nanotube and DNA, was depicted in Fig. 7(a). In this system, the local spin moments might be aligned by the induced current. The photo-induced organic magnets constructed of CT complexes were proposed in the previous our works [16]. Therefore, the photo-induction is also another possibility for the hole/electron doping. Lately, the newtechniques of laser manipulation and fixation of single Au nanoparticles were developed [17]. By use of this, organic metal hybrid system could be aligned on a certain substrates. Consequently, the new spintronics device as shown in Fig. 7(b) could be created. This material could be also controlled by the addition of an electric current that induced the hole/electron doping. Other possibilities to use this hybrid spin system are a superconductor and a drug delivering systems. If the hybrid spin system was arranged in a triangular ladder structure that was shown in Fig. 7(c), this system might be a spin mediated superconductor. On the other hand, the silica-based materials which can control the release of guest molecules with light have developed [18]. This kind of material can be easily modified by Au hybrid spin systems by use of the Au grafting methods [2–6]. This system was depicted in Fig. 7(d). Then, the obtained material could be guided to the goal by the induced magnetic field and the drug inside was released by light irradiation.

4. Conclusions

From the calculation results, it was found that the cationic Au_3 and neutral Au_{13} model systems have high spin ground states and the magnetic interaction of Au-organic spin molecule hybrid model systems were

dramatically changed depending on the hole or electron doping and were promising model systems for the nano-spin material, etc., that could be controlled by the induced external field.

Acknowledgements

This work has been supported by a Grant-in-Aid for Scientific Research on Priority Areas (Nos. 142064061 and 16350011) from the Ministry of Education, Culture, Sports, Science and Technology, Japan.

References

[1] M. Haruta, N. Yamanaka, T. Kobayashi, S. Iijima, J. Catal. 115 (1989) 301.
[2] M. Okumura, K. Tanaka, A. Ueda, M. Haruta, Solid State Ionics 95 (1997) 143.
[3] M. Okumura, S. Tsubota, M. Haruta, Catal. Lett. 51 (1998) 53.
[4] M. Okumura, S. Tsubota, M. Iwamoto, M. Haruta, Chem. Lett. (1998) 315.
[5] M. Okumura, M. Haruta, Chem. Lett. (2000) 396.
[6] M. Okumura, S. Tsubota, M. Haruta, J. Mol. Catal. A – Chem. 199 (2003) 73.
[7] M. Okumura, Y. Kitagawa, M. Haruta, K. Yamaguchi, Chem. Phys. Lett. 346 (2001) 163.
[8] Y. Maeda, M. Okumura, S. Tsubota, M. Kohyama, M. Haruta, Appl. Surf. Sci. 222 (2004) 409.
[9] Y. Yamamoto, T. Miura, M. Suzuki, N. Kawamura, H. Miyagawa, T. Nakamura, K. Kobayashi, T. Teranishi, H. Hori, Phys. Rev. Lett. 93 (2004) 116801.
[10] G. Harada, H. Sakurai, M. Matsushita, A. Izuoka, T. Sugawara, Chem. Lett. (2002) 1030.
[11] K. Yamaguchi, Y. Toyoda, M. Nakano, T. Fueno, Synth. Met. 19 (1987) 87.
[12] K. Yamaguchi, Y. Toyoda, T. Fueno, Synth. Met. 19 (1987) 81.
[13] M.J. Frisch, et al., Gaussian Inc., Pittsburgh PA, 1998.
[14] K. Yamaguchi, Y. Takahara, T. Fueno, in: V.H. Smith, et al. (Eds.), Applied Quantum Chemistry, D. Reidel Pub. Com., Lancaster, 1986, p. 155.
[15] S. Yamanaka, T. Kawakami, H. Nagao, K. Yamaguchi, Chem. Phys. Lett. 231 (1994) 25.
[16] M. Okumura, W. Mori, K. Yamaguchi, in: M. Doyama, et al. (Eds.), Computer Aided Innovation of New Materials, vol. II, Elsevier Science Publishers B.V., Amsterdam, 1993, p. 1785.
[17] S. Ito, H. Yoshikawa, H. Masuhara, Appl. Phys. Lett. 80 (2002) 482.
[18] N.K. Mal, M. Fujiwara, Y. Tanaka, Nature 421 (2003) 350.

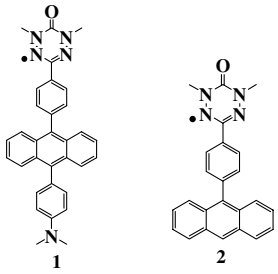


Fig. 1. Molecule studied in this work, **1** and previously reported stable radical, **2** with the excited quartet high-spin state.

orbital calculation was also carried out bath of the ground and the photo-excited spin states. The spin alignment on the photo-excited state was investigated by a time-resolved ESR (TRESR) experiment. In this paper, we also report a CT complex which has been synthesized using **1** as an electron donor and tetrafluoro-1,4-benzoquinone as the electron acceptor.

2. Experimental

2.1. Synthesis of stable radical *1*

Calbonic acid bis(1-methylhydrazide) was prepared according to the literature method [13]. Other reagents were used as purchased. Column chromatography was performed on alumina (Merk Aluminum Oxide 60). **1** was synthesized according to Scheme 1.

Sample was purified by the column chromatography on dichloromethane. Repeating recrystallization from Hexan/Dichlorometan gave **1** as red powder: m.p. >300 °C (Found: C, 77.18; H, 5.79; N, 13.81% requires: C, 77.08; H, 5.66; N, 14.05%).

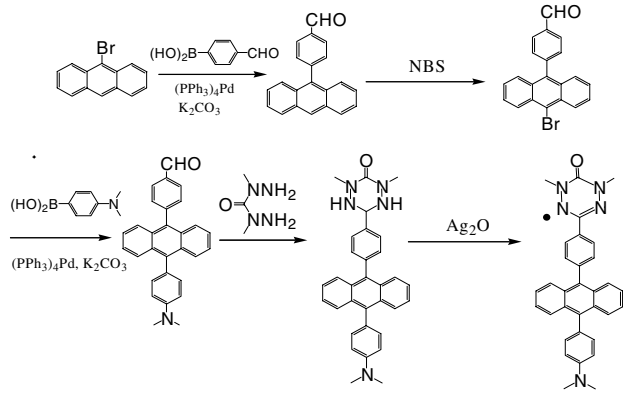
2.2. Preparation of CT complex

2.2.1. *1-BQF₄*

The CT complex was prepared under argon in 1,2-dichroloethane by mixing **1** with an excess argon in tetrafluoro-1,4-benzoquinone. The mixture was degassed in vacuum and cooled at −20 °C for three weeks. The mixture was evaporated under reduced pressure. The silver powder was purified by removing the contamination of tetrafluoro-1,4-benzoquinone in the precipitate using sublimation method.

2.3. Measurements

Oxidation potential of **1** was measured by the CV method using a Hokuto Dennko HSV-100 and UV–Vis absorption spectra were obtained with a Hitachi U-3000. Conventional ESR spectra were observed with a JEOL TE300 X-band ESR spectrometer. The ab initio



Scheme 1.

molecular orbital calculations were carried out based on the density functional theory (DFT) using GAUSSIAN 98 [14]. In the ab initio calculations, the STO 6-31G basis sets and UHF Becke 3LYP (UBecke 3LYP) hybrid method were employed. The photo-excited states were investigated by time-resolved ESR (TRESR) method. The detail of our TRESR setup was described in our previous paper [2]. The temperature in the ESR and TRESR measurements was controlled using an Oxford ESR 910 cold He gas flow system.

3. Results and discussion

The oxidation potential value of **1** in dichloromethane solution was 0.60 V on ferrocene which value was ca. 0.1 V smaller than **2**. The optical absorption band assigned to $\pi^* \leftarrow \pi$ transition arising from anthracene moiety was also shifted to longer wavelength. Their results were also supported by the ab intio calculation shown in Fig. 2. The calculated orbital energies and molecular orbitals of **1** and **2** were consistent with these experimental results. The energy location of π-HOMO of **1** becomes about 0.3 eV higher than that of **2**. These results show that the location of π-HOMO of **1** become

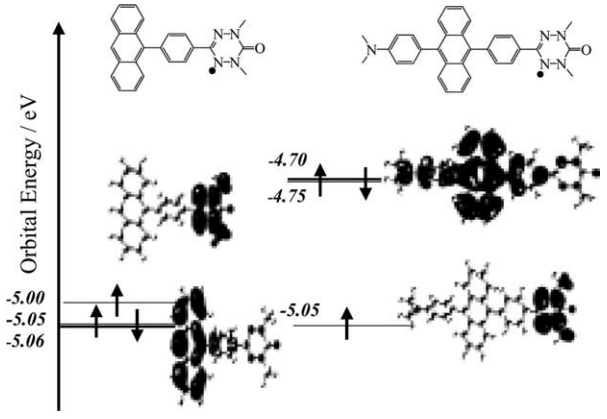


Fig. 2. Orbital energies and one-electron molecular orbitals of **1** and **3**.

higher in energy than that of **2** as the result of the attachment of dimethylamino group at the proper position. Although in **2** the energy of SOMO is located higher than that of HOMO, SOMO of **1** is located lower than the HOMO. This means that **1** will become more chemically stable compared with **2**.

The photo-excited state in **1** was investigated by TRESR experiments. Typical TRESR spectrum of **1** observed at 30 K in 2-MTHF glass matrix is shown in Fig. 3 together with the spectral simulation. The spectral simulation was carried out by the eigenfield/exact-diagonalization hybrid method [15–17] taking the electron spin polarization into account. The spectrum shows well resolved fine-structure splitting. The spectral simulation revealed that the observed TRESR spectrum of **1** has been unambiguously assigned as an excited quartet ($S = 3/2$) spin state (Q). The g value and fine-structure parameters for the quartet state have been determined to be $g(Q) = 2.0019$, $D(Q) = 0.0224\ \mathrm{cm}^{-1}$, $E(Q) = 0.003\ \mathrm{cm}^{-1}$.

The magnitude of the fine-structure parameter, D of **1** was 3% smaller than that of **2**. This result shows that the unpaired electron is slightly more delocalized in the whole molecule. However, no significant change was occurred in the molecular orbital with the unpaired electrons by an attaching dimethylamino group. The characteristic nature with the excited high-spin state is conserved in **2** and only the property of the electron donor is improved by an attaching dimethylamino group.

Fig. 4 shows the UV–Vis spectra of **1**, BQF_4 and **1**-BQF_4 charge-transfer complex. CT band was clearly observed in **1**-BQF_4.

X-band ESR spectra of **1**-BQF_4 complex in the ground state is shown in Fig. 5. This spectrum was observed at room temperature in solid phase. As shown in Fig. 5, this spectra was a very sharp line and the g value is determined to be 2.0019. This g value becomes a little smaller than the g value 2.0052 of **1**. This means that unpaired electron will move partially to the BQF_4 moiety as the result of the complex formation. Further experiments including the photo-excited state are in progress.

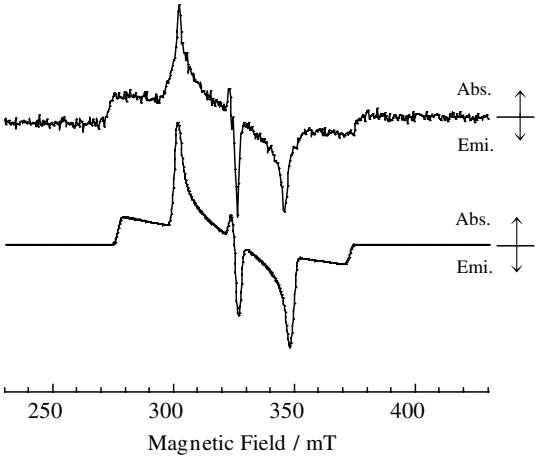


Fig. 3. Typical TRESR spectrum observed at 0.7 μs after LASER excitation.

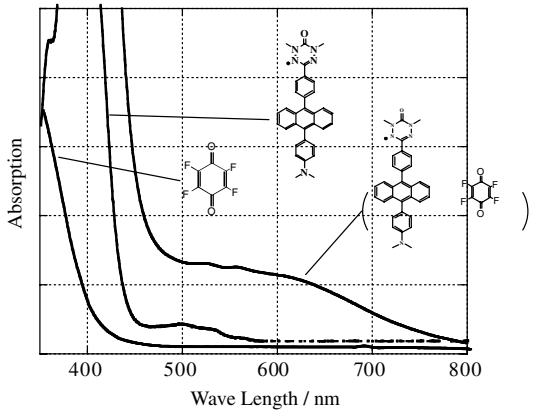


Fig. 4. Optical absorption spectra of **1**, BQF_4 and **1**-BQF_4 at room temperature. 1,2-Dichroloethane was used solvent.

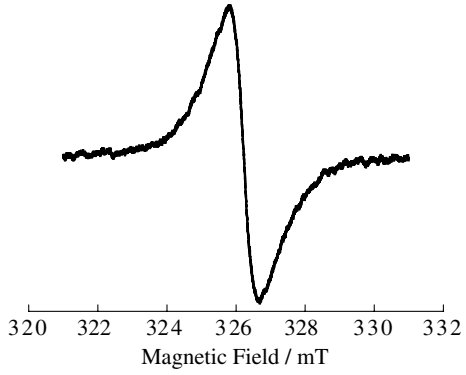


Fig. 5. X-band ESR spectra of **1**-BQF_4 observed at room temperature in solid phase. The microwave frequency is 9162.60 MHz.

4. Conclusions

1 was designed by the ab initio MO calculation and synthesized as the stable radical which electron donor property was improved compared with **1** and **2** previously reported. It is confirmed that **1** has the photo-excited high-spin quartet ($S = 3/2$) state as well as **2** by TRESR experiment. A CT complex **1**-BQF_4 was also synthesized using **1** as an electron donor.

Acknowledgements

This work was supported by the Grant-in-Aid for Scientific Research on the general (Nos. 13440211, 16350079) and Priority Area "Application of Molecular Spin" (Area No. 769, Proposal No. 15087208) from the

Ministry of Education, Culture, Sports, Science and Technology, Japan.

References

[1] Y. Teki, S. Miyamoto, K. Iimura, M. Nakatsuji, Y. Miura, J. Am. Chem. Soc. 122 (2000) 984.
[2] Y. Teki, S. Miyamoto, M. Nakatsuji, Y. Miura, J. Am. Chem. Soc. 123 (2001) 294.
[3] Y. Teki, M. Nakatsuji, Y. Miura, Mol. Phys. 100 (2002) 1385.
[4] Y. Teki, M. Nakatsuji, Y. Miura, Int. J. Mod. Phys. B 15 (2001) 4029.
[5] Y. Teki, Polyhedron 20 (2001) 1163.
[6] Y. Teki, M. Kimura, S. Narimtsu, K. Ohara, K. Mukai, Bull. Chem. Soc. Jpn. 77 (2004) 95.
[7] Y. Teki, S. Nakajima, Chem. Lett. 33 (2004) 1500.
[8] (a) C. Corvaja, M. Mggini, M. Prato, G. Scorrano, M. Venjin, J. Am. Chem. Soc. 117 (1995) 8857;
(b) N. Mizouchi, Y. Ohba, S. Yamauchi, J. Chem. Phys. 101 (1997) 5966.
[9] (a) K. Ishii, J. Fujiwara, Y. Ohba, S. Yamauchi, J. Am. Chem. Soc. 118 (1996) 13079;
(b) K. Ishii, J. Fujisawa, A. Adachi, S. Yamauchi, N. Kobayashi, J. Am. Chem. Soc. 120 (1998) 3152.
[10] P. Ceroni, F. Conti, C. Corvaja, M. Maggini, F. Paolucci, S. Roffia, G. Scorrano, A. Toffoetti, J. Phys. Chem. A 104 (2000) 156.
[11] (a) N. Mizouchi, Y. Ohba, S. Yamauchi, J. Phys. Chem. 103 (1999) 7749;
(b) F. Conti, C. Corvaja, A. Toffoletti, N. Mizouchi, Y. Ohba, S. Yamauchi, M. Maggini, J. Phys. Chem. 104 (2000) 4962;
(c) J. Fujiwara, Y. Iwasaki, Y. Ohba, S. Yamauchi, N. Koga, S. Karasawa, M. Fuhs, K. Mobius, S. Weber, Appl. Mogn. Reson. 21 (2001) 483.
[12] K. Ishii, Y. Hirose, N. Kobayashi, J. Phys. Chem 103 (1999) 1986.
[13] C. Hirel, K.E. Vostrikova, J. Pecaut, V.I. Ovcharenko, P. Rey, Chem. Eur. J. 7 (2001) 2007.
[14] The DFT calculation was carried out using GAUSSIAN 98, Revision A.ll, Gaussian, Inc., Pittsburgh, PA, 1998.
[15] G.G. Belford, R.L. Belford, J.F. Burkhalter, J. Magn. Reson. 11 (1973) 251.
[16] Y. Teki, I. Fujita, T. Takui, T. Kinoshita, K. Itoh, J. Am. Chem. Soc. 116 (1994) 11499.
[17] In the spectral simulation of the TRESR spectra, the calculation of ESP has been added as a subroutine to the computer program. More detailed procedures of the spectral simulation for high-spin organic molecules are similar to those described in our previous paper for the perturbation approach: Y. Teki, T. Takui, H. Yagi, K. Itoh, H. Iwamura, J. Chem. Phys. 83 (1985) 539.

vanadium–benzene, $V_n(C_6H_6)_{n+1}$ (see Fig. 1) [14–17], revealed that their magnetic moments increase monotonically with the layer number n [18]. The measured increase of magnetic moments indicates that the electron spins of the non-bonding d_σ electrons, localized on the V metal atoms, are aligned with a ferromagnetic ordering. This result provides the first example of magnetic spin alignment of magnetic sandwich complexes. The elucidation of the magnetic properties of isolated organometallic complexes will be an important task underlying the rational design of future novel magnetic materials, for example those based on single molecule magnets.

In this contribution, we present the results of Stern-Gerlach molecular beam deflection studies of 1D-organometallic multi-decker sandwich complexes: terbium–cyclooctatetraene $Tb_n(C_8H_8)_{n+1}$ (Fig. 1). Bonding in $Ln_n(C_8H_8)_{n+1}$ sandwich complexes (where Ln represents a lanthanide metal atom) has been found to be highly ionic in nature [19–21] as a result of charge-transfer from Ln metal atoms to C_8H_8 ligands. In the present study, terbium was selected from among the various lanthanide metals due to its large magnetic moment. Since 4f electrons are effectively shielded from interaction with external ligand fields by the outer-lying $5s^2$ and $5p^6$ electrons, the magnetic properties of Ln containing complexes are essentially ascribed to those of Ln free ions, Ln^{2+} and Ln^{3+}. Therefore, the unpaired 4f electrons within the Ln ions largely determine the magnetic properties of the $Ln_n(C_8H_8)_{n+1}$ complex, and the number of layers in a multi-decker sandwich complex, may provide a controllable parameter for the overall magnetic moments. There have been a few reports on the magnetic susceptibilities of the ionic sandwich lanthanide complexes: $K^+[Ln(C_8H_8)_2]^-$, $[Ln(C_8H_8)_2Cl\cdot 2THF]$ (Ln = Ce, Pr, Nd, Sm and Tb), $[(THF)_3K(C_8H_8)]_2$ Eu and $Ln(Pc)_2$ (Ln = Pr, Gd, Tb, Dy, Ho, Er, Tm, Yb and Lu; Pc = phthalocyanine) [22–26]. However, to our knowledge, there have been no reports on measurements of incremental magnetic moment for multi-decker sandwich complexes, except for the study of the f–f interactions in dinuclear lanthanide complexes [26]. In this work, we discuss the size dependence of magnetic moment for 1D $Tb_n(C_8H_8)_{n+1}$ complexes ($n = 1-5$) determined in a molecular beam employing the Stern-Gerlach deflection method.

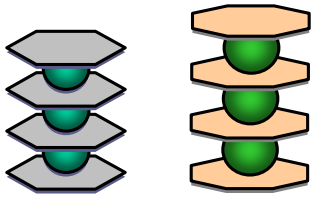


Fig. 1. Schematic structure of vanadium–benzene complex: $V_n(C_6H_6)_{n+1}$ and lanthanide–cyclooctatetraene complex: $Tb_n(C_8H_8)_{n+1}$ ($n = 3$).

2. Experimental

The magnetic moments of $Tb_n(C_8H_8)_{n+1}$ complexes were measured by molecular beam magnetic deflection – a variation on the classic Stern-Gerlach experiment used originally to determine the magnetic moments of atoms. In this approach, species that can be produced only in small quantities and/or that are highly reactive can be studied without the perturbing influences of solvents, matrices or self-reaction/polymerization. Furthermore, the use of a position-sensitive time-of-flight (PS-TOF) mass spectrometer for beam detection enables us to obtain deflection information for complexes with various compositions and sizes simultaneously. The experiments and analysis procedures have been described in detail elsewhere [27]. Briefly, metal atoms were produced by focusing the second harmonic output of Nd^{3+}:YAG laser (~30 mJ/pulse, 25 Hz) onto a metal rod of Tb within a fast flow source. The atomic vapor was carried by a continuous stream of helium into a flow tube reactor, where C_8H_8 (cyclooctatetraene) vapor was injected. The subsequent reaction of the metal atoms and C_8H_8 form a variety of product species, the dominant fraction of which consisted of the *full sandwich* complexes: $Tb_n(C_8H_8)_{n+1}$ The mixture of helium and organometallic complexes expanded into vacuum through a 1.5 mm diameter nozzle at the end of the flow tube. The resulting supersonic free jet was collimated into a molecular beam using a series of skimmers and orifices. The collimated molecular beam entered a high vacuum chamber, where it passed through the gap of a dipole gradient electromagnet capable of producing an inhomogeneous magnetic field, with gradients $\partial B/\partial z$ up to ~210 T/m and B fields up to ~1.2 T. The complexes were detected 0.9 m downstream of the deflection magnet using laser photoionization time-of-flight (TOF) mass spectrometry employing an ArF excimer laser as the photoionization source. The TOF spectrometer was operated in the position-sensitive mode [28], a technique which maps the spatial distribution of the molecular beam along the z axis (parallel to the magnetic field) onto the time domain. Between 800 and 2000 spectra were averaged in a digital oscilloscope with the magnetic field on, and then again with the field off. The deflection of the molecular beam was determined by quantitatively comparing the temporal profiles of the mass peaks in the field-on TOF spectrum with those of the field-off spectrum. The field-induced changes in PSTOF temporal profiles reflected shifts and/or broadening of the corresponding molecular beam spatial profiles.

In Stern-Gerlach studies of atoms and complexes such as those reported here, the z-component of magnetic moment μ_z of the species under investigation is given by

$$\mu_z = \frac{f}{t_{\mathrm{arr}}}\frac{mV^2}{LD\mu_{\mathrm{B}}}\frac{\Delta t}{\left(\frac{\partial B}{\partial z}\right)}, \qquad (1)$$

where the factor f is an instrumental constant, t_{arr} is the arrival time of the target complex, m is mass of the complex, V is a beam speed, D and L are the length of the magnet and the distance from the final collimating slit to the detector, Δt is the time difference (field-on versus field-off) of the TOF peak center of the complex, and $(\partial B/\partial z)$ is the magnetic gradient, respectively.

The quantity measured in determining net beam deflections is the change in the average position of deflected beam profile. Specifically, the beam deflections are quantitatively determined as the difference in first moments between the zero-field beam profile and the profile recorded with the field applied. For superparamagnetic complexes (i.e., those in which intramolecular spin relaxation occurs on a timescale faster than the flight time through the magnetic field) the peak shift can be described to good approximation the Langevin model [29], which can be simplified to the Curie Law under the condition of $\mu B \ll k_B T$,

$$\langle M_z \rangle = \frac{\mu^2 B}{3k_B T}. \quad (2)$$

Here, the time averaged effective magnetic moment $\langle M_z \rangle$ is related to the true moment μ. Then the magnetic moment μ in μ_B units can be obtained from the deformation of (1) with replacing μ_z into $\langle M_z \rangle$,

$$\mu = \frac{1}{\mu_B}\sqrt{\frac{f}{t_{arr}}\frac{mV^2}{LD}3k_B T\frac{\Delta t_{delay}}{B\left(\frac{\partial B}{\partial Z}\right)}}, \quad (3)$$

where Δt_{delay} is the shift of the peak, B is the magnetic field in T. The last term predicts that Δt_{delay} should be proportional to $B(\partial B/\partial z)$ in this model.

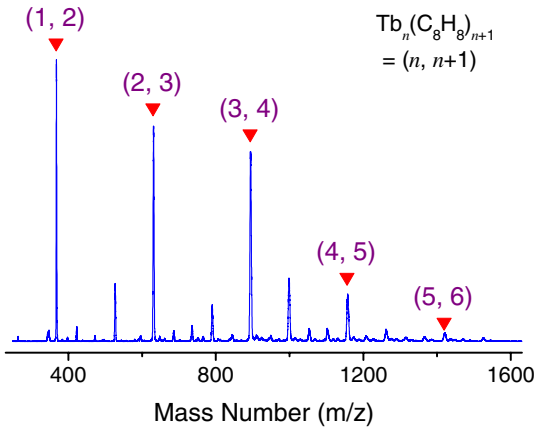


Fig. 2. Mass spectrum for $Tb_n(C_8H_8)_m$ complexes ($T = 146$ K). The regular progressions of mass peaks exhibit the dominant fraction of *full sandwich* complexes: $Tb_n(C_8H_8)_{n+1}$.

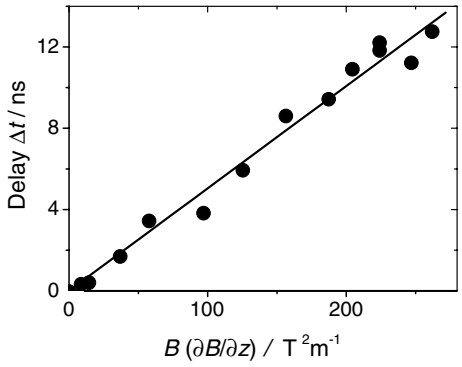


Fig. 3. Single-sided magnetic deflection of TOF peak delay Δt of $Tb_3(C_8H_8)_4$ at 150 K. Peak delay Δt varies linearly with the product of $B(\partial B/\partial z)$.

3. Results and discussion

Fig. 2 shows the photoionization mass spectra of terbium–cyclooctatetraene complexes generated at a source temperature of 146 K. Labeled peaks corresponding to "complete" sandwich $Tb_n(C_8H_8)_{n+1} = (n, n+1)$ complexes appear prominently. Small quantities of incomplete sandwich complexes (e.g., "half" sandwich complexes containing an uncapped metal atom, or complexes which contain excess ligand molecules) are also produced.

Fig. 3 shows a linear dependence of the spatial shift of the $Tb_3(C_8H_8)_4$ peak against the product of $B(\partial B/\partial z)$, as predicted by the Langevin/Curie model. It has been shown that many types of polynuclear metal clusters (Ni_n, Co_n, Fe_n and Gd_n) show one-side deflection behavior similar to that displayed by $Tb_3(C_8H_8)_4$ [6–12]. Other $Tb_n(C_8H_8)_{n+1}$ complexes ($n = 1, 2, 4, 5$) also exhibited one-sided peak shifts. These observations indicate the occurrence of spin relaxation and thus justifies the use of the Langevin model to determine the intrinsic moments of the $Tb_n(C_8H_8)_{n+1}$ complexes (vide infra). The occurrence of rapid spin relaxation demonstrates that the energy barrier for intramolecular spin reorientation due to internal magnetic anisotropy is negligible compared to $k_B T$ [30]. Intrinsic moments for $Tb_n(C_8H_8)_{n+1}$ obtained via Eq. (3), are plotted in Fig. 4. A monotonic increase of the magnetic moment with the size up to $n = 3$ is observed. Their absolute values are in the good agreement with the magnetic moment of a free Tb^{3+} ion ($4f^8$; 9.7 μ_B). Although the experimental uncertainty is large, deviation at $n = 1$ may attributed to the contribution of unpaired spins on the C_8H_8 ligands [31]. On the other hand, the magnetic moment drops at $n = 4$. For complexes of larger than $n = 4$, the increase in magnetic moment with each additional layer is about a half that measured for $n < 4$. This is ascribed to the particular oxidation states of Tb atoms comprising of the larger complexes. as reported previously [20,21], for longer sandwich complexes ($n > 2$), some of Tb atoms take on +2 oxidation states in addition +3 states since the

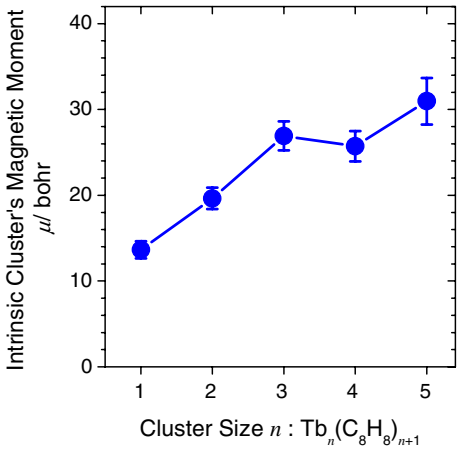


Fig. 4. Magnetic moments μ for $Tb_n(C_8H_8)_{n+1}$ ($n = 1 - 5$) complexes at $T = 146$ K.

C_8H_8 ligand can accommodate only two electrons. Although it is well known that Tb atom takes +3 and rarely +4 oxidation states in Tb complexes, unusual lower +2 oxidation state can exist for species isolated in a molecular beam. For $Tb(C_8H_8)_2$ and $Tb_2(C_8H_8)_3$, the oxidation state of Tb atom(s) is +3: the constituents of $Tb(C_8H_8)_2$ and $Tb_2(C_8H_8)_3$ can be formally expressed as $\{(C_8H_8)^{1.5-}\ Tb^{3+}\ (C_8H_8)^{1.5-}\}$ and $\{(C_8H_8)^{2-}\ Tb^{3+}\ (C_8H_8)^{2-}\ Tb^{3+}\ (C_8H_8)^{2-}\}$, respectively [33]. In the case of $Tb_3(C_8H_8)_4$, however, the oxidation states of the constituents can be formally expressed as $\{(C_8H_8)^{2-}\ Tb^{3+}\ (C_8H_8)^{2-}\ Tb^{2+}\ (C_8H_8)^{2-}\ Tb^{3+}\ (C_8H_8)^{2-}\}$, because four C_8H_8 ligands can accept 8 electrons in total. Similarly, for the case of $Tb_4(C_8H_8)_5$ complex, two Tb^{2+} ions exist in the middle of the complex, with the outermost Tb ions existing in +3 state. These charge distributions have reasonably been deduced from photoionization spectroscopy and chemical probe experiments [20,21]. Since the magnetic moment for Tb^{2+} ($4f^9$; 9.47 μ_B) is almost the same as that of Tb^{3+}, the lower magnetic moments measured for $Tb_4(C_8H_8)_5$ complex implies that interaction between the two central Tb^{2+} ions is antiferromagnetic. The increase of magnetic moment from $n = 4$ to $n = 5$ can be explained by the excess Tb^{2+} ion which cannot be coupled. Therefore, continued zigzag oscillation of magnetic moments is expected for $Tb_n(C_8H_8)_{n+1}$ complexes ($n \geqslant 3$). However, since only the entire magnetic moment is measured in the present molecular beam study, the size dependence may be blurred by coexistence of several low-lying electronic spin states.

The observed one-sided beam deflection behavior indicates that intramolecular spin relaxation (ISR) occurs for $Tb_n(C_8H_8)_{n+1}$ complexes. That ISR may occur at all in these Tb-COT systems is a result of their large density of rovibronic states ρ. In particular intramolecular spin relaxation can occur in isolated species only when the average spacing between rovibronic levels given by ρ^{-1} is less than spacing between Zeeman levels [32]. By comparison, the electronic structure of $V_n(C_6H_6)_{n+1}$ complexes are comparatively simple owing to the non-bonding character of d_σ orbitals which accommodate unpaired spin [17,18]. As a result, the density of states for $V_n(C_6H_6)_{n+1}$ complexes is sparse since there are no low-lying states which can be crossed in the magnetic field, and thus spin relaxation is not observed. In contrast, the density of states of $Tb_n(C_8H_8)_{n+1}$ complexes is dense due to existence of low-lying electronic states and mixing of these states in the presence of magnetic field [33]. It is thus reasonable to expect that this large density of states makes spin relaxation is facile in $Tb_n(C_8H_8)_{n+1}$ complexes. Note that it is very important to uncover the relationship between the magnetization relaxation and ligands through the control of degrees of vibrations and dimensionality. From our result on $Tb(C_8H_8)_2$, there appears to no evidence for slow magnetization relaxation, whereas $Tb(Pc)_2$ exhibits slow magnetization [34]. The observed one-side magnetic deflection of Tb-COT clusters is thus explained by fast magnetic relaxation. If these species showed slow spin relaxation (or none at all), magnetic deflection behavior should involve symmetric beam broadening as in isolated atoms. It is quite likely that the gas-phase magnetic beam deflection of $Tb(Pc)_2$ would be different from that of $Tb(C_8H_8)_2$.

In summary, the magnetic deflections of multiple-decker terbium–cyclooctatetraene organometallic complexes have been measured by a Stern-Gerlach molecular beam deflection method. $Tb_n(C_8H_8)_{n+1}$ sandwich complexes displayed one-side deflections which indicates the occurrence of fast intramolecular spin relaxation. The evolution of the magnetic moment with increasing size can be rationalized in terms of the number of Tb^{3+} ions. The drop of the magnetic moment for $Tb_4(C_8H_8)_5$ implies antiferromagnetic interaction of adjacent Tb^{2+} ions at the central portion of the complex. Size-selective soft-landing of gas-phase complexes onto nano-scale designed surfaces is an emerging approach [35] that is expected to open exciting new possibilities for exploiting these species as nano-sized magnetic building blocks in applications such as magnetic recording media.

Acknowledgments

This work was supported in part by the Office of Science, Division of Chemical Science, US-DOE under contract number W-31-109-ENG-38. This work is partly supported by the 21st Century COE program "KEIO Life Conjugate Chemistry" (KEIO-LCC) from the Ministry of Education, Culture, Sports, Science, and Technology, Japan.

References

[1] C. Kollmar, O. Kahn, Acc. Chem. Res. 26 (1993) 259.
[2] J.S. Miller, A.J. Epstein, Angew. Chem., Int. Ed. Engl. 33 (1994) 385.
[3] J.A. McCleverty, M.D. Ward, Acc. Chem. Res. 31 (1998) 842.
[4] A. Nakajima, K. Kaya, J. Phys. Chem. A 104 (2000) 176.
[5] W.D. Knight, R. Monot, E.R. Dietz, A.R. George, Phys. Rev. Lett. 40 (1978) 1324.
[6] D.M. Cox, D.J. Trevor, R.L. Whetten, E.A. Rohlfing, A. Kaldor, Phys. Rev. B 32 (1985) 7290.
[7] W.A. de Heer, P. Milani, A. Châtelain, Phys. Rev. Lett. 65 (1990) 488.
[8] W.A. de Heer, P. Milani, A. Châtelain, Z. Phys. D 19 (1991) 241.
[9] D.C. Douglass, A.J. Cox, J.P. Bucher, L.A. Bloomfield, Phys. Rev. B 47 (1993) 12874.
[10] I.M.L. Billas, A. Châtelain, W.A. de Heer, Science 265 (1994) 1682.
[11] I.M.L. Billas, A. Châtelain, W.A. de Heer, J. Mag. Mag. Mater. 168 (1997) 64.
[12] D. Gerion, A. Hirt, A. Châtelain, Phys. Rev. Lett. 83 (1999) 532.
[13] A. Amirav, G. Navon, Chem. Phys. 82 (1983) 253.
[14] K. Hoshino et al., J. Phys. Chem. 99 (1995) 3053.
[15] K. Miyajima et al., J. Phys. Chem. A 106 (2002) 10777.
[16] T. Yasuike, S. Yabushita, J. Phys. Chem. A 103 (1999) 4533.
[17] A. Nakajima;, K. Kaya, J. Phys. Chem. A 104 (2000) 176.
[18] K. Miyajima, A. Nakajima, S. Yabushita, M.B. Knickelbein, K. Kaya, J. Am. Chem. Soc. 126 (2004) 13202.
[19] W. Liu, M. Dolg, P. Fulde, J. Chem. Phys. 107 (1997) 3584.
[20] K. Miyajima, T. Kurikawa, M. Hashimoto, A. Nakajima, K. Kaya, Chem. Phys. Lett. 306 (1999) 256.
[21] T. Kurikawa, Y. Negishi, F. Hayakawa, S. Nagao, K. Miyajima, A. Nakajima, K. Kaya, J. Am. Chem. Soc. 120 (1998) 11766.
[22] F. Mares, K. Hodgson, A. Streitwieser Jr., J. Organomet. Chem. 24 (1970) C68.
[23] K.O. Hodgson, F. Mares, D.F. Starks, A. Streitwieser Jr., J. Am. Chem. Soc. 95 (1973) 8650.
[24] W.J. Evans, J.L. Shreeve, J.W. Ziller, Polyhedron 14 (1995) 2945.
[25] K.L. Trojan, J.L. Kendall, K.D. Kepler, W.E. Hatfield, Inorg. Chim. Acta. 198–200 (1998) 795.
[26] N. Ishikawa, T. Iino, Y. Kaizu, J. Am. Chem. Soc. 124 (2002) 11440.
[27] M.B. Knickelbein, J. Chem. Phys. 116 (2002) 9703.
[28] W.A. de Heer, P. Milani, Rev. Sci. Instrum. 62 (1991) 670.
[29] S.N. Khanna, S. Linderoth, Phys. Rev. Lett. 67 (1991) 742.
[30] P.J. Jensen, S. Mukherjee, K.H. Bennemann, Z. Phys. D 21 (1991) 349.
[31] M. Schultz, J.M. Boncella, D.J. Berg, T.D. Tilley, R.A. Andersen, Organometallics 21 (2002) 460.
[32] M.B. Knickelbein, J. Chem. Phys. 121 (2004) 5281.
[33] W. Liu, M. Dolg, P. Fulde, Inorg. Chem. 37 (1998) 1067.
[34] N. Ishikawa, M. Sugita, T. Ishikawa, S. Koshihara, Y. Kaizu, J. Am. Chem. Soc. 125 (2003) 8694.
[35] K. Judai, K. Sera, K. Yagi, T. Yasuike, S. Yabushita, A. Nakajima, K. Kaya, Chem. Phys. Lett. 334 (2001) 277.

thus the lowering of the lattice symmetry, and the presence of the rhombic (E) term in the spin Hamiltonian. It is thus of interest to examine, by solid state NMR spectroscopy, the role of the lattice-solvated molecules in the overall magnetic symmetry and structure of Mn_{12}–Ac and related compounds. To this effect, we have carried out ^{55}Mn NMR measurements on the recently synthesized compound $[Mn_{12}O_{12}(O_2CCH_2Br)_{16}(H_2O)_4]\cdot 4CH_2Cl_2$ (Fig. 1), henceforth as Mn_{12}–BrAc [19]. In particular, we examined the NMR spectra of single crystal as well as aligned powder of this compound. We found significant differences between the spectra from the single crystals versus aligned powder; specifically that the single crystals afford significantly higher spectral resolution than the aligned powder, and moreover, that the act of powdering introduces significant differences in the chemical structure of Mn_{12}–BrAc. Furthermore, angular dependence studies are now possible because of the use of single crystals. We conducted such studies with rotations in the *ac*-plane.

2. Synthesis and crystal growth

Mn_{12}–BrAc was synthesized by mixing Mn_{12}–Ac in toluene and then adding an excess of HO_2CCH_2Br, as described elsewhere [19]. Once the initial crystals of Mn_{12}–BrAc were formed, they were recrystallized by dissolving in dichloromethane and adding bromoacetic acid. Once dissolved, the solution was filtered and placed into small vials with a small amount of hexanes. A needle was pushed through the lid to assure slow evaporation. After a week, nice brick looking single crystals form.

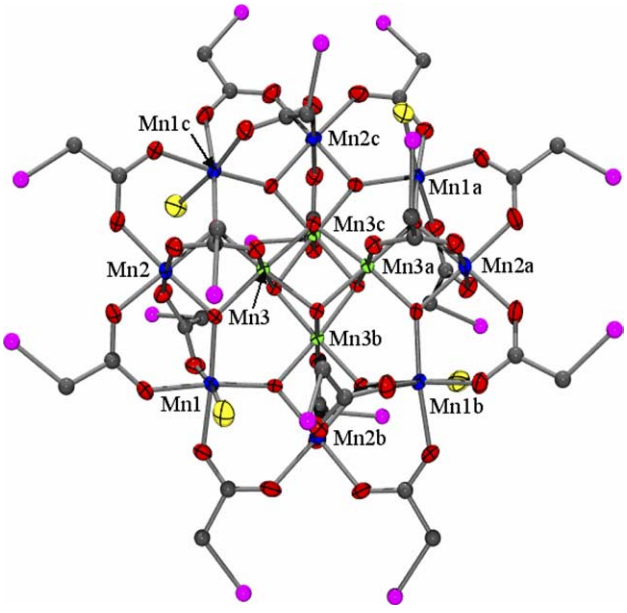


Fig. 1. ORTEP representation in PovRay format of Mn_{12}–BrAc.

3. NMR experimental details

^{55}Mn NMR measurements were made using a home built MAGRes2000 Integrated Wideband NMR spectrometer with quadrature detection and a home built high frequency probe [20,21]. The crystal samples were prepared by removing the crystal from its mother liquor and immediately covering in 5-min epoxy to prevent the sample from drying. Immediately after the epoxy was set, the sample was mounted into the coil and cooled in a dewar of liquid Helium. Aligned powder samples were made by crushing the crystals and then mixing with Stycast 1266 epoxy. On crushing the sample, it was noticed that the crystals went from a dark wet looking brown color to a light brown, dry powdery sample. The epoxy was then allowed to cure overnight at room temperature in a field of 8.5 T. Data was acquired for both samples at ~2 K, below the blocking temperature, T_B, of ~3 K because of fast T_2 times above this temperature. A Hahn echo pulse sequence was used while the frequency was scanned from 220 to 400 MHz, usually taking 0.1–0.2 MHz steps. Frequency scans were necessary because of the large peak widths (~5–20 MHz). Pulse lengths were on the order of hundreds of nanoseconds giving a bandwidth of roughly ~2 MHz. After the scan, the data was processed using a Fast Fourier Transform Sum (FFT Sum).

4. Results

We present here the comparison of single crystal ^{55}Mn NMR spectroscopic measurements of $[Mn_{12}O_{12}(O_2CCH_2Br)_{16}(H_2O)_4]\cdot 4CH_2Cl_2$ (Fig. 2, henceforth Mn_{12}–BrAc) and an aligned powder sample of Mn_{12}–BrAc. As will be seen, the ability to probe Mn sites represents a powerful tool to study factors such as symmetry-lower-

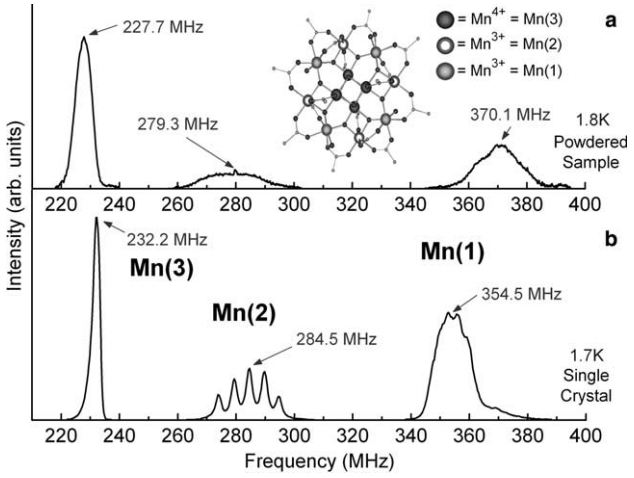


Fig. 2. Comparison of Mn_{12}–BrAc aligned powder vs. single crystal. Inset shows the core crystal structure and assigns the peaks.

ing in SMMs due to extrinsic perturbations and the ground state at each Mn ion. Mn_{12}–BrAc yield large single crystals suitable for ^{55}Mn NMR studies. Fig. 2 shows a comparison of ^{55}Mn NMR signals obtained from: (a) Mn_{12}–BrAc powder and (b) a Mn_{12}–BrAc single crystal, all in zero external field, $H_0 = 0$.

The aligned powder spectrum of Mn_{12}–BrAc, Fig. 2(a), shows three peaks corresponding to the three expected sites of the Mn ions [22,23]. The first peak (Mn(3)) at 227.7 MHz corresponds to the Mn^{4+} ions in the Mn_4O_4 core and has Full Width at Half Maximum (FWHM) of 6.52 MHz. The second peak (Mn(2)) at 279.3 MHz, with a FWHM of 24.74 MHz, is a result of four of the Mn^{3+} ions located in the crown of the molecule. No quadrupolar splitting is noticed. The last four Mn^{3+} ions located in the crown of the molecule produce the third peak (Mn(1)) at 370.1 MHz and a FWHM of 16.67 MHz. Again, no quadrupolar information can be extracted from this peak. Hyperfine fields can be calculated by using $\gamma_n^{55} = 10.5$ MHz/T resulting in fields of 21.69, 26.60, and 35.25 T corresponding to Mn(3), Mn(2), and Mn(1), respectively.

Upon examining the single crystal data (Fig. 2(b)) a sharp distinction is noticed. Resolution is far superior to that of the aligned powder and the peaks are actually shifted, up to ~16 MHz. The peak assignments are the same as the aligned powder. The narrow first peak has a frequency of 232.2 MHz, a FWHM of 2.89 MHz, and a hyperfine field of 22.11 T. The second quadrupolar split line has a central transition at 284.5 MHz, a FWHM of 2.91 MHz and an internal field of 27.10 T. Lastly, the third peak occurs at 354.5 MHz with a hyperfine field of 33.76 T. While the resolution is not great enough to measure the width of one of the quadrupolar split peaks, the FWHM for the entire peak is 13.82 MHz. All data should be contrasted with that obtained from the aligned powder.

The large resolution enhancement afforded by use of single crystals allows us to calculate the quadrupole coupling parameter e^2qQ for the second and third peaks through the quadrupole splitting, $\Delta\nu_Q$, and the equation for the energy [22,23]

$$\mathbf{E}_m = -\gamma_n \hbar H_0 m + \frac{e^2qQ}{4I(2I-1)}\left(\frac{3\cos^2\theta - 1}{2}\right)[3m^2 - I(I+1)],$$

where I and m are the nuclear spin and its projection quantum numbers, and θ the angle from the symmetry axis. From crystallographic data for Mn_{12}–BrAc, it is known that the local Jahn–Teller axes, and hence the principal hyperfine field directions of Mn(2) and Mn(1) ions are canted away from the c-axis at angles of 7.9° and 34.0°, respectively. With $I = 5/2$, $\Delta\nu_Q = 5.15 \pm 0.05$ MHz for the Mn(2) peak while $\Delta\nu_Q = 3.3 \pm 0.10$ MHz for the Mn(1) peak resulting in e^2qQ values of 35.33 ± 0.35 and 41.43 ± 1.26 MHz, respectively. No such information is obtainable from the oriented powder data (Fig. 2(a)).

Powdering the sample obviously changes the environment of the Mn ions, most likely due to the pressure and temperature change placed on the crystals when they are crushed. Further studies of these effects are underway to determine the exact cause of the transformation. More significant to this work is the knowledge that an aligned powder does not represent a statistical average of the crystal, as is seen by the large shift of the peaks in the aligned powdered spectra. It is thus suggested that work on aligned powders should be viewed with caution.

Yet another advantage to using single crystals is the ability to perform angular dependence studies. Angular dependence of the Mn(3) peak of Mn_{12}–BrAc was conducted from the easy to hard axis, as shown in Fig. 3. Rotation in the ac plane was prepared by cooling the crystal in zero field, so signals from both $m_s = \pm 10$ states are discernible, separated by twice the Zeeman frequency at the applied field (1 T here). The angular variation in the *ac*-plane is described by the following equation:

$$\textit{Peak Frequency} = \nu_{CF} \pm (^{55}\gamma/2\pi)(H_0)(\cos\theta).$$

ν_{CF} represents the central frequency and θ being the angle between H_0 and the c-axis. As the crystal is rotated, the effective field, H_{eff}, felt by the nuclei is just the sum of the projection of H_0 onto the hyperfine field, H_N ($H_{eff} = H_N \pm H_0\cos\theta$). Thus, a maximum in the splitting is seen when H_0 is parallel to the c-axis ($\theta = 0°$) while a minimum in the splitting is noticed when H_0 is perpendicular to the c-axis ($\theta = 90°$). One interesting result is the splitting observed when the crystallographic c-axis is perpendicular to the external field, H_0. When the crystal is in this configuration and an external field is applied, we observe two peaks as opposed to the expected one. We tentatively assign this to two different orientations of the hyperfine fields at the Mn^{4+} sites.

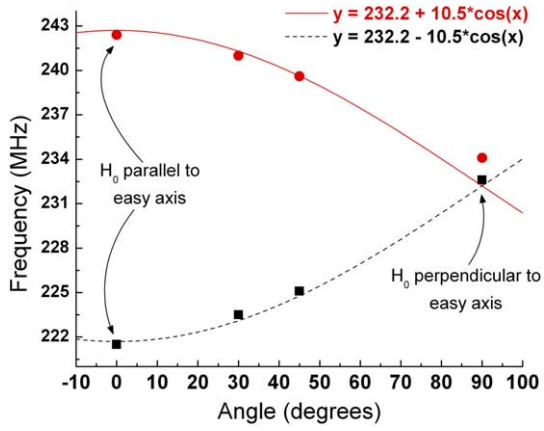


Fig. 3. Angular dependence in the *ac*-plane of a single crystal of Mn_{12}–BrAc.

5. Conclusion

Loss of information from aligned powdered samples is obvious by the shifts in frequency and loss of quadrupolar splitting. Single crystal measurements offer a new way to probe the magnetic properties of SMM by providing more accurate measurements of hyperfine fields and quadrupolar information. Angular dependence studies show that there is more work to be done to understand the magnetic structure of this molecule. The higher symmetry of Mn_{12}–BrAc, as a result of having no waters of hydration to allow hydrogen bonding, produces a less convoluted spectrum than Mn_{12}–Ac, suggesting that Mn_{12}–BrAc is a model system to study for understanding magnetic tunneling in the Mn_{12} family. Two recent studies [24–26] support this conclusion.

Acknowledgement

This work was supported by the NSF-DMR Grant # DMR 0103290.

References

[1] G. Christou, D. Gatteschi, D.N. Hendrickson, MRS Bulletin 25 (2000) 66.
[2] D. Gatteschi, R. Sessoli, Angew. Chem. Int. Ed. Eng 42 (2003) 26.
[3] T. Lis, Acta Crystallogrr. B36 (1980) 2042.
[4] S. Hill, J.A.A.J. Perenboom, N.S. Dalal, T. Hathaway, T. Stalcup, J.S. Brooks, Phys. Rev. Lett. 80 (1998) 2453.
[5] J.A.A.J. Perenboom, J.S. Brooks, S. Hill, T. Hathaway, N.S. Dalal, Phys. Rev. B 58 (1998) 330.
[6] S. Hill, S. Maccagnano, K. Park, R.M. Achey, J.M. North, N.S. Dalal, Phys. Rev. B 65 (2002) 224410.
[7] A. Mukhin, V.D. Travkin, A.K. Zvezdin, S.P. Lebedev, A. Caneschi, D. Gatteschi, Europhys. Lett. 44 (1998) 778.
[8] A. Mukhin, B. Gorshunov, M. Dressel, C. Sangregorio, D. Gatteschi, Phys. Rev. B 63 (2001) 214411.
[9] M. Dressel, B. Gorshunov, K. Rajagopal, S. Vongtragool, A.A. Mukhin, Phys. Rev. B 67 (2003) 060405.
[10] A.L. Barra, D. Gatteschi, R. Sessoli, Phys. Rev. B 56 (1997) 8192.
[11] R. Blinc, P. Cevc, D. Arcon, N.S. Dalal, R.M. Achey, Phys Rev. B 63 (2001) 212401.
[12] K. Park, M.A. Novotny, N.S. Dalal, S. Hill, P.A. Rikvold, Phys. Rev. B 65 (2002) 014426.
[13] K. Park, M.A. Novotny, N.S. Dalal, S. Hill, P.A. Rikvold, J. Appl. Phys. 91 (2002) 7167.
[14] S. Carretta, E. Liviotti, G. Amoretti, R. Caciuffo, A. Caneschi, D. Gatteschi, Phys. Rev. B 65 (2002) 052411.
[15] M. Hennion, L. Pardi, I. Mirebeau, E. Suard, R. Sessoli, A. Caneschi, Phys. Rev. B 56 (1997) 8819.
[16] I. Mirebeau, M. Hennion, H. Casalta, H. Andres, H.U. Gudel, A.V. Irodova, A. Caneschi, Phys. Rev. Lett. 83 (1999) 628.
[17] R. Caciuffo, G. Amoretti, A. Murani, R. Sessoli, A. Caneschi, D. Gatteschi, Phys. Rev. Lett. 81 (1998) 4744.
[18] A. Cornia, R. Sessoli, L. Sorace, D. Gatteschi, A.L. Barra, C. Daiguebonne, Phys. Rev. Lett. 89 (2002) 257201.
[19] H. Tsai, D. Chen, C. Yang, T. Jwo, C. Wur, G. Lee, Y. Wang, Inorg. Chem. Commun. 4 (2001) 511.
[20] R.M. Achey, P.L. Kuhns, A.P. Reyes, W.G. Moulton, N.S. Dalal, Phys. Rev. B 64 (2001) 064420.
[21] R.M. Achey, P.L. Kuhns, A.P. Reyes, W.G. Moulton, N.S. Dalal, Solid-State Commun. 121 (2002) 107.
[22] T. Kubo, T. Goto, T. Koshiba, K. Takeda, K. Awaga, Phys. Rev. B 65 (2002) 224425.
[23] Y. Furukawa, K. Watanabe, K. Kumagai, F. Borsa, T. Sasaki, N. Kobayashi, D. Gatteschi, Phys. Rev. B 67 (2003) 064426.
[24] A.G. Harter, N.E. Chakov, B. Roberts, R. Achey, A. Reyes, P. Kuhns, G. Christou, N.S. Dalal, Inorg. Chem. 44 (2005) 2122.
[25] S. Hill, R.S. Edwards, S.I. Jones, N.S. Dalal, J.M. North, Phys. Rev. Lett. 90 (2003) 217204.
[26] E. del Barco, A.D. Kent, E.M. Rumberger, D.N. Hendrickson, G. Christou, Phys. Rev. Lett. 91 (2003) 047203.

$(NH_4)_3CrO_8$ was synthesized by dissolving $(NH_4)_2CrO_4$ or CrO_3 in NH_4OH at room temperature. This solution was then cooled to −5 °C at which point H_2O_2 is added drop wise [6–10]. This process yields mm-size crystals. Crystals can be kept for more than a year at freezing temperatures. Decomposition occurs quickly if allowed to warm up and the compound can be explosive if pressure or heat is applied.

2.2. X-ray

Data were collected at 173 K on a Siemens SMART PLATFORM equipped with a CCD area detector and a graphite monochromator utilizing Mo Kα radiation ($\lambda = 0.71073$ Å). Cell parameters were refined using up to 8192 reflections. A full sphere of data (1850 frames) was collected using the ω-scan method (0.3° frame width). The first 50 frames were remeasured at the end of data collection to monitor instrument and crystal stability (maximum correction on I was <1%). Absorption corrections by integration were applied based on measured indexed crystal faces.

The structure was resolved by the Direct Methods in SHELXTL5, and refined using full-matrix least squares. The non-H atoms were treated anisotropically, whereas the hydrogen atoms located from a Difference Fourier map. N1 is located on a $\bar{4}$ symmetry center thus only one H atom exists in the asymmetric unit, and it was refined freely. N2 is located on a $\bar{4}2$ m center thus the four tetrahedrally oriented H atoms are heavily disordered. Two H atoms were found and were refined riding on their N2 atom. Because of symmetry, the H atoms around N2 are octahedrally oriented which is theoretically not correct for an ammonium cation but is close to two disordered sets that are related by 2-fold rotation or mirror symmetry. The asymmetric unit consists of 1/8 CrO_8^{3-} (located on a $\bar{4}2$ m center), 1/8 NH_4^+ (located on a $\bar{4}2$ m center), and another NH_4^+ ion located on a $\bar{4}$ symmetry element (1.4 in the asymmetric unit). Thus, the stoichiometry is $CrO_8(NH_4)_3$. The structure was also solved and refined in sub space groups of $I\bar{4}2$ m but these refinements did not provide any better results and did not remove the disorder of the H atoms around N2. A total of 26 parameters were refined in the final cycle of refinement using 254 reflections with $I > 2\sigma(I)$ to yield R_1 and wR_2 of 1.70% and 5.00%, respectively. Refinement was done using F^2.

2.3. Heat capacity and magnetization measurements

In order to detect a possible solid–solid or magnetic phase transition, we carried out heat capacity measurements over the range of 300 K down to 300 mK. These measurements were made with a Quantum Design Physical Properties Measurement System (QD PPMS) facility available at the National High Magnetic Field Laboratory in Tallahassee, Florida. dc magnetic susceptibility measurements were made using a Quantum Design SQUID magnetometer over a temperature range of 1.8–300 K.

2.4. Electron paramagnetic resonance spectroscopy

Electron paramagnetic resonance (EPR) spectroscopic measurements were carried out over a range of 2.8–295 K at X-band (~9.5 GHz), Q-band (35 GHz) and W-band (~93.5 GHz) using the Bruker (X- and Q-band) spectrometers; and a locally designed W-band system available as described earlier [11–14]. Both single crystals and powder samples were studied. Angular studies where done using a goniometer and the Q-band setup. The measured Zeeman splitting constants, g-values, clearly identified the compound as containing the Cr(5+) ion, based on our earlier reports [7,8,11–14].

3. Results and discussion

Fig. 1 shows a schematic of the CrO_8^{3-} moiety [11], which is the central part of our compound. Fig. 2 depicts the unit cell of $(NH_4)_3CrO_8$, based on our X-ray diffraction data as discussed above. The structure consists of essentially isolated Cr(5+), $3d^1$ ions and one thus expects little or no magnetic exchange interaction between the Cr(5+) ions, as we had envisaged. Indeed, magnetic susceptibility measurements, shown in Figs. 3 and 4, fully supported this behavior: the saturated magnetic moment corresponded to an $S = 1/2$ system (Fig. 3), while the magnetic susceptibility data followed the

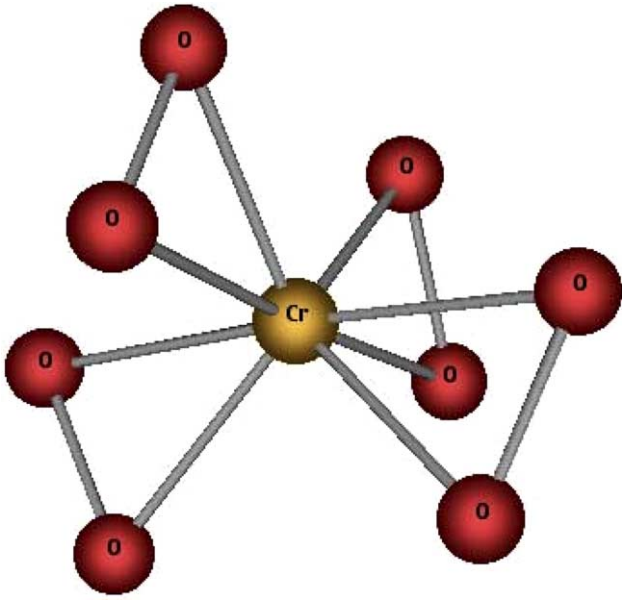


Fig. 1. Structure of CrO_8^{3-} ion.

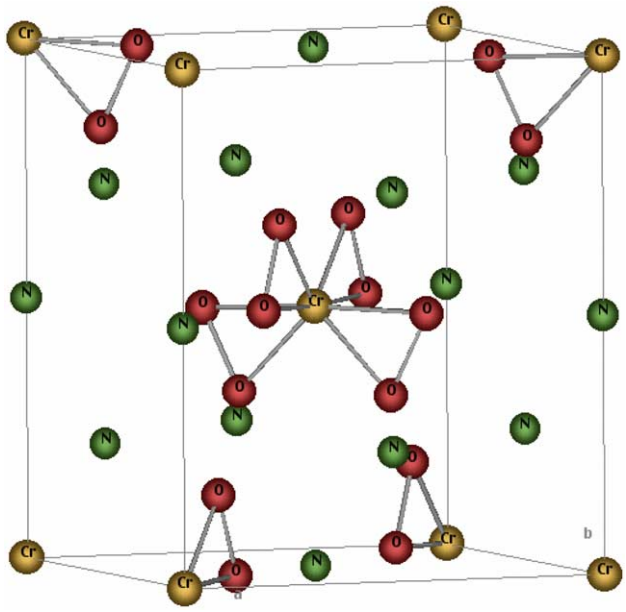


Fig. 2. Unit cell for $(NH_4)_3CrO_8$.

expected Curie–Weiss behavior (a straight line for the inverse susceptibility, $1/\chi$ versus T plot), as seen in Fig. 4. The Curie constant was $C = 0.320$ mol K/emu and $\theta = -0.8$ K showing a weak antiferromagnetic coupling, if any, similar to the other peroxychromates [7–13]. From the effective moment ($\mu_{eff}/\mu_\beta = 1.596$) we calculate, assuming $S = 1/2$, that $g_{iso} = 1.8429$, which was essentially in agreement with the variable temperature, variable frequency EPR data (Figs. 6 and 7, vide infra).

Heat capacity data (Fig. 5), on the other hand, exhibited a small but sharp peak at 137.5 K, which indicated the presence of some form of a order–disorder phase transition. $\Delta S = 4.70$ J/mol K was calculated over the peak by graphing $C_p * T$ versus T and then integrating; $\Delta S = \int C_p \frac{dT}{T}$. For a two state mixed system, the theoretically expected value is $\Delta S = R * \ln(2) = 5.76$ J/mol K,

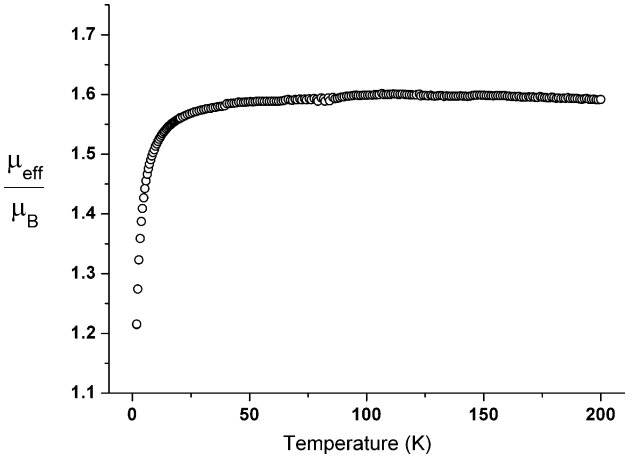


Fig. 3. Temperature dependence of magnetic moment of $(NH_4)_3CrO_8$.

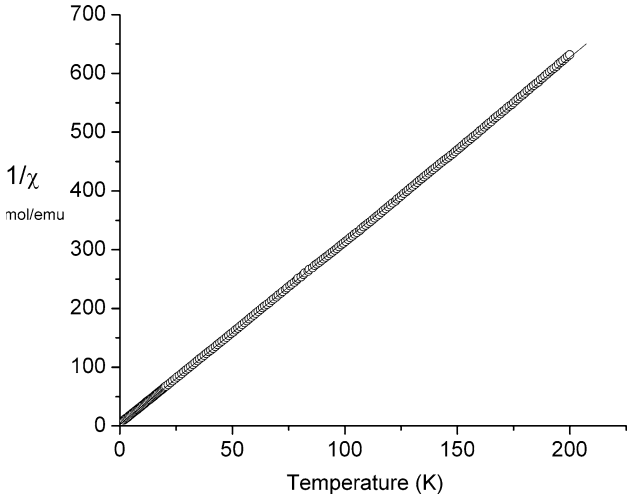


Fig. 4. Temperature dependence of $1/\chi$ for $(NH_4)_3CrO_8$. Red line is the fit to the Curie–Weiss Law.

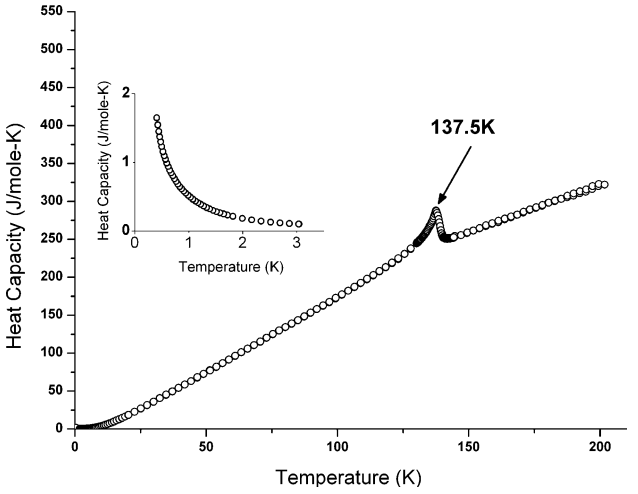


Fig. 5. Temperature dependence of heat capacity for $(NH_4)_3CrO_8$. The arrow highlights the solid–solid phase transition at 137.5 K. Inset shows heat capacity from 3 to 0.4 K.

which indicates that the phase transition can be ascribed to an order–disorder mechanism. The order–disorder process must involve the reorientational motion of the NH_4^+ groups. We rule out the order–disorder change in the CrO_8^{3-} units because other isostructural peroxychromates do not exhibit any such transition above 4 K. This postulate could be checked through X-ray structural studies around 137 K. The absence of any such anomaly in the magnetic susceptibility data (Fig. 4), clearly shows that the transition must be of a non-magnetic origin. This was supported by the absence of any noticeable anomalous change around 137.5 K in our detailed EPR measurements at the Q-band frequency (Fig. 7). The X, Q, and W-band EPR experiments yielded a $g_\parallel = 1.983 \pm 0.0005$ and $g_\perp = 1.950 \pm 0.0005$. These data yield $g_{iso} = \frac{1}{3}(g_\parallel + 2g_\perp) = 1.961 \pm$

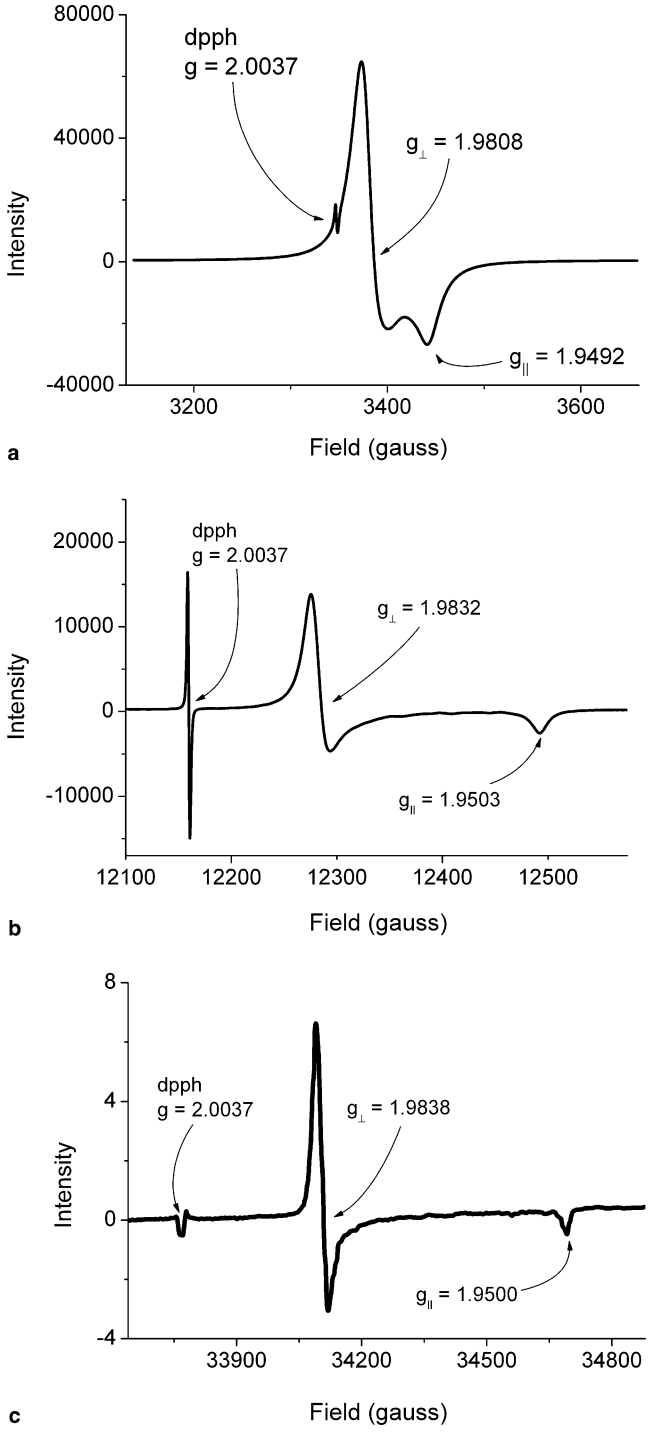


Fig. 6. EPR spectra of $(NH_4)_3CrO_8$ at: (a) X-band, 9.5 GHz; (b) Q-band, 34.5 GHz and (c) W-band, 94.5 GHz.

0.0005, in essential agreement with the above summarized magnetization measurements $g_{iso} = 1.843$. Angular dependence on a single crystal was done at Q-band frequency (Fig. 8). The crystal was rotated from the *c*-axis to the *a*-axis. The solid line corresponds to the fit of $g_{\text{eff}}^2 = g_{\perp}^2 \sin^2\theta + g_{\parallel}^2 \cos^2\theta$, giving $g_{\perp} = 1.9844 \pm 0.0005$ and $g_{\parallel} = 1.9522 \pm 0.0005$ which correspond well with the values calculated from the different frequencies measured. The line-width-at-half-height of the Q-band spectrum at 200 K, 9.84 gauss, allows calculation of an upper bound of the transverse relaxation; $T_2 = 5.8$ ns from the equation: $T_2 = \frac{1.3131\times10^{-7}}{g\Delta H_{\text{pp}}}$, where ΔH_{pp} is the width-at-half-height of the EPR peak. Further studies are needed to gain additional insight into the dynamics of this molecule. It is known that for a $3d^1$ ion in tetrahedral coordination the ground state can either be d_{z^2} or $d_{x^2-y^2}$ [10,15]. For the case of tetragonal elongation, $d_{x^2-y^2}$ is the ground state with $g_{\parallel} \approx g_e - \frac{8\lambda}{\Delta E}$ and $g_{\perp} \approx g_e - \frac{2\lambda}{\Delta E}$ where g_e is the free-electron *g*-value of 2.0023, and λ is the spin–orbit coupling constant. Thus, determination of the *g*-values will yield the ground state of this molecule. It was found for $(NH_4)_3CrO_8$ that $g_{\perp} > g_{\parallel}$ thus demonstrating that the ground state is indeed $d_{x^2-y^2}$ [7,8,15]. It should also be noted that no hyperfine interactions are seen as expected from the low percentage (9.50%) of Cr nuclei with nuclear spin.

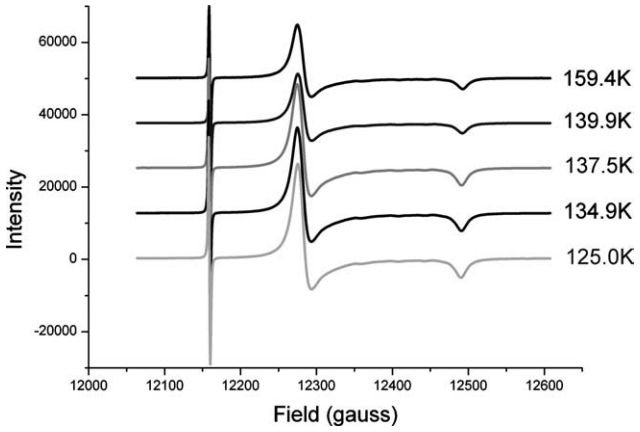


Fig. 7. Temperature dependence of Q-band EPR spectra for $(NH_4)_3CrO_8$. No change is noticeable at the phase transition temperature of 137.5 K.

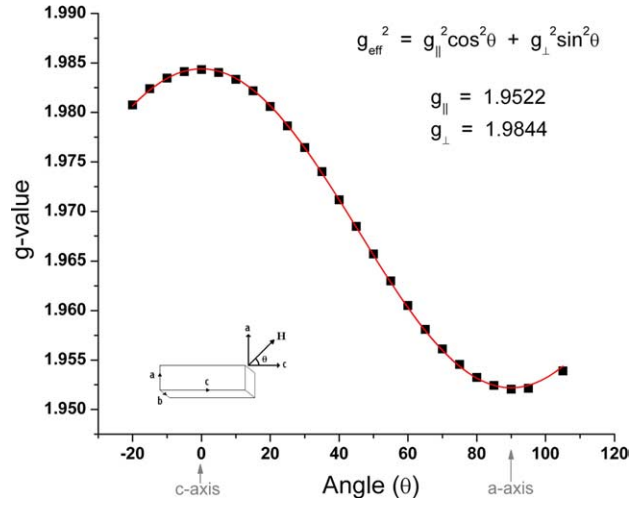


Fig. 8. Angular dependence of Q-band EPR spectra for $(NH_4)_3CrO_8$. Rotation is from the *c*-axis to the *a*-axis and was performed at 200 K.

4. Conclusion

The compound $(NH_4)_3CrO_8$, newly reported here, behaves as a simple $S = 1/2$ paramagnetic system, largely free from hyperfine and exchange interactions. Heat capacity, susceptibility, and EPR measurements support the hypothesis that the peak in the heat capacity is an order–disorder transition with no magnetic origin. Calculation of the entropy gives nice agreement to the theoretical prediction of a mixed two state system. This compound could serve as a model system and be a simple replacement for materials like V_{15}. Further studies along these lines should be fruitful.

Acknowledgements

This work was partially supported by the NSF Grant DMR 0103290 (NIRT).

K.A.A. acknowledges the National Science Foundation and the University of Florida for funding of the purchase of the X-ray equipment.

References

[1] G. Christou, D. Gatteschi, D.N. Hendrickson, MRS Bulletin 25 (2000) 66.
[2] D. Gatteschi, R. Sessoli, Angew. Chem. Int. Ed. Eng. 42 (2003) 26.
[3] A. Muller, J. Doring, Angew. Chem., Int. Ed. Engl. 27 (1991) 416.
[4] I. Chiorescu, W. Wernsdorfer, A. Muller, H. Bogge, B. Barbara, Phys. Rev. Lett. 84 (2000) 3454.
[5] D. Zipse, N.S. Dalal, R.T. Vasic, J.S. Brooks, P. Kogerler, Phys. Rev. B 71 (2005) 064417.
[6] E.H. Riesenfeld, Chem. Ber. 38 (1905) 4068.
[7] N.S. Dalal, J.M. Millar, M.S. Jagadeesh, M.S. Seehra, J. Chem. Phys. 74 (1981) 1916.
[8] X. Shi, N.S. Dalal, Biochem. Biophys. Res. Commun. 156 (1988) 137.
[9] C. Ramsey, B. Cage, P. Nguyen, K.A. Abboud, N.S. Dalal, Chem. Mater. 15 (2003) 92.
[10] C.M. Ramsey, N.S. Dalal, Mol. Cell. Biochem. 255 (2004) 113.
[11] B. Cage, W. Geyer, K.A. Abboud, N.S. Dalal, Chem. Mater. 13 (2001) 871.
[12] B. Cage, N.S. Dalal, Chem. Mater. 13 (2001) 880.
[13] R. Blinc, P. Cevc, D. Arcon, N.S. Dalal, R.M. Achey, Phys. Rev. B 63 (2001) 212401.
[14] B. Cage, A. Hasan, L. Pardi, J. Krzystek, L.C. Brunel, N.S. Dalal, J. Mag. Reson. 124 (1997) 495.
[15] J.A. Weil, J.R. Bolton, J.E. Wertz, Electron Paramagnetic Resonance, Wiley, 1994.

ferrimagnetic regions upon cooling below T_C. In this dark state, the diamagnetic regions contain low spin (LS) Fe^{2+}($S = 0$) and Co^{3+}(LS, $S = 0$) pairs, and primordial ferrimagnetic regions consist of antiferromagnetically coupled Fe^{3+}(LS, $S = 1/2$) and high spin (HS) Co^{2+}($S = 3/2$) pairs. Although the concentration of alkali atoms and H_2O molecules contribute, the relative population of each region is mainly determined by the Co/Fe ratio in the synthesis process [10,11]. Upon irradiation, there is a charge transfer within a diamagnetic region from Fe^{2+}(LS, $S = 0$) to Co^{3+}(LS, $S = 0$), resulting in a ferrimagnetic region with Fe^{3+}(LS, $S = 1/2$) and Co^{2+}(HS, $S = 3/2$). This photoinduced charge transfer increases the relative population of ferrimagnetic regions, and thus increases the net magnetization [14,18,19]. In our magneto-optical investigations, film **1** showed an increase, while film **2** showed a *decrease*, in the photoinduced magnetization when the surfaces of the films were oriented perpendicular ($\perp$) to the external magnetic field (H_E). Moreover, when film **2** was oriented parallel ($\parallel$) to H_E, the photoinduced magnetization *increased*. In this paper, the contrasting magnetic behavior exhibited by the two films and the field orientation dependent anisotropic magnetization of film **2** are presented and discussed within a dipolar field model.

2. Experimental details

Two separate solutions of 5×10^{-3}mol of cobalt (II) nitrate aqueous solution, and a mixed solution of 2×10^{-2} mol potassium ferricyanide and 1.25×10^{-2} mol rubidium nitrate were prepared. For sample film **1**, a thin mylar sheet (thickness $\sim$ 100 μm) was immersed sequentially in one solution after the other for 20 cycles, and each immersion was performed by dipping the mylar sheet in and out of the solution for 3–4 times. Sample film **2** was prepared in a similar manner, except after each cycle of immersion, the film was rinsed by H_2O and methanol. The resultant films were dried with nitrogen gas and cut into small squares ($\sim$10.5 mm^2), and they were subsequently used in standard SEM and SQUID magnetometer measurements.

For the magneto-optical studies, a bundle of optical fibers was located near the sample films stacked in a gel-cap, and then connected to a room temperature light source using a homemade probe. The magnetometer was used to measure the dc magnetization while a commercial halogen lamp was used as an unfiltered visible light source. For each sample film, the time dependent magnetization was measured upon irradiation with visible light at 5 K with H_E = 200 G ($\perp$ films). The temperature dependent zero-field-cooled (zfc) and field-cooled (fc) magnetizations were also measured from 5 to 30 K with H_E = 200 G ($\perp$ films). Similar magnetic measurements were made only for film **2** when $H_E \parallel$ film. The background magnetic contributions from the container and mylar sheet were measured separately and subtracted from the signals obtained from the samples.

3. Results and discussion

The mixed metal cyanides generally form as powders. The cubic structure normally has small structural coherence, which is responsible for the cluster-glass magnetic behavior that is commonly observed. The synthesis protocol for film **2** included an additional step of rinsing with H_2O and methanol after each cycle of immersion to the solutions, whereas film **1** was fabricated without this rinsing process. The additional rinsing step for film **2** was expected to remove the excess powder residue attached to the film. As a result, for film **1**, the particles that make up the powder are randomly deposited, giving rise to a bulk-like texture, see the SEM image in Fig. 1(a). For film **2**, the particles are more uniformly arranged parallel to the films, resulting in a quasi-two-dimensional texture within continuous patches approximately 600 nm^2 as shown in the SEM image in Fig. 1(b). Furthermore, the long-range ($\sim$50 μm) quality of the samples was confirmed by additional SEM studies of each film.

The time dependent magnetization of film **1** is shown in Fig. 2(a) when $H_E \perp$ film. Upon irradiation at 5 K with H_E = 200 G, the magnetization of film **1** increased about 50%. This increase in the photoinduced magnetization is consistent with the results from bulk materials obtained by others [10,13,15] and reflects the powder-like nature of film **1**, see Fig. 1(a). The temperature dependences of the magnetizations in both the dark and photoinduced states are shown in Fig. 2(b). The increase in the fc values with decreasing temperatures and

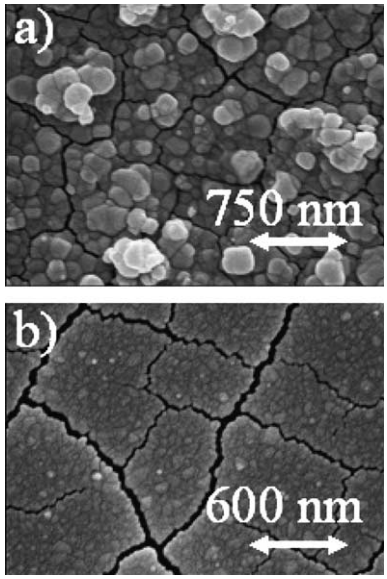


Fig. 1. SEM images of film **1** (a) and film **2** (b).

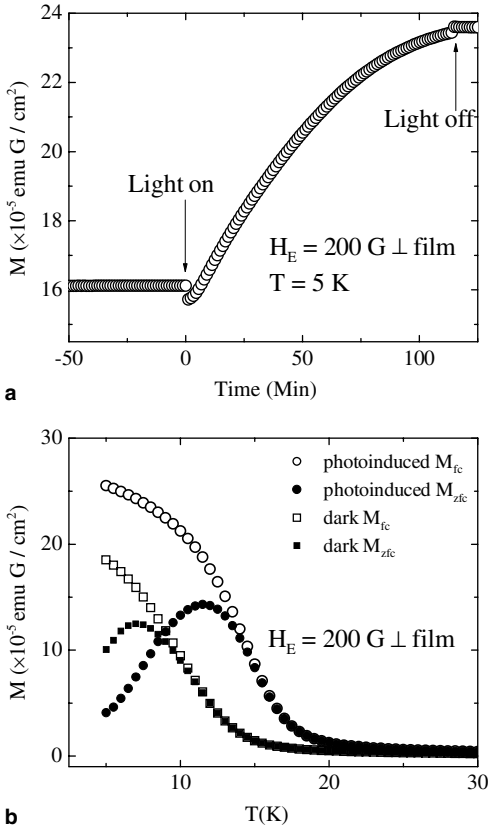


Fig. 2. Time dependent photoinduced magnetization (a) and temperature dependent magnetizations of film **1** when $H_E \perp$ film (b).

the maximum peak in the zfc magnetization are indications of cluster spin-glass behavior [16,21,22]. In a simple description specific to our samples, the cluster spin-glass state contains disordered interacting clusters, and each cluster consists of ferrimagnetically ordered Fe^{3+}(LS, $S = 1/2$) and Co^{2+}(HS, $S = 3/2$) regions. As a result of irradiation, the dark state $T_C \sim 15$ K increases to $T_C \sim 18$ K for the photoinduced state. In addition to the increase in T_C, the peak temperature (T_P) where the zfc magnetization value reaches its maximum has shifted from ~7 K in dark state to ~11.5 K in the photoinduced state. These changes in T_C and T_P in the photoinduced state can be easily interpreted within a cluster spin-glass description. More specifically, as a result of the irradiation, additional ferrimagnetic regions have been created, thereby resulting in increases in the size and concentration of the ferrimagnetic clusters. The larger clusters, whose magnetic correlation lengths are less restricted by the structural disorder (since T_C bulk ~ 21 K), are responsible for the increase of T_C in the photoinduced state. At the same time, the increased concentration of the clusters enhances the interactions between them and results in an increased T_P for the photoinduced states. Similar behavior was observed by another group in their study of a bulk material [16]. From the SEM images and the comparisons with the magnetic results of bulk materials reported by others, film **1** behaves as a powder-like film.

On the other hand, when film **2** was placed in $H_E \perp$ film, the magnetization of the film *decreased* upon irradiation, see Fig. 3(a). We previously used a dipolar field model to describe this type of decrease in the photoinduced magnetization [9]. In this model, a quasi-two-dimensional array of primordial ferrimagnetic regions produces a dipolar field that splays onto adjacent diamagnetic regions. Since the primordial ferrimagnetic moments are parallel to H_E, the direction of the dipolar field on the adjacent diamagnetic region is antiparallel to H_E when $H_E \perp$ film, and parallel to H_E when $H_E \parallel$ film. As a consequence, the net magnetic field seen by the diamagnetic region is a vector sum of the dipolar field and H_E. Upon irradiation when $H_E \perp$ film, the diamagnetic region undergoes a transition to a ferrimagnetic region, and the orientations of the net moment in the newly formed ferrimagnetic region will follow the net magnetic field. If the dipolar field is stronger than H_E, the net moment in the newly formed ferrimagnetic region will point antiparallel to H_E, and thus yield a *decrease* in the photoinduced net magnetization as experimentally shown in Fig. 3(a). An additional aspect of the dipolar field model is experimentally realized and is shown in Fig. 4,

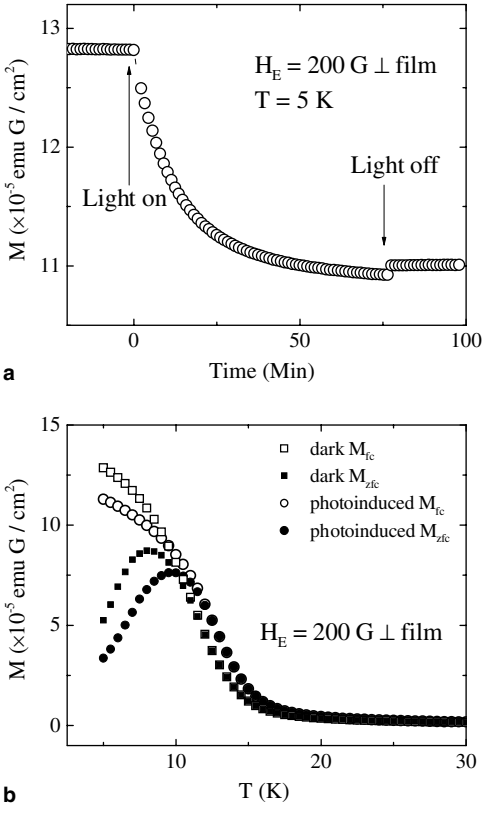


Fig. 3. Time dependent photoinduced magnetization (a) and temperature dependent magnetizations of film **2** when $H_E \perp$ film (b).

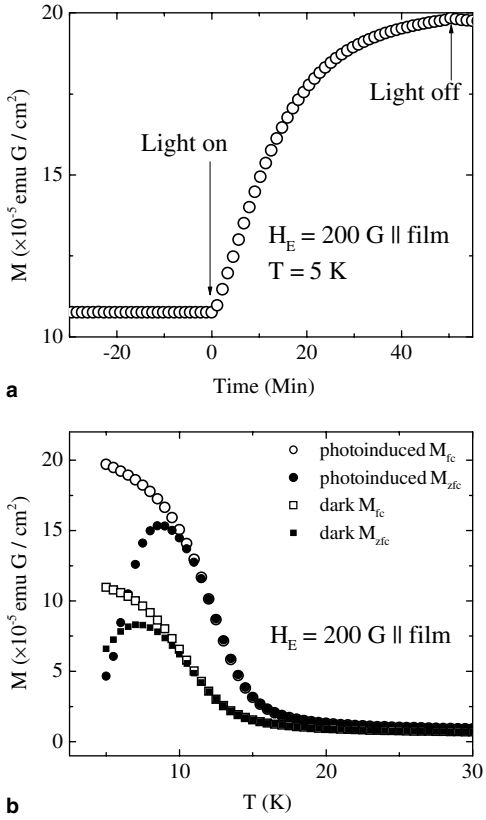


Fig. 4. Time dependent photoinduced magnetization (a) and temperature dependent magnetizations of film **2** when $H_E \parallel$ film (b).

where the photoinduced magnetization of film **2** *increases* when $H_E \parallel$ film.

In general, the behavior of the temperature dependent magnetization data of film **2** in both orientations (Fig. 3(b) for $H_E \perp$ film and Fig. 4(b) for $H_E \parallel$ film) is similar to the cluster spin-glass description of film **1**, Fig. 2(b). In both orientations of film **2**, the divergences between the zfc and fc magnetizations and the increases in T_P and T_C in the photoinduced state resemble the same behavior observed in film **1**. It is noteworthy that the photoinduced increase of T_C in film **2** ($H_E \perp$ film) is relatively smaller than the increases observed in film **1** ($H_E \perp$ film) and film **2** ($H_E \parallel$ film). This behavior of film **2** ($H_E \perp$ film) again indicates the quasi-two-dimensional nature of the film, where the dipolar field enhances the disorder within the cluster, and thereby yields a smaller increment of T_C in the photoinduced state when compared to the increase of T_C observed in the powder-like film.

4. Conclusions

We have generated magneto-optically active $Rb_jCo_k[Fe(CN)_6]_l \cdot nH_2O$ films using sequential deposition methods. The surface quality of the films was intentionally varied by modifying the synthesis protocol yielding a powder-like rough surface for film **1**, and a quasi-two-dimensional smooth surface for film **2**. Standard SEM images confirmed the quality of the film surfaces, and the dc magnetization measurements showed different photoinduced magnetic behavior between the two films. Upon irradiation at 5 K with an external magnetic field of 200 G perpendicular to the film surface, the magnetization of film **1** increased, whereas the magnetization of film **2** *decreased*. This contrasting behavior is consistent with a dipolar field model describing the phenomena and is related to the novel anisotropy of the photoinduced magnetism in film **2**, where the photoinduced magnetizations increases or decreases depending on the orientation of the film with respect to the external field. The ability to increase and decrease the photoinduced magnetization by reorientation of the film is a unique phenomenon that requires anisotropy. Consequently, the presence of this phenomenon allows us to differentiate between a quasi-two-dimensional film (film **2**) and a three-dimensional powder-like film (film **1**).

Acknowledgements

This work was supported, in part, by NSF DMR-9900855 (D.R.T.), NSF DMR-0113714 (M.W.M. and D.R.T.), ACS-PRF 36163-AC5 (M.W.M. and D.R.T.), NSF DGE-0209410 (E.C.), and NSF DMR-0305371 (M.W.M.). We gratefully acknowledge early contributions from J. T. Culp.

References

[1] O. Sato, T. Iyoda, A. Fujishima, K. Hashimoto, Science 272 (1996) 704.
[2] E. Dujardin, S. Ferlay, X. Phan, C. Desplanches, C. Cartier dit Moulin, P. Sainctavit, F. Baudelet, E. Dartyge, P. Veillet, M. Verdaguer, J. Am. Chem. Soc. 120 (1998) 11347.
[3] M. Verdaguer, A. Bleuzen, V. Marvaud, J. Vaissermann, M. Seuleiman, C. Desplanches, A. Scuiller, C. Train, R. Garde, G. Gelly, C. Lomenech, I. Rosenman, P. Veillet, C. Cartier, F. Villain, Coord. Chem. Rev. 190–192 (1999) 1023.
[4] J.T. Culp, J.-H. Park, D. Stratakis, M.W. Meisel, D.R. Talham, J. Am. Chem. Soc 124 (2002) 10083.
[5] J.T. Culp, J.-H. Park, I.O. Benitez, Y.D. Huh, M.W. Meisel, D.R. Talham, Chem. Mater. 15 (2003) 3431.
[6] J.T. Culp, J.-H. Park, M.W. Meisel, D.R. Talham, Polyhedron 22 (2003) 3059.
[7] J.T. Culp, J.-H. Park, I.O. Benitez, M.W. Meisel, D.R. Talham, Polyhedron 22 (2003) 2125.
[8] T. Yamamoto, Y. Umemura, O. Sato, Y. Einaga, Chem. Lett. 33 (2004) 500.
[9] J.-H. Park, E. Čižmár, M.W. Meisel, Y.D. Huh, F. Frye, S. Lane, D.R. Talham, Appl. Phys. Lett. 85 (2004) 3797.

[10] A. Bleuzen, C. Lomenech, V. Escax, F. Villain, F. Varret, C. Cartier dit Moulin, M. Verdaguer, J. Am. Chem. Soc. 122 (2000) 6648.
[11] V. Escax, A. Bleuzen, C. Cartier dit Moulin, F. Villain, A. Goujon, F. Varret, M. Verdaguer, J. Am. Chem. Soc. 123 (2001) 12536.
[12] M. Verdaguer, Science 272 (1996) 698.
[13] A. Goujon, O. Roubeau, F. Varret, A. Dolbecq, A. Bleuzen, M. Verdaguer, Eur. Phys. J. B 14 (2000) 115.
[14] K. Yoshizawa, F. Mohri, G. Nuspl, T. Yamabe, J. Phys. Chem. B 102 (1998) 5432.
[15] O. Sato, Y. Einaga, A. Fujishima, K. Hashimoto, Inorg. Chem. 38 (1999) 4405.
[16] D.A. Pejaković, J.L. Manson, J.S. Miller, A.J. Epstein, Phys. Rev. Lett. 85 (2000) 1994.
[17] C. Cartier dit Moulin, F. Villain, A. Bleuzen, M.-A. Arrio, P. Sainctavit, C. Lomenech, V. Escax, F. Baudelet, E. Dartyge, J.J. Gallet, M. Verdaguer, J. Am. Chem. Soc. 122 (2000) 6653.
[18] G. Champion, V. Escax, C. Cartier dit Moulin, A. Bleuzen, F. Villain, F. Baudelet, E. Dartyge, M. Verdaguer, J. Am. Chem. Soc. 123 (2001) 12544.
[19] T. Kawamoto, Y. Asai, S. Abe, Phys. Rev. Lett. 86 (2001) 348.
[20] M. Hanawa, Y. Moritomo, A. Kuriki, J. Tateishi, K. Kato, M. Takata, M. Sakata, J. Phys. Soc. Jpn. 72 (2003) 987.
[21] J.A. Mydosh, Spin Glasses, Taylor & Francis, Washington DC, 1993.
[22] J.T. Culp, J.-H. Park, M.W. Meisel, D.R. Talham, Inorg. Chem. 42 (2003) 2842.

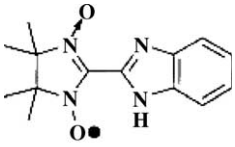


Fig. 1. The molecular structure of 2-BIMNN.

ESR measurements were carried out using a resonant cavity perturbation technique in combination with a broadband millimetre-wave vector network analyser (MVNA). The MVNA is a phase-sensitive, fully sweepable (8–350 GHz) super-heterodyne millimetre-wave source and detection system. A sample probe couples the network analyser via waveguides to a range of high-Q cavities situated in a 3He/4He cryostat inside the bore of a 17 T superconducting magnet. In comparison with conventional high-field ESR techniques, the system offers several advantages. The MVNA allows vector measurements, i.e., simultaneous measurements of both the amplitude and the phase of transmitted/reflected signal. The resonant cavity provides a well-defined millimetre-wave environment and substantially improved sensitivity to small samples over non-resonant methods. Careful coupling of radiation to and from the cavity (via the waveguide), combined with the ability to study very small samples, eliminates problems associated with standing waves in the sample probe. This, in turn, eliminates mixing of the dissipative and reactive responses of the sample under investigation and, when combined with a vector detection scheme, enables faithful extraction of ESR lineshapes (both the real and imaginary components), free from instrumental artifacts. The tunable cylindrical cavity gives the advantage of varying the frequency over quite a wide range, while the rectangular cavity allows angle-dependent experiments. The samples were oriented such that the applied magnetic field B was perpendicular to the c-axis, with the microwave field always parallel to the c-axis. Angle-dependence was also studied by rotating the c-axis away from B by an angle θ.

3. Results and discussion

We have performed electron spin resonance (ESR) measurements on 2-BIMNN single crystals in the temperature range 1.4–100 K (see Fig. 2). As the temperature was decreased from ~100 K, the linewidth was seen to broaden considerably below 20 K, reaching a maximum value at 10 K, and then decreasing again. This broadening of the linewidth at low temperature can be explained by a reduction of the exchange narrowing. The dominant broadening mechanism is the dipole–dipole interaction between adjacent spins along the c-axis. Other broadening mechanisms include the interchain exchange, interchain dipolar fields, hyperfine interactions, and possible single-ion anisotropies [6]. The maximum around 10 K has been reproduced in an experiment on a second crystal of 2-BIMNN. This feature may be due to a preferential alignment of spins below 10 K arising from the anisotropic dipolar interaction. Above 20 K, the ESR lines are Lorentzian, so the of the local field should be dynamic in this case.

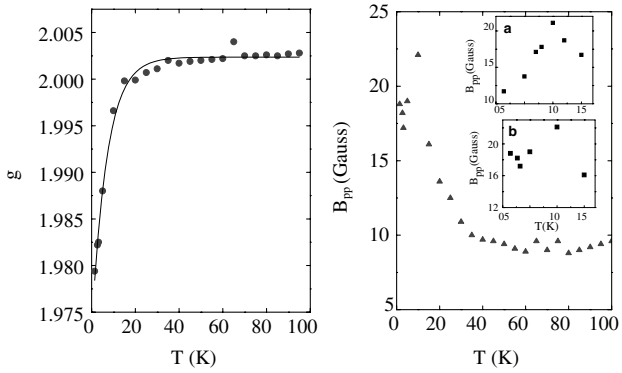


Fig. 2. Temperature dependence of the g value and the peak-to-peak linewidth B_{pp}. In the inset is shown the low temperature dependence of the linewidth for two different crystals.

A dramatic ESR lineshift to higher fields on cooling is observed below 20 K, corresponding to a decrease in the g-value. The g-value saturates above 20 K at the free electron value 2.00232. For ordinary free radicals, the difference in g between at low and high temperatures does not exceed 0.1%, whereas for the 2-BIMNN, the difference in g is an order of magnitude larger [7]. The downwards shift of the resonance field observed as the temperature decreases is what is expected in uniaxial low-dimensional magnetic systems, when the orientation of the crystal is orthogonal to the applied static field. Nagata et al. theorized that a weak uniaxial dipolar anisotropy was responsible for the g shift [8].

The g tensor is also related to the spin correlation function. Short-range magnetic order is known to have an increasing effect for low dimensions. Since the stacking axis of this 1-d radical magnet coincides with the long axis of the crystalline materials, one may conclude that magnetic effects due to short-range order could be responsible for the g-shift, but these effects are difficult to distinguish from those of the demagnetizing field [9,10].

An angle-dependent experiment was carried out on a single crystal. At 1.4 K, though the resonance field shows a pronounced angular dependence (Fig. 3), the linewidth is only weakly angle-dependent (Fig. 4). At 50 K, the g value changes slightly, though the trend is similar to that at 1.4 K; the linewidth can be considered to be constant. In the angular dependence of the g factor recorded at 1.4 and 50 K, we see that they cross each other at 44° and 146°. The angles are close to 90 ± 54°, where 54° is the magic angle. Fitting to the equation $g = g_1 + g_2\cos^2(\theta - \theta_0)$,

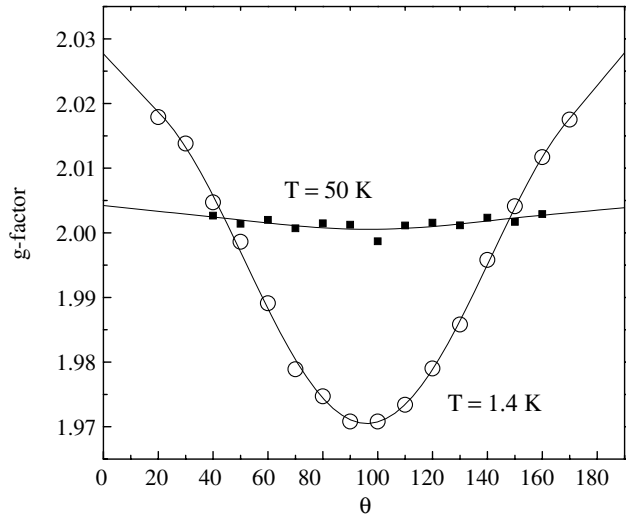


Fig. 3. The g-factors vs. θ at 1.4 and 50 K. The circles and squares are the experimental data at, respectively, 1.4 and 50 K. The lines show the fits to the data.

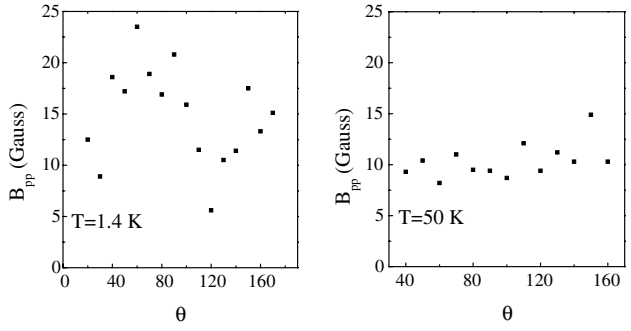


Fig. 4. The linewidths for different angles at 1.4 and 50 K, with resonance frequency 71.91 GHz.

we see that the data at 1.4 K gives a nice fit, giving the values $g_1 = 1.9704 \pm 0.0003$, $g_2 = 0.0511 \pm 0.0006$ and $\theta_0 = 6.1 \pm 0.3°$. The g-shift is seen to be more pronounced at low temperatures, where the effects of the short-range magnetic order are expected to become important in low-dimensional magnets. Boucher has shown that at least in the case of the 1-d antiferromagnetic compound TMMC, these effects should be attributed mostly to the anisotropy induced by the dipolar field rather than to the applied magnetic field [11].

We believe that the maximum observed in the temperature dependence of the linewidth of 2-BIMNN does not originate from a phase transition [6] but arises from the change of the dominant contribution from the long-time behaviour of the spin correlation function at high temperature to the short-time behaviour below 10 K. If this is the case, then we would expect the linewidth to be isotropic at 1.4 K, and from our experimental data where the errors on the linewidth for angular dependence studies are quite high, we can say that that is what we find. The angular dependence of the half-width follows the equation $\Delta H_{1/2} \propto |3\cos^2\theta - 1|^{4/3}$ at higher temperatures [4], but that is when the angular dependence of only the secular contribution is considered, which is expected to be dominant. In the low temperature data, we see no such dependence. The anisotropy of the linewidth not being detectable can be linked to the almost isotropic dipolar field expected from the highly symmetrical molecular arrangement [9].

Below 10 K, additional transitions in the ESR spectrum appear at fields below that of the main transition, as shown in Fig. 5. These features were observed in measurements on four different crystals of 2-BIMNN, and so we conclude that this is an intrinsic effect. They may be due either to a hitherto undiscovered structural phase transition [12] which sets in below 10 K or to the development of hyperfine structure [7] arising from the coupling between the substantially delocalised unpaired electron and the atomic nuclei on the nitronyl nitroxide group.

Frequency dependence studies were carried out at 1.4 and 50 K. The linewidth was not frequency dependent but the g-value changed slightly at 1.4 K, as shown in Fig. 6, increasing with frequency. This

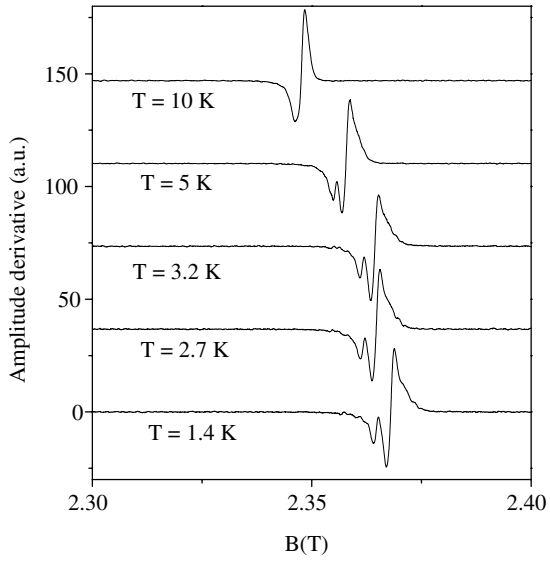


Fig. 5. The derivatives of the ESR absorption signals at different temperatures.

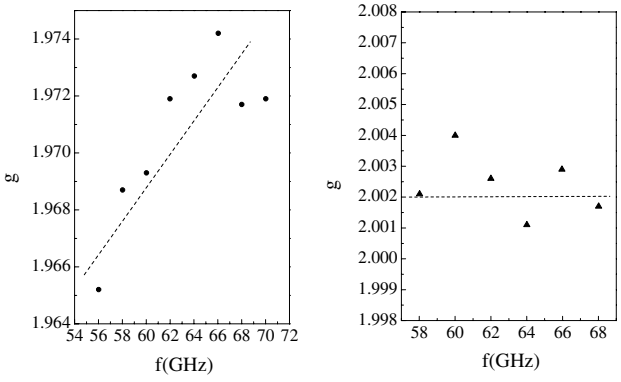


Fig. 6. g values at different frequencies at $T = 1.4$ K and $T = 50$ K.

possibly results from the field-dependence of the magnetic susceptibility which influences the difference of g from the free electron value.

References

[1] G.M. Rosen, B.E. Britigan, H.J. Halpern, S. Pou, Free Radicals: Biology and Detection by Spin Trapping, Oxford University Press Inc., 1999.
[2] S.J. Blundell, F.L. Pratt, J. Phys.: Condens. Matter 16 (2004) R771.
[3] T. Sugano, S.J. Blundell, W. Hayes, P. Day, Polyhedron 22 (2003) 2343.
[4] T. Sugano, Synthetic Metals, in press.
[5] N. Yoshioka, M. Irisawa, Y. Mochizuki, T. Kato, H. Inoue, S. Ohba, Chem. Lett. (1997) 252.
[6] T.T.P. Cheung, Z.G. Soos, R.E. Dietz, F.R. Merritt, Phys. Rev. B. 17 (1978) 1266.
[7] S.A. Al'tshuler, B.M. Kozyrev, Electron Paramagnetic Resonance, Academic Press, 1964.
[8] K. Nagata, Y. Tazuke, J. Phys. Soc. Jpn. 32 (1972) 337.
[9] P. Turek, Mol. Cryst. Liq. Cryst. 233 (1993) 191.
[10] J.L. Stanger, J.J. Andre, P. Turek, Y. Hosokoshi, M. Tamura, M. Kinoshita, P. Rey, J. Cirujeda, J. Veciana, Phys. Rev. B 55 (1997) 8398.
[11] J.P. Boucher, J. Magn. Magn. Mater. 15–18 (1980) 687.
[12] G.V. Mamin, V.N. Efimov, Magn. Res. Solids 3 (1997) 1.

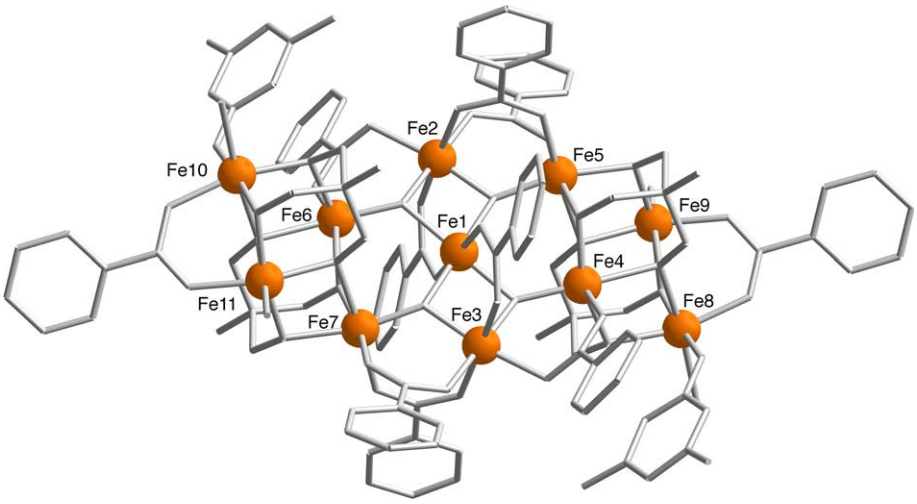


Fig. 1. Representation of the molecular structure of the Fe_{11} complex $[NEt_4][Fe_{11}O_4(O_2CPh)_{10}(thme)_4(dmhp)_2Cl_4]$ (H_3thme, 1,1,1-tris(hydroxymethyl)-ethane; dmhp, 4,6-dimethyl-2-hydroxypyrimidine). The Fe atoms are represented with spheres while the rest are indicated as sticks and the hydrogen atoms are omitted.

values, in order to advance in the understanding of the magnetic properties of such compound.

Due to the low symmetry of the complex, the spin Hamiltonian considering only the exchange coupling terms can be expressed as:

$$\begin{aligned}\hat{H} = &-J_1\left[\hat{S}_1\hat{S}_2 + \hat{S}_1\hat{S}_3\right] - J_2\left[\hat{S}_2\hat{S}_6 + \hat{S}_3\hat{S}_4\right] \\ &- J_3\left[\hat{S}_1\hat{S}_4 + \hat{S}_1\hat{S}_6\right] - J_4\left[\hat{S}_1\hat{S}_7 + \hat{S}_1\hat{S}_5\right] \\ &- J_5\left[\hat{S}_2\hat{S}_5 + \hat{S}_3\hat{S}_7\right] - J_6\left[\hat{S}_4\hat{S}_5 + \hat{S}_6\hat{S}_7\right] \\ &- J_7\left[\hat{S}_4\hat{S}_8 + \hat{S}_6\hat{S}_{10}\right] - J_8\left[\hat{S}_4\hat{S}_9 + \hat{S}_6\hat{S}_{11}\right] \\ &- J_9\left[\hat{S}_5\hat{S}_9 + \hat{S}_7\hat{S}_{11}\right] - J_{10}\left[\hat{S}_8\hat{S}_9 + \hat{S}_{10}\hat{S}_{11}\right], \end{aligned} \quad (1)$$

where $\hat{S}_i$ are the spin operators of each paramagnetic Fe(III) center. A detailed description of the procedure used to obtain the exchange coupling constants can be found in previous works [7–10] and a description of the Computational details is provided in Appendix A.

The large number of states ($6^{11} = 3.62 \times 10^8$ states) present in the Fe_{11} complex makes it impossible to perform a fitting of the measured magnetic susceptibility using the exact diagonalization approach to obtain all the J values as usually done for smaller molecules. In this case, the large number of exchange coupling constants also makes more difficult the fitting procedure because several sets of J values may fit perfectly the experimental data. Hence, the use of theoretical methods is especially important in this case to obtain a detailed description of the nature of the exchange interactions present in the Fe_{11} complex. The calculated exchange coupling constants using the PBE functional (see Appendix A for computational details) are presented in Table 1.

The calculated J values show similar trends to those obtained in the case of the Fe_8 and Fe_{19} complexes

Table 1
Description of the bridging ligands, average Fe···Fe distances and calculated exchange coupling constants J (cm^{-1}) for the Fe_{11} complex

	Bridging ligands	d(Fe···Fe) (Å)	J_{PBE}	J_{MCfit}
J_1	(μ_3-O)$_2$ (μ_2-O$_2$CPh)	2.846	−1.1	−0.14
J_2	(μ_3-O) (μ_2−O$_2$CPh)	3.414	−70.7	−70.4
J_3	μ_3-O	3.425	−48.5	−70.4
J_4	μ_3-O	3.478	−65.6	−70.4
J_5	(μ_3-O)$_2$ (μ_2-O$_2$CPh)$_2$	3.300	−70.5	−70.4
J_6	(μ_2-OR)$_2$	3.116	−16.9	−10.2
J_7	(μ_2-OR)$_2$	3.233	−19.7	−10.2
J_8	(μ_2-OR)$_2$	3.360	−16.8	−10.2
J_9	(μ_2-OR)$_2$	3.177	−13.1	−10.2
J_{10}	(μ_2-OR)$_2$ (μ_2-O$_2$CPh)	3.045	−14.6	−8.3

Values obtained using the classic Monte Carlo approach fitting of the experimental magnetic susceptibility curve are also indicated (J_{MCfit}).

[11,12]: (i) all the interactions are antiferromagnetic. (ii) The carboxylate ligands seem to play a minor role in comparison with the other bridging ligands. (iii) The single μ_3-O bridges (J_2, J_3, J_4 and J_5) usually provide the strongest coupling constants. (iv) Double oxo bridges, such as those corresponding to the J_1 interaction, result in weaker interactions than those provided by single bridges. This fact is probably due to the small Fe–O–Fe angle. (v) All the interactions through a double alkoxo bridge show similar strengths, with values close to $-20\ cm^{-1}$ (J_6, J_7, J_8, J_9 and J_{10}).

We have calculated the energies corresponding to all the single determinant distributions (2048 states), assuming that all the Fe(III) cations have M_s values of 5/2, using the calculated J values. We found that the ground state has $S = 15/2$ corresponding to the case in which the Fe4, Fe5, Fe6 and Fe7 atoms have opposite spin than the other iron atoms. The first excited single determinant state has $S = 5$ (Fe1, Fe2, Fe3, Fe9 and Fe11 with spin down), placed $126\ cm^{-1}$ above that the

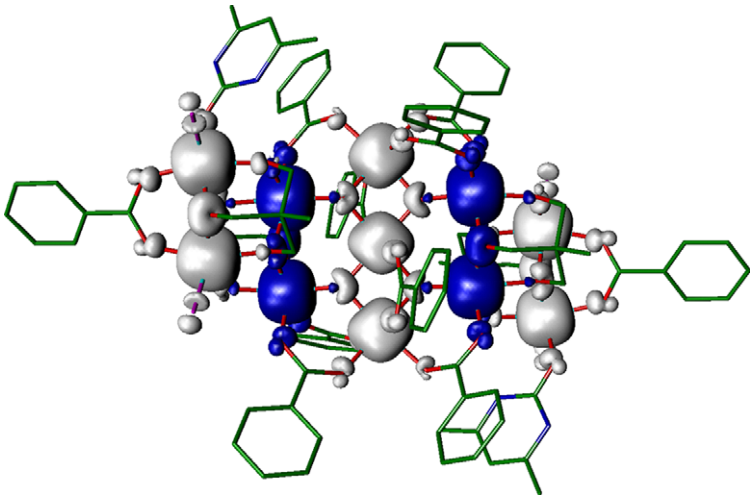


Fig. 2. Representation of the spin density map calculated at PBE level for the single-determinant ground state $S = 15/2$ of the Fe_{11} complex (clear and dark regions indicate positive and negative spin populations, respectively).

ground state. The spin density corresponding to the single determinant ground state is shown in Fig. 2. As expected, considering the d^5 electronic structure of the Fe(III) cation, the spin delocalization mechanism trough the σ system is the predominant one [13]. It is worth noting that in the case of the μ_3-O bridging ligands, the magnetic frustration is evidenced by a different sign of the spin density at the oxygen orbitals depending on their orientation relative to the Fe(III) cations with different spin sign. The presence of magnetic frustration could be responsible that the total spin of the system $S = 11/2$ cannot be described as a single determinant. In such cases, due to the frustration probably some M_s values of the Fe(III) cations will be smaller than 5/2 in order to stabilize the system.

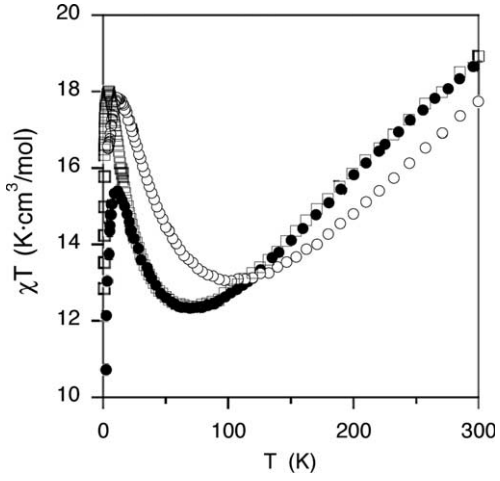


Fig. 3. Magnetic susceptibility curves of the Fe_{11} complex. The black circles correspond to experimental data. The white circles and squares were obtained directly from the DFT J values and from a fitting procedure using Monte Carlo simulations with the calculated values as starting point, respectively (see both sets of values in Table 1).

In order to compare our results with the available experimental data (see Fig. 3), we have performed Monte Carlo simulations to obtain a magnetic susceptibility curve based on the calculated J values (see Appendix A for a description of the simulations). The resulting susceptibility curve obtained from the calculated DFT J values nicely reproduces the expected values for a $S = 11/2$ ground state. The DFT results reproduce very well the experimental data taking into account that small changes in the J values modify considerably the shape of the magnetic susceptibility curve. The use of the calculated J values as starting point for a fitting procedure, using only four different J coupling constants corresponding to the exchange pathways through different bridging ligands, confirms that with small changes in the initial sets of values the experimental curve can be fitted (see Table 1). We have selected only four exchange coupling constants in order to avoid numerical problems during the fitting procedure.

2. Conclusions

The use of theoretical methods based on density functional theory provides a detailed knowledge of the exchange interaction present in the large Fe_{11} systems where it is not possible to extract such information from the magnetic susceptibility data. We have obtained basically the same trends and values than for other polynuclear Fe(III) complexes, [11,12] the μ_3-O bridging ligands are those with strongest antiferromagnetic coupling in comparison with the double oxo bridges. The use of the calculated J values in a Monte Carlo simulation gives a magnetic susceptibility curve very close to the experimental data despite of the limitations of the

classical Monte Carlo approach. Moreover, the fitting of the experimental results using as starting points the calculated J values results in a good fit with J values very close to those obtained from the DFT calculations.

Acknowledgments

The research has been supported by the Dirección General de Enseñanza Superior (DGES) and Comissió Interdepartamental de Ciència i Tecnologia (CIRIT) through Grants BQU2002-04033-C02-01 and 2001-SGR-0044, respectively. The computing resources were generously made available in the Centre de Computació de Cataluny a (CESCA) with a grant provided by Fundació Catalana per a la Recerc a (FCR) and the Universitat de Barcelona.

Appendix A

Electronic structure calculations have been performed using the SIESTA (Spanish Initiative for Electronic Simulations with Thousands of Atoms) code [14–17]. The generalized-gradient approximation (GGA) functional proposed by Perdew, Burke and Erzernhof (PBE) [18] was employed and pseudopotentials were generated according to the procedure of Trouiller and Martins [19] (see [12] for a more detailed description). We have used a numerical basis set of triple-ζ quality with polarization functions for the iron atoms and a double-ζ one with polarization functions for the main group elements. The values of 50 meV for the energy shift and 250 Ry for mesh cutoff provide a good compromise between accuracy and computer time to estimate the exchange coupling constants according to a previous study [12]. This approach provides good results despite the use of a GGA functional, that is well-known to give too large J values due to an overestimation of the spin delocalization [8], because the use of pseudopotentials partially compensates this problem.

The 11 calculations performed in order to obtain the 10 exchange coupling constants: the high spin state and ten additional calculations inverting the spin of some atoms, to indicate such spin distributions, we will write within parenthesis the atoms with spin down (1), (2,3), (4,6), (5,7), (8,10), (9,11), (1,2,3), (1,4,6), (5,7,9,11) and (4,5,6,7). Moreover, we have also calculated the first excited single determinant corresponding to a (1,2,3,9,11) spin distribution.

The magnetic susceptibilities have been calculated using Monte Carlo simulations with the Metropolis algorithm [20,21]. A sampling of states was generated to obtain the average magnetization M using Eq. (2) that includes the configurations that bring important contributions at temperature T.

$$\langle M\rangle = \frac{\sum_{i=1}^{n} M_i e^{-E_i/kT}}{\sum_{i=1}^{n} e^{-E_i/kT}}. \quad (2)$$

Thus, the magnetic susceptibility, χ_m, can be obtained from the fluctuations in the magnetization by employing Eq. (3), where $\langle M\rangle$ and $\langle M^2\rangle$ are the mean values of M and M^2.

$$\chi = (\langle M^2\rangle - \langle M\rangle^2)/kT. \quad (3)$$

The number of steps in the Monte Carlo simulation is different for each temperature, being $10^7/T$ (T in K). Hence, we have more steps in the sampling at low temperature because it is more difficult to describe correctly the magnetic behavior at such temperatures. At the beginning of the simulation 10% of the steps are employed for the thermalization of the system.

References

[1] J.S. Miller, M. Drillon (Eds.), Magnetism: Molecules to Materials Models and Experiments, Wiley-VCH, Weinheim, 2001.
[2] J.S. Miller, M. Drillon (Eds.), Magnetism: Molecules to Materials Molecule-based Materials, Wiley-VCH, Weinheim, 2001.
[3] J.S. Miller, M. Drillon (Eds.), Magnetism: Molecules to Materials Nanosized Magnetic Materials, Wiley-VCH, Weinheim, 2002.
[4] D. Gatteschi, J. Phys. Chem. B 104 (2001) 9780.
[5] D. Gatteschi, Angew. Chem., Int. Ed. 42 (2003) 246.
[6] L.F. Jones, E.K. Brechin, D. Collison, M. Helliwell, T. Mallah, S. Piligkos, G. Rajaraman, W. Wernsdorfer, Inorg. Chem. 42 (2003) 6601.
[7] E. Ruiz, P. Alemany, S. Alvarez, J. Cano, J. Am. Chem. Soc. 119 (1997) 1297.
[8] E. Ruiz, J. Cano, S. Alvarez, P. Alemany, J. Comp. Chem. 20 (1999) 1391.
[9] E. Ruiz, A. Rodríguez-Fortea, J. Cano, S. Alvarez, P. Alemany, J. Comp. Chem. 24 (2003) 982.
[10] E. Ruiz, S. Alvarez, A. Rodríguez-Fortea, P. Alemany, Y. Pouillon, C. Massobrio, in: J.S. Miller, M. Drillon (Eds.), Magnetism: Molecules to Materials, Wiley-VCH, Weinheim, 2001, p. 227.
[11] E. Ruiz, J. Cano, S. Alvarez, Eur. J. Chem. (in press).
[12] E. Ruiz, A. Rodríguez-Fortea, J. Cano, S. Alvarez, J. Phys. Chem. Solids 65 (2003) 799.
[13] J. Cano, E. Ruiz, S. Alvarez, M. Verdaguer, Comment Inorg. Chem. 20 (1998) 27.
[14] Siesta v. 1.3: E. Artacho, J.D. Gale, A. García, J. Junquera, R.M. Martin, P. Ordejón, D. Sánchez-Portal, J.M. Soler, SIESTA, 2003.
[15] E. Artacho, D. Sánchez-Portal, P. Ordejón, A. García, J.M. Soler, Phys. Stat. Sol. A 215 (1999) 809.
[16] J.M. Soler, E. Artacho, J.D. Gale, A. García, J. Junquera, P. Ordejón, D. Sánchez-Portal, J. Phys.: Condens. Matter 14 (2002) 2745.
[17] D. Sánchez-Portal, P. Ordejón, E. Artacho, J.M. Soler, Int. J. Quant. Chem. 65 (1997) 453.
[18] J. Perdew, K. Burke, M. Ernzerhof, Phys. Rev. Lett. 77 (1996) 3865.
[19] N. Trouiller, J.L. Martins, Phys. Rev. B 43 (1991) 1993.
[20] E. Boullant, J. Cano, Y. Journaux, S. Decurtins, M. Gross, M. Pilkington, Inorg. Chem. 40 (2001) 3900.
[21] C. Benelli, J. Cano, Y. Journaux, R. Sessoli, G.A. Solan, R.E.P. Winpenny, Inorg. Chem. 40 (2001) 188.

crystal using as only data the (microscopic) magnetic pair interactions (J_{AB}) between A and B constituent radicals of the crystal. These J_{AB} exchange interactions are computed for all unique A–B pairs present in the crystal using theoretical methods. This calculation only requires the crystal structure data of the system to be studied. This *bottom–up* approach enables to connect the macroscopic properties (magnetic susceptibility, for instance) with their microscopic origin, the J_{AB} exchange interactions. Consequently, it provides a rational analysis of the magnetic properties of a crystal. This approach has been successfully applied to well-known molecule-based crystals having dominant ferromagnetic or antiferromagnetic properties, and also to bulk ferromagnets [4,5]. Recently, we have also applied this approach to the study of through-bond magnetic crystals [6]. Let us mention here that these studies have shown that the microscopic J_{AB} exchange interactions are not always equal to the experimental J constant obtained from fitting the magnetic susceptibility curves to an empirical expression. Often, such empirical model is an over-simplification of the true topology of the magnetic interactions, and the J values are only averaged or effective constants.

In this work, we will apply our *bottom–up* approach to study the magnetism of the *meta*-(methoxy)phenyl nitronyl nitroxide crystal, *m*-(OMe)PhNN (see Fig. 1(a)). This crystal is sometimes identified by its REFCODE name [7], YISCIM. Our interest in this crystal is many-fold. First of all, its magnetism is not fully understood, because no information is available on its magnetic exchange pathways and their topology. The only experimental study available [8] indicates that the magnetic susceptibility of YISCIM obeys the Curie–Weiss law, being the paramagnetic θ equal to -0.97 K. Furthermore, room-temperature EPR studies on YISCIM [8] have allowed to conclude that $|J| = 1.6\ \mathrm{cm}^{-1}$. On the other hand, the molecular structure of *m*-(OMe)PhNN radical is very close to the structure of *para*-(methylthio)phenyl nitronyl nitroxide radical, *p*-(SMe)PhNN, whose crystal behaves as a bulk ferromagnet. It would thus be very interesting to find connections between the magnetic properties of these two radicals and the structure of these radicals and their corresponding crystals. Finally, once the analysis of YISCIM had started, we found a feature that makes its study even more attractive: it presents ferro and antiferromagnetic pathways of similar strength. This fact makes impossible to predict its dominating magnetic behavior based on the usual qualitative considerations. Only by using a quantitative methodology, like the *bottom–up* procedure employed here, one can determine the tendency of the magnetic susceptibility curve. In this work, we will also perform numerical simulations trying to investigate the conditions under which the competition between the ferro and antiferromagnetic exchange pathways results in a dominating ferro or antiferromagnetic macroscopic behavior.

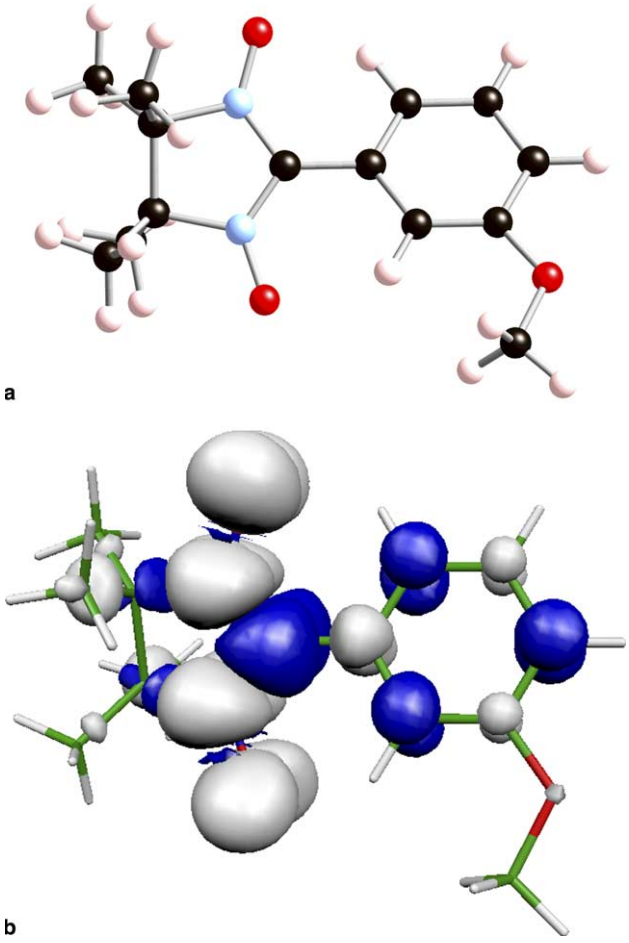


Fig. 1. Geometry (a) and spin distribution (b) of the *m*-(OMe)PhNN radical, computed at the B3LYP/6-31+G(d) level. The surface of 0.001 a.u. is displayed (white: positive values; blue: negative ones).

1.1. Computational details

Magnetism in organic solids is usually interpreted on a local (microscopic) scale via the exchange interaction J_{AB} between neighboring radicals A and B for all unique pairs present in the crystal. We have shown before [4–6] that it is possible to connect in a quantitative and accurate form the magnitude and topology of these J_{AB} pair exchange interactions with the macroscopic magnetic susceptibility $\chi(T)$, and other macroscopic magnetic properties (heat capacity $C_p(T)$, etc.). Such *bottom–up* procedure consists of the following four steps:

(1) *Analysis of the crystal packing*: All possible unique A–B radical pairs *di* present in the crystal that are good candidates to present sizable values of the microscopic magnetic interaction J_{AB} are identified.

(2) *Computation of the dimeric J_{AB} interactions*: The J_{AB} magnetic interactions are computed for all *di* pairs of radicals selected in the previous step, using the appropriate computational methods.

(3) *Definition of the magnetic topology of the crystal*: The magnetic topology is determined by inspection of the connectivity of the non-negligible J_{AB} pair interactions. Each radical can be seen as a point site, which is connected to another when $|J_{AB}|$ is larger than a given threshold (estimated as $|0.05|\ \mathrm{cm}^{-1}$ in our calculations).

(4) *Construction of a finite Heisenberg spin Hamiltonian that represents the problem and calculation of the macroscopic magnetic properties*: In this step, we search for the smallest subset of non-negligible J_{AB} pair interactions that describes the crystal magnetic topology in a balanced way (we have called it the *minimal magnetic model space*). Such model is then used to compute the matrix representation of the Heisenberg Hamiltonian[1]:

$$\hat{H} = -\sum_{A,B}^{N} J_{AB}\left(2\hat{S}_A \cdot \hat{S}_B + 1/2\hat{I}_{AB}\right), \qquad (1)$$

being $\hat{S}_A$ the spin operator associated with radical A, $\hat{I}_{AB}$ the identity operator, and N the number of radicals in the minimal magnetic model space. The only input data required to build this Heisenberg Hamiltonian are the J_{AB} values computed in step 2. The matrix representation of the Heisenberg Hamiltonian (1) is thus built in the basis of spin eigenfunctions of the minimal magnetic model space. It is then diagonalized and the resulting set of eigenvalues is used to compute the macroscopic magnetic property of interest (usually $\chi(T)$) applying the standard expressions of statistical mechanics.

This procedure, besides producing numerical values of $\chi(T)$ that present the same shape than the experimental $\chi(T)$ curve [4–6], provides a detailed understanding of the macroscopic measured properties in terms of J_{AB} pair interactions and their magnetic topology. One must realize here that both J_{AB} interactions and magnetic topology are only a function of the crystal packing. This is a specific advantage of the *bottom–up* procedure not encountered in many other methods currently available to analyze magnetic properties of crystals. The procedure is totally unbiased, and only requires an accurate crystal structure, which should be determined at a low enough temperature to avoid the distortion induced in the crystal by the thermal expansion. Otherwise, one can reach misleading conclusions [5c,6].

[1] The Heisenberg Hamiltonian (1) gives the same energy spectra than the usual one in which the second term is not present, but it is more convenient for our computer programs.

Besides the previous general considerations, it is interesting to comment a few specific points about how the above procedure has been applied to YISCIM crystal. First of all, concerning the selection of radical pairs (step 1), all *A–B* radical pairs whose ONCNO···ONCNO distance in YISCIM is smaller than 7.4 Å were selected to calculate their exchange interaction J_{AB}. This cutoff deliberately includes more pairs than the first nearest neighbors, which are the usual candidates in the literature. We chose the ONCNO···ONCNO distance because, in the case of the *m*-(OMe)PhNN radical, B3LYP/6-31+G(d) calculations indicate that the spin density is mostly delocalized on the ONCNO group (see Fig. 1). However, such large cutoff allowed us to investigate possible alternative magnetic pathways, as those involving the O of the CH_3O groups. The value of J_{AB} for all biradical pairs identified in step 1 was computed using density functional (DFT) methods [9]. More specifically, we used the B3LYP functional [10] and the 6-31+G(d) basis set [11]. The energy of the singlet was computed using the broken-symmetry approximation [12], which has been shown to give a reasonable good description of open-shell singlet states. The magnitude of J_{AB} was computed as $J_{AB} = E^{S}_{BS} - E^{T}$ because in our calculations the open-shell singlet state had both half-filled orbitals localized on one radical or on the other and, thus, their overlap was negligible ($S_{ab} = 0$). This fact reveals unnecessary the usual correction employed with Hartree–Fock wavefunctions (see [5c] and references therein for a more detailed discussion). All DFT calculations performed in this study were carried out using the GAUSSIAN 98 package [13].

2. Results and discussion

2.1. Electronic structure of the m-(OMe)PhNN radical

The *m*-(OMe)PhNN radical presents a doublet ground state at the geometry found in the YISCIM crystal. In such electronic state, the B3LYP/6-31+G(d) spin density (Fig. 1(b)) presents the usual spin distribution found within the nitronyl nitroxide family [14]: there is a region of high density on the ONCNO atoms of the five-membered ring (NO and central C atoms show positive and negative spin densities, respectively), and much smaller amounts on the C atoms of the phenyl Ph ring, with alternation of sign between adjacent atoms. In addition, the amount of spin on the C atom of the methoxy OMe group is negligible, and the spin density on the O atom of the same group is even smaller than that on the C atoms of the Ph skeleton. The spin density on all H atoms is negligible. The analysis of the atomic spin populations (obtained according to the Mulliken method) provides the same picture, as can be concluded by looking at the atoms having the

maximum of population: N(NO) = 0.31, O(NO) = 0.33, C(ONCNO) = −0.24, |C(Ph)| = 0.06, O(OMe) = 0.002, H < 0.001 electrons.

2.2. Determination of the magnetic topology

The crystal packing structure of the *m*-(OMe)PhNN radical (YISCIM crystal) has been determined at room-temperature by Angeloni et al. [8]. YISCIM crystallizes into the $P2_1$ space group (a = 6.391 Å, b = 11.230 Å, c = 10.228 Å, β = 107.78°) with two radical molecules per unit cell. The packing structure can be described by a set of *A* planes piled along the *c* axis (see Fig. 2(a)). Within each *A* plane the radicals are packed in a T shape, as shown in Fig. 2(b). Any given radical is related to four others by means of C–H···O hydrogen bonds. In two cases (indicated by I in Fig. 2(b)), the two radicals simultaneously form one C(sp^2)–H···ON and one C(sp^2)–H···OCH_3 hydrogen bonds (with H···O distances of 2.325 and 2.939 Å, respectively). In the other two cases (II in Fig. 2(b)), the radicals establish multiple C(sp^3)–H···ON involving the methyls and NO groups of the five-membered ring (the shortest H···O distance being 2.343 Å). Besides the hydrogen bonds, there are two other radicals related to the central radical by C–H···H–C interactions (III in Fig. 2(b)) (the shortest H···H distance being 2.473 Å). As a result of this packing there is no direct overlap between NO groups, being the shortest NO···ON distance within any *A* plane of 6.031 Å (later on this radical-pair will be identified as *d3*). However, there are many short NO···ON contacts between radicals in adjacent *A* planes, as we will see below.

A systematic analysis of the crystal packing, done by looking at the distances from a given radical to all its nearby surrounding radicals, shows that there are four radical pairs (identified below as *d1–d4*) whose ONCNO···ONCNO intermolecular distance is less than 7.4 Å. Notice that all pairs, except *d3*, correspond to contacts between radicals in adjacent *A* planes. In addition to the *d1–d4* pairs, we have also searched for those radical-pairs whose NO···OMe distance is shorter than 7.4 Å. For YISCIM, there is only one extra pair that has to be considered, hereafter identified as *d5*.

The *d1–d5* pairs of radicals define possible magnetic pathways for exchange interactions J_{AB} between the radicals. The topology of these *di* pairs within the crystal forms the complex three-dimensional network depicted in a schematic form in Fig. 3 (in this figure each radical is represented as a point site, for clarity purposes). The *d2* and *d5* pairs form planes along the crystallographic *ab*-axes, being these planes alternatively connected either by *d1, d3* or *d4* pairs. Notice the zigzag form of the connections made by *d1*, *d3* and *d4*.

The computed J_{AB} values for the *d1–d5* pairs are shown in Table 1: only three pairs, *J*(*d2*), *J*(*d3*) and

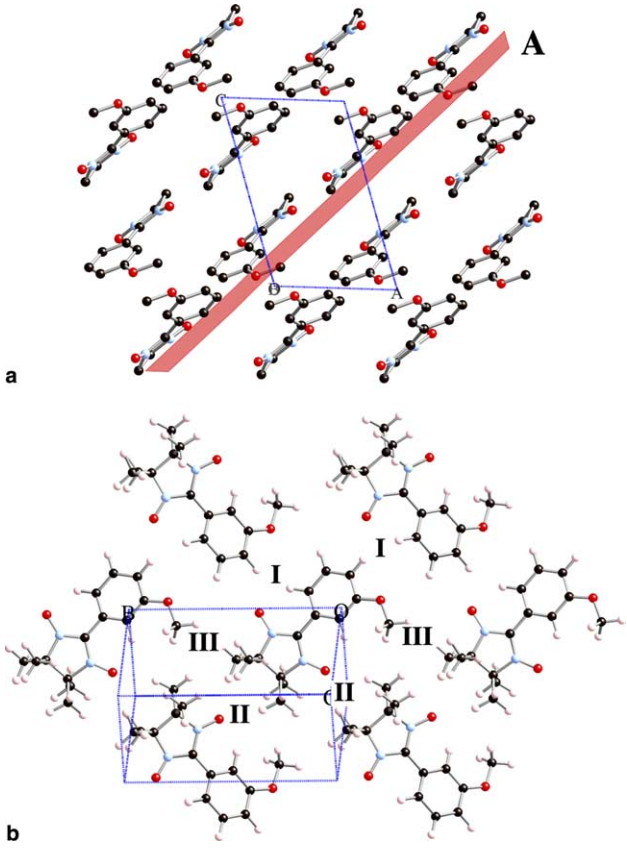


Fig. 2. View of the crystal structure of YISCIM: (a) view along the *b* axis, indicating one of the *A* planes; (b) view of one *A* plane along a perpendicular view (**I**, **II** and **III** refer to the different packing motifs within each *A* plane, see text for a more detailed description).

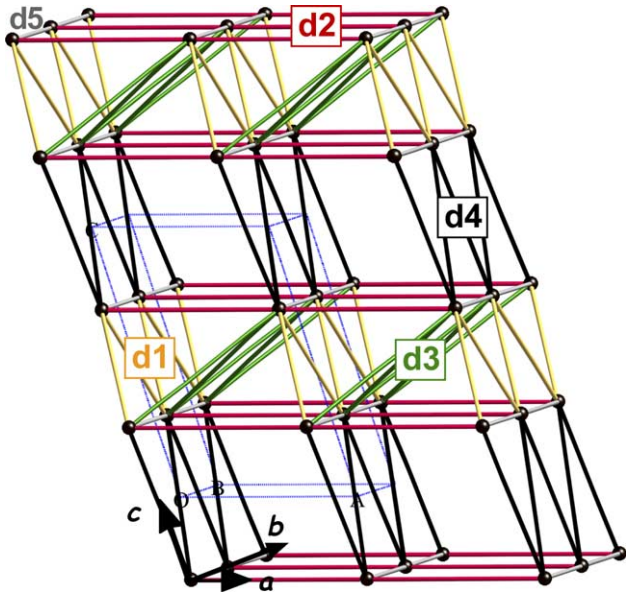


Fig. 3. Scheme of the packing of YISCIM, indicating the position and connectivity of the *di* radical-pairs that fulfill the distance cutoff criterion (*d1–d5*). Notice that each *m*-(OMe)PhNN radical has been replaced by a point site.

Table 1
Unrestricted DFT broken symmetry UB3LYP/6-31 + G(d) results for pair interaction $J(di)$ of all candidates (listed as shortest intermolecular NO···ON distance increases; the shortest NO···OMe distance is also given) for YISCIM

Dimer *di*	NO···ON (Å)	NO···OMe (Å)	$J(di)$ (cm^{-1})
d1	4.64	6.60	$\ll\|0.05\|$
d2	5.40	6.46	−0.20
d3	6.03	6.91	−0.11
d4	6.66	4.00	+0.22
d5	8.42	5.31	$\ll\|0.05\|$

Notice that *d1–d4* were chosen in terms of NO···ON distance criterion (<7.4 Å), while *d5* was selected due to presenting NO···OMe distances shorter than 7.4 Å (*d4* could have also been selected according to such criterion).

$J(d4)$, have values of J_{AB} larger than $|0.05|\ cm^{-1}$. It is worth noticing that the strength of J_{AB} is not proportional to the NO···ON distance, thus stressing the importance of the relative radical pair orientation, and/or of the other intermolecular interactions the radical pairs can establish between them.

The *magnetic topology* (Fig. 4(a)) is obtained by accounting for the connectivity of the radical-pairs having $J_{AB}(di)$ values larger than $|0.05|\ cm^{-1}$ (or by deleting those *di* pairs in Fig. 3 whose $J_{AB}(di)$ value is smaller than $|0.05|\ cm^{-1}$). In YISCIM (see Fig. 4(a)), the magnetic topology can be visualized as bent planes of connected $J(d3)$ and $J(d4)$ zigzag chains (green and black)

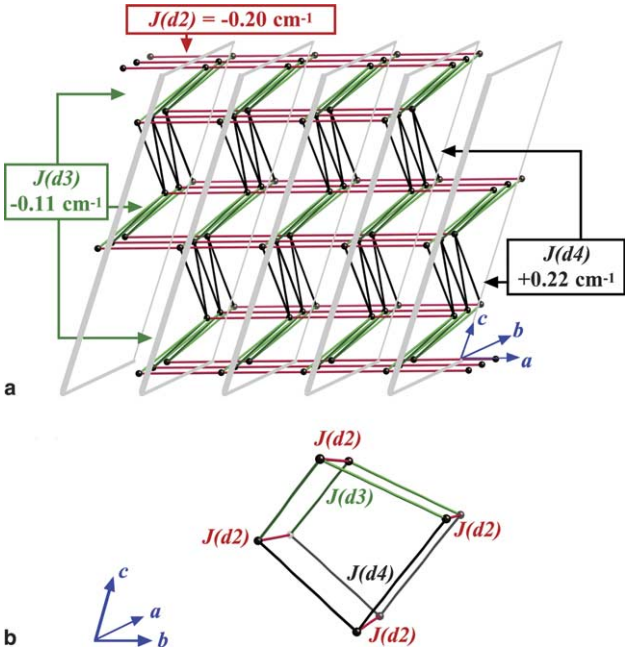


Fig. 4. (a) Magnetic topology of YISCIM: zigzag antiferromagnetic $J(d3)$ and ferromagnetic $J(d4)$ chains form bent *bc*-planes, that interact along the *a* axis through antiferromagnetic $J(d2)$ interaction. Notice that each *m*-(OMe)PhNN radical has been replaced by a point site. (b) Three-dimensional minimal magnetic model (8s), which consists of eight radicals forming a hexahedral figure.

running along the *bc* crystallographic axes, which are interconnected along the *a* axis by antiferromagnetic $J(d2)$ interactions (red). Within any *bc*-plane, one chain is ferromagnetic ($J(d4) = +0.22\ cm^{-1}$, in black), while the adjacent ones are antiferromagnetic ($J(d3) = -0.11\ cm^{-1}$, in green). The overall magnetic topology is three-dimensional, and does not follow any simple magnetic motif.

2.3. Construction of the Heisenberg Hamiltonian and calculation of the magnetic susceptibility

There are two conditions that one has to keep in mind when selecting the N magnetic centers (in this case of spin $S = 1/2$) that constitute the *minimal magnetic model space*: (i) the three-dimensional magnetic topology of the crystal must be recovered by extension of the minimal model along the (a,b,c) crystallographic axes, and (ii) all important J_{AB} interactions must be present with a weight and environment that mimics that found in the crystal (see Fig. 4(a)). When these considerations are applied to YISCIM, the smallest spin space that reproduces the magnetic topology of Fig. 4(a) is the hexahedral model depicted in Fig. 4(b). We have previously shown [5c] that a four sites model (hereafter identified as the 4s-model) is required to reproduce the magnetic susceptibility of a system whose magnetic topology is a two-dimensional layer (note that depending on J_{AB} values the 4s-model will be represented by a square, rectangle, or trapezoid). Thus, for YISCIM, two interacting layers should require two interconnected trapezoidal 4s-models as depicted in Fig. 4(b). We will identify such a minimal magnetic model as the 8s-model. Such 8s-model presents all types of J_{AB} interactions in a proportion and environment similar to that found in Fig. 4(a), and regenerates the zigzag planes by propagation along *b* and *c* axes, and the whole topology of Fig. 4(a) when further propagated along *a*.

With the set of spin eigenfunctions of the 8s-model and the values of the J_{AB} parameters of Table 1, we built the matrix representation of the Heisenberg Hamiltonian (1). The energy levels of this Heisenberg Hamiltonian were then computed by diagonalization of that matrix. These eigenvalues were used in the appropriate statistical formulae (see [4]) to compute the macroscopic magnetic susceptibility $\chi T(T)$ curve (Fig. 5(a)). This curve closely reproduces the experimental $\chi T(T)$ curve obtained in the 4.2–250 K temperature range (the experimental curve was obtained by taking the expression for the Curie–Weiss law, $\chi = C/(T-\theta)$, with $\theta = -0.97$ K [8] and using the Curie constant $C = 0.376$ emu K mol^{-1}). We have tested the convergence of our computed $\chi T(T)$ curves against an increase of the size of the minimal magnetic model space by extending the 8s-model space along (a,b,c) crystallographic axes (models $(8s) \times 1.5a$, $2a$, $2b$, $2c$, $1.5bc$). As shown in

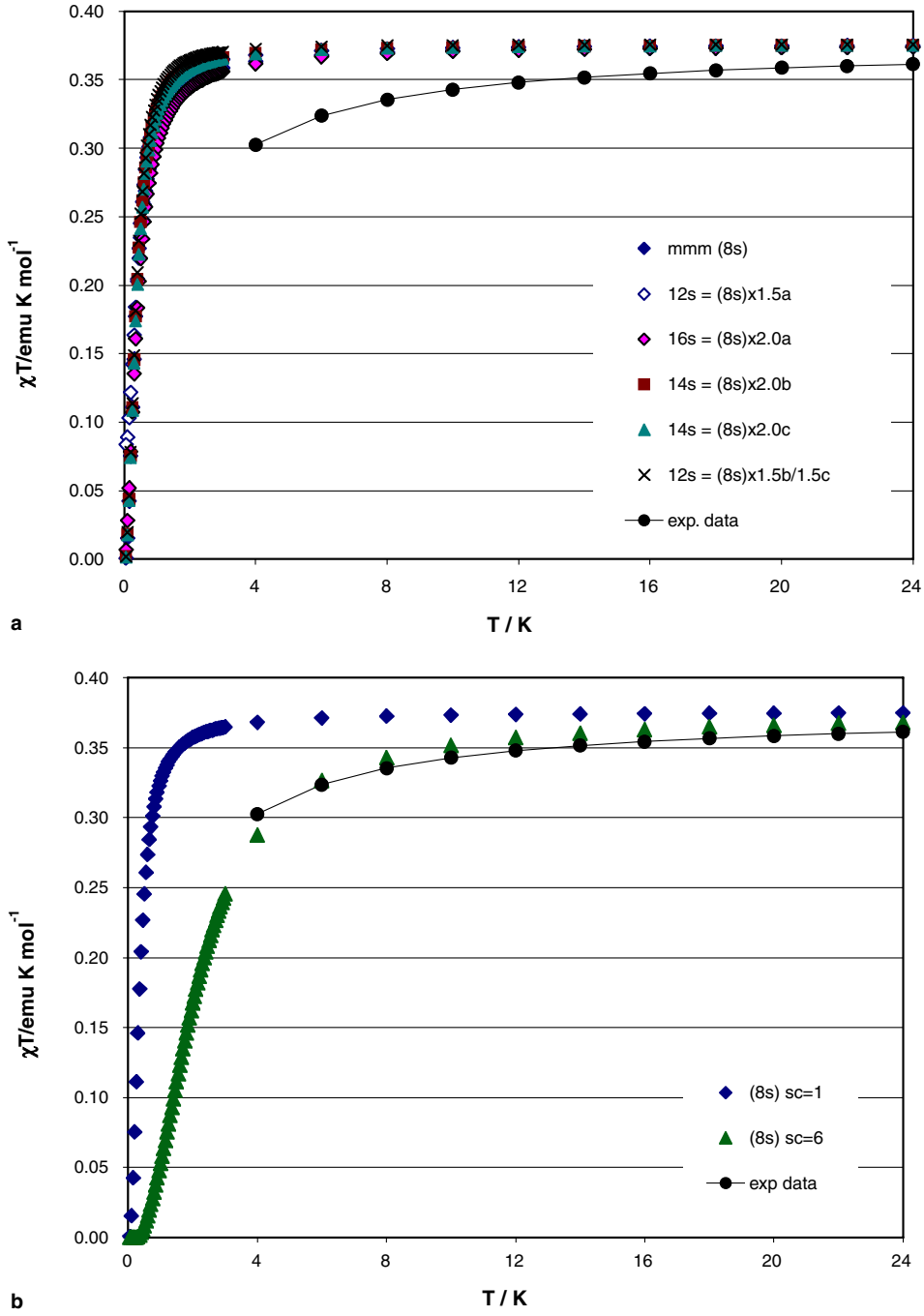


Fig. 5. Comparison between computed and experimental magnetic susceptibility $\chi T(T)$ of YISCIM: (a) results using (8s) model and its extension along (*a,b,c*) crystallographic axes; (b) an scaling factor of 6.00 is sufficient to reproduce the experimental curve.

Fig. 5(a), the $\chi T(T)$ curves obtained with the extended models nearly match the $\chi T(T)$ values computed using the 8s-model, although some numerical differences remain with the experimental curve. The small differences found between the computed and experimental curves can be recovered by the use of a scaling factor (Fig. 5(b)) as we will elaborate below. These magnetic susceptibility curves indicate that YISCIM behaves as a dominant antiferromagnet, despite the fact that it has one ferro and two antiferromagnetic J_{AB} interactions of similar magnitude and weight (Fig. 4(b)).

Let us focus now into the source of the difference between computed and experimental magnetic susceptibility curves. There are various possible causes. First of all [5a,6], we have recently come across the fact that the discrepancy between simulated and experimental data can be tracked down to the use of crystal coordinates determined at room temperature instead of using

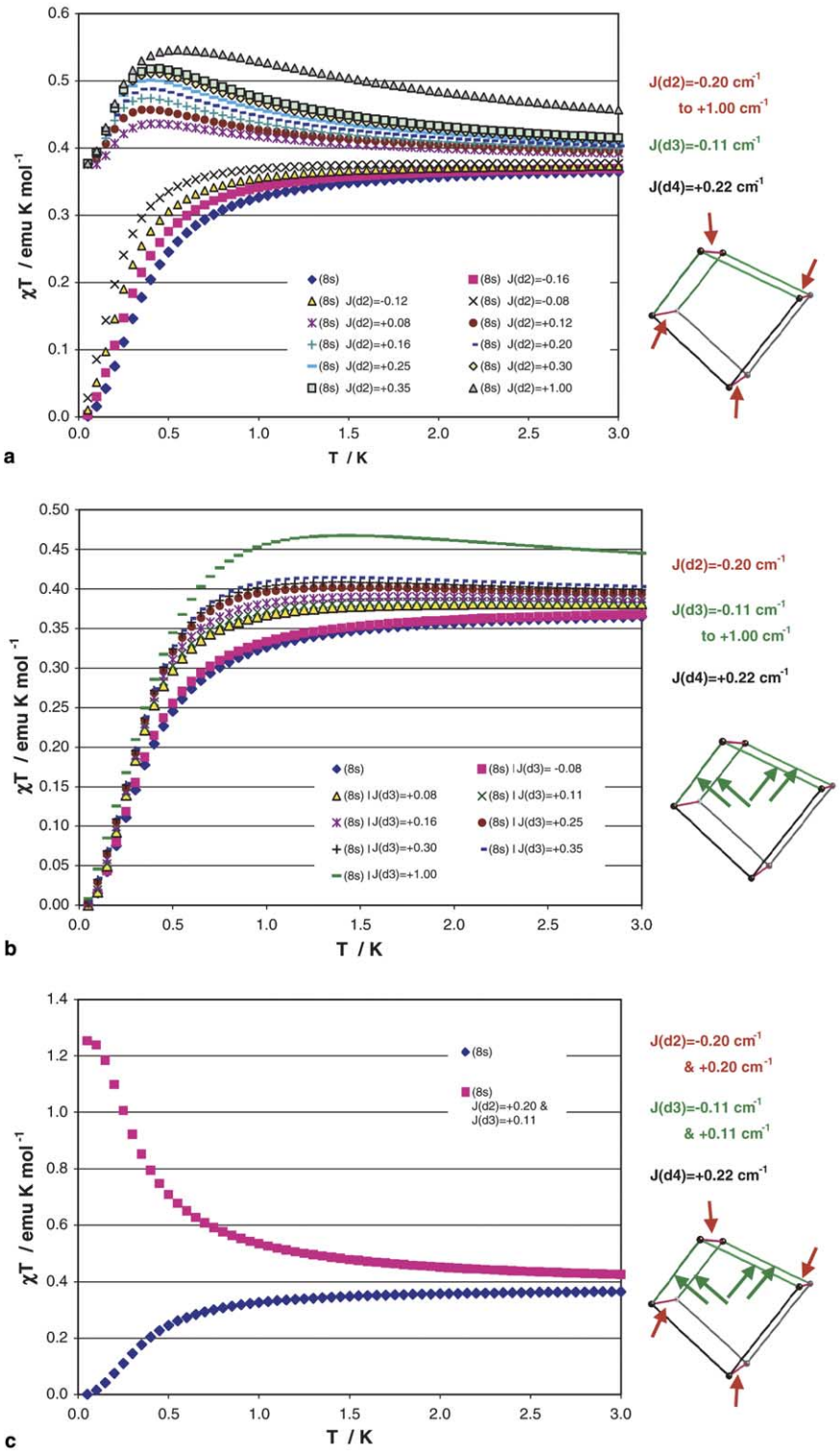


Fig. 6. Series of numerical simulations on the competition between FM and AFM J_{AB} pair interactions by systematically changing $J(d2)$ and $J(d3)$ values (see main text for discussion).

low-temperature structures. In another words, thermal expansion is not always isotropic and can induce subtle changes in the structure of the pairs that create non-negligible changes in the computed J_{AB} microscopic magnetic interactions. Besides the thermal expansion effect, there might be systematic errors in the computation of the J_{AB} due (i) to the use of DFT methods, instead of more sophisticated methods, or (ii) to collective

exchange effects, which are not considered in the dimer approach employed here. We have previously shown [4,5] that one can recover these discrepancies by multiplying the energies by a linear scaling factor, whose effect in the spectrum of energies of the Heisenberg Hamiltonian is just separating these energies uniformly. For YISCIM, the scaling factor that best matches the experimental data using the 8s-model is 6.0 (Fig. 5(b)). With this factor, the difference between the computed and experimental magnetic susceptibility curves becomes acceptable, specially considering that the computed $\chi T(T)$ curve has been obtained using the crystal structure determined at room temperature.

2.4. Numerical simulations on the competition between ferro and antiferromagnetic exchange pathways

Using the 8s minimal magnetic model space, we have carried out a few numerical studies changing systematically the values of the two antiferromagnetic J_{AB} pair interactions, in order to explore the reasons for the dominant antiferromagnetic behavior of the crystal and what pair interaction is the one responsible for the overall magnetic behavior. In all series of simulations, we have taken as a reference the values of $J(d2)$, $J(d3)$ and $J(d4)$ pair interactions computed using the room temperature crystal structure of YISCIM.

We first analyzed the effect of changing $J(d2)$ while keeping $J(d3)$ and $J(d4)$ constant using the computed values at room temperature ($J(d3) = -0.11$ and $J(d4) = +0.22\ \mathrm{cm}^{-1}$). Let us remind here that $J(d3)$ and $J(d4)$ define the topology of the *bc*-layer, which is represented by a trapezoidal 4s-model. Tests on such 4s-model showed that macroscopically has a dominant ferromagnetic behavior, contrarily to the antiferromagnetic behavior of the 8s minimal model. Therefore, we changed the $J(d2)$ parameter from -0.20 to $+1.0\ \mathrm{cm}^{-1}$, by steps of approximately $0.04\ \mathrm{cm}^{-1}$, expecting to achieve an overall ferromagnetic behavior. The computed magnetic susceptibility curves are collected in Fig. 6(a), together with that obtained using the original J_{AB} values computed using the YISCIM structure at room temperature. These curves show that by modifying the $J(d2)$ parameter it is possible to obtain the $\chi T(T)$ curve characteristic of a weak ferromagnet, but never the shape of a dominant ferromagnet.

We carried a second series of simulations (see Fig. 6(b)) changing the value of the $J(d3)$ parameter from -0.11 up to $+1.0\ \mathrm{cm}^{-1}$, while keeping $J(d2)$ and $J(d4)$ constant at their reference YISCIM values (-0.20 and $+0.22\ \mathrm{cm}^{-1}$, respectively). The conclusion is analogous to the previous simulation and no net dominant ferromagnetic behavior was obtained. With the changes introduced in this series, the *bc*-layers have become ferromagnetic and just the inter-layer antiferromagnetic $J(d2)$ interaction is responsible for the failure to obtain an overall ferromagnetic behavior. Only when all three J_{AB} parameters become ferromagnetic a net dominant ferromagnetic behavior for the magnetic susceptibility $\chi T(T)$ curve is finally obtained (see Fig. 6(c)).

We have thus found that small changes in the size of the $J(d2)$, $J(d3)$ and $J(d4)$ parameters close to the computed room temperature YISCIM values do not induce marked changes in the shape of the $\chi T(T)$ curves. This conclusion was unexpected to us, and suggests that more detailed and systematic studies should be done to determine the importance of the magnetic topology on these results. We plan to do so in a quantitative way, looking at the weight of the populations of the ferro versus antiferromagnetic states.

2.5. Comparing the magnetic properties of (OMe)PhNN and (SMe)PhNN crystals

The most remarkable similarity between the *m*-(OMe)PhNN radical and its thio-substituted counterpart is the nearly identical spin distribution that they present. Almost no spin density is present on the O and S atoms of the XMe (X = O or S) groups: the Mulliken spin population on the O(OMe) atom of the *m*-(OMe)PhNN radical and on the S(SMe) atom of the *m*-(SMe)PhNN radical is 0.002 and -0.007 electrons, respectively (the difference is almost negligible), while the population on the remaining atoms is nearly the same. Therefore, as the strength of the C–H···O and C–H···S intermolecular bonds is also similar, one could expect that the (OMe)PhNN and the (SMe)PhNN radicals would pack in a similar form and have similar magnetic properties. These expectations are confirmed in the *para* isomer of the radicals, as both present a dominant ferromagnetic behavior (in fact, the *p*-(SMe)PhNN crystal is one of the few purely organic bulk ferromagnets). A detailed study of these similarities is, however, out of the intended scope of this paper and will be the subject of a future communication.

3. Conclusions

A *bottom–up* theoretical procedure [4–6] has been applied to the room temperature crystal (YISCIM) of the *m*-(OMe)PhNN radical, a case of competing ferro and antiferromagnetic J_{AB} pair interactions whose overall behavior is that of a dominating antiferromagnet. We have computed the magnetic topology of this crystal and found it to consists of bent planes along the *bc*-directions, interconnected along the *a* axis by antiferromagnetic $J(d2)$ interactions. These *bc*-planes result from antiferromagnetic $J(d3)$ and ferromagnetic $J(d4)$ interactions forming zigzag chains.

The macroscopic magnetic susceptibility obtained from a magnetic topology like that of YISCIM cannot

be predicted using the usual qualitative considerations and requires of an appropriate numerical calculation, like that done in steps 3 and 4 of our bottom–up approach. For YISCIM, our computed magnetic susceptibility curve reproduces the overall shape of the experimental curve, although there are some numerical discrepancies between simulated and experimental $\chi T(T)$ data. These differences can originate from the use of a room temperature crystal structure (which surely presents thermal distortions with reference to the low temperature structure of interest), and/or small numerical errors due to the computational techniques employed. The discrepancies can however be recovered by the use of a linear scaling factor that multiplies the energy of all the magnetic states possible in our crystal. With a scale factor of 6.0 we have obtained the best agreement with the experimental $\chi T(T)$ data.

We have also explored, by means of numerical simulations in which the values of the J_{AB} pair interactions are slightly modified from the YISCIM computed values, forms of transforming the dominant antiferromagnetic behavior into a dominant ferromagnetic behavior. We have concluded that small changes in the antiferromagnetic $J(d2)$ and $J(d3)$ interactions do not induce a clear overall ferromagnetic behavior, but more detailed studies are required in order to understand why this is so.

Finally, a qualitative analysis has been done on the similarities between the (OMe)PhNN radical studied here and its sulphur-substituted counterpart, the (SMe)PhNN radical, which indicates that they should present a similar crystal packing and magnetic properties.

Acknowledgements

M.D. and J.J.N. acknowledge the Spanish "Ministerio de Ciencia y Tecnología" (# BQU2002-04587-C02-02), and the Catalan "CIRIT" (2001SGR-0044) for their continuous support. The authors also thank the CEPBA-IBM Research Institute, CEPBA and CESCA for allocation of CPU time in their computers. M.D. thanks the Spanish "Ministerio de Ciencia y Tecnología" for the award of a "Ramón y Cajal" Fellowship at Universitat de Barcelona. This project was partly supported by EPSRC (UK) under Grant GR/M86750 (ROPA).

References

[1] (a) J. Madox, Nature 335 (1988) 201;
(b) A. Gavezzotti, Acc. Chem. Res. 27 (1994) 309;
(c) J. Bernstein, Polymorphism in Molecular Crystals, Clarendon Press, Oxford, 2002;
(d) D. Braga, F. Grepioni, G. Orpen (Eds.), Crystal Engineering: From Molecules and Crystals to Materials, Kluwer, Dordrecht, 1999.

[2] (a) M. Deumal, J. Cirujeda, J. Veciana, J.J. Novoa, Adv. Mater. 10 (1998) 1461;
(b) M. Deumal, J. Cirujeda, J. Veciana, J.J. Novoa, Chem. Eur. J. 5 (1999) 1631.

[3] (a) H.M. McConnell, J. Chem. Phys. 39 (1963) 1910;
(b) H.M. McConnell, Proc. Robert A. Welch Found. Conf. Chem. Res. 11 (1967) 144;
(c) M. Deumal, J.J. Novoa, M.J. Bearpark, P. Celani, M. Olivucci, M.A. Robb, J. Phys. Chem. A 102 (1998) 8404;
(d) C. Kollmar, O. Kahn, Acc. Chem. Res. 26 (1993) 259.

[4] M. Deumal, M.J. Bearpark, J.J. Novoa, M.A. Robb, J. Phys. Chem. A 106 (2002) 1299.

[5] (a) M. Deumal, M.A. Robb, J.J. Novoa, Polyhedron 22 (2003) 1935;
(b) M. Deumal, C.P. Landee, J.J. Novoa, M.A. Robb, M.M. Turnbull, Polyhedron 22 (2003) 2235;
(c) M. Deumal, M.J. Bearpark, M.A. Robb, Y. Pontillon, J.J. Novoa, Chem. Eur. J. 10 (2004) 6422.

[6] M. Deumal, J. Ribas-Ariño, M.A. Robb, J. Ribas, J.J. Novoa, Molecules 9 (2004) 757.

[7] (a) Refcode according to Cambridge Crystallographic Database (CCSD): F.H. Allen, J.E. Davies, J.J. Galloy, O. Johnson, O. Kennard, C.F. Macrae, D.G. Watson, J. Chem. Inf. Comput. Sci. 31 (1991) 204;
(b) F.H. Allen, O. Kennard, Chem. Des. Automation News 8 (1993) 31.

[8] L. Angeloni, A. Caneschi, L. David, A. Fabretti, F. Ferraro, D. Gatteschi, A. le Lirzin, R. Sessoli, J. Mater. Chem. 4 (1994) 1047.

[9] (a) R.G. Parr, W. Yang, Density-Functional Theory of Atoms and Molecules, Oxford University Press, New York, 1989;
(b) W. Koch, M.C. Holthausen, A Chemist's Guide to Density Functional Theory, second ed., Wiley-VCH, Weinheim, 2000.

[10] (a) A.D. Becke, Phys. Rev. A 38 (1988) 3098;
(b) C. Lee, W. Yang, R.G. Parr, Phys. Rev. B 37 (1988) 785;
(c) A.D. Becke, J. Chem. Phys. 98 (1993) 5648.

[11] R. Ditchfield, W.J. Hehre, J.A. Pople, J. Chem. Phys. 54 (1971) 724.

[12] (a) L. Noodlemann, J. Chem. Phys. 74 (1981) 5737;
(b) L. Noodlemann, E.R. Davidson, Chem. Phys. 109 (1986) 131;
(c) E. Ruiz, P. Alemany, S. Alvarez, J. Cano, J. Am. Chem. Soc. 119 (1997) 1297;
(d) R. Caballol, O. Castell, F. Illas, I.D.R. Moreira, J.P. Malrieu, J. Chem. Phys. A 101 (1997) 7860;
(e) M. Nishino, Y. Shigeta, T. Soda, Y. Kitagawa, T. Onishi, Y. Yoshioka, K. Yamaguchi, Coord. Chem. Rev. 198 (2000) 265;
(f) J.-M. Mouesca, J. Chem. Phys. 113 (2000) 10505;
(g) F. Illas, I.D.R. Moreira, C. de Graaf, V. Barone, Theor. Chem. Acc. 104 (2000) 265.

[13] M.J. Frisch, G.W. Trucks, H.B. Schlegel, P.M.W. Gill, B.G. Johnson, M.A. Robb, J.R. Cheeseman, T. Keith, G.A. Petersson, J.A. Montgomery, K. Raghavachari, M.A. Al-Laham, V.G. Zakrzewski, J.V. Ortiz, J.B. Foresman, J. Cioslowski, B.B. Stefanov, A. Nanayakkara, M. Challacombe, C.Y. Peng, P.Y. Ayala, W. Chen, M.W. Wong, J.L. Andres, E.S. Replogle, R. Gomperts, R.L. Martin, D.J. Fox, J.S. Binkley, D.J. Defrees, J. Baker, J.J.P. Stewart, M. Head-Gordon, C. Gonzalez, J.A. Pople, GAUSSIAN 98, Gaussian, Inc., Pittsburgh, PA, 1999.

[14] M. Deumal, P. Lafuente, F. Mota, J.J. Novoa, Synth. Met. 122 (2001) 477.

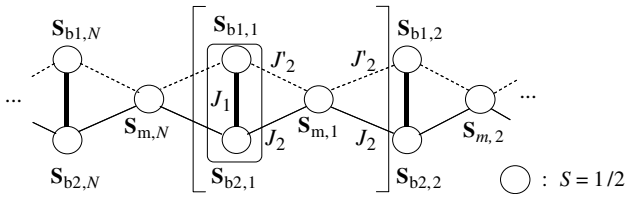


Chart 1. Schematic view of the Heisenberg spin Hamiltonian of the alternating biradical–monoradical chain system. The circles denote the $S = 1/2$ spins. J_1 represents the intramolecular coupling in the biradical, while J_2 and J'_2 denote the intermolecular exchange interactions.

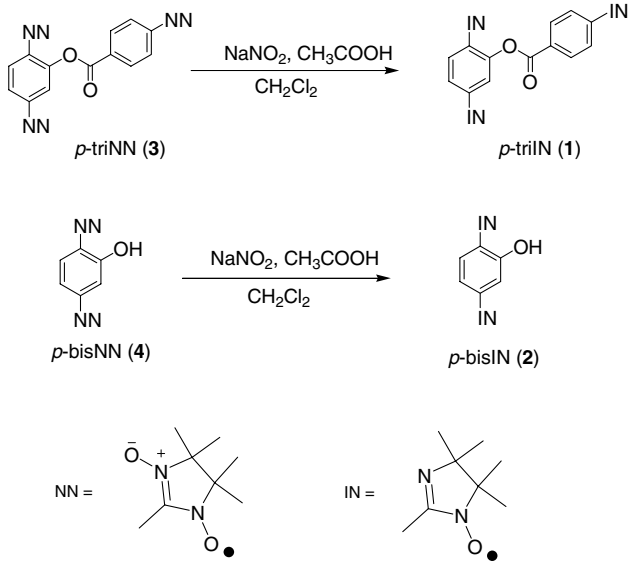
the generalized ferrimagnetism have never been disclosed until genuinely organic magnetism appeared.

The design of building blocks of molecule-based magnetic materials is one of the most important issues because the molecular packing of the building blocks in a crystalline solid state governs magnetic properties of the molecular assemblages. Referred to molecular crystal engineering, we have proposed an approach of single-component ferrimagnet, which consists of π-monoradical and π-biradical entities bridged by σ-bonds [4]. In this approach, the π-conjugation is effectively truncated at the σ-bond bridge and thus the amplitude of the exchange interactions between the two molecular entities $J(\sigma)$ and $J'(\sigma)$ are expected to be much smaller than that within the biradical entity $J(\pi)$, as illustrated in Chart 2:

$$|J(\sigma)|, \quad |J'(\sigma)| \ll |J(\pi)|. \tag{2}$$

The condition Eq. (2) gives the multiple magnetic degrees of freedom for the biradical and monoradical entities in the single molecule of the resultant triradical. When the triradical molecules are arranged to form a head-to-tail molecular packing, there is expected an alternating chain of the biradical and the monoradical moieties in a crystalline solid state, as depicted in Chart 2. The σ-bonds in the triradical are magnetically inactive as magnetic interaction pathway and play the role of only forming the structural framework, while the magnetic interactions are propagated by the through-space π-orbital overlaps between the molecular entities of the adjacent molecules in the crystalline solid. The conceptual advance of the molecular designing for the σ-bonded π-oligoradicals lies in the fact that inequivalent magnetic entities such as π-biradicals and π-monoradicals are forced to coexist in a crystalline solid state. A conventional ferrimagnetic spin alignment, i.e., an antiparallel coupling of $S = 1$ and $S = 1/2$ spins has been found for a triradical composed of a ground-state triplet biradical and a doublet monoradical [4]. In the present study, the approach of the σ-bonded π-oligoradicals is applied to the case of the constituent biradical entity with the singlet ($S = 0$) ground state, leading to a model compound for the generalized ferrimagnetism.

In our previous study, a nitronylnitroxide triradical (**3**, Scheme 1) has been synthesized and its magnetic properties examined [5]. In the triradical **3**, a π-conjugated biradical with a singlet ground state and a doublet monoradical are united by σ-bonds. The amplitude of $|J(\pi)|$ has been found to be larger than $|J(\sigma)|$ and $|J'(\sigma)|$ by three orders of magnitude; $2J(\pi)/k_B = -70$ K, $2|J(\sigma)|/k_B \sim 2|J'(\sigma)|/k_B \leqslant 0.01$ K [5]. The condition of Eq. (2) is fulfilled in the triradical **3**. The triradical **3** can be used as a building block for the generalized ferrimagnetism. We report here the designing and synthesis of a novel iminonitroxide triradical, *p*-triIN (**1**, Scheme 1), possessing a *para*-phenylene-based biradical moiety with a singlet ground



Scheme 1. Synthesis of *p*-triIN (**1**) and *p*-bisIN (**2**).

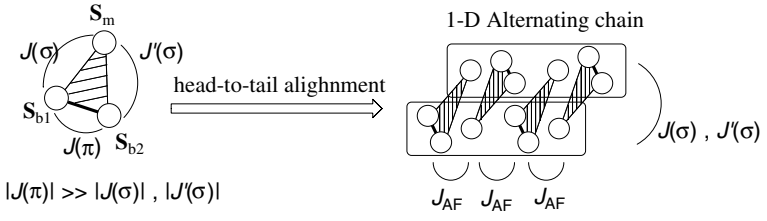


Chart 2. Schematic view of the single-component ferrimagnetic approach. The doubled chain with the intermolecular antiferromagnetic interactions J_{AF} (=J_2 and J'_2) is composed of the triradicals packed in a head-to-tail fashion. The exchange interactions between the chains correspond to the intramolecular magnetic couplings $J(\sigma)$ and $J'(\sigma)$.

state and a monoradical moiety as another model for the generalized ferrimagnetism. We present the magnetic properties of **1** and its parent biradical, *p*-bisIN (**2**, Scheme 1). Possible occurrence of the exotic ferrimagnetic spin alignment in the iminonitroxide triradical **1** is discussed from magnetic susceptibility measurements.

2. Experimental

2.1. Synthesis

The iminonitroxide triradical (**1**) and the biradical (**2**) were synthesized from the nitronylnitroxide triradical (**3**) [5] and biradical (**4**) [5], respectively, as shown in Scheme 1.

*p-triIN (**1**)*. Nitronylnitroxide triradical (**3**) (0.50 g, 0.75 mmol) was added to a suspension of $NaNO_2$ (0.47 g, 6.78 mmol) in CH_2Cl_2 (8 mL) and CH_3COOH (0.50 mL, 8.71 mmol). The reaction mixture was stirred for 10 min to give a bright orange solution. After filtration and neutralization with aqueous $NaHCO_3$, the organic layer was washed with water, and the aqueous phase was extracted with CH_2Cl_2 (100 mL). The combined organic phase was dried over $MgSO_4$. The solution was concentrated and chromatographed over a silica gel column. Elution with CH_2Cl_2/diethyl ether (9/1 in volume) followed by removal of the solvent in vacuo gave an orange product. Recrystallization from EtOH provided **1** as a pure orange solid (0.18 g, 0.29 mmol) (39%). Elemental analysis (C, H, N) of *p*-triIN (**1**). *Anal*. Calc. for *p*-triIN: C, 66.32; H, 7.04; N, 13.65. Found: C, 66.21; H, 7.11; N, 13.50%. IR(ν/cm^{-1}): 1375 (NO), 1741 (C=O). FAB$^+$ MS *m*/*z* 617.3 [M + 2H].

*p-bisIN (**2**)*. The biradical **2** was synthesized from **4** in the same way as that of **1**. Elemental analysis (C, H, N) of *p*-bisIN (**2**). *Anal*. Calc. for *p*-bisIN: C, 64.49; H, 7.58; N, 15.04. Found: C, 64.41; H, 7.59; N, 14.97%. Single crystals of **2** were obtained by recrystallization from a mixture of acetone and hexane.

2.2. Crystal structure analysis

Single-crystal diffraction data of **2** were collected on a Rigaku Mercury CCD diffractometer with graphite monochromated Mo Kα radiation at 108 K. The crystal structure was solved by using direct methods in a program package CRYSTALSTRUCTURE [6]. Anisotropic thermal parameters analysis was applied for non-hydrogen atoms. Hydrogen atoms with isotropic thermal parameters were refined as riding models.

2.3. Magnetic susceptibility measurements

Magnetic susceptibility was measured on a Quantum Design SQUID magnetometer MPMS-XL under the static magnetic field of 0.1 T in the temperature range down to 1.9 K. The magnetic responses were corrected with diamagnetic blank data of the sample holder obtained separately. The diamagnetic contribution of the sample itself was estimated from Pascal's constants.

3. Results and discussion

3.1. Crystal structure

The crystal data of *p*-bisIN (**2**) are listed in Table 1. Fig. 1 shows the molecular structure of **2**, which is located at the inversion center of the $P2_1/n$ lattice. A half of the molecule is crystallographically independent, indicating that the hydroxyl group of **2** (O2) is disordered in two positions with the occupancy ratio of 0.5:0.5, as found in the analogous compound **4** [5]. The oxygen atoms of nitroxide, O1 and O3, are disordered in two positions as well. The occupancy ratio of O3 (0.36) near the hydroxyl group is smaller than that of O1 (0.64) on the other side. In addition, the dihedral angle between the iminonitroxide plane (O1–N1–C1–N2–O3) and the phenyl plane (C8–C9–C10) is 18.21°, being smaller than that reported for **4** (33.37°) [5]. These are probably due to the difference in steric repulsion between the oxygen atoms of nitroxide and the hydroxyl group in the two positions.

3.2. Magnetic susceptibility

3.2.1. Biradical (**2**)

Magnetic susceptibility χ_m of **2** is shown in Fig. 2 in the $\chi_m T$ versus T plots. The $\chi_m T$ value at 298 K (0.73 emu mol^{-1} K) is slightly lower than that expected for two $S = 1/2$ spins (0.75 emu mol^{-1} K) with the *g*-factor of $g = 2.0$. With decreasing temperature the $\chi_m T$ value decreased to reach zero, as depicted in Fig. 2. These

Table 1
Selected X-ray crystallographic data of **2**

Compound	*p*-bisIN(**2**)
Chemical formula	$C_{20}H_{28}N_4O_3$
Crystal systems	monoclinic
Space group	$P2_1/n$
a (Å)	7.065(3)
b (Å)	14.449(5)
c (Å)	9.592(4)
β (°)	99.875(9)
V (Å^3)	964.7(6)
Z	4
D_{calc} (g cm^{-3})	1.275
T (K)	108
$R(I > 3\sigma(I))$[a]	0.068
R_w(all data)[b]	0.135

[a] $R = \sum ||F_o| - |F_c|| / \sum |F_o|$.

[b] $R_w = \sqrt{\sum w((|F_o| - |F_c|)^2 / \sum w(F_c)^2)}$.

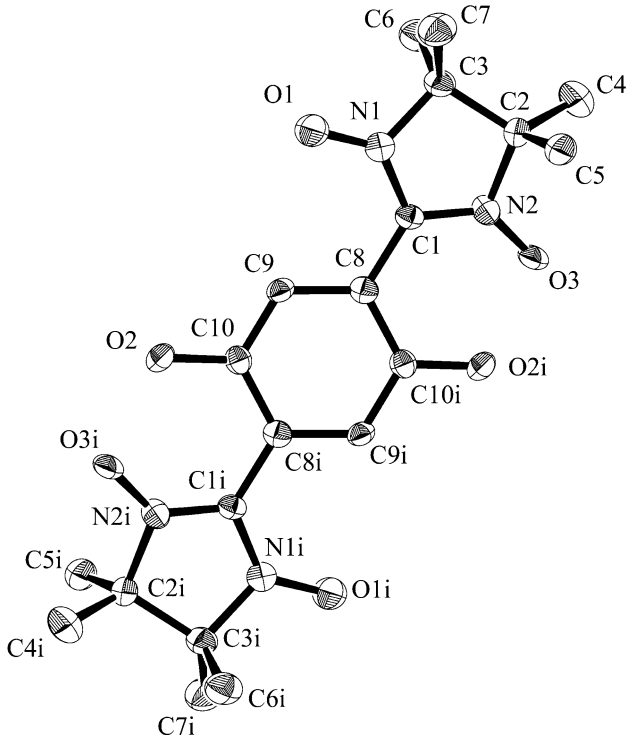


Fig. 1. ORTEP view of the molecular unit of *p*-bisIN (**2**) at the 50% probability level. Symmetry operation code for i is $-x+2$, $-y+1$, $-z+1$. The hydrogen atoms are omitted for the sake of clarity.

results indicate that a sizable intramolecular antiferromagnetic interaction is operative in **2**. The temperature dependence of magnetic susceptibility was analyzed by using the singlet–triplet model (the Bleany–Bowers model) [7]

$$\chi = \frac{Ng^2\mu_B^2}{3k_BT}\frac{2\alpha}{3+\exp(-2J(\pi)/k_BT)}. \quad (3)$$

The parameter $J(\pi)$ in Eq. (3) represents the intramolecular antiferromagnetic exchange interaction defined by the spin Hamiltonian of two $S = 1/2$ spins

$$H = -2J(\pi)S_1 \cdot S_2 \quad (4)$$

and α denotes the purity. The other symbols have their usual meanings. The *g*-factor is fixed as $g = 2.006$, which has been derived from an ESR spectrum. The best fit parameters are $\alpha = 0.96$, $2J(\pi)/k_B = -30.8 \pm 0.1$ K.[1]

[1] One of the disordered oxygen atoms (O3) of the nitroxide were found to have intermolecular short contacts with the other oxygen atom (O1) of the disordered nitroxide or the hydrogen atom attached to the phenyl carbon atom (C9) on the molecule neighboring along the *a*-axis: O3–O1 = 2.910(4) Å, O3–H(C9) = 2.747(1) Å. These contacts are expected to contribute to intermolecular antiferromagnetic interactions. The fitting with Eq. (3) has neglected the possible intermolecular interactions attributable to the contacts in order to avoid overparameterization. The amplitude of $2J(\pi)/k_B = -30.8$ K obtained from the fitting should contain the contribution form the intermolecular interactions and give only an estimate of the intramolecular exchange interaction.

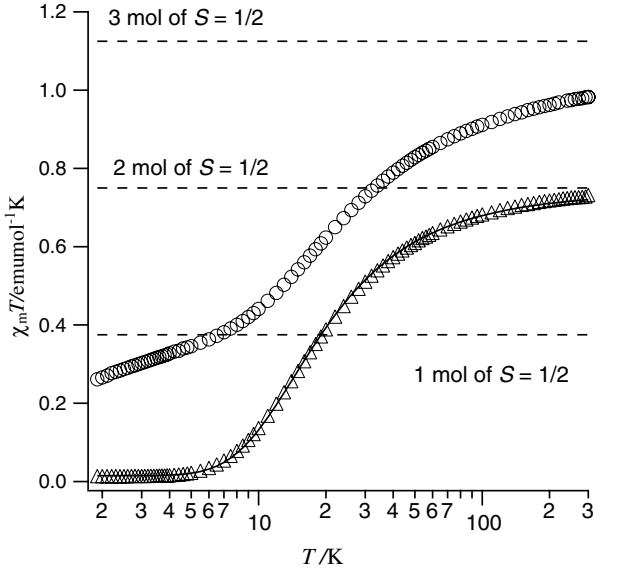


Fig. 2. Temperature dependence of the product χ_mT for *p*-triIN (**1**) (the circles) and *p*-bisIN (**2**) (the triangles). The solid line represents the theoretical calculation from Eq. (3). The horizontal dashed lines show the χ_mT values expected for 1, 2, and 3 moles of magnetically independent $S = 1/2$ spins.

The $2J(\pi)$ value of the iminonitroxide biradical **2** is smaller than that of previously reported nitronylnitroxide biradical **4** ($2J(\pi)/k_B = -82$ K) [5]. This result is consistent with previously reported theoretical calculations [8].

3.2.2. Triradical (*1*)

The temperature dependence of paramagnetic susceptibility χ_m for **1** is shown in Fig. 2 in the χ_mT versus T plots. At 298 K, the χ_mT value is 0.98 emu K mol^{-1}, which is slightly smaller than that for non-interacting three $S = 1/2$ spins (1.13 emu K mol^{-1}). Upon cooling, the χ_mT value for **1** decreased and passed across 0.38 emu mol^{-1} K, which is expected for one mol of $S = 1/2$ spin with $g = 2.0$, although the χ_mT value for **3** decreased down to a constant value of 0.38 emu mol^{-1} K below 10 K [9]. The magnetic behavior of **1** indicates that the ground state of the molecular assemblage of **1** in the crystal is diamagnetic.

In non-quantum terms, where the frustration effects inherent in the multicentered nature of the Hamiltonian in Chart 1 is neglected, the alternating assemblages of biradicals and monoradicals with three $S = 1/2$ spins in a repeating unit never affords any non-magnetic ground state. In this context, if the alternating molecular aggregation of the biradical and monoradical entities in **1** is made in the crystal, the non-magnetic ground state found in the susceptibility measurement is attributable to one of the exotic ground spin states that have been predicted in the theoretical model (Fig. 1) of the generalized ferrimagnetic spin assemblage. Another explanation of the non-magnetic ground state found for **1** is in possible interchain antiferromagnetic interactions.

Even when the single chain of **1** has the generalized ferrimagnetic spin alignment, interchain antiferromagnetic interactions bring about cancellation of magnetic moments as found in a ferrimagnetically short-range ordered chain [4]. The crystal structure analysis of **1** is currently underway in order to verify the occurrence of the generalized ferrimagnetism for **1** in the solid state.

4. Conclusion

The iminonitroxide triradical and biradical compounds **1** and **2** were synthesized by deoxygenation of the corresponding nitronylnitroxide radicals **3** and **4**, respectively. From the magnetic susceptibility measurements for **2**, the intramolecular exchange interaction within the *para*-phenylene-based biradical moiety has been found to be antiferromagnetic with the singlet–triplet energy gap of $2J(\pi)/k_B = -30.8$ K. The magnetic susceptibility of **1** in the crystalline solid state is indicative of the possible occurrence of an exotic non-magnetic ground state as predicted in the theory of generalized ferrimagnetism [3]. The occurrence of the non-magnetic ground state arises from the internal magnetic degree of freedom in the organic biradical and the multicentered intermolecular interactions, both of which have been neglected in conventional atom-based magnetics. The internal magnetic degree of freedom and the multicentered nature are essential in organic molecular-based magnetics.

5. Supplementary material

Full crystallographic details, excluding structure factors, have been deposited at the Cambridge Crystallographic Data Centre (http://www.ccdc.cam.ac.uk/). Any request to the CCDC for this material should quote the full literature citation and the deposition number CCDC No.: 249891. Copies of this information may be obtained free of charge from the Director, CCDC, 12 Union Road, Cambridge, CB2 1EZ, UK (fax: +44 1223 336033; e-mail: deposit@ccdc.cam.ac.uk or www: http://www.ccdc.cam.ac.uk/).

Acknowledgments

This work has been supported by Grants-in-Aid for Scientific Research from the Ministry of Education, Sports, Culture, Science and Technology, Japan. Financial support from PRESTO of Japan Science and Technology Agency (JST) is also acknowledged.

References

[1] For reviews of molecule-based magnetics, see:
(a) D. Gattesehi, O. Kahn, J.S. Miller, F. Palacio (Eds.), Molecular Magnetic Materials, KIuwer Academic, Dordrecht, 1991;
(b) H. Iwamura, J.S. Miller (Eds.), Mol. Cryst. Liq. Cryst. 232/233 (1993) 1-360, /1-366;
(c) J.S. Miller, A.J. Epstein (Eds.), Mol. Cryst. Liq. Cryst. 271–274 (1995) 1-216, /1-222/1-218/1-226;
(d) K. Itoh, J.S. Miller, T. Takui (Eds.), Mol. Cryst. Liq. Cryst. 305/306 (1997) 1-520, /1-586;
(e) O. Kahn (Ed.), Mol. Cryst. Liq. Cryst. 334/335 (1999) 1-706, /1-712;
(f) P.M. Lahti (Ed.), Magnetic Properties of Organic Materials, Marcel Dekker, New York, 1999;
(g) K. Itoh, M. Kinoshita (Eds.), Molecular Magnetism: New Magnetic Materials, Gordon & Breach, Amsterdam, 2000 (Kodansha as copublisher, Tokyo);
(h) G. Christou (Ed.), Polyhedron 20 (2001) 1115.
[2] (a) M. Tamura, Y. Nakazawa, D. Shiomi, K. Nozawa, Y. Hosokoshi, M. Ishikawa, M. Takahashi, M. Kinoshita, Chem. Phys. Lett. 186 (1991) 401;
(b) Y. Nakazawa, M. Tamura, N. Shirakawa, D. Shiomi, M. Takahashi, M. Kinoshita, M. Ishikawa, Phys. Rev. B 46 (1992) 8906.
[3] D. Shiomi, K. Sato, T. Takui, J. Phys. Chem. B 105 (2001) 2932.
[4] (a) D. Shiomi, T. Kanaya, K. Sato, M. Mito, K. Takeda, T. Takui, J. Am. Chem. Soc. 123 (2001) 11823;
(b) T. Kanaya, D. Shiomi, K. Sato, T. Takui, Polyhedron 20 (2001) 1397;
(c) D. Shiomi, M. Nishizawa, K. Kamiyama, S. Hase, T. Kanaya, K. Sato, T. Takui, Synth. Met. 121 (2001) 1810;
(d) C. Kaneda, D. Shiomi, K. Sato, T. Takui, Polyhedron 22 (2003) 1809;
(e) D. Shiomi, C. Kaneda, T. Kanaya, K. Sato, T. Takui, Appl. Magn. Reson. 23 (2003) 495.
[5] T. Ise, D. Shiomi, K. Sato, T. Takui, Synth. Met., in press.
[6] CRYSTALSTRUCTURE (ver. 3.6.0): Rigaku/Molecular Structure Corporation (2000–2004), 9009 New Trails Dr. The Woodlands, TX 77381, USA.
[7] B.D. Bleany, K. Bowers, Proc. R. Soc. Lond. A 214 (1952) 451.
[8] (a) P. Wautelet, L. Catala, A. Bieber, P. Turek, J.-J. Andre, Polyhedron 20 (2001) 1571;
(b) P. Wautelet, A. Bieber, P. Turek, J. Le Moigne, J.-J. Andre, Mol. Cryst. Liq. Cryst. 305 (1997) 55;
(c) L. Catala, J. Le Moigne, N. Kyritsakas, P. Rey, J.J. Novoa, P. Turek, Chem. Eur. J. 7 (2001) 2466.
[9] T. Ise, D. Shiomi, K. Sato, T. Takui, Chem. Mater., in press.

progress in terms of faculty of quantum chemistry computation enables us to run large size calculations. Not only accretion of CPU speed but also evolution of parallel execution are enable us to run huge MO calculations easily. Thus, we can apply theoretical calculation to large number of cluster size with sufficient numerical accuracy.

2. Molecular structures and calculation detail

The TTF-based donor salts are very familiar and important. Here, we employ the κ-$BETS_2FeCl_4$ crystal as one of the very interesting crystals that have been reported by many scientists. The X-ray structural study was measured in room temperature ($T = 295$ K) as experimental condition, although we have to employ the structural data for lower temperature [1,12]. Simple representation of BETS layers in κ-phases crystal was depicted in Fig. 1. In this figure, dimerized BETS pairs in two-dimensional donor sheet are found. Roman-face numbers (1, 2, 3,...) indicate each BETS molecule and italic-face alphabets (*A*, *B*, *p*, *q*) and numbers (*1*, *2*, *3*) indicate inter-molecule $J_{ab(M)}$ and inter-dimer $J_{ab(D)}$, respectively [13,14].

In this figure, some of clusters (i), (ii), (iii) and (iv) are worth studying. Cluster (i) has four BETS molecules with two holes and is a suitable model to investigate inter-dimer $J_{ab(D)}$ values. Clusters 56–78, 12–78 and 12–56 correspond to models for $J_{ab(D)}(n)$ ($n = 1, 2, 3$) values, respectively. In peculiar systems, triangular lattices with competitive antiferromagnetic J_{ab} values are important. Six BETS molecules with three holes are in cluster (ii), though spin frustration does not occur in this BETS complex. One-dimensional chain with periodic condition along this cluster is depicted in cluster (iii). This model is useful to investigate charge and spin density waves. For cluster (iv), larger size clusters are necessary, when eliminating edge-effects. If not only interacting pairs but also surrounding dimers are introduced in calculations, more accurate values can be given, though we encounter heavy calculations. As the following sections, we mainly discuss clusters (i) and (ii) and propose extended studies for clusters (iii) and (iv).

The effective exchange integrals based on Heisenberg Hamiltonian can describe spin properties. In series of our studies theoretical calculations by using of ab initio molecular orbital (MO) and density functional (DFT) methods were carried out [11]. Our calculations were carried out by GAUSSIAN-98 program packages, besides of periodic calculation by GAUSSIAN-03 Rev.C02 [15]. We used the simple basis sets included in Gaussian program packages. Moreover, our previous calculations

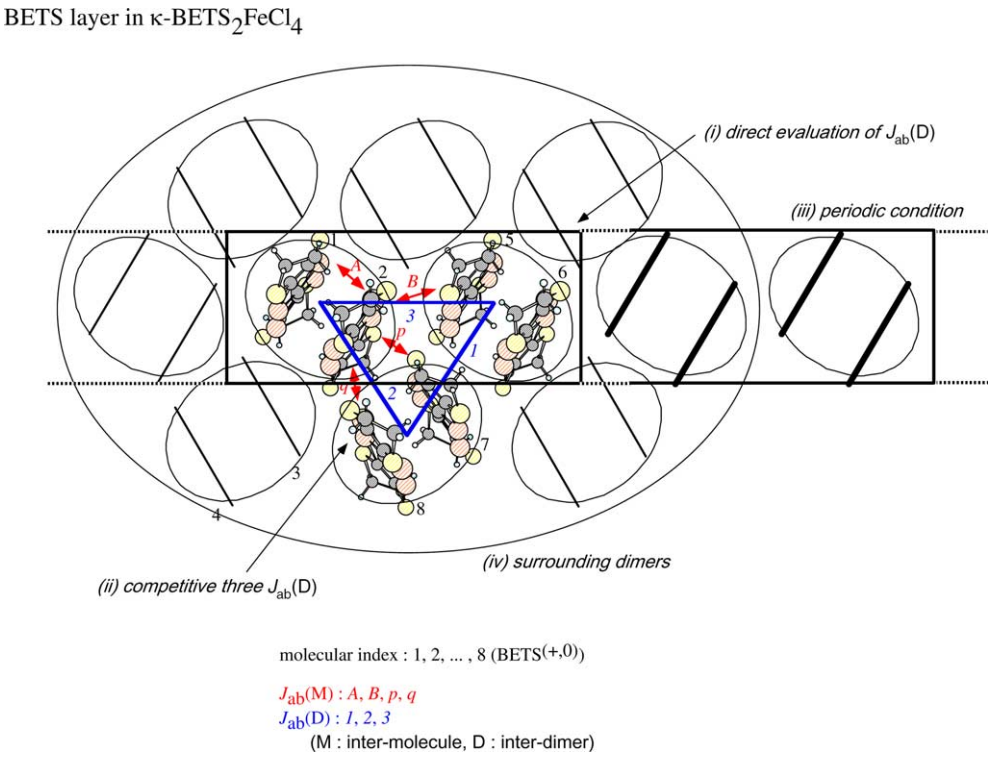


Fig. 1. Simple representation of BETS layers in κ-$BETS_2FeCl_4$ crystal. Roman-face numbers (1, 2, 3, ...) indicate each BETS molecule and italic-face alphabets (*A*, *B*, *p*, *q*) and numbers (*1*, *2*, *3*) indicate inter-molecule $J_{ab(M)}$ and inter-dimer $J_{ab(D)}$, respectively. Some of clusters (i), (ii), (iii) and (iv) are worth studying.

were concluded that our selection of the 6-31G basis set is suitable for these cases.

3. Theoretical background

In series of our studies, effective exchange integrals (J_{ab}) successfully describe magnetic interaction. The magnetic interaction between two localized electrons is usually described by the Heisenberg-type spin coupling Hamiltonian

$$H(HB) = -\sum 2J_{ab}S_a \cdot S_b, \tag{1}$$

where J_{ab} is the orbital-averaged effective exchange integral between the ath and bth sites with total spin operators S_a and S_b. Recent development of the ab initio computational techniques has made it possible to calculate the J_{ab} values directly. Broken-symmetry (BS) approach with the spin projected scheme [16], which eliminates the spin contamination problem, can evaluate J_{ab} values with the following equation:

$$J_{ab}^{(1)} = \frac{^{LS}E(X) - {}^{HS}E(X)}{^{HS}\langle S^2\rangle - {}^{LS}\langle S^2\rangle}, \tag{2}$$

where $^{Y}E(X)$ and $^{Y}\langle S_2\rangle(X)$ denote, respectively, total energy and total spin angular momentum for the spin state Y by the computational methods X.

Here, inter-molecule $J_{ab(M)}$ between two donor cations (namely, 2 holes in 2 molecules) and inter-dimer $J_{ab(D)}$ between two donor dimers (namely, 2 holes in 4 molecules) are defined as shown in Fig. 2(a). In our previous papers, we assume that $J_{ab(D)}$ values are related to $J_{ab(M)}$ values as the following equation (see our paper [11] in detailed).

$$J_{ab(D)} \cong \frac{1}{2}J_{ab(M)}(M_2M_3). \tag{3}$$

Here, we assume localization of spins in inner molecule (M_2,M_3) in system ($(M_1M_2)^{+}$–$(M_3M_4)^{+}$). However, in this assumption the interaction between two HOMOs from only inner molecules cannot describe whole of interaction $J_{ab(D)}$ as shown in Fig. 2(b). Thus, this procedure is remarkably insufficient to evaluate $J_{ab(D)}$ values. On the other hand, Fig. 2(c) shows that interaction between two MOs made from two HOMOs in each dimer ($(BETS_2)^{+\cdot}$) reproduces $J_{ab(D)}$ values correctly.

4. Detailed theoretical calculations

4.1. Direct evaluation of inter-dimer $J_{ab(D)}$ values

In this section, we focus on inter-dimer interaction in cluster (i) in Fig. 1, though all the results of these values were already reported : $J_1 = J_2 = -40.0\ cm^{-1}$ and $J_3 = -103.5\ cm^{-1}$ ($J_{ab(D)}(n) = J_n$) [11]. These values were reproduced from the calculated $J_{ab(M)}$ values with Eq. (3). In this paper, more extended treatment for $J_{ab(D)}$ is carried out. Now, our treatment is started for molecular pairs (12–56).

If we introduce two holes in four molecules ($(BETS_2)^{+\cdot}$–$(BETS_2)^{+\cdot}$), many types of spin structure

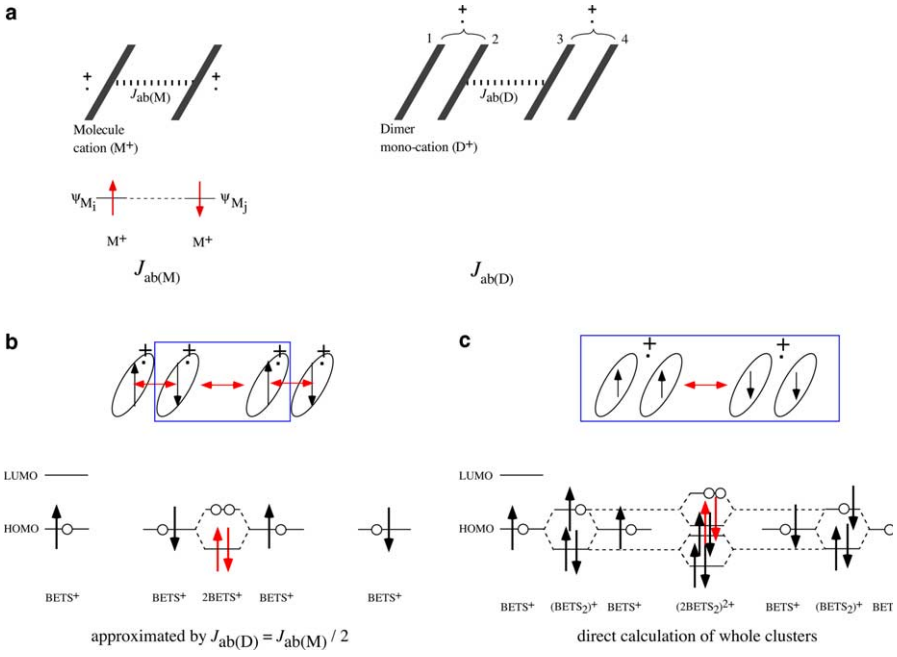


Fig. 2. (a) Simple illustration of inter-molecule $J_{ab(M)}$ and inter-dimer $J_{ab(D)}$ values. (b) Interaction between two HOMOs from only inner molecules contributes to $J_{ab(D)}$. (c) Interaction between two MOs made from two HOMOs in each dimer reproduces $J_{ab(D)}$.

are candidates for suitable magnetic interaction. In Fig. 3 several charge and spin density structure was illustrated. Initially, four types of spin structure +0–0+ (↑0–0↑, ↑0–0↓), 0+–+0 (0↑–↑0 and 0↑–↓0) were constructed with ab initio calculations. These structure is classified to the localized spin model, where holes exist in inner or outer positions. Ferro- or antiferro-magnetic spin arrangement is constructed in it. In Figs. 4(a) and (b) the obtained spin structure was summarized in order of total energies. These calculations were carried out under suppression of all geometrical symmetry. The UHF/6-31G methods in GAUSSIAN-98 program packages and SCF conversion were controlled in 10^{-5} level. In this threshold, more 1 cm^{-1} numerical accuracy for J values (1 a.u. = 2.194703205×10^5 cm^{-1}) is guaranteed.

However, in UB3LYP method, the localized spin structure is stabilized to the delocalized one during another types of SCF procedure as shown in Fig. 4(c). Each hole is shared in two BETS molecules and delocalized as Fig. 3. From these energy splitting between ↑↑–↑↑ and ↑↑–↓↓ states, J_3 value was successfully evaluated and antiferromagnetic interaction (-16.5 cm^{-1}) was concluded.

In addition, similar procedure was applied to molecular clusters 12–78 and 56–78, and $J_2 = -56.3$ cm^{-1} and $J_1 = -54.9$ cm^{-1} were evaluated as shown in Fig. 5. Though geometrical symmetry in BETS arrangement leads relation $J_2 = J_1$, there was slight difference between the obtained J_2 and J_1 values because of numerical error. If we compare these values to our previous reported values, it is found that all are antiferromagnetic and magnitude of J_3 values are slightly different.

4.2. Competition among J_1, J_2, J_3 interactions

In the previous section, three $J_{ab(D)}$ values could be evaluated in four molecular clusters. Competition among all dimers in two-dimensional BETS sheets is expected and more complicated. Next, in order to explain and understand correlation between three $J_{ab(D)}$ values, let us consider three dimer pairs as cluster (ii) in Fig. 1. Triangle structure is constructed by three types of $J_{ab(D)}$ parameters. For most peculiar example, Tamura and his co-workers reported frustrated spin structure, which is deduced from regular triangle geometry and all antiferromagnetic interaction [17]. In terms of theoretical studies, Yamanaka and his co-workers developed the GHF and GDFT methods that can calculate non-collinear type spins beyond RHF, UHF, etc., methods [18].

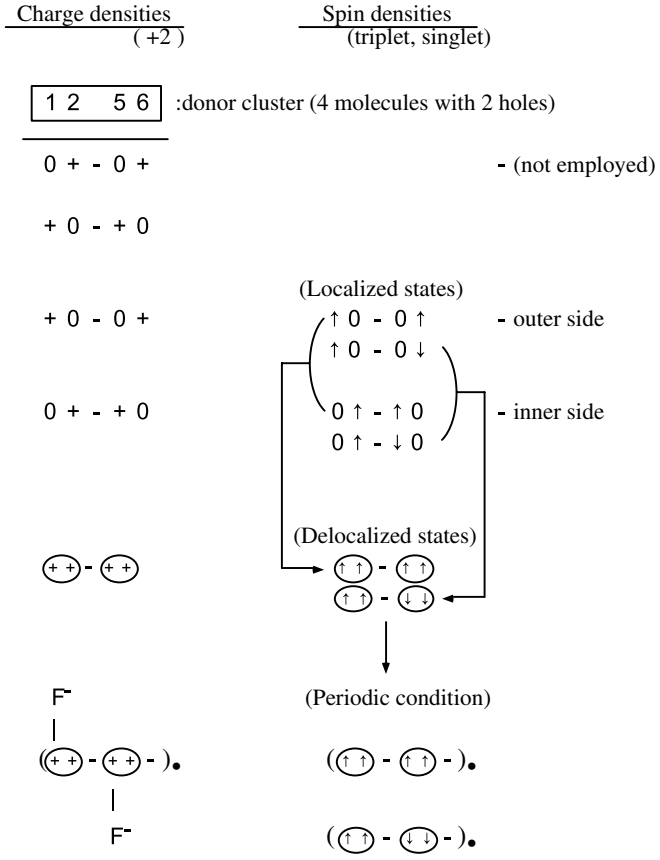


Fig. 3. All charge and spin density structure with localized, delocalized, periodic conditions.

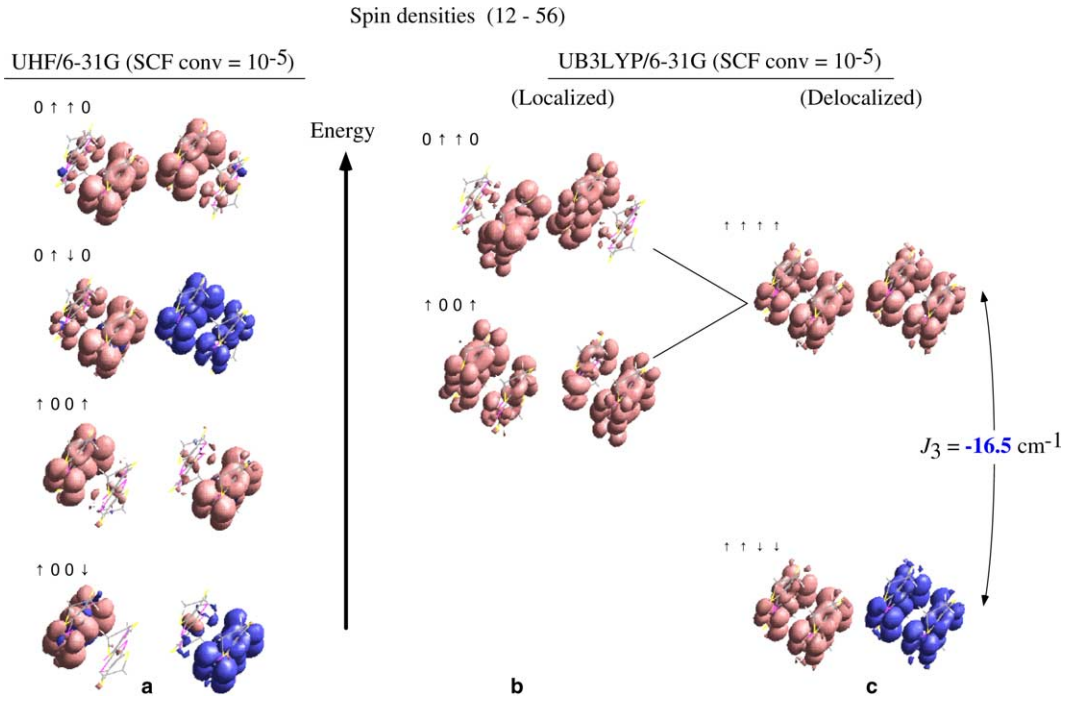


Fig. 4. Localized spin densities for cluster 12–56 by (a) UHF and (b) UB3LYP methods. (c) Delocalized spin densities and J_3 values.

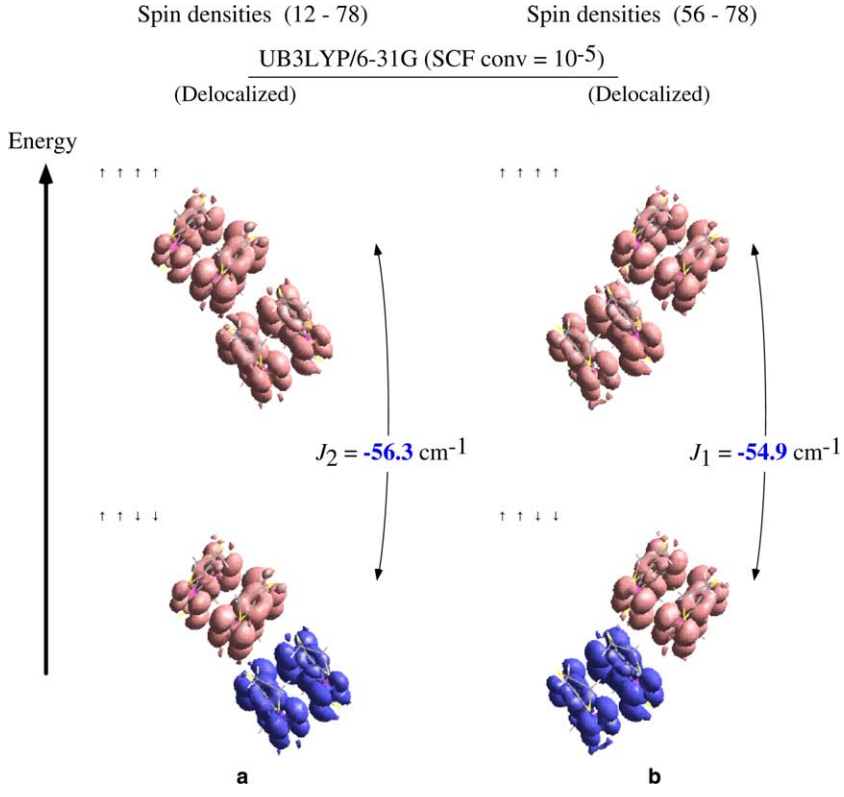


Fig. 5. Delocalized spin densities for cluster (a) 12–78 and (b) 56–78, and J_2 and J_1 values.

Fortunately, in this BETS system such extended treatment is not needed and spin frustration was not reported in experimental studies. All types of well controlled spin structure were illustrated in Fig. 6 by using of UB3LYP methods. In the spin structure, larger spin densities on inner molecules (2, 5, 7) were induced under SCF conversion ($= 10^{-5}$). Applying more tight SCF conversion ($= 10^{-7}$), larger spin densities moved

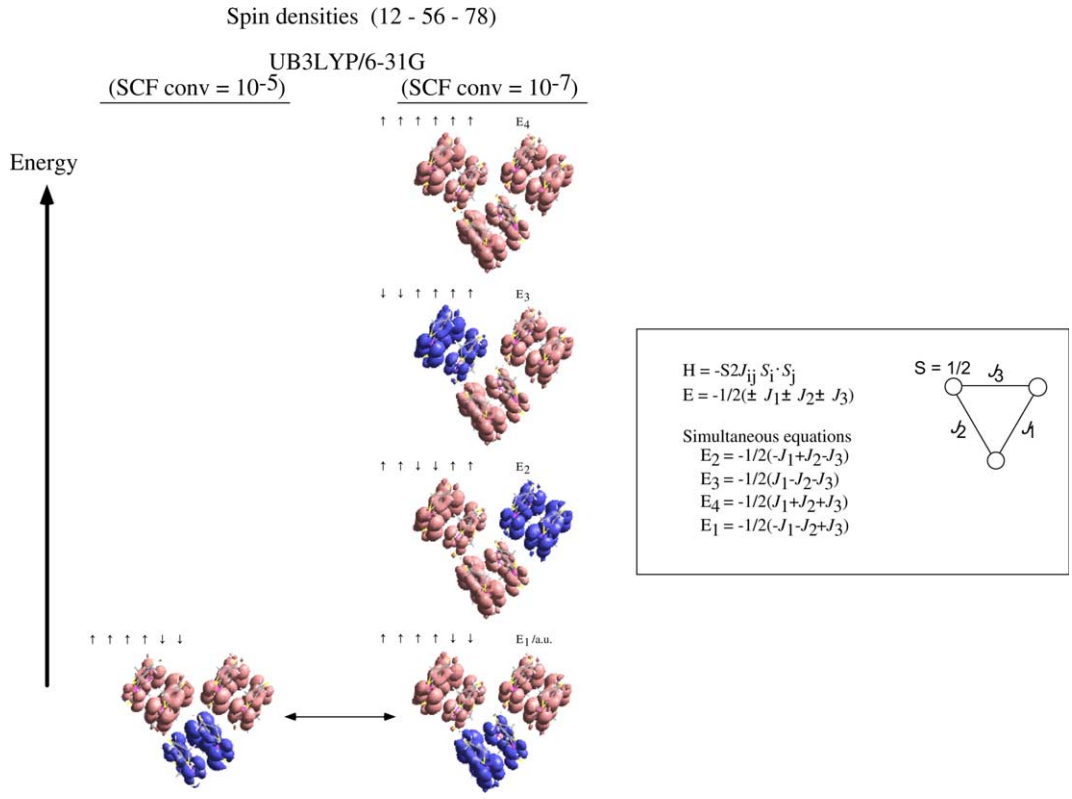


Fig. 6. All types of well controlled spin structure and simultaneous equations for J_1, J_2 and J_3.

to outer molecules (1, 6, 8). We can evaluate all $J_{ab(D)}$ values by solving simultaneous equations with total energy and spin structure. The results are $J_1 = -195.6\ cm^{-1}$, $J_2 = -185.0\ cm^{-1}$ and $J_3 = -174.8\ cm^{-1}$. Differ from the $J_{ab(D)}$ values obtained in the previous section is very large. Since complete delocalization of spins is not realized, large divergence of $J_{ab(D)}$ values appear. We report these values as tentative results and progress more accurate studies.

5. Discussion

Our calculations enabled us to obtain the accurate parameters $J_{ab(D)}$ as inter-dimer magnetic interaction in cluster models of BETS donors. Our direct calculations to large size of clusters were recognized very powerful way to obtain accurate magnetic interaction. The models of four BETS donors with two holes ($(BETS_2)^{+\cdot}$–$(BETS_2)^{+\cdot}$) is very good starting point. From the results, it is found that several spin structure appear and the localized and delocalized spin densities were induced according to calculated condition, such as initial SCF densities, SCF conversion criterion, etc. Three types of $J_{ab(D)}$ parameters, i.e. J_1, J_2 and J_3, were also given with total energies and simultaneous equation for total energy and spin structure.

In two-dimensional networks of BETS molecules, infinite BETS chains exist as cluster (iii) in Fig. 1. Usually, band calculations are most powerful and familiar treatment as well known. However, now we carried out ab initio MO calculation with periodic condition by newly introduced method in GAUSSIAN-03 program packages, though CRYSTAL program packages were used in our previous studies for calbene cluster etc. For example, chain $(12–56)_\infty$ is elongated, where one unit cell exhibits two holes par four BETS molecules as Fig. 3. Here, dummy two F^- anions introduced into unit cell for neutral charges. Both charge and spin density wave are very important physical properties and theoretical calculations for such chains can reveal them in detail. For example, delocalized spin densities in the highest spin ($(\uparrow\uparrow–\uparrow\uparrow)_\infty$) and the lowest spin ($(\uparrow\uparrow–\downarrow\downarrow)_\infty$) states appear in unit cell, where each hole delocalize in two molecules in one dimers.

In addition, calculations for each spin structure surrounding donors give more accurate results, since edge-effects are eliminated and valence between localized and delocalized electronic properties is well controlled. For example, number of molecules in cluster 12–56 with surrounding dimers for J_3 values is 20 as shown cluster (iv) in Fig. 1. In such calculations number of basis sets are very huge and SCF procedure is very difficult. However, we expect that calculations for large donor cluster will be feasible in near future.

Acknowledgements

This work has been supported by a Grant-in-Aid for Scientific Research on Priority Areas (Nos. 14204061 and 15750120) from Ministry of Education, Culture, Sports, Science and Technology, Japan.

References

[1] H. Kobayashi, A. Kobayashi, P. Cassoux, Chem. Soc. Rev. 29 (2000) 325.
[2] H. Akutsu, E. Arai, H. Kobayashi, H. Tanaka, A. Kobayashi, P. Cassoux, J. Am. Chem. Soc. 119 (1997) 12681.
[3] H. Akutsu, K. Kato, E. Ojima, H. Kobayashi, H. Tanaka, A. Kobayashi, P. Cassoux, Phys. Rev. B 58 (1998) 9294.
[4] H. Tanaka, A. Kobayashi, A. Sato, H. Akutsu, H. Kobayashi, J. Am. Chem. Soc. 121 (1999) 760.
[5] S. Uji et al., Nature 410 (2001) 908.
[6] K. Miyagawa, A. Kawamoto, Y. Nakazawa, K. Kanoda, Phys. Rev. Lett. 75 (1995) 1174.
[7] K. Kanoda, Physica C 282–287 (1997) 290.
[8] K. Kanoda, Hyperfine Interact. 104 (1997) 235.
[9] G. Saito, S. Kagoshima (Eds.), The Physics and Chemistry of Organic Superconductors, Springer, Berlin, 1990.
[10] T. Mori, H. Mori, S. Tanaka, Bull. Chem. Soc. Jpn. 72 (1999) 179.
[11] T. Kawakami, T. Taniguchi, S. Nakano, Y. Kitagawa, K. Yamaguchi, Polyhedron 22 (2003) 2051.
[12] H. Kobayashi, H. Tomita, T. Naito, A. Kobayashi, F. Sakai, T. Watanabe, P. Cassoux, J. Am. Chem. Soc. 118 (1996) 368.
[13] C. Hotta, H. Fukuyama, J. Phys. Soc. Jpn. 69 (2000) 2577.
[14] K.D. Carlson, U. Geiser, A.M. Kini, H.H. Wang, L.K. Montgomery, W.K. Kwok, M.A. Beno, J.M. Williams, C.S. Cariss, G.W. Crabtree, Inorg. Chem. 27 (1988) 965.
[15] M.J. Frisch, et al., J. A. Pople, Gaussian, Inc.
[16] T. Soda, Y. Kitagawa, T. Onishi, Y. Takano, Y. Shigeta, H. Nagao, Y. Yoshioka, K. Yamaguchi, Chem. Phys. Lett. 319 (2000) 223.
[17] M. Tamura, R. Kato, J. Phys.: Cond. Matt. 14 (2002) L729.
[18] S. Yamanaka, R. Takeda, T. Kawakami, S. Nakano, D. Yamaki, S. Yamada, K. Nakata, T. Sakuma, T. Takada, K. Yamaguchi, Int. J. Quant. Chem. 95 (2003) 512.

in Sr_2RuO_4 has been discussed in relation to the band structure and spin susceptibility by using a two-dimensional Hubbard model for three bands crossing the Fermi level [19]. The origin of the pairing mechanism has been discussed by two-dimensional Hubbard models with studies of the nature of both the normal and superconducting states.

Recently, we have presented a two-dimensional two-sublattice system, and have investigated two-band effects in magnetism and superconductivity by using a Hubbard model and an extended Hubbard model [20]. We have found that the effective exchange integral is expressed by the square of the on-site repulsion times the effective spin susceptibility. The results suggest that the ferromagnetic order appears by two-band effect. By hole- or electron-doping into the two-band system, antiferromagnetic order appears with disappearing the ferromagnetic order.

In this study, we investigate 4-band effects in magnetism by using the tight-binding model and the Hubbard model. For hole-doping into the system, the spin susceptibility between sites is calculated by using Green's function techniques. We discuss magnetic structure of the hole-doped systems in relation to band structure.

2. Many-band effects in magnetism

In this section, we present a two-dimensional 4-sublattice model and electronic band structures for some parameters in the sublattice model. The expression of spin susceptibility of the sublattice system is derived within the tight-binding approximation. We discuss many-band effects in magnetism of the many-band system in relation to hole- or electron-doping to the sublattice system.

2.1. Two-dimensional 4-sublattice model

In this study, we consider a two-dimensional 4-sublattice model as shown in Fig. 1. Hamiltonian within the tight-binding approximation of this system is written as

$$H_0 = \sum_{\boldsymbol{k},\sigma} \sum_{i,j=1}^{4} t_{ij}(\boldsymbol{k}) a^{\dagger}_{\boldsymbol{k}i\sigma} a_{\boldsymbol{k}i\sigma}, \tag{1}$$

where

$$t_{12}(\boldsymbol{k}) = 2t_{12} \cos\frac{k_x}{2} \exp\left(\mathrm{i}\frac{k_x}{2}\right), \tag{2}$$

$$t_{13}(\boldsymbol{k}) = 4t_{13} \cos\frac{k_x}{2} \cos\frac{k_y}{2} \exp\left(\mathrm{i}\frac{k_x}{2}\right) \exp\left(-\mathrm{i}\frac{k_y}{2}\right), \tag{3}$$

$$t_{14}(\boldsymbol{k}) = 2t_{14} \cos\frac{k_y}{2} \exp\left(-\mathrm{i}\frac{k_y}{2}\right), \tag{4}$$

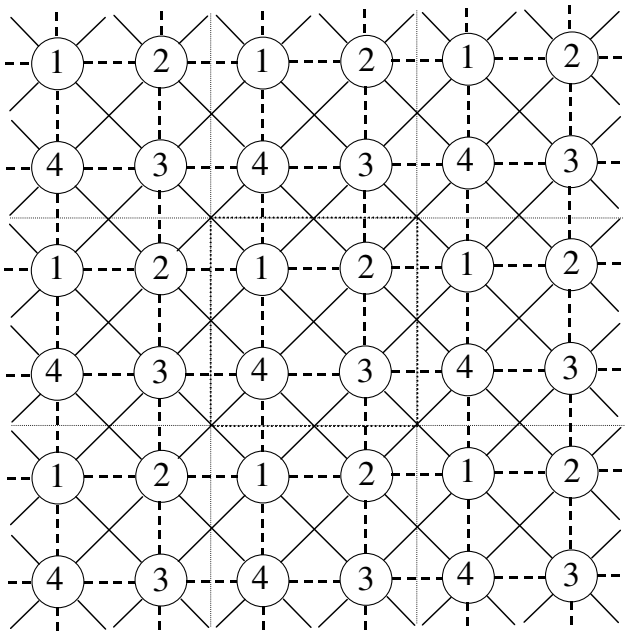


Fig. 1. Two-dimensional 4-sublattice system. The unit cell is composed of 4 sites. Transfer integral between sublattices i and j is t_{ij}.

$$t_{23}(\boldsymbol{k}) = 2t_{23} \cos\frac{k_y}{2} \exp\left(-\mathrm{i}\frac{k_y}{2}\right), \tag{5}$$

$$t_{24}(\boldsymbol{k}) = 4t_{24} \cos\frac{k_x}{2} \cos\frac{k_y}{2} \exp\left(-\mathrm{i}\frac{k_x}{2}\right) \exp\left(-\mathrm{i}\frac{k_y}{2}\right), \tag{6}$$

$$t_{34}(\boldsymbol{k}) = 2t_{34} \cos\frac{k_x}{2} \exp\left(-\mathrm{i}\frac{k_x}{2}\right). \tag{7}$$

t_{ij} $(i \neq j)$ is a transfer integral between the sublattices, and $t_{ji} = t^{*}_{ij}$. t_{ii} means a potential energy in each sublattice. Band structures of three cases in two-dimensional 4-sublattice system are shown in Fig. 2.

2.2. Spin susceptibility

In this subsection, we derive the expression of the spin susceptibility between sites within tight-binding approximation. From Eq. (1), the Green function for each band is written as

$$G_i(\boldsymbol{k}, \mathrm{i}\omega) = \frac{|\mathrm{i}\boldsymbol{k}\rangle\langle\mathrm{i}\boldsymbol{k}|}{\mathrm{i}\omega - \varepsilon_i(\boldsymbol{k})}. \tag{8}$$

Using the above equation and LCAO coefficients for site in sublattice, we obtain the Green function for site in sublattice as

$$g_{rs}(\boldsymbol{k}, \mathrm{i}\omega) = \sum_{i=1}^{4} \frac{\langle r|\mathrm{i}\boldsymbol{k}\rangle\langle\mathrm{i}\boldsymbol{k}|s\rangle}{\mathrm{i}\omega - \varepsilon_i(\boldsymbol{k})}. \tag{9}$$

From the above equation, the zz component of the spin susceptibility between sites is written as

$$\chi^{0}_{rs}(\boldsymbol{k}, \mathrm{i}\omega) = -\frac{1}{2}(g\mu_{\mathrm{B}})^2 F_{rs}(\boldsymbol{k}, \mathrm{i}\omega) \tag{10}$$

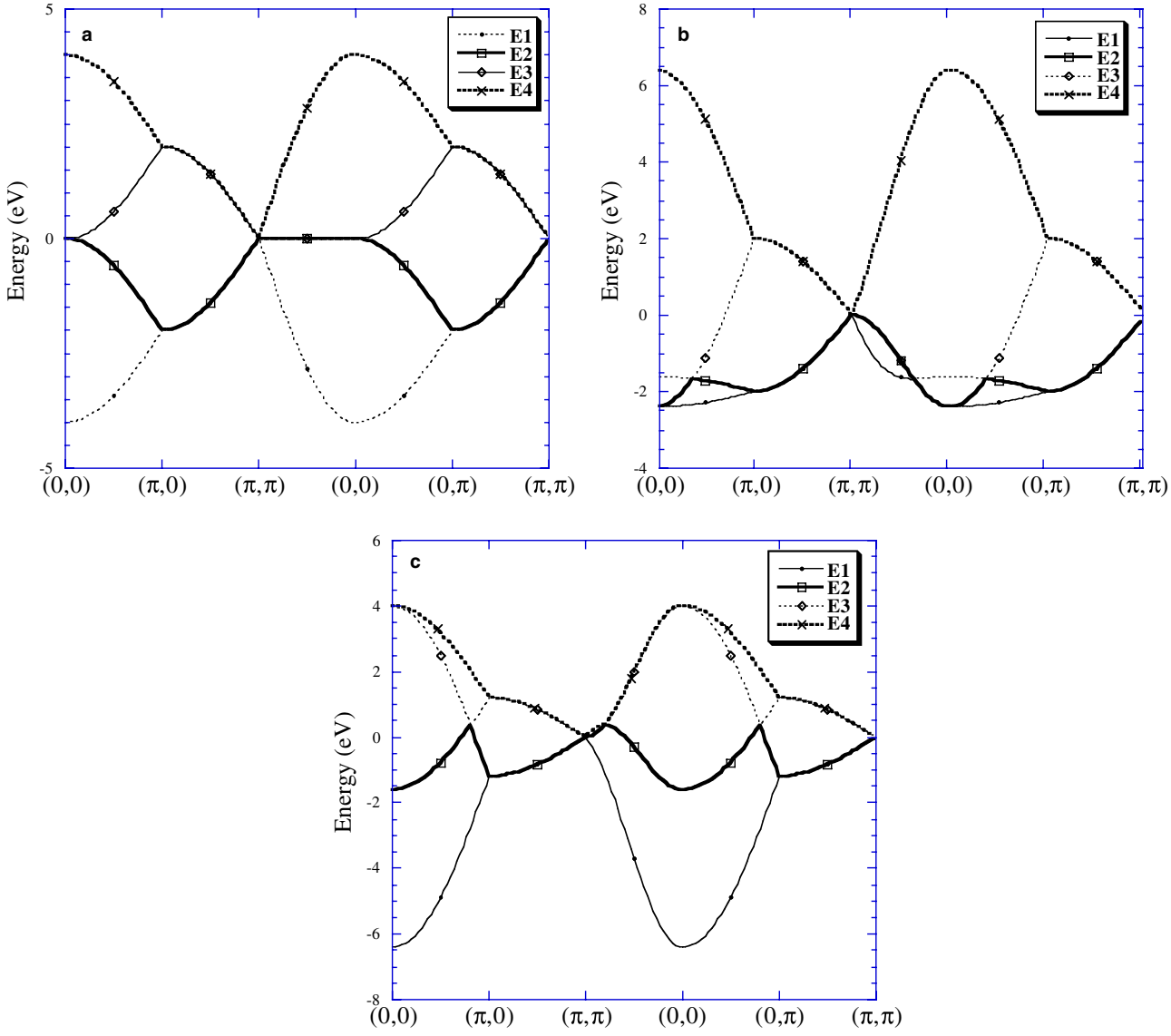


Fig. 2. Band structures: (a) $t_{12} = t_{14} = t_{23} = t_{34} = -1.0$ (eV), and other parameters are zero. This parameter set corresponds to square lattice system. The system is half-filling at $\mu = 0$; (b) $t_{13} = t_{24} = 0.6$, $t_{12} = t_{14} = t_{23} = t_{34} = -1.0$ (eV), and four potential energies are zero. Half-filling is at $\mu = -0.4$ eV. Fermi surface crosses three bands at half-filling. Some molecular crystals have similar band structure of this case; (c) $t_{13} = t_{24} = -1.0$, $t_{12} = t_{14} = t_{23} = t_{34} = 0.6$ (eV), and others are zero. Half-filling at $\mu = 0.18$ eV. Fermi surface crosses two-bands at half-filling.

with

$$F_{rs}(\boldsymbol{k}, \mathrm{i}\omega) = T \sum_{\boldsymbol{p}\nu} g_{rs}(\boldsymbol{p}, \mathrm{i}\nu) g_{sr}(\boldsymbol{p}+\boldsymbol{k}, \mathrm{i}\nu + \mathrm{i}\omega), \tag{11}$$

where r and s indicate site label in the unit cell as shown in Fig. 1. T is temperature, and g and μ_B are g-factor (=2.0023) and the Bohr magneton (=$|e|/2mc$), respectively. By summing over the Mastubara frequency ν, the spin susceptibility of Eq. (10) becomes

$$\chi^0_{rs}(\boldsymbol{k}, \mathrm{i}\omega) = -\frac{(g\mu_B)^2}{2} \sum_{\boldsymbol{p}} \sum_{i,j=1}^{4} \left[f(\varepsilon_i(\boldsymbol{p}+\boldsymbol{k})) - f(\varepsilon_j(\boldsymbol{p})) \right] \times \frac{\langle r|\mathrm{i}\boldsymbol{p}+\boldsymbol{k}\rangle\langle \mathrm{i}\boldsymbol{p}+\boldsymbol{k}|s\rangle\langle s|\mathrm{j}\boldsymbol{p}\rangle\langle \mathrm{j}\boldsymbol{p}|r\rangle}{\varepsilon_i(\boldsymbol{p}+\boldsymbol{k}) - \varepsilon_j(\boldsymbol{p}) - \mathrm{i}\omega}, \tag{12}$$

where f is the Fermi distribution function.

Fig. 3 shows the spin susceptibilities between sites $\mathrm{Re}\chi^0_{rs}(\boldsymbol{k}, \omega = 0)$ obtained from numerical calculations of Eq. (12) in the case of Fig. 2(a). Fig. 3(a) shows the real part of the spin susceptibility at half-filling. We find that χ^0_{11} for the same sublattice is positive with two sharp peaks at (0,0) and (π,π). The χ^0_{11} suggests that the direction of spin is parallel to the same site of other unit cells. From the spin susceptibility χ^0_{13} between sites 1 and 3, we can know that the direction of spins between diagonal states in unit cells is also parallel at half-filling. On the other hand, the spin susceptibility χ^0_{12} between nearest neighbor sites becomes negative, that is antiferromagnetic. Therefore, from Fig. 3(a), we find long-range antiferromagnetic order at half-filling.

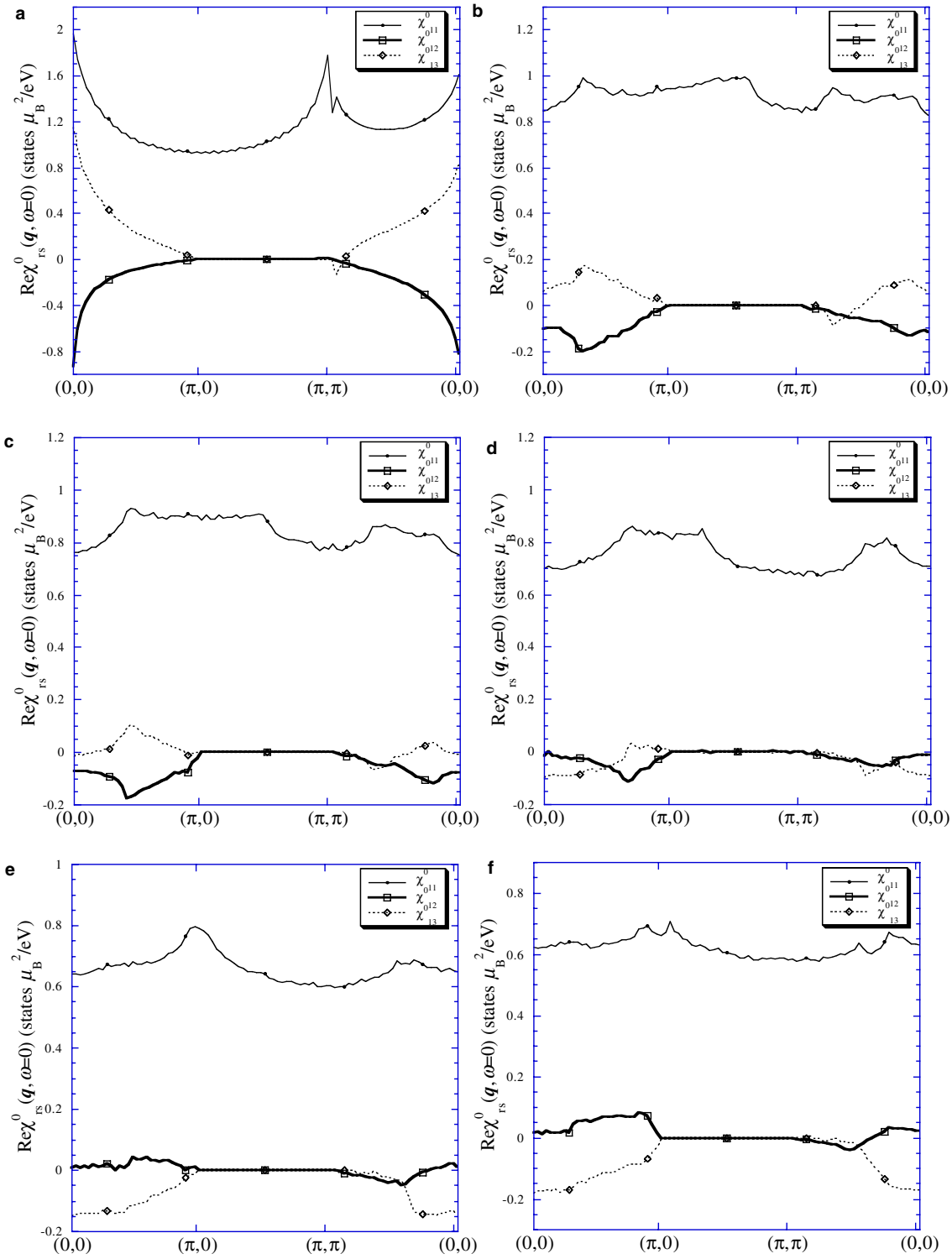


Fig. 3. Spin susceptibility in case $t_{12} = t_{14} = t_{23} = t_{34} = -1.0$ (eV) and others are zero: (a) spin susceptibility $\mathrm{Re}\chi^0_{rs}(\boldsymbol{q}, \omega = 0)$ at half-filling ($\mu = 0$); (b) $\mu = -0.5$ eV. The number of doped hole n_h away from half-filling per unit cell is 0.75; (c) $n_h = 1$ ($\mu = -2/3$); (d) $n_h = 1.5$ ($\mu = -1$); (e) $n_h = 2$ ($\mu = -4/3$); (f) $n_h = 2.25$ ($\mu = -1.5$).

Figs. 3(b)–(f) show the spin susceptibility of the system doped with holes away from half-filling. In Fig. 3(b), we find peaks around (π/3,0), (π,2π/3), and (2π/3,2π/3). These peaks arise from Fermi momenta of the hole-doped system. As increasing hole-doping, the spin susceptibilities of hole-doped system becomes smaller than those of half-filling as shown in Figs. 3(b) and (c). In Fig. 3(d), we can find region where the spin susceptibility between

diagonal sites becomes negative. The results as shown in Fig. 3(d) suggest that when we focus spin of a sublattice, the direction of spin of other sublattice is antiparallel except for the same site. In Fig. 3(e), we can find that the spin susceptibility between diagonal sites becomes negative and that χ^0_{12} almost vanishes. These results suggest that there is only antiferromagnetic spin correlation between diagonal sites. In Fig. 3(f), the spin susceptibilities of χ^0_{11} and χ^0_{12} are positive, and χ^0_{13} becomes negative. We can know ferromagnetic order along x-axis or y-axis, and also find antiferromagnetic order along orthogonal direction to the ferromagnetic order. From Fig. 3, we can find long-range antiferromagnetic order in the square lattice system around half-filling, and that the long-range antiferromagnetic order disappears in the case of hole-doped system. Interesting spin states appears, when the system is doped with holes.

2.3. Many-band systems

Next, we consider 4-band systems as shown in Figs. 2(b) and (c). Fig. 4 shows the spin susceptibilities of hole-doped system with the band structure as shown in Fig. 2(b). We find two peaks with negative value around $(0,3\pi/2)$ and $(3\pi/2,3\pi/2)$ in the spin susceptibility between diagonal sites as shown in Fig. 4(c), and from Fig. 4, we expect that the spin correlation of the system around half-filling weakly becomes almost antiferromagnetic. As increasing hole-doping, the system has antiferromagnetic order around chemical potential of $\mu = -1.0$. Fig. 5 shows the spin susceptibilities of the system as shown in Fig. 2(c). At half-filling, χ^0_{11} is positive in all region. On the other hand, χ^0_{12} and χ^0_{13} become negative around point (0,0). From Figs. 4 and 5, we can expect that magnetic properties of many-band system doped with hole become more complex and interesting than those of single- or two-band system.

2.4. Effective interactions and effective spin susceptibility in Hubbard model

In previous subsections, we have investigated the spin susceptibility of 4-band system doped with hole. From the spin susceptibility, we can know some physical

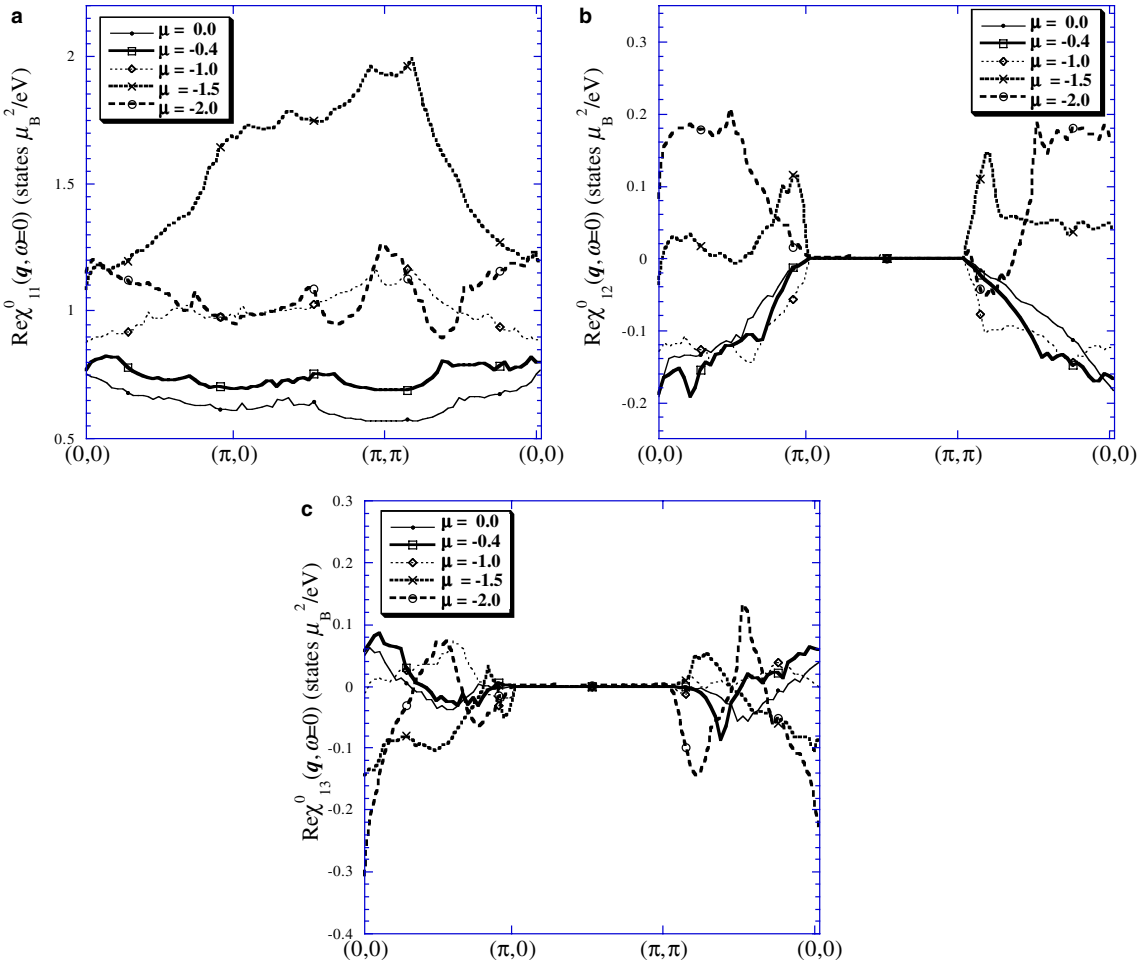


Fig. 4. Dependency of spin susceptibility on hole-doping in case $t_{13} = t_{24} = 0.6$, $t_{12} = t_{14} = t_{23} = t_{34} = -1.0$ (eV), and four potential energies are zero: (a) spin susceptibility $\chi^0_{11}(\boldsymbol{q})$; (b) spin susceptibility $\chi^0_{12}(\boldsymbol{q})$; (c) spin susceptibility $\chi^0_{13}(\boldsymbol{q})$.

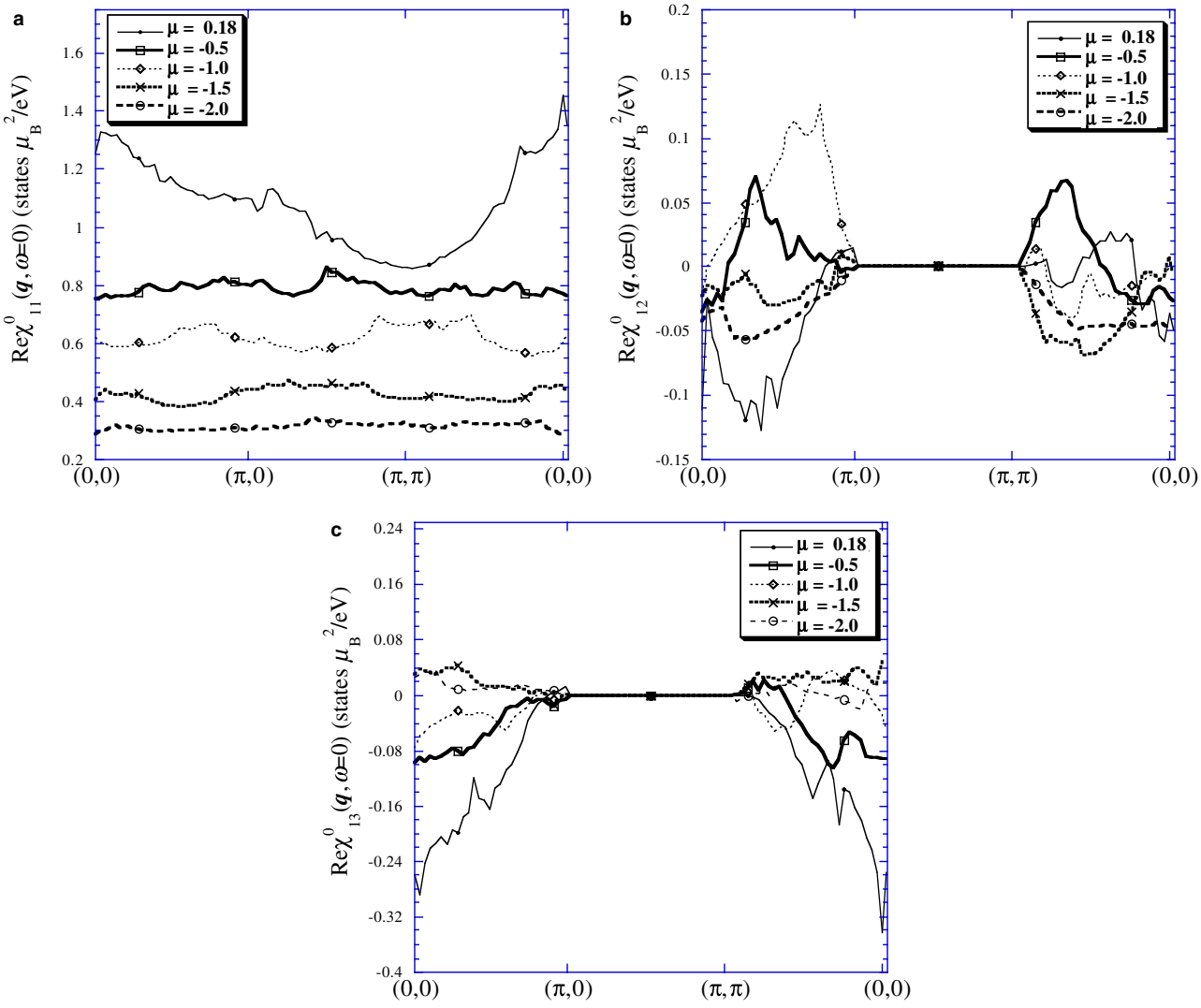


Fig. 5. Dependency of spin susceptibility on hole-doping in case $t_{13} = t_{24} = -1.0$, $t_{12} = t_{14} = t_{23} = t_{34} = 0.6$ (eV), and others are zero: (a) spin susceptibility $\chi^0_{11}(\boldsymbol{q})$; (b) spin susceptibility $\chi^0_{12}(\boldsymbol{q})$; (c) spin susceptibility $\chi^0_{13}(\boldsymbol{q})$.

properties such as effective interactions, magnetic properties and so on. In this subsection, we derive expressions of effective interactions by using the spin susceptibility within the random-phase approximation (RPA).

Effective interaction $V^{\sigma-\sigma}_{\text{eff}}(\boldsymbol{q})$ is written as

$$\begin{aligned} V^{\sigma-\sigma}_{\text{eff}}(\boldsymbol{q}) &= U + U\chi^0(\boldsymbol{q})U\chi^0(\boldsymbol{q})U \\ &\quad + U\chi^0(\boldsymbol{q})U\chi^0(\boldsymbol{q})U\chi^0(\boldsymbol{q})U\chi^0(\boldsymbol{q})U + \cdots, \\ &= U + U\chi^0(\boldsymbol{q})U\chi^0(\boldsymbol{q})V^{\sigma-\sigma}_{\text{eff}}(\boldsymbol{q}), \\ &= \left[1 - U\chi^0(\boldsymbol{q})U\chi^0(\boldsymbol{q})\right]^{-1}U, \end{aligned} \tag{13}$$

where U is a diagonal matrix ($U_{rs} = U_r\delta_{rs}$), and $\chi^0(\boldsymbol{q})$ is a matrix consisting of matrix element $\chi^0_{rs}(\boldsymbol{q})$. U_r means on-site coulomb potential at r-th site. Diagonal elements of $V^{\sigma-\sigma}_{\text{eff}}(\boldsymbol{q})$ mean the effective on-site coulomb potential.

By the similar procedure, we have effective interaction $V^{\sigma\sigma}_{\text{eff}}(\boldsymbol{q})$;

$$V^{\sigma\sigma}_{\text{eff}}(\boldsymbol{q}) = \left[1 - U\chi^0(\boldsymbol{q})U\chi^0(\boldsymbol{q})\right]^{-1}U\chi^0(\boldsymbol{q})U. \tag{14}$$

Note that diagonal elements of the matrix $V^{\sigma\sigma}_{\text{eff}}(\boldsymbol{q})$ always vanish.

Effective spin susceptibility $\chi(\boldsymbol{q})$ is also easily shown by the similar procedure.

$$\chi(\boldsymbol{q}) = \chi^0(\boldsymbol{q})\left[1 - U\chi^0(\boldsymbol{q})U\chi^0(\boldsymbol{q})\right]^{-1}. \tag{15}$$

From Eqs. (13) and (14), we can approximately derive an expression of the effective exchange integral J in the Heisenberg model. Recently, several computational methods of J have been presented [21–28]. We can approximately define the expression of the effective exchange integral $J^{\text{eff}}_{ab}(\boldsymbol{q})$ as

$$J^{\text{eff}}_{ab}(\boldsymbol{q}) = \left(V^{\sigma-\sigma}_{\text{eff}}(\boldsymbol{q}) - V^{\sigma\sigma}_{\text{eff}}(\boldsymbol{q})\right)_{ab} \tag{16}$$

$$= \frac{1}{2}\left(V^{\sigma-\sigma}_{\text{eff}}(\boldsymbol{q})\left[1 - \chi^0(\boldsymbol{q})U\right]\right)_{ab}. \tag{17}$$

Using Eq. (15), we can rewrite Eq. (17) as

$$J_{ab}^{\mathrm{eff}}(\boldsymbol{q}) = \left(\left[\chi^0(\boldsymbol{q}) \right]^{-1} \chi(\boldsymbol{q}) U \left[1 - \chi^0(\boldsymbol{q}) U \right] \right)_{ab}. \tag{18}$$

From the above equation, we can find that the effective exchange integral is proportional to the effective spin susceptibility between sublattices.

3. Concluding remarks

We have presented a two-dimensional 4-sublattice square lattice system and have investigated 4-band effects in magnetism by using spin susceptibility. The spin susceptibility of the sublattice system has been calculated, and the expression of the effective exchange integral in Heisenberg model has been derived within the random-phase approximation by using Hubbard model and the spin susceptibility. The effective exchange interaction arises from the spin susceptibility and the on-site coulomb interaction.

The present results suggest that in many-band system doped with hole, we can expect new magnetic properties or new magnetic state. We also expect that new magnetic properties arise from many-band effect in systems with spin frustration such as kagome lattice, triangular lattice, and so on. The many-band effect in hole-doped systems with spin frustration will be presented elsewhere [29].

Acknowledgements

H.N. is grateful for a financial support of the Ministry of Education, Science and Culture of Japan (Research No. 15550010). The author thanks Profs. K. Yamaguchi, and K. Nishikawa, Drs. H. Kawabe and T. Yoshimoto for their continued encouragement and helpful discussion.

References

[1] J. Nagamatsu, N. Nakamura, T. Muranaka, Y. Zentani, J. Akimitsu, Nature 410 (2001) 63.
[2] H. Suhl, B.T. Matthias, R. Walker, Phys. Rev. Lett. 3 (1959) 552.
[3] J. Kondo, Prog. Theor. Phys. 29 (1963) 1.
[4] H. Nagao, M. Nishino, Y. Shigeta, Y. Yoshioka, K. Yamaguchi, J. Chem. Phys. 113 (2000) 11237.
[5] N. Kristoffel, T. Örd, K. Rago, Europhys. Lett. 61 (2003) 109.
[6] H. Nagao, A.M. Yaremko, S.P. Kruchinin, K. Yamaguchi, in: J.F. Annett, S.P. Kruchinin (Eds.), New trends in superconductivity, NATO science series, II mathematics, physics and chemistry, vol. 67, Kluwer Academic Publishers, 2002, p. 155.
[7] H. Nagao, H. Kawabe, S.P. Kruchinin, D. Manske, K. Yamaguchi, Mod. Phys. Lett. B 17 (2003) 423.
[8] H. Nagao, M. Nishino, M. Mitani, Y. Yoshioka, K. Yamaguchi, Int. J. Quantum Chem. 65 (1997) 947.
[9] H. Nagao, M. Mitani, M. Nishino, Y. Shigeta, Y. Yoshioka, K. Yamaguchi, Int. J. Quantum Chem. 75 (1999) 549.
[10] J. Kondo, J. Phys. Soc. Jpn. 71 (2002) 1353.
[11] J.G. Bednorz, K.A. Mülller, Z. Phys. B 64 (1986) 189.
[12] D.M. Ginzberg, Physical Properties of High Temperature Superconductors, vols. 1–4, World Scientific, Singapore, 1990, 1992, 1994, 1996.
[13] Z.-X. Shen et al., Phys. Rev. Lett. 70 (1993) 1553.
[14] D.J. Scalapino, Phys. Rep. 250 (1995) 329.
[15] C.-H. Pao, N.E. Bickers, Phys. Rev. Lett. 72 (1994) 1870.
[16] P. Monthoux, D.J. Scalapino, Phys. Rev. Lett. 72 (1994) 1874.
[17] C. Timm, D. Manske, K.H. Bennemann, Phys. Rev. B 66 (2002) 094515.
[18] D. Manske, I. Eremin, K.H. Bennemann, Phys. Rev. B 67 (2003) 134520.
[19] I. Eremin, D. Manske, K.H. Bennemann, Phys. Rev. B 65 (2002) 220502.
[20] H. Nagao, Int. J. Quantum Chem. 100 (2005) 867.
[21] A.P. Ginsberg, J Am. Chem. Soc. 102 (1980) 111.
[22] L. Noodleman, E.R. Davidson, Chem. Phys. 109 (1986) 131.
[23] A. Bencini, F. Totti, C.A. Doul, K. Doclo, P. Fantucci, V. Barone, Inorg. Chem. 36 (1997) 5022.
[24] E. Ruiz, J. Cano, S. Alvarez, P. Alemany, J. Comput. Chem. 20 (1999) 1391.
[25] K. Yamaguchi, Y. Takahata, T. Fueno, in: V.H. Smith et al. (Eds.), Applied quantum chemistry, Reidel Boston, MA, 1986, p. 155.
[26] K. Yamaguchi, F. Jensen, A. Dorigo, K.N. Houk, Chem. Phys. Lett. 149 (1988) 537.
[27] K. Yamaguchi, T. Kawakami, Y. Takano, Y. Kitagawa, Y. Yamashita, H. Fujita, Int. J. Quantum Chem. 90 (2002) 370.
[28] K. Yamaguchi, in: R. Carbo, M. Klobukowski (Eds.), Self-consistent field theory and applications, Elsevier, Amsterdam, 1990, p. 727.
[29] H. Nagao (to appear).

ferrimagnetic ring S_xs_x ($S = 5/2$, $s = 1/2$, $x = 2$–8). The Hamiltonian of this system is given by

$$\hat{H}_{\rm sys} = \hat{H}_0 + \hat{H}_{\rm DM} + \hat{H}_{\rm z}, \tag{1}$$

$$\hat{H}_0 = \sum_{i=1}^{x} J_1[\mathbf{S}_{2i-1}\cdot\mathbf{s}_{2i} + \mathbf{s}_{2i}\cdot\mathbf{S}_{2i+1}] + \sum_{i=1}^{x} J_2\mathbf{s}_{2i-1}\cdot\mathbf{s}_{2i+1}, \tag{2}$$

$$\hat{H}_{\rm DM} = \sum_{i=1}^{x}[\mathbf{D}_{2i-1,2i}\cdot\mathbf{S}_{2i-1}\times\mathbf{s}_{2i} + \mathbf{D}_{2i,2i+1}\cdot\mathbf{s}_{2i}\times\mathbf{S}_{2i+1}] + \sum_{i=1}^{x}\mathbf{d}_{2i-1,2i+1}\cdot[\mathbf{s}_{2i-1}\times\mathbf{s}_{2i+1}], \tag{3}$$

$$\hat{H}_{\rm z} = -h\sum_{i=1}^{x}(s^z_{2i-1} + S^z_{2i}). \tag{4}$$

The total Hamiltonian $\hat{H}_{\rm sys}$ consists of three parts. The first one is the Heisenberg Hamiltonian $\hat{H}_0$ which determines the position of steps of the magnetization process. The second one is the Dzyaloshinsky–Moriya (DM) interaction, $\hat{H}_{\rm DM}$, which determines the form of the magnetization process near steps. The third one is the Zeeman term, $\hat{H}_{\rm z}$, which describe the effect of the magnetic field. h represents the magnetic field which is assumed to be parallel to the z-axis. In all definitions, $\mathbf{S}_i$ and $\mathbf{s}_i$ represents the spin operator at an $S = 5/2$ spin site and an $s = 1/2$ spin site, respectively. The periodic boundary condition, $\mathbf{s}_{2x+1} = \mathbf{s}_1$, is imposed. J_1 and J_2 represent the coupling constant with Heisenberg exchange interaction. $|\mathbf{D}_{i,j}| = D_{i,j}$ and $|\mathbf{d}_{i,j}| = d_{i,j}$ are parameters for DM interaction. These parameters are controllable in the calculation. We take J_1 as an energy unit and define dimensionless parameters: $\tilde{h} = h/J_1$, $\tilde{d}_{i,j} = d_{i,j}/J_1$, $\tilde{D}_{i,j} = D_{i,j}/J_1$, $\tilde{J}_2 = J_2/J_1$. In this paper, we investigate the two cases for $\tilde{J}_2$. One is the non-frustrated system, $\tilde{J}_2 = 0$. The other is a frustrated system, $\tilde{J}_2 = 2.15$. This parameter is determined as the optimum parameter in Mn_6R_6 [4]. For the sake of simplicity, we take the condition that $\mathbf{D}_{2i-1,2i} = \mathbf{D}_{2i,2i+1}$, $\mathbf{d}_{2i-1,2i+1} = 0$ in the case of $\tilde{J}_2 = 0$, and that $\mathbf{D}_{2i-1,2i} = \mathbf{D}_{2i,2i+1} = \mathbf{d}_{2i-1,2i+1}$ in the case of $\tilde{J}_2 = 2.15$.

In order to determine the DM interaction, we have to discuss the symmetries of the molecule. First, we examine the case of Mn_6R_6. The crystallographic data of atomic position tells us four symmetries of the molecule. The first one is C_i with the inversion center at the center of the two hexagons; one is the inner-hexagon that is composed of $s = 1/2$ spins and the other is the outer-hexagon that is composed of $S = 5/2$ spins. The second one is S_6 with the axis that is perpendicular to the hexagon and that goes thorough the inversion center. The third one is C_3 with the same axis. In addition to the above three symmetries, there exists an approximate symmetry. That is C_2 with the axis going through two apexes and the center of the inner-hexagon.

By considering these four symmetries of Mn_6R_6, we determine the DM interaction for S_xs_x. After a simple analysis, one obtain an arrangement of $\mathbf{d}_{i,j}$ of S_6s_6 depicted in Fig. 1 as well as a set of uniform $\mathbf{d}_{i,j}$ perpendicular to the hexagon. Note that the projections of $\mathbf{D}_{i,i+1}$ and $\mathbf{D}_{i+1,i+2}$ to the xy-plane are directed to the same direction as that of $\mathbf{d}_{i,i+2}$. For other S_xs_x when x is even, we suppose the same arrangement of $\mathbf{d}_{i,j}$. That is, $\mathbf{d}_{i,j}$ is perpendicular to the each side of the inner-polygon and forms the alternated array with respect to the direction of the center of the polygon. A similar pattern of DM interaction was discussed in the case of the nanoscale antiferromagnetic rings [6]. For the S_xs_x when x is odd, we assume the following symmetries. Note that C_i and S_x does not exist in the case that x is odd. First, let us consider the arrangement of $\mathbf{d}_{i,j}$ of S_5s_5. We suppose C_5 with the axis that is perpendicular to the pentagon and that goes through the center of the pentagon. We also consider C_2. The axis of C_2 connects two apexes in the different pentagon, inner-pentagon and outer-pentagon and goes thorough the common center of these pentagons. After a simple analysis, one obtains an arrangement of $\mathbf{d}_{i,j}$ of S_5s_5 depicted in Fig. 1 as well as

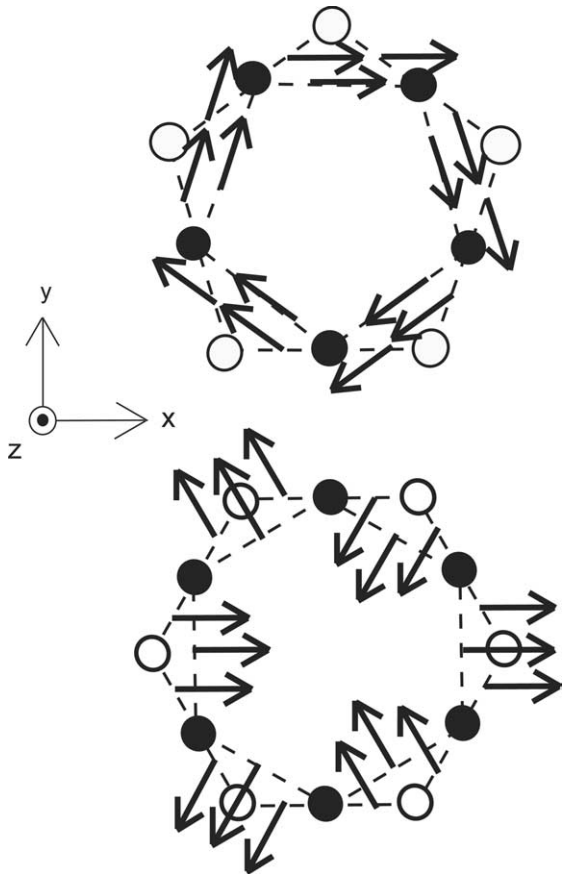


Fig. 1. The arrangement of $\mathbf{D}_{i,j}$ of S_5s_5 (upper side) and S_6s_6 (down side). The arrows show the projection of $\mathbf{D}_{i,j}$ on xy-plane. The black bullets represent $s = 1/2$ local spin sites and the white bullets represent $S = 5/2$ local spin sites.

a set of uniform $\mathbf{d}_{i,j}$. For the other odd-numbered S_xs_x ($x = 3, 7$), we also suppose the same symmetry and can obtain the same arrangement of $\mathbf{d}_{i,j}$. Considering the above arrangement of $\mathbf{D}_{i,j}$, we calculate the magnetization process ($T = 0$ [K]) and the field derivative of the magnetization, $\mathrm{d}M/\mathrm{d}\tilde{h}$ for the various size of S_xs_x. Applying the reduced matrix that is adopted by the effective basis method [7], we make the numerical diagonalization. The direction of the magnetic field is supposed to be perpendicular to the polygon in this paper. Therefore, components of $\mathbf{D}_{i,j}$ and $\mathbf{d}_{i,j}$ perpendicular to the polygons do not contribute to the magnetization process.

First, let us discuss the magnetization process and $\mathrm{d}M/\mathrm{d}\tilde{h}$.

In the non-frustrated case of S_xs_x ($\tilde{J}_2 = 0$, $\tilde{d}_{i,j} = 0$, $x = 2$–8), there is no width in all the peaks, that is, each peak forms the δ-function. Therefore, all the magnetization processes reveal step structures. In this case, regarding the peak structure, there is no qualitative difference among the systems with different x. That is, there is no remarkable size dependence of the magnetization process.

In the frustrated cases of S_xs_x ($\tilde{J}_2 = 2.15$, $\tilde{d}_{i,j} = 0.05$, $x = 2$–8), magnetization process and $\mathrm{d}M/\mathrm{d}\tilde{h}$ are drastically dependent on the size of the ring. We first discuss the magnetization process of S_6s_6 by comparing the experimental data of Mn_6R_6. Fig. 2(b) shows the magnetization process of S_6s_6. The magnetization M of the ground state at given field changes from $M = 12$ to $M = 18$. Every step indicates the position of the energy-level crossing between the case M and $M + 1$. The field derivative of the magnetization $\mathrm{d}M/\mathrm{d}\tilde{h}$ is shown in Fig. 2(a). The height of the peak increases from the first peak to the third peak. The height of the fourth peak is higher than the first peak and is lower than the second peak. The tendency of the former four peaks agrees with the four peaks that is experimentally observed for Mn_6R_6 [2], although the numerical third peak is comparably sharp. The main origin for the height of the experimental third peak may be the other factors, such as the thermal distribution and other anisotropy effects, for example, the dipole–dipole interaction. However, the DM interaction determined above is the primary origin for the peak structure that is experimentally observed. On the other hand, in the case of $\tilde{J}_2 = 0.0$ mentioned above, S_6s_6 is inconsistent with Mn_6R_6 with respect to the peak structure. For other cases of frustrated systems of S_xs_x, ($\tilde{J}_2 = 2.15$, $\tilde{d}_{i,j} = 0.05$, $x = 3, 5, 7$), Fig. 3 shows the magnetization process and the field derivative of magnetization. Interesting peak structure is observed in all cases, that is, changes of the height of the peaks in the magnetic fields is not monotonous. One of the present authors have reported that the lattice distortion makes the peak structure varied in antiferromagnetic ring [8]. But the origin for the curious peak structure in the present system is the frustration. In the case of S_xs_x, ($x = 4, 8$), all the peaks in each system form the δ-function. Therefore, the change of the number of the unit cell provides the drastic change of the magnetization process when the system has frustration. This size effect can be utilized as a finger print of each molecule.

Finally, we demonstrate another size dependence effect that is found in the translational quantum number, $k = (2\pi/x)n$ ($n = 0, 1, \ldots$), which is associated with the cyclic shift operation of the rings. The translational quantum number is a wave number in the wave function of a system. Because the DM interaction is generally small in comparison with exchange interaction, the wave

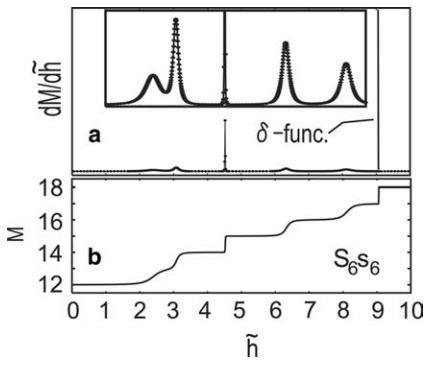


Fig. 2. The field derivative of magnetization, $\mathrm{d}M/\mathrm{d}\tilde{h}$, (a) and the magnetization process (b) in S_6s_6. The inset figure is enlarged one $1 < \tilde{h} < 8.7$. Only the sixth peak form the δ-function. This result is consistent with the experimental data of Mn_6R_6 [2].

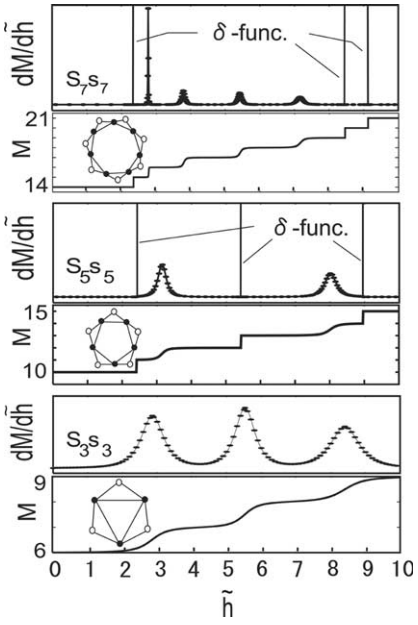


Fig. 3. The magnetization process and the field derivative of magnetization $\mathrm{d}M/\mathrm{d}h$ in S_xs_x ($x = 3, 5, 7$). The remarkable size dependence of magnetization process is observed.

number should not be affected by the DM interaction. Thus, we calculate k in the lowest energy eigenstate of $\hat{H}_0 + \hat{H}_z$ at given fields. The calculating results are divided into the following three features: (I) ($\tilde{J}_2 = 0$, $x = 2$–8): this parameter set corresponds to the non-frustrated case. In this case, $k = 0$ is always realized in the lowest energy eigenstate at any given field. Moreover, this feature does not depend on the number of unit cell; (II) ($\tilde{J}_2 = 2.15$, $x = 2, 4, 6, 8$): this parameter set corresponds to the frustrated case in which the number of the unit cell is even. In this system, k takes the value of 0 and π alternately; when M is even number, $k = 0$, when M is odd number, $k = \pi$; (III) ($\tilde{J}_2 = 2.15$, $x = 3, 5, 7$): this parameter set corresponds to the frustrated case in which the number of the unit cell is odd. Note that there are two kinds of frustration in this system. One is the triangle s–S–s, and another is the polygon which consists of s. Then, the feature of k is rather complicated. In case $x = 3$, while the magnetization of the lowest energy eigenstate is changed from $M = 6$ to $M = 9$, the k is realized $k = 0$, $\pm 2\pi/3$, $\pm 2\pi/3$, 0, respectively. In case $x = 5$, while the magnetization is changed from $M = 10$ to $M = 15$, the k is realized $k = 0$, $\pm 4\pi/5$, $\pm 2\pi/5$, $\pm 2\pi/5$, $\pm 4\pi/5$, 0, respectively. In case of $x = 7$, while the magnetization is changed from $M = 14$ to $M = 21$, the k is realized $k = 0$, $\pm 6\pi/7$, $\pm 2\pi/7$, $\pm 4\pi/7$, $\pm 2\pi/7$, $\pm 6\pi/7$, 0, respectively. The same result of the frustrated cases (II) and (III), is obtained in the $S = 1/2$ antiferromagnetic spin rings [9] in which the number of sites corresponds to the number of unit cell in the present systems. Note that, the drastic size dependence of $\mathrm{d}M/\mathrm{d}\tilde{h}$ appears in the situation of the parameter set of the feature (II) and (III). Therefore, the size dependence of the translational quantum number k appears only in the frustrated case but not in the non-frustrated case.

In summary, we have investigated the size dependence of the magnetic properties in nanoscale ferrimagnetic ring. We have investigated the two types of ferrimagnetic rings with Dzyaloshinsky–Moriya interaction. One is the frustrated system and the other is the non-frustrated system. As a result, in the non-frustrated case, the change of the number of unit cells does not provide the remarkable change about the magnetization process. On the other hand, in the frustrated cases, there are drastic size dependence of the magnetization process. This result indicates that the effect of frustration causes the size dependence of the magnetic properties in the ferrimagnetic ring. We also provide the information for the other aspect of the size dependence by calculating the translational quantum number in the lowest eigenstate at the given fields. It is clarified that the size dependence caused by the frustration is also found in the behavior of the translational quantum number of the ground state.

Acknowledgments

This work was partly supported by a Grant-in-Aid from the Ministry of Education, Culture, Sports, Science and Technology (MEXT) (No. 15GS0213), the MEXT Special Coordination Funds for Promoting Science and Technology (Nanospintronics Design and Realization), the 21st COE Program supported by the Japan Society for the Promotion of Science (JSPS), NEDO under the Materials and Nano-technology Program and ACT-JST. Numerical calculation have been done using the computer facilities of the Institute for Solid State Physics (ISSP) and the Japan Atomic Energy Research Institute (JAERI).

References

[1] A. Caneschi, D. Gatteshi, J. Laugier, P. Rey, R. Sessoli, C. Zanchini, J. Am. Chem. Soc. 110 (1988) 2795.
[2] V.V. Kostyuchenko, I.M. Markevtsev, A.V. Philoppov, V.V. Platonov, V.D. Selemir, O.M. Tatsenko, A.K. Zvezdin, A. Caneschi, Phys. Rev. B 67 (2003) 184412.
[3] H. Hori, S. Yamamoto, Phys. Rev. B 68 (2003) 054409.
[4] S. Tonooka, H. Nakano, K. Kusakabe, N. Suzuki, J. Phys. Soc. Jpn. 73 (2004) 1597.
[5] S. Tonooka, K. Kusakabe, N. Suzuki, H. Nakano, J. Phys.: Condens. Matter 16 (2004) S5739.
[6] H. Nakano, S. Miyashita, J. Phys. Soc. Jpn. 71 (2002) 2580.
[7] H. Nakano, S. Miyashita, J. Phys. Soc. Jpn. 70 (2001) 2151.
[8] H. Nakano, S. Miyashita, J. Phys. Chem. Solids 63 (2002) 1519.
[9] K. Bärwinkel, P. Hage, H.-J. Schumidt, J. Schnack, Phys. Rev. B 68 (2003) 054422.

that of frequency domain magnetic resonance spectroscopy (FDMRS), which combines the zero-field advantage of INS with HFEPR sensitivity [8].

Magnetic resonance and neutron scattering studies have focussed on the determination of spin Hamiltonian parameters, i.e., the fitting of a certain spin Hamiltonian to the observed peak positions. Much less attention has been paid to the lineshape of the magnetic resonance lines. The (inhomogeneously broadened) magnetic resonance lineshape of two other single molecule magnets, $Mn_{12}Ac$ and Fe_8 has been studied using both HFEPR and time-domain THz spectroscopy. HFEPR studies on Fe_8 showed that both distributions in the internal dipolar fields, and in the zero-field splitting parameters contribute to the linewidth [9,10]. In the case of $Mn_{12}Ac$ is was shown that the contribution of the dipolar fields to the linewidth is relatively unimportant, and that it is mainly governed by distributions in the zero-field splitting parameter D [9–11]. In the latter sample, the situation is made more complicated by the presence of different isomers [12]. One reason for the relative scarcity of lineshape studies is that lineshapes are often distorted in experiments using the simpler single pass transmission HFEPR setups. Apart from information on distributions of the ZFS parameters in the case of inhomogeneously broadened lines, in the case of homogeneously broadened lines, the excited state lifetime can be obtained. These lifetimes are currently of great interest, since single molecule magnets were proposed as promising candidates for application in quantum computing. In this proposal, three microwave pulses of a duration of 10^{-7} s have to be applied within the lifetime of a coherently populated state [13]. However, little is known about the dynamics of the magnetic microstates of SMMs. A rough indication comes from the prefactor in the Arrhenius law type of temperature dependence of the magnetization relaxation rate. For published SMMs this prefactor usually lies between 10^{-7} and 10^{-9} s^{-1}.

Here, we present a preliminary study of the zero-field splittings and the magnetic resonance lineshapes and –widths of two published SMMs, namely (PPh_4)-$[Mn_{12}O_{12}(O_2CEt)_{16}(H_2O)_4]$ ($[Mn_{12}^-]$) [14], and $[Mn_9O_7$-$(O_2CCH_3)_{11}(thme)(py)_3(H_2O)_2]$ ($[Mn_9]$) [15]. These systems are structurally rather similar, both having non-integer ground states, and idealized axial symmetry. $[Mn_{12}^-]$ has an $S = 19/2$ ground state, and $[Mn_9]$ an $S = 17/2$ ground state. The energy barriers towards relaxation of the magnetization were determined to be $\Delta E = 57$ K and $\Delta E = 27$ K for $[Mn_{12}]^-$ and $[Mn_9]$, respectively [14,15]. From magnetization measurements for $[Mn_9]$ a D value of $-0.29(3)$ cm^{-1} was determined [15], while a D value of -0.4 cm^{-1} was obtained for $[Mn_{12}^-]$ [14]. In the case of $[Mn_{12}^-]$, HFEPR measurements yielded a value of $D = -0.42$ cm^{-1} [14].

2. Experimental

The materials $[Mn_{12}]^-$ and $[Mn_9]$ were prepared as described [14,15]. Their identity and purity was checked by elemental analysis, X-ray unit cell determination, and IR-spectroscopy.

The FDMRS spectrometer has been described in the literature [8]. Briefly, it is a quasi-optical spectrometer in a Mach–Zehnder interferometer layout. It features backward wave oscillators as sources, which are vacuum tubes that produce strong, coherent radiation which is tunable over a wide frequency range. As detectors both room temperature Golay cells and helium-cooled Bolometers are used. The transmission spectra reported here employ only one arm of the interferometer; for phase spectra both arms are required. Measurements are possible with and without the application of a static external magnetic field, where the field can be parallel (Faraday geometry) or perpendicular (Voigt geometry) to the radiation propagation direction. The present measurements were performed in zero field on pressed powder pellets of 1 cm diameter and 3.449 mm thickness ($[Mn_{12}]^-$) and 1.456 mm thickness ($[Mn_9]$), respectively.

The analysis procedure was as follows: The spectra were normalised, i.e., divided by the highest temperature one, to remove the Fabry–Perot resonance induced oscillation of the baseline, and artefacts. Subsequently, the resonance frequencies were determined. The spin Hamiltonian parameters were fitted to these frequencies using matrix diagonalisation. Using the obtained parameters, the spectra were simulated using Fresnel formulas for transmission of a plane parallel sample, and the resonance line width was determined [8].

3. Results and discussion

In the transmission spectra for $[Mn_{12}]^-$ and $[Mn_9]$, two features were observed. First of all there is an oscillation in the baseline, which is due to Fabry–Perot-like interference of the radiation within the plan-parallel pellet. Second, several narrow lines are visible with intensities depending on the temperature. These narrow lines are attributed to magnetic resonance transitions between the magnetic microstates within the ground state $S = 19/2$ and $S = 17/2$ multiplets of $[Mn_{12}]^-$ and $[Mn_9]$, respectively. The spectra were normalised (Figs. 1 and 2) to remove the baseline oscillation. In this way, the resonance position can be determined with an accuracy of less than 1% or 0.03 cm^{-1}. For $[Mn_{12}]^-$, five resonance lines can be observed at 7.66, 7.04, 6.31, 5.41, and 4.71 cm^{-1}, respectively. Four resonance lines are present in the spectra recorded for $[Mn_9]$, namely at 3.79, 3.41, 2.95 and $\sim$2.50 cm^{-1}.

In general, the degeneracy of the magnetic microstates is lifted due to zero-field splitting, which, using a

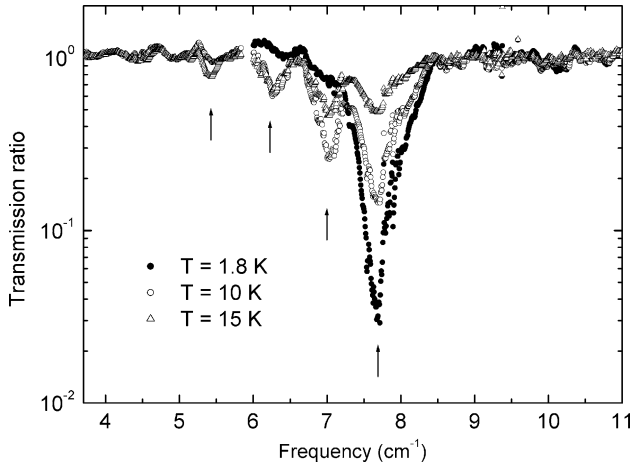


Fig. 1. FDMRS spectra recorded on a pressed powder pellet of $[Mn_{12}]^-$ at various temperatures as indicated. Arrows denote magnetic resonance transitions.

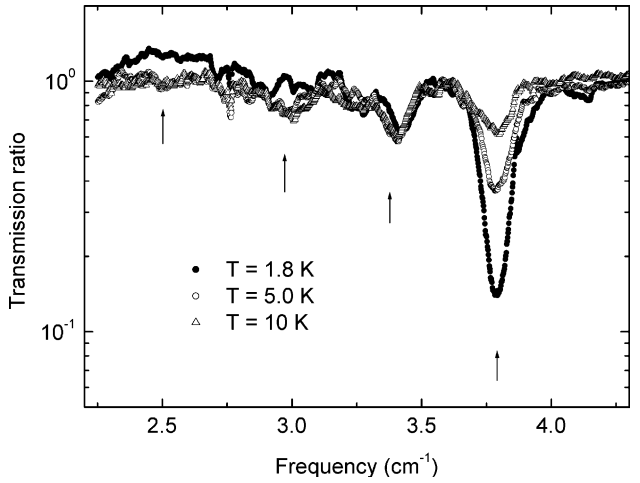


Fig. 2. FDMRS spectra recorded on a pressed powder pellet of $[Mn_9]$ at various temperatures as indicated. Arrows denote magnetic resonance transitions.

spin Hamiltonian approach, can be described as functions of the spin operators. In many studies of the magnetic anisotropy of molecular magnets, it has proven necessary to include not only second-order terms but also additional higher-order ones. Usually Stevens operator equivalents are used for these higher-order terms. In the present case, the following spin Hamiltonian was used to fit the spectra:

$$H = D\left[\hat{S}_Z^2 - \frac{1}{3}S(S+1)\right] + B_4^0\hat{O}_4^0.$$

From the fact that the highest frequency line in both samples has the highest intensity at low temperatures, we can immediately conclude that the leading term in the spin Hamiltonian must be negative, i.e., $D < 0$. The position of the highest-frequency resonance line gives an estimate of the second-order axial ZFS parameter, i.e., $D = -0.425\ \mathrm{cm}^{-1}$ for $[Mn_{12}]^-$, and $D = -0.237\ \mathrm{cm}^{-1}$ for $[Mn_9]$. A least squares fit of the spin Hamiltonian parameters to the observed resonance frequencies resulted in the following parameters: $D = -0.454 \pm 0.004\ \mathrm{cm}^{-1}$ and $B_4^0 = (+1.01 \pm 0.05) \times 10^{-5}\ \mathrm{cm}^{-1}$ for $[Mn_{12}]^-$, and $D = -0.247 \pm 0.005\ \mathrm{cm}^{-1}$, $B_4^0 = (+4.6 \pm 0.1) \times 10^{-6}\ \mathrm{cm}^{-1}$ for $[Mn_9]$. The fit was not improved by introduction of transverse anisotropy either in second or in fourth order. These parameters fit quite well with published ones based on magnetization measurements, and, in the case of $[Mn_{12}]^-$ with HFEPR data. In these latter studies it was stated that inclusion of fourth-order ZFS parameters did not improve the fit. In our fits a significant improvement was found, however. Interestingly, the magnitude of the B_4^0 parameter of $[Mn_{12}]^-$ is almost 2 orders of magnitude smaller than in the case of the parent $[Mn_{12}Ac]$ molecule [4,16–18]. The zero-field splitting of a total spin state of a single molecule magnet is to a large extent a linear combination of the zero-field splittings of the single ions, where the coefficients depend on the exchange coupling scheme [19]. Therefore, this drastic drop in magnitude is unexpected since neither the single ion anisotropies nor the exchange couplings are likely to change dramatically. Since the fourth-order anisotropy in the case of $[Mn_9]$ is even smaller, it would be interesting to see if such small B_4^0 values are a general feature of exchange coupled clusters with non-integer spin ground states. Another feature of interest is the positive sign of B_4^0 in both cases. In many cases, this parameter is negative for single molecule magnets, e.g., in the case of the aforementioned $Mn_{12}Ac$ [18], Fe_8, [20], or the $[Mn_4]_2$ dimer [21]. However, other examples of positive B_4^0 parameter are known, e.g., for some Mn_4SMMs [5].

Using the obtained spin Hamiltonian parameters, the magnetic resonance spectra were simulated at the lowest temperature of $T = 1.8$ K as shown in Figs. 3 and 4 for $[Mn_{12}]^-$ and $[Mn_9]$, respectively. As can be seen, the resonance line of $[Mn_9]$ can best be described by a Gaussian function which shows better agreement with the experiment than a Lorentzian one, especially at the edges of the resonance line. Interestingly, the contrary is true for $[Mn_{12}]^-$, where the resonance line is clearly Lorentzian. The Gaussian (*inhomogeneously* broadened) lineshape in the case of $[Mn_9]$ suggests that the linewidth is determined by distributions in the sample either a distribution in ZFS parameters or a distribution in the local magneto dipolar field. Within experimental error, the linewidth ($0.06 \pm 0.02\ \mathrm{cm}^{-1}$) does not change with temperature, which indicates that the distribution in D is the main source of inhomogeneous broadening. This linewidth is slightly smaller than that found for $[Mn_{12}Ac]$ ($0.09 \pm 0.01\ \mathrm{cm}^{-1}$) [22].

In contrast, the highest-frequency resonance line of $[Mn_{12}]^-$ appears to be *homogeneously* broadened,

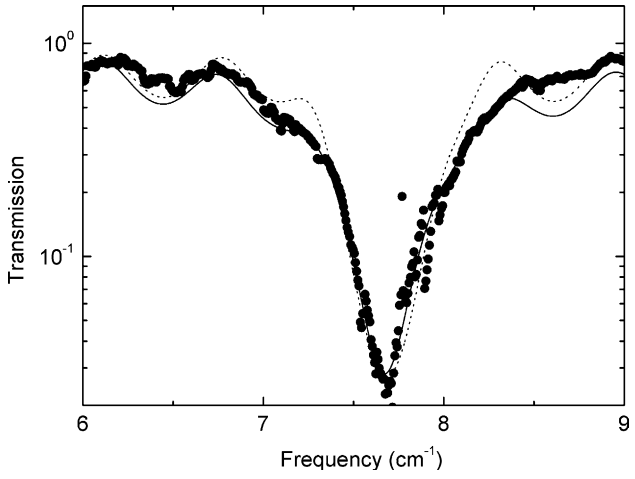


Fig. 3. FDMRS spectrum recorded on $[Mn_{12}^{-}]$ at $T = 1.8$ K, together with fits assuming Lorentzian (drawn) and Gaussian (dotted) lines.

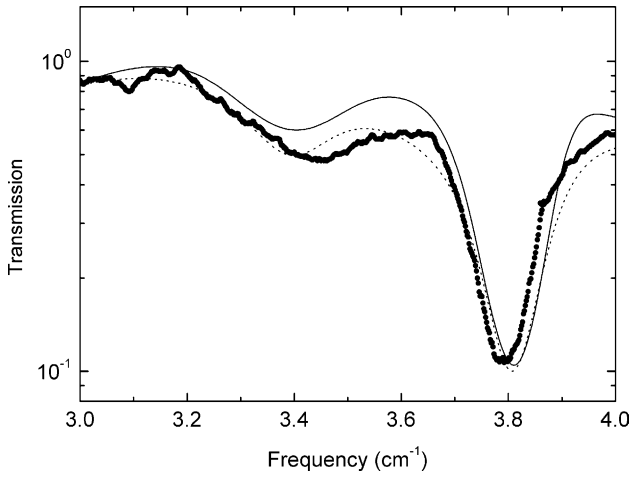


Fig. 4. FDMRS spectrum recorded on $[Mn_9]$ at $T = 1.8$ K, together with fits assuming Lorentzian (dotted) and Gaussian (drawn) lines.

which is quite uncommon. In fact most resonance lines recorded on molecular magnets by magnetic resonance spectroscopy (both HFEPR and FDMRS) are Gaussian shaped. The linewidth is slightly temperature dependent, going from 0.41 cm^{-1} (FWHM) at 1.8 K to 0.55 cm^{-1} at high temperatures. In case of homogeneously broadened resonance lines it is the excited state lifetime governed by spin–lattice or spin–spin relaxation, that determines the linewidth, through a Heisenberg type of uncertainty relation, which broadens the energies of short-lived states. In fact, on a quantitative level, the linewidth expressed as an angular frequency is given by $\omega = 2/\tau$, where τ is the relaxation time [23]. Conversely $\tau = \omega/2 = \pi\nu$. In the present case, that means that the excited state lifetime in the case of $[Mn_{12}^{-}]$ is 50–58 ps, depending on temperature. The prefactor in the Arrhenius analysis of the magnetization of the relaxation was determined to be 310 ps, which suggests that the dynamics of higher excited states are slightly slower. These lifetimes are short in comparison to other estimates of excited state lifetimes published in the literature. Thus, for certain Ni_4 clusters, spin–spin relaxation times of about 1 ns were reported [24]. In general, the relaxation from the excited state can take place through three types of processes [19]. The direct relaxation process is usually less important since the number of phonons is much smaller than the number of spins in concentrated magnetic media such as molecular magnets. Two two-phonon processes exist which rely on an intermediary state, which is real in the case of an Orbach process and virtual in the case of a Raman process. In exchange coupled clusters there are usually a number of levels present with energies comparable to kT. However, no large difference in exchange interactions, and therefore in number and energies of the excited spin levels is expected between $[Mn_{12}]^{-}$ and $[Mn_{12}Ac]$. This means that the origin of this short lifetime is as yet unclear.

In conclusion, we have determined the ZFS parameters of two non-integer single molecule magnets, $[Mn_9]$ and $[Mn_{12}]^{-}$, showing that frequency domain magnetic resonance spectroscopy (FDMRS) is excellently suited to this end. Furthermore, we have shown that the magnetic resonance linewidth is inhomogeneously broadened (Gaussian) in the case of $[Mn_9]$ and homogeneously broadened (Lorentzian) in the case of $[Mn_{12}]^{-}$. This allows the determination of the excited state lifetime in the latter case, which was determined to be 50–58 ps, depending on temperature. A consequence of such a short lifetime is that quantum computing schemes, based on coherent population of excited spin levels, will have to be carried out in shorter times than the excited state lifetime.

Acknowledgement

Financial support from the DFG is gratefully acknowledged.

References

[1] D. Gatteschi, R. Sessoli, Angew. Chem., Int. Ed. 42 (2003) 268.
[2] S.M.J. Aubin, M.W. Wemple, D.M. Adams, H.-L. Tsai, G. Christou, D.N. Hendrickson, J. Am. Chem. Soc. 118 (1996) 7746.
[3] A.-L. Barra, L.-C. Brunel, D. Gatteschi, L. Pardi, R. Sessoli, Acc. Chem. Res. 31 (1998) 460.
[4] S. Hill, J.A.A.J. Peerenboom, N.S. Dalal, T. Hathaway, T. Statcup, J.S. Brooks, Phys. Rev. Lett. 80 (1998) 2453.
[5] J. Yoo, A. Yamaguchi, M. Nakano, J. Krzystek, W.E. Streib, L.C. Brunel, H. Ishimoto, G. Christou, D.N. Hendrickson, Inorg. Chem. 40 (2001) 4604.
[6] R. Basler, C. Boskovic, G. Chaboussant, H.U. Gudel, M. Murrie, S.T. Ochsenbein, A. Sieber, Chemphyschem 4 (2003) 910.

[7] S. Carretta, J. van Slageren, T. Guidi, E. Liviotti, C. Mondelli, D. Rovai, A. Cornia, A.L. Dearden, F. Carsughi, M. Affronte, C.D. Frost, R.E.P. Winpenny, D. Gatteschi, G. Amoretti, R. Caciuffo, Phys. Rev. B 67 (2003) 104403.
[8] J. van Slageren, S. Vongtragool, B. Gorshunov, A.A. Mukhin, N. Karl, J. Krzystek, J. Telser, A. Muller, C. Sangregorio, D. Gatteschi, M. Dressel, Phys. Chem. Chem. Phys. 5 (2003) 3837.
[9] K. Park, M.A. Novotny, N.S. Dalal, S. Hill, P.A. Rikvold, Phys. Rev. B 6614 (2002) 4409.
[10] S. Hill, S. Maccagnano, K. Park, R.M. Achey, J.M. North, N.S. Dalal, Phys. Rev. B 6522 (2002) 4410.
[11] B. Parks, J. Loomis, E. Rumberger, D.N. Hendrickson, G. Christou, Phys. Rev. B 64 (2001) 184426.
[12] S. Hill, R.S. Edwards, S.I. Jones, N.S. Dalal, J.M. North, Phys. Rev. Lett. 90 (2003) 217204.
[13] M.N. Leuenberger, D. Loss, Nature 410 (2001) 789.
[14] S.M.J. Aubin, Z. Sun, L. Pardi, J. Krzystek, K. Folting, L.-C. Brunel, A.L. Rheingold, G. Christou, D.N. Hendrickson, Inorg. Chem. 38 (1999) 5329.
[15] E.K. Brechin, M. Soler, J. Davidson, D.N. Hendrickson, S. Parsons, G. Christou, Chem. Commun. (2002) 2252.
[16] A.A. Mukhin, V.D. Travkin, A.K. Zvezdin, S.P. Lebedev, A. Caneschi, D. Gatteschi, Europhys. Lett. 44 (1998) 778.
[17] I. Mirebeau, M. Hennion, H. Casalta, H. Andres, H.-U. Güdel, A.V. Irodova, A. Caneschi, Phys. Rev. Lett. 83 (1999) 628.
[18] A.-L. Barra, D. Gatteschi, R. Sessoli, Phys. Rev. B 56 (1997) 8192.
[19] A. Bencini, D. Gatteschi, EPR of Exchange Coupled Systems, Springer, Berlin, 1990.
[20] A.-L. Barra, D. Gatteschi, R. Sessoli, Chem. Eur. J. 6 (2000) 1608.
[21] S. Hill, R.S. Edwards, N. Aliaga-Alcalde, G. Christou, Science 302 (2003) 1015.
[22] S. Vongtragool, Ph.D. Thesis, University of Stuttgart, Stuttgart, 2004.
[23] N.M. Atherton, Principles of Electron Spin Resonance, Prentice-Hall, New York, 1993.
[24] E. Del Barco, A.D. Kent, E.C. Yang, D.N. Hendrickson, Phys. Rev. Lett. 93 (2004) 157202.

non-magnetic plate. The specimen was installed in the ^{3}He-refrigerator, so as to align the *b*-axis (the easy axis [6]) in the field direction of the magnetometer. The applied field, H_a, was corrected for the demagnetization effect to give the field seen by the sample, $H_{eff.}$. Only a rough estimation of demagnetization factor, N, was possible, because the shape is different piece by piece and is not ellipsoidal. However, the value of N does not affect any conclusion in this work. We applied N of approximately 0.4, to calculate, $H_{eff.} = H_a - 4\pi N M_V$, where M_V denotes the magnetization per unit volume.

While the new measurement system was being conceived, we always kept one thing in mind; ''Do not alter the MPMS.'' We have succeeded in designing a system that is easily attachable and detachable. Our MPMS is equipped with the ^{3}He cryostat only when temperatures lower than 1.8 K is necessary; otherwise it works just as a normal MPMS. The ^{3}He cryostat has been designed to be slim enough to fit into the sample space of Quantum Design's MPMS. The schematic drawing of the cryostat is shown in Fig. 1. It is the ''Sample in liquid''-type cryostat, meaning that the sample is soaked in the liquid ^{3}He. The lower end of the main pipe has a vacuum jacket to insulate the inside of the cryostat from the outside environment, which is actually the sample space in an ordinary usage of the MPMS and maintained at 1.6 K during the ^{3}He-temperature operation. Here the base temperature of the MPMS somewhat lower than the usual (around 1.8 K) is achieved by an auxiliary rotary pump, facilitating more efficient condensation of ^{3}He gas.

The principle of the measurement is that we scan the whole cryostat, including the sample, through the pick-up coil. In a way it is similar to magnetization measurements with a pressure cell. This method is advantageous in that the sample temperature is very stable during the scan. The problem is that the cryostat contributes to the background. It can be subtracted, however, unless it is too large. The current version has been designed for an Reciprocating Sample Oscillation (RSO)-type drive, although a version that is compatible with a standard DC-type drive is also possible. The present cryostat is supported at its neck by the top part of the moving rack of the RSO unit. On top of the drive we mount a box as a sample-space airlock, and a bellows inside the box interconnects between the ^{3}He cryostat and a flange, which is the port to a gas-handling system.

To hold a sample in position, we use the drinking straws that are used with the MPMS. Since the sample is thermally insulated from the outside of the cryostat, the temperature has to be measured in situ. To reduce the background from the thermometer, we have adopted a bare-chip Cernox (Lake Shore Cryotronics, Inc.) sensor, which gives a fairly small moment of 1×10^{-4} emu at 1.6 K and 1 T. It is accommodated in a polyimide tube and placed just above the sample. The total background from the current cryostat is about 6×10^{-4} emu at 0.5 K and 1 T. This is small enough to be neglected in the case reported herein and in most other cases. If necessary, we can subtract the background by measuring it separately.

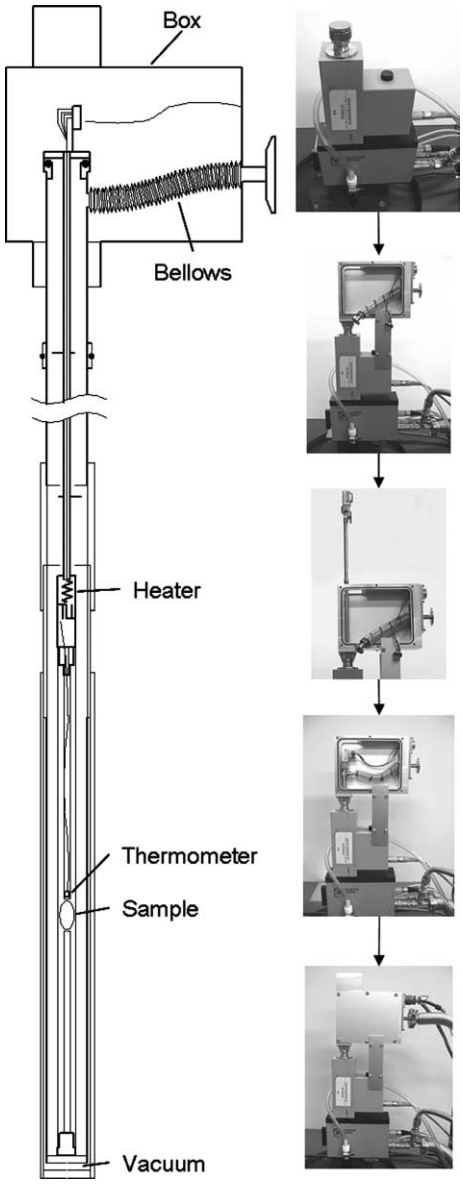


Fig. 1. (Left) Schematic drawing of our ^{3}He cryostat. (Right) Pictures showing the set-up procedure of the ^{3}He cryostat.

The usage of the new apparatus is as the following (see the pictures in Fig. 1). The normal MPMS has an O-ring seal made of acryl on the top opening of the RSO drive unit. We replace the seal with an O-ring compression fitting for a more secure connection. After warming up the sample space of the MPMS to around room temperature and venting with He gas, we fix the box on top of the RSO unit by inserting the bottom pipe of the box into the O-ring fitting. Then the ^{3}He cryostat is installed into the MPMS's sample space, and all the connections are made. When the box has been covered

and the inside of the ^{3}He cryostat has been evacuated, the system is ready to be cooled down.

Using ^{3}He gas as heat-exchange medium inside the cryostat, we first cool down the MPMS to around 5 K. Then the auxiliary rotary pump lowers the temperature to 1.6 K, at which ^{3}He gas is condensed. Finally the liquefied ^{3}He is pumped out to go below 0.5 K. We can reach 0.48 K within 30 min or so after starting to pump the liquid.

Fig. 2 shows the M–H characteristic of β-p-NPNN below and above T_c. The data above T_c, which were measured by a usual method without the ^{3}He-refrigerator, are consistent with those reported previously [4,5]. The saturation of the paramagnetic moment at the value close to $M_{sat}(1/2)$ was observed at 2 K. The static M–H curves below T_c clearly show that the ferromagnetic moment also saturates at $M_{sat}(1/2)$. Therefore, we conclude M_{sat} of β-p-NPNN is $M_{sat}(1/2)$ as expected for an ordinary spin-1/2 Heisenberg ferromagnet.

Another characteristic is the absence of hysteresis as shown in Fig. 3; the magnetization is almost reversible and the coercive force and residual magnetization are too small to be detected, unlike the previous result [4,5]. The small hysteresis observed by the dynamical method might have been an artifact due to the difference in the data-acquisition timing for M and H. Another thing that we would like to point out is that the field was applied along the easy axis in the present measurements to suppress the irreversible rotation of magnetization against the small dipolar anisotropy, whereas the field had not been along the easy axis in the previous ones. Thus β-p-NPNN is concluded to be a considerably soft magnet at least for the easy axis. This behavior is expected for an isotropic Heisenberg spins of the organic radicals, and is consistent with the specific heat [5] and μSR [6] results.

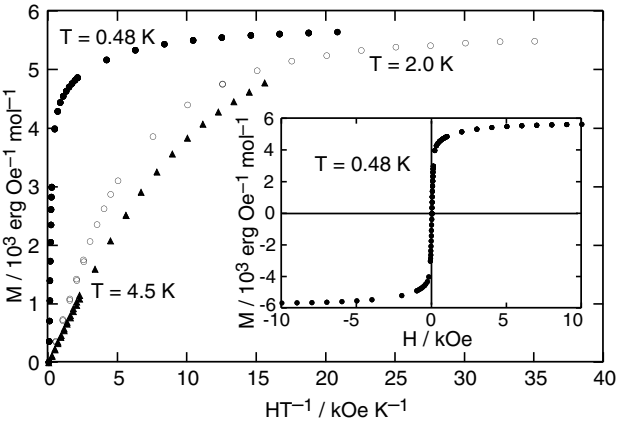


Fig. 2. Magnetization of β-p-NPNN below and above T_c plotted vs. H/T. The inset shows the overall M–H characteristic in the ferromagnetic state. Demagnetization correction is not made for the data in this figure.

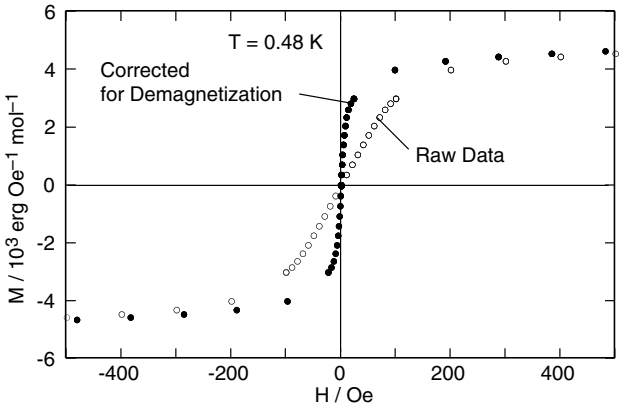


Fig. 3. Low field M–H curve of ferromagnetic β-p-NPNN at 0.48 K. The closed symbols show the data corrected for demagnetization effect, while open ones are without the correction. Both upward and downward field sweep data are shown. No hysteretic behavior is found.

In the ferromagnetic state, M rises rapidly below the applied field $H_a \approx 200$ Oe. It is also noted that M is still increasing slowly even in the high-field regime, $H_a > 1$ kOe, until it saturates near $H_a = 10$ kOe. This means that $H_a = 400$ Oe was too low to determine M_s. Since the magnetic anisotropy of β-p-NPNN is significantly small, the slow saturation can be related to the thermal fluctuation effect of a soft isotropic ferromagnet, rather than to the rotation of domain magnetization or to the domain wall displacement of hard magnets. If this is the case, the initial increase of M at low fields is regulated by the spontaneous magnetization, M_{sp}, which corresponds to the order parameter. This is followed by slow increase of M in the range, $M_{sp} < M < M_{sat}$, in the high field regime. The spontaneous magnetization $M_{sp}(T)$ decreases from $M_{sp}(0) = M_{sat}$ to zero as $T = T_c$ is approached. From the μSR measurement [7], $M_{sp} \approx 0.8\ M_{sat} = 4.5 \times 10^3$ erg Oe^{-1} mol^{-1} is inferred at $T = 0.48$ K ($T/T_c = 0.8$). This agrees with the initial rise of M observed in this work. In this way, the M–H characteristic of β-p-NPNN is understood in terms of the thermal fluctuation.

Acknowledgement

This work is supported by a Grant-in-Aid for Scientific Research (No. 15550135) from the Ministry of Education, Culture, Sports, Science and Technology, Japan.

References

[1] M. Tamura, Y. Hosokoshi, D. Shiomi, M. Kinoshita, Y. Nakazawa, M. Ishikawa, H. Sawa, T. Kitazawa, A. Eguchi, Y. Nishio, K. Kajita, J. Phys. Soc. Jpn. (2003).

[2] M. Kinoshita, Phil. Trans. Roy. Soc., Lond. Ser. A 357 (1999) 2855.
[3] M. Kinoshita, Jpn. J. Appl. Phys. 33 (1994) 5718.
[4] M. Tamura, Y. Nakazawa, D. Shiomi, K. Nozawa, Y. Hosokoshi, M. Ishikawa, M. Takahashi, M. Kinoshita, Chem. Phys. Lett. 186 (1991) 401.
[5] Y. Nakazawa, M. Tamura, N. Shirakawa, D. Shiomi, M. Ishikawa, M. Takahashi, M. Kinoshita, Phys. Rev. B 46 (1992) 8906.
[6] L.P. Le, A. Keren, G.M. Luke, W.D. Wu, Y.J. Uemura, M. Tamura, M. Ishikawa, M. Kinoshita, Chem. Phys. Lett. 206 (1993) 405.
[7] K. Takeda, K. Konishi, M. Tamura, M. Kinoshita, Phys. Rev. B. 53 (1996) 3374.
[8] M. Mito, T. Kawae, M. Takumi, K. Nagata, M. Tamura, M. Kinoshita, K. Takeda, Phys. Rev. B 56 (1997) 14255.
[9] N. Shirakawa, H. Horinouchi, Y. Yoshida, J. Magn. Magn. Mater. 272–276 (2004) e149.

(0.24 g, 1.0 mmol) was added to the resulting slurry and the mixture was stirred for 63 h at 90 °C. The reaction mixture was quenched with 100 ml water and yellow suspension was extracted with dichloromethane. Organic phase was evaporated and obtained crude products was purified with silica-gel column chromatography with dichloromethane/hexane (1/1, v/v) as an eluent to yield 0.24 g of $dppFc_2$ as orange powder (0.41 mmol, 41%). *Anal*. Calc. for $C_{31}H_{25}N_5Fe_2$: C, 64.28; H, 4.35; N, 12.09. Found: C, 64.18; H, 4.62; N, 12.11%. ^{1}H NMR (270 MHz, $CDCl_3$, 25 °C): δ 8.51(d, $J = 2.7$, 2H, pz), 7.89 (m, 3H, py), 6.54 (d, $J = 2.7$, 2H, pz), 4.79 (s, 4H, Cp), 4.34 (s, 4H, Cp), 4.11 (s, 10H, Cp).

2.1.2. $[Fe(dppFc_2)_2](BF_4)_2$

A solution of $Fe(BF_4)_2 \cdot 6H_2O$ (44 mg, 0.13 mmol) in degassed acetone (5 ml) was added to the orange suspension of $dppFc_2$ (35 mg, 0.06 mmol) in acetone (5 ml) and stirred for 30 min to obtain deep orange solution. Addition of diethylether to the deep orange solution gave brown powder. Recrystallization from acetonitrile and diethylether gave deep red crystals of $[Fe(dppFc_2)_2](BF_4)_2$. *Anal*. Calc. for $C_{62}H_{50}B_2F_8Fe_5N_{10} \cdot 4H_2O$: C, 51.00; H, 4.00; N, 9.59. Found: C, 51.18; H, 3.91; N, 9.50%.

2.2. X-ray crystallography

Each crystal of $dppFc_2$ and $[Fe(dppFc_2)_2](BF_4)_2 \cdot 3CH_3CN$ was mounted on a glass capillary, and data were collected at −30 °C (Bruker SMART APEX diffractometer coupled with a CCD area detector with graphite monochromated Mo Kα($\lambda = 0.71073$ Å) radiation). The structure was solved by direct methods and expanded by using Fourier techniques using SHELXTL program. Crystal data: [$dppFc_2$]: $C_{31}H_{25}Fe_2N_5$, $M = 579.26$, monoclinic space group $P2_1/n$, $a = 14.246(2)$, $b = 9.793(1)$, $c = 17.910(3)$ Å, $\beta = 90.055(3)°$, $V = 2498.6(7)$ Å^3, $Z = 4$. A total of 10 770 were collected ($1.83° < \theta < 23.26°$) of which 3580 unique reflections ($R_{int} = 0.0546$) were measured. Residual R and wR were 0.0424 and 0.1297, respectively, from the refinement on F^2 with $I > 2\sigma(I)$. [$[Fe(dppFc_2)_2](BF_4)_2 \cdot 3CH_3CN$]: $C_{62}H_{54}F_8Fe_5N_{13}B_2$, $M = 1506.11$, monoclinic space group $C2/c$, $a = 21.864(3)$, $b = 21.536(2)$, $c = 29.389(3)$ Å, $\beta = 102.721(2)°$, $V = 13498(3)$ Å^3, $Z = 8$. A total of 30 072 were collected ($1.34° < \theta < 23.30°$) of which 9712 unique reflections ($R_{int} = 0.0499$) were measured. Residual R and wR were 0.0539 and 0.1459, respectively, from the refinement on F^2 with $I > 2\sigma(I)$. Empirical absorption corrections by SADABS (G.M. Sheldrick, 1994) were carried out. In the structure analyses, non-hydrogen atoms were refined with anisotropic thermal parameters. Hydrogen atoms were included in calculated positions and refined with isotropic thermal parameters riding on those of the parent atoms.

2.3. Physical measurements

DC magnetic susceptibility data were collected by using a Quantum Design MPMS-XL SQUID magnetometer at temperatures ranging from 1.8 to 300 K. Cyclic voltammetry measurements were carried out in a standard one-compartment cell under N_2 equipped with a platinum-wire counter electrode, a grassy carbon electrode and a saturated calomel electrode (SCE) with an ALS 620A electrochemical analyzer.

3. Results and discussion

3.1. Descriptions of crystal structures: $dppFc_2$ and $[Fe(dppFc_2)_2](BF_4)_2 \cdot 3CH_3CN$

Single crystals of $dppFc_2$ for X-ray crystallography were obtained by slow evaporation of dichloromethane/hexane solution. An ORTEP diagram of $dppFc_2$ is shown in Fig. 1. $dppFc_2$ crystallizes in monoclinic space group $P2_1/n$. Two ferrocenyl groups are attached to 3-position of pyrazole rings and show an anti-parallel conformation with each other. Cyclopentadienyl rings are coplanar with three heterocyclic rings of tridentate ligand moiety, which indicates weak π-conjugation between them. $[Fe(dppFc_2)_2](BF_4)_2 \cdot 3CH_3CN$ crystallizes in monoclinic space group $C2/c$, and the unit cell contains two crystallographic independent molecules. Each central iron(II) ions show both significantly distorted octahedral surroundings composed of six nitrogen atoms from two tridentate $dppFc_2$ ligands (Fig. 2). Coordination bond lengths are in the range of 2.134(5)–2.190(4) Å, characteristic of bond lengths for a high spin iron(II) ion. Bite angles of tridentate ligands to iron(II) ion (N1–Fe1–N2 and N4–Fe1–N5) are 73.1(1)° and 72.67(9)°, respectively. Distortion can be quantified using Σ parameters defined by Guionneau et al. [19] Σ parameter is the sum of the deviations from 90° of the 12 bite angles in the coordination sphere, and the large Σ value represents large distortion of octahedron from ideal one. The Σ values are estimated to be 168.62° and 169.28° for two complex cations, which

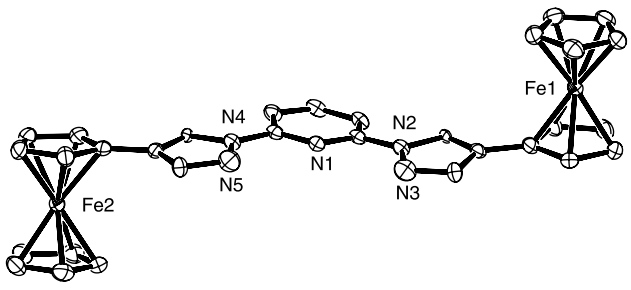


Fig. 1. ORTEP drawing of $dppFc_2$.

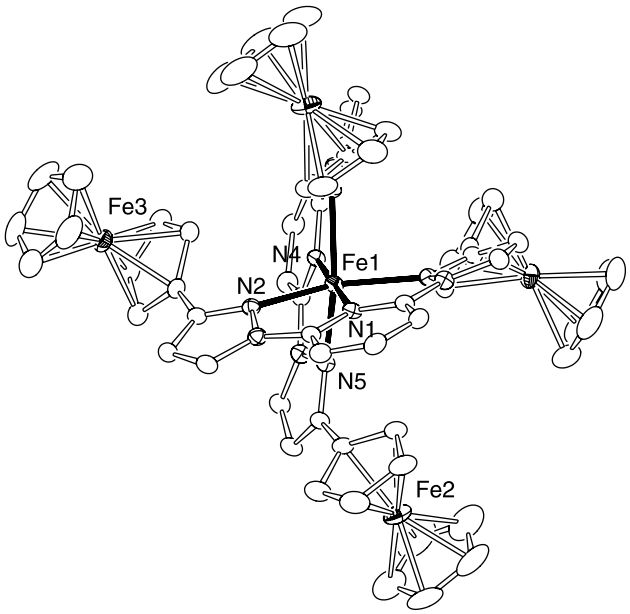


Fig. 2. ORTEP drawing of $[Fe(dppFc_2)_2]^{2+}$. Selected bond lengths (Å) and angles (°): Fe(1)–N(1) 2.134(5), Fe(1)–N(4) 2.135(5), Fe(1)–N(2) 2.181(4), Fe(1)–N(5) 2.185(3), Fe(2)–C(10) 2.018(4), N(1)–Fe(1)–N(2) 73.1(1), N(4)–Fe(1)–N(2) 106.9(1), N(1)–Fe(1)–N(5) 107.3(1), N(4)–Fe(1)–N(5) 72.67(9), N(2)#1–Fe(1)–N(5) 102.9(1), N(2)–Fe(1)–N(5) 87.1(1), N(1)–Fe(1)–N(5)#1 107.33(9), N(4)–Fe(1)–N(5)#1 72.7(1). Symmetry operation #1: $-x, y, -z + 1/2$.

show good agreement with the values for high spin iron(II) complexes with tridentate nitrogen ligands. In $[Fe(dppFc_2)_2](BF_4)_2 \cdot 3CH_3CN$, conformations of two ferrocenyl groups in the ligand are anti-parallel and two cyclopentadienyl rings are distorted from three heterocyclic rings plane with torsion angles of C8–C9–C10–C14 being 140.0(5)°, which may be due to the steric hindrance between ferrocenyl groups.

3.2. Redox properties of $dppFc_2$ and $[Fe(dppFc_2)_2](BF_4)_2$

In the electrochemical measurements, the tridentate ligand $dppFc_2$ undergoes reversible one-step $2e^-$ oxidation on two ferronenyl groups at $E^{0'} = 0.47$ V versus SCE. In the cyclic voltammogram of $[Fe(dppFc_2)_2](BF_4)_2$ with potential scans between 0.00 and 0.90 V versus SCE showed two irreversible redox couples (Fig. 3). The first couple of oxidation and re-reduction waves was observed at $E_1^{0'} = 0.47$ V versus SCE, which is same as the value of $dppFc_2$. In the first couple, re-reduction current is much larger than that in oxidation wave. When the positive limit of the potential scan is 0.55 V, the large re-reduction wave does not appear (Fig. 3). While the second redox couple at $E_2^{0'} = 0.63$ V showed smaller re-reduction current than that in oxidation. By comparison of the redox potentials, the first redox couple

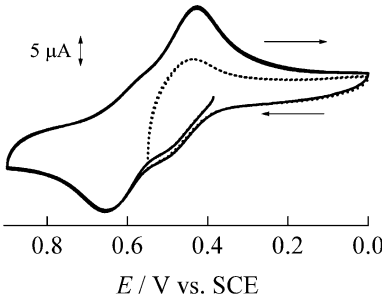
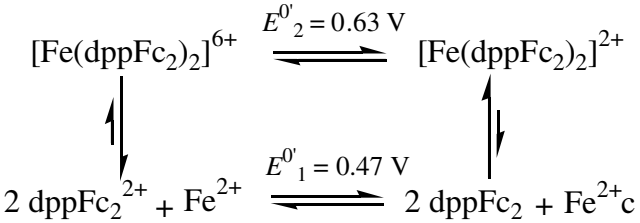


Fig. 3. Cyclic voltammogram of $[Fe(dppFc_2)_2](BF_4)_2$ at a glassy carbon electrode in 0.1 mol dm^{-3} $[Bu_4N][PF_6]$/MeCN at a scan rate of 0.1 V s^{-1}.

was assigned to $dppFc_2/dppFc_2^{2+}$ and irreversibility of two-step redox process in $[Fe(dppFc_2)_2]^{2+}$ can be interpreted by the EC mechanism and dissociation equilibrium in MeCN solution as shown in Scheme 1. Before oxidation of the two ferrocenyl moiety, $[Fe(dppFc_2)_2]^{2+}$ species is dominant in MeCN solution, while after the oxidation electronic repulsion between central iron(II) ion and ferrocenyl cations may cause the ligand dissociation.

3.3. Magnetic susceptibility measurements of $[Fe(dppFc_2)_2](BF_4)_2 \cdot 3CH_3CN$

Temperature dependence of magnetic susceptibilities for $[Fe(dppFc_2)_2](BF_4)_2 \cdot 3CH_3CN$ was measured in the temperature range of 2–300 K (Fig. 4). At room temperature the $\chi_m T$ value is 3.35 emu mol^{-1} K, which corresponds to the spin-only value for a non-interacting high spin Fe^{II} ion. $\chi_m T$ values are almost constant down to 80 K, followed by sudden decrease below 50 K which is due to the zero-field splitting of the high spin iron(II) ion. The temperature independent $\chi_m T$ values indicates $[Fe(dppFc_2)_2](BF_4)_2 \cdot 3CH_3CN$ is in the high spin state in all temperature range measured. An iron(II) complex with similar ferrocenyl-substituted tridentate ligand shows spin conversion between high- and low-spin state at T_c = ca. 370 K, in which ferrocenyl group attaches to 4-position on the pyridine ring with ester bond [20]. The absence of spin conversion in $[Fe(dppFc_2)_2](BF_4)_2 \cdot 3CH_3CN$ can be attributable to the steric hindrance



Scheme 1.

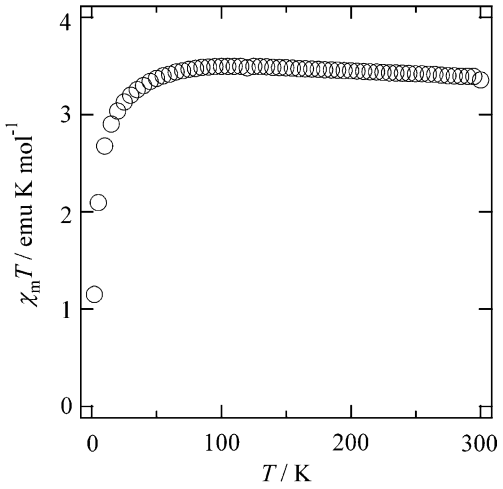


Fig. 4. Plot of $\chi_m T$ vs. T for $[Fe(dppFc_2)_2](BF_4)_2 \cdot 3CH_3CN$.

between ferrocenyl groups which causes significant distortion of coordination geometry and stabilizes the high spin state in the central iron(II) ion.

4. Conclusion

Tridentate ligand with two ferrocenyl groups give an opportunity to assemble four redox-active centre by coordination to iron(II) ion. The complex with four ferrocenyl groups undergoes two irreversible redox process in EC mechanism.

5. Supplementary material

Crystallographic data reported in this paper have been deposited with Cambridge Crystallographic Data Centre as supplementary publication no. CCDC 251833 and 251834. These data can be obtained free of charge via www.ccdc.cam.ac.uk/conts/retrieving.html (or from the Cambridge Crystallographic Data Centre, 12, Union Road, Cambridge CB2 1EZ, UK; fax: +44 1223 336 033; or deposit@ccdc.cam.ac.uk).

Acknowledgements

This work was partially supported by a Grant-in-aid for Scientific Researches from the Ministry of Education, Culture, Sports, Science and Technology, Japan, and by the COE and TARA projects of University of Tsukuaba.

References

[1] M. Kimura, T. Horai, T. Muto, K. Hanabusa, H. Shirai, Chem. Lett. (1999) 1129.
[2] S. Kelch, M. Rehahn, Macromolecules 32 (1999) 5818.
[3] U. Velten, B. Lahn, M. Rehahn, Macromol. Chem. Phys. 198 (1997) 2789.
[4] U.S. Schubert, C. Eschbaumer, Angew. Chem. Int. Ed. 41 (2002) 2892.
[5] U.S. Schubert, C.H. Weidl, C.N. Moorefield, G.R. Baker, G.R. Newkome, Polym. Preprints 40 (1999) 940.
[6] B.J. Holliday, C.A. Mirkin, Angew. Chem. Int. Ed. 40 (2001) 2022.
[7] A. Harriman, R. Ziessel, Chem. Commun. (1996) 1707.
[8] A.M. DeBlass, C. DeSantis, L. Fabbrizzi, M. Liccheli, P. Pallavicini, A. Poggi, in: V. Balzani (Ed.), Supramolecular Chemistry, Kluwer Academic Publishers, London, 1995, pp. 87–103.
[9] S. Achar, C.E. Immoos, M.G. Hill, V.J. Catalano, Inorg. Chem. 36 (1997) 2314.
[10] N. Sachsinger, C.D. Hall, J. Organomet. Chem. 531 (1997) 55.
[11] I.R. Butler, N. Burke, L.J. Hobson, H. Findenegg, Polyhedron 19 (1992) 2435.
[12] B. König, M. Nimtz, H. Zierg, Tetarahedron 22 (1995) 6267.
[13] U. Siemeling, U. Vorfeld, B. Neumann, H.G. Stammler, P. Zanello, F. Fabrizi de Biani, Eur. J. Inorg. Chem. (1999) 5.
[14] M.E. Padilla-Tosta, R. MartínezMánez, J. Soto, J.M. Loris, Tetrahedron 51 (1998) 12039.
[15] I.R. Butler, S.J. McDonald, M.B. Hursthouse, K.M. AdulMalik, Polyhedron 14 (1995) 529.
[16] J. Elhaïk, V.A. Money, S.A. Barrett, C.A. Kilner, I.R. Evans, M.A. Halcrow, J. Chem. Soc., Dalton Trans. (2003) 253.
[17] J.M. Holland, J.A. McAllister, C.A. Kilner, M. Thornton-Pett, A.J. Bridgeman, M.A. Halcrow, J. Chem. Soc., Dalton Trans. (2002) 548.
[18] N. Almirante, A. Cerri, G. Fedrizzi, G. Marazzi, M. Santagostinio, Tetrahedron Lett. 39 (1998) 3287.
[19] P. Guionneau, M. Marchivie, G. Bravic, J.-F. Létard, D. Chasseau, J. Mater. Chem. (2002) 2546.
[20] Unpublished data.

observed that the magnetic coupling is predominantly one-dimensional and ferromagnetic along the chain direction, with the latter feature setting $MnNi(NO_2)_4(en)_2$ apart from the usual antiferromagnetic alignment in other bimetallic chains. From the study of the bulk properties the coupling strength has been determined to $J_{\parallel\text{chain}}/k_B = 1.9$ K. In addition, from the anisotropy of the magnetic properties a zero field splitting of $D/k_B = -0.45$ K has been derived. In the presence of the zero field splitting D and together with a finite inter-chain coupling $J_{\perp\text{chain}}$, the intra-chain coupling $J_{\parallel\text{chain}}$ causes the system to undergo an antiferromagnetic transition below $T_N = 2.3$ K. In the antiferromagnetic phase the spins point along the easy crystallographic c-direction, with a ferromagnetic alignment within the a–b-plane and antiferromagnetic coupling along the c-axis. Extending the work from [7], by means of a high-temperature series expansion [8] the susceptibility of $MnNi(NO_2)_4(en)_2$ has been fitted, yielding values $J_{\parallel\text{chain}} = 2.8$ K, $D = -0.36$ K and $J_{\perp\text{chain}} = -0.036$ K.

Here, we present measurements of the lattice parameters and the magnetization under pressure on $MnNi(NO_2)_4(en)_2$. From the pressure dependence of the lattice parameters we derive the bulk modulus, which turns out to be comparatively small, and as it is typical for molecule-based magnetic materials. Furthermore, from the magnetization experiments we determine the pressure dependence of the antiferromagnetic transition temperature. We find only a very small increase with pressures as high as 8.2 kbar, which combined with the structural data corresponds to an unusally small magnetic Grüneisen parameter of $\Gamma_{mag} = 0.5(5)$. Finally, we discuss possible explanations for this small Grüneisen parameter.

2. Experimental

We have performed neutron powder diffraction and magnetization experiments under applied hydrostatic pressure. The neutron diffraction experiments have been carried out on non-deuterated material $MnNi(NO_2)_4(en)_2$ at the Berlin Neutron Scattering Center (BENSC) of the Hahn-Meitner Institut, utilizing the Focusing diffractometer E6 with a neutron wavelength $\lambda = 2.448$ Å at $T = 2$ K. The pressure has been generated by means of a clamped pressure cell. The applied pressure has been determined from the lattice parameter of NaCl, of which some powder was included in the sample space.

The magnetization experiments have been performed in a commercial SQUID at temperatures ranging from 1.75 to 300 K. Here, for the pressure experiments a clamped pressure cell, fitting into the sample space of the SQUID and as described previously [1], has been employed. This cell allows the determination of the magnetization at pressures up to ~10 kbar. As a pressure medium we use Fluorinert FC77, while the applied pressure has been determined from the superconducting transition temperature of a piece of indium in the sample space.

3. Results and discussion

In Fig. 1, we plot the neutron diffraction spectra of $MnNi(NO_2)_4(en)_2$ taken at 2 K at ambient pressure and 3 kbar, respectively. In the plot, in addition to the Bragg reflections from $MnNi(NO_2)_4(en)_2$, those from the pressure standard NaCl can be observed as indicated. With the large experimental background from incoherent scattering by hydrogen and the pressure cell the signal-to-noise ratio is comparatively small, prohibiting a full refinement of the data and limiting the resolution of the experiment. Within these limits, however, we find no indication for a change of the crystallographic symmetry of the overall lattice. Moreover, the Bragg reflections shift with pressure. Using a profile matching technique, we obtain a reduction of the lattice parameters of $\Delta a/a = 0.36\%$, $\Delta b/b = 0.98\%$ and $\Delta c/c = 2.1\%$. The experimental resolution is insufficient to detect additional scattering contributions in the antiferromagnetically ordered state below T_N.

From the reduction of the lattice parameters we derive the bulk modulus $B = V\frac{\Delta p}{\Delta V}$, which we evaluate to 8.8 GPa. This is a very small value, reflecting the softness of this molecule-based material. Typical intermetallic compounds, for instance, generally have bulk moduli of the order of 100 GPa (for comparison see for instance [9,10]).

In Fig. 2(a), we plot the temperature dependence of the magnetization of $MnNi(NO_2)_4(en)_2$ in a field of 0.05 T at various pressure values $p \leqslant 8.2$ kbar. At ambient pressure the reported behavior [7] from the transi-

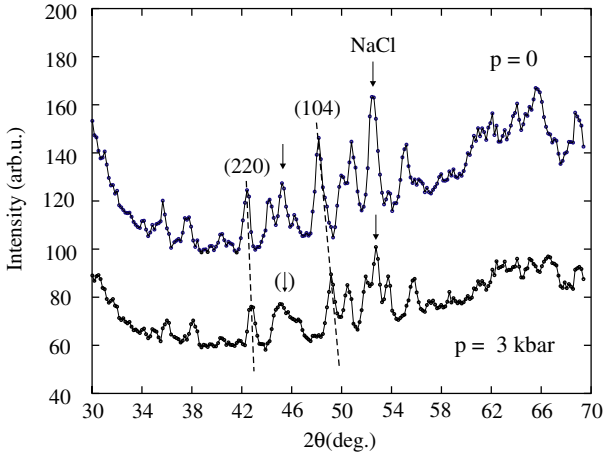


Fig. 1. The neutron diffraction spectra taken on $MnNi(NO_2)_4(en)_2$ taken at 2 K at ambient pressure and under applied pressure of 3 kbar. The positions of Bragg reflections from the pressure standard NaCl are indicated. Shifts of two selected reflections from the sample are marked by dashed lines. They differ considerably, indicating an anisotropic pressure response.

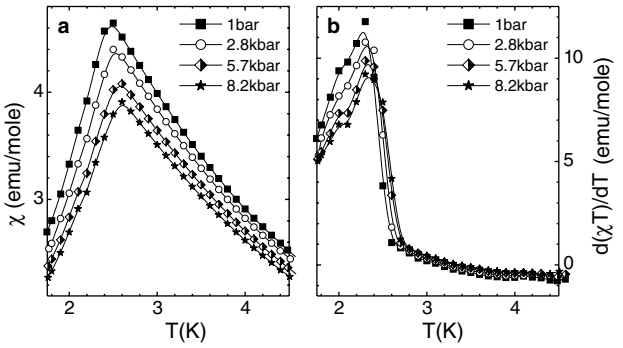


Fig. 2. (a) The temperature dependence of the magnetization of $MnNi(NO_2)_4(en)_2$ for externally applied pressure up to 8.2 kbar and an applied field of 0.05 T. (b) The temperature derivative $d(\chi T)/dT$ for the data from (a); for details see text.

tion into the antiferromagnetic state at low temperatures is reproduced. Within mean-field theory, the antiferromagnetic transition temperature is derived from the maximum of $d(\chi T)/dT$. Accordingly, in Fig. 2(b), we plot $d(\chi T)/dT$ as function of temperature, from which we obtain $T_N = 2.30$ K at ambient pressure.

With increasing pressure the antiferromagnetic peak shifts up slightly in temperature. From Fig. 2(b), we find an increase of T_N up to 2.41 K in 8.2 kbar, corresponding to an increase of T_N by less than 5(±4)%. The pressure response of T_N is summarized in Fig. 3.

To assess the relative strength of the pressure response it is common to determine the magnetic Grüneisen parameter defined as $\Gamma_{mag} = -\frac{d(\ln(T^*/T_0))}{d(\ln(V^*/V_0))}$. Here, T^* denotes the transition temperature under applied pressure with a unit cell volume V^*, while T_0 and V_0 represent the ambient pressure values. Assuming that the volume compression at low temperatures is linear with pressure up to 8.2 kbar, we obtain $\Gamma_{mag} = 0.5(5)$. This value is surprisingly small. For comparison, in our previous study on $FePM_2Cl_2$, we found $\Gamma_{mag} \sim 4$–7, which is a typical value for common magnets.

The antiferromagnetic transition temperature is determined by three energy scales, i.e., the values of $J_{\parallel chain}$, D and $J_{\perp chain}$. The zero field splitting D is a single ion effect and not expected to be strongly pressure dependent. The pressure effects on the inter- and intrachain coupling we can model by calculating "anisotropic" Grüneisen parameters, this way incorporating the highly anisotropic compression in our analysis.[1] Considering that $V^*/V_0 = (1-\frac{\Delta a}{a})(1-\frac{\Delta b}{b})(1-\frac{\Delta c}{c})$, we

[1] We have attempted to directly determine the pressure dependence of $J_{\parallel chain}$ and $J_{\perp chain}$ by fitting χ using high temperature series expansion as in [8]. Here, we assumed that the sample is aligned in the pressure such that the magnetic field B is parallel to the a-axis. Unfortunately, the pressure induced changes to χ in the temperature range relevant for the fit, 10–25 K, are too small, and thus the error bars to $J_{\parallel chain}$ and $J_{\perp chain}$ too large, as to allow an unambiguous conclusion on the pressure response of the magnetic exchange in $MnNi(NO_2)_4(en)_2$.

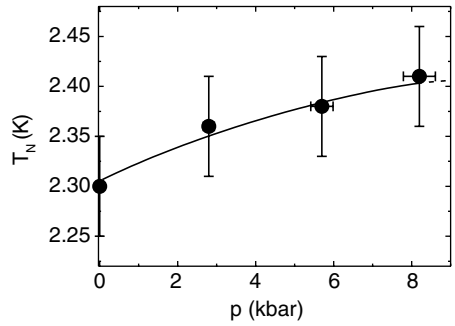


Fig. 3. The pressure dependence of T_N of $MnNi(NO_2)_4(en)_2$, as determined from the maximum of $d(\chi T)/dT$.

can derive corresponding expressions for the compression of the a–b-plane diagonal (the chain direction) and the c-axis. With the a–b-plane diagonal $d = \sqrt{a^2+b^2}$, we get $\Delta d/d = 0.50\%$. We define $\Gamma_{mag}(d) = -\frac{d(\ln(T^*/T_0))}{d(\ln((1-\frac{\Delta d}{d})^3))}$ and $\Gamma_{mag}(c) = -\frac{d(\ln(T^*/T_0))}{d(\ln((1-\frac{\Delta c}{c})^3))}$ and obtain values $\Gamma_{mag}(d) \sim 1$–2 and $\Gamma_{mag}(c) \sim 0.2$–0.3.

The very low value of $\Gamma_{mag}(c)$ indicates that in particular the c-axis compression is ineffective regarding the antiferromagnetic transition temperature. Then, one scenario to account for the small Grüneisen parameter would imply that any pressure induced increase of the magnetic exchange along the c-axis, which is mediated along van der Waals-bonded paths, is compensated by canting of the atoms and molecules making up the bond. In contrast, a second scenario would postulate magnetic frustration on the chain, where competing magnetic exchanges (for instance between nearest and next-nearest neighbors) limit the effect of pressure on the antiferromagnetic transition temperature. This latter scenario, however, appears to be very unlikely, since from the susceptibility study there is no evidence for frustration.

To test the scenario on the c-axis exchange high-resolution diffraction experiments under pressure would be necessary, this way to resolve the actual positions of all atoms and molecules. In addition, a uniaxial pressure experiments would be useful, as we would predict that for pressure applied along the c-axis almost no net increase of T_N should be observed, in contrast to an experiment with pressure along the a–b-diagonal.

4. Conclusions

In conclusion, we have performed high pressure experiments on the crystallographic structure and antiferromagnetically ordered phase of the bimetallic chain compound $MnNi(NO_2)_4(en)_2$. We obtain the bulk modulus at low temperatures, thus establishing the softness of the material. We determine the pressure response of the antiferromagnetic transition temperature T_N, which hardly increases up to 8.2 kbar. This weak response we tentatively attribute to the pressure effect of the magnetic exchange along the

crystallographic *c*-axis. Our findings demonstrate the importance in pressure experiments on molecule-based magnetic materials to establish at the same time the structural and magnetic properties as function of pressure.

Acknowledgments

We gratefully acknowledge SQUID access provided by D. Menzel and J. Schoenes at the IHO of the TU Braunschweig. This work has been supported by the Deutsche Forschungsgemeinschaft DFG under Contract No. SU229/6-1.

References

[1] A.U.B. Wolter, H.-H. Klauss, F.J. Litterst, T. Burghardt, A. Eichler, R. Feyerherm, S. Süllow, Polyhedron 22 (2003) 2139.
[2] M. Mito, T. Kawae, M. Takumi, K. Nagata, M. Tamura, M. Kinoshita, K. Takeda, Phys. Rev. B 56 (1997) R14255.
[3] M. Mito, T. Kawae, M. Hitaka, K. Takeda, T. Ishida, T. Nogami, Chem. Phys. Lett. 333 (2001) 69.
[4] A.U.B. Wolter, P. Wzietek, S. Süllow, F.J. Litterst, P. Auban-Senzier, D. Jérome, R. Feyerherm, H.-H. Klauss, J. Magn. Magn. Mat. 272–276 (2004) 1056.
[5] A.U.B. Wolter, P. Wzietek, S. Süllow, F.J. Litterst, P. Auban-Senzier, D. Jérome, R. Feyerherm, H.-H. Klauss, J. Phys. IV 114 (2004) 147.
[6] O. Kahn, E. Bakalbassis, C. Mathonière, M. Hagiwara, K. Katsumata, L. Ouahab, Inorg. Chem. 36 (1997) 1997.
[7] R. Feyerherm, C. Mathonière, O. Kahn, J. Phys.: Condens. Matter 13 (2001) 2639.
[8] N. Fukushima, A. Honecker, S. Wessel, W. Brenig, Phys. Rev. B 69 (2004) 174430.
[9] P. Haen et al., in: G. Oomi, H. Fuji, T. Fujita (Eds.), Transport and Thermal Properties of f Electron Compounds, Plenum Press, New York, 1993, p. 145.
[10] C. Wassilev-Reul, M. Kunz, M. Hanfland, D. Haeusermann, C. Geibel, F. Steglich, Physica B 230–232 (1997) 310.

in Fig. 1 [8,9]. The structure is cubic *Pm3m* at room temperature and elongated tetragonal or orthorhombic structure in the low temperature region both for NH_4MnF_3 and NH_4ZnF_3 [7,10–12]. Neutron magnetic scattering indicated that the antiferromagnetic ordering is essentially of the G-type according to Pickart et al. [13] and Gersch and Koeler [14] and in this arrangement, the magnetic lattice of Mn(II) ions is doubled in the three directions and each positive spin is surrounded by six negative spins. However, irregularity of the scattering suggests multi-axis structure of magnetic lattice [13]. We probed the magnetic characters of the magnetic lattice made by Mn(II) ions with local magnetic field caused by the Mn(II) spin at the deuterium site of ammonium ion. In this paper, we report characteristic behaviors of near-surface and inner spins of nano-particles determined by magnetic susceptibility measurement, and solid-state high-resolution and wide-line deuterium NMR spectrum. Particularly, internal magnetic field and critical behavior with approaching to Néel temperature in the antiferromagnetic phase were studied by solid-state wide-line deuterium NMR.

2. Experiments

2.1. Sample preparation

The bulk polycrystalline samples of ND_4MnF_3 (**1**) and $ND_4Mn_{0.5}Zn_{0.5}F_3$ (**3**) were prepared after a similar method reported by Silver [15] with using deuterated compounds, i.e., ND_4F and heavy water, instead of normal compounds. For the magnetically diluted compound **3**, a mixture of $MnCl_2$ and $ZnCl_2$ in equal mole was used as reactant. Nano-particle sample of ND_4MnF_3 (**2**) was synthesized by a reversed micelle method according to Roth and Hempelmann [16] with using deuterated reactant and deuterated ammonium-AOT as a surfactant. The surfactant of AOT-NH_4 was prepared by a cation exchange method reported in [17] and AOT-NH_4 was deuterated by several times of recrystallization from heavy water and AOT-ND_4 was dried in vacua.

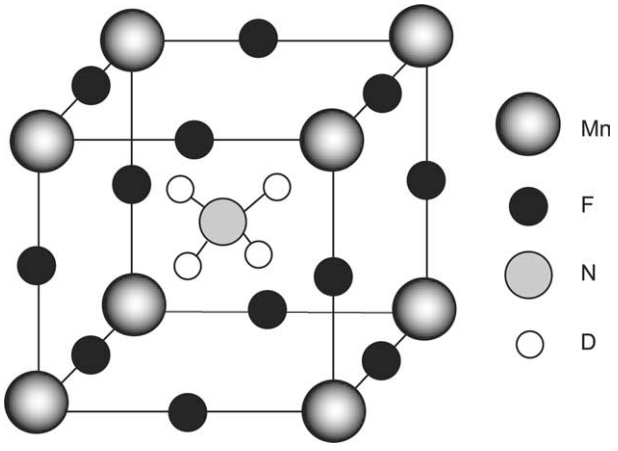


Fig. 1. Crystal structure of ND_4MnF_3. Cubic perovskite structure *Pm3m* in the room temperature phase and elongated tetragonal in the low temperature phase.

2.2. SEM and magnetic susceptibility measurements

The crystallite size was determined by scanning electron microscope (SEM) image. The particles were dispersed on mica and were coated by osmium by sputtering method.

Magnetic susceptibilities were measured with a MPMS SQUID magnetometer for samples of 29.9 mg of **1**, 12.4 mg of **2** and 27.4 mg of **3** between 5 and 300 K. The measurement was carried out with increasing temperature after cooling down to 5 K under zero external field (ZFC) or after field cooling (FC). The magnetic susceptibility of bulk compounds **1** and **3** was measured under magnetic field of 0.1 T, while under magnetic filed of 0.01, 0.1 and 1 T for the nano-particle **2**.

2.3. Solid-state high-resolution and wide-line deuterium NMR

Solid-state high-resolution deuterium NMR spectra in the paramagnetic phase were measured with magic angle spinning by a similar method described in [18] at the resonance frequency of 46.1 kHz and at spinning speed of ~7 kHz with a Bruker DSX300 spectrometer. The thermometer of the MAS NMR probe and an effect of spinning speed on temperature increase were carefully calibrated [18,19]. The MAS technique gives an isotropic shift of deuterium. The D-NMR shift was measured from the external second reference of CD_3OD (CD_3: 3.35 ppm).

Assuming a small zero field splitting, the observed isotropic shift δ_{iso} consists of the Fermi contact term, the dipole interaction term (pseudo contact) and the temperature independent diamagnetic term (chemical shift) as follows [20,21]:

$$\delta_{iso} = \delta_{Fermi} + \delta_{Pseudo} + \delta_{dia}, \quad (1)$$

$$\delta_{Fermi} + \delta_{Pseudo} = \frac{\mu_B}{3k_B T} \cdot \frac{A_C}{\gamma_D/2\pi} \cdot S(S+1). \quad (2)$$

Electron spin induced on the deuterium nucleus by electron spin of a magnetic metal ion causes a Fermi contact shift of the NMR resonance line, while anisotropy of the *g*-tensor of magnetic metal ions gives a pseudo contact shift. In the present case, the pseudo contact term (dipole term) is considered to be dominant. The coefficient A_C in Eq. (2) is defined as the hfcc of the deuterium

nucleus in Hz unit, which include principal values of anisotropic *g*-tensor.

Wide-line deuterium NMR spectra were measured for antiferromagnetic phase of **1**, **2** and **3** with a TECHMAG APOLLO NMR system at an external field of 7.0 T. The spectrum was measured by echo method. Since powder spectral width is extremely broadened in the antiferromagnetic phase, we measured echo signals at many different irradiation frequencies. The envelope of all the echo signals shows a line shape of the powder spectrum. In this measurement, a laboratory made cryostat was used for liquid helium temperature region.

3. Results and discussion

3.1. Determination of the crystallite size and structure

Powder X-ray diffraction pattern at room temperature was in agreement with a reported cubic *Pm3m* structure for all of the samples **1**, **2** and **3**. For the nano-particle sample **2**, broad diffraction peaks due to small size were observed in comparison with the bulk sample **1**. The size of the particle was determined to be ca. 30 nm by SEM as described below. In addition to the diffraction of ND_4MnF_3, a small amount of reactant of ND_4F was found as shown in Fig. 2. The amount of ND_4F was estimated to be 4% by solid-state high-resolution deuterium NMR spectrum as described in Section 3.2.

SEM images are shown in Fig. 3(a)–(c) for the sample **1**, **2** and **3**, respectively. This figure shows a smallest and isolated particle in what we found. Although major parts of nano-particles are closely assembled, each particle seems small as the isolated particle as shown in Fig. 3(b). TEM image is better to determine the size distribution of the nano-particles.

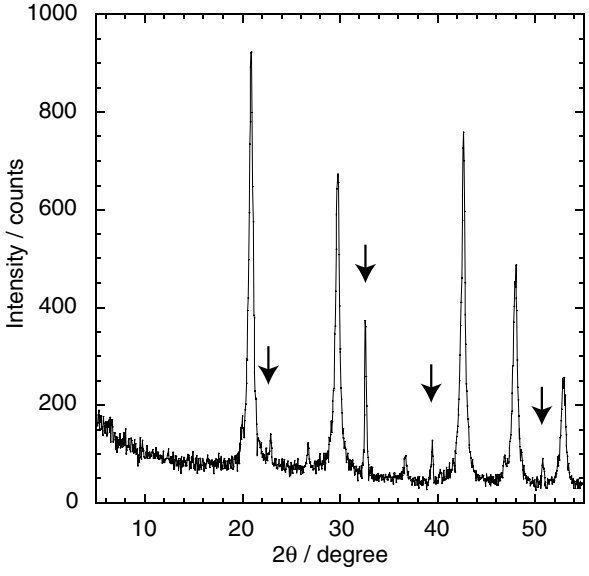


Fig. 2. X-ray powder diffraction pattern of nano-particles of ND_4MnF_3 (**2**). Small and sharp peaks indicated by arrows are due to a small amount of reactant of ND_4F.

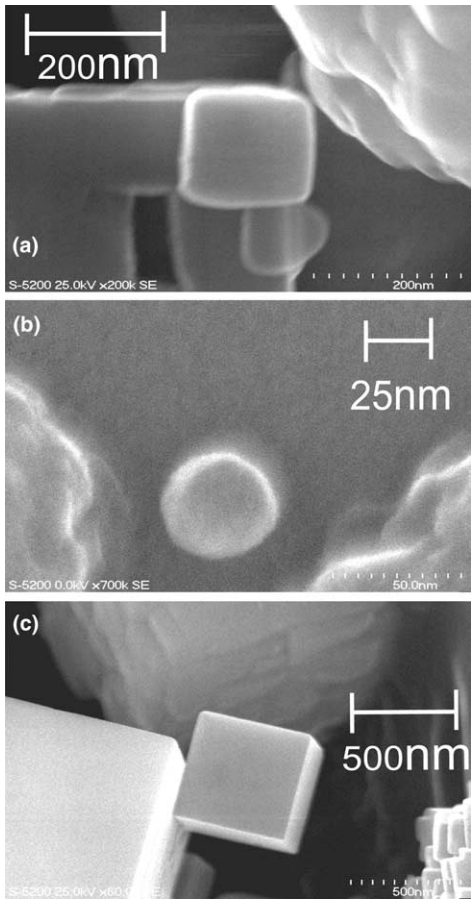


Fig. 3. Typical SEM images of **1** (a), **2** (b) and **3** (c).

3.2. Magnetic susceptibility

Magnetic susceptibility measured for **1**, **2** and **3** under ZFC condition was plotted as a function of temperature in Fig. 4(a). Magnetic susceptibility of sample **2** shows different behavior in the temperature region lower than ca. 20 K from that of bulk sample **1**. This difference can be ascribed to magnetic dipole moments made from near-surface spin. In a typical case of nano-particle of antiferromagnetic $KMnF_3$, magnetic susceptibility shows different behaviors for ZFC and FC, i.e., blocking of an orientation of residual magnetic moment near 10 K [1]. A similar behavior was reported for quenched ferrofluid system [6]. On the contrary, magnetic susceptibility of **2** under ZFC and FC showed almost the same temperature dependence and ZFC measurement showed no blocking behavior above 5 K. Namely, the blocking temperature is lower than 5 K for **2**. This result may be

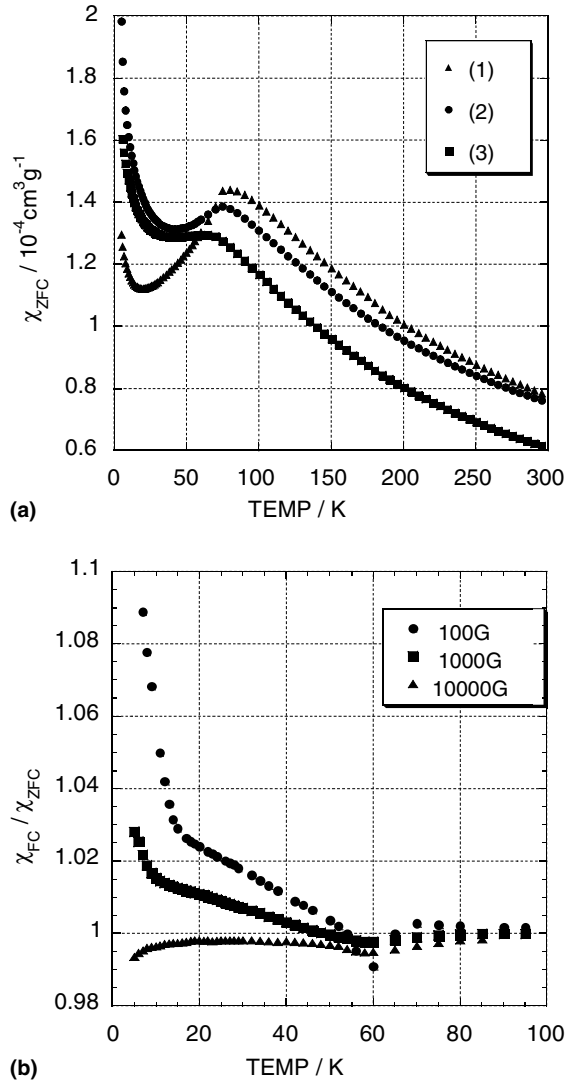


Fig. 4. (a) Magnetic susceptibility of **1**, **2** and **3** measured under zero field cooling and applied magnetic field of 0.1 T. (b) Field dependence of the ratio of magnetic susceptibility under field cooling (χ_{FC}) to that under zero field cooling (χ_{ZFC}) of 30 nm ND_4MnF_3 at different magnetic field of 0.01, 0.1 and 1 T.

ascribed to a relatively short relaxation time of orientation of the residual magnetic moment of **2**. Even in such a short relaxation time, the relaxation phenomena may be detected by field dependence of the magnetic susceptibility. So we measured in detail the susceptibility of nano-particle **2** under different applied fields of 0.01, 0.1 and 1 T. Fig. 4(b) shows the ratio of magnetic susceptibility under FC (χ_{FC}) to that under ZFC (χ_{ZFC}) for 30 nm particles. The ratio decreased with increasing external field and became almost unity at 1 T. This result means that the relaxation time of the orientation of the magnetic moment becomes shorter as the external magnetic field is increased. For example, magnetic moments, which were randomly oriented after ZFC, immediately align with respect to a direction of the external magnetic field of 1 T even at 5 K. The field dependence is particularly remarkable below 20 K. For investigating the near-surface spin state in a microscopic view point, we measured solid-state deuterium NMR spectrum. Magnetic behavior of Mn(II) ions can be detected through deuterium atom of ammonium ion.

3.3. Solid-state high-resolution deuterium NMR

Fig. 5 shows a comparison of solid-state high-resolution deuterium NMR spectra of **1**, **2** and **3** measured with the same experimental condition at 300 K in the paramagnetic phase. In order to compare the spectral line shapes among the three samples, peak positions of all the spectra were adjusted to the observed shift of the spectrum **2**. Particular attention was paid to the spectral shape and width. Compared with a spectrum of bulk ND_4MnF_3 (**1**), the signal of **2** has broad component as a tail, and the signal of **3** is remarkably asymmetric and skewed in the low frequency side. Now we consider the differences in the line shapes of the spectra. Width of the bulk sample **1** is the smallest and a center of this peak is shifted to higher frequency from diamagnetic ND_4F due to hyperfine coupling described in Eqs. (1) and (2). This hfc is brought about dominantly by eight Mn(II) ions in nearest neighbor around the ammonium ion shown in Fig. 1. For a bulk sample of magnetically diluted $ND_4Mn_{0.5}Zn_{0.5}F_3$, number of magnetic Mn(II) ions in the nearest neighbor is randomly distributed from 8 to 0 for individual ND_4^+ ion. For the smaller number of Mn(II) ion around the ND_4^+

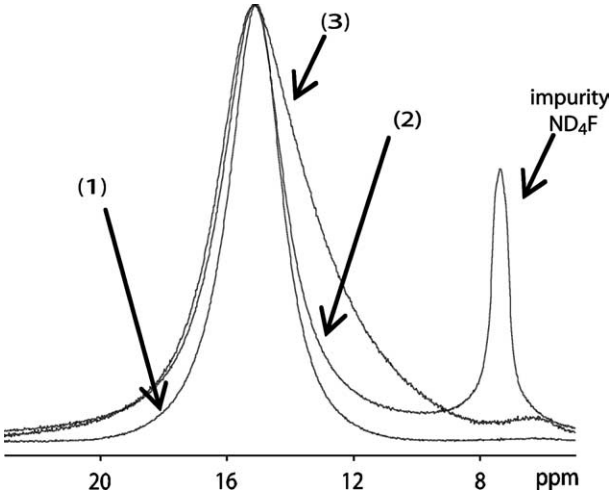


Fig. 5. Solid-state high-resolution deuterium NMR spectra of **1**, **2** and **3** at 300 K in the paramagnetic phase. In order to compare the spectral line shapes among the three samples, peak positions of all the spectra were adjusted to the observed shift of the spectrum **2**: −0.3 ppm and +1.0 ppm give the original shift of **1** and **3**, respectively.

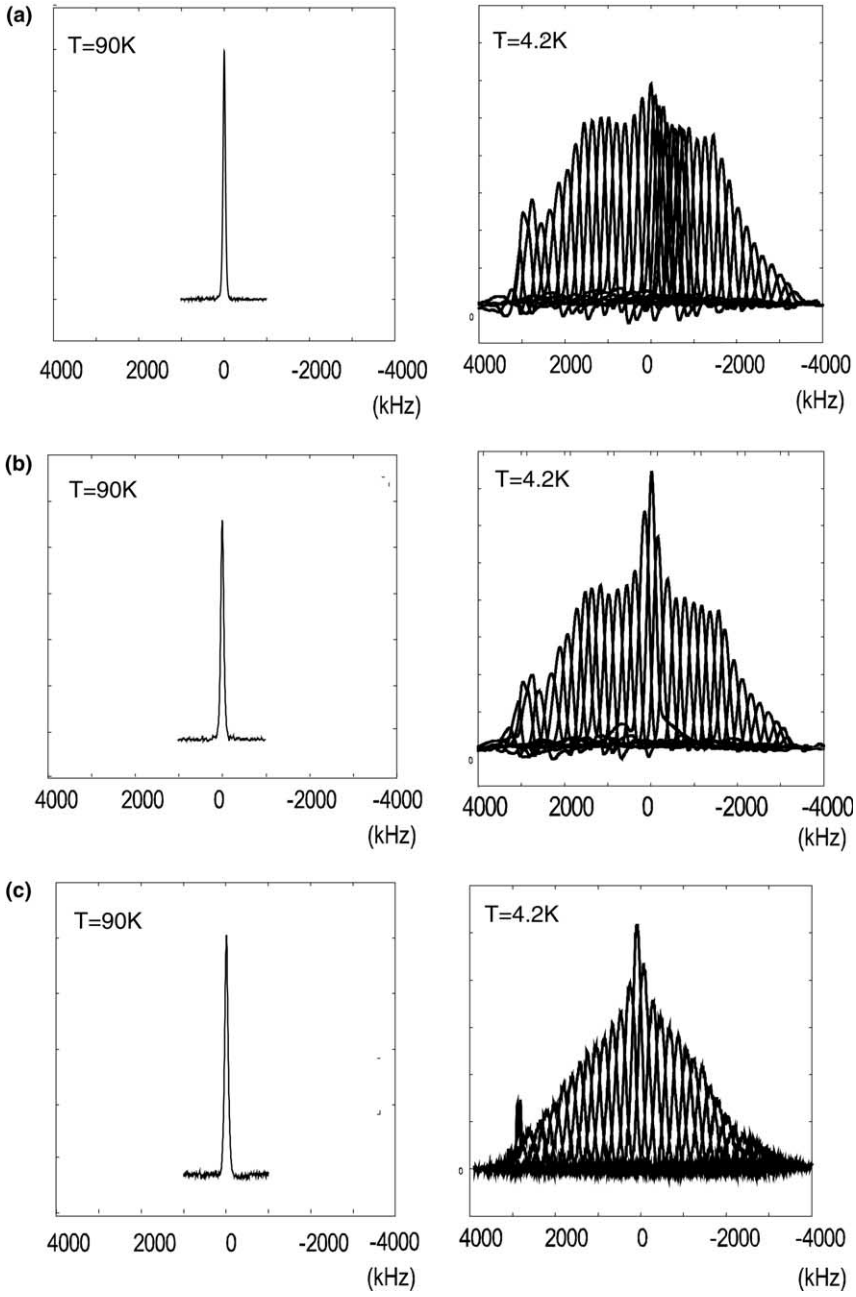


Fig. 6. Solid-state wide-line deuterium NMR spectra of **1** (a), **2** (b) and **3** (c) at 4.2 K in the antiferromagnetic phase and at 90 K in the paramagnetic phase. For the spectrum at 4.2 K, many echo signals measured with different irradiation frequencies were illustrated and a whole envelope is a powder pattern of the spectrum.

ion, the deuterium NMR of the ND_4^+ ions shows the lower frequency shift. Therefore, the deuterium NMR spectrum of $ND_4Mn_{0.5}Zn_{0.5}F_3$ has a long tail to the diamagnetic position. The spectrum of 30 nm ND_4MnF_3 (**2**) can be decomposed into two components, i.e., a sharp and a broad bottom components. We assigned broad component to the near-surface ammonium ions. The broadness may be brought about by a distribution of anisotropic *g*-tensor of Mn(II) ion near the surface. In addition, we also measured temperature dependence of these shift between 170 and 370 K. Slope of the peak shift plotted as a function of inverse temperature gave hfcc. The peak shift of sharp and broad component for nano-particle **2** gave small and almost the same values of hfcc = +8.4 and +8.6 kHz, respectively. Since deuterium atom of ND_4^+ has no direct bond with Mn(II) ion, a major origin of hfcc is magnetic dipole term.

3.4. Internal magnetic field and critical behavior determined by solid-state wide-line deuterium NMR

Fig. 6 shows wide-line deuterium NMR spectra of **1**(**a**), **2**(**b**) and **3**(**c**) at 90 K in the paramagnetic phase[1] and at 4.2 K in the antiferromagnetic phase. Full-width at half-maximum of the spectrum drastically broadened to 4 MHz in the antiferromagnetic phase. NMR signal of ND_4F as an impurity was not observed in the spectrum of **2**, because relaxation time of ND_4F is much longer than the repetition time for accumulation of the signal. The spectrum shows that deuterium atom of ND_4^+ ion looks at internal magnetic field of antiferromagnetically ordered electron spins of Mn(II) ions. In the spectrum of nano-particle **2**, narrow component with the width of 470 kHz was clearly observed, while such a narrow component was scarcely observed for bulk sample **1**. We assigned this narrow signal of the nano-particle **2** to the ammonium ions located in near-surface positions of the nano-particle. The narrow signal intimates a small internal magnetic field of near-surface region. The spectrum of magnetically diluted sample **3** is very different from the spectrum of the nano-particle **2**, since internal magnetic field distributes due to a random replacement of magnetic manganese ions with non-magnetic zinc ions.

In Fig. 7, temperature dependence of the spectrum width is shown for each sample. This figure represents the temperature dependence of the internal magnetic field for each sample **1**, **2** and **3**. The temperature variation of the internal magnetic field f can be written by the following empirical equation [24]:

$$f = f_0[1 + (T/T_N)^{\alpha}]^{\beta}. \quad (3)$$

The above function can be fitted to the bulk sample **1** as shown in Fig. 7(a). The value of $f_0 = 4100$ kHz was obtained for the internal magnetic field looked at the position of deuterium atom of ND_4^+ ion at zero temperature and the Néel temperature was determined to be $T_N = 70$ K. Parameter of $\alpha = 3.2$ represents the low temperature part of the internal magnetic field. The value of $\beta = 0.4$ is determined mainly by the internal magnetic field in the temperature range near T_N and closely related to the critical exponent. The function with the same parameters as for the bulk sample **1** is shown in Fig. 7(b) as dotted curve for comparing the critical behavior of the nano-particle **2** with the bulk sample **1**. In the nano-particle **2**, the internal magnetic field begins to decrease in the lower temperature region and shows a tail with approaching to 70 K, while the internal magnetic field in the low temperature limit is almost the same as that of the bulk sample. This behavior of the internal magnetic field of the nano-particle **2** does not resemble a behavior of magnetically diluted specimen **3**, in which much more gentle slope of temperature

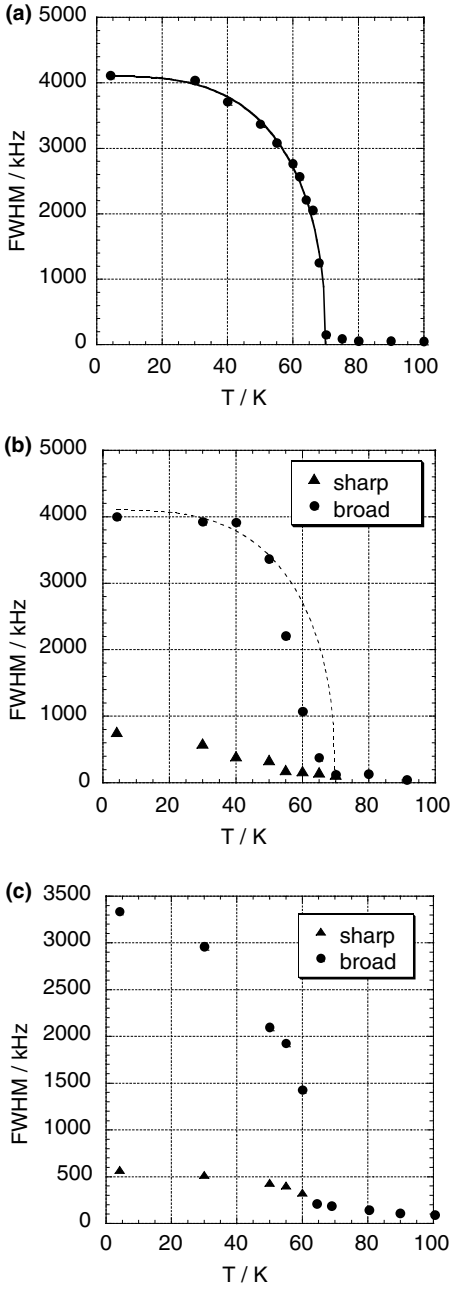


Fig. 7. Temperature variation of the internal magnetic field of **1** (a), **2** (b) and **3** (c) determined by temperature dependence of the full-width at half-maximum of wide-line deuterium NMR spectrum.

[1] Spectral shape can be expressed by a single gaussian for all of the sample and a half-width at half-maximum is 58, 69 and 92 kHz for **1**, **2** and **3**, respectively. The width is smaller than the peak to peak frequency of Pake doublet expected for the powder pattern of deuterium atom with quadrupole coupling of $e^2Qq/h = 180$ kHz of ND_4^+ ion without rotational motion [22,23]. This result indicates rapid rotational motion of the ND_4^+ ion in the crystalline lattice at 90 K for all of **1**, **2** and **3**. A rotational motion of the ND_4^+ ion may be expected in the lower temperature region as in the case of NH_4ZnF_3 [10]. However, the motion is not so rapid to average the internal magnetic field of ca. 4 MHz.

variation was observed as shown in Fig. 7(c). This behavior may be ascribed to a wide distribution of the magnetic domain size due to a random distribution of diamagnetic Zn(II) ions in the lattice. The near-surface spins of nano-particle **2** do not behave like a non-interacting curie spins, but have some ordering in small extent. If the near-surface spin of **2** had behaved as a curie spin, the width of the narrow component of deuterium NMR spectrum of **2** would be proportional to inverse temperature.

Acknowledgments

This research was supported by grant-in-aid for Scientific Research on Priority Areas ''Application of Molecular Spins'' (15087201) from the Ministry of Education, Culture, Sports, Science and Technology of Japan and partially by The Mitsubishi Foundation.

References

[1] Charles J. O'Conner, Vladimir Kolesnichenko, Everett Carpenter, Claudio Sangregorio, Wellie Zhou, Amar Kumbhar, Jessica Sims, Fabrice Agnoli, Synthetic Met. 122 (2001) 547.
[2] Eveerette E. Carpenter, Claudio Sangregorio, Charles J. O'Conner, Mol. Cryst. Liq. Cryst. 34 (1999) 641.
[3] Fabrice Agoli, Weili L. Zhou, Charles J. O'Conner, Adv. Mater. 13 (2001) 1697.
[4] Ki-Sub Kim, D. Demberelnyamaba, Huen Lee, Langmuir 20 (2004) 556.
[5] Young Sun, M.B. Salamon, K. Garnier, R.S. Averback, Phys. Rev. Lett. 91 (2003) 167206.
[6] Weili Luo, Sidney R. Nagel, T.F. Rosenbaum, R.E. Rosensweig, Phys. Rev. Lett. 67 (1991) 2721.
[7] R.B. Helmholdt, G.A. Wiegers, J. Baltolome, J. Phys. C13 (1980) 5081.
[8] M.A. Laguna, M.L. Sanjuán, V.M. Orera, J. Rubín, E. Palacios, M.C. Piqué, J. Bartolomé, J.F. Berar, J. Phys.: Condens. Matter 5 (1993) 283.
[9] R.B. Helmholt, G.A. Wiegers, J. Bartolome, J. Phyc. C: Solid State Phys. 13 (1980) 5081.
[10] H.B. Brom, J. Bartolome, Physica 111B (1981) 183.
[11] J. Bartolome, R. Navarro, D. Gonzalez, L.J. de Jongh, Physica 92B (1977) 23.
[12] R. Burriel, J. Bartolome, R. Navarro, D. Gonzalez, Proc. E.P.S. Conf. C.M.D., Antwerpen, Plenum Press, New York, 1980.
[13] S.J. Pickart, H.A. Alperin, R. Nathans, J. Phys. 25 (1964) 565.
[14] H. Gersch, W. Koehlwr, J. Phys. Chem. Solids 5 (1958) 180.
[15] J. Silver, J. Fluorine Chem. 8 (1976) 527.
[16] Marcel Roth, Rolf Hempelmann, Chem. Mater. 10 (1998) 78.
[17] Julian Eastoe, Brian H. Robinson, Richard K. Heenan, Langmuir 9 (1993) 2820.
[18] G. Maruta, S. Takeda, R. Imachi, T. Ishida, T. Nogami, K. Yamaguchi, J. Am. Chem. Soc. 121 (1999) 424.
[19] P.A. Beckmann, C. Dybowski, J. Magn. Reson. 146 (2000) 379.
[20] R. Kurland, B.R. McGervey, J. Magn. Reson. 2 (1970) 286.
[21] J.P. Jesson, in: G.N. La Mar, W. DeW. HorrocksJr., R.H. Holm (Eds.), NMR of Paramagnetic Molecules, Academic Press, New York, 1973.
[22] T. Chiba, Bull. Chem. Soc. Jpn. 43 (1970) 1939.
[23] T. Chiba, Bull. Chem. Soc. Jpn. 38 (1965) 490.
[24] A. Husman, S.J. Blaundell, Th. Jestädt, B.W. Lovett, I.M. Marshall, F.L. Pratt, L.E. Spring, P.D. Battle, M.J. Rosseinsky, Physica B 289–299 (2000) 69.

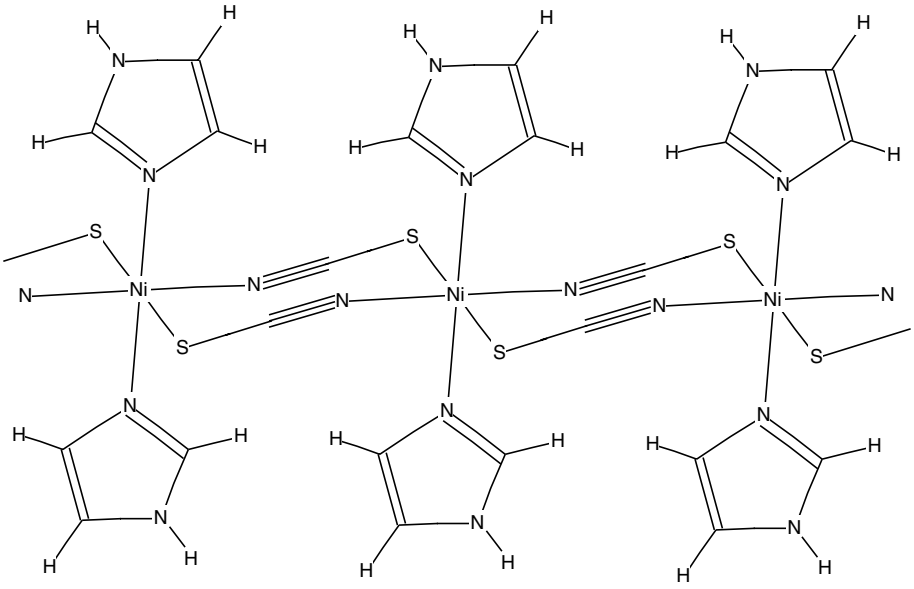


Fig. 1. One-dimensional chain structure of $Ni(NCS)_2(Him)_2$.

verify this theory are necessary to understand the intermolecular magnetic interaction in coordination compounds. In this work, we have employed Density functional theory (DFT) and NMR experiment [9] to elucidate role of the imidazole ligand in long range ordering.

Di-μ-thiocyanatobis(imidazole)nickel(II), $Ni(NCS)_2(Him)_2$, is a ferromagnet ($T_C = 5$ K) which consists of NCS-bridged one-dimensional Ni(II) chains as shown in Fig. 1 with the intrachain exchange interaction parameter ($2J$) of 8.0 cm^{-1} [3]. In this work, we determined electron spin density distribution of imidazole ligand in the compound by measuring solid-state high-resolution ^1H, ^2H, and ^{13}C NMR spectra in order to elucidate the interchain magnetic interaction essential for long-range order in the crystal. Partially or fully deuterated imidazole was used to prepare the sample and magic angle spinning (MAS) technique was employed to measure temperature dependence of the isotropic shifts of NMR signals. These experimental results indicate that unpaired electrons in the d-orbitals of the octahedral nickel(II) ion delocalize over the imidazole ligand. Consequently, we proposed an interchain superexchange pathway through N–H···S hydrogen bond.

2. Experimental

2.1. Preparations

1,2-Dideutero-imidazole was prepared by the literature method [10]. The degree of deuteration was estimated to be 70–80%. $Ni(NO_3)_2 \cdot 6D_2O$ was recrystallized from deuterium oxide. 1,2,4,5-Tetradeutero-imidazole (98% D, Cambridge Isotope Laboratories) and the other reagents were used as supplied. Non-deuterated sample of $Ni(NCS)_2(Him)_2$ (**1**) was prepared by a similar method described in [3]. $Ni(NO_3)_2 \cdot 6H_2O$ (2 mmol) and NaSCN (4 mmol) were dissolved in water (2 cm^3), then the aqueous solution was added to methanol solution (1 cm^3) of imidazole (4 mmol). The resulting blue solution was left to stand under N_2 gas flow at room temperature. Green crystal of $Ni(NCS)_2(Him)_2$ was obtained with violet crystal of $Ni(NCS)_2(Him)_4$. The products were separated by hand, washed with water and acetone, and dried in vacuo. Fully deuterated sample of $Ni(NCS)_2$(1,2,4,5-tetradeutero-Him)$_2$ (**4**) was prepared from 1,2,4,5-tetradeutero-imidazole with deuterated solvents of D_2O and CH_3OD. Partially deuterated samples of $Ni(NCS)_2$(1,2-dideutero-Him)$_2$ (**3**) and $Ni(NCS)_2$(2-deutero-Him)$_2$ (**2**) were prepared from 1,2-dideutero-imidazole with deuterated and protonated solvents, respectively.

2.2. NMR measurements

Solid-state high-resolution ^1H, ^2H, and ^{13}C NMR spectra of **1**–**4** were measured at a resonance frequencies of 300, 46.1, and 75.4 MHz, respectively, with a Bruker DSX300 spectrometer and a 4-mm CP/MAS probe. Temperature dependence of the spectra were measured for **3** from 300 to 200 K. MAS technique was used to obtain high-resolution spectra for the powder samples, whereas cross polarization or ^1H decoupling was not employed. The spinning rates of the samples were 9–10 kHz. The free induction decay (FID) of ^1H-MAS-NMR was accumulated from the first rotational echo after a $\pi/2$ pulse. For ^2H- or ^{13}C-MAS-NMR, π pulse

was applied at the first rotational echo after a π/2 pulse,then the FID was accumulated from the second rotational echo. The repetition time for each spectrum was 0.5 s. The thermometer of the MAS probe was calibrated against the isotropic chemical shift of the ^{207}Pb-MAS-NMR spectrum of $Pb(NO_3)_2$ [11]. The uncertainty of the temperature measurement after the calibration was 4 K, and the temperature fluctuation during the accumulation was within 1 K. The differences between the sample temperature T and the bearing gas temperature T_b, which was read from the thermometer, were 27 K at T = 202 and 7 K at T = 304 K for a spinning rate of 9 kHz.[1] ^{1}H, ^{2}H, and ^{13}C NMR shifts were measured from tetramethylsilane.

2.3. Computational methods

Using the GAUSSIAN-98 software package [12], we performed UB3LYP calculation on $[Ni(NCS)_2(SCN)_2(Him)_2]^{2-}$ as a molecular model for the coordination polymer. The geometric structure of the model was extracted from the crystal structure [3] determined by X-ray diffraction. The Wachters–Hay basis set [13,14] was used for Ni atom and the 6-31G(d,p) basis set was used for H, C, N, S atoms.

3. Results and discussion

3.1. NMR peak assignment

The observed isotropic lines in the ^{2}H-MAS-NMR spectra were accompanied by typically 30 spinning sidebands (SSBs) spaced at the spinning frequencies. This is because the anisotropic quadrupole interactions of the deuterons are much larger than the spinning frequencies. We confine ourselves to the isotropic part of the spectra though it is possible, in principle, to analyze the SSBs to deduce the anisotropic hyperfine interaction [15]. Fig. 2(a) shows the central part of the ^{2}H NMR spectrum of **3** measured at a spinning frequency of 9 kHz. Two isotropic lines corresponding to 1,2-deuterons of the imidazole ligand were observed at 69 and 46 ppm. A signal at 6 ppm was assigned to a trace of solvent because it flanked no SSBs. In the ^{2}H NMR spectrum of **2**, in which only 2-position of the imidazole ligand is deuterated, the peak at 69 ppm was disappeared. Thus, we assigned this peak to 1-deuteron and the peak at 46 ppm to 2-deuteron of imidazole. Fig. 2(b) shows the ^{1}H NMR spectrum of **3** measured at a spinning frequency of 9 kHz. An isotropic line at 52 ppm was assigned to unresolved signals of 4,5-protons of the imidazole ligand. This overlap of the two

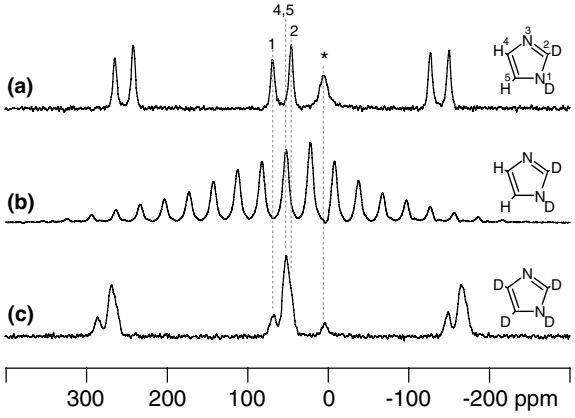


Fig. 2. (a) ^{2}H-MAS-NMR spectrum of **3** at 9 kHz and 304 K. (b) ^{1}H-MAS-NMR spectrum of **3** at 9 kHz and 304 K. (c) ^{2}H-MAS-NMR spectrum of **4** at 10 kHz and 306 K. Asterisk indicates trace of solvent.

peaks could not be removed in the ^{2}H-MAS-NMR spectrum of fully deuterated **4** at a spinning frequency of 10 kHz as shown Fig. 2(c). In this spectrum, the signal of 2-deuteron also overlapped those of 4,5-deuterons. We, therefore, measured temperature dependence of ^{2}H- and ^{1}H-MAS-NMR spectra of **3** to obtain the hyperfine coupling constants of the hydrogen atoms of the imidazole ligand.

Fig. 3(a) shows ^{13}C-MAS-NMR spectrum of **1** at a spinning frequency of 10 kHz and 306 K. Three isotropic lines were observed at 564, 318, 278 ppm though four inequivalent carbon sites exist in the crystal. We considered that the signal of ^{13}C in the thiocyanate ligand broadened out to baseline because of its fast transverse relaxation rate T_2^{-1} caused by large hyperfine coupling constants (hfcc) of this nucleus. We, consequently, assigned all the observed three lines to ^{13}C in the imidazole ligand. The peak at 318 ppm and its SSBs sharpened when protons of 1,2-position were substituted by

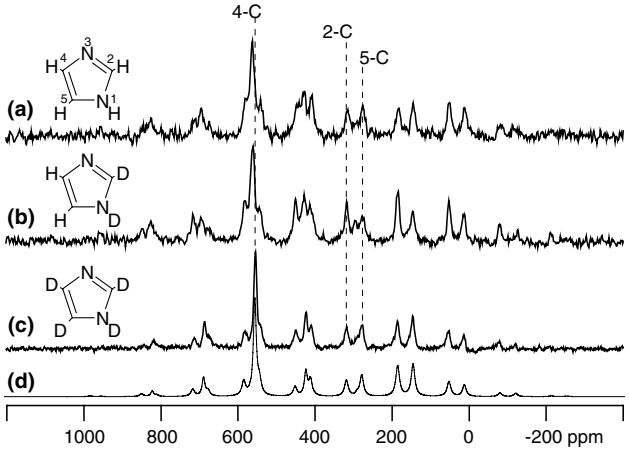


Fig. 3. ^{13}C-MAS-NMR spectra of: (a) **1**, (b) **3**, (c) **4** at a spinning frequency of 10 kHz and 306 K. Three isotropic lines of 561, 318 and 277 ppm are assigned to 4-, 2-, and 5-carbon, respectively. (d) ^{13}C-MAS-NMR spectrum synthesized with the parameters Δ^{calc} and η^{calc}.

[1] The difference $T - T_b$ originates from frictional heating, heat from the driving gas of room temperature, and uncalibrated T_b.

Table 1
Anisotropic and asymmetric parameters in 2,4,5-carbon of the imidazole ligand of $Ni(NCS)_2(Him\text{-}d_4)_2$ at 306 K

Position	δ_{iso} (ppm)	Δ^{exp} (ppm)	Δ^{calc} (ppm)	η^{exp}	η^{calc}
2-Carbon	318	520	530	0.8	0.4
4-Carbon	555	240	207	0.8	0.6
5-Carbon	278	440	450	0.7	0.6

deuterons as shown in Fig. 3(b). This narrowing is explained by the facts that (i) ^{13}C–^{1}H dipolar interaction is not completely removed under our MAS condition and (ii) the nuclear–nuclear dipolar interaction can be reduced chemically by deuteration. The degree of the reduction should be most significant for the adjacent carbon. Thus, we assigned the peak at 318 ppm to 2-carbon. When all the protons were substituted by deuterons, all the lines in ^{13}C NMR spectrum sharpened as shown in Fig. 3(c). We analyzed the SSB pattern of this spectrum to assign the remaining two peaks. In general, we can extract the principal values δ_{xx}, δ_{yy}, δ_{zz} of the NMR shift tensor from SSB pattern of ^{13}C-MAS-NMR spectrum [16]. These parameters can be expressed by another set of parameters, $\delta_{iso} = (\delta_{xx} + \delta_{yy} + \delta_{zz})/3$, $\Delta = \delta_{zz} - \delta_{iso}$, $\eta = (\delta_{xx} - \delta_{yy})/\Delta$, where $|\delta_{zz}| \geqslant |\delta_{xx}| \geqslant |\delta_{yy}|$. Using WIN-FIT [17] program, we fitted the ^{13}C-MAS-NMR spectrum of **4** with CSA mas model. The optimized parameters, δ_{iso}, Δ^{exp}, η^{exp}, are listed in Table 1. We found that the position of the isotropic line δ_{iso} of the signal at the highest frequency shifted from 564 ppm for **1** and **3** to 555 ppm for **4** by deuteration. The other two peak (318 and 278 ppm) remained the same within experimental errors. The cause of this shift is not fully understood at present. we guess that it was due to a slight modification of the crystal structure caused by deuterium substitution. The anisotropic parameter Δ^{exp} of the highest frequency peak was smaller than those of the other peaks, indicating this signal can be assigned to 4-carbon of which distance from nickel atom is long. To confirm this speculation, we computed anisotropic parameter Δ^{calc} and the asymmetric parameter η^{calc} for each carbon site from crystal structure parameters as discussed below.

Supposing the nuclear–nuclear dipolar interaction is decoupled, the NMR shift tensor is given as a sum of the hyperfine tensor and the chemical shift tensor [18]. The anisotropic part of the hyperfine tensor, which comes from electron–nuclear dipolar interaction, can be estimated by a point dipole model [19]. We put a point dipole bearing effective moment of $\mu_{eff} = g\sqrt{S(S+1)} = 2.18\sqrt{2}$ on each octahedral NiS_2N_4 unit. The spin distribution was taken to be 76% (nickel), 5% (sulfur), 4% (nitrogen of the thiocyanate), and 3% (nitrogen of the imidazole) on the basis of the DFT calculation. NiS_2N_4 units within 30 Å of the carbon were taken into account to calculate the dipolar field at 2,4,5-positions of the imidazole. The chemical shift tensor of each carbon was estimated from UB3LYP calculation on the molecular model. The hyperfine and the chemical-shift tensors were added together and diagonalized to obtain Δ^{calc} and η^{calc}. The parameters computed for each carbon site are listed in Table 1. The computed anisotropic parameters Δ^{calc} were consistent with Δ^{exp}, whereas agreement between asymmetric parameters η^{calc} and η^{exp} was not very good. This is probably due to low accuracy of the estimates of the chemical shift tensor. However, the agreement was sufficient for the purpose of assigning the two signals at 555 and 278 ppm to 4-carbon and 2-carbon, respectively. The ^{13}C-MAS-NMR spectrum of **4** is well reproduced by a spectrum synthesized with the parameters Δ^{calc} and η^{calc} (Fig. 3(d)), supporting the peak assignment.

3.2. Determination of the hyperfine coupling constants

The hfcc of the ^{1}H, ^{2}H and ^{13}C of the imidazole ligand were determined from the temperature dependence of the isotropic NMR shifts δ_{iso} measured for **3** using the following procedure.

The isotropic shift of a ligand nucleus in a paramagnetic metal complex consists of the Fermi contact term, the pseudo-contact term, and the diamagnetic term

$$\delta_{iso} = \delta_{Fermi} + \delta_{pc} + \delta_{dia}. \quad (1)$$

Kurland and McGarvey [20] gave a expressions for δ_{Fermi} and δ_{pc} of tetragonally distorted octahedral Ni^{2+} ($S = 1$) complex as

$$\delta_{Fermi} = \frac{2g_{iso}\mu_B A}{3k_B T(\gamma_{nuc}/2\pi)}\left[1 - \frac{g_\parallel - g_\perp}{9g_{iso}}\frac{D}{k_B T}\right], \quad (2)$$

$$\delta_{pc} = \frac{2\mu_B^2(g_\parallel^2 - g_\perp^2)}{9k_B T}\frac{3\cos^2\Omega - 1}{R^3}\left[1 - \frac{g_\parallel^2 - g_\perp^2/2}{3(g_\parallel^2 - g_\perp^2)}\frac{D}{k_B T}\right], \quad (3)$$

where A is the hfcc in hertz, T is the absolute temperature, γ_{nuc} is the gyromagnetic ratio of the nucleus, $g_\parallel$ and $g_\perp$ are the parallel and perpendicular components of the g tensor, D is the zero field splitting parameter, R is the length of a vector from the metal to the nucleus, Ω is the angle between the vector and z-axis, and the other terms have their usual meanings. The zero field splitting of $Ni(NCS)_2(Him)_2$ is so small ($D/k_B T < 2 \times 10^{-3}$ for $T > 200$ K) that we dropped the second terms of these equations. The intrachain magnetic interaction of the coordination polymer was included by substituting $T \to T - \theta$ where θ is the Weiss temperature. Then we obtained

$$\delta_{Fermi} = \frac{2g_{iso}\mu_B A}{3k_B(T - \theta)(\gamma/2\pi)}, \quad (4)$$

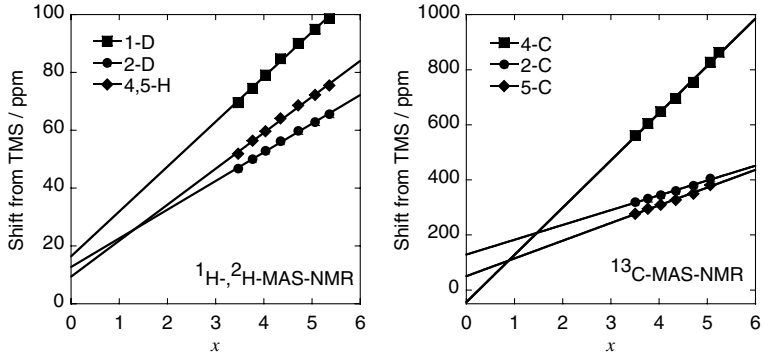


Fig. 4. Temperature dependence of the isotropic shifts of ^{1}H-, ^{2}H- and ^{13}C-MAS-NMR of **3**. The variable x is defined to be $x = 1000/(T/\mathrm{K} - 15.3)$ and is proportional to the magnetic susceptibility. The solid lines are the result of fitting to Eq. (9).

$$\delta_{\mathrm{pc}} = \frac{2\mu_{\mathrm{B}}^2(g_{\parallel}^2 - g_{\perp}^2)}{9k_{\mathrm{B}}(T-\theta)} \frac{3\cos^2\Omega - 1}{R^3}. \tag{5}$$

To determine A from the temperature dependence of δ_{iso}, we estimated the other parameters $g_{\parallel}$, $g_{\perp}$, and θ from published data. The Weiss temperature were estimated from the intrachain magnetic coupling constant $2J = 8.0\ \mathrm{cm}^{-1}$ [3], using

$$\theta = \frac{2zS(S+1)}{3k_{\mathrm{B}}}J, \tag{6}$$

where z is the number of the neighboring atoms and is equal to two for a simple magnetic chain. The estimated value of θ is 15.3 K. The g values of tetragonally distorted octahedral Ni^{2+} ($S = 1$) complex can be expressed as

$$g_{\perp} = 2.0023 - \frac{8\lambda}{\Delta E(^3\mathrm{B}_{1\mathrm{g}} \rightarrow {}^3\mathrm{E}_{\mathrm{g}})}, \tag{7}$$

$$g_{\parallel} = 2.0023 - 8\frac{8\lambda}{\Delta E(^3\mathrm{B}_{1\mathrm{g}} \rightarrow {}^3\mathrm{B}_{2\mathrm{g}})}, \tag{8}$$

where λ is the spin–orbit coupling constant and ΔE are the excitation energies. Using the literature values of $\Delta E(^3\mathrm{B}_{1\mathrm{g}} \rightarrow {}^3\mathrm{E}_{\mathrm{g}}) = 7480\ \mathrm{cm}^{-1}$, $\Delta E(^3\mathrm{B}_{1\mathrm{g}} \rightarrow {}^3\mathrm{B}_{2\mathrm{g}}) = 12\,130\ \mathrm{cm}^{-1}$, and $g_{\mathrm{iso}} = 2.18$ [3], we obtained $g_{\perp} = 2.21$ and $g_{\parallel} = 2.13$. The geometric parameters R were taken from the crystal structure, whereas Ω were approximated by zero for all the nuclei in the imidazole ligand, on the assumption that S–Ni–S was the symmetric axis. We finally obtained an expression of the isotropic NMR shift as

$$\delta_{\mathrm{iso}}/\mathrm{ppm} = \left[\frac{22.9 \times A/\mathrm{MHz}}{\gamma_{\mathrm{nuc}}/\gamma_{^1\mathrm{H}}} + \frac{47}{(R/\text{Å})^3}\right]x + \delta_{\mathrm{dia}}/\mathrm{ppm}, \tag{9}$$

where x is defined as

$$x = \frac{1000}{T/\mathrm{K} - 15.3}, \tag{10}$$

and δ_{dia} is assumed to be independent of temperature.

Temperature dependence of the isotropic shifts of ^{1}H-, ^{2}H- and ^{13}C-MAS-NMR of **3** were fitted by Eq. (9) as shown in Fig. 4. The experimental values of A are listed in Table 2 where the hfccs of deuteron were converted to those of proton by multiplying by the gyromagnetic ratio $\gamma_{^1\mathrm{H}}/\gamma_{^2\mathrm{H}}$. We observed that A of H and C are all positive values. The sign of A^{calc} obtained from DFT calculation were also positive and the $(A^{\mathrm{calc}} - A^{\mathrm{exp}})/A^{\mathrm{exp}}$ were within ±20% for carbon. This agreement between the experimental and theoretical hfcc encouraged us to utilize the calculated atomic spin density ρ^{calc} for discussing the spin density distribution of the imidazole ligand.

3.3. Spin density distribution of the imidazole ligand and possible interchain pathway

The positive signs of A of H and C can be explained by σ spin delocalization mechanism [21]. An octahedral Ni^{2+} ($S = 1$) complex has a $(t_{2g})^6(e_g)^2$ configuration and e_g orbitals are the SOMO of this complex. One of the e_g orbitals is composed of $d_{x^2-y^2}$ orbital of the nickel ion and σ orbitals of the ligand

$$e_{\mathrm{g}} = c_{\mathrm{d}}d_{x^2-y^2} + \sum_{k=1}^{4} c_k\sigma_k, \tag{11}$$

where c_{d} and c_k are appropriate coefficients. In the case of nickel–imidazole complexes, one of the σ orbitals is the n-orbital or a molecular orbital occupied by lone

Table 2
Hyperfine coupling constant A (MHz) and atomic spin density ρ of the imidazole ligand in $Ni(NCS)_2(Him)_2$ crystal

Position	A^{exp}	A^{calc}	ρ^{calc}
1-^{14}N		+0.81	+0.001
2-^{13}C	+0.57	+0.46	−0.007
3-^{14}N		+18.5	+0.057
4-^{13}C	+0.69	+0.85	−0.003
5-^{13}C	+1.88	+1.88	+0.003
1-^{1}H	+0.66	+0.45	
2-^{1}H	+0.37	+0.52	
4-^{1}H	+0.48	+0.63	
5-^{1}H	+0.53	+0.36	

electron-pair, which is mainly composed of an atomic orbital (AO) of 3-nitrogen. The coefficients of Eq. (11) is related to the spin delocalization from nickel into 3-nitrogen and the degree of the delocalization was $|c_{\mathrm{Him}}|^2 \simeq 0.06$ for $Ni(NCS)_2(Him)_2$ as is seen in Table 2. The electron spin is delocalized over the whole imidazole ligand because the n-orbital is not only composed of the AO of 3-nitrogen, but also of s-orbitals of hydrogen atoms and sp^2 orbitals of carbon atoms of the ligand. Though the contributions from these other AOs are small compared to that of the 3-nitrogen, the result that *all* of the observed A of H and C are positive values indicates that the σ spin delocalization is the dominant mechanism.

The other possible mechanism that induces spin density distribution is spin polarization mechanism, originally introduced by McConnell and Chesnut [22] to explain negative spin densities in aromatic radicals. It states that in molecular orbital theory the most likely spot to find a negative spin density is on a carbon atom which has zero spin density in the ground state configuration. Subsequently, it was extended to deal with non-aromatic radicals such as nitroxide or nitronyl nitroxide. It is sometimes referred to as alternation rule because the sign of the spin density alternates through successive bonds [23]. In the imidazole ligand of $Ni(NCS)_2(Him)_2$, the spin source that induces π spin polarization is the p_z orbital of 3-nitrogen of which electron spin is induced by n–π spin polarization. The alternation rule predicts negative spin densities on 2- and 4-carbon atoms and positive spin densities on 1-nitrogen and 5-carbon from this spin source. The calculated atomic spin densities ρ^{calc} listed in Table 2 are explained by this alternation rule but the experimental and theoretical hfccs are not. We thus concluded that the spin polarization dominates atomic spin densities of the π-electron systems in the imidazole ligand but the σ-electron systems is dominated by σ spin delocalization. The effect of the spin polarization on the σ-electron systems can be seen from the difference between hfcc of 5-carbon and those of 2,4-carbon in magnitude. Larger hfcc of 5-carbon indicates that the σ spin delocalization and the π spin polarization work cooperatively at this site but counterwork on 2,4-carbon atoms. It should be emphasized that the effect of the π spin polarization is negligible on hydrogen atoms, judging from the value of hfcc, and this positive spin densities of s-orbitals of the hydrogen atoms are brought by the σ spin delocalization. In other words, SOMO of this complex extends into the whole imidazole ligand.

The observed spin density distribution of the imidazole ligand in $Ni(NCS)_2(Him)_2$ qualitatively agreed with those of $[Ni(Him)_6]^{2+}$ [21] and $Cu(Him)_2Cl_2$ [24]. The nature of σ delocalization is independent of environment. Here, we briefly discuss the intermolecular magnetic interaction via the imidazole ligand. On the basis of above discussion, the $d_{x^2-y^2}$-based SOMO of $Ni(NCS)_2(Him)_2(SCN)_2$ unit is extended to 1-hydrogen that forms hydrogen bond with a sulfur atom of an adjacent chain as shown in Fig. 5(a). A p-orbital of this sulfur atom has MO coefficient of the other SOMO mainly composed of d_{z^2} of the nickel atom. Therefore, orthogonal SOMO–SOMO interaction occurs at N–H···S hydrogen bond. This causes a ferromagnetic interaction between the chains. In the case of $Cu(Him)_2Cl_2$, the $d_{x^2-y^2}$-based SOMO extended to 1-hydrogen has finite overlap integral between the SOMO of the adjacent Cu(II) complex (Fig. 5(b)). Thus, antiferromagnetic interaction occurs at N–H···Cl hydrogen bond. Imidazole ligand acts as either ferromagnetic or antiferromagnetic exchange coupler, depending on the crystal packing.

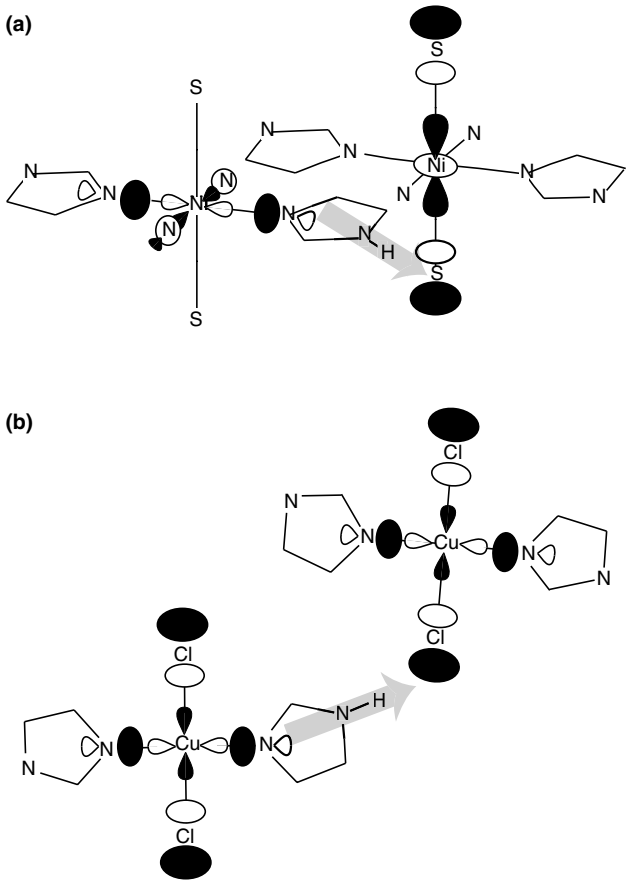


Fig. 5. Interchain SOMO–SOMO interactions via imidazole ligands in (a) $Ni(NCS)_2(Him)_2$ and (b) $Cu(Him)_2Cl_2$. Black and white represent opposite signs of the SOMO. The gray arrows indicate the delocalized SOMOs which extend onto the chain-bridging imidazole ligands. (a) Ferromagnetic interaction between the $d_{x^2-y^2}$-based and the d_{z^2}-based SOMOs. N–H bond is directed toward the *node* of the p-orbital of the sulfur. N···S distance is 3.38 Å and N···S–Ni angle is 92.7° [3]. (b) Antiferromagnetic interaction between the $d_{x^2-y^2}$-based SOMOs. N–H bond is directed toward the outer *lobe* of the p-orbital of the chlorine. N···Cl distance is 3.16 Å and N···Cl–Cu angle is 135.2° [7].

Acknowledgements

This research was supported by Grant-in-Aid for Scientific Research (Nos. 14740371 and 15087201) from the Ministry of Education, Culture, Sports, Science and Technology of Japan.

References

[1] S.J. Blundell, F.L. Pratt, J. Phys. 16 (2004) R771.
[2] J.V. Yakhmi, Macromol. Symp. 212 (2004) 141.
[3] B. Żurowska, J. Mroziński, M. Julve, F. Lloret, A. Maslejova, W. Sawka-Dobrowolska, Inorg. Chem. 41 (2002) 1771.
[4] J. Cano, P.S. Alemany, M. Verdaquer, E. Ruiz, Chem. Eur. J. 4 (1998) 476.
[5] F. Fabrizi de Biani, E. Ruiz, J. Cano, J.J. Novoa, S. Alvarez, Inorg. Chem. 39 (2000) 4271.
[6] B. Gillon, in: J.S. Miller, M. Drillon (Eds.), Magnetism: Molecules to Materials, Wiley–VCH, Weinheim, 2001, p. 357.
[7] B.K.S Lundberg, Acta Chem. Scand. 26 (1972) 3977.
[8] W.E. Estes, W.E. Hatfield, J.A.C. van Ooijen, J. Reedijk, J. Chem. Soc., Dalton Trans. (1980) 2125.
[9] F.H. Köhler, in: J.S. Miller, M. Drillon (Eds.), Magnetism: Molecules to Materials, Wiley–VCH, Weinheim, 2001, p. 379.
[10] R.J. Gillespie, A. Grimison, J.H. Ridd, R.F.M. White, J. Chem. Soc. (1958) 3228.
[11] A. Bielecki, D.P. Burum, J. Magn. Reson. A 116 (1995) 215.
[12] M.J. Frisch, G.W. Trucks, H.B. Schlegel, G.E. Scuseria, M.A. Robb, J.R. Cheeseman, V.G. Zakrzewski, J.A. Montgomery Jr., R.E. Stratmann, J.C. Burant, S. Dapprich, J.M. Millam, A.D. Daniels, K.N. Kudin, M.C. Strain, O. Farkas, J. Tomasi, V. Barone, M. Cossi, R. Cammi, B. Mennucci, C. Pomelli, C. Adamo, S. Clifford, J. Ochterski, G.A. Petersson, P.Y. Ayala, Q. Cui, K. Morokuma, P. Salvador, J.J. Dannenberg, D.K. Malick, A.D. Rabuck, K. Raghavachari, J.B. Foresman, J. Cioslowski, J.V. Ortiz, A.G. Baboul, B.B. Stefanov, G. Liu, A. Liashenko, P. Piskorz, I. Komaromi, R. Gomperts, R.L. Martin, D.J. Fox, T. Keith, M.A. Al-Laham, C.Y. Peng, A. Nanayakkara, M. Challacombe, P.M.W. Gill, B. Johnson, W. Chen, M.W. Wong, J.L. Andres, C. Gonzalez, M. Head-Gordon, E.S. Replogle, J.A. Pople, GAUSSIAN-98, Revision A.11.1, Gaussian, Inc., Pittsburgh, PA, 2001.
[13] A.J.H. Wachters, J. Chem. Phys. 52 (1970) 1033.
[14] P.J. Hay, J. Chem. Phys. 66 (1977) 4377.
[15] H. Lee, T. Polenova, R.H. Beer, A.E. McDermott, J. Am. Chem. Soc. 121 (1999) 6884.
[16] J. Herzfeld, A.E. Berger, J. Chem. Phys. 73 (1980) 6021.
[17] WIN-FIT, ver. 950425, Bruker-Franzen Analytik.
[18] C.P. Slichter, Principles of Magnetic Resonance, third ed., Springer, Berlin, 1990, chapter 4.
[19] T. Sandreczki, D. Ondercin, R.W. Kreilick, J. Magn. Reson. 34 (1979) 171.
[20] R.J. Kurland, B.R. McGarvey, J. Magn. Reson. 2 (1970) 286.
[21] M. Wicholas, R. Mustacich, B. Johnson, T. Smedley, J. May, J. Am. Chem. Soc. 97 (1975) 2113.
[22] H.M. McConnell, D.B. Chesnut, J. Chem. Phys. 27 (1957) 984.
[23] G. Maruta, S. Takeda, R. Imachi, T. Ishida, T. Nogami, K. Yamaguchi, J. Am. Chem. Soc. 121 (1999) 424.
[24] G. Maruta, S. Takeda, preliminary results of ^{2}H, ^{13}C-MAS-NMR experiment: $A_{^{13}C} = 0.6 \sim 4.6$ MHz, $A_{^{1}H} = 0.81 \sim 2.20$ MHz.

are seven structurally-characterized polynuclear copper(II) complexes which are bridged by two unsubstituted pyrazolate anions, $C_3H_3N_2^-$, (Fig. 1(a)) [23–27]. These are antiferromagnetically-coupled coordination polymer [23] and binuclear complexes [24–27] with $-2J$ values of 143–270 cm^{-1}. The superexchange pathway has been proposed to be the π system of the pyrazolates for the polymeric complex [23], while the σ system has been proposed for the others on the basis of extended Hückel MO calculations.

In this paper, we investigate poly- and bi-nuclear copper(II) complexes $[Cu(pz)_2]_n$ (**1**) and $[Cu_2(pz)_2(NO_3)(H_2O)(phen)_2]NO_3$ (**2**) (Hpz = pyrazole, phen = 1,10-phenanthroline) which have simple pyrazolate ligands as bridges. In **1**, coordination geometry around the copper atom is a distorted tetrahedron having exact D_2 symmetry and in **2** is the geometry between trigonal bipyramidal and square pyramidal. These complexes have electron spin of $S = 1/2$ at copper(II) ion. It has been reported that the $-2J$ value of **1** and **2** is 162, 143 cm^{-1}, respectively, indicating the existence of an antiferromagnetic interaction. Delocalized or polarized electron spin of the bridging pyrazolate is believed to mediate antiferromagnetic exchange interaction [23,27]. There is continuing interest in molecular orbitals that determine the local magnetic structures of paramagnetic complexes. We measured solid-state high-resolution NMR spectra of deuterated analogues of the complexes to elucidate which molecular orbital works as superexchange pathway.

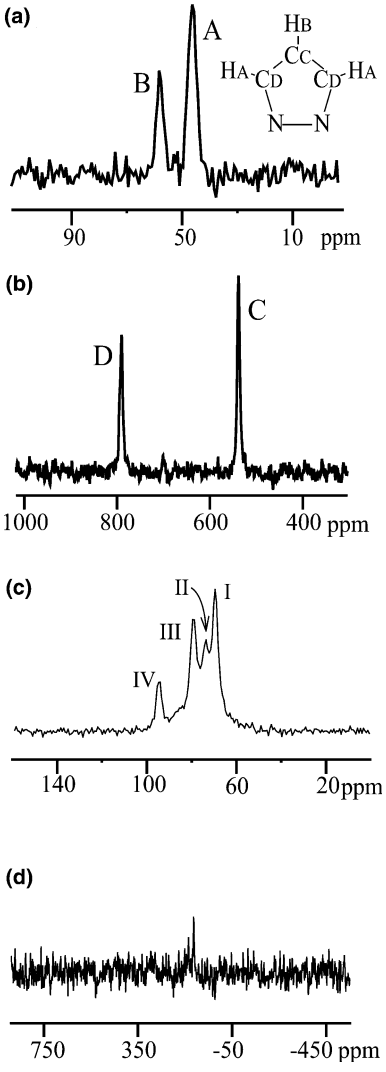


Fig. 1. Solid-state high-resolution NMR spectra of deuterated complexes **1**-d_6 and **2**-d_6: (a) ^2H NMR spectrum of **1**-d_6 at 276 K, (b) ^{13}C NMR spectrum of **1**-d_6 at 276 K, (c) ^2H NMR spectrum of **2**-d_6 at 190 K, (d) ^{13}C NMR spectrum of **2**-d_6 at 300 K. Additionally, alphabetical scheme for the hydrogen and carbon atoms of pyrazolate ligand is described for (a) and (b).

2. Experimental

2.1. Sample preparation

Perdeuterated pyrazole was prepared by catalytic exchange reaction [28]. Deuterated analogues of **1** and **2** were prepared in a similar manner to the literature methods [23,27] using the perdeuterated pyrazole. The samples **1**-d_6 and **2**-d_6 were identified with elemental analysis and powder X-ray diffraction.

2.2. Solid-state high-resolution NMR

^2H MAS NMR and the ^{13}C MAS NMR spectra of **1**-d_6 and **2**-d_6 were measured by a modified TOSS pulse sequence[1] [29] for powder crystalline samples at an external magnetic field of 7.05 T with a Bruker DSX300 spectrometer. A simple π-echo pulse sequence was also employed to measure the spinning sideband patterns. The spinning speeds of the samples were 7 and 9 kHz for **1**-d_6 and **2**-d_6, respectively. The ^2H and ^{13}C NMR spectra were measured from 190 to 350 K. The thermometer of the MAS NMR probe and an effect of the spinning speed on temperature-increase were carefully calibrated using $Pb(NO_3)_2$. The uncertainty of the temperature measurement after the calibration was 4 K, and the temperature fluctuation during the accumulation was within 1 K [12]. The NMR shifts were measured from TMS using methanol-d_4 (^2H) and hexamethylbenzene (^{13}C) as the second reference.

2.3. Electronic structure calculations

Density functional theory (DFT) calculations were performed at the level of UB3LYP/LanL2DZ using GAUSSIAN 98 program package [30]. We used $[Cu_2(pz)_2Cl_4]^{2-}$ as a molecular model of **1** because

[1] Cross polarization and ^1H-decoupling, which were usually implemented in TOSS sequences, were not employed in our experiments.

DFT calculations of one-dimensional polymeric complex is difficult. In the model molecule, copper atoms are bridged by two pyrazolate ligands and each copper ion is coordinated by two chlorine atoms. As a model of **2** $[Cu_2(pz)_2(NO3)(H_2O)(phen)_2]^+$ itself was used. The geometrical parameters were taken from their crystal structures.

3. Results and discussion

3.1. Spin densities of polynuclear copper(II) complex $[Cu(pz)_2]_n$

Figs. 1(a) and (b) show ^2H and ^{13}C MAS NMR spectra of **1**-d_6 at 276 K, respectively. Two peaks were observed both in ^2H NMR spectrum (A and B in Fig. 1(a)) and in ^{13}C NMR spectrum (C and D in Fig. 1(b)). These peaks were assigned to nuclei of the pyrazolate ligand as shown in Fig. 1. This assignment was based on the relative intensity of the NMR signals including spinning sidebands (data not shown). High frequency shifts were observed for the four NMR signals, indicating positive HFCCs of these nuclei. Since paramagnetic shift δ_{para} is proportional to the magnetic susceptibility χ

$$\delta_{iso} = \delta_{para} + \delta_{dia} = \frac{A_N \cdot \chi}{N_A(\gamma_N/2\pi)g\beta} + \delta_{dia}, \quad (1)$$

where the HFCC (A_N in hertz) can be determined from the temperature dependence of the isotropic shift δ_{iso} with the help of the magnetic susceptibility. In Eq. (1), N_A is the Avogadro constant, γ_N is gyromagnetic ratio of the nucleus, g is the isotropic g value of the complex, β is the Bohr magneton, and δ_{dia} is the temperature-independent chemical shift [31]. Temperature dependences of ^2H and ^{13}C NMR spectra of **1**-d_6 are summarized in Figs. 2(a) and (b). The NMR signals were shifted to higher frequencies with decreasing temperature. Magnetic susceptibility of **1** was interpreted in terms of one-dimensional antiferromagnetic Heisenberg model [32]:

$$\chi = \frac{N_A g^2 \beta^2}{kT} \cdot \frac{0.250 + 0.14995x^{-1} + 0.30094x^{-2}}{1 + 1.986x^{-1} + 0.68854x^{-2} + 6.0626x^{-3}}, \quad (2)$$

where $x = kT/|J|$. The magnetic-exchange coupling constant, $-2J$ and the g value of **1** are reported as 162 cm^{-1} and 2.13, respectively [23]. Because the paramagnetic shift is proportional to the magnetic susceptibility, the observed ^2H NMR isotropic shifts of **1**-d_6 were plotted as a function of the magnetic susceptibility of **1** (Fig. 3). From the slope of the line, we determined the HFCCs of deuteron in the use of Eq. (1) as listed in Table 1. The HFCCs of carbon were also deduced in the same manner. Here, we mention the observed

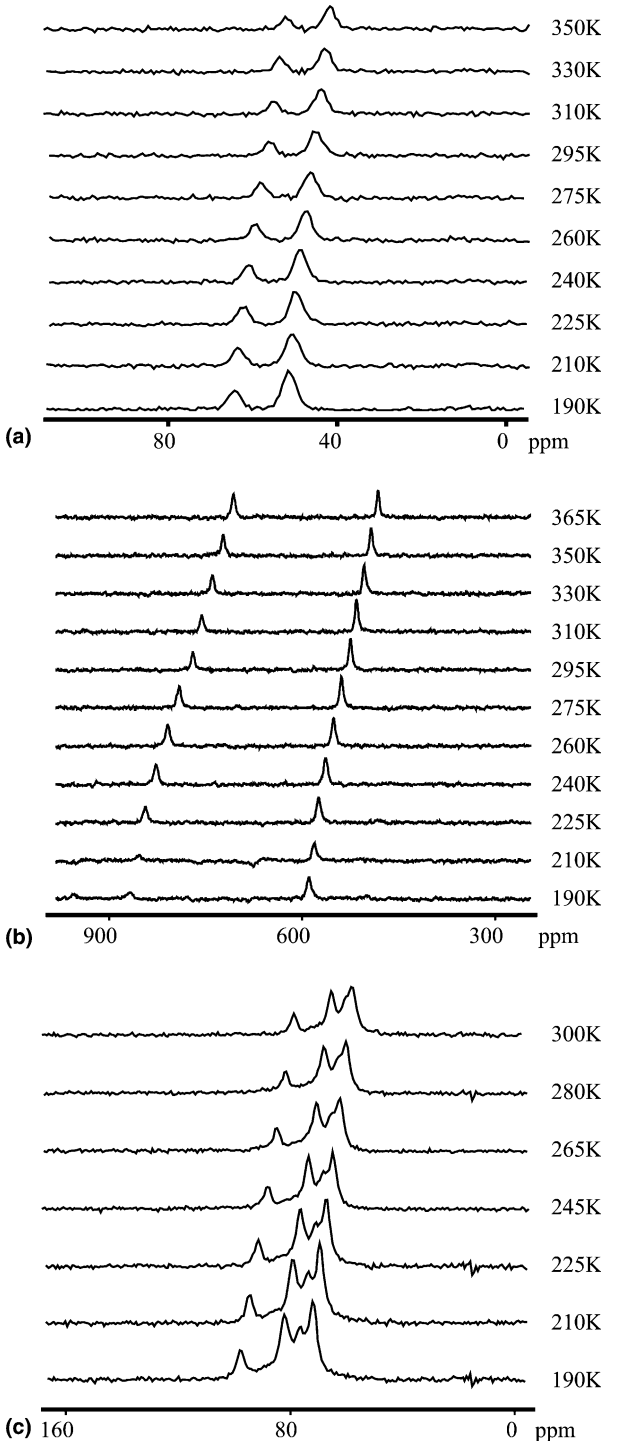


Fig. 2. Temperature dependence of the MAS NMR spectra: (a) ^2H NMR spectra of **1**-d_6, (b) ^{13}C NMR spectra of **1**-d_6, (c) ^2H NMR spectra of **2**-d_6.

HFCCs (A_N) is composed of the Fermi contact (A_{Fermi}) and the pseudo contact (A_{pseudo}) terms [31]

$$A_N = A_{Fermi} + A_{pseudo}, \quad (3)$$

$$A_{pseudo} = \frac{1}{3}\frac{\gamma_N}{2\pi} g\beta \left(\frac{g_\parallel^2}{g^2} - \frac{g_\perp^2}{g^2}\right) \frac{1}{r^3}(3\cos^2\theta - 1), \quad (4)$$

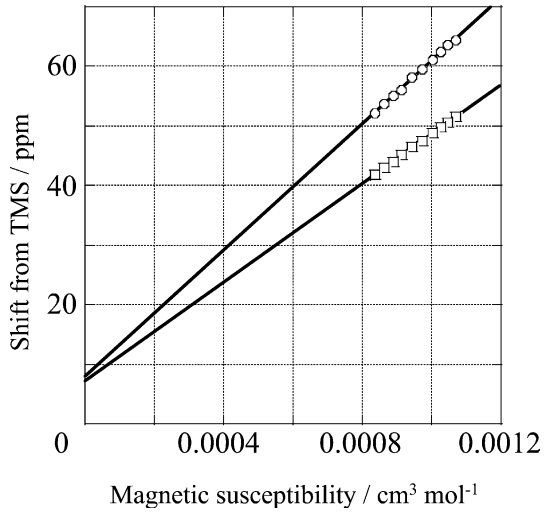


Fig. 3. A plot of the isotropic shifts as a function of magnetic susceptibility in ^{2}H NMR spectra of **1**-d_6: ○, the shifts derived from peak B; □, the shifts derived from peak A.

where r is the length of a vector r from the copper ion to the nucleus, θ is the polar angles of the vector with respect to the principal axis of g-tensor. However, values of the A_{pseudo} were estimated to be less than 0.05 and 0.1 MHz for ^{2}H and ^{13}C NMR shifts of **1**-d_6, respectively, which shows the contribution of A_{pseudo} to the observed A_N is vanishingly low. Thus, we can regard the observed HFCCs as Fermi contact term A_{Fermi}. Then the s-electron spin densities for H and C atoms of **1**-d_6 were determined from A_N as

$$A_{\text{Fermi}} = \rho^{\text{s}} A_{\text{f}}, \tag{5}$$

where ρ^{s} is the s-electron spin density of the atom and A_{f} is the value of the HFCC when the s orbital is singly occupied ($\rho^{\text{s}} = 1$). The experimental s-electron spin densities and computed atomic spin densities ρ^{atom} are also listed in Table 1.

Table 1
HFCCs and electron spin densities in **1**-d_6 and **2**-d_6

	NMR experiment		DFT calculation	
	HFCC (MHz)	s-Electron spin density	HFCC (MHz)	Atomic spin density
1-d_6				
A	+0.31	+0.001	+0.29	+0.001
B	+0.39	+0.002	+0.24	+0.000
C	+7.81	+0.003	+5.58	+0.006
D	+5.30	+0.002	+9.79	−0.001
2-d_6				
I	+0.32	+0.001		
II	+0.37	+0.002		
III	+0.38	+0.002		
IV	+0.44	+0.002		
H1			+0.28	+0.001
H2			+0.37	+0.001
H3			+0.45	+0.001
H4			+0.45	+0.001
H5			+0.40	+0.001
H6			+0.42	+0.001

3.2. Magnetic interaction path of polynuclear copper(II) complex $[Cu(pz)_2]_n$

We found that the s-electron spin densities of carbon and hydrogen atoms in pyrazolate are all positive values. Here, we discuss the magnetic interaction path of **1** on the basis of the NMR results with the help of molecular orbitals. There are two candidates for the interaction pathway in terms of molecular orbital theory: π-electron system and σ-electron system in the pyrazolate anion. The π-electron system of the anion is a 6-electron 5-orbital system including HOMO and LUMO of an imaginary isolated pyrazolate ligand. The σ-electron system of the anion is a 4-electron 2-orbital system mainly composed of two lone electron-pair of the two nitrogen atoms. We obtained these orbitals by extended Hückel MO calculations on an isolated pyrazolate anion and the qualitative character of these systems was not changed by higher level of calculation. When the pyrazolate coordinates to paramagnetic metal ions, electron spin densities is induced by delocalization and/or polarization mechanisms and the spin density distribution of the ligand depends on which mechanism is dominant. In the π-system, the s-electron spin densities of H and C atoms in pyrazolate ligand are zero at the first approximation because they are on the node of the π-orbitals. However, the s-electron spin density can be finite on the constituent atoms due to spin polarization mechanism [33]. Spin polarization is that on any CH σ-bond unpaired electron in 2p π-orbital attracts the electron of the same spin of CH σ-bonding electron pair. As a result, the sign of s-electron spin density of a carbon atom is equal to that of π-electron spin density, and the adjacent hydrogen atom has the opposite sign to the unpaired π-electron. Therefore, CH σ-bonding spin on the H site is consequently opposite in sign to the s-electron spin on the C site if the π-spin polarization is dominant. On the other hand, in the σ-system, s-orbitals of H and C atoms have non-zero MO coefficients of the nonbonding orbitals which are mainly localized on N atoms. Thus the signs of the s-electron spin densities on the H and C sites become all positive when the N atoms have positive spin densities. In experimental NMR data, the signs of s-electron spin densities on the H and C sites of pyrazolate ligand were all positive. Therefore the magnetic interaction path of **1** cannot be the π-system on the assumption that the magnetic interaction path should dominate the local magnetic structure of the ligand. Consequently, the path of **1** is the σ-system in view of the property of the σ-orbitals. We obtained the HFCCs (A_{Fermi}) and atomic electron spin densities ρ^{atom} of **1** using the DFT calculations. The calculated values of A_{Fermi} were 0.29, 0.24, 5.58 and 9.79 MHz

for the peak A, B, C and D, respectively, and atomic spin densities were positive except for peak D. This small negative value of ρ^{atom} indicates that π-spin polarization occurs slightly with the dominant σ-delocalization mechanism. We concluded that the dominant magnetic interaction path in **1** is the σ-electron system of the pyrazole ligand.

3.3. Spin densities and magnetic interaction path of binuclear copper(II) complex $[Cu_2(pz)_2(NO_3)(H_2O)(phen)_2]NO_3$

Figs. 1(c) and (d) illustrate ^2H and ^{13}C MAS NMR spectra of **2**-d_6 at 190 and 300 K, respectively. As shown in Fig. 1(d), we could not observe a ^{13}C NMR signal of **2**-d_6 under our experimental condition. A peak around 150 ppm is probably due to impurity or background. The reason is ascribable to longer electron spin relaxation time T_{1e} of **2**-d_6 or heteronuclear dipole–dipole interactions between protons in 1,10-phenanthroline ligand and carbon nuclei. We observed four ^2H NMR signals of I, II, III and IV as shown in Fig. 1(c). Because $[Cu_2(pz)_2(NO_3)(H_2O)(phen)_2]^+$ has no symmetry element, complex **2**-d_6 has six non-equivalent deuterium atoms in the two pyrazolate ligands. One-to-one assignment of the four peaks to the six hydrogen of the pyrazolate ligands could not be achieved. It is, however, obvious that all of the four signals have positive HFCCs from their high frequency shifts as is observed for **1**-d_6. The temperature dependence of ^2H MAS NMR spectrum is shown in Fig. 2(c). All of the four peaks were shifted to higher frequencies with decreasing temperature. Magnetic susceptibility of **2** was interpreted with singlet–triplet model [27].

$$\chi = \left(\frac{N_A g^2 \beta^2}{kT}\right)\left[3 + \exp\left(\frac{-2J}{kT}\right)\right]^{-1}, \quad (6)$$

where $-2J$ and g value of **2** are reported as 143 and 2.14 cm^{-1}, respectively [27]. The four paramagnetic shifts in the ^2H MAS NMR spectrum of **2**-d_6 were plotted as a function of the magnetic susceptibility, then the HFCCs and electron spin densities in **2**-d_6 were obtained in a similar manner to **1**-d_6. The HFCCs and the spin densities are listed in Table 1. As were obtained for **1**, the pseudo contact term was evaluated for **2** using Eq. (4). Values of the A_{pseudo} are estimated to be less than 0.05 MHz for ^2H shifts. As compared to the HFCCs on Table 1, contribution of the A_{pseudo} to the obtained HFCCs is vanishingly low again. Therefore the experimental HFCCs in **2**-d_6 can be also thought of as Fermi contact term. The HFCCs and atomic spin densities from the DFT calculations in **2** were obtained as shown in Table 1, and the numbering scheme for the hydrogen atoms is shown in Fig. 4. Here, we compared the result of the calculations with the experimental

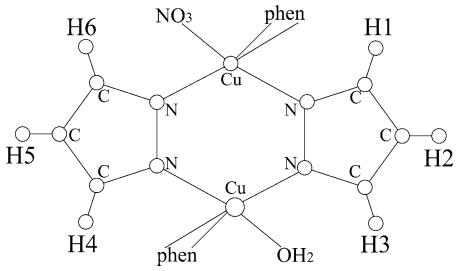


Fig. 4. Numbering scheme for the hydrogen atoms of **2**.

values in **2**-d_6 to assign I, II, III and IV to hydrogen atoms of the pyrazolate ligands. The one-to-one assignment could not be also achieved. However, the experimental HFCC fell within 0.32–0.44 MHz and the calculated HFCC fell within 0.28–0.45 MHz. We concluded that the HFCCs of the pyrazolate ligands are similar positive values to each other.

Electron spin densities on H sites in **2**-d_6 as well as in **1**-d_6 were all positive values. As discussed in the magnetic interaction of **1**, either σ or π orbital of pyrazolate ligand is the magnetic interaction path in the binuclear complex **2**. If π-orbitals are used, signs of the spin densities on H sites in **2**-d_6 would not be all the same. The signs deduced from the experiment on **2**-d_6 correspond with properties of the σ-system. The magnetic interaction path of **2**-d_6 is also σ-orbitals of pyrazolate ligands.

It should be noted that the HFCCs of **1**-d_6 and **2**-d_6 are almost the same values, which indicates that the spin density distribution are almost the same at the pyrazolate ligands in the both compounds. Moreover, the $-2J$ values of the these compounds are approximately the same though they are very different in coordination geometry. Plass et al. [21] reported that their mono-imidazolate-bridged binuclear copper(II) complexes $[Cu_2(dien)_2(L)](ClO_4)_3$ (L:imizolate or substituted imidazolates) have no simple magneto-structural correlation and concluded that the magnetic interactions between the copper(II) ions is dominated by the σ exchange pathway through the bridging imidazolate ligand. However, it should be stressed that there *is* a magneto-structural correlation in bis-pyrazolate-bridged copper(II) complex [27]. Matsushima et al. found that square–planar and square–pyramidal complexes, which have the well-defined $d_{x^2-y^2}$ orbital as the magnetic orbital, have larger $-2J$ values than trigonal bipyramidal complexes. The magnetic orbitals of the latter compounds are so distorted from the $d_{x^2-y^2}$ orbital that the orbital-overlap integrals between copper(II) centers and pyrazolate ligands decrease. The distorted tetrahedral geometry around the copper atom in **1** also deviate the magnetic orbital from the ideal $d_{x^2-y^2}$ orbital. This is the reason why antiferromagnetic interaction in **1** is as weak as in **2**.

4. Conclusion

We investigated magnetic interaction paths for complex **1** and **2**, which include heterocyclic ligand, by means of solid-state MAS NMR measurement. We found the electron spin of $S = 1/2$ of Cu(II) ion in **1** and **2** delocalize over the pyrazolate ligand via σ-orbitals. The experimental values of HFCCs agreed with those calculated on the basis of DFT. It is important that the observed s-electron spin densities are all positive values in **1**-d_6 and **2**-d_6. Taking molecular orbitals of pyrazolate ligand into account, the NMR result cannot be explained by π-spin polarization. We concluded that the magnetic interaction paths of **1** and **2** are not π but σ-electron system of the pyrazolate.

Acknowledgements

This research was supported by Grant-in-aid for Young Scientists (No. 14740371) and for Scientific Research on Priority Areas "Application of Molecular Spins" (No. 15087201) from the Ministry of Education, Culture, Sports, Science and Technology of Japan.

References

[1] A. Lascialfari, Z.H. Jang, F. Borsa, P. Carretta, D. Gatteschi, Phys. Rev. Lett. 81 (1998) 3773.
[2] R.M. Achey, P.L. Kuhns, A.P. Reyes, W.G. Moulton, N.S. Dalal, Phys. Rev. B64 (2001) 064420.
[3] S. Takaishi, Y. Tobu, H. Kitagawa, A. Goto, T. Shimizu, T. Okubo, T. Mitani, R. Ikeda, J. Am. Chem. Soc. 126 (2004) 1614.
[4] F.H. Köhler, in: J.S. Miller, M. Drillon (Eds.), Magnetism: Molecules to Materials, WILEY-VCH, Weinheim, 2001, p. 379.
[5] K. Liu, D. Ryan, K. Nakanishi, A. McDermott, J. Am. Chem. Soc. 117 (1995) 6897.
[6] M. Crozet, M. Chaussade, M. Bardet, L. Emsley, B. Lamotte, J.M. Mouesca, J. Phys. Chem. A 104 (2000) 9990.
[7] S. Ganapathy, V.P. Chacko, R.G. Bryant, M.C. Etter, J. Am. Chem. Soc. 108 (1986) 3159.
[8] Y. Ishii, N.P. Wickramasinghe, S. Chimon, J. Am. Chem. Soc. 125 (2003) 3438.
[9] A.N. Clayton, C.M. Dobson, C.P. Grey Soc., J. Chem. Soc., Chem. Commun. (1990) 72.
[10] C.J. Groombridge, M.J. Perkins, J. Chem. Soc., Chem. Commun. (1991) 1164.
[11] K. Liu, J. Williams, H. Lee, M.M. Fitzgerald, G.M. Jensen, D.B. Goodin, A.E. McDermott, J. Am. Chem. Soc. 120 (1998) 10199.
[12] G. Maruta, S. Takeda, R. Imachi, T. Ishida, T. Nogami, K. Yamaguchi, J. Am. Chem. Soc. 121 (1999) 424.
[13] H. Heise, F.H. Köhler, F. Mota, J.J. Novoa, J. Veciana, J. Am. Chem. Soc. 121 (1999) 9659.
[14] J. Blumel, M. Herker, W. Hiller, F.H. Köhler, Organometallics 15 (1996) 3474.
[15] Y. Paik, J.P. Osegovic, F. Wang, W. Bowden, C.P. Grey, J. Am. Chem. Soc. 123 (2001) 9367.
[16] T.P. Spaniol, A. Kubo, T. Terao, J. Chem. Phys. 106 (1997) 5393.
[17] I. Sack, S. Vega, J. Magn. Reson. 145 (2000) 52.
[18] V.H. Crawford, H.W. Richardson, J.R. Wasson, D.J. Hodgson, W.E. Hatfield, Inorg. Chem. 15 (1976) 2107.
[19] P. Jeffrey, J.C. Thibeault, R. Hoffmann, J. Am. Chem. Soc. 97 (1975) 4884.
[20] S. Brooker, Eur. J. Inorg. Chem. (2002) 2535.
[21] W. Plass, A. Pohlmann, P.S. Subramanian, D. Srinivas, Z. Anorg. Allg. Chem. 628 (2002) 1377.
[22] G. La Monica, G.A. Ardizzoia, Coord. Chem. Rev. 46 (1997) 151.
[23] M.K. Ehlert, S.J. Rettig, A. Storr, R.C. Thompson, J. Trotter, Can. J. Chem. 69 (1991) 432.
[24] M.G.B. Drew, P.C. Yates, F.S. Esho, J. Trocha-Grimshaw, A. Lavery, K.P. Mckillop, S.M. Nelson, J. Nelson, J. Chem. Soc., Dalton. Trans. (1988) 2995.
[25] D. Ajò, A. Bencini, F. Mani, Inorg. Chem. 27 (1988) 2437.
[26] E. Spodine, A.M. Atria, J. Valenzuela, J. Jalocha, J. Manzur, A.M. Garcia, M.T. Garland, O. Pena, J.Y. Saillard, J. Chem. Soc., Dalton Trans. (1999) 3029.
[27] H. Matsusima, H. Hamada, K. Watanabe, M. Koikawa, T. Tokii, J. Chem. Soc., Dalton Trans. (1999) 971.
[28] P. Frediani, D. Rovaib, M. Muniz-Mirandab, A. Salvinia, M. Caporalia, Catal. Commun. 2 (2001) 125.
[29] W.T. Dixon, J. Chem. Phys. 77 (1982) 1800.
[30] M.J. Frisch, G.W. Trucks, H.B. Schlegel, G.E. Scuseria, M.A. Robb, J.R. Cheeseman, V.G. Zakrzewski, J.A. Montgomery Jr., R.E. Stratmann, J.C. Burant, S. Dapprich, J.M. Millam, A.D. Daniels, K.N. Kudin, M.C. Strain, O. Farkas, J. Tomasi, V. Barone, M. Cossi, R. Cammi, B. Mennucci, C. Pomelli, C. Adamo, S. Clifford, J. Ochterski, G.A. Petersson, P.Y. Ayala, Q. Cui, K. Morokuma, P. Salvador, J.J. Dannenberg, D.K. Malick, A.D. Rabuck, K. Raghavachari, J.B. Foresman, J. Cioslowski, J.V. Ortiz, A.G. Baboul, B.B. Stefanov, G. Liu, A. Liashenko, P. Piskorz, I. Komaromi, R. Gomperts, R.L. Martin, D.J. Fox, T. Keith, M.A. Al-Laham, C.Y. Peng, A. Nanayakkara, M. Challacombe, P.M.W. Gill, B. Johnson, W. Chen, M.W. Wong, J.L. Andres, C. Gonzalez, M. Head-Gordon, E.S. Replogle, J.A. Pople, GAUSSIAN 98, Revision A.11.1, Gaussian, Inc., Pittsburgh, PA, 2001.
[31] I. Bertini, C. Luchinat, Coord. Chem. Rev. 150 (1996) 1.
[32] W.E. Estes, W.E. Hatfield, J.A.C. van Ooijen, J. Reedijk, J. Chem. Soc., Dalton Trans. (1980) 2121.
[33] H.M. McConnell, D.B. Chesnut, J. Chem. Phys. 28 (1958) 107.

BH_3) [16,17]. We found the changes of the spin-crossover temperature T_c with S/BH_3 substitution depends on the enthalpy, presumably arising from the ligand-field strength. To get the further insight into the cooperativity between dinuclear complexes and the synergy between the intra-dimer magnetic exchange coupling and the spin-crossover phenomenon, we report here the synthesis and magnetic characterization of $[\{M(NCS)(4\text{-Phpy})\}_2(\mu\text{-bpypz})_2]$ ($M = Co^{2+}$ and Fe^{2+}). As the additional axial pyridine derivatives and the metal ions are replaceable for the bpypz-bridged dinuclear complexes, the role of these items on the spin-crossover is investigated.

2. Experimental

2.1. Syntheses

2.1.1. Preparation of the starting complexes

The starting complex *trans*-$[Fe(NCS)_2(py)_4]$ was obtained by a method given in the literature [18]. *trans*-$[Co(NCS)_2(py)_4]$ was obtained by the analogous method to *trans*-$[Fe(NCS)_2(py)_4]$; to an aqueous solution (250 mL) containing 14.58 g of $Co(NO_3)_2 \cdot 6H_2O$ and pyridine (20 mL) was slowly added an aqueous solution (100 mL) containing 8.04 g of NaNCS. The pink precipitate obtained was filtered off and washed with 10 mL portions of ethanol–pyridine (9:1). After drying in vacuo, a pink powder was obtained.

2.1.2. $[\{Co(NCS)(4\text{-Phpy})\}_2(\mu\text{-bpypz})_2]$

A methanolic solution (2 mL) of *trans*-$[Co(NCS)_2(py)_4]$ (3 mmol L^{-1}) was transferred to a glass tube, and then a methanolic solution of 2 mL of Hbpypz (3 mmol L^{-1}) and 4-Phpy (10 mmol L^{-1}) was poured into the glass tube without mixing the solutions. Orange crystals began to form at ambient temperature in 2 weeks. One of these crystals was used for X-ray crystallography. Physical measurements were conducted on a polycrystalline powder that was synthesized as follows: Hbpypz (0.022 g, 0.099 mmol) was dissolved in 12 mL of a methanol solution of 4-Phpy (0.022 g, 0.14 mmol) with a 10% methanol solution of tetra-*n*-butylammonium hydroxide $(n\text{-Bu})_4NOH$ (0.26 g, 0.10 mmol). To this solution was added 15 mL of a methanol solution of *trans*-$[Co(NCS)_2(py)_4]$ (0.049 g, 0.10 mmol) under an N_2 stream. An orange precipitate was obtained and after stirring this reaction mixture for 2 h, the precipitate was filtered off and washed with methanol. The solid was then dried in vacuo. Yield 71%. Calc. for $C_{50}H_{36}N_{12}S_2Co_2$: C, 60.85; H, 3.68; N, 17.04. Found: C, 59.61; H, 3.48; N, 17.54%. The homogeneity of the powder sample was confirmed by comparison of the observed powder diffraction pattern with that calculated from the single-crystal data.

2.1.3. $[\{Fe(NCS)(4\text{-Phpy})\}_2(\mu\text{-bpypz})_2]$

Hbpypz (0.074 g, 0.033 mmol) was dissolved in 36 mL of a methanol solution of 4-Phpy after deprotonating with a 10% methanol solution of tetra-*n*-butylammonium hydroxide $(n\text{-Bu})_4NOH$ (0.87 g, 0.34 mmol). To this solution was added 15 mL of a methanol solution of *trans*-$[Fe(NCS)_2(py)_4]$ (0.16 g, 0.33 mmol) under an N_2 stream. A yellow precipitate was obtained and after stirring this reaction mixture for 2 h, the precipitate was filtered off and washed with methanol. The solid was then dried in vacuo. Yield 71%. Calc. for $C_{50}H_{36}N_{12}S_2Fe_2$: C, 61.23; H, 3.70; N, 17.14. Found: C, 60.10; H, 3.52; N, 16.72%.

2.2. Physical measurements

Magnetic susceptibility data were recorded over the temperature range from 2 to 300 K in the presence of a magnetic field between 50 and 5000 G with a SQUID susceptometer (Quantum Design, San Diego, CA). All data were corrected for diamagnetism, which was calculated from Pascal's tables. Least squares fitting of the magnetic susceptibility to appropriate equations with Heisenberg Hamiltonian ($H = -JS_i \cdot S_i$) were performed for the cobalt complex. X-ray powder diffraction data were collected on a Rigaku MultiFlex diffractometer by using Cu Kα radiation.

2.3. Crystallographic data collection and refinement of the structure

Data collection of **1** was carried out by a Rigaku Mercury charge coupled device (CCD) system with graphite-monochromated Mo Kα radiation. Crystallographic data are given in Table 1. The structure was solved by a standard direct method (TEXSAN crystallographic software package of the Molecular Structure

Table 1
Crystallographic data for **1**

Formula	$C_{50}H_{36}Co_2N_{12}S_2$
Molecular weight	986.90
Crystal system	triclinic
Space group	$P\bar{1}$ (No. 2)
Z	1
T (K)	200
a (Å)	9.271(4)
b (Å)	10.657(4)
c (Å)	12.968(5)
α (°)	93.71(1)
β (°)	108.02(1)
γ (°)	105.69(1)
V (Å^3)	1157.6(8)
D_{calc} (g cm^{-3})	1.416
μ (cm^{-1})	8.57
R_1/wR_2[a]	0.0362/0.1094

[a] $R_1 = \sum||F_o| - |F_c||/\sum|F_o|$; $wR_2 = [\sum w(|F_o| - |F_c|)^2/\sum|F_o|^2]^{1/2}$.

Corp. and Rigaku). Full-matrix least-squares refinements were carried out with anisotropic thermal parameters for all non-hydrogen atoms. All the hydrogen atoms were placed in the calculated positions and fixed. CCDC reference number is CCDC 251440.

3. Results and discussion

3.1. Structure of [{Co(NCS)(4-Phpy)}$_2$(μ-bpypz)$_2$] (1)

An ORTEP drawing of the structure around the cobalt ions in **1** with the atom numbering scheme is shown in Fig. 1(a). The structure of **1** shows that the desired coordination has been achieved with the cobalt atoms being coordinated to two bpypz to form a dinuclear complex [19]. The dinuclear unit is centrosymmetric, thus, the only one kind of cobalt and ligands exist in the molecule. Each cobalt atom is bound to the four nitrogen atoms of two pyridyl and two pyrazolate moieties in bpypz in the basal plane and two nitrogen atoms of 4-Phpy and NCS^- anion at the axial positions (2.190(4) Å (Co–N(1)), 2.059(3) Å (Co–N(2)), 2.046(3) Å (Co–N(3)), 2.216(4) Å (Co–N(4)), 2.168(4) Å (Co–N(6)), 2.095(4) Å (Co–N(21))) forming a distorted octahedral environment as clearly seen from the top and side views of the molecule. The dihedral angle between pyridyl and phenyl rings in 4-Phpy is 20°, the value of which is smaller than those of [Ta(NMe$_2$)Cl$_3$(4-Phpy)] (40°) [20] and [Ni(4-Phpy)$_2$(DBM)$_2$] (DBM = dibenzoylmethane) (30°) [21]. The efficient packing presumably compensates for

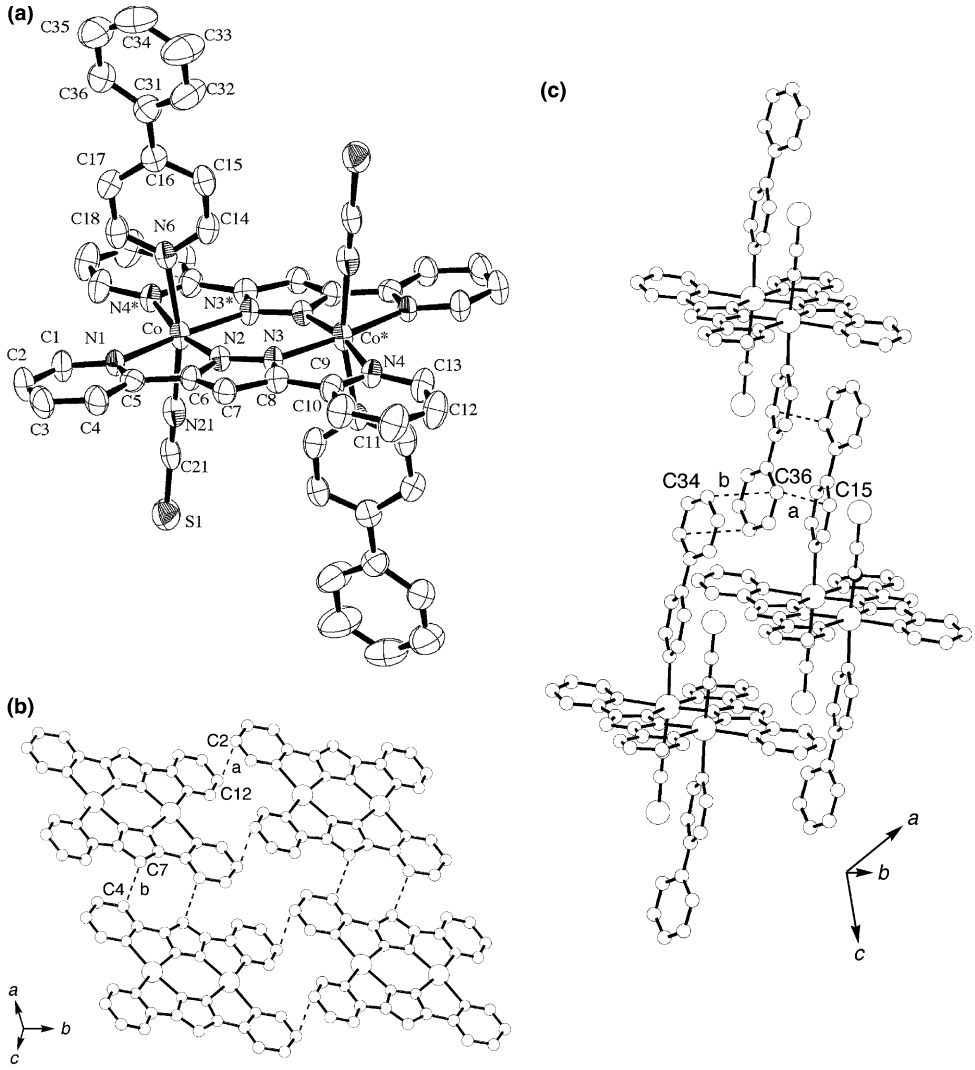


Fig. 1. (a) ORTEP drawing of **1** with atom numbering scheme. Thermal ellipsoids are set at 50% probability and hydrogen atoms have been omitted for clarity. Selected bond distances (Å): Co–N1 2.190(4), Co–N2 2.059(3), Co–N3* 2.046(3), Co–N4* 2.216(4), Co–N6 2.168(4), Co–N21 2.095(4). (b) Emphasizing the π–π stacking interactions between two bpypz ligands of consecutive **1** dimers: *a* (C2–C12) = 3.46 Å, *b* (C4–C7) = 3.42 Å. 4-Phenylpyridine ligands and NCS^- anions have been omitted for clarity. (c) Emphasizing π–π stacking interactions between consecutive 4-phenylpyridine ligands: *a* (C15–C36) = 3.51 Å, *b* (C34–C36) = 3.73 Å.

any unfavorable H—H contact that results in the coordinated 4-Phpy (vide infra). Interestingly, **1** forms a layer by the two types of π–π stacking interactions between the adjacent bpypz ligands of the neighbor dimers (Fig. 1(b)): (1) between pyridyl rings and (2) between pyridyl and pyrazole rings on the adjacent complexes. The layers are connected by additional π–π stacking interactions between adjacent 4-Phpy ligands (Fig. 1(c)) to form a three-dimensional structure.

3.2. Structure of [{Fe(NCS)(4-Phpy)}$_2$(μ-bpypz)$_2$] (2)

Despite many efforts, we did not succeed in growing single crystals of **2** suitable for single crystal X-ray analysis and we used powder diffraction pattern to determine the structure. Fig. 2 shows the diffractograms of compounds **1** and **2** accompanied with the simulated pattern obtained from the crystal structure of **1**. The X-ray diffraction patterns show **1** and **2** to be isomorphous at room temperature, and thus, the dinuclear iron(II) structure is confirmed to be formed.

3.3. Magnetic properties

Fig. 3 shows temperature dependence of the magnetic susceptibilities of the compounds **1** and **2**. The $\chi_M T$ value of **1** in the higher temperature region is about 5.4 emu K mol^{-1}, which is larger than the spin only value for two Co(II) site (3.752 emu K mol^{-1}). This behavior is typical of the high spin Co(II) ion in a distorted octahedral environment, and a large orbital contribution to the magnetic moment should be considered. However, at lower temperature the $\chi_M T$ value dramatically decreases in a manner indicative of intramolecular antiferromagnetic coupling between high spin cobalt(II) ions with a low-lying spin singlet as the ground state. Thus we have attempted to fit the essential feature of the experimental susceptibility by using the simple classical spin approach ($H = -JS_A \cdot S_B$), to give a fitting with $J = -8.78$ cm^{-1} and $g = 2.49$. No spin transition occurs in **1** while J value correlates well to the related high spin cobalt(II) dinuclear complexes reported [22].

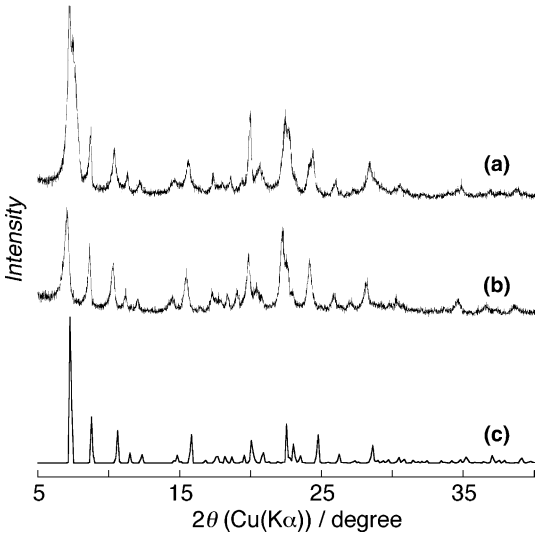


Fig. 2. Powder X-ray diffraction patterns of **1** (a) and **2** (b). (c) shows the simulated pattern obtained from the crystal structure of **1**.

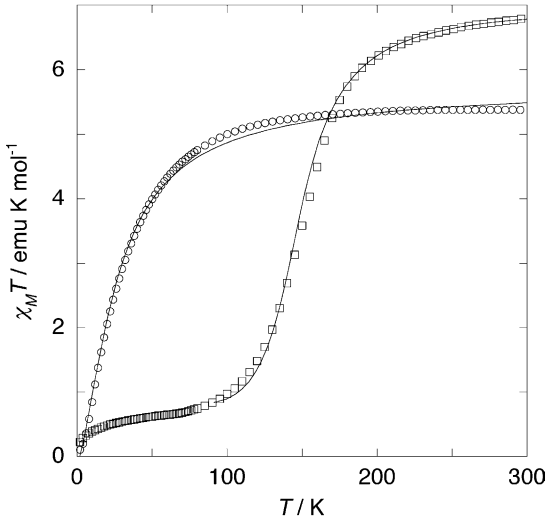


Fig. 3. Temperature dependence of $\chi_M T$ plots for **1** (○) and **2** (□). The solid lines are the fit of the data; see the text for the fitting parameters.

On the other hand, compound **2** shows a spin-crossover phenomenon. The substitution of the metal ion from cobalt to iron leads to the emergence of the spin-crossover. This may be due to the difference in the stability of the low spin phases. The temperature dependence of the $\chi_M T$ value is reversible in both the cooling and warming mode with no hysteresis. The $\chi_M T$ value decreases on lowering the temperature, and then it remains nearly constant at 0.6 emu K mol^{-1}, the value of which corresponds to a mixture of low spin and high spin ions, with the molar fractions 0.17 and 0.83, respectively. Below 40 K, the $\chi_M T$ value slightly decreases, reaching a value of 0.2 emu K mol^{-1} at 2 K. This decrease in the low temperature range may be attributed to the antiferromagnetic coupling of the residual HS sites as seen in the cobalt complex shown above. The spin-crossover temperature T_c (150 K) of complex **2** is higher than that of [{Fe(NCS)(py)}$_2$(μ-bpypz)$_2$] (127 K) [23]. The detailed comparison in spin-crossover behavior between these two complexes could be made by the least-squares fitting of the magnetic susceptibility using the regular solution model through Eq. (1) [24].

$$\ln[(1-\gamma_{HS})/\gamma_{HS}] = \Delta H_{HL} + \Gamma(1-2\gamma_{HS})/RT - \Delta S_{HL}/R, \quad (1)$$

where γ_{HS} is the high spin fraction, Γ is an interaction parameter, and ΔH_{HL} and ΔS_{HL} are the enthalpy and entropy change associated with the spin transitions.

The cooperative factor of the spin transition is defined by $C = \Gamma/2RT_c$. A good simulation of the magnetic susceptibility is achieved with $\Delta H_{HL} = 7.18$ kJ mol^{-1}, $\Delta S_{HL} = 47.9$ J K^{-1} mol^{-1}, $\Gamma = 1.08$ kJ mol^{-1} and $C = 0.433$ as indicated by the solid curve in Fig. 3. ΔH_{HL} for **2** is larger than that for [{Fe(NCS)(py)}$_2$(μ-bpypz)$_2$] (5.96 kJ mol^{-1}) whereas ΔS_{HL} is similar to each other ($\Delta S_{HL} = 46.6$ J K^{-1} mol^{-1} for [{Fe(NCS)(py)}$_2$-(μ-bpypz)$_2$]) [23]. Thus, the difference of T_c with the substitution of pyridine moiety for [{Fe(NCS)(X-py)}$_2$-(μ-bpypz)$_2$] is attributed in their enthalpy difference. This is similar to the replacement of NCS^- to $NCBH_3^-$ moiety for [{Fe(NCX)(py)}$_2$(μ-bpypz)$_2$], but is different from the case for the series of compounds [Fe(PM-L)$_2$(NCX)$_2$] in which ΔS_{HL} is significantly affected by the S/Se substitution of X in NCX^- [24]. Interestingly, the cooperative factor C of **2** is smaller than that of [{Fe(NCS)(py)}$_2$(μ-bpypz)$_2$] indicating that the spin-crossover behavior for **2** is more gradual than that for [{Fe(NCS)(py)}$_2$(μ-bpypz)$_2$] [23]. This may reflect the difference in the crystal packing structure due to the substitution from py to 4-Phpy. Moreover, the spin-crossover in the present dinuclear complex occurs apparently in terms of a single molecular basis rather than by intermolecular interactions as claimed for *cis*-[Fe(NCBH$_3$)$_2$(phen)$_2$] [25]. On the other hand, we have very recently revealed that [{Fe(NCBH$_3$)(4-Phpy)}$_2$-(μ-bpypz)$_2$] shows the non-stepwise direct two step spin-crossover through the intermediate magnetic state with the coexistence of [HS–HS] and [LS–LS] dinuclear spin states while the X-ray diffraction patterns show [{Fe(NCX)(4-Phpy)}$_2$(μ-bpypz)$_2$] (X = S, BH$_3$) to be isomorphous at room temperature [17]. Therefore, the intermediate magnetic state can be affected by the subtle change in the molecular structure or the intermolecular interactions such as π–π stacking interactions.

4. Conclusions

We have described the synthesis, structure and magnetic properties of dinuclear complexes using bpypz as the linking ligand. The iron(II) complex exhibits that the spin-crossover occurs with a single HS–HS to LS–LS process, as in the case of the μ-pypz complex [15] while no spin transition occurs in the cobalt(II) complex. The changes in the thermodynamic parameters on the spin-transition of the iron complex are in accordance with those for the corresponding spin-crossover mononuclear iron(II) complexes. The difference of T_c with the substitution of pyridine moiety from py to 4-Phpy for [{Fe(NCS)(X-py)}$_2$(μ-bpypz)$_2$] is attributed in their enthalpy difference. This is similar to the replacement of NCS^- to $NCBH_3^-$ moiety for [{Fe(NCX)(py)}$_2$-(μ-bpypz)$_2$]. However, the spin transition behavior of the dinuclear complexes cannot be easily understood as exemplified in the comparison between [{Fe(NCX)-(4-Phpy)}$_2$(μ-bpypz)$_2$] since it can be affected by the synergy between the inter- and intramolecular interactions. Therefore, further exploration into this series of compounds could give a clue to deeper understanding spin-crossover phenomena in dinuclear complexes.

Acknowledgments

This research was supported by a Grant-in-Aid for Scientific Research (No. 15550050), and by a Grant-in-Aid for Scientific Research on Priority Area (No. 417) from the Ministry of Education, Culture, Sports, Science and Technology, Japan.

References

[1] P. Gütlich, Y. Garcia, H.A. Goodwin, Chem. Soc. Rev. 29 (2000) 419.
[2] J.A. Real, A.B. Gaspar, V. Niel, M.C. Muñoz, Coord. Chem. Rev. 236 (2003) 121.
[3] O. Kahn, C.J. Martinez, Science 279 (1998) 44.
[4] G.J. Halder, C.J. Kepert, B. Moubaraki, K.S. Murray, J.D. Cashion, Science 298 (2002) 1762.
[5] A. Michalowicz, J. Moscovici, B. Ducourant, D. Cracco, O. Kahn, Chem. Mater. 7 (1995) 1833.
[6] Y. Garcia, O. Kahn, L. Rabardel, B. Chansou, L. Salmon, J.P. Tuchagues, Inorg. Chem. 38 (1999) 4663.
[7] P.J. Koningsbruggen, Y. Garcia, O. Kahn, L. Fournès, H. Kooijman, A.L. Spek, J.G. Haasnoot, J. Moscovici, K. Provost, A. Michalowicz, F. Renz, P. Gütlich, Inorg. Chem. 39 (2000) 1891.
[8] S. Hayami, K. Hashiguchi, G. Juhász, M. Ohba, H. Okawa, Y. Maeda, K. Kato, K. Osaka, M. Takata, K. Inoue, Inorg. Chem. 43 (2004) 4124.
[9] A. Real, J. Zarembowitch, O. Kahn, X. Solans, Inorg. Chem. 26 (1987) 2939.
[10] R. Claude, J.-A. Real, J. Zarembowitch, O. Kahn, L. Ouahab, D. Grandjean, K. Boukheddaden, F. Varret, A. Dworkin, Inorg. Chem. 29 (1990) 4442.
[11] J.-A. Real, H. Bolvin, A. Bousseksou, A. Dworkin, O. Kahn, F. Varret, J. Zarembowitch, J. Am. Chem. Soc. 114 (1992) 4650.
[12] J.A. Real, I. Castro, A. Bousseksou, M. Verdaguer, R. Burriel, M. Castro, J. Linares, F. Varret, Inorg. Chem. 36 (1997) 455.
[13] J.-F. Létard, J.A. Real, N. Moliner, A.B. Gaspar, L. Capes, O. Cador, O. Kahn, J. Am. Chem. Soc. 121 (1999) 10630.
[14] V. Ksenofontov, A.B. Gaspar, V. Niel, S. Reiman, J.A. Real, P. Gütlich, Chem. Eur. J. 10 (2004) 1291.
[15] B.A. Leita, B. Moubaraki, K.S. Murray, J.P. Smith, J.D. Cashion, Chem. Commun. (2004) 156.
[16] N. Suemura, M. Ohama, S. Kaizaki, Chem. Commun. (2001) 1538.
[17] K. Nakano, S. Kawata, K. Yoneda, A. Fuyuhiro, T. Yagi, S. Nasu, S. Morimoto, S. Kaizaki, Chem. Commun. (2004) 2892.
[18] G.B. Kauffman, R.A. Alberts, F.L. Harlan, Inorg. Synth. 12 (1970) 251.
[19] M. Munakata, P.L. Wu, M. Yamamoto, T. Kuroda-Sowa, M. Maekawa, S. Kawata, S. Kitagawa, J. Chem. Soc., Dalton Trans. (1995) 4099.
[20] S.W. Schweiger, D.L. Tillison, M.G. Thorn, P.E. Fanwick, I.P. Rothwell, J. Chem. Soc., Dalton Trans. (2001) 2401.

[21] D.V. Soldatov, G.D. Enright, J.A. Ripmeester, Chem. Mater. 14 (2002) 348.
[22] S. Brooker, D.J. Geest, R.J. Kelly, P.G. Plieger, B. Moubaraki, K.S. Murray, G.B. Jameson, J. Chem. Soc., Dalton Trans. (2002) 2080.
[23] K. Nakano, N. Suemura, S. Kawata, A. Fuyuhiro, T. Yagi, S. Nasu, S. Morimoto, S. Kaizaki, Dalton Trans. (2004) 982.
[24] L. Capes, J.-F. Létard, O. Kahn, Chem. Eur. J. 6 (2000) 2246.
[25] K.F. Purcell, M.P. Edwards, Inorg. Chem. 23 (1984) 2620.

were obtained upon diffusion of Et_2O after two weeks (~15%). Elemental *Anal*. Calc. for $C_{151}H_{172}N_{66}O_{46}F_{10}Mn_{26}$: C, 34.44; H, 3.29; N, 17.56; F, 3.61. Found: C, 34.65; H, 3.09; N, 17.89; F, 3.55%. Crystal data: $C_{151.50}H_{196}F_{10}Mn_{26}N_{66}O_{46.50}$, $M = 5304.18$, brown blocks, triclinic $P\bar{1}$, $a = 17.9570(10)$, $b = 24.0865(14)$, $c = 27.3871(16)$ Å, $\alpha = 98.907(2)$, $\beta = 95.758(2)$, $\gamma = 101.778(2)°$, $V = 11349.2(11)$ Å^3, $T = 150(2)$, $Z = 2$, $\mu = 1.48$ mm^{-1}, Synchrotron radiation (CCLRC Daresbury Laboratory, Station 9.8 = 0.6867 Å) Bruker AXS SMART 1K CCD diffractometer [5], narrow frame ω rotations, and corrected semi-empirically for absorption and incident beam decay (transmission 0.88–0.97) 37727 reflections collected, 23486 unique, ($R_{int} = 0.0521$), $2\theta_{max} = 40.14$ 2581 parameters, $R_1 = 0.0786$ [13934 data with $I > 2\sigma(F)$], $wR_2 = 0.2218$ for 2581 parameters. CCDC 194440.

2.1.2. Synthesis of $[Mn_{10}O_6(OH)_2(Bta)_8(py)_8F_8] \cdot 0.75H_2O \cdot 0.5BtaH \cdot 1.4CH_3OH$ (2)

Anhydrous MnF_3 (0.5 g) and benzotriazole (BtaH) (1.6 g) were heated in methanol (20 ml, 50 °C) under aerobic conditions for 10 min. The resulting black solution was filtered and pyridine (1.00 cm^3) added dropwise. Black crystals of **2** were obtained upon diffusion of Et_2O into the solution after two weeks (~20%). Elemental *Anal*. Calc. for $C_{88}H_{74}N_{32}O_8F_8Mn_{10}$: C, 43.87; H, 3.10; N, 18.60; F, 6.30. Found: C, 43.58; H, 2.88; N, 17.98; F, 6.45%. Crystal data: $C_{92.40}H_{83.60}F_8Mn_{10}N_{33.50}O_{10.15}$, $M = 2527.13$, brown blocks, triclinic $P\bar{1}$, $a = 17.5090(12)$, $b = 18.1168(13)$, $c = 18.6737(13)$ Å, $\alpha = 90.541(2)$, $\beta = 99.171(2)$, $\gamma = 98.173(2)°$, $V = 5785.2(7)$ Å^3, $T = 150(2)$, $Z = 2$, $\mu = 1.131$ mm^{-1}, Synchrotron radiation (CCLRC Daresbury Laboratory, Station 9.8 = 0.6867 Å) Bruker AXS SMART 1K CCD diffractometer [5], narrow frame ω rotations, and corrected semi-empirically for absorption and incident beam decay (transmission 0.88–0.97) 37509 reflections collected, 19469 unique, ($R_{int} = 0.0761$), $2\theta_{max} = 40.14$ 2581 parameters, $R_1 = 0.0786$ [13934 data with $I > 2\sigma(F)$], $wR_2 = 0.2218$ for 2581 parameters. CCDC 234429.

2.1.3. Synthesis of $[NHEt_3]_2[Mn_3O(Bta)_6F_3]$ (3) · 2 MeOH

Anhydrous MnF_3 (0.5 g) and benzotriazole (BtaH) (1.6 g) were heated in methanol (20 ml, 50 °C) under aerobic conditions for 10 min. The resulting black solution was filtered and triethylamine (0.33 cm^3) added. Upon evaporation in air green crystals of **2** were obtained after 24 h (~80%). Elemental *Anal*. Calc. for $C_{49}H_{60}N_{20}O_2F_3Mn_3$: C, 50.09; H, 4.90; N, 24.34; F, 4.82; Mn, 14.32. Found: C, 49.50; H, 5.01; N, 24.04; F, 4.78; Mn, 14.55%. Crystal data for **3** $C_{50}H_{64}F_3Mn_3N_{20}O_3$, $M = 1215.03$, green plates, monoclinic $P2(1)/c$, $a = 21.440(2)$, $b = 12.5632(12)$, $c = 20.0675(19)$ Å, $\alpha = 90$, $\beta = 91.643(2)$, $\gamma = 90°$, $V = 5403.0(9)$ Å^3, $T = 100(2)$, $Z = 4$, $\mu = 0.764$ mm^{-1}. A Bruker SMART APEX CCD diffractometer, $\lambda = 0.71073$ Å with 0.3° ω frame rotations collected 42491 reflections, 12792 unique, ($R_{int} = 0.0743$), $2\theta_{max} = 57.28$, 722 parameters, $R_1 = 0.0417$, $wR_2 = 0.0717$ [7057 data with $I > 2\sigma(F)$]. CCDC 234430.

2.1.4. Synthesis of $[Mn_8O_4(Me_2Bta)_6(OMe)_2F_8(Me_2BtaH)(MeOH)_8] \cdot 3\ MeOH$ (4)

Anhydrous MnF_3 (0.5 g) and dimethylbenzotriazole (Me_2BtaH) (1.6 g) were heated in methanol (20 ml, 50 °C) under aerobic conditions for 10 min. The resulting black solution was filtered and upon evaporation in air black crystals of **4** were obtained after 24 h (~80%). Elemental *Anal*. Calc. for $C_{66}H_{94}N_{21}O_{14}F_8Mn_8$: C, 39.67; H, 4.79; N, 14.72; F, 7.61. Found: C, 39.95; H, 4.03; N, 14.96; F, 8.11%. Crystal data: $C_{68.5}H_{86}F_8Mn_8N_{21}O_{17}$, $M_r = 2067.10$, monoclinic, space group, $P21/c$ $a = 52.079(7)$, $b = 15.469(2)$, $c = 24.016(3)$ Å, $\alpha = 90.00$, $\beta = 91.495(3)$, $\gamma = 90.00°$, V=19341(4) Å^3, $T = 100(2)$ K, $Z = 8$, 109583 reflections collected, 39375 unique ($R_{int} = 0.1355$), $R(F) = 0.0741$ and $wR_2 = 0.2055$ using 10703 reflections with $I > 2\sigma(I)$. CCDC 224233.

2.1.5. Synthesis of $[Mn_{13}O_{12}(Me_2Bta)_{12}F_6(MeOH)_{10}(H_2O)_2] \cdot 3\ MeOH \cdot H_2O$ (5)

Anhydrous MnF_3 (0.5 g) and dimethylbenzotriazole (Me_2BtaH) (1.6 g) were heated in methanol (20 ml, 50 °C) under aerobic conditions for 20 min. The resulting black solution was filtered and upon evaporation in air, black crystals of **4** were obtained after 24 h. Elemental *Anal*. Calc. for $C_{106}H_{140}N_{36}O_{24}F_6Mn_{13}$: C, 40.67; H, 4.51; N, 16.11; F, 3.64. Found: C, 39.83; H, 4.12; N, 16.58; F, 4.21%. Crystal data for **5**: $C_{110.5}H_{155.5}F_6Mn_{13}N_{36}O_{27}$, $M_r = 3252.43$, crystal dimension = 0.06 × 0.04 × 0.01 mm^3, triclinic, space group, $P\bar{1}$ $a = 17.5604(13)$, $b = 17.7334(13)$, $c = 30.679(2)$ Å, $\alpha = 89.695(2)$, $\beta = 73.548(2)$, $\gamma = 60.850(2)°$, $V = 7901.1(10)$ Å^3, $T = 150(2)$ K, $Z = 2$, $\rho = 1.37$ Mg/m^3, 29859 reflections collected, 19051 unique ($R_{int} = 0.0426$), $R(F) = 0.0849$ and $wR_2 = 0.2400$ using 13869 reflections with $I > 2\sigma(I)$. The data were collected on SRS at CCLRC Daresbury using a Bruker AXS SMART CCD area detector. CCDC 224232.

3. Results and discussion

3.1. Description of structures

The structure of $[Mn^{III}_{26}O_{17}(OH)_8(OMe)_4F_{10}1111(Bta)_{22}(MeOH)_{14}(H_2O)_2]$ (**1**) is shown in Fig. 1. The $[Mn^{III}_{26}O_{17}(OH)_8(OMe)_4]^{32+}$ core of **1** can be described as a central distorted tetra-face-capped octahedron

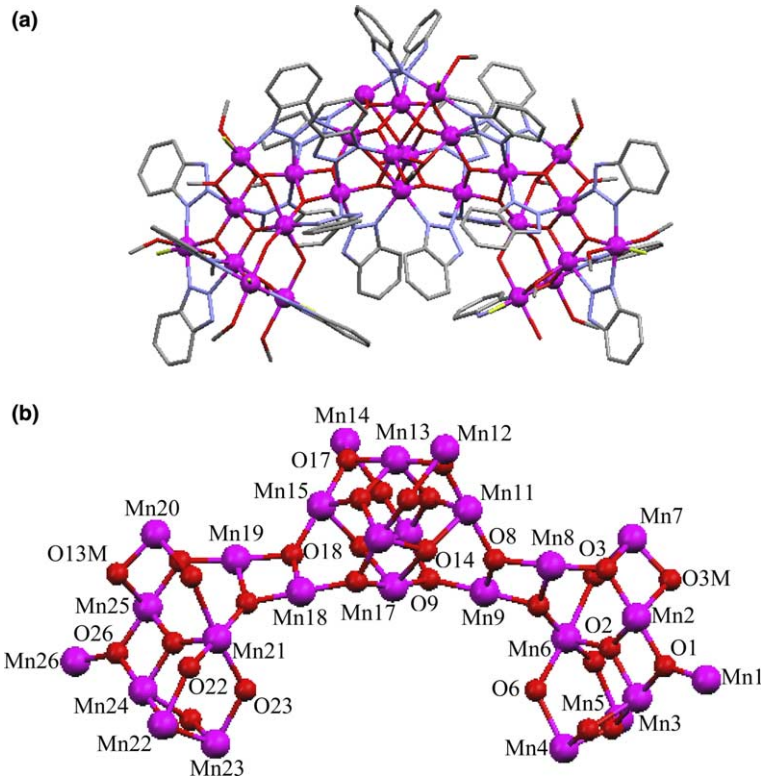


Fig. 1. The structure of complex **1** (a) and its metal-oxygen core (b) showing the aggregated $\{Mn_3O\}$ units (Mn = pink, O = red, N = blue, F = green, C = grey).

(Mn9–Mn18), either side of which are attached two vertex-sharing tetrahedra (Mn2–Mn8 and Mn19–Mn25), centred on Mn6 and Mn21. A pseudo C_2-axis passes through the direction defined by Mn13 and Mn17, situated at the "top" of the molecule. The O^{2-} ions all bridge in their usual μ_3-fashion forming $\{Mn_3O\}^{7+}$ units. The OH^- ions are of two types: four are μ_3-bridging (O10, O11, O14, O16) and are situated within the tetra-face-capped octahedron, while the remaining ions are μ_2-bridging (O5, O6, O12, O15, O22, O23) and are situated both in the tetra-face-capped octahedron (O12 and O15) and within the two vertex-sharing tetrahedra (O5, O6, O22 and O23). The 22 deprotonated Bta^- ligands are of two types: four use all three nitrogens to bond to three Mn^{3+} centers while the remaining 18 use only two nitrogen atoms to bond to two Mn^{3+} centers, the third nitrogen atom H-bonds to adjacent MeOH, H_2O or OH^- ligands. The four MeO^- ions are all μ_2-bridging, but there are also two MeOH molecules which act as μ_2-bridges (O7M, O12M) between Mn6–Mn7 and Mn20–Mn21, respectively. In each case, the O-atom of the MeOH molecule is not deprotonated, as confirmed by the observed bond lengths (2.393–2.476 Å), BVS analysis and the presence of a H-bond between each O-atom and an unbound N-atom of a μ_2-bridging Bta^- ligand (e.g., O7M–N73, 2.738 Å). The 10 F^- ions are all terminal with bond lengths ranging from 1.800(8) to 1.844(8) Å. The Mn centers all lie in distorted octahedral geometries and display the Jahn–Teller elongations expected for high spin Mn^{3+}, although these axes are not co-parallel.

The structure of $[Mn^{III}_{10}O_6(OH)_2(Bta)_8(py)_8F_8]$ (**2**) is shown in Fig. 2. The core of the decametallic structure of **2** can be described as a "super-tetrahedron", consisting of a tetrahedral array of Mn^{3+} ions (Mn1, Mn5, Mn7 and Mn9), with Mn^{3+} ions Mn2, Mn3, Mn4, Mn6, Mn8 and Mn10 capping each edge (Fig. 2(b)). The Mn ions comprising the tetrahedron are each bonded to three edge capping Mn ions via one μ_3-oxide (O1, O5, O6 and O7) and one μ_2-fluoride bridge (F5–F8). The F^- bridges are all asymmetric displaying one short (~1.86 Å) and one long (~2.1–2.14 Å) bond length, as a consequence of at least one Mn–F bond lying on a Jahn–Teller axis. The edge-capping metal centers are bonded to each other via a combination of μ_3-oxides and μ_3-hydroxides. The OH^- ions (O2, O3, O4 and O8) only bridge between the edge-capping centers. Each Bta^- anion bridges between apex and edge-capping Mn^{3+} centers in a μ_2-fashion, while each pyridine ligand bonds terminally. The co-ordination at each apical Mn ion is completed by a terminal fluoride ion (F1–F4). These F^- ions H-bond to water molecules in the lattice, which in turn H-bond to the MeOH molecules of solvation, which in turn H-bond to the BtaH molecule of crystallization. Each Mn center displays a distorted

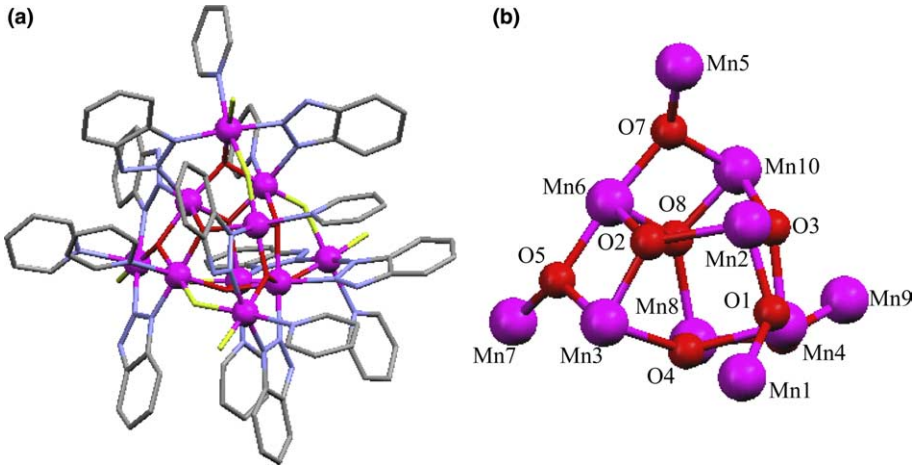


Fig. 2. The structure of complex **2** and its metal-oxygen core of aggregated $\{Mn_3O\}$ units (Mn = pink, O = red, N = blue, F = green, C = grey).

octahedral geometry, with the expected Jahn–Teller elongations.

The structure of the anion of $[NHEt_3]_2[Mn^{III}{}_3O(Bta)_6F_3]$ (**3**) is shown in Fig. 3. The $[Mn_3O(Bta)_6F_3]^{2-}$ anion in **3** consists of three Mn^{3+} centers arranged in a triangle, linked by one central μ_3-oxide (O3). Each μ_2-Bta^- ligand bridges two Mn centers along one edge of the triangle. The co-ordination at each metal center is completed by a terminal fluoride ion (F1–F3). The Mn^{3+} ions are in Jahn–Teller distorted octahedral geometries, but the JT axes are not co-parallel, defined by N2–Mn1–N5; N17–Mn2–N14 and N8–Mn3–N11. The angles around the central O^{2-} range from 119.3° to 120.6°. Despite each edge of the triangle having the same bridges, the $\{Mn_3O\}$ unit tends towards being isosceles with the Mn3–Mn1 and Mn3–Mn2 distances being 3.260 Å in length with the Mn1–Mn2 distance slightly shorter at 3.226 Å. The MeOH solvent molecules are H-bonded to either an unbound N-atom of a Bta^- ligand (e.g., N18–O1, 2.737 Å) or to the cation (e.g., N20–O1, 2.695 Å).

$[Mn^{III}{}_8O_4(Me_2Bta)_6(OMe)_2F_8(Me_2BtaH)(MeOH)_8]$ (**4**, Fig. 4) crystallizes in good yield after 2 weeks, in the monoclinic space group $P2_1/c$. The core of **4** consists of a central $[Mn_4O_2]^{8+}$ butterfly unit (Mn3–Mn6), the body atoms of which (Mn3, Mn6) are also part of a peripheral $[Mn_3O]^{7+}$ triangular unit. The $[Mn_4O_2]$ butterfly is near planar with Mn4 and Mn5 approximately 10° above the 'plane' defined by Mn3, Mn6, O8 and O12. The two peripheral $[Mn_3O]$ triangles are perpendicular to this plane, attached via an O^{2-} ion (O2, O11) forming a $[Mn_8O_4]^{16+}$ core. Two MeO^- (O1, O10) and two F^- (F7, F8) ions act as μ_2-bridges, the MeO^- bridging one side of the $[Mn_3O]$ unit and the F^- linking the $[Mn_3O]$ unit to the central $[Mn_4O_2]$ butterfly. The F^- bridges are asymmetric as, in each case, one Mn–F bond lies on a Jahn–Teller axis. The six Me_2Bta^- ligands all bond in a μ_2-fashion and the remaining six F^- ions and eight MeOH molecules all are terminal. There is one protonated Me_2BtaH ligand present, bonded in a monodentate fashion to Mn7. It H-bonds to a terminal F^- ion on an adjacent molecule (e.g., N19–F6, 2.629 Å). The Mn^{3+} ions are all six-coordinate and in distorted octahedral geometries, with one exception: Mn7 is 5-coordinate and square-based pyramidal with the nearest atom to the 'vacant' coordination site the oxygen of a MeOH molecule bonded to Mn5 (O13–Mn7, 2.701 Å). All the Mn ions display the Jahn–Teller elongations expected of high spin Mn^{3+} ions, although these are not all co-parallel.

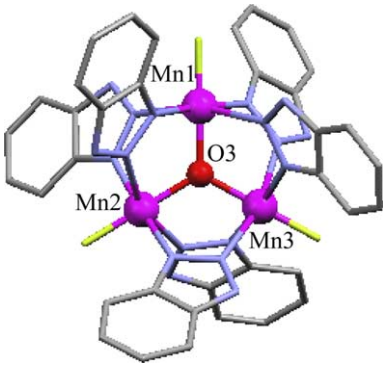


Fig. 3. The structure of complex **3** (Mn = pink, O = red, N = blue, F = green, C = grey).

$[Mn^{IV}{}_3Mn^{III}{}_{10}O_{12}(Me_2Bta)_{12}F_6(MeOH)_{10}(H_2O)_2]$ (**5**, Fig. 5) crystallizes, after 2 weeks, in the triclinic space group $P\bar{1}$. The core of **5** consists of a $[Mn^{IV}{}_3Mn^{III}{}_4O_{12}]$ hexagon centered on Mn1. The Mn^{4+} ions (Mn1, Mn3, Mn3A) form a linear $[Mn_3O_4]$ trimer through the center of the hexagon with the Mn^{3+} ions (Mn2, Mn4 and symmetry equivalents) attached on either side. The 12 O^{2-} ions are all μ_3-bridging and are of two types: six are bound to the central Mn^{4+} ion and link this ion to the outer six Mn ions of the hexagon. The remaining six O^{2-} ions bridge between the

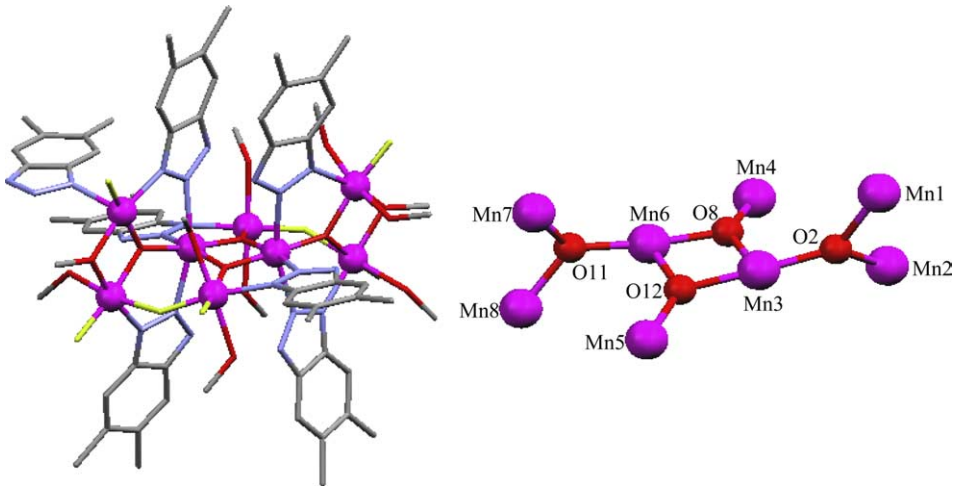


Fig. 4. The structure of complex **4** and its metal-oxygen core showing the aggregated $\{Mn_3O\}$ units (Mn = pink, O = red, N = blue, F = green, C = grey).

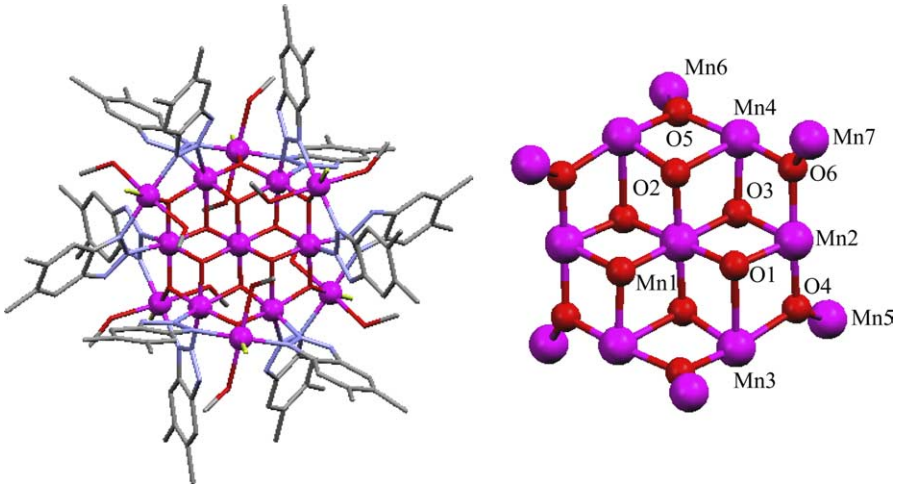


Fig. 5. The structure of complex **5** and its metal-oxygen core showing the aggregated $\{Mn_3O\}$ units.

outer Mn ions of the centered-hexagon and the remaining six Mn^{3+} ions (Mn5, Mn6, Mn7) that are located, alternately, above and below the plane of the $[Mn^{IV}{}_3Mn^{III}{}_4O_{12}]$ core. The μ_2-Me_2Bta^- ligands are all deprotonated and link the Mn ions in the central hexagon to the Mn ions above and below this plane. The coordination of these six Mn ions is completed by a terminal F^- ion and either two MeOH molecules (for example, Mn6, Mn7) or one MeOH and one H_2O molecule (Mn5). All the Mn^{3+} ions show the expected Jahn–Teller elongations, although they are not co-parallel.

The oxidation states of the Mn ions in each compound were determined by a combination of bond lengths (the observed Jahn–Teller elongations), charge balance considerations and bond valence sum (BVS) calculations. The inorganic bridges were determined in a similar fashion, in conjunction with microanalysis. Full details of bond lengths and angles for complexes **1**–**5** can be found in the deposited cif files.

3.2. Discussion and structural comparison

As in most Mn cluster chemistry it is extremely unlikely that complexes **1**–**5** are the only ones present in solution at any one given time. Thus, the loss of F^- ions and the appearance of OH^-, O^{2-} and MeO^- ions, is also likely to involve the deprotonation/protonation, structural rearrangements and redox chemistry of other species present in solution.

However, complexes **1**–**5** can all be described as aggregated $\{Mn_3O\}$ triangular units: **1** consists of 20 triangular units; **2** is made from eight edge-sharing units; **3** consists of one triangular unit; **4** contains four edge- and vertex-sharing units; and **5** contains 12 such units. This perhaps suggests that triangular $[Mn_3OF_3]^{4+}$ units may

be present in all of the above solutions and that the identity of the isolated crystalline product is then dependent on the nature of the added ligand or base.

For complexes **1**–**3**: the reaction performed with no base produces the largest cluster (**1**) with the lowest Mn:F ratio and was isolated in the lowest yield. The introduction of a weakly coordinating base (py, $pK_a = 5.25$) produces the second largest cluster (**2**), and the introduction of a strong non-coordinating base (NEt_3, $pK_a = 11.01$) that also acts as a cation on protonation produces the smallest cluster (**3**) in the largest yield. When NEt_3 is added, complex **3** is isolated instantly in high yield, as it not only deprotonates the BtaH ligands, but the resultant cations $\{HNEt_3\}^+$ stabilize the complex. Pyridinium ions, on the other hand, are 'poor' cations (in crystallization terms) but pyridine molecules are frequently seen to act as terminal ligands in Mn^{3+}clusters. This allows time for the hydrolysis and aggregation of the $\{Mn_3OF_3\}$ units into larger fragments, crystallizing as complex **2** after 1 week in a comparitively moderate yield. When no base is added (and thus there is no direct deprotonation of the BtaH ligands) the hydrolysis process is even longer (~2 weeks) and complex **1** crystallizes, but in poor yield.

The reaction which produces complex **4** is similar to that which produces **1**, but where the BtaH has been replaced by Me_2BtaH. Thus, it is reasonable to assume that the observed differences in the product must be due to the effect of the methyl substituents on both the reactivity of the ligand itself and the changes in intermolecular interactions/packing/solubility. For example, in complex **1** the Bta^- ligands bond in both a μ_3 and μ_2-fashion whereas in complex **4** the Me_2Bta^- ligands all bond in a μ_2-fashion.

Complex **4** is related to complex **5** and could be thought of as an 'intermediate' in the formation of **5**: again both clusters are comprised of aggregated $\{Mn_3O\}$ units and the $[Mn_8O_4]$ unit present in **4** can be seen three times in the core of **5**. For example, in **5**, the unit containing Mn1, Mn2, Mn3 and Mn5 forms the $[Mn_4O_2]$ butterfly unit with O1 and O4, with the peripheral $[Mn_3O]$ units sharing Mn2 and Mn3 with the butterfly and containing Mn4A, Mn7A and O5, and Mn4, Mn6 and O5, respectively. The three fused $[Mn_8O_4]$ units all share the central Mn atom, Mn1. Each $[Mn_8O_4]$ then shares a $[Mn_4O_2]$ unit with its nearest neighbour with only one Mn ion in each unit unshared (e.g., Mn5, Mn7 and Mn6A).

The central $[Mn^{IV}_3Mn^{III}_4O_{12}]$ core of **5** is reminiscent of the hexagonal close-packed structure present in CdI_2 and is similar to the cores found in $[Mn_7(OH)_3Cl_3(hmp)_9]^{2+}$ [6], $[Mn_7(OMe)_{12}(dbm)_6]$ [7] and the alkali metal containing species $[NaMn_6(OMe)_{12}(dbm)_6]^+$[8] as well as larger molecules such as $[Mn_{16}]$ [9], and $[Mn_{21}]$ [10].

Full analysis of the magnetic data for complexes **1**–**5** will be given elsewhere.

4. Conclusions

Complexes **1**–**5** represent the first examples of manganese clusters derived from MnF_3 and are rare examples of Mn^{3+} and Mn^{4+}/Mn^{3+} clusters stabilized by N-donor ligands.

Our original approach was to use 'melt' type reactions whereby the MnF_3 and organic ligand mixture was heated to the melting point of the organic ligand under an inert atmosphere. As the reaction proceeds the MnF_3 dissolves in the organic ligand and the product can be extracted from the 'melt' into a number of solvents. The reason for choosing a 'melt' type of reaction was to overcome the relative insolubility of MnF_3 in common organic solvents. The formation of complexes **1**–**5** directly from hot MeOH solutions thus provides an alternative and potentially much simpler route from which to obtain high nuclearity Mn clusters.

This work shows therefore that MnF_3 is an excellent precursor for synthesizing high nuclearity Mn^{3+} clusters. It provides a source of Mn^{3+} without the need for oxidising Mn^{2+} species or the use of the triangular $[Mn_3O(O_2CR)_6(L)_3]^{0/+}$ species. Complexes **1**–**5** were all made from similar reactions, where the identity of the cluster isolated is controlled by the nature of the ligand and base added. Complex **1** is the third largest Mn cluster reported; complex **2** is rare example of a cluster with a 'supertetrahedral' metal core; complex **3** is a rare example of an oxo-centered trimetallic cluster in which the M^{3+} centres are bridged by ligands other than carboxylates and complex **5** is only the second example of a tridecametallic Mn cluster.

5. Supplementary material

Crystallographic data have been deposited with the Cambridge Crystallographic Data Centre. Copies of this information may be obtained from The Director, CCDC, 12 Union Road, Cambridge, CB2 1EZ, UK (fax: +44 1223 336 033; e-mail: deposit@ccdc.cam.ac.uk or http://www.ccdc.cam.ac.uk).

Acknowledgments

This work was supported by Lloyd's of London Tercentenary Foundation and the EPSRC. We also thank the EPSRC-UKCCF for computer time on the Columbus system, and CCLRC for access to Station 9.8 for data collection.

References

[1] (a) See for example: E.K. Brechin, M. Soler, G. Christou, J. Davidson, D.N. Hendrickson, S. Parsons, W. Wernsdorfer, Polyhedron 22 (2003) 1771;
(b) E.K. Brechin, M. Soler, G. Christou, M. Helliwell, S.J. Teat, W. Wernsdorfer, Chem. Commun. (2003) 1276;
(c) M. Soler, W. Wernsdorfer, K. Folting, M. Pink, G. Christou, J. Am. Chem. Soc. 126 (2004) 2156, and references therein;
(d) A.J. Tasiopolous, A. Vinslava, W. Wernsdorfer, K.A. Abboud, G. Christou, Angew. Chem., Int. Ed. 43 (2004) 2117.

[2] (a) See for example: E.K. Brechin, C. Boskovic, W. Wernsdorfer, J. Yoo, A. Yamaguchi, E.C. Sañudo, T.R. Concolino, A.L. Rheingold, H. Ishimoto, D.N. Hendrickson, G. Christou, J. Am. Chem. Soc. 124 (2002) 9710;
(b) D.N. Hendrickson, G. Christou, H. Ishimoto, J. Yoo, E.K. Brechin, A. Yamaguchi, E.M. Rumberger, S.M.J. Aubin, Z. Sun, G. Aromí, Polyhedron 20 (2001) 1479.

[3] (a) N.V. Gerbeleu, Y.T. Struchkov, G.A. Timco, A.S. Batsanov, K.M. Indrichan, G.A. Popovic, Dokl. Chem. 313 (1991) 232;
(b) N.V. Gerbeleu, Y.T. Struchkov, G.A. Timco, A.S. Batsanov, K.M. Indrichan, G.A. Popovic, Dokl. Akad. Nauk SSSR 313 (1991) 1459;
(c) F.K. Larsen, J. Overgaard, S. Parsons, E. Rentschler, A.A. Smith, G.A. Timco, R.E.P. Winpenny, Angew. Chem., Int. Ed. 42 (2003) 5978.

[4] I. Dugdale, J.B. Cotton, Corros. Sci. 3 (1963) 69.

[5] (a) J. Cernik, W. Clegg, C.R.A. Catlow, G. Bushnell-Wye, J.V. Flaherty, G.N. Greaves, I. Burrows, D.J. Taylor, S.J. Teat, M. Hamichi, J. Synchroton radiat. 4 (1997) 279;
(b) SMART version 5.054, Bruker AXS Inc., Madison, WI, USA, 1998;
(c) SAINT version 6.02a, Bruker AXS Inc., Madison, WI, USA, 2000;
(d) G.M. Sheldrick, SADABS, program for scaling and correction of area detector data, University of Gottinghen, 1997;
(e) G.M. Sheldrick, SHELXTL, Version 5.10, Bruker AXS Inc., Madison, WI, USA, 2000.

[6] M.A. Bolcar, S.M.J. Aubin, K. Folting, D.N. Hendrickson, G. Christou, Chem. Commun. (1997) 1485.

[7] G.A. Abbati, A. Cornia, A.C. Fabretti, A. Caneschi, D. Gatteschi, Inorg. Chem. 37 (1998) 3759.

[8] G.A. Abbati, A. Cornia, A.C. Fabretti, A. Caneschi, D. Gatteschi, Inorg. Chem. 37 (1998) 1430.

[9] D.J. Price, S.R. Batten, M. Moubaraki, K.S. Murray, Chem. Commun. (2002) 762.

[10] J.T. Brockman, J.C. Huffman, G. Christou, Angew. Chem., Int. Ed. 41 (2002) 2506.

immediately affords a red-brown solution which was then stirred for a further hour. The complex $[Mn_2(Hthme)_2(bpy)_2](ClO_4)_2$ (**1**) was obtained in high yield (~50 %) via diethylether diffusion after 3 days. Elemental *Anal.* Calc. for $Mn_2C_{30}H_{36}O_{14}Cl_2$: C, 42.02; H, 4.23; N, 6.53. Found: C, 42.00; H, 4.11; N, 6.50%.

2.2. X-ray crystallography and structure solution

A crystal was mounted using a drop of fomblin (perfluoropolymethylisopropyl ether) oil in a Hamilton Cryoloop and data were collected on a Bruker Smart Apex CCD diffractometer at 100 K using Mo radiation. The structure was solved by direct methods.

The asymmetric unit contains half the dimer, together with a ClO_4^- ion. The non-H atoms were refined anisotropically. H atoms bonded were included in calculated positions. It was clear from the diffraction pattern that the crystal was a non-merohedral twin, and the *R* value initially was about 9.9%. However, accounting for the twinning using the matrix −1000−10−0.489−0.3051 (a 180° rotation about the 001 reciprocal lattice direction) and including the BASF and HKLF 5 commands, led to a refined scale factor of 0.275 for the twinned component, and a much improved R value of 5.86%. CCDC 255232. Crystallographic parameters are collected in Table 1.

2.3. Crystal structure

The centrosymmetric cation of **1** (Fig. 1) contains two Mn^{III} ions (Mn···Mn separation, 3.0964(14) Å) bridged by two μ_2-oxygens from the two $Hthme^{2-}$ ligands. The other two arms are both terminal but differ in that one is deprotonated (O3···Mn, 1.798(3) Å) and one is protonated (O1···Mn, 1.990(4) Å), with the protonated arm H-bonded to the ClO_4^- counter ion (O1···O4, 3.022(4) Å). The coordination sphere of each manganese centre is completed by a chelating bpy ligand. The Mn^{III} ions are in distorted octahedral geometries (*cis*, 78.0–98.7°; *trans*, 167.4–168.7°) but do not display an obvious Jahn-Teller elongation, with each of the six bonds distinctly different (Table 2). It appears that the trigonal field of the $Hthme^{2-}$ ligand causes a rhombic distortion of the Mn^{III} ion preventing the expected Jahn-Teller elongation along O1–Mn1–O2A: although the Mn–O2A bond is much longer (2.114 Å) than the other bonds, the Mn–O1 bond (1.990 Å) is not.

Table 1
Crystal data and structure refinement for complex **1**

	1[Mn_2]
Formula	$C_{30}H_{34}Cl_2Mn_2N_4O_{14}$
M (g mol^{-1})	855.39
Crystal system	triclinic
Space group	$P\bar{1}$
Unit cell dimensions	
a (Å)	8.254(3)
b (Å)	10.002(3)
c (Å)	10.374(3)
α (°)	81.248(5)
β (°)	78.557(5)
γ (°)	88.519(5)
V (Å^3)	829.6(5)
T (K)	100(2)
Z	1
ρ_{calc} (g cm^{-3})	1.712
Crystal shape/colour	brown-green block
Crystal size [mm]	0.25 × 0.10 × 0.03
μ (mm^{-1})	1.000
Unique data	5951
Unique data, ($I > 2\sigma(F)$)	4988
R_1, wR_2	0.0586, 0.1445
Goodness-of-fit	1.101

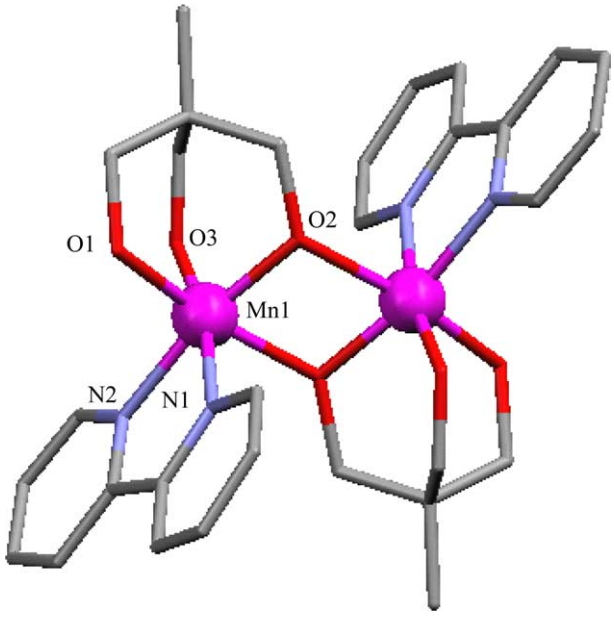


Fig. 1. The structure of the cation of **1**. Selected interatomic distances [Å] and angles [°], Mn–O1,1.990(3); Mn–O2, 1.878(3); Mn–O3,1.798(3); Mn–O2A, 2.114(3); Mn–N1, 2.081(3); Mn–N2, 2.034(3) and Mn1–O2–Mn1A, 101.6(1).

The oxidation state of the Mn ions was confirmed by BVS analysis. The cations of **1** pack in columns with each molecule stacked directly upon the next (Fig. 2), such that the π-rings of adjacent bpy ligands interact though are not fully eclipsed (C···C, ~3.5 Å), with the ClO_4^- anions filling the channels between these columns.

3. Magnetic measurements

3.1. Bulk measurements

Solid state dc magnetization measurements were performed on **1** in the range 1.8–300 K in a field of 5.0 kG (Fig. 3). The $\chi_M T$ value of approximately 6.3 cm^3 K mol^{-1} at 300 K remains constant as the

Table 2
Selected bond lengths (Å) and angles (°) for complex **1**

Mn(1)–O(3)	1.798(3)
Mn(1)–O(2)	1.878(3)
Mn(1)–O(1)	1.990(4)
Mn(1)–N(2)	2.034(3)
Mn(1)–N(1)	2.081(3)
Mn(1)–O(2)A	2.114(3)
Mn(1)–Mn(1)A	3.0964(14)
O(3)–Mn(1)–O(2)	93.72(13)
O(3)–Mn(1)–O(1)	91.16(14)
O(2)–Mn(1)–O(1)	90.70(14)
O(3)–Mn(1)–N(2)	92.45(13)
O(2)–Mn(1)–N(2)	168.67(11)
O(1)–Mn(1)–N(2)	98.67(14)
O(3)–Mn(1)–N(1)	168.73(14)
O(2)–Mn(1)–N(1)	96.73(12)
O(1)–Mn(1)–N(1)	84.53(12)
N(2)–Mn(1)–N(1)	77.97(12)
O(3)–Mn(1)–O(2)A	95.79(13)
O(2)–Mn(1)–O(2)A	78.43(11)
O(1)–Mn(1)–O(2)A	167.43(14)
N(2)–Mn(1)–O(2)A	91.51(11)
N(1)–Mn(1)–O(2)A	90.43(11)

temperature is decreased until ca. 150 K when it begins to increase to a maximum value of 7.6 cm^3 K mol^{-1} at 25 K before decreasing rapidly to 6.5 cm^3 Kmol^{-1} at 5 K. This suggests that the exchange between the metal centres is ferromagnetic with the low temperature decrease assigned to zero-field splitting and/or intermolecular interactions. In order to fit the data, the Hamiltonian given in Eq. (1) was employed.

$$\hat{H} = -2J\hat{S}_{1a}\hat{S}_{1b}. \quad (1)$$

The fit at high temperatures (>50 K) to the experimental $\chi_M T$ data suggests a ground state spin of $S = 4$ with the following parameters: $g = 1.99$ and $J = +2.13$ cm^{-1}.

In order to confirm the ground state spin, magnetization data were collected in the ranges 1.8–10 K and 10–70 kG (Fig. 3). The data were fit, assuming only the ground state is populated, to give $S = 4$, $g = 1.71$ and

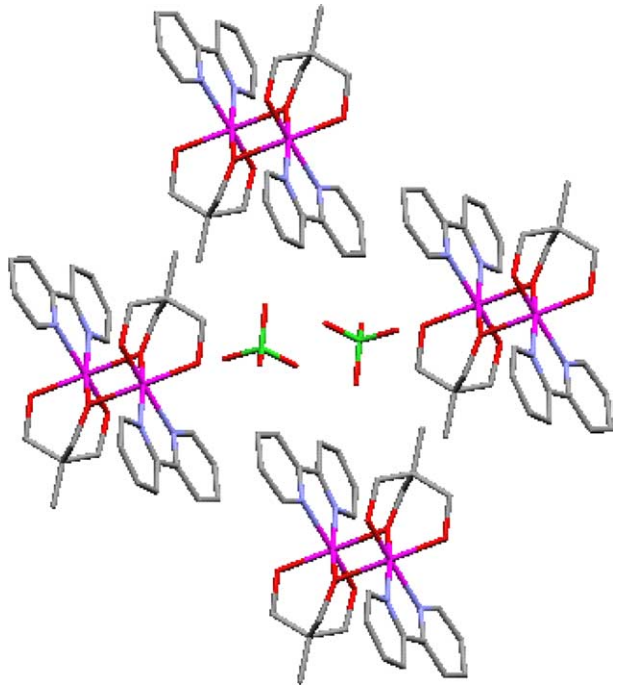


Fig. 2. The packing of **1** in the crystal.

$D = -0.65$ cm^{-1}. Given the value and sign of S and D, ac magnetization measurements were performed to see if **1** acts as an SMM. However measurements taken in the 1.8–10 K range in a 3.5 G ac field oscillating at 50–1000 Hz gave no out-of-phase signal. The obtained g-value is rather low for Mn^{III} and multi-frequency EPR and INS experiments are currently underway to probe the magnetic behaviour of **1** more thoroughly.

3.2. Single crystal measurements

Single crystal magnetic measurements were performed on **1** using an array of micro-squids. Fig. 4 shows hysteresis loops for **1** at temperatures below 1.2 K and at various sweep rates, with the field applied in

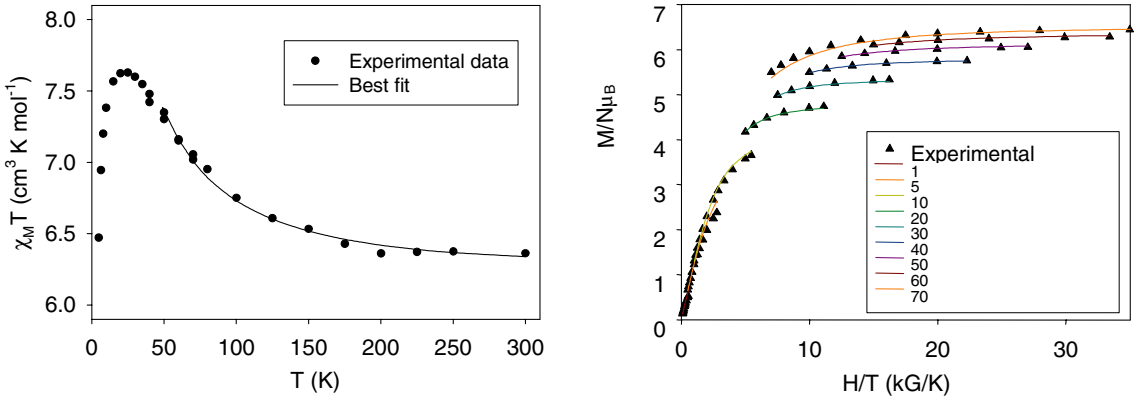


Fig. 3. Plot of $\chi_M T$ vs. T for complex **1**. The solid line is a fit to the data with $J = +2.13$ cm^{-1} and $g = 1.99$ (left). Plot of reduced magnetization vs. H/T for **1**, in the temperature range 1.8–10 K and 10–70 kG. The solid lines are fits of the data to an $S = 4$ state with $g = 1.71$ and $D = -0.65$ cm^{-1} (right).

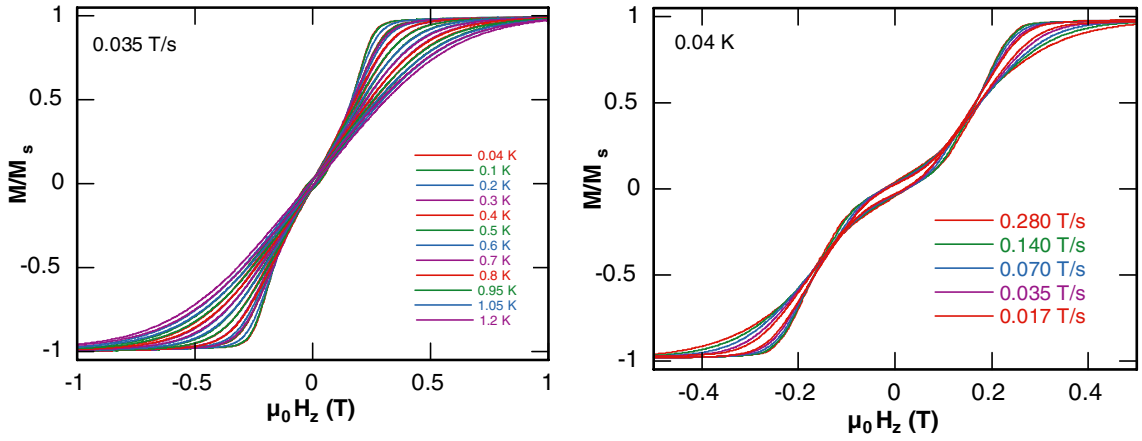


Fig. 4. Magnetization (M) of **1** (plotted as fraction of maximum value M_s vs. applied field $\mu_0 H$). The resulting loops are shown at different temperatures (left) and different field sweep rates (right).

the direction of the easy axis of the molecule. The hysteresis loops have a small coercive field and two step-like features. These step-like features however, do not originate at zero-field, the first step being shifted by approximately −0.2 T. The measurements taken at 0.04 K in particular show small openings in the loops at different sweep rates indicative of slow relaxation of the magnetization. The small coercive field and the overall shape of the loops suggest the presence of strong intermolecular interactions consistent with the extensive intermolecular interactions throughout the crystal lattice as mediated via the π–π stacking of the bpy rings and the H-bonding interactions of the ClO_4^- ions. In principle therefore, complex **1** can be regarded as an exchange-biased SMM [8] although it is clearly difficult to separate the intermolecular interactions and the SMM behaviour. Studies of analogues of complex **1** that contain different peripheral ligands and which pack differently are currently in progress and will be reported in full elsewhere.

4. Theoretical calculations

The broken symmetry model developed by Noodleman [9] has been widely used to compute J-values using HF or DFT calculations. For binuclear transition metal complexes the following equation has been advocated by Ruiz et al. [10]:

$$J = \frac{2(E_{BS} - E_{HS})}{S_{HS}(S_{HS} + 1)}. \quad (2)$$

The combination of a hybrid B3LYP [11] functional with Ahlrichs' TZV [12] basis set as implemented on GAUSSIAN 98 [13] has been shown previously to give good numerical estimates of J-values, and therefore all the calculations on complex **1** were performed using this methodology. To avoid convergence problems, the initial guess for the calculations was generated using JAGUAR [14] and this guess was then transferred to GAUSSIAN to proceed further. Calculations performed on the full structure of **1**, ($[Mn_2(Hthme)_2(bpy)_2](ClO_4)_2$), gives the estimate of $J = -0.55$ cm^{-1}. The calculations thus support a weak exchange between the metal centres, but give the wrong sign in comparison to the experimental data – although the overall numerical difference between the two is small, making the change in sign unsurprising. Over-estimation of J-values using the DFT-BS approach has been encountered previously [10,15]. Calculations were also performed on a model complex of **1**, in which the terminal bpy ligands were replaced with NH_3 molecules and including only the cation: $[Mn_2(Hthme)_2(NH_3)_4]^{2+}$. This gives $J = -1.1$ cm^{-1}, suggesting that the terminal ligands have significant influence on the coupling.

Spin density distributions provide information about the mechanism of the exchange interaction. The high spin state spin density plot of **1** is shown in Fig. 5. The white

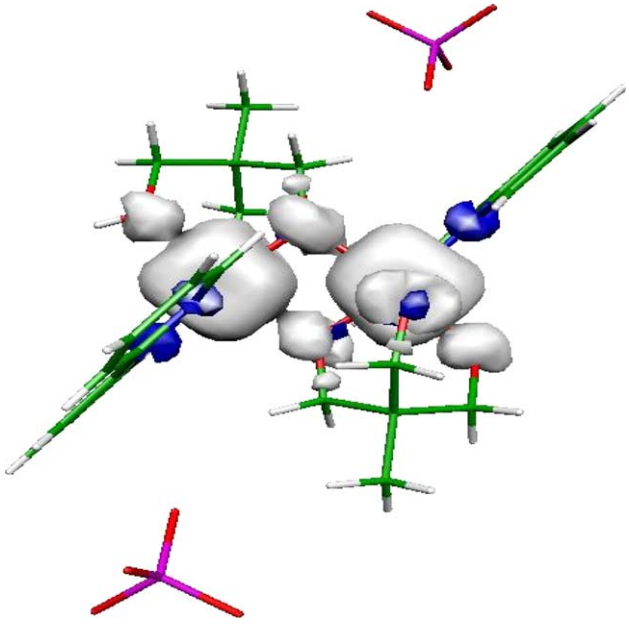


Fig. 5. The high spin state spin density plot of complex **1**.

colour represents a positive spin density and the blue colour represents a negative spin density. It is clear from the figure that in this case both spin delocalisation and spin polarisation mechanisms operate. Previously we have shown that for Mn(III) ions, the Jahn-Teller axis favours a spin delocalisation mechanism with the other axes favouring spin polarisation [16]. Here the O1–Mn1–O2A axis favours spin delocalisation, and the others show a predominantly spin polarisation mechanism. Therefore we can conclude that the O1–Mn1–O2A axis is indeed the Jahn-Teller axis of the molecule.

5. Conclusions

Reaction of H_3thme with $[Mn_2O_2(bpy)_4](ClO_4)_3$ produces the dimetallic complex $[Mn_2(Hthme)_2(bpy)_2](ClO_4)_2$. Magnetic measurements suggest the presence of a weak ferromagnetic interaction between the Mn^{III} ions. Low temperature single crystal measurements show the co-existence of SMM behaviour and strong intermolecular interactions. DFT calculations support a weak exchange between the metal centres, and also provide an insight into the mechanism of the exchange. Spin density distributions help to identify the Jahn-Teller axis of the Mn ions.

Acknowledgements

The authors thank Lloyds of London Tercentenary Foundation, the EPSRC (UK), the NSF (USA), and the EPSRC UKCCF for computer time on the Columbus and Proton systems.

References

[1] (a) V.L. Pecoraro (Ed.), Manganese Redox Enzymes, VCH Publishers, New York, 1992;
(b) G. Christou, Acc. Chem. Res. 22 (1989) 328.
[2] G. Christou, D. Gatteschi, D.N. Hendrickson, R. Sessoli, MRS Bull. 25 (2000) 66.
[3] See for example;
(a) D.N. Hendrickson, G. Christou, H. Ishimoto, J. Yoo, E.K. Brechin, A. Yamaguchi, E.M. Rumberger, S.M.J. Aubin, Z. Sun, G. Aromí, Polyhedron 20 (2001) 1479;
(b) D. Gatteschi, R. Sessoli, A. Cornia, Chem. Commun. (2000) 725;
(c) C. Boskovic, E.K. Brechin, W.E. Streib, K. Folting, D.N. Hendrickson, G. Christou, J. Am. Chem. Soc. 124 (2002) 3725;
(d) E.K. Brechin, C. Boskovic, W. Wernsdorfer, J. Yoo, A. Yamaguchi, E.C. Sañudo, T. Concolino, A.L. Rheingold, H. Ishimoto, D.N. Hendrickson, G. Christou, J. Am. Chem. Soc. 124 (2002) 9710;
(e) E.K. Brechin, M. Soler, J. Davidson, D.N. Hendrickson, S. Parsons, G. Christou, Chem. Commun. (2002) 2252;
(f) A.J. Tasiopoulos, A. Vinslava, W. Wernsdorfer, K.A. Abboud, G. Christou, Angew. Chem. Int. Ed. 43 (2004) 2117.
[4] E.K. Brechin, J. Yoo, M. Nakano, J.C. Huffman, D.N. Hendrickson, G. Christou, Chem. Commun. (1999) 783.
[5] J. Yoo, A. Yamaguchi, M. Nakano, J. Krzystek, W.E. Streib, L.-C. Brunel, H. Ishimoto, G. Christou, D.N. Hendrickson, Inorg. Chem. 122 (2001) 12469.
[6] S.M.J. Aubin, N.R. Dilley, M.W. Wemple, M.B. Maple, G. Christou, D.N. Hendrickson, J. Am. Chem. Soc. 120 (1998) 869.
[7] S.R. Cooper, M. Calvin, J. Am. Chem. Soc. 99 (1977) 6623.
[8] (a) W. Wernsdorfer, N. Aliaga-Alcalde, D.N. Hendrickson, G. Christou, Nature 416 (2002) 406;
(b) E.C. Yang, W. wernsdorfer, S. Hill, R.S. Edwards, M. Nakano, S. maccagnano, L.N. Zakharov, A.L. Rheingold, G. Christou, D.N. Hendrickson, Polyhedron 22 (2003) 1727.
[9] L. Noodleman, J. Chem. Phys. 74 (1981) 5737.
[10] E. Ruiz, S. Alvarez, A. Rodriguez-Fortea, P. Alemany, Y. Pouillon, C. Massobrio, in: J.S. Miller, M. Drillon (Eds.), Magnetism: Molecules to Materials, vol. II, Wiley-VCH, Weinheim, 2001.
[11] A.D. Becke, J. Chem. Phys. 98 (1993) 5648.
[12] A. Schäfer, C. Huber, R. Ahlrichs, J. Chem. Phys. 100 (1994) 5829.
[13] M.J. Frisch, G.W. Trucks, H.B. Schlegel, G.E. Scuseria, M.A. Robb, J.R. Cheeseman, V.G. Zakrzewski, J.A. Montgomery Jr., R.E. Stratmann, J.C. Burant, S. Dapprich, J.M. Millam, A.D. Daniels, K.N. Kudin, M.C. Strain, O. Farkas, J. Tomasi, V. Barone, M. Cossi, R. Cammi, B. Mennucci, C. Pomelli, C. Adamo, S. Clifford, J. Ochterski, G.A. Petersson, P.Y. Ayala, Q. Cui, K. Morokuma, N. Rega, P. Salvador, J.J. Dannenberg, D.K. Malick, A.D. Rabuck, K. Raghavachari, J.B. Foresman, J. Cioslowski, J.V. Ortiz, A.G. Baboul, B.B. Stefanov, G. Liu, A. Liashenko, P. Piskorz, I. Komaromi, R. Gomperts, R.L. Martin, D.J. Fox, T. Keith, M.A. Al-Laham, C.Y. Peng, A. Nanayakkara, M. Challacombe, P.M.W. Gill, B. Johnson, W. Chen, M.W. Wong, J.L. Andres, C. Gonzalez, M. Head-Gordon, E.S. Replogle, J.A. Pople, GAUSSIAN 98, Revision A.11.3, Gaussian Inc., Pittsburgh, PA, 2002.
[14] JAGUAR 5.0, Schrodinger Inc., Portland, OR, 2003.
[15] (a) A. Abu-Nawwas, J. Cano, P. Christian, T. Mallah, G. Rajaraman, S.J. Teat, R.E.P. Winpenny, Y. Yasuhiko, Chem. Commun. (2004) 314;
(b) G. Rajaraman, J. Cano, E.K. Brechin, E.J.L. McInness, Chem. Commun. (2004) 1476;
(c) G. Rajaraman, M. Murugesu, M. Soler, W. Wernsdorfer, M. Helliwell, S.J. Teat, G. Christou, E.K. Brechin, J. Am. Chem. Soc. 126 (2004) 15445.
[16] L.F. Jones, G. Rajaraman, J. Brockman, M. Murugesu, J. Raftery, S.J. Teat, W. Wernsdorfer, G. Christou, E.K. Brechin, D. Collison, D., Chem. Eur. J. 10 (2004) 5180.

as a function of momentum and energy transfer provides useful information on the magnetic scattering function $S(Q,\omega)$, which contains the details about the magnetic exchange interactions and anisotropy splittings [6]. The focus of the present study is aimed at the determination of the anisotropy splitting of the ground state of **1**.

To date no experimental study has provided direct information on the nature and energies of energy splitting in the ground state of **1**. As a first approximation a giant spin model can be used to describe the ground state, assuming that it is well isolated from the excited spin states. An effective Hamiltonian then describes the zero field splitting of the giant spin ground state. The low C_1 symmetry of **1** allows for many higher order crystal field terms in the effective spin Hamiltonian. The fact that the Jahn–Teller axes of the four Mn^{III} ions all lie roughly perpendicular to the plane of the $[Mn_4^{III}Mn_2^{II}O_6]$ ring justifies the use of an axial Hamiltonian in first order

$$H_{\text{axial}} = D[\hat{S}_z^2 - S(S+1)/3] + B_4^0\hat{O}_4^0 \quad (1)$$

with $\hat{O}_4^0 = 35\hat{S}_z^4 - [30S(S+1) - 25]\hat{S}_z^2 - 6S(S+1) + 3S^2(S+1)^2$. The first term of (1) splits the ground state in $S + 1/2$ Kramer's doublets. For a negative D value the $M_S = \pm S$ doublet lies lowest in energy.

A ground state spin of $S = 17/2$ has been postulated for **1** on the basis of magnetic powder measurements [4]. Eq. (1) splits this ground state into nine $\pm M_S$ Kramer's doublets. An alternative solution with $S = 19/2$ has also been postulated, which would give rise to 10 Kramer's doublets [4]. The INS selection rule $\Delta M_S = \pm 1$ predicts eight or nine transitions for an $S = 17/2$ or $S = 19/2$ ground state, respectively. The intensity for an $|M_S| \rightarrow |M_S + 1|$ INS transition can be calculated as [7]

$$I(|M_S| \rightarrow |M_S+1|) \propto P(\pm M_S) \cdot \begin{pmatrix} S & 1 & S \\ -M_S & 1 & M_S+1 \end{pmatrix} \cdot \begin{pmatrix} S & 1 & S \\ -M_S-1 & 1 & M_S \end{pmatrix} \quad (2)$$

with $P(\pm M_S)$ being the Boltzmann population of the initial state $\pm M_S$. The brackets are 3-j symbols.

2. Experimental

2.1. Synthesis

$[Mn_3O(OAc)_6(py)_3] \cdot py$ was dissolved in MeCN with 1 equivalent of the ligand 1,1,1-tris(hydroxymethyl)ethane (H_3thme) and stirred for 12 h. The solution was then filtered and Et2O added slowly. Crystals of $[Mn_9O_7(OAc)_{11}(thme)(py)_3(H_2O)_2]$ (**1**) were obtained after 1 week.

2.2. Physical measurements

The INS experiments were performed on the inverted geometry time-of-flight spectrometer IRIS at the pulsed neutron spallation source ISIS at the Rutherford Appleton Laboratory, UK, using the PG002 graphite analyser with an analysing energy of 1.84 meV. Data were collected at three temperatures 1.6, 12, and 20 K and corrected for the background and detector efficiency by means of empty cell measurements and a vanadium reference. The time-of-flight to energy conversion and the data reduction were done using the program GUIDE. The instrumental resolution derived from a vanadium metal reference at the elastic position was 18 eV. On IRIS, the ZnS detector banks cover the angular range $2\theta = 20$–$160°$ giving access to a momentum transfer range $Q = 0.3$–1.8 Å^{-1} at the elastic position.

A 2.5 g fresh polycrystalline sample of undeuterated $[Mn_9O_7(OAc)_{11}(thme)(py)_3(H_2O)_2]$ was used. The sample was placed under Helium in an aluminum hollow cylinder can with an outer diameter of 23 mm and a sample thickness of 2 mm. The container was inserted in a standard ILL orange cryostat.

3. Results and discussion

Fig. 1 shows the INS spectra of **1** measured at 1.6 K (10 h), 12 K (31 h) and 20 K (25 h), summed over all scattering angles. Positive and negative energy transfer corresponds to neutron energy loss and gain, respectively. The 1.6 K spectrum exhibits one strong band at 3.72 cm^{-1} on the loss side with a second one coming up as a shoulder at lower energy. A series of hot bands is observed at 12 and 20 K. At this latter temperature,

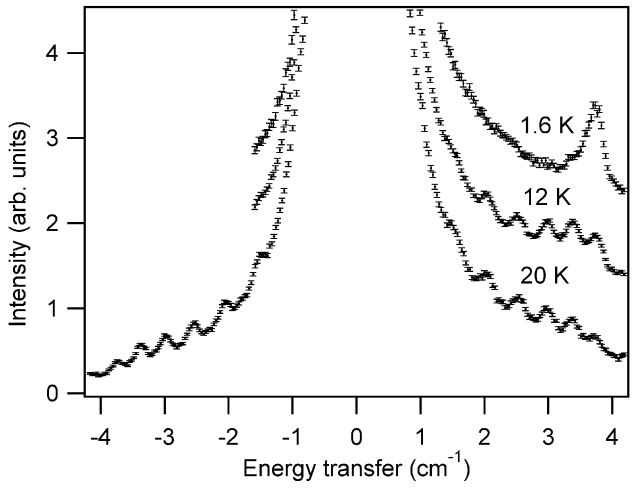


Fig. 1. INS spectra measured on IRIS with an analysing energy of 1.84 meV at 1.6 K (10 h), 12 K (31 h) and 20 K (25 h), summed over all scattering angles.

we measured the energy gain and the loss side. The peak energies are the same on both sides, and we can identify six distinct maxima and a shoulder on the elastic line on either side of the spectrum. The peaks exhibit an almost regular picket fence pattern with decreasing peak separations towards higher energy transfer. On the basis of their temperature and Q-dependence it is possible to assign the 14 observed bands to $\Delta M_S = \pm 1$ transitions within the ground state multiplet. The progression of the peak positions is limiting the possible number of transitions in the ground state multiplet to exactly eight on either side. Therefore, we can clearly rule out the possibility of an $S = 19/2$ ground state. Our data unambiguously confirms the $S = 17/2$ ground state.

Fig. 2(a) shows the spectrum measured at 20 K after subtracting the non-magnetic background. The peaks labelled I–VII correspond to the transitions shown in Fig. 3, which shows the energy splitting pattern of the $S = 17/2$ derived from our data. Least-squares calculations using Eq. (1) and the peak positions determined by INS yield the following best parameter set: $D = -0.249(5)\ \mathrm{cm}^{-1}$, $B_4^0 = 7(4) \times 10^{-6}\ \mathrm{cm}^{-1}$. The value

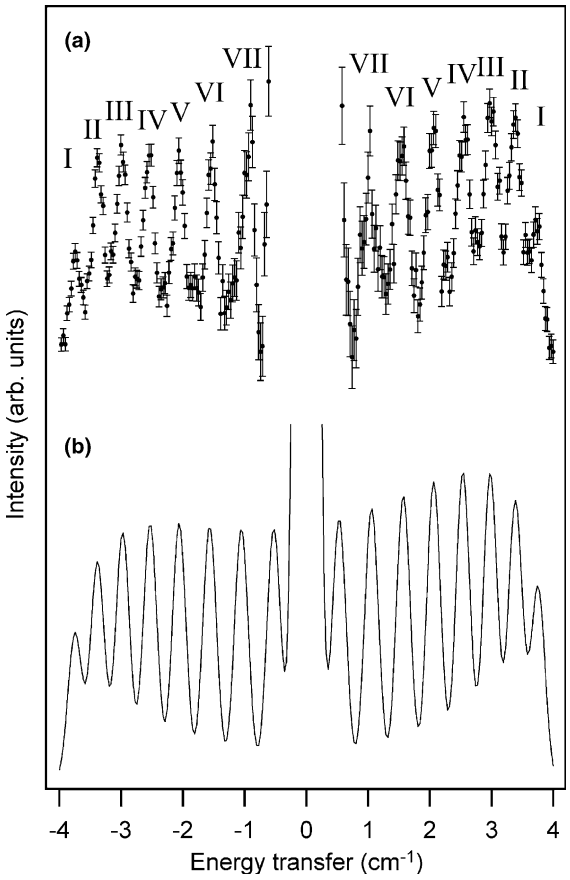


Fig. 2. (a) INS spectrum of Mn_9 measured at 20 K and corrected for background. (b) Calculated spectrum at 20 K using Eqs. (1) and (2) with the parameters $D = -0.249\ \mathrm{cm}^{-1}$ and $B_4^0 = 7 \times 10^{-6}\ \mathrm{cm}^{-1}$. The labelling of the peaks corresponds to the transitions in Fig. 3.

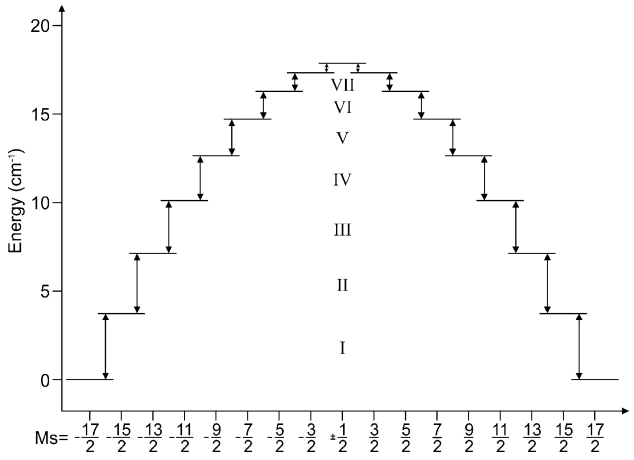


Fig. 3. Calculated anisotropy splitting of the $S = 17/2$ ground state according to the Hamiltonian of Eq. (1) with parameter values $D = -0.249\ \mathrm{cm}^{-1}$ and $B_4^0 = 7 \times 10^{-6}\ \mathrm{cm}^{-1}$ The double arrows correspond to the allowed $\Delta M_S = \pm 1$ INS transitions.

of the axial anisotropy parameter D is in good agreement with the D values of -0.29 and $-0.25\ \mathrm{cm}^{-1}$ derived from powder and single crystal magnetic measurements, respectively [8]. A Hamiltonian without the fourth order term $B_4^0 \hat{O}_4^0$ could not account for the observed decrease of the energy intervals with increasing energy transfer. The B_4^0 parameter must be positive, which is not without precedent in the spin cluster literature. Positive B_4^0 values have been reported for example for the classical single molecule magnet Fe_8 and for a Mn_4 butterfly single molecule magnet [9,10].

Fig. 2(b) shows a calculated spectrum at 20 K using Eqs. (1) and (2) with the best fit parameters. The peak positions and relative intensities are in excellent agreement with the experimental data shown in Fig. 2(a). For energy transfers below $\pm 1\ \mathrm{cm}^{-1}$ the experimental data are dominated by the elastic line, and the eighth peak predicted by the calculations is not observable. The non-magnetic scattering is orders of magnitude more intense than the magnetic scattering in the region of the elastic line, thus swamping the magnetic part.

Physically, the strong central line with the pronounced tails in Fig. 1 originates from elastic and quasi-elastic non-magnetic scattering processes. Its intensity is enhanced by the presence of a large number of hydrogen atoms in the measured sample. Hydrogen is a strong incoherent nuclear scatterer. This is exploited in molecular vibrational spectroscopy [11]. At the low energy transfer of our experiment, it leads to an enhanced elastic line including tails as well as a higher background. For a more accurate determination of the peak VII in Fig. 2(a), it would be necessary to measure a deuterated sample. The incoherent nuclear scattering cross-section of deuterium is 40 times smaller than the one of hydrogen; therefore, the effects described above are reduced

drastically. Deuteration is often considered a prerequisite for a successful magnetic INS experiment, but the present study shows that data of remarkable quality can be obtained with an undeuterated sample in the energy transfer range between 1 and 4 cm^{-1} also. We have recently studied a number of undeuterated molecular spin clusters by INS and made similar observations [12,13]. The energy transfer region, in which magnetic cluster excitations can be observed despite the presence of hydrogen atoms, covers the range from about 1 to 30 cm^{-1}. We ascribe this to a low density of vibrational states with significant hydrogen contribution in this "lucky window".

4. Conclusions

INS measurements unambiguously prove the $S = 17/2$ ground state of **1**. Analysis of the INS transitions within the zero field split ground state lead to a very accurate determination of the axial anisotropy parameter D and the crystal field parameter B_4^0. The experimental INS results of this study are of remarkable quality, despite the presence of a large number of hydrogen atoms in the sample.

References

[1] G. Christou, D. Gatteschi, D.N. Hendrickson, R. Sessoli, MRS Bull. 25 (2000) 66.
[2] H. Miyasaka, R. Clérac, W. Wernsdorfer, L. Lecren, C. Bonhomme, K.-I. Sugiura, M. Yamashita, Angew. Chem., Int. Ed. 43 (2004) 2801.
[3] A.J. Tasiopoulos, A. Vinslava, W. Werndorfer, K.A. Abboud, G. Christou, Angew. Chem., Int. Ed. 43 (2004) 2117.
[4] E.K. Brechin, M. Soler, J. Davidson, D.N. Hendrickson, S. Parsons, G. Christou, Chem. Commun. (2002) 2252.
[5] R. Basler, C. Boskovic, G. Chaboussant, H.U. Güdel, M. Murrie, S.T. Ochsenbein, A. Sieber, Chem. Phys. Chem. 4 (2003) 910.
[6] P. Böni, A. Furrer, J. Schefer, Principles of neutron scattering, in: Proceedings of the Eighth Summer School on Neutron Scattering, World Scientific, Singapore, 2000.
[7] J.R. Birgeneau, J. Phys. Chem. Solids 33 (1972) 59.
[8] E.K. Brechin, M. Soler, G. Christou, J. Davidson, D.N. Hendrickson, S. Parsons, W. Wernsdorfer, Polyhedron 22 (2003) 1771.
[9] R. Caciuffo, G. Amoretti, A. Murani, R. Sessoli, A. Caneschi, D. Gatteschi, Phys. Rev. Lett. 81 (1998) 4744.
[10] J. Yoo, A. Yamaguchi, M. Nakano, J. Krzystek, W.E. Streib, L.-C. Brunel, H. Ishimoto, G. Christou, D.N. Hendrickson, Inorg. Chem. 40 (2001) 4604.
[11] G.F. Longster, J.W. White, Mol. Phy. 17 (1969) 1.
[12] H. Andres, R. Basler, H.U. Güdel, G. Aromi, G. Christou, H. Büttner, B. Ruffle, J. Am. Chem. Soc. 122 (2000) 12469.
[13] C. Boskovic, A. Sieber, G. Chaboussant, H.U. Güdel, J. Ensling, W. Wernsdorfer, A. Neels, G. Labat, H. Stoeckli-Evans, S. Janssen, Inorg. Chem. 43 (2004) 5053.

2. The model

Each magnetic cluster can be described by the following spin Hamiltonian:

$$H = \sum_{i>j} J_{ij}\mathbf{s}_i \cdot \mathbf{s}_j + \sum_i \sum_{k,q} b_k^q(i) O_k^q(\mathbf{s_i}) + \sum_{i>j} \mathbf{s}_i \cdot \mathbf{D}_{ij} \cdot \mathbf{s}_j - g\mu_B \sum_i \mathbf{B} \cdot \mathbf{s}_i, \quad (1)$$

where $\mathbf{s}_i$ are spin operators of the ith ion in the molecule ($s_i = 5/2$ for Fe^{3+}). The first term is the isotropic Heisenberg exchange interaction; the exchange constants J_{ij} used in this work are those determined from susceptibility [12]. In the second term, which describes the local crystal-fields (CFs), the Stevens operator equivalents $O_k^q(\mathbf{s_i})$ and the CF parameters $b_k^q(i)$ for the ith ion appear [13]. The rank k is even and not larger than 4 for d-electrons, and $q = -k,\ldots,k$. The third term represents the dipolar anisotropic intra-cluster spin–spin interactions. The last term is the Zeeman coupling with an external field $\mathbf{B}$.

The rotationally invariant Heisenberg term conserves the modulus $\sqrt{S(S+1)}$ of the total spin $\mathbf{S} = \sum_i \mathbf{s}_i$. Hence, when this term is dominant (*strong-exchange limit*), the energy spectrum of H consists of several multiplets with an almost definite value of S. On the other hand, the crystal fields and the anisotropic dipolar interactions are responsible for S mixing. When the latter is neglected, H can be projected onto each S multiplet to give $H_{ZF} + H_Z$, where the zero-field Hamiltonian (for the approximate D_2 symmetry of Fe_8) is

$$H_{ZF} = B_2^0 O_2^0(\mathbf{S}) + B_2^2 O_2^2(\mathbf{S}) + B_4^0 O_4^0(\mathbf{S}) + B_4^2 O_4^2(\mathbf{S}) + B_4^4 O_4^4(\mathbf{S}), \quad (2)$$

and $H_Z = -g\mu_B \mathbf{B} \cdot \mathbf{S}$ is the Zeeman contribution. The parameters B_K^Q are calculated from $b_k^q(i)$ and $\mathbf{D}_{ij}$ by CF and dipolar projection coefficients. This approach, applied to the $S = 10$ ground manifold of Fe_8, has allowed to interpret inelastic neutron scattering (INS) data very satisfactorily [7,8]. For a cluster of interacting spins, the magnetic cross-section is given by [14]

$$\frac{\partial^2\sigma}{\partial\Omega\,\partial\omega} \propto \sum_{n,m} \exp\left(-\frac{E_n}{kT}\right) \sum_{\alpha,\beta} \left(\delta_{\alpha,\beta} - \frac{Q_\alpha Q_\beta}{Q^2}\right) \times \sum_{l,j} \{g_l F_l(Q)\}\{g_j F_j(Q)\} \exp(i\mathbf{Q}\cdot\mathbf{R}_{lj}) \times \langle n|s_l^\alpha|m\rangle\langle m|s_j^\beta|n\rangle \delta(\hbar\omega + E_n - E_m), \quad (3)$$

where $\mathbf{R}_{lj} = \mathbf{R}_l - \mathbf{R}_j$, $\mathbf{Q}$ is the scattering vector, $F_l(Q)$ is the magnetic form factor and g_l the g-factor of the lth ion, $\alpha,\beta = x,y,z$, and $|n\rangle$ is a cluster wavefunction with energy E_n. Within a single multiplet with well-defined total spin S, the matrix elements of the local spin operators $\mathbf{s}_l$ which appear in Eq. (3) are proportional to those of the total spin $\mathbf{S}$, with proportionality coefficients d_l. As a consequence, putting $\mathbf{z}' = \mathbf{Q}/Q$, the cross-section can be rewritten as

$$\frac{\partial^2\sigma}{\partial\Omega\,\partial\omega} = A(Q) \sum_{n,m} \exp\left(-\frac{E_n}{kT}\right) \delta(\hbar\omega + E_n - E_m) |\langle n|S_\perp|m\rangle|^2, \quad (4)$$

where $S_\perp$ is the component of $\mathbf{S}$ perpendicular to $\mathbf{Q}$ and the first factor, which depends only on Q, is given by

$$A(Q) \propto \sum_{l,j} \{d_l g_l F_l(Q)\}\{d_j g_j F_j(Q)\} \exp\left(iQR_{lj}^{z'}\right). \quad (5)$$

For a powder sample, the physical quantity of interest is the average of the cross-section made over all the possible orientations of $\mathbf{Q}$ in space. In principle, the above factorization is not possible in this framework. However, it can still be shown that

$$\frac{\partial^2\sigma}{\partial\Omega\,\partial\omega} \propto \frac{2}{3}\left(|\langle n|S_x|m\rangle|^2 + |\langle n|S_y|m\rangle|^2 + |\langle n|S_z|m\rangle|^2\right) \quad (6)$$

if one of the following conditions is met: (i) the studied molecule has uniaxial anisotropy (z being the symmetry direction), or (ii) $Q \simeq 0$.

The analysis of experimental INS spectra for Fe_8 by means of Eqs. (2) and (6) allowed to obtain a reliable set of CF parameters ($B_2^0 = -9.75\times10^{-2}$ K, $B_2^2 = -4.66\times10^{-2}$ K, $B_4^0 = 1.0\times10^{-6}$ K, $B_4^2 = 1.2\times10^{-7}$ K, $B_4^4 = 8.6\times10^{-6}$ K) [7,8]. Although Fe_8 does not meet condition (i), the calculated eigenfunctions are not too different from those of an uniaxial system, suggesting that use of Eq. (6) as a satisfactory approximation is allowed. Moreover, the maximum value of Q (1.28 $Å^{-1}$) relative to the INS experiment in question is small enough to reproduce the correct intensity ratios by using this simple equation. We have numerically checked that the INS spectrum calculated by using Eq. (6) agrees well with that computed by the rigorous treatment. Very similar sets of parameters were later found by optical spectroscopy [9] and electron paramagnetic resonance (EPR) [10]. Diagonalization of the Hamiltonian (2) also allows to estimate the tunnel splitting Δ once the CF parameters are known; for instance, with the above parameters, the zero-field gap between the two lowest-lying levels is $\Delta_0 = 4.44\times10^{-11}$ K.

A precise value of the tunneling gap can be obtained by magnetization measurements. In particular, Δ was estimated for Fe_8 by saturating the sample, then measuring the fraction of clusters which reversed their spin at a level anticrossing induced by an applied field swept at a constant rate (dB/dt) [6]. The tunneling probability Π is linked to Δ through the Landau–Zener formula

$$\Pi = 1 - \exp\left(-\frac{\pi\Delta^2}{4\hbar g\mu_B S(dB/dt)}\right). \quad (7)$$

Unfortunately, the so-obtained magnitude of the tunneling gap is not compatible with the estimates based on

spectroscopic data; for instance, the zero-field gap is of the order of 10^{-7} K, more than three orders of magnitude larger than the calculated value. This huge discrepancy seriously hinders any attempt to reach a satisfactory theoretical modeling of the quantum tunneling of the magnetization.

On the other hand, Eq. (2) is known to be valid only in the strong-exchange limit. In order to evaluate S-mixing effects, we followed the method developed in [15], in which S-mixing is included up to the second order in the anisotropy by a unitary transformation applied to the complete Hamiltonian (1). The system can be still described as an effective spin $S = 10$, provided the spin-Hamiltonian (2) is properly modified. The perturbational procedure consists in performing a unitary transformation on H such that the off-diagonal blocks (i.e., those responsible for S mixing) of the transformed Hamiltonian are zero up to second order in the anisotropy. Hence, in the new basis, states belonging to different multiplets are uncoupled and the system can be described as an effective spin multiplet, like in the strong-exchange limit. The advantage of using this method with respect to large-scale numerical diagonalization (e.g., using the Lanczos algorithm) is that it allows to reduce drastically the calculation times and to recover the simple and physically transparent single-spin formalism. The modified Hamiltonian H'_{ZF} can be written as

$$H'_{\mathrm{ZF}} = \sum_{K,Q} C_K^Q O_K^Q, \tag{8}$$

where $K \leqslant 8$ and even, and $-K \leqslant Q \leqslant K$. The new C_K^Q parameters are obtained by adding the mixing contribution $\tilde{B}_K^Q$ to the old B_K^Qs; this implies that the CF parameters determined by INS are to be regarded as C_K^Qs, rather than B_K^Qs. Apart from renormalizing the value of the parameters which appear in Eq. (2), S mixing adds new terms, otherwise forbidden (those with $K > 4$), to the effective Hamiltonian, thus opening new highly efficient tunneling channels. The parameters $\tilde{B}_K^Q$ are given by linear combinations of products of matrix elements of the tensor operators $T_{q'}^{(k')}$ and $T_{q''}^{(k'')}$ which describe the local CF and dipole–dipole coupling [16], with $Q = q' + q''$ and $K \leqslant k' + k''$. Concerning the local CF term, we do not include the b_4^0s and b_4^2s since the corresponding parameters in the projected Hamiltonian (2) have been found negligible and/or not relevant to calculate the tunnel splitting. By combining the tensor operators related to the remaining local parameters, three new Stevens operators appear in Eq. (2) (O_6^4, O_6^6, and O_8^8), whose coefficients are given by

$$\tilde{B}_6^4 = \sum_{i,j} b_2^0(i) b_4^4(j) \Xi_{(1)}(i,j) + \sum_i b_4^4(i) \Upsilon_{(1)}(i), \tag{9a}$$

$$\tilde{B}_6^6 = \sum_{i,j} b_2^2(i) b_4^4(j) \Xi_{(2)}(i,j) + \sum_i b_4^4(i) \Upsilon_{(2)}(i), \tag{9b}$$

$$\tilde{B}_8^8 = \sum_{i,j} b_4^4(i) b_4^4(j) \Xi_{(3)}(i,j) \tag{9c}$$

with

$$\Xi_{(1)}(i,j) = \sqrt{6} \sum_{S''=S-2}^{S+2} e_{64}^{S-S''} \times \sum_{\alpha''} \frac{\langle \alpha S \| T^{(2)}(i) \| \alpha'' S'' \rangle \langle \alpha S \| T^{(4)}(j) \| \alpha'' S'' \rangle}{E_{0\alpha''S''} - E_0}, \tag{10a}$$

$$\Xi_{(2)}(i,j) = \sum_{S''=S-2}^{S+2} c_{66}^{S-S''} \times \sum_{\alpha''} \frac{\langle \alpha S \| T^{(2)}(i) \| \alpha'' S'' \rangle \langle \alpha S \| T^{(4)}(j) \| \alpha'' S'' \rangle}{E_{0\alpha''S''} - E_0}, \tag{10b}$$

$$\Xi_{(3)}(i,j) = \sum_{S''=S-4}^{S+4} c_{88}^{S-S''} \times \sum_{\alpha''} \frac{\langle \alpha S \| T^{(4)}(i) \| \alpha'' S'' \rangle \langle \alpha S \| T^{(4)}(j) \| \alpha'' S'' \rangle}{E_{0\alpha''S''} - E_0}, \tag{10c}$$

$$\Upsilon_{(1)}(i) = -\sum_{j,k} J_{jk}^v \sum_{S''=S-2}^{S+2} e_{64}^{S-S''} \times \sum_{\alpha''} \frac{\langle \alpha S \| T^{(2)}(11|jk) \| \alpha'' S'' \rangle \langle \alpha S \| T^{(4)}(i) \| \alpha'' S'' \rangle}{E_{0\alpha''S''} - E_0}, \tag{10d}$$

and

$$\Upsilon_{(2)}(i) = -\sqrt{2} \sum_{j,k} J_{jk}^u \sum_{S''=S-2}^{S+2} c_{66}^{S-S''} \times \sum_{\alpha''} \frac{\langle \alpha S \| T^{(2)}(11|jk) \| \alpha'' S'' \rangle \langle \alpha S \| T^{(4)}(i) \| \alpha'' S'' \rangle}{E_{0\alpha''S''} - E_0}. \tag{10e}$$

In the preceding expressions i, j and k label magnetic ions, $T^{(k)}(i)$ and $T^{(2)}(11|jk)$ are the tensor operators describing the local CF and dipole–dipole interactions [16] respectively. $J_{jk}^{u,v}$ are defined in terms of the elements of the dipole–dipole tensor $\mathbf{D}_{ij}$ in [16]. The $c_{kk}^{S-S''}$ and $e_{kq}^{S-S''}$ coefficients are defined according to the theory developed in [15,17] as

$$c_{66}^{\Delta S} = \frac{a_6^{\Delta S}}{\sqrt{\prod_{\ell=-3}^{+3} (2S - n - \Delta S)(2S - n - \Delta S + 2)}} \tag{11a}$$

and

$$c_{88}^{\Delta S} = \frac{a_8^{\Delta S}}{\prod_{\ell=-4}^{+4} (2S - n - \Delta S + 1)}, \tag{11b}$$

Table 1
The numerical coefficients $a_k^{\Delta S}$ which appear in Eqs. (11a) and (11b)

ΔS	$a_6^{\Delta S}$	$a_8^{\Delta S}$
0	$-4\sqrt{105}$	-140
±1	$8\sqrt{14}$	112
±2	$-4\sqrt{7}$	-56
±3	0	16
±4	0	2

with $e_{64}^{\Delta S} = (\sqrt{6}/11)c_{66}^{\Delta S}$ and the numerical coefficients $a_k^{\Delta S}$ listed in Table 1. Similar expressions are found for rank-4 mixing contributions, which renormalize the "bare" values of the B_4^q parameters in Eq. (2).

3. Results and discussion

According to the theory outlined in the previous section, new higher-order terms appear in the effective Hamiltonian describing the ground multiplet. We will now estimate the effect of these terms on the zero-field tunnel splitting. In order to compute the C_K^Qs, it is necessary to know both the local CF parameters $b_k^q(i)$ and the dipole–dipole coupling $J_{jk}^{u,v}$. While the point-dipole approximation is generally appropriate for the latter, the $b_k^q(i)$s cannot be determined ab initio reliably. Therefore, by numerically inverting the second-order functions $C_K^Q(\{b_k^q(i)\})$, we determine the possible sets of local parameters $\{b_k^q(i)\}$ consistent with INS, i.e., such that the values $C_K^Q(\{b_k^q(i)\})$ for $K \leqslant 4$ coincide with those determined by INS (within experimental error bars). Even by neglecting all $b_k^q(i)$ with $q \neq 0,2,4$ (i.e., those not contributing to H_{ZF}) and by imposing the D_2 molecular symmetry on the local CF, there are still more unknown parameters than constraints, and we find therefore that there are infinitely many sets allowed by INS. For these sets, the distribution of the calculated values of the tunnel splitting Δ is shown in Fig. 1 by a histogram of the log-increments $\log(\Delta/\Delta_0)$. In Fig. 1(a) the local CF parameters $b_k^q(i)$ vary on a grid bounded by $|b_2^q(i)| < 8$ K, $|b_4^q(i)| < 0.4$ K, whilst Fig. 1(b) the grid bounds are restricted to $|b_2^q(i)| < 4$ K, $|b_4^q(i)| < 0.04$ K. Although no upper bound for the $b_k^q(i)$s can be directly deduced from experiments, local second-order parameters of a few K are a reasonable choice for Fe^{3+} in low-symmetry environments [18]; typical ratios of fourth- to second-order CF parameters range (in modulus) between 0.01 and 0.1. Fig. 1 shows that the effect of S mixing is huge, since it enhances the tunnel splitting by several orders of magnitude. In particular, the arrows indicate the ratio between the measured value of Δ and Δ_0, which falls well inside both distributions.

By itself, this proves that S mixing can recover the discrepancy between the measured and computed zero-field value of Δ. It remains to be proven that also the measured oscillations of Δ in a transverse magnetic field and its behavior in correspondence of anticrossings with excited states can be accounted for. Once again, we have more free parameters than needed; however, numerical calculations show that, among the new parameters, the most influent on Δ are those of sixth-order (in our case, C_6^4 and C_6^6). The CF parameters with $K \leqslant 4$ must obviously be kept fixed as determined by INS spectroscopy. The measured oscillations of Δ as a function of the transverse field are well reproduced with the choice $C_6^4 = -1.8 \times 10^{-7}$ K and $C_6^6 = -1.15 \times 10^{-7}$ K, which give a zero-field value $\Delta = 1.1 \times 10^{-7}$ K. We stress that this is not the unique possible set; however, to show that the order and sign of these parameters are realistic in Fe_8, the distribution $P(C_6^6)$ of values of C_6^6 calculated on the same grids as described above are reproduced in the insets of Fig. 1. The same numerical check was performed for C_6^4. It must be noticed that the computed

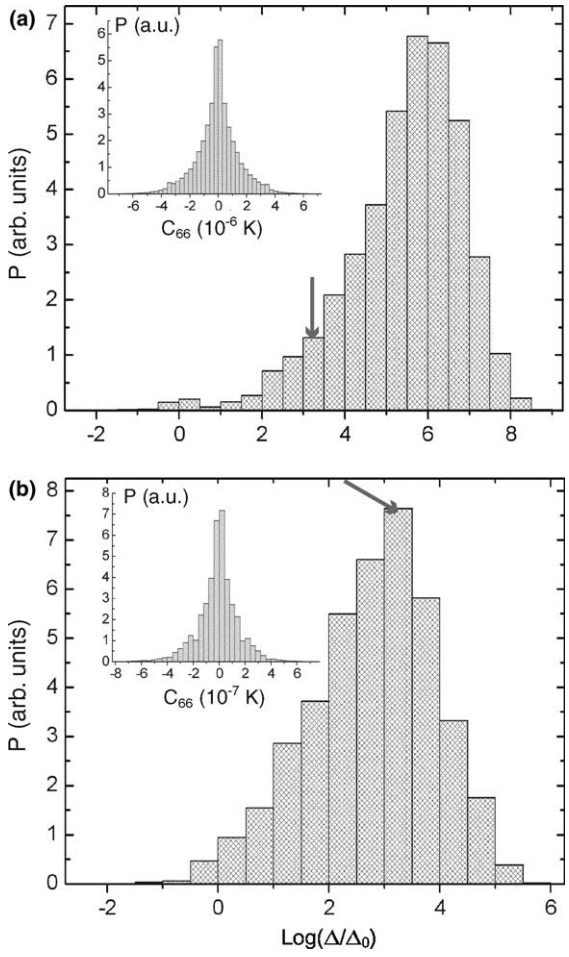


Fig. 1. Calculated distribution of values of the zero-field tunnel splitting Δ normalized to the value $\Delta_0 = 4.44 \times 10^{-11}$ K obtained without S-mixing. The local CF parameters $b_k^q(i)$ vary on grids [different in (a) and (b)] as defined in the text. Arrows indicate the measured ratios. Insets show the distribution of values of C_6^6 on the same grids.

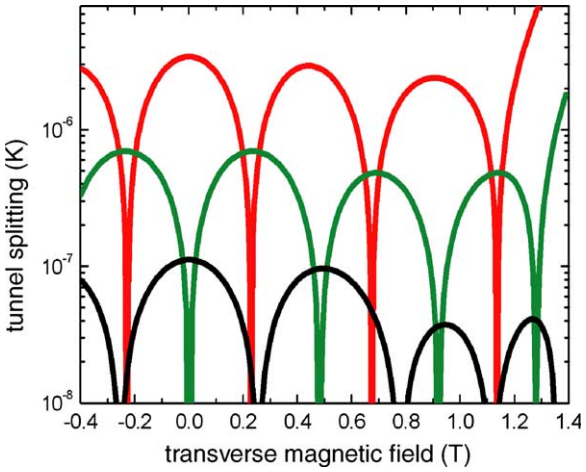


Fig. 2. Calculated tunnel splitting as function of an applied transverse magnetic field with $B_z = 0$ ($n = 0$), and AC gaps involving the excited states $|-10\rangle$ and $|10 - n\rangle$ ($n = 1, 2$) with $B_z = B_{AC} \sim n \cdot 0.22$ T ($n = 1, 2$); the parameters used are given in the text.

INS spectra are indistinguishable when the additional parameters are included or not, apart from an irrelevant shift (~20 μeV) of the shoulder at 0.16 meV [11] (see Fig. 2).

4. Conclusions

By accounting for *S*-mixing perturbatively, we have shown that the discrepancy between spectroscopic and relaxation measurements in Fe_8 can be overcome. Although a unique determination of the C_K^Qs is not possible, the crucial point we demonstrated is that high-rank terms, which are allowed only if *S*-mixing is considered, are essential to describe consistently relaxation and spectroscopic data, since they open highly efficient tunnel channels. Since Fe_8 displays a relatively small degree of *S*-mixing, we expect the tunnel splitting of many magnetic clusters to be influenced even more heavily by such a mechanism. In particular, the degree of *S*-mixing is strongly influenced by the topology of the molecule; therefore this feature, together with the height of the anisotropy barrier, must be taken into account when designing new nanomagnets.

References

[1] D. Gatteschi, R. Sessoli, Angew. Chem. Int. Ed. 42 (2003) 268.
[2] R. Sessoli, D. Gatteschi, A. Caneschi, M.A. Novak, Nature (London) 365 (1993) 141.
[3] D. Gatteschi, A. Caneschi, L. Pardi, R. Sessoli, Science 265 (1994) 1054.
[4] N.V. Prokof'ev, P.C.E. Stamp, Phys. Rev. Lett. 80 (1998) 5794.
[5] C. Sangregorio, T. Ohm, C. Paulsen, R. Sessoli, D. Gatteschi, Phys. Rev. Lett. 78 (1997) 4645.
[6] W. Wernsdorfer, R. Sessoli, Science 284 (1999) 133.
[7] R. Caciuffo, G. Amoretti, A. Murani, R. Sessoli, A. Caneschi, D. Gatteschi, Phys. Rev. Lett. 81 (1998) 4744.
[8] G. Amoretti, R. Caciuffo, J. Combet, A. Murani, A. Caneschi, Phys. Rev. B 62 (2000) 3022.
[9] A. Mukhin, B. Gorshunov, M. Dressel, C. Sangregorio, D. Gatteschi, Phys. Rev. B 63 (2001) 214411.
[10] S. Hill, S. Maccagnano, Kyungwha Park, R.M. Achey, J.M. North, N.S. Dalal, Phys. Rev. B 65 (2002) 224410.
[11] S. Carretta, E. Liviotti, N. Magnani, P. Santini, G. Amoretti, Phys. Rev. Lett. 92 (2004) 207205.
[12] A.L. Barra, D. Gatteschi, R. Sessoli, Chem. Eur. J. 6 (2000) 1608.
[13] A. Abragam, B. Bleaney, Electron Paramagnetic Resonance of Transition Ions, Clarendon Press, Oxford, 1970.
[14] W. Marshall, S.W. Lovesey, Theory of Thermal Neutron Scattering, Clarendon Press, Oxford, 1971.
[15] E. Liviotti, S. Carretta, G. Amoretti, J. Chem. Phys. 117 (2002) 3361.
[16] J.J. Borras-Almenar, J.M. Clemente-Juan, E. Coronado, B.S. Tsukerblat, Inorg. Chem. 38 (1999) 6081.
[17] S. Carretta, E. Liviotti, N. Magnani, G. Amoretti, J. Appl. Phys. 93 (2003) 7822.
[18] E. Siegel, K.A. Müller, Phys. Rev. B 19 (1979) 109.

field (H_{SF}) and the AF-P transition field (H_C) with high accuracy.

2. Experiments

γ-Phase single crystals were grown by the evaporation method. The acetonitrile solution of NPNN has been kept in an incubator at 60°. Several dark-greenish single crystals, having typical dimension of $0.5 \times 0.5 \times 0.2\ mm^3$, are obtained within 24 h. The previous paper reported the instability of γ-phase under the room temperature [3]. To avoid the degeneration to the stable β-phase, we held the γ-phase crystals in a refrigerator. Before performing the experiments, we carefully selected single crystals without twin boundary and contaminations of the other phase by X-ray diffraction.

In the ESR measurements, homemade LC resonator with the resonant frequency of ~300 MHz was used. The resonant frequency ($2\pi f = 1/\sqrt{LC}$) can be tuned from 200 to 300 MHz (EPR resonance field corresponds to about 70–100 G) by adjusting the capacitance of flat condenser. The samples were directly cooled by the ^{3}He. The temperature was monitored by the vapor pressure of ^{3}He gas and by the Cernox resistive thermometer equipped around LC resonator. The lowest temperature attained is about 0.4 K. ESR absorption signals were obtained by monitoring the reflection intensity from the resonator through the scalar network analyzer (Agilent Technology, 8719ET). In this experiment, the radio frequency (RF) is set to be about 286 MHz.

In the magnetic torque measurements [4], we used a piezo-resistive cantilever, which is fabricated by Seiko Instruments Inc. for atomic force microscopy (AFM). The small sample is attached at the tip of cantilever using epoxy, and placed at the center of magnet. The sample mounted on the cantilever is shown in the inset of Fig. 1. The magnetic torque is proportional to the off-balance voltage of the bridge circuit, which detected by the lock in amplifier (Stanford Research System SR830). The sample mounted on cantilever is directly cooled by the ^{3}He. The system is so sensitive to observe a spin–flop transition even if the very small sample, whose dimension was $0.25 \times 0.10 \times 0.10\ mm^3$, was used. The magnetic field applied to the *bc*-plane in the torque measurements.

3. Results and discussion

3.1. ESR

The EPR signals are broadened with decreasing temperature, independently from the magnetic field direction, and disappeared below 0.6 K. At the lowest temperature, no trace of the ferromagnetic resonance,

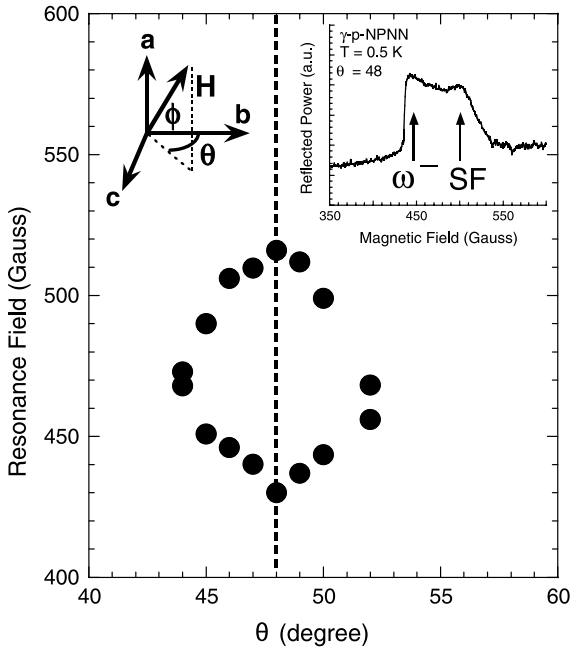


Fig. 1. Angular dependence of the resonance field of ω^- and SF-mode. The inset figure shows the typical AFMR signal. The resonance positions of ω^- and spin–flop (SF)-mode are depicted by the arrows. The angles, θ and ϕ are shown in the inset.

which was observed in the β-phase crystals, is obtained. After EPR signals disappeared, the AFMR signals emerge in different magnetic field. The observed AFMR signal is decomposed by two resonant modes: the lower-field edge of AFMR signal corresponds to the ω^- mode and the higher-field edge corresponds to the spin–flop (SF) mode. Fig. 1 shows the observed AFMR signal and the angular dependence of the ω^- and SF-mode. The angles for applied magnetic field, θ and ϕ, relative to the crystal axis are defined in the inset. These AFMR signals can be observed in the narrow angular region: $44° < \theta < 55°$ and $0° < \phi < 60°$. The typical angular dependence of AFMR around the spin-easy axis was clearly observed within the *bc*-plane. Around $\theta = 48 \pm 10$ and $\phi = 0°$, the maximum separation between the resonance fields for two AFMR modes is obtained. This result indicates that the spin-easy axis is parallel to this direction. It is noted that the spin-easy axis almost points toward the phenyl ring from the ONCNO fragments.

Fig. 2 shows the frequency (ω/γ)-field (H) relation of the AFMR. The resonance field of low-field edge signal increases with decreasing the RF frequency. The inseparability of signals is possibly because the measured temperature is approximate to the Neel temperature. To investigate the AFMR, we applied the two-sublattice model with orthorhombic anisotropy [5]. This assumption is reasonable because that the magnetic coupling in the *bc*-plane is ferromagnetic and the dominant anisotropy term should be caused by the dipole–dipole

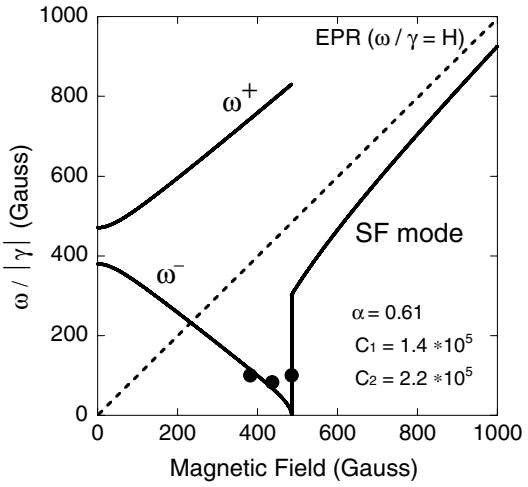


Fig. 2. Frequency (ω/γ)-field relation. The solid lines are the fitting curves with $C_1 = 1.4 \times 10^5$, $C_2 = 2.2 \times 10^5$ and $\alpha = 0.61$. The dashed line indicates the EPR relation; $\omega/\gamma = H$.

interaction. Using this model, the frequency–field relation is well reproduced (see Fig. 2). The solid lines are the fitting curves with the parameters as follow:

$$AK_1 = 7.2 \times 10^4(\mathrm{G}^2), \quad AK_2 = 1.1 \times 10^5(\mathrm{G}^2), \ \alpha = 0.61,$$

where A is the molecular field coefficient, K_1 and K_2 are the orthorhombic anisotropy parameters and $\alpha = 1 - \chi_{\|}/\chi_{\perp}$. The specific heat measurements under the applied magnetic field indicated the existence of one-dimensional ferromagnetic fluctuation. The overall temperature dependences of the specific heat had been well understood by the mean-field theory incorporated in the one-dimensional Heisenberg model [3]. Two interchain couplings were estimated to be $J' = (J_{13}) = 0.224$ K and $J'' = -0.176$ K. Using the antiferromagnetic interchain-coupling constant; we evaluate the orthorhombic anisotropy parameters and get $K_1/M = 55$ G and $K_2/M = 84.6$ G. The spin–flop field, H_{SF} is estimated to be 486 G, which is larger than H_{SF} (~50 G) for the high-pressure antiferromagnetic phase of β-phase [6]. The resonance field of the spin–flop mode hardly depended on temperature while that of ω^- mode depended on temperature. To investigate the magnetic parameters precisely, experiment at lower temperature is required.

3.2. Magnetic torque measurement

Fig. 3 shows the magnetic torque curve as a function of magnetic field. The angle θ is defined in the inset of Fig. 1 and the magnetic field is rotated in the *bc*-plane. At 1.5 K, the magnetic torque approximately increases proportional to the square of magnetic field strength. No structure was observed up to 8000 G (see the inset of Fig. 3). On the contrary, at 0.4 K ($<T_N$), two structures clearly emerge at 470 and 2100 G when the magnetic field is applied around $\theta = 40°$. The lower-field structure has a remarkable angular dependence. This anomaly around 470 G was observed in a very narrow angular region. The most pronounced structure was obtained around $\theta = 40°$. This direction corresponds well to the spin-easy axis observed in AFMR measurements. The magnetic field of 470 G is also consistent with the spin–flop transition field. The higher-field structure is observed in all magnetic field directions with weak angular dependence. Therefore, we assign H_C as the transition filed between AF and paramagnetic phase. The obtained H_C is consistent with the calculated result using the quasi-one-dimensional Heisenberg ferromagnetic model, in which H_C was estimated about 2200 G at 0.4 K [3].

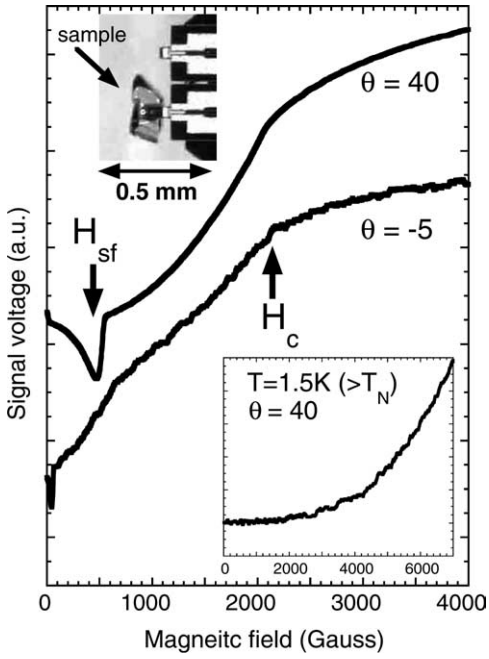


Fig. 3. Magnetic field dependence of the magnetic torque of γ-phase single crystal at 0.4 K. The inset figure shows the torque curve at 1.5 K. The magnetic field direction, θ, is defined in Fig. 1. The picture shows the sample mounted on the cantilever.

4. Conclusion

We have performed low-temperature ESR and magnetic torque measurements of γ-*p*-NPNN. Using the low frequency and low-temperature ESR technique, two AFMR modes along spin-easy axis can be observed for the first time. The frequency–field relation is well reproduced by the usual AFMR theory with the orthorhombic anisotropy parameters. We estimated the exchange and anisotropy parameters. In the magnetic torque measurement using small single crystal, we can observe the SF and AF-P transitions at 470 and 2100 G, respectively. Both AFMR and magnetic torque

measurements directly establish the antiferromagnetic ground state of γ-*p*-NPNN.

References

[1] M. Tamura, Y. Hosokoshi, D. Shiomi, M. Kinoshita, Y. Nakazawa, M. Ishikawa, H. Sawa, T. Kitazawa, A. Eguchi, Y. Nishio, K. Kajita, J. Phys. Soc. Jpn. 72 (2003) 1735.
[2] M. Tamura, Y. Nakazawa, D. Shiomi, K. Nozawa, Y. Hosokoshi, M. Ishikawa, M. Takahashi, M. Kinoshita, Chem. Phys. Lett. 186 (1991) 401.
[3] Y. Nakazawa, M. Tamura, N. Shirakawa, D. Shiomi, M. Takahashi, M. Kinoshita, M. Ishikawa, Phys. Rev. B 46 (1992) 8906.
[4] E. Ohmichi, T. Osada, Rev. Sci. Instrum. 73 (2002) 3022.
[5] T. Nagamiya, K. Yoshida, R. Kubo, Adv. Phys. 4 (1955) 1.
[6] M. Mito, T. Kawae, M. Takumi, K. Nagata, M. Tamura, M. Kinoshita, K. Takeda, Phys. Rev. B 56 (1997) R14225.

reported [7]. The typical shape of single crystal for the low-frequency (LF) ESR experiment is depicted in the inset of Fig. 1(a), whose diameter is about 0.6 mm. The alignment of crystal axes was also determined by the X-ray diffraction measurement.

In order to avoid the saturation effects, we developed the LF-ESR system. The resonator was constructed by the LC circuit, in which both the condenser (C) and pick-up coil (L) are put in parallel. The resonance frequency ($2\pi f = 1/\sqrt{LC}$) can be tuned by adjusting the capacitance and we mainly used the LC resonator with the resonant frequency of ~300 MHz, which corresponds to the EPR resonance field of about 100 G. The magnetic field is controlled by the Bruker ER032M and is monitored by the Hall magnetometer. As the high power of oscillating magnetic field easily saturate the resonance line [7], we adjusted the rf power carefully so that the line shapes might not be distorted. The samples were directly cooled by the ^{3}He. The temperature was monitored by the vapor pressure of ^{3}He gas (MKS Baratron) and by the Cernox resistive thermometer equipped around the LC resonator. The lowest temperature attained is about 0.4 K. ESR absorption signals were obtained by monitoring the reflection intensity from the resonator through the scalar network analyzer (Agilent Technology, 8719ET).

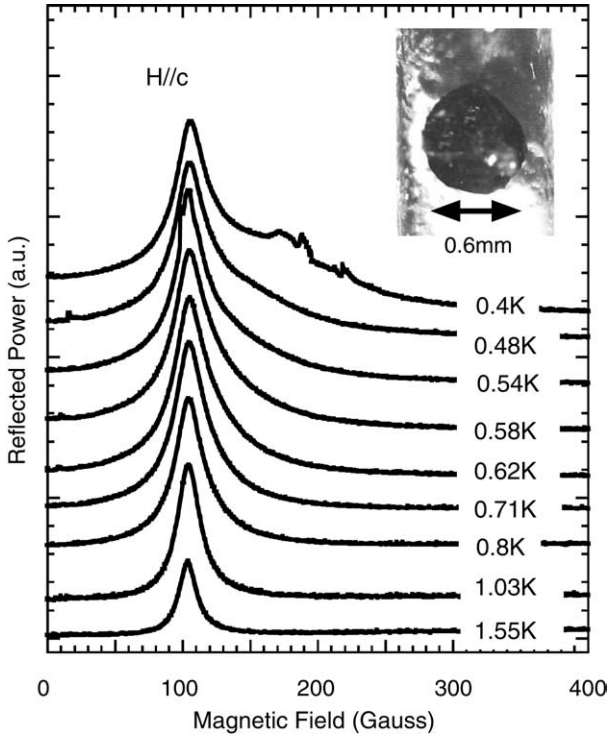


Fig. 1. Temperature dependence of ESR spectra for H//*c*. The inset shows the picture of spherically molded single crystal of β-*p*-NPNN, whose diameter is about 0.6 mm.

3. Results and discussion

Fig. 2 shows typical ESR absorption signals at different temperatures for H//*c*. The applied rf is about 289 MHz, corresponding to the EPR resonance field of 103 G. As temperature is decreased, the signals at EPR position increase its intensity with slight increase of the line-width, but are observed at the lowest temperature. Below 0.8 K, new absorption signals are gradually developed at the higher field shoulder of EPR signals. These absorption signals can be observed in all magnetic field direction. We marked these signals HF. The observed spectra were well fitted by assuming two symmetric

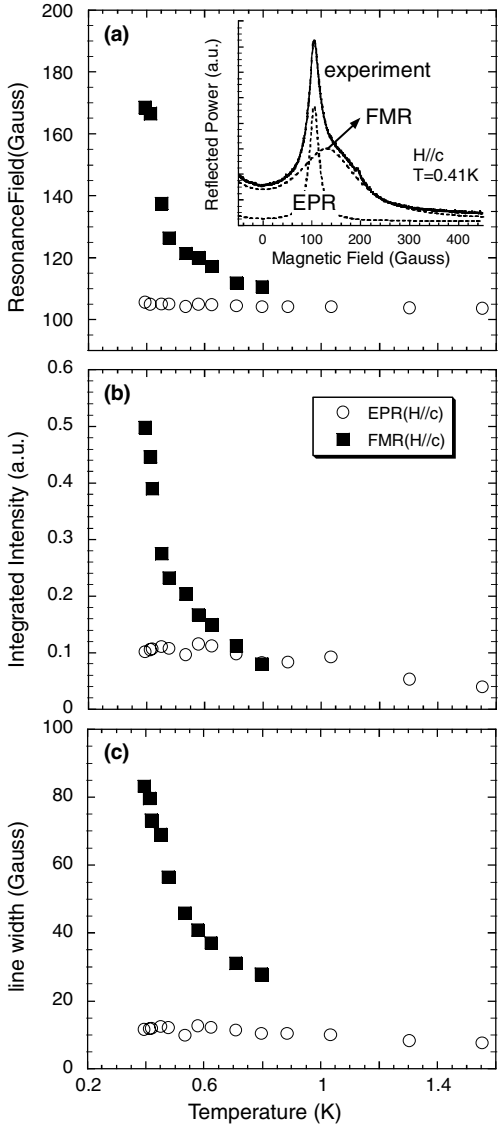


Fig. 2. Temperature dependence of ESR parameters for H//*c*. (a) The resonance fields, (b) the integrated intensity and (c) the line width are shown. The inset figure in (a) shows the typical spectrum at 0.5 K. The ESR spectra were decomposed by two symmetric Lorentzian absorption; EPR and HF(FMR). The open circles and closed squares are parameters for EPR and HF(FMR) components, respectively.

Lorentzian signals. In the inset of Fig. 2(a), both the spectrum and the decomposed two Lorentzian signals are indicated. Figs. 2(a)–(c) show the temperature dependences of resonance fields, integrated intensity and line width for two components, respectively, where the magnetic fields are applied parallel to the *c*-axis. Because the resonance fields of lower field signals are almost independent from temperature as well as the angle between the magnetic field and the crystal axis, we could assign these signals at low temperatures as residual EPR signals. The sample preparation procedure for making the spherical shape may cause some impurities on the surface of the crystals. Contrary to the EPR signals, the parameters for HF signals have remarkable temperature dependence. The resonance fields shift to the higher field side, i.e., the lower *g*-factor side as the temperature is decreased. This result indicates the existence of internal magnetic field acting on the spin system. The integrated intensity of HF signal is several times stronger than that of EPR signal. The resonance fields of HF signals also depend on the magnetic field direction. The angular dependence of resonance fields at the lowest temperature for H//*bc*-plane is presented in Fig. 3. When the magnetic field is tilted away from the *c*-axis, it is difficult to estimate the resonance field of HF signals correctly due to the overlapping of HF signals on the EPR signals. Contrary to the *bc*-plane, it should be noted that the ESR spectra are nearly isotropic in the *ab*-plane. This suggests

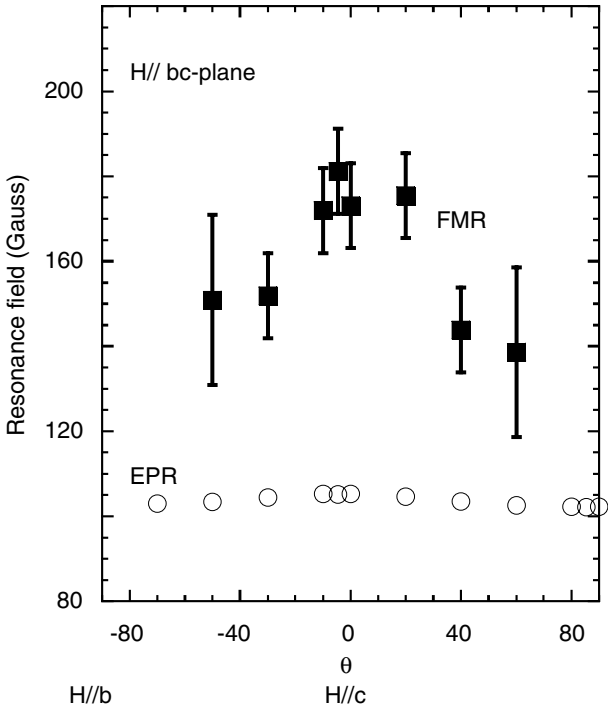


Fig. 3. Angular dependence of resonance fields at 0.4 K. The magnetic field is applied within the *bc*-plane. The open circles and closed squares indicate the resonance fields for EPR and HF(FMR) components, respectively.

that the HF signals should have no clear angular dependence. From these experimental results, we can judge the HF signals as a ferromagnetic resonance (FMR). This is the first evidence for observing the symmetric FMR signals in the β-*p*-NPNN. The higher field shift for H//*c* as well as the isotropic behavior in the *ab*-plane indicate that the *spin hard* axis aligns parallel to the *c*-axis. The dipolar field calculation also supports this result [1].

In order to estimate the FMR, we assume a uniaxial anisotropy and ignore the demagnetizing field term in a magnetic free energy density because the crystal has a roughly spherical shape. When the magnetic field is applied perpendicular to the spin-easy axis, the FMR relation is written by the usual Kittel's formula

$$\frac{\omega}{\gamma} = \sqrt{H(H - 2H_K)}, \quad H > 2H_K,$$

where $H_K = KM$ is the anisotropy field and M is the spontaneous magnetization. Using this expression, we can estimate the anisotropy field as $2H_K = 121 \pm 20$ G. This result may be consistent with the small saturation field of magnetization as well as with the small coercive force [2,3]. However, this value is smaller than the calculated results of dipole interaction [1]. Since the magnetic anisotropy field depends on the spontaneous magnetization, it should be compared with the extrapolated value toward $T = 0$. The temperature dependence of spontaneous magnetization had been estimated by the temperature dependence of muon spin precession frequency [4]. Their temperature dependence follows $[1 - (T/Tc)^{\alpha}]^{\beta}$ formula with the exponents; $\alpha = 1.86$ and $\beta = 0.32$. Therefore, the reduced factor of spontaneous magnetization at 0.4 K, at which our LF-ESR measurements have been done, is estimated to be about $M(T)/M_0 \approx 0.86$. Though there may not be a formula on the temperature dependence of the magnetic anisotropy, which can be applied to all systems, we apply the temperature dependence of uniaxial anisotropy for localized spin magnet model [8]. In this model, the anisotropy constant depends on the following formula; $K(T)/K_0 \propto [M(T)/M_0]^3$ at low temperatures, whilst $K(T)/K_0 \propto [M(T)/M_0]^2$ at higher temperatures, where $M(T)$ is the spontaneous magnetization at T. Therefore, in the case of β-*p*-NPNN, the magnetic anisotropy at $T = 0$ is obtained to be $H_K(0) \approx 130$ G. This value is rather consistent with the calculation for the dipole-sum, but it is necessary to measure FMR at lower temperature in order to investigate the anisotropy constant correctly.

4. Conclusion

The low-temperature and radio-frequency (rf) ESR were performed using the spherically-molded single crystals of β-*p*-NPNN. The FMR signals could be observed below 0.8 K, especially for H//*c*. The higher field

shift of FMR for H//c indicates that the spin-hard axis is parallel to this direction. We applied the usual Kittel's FMR relation with uniaxial anisotropy and estimate the magnetic anisotropy field of H_K = 61 G at 0.4 K.

References

[1] M. Kinoshita, J. Appl. Phys. 33 (1994) 5718, and references therin.
[2] M. Tamura, Y. Nakazawa, D. Shimomi, K. Nozawa, Y. Hosokoshi, M. Ishikawa, M. Takahashi, M. Kinoshita, Chem. Phys. Lett. 186 (1991) 401.
[3] Y. Nakazawa, M. Tamura, N. Shirakawa, D. Shiomi, M. Takahashi, M. Kinoshita, M. Ishikawa, Phys. Rev. B 46 (1992) 8906.
[4] L.P. Le, A. Keren, G.M. Luke, W.D. Wu, Y.J. Uemura, M. Tamura, M. Ishikawa, M. Kinoshita, Chem. Phys. Lett. 206 (1993) 405.
[5] A. Zheludev, E. Ressouche, J. Schweizer, P. Turek, M. Wan, H. Wang, J. Mag. Mater. 135 (1994) 233.
[6] P. Turek, Mol. Cryst. Liq. Cryst. 233 (1993) 191.
[7] K. Oshima, H. Kawanoue, Y. Haibara, H. Yamazaki, K. Awaga, M. Tamura, M. Kinoshita, Synth. Met. 71 (1995) 1821.
[8] H.B. Callen, E. Callen, J. Phys. Chem. Solids. 27 (1966) 1271.

calculation, the non-collinear magnetic clusters, which has a three-dimensional magnetic arrangement, was obtained as the ground state at Fe_3O_5 [2].

The atomic structure of charged clusters could be different from that of neutral cluster. To compare with the available experimental data of EA [3], in the present work, we report the ground state geometry and magnetic structure for the anion iron oxide clusters, $Fe_nO_m^-$ $(n = 3, 4)$ and their vertical detachment energies (VDE). We discuss the dependence of VDE with respect to the number of oxygen atoms.

2. Calculation method

We have used the first principles molecular dynamics [6], which is based on the density functional theory [7,8] with ultra-soft pseudo potentials [9–11] and plane-waves, to optimize the configuration of clusters. This scheme allows us to take the simultaneous optimization in both of atomic and electronic degrees of freedom. The clusters were placed in a large cubic cell of side 20 a.u. with the periodic boundary condition. The energy cutoffs are 24 Ry for plane-wave expansion of electron wave functions at the Γ point and 250 Ry for the augmented electron density [10,11]. We used the generalized gradient approximation (called PW91) for the exchange-correlation energy [12]. To treat the metallic property that there are some degenerate states around the Fermi level, as in the calculation of neutral clusters, we introduced the additional freedom of partial occupations [13–15]. Consequently, the values presented for magnetization were obtained by integrating spin densities, resulting in non-integer value. The contribution of uniform charge to the Hartree potential has been evaluated with the real space integration in the real cell, as used in the previous study [16].

In pure iron clusters, there are ferromagnetic and antiferromagnetic interactions between magnetic moments on atoms [17,18]. Due to this property, non-collinear magnetic structures could appear in the optimization process of atomic and electronic configurations. Therefore, we have used the scheme of non-collinear magnetism [17,19], as well as the usual spin polarized scheme for density functional calculations. Because iron oxide clusters having many oxygen atoms favor antiferromagnetic configurations, the collinear scheme sometimes encounters the difficulty that the system falls down to a metastable spin configuration. The non-collinear scheme, in which the atomic magnetic moments could rotate gradually at the cost of low energies, efficiently seek the ground state spin configuration.

3. Results and discussion

3.1. $Fe_3O_m^-$

The stable sites for O atoms are categorized into the bridge and surface sites. The latter is a site above the center of the triangle consisting of Fe atoms. The edge site of O (the oxygen atom is bonded at a single Fe atom) usually gives a higher energy. We present the geometry and magnetic arrangement of the ground state

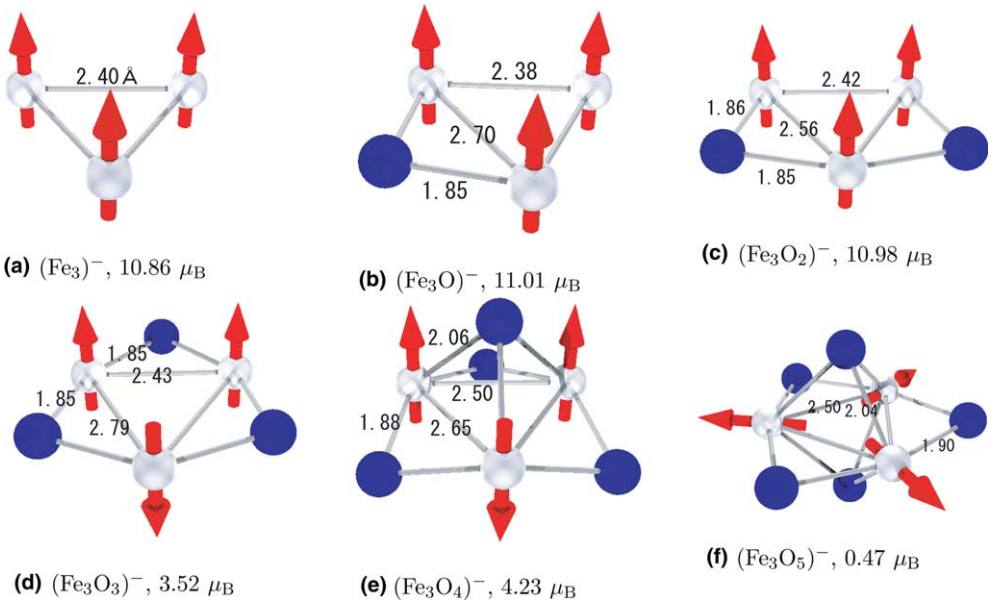


Fig. 1. The ground state geometry and magnetic configuration for the anion clusters, $Fe_3O_m^-$ $(m = 0–5)$, with the bond length in Å and the magnetization in μ_B: (a) $(Fe_3)^-$, 10.86 μ_B; (b) $(Fe_3O)^-$, 11.01 μ_B; (c) $(Fe_3O_2)^-$, 10.98 μ_B; (d) $(Fe_3O_3)^-$, 3.52 μ_B; (e) $(Fe_3O_4)^-$, 4.23 μ_B; (f) $(Fe_3O_5)^-$, 0.47 μ_B.

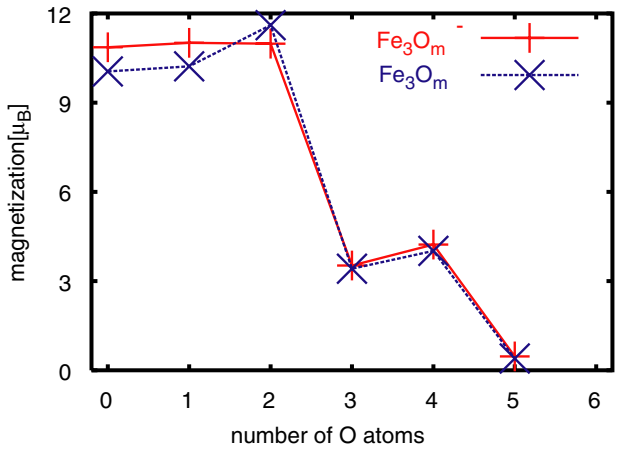


Fig. 2. The oxidation dependences of total magnetization for Fe_3O_m and $Fe_3O_m^-$ ($m = 0$–5).

configurations for $Fe_3O_m^-$ ($m = 0$–5) in Fig. 1. Oxygen atoms favor the bridge site in $Fe_3O_m^-$ ($m = 1$–3). When adding O atoms ($Fe_3O_m^-$ ($m = 4, 5$)), they occupy into the surface site. This shows a similar configuration as in the neutral clusters [2].

The pure anion Fe cluster has the ferromagnetic ground state. The ferromagnetic arrangement survives to $Fe_3O_2^-$. Increasing the number of O atoms, the arrangement changes to antiferromagnetic one at $m \geqslant 3$, as shown in Fig. 2. This is due to the antiferromagnetic interaction of superexchange mechanism through O atoms. Whereas this antiferromagnetic interaction between Fe atom may become strong as the number of oxygen atoms increases.

At the largest number of O atoms, the cluster of $Fe_3O_5^-$ (see Fig. 1(f)) has non-collinear magnetic arrangement as the neutral one [2]. The atomic magnetic moments on Fe form the angle of 120° in a plane. The stability of non-collinearity results from a competition among the strong symmetric antiferromagnetic interactions between Fe atoms.

In comparison with the neutral clusters, generally, effects of additional electron gives longer bond lengths. In the ferromagnetic clusters, $Fe_3O_m^-$ ($m = 0$–2), the Fe–Fe bond becomes longer by about 0.15 Å than that in the corresponding neutral one. In the antiferromagnetic cluster of $Fe_3O_m^-$ ($m = 3, 4$), the ferromagnetic bond between Fe atoms (the Fe–Fe bond with ferromagnetic arrangement) becomes longer by about 0.05 Å, while the antiferromagnetic bond becomes longer by 0.1 Å. As a general tendency in antiferromagnetic clusters, the adding electron increases antiferromag-

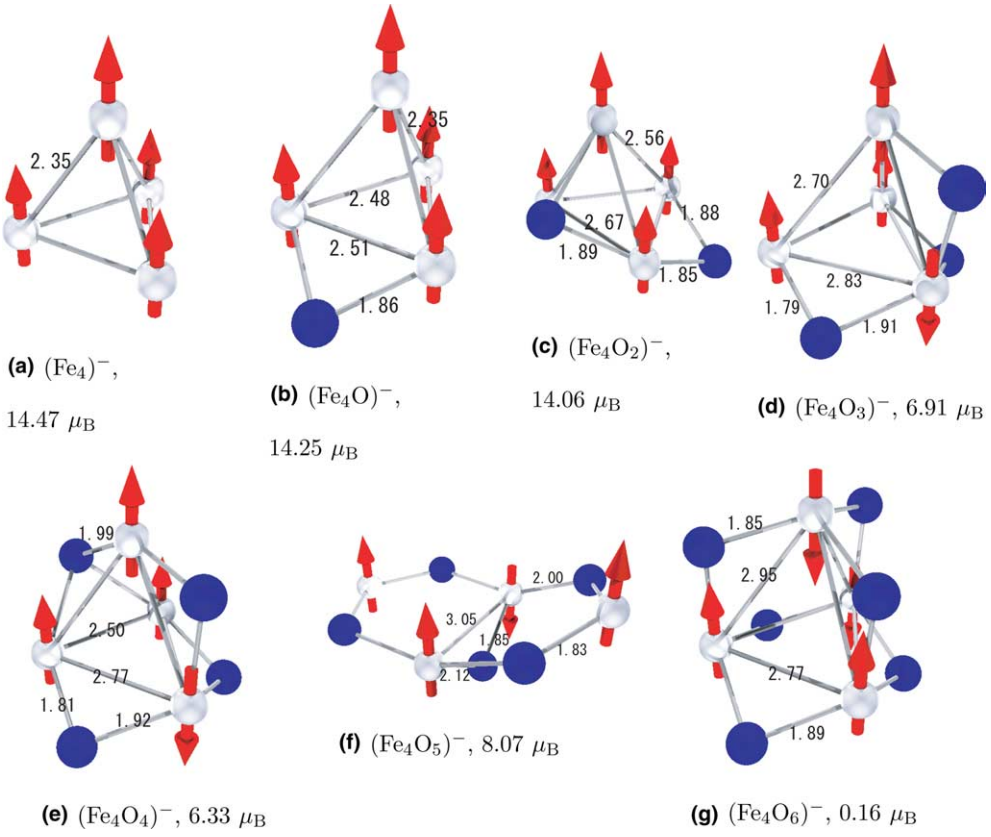


Fig. 3. The ground state geometry and magnetic configuration for the anion clusters, $Fe_4O_m^-$ ($m = 0$–6), with the bond length in Å and the magnetization in μ_B: (a) $(Fe_4)^-$, 14.47 μ_B; (b) $(Fe_4O)^-$, 14.25 μ_B; (c) $(Fe_4O_2)^-$, 14.06 μ_B; (d) $(Fe_4O_3)^-$, 6.91 μ_B; (e) $(Fe_4O_4)^-$, 6.33 μ_B; (f) $(Fe_4O_5)^-$, 8.07 μ_B; (g) $(Fe_4O_6)^-$, 0.16 μ_B.

netic bonds between Fe atoms more than ferromagnetic bonds.

3.2. $Fe_4O_m^-$

The geometry and magnetic arrangement for the ground state clusters, $Fe_4O_m^-$, are shown in Fig. 3. The low energy configurations for Fe_4^- have tetrahedral (Fig. 3(a)) and plane structures. The former is more stable by 2.75 eV than the latter. Three stable clusters were obtained for Fe_4O^-; the most stable is shown in Fig. 3(b), the second stable one has an O atom at a surface site (+0.28 eV), and the third one has a plane structure (+1.79 eV vs. the most stable one).

In the neutral cluster of Fe_4O_3, two O atoms are added to the bridge sites between two Fe atoms and the other O atom is added to the surface site. In the anion cluster, unlike the neutral one, three O atoms are added to the bridge sites, and the magnetic arrangement changes from ferromagnetic to antiferromagnetic one, as shown in Fig. 4. This indicates that the adding electron induces antiferromagnetic interaction.

We obtained the stable cluster of plane structure, as well as the three-dimensional structure for $Fe_4O_4^-$. The former is at the energy of 1.7 eV above the most stable one (Fig. 3(e)). For $Fe_4O_5^-$, we obtained the stable cluster of plane-like structure (Fig. 3(f)). The plane structure might be due to an incommensurate situation on the number of O atoms. While the tetrahedron of Fe_4 has six Fe–Fe bonds, which reserves six bridge sites, an unoccupied bridge site of O atom would deform a three-dimensional structure for $Fe_4O_5^-$. In deed, for $Fe_4O_6^-$, all of the bridge sites are occupied by O atoms, resulting to the stable cluster.

As in $Fe_3O_m^-$, effects of the additional electron appeared in the longer bond lengths by about 0.1 Å for Fe–Fe bond and by about 0.05 Å for Fe–O bond.

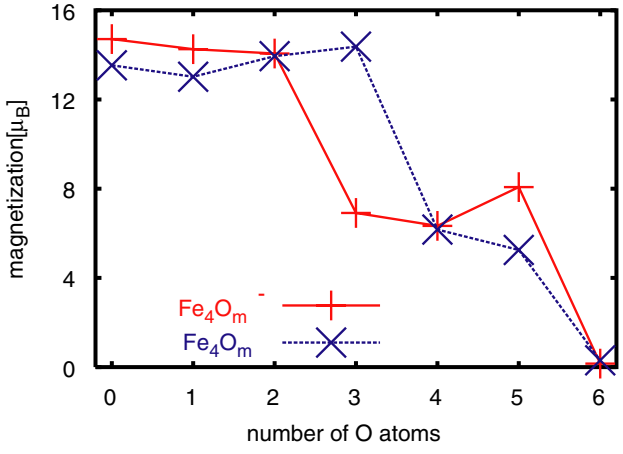


Fig. 4. The oxidation dependences of total magnetization for Fe_4O_m and $Fe_4O_m^-$ ($m = 0$–6).

3.3. Vertical detachment energy

The VDEs of the ground state geometry for $Fe_nO_m^-$ ($n = 3, 4$) are shown as a function of the number of O atoms in Fig. 5. The VDE of $Fe_3O_m^-$ is in agreement with the experimental data [3] without $Fe_3O_5^-$. In the photoelectron spectrum of $Fe_3O_5^-$ [3], there is a relatively long tail in the low binding energies, which implies the existence of minor clusters having low EAs. To extract this implication in experimental data, we estimated the length of tail from the spectrum and present a vertical bar in Fig. 5.

For $Fe_4O_m^-$, the calculated VDEs generally are lower than the experimental one. This shows a contrast with a general property of local density functional calculations which usually gives larger energies [16,20].

The VDE of $Fe_4O_m^-$ is in fair agreement with the experimental data in the tendency of oxidation [3]. However, some clusters show a difference between calculation and experiment. As a general property, spectrum

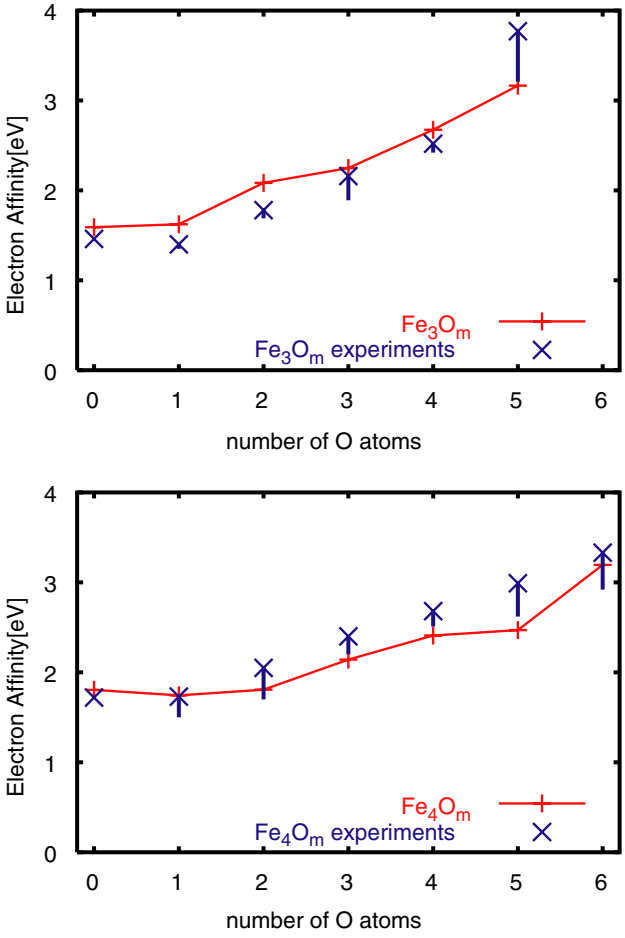


Fig. 5. The vertical detachment energy of $Fe_3O_m^-$ and $Fe_4O_m^-$ clusters as a function of the number of O atoms. The plus and cross specify the calculated VDE and the EA of experiment[3], respectively. The lines are for the guide of eye. The vertical bar from the cross indicates a length of low-energy tail in the photoelectron spectrum by Wang et al.

of $Fe_4O_m^-$ have longer tail than the smaller clusters, $Fe_nO_m^-$ ($n = 1$–2). This seems to be correlated with the large difference in $Fe_4O_m^-$.

4. Summary

We have determined the ground state geometry and magnetic arrangement for the anion iron clusters, $Fe_3O_m^-$ ($m = 1$–5) and $Fe_4O_m^-$ ($m = 1$–6), which had been obtained in the gas phase experiment. In the structural optimization, the first O atom favors a bridge site, and the second O atom occupies another bridge site in $Fe_3O_2^-$ and the surface site in $Fe_4O_2^-$. These behaviors are similar to the neutral clusters. Compared with the neutral clusters, the anion clusters are stabilized with bond elongation by $\sim$0.1 Å for Fe–Fe bonds and $\sim$0.05 Å for Fe–O bonds. We evaluated the VDEs and discussed the behavior with respect to the number of O atoms. The VDE of $Fe_3O_m^-$ is in good agreement with the experimental data without $Fe_3O_5^-$. For $Fe_4O_m^-$, the calculated VDEs generally show lower values than the experimental one.

Acknowledgments

This work was supported by the Japan Society for the Promotion of Science (JSPS) under Project No. 13640328. The calculation in this work was partially carried out using the facilities of the Supercomputer Centre, Institute for Solid State Physics, University of Tokyo. The author (T.O.) is grateful for a financial support of Grant-in Aid for Scientific Research by JSPS (Project No. 16310081).

References

[1] I.M.L. Billas, A. Chatelain, W.A. De Heer, Science 265 (1994) 1682.
[2] H. Shiroishi, T. Oda, I. Hamada, N. Fujima, Eur. Phys. J. D. 24 (2003) 85.
[3] L.S. Wang, H. Wu, S. Desai, Phys. Rev. Lett. 76 (1996) 4853.
[4] H. Wu, L.S. Wang, S. Desai, J. Am. Chem. Soc. 76 (1996) 5296.
[5] J. Fan, L.S. Wang, J. Chem. Phys. 102 (1995) 8714.
[6] R. Car, M. Parrinello, Phys. Rev. Lett. 55 (1985) 2471.
[7] P. Hohenberg, W. Kohn, Phys. Rev. 136B (1964) 864.
[8] W. Kohn, L.J. Sham, Phys. Rev. A 140 (1965) 1133.
[9] D. Vanderbilt, Phys. Rev. B 41 (1990) 7892.
[10] A. Pasquarello, K. Laasonen, R. Car, C. Lee, D. Vanderbilt, Phys. Rev. Lett. 69 (1992) 1982.
[11] K. Laasonen, A. Pasquarello, R. Car, C. Lee, D. Vanderbilt, Phys. Rev. B 47 (1993) 10142.
[12] J.P. Perdew, J.H. Chevary, S.H. Vosko, K.A. Jackson, M.R. Pederson, D.J. Singh, C. Fiolhais, Phys. Rev. B 46 (1992) 6671.
[13] N.D. Mermin, Phys. Rev. B 137 (1965) A1441.
[14] N. Marzari, D. Vanderbilt, M.C. Payne, Phys. Rev. Lett. 79 (1997) 1337.
[15] T. Oda, J. Phys. Soc. Jpn. 71 (2002) 519.
[16] H. Shiroishi, T. Oda, I. Hamada, N. Fujima, Mol. Simul. 30 (2004) 911.
[17] T. Oda, A. Pasquarello, R. Car, Phys. Rev. Lett. 80 (1998) 3622.
[18] N. Fujima, T. Oda, Eur. Phys. J. D. 24 (2003) 89.
[19] T. Oda, A. Pasquarello, Phys. Rev. B 70 (2004) 134402.
[20] M. Castro, D.R. Salahub, Phys. Rev. B 49 (1994) 11842.

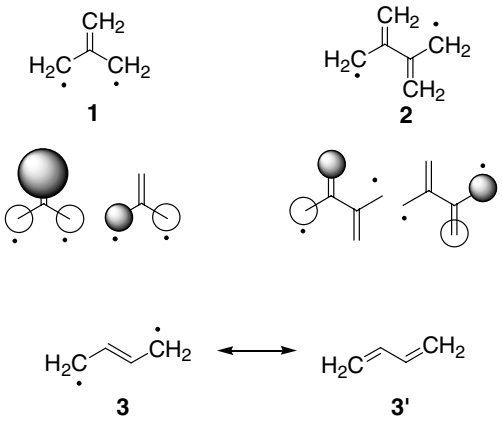


Fig. 1. The molecular structure and the shape of the orbitals of trimethylenemethane (**1**), tetramethyleneethane (**2**), and butadiene (**3′**).

molecule therefore exists as a normal closed-shell Kekulé molecule. 1,3-Butadiene (**3′**) is an example of a normal Kekulé molecule; it has the resonant biradical structure, 2-butene-1,4-diyl (**3**). In this case, the closed-shell structure **3′** is the ground state, so the ground electronic state has no unpaired electrons. In other words, the magnetic interaction between the two spins in the structure **3** is strongly antiferromagnetic.

The magnetic interactions in the disjoint and non-disjoint biradicals have been theoretically and experimentally investigated to conclude that while TMM (**1**) has a ground triplet state, the singlet and triplet states of TME (**2**) are nearly degenerate [7,8].

Photochromism is a reversible phototransformation of a chemical species between two forms having different absorption spectra [9–11]. Photochromic compounds reversibly change not only the absorption spectra but also their geometrical and electronic structures. The geometrical and electronic structural changes induce some changes in physical properties, such as fluorescence, refractive index, polarizability, and electric conductivity. When the photochromic compounds are used as "spin couplers", the magnetic interaction can be controlled by photoirradiation. Not only our group but also others [12–17] have recently been interested in the photocontrol of magnetism of organic radical-based magnetic materials.

Diarylethenes with heterocyclic aryl groups are well known as thermally irreversible, highly sensitive, and fatigue-resistant photochromic compounds (Fig. 2) [18].

The difference in color is due to the differences in the geometrical and electronic structures. In the open-ring isomer, free rotation is possible between the ethene moiety and the aryl group. Therefore, the open-ring isomer is non-planar and the π-electrons are localized in the two aryl groups. On the other hand the closed-ring isomer has bond-alternative polyene structure and the

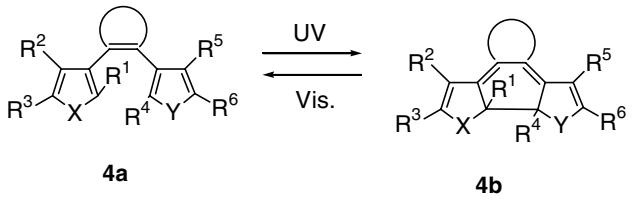


Fig. 2. Photochromism of diarylethene.

π-electrons are delocalized throughout the molecule. These geometrical and electronic structural differences resulted in some differences in the physical properties. For example, the closed-ring isomer has a high polarizability, because the closed-ring isomer has more delocalized π-electrons [19,20]. Not only the change in polarizability, but also the switching in fluorescence [21] and electronic conduction [22] have been developed.

2. Diarylethene as a photoswitch

There is a characteristic feature in the electronic structural changes of diarylethenes. Fig. 3 shows the open-ring isomer **5a** and closed-ring isomer **5b** of the radical-substituted diarylethenes with simplified structures. While there is no resonant closed-shell structure for **5a**, there does exist **5b′** as the resonant quinoid-type closed-shell structure for **5b**. **5a** is a non-Kekulé biradical, and **5b** is a normal Kekulé molecule. In other words, **5a** has two unpaired electrons, while **5b** has no unpaired electrons. The calculated shapes of two SOMOs of **5a**

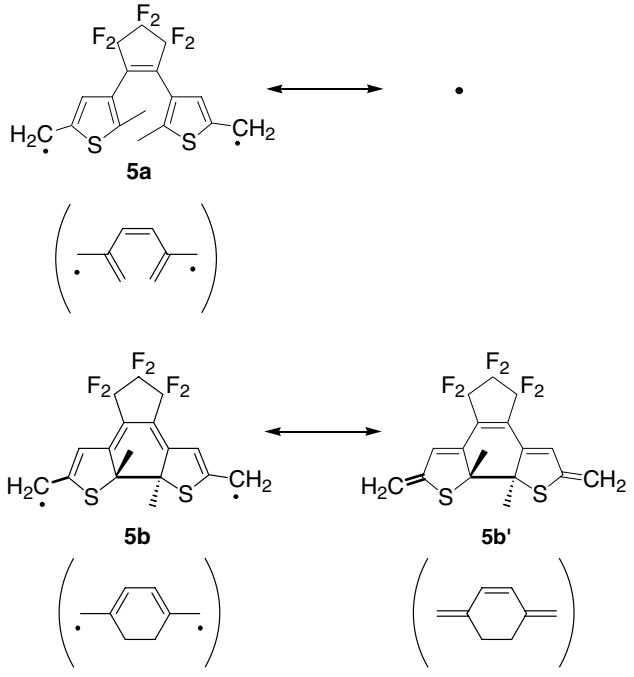


Fig. 3. The open-ring isomer **5a** and the closed-ring isomer **5b** of the radical-substituted diarylethene.

are separated in the molecule and there is no overlap. This configuration is a typical disjoint biradical, in which the intramolecular radical–radical interaction is weak. In the open-ring isomer, the bond-alternation is discontinued at the 3-position of the thiophene rings. This is the origin of the disjoint nature of the electronic configuration of **5a**. **5a** is a disjoint non-Kekulé biradial and corresponds to tetramethyleneethane (**2**) in the former example. However, the closed-ring isomer **5b**′ is a normal Kekulé molecule. In this case, the ground electronic state has no unpaired electrons. In this singlet ground state, the magnetic interaction is strongly antiferromagnetic. **5b**′ corresponds to butadiene **3**′ in the former example.

The electronic structural change of radical-substituted diarylethenes accompanying the photoisomerization is the transformation of a disjoint non-Kekulé structure to a closed-shell Kekulé structure. One may infer from the above consideration that the interaction between spins in the open-ring isomer of diarylethene is weak, while significant antiferromagnetic interaction takes place in the closed-ring isomer. In other words, the open-ring isomer is "OFF" state and the closed-ring isomer is "ON" state.

3. Photoswitching of magnetic interaction

Photochromic biradical **6a** was designed and synthesized by choosing 1,2-bis(2-methyl-1-benzothiophen-3-yl)perfluorocyclopentene as a photochromic spin coupler and nitronyl nitroxides as spin sources (Fig. 4) [23,24]. The schematic representation is also shown in Fig. 4.

In solution, **6a** showed ideal photochromic behavior by irradiation with UV and visible light (Fig. 5). Although the radical moiety absorbs in the region from 550 to 700 nm, this did not prevent the photochromic reaction. Almost 100% photochemical conversions were observed in both the cyclization from open-ring isomer **6a** to closed-ring isomer **6b** and the cycloreversion from **6b** to **6a**. For the practical use of photochromic devices, high conversion is one of the most important characteristics.

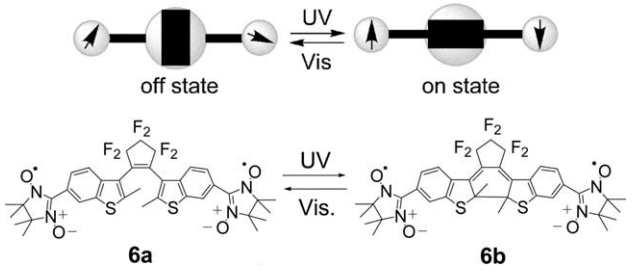


Fig. 4. Photoswitching of intramolecular magnetic interaction. top: schematic representation, bottom: synthesized molecule.

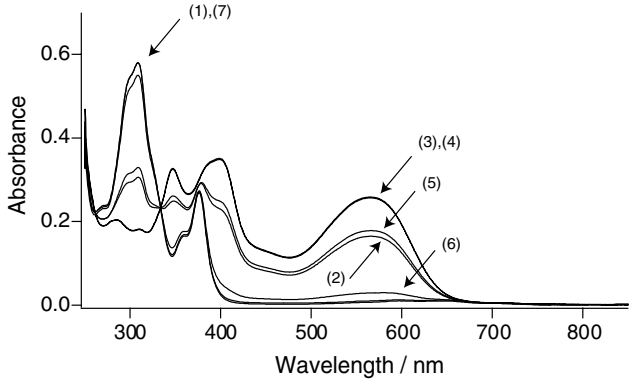


Fig. 5. The photochromic reaction of **6** (in EtOAc, 1.7×10^{-5} M): (1) the open-ring isomer; (2) irradiated with 313 nm light for 1 min; (3) for 5 min; (4) for 10 min; (5) irradiated with 578 nm light for 5 min; (6) for 30 min; (7) for 60 min.

Magnetic susceptibilities of **6a** and **6b** were measured on a SQUID susceptometer in microcrystalline form. χT–T plots are shown in Fig. 6. The data were analyzed in terms of a modified singlet–triplet two-spin model (the Bleaney–Bowers-type), in which two spins ($S = 1/2$) couple antiferromagnetically within a biradical molecule by exchange interaction J. The best-fit parameters obtained by means of a least-squares method were $2J/k_B = -2.2 \pm 0.04$ K for **6a** and $2J/k_B = -11.6 \pm 0.4$ K for **6b**. Although the interaction ($2J/k_B = -2.2$ K) between the two spins in the open-ring isomer **6a** was weak, the spins of **6b** have a remarkable antiferromagnetic interaction ($2J/k_B = -11.6$ K).

The open-ring isomer **6a** had a twisted molecular structure and a disjoint electronic configuration. On the other hand, the closed-ring isomer **6b** had a planar molecular structure and a non-disjoint electronic configuration. The photoinduced change in magnetism agrees well with the prediction that the open-ring isomer has an "OFF" state and the closed-ring isomer has an "ON" state.

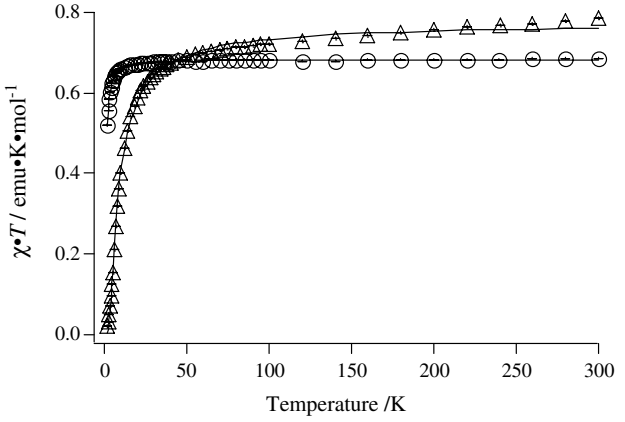


Fig. 6. Temperature dependence of the magnetic susceptibility of **6a** (O) and **6b** (Δ) (χT–T plot).

Although the switching of exchange interaction was detected by a susceptibility measurement of biradical **6**, both open- and closed-ring isomers **6a** and **6b** had 9-line ESR spectra because the exchange interaction between the two radicals was much stronger than the hyperfine coupling constant in both isomers. For one to detect the change of the exchange interaction by ESR spectroscopy, the value of the interaction should be comparable to the hyperfine coupling constant. Therefore, biradicals **7** ($n = 1, 2$), in which *p*-phenylene spacers are introduced to control the strength of the exchange interaction, were designed and synthesized (Fig. 7) [25,26].

As described earlier, when two nitronyl nitroxides are magnetically coupled via an exchange interaction, the biradical gives a 9-line ESR spectrum. If the exchange interaction is weaker than the hyperfine coupling, the two nitroxide radicals are magnetically independent and give a 5-line spectrum. In intermediate situations, the spectrum becomes complex.

Diarylethenes, **7a**, ($n = 1, 2$) also underwent reversible photochromic reactions by alternative irradiation with UV and visible light. The changes in the ESR spectra accompanying the photochromic reaction were examined for diarylethenes, **7a**, ($n = 1, 2$). Fig. 8 shows the ESR spectra at different stages of the photochromic reaction of **7a** ($n = 1$). The ESR spectrum of **7a** ($n = 1$) showed a complex of 15 lines. This suggests that the two spins of nitronyl nitroxide radicals were coupled by an exchange interaction that is comparable to the hyperfine coupling constant. Upon irradiation with 366 nm light, the spectrum converted completely to a 9-line spectrum, corresponding to the closed-ring isomer **7b** ($n = 1$). The 9-line spectrum indicates that the exchange interaction between the two spins in **7b** ($n = 1$) is much stronger than the hyperfine coupling constant.

The ESR spectral change was also observed for **7a** ($n = 2$). The open-ring isomer **7a** ($n = 2$) had a 5-line spectrum, while the closed-ring isomer **7b** ($n = 2$) had a distorted 9-line spectrum. A simulation of the ESR spectra was performed. The exchange interaction decreases with the increase in the π-conjugated chain length, as shown in Table 1. The exchange interaction change in **7a** ($n = 1, 2$) upon photoirradiation was more than 30-fold. This result shows a very large switching effect of diarylethenes and suggests the superiority of diarylethenes as molecular switching units. Although the absolute value of the exchange interaction is small, the information of the spins can be clearly transmitted through the closed-ring isomer, and the switching can be detected by ESR spectroscopy.

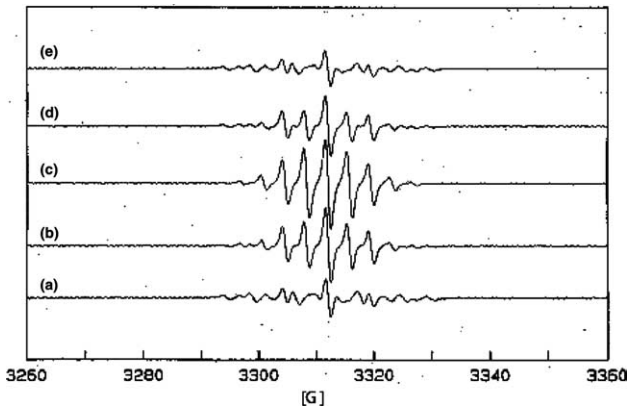


Fig. 8. ESR spectral change of **7a** ($n = 1$) along with photochromism (benzene solution, 1.1×10^{-4} M): (a) initial; (b) irradiation with 366 nm light for 1 min; (c) 4 min; (d) irradiation with >520 nm light for 20 min; (e) 50 min.

Table 1
Magnetic interaction between two nitronyl nitroxide connected by diarylethene photoswitches

	Open-ring isomer		Closed-ring isomer	
	ESR line shape	$\lvert 2J/k_B\ \mathrm{K}\rvert$	ESR line shape	$\lvert 2J/k_B\ \mathrm{K}\rvert$
6	9 lines	2.2	9 lines	11.6
7 ($n = 1$)	15 lines	$\begin{cases} 1.2 \times 10^{-3} \\ < 3 \times 10^{-4} \end{cases}$	9 lines	>0.04
7 ($n = 2$)	5 lines	$<3 \times 10^{-4}$	distorted 9 lines	0.010
8 ($n = 1$)	13 lines	$\begin{cases} 5.6 \times 10^{-3} \\ < 3 \times 10^{-4} \end{cases}$	9 lines	>0.04
8 ($n = 2$)	5 lines	$<3 \times 10^{-4}$	9 lines	>0.04

Oligothiophenes are good candidates for conductive molecular wires. The thiophene-2,5-diyl moiety has been used as a molecular wire unit for energy and electron transfer and can serve as a stronger magnetic coupler than *p*-phenylene [27,28]. Therefore, diarylethenes, **8a**, ($n = 1, 2$) having one nitronyl nitroxide radical at each end of a molecule containing oligothiophene spacers was synthesized and their photo- and magnetochemical properties were studied (Fig. 9).

Photochromic reactions and an ESR spectral change was also observed for **8a** ($n = 1, 2$). Table 1 lists the exchange interaction between the two diarylethene-bridged

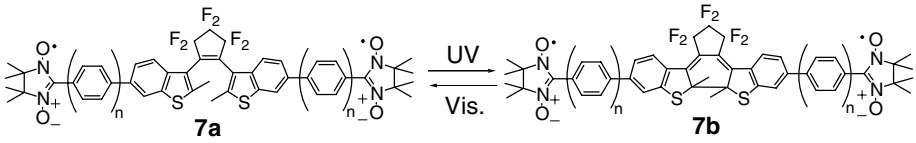


Fig. 7. Photoswitching using *p*-phenylene spacer.

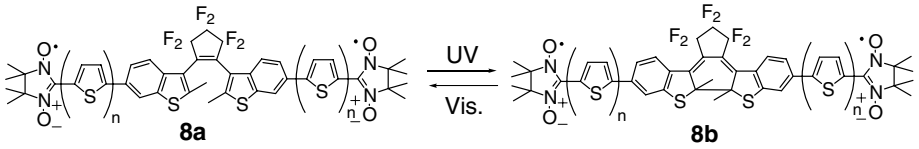


Fig. 9. Photoswitching using thiophene-2,5-diyl spacer.

nitronyl nitroxide radicals. For all five biradicals, the closed ring isomers have stronger interactions than the open-ring isomers. The exchange interactions through oligothiophene spacers were stronger than the corresponding biradicals with oligophenylene spacers. The efficient π-conjugation in thiophene spacers resulted in strong exchange interactions between the two nitronyl nitroxide radicals. In the case of bithiophene spacers, the exchange interaction difference between open- and closed-ring isomers was estimated to be more than 150-fold.

4. Reversed photoswitching using bis(2-thienyl)ethene

Photoswitching using bis(2-thienyl)ethene (**9**) (Fig. 10), in which 2-thienyl group is connected to the perfluorocyclopentene ring, was performed [29]. In the case of regular bis(3-thienyl)ethenes, the bond alternation is discontinued in the open-ring isomer, but in the closed-ring isomer, the π-electron is delocalized throughout the molecule. Therefore the open-ring isomer is in "OFF" state due to the disconnection of the π-system and the closed-ring isomer is in "ON" state due to the delocalization of the π-conjugated system. The situation is reversed when thiophene rings are substituted to the ethene moiety at 2-position. The bond alternation is continued throughout the molecule in the open-ring isomer, while in the closed-ring isomer two aryl rings are separated by the sp^3 carbon and sulfur atoms. The magnetic interaction between the two unpaired electrons at 5-positions in the closed-ring isomer is expected to become much weaker than that in the open-ring isomer. In other words, the open-ring isomer is in "ON" state and the closed-ring isomer in "OFF" state.

The synthesized bis(2-thienyl)ethene (**9a**) did not undergo photochromism, but the precursor underwent photochromic reaction. The closed-ring isomer of the precursor was obtained and the closed-ring isomer was transformed to the desired molecule. The obtained closed-ring isomer **9b** was converted to the open-ring isomer **9a** by irradiation with visible light. The ESR spectrum of the closed-ring isomer **9b** was a five-line spectrum, but the spectrum of the open-ring isomer **9a** was a distorted 9 lines. This suggests that there are stronger magnetic interaction in the open-ring isomer than in the closed-ring isomer. The switching direction is reversed by using bis(2-thienyl)ethene.

5. Photoswitching using array of photochromic molecules

In the previous section it was demonstrated that the exchange interaction between two nitronyl nitroxide radicals located at either end of a diarylethene was photoswitched reversibly by alternate irradiation with ultraviolet and visible light. The difference in the exchange interaction between the two switching states was more than 150-fold. ESR spectra can be used as a good tool for detecting small magnetic interaction changes in the molecular systems. In this section photoswitching of intramolecular magnetic interaction using a diarylethene dimer will be presented [30].

When a diarylethene dimer is used as a switching unit, there are three kinds of photochromic states: open–open (OO), closed–open (CO), and closed–closed (CC). From the analogy of an electric circuit, one may infer that the dimer has two switching units in series. Diarylethene dimer **10**, which has 28 carbon atoms between two nitronyl nitroxide radicals, was synthesized (Fig. 11). When the two radicals are separated by the 28 conjugated carbon atoms, the 5-line and 9-line spectra were clearly distinguishable upon irradiation. A *p*-phenylene spacer was introduced so that the cyclization reaction could occur at both diarylethene moieties. Bond alternation is discontinued at the open-ring moieties of **10(OO)** and **10(CO)**. As a result, the spins at either end of **10(OO)** and **10(CO)** cannot interact with each other. On the

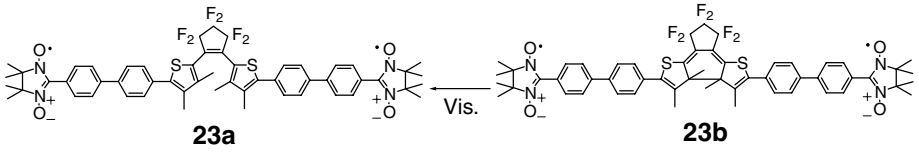


Fig. 10. Photoswitching using bis(2-thienyl)ethene.

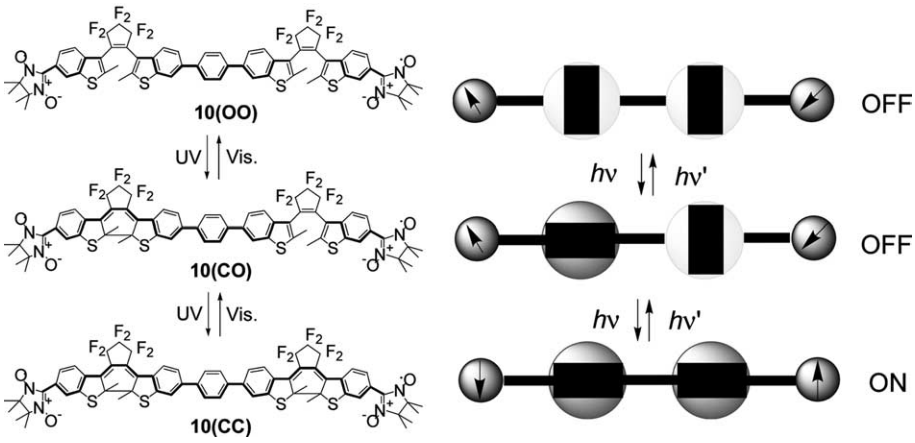


Fig. 11. Photochromic reaction and schematic illustration of diarylethene **10**.

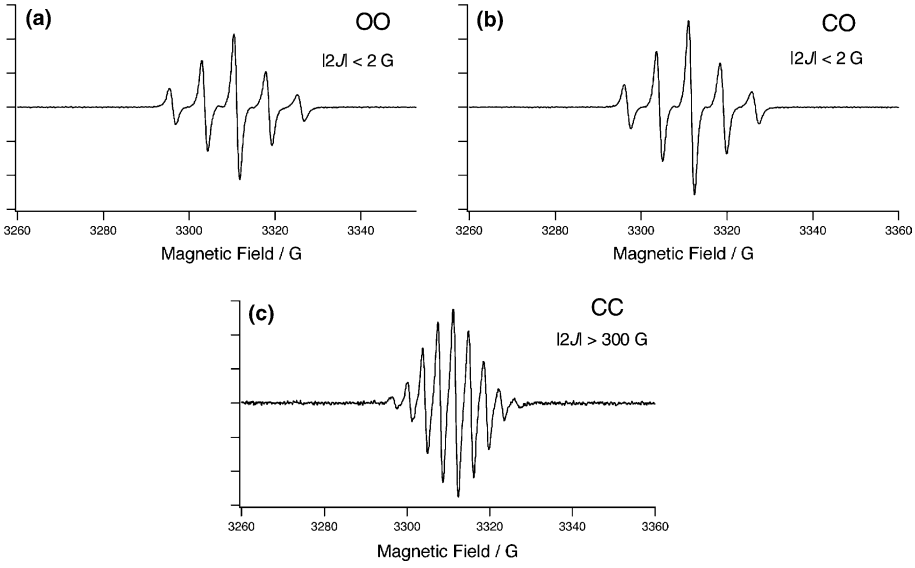


Fig. 12. ESR spectra of (a) **10(OO)**, (b) **10(CO)**, and (c) **10(CC)**.

other hand, the π-system of **10(CC)** is delocalized throughout the molecule and the exchange interaction between the two radicals is expected to occur.

ESR spectra of isolated **10(OO)**, **10(CO)**, and **10(CC)** were measured in benzene at room temperature (Fig. 12). The spectra of **10(OO)** and **10(CO)** were 5-line spectra, suggesting that the exchange interaction between the two nitronyl nitroxide radicals is much weaker than the hyperfine coupling constant ($2J/k_B < 3 \times 10^{-3}$ K).

However, the spectrum of **10(CC)** was a clear 9-line spectrum, indicating that the exchange interaction between the two spins is much stronger than the hyperfine coupling constant ($2J/k_B > 0.04$ K). The result indicates that each diarylethene chromophore serves as a switching unit to control the magnetic interaction. The magnetic interaction between terminal nitronyl nitroxide radicals was controlled by the switching units in series.

6. Conclusions

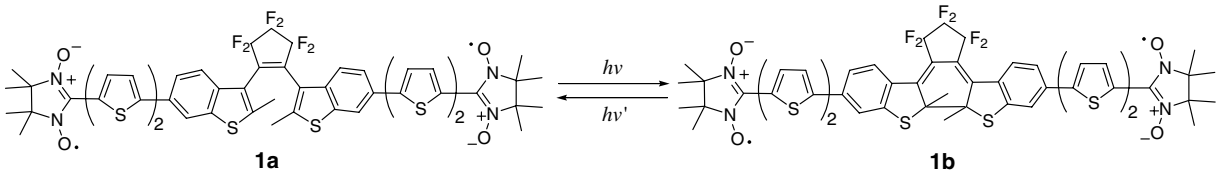
Since the report of the quintet ground state of *m*-phenylenebis(phenylmethylene), the field of molecular magnetism has emerged. This inherently interdisciplinary field has developed by expanding its scope to organic, inorganic, physical chemistry, and solid state physics. Starting from some basic considerations of the interaction mechanism, several aspects of the intramolecular magnetic interaction has been overviewed. The difference between the disjoint and non-disjoint biradicals brought to fruition the realization of the reversible photoswitching system. The photochromism of diarylethene is suitable for the switching system. This system has the possibility to be applied to the molecular-scale information processing system [31].

Acknowledgements

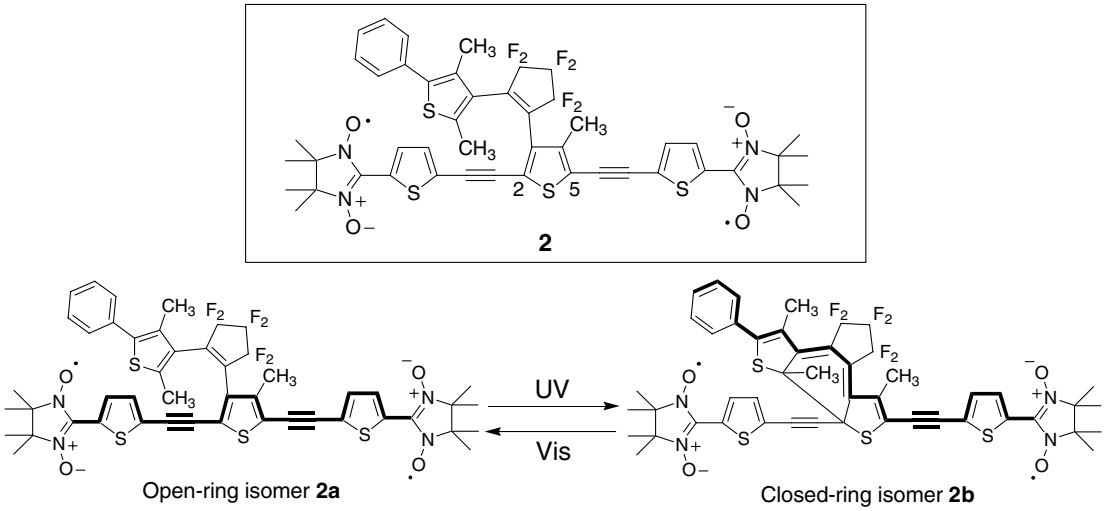
The authors are grateful for the supports from Japan Science and Technology Agency and the Ministry of Education, Science, Culture, and Sports, Japan.

References

[1] O. Kahn, Molecular Magnetism, VCH, New York, 1993.
[2] J.S. Miller, A.J. Epstein, Angew. Chem., Int. Ed. 33 (1994) 385.
[3] C. Benelli, D. Gatteschi, Chem. Rev. 102 (2002) 2369.
[4] J.S. Miller, M. Drillon (Eds.), Magnetism: Molecules to Materials, Wiley-VCH, Weinheim, 2001.
[5] H. Iwamura, N. Koga, Acc. Chem. Res. 26 (1993) 346.
[6] W.T. Borden, E.R. Davidson, J. Am. Chem. Soc. 99 (1977) 4587.
[7] K. Matsuda, H. Iwamura, J. Am. Chem. Soc. 119 (1997) 7412.
[8] K. Matsuda, H. Iwamura, J. Chem. Soc., Perkin Trans. 2 (1998) 1023.
[9] B.L. Feringa (Ed.), Molecular Switches, Wiley-VCH, Weinheim, 2001.
[10] G.H. Brown, Photochromism, Wiley-Interscience, New York, 1971.
[11] H. Dürr, H. Bouas-Laurent, Photochromism: Molecules and Systems, Elsevier, Amsterdam, 2003.
[12] K. Tanaka, F. Toda, J. Chem. Soc., Perkin Trans. 1 (2000) 873.
[13] L. Xu, T. Sugiyama, H. Huang, Z. Song, J. Meng, T. Matsuura, Chem. Commun. (2003) 2328.
[14] H. Kurata, T. Tanaka, M. Oda, Chem. Lett. (1999) 749.
[15] H. Kurata, Y. Takehara, T. Kawase, M. Oda, Chem. Lett. (2003) 538.
[16] Y. Teki, S. Miyamoto, M. Nakatsuji, Y. Miura, J. Am. Chem. Soc. 123 (2001) 294.
[17] T. Kaneko, H. Akutsu, J. Yamada, S. Nakatsuji, Org. Lett. 5 (2003) 2127.
[18] M. Irie, Chem. Rev. 100 (2000) 1685.
[19] T. Kawai, N. Fukuda, D. Dröschl, S. Kobatake, M. Irie, Jpn. J. Appl. Phys. 38 (1999) L1194.
[20] J. Chauvin, T. Kawai, M. Irie, Jpn. J. Appl. Phys. 40 (2001) 2518.
[21] G.M. Tsivgoulis, J.-M. Lehn, Angew. Chem., Int. Ed. 34 (1995) 1119.
[22] T. Kawai, T. Kunitake, M. Irie, Chem. Lett. (1999) 905.
[23] K. Matsuda, M. Irie, J. Am. Chem. Soc. 122 (2000) 7195.
[24] K. Matsuda, M. Irie, Chem. Lett. (2000) 16.
[25] K. Matsuda, M. Irie, J. Am. Chem. Soc. 122 (2000) 8309.
[26] K. Matsuda, M. Irie, Chem. Eur. J. 7 (2001) 3466.
[27] K. Matsuda, M. Matsuo, M. Irie, Chem. Lett. (2001) 436.
[28] K. Matsuda, M. Matsuo, M. Irie, J. Org. Chem. 66 (2001) 8799.
[29] K. Matauda, M. Matsuo, S. Mizoguti, K. Higashiguchi, M. Irie, J. Phys. Chem. B 106 (2002) 11218.
[30] K. Matsuda, M. Irie, J. Am. Chem. Soc. 123 (2001) 9896.
[31] C. Joachim, J.K. Gimzewski, A. Aviram, Nature 408 (2000) 541.



Scheme 1. Photochromism of diarylethene possessing long π-conjugated chains.



Scheme 2. Photochromic reaction of diarylethene **2** which has extended π-conjugated chain at the 2,5-position of the thiophene unit.

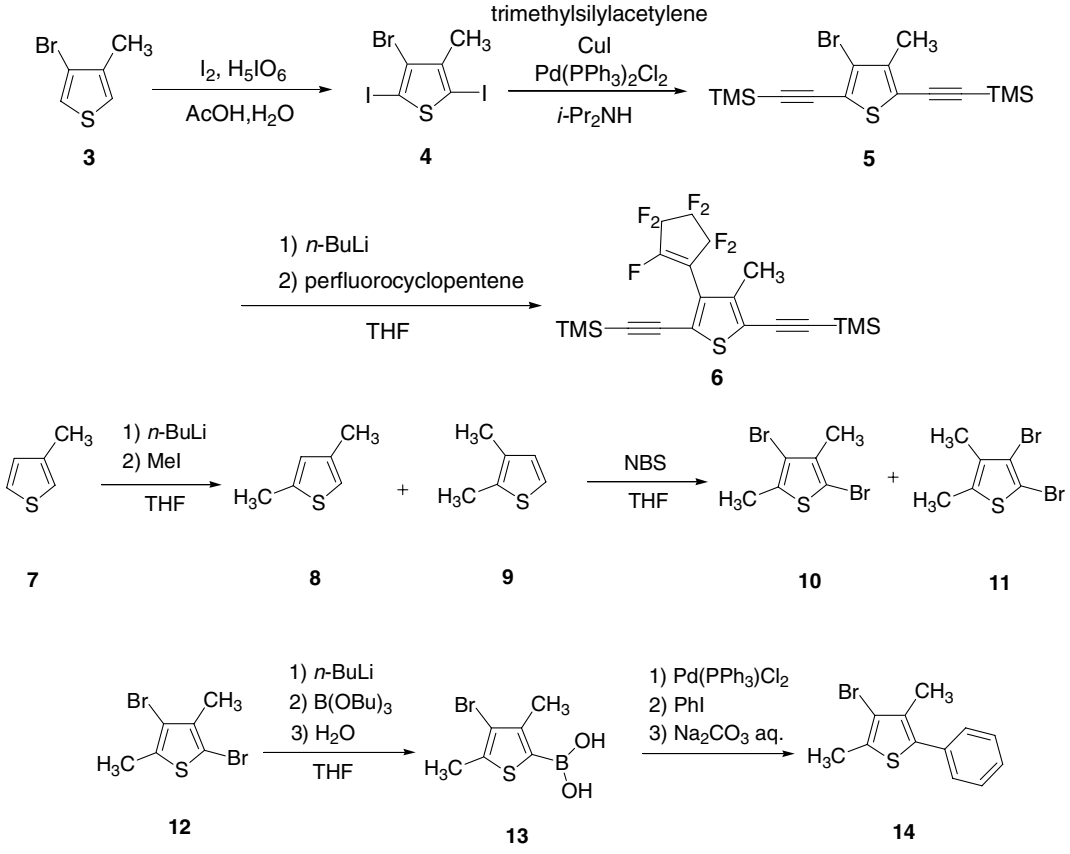
undergo photochromic reaction. In the open-ring isomer, two nitronyl nitroxide radicals are connected by the π-conjugated chain. When the open-ring isomer undergoes photocyclization upon irradiation with UV light, π-conjugated chain is disconnected at the 2-position of the thiophene ring and the intramolecular magnetic interaction may be suppressed. In other words, the open-ring isomer is in the ON state and the closed-ring isomer is in the OFF state.

In the open-ring isomer, the thiophene ring keeps its structure, so the π-conjugated chain is not perturbed by the introduction of the photochromic unit. In the closed-ring isomer, the hybridization of the carbon atom at the 2-position of the thiophene ring change from sp^2 to sp^3. The π-system is disconnected in this form (Scheme 2).

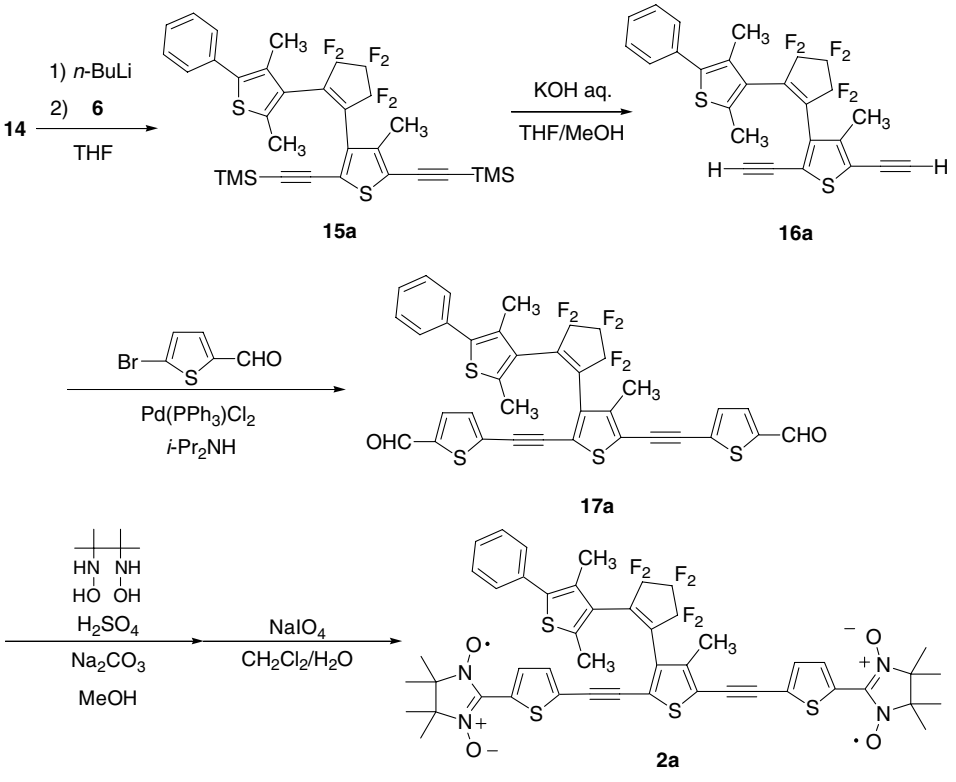
2.2. Synthesis of diarylethene diradical

In this study, we use a bis(ethynyl)-substituted diarylethene as a core component of the diradical. Thienylene–ethynylene unit was introduced because this unit is a building block of the π-conjugated polymers or oligomers [5]. Synthesis of **2a** was performed according to Schemes 3 and 4. Syntheses of thiophene units **6** and **14** were performed according to Scheme 3 [2]. A thiophene unit with extended π-conjugated chain, **5**, was prepared from 3-bromo-4-methylthiophene by two steps. Iodination of 3-bromo-4-methylthiophene **3** by iodine and orthoperiodic acid in acetic acid and water (3:2) gave 3-bromo-1,5-diiodo-4-methylthiophene **4** (96% yield). 3-Bromo-4-methyl-2,5-bis(trimethylsilylethynyl)thiophene **5** was given by Sonogashira coupling reaction of trimethylsilylacetylene with diiodothiophene **4** at the 2,5-position of thiophene ring (40%). Another unit, **14**, was prepared from 3-bromo-4-methylthiophene in three steps. Methylation of 3-methylthiophene **7** gave 2,4-dimethylthiophene **8** and 2,3-dimethylthiophene **9** as a mixture (85%). Bromination of the mixture of **8** and **9** by *N*-bromosuccinimide in THF gave 2,4-dibromo-3,5-dimethylthiophene **10** and 2,3-dibromo-4,5-dimethylthiophene **11** in 90% yield. Compounds **10** and **11** can be separated easily by column chromatography(eluent: *n*-hexane). 3-Bromo-2,5-dimethyl-4-phenylthiophene **14** was given by Suzuki coupling reaction of thienyl boronic acid **13** and iodobenzene (81%).

Unsymmetrical diarylethene **15a** was synthesized by the coupling of lithiated **14** with **6** (79%). Diarylethene protected by trimethylsilyl substituent **15a** can be easily desilylated by KOH aq. in THF/MeOH to give **16a** quantitatively. Sonogashira coupling with 2-bromothiophenecarboxaldehyde gave the dialdehyde **17a** (20%), which was converted in two steps into nitronyl nitroxide radical **2a** as a green amorphous solid by 9%. For all compounds, the structures were confirmed by NMR, elemental analysis and mass spectrometry.



Scheme 3. Syntheses of thiophene unit **6** and **14**.



Scheme 4. Synthesis of diarylethene diradical **2a**.

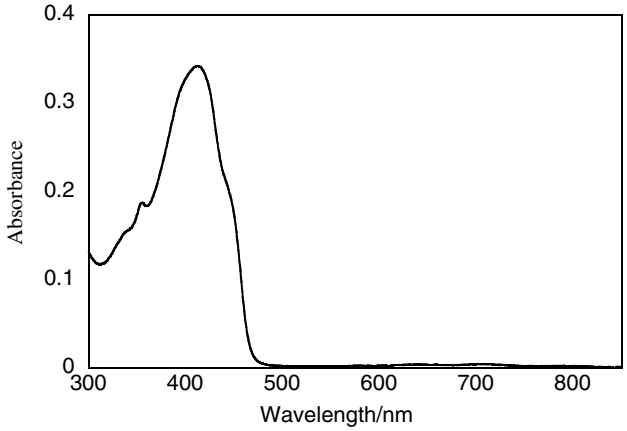


Fig. 1. Absorption spectrum of diradical **2a** (8.9×10^{-5} M ethyl acetate solution).

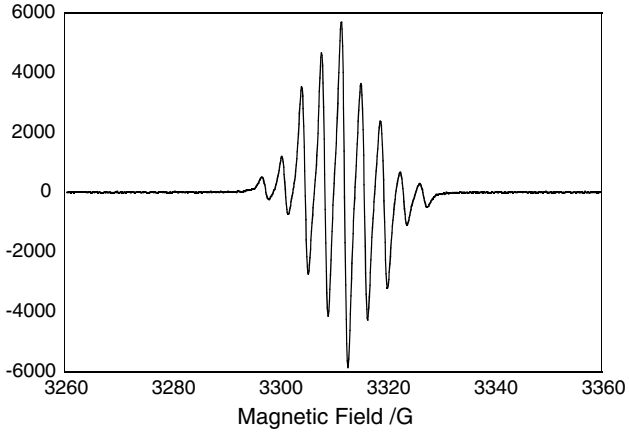


Fig. 2. ESR spectrum of diradical **2a** in toluene at room temperature (9.32 GHz). $g = 2.0065$, $a_N = 7.5$ G.

2.3. Absorption and ESR spectra of diradicals *2a*

Fig. 1 shows the absorption spectrum of **2a**. The small absorption around 550–650 nm is due to nitronyl nitroxide substituents [4c]. The absorption maximum of **2a** was located at 409 nm. A long π-conjugated chain composed of two nitronyl nitroxide radicals, two ethynyl groups, and three 2,5-thienyl groups contributes to the absorption band.

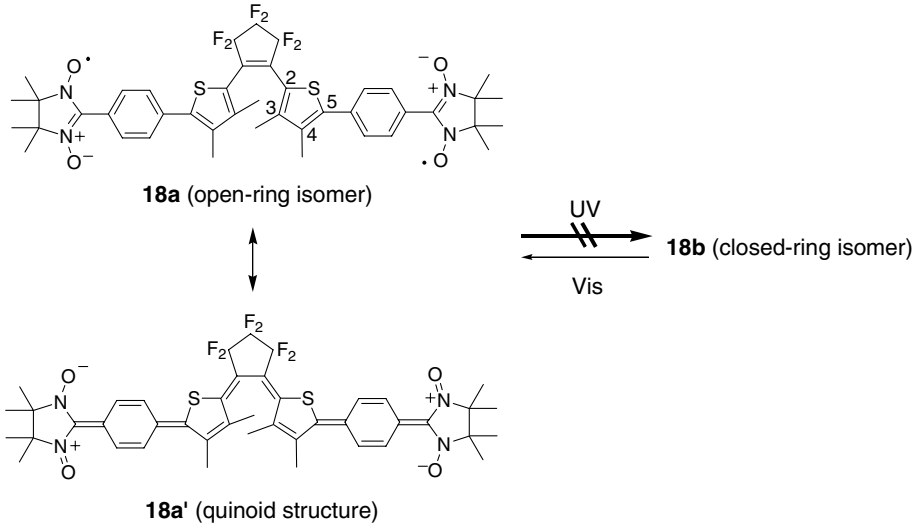
Fig. 2 shows the ESR spectrum observed for the open-ring isomer **2a** in toluene. **2a** has a nine-line spectrum, suggesting that the exchange interaction between the two nitronyl nitroxide radicals is larger than the hyperfine coupling constant ($0.04\ \mathrm{K} < |2J/k_B|$).

2.4. Photochemical behavior of diradical *2a*

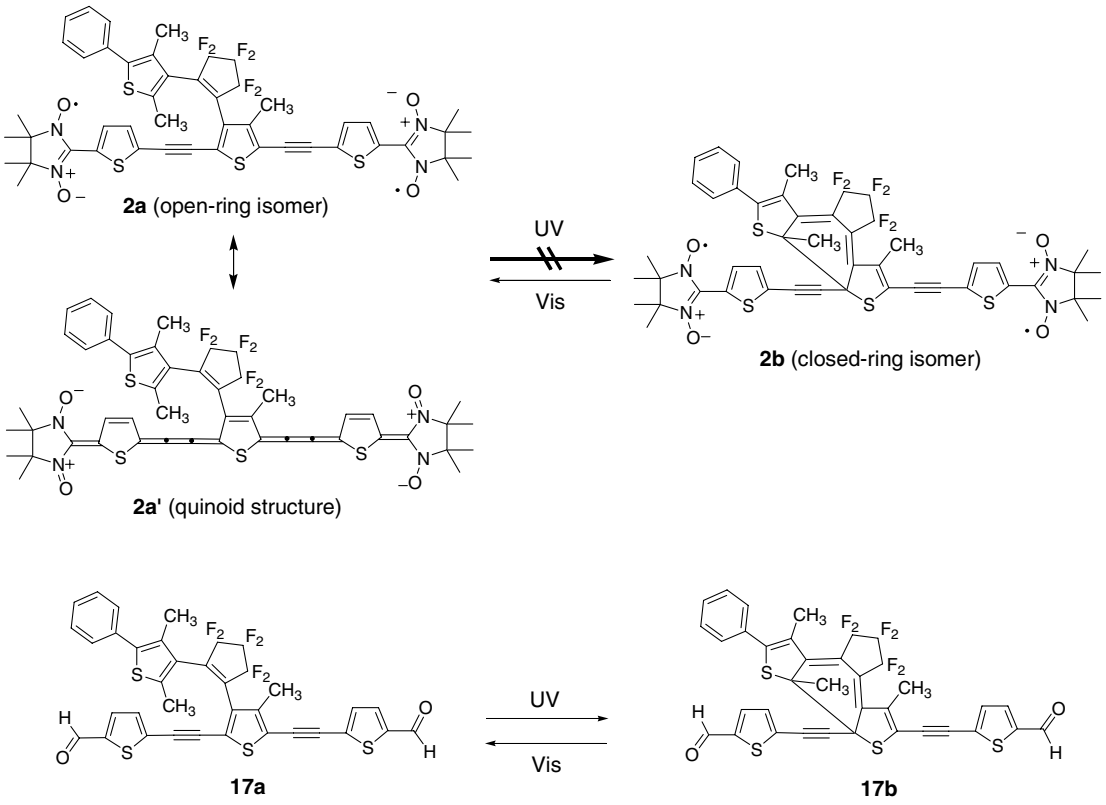
2a did not show any absorption spectral change upon irradiation with 365 nm light. Bis(2-thienyl)ethene having two nitronyl nitroxide **18a** has been reported not to undergo photocyclization [4f]. As discussed in the report, the open-ring isomer of bis(2-thienyl)ethene diradical **18a** has a resonant quinoid structure. The contribution of the quinoid structure **18a′** stabilizes the open-ring isomer and suppresses photocyclic reaction (see Scheme 5).

2a has similar quinoid structure **2a′**, as shown in Scheme 6. Therefore, stabilization of the open-ring isomer **2a** due to the formation of the quinoid structure **2a′** is considered to suppress the photocyclization of diarylethene **2a** and the solution of **2a** did not change the color.

Precursors of **2a**, such as **15a**, **16a** and **17a**, showed photochromism upon irradiation with UV light. Fig. 3 shows the absorption spectral change of compound **17a**. Upon irradiation with 365 nm light, a new 614 nm band due to **17b** appeared. Upon irradiation with 578 nm light, the spectrum converted back to the original one. The difference in the structure of the end groups controlled the photochromic reactivity. Dialde-



Scheme 5. Nitronyl nitroxide **18a** [4] and the photoreaction mechanism.



Scheme 6. Possible photoreaction mechanism of diarylethene **2** and **17**.

hyde **17a** does not have a resonant quinoid structure, wile diradicals **2a** has the quinoid structure which suppressed the photochromic reaction.

3. Summary

A new diarylethene diradical having 4-methyl-2, 5-bis(thienylethynyl)-3-thienyl unit **2a** was synthesized. The ESR spectrum of **2a** showed nine lines, suggesting that there is a strong interaction in the π-conjugated chain. Diarylethene **2a** did not show any photochromic reactivity upon irradiation with UV light, because the resonant quinoid structure **2a**′ suppressed the photocyclic reaction. The photoreactivity of the diarylethenes were found to be largely affected by the structure of the end groups.

4. Experimental

4.1. General

^{1}H NMR spectra were recorded on Varian Gemini 200 instruments. UV–Vis spectra were recorded on a Hitachi U-3310 spectrophotometer. Mass spectra were obtained on JEOL JMS-GC mateII. Melting points were not corrected.

All reactions were monitored by thin-layer chromatography carried out on 0.2-mm E. Merck silica gel plates (60F-254). Column chromatography was performed on silica gel (Kanto, 63-210 mesh).

4.2. Synthetic procedure

4.2.1. 3-Bromo-2,5-diiodo-4-methylthiophene (*4*)

To a solution of 3-bromo-4-methylthiophene (5.0 g, 28.2 mmol) in acetic acid (30 mL) was added water (22 mL), conc. H_2SO_4 (5.2 mL), orthoperiodic acid (2.0 g, 8.8 mmol), and iodine (6.76 g, 26.6 mmol). The reaction mixture was refluxed for 3 h and cooled down to room temperature. After the addition of ice water, the reaction mixture was neutralized with sodium hydroxide, poured into water, extracted with ethyl acetate, washed with water, dried over magnesium sulfate, and concentrated. Column chromatography (silica, hexane:ethyl acetate = 5:1) gave compound **4** (11.19 g, 92%) as a colorless needle: m.p. 79.5–80.5 °C; ^{1}H NMR ($CDCl_3$, 200 MHz) δ 2.34 (s, 3H). *Anal.* Calc. for $C_6H_3BrI_2S$: C, 14.00; H, 0.71. Found: C, 14.05; H, 0.70%.

4.2.2. 3-Bromo-4-methyl-2,5-bis(trimethylsilylethynyl)thiophene (*5*)

To a solution of diiodinated compound **7** (9.43 g, 22 mmol) in triethylamine (40 mL) was added

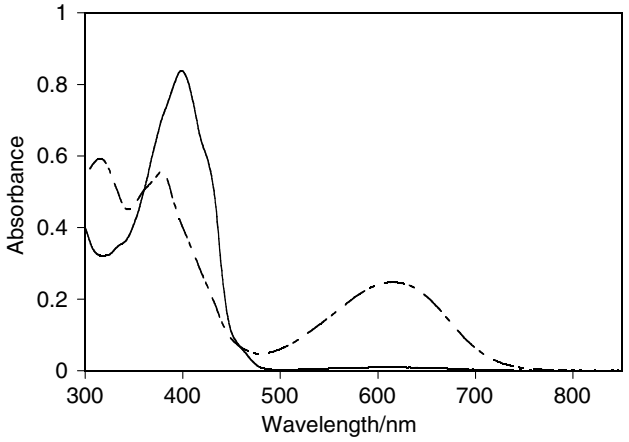


Fig. 3. Absorption spectra of diarylethene **17** (1.9×10^{-5} M ethyl acetate solution): open-ring isomer **17a** (——), in the photostationary state under irradiation with 365 nm light (– – –).

$Pd(Ph_3P)_2Cl_2$ (0.93 g, 1.3 mmol) and CuI (0.34 g, 1.8 mmol). A solution of trimethylsilylacetylene (4.32 g, 44 mmol) in triethylamine (440 mL) was added dropwise to the reaction mixture at room temperature, and stirred for 4 h at 60 °C. The reaction mixture was cooled down to room temperature, filtered out brown solid. The solution was poured into water, extracted with ether, washed with water, dried over magnesium sulfate, and concentrated. Column chromatography (silica, hexane) gave compound **5** (3.42 g, 42%) as a colorless needle: m.p. 104.5–106.5 °C; ^{1}H NMR ($CDCl_3$, 200 MHz) δ 0.26 (s, 9H), 0.27 (s, 9H), 2.25 (s, 3H). *Anal.* Calc. for $C_{15}H_{21}BrSSi_2$: C, 48.76; H, 5.73. Found: C, 48.78; H, 5.73%.

*4.2.3. 1-[4-Methyl-2,5-bis(trimethylsilylethynyl)-3-thienyl]-perfluorocyclopentene (**6**)*

n-Butyllithium in hexane (1.6 N, 4.59 mL, 7.04 mmol) was added to a solution of bromothiophene derivative **5** (2.59 g, 7.0 mmol) in THF (200 mL) at −78 °C under argon atmosphere. After the mixture was stirred for 30 min, perfluorocyclopentene (4.58 g, 21 mmol) was added in one portion. The solution was allowed to warm to 10 °C with stirring. Water was added to the reaction mixture. The reaction mixture was extracted with ether, washed with water, dried over magnesium sulfate, and concentrated. Column chromatography (silica, hexane) gave compound **6** (2.75 g, 79%) as a colorless wax: ^{1}H NMR ($CDCl_3$, 200 MHz) δ 0.21 (s, 9H), 0.26 (s, 9H), 2.21 (s, 3H). *Anal.* Calc. for $C_{20}H_{21}F_7SSi_2$: C, 49.77; H, 4.39. Found: C, 50.07; H, 4.50%.

*4.2.4. 1-[2,4-Dimethyl-5-phenyl-3-thienyl]-2-[4-methyl-2,5-bis(trimethylsilylethynyl)-3-thienyl]-perfluorocyclopentene (**15a**)*

n-Butyllithium in hexane (1.6 N, 3.03 mL, 4.84 mmol) was added to a solution of 3-bromo-2,5-dimethyl-5-phenyl thiophene **14** (2.59 g, 4.4 mmol) in THF (25 mL) at −78 °C under argon atmosphere. After the mixture was stirred for 30 min, solution of monosubstituted perfluorocyclopentene **6** (1.93 g, 3.95 mmol) in THF (10 mL) was added dropwise. The solution was allowed to warm to 10 °C with stirring. Water was added to the reaction mixture. The reaction mixture was extracted with ether, washed with water, dried over magnesium sulfate, and concentrated. Column chromatography (silica, hexane:CH_2Cl_2 = 10:1) gave compound **15a** (2.35 g, 76%) as a colorless powder: m.p. 57.5–59.5 °C; ^{1}H NMR ($CDCl_3$, 200 MHz) δ 0.09–0.15 (m, 18H), 1.95–2.52 (m, 9H), 7.24–7.44 (m, 5H). *Anal.* Calc. for $C_{32}H_{32}F_6S_2Si_2$: C, 59.05; H, 4.96. Found: C, 58.80; H, 4.99%.

*4.2.5. 1-[2,5-Bis(5-formyl-2-thienylethynyl)-4-methyl-3-thienyl]-2-[2,4-dimethyl-5-phenyl-3-thienyl]-perfluorocyclopentene (**17a**)*

To a solution of diarylethene **15a** (651 mg, 1.0 mmol) in THF (20 mL) and methanol (10 mL) was added potassium hydroxide in water (20 wt%, 0.25 mL) with stirring. After the mixture was stirred for 30 min, the reaction mixture was extracted with ether, washed with water, dried over magnesium sulfate, and concentrated. Column chromatography (silica, hexane) gave desilylated compound **16a** (461 mg, 86%) as a dark brown wax.

A solution of desilylated compound **16a** (461 mg, 0.86 mmol) in diisopropylamine (20 mL) was added to solution of 2-bromo-5-thiophenecarboxaldehyde (172 mg, 0.9 mmol), $Pd(PPh_3)_2Cl_2$ (151 mg, 0.22 mmol) and copper iodide (41 mg, 0.22 mmol) in diisopropylamine (10 mL) at room temperature under argon atmosphere and then stirred for 5 h at 60 °C. The reaction mixture was cooled down to room temperature, filtered out brown solid. The solution was poured into water, extracted with ether, washed with water, dried over magnesium sulfate, and concentrated. Column chromatography (silica, hexane:ethyl acetate = 3:2) gave compound **17a** (129 g, 20%) as a dark green powder: m.p. 60.5–62.5 °C; ^{1}H NMR ($CDCl_3$, 200 MHz) δ 2.05–2.55 (m, 9H), 7.20–7.50 (m, 7H), 7.69 (d, J = 4.2 Hz, 2H), 9.89 (s, 2H). UV–Vis (AcOEt) $\lambda_{max}(\varepsilon)$ 399 (4.4×10^4) nm; FAB HRMS (*m*/*z*) $[M]^+$ Calc. for $C_{40}H_{20}F_6N_4O_2S_4$: 726.0250. Found: 726.0231.

*4.2.6. 1-[2,4-Dimethyl-5-phenyl-3-thienyl]-2-[4-methyl-2,5-bis(5-(1-oxyl-3-oxide-4,4,5,5-tetramethylimidazolin-2-yl)-thienylethynyl)-3-thienyl]hexafluorocyclopentene (**2a**)*

A solution of bisformylated derivative **17a** (129 mg, 0.18 mmol), 2,3-bis(hydroxyamino)-2,3-dimethylbutane sulfate (262 mg, 1.07 mmol), potassium carbonate (152 mg, 1.10 mmol) in dry methanol (10 mL) and benzene (5 mL) was refluxed for 18 h. The reaction mixture was poured into water, extracted with ethyl acetate, washed with water, dried over magnesium sulfate, and concentrated to give tetrahydroxylamine as an orange solid. Purification was not performed.

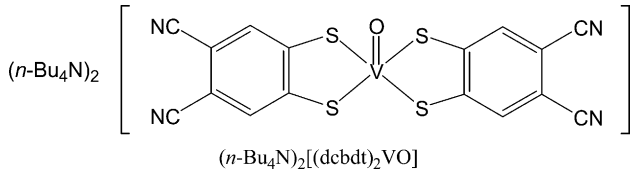
To a solution of tetrahydroxylamine in dichloromethane (10 mL) was added a solution of sodium periodate (34 mg, 0.16 mmol) in water (20 mL). The mixture was stirred for 30 min in the open air. The organic layer was separated, washed with water, dried over magnesium sulfate, and concentrated. Purification was performed by column chromatography (silica, CH_2Cl_2:ethyl acetate = 100:1). **2a** was obtained as a green amorphous solid (15 mg, 9%): m.p. 98.5–100.5 °C; EPR (toluene) 1:4:10:16:19:16:10:4:1, nine lines, $g = 2.0065$, $a_N = 7.5$ G. UV–Vis (AcOEt) $\lambda_{max}(\varepsilon)$ 358 (2.5×10^4), 409 (3.9×10^4) nm; FAB HRMS (*m*/*z*) $[M + 2]^+$ Calc. for $C_{48}H_{44}F_6N_4O_4S_4$: 982.2150. Found: 982.2166.

Acknowledgment

This work was supported by PRESTO, JST.

References

[1] (a) G.H. Brown, Photochromism, Wiley-Interscience, New York, 1971;
(b) H. Dürr, H. Bouas-Laurent, Photochromism: Molecules and System, Elsevier, Amsterdam, 2003.
[2] M. Irie, Chem. Rev. 100 (2000) 1685.
[3] S. Nakatsuji, Chem. Soc. Rev. (2004) 348.
[4] (a) K. Matsuda, M. Irie, Chem. Lett. (2000) 16;
(b) K. Matsuda, M. Irie, J. Am. Chem. Soc. 122 (2000) 7252;
(c) K. Matsuda, M. Irie, J. Am. Chem. Soc. 122 (2000) 8309;
(d) K. Matsuda, M. Matsuo, M. Irie, Polyhedron 20 (2001) 1391;
(e) K. Matsuda, M. Matsuo, M. Irie, J. Org. Chem. 66 (2001) 8799;
(f) K. Matsuda, M. Matsuo, S. Mizoguti, K. Higashiguchi, M. Irie, J. Phys. Chem. B 106 (2002) 11218;
(g) K. Takayama, K. Matsuda, M. Irie, Chem. Eur. J. 9 (2003) 5605.
[5] K. Morimitsu, S. Kobatake, M. Irie, Tetrahedron Lett. 45 (2004) 1155.



$(n\text{-}Bu_4N)_2[(dcbdt)_2VO]$

Scheme 1.

Here we report the synthesis, crystal structure, magnetic susceptibility, ESR spectrum and its theoretical investigation of $(n\text{-}Bu_4N)_2[(dcbdt)_2VO]$ (see Scheme 1).

2. Experimental

2.1. Synthesis of $(n\text{-}Bu_4N)_2[(dcbdt)_2VO]$

4,5-Dicyanobenzene-1,2-dithiol (H_2dcbdt) (135.0 mg, 0.702 mmol) prepared in accordance with literature [10] was dissolved in 5 ml in methanol solution of NaOMe (83.4 mg, 1.54 mmol). To this solution a solution of anhydrous VCl_3 (55.2 mg, 0.35 mmol) in 5 ml of tetrahydrofuran was added and this solution was exposed to air. After exposure for 30 min n-Bu_4NBr (905.2 mg, 2.81 mmol) was added. The dropwise addition of 20 ml of water caused precipitation of the product as light brown powder. This precipitate were recrystallized from acetone–i-PrOH (1:2) and dried in air to give 283.5 mg (87%) of product. The composition of $(n\text{-}Bu_4N)_2[(dcbdt)_2VO]$ was determined by X-ray structure analysis.

2.2. The X-ray crystallographic study of $(n\text{-}Bu_4N)_2[(dcbdt)_2VO]$

The X-ray diffraction data were collected at 90 K on a Bruker ASX APEX CCD area detector with graphite monochromated Mo Kα radiation ($\lambda = 0.71073$ Å). Data collection and cell refinement were performed on Bruker SMART and Bruker SAINT programs [15,16]. Crystallographic data are gathered in Table 1.

The structure was solved by direct methods (SHELXS-97) [17] and refined on F_o^2 with full-matrix least squares analysis. The calculations were carried out with Bruker SHELXTL crystallographic package [18]. The final cycle of least-square refinement on F_o^2 for 5802 data and 283 parameters converged to $wR_2(F_o^2) = 0.1081$ for all data and to $R = 0.0465$ for 4470 data with $I \geqslant 2\sigma(F^2)$. H-atom positions were calculated at C–H distances of 0.95 Å for benzene rings and 0.99 Å for alkyl groups and they were included in the final calculations but not refined. The drawings of the molecular structures were produced using ORTEP-III [19]. The atomic scattering factors were taken from International Tables for X-ray Crystallography [20].

Table 1
Crystal data and structure refinement for $(n\text{-}Bu_4N)_2[(dcbdt)_2VO]$

Empirical formula	$C_{24}H_{38}N_3O_{0.50}S_2V_{0.50}$
Formula weight	466.16
Temperature (K)	90
Wavelength (Å)	0.71073
Crystal system	monoclinic
Space group	$C2$
Unit cell dimensions	
a (Å)	19.290(2)
b (Å)	13.7930(16)
c (Å)	9.6121(11)
α (°)	90
β (°)	90.969(2)
γ (°)	90
Volume (Å^3)	2557.1(5)
Z	4
Density (calculated) (Mg/m^3)	1.211
Absorption coefficient (mm^{-1})	0.397
$F(000)$	1002
Crystal size (mm)	$0.38 \times 0.14 \times 0.12$
θ Range for data collection (°)	1.82–27.48
Index ranges	$-24 \leqslant h \leqslant 25$, $-17 \leqslant k \leqslant 17$, $-12 \leqslant l \leqslant 12$
Reflections collected	15320
Independent reflections [R_{int}]	5802 [0.0327]
Completeness to $\theta = 27.48°$ (%)	99.7
Absorption correction	empirical
Maximum and minimum transmission	0.9539 and 0.8637
Refinement method	full-matrix least-squares on F^2
Data/restraints/parameters	5802/7/283
Goodness-of-fit on F^2	1.034
Final R indices [$I > 2\sigma(I)$]	$R_1 = 0.0465$, $wR_2 = 0.1081$
R indices (all data)	$R_1 = 0.0655$, $wR_2 = 0.1175$
Absolute structure parameter	0.52(5)
Largest differential peak and hole (e Å^{-3})	0.406 and −0.349

2.3. ESR and magnetic susceptibility measurement

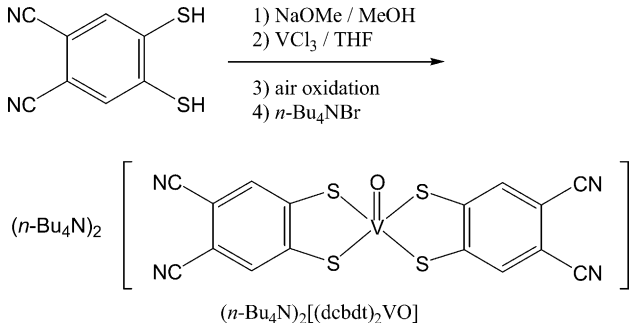
The powder ESR spectrum of $(n\text{-}Bu_4N)_2[(dcbdt)_2VO]$ was recorded by using Bruker 300E spectrometer at room temperature.

Magnetic susceptibilities (χ_{obs}) were measured in the temperature range 4–300 K at applied field of 500 Oe using SQUID magnetometer (MPMS XL, Quantum Design). The paramagnetic susceptibility (χ_p) was obtained by subtracting the diamagnetic contributions, calculated using Pascal's constant, from χ_{obs}.

3. Result and discussion

3.1. Synthesis of $(n\text{-}Bu_4N)_2[(dcbdt)_2VO]$

The H_2dcbdt was synthesized in accordance with the literature [10]. The $(n\text{-}Bu_4N)_2[(dcbdt)_2VO]$ was obtained by the reaction of VCl_3 with Na_2dcbdt. VCl_3 in a THF solution was added to a MeOH solution containing 2 equiv. of Na_2dcbdt. After the solution was stirred for



Scheme 2.

30 min and exposed to air for 30 min at room temperature, to the obtained deep purple solution water was added to give light brown powder. Recrystallization from acetone–*i*-PrOH resulted the isolation of light brown platelet crystals in 87% yield (see Scheme 2).

Table 2
Atomic coordinates ($\times 10^4$) and equivalent isotropic displacement parameters (Å $\times 10^3$) for $(n\text{-Bu}_4\text{N})_2[(\text{dcbdt})_2\text{VO}]$

	x	*y*	*z*	U_{eq}
V(1A)	10000	2149(1)	10000	26(1)
V(1B)	10000	1421(1)	10000	26(1)
O(1A)	10000	3329(3)	10000	42(1)
O(1B)	10000	293(7)	10000	42(1)
S(1)	9661(1)	1778(1)	7671(1)	30(1)
S(4A)	8865(1)	1648(2)	10599(3)	36(1)
S(4B)	8870(1)	1951(4)	10575(7)	36(1)
N(1)	5963(1)	1797(3)	7691(2)	45(1)
N(2)	6892(1)	1814(3)	4251(2)	45(1)
N(3)	5000	4078(3)	5000	33(1)
N(4)	10000	4512(3)	5000	30(1)
C(1)	8754(1)	1768(3)	7737(2)	29(1)
C(2)	8368(1)	1781(3)	6483(2)	30(1)
C(3)	7646(1)	1785(3)	6508(2)	34(1)
C(4)	7241(1)	1803(3)	5227(2)	35(1)
C(5)	8408(1)	1770(3)	9014(2)	36(1)
C(6)	7681(1)	1771(3)	9016(2)	38(1)
C(7)	7304(1)	1781(3)	7772(2)	35(1)
C(8)	6554(1)	1786(3)	7762(2)	37(1)
C(11)	4425(2)	4748(3)	4467(4)	34(1)
C(12)	9431(2)	3840(2)	4451(4)	33(1)
C(13)	10263(2)	5167(2)	3851(5)	37(1)
C(14)	3796(2)	4242(2)	3839(4)	37(1)
C(15)	8802(2)	4350(3)	3799(4)	36(1)
C(16)	5269(2)	3430(2)	3858(4)	37(1)
C(17)	8257(2)	3593(3)	3415(5)	48(1)
C(18)	3241(2)	4996(3)	3503(4)	42(1)
C(19)	10802(2)	5372(3)	1512(5)	57(1)
C(20)	5777(2)	3244(3)	1497(5)	49(1)
C(21)	2607(2)	4574(3)	2767(5)	53(1)
C(22)	5568(2)	3956(3)	2634(5)	44(1)
C(23)	7625(2)	4013(3)	2706(5)	51(1)
C(24)	10588(2)	4654(3)	2618(4)	39(1)
C(25)	11135(3)	4881(4)	286(6)	74(2)
C(26)	6077(3)	3772(4)	261(6)	65(1)

U_{eq} is defined as one third of the trace of the orthogonalized U_{ij} tensor.

3.2. Molecular and crystal structure of $(n\text{-Bu}_4\text{N})_2[(\text{dcbdt})_2\text{VO}]$

Final atomic coordinates for the non-hydrogen atoms are in Table 2.

The asymmetric unit contains one *n*-Bu_4N entity and half molecule of $[(\text{dcbdt})_2\text{VO}]$. The structure of $[(\text{dcbdt})_2\text{VO}]^{2-}$ is depicted in Fig. 1.

The selected bond lengths for the $[(\text{dcbdt})_2\text{VO}]^{2-}$ ion are in Table 3.

The vanadium atom is in a square-pyramidal coordination environment, the basal positions being occupied by sulfur atoms (S1, S4A, S1*, S4A* or S1, S4B, S1*, S4B*) of two bidentate dcbdt^{2-} ligands, and possesses idealized C_{2v} symmetry which disorders the VO group about two positions with 66% and 34% occupancies. The V(1A)–O(2A) distance [1.628(5) Å] is consistent with the presence of a vanadium–oxygen double bond (i.e., the vanadyl $V{=}O^{2+}$ moiety) but is slightly longer than that normally found in this geometry ($\leqslant$1.60 Å) in the absence of a sixth ligand *trans* to the oxygen [21]. The V–S bond lengths, V(1A)–S(1) 2.3772(6) Å, V(1A)–S(4A) 2.3755(8) Å, V(1B)–S(1) 2.3731(7) Å and V(1B)– S(4B) 2.3742(9) Å, are in the typical range, 2.36–2.38 Å of other bis(dithiolato) oxovanadium complexes [22,23].

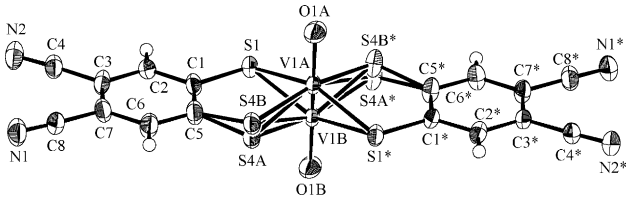


Fig. 1. Atomic numbering scheme for $[(\text{dcbdt})_2\text{VO}]$ anion of $(n\text{-Bu}_4\text{N})_2[(\text{dcbdt})_2\text{VO}]$.

Table 3
Selected bond lengths (Å) for $(n\text{-Bu}_4\text{N})_2[(\text{dcbdt})_2\text{VO}]$

V(1A)–O(1A)	1.628(5)
V(1B)–O(1B)	1.556(10)
V(1A)–S(4A)	2.3755(8)
V(1A)–S(1)	2.3772(6)
V(1B)–S(1)	2.3731(7)
V(1B)–S(4B)	2.3742(9)
S(1)–C(1)	1.7518(19)
S(4A)–C(5)	1.756(4)
S(4B)–C(5)	1.750(7)
C(1)–C(2)	1.406(3)
C(2)–C(3)	1.391(3)
C(3)– C(7)	1.392(3)
C(3)–C(4)	1.448(3)
C(6)–C(7)	1.389(3)
C(5)–C(6)	1.403(3)
C(5)–C(1)	1.407(3)
C(7)–C(8)	1.445(3)
C(8)–N(1)	1.141(3)
C(4)–N(2)	1.145(3)

Figs. 2(a) and (b) show projections of the crystal structure down to the *ac* and *ab* planes.

The structure consists of layers of $[(dcbdt)_2VO]^{2-}$ ions in the *ac* plane alternating with layers of *n*-Bu_4N^+ ions along the *b* direction. $[(dcbdt)_2VO]^{2-}$ ions are separated by *n*-Bu_4N^+ ions layer preventing any short anion-anion interactions. Some van der Waals contacts are observed between $[(dcbdt)_2VO]^{2-}$ ions and *n*-Bu_4N^+ ions. Indeed interatomic distances rather shorter than the sum of van der Waals radii of S···H (2.90 Å), C···H (2.79 Å) and N···H (2.63 Å) are observed between sulfur, carbon and nitrogen atoms of dcbdt ligands and hydrogen atoms of *n*-Bu_4N^+ ions [24].

3.3. Powder ESR spectrum of $(n\text{-}Bu_4N)_2[(dcbdt)_2VO]$ and its theoretical analysis

Fig. 3(a) shows the powder ESR derivative spectrum of $(n\text{-}Bu_4N)_2[(dcbdt)_2VO]$ measured at room temperature with a microwave frequency $\nu = 9.372844$ GHz. The spectrum consists of eight hyperfine structure lines due to the interaction of the unpaired electron with the ^{51}V nuclear spin ($I = 7/2$, 100%) as will be described below. The isotropic *g* value and hyperfine coupling constant $A(^{51}V)$ are $g = 1.990$ and $|A| = 84.6 \times 10^{-4}\ cm^{-1}$. These data indicate the valence state of V atom is IV.

We theoretically analyze the observed ESR derivative spectrum using a simple model of an electron spin **S** with

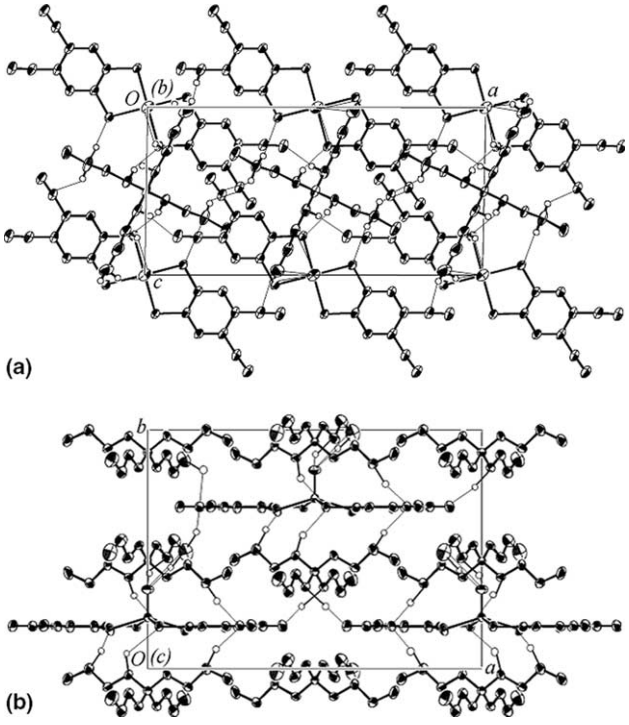


Fig. 2. Crystal structure of $(n\text{-}Bu_4N)_2[(dcbdt)_2VO]$: (a) projection down the *ac* plane and (b) projection down the *ab* plane. In (a) and (b), thin solid lines show van der Waals contacts.

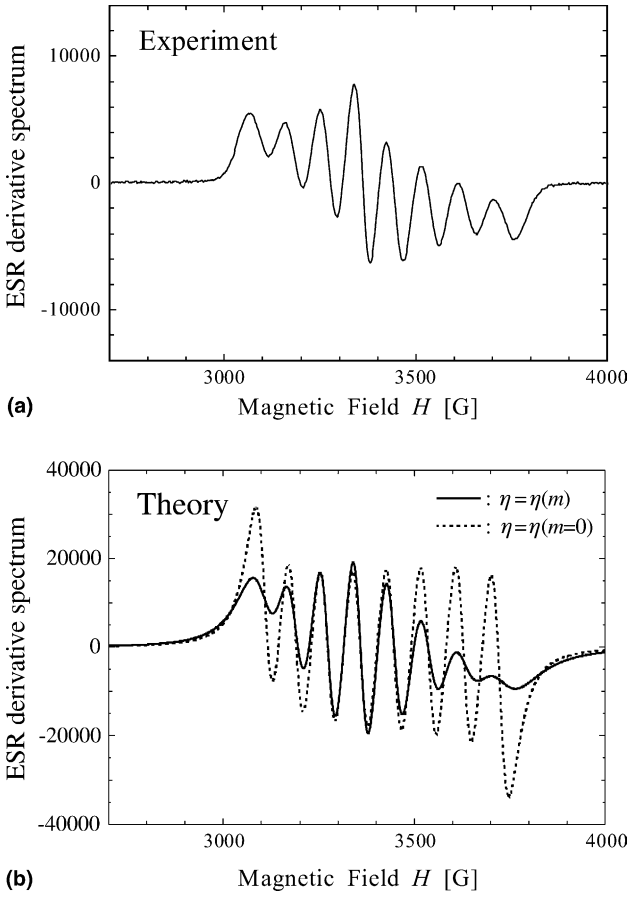


Fig. 3. ESR derivative spectrum vs. magnetic field *H*. (a) Experimental spectrum and (b) calculated spectrum, $dI(H)/dH$. In (b), spectra with $\eta(m)$ and $\eta(m = 0)$ are shown by the solid curve and the dotted one, respectively.

$S = 1/2$ coupled to a nuclear spin **I** with $I = I$. The Hamiltonian is given by,

$$\hat{H} = hS_z - h'S_z + A\mathbf{I}\cdot\mathbf{S}, \tag{1}$$

with $h = g\mu_B H$, and $h' = g_N\mu_N H$, where g (g_N) is the electron *g*-factor (the nuclear *g*-factor), $\mu_B(\mu_N)$ is the Bohr magneton (the nuclear magneton), and *A* is the hyperfine coupling constant. The first, second, and third terms represent the Zeeman interaction for **S**, that for **I**, and the hyperfine interaction, respectively. When the base of the Hamiltonian is represented by $|M,m\rangle$, which is a state with $S_z = M$ and $I_z = m$, eigenvalues and eigenstates within the second order perturbation are obtained as $E_{M,m}$ and $|M,m)$, respectively:

$$E_{-1/2,m} = -\varepsilon(m) - \zeta(m), \tag{2}$$

$$|-1/2,m) = C_1(m)|-1/2,m\rangle, \tag{3}$$

for $S_z = -1/2$ and $I_z = m$, and

$$E_{1/2,m} = \varepsilon(m) - \zeta(m), \tag{4}$$

$$|1/2,m) = C_2(m)|1/2,m\rangle, \tag{5}$$

for $S_z = 1/2$ and $I_z = m$, with

$$\varepsilon(m) = \frac{h + Am}{2} + \frac{A^2[I(I+1) - m^2]}{4(h+h')}, \tag{6}$$

$$\zeta(m) = \left[h' + \frac{A^2}{4(h+h')}\right]m, \tag{7}$$

$$C_1(m) = 1 - \frac{A\sqrt{I(I+1) - m(m-1)}}{2(h+h')} \times \left[1 - \frac{A(2m-1)}{2(h+h')} + \frac{A\sqrt{I(I+1) - m(m-1)}}{4(h+h')}\right], \tag{8}$$

$$C_2(m) = 1 + \frac{A\sqrt{I(I+1) - m(m+1)}}{2(h+h')} \times \left[1 - \frac{A(2m+1)}{2(h+h')} - \frac{A\sqrt{I(I+1) - m(m+1)}}{4(h+h')}\right]. \tag{9}$$

Within the linear response theory [25], we obtain an analytic expression of the intensity, which corresponds to an imaginary part of the dynamical susceptibility [26], as follows:

$$I(H) = \frac{1}{\sum_{m'} \exp[\beta\zeta(m')]\cosh[\beta\varepsilon(m')]} \times \sum_m \frac{\exp[\beta\zeta(m)]\sinh[\beta\varepsilon(m)][C_1(m)C_2(m)]^2\eta}{[h\nu - 2\varepsilon(m)]^2 + \eta^2}, \tag{10}$$

with $\beta = 1/(k_B T)$, where η is the infinitesimal quantity. Note here that the transition is allowed only for $|-1/2,m) \rightarrow |1/2,m)$.

The above model is now applied to the present system. We use $I = 7/2$, $\nu = 9.372844$ GHz, $T = 300$ K, and $g_N = 1.47$ [23]. Furthermore, we choose $A = -79.44 \times 10^{-4}$ cm^{-1}, $g = 1.97$, and $\eta = 40.73 \times 10^{-4}$ cm^{-1} so as to fit the peak position of experimental results. In Fig. 3(b), the calculated derivative spectrum $dI(H)/dH$ is shown by the dotted curve. The eight peaks appear reflecting the transition of $|-1/2,m) \rightarrow |1/2,m)$ for $m = -7/2, -5/2, -3/2, \ldots, 7/2$. Based on the agreement of the number of peaks between the calculated spectrum and the experimental one, we understand that this transition was actually observed in the experiment. On the other hand, heights and widths of peaks are largely different from the experimental ones. We therefore try to reproduce them partially well by assuming η to be $\eta(m) = \eta(1 + am + bm^2)$, where a and b are considered to arise from the anisotropy of g and A [27]. When $a = 0.1$ and $b = 0.075$ are chosen, the calculated spectrum agrees fairly well with the experimental one [see solid curve of Fig. 3(b)].

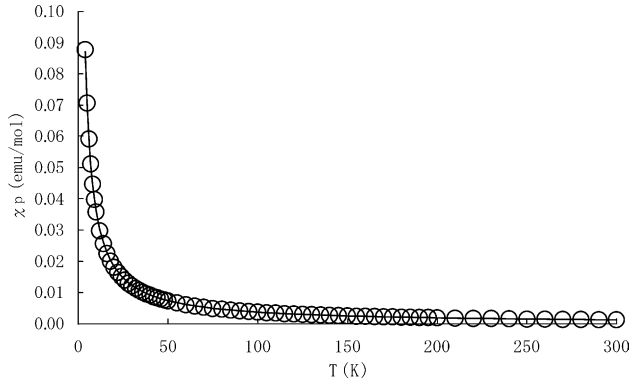


Fig. 4. Temperature dependence of paramagnetic susceptibility (χ_p) for $(n\text{-}Bu_4N)_2[(dcbdt)_2VO]$. The solid lines was reproduced by choosing appropriate values of the C and θ values in the equation $\chi_p(T) = C/(T - \theta)$.

3.4. Magnetic susceptibility of $(n\text{-}Bu_4N)_2[(dcbdt)_2VO]$

The temperature dependence of the paramagnetic susceptibility (χ_p) was investigated in the temperature range 5–300 K for $(n\text{-}Bu_4N)_2[(dcbdt)_2VO]$ and result is shown in Fig. 4.

The temperature dependence of χ_p obeyed a Curie-Weiss law, $\chi_p = C/(T - \theta)$, where C is the Curie constant and θ the Weiss temperature. By fitting C and θ values in $\chi_p = C/(T - \theta)$ the observed χ_p versus T behavior was well reproduced for the complex using the values of $C = 0.372$ emu K mol^{-1} and $\theta = -0.371$ K. The obtained C value correspond to the value (0.373 emu K mol^{-1}) that calculated by the equation of $C = N\mu_B^2 g^2 S(S+1)/3k_B$, where N is Avogadro number, μ_B the Bohr magneton, k_B Boltzmann constant, S the spin magnetic quantum number ($S = 1/2$ for V(IV)), and g an average g factor of the V(IV) spin (1.99 from ESR measurement of the complex), respectively. The C and θ values obtained suggest that a complete $S = 1/2$ spin resides on oxovanadium complex and that the intermolecular spin–spin interaction is very weakly antiferromagnetic. Such spin–spin interaction can be well understood from its crystal structures, in which there is no direct contact between the neighboring oxovanadium complex anions.

4. Supplementary material

Crystallographic data for the structural analysis have been deposited with the Cambridge Crystallographic Data Center, CCDC No. 273084 for $(n\text{-}Bu_4N)_2[(dcbdt)_2VO]$. Copies of this information may be obtained free of charge on application to The Director, CCDC, 12 Union Road, Cambridge, CB2 1EZ, UK (fax: +44 1223 336033; e-mail: deposit@ccdc.cam.ac.uk or www: http://www.ccdc.cam.ac.uk).

Acknowledgements

We thank Dr. Kenji Yoza, Bruker AXS for the crystal structure analysis. This work was partially supported by a grant-in-aid for scientific research (No. 16750114) from JSPS and Joint Studies Program with Professor Katsuya Inoue of the Institute for Molecular Science.

References

[1] H.B. Gray, Transition Met. Chem. 1 (1965) 239.
[2] G.N. Schrauzer, Transition Met. Chem. 4 (1968) 299.
[3] J.A. McCleverty, Prog. Inorg. Chem. 10 (1968) 49.
[4] D. Cpicivanis, Prog. Inorg. Chem. 11 (1970) 233.
[5] R. Eisenverg, Prog. Inorg. Chem. 12 (1970) 295.
[6] S. Alvarez, V. Ramon, R. Hoffman, J. Am. Chem. Soc. 107 (1985) 6253.
[7] R.P Burns, C.A. McAuliffe, Adv. Inorg. Chem. Radiochem. 22 (1986) 303.
[8] L. Alcácer, H. Novais, in: J.S. Miller (Ed.), Extended Linear Chain Compound, vol. 3, Plenum Press, New York, 1983 (Chapter 6).
[9] P. Cassoux, L. Valade, H. Kobayashi, A. Kobayashi, R.A. Clark, A.E. Underhill, Coord. Chem. Rev. 110 (1991) 115.
[10] D. Simão, H. Alves, D. Belo, S. Rabaça, E.B. Lopes, I.C. Santos, V. Gamma, M.T. Duarte, R.T. Henriques, H. Novais, M. Almeida, Eur. J. Inorg. Chem. 3119 (2001).
[11] H. Alves, D. Simão, H. Novais, I.C. Santos, C. Giménez-Saiz, V. Gama, J.C. Waerenborgh, R.T. Henriques, M. Almeida, Polyhedron 22 (2003) 2481.
[12] R. Eisenberg, H.B. Gray, Inorg. Chem. 6 (1967) 1844.
[13] W.E. Broderick, E.M. McGhee, M.R. Godfrey, B.M. Hoffman, J.A. Ibers, Inorg. Chem. 28 (1989) 2902.
[14] C. Livage, M. Fourmigué, P. Batail, E. Canadell, C.M. Cowie, M.J. Bennett, Inorg. Chem. 15 (1976) 1595.
[15] Bruker SMART (version 5.628): Bruker AXS Inc., Madison, WI, USA, 2000.
[16] Bruker SAINT-plus (version 6.45): Bruker AXS Inc., Madison, WI, USA, 2002.
[17] G.M. Sheldrick, SHELX-97, An Integrated System for Solving and Refining Crystal Structures from Diffraction Data, University of Göttingen, Germany, 1997.
[18] Bruker SHELXTL package (version 6.10): Bruker AXS Inc., Madison, WI, USA, 2000.
[19] Michael N. Burnett, Carroll K. Johnson, ORTEP-III: Oak Ridge thermal ellipsoid plot program for crystal structure illustrations, Oak Ridge National Laboratory Report ORNL-6895, 1996.
[20] D.T. Cromer, J.T. WaberInternational Table for X-ray Crystallography, vol. 4, Kynoch Press, Birmingham, 1974.
[21] J. Selbin, Coord. Chem. Rev. 1 (1966) 293.
[22] J.K. Money, J.C. Huffman, G. Christou, Inorg. Chem. 24 (1985) 2397.
[23] D. Collison, F.E. Mabbs, J. Temperley, J. Chem. Soc., Dalton Trans. (1988) 309.
[24] A. Bondi, J. Phys. Chem. 68 (1964) 441.
[25] R. Kubo, J. Phys. Soc. Jpn. 12 (1957) 570.
[26] The dynamical susceptibility is written as, $\phi^{-+}(h\nu) = \sum_{m,n} (\rho_n - \rho_m)\langle m \mid S_- \mid n\rangle\langle n \mid S_+ \mid m\rangle/(h\nu + E_m - E_n)$, where E_m and $|m\rangle$ denote the eigenvalue and the eigenstate of the Hamiltonian, respectively, and $\rho_n = \exp(-\beta E_n)/\sum_m \exp(-\beta E_m)$ with $\beta = 1/k_B T$. For example, see S. Kokado, N. Suzuki, J. Phys. Soc. Jpn. 66 (1997) 3605.
[27] For example, see R.N. Rogers, G.E. Pake, J. Chem. Phys. 33 (1960) 1107.

Metal–complex compounds are constructed with metal ions and organic ligands, and various high-Tc ferromagnets and ferrimagnets have been reported in Prussian Blue type of system as follows: $CsMn^{II}[Cr^{III}(CN)_6]$ (ferrimagnet, Tc = 90 K) [16], $CsNi^{II}[Cr^{III}(CN)_6]$ (ferromagnet, Tc = 90 K) [17], $Cs_2Mn^{II}[V^{II}(CN)_6]$ (ferrimagnet, Tc = 125 K) [18], $Cs_{0.75}Cr_{1.125}^{II}[Cr^{III}(CN)_6]$ (ferrimagnet, Tc = 190 K) [19], $Cr_3^{II}[Cr^{III}(CN)_6]_2 \cdot 10H_2O$ (ferrimagnet, Tc = 240 K) [19], and $V[Cr(CN)_6]_{0.86} \cdot 2.8H_2O$ (ferrimagnet, Tc = 315 K) [20]. They possess large spontaneous magnetization due to the high spin state. However, their crystal structures have not been solved yet, and the correlation between magnetic property and crystal structure has been unknown.

Dimetallic ferrimagnet $[Mn(L)]_3[Cr(CN)_6]_2 \cdot n_2O$ [21,22] series have an eminent transition temperature of about 70 K in the structurally characterized molecule-based magnets; (1) L = en (ethylenediamine), n = 4, Tc = 69 K, (2) L = glya (glycine amide), n = 2.5, Tc = 71 K, (3) no L, n = 12, Tc = 63 K. This dimetallic system has an ideal three-dimensional network, extended by Cr^{III}–CN–Mn^{II} linkage, and the antiferromagnetic interaction between Cr^{III} ion and Mn^{II} one results in the appearance of huge spontaneous moment for S = 9/2. The crystal structure with the antiferromagnetic molecule stacking is assumed to be generally stable under external stress. Thus, we have focused our attention on this series as a target of material control for high Tc by using pressure, and have investigated the pressure effects on $[Mn(en)]_3[Cr(CN)_6]_2 \cdot 4H_2O$ firstly.

2. Experimental

The preparation of $[Mn(en)]_3[Cr(CN)_6]_2 \cdot 4H_2O$ has been described elsewhere [21]. Fig. 1 shows a cubic picture of the unit cell. The crystal structure belongs to a monoclinic system of space group $C2/c$ (#15) with lattice parameters a = 24.505(7) Å, b = 11.323(4) Å, c = 14.810(4) Å, β = 120.69(2)° and V = 3533(1) Å^3. Three-dimensional network is constructed by the alternative array of $[Cr(CN)_6]^{3-}$ and $[Mn(en)]^{2+}$ ions. The network comprises defective cubes with three Cr atoms, three Mn(1) atoms, and one Mn(2) atom at the seven corners and eight Cr–CN–Mn edges. The Mn–N–C bond angle ranges between 145.7(3)° and 167.4(3)°. The shortest Cr···Mn(1), Cr···Mn(2), and Mn(1)···Mn(2) distances are 5.1553(8), 5.2842(8), and 6.659(1) Å, respectively. The water molecules reside in cavities of the network and form hydrogen bonds with the cyano nitrogen atoms as O–H···N.

The magnetic measurements have been performed in the pressure region up to P = 4.7 GPa and the temperature range from 5 to 200 K. Pressure has been attained using a diamond anvil cell (DAC) [23], which can be inserted into a superconducting quantum interference device (SQUID) magnetometer (Quantum Design, MPMS-5S). The tip diameter of diamond anvils was 0.5 mm. In the center of the gaskets made of Cu–Be, the sample space with diameter 0.2 mm was holed. A very small quantity of sample and some pieces of ruby were held with a transmitting medium into the sample space. The value of pressure was determined by the measurement of the shift of R1 ruby fluorescence at room temperature [24]. The pressure-increase by cooling down to liquid-helium temperature has been estimated to be at most about 14% of the pressure value at room temperature [23]. The magnetic measurements have been done under magnetic field H = 0.5 T, which is enough to saturate the magnetic moment in the ordered state of $[Mn(en)]_3[Cr(CN)_6]_2 \cdot 4H_2O$.

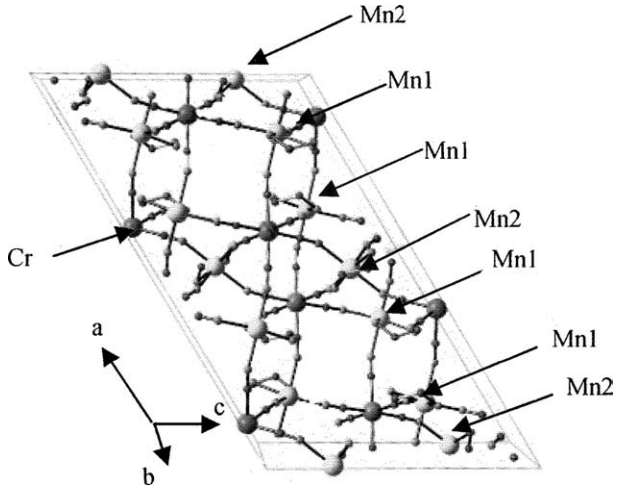


Fig. 1. Projection of the 3D network structure of $[Mn(en)]_3[Cr(CN)_6]_2 \cdot 4H_2O$ (en and H_2O are omitted).

3. Experimental results and discussion

Fig. 2 shows temperature dependence of the magnetization for $[Mn(en)]_3[Cr(CN)_6]_2 \cdot 4H_2O$ at H = 0.5 T in the pressure region up to 4.7 GPa. The accurate weight of the used sample could not be measured, but it is estimated to be about 4 μg from the value of magnetization at low temperature. Therefore, M in the vertical axis represents the actual measurement value. At ambient pressure, M rapidly increases below 80 K. For the sake of convenience, here we define Tc as the temperature below which M rapidly starts to increase. Fig. 3 shows pressure dependence of Tc for $[Mn(en)]_3[Cr(CN)_6]_2 \cdot 4H_2O$. With increasing pressure, the development of magnetization shifts toward higher temperatures. For $P \leqq 3.0$ GPa, Tc linearly increases against pressure as dTc/dP = +15.3 K/GPa, which is smaller than dTc/dP = +21.9 K/GPa of the similar antiferromagnetic system, the genuine organic radial week-ferromagnet, p-NC · C_6F_4 · CNSSN

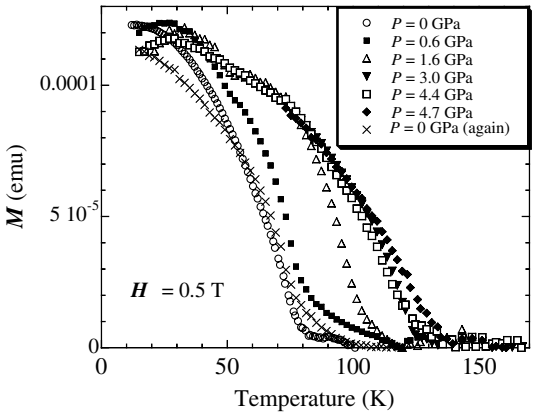


Fig. 2. Pressure dependence of magnetization (M) for $[Mn(en)]_3[Cr(CN)_6]_2 \cdot 4H_2O$ in the pressure region up to 4.7 GPa. The measurement has been done under the external magnetic field of $H = 0.5$ T.

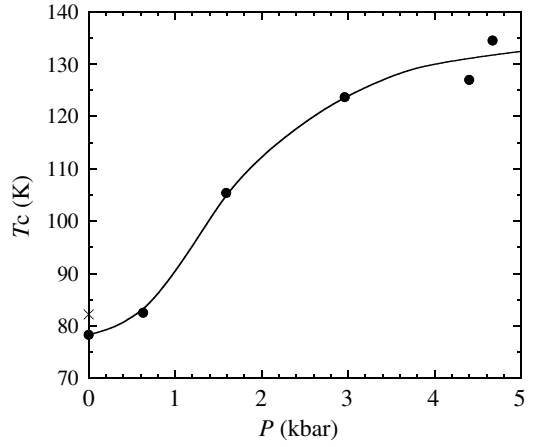


Fig. 3. Pressure dependence of the transition temperature (Tc) for $[Mn(en)]_3[Cr(CN)_6]_2 \cdot 4H_2O$. The value of Tc after releasing pressure of 4.7 GPa is marked with a cross.

[6]. The enhancement of Tc tends to saturate for $P \geqq 3.0$ GPa. Finally at $P = 4.7$ GPa, Tc reaches 136 K, which would be a record of Tc in the structurally characterized molecule-based magnet system. As for the state after releasing pressure of 4.7 GPa, the value of Tc is nearly consistent with that of the initial state as shown in Fig. 2. On the other hand, the amount of saturated magnetization hardly changes in the considered pressure region. To sum up, it is assumed that the antiferromagnetic state of $[Mn(en)]_3[Cr(CN)_6]_2 \cdot 4H_2O$ does not have high sensitivity, comparing to the organic system, and remains stable keeping elasticity under pressure. The latter characteristic is desirable for the artificial material control using pressure.

Here, we discuss the mechanism for the pressure dependence of Tc. The enhancement of Tc must be triggered by the enhancement of intermolecular interaction due to the increase of orbital-overlapping. The linearity of dTc/dP is not maintained for $P \geqq 3.0$ GPa, where the intermolecular shrinkage might be restricted, due to the effect of van der Waals force. This makes us expect that any change in the structural data appears at around $P = 3.0$ GPa. The structural analysis experiment under pressure is currently underway. Here we stress that the saturated moment hardly changes in the pressure region up to $P = 4.7$ GPa. The result suggests that the interaction network is not destroyed in the considered pressure region. In fact, there is reproducibility of magnetic properties after leasing pressure of 4.7 GPa, and it can be concluded that the crystal structure of this compound is strong against huge external stress. In the recent powdered structural analysis experiment, remarkable broadening of diffraction peak is observed for $P > 3.0$ GPa, where the sign of transformation to an amorphous state appears. We suppose that the state with Tc of 136 K at $P = 4.7$ GPa has some structural defect, but the interaction network itself survives.

4. Conclusion

We have studied the pressure effects on the dimetallic ferrimagnet $[Mn(en)]_3[Cr(CN)_6]_2 \cdot 4H_2O$ through the magnetic measurements in the pressure region up to $P = 4.7$ GPa. This ferrimagnet originally has an eminent transition temperature Tc of 69 K at ambient pressure. The artificial control by applying hydrostatic pressure makes Tc largely increase up to 136 K at $P = 4.7$ GPa, which would be a record of Tc in the structurally characterized molecule-based magnet system. As for the saturated moment, the amount hardly changes for $P \leqq 4.7$ GPa. There might remain large possibility in the material control by using the external stress under the further pressure. The powdered structural analysis experiments are being performed. The Rietveld structural analysis would clear the mechanism for the pressure-induced enhancement of Tc.

Acknowledgements

This work has been supported by Giant-in-Aids from the Japan Society for the Promotion of Science and CREST projects, Japan Science and Technology Agency (JST).

References

[1] See, for example K. Itoh, M. Kinoshita (Eds.), Molecular Magnetism: New Magnetic Materials, Kodansha/Gordon & Breach, Tokyo/New York, 2000.
[2] M. Kinoshita, P. Turek, M. Tamura, K. Nozawa, D. Shiomi, Y. Nakazawa, M. Ishikawa, M. Takahashi, K. Awaga, T. Inabe, Y. Maruyama, Chem. Lett. (1911) 1225.
[3] W. Fujita, K. Awaga, Chem. Phys. Lett. 388 (2004) 186.

[4] A.J. Banister, N. Bricklebank, I. Lavender, J.M. Rawson, C.I. Gregory, B.K. Tanner, W. Clegg, M.R.J. Elsegood, F. Palacio, Angew. Chem., Int. Ed. Engl. 35 (1999) 2533.
[5] F. Palacio, G. Antorrena, M. Castro, R. Burriel, J. Rawson, J.N.B. Smith, C. Ritter, Phys. Rev. Lett. 79 (1997) 2336.
[6] M. Mito, T. Kawae, K. Takeda, S. Takagi, Y. Matsushita, H. Deguchi, J.M. Rawson, F. Palacio, Polyhedron 20 (2001) 1509.
[7] P.-M. Allemand, K.C. Khemani, A. Koch, F. Wudl, K. Holczer, S. Donovan, G. Gruner, J.D. Thompson, Science 253 (1991) 301.
[8] A. Mrzel, P. Cevc, A. Omerzu, D. Mihailovič, Phys. Rev. B 53 (1996) R2922.
[9] K. Takeda, K. Konishi, M. Tamura, M. Kinoshita, Phys. Rev. B 53 (1996) 3374.
[10] M. Mito, T. Kawae, M. Takumi, K. Nagata, M. Tamura, M. Kinoshita, K. Takeda, Phys. Rev. B 56 (1997) 14255.
[11] K. Takeda, M. Mito, T. Kawae, M. Takumi, K. Nagata, M. Tamura, M. Kinoshita, J. Phys. Chem. B 102 (1998) 671.
[12] M. Mito, T. Kawae, M. Hitaka, K. Takeda, T. Ishida, T. Nogami, Chem. Phys. Lett. 333 (2001) 69.
[13] K. Takeda, M. Mito, K. Kinoshita, Miguel.A. Novak, Polyhedron 22 (2003) 2287.
[14] K. Mizoguchi, M. Machino, H. Sakamoto, T. Kawamoto, M. Tokumoto, A. Omerzu, D. Mihailovič, Phys. Rev. B 63 (2001) 140417.
[15] T. Kawamoto, M. Tokumoto, H. Sakamoto, K. Mizoguchi, J. Phys. Soc. Jpn. 70 (7) (2001) 1892.
[16] W.D. Griebler, D. Babel, Z. Naturforsch. B 37 (1982) 832.
[17] V. Gadet, T. Mallah, I. Castro, M. Verdaguer, J. Am. Chem. Soc. 114 (1992) 9213.
[18] W.R. Entley, G.S. Girolami, Science 268 (1995) 397.
[19] T. Mallah, S. Thiébaut, M. Verdaguer, P. Veillet, Science 262 (1993) 1554.
[20] S. Ferlay, T. Mallah, R. Ouahés, P. Veillet, M. Verdaguer, Nature 378 (1995) 701.
[21] M. Ohba, N. Usuki, N. Fukita, H. Ōkawa, Angew. Chem. Int. Ed. 38 (1999) 1795.
[22] N. Usuki, M. Yamada, M. Ohba, H. Ōkawa, J. Solid State Chem. 159 (2001) 328.
[23] M. Mito, M. Hitaka, T. Kawae, K. Takeda, T. Kitai, N. Toyoshima, Jpn. J. Appl. Phys. 40 (2001) 6641.
[24] G.J. Piermarini, S. Block, J.D. Barnett, R.A. Forman, J. Appl. Phys. 46 (1975) 2774.

intermolecular linkages through S···S or S···N interatomic contacts. In some cyclic thiazyl, ferromagnetic and weak-ferromagnetic ordered states with high transition temperature above 1.0 K have been found in such compounds as *p*-O_2N–C_6F_4–CNSSN (T_C = 1.3 K) [16] and *p*-NC–C_6F_4–CNSSN (T_N = 35.5 K) [17,18]. Thus, intermolecular linkages through the S···S or S···N interatomic contacts may allow strong intermolecular magnetic interactions to take place. In the pressurized sulfur-based system, there might be a risk of collapse of the ferromagnetic molecular stacking, but a remarkable enlargement of molecular overlapping should occur. In any case, as a method of searching high-T_C magnets, pressure experiments must constitute a very attractive physical approach. In this study, pressure effects on the organic ferromagnet, γ-BBDTA · $GaCl_4$, have been investigated through ac magnetic susceptibility measurements in the pressure region up to 16.2 kbar.

2. Experimental

The thiazyl organic crystal, BBDTA · $GaCl_4$, was prepared according to the procedure described elsewhere [8]. The molecular structure is shown in Fig. 1. The γ-phase crystallizes in the monoclinic system *C*2/*c* with a = 11.260(5) Å, b = 10.851(6) Å, c = 13.209(7) Å, β = 114.853(2)° and V = 1464.44(13)Å^3. On the other hand, the diamagnetic α- and β-phases crystallize in the triclinic system.

Measurements of the ac magnetic susceptibilities, χ_{ac}, were performed with the ac field of amplitude 2 Oe (peak-to-peak) and frequency 100 Hz using a superconducting quantum interference device (SQUID) magnetometer (Quantum Design MPMS-5S). Pressure was attained using a piston-cylinder type of pressure cell (Kyowa-Seisakusho Co. Ltd., CR-PSC-KY05-1) in the region up to 16.2 kbar. The powdered sample of the γ-phase of BBDTA · $GaCl_4$ was held into a Teflon cell, which prevented leakage of pressure, with a pressure transmitting medium, Apienzon-J grease, and a piece of superconducting metal, Sn. The pressure value at liquid helium temperature was estimated from the shift of the superconducting transition temperature of Sn [19]. A series of ac magnetic measurements have been performed through three runs, whose pressure region is as follows: 0–8.22 kbar for the first, 0–8.45 kbar for the second and 0–16.2 kbar for the third.

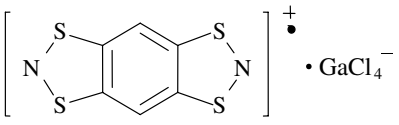


Fig. 1. Molecular structure of the γ-phase of BBDTA · $GaCl_4$.

3. Results and discussion

The temperature dependence of the real component (χ') of χ_{ac} for the γ-phase BBDTA · $GaCl_4$ in the first run is shown in Fig. 2. The enlarged one for 1.96–8.22 kbar is done in the inset of Fig. 2. A part of results for the second and third runs is shown in Fig. 3. At ambient pressure, a rapid increase of the magnitude of χ' appears at around 7.0 K of T_C. We estimate the value of T_C as the temperature, in which the extrapolating lines in the region with the rapid increase of χ' and in the paramagnetic region cross.

Under hydrostatic pressure, the magnitude of χ' is remarkably suppressed, and decreases down to about a half of the initial with little pressure of 0.10 kbar. At around 2.0 kbar, there remains only the magnetic signal

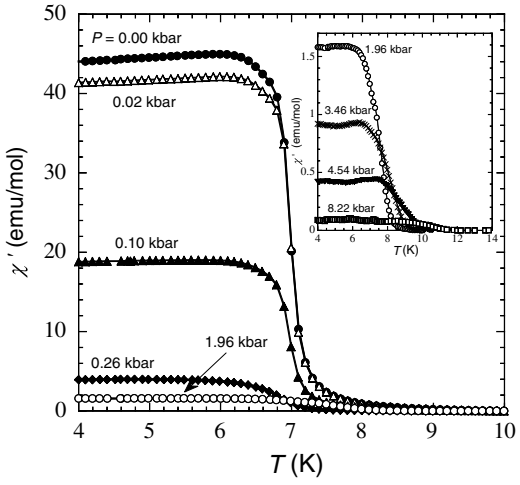


Fig. 2. Temperature dependence of the real component of the ac magnetic susceptibility, χ', for the γ-phase of BBDTA · $GaCl_4$ in the first run. The inset is the enlarged figure for $0.63 \leqq P \leqq 8.22$ kbar.

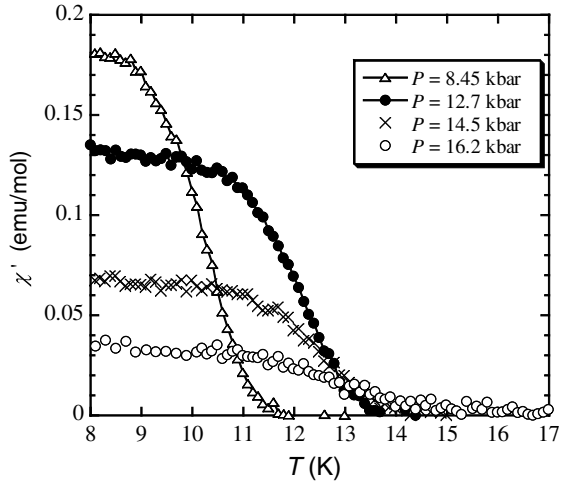


Fig. 3. Temperature dependence of χ' for the γ-phase of BBDTA · $GaCl_4$ in the second and third runs ($P \leqq 16.2$ kbar).

for 3.5% of the initial, and the amount is finally suppressed down to 0.07% of the initial at 16.2 kbar. Thus, γ-BBDTA · $GaCl_4$ is extremely unstable against the external stress.

The application of pressure suppresses the magnitude of χ', while it enhances the T_C. The pressure dependence of T_C is shown in Fig. 4, and T_C increases with linear fashion against pressure in the considered pressure region. The amount of the gradient, dT_C/dP, is estimated to be $+5.1 \times 10^{-1}$ K/kbar. The normalized gradient with the value of $T_C(P = 0)$, $dT_C/T_C(P = 0)/dP$, is $+7.3 \times 10^{-2}$/kbar, which is larger than those in few ferromagnets, whose T_C's increase under pressure; $dT_C/T_C(P = 0)/dP = +1.8 \times 10^{-2}$/kbar for 2,5-difluorophenyl-α-nitronyl nitroxide (2,5-DFPNN; $T_C(P = 0) = 0.45$ K) [6] and $+5.0 \times 10^{-2}$/kbar for *p*-O_2N–C_6F_4–CNSSN ($T_C(P = 0) = 1.3$ K) [20]. The γ-BBDTA · $GaCl_4$ is sensitive to pressure, comparing to the other organic radical ferromagnets. Finally, T_C of the γ-phase BBDTA · $GaCl_4$ arrives at 14.5 K at $P = 16.2$ kbar, and nearly approaches 16 K for TDAE-C_{60} [21]. The tremendous increase of T_C could be realized just on the base of compact intermolecular linkage through S···S and S···N paths. This experiment might be evaluated as a valuable artificial material control using external stress like pressure.

Here, we will discuss the mechanism for both (1) the pressure-induced suppression of the magnetic signal and (2) the enhancement of T_C. These phenomena are inconsistent each other in the case of the bulk-ferromagnet, and these origins have to be considered each other. As for the origin of (1), we assume the structural transition from the ferromagnetic γ-phase to diamagnetic α- and/or β-phases, whose structure has originally higher stability than that of the γ-phase. The structural analysis experiments under pressure are being performed now, and the direct proof will be detected soon. Next, as for (2), we suppose that the pressure-induced enhancement of intermolecular interaction in the surviving γ-phase results in the enhancement of T_C. In fact, T_C could exceed 16 K, T_C of TDAE-C_{60}, at around 18 kbar. The measurements in the further pressure region are, however, very difficult from both the view points of the measurement sensitivity and the limit of pressure in the piston cylinder type of cell.

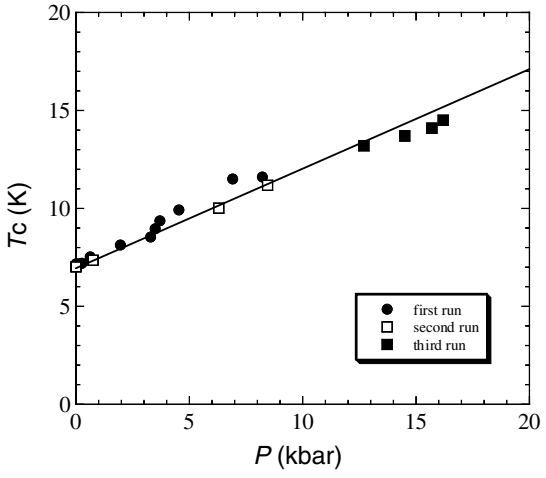


Fig. 4. Pressure dependence of the Curie temperature T_C for the γ-phase of BBDTA · $GaCl_4$. The straight line has the gradient of $dT_C/dP = +5.1 \times 10^{-1}$ K/kbar.

4. Summary

The pressure effects on the thiazyl organic ferromagnet, γ-BBDTA · $GaCl_4$, with $T_C = 7.0$ K, have been investigated through ac magnetic susceptibility measurements under the hydrostatic pressure region up to 16.2 kbar. The Curie temperature is enhanced by applying pressure and reached to 14.5 K at 16.2 kbar. Under further pressure, this material might show a ferromagnetic transition over 16 K, which is the highest T_C in the organic materials. On the other hand, the real component of the ac susceptibility decreases with increasing pressure; it is suppressed to 3.5% of the initial value at 2.0 kbar and 0.07% at 16.2 kbar. Those pressure effects could be explained with two factors: a pressure-induced structural transformation from the ferromagnetic γ-phase to diamagnetic α- and/or β-phases and an enhancement of intermolecular interactions in the surviving γ-phase.

Acknowledgments

This work was supported by the Grant-in-Aid for Scientific Research on Priority Areas "Application of Molecular Spins" (Area No. 769) from Ministry of Education, Culture, Sports, Science and Technology (MEXT).

References

[1] K. Takeda, K. Konishi, M. Tamura, M. Kinoshita, Phys. Rev. B 53 (1996) 3374.
[2] M. Mito, H. Nakano, M. Ito, M. Hitaka, T. Kawae, K. Konishi, K. Mukai, K. Takeda, Czech. J. Phys. 46 (Suppl. S4) (1996) 2107.
[3] M. Mito, T. Kawae, M. Takumi, K. Nagata, M. Tamura, M. Kinoshita, K. Takeda, Phys. Rev. B 56 (1997) 14255.
[4] K. Takeda, M. Mito, T. Kawae, M. Takumi, K. Nagata, M. Tamura, M. Kinoshita, J. Phys. Chem. B 102 (1998) 671.
[5] M. Mito, T. Kawae, M. Hitaka, K. Takeda, T. Ishida, T. Nogami, Chem. Phys. Lett. 333 (2001) 69.
[6] M. Mito, H. Deguchi, T. tanimoto, T. Kawae, S. Nakatsuji, H. Morimoto, H. Anzai, H. Nakao, Y. Murakami, K. Takeda, Phys. Rev. B 67 (2003) 024427.
[7] K. Takeda, M. Mito, K. Kinoshita, M.A. Novak, J.L. Tholence, A. Rassat, Polyhedron 22 (2003) 2287.
[8] W. Fujita, K. Awaga, Chem. Phys. Lett. 388 (2004) 186.

[9] M. Kinoshita, P. Turek, M. Tamura, K. Nozawa, D. Shiomi, Y. Nakazawa, M. Ishikawa, M. Takahashi, K. Awaga, T. Inabe, Y. Maruyama, Chem. Lett. (1911) 1225.
[10] See, for example, K. Itoh, M. Kinoshita (Eds.), Molecular Magnetism – New Magnetic Materials, Kodansha, Gordon and Breach, New York, 2000.
[11] R. Chiarelli, M.A. Novak, A. Rassat, J.L. Tholence, Nature (London) 363 (1993) 147.
[12] T. Sugawara, M. Matsushita, A. Izuoka, N. Wada, N. Takeda, M. Ishikawa, J. Chem. Soc., Chem. Commun. (1994) 1723.
[13] T. Nogami, T. Ishida, H. Tsuboi, H. Yoshikawa, H. Yamamoto, M. Yasui, F. Iwasaki, H. Iwamura, N. Takeda, M. Ishikawa, Chem. Lett. (1995) 635.
[14] K. Mukai, K. Konishi, K. Nedachi, K. Takeda, J. Phys. Chem. 100 (1996) 9658.
[15] S. Nakatsuji, H. Morimoto, H. Anzai, J. Kawashima, K. Maeda, M. Mito, K. Takeda, Chem. Phys. Lett. 296 (1998) 159.
[16] A. Alberola, R.J. Less, C.M. Pask, J.M. Rawson, F. Palacio, P. Oliete, C. Paulsen, A. Yamaguchi, R.D. Farley, D.M. Murphy, Angew. Chem., Int. Ed. Engl. 42 (2003) 4782.
[17] A.J. Banister, N. Bricklebank, I. Lavender, J.M. Rawson, C.I. Gregory, B.K. Tanner, W. Clegg, M.R.J. Elsegood, F. Palacio, Angew. Chem., Int. Ed. Engl. 35 (1996) 2533.
[18] F. Palacio, G. Antorrena, M. Castro, R. Burriel, J. Rawson, J.N.B. Smith, C. Ritter, Phys. Rev. Lett. 79 (1997) 2336.
[19] L.D. Jennings, C.A. Swenson, Phys. Rev. 112 (1958) 31.
[20] K. Takeda, private communication.
[21] B. Narymbetov, A. Omerzu, V.V. Kabanov, M. Tokumoto, H. Kobayashi, D. Mihailovic, Nature 407 (2000) 883.

known [1–10], there is a continuing need for new examples to improve our understanding of this phenomenon. Efforts along these lines have been concentrated in two directions: (i) development of synthetic routes to new high nuclearity metal complexes [4,5], and (ii) modifications of known SMMs in a controlled fashion [6–10]. The best and most thoroughly studied SMMs to date are members of the $[Mn_{12}O_{12}(O_2CR)_{16}(H_2O)_4]$ ($[Mn_{12}]$) family. A number of $[Mn_{12}]$ derivatives have been prepared in their neutral [1,6–8], one-electron [6f,9] or two-electron [10] reduced versions with a variety of carboxylate [6,9,10], mixed carboxylate [7], and mixed carboxylate/non-carboxylate [8] ligands. In all such modifications, the $[Mn_{12}(\mu_3\text{-}O)_{12}]$ core remains essentially the same.

In the present work, we report three new developments: (i) A new synthetic procedure in Mn cluster chemistry involving reductive aggregation of permanganate (MnO_4^-) ions in MeOH/benzoic acid solution; (ii) the products of this synthetic procedure which include two new compounds, the $N^nBu_4^+$ salts of the new $[Mn_{12}O_{12}(OMe)_2(O_2CPh)_{16}(H_2O)_2]^{2-}$ (**2**) cluster anion, a structural derivative of the well studied $[Mn_{12}]$ complexes, and the polymer $[Mn(OMe)(O_2CPh)_2]_n$ (**3**); and (iii) the establishment that the anion of **2** is a new SMM.

2. Experimental

2.1. Syntheses

All manipulations were performed under aerobic conditions with the use of materials as received unless otherwise indicated; water was distilled in-house. Elemental analyses were performed by the in-house facilities of the Chemistry Department, University of Florida.

2.1.1. Preparation of $(N^nBu_4)_2[Mn_{12}O_{12}(O_2CPh)_{16}(OMe)_2(H_2O)_2]$ (2)

Freshly prepared $(N^nBu_4)MnO_4$ (1.0 g, 2.8 mmol) was added in small portions to a solution of benzoic acid (5.0 g, 40.9 mmol) in MeOH (15 ml), and the mixture stirred for ~5 min. The resulting purple solution was left undisturbed at room temperature overnight. During this time, the color slowly turned dark brown, and black crystals slowly formed. The latter, which were found to be poor diffractors of X-rays, were collected by filtration, washed with MeOH (2 × 10 ml) and dried in vacuo. The material was recrystallized from CH_2Cl_2/hexanes to give a mixture of diamond-shaped crystals of $2 \cdot 2H_2O \cdot 4CH_2Cl_2$ (**2a**) and needle-shaped crystals of $2 \cdot 2H_2O \cdot CH_2Cl_2$ (**2b**) in an overall yield of 0.12 g (15 % based on Mn). These were collected by filtration, washed with hexanes, and dried in vacuo. Both **2a** and **2b** were good diffractors of X-rays, as long as they were kept in contact with the mother liquor to prevent solvent loss. *Anal.* Calc. for $C_{146}H_{166}N_2O_{50}Mn_{12}$ ($2 \cdot 2H_2O$): C, 51.45; H, 4.91; N, 0.82. Found: C, 51.26; H, 4.72; N, 0.70%. Selected IR data (KBr, cm^{-1}): 3430(s, br), 3065(w) 2965(w), 2925(w), 2875(w), 1598(s), 1560(s), 1532(s), 1492(m), 1448(m), 1417(s), 1306(w), 1177(m), 1069(w), 1026(m), 838(w), 718(s), 675(s), 625(m, br), 499(m).

2.1.2. Preparation of $[Mn(OMe)(O_2CPh)_2]_n$ (3)

Compound **3** was prepared by employing the same synthetic procedure as for **2** with the only difference being that the purple solution was left to stand at room temperature for a long period of time (~2 weeks). The yield was 70%. *Anal.* Calc. for $C_{15}H_{13}MnO_5$ (**3**): C, 54.90; H: 3.99. Found: C, 54.67; H, 3.83%. Selected IR data (KBr, cm^{-1}): 3421(m, br), 3065(m), 3023(w), 2940(w), 1693(m), 1592(s), 1552(s), 1491(m), 1448(m), 1386(s), 1306(m), 1177(m), 1159(w), 1143(w), 1069(m), 1026(m), 992(m), 937(w), 841(w), 816(w), 716(s), 683(m), 610(m), 558(m), 483(m).

3. Results and discussion

3.1. Syntheses

The synthesis of normal $[Mn_{12}]$ compound **1** consists of the comproportionation reaction between $Mn(O_2CMe)_2 \cdot 4H_2O$ and $KMnO_4$ in 60% aqueous acetic acid [11]. In contrast, the new synthetic procedure in the present work is part of a wider investigation of the reduction of MnO_4^- in alcohol/carboxylic acid mixtures. The present results were obtained from a MeOH/$PhCO_2H$ medium. Thus, addition of $(N^nBu_4)MnO_4$ to a methanolic solution of benzoic acid results in the formation of a dark brown solution from which subsequently were obtained essentially black crystals. Recrystallization from CH_2Cl_2/hexanes results in the formation of two types of black crystals in a total, overall yield of 15% yield. When the dark brown solution was left for ~2 weeks to stand at room temperature brown crystals of **3** were formed in high yield. Since the average oxidation state of **2** (8 Mn^{III}, 4 Mn^{IV}) is higher than that of **3** (Mn^{III}), it seems reasonable to assume that the formation of the latter is a result of further reduction of Mn^{IV} ions by MeOH, i.e., the longer crystallization times allow the formation of products that are further reduced.

3.2. Description of structures

3.2.1. $[Mn_{12}O_{12}(OMe)_2(O_2CPh)_{16}(H_2O)_2]^{2-}$

Both types of crystals of **2**, diamond-like **2a** and needle-like **2b**, were crystallographically characterized, and found to be $(N^nBu_4)_2[Mn_{12}O_{12}(OMe)_2(O_2CPh)_{16}(H_2O)_2] \cdot 2H_2O \cdot 4CH_2Cl_2$ (**2a**) and $(N^nBu_4)_2[Mn_{12}O_{12}$-

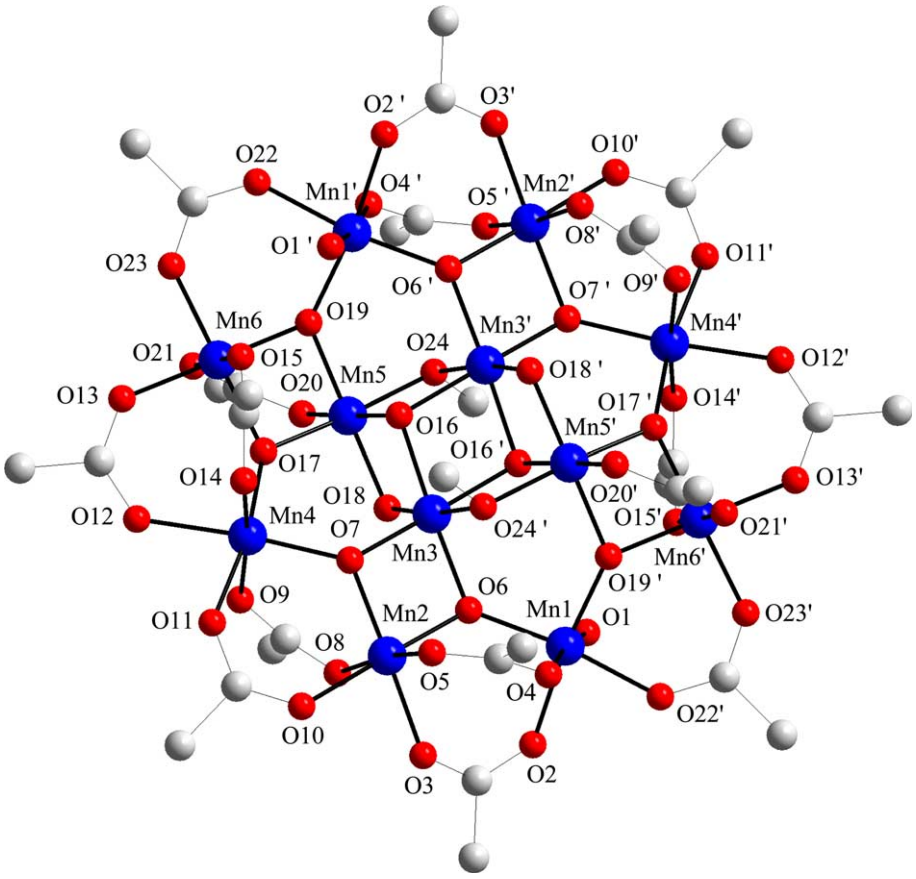


Fig. 1. Labeled ORTEP plot (at the 50% probability level) of the anion of **2a**. For clarity, the benzoate rings have been omitted, except for the *ipso*-carbon atom of each ring. Color scheme: Mn (blue), O (red), C (grey).

$(OMe)_2(O_2CPh)_{16}(H_2O)_2]\cdot 2H_2O\cdot CH_2Cl_2$ (**2b**). Both contain the same dianion, abbreviated $[Mn_{12}']^{2-}$. Complex **2a** crystallizes in the orthorhombic space group *Pbca* with its asymmetric unit containing half the $[Mn_{12}']^{2-}$ cluster and one $N^nBu_4^+$ cation, as well as one H_2O and two disordered CH_2Cl_2 solvent molecules. The $[Mn_{12}']^{2-}$ anion of **2a** (Fig. 1) contains a central $[Mn^{IV}_4(\mu_3\text{-}O)_2(\mu\text{-}O)_2(\mu\text{-}OMe)_2]^{6+}$ unit surrounded by a non-planar ring of eight Mn^{III} atoms that are connected to the central Mn_4 unit by eight bridging $\mu_3\text{-}O^{2-}$ ions. The metal oxidation states and their trapped-valence nature were determined by inspection of the Mn–O bond lengths, Mn bond valence sum calculations[2] [12] and the presence of Mn^{III} Jahn–Teller elongation axes for the Mn atoms in the outer ring. The outer Mn_8 ring is very similar to that in normal $[Mn_{12}]$ compound **1**, but the latter has a central $[Mn_4(\mu_3\text{-}O)_4]^{8+}$ cubane. The central $[Mn^{IV}_4O_4(OMe)_2]^{6+}$ unit of **2a** comprises a planar Mn_4 rhombus with two $\mu_3\text{-}O^{2-}$ ions (O16, O16′), one above and one below the Mn_4 plane, and a $\mu\text{-}O^{2-}$ (O18, O18′) or $\mu\text{-}MeO^-$ (O24, O24′) ion bridging each edge of the rhombus. The central unit can thus be described either as a face-sharing dicubane unit with two missing vertices, or as two edge-sharing, oxide-capped Mn_3 triangular units. Tetranuclear complexes possessing a core very similar to this central unit of the anion of **2a** have been observed previously with Mn [5a,5b], as well as with other transition metals [13]. Peripheral ligation is completed by 16 bridging benzoate groups and two terminal water molecules. All Mn atoms are six-coordinate with near octahedral geometries.

Complex **2b** crystallizes in the triclinic space group $P\bar{1}$, and its asymmetric unit consists of a half cluster and two halves of $N^nBu_4^+$ cations disordered around inversion centers, as well as one disordered H_2O molecule and half a CH_2Cl_2. The structure of the anion of **2b** is essentially identical to that of **2a**, except for some disorder in the peripheral benzoate rings.

For both **2a** and **2b**, there are Jahn–Teller (JT) distortions at the Mn^{III} ions in the outer ring, consistent with high-spin Mn^{III} in near-octahedral geometry. The JT distortion takes the form of an axial elongation, with the elongation axes axial to the Mn_{12} disk-like core and thus roughly parallel to each other. Axially elon-

[2] Bond valence sum calculations for Mn^{III} and Mn^{IV} ions of **2a** and **2b** gave oxidation state values of 2.89–3.02 and 4.00–4.18, respectively.

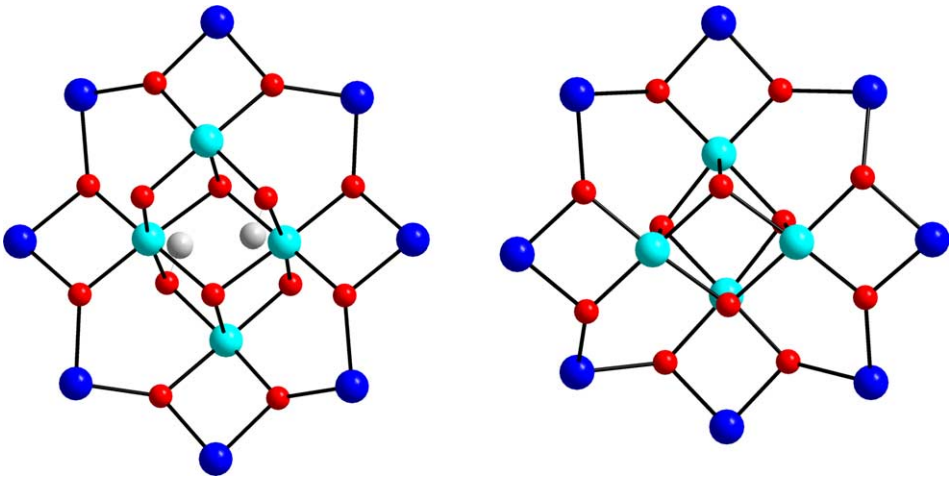


Fig. 2. Comparison of the cores of the anion of **2a** (left) and normal [Mn_{12}] complex **1** (right). Color scheme: Mn^{4+} (cyan), Mn^{3+} (blue), O (red), C (grey).

gated Mn–O bonds are typically at least 0.1–0.2 Å longer than the others. However, there is one anomaly: for **2a** (Fig. 1), the JT elongated bonds at Mn4 (Mn4–O9 = 2.074(4), Mn4–O14 = 2.080(5) Å) are not as long as those at the other Mn^{III} ions (2.112(5)–2.250(5) Å), and *trans* bonds Mn4–O7 (1.958(4) Å) and Mn4–O12 (2.060(5) Å) are longer than expected, especially Mn–O7, which is unusually long for a Mn–O^{2-} bond (compare Mn–O^{2-} bonds at the other Mn^{III} ions of 1.876(4)–1.905(4) Å). A similar anomalous situation is present at Mn1 of **2b**. This structural feature at Mn atoms Mn4 of **2a** and Mn1 of **2b** will prove crucial to understanding the magnetic data below, and we will thus return to this point later.

The anions of complexes **2a** and **2b** are remarkably similar to normal [Mn_{12}] clusters, such as **1**, with the main difference being the structure of the central cores. These are compared in Fig. 2. In fact, the core of the anions of **2a** and **2b** could be considered the result of partial methanolysis of the central $[Mn_4O_4]^{8+}$ cubane of **1**, leading to incorporation of two MeO^- bridges and a change in the core structure (although we do not claim that this corresponds to its means of formation in the reaction mixture). It is also interesting to note that complexes **1** and **2** are the smallest nuclearity members of a larger family of [Mn^{III}_x, Mn^{IV}_y] clusters in which there is an outer Mn^{III}_x ring around a central Mn^{IV}_y core. This family currently comprises normal [Mn_{12}] complexes (such as **1**) and **2a/2b** ($x = 8, y = 4$), the Mn_{16} cluster $[Mn_{16}O_{16}(OMe)_6(O_2CMe)_{16}(MeOH)_3(H_2O)_3]$ ($x = 10$, $y = 6$) [4c,14], and the Mn_{21} cluster $[Mn_{21}O_{24}(OMe)_8(O_2CCH_2{}^tBu)_{16}(H_2O)_{10}]$ ($x = 12, y = 9$) [15].

3.2.2. $[Mn(OMe)(O_2CPh)_2]_n$

Compound **3** crystallizes in the triclinic space group $P\bar{1}$ and its asymmetric unit consists of a [Mn(μ-O_2CPh)$_2$(μ-OMe)Mn] portion of the chain. The compound contains a linear chain of repeating [Mn^{III}(μ-OMe)(μ-O_2CPh)$_2$$Mn^{III}$] units (Fig. 3). The structure of **3** is similar to that of {[Mn(OH)(O_2CMe)$_2$] · HO_2CMe · H_2O} (**4**) reported recently [16], which is also a linear chain, except that (i) there are OMe^- bridging groups instead of OH^-, (ii) the carboxylate ligands are $PhCO_2^-$ instead of $MeCO_2^-$, and (iii) there are no solvents of crystallization in contrast to **4** where solvents of crystallization are participating in the formation of a hydrogen-bonding network between chains. The Mn···Mn separations in **3** are 3.388(1) Å, identical to the 3.384(1) Å value of those in **4**. All the $PhCO_2^-$ groups are in their familiar *syn*,*syn*-bridging modes. The metal oxidation state and its trapped-valence nature were determined by inspection of the Mn–O bond

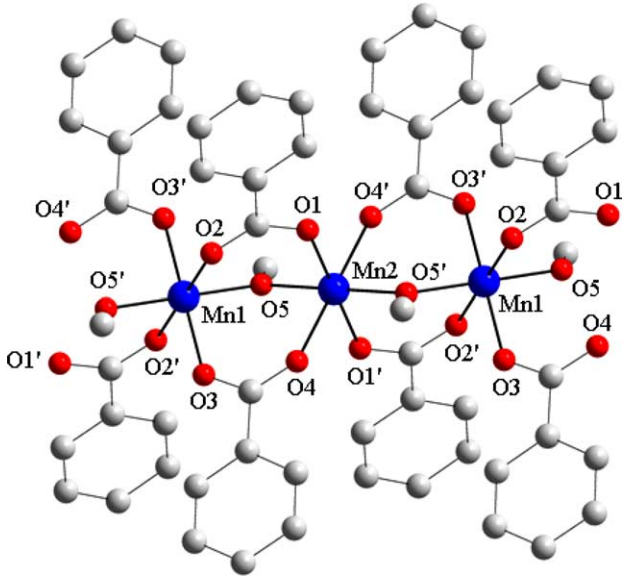


Fig. 3. Labelled ORTEP plot (at the 50% probability level) of a small section of the polymeric chain of [Mn(OMe)(O_2CPh)$_2$]$_n$ (**3**).

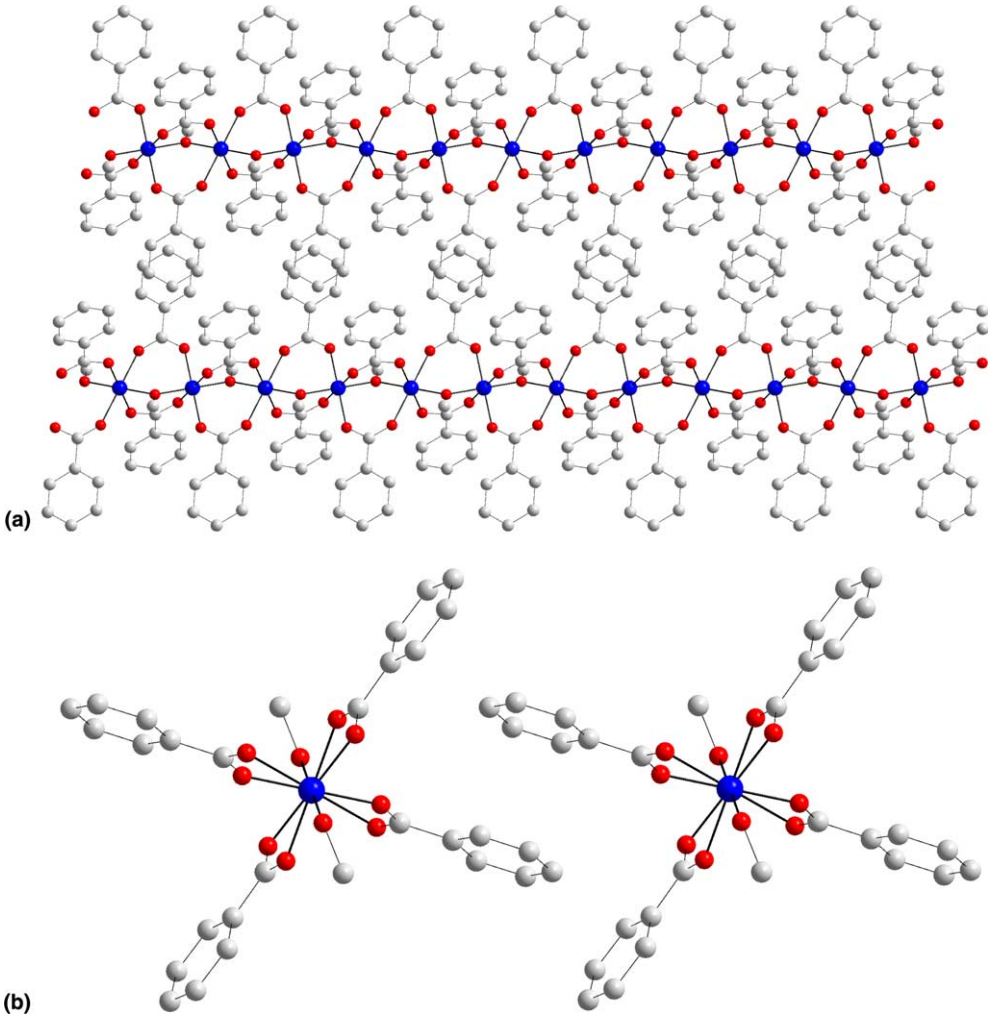


Fig. 4. (a) A section of two adjacent chains of **3** emphasizing (i) the π-stacking between the benzoate rings of the two neighboring chains, (ii) the fact that the chains run parallel in the crystal. (b) A view along the chain axis of **1**.

lengths, Mn bond valence sum calculations[3] [12] and the presence of Mn^{III} Jahn–Teller elongation axes for the two independent Mn atoms of the chain. The Jahn–Teller elongation axes are the O(2)–Mn(1)–O(2′) and O(4′)–Mn–O(2), which are parallel. It is interesting to note that the [Mn(μ-OMe)(μ-$O_2CR)_2$Mn] triply bridged unit is unprecedented in any Mn cluster of any nuclearity. This could be partially due to the fact that the list of Mn complexes containing methoxy groups is not extensive. A close examination of the packing of **3** shows that the chains all run parallel in the crystal, and in the absence of solvent molecules of crystallization there are no hydrogen-bonding interactions holding the neighboring chains together. However, a closer look reveals the existence of π-stacking interactions between the benzoate rings of neighboring chains (average C···C separation = 3.719 Å). This is emphasized in Fig. 4, which shows a small part of two adjacent chains from a viewpoint perpendicular to the chains (Fig. 4(a)) and along the chains (Fig. 4(b)).

3.3. Magnetism studies

3.3.1. $[Mn_{12}O_{12}(OMe)_2(O_2CPh)_{16}(H_2O)_2]^{2-}$

The structural similarity between complexes **1** and **2** suggested the possibility that the latter might also be a SMM, just like the former. This was therefore investigated by AC magnetic susceptibility measurements on a polycrystalline sample of **2** (containing both **2a** and **2b**) in the temperature range 1.8–10 K using a 3.5 G AC field oscillating at 5–500 Hz frequencies (ν). These studies revealed two frequency-dependent out-of-phase χ''_m AC signals (Fig. 5), one in the higher temperature (HT) range of 3–5 K, and a second one at lower temperatures (LT) whose peaks clearly occur at temperatures below the operating limit of our SQUID (superconducting quantum interference device) instrument (1.8 K).

[3] Bond valence sum calculations for the two independent Mn^{III} ions of **3** gave oxidation state values of 2.98 for both of them.

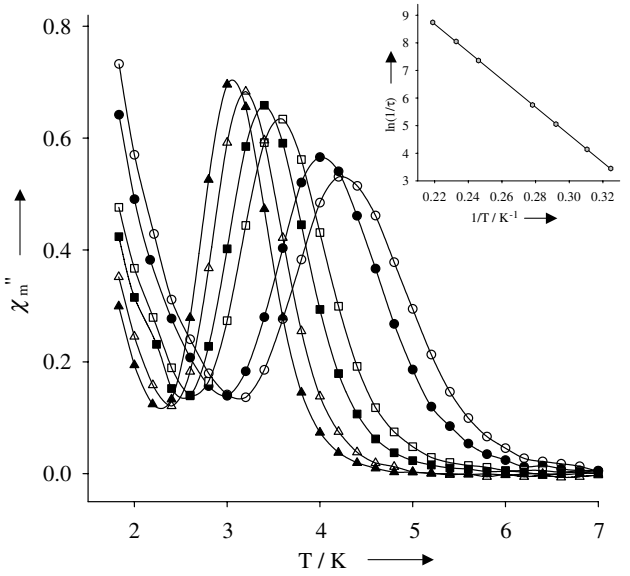


Fig. 5. Plot of χ''_m vs. T for a microcrystalline sample of **2** at 500 (○), 250 (●), 50 (□), 25 (■), 10 (△), 5 (▲) Hz. Inset: Plot of the natural logarithm of relaxation rate, $\ln(1/\tau)$ vs. inverse temperature using the χ''_m vs. T data for the slower-relaxing species (higher temperature data). The solid line is a fit to the Arrhenius equation; see the text for the fitting parameters.

The LT and HT χ''_m signals correspond to faster and slower relaxation rates, respectively. The peak of a χ''_m versus T plot represents the temperature at which the magnetization relaxation rate equals the angular frequency $\omega(=2\pi\nu)$, and the χ''_m versus T data at different frequencies (ν) were therefore used as a source of kinetic data to construct an Arrhenius plot (Fig. 5, inset) based on the Arrhenius equation of Eq. (1), where $1/\tau$ is the relaxation rate (τ is the relaxation time), $1/\tau_0$ is the pre-exponential factor, U_{eff} is the effective relaxation barrier,

$$1/\tau = 1/\tau_0 \exp(-U_{eff}/kT) \quad (1)$$

and k is the Boltzmann constant. The fit of the data to Eq. (1) gave $U_{eff} = 50.1$ K and $1/\tau_0 = 3.61 \times 10^8$ s^{-1}. This U_{eff} value is smaller than that of normal [Mn_{12}] complexes; complex **1**, for example, has a U_{eff} of 60–65 K.

The observation of out-of-phase AC signals suggests that **2** might be an SMM, although such signals by themselves are not proof of an SMM. It is also tempting to assume that the two χ''_m signals in Fig. 3 are due to the two crystal forms, diamond-like **2a** and needle-like **2b**. To confirm whether **2a** and/or **2b** are indeed SMMs, and to assess any difference between the two forms, magnetization versus DC field sweep studies were performed on single crystals of **2a** and **2b** using a micro-SQUID apparatus [17]. The resulting hysteresis loops are shown in Fig. 6, and their coercivities (i) increase with decreasing T at a constant field sweep rate, and (ii) increase with increasing sweep rate at a constant T

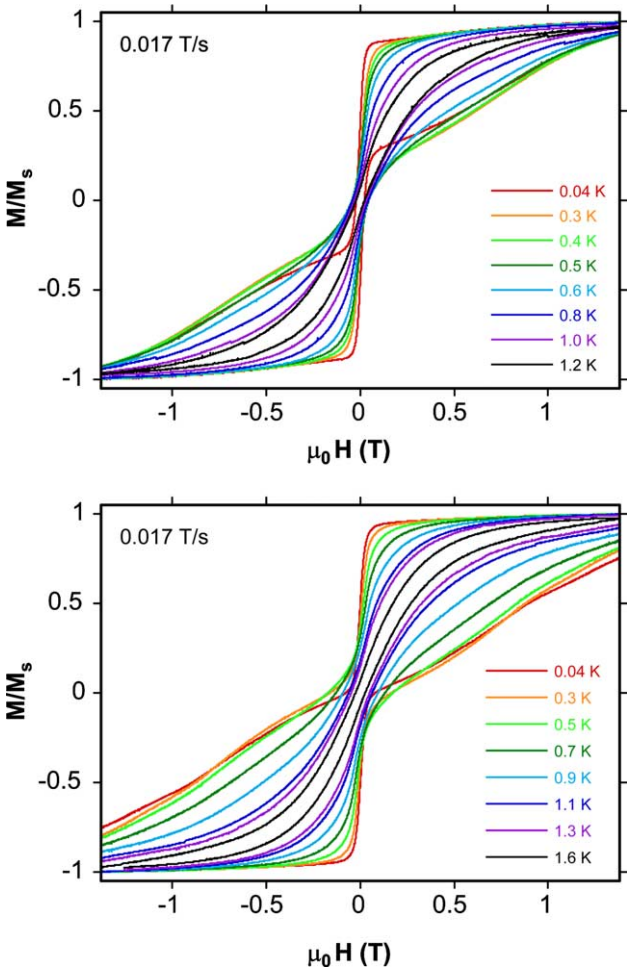


Fig. 6. Magnetization (M) vs. applied magnetic field ($\mu_0 H$) hysteresis loops for a single crystal (wet with mother liquor) of **2a** (top) and **2b** (bottom) at the indicated temperatures. M is normalized to its saturation value, M_s.

(not shown). This is as expected for the superparamagnet-like properties of a SMM.

However, it is clear that the observed properties (hysteresis loops) of **2a** and **2b** are very similar, and this is totally inconsistent with the two very different AC signals in Fig. 5 and the at-first-glance 'obvious' conclusion that the two signals are due to the two crystal forms. In fact, the hysteresis loops of both **2a** and **2b** each suggest a mixture of faster-relaxing (LT) and slower-relaxing (HT) forms, the former being responsible for the large decrease in magnetization at zero field, and the latter being responsible for the subsequent feature at higher fields. The relative proportions of these two features suggest comparable amounts of the LT and HT forms in each crystal, with perhaps a slightly greater amount of the former, and this is again consistent with the relative proportion of LT and HT AC signals in Fig. 5. Note that the AC and hysteresis studies were performed on wet single-crystals and microcrystals suspended in solid eicosane, respectively, and thus not strictly speaking on

the same material. Nevertheless, we conclude that (i) complex **2** is a new SMM; (ii) the different space groups of diamond-like **2a** and needle-like **2b** lead to only small differences in the magnetic properties of the $[Mn_{12}O_{12}(OMe)_2(O_2CPh)_{16}(H_2O)_2]^{2-}$ anion; and (iii) there are faster- and slower-relaxing forms of complex **2** that co-crystallize in the same crystal. In fact, point (iii) has long been known to also be the case for **1**, whose crystals contain about 5% of the faster-relaxing form; complex **2** thus differs from **1** only in the relative amounts of the two forms.

For normal $[Mn_{12}]$ complexes, we have reported elsewhere that crystals of pure faster-relaxing forms can be prepared with, for example, ^{t}butylacetate as the carboxylate group [6d,6g]. Crystallography on such crystals has allowed the origin of the faster-relaxing form to be identified as the abnormal orientation of one of the Mn^{III} JT elongation axes being disposed equatorial rather than axial to the Mn_{12} disk-like plane, and thus pointing to a core O^{2-} ion. We have named this 'Jahn–Teller isomerism'. The same is likely to be the origin of the two forms of **2**. Indeed, this takes us back full circle to the crystal structures described above, because it rationalizes the unusual Mn–O bond lengths at Mn4 for **2a** and Mn1 for **2b**. For **2a**, for example, an approximately equal mixture of (a) slower-relaxing species with the JT axis at Mn4 in the normal position along the O9–Mn4–O14 axis, and (b) faster-relaxing species with the JT axis at Mn4 abnormally aligned along the O7–Mn4–O12 axis will lead to the crystallographic average result that the O9–Mn4–O14 and O7–Mn4–O12 bond lengths are shorter and longer, respectively, than they should be, which is what is seen. Similarly for **2b**, we thus feel that the crystallographic data support the conclusion from the magnetic studies that crystals of **2a** and **2b** comprise a mixture of slower- and faster-relaxing species resulting from normal and abnormal orientations, respectively, of a Mn^{III} JT elongation axis. As with normal $[Mn_{12}]$ complexes, it will require crystallization of pure crystals of the different forms of **2** to allow more detailed study, and this is a current objective.

3.3.2. $[Mn(OMe)(O_2CPh)_2]_n$

Solid state dc magnetic susceptibility data were collected in the 5.0–300 K range in a 5 kG (0.5 T) field. The data for **3** are plotted as $\chi_m T$ versus T in Fig. 7. The $\chi_m T$ value of 2.59 $cm^3\ mol^{-1}$ K at 300 K is lower than the expected value of 3 $cm^3\ mol^{-1}$ K for an isolated Mn^{III} center, and decreases steadily to 0.18 $cm^3\ mol^{-1}$ K at 8 K, and then increases smoothly to 0.21 at 5 K. These data suggest that the existence of strong antiferromagnetic interactions between the Mn^{III} centers of the chain resulting in a diamagnetic ground state (S = 0). This is not surprising because triply bridged Mn_2^{III} (and $Mn^{II}Mn^{III}$) dinuclear units are almost always antiferromagnetically coupled, although a dinuclear complex with the $[Mn(\mu\text{-}OMe)(\mu\text{-}O_2CR)_2Mn]$ core is not known for direct comparison. The very small increase at $T < 8$ K could be due to weak ferromagnetic interactions between the chains. This behavior is very similar to that observed for **4**, where however this behavior is more pronounced, presumably due to the stronger interactions between chains mediated by the strong hydrogen-bonding in **4**.

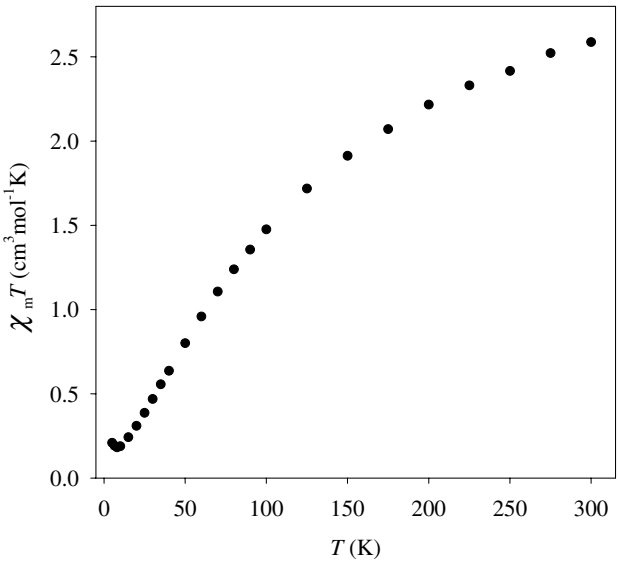


Fig. 7. A plot of $\chi_m T$ vs. T for **3**.

4. Conclusions

The new reductive aggregation procedure has led to two new compounds. The first is a variant of the $[Mn_{12}]$ family of SMMs and the second a Mn^{III} polymer. The latter is an antiferromagnetically coupled chain. In contrast, the anion of **2** is a structural variant of normal $[Mn_{12}]$ complexes, and like them is an SMM. It also displays both faster- and slower-relaxing magnetization dynamics that we assign to the presence of JT isomerism. We have in the past obtained many derivatives of $[Mn_{12}]$ complexes, for example by carboxylate substitution [6,7], one- and two-electron reduction [6f,9,10], introduction of non-carboxylate ligands [8], etc., and similar derivatization of **2** may also prove possible, in which case it is merely the prototype of what could become a large new family of related SMMs.

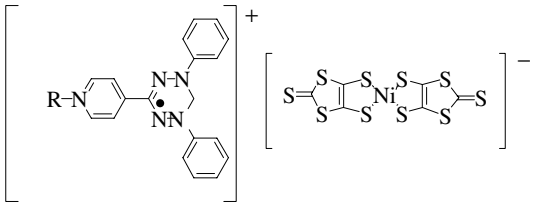
References

[1] (a) R. Sessoli, H.-L. Tsai, A.R. Schake, S. Wang, J.B. Vincent, K. Folting, D. Gatteschi, G. Christou, D.N. Hendrickson, J. Am. Chem. Soc. 115 (1993) 1804;
(b) R. Sessoli, D. Gatteschi, A. Caneschi, M.A. Novak, Nature 365 (1993) 141.

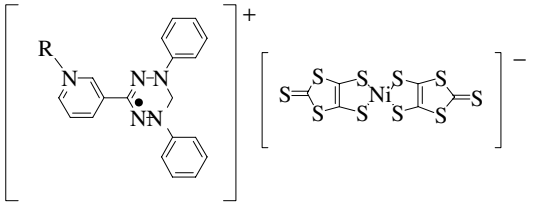
[2] S.M.J. Aubin, M.W. Wemple, D.M. Adams, H.-L. Tsai, G. Christou, D.N. Hendrickson, J. Am. Chem. Soc. 118 (1996) 7746.
[3] (a) G. Christou, D. Gatteschi, D.N. Hendrickson, R. Sessoli, MRS Bull. 25 (2000) 66;
(b) D. Gatteschi, R. Sessoli, Angew. Chem. Int. Ed. 42 (2003) 268.
[4] (a) A.J. Tasiopoulos, W. Wernsdorfer, B. Moulton, M.J. Zaworotko, G. Christou, J. Am. Chem. Soc. 125 (2003) 15274;
(b) A.J. Tasiopoulos, A. Vinslava, W. Wernsdorfer, K.A. Abboud, G. Christou, Angew. Chem. Int. Ed. 43 (2004) 2117;
(c) D.J. Price, S.R. Batten, B. Moubaraki, K.S. Murray, Chem. Commun. (2002) 762;
(d) S.M.J. Aubin, N.R. Dilley, L. Pardi, J. Krzystek, M.W. Wemple, L.-C. Brunel, M.B. Maple, G. Christou, D.N. Hendrickson, J. Am. Chem. Soc. 120 (1998) 4991;
(e) M. Soler, W. Wernsdorfer, K. Folting, M. Pink, G. Christou, J. Am. Chem. Soc. 126 (2004) 2156;
(f) E.K. Brechin, M. Soler, G. Christou, M. Helliwell, S.J. Teat, W. Wernsdorfer, Chem. Commun. (2003) 1276.
[5] (a) E.K. Brechin, J. Yoo, M. Nakano, J.C. Huffman, D.N. Hendrickson, G. Christou, Chem. Commun. (1999) 783;
(b) J. Yoo, E.K. Brechin, A. Yamaguchi, M. Nakano, J.C. Huffman, A.L. Maniero, L.-C. Brunel, K. Awaga, H. Ishimoto, G. Christou, D.N. Hendrickson, Inorg. Chem. 39 (2000) 3615;
(c) E.K. Brechin, M. Soler, J. Davidson, D.N. Hendrickson, S. Parsons, G. Christou, Chem. Commun. (2002) 2252;
(d) L.F. Jones, E.K. Brechin, D. Collison, A. Harrison, S.J. Teat, W. Wernsdorfer, Chem. Commun. (2002) 2974;
(e) M. Moragues-Canovas, M. Helliwell, L. Ricard, E. Riviere, W. Wersdorfer, E. Brechin, T. Mallah, Eur. J. Inorg. Chem. (2004) 2219;
(f) C.J. Milios, C.P. Raptopoulou, A. Terzis, F. Lloret, R. Vicente, S.P. Perlepes, A. Escuer, Angew. Chem. Int. Ed. 43 (2004) 210;
(g) A.K. Boudalis, B. Donnadieu, V. Nastopoulos, J.M. Clemente-Juan, A. Mari, Y. Sanakis, J.-P. Tuchagues, S.P. Perlepes, Angew. Chem. Int. Ed. 43 (2004) 2266;
(h) H. Andres, R. Basler, A.J. Blake, C. Cadiou, G. Chaboussant, C.M. Grant, H.-U. Güdel, M. Murrie, S. Parsons, C. Paulsen, F. Semadini, V. Villar, W. Wernsdorfer, R.E.P. Winpenny, Chem. Eur. J. 8 (2002) 4867.
[6] (a) S.M.J. Aubin, Z. Sun, I.A. Guzei, A.L. Rheingold, G. Christou, D.N. Hendrickson, Chem. Commun. (1997) 2239;
(b) Z. Sun, D. Ruiz, E. Rumberger, C.D. Incarvito, K. Folting, A.L. Rheingold, G. Christou, D.N. Hendrickson, Inorg. Chem. 37 (1998) 4758;
(c) D. Ruiz, Z. Sun, B. Albela, K. Folting, J. Ribas, G. Christou, D.N. Hendrickson, Angew. Chem. Int. Ed. 37 (1998) 300;
(d) Z. Sun, D. Ruiz, N.R. Dilley, M. Soler, J. Ribas, K. Folting, M.B. Maple, G. Christou, D.N. Hendrickson, Chem. Commun. (1999) 1973;
(e) S.M.J. Aubin, Z. Sun, H.J. Eppley, E.M. Rumberger, I.A. Guzei, K. Folting, P.K. Gantzel, A.L. Rheingold, G. Christou, D.N. Hendrickson, Inorg. Chem. 40 (2001) 2127;
(f) H.J. Eppley, H.-L. Tsai, N. de Vries, K. Folting, G. Christou, D.N. Hendrickson, J. Am. Chem. Soc. 117 (1995) 301;
(g) M. Soler, W. Wernsdorfer, Z. Sun, J.C. Huffman, D.N. Hendrickson, G. Christou, Chem. Commun. (2003) 2672.
[7] M. Soler, P. Artus, K. Folting, J.C. Huffman, D.N. Hendrickson, G. Christou, Inorg. Chem. 40 (2001) 4902.
[8] (a) P. Artus, C. Boskovic, J. Yoo, W.E. Streib, L.-C. Brunel, D.N. Hendrickson, G. Christou, Inorg. Chem. 40 (2001) 4199;
(b) C. Boskovic, M. Pink, J.C. Huffman, D.N. Hendrickson, G. Christou, J. Am. Chem. Soc. 123 (2001) 9914;
(c) N.E. Chakov, W. Wernsdorfer, K.A. Abboud, D.N. Hendrickson, G. Christou, Dalton Trans. (2003) 2243.
[9] (a) S.M.J. Aubin, Z. Sun, L. Pardi, J. Krzystek, K. Folting, L.-C. Brunel, A.L. Rheingold, G. Christou, D.N. Hendrickson, Inorg. Chem. 38 (1999) 5329;
(b) T. Kuroda-Sowa, M. Lam, A.L. Rheingold, C. Frommen, W.M. Reiff, M. Nakano, J. Yoo, A.L. Maniero, L.-C. Brunel, G. Christou, D.N. Hendrickson, Inorg. Chem. 40 (2001) 6469.
[10] (a) M. Soler, S.K. Chandra, D. Ruiz, E.R. Davidson, D.N. Hendrickson, G. Christou, Chem. Commun. (2000) 2417;
(b) M. Soler, W. Wernsdorfer, K.A. Abboud, J.C. Huffman, E.R. Davidson, D.N. Hendrickson, G. Christou, J. Am. Chem. Soc. 125 (2003) 3576.
[11] T. Lis, Acta Crystallogr., Sect. B 36 (1980) 2042.
[12] W. Liu, H.H. Thorp, Inorg. Chem. 32 (1993) 4102.
[13] (a) For example, see M.J. Manos, A.J. Tasiopoulos, E.J. Tolis, N. Lalioti, J.D. Woolins, A.M.Z. Slawin, M.P. Sigalas, T.A. Kabanos, Chem. Eur. J. 9 (2003) 695;
(b) H. Kang, S. Liu, S.N. Shaikh, T. Nicholson, J. Zubieta, Inorg. Chem. 28 (1989) 920.
[14] P. King, W. Wernsdorfer, K.A. Abboud, G. Christou, Inorg. Chem. 43 (2004) 7315.
[15] J.T. Brockman, J.C. Huffman, G. Christou, Angew. Chem. Int. Ed. 41 (2002) 2506.
[16] (a) A.J. Tasiopoulos, N.C. Harden, K.A. Abboud, G. Christou, Polyhedron 22 (2003) 133;
(b) D.J. Price, S.R. Batten, B. Moubaraki, K.S. Murray, Polyhedron 22 (2003) 2167.
[17] W. Wernsdorfer, E. Bonet Orozco, K. Hasselbach, A. Benoit, D. Mailly, O. Kubo, H. Nakano, B. Barbara, Phys. Rev. Lett. 79 (1997) 4014.

semiconductors consisting of open-shell radical cation donor and metal complex anion acceptor have been reported for the (1:1) salt of $Ni(dmit)_2$ anion with the *p*-EPYNN (*p*-*N*-ethylpyridinium α-nitronyl nitroxide) and the Me_3N^+–TEMPO (=*N*,*N*,*N*-trimethyl(1-oxyl-2,2,6,6-tetramethylpiperidine-4-yl)ammonium) radical cations [8,9].

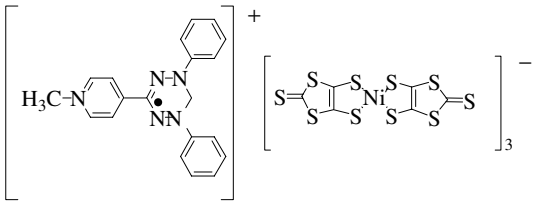
Verdazyl radicals show a high chemical and thermal stability and can be isolated as solvent-free pure radicals in crystalline states [10]. The magnetic properties of these verdazyl radical crystals have been studied extensively, and several interesting magnetic properties such as ferromagnetism, weak ferromagnetism, antiferromagnetism, spin-Peierls transition, and spin frustration have been reported [11–17]. Recently, first two examples of molecular paramagnetic semiconductors consisting of verdazyl radical cation and metal complex anion have been reported for the $Ni(dmit)_2$ salts of 3-[4-(trialkylammonio)phenyl]-1,5-diphenyl-6-oxoverdazyl radical cations [18,19]. Further, we prepared the (1:1) and (1:2) salts of 3-(4- and 3-alkyl-pyridinium)-1,5-diphenylver-dazyl (alkyl = ethyl and methyl) radical cations with TCNQ anion, and found that the (1:2) salts are genuine organic paramagnetic semiconductors [20,21]. However, the examples of the molecular complexes between the open-shell radical cation and electron acceptor anion are very limited. In the present work, we prepared five kinds of (1:1) and (1:3) salts **1**–**5** of 3-(4- and 3-alkyl-pyridinium)-1,5-diphenylverdazyl (alkyl = ethyl and methyl) radical cations with $Ni(dmit)_2$ anion (see Fig. 1), and studied the structural, magnetic and conducting properties of these radical salts.



$R = C_2H_5$: $[p\text{–EtPyDV}]^+[Ni(dmit)_2]^-$ (1)
$R = CH_3$: $[p\text{–MePyDV}]^+[Ni(dmit)_2]^-$ (3)



$R = C_2H_5$: $[m\text{–EtPyDV}]^+[Ni(dmit)_2]^-$ (2)
$R = CH_3$: $[m\text{–MePyDV}]^+[Ni(dmit)_2]^-$ (4)



$[p\text{-MePyDV}]^+[Ni(dmit)_2]_3^-$ (5)

Fig. 1. Chemical structures of the (1:1) and (1:3) salts of 3-(4- and 3-alkyl-pyridinium)-1,5-diphenylverdazyl radical cations (alkyl = ethyl and methyl) with $Ni(dmit)_2$ anion.

2. Experimental

2.1. Syntheses

The preparations of 3-(4-pyridyl)-1,5-diphenyl-verdazyl (*p*-PyDV) and 3-(3-pyridyl)-1,5-diphenyl-verdayl (*m*-PyDV) radicals were reported in a previous work [17]. The preparations of the iodide salts, 3-(4- and 3-alkyl-pyridinium)-1,5-diphenylverdazyl iodides (alkyl = ethyl and methyl), $[p\text{-EtPyDV}]^+I^-$ (**6**), $[m\text{-EtPyDV}]^+I^-$ (**7**), $[p\text{-MePyDV}]^+I^-$ (**8**), and $[m\text{-MePyDV}]^+I^-$ (**9**), were reported in previous papers [20,21].

Preparations of the charge transfer salts **1**–**5** are as follows.

2.1.1. $[p\text{-}EtPyDV]^+[Ni(dmit)_2]^-$ (*1*)

To stirred solution of $[p\text{-EtPyDV}]^+[I]^-$ (47.0 mg, 0.100 mmol) in methanol (50 ml), $[n\text{-}Bu_4N]^+[Ni(dmit)_2]^-$ (69.4 mg, 0.100 mmol) in methanol (250 ml) was added and stirring was continued for 2 h under nitrogen atmosphere. The black-violet solids precipitated were filtered and washed with diethyl ether. Recrystallization of the residue from acetonitrile–diethyl ether afforded the product as black-violet prismatic crystals (43 mg, 54%): m.p. = 190.0–191.5 °C; UV (acetonitrile) λ_{max} ($\log\varepsilon$): 747 (3.37), 617 (3.59), 543 (4.03), 436 (4.26), 380 (4.56), 315 (4.59), 241 (4.64). *Anal.* Calc. for $C_{27}H_{21}N_5S_{10}Ni$: C, 40.80; H, 2.66; N, 8.81. Found: C, 40.58; H, 2.62; N, 8.46%.

The radical salts **2**, **3**, and **4** were prepared similarly.

2.1.2. $[m\text{-}EtPyDV]^+[Ni(dmit)_2]^-$ (*2*)

Dark-green powder crystals: m.p. = 199.0–201.0 °C; UV (acetonitrile) λ_{max} ($\log\varepsilon$) 735 (3.59), 625 (3.64), 443 (4.31), 389 (4.39), 314 (4.64), 240 (4.58). *Anal.* Calc. for $C_{27}H_{21}N_5S_{10}Ni$: C, 40.80; H, 2.66; N, 8.81. Found: C, 40.67; H, 2.61; N, 8.71%.

2.1.3. $[p\text{-}MePyDV]^+[Ni(dmit)_2]^-$ (*3*)

Dark-green powder crystals: m.p. > 300.0 °C; UV (acetonitrile) λ_{max} ($\log\varepsilon$) 747 (3.36), 619 (3.59), 543 (4.13), 436 (4.26), 379 (4.56), 350 (4.51), 315 (4.60),

240 (4.65). *Anal*. Calc. for $C_{26}H_{19}N_5S_{10}Ni$: C, 39.99; H, 2.45; N, 8.97. Found: C, 40.82; H, 2.57; N, 9.14%.

2.1.4. [m-MePyDV]$^+$[Ni(dmit)$_2$]$^-$ (4)

Black-violet powder crystals: m.p. > 300.0 °C; UV (acetonitrile) λ_{max} (log ε) 736 (3.34), 619 (3.61), 439 (4.30), 392 (4.41), 315 (4.58), 241 (4.63). *Anal*. Calc. for $C_{26}H_{19}N_5S_{10}Ni$: C, 39.99; H, 2.45; N, 8.97. Found: C, 40.15; H, 2.55; N, 9.05%.

2.1.5. [p-MePyDV]$^+$[Ni(dmit)$_2$]$_3^-$ (5)

For the preparation of (1:3) salt **5**, the air oxidation of a solution containing the [*p*-MePyDV]$^+$[Ni(dmit)$_2$]$^-$ (**3**) (30 mg), acetic acid (20 ml) and acetic anhydride (20 ml) in acetone (300 ml) was carried out at room temperature [6,7]. Black fine crystals obtained show a high melting point and are insoluble in the usual organic solvents. The result of the elemental analysis indicates the formation of a (1:3) salt, [*p*-MePyDV]$^+$[Ni–(dmit)$_2$]$_3^-$ (**5**) [7]. M.p. > 300 °C; *Anal*. Calc. for $C_{38}H_{19}N_5S_{30}Ni_3$: C, 27.11; H, 1.14; N, 4.16. Found: C, 26.85; H, 1.27; N, 3.97%.

2.2. Measurements

The magnetic susceptibility (χ_M) was measured in the temperature range of 1.8–300 K by a SQUID magnetometer. The χ_M of all samples has been corrected for the diamagnetic contribution ($\chi_{dia} = -0.399 \times 10^{-3}$ emu/mol for salts **1** and **2**, -0.388×10^{-3} emu/mol for salts **3** and **4**, and -0.757×10^{-3} emu/mol for salt **5**), calculated by Pascal's method. The conductivity measurements of salts **1**–**5** were performed for the pressed pellet samples of salts, using the standard dc four-probe method.

2.3. Structure determination

The X-ray measurements of the [*p*-EtPyDV]$^+$[Ni(dmit)$_2$]$^-$ salt (**1**) and [*p*-EtPyDV]$^+$I$^-$ salt (**6**) were carried out on a Rigaku AFC5R diffractometer with graphite-monochromated Mo Kα (λ = 0.71069 Å) radiations. The structure was solved by the direct method.

3. Results

3.1. UV–Vis spectra of salts 1–5

Absorption spectra of [*m*-MePyDV]$^+$[Ni(dmit)$_2$]$^-$ (**4**), [*m*-MePyDV]$^+$I$^-$ (**9**), and [*n*-Bu$_4$N]$^+$[Ni(dmit)$_2$]$^-$ salts are measured in acetonitrile solvent. As shown in Fig. 2, the absorption spectrum of **4** can be well explained by the addition of [*m*-MePyDV]$^+$I$^-$ (**9**) and [*n*-Bu$_4$N]$^+$[Ni(dmit)$_2$]$^-$, suggesting the (1:1) complex formation between the [*m*-MePyDV]$^+$ cation and the [Ni(dmit)$_2$]$^-$ anion [18]. Similarly, the absorption spectra of salts **1**–**3** in acetonitrile can be well explained by an addition of those of corresponding iodide salts and [*n*-Bu$_4$N]$^+$[Ni(dmit)$_2$]$^-$, respectively. The electronic structures of the verdazyl radical cation and Ni(dmit)$_2$ anion moieties in salts **1**–**4** are thought to be similar to those in corresponding iodide salts **6**–**9** and [*n*-Bu$_4$N]$^+$[Ni(dmit)$_2$]$^-$, respectively. The (1:3) salt **5** crystals are insoluble in the usual organic solvents, and we could not measure the optical spectrum of salt **5** in solution.

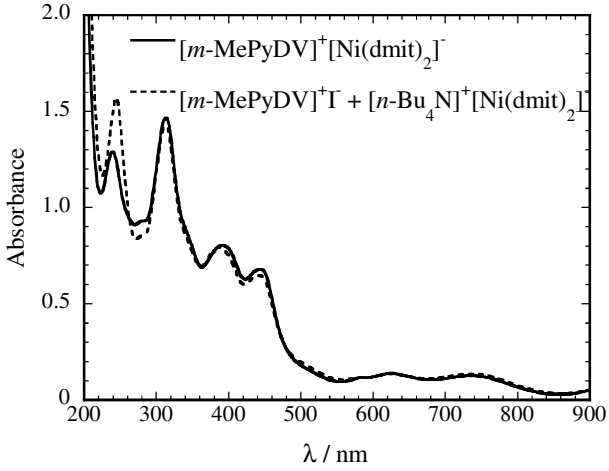


Fig. 2. UV–Vis spectra of the (1:1) [*m*-MePyDV]$^+$[Ni(dmit)$_2$]$^-$ salt (**4**) in acetonitrile.

3.2. Crystal structures of salts 1 and 6

The crystal structure could be determined for the [*p*-EtPyDV]$^+$[Ni(dmit)$_2$]$^-$ salt (**1**) and the [*p*-EtPyDV]$^+$-I$^-$ salt (**6**) (see Table 1). The crystal structures of salts **1** and **6** are shown in Fig. 3(a) and (b), respectively. The bond lengths and bond angles of verdazyl moieties (N1–N2–C1–N3–N4–C2) in salts **1** and **6** are similar to corresponding those of the neutral 1,3,5-triphenylverdazyl (TPV) (data are not shown) [22]. However, the dihedral angles (8.965° and 2.380°) between least-squares plane (N1–N2–N3–N4 plane) of verdazyl ring and those of N1- and N4-phenyl rings in salt **1** are much smaller than those of the iodide salt **6** (9.255° and 28.925°) and TPV (27.8(4)° and 40.2(4)°), respectively. In TPV, the verdazyl ring has an unsymmetrical boat configuration, with both C1 and C2 out of the nitrogen plane on the same side. C1 is displaced by only +0.099 Å, while C2 is displaced by +0.590 Å. The verdazyl ring in iodide salt **6** also shows similar structure to that of TPV. On the other hand, in salt **1**, the deviations (−0.007(16) and +0.140(17) Å) of C1 and C2 atoms out of N1–N2–N3–N4 plane are very small, indicating that the verdazyl molecule has planar structure.

Table 1
Crystal data, experimental conditions, and refinement details of salts **1** and **6**

	[*p*-EtPyDV]$^+$[Ni(dmit)$_2$]$^-$ (**1**)	[*p*-EtPyDV]$^+$I$^-$ (**6**)
Empirical formula	$C_{27}H_{21}N_5NiS_{10}$	$C_{21}H_{21}N_5I$
Formula weight	794.80	470.33
Crystal color	black, prismatic	purple, prismatic
Crystal system	triclinic	monoclinic
Space group	$P\bar{1}$(#2)	$P2_1/c$(#14)
Unit cell dimensions		
a (Å)	11.866(3)	8.771(2)
b (Å)	16.556(4)	8.851(3)
c (Å)	9.267(2)	26.166(2)
α (°)	105.94(2)	
β (°)	111.93(2)	96.83(1)
γ (°)	79.72(3)	
V (Å^3)	1618.0(8)	2016.8(8)
Z	2	4
D_x (g cm^{-3})	1.631	1.549
μ (cm^{-1}) (Mo Kα)	12.74	16.04
Crystal size/mm	0.03 × 0.10 × 0.50	0.25 × 0.23 × 0.10
Number of reflections measured	5999	5262
Number of unique reflections (R_{int})	5745 (0.079)	4641 (0.026)
R, R_w	0.180, 0.221	0.067; 0.101

The bond lengths and bond angles of the Ni(dmit)$_2$ anion in salt **1** are also similar to corresponding those in the [*n*-Bu$_4$N]$^+$[Ni(dmit)$_2$]$^-$ salt (data are not shown) [23]. The result indicates that the Ni(dmit)$_2$ moiety in salt **1** is considered to exist as monoanion [Ni(dmit)$_2$]$^-$ with $S = 1/2$ [8]. The dihedral angles between least-squares planes of two dmit rings in salt **1** is 4.683°, indicating the planarity of the Ni(dmit)$_2$ moiety.

Molecular packing of salt **1** is shown in Fig. 4. The unit cell of salt **1** contains two Ni(dmit)$_2$ anions and two verdazyl cations [*p*-EtPyDV]$^+$. The Ni(dmit)$_2$ anion molecules in salt **1** form a dimer ([Ni(dmit)$_2$] (A)–[Ni(dmit)$_2$] (B)) having intra-dimer contacts of ca. 3.6–3.8 Å (see Table 2). The dimer molecules are sandwiched between two verdazyl cation molecules, forming a linear tetramer ([*p*-EtPyDV]$^+$ (A)–[Ni(dmit)$_2$] (A)–[Ni(dmit)$_2$] (B)–[*p*-EtPyDV]$^+$ (B)) in the crystal. The Ni(dmit)$_2$ anion dimers are connected to each other through short S–S contacts (S8–S9 = 3.566(4) Å, S9–S9 = 3.811(7) Å, and S5–S8 = 3.934(5) Å) between Ni(A) and Ni(C).

3.3. Conductivities of salts 1–5

The room-temperature conductivities (σ_{RT}'s) for salts **1**, **2**, **3**, and **4** are 2.3×10^{-5}, 1.1×10^{-3}, 1.4×10^{-5}, and 5.4×10^{-6} S cm^{-1}, respectively, as listed in Table 3. As shown in Fig. 5, the salts **1**, **2**, **3** and **4** show semiconductive behavior with activation energy values (E_A's) of 0.28, 0.52, 0.21 and 0.33 eV at the temperature range of 219–298, 250–283, 246–279 and 269–298 K, respectively. The conductivity of the (1:3) salt **5** at 20 °C was $\sigma = 1.0$ S cm^{-1} with an activation energy $E_A = 0.048$ eV (data are not shown), and is three to five orders of magnitude larger than those of the (1:1) salts **1**–**4**.

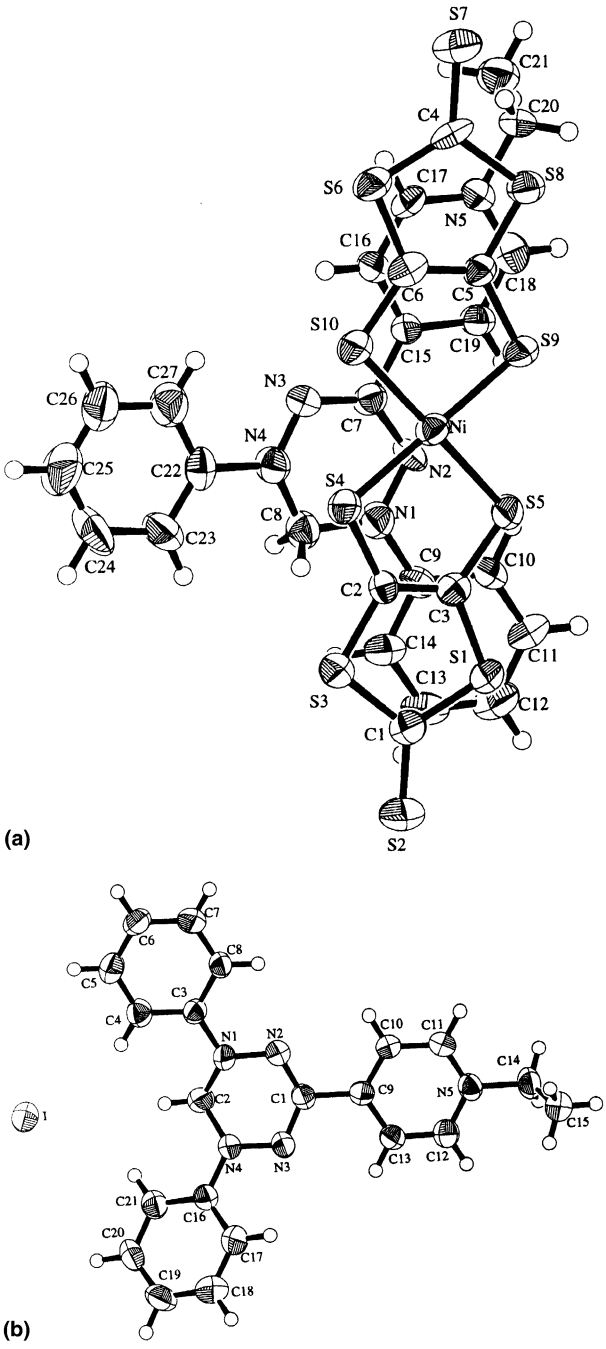


Fig. 3. Molecular structures of (a) the Ni salt **1** and (b) the iodide salt **6** with the atom numbering scheme.

3.4. Magnetic susceptibilities of salts 1–5

Fig. 6 shows a plot of $\chi_M T$ versus T for salts **1**–**5**. The value of $\chi_M T$ for the [*p*-EtPyDV]$^+$[Ni(dmit)$_2$]$^-$ salt (**1**) is 0.243 K emu/mol at 300 K (see Table 3), and decreases

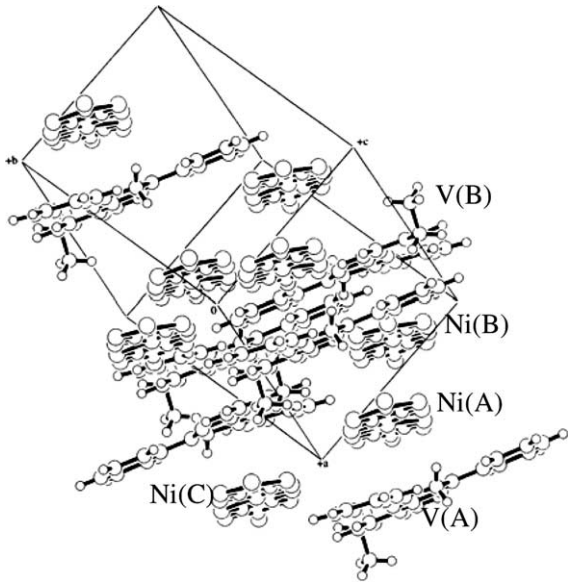


Fig. 4. Molecular packing in salt **1**, showing the formation of magnetic linear tetramer, [verdazyl cation (A)–Ni(dmit)$_2$ anion (A)–Ni(dmit)$_2$ anion (B)–verdazyl cation (B)].

by lowering the temperature, indicating AFM interaction in salt **1**. As shown in Fig. 7, the χ_M of salt **1** decreases slowly by lowering the temperature from 300 K, shows a minimum around 160 K, and increases rapidly below 20 K.

The value of $\chi_M T$ for the [*m*-EtPyDV]$^+$[Ni(dmit)$_2$]$^-$ salt (**2**) is 0.685 K emu/mol at 300 K, and is close to the sum of those (0.376 and 0.392 K emu/mol) expected for non-interacting $S = 1/2$ spin system with *g*-values $g_V^+ = 2.0032$ for [*m*-EtPyDV]$^+$I$^-$ [21] and $g_{Ni}^- = 2.0472$ for [*n*-Bu$_4$N]$^+$[Ni(dmit)$_2$]$^-$ [18], respectively, suggesting that both the spins of verdazyl cation and Ni(dmit)$_2$ anion contribute to the magnetism of salt **2**. $\chi_M T$ for salt **2** decreases gradually by decreasing the temperature, shows the plateau between 30 and 60 K, and increases by decreasing the temperature. Below 30 K, the susceptibility of salt **2** follows the Curie–Weiss law with a Curie constant of 0.376 K emu/mol and a positive Weiss constant of $+2.2 \pm 0.2$ K (see Fig. 8(b)). The $\chi_M T$ (0.388 K emu/mol) of salt **2** at the plateau (30–60 K) amounts to about one half of the value (0.768 emu K/mol) calculated on the basis of two $S = 1/2$ spins per one formula unit of the salt, as shown in Fig. 8(a). The additional susceptibility above 60 K is considered to be a thermally activated species which is nonmagnetic at lower temperatures. This magnetic contribution is tentatively assigned to the dimer of the Ni(dmit)$_2^-$ radical anions. The susceptibility at lower temperatures is, therefore, attributed to the verdazyl radical cations.

The χ_M of the [*p*-MePyDV]$^+$[Ni(dmit)$_2$]$^-$ salt (**3**) decreases gradually by decreasing temperature from 300 K, and shows a minimum at about $T_{min} = 170$ K (data are not shown). The susceptibility increases by

Table 2
Pertinent intermolecular contacts (*r*/Å) in [*p*-EtPyDV]$^+$[Ni(dmit)$_2$]$^-$ (**1**)

Ni(A)–Ni(B) Ni–Ni 4.278(3) (r < 4.00 Å)		Ni(A)–Ni(C) Ni–Ni > 5.00 (r < 4.00 Å)		Ni(A)–V(A) (r < 4.00 Å)		V(A)–V(B) N(*i*)–N(*j*) (*i*, *j* = 1,2,3,4) (r < 5.00 Å)	
Ni–S10	3.815(4)	S5–S8	3.934(5)	Ni–N2	3.771(9)	N1–N1	4.29(2)
Ni–C6	3.87(1)	S8–S9	3.566(4)	Ni–N3	3.684(9)		
S2–S7	3.970(5)	S9–S9	3.811(7)	S4–N1	3.936(9)		
S3–S7	3.614(5)			S4–N3	3.69(1)		
S4–S8	3.819(5)			S4–N4	3.30(1)		
S4–C5	3.59(1)			S5–N1	3.79(1)		
S4–C6	3.81(1)			S5–N2	3.67(1)		
C2–C4	3.63(2)			S10–N3	3.597(9)		
				C2–N1	3.62(2)		
				C2–N4	3.90(1)		
				C3–N1	3.56(1)		

Table 3
Conductivity (σ_{RT}), activation energy (E_A), $\chi_M T$ value (at 300 K), and magnetism of salts **1**–**5**

Salts	σ_{RT} (S cm^{-1})	E_A (eV)	$\chi_M T$ (K emu/mol)	magnetism
[*p*-EtPyDV]$^+$[Ni(dmit)$_2$]$^-$ (**1**)	2.3×10^{-5}	0.28	0.243	linear tetramer ($2J_1/k_B = -780$ K, $2J_2/k_B = -200$ K) + Curie impurity (5.3%)
[*m*-EtPyDV]$^+$[Ni(dmit)$_2$]$^-$ (**2**)	1.1×10^{-3}	0.52	0.685	1D-Ferro ($2J/k_B = +2.5$ K) + S–T ($2J/k_B = -320$ K)
[*p*-MePyDV]$^+$[Ni(dmit)$_2$]$^-$ (**3**)	1.4×10^{-5}	0.21	0.288	linear tetramer
[*m*-MePyDV]$^+$[Ni(dmit)$_2$]$^-$ (**4**)	5.4×10^{-6}	0.33	0.713	alternating chain ($T_{max} = 100 \pm 2$ K, $2J_1/k_B = -165$ K, $\alpha = J_2/J_1 = 0.6$) + Curie impurity (5.4%)
[*p*-MePyDV]$^+$[Ni(dmit)$_2$]$_3^-$ (**5**)	1.0	0.048	0.641	Curie–Weiss law ($C = 0.684$ (emu K)/mol, $\theta = -17$ K)

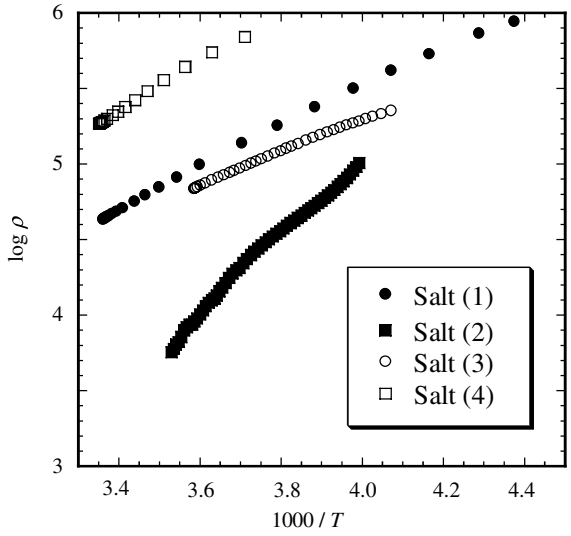


Fig. 5. Temperature dependence of the resistivity (ρ) of the (1:1) salts **1**–**4** at ambient pressure.

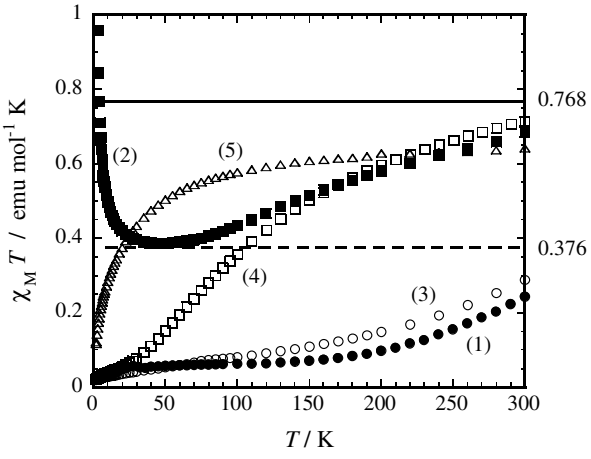


Fig. 6. Temperature dependence of the product $\chi_M T$ for salts **1**–**5**.

decreasing temperature below 170 K. The value of $\chi_M T$ for **3** is 0.288 K emu/mol at 300 K, and decreases by lowering the temperature, indicating AFM interaction in **3**, as shown in Fig. 6. The magnetic behavior of salt **3** is very similar to that of salt **1**.

The χ_M of the $[m\text{-MePyDV}]^+[Ni(dmit)_2]^-$ salt (**4**) shows a broad maximum at $T_{max} = 100 \pm 2$ K, as shown in Fig. 9. An increase in susceptibility below 26 K was observed, which is probably due to Curie impurities. The value (0.713 K emu/mol) of $\chi_M T$ at 300 K observed for salt **4** is similar to the sum of those (0.376 and 0.392 K emu/mol) for $S = 1/2$ spin system with $g_V^+ = 2.0033$ [21] and $g_{Ni}^- = 2.0472$ [18], suggesting that both the spins of verdazyl cation and $[Ni(dmit)_2]^-$ anion contribute to the magnetism of salt **4**.

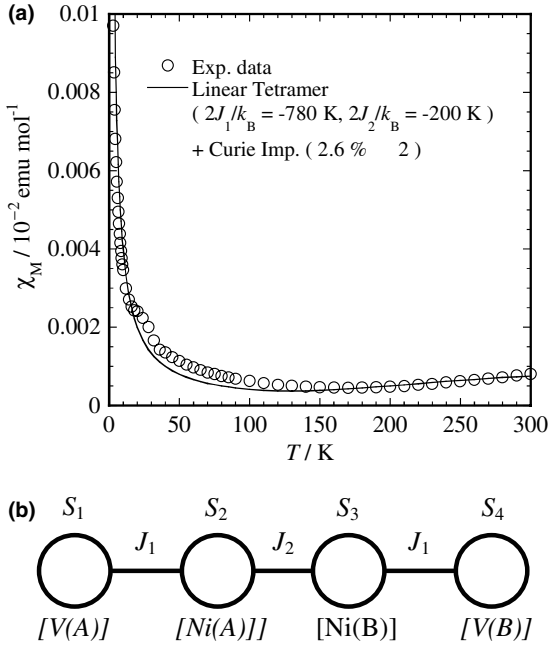


Fig. 7. (a) Temperature dependence of the magnetic susceptibility of salt **1**. The solid curve is the theoretical susceptibility calculated using Eq. (2) in [24]. (b) Scheme 1.

The χ_M of the $[p\text{-MePyDV}]^+[Ni(dmit)_2]_3^-$ salt (**5**) increases monotonically by lowering the temperature, and follows the Curie–Weiss law with $C = 0.684$ K emu/mol and $\theta = -17.0$ K.

4. Discussion

4.1. Magnetic properties of salts *1* and *3*

The χ_M of salt **1** is shown in Fig. 7. As described in a previous section, the $Ni(dmit)_2$ anion molecules in salt **1** form a dimer ($Ni(dmit)_2$ (A)–$Ni(dmit)_2$ (B)) with short intra-dimer contacts of ca. 3.6–3.7 Å, suggesting strong AFM exchange interaction. However, the χ_M of **1** can not be explained by a simple dimer model. In salt **1**, the dimer molecules are sandwiched between two verdazyl cation molecules, forming linear tetramer ($[p\text{-EtPyDV}]^+$ (A)–$[Ni(dmit)_2]^-$ (A)–$[Ni(dmit)_2]^-$ (B)–$[p\text{-EtPyDV}]^+$ (B)) (see Fig. 4 and Table 2). As described in a previous section, the verdazyl cation molecule in salt **1** has planar structure, and we can expect close contacts between verdazyl cation and $Ni(dmit)_2$ anion molecules. In fact, there are many short contacts between the Ni, S(i) and C(i) atoms in the $Ni(dmit)_2$ anions and the N(j) atoms (j = 1, 2, 3, and 4) in the hydrazidinyl moiety (N1–N2–C7–N3–N4–C8), having large unpaired spin densities, of verdazyl cations [17]. The result suggests strong exchange interaction between the verdazyl cation and the $Ni(dmit)_2$ anion molecules.

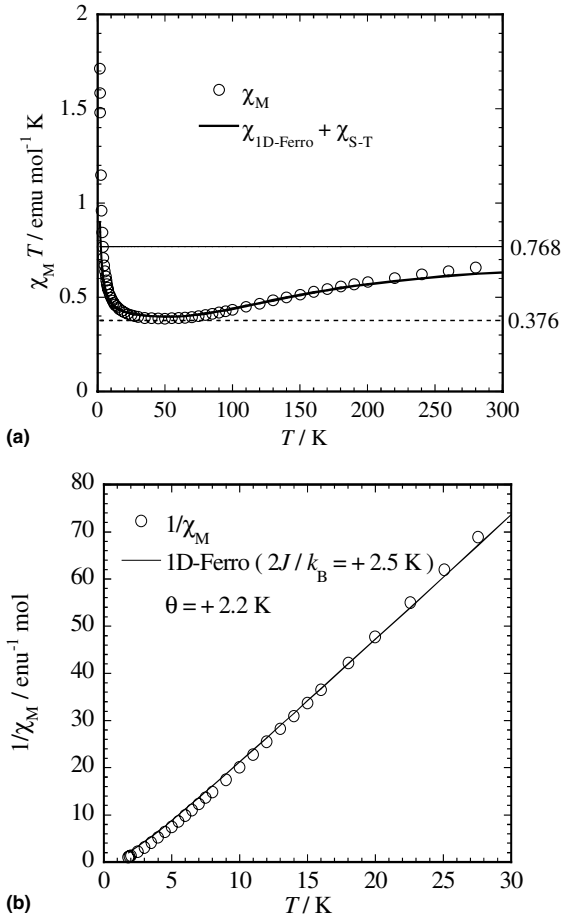


Fig. 8. (a) Temperature dependence of the product $\chi_M T$ (○) for salt **2**. The solid curve is the theoretical susceptibility calculated using Eq. (2). (b) Inverse molar magnetic susceptibility ($1/\chi_M$) of salt **2** at low temperatures. The observed values (open circles) obey the theoretical results for the 1D isotropic Heisenberg ferromagnet (Eq. (3)) with $2J/k_B$ = +2.5 K indicated by the solid line.

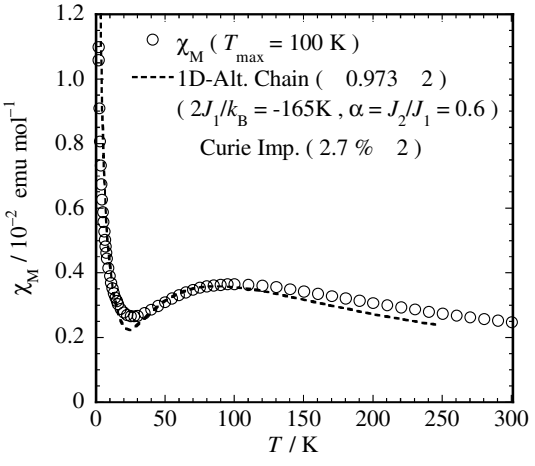


Fig. 9. Temperature dependence of the magnetic susceptibility (χ_M) (○) of salt **4**. The dashed curve is the theoretical susceptibility calculated by using Eq. (5).

In such a case, the χ_M of salt **1** may be explained by a four-spin Heisenberg Hamiltonian,

$$H = -2J_1(S_1S_2 + S_3S_4) - 2J_2S_2S_3,$$
$$S_1 = S_2 = S_3 = S_4 = 1/2, \quad (1)$$

where J_1 is the exchange interaction between an edge verdazyl cation and a central Ni(dmit)$_2$ anion and J_2 is the interaction between two central Ni(dmit)$_2$ anions. The model is shown in Fig. 7(b). This Hamiltonian has been solved exactly by Rubenacker et al. [24] to obtain the energy levels and magnetic susceptibility. Using the Eq. (2) in [24], we have fitted our data to this model, where the g-value (g = 2.0221 at 300 K) observed for salt **1** was used tentatively for the calculation of the susceptibility. The calculated susceptibility is shown by solid curve in Fig. 7(a). The best fit parameters obtained are $2J_1/k_B = -780$ K and $2J_2/k_B = -200$ K. The $2J_2/k_B$ value (−200 K) for the dimer is similar to that (−320 K) for the Ni(dmit)$_2$ dimer in salt **2**, as described later. The Ni(dmit)$_2$ (A) molecule connects with the Ni(dmit)$_2$ (C) molecule with short inter-dimer S···S contacts (see Fig. 4 and Table 2). Therefore, we can expect some interaction between two Ni(dmit)$_2$ molecules (A) and (C). The difference between the experimental and theoretical values of susceptibility of salt **1** may be due to such an interaction.

The susceptibility of the [*p*-MePyDP]$^+$[Ni(dmit)$_2$]$^-$ salt (**3**) is similar to that of salt **1**. The result suggests that salt **3** also forms a magnetic linear tetramer as observed for salt **1**.

4.2. Magnetic property of salt 2

The susceptibility of salt **2** can be explained by the two term contributions (Eq. (2)).

$$\chi_M = \chi_{1D\text{-}Ferro} + \chi_{S\text{–}T}, \quad (2)$$

where the first and second terms represent the contributions from quasi one-dimensional (1D) FM Heisenberg linear-chain system [25] and singlet–triplet (S–T) equilibrium system, respectively. $\chi_{1D\text{-}Ferro}$ and $\chi_{S\text{–}T}$ are given by Eqs. (3) and (4), respectively.

$$\chi_{1D\text{-}Ferro} = (N_o g^2 \mu_B^2 / 4k_B T)[1 + (J/k_B T)], \quad (3)$$

$$\chi_{S\text{–}T} = (N_o g^2 \mu_B^2 / k_B T)[1/(3 + e^{-2J/k_B T})]. \quad (4)$$

The susceptibility of salt **2** follows the Curie–Weiss law with positive Weiss constant of +2.2 K in the temperature region between 10 and 40 K. A plot of $1/\chi_M$ against T is no longer linear at low temperature (<10 K). Therefore, the low-temperature behavior of the susceptibility of salt **2** was analyzed on the basis of the quasi-1D FM Heisenberg model. In fact, the susceptibilities of salt **2** below 40 K are well reproduced by Eq. (3) with $2J/k_B$ = +2.5 ± 1.0 K and g = 2.00, as shown in Fig. 8(b). Above ca. 50 K, however, χ_MT increases with increasing

temperature, as shown in Fig. 8(a). This increase indicates that thermal magnetic excitation occurs in addition to the 1D FM linear-chain spins. The experimental data are interpreted by the S–T model (Eq. (4)) with $2J/k_B = -320$ K. As shown in Fig. 8(a), the experimental curve can be well reproduced by Eq. (2).

4.3. Magnetic property of salt 4

The susceptibility of salt **4** shows a broad maximum at $T_{max} = 100 \pm 2$ K. The susceptibility of **4** can be well explained by the sum of the two contributions;

$$\chi_M = C_{1D\text{-}Alt}\chi_{1D\text{-}Alt} + C_{Curie}\chi_{Curie}, \quad (5)$$

where $C_{1D\text{-}Alt} + C_{Curie} = 2$, and the first and second terms represent the contributions from the 1D AFM Heisenberg alternating-chain system [26] and from the Curie impurity, respectively. C_i is the fraction of each term. The dashed curve in Fig. 9 is a theoretical curve with $C_{1D\text{-}Alt} = 2 \times 0.973$ and $C_{Curie} = 2 \times 0.027$ and $2J_1/k_B = -165$ K (alternation parameter $\alpha = J_2/J_1 = 0.6$). The result shows that both the spins of verdazyl cation and $Ni(dmit)_2$ anion contribute to the magnetism of salt **4**.

4.4. Conducting properties of salts 1–5

Recently, we prepared several kinds of (1:1) and (1:3) salts of open-shell 6-oxoverdazyl radical cations with $Ni(dmit)_2$ anion, and found that the (1:3) salts are molecular paramagnetic semiconductors [18,19]. On the other hand, the (1:1) salts showed the property as paramagnetic insulators, as observed for the usual (1:1) salts of $Ni(dmit)_2$ anion with closed-shell electron donor cations, such as tetra-alkyl-ammonium cations, alkali metal cations, etc [6,7].

However, in the present work, all the (1:1) salts **1**–**4** studied were found to be semiconductors, against to our expectation. As described above, salt **1** forms a magnetic linear tetramer in which the strong exchange interaction between $Ni(dmit)_2$ (A) and verdazyl (B) spins in addition to that between $Ni(dmit)_2$ (A) and (B) spins was observed. Such an interaction will induce a delocalization of conduction electron from $Ni(dmit)_2$ dimer moieties to verdazyl moieties, and, thus, a decrease in the on-site Coulomb repulsion. Further, comparatively short S–S contacts were observed between $Ni(dmit)_2$ (A) and (C) anions, as listed in Table 2. As a result, salt **1** may show semiconductive behavior. Salt **3** showed the magnetic property similar to that of salt **1**. Further, strong interaction between verdazyl cation and $Ni(dmit)_2$ anion was observed for salt **4**, suggesting a decrease in the on-site Coulomb repulsion in **4**. The crystal structure analyses will be necessary to discuss the details of the semiconductive behavior observed for the (1:1) salts **2**–**4**. On the other hand, the conductivity of the (1:3) salt **5** at 20 °C was $\sigma = 1.0$ S cm^{-1} with an activation energy $E_A = 0.048$ eV. This value is three to five orders of magnitude larger than those of the (1:1) salts **1**–**4**.

The examples of the organic/inorganic hybrid system which shows the magnetism and conductivity are very limited, because of the difficulty in molecular design of the complexes. The present work provides five examples of new molecular magnetic semiconductors consisting of open-shell verdazyl radical cation and metal complex anion. Especially, FM interaction was observed for salt **2** at 1.8–40 K. We may expect FM order for salt **2** at lower temperature.

5. Supplementary material

Crystallographic data for the structural analysis have been deposited with the Cambridge Crystallographic Data Centre, deposition number CCDC No. 249719. Copies of this information may be obtained free of charge from: The Director, CCDC, 12 Union Road, Cambridge CB2 1EZ, UK, fax: +44 1223 336 033, e-mail: deposit@ccdc.cam.ac.uk or www: http://www.ccdc.cam.ac.uk), or on the web http://www.ccdc.cam.ac.uk.

Acknowledgements

We are very grateful to Prof. Yohji Misaki and Dr. Masateru Taniguchi of Kyoto University for their kind help in the measurement of conductivity of salts **2** and **3**. We are also very grateful to Prof. Katsuya Inoue and Dr. Kentaro Suzuki of Institute for Molecular Science for their kind help in SQUID measurement. This work was partly supported by the Grant-in-Aid for Scientific Research on Priority Areas (B) of Molecular Conductors and Magnets (Area No. 730/11224205) from the Ministry of Education, Science, Sports and Culture, Japan. This work was partly supported by the Joint Study Program (2002–2003) of the Institute for Molecular Science.

References

[1] M. Kurmoo, A.W. Graham, P. Day, S.J. Coles, M.B. Hursthouse, J.L. Caulfield, J. Singleton, F.L. Pratt, W. Hayes, L. Ducasse, P. Guionneau, J. Am. Chem. Soc. 117 (1995) 12,209.
[2] E. Ojima, H. Fujiwara, K. Kato, H. Kobayashi, H. Tanaka, A. Kobayashi, M. Tokumoto, P. Cassoux, J. Am. Chem. Soc. 121 (1999) 5581.
[3] E. Coronado, J.R. Galan-Mascaros, C.J. Gomez-Garcia, V. Laukhin, Nature 408 (2000) 447.
[4] H. Fujiwara, E. Fujiwara, Y. Nakazawa, B.Z. Narymbetov, K. Kato, H. Kobayashi, A. Kobayashi, M. Tokumoto, P. Cassoux, J. Am. Chem. Soc. 123 (2001) 306.
[5] L. Martin, S.S. Turner, P. Day, P. Guionneau, J.K. Howard, D.E. Hibbs, M.E. Light, M.B. Hursthouse, M. Uruichi, K. Yakusi, Inorg. Chem. 40 (2001) 1363.
[6] P. Cassoux, L. Valade, H. Kobayashi, A. Kobayashi, R.A. Clark, A.E. Underhill, Coord. Chem. Rev. 110 (1991) 115.

[7] A.E. Pullen, R.-M. Olk, Coord. Chem. Rev. 188 (1999) 211, and references are cited therein.
[8] H. Imai, H. Otsuka, T. Naito, K. Awaga, T. Inabe, J. Am. Chem. Soc. 121 (1999) 8098.
[9] S. Aonuma, H. Casellas, C. Faulmann, B. Garreau de Bonneval, I. Malfant, P. Cassoux, P.G. Lacroix, Y. Hosokoshi, K. Inoue, J. Mater. Chem. 11 (2001) 337.
[10] R. Kuhn, F.A. Neugebauer, H. Trischmann, Angew. Chem. 67 (1964) 691.
[11] K. Mukai, K. Konishi, K. Nedachi, K. Takeda, J. Phys. Chem. 100 (1996) 9658.
[12] R.K. Kremer, B. Kanellakopulos, P. Bele, H. Brunner, F.A. Neugebauer, Chem. Phys. Lett. 230 (1994) 255.
[13] S. Tomiyoshi, T. Yano, N. Azuma, M. Shoga, K. Yamada, J. Yamauchi, Phys. Rev. B 49 (1994) 16031.
[14] M. Mito, H. Nakano, T. Kawae, M. Hitaka, S. Takagi, H. Deguchi, K. Suzuki, K. Mukai, K. Takeda, J. Phys. Soc. Jpn. 66 (1997) 2147.
[15] K. Mukai, Y. Shimobe, J.B. Jamali, N. Achiwa, J. Phys. Chem. B 103 (1999) 10876.
[16] K. Mukai, M. Yanagimoto, S. Tanaka, M. Mito, T. Kawae, K. Takeda, J. Phys. Soc. Jpn. 72 (2003) 2312.
[17] K. Mukai, M. Matsubara, H. Hisatou, Y. Hosokoshi, K. Inoue, N. Azuma, J. Phys. Chem. B 106 (2002) 8632.
[18] K. Mukai, T. Hatanaka, N. Senba, T. Nakayashiki, Y. Misaki, K. Tanaka, K. Ueda, T. Sugimoto, N. Azuma, Inorg. Chem. 41 (2002) 5066.
[19] K. Mukai, N. Senba, T. Hatanaka, H. Minakuchi, K. Ohara, M. Taniguchi, Y. Misaki, Y. Hosokoshi, K. Inoue, N. Azuma, Inorg. Chem. 43 (2004) 566.
[20] K. Mukai, S. Jinno, Y. Shimobe, N. Azuma, Y. Hosokoshi, K. Inoue, M. Taniguchi, Y. Misaki, K. Tanaka, Polyhedron 20 (2001) 1537.
[21] K. Mukai, S. Jinno, Y. Shimobe, N. Azuma, M. Taniguchi, Y. Misaki, K. Tanaka, K. Inoue, Y. Hosokoshi, J. Mater. Chem. 13 (2003) 1614.
[22] D.E. Williams, Acta Crystallogr., Sect. B 29 (1975) 96.
[23] O. Lindqvist, L. Anderson, J. Sieler, G. Steimecke, E. Hoyer, Acta Chem. Scand., Ser. A 36 (1982) 855.
[24] G.V. Rubenacker, J.E. Drumheller, K. Emerson, R.D. Willet, J. Magn. Magn. Mater. 54 (1986) 1483.
[25] J.C. Bonner, M.E. Fisher, Phys. Rev. 135 (1964) A640.
[26] J.C. Bonner, H.W.J. Blote, J.W. Bray, I.S. Jacobs, J. Appl. Phys. 50 (1979) 1810.

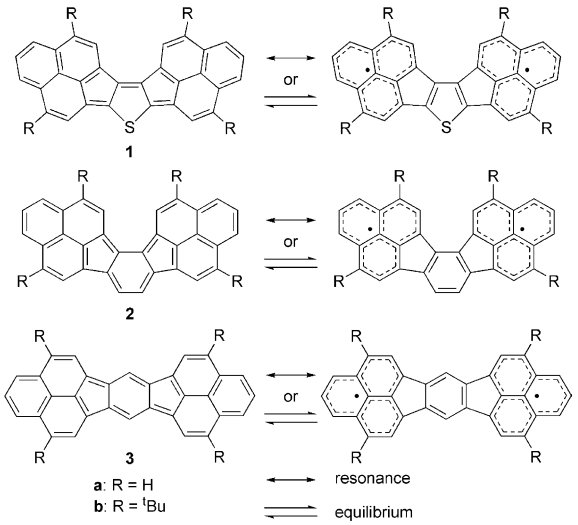


Fig. 1. Kekulé and biradical structures of phenalenyl-based amphoteric redox compounds.

Yanagimoto P1100 spectrometer. Cyclic voltammogram of the compound was recorded with glassy carbon working electrode and Pt counter electrode in CH_2Cl_2 containing 0.1 M $(n\text{-}Bu)_4NClO_4$ as the supporting electrolyte. The experiments employed a saturated calomel electrode (SCE) as a reference. Electrochemical experiments were done under an argon atmosphere at room temperature. For the X-ray crsytal structure analysis, data collection were performed on Enraf-Nonius CAD-4 diffractometer (Mo Kα, $\lambda = 0.71069$ Å) at 9 K for **1** and on Rigaku AFC7R diffractometer (Mo Kα, $\lambda = 0.71069$ Å) at rt for **3**.

2.1. Computational detail

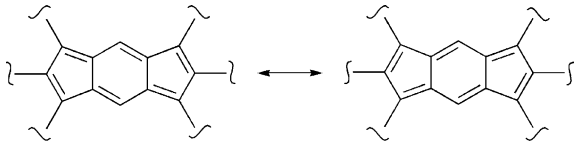
All calculations reported in this paper were performed with the GAUSSIAN 98 program [6]. All geometry optimizations were carried out at the B3LYP level of density functional theory with the 6-31G** basis set. Excitation energy was computed using time-dependent density funcutional theory (TD-RB3LYP) with 6-31G** basis set in the RB3LYP optimized geometry. Singlet biradical character was estimated with the symmetry-broken UB3LYP/6-31G** method with a geometry optimization and with the CASSCF(2,2) method in the RB3LYP optimized geometry.

3. Results and discussion

3.1. Calculated biradicaloid character of *1a–3a*

3.1.1. Closed- and open-shell singlet state

Optimization at the RB3LYP/6-31G** level gave structures in C_{2v}, C_{2v}, and D_{2h} symmetry for **1a**, **2a**, and **3a**, respectively. Strong bond alternations are observed in the central conjugated rings for **1a** and **2a** as shown in Fig. 2 (Kekulé structure). In the restricted DFT solution, thienoquinodimethane and *o*-quinodimethane structures contribute largely to the ground electronic state in **1a** and **2a**. In the case of **3a**, the bond alternation is slightly reduced due to the resonance of the following structures.



However, *p*-quinodimethane structure would contribute to the ground electronic state in **3a**. The RDFT calculations of **1a**–**3a** reveal quite small HOMO–LUMO gaps; 1.238, 0.851, 1.251 eV for **1a**, **2a**, and **3a**, respectively. As shown in Fig. 3, the frontier orbitals of **1a**–**3a** retain the NBMO character of phenalenyl radical and the spatial overlap between HOMO and LUMO are quite large.

As mentioned above, quinoid compounds tend to show biradicaloid characters. The contribution of quinoid structures to the ground electronic state of **1a**–**3a** will lead to the biradicaloid character for **1a**–**3a**. The frontier orbitals of **1a**–**3a** support this idea. For a compound with a large spatial overlap and a small energy gap between HOMO and LUMO, a large exchange

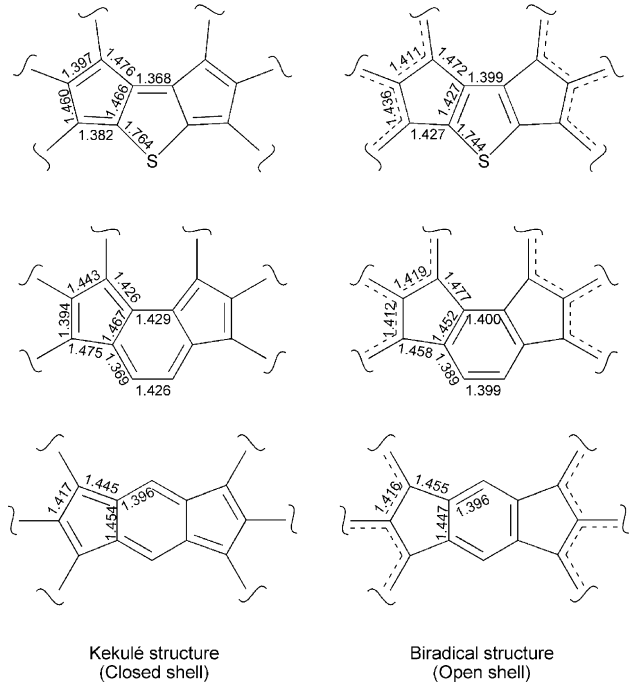


Fig. 2. Calculated geometries of closed- and open-shell singlet state for **1a**–**3a**.

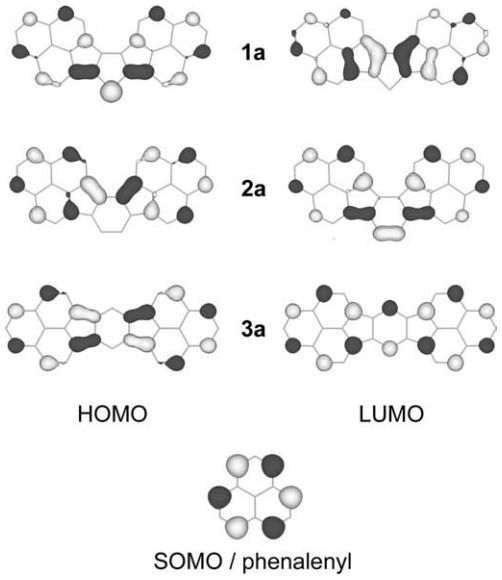


Fig. 3. Molecular orbitals of **1a**–**3a** and phenalenyl radical calculated with RB3LYP/6-31G**.

interaction ($K_{H,L}$) of the frontier orbitals is expected and should lead to a pronounced biradical character of the system. Whereas the exchange interaction $K_{H,L}$ is generally related to the stabilization of a triplet biradical state, a large $K_{H,L}$ will also contribute to the substantial admixture of a doubly excited configuration into a ground state configuration, i.e. a singlet biradical character [7].

The singlet biradical character of a molecule can be estimated by the energy-lowering of the symmetry broken unrestricted DFT solution compared to the restricted DFT solution [8]. The broken symmetry UB3LYP/6-31G** calculation of **1a**–**3a** with the re-optimized geometries gave the substantial energy lowering as summarized in Table 1. The open-shell UB3LYP solutions are 6.42–35.38 kJ/mol below the closed-shell RB3LYP solutions. Natural orbital analysis of the broken symmetry UB3LYP solution reveals the LUMO-occupation numbers of 0.72, 0.99, and 0.37 for **1a**, **2a**, and **3a**, respectively. These occupation numbers suggest the order of increasing biradicaloid character as **3a** < **1a** < **2a** [11]. Qualitatively similar trend is found in the spin contamination $\langle S^2\rangle$. The molecular geometries of **1a**–**3a** show the reduced bond alternations and the revival of aromaticity in the central thiophene and benzene ring. The averaged bond length between the central aromatic ring and the phenalenyl moieties become close to that of the sp^2–sp^2 single bond (1.48 Å). Spin densities of the open-shell singlet (singlet biradical) state of **1a**–**3a** show a similar distribution pattern to that of phenalenyl radical (Fig. 4). Unpaired electrons mainly reside on the two phenalenyl moieties with anti-parallel spins in the each molecule. These findings indicate that phenalenyl-based amphoteric redox compounds **1a**–**3a** possess the singlet biradical character in the ground state, which is best described as the resonance structure of Kekulé and biradical form shown in Fig. 1.

Table 1
Energy gaps (kJ/mol) between the singlet and the triplet state, and the spin contamination of the open-shell singlet state and the triplet state

	1a	2a	3a
ΔE (CS–OS)[a]	7.08	35.38	6.42
$\langle S^2\rangle$[b]	1.01	1.09	0.65
ΔE (T–OS)[c]	3.99	0.96	29.56
$\langle S^2\rangle$[d]	2.07	2.07	2.08

[a] Closed-shell singlet (CS) minus open-shell singlet (OS) energy.
[b] Spin contamination of the open-shell singlet.
[c] Triplet (T) minus open-shell singlet energy. Open-shell singlet energies were scaled to correct for the spin contaminations in the singlet states using ΔE (T–OS)=ΔE (T–OS)^{unscaled} $\langle S^2\rangle_T/(\langle S^2\rangle_T - \langle S^2\rangle_{OS})$ [9,10].
[d] Spin contamination of the triplet.

3.1.2. Triplet state

A large exchange interaction ($K_{H,L}$) of the frontier orbitals lead to the stabilization of the triplet state. Table 1 shows the energy gap between the ground open-shell singlet and the excited triplet state of **1a**–**3a**. The ΔE (T–OS) of **1a** and **2a** are substantially small, whereas **3a** gives a relatively large gap. This implies the small preference for the promotion of an electron from the HOMO to the LUMO in **3a**. As mentioned above, the singlet biradical character of **3a** is smaller than those of **1a** and **2a**. These findings suggest the smaller biradicaloid character of **3a** in comparison with **1a**

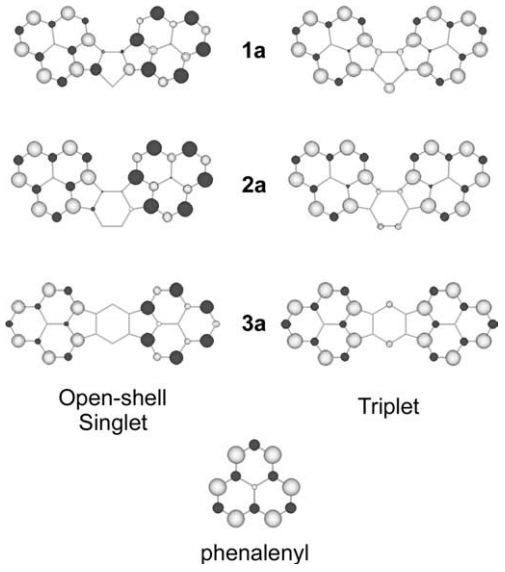


Fig. 4. Spin densities of open-shell singlet and triplet state for **1a**–**3a** along with that of phenalenyl radical (UB3LYP/6-31G**). Light and dark surfaces represent positive and negative spin densities, respectively.

and **2a**. One reason for the difference may be derived from the HOMO–LUMO gaps. TD-RB3LYP calculation for the singlet states (CS) gave the order of increasing transition energy as **2a** (0.614 eV) < **1a** (0.815 eV) ≪ **3a** (1.594 eV), which originated mainly from single-electron HOMO–LUMO excitations.

Unpaired electrons mainly reside on the two phenalenyl moieties with parallel spins in the each molecule (Fig. 4). Similar to the open-shell singlet states, the distribution pattern of the unpaired electrons for the excited triplet state is almost identical to that of phenalenyl radical. Thus, the triplet state is best described as the biradical form shown in Fig. 1.

3.2. Experimental biradicaloid character of *1b–3b*

In general, planer conjugated polycyclic compounds are sparingly soluble in most organic solvents. Furthermore, biradicaloid compounds are highly reactive species, which prevents the isolation and purification of the compounds. In order to overcome these negative aspects, we have introduced *tert*-butyl groups into the parent system of **1a**–**3a** [3–5].

3.2.1. Singlet state

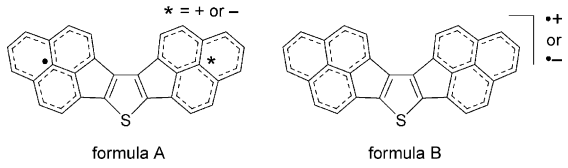
There are few ways of probing singlet biradical characters. ESR spectroscopy, which is a most powerful method for investigating open-shell species, usually gives a negative result for singlet biradical species due to the absence of signals. Cyclic voltammetry would provide suggestive information to the singlet biradical character, because electronic coupling of two unpaired electrons should be different between Kekulé and biradical structures. The Kekulé structure, in which two unpaired electrons are strongly coupled, will give the delocalized frontier orbitals over the entire molecules, which lead to a relatively large difference between the first and second redox potentials (ΔE^{ox} and ΔE^{red}, see Table 2) due to the on-site coulomb repulsion. On the other hand, the biradical structure, in which the electronic coupling is small or non-existing, will provide the frontier orbitals localized on the each radical moiety, which lead to substantially small ΔE^{ox} and ΔE^{red} values [12].

Table 2
Electrochemical data of amphoteric redox compounds (V vs. SCE)

	E_2^{ox}	E_1^{ox}	E_1^{red}	E_2^{red}	ΔE^{oxa}	ΔE^{redb}	E_1^{sumc}
1b	+0.94	+0.47	−0.53	−0.90	0.47	0.37	1.00
2b	+0.75	+0.42	−0.58	−0.96	0.33	0.38	1.00
3b	+0.84	+0.48	−0.67	−1.25	0.36	0.58	1.15

[a] $\Delta E^{ox} = E_2^{ox} - E_1^{ox}$.
[b] $\Delta E^{red} = E_1^{red} - E_2^{red}$.
[c] $E_1^{sum} = E_1^{ox} + (-E_1^{red})$.

The amphoteric redox compounds **1b**–**3b** shows the relatively large values for ΔE^{ox} and ΔE^{red}; indicating the strong coupling of the two electrons. The delocalization of the frontier orbitals could be estimated from the spin distribution pattern of the redox species, i.e. the radical cation and radical anion species of **1b**–**3b**. The ESR spectroscopy of the monovalent radical species revealed the spin delocalization over the entire molecules, which is best described as the formula B instead of the formula A.



formula A formula B

According to the Robin and Day scheme [13], the monovalent radical species of **1b**–**3b** can be placed in the class III category that includes fully-delocalized system. Thus the CV and ESR studies imply the large contribution of the Kekulé structure to the ground singlet state of **1b**–**3b**.

However, the trend of the calculated singlet biradicaloid character is qualitatively in line with those of the E_1^{sum} values and the HOMO–LUMO electron transition energies for **1b**–**3b**. The smallest biradicaloid **3b** shows the largest E_1^{sum} value (Table 2) and HOMO–LUMO transition energy (0.92, 1.00, and 1.64 eV for **1b**, **2b**, and **3b**, respectively). The largest HOMO–LUMO gap for **3b** may be responsible for the smallest biradicaloid character.

In contrast to the CV and ESR results, the indicative result for the singlet biradical contribution to the ground state has been obtained by X-ray crystallographic analysis for **1b**. The X-ray analysis reveals that **1b** forms two kinds of dimeric pairs with substantially short non-bonding contacts of ~3.1 Å between each thiophene rings as shown in Fig. 5. Terminal rings are separated by over 4.2 Å due to the steric repulsion between *tert*-Bu groups and six-membered rings. The van der Waals contact of carbon atoms only exists within central dicyclopenta[*b*; *d*]thiophene units. Attractive interaction for the dimerization should be an intermolecular charge-transfer (CT) interaction through the double excitation configuration $^1\Phi_{H,H\rightarrow L,L}$, i.e. a singlet biradical contribution. Based on the CASSCF(2,2) calculation of **1b**, the occupation numbers of HOMO and LUMO are 1.9 and 0.1, respectively. In this case, a LUMO–LUMO interaction will lead to a stabilization of the system, because a newly formed 'LUMO' of the dimer, which is more stabilized than the original LUMO, can accommodate at least 0.2 electron (Fig. 6). In addition, a HOMO–HOMO interaction seems to contribute the stabilization

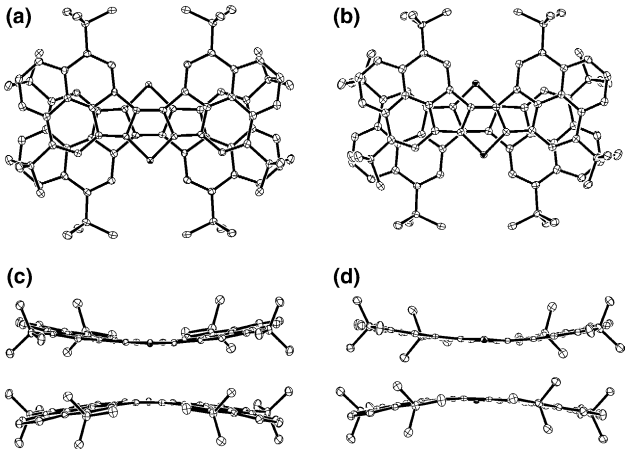


Fig. 5. Crystal structures of **1b**. Top view of the dimeric pair A (a) and B (b), and side view of the dimeric pair A (c) and B (d). Hydrogen atoms were omitted for clarity.

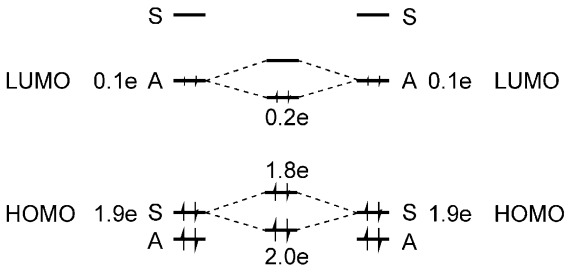


Fig. 6. Schematic drawing of the molecular orbital interaction of the dimeric **1b** through the double excitation configuration $^1\Phi_{H,H\rightarrow L,L}$. 'S' and 'A' denote the symmetry of the molecular orbitals.

of the system, because a newly formed 'HOMO' of the dimer would contain only 1.8 electrons, which result in the suppression of a four-electron repulsion generally arisen from the interaction between fully occupied orbitals.[1]

The large discrepancy is found in the LUMO occupation numbers between the broken-symmetry UB3LYP and the CASSCF(2,2) calculations (0.72e versus 0.1e) for **1a**. On the basis of the CV and ESR results, the UB3LYP calculation seems to overestimate the static electron correlation. The molecular geometry obtained by the X-ray analysis is almost in the middle point between the Kekulé and biradical structures calculated by the B3LYP method (Fig. 7). To estimate more accurate biradical characters, larger size of post HF calculations are highly demanded.

[1] In general, the π–π interaction of aromatic systems is affected by various electronic factors. The well-known attractive forces are derived from electrostatic interactions between electron-deficient and electron-rich sites. However, this interaction is not likely effective for the dimers of **1b**, because the overlap of positive and negative charges is small on the basis of the Mulliken charge analysis.

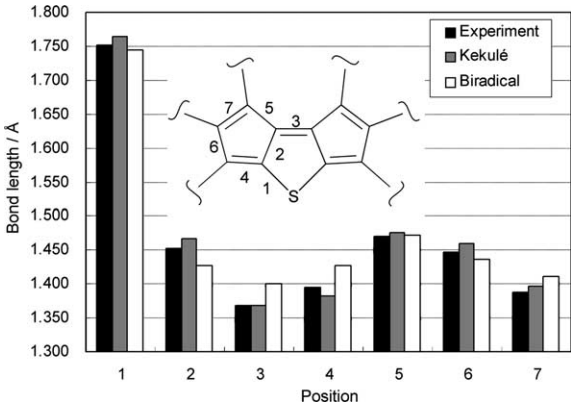


Fig. 7. Experimental and theoretical bond lengths of the central rings of **1b**. The experimental data are the averaged bond lengths.

3.2.2. Triplet state

As described above, **1a** and **2a** possess the substantially small energy gaps between the singlet and triplet state. This finding suggests that **1b** and **2b** should be in thermal equilibrium with triplet states even at room temperature. ^{1}H NMR spectra of **1b** and **2b** give no signals in the aromatic region at room temperature. Although on cooling a broad band appears in the aromatic region, sharp signals can not be obtained even at −90 °C. The equilibrium with the thermally accessible triplet state would cause the line broadening of the NMR signals. The ESR measurement of the solid **1b** affords typical spectra for triplet species ($|D|$ = 17.2 mT, $|E|$ = 3.9 mT) and temperature dependence of the half-field signal indicates the thermal excitation to the triplet state with the energy gap (ΔE_{S-T}) of ~5 kJ/mol. From the D value, the average distance between the two interacting spins can be estimated to be 5.5 Å, which is smaller than the intramolecular distance between the centers of the two phenalenyl moieties of **1b** (8.4 Å).

The less biradicaloid **3b** also shows the NMR signal broadening at room temperature. In contrast to **1b** and **2b**, on cooling to −30 °C the broad signals become sharp and four peaks appear at 7.69, 7.10, 7.04, and 6.98 ppm. The ESR spectrum of the solid **3b** affords the fine structure typical for triplet species ($|D|$ = 9.6 mT, $|E| \leqslant 0.2$ mT, ΔE_{S-T} = 20.4 kJ/mol) above room temperature.

4. Conclusion

The phenalenyl-based amphoteric redox compounds show appreciable biradicaloid characters. The most biradicaloid compounds are very reactive and then are observable only in a low-temperature matrix, whereas **1b**–**3b** can be isolated in air at room temperature. The difference of the stability should be arisen from the spin delocalization over the phenalenyl units. The connection

of two phenalenyl radical units with various quinoid compounds will lead to the wide variety of biradicaloid compounds isolable in air. The stable biradicaloid compounds will open the opportunity to investigate the solid state properties such as crystal packing, magnetism, and electro-conductive behavior on the basis of the new sort of idea.

Acknowledgement

This work is supported by a Grant-in-Aid for Scientific Research on Priority Areas (No. 15750034, and Area No. 769, Proposal No. 15087202) from the Ministry of Education, Culture, Sports, Science and Technology (MEXT), Japan.

References

[1] C.R. Flynn, J. Michl, J. Am. Chem. Soc. 96 (1974) 3280.
[2] Recent review K. Nakasuji, T. Kubo, Bull. Chem. Soc. Jpn. 77 (2004) 1791.
[3] T. Kubo, M. Sakamoto, M. Akabane, Y. Fujiwara, K. Yamamoto, M. Akita, K. Inoue, T. Takui, K. Nakasuji, Angew. Chem. Int. Ed. 43 (2004) 6474.
[4] T. Kubo, K. Yamamoto, K. Nakasuji, T. Takui, Tetrahedron Lett. 42 (2001) 7997.
[5] K. Ohashi, T. Kubo, T. Masui, K. Yamamoto, K. Nakasuji, T. Takui, Y. Kai, I. Murata, J. Am. Chem. Soc. 120 (1998) 2018.
[6] M.J. Frisch, G.W. Trucks, H.B. Schlegel, G.E. Scuseria, M.A. Robb, J.R. Cheeseman, V.G. Zakrzewski, J.A. Montgomery, Jr., R.E. Stratmann, J.C. Burant, S. Dapprich, J.M. Millam, A.D. Daniels, K.N. Kudin, M.C. Strain, O. Farkas, J. Tomasi, V. Barone, M. Cossi, R. Cammi, B. Mennucci, C. Pomelli, C. Adamo, S. Clifford, J. Ochterski, G.A. Petersson, P.Y. Ayala, Q. Cui, K. Morokuma, D.K. Malick, A.D. Rabuck, K. Raghavachari, J.B. Foresman, J. Cioslowski, J.V. Ortiz, A.G. Baboul, B.B. Stefanov, G. Liu, A. Liashenko, P. Piskorz, I. Komaromi, R. Gomperts, R.L. Martin, D.J. Fox, T. Keith, M.A. Al-Laham, C.Y. Peng, A. Nanayakkara, C. Gonzalez, M. Challacombe, P.M.W. Gill, B.G. Johnson, W. Chen, M.W. Wong, J.L. Andres, M. Head-Gordon, E.S. Replogle and J.A. Pople, Gaussian, Inc., Pittsburgh, PA, 1998.
[7] D.R. McMasters, J. Wirz, J. Am. Chem. Soc. 123 (2001) 238.
[8] V. Bachler, G. Olbrich, F. Neese, K. Wieghardt, Inorg. Chem. 41 (2002) 4179.
[9] K. Yamaguchi, F. Jensen, A. Dorigo, K.N. Houk, Chem. Phys. Lett. 149 (1988) 537.
[10] T. Soda, Y. Kitagawa, H. Onishi, Y. Takano, Y. Shigeta, H. Nagao, Y. Yoshioka, K. Yamaguchi, Chem. Phys. Lett. 319 (2000) 223.
[11] D. Döhnert, J. Koutecký, J. Am. Chem. Soc. 102 (1980) 1789.
[12] F.A. Cotton, J.P. Donahue, C.A. Murillo, J. Am. Chem. Soc. 125 (2003) 5436.
[13] M.B. Robin, P. Day, Adv. Inorg. Radiochem. 10 (1967) 247.

2.1. Preparation of *1–4*

The metal complexes (70 μmol) were dissolved in trifluoroacetic acid (5 mL). Ethanol of 5 mL was added to the solution and the mixture allowed to stand for a few days at 4 °C to give crystalline **1–4**. **1** (Yield 29%); m.p. >300 °C. *Anal.* Calc. for $C_{20}H_{24}F_6N_4O_4CuS_4$: C, 34.80; H, 3.50; N, 8.12. Found: C, 34.80; H, 3.48; N, 7.97%. **2** (Yield 50%); m.p. >300 °C. *Anal.* Calc. for $C_{20}H_{24}F_6N_4O_4NiS_4$: C, 35.05; H, 3.53; N, 8.17. Found: C, 35.19; H, 3.49; N, 7.92%. **3** (70%); m.p. >300 °C. *Anal.* Calc. for $C_{20}H_{24}F_6N_4O_4PdS_4$: C, 32.77; H, 3.30; N, 7.64. Found: C, 32.92; H, 3.28; N, 7.50%. **4** (Yield 50%); m.p. >300 °C. *Anal.* Calc. for $C_{20}H_{24}F_6N_4O_4PtS_4$: C, 29.23; H, 2.94; N, 6.82. Found: C, 29.56; H, 3.00; N, 6.68%.

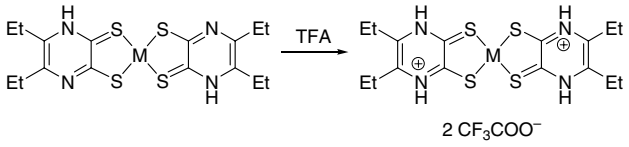
2.2. X-ray crystallography

Data collection were performed on Rigaku RAXIS-RAPID Imaging Plate (Mo Kα, $\lambda = 0.71069$ Å) for **1** and **2** and on Rigaku MSC Mercury CCD (Mo Kα, $\lambda = 0.71069$ Å) for **3** and **4**. The structure was solved with direct methods and refined with full-matrix least squares (SHELX-97). Crystalographic data are listed in Table 1.

3. Results and discussion

3.1. Preparation and crystal structure of *1–4*

The TFA-free metal complexes were dissolved in TFA–EtOH and were recrystallized at 4 °C to give X-ray quality single crystals **1–4** (Scheme 1). Complexes



Scheme 1. Preparation of **1–4**.

1–4 show almost same crystal structures with an extended two-dimensional hydrogen bonded network consisting of a crystallographically independent metal complex and bridging TFA linkers (Figs. 1, 2, and Table 2). Hydrogen atoms experimentally found on all nitrogen atoms of pyrazine rings form hydrogen bonds to the carboxy oxygen atoms of trifluoroacetate. The reduced bond alternation on the pyrazine rings are

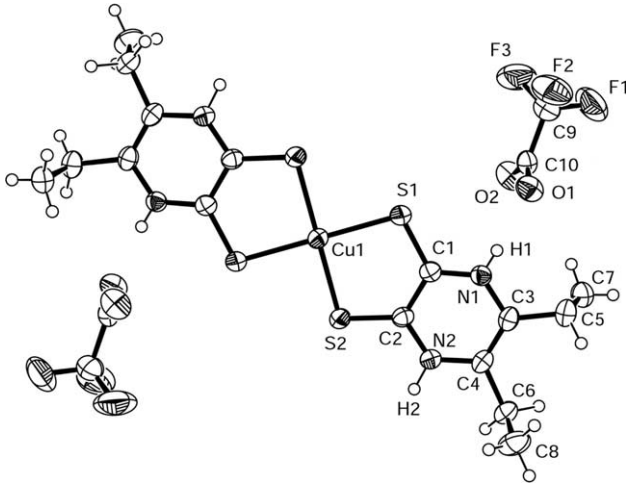


Fig. 1. ORTEP drawing of **1** with thermal ellipsoids drawn at 50% probability.

Table 1
Crystallographic data for **1–4**

Parameter	1	2	3	4
Formula	$C_{20}H_{24}CuF_6N_4O_4S_4$	$C_{20}H_{24}F_6N_4NiO_4S_4$	$C_{20}H_{24}F_6N_4O_4PdS_4$	$C_{20}H_{24}F_6N_4O_4PtS_4$
Formula weight	690.21	685.38	733.07	821.76
Crystal system	monoclinic	monoclinic	monoclinic	monoclinic
Space group	$P2_1/n$ (no. 14)	$P2_1/n$ (no. 14)	$P2_1/n$ (no. 14)	$P2_1/n$ (no. 14)
a (Å)	8.6077(1)	8.498(1)	8.612(3)	8.596(2)
b (Å)	13.6280(1)	13.663(1)	13.621(4)	13.690(3)
c (Å)	12.1470(6)	12.059(2)	12.175(4)	12.150(3)
β (°)	102.427(1)	101.641(3)	102.715(6)	103.081(5)
V (Å^3)	1391.54(7)	1371.5(3)	1393.2(8)	1392.7(6)
Z	2	2	2	2
T (K)	200	200	200	200
ρ_{calc}	1.647	1.660	1.747	1.960
μ (Mo Kα, cm^{-1})	1.160	1.088	1.041	5.413
Unique reflections ($I > 2\sigma$)	1543	2128	2192	2178
Number of parameters	178	178	178	178
Goodness-of-fit	1.095	1.023	0.875	0.900
R_1, wR_2 ($I > 2\sigma$)	0.0449, 0.0998	0.0572, 0.1123	0.0315, 0.0552	0.0248, 0.0438

$R_1 = \sum\|F_o| - |F_c\|/\sum|F_o|$; GOF $= [\sum[w(F_o^2 - F_c^2)^2]/(n-p)]^{1/2}$; $wR_2 = [\sum[w(F_o^2 - F_c^2)^2]/\sum[w(F_o^2)^2]]^{1/2}$, where $w = 1/\sigma^2(F_o^2) + (aP)^2 + bP$, $P = (F_o^2 + 2F_c^2)/3$.

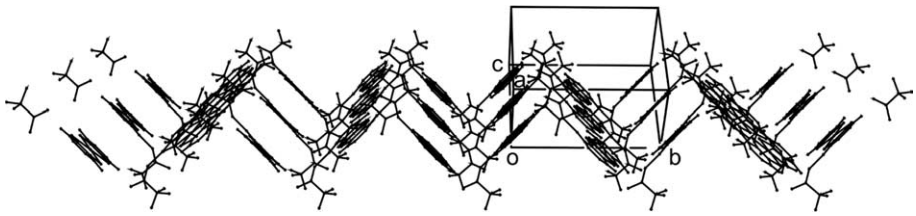


Fig. 2. Zigzag 2D sheet structure of **1**.

Table 2
Selected bond lengths and angles for **1**–**4**

	1	2	3	4
M–S2	2.265(1)	2.1694(9)	2.288(1)	2.284(1)
M–S1	2.267(1)	2.1710(9)	2.2886(9)	2.285(1)
S1–C1	1.691(4)	1.703(4)	1.705(3)	1.703(4)
S2–C2	1.686(4)	1.685(4)	1.693(3)	1.692(4)
N1–C1	1.336(6)	1.324(4)	1.343(3)	1.342(5)
N1–C3	1.367(6)	1.364(4)	1.373(3)	1.369(5)
N2–C2	1.352(5)	1.337(4)	1.344(3)	1.341(4)
N2–C4	1.377(6)	1.374(4)	1.376(3)	1.372(5)
C1–C2	1.435(6)	1.428(5)	1.426(4)	1.431(5)
C3–C4	1.354(6)	1.368(5)	1.353(4)	1.356(5)
S2–Ni1–S1	91.42(4)	92.74 (3)	90.17(3)	89.94(4)
C1–S1–Ni1	101.8(1)	103.1(1)	102.4(1)	102.7(1)
C2–S2–Ni1	101.5(1)	103.1(1)	102.5(1)	103.1(1)
C1–N1–C3	126.0(3)	124.6(3)	124.1(3)	124.1(3)
C2–N2–C4	124.5(3)	124.8(3)	124.9(3)	124.7(3)
N1–C1–C2	116.9(4)	118.2(3)	117.8(3)	117.5(3)
N1–C1–S1	121.3(3)	122.1(2)	120.3(2)	120.5(3)
C2–C1–S1	121.8(3)	119.7(3)	121.9(2)	121.9(3)
N2–C2–C1	116.6(4)	116.5(3)	116.7(3)	116.9(3)
N2–C2–S2	120.4(3)	122.4(2)	120.7(2)	121.1(3)
C1–C2–S2	123.0(3)	121.1(3)	122.6(2)	122.0(3)
N1–C3–C4	117.3(4)	118.1(3)	118.6(3)	118.7(3)
C3–C4–N2	118.7(4)	117.7(3)	118.0(3)	118.0(3)

observed for the protonated complexes **1**–**3** in comparison with the corresponding unprotonated complexes. Geometries for N–H ⋯ O, i.e. $d_{NH\cdots O}$ = 1.67 − 1.88 Å, $d_{N\cdots O}$ = 2.65 − 2.69 Å, θ_{N-H-O} = 166.1°–178.5°, are almost same as the values found in pyridine–carboxylic acid dimers [2]. The N ⋯ O distances of 2.65–2.69 Å indicate strong hydrogen bond interactions between the metal complexes and trifluoroacetate molecules. The four trifluoroacetate molecules binds to the one metal complex and the trifluoroacetate is hydrogen bonded to another metal complex. The two metal complexes are almost orthogonal, with an angle of about 89° between the two planes. Thus, the complexes **1**–**4** form the 2D zigzag sheet through hydrogen bonds.

Regarding the interaction between the 2D sheet, the trifluoroacetate molecules play an important role in binding the sheets as shown in Fig. 3. Negative trifluoroacetate molecules come close to the positive pyrazine rings whose charges are induced by protonation. An oxygen atom and three fluorine atoms of the trifluoroacetate point to the positive pyrazine ring. Table 3 shows the distance of C–F ⋯ π and C–O ⋯ π. To estimate the inter-

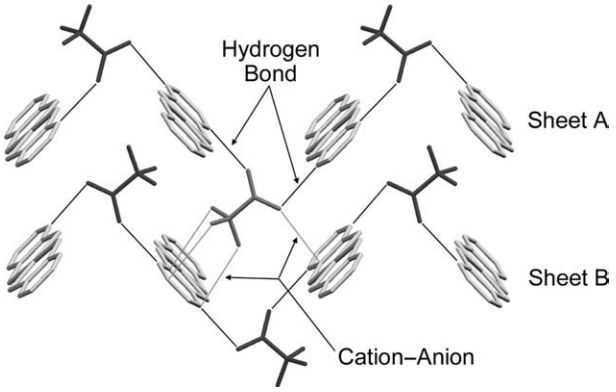


Fig. 3. Intra- and inter-sheet interaction of the 2D zigzag sheet of **1**. Et groups and hydrogen atoms are omitted for clarity.

Table 3
Distances (Å) of C–F ⋯ π and C–O ⋯ π of **1**–**4**

	1	2	3	4
C–F ⋯ π[a]	3.23	3.22	3.23	3.22
C–O ⋯ π	3.13	3.11	3.10	3.10

[a] The shortest C–F ⋯ π distances.

sheet interaction, electrostatic potential was calculated using the DFT method (UB3LYP/LANL2DZ). The electrostatic potential shown in Fig. 4 reveals that the pyrazine rings are more positive relative to the central MS_4 unit and Et groups. On the other hand, negative charges would reside on the F and O atoms of the trifluoroacetate molecules. This electrostatic interaction (cation–anion) is responsible for stacking of the 2D sheets.

3.2. Magnetic behavior of *1*

As described above, hydrogen bond has been extensively demonstrated not only to be a useful tool for



Fig. 4. Electrostatic potential surface for **1** calculated with UB3LYP/LANL2DZ: More positive site (dark), less positive site (light).

crystal engineering but also to propagate ferromagnetic interactions. To estimate magnetic exchange coupling through TFA, the magnetic susceptibility measurement of **1** was carried out using a SQUID magnetometer at 2–290 K. The χT value at room temperature equals 0.381 emu K mol^{-1}, which is close to the calculated value for uncorrelated $S = 1/2$ spins. In the whole temperature range the χT value shows no dramatic changes, indicating the absence of strong magnetic interactions between the Cu complexes (Fig. 5). The DFT calculation (UB3LYP/LANL2DZ) of the Cu complex surrounded by eight trifluoroacetate molecules indicates that an unpaired electron resides mainly on the central CuS_4 unit (93%) and that no spin density is localized on oxygen atoms of the trifluoroacetate (<1%). Fig. 6 shows the spin density of **1** · 8TFA. Furthermore, long Cu–Cu distance of 8.61 Å and no van der Waals contact between the CuS_4 units prevent strong magnetic interactions. The absence of the strong magnetic interaction results in the isolated spin sites. Thus, the Cu complex **1** shows paramagnetic behavior at 2–290 K.

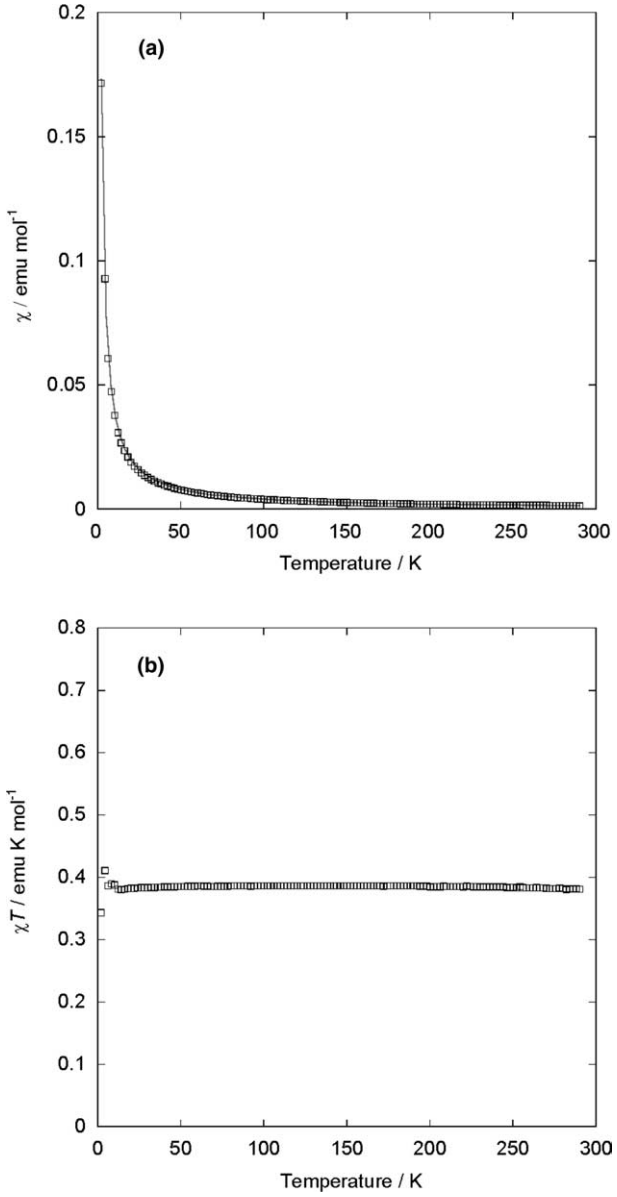


Fig. 5. Temperature dependence of the magnetic susceptibility of **1**. (a) χ–T plot and (b) χT–T plot.

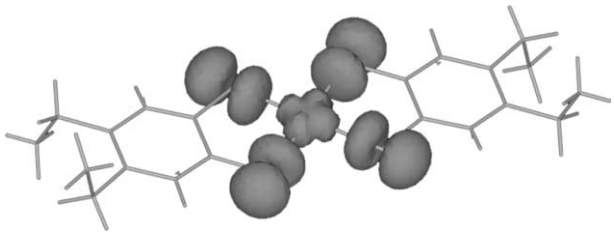


Fig. 6. Spin density of **1** · 8TFA. TFA molecules are omitted for clarity.

4. Conclusions

The bis(pyrazinedithiolate)metal complex have formed the 2D zigzag sheet structure bridged by trifluoroacetic acid molecules. The SQUID measurement has revealed that the Cu complex shows the paramagnetic behavior. The DFT calculation has suggested the spin localization on the CuS_4 core with no contribution of TFA molecules to propagating the spin.

5. Supplementary material

Crystallographic data for the structural analyses have been deposited with the Cambridge Crystallographic Data Centre, CCDC Nos. 200418, 200419, 200420, and 200421. Copies of this information may be obtained free of charge from The Director, CCDC, 12 Union Road, Cambridge, CB2 1EZ, UK (fax: +44 1223 336 033; e-mail: deposit@ccdc.cam.ac.uk or www: http://www.ccdc.cam.ac.uk).

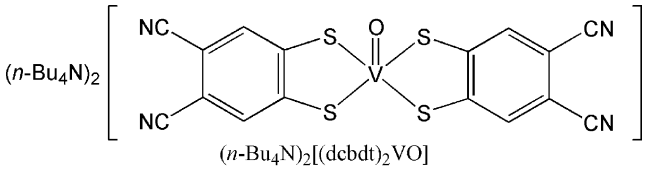
Acknowledgment

This work is supported by a Grant-in-Aid for Scientific Research on Priority Areas (No. 15750034, and Area No. 769, Proposal No. 15087202) from the Ministry of Education, Culture, Sports, Science and Technology (MEXT), Japan.

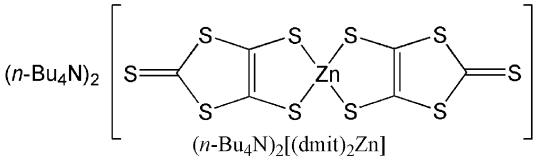
References

[1] D. Gatteschi, Adv. Mater. 6 (1994) 635.
[2] M. Kinoshita, Jpn. J. Appl. Phys. 33 (1994) 5718.

[3] H.O. Stumpf, L. Ouahab, Y. Pei, D. Grandjean, O. Kahn, Science 261 (1993) 447.
[4] T. Steiner, Angew. Chem. Int. Ed. 41 (2002) 48.
[5] E. Bosch, R. Radford, C.L. Barnes, Org. Lett. 3 (2001) 881.
[6] P.J. Fagan, M.D. Ward, Perspectives Supramol. Chem. 2 (1996) 107.
[7] P. Metrangolo, G. Resnati, Chem. Eur. J. 7 (2001) 2511.
[8] C.G. Claessens, J.F. Stoddart, J. Phys. Org. Chem. 10 (1997) 254.
[9] D.A. Dougherty, Science 271 (1996) 163.
[10] J.C. Ma, D.A. Dougherty, Chem. Rev. 97 (1997) 1303.
[11] G.W. Gokel, S.L.D. Wall, E.S. Meadows, Eur. J. Org. Chem. (2000) 2967.
[12] J. Veciana, J. Cirujeda, C. Rovira, J.V. Gancedo, Adv. Mater. 7 (1995) 221.
[13] M.M. Matsushuta, A. Izuoka, T. Sugawara, T. Kobayashi, N. Wada, N. Takeda, M. Ishikawa, J. Am. Chem. Soc. 119 (1997) 4369.
[14] H. Muhonen, Inorg. Chem. 25 (1986) 4692.
[15] T. Kubo, M. Ohashi, K. Miyazaki, A. Ichimura, K. Nakasuji, Inorg. Chem. 43 (2004) 7301.
[16] M.J. Frisch, G.W. Trucks, H.B. Schlegel, G.E. Scuseria, M.A. Robb, J.R. Cheeseman, V.G. Zakrzewski, J.A. Montgomery, R.E. Stratmann, J.C. Burant, S. Dapprich, J.M. Millam, A.D. Daniels, K.N. Kudin, M.C. Strain, O. Farkas, J. Tomasi, V. Barone, M. Cossi, R. Cammi, B. Mennucci, C. Pomelli, C. Adamo, S. Clifford, J. Ochterski, G.A. Petersson, P.Y. Ayala, Q. Cui, K. Morokuma, D.K. Malick, A.D. Rabuck, K. Raghavachari, J.B. Foresman, J. Cioslowski, J.V. Ortiz, B.B. Stefanov, G. Liu, A. Liashenko, P. Piskorz, I. Komaromi, R. Gomperts, R.L. Martin, D.J. Fox, T. Keith, M.A. Al-Laham, C.Y. Peng, A. Nanayakkara, C. Gonzalez, M. Challacombe, P.M.W. Gill, B. Johnson, W. Chen, M.W. Wong, J.L. Andres, C. Gonzalez, M. Head-Gordon, E.S. Replogle, J.A. Pople, GAUSSIAN-98 (Revision A.6), Gaussian Inc., Pittsburgh, PA, 1998.



$(n\text{-Bu}_4\text{N})_2[(\text{dcbdt})_2\text{VO}]$



$(n\text{-Bu}_4\text{N})_2[(\text{dmit})_2\text{Zn}]$

Scheme 1.

2. Experimental

$(n\text{-Bu}_4\text{N})_2[(\text{dmit})_2\text{Zn}]$ was used as purchased from Tokyo-Kasei Ltd. $(n\text{-Bu}_4\text{N})_2[(\text{dcbdt})_2\text{VO}]$ was prepared as follows. 4,5-dicyanobenzene-1,2-dithiol (H_2dcbdt) (135.0 mg, 0.702 mmol) prepared in accordance with the literature [9] was dissolved in 5 ml methanol solution of NaOMe (83.4 mg, 1.54 mmol). To this solution, a solution of anhydrous VCl_3 (55.2 mg, 0.35 mmol) in 5 ml of tetrahydrofuran was added and exposure of this solution to air. After exposure for 30 min n-Bu_4NBr (905.2 mg, 2.81 mmol) was added. The dropwise addition of 20 ml of water caused the product to precipitate as light brown powder. This precipitate were recrystallized from acetone–i-PrOH (1:2) and dried in air to give 283.5 mg (87%) of product. The composition of $(n\text{-Bu}_4\text{N})_2[(\text{dcbdt})_2\text{VO}]$ was determined by X-ray structure analysis [8].

Silicon (Si (1 0 0)) (Shin-etsu Silicon, Japan), magnesium oxide and glass (Matsunami, Japan) substrates were used as purchased. Dipping process was performed as follows. A solution of bisdithiolene metal complexes (1.0×10^{-2} mol) in freshly distilled acetone (2.5 ml) was introduced into a weighing bottle. To this bottle, substrates were dipped under ambient and highly humidified condition. Deposits of corresponding bisdithiolene metal complexes grew on the surface of several substrates during solvent evaporation.

The deposits were examined with an analytic scanning electron microscope (JSM-6360LA, JEOL Ltd.) and a scanning probe microscope (SPI 3700, SII Nanotechnology Inc.).

3. Results and discussion

An X-ray structure analysis indicated that $[(\text{dcbdt})_2\text{VO}]$ moieties were surrounded by n-Bu_4N cations and there was no direct interaction among these moieties. Although there was no direct interaction among them, several S···H, C···H and N···H van der Waals contacts between n-Bu_4N cations and $[(\text{dcbdt})_2\text{VO}]$ moieties were observed. The ESR and SQUID measurement showed that the vanadium atom is in the state of V(IV) ($S = 1/2$) and these magnetic moments interacted with each other very weakly antiferromagnetically (−0.371 K of Weiss temperature). The detail of molecular and crystal structure, and magnetic properties of newly obtained $(n\text{-Bu}_4\text{N})_2[(\text{dcbdt})_2\text{VO}]$ have been reported separately [8].

Fig. 1 shows SEM images of the $(n\text{-Bu}_4\text{N})_2[(\text{dmit})_2\text{Zn}]$ deposits on a polished surface of silicon substrates. The shapes of deposits are largely affected by the experimental conditions. The deposits of this complex is formed by well defined diamond and hexagonal shaped micro-sized (almost millimeter sized) crystals under ambient condition (Fig. 1(a)). On the other hand, the deposits under highly humidified condition consist of

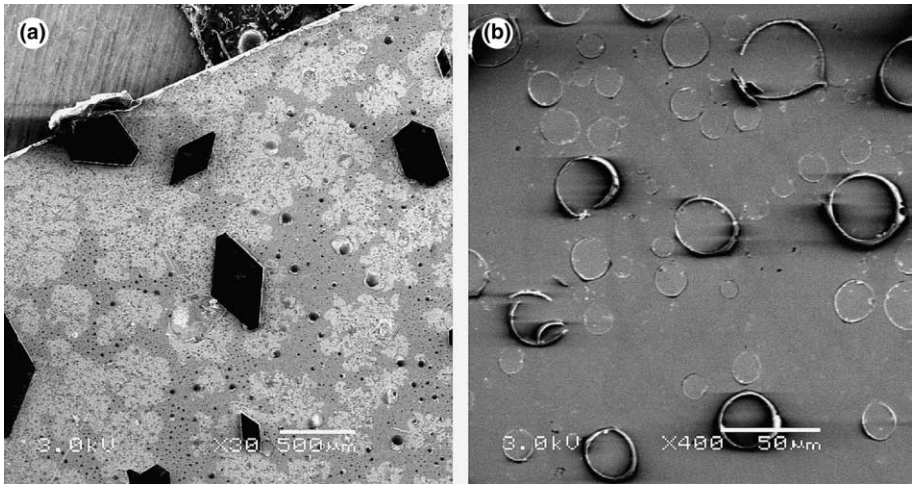


Fig. 1. SEM images of deposits of $(n\text{-Bu}_4\text{N})_2[(\text{dmit})_2\text{Zn}]$ on a polished surface of silicon substrates under (a) ambient and (b) highly humidified conditions.

micro-scale rings. The internal and external diameter lies from 10 and 30 μm, and from 15 to 40 μm (Fig. 1(b)).

On the contrary to the zinc complex, deposits of (n-$Bu_4N)_2$[$(dcbdt)_2VO$] show quite different morphologies under ambient condition. On glass substrate prismatic micro-crystals are observed under an optical microscope as was seen from the deposits of the zinc complex. SEM images of the micro-crystals show that a lot of micro-scale porous structures exist on the surface of it (Fig. 2). The diameter of these pores lies from 2 to 180 μm. On magnesium oxide substrate the deposit consists of bead structures with a diameter around 5 μm (Fig. 3). When a non-polished surface of a silicon substrate is used, the surface is covered with a two-dimensional network (Fig. 4). Furthermore when a polished surface of silicon substrates is used, two kinds of morphologies are observed (Fig. 5(a)). One of them is a needle like micro-crystal with the thickness of 5–8 μm and the length of 20–150 μm (Fig. 5(b)). The other one is a micro-scale ring (Fig. 5(c)). The internal diameter lies from 1 to 10 μm and the external diameter lies from 10 to 20 μm. The AFM image reveals that the micro-scale ring with a diameter of 20 μm has 640 nm thickness. Same procedure under highly humidified condition diminish the size of the micro-scale rings. Mainly obtained smaller rings have an internal diameter around 2.0 μm and an external diameter around 4 μm (Fig. 5(d)).

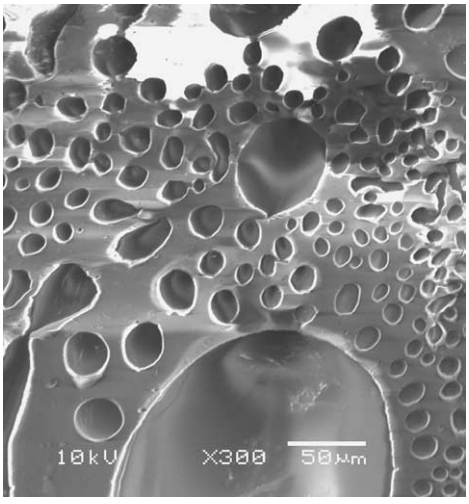


Fig. 2. A SEM image of deposits of (n-$Bu_4N)_2$[$(dcbdt)_2VO$] on a glass substrate.

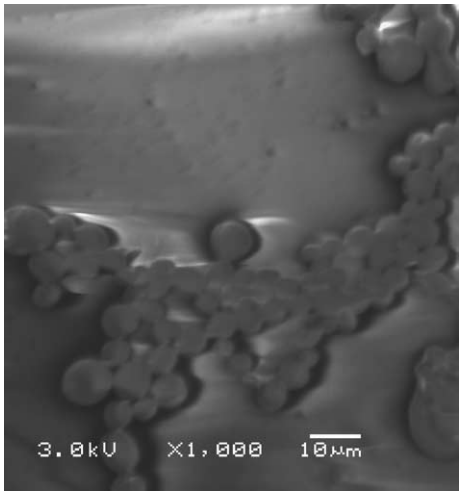


Fig. 3. A SEM image of deposits of (n-$Bu_4N)_2$[$(dcbdt)_2VO$] on a magnesium oxide substrate.

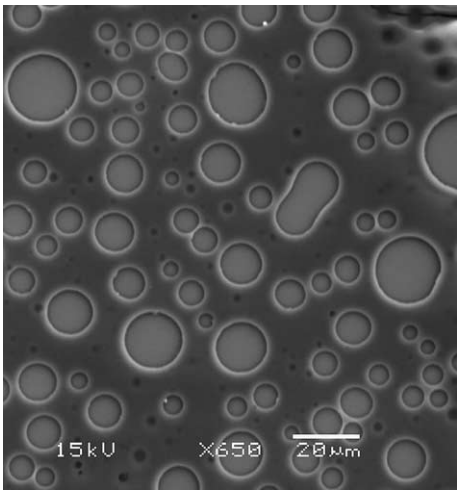


Fig. 4. A SEM image of deposits of (n-$Bu_4N)_2$[$(dcbdt)_2VO$] on a non-polished surface of a silicon substrate.

Although any explanation for formation of micro-scale rings on polished silicon surface must remain somewhat speculative at this stage, the observed micro-scale ring is reminiscent of the micro-porous films formed in the solvent evaporation of many materials, such as block copolymers, amphiphilic polyion complexes, such as organic/inorganic hybrids and homopolymers, such as polystyrene [10]. In these systems, water droplets condensed from moisture on the evaporating solutions act as the template to direct formation of the honeycomb patterns. The speculative formation of the new micro-scale rings could be explained as follows. The micrometer sized droplets of acetone solution of dithiolene metal complexes disperse on the polished surface of the silicon wafer randomly. The evaporation of the acetone leads to a cooling of the solution due to the heat of evaporation and water vapor condenses on the surface of the acetone solution droplets. Micro-sized water droplets grow in the middle of the solution droplets by further evaporation of acetone. This water droplet acts as the template to form the hole of the micro-scale rings.

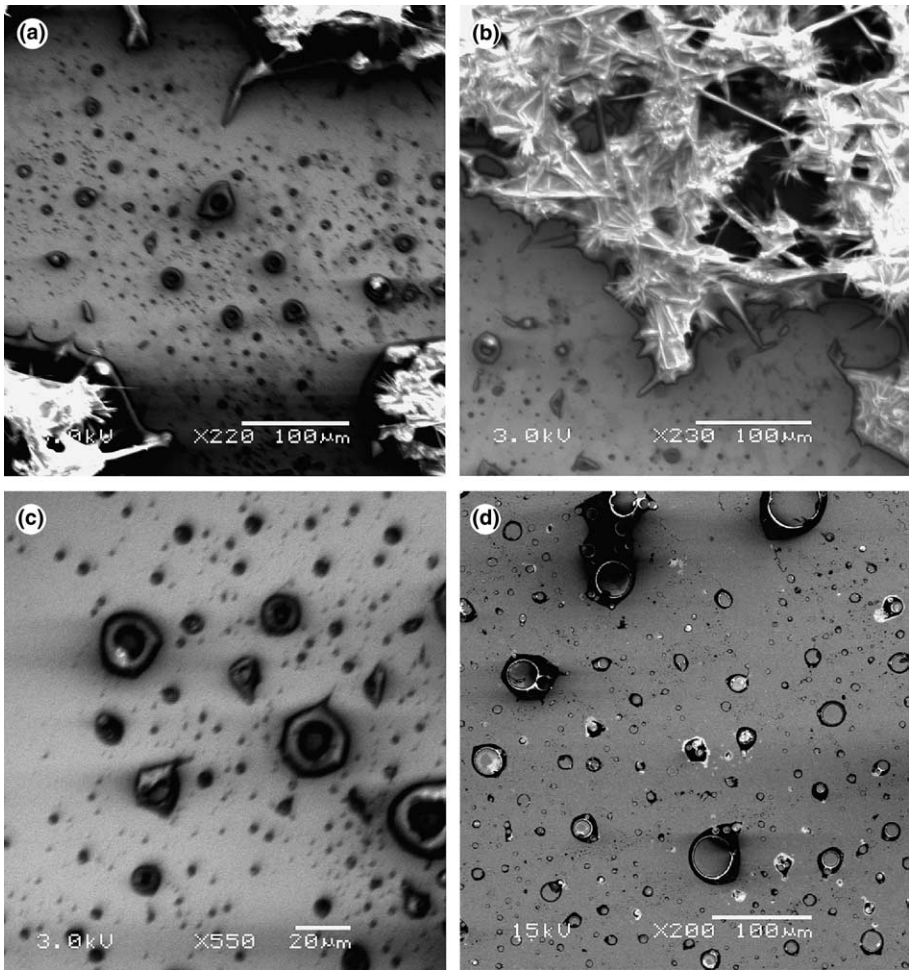


Fig. 5. SEM images of (a) deposits, (b) micro-crystals and (c) micro-scale rings on a polished surface of silicon substrates under ambient and (d) highly humidified conditions.

4. Summary

We have successfully fabricated porous, bead, two-dimensional network and micro-scale rings structures of $(n\text{-}Bu_4N)[(dcbdt)_2VO]$ and $(n\text{-}Bu_4N)_2[(dmit)_2Zn]$ on several substrates using a simple and easy chemical deposition method for the first time. We believe that this simple and easy fabrication method makes it suitable for practical applications such as new information storage and low cost nano-scale lithography as well as scientific research.

In particular, we take strong interest in an application of the ring to the magnetic storage, because each vanadium atom in the ring has the magnetic moment and these moments interact with each other. For example, when nano-scale rings can be two-dimensionally arrayed, they could become a high density storage media. Here, for each ring, the record may be performed by changing the magnetic state, where the change is realized by changing the magnitude of exchange interactions, and so on. On the other hand, the read may be done by microscopy utilizing the electron spin resonance [11] or the spin dependent transport [12].

We are now theoretically investigating properties about the magnetic storage, and the results will be reported elsewhere.

Acknowledgment

This work was partially supported by a grant-in-aid for scientific research (No. 16750114) from JSPS.

References

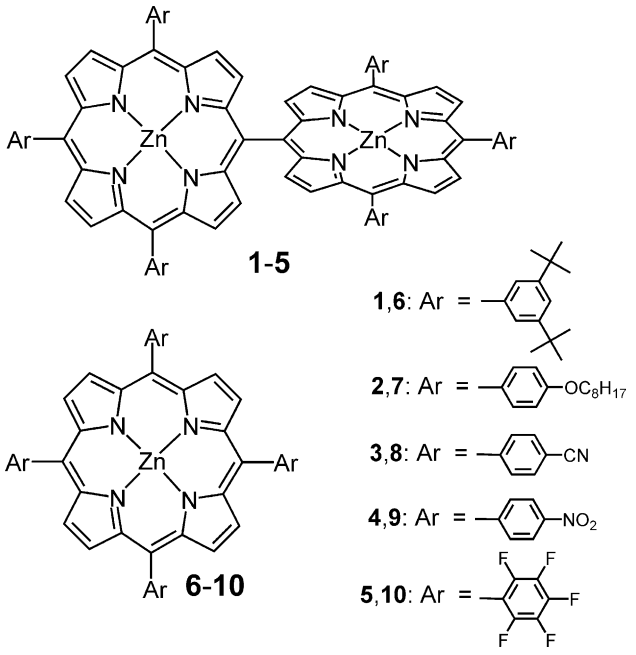
[1] J. Fraxedas, Adv. Mater. 14 (2002) 1603.
[2] J.A. McCleverty, Prog. Inorg. Chem. 10 (1968) 49.
[3] R.P Burns, C.A. McAuliffe, Adv. Inorg. Chem. Radiochem. 22 (1986) 303.
[4] P. Cassoux, L. Valade, H. Kobayashi, A. Kobayashi, R.A. Clark, A.E. Underhill, Coord. Chem. Rev. 110 (1991) 115.
[5] R. Eisenberg, H.B. Gray, Inorg. Chem. 6 (1967) 1844.

[6] W.E. Broderick, E.M. McGhee, M.R. Godfrey, B.M. Hoffman, J.A. Ibers, Inorg. Chem. 28 (1989) 2902.
[7] C. Livage, M. Fourmigué, P. Batail, E. Canadell, C.M. Cowie, M.J. Bennett, Inorg. Chem. 15 (1976) 1595.
[8] T. Suzuki, K. Ueda, R. Kita, S. Kokado, K. Harigaya, Polyhedron, this issue.
[9] D. Simõ, H. Alves, D. Belo, S. Rabaça, E.B. Lopes, I.C. Santos, V. Gamma, M.T. Duarte, R.T. Henriques, H. Novais, M. Almeida, Eur. J. Inorg. Chem. 3119 (2001).
[10] O. Karthaus, N. Maruyama, X. Cieren, M. Shimomura, H. Hasegawa, T. Hashimoto, Langmuir 16 (2000) 6071.
[11] In fact, quite recently, the magnetic resonance force microscopy detected a single spin. D. Rugar, R. Budakian, H.J. Mamin, B.W. Chui, Nature 430 (2004) 329.
[12] For example, as for the spin polarized scanning tunneling microscopy, see S. Heinze, M. Bode, A. Kubetzka, O. Pietzsch, X. Nie, S. Blügel, R. Wiesendanger, Science 288 (2000) 1805.

Similar π-systems are constructed by connecting bulky π-radicals. Poly(π-radical anion) of oligo(9,10-anthrylenes) is a good example [7]. In this case, π-radicals reside on anthracene π-planes, which are aligned sterically in an almost orthogonal orientation, and thermally excited high-spin states were observed. In order to realize a high-spin state as a ground state, perfect orthogonality is necessary, and the torsional angle between the spin-carrying π-systems should be close to 90°.

Recently, directly *meso*-linked porphyrin arrays have been synthesized and investigated [8,10–12]. The characteristics of these porphyrin arrays are orthogonal orientation of π-systems derived from steric hindrance between adjacent porphyrin macrocycles. The torsional angles of the neighboring π-planes have been estimated to be nearly 90° in a solution, based on the excitonic coupling of the Soret band absorption [10,11,13]. X-ray crystallographic analyses of another derivative of directly *meso*-linked dimer revealed that the torsional angle is also large in a crystal [12]. Therefore, this π-system is convenient for spin alignment based on spacially orthogonal alignment of molecular orbitals. For the formation of π-radical cation, Zn(II) porphyrin derivatives have been well investigated since the central zinc atom is inactive to the redox reaction. Furthermore, π-radical cations of Zn(II) porphyrin derivatives are relatively stable because of the electron donating character.

From these viewpoints, we have investigated the poly(π-radical cation)s of directly *meso*-linked Zn(II) porphyrin arrays. In our preliminary report [8], high-spin states of the poly(π-radical cation)s of the porphyrin arrays were observed in terms of ESR spectroscopy. It was also found that bis(π-radical cation) of directly *meso*-β-linked Zn(II) porphyrin dimer is a triplet species which obeys Curie law [9]. For the further investigation of directly *meso*-linked porphyrin dimer, substituent effect at the *meso*-position was confirmed. Since the highest occupied molecular orbital (HOMO) of ordinary tetraphenylporphyrin derivative has A_{2u} symmetry, the spin density of the π-radical cation is high at the *meso*-position. The magnetic interaction between two π-radicals which reside each porphyrin unit should be strongly dependent on the spin density at the *meso*-positions of the nearest neighbor. If the electron-donating ability of the *meso*-aryl substituents is increased, electron density at the *meso*-positons is also increased, leading to larger magnetic interaction between two π-radical cations. In order to discuss about this effect, a series of directly *meso*-linked Zn(II) porphyrin dimers bearing various *meso*-substituents (**1**–**5**) were prepared, and the property of the bis(π-radical cation) of dimer **2** is compared with that of dimer **1**, which carries *meso*-(3,5-di-*tert*-butylphenyl) substituents.



2. Experimental

These porphyrin dimers were prepared by oxidative coupling of corresponding Zn(II) 5,10,15-triphenylporphyrin derivatives. Chloroform solution of $NaAuCl_4$ was prepared by dipping $NaAuCl_4 \cdot 2H_2O$ powder into same volume of dimethylformamide followed by dilution with chloroform. ESR spectra were recorded on a JEOL JES-TE300 spectrometer, equipped with an RMC liquid helium transfer system and a Scientific Instruments 9650 digital temperature controller. Zero field splitting parameters were evaluated from high field approximation.

3. Results and discussion

3.1. Preparation and characterization of dimers

Directly *meso*-linked porphyrin arrays have been prepared by either of cyclization reaction using *meso*-formylporphyrins [10a] or oxidative coupling reaction [10b,11]. For oxidative coupling method, silver ion salts are commonly used, since further oxidation of the resulted porphyrin arrays leads the formation of ring-fused species [11]. In this study, however, silver ion salts were not effective for the oxidation of triarylporphyrins with electron-withdrawing substituents. Therefore, these triarylporphyrins were oxidized electrochemically, and corresponding dimers were successfully obtained with relatively good yields. Usually, the resulted dimer is more oxidizable than the starting monomer. If the

oxidation reaction is performed continuously, oxidation of dimer should occur more frequently than that of monomer. Electron-donating substituents will contribute to this tendency while electron-withdrawing substituents will disturb it. This effect might be the reason for the relatively good yield of the electrochemically generated dimers.

UV–Vis absorption spectra of these directly *meso*-linked porphyrin dimers showed split Soret bands around 420 and 460 nm (Table 1), that is, one lower-energy absorption of the excitonically coupled transition dipole parallel to the *meso–meso* linkage and the other higher-energy absorption of the transition dipoles perpendicular to the linkage. The higher-energy absorption is sensitive to the torsional angle. If the dipoles are uncoupled by the rectangular crossing due to the orthogonal structure, the excitation energy is similar to the corresponding monomer. In fact, as seen in Table 1, the higher-energy Soret bands of dimers **1**–**5** is similar to the corresponding monomers **6**–**10**.

Cyclic voltammograms of these dimers showed two reversible redox waves (Table 2). The first oxidation potentials of these dimers are distributed to wide range while the separations between the first and the second potentials are almost same. The similarity and small value of ΔE indicate that these oxidation processes are successive oxidation from each porphyrin rings and that the Coulombic effect between two porphyrin rings is similar in these dimers.

3.2. Chemical oxidation of dimers to mono(π-radical cation)s

When a chloroform solution of dimer **1** was treated with a small amount of $NaAuCl_4$ in chloroform, the lower energy absorption of Soret band (450 nm) decreased, whereas the higher energy absorption of Soret band (410 nm) remained, as shown in Fig. 1(a). Based on the exciton coupling theory, the former absorption is assigned to the coupled transition dipole parallel to the *meso–meso* linkage of the neutral dimer, and the latter one is assigned to the transition dipole perpendicular to the linkage, which resides on one neutral porphyrin macrocycle. Therefore, the decrease of the higher energy absorption of Soret band indicates that the loss of the coupled transition dipole. The broad absorption band appeared at longer wavelength region (~650 nm) is derived from π-radical cation of a porphyrin. Oxidation of either porphyrin moiety of the dimer to a π-radical cation causes the loss of the exciton coupling. The remaining slightly increased higher energy absorption of Soret band indicates that the other porphyrin moiety is kept neutral.

The ESR spectrum of the oxidized species was observed as a single peak at 10 K, indicating the generation of mono(π-radical cation) $\mathbf{1}^{+\cdot}$. At room temperature, the

Table 1
Absorption maxima of monomers **6**–**10** and dimers **1**–**5** in chloroform

	λ_{max} (nm)			λ_{max} (nm)			ΔE_{Soret} (cm^{-1})
	Soret	Q		Soret		Q	
6	423.5	551	**1**	421	458.5	561.5	1943
7	425.5	553.5	**2**	424.5	460	565	1818
8	426.5	556	**3**	424.5	458	564	1723
9	427.5	555	**4**	426	461.5	564	1806
10	420	550.5	**5**	419.5	455.5	563	1884

Table 2
Redox potentials of monomers **6**–**10** and dimers **1**–**5** in 0.1 M Bu_4NBF_4–CH_2Cl_2 vs. Ag/Ag^+ at room temperature

	$E^{ox1}_{1/2}$ (V)	$E^{ox2}_{1/2}$ (V)		$E^{ox1}_{1/2}$ (V)	$E^{ox2}_{1/2}$ (V)	ΔE (V)
6	0.45	0.83	**1**	0.44	0.58	0.14
7	0.40	0.77	**2**	0.43	0.55	0.12
8	0.68	0.98	**3**	0.62	0.77	0.15
10	1.02		**5**	0.84	0.98	0.14

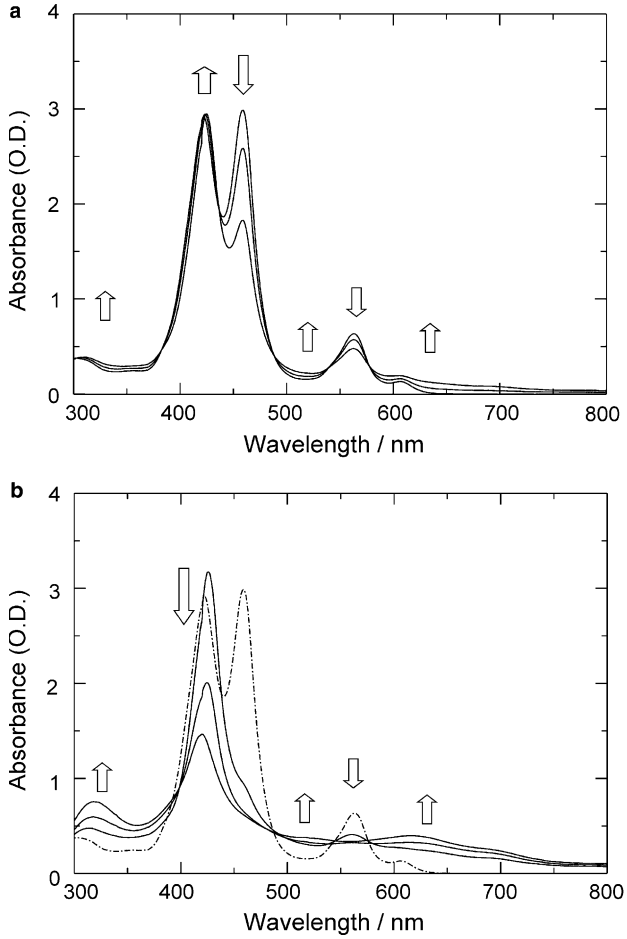


Fig. 1. In situ absorption spectral changes due to the progress of the oxidation of dimer **1** at room temperature by the treatment with $NaAuCl_4$ in chloroform. (a) The first oxidation stage from **1** to $\mathbf{1}^{+\cdot}$ and (b) the second oxidation stage from to $\mathbf{1}^{+\cdot}$ to $\mathbf{1}^{2+\cdot\cdot}$. The dotted broken line corresponds to the starting neutral dimer **1**.

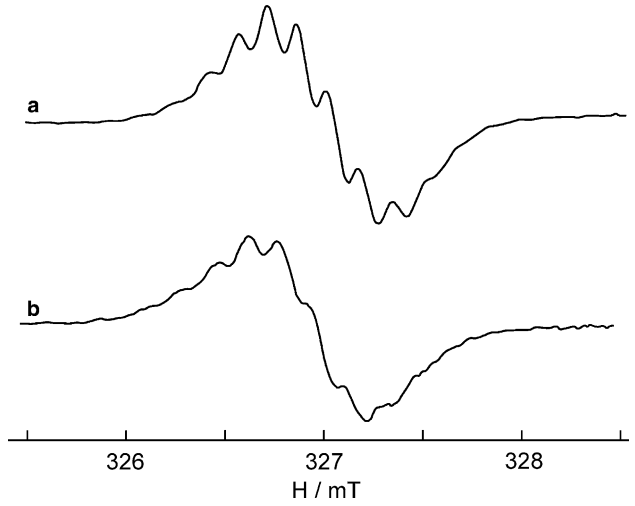


Fig. 2. ESR spectra of (a) π-radical cation of monomer **6**, and (b) mono(π-radical cation) of dimer **1** in chloroform at room temperature. 9.1662 GHz (1 mW) microwave and 63 μT field modulation were used.

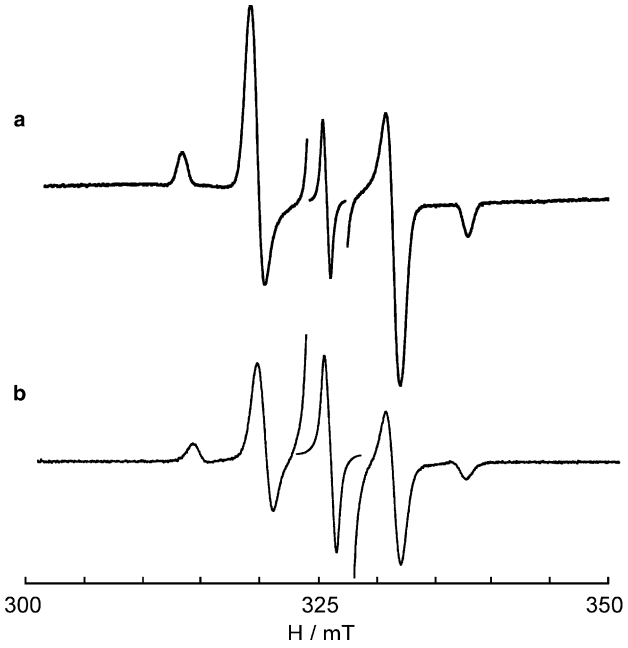


Fig. 3. ESR spectra of bis(π-radical cation) of (a) dimer **1**, and (b) dimer **2** in chloroform at 100 K. 9.1492 GHz (for **1**) or 9.1504 GHz (for **2**) microwave (0.2 mW) and 1 mT field modulation were used.

ESR signal showed a hyperfine-splitting structure due to four equivalent nitrogen atoms as shown in Fig. 2(b). The hyperfine coupling constant and g value ($a_N = 1.57$ G, $g = 2.0037$) are almost the same as those of the corresponding monomer **6** ($a_N = 1.51$ G, $g = 2.0031$, Fig. 2(a)). These results suggest that the π-radical remains on the single porphyrin ring and hardly penetrates the adjacent porphyrin ring because of the small overlap integral between the orthogonal π-systems.

3.3. Diradical formation of dimers

A cyclic voltammogram of dimer **1** has a pair of reversible peaks at 0.47 and 0.60 V versus Ag^+/Ag. The small difference in these potentials suggests that the redox processes are successive one-electron oxidations of each porphyrin ring of dimer **1**, that is, the first one is the formation of mono(π-radical cation) $\mathbf{1}^{+\cdot}$ at one porphyrin ring, and the second one is the oxidation at the other ring to bis(π-radical cation) $\mathbf{1}^{2+\cdot\cdot}$. This is not the case of the formation of a single porphyrin π-dication connected with a neutral porphyrin in the dimer, where the unsymmetrical oxidation is energetically unfavorable. Therefore, further oxidation of mono(π-radical cation) $\mathbf{1}^{+\cdot}$ should afford diradical species. In the CV time scale, diradical $\mathbf{1}^{2+\cdot\cdot}$ is stable enough to give a reversible voltammogram, whereas continuous electrolysis affords the ring-fused compounds, as reported recently [11]. The redox potentials of dimer **2** were observed at 0.43 and 0.55 V, which were lower than those of dimer **1**. Such tendency is derived from electron donating nature of the octyloxy groups, and the result indicates that generation of bis(π-radical cation) of dimer **2** is easier than dimer **1**. The difference between the first and the second potentials of dimer **2** is almost same as that of dimer **1**, indicating that the difference is caused by Coulombic effect.

An additional treatment of the solution of the mono(π-radical cation) of dimer **1** by $NaAuCl_4 \cdot 2H_2O$ caused a spectral change in low temperature ESR. Along with the decreased central monoradical signal, a set of fine-structured signals due to a triplet diradical were observed, as shown in Fig. 3(a). Half-field forbidden transition ($\Delta m_s = \pm 2$) signal was also observed at $g = 4.003$. The zero-field-splitting parameters at 110 K were determined to be $|D| = 1.19 \times 10^{-2}$ cm^{-1} and $|E| = 3.0 \times 10^{-4}$ cm^{-1}, respectively. Although these values slightly deviated with a change of temperature, the spectral line shape was qualitatively kept. The large D value indicates that each component of the diradical resides nearby, and the small E value is due to an axis symmetry. On the basis of the point dipole approximation, the D value is translated as two spins with ca. 6.0 Å distance. The distance calculated from the ESR D value is shorter than the center-to-center distance of two porphyrins (8.4 Å). Such tendency may be derived from the contribution of spin density at the *meso*-positions of the nearest neighbor.

During the second stage of oxidation, the higher energy absorption of the Soret band (410 nm) assigned to the remaining neutral porphyrin macrocycle decreased, indicating the formation of a bis(π-radical cation) $\mathbf{1}^{2+\cdot\cdot}$ (Fig. 1(b)).

The bis(π-radical cation) of dimer **2** was also generated by the same manner, and it showed similar ESR

spectrum (Fig. 3(b)). The similar zero-field-splitting parameter values of these two bis(π-radical cation)s indicate that the structure or the distribution of each π-radical is almost same.

3.4. Singlet–triplet energetics of π-diradicals

The temperature dependence of the $\Delta m_s = \pm 1$ signal intensity is unprecedented feature, as shown in Fig. 4. At temperatures lower than 120 K, the triplet spectrum kept almost the same signal, although the intensity increased gradually as the temperature increased. On the other hand, an abrupt increase and decrease of the signal intensity was observed at 130–190 K with keeping the similar line shape. This behavior is reversible with increasing and decreasing the temperatures. The temperature where signal intensity grows up is higher for dimer **2** than dimer **1**. Maximum signal intensity of $\mathbf{1}^{2+\bullet\bullet}$ was observed at 165 K, and that of $\mathbf{2}^{2+\bullet\bullet}$ was at 180 K.

The plots of the triplet ESR signal intensity versus the inversed temperature, however, cannot be rationalized as a thermally excited species with a single energy gap, which is represented by the following equation:

$$I = (C/T)[\exp(-\Delta E/k_B T)/\{1 + 3\exp(-\Delta E/k_B T)\}]. \quad (1)$$

Although the intensity change at the lower temperature region may be reproduced as a summation of plural components with different singlet–triplet energy gaps, at least three components ($\Delta E/k_B = 200$, 100, and 40 K, with a ratio of 2.5:1.2:1, for $\mathbf{1}^{2+\bullet\bullet}$) are needed for the good fit (Fig. 5). In this case, the number of components (three) does not have any meaning, and there should be a large number of components. These three components are just representatives of various components. The singlet–triplet energy gap depends on the overlap integral, which are closely related with the dihedral angle between two spin-carrying sites. If there are several kinds of bis(π-radical cation)s of the *meso*-linked dimers with different dihedral angles in the frozen solution, these bis(π-radical cation)s should exhibit various singlet–triplet energy gaps. The temperature dependence at lower temperatures indicates such situation. When the temperature is raised up to 130 K, molecular motion around the *meso–meso* linkage may take place. Under this circumstance, the averaged molecular symmetry is considered to be nearly D_{2d}, and the dihedral angle between two porphyrin rings should be almost 90°. Therefore, the singlet–triplet energy gap is minimized to cause the abrupt increase of the signal intensity.

The rotation around the *meso–meso* linkage will cause changes in zero-field splitting parameters. In fact, slight shift of signal positions was observed between 120–160 K. In the case of symmetrical diradicals, such as C_{60}^{2-}, it has been discussed that some nearly degenerated states are averaged dynamically with variable factors to cause change in ESR spectra along with temperature variation [14]. The dynamic Jahn–Teller effect may operate in the present case.

When orbital interaction between the neighboring *meso*-positions is considered, the magnitude of the

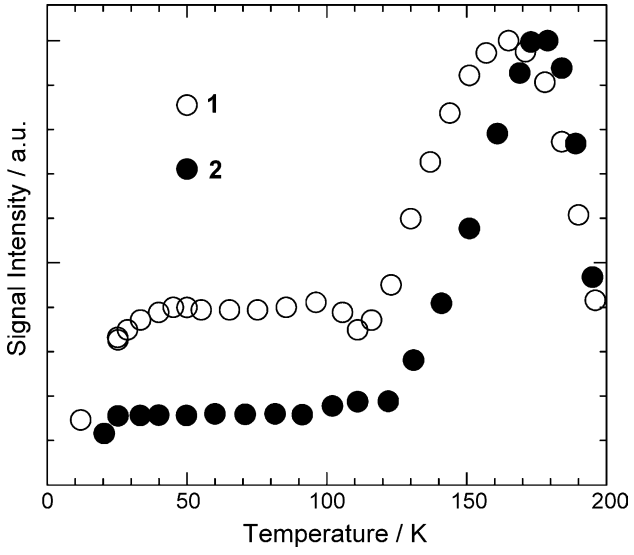


Fig. 4. Temperature dependence of triplet ESR signal intensity of bis(π-radical cation) of dimer **1** (open circles) and dimer **2** (closed circles) in chloroform.

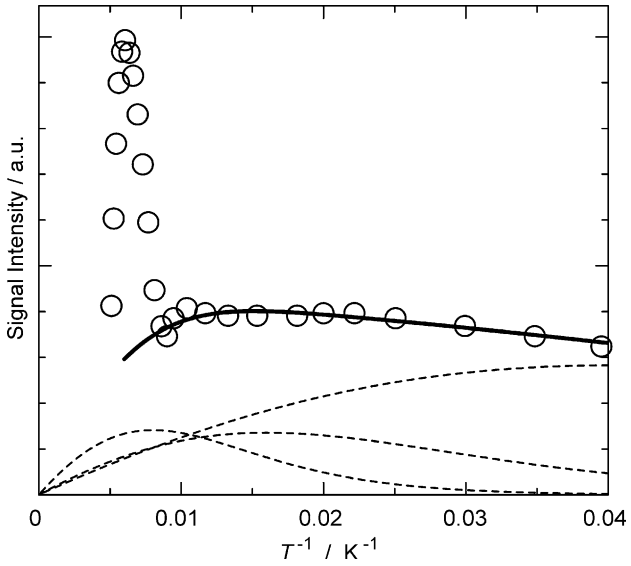


Fig. 5. Fitting of temperature dependence plots of triplet ESR signal intensity of bis(π-radical cation) of dimer **1**. The open circles are experimental data and the solid line shows the summation of three components, which are drawn with dotted lines. The dotted lines show the theoretical curves derived from Eq. (1) for singlet–triplet energy gap $\Delta E/k_B$ = 200, 100, or 40 K, with a factor (included in C) of 2.5, 1.2, or 1.0, respectively.

interaction depends on the orbital coefficients at the *meso*-positions of the nearest neighbor. If electron-donating ability of the *meso*-substituents is increased, the electron density at the *meso*-positions is also increased. Therefore, magnetic interaction in bis(π-radical cation) of dimer is expected to be modulated with the electron-donating ability of the *meso*-substituents. In fact, replacement of *meso*-(3,5-di-*tert*-butylphenyl) group of dimer **1** to *meso*-octyloxypheny group (**2**) caused the shift of the characteristic temperatures to the higher side (Fig. 4).

Drastic change in magnetic susceptibility is frequently found in the crystalline state. Such phenomena are usually based on cooperative effects. Sometimes the balance of enthalpy and entropy contributions causes a phase-transition like behavior. In spin-crossover systems, high temperature high-spin phase and low temperature low-spin phase are observed. The temperature dependence of the bis(π-radical cation)s of directly *meso*-linked porphyrin dimers reminds us such behavior.

4. Conclusion

A series of directly *meso*-linked Zn(II) porphyrin dimers were prepared, and two of them were chemically oxidized to bis(π-radical cation)s. The temperature dependence of ESR triplet signal intensity showed anomalous feature, which was rationalized in terms of molecular motion. This result may imply that the orthogonality between two porphyrin rings is not yet enough. If the perfect orthogonality is achieved in a moment of the rotation around the *meso–meso* linkage at high temperature, degeneracy or crossover between singlet and triplet states may take place. Comparison of diradical $\mathbf{2}^{2+\bullet\bullet}$ with diradical $\mathbf{1}^{2+\bullet\bullet}$ revealed that the magnetic interaction in these π-diradicals is modulated by the electron-donating ability of the *meso*-aryl substituents.

Acknowledgement

This work was supported by a Grant-in-Aid for Scientific Research on Priority Areas (417) from the Ministry of Education, Culture, Sports, Science, and Technology (MEXT) of the Japanese Government.

References

[1] (a) R. Breslow, H.W. Chang, R. Hill, E. Wasserman, J. Am. Chem. Soc. 89 (1967) 1112;
(b) T.J. LePage, R. Breslow, J. Am. Chem. Soc. 109 (1987) 6412.
[2] (a) A. Rajca, Chem. Rev. 94 (1994) 871;
(b) W.T. Borden, H. Iwamura, J.A. Berson, Acc. Chem. Res. 27 (1994) 109.
[3] (a) H. Nishide, T. Kaneko, T. Nii, K. Katoh, E. Tsuchida, P.M. Lahti, J. Am. Chem. Soc. 118 (1996) 9695;
(b) H. Nishide, T. Kaneko, S. Toriu, Y. Kuzumaki, E. Tsuchida, Bull. Chem. Soc. Jpn. 69 (1996) 499.
[4] (a) P.M. Lahti (Ed.), Magnetic Properties of Organic Materials, Marcel Dekker, New York, 1999;
(b) K. Itoh, M. Kinoshita (Eds.), Molecular Magnetism–New Magnetic Materials, Kodansha/Gordon & Breach, Tokyo, 2000;
(c) D.A. Shultz, H. Lee, R.K. Kumar, K.P. Gwaltney, J. Org. Chem. 64 (1999) 9124;
(d) H. Nishide, T. Ozawa, M. Miyasaka, E. Tsuchida, J. Am. Chem. Soc. 123 (2001) 5942;
(e) A. Rajca, J. Wongsriratanakul, S. Rajca, Science 294 (2001) 1503.
[5] L. Salem, C. Rowland, Angew. Chem. Int. Ed. 11 (1972) 92.
[6] (a) M. Ballester, J. Castañer, J. Riera, G. de la Fuente, M. Camps, J. Org. Chem. 50 (1985) 2287;
(b) E. Molins, C. Miravitlles, E. Espinosa, M. Ballester, J. Org. Chem. 67 (2002) 7175.
[7] (a) M. Hoshino, K. Kimura, M. Imamura, Chem. Phys. Lett. 20 (1973) 193;
(b) M. Baumgarten, U. Müller, A. Bohnen, K. Müllen, Angew. Chem., Int. Ed. Engl. 31 (1992) 448;
(c) U. Müller, M. Baumgarten, J. Am. Chem. Soc. 117 (1995) 5840.
[8] H. Segawa, D. Machida, Y. Senshu, J. Nakazaki, K. Hirakawa, F. Wu, Chem. Commun. (2002) 3032.
[9] H. Segawa, Y. Senshu, J. Nakazaki, K. Susumu, J. Am. Chem. Soc. 126 (2004) 1354.
[10] (a) K. Susumu, T. Shimidzu, K. Tanaka, H. Segawa, Tetrahedron Lett. 37 (1996) 8399;
(b) F. Wu, H. Segawa, Photogr. Sci. Photochem. 17 (1999) 316.
[11] (a) A. Osuka, H. Shimidzu, Angew. Chem., Int. Ed. Engl. 36 (1997) 135;
(b) N. Yoshida, H. Shimidzu, A. Osuka, Chem. Lett. (1998) 55;
(c) T. Ogawa, Y. Nishimoto, N. Yoshida, N. Ono, A. Osuka, Angew. Chem. Int. Ed. 38 (1999) 176;
(d) H.S. Cho, N.W. Song, Y.H. Kim, S.C. Jeoung, S. Hahn, D. Kim, S.K. Kim, N. Yoshida, A. Osuka, J. Phys. Chem. A 104 (2000) 3287;
(e) Y.H. Kim, D.H. Jeong, D. Kim, S.C. Jeoung, H.S. Cho, S.K. Kim, N. Aratani, A. Osuka, J. Am. Chem. Soc. 123 (2001) 76;
(f) D. Kim, A. Osuka, J. Phys. Chem. A 107 (2003) 8791.
[12] R.G. Khoury, L. Jaquinoid, K.M. Smith, Chem. Commun. (1997) 1057.
[13] M. Kasha, H.R. Rawls, M.A. El-Bayoumi, Pure Appl. Chem. 11 (1965) 371.
[14] M.M. Khaled, R.T. Carlin, P.C. Trulove, G.R. Eaton, S.S. Eaton, J. Am. Chem. Soc. 116 (1994) 3465.

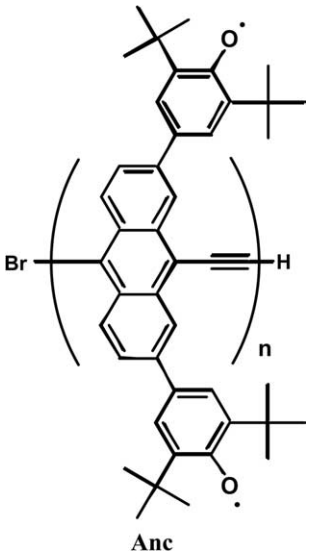


Chart 1.

2. Experimental

2.1. Materials

The monomers, 2,7-bis(4-acetoxy-3,5-di-*tert*-butylphenyl)-10-bromo-9-(3-hydroxy-3-methyl-1-butynyl)anthracene (**A1a**) and 2,7-bis(4-acetoxy-3,5-di-*tert*-butylphenyl)-9-bromo-10-(3-hydroxy-3-methyl-1-butynyl) anthracene (**B1a**), were synthesized as previously described [2]. Other conventional reagents were used as received or purified by conventional method.

2.2. Polymerization and fractionation

Polymerization was carried out by modifying the conditions described in [2,4]. The monomer **A1a** (166 mg, 0.2 mmol), tetrakis(triphenylphosphine)palladium(0) (2.3 mg, 0.002 mmol), and copper iodide (0.38 mg, 0.002 mmol) were placed in an Schlenk tube under a nitrogen atmosphere. Freshly distilled toluene (2 ml) was transferred to the tube, and the monomers were dissolved with stirring. 5 M KOH methanol solution (0.02 ml) was added to the monomer solution, and the mixture was heated at 110 °C for 3 h. After cooling, the reaction mixture was poured into methanol to yield polymer precipitate. The methanol soluble fraction was purified by silica gel column separation with chloroform and hexane/ethyl acetate (16/3 v/v) as an eluent to give the dimer **A2a** and the trimer **A3a**. The precipitate was purified by preparative GPC with chloroform as an eluent to give the monodisperse oligomers **A2a**–**A5a**. The dimer **B2a** was synthesized as described above.

A2a: Yield 8.7%. TLC (hexane/ethyl acetate = 4/1 v/v): $R_f = 0.28$. IR (KBr, cm^{-1}) 3460 (ν_{O-H}), 2968–2860 (ν_{C-H}, *tert*-butyl), 1768 ($\nu_{C=O}$). ^1H NMR ($CDCl_3$, 500 MHz; ppm) δ 1.27 (s, 36H, *tert*-butyl), 1.45 (s, 36H, *tert*-butyl), 1.87 (s, 6H, CH_3), 2.22 (s, 1H, OH), 2.32 (s, 6H, $COCH_3$), 2.41 (s, 6H, $COCH_3$), 7.77 (s, 4H, PhH), 7.79 (s, 4H, PhH), 7.87 (dd, 2H, $J = 8.9$, 1.7 Hz, ArH), 7.99 (dd, 2H, $J = 9.2$, 1.7 Hz, ArH), 8.71 (d, 2H, $J = 9.2$ Hz, ArH), 8.81 (d, 2H, $J = 1.7$ Hz, ArH), 8.92 (d, 2H, $J = 8.8$ Hz, ArH), 9.12 (d, 2H, $J = 1.7$ Hz, ArH). ^{13}C NMR ($CDCl_3$; ppm): δ 22.61, 22.73, 31.35, 31.39, 31.51, 31.60, 31.79, 35.57, 35.69, 66.23, 79.19, 98.35, 98.88, 107.60, 118.00, 118.25, 118.36, 124.43, 124.53, 124.71, 125.56, 125.61, 127.45, 127.52, 127.64, 127.71, 129.09, 129.57, 131.36, 132.76, 133.85, 136.82, 137.56, 139.46, 139.71, 143.05, 147.99, 148.07, 170.97, 171.15.

A3a: Yield 5.0%. TLC (hexane/ethyl acetate = 4/1 v/v): $R_f = 0.17$. ^1H NMR ($CDCl_3$, 500 MHz; ppm) δ 1.27 (s, 36H, *tert*-butyl), 1.30 (s, 36H, *tert*-butyl), 1.46 (s, 36H, *tert*-butyl), 1.87 (s, 6H, CH_3), 2.04 (s, 1H, OH), 2.31 (s, 6H, $COCH_3$), 2.32 (s, 6H, $COCH_3$), 2.41 (s, 6H, $COCH_3$), 7.76 (s, 4H, PhH), 7.80 (s, 4H, PhH), 7.81 (s, 4H, PhH), 7.91 (dd, 2H, $J = 9.0$, 1.7 Hz, ArH), 7.94 (dd, 2H, $J = 9.0$, 2.0 Hz, ArH), 8.01 (dd, 2H, $J = 9.3$, 1.7 Hz, ArH), 8.74 (d, 2H, $J = 9.3$ Hz, ArH), 8.83 (d, 2H, $J = 1.7$ Hz, ArH), 8.99 (d, 2H, $J = 9.0$ Hz, ArH), 9.01 (d, 2H, $J = 9.0$ Hz, ArH), 9.17 (br, 4H, ArH).

A4a: Yield 1.8% (estimated from chromatogram of GPC). TLC (hexane/ethyl acetate = 4/1 v/v): $R_f = 0.08$. ^1H NMR ($CDCl_3$, 500 MHz; ppm) δ 1.27 (s, 36H, *tert*-butyl), 1.29 (s, 36H, *tert*-butyl), 1.31 (s, 36H, *tert*-butyl), 1.47 (s, 36H, *tert*-butyl), 1.88 (s, 6H, CH_3), 2.31 (s, 6H, $COCH_3$), 2.316 (s, 6H, $COCH_3$), 2.32 (s, 6H, $COCH_3$), 2.41 (s, 6H, $COCH_3$), 7.78 (s, 4H, PhH), 7.79 (s, 4H, PhH), 7.81 (s, 8H, PhH), 7.92 (dd, 2H, $J = 9.0$, 1.7 Hz, ArH), 7.96 (dd, 2H, $J = 9.0$, 2.0 Hz, ArH), 7.98 (dd, 2H, $J = 9.0$, 2.0 Hz, ArH), 8.01 (dd, 2H, $J = 9.3$, 1.7 Hz, ArH), 8.74 (d, 2H, $J = 9.3$ Hz, ArH), 8.83 (d, 2H, $J = 1.7$ Hz, ArH), 9.01 (d, 2H, $J = 9.0$ Hz, ArH), 9.03 (d, 2H, $J = 9.0$ Hz, ArH), 9.08 (d, 2H, $J = 9.0$ Hz, ArH), 9.18 (br, 4H, ArH), 9.22 (d, 2H, $J = 1.7$ Hz, ArH).

A5a: Yield 1.0% (estimated from chromatogram of GPC). TLC (hexane/ethyl acetate = 4/1 v/v): $R_f = 0.06$. ^1H NMR ($CDCl_3$, 500 MHz; ppm) δ 1.28 (s, 36H, *tert*-butyl), 1.302 (s, 36H, *tert*-butyl), 1.305 (s, 36H, *tert*-butyl), 1.31 (s, 36H, *tert*-butyl), 1.47 (s, 36H, *tert*-butyl), 1.88 (s, 6H, CH_3), 2.315 (s, 6H, $COCH_3$), 2.318 (s, 6H, $COCH_3$), 2.32 (s, 6H, $COCH_3$), 2.33 (s, 6H, $COCH_3$), 2.41 (s, 6H, $COCH_3$), 7.79 (s, 4H, PhH), 7.80 (s, 4H, PhH), 7.81 (m, 12H, PhH), 7.91–8.03 (m, 10H, $J = 9.3$, 1.7 Hz, ArH), 8.74 (d, 2H, $J = 9.3$ Hz, ArH), 8.83 (d, 2H, $J = 1.7$ Hz, ArH), 9.01 (d, 2H, $J = 9.0$ Hz, ArH), 9.04 (d, 2H, $J = 9.0$ Hz, ArH), 9.10 (d, 2H, $J = 9.0$ Hz, ArH), 9.11 (d, 2H, $J = 9.0$ Hz, ArH), 9.19 (br, 4H, ArH), 9.23 (br, 4H, ArH).

B2a: Yield 5.0%. TLC (hexane/ethyl acetate = 4/1 v/v): $R_f = 0.26$. IR (KBr, cm^{-1}) 3460 (ν_{O-H}), 2972–2860 (ν_{C-H}, *tert*-butyl), 1762 ($\nu_{C=O}$). ^1H NMR ($CDCl_3$,

500 MHz; ppm) δ 1.27 (s, 36H, *tert*-butyl), 1.45 (s, 36H, *tert*-butyl), 1.92 (s, 6H, CH_3), 2.32 (s, 6H, $COCH_3$), 2.41 (s, 6H, $COCH_3$), 7.74 (s, 4H, PhH), 7.76 (s, 4H, PhH), 7.85 (dd, 2H, J = 8.9, 1.6 Hz, ArH), 7.97 (dd, 2H, J = 8.9, 1.6 Hz, ArH), 8.68 (d, 2H, J = 8.9 Hz, ArH), 8.80 (d, 2H, J = 1.6 Hz, ArH), 8.96 (d, 2H, J = 8.9 Hz, ArH), 9.08 (d, 2H, J = 1.6 Hz, ArH). ^{13}C NMR ($CDCl_3$; ppm): δ 22.63, 22.74, 31.38, 31.53, 31.85, 35.56, 35.66, 66.35, 78.99, 98.29, 99.01, 106.84, 117.77, 118.11, 118.49, 124.62, 125.51, 125.84, 126.05, 126.93, 127.73, 127.75, 127.77, 127.88, 130.88, 130.98, 131.36, 132.34, 132.83, 137.20, 137.64, 139.69, 140.44, 142.97, 147.95, 148.08, 171.01, 171.12.

2.3. Deprotection and oxidation

The dimer **B2a** (23 mg, 0.015 mmol) was dissolved in THF (2 ml) under a nitrogen atmosphere. DMSO (6 ml) was added to the solution, then aqueous 2.5 M KOH (0.6 ml) was added to its suspension. The mixture was stirred at 50 °C for 12 h, cooled to room temperature, and neutralized with aqueous 3 N HCl. The organic product was extracted with chloroform, washed with water, and dried over anhydrous sodium sulfate. The solvent was evaporated, and the crude product was purified by silica gel column separation with hexane/ethyl acetate (4/1 v/v) as an eluent to give the dimer **B2b**.

B2b: Yield 27%. TLC (hexane/ethyl acetate = 4/1 v/v): R_f = 0.27. IR (KBr, cm^{-1}) 3636 (ν_{O-H}), 3315 ($\nu_{\equiv C-H}$), 2970–2860 (ν_{C-H}, *tert*-butyl). ^{1}H NMR ($CDCl_3$, 500 MHz; ppm) δ 1.26 (s, 36H, *tert*-butyl), 1.38 (s, 36H, *tert*-butyl), 4.13 (s, 1H, $\equiv$C–H), 5.28 (s, 2H, OH), 5.38 (s, 2H, OH), 7.63 (s, 4H, PhH), 7.67 (s, 4H, PhH), 7.81 (dd, 2H, J = 9.0, 1.7 Hz, ArH), 7.97 (dd, 2H, J = 9.0, 1.7 Hz, ArH), 8.73 (d, 2H, J = 9.0 Hz, ArH), 8.76 (d, 2H, J = 1.7 Hz, ArH), 8.95 (d, 2H, J = 9.0 Hz, ArH), 9.08 (d, 2H, J = 1.7 Hz, ArH). ^{13}C NMR ($CDCl_3$; ppm): δ 29.70, 30.22, 30.37, 34.43, 34.55, 80.50, 89.49, 94.08, 99.28, 117.17, 117.82, 118.55, 123.57, 124.16, 124.45, 124.95, 126.95, 127.64, 127.72, 131.04, 131.35, 131.54, 131.82, 131.96, 132.93, 136.42, 136.48, 140.18, 140.93, 154.05, 154.09.

The dimer **B2c** was prepared by chemical oxidation of the corresponding hydroxyl precursors with PbO_2 under nitrogen in a glovebox as follows. A degassed toluene solution of the dimer **B2b** (10 mM per phenol unit) was treated with 10 equivalents of recently prepared PbO_2, and was vigorously stirred for 1 h. After filtration the solution was used for spectroscopic and magnetic measurement.

2.4. Measurements

Solutions for ESR experiments were prepared under nitrogen in a glovebox and placed in quartz tubes sealed with septa and Parafilm. ESR spectra were taken on a JEOL JES-2XG ESR spectrometer with 100 KHz field modulation in the X-band frequency region. Signal positions were calibrated against an external standard of Mn^{2+}/MgO (g = 1.981). The 77 K ESR spectra were measured for the toluene glass sample using a small Dewar flask containing the liquid nitrogen, which was inserted into the cavity of the spectrometer. The spin concentrations of each sample were determined by careful double integration of the ESR signal calibrated with that of the 2,2,6,6-tetramethyl-1-piperidinyloxy (TEMPO) standard solution.

For magnetic measurement, the solution of polyradical immediately after oxidation was used to give the sample diluted with diamagnetic toluene. The sample solution was contained in a diamagnetic capsule. Magnetization was measured using a Quantum Design MPMS-7 SQUID magnetometer. The magnetization was measured from 0.5 to 7 T at 2 K. The static magnetic susceptibility was measured from 2 to 100 K in a field of 0.5 T. The mean-field correction parameter, θ, corresponding to small intermolecular (antiferro)magnetic interaction was determined from curve fitting using the product of molar magnetic susceptibility (χ_{mol}) and T versus T data. The spin concentrations of each sample were determined by analyzing the saturated magnetization at 2 K using a SQUID magnetometer.

IR spectra were obtained using a Hitachi IR 270-30 spectrometer. NMR (^{1}H, ^{13}C) spectra were measured using a Varian Unity 500SW (500 MHz). UV–Vis absorption spectra were recorded on a JASCO Ubest V-550DS UV–Vis spectrometer.

3. Results and discussion

3.1. Synthesis and characterization of oligomers

We synthesized monomers, 2,7-bis(4-acetoxy-3,5-di-*tert*-butylphenyl)-10-bromo-9-(3-hydroxy-3-methyl-1-butynyl)anthracene (**A1a**) and 2,7-bis(4-acetoxy-3,5-di-*tert*-butylphenyl)-9-bromo-10-(3-hydroxy-3-methyl-1-butynyl)anthracene (**B1a**), which had ethynyl and bromo groups to be linked with head-to-tail bonds by self-condensation. The polymerization of these monomers were carried out in the presence of the Pd(0) complex catalyst and the appropriate base, combining the deprotection of the ethynyl group and the cross-coupling to the aromatic halide to circumvent an oxidative coupling side reaction to produce diyne linkages. The methanol-soluble reddish brown solid and the methanol-insoluble dark blue solid were obtained by precipitation from the polymerization mixtures into methanol. The methanol-soluble fraction was further purified by silica gel column separation to give the dimer **A2a** and the trimer **A3a**. The monodisperse oligomers **A2a**–**A5a** were fractionated from the methanol-insoluble fraction

by preparative GPC. The relative amounts of oligomers in the methanol-insoluble fraction were calculated from the chromatogram of GPC as **A2a/A3a/A4a/A5a** = 9/20/19/11. The precise degree of polymerization was determined from ^{1}H NMR; the ratio of the peak areas of the terminal hydroxyisopropyl group and the aromatic region, and the number of chemical shifts in the aromatic region (Fig. 1). The degree of polymerization was controlled by amount of the base, and the dimer **A2a** was obtained in 8.7% yield when 0.5 equiv. of KOH was used (see Scheme 1).

The oligomers were soluble in organic solvent such as chloroform, tetrahydrofuran, aromatic hydrocarbons. The color of chloroform solution changed with degree of polymerization as orange (**A2a**), reddish orange (**A3a**), red (**A4a**) and reddish violet (**A5a**). The UV–Vis spectra of oligomers **A2a**–**A5a** show absorption maxima (λ_{max}) at 480 (**A2a**), 515 (**A3a**), 534 (**A4a**) and 543 (**A5a**) nm, respectively (Fig. 2). The λ_{max} of **A5a**, i.e., even 5-mer, shifted to longer wavelength compared with the previously reported λ_{max} for poly(1,4-phenyleneethynylene)s (360–450 nm) and poly[(9,10-anthryleneethynylene)-alt-(1,4-phenyleneethynylene)]s (450–540 nm) [5], which suggests that the electronic structure of the planar and π-conjugated anthracene skeleton contributes to developing the π-conjugation system throughout the backbone.

3.2. Polyradical formation of dimer

The dimer **B2a** was converted to the corresponding hydroxyl dimer **B2b** after complete elimination of the protecting acetyl group by treatment with alkaline solution. The dimer **B2c** was obtained by oxidizing **B2b** by treatment of the solution with fresh PbO_2. The dimer **B2c** was appropriately stable for maintaining the initial spin concentration under the ESR and SQUID measurement conditions, although the spin concentration of **B2c** was ca. 0.2 spin/phenoxyl unit in this oxidative condition (see Scheme 2).

The ESR spectrum of **B2c** showed broad hyperfine structures at g = 2.0041 indicating the formation of the phenoxyl radical, and the coupling of the protons of the phenoxyl ring and the anthracene skeleton, although it was difficult to analyze the spectrum because of the mono-, di- and triradical species included in **B2c** at

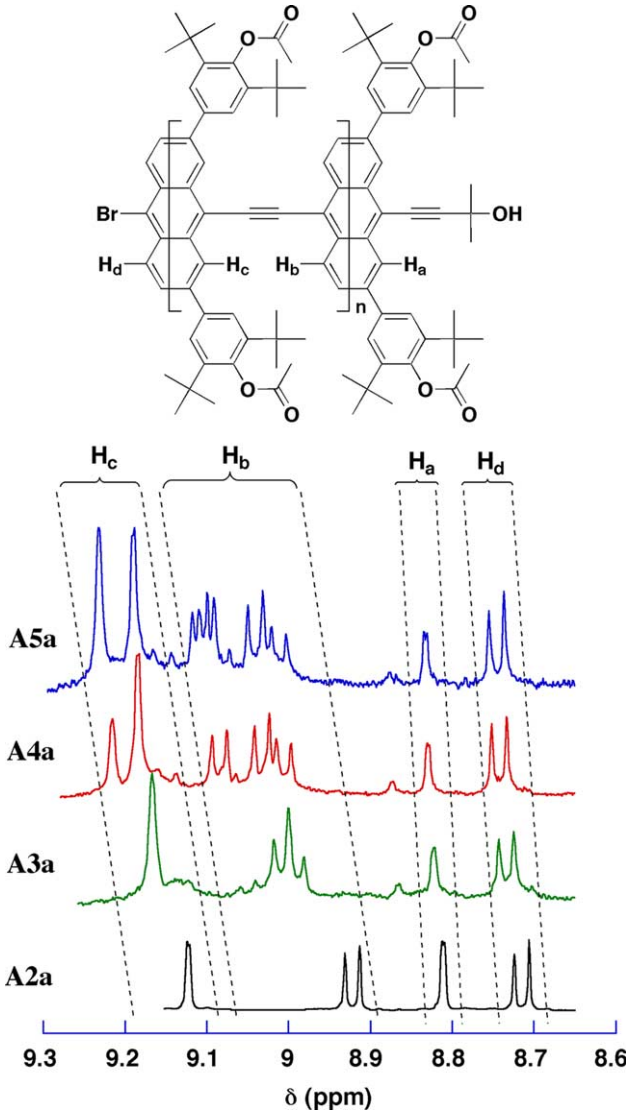
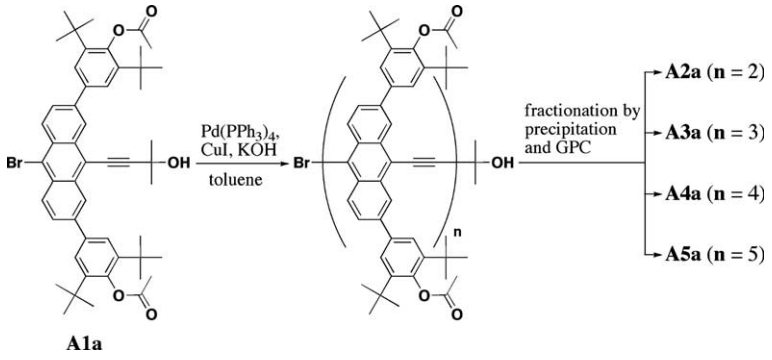


Fig. 1. ^{1}H NMR (500 MHz) spectra of **A2a**, **A3a**, **A4a** and **A5a**.



Scheme 1.

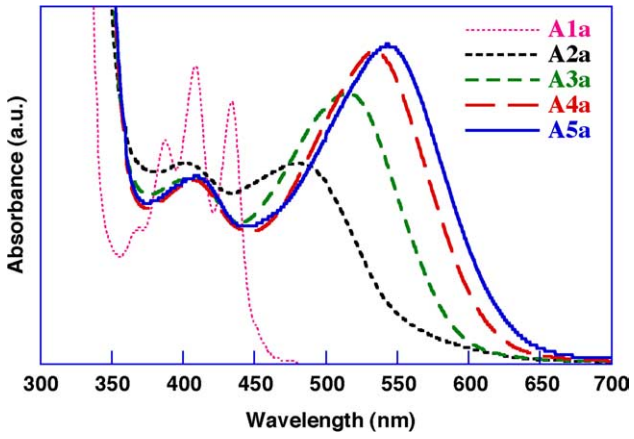
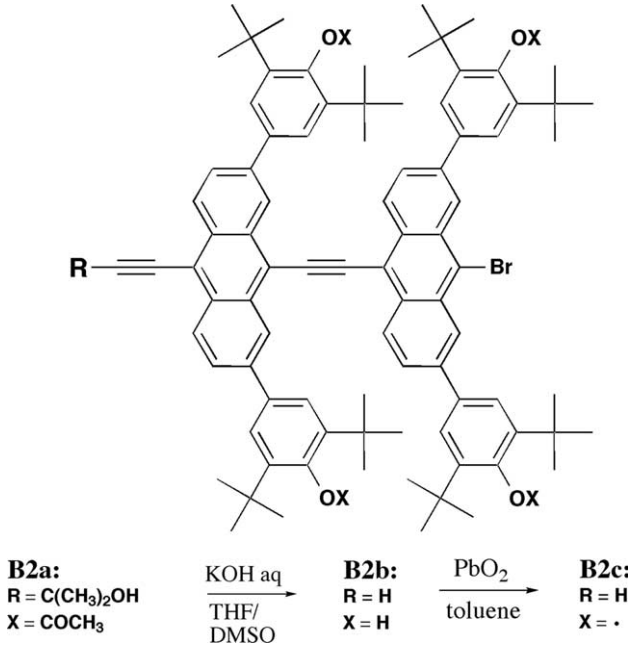


Fig. 2. UV–Vis absorption spectra of **A1a**, **A2a**, **A3a**, **A4a** and **A5a** in chloroform.



Scheme 2.

low spin concentration. The $\Delta m_s = \pm 2$ forbidden transition is clearly observed at $g = 4$ in frozen toluene glass of **B2c** at 77 K, although clear fine-structures that give zero-field splitting parameters D or E are not detected at $g = 2$ because of the presence of the several conformers and/or the mono-, di- and triradical species (Fig. 3).

3.3. Magnetic interaction of polyradical dimer

The magnetization (2–15 K, 0.5–7 T) and magnetic susceptibility (2–100 K at 0.5 T) of dimer **B2c** were measured using a SQUID magnetometer in order to estimate the intramolecular spin coupling in the polyradical. The sample was prepared as the frozen glass diluted in diamagnetic toluene to minimize intermolecular interactions. The magnetization (M) normalized by saturated magnetization (M_s), M/M_s, versus the ratio of magnetic field (H) and the effective temperature ($T - \theta$) plots of **B2c** were located almost on the theoretical Brillouin curves of $S = 2/2$, which was consistent with the low spin concentration of **B2c** including the mono-, di- and triradical species. The $\chi_{mol}T$ versus T plots of **B2c** are shown in Fig. 4, where χ_{mol} is the molar paramagnetic susceptibility based on per mol of exact phenoxyl. We have already reported that the $\chi_{mol}T$ value of monomeric diradical, 4,4′-(2,7-anthrylene)bis(2,6-di-*tert*-butylphenoxyl), was an approximately constant value below 100 K, which was larger than the theoretical value for $S = 1/2$ ($\chi_{mol}T = 0.375$) and almost agreed with the value for $S = 2/2$ ($\chi_{mol}T = 0.5$). The $\chi_{mol}T$ value of monomeric diradical indicated strong ferromagnetic coupling ($2J' > 10^2\ cm^{-1}$) between two phenoxyls through the anthracene unit. Therefore, the spin coupling constant through the dianthrylacetylene unit, J, of **B2c** was determined by curve fitting of the $\chi_{mol}T$ versus T data in consideration of a large enough spin coupling constant between two phenoxyls through the

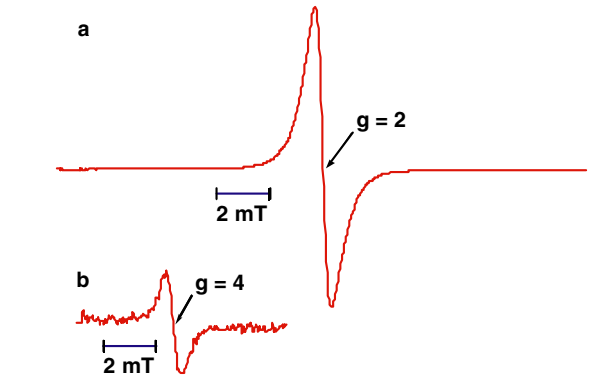


Fig. 3. ESR spectra of **B2c** (10 mM, spin conc. = 0.20 spin/phenoxyl unit) in frozen toluene glass at 77 K: (a) at $g = 2$ and (b) at $g = 4$.

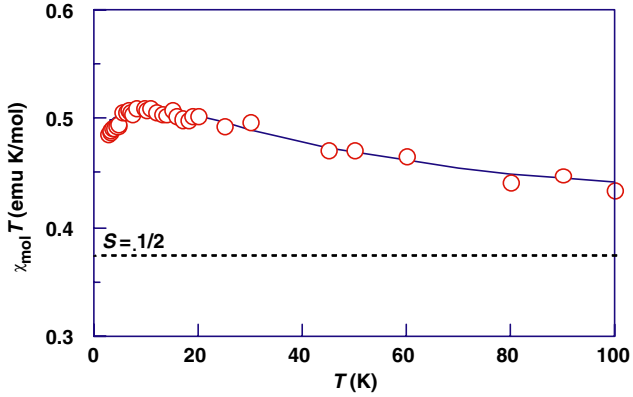


Fig. 4. $\chi_{mol}T$ vs. T plots (○) of **B2c** (10 mM, spin conc. = 0.20 spin/phenoxyl unit) in frozen toluene glass. Solid line: Theoretical curve calculated using Eq. (1) with $2J = 34\ cm^{-1}$, $\theta = -0.1$ K, $x_1 = 0.58$, $x_2 = 0.22$, $x_3 = 0.018$, $x'_1 = 0.15$, and $x'_2 = 0.037$.

anthracene unit ($J' \gg kT$). The curve fitting of the $\chi_{mol}T$ versus T data was performed using an expression for the sum of the mono-, di-, tri- and tetraradical species.

$$\chi_{mol}T = \frac{N_A g^2 \mu_B^2 T}{k(T-\theta)} \left\{ \frac{x_3(10+2\exp(-4J/kT))}{4(5+3\exp(-4J/kT)+\exp(-6J/kT))} + \frac{x_2(10+\exp(-3J/kT))}{3(8+4\exp(-3J/kT))} - \frac{x_1}{(3+\exp(-2J/kT))} + \frac{x_2'}{3} + \frac{x_1'}{4} \right\}, \quad (1)$$

where θ, x_1, x_2 and x_3 are the Weiss constant for a weak intermolecular magnetic interaction, and the fractions of the di-, tri- and tetraradical species, respectively, and x_1' and x_2' are the fractions of the mono- and diradical species without the spin coupling through the dianthrylacetylene unit. The $2J$ value of **B2c** was $34 \pm 1\ cm^{-1}$, which agreed with the $2J$ value of the corresponding oligomeric diradical which had one pendant phenoxyl in one anthracene unit ($2J = 31 \pm 3\ cm^{-1}$) [6]. It has been known that the coplanarity of π-conjugated pendant polyradicals throughout the backbone and the pendant side chain is significantly effective in the magnitude of the spin coupling constant [1]. For example, the expected ferromagnetic interactions have not been observed for any poly(phenylacetylene)-based pendant polyradicals, because the coplanarity both in the poly(phenylacetylene) skeleton itself and in the dihedral angle with a pendant radical were significantly distorted by the sterically bulky pendant groups [7]. The $2J$ value of **B2c** indicates that the poly(9,10-anthryleneethynylene)-based polyradical has less steric hindrance between the side chain radicals and the poly(9,10-anthryleneethynylene) backbone even if the polyradical has two pendant phenoxyls in one anthracene unit.

4. Conclusions

The poly(9,10-anthryleneethynylene)s with pendant phenol residue at the 2- and 7-positions were synthesized via polymerization of the corresponding bromoethynylanthracene monomer in the presence of the Pd(0) complex catalyst and the appropriate base. The degree of polymerization was controlled by amount of the base, and the monodisperse oligomers **A2a**–**A5a** were fractionated by precipitation into methanol followed by preparative GPC. The $2J$ value of **B2c**, $34 \pm 1\ cm^{-1}$, verified the moderately strong ferromagnetic coupling through the dianthrylacetylene unit for the corresponding poly(9,10-anthryleneethynylene)-based polyradical **Anc**.

Acknowledgments

This work was partially supported by a Grant-in-Aid for Exploratory Research (Nos. 16655083 and 15655039), and for Scientific Research (No. 16350061) from JSPS, by a Grant for the Promotion of Niigata University Research Projects, and by the Asahi Glass Foundation. We thank for Prof. H. Nishide (Waseda Univ.) for the use of their SQUID magnetometer.

References

[1] H. Nishide, T. Kaneko, in: P.M. Lahti (Ed.), Magnetic Properties of Organic Materials, vol. 279, Marcel Dekker Inc., New York, 1999, p. 285.
[2] T. Kaneko, T. Makino, H. Miyaji, M. Teraguchi, T. Aoki, M. Miyasaka, H. Nishide, J. Am. Chem. Soc. 125 (2003) 3554.
[3] T. Kaneko, T. Makino, H. Miyaji, A. Onuma, M. Teraguchi, T. Aoki, Polyhedron 22 (2003) 1845.
[4] T. Kaneko, T. Matsubara, T. Aoki, Chem. Mater. 14 (2002) 3898.
[5] (a) U.H.F. Bunz, Chem. Rev. 100 (2000) 1605;
(b) R. Giesa, J. Macromol. Sci. Rev. Macromol. Chem. Phys. C36 (1996) 631.
[6] T. Kaneko, T. Makino, G. Sato, T. Aoki, Polyhedron 20 (2001) 1291.
[7] H. Nishide, T. Kaneko, M. Igarashi, E. Tsuchida, N. Yoshioka, P.M. Lahti, Macromolecules 27 (1994) 3082.

The three-dimensional structure for the first time of a plant-type [2Fe–2S] Fd was reported in a crystallographical approach by Fukuyama et al. A small cluster modeling the active center of the Fd have been proposed by Tsukihara et al. [2], which is a peptide having twenty amino acid residues. It consists of the Fe_2S_2 core and the amino acid chain of the first shell in Fd. The details of the atomic structure revealed the existence of hydrogen bonds around the Fe_2S_2 core, which implied the stability of the local structure around the active site. Ten years later, the model peptide was reproduced by Ueyama et al. [3] by using a chemical procedure in a solvent of *N*,*N*-dimethylformamide (DMF). This cluster indicated the value of redox potential to be similar to that of natural Fd.

The theoretical approach to the active center of Fd has been progressed in the study of the series for Fe_2S_6, Fe_3S_7, Fe_4S_8 clusters. The applications of the localized spin systems have been successfully contributed to the understanding of antiferromagnetic arrangement about Fe magnetic moments in these clusters [4,5]. The results of density functional theory have also supported results of the magnetic structure of clusters [5,6]. The total number of residues in Fd's is usually about a hundred, the whole of which is too demanding to calculate with ab initio approach. Taking solvent effects, the environment effect has been studied for quantitative explanation of the redox potential [7].

As a first step from the previous work on the understanding of electronic structures, we study the Fe_2S_6 cluster which includes amino acid residues explicitly. Inclusion of residues would be important for the understanding of electron transfer because some of the residues around the Fe_2S_2 core is on the surface of Fd, as shown in experiment [1].

The antiferromagnetic coupling in Fe_2S_2 core has been one of the central issues of the model system. The relationship with amino acid residues has never been definitive in the electronic structure study. In this work, by using a state-of-the-art ab initio density functional calculation [8,9], we show the electronic structure of active site including the first shell of residues and speculate on the process of electron transfer from Fd to FNR.

2. Model system and calculation method

In this work, we required the properties of the model system: (1) that the cluster had several amino acid residues, which are accessible by the present ability of ab initio electronic structure calculation, (2) that the cluster had a hydrogen bond in itself, (3) that the cluster was expected to show a realistic property for redox potential, and (4) that the cluster had been synthesized with a chemical method artificially. Fortunately, there was a peptide, which was designed by Tsukihara et al. [2] and reproduced by Ueyama et al. [3]. This peptide sequence of cluster is based in our work.

To set up an atomic coordinate of the model cluster, we took the coordinate of a crystallographic data [10].[1] The coordinate of hydrogen atoms was assumed by the routine in AMBER code [11]. This treatment has given reasonable results for all clusters calculated in this work. In the Fd, the successive chains, Pro 38–Gly 51 and Leu 77–Val 80 were used for the model cluster. The sulfur atoms at the side chains in Cys's 41, 46, 49, and 79 are bridged to Fe atoms in the Fe_2S_2 core cluster. The two residues, Pro and Leu were inserted between Gly 51 and Leu 77, forming a structure of beta turn with a NH–O hydrogen bond. Consequently, the model cluster keeps a single successive chain, which may stabilize it even if in solvent. The N-terminus and C-terminus were terminated with the acetyl group (CH_3CO–) and the amino group (–NH_2), respectively, as the cluster obtained in [3]. The resulting configuration of cluster seems to be very similar to that of Fig. 12 in [2]. The full representation of the molecule is given in Table 1 and the schematic diagram is shown in Fig. 1. As shown in Fig. 2, one of the Fe atoms is indirectly connected with the other Fe atoms through the bridging of two S atoms ("bridging sulfur"). Each Fe atom is tetrahedrally surrounded by four S atoms, two of which bridge sulfur and the other two ("cysteine sulfur") come from the cysteine amino acid residues. The atomic structure of the two termini and the two inserted residues is locally optimized by using the forces on atoms and all the other parts of atomic configurations are fixed on the experimental data 1 in the present electronic structure calculation. The theoretical determination of structural properties for clusters could be an interesting problem, but we mainly kept the experimental configuration to see the environmental dependence of amino acid.

The peptide molecule of 20 amino acids (call 20-peptide), which is mentioned above, has three NH–S hydrogen bonds around the Fe_2S_6 cluster. These hydrogen bonds are connections between S(1) and N in Ala 6, S(5) and N in Ser 3, and S(5) and N in Arg 5. These N atoms are of the main chain of the peptide. The distances are 3.0–3.3 Å. It is known that the hydrogen bonds induce large distortion in the resulting structure of the experiment [10].

The structural properties of the local coordinate around the Fe_2S_6 cluster are summarized in Table 2, which reveal that the tetrahedral coordination around each Fe atom is distorted largely. The core cluster of Fe_2S_2 form a plane in an ideal cluster [6], but the real

[1] PDB file for Spirulina platensis: the accession code is 4FXC at the Web site of Protein Data Bank (http://www.rcsb.org.bdb/index.html).

Table 1
Iron–sulfur molecules which model the active site of ferredoxin

Label	Cluster
H-terminus	$[(FeS)_2(SH)_4]$
CH_3-terminus	$[(FeS)_2(S–CH_3)_4]$
Cys-terminus	$[(FeS)_2(Ac–Cys–NH_2)_4]$
7-Peptide	$[(FeS)_2(Ac–Ser–Cys–Ala–Ala–NH_2)\ (Ac–Cys–NH_2)_3]$
20-Peptide	$[(FeS)_2(CH_3CO–Pro–Tyr–Ser–Cys–Arg–\ Ala–Gly–Ala–Cys–Ser–Thr–Cys–Ala–\ Gly–Pro–Leu–Leu–Thr–Cys–Val–NH_2)]$
20-Peptide + Glu	$[(FeS)_2(CH_3CO–Pro–Tyr–Ser–Cys–Arg–\ Ala–Gly–Ala–Cys–Ser–Thr–Cys–Ala–\ Gly–Pro–Leu–Leu–Thr–Cys–Val–NH_2)\ (Ac–Glu–NH_2)]$

Ac specifies the acetyl group (CH_3CO–).

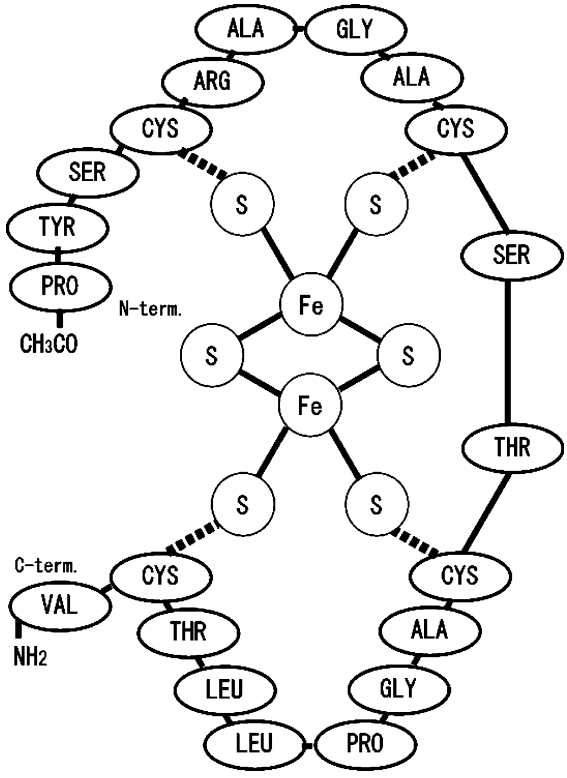


Fig. 1. Schematic peptide sequence for the peptide of 20 amino acids (20-peptide).

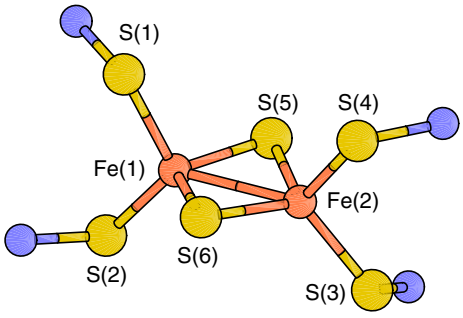


Fig. 2. Iron-sulfur cluster Fe_2S_6 of plant-type ferredoxin. The numbering besides the atoms is used in this work.

system has a dihedral angle (Table 2). These distortions could be related with the hydrogen bonds existing around the active center [10].

Table 2
Properties of bond lengths (in Å) and bond angles (in °) in the iron–sulfur cluster

Distances (Å)	
Fe(1)–Fe(2): 2.64	
Fe(1)–S(1,2): 2.28, 2.26	Fe(2)–S(3,4): 2.26, 2.27
Fe(1)–S(5,6): 2.17, 2.20	Fe(2)–S(5,6): 2.23, 2.22
Angles (°)	
S(1)–Fe(1)–S(2,5,6): 115, 108, 95.3	
S(2)–Fe(1)–S(5,6): 115, 115	S(5)–Fe(1)–S(6): 107
S(3)–Fe(2)–S(4,5,6): 103, 114, 122	
S(4)–Fe(2)–S(5,6): 113, 98.9	S(5)–Fe(2)–S(6): 104
Fe(1)–S(5)–Fe(2): 73.5	Fe(1)–S(6)–Fe(2): 73.5
Dihedral angles (°)	
S(5)–Fe(1)–Fe(2)–S(6): 168	S(1)–Fe(1)–Fe(2)–S(3,4): 178, 1.3
S(1)–Fe(1)–Fe(2)–S(5): 93.0	S(2)–Fe(1)–Fe(2)–S(3,4): 7.0, 169

To examine the role of amino acid residues, we have prepared five other model molecules, which preserve the local coordinate of Fe_2S_6 cluster, but have a different environment. The two molecules have the hydrogen and CH_3 termini, respectively, for the four termini of S atoms on Fe_2S_6. Another molecule has four Cys residues and one other molecule has four Cys and three residues. In the latter, the three residues are connected to the first Cys. The last molecule is a complex between the molecule of 20 amino acids and the Glu residue, forming a salt-bridge between the Arg and the Glu. The termini of amino acid residues in all of the five molecules are terminated with the acetyl and amino groups for N-terminus and C-terminus, respectively, as performed in the peptide of 20 amino acids. These clusters are summarized in Table 1.

To construct models for the electron transfer about Fd, the termination of Fe_2S_6 is presumably important. It is known that the extension of orbitals is observed in electronic structure calculations for the reducing electron [6]. For example, the electron was delocalized onto the CO groups in the Cys terminus [12]. In the real system, the terminus locates outside the first peptide shell. Therefore, to minimize the effect of terminus and to coincide with the synthetic molecules [3], this work uses the Ac and NH_2 groups for terminus on residue, which form a bond similar to that of the peptide bond.

The electronic structure calculation for the model clusters is based on the density functional approach [8,9]. We used ultrasoft-type pseudo-potentials [13–15] to include core–valence interactions and plane-wave basis to represent wave functions and electron densities. These pseudo-potentials are capable to deal with valence electrons in magnetic transition metal elements as well as other organic elements. The energy cut-offs of 25 and 250 Ry were taken for wave function and electron density, respectively. We used the exchange-correlation functional by Perdew et al. [16], which is known as PW91. To optimize the electronic degrees of freedom, we used the damped dynamics of Car–Parrinello's scheme [17,18], which has the property that the wave function could be updated from a scratch.

The molecule of interest was placed at the center of a cubic box and the wave function was solved with the periodic boundary condition. The molecule was separated by more than 6 Å with that in periodic image cells. This separation never disturbs the structure of valence electrons due to the fully damped electron density at the edge of the molecule. In biological molecules, the number of electrons assumed is important. The oxidized state studied here corresponds to the anion cluster having charges of 2− except for the 20-peptide molecule. The latter has 1− due to the formal charge of +1 at the side chain of Arg.

To analyze molecular orbitals, we introduced the quantity of local orbital component, which is defined as the sum of number of electrons contributed from specified orbitals. The contribution of local orbital components to magnetization can be estimated for each molecular level. The magnetization on atoms is estimated by integrating the spin density within the radius: 0.90, 0.90, 0.69, 0.69, 0.74, and 0.42 Å for Fe, S, O, N, C, and H, respectively.

3. Results

3.1. 20-Peptide molecule

The damped dynamics of Car–Parrinello scheme [17,18] provided that the system was converged to an antiferromagnetic cluster. The total magnetization of the whole cluster was vanishing. To find any other lower-energy magnetic configuration, we used the efficient scheme of non-collinear magnetism [19,20], however, obtaining the same antiferromagnetic configuration. In Fig. 3, we present the energy levels of the eigenstate and the local components around the Fermi level.

Asymmetry distribution of eigenvalues between spin-up and spin-down states (top panel in Fig. 3) is caused by the distortion on the tetrahedral geometry of S atoms. The exchange splitting of ~5 eV in Fe 3d orbitals stabilizes the system of the cluster. The level structure on

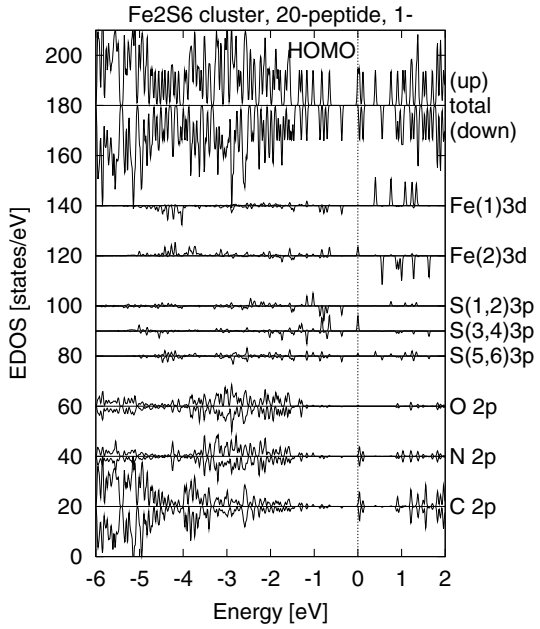


Fig. 3. Energy levels of eigenstate and their local components in the oxidized state for the 20-peptide clusters. In each panel the level of spin-up and spin-down states is shown separately. The origin of energy is taken at the HOMO level. The energy levels are broadened by the Gaussian function of the width 0.02 eV. The vertical dotted line indicates the HOMO level.

Fe atoms shows a consistency with the formal valence of Fe^{3+}, showing five levels above the Fermi level clearly. The characteristic field induced by tetrahedral geometry of S atoms is not so impressive. The S 3p orbitals are mainly just below the Fermi level, which reveals that the closed shell electron configuration forms on S atoms. The orbital components of O 2p, N 2p and C 2p exists mainly below the Fermi level.

The occupied molecular orbitals below the Fermi level mainly consist of S 3p orbitals. These orbitals show a strong hybridization with Fe 3d orbitals in the same spin state, resulting in an induction of polarized spin density on cysteine S atoms (see Table 3). At the highest occupied molecular orbital (HOMO) levels in both spin states, there exists the Fe 3d component which belongs to the spin state parallel to the magnetization of Fe atoms (majority spin state).

The unoccupied molecular orbitals above the Fermi level are the hybridized states between N 2p and C 2p and the minority spin states of Fe 3d orbitals. The former is identified to the orbitals on the side chain of Arg, which is placed just above the HOMO level, and on the main chain around the residues of Ala 13, Gly 14 and Pro 15, which are at the energies above 0.8 eV. It is noted that the empty energy level of Arg corresponds to a plus charge on the side chain of it. The lowest unoccupied molecular orbital (LUMO) level of this molecule is formally determined to be the state of Arg.

Table 3
Energy level differences (in eV) of S 3p(HOMO(up))–Fe 3d(the lowest minority spin state) and HOMO(up)–HOMO(down), and atomic magnetization (in μ_B) in Fe_2S_6 cluster for calculated molecules

Molecule	S 3p–Fe 3d	HOMO(up)–HOMO(down)	Fe(1)	Fe(2)	S(1)	S(2)	S(3)	S(4)	S(5)	S(6)
H-terminus	0.98	0.14	−3.08	3.11	−0.10	−0.09	0.09	0.10	−0.04	0.02
CH_3-terminus	0.76	0.17	−3.06	3.09	−0.12	−0.11	0.11	0.12	−0.01	−0.01
Cys-terminus	0.53	0.28	−3.04	3.09	−0.15	−0.11	0.13	0.11	0.00	−0.01
7-Peptide	0.46	0.35	−3.05	3.08	−0.14	−0.11	0.14	0.13	−0.01	−0.03
20-Peptide	0.40	0.37	−3.06	3.08	−0.13	−0.12	0.15	0.14	−0.02	−0.04
20-Peptide + Glu	0.40	0.38	−3.06	3.08	−0.13	−0.12	0.15	0.14	−0.02	−0.04

The latter is estimated to be an integration of spin density within the atomic radius defined in Section 2.

Fig. 3 shows that, above the Fermi level, the hybridization with S 3p orbitals on the cysteine sulfur (S(1)–S(4)) is relatively weak compared with that of the bridging sulfur. This implies weaker bonds between Fe and cysteine sulfurs and stronger bonds between Fe and bridging sulfurs. This indication is consistent with the picture that the Fe_2S_2 core is not bonded to a polypeptide protein, but rather bound in it. The lowest unoccupied level of Fe 3d is localized on single Fe atom. This orbital has distributions to the direction in which the vector to S atoms does not exist.

3.2. Comparison with the 20-peptide + Glu complex

In the electronic structure of 20-peptide cluster, the orbitals of Arg are indicated to be placed just on the Fermi level. Taking into account the location of Arg, which is on the surface of Fd, the Arg state could vary depending on the environment of Fd. As explicitly pointed out by Kurisu et al., the salt-bridge between the Arg and Glu in Fd plays an important role in stabilizing Fd. To see effects of the salt-bridge, we constructed the complex of 20-peptide + Glu cluster (Table 1) and also performed the electronic structure calculation. The atomic configuration of Glu is taken from the result of X-ray diffraction for Fd 1.

Fig. 4 shows the energy levels of the complex in the same way as for the 20-peptide molecule. It clearly indicates that the state of Arg disappears from the vicinity of the Fermi level. This state, which has provided a plus charge on Arg, is raised above 2 eV due to the occupied orbitals of the Glu residue. The apparent characteristic for the orbitals on Glu appeared below the HOMO level, as observed at O 2p in Fig. 4.

3.3. Comparison with the smaller molecules

Unlike the 20-peptide molecule, the 7-peptide molecule has decouplings in the main peptide chain. This structural property might lower the stability of the molecule. It, however, still keeps the three NH–S hydrogen bonds in the 20-peptide molecule, while the Cys-terminus molecule has only one NH–S hydrogen bond of connection between S(5) and N of the amino group at C-terminus on the first Cys.

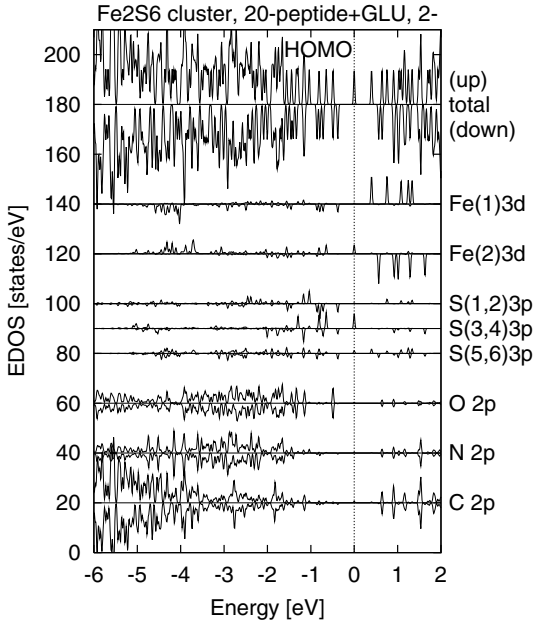


Fig. 4. Energy levels of the eigenstate and their local components in the oxidized state for the 20-peptide + Glu complex. See Fig. 3 for the scheme of the figure.

Figs. 5 and 6 present the eigen energy levels of electrons for the 7-peptide and Cys-terminus molecules, respectively. These molecules seem to almost keep the electronic structure of larger molecules (20-peptide, 20-peptide + Glu) on Fe_2S_6. The Fe 3d component in the energies at about −4 eV shows sharpening of the level compared with the larger molecules. This indicates a stronger hybridization with S 3p orbitals in the larger molecules. Although there are eight termini for residues in the smaller molecules, the orbitals originated from the terminus are not observed in vicinity of the Fermi level.

The HOMO and LUMO levels change gradually from the small molecules to the larger molecules. In Table 3, we reported the gap between the HOMO(S 3p) and the lowest Fe 3d minority-spin level. This indicates the energy necessary to place an electron at the Fe 3d level, if each electron orbital does not change (Koopmans theorem). In the real system, adding of electrons changes orbitals of the electron. In the present case the energy much larger than the gap was usually necessary to place an electron (preliminary calculations indicate

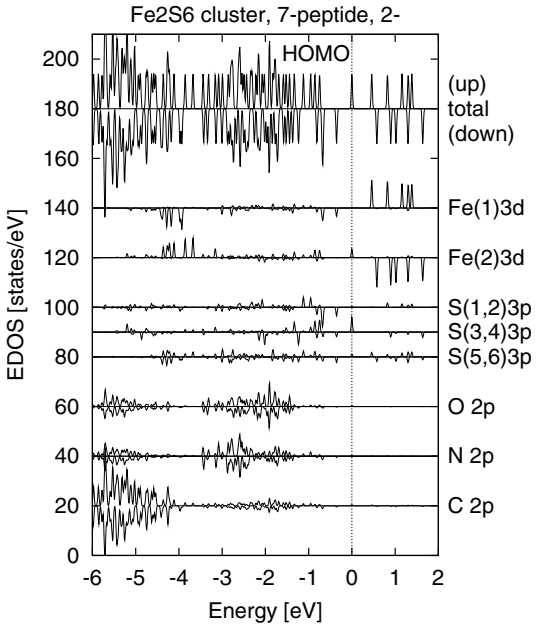


Fig. 5. Energy levels of the eigenstate and their local components in the oxidized state for the 7-peptide molecule. See Fig. 3 for the scheme of the figure.

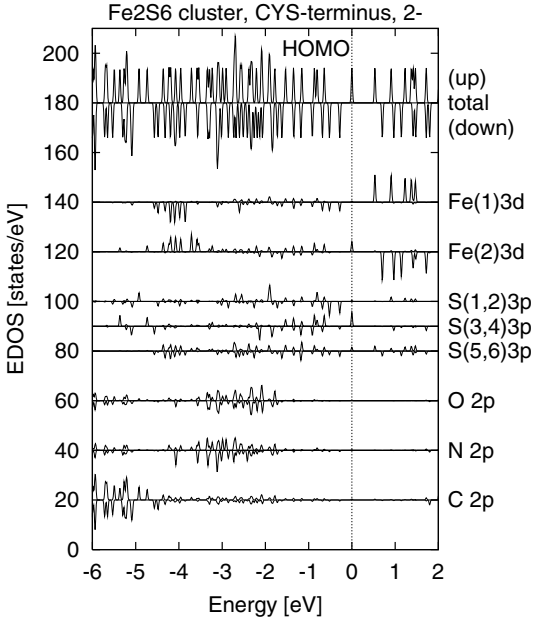


Fig. 6. Energy levels of the eigenstate and their local components in the oxidized state for the Cys-terminus molecule. See Fig. 3 for the scheme of the figure.

2–3 eV for the free standing molecules). The gap of S 3p–Fe 3d for H-terminus (0.98 eV) agrees with the value of Noodleman and Baerends (0.89 eV) [6]. This value decreases as the size of the molecule increases.

Table 3 also reports the level difference between the HOMOs of spin-up and spin-down states. This value scales the asymmetry of spin-up and spin-down states at the Fermi level. The value increases as the size of the molecule increases. Although we used the same configuration for the local coordinate in the Fe_2S_6 cluster, the change in value appeared. The asymmetry at the Fermi level is attributed to the NH–S hydrogen bonds, which are concentrated in the region of Fe(1) having spin-down polarization. These bonds relatively stabilize the levels of 3p orbitals on S(1) and S(2), resulting in lowering the HOMO level of spin-down state. As shown in Table 3, the Cys-terminus molecule which gets a hydrogen bond shows larger increase from the value of CH_3-terminus one. At the 7-peptide molecule which has full three hydrogen bonds, the value increases significantly.

3.4. Magnetic configuration

The antiferromagnetic configuration of Fe atomic magnetic moments is obtained for all molecules. The hybridization between Fe 3d and S 3p orbitals induces spin polarization on S atoms. In Table 3, atomic magnetizations are reported. The molecular dependency is not remarkable. The magnetizations on S(5) and S(6) are averaged on atomic region, resulting in small values.

4. Discussion and summary

While the Arg residue in a salt-bridge was proposed in the experiment for stabilizing electrostatically Fd itself or the complex between Fd and FNR, our calculation shows the existence of its levels around the Fermi level and implies interesting roles in the process of electron transfer. The state on Arg provides a hole orbital to the carrier electron. When the salt-bridge breaks, the electron could be around the side chain of Arg with help of a small energy perturbation. The occupation of the electron in the hole of Arg (the plus charge on Arg is compensated with the electron charge) cancels the electrostatic energy contributed from the carrier electron. If the salt-bridge is formed with help of other strong energies, the electron would overflow into Fe sites and be ready to transfer to FNR. Thus, as a speculation, the orbitals on Arg could be an electron sink and the salt-bridge on Arg could be a switch of electron transfer.

In summary, we have studied electronic structures of the model molecule, which have 20 amino acids, for the oxidized active site of Fd. The antiferromagnetic configuration has been obtained for the couple of Fe magnetic moment. The HOMO level of the molecule lies at the top of S 3p orbitals. Reflecting the distortion of Fe_2S_6 cluster, the asymmetry of spin-up and spin-down states is observed at the HOMO level and is found to correlate with the existence of hydrogen bonds. The electronic structure on Fe atoms is consistent with the formal valence of Fe^{3+}, implying that the reducing electron

occupies the minority spin state of Fe 3d orbitals unless the Arg residue in the molecule breaks its salt-bridge with Glu residue. The result of our work greatly supports an important relation between the salt-bridges and the mechanism of electron transfer. The study on reduced states is under calculation.

Acknowledgments

The calculation in this work was partially carried out using the facilities of the Supercomputer Center, Institute for Solid State Physics, University of Tokyo. The authors acknowledge the computational resources by the Research Center for Computational Science, Okazaki National Research Institutes. This work was financially supported by the Japan Society for the Promotion of Science under Grant-in Aid for Scientific Research No. 16310081. The author (H.N.) is grateful for a financial support from the Ministry of Education, Science and Culture of Japan (Research No. 15550010).

References

[1] G. Kurisu, M. Kusunoki, E. Katoh, T. Yamazaki, K. Teshima, Y. Onda, Y. Kimata-Ariga, T. Hase, Nature Struct. Biol. 8 (2001) 117.
[2] T. Tsukihara, M. Kobayashi, M. Nakamura, Y. Katsube, K. Fukuyama, T. Hase, K. Wada, H. Matsubara, Biosystems 15 (1982) 243.
[3] N. Ueyama, S. Ueno, A. Nakamura, K. Wada, H. Matsubara, S. Kumagai, S. Sakakibara, T. Tsukihara, Biopolymers 32 (1992) 1535.
[4] R.H. Sands, W.R. Dunham, Q. Rev. Biophys. 7 (1997) 443.
[5] L. Noodleman, C.Y. Peng, D.A. Case, J.-M. Mouesca, Coord. Chem. Rev. 144 (1995) 199.
[6] L. Noodleman, E.J. Baerends, J. Am. Chem. Soc. 106 (1984) 2316.
[7] R.A. Torres, T. Lovell, L. Noodleman, D.A. Case, J. Am. Chem. Soc. 125 (2003) 1923.
[8] P. Hohenberg, W. Kohn, Phys. Rev. 136 (1964) B864.
[9] W. Kohn, L.J. Sham, Phys. Rev. 140 (1965) A1133.
[10] K. Fukuyama, T. Hase, S. Matsumoto, T. Tsukihara, Y. Katsube, N. Tanaka, M. Kakudo, K. Wada, H. Matsubara, Nature 286 (1980) 522.
[11] D.A. Pearlman, D.A. Case, J.W. Caldwell, W.S. Ross, T.E. Cheatham III, S. DeBolt, D. Ferguson, G. Seibel, P. Kollman, Comput. Phys. Commun. 91 (1995) 1.
[12] R. Morales, M. Frey, J.-M. Mouesca, J. Am. Chem. Soc. 124 (2002) 6714.
[13] D. Vanderbilt, Phys. Rev. B 41 (1990) 7892.
[14] A. Pasquarello, K. Laasonen, R. Car, C. Lee, D. Vanderbilt, Phys. Rev. Lett. 69 (1992) 1982.
[15] K. Laasonen, A. Pasquarello, R. Car, C. Lee, D. Vanderbilt, Phys. Rev. B 47 (1993) 10142.
[16] J.P. Perdew, J.H. Chevary, S.H. Vosko, K.A. Jackson, M.R. Pederson, D.J. Singh, C. Fiolhais, Phys. Rev. B 46 (1992) 6671.
[17] R. Car, M. Parrinello, Phys. Rev. Lett. 55 (1985) 2471.
[18] F. Tassone, F. Mauri, R. Car, Phys. Rev. B 50 (1994) 10561.
[19] T. Oda, A. Pasquarello, R. Car, Phys. Rev. Lett. 80 (1998) 3622.
[20] T. Oda, A. Pasquarello, Phys. Rev. B 70 (2004) 134402.

yield chemically pure crystals of either the HT or LT forms. In some cases, ac susceptibility measurements show that a single-crystal can either have a HT or LT peak, but *not* both. The majority of crystal structures reported for $[Mn_{12}O_{12}(O_2CR)_{16}(H_2O)_4]$ complexes exhibit HT behavior and have activation energies towards magnetization reversal of $U_{eff} = 60–70$ K. A much smaller family of $[Mn_{12}O_{12}(O_2CR)_{16}(H_2O)_4]$ are LT and have activation energies in the 20–40 K range. Crystal structures of each isomer can be solved. The LT form has an abnormally oriented Jahn–Teller axis in the coordination geometry of one or more of the Mn^{III} ions. These abnormal Jahn–Teller axes are oriented towards a μ_3-oxide which, topographically, reside near the plane of the disc-like shape of the $[Mn_{12}O_{12}]$ core. The HT form does not have an abnormally oriented Jahn–Teller axis at a Mn^{III} ion. This phenomenon has been coined "Jahn–Teller isomerism" (JTI). In this paper, we report the characterization of a new LT complex, $[Mn_{12}O_{12}(O_2CC_6H_4\text{-}2\text{-}CH_3)_{16}(H_2O)_4] \cdot S$.

2. Experimental

2.1. Synthesis

All solvents and reagents were used as received. All reactions were performed under aerobic conditions.

$[Mn_{12}O_{12}(O_2CC_6H_4\text{-}2\text{-}CH_3)_{16}(H_2O)_4] \cdot CH_2Cl_2 \cdot 2H_2O$ (complex **1**). Multiple treatments of a toluene slurry of $Mn_{12}Ac$ (4.0 g, 1.94 mmol) with a large excess of 2-methylbenzoic acid (8.7 g, 63.9 mmol) followed by solvent removal and washing of the excess carboxylate ligand with ethanol yields the product $[Mn_{12}O_{12}(O_2CC_6H_4\text{-}2\text{-}CH_3)_{16}(H_2O)_4]$. *Anal.* calc. for $C_{128}H_{120}Mn_{12}O_{48}$: C, 49.8; H, 3.9. Found: C, 50.3; H, 3.8%. Crystallization solvents were saturated with 2-methylbenzoic acid before their use. Crystallization is achieved by layering a CH_2Cl_2 solution of complex **1** with hexanes. Over a period of three weeks, block shaped crystals with the formula $[Mn_{12}O_{12}(O_2CC_6H_4\text{-}2\text{-}CH_3)_{16}(H_2O)_4] \cdot 2H_2O \cdot CH_2Cl_2$ precipitate from the solution.

2.2. Physical measurements

High frequency electron paramagnetic resonance (HFEPR) measurements were performed on home made instrumentation described elsewhere [26]. Low temperature magnetization versus field data were collected using a micro-Hall effect magnetometer which is described in [27]. Practical considerations of the crystal morphology for complex **1** meant that the magnetic field orientation for the data presented in both the single-crystal HFEPR and single-crystal magnetization studies was ~45° away from the easy axis of **1**.

3. Results and discussion

3.1. Description of structure

Several relevant crystal structure parameters are listed in Table 1 for complex **1**. The crystal structure for $[Mn_{12}O_{12}(O_2CC_6H_4\text{-}2\text{-}CH_3)_{16}(H_2O)_4] \cdot CH_2Cl_2 \cdot 2H_2O$ (**1**) is illustrated in Fig. 1. Complex **1** crystallizes in the monoclinic *C2/c* space group. The atoms Mn(5) and Mn(5a), which are related by a crystallographic C2 axis, have an unusually oriented Jahn–Teller axis. This abnormally oriented Jahn–Teller axis contains an oxide ion, O(1), a situation which is highly unusual: JT elongation axes usually orient so as to avoid the strong Mn(III)–O^{2-} bonds, normally the shortest bonds about a Mn(III) ion. These abnormally oriented Jahn–Teller axes reside nearly in the plane of the ring formed by the the eight Mn(III) surrounding the cubane core. The other six Mn(III) ions have their Jahn–Teller elongation axis situated essentially parallel to each other and orthoganol to the plane of the ring of Mn(III) ions.

3.2. Alternating current magnetic susceptibility studies

Ac magnetic susceptibility data were collected for a single-crystal sample of complex **1** in the 1.8–10 K range with a 3 Oe ac field oscillating in the frequency range of 50–1000 Hz. The external dc magnetic field was fixed at zero. Complex **1** is a LT form and exhibits an out-of-phase peak in its ac susceptibility in the 2–4 K region as seen in Fig. 2. The appearance of frequency dependent peaks in the out-of-phase ac susceptibility is evidence for slow magnetization relaxation dynamics relative to the frequency of the applied oscillating ac field. The magnetization relaxation rates can be

Table 1
Crystallographic parameters for complex **1**

Complex	**1**
Solvate (S)	$CH_2Cl_2 \cdot 2H_2O$
Crystal system	monoclinic
Space group	*C2/c*
Crystal habit	block
a (Å)	17.4305(9)
b (Å)	38.214(2)
c (Å)	21.0129(11)
α (°)	90
β (°)	98.5610(10)
γ (°)	90
V (Å^3)	13840.6(12)
Z	4
Temperature (K)	100(2)
Reflections collected	43649
Number of observed reflections	13003
Independent reflections	15785
Final *R* indices [$I > 2\sigma(I)$]	$R_1 = 0.0837$
R indices (all data)	$R_1 = 0.0960$
Goodness-of-fit on F^2	0.870

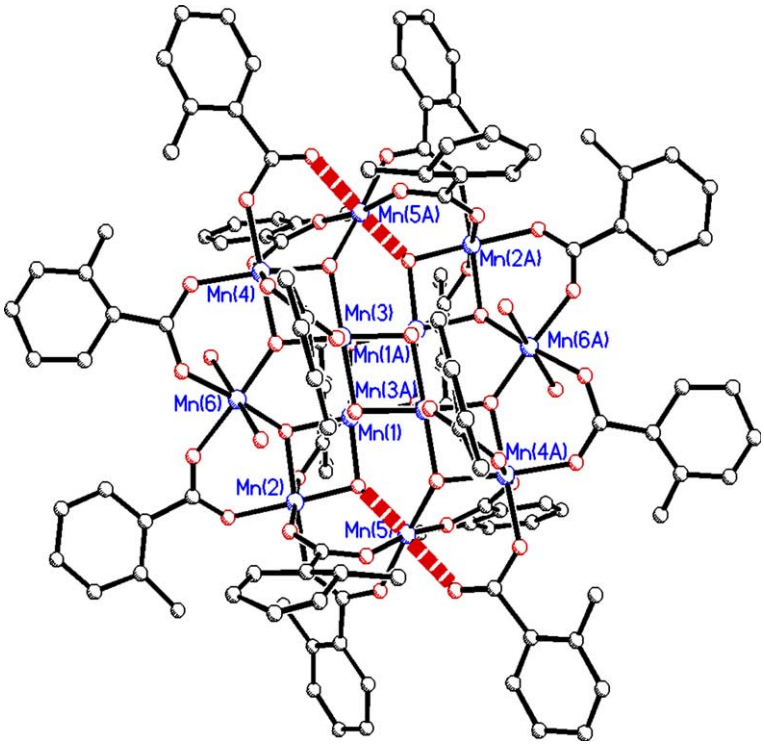


Fig. 1. ORTEP representation of the LT complex $[Mn_{12}O_{12}(O_2CC_6H_4\text{-}2\text{-}CH_3)_{16}(H_2O)_4]\cdot CH_2Cl_2\cdot 2H_2O$ (complex **1**). The thick dashed lines represent abnormally oriented Jahn–Teller axes.

quantified by analyzing the frequency dependencies of the χ''_M signals for the two complexes as shown in Fig. 2. Data were collected for several ac frequencies in the 50–1000 Hz range and the maxima of the χ''_M were used in conjunction with the Arrhenius equation

$$\ln(1/\tau) = \ln(1/\tau_0) - U_{\text{eff}}/kT \quad (1)$$

to calculate the barrier towards magnetization reversal as $U_{\text{eff}} = 29$ K for complex **1**. Complex **1** has an activation energy towards magnetization reversal, U_{eff}, that is nearly half of its parent compound, $Mn_{12}Ac$, which has an activation energy of $U_{\text{eff}} = 62$ K.

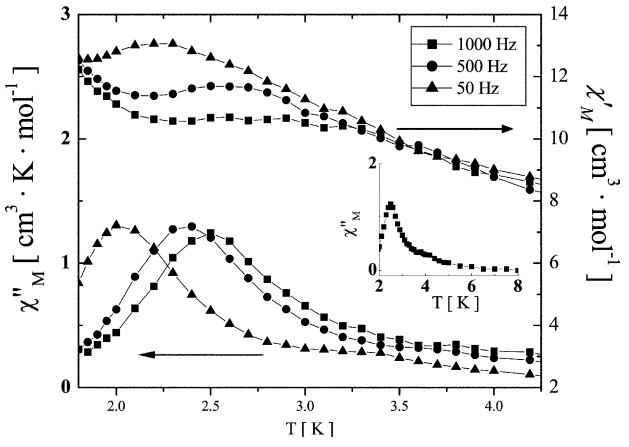


Fig. 2. Plot of the variable-temperature ac susceptibility for a single crystal of complex (**1**) collected for several frequencies. The in-phase responses are shown in the upper part of the plot, whereas the out-of-phase responses are shown in the lower part.

3.3. Magnetization versus magnetic field hysteresis

Fig. 3 shows the single-crystal magnetization hysteresis data for complex **1** measured at 0.38 K for two

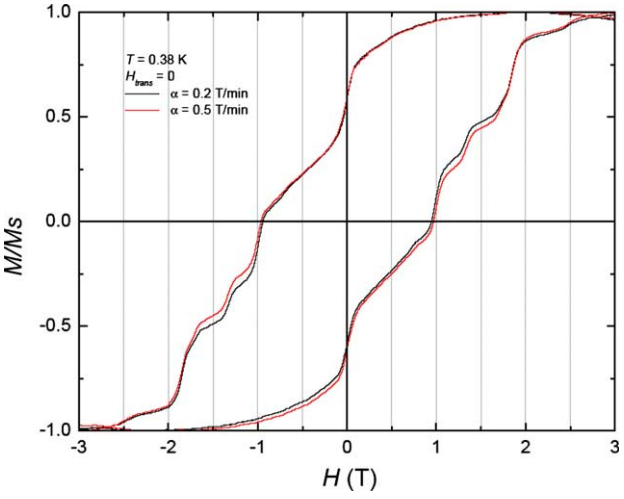


Fig. 3. Plot of the normalized magnetization (M/M_S) vs. magnetic field (H), where M_S is the saturation magnetization. Data were collected on a single crystal at a temperature of 0.38 K and scanning rates of 0.2 and 0.5 T/min with the longitudinal magnetic field ~45° away from the easy axis.

different sweep rates, 0.2 and 0.5 T/min. The applied magnetic field was ~45° away from the easy axis of magnetization. A complex hysteresis loop is observed. The observation of an appreciable coercive field along with magnetic field sweep rate dependent steps in the hysteresis loop for the field interval between 1 and 3 T confirms the single-molecule magnet behavior of **1**. The steps are due to quantum tunneling of the magnetization. There is also a large step observed at zero magnetic field.

3.4. High frequency EPR (HFEPR) studies

In order to determine the ground state spin Hamiltonian parameters for complex **1**, HFEPR data of a single-crystal sample were collected. The spectra are shown in Fig. 4 for a microwave frequency of 324 GHz and at temperatures of 2, 4, 6, 8, 10, 12, 14, and 16 K. The frequency dependence of several resonances were simulated using an $S = 10$ spin Hamiltonian. The Zeeman interaction, axial zero-field splitting, $D(\hat{S}_z^2)$, and the fourth order zero-field term, $B_4^0\hat{O}_4^0$, were included in the analysis. Fig. 5 depicts the results obtained from the simulations of the resonances, which are consistent with the following parameters: $g_z = g_x = g_y = 2.0$, $D = -0.47$ cm^{-1}, and $B_4^0 = -2.0 \times 10^{-5}$ cm^{-1}.

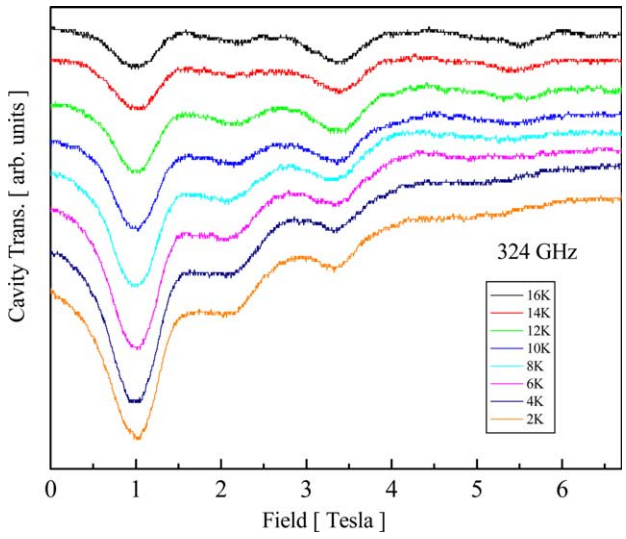


Fig. 4. HFEPR spectra measured at 324 GHz for a single-crystal sample of complex **1**. Data were collected at the temperatures of 2, 4, 6, 10, 12, 14, and 16 K with the magnetic field oriented ~40° to the easy axis direction.

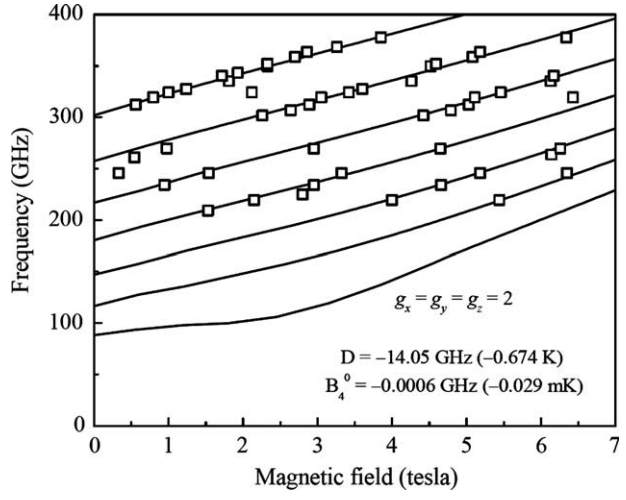


Fig. 5. Zeeman diagram for the spin Hamiltonian associated with the $S = 10$ ground state of complex **1** with the magnetic field oriented ~40° to the easy axis direction. The solid lines represent the energy spectrum obtained from the simulation to the resonances.

4. Conclusion

The synthesis and crystal structure of a LT Mn_{12} complex are reported. Steps, with the most pronounced having field intervals of ~0.8 T, are observed in magnetization hysteresis plots collected for a single crystal at millikelvin temperatures. These steps confirm that **1** behaves as a single-molecule magnet. HFEPR data collected on this sample allowed for the quantitative characterization of the spin Hamiltonian parameters $g_z = g_x = g_y = 2.0$, $D = -0.47$ cm^{-1}, and $B_4^0 = -2.0 \times 10^{-5}$ cm^{-1}. The resonance positions of the steps seen in the magnetization hysteresis plot are consistent with the parameters obtained from the EPR studies when the ~45° angle between the easy axis and magnetic field is taken into consideration ($0.8\cos(45°) \approx 0.5$).

Acknowledgments

This work was supported by the National Science Foundation (CHE0350615, DMR0103290 and DMR0239481). S.H. is a Cottrell scholar of the Research Corporation.

References

[1] G. Christou, D. Gatteschi, D.N. Hendrickson, R. Sessoli, MRS Bull. 25 (11) (2000) 66.
[2] D. Gatteschi, R. Sessoli, Angew. Chem. Int. Ed. 42 (3) (2003) 268.
[3] R. Sessoli, H.L. Tsai, A.R. Schake, S.Y. Wang, J.B. Vincent, K. Folting, D. Gatteschi, G. Christou, D.N. Hendrickson, J. Am. Chem. Soc. 115 (5) (1993) 1804.
[4] D. Ruiz-Molina, G. Christou, D.N. Hendrickson, Mol. Cryst. Liq. Cryst. 343 (2000) 335.
[5] M. Soler, S.K. Chandra, D. Ruiz, J.C. Huffman, D.N. Hendrickson, G. Christou, Polyhedron 20 (11–14) (2001) 1279.
[6] M. Soler, S.K. Chandra, D. Ruiz, E.R. Davidson, D.N. Hendrickson, G. Christou, Chem. Commun. (24) (2000) 2417.
[7] P. Gerbier, D. Ruiz-Molina, N. Domingo, D.B. Amabilino, J. Vidal-Gancedo, J. Tejada, D.N. Hendrickson, J. Veciana, Monatsh Chem. 134 (2) (2003) 265.
[8] T. Kuroda-Sowa, M. Lam, A.L. Rheingold, C. Frommen, W.M. Reiff, M. Nakano, J. Yoo, A.L. Maniero, L.C. Brunel, G. Christou, D.N. Hendrickson, Inorg. Chem. 40 (25) (2001) 6469.

[9] A.R. Schake, H.L. Tsai, N. Devries, R.J. Webb, K. Folting, D.N. Hendrickson, G. Christou, J. Chem. Soc., Chem. Commun. 5 (2) (1992) 181.
[10] A.R. Schake, H.L. Tsai, R.J. Webb, K. Folting, G. Christou, D.N. Hendrickson, Inorg. Chem. 33 (26) (1994) 6020.
[11] H.L. Tsai, T.Y. Jwo, G.H. Lee, Y. Wang, Chem. Lett. (4) (2000) 346.
[12] H.L. Tsai, D.M. Chen, C.I. Yang, T.Y. Jwo, C.S. Wur, G.H. Lee, Y. Wang, Inorg. Chem. Commun. 4 (9) (2001) 511.
[13] G. Aromi, S.M.J. Aubin, M.A. Bolcar, G. Christou, H.J. Eppley, K. Folting, D.N. Hendrickson, J.C. Huffman, R.C. Squire, H.L. Tsai, S. Wang, M.W. Wemple, Polyhedron 17 (17) (1998) 3005.
[14] H.J. Eppley, S.M.J. Aubin, M.W. Wemple, D.M. Adams, H.L. Tsai, V.A. Grillo, S.L. Castro, Z.M. Sun, K. Folting, J.C. Huffman, D.N. Hendrickson, G. Christou, Mol. Cryst. Liq. Cryst. A 305 (1997) 167.
[15] D. Ruiz, Z.M. Sun, B. Albela, K. Folting, J. Ribas, G. Christou, D.N. Hendrickson, Angew. Chem., Int. Ed. Engl. 37 (3) (1998) 300.
[16] S.M.J. Aubin, Z. Sun, E.M. Rumberger, D.N. Hendrickson, G. Christou, J. Appl. Phys. 91 (10) (2002) 7158.
[17] S.M.J. Aubin, Z.M. Sun, H.J. Eppley, R.M. Rumberger, I.A. Guzei, K. Folting, P.K. Gantzel, A.L. Rheingold, G. Christou, D.N. Hendrickson, Polyhedron 20 (11–14) (2001) 1139.
[18] M. Soler, W. Wernsdorfer, Z.M. Sun, J.C. Huffman, D.N. Hendrickson, G. Christou, Chem. Commun. (21) (2003) 2672.
[19] N. Soler, W. Wernsdorfer, Z.M. Sun, D. Ruiz, J.C. Huffman, D.N. Hendrickson, G. Christou, Polyhedron 22 (14–17) (2003) 1783.
[20] S.M.J. Aubin, Z.M. Sun, H.J. Eppley, E.M. Rumberger, I.A. Guzei, K. Folting, P.K. Gantzel, A.L. Rheingold, G. Christou, D.N. Hendrickson, Inorg. Chem. 40 (9) (2001) 2127.
[21] D. Ruiz, Z.M. Sun, S.M.J. Aubin, E. Rumberger, C. Incarvito, K. Folting, A.L. Rheingold, G. Christou, D.N. Hendrickson, Mol. Cryst. Liq. Cryst. A 334 (1999) 1125.
[22] Z.M. Sun, D. Ruiz, N.R. Dilley, M. Soler, J. Ribas, K. Folting, M.B. Maple, G. Christou, D.N. Hendrickson, Chem. Commun. (19) (1999) 1973.
[23] Z.M. Sun, D. Ruiz, E. Rumberger, C.D. Incarvito, K. Folting, A.L. Rheingold, G. Christou, D.N. Hendrickson, Inorg. Chem. 37 (19) (1998) 4758.
[24] S.M.J. Aubin, Z.M. Sun, I.A. Guzei, A.L. Rheingold, G. Christou, D.N. Hendrickson, Chem. Commun. (22) (1997) 2239.
[25] S.M.J. Aubin, Z.M. Sun, I.A. Guzei, A.L. Rheingold, G. Christou, D.N. Hendrickson, Chem. Commun. (22) (1997) 2239.
[26] M. Mola, S. Hill, P. Goy, M. Gross, Rev. Sci. Instrum. 71 (1) (2000) 186.
[27] A.D. Kent, S. von Molnar, S. Gider, D.D. Awschalom, J. Appl. Phys. 76 (10) (1994) 6656.

during the time evolution. The most powerful quantum algorithms, such as the one by Shor for factorizing large integers, where shown to require proper sequences of single- and two-qubit gates, i.e., unconditional rotations of single subsystems and unitary transformations of interacting couples [2]. Indeed, this selective addressing of the different qubits and the timely tuning of the couplings between them are among the most experimentally demanding achievements on the way to the QIP implementation.

Very recently, Meier, Levy, and Loss [3] have asserted the suitability to the application of this approach of those antiferromagnetic spin clusters characterized by a ground-state doublet, each cluster corresponding to an effective two-level system. One of the main advantages with respect to previously proposed single-spin encodings (i.e., one qubit per electron spin) [4] would arise from the largest size of the molecules, and from the resulting reduction of the spatial resolution which is required for the selective addressing of the qubits by means of pulsed magnetic fields. On the other hand, a number of issues arising from the multi-spin encoding of the qubit remains to be considered. In particular, an unwanted population loss from the ground-state doublet to the higher states (leakage) might occur during the manipulation: can the energy separation between the computational and the additional states of each molecule, as well as the molecule symmetries, be engineered in order to keep the leakage negligible throughout the time evolution? Besides making the higher energy levels harmless, is it possible to exploit them as a computational resource, and to develop a system-specific route to the implementation of the quantum gates? More generally, do the permanent intercluster couplings (such as the ones demonstrated in analogous molecular magnets [5]) allow the realization of both the conditional and unconditional dynamics?

In the present paper, we address some of these open questions. In particular, we consider the antiferromagnetic heterometallic ring $\{[Me_2NH_2]^+[Cr_7NiF_8(O_2CCMe_3)_{16}]^-\}$, Cr_7Ni in short [6], where the substitution of one $Cr^{III}(S = 3/2)$ ion with a $Ni^{II}(S = 1)$ provides an extra spin to the otherwise compensated molecule. We first show that Cr_7Ni is a suitable candidate for the qubit encoding, for it possesses an energetic spectrum and symmetries that allow to perform the required rotations within the computational space, while keeping the occupation of the excited states negligible. We also report preliminary characterization of Cr_7Ni-dimers in which couples of Cr_7Ni clusters are linked by diamines. Finally, we propose a scheme for selectively turning on and off the effective qubit–qubit coupling, by exploiting the presence of specific auxiliary states which belong to the excited $S = 3/2$ quadruplet, and in spite of the permanent nature of the intercluster interaction.

2. The molecular Cr_7Ni ring as qubit

In order to characterize the lowest-lying states of the Cr_7Ni molecule, we have performed low-temperature specific heat measurements. This is a powerful technique, since the observed Schottky anomaly is directly related to the pattern of the lowest energy eigenvalues. Measurements at zero magnetic field are particularly important, since they are obtained without any perturbing field. Although the energy level scheme is similar for most of these cyclic spin system, the presence of a huge lattice contribution and the need to simultaneously determine different microscopic parameters of the spin Hamiltonian require more experimental data. The lattice contribution is dominant above ~5 K and it does not change upon the application of a magnetic field, so it can be essentially determined by fitting data at high temperature. Conversely, the Schottky anomaly dominates at low temperatures and it changes upon the application of an external field **B**, as a consequence of Zeeman splitting of the lowest multiplets (see Fig. 1). Thus, the independent fit of few experimental curves obtained at different values of **B** allows the determination of the microscopic parameters appearing in the following spin Hamiltonian:

$$\mathscr{H} = \sum_{i=1}^{8} J_i \mathbf{s}_i \cdot \mathbf{s}_{i+1} + \sum_{i=1}^{8} d_i [s_{z,i}^2 - s_i(s_i+1)/3] + \sum_{i<j=1}^{8} \mathbf{s}_i \cdot \mathbf{D}_{ij} \cdot \mathbf{s}_j + \mu_B \sum_{i=1}^{8} g_i \mathbf{B} \cdot \mathbf{s}_i,$$

the first term corresponds to the dominant antiferromagnetic Heisenberg exchange between nearest neighbouring spins, with an antiferromagnetic character; the second and third anisotropic terms account for the

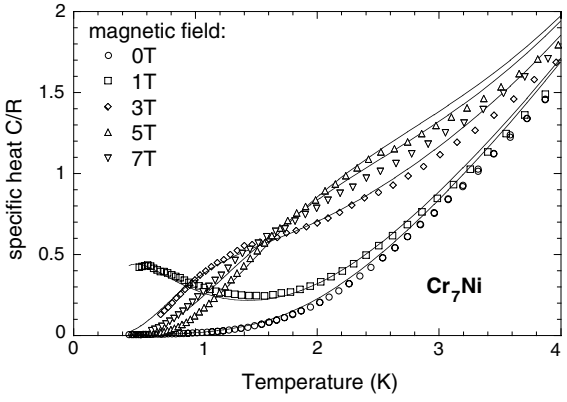


Fig. 1. Temperature dependence of the specific heat $C(T,H)$ (normalized to the gas constant R) of molecular Cr_7Ni ring: the evolution of the magnetic contribution (Schottky anomaly) in different magnetic fields should be noted. Unbroken lines are the best fit curves of the experimental data obtained as described in the text.

intracluster dipole–dipole interaction and for the coupling to the crystal field, respectively; finally, we consider the Zeeman coupling to the external field, with $g_{Cr} = 1.98$ and $g_{Ni} = 2.2$, respectively. The microscopic parameters entering the spin Hamiltonian were determined by fitting the magnetic-field dependent specific heat data: $J_{Cr}/k_B = (17.0 \pm 1.5)$ K, $J_{Ni}/J_{Cr} = 0.9$, $|d_i|/k_B = (0.3 \pm 0.15)$ K (for all the spin sites). The resulting ground state at zero field consists in a doublet with total spin $S = 1/2$, whilst the first excited multiplet approximately corresponds to $S = 3/2$. In fact, the presence of the anisotropy and Zeeman terms mixes different multiplets, and the total spin S is no longer a good quantum number (our two-step procedure, developed in [7], allows us to properly take into account such S-mixing). We have recently performed high-field torque-magnetometry experiments on a Cr_7Ni single crystal [8], and found that S-mixing has important effects at the level (anti-) crossing. Conversely, our calculations show that the mixing of different multiplets is little at low fields and does not significantly influence the implementation of the qubit operations; in particular, the ground state doublet has an approximated Kramers nature, imposed by the system symmetry, and an energy separation of $\Delta_0/k_B = 13$ K from the $S = 3/2$ multiplet. Further inelastic-neutron-scattering (INS) [9] and high field torque-magnetometry experiments agree well with the above estimates and allow a refined estimate of the exchange and anisotropy parameters (the accuracy of the specific heat data fit gives an error bar of 10% for the microscopic parameters, error that largely accounts for the values independently obtained by different experiments, cfr. [8,9]). In particular, the sign of the torque signal showed that the $S = 3/2$ multiplet has an easy plane anisotropy thus implying a negative d_i. Also the INS-data confirm the dominant axial character of the anisotropy, and the irrelevance of further (i.e., rhombic or higher order) anisotropic terms to the fitting of the experimental results. We thus conclude that the influence of such terms on the dynamics of this spin system and can be safely neglected for the purpose of the QIP implementation.

Based on these results, we identify the computational basis with the ground-state doublet $S = 1/2$: $|0\rangle \equiv |S_z = -1/2\rangle$ and $|1\rangle \equiv |S_z = +1/2\rangle$. The energy separation between these states and the next excited one, $\Delta_0/k_B \approx 13$ K, allows the cluster to be considered as an effective two-level system; the application of a static magnetic field perpendicular to the ring plane, $\mathbf{B}_0 = B_0\mathbf{z}$, reduces the value of Δ_0. On the other hand, the qubit initialization to its $|0\rangle$ state requires the ring to be cooled at a temperature which is much lower than the energy splitting between the computational states, i.e., $T < \mu_B B_0/k_B$, and it is therefore favoured by a high B_0. A reasonable compromise turns out to be $B_0 \approx 2T$, which implies $T \leqslant 1$ K.

Any quantum algorithm can be obtained by combining general one-qubit rotations with a non-trivial two-qubit gate (a CNOT, or an equivalent one). In the present case, the gating can be realized by applying sequences of pulsed magnetic fields $\mathbf{B}_1(t)$ orthogonal to the static field $\mathbf{B}_0$. As already mentioned, one of the main sources of errors that comes with the use of effective, rather than true, two-level systems is represented by the population loss to the cluster excited states, the so-called "*leakage*", which is given by $L = 1 - [|\langle 0|\psi(t)\rangle|^2 + |\langle 1|\psi(t)\rangle|^2]$. Quite generally, the longer are the field pulses that are used for the state manipulation, the better they spectrally resolve the required transitions, thus avoiding leakage. However, our simulations show that the relatively large value of Δ_0 in the present systems, allows to keep L below 10^{-4} even for a gating time (i.e., pulse duration) of the order of 150 ps [10].

On long enough time scales, the coupling of the system with the solid-state environment spoils its coherent evolution and causes decoherence. A quantitative evaluation of the decoherence rate for the present system requires specific experimental and theoretical work, that still needs to be carried out. Here, we simply point out that that the main decoherence source for the Cr_7Ni rings is expected to consist in the (super-)hyperfine coupling between the Cr electron spin and the closest nucleus of F. A preliminary evaluation of the decoherence time can be obtained by magnetization measurements with resonant photon absorbtion on Cr_7Ni, which give $\tau_d \sim 25$ ns [11] . This, however, should only be considered as a lower bond for τ_d, since these experiments are carried out on bulk crystals, whose coherence is limited by the inhomogeneous broadening, i.e., from possible differences between the rings of the bulk. Thus, while the chemical substitution of F with other chemical groups might certainly contribute to an increase of τ_d, the present value of the τ_d/τ_c ratio is already large enough for a large number of quantum gates to be performed in these systems. It is also worth mentioning that working in the *mK* temperature region and using static fields $\mathbf{B}_0$ of few Tesla, it is possible to polarize the nuclear spins and make large the mismatch between nuclear and electronic energy gaps thus, in principle, vanishing the effects of this mechanism of decoherence.

3. Possible routes for implementation of multiple-qubit gates

The implementation of the two-qubit gate in molecular magnets does certainly provide further challenging issues. In fact, not only it requires the realization of intercluster molecular links, such as the ones that have been demonstrated between Mn_4 dimers [5], but also a timely switch (on and off) of the coupling during gating. Here, we firstly report preliminary experimental results

on "Cr_7Ni-dimers", and then we propose a computational scheme that allows the above switching even in presence of an untuneable intercluster interaction.

We measured the magnetic and thermal properties of two "Cr_7Ni-dimers", namely $\{[Cr_7NiF_8(O_2CCMe_3)_{16}]_2[H_3N(CH_2)_9NH_3]\}$ (labelled as GT67) and $\{[Cr_7NiF_8(O_2CCMe_3)_{16}]_2[H_3N(CH_2)_8NH_3]\}$ (labelled as GT100) whose unit cell comprises two Cr_7Ni rings linked by diamines of different lengths. The preparation and structural characterization of these derivatives will be reported elsewhere [12]. In Fig. 2, we plot the ac susceptibility χ_{ac} measured on ca. 50 mg powders of each derivative and we compare them with that of Cr_7Ni. In Fig. 3, we report the dc magnetization measured at 0.4 K on small grains (ca. $200 \times 200 \times 200\ \mu m^3$) of each compound by mean of home-made Hall micro-probes. Only half unit cell of GT100 and GT67 was considered for a proper data normalization. It turns out that the behaviour of these two derivatives is very close to that of the original molecular Cr_7Ni ring in the range of temperature (0.4–100 K) and magnetic field we explored. Briefly, the $\chi_{ac}T$ product saturates to the value of the Curie constant $g^2\mu^2N_AS(S+1)/3k_B$ correspondent to $S = 1/2$ at low temperature whilst the bump at ~40 K in the χ_{ac} versus T curve is due to the population of excited states. The magnetization measured at 0.4 K fits the Brillouin curve calculated for $S = 1/2$ and no anomaly is evident at low field. In Fig. 4, we also report the low temperature specific heat $C(T)$ of the GT67 and GT100 compounds and we compare results with data obtained for molecular Cr_7Ni wheels after proper normalization. The experimental data, overlap each others except for the deviation of the specific heat curve of GT100 below 1 K. Different samples were measured and according to our experience the $C(T)$ behaviour below 1 K turns out to be sample dependent and it also change upon the application of weak magnetic field (~0.1 T). This is not surprising since the absolute value of $C(T)$ drops below 1 K – even for Cr_7Ni – so it is likely that the $C(T)$ is influenced by the presence of even very small amount of magnetic impurities or defected wheels. Further work is thus needed in order to probe the presence of an intercluster coupling. However, these results show that the basic Cr_7Ni wheels are essentially preserved in all these derivatives if looked at large energy scale and we may, at

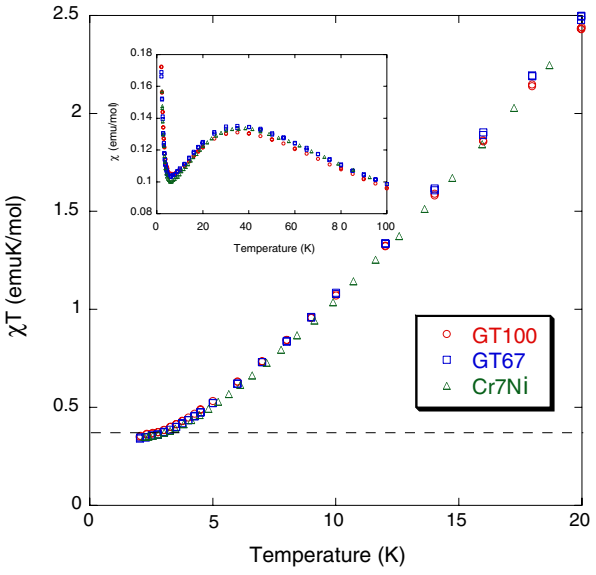


Fig. 2. The behaviour of ac susceptibility χ_{ac} measured at $f = 90$ Hz and $H_{ac} = 15$ Oe. In the main graph, the product χT as a function of temperature of Cr_7Ni and (Cr_7Ni)-dimers, referred as GT67 and GT100, respectively, in the text, is plotted. Note that χT tends to saturate close to the value of the Curie constant $g^2\mu^2N_AS(S+1)/3k_B$ correspondent to $S = 1/2$ at low temperature. Inset: temperature dependence of the ac susceptibility χ_{ac} for the same derivatives.

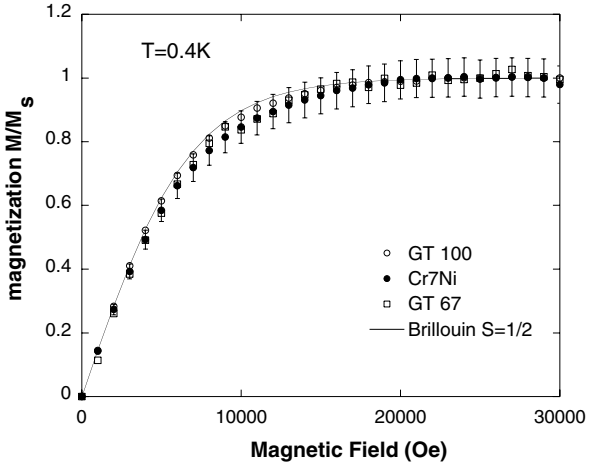


Fig. 3. Magnetization, normalized to the saturation values, of the Cr_7Ni ring and two (Cr_7Ni)-dimers, referred as GT67 and GT100 in the text, measured at 0.4 K. The observed behaviours for the different compounds are close, within our experimental accuracy, one to the others and to the Brillouin curve calculated for $S = 1/2$.

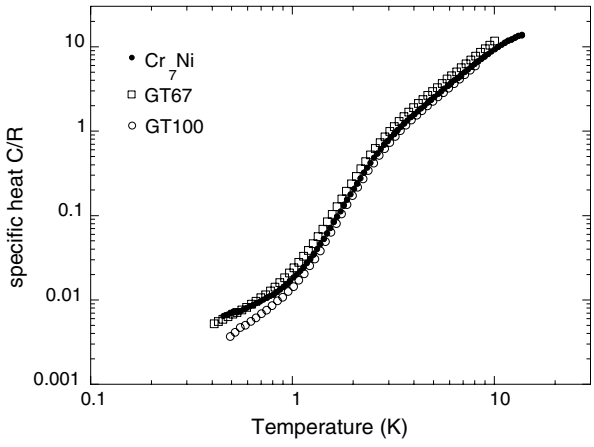


Fig. 4. Specific heat C, normalized to the gas constant R, of the molecular Cr_7Ni ring and the two (Cr_7Ni) dimers named GT67 and GT100, respectively, in the text.

least, give an upper bond of c.a. 1 K for such coupling between Cr_7Ni wheels in the studied dimers. A close inspection of the crystal structure of these derivatives also shows little overlap between the wavefunctions of the Cr ions and the diamines and this further corroborates the weakness of the expected coupling. We believe that the preparation and characterization of molecular dimers will be an interesting issue to pursue in the next years. We just mention here that other chemical strategies are currently explored and results will be presented elsewhere [12] and in the following we briefly present a possible scheme for the implementation of the required two-qubit gate, namely the CNOT.

We assume that a permanent link exists between two molecular qubits, hereafter named A and B, both characterized by the above-mentioned antiferromagnetic ordering of the respective ground states, and thus by an (approximately) antiparallel alignment of two sublattices (see Fig. 5). We assume the link to be preferentially coupled to one of the two sublattices of A, while it interacts – weakly asymmetrically – with the two sublattices of B, e.g., via local interactions to the neighbouring spins i and $i+1$. In this case, the overall effective interaction is proportional to the $\langle \mathbf{s}_i \rangle + \langle \mathbf{s}_{i+1} \rangle$, and thus vanishes when B is in its ground state (being $\langle \mathbf{s}_i \rangle \approx -\langle \mathbf{s}_{i+1} \rangle$), whilst it becomes finite if B is driven to an excited states (say $|2\rangle$) lacking such antiparallel alignment of the neighbouring spins. The $S = 1/2$ and $S = 3/2$ spin eigenstates of Cr_7Ni, for example, fulfil such requirements. The resulting energetic spectra of the AB system allows the implementation of a controlled-Z gate, which is equivalent to CNOT and is defined by the following transformation of the basis states: $|0\rangle_A \otimes |0\rangle_B \rightarrow |0\rangle_A \otimes |0\rangle_B$, $|0\rangle_A \otimes |1\rangle_B \rightarrow |0\rangle_A \otimes |1\rangle_B$, $|1\rangle_A \otimes |0\rangle_B \rightarrow |1\rangle_A \otimes |0\rangle_B$, $|1\rangle_A \otimes |1\rangle_B \rightarrow -|1\rangle_A \otimes |1\rangle_B$, as depicted in the true table of Fig. 5(b). In fact, the energy of the transition from $|1\rangle_B$ to $|2\rangle_B$ are renormalized by the interaction between A and B; the applied magnetic field frequency can thus be tuned depending in such a way that it is in resonance with the above transition only if cluster A is in the $|1\rangle_A$ state. The sequential application of two such π-pulses, separated by proper time delay τ, thus excites and de-excites B, inducing an additional phase $\theta = [-\tau(E_2 - E_1)2\pi/h]$ to $|1\rangle_A \otimes |1\rangle_B$ (in particular the controlled-Z corresponds to $\theta = \pi$). Numerical simulations with sequences of pulsed magnetic fields indicate that the time required to excite molecule in its auxiliary state is only few times longer than the single qubit gating time estimated in equivalent condition whilst the leakage to the lowest stats out of the computational basis remain very low ($L < 10^{-4}$). The details of this scheme as well as numerical simulations with the actual energy level of Cr_7Ni rings and possible exchange coupling between A and B will be presented elsewhere [10,13]. The important point we would like to stress here is that excited states of molecular qubit that can be efficiently exploited for the quantum-gate implementation.

In conclusion, we show that heterometallic molecular clusters with dominant antiferromagnetic internal coupling are suitable electronic spin systems for the implementation of the Shor's quantum algorithm. One main advantage in using molecular clusters is the size of the qubit that will help in the addressing to single quantum object. We also underlined a further resource of molecular clusters made by their excited states that in a proper computational scheme may constitute an important feature to consider.

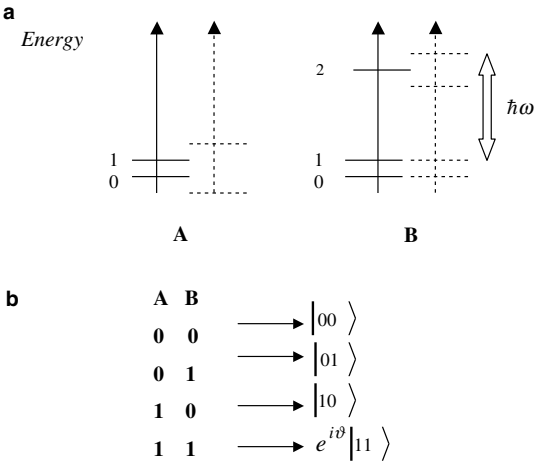


Fig. 5. Scheme for two qubit gate. (a) Continuous lines represent the energy levels for isolated cluster qubits; dotted lines sketch a possible patter of the energy levels when B is excited to its auxiliary state $|2\rangle$ and the coupling between the A and B molecules is active. By making use of the axilliary state $|2\rangle$ of molecule B and suitable time for rotation it can be possible to realize a controlled-Z as depicted in the true table (b).

Acknowledgements

This work was partially founded by the FIRB project RBNE01YLKN supported by the Italian Ministry of University and Research. Collaboration between the different teams was supported by EC- RTN-QUEMOLNA Contract No. MRTN-CT-2003-504880.

References

[1] M. Leuenberger, D. Loss, Nature 410 (2001) 789.
[2] M.A. Nielsen, I.L. Chuang, Quantum Computation and Quantum Information, Cambridge University Press, 2000.
[3] F. Meier, J. Levy, D. Loss, Phys. Rev. Lett. 90 (2003) 047901.
[4] D. Loss, D.P. DiVincenzo, Phys. Rev. A 57 (1998) 120.
[5] W. Wernsdorfer, N. Aliaga-Alcalde, D.N. Hendrickson, G. Christou, Nature 416 (2002) 406.
[6] F.K. Larsen, E.J.L. McInnes, H. El Mkami, J. Overgaard, S. Piligkos, G. Rajaraman, E. Rentschler, A.A. Smith, G.M. Smith, V. Boote, M. Jennings, G.A. Timco, R.E.P. Winpenny, Angew. Chem., Int. Ed. 42 (2003) 101.

[7] E. Liviotti, S. Carretta, G. Amoretti, J. Chem. Phys. 117 (2002) 3361.
[8] S. Carretta, P. Santini, G. Amoretti, M. Affronte, A. Ghirri, I. Sheikin, S. Piligkos, G.A. Timco, R.E.P. Winpenny, Phys. Rev. Lett.; cond-mat/0412628 (submitted).
[9] R. Caciuffo, T. Guidi, G. Amoretti, S. Carretta, E. Liviotti, P. Santini, Phys. Rev. B; cond-mat/0412169 (submitted).
[10] F. Troiani, A. Ghirri, M. Affronte, S. Carretta, G. Amoretti, S. Piligkos, G. Timco, R.E.P. Winpenny, cond-mat/0405507, 2004.
[11] W. Wernsdorfer, private communication.
[12] G.Timco, R.E.P. Winpenny, unpublished.
[13] F. Troiani, M. Affronte, S. Carretta, P. Santini, Phys. Rev. Lett cond-mat/0411113 (submitted).

example are the molecular-based Gd(hfac)$_3$NITR chains recently synthesized [6,7] [hfac is hexafluoro-acetylacetonate and NITR is 2-R-4,4,5,5-tetramethyl-4,5-dihydro-1H-imidazolyl-1-oxyl 3-oxide], where R = isopropyl, ethyl, methyl, phenyl (hereafter denoted by *i*Pr, Et, Me, Ph, respectively). Their magnetic properties are determined by Gd^{3+} rare-earth ions (with spin $S = 7/2$), and nitronyl nitroxide organic radicals R (with $s = 1/2$), alternating along the chain and interacting via competing nearest neighbour (NN) and next nearest neighbour (NNN) exchange coupling (see Fig. 1). EPR measurements [8] confirmed the 1D nature of the structure, while X-ray diffraction data showed that the chains are well separated from each other, with an interchain Gd–Gd distance of 10.5 Å. As a consequence, the interchain interactions, of dipolar nature, turn out to be much weaker with respect to the intrachain ones.

The first experimental magnetic susceptibility data in the various compounds with different organic radical R [9] showed a quite different behaviour of the quantity $\chi_M T$, depending on the radical nature. In fact for the compounds with R = *i*Pr and Et, $\chi_M T$ was found to decrease with decreasing T, a behaviour which resembles that of an antiferromagnet; in contrast, for the compounds with R = Me and Ph, $\chi_M T$ was found to diverge with decreasing T, a typical ferromagnetic behaviour.

The model Hamiltonian for these compounds can be represented as

$$H = H_{\text{intra}} + H_{\text{inter}}. \tag{1.1}$$

The first term on the right hand side of Eq. (1.1) includes the competing exchange interactions along the chains ($J_{z1} > 0$ is the NN ferromagnetic intrachain exchange, while $J_{z2} < 0$ and $J'_{z2} < 0$ are the NNN antiferromagnetic ones, see Fig. 1), as well as an effective single-ion anisotropy ($D > 0$) acting on the Gd $S = 7/2$ spins and favouring them to lie in the xy plane perpendicular to the chain axis, z:

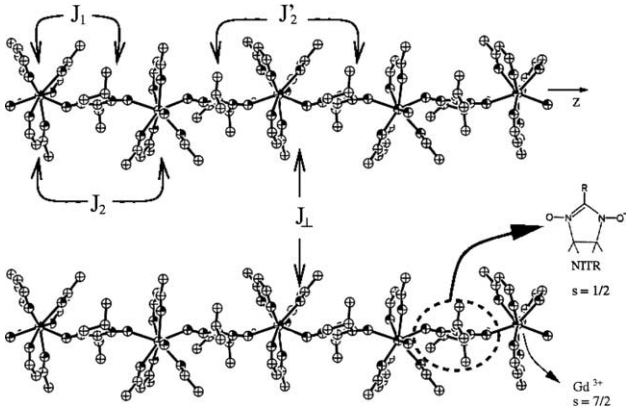


Fig. 1. Structure representation of the compound Gd(hfac)$_3$NITR [8]: gadolinium atoms with spin $S = 7/2$, and the group structure NITR with total spin $s = 1/2$. Here, it is also reported J_{z1} (ferromagnetic), $J_{z2}J'_{z2}$ (antiferromagnetic), and $J_\perp$ (ferro or antiferromagnetic) as NN, NNN intrachain and NN intrachain interaction, respectively.

$$H_{\text{intra}} = \sum_{i=1}^{M}\sum_{n=1}^{N/2}\Big[-J_{z1}(\vec{S}_{i,2n-1}\cdot\vec{s}_{i,2n} + \vec{s}_{i,2n}\cdot\vec{S}_{i,2n+1}) + D(S^z_{i,2n-1})^2 - J'_{z2}(\vec{S}_{i,2n-1}\cdot\vec{S}_{i,2n+1}) - J'_{z2}(\vec{s}_{i,2n}\cdot\vec{s}_{i,2n+2})\Big]. \tag{1.2}$$

The index n refers to the spin position along the ith chain. Different chains interact through a weak ferromagnetic (or antiferromagnetic) exchange ($|J_\perp/J_{z1,2}| \ll 1$):

$$H_{\text{inter}} = \sum_{\langle i,j\rangle}\sum_{n=1}^{N} -J_\perp(\vec{X}_{i,n}\cdot\vec{X}_{j,n}), \tag{1.3}$$

where $\vec{X}_{i,n} = \vec{S}_{i,n}(Gd^{3+}), \vec{s}_{i,n}(\text{NITR})$. Thus, the total Hamiltonian is a collection of M weakly interacting chains [10].

For the planar 1D model with equal spins and competing NN and NNN exchange interactions, Harada [11] showed that, for sufficiently strong NNN exchange, a helical ground state is energetically favored, with a twofold chiral degeneracy associated with the clockwise and counter-clockwise turn of the spins along the chain (see Fig. 2). The chirality order parameter related to a NN spin pair can be defined as (a is the lattice step and Q is the pitch of the helix)

$$k_i = \frac{[\vec{S}_i\cdot\vec{S}_{i+1}]^z}{|\sin aQ|}, \tag{1.4}$$

and for the planar 1D model it takes the values ± 1 at $T = 0$. In the present case of two different kinds of spins alternating along the chain, the wave number Q that determines the pitch of the helical order is found to be (hereafter we put $a = 1$)

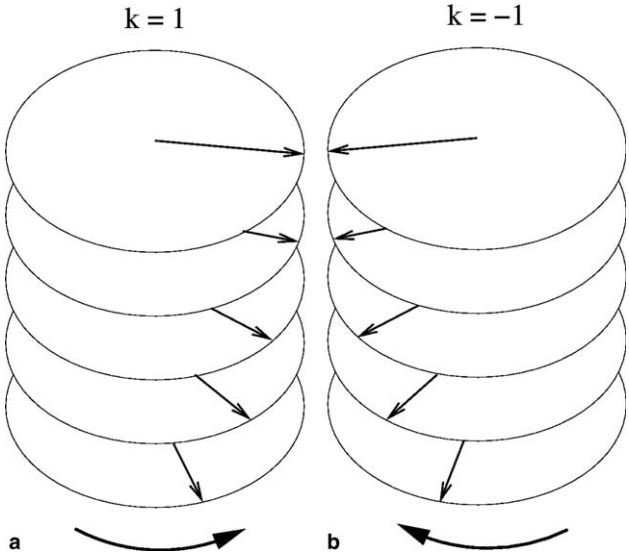


Fig. 2. Helical ground state configuration of a spin chain with easy-plane anisotropy and $S = s$ at $T = 0$. (a) Helical ground state with counter-clockwise turn of the spins ($k = 1$); (b) helical ground state with clockwise turn of the spins ($k = -1$).

$$\pm Q = \pm\cos^{-1}\left(\frac{1}{2(\delta+\delta')}\right), \quad (1.5)$$

where $\delta' = (|J_{z2}|S^2)/(J_{z1}sS)$ and $\delta = (|J'_{z2}|s^2)/(J_{z1}sS)$. Therefore the helical order is possible only if the ratio between NNN and NN exchange coupling exceeds a threshold value, i.e. $2(\delta+\delta') > 1$.

By transfer matrix computations of the model (1.2), it was possible to provide a first classification according to the different nature of the organic radical R [9]. The chains with helix pitch Q (at $T = 0$) close to $\pi/2$ are called *fully frustrated* magnetic chains: this is the case of the molecular chains with R = *i*Pr ($Q = 0.399\pi$) and R = Et ($Q = 0.397\pi$). In contrast, the chains with helix pitch Q significantly smaller than $\pi/2$ are called *weakly frustrated* magnetic chains: this is the case of the molecular chains with R = Me ($Q = 0.206\pi$) and R = Ph ($Q = 0.175\pi$).

In this paper we present recent specific heat and muon spin relaxation data in the molecular-based Gd(hfac)$_3$NITR chains with R = *i*Pr and R = Ph, and we compare their magnetic properties according to their different degree of frustration.

For Gd(hfac)$_3$NITiPr (hereafter denoted by Gd-*i*Pr), recent specific heat data [12] are reported in Fig. 3 versus temperature. The heat capacity of thin pellets of pressed microcrystals was measured in different cryogenic systems and using three different calorimeters and techniques. In zero field a λ-type anomaly is clearly visible at $T_0 = 2.08$ K, while below 1 K the specific heat scales to zero with a quasi-linear T-law. Moreover such λ-type anomaly is completely removed by the application of an external magnetic field of 5 T, thereby proving the magnetic origin of the transition. A further feature of the λ-peak is the absence of latent heat, which indicates that the phase transition is of the second order. An analysis of the residual magnetic entropy removed in the low-temperature region $T < T_0$ below the λ-anomaly provides a rather high value (59% of the total magnetic entropy). This result suggests the absence of a strong short-range order at these temperatures, in contrast with the usual behaviour of quasi-1D magnets (like TMMC, see [13]).

The low-temperature susceptibility data for Gd–*i*Pr reported in [10] clearly showed that $\chi(T)$ does not present any anomaly at $T \sim 2$ K. Such an experimental result quite excludes the possibility of a phase transition to 3D helical long range order. The behaviour [10] observed in the susceptibility data is in full agreement with more recent measurements of the muon longitudinal relaxation rate λ of Gd–*i*Pr as a function of temperature [12], for both $H = 0$ and for a longitudinal field $H = 500$ Oe. In fact, as shown in Fig. 4, no divergence is observed in $\lambda(T)$ close to 2 K, where the specific heat shows the anomaly previously discussed, thus indicating that this temperature does not mark any transition to a long-range order for the two-spin correlation function. Moreover, see inset of Fig. 4, the analysis of the zero-field muon asymmetry $A(t)$ versus time below T_0 (analyzed by a stretched exponential decay $A(t) \approx A_0 e^{-\sqrt{\lambda t}}$) shows the absence of long range magnetic order at muon site in the whole investigated T-range. In presence of long-range magnetic order, one should observe an oscillation in the asymmetry, caused by the precession of the muon spin around the local field itself.

It clearly appears that, while the four-spin correlation function (probed by the magnetic specific heat, Fig. 3) unequivocally shows a magnetic phase transition at $T \sim 2$ K, the two-spin correlation function (probed by susceptibility [10], and by μ^+ SR, Fig. 4) does not show any anomaly related to a transition to conventional 3D helical long range order. Taking also into account that

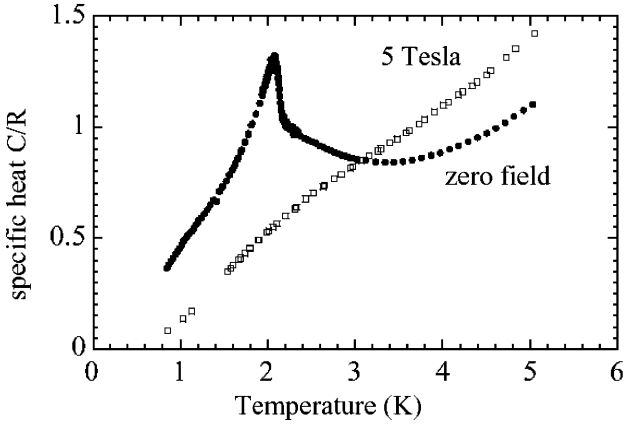


Fig. 3. Specific heat vs. temperature of Gd–*i*PR. Filled circles: zero field measurements; open squares: 5 T measurements.

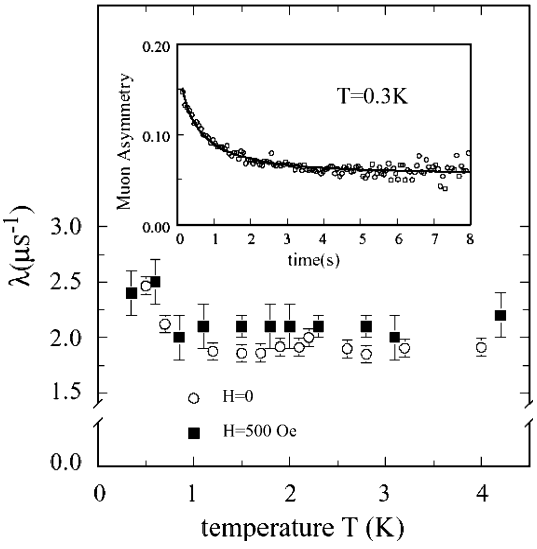


Fig. 4. Muon longitudinal relaxation rate measured in Gd–*i*Pr as a function of temperature with field $H = 0$ (open circles) and $H = 500$ Oe (filled squares). Inset: measured muon asymmetry below T_0 (open circles) and fit (line).

at very low temperatures (0.175–0.8 K) a linear T-dependence of the magnetic specific heat was observed in Gd–*i*Pr (a clear indication for isotropic 1D magnetic behaviour), one can reasonably conclude that our new experimental data in this molecular magnetic compound provide evidence for the onset, below $T_0 = 2.08$ K, of an ordered chiral phase in the absence of 3D helical long-range order.

New specific heat in the range 29–200 mK have been performed, quite recently. Such data (which will be published soon in a next article [14]) present, for $T_N = 39$ mK, an anomaly which cannot be reproduced by a Schottky-like contribution. In contrast, such anomaly displays a sharp λ-shape, signaling the onset of a phase transition to 3D helical long-range order, well separated in temperature from the chiral transition at $T_0 = 2.08$ K.

Such experimental data in Gd–*i*Pr fully confirm Villain's conjecture. In fact, some years ago he suggested [15] that quasi-1D planar helimagnets may have – in addition to the low-temperature 3D helimagnetic phase and to the high-temperature paramagnetic one – a chiral phase, stable at intermediate temperatures $T_N < T < T_0$, characterized by spontaneous breaking of the translational invariance without violation of the overall invariance with respect to spin rotation and time reversal. The chiral phase is similar to a collection of cork-screw all turning concordantly, whereas their phase are random (see Fig. 5).

Due to the Ising nature of chirality, T_0 results greater than T_N, because the chirality–chirality correlation function is stronger than the usual spin–spin correlation one. In fact the chiral correlation length ξ_k, defined via the chirality–chirality correlation function:

$$\langle k_n k_{n+p} \rangle \propto e^{-\frac{|p|}{\xi_k}}, \tag{1.6}$$

diverges exponentially as temperature is decreased (J is the exchange constant)

$$\xi_k \propto e^{\frac{|J|}{k_B T}}, \tag{1.7}$$

while the spin–spin correlation function

$$\langle \vec{s}_1 \cdot \vec{s}_{2n+1} \rangle \propto e^{-\frac{2n}{\xi_{XY}}}, \tag{1.8}$$

diverges as a power law

$$\xi_{XY} \propto \frac{Js^2}{k_B T}. \tag{1.9}$$

The Villain's conjecture appears to be verified in the molecular magnetic chain Gd–*i*Pr: in fact, an anomaly is expected at T_0 for the physical properties related to Eq. (1.6) (such as the magnetic specific heat), while the quantities related to Eq. (1.8) (such as the magnetic susceptibility and μ^+SR) are expected to behave critically only at T_N.

In order to interpret the experimental results in Gd–*i*Pr, a theoretical approach based on Villain's conjecture has been developed [16]. The model is built by rescaling on the XY spin variables; consequently, one obtains an order parameter with Ising-like symmetry that describes the chiral order, investigable by mean field approach. Such order is established by a second order phase transition, as experimentally observed in the specific heat data. Further indication for a second order chiral phase transition is provided by a more refined renormalization group analysis. Besides, preliminary numerical analysis via the Monte-Carlo technique seem to confirm the presence of two well-separated transition temperatures, as estimated both experimentally and theoretically [17].

It is worth noticing that such a behavior is peculiar of Gd–iPr chains. In fact, for the Gd(hfac)$_3$NITPh molecular magnetic chain (hereafter denoted by Gd–Ph), where the frustration is smaller than for Gd–*i*Pr, the new specific heat data, shown in Fig. 6(a), suggest the existence of a single λ-anomaly at $T_N = 0.63$ K. Below T_N, at very low temperature $C(T) \propto T^\alpha$ (where α is between 2 and 3), displaying an evident crossover to a linear behaviour when the temperature increases (see Fig. 6(b)). Such a behaviour can be easily understood in terms of a free spin wave contribution within a 3D model with strongly anisotropic interactions [18]. In Fig. 6(b) we show that spin wave theory is able to correctly reproduce the measured temperature dependence of the specific heat of Gd–Ph. Furthermore, providing an exact solution for the single chain by the transfer matrix method and treating the interchain interactions in a mean-field approximation, we find a transition temperature

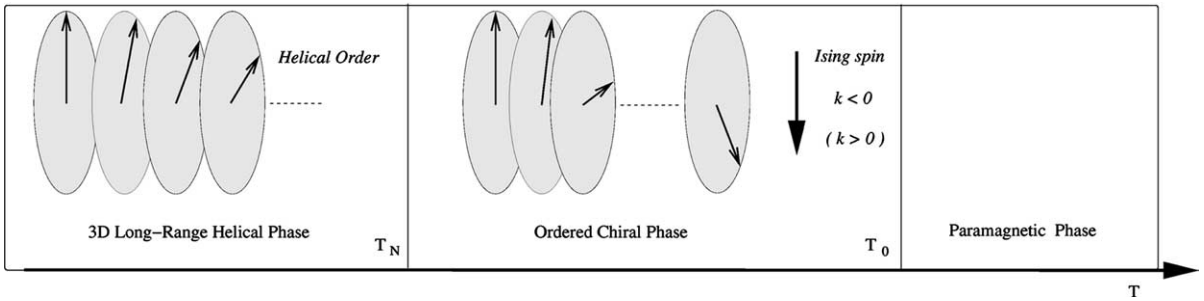


Fig. 5. Schematic representation of Villain's conjecture for the phase diagram of a quasi-one-dimensional helimagnet.

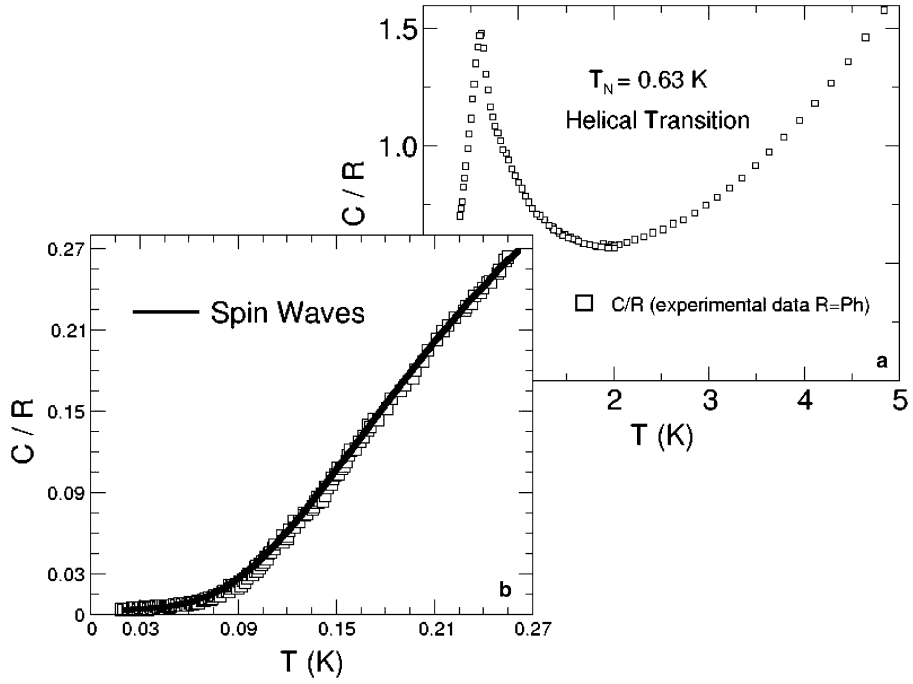


Fig. 6. (a) Specific heat data for Gd–Ph. (b) Fit obtained by 3D spin wave theory (solid line) and specific heat data (open squares) at temperatures below T_N.

$T_N^{\text{theor}} = 0.64$ K, in close agreement with the experimental value [18]. In conclusion, differently from the fully frustrated compound Gd–*i*Pr, the weakly frustrated Gd–Ph magnetic chain does not show the presence of a chiral order at any temperature. Rather, our theoretical analysis suggests that the phase transition observed at $T_N = 0.63$ K is related to the onset of the usual 3D helical long range order.

References

[1] H.J. Mikeska, M. Steiner, Adv. Phys. 40 (1991) 191.
[2] M. Hase, I. Terasaki, K. Uchinokura, Phys. Rev. Lett. 70 (1993) 3651.
[3] S.E. Nagler et al., Phys. Rev. Lett. 49 (1984) 599.
[4] B.D. Gaulin, in: H.T. Diep (Ed.), Magnetic Systems with Competing Interactions, World Scientific, Singapore, 1994, p. 335.
[5] G. Toulouse, Comm. Phys. 2 (1977) 115.
[6] D. Gatteschi et al. (Eds.), Magnetic Molecular Materials, NATO ASI Ser. E, 198, Kluwer, Dordrecht, 1991.
[7] D. Gatteschi, R. Sessoli, J. Magn. Magn. Mater. 104–107 (1992) 2092.
[8] C. Benelli et al., Inorg. Chem. 29 (1990) 4223.
[9] F. Bartolomé et al., Phys. Rev. Lett. 77 (1996) 382.
[10] M. Affronte et al., Phys. Rev. B 59 (1999) 6282.
[11] I. Harada, J. Phys. Soc. Jap. 52 (1984) 1643.
[12] A. Lascialfari et al., Phys. Rev. B 67 (2003) 224408.
[13] F. Borsa et al., PRB 28 (1983) 5173.
[14] E. Olivieri, F. Cinti, G. Ventura, A. Rettori, et al., in preparation.
[15] J. Villain, in: C. Weil et al. (Eds.), Proc. 13th IUPAP Conf. Statis. Phys., Ann. Isr. Phys. Soc., 2, 1978, p. 565.
[16] F. Cinti, A. Rettori, J. Villain, in preparation.
[17] T. Roscilde et al., in preparation.
[18] F. Cinti, Ph.D Thesis, Modena University, 2003.

long-range magnetic order below $T_N = 1.87$ K, probably of antiferromagnetic nature.

The communication is organized as follows. Firstly, we introduce the Reader to the magnetocaloric effect. In the following section, we describe the magnetic structure of the Fe_{14} cluster core. Then, we present and discuss the magnetization and specific heat experiments, whose results are used in the last section to calculate the MCE parameters.

Magnetization measurements down to 2 K and specific heat measurements using the relaxation method down to ≈0.35 K, were carried out in a PPMS (Quantum Design Inc.) apparatus for the $0 < H < 7$ T magnetic field range. Magnetization and susceptibility measurements below 2 K were performed by means of a home-made Hall probe appositely installed in the same commercial apparatus. In this case the samples used consisted of a collection of small grains of ca. 10^{-3} mm^3.

2. Magnetocaloric effect

When a material is magnetized by application of a magnetic field H, the entropy associated with the magnetic degrees of freedom, S_m, is changed as the field changes the magnetic order of the material. The MCE and the associated principle of adiabatic demagnetization is readily understood looking at Fig. 1. The system, assumed to be a paramagnetic material, is initially in state A(T_i, H_i), at temperature T_i and field H_i. Under adiabatic conditions (i.e., when the total entropy of the system remains constant during the magnetic field change), the magnetic entropy change must be compensated for by an equal but opposite change of the entropy associated with the lattice, resulting in a change in temperature of the material. That is, the adiabatic field change $H_i \rightarrow H_f$ brings the system to state B(T_f, H_f) with the temperature change $\Delta T_{ad} = T_f - T_i$ (horizontal arrow in Fig. 1). If otherwise the magnetic field is isothermally changed to H_f in a reversible process, the system goes to state C(T_i, H_f) with the magnetic entropy change ΔS_m (vertical arrow in Fig. 1). Both ΔS_m and ΔT_{ad} represent the characteristic parameters of the MCE. It is easy to see that if the magnetic change ΔH reduces the entropy ($\Delta S_m < 0$), then ΔT_{ad} is positive, whereas if ΔH is such that $\Delta S_m > 0$, then $\Delta T_{ad} < 0$ (Fig. 1).

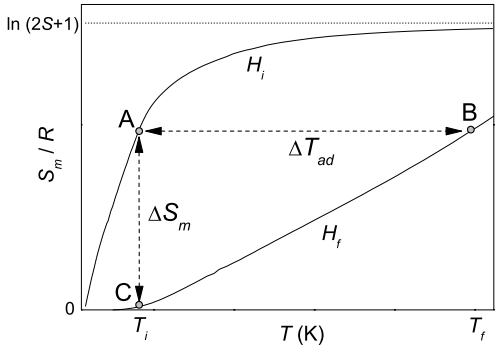


Fig. 1. Molar magnetic entropy of a (super)paramagnet with spin S per formula unit, as a function of temperature, for magnetic field H_i and $H_f > H_i$. AB process: adiabatic magnetization providing ΔT_{ad}. AC process: isothermal magnetization providing ΔS_m.

Large magnetic moments are often attainable in superparamagnetic clusters, resulting therefore in large entropies. Moreover, for certain ranges of field, temperature and cluster size, it is easier in superparamagnets than in pure materials to change the magnetic entropies by application of a field [6,7]. Obviously, this leads to an interest in superparamagnets in terms of MCE. The picture depicted in Fig. 1 is still valid for a superparamagnet with S as net cluster moment, provided that it is at temperatures above the blocking temperature. The cluster magnetic anisotropy, which indeed determines the blocking temperature, can be considered as a drawback in the MCE efficiency of superparamagnets. This because, by shifting the maxima of $\Delta S_m(T)$ and $\Delta T_{ad}(T)$ towards higher temperatures, it tends to lower the values of the MCE response [6,7,12]. Ideal candidates for MCE applications, would then be magnetic clusters with large S and small anisotropy.

3. Fe_{14} molecular nanocluster

In what follows, we focus on the Fe_{14} compound, nominally $Fe_{14}(bta)_6O_6(OMe)_{18}Cl_6$ [11]. Fig. 2 shows the highly symmetric core, comprising 14 Fe^{3+} $s = \frac{5}{2}$ spins, which can be described as a hexacapped hexagonal bipyramid with the caps on alternate faces. The three face capping iron ions [Fe2, Fe3, Fe4 and symmetry equivalents] and the apical iron [Fe1 and symmetry equivalent] on either half of the molecule form two $[Fe_4(bta)_3Cl_3]$ units each separated from a central $\{Fe_6\}$ ring, which has an almost planar symmetry. The Fe–O–Fe bridges fall into two categories: those that connect the apical iron ions [Fe1 and symmetry equivalent] to the face cap and equatorial iron ions, and those characterized by much smaller angles that connect all other iron ions. If we assume that the larger angles will lead to the strongest antiferromagnetic exchange, thus dominating the other interactions, then we are left with a situation whereby the spins on Fe1 and symmetry equivalent are antiferromagnetically coupled to all other spins, which should lead to 12 $s = \frac{5}{2}$ spins up and two $s = \frac{5}{2}$ spins down, and an overall $S = 25$ cluster spin ground-state (Fig. 2). Although a full description of the electronic configuration of the Fe_{14} cluster core is still not available, preliminary density functional and Monte Carlo calculations [13] support such a very large value for the spin ground-state.

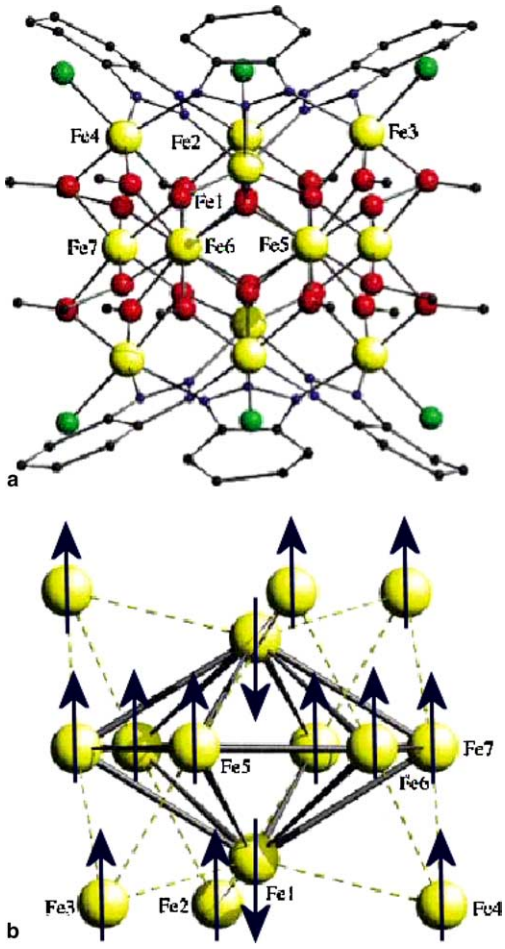


Fig. 2. (a) Molecular structure of $Fe_{14}(bta)_6O_6(OMe)_{18}Cl_6$. Colour scheme: Fe, yellow; O, red; N, blue; Cl, green. After [11]. (b) Sketch of the symmetric core containing 14 exchange-coupled Fe^{3+} ions, yielding a total spin $S = 25$. The arrows illustrate the alignment of the Fe^{3+} $s = \frac{5}{2}$ spins inside the cluster.

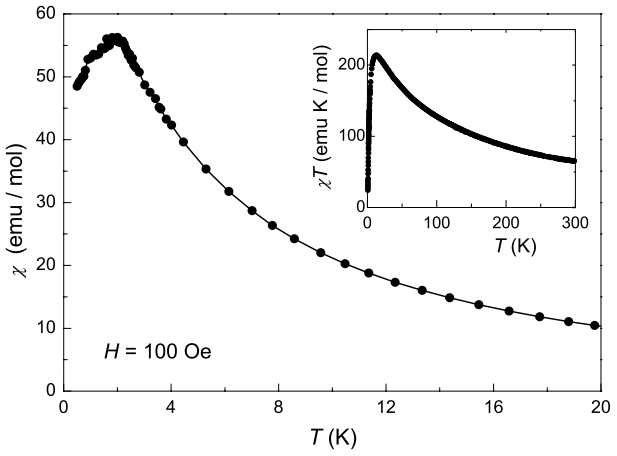


Fig. 3. Temperature dependence of the DC-susceptibility of Fe_{14} taken for $H = 100$ Oe, showing the transition to a long-range ordered state at $T_N = (1.9 \pm 0.1)$ K. Line is guide to the eye. Inset: temperature dependence of χT.

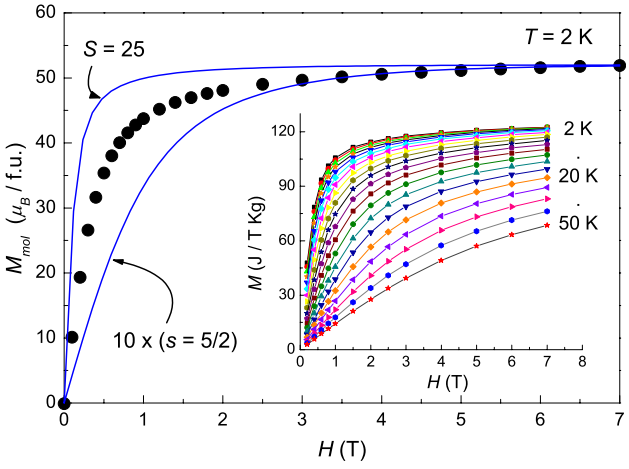


Fig. 4. Field dependence of the experimental molar magnetization for $T = 2$ K together with the calculated magnetizations for a single $S = 25$ spin and for the uncoupled sum of 10 $s = \frac{5}{2}$ spins. Inset: Magnetization isotherms used to estimate the entropy change ΔS_m shown below in Fig. 7.

4. Experimental results

Fig. 3 shows the temperature dependence of the DC-susceptibility of Fe_{14} measured for an applied field of $H = 100$ Oe. Data down to 2 K are collected using a commercial calibrated magnetometer, whereas data from ~10 K down to 0.35 K are taken with Hall micro-probe. The latter, initially in arbitrary units, are successively properly scaled with the high-T data taken with the commercial magnetometer. The main feature of Fig. 3 is given by the sharp peak at $T_N = (1.9 \pm 0.1)$ K, that, in view also of the specific heat data presented below, we tentatively attribute to the transition to a long-range magnetically ordered phase. The maximum value of χ at T_N corresponds to $\chi_{max} \simeq 56$ emu/mol (Fig. 3), which is smaller than that expected for paramagnetic $S = 25$ spin,[2] suggesting that a full ordered $S = 25$ magnetic state inside the cluster is not achieved at T_N. The observed behaviour is compatible with an antiferromagnetic nature of the ordered phase, as evidenced by the sharp decrease in the temperature dependence of χT below 13 K (inset of Fig. 3). Fig. 4 shows the molar saturation magnetization which tends to the limiting value of $M_{mol} \simeq 50\ \mu_B$ (for $T = 2$ K), in agreement thus with spin $S = 25$ and $g = 2$. However, the magnetization does not vary according to the Brillouin function for $S = 25$, that is displayed in the Figure for comparison. On basis of the ordered arrangement of Fig. 2, one should expect a net total spin per cluster resulting from the sum of 10 iron spins. Together with the experimental magnetization, therefore, we also plotted the magnetization of 10 uncoupled $s = \frac{5}{2}$

[2] For $S = 25$ and assuming $g = 2$, the Curie constant has the value of $C = 162$ emu/Kmol. Therefore, the expected susceptibility at $T_N = 1.9$ K should not be less than $C/T_N \approx 85$ emu/mol, which is not observed.

spins (Fig. 4, for $T = 2$ K). It can be observed that the experimental data lie above the uncoupled case and below the magnetization for $S = 25$. In agreement with susceptibility data, such a behaviour suggests that superexchange intracluster interactions tend to align the iron spins as depicted in Fig. 2. However, this is not fully achieved without applying the field, likely because (i) degrees of freedom inside the cluster allow spin states other than $S = 25$ to contribute, and/or (ii) intercluster interactions, responsible for the long-range ordering, are similar in magnitude to the intracluster ones. In the inset of Fig. 4, we also plot systematic magnetization measurements, in the magnetic field range $0 \leqslant H \leqslant 7$ T and in the temperature range $2 \leqslant T \leqslant 50$ K, that we shall use below to estimate the MCE of the Fe_{14} molecular nanocluster.

Fig. 5 shows the collected specific heat data C/R of the molecular Fe_{14} compound as a function of temperature for applied magnetic field $H = 0$ and 7 T. The main feature is the λ-type anomaly in the zero-field specific heat at $T_N = (1.87 \pm 0.02)$ K, revealing the onset of long-range ordering and corroborating the interpretation of the susceptibility data. This anomaly is quickly removed by the application of an external field of 1 T (not shown here), proving its magnetic origin. The λ-type anomaly is more clearly seen in Fig. 6, where we show the specific heat C_{order} associated only with electronic spins contributing to the ordering mechanism. Such a curve is obtained as depicted in the inset: we drew a linear contribution of the specific heat at low temperatures that we subtracted to the total specific heat obtaining the residual C_{order}. The relative height of the transition peak amounts to $\approx 1.2R$. This value is apparently a bit too low for a very large spin as that of Fe_{14}. However, this is understandable if one

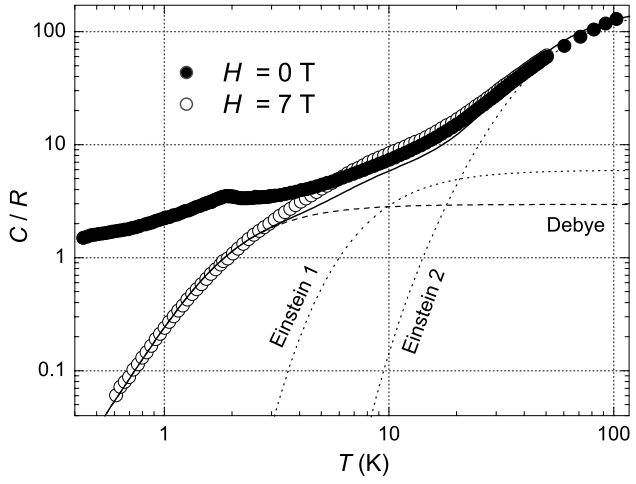


Fig. 5. Temperature dependence of the total specific heat of Fe_{14} for applied magnetic field $H = 0$ and 7 T. Solid line is the total lattice contribution, whereas the dashed and dotted lines are the Debye and Einstein contributions, respectively.

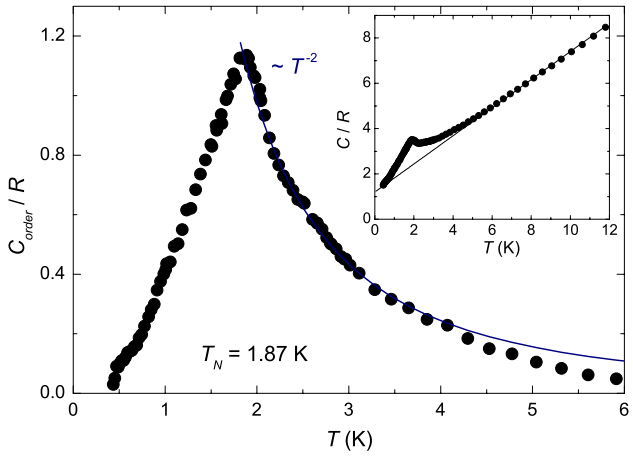


Fig. 6. Temperature dependence of the ordering specific heat C_{order}, from which the ordering temperature $T_N = (1.87 \pm 0.02)$ K is deduced. Solid line is a fit to $C_m \propto T^{-2}$ (see text). Inset: total specific heat vs. T in linear coordinates showing the linear contribution (solid line) used to obtain C_{order}.

considers that the large specific heat contribution that we subtracted to get C_{order}, leaves a relatively small amount of entropy for the electronic spins to order. Above the transition temperature, C_{order} is well described by an asymptotic term of the magnetic anomaly [14] according to $C_{order}/R = a\ T^{-2}$, where $a = 3.9$ K^2 (Fig. 6).

We estimated the lattice contribution C_{latt} for the specific heat data of Fig. 5. This contribution can be modelled with the sum of a Debye curve, which describes the contribution of acoustic modes, plus an Einstein oscillator term that probably arises from intramolecular vibrational modes. The overall fit provides $\theta_D \simeq 10$ K and $\theta_E^{(1)} \simeq 25$ K for the Debye and Einstein temperatures, respectively. The specific heat data measured above 20 K show a second step-like increase, indicating the existence of higher energy vibrational modes, that we modelled with an additional Einstein term providing $\theta_E^{(2)} \simeq 68$ K . The determination of these modes has some uncertainty since the analysis of the specific heat data has different free parameters in this temperature range. We note that these values of θ_D and $\theta_E^{(i)}$, although commonly found in the specific heat analysis of molecular magnets, are very low. It is also worth noting that small amount of disordered solvent contained in the molecular crystal may also contribute to C_{latt} at these temperatures. These facts question the consistency of the Debye–Einsten model itself and we believe that the θ_D and $\theta_E^{(i)}$ values should be considered as phenomenological parameters rather than true features of the acoustic and optical phonon modes. Moreover, anticipating the discussion below, an excess of entropy is seen to occur in the temperature range around 6 K, introducing therefore an additional uncertainty in the determination of θ_D and $\theta_E^{(i)}$.

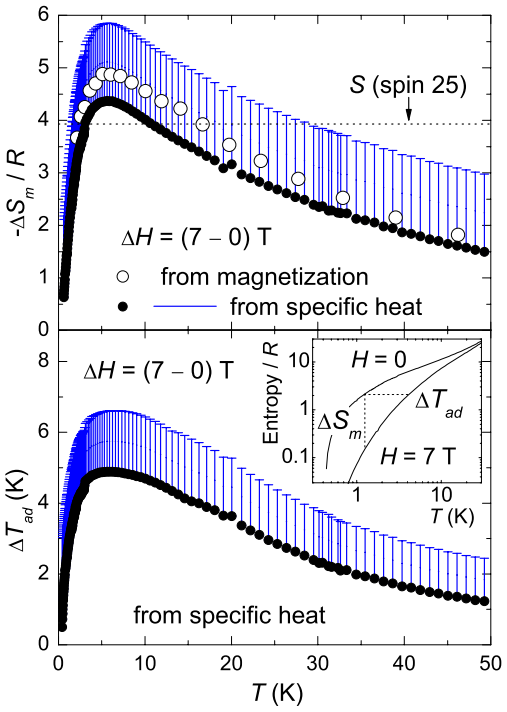


Fig. 7. (Top) Temperature dependence of the isothermal magnetic entropy change ΔS_m as obtained from specific heat (filled dots and bars, see text) and magnetization data (empty dots), both for $\Delta H = (7–0)$ T. Shown as dotted line is the limiting entropy of a $S = 25$ spin system. (Bottom) Temperature dependence of the adiabatic temperature change ΔT_{ad} as obtained from specific heat data (filled dots and bars, see text) for $\Delta H = (7–0)$ T. In the inset: experimental entropy of Fe_{14} vs. temperature for $H = 0$ and 7 T.

5. Evaluation of MCE

In what follows, we evaluate the magnetocaloric effect for the Fe_{14} molecular compound from experimental data, as described in [15,16]. This procedure includes the evaluation of the isothermal magnetic entropy change ΔS_m and adiabatic temperature change ΔT_{ad} from measured specific heat. For comparison, we evaluate ΔS_m also from magnetization data.

MCE from specific heat. From the specific heat data of Fig. 5 we firstly determine the total entropies at applied magnetic fields $H = 0$ and 7 T as functions of temperature using the following equation:

$$S(T)_H = \int_0^T \frac{C(T)_H}{T} \mathrm{d}T. \qquad (1)$$

The result of the numerical integration $S(T)_H$ is plotted in the bottom inset of Fig. 7 for both applied fields. Then we calculate the magnetic entropy change and adiabatic temperature change, for this field change $\Delta H = (7–0)$ T, as $\Delta S_m(T)_{\Delta H} = [S(T)_{7\,T} - S(T)_0]_T$ and $\Delta T_{ad}(T)_{\Delta H} = [T(S)_{7\,T} - T(S)_0]_S$, respectively.[3] The results are displayed as filled dots in Fig. 7. It can be seen that, for $\Delta H = (7–0)$ T, Fe_{14} reaches a maximum $-\Delta S_m$ of $\approx 4.5R$ (or equivalently ≈ 15.9 J/kg K) and ΔT_{ad} of ≈ 5 K, both at $T \simeq 6$ K. It is worth to mention that we calculate the entropy starting from the lowest experimentally achieved temperature (≈ 0.35 K) and, obviously, not from $T = 0$ K as requested by Eq. (1). Therefore, the so-obtained $\Delta S_m(T)$ and $\Delta T_{ad}(T)$ should be considered as underestimates. Upper limits are roughly obtained by extrapolating linearly the experimental specific heat below T_N for $T \to 0$ K. The results, plotted in Fig. 7 as bars, show that we estimate at $T = 6$ K for $\Delta H = (7–0)$ T the magnetic entropy change and adiabatic temperature change as $-\Delta S_m = (5.0 \pm 0.8)$ R, or equivalently (17.6 ± 2.8) J/kg K, and $\Delta T_{ad} = (5.8 \pm 0.8)$ K, respectively. It is important to note that, since the entropy expected for a $S = 25$ spin system is $R \ln(2S + 1) \simeq 3.9R$, the experimental magnetic entropy change is much larger than the maximum allowed (shown in the top panel of Fig. 7 as dotted line) assuming a spin $S = 25$ for the Fe_{14} nanocluster. Obviously, the maxima in $-\Delta S_m(T)$ and $\Delta T_{ad}(T)$ are originated to large extent by this excess of magnetic entropy which is then removed by the applied field. One may thus wonder where this excess of magnetic entropy is coming from. Recalling the incomplete achievement of the $S = 25$ spin state deduced from magnetization and susceptibility measurements, it is reasonable to formulate the hypothesis that spin states other than $S = 25$ are contributing in this low-temperature range. Additionally, the transition to the long-range magnetic ordered state is certainly contributing as well to the MCE parameters below ~ 2 K. However, on basis of the relatively low values of the C_{order} data of Fig. 6, we do not expect this contribution to be the dominant one. Indeed, no apparent anomaly is seen in $\Delta S_m(T)$ and $\Delta T_{ad}(T)$ at T_N.

MCE from magnetization. In an isothermal process of magnetization, the total magnetic entropy change ΔS_m due to the application of a magnetic field, can be derived from Maxwell relations by integrating over the magnetic field change $\Delta H = H_f - H_i$, i.e.,

$$\Delta S_m(T)_{\Delta H} = \int_{H_i}^{H_f} \left(\frac{\partial M(T,H)}{\partial T}\right)_H \mathrm{d}H. \qquad (2)$$

From the magnetization data of Fig. 4, we therefore calculate $\Delta S_m(T)$ using Eq. (2). The so-obtained magnetic entropy change for the magnetic field change $\Delta H = (7–0)$ T[4] is displayed as function of temperature in the top panel of Fig. 7, together with ΔS_m as obtained from specific heat data for comparison. It can be noticed that, within the bars, the result fully agrees with the

[3] Note that the estimation of the lattice contribution is irrelevant for our calculations, since we consider the difference between the total entropies at different fields.

[4] For practical reasons, the measurements at the lowest applied field were carried out for $H_i = 10^{-3}$ T, which in our calculations was approximated to zero-applied field.

previous estimate inferred from specific heat, suggesting that both (independent) procedures can be effectively used to characterize the Fe_{14} molecular nanocluster with respect to its magnetocaloric properties.

6. Concluding remarks

The values of $\Delta S_m(T)$ and $\Delta T_{ad}(T)$ obtained in Fe_{14} are exceptionally large, even more than the ones obtained with intermetallic materials known to be, so far, the best magnetic refrigerant materials in the temperature range below 10 K [2,17]. For instance, the best representative is the recently studied [17] $(Er_{1-x}Dy_x)Al_2$ alloy that, for $x \geqslant 0.5$ concentrations, presents MCE parameters below 10 K which are at least 30% smaller than that of Fe_{14}. Among systems of superparamagnetic particles and molecular magnets, the gap is even more pronounced. For instance, because of their well-defined spin ground-state in this temperature and field range, it is easy to show that the well known Fe_8 and Mn_{12}-ac molecular nanoclusters, i.e., cannot exceed values of $-\Delta S_m \simeq 12.5$ and 11 J/kg K, respectively, thus much smaller than that of Fe_{14}. Moreover in these materials, as in most molecular magnets, an additional complication (with respect to MCE parameters) is added by the cluster magnetic anisotropy. Because of this, cluster spins are usually blocked in the liquid helium temperature range, causing the spin–lattice relaxation to slow down dramatically. Therefore, cluster spins tend to loose thermal contact with the lattice [18–20] resulting in lower magnetic entropies and, consequently, lower MCE parameters. Ideally, it is desirable to keep the spin–lattice relaxation at sufficiently high rates down to lowest temperatures, in order to have a more efficient material in terms of MCE. This route was already recently tried [21] with heterometallic octanuclear molecular rings of type Cr_7Cd, that can be seen as an ordered arrangement of well-separated paramagnetic spins, having fast relaxations in the whole (experimental) temperature range. In terms of MCE parameters, the only limitation of this material is given by the cluster spin value itself ($S = \frac{3}{2}$) allowing not more than $-\Delta S_m \simeq 5.1$ J/kg K as experimentally reported to occur for $T < 2$ K [21].

Summing up, the above-reported experiments on the Fe_{14} molecular nanocluster show that for a better description of its magnetic and thermal properties we should go beyond the standard giant spin model to take into account internal degrees of freedom inside the cluster. Nevertheless, in this preliminary communication we can already conclude that Fe_{14} is unique in terms of MCE due to the combination of the following characteristics: (i) unusually large spin ground-state; (ii) very low cluster magnetic anisotropy; (iii) excess of entropy coming from low-lying excited S states; (iv) long-range magnetic ordering. For these reasons, Fe_{14} has therefore high potentiality to work as magnetic refrigerant within a temperature range below 10 K.

Acknowledgements

This work was partially funded by the Italian Ministry of Education, University and Research under FIRB Project No. RBNE01YLKN. The collaboration between different involved teams was supported by the European Community under Contract No. MRTN-CT-2003-504880 "QuEMolNa".

References

[1] C. Zimm, A. Jastrab, A. Sternberg, V.K. Pecharsky, K.A. Gschneidner Jr., M. Osborne, I. Anderson, Adv. Cryog. Eng. 43 (1998) 1759.
[2] V.K. Pecharsky, K.A. Gschneidner Jr., J. Magn. Magn. Mater. 200 (1999) 44.
[3] K.A. Gschneidner Jr., A.O. Pecharsky, V.K. Pecharsky, in: R.S. Ross Jr. (Ed.), Cryocoolers II, Kluwer Academic/Plenum Press, New York, 2001, p. 433.
[4] P. Debye, Ann. Phys. 81 (1926) 1154.
[5] W.F. Giauque, J. Am. Chem. Soc. 49 (1927) 1864.
[6] R.D. McMichael, R.D. Shull, L.J. Swartzendruber, L.H. Bennett, R.E. Watson, J. Magn. Magn. Mater. 111 (1992) 29.
[7] L.H. Bennett, R.D. McMichael, H.C. Tang, R.E. Watson, J. Appl. Phys. 75 (1994) 5493.
[8] T. Kinoshita, S. Seino, H. Maruyama, Y. Otome, K. Okitsu, T. Nakayama, K. Niihara, T. Nakagawa, T.A. Yamamoto, J. Alloys Comp. 365 (2004) 281.
[9] F. Torres, J.M. Hernández, X. Bohigas, J. Tejada, Appl. Phys. Lett. 77 (2000) 3248.
[10] F. Torres, X. Bohigas, J.M. Hernández, J. Tejada, J. Phys.: Condens. Matter 15 (2003) L119.
[11] D.M. Low, L.F. Jones, A. Bell, E.K. Brechin, T. Mallah, E. Rivière, S.J. Teat, E.J.L. McInnes, Angew. Chem., Int. Ed. 42 (2003) 3781.
[12] X.X. Zhang, H.L. Wei, Z.Q. Zhang, L. Zhang, Phys. Rev. Lett. 87 (2001) 157203.
[13] G. Rajaraman, J. Cano, E.K. Brechin, E.J.L. McInnes, Chem. Commun. (2004) 1476.
[14] L.J. de Jongh, A.R. Miedema, Adv. Phys. 50 (2001) 947.
[15] V.K. Pecharsky, K.A. Gschneidner Jr., J. Appl. Phys. 86 (1999) 565.
[16] J.S. Lee, Phys. Status Solidi B 241 (2004) 1765.
[17] A.L. Lima, K.A. Gschneidner Jr., V.K. Pecharsky, A.O. Pecharsky, Phys. Rev. B 68 (2003) 134409.
[18] M. Evangelisti, F. Luis, F.L. Mettes, N. Aliaga, G. Aromí, G. Christou, L.J. de Jongh, Polyhedron 22 (2003) 2169.
[19] F. Luis, F. Mettes, M. Evangelisti, A. Morello, L.J. de Jongh, J. Phys. Chem. Solids 65 (2004) 763.
[20] M. Evangelisti, F. Luis, F.L. Mettes, N. Aliaga, G. Aromí, J.J. Alonso, G. Christou, L.J. de Jongh, Phys. Rev. Lett. 93 (2004) 117202.
[21] M. Affronte, A. Ghirri, S. Carretta, G. Amoretti, S. Piligkos, G.A. Timco, R.E.P. Winpenny, Appl. Phys. Lett. 84 (2004) 3468.

To date, five different crystal structures, based upon four structurally similar perfluoroaryl-dithiadiazolyl radicals, have been reported in which the tendency for dimerization has been inhibited [6–11].

The magnetic behaviour of these paramagnetic compounds is extremely varied and strongly dependent on the crystal structure. One of the most interesting, the β-phase of the *p*-$NCC_6F_4CNSSN^{\cdot}$, exhibits weak ferromagnetism below 36 K [12]. In this compound, the magnetic interactions are antiferromagnetic but the magnetic space group allows the canting of the spins, which results in a weak ferromagnetism. Both the α-phase of this dithiadiazolyl radical [7] and *p*-$BrC_6F_4CNSSN^{\cdot}$ [9] are paramagnetic with negative Curie–Weiss constants, also indicative of dominant antiferromagnetic interactions. In contrast, the *p*-$O_2NC_6F_4CNSSN^{\cdot}$ radical shows dominant ferromagnetic interactions and a ferromagnetic transition at 1.32 K [10]. Recently, we reported the perfluorobiphenyl derivative, *p*-$NCC_6F_4C_6F_4CNSSN^{\cdot}$, which is also monomeric but exhibits near perfect Curie behaviour indicative of negligible magnetic exchange between paramagnetic centres [11].

In this work we have performed an ab initio study of the magnetic interactions in the first four compounds described above. This study has provided us with a good theoretical understanding of the magnetic exchange pathways which provide a clear rationale of not only the long- or short-range nature of the magnetic order, but also whether the ordering is ferro or antiferromagnetic. The enhanced understanding of the exchange pathway is of great importance in order to develop new synthetic targets in which the magnetic interactions can be predicted in a well-defined manner based on the nature of the intermolecular geometry.

The magnetic behaviour of these compounds has been investigated by the use of the Heisenberg–Dirac–van Vleck spin Hamiltonian:

$$H = -\sum_{ij} J_{ij} S_i \cdot S_j,$$

where J_{ij} is the magnetic coupling constant between the i and j magnetic centres with total spin operators S_i and S_j, respectively.

The theoretical analysis of the exchange pathway under the Heisenberg model for isotropic exchange can be divided into two steps. The first step is to identify all the radical pairs whose magnetic coupling constants could be considered significant. Since both the direct exchange and dipolar exchange depend strongly on intermolecular separation r between the magnetic centres (as $\exp(-r)$ [13] and r^{-3}, respectively), pair selection has been performed using a simple distance cut-off criterion. As almost all the spin density is located on the dithiadiazolyl ring [14,15], only radical pairs with an intermolecular contact between heterocyclic rings shorter than 7 Å have been selected. In the second step, the magnetic coupling constants for the selected radical pairs have been computed. The magnetic coupling constant, J, has been determined within the DFT broken-symmetry approach using the scheme proposed by Yamaguchi [16] in which the magnetic interaction constant is calculated by

$$J = -\frac{(E_{BS} - E_{HS})}{(\langle S^2\rangle_{BS} - \langle S^2\rangle_{HS})},$$

where E_x and $\langle S^2\rangle_x$ denote the total energy and the total spin angular momentum, respectively, for the spin state X (i.e., the broken symmetry singlet and high spin triplet states). All the calculations have been carried out using the hybrid exchange-correlation functional B3LYP [17] and the 6-311G* basis set [18] implemented in the GAUSSIAN98 package [19].

Table 1
Computed magnetic coupling constants for the four dithiadiazolyl compounds studied in this work

Units: cm^{-1}	α-NC–	β-NC–	O_2N–	Br–
J_1	7.578	−31.380	1.1457	−7.618
J_2	0.004	−0.035	0.0351	7.519
J_3	−8.801	−0.007	−0.0263	−8.250
J_4	0.189	<±0.005	−0.0373	−0.087
J_5	<±0.005			−0.107
J_6	<±0.005			0.010
J_7	<±0.005			0.063
J_8	<±0.005			
J_9	−0.017			

In the following sections we analyse the magnetic behaviour of each of the four structures with respect to the magnetic coupling constants obtained from our computations (see Table 1).

1. β-Phase of p-NC–C_6F_4–$CNSSN^{\cdot}$

The β-phase of *p*-$NCC_6F_4CNSSN^{\cdot}$ exhibits a transition to a canted antiferromagnetic phase at 36 K [12] resulting in a weak spontanous magnetization. This weak-ferromagnetic transition has been established by different experimental techniques including neutron diffraction, heat capacity, magnetic measurements [12] single-crystal EPR and muon experiments [20–22]. Previously, the magnetic system has been described with only one antiferromagnetic interaction which propagates in a diamond-like network. Furthermore, the possible magnetic pathway via the contact between the cyano group and the dithiadiazolyl ring has been proved experimentally to be negligible [23]. Finally, the magnetic susceptibility at high temperature follows a Curie–Weiss law with $\theta = -59$ K.

Four possible magnetic exchange pathways are obtained based on the distance cut-off criterion. Fig. 1 illustrates how three of these interactions propagate the magnetic exchange through the lattice. The fourth magnetic pathway has been omitted for clarity but generates

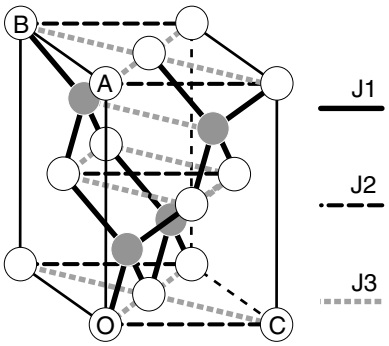


Fig. 1. Scheme showing the magnetic exchange pathway proposed for the β-phase of the *p*-NC–C_6F_4–CNSSN$^{\cdot}$ radical. It can be observed that the J_1 pathway propagates as a diamon-like 3D network.

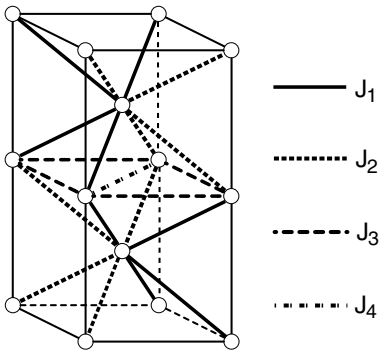


Fig. 2. Scheme representing the four magnetic pathways that fulfil the distance cut-off criterium for the ferromagnetic *p*-O_2N–C_6F_4–CNSSN$^{\cdot}$ radical.

a diamond-like network in a similar manner to J_1. The DFT calculations of the magnetic coupling constants for these four possible magnetic pathways are presented in Table 1. They indicate a single dominant exchange pathway (J_1) via the closest intermolecular S···N contact between heterocyclic rings ($d_{S\cdots N} = 3.488$ Å) which propagates through the lattice in a diamond-like motif. This is in agreement with the analysis made by Antorrena et al. [9]. The mean-field approximation, using the value of the computed J_1 interaction, predicts an antiferromagnetic transition at 45 K, a value in good agreement with the experimental value of 36 K.

2. *p*-O_2N–C_6F_4–CNSSN$^{\cdot}$

The *p*-$O_2NC_6F_4CNSSN^{\cdot}$ radical [10] is one of two S-based free radical ferromagnets; the other being the radical cation [BBDTA][$GaCl_4$]·MeCN [24]. The high temperature magnetic susceptibility of *p*-$O_2NC_6F_4CNSSN^{\cdot}$ shows Curie–Weiss behaviour with $\theta = 1.6 \pm 0.1$ K. The positive value of the Curie–Weiss constant indicates the presence of ferromagnetic interactions between the $S = 1/2$ centres. Low temperature a.c. magnetic susceptibility studies on a single crystal confirm a long-range ferromagnetic transition at 1.32 ± 0.02 K.

This derivative also exhibits four magnetic pathways which fulfil the distance cut-off criterion. These are represented in Fig. 2. Whilst the J_1 and J_2 magnetic pathways generate a 3D network connecting radicals in different planes perpendicular to the *c*-axis, the remaining two interactions connect radicals within the *ab* plane. The computations of the magnetic coupling constants for the four interactions (see Table 1) show that the J_1 magnetic interaction is the dominant one and should lead to ferromagnetic interactions propagating through 3D. In a mean-field approximation calculation with the J_1 magnetic interaction determined by our ab initio calculations, we calculate a ferromagnetic transition at 1.64 K, very close to the experimental ferromagnetic transition temperature (1.3 K).

In both of these two structures, there is a single magnetic interaction which propagates throughout the 3D structure giving rise to long-range magnetic order. The DFT calculations not only reproduce the sign of the exchange interaction but also good estimates of the strength of the exchange interaction (evidenced by the ordering temperatures). As with other organic radicals, the spin can be considered to be Heisenberg-like (with very little single-ion anisotropy) and is only expected to exhibit long-range order once a 3D network is established. The dominant exchange pathway determined for both these radials also predicts the correct (3D) lattice dimensionality. We now turn our attention to two other dithiadiazolyl radicals which show no clear evidence for long-range magnetic order.

3. α-Phase of it p-NC–C_6F_4–CNSSN$^{\cdot}$

This compound has been successfully crystallized once and appears to be a meta-stable phase. Its crystal structure has been reported and the temperature dependence of the magnetic susceptibility measured on a Faraday balance [7]. Above 100 K, the susceptibility follows a Curie–Weiss law with $\theta = -25$ K, whereas in the low temperature range there is a maximum in χ around 8 K.

The low symmetry of the space group (triclinic $P\bar{1}$) leads to a large number of chemically distinct pairs of near-neighbour contacts. In addition to a magnetic pathway (J_9) extending through CN···S contacts (analogous to the β-phase which is determined to be of the order of 10^{-2} cm^{-1}), there are a further eight other possible magnetic pathways which fulfil the distance cut-off criterion. The computed magnetic coupling constants are listed in Table 1. The two strongest interactions J_1 and J_3 are 1–2 orders of magnitude greater than the other exchange interactions and form a linear chain with alternating ferromagnetic and antiferromagnetic interactions. The effect of the other interactions would be a dimensionality crossover from 2D to 3D behaviour, and would be expected below 1 K. The

magnitude of J_1/k_B and J_3/k_B obtained are of similar value to the temperature of the maximum in the magnetic susceptibility. However, with the calculated J_1 and J_3 magnetic coupling constants the Curie–Weiss constant at most would be about -1 K, instead of $\theta = -25$ K. However, because of problems with the accuracy of the temperature control in the reported magnetic measurements [7] a more detailed analysis should be reserved until more reliable data are available.

4. *p*-Br–C_6F_4–CNSSN$^{\bullet}$

In this compound, the magnetic susceptibility above 60 K follows a Curie–Weiss law with $\theta = -27$ K. With this value of θ, the mean-field approximation predicts an antiferromagnetic transition at 27 K, whereas in a low-dimensional system a broad peak around 27 K would be expected. Nevertheless, the experimental magnetic susceptibility down to 1.8 K shows neither an antiferromagnetic transition nor a broad peak, but increases continually with decreasing temperature [9]. The absence of a λ-type maximum in χ mitigates against a long-range antiferromagnetically ordered phase, but gives little evidence on the true nature of the exchange interactions and lattice dimensionality.

Amongst the seven possible magnetic pathways obtained from the distance cut-off criterion, there appear to be three significant interactions (Table 1) which are 1–2 orders of magnitude stronger than the remaining interactions. The magnetic motif, see Fig. 3, generated by these three strongest interactions is strongly 2D and can be described as a square network, where the J_3 interaction propagates along the column and J_1 and J_2 alternate through the rows. Each $\ldots J_1$–J_2–J_1–$J_2\ldots$ row is shifted with respect to the neighbouring rows. The 2D nature of the magnetic network clearly explains the lack of magnetic order above 1.8 K. Furthermore, the magnetic network exhibits clear frustration which may explain the lack of a broad maximum in χ characteristic of the short-range ordering of low-dimensional systems without frustration. However, the complexity of the exchange pathway currently precludes a simple analysis of the data and further modelling of the susceptibility data using Monte Carlo methods is planned.

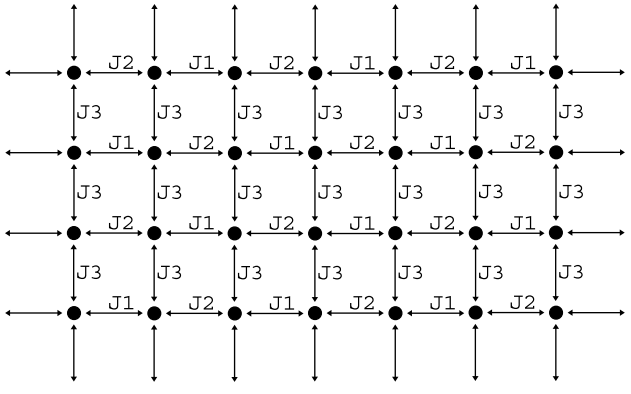


Fig. 3. 2D square network generated by the three strongest computed interactions in the *p*-Br–C_6F_4–CNSSN$^{\bullet}$ radical. The J_3 interaction propagates along the column, and J_1 and J_2 alternate through the rows.

We have shown that ab initio calculations of the magnetic exchange may provide a better understanding of the mechanisms which govern both the nature and strength of the interaction between thiazyl-based radicals. Moreover, a consideration of the dimensionality of the exchange pathway provides an excellent correlation with the observation (or absence) of bulk magnetic order. Notably, these calculations have demonstrated the existence of both ferro and antiferromagnetic coupling constants >10 K. Judicious control of the nature of the crystal structure may lead to organic magnets with high transition temperatures. Further studies are in progress.

References

[1] (a) K. Awaga, Y. Maruyama, Chem. Phys. Lett. 158 (1989) 556; (b) M. Tamura, Y. Nakazawa, D. Shiomi, K. Nozawa, Y. Hosokoshi, M. Ishikawa, M. Takahashi, M. Kinoshita, Chem. Phys. Lett. 186 (1991) 401.
[2] Paul M. Lathi (Ed.), Magnetic Properties of Organic Materials, Marcel Dekker, New York, 1999.
[3] J.M. Rawson, F. Palacio, Struct. Bonding 100 (2001) 94.
[4] J. Rawson, A. Banister, I. Lavender, Adv. Heterocycl. Chem. 62 (1995) 137.
[6] (a) J. Rawson, R.L.J. Smith, F. Palacio, G. Antorrena, Mol. Cryst. Liq. Cryst. 334 (1999) 275;
(b) G. Antorrena, F. Palacio, J.M. Rawson, J.N.B. Smith, in: J. Veciana, C. Rovira, D.B. Amabilino (Eds.), Supramolecular Engineering of Synthetic Metallic Materials: Conductors and Magnets. NATO-ARW, Sitges (1998), Kluwer Academic Publishers, Dordrecht, NATO-ASI Ser. C518 (1999) 217.
[7] A.J. Banister, N. Bricklebank, W. Clegg, M.R.S. Elsegood, C.I. Gregory, I. Lavender, J.M. Rawson, B.K. Tanner, J. Chem. Soc., Chem. Commun. (1996) 680, N.B. The magnetic measurements were measured on a Faraday Balance. A sample of the β-phase of p-$NCC_6F_4CNSSN^{\bullet}$ measured on the same equipment appeared to order at 38 K (cf. transition temperatures recorded with a variety of other techniques at 35.5–36.0 K). This small discrepancy in temperature underlines the need for further investigations of the α-phase.
[8] A.J. Banister, N. Bricklebank, I. Lavender, J.M. Rawson, C.I. Gregory, B.K. Tanner, W. Clegg, M.R.J. Elsegood, F. Palacio, Angew. Chem., Int. Ed. Engl. 35 (1996) 2533.
[9] G. Antorrena, J.E. Davies, M. Hartley, F. Palacio, J.M. Rawson, J.N.B. Smith, A. Steiner, J. Chem. Soc., Chem. Commun. (1999) 1393.
[10] A. Alberola, R.J. Less, C.M. Pask, J.M. Rawson, F. Palacio, P. Oliete, C. Paulsen, A. Yamaguchi, R.D. Farley, Angew. Chem., Int. Ed. 42 (2003) 4782.
[11] A. Alberola, R.J. Less, F. Palacio, C.M. Pask, J.M. Rawson, Molecules 9 (2004) 771.
[12] F. Palacio, G. Antorrena, M. Castro, R. Burriel, J.M. Rawson, J.N.B. Smith, N. Bricklebank, J. Novoa, C. Ritter, Phys. Rev. Lett. 79 (1997) 2336.

[13] C. Herring, in: G. Rado, H. Suhl (Eds.), Magnetism IIB, Direct Exchange between Well-separated Atomsress, Academic Press, New York, 1966, p. 5.
[14] J. Luzón, J. Campo, F. Palacio, G.J. McIntyre, A.E. Goeta, E. Ressouche, C.M. Pask, J.M. Rawson, Physica B 335 (2003) 1.
[15] P.J. Alonso, G. Antorrena, J.I. Martínez, J.J. Novoa, F. Palacio, J.M. Rawson, J.N.B. Smith, Appl. Magn. Reson. 20 (2001) 231.
[16] H. Nagao, M. Nishino, Y. Shigeta, T. Soda, Y. Kitagawa, T. Onishi, Y. Yoshioka, K. Yamaguchi, Coord. Chem. Rev. 198 (2000) 265.
[17] A.D. Becke, J. Chem. Phys. 98 (1993) 5648.
[18] R. Krishnan, J.S. Binkley, R. Seeger, J.A. Pople, J. Chem. Phys. 72 (1980) 650.
[19] M.J. Frisch et al., Gaussian 98, Revision A.11.3, Gaussian Inc., Pittsburgh, PA, 2002.
[20] F.L. Pratt, A.E. Goeta, F. Palacio, J.M. Rawson, J.N.B. Smith, Physica B 289–290 (2000) 119.
[21] J.M. Rawson, A. Alberola, H. El-Mkami, G.M. Smith, J. Phys. Chem. Sol. 65 (2004) 727.
[22] A. Alberola, C.M. Pask, J.M. Rawson, E.J.L. McInnes, J. Wolowska, H. El Mkami, G.M. Smith, J. Phys. Chem. B 107 (2003) 14158.
[23] P.J. Langley, J.M. Rawson, J.N.B. Smith, M. Schuler, R. Bachmann, A. Schweiger, F. Palacio, G. Antorrena, G. Gescheidt, A. Quintel, J. Mater. Chem. 9 (1999) 1431.
[24] W. Fujita, K. Awaga, Chem. Phys. Lett. 357 (2002) 385.

py_4C (8.1 mg; 0.025 mmol) and an ether solution (1 mL) of dehydrated $Cu(hfac)_2$ (23.9 mg; 0.050 mmol) were combined and heated at 40 °C for 24 h after diluted with 3 mL of hexane. Greenish blue plates of $[Cu(hfac)_2(py_4C)]$ were precipitated and separated on a filter. The yield was 16.7 mg (83%). *Anal.* Calc. for $C_{31}H_{18}N_4O_4Cu_1F_{12}$: C, 46.42; H, 2.26; N, 6.99. Found: C, 45.85; H, 2.27; N, 6.84%.

Similarly a reaction mixture was prepared and refluxed in hexane for 1 day. After the mixture was allowed to stand at room temperature for a few days, green plates of $[Cu(hfac)(py_4C)\cdot Cu(hfac)_3]$ were precipitated and isolated on a filter. The yield was 6.2 mg (19%). *Anal.* Calc. for $C_{41}H_{20}N_4O_8Cu_2F_{24}$: C, 38.48; H, 1.58; N, 4.38. Found: C, 38.27; H, 1.63; N, 5.31%.

X-ray diffraction data of a single crystal of $[Cu(hfac)_2(py_4C)]$ and $[Cu(hfac)(py_4C)\cdot Cu(hfac)_3]$ were collected on a Rigaku R-axis RAPID diffractometer with graphite monochromated Mo Kα radiation ($\lambda = 0.71069$ Å). The structures were solved by direct methods and expanded using Fourier techniques in the CrystalStructure program package [16]. Thermal displacement parameters were refined anisotropically for non-hydrogen atoms. Hydrogen atoms were located at calculated positions. CCDC reference numbers 252026 and 252027.

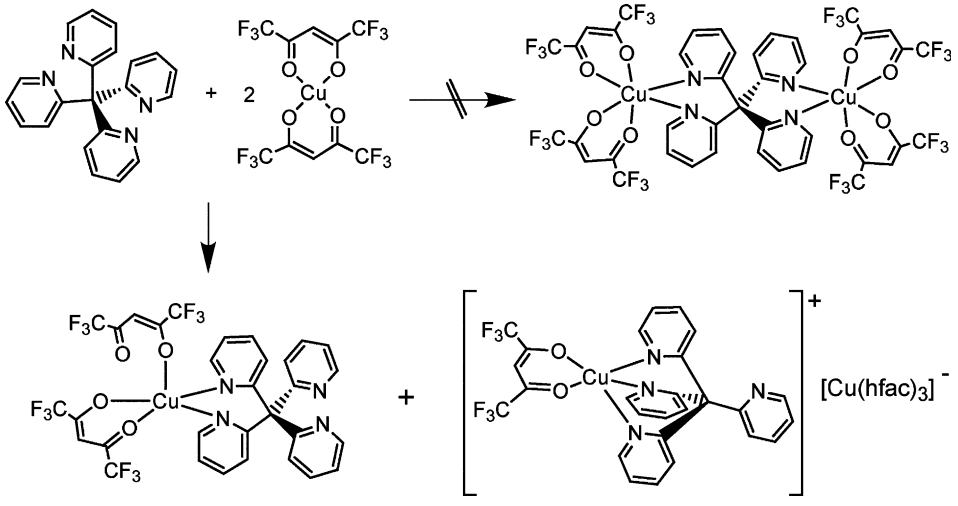
Magnetic susceptibilities of randomly oriented polycrystalline samples were measured on a Quantum Design MPMS SQUID magnetometer at an applied field of 5×10^3 Oe in a temperature range 1.8–100 K. The magnetic responses were corrected with diamagnetic blank data of the sample holder obtained separately. The diamagnetic contribution of the sample itself was estimated from Pascal's constants.

3. Results and discussion

We planned to prepare the target dinuclear copper(II) complex $[\{Cu(hfac)_2\}_2(py_4C)]$ in which two pyridine nitrogen atoms are coordinated to each copper(II) ion, as shown in Scheme 1. However, we obtained so far only $[Cu(hfac)_2(py_4C)]$ and $[Cu(hfac)(py_4C)\cdot Cu(hfac)_3]$ instead of $[\{Cu(hfac)_2\}_2(py_4C)]$. Their molecular structures were unequivocally determined by means of X-ray crystallographic analysis (Fig. 1). Selected crystallographic parameters are listed in Table 1.

The copper(II) ion in $[Cu(hfac)_2(py_4C)]$ is penta-coordinate, giving a square pyramidal configuration. Two nitrogen atoms (N1 and N2) are coordinated to Cu1 at equatorial sites, while N3 and N4 are free from coordination. One hfac ligand forms a chelate ring on the equatorial plane. The other hfac located at the axial site in a monodentate manner. The axial Cu1–O3 bond (2.156(4) Å) is longer than the equatorial bonds (1.955(3), 1.950(3), 1.981(4), and 1.960(4) Å for Cu1–O1, Cu1–O2, Cu1–N1, and Cu1–N2, respectively).

We could not elucidate the molecular structure of $[Cu(hfac)(py_4C)\cdot Cu(hfac)_3]$ only from the elemental analysis which should be the same as that of the target compound, but the molecular structure was clarified by means of X-ray crystallographic analysis as depicted in Fig. 1(b). The product consists of an ion pair: $[Cu(hfac)(py_4C)]^+$ and $[Cu(hfac)_3]^-$. The copper(II) ion (Cu1) in $[Cu(hfac)(py_4C)]^+$ is penta-coordinate. Two nitrogen atoms (N1 and N2) are coordinated to Cu1 at equatorial sites, and one nitrogen (N3) occupies an axial position. The Cu1–N3 bond length (2.205(4) Å) is considerably longer than those of Cu1–N1 and Cu1–N2 (1.973(5) and 1.969(4) Å, respectively). One hfac ligand forms a chelate ring on the equatorial plane. The Cu1–O1 and Cu1–O2 bond lengths are 1.946(3) and 1.952(5) Å, respectively.



Scheme 1.

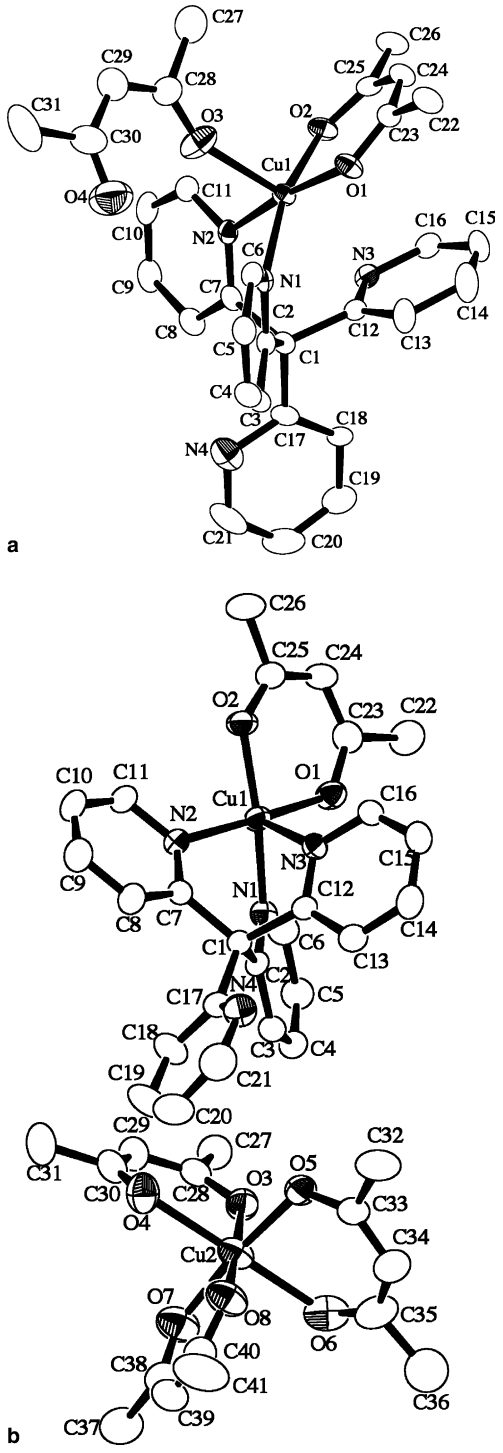


Fig. 1. Ortep drawings of: (a) $[Cu(hfac)_2(py_4C)]$; and (b) $[Cu(hfac)(py_4C)\cdot Cu(hfac)_3]$ with thermal ellipsoids at the 50% and 30% probability levels, respectively. Hydrogen and fluorine atoms are omitted for the sake of clarity.

The counter anion consists of a paramagnetic copper(II) ion and three hfac ligands. The Cu2–O4 and Cu2–O6 are assigned as axial because these bond lengths (2.236(5) and 2.219(6) Å, respectively), are much longer than other Cu2-O bonds (1.951(4)–2.041(4) Å).

Table 1
Selected crystallographic parameters

Compounds	$[Cu(hfac)_2(py_4C)]$	$[Cu(hfac)(py_4C)\cdot Cu(hfac)_3]$
Formula	$C_{31}H_{18}CuF_{12}N_4O_4$	$C_{41}H_{20}Cu_2F_{24}N_4O_8$
Crystal system	monoclinic	triclinic
Space group	$P2_1/n$	$P\bar{1}$
a (Å)	18.643(8)	12.6518(5)
b (Å)	8.657(4)	14.3309(5)
c (Å)	18.748(9)	14.4301(5)
α (°)	90	74.170(1)
β (°)	95.26(4)	78.1090(7)
γ (°)	90	78.012(1)
V (Å)^3	3012(2)	2431.0(2)
Z	4	2
μ (mm^{-1})	0.846	1.022
d_{calc} (g cm^{-3})	1.768	1.748
$R(F)(I > 2\sigma(I))$[a]	0.058	0.070
$R_w(F^2)$ (all data)[b]	0.087	0.088
T (K)	90	296

[a] $R = \sum(\|F_o\|-|F_c\|)/\sum|F_o|$.
[b] $R_w = [\Sigma w(|F_o|-|F_c|)^2/\sum w|F_c|^2]^{1/2}$.

The magnetic properties were obtained on a SQUID magnetometer. The magnetic susceptibility of $[Cu(hfac)_2(py_4C)]$ obeyed the Curie-law. The Curie constant in $\chi_{mol} = C/T$ was determined to be 0.436 cm^3 K mol^{-1}, which corresponds to $S = 1/2$ species with $g = 2.16$. No appreciable magnetic interaction was observed, being in agreement with the crystal structure determined.

The magnetic susceptibility of $[Cu(hfac)(py_4C)\cdot Cu(hfac)_3]$ also behaved as an ideal paramagnet. The Curie constant was 0.883 cm^3 K mol^{-1}, which corresponds to the sum of two $S = 1/2$ species with $g = 2.13$ on the average of the cationic and anionic paramagnetic portions.

In summary, the desired spiro-fused structure was not characterized in obtained complexes. Usually copper(II) ions are ready to undergo Jahn-Teller distortion which stabilizes a penta-coordinate square pyramid or a square plane. The proposed synthetic scheme is based on hexa-coordinate metal ions and we have unsuccessful results on the dinuclear copper(II) complex containing a py_4C bridge. Steric congestion of hfac ligands should also be taken into consideration for further study. We tried to prepare oxovanadium(II) derivatives using $VO(hfac)_2$ in place of $Cu(hfac)_2$, but no meaningful products were separated. Very recently we have found that the reaction of py_4C and $Mn(hfac)_2$ afforded dinuclear complex. Details will be reported elsewhere [17].

Acknowledgements

This work was supported by a Grant-in-Aid for Scientific Research on Priority Areas of "Molecular Conductors" (No. 15073101) and by Grants-in-Aid for

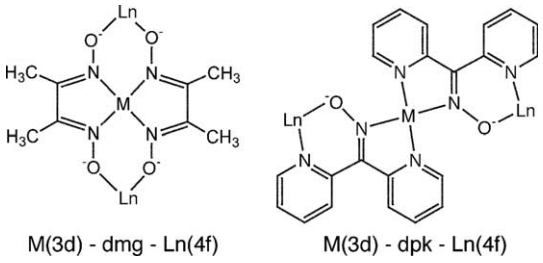
Scientific Research (Nos. 16550121 and 15550115) from the Ministry of Education, Culture, Sports, Science and Technology, Japan. One of the authors (T.I.) thanks Research Foundation For Materials Science, Japan.

Appendix A. Supplementary data

Supplementary data associated with this article can be found, in the online version, at doi:10.1016/j.poly.2005.03.155.

References

[1] C. Joachim, J.K. Gimzewski, A. Aviram, Nature 408 (2000) 541.
[2] J.M. Tour, R. Wu, J.S. Schumm, J. Am. Chem. Soc. 112 (1990) 5662.
[3] R. Wu, J.S. Schumm, D.L. Pearson, J.M. Tour, J. Org. Chem. 61 (1996) 6906.
[4] A. Aviram, J. Am. Chem. Soc. 110 (1988) 5687.
[5] A. Ito, M. Urabe, K. Tanaka, Angew. Chem. Int. Ed. 42 (2003) 921.
[6] L. McElwee-White, W.A. Goddard III, D.A. Dougherty, J. Am. Chem. Soc. 106 (1984) 3461.
[7] L. McElwee-White, D.A. Dougherty, J. Am. Chem. Soc. 106 (1984) 3466.
[8] N.L. Frank, R. Clérac, J.-P. Sutter, N. Daro, O. Kahn, C. Coulon, M.T. Green, S. Golhen, L. Ouahab, J. Am. Chem. Soc. 122 (2000) 2053.
[9] M.E. Itkis, X. Chi, A.W. Cordes, R.C. Haddon, Science 296 (2002) 1443.
[10] X. Chi, M.E. Itkis, B.O. Patrick, T.M. Barclay, R.W. Reed, R.T. Oakley, A.W. Cordes, R.C. Haddon, J. Am. Chem. Soc. 121 (1999) 10395.
[11] M. Ooishi, M. Seino, R. Imachi, T. Ishida, T. Nogami, Tetrahedron Lett. 43 (2002) 5521.
[12] T. Ishida, M. Ooishi, T. Nogami, Abstract Book of "IMS COE Symposium on Electronic Properties of Molecular Assemblies, 2001, p. 109.
[13] T. Ishida, T. Kawakami, S.-i. Mitsubori, T. Nogami, K. Yamaguchi, H. Iwamura, J. Chem. Soc., Dalton Trans. (2002) 3177.
[14] K. Matsumoto, M. Kannami, M. Oda, Tetrahedron Lett. 44 (2003) 2861.
[15] K. Matsumoto, M. Kannami, M. Oda, Chem. Lett. 33 (2004) 1096.
[16] CrystalStructure, Single Crystal Structure Analysis Software Version 3.5.1, Rigaku/MSC, 9009 New Trails Drive, The Woodlands, TX 77381, USA, 2003.
[17] A. Okazawa, T. Ishida, T. Nogami, Chem. Lett. 33 (2004) 1478.



Scheme 1. M–dmg–Ln and M–dpk–Ln building blocks.

2. Experimental

The starting materials, [Ni(dpk)$_2$(phen)] and [Ni(dpk)$_2$(py)$_2$], were prepared according to the method of [Ni(pao)$_2$(py)$_2$] (pao = pyridine-2-aldoximate) [11]. The following complexation procedure is typical. After azeotropic distillation of *n*-heptane and water from a *n*-heptane solution (150 mL) containing 328 mg (0.40 mmol) of [Dy(hfac)$_3$(H$_2$O)$_2$] [12], ca. 10 mL of dry ether was added to the residue to give a yellow clear solution. A dry dichloromethane solution (10 mL) containing 128 mg (0.20 mmol) of [Ni(dpk)$_2$(phen)] was added to the above solution and the combined solution was allowed to stand at room temperature after the removal of orange powder precipitated. Orange crystals of [{Ln(hfac)$_3$}$_2${Ni(dpk)$_2$(phen)}] (**1Dy**) were grown and collected on a filter. The yield was 255 mg (0.12 mmol; 58%).

X-ray diffraction data of a single crystal of **1Ln** and **2Ln** were collected on a Rigaku R-axis RAPID diffractometer with graphite monochromated Mo Kα (λ = 0.71069 Å) radiation at 90 K. The structures were solved by direct methods and expanded using Fourier techniques in the CRYSTALSTRUCTURE program package [13]. Thermal displacement parameters were refined anisotropically for non-hydrogen atoms. Hydrogen atoms were located at calculated positions. Selected crystallographic parameters are as follows. **1Dy**: $C_{64}H_{38}Dy_2F_{36}N_8O_{18}Ni_1$, monoclinic, *C*2/*c*, a = 25.44(1) Å, b = 16.119(9) Å, c = 21.91(1) Å, β = 112.29(4)°, V = 8310(7) Å^3, Z = 4, d_{calc} = 1.818 g cm^{-3}, μ(Mo Kα) = 2.155 mm^{-1}, $R(F)$ ($I > 2\sigma(I)$) = 0.066, and $R_w(F^2)$ (all data) = 0.102 for 8940 unique reflections. **2Dy**: $C_{62}H_{32}Dy_2F_{36}N_8O_{14}Ni_1$, monoclinic, $P2_1/n$, a = 10.963(6) Å, b = 14.812(8) Å, c = 23.73(1) Å, β = 100.63(5)°, V = 3786(3) Å^3, Z = 2, d_{calc} = 1.912 g cm^{-3}, μ(Mo Kα) = 2.357 mm^{-1}, $R(F)$ ($I > 2\sigma(I)$) = 0.056, and $R_w(F^2)$ (all data) = 0.069 for 7988 unique reflections.

Magnetic susceptibilities of polycrystalline samples of **1Ln** and **2Ln** were measured on a Quantum Design MPMS SQUID magnetometer at an applied magnetic field of 500 Oe over a temperature range 1.8–300 K. The magnetic responses were corrected with diamagnetic blank data of the sample holder obtained separately. The diamagnetic contribution of the sample itself was estimated from Pascal's constant. Ac magnetic susceptibility was measured on a Quantum Design PPMS ac/dc magnetometer in a temperature range down to 2.0 K. The polycrystalline sample of **1Ln** and **2Ln** were fixed with mineral oil in all magnetic measurements.

3. Results and discussion

3.1. Crystal structure analysis

We prepared ten kinds of complexes, **1Ln** and **2Ln** (Ln = La, Tb, Dy, Ho, Er). The crystal structures of **1Ln** (Ln = Tb, Dy, Ho, Er) and **2Ln** (Ln = Dy, Ho) were analyzed by means of single-crystal X-ray diffraction study. Fig. 1(a) and (b) shows the ORTEP drawings of **1Dy** and **2Dy**, respectively, indicating that three metal ions are arranged in a linear array, and also that the ligands or metal ions did not scramble during the synthesis. The central [Ni(dpk)$_2$ (L)$_2$] ((L)$_2$ = phen, (py)$_2$) structure was completely remained from the starting materials. The cell parameters of other complexes are summarized in Table 1. Compounds **1Tb**, **1Ho**, and **1Er** have isomorphous crystal structures to **1Dy**. Actually, though the *R* factors in the refinement were somewhat unsatisfactory ($R \geqslant 0.1$), the molecular structures of **1Tb**, **1Ho**, and **1Er** were preliminarily solved and refined to be practically the same molecular structures as that of **1Dy**. Unfortunately, **2Tb** and **2Er** did not afford good single crystals suitable for X-ray diffraction study. Preliminary X-ray diffraction analysis indicated that **2Dy** and **2Ho** were isomorphous to each other.

The molecular structure of **1Dy** (Fig. 1(a)) has a two-fold axis along the center of phen and Ni1. The Ni1 ion has an octahedral geometry with a slight Jahn–Teller distortion, which is characteristic of high-spin Ni^{II} (S = 1), as indicated by the Ni–N bond-lengths of 2.082(9)–2.110(9) Å. The Ni and Dy ions are bridged by the N–O groups from dpk with the Dy1–O1–N3–Ni1 torsion angle of −138.1(6)°. The N2–Ni1–N2# and N3–Ni1–N3# angles are 100.1(3)° and 175.1(3)°, respectively (the symmetry operation code for # is $-x$, $+y$, $1/2 - z$). Owing to the molecular symmetry, three metal ions are arranged in a V-shaped manner, but actually the Dy1–Ni1–Dy1# array was very close to linear, as indicated by the Dy1–Ni1–Dy1# angle of 177.14(5)°. The Dy1 are octa-coordinate with three hfac chelates and additional N and O atoms from dpk. The O1–Dy1 distance (2.246(9) Å) is shorter than other O–Dy1 bonds (2.347(8)–2.389(9) Å).

The molecular structure of **2Dy** (Fig. 1(b)) has an inversion center at the Ni ion, and therefore three metal ions are arranged in a strictly linear manner. The N$_6$ geometry around N1 also shows a small Jahn–Teller

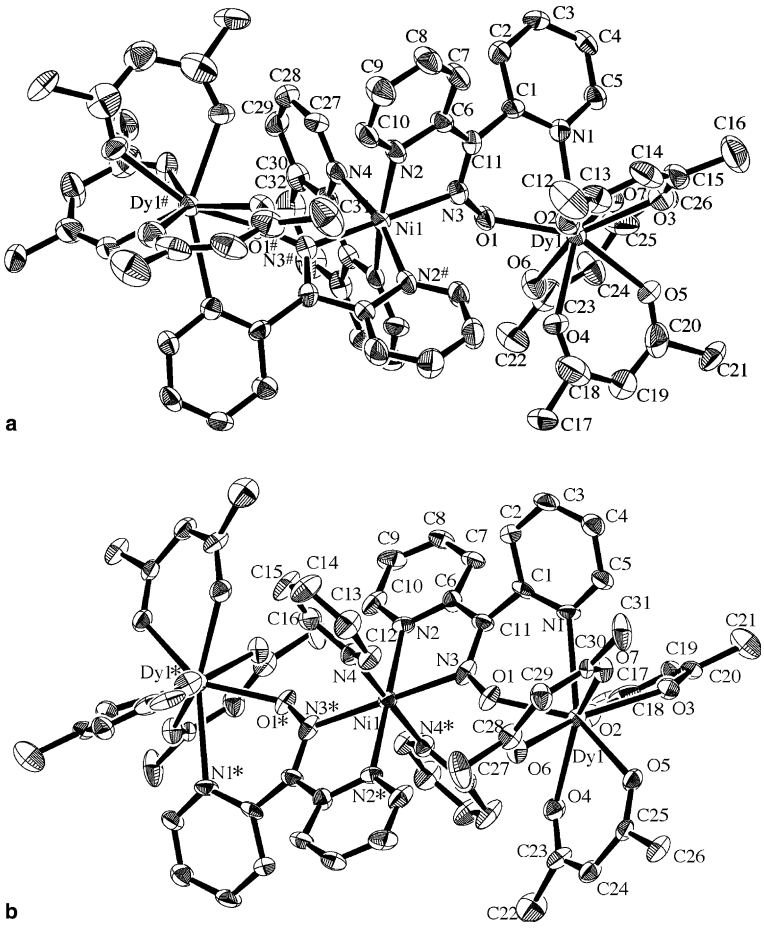


Fig. 1. ORTEP drawings of **1Dy** (a) and **2Dy** (b) with thermal ellipsoids at the 50% probability level. Hydrogen and fluorine atoms are omitted for the sake of clarity. The symmetry operation codes for # and * are $-x$, $+y$, $1/2 - z$, and $-x$, $1 - y$, $-z$, respectively.

Table 1
Cell parameters of **1Ln** (Ln = Tb, Dy, Ho, Er) and **2Ln** (Ln = Dy, Ho)

Compounds	**1Tb**	**1Dy**	**1Ho**	**1Er**	**2Dy**	**2Ho**
Space group	*C*2/*c*	*C*2/*c*	*C*2/*c*	*C*2/*c*	$P2_1/n$	$P2_1/n$
a (Å)	25.56(2)	25.44(1)	25.885(3)	25.579(2)	10.963(6)	10.871(7)
b (Å)	15.80(1)	16.119(9)	15.967(2)	15.994(1)	14.812(8)	14.773(8)
c (Å)	21.79(2)	21.91(1)	22.020(2)	21.899(2)	23.73(1)	23.50(2)
β (°)	112.65(7)	112.29(4)	112.844(4)	112.737(2)	100.63(5)	100.50(7)
V (Å^3)	8122(10)	8310(7)	8387(1)	8262(1)	3786(3)	3710(4)
Z	4	4	4	4	2	2
T (K)	90	90	100	100	90	100

distortion (the Ni1–N bond lengths are 2.118(9)–2.155(8) Å). The Ni and Dy ions are bridged by the N–O groups from dpk with the Dy1–O1–N3–Ni1 torsion angle of −143.7(5)°. The Dy1 are octa-coordinate like **1Dy**. The O1–Dy1 distance is the shortest (2.221(7) Å) among all of the O–Dy1 bonds (2.359(7)–2.440(7) Å).

3.2. Magnetic properties

In order to elucidate whether magnetic coupling between Ni–Ln is ferro- or antiferromagnetic, we measured temperature dependence of the dc magnetic susceptibility. Fig. 2(a) and (b) shows the temperature dependence of the product $\chi_{mol}T$ for **1Ln** and **2Ln** (Ln = Tb, Dy, Ho, Er), respectively. The observed $\chi_{mol}T$ decreases on cooling are due to the single-ion property such as the crystal field effect reducing the orbital angular momentum of the Dy ions and also due to magnetic coupling effects between the Dy and Ni ions. For all of the complexes, the $\chi_{mol}T$ value showed a monotonic decrease, indicating the absence of ferro- or ferrimagnetic coupling. Furthermore, rapid decreases below ca. 5 K suggest the presence of weak antiferromagnetic coupling

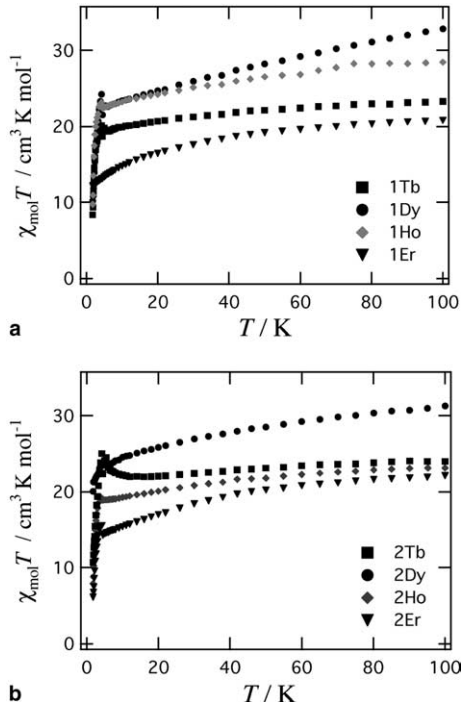


Fig. 2. Temperature dependence of the product $\chi_{mol}T$ for **1Ln** (a) and **2Ln** (b).

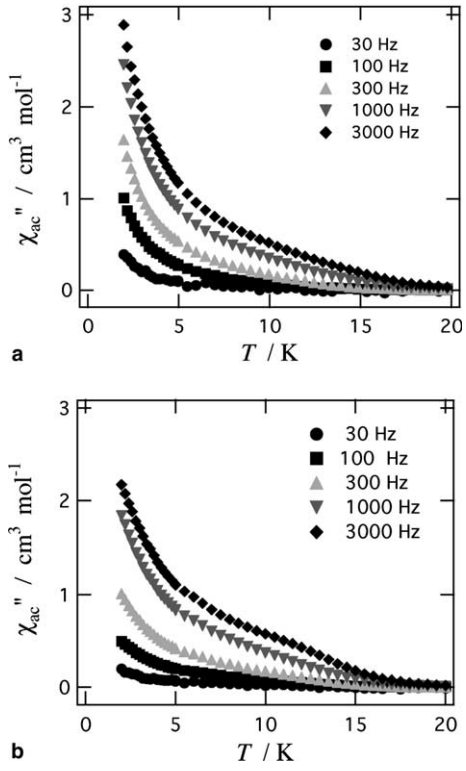


Fig. 3. Temperature and frequency dependence of the out-of-phase ac magnetic susceptibility χ''_{ac} for **1Dy** (a) and **2Dy** (b).

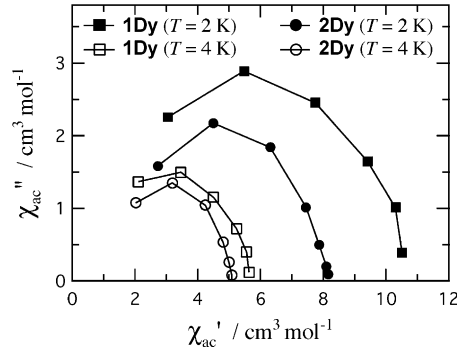


Fig. 4. Cole–Cole diagram (χ''_{ac} vs. χ'_{ac} plot) for **1Dy** and **2Dy** measured at 2.0 and 4.0 K.

between the Ln and Ni ions. Small humps are found around 5 K, which are accompanied by some wasted time in the cryostat process around 4.5 K. The Ni^{II} high spin state ($S = 1$) was confirmed by the magnetic measurements on **1La** and **2La**.

We measured the ac magnetic susceptibility (χ'_{ac} and χ''_{ac} for in-phase and out-of-phase susceptibilities, respectively) of **1Ln** and **2Ln**. The data were obtained with 5 G ac fields (10–10^4 Hz) at a zero dc field. Fig. 3(a) and (b) shows the frequency dependence of χ''_{ac} for **1Dy** and **2Dy**. Upon cooling, the χ''_{ac} of **1Dy** showed a notable increase below ca. 20 K (Fig. 3(a)), whereas those of **1Tb**, **1Ho**, and **1Er** did not show any meaningful increase. Furthermore, the χ''_{ac} frequency dependence of **1Dy** was very significant; the χ''_{ac} value showed drastic upsurge as the ac field frequency was elevated from 10 to 10^4 Hz.

As for the series of **2Ln**, **2Dy** similarly exhibited an increase of χ''_{ac} below ca. 17 K (Fig. 3(b)). The measurements on **2Tb**, **2Ho**, and **2Er** gave results similar to the case of the series of **1Ln**; only the Dy derivative showed a significant χ''_{ac} increase and frequency dependence. This frequency dependence seems to be an indication of blocking behavior usually observable for SMMs due to slow magnetization relaxation [2].

According to analysis of the Cole–Cole diagram [14], we plotted the χ''_{ac} data against χ'_{ac} at 2.0 and 4.0 K for **1Dy** and **2Dy** (Fig. 4). They clearly show semicircles, suggesting the χ''_{ac} increase is due to relaxation slowing down. The decrease of χ''_{ac} value in Fig. 4 is incomplete because the ac field could be applied in a frequency range up to 10^4 Hz. These findings suggest that **1Dy** and **2Dy** might become SMMs, but it will take place only at a very low temperature; i.e., the blocking temperature (T_B) will be much lower than 2 K. From a close look at Fig. 3(a) and (b), rather long tails of χ''_{ac} could be found in spite of the low T_B. There seems to be a shoulder around 12 K in Fig. 3(b). The origin is not clear so far.

Matsumoto et al. [7] developed the tetranuclear $[CuLTb(hfac)_2]_2$ and $[CuLDy(hfac)_2]_2$ as SMMs involving intramolecular ferromagnetic coupling. We have very recently reported pentanuclear $[Tb_4Cu_1]$ with a ground high-spin state behaving as an SMM [6].

Intramolecular ferro- and/or ferrimagnetic interactions leading to ground high-spin states are preferable for slowing the magnetization relaxation, because the energy barrier can be described as $\Delta = |D|S^2$ [2]. On the other hand, Kaizu et al. [9] reported the mononuclear phthalocyanine Tb and Dy salts were SMMs. They discussed the advantage of Tb and Dy ions over other lanthanide ions in the single-ion level. The situation of the present complexes **1Dy** and **2Dy** seems similar to that of the phthalocyanine-salts case, since no ferromagnetic coupling was characterized within a molecule. However, the SMM properties of **1Dy** and **2Dy** could not be attributed solely to Dy single-ion properties. We confirmed that the starting material $Dy(hfac)_3(H_2O)_2$ showed no frequency dependence of the χ''_{ac}. Very recently, we found that an isomorphous copper(II) derivative exhibited much slower magnetization relaxation; an obvious χ''_{ac} peak appeared above 2 K [10]. The role of 3d metal ions is essential.

4. Summary

We have reported the structural and magnetic characterization of **1Ln** and **2Ln**. The dpk monoanion works as a coupler between 3d and 4f metal ions. Lanthanide ions are supposed to be promising candidates for the SMM elements because of the large spin and oribital angular momenta and large magnetic anisotropy. We have developed **1Dy** and **2Dy** as a new class of SMMs.

Acknowledgements

This work was supported by a Grant-in-Aid for Scientific Research on Priority Areas of "Molecular Conductors" (No. 15073101) and by Grants-in-Aid for Scientific Research (Nos. 16550121 and 15550115) from the Ministry of Education, Culture, Sports, Science and Technology, Japan. One of the authors (T.I.) thanks Research Foundation For Materials Science, Japan.

Appendix A. Supplementary data

CCDC reference numbers 250361 and 250362. Crystallographic data reported in this paper has been deposited with the Cambridge Crystallographic Data Centre, 12, Union Road, Cambridge CB2 1EZ, UK (fax: +44 1223 336 033; deposit@ccdc.cam.ac.uk or www: http://www.ccdc.cam.ac.uk). Supplementary data associated with this article can be found, in the online version, at doi:10.1016/j.poly.2005.03.154.

References

[1] D. Gatteschi, A. Caneschi, L. Pardi, R. Sessoli, Science 265 (1994) 1054.
[2] G. Christou, D. Gatteschi, D.N. Hendrickson, R. Sessoli, MRS Bull. 25 (2000) 66.
[3] F. Lloret, R. Ruiz, B. Cervera, I. Castro, M. Julve, J. Faus, J.A. Real, F. Sapiña, Y. Journaux, J.C. Colin, M. Verdaguer, J. Chem. Soc., Chem. Commun. (1994) 2615.
[4] R. Clérac, H. Miyasaka, M. Yamashita, C. Coulon, J. Am. Chem. Soc. 124 (2002) 12837.
[5] Y. Kobayashi, S. Ueki, T. Ishida, T. Nogami, Chem. Phys. Lett. 378 (2003) 337.
[6] S. Ueki, M. Sahlan, T. Ishida, T. Nogami, Synth. Met. in press.
[7] S. Osa, T. Kido, N. Matsumoto, N. Re, A. Pochaba, J. Mrozinski, J. Am. Chem. Soc. 126 (2004) 420.
[8] F.C.M. Zaleski, E.C. Depperman, J.W. Kampf, M.L. Lirk, V.L. Pecoraro, Angew. Chem., Int. Ed. 43 (2004) 3912.
[9] N. Ishikawa, M. Sugita, T. Ishikawa, S.-y. Koshihara, Y. Kaizu, J. Am. Chem. Soc. 125 (2003) 8694.
[10] F. Mori, T. Nyui, T. Ishida, T. Nogami, K.-Y. Choi, H. Nojiri, in preparation.
[11] R.A. Crause, D.H. Busch, J. Am. Chem. Soc. 82 (1960) 4830.
[12] M.F. Richardson, W.F. Wagner, D.E. Sands, J. Inorg. Nucl. Chem. 30 (1968) 1275.
[13] CRYSTALSTRUCTURE, Single Crystal Structure Analysis Software Version 3.5.1, Rigaku/MSC, 9009 New Trails Drive, The Woodlands, TX 77381, USA, 2003.
[14] K.S. Cole, H.R. Cole, J. Chem. Phys. 9 (1941) 341.

2. Experimental

The new ligand 5bpno was prepared by lithiation of 5-bromo-2,2′-bipyridine [16] followed by the reaction with 2-methyl-2-nitrosopropane to give 5-(*N*-*t*-butylhydroxylamino)-2,2′-bipyridine in 59% yield. Mp. 124–125 °C. Subsequent oxidation of the hydroxylamine with freshly prepared Ag_2O in benzene gave 2,2′-bipyridin-5-yl *t*-butyl nitroxide (5bpno) in 15% yield. Mp. 139–141 °C (dec.). ESR (r.t., benzene) $g = 2.0063$, $a_N = 12.3$ G. The moleuclar structure was confirmed by means of X-ray crystallographic analysis.[1]

In a typical procedure, 50 mg of 5bpno and stoichiometric amount of metal salts were dissolved in 3 mL of methanol, and the resultant solution was kept in a refrigerator overnight giving the polycrystals of the desired complex in 10–30% yield. The products were isolated on a filter and subjected to elemental analysis, X-ray diffraction study, and magnetic measurements without further purification.

The elemental analysis measured on a Fisons EA-1108 by a usual combustion method indicated the following composition. $[Mn^{II}(5bpno)_3(ClO_4)_2]$: Calc. for $C_{42}H_{48}N_9O_{11}Cl_2Mn$: C, 51.44; H, 4.93; N, 12.85. Found: C, 51.00; H, 5.08; N, 12.17%. $[Mn^{II}(5bpno)(CH_3OH)_2Cl_2]$: Calc. for $C_{16}H_{24}N_3O_3Cl_2Mn$: C, 44.46; H, 5.60; N, 9.72. Found: C, 45.90; H, 5.57; N, 9.99%. $[Cu^{II}(5bpno)_2(ClO_4)_2]$: Calc. for $C_{28}H_{32}N_6O_{10}Cl_2Cu$: C, 45.02; H, 4.32; N, 11.25. Found: C, 45.56; H, 4.66; N, 10.98%. $[Cu^{II}(5bpno)Cl_2]$: Calc. for $C_{44}H_{16}N_3OCl_2Cu$: C, 44.63; H, 4.28; N, 11.15. Found: C, 43.62; H, 4.24; N, 10.28%.

X-ray diffraction data of a single crystal of $[Cu(5bpno)_2(ClO_4)_2]$ were collected on a Rigaku R-axis RAPID diffractometer with graphite-monochromated Mo Kα radiation ($\lambda = 0.71069$ Å) at 100 K. The structure was solved by direct methods and expanded using Fourier techniques in the CrystalStructure program package [17]. Numerical absorption correction was used. Thermal displacement parameters were refined anisotropically for non-hydrogen atoms and isotropically for hydrogen atoms. All the hydrogen atoms were found experimentally. Full-matrix least-squares methods were applied using all of the unique diffraction data. Selected crystallographic parameters of $[Cu(5bpno)_2(ClO_4)_2]$ are: $C_{56}H_{64}Cl_4Cu_2N_{12}O_{20}$, monoclinic, $P2_1/n$, $a = 15.012(6)$, $b = 14.469(4)$, $c = 15.881(6)$ Å, $\beta = 114.07(3)°$, $V = 3149(2)$ Å^3, $Z = 2$, $d_{calc} = 1.575$ g cm^{-3}, μ (Mo Kα) = 0.929 mm^{-1}, $R(F)(I > 2\sigma(I)) = 0.042$, and $R_w(F^2)$ (all data) = 0.069 for 7145 unique reflections. CCDC reference number 250190.

Magnetic susceptibilities of polycrystalline samples were measured on a Quantum Design MPMS SQUID magnetometer at an applied magnetic field of 5 kOe over a temperature range 1.8–300 K. The magnetic responses were corrected with diamagnetic blank data of the sample holder obtained separately. The diamagnetic contribution of the sample itself was estimated from Pascal's constant.

3. Results

3.1. Crystal structure analysis

As Fig. 1 shows, the Cu ion in $[Cu(5bpno)_2(ClO_4)_2]$ was tetra-coordinate with four nitrogen atoms forming two chelate rings like bpy complexes, while the nitroxide groups did not participate in coordination. The Cu1 coordination sphere is basically assigned to a square plane, being in agreement with the divalent copper geometry. The axial sites are practically vacant; however, there seem very weak interactions as indicated by rather long Cu1–O4, Cu1–O6, Cu1–O3$^{\#}$, and Cu1–O5$^{\#}$ distances (3.070(2), 3.147(2), 3.020(2), and 2.891(2) Å, respectively), where the symmetry operation code of # is $3/2 - x$, $-1/2 + y$, $1/2 + z$. Two five-membered chelate rings are inclined as indicated by the dihedral angle of 39.5(1)° between the two averaged plane (Cu1–N1–C1–C6–N2 and Cu1–N4–C15–C20-N5) probably owing to the van der Waals repulsion between H3–H19 and H7–H23 and also between the *t*-Bu-N(O·) groups.

Interestingly, two 5bpno ligands have a *syn* configuration, i.e., two nitroxide groups are closely located with the inter-atomic O1–O2 distance of 4.593(3)Å. The magnetic study on $[Cu(5bpno)_2(ClO_4)_2]$ revealed the presence of antiferromagnetic interaction (see below). The intramolecular O1–O2 through-space orbital contact may lead to antiferromagnetic interaction and disturb interpretation of through-bond metal–radical magnetic interactions. Since the square planer geometry is characteristic of copper(II) complexes and the N–O–O–N proximity is expected only for this geometry, the observed magnetic interactions in the other complexes, $[Mn(5bpno)_3(ClO_4)_2]$, $[Mn(5bpno)(CH_3OH)_2Cl_2]$, and $[Cu(5bpno)Cl_2]$, can be attributed mainly to the metal–radical interactions.

[1] We found polymorphism in the crystals of 5bpno. Phase α: $C_{14}N_3O_1H_{16}$, monoclinic, $P2_1/n$, $a = 6.1429(3)$, $b = 12.9498(3)$, $c = 15.9699(7)$ Å, $\beta = 96.148(6)°$, $V = 1263.09(9)$ Å^3, $Z = 4$, $d_{calc} = 1.274$ g cm^{-3}, μ(Mo Kα) = 0.083 mm^{-1}, $T = 100$ K, $R(F)(I > 2\sigma(I)) = 0.059$, and $R_w(F^2)$ (all data) = 0.027 for 2862 unique reflections. Phase β: $C_{14}N_3O_1H_{16}$, orthorhombic, *Pbca*, $a = 8.406(4)$, $b = 10.191(4)$, $c = 30.60(1)$ Å, $V = 2621(1)$ Å^3, $Z = 8$, $d_{calc} = 1.228$ g cm^{-3}, μ(Mo Kα) = 0.080 mm^{-1}, $T = 100$ K, $R(F)(I > 2\sigma(I)) = 0.060$, and $R_w(F^2)$ (all data) = 0.043 for 2889 unique reflections. CCDC reference numbers 250188 and 250189. The *t*-Bu-N(–O·) groups in the α- and β-phase crystals have *anti*- and *syn*-conformations of the nitroxide oxygen atom, respectively, with respect to the adjacent pyridine ring.

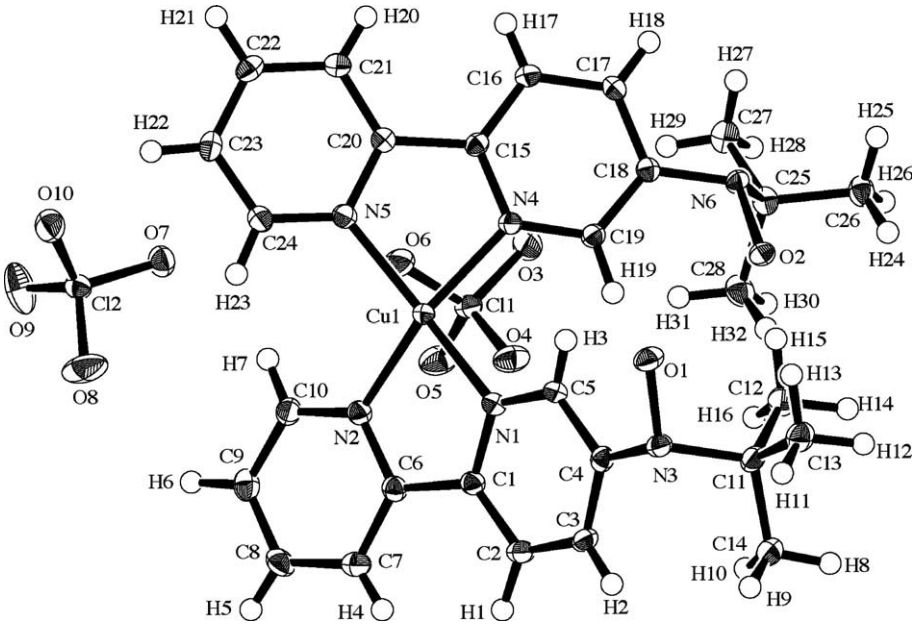


Fig. 1. Ortep drawing of $[Cu(5bpno)_2(ClO_4)_2]$ with thermal ellipsoids at the 50% probability level for non-hydrogen atoms. Atom numbering scheme is also shown.

Relatively short intermolecular radical–radical contacts were found with the O2–N6‡ and O2–O2‡ distances of 2.804(4) and 3.167(3) Å, which are shorter than or close to the sum of the van der Waals radii (3.07 and 3.04 Å for N–O and O–O, respectively [18]; the symmetry operation code for ‡ is $5/2 - x$, $3/2 + y$, $1/2 - z$). Antiferromagnetic coupling is expected as in the case of the intramolecular one at O1–O2.

Unfortunately, only $[Cu(5bpno)_2(ClO_4)_2]$ gave good crystals suitable for single-crystal X-ray diffraction analysis.

3.2. Magnetic properties

Fig. 2 shows the results of magnetic measurements on four complexes investigated here. In a high temperature region, the observed $\chi_{mol}T$ value of $[Mn(5bpno)_3(ClO_4)_2]$ was 5.5 cm^3 K mol^{-1}, which agrees well with the theoretical spin only value of 5.5 cm^3 K mol^{-1} for a species containing one $S_{Mn} = 5/2$ and three $S_{radical} = 1/2$ spins. The presence of ferromagnetic interaction was clearly indicated by the upsurges of the $\chi_{mol}T$ values on cooling. The $\chi_{mol}T$ value reached to a maximum 6.34 cm^3 K mol^{-1} at 14 K and then decreased sharply owing to secondary antiferromagnetic interaction.

Although the X-ray crystallographic analysis on $[Mn(5bpno)_3(ClO_4)_2]$ was unsuccessful, we assume a tris(bpy)-type N_6-coordination structure, and a Mn-centered triangular model can be proposed for the spin–spin exchange interaction. The three radical sites may not be crystallograpihcally equivalent and there may be some isomers of $[Mn(5bpno)_3^{2+}]$, but one exchange

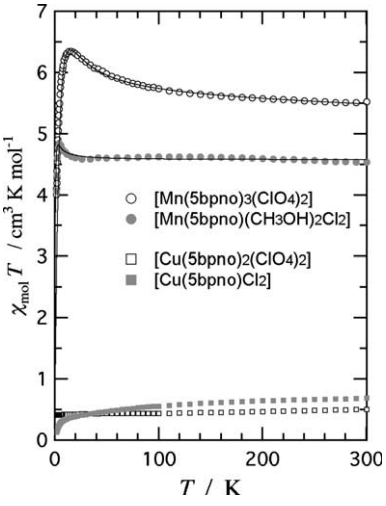


Fig. 2. Temperature dependence of the product $\chi_{mol}T$ for $[Mn(5bpno)_3(ClO_4)_2]$, $[Mn(5bpno)(CH_3OH)_2Cl_2]$, $[Cu(5bpno)_2(ClO_4)_2]$, and $[Cu(5bpno)Cl_2]$. The solid lines represent calculated curves. See the text for the equations and parameters.

parameter J is introduced as an average. Accordingly, we obtained the Heisenberg spin Hamiltonian $H = -2J(S_1 \cdot S_2 + S_1 \cdot S_3 + S_1 \cdot S_4)$ and the following expression of the molar magnetic susceptibility (Eq. (1)), by application of Kambe's vector coupling method [19] and the van Vleck equation:

$$\chi_{mol} = \frac{N_A g^2 \mu_B^2}{3k_B(T-\theta)} \frac{A}{B}, \quad (1)$$

where $A = 180 + 84\exp(-8J/k_BT) + 168\exp(-5J/k_BT) + 30\exp(-14J/k_BT) + 60\exp(-11J/k_BT) + 6\exp(-18J/k_BT)$,

$B = 9 + 7\exp(-8J/k_BT) + 14\exp(-5J/k_BT) + 5\exp(-14J/k_BT) + 10\exp(-11J/k_BT) + 3\exp(-18J/k_BT)$.

The intermolecular interaction is evaluated by a Weiss mean-field parameter θ. The best-fit curve is superposed in Fig. 2 with the optimized parameters of $J/k_B = +3.73(6)$ K, $g = 2.01(1)$, and $\theta = -4.67(4)$ K. The fit seems considerably good, indicating that the proposed model is plausible.

The observed $\chi_{mol}T$ value of [Mn(5bpno)-$(CH_3OH)_2Cl_2$] was 4.5 cm^3 K mol^{-1} at 300 K, which is slightly smaller than the theoretical spin only value of 4.75 cm^3 K mol^{-1}. With a decrease of temperature the $\chi_{mol}T$ reached to 4.84 cm^3 K mol^{-1} at 4.2 K which is larger than the spin only value, indicating the presence of ferromagnetic interaction in spite of possible impurity contaminated. Intramolecular ferromagnetic and intermolecular antiferromagnetic interactions are assumed since the $\chi_{mol}T$ value decreased in a lower temperature region just like $[Mn(5bpno)_3(ClO_4)_2]$.

Despite the lack of structural information on $[Mn(5bpno)(CH_3OH)_2Cl_2]$, a hexa-coordinate structure around the Mn ion is rationally proposed by the ligation of two nitrogens from 5bpno, two oxygens from metanol, and two chloride ions. Theoretical fit to a two-centered model for S_{Mn} and $S_{radical}$ (Eq. (2)) gave the optimized parameters as follows: $J/k_B = +0.76(11)$ K, $g = 1.96(1)$, and $\theta = -0.359(6)$ K. The calculated curve successfully reproduced the experimental data (Fig. 2). The optimized g value is somewhat lower than expected for the average of manganese(II) and radical spins, probably because the specimen contains some impurity. Assuming the g value of 2.00, the purity factor is estimated to be 0.96.

$$\chi_{mol} = \frac{N_A g^2 \mu_B^2}{k_B(T-\theta)} \frac{28 + 10\exp(-6J/k_BT)}{7 + 5\exp(-6J/k_BT)} \quad (2)$$

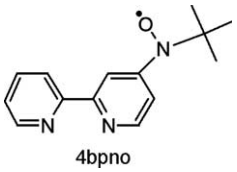
On the other hand, the $\chi_{mol}T$ value of $[Cu(5bpno)Cl_2]$ monotonically decreased on cooling, indicating the presence of dominant antiferromagnetic interaction. The observed $\chi_{mol}T$ value was 0.69 cm^3 K mol^{-1} at 300 K, which is slightly smaller than the theoretical spin only value of 0.75 cm^3 K mol^{-1} from $S_{Cu} = 1/2$ and $S_{radical} = 1/2$. The data were analyzed on the singlet–triplet model [20], only giving an unsatisfactory fit. The exchange parameter J/k_B was preliminarily estimated to be ca. −8 K. Because of the lack of structural information on $[Cu(5bpno)Cl_2]$, we could not propose any magnetic exchange models, but nonetheless the experimental results strongly suggest that the Cu–5bpno interaction is antiferromagnetic, in sharp contrast to the ferromagnetic Mn–5bpno.

The observed antiferromagnetic interaction in $[Cu(5bpno)_2(ClO_4)_2]$ is much larger than [Cu(5bpno)-Cl_2]. The $\chi_{mol}T$ value of $[Cu(5bpno)_2(ClO_4)_2]$ was 0.50 cm^3 K mol^{-1} at 300 K, which is very small for three-1/2 spin species and actually smaller than that of $[Cu(5bpno)Cl_2]$ having two 1/2-spins (Fig. 2). With a decrease of temperature the $\chi_{mol}T$ value decreases but the temperature dependence is somewhat insensitive to reach 0.41 cm^3 K mol^{-1} at 2 K. This value corresponds to $S = 1/2$ and $g = 2.1$, being typical of copper(II) ions. Therefore, two radical spins are antiferromagnetically correlated. As the X-ray crystallographic analysis suggested (Fig. 1), a possible explanation is that the observed antiferromagnetic coupling is assigned to the intramolecular O1–O2 contacts. The Cu–5bpno magnetic interaction is buried with the strong radical–radical interaction.

4. Discussion

The mutual geometry between radical and metal spins is designed to be a "*meta*" position in the present study. High-spin organic molecules in which the *meta*-phenylene bridges are used as a ferromagnetic coupler are accessible when non-bonding molecular orbitals are present due to π-topological symmetry [21–24]. The application of the spin-polarization mechanism of organic high-spin molecules to transition metal complexes is not sufficiently understood with respect to limitation of the π-conjugation regime [25–32]. Iwamura and co-workers [33–35] have reported the pioneering works on the magnetic exchange interactions between radical and metal spins across a pyridine skeleton. Two manganese(II) complexes have been proposed using 3-pyridyl and 4-pyridyl *t*-butyl nitroxide radicals (3NOPy and 4NOPy, respectively), and actually they obtained $[Mn(hfac)_2(3NOPy)]_2$ and $[Mn(hfac)_2(4NOPy)_2]$ (hfac denotes 1,1,1,5,5,5-hexafluoropentane-2,4-dionate). The latter clearly showed antiferromagnetic coupling between Mn and radical spins across the 4-pyridyl group. In the former complex, however, the nitroxide oxygen atoms are coordinated to the Mn ions giving strong antiferromagnetic coupling, and therefore the magnetic coupling across the 3-pyridyl group could not be determined [33,34]. The present work on $[Mn(5bpno)_3(ClO_4)_2]$ and $[Mn(5bpno)(CH_3OH)_2Cl_2]$ recovers their missing data; it was proved to be ferromagnetic.

Most important discussion arises in comparison of the present results with those of isomeric structures. The magnetic interactions across a 4-pyridyl group have been investigated by using 2,2′-bipyridin-4-yl *t*-butyl nitroxide (abbreviated as 4bpno hereafter) [35]. Antiferromagnetic and ferromagnetic couplings have been characterized in $[M(hfac)_2(4bpno)]$ for $M = Mn^{II}$ and Cu^{II}, respectively. The X-ray crystallographic analysis revealed that the nitrogen atoms in the bpy moiety were coordinated to the Mn ion while the nitroxide group were free from coordination [35].



The observed magnetic exchange interactions are qualitatively summarized in Table 1. The sign of the intramolecular exchange interactions are altered:

(1) By replacing metal ions between Mn^{II} and Cu^{II}.
(2) By changing the substituted positions between *meta* and *para*.

In phenyl nitroxide derivatives, it is well known that positive spin densities are polarized at *ortho* and *para* carbons while negative spin densities are at *meta* carbons in the adjacent phenyl ring [36–39]. Similar spin-polarization may take place in pyridyl nitroxide derivatives. The copper $d_{x^2-y^2}$ magnetic orbital has a σ-character and cannot participate in the π-conjugation. On the other hand, the high-spin Mn^{II} has magnetic t_{2g} orbitals, which can afford dπ–pπ conjugation with the pyridine N atom. As Fig. 3(a) shows, the ferromagnetic coupling in the Mn–5bpno complexes is interpreted based on the spin-polarization mechanism like *meta*-phenylene-bridged high-spin organic compounds. The orthogonal geometry between $2p_z$(N) and $3d_{x^2-y^2}$(Cu) leads to the spin-polarization at the Cu ion with the same sign of the N atom (Fig. 3(b)). Since the N atom has negative spin density, the Cu ion is negatively spin-polarized. Thus, the nitroxide radical and copper spins are antiferromagnetically correlated. Furthermore, the change of magnetic interactions between 5bpno and 4bpno complexes is perfectly explained by spin-alternating character throughout the π-electron system.

The manganese(II) ion simultaneously has dπ and dσ spins. A σ-type spin-polarization pathway is also possible. The magnetic interaction is more complex because many kinds of magnetic interactions are present, and the total magnetic exchange interaction is defined with the sum of ferromagnetic and antiferromagnetic terms [40]. The experimental results suggest that the ferromagnetic term surpasses the antiferromagnetic terms in $[Mn(5bpno)_3(ClO_4)_2]$ and $[Mn(5bpno)(CH_3OH)_2Cl_2]$.

Table 1
Magnetic interaction between paramagnetic ligands and metal spins

	5bpno	4bpno
Mn^{II} (d^5)	Ferromagnetic	Antiferromagnetic
Cu^{II} (d^9)	Antiferromagnetic	Ferromagnetic
Reference	This work	Ref. [35]

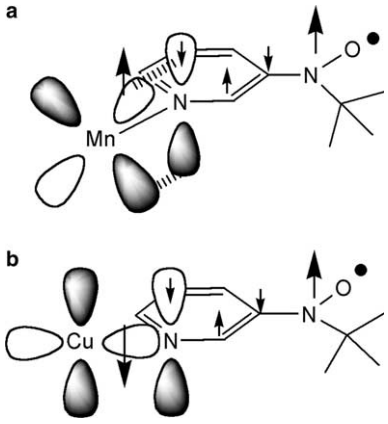


Fig. 3. Spin-polarization mechanisms in (a) Mn– and (b) Cu–5bpno complexes. An additional pyridine ring in 5bpno is omitted for the sake of clarity.

In summary, the magnetic measurements revealed the presence of ferromagnetic couplings in $[Mn^{II}(5bpno)_3(ClO_4)_2]$ and $[Mn^{II}(5bpno)(CH_3OH)_2Cl_2]$. The magnetic exchange couplings between the manganese(II) and radical spins through the intervening pyridine ring can be explained in terms of the spin-polarization involving pπ–dπ-type conjugation. The metal–radical magnetic interactions are controllable by means of designing the substitution positions. This work may provide a molecular design using 4-pyridyl and 5-(2,2′-bipyridyl) groups for organic–inorganic hybrid ferromagnetic materials.

Acknowledgments

This work was supported by a Grant-in-Aid for Scientific Research on Priority Areas of "Molecular Conductors" (No. 15073101) and by Grants-in-Aid for Scientific Research (Nos. 16550121 and 15550115) from the Ministry of Education, Culture, Sports, Science and Technology, Japan.

References

[1] A. Caneschi, D. Gatteschi, R. Sessoli, Acc. Chem. Res. 22 (1989) 392.
[2] J.M. Manriquez, G.T. Yee, R.S. McLean, A.J. Epstein, J.S. Miller, Science 252 (1991) 1415.
[3] K. Inoue, T. Hayamizu, H. Iwamura, D. Hashizume, Y. Ohashi, J. Am. Chem. Soc. 118 (1996) 1803.
[4] T. Ise, T. Ishida, D. Hashizume, F. Iwasaki, T. Nogami, Inorg. Chem. 42 (2003) 6106.
[5] D. Luneau, P. Rey, J. Laugier, P. Fries, A. Caneschi, D. Gatteschi, R. Sessoli, J. Am. Chem. Soc. 113 (1991) 1245.
[6] D. Luneau, P. Rey, J. Laugier, E. Belorizky, A. Conge, Inorg. Chem. 31 (1992) 3578.
[7] K. Fegy, K.E. Vostrikova, D. Luneau, P. Rey, Mol. Cryst. Liq. Cryst. 305 (1997) 69.

[8] K. Fegy, D. Luneau, T. Ohm, C. Paulsen, P. Rey, Angew. Chem., Int. Ed. Engl. 37 (1998) 1270.
[9] H. Mori, O. Nagao, M. Kozaki, D. Shiomi, K. Sato, T. Takui, K. Okada, Polyhedron 20 (2001) 1663.
[10] J. Omata, T. Ishida, D. Hashizume, F. Iwasaki, T. Nogami, Inorg. Chem. 40 (2001) 3954.
[11] T. Matsuyama, Y. Iwata, T. Ishida, T. Nogami, Synth. Met. 133–134 (2003) 611.
[12] C. Aoki, T. Ishida, T. Nogami, Inorg. Chem. 42 (2003) 7616.
[13] S. Yamada, T. Ishida, T. Nogami, Dalton Trans. (2004) 898.
[14] A. Zheludev, V. Barone, M. Bonnet, B. Delley, A. Grand, E. Ressouche, P. Rey, R. Subra, J. Schweizer, J. Am. Chem. Soc. 116 (1994) 2019.
[15] J.F.W. Keana, Chem. Rev. 78 (1978) 37.
[16] F.M. Romero, R. Ziesel, Tetrahedron Lett. 36 (1995) 6471.
[17] CrystalStructure, Single Crystal Structure Analysis Software Version 3.5.1, Rigaku/MSC, 9009 New Trails Drive, The Woodlands, TX 77381, USA, 2003.
[18] A. Bondi, J. Phys. Chem. 68 (1964) 441.
[19] K. Kambe, J. Phys. Soc. Jpn. 5 (1950) 48.
[20] B. Bleaney, K.D. Bowers, Proc. R. Soc. Lond. A 214 (1952) 451.
[21] H. Iwamura, Adv. Phys. Org. Chem. 26 (1990) 179.
[22] A. Rajca, Chem. Rev. 94 (1994) 871.
[23] N. Mataga, Theor. Chim. Acta 10 (1967) 372.
[24] J.C. Longuet-Higgins, J. Chem. Phys. 18 (1950) 265.
[25] T. Ishida, S.-i. Mitsubori, T. Nogami, N. Takeda, M. Ishikawa, H. Iwamura, Inorg. Chem. 40 (2001) 7059.
[26] T. Ishida, T. Kawakami, S.-i. Mitsubori, T. Nogami, K. Yamaguchi, H. Iwamura, J. Chem. Soc., Dalton Trans. (2002) 3177.
[27] T. Glaser, M. Heidemeier, S. Grimme, E. Bill, Inorg. Chem. 43 (2004) 5192.
[28] I. Fernández, R. Ruiz, J. Faus, M. Julve, F. Lloret, J. Cano, X. Ottenwaelder, Y. Journaux, M.C. Muñoz, Angew. Chem. Int. Ed. 40 (2001) 3039.
[29] J.A. McCleverty, M.D. Ward, Acc. Chem. Res. 31 (1998) 842.
[30] F. Lloret, G. De Munno, M. Julve, J. Cano, R. Ruiz, A. Caneschi, Angew. Chem. Int. Ed. 37 (1998) 135.
[31] H. Oshio, J. Chem. Soc., Chem. Commun. (1991) 240.
[32] L.C. Francesconi, D.R. Corbin, D.N. Hendrickson, G.D. Stucky, Inorg. Chem. 18 (1979) 3074.
[33] M. Kitano, Y. Ishimaru, K. Inoue, N. Koga, H. Iwamura, Inorg. Chem. 33 (1994) 6012.
[34] Y. Ishimaru, M. Kitano, H. Kumada, N. Koga, H. Iwamura, Inorg. Chem. 37 (1998) 2273.
[35] H. Kumada, A. Sakane, N. Koga, H. Iwamura, J. Chem. Soc., Dalton Trans. 10 (2000) 911.
[36] A.R. Forrester, S.P. Hepburn, G. McConnachie, J. Chem. Soc., Parkin Trans. I (1974) 2213.
[37] J. Goldman, T.E. Petersen, K. Torssell, Tetrahedron 29 (1973) 3833.
[38] H.G. Aurich, E. Deuschle, I. Lotz, J. Chem. Res. (S) (1977) 248.
[39] M. Nakagawa, T. Ishida, M. Suzuki, D. Hashizume, M. Yasui, F. Iwasaki, T. Nogami, Chem. Phys. Lett. 302 (1999) 125.
[40] O. Kahn, Molecular Magnetism, VCH, New York, 1993, p. 145 (Chapter 8).

Ferromagnetic ordering with blue light irradiation at low temperature was found for $Cu_2[Mo(CN)_8]\cdot 8H_2O$ [2,3]. The critical temperature was 35 K and this photoinduced phase was transformed to the original form with increasing temperature up to 200 K. Reversible change of the magnetism with blue and red light irradiation was found at low temperature [3]. In this change of the magnetism, a reduction of Cu(II) to Cu(I) occurs by electron transfer from Mo(IV) ion with blue light irradiation. The coordination structure of this reducible Cu(II) ion before irradiation must be crucial for the photoinduced ferromagnetism. However, detailed structure of this compound is not known. Therefore, we tried to elucidate the local structure of $Cu_2[Mo(^{13}CN)_8]\cdot 8H_2O$ (**1**) by a measurement of hyperfine coupling constant (hfcc) of ^{13}C atoms of ^{13}C enriched cyanide ions. The hfcc of a CN ligand must be sensitive to its coordination bond and local magnetic structures of a variety of polycyanide complexes [8,9]. We studied the plus and minus sign and the magnitude of hfcc of ^{13}C enriched cyanide ions of **1** and of closely related structure-known polycyanide complexes of $Fe_2^{II}[Mo^{IV}(^{13}CN)_8]\cdot 8H_2O$ (**2**), $Mn_2^{II}[Mo^{IV}(^{13}CN)_8]\cdot 8H_2O$ (**3**), $[Cu^{II}(bpy)_2]_2[Mo^{IV}(^{13}CN)_8]\cdot 5H_2O\cdot CH_3OH$ (**4**), UV-irradiated $K_4[Mo^{IV}(^{13}CN)_8]\cdot 2D_2O$ (**5**), $Cs_3[Mo^{V}(^{13}CN)_8]\cdot 2H_2O$ (**6**), $[Cu_2^{II}(tren)_2{}^{13}CN](BF_4)_3$ (**7**), and $[Ni_2^{II}(tetren)_2{}^{13}CN](ClO_4)_3$ (**8**) by temperature dependence of solid-state ^{13}C NMR spectrum.

Broad-line ^{13}C NMR spectrum of higher spin system has been reported for Mn_{12}-acetate cluster [10–12]. Methyl groups of acetate ions were enriched with ^{13}C isotope. Although the methyl carbon atoms are apart from the magnetic Mn ions, the spectrum width is larger than 4000 ppm for powder sample at 250 K and no magic angle spinning spectrum was reported. In our case, the carbon atoms of cyanide ions closely locate to magnetic metal ions.

2. Experimental

2.1. Sample preparations

2.1.1. $K_4[Mo^{IV}(^{13}CN)_8]\cdot 2H_2O$ (5)

Warning! Although we have experienced no difficulties, this procedure may produce HCN gas. 99% ^{13}C enriched specimen was synthesized by a similar method reported for normal compound [13]. 1.0 g of MoO_3 and 4.6 g of 99% ^{13}C enriched $K^{13}CN$ were milled in a mortar. 7.5 ml of H_2O was slowly added to the milled mixture in drop-wise at 0 °C and then 1.1 g of 85% aqueous $(NH_2)_2$ was added. Under ambient temperature, 4.5 ml conc. HCl was added very slowly to the above solution in 1 h. Resulting solution was heated up to 86 °C for 1 h and was cooled down to room temperature. Pouring the solution into 85 ml of CH_3OH results in immediate precipitation of brown yellow powder. 12.5 ml aqueous solution of the filtered powder was heated to boil with activated carbon. The solution was filtered and poured into 85 ml of CH_3OH results in immediate precipitation of yellow powder. The treatment with activated carbon and recrystallization were repeated three times. The last treatment with D_2O instead of H_2O gave a deuterated analogue of $K_4[Mo^{IV}(^{13}CN)_8]\cdot 2D_2O$. *Anal*. Calc. for **5**: C, 20.6; H, 0.79; N, 22.2. Found: C, 19.25; H, 0.96; N, 22.95%.

2.1.2. $Cu_2^{II}[Mo^{IV}(^{13}CN)_8]\cdot 8H_2O$ (1)

Slow addition of 0.2 M aqueous solution of $CuCl_2$ to 0.2 M aqueous solution of $K_4[Mo^{IV}(^{13}CN)_8]$ gave red-purple powder [2]. Filtrated powder was dried in a desiccator. *Anal*. Calc. for **1**: C, 16.70; H, 2.80; N, 19.48. Found: C, 16.95; H, 2.58; N, 19.97%. The same procedure with heavy water solution and deuterated analogue of **5** gave $Cu_2[Mo(^{13}CN)_8]\cdot 8D_2O$.

2.1.3. $Fe_2^{II}[Mo^{IV}(^{13}CN)_8]\cdot 8H_2O$ (2)

Compound **2** was synthesized after the reference [14] with 99% ^{13}C enriched **5** instead of normal compound. *Anal*. Calc. for **2**: C, 17.44; H, 2.77; N, 20.35. Found: C, 15.88; H, 2.86; N, 18.80%. Powder X-ray diffraction pattern agreed well with the structure determined for a single crystal [15]. The compound **2** may be oxidized in the air. A fresh yellow powder sample became blue in a few days in the air. Evacuation of the virgin yellow powder led to color change to green-yellow. Electronic sate may be changed due to a loss of crystal water. Therefore, for the NMR measurement, a fresh yellow sample was sealed into a glass ample with N_2 gas for preventing a loss of crystal water and an effect of oxygen.

2.1.4. $Mn_2^{II}[Mo^{IV}(^{13}CN)_8]\cdot 8H_2O$ (3)

Compound **3** was synthesized after the reference [15] with 99% ^{13}C enriched **5** instead of normal compound. *Anal*. Calc. for **3**: C, 17.22; H, 2.86; N, 20.09. Found: C, 16.66; H, 2.55; N, 20.05%.

2.1.5. $[Cu^{II}(bpy)_2]_2[Mo^{IV}(^{13}CN)_8]\cdot 5H_2O\cdot CH_3OH$ (4)

Polycrystalline sample of **4** was obtained after the method of reference [1] with 99% ^{13}C enriched **5** instead of normal compound. *Anal*. Calc. for **4**: C, 49.98; H, 3.91; N, 19.62. Found: C, 47.31; H, 4.08; N, 18.53%. Powder X-ray diffraction pattern agreed well with the structure determined for a single crystal [1].

2.1.6. $Cs_3[Mo^{V}(^{13}CN)_8]\cdot 2H_2O$ (6)

Polycrystalline sample of **6** was obtained after the method of reference [16] with 99% ^{13}C enriched **5** instead of normal compound. *Anal*. Calc. for **6**: C, 13.00; H, 0.55; N, 15.17. Found: C, 12.96; H, 0.72; N, 15.18%. Powder X-ray diffraction pattern agreed well with the structure determined for a single crystal [17].

2.1.7. $[Cu_2^{II}(tren)_2{}^{13}CN](BF_4)_3$ (7) and $[Ni_2^{II}(tetren)_2{}^{13}CN](ClO_4)_3$ (8)

Blue crystals of **7** and purple crystals of **8** were obtained after the methods of reference [18] by slow evaporation of the solvent. Colorless crystals also appeared and were taken off. *Anal.* Calc. for **7**: C, 22.12; H, 5.14; N, 17.86. Found: C, 21.85; H, 5.06; N, 17.64%. *Anal.* Calc. for **8**: C, 24.35; H, 5.73; N, 18.38. Found: C, 24.65; H, 5.46; N, 18.73%. Powder X-ray diffraction patterns of **6** and **7** agreed well with the respective structure reported for each single crystal [18].

2.2. Solid-state NMR

The ^{13}C NMR spectrum was measured by an echo pulse sequence for static powder crystalline sample at an external magnetic field of 7.05 T with a Bruker DSX300 spectrometer. Various irradiation frequencies were used to cover the wide spectrum. The envelope of all the echo signals displays a whole spectral line shape. When a line shape is almost symmetric, we assume that the isotropic shift is the center of the spectrum. The shift was measured from external second reference of the powder crystalline sample of $K^{13}CN$ (169.6 ppm from TMS). Assuming a small zero-field splitting, the observed isotropic shift δ_{iso} consists of the Fermi contact term, the dipole interaction term (pseudo contact) and the temperature independent diamagnetic term (chemical shift) as follows [19,20]:

$$\delta_{iso} = \delta_{Fermi} + \delta_{Pseudo} + \delta_{dia}, \quad (1)$$

$$\delta_{Fermi} + \delta_{Pseudo} = \frac{\mu_B}{3k_B T}\frac{A_C}{\gamma_C/2\pi}S(S+1). \quad (2)$$

Electron spin induced on the ^{13}C nucleus by electron spin of a magnetic metal ion causes a Fermi contact shift of the NMR resonance line, while anisotropy of the *g*-tensor of magnetic metal ions gives a pseudo-contact shift. The coefficient A_C in Eq. (2) is defined as the hfcc of the ^{13}C nucleus in Hz unit, which includes principal values of anisotropic *g* tensor.

Magic angle spinning ^{13}C and ^{2}H NMR (MAS NMR) spectra were measured by a similar method described in reference [21] at a resonance frequency of 75.4 and 46.1 MHz, respectively, and at a magic angle spinning speed of ca. 9 kHz with a Bruker DSX300 spectrometer. The MAS technique gives a high resolution spectrum with an isotropic shift in some cases. The thermometer of the MAS NMR probe and an effect of spinning speed on temperature increase were carefully calibrated [21,22]. Uncertainty of the temperature measurement was within ±2 K. The ^{2}H NMR shift was measured from the external second reference of CD_3OD (CD_3: 3.35 ppm).

3. Results and discussion

3.1. Hyperfine coupling constants of cyanide ions and local coordination structures of 1

Fig. 1 illustrates a typical ^{13}C NMR spectrum of cyanide ions of **1**. We found two distinct signals corresponding to two different electronic states of the cyanide ions. Largely shifted values from the diamagnetic shift of $K^{13}CN$ (origin of abscissa) indicates an effect of electronic spins of Cu^{II} ions in this compound **1**, in which Mo^{IV} ions are diamagnetic. Since each peak exhibited a small anisotropy and was almost symmetric, the isotropic shift described in Eqs. (1) and (2) was determined as the maximum point of the peak. Temperature dependence of the isotropic shift is plotted as a function of inverse temperature in Fig. 2 for both high and low frequency peaks. This figure indicates a good linear relation between the isotropic shift and inverse temperature as suggested in Eqs. (1) and (2). The hfcc of each peak was determined from the slope of this figure to be +19 and −2.0 MHz for high and low frequency peak, respectively. The plus and minus sign of the hfcc indicates that there are two different coordination structures for the cyanide ions. Nitrogen atoms of the cyanide ions are coordinated to Cu^{II} ions. Intensity ratio of the two signals suggests almost 3:1 population of different coordination structures.

To estimate the coordination structures of cyanide ions around magnetic metal ions, we determined the hfcc of cyanide ions for two other compounds **2** and **3**, which have a similar unit formula to **1**. The crystal structure of **2** is known, and **2** and **3** are believed to be isomorphous [1]. The coordination structure of **2** is illustrated in Fig. 3, where Fe^{II} ion has square-planner N-coordination of four cyanide ions and axial coordination of two water molecules. Typical ^{13}C NMR spectrum is shown in Fig. 4(a) and (c) for **2** and **3**, respectively. Only a single peak was observed both for

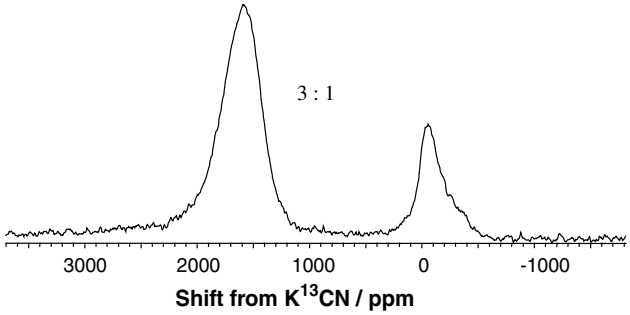


Fig. 1. Typical ^{13}C NMR spectrum of 99% ^{13}C enriched cyanide ions of $Cu_2^{II}[Mo^{IV}(^{13}CN)_8]\cdot 8H_2O$ (**1**) at 294 K. The spectrum was measured with a spin echo technique. The envelope of many echo signals is illustrated. Magic angle spinning (MAS) at 10 kHz indicated no resolution enhancement for the higher frequency peak, whereas MAS technique was effective for the low frequency signal.

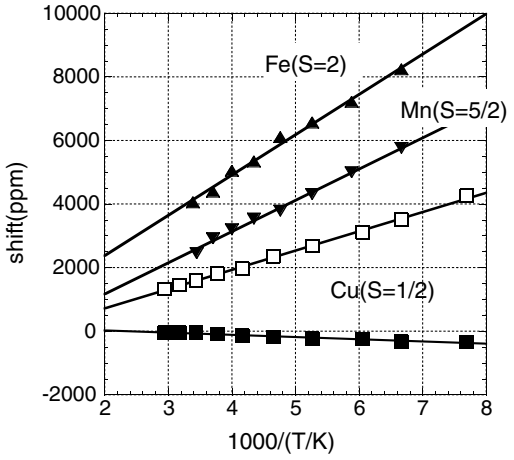


Fig. 2. Temperature dependence of isotropic ^{13}C NMR shift of $Cu_2^{II}[Mo^{IV}(^{13}CN)_8]\cdot 8H_2O$ (**1**) ■, low frequency peak and □, high frequency peak; ▲, $Fe_2^{II}[Mo^{IV}(^{13}CN)_8]\cdot 8H_2O$ (**2**); ▼, $Mn_2^{II}[Mo^{IV}(^{13}CN)_8]\cdot 8H_2O$ (**3**). The origin of the abscissa is the diamagnetic shift of polycrystalline sample of $K^{13}CN$. The hyperfine coupling constants determined from the slopes of this figure with Eqs. (1) and (2) are +19 MHz (high frequency peak) and −2.0 MHz (low frequency peak) for **1**, +4.9 MHz for **2**, and +2.3 MHz for **3**.

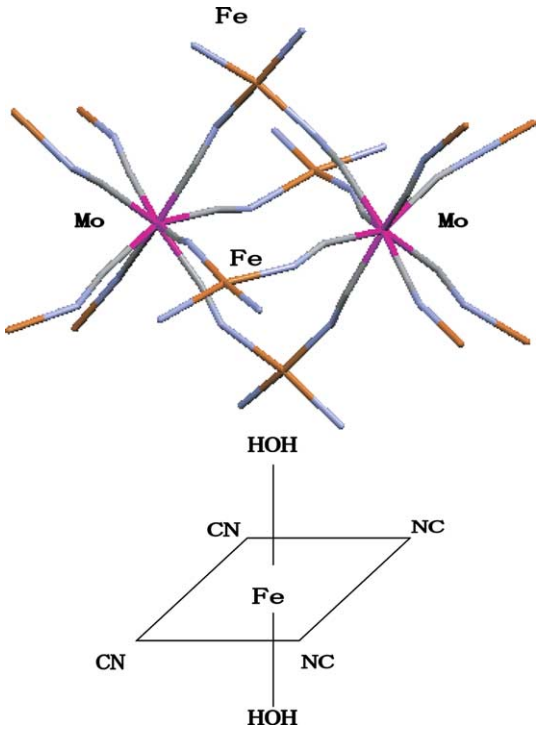


Fig. 3. Structure of coordination network of $Fe_2^{II}[Mo^{IV}(^{13}CN)_8]\cdot 8H_2O$ (**2**) after reference [12].

2 and **3**. A small signal near 0 ppm is impurity due to slight decomposition.[2] The spectrum is almost symmetric and the isotropic shift was determined as the center of the signal. Temperature dependence of the ^{13}C NMR shifts is plotted in Fig. 2 for **2** and **3** together with **1**. Positive slope for **2** and **3**, which have square planar N-coordination structure around the magnetic metal center, resembles the slope of high frequency peak of **1**. Thus we assigned the high frequency peak of ^{13}C NMR spectrum of **1** to the cyanide ions that have square planar like N-coordination to Cu^{II} ion in **1**. The derived values of hfcc are summarized in Table 1.

Low frequency peak of **1** indicates that a part of cyanide ions of **1** exhibits negative hfcc and their N-coordination structures are different from the square planar structure. The negative hfcc was observed for **4**, which has an N-coordination to Cu(II) ion in an equatorial plane of trigonal bipyramidal structure as shown in Fig. 5. A typical ^{13}C NMR spectrum of **4** is illustrated in Fig. 6. Three different isotropic peaks, i.e. α, β, γ, were identified. Two of eight cyanide ions of **4** are directly coordinated to magnetic Cu(II) ions and their ^{13}C NMR signals should exhibit broader width and largest magnitude of hfcc, while other six cyanide ions are free of coordination. The peak γ, which shows largest width, was assigned to the cyanide ions coordinated to Cu(II) ions. Fig. 7 shows their shifts plotted as a function of inverse temperature and the peak γ exhibits the largest magnitude of hfcc. The sign of the hfcc of the peak γ is negative, which is similar to the low frequency peak of **1**. It is considered that the N-coordination geometry of the cyanide ion with a negative hfcc of **1** is largely deformed from the square planar. It is not clear at present whether two distinct Cu(II) ions exist in **1**, one of which is a square planar type and the other is largely deformed from the square planar, or all the Cu(II) ions are deformed form the square planar, in which three of the four N-coordination bonds are similar to the square planar and the rest one is deformed from the square planar type. Any how, such native deformation of N-coordination bond from the square planar structure in **1** is probably relevant to stabilize the reduced Cu(I) ion, which is produced by blue light irradiation.

We also investigated the motional behavior of crystal water molecules of deuterated analogue of **1**. Solid-state ^2H NMR spectrum is narrow, which indicates rapid and almost isotropic rotation of the crystal water molecule (D_2O) at 295 K. A similar behavior was observed for Prussian-blue analogue [23,24]. Magic angle spinning ^2H NMR spectrum showed an intense peak at 6.5 ppm at 295 K. This shift value is almost typical for diamagnetic

[2] The compound **2** decomposed in the air. A fresh yellow powder sample became dark blue in a few days in the air. The blue sample exhibited a completely different ^{13}C NMR signal from virgin yellow sample as shown in Fig. 4(b). The signal of blue sample locates near 0 and 3000 ppm, one of which near 0 ppm is the almost the same shift observed as a small peak in Fig. 4(a). Evacuation of the virgin yellow powder led to color change to yellow-green. Electronic sate of **2** may be slightly hanged due to a loss of crystal water. Therefore, for the NMR measurement of **2**, a fresh yellow sample was sealed into a glass ample with N_2 gas for preventing a loss of crystal water and an effect of oxygen.

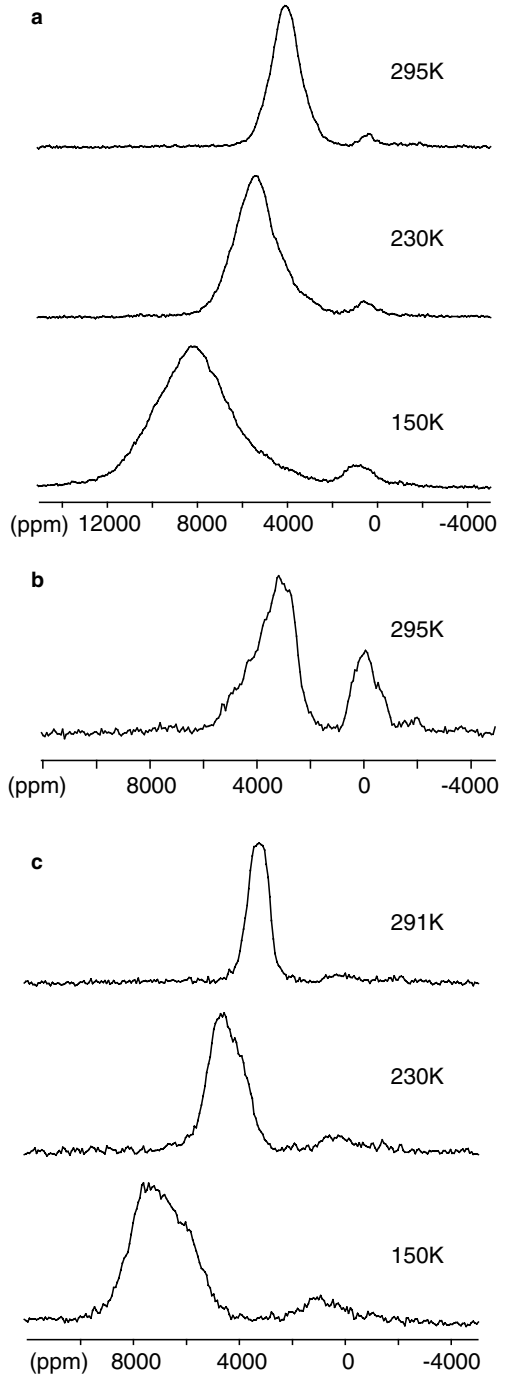


Fig. 4. Typical ^{13}C NMR spectrum of 99% ^{13}C enriched cyanide ions of: (a) $Fe_2^{II}[Mo^{IV}(^{13}CN)_8]\cdot 8H_2O$ (**2**), (b) a specimen of **2** stored in the air and (c) $Mn_2^{II}[Mo^{IV}(^{13}CN)_8]\cdot 8H_2O$ (**3**). Each spectrum is constructed with many echo signals measured with different excitation frequencies. The origin of the abscissa is the diamagnetic shift of polycrystalline sample of $K^{13}CN$.

compounds and suggests no strong interaction between the crystal water molecules and the magnetic Cu(II) ion in contrast to the crystal structure of Fe(II) compound **2**, in which crystal water molecules directly coordinate to the Fe(II) ion. A small peak of MAS ^2H NMR was also observed at 28 ppm. However, the intensity was only 3%

Table 1
Hyperfine coupling constant of ^{13}C nucleus of compounds **1**, **2**, **3**, and **4**

Compound	**1**	**2**	**3**	**4**
Spin S of magnetic metal ion	Cu(II)	Fe(II)	Mn(II)	Cu(II)
	1/2	2	5/2	1/2
Hfcc	+19 MHz (not known)	+4.9 MHz (SQP)	+2.3 MHz (SQP)	
				+0.44 MHz
				−0.24 MHz
	−2 MHz (not known)			−0.79 MHz (EP-TBP)

Compounds are $Cu_2^{II}[Mo^{IV}(^{13}CN)_8]\cdot 8H_2O$ (**1**), $Fe_2^{II}[Mo^{IV}(^{13}CN)_8]\cdot 8H_2O$ (**2**), $Mn_2^{II}[Mo^{IV}(^{13}CN)_8]\cdot 8H_2O$ (**3**), and $[Cu^{II}(bpy)_2]_2[Mo^{IV}(^{13}CN)_8]\cdot 5H_2O\cdot CH_3OH$ (**4**). SQ represents the square planer structure and EP-TBP means equatorial plane of trigonal bipyramidal.

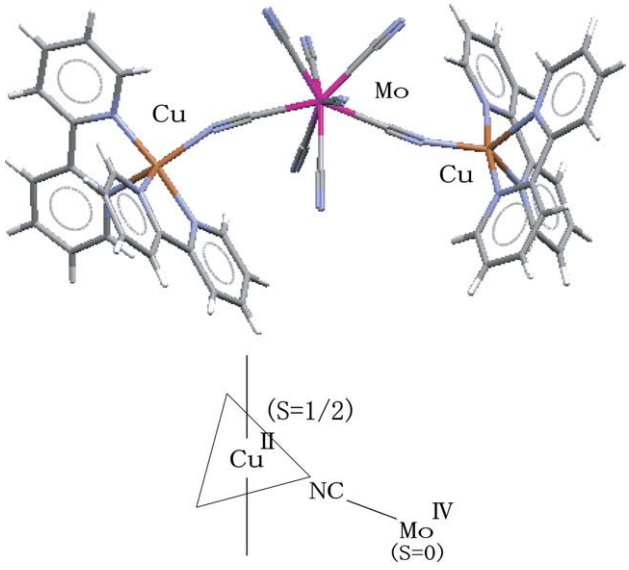


Fig. 5. Molecular and coordination structure of $[Cu^{II}(bpy)_2]_2[Mo^{IV}(^{13}CN)_8]\cdot 5H_2O\cdot CH_3OH$ (**4**) [1].

of the peak at 6.5 ppm and the small peak was tentatively assigned to an impurity.

*3.2. Photoreaction of **5** in aqueous solution and in the crystalline phase, and ^{13}C NMR spectrum of $[Mo^V(^{13}CN)_8]^{3-}$ ion*

To obtain an information about hfcc of ^{13}C atom given by photoinduced Mo(V) ion ($S = 1/2$) in the crystalline phase of $K_4[Mo^{IV}(^{13}CN)_8]\cdot 2D_2O$ (**5**), we measured ^{13}C NMR spectrum for ca. 50 mg of light irradiated powder specimen of **5**. By irradiation with a light (ca. 300–800 nm) of a Xe lamp at room temperature for a few days, we observed a very broad ^{13}C NMR spectrum overlapped by a sharp central line of a diamagnetic species of **5** as shown in Fig. 8(a). Signal-to-noise ratio is

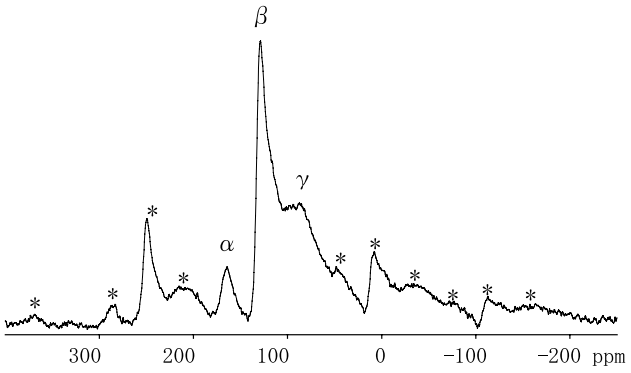


Fig. 6. A typical magic angle spinning ^{13}C NMR spectrum of cyanide ions of 99% ^{13}C enriched sample of $[Cu^{II}(bpy)_2]_2[Mo^{IV}(^{13}CN)_8]\cdot 5H_2O\cdot CH_3OH$ (**4**), which was measured at 300 K with a spinning speed of 9 kHz. The shift was measured from TMS and a second reference of $K^{13}CN$ (169.6 ppm from TMS) was used. α, β and γ indicate signals of isotropic shift. Peaks indicated by asterisks are spinning side bands, which were clearly distinguished from the isotropic shifts by using several different spinning speeds.

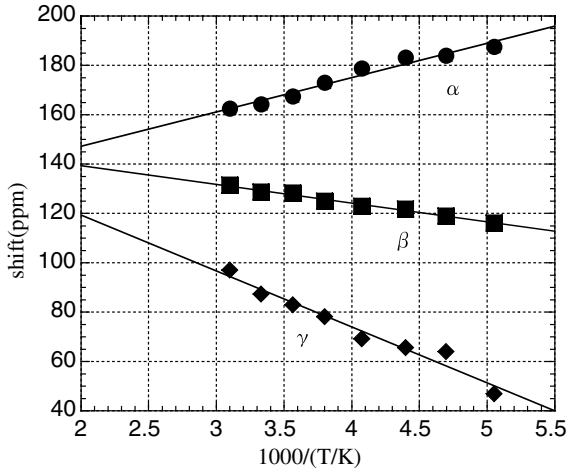


Fig. 7. Temperature dependence of the isotropic shift of ^{13}C NMR lines indicated by α, β and γ in Fig. 6. Each temperature slope gave hfcc of +0.44 (α), −0.24 (β) and −0.79 MHz (γ), respectively.

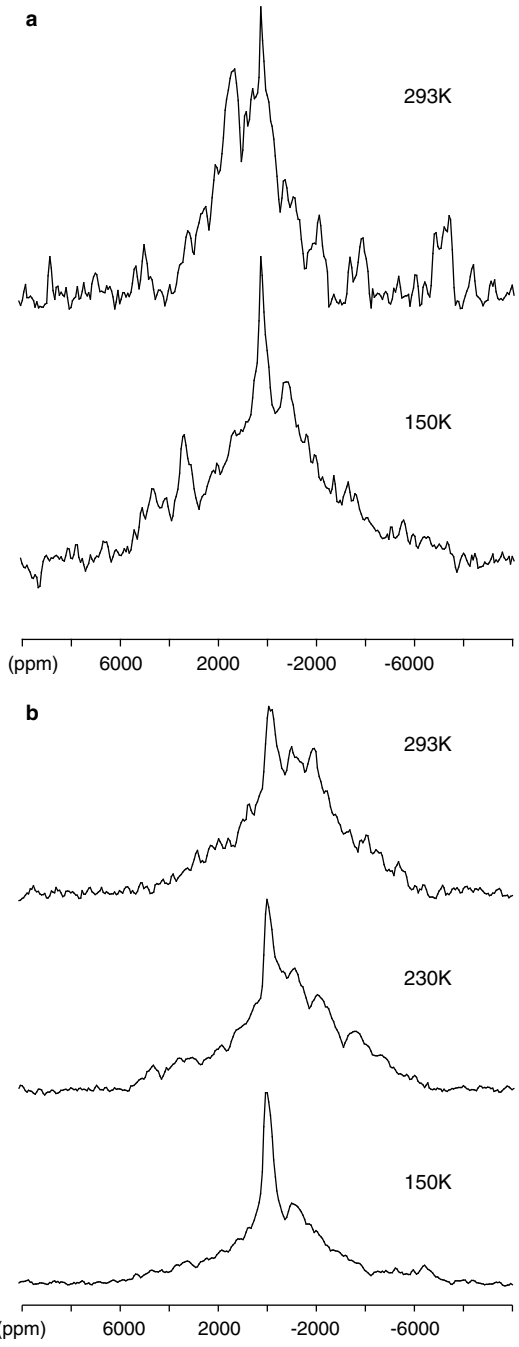


Fig. 8. ^{13}C NMR spectrum of cyanide ion of $[Mo^V(^{13}CN)_8]^{3-}$ of (a) UV-irradiated $K_4[Mo^{IV}(^{13}CN)_8]\cdot 2D_2O$ (**5**) and (b) $Cs_3[Mo^V(^{13}CN)_8]\cdot 2H_2O$ (**6**). The origin of the abscissa is the diamagnetic shift of polycrystalline sample of $K^{13}CN$. The signal near 0 ppm was assigned to decomposed fragment, which is diamagnetic.

bad because of conversion from Mo(IV) to Mo(V) is not enough. The amount of the conversion from Mo(IV) to Mo(V) was estimated to be ca. 1.4% from the MAS ^2H NMR spectrum of OD^- ion produced by a reduction of D_2O molecule as shown in Fig. 9.[3] Intensity of the sharp signal of diamagnetic **5** with long relaxation time was diminished by short repetition time for accumulation of the signal. The signal of ^{13}C NMR of $[Mo^V(^{13}CN)_8]^{3-}$ is very broad and a center of the broad signal is almost temperature independent in contradiction to a prediction by Eqs. (1) and (2). To clarify this behavior, we also studied ^{13}C NMR spectrum of $Cs_3[Mo^V(^{13}CN)_8]\cdot 2H_2O$ (**6**) in the crystalline phase. The spectrum is also very broad and almost temperature independent as illustrated in

[3] It is noted that reduction of the crystal water molecule hydrogen-bonded to the N atom of Mo(IV)–CN by an electron transfer from Mo(IV) ion with UV-irradiation was concluded in the crystalline phase. Such a reaction was proposed in solution and in the solid state [7].

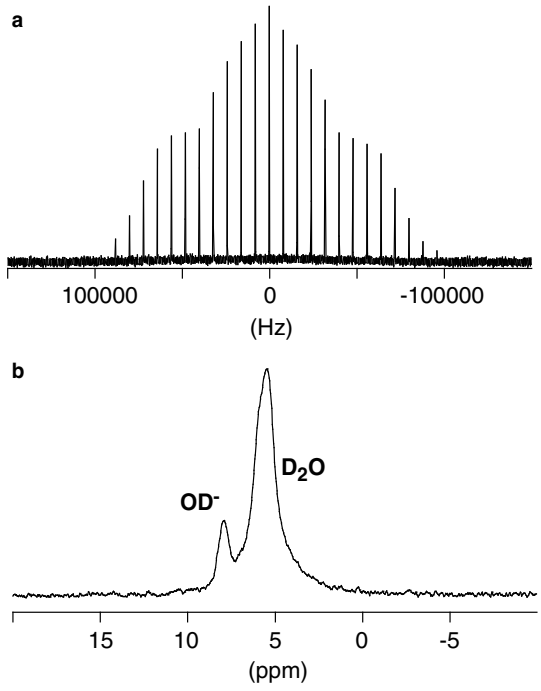


Fig. 9. Magic angle spinning ^{2}H NMR spectrum of UV-irradiated $K_4[Mo^{IV}(^{13}CN)_8]\cdot 2D_2O$ (**5**). (a) Full-width spectrum including spinning side bands and (b) isotropic shift. The full width spectrum (a) indicates 180° flip motion of D_2O molecule in the solid state around the molecular C_2 axis. A small signal at 7.9 ppm of (b) was assigned to OD^- ion produced by UV-irradiation, $Mo^{IV} + D_2O \rightarrow Mo^{V} + OD^- + 1/2D_2$ (↑). The intensity of this signal is 1.4% of total intensity of D signals including all of the spinning side bands. A large signal at 5.4 ppm is crystal water molecule, which is independent of UV-irradiation. The signal of OD^- ion showed no spinning side band, which indicates rapid isotropic rotation of OD^- ion in the crystalline lattice of **5**.

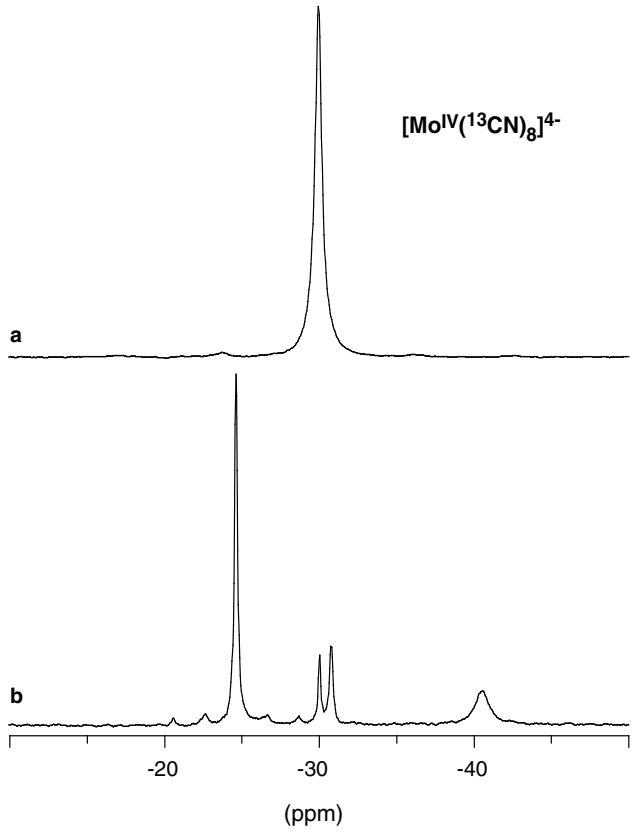


Fig. 10. ^{13}C NMR spectrum of cyanide ion of D_2O solution of $K_4[Mo^{IV}(^{13}CN)_8]\cdot 2D_2O$ (a) before and (b) after UV-irradiation. The origin of the abscissa is the diamagnetic shift of polycrystalline sample of $K^{13}CN$. Since the reaction product was not identified, signal assignment was impossible for spectrum (b). Two spectra were measured with MAS NMR probe for solid.

Fig. 8(b). For these compounds, relaxation time of electron spin may not be matched to the assumed condition to derive the Eqs. (1) and (2) for ^{13}C NMR in the solid state.

In contrast to the above result for the crystalline phase, well resolved ^{13}C NMR signals were observed for light irradiated D_2O solution of a deuterated analogue of **5** as illustrated in Fig. 10. Color of the solution changed immediately from yellow to green by light irradiation under a similar condition to the polycrystalline phase. The observed shifts of ^{13}C NMR signals for the irradiated solution are not so large, suggesting that the paramagnetic species of $[Mo^{V}(^{13}CN)_8]^{3-}$ was not detected. The hfcc of carbon nucleus of $[Mo^{V}(^{13}CN)_8]^{3-}$ was estimated from quantum mechanical calculation based on UB3LYP/LanL2DZ for an anti-prism coordination structure of $[Mo^{V}(^{13}CN)_8]^{3-}$ in crystalline phase of **6**. The values are −26.9 to −31.7 MHz. All the values are negative and the magnitude is similar to the value of |33| MHz determined by ESR for the $[Mo^{V}(CN)_8]^{3-}$ ion in an aqueous solution of $K_3[Mo^{V}(CN)_8]$ [25].

3.3. A possible effect of polymeric sequential coordination structure on the linewidth of ^{13}C NMR spectrum of cyanide ion

To investigate further what is the origin of very broad and almost temperature independent ^{13}C NMR spectrum observed for UV irradiated **5** and for **6**, we tried to measure the ^{13}C NMR spectrum for Cu(II) and Ni(II) dimmer compounds of **7** and **8** in their crystalline phase. We suspected that isolated electron spin or localized exchange interactions closed within a molecule would bring about a very broad ^{13}C NMR spectrum. Our ^{13}C NMR measurements for three-dimensional polymeric cyanide complexes such as Prussian-blue analogues [25] and for one-dimensional Ni(II) and Cu(II) chain complexes [26,27], which have extended exchange interactions, showed narrower and temperature dependent spectrum and we were able to apply Eqs. (1) and (2). An exception is hexacyanoferrate ion $[Fe^{III}(^{13}CN)_6]^{3-}$ in the solid state [23]. This compound showed relatively narrow and temperature dependent ^{13}C NMR spectrum. The compounds **7** and **8** are dinuclear complex of Cu(II) and Ni(II), in

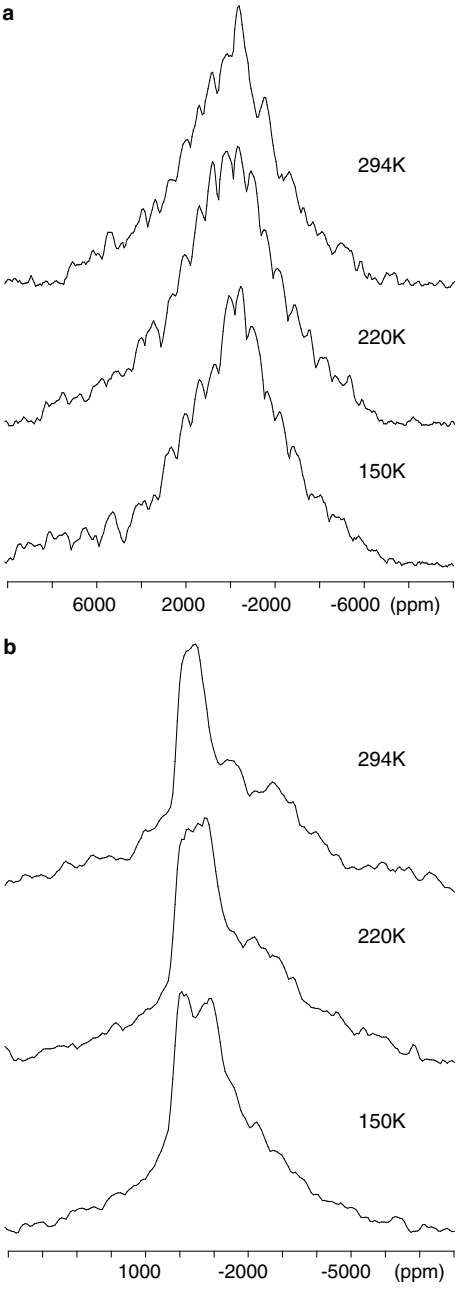


Fig. 11. ^{13}C NMR spectrum of cyanide ion of (a) $[Cu_2^{II}(tren)_2{}^{13}CN](BF_4)_3$ (**7**) and (b) $[Ni_2^{II}(tetren)_2{}^{13}CN](ClO_4)_3$ (**8**). The origin of the abscissa is the diamagnetic shift of polycrystalline sample of $K^{13}CN$.

which two identical magnetic metal ions are linked by a cyanide ion and relatively large antiferromagnetic interaction is closed within a molecule in the solid state [18]. Typical ^{13}C NMR spectra for **7** and **8** are illustrated in Fig. 11. Very broad and almost temperature independent spectrum was found both for Cu(II) (**7**) and Ni(II) (**8**). A condition of relaxation time of electron spin may be not matched with an assumption for Eqs. (1) and (2). It requires a detailed investigation of spin-lattice relaxation of electron spin to clarify the mechanism of this behavior.

Acknowledgments

This research was supported by grant-in-aid for Scientific Research on Priority Areas "Application of Molecular Spins" (15087201) and 14740371 from the Ministry of Education, Culture, Sports, Science and Technology of Japan and partially by The Mitsubishi Foundation.

References

[1] G. Rombaut, M. Verelst, S. Golhen, L. Ouahab, C. Mathonière, O. Kahn, Inorg. Chem. 40 (2001) 1151.
[2] S. Ohkoshi, N. Machida, Z.J. Zhong, K. Hashimoto, Synth. Met. 122 (2001) 523.
[3] S. Ohkoshi, N. Machida, Y. Abe, Z. Zhuang, K. Hasimoto, Chem. Lett. (2001) 312.
[4] W.L. Waltz, A.W. Adamson, J. Phys. Chem. 73 (1969) 4250.
[5] M. Shirom, Y. Siderer, J. Chem. Phys. 58 (1973) 1250.
[6] A. Vogler, W. Losse, H. Kunkely, J. Chem. Soc., Chem. Commun. (1979) 178.
[7] G. Rombaut, S. Golhen, L. Ouahab, C. Mathonière, O. Kahn, J. Chem. Soc., Dalton Trans. (2000) 3609.
[8] S. Takeda, Y. Umehara, H. Hara, G. Maruta, Mol. Cryst. Liq. Cryst. 379 (2002) 253.
[9] H. Ishiyama, G. Maruta, T. Kobayashi, S. Takeda, Polyhedron 22 (2003) 1981.
[10] R.M. Achey, P.L. Kuhns, W.G. Moulton, A.P. Reyes, N.S. Dalal, Polyhedron 20 (2001) 1745.
[11] R.M. Achey, P.L. Kuhns, A.P. Reyes, W.G. Moulton, N.S. Dalal, Phys. Rev. B 64 (2001) 064420.
[12] R.M. Achey, P.L. Kuhns, A.P. Reyes, W.G. Moulton, N.S. Dalal, Solid State Commun. 121 (2002) 107.
[13] R.M. Achey, P.L. Kuhns, A.P. Reyes, W.G. Moulton, N.S. Dalal, Inorg. Synth. X1 (2002) 55.
[14] G.F. McKnight, G.P. Haifgt Jr., Inorg. Chem. 12 (1973) 3007.
[15] A.K. Sra, G. Rombaut, F. Lahiête, S. Golhen, L. Ouahab, C. Mathoniere, J.V. Yakhni, O. Kahn, New J. Chem. 24 (2000) 871.
[16] L.D.C. Box, J.G. Leipoldt, S.S. Basson, Z. Anorg. Allg. Chem. 415 (1975) 81.
[17] S.S. Basson, J.G. Leipoldt, D.C. Bok, J.S. van Vollechoven, P.J. Cilliers, Acta Crystallogr., Sect. B 36 (1980) 1765.
[18] A. Rodrigetz-Fortea, P. Alemany, S. Alvarez, E. Ruiz, A. Scuiller, C. Decroix, V. Marvaud, J. Vaissermann, M. Verdaguer, Inorg. Chem. 40 (2001) 5868.
[19] R. Kurland, B.R. McGervey, J. Magn. Reson. 2 (1970) 286.
[20] J.P. Jesson, in: G.N. La Mar, W.DeW. Horrocks, R.H. Holm (Eds.), NMR of Paramagnetic Molecules, Academic Press, New York, 1973.
[21] G. Maruta, S. Takeda, R. Imachi, T. Ishida, T. Nogami, K. Yamaguchi, J. Am. Chem. Soc. 121 (1999) 424.
[22] P.A. Beckmann, C. Dybowski, J. Magn. Reson. 146 (2000) 379.
[23] S. Takeda, Y. Umehara, H. Hara, G. Maruta, Mol. Cryst. Liq. Cryst. 379 (2002) 253.
[24] H. Ishiyama, G. Maruta, T. Kobayashi, S. Takeda, Polyhedron 22 (2003) 1981.
[25] B.R. McGarvey, Inorg. Chem. 5 (1966) 476.
[26] G. Maruta, S. Takeda, Polyhedron 24 (2005) 2424.
[27] T. Oomomo, G. Maruta, S. Takeda, Polyhedron 24 (2005) 2431.

rautomerism, in which the electron transfer is limited within a small molecule. Transition metal complexes of Mn [1–3], Co [3–8] and Rh [9] with ligands derived from 1,2-benzoquinone show this type of valence tautomerism in solution and in the solid state in some cases [5,8].

A cobalt complex with two 3,5-di-*t*-butyl-1,2-benzoquinone and a chelating nitrogen donor ligand of 2,2-bipyridine (bpy) has been reported to undergo a valence tautomeric interconversion between *low-spin* $[Co^{III}(SQ)(Cat)(bpy)]$ and *high-spin* $[Co^{II}(SQ)_2(bpy)]$ in solution and also in the solid state [4,5]. In this molecule an intramolecular electron transfer converts the high-spin Co(II) into a low-spin Co(III) ion, and one of the ligands is reduced from a SQ to a Cat ligand by one electron. The dynamic processes that are possible for such a valence tautomeric complex are illustrated in Fig. 1. Transition of a spin state occurs in 1,2-benzoquinone moiety and in cobalt ion. Respective change can be observed independently by solid-state high-resolution NMR spectrum. Interconversion dynamics between SQ and Cat may be detected directly by ^{13}C NMR spectrum of these ligands, while the spin state of cobalt ion can be monitored by ^{2}H NMR spectrum of deuterated bpy ligand. We also intend to take an information about magnetic coupling among the three spin species, i.e., two SQ ($S = 1/2$) and Co(II) ion ($S = 3/2$) in the high spin isomer.

Magnetic susceptibility of [Co(3,5-di-*t*-butyl-1,2-benzoquinone)$_2$(2,2′-bipyridine)] · $x(C_6H_5CH_3)$ in the solid state has been reported by two groups [5,10]. The temperature behavior of effective moment is slightly different between them. This compound includes toluene as a crystal solvent. The valence tautomeric interconversion is known to be sensitive to molecular environment and an amount of crystal solvent [8]. Therefore, we investigated stable and metastable phases of this compound, which include toluene molecules as a crystal solvent in different amount.

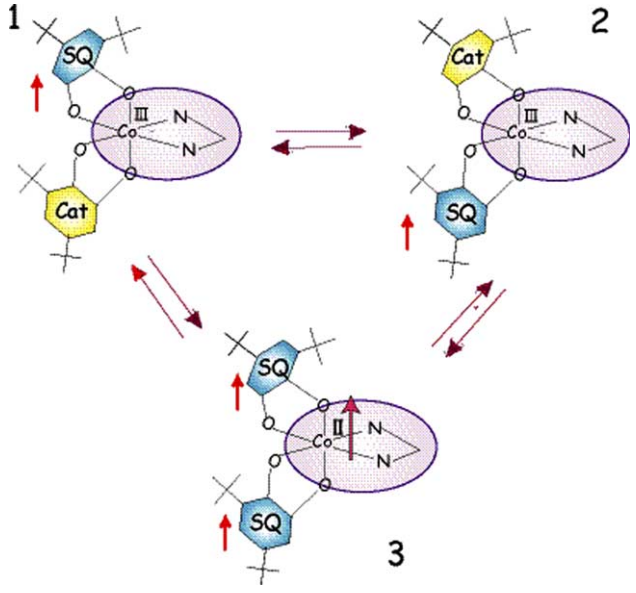


Fig. 1. Possible intramolecular electron transfer processes present for a valence tautomeric complex [Co(3,5-di-*t*-butyl-1,2-benzoquinone)$_2$(2,2′-bipyridine)].

2. Experiment

2.1. Sample preparation

[Co(3,5-di-*t*-butyl-1,2-benzoquinone)$_2$(2,2′-bipyridine)] · $0.5(C_6H_5CH_3)$ was prepared from a tetramer $[Co^{II}$(3,5-di-*t*-butyl-1,2-benzoquinone)$_2]_4$ according to the procedure reported in [4]. Fifteen ml toluene solution of 0.061 g of 2,2′-bpy was added drop-wise to a 50-ml toluene solution of 0.20 g of the tetramer under stirring and argon atmosphere. After 3.5 h reaction, solvent was evaporated. For the preparation of partially deuterated compound of [Co(3,5-di-*t*-butyl-1,2-benzoquinone)$_2$-(2,2′-bipyridine-d_8)] · $0.5(C_6H_5CH_3)$, fully deuterated 2,2′-bpy was used instead of normal 2,2′-bpy. The tetramer $[Co^{II}$(3,5-di-*t*-butyl-1,2-benzoquinone)$_2]_4$ was prepared according to the procedure reported in [11]. All manipulations were carried out under argon atmosphere. Elemental analysis gave C: 70.57% (71.02), H: 8.32% (7.47), N: 3.48% (3.99), and C: 69.41% (70.23), H: 8.41% (8.50), N: 3.41% (3.95), for normal and deuterated bpy-d_8, respectively, where the values in parentheses are calculated for a formula of [Co(3,5-di-*t*-butyl-1,2-benzoquinone)$_2$(2,2′-bipyridine)] · $0.5(C_6H_5CH_3)$ and [Co(3,5-di-*t*-butyl-1,2-benzoquinone)$_2$(2,2′-bipyridine-d_{18})] · $0.5(C_6H_5CH_3)$. The normal sample once heated up to 390 K showed a loss of relative content of C and H, and an increase of N, i.e., C: 69.62%, H: 8.22%, N: 3.52%, indicating a partial loss of toluene molecule.

2.2. Powder X-ray diffraction, TG–DTA and magnetic susceptibility measurements

Powder X-ray diffraction was measured at room temperature to monitor the phase change on thermal treatment by use of Cu Kα irradiation with Rint 2000 (Rigaku) equipped at Inorganic Chemistry Laboratory. Thermogravimetry combined with differential thermal analysis (TG–DTA) was measured between 290 and 480 K with TG/DTA 220U (Seiko Epson) under argon gas flow condition. Speed of temperature increase was 10 K/min. Direct current magnetic susceptibility was measured between 6 and 390 K at an external magnetic field of 1 T with SQUID magnetometer (Quantum Design MPMS 5) equipped at Inorganic Chemistry Laboratory.

2.3. Solid-state high-resolution ^{13}C and ^{2}H NMR

The magic angle spinning ^{13}C and ^{2}H NMR spectra were measured between 197 and 367 K for polycrystalline sample at a magic angle spinning speed of ca. 9 kHz and at a resonance frequency of 75.4 and 46.1 MHz, respectively, with a Bruker DSX300 spectrometer. Polycrystalline sample was packed into the center of a zirconia rotor of 4 mm diameter within a length of ca. 5 mm to minimize the temperature gradient of the sample. The thermometer of the MAS NMR probe and an effect of spinning speed on temperature increase were carefully calibrated [12,13]. The shifts of ^{13}C and ^{2}H NMR lines were measured from an external second reference of hexamethylbenzene (CH_3: 17.17 ppm) and from an external second reference of CD_3OD (CD_3: 3.35 ppm), respectively.

3. Results and discussion

3.1. Irreversible phase transformation, stable and metastable phase

Powder X-ray diffraction patterns of virgin samples of normal and bpy-deuterated compounds agreed with the reported crystal structure [4]. Thermogravimetry combined with differential thermal analysis (TG–DTA) indicated an exothermic peak accompanied with 1.5% and 2% weight loss at 369 and 359 K for normal and bpy-deuterated virgin sample, respectively, as shown in Fig. 2(a) and (b). The exothermic peak in DTA indicates a transformation from metastable to stable crystal phase. It is noted that the virgin crystal is in metastable state. The weight loss is probably due to partial loss of toluene as crystal solvent. Elemental analysis of the specimen once heated up to 390 K showed a small decrease of relative content of C and H, and an increase of N compared with the virgin sample. Further increase of temperature induced melting at 459 and 460 K accompanied with 12% and 15% weight loss for normal and bpy-deuterated sample, respectively. All crystal solvent molecules were lost and partial decomposition of the sample occurred. The normal compound once heated up to 390 K showed no anomaly around 370 K and exhibited a melting temperature 461 K as shown in Fig. 2(c). This melting was accompanied with 10% weight loss. Powder X-ray diffraction pattern of the compound once heated up to 390 K, i.e., the stable phase, was different from the pattern of the virgin sample both for normal and bpy-deuterated specimens as indicated in Fig. 3. The virgin sample in metastable phase showed no valence tautomeric interconversion, whereas the specimen in stable phase exhibited reversible interconversion as described below.

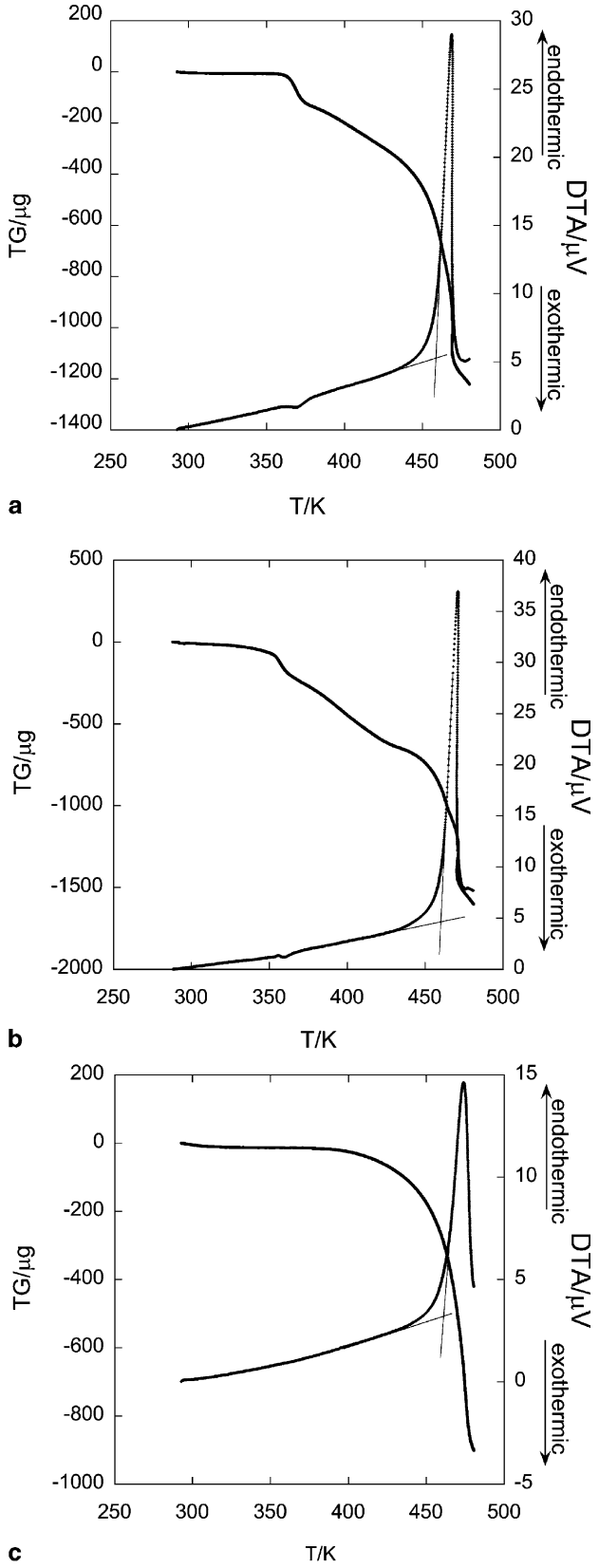


Fig. 2. TG–DTA curves of: (a) normal, (b) bpy-deuterated and (c) once heated up to 390 K sample of [Co(3,5-di-*t*-butyl-1,2-benzoquinone)$_2$(2,2′-bipyridine)] · x($C_6H_5CH_3$). Speed of temperature increase is 10 K/min.

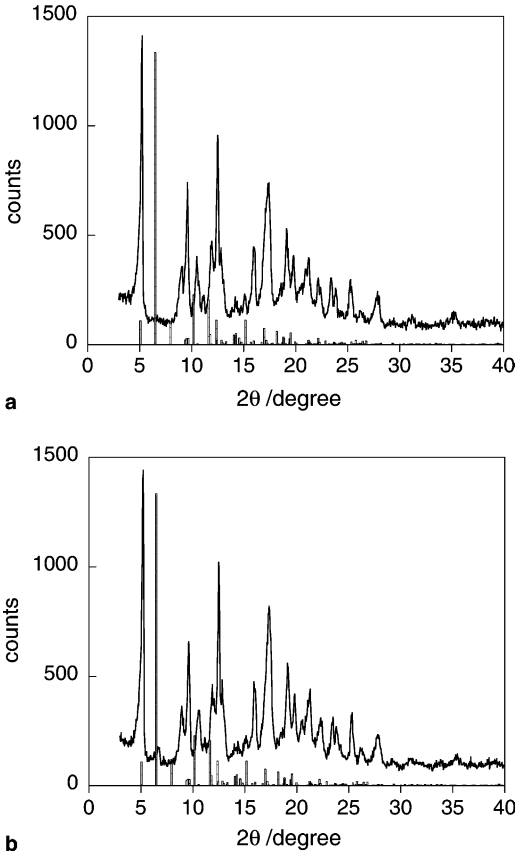


Fig. 3. Powder X-ray diffraction pattern of: (a) normal and (b) bpy-deuterated [Co(3,5-di-*t*-butyl-1,2-benzoquinone)$_2$(2,2′-bipyridine)] · x($C_6H_5CH_3$) in the stable phase, which were once heated up to 390 K. Vertical lines drawn on the abscissa are diffraction peaks calculated from a reported crystal structure [4].

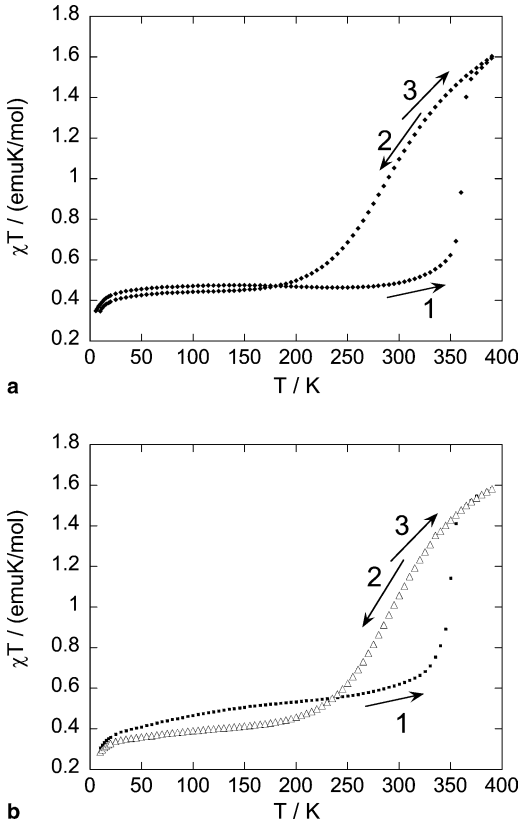


Fig. 4. Thermal hysteresis of magnetic susceptibility χ of: (a) [Co-(3,5-di-*t*-butyl-1,2-benzoquinone)$_2$(2,2′-bipyridine)] · x($C_6H_5CH_3$) and (b) its bpy-deuterated analogue. Three successive runs 1, 2 and 3 in order were carried out to ensure the thermal hysteresis of χ. Molecular formula [Co(3,5-di-*t*-butyl-1,2-benzoquinone)$_2$(2,2′-bipyridine)] · 0.5 ($C_6H_5CH_3$) or its bpy-duterated analogue of the virgin sample was used to calculate the values of χ, although 1.5 ~ 2% weight loss occurred after heating up to 390 K during the first run.

3.2. Valence tautomeric interconversion in the stable phase

Thermal hysteresis of magnetic susceptibility is shown in Fig. 4(a) and (b) for normal and bpy-deuterated compound, respectively. After the sample was cooled down to 6 K from room temperature, three runs for the measurements were continued. In the first step, the magnetic susceptibility was measured in a heating process up to 390 K. Then, two successive measurements were continued on cooling down to 6 K and again on heating up to 390 K both for normal and bpy-deuterated sample. The first run for the virgin sample, which is metastable phase and its crystal structure is known [4], indicated onset of an increase of effective magnetic moment near 300 K. This may be a low temperature tail of valence tautomeric interconversion in the metastable phase or a pre-transition effect related to the metastable to stable transformation. A sharp increase of the effective magnetic moment around 360 K is due to the phase transformation to the stable phase.

After the phase change occurred, a reversible temperature dependence of the effective magnetic moment was observed, which is the valence tautomeric interconversion between *low-spin* [Co^{III}(SQ)(Cat)(bpy)] · x($C_6H_5CH_3$) and *high-spin* [Co^{II}(SQ)$_2$(bpy)] · x($C_6H_5CH_3$) in the new crystalline phase as mentioned in Section 3.1. For a valence tautomeric equilibrium between the two different spin species a (low temperature form) and b (high temperature form), which exhibit magnetic susceptibility χ_a and χ_b, respectively, the observed magnetic susceptibility χ can be expressed in a following formula:

$$\chi = \chi_a f_a + \chi_b f_b = \frac{C_A}{T} f_a + \frac{C_B}{T} f_b,$$
$$\chi T = 0.125 \left(\frac{\mu_{eff}}{\mu_B}\right)^2 = C_A f_a + C_B f_b, \quad (1)$$

where the fractions f_a and f_b can be written by

$$f_a = \frac{\exp(-\frac{\Delta S}{R} + \frac{\Delta H}{RT})}{1 + \exp(-\frac{\Delta S}{R} + \frac{\Delta H}{RT})},$$
$$f_b = \frac{1}{1 + \exp(-\frac{\Delta S}{R} + \frac{\Delta H}{RT})}. \quad (2)$$

Eq. (1) was fitted to the observed magnetic susceptibility as shown in Fig. 5 to deduce the values of entropy and enthalpy change related to the valence tautomeric interconversion and to estimate the total spin of the high temperature species in the stable phase. The best fit gave the values of $\Delta S = 53\ \mathrm{J\ K^{-1}\ mol^{-1}}$ and $\Delta H = 17\ \mathrm{kJ\ mol^{-1}}$, which are smaller than those reported for a phase probably different from the present study [5,10]. Preliminary measurement of heat capacity for the stable phase showed a very broad anomaly around 280 K. The behavior is similar to the heat capacity of similar compound of [Co(3,6-di-*t*-butyl-1,2-benzoquinone)$_2$(2,2′-bipyridine)], for which similar values of $\Delta S = 48\ \mathrm{J\ K^{-1}\ mol^{-1}}$ and $\Delta H = 15\ \mathrm{kJ\ mol^{-1}}$ were reported [14]. Magnitude of spin for the high temperature species was estimated to be $S = 3/2$, since the values of $(\mu_{\mathrm{eff}}/\mu_{\mathrm{B}})$ for the low and high temperature species were determined to be 1.9 and 4.0, respectively. Assuming an isotropic g tensor ($g = 2$), effective moment $(\mu_{\mathrm{eff}}/\mu_{\mathrm{B}})$ is 1.7, 3.9 and 5.9 for $S = 1/2$, 3/2 and 5/2, respectively. Entropy difference between the two species due to a change of spin multiplicity is $11.5\ \mathrm{J\ K^{-1}\ mol^{-1}}$, which is much smaller than the observed value of $53\ \mathrm{J\ K^{-1}\ mol^{-1}}$. This large entropy change may be ascribed to a change of vibrational density of state, since metal ligand coordination bond length of *high-spin* Co(II) form is longer than that of *low spin* Co(III) form by ca. 0.02 nm, and vibrational frequencies becomes smaller for high temperature high spin Co(II) species [4,8,15,16]. The valence tautomeric interconversion can be characterized as entropy driven process. Since the total spin of [Co$^{\mathrm{II}}$(SQ)$_2$(bpy)] as the high temperature species is composed of two SQ ($S = 1/2$) moieties and one Co$^{\mathrm{II}}$ ion ($S = 3/2$), an expected maximum spin state will be $S = 5/2$ in the case of parallel alignment of all of the spin components. However, the experimentally estimated value is $S = 3/2$. Thus, a strong antiferromagnetic coupling is expected among some of the spin components. The spin coupling will be elucidated by solid-state high-resolution NMR spectrum.

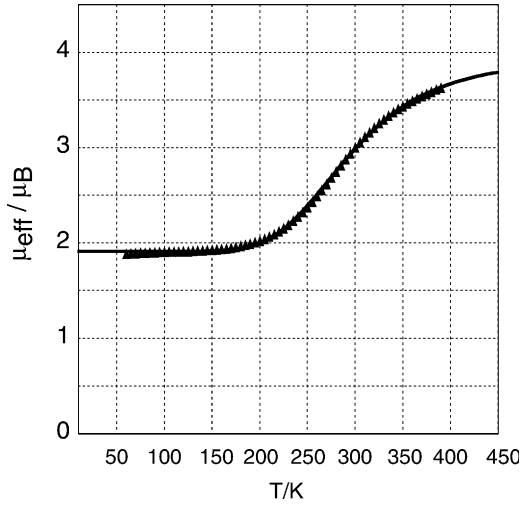


Fig. 5. Temperature dependence of effective magnetic moment due to valence tautomeric interconversion in the stable phase for normal compound. Solid curve is the result of fitting. Values of $\Delta S = 53\ \mathrm{J\ K^{-1}\ mol^{-1}}$ and $\Delta H = 17\ \mathrm{kJ\ mol^{-1}}$ were deduced for the conversion. For the bpy deuterated compound, almost the same results were obtained as those for the normal compound.

3.3. Interconversion between Cat and SQ, and antiferromagnetic interaction between two SQ ligands

Temperature variation of solid-state high-resolution ^{13}C MAS NMR spectrum measured with magic angle spinning (MAS) for a metastable virgin sample is illustrated in Fig. 6. The measurement was conducted from 303 K down to 186 K for the first run followed by the second run from 316 to 353 K. In the low temperature region such as 186 K, a relatively sharp peak (γ) at 30 ppm, which is temperature independent, was clearly observed. Since this shift is typical for methyl carbon of diamagnetic 3,5-di-*t*-butyl-1,2-benzoquinone [17], the diamagnetic Cat ligand was distinguished from spin bearing SQ ligand. Broad peaks (α and β) around $100 \sim 150$ ppm at 186 K were tentatively assigned to methyl carbons of SQ overlapped by some other carbon

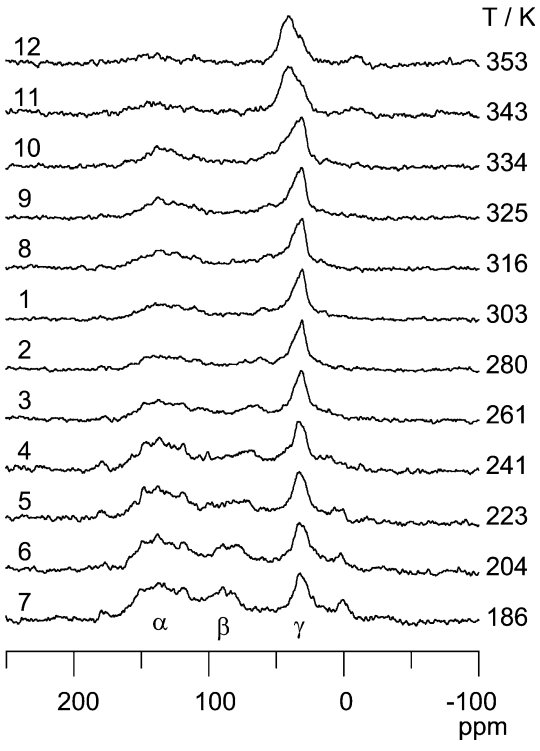


Fig. 6. Temperature variation of ^{13}C MAS NMR spectrum of [Co(3,5-di-*t*-butyl-1,2-benzoquinone)$_2$(2,2′-bipyridine)] · x($C_6H_5CH_3$) in the virgin metastable phase. To make the phase relation clear, successive measurements were carried out from number 1 to 12 in order. Above 343 K partial phase change occurred from metastable to stable phase. α and β were assigned to the signals of SQ ($S = 1/2$) and γ was assigned to Cat ($S = 0$).

signals. The peak at 30 ppm of Cat is temperature independent up to 325 K. This result indicates that no interconversion between Cat and SQ states occurs below 325 K. The profile of SQ signals is temperature dependent because of hyperfine coupling in a SQ ligand. No dynamic process of interconversion between Cat and SQ occurred below 325 K in the metastable phase. Sudden change was observed at 343 K, which indicates a partial phase change. This thermal treatment brought about additional peaks in the spectrum at 303 K, which was measured after heating up to 353 K, due to mixing of stable and metastable phases. Although an onset of increase of effective moment was observed in the metastable virgin sample below 325 K as indicated in Fig. 4, the dynamic process is slower than $10^3\ s^{-1}$, even if it occurs. ^2H MAS NMR spectrum of the metastable virgin sample of deuterated bpy-d_8 analogue is illustrated in Fig. 7. The peak near 8 ppm is temperature independent and indicates that the central metal ion directly bonded to bpy-d_8 is diamagnetic Co(III) state up to 331 K.

In contrast to the metastable phase, ^{13}C MAS NMR signals of stable phase were observed near 55 (b) and 95 ppm (a) at 186 K, just in between the signals of Cat and SQ. The peak (b) at 55 ppm is an average of 30 (Cat, γ) and 90 (SQ, β) ppm peaks and the peak (a) at 95 ppm is an average of 30 (Cat, γ) and 150 (SQ, α) ppm peaks in Fig. 6. Both 55 and 95 ppm signals are temperature dependent as shown in Fig. 8. This result clearly indicates that dynamic interconversion between Cat and SQ states were directly observed by the NMR spectrum.

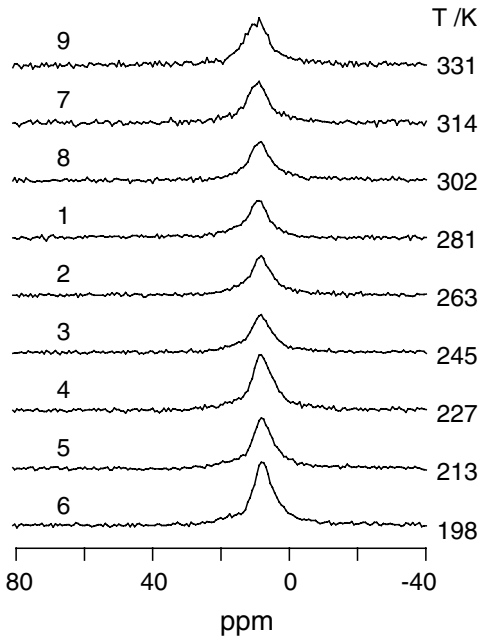


Fig. 7. Temperature variation of ^2H MAS NMR spectrum of [Co(3,5-di-*t*-butyl-1,2-benzoquinone)$_2$(2,2′-bipyridine-d_8)] · $x(C_6H_5CH_3)$ in the virgin metastable phase. To make the phase relation clear, successive measurements were carried out from number 1 to 9 in order.

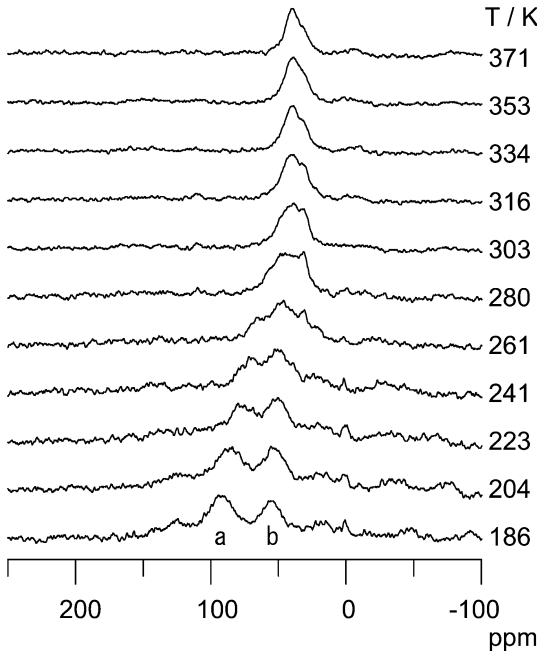


Fig. 8. Temperature variation of ^{13}C MAS NMR spectrum of [Co(3,5-di-*t*-butyl-1,2-benzoquinone)$_2$(2,2′-bipyridine)] · $x(C_6H_5CH_3)$ in the stable phase. Reversible change of the spectrum was confirmed. The signals (a) and (b) were assigned to the methyl groups of 5-*t*-Bt and 3-*t*-Bt, respectively, in averaged state of Cat ($S = 0$) and SQ ($S = 1/2$).

The conversion rate is much larger than NMR time scale of ca. $5 \times 10^4\ s^{-1}$ even in the low temperature region such as 186 K. This conversion is associated with a small energy difference between the two relevant species, since the averaged shift is almost the midpoint between the Cat and SQ. It is suggested that the energy difference between *low-spin* [Co^{III}(Cat)(SQ)] (**1**) and *low-spin* [Co^{III}(SQ)(Cat)] (**2**) shown in Fig. 1 is small enough in the stable phase. The two peaks at 55 (b) and 95 ppm (a) at 186 K in the stable phase were assigned to methyl groups of 3-*t*-Bt group and those of 5-*t*-Bt group of 3,5-di-*t*-butyl-1,2-benzoquinone as an averaged state of Cat ad SQ. Since 3,5-di-*t*-butyl-1,2-semiquinone ($S = 1/2$) has an electronic structure to exhibit a smaller hyperfine coupling on 3 and 6 positions and larger hyperfine coupling on 4 and 5 positions [18], a smaller and a larger paramagnetic shift are expected for 3 and 5 position, respectively.

Assuming a small zero field splitting, the temperature dependence of the paramagnetic isotropic shift δ_{iso} can be written by the Fermi contact term, the dipole interaction term (pseudo contact) and the temperature independent diamagnetic term (chemical shift) as follows [19,20]:

$$\delta_{iso} = \delta_{Fermi} + \delta_{Pseudo} + \delta_{dia},$$
$$\delta_{Fermi} + \delta_{Pseudo} = \frac{\mu_B}{3k_B T}\frac{A}{\gamma_C/2\pi}S(S+1). \quad (3)$$

Electron spin induced on the ^{13}C nucleus brings about a Fermi contact shift of the NMR resonance line, while

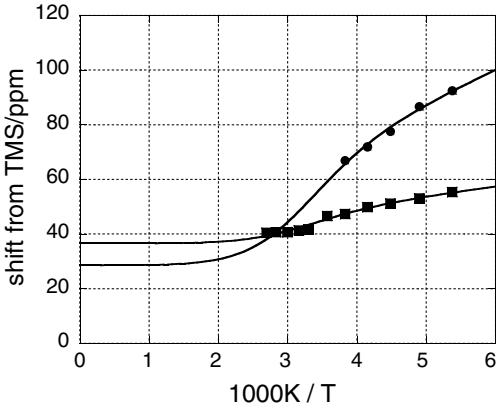


Fig. 9. Temperature dependence of the isotropic shift of ^{13}C MAS NMR of methyl groups of [Co(3,5-di-*t*-butyl-1,2-benzoquinone)$_2$-(2,2′-bipyridine)] · $x(C_6H_5CH_3)$ in the stable phase. Closed circles represent the sift of 5-*t*-Bt groups in averaged state of Cat ($S = 0$) and SQ ($S = 1/2$) ((a) in Fig. 8), while closed squares show the shift of 3-*t*-Bt groups ((b) in Fig. 8). Solid curves are fitting of Eq. (4) for the valence tautomeric interconversion between *low-spin* Co(III) form and *high-spin* Co(II) form.

anisotropy of the *g*-tensor of electron spin gives a pseudo-contact shift. The coefficient A in Eq. (3) is defined as the hyperfine coupling constant (hfcc) of the ^{13}C nucleus in Hz unit for a given electron spin S. In the case of valence tautomeric interconversion, the observed isotropic shift can be written in the same formula as Eqs. (1) and (2):

$$\begin{aligned}\delta_{\mathrm{obs}} &= \delta^{\mathrm{a}}_{\mathrm{iso}} f_{\mathrm{a}} + \delta^{\mathrm{b}}_{\mathrm{iso}} f_{\mathrm{b}} \\ &= \frac{\mu_{\mathrm{B}}}{3k_{\mathrm{B}}T}\frac{1}{\gamma_{\mathrm{C}}/2\pi}\left(A_{\mathrm{a}}S^{\mathrm{a}}(S^{\mathrm{a}}+1)f_{\mathrm{a}}\right. \\ &\quad \left. + A_{\mathrm{b}}S^{\mathrm{b}}(S^{\mathrm{b}}+1)f_{\mathrm{b}}\right) + \delta_{\mathrm{dia}}. \end{aligned} \quad (4)$$

Here, A_{a} and A_{b} are effective hyperfine coupling constants of the low and high temperature valence tautomeric isomers, respectively. Fractions of the two isomers were determined by magnetic susceptibility measurement as described in Section 3.2. Almost negligible hfcc for the high temperature isomer gave a fit to the observed temperature dependence of the isotropic shift as illustrated in Fig. 9. The negligible hfcc of the SQ ($S = 1/2$) for the high temperature [$Co^{II}(SQ)_2$] isomer suggests that strong antiferromagnetic interaction operates between the two SQ ligands to cancel the polarized spins on their *t*-Bt groups and the spin of $S = 3/2$ of Co^{II} ion remains in the *high-spin* [$Co^{II}(SQ)_2$] isomer. The effective hfcc's of methyl groups were estimated to be 0.11 and 0.38 MHz for 3 and 5 position of averaged state of Cat and SQ in the low spin [Co^{III}(Cat)(SQ)] isomer in the stable phase. Increase of the averaged magnitude of electron spin of cobalt ion as temperature increased was detected by ^2H MAS NMR of deuterated bpy-d_8, which is directly coordinated to the cobalt ion. Although the quality of the spectrum is not enough for quantitative discussions, splits of the peak accompanied by broadening were observed as the temperature was increased.

Acknowledgements

The authors thank Profs. H. Kawaji and T. Atake for the heat capacity measurement. This research was supported by Grant-in-Aid for Scientific Research on Priority Areas "Application of Molecular Spins" (15087201) and 14740321 from the Ministry of Education, Culture, Sports, Science and Technology of Japan and partially by The Mitsubishi Foundation.

References

[1] M.W. Lynch, D.N. Hendrickson, B.J. Fitzgerald, C.G. Pierpont, J. Am. Chem. Soc. 106 (1984) 2041.
[2] S.A. Attia, C.G. Pierpont, Inorg. Chem. 34 (1995) 1172.
[3] C.G. Pierpont, Coord. Chem. Rev. 216–217 (2001) 99.
[4] R.M. Buchanan, C.G. Pierpont, J. Am. Chem. Soc. 102 (1980) 4951.
[5] O.S. Jun, C.G. Pierpont, Inorg. Chem. 33 (1994) 2227.
[6] G.A. Abakumov, V.K. Cherkasov, M.P. Bubnov, O.G. Ellert, Z.B. Dobrokhotova, L.N. Zarkharov, Y.T. Struchovkov, Dokl. Akad. Nauk. 328 (1993) 12.
[7] D.M. Adams, A. Dei, A.L. Rheingold, D.N. Hendrickson, Angew. Chem., Int. Ed. Engl. 32 (1993) 880.
[8] D.M. Adams, A. Dei, A.L. Rheingold, D.N. Hendrickson, J. Am. Chem. Soc. 115 (1993) 8221.
[9] G.A. Abakumov, G.A. Razuvaev, V.I. Nevodchikov, V.K. Cherkasov, J. Organomet. Chem. 341 (1988) 485.
[10] A. Yamaguchi, K. Awaga, J. Mater. Chem. 11 (2001) 2142.
[11] R.M. Buchanan, B.J. Fizgerald, C.G. Pierpont, Inorg. Chem. 18 (1979) 3439.
[12] G. Maruta, S. Takeda, R. Imachi, T. Ishida, T. Nogami, K. Yamaguchi, J. Am. Chem. Soc. 121 (1999) 424.
[13] P.A. Beckmann, C. Dybowski, J. Magn. Reson. 146 (2000) 379.
[14] B.V. Lebedev, N.N. Smirnova, G.A. Abakumov, V.K. Cherkasov, M.P. Bubnov, J. Chem. Thermodyn. 34 (2002) 2093.
[15] D.M. Adams, D.N. Hendrickson, J. Am. Chem. Soc. 118 (1996) 11515.
[16] C.G. Pierpont, R.M. Buchanan, Coord. Chem. Rev. 38 (1981) 45.
[17] Integrated Spectral Data Base System for Organic Compounds, SDBSWeb: <http://www.aist.go.jp/RIODB/SDBS/>.
[18] S. Patai (Ed.), The Chemistry of the Quinonoid Compounds, Part 1, Wiley, New York, 1974.
[19] R. Kurland, B.R. McGervey, J. Magn. Reson. 2 (1970) 286.
[20] J.P. Jesson, in: G.N. La Mar, W.DeW. Horrocks, R.H. Holm (Eds.), NMR of Paramagnetic Molecules, Academic Press, 1973.

2. Results and discussion

2.1. Preparation and magnetic properties of azoxy- and azobenzene derivatives with aminoxyls

4,4′-Dihydroxyazoxybenzene **1a** [7] prepared by the zinc reduction of *p*-nitrophenylacetate followed by the alkaline hydrolysis of the acetyl groups was reacted with two molar amounts of aminoxyl-substituted bromoundecanoxycarbonyl derivatives (**3**, **4**) to give the corresponding biradical **5a** and **5b** in 34%, 42% yields, respectively. Similar reaction of 4-hydroxyazobenzene **2a** [8] prepared by the treatment of *p*-hydroxybenzene diazonium chloride with ammoniac cupric sulfate solution gave the biradicals with an azobenzene core (**6a**, **6b**) in 31%, 29% yields, respectively. By the derivatization of commercially available 4-hydroxyazobenzene with **2b**, the monoradicals with an azobenzene core (**8a**, **8b**) were prepared in the similar manner in 71% yield for **8a** and 72% yield for **8b** [9], while the monoradicals with an azoxybenzene core (**7a**, **7b**) were obtained from 4-hydroxylazoxybenzene **1b**, which was derived from the oxidation of the azobenzene **2b** with *m*-chloroperbenzoic acid (MCPBA), in 76% and 53% yield, respectively (Scheme 1). The thermotropic properties of the radicals thus prepared were examined by the DSC measurements and no endothermic peak but that of melting point could so far be discerned for any monoradicals as well as biradicals thus prepared.

The magnetic data were obtained by using SQUID susceptometer between the temperature range from 2 to 300 K and the data for the biradicals and the monoradicals are summarized in Table 1. Thus, antiferromagnetic interactions were observed in all of the biradical compounds **5** and **6** and the behavior being based on Curie–Weiss (CW) law was apparent for the PROXYL-based derivatives, i.e., **5b** and **6b**. On the contrary, the behavior being well expressed by singlet–triplet (ST) model was found for the TEMPO-based biradicals **5a** and **6a** with relatively large *J*-values of −33.9 K for **5a** and −38.5 K for **6a**, respectively. Since similar magnetic behaviors have also been observed in the related biradicals with a naphthalene or a biphenyl core [10], the molecules in the biradicals with extended long alkyl groups could be well anticipated to have the similar structural features in the solid-state with a hand-in-hand fashion especially for the TEMPO-based biradicals **5a** and **6a**, although their crystal structures are not clarified yet because of the lack of single crystals suitable for the X-ray analysis. On the contrary, weak intermolecular magnetic interactions were observed for the corresponding monoradicals **7** and **8**, in which only weak ferromagnetic interactions based on CW model were found for **8a**, while antiferromagnetic interactions on ST model were dominant for the other monoradicals.

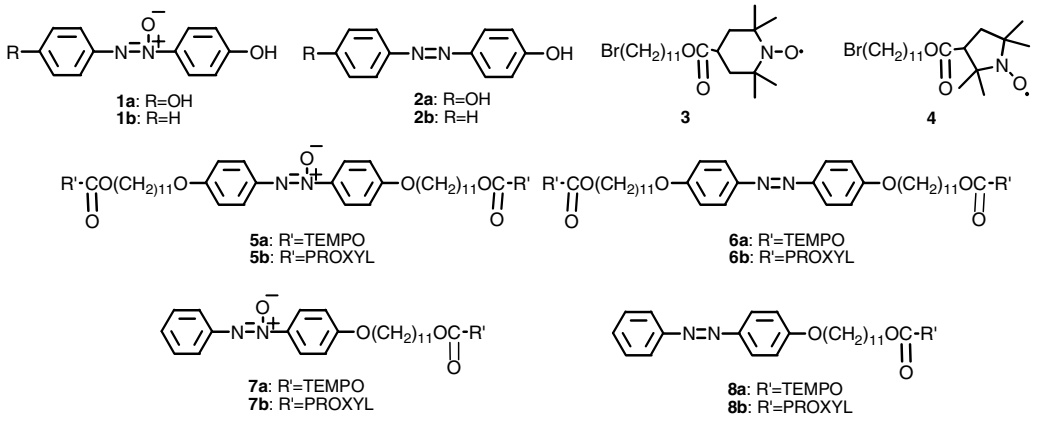
Table 1
Magnetic data of radical compounds

Compound	Magnetic interaction	C (emu K mol^{-1})	θ (K)	J (K)
5a	antiferromagnetic[a]			−33.9
5b	antiferromagnetic[b]	0.77	−1.07	
6a	antiferromagnetic[a,c]			−38.5
6b	antiferromagnetic[b,c]	0.76	−2.72	
7a	antiferromagnetic[a]			−14.8
7b	antiferromagnetic[a]			−3.7
8a	ferromagnetic[b,c]	0.38	0.09	
8b	antiferromagnetic[a,c]			−4.2

[a] Fitting for ST model.
[b] Fitting for CW law.
[c] Ref. [8].

2.2. Photo-responsive properties of the azobenzene derivatives

An azobenzene unit is known to give in a molecular/supramolecular system not only a mesogenic property but also a photo-responsive property and hence latter



Scheme 1.

properties of the azobenzene derivatives thus prepared were studied at the same time. Irradiation of the *trans*-isomers of the biradicals **6a** or **6b** with the light of 365 nm in dichloromethane solution gave gradually the corresponding *cis*-isomers, which could be isolated in the solid-state. However, the corresponding *cis*-isomers were found to be fairly unstable and they were smoothly reverted back to the original *trans*-isomers even when kept in the dark and stored in a refrigerator. We then turned our attention to the monoradicals with an azobenzene unit **8a** or **8b**.

When the *trans*-isomer of the monoradical with a TEMPO-substituent (**8a**) was irradiated with the light of 365 nm in dichloromethane solution, an absorption maximum at around 350 nm shifted gradually to a newly developed absorption at around 440 nm with an isosbestic point at 410 nm, while the reverse change was found to occur by irradiation of the latter solution with a fluorescent lamp or merely exposing the solution in the diffused light (Scheme 2). The forward and the backward reaction could be repeated for several times without appreciable decay as shown in Fig. 1 and the *cis*-isomer **9a** with the absorption at 440 nm could be isolated in the solid states. Fortunately, the *cis*-isomer **9a** was found to be more stable and durable than the previous *cis*-isomers of the biradicals **6a** or **6b** without appreciable change when kept in the dark and stored in a refrigerator. In turn, the backward reaction took place by the exposure of the solid material in the diffused light at ambient temperature for several hours and hence a reversible system could be constructed in this case [9]. At the same time, the original magnetic behavior of CW model with only weak ferromagnetic interactions ($\theta = 0.09$ K) was found to be changeable to the behavior of ST model with relatively strong magnetic interactions ($J = -37$ K) as shown in Fig. 2. Thus, an organic photo-responsive spin system has been available, in which photo-induced switching behavior of their intermolecular spin–spin interactions is observed.

The photo-isomerization of the *trans*-isomer of the azobenzene derivative with a PROXYL group (**8b**) was next examined and found to occur similarly by irradiation to give the corresponding *cis*-isomer **9b** as a relatively stable solid. The magnetic behavior of the *trans*-isomer **8b** was being based on ST model with relatively small intermolecular magnetic interactions

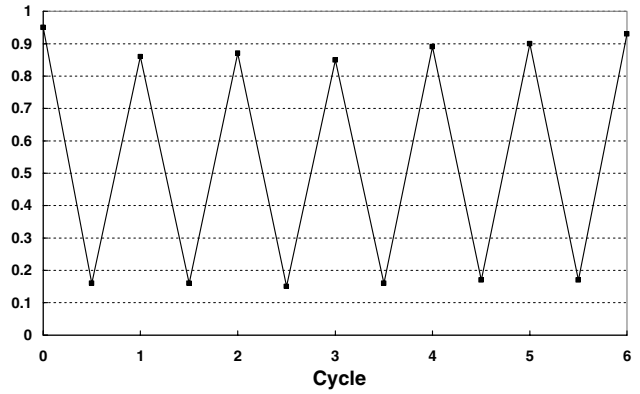


Fig. 1. Absorption changes observed at 346 nm by alternating irradiation at 365 nm and with a fluorescent light in dichloromethane over 6 cycles.

($J = -4.2$ K) and larger magnetic interactions with $J = -7.7$ K was observed in the corresponding *cis*-isomer, even though the behavior was also that of ST

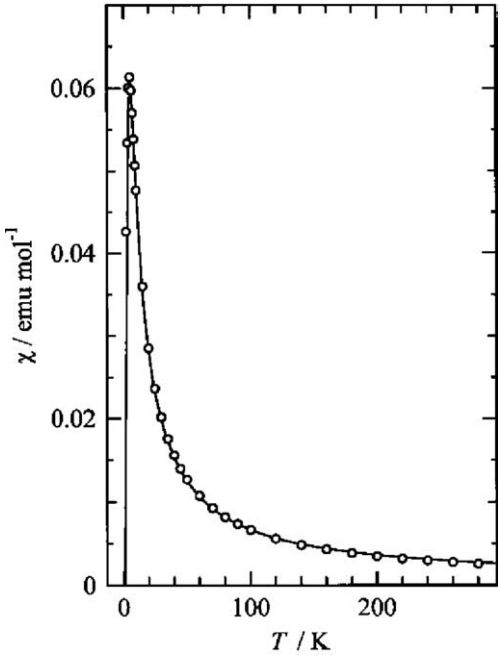
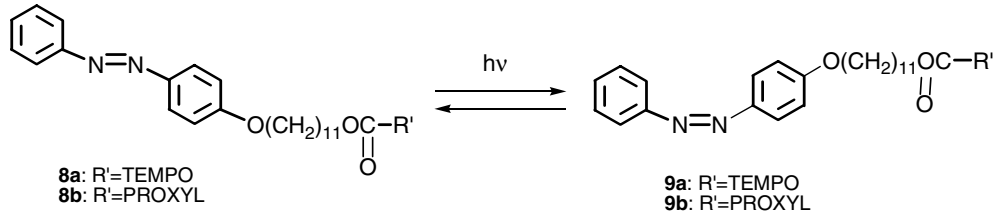


Fig. 2. Temperature dependence of magnetic susceptibility for a polycrystalline sample of *cis*-azobenzene derivative with TEMPO-substituent **9a**. The solid line corresponds to the best fit to a ST model with $J = -36.7$ K (spin concentration is estimated to be 64.3%).



Scheme 2.

model. The *cis*-isomer **9b** was found to give more slowly back to the *trans*-isomer **8b** than that of the corresponding biradical **6b** described above at ambient temperature and hence it could be handled at usual condition like the *cis*-isomer with TEMPO-substituent **9a**.

In summary, we have prepared several aminoxyl radicals and biradicals having an azoxy- or azobenzene core on one hand and a long alkyl group on the other hand and found that the biradicals with TEMPO substituents at their ends showed relatively large antiferromagnetic interactions being well expressed by ST model, while only weak antiferromagnetic interactions were observed in the corresponding PROXYL derivatives. The photoresponsive magnetic properties were observed in a couple of monoaminoyl-substituted azobenzene derivatives **8a** and **8b** and more appreciable change of the intermolecular magnetic interactions could be discerned in the TEMPO derivatives (**8a** and **9a**) than that of the PROXYL derivatives (**8b** and **9b**).

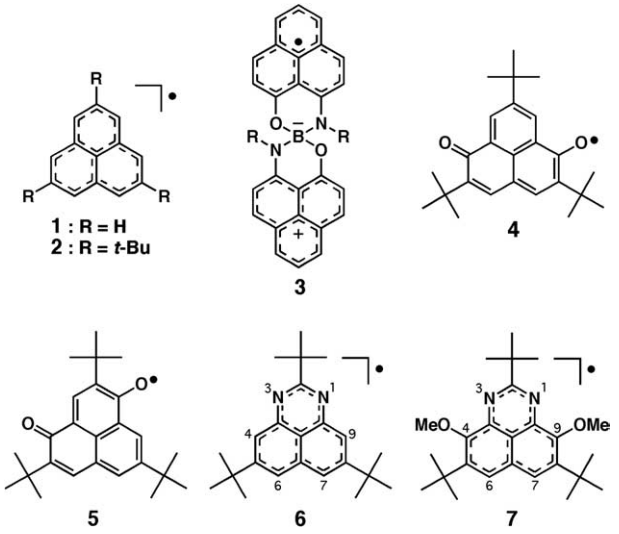
Acknowledgments

This work was supported by a Grant-in-Aid for Scientific Research (No. 13440213) from the Japan Society for the Promotion of Science (JSPS), which is gratefully acknowledged.

References

[1] (a) P.M. Lahti (Ed.), Magnetic Properties of Organic Materials, Marcel Dekker, Inc., New York, Basel, 1999;
(b) K. Itoh, M. Kinoshita (Eds.), Molecular Magnetism, Kodansha/Gordon and Breach Science Publishers, Tokyo, 2000;
(c) J. Veciana (Ed.), Structure and Bonding, π–Electron Magnetism: From Molecule to Magnetic Materials, vol. 100, Springer-Verlag, Berlin, 2001;
(d) J.S. Miller, M. Drillon (Eds.), Magnetism: Molecules to Materials, vols. I–IV, Wiley-VCH, Weinheim, 2001–2002.
[2] S. Nakatsuji, Chem. Soc. Rev. 33 (2004) 348.
[3] S. Nakatsuji, Adv. Mater. 13 (2001) 1719.
[4] T. Kaneko, H. Akutsu, J. Yamada, S. Nakatsuji, Org. Lett. 5 (2003) 2127.
[5] J.-L. Gallani, C. Bourgogne, S. Nakatsuji, Langmuir 20 (2004) 10062.
[6] K. Hamachi, K. Matsuda, T. Itoh, H. Iwamura, Bull. Chem. Soc. Jpn. 71 (1998) 2937.
[7] N.J. Leonald, J.W. Curry, J. Org. Chem. 17 (1952) 1071.
[8] R. Willstatter, M. Benz, Chem. Ber. 39 (1906) 3492.
[9] H. Fujino, T. Amano, H. Akutsu, J. Yamada, S. Nakatsuji, Chem. Commun. (2004) 2310.
[10] T. Amano, H. Akutsu, J. Yamada, S. Nakatsuji, Chem. Lett. 33 (2004) 382.

clarified its spin structure and crystal structure [9]. It turned out that the incorporation of nitrogen atoms induced small but measurable change of spin density distribution on phenalenyl, which led to a difference of crystal structure and physical properties between **6** and **2** [9a,b]. For further elucidation of the heteroatomic effects on the properties and spin structure of phenalenyl system, we have designed *tert*-butylated 4,9-dimethoxy-1,3-diazaphenalenyl (**7**) as the first example of an azaphenalenyl system having alkoxy substituents. We expected that the introduction of methoxy groups at 4- and 9-positions could strongly affect the electronic spin structure of the 1,3-diazaphenalenyl π-system and their properties, because large spin densities of 1,3-diazaphenalenyl system exist at 1-, 3-, 4-, 6-, 7-, and 9-positions. In this paper, we report on the first generation of dimethoxy-substituted azaphenalenyl radical **7** and effects of the methoxy group in a 1,3-diazaphenalenyl π-system.



2. Experimental

2.1. General

All chemicals were reagent grade and used without further purification. 2,7-Di-*tert*-butyl-3,6-dimethoxynaphthalene (**8**) was prepared from 2,7-dimethoxynaphthalene according to the reported procedure [7b]. *p*-Chloranil was recrystallized from benzene. Active PbO_2 was prepared according to the reported procedure [7b,10]. All reactions requiring anhydrous conditions were performed under argon atmosphere. Toluene and *N*,*N*-dimethylacetamide (DMA) were dried and distilled over CaH_2 under argon prior to use. Xylene (mixture of isomers) was dried by the filtration through the Alumina Super I (ICN BIOMEDICALS) column. ^{1}H NMR spectra were recorded on a JEOL EX-270 spectrometer with $CDCl_3$ and Me_4Si as an internal standard. EI-MS spectra were recorded at 70 eV on a Shimadzu QP-5000. Infrared spectra were recorded using KBr plates and CCl_2CCl_2 solution on Perkin–Elmer FT 1640 IR. Melting points were recorded with a Yanaco micro melting point apparatus and were uncorrected. The liquid-phase ESR spectra were recorded at 270–290 K on an X-band Bruker ESR/ENDOR spectrometer ESP300/350. R_f values on TLC were recorded on E. Merck precoated (0.25 mm) silica gel 60 F_{254}. The plates were sprayed with a solution of 10% phosphomolybdic acid in 95% EtOH and then heated until the spots became clearly visible. Silica gel 60 (100–200 mesh) was used for column chromatography. Deactivated silica gel was prepared by mixing silica gel with 6% water.

2.2. Synthesis of 3,6-di-tert-butyl-1,8-dinitro-2,7-dimethoxynaphthalene (*9*)

2,7-Di-*tert*-butyl-3,6-dimethoxynaphthalene (**8**) (10 g, 33 mmol), $Cu(NO_3)_2 \cdot 3H_2O$ (16.0 g, 66 mmol) and acetic anhydride (300 mL) were placed in a 1-L three-necked round-bottomed flask and stirred at room temperature for 14 h. Most of the acetic anhydride was removed by distillation at 60 °C, and the residue was mixed with H_2O (~300 mL). The resulting mixture was stirred for 30 min, and was mixed with CH_2Cl_2. The organic layer was separated, and the aqueous layer was extracted with CH_2Cl_2. The combined organic layer was washed with saturated aqueous $NaHCO_3$, and dried over Na_2SO_4, then filtered and concentrated under reduced pressure, to give the desired compound (11.6 g, 90%) as a yellowish orange solid: mp 203–205 °C; TLC R_f 0.40 (5:1 hexane/ethyl acetate); ^{1}H NMR (270 MHz, $CDCl_3$) δ 1.47 (s, 18H), 3.89 (s, 6H), 7.86 (s, 2H); *m*/*z* 390 (M^+, 9%), 344 ($M^+ - NO_2$, 58%); *Anal.* Calc. for $C_{20}H_{26}N_2O_6$: C, 61.53; H, 6.71; N, 7.18. Found: C, 61.37; H, 6.71; N, 7.21%.

2.3. Synthesis of 1,8-diamino-3,6-di-tert-butyl-2,7-dimethoxynaphthalene (*10*)

Dinitro derivative **9** (1.99 g, 5.12 mmol), Sn (2.61 g, 22.0 mmol) and $SnCl_2 \cdot 2H_2O$ (9.06 g, 40.2 mmol) were placed in a 300-mL round-bottomed flask equipped with reflux condenser. To this mixture was added concentrated HCl (50 mL) and acetic acid (100 mL) at room temperature. This reaction mixture was stirred at 90 °C for 6.5 h. After being cooled to room temperature, the resulting mixture was extracted with CH_2Cl_2/hexane solution and the organic layer was washed with 2 M HCl aq, 0.1 M pH 7.0 phosphate buffer solution, saturated aqueous $NaHCO_3$ and 10% aqueous NaOH, successively. The organic layer was dried over Na_2SO_4,

then filtered and concentrated under reduced pressure. The residual solid was subjected to deactivated silica gel column chromatography with a 20:1–15:1 mixture of hexane and ethyl acetate as eluent, to give diamino derivative **10** (957 mg, 59%) as deep orange powder. This compound was used for next reaction without further purification due to its low stability: TLC R_f 0.63 (2:1 hexane/ethyl acetate); ^{1}H NMR (270 MHz, $CDCl_3$) δ 1.44 (s, 18H), 3.82 (s, 6H), 4.4–4.6 (br, 4H), 7,06 (s, 2H); EI-MS, *m*/*z* 330 (M^+, 42%), 315 ($M^+ - CH_3$, 100%).

2.4. Synthesis of 2,5,8-tri-tert-butyl-4,9-dimethoxy-1,3-diazaphenalene (*11*)

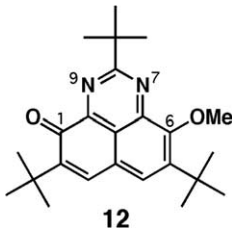
Diamino derivative **10** (162 mg, 0.49 mmol) was placed in a 50-mL Schlenk tube equipped with a reflux condenser and mixed with xylene (5 mL), pivalaldehyde (0.1 mL, 0.9 mmol), *p*-TsOH · H_2O (27 mg) and 5% Pd/C (270 mg). This mixture was refluxed at 160 °C for 15 h. After being cooled to room temperature, this reaction mixture was directly treated with the Na_2SO_4 and passed through a Celite column to removed water and Pd/C, and rinsed with CH_2Cl_2. After being concentrated under reduced pressure, the residual solid was subjected to deactivated silica gel column chromatography with a 5:1 mixture of hexane and CH_2Cl_2 as eluent, to give 1,3-diazaphenalene derivative **11** (121 mg, 63%) as orange powder: m.p. 71–73 °C; TLC R_f 0.57 (5:1 hexane/ethyl acetate); TLC (alumina) R_f 0.61 (5:1 hexane/ethyl acetate); ^{1}H NMR (270 MHz, $CDCl_3$) δ 1.38 (s, 9H), 1.39 (s, 9H), 1.41 (s, 9H), 3.72 (s, 3H), 4.03 (s, 3H), 6.93 (s, 1H), 7.0–7.1 (br, 1H), 7.04 (s, 1H); EI-MS, *m*/*z* 396 (M^+, 71%), 381 ($M^+ - CH_3$, 100%); *Anal*. Calc. for $C_{25}H_{36}N_2O_2 \cdot (CH_2Cl_2)_{0.05}$: C, 75.07; H, 9.08; N, 6.99. Found: C, 75.01; H, 9.04; N, 6.82%.

2.5. ESR/ENDOR/TRIPLE spectroscopies of the radical 7

A toluene solution of 1,3-diazaphenalene derivative **11** (8×10^{-5} M) and *p*-chloranil (ca. 0.5 mg) was placed in an ESR tube, degassed by the freeze-pump-thaw method, and sealed. ESR measurements were performed at 290 K. ^{1}H and ^{14}N ENDOR/TRIPLE spectra were measured at 270 K.

2.6. Preparation of the radical 7 in the solid state

1,3-Diazaphenalene derivative **11** (10 mg, 0.026 mmol) was placed in a 50-mL Schlenk tube and dissolved with degassed toluene (3 mL). To this mixture was added active PbO_2 (30 mg, 0.13 mmol), then this mixture was degassed and filled with argon. After being stirred at room temperature for 1 min, the resulting mixture was filtered through a Celite column under argon atmosphere, and rinsed with degassed toluene. The filtrates were concentrated in vacuo, to give the crude radical as a green solid (about 1:1 mixture of radical **7** and phenalenone derivative **12** in TLC spectroscopy): TLC (alumina) R_f 0.82 for **7**, and 0.61 for **12** (5:1 hexane/ethyl acetate).



12

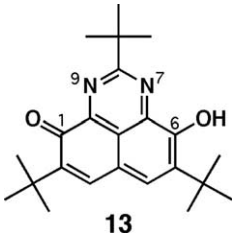
2.7. Generation of 7,9-diazaphenalenone derivative *12*

1,3-Diazaphenalene derivative **11** (10 mg, 0.026 mmol) was placed in a 50-mL Schlenk tube and dissolved with degassed toluene (3 mL). To this mixture was added active PbO_2 (60 mg, 0.25 mmol), and then this mixture was degassed and filled with argon. After being stirred at room temperature for 45 min, the resulting mixture was filtered through a Celite column under argon atmosphere, and rinsed with toluene. The filtrates were concentrated in vacuo, to give the phenalenone **12** as a reddish orange solid (13 mg, quant). Analytically pure sample was prepared by deactivated silica gel column chromatography with a 250:1 mixture of hexane and ethyl acetate as eluent: m.p. 173–175 °C; TLC R_f 0.60 (5:1 hexane/ethyl acetate); TLC (alumina) R_f 0.61 (5:1 hexane/ethyl acetate); ^{1}H NMR (270 MHz, $CDCl_3$) δ 1.41 (s, 9H), 1.51 (s, 9H), 1.60 (s, 9H), 4.46 (s, 3H), 7.46 (s, 1H), 7.63 (s, 1H); EI-MS, *m*/*z*380 (M^+, 65%), 365 ($M^+ - CH_3$, 100%); IR (KBr) 2960, 1644 cm^{-1}; *Anal*. Calc. for $C_{24}H_{32}N_2O_2$: C, 75.75; H, 8.48; N, 7.36. Found: C, 75.48; H, 8.48; N, 7.25%.

2.8. Conversion of *12* to 6-hydroxy-7,9-diazaphenalenone derivative *13*

7,9-Diazaphenalenone derivative **12** (13 mg) was placed in a 30-mL round-bottomed flask and dissolved with DMA (2.0 mL). To this mixture was added LiI (91 mg, 0.68 mmol) and stirred at 180 °C for 3 h. After being cooled to room temperature, 0.1 M, pH 7.0, phosphate buffer solution was added to this mixture. The resulting mixture was extracted with ethyl acetate. The organic layer was washed with saturated aqueous NaCl and water, and dried over Na_2SO_4, then filtered and concentrated under reduced pressure, to give 6-hydroxy-7,9-diazaphenalenone **13** as a deep red solid (11 mg, crude yield 88%). Analytically pure sample was prepared by

recrystallization from a mixture of hexane and CH_2Cl_2: m.p. 206–208 °C; TLC R_f 0.52 (5:1 hexane/ethyl acetate); ^{1}H NMR (270 MHz, $CDCl_3$) δ 1.41 (s, 9H), 1.53 (s, 9H), 1.59 (s, 9H), 7.47 (s, 1H), 7.62 (s, 1H), 8.5–8.6 (br, 1H); *m/z* 366 (M^+, 100%); IR (KBr) 3386, 2958, 1652 cm^{-1}; IR (CCl_2CCl_2) 3389, 2959, 1653 cm^{-1}; *Anal.* Calc. for $C_{23}H_{30}N_2O_2 \cdot (CH_2Cl_2)_{0.05}$: C, 74.67; H, 8.18; N, 7.56. Found: C, 74.44; H, 8.32; N, 7.48%.



13

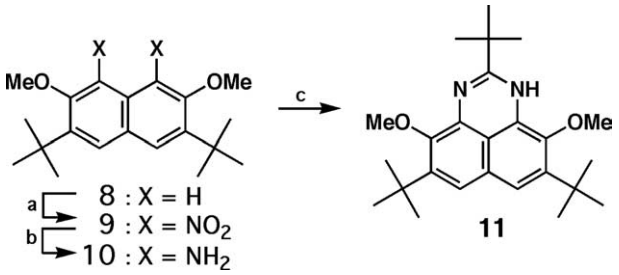
3. Results and discussion

3.1. Synthesis of the radical precursor *11*

The radical precursor, 1,3-diazaphenalene derivative **11**, was synthesized from di-*tert*-butyl-dimethoxynaphthalene **8** in three steps (Scheme 1).[1] Two nitro groups were effectively introduced to dimethoxynaphthalene **8** at the 1,8-positions with $Cu(NO_3)_2 \cdot 3H_2O$ and acetic anhydride [11]. Dinitro derivative **9** was converted to diamino derivative **10** with Sn and $SnCl_2 \cdot 2H_2O$ under acidic conditions. Condensation with pivalaldehyde in the presence of *p*-TsOH · H_2O followed by dehydrogenation with Pd/C gave 1,3-diazaphenalene derivative **11** [12].

3.2. Stability of the radical 7 in a solution and the solid state

The ESR signal intensity of radical **7** generated by treatment of **11** with *p*-chloranil in a degassed toluene solution decreased to one-fifth of its original magnitude at −30 °C after a week in a sealed ESR tube. The radical **7** was also generated by the treatment of active PbO_2 in degassed toluene solution. When the reaction time was longer than 1 min, the radical **7** was transformed completely to the 7,9-diazaphenalenone derivative **12** as proven by NMR, IR, and EI-MS spectra. The molecular structure of **12** was also confirmed by conversion to 6-hydroxy-7,9-diazaphenalenone derivative **13**.[2] The



Scheme 1. Synthesis of **11**. Reagents and conditions: (a) 2 equiv $Cu(NO_3)_2 \cdot 3H_2O$, Ac_2O, rt, 14 h, 90%; (b) 4.5 equiv Sn, 7.8 equiv $SnCl_2 \cdot 2H_2O$, conc. HCl aq–AcOH (1:2), 100 °C, 6.5 h, 59%; (c) 1.8 equiv *t*-BuCHO, cat Pd/C, cat *p*-TsOH · H_2O, xylene, reflux, 5 h, 63%.

mixture of **7** and **12** as a green solid was obtained when the reaction was worked up within 1 min (TLC spectroscopy indicated that the ratio of **7**:**12** was about 1:1). TLC spectroscopy showed that the crude radical solid stored at −30 °C under air atmosphere for a week was completely transformed to **12**. These observations indicate that the stability of **7** in a degassed solution and the solid states is lower than the parent 1,3-diazaphenalenyl **6**, which is stable in degassed solution and the solid state for a long period of time [9a,b].

3.3. Clarification of spin structure in terms of ESR/ENDOR/TRIPLE spectroscopies

A hyperfine ESR spectrum of the radical **7** observed from a degassed toluene solution of radical precursor **11** (8×10^{-5} M) with *p*-chloranil at 290 K is shown in Fig. 1(a). In order to determine the magnitudes and relative signs of hyperfine coupling constants (hfcc's), the liquid-phase ^{1}H and ^{14}N ENDOR/TRIPLE spectra were measured (Fig. 1(c) and (d)). The ^{1}H and ^{14}N ENDOR spectrum showed four pairs of lines which were attributable to two protons and two nitrogen atoms on the phenalenyl skeleton, the methoxy group's protons, and *tert*-butyl protons, respectively. Furthermore, the ^{1}H and ^{14}N TRIPLE spectrum confirmed the relative signs of hfcc's of the protons and nitrogen atoms except for the *tert*-butyl protons. The observed ESR spectrum was successfully simulated by the use of the hfcc's obtained from ^{1}H and ^{14}N ENDOR spectrum (Fig. 1(b)). The experimental and calculated values of hfcc's and *g*-value of **7** were summarized in Table 1. Assignments were carried out with the help of theoretically calculated hfcc's (Fermi contact analysis using DFT calculation). The calculated values underestimate the observed ones, but the trend of relative magnitude and absolute signs reproduce well the experimental results. These observed hfcc's suggest that the unpaired electron of the radical delocalizes on the phenalenyl skeleton and the oxygen atoms of the methoxy group.

[1] 1,3-Diazaphenalene **11** was a synthetic intermediate of the 7,9-diaza-6-oxophenalenoxyl derivative, see Section 2.4 and [7f].

[2] 6-Hydroxy-7,9-diazaphenalenone derivative **13** was also a synthetic intermediate of the 7,9-diaza-6-oxophenalenoxyl, see Section 2.8 and [7f].

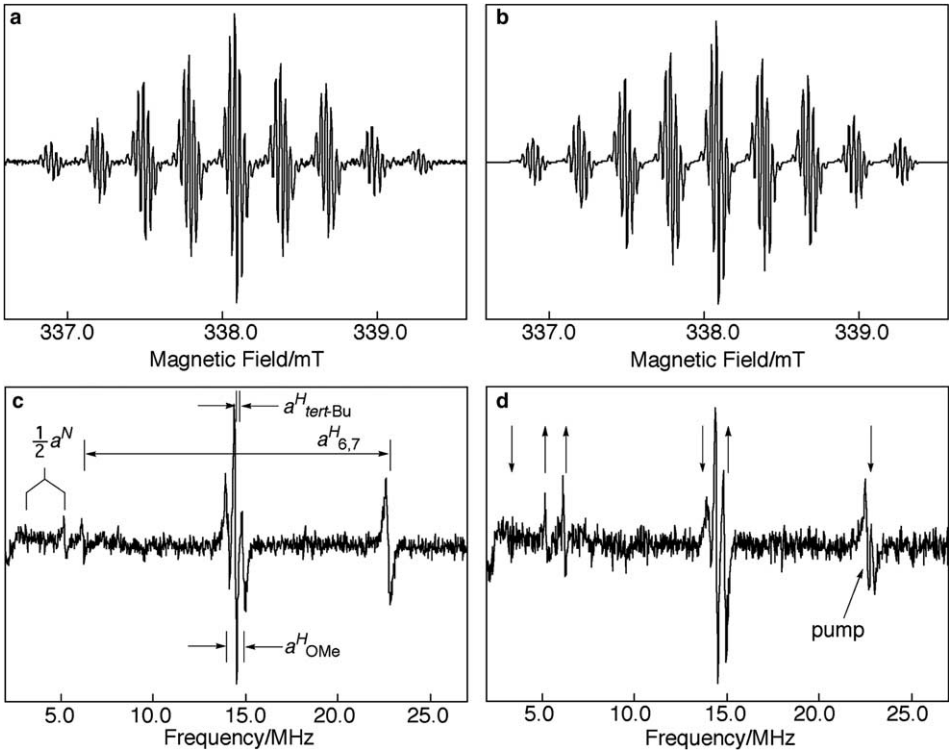


Fig. 1. Observed hyperfine ESR (a, 290 K), simulated (b), ^{1}H and ^{14}N ENDOR (c, 270 K), and ^{1}H and ^{14}N TRIPLE (d, pump frequency: 22.71 MHz, 270 K) spectra for **7** generated by the treatment of **11** with *p*-chloranil in a toluene solution (8×10^{-5} M). The microwave frequency used for the ESR measurement was 9.489354 GHz. The observed *g*-value is 2.0035.

Table 1
Hyperfine coupling constants (hfcc's) of ^{1}H and ^{14}N nuclei[a] and *g*-values

Radical	a^H					a^N	*g*-value
	4,9	6,7	OMe	2-*t*-Bu	5,8-*t*-Bu	1,3	
7		−0.590 (−0.452)	+0.032 (+0.146)[c]	±0.0025[b] (+0.0046)	±0.0025[b] (−0.0008)	+0.299 (+0.260)	2.0035
6[d]	−0.638	−0.715		+0.006	+0.021	+0.292	2.0033

[a] The experimental hfcc's were determined by spectral simulation with the help of ^{1}H and ^{14}N ENDOR in a toluene solution. The relative signs of the hfcc's were determined in terms of ^{1}H-TRIPLE spectroscopy. Values in parentheses were results of Fermi contact analysis by the DFT method (using GAUSSIAN-03 at the UBLYP/6-31G**//UBLYP/6-31G**) [13].
[b] The sign was experimentally unknown.
[c] The marked deviation seen in the protons on the methoxy groups is likely because the calculation does not take the dynamic rotational motion into consideration.
[d] Ref. [9a].

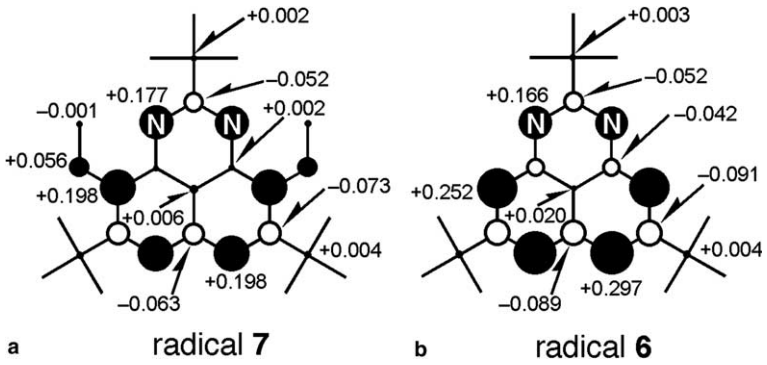


Fig. 2. Spin density distributions calculated at the UBLYP/6-31G**//UBLYP/6-31G** level of theory for (a) radical **7** and (b) **6**. Vacant and filled circles denote negative and positive spin densities, respectively.

3.4. Comparison of the spin densities of 7 with those of 6

The experimental values of hfcc's and *g*-value of the parent 1,3-diazaphenalneyl radical **6** are also summarized in Table 1 [9a,b]. The slightly larger *g*-value (2.0035) of **7** than that of **6** (2.0033) indicates the contribution of unpaired electrons on the oxygen atoms of the methoxy group. Interestingly, the hfcc's of the protons at the 6- and 7-positions of **7** are smaller than those of **6**. This observation shows that the spin densities at the 6- and 7-positions decrease.

In order to clarify the difference of the electronic spin structures between **7** and **6**, we have carried out density functional theory calculations for **7** and **6** by using GAUSSIAN-03 at the UBLYP/6-31G**//UBLYP/6-31G** level (Fig. 2(a) and (b)) [13]. It showed that a robust π-spin polarized and delocalized nature similar to the parent 1,3-diazaphenalenyl **6** is maintained in **7**, and that large spin densities exist on not only nitrogen and carbon atoms at 1-, 3-, 4-, 6-, 7-, and 9-positions but also the two oxygen atoms at the methoxy groups of **7**. By comparing the spin densities of **7** with those of **6**, it turns out that the spin densities at the 6- and 7-positions decrease. This is consistent with the hfcc's of the protons at the 6- and 7-positions described above. In addition, the small but measurable increase in the spin density of nitrogen atoms in the DFT calculation corresponds to the small increase of observed hfcc's on nitrogen atoms of the radical **7**.

4. Summary

Dimethoxy-substituted 1,3-diazaphenalenyl radical **7** was generated, and its solution and solid-state stability has been studied. The stability of **7** in both solution and solid states was found to be lower than the parent 1,3-diazaphenalenyl **6** that showed a high stability enough to be isolated in air. The spin structure was clarified by ESR/ENDOR/TRIPLE spectroscopies and theoretical calculation, which shown that the unpaired electron of **7** delocalizes onto the phenalenyl skeleton and oxygen atoms of methoxy groups. By comparing the hfcc's obtained by ESR measurements and the spin densities calculated by DFT method of **7** with those of **6**, it is clarified that the spin densities at 6- and 7-positions of **7** decrease while those of the 1- and 3-positions (on nitrogen atoms) increase. We believe that this study will be helpful to design new heteroatom-incorporated phenalenyl derivatives, and to control their electronic-spin structure and properties. The origin of the instability of **7** is under consideration, and the syntheses of other azaphenalenyl derivatives are in progress.

Acknowledgements

This work was partially supported by PRESTO-JST, Grant-in-Aid for Scientific Research in Priority Areas "Application of Molecular Spins" (Area No. 769) from Ministry of Education, Culture, Sports, Science, and Technology, Japan, and 21COE program "Creation of Integrated EcoChemistry of Osaka University".

References

[1] Recent overview of molecule-based magnets, see, e.g.: K. Itoh, M. Kinoshita (Eds.), Molecular Magnetism, Gordon & Breach/Kodansha, New York/Tokyo, 2000, pp. 1–347.
[2] (a) R.C. Haddon, Nature 256 (1975) 394–396;
(b) R.C. Haddon, Aust. J. Chem. 28 (1975) 2343–2351.
[3] (a) K. Tamaki, Y. Morita, J. Toyoda, H. Yamochi, G. Saito, K. Nakasuji, Tetrahedron Lett. 38 (1997) 4583–4586;
(b) X. Chi, M.E. Itkis, B.O. Patrick, T.M. Barclay, R.W. Reed, R.T. Oakley, A.W. Cordes, R.C. Haddon, J. Am. Chem. Soc. 121 (1999) 10395–10402;
(c) M.E. Itkis, X. Chi, A.W. Cordes, R.C. Haddon, Science 296 (2002) 1443–1445;
(d) J.S. Miller, Angew. Chem., Int. Ed. 42 (2003) 27–29.
[4] K. Goto, T. Kubo, K. Yamamoto, K. Nakasuji, K. Sato, D. Shiomi, T. Takui, M. Kubota, T. Kobayashi, K. Yakushi, J. Ouyang, J. Am. Chem. Soc. 121 (1999) 1619–1620.
[5] (a) X. Chi, M.E. Itkis, K. Kirschbaum, A.A. Pinkerton, R.T. Oakley, A.W. Cordes, R.C. Haddon, J. Am. Chem. Soc. 123 (2001) 4041–4048;
(b) X. Chi, M.E. Itkis, R.W. Reed, R.T. Oakley, A.W. Cordes, R.C. Haddon, J. Phys. Chem. B 106 (2002) 8278–8287;
(c) X. Chi, M.E. Itkis, F.S. Tham, R.T. Oakley, A.W. Cordes, R.C. Haddon, Int. J. Quantum Chem. 95 (2003) 853–865;
(d) S.K. Pal, M.E. Itkis, R.W. Reed, R.T. Oakley, A.W. Cordes, F.S. Tham, T. Siegrist, R.C. Haddon, J. Am. Chem. Soc. 126 (2004) 1478–1484.
[6] Haddon and co-workers also demonstrated the crystal structure and electronic properties of perchlorophenalenyl, see:
(a) P.A. Koutentis, Y. Chen, Y. Cao, T.P. Best, M.E. Itkis, L. Beer, R.T. Oakley, A.W. Cordes, C.P. Brock, R.C. Haddon, J. Am. Chem. Soc. 123 (2001) 3846–3871;
(b) P.A. Koutentis, R.C. Haddon, R.T. Oakley, A.W. Cordes, C.P. Brock, Acta Crystallogr., Sect. B 57 (2001) 680–691.
[7] (a) K. Hatanaka, Y. Morita, T. Ohba, K. Yamaguchi, T. Takui, M. Kinoshita, K. Nakasuji, Tetrahedron Lett. 37 (1996) 873–876;
(b) Y. Morita, T. Ohba, N. Haneda, S. Maki, J. Kawai, K. Hatanaka, K. Sato, D. Shiomi, T. Takui, K. Nakasuji, J. Am. Chem. Soc. 122 (2000) 4825–4826;
(c) Y. Morita, S. Maki, K. Fukui, T. Ohba, J. Kawai, K. Sato, D. Shiomi, T. Takui, K. Nakasuji, Org. Lett. 3 (2001) 3099–3102;
(d) Y. Morita, J. Kawai, N. Haneda, S. Nishida, K. Fukui, S. Nakazawa, D. Shiomi, K. Sato, T. Takui, T. Kawakami, K. Yamaguchi, K. Nakasuji, Tetrahedron Lett. 42 (2001) 7991–7995;
(e) Y. Morita, J. Kawai, K. Fukui, S. Nakazawa, K. Sato, D. Shiomi, T. Takui, K. Nakasuji, Org. Lett. 5 (2003) 3289–3291;
(f) We have also reported the nitrogen incorporated 6-oxophenalenoxyl, see:Y. Morita, S. Suzuki, J. Kawai, S. Nishida, K. Fukui, S. Nakazawa, K. Sato, D. Shiomi, T. Takui, K. Nakasuji, Synth. Met. 137 (2003) 1209–1210.
[8] (a) Y. Morita, S. Nishida, J. Kawai, K. Fukui, S. Nakazawa, K. Sato, D. Shiomi, T. Takui, K. Nakasuji, Org. Lett. 4 (2002) 1985–1988;

(b) Y. Morita, S. Nishida, J. Kawai, K. Fukui, S. Nakazawa, K. Sato, D. Shiomi, T. Takui, K. Nakasuji, Polyhedron 22 (2003) 2209–2213.

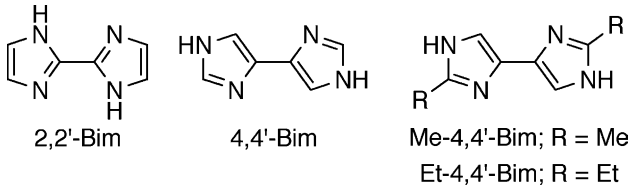
[9] (a) Y. Morita, T. Aoki, K. Fukui, S. Nakazawa, K. Tamaki, S. Suzuki, A. Fuyuhiro, K. Yamamoto, K. Sato, D. Shiomi, A. Naito, T. Takui, K. Nakasuji, Angew. Chem., Int. Ed. 41 (2002) 1793–1796;
(b) Y. Morita, K. Fukui, S. Suzuki, T. Aoki, S. Nakazawa, K. Tamaki, A. Fuyuhiro, K. Yamamoto, K. Sato, D. Shiomi, A. Naito, T. Takui, K. Nakasuji, Polyhedron 22 (2003) 2199–2204;
(c) First metal complex of azaphenalene derivative with pyrimidine moiety, see: Y. Morita, S. Suzuki, K. Fukui, S. Nakazawa, K. Sato, D. Shiomi, T. Takui, K. Nakasuji, Polyhedron 22 (2003) 2215–2218;
(d) Other azaphenalenyl radical, see: S. Zheng, J. Lan, S.I. Khan, Y. Rubin, J. Am. Chem. Soc. 125 (2003) 5786–5791.

[10] R. Kuhn, I. Hammer, Chem. Ber. 83 (1950) 413–414.

[11] (a) I.C. Calder, P.J. Garratt, H.C. Longuet-Higgins, F. Sondheimer, R. Wolovsky, J. Chem. Soc. C (1967) 1041–1044;
(b) E.P. Woo, F. Sondheimer, Tetrahedron 26 (1970) 3933–3939.

[12] 1,3-Diazaphenalene (perimidine) derivatives are generally prepared from 1,8-diaminonaphthalene and the corresponding aldehyde, see:
(a) V. Paragamian, M.B. Baker, B.M. Puma, J. Reale Jr., J. Heterocycl. Chem. 5 (1968) 591–597;
(b) A.L. Llamas-Saiz, C. Foces-Foces, D. Sanz, R.M. Claramunt, J. Dotor, J. Elguero, J. Catalán, J.C. del Valle, J. Chem. Soc., Perkin Trans. 2 (1995) 1389–1398.

[13] M.J. Frisch, G.W. Trucks, H.B. Schlegel, G.E. Scuseria, M.A. Robb, J.R. Cheeseman, J.A. Montgomery Jr., T. Vreven, K.N. Kudin, J.C. Burant, J.M. Millam, S.S. Iyengar, J. Tomasi, V. Barone, B. Mennucci, M. Cossi, G. Scalmani, N. Rega, G.A. Petersson, H. Nakatsuji, M. Hada, M. Ehara, K. Toyota, R. Fukuda, J. Hasegawa, M. Ishida, T. Nakajima, Y. Honda, O. Kitao, H. Nakai, M. Klene, X. Li, J.E. Knox, H.P. Hratchian, J.B. Cross, V. Bakken, C. Adamo, J. Jaramillo, R. Gomperts, R.E. Stratmann, O. Yazyev, A.J. Austin, R. Cammi, C. Pomelli, J.W. Ochterski, P.Y. Ayala, K. Morokuma, G.A. Voth, P. Salvador, J.J. Dannenberg, V.G. Zakrzewski, S. Dapprich, A.D. Daniels, M.C. Strain, O. Farkas, D.K. Malick, A.D. Rabuck, K. Raghavachari, J.B. Foresman, J.V. Ortiz, Q. Cui, A.G. Baboul, S. Clifford, J. Cioslowski, B.B. Stefanov, G. Liu, A. Liashenko, P. Piskorz, I. Komaromi, R.L. Martin, D.J. Fox, T. Keith, M.A. Al-Laham, C.Y. Peng, A. Nanayakkara, M. Challacombe, P.M.W. Gill, B. Johnson, W. Chen, M.W. Wong, C. Gonzalez, J.A. Pople, GAUSSIAN-03: Revision C.02, Gaussian, Inc., Wallingford, CT, 2004.



Drawing 1.

supramolecular assemblies based on 4,4′-Bim system by the introduction of alkyl substituents with the aim to control H-bonding pattern and networks in terms of the steric effects. Recently, Turnbull and coworkers [10] have reported the crystal structures of methyl-substituted 4,4′-Bim (Me-4,4′-Bim) as the dihydrate and trifluoroacetic acid salt including their H-bonded networks. In this report, we have newly synthesized 2-ethyl-substituted 4,4′-Bim (Et-4,4′-Bim), and revealed its crystal structure together with its hydrate. Moreover, we have disclosed crystal structure of anhydrous Me-4,4′-Bim, demonstrating a substantial effect of water molecule on forming H-bonded networks. These continuous and systematic studies provide a unique opportunity for the creation of supramolecular assemblies based on 4,4′-Bim system (see Drawing 1).

2. Experimental

2.1. Materials and methods

^{1}H NMR spectra were recorded on a JEOL EX-270 spectrometer with Me_4Si as an internal standard. Infrared spectra were recorded using KBr plates on JASCO FT/IR-660M. EI-MS spectra were recorded at 70 eV on a Shimadzu QP-5000. Melting points were measured by a Yanaco micro melting point apparatus and were uncorrected. Elemental analyses were performed at the Analytical Center of Graduate School of Science, Osaka University. R_f values on TLC were recorded on E. Merck precoated (0.25 mm) silica gel 60 F_{254}. The plates were sprayed with a solution of 10% phosphomolybdic acid in 95% EtOH and then heated until the spots become clearly visible. Triphenylmethyl (Tr)-protected Me-4,4′-Bim was prepared by the reported procedure [11]. DMF was dried over CaH_2 and distilled under reduced pressure prior to use. The reaction requiring anhydrous conditions was performed under an argon atmosphere.

2.2. Synthesis of Me-4,4′-Bim and Et-4,4′-Bim

2.2.1. 2-Ethyl-4,5-diiodoimidazole (2)

Iodine (26.8 g, 106 mmol) was placed in a 1-L round-bottomed flask and dissolved with $CHCl_3$ (130 mL). To this solution was added 2-ethylimidazole (**1**) (5.04 g, 52.4 mmol) in 2 M NaOH aqueous solution (130 mL, 260 mmol), and the mixture was stirred at room temperature for 18 h. To the resulting mixture was added a saturated $Na_2S_2O_3$ aqueous solution (100 mL), then the $CHCl_3$ layer was separated. The aqueous layer was neutralized to pH 7 with acetic acid. The resulting solid was collected by filtration and then washed with water (100 mL), to give **2** (17.7 g, 97%) as light reddish yellow powder: R_f 0.49 (1:3 hexane/ethyl acetate); ^{1}H NMR ($CDCl_3$) δ 1.28 (t, 3H, J = 7.7 Hz), 2.78 (q, 2H, J = 7.7 Hz); IR (KBr) 3100–2300, 2974, 1550 cm^{-1}; EI-MS, *m/z* 348 (M^+, 100%).

2.2.2. 2-Ethyl-4-iodoimidazole (3)

Diiodoimidazole **2** (12.9 g, 37.1 mmol) and Na_2SO_3 (39.1 g, 310 mmol) were placed in a 2-L round-bottomed flask and suspended in 30% EtOH aqueous solution (620 mL). This mixture was refluxed for 17 h. EtOH was removed by distillation under reduced pressure. The residue was extracted with ethyl acetate (600 mL). The organic layer was washed with a saturated NaCl aqueous solution (600 mL) and dried over Na_2SO_4, then filtered and concentrated under reduced pressure to give **3** (7.39 g, 90%) as light yellow powder: m.p. 146–147 °C; R_f 0.49 (ethyl acetate); ^{1}H NMR ($CDCl_3$) δ 1.31 (t, 3H, J = 7.7 Hz), 2.78 (q, 2H, J = 7.7 Hz), 7.01 (s, 1); IR (KBr) 3100–2400, 2975, 1564 cm^{-1}; EI-MS, *m/z* 222 (M^+, 100%). *Anal.* Calc. for $C_5H_7IN_2$: C, 27.05; H, 3.18; N, 12.62. Found: C, 27.45; H, 3.13; N, 12.73%.

2.2.3. N-triphenylmethyl-2-ethyl-4-iodo-imidazole (4)

Iodoimidazole **3** (5.05 g, 22.9 mmol) and Et_3N (6.40 mL, 46.0 mmol) were dissolved in DMF (50 mL) in a 100-mL round-bottomed flask. To this solution was add TrCl (12.8 g, 45.8 mmol) and stirred at room temperature for 51 h. The resulting mixture was poured into water (100 mL) and extracted with ethyl acetate (300 mL). The organic layer was washed with a saturated NaCl aqueous solution (300 mL) and dried over Na_2SO_4, then filtered and concentrated under reduced pressure. The residue was recrystallized from ethyl acetate/ether to give **4** (5.31 g, 50%) as a white powder: m.p. 191–192 °C; R_f 0.21 (CH_2Cl_2); ^{1}H NMR ($CDCl_3$) δ 0.77 (t, 3H, J = 7.4 Hz), 1.90 (q, 4H, J = 7.4 Hz), 6.70 (s, 1), 7.07–7.18 (m, 6), 7.29–7.37 (m, 9); IR (KBr) 3160, 2986, 2966 cm^{-1}; FAB-MS, *m/z* 465 ($M^+ + 1$). *Anal.* Calc. for $C_{24}H_{21}IN_2$: C, 62.08; H, 4.56; N, 6.03. Found: C, 62.15; H, 4.47; N, 6.06%.

2.2.4. N,N′-bis(triphenylmethyl)-2,2′-diethyl-4,4′-biimidazole (5)

Tr-protected 4-iodo-imidazole **4** (1.00 g, 2.16 mmol), Et_3N (0.60 mL, 4.31 mmol) and $Pd(PPh_3)_4$ (132 mg, 0.11 mmol) were placed in a 10-mL thick-walled ampule tube and dissolved with DMF (3 mL). The reaction

mixture was degassed by a repeated freeze-pump-thaw method, then the tube was sealed. After being stirred at 110 °C for 45 h, the tube was opened at room temperature, and the precipitate was collected by filtration. The combined solid were washed with water (20 mL), ethyl acetate (10 mL) and ether (10 mL) to give **5** (394 mg, 58%) as a grayish white powder: m.p. 265–268 °C; R_f 0.62 (ethyl acetate); ^{1}H NMR ($CDCl_3$) δ 0.74 (t, 6H, J = 7.4 Hz), 1.90 (q, 4H, J = 7.4 Hz), 7.14–7.20 (m, 14 H), 7.24–7.30 (m, 18H); IR (KBr) 2922 cm^{-1}; FAB-MS, m/z 674 (M^+ + 1).

2.2.5. 2,2′-Dimethyl-4,4′-biimidazole (Me-4,4′-Bim)

Tr-protected 2,2′-dimethyl-4,4′-biimidazole (1.94 g, 3.01 mmol) and EtOH (22.5 mL) were placed in a 100-mL round-bottomed flask. To this suspension was added 1 M HCl aqueous solution (12 mL, 12 mmol) and this mixture was refluxed for 3 h. EtOH was removed by distillation under reduced pressure. Water (20 mL) was added to the residue, then filtered. The filtrate was neutralized with a saturated K_2CO_3 aqueous solution. The mixture was concentrated under reduced pressure. The residue was dissolved with EtOH (20 mL) and filtered, then the filtrate was concentrated under reduced pressure, to give Me-4,4′-Bim (403 mg, 83%) as a white powder: m.p. 260–262 °C (dec.); R_f 0.30 (MeOH); ^{1}H NMR (DMSO-d_6, 80 °C) δ 2.25 (s, 6H), 6.90 (s, 2H), 11.4 (brs, 2H); IR (KBr) 3500–2400, 3064, 1680, 1560 cm^{-1}; EI-MS, m/z 162 (M^+, 100%). *Anal.* Calc. for $C_8H_{10}N_4 \cdot (H_2O)_{0.3}$: C, 57.33; H, 6.37; N, 33.43. Found: C, 57.50; H, 6.43; N, 33.30%.

2.2.6. 2,2′-Diethyl-4,4′-biimidazole (Et-4,4′-Bim)

Following the same procedure as that for Me-4,4′-Bim, Et-4,4′-Bim was obtained as a white powder (94% yield): m.p. 269–271 °C; R_f 0.46 (MeOH); ^{1}H NMR (DMSO-d_6, 80 °C) δ 1.21 (t, 6H, J = 7.4 Hz), 2.61 (q, 4H, J = 7.4 Hz), 6.92 (s, 2H); IR (KBr) 3300–2300, 2973, 1647, 1578 cm^{-1}; EI-MS, m/z 190 (M^+, 100%). *Anal.* Calc for $C_{10}H_{14}N_4$: C, 63.13; H, 7.42; N, 29.45. Found: C, 62.97; H, 7.25; N, 29.17%.

2.3. X-ray crystallographic studies of Me-4,4′-Bim, Et-4,4′-Bim and Et-4,4′-Bim dihydrate

X-ray crystallographic measurements for single crystals were made on Rigaku Mercury CCD area detector with graphite monochromated Mo Kα radiation (λ = 0.7107 nm). All structures were determined by direct method using SHELXLS-86 and refined by least squares on F^2 with SHELXL-97. All non-hydrogen atoms were refined anisotropically and all hydrogen atoms were included but not refined. Crystal data and experimental details of the structure determination are listed in Table 1.

Table 1
Crystal data and structure refinement parameters for Me-4,4′-Bim, Et-4,4′-Bim and Et-4,4′-Bim · 2H_2O

	Me-4,4′-Bim	Et-4,4′-Bim	Et-4,4′-Bim · 2H_2O
Empirical formula	$C_8H_{10}N_4$	$C_{10}H_{14}N_4$	$C_{10}H_{18}N_4O_2$
Formula weight	162.20	190.25	226.28
Temperature (K)	200	200	200
Crystal system	trigonal	monoclinic	monoclinic
Space group	$R-3$	$C2/c$	$P2_1/c$
a (Å)	21.067(4)	15.132(2)	10.948(2)
b (Å)	21.067(4)	7.7829(9)	8.617(2)
c (Å)	4.996(1)	9.219(1)	13.171(3)
α (°)	90	90	90
β (°)	90	103.817(2)	102.724(9)
γ (°)	120	90	90
V (Å)^3	1920.2(7)	1054.3(2)	1211.9(4)
Z	9	4	4
D_{calc} (g cm^{-1})	1.262	1.199	1.240
μ (Mo Kα) (cm^{-1})	0.83	0.77	0.89
2θ Range (°)	7.8–55.0	7.1–55.0	6.0–55.0
Unique reflections	969	1127	2769
Observed data [$I > 2\sigma(I)$]	831	998	1346
Refined parameters	55	64	145
R_1, wR_2	0.070, 0.222	0.069, 0.223	0.043, 0.100
Goodness-of-fit	1.17	1.05	0.80

3. Results and discussion

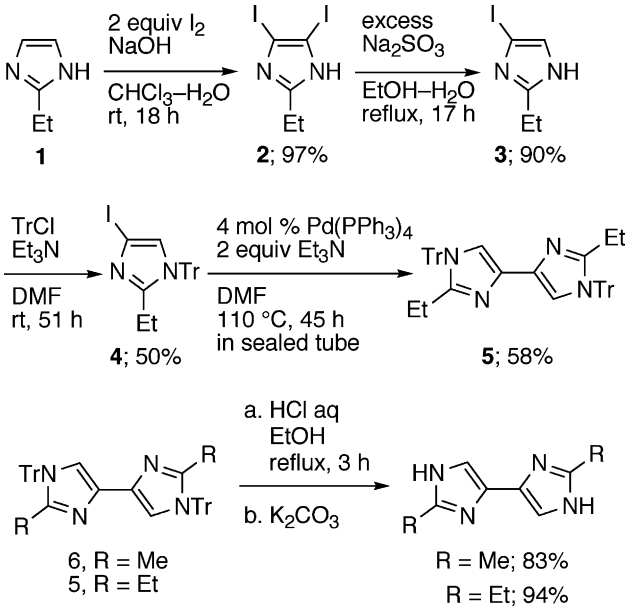
3.1. Syntheses of R-4,4′-Bim

Tr-protected Et-4,4′-Bim (**5**) were synthesized in four steps from 2-ethylimidazole (**1**) according to the procedure for Tr-protected Me-4,4′-Bim (Tr = triphenylmethyl) [11]. Imidazole **1** was converted into 2-ethyl-4-iodoimidazole (**3**) by iodination followed by the reductive removal of iodine atom at 5-position. The amino group of **3** was protected by TrCl using Et_3N, to give Tr-protected iodoimidazole **4**. Homo-coupling reaction of **4** in the presence of catalytic amount of $Pd(PPh_3)_4$ and excess amount of Et_3N in a sealed tube gave Tr-protected Et-4,4′-Bim **5**. The deprotection reaction of **5** and Tr-protected Me-4,4′-Bim **6** were carried out by the treatment with excess HCl and following neutralization using K_2CO_3, to give neutral Me- and Et-4,4′-Bim (Scheme 1). Single crystals of anhydrous Me- and Et-4,4′-Bim suitable for X-ray crystal structure analysis were obtained by vapor-diffusion method from MeOH solution using $CHCl_3$ and acetone, respectively. Dihydrate Et-4,4′-Bim was crystallized by cooling of hot aqueous solution of Et-4,4′-Bim.

3.2. Crystal structures of Me-4,4′-Bim, Et-4,4′-Bim and Et-4,4′-Bim · 2H_2O

3.2.1. Me-4,4′-Bim

Me-4,4′-Bim anhydrate crystallized in the trigonal system. The molecular structure is nearly planar with



Scheme 1.

the dihedral angle of 1.4 °, and the methyl group lies in the plane of imidazole ring (Fig. 1(a)). The molecule possesses *trans*-conformation with the inversion center on the central C–C bond. The planar molecular structure with *trans*-conformation in this crystal structure shows the resemblance to those of Me-4,4′-Bim dihydrate and trifluoroacetic acid salt [10]. Interestingly, the imidazole rings of Me-4,4′-Bim molecules are linked by direct N(1)–H···N(2) H-bondings to form a six-membered cyclic motif in each imidazole ring (Fig. 1(b)). The closest N(1)···N(2) distance is 2.85 Å, and the dihedral angle between two imidazole rings linked by the H-bond is ca. 76°. The cyclic motif stacks along the *a*-axis to construct a tube-like cavity surrounded by methyl groups with ~3 Å of diameter. The interplanar distance of the stacking is 3.5 Å, and noticeable overlap on the biimidazole skeleton is not found (Fig. 1(c)). The H-bonding interactions construct a three-dimensional network in the crystal (Fig. 1(d)).

3.2.2. Et-4,4′-Bim

In the crystal structure of Et-4,4′-Bim anhydrate, one imidazole-ring and ethyl group are crystallographically independent. Similar to the molecular structure of Me-4,4′-Bim, Et-4,4′-Bim possesses the nearly planar molecular structure (dihedral angle of 1.3°) and the *trans*-conformation (Fig. 2(a)). The hydrogen atoms of N–H groups (H1a and H1b) are positionally disordered

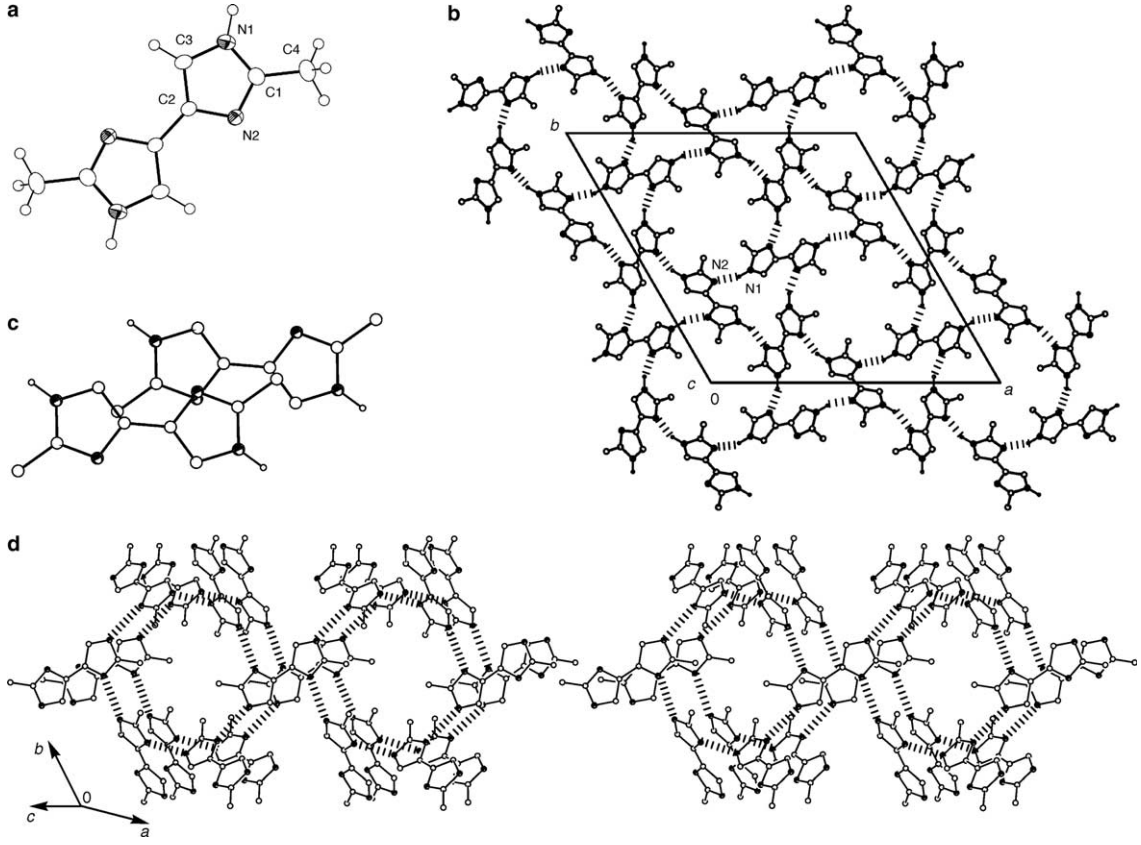


Fig. 1. Crystal structure of Me-4,4′-Bim. ORTEP view of the molecular structure, showing the atomic labelling scheme (a). Perspective view along the *c*-axis, showing the H-bonded cyclic motifs and cavity (b). Overlap mode in a stacking structure (c). Stereoview of the crystal packing, showing the three-dimensional H-bonded network (d). Dotted lines show the H-bonding interactions. H-bonding distances (D···A in Å): N(1)···N(2), 2.85.

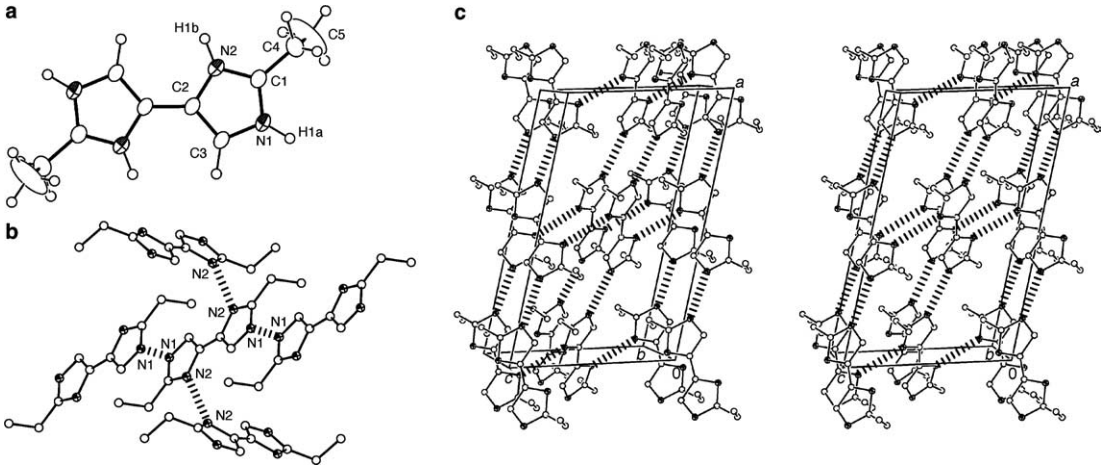


Fig. 2. Crystal structure of Et-4,4′-Bim. ORTEP view of the molecular structure, showing the atomic labelling scheme (a). Partial packing of Et-4,4′-Bim, illustrating the H-bonding scheme (b). Stereoview of the crystal packing, showing the three-dimensional H-bonded network (c). The hydrogen atoms of N–H groups (H1a and H1b) were located and refined as half-occupancy atoms. Dotted lines show the H-bonding interactions. H-bonding distances (D···A in Å): N(1)···N(1), 2.81; N(2)···N(2), 2.92.

and were treated as half occupancy atoms during refinement (Fig. 2(a)). In this structure, two types of H-bonding interaction are observed (Fig. 2(b)). One is N(1)–H···N(1) interaction which connect Et-4,4′-Bim molecules along the [1 1 0] and [−1 1 0] directions. The other is N(2)–H···N(2) interaction elongated along the

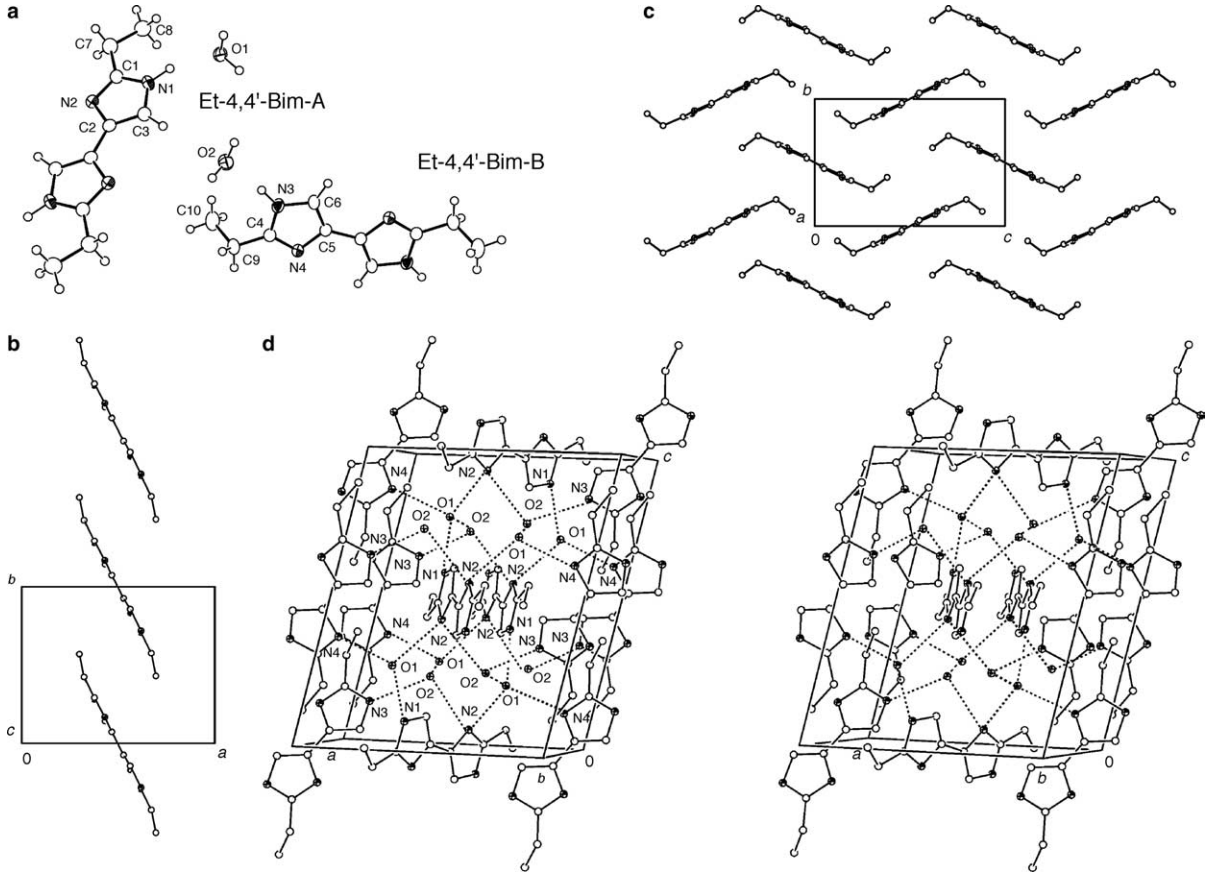


Fig. 3. Crystal structure of Et-4,4′-Bim · $2H_2O$. ORTEP view of the molecular structure, showing the atomic numbering scheme (a). Stacking structure of Et-4,4′-Bim-B molecules viewed along the *c*-axis (b). Arrangement of Et-4,4′-Bim-B molecules in the *bc* plane (c). Stereoview of the crystal packing, showing the H-bonding interactions and a channel structure (d). Dotted lines show the H-bonding interactions. H-bonding distances (D···A in Å): N(1)···O(1), 2.87; N(2)···O(1), 2.94; N(2)···O(2), 2.98; N(3)···O(2), 2.88; N(4)···O(1), 2.79; O(1)···O(2), 2.89.

a-axis. The distances of N(1)–H···N(1) and N(2)–H···N(2) H-bondings are 2.81 and 2.92 Å, respectively. Neighboring Et-4,4′-Bim molecules linked by N(1)–H···N(1) H-bonding are parallel, while dihedral angle between those linked by N(2)–H···N(2) H-bonding 82° (Fig. 2(b)). These H-bonding interactions build up a three-dimensional network (Fig. 2(c)). Notably, the formation of H-bonding interactions between same kinds of nitrogen atoms is the most noticeable difference with the H-bonding nature of Me-4,4′-Bim in which the H-bonding is formed between different nitrogen atoms, N(1) and (2).

3.2.3. Et-4,4′-Bim · $2H_2O$

With in a unit cell, there are two crystallographically independent Et-4,4′-Bim (Et-4,4′-Bim-A and -B) and water molecules. Both of Et-4,4′-Bim-A and -B molecules possess the inversion centers on central C–C bonds (Fig. 3(a)). Their planar structures with *trans*-conformation is similar to that shown in the crystal structure of Et-4,4′-Bim anhydrate. The Et-4,4′-Bim-A molecule stacks with 3.9 Å of face-to-face distance to form columnar structure parallel to the *b*-axis (Fig. 3(b)). Within this column, noticeable overlap is not found. On the other hand, Et-4,4′-Bim-B molecules are arranged in herringbone structure along the *bc* plane (Fig. 3(c)). In contrast to the formation of direct N–H···N H-bonding in anhydrous Et-4,4′-Bim, all nitrogen atoms on Et-4,4′-Bim molecules of this crystal form H-bondings with water molecules. These H-bonding interactions through water molecules connect Et-4,4′-Bim molecules, resulting in the construction of three-dimensional H-bonded network (Fig. 3(d)). In addition to these structural features, a channel structure parallel to the *b*-axis was observed in this crystal structure, which is fulfilled by the water molecules (Fig. 3(d)).

4. Conclusion

The synthesis and crystal structural analysis of new 4,4′-Bim derivative, Et-4,4′-Bim, including its dihydrate were demonstrated. Furthermore, we revealed the characteristic H-bonded structure of anhydrous Me-4,4′-Bim. In these crystal structures, the difference of alkyl-substituent strongly affects the H-bonding pattern, N(1)···N(2) in anhydrate Me-4,4′-Bim, and N(1)···N(1) and N(2)···N(2) in anhydrate Et-4,4′-Bim. In the crystal structure of dihydrate Et-4,4′-Bim, including of water molecules prevented the formation of direct N–H···N H-bondings and changed the H-bonded network and molecular packing. The construction of channel structures of anhydrate Me-4,4′-Bim and dihydrate Et-4,4′-Bim shows their potential to bind small guest molecules. These observations indicate that 4,4′-Bim system is useful and interesting ligands of assembled metal complexes and component molecule of H-bonded charge-transfer complexes exhibiting interesting conducting, magnetic and host–guest properties based on the characteristic H-bonding structures. Further studies on 2,2′-substituted-4,4′-Bim system is in progress for the construction of their assembled metal complexes and CT complexes.

5. Supplementary material

Crystallographic data for the structural analysis have been deposited with Cambridge Crystallographic Data Centre, CCDC Reference Nos. 250710–250712. Copies of this information may be obtained free of charge from The Director, CCDC, 12 Union Road, Cambridge CB2 1EZ, UK (fax: +44 1233 336 033; e-mail: deposit@ccdc.cam.ac.uk or http://www.ccdc.cam.ac.uk).

Acknowledgments

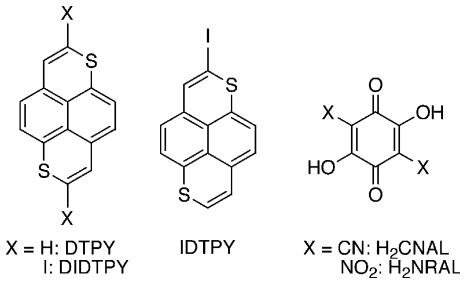
This work was partially supported by a Grant-in-Aid for Scientific Research (No. 16350074) from the Ministry of Education, Culture, Sports, Science, and Technology, Japan, by PRESTO-JST, by a grant of The Asahi Glass Foundation and by 21COE program "Creation of Integrated EcoChemistry of Osaka University".

References

[1] (a) J.-M. Lehn, Supramolecular Chemistry: Concepts and Perspective, VCH, Weinheim, 1995;
(b) J.W. Steed, J.L. Atwood, Supramolecular Chemistry, Wiley, Chichester, 2000.
[2] K. Nakasuji, K. Sugiura, T. Kitagawa, J. Toyoda, H. Okamoto, K. Okaniwa, T. Mitani, H. Yamamoto, I. Murata, A. Kawamoto, J. Tanaka, J. Am. Chem. Soc. 113 (1991) 1862.
[3] (a) K. Tamaki, Y. Morita, J. Toyoda, H. Yamochi, G. Saito, K. Nakasuji, Tetrahedron Lett. 38 (1997) 4583;
(b) Y. Morita, E. Miyazaki, T. Yokoyama, T. Kubo, E. Mochizuki, Y. Kai, K. Nakasuji, Synth. Met. 135–136 (2003) 617;
(c) Y. Morita, T. Murata, K. Tamaki, H. Yamochi, G. Saito, K. Nakasuji, Synth. Met. 135–136 (2003) 657;
(d) Y. Morita, S. Maki, M. Ohmoto, H. Kitagawa, T. Okubo, T. Mitani, K. Nakasuji, Org. Lett. 4 (2002) 2185;
(e) T. Murata, Y. Morita, K. Fukui, K. Sato, D. Shiomi, T. Takui, M. Maesato, H. Yamochi, G. Saito, K. Nakasuji, Angew. Chem. Int. Ed. 43 (2004) 6343;
(f) M.B. Zaman, Y. Morita, J. Toyoda, H. Yamochi, G. Saito, N. Yoneyama, T. Enoki, K. Nakasuji, Chem. Lett. 26 (1997) 729;
(g) M.B. Zaman, J. Toyoda, Y. Morita, S. Nakamura, H. Yamochi, G. Saito, K. Nishimura, N. Yoneyama, T. Enoki, K. Nakasuji, J. Mater. Chem. 11 (2001) 2211.
[4] (a) M. Mitsumi, J. Toyoda, K. Nakasuji, Inorg. Chem. 34 (1995) 3367;
(b) H. Kitagawa, T. Mitani, T. Itoh, J. Toyoda, K. Nakasuji, Synth. Met. 71 (1995) 1919;
(c) T. Itoh, J. Toyoda, M. Tadokoro, H. Kitagawa, T. Mitani, K. Nakasuji, Chem. Lett. 24 (1995) 41.

[5] (a) D.T. Cromer, R.R. Ryan, C.B. Storm, Acta Crystallogr. C 43 (1987) 1435;
(b) S. Bélanger, A.L. Beauchamp, Acta Crystallogr. C 52 (1996) 2588;
(c) W.E. Allen, C.J. Fowler, V.M. Lynch, J.L. Sessler, Chem. Eur. J. 7 (2001) 721;
(d) K. Ramírez, J.A. Reyes, A. Briceño, R. Atencio, Crystengcomm 4 (2002) 218.
[6] T. Akutagawa, G. Saito, M. Kusunoki, K. Sakaguchi, Bull. Chem. Soc. Jpn. 69 (1996) 2487.
[7] (a) K.D. Benkstein, J.T. Hupp, C.L. Stern, Angew. Chem. Int. Ed. 39 (2000) 2891;
(b) M. Tadokoro, K. Nakasuji, Coord. Chem. Rev. 198 (2000) 205;
(c) M. Tadokoro, H. Kanno, T. Kitajima, H.-S. Umemoto, N. Nakanishi, K. Isobe, K. Nakasuji, Proc. Natl. Acad. Sci. USA 99 (2002) 4950;
(d) J. Ramón, G. Mascarós, K.R. Dunbar, Angew. Chem. Int. Ed. 42 (2003) 2289.
[8] Y. Morita, T. Murata, S. Yamada, M. Tadokoro, A. Ichimura, K. Nakasuji, J. Chem. Soc., Perkin Trans. 1 (2002) 2598.
[9] Y. Morita, T. Murata, K. Fukui, M. Tadokoro, K. Sato, D. Shiomi, T. Takui, K. Nakasuji, Chem. Lett. 33 (2004) 188.
[10] W. Zhang, C.P. Landee, R.D. Willett, M.M. Turnbull, Tetrahedron 59 (2003) 6027.
[11] M.D. Cliff, S.G. Pyne, Synthesis (1994) 681.

optical and electric properties and crystal structures of IDTPY itself, H_2NRAL complex with a diaqua oxonium ($H_5O_2^+$) and NO_3^- salt of IDTPY.



2. Experimental

2.1. Materials and methods

IDTPY was synthesized according to our previous report [7]. Chlorobenzene used for electrooxidation was distilled over CaH_2. All chemicals were of reagent grade and used without further purification. Infrared and electronic spectra were recorded using KBr pellets on Perkin–Elmer 1600 series FT-IR and Shimadzu UV-3100PC, respectively. The alternating current electric conductivity measurements for compressed pellets were performed by a conventional two-probe method using gold paint and Au wire (25 μm ∅). Melting points were measured by a Yanaco micro melting point apparatus and were uncorrected. Elemental analyses were performed at the Analytical Center of Graduate School of Science, Osaka University.

2.2. General procedure for syntheses of the CT complexes of IDTPY

IDTPY was placed in a 20-mL round-bottomed flask and dissolved with CH_2Cl_2. To this solution was added the CH_2Cl_2 solution of acceptor, and the resulting precipitates were collected.

2.2.1. IDTPY–DDQ complex

Dark violet powder. m.p. 218–219 °C (dec); IR (KBr) 2212, 1560, 1515, 1472 cm^{-1}; UV (KBr) 1252, 532 nm; *Anal*. Calc. for $(C_{14}H_7S_2I)(C_8N_2O_2Cl_2)$: C, 44.54; H, 1.19; N, 4.72. Found; C, 44.87; H, 1.23; N, 5.16%.

2.2.2. IDTPY–$(H_2CNAL)_{1.5}$ complex

Dark violet powder. m.p. 238–240 °C (dec); IR (KBr) 2227, 2212, 1540, 1516, 1472 cm^{-1}; UV (KBr) 1246, 538, 268 nm; *Anal*. Calc. for $(C_{14}H_7S_2I)(C_8H_2N_2O_4)_{1.5}$: C, 47.94; H, 1.55; N, 6.45. Found: C, 47.85; H, 1.59; N, 6.33%.

2.2.3. $IDTPY^{\bullet+} \cdot NRAL^{2-} \cdot H_5O_2^+$ complex

Dark green microcrystals. m.p. 133–135 °C (dec); IR (KBr) 1560, 1514, 1472 cm^{-1}; UV (KBr) 1058, 544, 240 nm; *Anal*. Calc. for $(C_{14}H_7S_2I)(C_6N_2O_8)(H_5O_2)$: C, 38.05; H, 1.92; N, 4.44. Found: C, 38.25; H, 1.86; N, 4.80%.

2.3. Synthesis of the $IDTPY^{\bullet+} \cdot NO_3^-$ salt

IDTPY (7.3 mg, 0.020 mmol) was placed in a 20-mL round-bottomed flask and dissolved with chlorobenzene (10 mL). To this solution was added $Bu_4N^+NO_3^-$ (18.3 mg, 0.060 mmol) and transferred to a 10-mL V-shape tube. Electrooxidation was conducted under constant current of 3 μA for 10 days at room temperature, to give the $IDTPY^{\bullet+} \cdot NO_3^-$ salt (3.7 mg) as black microblocks. mp 154–156 °C (dec); IR (KBr) 1678, 1552, 1515, 1476 cm^{-1}; UV (KBr) 1158, 542 nm; *Anal*. Calc. for $(C_{14}H_7S_2I)(NO_3)$: C, 39.27; H, 1.65; N, 3.27. Found; C, 40.02; H, 1.79; N, 3.00%.

2.4. X-ray structure analyses of IDTPY, $IDTPY^{\bullet+} \cdot NRAL^{2-} \cdot H_5O_2^+$ complex, and $IDTPY^{\bullet+} \cdot NO_3^-$ salt

Single crystals of IDTPY suitable for X-ray analysis were obtained by slow evaporation of its CH_2Cl_2 solution at room temperature. X-ray data of IDTPY and $IDTPY^{\bullet+} \cdot NO_3^-$ were collected on a Rigaku/MSC Mercury CCD with graphite monochromated Mo Kα ($\lambda = 0.71070$ Å) radiation. Crystallographic measurement for $IDTPY^{\bullet+} \cdot NRAL^{2-} \cdot H_5O_2^+$ was made on Rigaku RAXIS-RAPID Imaging Plate with graphite monochromated Mo Kα ($\lambda = 0.71075$ Å) radiation. The structures were solved by direct methods using SIR92 [10] for IDTPY and $IDTPY^{\bullet+} \cdot NO_3^-$, and SHELXS-86 [11] for $IDTPY^{\bullet+} \cdot NRAL^{2-} \cdot H_5O_2^+$, and refined by full-matrix least squares methods based on F^2. The non-hydrogen atoms were refined anisotropically. The crystallographic data are summarized in Table 1. The extent of disorder in the $IDTPY^{\bullet+} \cdot NO_3^-$ salt was determined by refining the site occupancies of the I1, I2, S1, S2, C2 and C8 sites which were at averaged positions as follows: 50.4 electrons at I1, 2.6 electrons at I2, 14 electrons at S1 and S2, and 10 electrons at C2 and C8.

3. Results and discussion

3.1. Syntheses of CT complexes and salt of IDTPY

The CT complexes of IDTPY with DDQ, H_2CNAL and H_2NRAL were synthesized by the mixed method. The $IDTPY^{\bullet+} \cdot NO_3^-$ salt was prepared and crystallized by the electrooxidation in a chlorobenzene solution under a constant current of 3 μA. The molecular ratios of

Table 1
Crystallographical data for IDTPY, $IDTPY^{\bullet+} \cdot NRAL^{2-} \cdot H_5O_2^+$ complex and $IDTPY^{\bullet+} \cdot NO_3^-$ salt

Compound	IDTPY	$IDTPY^{\bullet+} \cdot NRAL^{2-} \cdot H_5O_2^+$	$IDTPY^{\bullet+} \cdot NO_3^-$
Formula	$C_{14}H_7S_2I$	$C_{20}H_{12}O_{10}N_2S_2I$	$C_{14}H_7O_3NS_2I$
Formula weight	366.23	631.35	428.24
Crystal size (mm)	$0.12 \times 0.05 \times 0.01$	$0.15 \times 0.11 \times 0.06$	$0.15 \times 0.05 \times 0.02$
Crystal system	monoclinic	triclinic	triclinic
Space group	$P2_1/c$	$P\bar{1}$	$P\bar{1}$
Unit cell dimensions			
a (Å)	4.1167(9)	9.167(8)	7.249(2)
b (Å)	14.799(4)	9.088(9)	9.353(4)
c (Å)	19.997(5)	12.83(2)	10.931(1)
α (°)		90.41(3)	69.81(4)
β (°)	94.996(9)	101.70(3)	75.93(5)
γ (°)		103.69(3)	89.63(6)
V (Å^3)	1213.7(5)	1014(6)	672.3(4)
Z	4	2	2
D_{calc} (g cm^{-3})	2.004	2.066	2.115
T (K)	200	150	200
μ(Mo Kα) (mm^{-1})	2.954	1.852	2.701
Number of reflections collected	11960	9545	8934
Number of independent reflections	1130[a]	2887[a]	2135[b]
Number of parameters refined	154	316	200
Final R indices	$R_1 = 0.058$, $wR_2 = 0.094$	$R_1 = 0.068$, $wR_2 = 0.217$	$R_1 = 0.071$, $wR_2 = 0.162$
Goodness-of-fit	0.95	1.05	1.02

[a] $I > 2.0\sigma(I)$.
[b] $I > 1.0\sigma(I)$.

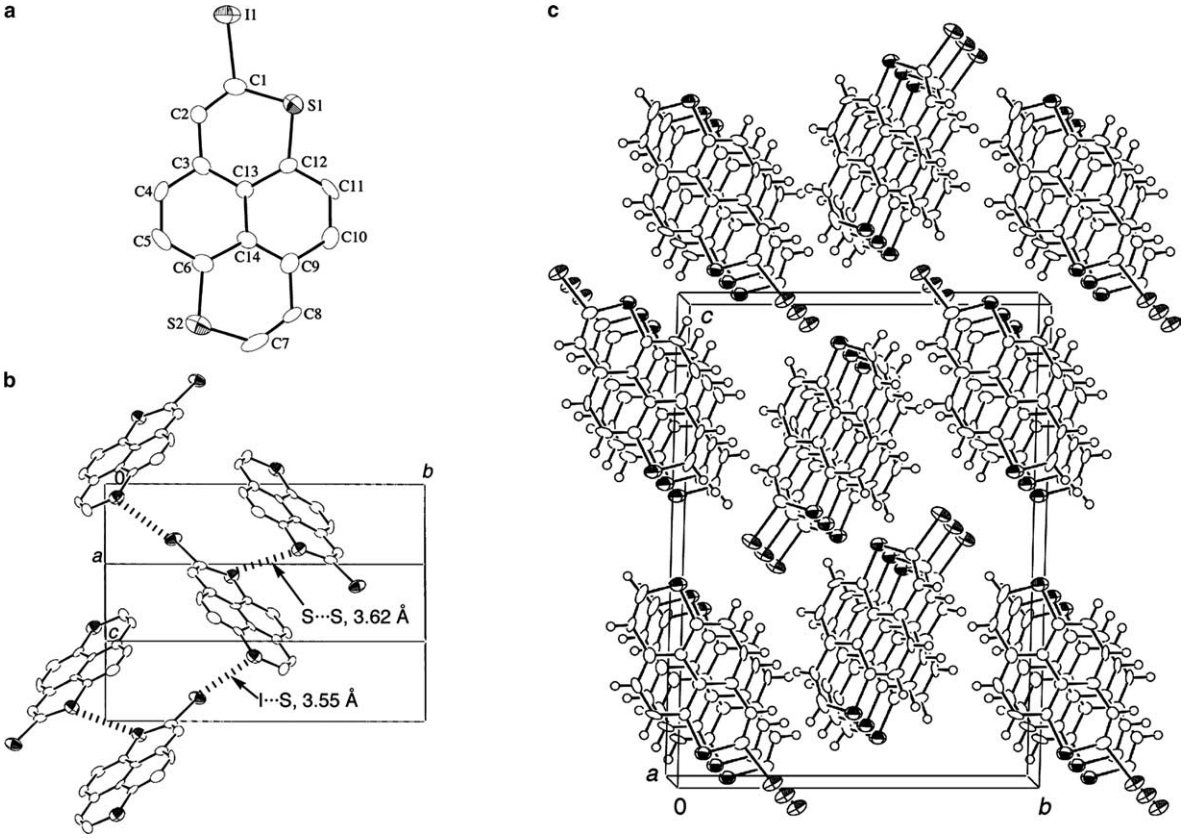


Fig. 1. Crystal structure of IDTPY. Molecular structure of IDTPY with atomic numbering (a), intermolecular strong I···S (3.55 Å) and weak S···S (3.62 Å) interactions (b), and packing diagram along the *a*-axis (c). Hydrogen atoms in (a) and (b) are omitted for clarity.

donor and acceptor of their CT complexes and salt were determined by elemental analyses and X-ray analyses.

3.2. X-ray diffraction studies of IDTPY, $IDTPY^{\bullet+}\cdot NRAL^{2-}\cdot H_5O_2^{+}$ and $IDTPY^{\bullet+}\cdot NO_3^{-}$

3.2.1. Crystal structure of IDTPY

IDTPY crystallizes in a monoclinic system, $P2_1/c$. A crystal structure of IDTPY was shown in Fig. 1. There are intermolecular strong I···S (3.55 Å) and weak S···S (3.62 Å) interactions within the sum of van der Waals radii (3.78 and 3.60 Å, respectively), forming the two-dimensional sheet structure through these interactions (Fig. 1(b)). IDTPY forms a uniform columnar structure along the *a*-axis with an interplanar distance of 3.5 Å (Fig. 1(c)). These non-covalent interactions such as halogen-bonding and π···π interaction shown in the crystal of IDTPY were also observed in that of DIDTPY [7].

3.2.2. Crystal structure of $IDTPY^{\bullet+}\cdot NRAL^{2-}\cdot H_5O_2^{+}$

The CT complex crystallizes in a triclinic system, $P\bar{1}$. The H_2NRAL complex of IDTPY with $H_5O_2^{+}$ is composed of $IDTPY^{\bullet+}$, $NRAL^{2-}$, and $H_5O_2^{+}$ in 1:1:1 ratio (Fig. 2(a)). In bond distances of the IDTPY molecule, S(1)–C(1) and C(12)–S(1) bonds are shortened by 0.05 Å, and C(1)–C(2) and C(2)–C(3) bonds are elongated by 0.02–0.06 Å compared with those of IDTPY (Tables 2 and 3), indicating that an ionicity of IDTPY is +1 [6b]. Furthermore, a very strong hydrogen-bond-

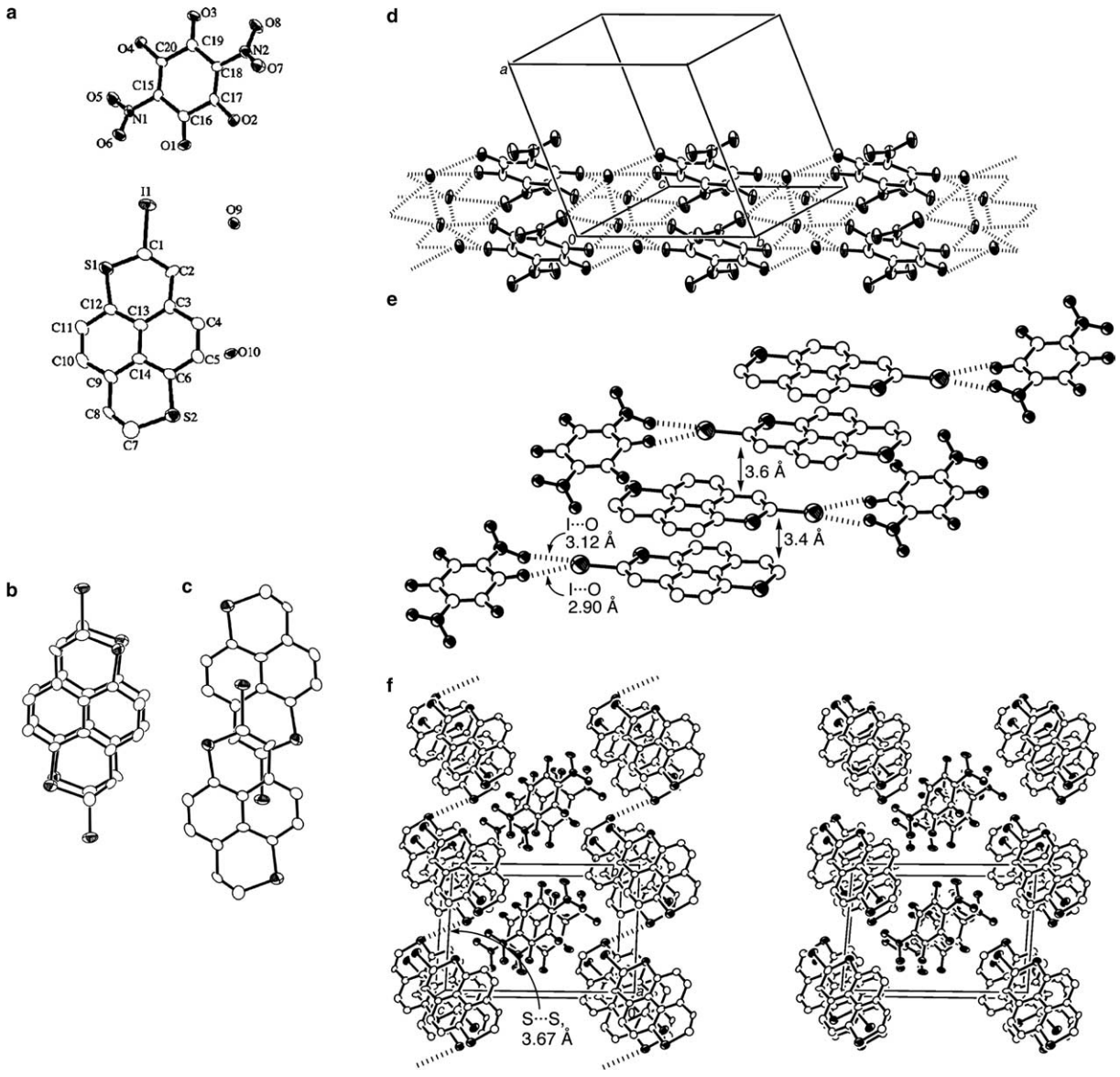


Fig. 2. Crystal structure of $IDTPY^{\bullet+}\cdot NRAL^{2-}\cdot H_5O_2^{+}$. Atomic numbering (a), overlap modes of intradimer and interdimer of $IDTPY^{\bullet+}$ ((b) and (c)), hydrogen-bonded chain structure through $H_5O_2^{+}$ and $NRAL^{2-}$ (d), I···O interactions between $IDTPY^{\bullet+}$ and $NRAL^{2-}$ (e), and the stereo view along the *a*-axis (f). Hydrogen atoms and $H_5O_2^{+}$ (in (e) and (f)) are omitted for clarity.

Table 2
Selected bond distances (Å) for IDTPY

Bond distances (Å)	
C(12)–S(1)	1.77(1)
S(1)–C(1)	1.75(1)
C(1)–C(2)	1.33(1)
C(2)–C(3)	1.47(2)
C(6)–S(2)	1.77(1)
S(2)–C(7)	1.71(1)
C(7)–C(8)	1.34(2)
C(8)–C(9)	1.48(2)
C(1)–I(1)	2.08(1)

Table 3
Selected bond distances (Å) for $IDTPY^{\bullet+} \cdot NRAL^{2-} \cdot H_5O_2^+$

Bond distances (Å)	
C(12)–S(1)	1.717(10)
S(1)–C(1)	1.700(9)
C(1)–C(2)	1.39(1)
C(2)–C(3)	1.49(1)
C(6)–S(2)	1.737(10)
S(2)–C(7)	1.843(9)
C(7)–C(8)	1.18(1)
C(8)–C(9)	1.50(1)
C(1)–I(1)	2.076(10)

ing (O···O distance, 2.43 Å) observed between crystal waters suggests the existence of $H_5O_2^+$ [12]. Considering molecular ratio of these components, the ionicity of the H_2NRAL moiety is determined as −2.

A dimeric structure of $IDTPY^{\bullet+}$ with intra- and interdimer distances of 3.4 and 3.6 Å is formed in the crystal (Fig. 2(b) and (c)). Multiple hydrogen-bondings (2.73–2.85 Å) between $H_5O_2^+$ and $NRAL^{2-}$ molecules, and dimeric pair of $NRAL^{2-}$ molecules with an intradimer distance of 3.4 Å were constructed, resulting in the formation of one-dimensional chain structure along the *b*-axis (Fig. 2(d)). There are two short I···O contacts (2.90 and 3.12 Å) between $IDTPY^{\bullet+}$ and $NRAL^{2-}$ molecules (Fig. 2(e)). The dimer of $IDTPY^{\bullet+}$ was connected with a weak S···S interaction (3.67 Å) along the *b*-axis (Fig. 2(f)). These π···π, I···O and S···S interactions might hamper the alternated stacking motif.

3.2.3. Crystal structure of the $IDTPY^{\bullet+} \cdot NO_3^-$

In the NO_3^- salt of IDTPY, a molecular ratio of donor and counter anion is 1:1, indicating that an ionicity of IDTPY is +1. $IDTPY^{\bullet+} \cdot NO_3^-$ crystallizes in a

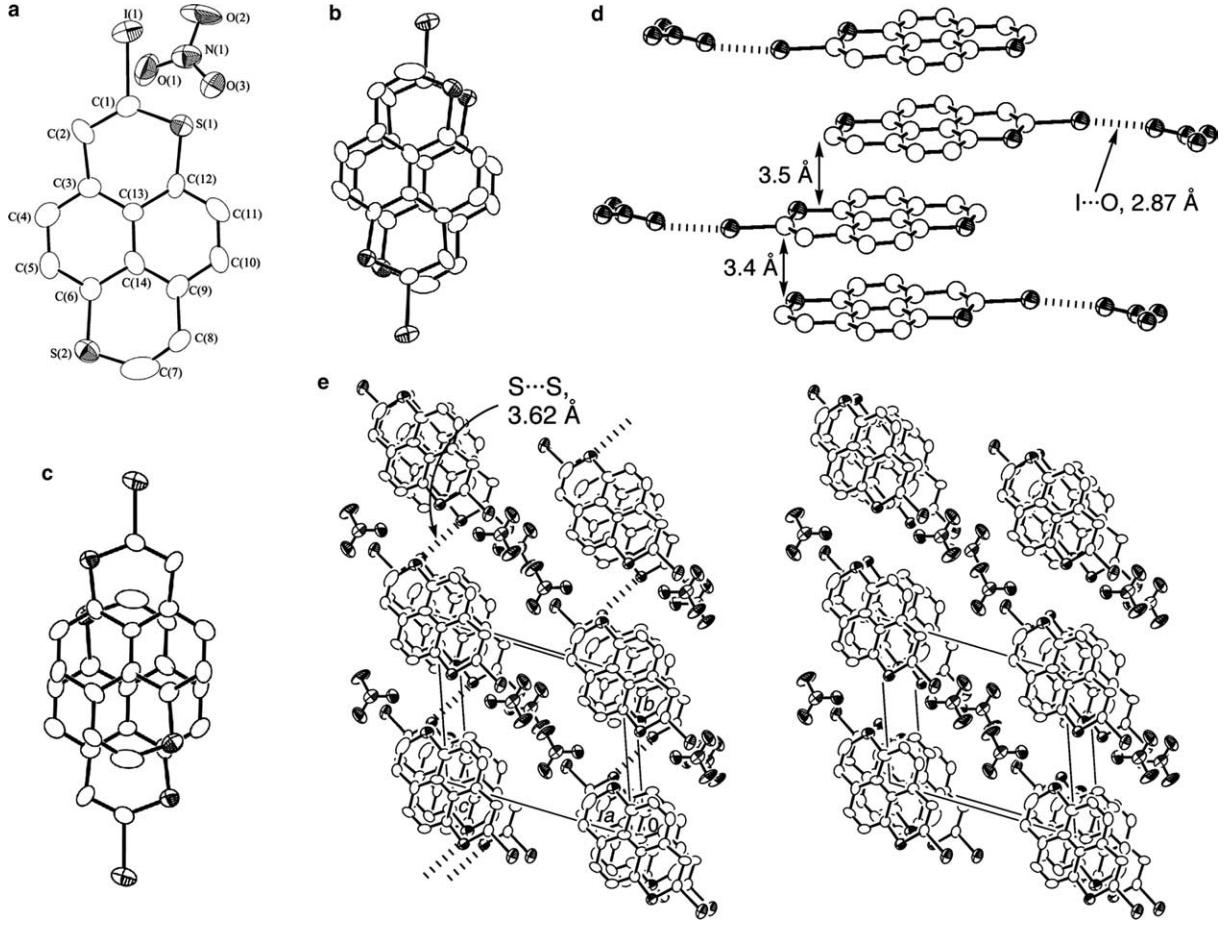


Fig. 3. Molecular structure of $IDTPY^{\bullet+} \cdot NO_3^-$ with atomic numbering (a), overlap modes of intradimer and interdimer of $IDTPY^{\bullet+}$ ((b) and (c), respectively), columnar stacking structure of $IDTPY^{\bullet+}$ and short I···O interaction between $IDTPY^{\bullet+}$ and NO_3^- (d), and packing diagram along the *a*-axis (e). Hydrogen and disordered iodine (except for (a)) atoms are omitted for clarity.

Table 4
Selected physical data for CT complexes and salt of IDTPY

	IDTPY–DDQ	IDTPY–$(H_2CNAL)_{1.5}$	$IDTPY^{\bullet+} \cdot NRAL^{2-} \cdot H_5O_2^+$	$IDTPY^{\bullet+} \cdot NO_3^-$
ν_{CN} (cm^{-1})	2212	2212, 2227		
CT band (cm^{-1})	8000	8000	9500	8600
σ_{rt} (S cm^{-1})	8.7×10^{-4}	4.9×10^{-4}	7.3×10^{-6}	1.5×10^{-2}
E_a (meV)	189	240	397	123

triclinic system, $P\bar{1}$. Iodine (I1, I2), sulfur (S1, S2) and carbon (C2, C8) atoms of $IDTPY^{\bullet+}$ are disordered by the ratio of 95:5 (in I1 and I2) and 3:1 (in S1 and C2, S2 and C8), respectively (Fig. 3(a)). $IDTPY^{\bullet+}$ forms a columnar structure with a dimeric pair of $IDTPY^{\bullet+}$ with intradimer and interdimer distance of 3.4 and 3.5 Å, respectively (Fig. 3(b)–(d)). There is a short I···O contact (2.87 Å) between $IDTPY^{\bullet+}$ and NO_3^- (Fig. 3(d)). Furthermore, a weak S···S interaction (3.62 Å) between columns of $IDTPY^{\bullet+}$ was shown, resulting in the construction of a two-dimensional sheet structure (Fig. 3(e)).

3.3. Optical properties

In order to elucidate and characterize electronic structures of the CT complexes and salt of IDTPY, we measured infrared and electronic spectra in KBr pellets. In the infrared spectra of the IDTPY–$(H_2CNAL)_{1.5}$ complex, nitrile stretching frequencies due to H_2CNAL moieties were observed at 2212 and 2227 cm^{-1} (Table 4), suggesting the co-existence of two chemical species of $HCNAL^-$ and H_2CNAL.[1] In the IDTPY–DDQ complex, the CN stretching frequency of 2212 cm^{-1} indicates a completely charge-transfered ionic nature of this complex [13].

Electronic spectra of these CT complexes and salt were shown in Fig. 4. An intramolecular transition due to $IDTPY^{\bullet+}$ was shown at 18 000 cm^{-1} in the electronic spectrum of IDTPY–DDQ (Fig. 4(a)). In other CT complexes and salt of IDTPY, the strong absorptions (18000 cm^{-1}) due to the intramolecular transition of $IDTPY^{\bullet+}$ (Fig. 4(b)–(d)) suggest that ionicities of IDTPY moieties were to be +1. In the H_2NRAL complex and NO_3^- salt of IDTPY, CT bands due to the intradimer transitions of the $IDTPY^{\bullet+}$ dimer were observed around 8000–9500 cm^{-1} (Table 4 and Fig. 4(c) and (d)). In other CT complexes of IDTPY, CT bands were measured around 8000 cm^{-1}, which might be assignable to the CT transition between donors, or donor and acceptor (Fig. 4(a) and (b)).

[1] In the IR spectra, the nitrile stretching frequencies due to $Bu_4N^+ \cdot HCNAL^-$ and $H_2CNAL \cdot 6H_2O$ are observed at 2206 and 2236 cm^{-1}, respectively. See also [4a].

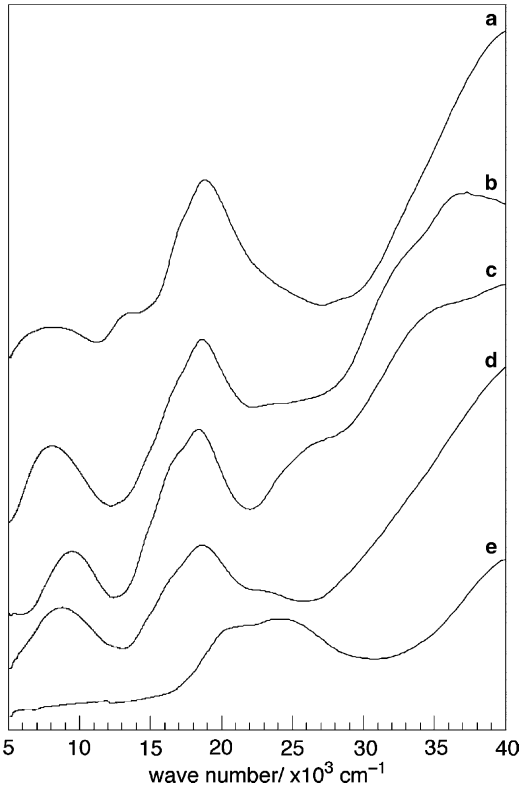


Fig. 4. Electronic spectra of IDTPY–DDQ (a), IDTPY–$(H_2CNAL)_{1.5}$ (b), $IDTPY^{\bullet+} \cdot NRAL^{2-} \cdot H_5O_2^+$ (c), $IDTPY^{\bullet+} \cdot NO_3^-$ (d) and IDTPY (e) in KBr pellets.

3.4. Electric conductivities

Electric conductivities of the CT complexes and salt of IDTPY were measured by two-probe method in compressed pellets. Their room temperature electric conductivities (σ_{rt}) and activation energies (E_a) are summarized in Table 4. These CT complexes and salt were semiconductors with 1.5×10^{-2}–7.3×10^{-6} S cm^{-1}.

4. Conclusion

The new CT complexes and salt of IDTPY with DDQ, H_2CNAL, $NRAL^{2-}$ and NO_3^- were synthesized. These CT complexes and salt with CT bands around 8000–9500 cm^{-1} were semiconductors. We demonstrated that strong intermolecular halogen-bondings through the iodine atom of IDTPY played an important

role in the formation of multi-dimensional structures of IDTPY, $IDTPY^{\bullet+} \cdot NRAL^{2-} \cdot H_5O_2^{+}$ and $IDTPY^{\bullet+} \cdot NO_3^{-}$. These results urge us to synthesize further DTPY derivatives with an iodine atom and to explore their CT complexes and salts, which contributes to not only the conductive materials science but also supramolecular chemistry.

5. Supplementary data

Crystallographic data for the structural analyses has been deposited with the Cambridge Crystallographic Data center, CCDC Nos. 251160–251162 for IDTPY, $IDTPY^{\bullet+} \cdot NRAL^{2-} \cdot H_5O_2^{+}$ and $IDTPY^{\bullet+} \cdot NO_3^{-}$. Copies of these informations may be obtained free of charge from The Director, CCDC, 12 Union Road, Cambridge CB2 IEZ, UK (fax: +44 1223 336 033; e-mail: deposit@ccdc.cam.ac.uk or http://www.ccdc.cam.ac.uk).

Acknowledgements

This work was partially supported by PRESTO-JST, Grant-in-Aid for Scientific Research (No. 16350074) from the Ministry of Education, Culture, Sports, Science, and Technology, Japan, 21COE program "Creation of Integrated EcoChemistry of Osaka University", and by a grant of The Asahi Glass Foundation.

References

[1] For recent overviews of organic conductor and superconductor based on a TTF skeleton, see:
(a) T. Ishiguro, K. Yamaji, G. Saito, Organic Superconductors, second ed., Springer, Tokyo/Berlin, 1998;
(b) J. Yamada, T. Sugimoto, TTF Chemistry: Fundamentals and Applications of Tetrathiafulvalene, Kodansha/Springer, Tokyo, 2004.

[2] Organic conductors of TTF derivatives with hydrogen-bonding, see:
(a) A. Dolbecq, M. Fourmigué, P. Batail, Chem. Mater. 6 (1994) 1413;
(b) A.J. Moore, M.R. Bryce, A.S. Batsanov, J.N. Heaton, C.W. Lehmann, J.A.K. Howard, N. Bobertson, A.E. Underhill, I.F. Perepichka, J. Mater. Chem. 8 (1998) 1541;
(c) G. Ono, A. Izuoka, T. Sugawara, Y. Sugawara, J. Mater. Chem. 8 (1998) 1703;
(d) K. Balodis, S. Khasanov, C. Chong, M. Maesato, H. Yamochi, G. Saito, O. Neilands, Synth. Met. 133–134 (2003) 353.

[3] Organic conductors of TTF derivatives with halogen-bonding, see:
(a) T. Imakubo, H. Sawa, R. Kato, Synth. Met. 73 (1995) 117;
(b) M. Iyoda, H. Suzuki, S. Sasaki, H. Yoshino, K. Kikuchi, K. Saito, I. Ikemoto, H. Matsuyama, T. Mori, J. Mater. Chem. 6 (1996) 501;
(c) H.M. Yamamoto, J.-I. Yamaura, R. Kato, J. Am. Chem. Soc. 120 (1998) 5905;
(d) T. Devic, M. Evain, Y. Moëlo, E. Canadell, P. Auban-Senzier, M. Fourmigué, P. Batail, J. Am. Chem. Soc. 125 (2003) 3295.

[4] Our recent studies on the TTF chemistry with hydrogen-bonded functionalities, see:
(a) Y. Morita, S. Maki, M. Ohmoto, H. Kitagawa, T. Okubo, T. Mitani, K. Nakasuji, Org. Lett. 4 (2002) 2185;
(b) Y. Morita, S. Maki, M. Hori, M. Ohmoto, E. Mochizuki, Y. Kai, H. Kitagawa, T. Mitani, K. Nakasuji, Synth. Met. 135–136 (2003) 537;
(c) Y. Morita, S. Maki, M. Ohmoto, H. Kitagawa, T. Okubo, T. Mitani, K. Nakasuji, Synth. Met. 135–136 (2003) 541;
(d) T. Murata, Y. Morita, K. Fukui, K. Sato, D. Shiomi, T. Takui, M. Maesato, H. Yamochi, G. Saito, K. Nakasuji, Angew. Chem., Int. Ed. 43 (2004) 6343.

[5] (a) G.R. Desiraju, R.L. Harlow, J. Am. Chem. Soc. 111 (1989) 6757;
(b) J.P.M. Lommerse, A.J. Stone, R. Taylor, F.H. Allen, J. Am. Chem. Soc. 118 (1996) 3108;
(c) T. Metrangolo, G. Resnati, Chem. Eur. J. 7 (2001) 2511.

[6] (a) N. Thorup, G. Rindorf, C.S. Jacobsen, K. Bechgaard, I. Johannsen, K. Mortensen, Mol. Cryst. Liq. Cryst. 120 (1985) 349;
(b) K. Nakasuji, H. Kubota, T. Kotani, I. Murata, G. Saito, T. Enoki, K. Imaeda, H. Inokuchi, M. Honda, C. Katayama, J. Tanaka, J. Am. Chem. Soc. 108 (1986) 3460;
(c) K. Nakasuji, M. Sasaki, T. Kotani, I. Murata, T. Enoki, K. Imaeda, H. Inokuchi, A. Kawamoto, J. Tanaka, J. Am. Chem. Soc. 109 (1987) 6970.

[7] Y. Morita, E. Miyazaki, J. Toyoda, K. Nakasuji, Bull. Chem. Soc. Jpn. 76 (2003) 205.

[8] (a) Y. Morita, E. Miyazaki, S. Maki, J. Toyoda, H. Yamochi, G. Saito, K. Nakasuji, Mol. Cryst. Liq. Cryst. 379 (2002) 77;
(b) Y. Morita, E. Miyazaki, H. Yamochi, G. Saito, K. Nakasuji, Synth. Met. 135–136 (2003) 581.

[9] (a) M.D. Zaman, Y. Morita, J. Toyoda, H. Yamochi, G. Saito, N. Yoneyama, T. Enoki, K. Nakasuji, Chem. Lett. 26 (1997) 729;
(b) M.D. Zaman, J. Toyoda, Y. Morita, S. Nakamura, H. Yamochi, G. Saito, K. Nishimura, N. Yoneyama, T. Enoki, K. Nakasuji, J. Mater. Chem. 11 (2001) 2211.

[10] A. Altomare, M.C. Burla, M. Camalli, M. Cascarano, C. Giacovazzo, A. Guagliardi, G. Polidori, J. Appl. Crystallogr. 27 (1994) 435.

[11] G.M. Sheldrick, in: G.M. Sheldrick, C. Kruger, R. Goddard (Eds.), Crystallographic Computing, vol. 3, Oxford University Press, Oxford, 1985, pp. 175–189.

[12] G.R. Jeffrey, An Introduction to Hydrogen Bonding, Oxford University Press, New York, 1997, pp. 44–48.

[13] J.S. Miller, P.J. Krusic, D.A. Dixon, W.M. Reiff, J.H. Zhang, E.C. Anderson, A.J. Epstein, J. Am. Chem. Soc. 108 (1986) 4459.

6.65; N, 17.34. Found: C, 69.50; H, 6.78; N, 17.45%. ESR (benzene): $g = 2.0066$, $a_N = 11.70$, $a_H = 2.11$ (2H) and 0.94 G (2H). UV–Vis (λ_{max}, THF; nm [M^{-1} cm^{-1}]): 319 [37 000], 500 [5400].

3. Crystallographic characterization

Analysis was carried out on a Bruker-Nonius KappaCCD diffractometer using Mo Kα radiation, $\lambda = 0.71073$ Å, $\mu = 0.081$ mm^{-1}, $T = 293$ K. Red needle, formula $C_{14}H_{16}N_3O$, MW = 242.3, $0.65 \times 0.35 \times 0.15$ mm, triclinic, $P\bar{1}$, $a = 8.6102(2)$ Å, $b = 12.2878(3)$ Å, $c = 12.5928(3)$ Å, $Z = 4$, $V = 1293.19(5)$ $Å^3$, density (calc.) = 1.245 g/cm^3, $F(000) = 516$, N = unique 4512 reflections were measured using ω scans to $2\theta_{max} = 50.02°$. The structure was solved by direct methods and refined on F_0^2 (with full-matrix least-squares using SHELXTL97 [6]) using 325 parameters with 358 reflections having $I > 2\sigma$ to give $R_1 = 0.0466$, $wR_2 = 0.1188$: for all reflections, $R_1 = 0.0604$, $wR_2 = 0.1298$. See Table 1 for selected bond lengths and angles. Fig. 1 gives an ORTEP representation with the numbering scheme used in this article. Full crystallographic details may be found in CIF format with the Cambridge Crystallographic Databank, CCDC Deposition No. 178242.

4. Magnetic characterization

Magnetization measurements for **1** were carried out on a Quantum Design SQUID MPMS magnetometer at the University of Massachusetts Amherst Nanomagnetics Characterization Facility (NSF CTS-0116498) on polycrystalline samples placed in gelatin capsules and held in place with a small amount of cotton. Measurements were made using an external magnetic field of 1000 Oe over a temperature range of 1.8–300 K. Before measurements, a helium purge procedure was carried out to avoid oxygen contamination. Final measurements were corrected for temperature independent contributions. The results are discussed in the following section.

5. Results and discussion

In the crystal structure of **1**, there are two distinct geometries, which we shall denote **1a** and **1b**. The major difference between the forms is the nitroxide-phenyl torsional angle, 23.9° and 8.4° in **1a** and **1b**, respectively. The interannular torsional angles are quite similar, 35.8° and 37.1° in **1a** and **1b**, respectively. Throughout the lattice, **1** forms chains through an aryl C–H to pyrimidine nitrogen contacts along the *b*-axis, via (**1a**)*meta*-CH···ON(**1b**) contacts of 2.71 Å, and (**1b**)NO···*ortho*-HC(**1a**) of 2.81 Å. The chains align in

Table 1
Selected bond lengths, angles, and distances for radical **1**

Bond lengths	
O(1)–N(3)	1.2831(18)
O(2)–N(6)	1.2805(18)
N(1)–C(1)	1.320(2)
N(1)–C(2)	1.331(2)
N(2)–C(1)	1.328(2)
N(2)–C(4)	1.335(2)
N(3)–C(8)	1.4146(19)
N(3)–C(11)	1.507(2)
N(4)–C(15)	1.318(2)
N(4)–C(16)	1.333(2)
N(5)–C(15)	1.321(2)
N(5)–C(18)	1.333(2)
N(6)–C(22)	1.422(2)
N(6)–C(25)	1.503(2)
C(2)–C(3)	1.381(2)
C(3)–C(4)	1.387(2)
C(3)–C(5)	1.479(2)
C(5)–C(6)	1.390(2)
C(5)–C(10)	1.390(2)
C(6)–C(7)	1.373(2)
C(7)–C(8)	1.389(2)
C(8)–C(9)	1.392(2)
C(9)–C(10)	1.377(2)
C(16)–C(17)	1.382(2)
C(17)–C(18)	1.386(2)
C(17)–C(19)	1.481(2)
C(19)–C(20)	1.388(2)
C(19)–C(24)	1.392(2)
C(20)–C(21)	1.380(2)
C(21)–C(22)	1.389(2)
C(22)–C(23)	1.384(2)
C(23)–C(24)	1.375(2)
Bond angles	
O(1)–N(3)–C(8)	116.78(13)
O(1)–N(3)–C(11)	117.14(13)
O(2)–N(6)–C(22)	115.84(13)
O(2)–N(6)–C(25)	118.11(13)
Torsional angles	
O(1)–N(3)–C(8)–C(9)	8.2 (**1a**)
O(2)–N(6)–C(22)–C(23)	24.1 (**1b**)
C(10)–C(5)–C(3)–C(4)	37.2 (**1a**)
C(24)–C(19)–C(17)–C(18)	36.2 (**1b**)
Intermolecular distances and angles	
O(1)···H(20)	2.72 (**1a**–**1b**)
O(1)···H(21)	3.13 (**1a**–**1b**)
O(2)···H(7)	2.81 (**1b**–**1a**)
O(2)···H(8)	3.09 (**1b**–**1a**)
H(4)···N(4)	2.58 (**1a**–**1b**)
H(18)···N(1)	2.74 (**1b**–**1a**)
Intermolecular stacking distances	
C(5)···C(9′)	3.845 (**1a**–**1a**′)
C(6)···C(10′)	3.782 (**1a**–**1a**′)
C(6)···C(10′)–C(5)	99.4 (**1a**–**1a**′)
H(14)···H(48′)	3.22 (**1b**–**1b**′)
Phenyl to phenyl	
Plane to plane distance	3.77 (**1a**–**1a**′)

See Fig. 1 for atom numbering.
All distances in angstroms, all angles in degrees, esd for molecular parameters in parentheses.

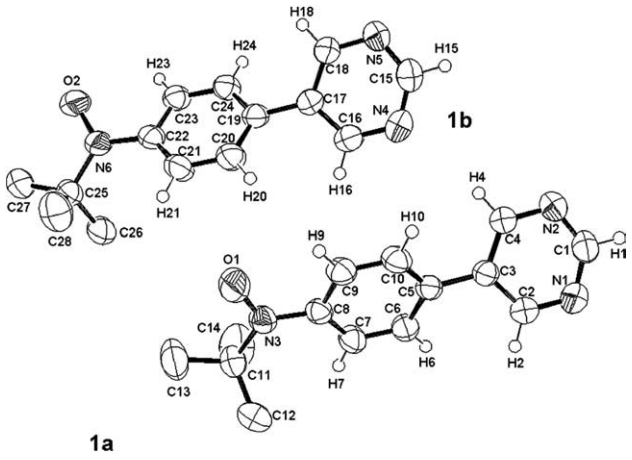


Fig. 1. Crystallographic numbering scheme for **1**. See also Tables 1 and 2.

antiparallel fashion, held together by contacts from the nitroxide oxygens of **1b** to the aryl CH *meta* to the nitroxide of **1a**′ in an adjacent chain, with (**1a**′)NO···HC-pyrimidine(**1b**) 2.95 Å. The latter contacts yield a set of approximately in-plane dimerization contacts between **1a** and **1b** forms. The intrachain NO···H(C) angles are 170.8° (**1a**–**1b**) and 118.4° (**1b**–**1a**), and the interchain angle 135.3° (**1a**′–**1b**). These alternating **1a**–**1b** 1-D chains yield fairly close intermolecular contacts that are possible sites for exchange interactions. The various intra-chain and inter-chain contacts are shown in Fig. 2.

In addition to the nitroxide to HC contact chains described above, pseudo-*para* **1a**:**1a**′ stacked pairs occur among the **1a** sites only, with 3.77 Å between phenyl rings, as is also shown in Fig. 2. This should provide some degree of π-overlap between the phenyl units of the **1a**:**1a**′ dimers. There is *no* comparable stacking or dimeric association of the **1b** molecules.

Finally, there are no nitroxide–nitroxide contacts closer than 5.8 Å to provide more direct spin-pairing contacts between these main spin density sites of **1**. Any intermolecular exchange mechanisms must therefore occur by more indirect pathways, such as spin polarization across close interatomic contacts between sites of small to modest spin population.

In the magnetic measurements, the high temperature limit of χT is reasonably close to the value of 0.375 emu K/Oe mol expected for $S = 1/2$ spin carriers, as shown in Fig. 3. A Curie–Weiss fit of $1/\chi$ versus T for $T > 100$ K gives $C = 0.342$ emu K/Oe mol, $\theta = (+)0.02$ K. The value for the Curie constant corresponds to $S = 1/2$ spin carriers with $g = 1.91$. The Weiss constant shows that the high temperature behavior is essentially paramagnetic. As the temperature drops below 100 K, however, there is significant antiferromagnetic (AFM) deviation from ideal Curie–Weiss behavior, indicating significant intermolecular exchange.

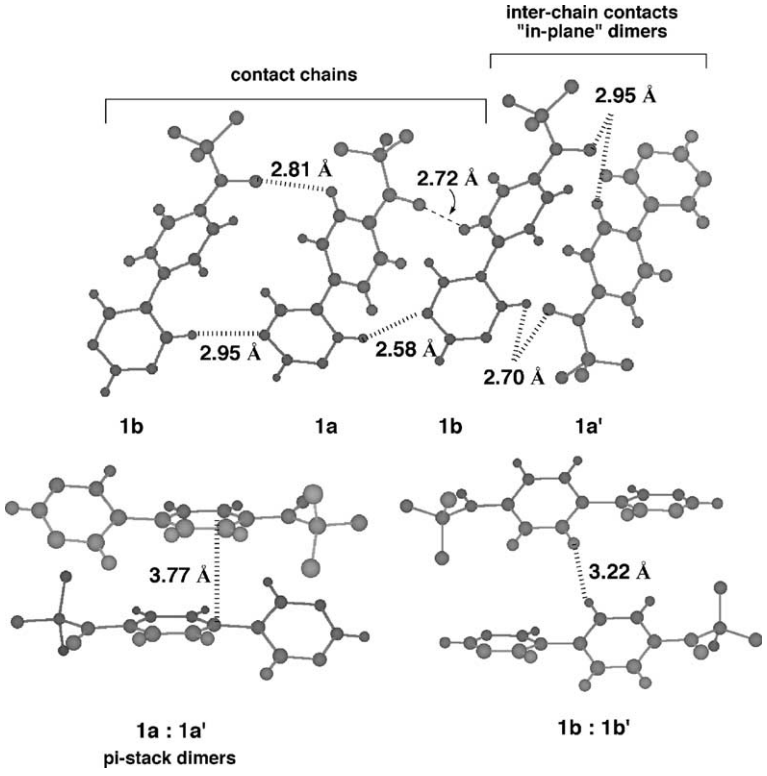


Fig. 2. Scheme of crystallographic contacts in **1**.

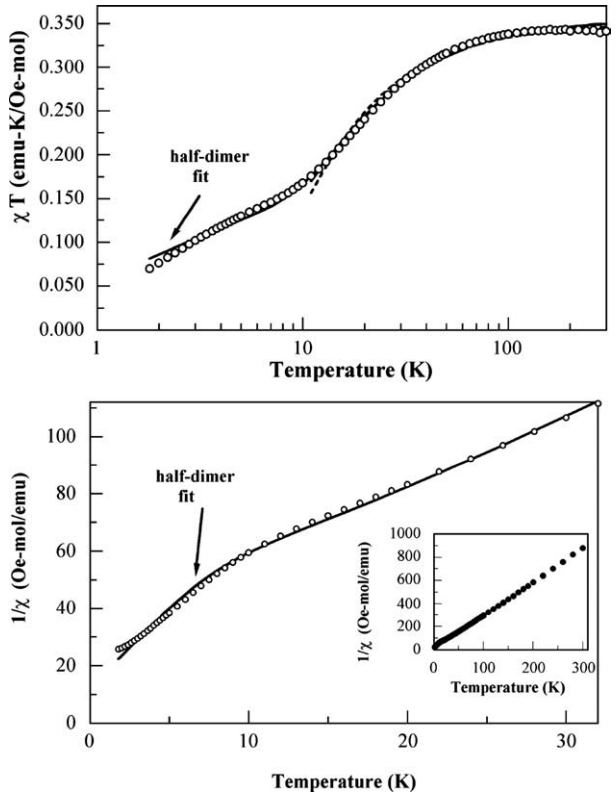


Fig. 3. χT vs. T (above) and $1/\chi$ vs. T (below) plots for **1** at 1000 Oe. The upper plot shows fits to Eqs. (1) (---) and (2) (-●-) for $T > 10$ K, to Eq. (3) (—) across the full temperature range measured. Eqs. (1) and (2) fits virtually overlap. The lower plot shows the fitted curve from Eq. (3) (—). The inset in the lower plot shows the full temperature range $1/\chi$ vs. T data.

Based on the close contacts models shown in Fig. 2, the magnetic behavior could reasonably be fit either to alternating chain or dimer models. The **1a**···**1b**···**1a** contacts could provide an alternating 1-D chain exchange mechanism throughout the solid, involving all molecules. The **1a**′(CH)···**1b**(ON) contacts (Fig. 2) could provide a spin-pairing contact mechanism between all **1a**′:**1b** pairs. Quite differently, the π-stacked **1a**:**1a**′ dimers could provide spin pairing of half of the molecules in the cell, with no obvious analogous mechanism for **1b**:**1b**′ spin pairing. A **1a**:**1a**′ spin-pairing mechanism could be further aided by the planarity of the **1a** form – which thus should be more spin-delocalized – by comparison to the twisted **1b** form. It is not clear based on inspection which (if any) of these interactions would dominate the magnetic behavior of the overall material, or whether the result would be a complex mix of all these interactions.

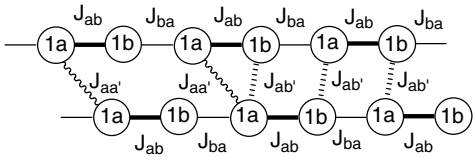
We fit the χT versus T data to both Bleaney–Bowers [7] dimer (**1a**′–**1b** pairings) and Bonner–Fisher [8] 1-D AFM chain (**1a**–**1b**) models. The former is the typical, simple spin-pairing model given by Eq. (1) with exchange constant $J_{ab'}/k$ between **1a** and **1b**. The latter models an alternating 1-D Heisenberg chain system of $S = 1/2$ spin units with two different, alternating exchange constants J_{ab}/k and $J_{ba}/k = \alpha \cdot J_{ab}/k$ using Eq. (2) [8c]. Finally, we fit the data to the model of Eq. (3) in which half the spins are paired with a significant exchange constant $(J/k)_{aa'}$(**1a**:**1a**′), and the others have paramagnetic, Curie-type behavior, a "half-dimer" model, with a mean field term (θ) included. The constants and variables used in the equations are defined as follows: N is the Avogadro's number, g the Lande factor, β the Bohr magneton constant, k the Boltzmann constant, T the Kelvin temperature, χ the paramagnetic susceptibility, θ the mean field term, J/k the exchange energy. The coefficients A–F for Eq. (2) are given elsewhere [8c], and incorporate $\alpha = J_{ab}/J_{ba}$ as a fittable exchange alternation parameter. Scheme 1 shows the possible interactions involved

$$\chi_{BB} = \frac{N_{dimer} g^2 \beta^2}{kT}(1/(3 + e^{-2J/kT})) \quad (\text{where } J = J_{ab'}), \tag{1}$$

$$\chi_{BF} = \frac{N g^2 \beta^2}{kT}\left(\frac{A + Bx + Cx^2}{1 + Dx + Ex^2 + Fx^3}\right) \quad (\text{where } x = |J_{ab}/kT|), \tag{2}$$

$$\chi_{half-dimer} = \frac{g^2 \beta^2}{k(T - \theta)} \times \left[0.5 N_{dimer}(1/(3 + e^{-2J/kT})) + 0.5 N_{monomer}\frac{g^2 \beta^2}{k}\right] \quad (\text{where } J = J_{aa'}). \tag{3}$$

Fig. 3 and Table 2 summarize the results. The single Bleaney–Bowers and alternating chain fits in the figure are shown only for $T > 10$ K, since both models gave substantial deviations from the $\chi T(T)$ data at lower temperatures. The fit to the half-dimer model was by far the best over the full temperature range studied, yielding a half-dimeric AFM spin-pairing interaction of $J/k = (-)15.9$ $K = (-)130$ J/mol, with $g = 1.95$ and a mean field Weiss constant of $\theta = (-)2.2$ K. Based on the superior agreement of experiment to this fit combined with the crystallographic evidence, we feel that the half-dimer spin pairing through the **1a**:**1a**′



Scheme 1. Potential close exchange contacts in **1**. See Fig. 3 and Eqs. (1) and (2).

Table 2
Exchange constants derived from fits of Eqs. (1)–(3) to data of Fig. 3

Model	Exchange (J/k)	θ	g(calc.)
BB	(−)9.8 K		1.94
BF	(−)7.0 K ($\alpha = 0.82$)		1.95
Half-dimer	(−)15.9 K	(−)2.2 K	1.95

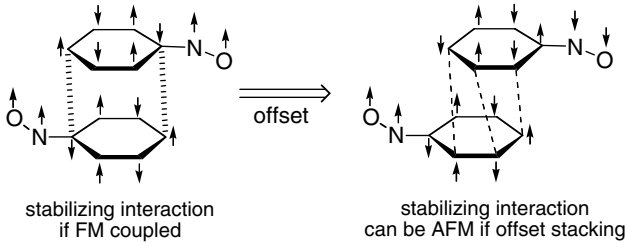
Eqs. (1) and (2) fits (BB and BF, respectively) were out carried for $T > 10$ K, the fit to Eq. (3) is across the full range of data. For the BF model, $J = J_{ab}$, $\alpha J = J_{ba}$.

dimer-stacks is the dominant magnetic exchange interaction in the crystal, although additional weaker interactions may be present.

We were initially surprised that the half-dimer model fit the magnetic behavior as well as Fig. 3 shows, given the multiple possible exchange paths that are present. But, the close π-stacking overlap in the **1a**:**1a**′ pairs appears to provide the most effective exchange among a set of weak exchange mechanisms, with the **1b** molecules having no effective intermolecular exchange interactions detectable under our conditions. ESR hyperfine analysis and computational modelling show [5b] that no site on the pyrimidine ring of **1** has >0.6% absolute spin population, so the (**1a**′)NO···HC-pyrimidine(**1b**) contact is unlikely to be a significant exchange contributor, consistent with the poor fit to the single spin-pairing model of Eq. (1). By comparison, UB3LYP/6-31G* computations [9][2] on the **1a**:**1a**′ dimer stacks at the crystallographic geometry show that the AFM exchange coupled state is favored over the FM coupled triplet by 100 J/mol, which corresponds to $2J/k = (-)12$ K. This is less than half the experimental half-dimer model exchange coupling of $2J/k = (-)260$ J/mol, but qualitatively correct. Given that the intradimer stacking may become smaller with stronger interactions at very low temperatures, the agreement of theory and experiment is encouraging.

Interestingly, a simple McConnell I model analysis of the **1a**:**1a**′ dyads predicts that they would be FM coupled *if* perfectly pseudo-*para* stacked (Scheme 2) [10]. However, the **1a**:**1a**′ dyads are offset relative to perfect *para*-packing. Yamaguchi et al. [11] have shown computationally that such offsets have a strong influence on qualitative application of the McConnell I approach, which accounts for the fact that this model is very difficult to apply in experimental practice. The offset apparently leads to AFM exchange that we attribute to the half of the molecules in the solid that form the **1a**:**1a**′ dyads, based on the computations described above.

[2] Computations were carried out at the fixed crystallographic geometry of a π-stacked A–A′ dyad of **2**, using a broken-symmetry wavefunction for the singlet state, replacing the *tert*-butyl groups with hydrogen atoms, and ignoring zero point energy corrections. For the singlet multiplicity computation of the π-stacked dyad, $\langle S^2 \rangle = 1.02$.



Scheme 2. FM exchange of aryl nitroxide radicals stacked in perfect pseudo-*para* orientation, vs. possible AFM exchange if the stacking is offset.

6. Conclusions

Multiple intermolecular contacts between small spin density sites in organic solids can confound the expectations of simplified explanations that seek to correlate overlap between large spin density sites with magnetic behavior, as others have noted [3]. Studies such as this one can help to determine which kinds of interactions tend to dominate in such situations, when multiple exchange pathways are plausible based on crystallography.

Acknowledgments

This work was supported by the National Science Foundation (CHE 9809548). We thank Dr. A. Chandrasekaran of the UMass-Amherst X-ray Structural Characterization Center (NSF CHE-9974648) for crystallographic analyses. We also acknowledge support for the UMass-Amherst Nanomagnetics Characterization Facility from NSF CTS-0116498.

References

[1] For some general reviews see:
(a) O. Kahn, Molecular Magnetism, VCH, New York, NY, 1993;
(b) P.M. Lahti (Ed.), Magnetic Properties of Organic Molecules, Marcel Dekker, New York, NY, 1999;
(c) K. Itoh, M. Kinoshita (Eds.), Molecular Magnetism: New Magnetic Materials, Gordon & Breach, Newark, NJ, 2000;
(d) J.S. Miller, A.J. Epstein, MRS Bull. 25 (2000) 21;
(e) J. Veciana, H. Iwamura, MRS Bull. 25 (2000) 41;
(f) L. Ouahab, Coord. Chem. Rev. 178–180 (1998) 1501;
(g) R.G. Hicks, Austr. J. Chem. 54 (2001) 597;
(h) M.T. Lemaire, Pure Appl. Chem. 7 (2004) 277.
[2] (a) M. Takahashi, P. Turek, Y. Nakazawa, M. Tamura, K. Nozawa, D. Shiomi, M. Ishikawa, M. Kinoshita, Phys. Rev. Lett. 67 (1991) 746;
(b) M. Tamura, Y. Nakazawa, D. Shiomi, K. Nozawa, Y. Hosokoshi, M. Ishikawa, M. Takahashi, M. Kinoshita, Chem. Phys. Lett. 186 (1991) 401.
[3] (a) J. Veciana, J.J. Novoa, M. Deumal, J. Cirujeda, in: P.M. Lahti (Ed.), Magnetic Properties of Organic Materials, Marcel-Dekker, New York, NY, 1999, pp. 573–600;

(b) M. Deumal, J.J. Novoa, M.J. Bearpark, P. Celani, M. Olivucci, M.A. Robb, J. Phys. Chem. A 102 (1998) 8404;
(c) J.J. Novoa, M. Deumal, P. LaFuente, M.A. Robb, Mol. Cryst. Liq. Cryst. Sci. Technol. A 335 (1999) 1315.

[4] (a) J.R. Ferrer, P.M. Lahti, C. George, G. Antorrena, F. Palacio, Chem. Mater. 11 (1999) 2205;
(b) P.M. Lahti, B. Esat, J.R. Ferrer, Y. Liu, K.A. Marby, C. Xie, C. George, G. Antorrena, F. Palacio, Mol. Cryst. Liq. Cryst. 334 (1999) 285;
(c) Y. Liao, C. Xie, P.M. Lahti, R.T. Weber, J. Jiang, D.P. Barr, J. Org. Chem. 64 (1999) 5176;
(d) J.R. Ferrer, P.M. Lahti, C. George, P. Oliete, M. Julier, F. Palacio, Chem. Mater. 13 (2001) 2447;
(e) P.M. Lahti, Y. Liao, M. Julier, F. Palacio, Synth. Met. 122 (2001) 485;
(f) P.M. Lahti, J.R. Ferrer, C. George, P. Oliete, M. Julier, F. Palacio, Polyhedron 20 (2001) 1465;
(g) Y. Liao, M. Baskett, P.M. Lahti, F. Palacio, Chem. Commun. (2002) 252;
(h) Y. Miyazaki, T. Sakakibara, J.R. Ferrer, P.M. Lahti, G. Antorrena, F. Palacio, M. Sorai, J. Phys. Chem. B 106 (2002) 8615;
(i) B. Esat, P.M. Lahti, M. Julier, F. Palacio, Cryst. Eng. Commun. (2002) 1;
(j) L.M. Field, P.M. Lahti, Chem. Mater. 15 (2003) 2861;
(k) P. Taylor, P.R. Serwinski, P.M. Lahti, Chem. Commun. (2003) 1400.

[5] (a) L.M. Field, P.M. Lahti, F. Palacio, Chem. Commun. (2002) 636;
(b) L.M. Field, P.M. Lahti, F. Palacio, A. Paduan-Filho, J. Am. Chem. Soc. 125 (2003) 10110.

[6] G.M. Sheldrick, SHELXL97, Program for Crystal Structure Refinement, University of Göttingen, Göttingen, Germany, 1997.

[7] B. Bleaney, K.D. Bowers, Proc. R. Soc. Lond. A (1952) 214.

[8] (a) J.C. Bonner, M.E. Fisher, Phys. Rev. A 135 (1964) 650;
(b) J.C. Bonner, Ph.D. Dissertation, University of London, UK, 1968.;
(c) W.E. Hatfield, W.E. Estes, W.E. Marsh, M.W. Pickens, L.W. ter Haar, R.R. Weller, in: J.S. Miller (Ed.), Extended Linear Chain Compounds, vol. 3, Plenum Press, New York, NY, 1983, p. 113ff.

[9] Computations were carried out using Gaussian 03: M.J. Frisch, G.W. Trucks, H.B. Schlegel, G.E. Scuseria, M.A. Robb, J.R. Cheeseman, J.A.J. Montgomery, T. Vreven, K.N. Kudin, J.C. Burant, J.M. Millam, S.S. Iyengar, J. Tomasi, V. Barone, B. Mennucci, M. Cossi, G. Scalmani, N. Rega, G.A. Petersson, H. Nakatsuji, M. Hada, M. Ehara, K. Toyota, R. Fukuda, J. Hasegawa, M. Ishida, T. Nakajima, Y. Honda, O. Kitao, H. Nakai, M. Klene, X. Li, J.E. Knox, H.P. Hratchian, J.B. Cross, C. Adamo, J. Jaramillo, R. Gomperts, R.E. Stratmann, O. Yazyev, A.J. Austin, R. Cammi, C. Pomelli, J.W. Ochterski, P.Y. Ayala, K. Morokuma, G.A. Voth, P. Salvador, J.J. Dannenberg, V.G. Zakrzewski, S. Dapprich, A.D. Daniels, M.C. Strain, O. Farkas, D.K. Malick, A.D. Rabuck, K. Raghavachari, J.B. Foresman, J.V. Ortiz, Q. Cui, A.G. Baboul, S. Clifford, J. Cioslowski, B.B. Stefanov, G. Liu, A. Liashenko, P. Piskorz, I. Komaromi, R.L. Martin, D.J. Fox, T. Keith, M.A. Al-Laham, C.Y. Peng, A. Nanayakkara, M. Challacombe, P.M.W. Gill, B. Johnson, W. Chen, M.W. Wong, C. Gonzalez, J.A. Pople, Gaussian 03, Revision B.03, Pittsburgh, PA, 2003.

[10] H.M. McConnell, J. Chem. Phys. 39 (1963) 1910.

[11] K. Yamaguchi, T. Kawkami, A. Oda, Y. Yoshioka, in: P.M. Lahti (Ed.), Magnetic Properties of Organic Molecules, Marcel Dekker, New York, NY, 1999, p. 403ff.

2. Experimental

2.1. 1-Bromo-3-N-tert-butyl-N-hydroxylaminobenzene (3)

A solution of 11.3 mL (17.0 mmol) *n*-butyllithium (1.5 M in hexanes) was added to a solution of 4.00 g (17.0 mmol) 1,3-dibromobenzene in diethyl ether (80 mL) under argon at −78 °C. The suspension was allowed to stir for 30 min, warmed to room temperature at which time it went into solution, and then cooled to −78 °C. A solution of 2.22 g (25.4 mmol) of 2-methyl-2-nitrosopropane in diethyl ether (15 mL) was added, and the reaction was left to stir overnight at ambient temperature. Aqueous saturated ammonium chloride (25 mL) was added and the organic layer was separated and washed with water. The aqueous layer was extracted with diethyl ether and the combined organic layers were dried over magnesium sulfate. Evaporation of the solvent yielded pale yellow crystals (air-sensitive!) that were dried under vacuum and used immediately in the next step.

2.2. 1-Bromo-3-N-(tert-butyl-N-tert-butyldimethylsiloxylamino)benzene (4)

All of product **3** from the previous step was dissolved in DMF (20 mL) and added to 5.11 g (33.9 mmol) of *tert*-butylchlorodimethylsilane plus 3.46 g (50.8 mmol) of imidazole in a dry flask. The resulting solution was stirred under argon for 24 h at 50 °C. Distilled water (20 mL) was added, and the solution was extracted with hexanes. The combined organic layers were dried over magnesium sulfate and evaporated under reduced pressure. Purification by column chromatography on silica gel with hexanes yielded 5.35 g (89%) of protected hydroxylamine **2** as a clear colorless oil. ^{1}H NMR (200 MHz, $CDCl_3$): δ −0.12 (broad s, 6H), 0.90 (s, 9H), 1.09 (s, 9H), 7.04–7.24 (m, 3H), 7.43 (s, 1H).

2.3. 1-[N-tert-Butyl-N-(tert-butyldimethylsiloxy)amino]-3-benzoic acid (5)

A solution of 9.1 mL of *tert*-butyllithium (1.5 M solution, 13.7 mmol) was added dropwise to 2.23 g (6.21 mmol) of **4** in dry THF at −78 °C, and allowed to stir 2 h. The solution was allowed to warm to room temperature, then cooled to −78 °C, added to an excess of Dry Ice via cannula, and left to stir until all CO_2 bubbling ceased. HCl (20 mL of a 1 M solution) was added and the solution was extracted with dichloromethane, concentrated, and recrystallized from hot dichloromethane to yield 0.982 g (49%) of clear colorless crystals, m.p. 157–158 °C. ^{1}H NMR (400 MHz, $CDCl_3$): δ −0.12 (broad s, 6H), 0.92 (s, 9H), 1.11 (s, 9H), 7.33 (t, 1H, $J = 7.84$ Hz), 7.52 (broad d, 1H, $J = 6.32$ Hz), 7.84–7.87 (doublet of triplets, 1H), 7.99 (broad s, 1H). *Anal*. Calc. for $C_{17}H_{29}NO_3Si$: C, 63.12; H, 9.04; N, 4.33. Found: C, 62.92; H, 8.97; N, 4.30%. IR (KBr, cm^{-1}) 1697 (C=O).

2.4. 3-(N-tert-Butyl-N-hydroxylamino)benzoic acid (6)

Concentrated HCl (5 mL) was added to a solution of 0.555 g (1.72 mmol) of protected *meta*-benzoic acid in 10 mL of ethanol. The solution was stirred until deprotection was complete as evidenced by thin layer chromatography, concentrated under vacuum and then diluted with distilled water (5 mL). The resulting solution was brought to pH 2–3 with 2 M sodium hydroxide and extracted with ethyl acetate. The combined organic portions were dried over magnesium sulfate and evaporated under reduced pressure to a pale yellow crystalline powder. This was recrystallized from acetone to yield 0.228 g (64%) of **6** as pale orange crystals, m.p. 197–199 °C. ^{1}H NMR (400 MHz, DMSO): δ 1.07 (s, 9H), 7.34–7.41 (m, 2H), 7.63–7.66 (doublet of triplets, 1H), 7.80 (t, 1H), 8.42 (s, 1H), 12.8727 (s, 1H). IR (KBr disk, cm^{-1}): 3275 (strong, N–OH), 3100–2500 (medium, broad, OH overlaying C–H stretch), 1701 (strong, C=O stretch). *Anal*. Calc. for $C_{11}H_{15}NO_3$: C, 63.14; H, 7.23; N, 6.69%. Found: C, 62.93; H, 7.27; N, 6.51%. The structure of this compound was confirmed by single crystal X-ray diffractometry, the details of which were submitted to the Cambridge Crystallographic Databank, CCDC deposition # 251475.

2.5. 3-N-(tert-Butyl-N-aminoxyl)benzoic acid (2)

A solution of 0.15 g (0.072 mmol) of **6** in 30 mL of distilled ether was vigorously stirred under argon with 0.34 g (0.14 mmol) of lead dioxide for 1 h. A product-isolation flask was pre-treated with a dilute solution of dichlorodimethylsilane in dichloromethane, then dried under nitrogen. (If the isolation flask is not silanized, the final product sticks tenaciously to the sides, and cannot be scraped off.) The red solution of product was then filtered through a glass frit into the isolation flask. Evaporation of the solvent gave an essentially quantitative yield of red crystalline solid **2** that was used as is for magnetic and crystallographic analysis. Decomposition point 83–86 °C. UV (MeOH, $\lambda_{max}(\varepsilon = M^{-1}\,cm^{-1})$): 289 nm (4700), 393 nm (790). UV (benzene, $\lambda_{max}(\varepsilon = M^{-1}\,cm^{-1})$): 298 nm (7800), 400 nm (1100). IR (KBr, cm^{-1}) 3420 (strong, OH stretch), 1695 (strong, C=O). High resolution MS (EI, m/z): Calc. for $C_{11}H_{14}NO_3$: 208.0974. Found: 208.0972. *Anal*. Calc. for $C_{11}H_{14}NO_3$: C, 63.45; H, 6.78; N, 6.73. Found: C, 60.25; H, 6.59; N, 6.20%. ESR (9.653 GHz, toluene, room temperature): $a(N) = 12.24$ gauss (1 N), $a(H_1 = 1.97$ gauss (3H), $a(H_2 = 0.90$ gauss (1H). Details

of single crystal X-ray diffraction studies are given in a subsequent section below.

3. Synthesis and characterization

The synthesis of **2** is shown in Fig. 1. 1,3-Dibromobenzene was treated with butyl lithium followed by 2-methyl-2-nitrosopropane [5] to make the corresponding hydroxylamine **3**, which was protected with *tert*-butylchlorodimethylsilane to make previously reported [6] compound **4**. This was metallated, treated with CO_2 to give **5**, and deprotected to **6**, a colorless solid that was oxidized with PbO_2 in diethyl ether to give the desired radical **2** as a red crystalline solid. The product nitroxide appears to be highly stable, and can be stored without apparent decomposition for months.

The UV–Vis spectrum of **2** shows absorptions at 290–300 and 390–400 nm, which di not exhibit substantial solvent polarity effects in methanol versus benzene. Interestingly, addition of silica gel completely decolorized benzene solutions of **2**, as we shall describe further below. The infrared spectrum of **2** in KBr shows a strong OH stretching mode as well as the expected carbonyl stretch at 1695 cm^{-1}. The IR and the crystallography (below) show that the carboxylic acid OH groups are strongly hydrogen bonded. The solution ESR spectrum at 9.8 GHz shows hyperfine coupling (hfc) as follows: $a(N) = 12.2$ gauss, $a_1(3H) = 2.0$ gauss, $a_2(1H) = 0.9$ gauss, all obtained in toluene solvent. The larger protic hfc are attributed to the C–H that are *ortho* and *para* to the nitroxide, the smaller to the *meta* C–H. Line broadening of ESR spectra was observed under some room temperature conditions, but typically could be resolved to restore the monoradical spectrum upon cooling to 200–220 K, so long as the concentration was not so high as to give collisional line broadening. We did not observe any peaks consistent with triplet state radical pair formation in toluene at room temperature,

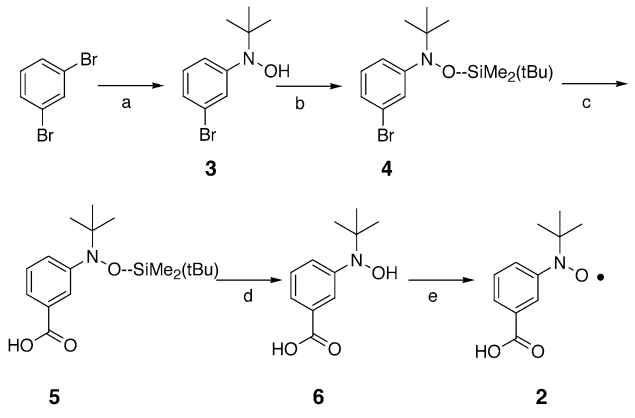


Fig. 1. Synthetic route to make radical **2**. (a) *n*-BuLi in Et_2O, −78 °C, then $Me_2CN{=}O$, then aq workup; (b) Cl–$SiMe_2$(*t*Bu)/imidazole in DMF, heat, 89%; (c) *t*-BuLi in THF, −78 °C, then CO_2, then aq HCl, 49%; (d) conc. HCl, room temperature, 64%; (e) PbO_2 in Et_2O, room temperature, ~100%.

Table 1
Selected molecular and intermolecular structural parameters for radical **2**

Bond lengths	
O(1)–N(1)	1.288(3)
O(1A)–N(1A)	1.292(3)
O(2)–C(8)	1.241(3)
O(2A)–C(8A)	1.232(4)
O(3)–C(8)	1.318(3)
O(3A)–C(8A)	1.311(4)
N(1)–C(1)	1.421(4)
N(1A)–C(1A)	1.416(4)
N(1)–C(7)	1.512(4)
N(1A)–C(7A)	1.510(4)
C(1)–C(2)	1.393(4)
C(1)–C(6)	1.398(4)
C(2)–C(3)	1.382(4)
C(3)–C(4)	1.395(4)
C(3)–C(8)	1.477(4)
C(4)–C(5)	1.384(4)
C(5)–C(6)	1.388(4)
C(1A)–C(2A)	1.394(4)
C(1A)–C(6A)	1.406(4)
C(2A)–C(3A)	1.394(4)
C(3A)–C(4A)	1.394(4)
C(3A)–C(8A)	1.483(4)
C(4A)–C(5A)	1.376(4)
C(5A)–C(6A)	1.386(4)
O(3)–H(1)	1.19
O(3A)–H(1A)	1.05
Bond angles	
O(1)–N(1)–C(1)	116.6(2)
O(1)–N(1)–C(7)	117.5(2)
O(1A)–N(1A)–C(1A)	116.1(2)
O(1A)–N(1A)–C(7A)	117.5(2)
Torsional angles	
O(2A)–C(8A)–C(3A)–C(2A)	3.4
O(2)–C(8)–C(3)–C(2)	5.5
O(1)–N(1)–C(1)–C(2)	22.0
O(1A)–N(1A)–C(1A)–C(2A)	0.8
Intermolecular distances and angles	
O(2)–H(1A)	1.58 (a)
O(2A)–H(1)	1.43 (a)
O(1)–H(6)C(6)	2.51 (b)
O(1a)–H(6a)C(6a)	2.74 (b)
O(1)–H(5)C(5)	2.85 (b)
O(1a)–H(5a)C(5a)	3.06 (b)
O(2)–H(1A)–O(3A)	173 (a)
O(2A)–H(1)–O(3)	167 (a)
Inter-ring plane-to-plane angle	
O(2)–N(3)–C(3A)–C(2A)	176

All distances in angstroms, all angles in degrees, esd for selected parameters in parentheses. (a) Carboxylic acid hydrogen bond, (b) nitroxide to aryl CH 1-D chain contact. Distances and angles using hydrogen atom positions were assigned using models described in CCDC deposition number 251476, and so are given to three significant digits.
See Fig. 2 for atom numbering.

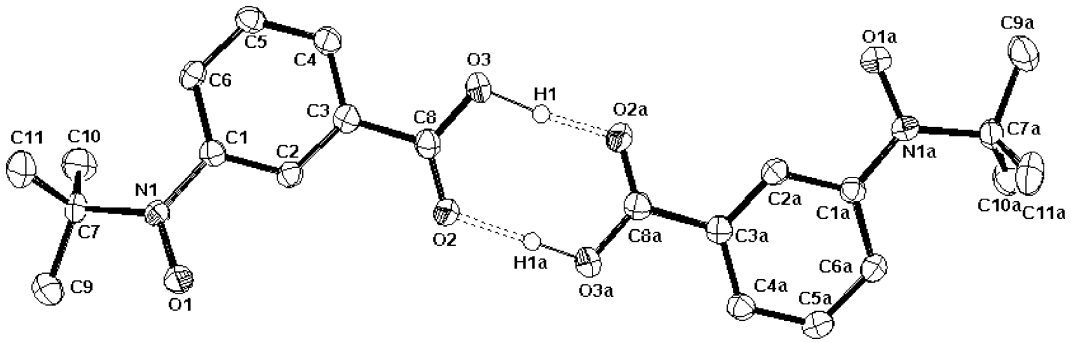


Fig. 2. Crystallographic numbering scheme for **2**. See also Table 1. Form B to left, form A to right.

nor any triplet state turning points or a half-field transition in frozen toluene or in KBr matrices at 77 K.

4. Crystallography

Crystals of **2** were obtained by crystallization in dichloromethane using glassware silanized with dichlorodimethylsilane. Crystallographic details are given below and in Table 1. Fig. 2 shows an ORTEP style representation.

4.1. Radical (2)

Analysis was carried out on a Bruker-Nonius KappaCCD diffractometer using Mo Kα radiation, $\lambda = 0.71073$ Å, $\mu = 0.092\ \mathrm{mm}^{-1}$, $T =$ 100(2) K. Red needle, formula $C_{11}H_{14}NO_3$, $M_w =$ 208.23, $1.10 \times 0.15 \times 0.03$ mm, orthorhombic, $Pca2_1$ (#29), $a =$ 18.5303(7) Å, $b = 6.2148(2)$ Å, $c = 18.9709(7)$ Å, $Z =$ 8, $V = 2184.73(14)$ Å^3, $D_{calc} = 1.266$ g/cm^3, $F(000) = 888$, $N =$ unique 3561 reflections were measured using ω scans to $2\theta_{max} = 50.06°$. The structure was solved by direct methods and refined on F_0^2 (full matrix least squares using SHELXTL97 [7]) using 279 parameters with 2848 reflections having $I > 2\sigma$ to give $R_1 = 0.0481$, $wR_2 = 0.0956$: for all reflections, $R_1 = 0.0718$, $wR_2 = 0.1059$. The absolute structure parameter was −0.9(15). The COOH hydrogens were located from the difference Fourier analysis and refined freely at an isotropic level. Full details were deposited in CIF format with the Cambridge Crystallographic Databank, CCDC deposition # 251476.

5. Magnetic studies

Magnetization measurements for **2** were carried out on a Quantum Design SQUID MPMS magnetometer on polycrystalline samples placed in gelatin capsules and held in place with a small amount of cotton. Measurements were made using external magnetic fields of 500–1000 oersted over a temperature range of 1.8–300 K. Before measurements, a helium purge procedure was carried out to avoid oxygen contamination. Final measurements were corrected for temperature independent contributions. Fig. 3 shows the results.

6. Results and discussion

There are two different structures that form a classic carboxylic acid hydrogen bonded dimer of **2** in its crystal lattice, shown as A and B in Fig. 4. The nitroxide group is nearly coplanar with the phenyl ring in one structure (form A), and somewhat twisted in the other (form B, Table 1). The carboxylic acid moieties are nearly coplanar in both structures, with dihedral torsions of only 3.3° and 5.4°. Save for the difference in nitroxide torsions, the dimer would be essentially centrosymmetric. The two phenyl rings are twisted only 4.7° relative to one another in the hydrogen bonded dyad. Within the crystal structure are no intermolecular nitroxide to nitroxide contacts closer than 6 Å. Thus, there are no spin pairing contacts involving sites of large spin density in the lattice of **2**. There are also no coplanar or nearly coplanar phenyl–phenyl stacking interactions. But, in addition to the hydrogen bonded dimers, **2** forms 1-D chains of nitroxide oxygens to one of the *ortho* aryl CH units. The (N)–O···H–(C) distances are 2.5 Å in one chain, 2.7 Å in the other. The phenyl groups of Ph–NO···H–Ph–NO chains are not coplanar, but rather are all canted about 34° relative to the vector of chain formation, the crystallographic *b*-axis (see Fig. 4). Overall, each crystallographic form of **2** forms chains (A–A–A, B–B–B), which are then linked in an antiparallel fashion by the carboxylic acid hydrogen bonds. There are no π-stacking contacts, but rather formation of herringbone type arrays among the 1-D chains. The combination of the hydrogen bonds and 1-D chain contacts gives rise to ribbons of close contacts between the nitroxide NO units and aryl C–H moieties (Fig. 4).

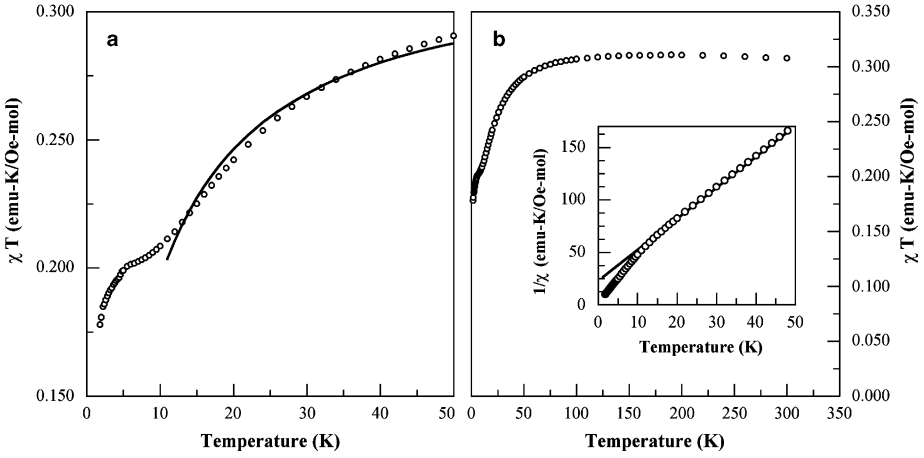


Fig. 3. χT versus T plot at 1000 Oe for **2** at lower temperatures (a) and across full temperature range measured (b). Solid line to left is fit to a spin pairing model for $T > 10$ K data. Inset to left is $1/\chi$ versus T plot, showing the Curie–Weiss fit for $T > 20$ K as a solid line.

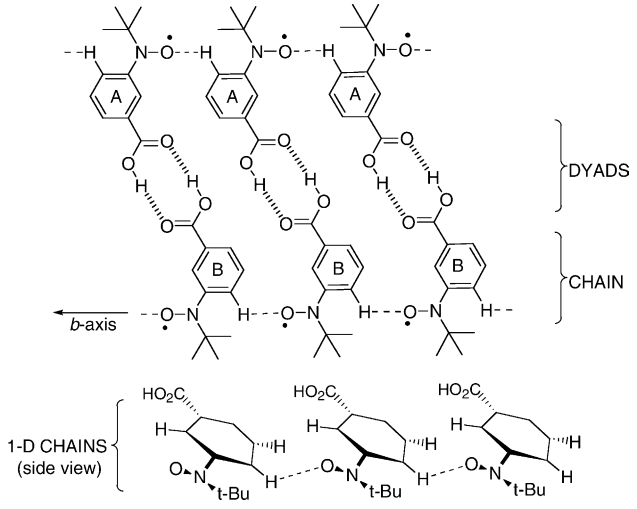


Fig. 4. Schematic representation of close contact motifs in crystalline **2**. Labels "A" and "B" refer to crystallographically distinguishable forms of **2**.

The χT versus T plot for **2** exhibits a higher temperature plateau consistent (though somewhat low) with the value expected for discrete $S = 1/2$ species, but turns down at lower temperatures, showing the onset of antiferromagnetic exchange interactions. The $1/\chi$ versus T plot (Curie–Weiss plot) shows a change in slope at about 10 K. The data correspond to $C \sim 0.31$ emu-K/Oe-mol with $\theta = (-)3.8$ K in the higher temperature range, and C ~ 0.23 emu-K/Oe-mol with $\theta = (-)1.5$ K below 10 K. These results were closely reproducible for three separately synthesized and purified samples of **2**. Elemental analyses for **2** also were reproducible, but low in carbon, commensurate with the low Curie constant. Despite the low carbon in the elemental analysis, the reproducibility of magnetic behavior argues that sample composition is consistent.

The low value of the high temperature Curie constant may be due to water adsorption in the samples, although we could not find solvation water (or any other solvent incorporation) in the crystal diffraction analysis, even at 100 K. The affinity of **2** for some hydrogen bonding environments is notable, particularly its tendency to adsorb to silica based materials out of nonpolar solvents. When isolated by solvent evacuation, radical **2** adsorbs tenaciously to Pyrex, unless the Pyrex is first silanized to reduce the presence of surface hydroxyl groups. Also, dilute solutions of **2** in benzene are completely decolorized by addition of silica gel; a decrease in color is observed for ether solutions, though not complete decolorization. Filtration of the resultant yellow silica gels and stirring in methanol recovers a yellow-colored solution. Fig. 5 shows the ESR spectra of silica gel with **2** adsorbed from benzene and ether solutions. both show the radical, albeit in somewhat different environments with different lineshapes. The results show that **2**

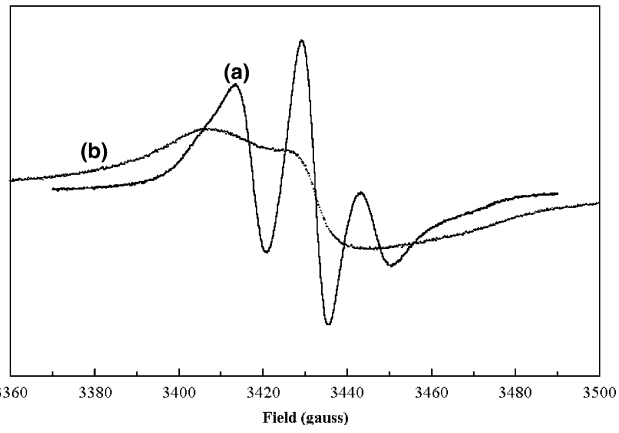


Fig. 5. ESR spectra of **2** adsorbed onto silica gel from benzene (a) and diethyl ether (b). Both spectra shown at room temperature at 9.647 GHz (the spectra do not change significantly upon cooling to 77 K).

adsorbs strongly to silica. We intend to investigate the scope of this effect for covering surfaces and nanoparticles with **2**.

The lower temperature antiferromagnetic (AFM) downturn in **2** shows that there are intermolecular exchange interactions. Since there are no close nitroxide–nitroxide contacts, the exchange pathway presumably follow some indirect spin polarization or similar pathway. Based on the crystallography, either spin pairing through the carboxylic acid hydrogen bond, or 1-D chains along the nitroxide to aryl CH contacts, seem possible.

The analysis is complicated by the change in slope at 10 K, which indicates a change in behavior. For the data above 10 K, a Bleaney–Bowers spin-pairing model [8] represented by Eq. (1) gives a moderately good fit for $J/k = (-)1.6$ K, $\theta = (-)5.0$ K, where all the physical constants have the usual meanings and values. But, the large value of the Weis constant shows that the model does not well represent all the interactions within the sample,

$$\chi = \left(\frac{Ng^2\beta^2}{kT}\right)\frac{2e^{2J/kT}}{1+3e^{2J/kT}}. \quad (1)$$

The change in behavior at $T < 10$ *K* is consistent with the presence of at least two different exchange mechanisms [9]. There are two crystallographically different molecules of **2**, but the closest dimeric contacts all occur between forms A and B, not for A–A or B–B dyads (at least down to 100 K). The only close A–A and B–B type contacts occur along the nitroxide to aryl CH chains. However, the χT versus T data do not fit well to a simple Bonner–Fisher 1-D antiferromagnetic chain over the full temperature range [10]. Possibly some sort of conformational or phase change occurs at 10 K to alter the array of close contacts between molecules of **2**, resulting in the observed alteration of the Curie–Weiss plot. Alternatively, the change in slope may mirror lower and higher temperature limits for two exchange mechanisms (whether or not there is a change in structure at 10 K). We can crudely estimate the presumptive exchange strengths in the two temperature ranges using Eq. (2) [11], where J/k is an exchange constant, $S = 1/2$, and z is the number of nearest neighbors interacting with a $S = 1/2$ site. Using the Weiss constants of $(-)3.8$ K and $(-)1.5$ K for the higher and lower temperature portions of the Curie–Weiss plot (see above), $J_1/k = (-)7.6$ K $= (-)63$ J/mol at higher temperature, $J_2/k = (-)3.0$ K $= (-)25$ J/mol at lower temperature, both assuming that $z = 1$. It is reasonable to relate these to the spin pairing and chain exchange mechanisms that are

$$\theta = \frac{2zJS(S+1)}{3k} \quad (2)$$

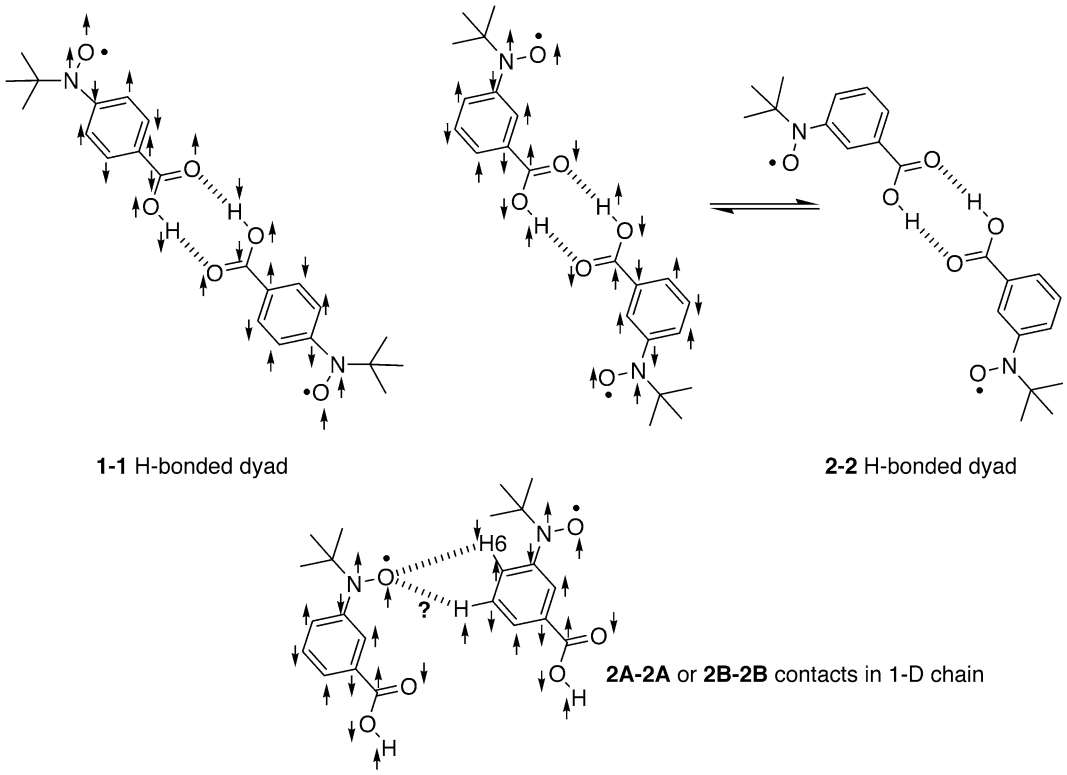
based on the crystallography of **2**, even though this is difficult to prove outright from the data. Still, this leads to questions about the proposed exchange mechanisms. Is the AFM exchange mechanism dominated by close contacts in the carboxylic acid hydrogen bonded dyads? Does the 1-D chain of nitroxide to aryl HC contacts play an identifiable role?

The overall AFM exchange in polycrystalline **2** is worth comparing to the behavior of **1** reported by Veciana and coworkers [4], who *also* observed net AFM downturn in the solid state, but who observed triplet radical pair ESR spectra for **1** *in solution*. The triplet ESR signal variation of **1** with temperature in frozen solution indicated that the triplet–singlet splitting was 4 K (33 J/mol) favoring the triplet state. They interpreted the triplet spectrum as occurring by a spin polarization mechanism that exchange links the nitroxide units in a ferromagnetic (FM) manner through the hydrogen bonded carboxylic acid groups. Scheme 1 shows the qualitative spin polarizations in the dyad. They suggested that this same FM interaction in the solid state is overwhelmed by an additional, AFM interaction, giving the net overall AFM exchange behavior of **1** in the solid. They tentatively suggested that the solid state AFM interaction occurred by π–π overlap mechanism between stacked dyads. There are no π-stacks in **2**, by comparison.

We found no evidence of triplet radical pairing for **2** in solution either at room temperature or at 77 K, even in nonpolar solvents, even though a similar spin polarization analysis to that carried out for **1** again suggests the possibility of FM exchange linkage. In solution, the presence of multiple conformational isomers of **2**–**2** dyads (see Scheme 1) may broaden below detection any ESR lines from triplet spin pairing, an effect that should be less pronounced in pseudo-*para* **1**–**1** dyads.

The solid state results for **2** are difficult to explain qualitatively by clear relationship to a single crystallographic feature or motif. UB3LYP/6-31G* computations [12][1] using the 100 K crystallographic geometry of **2** (but replacing the *tert*-butyl groups with hydrogens) favor the triplet over the singlet state by only by 35 J/mol, and show no more than 0.5% absolute value of spin densities on carboxylic acid O2, C8, O3, and H1 in Fig. 2. These computations thus do not seem to explain the observed bulk AFM (not FM) magnetic behavior. Qualitatively, the chains of 1-D contacts in **2** might also be considered to lead to FM exchange (Scheme 1), although the canting of the phenyl rings within the 1-D chains could alter the nature of this exchange mechanism. But, model dyad computations for

[1] Computations were carried out at the fixed crystallographic geometry of dyads of **2**, using a broken-symmetry wavefunction for the singlet state, replacing the *tert*-butyl groups with hydrogen atoms, and ignoring zero point energy corrections. For the singlet multiplicity calculation of the hydrogen bonded dyad, $\langle S^2\rangle = 1.016$; for the dyads of the A–A–A and B–B–B chains, $\langle S^2\rangle = 1.016$ and 1.019, respectively.



Scheme 1. Putative spin polarization exchange mechanisms for **1** and **2** based on qualitiative expected spin density distribution in each. The 1-D chain model shows both the closest contact between NO and an *ortho* C–H, and a possible contact to a *meta* C–H – as pictured, the *ortho*-contact is assumed to dominate. See the text for additional discussion.

the A–A–A and B–B–B chains instead give slight AFM exchange preferences (singlet state preferred) by 20 and 6 J/mol, respectively [12][1].

The latter results suggest that the simple FM chain exchange model of Scheme 1 – analyzed as proceeding solely through the C–H bonds *ortho* to the nitroxides – is oversimplified, maybe due to noncoplanarity of the aryl nitroxide units in the chains. Interaction through the *meta* C–H bonds also might contribute to the bulk AFM behavior seen in **2** (dotted interaction in Scheme 1). In principle, the two slightly different chains in **2** might even correlate with the multiple AFM exchange constants that are suggested by the magnetic data. This would be consistent with the computational and crystallographic evidence, but we cannot confidently advance a two-chain model as clearly explaining the observed magnetic behavior[2]. For example, we might also get increased geometric difference between the molecules in the two chains at reduced temperatures, even leading to a phase change in the crystal structure. The situation is just too complex to resolve clearly with the data available at present.

The clearest conclusion from the data is that multiple, competing exchange mechanisms exist in **2**. Spin polarization pathways that are most easily identified by the close atomic contacts in the crystal structure are weak, and may even be overwhelmed by through-space dipolar, mean-field type AFM exchange interactions in the bulk solid, giving the overall observed behavior.

7. Conclusions

3-(*N*-*tert*-Butyl-*N*-aminoxyl)benzoic acid has a number of crystallographic similarities to previously [4] reported isomer 4-(*N*-*tert*-butyl-*N*-aminoxyl)benzoic acid, but behaves rather differently in terms of solution ESR spectroscopy. Polycrystalline magnetic susceptibilities of both show AFM dominant exchange behavior, although the change in molecular connectivity has a substantial effect on the solution dyad ESR behavior. The similarity of solid state magnetic behaviors suggests that multiple weak exchange forces are involved in **1**–**2** that are subtly balanced, rendering any solid state

[2] Efforts to fit the magnetic behavior of **2** to a 1:1 mix of Bonner–Fisher [9] chains with two different exchange constants were not a significant improvement over other fits that we attempted, unless an unexpectedly large paramagnetic term was added. In the latter situation, the difference between the two fitted 1-D chain exchange constants was very large, with one being only about 0.05 J/mol and the other about 14 J/mol. We felt that this difference between exchange constants in a two-chain fit was not physically reasonable given the geometric similarity of the two chains at 100 K, unless a phase change or molecular geometry change causes a substantial difference between the A and B forms of **2** at low temperatures.

structure-property analysis quite difficult, as well as extrapolation in solution experiments or by computation from simplified dyad models to solid state behavior.

Acknowledgements

This work was supported by the National Science Foundation (CHE 9809548 and CHE 0415716). We thank Dr. A. Chandrasekaran of the UMass-Amherst X-ray Structural Characterization Center (NSF CHE-9974648) for crystallographic analyses, and Dr. G. Dabkowski for elemental analyses. We also acknowledge support for the UMass-Amherst Nanomagnetics Characterization Facility from NSF CTS-0116498.

References

[1] See for example (a) M.C. Etter, Acc. Chem. Res. 23 (1990) 120;
(b) J. Bernstein, M.C. Etter, L. Leiserowitz, Struct. Correl. 2 (1994) 431;
(c) P. Schuster, NATO Advanced Study Institutes Series, Series C: Mathematical and Physical Sciences C39 (1978) 229–255. For specific reference to hydrogen bonds in radicals, see for example the following and citations therein;
(d) J. Cirujeda, E. Hernàndez-Gasió, C. Rovira, J.-L. Stanger, P. Turek, J. Veciana, J. Mater. Chem. 5 (1995) 243;
(e) J. Zhang, M. Baumgarten, Chem. Phys. 222 (1997) 1.

[2] (a) D. Gatteschi, O. Kahn, J.S. Miller, F. Palacio, Magnetic Molecular Materials, Kluwer Academic Publishers, Dordrecht, The Netherlands, 1991;
(b) O. Kahn, Molecular Magnetism, VCH, New York, NY, 1993;
(c) J.S. Miller, Magnetism: Molecules to Materials, Wiley, New York, NY, 1999;
(d) P.M. Lahti (Ed.), Magnetic Properties of Organic Molecules, Marcel Dekker, New York, NY, 1999;
(e) J.S. Miller, A.J. Epstein, MRS Bulletin 25 (2000) 21;
(f) J. Veciana, H. Iwamura, MRS Bulletin 25 (2000) 41;
(g) L. Ouahab, Coord. Chem. Rev. 178–180 (1998) 1501;
(h) R.G. Hicks, Austr. J. Chem. 54 (2001) 597;
(i) M.T. Lemaire, Pure Appl. Chem. 7 (2004) 277;
(j) J. Cirujeda, E. Hernndez-Gasi, F. Lanfranc de Panthou, J. Laugier, M. Mas, E. Molins, C. Rovira, J.J. Novoa, P. Rey, J. Veciana, Mol. Cryst. Liq. Cryst. 271 (1995) 1.

[3] (a) J.R. Ferrer, P.M. Lahti, C. George, G. Antorrena, F. Palacio, Chem. Mater. 11 (1999) 2205;
(b) P.M. Lahti, B. Esat, J.R. Ferrer, Y. Liu, K.A. Marby, C. Xie, C. George, G. Antorrena, F. Palacio, Mol. Cryst. Liquid Cryst. 334 (1999) 285;
(c) Y. Liao, C. Xie, P.M. Lahti, R.T. Weber, J. Jiang, D.P. Barr, J. Org. Chem. 64 (1999) 5176;
(d) J.R. Ferrer, P.M. Lahti, C. George, P. Oliete, M. Julier, F. Palacio, Chem. Mater. 13 (2001) 2447;
(e) P.M. Lahti, Y. Liao, M. Julier, F. Palacio, Synth. Met. 122 (2001) 485;
(f) P.M. Lahti, J.R. Ferrer, C. George, P. Oliete, M. Julier, F. Palacio, Polyhedron 20 (2001) 1465;
(g) Y. Liao, M. Baskett, P.M. Lahti, F. Palacio, Chem. Commun. (2002) 252;
(h) Y. Miyazaki, T. Sakakibara, J.R. Ferrer, P.M. Lahti, G. Antorrena, F. Palacio, M. Sorai, J. Phys. Chem. B 106 (2002) 8615;
(i) B. Esat, P.M. Lahti, M. Julier, F. Palacio, Cryst. Eng. Commun. 11 (2002) 59;
(j) L.M. Field, P.M. Lahti, Chem. Mater. 15 (2003) 2861;
(k) P. Taylor, P.R. Serwinski, P.M. Lahti, Chem. Commun. (2003) 1400.

[4] D. Maspoch, L. Catala, P. Gerbier, D. Ruiz-Molina, J. Vidal-Gancedo, K. Wurst, C. Rovira, J. Veciana, Chem. Eur. J. 8 (2002) 3635.

[5] J.C. Stowell, J. Org. Chem. 36 (1971) 3055.

[6] Y. Liao, C. Xie, P.M. Lahti, R.T. Weber, J. Jiang, D.P. Barr, J. Org. Chem. 64 (1999) 5176.

[7] G.M. Sheldrick, SHELXTL97 Program for the Refinement of Crystal Structures, University of Göttingen, Germany.

[8] B. Bleaney, K.D. Bowers, Proc. R. Soc. London A (1952) 214.

[9] (a) Examples include the following: Y. Hosokoshi, M. Tamura, D. Shiomi, N. Iwasawa, K. Nozawa, M. Kinoshita, H.A. Katori, T. Goto, Physica B 201 (1994) 497;
(b) Y. Hosokoshi, M. Tamura, K. Nozawa, S. Suzuki, H. Sawa, R. Kato, M. Kinoshita, Mol. Cryst. Liq. Cryst. 271 (1995) 115;
(c) B. Esat, P.M. Lahti, M. Julier, F. Palacio, Cryst. Eng. Commun. (2002) 1.

[10] The 1-D chain fit model that we attempted to fit to the data of Fig. 3 is described in:
(a) J.C. Bonner, M.E. Fisher, Phys. Rev. A 135 (1964) 650;
(b) J.C. Bonner, Ph. D. Dissertation, University of London, UK, 1968.

[11] See for example J.S. Smart, Effective Field Theories of Magnetism, W.B. Saunders, Philadelphia, PA, 1966, 25ff.

[12] Computations were carried out using Gaussian 03: M.J. Frisch, G.W. Trucks, H.B. Schlegel, G.E. Scuseria, M.A. Robb, J.R. Cheeseman, J.A.J. Montgomery, T. Vreven, K.N. Kudin, J.C. Burant, J.M. Millam, S.S. Iyengar, J. Tomasi, V. Barone, B. Mennucci, M. Cossi, G. Scalmani, N. Rega, G.A. Petersson, H. Nakatsuji, M. Hada, M. Ehara, K. Toyota, R. Fukuda, J. Hasegawa, M. Ishida, T. Nakajima, Y. Honda, O. Kitao, H. Nakai, M. Klene, X. Li, J.E. Knox, H.P. Hratchian, J.B. Cross, C. Adamo, J. Jaramillo, R. Gomperts, R.E. Stratmann, O. Yazyev, A.J. Austin, R. Cammi, C. Pomelli, J.W. Ochterski, P.Y. Ayala, K. Morokuma, G.A. Voth, P. Salvador, J.J. Dannenberg, V.G. Zakrzewski, S. Dapprich, A.D. Daniels, M.C. Strain, O. Farkas, D.K. Malick, A.D. Rabuck, K. Raghavachari, J.B. Foresman, J.V. Ortiz, Q. Cui, A.G. Baboul, S. Clifford, J. Cioslowski, B.B. Stefanov, G. Liu, A. Liashenko, P. Piskorz, I. Komaromi, R.L. Martin, D.J. Fox, T. Keith, M.A. Al-Laham, C.Y. Peng, A. Nanayakkara, M. Challacombe, P.M.W. Gill, B. Johnson, W. Chen, M.W. Wong, C. Gonzalez, J.A. Pople, GAUSSIAN 03, Revision B.03, Pittsburgh, PA, 2003.

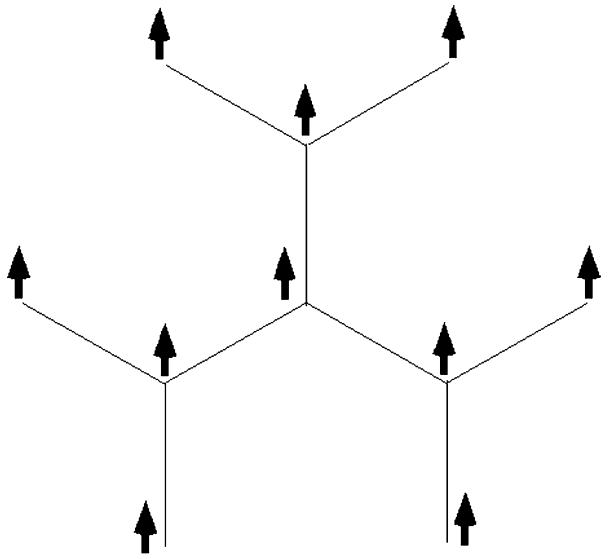


Fig. 1. Sample of the dendritic architecture of the spin aggregate. This structure is called Cayley-tree type.

For the diagonalization of the Hamiltonian, we utilize the basis which constructed from a direct product of a state vector for each spin $\{|\varphi_{i_k}^k\rangle\}$:

$$\left|\varphi_{i_1}^1\varphi_{i_2}^2\cdots\varphi_{i_N}^N\right\rangle \equiv \left|\varphi_{i_1}^1\right\rangle \otimes \left|\varphi_{i_2}^2\right\rangle \otimes \cdots \otimes \left|\varphi_{i_N}^N\right\rangle, \tag{2}$$

where i_k represents a state for each spin:

$$|\varphi_1^k\rangle \equiv |\alpha^k\rangle \quad \text{(up spin)}, \tag{3}$$

$$|\varphi_2^k\rangle \equiv |\beta^k\rangle \quad \text{(down spin)}. \tag{4}$$

By diagonalizing the Hamiltonian H_0, we obtain new states with eigenenergies $\{E_k\}$ and eigenstates $\{|i\rangle\}$;

$$H_0\,|i\rangle = E_i\,|i\rangle. \tag{5}$$

In order to perform the spin dynamics from a ferromagnetic state to a thermally-stable state, we choose the lowest M (=$2S+1$) states with the same value of the multiplicity $\boldsymbol{S}^2 = S(S+1) = (N/2)(N/2+1)$. These states are represented by

$$\begin{aligned} |1\rangle &= |\alpha^1\alpha^2\cdots\alpha^N\rangle,\\ |2\rangle &= \frac{1}{\sqrt{10}}\left(|\beta^1\alpha^2\cdots\alpha^N\rangle + |\alpha^1\beta^2\cdots\alpha^N\rangle + \cdots |\alpha^1\alpha^2\cdots\beta^N\rangle\right),\\ &\vdots\\ |M\rangle &= |\beta^1\beta^2\cdots\beta^N\rangle. \end{aligned} \tag{6}$$

The total spin Hamiltonian is assumed to be

$$H_{\mathrm{S}} = H_0 + H', \tag{7}$$

where

$$H' = -d_z\sum_i (S_i^z)^2 - \omega\sum_{i<j}\frac{3(\boldsymbol{S}_i\cdot\boldsymbol{e}_{ij})(\boldsymbol{e}_{ij}\cdot\boldsymbol{S}_j) - \boldsymbol{S}_i\cdot\boldsymbol{S}_j}{r_{ij}^3}. \tag{8}$$

The first sum represents a uniaxial anisotropy, here, for $d_z>0$, favoring the z axis as easy axis of the system [10]. The second sum is the dipole–dipole interaction with the strength ω . The $\boldsymbol{e}_{ij}$ are unit vectors pointing from a spin i to j, and r_{ij} is the distance between these spins. By using the states $|i\rangle$ as a basis and diagonalizing the Hamiltonian H', we get a new model involving an anisotropic effect;

$$H'\,|\psi_k\rangle = \omega_k\,|\psi_k\rangle. \tag{9}$$

These spins interact with nuclear vibration, i.e., phonons whose states are represented by $\{|q_{(i,j)}\rangle\}$ with the frequency $\{\Omega_{q_{(i,j)}}\}$ · $q_{(i,j)}$ means the phonon state coupled with both of the bases i and j. The Hamiltonian, H_{R}, for the phonon is given by

$$H_{\mathrm{R}} = \sum_{(i,j)}\sum_{q_{(i,j)}} \Omega_{q_{(i,j)}} c^+_{q_{(i,j)}} c_{q_{(i,j)}}, \tag{10}$$

where $\sum_{(i,j)}$ means the summation over all possible pairs of i and j . $c^+_{q_{(i,j)}}$ and $c_{q_{(i,j)}}$ represent the creation and annihilation operators concerning a phonon state $|q_{(i,j)}\rangle$, respectively. These operators satisfy the following commutation relations:

$$\left[c_{q_{(i,j)}}, c^+_{q'_{(i',j')}}\right] = \delta_{ii'}\delta_{jj'}\delta_{q_{(i,j)}q'_{(i',j')}}(1-\delta_{ij}) + \delta_{ij'}\delta_{ji'}\delta_{q_{(i,j)}q'_{(i',j')}}, \tag{11}$$

$$\left[c_{q_{(i,j)}}, c_{q'_{(i',j')}}\right] = \left[c^+_{q_{(i,j)}}, c^+_{q'_{(i',j')}}\right] = 0. \tag{12}$$

The interaction Hamiltonian, H_{SR}, for spin–phonon coupling is assumed to be [11]

$$H_{\mathrm{SR}} = \sum_{i,j,q_{(i,j)}} |i\rangle\langle j|\,(\kappa^*_{(i,j),q_{(i,j)}} c^+_{q_{(i,j)}} + \kappa_{(i,j),q_{(i,j)}} c_{q_{(i,j)}}),\quad (i,j=1,2,\ldots,M), \tag{13}$$

where $\kappa_{(i,j),q_{(i,j)}}$ represents a coupling constant between a pair of spins (i and j) and phonon $q_{(i,j)}$.

The total Hamiltonian, H, is described by

$$H = H_{\mathrm{S}} + H_{\mathrm{R}} + H_{\mathrm{SR}}. \tag{14}$$

In order to examine the spin dynamics [12,13] involving the effects of the interaction between spins and phonons, we can use a reduced density operator, ρ, for the spin system;

$$\rho = \mathrm{tr}_{\mathrm{R}}[\chi], \tag{15}$$

where χ is the density operator for the total system, and $\mathrm{tr}_{\mathrm{R}}[\,]$ represents that we take the trace over the phonon states, that is, $\mathrm{tr}_{\mathrm{R}}\{\cdots R_0\}$, when R_0 is the thermal-equilibrium density operator of phonon states.

2.2. Quantum master equation approach involving spin–phonon coupling

We start with a quantum master equation (in the interaction picture) in the Born–Markov approximation [13,14]:

$$\tilde{\rho} = -\int_0^t \mathrm{d}t' \mathrm{tr}_\mathrm{R}\left\{\left[\widetilde{H}_\mathrm{SR}(t), \left[\widetilde{H}_\mathrm{SR}(t'), \tilde{\rho}(t)R_0\right]\right]\right\}, \tag{16}$$

where $\tilde{\rho}$ denotes the reduced density operator of spin system in the interaction picture. The interaction Hamiltonian in the interaction picture $\widetilde{H}_\mathrm{SR}(t)$ is defined as

$$\widetilde{H}_\mathrm{SR}(t) = \mathrm{e}^{\mathrm{i}(H_\mathrm{S}+H_\mathrm{R})t} H_\mathrm{SR} \mathrm{e}^{-\mathrm{i}(H_\mathrm{S}+H_\mathrm{R})t}. \tag{17}$$

Using Eqs. (10), (13) and (17), we have

$$\widetilde{H}_\mathrm{SR}(t) = \sum_{i,j,q_{(i,j)}} \mathrm{e}^{\mathrm{i}H_\mathrm{S}t}\,|i\rangle\langle j| \times \mathrm{e}^{-\mathrm{i}H_\mathrm{S}t}\left\{\kappa^*_{(i,j),q_{(i,j)}} c^+_{q_{(i,j)}} \mathrm{e}^{\mathrm{i}\Omega_{q_{(i,j)}}t} + \kappa_{(i,j),q_{(i,j)}} c_{q_{(i,j)}} \mathrm{e}^{-\mathrm{i}\Omega_{q_{(i,j)}}t}\right\}, \tag{18}$$

where we have used

$$\mathrm{e}^{\mathrm{i}H_\mathrm{R}t} c^+_{q_{(i,j)}} \mathrm{e}^{-\mathrm{i}H_\mathrm{R}t} = c^+_{q_{(i,j)}} \mathrm{e}^{\mathrm{i}\Omega_{q_{(i,j)}}t}, \tag{19}$$

$$\mathrm{e}^{\mathrm{i}H_\mathrm{R}t} c_{q_{(i,j)}} \mathrm{e}^{-\mathrm{i}H_\mathrm{R}t} = c_{q_{(i,j)}} \mathrm{e}^{-\mathrm{i}\Omega_{q_{(i,j)}}t}. \tag{20}$$

The right-hand side of Eq. (16) has four terms:

$$\rho^{\tilde{V}} = -\int_0^t \mathrm{d}t' \mathrm{tr}_\mathrm{R}\left\{\widetilde{H}_\mathrm{SR}(t)\widetilde{H}_\mathrm{SR}(t')\tilde{\rho}(t)R_0 - \widetilde{H}_\mathrm{SR}(t')\tilde{\rho}(t)R_0\widetilde{H}_\mathrm{SR}(t) - \widetilde{H}_\mathrm{SR}(t)\tilde{\rho}(t)R_0\widetilde{H}_\mathrm{SR}(t') + \tilde{\rho}(t)R_0\widetilde{H}_\mathrm{SR}(t')\widetilde{H}_\mathrm{SR}(t)\right\}. \tag{21}$$

Using Eq. (18), the first term in the right-hand side of Eq. (21) is rewritten as

$$\begin{aligned} &-\int_0^t \mathrm{d}t' \mathrm{tr}_\mathrm{R}\left\{\widetilde{H}_\mathrm{SR}(t)\widetilde{H}_\mathrm{SR}(t')\tilde{\rho}(t)R_0\right\} \\ &= -\sum_{i,j,q_{(i,j)}} \int_0^t \mathrm{d}t' \left\{\mathrm{e}^{\mathrm{i}H_\mathrm{S}t}\,|i\rangle\langle j|\mathrm{e}^{-\mathrm{i}H_\mathrm{S}(t-t')}\,|i\rangle \right. \\ &\times \langle j|\mathrm{e}^{\mathrm{i}H_\mathrm{S}(t-t')}\rho\mathrm{e}^{-\mathrm{i}H_\mathrm{S}t}(1-\delta_{ij}) + \mathrm{e}^{\mathrm{i}H_\mathrm{S}t}\,|i\rangle\langle j|\,\mathrm{e}^{-\mathrm{i}H_\mathrm{S}(t-t')}|j\rangle \\ &\times \left.\langle i\,|\mathrm{e}^{\mathrm{i}H_\mathrm{S}(t-t')}\rho\mathrm{e}^{-\mathrm{i}H_\mathrm{S}t}\right\}\left[\left|\kappa_{(i,j),q_{(i,j)}}\right|^2\left\{\bar{n}(\Omega_{q_{(i,j)}},T)\mathrm{e}^{\mathrm{i}\Omega_{q_{(i,j)}}(t-t')} \right.\right. \\ &\left.\left. + (\bar{n}(\Omega_{q_{(i,j)}},T)+1)\mathrm{e}^{-\mathrm{i}\Omega_{q_{(i,j)}}(t-t')}\right\}\right] \end{aligned} \tag{22}$$

where we have used

$$\mathrm{tr}_\mathrm{R}\left(c^+_{q_{(i,j)}} c^+_{q'_{(i',j')}} R_0\right) = \mathrm{tr}_\mathrm{R}\left(c_{q_{(i,j)}} c_{q'_{(i',j')}} R_0\right) = 0, \tag{23}$$

$$\mathrm{tr}_\mathrm{R}\left(c^+_{q_{(i,j)}} c_{q'_{(i',j')}} R_0\right) = \left\{\delta_{ii'}\delta_{jj'}\delta_{q_{(i,j)}q'_{(i',j')}}(1-\delta_{ij}) + \delta_{ij'}\delta_{i'j}\delta_{q_{(i,j)}q'_{(i',j')}}\right\}\bar{n}(\Omega_{q_{(i,j)}},T), \tag{24}$$

$$\mathrm{tr}_\mathrm{R}\left(c_{q_{(i,j)}} c^+_{q_{(i',j')}} R_0\right) = \left\{\delta_{ii'}\delta_{jj'}\delta_{q_{(i,j)}q'_{(i',j')}}(1-\delta_{ij}) + \delta_{ij'}\delta_{i'j}\delta_{q_{(i,j)}q'_{(i',j')}}\right\}\left(\bar{n}(\Omega_{q_{(i,j)}},T)+1\right), \tag{25}$$

with

$$\bar{n}(\Omega_{q_{(i,j)}},T) = \left[\mathrm{e}^{(\Omega_{q_{(i,j)}}/k_\mathrm{B}T)} - 1\right]^{-1}. \tag{26}$$

$\bar{n}(\Omega_{q_{(i,j)}},T)$ denotes the mean phonon number for a phonon with frequency $\Omega_{q_{(i,j)}}$ in thermal equilibrium at temperature T. Because H_S remains in the right-hand side of Eq. (22), we insert the completeness relation with respect to eigenstates of H_S:

$$\sum_k |\psi_k\rangle\langle\psi_k| = 1 \tag{27}$$

into Eq. (22). As a result, Eq. (22) now becomes

$$\begin{aligned} &-\int_0^t \mathrm{d}t' \mathrm{tr}_\mathrm{R}\left\{\tilde{H}_\mathrm{SR}(t)\tilde{H}_\mathrm{SR}(t')\tilde{\rho}(t)R_0\right\} \\ &= -\sum_{i,j,q_{(i,j)}}\sum_{k,m,n}\int_0^t \mathrm{d}t' \left\{\mathrm{e}^{\mathrm{i}H_\mathrm{S}t}\,|i\rangle\langle j|\psi_k\rangle\langle\psi_k|i\rangle\langle j|\psi_m\rangle \right. \\ &\times \langle\psi_m|\rho|\psi_n\rangle\langle\psi_n|\mathrm{e}^{-\mathrm{i}H_\mathrm{S}t}(1-\delta_{ij}) + \mathrm{e}^{\mathrm{i}H_\mathrm{S}t}\,|i\rangle\langle j|\psi_k\rangle \\ &\times \left.\langle\psi_k|j\rangle\langle i|\,\psi_m\rangle\langle\psi_m|\rho|\,\psi_n\rangle\langle\psi_n|\mathrm{e}^{-\mathrm{i}H_\mathrm{S}t}\right\} \\ &\cdot \left[\left|\kappa_{(i,j),q_{(i,j)}}\right|^2\left\{\bar{n}(\Omega_{q_{(i,j)}},T)\mathrm{e}^{\mathrm{i}(\Omega_{q_{(i,j)}}-\omega_k+\omega_m)(t-t')} \right.\right. \\ &\left.\left. + (\bar{n}(\Omega_{q_{(i,j)}},T)+1)\mathrm{e}^{\mathrm{i}(-\Omega_{q_{(i,j)}}-\omega_k+\omega_m)(t-t')}\right\}\right]. \end{aligned} \tag{28}$$

In the Markov approximation, it is possible to evaluate the time integral in the right-hand side of Eq. (28). This approximation is acceptable when the order of t is much larger than that of t' [13]. In this case, we can assume t to be infinity. Under this approximation, Eq. (28) is expressed by

$$\begin{aligned} &-\int_0^t \mathrm{d}t' \mathrm{tr}_\mathrm{R}\left\{\tilde{H}_\mathrm{SR}(t)\tilde{H}_\mathrm{SR}(t')\tilde{\rho}(t)R_0\right\} \\ &= -\sum_{i,j}\sum_{k,m,n}\left(\mathrm{e}^{\mathrm{i}H_\mathrm{S}t}\,|i\rangle\langle j|\psi_k\rangle\langle\psi_k|i\rangle\langle j|\psi_m\rangle \right. \\ &\times \langle\psi_m|\rho\,|\psi_n\rangle\langle\psi_n|\mathrm{e}^{-\mathrm{i}H_\mathrm{S}t}(1-\delta_{ij}) + \mathrm{e}^{\mathrm{i}H_\mathrm{S}t}\,|i\rangle\langle j|\psi_k\rangle \\ &\times \left.\langle\psi_k|j\rangle\langle i|\psi_m\rangle\langle\psi_m|\rho|\psi_n\rangle\langle\psi_n|\mathrm{e}^{-\mathrm{i}H_\mathrm{S}t}\right)\gamma_{(i,j)}(\omega_m-\omega_k), \end{aligned} \tag{29}$$

where

$$\gamma_{(i,j)}(\omega_m-\omega_k) = \sum_{q_{(i,j)}}\left|\kappa_{(i,j),q_{(i,j)}}\right|^2\left\{\bar{n}(\Omega_{q_{(i,j)}},T)\delta(\Omega_{q_{(i,j)}}-\omega_k+\omega_m) + (\bar{n}(\Omega_{q_{(i,j)}},T)+1)\delta(-\Omega_{q_{(i,j)}}-\omega_k+\omega_m)\right\}. \tag{30}$$

Similarly, from the second, third and fourth terms in the right-hand side of Eq. (21), we, respectively, obtain

$$\begin{aligned} &-\int_0^t \mathrm{d}t' \mathrm{tr}_\mathrm{R}\left\{-\tilde{H}_\mathrm{SR}(t')\tilde{\rho}(t)R_0\tilde{H}_\mathrm{SR}(t')\right\} \\ &= -\sum_{i,j}\sum_{k,m,n}\left(-\mathrm{e}^{\mathrm{i}H_\mathrm{S}t}\,|\psi_k\rangle\langle\psi_k|i\rangle \right. \\ &\times \langle j|\psi_m\rangle\langle\psi_m|\rho|\psi_n\rangle\langle\psi_n|i\rangle\langle j|\mathrm{e}^{-\mathrm{i}H_\mathrm{S}t}(1-\delta_{ij}) \\ &- \mathrm{e}^{\mathrm{i}H_\mathrm{S}t}|\psi_k\rangle\langle\psi_k|i\rangle\langle j|\psi_m\rangle \\ &\times \left.\langle\psi_m|\rho|\psi_n\rangle\langle\psi_n|i\rangle\langle j|\mathrm{e}^{-\mathrm{i}H_\mathrm{S}t}\right)\gamma_{(ij)}(\omega_m-\omega_k), \end{aligned} \tag{31}$$

$$
\begin{aligned}
&-\int_0^t \mathrm{d}t' \mathrm{tr}_{\mathrm{R}}\{-\tilde{H}_{\mathrm{SR}}(t')\tilde{\rho}(t)R_0\tilde{H}_{\mathrm{SR}}(t')\}\\
&\quad=-\sum_{i,j}\sum_{k,m,n}\big(-\mathrm{e}^{\mathrm{i}H_{\mathrm{S}}t}|i\rangle\langle j|\psi_m\rangle\\
&\qquad\times\langle\psi_m|\rho|\psi_n\rangle\langle\psi_n|i\rangle\langle j|\psi_k\rangle\langle\psi_k|\mathrm{e}^{-\mathrm{i}H_{\mathrm{S}}t}(1-\delta_{ij})\\
&\qquad-\mathrm{e}^{\mathrm{i}H_{\mathrm{S}}t}|i\rangle\langle j|\psi_m\rangle\langle\psi_m|\rho|\psi_n\rangle\\
&\qquad\times\langle\psi_n|i\rangle\langle j|\psi_k\rangle\langle\psi_k|\mathrm{e}^{-\mathrm{i}H_{\mathrm{S}}t}\big)\gamma_{(ij)}(\omega_m-\omega_k),
\end{aligned}
\tag{32}
$$

and

$$
\begin{aligned}
&-\int_0^t \mathrm{d}t' \mathrm{tr}_{\mathrm{R}}\{\tilde{\rho}(t)R_0\tilde{H}_{\mathrm{SR}}(t)\tilde{H}_{\mathrm{SR}}(t')\}\\
&\quad=-\sum_{i,j}\sum_{k,m,n}\big(\mathrm{e}^{\mathrm{i}H_{\mathrm{S}}t}|\psi_m\rangle\langle\psi_m|\rho|\psi_n\rangle\langle\psi_n|i\rangle\langle j|\psi_k\rangle\\
&\qquad\times\langle\psi_k|i\rangle\langle j|\mathrm{e}^{-\mathrm{i}H_{\mathrm{S}}t}(1-\delta_{ij})+\mathrm{e}^{\mathrm{i}H_{\mathrm{S}}t}|\psi_m\rangle\langle\psi_m|\rho|\psi_n\rangle\\
&\qquad\times\langle\psi_n|i\rangle\langle j|\psi_k\rangle\langle\psi_k|i\rangle\langle j|\mathrm{e}^{-\mathrm{i}H_{\mathrm{S}}t}\big)\gamma_{(ij)}(\omega_m-\omega_k).
\end{aligned}
\tag{33}
$$

Using Eqs. (29), (31), (32) and (33), we get the quantum master equation involving the spin–phonon coupling in the Schrödinger picture:

$$
\begin{aligned}
\rho^{\dot{\tilde{V}}}_{\alpha\beta}&=-i(\omega_\alpha-\omega_\beta)\rho_{\alpha\beta}-\sum_{m,n}^{M}\Gamma_{\alpha\beta;mn}\rho_{mn}\\
&\quad+iB\sum_{n}^{M}(S_{\alpha n}\rho_{n\beta}-\rho_{\alpha n}S_{n\beta})\quad(\alpha\neq\beta)
\end{aligned}
\tag{34}
$$

and

$$
\rho^{\dot{\tilde{V}}}_{\alpha\alpha}=-\sum_{m}^{M}\Gamma_{\alpha\alpha;mm}\rho_{mm}+iB\sum_{n}^{M}(S_{\alpha n}\rho_{n\alpha}-\rho_{\alpha n}S_{n\alpha}),
\tag{35}
$$

where

$$
\begin{aligned}
\Gamma_{\alpha\beta;mn}&=\sum\nolimits_{k}^{M}\sum_{i,j}^{N}\Big[\delta_{\beta n}\{(1-\delta_{ij})C^*_{\alpha i}C_{kj}C^*_{ki}C_{mj}\\
&\quad+C^*_{\alpha i}|C_{kj}|^2C_{mi}\}\gamma_{(i,j)}(\omega_m-\omega_k)\\
&\quad+\delta_{\alpha m}\{(1-\delta_{ij})C^*_{ni}C_{kj}C^*_{ki}C_{\beta j}\\
&\quad+C^*_{ni}|C_{kj}|^2C_{\beta i}\}\gamma_{(i,j)}(\omega_n-\omega_k)\Big]\\
&\quad-\sum_{i,j}^{N}\Big[\{(1-\delta_{ij})C^*_{\alpha i}C_{mj}C^*_{ni}C_{\beta j}+C^*_{\alpha i}C_{mj}C^*_{nj}C_{\beta i}\}\}\\
&\quad\times\{\gamma_{(i,j)}(\omega_m-\omega_\alpha)+\gamma_{(i,j)}(\omega_n-\omega_\beta)\}\Big],
\end{aligned}
\tag{36}
$$

$$
\begin{aligned}
\Gamma_{\alpha\alpha;mm}&=\delta_{\alpha m}\sum_{k}^{M}\sum_{i,j}^{N}\Big[2\{(1-\delta_{ij})C^*_{\alpha i}C_{kj}C^*_{ki}C_{\alpha j}\\
&\quad+|C_{\alpha i}|^2|C_{kj}|^2\}\gamma_{(i,j)}(\omega_m-\omega_k)\Big]\\
&\quad-\sum_{i,j}^{N}\Big[2\{(1-\delta_{ij})C^*_{\alpha i}C_{mj}C^*_{mi}C_{\alpha j}\\
&\quad+|C_{\alpha i}|^2|C_{mj}|^2\}\gamma_{(i,j)}(\omega_m-\omega_\alpha)\Big]
\end{aligned}
\tag{37}
$$

and

$$
\gamma_{(i,j)}(\omega)=\frac{2\gamma^0_{(i,j)}}{1+\exp(-\omega/k_{\mathrm{B}}T)}.
\tag{38}
$$

This factor $\gamma_{(i,j)}(\omega)$ is taken to satisfy the thermal equilibrium condition [11]; $\gamma^0_{(i,j)}$ indicates the high-temperature limit of $\gamma_{(i,j)}(\omega)$ and k_{B} is the Boltzmann constant. The third and second terms on the right-hand side of Eqs. (34) and (35) represent the interaction between the spin-aggregate system and the external magnetic field, respectively. B represents the magnetic amplitude. We have solved Eqs. (34) and (35) numerically using the fourth-order Runge–Kutta method.

3. Concluding remarks

We formulated a master equation approach involving the effects of the interaction between spins and phonons in the Markov approximation. This calculation relates to the method of the calculation in the quantum computer. Coherent states of spins have received current interest in relation to quantum computing [14]. For example, the resonating state of spins is expressed by the superposition of two states $|\alpha\rangle$ and $|\beta\rangle$:

$$
|\Psi\rangle=\cos\theta\,|\,\alpha\rangle+\mathrm{e}^{\mathrm{i}\phi}\sin\theta|\beta\rangle,
\tag{39}
$$

where ϕ is the phase factor. If the states $|\alpha\rangle$ and $|\beta\rangle$ are regarded as classical bits 0 and 1, respectively, in conventional computer, the quantum bit (qubit) in quantum computer is defined as the above superposed state $|\Psi\rangle$. A quantum computer based on electron spins as qubits have actively studied [15,16]. Recently, we have reviewed spin and pseudo spin models for several kinds of two-level systems in relation to quantum computing [8]. However, the control of decoherence between monomers is one of the bottle necks for many qubit systems in future quantum devices. In fact, the coherence in the mesoscopic quantum systems is rapidly destroyed by coupling with other freedom of reservoirs such as phonons [17–21]. We consider that the dynamics is important for understanding the relation between the architectures and the function of the spin aggregate. As for such a device, it is necessary to perform the spin dynamics involving the effect of the reservoirs for the several spin systems which possess the many novel architectures. At the next stage, therefore, we apply the present approach to the dendritic spin systems, as well as aggregates with other spatial dimensions, in order to elucidate the structure dependence (dipole–dipole interaction) of spin dynamics.

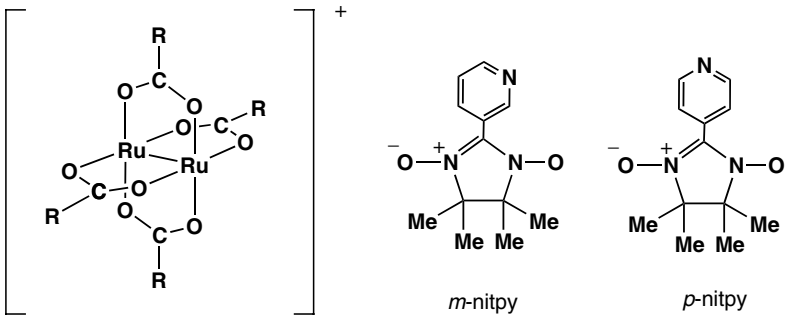
Acknowledgements

M.T.'s work was supported by Research Fellowships of the Japan Society for the Promotion of Science for

Young Scientists. This work was supported by Grant-in-Aid for Scientific Research (Nos. 14204061 and 14340184) from Japan Society for the promotion of Science (JSPS).

References

[1] D.A. Tomalia, A.M. Naylor, W.A. Goddard III, Angew. Chem. Int. Ed. Engl. 29 (1990) 138.
[2] C. Devadoss, P. Bharathi, J.S. Moore, J. Am. Chem. Soc. 118 (1996) 9635.
[3] R. Kopelman, M. Shortreed, Z.-Y. Shi, W. Tan, Z. Xu, J.S. Moore, A. Bar-Haim, J. Klafter, Phys. Rev. Lett. 78 (1997) 1239.
[4] M.R. Shortreed, S.F. Swallen, Z.-Y. shi, W. Tan, Z. Xu, C. Devadoss, J.S. Moore, R. Kopelman, J. Phys. Chem. B 101 (1997) 6318.
[5] M. Nakano, M. Takahata, H. Fujita, S. Kiribayashi, K. Yamaguchi, Chem. Phys. Lett. 323 (2000) 249.
[6] M. Takahata, M. Nakano, H. Fujita, K. Yamaguchi, Chem. Phys. Lett. 363 (2002) 422.
[7] M. Takahata, M. Nakano, K. Yamaguchi, J. Theor. Comp. Chem. 2 (2003) 459.
[8] K. Yamaguchi, M. Nakano, H. Nagao, M. Okumura, S. Yamanaka, T. Kawakami, D. Yamaki, M. Nishino, Y. Shigeta, Y. Kitagawa, Y. Takano, M. Takahata, R. Takeda, Bull. Korean Chem. Soc. 24 (2003) 864.
[9] H. Haken, Quantenfeldtheorie Des Festkörpers, B.G. Teubner, Stuttgart, 1973.
[10] D. Hinzke, U. Nowak, Phys. Stat. Sol. 189 (2002) 475.
[11] J.A. Leegwater, J.R. Durrant, D.R. Klug, J. Phys. Chem. B 101 (1997) 7205.
[12] R. Kubo, M. Toda, N. Hashitume, Statistical Physics II, Springer, 1991.
[13] H.J. Carmichael, Statistical Methods in Quantum Optics 1, Springer-Verlag, Berlin, 1999.
[14] M.A. Nielsen, I.L. Chuang, Quantum Computation and Quantum Information, Cambridge University Press, 2001.
[15] D. Loss, D.P. DiVincenzo, Phys. Rev. A 57 (1998) 120.
[16] A. Imamoglu, D.D. Awschalom, G. Burkard, D.P. DiVincenzo, D. Loss, M. Sherwin, A. Small, Phys Rev. Lett. 83 (1999) 4204.
[17] D. Chandler, P.G. Wolyness, J. Chem. Phys. 74 (1981) 4078.
[18] B. Carmeli, D. Chandler, J. Chem. Phys. 82 (1985) 3400.
[19] E. Joos, H.D. Zeh, C. Kiefer, D. Giulini, J. Kupsch, I.-O. Stamatescu, Decoherence and the Appearance of a Classical World in Quantum Theory, Springer-Verlag, Berlin, Heidelberg, 1996.
[20] Y. Imry, Introduction to Mesoscopic Physics, Oxford University Press, 2002.
[21] Ph. Blanchard, D. Giulini, E. Joos, C. Kiefer, I.-O. Stamatescu (Eds.), Decoherence: Theoretical, Experimental, and Conceptual Problems, Springer-Verlag, Berlin, Heidelberg, 2000.



$[Ru_2(O_2CR)_4]^+$; R = CMe_3 (piv) and Et (pro)

Fig. 1. Chemical structures of ruthenium(II,III) carboxylates and pyridyl nitronyl nitroxides.

interaction through the pyridyl group is weak, it plays an important role in their magnetic properties because *m*- and *p*-nitpy magnetically couple with the Ru(II,III) dimer through the coordinating pyridyl groups with the opposite ways; *m*-nitpy gives the antiferromagnetic interaction and *p*-nitpy the ferromagnetic interaction. The ferromagnetic behavior observed for **1** was interpreted by taking into consideration that the *p*-nitpy ferromagnetically interacts with Ru(II,III) dimer through the pyridyl nitrogen ($J' = 0.45$ cm^{-1}) as well as through the nitroxide oxygen ($J = 20$ cm^{-1}). In this manner, the antiferromagnetic behavior of $[Ru_2(piv)_4(m\text{-nitpy})]_n(BF_4)_n \cdot nH_2O$ was considered to be due to the antiferromagnetic interaction ($J' = -0.4$ cm^{-1}) through the coordinated pyridyl group in spite of the ferromagnetic interaction through the N–O group ($J = 0.3$ cm^{-1}). At the stage, however, we did not have the crystal structure of the Ru(II,III) polymer with *m*-nitpy at hand. In the present study, we employed ruthenium(II,III) propionate as the dimer and obtained polymer chain complexes $[Ru_2(pro)_4(m\text{- and } p\text{-nitpy})]_nX_n$ and adduct dimer complexes $[Ru_2(pro)_4(m\text{- and } p\text{-nitpy})_2]X$ ($X = BF_4$ and PF_6) as in the case of ruthenium(II,III) pivalate with the pyridyl radicals. Herein, we report on the magnetic properties of these complexes. The crystal structures of the polymer complex of *m*-nitpy and adduct dimer of *p*-nitpy were also determined.

2. Experimental

2.1. Synthesis

All manipulations were performed under anaerobic conditions using standard Schlenk techniques. The tetrafluoroborate and hexafluorophosphate salts, $[Ru_2(pro)_4(H_2O)_2]BF_4$ and $[Ru_2(pro)_4(H_2O)_2]PF_6$, were prepared according to a method described in the literature [25]. The axial water molecules of these salts were removed before use by heating under vacuum. The nitronyl nitroxide radicals, *p*-nitpy and *m*-nitpy, were obtained according to a method described in the elsewhere [26,27].

2.1.1. $[Ru_2(pro)_4(m\text{-nitpy})]_n(PF_6)_n \cdot nCH_2Cl_2$ (**4**)

A 10.0 mg (0.0148 mmol) portion of $[Ru_2(pro)_4(H_2O)_2]PF_6$ was employed for a reaction with *m*-nitpy (3.5 mg, 0.015 mmol) in CH_2Cl_2 (5 cm^3) under argon. Onto the reacted solution was slowly added hexane–dichloromethane (13 cm^3); the resulting solution was allowed to stand for two weeks at room temperature to deposit deep blue crystals, which were collected by filtration. The yield was 7.9 mg (59% based on $[Ru_2(pro)_4(H_2O)_2]PF_6$). *Anal.* calc. for $C_{25}H_{38}PCl_2F_6N_3O_{10}Ru_2$ (**4**): C, 31.32; H, 4.00; N, 4.38. Found: C, 31.27; H, 4.05; N, 4.32%. IR (cm^{-1}): $\nu(CH_3)$ 2991, 2948, ν(asym-(COO)) 1454, ν(sym(COO)) 1431, ν(NO) 1377, $\nu(PF_6^-)$ 846. Diffuse reflectance spectrum λ_{max}/nm 266, 369, 626sh, 962br. μ_{eff} (300 K)/μ_B 4.66.

2.1.2. $[Ru_2(pro)_4(m\text{-nitpy})_2]BF_4$ (**5**)

This compound was obtained as deep blue crystals by the reaction of $[Ru_2(pro)_4(H_2O)_2]BF_4$ (20.0 mg, 0.0324 mmol) of *m*-nitpy (15.4 mg, 0.0657 mmol) in CH_2Cl_2/hexane using the same method as that of **4**. The yield was 24.6 mg (72.3% based on $[Ru_2(pro)_4(H_2O)_2]BF_4$). *Anal.* calc. for $C_{36}H_{52}BF_4N_6O_{12}Ru_2$ (**5**): C, 41.19; H, 4.99; N, 8.01. Found: C, 41.03; H, 4.96; N, 7.95%. IR (cm^{-1}): $\nu(CH_3)$ 2979, 2943, ν(asym(COO)) 1465, ν(sym(COO)) 1421, ν(NO) 1376, $\nu(BF_4^-)$ 1055. Diffuse reflectance spectrum λ_{max}/nm 260, 359, 599, 652sh, 906br. μ_{eff} (300 K)/μ_B 4.85.

2.1.3. $[Ru_2(pro)_4(p\text{-nitpy})]_n(BF_4)_n \cdot nCH_2Cl_2$ (**6**)

This compound was obtained as deep green crystals by the reaction of $[Ru_2(pro)_4(H_2O)_2]BF_4$ (10.2 mg, 0.0165 mmol) of *p*-nitpy (4.1 mg, 0.018 mmol) in

CH_2Cl_2/hexane using the same method as that of **4**. The yield was 8.7 mg (61% based on $[Ru_2(pro)_4(H_2O)_2]BF_4$). *Anal.* calc. for $C_{25}H_{38}BCl_2F_4N_3O_{10}Ru_2$ (**6**): C, 33.34; H, 4.25; N, 4.67. Found: C, 33.32; H, 4.23; N, 4.56%. IR (cm^{-1}): $\nu(CH_3)$ 2984, 2948, ν(asym(COO)) 1471, ν(sym(COO)) 1429, ν(NO) 1374, $\nu(BF_4^-)$ 1057. Diffuse reflectance spectrum λ_{max}/nm 232, 639sh, 983br. μ_{eff} (300 K)/μ_B 4.50.

2.1.4. $[Ru_2(pro)_4(p\text{-nitpy})_2]BF_4$ (7)

This compound was obtained as deep green crystals by the reaction of $[Ru_2(pro)_4(H_2O)_2]BF_4$ (20.0 mg, 0.0324 mmol) of *p*-nitpy (15.4 mg, 0.0657 mmol) in CH_2Cl_2/hexane using the same method as that of **4**. The yield was 25.3 mg (74.3% based on $[Ru_2(pro)_4(H_2O)_2]BF_4$). *Anal.* calc. for $C_{36}H_{52}BF_4N_6O_{12}Ru_2$ (**7**): C, 41.19; H, 4.99; N, 8.01. Found: C, 41.12; H, 5.01; N, 8.29%. IR (cm^{-1}): $\nu(CH_3)$ 2986, 2943, ν(asym(COO)) 1458, ν(sym(COO)) 1430, ν(NO) 1376, $\nu(BF_4^-)$ 1066. Diffuse reflectance spectrum λ_{max}/nm 266, 363, 429, 633sh, 1142br. μ_{eff} (300 K)/μ_B 5.21.

2.2. Measurements

Elemental analyses for carbon, hydrogen, and nitrogen were conducted using a Perkin–Elmer 2400 Series II CHNS/O Analyzer. Infrared spectra were measured with a JASCO MFT-2000 FT-IR Spectrometer in the 4000–600 cm^{-1} region. The electronic spectra were measured with a Shimadzu UV–Vis-NIR Recording Spectrophotometer Model UV-3100. The temperature dependence of the magnetic susceptibilities was measured with a Quantum Design MPMS-5S SQUID susceptometer operating at a magnetic field of 0.5 T over a temperature range of 4.5–300 K. The susceptibilities were corrected for the diamagnetism of the constituent atoms using Pascal's constants [28]. The effective magnetic moments were calculated from the equation $\mu_{eff} = 2.828\sqrt{\chi T}$, where χ is the magnetic susceptibility per mole of $Ru^{II,III}{}_2$-radical unit.

2.3. X-ray crystal structure analyses

Diffraction data were collected on an Enraf-Nonius CAD4 diffractometer using graphite-monochromated Mo Kα radiation at 25 ± 1 °C. Crystal data are given in Table 1. The structure was solved by direct methods, and refined by full-matrix least-squares methods. All non-hydrogen atoms were refined with anisotropic thermal parameters. The hydrogen atoms were inserted at their calculated positions and fixed there. All of the calculations were carried out on a VAX station 4000 90A computer utilizing the MoLEN program package [29].

Table 1
Crystal data of **4** and **7**

Complex	**4**	**7**
Formula	$C_{25}H_{38}PCl_2F_6N_3O_{10}Ru_2$	$C_{36}H_{52}BF_4N_6O_{12}Ru_2$
Formula weight	958.80	1050.0
Crystal system	monoclinic	monoclinic
Space group	$P2_1/c$	$C2/c$
a (Å)	13.419(4)	12.813(6)
b (Å)	12.637(2)	26.479(4)
c (Å)	22.441(6)	13.353(6)
β (°)	97.79(1)	98.59(2)
V (Å^3)	3770(2)	4479(3)
Z	4	4
D_c (g cm^{-3})	1.68	1.56
D_m (g cm^{-3})	1.69	1.54
μ(Mo Kα) (cm^{-1})	10.45	7.377
Crystal size (mm)	$0.65 \times 0.50 \times 0.38$	$0.62 \times 0.40 \times 0.32$
2θ Range (°)	1.0–51.0	1.0–51.0
Total number of reflections measured	7387	4272
Number of unique reflections with $I \geqslant 3\sigma(I)$	5577	2404
$F(000)$	1920	2140
Final number of variables	413	285
R	0.053	0.069
R_w	0.068	0.079

$R = \sum||F_o| - |F_c||/\sum|F_o|$, $R_w = [\sum w(|F_o| - |F_c|)^2/\sum w|F_o|^2]^{1/2}$.

3. Results and discussion

3.1. Description of crystal structures

3.1.1. $[Ru_2(pro)_4(m\text{-nitpy})]_n(PF_6)_n \cdot nCH_2Cl_2$ (4)

The crystal structure of **4** is depicted in Fig. 2. The selected bond distances and angles are listed in Table 2. The zigzag chain structure is built up by alternated arrangement of Ru(II,III) dimer and *m*-nitpy, like the case of $[Ru_2(piv)_4(p\text{-nitpy})]_n(BF_4)_n$ [23]. One of the two N–O groups of *m*-nitpy coordinates to the Ru(II,III) dimer by the Ru1–O9 separation of 2.295(4) Å. The other nitroxide oxygen designated by O10 is free from the coordination. The pyridyl nitrogen alternatively participates in the coordination with an axial Ru2–N3 distance of 2.271(5) Å. The N–O bond lengths of the *m*-nitpy molecule (1.297(7) Å for N1–O9 and 1.256(8) Å for N2–O10) indicate that the nitroxide is in a free radical form, although the coordinated N–O bond (N1–O9) is slightly elongated due to the axial coordination similarly to the case of $[Ru_2(piv)_4(p\text{-nitpy})]_n(BF_4)_n$ [23]. The Ru1–Ru2 bond distance of the dimer core, the axial sites of which are occupied by the nitroxide oxygen and pyridyl nitrogen, is 2.278(1) Å, which is nearly the same as that (2.272(1) Å) for $[Ru_2(piv)_4(p\text{-nitpy})]_n$-$(BF_4)_n$ [23].

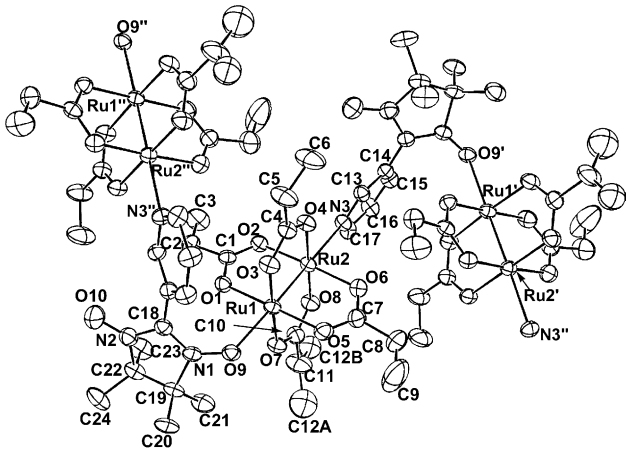


Fig. 2. ORTEP drawing of the structure of **4**. The hydrogen atoms, PF_6^- ions, and CH_2Cl_2 molecules are omitted for clarity.

Table 2
Selected bond distances (Å) and angles (°) of **4** and **7** with their estimated deviations in parentheses

4	
Ru1–Ru2	2.278(1)
Ru1–O1	2.026(4)
Ru1–O3	2.026(4)
Ru1–O5	2.027(5)
Ru1–O7	2.018(4)
Ru1–O9	2.295(4)
Ru2–O2	2.023(5)
Ru2–O4	2.024(4)
Ru2–O6	2.031(5)
Ru2–O8	2.013(4)
Ru2–N3	2.271(5)
O9–N1	1.297(7)
O10–N2	1.256(8)
Ru2–Ru1–O9	176.9(1)
Ru1–Ru2–N3	177.1(1)
Ru1–O9–N1	120.0(3)
7	
Ru–Ru′	2.277(1)
Ru–O1	2.000(7)
Ru–O2	1.990(8)
Ru–O3	2.013(7)
Ru–O4	2.011(7)
Ru–N3	2.294(8)
O5–N1	1.25(1)
O6–N2	1.26(1)
Ru′–Ru–N3	174.7(2)

3.1.2. $[Ru_2(pro)_4(p\text{-nitpy})_2]BF_4$ (7)

The bis-niroxide adduct structure of **7** is depicted in Fig. 3. A crystallographic inversion center is located at the midpoint of the Ru–Ru′ bond of the Ru(II,III) core. The Ru–Ru′ and axial Ru–N3 distances are 2.277(1) and 2.294(8) Å, respectively, which are comparable to the corresponding ones in the previously reported bis-adduct complex of *p*-nitpy [22]. The two N–O groups

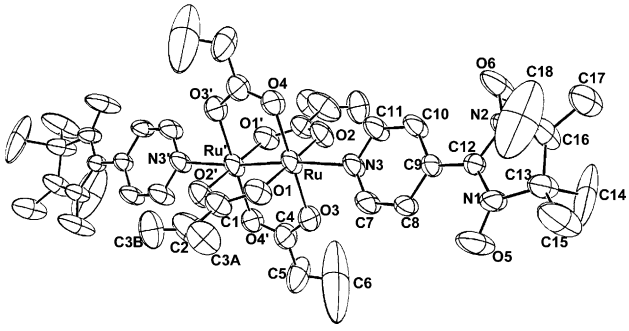


Fig. 3. ORTEP drawing of the structure of **7**. The hydrogen atoms and BF_4^- ions are omitted for clarity.

of *m*-nitpy are both free from the coordination and their bonds lengths 1.25(1) Å (for N1–O5) and 1.26(1) Å (for N2–O6) indicate that the *p*-nitpy molecule exists as a free radical [22]. The nearest O···O distance between the N–O groups of the radicals of the neighboring Ru(II,III) cationic units is 3.48(1) Å for O6···O6 $(1-x,-y,-z)$, which is relatively shorter than that (3.79(1) Å) for **3** [22].

3.2. Structural comparison of Ru(II,III) complexes with pyridyl nitroxide radicals

In Table 3, structural parameters of Ru(II,III) dimers with pyridyl nitoroxide radicals are listed. The structural effect on the polymer and bis-adduct structures due to the change from *t*-butyl to propyl group in the dimeric core cannot be found. The Ru–Ru bond distances are nearly the same (2.27–2.28 Å) and the axial Ru–N_{py} and Ru–O_{ax} distances and Ru–O_{ax}–N angle are similar among the listed complexes (Ru–N_{py} = 2.27–2.30 Å; Ru–O_{ax} = 2.286(7) and 2.295(4) Å; Ru–O_{ax}–N = 125.3(6)° and 120.3(3)°). It is also noticeable that there is no significant difference in the Ru–Ru and Ru–N_{py} distances between the polymer complexes (**1** and **4**) and bis-adduct complexes (**2**, **3**, and **7**). This may be related to the fact that polymer and bis-adduct complexes were obtained only by changing the molar ratio of the radicals and Ru(II,III) cationic dimers employed for the reactions.

3.3. Magnetic properties

Temperature dependences of magnetic moments are shown for complexes **4**–**7** in Figs. 4–7, respectively, in which the solid lines are drawn with the parameters listed in Table 4 (g_M and g_R are the *g* factors of the Ru(II,III) core and the nitroxide radical, respectively. *D* is the parameter for the zero-field splitting for the Ru(II,III) core. *J*, *J*′, and *J*″ are the parameters for the magnetic interaction defined in Fig. 8). The magnetic models for the analyses are illustrated in Fig. 8, details of the quantum treatments for each model being found

Table 3
Structural parameters of Ru(II,III) dimers with pyridyl nitroxide radicals

Complexes	Ru–Ru	Ru–O_{ax} [Ru–N_{py}]	∠Ru–O_{ax}–N	N–O	Ref.
1	2.272(1)	2.286(7) [2.260(9)]	125.3(6)	1.30(1) 1.27(1)	[22]
2	2.276(1)	[2.269(3)]		1.273(4) 1.274(4)	[22]
3	2.282(1)	[2.282(6)]		1.27(1) 1.27(1)	[22]
4	2.277(1)	2.295(4)	120.3(3)	1.297(7) 1.256(8)	this work
7	2.277(1)	[2.294(8)]		1.25(1) 1.26(1)	this work

elsewhere [22,23]. Table 4 contains the used model types as well as the magnetic parameters for the complexes **1**–**7**. The magnetic moment of **6** gradually decreases with lowering of temperature and reaches a minimum value around 90 K (Fig. 6). Upon further cooling, the magnetic moment increases gradually, reaching a maximum value of 4.81 μ_B at 14 K, and then decreases. In Fig. 6, the dashed line is drawn by the equation based on the model A, the parameters being set at $g_M = 2.06$, $g_R = 2.0$, $J = 20$ cm^{-1}, $J' = 0.4$ cm^{-1}, and $D = 80$ cm^{-1}. Unfortunately, we could not simulate the temperature-dependent profile properly. However, the behavior below 100 K is very similar to that of **1** [23]. Hence, it is certain that **6** has a polymer structure and *p*-nitpy ferromagnetically couples with Ru(II,III) dimer through the N–O and pyridyl groups. In fact, the positive J and J' values were also obtained in the best fitting using $D = 300$ cm^{-1}, which could support the existence the ferromagnetic interaction through the N–O and pyridyl groups. On the contrary, the magnetic moment of **4** de-

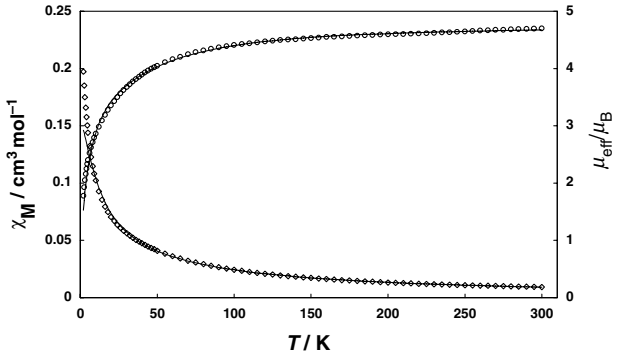


Fig. 4. Effective magnetic moments (○) and magnetic susceptibility data (◇) of **4**. The solid line was calculated from the spin coupling model A with the parameters in Table 4.

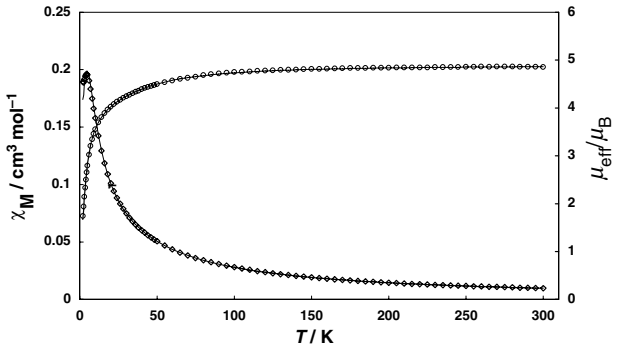


Fig. 5. Effective magnetic moments (○) and magnetic susceptibility data (◇) of **5**. The solid line was calculated from the spin coupling model B with the parameters in Table 4.

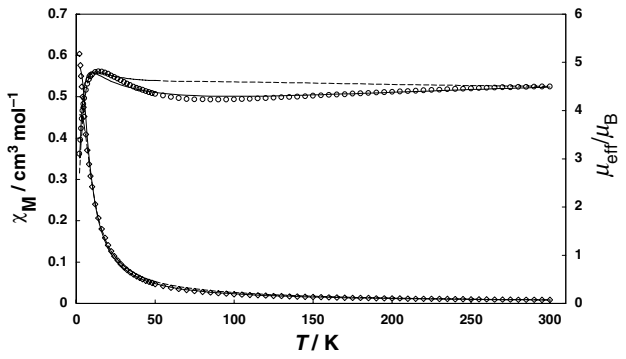


Fig. 6. Effective magnetic moments (○) and magnetic susceptibility data (◇) of **6**. The solid line was calculated from the spin coupling model A with the parameters in Table 4.

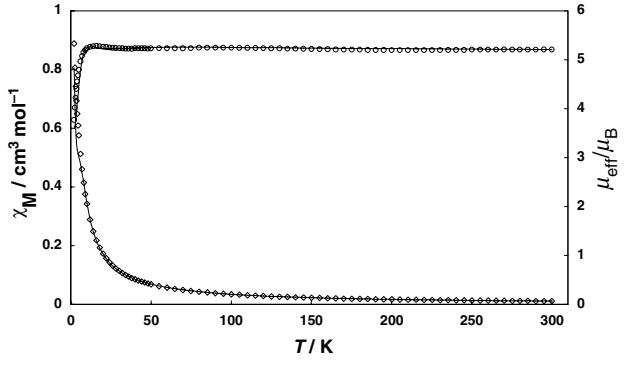


Fig. 7. Effective magnetic moments (○) and magnetic susceptibility data (◇) of **7**. The solid line was calculated from the spin coupling model B with the parameters in Table 4.

Table 4
Fitting parameters for the magnetic data

Complexes	g_M	g_R	D (cm^{-1})	J (cm^{-1})	J' (cm^{-1})	J'' (cm^{-1})	Model	Ref.
1	2.23	2.00	50	20	0.45		A	[23]
2	2.3	2.0	50		−1.0	0	B	[22]
3	2.09	2.0	50		1.4	−6.0	B	[22]
4	2.3	2.0	60	5	−1.7		A	this work
5	2.19	2.0	45		−1.6	0	B	this work
6	2.25	2.0	300	12	0.35		A	this work
7	2.35	2.0	35		1.45	−6.0	B	this work

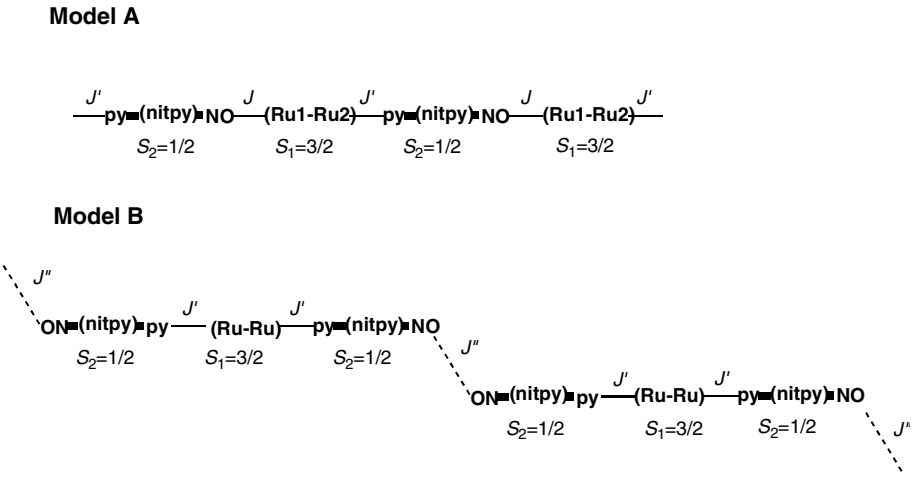


Fig. 8. Spin coupling models.

creases steadily with lowering of the temperature. This behavior obviously comes from the antiferromagnetic interaction through the pyridyl group of *m*-nitpy ($J' = -1.7$ cm^{-1}) because the interaction through the N–O group is ferromagnetic ($J = 5$ cm^{-1}). According to our previously reported proposal [24], the axial bond angle value of ∠Ru1–O9–N1 = 120.0(3)° is in the range for the ferromagnetic interaction between the ruthenium(II,III) core and the radical. In Table 4, two pairs of bis-adduct complexes consisting of *m*- and *p*-nitpy are included. A pair of **2** and **5** has the antiferromagnetic interaction through pyridyl group of *m*-nitpy [$J' = -1.0$ (for **2**) and −1.6 cm^{-1} (for **5**)]. The other pair of **3** and **7** has the ferromagnetic interaction through pyridyl group of *p*-nitpy [$J' = 1.4$ (for **3**) and 1.45 cm^{-1} (for **7**)]. The difference can be interpreted by the consideration for the number of carbon and nitrogen atoms on the π-system between the Ru(II,III) dimer and the N–O group based on the spin-polarization mechanism [22].

4. Conclusions

In this study, we obtained adduct polymer complexes $[Ru_2(pro)_4(m\text{- and }p\text{-nitpy})]_nX_n$ and dimer complexes $[Ru_2(pro)_4(m\text{- and }p\text{-nitpy})_2]X$ ($X = BF_4$ and PF_6) as in the case of ruthenium(II,III) pivalate with the pyridyl radicals. It was found that the difference of alkyl group on the carboxylate ion of the Ru(II,III) dimer core does not give any important effect on the structures and magnetic properties for the obtained polymer and bis-adduct complexes. The magnetic investigations on the pyridyl nitroxide complexes of ruthenium(II,III) propionate and ruthenium(II,III) pivalate show that the pyridyl group can mediate ferro- or antiferromagnetically the interaction depending on the position on the coordinated nitrogen atom on the pyridyl ring; *m*-nitpy gives the antiferromagnetic interaction and *p*-nitpy the ferromagnetic interaction in combination with Ru(II,III) dimer.

5. Supplementary data

Crystallographic data for the structural analysis have been deposited with the Cambridge Crystallographic Data Center, CCDC Nos. 256932 and 256933 for complexes **4** and **7**, respectively. Copies of this information may be obtained free of charge from The Director, CCDC, 12 Union Road, Cambridge CB2 1EZ, UK (fax: +44 1223 336 033; e-mail: deposit@ccdc.cam.ac.uk or on the web: http://www.ccdc.cam.ac.uk).

Acknowledgment

The present work was partially supported by Grants-in-Aid for Scientific Research (Nos. 14540516 and 16550062) from the Ministry of Education, Culture, Sports, Science, and Technology.

References

[1] F.A. Cotton, R.A. Walton, Multiple Bonds between Metal Atoms, 2nd ed., Oxford University Press, New York, 1993.
[2] K.R. Dunber, J. Cluster Sci. 5 (1994) 125.
[3] F.A. Cotton, Inorg. Chem. 37 (1998) 5710.
[4] M.A.S. Aquino, Coord. Chem. Rev. 170 (1998) 141.
[5] M.H. Chisholm, Acc. Chem. Res. 33 (2000) 53.
[6] F.A. Cotton, C. Lin, C.A. Murillo, Acc. Chem. Res. 34 (2001) 759.
[7] J.G. Norman, G.E. Renzoni, D.A. Case, J. Am. Chem. Soc. 101 (1979) 5256.
[8] F.A. Cotton, Y. Kim, T. Ren, Inorg. Chem. 31 (1992) 2723.
[9] J. Telser, R. Drago, Inorg. Chem. 23 (1984) 3114.
[10] F.D. Cukiernik, A.-M.G. Godquin, R. Maldivi, J.-C. Marchon, Inorg. Chim. Acta 215 (1994) 203.
[11] E.J. Beck, K.D. Drysdale, L.K. Thompson, L. Li, C.A. Murphy, M.A.S. Aquino, Inorg. Chim. Acta 279 (1998) 121.
[12] D. Yoshioka, M. Handa, H. Azuma, M. Mikuriya, I. Hiromitsu, K. Kasuga, Mol. Cryst. Liq. Cryst. 342 (2000) 133.
[13] M. Handa, D. Yoshioka, Y. Sayama, K. Shiomi, M. Mikuriya, I. Hiromitsu, K. Kasuga, Chem. Lett. (1999) 1033.
[14] D. Yoshioka, M. Mikuriya, M. Handa, Bull. Chem. Soc. Jpn. 77 (2004) 2205.
[15] H. Miyasaka, C.S.C. Fernandez, R. Clerac, K.R. Dunbar, Angew. Chem. Int. Ed. 39 (2000) 3831.
[16] H. Miyasaka, R. Clerac, C.S.C. Fernandez, K.R. Dunbar, Inorg. Chem. 40 (2001) 1663.
[17] Y. Liao, W.W. Shum, J.S. Miller, J. Am. Chem. Soc. 124 (2002) 9336.
[18] D. Yoshioka, M. Mikuriya, M. Handa, Chem. Lett. (2002) 1044.
[19] M. Handa, Y. Sayama, M. Mikuriya, R. Nukada, I. Hiromitsu, K. Kasuga, Bull. Chem. Soc. Jpn. 71 (1998) 119.
[20] Y. Sayama, M. Handa, M. Mikuriya, I. Hiromitsu, K. Kasuga, Bull. Chem. Soc. Jpn. 74 (2001) 2129.
[21] Y. Sayama, M. Handa, M. Mikuriya, R. Nukada, I. Hiromitsu, K. Kasuga, in: G. Ondrejovic, A. Sirota (Eds.), Coordination Chemistry at the Turn of the Century, Slovak Technical University Press, Blatislava, 1999, pp. 447–452.
[22] Y. Sayama, M. Handa, M. Mikuriya, I. Hiromitsu, K. Kasuga, Bull. Chem. Soc. Jpn. 73 (2000) 2499.
[23] (a) Y. Sayama, M. Handa, M. Mikuriya, I. Hiromitsu, K. Kasuga, Chem. Lett. (1998) 777;
(b) M. Handa, Y. Sayama, M. Mikuriya, I. Hiromitsu, K. Kasuga, Mater. Sci. 21 (2003) 199.
[24] (a) Y. Sayama, M. Handa, M. Mikuriya, I. Hiromitsu, K. Kasuga, Chem. Lett. (1999) 453;
(b) Y. Sayama, M. Handa, M. Mikuriya, I. Hiromitsu, K. Kasuga, Bull. Chem. Soc. Jpn. 76 (2003) 769.
[25] M.C. Barral, R. Jimenez-Aparicio, J.L. Priego, E.C. Royer, E. Gutierrez-Puebla, C.R. Valero, Polyhedron 11 (1992) 2209.
[26] E.F. Ullman, L. Gall, J.H. Osiecki, J. Org. Chem. 35 (1970) 3623.
[27] M.S. Davis, M. Morokuma, R.W. Kreilick, J. Am. Chem. Soc. 94 (1972) 5588.
[28] P.W. Selwood, Magnetochemistry, Interscience Publishers, New York, 1956, p. 78 and 91.
[29] C.K. Fair, MolEN Structure Determination Systems, Delft Instrument, Delft, 1990.

residues, which are His46, Cys112, His117, Met121, and Gly45. The copper ion is strongly coordination to His46, Cys112, and His117 and is weakly bonding to other residues. The active site of azurin has a distorted trigonal bipyramidal structure.

The geometry of the active site of azurin has been estimated by the density functional theory (DFT) with B3LYP method [8] and quantum mechanics/molecular mechanics (QM/MM) method [9]. The hyperfine coupling constants in the active site has been calculated by DFT with UB1LYP [10] and B3LYP [11] methods, and also by QM/MM approach [12]. The electronic structure and the g-tensor of the active site of azurin have been investigated by ab initio multireference determinantal configuration interaction (MRD-CI) calculations [13].

In this study, we present a cluster model for the active site of oxidized azurin and investigate the electronic structure of the cluster model by the density functional methods. Dependency of electronic properties such as partial charge and partial spin densities in the cluster model on the cluster structure is investigated. We estimate force constants between the copper ions and coordinate-bonded atoms in residues around the copper ion. We discuss the electronic structures of the cluster model in relation to the active site of oxidized azurin by a simple Hubbard model for the active site.

2. Model and method

We consider a cluster model which consists of a copper ion and five residues as shown in Fig. 1. For the configuration of the cluster model, we use the coordinate of atoms around the active site of *Pseudomonas aeruginosa* azurin in Protein Data Bank (PDB), code 4AZU, which is determined by X-ray diffraction at pH 5.5 [7]. The configuration of hydrogen atoms in the cluster model is determined by HF/3-21G* geometry optimization with fixed other all atoms. Ligand distance, angle, and dihedral angle of our cluster model used in this study are summarized in Table 1. In this study, we calculate electronic properties of the cluster model in a condition that the total charge of the cluster model is +1 as $[Cu(His46)(Cys112)(His117)(Met121)(Gly45)]^{+}$ with the geometry as shown in Fig. 1.

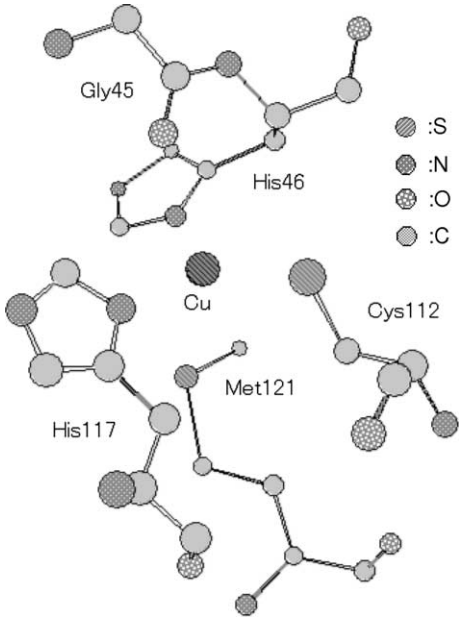


Fig. 1. Cluster model of oxidized azurin.

Table 1
Ligand distances, angles, and dihedral angles of active site model used in this study

	Parameter
Distance (Å)	
Cu–O(Gly45)	2.955
Cu–N(His46)	2.064
Cu–S(Cys112)	2.267
Cu–N(His117)	1.978
Cu–S(Met121)	3.164
Angle (°)	
N(His117)–Cu–N(His46)	108.3
S(Cys112)–Cu–N(His117)	123.7
S(Cys112)–Cu–S(Met121)	110.5
S(Cys112)–Cu–O(Gly45)	100.3
Dihedral angle (°)	
N(His117)–Cu–S(Cys112)–C_β	91.6
S(Cys112)–Cu–N(His46)–C_γ	−13.6
S(Cys112)–Cu–N(His117)–C_γ	−40.7
S(Cys112)–Cu–S(Met121)–C_γ	46.9
S(Cys112)–Cu–O(Gly45)–C	82.8

We perform density functional calculations with Becke's three-parameter hybrid exchange functional [14] and the Lee–Yang–Parr correlation functional [15] (B3LYP) for the cluster model by GAUSSIAN98 program package [16]. We calculate the distribution of partial charge and partial spin densities on some atoms by Mulliken population analysis (MPA) and natural population analysis (NPA) [17] with 6–31G** basis set [18]. The potential energy surfaces are also calculated by B3LYP with 6–31G** basis.

3. Results and discussion

In this study, we calculate electronic properties such as total energy, partial charge and spin densities for various cluster structures, and discuss the dependency of those properties on the cluster structure.

3.1. Potential energy surface and parameters

We show potential energy surfaces (PES) for Cu–X (X = S(Cys112), N(His117), S(Met121)) by B3LYP/6-31G** in Fig. 2(a). These calculations are performed to construct PES along the Cu–X. The internal coordi-

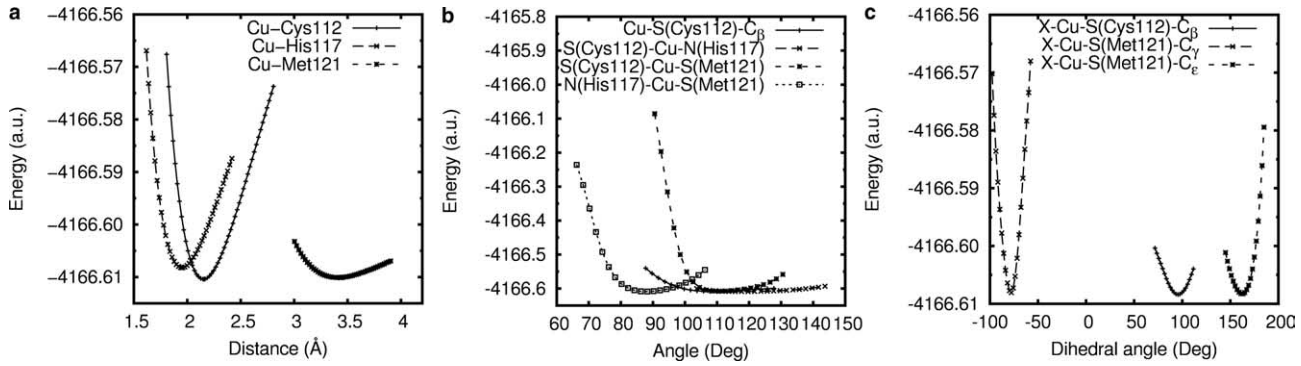


Fig. 2. Potential energy surfaces. (a) Potential energy surface for distance between Cu and X (X = S(Cys112), N(His117), S(Met121)). (b) Potential energy surface for angle X–Cu–Y ((X,Y) = (S(Cys112),N(His117)), (S(Cys112),S(Met121)), (N(His117),S(Met121))). (c) Potential energy surface for dihedral angle X–Cu–Y–Z (X = N(His117), (Y,Z) = (S(Cys112),C_β), (S(Met121),C_γ), (S(Met121),C_ϵ)).

nates other than the varying ones are fixed at the initial geometry. We find that the equilibrium bond lengths of Cu–S(Cys112) and Cu–N become 2.157 and 1.948 Å, respectively. These equilibrium distances are shorter than those of experimental structures. The equilibrium bond length of Cu–S(Met121) becomes 3.342 Å which is longer than that of X-ray diffraction crystallography.

Fig. 2(b) shows PESs for angle of X–Cu–Y ((X,Y) = (S(Cys112),N), (S(Cys112),S(Met121)), (N,S-(Met121))) and for Cu–S(Cys112)–C_β. The equilibrium angles are 119.687°, 110.536°, 88.231°, and 107.736°, respectively. The angle of S(Cys112)–Cu–N is smaller than that of the experimental result, and N–Cu–S(Met121) is larger than that. Other two angles become just values of experimental data.

Fig. 2(c) shows PESs for dihedral angle of X–Cu–Y–Z (X = N, and (Y,Z) = (S(Cys112),C_β), (S(Met121),C_γ), (S(Met121),C_ϵ)). These equilibrium dihedral angles are 95.625°, −77.727°, and 163.075°, respectively. The present results of PES for distance, angle, and dihedral angles summarizes in Table 2.

From these PES calculations, we estimate parameters of model potentials for distance, angle, and dihedral angle related to the copper ion. Potential of the distance is often evaluated by Morse and harmonic potential functions, $V_M(r)$ and $V_H(r)$, written as:

$$V_M(r, D_e) = D_e(1 - \exp[-\alpha(r - r_c)])^2, \quad (1)$$

$$V_H(r, K_r) = K_r(r - r_c)^2, \quad (2)$$

where D_e and α are constant fitting parameters, and r_c means equilibrium bonding distance, and K_r is a constant parameter. Potentials for angle and dihedral angle are evaluated by:

$$V(\theta, K_\theta) = K_\theta(\theta - \theta_c)^2, \quad (3)$$

$$V(\phi, K_\phi) = K_\phi[1 - \cos(\phi - \phi_c)], \quad (4)$$

where K_θ and K_ϕ are fitting parameters, and θ_c and ϕ_c are equilibrium angle and dihedral angle, respectively.

Table 2
Ligand distance, angle, and dihedral angle, and fitting parameters

Distance	r_c (Å)	r_{PDB} (Å)	K_r (kcal/mol)
Cu–S(Cys112)	2.157	2.267	130.948
Cu–N(His116)	1.948	1.978	128.449
Cu–S(Met121)	3.342	3.164	29.150
Angle	θ_c (°)	θ_{PDB} (°)	K_θ (kcal/mol rad^2)
Cu–S(Cys112)–C_β	107.736	107.736	34.857
S(Cys112)–Cu–N(His117)	119.687	123.686	11.950
S(Cys112)–Cu–S(Met121)	110.536	110.536	95.530
N(His117)–Cu–S(Met121)	88.231	86.231	112.133
Dihedral angle	ϕ_c (°)	ϕ_{PDB} (°)	K_ϕ (kcal/mol rad^2)
N(His117)–Cu–S(Cys112)–C_β	95.625	91.625	0.255
N(His117)–Cu–S(Met121)–C_ϵ	163.075	165.075	0.425
N(His117)–Cu–S(Met121)–C_γ	−77.727	−77.727	1.772
S(Cys112)–Cu–S(Met121)–C_ϵ	−72.252	−70.252	0.428
S(Cys112)–Cu–S(Met121)–C_γ	46.946	46.946	1.773
S(Met121)–Cu–S(Cys112)–C_β	−9.892	−7.892	0.255

These fitting parameters determined from these calculations as shown in Fig. 2 are summarized in Table 2.

3.2. Charge density and spin density

Fig. 3 shows dependency of partial charge and spin densities on various cluster structures estimated by Mulliken population analysis. We show partial charge densities on the copper ion, the sulfur and nitrogen ions for various distances between Cu and X (X = S(Cys112), N(His117), S(Met121)) in Fig. 3(a)–(c), respectively. From Fig. 3(a), we can find that the partial charge on Cu ion becomes larger, when the distance between Cu and S(Cys112) increases. On the other hand, the partial charge on S ion in Cys112 becomes smaller. Partial charge on other ions hardly varies. From Fig. 3(b) and (c), we also find that each partial charge is almost constant for change of distance between Cu and N(His117) or Cu and S(Met121).

Dependency of partial spin on the distance between Cu and X (X = S(Cys112), N(His117), S(Met121)) is shown in Fig. 3(d)–(f), respectively. We can find that

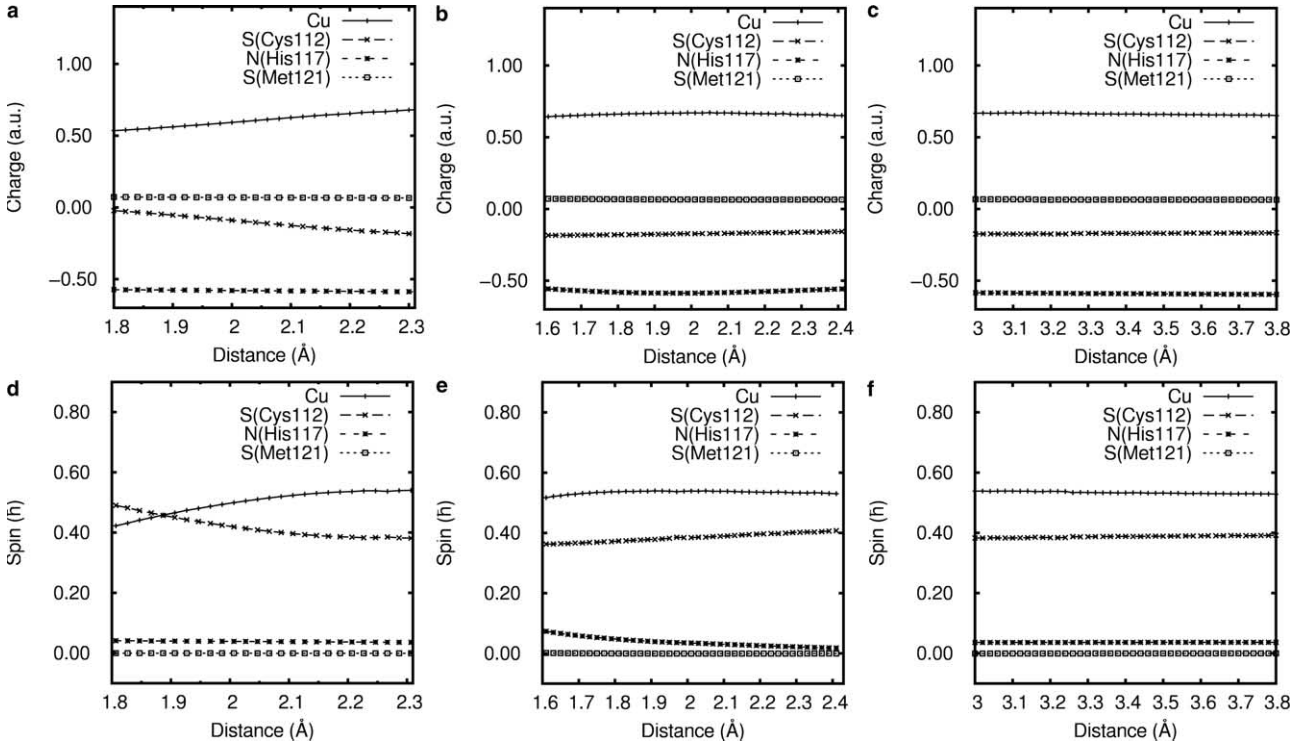


Fig. 3. Atomic charge and spin density. (a) Partial charge densities of Cu, S(Cys112), N(His117), and S(Met121) for various distances between Cu and S(Cys112) atoms. (b) Partial charge densities for various distances between Cu and N(His117) atoms. (c) Partial charge densities for various distances between Cu and S(Met121) atoms. (d) Partial spin densities of Cu, S(Cys112), N(His117), and S(Met121) for various distances between Cu and S(Cys112) atoms. (e) Partial spin densities for various distances between Cu and N(His117) atoms. (f) Partial spin densities for various distances between Cu and S(Met121) atoms.

the partial spin on copper ion increases, if the distance between Cu and S(Cys112) becomes larger, and that the partial spin density on the sulfur ion in Cys112 decreases. Others are almost constant for varying the distances. From Fig. 3, we can find that partial charge and spin depend upon the varying distance between the copper and sulfur(Cys112) ions.

3.3. Simple Hubbard model for active site

In this section, we present a simple Hubbard model to understand the electronic structure of the active site of oxidized azurin, and discuss charge and spin densities around the active site by using the simple model in relation to a strongly correlated electron systems. In this study, we focus on $d_{x^2-y^2}$ orbital of the copper ion and p_y orbital of sulfur ion in Cys112 in the active site as shown in Fig. 4(a), and we consider a Hubbard Hamiltonian of this model (see Appendix A).

From the Hubbard model for the active site of azurin, we can find the ground state energy for 3-electron and 4-electron systems as shown in Fig. 4(b) (see Appendix A). When $t/U < 1$, the ground state energy becomes larger than that of $t/U > 1$ because of the on-site repulsion U. The ground state energy of 4-electron system is larger than that of 3-electron system. The partial electronic charge on each orbital is shown in Fig. 4(c). When $t/U < 1/3$, partial charge of p-orbital is larger than that of d-orbital because of the on-site repulsion U, and the partial charge of d-orbital becomes 1 in the case of $t/U \ll 0$. On the other hand, from Fig. 4(d), partial spin of p-orbital is smaller than that of d-orbital, when $t/U < 1/3$.

When the distance between copper and sulfur ions increases, the transfer integral t becomes smaller. Therefore, t/U becomes smaller as the increase of the distance. From Fig. 4(c), we can find the tendency of the decrease of partial electronic charge in copper ion. The decrease implies that partial charge on the copper ion becomes larger. On the other hand, From Fig. 4(d), partial spin becomes larger as the increase of the distance. In this case, we can estimate $t/U \sim 0.29$ form Fig. 3(a) and (b). These tendency derived from the simple Hubbard model are good agreement with those from quantum chemical calculations.

In the high-Tc superconductivity, copper ions play an important role of the strong electron correlation, and it is well known that the on-site repulsion U of the copper ion is large (about 8 eV). In the case of the active site of oxidized azurin, we can expect that the copper ion also play a chemical role of electronic structure, functionalities in azurin.

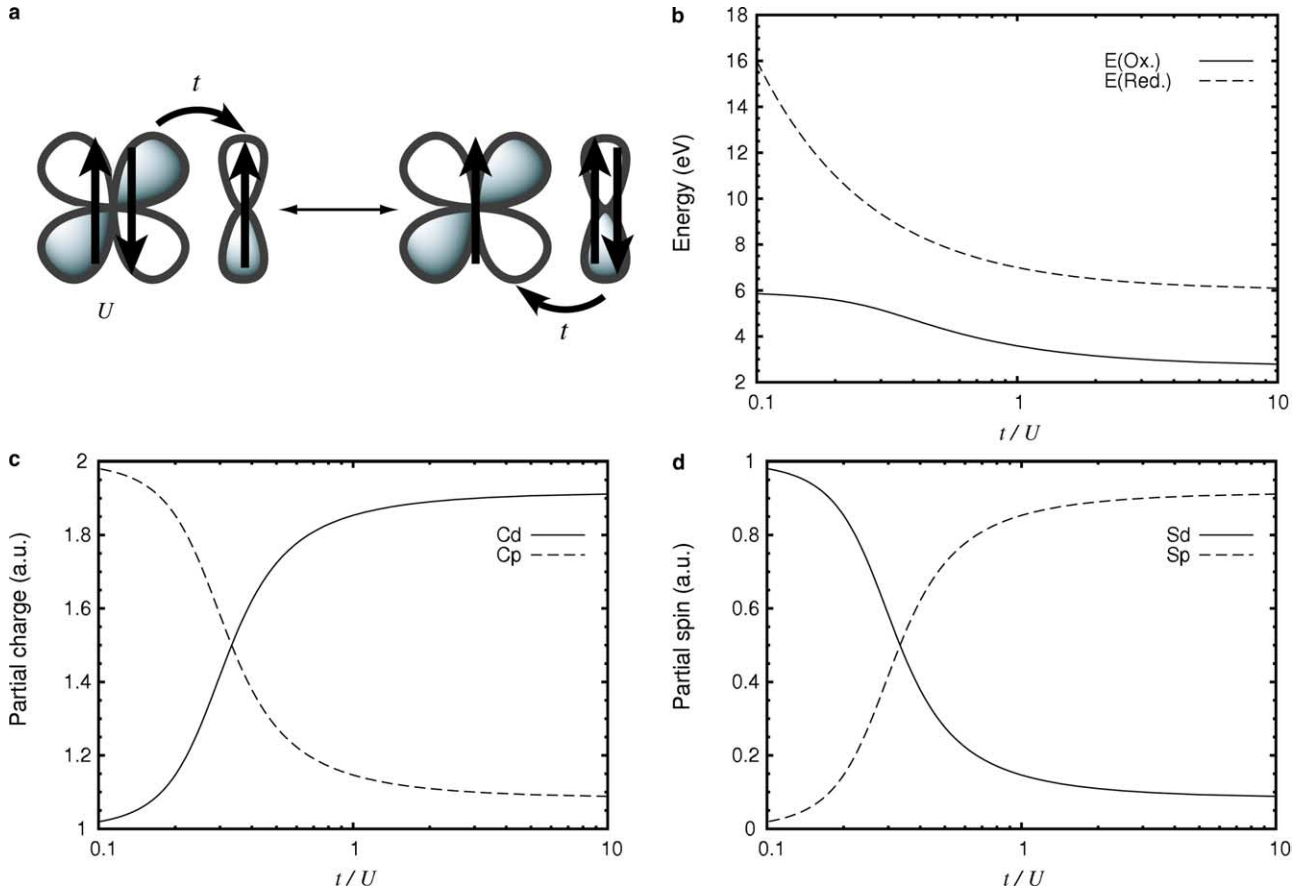


Fig. 4. Simple Hubbard model for active site of azurin. (a) 2-Site 3-electron system with $d_{x^2-y^2}$ of the copper ion and p_y of the sulfur ion in Cys112. (b) Total energy for 3- and 4-electron systems. We use parameters of $\epsilon_d = 0.0$, $\epsilon_p = 3.0$, $t = 1.0$ (eV). (c) Partial charge on each orbital. (d) Partial spin on each orbital. We have $C_d = C_p$ and $S_d = S_p$ in $t/U = 1/3$ form Eqs. (A.16) and (A.17).

4. Concluding remarks

We have presented a cluster model for the active site of oxidized azurin and have investigated electronic structure of the cluster model by density functional calculations. We have calculated the potential energy surfaces for distances between the copper and coordinate-bonded atoms, angles, and dihedral angles related the copper ion. Partial charge and spin densities on each atom have been also calculated. The dependency of the partial charge and spin densities on the change of the distance has been discussed in relation to the strong electron correlation on d-orbital of the copper ion. The partial charge and spin on the copper and sulfur ions in Cys112 depend upon only the distance between them. Partial charge and spin densities on other atoms are almost constant. We have estimated parameters of some effective energy potentials for distance, angle, and dihedral angle. The contributions of electronic structure from excellent basis set and methods will be presented elsewhere.

Acknowledgement

H.N. is grateful for a financial support of the Ministry of Education, Science and Culture of Japan (Research No. 15550010).

Appendix A

Here, we briefly present the simple Hubbard model for the active site of azurin. The Hubbard Hamiltonian of the model is written as

$$H = H_0 + H_1 + H_2, \tag{A.1}$$

where

$$H_0 = \sum_\sigma (\varepsilon_d d^\dagger_\sigma d_\sigma + \varepsilon_p p^\dagger_\sigma p_\sigma), \tag{A.2}$$

$$H_1 = t \sum_\sigma \left(d^\dagger_\sigma p_\sigma + p^\dagger_\sigma d_\sigma\right), \tag{A.3}$$

$$H_2 = U d^\dagger_\uparrow d^\dagger_\downarrow d_\downarrow d_\uparrow. \tag{A.4}$$

H_1 means kinetic part between d and p orbitals with the transfer integral t, and H_0 is the unperturable Hamilton with orbital energies ε_d and ε_p for d and p orbitals, respectively. H_2 indicates interaction part with on-site coulomb repulsion U on the d-orbital. $d^\dagger_\sigma$ (d_σ) is a creation (annihilation) operator at $d_{x^2-y^2}$ orbital with spin σ, and $p^\dagger_\sigma$ and p_σ mean a creation and an annihilation operator at p_y orbital, respectively.

For this model, we consider two electronic states as:

$$|\varphi_1\rangle = d^\dagger_\uparrow d^\dagger_\downarrow p^\dagger_\uparrow |0\rangle, \tag{A.5}$$

$$|\varphi_2\rangle = d^\dagger_\uparrow p^\dagger_\uparrow p^\dagger_\downarrow |0\rangle. \tag{A.6}$$

State $|\varphi_1\rangle$ includes two d-electrons and one p-electron, and state $|\varphi_2\rangle$ includes one d-electron and two p-electrons. We consider a superposition of two states as

$$|\phi\rangle = \frac{1}{\sqrt{1+g^2}}(|\varphi_1\rangle + g|\varphi_2\rangle). \tag{A.7}$$

By using the wavefunction of Eq. (A.7) and Hamiltonian of Eq. (A.1), we obtain the eigenvalue problem as

$$\boldsymbol{H}|\phi\rangle = E|\phi\rangle, \tag{A.8}$$

where

$$\boldsymbol{H} = \begin{pmatrix} 2\varepsilon_d + \varepsilon_p + U & -t \\ -t & \varepsilon_d + 2\varepsilon_p \end{pmatrix}. \tag{A.9}$$

From Eq. (A.8), we have the eigenvalue and the wavefunction of the ground state as

$$E_{GS} = -\frac{1}{2}\left[\sqrt{(\varepsilon_d - \varepsilon_p + U)^2 + 4t^2} - 3(\varepsilon_d + \varepsilon_p) - U\right] \tag{A.10}$$

and

$$|\phi_{GS}\rangle = \frac{t|\varphi_1\rangle + \left(2\varepsilon_d + \varepsilon_p + U - E_{GS}\right)|\varphi_2\rangle}{\sqrt{t^2 + \left(2\varepsilon_d + \varepsilon_p + U - E_{GS}\right)^2}}. \tag{A.11}$$

Here, we define a partial charge and a partial spin of each orbital as:

$$C_d = \langle\phi|\sum_\sigma d^\dagger_\sigma d_\sigma|\phi\rangle, \tag{A.12}$$

$$C_p = \langle\phi|\sum_\sigma p^\dagger_\sigma p_\sigma|\phi\rangle, \tag{A.13}$$

$$S_d = \langle\phi|(d^\dagger_\uparrow d_\uparrow - d^\dagger_\downarrow d_\downarrow)|\phi\rangle, \tag{A.14}$$

$$S_p = \langle\phi|(p^\dagger_\uparrow p_\uparrow - p^\dagger_\downarrow p_\downarrow)|\phi\rangle, \tag{A.15}$$

where C_d (S_d) and C_p (S_p) mean partial charge (spin) on the d and p orbitals, respectively. From Eqs. (A.11)–(A.15), we have:

$$C_d = \frac{2t^2 + \left(2\varepsilon_d + \varepsilon_p + U - E_{GS}\right)^2}{t^2 + \left(2\varepsilon_d + \varepsilon_p + U - E_{GS}\right)^2}, \tag{A.16}$$

$$C_p = \frac{t^2 + 2\left(2\varepsilon_d + \varepsilon_p + U - E_{GS}\right)^2}{t^2 + \left(2\varepsilon_d + \varepsilon_p + U - E_{GS}\right)^2}, \tag{A.17}$$

$$S_d = \frac{\left(2\varepsilon_d + \varepsilon_p + U - E_{GS}\right)^2}{t^2 + \left(2\varepsilon_d + \varepsilon_p + U - E_{GS}\right)^2}, \tag{A.18}$$

$$S_p = \frac{t^2}{t^2 + \left(2\varepsilon_d + \varepsilon_p + U - E_{GS}\right)^2}. \tag{A.19}$$

References

[1] A. Nakamura, N. Ueyama, K. Yamaguchi, Organometallic Conjugation – Structures, Reactions and Functions of d–d and d–π Conjugated Systems-KODANSHA, Springer, Berlin, 2002 (references therein).
[2] K.W. Penfield, A.A. Gewirth, E.I. Solomon, J. Am. Chem. Soc. 107 (1985) 4519.
[3] E.I. Solomon, M.J. Baldwin, M.D. Lowery, Chem. Rev. 92 (1992) 521.
[4] J.A. Guckert, M.D. Lowery, E.I. Solomon, J. Am. Chem. Soc. 117 (1995) 2817.
[5] E.I. Solomon, R.K. Szilagyi, S.D. George, L. Basumallick, Chem. Rev. 104 (2004) 419.
[6] E.T. Adman, Adv. Protein Chem. 42 (1991) 145.
[7] H. Nar, A. Messerschmidt, R. Hunber, M. van de Kamp, G.W. Canters, J. Mol. Biol. 221 (1991) 765.
[8] U. Ryde, M.H.M. Ollson, B.O. Roos, A.C. Borin, Theor. Chem. Acc. 105 (2001) 452.
[9] U. Ryde, M.H.M. Olsson, Int. J. Quantum Chem. 81 (2001) 335.
[10] A.R. Jaszewski, J. Jezierska, Chem. Phys. Lett. 343 (2001) 571.
[11] M. Swart, Density functional theory applied to copper proteins, PhD Thesis, Rijkuniversiteit Groningen, Groningen, 2002.
[12] S. Moon, S. Patchkovskii, D.R. Salahub, J. Mol. Struct. (Theochem.) 632 (2003) 287.
[13] M. van Gastel, J.W.A. Coremans, H. Sommerdijk, M.C. van Hemert, E.J.J. Groenen, J. Am. Chem. Soc. 124 (2002) 2035.
[14] A.D. Becke, J. Chem. Phys. 98 (1993) 5648.
[15] C. Lee, W. Yang, R.G. Parr, Phys. Rev. B 37 (1988) 785.
[16] M.J. Frisch, G.W. Trucks, H.B. Schlegel, G.E. Scuseria, M.A. Robb, J.R. Cheeseman, V.G. Zakrzewski, J.A. Montgomery, Jr., R.E. Stratmann, J.C. Burant, S. Dapprich, J.M. Millam, A.D. Daniels, K.N. Kudin, M.C. Strain, O. Farkas, J. Tomasi, V. Barone, M. Cossi, R. Cammi, B. Mennucci, C. Pomelli, C. Adamo, S. Clifford, J. Ochterski, G.A. Petersson, P.Y. Ayala, Q. Cui, K. Morokuma, N. Rega, P. Salvador, J.J. Dannenberg, D.K. Malick, A.D. Rabuck, K. Raghavachari, J.B. Foresman, J. Cioslowski, J.V. Ortiz, A.G. Baboul, B.B. Stefanov, G. Liu, A. Liashenko, P. Piskorz, I. Komaromi, R. Gomperts, R.L. Martin, D.J. Fox, T. Keith, M.A. Al-Laham, C.Y. Peng, A. Nanayakkara, M. Challacombe, P.M.W. Gill, B. Johnson, W. Chen, M.W. Wong, J.L. Andres, C. Gonzalez, M. Head-Gordon, E.S. Replogle, J.A. Pople, Gaussian 98, Revision A.11.4, Gaussian, Inc., Pittsburgh, PA, 2002.
[17] A.E. Reed, R.B. Weinstock, F. Weinhold, J. Chem. Phys. 83 (1985) 735.
[18] W.J. Hehre, L. Radom, P.v.R. Schleyer, J.A. Pople, Ab Initio Molecular Orbital Theory, Wiley-Interscience, New York, 1986.

bonding residues near the metal site to assist in catalysis, and (10) imposing a unique geometry on the metal site.

Recently, the blue copper proteins including azurin have been investigated experimentally and theoretically by many groups [1,6–12]. The geometry of the active site of azurin has been estimated by the density functional theory (DFT) with B3LYP method [7] and quantum mechanics/molecular mechanics (QM/MM) method [8]. The hyperfine coupling constants in the active site have been calculated by DFT with B1LYP [9] and B3LYP [10] methods, and also by QM/MM approach [11]. The electronic structure and the *g*-tensor of the active site of azurin have been investigated by ab initio multireference determinantal configuration interaction (MRD-CI) calculations [12].

Solvent effects on electronic structure of molecules have been investigated by many chemists and physicists to understand molecular structure, mechanism of chemical reactions in solution, etc. by using quantum-chemical calculations and molecular dynamics simulations. Physical properties such as geometry of molecules and charge distribution in solution often vary from those in vacuum [13]. Ryde et al. [7] have also performed a geometry optimization of the active site of blue copper proteins including azurin by quantum-chemical calculations with polarizable continuum model (PCM) [14]. Their results suggest that weak axial bond of Cu–S(Met121) in solution is more elongated than that in vacuum.

In this study, we investigate solvent effects on electronic structure of active site of oxidized azurin by density functional calculations. A cluster model for the active site of oxidized azurin is presented, and we calculate physical properties such as charge density and spin density of the model cluster involving solvent effects. We also present the dependence of those properties on the dielectric constant. Finally, we discuss the charge or electron transfer in the active site of azurin in relation to solvent effect.

2. Computational method

We present a cluster model for the active site of oxidized azurin and methods used in this study.

2.1. Computational model for active site

We consider a cluster model, which consists of a copper ion and five residues as shown in Fig. 1, for the active site of oxidized azurin. In the configuration of the cluster model, we use the coordinate of atoms around the active site of *Pseudomonas aeruginosa* azurin (code 4AZU) in Protein Data Bank, which is determined by X-ray diffraction results at pH 5.5 [6]. The configuration of all hydrogen atoms in the cluster model is determined by Hartree–Fock/3-21G* geometry optimization with fixed configuration of other all atoms. Ligand distances, angles, and dihedral angles of the cluster model used in this study are summarized in Table 1. In the calculations of this study, we use a condition that the total charge of the cluster model is +1.

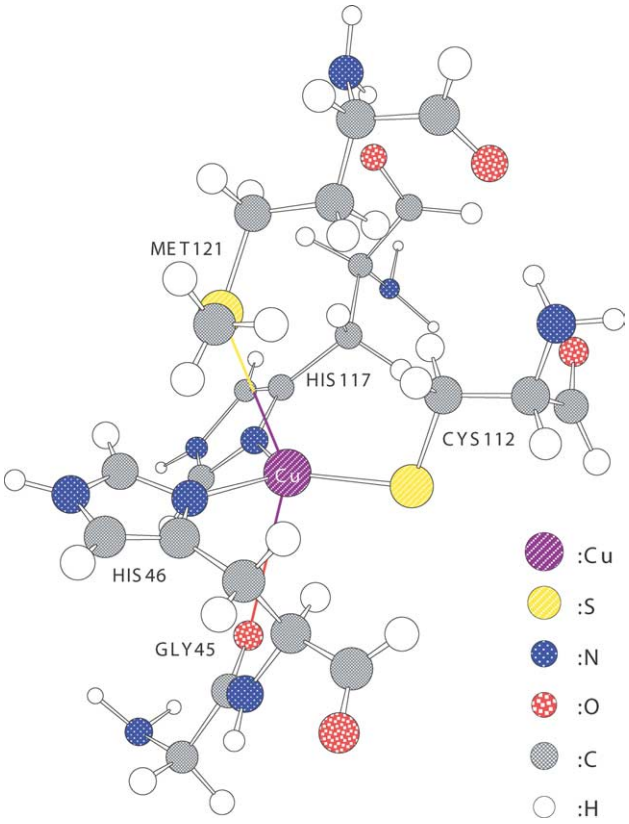


Fig. 1. Cluster model for active site of oxidized azrin.

2.2. Solvent effect using polarizable continuum model

We perform density functional calculations with Becke's three-parameter hybrid exchange functional [15] and the Lee–Yang-Parr correlation functional [16] (B3LYP) for the cluster model as shown in Fig. 1 by GAUSSIAN 03 program package [17]. We calculate partial charge and partial spin density on each atom by Mulliken population analysis (MPA) and natural population analysis (NPA) [18] with 6-31G* split-valence basis set [19].

For investigation of electronic structure of the active site of oxidized azurin in solution, we use polarizable continuum model (PCM) [14] in DFT calculations. An integral equation formulation model (IEF-PCM) [20] is adopted. In present calculations, values of dielectronic constant ϵ_r are arbitrarily selected in the region from 2 to 78.

3. Results and discussion

3.1. Spin density and charge density in vacuum

Fig. 2(a) shows the singly occupied molecular orbital (SOMO) of the cluster model by unrestricted B3LYP/6-

Table 1
Ligand distances, angles, and dihedral angles of active site model used in this study

	Parameter
Distance (Å)	
Cu–O(Gly45)	2.955
Cu–N(His46)	2.064
Cu–S(Cys112)	2.267
Cu–N(His117)	1.978
Cu–S(Met121)	3.164
Angle (°)	
N(His117)–Cu–N(His46)	108.3
S(Cys112)–Cu–N(His117)	123.7
S(Cys112)–Cu–S(Met121)	110.5
S(Cys112)–Cu–O(Gly45)	100.3
Dihedral angle (°)	
N(His117)–Cu–S(Cys112)–C_β	91.6
S(Cys112)–Cu–N(His46)–C_γ	−13.6
S(Cys112)–Cu–N(His117)–C_γ	−40.7
S(Cys112)–Cu–S(Met121)–C_γ	46.9
S(Cys112)–Cu–O(Gly45)–C	82.8

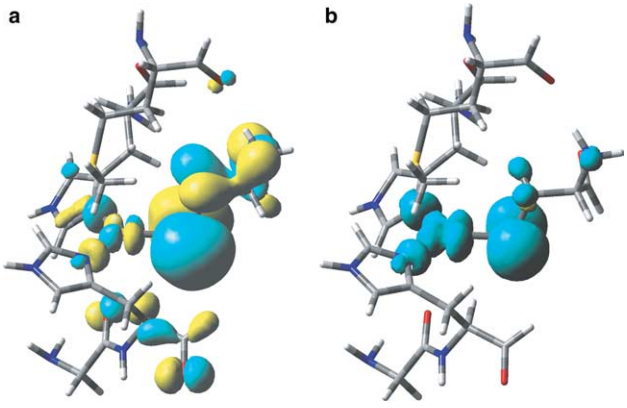


Fig. 2. SOMO and spin density of the cluster model. (a) Distribution of SOMO (isovalue = 0.02 a.u., and orbital energy = −9.1931 eV). (b) Distribution of spin density (isovalue = 0.0012 a.u.).

31G* calculation. We can find $3d_{x^2-y^2}$ orbital π antibonded to the sulfur atom in the Cys112 and σ antibonded to the nitrogen atoms in His46 and His117. SOMO distributes on the nitrogen atoms in His46 and His117, and is not much on other atoms in His46 and His117. On the other hand, we can find that the distribution of SOMO widely lies over Cys112. SOMO largely distributes on the sulfur atom, two H atoms in $C_\beta H_2$ in Cys112, and the nitrogen atom in backbone of Cys112. We also find small distribution of SOMO around O atom in Gly45. Fig. 2(b) shows the spin density of the cluster model. The spin density distributes around copper ion, S(Cys112), N(His46) and N(His117) atoms, and we also find small distribution of spin density on the H atoms in $C_\beta H_2$ and the nitrogen atom in backbone of Cys112. In three coordination bonds to copper ion, SOMO widely distributes to only the bonding direction to the side of Cys112. These results suggest that histidine or imidazole has a role of restraint of spatial distribution for the direction of the coordination-bonding of the nitrogen atom to the copper ion.

Table 2 summarizes the atomic charge and spin density of the cluster model in vacuum by MPA and NPA. From partial spin density by MPA in Table 2, we find the largest value about 53.2% on the copper ion and the second largest value about 38.8% on the sulfur ion in Cys112. From NPA, we find that the valence of the copper ion becomes 1.26. Atomic charges and Mulliken spin densities of the similar cluster model to the present model in vacuum have been presented in [12].

3.2. Spin density and atomic charge in solution

Tables 3 and 4 show the spin densities and the charge distribution for various dielectric constants, respectively. The dielectric constants ϵ_r is varied from 2 to 78. In general, $\epsilon_r = 78$ corresponds to water molecule. We find asymptotical changes of spin density and atomic charge between the copper ion and the sulfur ion in Cys112. As increasing ϵ_r, the spin density of Cu ion becomes increasing, and the spin density of S_γ(Cys112) is decreasing. On the other hand, the atomic charge of Cu ion increases from 0.644 to 0.681, and the atomic charge of S_γ(Cys112) decreases from −0.160 to −0.233. These changes of atomic charge and spin densities suggest that electron with β spin on copper ion slightly moves to the sulfur ion in Cys112 in the case of increasing the dielectric constant. From this electron transfer, the spin density of the copper ion becomes larger than that in vacuum, and the charge distribution also becomes larger.

3.3. A simple model for solvent effect

In this subsection, we briefly discuss the solvent effects of electronic properties presented in previous subsection by using a simple Hubbard model [21–23]. In this study, we focus $d_{x^2-y^2}$ orbital of the copper ion and p_y orbital of sulfur ion in Cys112 in the active site of azurin. We assume on-site repulsion U on only copper site, because it is well known that the on-site coulomb repulsion U of the copper ion is large (about 8 eV). Therefore, for the most simple case, we can consider a 2-site system with 3 electrons as a simple model for the active site. By solving electronic structure of this simple model, we can find that partial charge of d orbital becomes larger than that of p orbital, when $t/U \gg 1$, and that partial spin of d orbital becomes smaller. On the other hand, in the case of $t/U \ll 1$, partial charge on d orbital becomes smaller, and partial spin on d orbital becomes larger, because of the large on-site repulsion. In the case of the active site of oxidized azurin,

Table 2
Partial atomic charges and partial spin densities on each atom by Mulliken population analysis (MPA) and natural population analysis (NPA)

Residue	Atom	MPA		NPA
		Atomic charge (a.u.)	Spin density (%)	Atomic charge (a.u.)
Cys112	Cu	0.6448	53.227	1.2605
	C_α	−0.0080	−0.007	−0.1594
	C_β	−0.4464	−1.520	−0.5852
	S_γ	−0.1603	38.769	−0.3691
His46	C_γ	0.2931	−0.052	0.1339
	$N_{\delta1}$	−0.5662	2.415	−0.6495
	$C_{\delta2}$	0.2263	−0.301	0.1956
	$C_{\epsilon1}$	−0.5139	0.025	−0.5038
	$N_{\epsilon2}$	−0.0195	0.268	−0.0798
His117	C_γ	0.2728	−0.126	0.1460
	$N_{\delta1}$	−0.5264	3.601	−0.6627
	$C_{\delta2}$	0.2308	−0.424	0.1899
	$C_{\epsilon1}$	0.0138	0.341	−0.0742
	$N_{\epsilon2}$	−0.5239	0.047	−0.5012
Gly45	C	0.5979	−0.015	0.6871
	O	−0.5303	0.022	−0.7012
	C_α	−0.2391	−0.001	−0.3368
Met121	C_γ	0.1987	−0.023	−0.5907
	S_δ	0.0769	−0.051	0.1822
	C_ϵ	−0.1603	0.005	−0.5678

we can expect that the transfer integral becomes smaller than the on-site repulsion on the copper ion in the active site.

Next, we consider a simple model for solvent effects. We assume the effective electron–electron interaction W between sites in the system and solvent molecules. The effective interaction is clearly related to the polarization of the solvent molecules. If solvent molecules have large dielectric constant, the effective interaction W becomes large. In the frame work of a random phase approximation [24,25], the effective on-site coulomb potential U_{eff} on the d orbital can be written as

$$U_{\text{eff}} = \frac{U}{1 - U^2 W^2}. \quad (1)$$

From Eq. (1), we find that the effective interaction U_{eff} becomes larger than the bare interaction U, when the dielectric constant is larger than that in vacuum. Therefore, from Eq. (1), we can expect that spin density of copper ion in the active site of oxidized azurin in solution with large dielectric constant becomes larger than that in vacuum. This effect arises from the strong electron correlation on the copper ion. Since on-site coulomb interactions of p orbitals are small, the solvent effects of electronic correlation in p orbital might be small.

4. Concluding remarks

In this study, we have presented a computational model for the active site of oxidized azurin and have investigated the electronic structure of the active site model by using the density functional methods with polarizable continuum model. The partial atomic charge and spin density on some ions have been calculated for various dielectric constants. We have presented a simple model for the active site of oxidized azurin by a Hubbard model, and have discussed the dependence of the charge and spin distributions on the dielectric constants.

For the cluster model in vacuum, the distribution of SOMO and the spin density widely lie over Cys112. The distribution of them over histidines is not so much.

Table 3
Dependency of spin density (%) on dielectric constant by MPA

ϵ_r	Vacuum	2	4	8	16	24	32	78
Cu	53.227	55.803	57.630	58.788	59.462	59.704	59.830	60.059
S_γ(Cys112)	38.769	36.151	34.127	32.793	32.002	31.714	31.565	31.290
C_β(Cys112)	−1.520	−1.437	−1.370	−1.324	−1.297	−1.287	−1.282	−1.272
$N_{\delta1}$(His117)	3.601	3.871	4.074	4.206	4.283	4.312	4.326	4.353
O(Gly45)	0.022	0.005	0.004	0.003	0.003	0.003	0.002	0.002
S_δ(Met121)	−0.051	−0.057	−0.061	−0.064	−0.065	−0.066	−0.066	−0.067

Table 4
Dependency of atomic charge (a.u.) on dielectric constant by MPA

ϵ_r	Vacuum	2	4	8	16	24	32	78
Cu	0.644	0.660	0.670	0.676	0.679	0.680	0.680	0.681
S_γ(Cys112)	−0.160	−0.185	−0.205	−0.212	−0.228	−0.231	−0.233	−0.236
C_β(Cys112)	−0.446	−0.444	−0.442	−0.440	−0.439	−0.439	−0.439	−0.439
$N_{\delta1}$(His117)	−0.526	−0.580	−0.583	−0.585	−0.586	−0.587	−0.587	−0.587
O(Gly45)	−0.530	−0.414	−0.429	−0.438	−0.443	−0.448	−0.446	−0.447
S_δ(Met121)	0.077	0.076	0.075	0.075	0.074	0.074	0.074	0.074

In solution, the partial spin and charge of the copper ion become larger than that in vacuum, when the dielectric constant is larger. The spin and charge of sulfur ion in Cys112 become smaller. These results suggest that electron with β spin moves from the copper ion to the sulfur ion, if the dielectric constant becomes larger. We have found the electron moving because of the strong electron correlation on the copper ion by using a Hubbard model.

Since the active site of azurin is surrounded by many residues, the electronic structure of active site of azurin is weakly interacted with solvent molecules. We need to consider larger systems and to use other excellent computational methods such as QM/MM method. The contribution to the electronic structure of the active site of azurin from neighbor residues around the active site will be presented elsewhere. Electronic structure of another cluster model terminated by H atoms for N- and C- termini in each residue in the cluster model presented in this study will be also presented elsewhere. The electronic structure of the new model also becomes the same tendency to the present model.

Acknowledgement

H.N. is grateful for a financial support of the Ministry of Education, Science and Culture of Japan (Research No. 15550010).

References

[1] E.T. Adman, Adv. Protein Chem. 42 (1991) 145.
[2] K.W. Penfield, A.A. Gewirth, E.I. Solomon, J. Am. Chem. Soc. 107 (1985) 4519.
[3] E.I. Solomon, M.J. Baldwin, M.D. Lowery, Chem. Rev. 92 (1992) 521.
[4] J.A. Guckert, M.D. Lowery, E.I. Solomon, J. Am. Chem. Soc. 117 (1995) 2817.
[5] E.I. Solomon, R.K. Szilagyi, S.D. George, L. Basumallick, Chem. Rev. 104 (2004) 419.
[6] H. Nar, A. Messerschmidt, R. Hunber, M. van de Kamp, G.W. Canters, J. Mol. Biol. 221 (1991) 765.
[7] U. Ryde, M.H.M. Ollson, B.O. Roos, A.C. Borin, Theor. Chem. Acc. 105 (2001) 452.
[8] U. Ryde, M.H.M. Olsson, Int. J. Quantum Chem. 81 (2001) 335.
[9] A.R. Jaszewski, J. Jezierska, Chem. Phys. Lett. 343 (2001) 571.
[10] M. Swart, Density functional theory applied to copper proteins, Ph.D. Thesis, Rijkuniversiteit Groningen, Groningen, 2002.
[11] S. Moon, S. Patchkovskii, D.R. Salahub, J. Mol. Struct. (Theochem) 632 (2003) 287.
[12] M. van Gastel, J.W.A. Coremans, H. Sommerdijk, M.C. van Hemert, E.J.J. Groenen, J. Am. Chem. Soc. 124 (2002) 2035.
[13] M.L.J. Drummond, Prog. Biophys. Mol. Biol. 47 (1986) 1.
[14] S. Miertuš, E. Scrocco, J. Tomasi, Chem. Phys. 55 (1981) 117.
[15] A.D. Becke, J. Chem. Phys. 98 (1993) 5648.
[16] C. Lee, W. Yang, R.G. Parr, Phys. Rev. B 37 (1988) 785.
[17] M.J. Frisch, G.W. Trucks, H.B. Schlegel, G.E. Scuseria, M.A. Robb, J.R. Cheeseman, J.A. Montgomery Jr., T. Vreven, K.N. Kudin, J.C. Burant, J.M. Millam, S.S. Iyengar, J. Tomasi, V. Barone, B. Mennucci, M. Cossi, G. Scalmani, N. Rega, G.A. Petersson, H. Nakatsuji, M. Hada, M. Ehara, K. Toyota, R. Fukuda, J. Hasegawa, M. Ishida, T. Nakajima, Y. Honda, O. Kitao, H. Nakai, M. Klene, X. Li, J.E. Knox, H.P. Hratchian, J.B. Cross, C. Adamo, J. Jaramillo, R. Gomperts, R.E. Stratmann, O. Yazyev, A.J. Austin, R. Cammi, C. Pomelli, J.W. Ochterski, P.Y. Ayala, K. Morokuma, G.A. Voth, P. Salvador, J.J. Dannenberg, V.G. Zakrzewski, S. Dapprich, A.D. Daniels, M.C. Strain, O. Farkas, D.K. Malick, A.D. Rabuck, K. Raghavachari, J.B. Foresman, J.V. Ortiz, Q. Cui, A.G. Baboul, S. Clifford, J. Cioslowski, B.B. Stefanov, G. Liu, A. Liashenko, P. Piskorz, I. Komaromi, R.L. Martin, D.J. Fox, T. Keith, M.A. Al-Laham, C.Y. Peng, A. Nanayakkara, M. Challacombe, P.M.W. Gill, B. Johnson, W. Chen, M.W. Wong, C. Gonzalez, J.A. Pople, GAUSSIAN 03, Revision B.05, Gaussian, Inc., Pittsburgh, PA, 2003.
[18] A.E. Reed, R.B. Weinstock, F. Weinhold, J. Chem. Phys. 83 (1985) 735.
[19] W.J. Hehre, L. Radom, P.v.R. Schleyer, J.A. Pople, Ab Initio Molecular Orbital Theory, Wiley-Interscience, New York, 1986.
[20] E. Cancès, B. Mennucci, J. Tomasi, J. Chem. Phys. 107 (1997) 3032.
[21] J. Hubbard, Proc. Roy. Soc. (London) A281 (1961) 401.
[22] J. Hubbard, Proc. Roy. Soc. (London) A276 (1963) 238.
[23] J. Hubbard, Proc. Roy. Soc. (London) A277 (1964) 237.
[24] D. Bohm, D. Pines, Phys. Rev. 92 (1953) 609.
[25] D. Pines, Phys. Rev. 92 (1953) 626.

2. Methods

We write the Ising spin Hamiltonian in the form

$$H = -\sum_{(ij)} J_{ij} S_i S_j. \quad (1)$$

where $S_i = \pm 1$ denotes the two states of the site i. We call the two states the L state for $S_i = -1$ and the H state for $S_i = 1$, respectively. The parameter $J_{ij}(>0)$ is the coupling energy between the nearest neighbor sites i and j. As the impurities, we introduce fixed spins that only have a single state, $S_i = 1$, or -1. Even in the presence of the fixed spins, the ground state is doubly degenerate 'ferromagnetic' phase where all of the variable spins are in the same state. We call these two global states the L and H phases, respectively.

In this paper, we consider a simple cubic spin lattice with three-dimensional periodic boundary conditions. The location of the fixed spins is schematically shown in Fig. 1. The system is identified by three parameters, N_a, N_i, and N_p. Fig. 1(a) and (b) shows the structures for the case of $N_p = 1$ and $N_p = 4$, for example. N_a indicates the number of spins on a side of cubic lattice. The system includes N_a^3 spins. In this paper, we fixed $N_a = 48$. In the case of $N_p = 1$ as shown in Fig. 1(a), we introduce fixed spins as two clusters whose size is $N_i \times N_i \times N_i$. One of the clusters I_H is located at the position of $(1/4, 1/4, 1/4)$, where the length unit is the side of the cubic. The other, I_L, is at $(3/4, 3/4, 3/4)$. The Ising spins in I_L and those in I_H is fixed with $S_i = -1$ and $S_i = 1$, respectively. In the case of $N_p > 1$, the system forms $N_p \times N_p \times N_p$ superstructure of the system of $N_p = 1$ as shown in Fig. 1(b). The number of clusters I_L and I_H are, respectively, given by N_p^3. The number of the fixed spins in each cluster is given by N_i^3 as well as the $N_p = 1$ case.

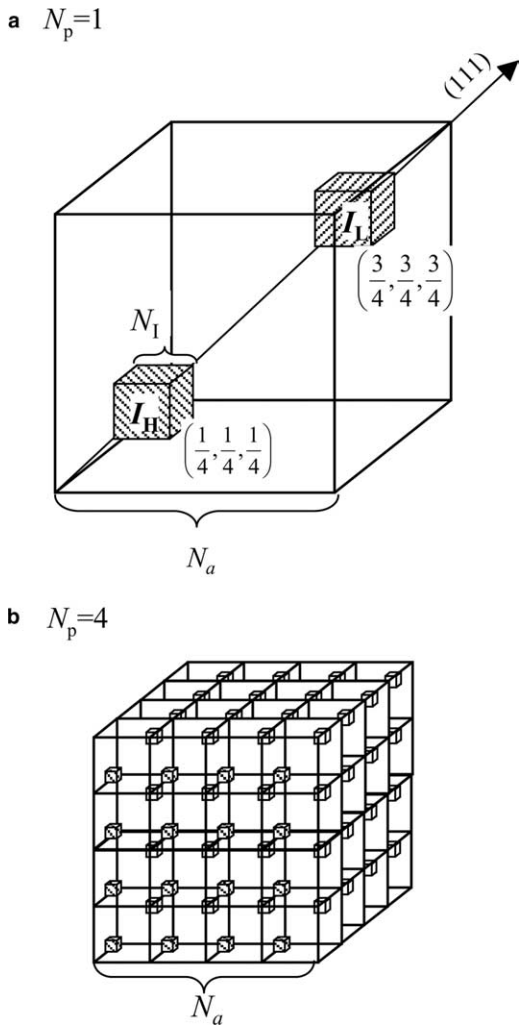


Fig. 1. Schematic structure of the calculated model for (a) $N_p = 1$ and (b) $N_p = 4$.

We studied the phase switching kinetics from one phase to another at finite temperatures by a means of a classical Monte Carlo simulation technique. The effect of photoexcitation is incorporated by external random flippings. Details of the actual procedure of the Monte Carlo simulations were described elsewhere [22,25]. In this paper, we assume the L phase as the initial state of the system and that the excitation occurs only when the spin is in the initial (L) state. Note that the backward transition from the H phase exhibits the same behavior because of symmetry with respect to the inversion of the spin direction.

The spin flipping rate at each site j is the sum of the external and thermal terms: $w_j = w_j^P + w_j^T$. The external term w_j^P corresponds to the selective photoexcitation. We consider selective excitation from L to H state, we set $w_j^P(L \to H) = W$ and $w_j^P(H \to L) = 0$. In each Monte Carlo step (MCS), both thermal and external spin-flip trials are performed at every site once on average. For the thermal flipping rate w_j^T, the heat bath model is used. We use $k_B T = J$, which is chosen lower than the order–disorder phase transition (Curie) temperature T_C, above which the bistability is lost. For example, $T_C = 4.51J$ for a cubic lattice with $N_i = 0$.

3. Result

We investigated the kinetics of the photoinduced switching with the excitation rate suddenly raised at $t = 0$ from 0 to a constant value W. The fraction of the H state, n_H, is plotted for $N_p = 1$ as a function of the excitation time t for strong and weak excitation ($W = 0.13$ and 0.10/MCS) in Fig. 2. For comparison, we draw the cases of $N_i = 12$ (doping fixed spins) and $N_i = 0$ (no fixed spins). At $t < 0$, the system is in an equilibrium state with $n_H \sim 0$. After the start of excitation at $t = 0$, n_H increases and approaches almost unity in some cases, indicating the completion of phase switching. With $W = 0.13$/MCS, the phase switching accomplishes

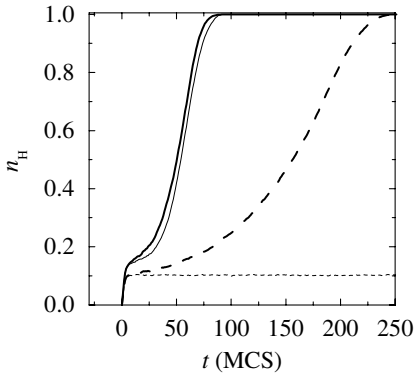


Fig. 2. Time evolution of n_H under continuous excitation on the system of $N_p = 1$ and $N_a = 48$ at $k_B T = J$. The thick and thin lines represent the cases with $N_i = 12$ and that with $N_i = 0$ (without fixed spins), respectively. The solid and broken lines are drawn for the excitation rate $W = 0.13$/MCS and for $W = 0.10$/MCS. The continuous excitation corresponding to photoirradiation is applied only at $t > 0$.

in almost the same time in the both cases. In the case of $W = 0.10$/MCS, on the other hand, the phase switching is observed only in the $N_i = 12$ case, indicating that the phase switching occurs under weaker excitation in the presence of fixed spins than the case without fixed spins.

The time of continuous excitation required for the phase switching, t_p, depends on the excitation intensity W. The W dependence of t_p is shown in Fig. 3 for various N_i with $N_p = 1$. Here, t_p is defined as the time of n_H exceeding $1 - n_H^0$, where n_H^0 represents n_H in an equilibrium state at $W = 0$. We used the average of 10 Monte Carlo samples to derive t_p. There is a threshold excitation rate W_c only above which the phase switching occurs for each N_i, and t_p diverges at above W_c. The threshold W_c is reduced significantly with increasing N_i.

The dependence of the threshold W_c on N_i and N_p is plotted in Fig. 4. We investigated two kinds of fixed spin distribution: (a) various N_i with fixing $N_p = 1$ and (b) various N_p with fixing $N_i = 1$. The x-axis in Fig. 4 means

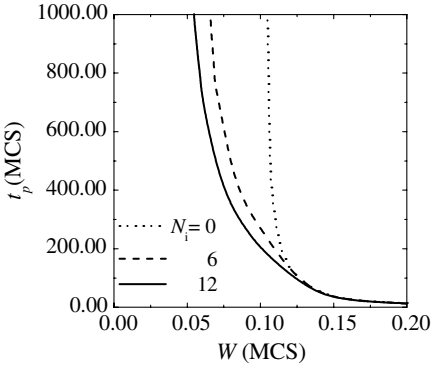


Fig. 3. Dependence of conversion time t_p on the excitation intensity W for various fixed spin cluster sizes N_i with $N_p = 1$ and $N_a = 48$ at $k_B T = J$.

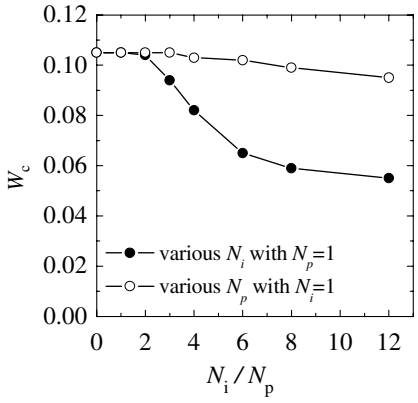


Fig. 4. Dependence of the threshold excitation rate W_c upon N_i and N_p at $k_B T = J$.

N_i for (a) and N_p for (b), respectively. Because number of fixed spins in the system is given by $N_i^3 N_p^3$, the same position along the x-axis indicates the same number of fixed spins in the system. The dependence of W_c on the number of fixed spins are clearly different between two systems. In the (a) case, W_c significantly decreases as N_i increases. At $N_i = 12$, W_c reaches about a half intensity compared with the case of $N_i = 0$. However, W_c is almost independent on N_p in the (b) case. These result shows W_c does not depend on the fraction of the fixed spins but the size of fixed spin clusters.

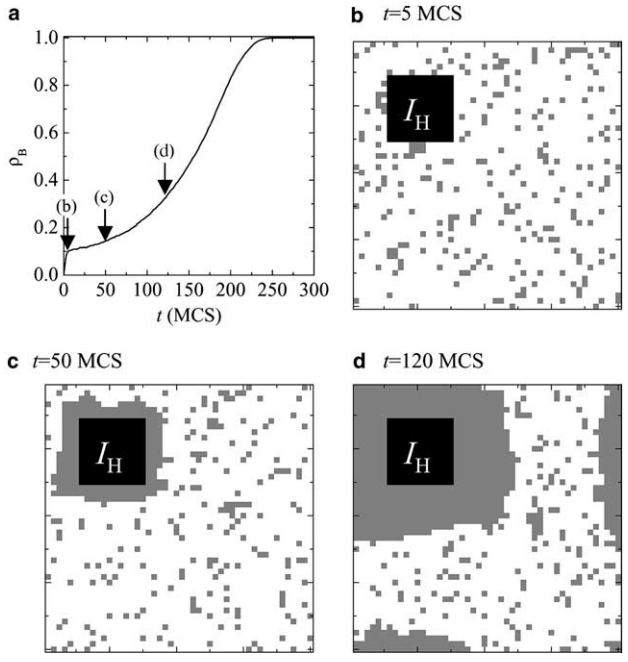


Fig. 5. (a) Fraction of the units in the H state n_H during the process of a photoinduced switching from the L phase to the H phase of the $48 \times 48 \times 48$ simple cubic lattice with $N_i = 12$ and $N_p = 1$. (b)–(d) Snapshots along the plane on $z = 1/4$ at $t = 5$,50, and 120 MCS with excitation rate $W = 0.12$/MCS. The white and gray region represent the units in $S_i = -1$ (initial) and in $S_i = -1$ (final), respectively. The region I_H represents the fixed spins with $S_i = 1$.

The reason why W_c depends on the cluster size is understood from the mechanism of the photoinduced switching. In our model, the photoinduced switching proceeds as a nucleation of the final phase and following its growth [24,25]. In the initial stage of the switching, the nucleus of the final phase appears. When the size of nucleus goes beyond a threshold, the growth of the final phase proceeds drastically. If the assembly of the final phase exists in advance, it can behave as the nucleus in the phase switching. For example, in the switching from the L phase to the H phase, the fixed spin cluster I_H plays a role of the nucleus. How the phase switching proceeds in the presence of the cluster is clearly understood with snapshots of the spin states in the switching process shown in Fig. 5. In Fig. 5(c), we found that the phase switching starts around the I_H cluster. The nucleus grows only when its size beyond a threshold in the switching. Therefore, as N_i increases, the switching is easy to appear as shown in Fig. 4

4. Conclusion

We demonstrated that the threshold of excitation intensity required for the phase switching can be reduced by introducing fixed spin clusters whose state is the same as the final phase. Our result implies that the photoinduced switching property of the complexes can be controlled by introducing impurities, although researchers generally try to exclude impurities to make a good sample in material synthesis. We expect that our idea will be a new guideline to improve properties of inorganic complexes.

Acknowledgements

This work was partly supported by NEDO under the Nanotechnology Materials Program, and by Ministry of Education, Science, Sports and Culture, Grant-in-Aid for Young Scientists (B), 16740181, 2004.

References

[1] O. Sato, T. Iyoda, A. Fujishima, K. Hashimoto, Science 272 (1996) 704.
[2] O. Sato, S. Hayami, Y. Einaga, Z.Z. Gu, Bull. Chem. Soc. Jpn. 76 (2003) 443.
[3] O. Sato, Y. Einaga, T. Iyoda, A. Fujishima, K. Hashimoto, J. Electrochem. Soc. 144 (1997) L11.
[4] N. Shimamoto, S. Ohkoshi, O. Sato, K. Hashimoto, Inorg. Chem. 41 (2002) 678.
[5] V. Escax, A. Bleuzen, J.P. Itie, P. Munsch, F. Varret, M. Verdaguer, J. Phys. Chem. B 107 (2003) 4763.
[6] H. Tokoro, S. Ohkoshi, K. Hashimoto, Appl. Phys. Lett. 82 (2003) 1245.
[7] A. Bleuzen, V. Escax, A. Ferrier, F. Villain, M. Verdaguer, P. Munsch, J.P. Itie, Angew. Chem. Int. Ed. 43 (2004) 3728.
[8] S. Decurtins, P. Gütlich, C.P. Kohler, H. Spiering, A. Hauser, Chem. Phys. Lett. 105 (1984) 1.
[9] P. Gütlich, Y. Garcia, T. Woike, Coord. Chem. Rev. 219 (2001) 839.
[10] A. Hauser, J. Jeftic, H. Romstedt, R. Hinek, H. Spiering, Coord. Chem. Rev. 192 (1999) 471.
[11] M. Marchivie, P. Guionneau, J.A. Howard, G. Chastanet, J.F. Létard, A.E. Goeta, D. Chasseau, J. Am. Chem. Soc. 124 (2002) 194.
[12] C. Enachescu, U. Oetliker, A. Hauser, J. Phys. Chem. B 106 (2002) 9540.
[13] X.J. Liu, Y. Moritomo, T. Kawamoto, A. Nakamoto, N. Kojima, Phys. Rev. B 67 (2003) 012102.
[14] X.J. Liu, Y. Moritomo, T. Kawamoto, A. Nakamoto, N. Kojima, J. Phys. Soc. Jpn. 72 (2003) 1615.
[15] J.F. Létard, L. Capes, G. Chastanet, N. Moliner, S. Letard, J.A. Real, O. Kahn, Chem. Phys. Lett. 313 (1999) 115.
[16] O. Sato, Acc. Chem. Res. 36 (2003) 692.
[17] Y. Einaga, O. Sato, T. Iyoda, A. Fujishima, K. Hashimoto, J. Am. Chem. Soc. 121 (1999) 3745.
[18] D.A. Pejaković, C. Kitamura, J.S. Miller, A.J. Epstein, Phys. Rev. Lett. 88 (2002) 5-057202.
[19] Y. Arimoto, S. Ohkoshi, Z.J. Zhong, H. Seino, Y. Mizobe, K. Hashimoto, J. Am. Chem. Soc. 125 (2003) 9240.
[20] H. Matsuzaki, W. Fujita, K. Awaga, H. Okamoto, Phys. Rev. Lett. 91 (2003) 1.
[21] T. Kawamoto, Y. Asai, S. Abe, Phys. Rev. Lett. 86 (2001) 348.
[22] T. Kawamoto, S. Abe, Phys. Rev. B 68 (2003) 235112.
[23] T. Kawamoto, S. Abe, Appl. Phys. Lett. 80 (2002) 2562.
[24] T. Kawamoto, S. Abe, Phase Transit. 75 (2002) 753.
[25] T. Kawamoto, S. Abe, in: K. Nasu (Ed.), Photoinduced Phase Transitions, World Scientific, Singapore, 2004 (Chapter 5).
[26] T. Kawamoto, Y. Moritomo, S. Abe, J. Phys. Soc. Jpn. 73 (2004) 3471.
[27] K. Takahashi, Z. Phys. B 71 (1988) 205.
[28] H. Constant-Machado, J. Linarès, F. Varret, J.G. Haasnoot, J.P. Martin, J. Zarembowitch, A. Dworkin, A. Bousseksou, J. Phys. I 6 (1996) 1203.
[29] T. Kohlhaas, H. Spiering, P. Gütlich, Z. Phys. B 102 (1997) 455.
[30] J. Linarès, J. Nasser, A. Bousseksou, K. Boukheddaden, F. Varret, J. Magn. Magn. Mater. 140 (1995) 1503.
[31] O. Sakai, M. Ishii, T. Ogawa, K. Koshino, J. Phys. Soc. Jpn. 71 (2002) 2052.
[32] I. Shteto, K. Boukheddaden, F. Varret, Phys. Rev. E 60 (1999) 5139.
[33] H. Romstedt, H. Spiering, P. Gütlich, J. Phys. Chem. Solids 59 (1998) 1353.
[34] C. Conséjo, G. Molnár, M. Goiran, A. Bousseksou, Polyhedron 22 (2003) 2441.
[35] M. Nishino, K. Boukheddaden, S. Miyashita, F. Varret, Phys. Rev. B 68 (2003) 224402.

the magnetic moment, is the essential feature for a molecule to function as an SMM. A twelve-nuclei manganese complex Mn_{12}-ac is one of the most extensively-studied SMM with the largest energy barrier of 66 K due to its $S = 10$ ground state and large negative D parameter [3]. Although there are many efforts to find new SMMs [4], Mn_{12} complex family still possesses the best structural and magnetic properties for showing single-molecular magnetic behavior at the highest temperature, and they have been paid a great deal of attention.

Chemical modifications so far done for Mn_{12}-ac complex include substitutions of bridging acetates to other carboxylates [1,2,5] and partial substitutions of a peripheral Mn^{III} ion to an Fe^{III} ion [6a] or a Cr^{III} ion [6b]. A substitution of carboxylate anions to non-carboxylate oxo anions such as NO_3^-, RSO_3^-, and $R_2PO_2^-$ would expand the possibility of the chemical modification in Mn_{12} complexes [7]. Although most of Mn_{12} complexes have four coordinating water molecules, only few examples, such as $[Mn_{12}O_{12}(O_2CEt)_{16}(H_2O)_3]\cdot 4H_2O$ [5a], $[Mn_{12}O_{12}(O_2CEt)_{16}(H_2O)_3]$ [8a], $(Ph_4P)[Mn_{12}O_{12}(O_2CH_2Cl)_{16}(H_2O)_3]$ [8b], $(PhP_4)_2[Mn_{12}O_{12}(O_2CH_2Cl)_{16}(H_2O)_3]$ [8c], and $(Ph_4P)[Mn_{12}O_{12}(O_2CC_4H_3S)_{16}(H_2O)_2]$ [5f], are known to have two or three coordinating water molecules with five-coordinating Mn^{III} ions. Herein, we report eight Mn_{12} derivatives with diphenylphosphate bridges including one-electron reduced anion complexes. Two crystal structures among them were determined by single crystal X-ray analyses [7e,7f].

2. Experimental

2.1. Compound preparation

All chemicals and solvents were used as received. The $[Mn_{12}O_{12}(CH_3COO)_{16}(H_2O)_4]\cdot 4CH_3COOH\cdot 2H_2O$ [9] (Mn_{12}-ac), $[Mn_{12}O_{12}(O_2CEt)_{16}(H_2O)_3]\cdot 4H_2O$ [5a] (Mn_{12}-pr), and $[Mn_{12}O_{12}(PhCOO)_{16}(H_2O)_4]\cdot PhCOOH\cdot CH_2Cl_2$ [4c] (Mn_{12}-bz) were prepared by the literature method.

2.2. $[Mn_{12}O_{12}(OAc)_{12}(dpp)_4]\cdot 6.1CH_2Cl_2\cdot 0.4H_2O$ (**1**$\cdot 6.1CH_2Cl_2\cdot 0.4H_2O$)

To a solution of Mn_{12}-ac (1.86 g, 1.0 mmol) in CH_3CN (100 ml) was added 4 equiv of diphenylphosphate (dppH, 1.01 g, 4.0 mmol). The mixture was stirred overnight in a closed flask and the solution was evaporated to dryness. To the residue was added toluene (100 ml), and the solution was stirred for 4 h, and then it was evaporated to dryness. The addition and removal of toluene were repeated four times. The residue was dissolved in CH_2Cl_2 (20 ml) and filtered. Hexane was added to the filtrate and the solution was allowed to stand at room temperature for two weeks. Black block-shaped crystals of **1**$\cdot 6.1CH_2Cl_2\cdot 0.4H_2O$ suitable for X-ray analysis were obtained from CH_2Cl_2/hexane. The crystals were isolated by filtration and dried in vacuo. The yield was 2.35 g (89%). *Anal.* Calc. for **1** ($C_{72}H_{76}Mn_{12}O_{52}P_4$): C, 33.83; H, 3.00. Found: C, 33.70; H, 3.14%. Selected IR data (KBr pellet cm^{-1}): 3069(w), 1581(s), 1491(s), 1441(s), 1379(m), 1330(m), 1201(m), 1092(s), 936(m), 670(m), 644(m), 611(m).

2.3. $[Mn_{12}O_{12}(OAc)_8(dpp)_8(H_2O)_2]$ (**2**)

A method similar to that used for synthesis of **1** was employed but using 8 equiv dppH. As a large amount of hexane was added to the filtrate of CH_2Cl_2 solution, the brown precipitate was collected by filtration, and washed with hexane, and dried in vacuo. The yield was 92%. *Anal.* Calc. for **2** ($C_{112}H_{108}Mn_{12}O_{62}P_8$): C, 40.12; H, 3.25. Found: C, 40.19; H, 3.28%. Selected IR data (KBr pellet cm^{-1}): 3069(w), 1591(s), 1491(s), 1440(m) 1382(m), 1332(m), 1198(s), 1107(s), 940(m), 779(m), 689(m), 532(m).

2.4. $[Ph_4P][Mn_{12}O_{12}(OAc)_{12}(dpp)_4(H_2O)_4]$ (**3**)

To a stirred dark brown solution of complex **1** (256 mg, 0.1 mmol) in CH_3CN (50 ml) was added solid Ph_4PI (46.7 mg, 0.1 mmol). The solution was stirred for 1 h. The I_2 in the resultant solution was removed by extraction in hexane (25 ml) for six times, and the solution was evaporated to dryness. The residue was dissolved in CH_2Cl_2 (6 ml). The brown powder was collected by filtration after addition of a large amount of hexane, and washed with hexane, and dried in vacuo. The yield was 249 mg (86%). *Anal.* Calc. for **3** ($C_{96}H_{104}Mn_{12}O_{56}P_5$): C, 38.85; H, 3.53. Found: C, 38.95; H, 3.36%. Selected IR data (KBr pellet cm^{-1}): 3067(w), 1590(s), 1491(s), 1440(s) 1389(m), 1334(m), 1203(m), 1095(s), 932(m), 779(m), 690(m), 669(m), 612(m), 528(m).

2.5. $[Ph_4P][Mn_{12}O_{12}(OAc)_8(dpp)_8(H_2O)_4]$ (**4**)

A method similar to that used for synthesis of **3** was applied to but replacing **1** with **2**. The yield was 90%. *Anal.* Calc. for **4** ($C_{136}H_{132}Mn_{12}O_{64}P_9$): C, 43.81; H, 3.57. Found: C, 44.06; H, 3.55%. Selected IR data (KBr pellet cm^{-1}): 3066(w), 1591(s), 1491(s), 1440(s) 1387(m), 1334(m), 1201(s), 1105(s), 1026(m), 934(m), 779(m), 690(m), 607(m), 529(m).

2.6. $[Mn_{12}O_{12}(OBz)_{12}(dpp)_4(H_2O)_4]\cdot 4CH_2Cl_2$ (**5**$\cdot 4CH_2Cl_2$)

To a solution of Mn_{12}-bz in CH_2Cl_2 was added 4 equiv of diphenylphosphate. The mixture was stirred about 1 h. Hexane was added to the filtrate; then the solution was

allowed to stand at room temperature for five days. Black block crystals $\mathbf{5}\cdot 4CH_2Cl_2$ suitable for X-ray analysis were obtained from CH_2Cl_2/hexane. The crystals were isolated by filtration and dried in vacuo. The yield was ca. 30%. *Anal.* Calc. for **5** ($C_{132}H_{108}O_{56}P_4Mn_{12}$): C, 47.00; H, 3.23; Mn, 19.54. Found: C, 46.84; H, 3.28; Mn, 18.89%. Selected IR data (KBr pellet cm^{-1}): 3066(w), 1595(m), 1562(m), 1491(s), 1415(s), 1348(m), 1201(m), 1088(s), 1025(w), 938(m), 687(m), 616(w), 517(m).

2.7. $[Mn_{12}O_{12}(OBz)_8(dpp)_8(H_2O)_4]$ (6)

A method similar to that used for synthesis of **5** was employed but using 8 equiv dppH. As a large amount of hexane was added to the filtrate of CH_2Cl_2 solution, the brown precipitate was collected by filtration, and washed with hexane, and dried in vacuo. The yield was 79%. *Anal.* Calc. for **6** ($C_{152}H_{128}Mn_{12}O_{64}P_8$): C, 46.98; H, 3.32; Mn, 16.79. Found: C, 46.84; H, 3.49; Mn, 15.94%. Selected IR data (KBr pellet cm^{-1}): 3067(w), 1592(s), 1560(w), 1492(s), 1415(s) 1355(m), 1199(s), 1105(s), 1025(w), 941(m), 779(m), 719(m), 688(m), 615(w), 523(m).

2.8. $[Ph_4P][Mn_{12}O_{12}(OBz)_{12}(dpp)_4(H_2O)_4]$ (7)

To a stirred dark brown solution of complex **5** (337 mg, 0.1 mmol) in CH_3CN (50 ml) was added solid Ph_4PI (46.6 mg, 0.1 mmol). The solution was stirred for 1 h. The I_2 in the resultant solution was removed by extraction in hexane (25 ml) for six times, and the solution was evaporated to dryness. The residue was dissolved in CH_2Cl_2 (6 ml). The brown powder was collected by addition of a large amount of hexane, and washed by hexane, and dried in vacuo. The yield was 333 mg (90%). *Anal.* Calc. for $\mathbf{7}\cdot CH_2Cl_2$ ($C_{157}H_{130}Cl_2Mn_{12}O_{56}P_5$): C, 49.65; H, 3.45; Mn, 17.36. Found: C, 49.47; H, 3.60; Mn, 16.96%. Selected IR data (KBr pellet cm^{-1}): 3065(w), 1594(m), 1560(m), 1518(m), 1492(s), 1416(s), 1361(m), 1202(m), 1092(s), 1026(w), 933(m), 720(s), 688(m), 616(w), 526(m).

2.9. $[Ph_4P][Mn_{12}O_{12}(OBz)_8(dpp)_8(H_2O)_4]$ (8)

A method similar to that used for synthesis of **7** was applied to but replacing **5** with **6**. The yield was 91%. *Anal.* Calc. for **8** ($C_{176}H_{148}Mn_{12}O_{64}P_9$): C, 50.03; H, 3.53; Mn, 15.60. Found: C, 49.54; H, 3.65; Mn, 16.05%. Selected IR data (KBr pellet cm^{-1}): 3065(w), 1593(m), 1560(m), 1523(m), 1492(s), 1416(s), 1361(m), 1202(m), 1105(s), 1026(m), 934(m), 778(m), 720(m), 689(m), 614(w), 526(m).

2.10. $[Mn_{12}O_{12}(O_2CC_2H_5)_{12}(dpp)_4(H_2O)_4]$ (9)

A similar method to the synthesis of **1** was applied but using Mn_{12}-pr (2.09 g, 1.0 mmol) in CH_3CN (100 ml) and 4 equiv of diphenylphosphate (dppH, 1.01 g, 4.0 mmol). The brown precipitates were collected after 1 week and dried in vacuo. The yield was 80%. *Anal.* Calc. for **2** ($C_{84}H_{108}Mn_{12}O_{56}P_4$): C, 36.07; H, 3.89. Found: C, 35.15; H, 3.69%.

2.11. Physicochemical measurements

Direct current (dc) and alternating current (ac) magnetic susceptibility data were collected on fresh microcrystalline samples restrained in eicosane to prevent torquing on a Quantum Design MPMS2 or MPMS7 SQUID magnetometer equipped with a 1 or 7 T magnet and capable of achieving temperatures of 1.7–400 K. A diamagnetic correction to the observed susceptibilities was applied using Pascal's constants. The magnitude of ac field was fixed to 0.3 mT, oscillating at frequency in the range of 5–997 Hz. Infrared spectra were recorded on KBr pellets using a JASCO FT/IR-430 spectrophotometer. ^1H NMR spectra were measured on a JEOL GSX 270 FT NMR spectrometer at room temperature. Tetramethylsilane was used as an internal reference for ^1H NMR measurement. Metal composition ware analyzed by Shimadzu AA-6200 Atomic Absorption Flame Emission Spectrophotometer.

2.12. X-ray structure analysis

Diffraction data for $\mathbf{1}\cdot 6.1CH_2Cl_2\cdot 0.4H_2O$ and $\mathbf{5}\cdot 4CH_2Cl_2$ were collected at −123 °C on a Rigaku/MSC Mercury CCD area detector with Rigaku AFC10 diffratometer equipped with graphite monochromated Mo Kα radiation. Crystal data and details of measurements for $\mathbf{1}\cdot 6.1CH_2Cl_2\cdot 0.4H_2O$ and $\mathbf{5}\cdot 4CH_2Cl_2$ are summarized in Table 1, and selected bond lengths and angles for **1** and **5** are given in Tables 2 and 3, respectively. The both structures were solved by direct method and expanded using Fourier techniques. The non-hydrogen atoms were refined anisotropically. Hydrogen atoms were included but not refined. Reliability factors are defined as $R = \sum||F_o| - |F_c||/\sum|F_o|$ and $R_w = \left[\sum w(F_o^2 - F_c^2)^2 / \sum w(F_o^2)^2\right]^{1/2}$. The final R and R_w values are also listed in Table 1.

3. Results and discussion

3.1. Crystal structure of $[Mn_{12}O_{12}(OAc)_{12}(dpp)_4]\cdot 6.1CH_2Cl_2\cdot 0.4H_2O$ ($\mathbf{1}\cdot 6.1CH_2Cl_2\cdot 0.4H_2O$)

The complex crystallizes in the monoclinic space group $P2_1/n$, with four formula units in the unit cell. A molecular core structure of **1** is shown in Fig. 1 together with the numbering scheme for some selected

Table 1
Crystallographic Data for $\mathbf{1}\cdot 6.1CH_2Cl_2\cdot 0.4\,H_2O$ and $\mathbf{5}\cdot 4CH_2Cl_2$

	$\mathbf{1}\cdot 6.1CH_2Cl_2\cdot 0.4H_2O$	$\mathbf{5}\cdot 4CH_2Cl_2$
Formula	$C_{78.1}H_{89.0}Cl_{12.2}Mn_{12}O_{52.4}P_4$	$C_{136}H_{116}Cl_8Mn_{12}O_{56}P_4$
Formula weight	3081.81	3713.15
Crystal color, habit	black block	black block
Crystal size (mm^3)	$0.28\times0.25\times0.13$	$0.30\times0.30\times0.30$
Crystal system	monoclinic	monoclinic
Space group	$P2_1/n$ (#14)	$P2/n$ (#13)
T (°C)	−123.0	−123.0
Unit cell dimensions		
a (Å)	14.8881(7)	18.792(5)
b (Å)	29.168(1)	16.406(4)
c (Å)	27.426(1)	24.815(6)
β (°)	94.468(3)	91.639(4)
V ($Å^3$)	11873.8(10)	7647(3)
Z	4	2
D_{calc} ($g\,cm^{-3}$)	1.724	1.412
Diffractometer	Rigaku/MSC mercury CCD	
μ (cm^{-1})	16.48	12.22
Radiation, λ (Å)	0.71070	0.71070
R^a, $R_w{}^b$	0.073, 0.168	0.0706, 0.1542
GOF	1.16	1.124

[a] $R=\sum||F_o|-|F_c||/\sum|F_o|$.
[b] $R_w=\left[\sum w(F_o^2-F_c^2)^2/\sum w(F_o^2)^2\right]^{1/2}$.

atoms. The eight Mn^{III} ions can be divided into two groups: four Mn^{III} ions with six coordination and four Mn^{III} ions with square pyramidal five coordination, which are arranged in 1:1:1:1 form with alternating up and down positions. The peripheral bridging ligands are categorized in three groups. They are eight equatorial acetates, four axial acetates and four axial dpp. The axial acetate groups are bridging Mn^{IV} and Mn^{III} ions whereas the dpp are bridging two types of Mn^{III} ions with alternating up and down positions. Each Mn^{III} ion in square pyramidal coordination is located about 0.2 Å above from the basal plane towards the apical oxygen atom. The exact distances are 0.215, 0.209, 0.200, and 0.187 Å for Mn8, Mn6, Mn10, and Mn12, respectively. The most interesting feature of this complex is the absence of any coordinating water molecules. This is the first observation in Mn_{12} complexes so far reported. The central $[Mn^{IV}{}_4O_4]^{8+}$ cubane and the outer ring of eight Mn^{III} ions are connected by eight μ^3-O^{2-} bridges. It should be noted that one phenoxy hydrogen atom of each dpp^- ligand is located near the vacant site of each five-coordinate Mn^{III} ion, as if it blocked water coordination. This situation is different from the case of **5**, where all phenoxy groups of dpp^- are directed to the out side of the molecule (vide infra). Those Mn···H distances are 3.490, 3.373, 3.170, and 3.158 Å for Mn8, Mn6, Mn10, and Mn12, respectively. This order is parallel to the decrease of the dislocation from the basal plane for each five-coordinate Mn^{III} ions (vide supra), indicating a strong correlation between them. This implies there is non-negligible Mn···H interaction.

3.2. Crystal structure of $[Mn_{12}O_{12}(OBz)_{12}(dpp)_4(H_2O)_4]\cdot 4CH_2Cl_2$ ($\mathbf{5}\cdot 4CH_2Cl_2$)

The complex crystallizes in the monoclinic space group $P2/n$, with two formula units in the unit cell. A molecular core structure of **5** is shown in Fig. 2 together with the numbering scheme for some selected atoms. Just like most of Mn_{12} complexes, the central $[Mn^{IV}{}_4O_4]^{8+}$ cubane and the outer ring of eight Mn^{III} ions are connected by eight μ^3-O^{2-} bridges. The peripheral bridging ligands are categorized in three groups. They are eight equatorial benzoate, four axial benzoate, and four axial dpp. The axial benzoate groups are bridging Mn^{III} and Mn^{IV} ions whereas the dpp are bridging two types of Mn^{III} ions with alternating up and down positions. In contrast to **1**, complex **5** contains four coordinating water molecules that are arranged in the 1:1:1:1 fashion with alternating up and down positions. All phenoxy groups of dpp are directing outwards, which enables water coordination. Four water oxygen atoms are involved in the elongated Mn–O bonds. The eight Jahn–Teller axes of Mn^{III} ions are roughly parallel to the crystallographic b-axis with angles of 15–38°. This is consistent with the observation of only a high-temperature (HT) phase in ac magnetization measurement.

3.3. ^1H NMR spectroscopy

In order to understand the coordinating condition of the five-coordinating Mn^{III} ions, the NMR method was applied to **1**. The ^1H NMR spectrum of **1** in CD_2Cl_2 is shown in Fig. 3(a). A broad signal **A** at 12.2 ppm was observed together with CH_3 (equatorial) protons (40–50 ppm), CH_3 (axial) protons (15–18 ppm), and phenyl protons (6–10 ppm). When a small amount of H_2O was added (Fig. 3(b)), a broad signal **B** due to coordinated water protons appeared at 28.5 ppm and the signal **A** shifted to higher field (10.3 ppm). A subsequent addition of a small amount of D_2O induced a disappearance of the signal **B** and a coalescence of the signal **A** into phenyl protons (Fig. 3(c)). These observations suggest that the signal **A** is due to a part of phenyl protons in the vicinity of Mn^{III} vacant sites, which are affected by the water coordination. Changes in spectral features of both CH_3 protons during the addition of water together with the observation of the signal **A** indicate that at least one phenoxy group of each dpp is almost fixed near the Mn^{III} vacant site during the NMR time scale and disturbing water coordination to the Mn^{III} ion. This is the first observation of an Mn_{12} complex with stable vacant sites on Mn^{III} ions in solution, which implies that **1** is a good candidate for a building block to form an

Table 2
Selected bond lengths (Å) and angles (°) for $\mathbf{1} \cdot 6.1CH_2Cl_2 \cdot 0.4H_2O$

Mn(1)–O(1)	1.909(3)	Mn(3)–O(17)	1.896(3)	Mn(6)–O(39)	1.933(3)	Mn(9)–O(45)	1.963(3)
Mn(1)–O(2)	1.905(3)	Mn(4)–O(1)	1.903(3)	Mn(7)–O(6)	1.912(3)	Mn(10)–O(9)	1.894(3)
Mn(1)–O(4)	1.898(3)	Mn(4)–O(3)	1.902(3)	Mn(7)–O(7)	1.912(3)	Mn(10)–O(10)	1.869(3)
Mn(1)–O(5)	1.877(3)	Mn(4)–O(4)	1.912(3)	Mn(7)–O(16)	2.182(3)	Mn(10)–O(30)	2.042(4)
Mn(1)–O(12)	1.870(3)	Mn(4)–O(10)	1.866(3)	Mn(7)–O(25)	2.127(3)	Mn(10)–O(46)	1.932(4)
Mn(1)–O(13)	1.907(3)	Mn(4)–O(11)	1.870(3)	Mn(7)–O(40)	1.949(3)	Mn(10)–O(47)	1.943(3)
Mn(2)–O(1)	1.908(3)	Mn(4)–O(19)	1.903(3)	Mn(7)–O(41)	1.955(4)	Mn(11)–O(10)	1.909(3)
Mn(2)–O(2)	1.911(3)	Mn(5)–O(5)	1.899(3)	Mn(8)–O(7)	1.896(3)	Mn(11)–O(11)	1.908(3)
Mn(2)–O(3)	1.907(3)	Mn(5)–O(12)	1.912(3)	Mn(8)–O(8)	1.862(3)	Mn(11)–O(20)	2.204(4)
Mn(2)–O(6)	1.864(3)	Mn(5)–O(14)	2.191(3)	Mn(8)–O(26)	2.060(4)	Mn(11)–O(33)	2.155(3)
Mn(2)–O(7)	1.875(3)	Mn(5)–O(21)	2.142(3)	Mn(8)–O(42)	1.939(4)	Mn(11)–O(48)	1.921(3)
Mn(2)–O(15)	1.905(3)	Mn(5)–O(37)	1.961(3)	Mn(8)–O(43)	1.946(3)	Mn(11)–O(49)	1.957(3)
Mn(3)–O(2)	1.907(3)	Mn(5)–O(52)	1.937(4)	Mn(9)–O(8)	1.923(3)	Mn(12)–O(11)	1.884(3)
Mn(3)–O(3)	1.908(3)	Mn(6)–O(5)	1.887(3)	Mn(9)–O(9)	1.903(3)	Mn(12)–O(12)	1.868(3)
Mn(3)–O(4)	1.908(3)	Mn(6)–O(6)	1.870(3)	Mn(9)–O(18)	2.191(4)	Mn(12)–O(34)	2.056(3)
Mn(3)–O(8)	1.864(3)	Mn(6)–O(22)	2.068(3)	Mn(9)–O(29)	2.116(4)	Mn(12)–O(50)	1.968(3)
Mn(3)–O(9)	1.866(3)	Mn(6)–O(38)	1.938(3)	Mn(9)–O(44)	1.936(4)	Mn(12)–O(51)	1.937(4)
O(1)–Mn(1)–O(2)	83.3(1)	O(4)–Mn(3)–O(9)	94.4(1)	O(6)–Mn(6)–O(38)	162.5(1)	O(18)–Mn(9)–O(44)	88.0(1)
O(1)–Mn(1)–O(4)	83.6(1)	O(4)–Mn(3)–O(17)	92.5(1)	O(6)–Mn(6)–O(39)	91.0(1)	O(18)–Mn(9)–O(45)	87.2(2)
O(1)–Mn(1)–O(5)	89.8(1)	O(8)–Mn(3)–O(9)	86.2(1)	O(22)–Mn(6)–O(38)	92.9(1)	O(29)–Mn(9)–O(44)	88.3(2)
O(1)–Mn(1)–O(12)	92.2(1)	O(8)–Mn(3)–O(17)	92.8(1)	O(22)–Mn(6)–O(39)	91.1(1)	O(29)–Mn(9)–O(45)	93.7(1)
O(1)–Mn(1)–O(13)	174.6(1)	O(9)–Mn(3)–O(17)	94.2(1)	O(38)–Mn(6)–O(39)	82.9(1)	O(44)–Mn(9)–O(45)	89.1(1)
O(2)–Mn(1)–O(4)	82.0(1)	O(1)–Mn(4)–O(3)	82.0(1)	O(6)–Mn(7)–O(7)	84.2(1)	O(9)–Mn(10)–O(10)	95.7(1)
O(2)–Mn(1)–O(5)	94.9(1)	O(1)–Mn(4)–O(4)	83.4(1)	O(6)–Mn(7)–O(16)	85.9(1)	O(9)–Mn(10)–O(30)	97.2(1)
O(2)–Mn(1)–O(12)	175.2(1)	O(1)–Mn(4)–O(10)	175.0(1)	O(6)–Mn(7)–O(25)	89.6(1)	O(9)–Mn(10)–O(46)	88.1(1)
O(2)–Mn(1)–O(13)	92.6(1)	O(1)–Mn(4)–O(11)	94.5(1)	O(6)–Mn(7)–O(40)	95.0(1)	O(9)–Mn(10)–O(47)	166.3(1)
O(4)–Mn(1)–O(5)	173.0(1)	O(1)–Mn(4)–O(19)	92.4(1)	O(6)–Mn(7)–O(41)	175.2(1)	O(10)–Mn(10)–O(30)	97.2(1)
O(4)–Mn(1)–O(12)	96.2(1)	O(3)–Mn(4)–O(4)	83.6(1)	O(7)–Mn(7)–O(16)	87.9(1)	O(10)–Mn(10)–O(46)	165.2(2)
O(4)–Mn(1)–O(13)	92.5(1)	O(3)–Mn(4)–O(10)	96.6(1)	O(7)–Mn(7)–O(25)	96.3(1)	O(10)–Mn(10)–O(47)	91.6(1)
O(5)–Mn(1)–O(12)	86.4(1)	O(3)–Mn(4)–O(11)	173.1(1)	O(7)–Mn(7)–O(40)	174.5(1)	O(30)–Mn(10)–O(46)	96.5(2)
O(5)–Mn(1)–O(13)	93.9(1)	O(3)–Mn(4)–O(19)	91.9(1)	O(7)–Mn(7)–O(41)	92.7(1)	O(30)–Mn(10)–O(47)	93.3(2)
O(12)–Mn(1)–O(13)	91.9(1)	O(4)–Mn(4)–O(10)	91.7(1)	O(16)–Mn(7)–O(25)	173.5(1)	O(46)–Mn(10)–O(47)	82.0(1)
O(1)–Mn(2)–O(2)	83.2(1)	O(4)–Mn(4)–O(11)	90.1(1)	O(16)–Mn(7)–O(40)	86.7(1)	O(10)–Mn(11)–O(11)	84.1(1)
O(1)–Mn(2)–O(3)	81.7(1)	O(4)–Mn(4)–O(19)	174.2(1)	O(16)–Mn(7)–O(41)	90.3(1)	O(10)–Mn(11)–O(20)	86.6(1)
O(1)–Mn(2)–O(6)	95.6(1)	O(10)–Mn(4)–O(11)	86.4(1)	O(25)–Mn(7)–O(40)	89.1(1)	O(10)–Mn(11)–O(33)	87.9(1)
O(1)–Mn(2)–O(7)	172.8(1)	O(10)–Mn(4)–O(19)	92.4(1)	O(25)–Mn(7)–O(41)	94.4(1)	O(10)–Mn(11)–O(48)	95.7(1)
O(1)–Mn(2)–O(15)	92.5(1)	O(11)–Mn(4)–O(19)	94.2(1)	O(40)–Mn(7)–O(41)	87.7(1)	O(10)–Mn(11)–O(49)	174.5(1)
O(2)–Mn(2)–O(3)	83.6(1)	O(5)–Mn(5)–O(12)	84.7(1)	O(7)–Mn(8)–O(8)	95.3(1)	O(11)–Mn(11)–O(20)	85.5(1)
O(2)–Mn(2)–O(6)	92.0(1)	O(5)–Mn(5)–O(14)	88.6(1)	O(7)–Mn(8)–O(26)	96.6(1)	O(11)–Mn(11)–O(33)	94.9(1)
O(2)–Mn(2)–O(7)	89.9(1)	O(5)–Mn(5)–O(21)	96.1(1)	O(7)–Mn(8)–O(42)	89.4(1)	O(11)–Mn(11)–O(48)	175.4(1)
O(2)–Mn(2)–O(15)	174.3(1)	O(5)–Mn(5)–O(37)	92.0(1)	O(7)–Mn(8)–O(43)	165.7(1)	O(11)–Mn(11)–O(49)	92.4(1)
O(3)–Mn(2)–O(6)	175.0(1)	O(5)–Mn(5)–O(52)	75.4(1)	O(8)–Mn(8)–O(26)	101.6(1)	O(20)–Mn(11)–O(33)	174.4(1)
O(3)–Mn(2)–O(7)	95.6(1)	O(12)–Mn(5)–O(14)	85.4(1)	O(8)–Mn(8)–O(42)	164.9(1)	O(20)–Mn(11)–O(48)	89.9(1)
O(3)–Mn(2)–O(15)	92.1(1)	O(12)–Mn(5)–O(21)	86.6(1)	O(8)–Mn(8)–O(43)	90.5(1)	O(20)–Mn(11)–O(49)	88.8(1)
O(6)–Mn(2)–O(7)	86.7(1)	O(12)–Mn(5)–O(37)	174.3(1)	O(26)–Mn(8)–O(42)	92.1(1)	O(33)–Mn(11)–O(48)	89.7(1)
O(6)–Mn(2)–O(15)	92.1(1)	O(12)–Mn(5)–O(52)	95.4(1)	O(26)–Mn(8)–O(43)	95.0(1)	O(33)–Mn(11)–O(49)	96.7(1)
O(7)–Mn(2)–O(15)	94.3(1)	O(14)–Mn(5)–O(21)	170.3(1)	O(42)–Mn(8)–O(43)	81.9(2)	O(48)–Mn(11)–O(49)	87.4(1)
O(2)–Mn(3)–O(3)	83.7(1)	O(14)–Mn(5)–O(37)	89.9(1)	O(8)–Mn(9)–O(9)	83.5(1)	O(11)–Mn(12)–O(12)	94.7(1)
O(2)–Mn(3)–O(4)	81.7(1)	O(14)–Mn(5)–O(52)	86.8(1)	O(8)–Mn(9)–O(18)	87.2(1)	O(11)–Mn(12)–O(34)	96.7(1)
O(2)–Mn(3)–O(8)	97.1(1)	O(21)–Mn(5)–O(37)	98.4(1)	O(8)–Mn(9)–O(29)	92.1(1)	O(11)–Mn(12)–O(50)	87.9(1)
O(2)–Mn(3)–O(9)	173.5(1)	O(21)–Mn(5)–O(52)	88.5(1)	O(8)–Mn(9)–O(44)	94.7(1)	O(11)–Mn(12)–O(51)	168.9(1)
O(2)–Mn(3)–O(17)	91.2(1)	O(37)–Mn(5)–O(52)	87.6(1)	O(8)–Mn(9)–O(45)	173.1(2)	O(12)–Mn(12)–O(34)	100.4(1)
O(3)–Mn(3)–O(4)	83.5(1)	O(5)–Mn(6)–O(6)	95.4(1)	O(9)–Mn(9)–O(18)	87.6(1)	O(12)–Mn(12)–O(50)	164.9(1)
O(3)–Mn(3)–O(8)	91.1(1)	O(5)–Mn(6)–O(22)	96.5(1)	O(9)–Mn(9)–O(29)	96.1(1)	O(12)–Mn(12)–O(51)	91.9(1)
O(3)–Mn(3)–O(9)	90.8(1)	O(5)–Mn(6)–O(38)	88.3(1)	O(9)–Mn(9)–O(44)	175.3(1)	O(34)–Mn(12)–O(50)	94.0(1)
O(3)–Mn(3)–O(17)	173.9(1)	O(5)–Mn(6)–O(39)	168.7(1)	O(9)–Mn(9)–O(45)	92.2(1)	O(34)–Mn(12)–O(51)	90.9(1)
O(4)–Mn(3)–O(8)	174.6(1)	O(6)–Mn(6)–O(22)	103.7(1)	O(18)–Mn(9)–O(29)	176.1(1)	O(50)–Mn(12)–O(51)	83.4(1)

assemblage of an Mn_{12} SMM. On the other hand, in the ^1H NMR spectrum of **9** in CD_2Cl_2 shown in Fig. 4, a signal assigned to the coordinating water proton can be observed at around 32 ppm. This signal was disappeared when a small amount of D_2O was added, indicating the validity of the assignment. This clearly shows **9** contains coordinating water molecules similar to **5**. This means phenoxy groups of dpp in **9** are directed to

Table 3
Selected bond lengths (Å) and angles (°) for $\mathbf{5}\cdot 4CH_2Cl_2$

Mn(1)–O(1)	1.935(3)	Mn(4)–O(3)	1.880(3)
Mn(1)–O(1′)	1.917(3)	Mn(4)–O(4)	1.935(3)
Mn(1)–O(2)	1.898(3)	Mn(4)–O(12)	1.986(3)
Mn(1)–O(3)	1.858(3)	Mn(4)–O(13)	1.945(3)
Mn(1)–O(6)	1.872(3)	Mn(4)–O(20)	2.112(3)
Mn(1)–O(7)	1.900(3)	Mn(4)–O(27)	2.227(3)
Mn(2)–O(1)	1.889(3)	Mn(5)–O(4)	1.923(3)
Mn(2)–O(2)	1.946(3)	Mn(5)–O(5)	1.882(3)
Mn(2)–O(2′)	1.919(3)	Mn(5)–O(10)	2.248(3)
Mn(2)–O(4)	1.880(3)	Mn(5)–O(14)	1.920(3)
Mn(2)–O(5)	1.861(3)	Mn(5)–O(15)	1.944(3)
Mn(2)–O(9)	1.902(3)	Mn(5)–O(23)	2.185(3)
Mn(3)–O(3)	1.879(3)	Mn(6)–O(5)	1.880(3)
Mn(3)–O(6)	1.919(3)	Mn(6)–O(6)	1.932(3)
Mn(3)–O(8)	2.281(3)	Mn(6)–O(16)	1.968(3)
Mn(3)–O(11)	1.932(3)	Mn(6)–O(17)	1.951(3)
Mn(3)–O(18)	1.920(3)	Mn(6)–O(24)	2.112(3)
Mn(3)–O(19)	2.163(3)	Mn(6)–O(28)	2.220(3)
O(1)–Mn(1)–O(1)	80.5(1)	O(3)–Mn(4)–O(4)	92.7(1)
O(1)–Mn(1)–O(2)	83.7(1)	O(3)–Mn(4)–O(12)	90.8(1)
O(1)–Mn(1)–O(3)	94.8(1)	O(3)–Mn(4)–O(13)	172.0(1)
O(1)–Mn(1)–O(6)	175.2(1)	O(3)–Mn(4)–O(20)	93.0(1)
O(1)–Mn(1)–O(7)	88.2(1)	O(3)–Mn(4)–O(27)	84.8(1)
O(1)–Mn(1)–O(2)	84.1(1)	O(4)–Mn(4)–O(12)	175.6(1)
O(1)–Mn(1)–O(3)	173.4(1)	O(4)–Mn(4)–O(13)	92.1(1)
O(1)–Mn(1)–O(6)	99.4(1)	O(4)–Mn(4)–O(20)	94.5(1)
O(1)–Mn(1)–O(7)	92.0(1)	O(4)–Mn(4)–O(27)	92.3(1)
O(2)–Mn(1)–O(3)	90.8(1)	O(12)–Mn(4)–O(13)	84.2(1)
O(2)–Mn(1)–O(6)	91.5(1)	O(12)–Mn(4)–O(20)	88.1(1)
O(2)–Mn(1)–O(7)	171.5(1)	O(12)–Mn(4)–O(27)	85.3(1)
O(3)–Mn(1)–O(6)	84.9(1)	O(13)–Mn(4)–O(20)	93.1(1)
O(3)–Mn(1)–O(7)	92.4(1)	O(13)–Mn(4)–O(27)	88.6(1)
O(6)–Mn(1)–O(7)	96.7(1)	O(20)–Mn(4)–O(27)	173.0(1)
O(1)–Mn(2)–O(2)	83.6(1)	O(4)–Mn(5)–O(5)	83.3(1)
O(1)–Mn(2)–O(2)	84.4(1)	O(4)–Mn(5)–O(10)	89.6(1)
O(1)–Mn(2)–O(4)	90.3(1)	O(4)–Mn(5)–O(14)	93.9(1)
O(1)–Mn(2)–O(5)	90.7(1)	O(4)–Mn(5)–O(15)	173.2(1)
O(1)–Mn(2)–O(9)	172.8(1)	O(4)–Mn(5)–O(23)	98.0(1)
O(2)–Mn(2)–O(2)	80.0(1)	O(5)–Mn(5)–O(10)	85.4(1)
O(2)–Mn(2)–O(4)	173.8(1)	O(5)–Mn(5)–O(14)	176.9(1)
O(2)–Mn(2)–O(5)	94.0(1)	O(5)–Mn(5)–O(15)	94.2(1)
O(2)–Mn(2)–O(9)	89.4(1)	O(5)–Mn(5)–O(23)	92.4(1)
O(2)–Mn(2)–O(4)	100.3(1)	O(10)–Mn(5)–O(14)	93.3(1)
O(2)–Mn(2)–O(5)	172.6(1)	O(10)–Mn(5)–O(15)	83.8(1)
O(2)–Mn(2)–O(9)	92.8(1)	O(10)–Mn(5)–O(23)	171.9(1)
O(4)–Mn(2)–O(5)	85.1(1)	O(14)–Mn(5)–O(15)	88.5(1)
O(4)–Mn(2)–O(9)	96.8(1)	O(14)–Mn(5)–O(23)	89.2(1)
O(5)–Mn(2)–O(9)	91.5(1)	O(15)–Mn(5)–O(23)	88.5(1)
O(3)–Mn(3)–O(6)	83.0(1)	O(5)–Mn(6)–O(6)	93.1(1)
O(3)–Mn(3)–O(8)	84.3(1)	O(5)–Mn(6)–O(16)	90.8(1)
O(3)–Mn(3)–O(11)	95.6(1)	O(5)–Mn(6)–O(17)	174.9(1)
O(3)–Mn(3)–O(18)	174.2(1)	O(5)–Mn(6)–O(24)	94.4(1)
O(3)–Mn(3)–O(19)	91.5(1)	O(5)–Mn(6)–O(28)	85.7(1)
O(6)–Mn(3)–O(8)	91.4(1)	O(6)–Mn(6)–O(16)	175.2(1)
O(6)–Mn(3)–O(11)	175.2(1)	O(6)–Mn(6)–O(17)	90.7(1)
O(6)–Mn(3)–O(18)	92.6(1)	O(6)–Mn(6)–O(24)	95.2(1)
O(6)–Mn(3)–O(19)	97.9(1)	O(6)–Mn(6)–O(28)	93.8(1)
O(8)–Mn(3)–O(11)	83.8(1)	O(16)–Mn(6)–O(17)	85.2(1)
O(8)–Mn(3)–O(18)	91.9(1)	O(16)–Mn(6)–O(24)	87.3(1)
O(8)–Mn(3)–O(19)	169.3(1)	O(16)–Mn(6)–O(28)	83.7(1)
O(11)–Mn(3)–O(18)	88.4(1)	O(17)–Mn(6)–O(24)	88.7(1)
O(11)–Mn(3)–O(19)	86.7(1)	O(17)–Mn(6)–O(28)	90.6(1)
O(18)–Mn(3)–O(19)	92.9(1)	O(24)–Mn(6)–O(28)	171.0(1)

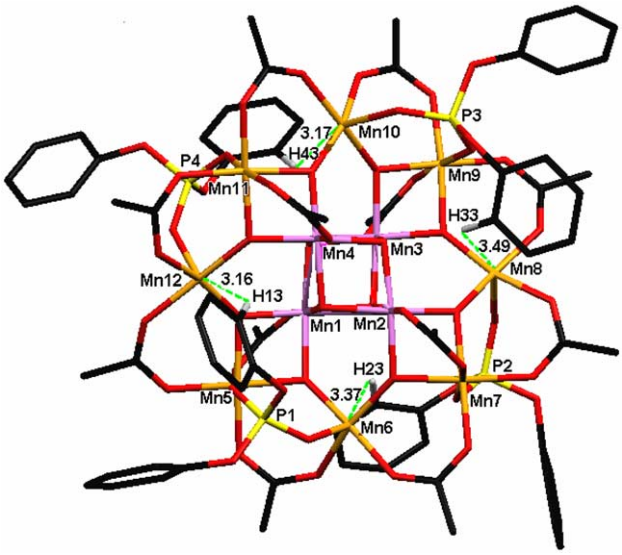


Fig. 1. A drawing of a molecular structure of complex **1**, with the atom numbering scheme for selected atoms. Four Mn^{III} ions, Mn6, Mn8, Mn10, Mn12, show five-coordination together with four Mn···H approaches. Other hydrogen atoms are omitted for clarity.

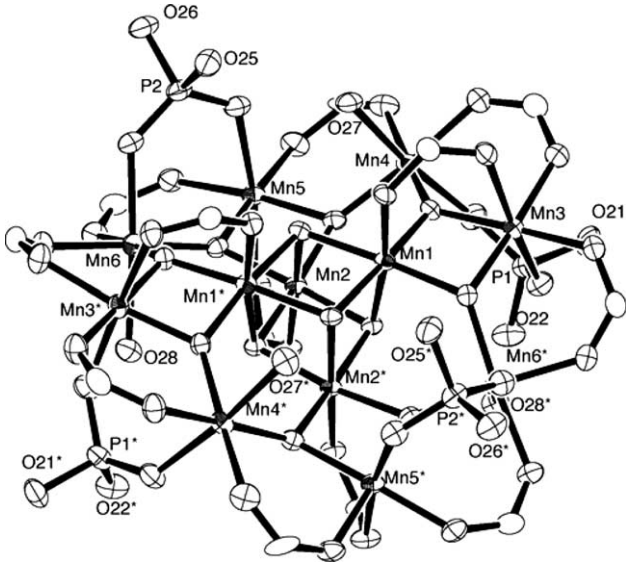


Fig. 2. An ORTEP view of **2** with atom numbering scheme for selected atoms. Phenyl groups and hydrogen atoms of water molecules are omitted for clarity.

outwards of the molecule like **5** as shown in Fig. 2, while those in **1** are in the proximity of the Mn12 core. The difference comes from the alkyl chain lengths of carboxylates, methyl and ethyl. A possible explanation is the difference of the extent of a hydrophobic space generated by alkyl chains of peripheral carboxyl groups. Compared to **9**, the extent of a hydrophobic space in **1** is small, which causes such a drastic change in locations of phenoxy groups and disturbances of water-coordination.

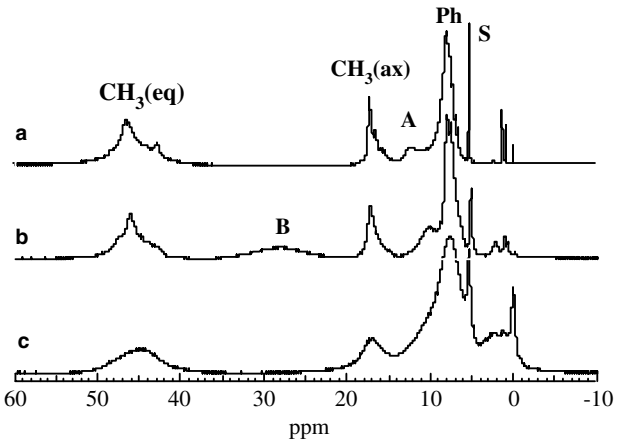


Fig. 3. The ^{1}H NMR spectra of complex **1** in CD_2Cl_2 during addition of water. (a), initial, (b) after adding a small amount of H_2O, and (c) after a subsequent addition of a small amount of D_2O.

3.4. Dc magnetic susceptibility

Solid-state, variable temperature magnetic susceptibility measurements were performed on a freshly prepared sample of **1**–**9** (figure see supporting materials), suspended in eicosane to prevent torquing. Dc magnetic susceptibility (χ_M) data were collected from 2 to 280 K at 1.0 T magnetic field. As the temperature increase, the $\chi_M T$ value of **1** shown a maximum of 43.4 cm^3 K mol^{-1} at 13.3 K and a broad minimum of 16.0 cm^3 K mol^{-1} at around 200 K and again increases slightly to 16.9 cm^3 K mol^{-1} at 280 K. Similar behaviors were observed for complex **2**–**9** and the data were summarized in Table 4.

3.5. Ac magnetic susceptibility

The observation of frequency-dependent out of phase signal, χ''_M , in ac magnetic susceptibility is an important indicator of SMMs, which show slow magnetization relaxation. Therefore, ac susceptibility data can be used not only to determine whether a molecule functions as a SMM but also to obtain the effective energy barrier U_{eff} for the magnetization relaxation. Ac magnetic susceptibility measurements of freshly prepared complexes **1**–**9** at several frequencies for the temperature range of 1.7–10.0 K were carried out to investigate the dynamic behavior of their magnetic moments. Figs. 5 and 6 show plots of $\chi'_M T$ vs T (top) and χ''_M vs T (bottom) for neutral complexes **1** and **5**, respectively, where χ'_M is in-phase ac susceptibility. Ac magnetic susceptibilities for other complexes are shown in supplemental data as Figure S3–S9. As temperature decreases, these values start to decrease at certain temperature depending on frequency. As expected for SMMs, the decrease of $\chi'_M T$ value corresponds to the appearance of out-of-phase signal (χ''_M). For most of neutral Mn_{12} complexes, there are two χ''_M peaks: high-temperature (HT) and low-temperature (LT) phases. On the other hand, only one peak was detected in reduced salts of Mn_{12} complexes. It is quite interesting that there is only a peak (HT) for neutral dpp substituted complexes **1**, **2**, and **5**. This indicates the substitution of dpp^- from axial position induces a parallel alignment of J–T axes of Mn(III) ions. The reason for a presence of a small amount of LT phase in complexes 6 and 9, as shown Figure S6 and S9, respectively, is probably ascribed to a presence of dpp^- substitution isomers in equatorial position [7b].

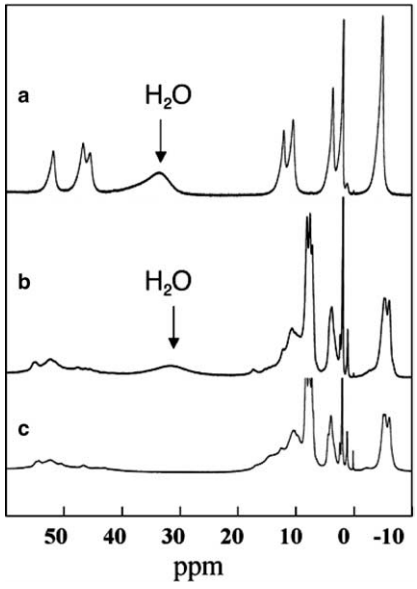


Fig. 4. The ^{1}H NMR spectra of (a) Mn_{12}-pr, (b) complex **9** in CD_2Cl_2, (c) after addition of a small amount of D_2O to (b).

Table 4
Dc magnetic susceptibility for **1**–**8**

	$(\chi_M T)_{max}$ (T)	$(\chi_M T)_{min}$ (T)	$(\chi_M T)_{280\,K}$
1	43.4 (13.3)	16.0 (200)	16.9
2	48.2 (10.0)	17.2 (200)	17.7
3	49.4 (10.0)	17.6 (180)	18.6
4	48.3 (10.0)	18.3 (180)	19.6
5	50.6 (14.0)	18.7 (200)	19.6
6	42.7 (10.0)	16.5 (160)	18.3
7	53.3 (10.0)	19.6 (180)	21.1
8	52.6 (10.0)	19.4 (180)	20.4
9	45.5 (14.0)	16.8 (200)	17.8

The frequency dependence of the χ''_M peak temperature can be analyzed by Arrhenius law. On the basis of the plots of the natural logarithm of the relaxation time τ evaluated from $1/(2\pi\nu)$, where ν is the ac frequency, versus the inverse of the χ''_M peak temperature T, the effective energy barrier U_{eff} and the pre-exponential factor τ_0 can be estimated by the following equation [10]:

$$\tau = \tau_0 \exp\left(\frac{U_{eff}}{k_B T}\right), \quad (1)$$

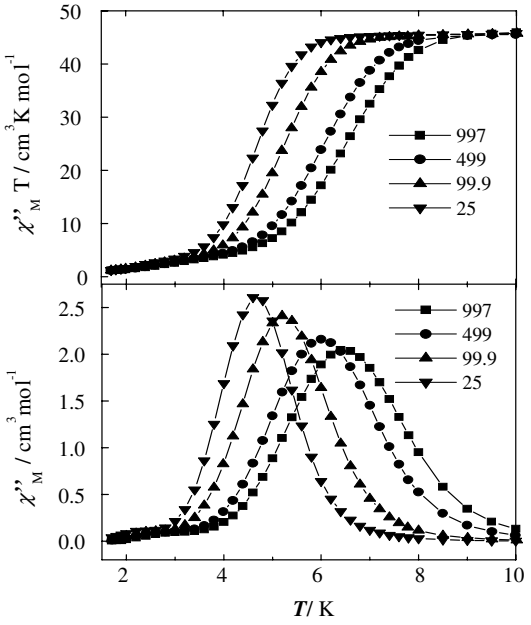


Fig. 5. Plots of $\chi'_M T$ vs T (top) and χ''_M vs T (bottom) for a polycrystalline sample of complex **1** in a 0.3 mT ac field oscillating at the indicated frequencies.

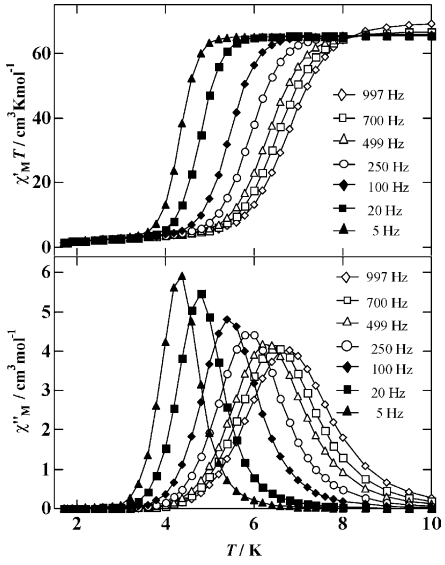


Fig. 6. Plots of $\chi'_M T$ vs T (top) and χ''_M vs T (bottom) for complex **5** in a 0.3 mT ac field oscillating at the indicated frequencies.

where k_B is the Boltzmann constant. The Arrhenius plots for **1**–**9** are shown in Fig. 7. The solid lines show the results of least-squares fits of the ac susceptibility relaxation data to Eq. (1). The pre-exponential factors τ_0 and the effective energy barriers U_{eff} of HT phases for **1**–**9** are given in Table 5. These values are somewhat smaller than those obtained for neutral Mn_{12} complexes, such as $[Mn_{12}O_{12}(NO_3)_4(O_2CCH_2\ Bu^t)_{12}(H_2O)_4]$ (72 K [7a]), and for the one-electron reduced Mn_{12} complexes, such as $(Ph_4P)[Mn_{12}O_{12}(O_2CEt)_{16}(H_2O)_4]$ (60.2 K [11]), $(Ph_4P)[Mn_{12}O_{12}(O_2CC_4H_3S)_{16}(H_2O)_2]$ (57.1 K [5f]) or

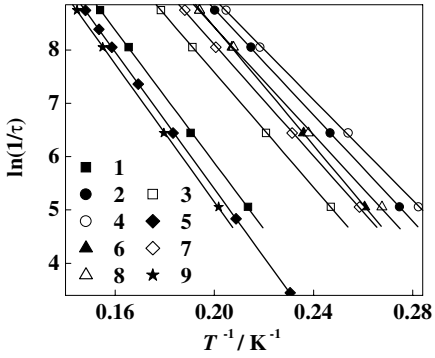


Fig. 7. Plots of the natural logarithm of the inverse of the magnetization relaxation time $\ln(1/\tau)$ vs the inverse of the absolute temperature of the χ''_M peaks for complexes **1**–**9**, solid lines represent least-squares fits of the data to the Arrhenius equation (see the text).

Table 5
The U_{eff} and τ^0 for complexes **1**–**8**

Complex	τ^0/s	U_{eff}/K
1	1.09×10^{-8}	62.5
2	7.47×10^{-9}	49.7
3	1.06×10^{-8}	53.9
4	1.03×10^{-8}	47.2
5	1.21×10^{-8}	64.2
6	3.27×10^{-9}	55.5
7	8.66×10^{-9}	52.3
8	9.05×10^{-9}	50.5
9	1.05×10^{-8}	64.6

$(Ph_4P)[Mn_{12}O_{12}(O_2CPh)_{16}(H_2O)_4]$ (55 K [12], 57.5 K [13]). To investigate the effect of the substitution of dpp^- ligands, the energy barriers of a freshly prepared Mn_{12}ac, **1** and **2** were compared. They are 72.7 K[1], 62.5 to 53.9 K, respectively. As the number of substituted dpp^- ligands increases, the U_{eff} values decrease monotonically. This rule was also observed about complexes Mn_{12}-bz, **5** and **6**, whose U_{eff} values decrease from 73.8 K,[1] 64.2 to 55.5 K, respectively. Since a U_{eff} is expressed as $|\mathbf{D}|S^2$ and an $S = 10$ ground state is also valid for complexes Mn_{12}-ac, **1** and **2** from low-temperature dc magnetization data, a molecular **D** is responsible to account for the decrease of U_{eff}. A molecular **D** can be estimated as a sum of single-ion **D**'s of Mn(III) ions, then both the alignment of J–T axes [14] and single-ion D-values [15] are important factors. Although we compared alignments of J–T axes of Mn(III) ions in complexes Mn_{12}-ac and **1** thoroughly, there are no significant differences between them. Therefore, a decrease of the single-ion D-values of each Mn(III) ion coordinated by dpp^- is the main reason for decrease of U_{eff} values.

[1] We measured the ac magnetic susceptibility of the freshly prepared Mn_{12}-ac and Mn_{12}-bz, and analyzed the data by Arrhenius law to obtain the effective energy U_{eff} of 72.7 and 73.8 K, respectively.

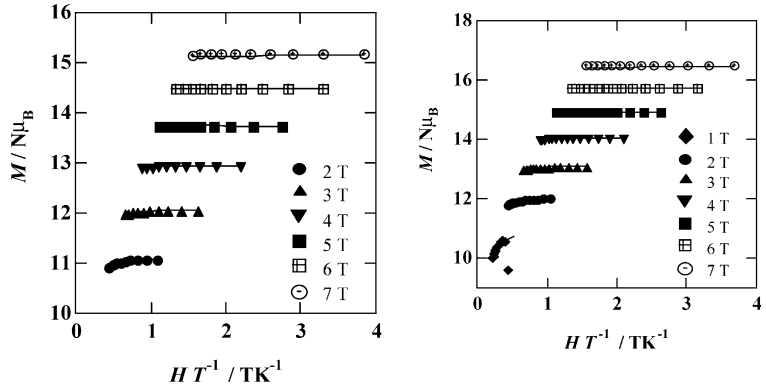


Fig. 8. Reduced magnetization data for **1** (left) and **5** (right) with different external fields. Lines show the best-fit assuming $S = 10$, $g = 1.78$, and $D = -0.60$ K for **1** and $S = 10$, $g = 1.92$, and $D = -0.63$ K for **5**.

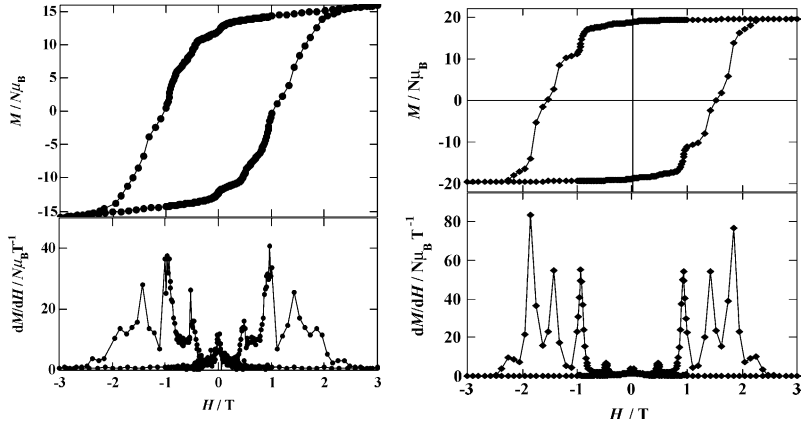


Fig. 9. A magnetization hysteresis loop for oriented crystals of **1** (left) and **5** (right) in an eicosane matrix measured at 1.9 K (top) and the corresponding first derivatives dM/dH (bottom).

3.6. Reduced magnetization

In order to determine S and D values, magnetization data $M/(N\mu_B)$ were collected for **1** and **5** fixed with an eicosane matrix under a 2–7 T field at temperatures between 1.9 and 4.5 K. The observed data were fitted with a magnetization fitting program "axfit" [16] assuming an $S = 10$ ground state. The lines in Fig. 8 shows the best fit for an $S = 10$ ground state with the parameters of $g = 1.78$ and $D = -0.60$ K for **1** and for an $S = 10$ ground state with the parameters of $g = 1.92$ and $D = -0.63$ K for **5**, respectively. Although a fit with a similar quality was also obtained by using $g = 1.98$ and $D = -0.74$ K assuming $S = 9$ ground state for **1**, this possibility might be excluded because the largest $|D|$ value of 0.74 K so far reported for Mn_{12} complexes is somewhat mysterious for **1** containing four five-coordinate Mn^{III} ions. Our model calculations using the AOM method[2] [17] showed that a single ion $|D|$ value for a five-coordinate Mn^{III} ion (2.0 cm^{-1}) is clearly smaller than those for six-coordinate Mn^{III} ions (2.3–3.2 cm^{-1}). The results of magnetization hysteresis loop also testified this conclusion and HF-EPR measurements will give more definitive conclusion.

3.7. Magnetization hysteresis loops

Especially for SMM, step-like sudden decreases of magnetization can be also seen, which are attributed to the quantum tunneling of magnetization. Since complex **1** and **5** are SMMs, it was of interest to investigate their magnetization response to a changing dc field. This experiment was performed using some single crystals of **1** or **5** that had been placed in a capsule with eicosane and oriented with their easy axes parallel by exposing them to a 7.0 T external magnetic field at 325 K, then allowed eicosane to cool and solidify at room temperature, to trap the crystals of **1** or **5** in their parallel orientation.

$$H_{S,-S+n} = nD/(g\mu_B). \quad (2)$$

The magnetization hysteresis loop measured for the field-oriented single crystals at 1.9 K are shown in Fig. 9 (left: **1**; right: **5**). The magnetization saturates

[2] A program ZAOM was used for calculation. AOM parameters were adopted from Ref. [17].

completely at fields above 2.3 T to ca. 16 $N\mu_B$. Hysteresis is seen with a coercive field of 1.0 T. In the bottom of the Fig. 9 are shown the first derivatives of the hysteresis plots. As the field is decreased from +3 T, the first step can be seen at zero fields, followed by steps at −0.49, −0.98, −1.43, and −2.38 T for **1**, and −0.47, −0.93, −1.42, −1.84, and −2.26 T for **5**. The steps correspond to increases in the rate of the change of the magnetization, and are attributable to resonant tunnelings between two sublevels of $m_s = S$ and $m_s = -S + n$, where $n = 0$, 1, 2, 3, and 4. Since the condition that the quantum tunneling occurs can be expressed as Eq. (2), [4b] we can predict a step interval of 0.50 T calculated as $|D|/(g\mu_B)$ using D (−0.60 K) and g (1.78) obtained from the reduced magnetization analysis of **1**. This value is in agreement with the observed one (about 0.49 T), indicating the validity of the reduced magnetization analysis. If using D (−0.74 K) and g (1.98), the step value can be calculated to be 0.56 T, which is inconsistent with the observed results, indicating the conclusion with $S = 10$ is valid for **1**. Similar to **1**, using the observed ΔH of 0.46 T for **5**, we estimate the value $|D|/g$ to be 0.31 K, which is fairly comparable to 0.33 K calculated by using the g and D values obtained from the reduced magnetization experiment.

4. Conclusion

Nine Mn_{12} derivatives with diphenylphosphate bridges, **1**–**9**, have been successfully isolated and studied, which indicate SMM behavior on ac susceptibility, and two complexes (**1** and **5**) were characterized by X-ray. Complex **1** has no coordinating water with four five-coordinate Mn^{III} ions while complex **5** has water coordination as usual. This is the first Mn_{12} derivative without coordinating water molecules. The difference comes from directions of phenoxy groups of dpp, which is induced by a difference of carboxylates. A contraction of a hydrophobic space in **1** compared to **5** or **9** causes a drastic change in locations of phenoxy groups and disturbances of water-coordination. NMR measurements of **1** showed a water coordination occurs when water was added in CD_2Cl_2 solution. The magnetization hysteresis loops of **1** and **5** show the quantum tunneling of magnetization. The substitution of dpp ligands results in the decrease of U_{eff}.

Acknowledgements

This work was supported in part by a Grant-in-Aid for Science Research from the Ministry of Education, Science and Culture, Japan. The authors are grateful to Kinki University for the financial support.

Appendix A. Supplementary data

Supplementary data for the two structures are available from the Cambridge Crystallographic Data Centre, 12, Union Road, Cambridge CB2 1EZ, UK (fax: +44 1223 336033; e-mail: deposit@ccdc.cam.ac.uk, or www: http://www.ccdc.cam.ac.uk), on request quoting the deposition Nos. CCDC 233090 for **1** and CCDC-183754 for **5**. Direct current variable temperature magnetic susceptibility; Multiple-frequency ac magnetic susceptibility. Supplementary data associated with this article can be found, in the online version, at doi:10.1016/j.poly. 2005.03.139.

References

[1] (a) R. Sessoli, D. Gatteschi, A. Caneschi, M.A. Novak, Nature 365 (1993) 141;
(b) R. Sessoli, H.-L. Tsai, A.R. Schake, S. Wang, J.B. Vincent, K. Folting, D. Gatteschi, G. Christou, D.N. Hendrickson, J. Am. Chem. Soc. 115 (1993) 1804.
[2] (a) W. Wernsdorfer, N. Aliaga-Alcalde, D.N. Hendrickson, G. Christou, Nature 416 (2002) 406;
(b) E. Coronado, F. Palacio, J. Veciana, Angew Chem. Int. Ed. 42 (2003) 2570;
(c) D. Gatteschi, R. Sessoli, Angew Chem. Int. Ed. 42 (2003) 268;
(d) A.J. Tasiopoulos, A. Vinslava, W. Wernsdorfer, K.A. Abboud, G. Christou, Angew Chem. Int. Ed. 43 (2004) 2117.
[3] I. Mirebeau, M. Hennion, H. Casalta, H. Andres, H.U. Gudel, A.V. Irodova, A. Caneschi, Phy. Rev. Lett. 83 (1999) 628.
[4] (a) B. Schwarzschild, Phys. Today January (1997) 17;
(b) J.R. Friedman, M.P. Sarachik, J. Tejada, R. Ziolo, Phys. Rev. Lett. 76 (1996) 3830;
(c) R. Sessoli, H.L. Tsai, A.R. Schake, S. Wang, J.B. Vincent, K. Folting, D. Gatteschi, G. Christou, D.N. Hendrickson, J. Am. Chem. Soc. 115 (1993) 1804;
(d) E.M. Chudnovsky, Science 274 (1996) 938.
[5] (a) H.J. Eppley, H.L. Tsai, N.D. Vries, K. Folting, G. Christou, D.N. Hendrickson, J. Am. Chem. Soc. 117 (1995) 301;
(b) T. Kuroda-Sowa, T. Nogami, M. Maekawa, M. Munakata, Mol. Cryst. Liq. Cryst. 379 (2002) 179;
(c) T. Kuroda-Sowa, M. Lam, A.L. Rheingold, C. Frommen, W.M. Reiff, M. Nakano, J. Yoo, A.L. Maniero, L.C. Brunel, G. Christou, D.N. Hendrickson, Inorg. Chem. 40 (2001) 6469;
(d) S.M.J. Aubin, M.W. Wemple, D.A. Adams, H.L. Tsai, G. Christou, D.N. Hendrickson, J. Am. Chem. Soc. 118 (1996) 7746;
(e) M. Soler, W. Wernsdorfer, K.A. Abboud, J.C. Huffman, E.R. Davidson, D.N. Hendrickson, G. Christou, J. Am. Chem. Soc. 125 (2003) 3576;
(f) T. Kuroda-Sowa, T. Nogami, H. Konaka, M. Maekawa, M. Munakata, H. Miyasaka, M. Yamashita, Polyhedron 22 (2003) 1795.
[6] (a) A.R. Schake, H.L. Tsai, N.D. Vires, K. Folting, D.N. Hendrickson, G. Christou, J. Chem. Soc., Chem. Commun. (1992) 181;
(b) J.Y. Li, H. Xu, J.Z. Zou, Z. Xu, X.Z. You, K.B. Yu, Polyhedron 15 (1996) 3325.
[7] (a) P. Artus, C. Boskovic, J. Yoo, W.E. Streib, L.C. Brune, D.N. Hendrickson, G. Christou, Inorg. Chem. 40 (2001) 4199;
(b) C. Boskovic, M. Pink, J.C. Huffman, D.N. Hendrickson, G. Christou, J. Am. Chem. Soc. 123 (2001) 9914;
(c) N.E. Chakov, W. Wernsdorfer, K.A. Abboud, D.N. Hendrickson, G. Christou, Dalton Trans. (2003) 2243;

(d) T. Kuroda-Sowa, T. Handa, T. Kotera, M. Maekawa, M. Munakata, H. Miyasaka, M. Yamashita, Chem. Lett. 33 (2004) 540;
(e) T. Kuroda-Sowa, S. Fukuda, S. Miyoshi, M. Maekawa, M. Munakata, H. Miyasaka, M. Yamashita, Chem. Lett. 31 (2002) 682;
(f) G.Q. Bian, T. Kuroda-Sowa, H. Konaka, M. Hatano, M. Maekawa, M. Munakata, H. Miyasaka, M. Yamashita, Inorg. Chem. 43 (2004) 4790.

[8] (a) S.M.J. Aubin, Z.M. Sun, H.J. Eppley, E.M. Rumberger, I.A. Guzei, K. Folting, P.K. Gantzel, A.L. Rheingold, G. Christou, D.N. Hendrickson, Inorg. Chem. 40 (2001) 2127;
(b) H.L. Tsai, T.Y. Jwo, G.H. Lee, Y. Wang, Chem. Lett. 29 (2000) 346;
(c) M. Soler, S.K. Chandra, D. Ruiz, J.C. Huffman, D.N. Hendrickson, G. Christou, Polyhedron 20 (2001) 1279.

[9] T. Lis, Acta Crystallog. Sect. B B36 (1980) 2042.

[10] S.M.J. Aubin, M.W. Wemple, D.A. Adams, H.L. Tsai, G. Christou, D.N. Hendrickson, J. Am. Chem. Soc. 118 (1996) 7746.

[11] S.M.J. Aubin, S. Spagna, H.J. Eppley, R.E. Sager, G. Christou, D.N. Hendrickson, Chem. Commun. (1998) 803.

[12] K. Takeda, K. Awaga, Phys. Rev. B 56 (1997) 14560.

[13] S.M.J. Aubin, Z. Sun, L.A. Pardi, J. Krzystek, K. Folting, L.C. Brunel, A.L. Rheingold, G. Christou, D.N. Hendrickson, Inorg. Chem. 38 (1999) 5329.

[14] (a) Z. Sun, D. Ruiz, N.R. Dilley, M. Soler, J. Ribas, K. Folting, M.B. Maple, G. Christou, D.N. Hendrickson, Chem. Commun. (1999) 1973;
(b) Z. Sun, D. Ruiz, E. Rumberger, C.D. Incarvito, K. Folting, A.L. Reingold, G. Christou, D.N. Hendrickson, Inorg. Chem. 37 (1998) 4758;
(c) D. Ruiz, Z. Sun, B. Albela, K. Folting, J. Libas, G. Christou, D.N. Hendrickson, Angew Chem. Int. Ed. 37 (1998) 300.

[15] (a) A.L. Barra, D. Gatteschi, R. Sessoli, Phys. Rev. B 56 (1997) 8192;
(b) G.Q. Bian, T. Kuroda-Sowa, N. Gunjima, M. Maekawa, M. Munakata, Inorg. Chem. Commun. 8 (2005) 208.

[16] J. Yoo, A. Yamaguchi, M. Nakano, J. Krzystek, W.E. Streib, L.C. Brunel, H. Ishimoto, G. Christou, D.N. Hendrickson, Inorg. Chem. 40 (2001) 4604.

[17] A. Cornia, R. Sessoli, D. Gatteschi, A.L. Barra, C. Daiguebonne, Phys. Rev. Lett. 89 (2002) 257201.

value of the paramagnetic center (roughly as $S(S+1)$), as well as on the concentration of the paramagnetic agent in the media. At low concentrations there is a linear dependence of R_1 and R_2 on the concentration.

The notion of relaxivity is used to allow one to compare the effectiveness of different relaxation agents (contrast agents) independently of the concentration used. It is defined as $r_{1,2} = R_{1,2}/c$, where c is the concentration. A competitive value in medical diagnostics is 4–5 s^{-1} mM^{-1}, recorded at magnetic fields of 2–3 T [1].

Recently, superparamagnetic iron oxide particles have attracted much attention as contrast agents, due to their extremely large spin values [2]. Single-molecule magnets, by contrast, offer superparamagnetism in uniquely small particles [3,4], that would be very powerful as contrast agents. Our attention was attracted to a report that the classic compound "Fe_8" provided contrast similar to that offered by the commercial compound Magnevist (GdDTPA) [5], and we report here a critical examination of its usefulness.

2. Experimental

2.1. Synthesis

The intermediate complex $Fe(tacn)Cl_3$ and crystals of Fe_8 ($C_{36}H_{120}O_{23}N_{18}Fe_8Br_8$) were obtained according to the method of Wiegardt [6,7]. The bright yellow precipitate formed from reacting tacn (1,4,7-triazacyclononane) ligand, purchased from Aldrich, and $FeCl_3 \cdot 6H_2O$ in ethanol, and was isolated and dried. The product was dissolved in a mixture of H_2O and pyridine. After 15 min, NaBr was added to the solution and the mixture was cooled to 200 °C and allowed to stand for 24 h. The brown crystals were isolated, washed and subjected to physical studies.

2.2. Physical measurements

Low temperature (0.4 K) magnetization versus field data were collected using a micro-Hall effect magnetometer which is described in [8].

Relaxivity measurements were conducted at 9.4 T on a Bruker AV 400 MHz narrow-bore NMR spectrometer in a standard 5 mm quartz tube. T_1 and T_2 were determined by routine inversion-recovery and CPMG sequences, respectively. The relaxation agents were dissolved in 99% D_2O to avoid both receiver saturation and radiation damping effects due to the appearance of a strong H_2O signal in the NMR measurements [9]. The water relaxation rates reported refer to the residual H_2O in the sample. All NMR measurements were taken at 25 °C.

The pH was adjusted in the samples by adding small amounts of NaOH to the solution. pH determinations were conducted with a standard glass combination pH electrode. The values reported are uncorrected for the presence of D_2O as the main solvent (pD = pH − 0.4). Physical studies comparing the relaxivity of the compounds and their dependence on concentration were done in 0.1 M HEPES buffer at pH 7 (purchased from Sigma). The lyophilized sample of Fe_8 was prepared by dissolving the crystals in water and immediately freezing them using dry ice. The water was removed using a standard lyophilizer.

3. Results and discussion

3.1. Characterization of Fe_8

Crystals of Fe_8 gave magnetic behavior consistent with that previously reported [10]. Steps in the hysteresis curves were observed at regular field intervals consistent with the $S = 10$ ground state and the spin-Hamiltonian parameters reported for Fe_8. We note that the hysteresis steps, while well defined, were broad, perhaps indicative of crystal defects.

3.2. Determination of relaxivity

As shown in Fig. 1, relaxivity was measured in aqueous solutions buffered at a pH of 7. Fe_8 gave a much

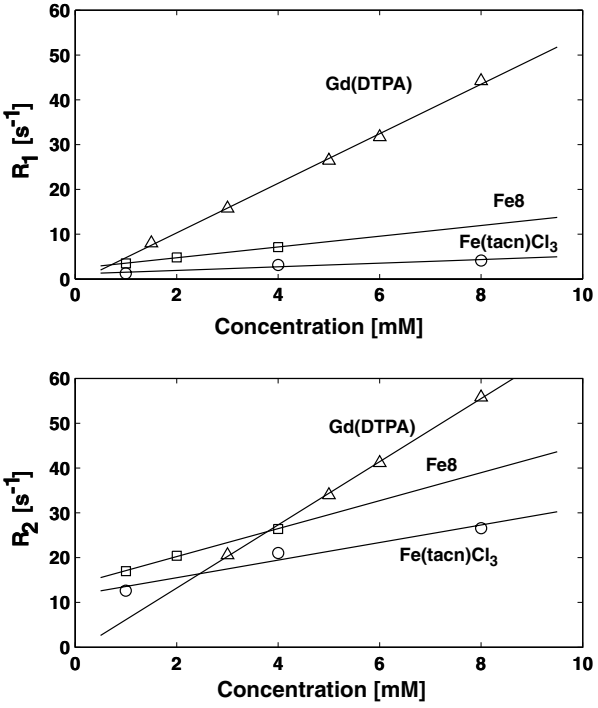


Fig. 1. Plot of R_1 and R_2 parameters vs. concentration of aqueous solutions of Gd(DTPA), $Fe(tacn)Cl_3$, and Fe_8, determined by inversion recovery and CPMG sequences on a 400 MHz NMR spectrometer.

lower T_1 relaxivity ($1.2\ s^{-1}\ mM^{-1}$) than the commercially used reference, GdDTPA ($5.5\ s^{-1}\ mM^{-1}$). Since this is in contrast to previous studies [5] we also investigated the relaxivity of the precursor complex $Fe(tacn)Cl_3$ ($0.4\ s^{-1}\ mM^{-1}$). The relaxation constants were monitored over a 24 h period, and were found to be approximately constant in solutions buffered at neutral pH. The r_2 parameters were measured as $3.1\ s^{-1}\ mM^{-1}$ (Fe_8), $7.0\ s^{-1}\ mM^{-1}$ (GdDTPA), and $2.0\ s^{-1}\ mM^{-1}$ ($Fe(tacn)Cl_3$).

3.3. Examination of solution species

Aqueous solution equilibria of iron complexes can be complex, and it would be appropriate to question the nature of solution species that would form upon dissolving the Fe_8 complex [11,12]. The relaxivity data indicate that Fe_8 does not decompose fully and exclusively to form $Fe(tacn)Cl_3$. If complete decomposition took place its relaxivity would be at least six times larger than the one for $Fe(tacn)Cl_3$ (considering the presence of only six ligands in Fe_8). Indeed, Fe(III) itself can show appreciable relaxivity in aqueous solution (for a review, see [13]). The fairly weak relaxivity shown for the solution prepared from Fe_8 suggests that some clustering of Fe persists in solution, resulting however in antiferromagnetic coupling, lower overall spin, and therefore lower contrast.

Among the many experiments that were attempted to shed light on solution speciation, perhaps the most definitive was that the Fe_8 was dissolved in water at a concentration of 1 mM and immediately frozen, then lyophilized to remove the water in the gentlest manner possible. A brown powder was obtained that was examined for superparamagnetism. The data indicated that the powder did not have a significant amount of Fe_8 (Fig. 2). It appeared to be a low-spin substance, with spin ~3/2. At 0.4 K there was no (or very small) hysteresis. The data were noisy because of the small amount of material.

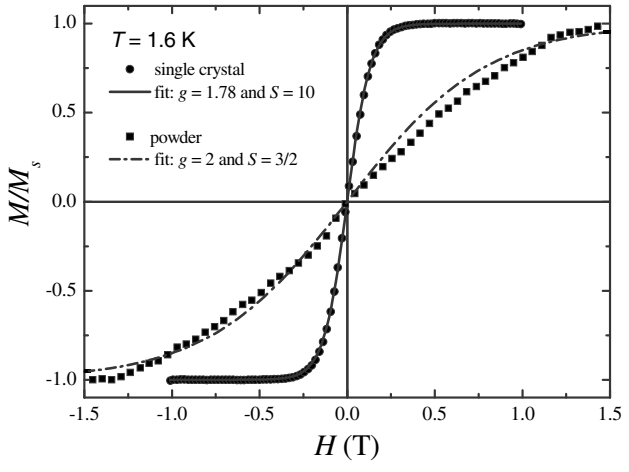


Fig. 2. Hysteresis curves for a single crystal of Fe_8 and grains/powder resulting from lyophilization of an aqueous solution of Fe_8 at 1.6 K. The powder appeared to be a low-spin ~3/2 at 0.4 K with no (or very small) hysteresis.

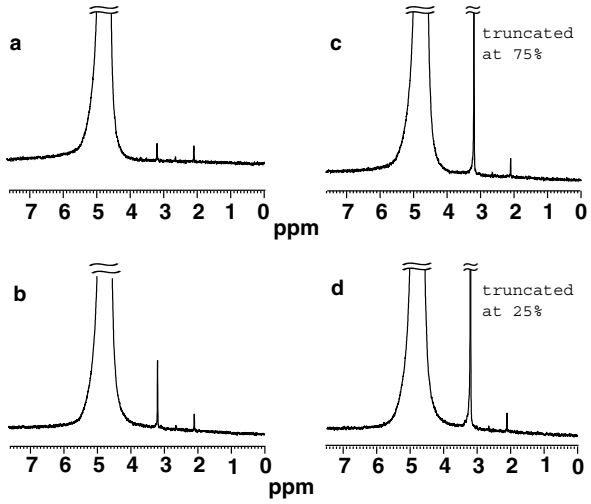


Fig. 3. ^1H NMR spectra of Fe_8 (at $c = 4$ mM) in 99% D_2O, at (a) immediately after dissolving, (b) 30 min (c) 120 min, and (d) 240 min after dissolving.

The ^1H NMR spectra of the solutions of the Fe_8 complexes were examined to assess whether a solution species could be assigned. The single peak at δ 3.2 increased substantially in intensity over 3 h as illustrated in Fig. 3. This peak coincides in shift with the one observed for $Fe(tacn)Cl_3$ and we therefore conclude that at least partial decomposition into this precursor compound occurs. Signals corresponding to that of free ligand (δ 2.8 ppm) were not observed.

3.4. Environmental dependence of relaxivity

During the course of examination of the solution species formed by Fe_8, a very strong dependence on pH was observed. As shown in Fig. 4, an increase of pH from neutral to 11 resulted in more than a 5-fold increase in R_1 for the Fe_8 complex. In contrast, the R_1 for GdDTPA was nearly constant over this range, and decreased for $Fe(tacn)Cl_3$. This data provides additional evidence for decomposition/rearrangement processes of Fe_8 in solution. The R_2 parameters, however, did not change as dramatically over this pH range.

The increase in pH of the solutions of Fe_8 were accompanied by complex changes in ^1H NMR spectra. At neutral pH, a single peak at δ 3.2 dominated the spectrum, while a smaller peak at δ 2.2 was present. At pH 7.6 a peak at 2.9 ppm appeared. The peak at 2.2 ppm grows larger up to a pH of 9 and becomes smaller again when approaching a pH of 10.7. At pH 11.3 small peaks appear at 3.0, 2.9, and 2.8 ppm (apparently

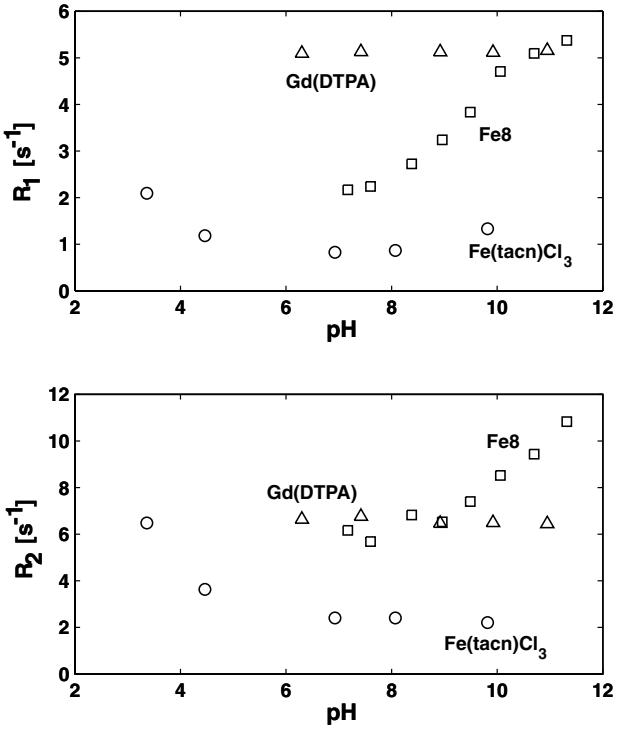


Fig. 4. pH-dependence of the relaxation parameters R_1 and R_2 for Fe_8 (squares), $Fe(tacn)Cl_3$ (circles), and Gd(DTPA) (triangles) (pH values are uncorrected for the presence of the large D_2O concentration).

corresponding to free ligand). In addition, a large peak is visible at 2.23 ppm. Thus, significant changes in solution speciation occurred with increasing pH, and some of these new species are likely to be responsible for the increased relaxivity.

Dependence of relaxivity on pH is of interest in the burgeoning field of molecular imaging in which "smart" contrast agents are desired as reporters of molecular processes in living systems [14,15]. However, further work will be required to determine whether Fe clusters may be of use for such purposes.

4. Conclusion

In contrast to the earlier report [5], Fe_8 in neutral, aqueous solution did not show stronger relaxivity than GdDTPA. This is corroborated by measurements of the magnetic properties before and after dissolving Fe_8, as well as solution NMR spectra and measured R_1 and R_2 parameters under various conditions. However, we found the relaxation properties of this compound to be highly dependent upon pH, a behavior that is of interest in the development of environment-sensitive contrast agents.

Acknowledgements

This work was supported by the National Science Foundation, Grant #NSF-DMR-0103290, and the NYU Whitehead Fellowship for Junior Faculty in the Biomedical and Biological Sciences. New York University is a member institution of the New York Structural Biology Center supported by NIH Grant 1P41 GM66354. NYU's NMR facilities were supported by a NSF grant MRI-0116222. We acknowledge Dr. Chin Lin and the Molecular Imaging and Contrast Agent Working Group at NYU.

References

[1] E. Tóth, L. Helm, A. Merbach, Top. Curr. Chem. 221 (2002) 61.
[2] Y.-X.J. Wang, S.M. Hussain, G.P. Krestin, Eur. Radiol. 11 (2001) 2319.
[3] R. Sessoli, D. Gatteschi, Angew. Chem. Int. Ed. Engl. 42 (2003) 268.
[4] J.R. Friedman, M.P. Sarachik, J. Tejada, R. Ziolo, Phys. Rev. Lett. 76 (1996) 3830.
[5] E. Rodriguez, A. Roig, E. Molins, M.R. Quintero, C. Arús, M. Cabañas, S. Cerdán, C.M Sanfeliu, in: VIIth International Conference on Molecule-based Magnets 2002, Valencia, Spain, abstract D-73.
[6] K. Wiegardt, K. Pohl, I. Jibril, G. Huttner, Angew. Chem., Int. Ed. Engl. 23 (1984) 77.
[7] K. Wiegardt, K. Pohl, W. Gebert, Angew. Chem. Int. Ed. Engl. 22 (1983) 727.
[8] A.D. Kent, S. von Molnar, S. Gider, D.D. Awschalom, J. Appl. Phys. 76 (1994) 6656.
[9] A. Vlassenbroek, J. Jeener, P. Broekaert, J. Chem. Phys. 103 (1995) 5886.
[10] W. Wernsdorfer, R. Sessoli, Science 284 (1996) 133.
[11] C.M. Flynn, Chem. Rev. 84 (1984) 31.
[12] N.N. Greenwood, A. Earnshaw, Chemistry of the Elements, Pergamon Press, Oxford, 1984.
[13] R.B. Lauffer, Chem. Rev. 87 (1987) 901.
[14] J.A. Helpern, J.C. Curtis, D. Hearshen, M.B. Smith, K.M.A. Welch, Magn. Reson. Med. 5 (1987) 302.
[15] V. Jacques, J.F. Desreux, Top. Curr. Chem. 221 (2002) 123.

(spin 1), and four alkoxide hmp-oxygen atoms at alternating corners. The molecule has S_4 site symmetry. Ferromagnetic exchange interactions between the four Ni^{II} ions lead to a $S = 4$ ground state at low temperature, which has been confirmed by high frequency Electron Paramagnetic Resonance (EPR) and magnetic relaxation experiments [12,13]. These molecules have a zero field splitting of the form $-DS_z^2$. This uniaxial anisotropy term in the Hamiltonian leads to an energy barrier $DS^2 \sim 12$ K that separates opposite projections of the spin of the molecule along the easy axis, $S_z = \pm 4$.

The spin Hamiltonian of Ni_4 is to first approximation:

$$H = -DS_z^2 - \mu_B \overrightarrow{S} \cdot \hat{g} \cdot \overrightarrow{H} + H'. \quad (1)$$

The second term is the Zeeman energy ($\hat{g} = (g_x, g_y, g_z)$, $\mu_0 = 1$ and H is in tesla). The last term includes high order transverse anisotropy terms (i.e., $C(S_+^4 + S_-^4)$). An external magnetic field, H_z, applied along the easy axis of the molecules tilts the double well potential favoring those spin projections aligned with the field. When the magnitude of the longitudinal field is $H_z = kD/g\mu_B$ (with k an integer), spin levels on opposite sides of the barrier have the same energy. These field values are known as *resonant fields*. The inset of Fig. 2 shows the behavior of the lowest states as a function of longitudinal magnetic field in the vicinity of resonance $k = 0$ ($H_z = 0$). When the system is near this resonance off-diagonal terms in the Hamiltonian, such as a Zeeman term due to an external transverse magnetic field lead to an energy splitting between symmetric, $|S\rangle$ and anti-symmetric $|A\rangle$ linear combinations of |up⟩ and |down⟩ states, known as the tunnel splitting, Δ. The frequency of QTM between |up⟩ and |down⟩ states is proportional to the tunnel splitting ($f = \Delta/h$). It is possible to write the energy eigenstates as:

$$\begin{aligned} |S\rangle &= \frac{1}{2}(|\text{up}\rangle + |\text{down}\rangle), \\ |A\rangle &= \frac{1}{2}(|\text{up}\rangle - |\text{down}\rangle), \end{aligned} \quad (2)$$

where

$$\begin{aligned} |\text{up}\rangle &= \frac{\sqrt{2}}{2}\sum_m (a_m + b_m)|m\rangle, \\ |\text{down}\rangle &= -\frac{\sqrt{2}}{2}\sum_m (a_m - b_m)|m\rangle. \end{aligned} \quad (3)$$

The value of the coefficients, a_m and b_m, depend on the external applied field. At zero longitudinal field ($k = 0$) and in the absence of transverse fields, all coefficients are zero except for a_{+4} and b_{-4}. In this situation, the two lowest levels are $|S\rangle = \frac{1}{\sqrt{2}}(|+4\rangle + |-4\rangle)$ and $|A\rangle = \frac{1}{\sqrt{2}}(|+4\rangle - |-4\rangle)$, corresponding to superpositions of opposite spin projections along the easy magnetic axis. In the presence of a strong transverse field this situation changes. Now, the states |up⟩ and |down⟩ are tilted away from the easy axis but still have well defined and opposite z-axis magnetizations, provided the transverse field is less than the anisotropy field, $H_a = 2DS/(g\mu_B) = 4.5$ T.

A transverse field is necessary to increase the tunnel splitting into a range where it is comparable or larger than the thermal energy ($k_B T$). In the experiments described below we use transverse fields from 2.2 to 3.6 T, for which the tunnel splitting ranges from 5 to 30 GHz.

2. Experimental

The experiment consists in sweeping an external longitudinal field across resonance $k = 0$ and measuring the magnetization of the sample in the presence of microwave radiation (see inset of Fig. 2). Photon induced transitions (PIT) between symmetric and anti-symmetric spin-states lead to changes of the average magnetization of the sample when the radiation energy coincides with the energy separation between levels. Note that this is only possible when the longitudinal field is not zero. When $H_z = 0$, both symmetric and anti-symmetric superposition states have zero z-axis projection and therefore transitions between them will not change the magnetization of the sample.

In order to induce transitions between $|S\rangle$ and $|A\rangle$ states the magnetic field component of the electromagnetic radiation, H_{ac}, must be aligned with the easy axis direction, $\hat{z}$. In this case, the rate of PITs (at $T = 0$) is given by:

$$\Gamma = \frac{\pi}{2}\left(\frac{g\mu_B}{\hbar}H_{ac}\right)^2 |\langle S|S_z|A\rangle|^2 f(\omega), \quad (4)$$

where $\langle S|S_z|A\rangle$ is the matrix element coupling the external radiation field and the spin of the molecule. On one hand, this probability depends on the magnitude of the ac field (i.e., the radiation power), which is determined by both the source power and the device that is used to irradiate the sample (i.e., the quality factor of the antenna). On the other hand the PIT probability depends on the magnitude of the external magnetic fields as follows: (1) for a given longitudinal field, the larger the transverse field (i.e., the larger tunnel splitting) the higher the probability, and (2) for a given transverse field, the probability increases as the longitudinal field decreases (see inset of Fig. 3), being maximum for $H_L = 0$. However, in this case, as mentioned above, PIT do not induce changes in the magnetization. A picture of the range of longitudinal fields for which PITs are allowed can be seen in the inset of Fig. 2. The departure of the energy splitting from a straight line (i.e., the simple Zeeman splitting), illustrated with the dashed line in this figure is due to the tunnel splitting.

In the experiment we sweep the longitudinal field at a given rate, $\alpha = dH_L/dt$, across the resonance, in the

presence of a constant transverse field, H_T, while we monitor the magnetization. For high transverse fields one finds the equilibrium magnetization, $M_{eq}(H_L,H_T,T)$. However, when the energy difference, E, between the two states matches the energy of the radiation, $\hbar\omega$, PITs change the populations of each state and thus the sample magnetization. This effect is manifested as a dip or peak in the magnetization curve whose shape is determined by $f(\omega)$, which is a Lorentzian function:

$$f(\omega) = \frac{1}{\pi}\frac{\tau_2}{1+(\omega-\omega_0)^2\tau_2^2}, \quad (5)$$

where $\omega_0 = E/\hbar$ and τ_2 is the transverse relaxation time. Therefore, the width of the peak will give us information about the decoherence time.

At a finite temperature, $T > 0$, the ratio between equilibrium populations of the two lowest states is $N_2/N_1 = \exp(-E/k_BT)$. Any non-equilibrium population will decay exponentially according to $d(n_2 - n_1)/dt = [(N_2 - N_1) - (n_2 - n_1)]/\tau_1$, where n_1 and n_2 are the instantaneous level populations and τ_1 is the energy longitudinal relaxation time. In the presence of radiation the evolution of the populations of these states is determined by the PIT rate, Γ, given in Eq. (4) in the form $d(n_2 - n_1)/dt = -2\Gamma(n_2 - n_1)$. Combining these two expressions we find:

$$n_d = n_0\left(1 - \frac{1}{1+2\tau_1\Gamma}\right)e^{-(\tau_1+2\Gamma)t/\tau_1} + \frac{n_0}{1+2\tau_1\Gamma}, \quad (6)$$

where $n_d = n_2 - n_1$ and $n_0 = N_2 - N_1$. From this is it clear that n_0 must not be zero. In other words, we need to work at a temperature for which the excited state population is small. Taking into account that the lowest temperature we can achieve in our experiment is 0.38 K, we need to work with frequencies of at least $f = E/h = 10$ GHz, in order to have $n_0 > 0.7$ (for 20 GHz, $n_0 = 0.91$).

We have used a high sensitivity micro-Hall magnetometer [14] to measure the longitudinal component of the magnetization of a millimeter-sized single crystal of Ni_4 that is placed over the magnetometer, with one of its faces parallel to the plane of the sensor. A thin superconducting circular loop ($\phi \sim 2$ mm) is placed perpendicular to the easy anisotropy axis of the crystal (see inset of Fig. 1). This loop shorts the end of a 2.4 mm coaxial line, connecting the inner and outer conductors. The coaxial line is made up of Cu and Stainless Steel sections to minimize power losses (~15 dB) and thermal conduction. The line is about 1.5 m long and connects the loop to an Agilent PNA 50 GHz Vector Network Analyzer. This system allows us to work with frequencies up to 50 GHz and makes possible the characterization of the resonances of the loop. All the measurements were done by using different loop resonances to maximize the power that is converted to ac magnetic field

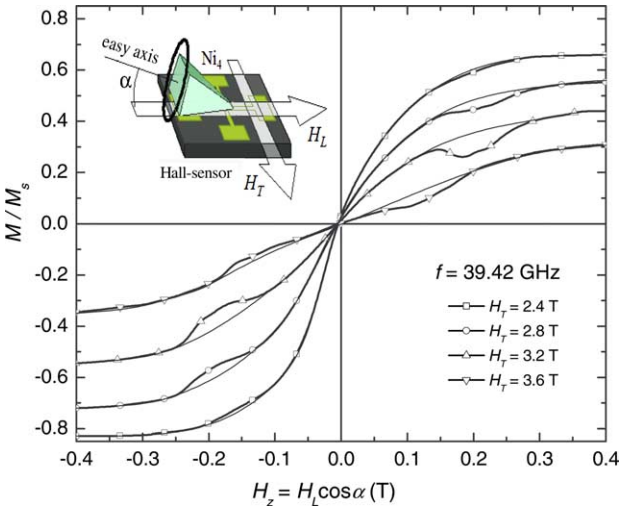


Fig. 1. Several magnetization curves recorded by sweeping the longitudinal field at a constant rate across zero field resonance in the presence of CW microwave radiation of $f = 39.8$ GHz for transverse fields values from 2.4 to 3.6 T. The thin lines correspond to equilibrium magnetization in the absence of radiation. The inset shows the setup.

at the sample position. A high field superconducting vector magnet was used to apply magnetic fields in arbitrary directions with respect to the axes of the crystal. In this case, both transverse and longitudinal magnetic fields were applied in the plane of the magnetometer. A ^{3}He cryostat is used to cool the sample to a temperature of 0.38 K.

3. Results and discussion

Fig. 1 shows several magnetization curves measured in presence of continuous wave (CW) microwave radiation of $f = 39.42$ GHz. The longitudinal magnetic field, H_z[2], was swept at a constant rate from −0.4 to 0.4 T. Different curves correspond to different transverse fields from $H_T = 2.4$–3.6 T. The thin lines represent the equilibrium magnetizations (or magnetization in the absence of microwave radiation). Deviations of the magnetization from M_{eq} are observed (peaks/dips) at opposite polarities of the longitudinal magnetic field[3], indicating PITs between spin levels with opposite net magnetization. The temperature of the sample was monitored during the whole field sweep and showed variations that

[2] The longitudinal magnetic field, H_z, represented in Fig. 1 has been calculated taking into account the misalignment, $\alpha = 20°$, between the applied field, H_L, (in the plane of the sensor) and the easy-axis of the single crystal, and is given by the relation $H_z = H_L\cos\alpha$.

[3] The small asymmetries observed between the longitudinal field positions and magnitudes of the peak and dip at opposite polarities is due to a second misalignment, $\theta = 5.3°$, between H_L and the projection of the easy axis of the crystal into the plane of the sensor. This misalignment produces variations of the transverse field felt by the molecules when the longitudinal field varies, explaining the asymmetry between PITs at opposite polarities of H_z.

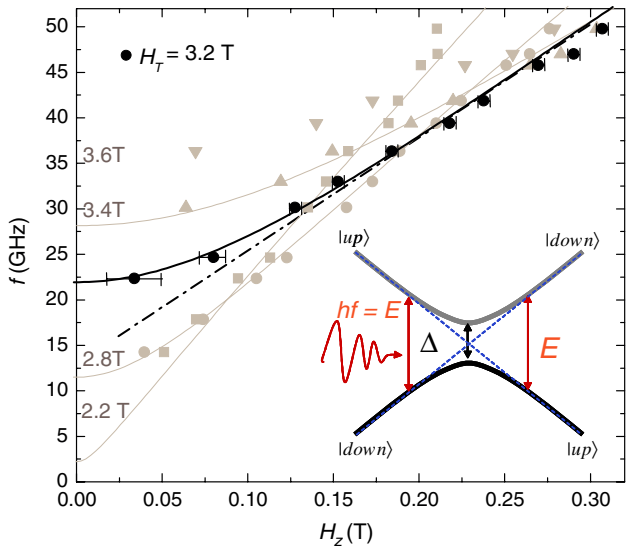


Fig. 2. Frequency-field plot of the positions of the PIT's dips of the sample magnetization. The result corresponding to $H_T = 3.2$ T has been highlighted (back solid circles) in order to show the curvature of the PITs frequency-field behavior in the vicinity of zero-field resonance. Grey circles correspond to other transverse field values. The solid lines are fit of the data using Hamiltonian of Eq. (1). The inset shows energies of the lowest lying levels of the Ni_4 molecule close to zero-field.

were less than 0.01 K at the positions of the peaks and dips. Note that a change of temperature of 1 K would be necessary to explain the magnetization changes observed in the peaks/dips, indicating that these magnetization variations are induced by population changes induced by absorption of microwave radiation and not by heating of the sample. The observed structure of the peaks/dips (each peak/dip is indeed composed by three peaks) is discussed in [10] and has also been observed in high-frequency EPR measurements [13] and ascribed to different Ni_4 species or microenvironments with slightly different values of the uniaxial anisotropy parameter, D.

We repeated the same measurements for different microwave frequencies from 14 to 50 GHz for the transverse fields, $H_T = 2.2$–3.6 T. For this experiment we chose the microwave powers so that the sample temperature was the same in all the measurements[4]. In Fig. 2 we show the behavior of the PIT dips (positive field polarity) in a frequency-field plot. In this figure results corresponding to $H_T = 3.2$ T (black solid circles) has been highlighted in order to clearly show the characteristics with microwave frequency and longitudinal field. (Results for negative polarities of H_z and a more detailed discussion can be found in [10].) It is clear that the PIT dip position deviates from the linear behavior (dashed line) on approaching the center of the resonance. This result is a direct measurement of the behavior of the energy difference between the two lowest spin states of the molecule (inset of Fig. 2) and *the curvature at the vicinity of the zero-field resonance constitutes an unambiguous signature of quantum superposition states with opposite magnetizations*. The solid lines are fits of the data by direct diagonalization of Hamiltonian of Eq. (1) using $D = 0.765$ K, $B = 7.9 \times 10^{-3}$ K, $C = 3.25 \times 10^{-5}$ K, $g_z = 2.3$, $g_x = g_y = 2.23$. These values are in excellent agreement with those found from high frequency EPR experiments [13]. This illustrates that the tunnel splitting, Δ (at $H_z = 0$), varies from 2 to 35 GHz for transverse fields ranging from 2.2 to 3.6 T [10].

Fig. 3 shows curves corresponding to the difference $M - M_{eq}$ for several frequencies from 18 to 47 GHz measured while a transverse field of 3 T was applied. The curves have been normalized by the equilibrium magnetization, $M_{eq}(H_z)$. This normalization allows the behavior of the magnitude of the PITs dip as a function of the longitudinal field to be seen. The magnitude of the PITs dip for different field values gives an estimate of the absorption of microwave radiation of a given frequency. The results show that the dip maximum amplitude decreases with field (see dashed line connecting dip's maxima in Fig. 3). From Eq. (4) we know that the maximum amplitude of the PIT's dip, which occurs at $\omega = \omega_0$, depends on the magnitude of the microwave field, on the matrix element coupling the external radiation field

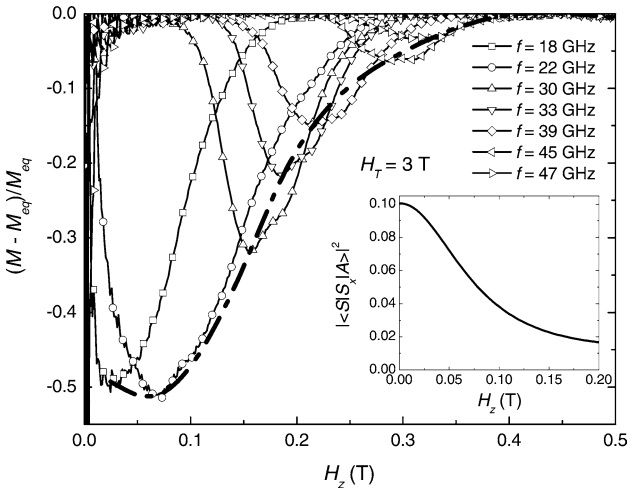


Fig. 3. Normalized change of the magnetization due to PITs at different microwave frequencies in the presence of a 3 T transverse applied field. The dashed-dotted line connecting the dip amplitudes has a minimum at ~0.06 T, which is not expected if the amplitude is governed solely by the matrix element in Eq. (4). The inset shows the square of this matrix element as a function of the longitudinal magnetic field for a transverse field of 3 T.

[4] For frequencies over 40 GHz the temperature of the sample was slightly smaller than at lower frequencies due to limitations of the microwave source at high frequencies and higher losses in the coaxial lines. Nevertheless, this temperature difference is not crucial for the analysis of this paper.

and the spin of the molecule, $\langle S|S_z|A\rangle$, and on τ_2, through the Lorentzian function of Eq. (5). While H_{ac} is independent of the longitudinal field and frequency,[4] the matrix element decreases with the longitudinal field as shown in the inset of Fig. 3, having a maximum at zero-field, indicating that the amplitude of the PIT's dip should monotonically decrease with longitudinal field as seen in the experiment. We note that a varying τ_1 would affect the behavior of the PIT's dips/peaks amplitude since the instantaneous population difference $n_d = n_1 - n_2$, and thus the magnetization, are τ_1-dependent, as seen in Eq. (6). This could explain the slight decrease of the peak's amplitude observed at $f = 18$ GHz in Fig. 3, which would be due to an increase in the longitudinal relaxation rate, $1/\tau_1$, in the vicinity of the resonance.

A signature of an increase of the longitudinal relaxation time, τ_1, with field or frequency is clearly observed in Fig. 4, which shows several $(M - M_{eq})/M_{eq}$ curves measured at different sweep rates of the longitudinal field and two different sweep directions: from negative to positive (up) and from positive to negative (down). The measurements were done in the presence of microwave radiation of 39.8 GHz and a transverse field of 3.2 T. The curves depend on the field sweep direction. When the field is swept from negative to positive the peak's ($H_z < 0$) amplitude decreases with increasing sweep rate (the peak's width remains almost constant) while the dip's ($H_z > 0$) width increases with increasing sweep rate (the dip's amplitude remains almost constant). The result for the opposite sweep direction is just equivalent but inverted. This broadening of the peaks/dips with increasing sweep rate is indicative of slow energy relaxation processes of the excited state (antisymmetric state). An estimation of the longitudinal relaxation time, from the width of the peaks shown in Fig. 4, gives $\tau_1 \sim 13$ s for negative-to-positive sweep direction and $\tau_1 \sim 19$ s for positive-to-negative sweep direction. The difference in these relaxation times is probably related to the transverse field, which varies slightly with the longitudinal field due to a misalignment of the sample with respect to the applied longitudinal field direction[3]. Moreover, this shows that τ_1 increases with longitudinal field, and thus with frequency, because the broadening only appears in one side of the peaks/dips (far from the resonance). This trend has also been observed in measurements with pulsed-microwave radiation (see [10] for details).

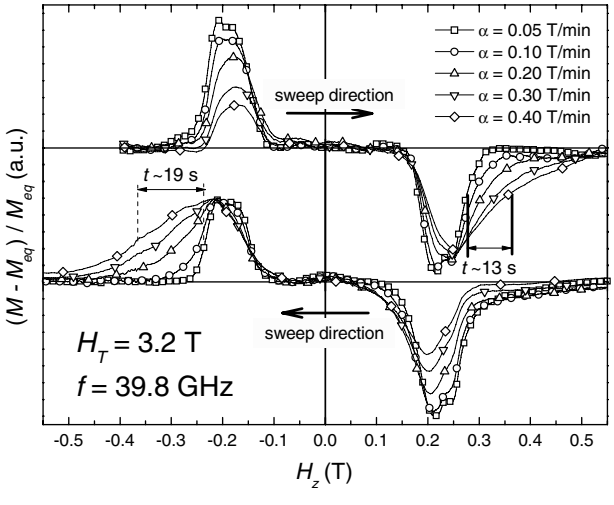


Fig. 4. $(M - M_{eq})/M_{eq}$ curves for different longitudinal field sweep rates from 0.05 to 0.4 T/min measured in the presence of microwave radiation of 39.8 GHz and a transverse field of 3.2 T. The asymmetric broadening of the peaks/dips for high sweep rates is indicative of a long energy relaxation time which increases with field and thus with frequency.

Relaxation processes must transfer energy to the environment, leading, for example, to generation of phonons or photons. The occurrence of each of these phenomena depends on the energy of the transitions and the temperature of the system (i.e., energy distribution of phonon or photon modes). The extracted relaxation times found here may indicate a very long spin-lattice relaxation time. However, slow relaxation processes could also be associated with poor thermal coupling between the sample and bath. We note that the phase space available for phonon generation increases with frequency. Therefore, since our experiments show that energy relaxation time increases with frequency, this result is not consistent with a spin-phonon bottleneck of the type studied in [15]. These experiments constitute an excellent means for studying the spin-environment coupling that govern quantum dynamics in SMMs.

We also note that the width of the PITs peaks/dips at different microwave powers provide a lower bound on the decoherence time, $\tau_\phi > 0.5$ ns (see [10]). Interestingly, a very similar decoherence time, $\tau_\phi = 1$ ns, has been recently reported by Hill et al. [16] through high frequency EPR experiments carried out in a single crystal of Mn_4-based SMMs ($S = 9/2$), in which exchange interaction between pairs of adjacent molecules (dimers) generate entanglement of the spin states of both molecules.

Improvement of the resonance circuit used to irradiate the sample, higher radiation powers and short pulses of radiation are necessary to carry out spin-echo experiments and to create Rabi oscillations. The Rabi frequency is determined by the magnitude of the ac magnetic field, $\Gamma_R \approx \frac{g\mu_B}{h} H_{ac} S$, and in our best case (at present) is of the order of ~100 kHz. Antiferromagnetic molecular magnets with an uncompensated electronic or nuclear spin that tracks the Neel vector for readout are also excellent candidates for long coherence times in mesoscopic spin-systems and for use in quantum computation [17,18].

Acknowledgements

We acknowledge Eugene Chudnovsky, Dmitry Garanin and Steve Hill for helpful and stimulating discussions of this work. This research was supported by NSF (Grant Nos. DMR-0103290, 0114142, and 0315609).

References

[1] J.R. Friedman et al., Phys. Rev. Lett. 76 (1996) 3830.
[2] J.M. Hernandez et al., Europhys. Lett. 35 (1996) 301.
[3] L. Thomas et al., Nature (London) 383 (1996) 145.
[4] W. Wernsdorfer, R. Sessoli, Science 284 (1999) 133.
[5] L. Bokacheva, A.D. Kent, M.A. Walters, Phys. Rev. Lett. 85 (2000) 4803.
[6] J. Tejada et al., Appl. Phys. Lett. 84 (2004) 2373.
[7] L. Sorace et al., Phys. Rev. B 68 (2003) 220407(R).
[8] W. Wernsdorfer, A. Muller, D. Mailly, B. Barbara, Europhys. Lett. 66 (2004) 861.
[9] M. Bal et al., Phys. Rev. B 70 (2004) 100408.
[10] E. del Barco, A.D. Kent, E.C. Yang, D.N. Hendrickson, Phys. Rev. Lett. 93 (2004) 157202.
[11] M. Leuenberger, D. Loss, Nature (London) 410 (2001) 789.
[12] E.C. Yang et al., Polyhedron 22 (2003) 1727.
[13] R.S. Edwards et al., J. Appl. Phys. 93 (2003) 7807.
[14] A.D. Kent, S. von Molnar, S. Gider, D.D. Awschalom, J. Appl. Phys. 76 (1994) 6656.
[15] I. Chiorescu et al., Phys. Rev. Lett. 84 (2000) 3454.
[16] S. Hill, R.S. Edwards, N. Aliaga-Alcalde, G. Crhistou, Science 302 (2003) 1015.
[17] A. Chiolero, D. Loss, Phys. Rev. Lett 80 (1998) 169.
[18] F. Meier, J. Levy, D. Loss, Phys. Rev. Lett. 90 (2003) 047901.

The similar structures in the active site have been found in several proteins such as ribonucleotide reductase [18,19], methane monooxygenase [20], purple acid phosphatase [21] and rubrerythrin [22]. Inorganic models as $[Fe_2O(CH_3CO_2)_2(Hbpz_3)_2]$ [23–26], $[Fe_2O(CH_3CO_2)_2(Me_3TACN)_2]$ [27] and their derivatives [28–30] were synthesized [31–33]. These μ-oxo bridged iron complexes show strong antiferromagnetic coupling. Interestingly, these magnetic interactions are particularly sensitive to the electronic environments over μ-oxo. The protonation of the μ-oxo remarkably decreases the magnetic interactions. This characteristic change is common to all μ-oxo-bridged binuclear iron complexes.

It is hard to treat the magnetic properties of transition metal oxides with computational calculations, because strong electron correlations and spin correlations are involved in these problems. Detail theoretical investigations about magnetic interactions and chemical bonds in these compounds are necessary and interesting from the view point of quantum chemistry. For past decades, we have investigated several metal oxides using both broken-symmetry (BS) and symmetry-adapted (SA) methods, and the reliabilities of these methods were examined. Recent development of BS density-functional methods enabled us to perform first-principle calculations to whole realistic transition metal oxides, which are synthetic models of Hr and manganese compounds [34,35]. Previously, magnetic interactions and nature of chemical bonds in μ-oxo bridged diiron model compound of Hr have been clarified based on density-functional theory. These compounds contain the symmetric coordination environment, but which are definitely different from the real proteins of Hr. Some other theoretical calculations have been reported. Chen et al. calculated on the dependence of the magnetic interactions on Fe–O distance [36]. Rodriguez et al. performed fundamental studies of magnetic interactions on Hr model compounds [37]. The bioxygen binding mechanisms of Hr are studied by Solomon et al. [11,38]. Using quantum mechanical/molecular mechanical (QM/MM) method, the binding energy of dioxygen to Hr were calculated by Wirstam et al. [10]. All these theoretical calculations use BS methodology to describe the electronic and magnetic structures in diiron cores.

In this work, electronic structures and magnetic interactions of the binuclear iron center in oxy-Hr, deoxy-Hr, and met-Hr are studied with density-functional theory. The effective-exchange integrals, J are calculated and the differences in the magnetic interaction are analyzed in terms of molecular orbitals. The magnetic interactions are compared with the one from the model compounds, and relations to the role in electron- and proton-transfer in oxygen bonding process in Hr are examined. This study would be also helpful to the magnetic properties for other metalloproteins containing μ-oxo-bridged binuclear irons.

2. Theoretical backgrounds

2.1. Hybrid DFT computations

The density-functional theory (DFT) is based on Hohenberg-Kohn theorems [39]. These theorems state that ground state energy (E) of Schrödinger equation is determined by only minimizing electron density $\rho(\mathbf{r})$,

$$E_G = \underset{\rho}{\mathrm{Min}}[\rho]. \tag{1}$$

The practical treatment of Eq. (1) was provided by Kohn and Sham. They introduced molecular orbital ϕ to obtain total electron density which satisfy the one-electron equation as,

$$\rho = \sum_i^N \int \phi_i^*(\mathbf{r})\phi_i(\mathbf{r})\,\mathrm{d}r, \tag{2}$$

$$\left(-\frac{1}{2}\nabla^2 + v_{\mathrm{eff}}(\mathbf{r})\right)\phi_i = \varepsilon_i\phi_i, \tag{3}$$

where v_{eff} is effective potential, which contain exchange-correlation potentials, classical coulombic interactions and nuclear interactions. The exchange-correlation potentials are defined by

$$E_{\mathrm{XC}} = C_1E_{\mathrm{X}}^{\mathrm{HF}} + C_2E_{\mathrm{X}}^{\mathrm{Slater}} + C_3\Delta E_{\mathrm{X}}^{\mathrm{Becke88}} + C_4E_{\mathrm{c}}^{\mathrm{VWN}} + C_5\Delta E_{\mathrm{c}}^{\mathrm{LYP}}, \tag{4}$$

where C_i are mixing coefficients. B2LYP method [40] using in this study has optimized exchange-correlation potential term for magnetic interaction in μ-oxo diiron inorganic model compounds [34]. The parameter sets are $(C_1,\ C_2,\ C_3,\ C_4,\ C_5) = (0.25,\ 0.75,\ 0.75,\ 1.0,\ 1.0)$. The parameter sets in other methods are (0.5, 0.5, 0.5, 1.0, 1.0) and (0.2, 0.8, 0.72, 1.0, 0.81) for BHandHLYP and B3LYP, respectively.

2.2. Effective-exchange integrals

The effective-exchange interactions between spins at iron atoms are described by spin Hamiltonian, the Heisenberg model (HB),

$$H(\mathrm{HB}) = -2\sum J_{\mathrm{ab}}\mathbf{S}_{\mathrm{a}}\cdot\mathbf{S}_{\mathrm{b}}, \tag{5}$$

where $\mathbf{S}_{\mathrm{a}}$ and $\mathbf{S}_{\mathrm{b}}$ represent spins at sites a and b, respectively. The effective-exchange integrals J_{ab} are experimentally determined by the measurement of magnetic susceptibility. J_{ab} values are estimated from the approximate spin projection (AP) procedure as

$$J_{\mathrm{ab}}(\mathrm{AP}-X) = \frac{E_{\mathrm{X}}^{\mathrm{LS}} - E_{\mathrm{X}}^{\mathrm{HS}}}{\langle \boldsymbol{S}^2\rangle_{\mathrm{X}}^{\mathrm{HS}} - \langle \boldsymbol{S}^2\rangle_{\mathrm{X}}^{\mathrm{LS}}}, \tag{6}$$

where $\langle \boldsymbol{S}^2\rangle$ is the expectation value of squared magnitudes of spin angular momentums and subscript X means calculation methods such as HF and DFT [41–43].

2.3. Natural orbital analysis

Natural orbital (NO) is obtained by eigenvector of diagonalization of all electron density as

$$\rho(\mathbf{x}',\mathbf{x}) = \sum_i n_i \varphi_i^*(\mathbf{x}')\varphi_i(\mathbf{x}). \tag{7}$$

Each eigenvalue for NOs corresponds to occupation number n_i. NO is symmetry adapted and is useful for orbital interaction analysis in broken-symmetry calculations using unrestricted orbitals. Chemical indices indicate the characteristic feature of orbitals and enable us to perform quantitative analysis of chemical bonds or magnetic interactions [34,44]. They are the effective bond order b, the information entropy I_n, the diradical character Y, the spin density Q, unpaired electron density U and the projected effective bond order B. In these chemical indices, only effective bond orders b and B are discussed here.

The spin-polarized orbitals of BS solution have the following relationship with natural orbitals and its occupation numbers,

$$\varphi_\pm = \frac{1}{\sqrt{2(1 \pm T)}}(\phi_\alpha \pm \phi_\beta), \tag{8a}$$

$$n_\pm = 1 \pm T, \tag{8b}$$

where φ_+ (φ_-) is (anti)bonding natural orbital and n_+ (n_-) is its occupation numbers. T is the orbital overlaps between alpha and beta spin-polarized orbitals. These occupation numbers are projected to $n_\pm^{\mathrm{AP}}$ by the AP procedure,

$$n_\pm^{\mathrm{AP}} = \frac{4n_\pm^2}{4 + (n_+ - n_-)^2}. \tag{9}$$

The effective bond order b and the projected effective bond order B are defined by difference between the occupation numbers of the bonding and antibonding natural orbitals,

$$b = \frac{n_+ - n_-}{2} \tag{10}$$

$$B = \frac{n_+^{\mathrm{AP}} - n_-^{\mathrm{AP}}}{2}. \tag{11}$$

If the bond-order value is equal to 0.0, spin is localizing in one site and its orbital is complete diradical. In contrast, the bond-order value is equal to 1.0, spin is delocalizing over sites and their orbitals are complete closed-shells. The b value is equal to the orbital overlap T and the B value is always larger than the b value. The orbital which has the largest bond-order value is the main interaction pathway among spin sites. The bond-order values reveal strength of orbital interactions. Magnetic interactions become clear by this natural orbital analysis.

As the similar procedure for natural orbitals, spin natural orbital (SNO) is obtained by diagonalization of all electron spin density matrix. Each eigenvalue for SNOs corresponds to spin occupation number n_i^{SNO} with alpha spin considered positive. The spin natural orbital illustrates broke-symmetry and is useful for the analysis for BS solution. The spin natural orbitals of BS solution are composed of natural orbitals with the following relationship as

$$\varphi_\pm^{\mathrm{SNO}} = \frac{1}{\mathrm{Norm}}(C\phi_\alpha + \phi_\beta), \tag{12a}$$

$$n_\pm^{\mathrm{SNO}} = \pm\sqrt{1 - T^2}, \tag{12b}$$

$$C = -\frac{1 \pm \sqrt{1 - T^2}}{T}, \tag{12c}$$

where Norm is normalization factor. These SNOs are especially useful for the analysis of spin densities at BS states. The occupation number of SNO n_+^{SNO} is the same as unpaired electron density U of chemical indices.

2.4. Computational detail

All the calculations were performed with GAUSSIAN98 program package [45]. 6-31G* basis sets given by Pople et al. [46,47] were used for hydrogen, carbon, nitrogen and oxygen atoms. Huzinaga MIDI basis plus Hay's diffuse basis were used for iron atoms [48,49]. All the position coordinates of non-hydrogen atoms were taken from the X-ray crystallographic structures in the Protein Data Bank (PDB). The PDB codes used in this study are 1HMO, 1HMD and 2HMQ for oxy-Hr, deoxy-Hr and met-Hr, respectively. These Hrs were obtained from *Themiste Dyscrita* (Sipunculid worm) and its structures are determined at 1.66 Å resolution of the met-Hr and at 2.0 Å of the oxy-Hr or deoxy-Hr [13,14]. The Hr model structures used in this study are shown in Fig. 1.

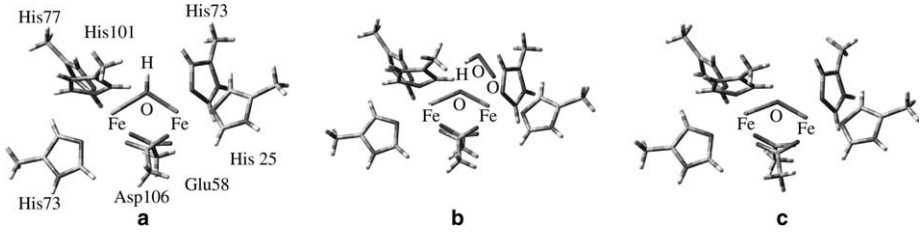


Fig. 1. The active site structure of Hr: (a) oxy form (PDB code: 1HMO) (b) deoxy form (1HMD) and (c) met form (2HMQ).

3. Calculated results

3.1. Met form

3.1.1. Effective-exchange integral

Calculated effective-exchange integral by UB2LYP method is $-J(\mathrm{AP}) = 131.6\ \mathrm{cm}^{-1}$ which is in agreement with experimental value $134\ \mathrm{cm}^{-1}$ [50]. Calculated $-J$ values are 18.92, 69.33, 153.98 and $318.19\ \mathrm{cm}^{-1}$ by UHF, UBHandHLYP, UB3LYP and UBLYP, respectively. These methods have different weight of Hartree-Fock exchange term in exchange-correlation potential. The pure DFT BLYP overestimates more than double while Hartee-Fock underestimate it less than one-seventh. Among these methods, hybrid-DFT as UB2LYP and UB3LYP is in qualitatively agreement with experimental values. The magnetic interactions J have a tendency to be smaller by the weight of Hartree-Fock exchange term in exchange-correlation potential. The B2LYP has larger share of Hartree–Fock exchange potential than B3LYP. The B2LYP predicts appropriate strength of magnetic interaction, this method can depict proper shapes of magnetic orbitals than other methods. Next, orbital interactions from UB2LYP are analyzed.

3.1.2. Orbital interactions

There are five bonding NOs and five antibonding NOs involving a magnetic interactions in met-Hr. They consist of iron d-orbitals and ligand orbitals, which are spin site orbitals and their delocalizing orbitals. The bonding and antibonding orbitals are different in the node at spin site and are pairing in a type of interactions. There are five types in this d-electron interacting system. They are named as σ, π_1, π_2, δ_1, δ_2 as elements from an approximate C_{2v} symmetry group in the active site. In Fig. 2 these NOs are shown in the order of their occupation numbers. The B values, which are projected effective bond order, for π_1, σ, π_2, δ_2, δ_1 are 0.29, 0.27, 0.24, 0.04, 0.026, respectively. This result indicates that σ and π interaction through p orbitals at μ-oxo are fairly stronger than δ interactions through carboxylic group of acetate. Strong antiferromagnetic interactions are mediated by μ-oxo bridge. Mulliken spin densities on the iron sites in BS state are 4.16 and −4.06. These spin densities are typical for high spin Fe(III) system of d5 electrons because contributions for the spin density are 0.799, 0.773, 0.845, 0.826, 0.943 from each interactions π_1, σ,π_2, δ_2, δ_1, respectively. The orbital interactions contribute to decrease to the spin density in iron spin sites.

3.2. Deoxy form

3.2.1. Effective-exchange integral

Calculated effective-exchange integral by UB2LYP method is $-J(\mathrm{AP}) = 18.88\ \mathrm{cm}^{-1}$ which is in agreement with experimental value $13\ \mathrm{cm}^{-1}$ [38]. Weak antiferromagnetic interactions between diirons are computationally reproduced. Calculated $-J$ values are −3.15, 9.64, 22.44 and $19.85\ \mathrm{cm}^{-1}$ by UHF, UBHandHLYP, UB3LYP and UBLYP, respectively. There is the same tendency to these results that the pure DFT BLYP overestimates while Hartee-Fock underestimates the J value.

3.2.2. Orbital interactions

The electron configurations in iron sites of deoxy-Hr are d6 high spin state and δ_1 orbitals are double occupied. For this reason, the types of interacting orbitals are other orbital interactions as σ, π_1, π_2, δ_2. These NOs (not shown) are similar in shape to that of Met-Hr in Fig. 2. These B values by UB2LYP are 0.2007, 0.1180, 0.0663, 0.0259, respectively. Compared with the B values of met-Hr and Oxy-Hr, these B values are smaller. Especially B value for π_1 becomes small. π_1 orbital interaction is superexchange (SE) interaction through protonated p orbital at μ-hydroxo. The SE interaction through μ-hyroxo in deoxy-Hr are smaller than the SE interaction through μ-oxo. The spin densities at iron sites are 3.78 and −3.73. This spin densities are close to the high spin Fe(II) system of d6 electrons. This is the reason that the spins in iron sites are localizing and their orbital interactions are small. Other electron configuration state as the distal iron having π_1

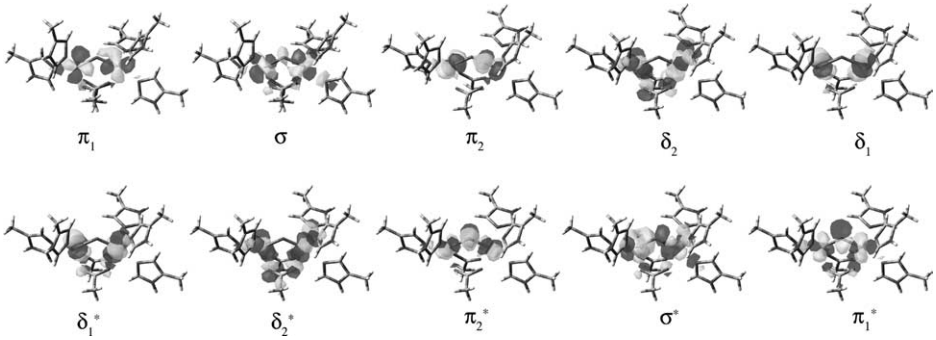


Fig. 2. Natural orbitals for the antiferromagnetic spin state of Met-Hr by UB2LYP/DZP. These orbitals are in the order of their occupation numbers.

double occupied electrons and proximal iron having δ_1 electrons which are important configuration to react with dioxygen are 1.78 kcal mol^{-1} above the δ_1 double occupied configuration one by UB3LYP at antiferromagnetic coupling state. These state are nearly degenerating in deoxy-Hr.

3.3. Oxy form

3.3.1. Effective-exchange integral

Calculated effective-exchange integral by UB2LYP method is $-J(\mathrm{AP}) = 75.60\ \mathrm{cm}^{-1}$ which is in agreement with experimental value 77 cm^{-1} [50]. The strong antiferromagnetic interactions between diirons are computationally reproduced. Calculated $-J$ values (cm^{-1}) by UHF, UBH and HLYP, UB3LYP and UBLYP are 30.46, 50.91, 121.94 and 334.13, respectively. There is also the same tendency to these results that the pure DFT BLYP overestimates while Hartee-Fock underestimates the J value. The calculated J values are given in Table 1 with experimental values.

3.3.2. Orbital interactions

As is the met form, the orbital interactions are π_1, σ, π_2, δ_1, δ_2 according to the strength. The B values for π_1, σ, π_2, δ_1, δ_2 are 0.89, 0.41, 0.33, 0.05, 0.03, respectively. As is the met form, σ and π interactions through p orbitals at μ-oxo are fairly stronger than δ interactions through carboxylic group of acetate. Strong antiferromagnetic interactions are mediated by μ-oxo bridge in oxy-Hr. Natural orbitals for σ and π_1 are mixing for orbital interactions to dioxygen. These orbital interactions to dioxygen are discussed in next section. Mulliken spin densities on the iron sites in BS state are 3.98 and −3.70. These spin densities are contributed by 0.451, 0.822, 0.915, 0.913, 0.928 from each interactions π_1, σ, π_2, δ_1, δ_2, respectively. The spin densities in iron sites depend on method. The iron spin density is 4.70, 4.31, 3.93, 3.60 by UHF, UBHandHLYP, UB3LYP and UBLYP, respectively. Molecular orbitals and their orbital interactions are also highly depending on methods. We discuss these properties by UB2LYP method which properly represents magnetic interactions in consistent with experimental values. In Table 2, the occupation numbers with assignments of orbital symmetries for met-Hr, deoxy-Hr, and oxy-Hr are given.

Table 1
Effective-exchange integrals[a] J calculated[b] for hemerythrin active site

State	$-J_{ab}$(AP)	exp.	Ref.
Met form	131.64	134	[50]
Deoxy form	18.88	13	[38]
Oxy form	75.60	77	[50]

[a] cm^{-1}.
[b] UB2LYP/DZP.

Table 2
Occupation numbers and quasi-symmetry[a] of the natural orbitals[b] for hemerythrin active site

Met form	π_1	σ	π_2	δ_2	δ_1
	1.2948	1.2657	1.2443	1.0442	1.0259
Deoxy form	δ_1	σ	π_2	π_1	δ_2
	1.9972	1.1014	1.0592	1.0332	1.0129
Oxy form	π_1	σ	π_2	δ_1	δ_2
	1.6084	1.2145	1.1695	1.0270	1.0156

[a] Orbital symmetry in Fe–O–Fe quasi-C_{2v} group.
[b] Antiferromagnetic spin state by UB2LYP/DZP.

3.3.3. Oxygen binding states in oxy-Hr

Natural orbitals in oxy-Hr are dissymmetric for the interactions with oxygen orbitals. The double occupied orbitals in dioxygen are delocalizing over iron spin sites. They are σ bonding and π bonding with proximal iron named as $\sigma(\mathrm{Fe}(\pi_1^*) + \mathrm{O}_2)$, and π $(\mathrm{Fe}(\delta_2) + \mathrm{O}_2)$, respectively, and their occupation numbers are 1.9966 and 1.9944. Strong orbital delocalization from hydroperoxide to iron atoms are seen (Fig. 3).

3.4. Comparison to Hr model compounds

Magnetic interaction analysis for Hr model compounds as $[Fe_2O(CH_3CO_2)_2(Hbpz_3)_2]$ and $[Fe_2O(CH_3CO_2)_2(Me_3TACN)_2]$ have reported [34]. Their magnetic interactions in μ-oxo are σ, π_1, π_2, δ_1, δ_2 type in the order of strength. In μ-hydroxo state, all the SE interaction are weakened and especially π_1 type interaction drastically reduced by protonation over μ-oxo, just as Hr active sites in this study. These magnetic interaction changes in Hr are essentially identical to Hr model compounds, which have no dioxygen bonding capability. Then the magnetic interactions are through μ-oxo and their changes are inherent to the Fe–O–Fe core.

3.5. ET process in Hr

The dioxygen binding mechanism in Hr had been studied by Solomon et al. using DFT calculations [11]. In their results, ETPT process is indicated, which is coupling mechanism of electron transfer (ET) and proton transfer (PT). The mechanism is composed of two step electron transfers (Fig. 4). In the first step one electron transfer from distal iron to dioxygen and proton tunnel-

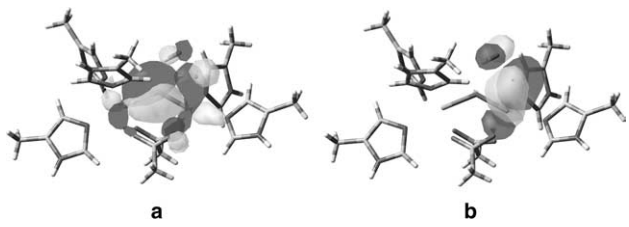


Fig. 3. Double occupied natural orbitals for the antiferromagnetic state of oxy-Hr by UB2LYP/DZP. (a) σ bonds $(\mathrm{Fe}(\pi_1^*) + \mathrm{O}_2)$ and (b) π bonds $(\mathrm{Fe}(\delta_2) + \mathrm{O}_2)$.

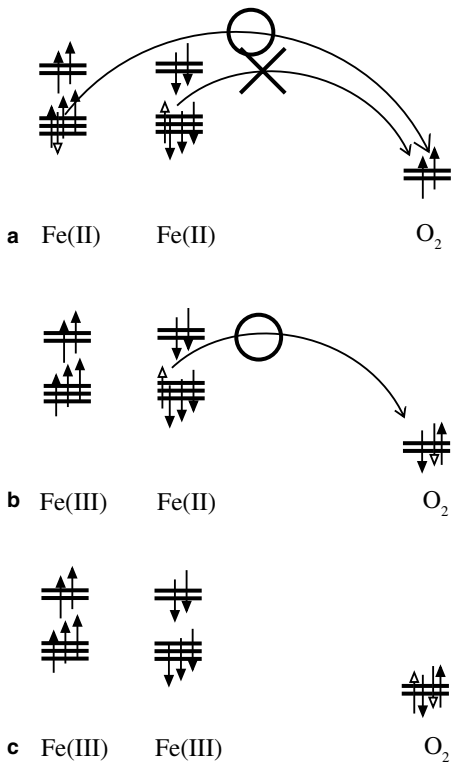


Fig. 4. Reversible dioxygen binding mechanism (ETPT) proposed by Solomon et al. for Hr. (a) deoxy-Hr. (b) Mixed-valence intermediate state. (c) Oxy-Hr.

ing occur at the same time from hydroxy to peroxide (ETPT). Then σ bond is formed between iron and oxygen of hydroperoxide. In the second step, one electron transfer occur from the proximal iron and π bonding is formed. The double occupied natural orbital in Fig. 3 are corresponding to the two step ET interactions.

4. Conclusion

The active sites from Hrs were calculated by DFT to clarify the oxygen binding states and its relation to magnetic properties. Natural orbitals were utilized for orbital interactions. The following results are concluded:

1. Calculated effective-exchange interactions in B2LYP method were in good agreement with experimental values for deoxy-Hr, oxy-Hr and met-Hr.
2. From natural orbital analysis, magnetic interactions in oxy-Hr, deoxy-Hr and met-Hr are elucidated. The iron spin sites are interacting each other in a form of The σ, π_1, π_2, δ_1, δ_2 type in met-Hr and in deoxy-Hr. The σ, π_1, π_2 type interactions were through μ-oxo and these interactions are relatively strong in oxy-Hr and met-Hr compared to the δ_1, δ_2 type interactions through carboxyl group of acetic acids. But in deoxy-Hr, main orbital interactings as σ, π_1, π_2 are decreased. Especially at π_1, whose intermediate orbital is protonated p orbital of oxygen at μ-hydroxo in deoxy-Hr. For this reason, magnetic interactions in deoxy-Hr are weakened.
3. Natural orbitals in oxy-Hr allowed to understand oxygen binding state well. π_1 type interaction orbital also plays key role in a process of dioxygen binding process. The natural orbital $\sigma(Fe(\pi_1) + O_2)$ represents first step electron transfer path in ETPT process. By this electron transfer from distal iron to dioxygen, σ bond between dioxygen and proximal iron atom is formed. Then π bond form by second electron transfer from δ_2 type orbital from proximal iron atom and they corresponds to $\pi(Fe(\delta_2) + O_2)$ of natural orbital.

Acknowledgement

This work is supported by the Grant-in-Aid for the 21st Century COE "Creation of Integrated EcoChemistry" from the Ministry of Education, Culture, Sports, Science and Technology (MEXT) of Japan and a Grant-in-Aid for Scientific Research on Priority Areas (Nos. 16750049 and 14204061) from Ministry of Education, Culture, Sports, Science and Technology, Japan.

References

[1] H. Eklund, Handbook of Metalloproteins, Willey, New York, 699–711.
[2] S.J. Lippard, J.M. Berg, Principles of Bioinorganic Chemistry, University Science Books, 1994.
[3] Andrew L. Feig, Stephen J. Lippard, Chem. Rev. 94 (1994) 759.
[4] R.E. Stenkamp, L.C. Siecker, L.H. Jensen, J. Sanders-Loehr, Nature 291 (1981) 263.
[5] Ronald E. Stenkamp, Larry C. Sieker, Lyle H. Jensen, Joann S. Loehr, J. Mol. Biol. 100 (1976) 23.
[6] Joann S. Loehr, Kathe N. Meyerhoff, Larry C. Sieker, Lyle H. Jensen, J. Mol. Biol. 91 (1975) 521.
[7] Ronald E. Stenkamp, Larry C. Sieker, Lyle H. Jensen, J. Mol. Biol. 126 (1978) 457.
[8] Joann S. Loehr, Peter J. Lammers, Bernadine Brimhall, Mark A. Hermodson, J. Biol. Chem. 253–316 (1978) 5726.
[9] Ke Zhang, E.A. Stern, F. Ellis, Biochemistry 27 (1988) 7470.
[10] Maria Wirstam, Stephen J. Lippard, Richard A. Friesner, J. Am. Chem. Soc. 125 (2003) 3980.
[11] Edward I. Solomon, Inorg. Chem. 40 (2001) 3656.
[12] Richard A. Friesner, Mu-Hyun Baik, Benjamin F. Gherman, Victor Guallar, Maria Wirstam, Robert B. Murphy, Stephen J. Lippard, Coord. Chem. Rev. 238–239 (2003) 267.
[13] Margaret A. Holmes, Isolde Le Trong, Stewart Turley, Larry C. Sieker, Ronald E. Stenkamp, J. Mol. Biol. 218 (1991) 583.
[14] Margaret A. Holmes, Ronald E. Stenkamp, J. Mol. Biol. 220 (1991) 723.
[15] Ronald E. Stenkamp, Larry C. Sieker, L.H. Jensen, John D. McCallum, Joann Sanders-Loehr, Biochemistry 82 (1985) 713.
[16] Markus Metz, Edward I. Solomon, J. Am. Chem. Soc. 123 (2001) 4938.

[17] Ronald E. Stenkamp, Larry C. Sieker, Lyle H. Jensen, J. Am. Chem. Soc. 106 (1984) 618.
[18] Robert C. Scarrow, Michael J. Maroney, Sharon M. Palmer, Lawrence Que Jr., J. Am. Chem. Soc. 108 (1986) 6832.
[19] Robert C. Sacrrow, Michael J. Maroney, Sharon M. Palmer, Lawrence Que Jr., A. Lawrence Roe, Scott P. Salowe, JoAnne Stubbe, J. Am. Chem. Soc. 109 (1987) 7857.
[20] Agneta Ericson, Britt Hedman, Keith O. Hodgson, J. Am. Chem. Soc. 110 (1988) 2330.
[21] S.M. Kauzlarich, B.K. Teo, T. Zirino, S. Burman, J.C. Davis, B.A. Averill, Inorg. Chem. 25 (1986) 2781.
[22] Shi Jin, Donald M. Kurtz Jr., Zhi-Jie Kiu, John Rose, Bi-Cheng Wang, J. Am. Chem. Soc. 124 (2002) 9845.
[23] William H. Armstrong, Stephen J. Lippard, J. Am. Chem. Soc. 105 (1983) 4837.
[24] William H. Armstrong, Stephen J. Lippard, J. Am. Chem. Soc. 106 (1984) 4632.
[25] William H. Armstrong, Alan Spool, Georgia C. Papaefthymiou, Richard B. Frankel, Stephen J. Lippard, J. Am. Chem. Soc. 106 (1984) 3653.
[26] Roman S. Czernuszewicz, John E. Sheats, Thomas G. Spiro, Inorg. Chem. 26 (1987) 2063.
[27] JudithAnn R. Hartman, R. Lynn Rardin, Phalguni Chaudhuri, Klaus Pohl, Karl Wieghardt, Bernhard Nuber, Johannes Weiss, Georgia C. Papaefthymiou, Richard B. Frankel, Stephen J. Lippard, J. Am. Chem. Soc. 109 (1987) 7387.
[28] Alan Spool, Ian D. Williams, Stephen J. Lippard, Inorg. Chem. 24 (1985) 2156.
[29] Robert H. Beer, William B. Tolman, Simon G. Bott, Stephen J. Lippard, Inorg. Chem. 30 (1991) 2082.
[30] Chuan He, Amy M. Barrios, Dongwhan Lee, Jane Kuzelka, Roman M. Davydov, Stephen J. Lippard, J. Am. Chem. Soc. 122 (2000) 12683.
[31] Britt Hedman, Man Sung Co, William H. Armstrong, Keith O. Hodgson, Stephen J. Lippard, Inorg. Chem. 25 (1986) 3708.
[32] Joann Sanders-Loehr, Willian D. Wheeler, Andrew K. Shiemke, Bruce A. Averill, Thomas M. Loehr, J. Am. Chem. Soc. 111 (1989) 8084.
[33] Petra N. Turowski, William H. Armstrong, Shuncheng Liu, Seth N. Brown, Stephen J. Lippard, Inorg. Chem. 33 (1994) 636.
[34] M. Shoji, Y. Nishiyama, Y. Maruno, K. Koizumi, Y. Kitagawa, S. Yamanaka, T. Kawakami, M. Okumura, K. Yamaguchi, Int. J. Quant. Chem. 100 (2004) 887.
[35] K. Koizumi, M. Shoji, Y. Nishiyama, Y. Maruno, Y. Kitagawa, K. Soda, S. Yamanaka, M. Okumura, K. Yamaguchi, Int. J. Quant. Chem. 100 (2004) 943.
[36] Zhida Chen, Zhitao Xu, Lei Zhang, Feng Yan, Zhenyang Lin, J. Phys. Chem. A 105 (2001) 9710.
[37] Jorge H. Rodriguez, James K. McCusker, J. Chem. Phys. 116 (2002) 6253.
[38] T.C. Brunold, E.I. Solomon, J. Am. Chem. Soc. 121 (1999) 8277–8287.
[39] P. Geerlings, F. De Proft, W. Langenaeker, Chem. Rev. 103 (2003) 1793.
[40] K. Kitagawa, T. Soda, Y. Shigeta, S. Yamanaka, Y. Yoshioka, K. Yamaguchi 84 (2001) 592–600.
[41] K. Yamaguchi, S. Yabushita, T. Fueno, in: V.H. Smith Jr., H.F. Schaefer III, K. Morokuma, S. Reidel (Eds.), Applied Quantum Chemistry, Dordercht, 1986, p. 155.
[42] K. Yamaguchi, H. Fukui, T. Fueno, Chem. Lett. 625 (1986).
[43] K. Yamaguchi, T. Tsunekawa, Y. Toyoda, T. Fueno, Chem. Phys. Lett. 143 (1988) 371.
[44] H. Isobe, Y. Takano, Y. Kitagawa, T. Kawakami, S. Yamanaka, K. Yamaguchi, K.N. Houk, Mol. Phys. 100 (2002) 717.
[45] M.J. Frisch, G.W. Trucks, H.B. Schlegel, G.E. Scuseria, M.A. Robb, J.R. Cheeseman, V.G. Zakrzewski, J.A. Montgomery Jr., R.E. Stratmann, J.C. Burant, S. Dapprich, J.M. Millam, A.D. Daniels, K.N. Kudin, M.C. Strain, O. Farkas, J. Tomasi, V. Barone, M. Cossi, R. Cammi, B. Mennucci, C. Pomelli, C. Adamo, S. Clifford, J. Ochterski, G.A. Petersson, P.Y. Ayala, Q. Cui, K. Morokuma, N. Rega, P. Salvador, J.J. Dannenberg, D.K. Malick, A.D. Rabuck, K. Raghavachari, J.B. Foresman, J. Cioslowski, J.V. Ortiz, A.G. Baboul, B.B. Stefanov, G. Liu, A. Liashenko, P. Piskorz, I. Komaromi, R. Gomperts, R.L. Martin, D.J. Fox, T. Keith, M.A. Al-Laham, C.Y. Peng, A. Nanayakkara, M. Challacombe, P.M.W. Gill, B. Johnson, W. Chen, M.W. Wong, J.L. Andres, C. Gonzalez, M. Head-Gordon, E.S. Replogle, J.A. Pople, Gaussian 98, Revision A.11.3, Gaussian Inc., Pittsburgh, PA, 2002.
[46] P.C. Hariharan, J.A. Pople, Theo. Chem. Acta 28 (1973) 213.
[47] W.J. Hehre, R. Ditchdield, J.A. Pople, J. Chem. Phys. 56 (1972) 2257.
[48] S. Huzinaga, Gaussian Basis Sets for Molecular Calculations, Elsevier, Amsterdam, Oxford, New York, Tokyo, 1984.
[49] P.J. Hay, J. Chem. Phys. 66 (1977) 4377.
[50] J.W. Dawson, H.B. Gray, H.E. Hoenig, G.R. Rossman, J.M. Schredder, R.-H. Wang, Biochemistry 11 (1972) 461–465.

It is necessary for the accurate investigations of such compounds to calculate and explain such interactions as SSC interactions within molecular orbital levels, since most of triplet carbenes were determined by the usage of EPR. Especially, high level ab initio studies can be significantly useful not just for inquiring into the origin of magnetic anisotropy but also to the flexible and systematic molecular designs, as well as the interpretation of spectra and the determination of molecular structures.

It was difficult to study ZFSs theoretically, because the electron correlation problems are deeply involved and even more so in excited spin states. Only ab initio studies of ZFSs have been carried out for such small molecules as CH_2, SiH_2, O_2, H_2CO [11–14]. Although semi-empirical methods have often been used and ab initio calculations are still difficult due to the much computing costs for aromatic and heterocyclic hydrocarbons.

In this study, theoretical studies of zero-field splitting energies from the spin–spin coupling contributions for ground triplet molecules [15] are reported. An efficient method for ZFS by the hybrid-density-functional theory (HDFT) is proposed, which can be applied up to relatively large molecules. First, this procedure is discussed for typical organic biradicals. Next, its detailed applications for traditional problems of such carbenes as vinylmethylene, phenylcarbene, and diphenylcarbenes are discussed from the viewpoint of the calculated ZFSs parameters, magnetic axes and spin orbitals.

2. Theoretical backgrounds

2.1. Anisotropy in spin hamiltonian

An anisotropic term in spin-Hamiltonian is constructed from the total spin operators as the form

$$H_{\mathrm{AS}} = \sum_{i,j} \mathbf{D}_{ij} S_i S_j, \quad (i,j = x,y,z), \tag{1}$$

where $\mathbf{D}_{ij}$ is a traceless symmetric rank-two tensor. Diagonalization of the $\mathbf{D}$ tensor can represent Eq. (1) in a principal axis (X, Y, Z) coordinate system as

$$H_{\mathrm{AS}} = D\left(S_Z^2 - \frac{1}{3}S^2\right) + E(S_X^2 - S_Y^2), \tag{2}$$

where D and E are the independent parameters: $D = -3/2\boldsymbol{D}_{ZZ}$ and $E = 1/2(\boldsymbol{D}_{YY} - \boldsymbol{D}_{XX})$. The Z is the main axis. D is the principle value and $E < |D/3|$, which represents anisotropy within XY plane. D and E values for organic radical are experimentally determined by EPR fine structure around the large signal $g = 2.0$. The magnetic axis is rarely determined by EPR study in solid crystals. The axes direction and the sign of E value change depending on the orientation definitions. The labels of the axes of EPR are conventionally chosen so as to make $DE < 0$. The energy surface of spin anisotropy is an ellipsoid with two different axes. The spin ellipsoid looks like a disc if $D > 0$, and the spin ellipsoid resembles a bar or a rugby ball if $D < 0$.

2.2. The origin of anisotropy in real Hamiltonian

The SOC and SSC expressions for the magnetic anisotropy are obtained under relativistic correction of the Breit–Pauli Hamiltonian [16–20]. The spin–orbit term is

$$\widehat{\mathbf{H}}^{\mathrm{SO}} = \frac{e^2\hbar}{2m^2c^2}\left(\sum_{n,i} Z_n \frac{\mathbf{S}(i)\cdot\mathbf{M}^n(i)}{\mathbf{r}_{ni}^3} - \sum_{i\neq j}\frac{2\mathbf{S}(i)\cdot\mathbf{M}^i(j) + \mathbf{S}(i)\cdot\mathbf{M}^j(i)}{\mathbf{r}_{ij}^3}\right), \tag{3}$$

where $\mathbf{S}(i)$ is a spin angular momentum operator. $\mathbf{M}^n(i)$ is a gauge-invariant angular momentum operator of ith electron defined as

$$\mathbf{M}^n(i) = \mathbf{r}_{in}\cdot\mathbf{p}_i. \tag{4}$$

The first term in Eq. (3) is the sum over the one-electron SOCs in the Coulomb field of nuclei n. The second term is the interaction of electron spin i with the magnetic field induced by the orbital current of jth electron. In most of organic free radicals, the orbital angular momentum is quenched and SOC is much smaller than SSC.

The spin–spin term is

$$\widehat{\mathbf{H}}^{\mathrm{SS}} = \frac{e^2\hbar^2}{m^2c^2}\sum_{i<j}\frac{\mathbf{r}_{ij}^2(\mathbf{S}(i)\cdot\mathbf{S}(j)) - 3(\mathbf{r}_{ij}\cdot\mathbf{S}(i))(\mathbf{r}_{ij}\cdot\mathbf{S}(j))}{\mathbf{r}_{ij}^5}, \tag{5}$$

which means the spin–spin dipolar coupling. This term is the main interaction of the ZFSs in organic radicals and the g-factors is near to the value for a free electron ($g_e = 2.0023$).

2.3. Spin orbitals

The unrestricted wave function method is employed in this HDFT study. These orbitals are spin-polarized and negative spin density is found over atoms. The spin orbitals are obtained from natural (spin) orbitals with occupation number 1.0, so-called singly occupied natural orbital (SONO). Natural orbitals (NOs) are obtained as an eigenvector by the diagonalization of all electron (or charge) density as

$$\rho(\mathbf{r}',\mathbf{r}) = \sum_i n_i\varphi_i^*(\mathbf{r}')\varphi_i(\mathbf{r}). \tag{6}$$

Each eigenvalue of NOs corresponds to occupation number n_i ($0 \leqslant n_i \leqslant 2$). Similar procedure to Eq. (6) provides spin natural orbital (SNO) from all electron spin density. Each eigenvalue of SNOs corresponds to spin occupation number n_i^{SNO} (in [0, 1]) where α spin is defined to be positive. The SONOs and HOMOs of α orbitals are almost the same, but this NO procedure

theoretically means the spin projection into pure high spin states from spin-contaminated states. These non-SONO NOs (i.e., HONOs) and its occupation numbers can analyse spin polarizations and magnetic interactions quantitatively [21,22].

The total spin orbitals are derived by the antisymmetrization of spin orbitals. An expectation value of an operator $\widehat{O}$ for magnetic properties is obtained as:

$$E = \langle \Phi | \widehat{O} | \Phi \rangle. \tag{7}$$

For the triplet states of organic biradicals, only two SONOs affect for their magnetic properties. The total spin orbitals are

$$|^3\Phi\rangle = |\varphi_i\varphi_j\rangle = \frac{1}{\sqrt{2}}(\varphi_i\varphi_j - \varphi_j\varphi_i), \tag{8}$$

and the anisotropic **D** tensor is obtained by the SSC contribution to the ZFS, as

$$\mathbf{D} = \mathbf{H}^{SS} = \langle {}^3\Phi | \widehat{\mathbf{H}}^{SS} | {}^3\Phi \rangle. \tag{9}$$

3. Computational procedures

The present study was started with coding a new computer programs called "GSO-ZFS", in order to calculate SSC. The two electron integrals in Eq. (1) were calculated by differentiating two-electron integrals based on the Obara–Saika methodology [23–26]. This computational procedure is described as below. First, ab initio MO calculations are performed for the molecular structures of the ground triplet state and spin orbitals with GAUSSIAN 98 program packages [27] using UB3LYP//6-31G method [28,29]. The **D** of SSC interaction is then evaluated by GSO-ZFS. ZFS parameters D, E and magnetic axis are provided by the diagonalization of **D**. the g-factor is fixed to be 2.0.

In the triplet states, two SONOs were selected for the SSC calculation. In general $2S$ spin orbitals are necessary for the SSC calculation in the highest $2S+1$ spin multiplicity state. The SNOs are necessary for evaluating SCC from unrestricted orbital calculations because of the separation from the slight spin contaminations by spin polarization. The SSC interactions between these spin orbitals were evaluated by the effective total spin wave functions of the antisymmetrized spin orbitals. If the spin state is of the excited one, multi-reference configuration interaction (MR-CI) and MR-SCF calculations will be necessary for the SSC calculations.

4. Calculated results and discussions

4.1. Applications to typical organic biradicals

D and E for typical organic biradicals depicted in Fig. 1 [5,16] were calculated by the method described above.

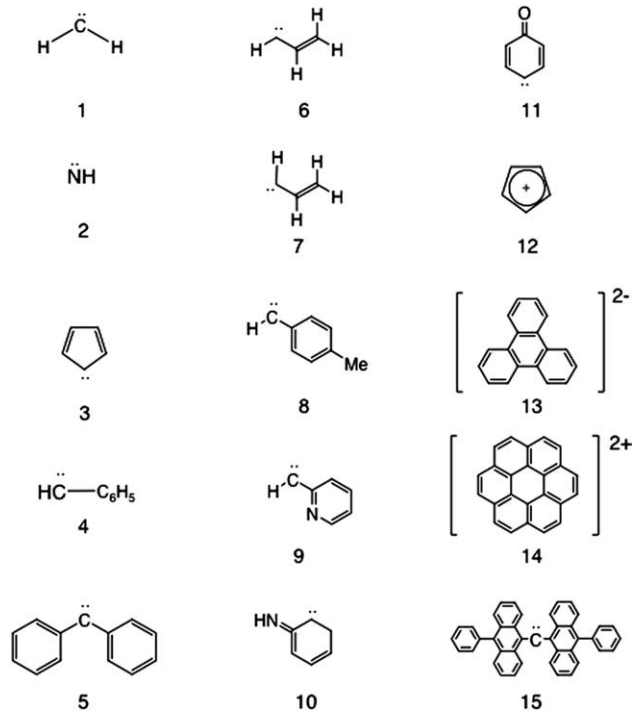


Fig. 1. Molecular structures of typical organic biradicals (**1**: carbene, **2**: nitrene, **3**: cyclopentadienylidene, **4**: phenylcarbene, **5**: diphenylcarbene, **6**: vinylcarbene (s-*E*), **7**: vinylcarbene (s-*Z*), **8**: *p*-tolylcarbene, **9**: pyridylcarbene, **10**: iminocyclohexadienylidene, **11**: 4-oxo-2,6-cyclohexadienylidene, **12**: ferrocene cation, **13**: triphenylene, **14**: coronene dication, **15**: bis[9-(10-phenyl)anthryl]carbene).

The results are summarized in Table 1 with their experimental values, indicating these calculated D and E values were in good agreements with their experimental values. All of these organic biradicals have positive D values because their spin orbitals distribute over one ring. In contrast of such spin distributions, if spins stay away each other, the D value is expected to have negative sign by the application of the point dipole approximation. These D values are often used for the experimental measurement between two spin sites.

The largest D value was obtained for **2** because the spin orbitals are the closest to each other. Also the D of carbene (**1**) was large for the same reason. Among carbene derivatives, the smallest D was obtained for **15** because each spin orbital at carbene centre is delocalized over the anthryl moieties and spins are distant each other [3,30,31]. E value shows how bending the carbene centre is. Such linear biradicals as **15** and **2** have characteristically 0 values of E, so do such molecules with more than C_3 symmetry as **12** and **13**.

Cyclopropenyl cation **13** has a 4π-electron cyclic system. It has the triplet ground state in order to keep C_5 symmetry of the molecular structure [32–35]. Coronene **14** takes thermally accessible triplet state in dication state [36], which is extremely stable at ambient room temperature, decomposing above 50–70 °C. The molec-

Table 1
D and *E* for the triplet ground states of organic molecules

No.	Molecules	Ab initio calculation[a]			Exp.			Ref.
		D (cm^{-1})	$-E$ (cm^{-1})	$-E/D$	$\|D\|$ (cm^{-1})	$\|E\|$ (cm^{-1})	$\|E/D\|$	
1	carbene	0.8104	0.0576	0.0711	0.7567	0.0461	0.0609	[44]
2	NH	1.698	0.0000	0.0000	1.86	0.0000	0.0000	[49]
3	C_5H_4	0.4412	0.0164	0.0373	0.4089	0.0120	0.0293	[48]
4	HCPh	0.5193	0.0346	0.0667	0.5150	0.024	0.0487	[42]
5	diphenylcarbene	0.3570	0.0125	0.0335	0.4055	0.0194	0.0478	[42]
6	$HCCHCH_2$ (s-*E*)	0.3762	0.0296	0.0787	0.4093	0.0224	0.0547	[40]
7	$HCCHCH_2$ (s-*Z*)	0.4355	0.0219	0.0504	0.4578	0.0193	0.0422	[40]
8	*p*-MePhCH	0.512	0.0343	0.0670	0.516	0.0240	0.0465	[45]
9	HCC_5NH_4	0.5443	0.0358	0.0658	0.537	0.027	0.0503	[46]
10	HNC_6H_4	0.0847	0.0048	0.0567	0.1704	0.0025	0.0150	[47]
11	C_6H_4O	0.2057	0.0036	0.0174	0.3179	0.0055	0.017	[7]
12	$C_5H_5^+$	0.1269	0.0000	0.0000	0.1868	0.0000	0.0000	[6]
13	$tripen^{2-}$	0.0485	0.0000	0.0000	0.0460	0.0088	0.0000	[32]
14	$coronen^{2+}$	0.1145	0.0000	0.0000	0.0591	0.0000	0.0000	[36]
14′	$coronen^{2-}$	0.0394	0.0000	0.0000	0.0542	0.0000	0.0000	[37]
15	PhAtCAtPh	0.0391	0.0000	0.0000	0.105	0.0004	0.0000	[3]

[a] Spin–spin coupling contributions.

ular structure of this dication spin state has D_{6h} symmetry, but the structure of the ground state with the singlet spins has D_{2h} symmetry under the influence of its Jahn–Teller distortions. We implemented geometry optimization for **14** to evaluate the structural distortion effect and the S-T gas. UB3LYP//6-31G showed that the total energy of the singlet state with D_{2h} was more stable than the one of the triplet spin state with D_{6h} by 147.5 kcal mol^{-1}. The Jahn–Teller distortions had small contributions to molecular stability for the singlet state of **14**, since the energy gap between the singlet structure and that of the triplet was only 8.4 kcal mol^{-1}. Hence, it is found that the observed EPR signals for $\mathbf{14}^{2+}$ are arise from its thermally excited triplet spin state. The temperature dependency in EPR signal intensity experimentally estimated S–T gap to be 1.4 kcal mol^{-1}. Also $\mathbf{14}^{2-}$ takes the thermally excited biradical state with 23 kcal mol^{-1} S–T gap [37]. In contrast, our UB3LYP//6-31G calculations evaluated the triplet spin state of $\mathbf{14}^{2-}$ to be slightly more stable by 2.1 kcal mol^{-1} (UB3LYP//6-31 + G* also did by 1.6 kcal mol^{-1}). Such phenomena as triplet stability in dianion and dication states resulted from the doubly degeneration of HOMO and LUMO orbitals in the neutral state of coronene.

Thermally excited triplet spin states were also observed in dianion state on strong Jahn–Teller distortions in hexabenzocoronene (HBC) derivatives that are more conjugated polycyclic aromatic hydrocarbons [38]. The HBCs have some characteristic features that HOMOs and LUMOs are nearly triple degenerated, and take such high-oxidized state as tetra anion. EPR observation then indicated that HBCs took quartet spin state, not triplet. These biradicals have π-conjugated spin orbitals and their magnetic hard axis (*Z*) is vertical to the aromatic rings from the result of our calculations. As the number of aromatic ring increases, *D* values decreases, simply due to the spin orbitals delocalized over the aromatic ring and increase in average spin-spin distances. EPR observed *D* and *E* value from HBC dianions are so small: 0.00145 and 0.00005, respectively. Since the molecular structure of coronene (**14**) has C_3 symmetry and the observed *E* value is characteristic zero value.

Only bis[9-(10-phenyl)anthryl]carbene **15** [3,39]was calculated by UB3LYP//4-31G because it is a relatively large molecule. The optimized bond angle at the carbene centre (θ) was evaluated to be 179.7°. The carbene was slightly bent and had small *E* value. The spin orbitals were much delocalized to each side of anthryl moieties. It is concluded that the weak carbene nature makes the carbene centre almost linear geometry.

More detailed discussions for triplet carbene, vinylmethylene and diphenylcarbene are given below.

4.2. Triplet carbene

Bond angles at the carbene centre (θ) have been experimentally estimated based on *E*/*D* values [39,40], which is also important for the delocalization nature of the spin orbitals at the carbene centre. The relationship of the ZFS values to θ was investigated by the calculations using UHF, UBHandHLYP, UB3LYP, and UBLYP. CH bond length was fixed to 1.10 Å. The results are displayed in Fig. 2. At the linear structure, $D = 0.8$ and $E = 0$. When θ decreases from 180°, *D* decreases while *E* increases. Therefore, *E*/*D* values decrease with the bond angle θ (Fig. 3). The decrease in *E*/*D* values is that spin orbitals are inhomogeneous between *YZ*-plane and *ZX*-plane where carbene locates because of the presence of hydrogen. The differences in

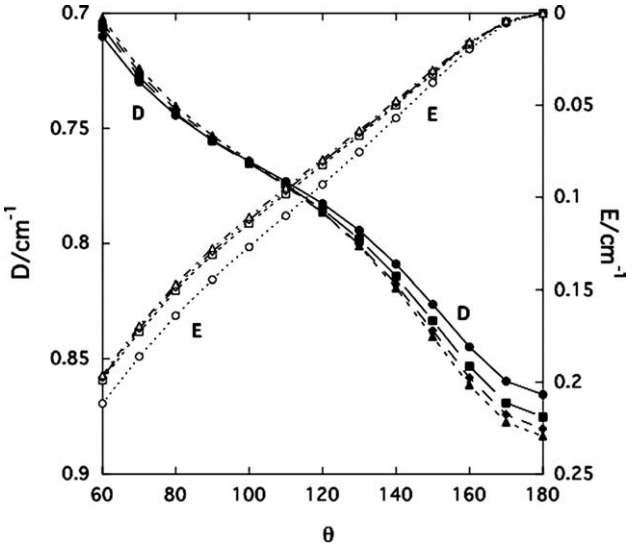


Fig. 2. D (solid symbols) and E (open symbols) values dependence of carbene as a function of the bond angle θ of carbene centre. D values are UHF (●), UBHandHLYP (■), UB3LYP (♦) and UBLYP (▲). E values are UHF (○), UBHandHLYP (□), UB3LYP (◇) and UBLYP (△).

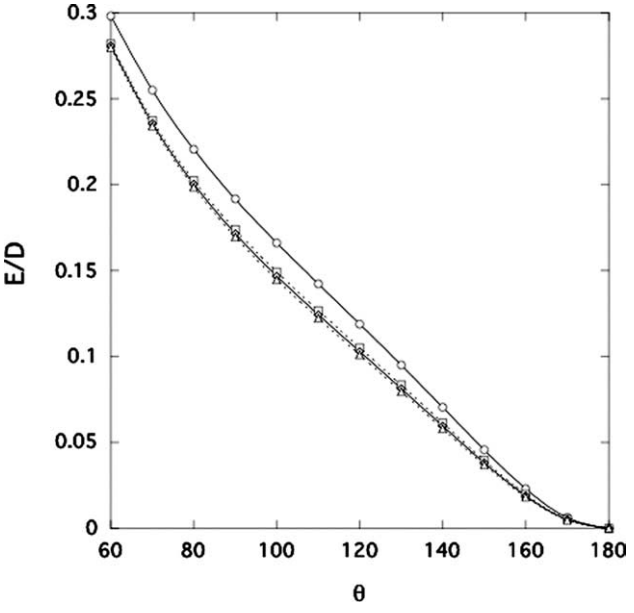


Fig. 3. E/D values dependences of carbene as a function of bond angle θ of carbene centre calculated by UHF (○), UBHandHLYP (□), UB3LYP (◇) and UBLYP (△).

computational methods of HF, BHandHLYP, B3LYP, BLYP are small, indicating that the differences in the shape of spin orbitals are almost the same as the ones for the SSC interactions. The total spin orbitals are then antisymmetrized by the Slater determinants in the process of the SSC calculation. Consequently, the spin correlations exist for all the spin orbitals, even by the pure

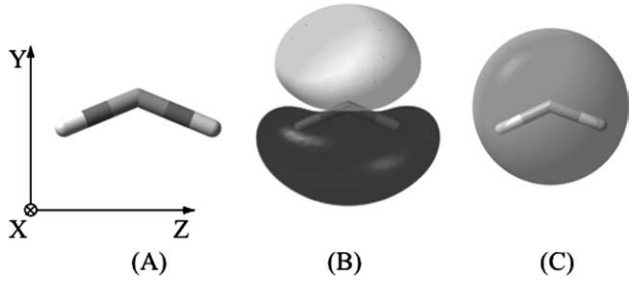


Fig. 4. Triplet carbene. The optimized molecular structure with the magnetic axes (A) and spin orbitals (B, C).

DFT (BLYP). Magnetic hard axis (Z) was parallel to the line connecting the two hydrogen atoms, while Magnetic easy plane (XY-plane) was vertical to the Z-axis. Therefore, two spin orbitals of carbenes are consisted of p_x and p_y orbitals, respectively (Fig. 4). The ZFS values D/cm^{-1} and E/cm^{-1} in the optimized structure were 0.8104 and −0.0576, respectively, as shown in Table 1. These values are slightly larger than experimental values: 0.7567 and −0.0461, respectively. Havlas et al. have reported $D = 0.8043\ \mathrm{cm}^{-1}$ and $E = -0.0428\ \mathrm{cm}^{-1}$ for carbene by CISDTQ/cc-pVDZ methods [11], which is comparable to our values. The SOC interaction causes a slightly smaller contributions than SSC by $D' = D + 0.0023\ \mathrm{cm}^{-1}$ and $E' = E + 0.0001\ \mathrm{cm}^{-1}$ [11,20].

4.3. Isomers of vinylmethylene

There are two isomers of vinylmethylene: s-E and s-Z, and EPR signals for each of these isomers have been observed. It is interest that whether we can theoretically distinguish the difference in fine structures of ZFS for those isomers, or not. Geometry optimizations were performed for each isomer. The θ s were 136.0° and 136.6° for s-E and s-Z, respectively. Fig. 5A displays that the spin orbital perpendicular to the methylene plane is delocalized over the π-orbitals for each s-E and s-Z isomers. The spin orbital populations on the C_2 atom were almost zero at the node of the spin orbitals. On the contrary, the other spin orbitals (σ type spin orbital) parallel to methylene plane localized at carbene centre (see Fig. 5C). The calculated D value of s-Z was larger than that of s-E, while E values of s-Z were smaller than that of s-E (Table 1). These results were consistent with experimental ones. Magnetic axis and spin orbitals are shown in Fig. 5A. As is already pointed by R.S. Hutton et al. [40], spin orbitals spread into Z-axis of the s-E isomer and the corresponding spin orbitals spread over XZ direction of the s-Z isomers. These spin orbitals clearly shows that the difference in delocalization direction affects the D value. The UB3LYP/6-31G calculated the s-E isomer to be more stable than s-Z by $0.207\ \mathrm{kcal\ mol}^{-1}$. The signal rates of s-$Z$/s-E in EPR are

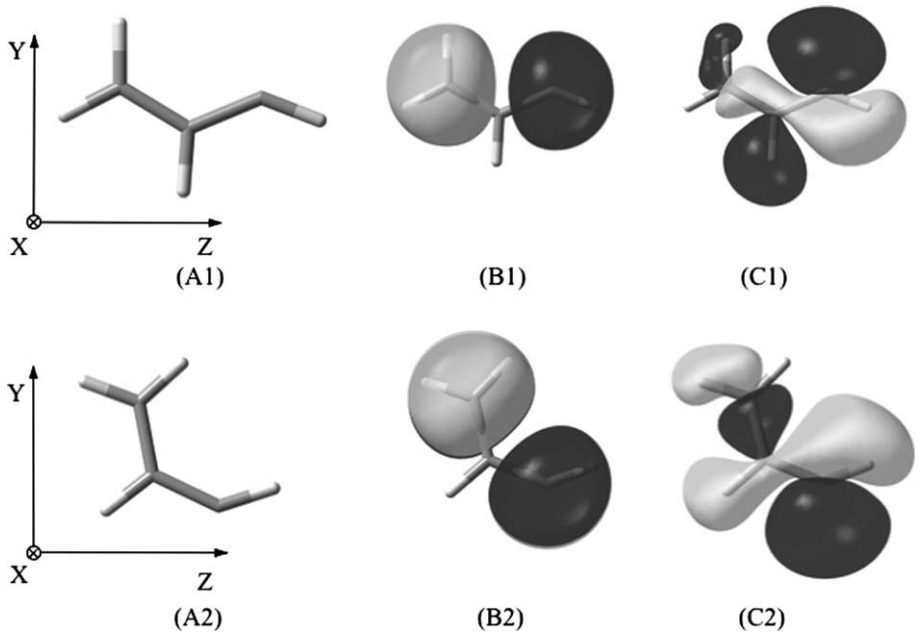


Fig. 5. Vinylcarbene of s-*E* (1) and s-*Z* (2) isomers. Each optimized molecular structures with their magnetic axes (A) and two spin orbitals (B, C).

0.05–0.65 depending on temperature and solvents. This experimental result agrees with our calculation result, showing s-*E* is thermodynamically more stable.

4.4. Phenylcarbene

The ground state structure of phenylcarbene is investigated by ZFSs. The molecular structure of phenylcarbene is considered to be either: the phenyl group is parallel or vertical to carbene C–H plane (denoted by **q0** and **q90**, respectively). Each of these structures wass theoretically optimized. It was revealed that **q0** was more stable than **q90** by 4.335 kcal mol^{-1}. The stable optimized structure **q0** was in agreement with other ab initio calculation results by Geise et al. [41]. For isomers **q0** and **q90**, $(D,\ E) = (0.5193, -0.0346)$ cm^{-1} and $(0.6005, -0.0308)$ cm^{-1}, respectively. The D for **q0** was closer to the experimental value $|D| = 0.5150$ cm^{-1}, while the experimental value $|E| = 0.024$ cm^{-1} was smaller than the calculated results. These spin orbitals for each isomer resembled each other and ZFS values were relatively equal (Fig. 6).

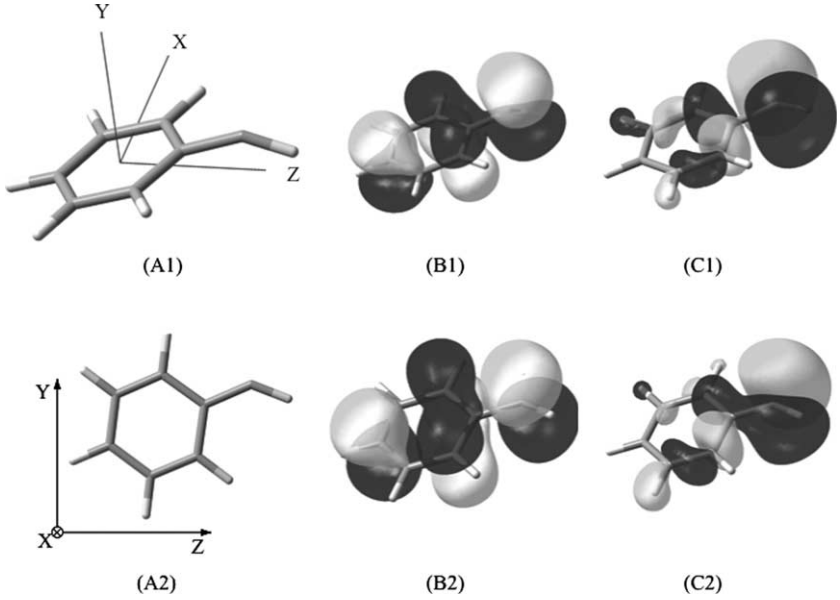


Fig. 6. Phenylcarbene of **q90** (1) and **q0** (2). Each optimized molecular structures with their magnetic axes (A) and two spin orbitals (B, C).

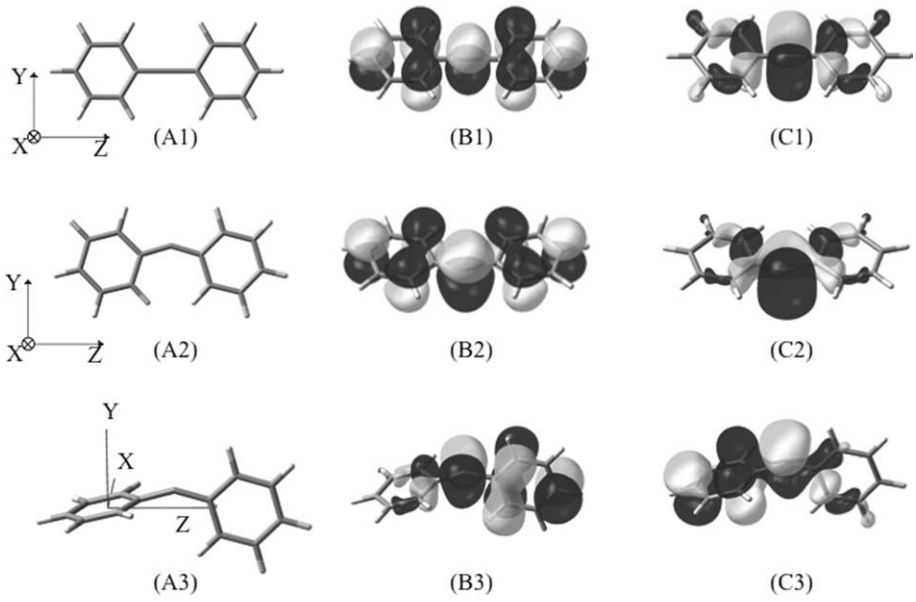


Fig. 7. Structures of diphenylcarbene: **a1** (1), **a2** (2) and **b** (3). Each optimized molecular structures with their magnetic axes (A) and two spin orbitals (B, C).

4.5. Diphenylcarbene

The molecular structure of diphenylcarbene is classical problem in EPR studies [5,17,18,31,43]. There are three conceivable structures. The first one (**a1**) is that phenylcarbenes are parallel each other and carbene centre is liner, i.e., $\theta = 0°$ (Fig. 7-2). The second one (**a2**) is that **a1** is bent at carbene centre in the phenyl ring plane so as the whole structure is within one plane (Fig. 7-1). The third one (**b**) is that the phenyl ring is vertical each other and carbene centre is bent (Fig. 7-3). The experimental ZFS values proposed that ground state is **a2.** (The most stable structure seems to **b**, because two spin orbitals at carbene centre can spread over each phenyl rings) We then decide the structure theoretically, especially using the calculated ZFS values.

In optimizing the forth geometry **a1**′, which is bent at carbene centre in the vertical direction, **a1**′ fell into the geometry **a1** and was revealed to be unstable. The angle θ optimized to be 147.0° and 149.0° for **a2** and **b**, respectively. The most stable structure of these three structures was decided to be **a2** by UB3LYP//6-31G. Energy gap between **a2** and **a1** was 85.58 kcal mol^{-1}, and that between **a2** and **b** were 81.28 kcal mol $^{-1}$. In **a1** and **a2**, one spin orbital vertical to the phenyl ring was delocalized onto π-orbitals over both phenyl rings and the other spin orbital was localized at the carbene centre. The carbene centre was in line and $E \approx 0$ at the structure **a1**. ZFS values were as $(D, E) = (0.3740, -0.00185)$ cm^{-1} and $(0.3774, -0.01657)$ cm^{-1} for **a1** and **a2**, respectively. On the other hand, the spin orbital at the carbene centre was delocalized over the next phenyl rings each other at the structure **b**. And the D value is rather smaller because average distances between spins are relatively longer than **a1** and **a2**. ZFS values for **b** were evaluated to be $(D, E) = (0.3569, -0.01254)$ cm^{-1}, while Experimental ZFS values are $|D| = 0.4055$ cm^{-1} and $|E| = 0.0194$ cm^{-1} [39]. Spin orbitals and magnetic axis are shown in Fig. 7. The most stable structure of phenylcarbene was estimated as **a2**, which reproduces experimental values. It is proved that molecular structure can be determined from the ab initio calculation of ZFS values.

5. Conclusion

The results of this approach were in good agreement with experimental values at moderate computational cost. By using this method, theoretical applications to organic biradicals are further examined for carbene structures, isomers of vinylcarbenes and diphenylcarbenes. We showed this calculation procedure was accurate enough for these the ZFS calculations and effective for the theoretical investigations for organic radicals. This means that high spin states in organic radicals are close to that of the single particle picture. It was also found that the SSC between spin orbitals are the dominant factor for the ZFS and the contributions from the SOC to the ZFS will be vanishingly small. This method has been quit valid in studies of organic ferromagnets.

Acknowledgement

This work has been supported by the 21 Century COE program entitled 'The Creation of Integrated Eco-Chemistry' in Osaka University and Grants-in-Aid for

Scientific Research on Priority Areas (Nos. 16750049 and 14204061) from Ministry of Education, Culture, Sports, Science and Technology, Japan.

References

[1] Y. Teki, S. Miyamoto, M. Nakatsuji, Y. Miura, J. Am. Chem. Soc. 123 (2001) 294.
[2] Y. Teki, S. Miyamoto, K. Iimura, M. Nakatsuji, Y. Miura, J. Am. Chem. Soc. 122 (2000) 984.
[3] H. Tomioka, E. Iwamoto, H. Itakura, K. Hirai, Nature 412 (2001) 626.
[4] T.J. LePage, R. Breslow, J. Am. Chem. Soc. 109 (1987) 6412.
[5] J.S. Miller, J.C. Calabrese, H. Rommelmann, S.R. Chittipeddi, J.H. Zhang, W.M. Reiff, A.J. Epstein, J. Am. Chem. Soc. 109 (1987) 769.
[6] M. Saunders, R. Berger, A. Jaffe, J.M. McBride, J. O'Neill, R. Breslow, J.M. Hoffman Jr., C. Perchonock, E. Wasserman, R.S. Hutton, V.J. Kuck, J. Am. Chem. Soc. 95-9 (1973) 3017.
[7] Y. Teki, T. Takui, K. Itoh, H. Iwamura, K. Kobatashi, J. Am. Chem. Soc. 108 (1986) 2147.
[8] S. Karasawa, H. Kumada, N. Koga, H. Iwamura, J. Am. Chem. Soc. 123 (2001) 9685.
[9] K. Itoh, Chem. Phys. Lett. 1 (1967) 235.
[10] E. Wasserman, R.S. Hutton, Acc. Chem. Res. 10 (1977) 27.
[11] Z. Havlas, J.W. Downing, J. Michl, J. Phys. Chem. A 102 (1998) 5681.
[12] O. Vahtras, O. Loboda, B. Minaev, H. Agren, K. Ruud, Chem. Phys. 279 (2002) 133.
[13] J. Mahlmann, M. Klessinger, Int. J. Quantum Chem. 77 (2000) 446.
[14] Z. Havlas, J. Michl, J. Mol. Struct. Theochem. 398–399 (1997) 281.
[15] W. Sander, G. Bucher, S. Wierlacher, Chem. Rev. 93 (1993) 1583.
[16] G. Breit, Phys. Rev. 35 (1930) 1447.
[17] E. Wasserman, L.C. Snyder, W.A. Yager, J. Chem. Phys. 41-6 (1964) 1763.
[18] I.V. Khudyakov, Y.A. Serebrennikov, N.J. Turro, Chem. Rev. 93 (1993) 937.
[19] R. McWeeny, Spins in Chemistry, Dover pub. Inc., Mineola, New York, 2004.
[20] R. Takeda, S. Yamanak, M. Shoji, K. Yamaguchi, Density functional study of zero-field splitting, Polyhedron (in press).
[21] M. Shoji, Y. Nishiyama, Y. Maruno, K. Koizumi, Y. Kitagawa, S. Yamanaka, T. Kawakami, M. Okumura, K. Yamaguchi, Int. J. Quantum Chem. 100 (2004) 887.
[22] M. Shoji, T. Hamamoto, K. Koizumi, H. Isobe, Y. Kitagawa, Y. Takano, S. Yamanaka, K. Yamaguchi, Theoretical study on the magnetic interactions of active site in hemerythrin, (in press).
[23] S. Obara, A. Saika, J. Chem. Phys. 89 (1988) 1540.
[24] S. Obara, A. Saika, J. Chem. Phys. 84 (1986) 3963.
[25] S. Obara, A. Saika, J. Chem. Phys 89 (1988) 1540.
[26] M. Honda, K. Sato, S. Obara, J. Chem. Phys. 94 (5) (1991) 3790.
[27] M.J. Frisch, G.W. Trucks, H.B. Schlegel, G.E. Scuseria, M.A. Robb, J.R. Cheeseman, V.G. Zakrzewski, J.A. Montgomery Jr., R.E. Stratmann, J.C. Burant, S. Dapprich, J.M. Millam, A.D. Daniels, K.N. Kudin, M.C. Strain, O. Farkas, J. Tomasi, V. Barone, M. Cossi, R. Cammi, B. Mennucci, C. Pomelli, C. Adamo, S. Clifford, J. Ochterski, G.A. Petersson, P.Y. Ayala, Q. Cui, K. Morokuma, N. Rega, P. Salvador, J.J. Dannenberg, D.K. Malick, A.D. Rabuck, K. Raghavachari, J.B. Foresman, J. Cioslowski, J.V. Ortiz, A.G. Baboul, B.B. Stefanov, G. Liu, A. Liashenko, P. Piskorz, I. Komaromi, R. Gomperts, R.L. Martin, D.J. Fox, T. Keith, M.A. Al-Laham, C.Y. Peng, A. Nanayakkara, M. Challacombe, P.M.W. Gill, B. Johnson, W. Chen, M.W. Wong, J.L. Andres, C. Gonzalez, M. Head-Gordon, E.S. Replogle, J.A. Pople, GAUSSIAN 98, Revision A.11.3, Gaussian, Inc., Pittsburgh, PA, 2002.
[28] P.C. Hariharan, J.A. Pople, Theo. Chem. Acta. 28 (1973) 213.
[29] W.J. Hehre, R. Ditchdield, J.A. Pople, J. Chem. Phys. 56 (1972) 2257.
[30] M. Shoji, T. Taniguchi, T. Kawakami, K. Yamaguchi, Polyhedron 22 (2003) 2067.
[31] E. Iwamoto, K. Hirai, H. Tomioka, J. Am. Chem. Soc. 125 (2003) 14664.
[32] H.V. Willigen, J.A.M.V. Broekhoven, E.D. Boer, Mol. Phys. 12–6 (1967) 533.
[33] R.D. Bach, R.F. Richter, J. Am. Chem. Soc. 94–13 (1972) 4749.
[34] J.S. Miller, D.A. Dixon, J.C. Calabrese, C. Vazquez, P.J. Krusic, M.D. Ward, E. Wasserman, R.L. Harlow, J. Am. Chem. Soc. 112 (1990) 381.
[35] J. Thomaides, P. Maslak, R. Breslow, J. Am. Chem. Soc. 110 (1988) 3970.
[36] P.J. Krusic, E. Wasserman, J. Am. Chem. Soc. 113 (1991) 2322.
[37] M. Glasbeek, J.D.W. van Voorst, G.J. Hoijtink, J. Chem. Phys. 45 (1966) 1852.
[38] L. Gherghel, J.D. Brand, M. Baumgarten, K. Mullen, J. Am. Chem. Soc. 121 (1999) 8104.
[39] R.W. Murray, A.M. Trozzolo, E. Wasserman, W.A. Yager, J. Am. Chem. Soc. 84 (1962) 3213.
[40] R.S. Hutton, M.L. Manion, H.D. Roth, E. Wasserman, J. Am. Chem. Soc. 96–14 (1974) 4680.
[41] C.M. Geise, C.M. Hadad, J. Org. Chem. 65 (2000) 8356.
[42] E. Wasserman, A.M. Trozzolo, W.A. Yager, R.W. Murray, J. Chem. Phys. 40 (1964) 2408.
[43] A.M. Trozzolo, E. Wasserman, in: R.A. Moss, M. Jones Jr. (Eds.), Carbenes, John Wiley & Sons, Inc., New York, 1987, pp. 185–206 (Chapter 5).
[44] J. Nolte, F. Temps, H.G. Wagner, M. Wolf, T.J. Sears, J. Chem. Phys. 100 (1994) 8706.
[45] O.L. Chapman, R.J. McMahon, P.R. West, J. Am. Chem. Soc. 106 (1984) 7973.
[46] O.L. Chapman, R.S. Sheridan, J.P. LeRoux, J. Am. Chem. Soc. 100 (1978) 6245.
[47] D.J. Graham, T.S. Lin, Chem. Phys. 73 (1982) 411.
[48] E. Wasserman, L. Barash, A.M. Trozzolo, R.M. Murray, W.A. Yager, J. Am. Chem. Soc. 86 (1964) 2304.
[49] R.N. Dixon, Can. J. Phys. 37 (1959) 1171.

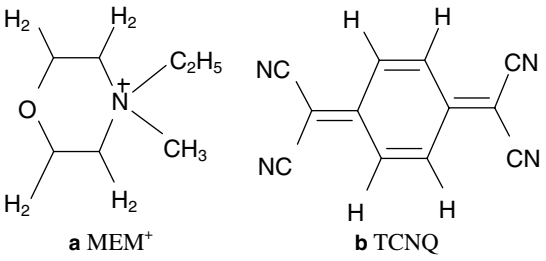


Fig. 1. Molecular structure of (a) MEM and (b) TCNQ.

temperature and orientation of the crystal. The ESR spectrum is significantly deformed by pressurization and the experimental results suggest that there are some different kinds of spins in the salt under pressure.

2. Experimental

2.1. Sample preparation

The salt, MEM–$[TCNQ]_2$, is made by a standard method and its single crystals are grown by slow cooling of acetonitrile solution of the salt. Being cut into a small rectangular single crystal of about $0.3 \times 0.3 \times 0.5$ mm^3, it is fixed in Stycast 1226 as schematically shown in Fig. 2(a), where a polyester sheet is used to arrange the crystal axis of the single crystal. The sample used for the ESR measurement is 1.0 mm in diameter and 1.0 mm in length. A very small piece of lead is inserted near the single crystal in order to determine the pressure by observing the change of the superconducting transition temperature. The uniaxial pressure is applied along the length of the sample.

2.2. ESR measurements under uniaxial pressure

The ESR spectra under uniaxial pressure were measured by a conventional X-band ESR instrument, JOEL JES-RE2X, with a cryostat and a hand-made pressure cell in the temperature range from 1.5 to 300 K. As shown in Fig. 2(b), the pressure cell is pressure-clamping type and made by ourselves. It is made of a kind of hard plastic material supplied by Nippon Polypenco Ltd. As the cell is inserted into the center of the cylindrical cavity of the ESR instrument, it should be made of non-magnetic, non-conductive and low-dielectric loss material. We tested some kind of material supplied by Nippon Polypenco Ltd. and selected suitable one for the pressure cell. As the cell is rather small, we need skilful techniques to make it. The maximum pressure obtained in the cell is up to 2 kbar. However, more pressure is not necessarily indispensable for the salt, MEM–$[TCNQ]_2$, because the salt shows the significant change in the susceptibility even below 2 kbar.

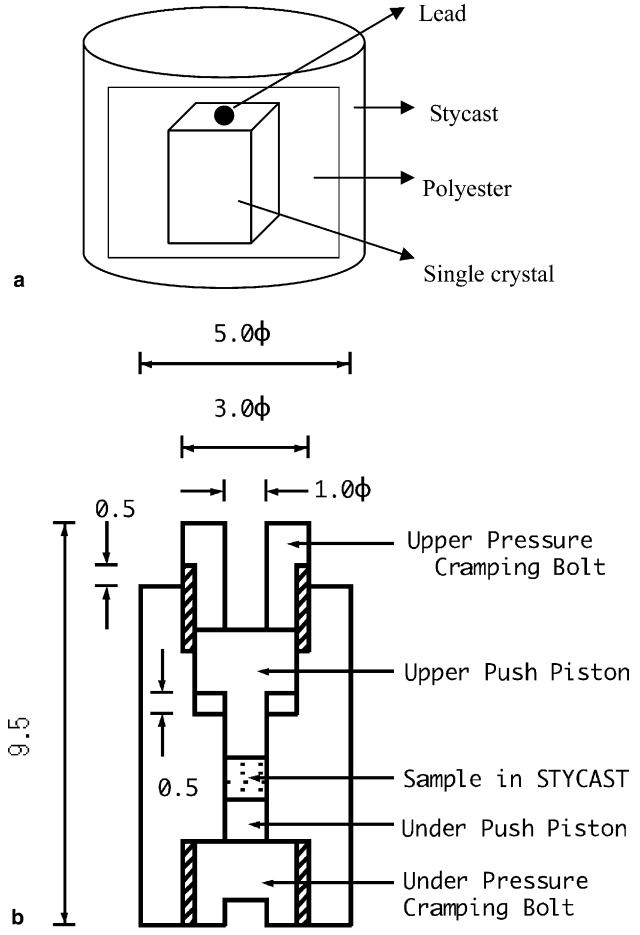


Fig. 2. (a) Schematic figure of the sample for the measurement of ESR under uniaxial pressure. A single crystal is fixed in Stycast 1226 with a small piece of lead for pressure measurement. The sample is 1.0 mm in diameter and 1.0 mm in length. (b) Design of a pressure cell for the ESR measurement under uniaxial pressure. The cell is made of a kind hard plastic material supplied by Nippon Polypenco Ltd.

3. Results and discussion

Under ambient pressure (1 bar), each ESR spectrum of a single crystal of the salt shows a single and symmetrical absorption at any temperatures and orientations of the crystal, though the linewidth of the absorption rather depends on the temperature and orientation. Even if a single crystal is fixed in Stycast 1226, the ESR spectrum of the crystal at ambient pressure is not so different from that of the crystal free from Stycast. No ESR absorption resulting from Stycast is observed at any temperatures. On the other hand, the ESR spectrum is deformed by pressurization. The ESR spectra at 300 K of a single crystal under uniaxial pressure of 1 kbar along *a*-axis are shown in Fig. 3, where the angle is the one between *c*-axis and the external field. The ESR spectrum under uniaxial pressure is deformed and rather different from that under ambient pressure. There are at least two absorptions in the

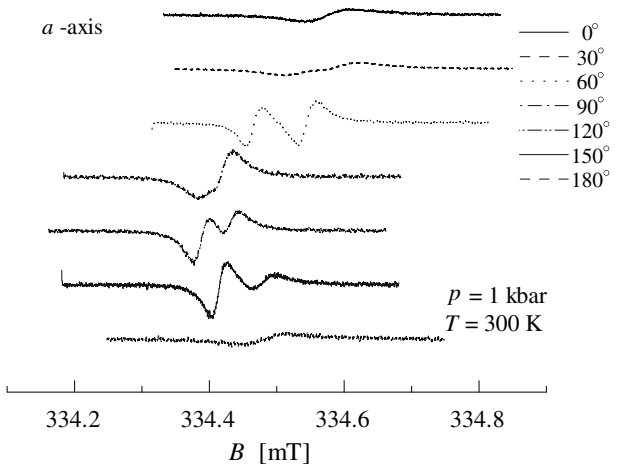


Fig. 3. Angular variations of the ESR spectrum at 300 K of a single crystal under uniaxial pressure of 1 kbar along *a*-axis.

spectrum and the spectrum fairly depends on the orientation. In the liquid helium temperature region, the ESR spectrum becomes more complicated and also significantly depends on the orientation for the external field. The spectrum shown in Fig. 4(a) is an example which shows three absorptions.

The deformed ESR spectrum at low temperatures can be well separated into three independent single absorptions under the assumption that the spectrum is composed of three independent Lorentzian absorptions as follows:

$$I(B) = \frac{a}{1 + b(B - B_0)^2}$$

(Lorentzian absorption),

$$I'(B) = \frac{-2ab(B - B_0)}{[1 + b(B - B_0)^2]^2}$$

(The derivative form of Lorentzian absorption).

The parameters a and b are related to the intensity and the linewidth of the ESR absorption, respectively. The parameter B_0 is the center field of the ESR absorption. These parameters of the three Lorentzian absorptions were determined so as to fit the measured ESR spectrum at each temperature and orientation. The obtained three absorptions (Absorp.-1, -2 and -3) at 4.2 K are shown in Fig. 4(b) with the measured ESR spectrum. The fitting seems to be very well. The same analyses were carried out and the temperature dependence of the linewidth and intensity of these three absorptions were obtained.

At low temperatures, both of the intensity and linewidth of Absorp.-3 fairly increase as the temperature is decreased, which suggests that Absorp.-3 results from the free spins produced by pressurization. On the other hand, the other two absorptions, Absorp.-1 and Absorp.-2, seem to result from the spin-pairs.

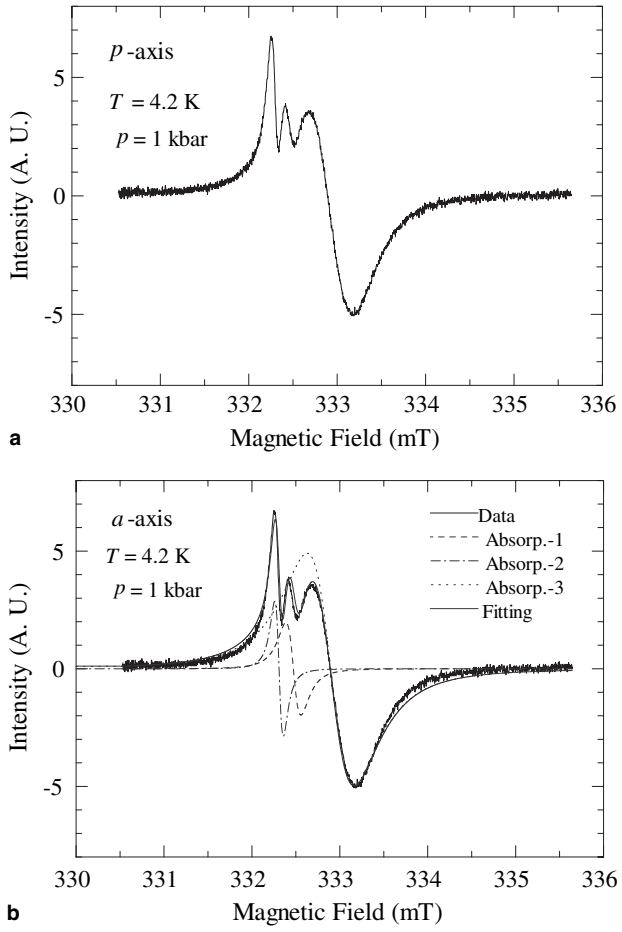


Fig. 4. (a) ESR Spectrum at 4.2 K of a single crystal under uniaxial pressure of 1 kbar along *a*-axis. (b) ESR Spectrum shown in (a) is separated into three single absorptions.

4. Conclusion

The ESR spectrum of a single crystal of a salt, MEM–$[TCNQ]_2$, under uniaxial pressure of 1 kbar is rather deformed compared to that under ambient pressure and it fairly depends on the temperature and orientation of the crystal. The spectrum at low temperatures can be well separated into three independent absorptions, Absorp.-1, -2 and -3. The intensity and linewidth of Absorp.-3 increase with decreasing temperature, which suggests that the origin of the increase of the static susceptibility at low temperatures is the free spins and related to Absorp.-3. The other two absorptions, Absorp.-1 and Absorp.-2, seem to result from the spin-pairs.

Acknowledgements

This work was partially supported by a Grant-in-Aid for Scientific Researches from the Ministry of Education, Culture, Sports, Science and Technology, Japan. The hard plastic material used for the pressure cell for the ESR measurements under uniaxial pressure was

supplied by Nippon Polypenco Limited. The ESR measurements were carried out at The center for Instrumental Analysis, Kyushu Institute of Technology.

References

[1] J.W. Bray, L.V. Interrante, I.S. Jacobs, J.C. Bonner, Extended Linear Chain Compound, vol. 3, Plenum Press, New York, 1983, pp. 353.
[2] S. Huizinga, J. Kommandeur, G.A. Sawatzky, B.T. Thole, K. Kopinga, W.J.M. de Jonge, J. Roos, Phys. Rev. B19 (1979) 4723.
[3] J.C. Bonner, M.E. Fisher, Phys. Rev. 135 (1964) A640.
[4] H. Nojiri, T. Hamamoto, O. Fujita, J. Akimitsu, S. Takagi, M. Motokawa, J. Magn. Magn. Mater. 177–181 (1998) 687.
[5] D. Bloch, J. Voiron, C. Vettier, J.W. Bray, S. Oostra, Physica 119B (1983) 43.
[6] S. Takagi, Y. Matsushita, Y. Yoshida, H. Deguchi, Mol. Cryst. Liq. Cryst. 376 (2002) 377.

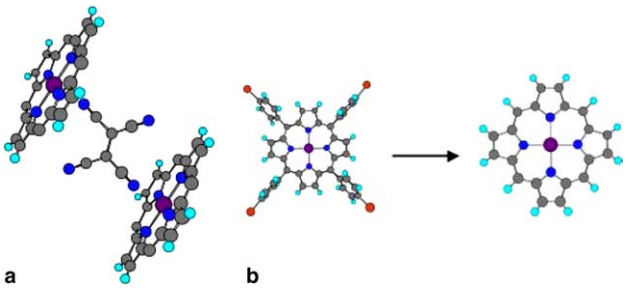


Fig. 1. Structure of the reduced model complex which is calculated in this work (a) and the way to cut ligands from the porphyrin ring (b).

In this study, we introduce a model complex which consists of two porphyrin rings and one TCNE as illustrated in Fig. 1(a). We calculate the electronic states of the model complex by using unrestricted hybrid DFT (UB3LYP, UB2LYP [5]) and UHF. We compared calculated results with experimental one. In the model complex MnTBrPP–TCNE ring was reduced to the manganese porphyrin as illustrated in Fig. 1(b). All calculations were performed by using GAUSSIAN 98 program package [6].

2. Theoretical background

2.1. Effective exchange integrals

The Heisenberg Hamiltonian is employed to describe localized spin interaction defined as

$$\widehat{H} = -2\sum_{a,b} J_{ab}\mathbf{S_a}\mathbf{S_b}, \tag{1}$$

where $\mathbf{S_c}$ ($\mathbf{c} = \mathbf{a}$ and $\mathbf{b}$) denotes the spin operator at the site c, and J_{ab} is the effective exchange integrals between sites a and b. The 3-site model Hamiltonian can be written as

$$H = -2\sum_{ab} J_{ab}\mathbf{S_a}\mathbf{S_b} = -2J(\mathbf{S_1}\mathbf{S_2} + \mathbf{S_2}\mathbf{S_3}). \tag{2}$$

The spin site of $\mathbf{S}_1$ and $\mathbf{S}_3$ are on the manganese, and $\mathbf{S}_2$ is on TCNE as illustrated in Fig. 2. The effective exchange integral between site 1 and 3 (J_{13}) assumed to be zero, and J_{12} equals to J_{23}. This assumption comes from the fact that experimental result was discussed only the neighboring spin sites in the one-dimensional chain molecule. The manner of spin alignment is shown in Fig. 3. The total spin operator is given by:

$$\mathbf{S} = \mathbf{S_1} + \mathbf{S_2} + \mathbf{S_3}, \tag{3}$$

$$\mathbf{S^2} = \mathbf{S_1^2} + \mathbf{S_2^2} + \mathbf{S_3^2} + \mathbf{2S_1S_2} + \mathbf{2S_2S_3} + \mathbf{2S_1S_3}. \tag{4}$$

Using the expression of (4), the model Hamiltonian can be written as

$$-2J(\mathbf{S_1}\mathbf{S_2} + \mathbf{S_2}\mathbf{S_3}) = J(-\mathbf{S^2} + \mathbf{S_1^2} + \mathbf{S_2^2} + \mathbf{S_3^2} + \mathbf{2S_1S_3}). \tag{5}$$

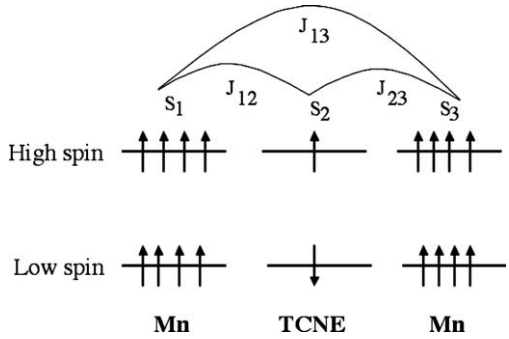


Fig. 2. The two types of electron configuration namely, high-spin and low-spin states.

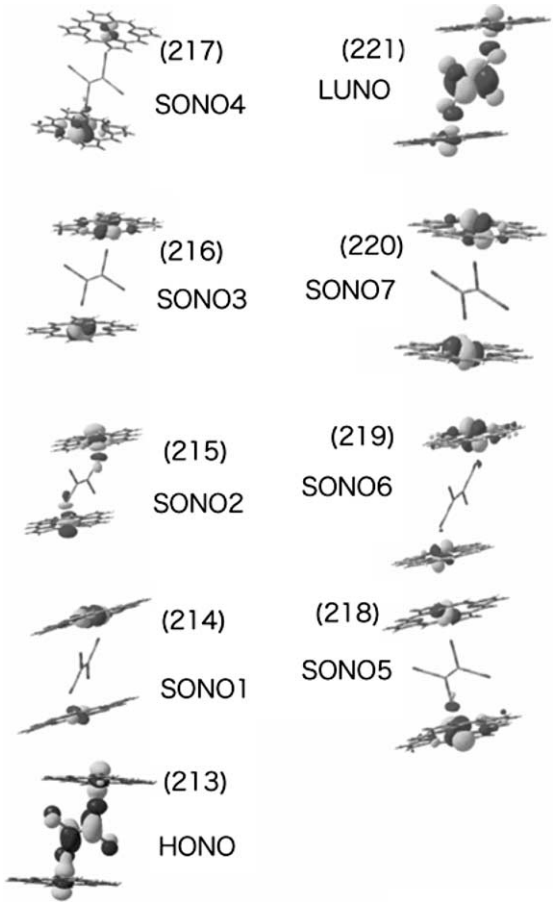


Fig. 3. The picture of natural orbitals and their orbital number.

Then we can obtain energy expectation values for the low spin (LS) and high spin (HS) states as:

$$E_{LS} = J(-\langle\mathbf{S^2}\rangle_{LS} + \langle\mathbf{S_1^2}\rangle_{LS} + \langle\mathbf{S_2^2}\rangle_{LS} + \langle\mathbf{S_3^2}\rangle_{LS} + 2\langle\mathbf{S_1S_3}\rangle_{LS}), \tag{6}$$

$$E_{HS} = J(-\langle\mathbf{S^2}\rangle_{HS} + \langle\mathbf{S_1^2}\rangle_{HS} + \langle\mathbf{S_2^2}\rangle_{HS} + \langle\mathbf{S_3^2}\rangle_{HS} + 2\langle\mathbf{S_1S_3}\rangle_{HS}). \tag{7}$$

The $\langle\mathbf{S_1S_3}\rangle$ term is the same in both high and low spin state as illustrated in Fig. 2.

From Eqs. (6) and (7) we can derive approximate spin projected (AP) J scheme

$$J = \frac{E_{LS} - E_{HS}}{\langle \mathbf{S^2} \rangle_{HS} - \langle \mathbf{S^2} \rangle_{LS}}. \quad (8)$$

2.2. Computational methods

2.2.1. Hybrid density functional theory

The Kohn–Sham (KS) density functional theory (DFT) [7] is one of the most popular approaches in computational chemistry. The energy expression is given by

$$E = T_0[\{\psi_i\}] + V_{Ne}[\rho] + V_{clmb}[\rho] + E_{xc}[\rho], \quad (9)$$

where T_0, V_{Ne} and V_{clmb} are the kinetic energy of electron, nuclear attraction energy and classical coulomb term, respectively. The exchange correlation potentials are generally defined by

$$E_{xc} = C_1 E_X^{HF} + C_2 E_X^{Slater} + C_3 E_X^{Becke88} + C_4 E_C^{VWN} + C_5 E_C^{LYP}, \quad (10)$$

where E_X^{HF}, E_X^{Slater}, and $E_X^{Becke88}$ denote the HF, Slater, and Becke's exchange functionals, respectively. E_C^{VWN} and E_C^{LYP} denote the Vosko, Wilk, and Nusair (VWN) [8] and Lee, Yang, and Parr (LYP) [9] correlation functionals, respectively. $\{C_i\}_{i=1-5}$ are the parameters. They are 0.2, 0.8, 0.72, 1.0, 0.81 and 0.5, 0.5, 0.5, 1.0, 1.0, for UB3LYP and UB2LYP, respectively [10].

2.2.2. The basis sets

Calculations were performed by the use of Huzinaga's MIDI + P basis sets (533(21)/53(21)/(41)) for transition metals and 6-31G* basis sets by Pople et al. for other molecules [11].

2.3. Natural orbital analysis

In order to understand the magnetic interaction between manganese and TCNE, it is desirable to use the picture of the molecular orbital because the Heisenberg model is closely related to the valence-bond picture. The natural orbital (NO) is determined by diagonalizing their first-order density matrix as

$$\rho(r, r') = \sum n_i \phi_i(r) \phi_i(r')^*, \quad (11)$$

where n_i and ϕ_i denote the occupation number and NO, respectively. The occupation numbers of bonding and antibonding orbitals take 2.0 and 0.0, respectively. Occupation numbers of magnetic NOs take near 1.0. The bonding magnetic orbitals are generally given by the in- and out-of phase combination of the bonding (ϕ_i) and antibonding (ϕ_i^*) orbitals

$$\psi_i^{\pm} = \cos\theta \phi_i \pm \sin\theta \phi_i^*, \quad (12)$$

where θ is the orbital mixing coefficient. The mixing provides magnetic orbitals (ψ_i^+ and ψ_i^-) which are localized on different magnetic sites. The orbital overlap (T_i) [12,13] between magnetic orbitals is defined to elucidate their localizability.

$$T_i = \langle \psi_i^+ | \psi_i^- \rangle = \cos^2\theta - \sin^2\theta = \cos 2\theta. \quad (13)$$

The occupation numbers of NOs are given by the orbital overlap as

$$n_i = 1 + T_i. \quad (14)$$

2.4. Chemical indices

Several chemical indices have been introduced by the use of occupation numbers of SONO in order to investigate character of magnetic orbitals. Using chemical indices we can elucidate a nature of a chemical bond by broken symmetry (BS) calculations. Chemical indices are equally defined both by BS and symmetry adapted (SA) methods. The examples of SA methods are CI, CASCI, and CASSCF.

The effective bond order (b_i) [12,13] is defined by

$$b_i = \frac{n_i - n_i^+}{2} = T_i. \quad (15a)$$

It varies from zero to one, depending on the strength of a covalent bond. The information entropy [14–16] is employed to express the character of a chemical bond. The Jaynes information entropy (I_i) is modified as the measure of a chemical bond.

$$I_i = \frac{2\ln 2 - n_i \ln n_i}{2\ln 2}. \quad (15b)$$

Since α and β spins occupy the different MOs in Eq. (12), under the BS approximation, the spin density index (Q_i) [12,13] appears only in the LS state as

$$Q_i = \sqrt{n_i(2 - n_i)} = \sqrt{1 - T_i^2}. \quad (15c)$$

This means that the α and β spins are populated on each magnetic orbital. The unpaired electron density (U_i) [18] is defined as the deviation of SA or BS wave functions from the single Slater determinant and can be expressed as

$$U_i = n_i(2 - n_i) = 1 - T_i^2. \quad (15d)$$

The U_i value is responsible for the electron localization via the Coulomb repulsion in diradical species. The diradical character (Y_i) is defined by the weight of the doubly excited configuration (W_D) as

$$Y_i = 2W_D = 1 - \frac{2T_i}{1 + T_i^2} = \frac{n_i^2 - 4n_i + 4}{n_i^2 - 2n_i + 2} \quad (15e)$$

3. Result and discussion

3.1. Effective exchange integrals

We performed ab initio calculation of the manganese porphyrin dimer which is a reduced model of one dimensional chain molecules. We deduced total energy and the square of spin magnitude, $\langle \mathbf{S}^2 \rangle$ from calculation for the estimation of effective exchange integrals. The J values calculated by three calculation methods are shown in Table 1.

All results show antiferromagnetic coupling, i.e., all of the J value are negative. The experimental value is $-178\ \mathrm{cm}^{-1}$ by Seiden expression model [2]. The UB3LYP calculation reproduced the antiferromagnetic nature of chain magnet. The strength of antiferromagnetic interactions of the model complexes increase in the order $|J(\mathrm{APUHF})| < |J(\mathrm{APUB2LYP})| < |J(\mathrm{APUB3LYP})|$. This tendency stems from a degree of correction in dynamical correlation effect and it is consistent with our previous result [17].

3.2. Spin and charge density populations

Table 2 shows the spin density population in case of low-spin state. The table shows the result of three methods, namely, UHF, UB2LYP and UB3LYP. The spin density populations on TCNE are net spin on itself. The magnitudes for one α spin ($S = 1/2$) and β spin ($S = -1/2$) are defined to be 1.0 and −1.0, respectively. Here, we define the spin populations on manganese as positive and define the spin populations on TCNE as negative. The spin population shows that manganese has four spin moments ($S = 4/2$) and TCNE has one spin moment ($S = 1/2$). This shows clearly the electronic structure of $\mathrm{Mn^{III}}$–$\mathrm{TCNE^{-}}$–$\mathrm{Mn^{III}}$.

Table 3 shows the Mulliken charge density populations of the results by three methods. Charge density populations labeled TCNE and porphyrin in the table are net charge. The charge density populations indicate $\mathrm{Mn^{III}}$ and $\mathrm{TCNE^{-}}$.

Table 1
The calculated J (in cm^{-1}) values by three methods

Method	UHF	UB2LYP	UB3LYP
	−26.67	−52.21	−106.7

Table 2
Spin density population on Mn and TCNE

	Mn(1)	Mn(2)	TCNE
UB3LYP	3.99	3.99	−0.86
UB2LYP	4.11	4.11	−0.90
UHF	4.25	4.25	−0.80

The value of TCNE is summed for all atoms which construct TCNE.

Table 3
Charge density population on Mn, TCNE and porphyrin ring

	Mn(1)	Mn(2)	TCNE	Porphyrin
UB3LYP	1.20	1.20	−0.56	−0.84
UB2LYP	1.43	1.43	−0.68	−1.18
UHF	1.79	1.79	−0.80	−1.78

The values of TCNE and porphyrin ring are summed for all atoms which construct them.

The charge density populations on manganese do not correspond to its formal charge III, but it is about 1.5 indeed. This tendency comes from donations by porphyrin ring. This is consistent with our previous result which used manganese(III) porphyrin dimer [17]. The population of charge density is symmetric.

3.3. Gross orbital population

Table 4 shows the gross orbital population of d-orbitals of manganese for low-spin state. The calculation method is UB3LYP. Since Mn(III) have four electrons in five d-orbitals, it has one hole in the d-orbitals. Table 4 shows that the hole is in $d_{x^2-y^2}$ which orients to the porphyrin ring. This hole in $d_{x^2-y^2}$ orbital stems from the energy splitting due to the ligand field.

3.4. Natural orbital analysis and occupation number

The NOs and their orbital numbers are schematically depicted in Fig. 3. The numbers of NOs and their occupation numbers are shown in Table 5 in case of low-spin state. Fig. 3 depicts NOs of magnetic orbitals that have

Table 4
The gross orbital population for manganese d-orbital

	Mn(1)	Mn(2)
d_{z^2}	0.842	0.842
d_{xz}	0.824	0.824
d_{yz}	0.826	0.826
$d_{x^2-y^2}$	0.474	0.474
d_{xy}	0.799	0.799

The calculation method is UB3LYP.

Table 5
Occupation numbers and their chemical indices

The number of NO	Occupation number	Q_n	U_n	I_n	Y_n
221	0.70				
220	1.00	100	100	100	100
219	1.00	100	100	100	100
218	1.00	100	100	100	100
217	1.00	100	100	100	100
216	1.00	100	100	100	100
215	1.00	100	100	100	100
214	1.00	100	100	100	100
213	1.30	95	91	75	56

All chemical indices are multiplied by 100 and expressed in %.

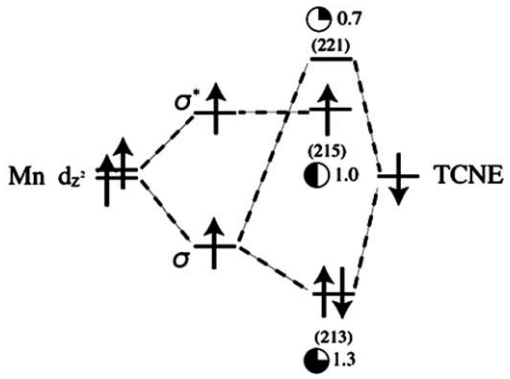


Fig. 4. Schematic view of orbitals. Their bond numbers and occupation numbers.

the occupation numbers around 1.0 (SONO) . The other NO's occupation number are almost 2.0 or 0.0. Eight electrons in d-orbitals of manganese, and one electron of TCNE are the origin of the nine NOs. The way of interaction between SONOs is shown in the pictures. Fig. 4 illustrates the way of construction of the σ-type bonding and antibonding SONOs. They are constructed from two electrons in d_{z^2} orbitals and one electron from TCNE. This one electron on TCNE is the result of charge transfer from manganese. First, two d_{z^2} orbitals on manganese make one bonding and one antibonding orbitals, namely in-phase and out-of-phase orbitals. Next, the in-phase orbital between two manganese interacts with the orbital on TCNE and three σ-type orbitals, bonding, nonbonding, and antibonding orbitals are exhibited.

The SONOs which have π and δ-type interactions take 1.0 in occupation numbers and do not interact with TCNE. This tendency stems from the ferrimagnetic behavior of the system, namely the net spin moment is not zero. From these results, we elucidated a ferrimagnetic structure of one-dimensional manganese porphyrin systems.

3.5. Chemical indices

Using the occupation number of magnetic orbitals, the chemical indices can be obtained. Table 5 shows the chemical indices such as information entropy (I), spin density index (Q), unpaired electron density (U), and diradical character (Y) are deduced from the occupation number of NOs. The orbital numbers of the NOs are from 213 to 220. The method of calculation is UB3LYP. The all chemical indices are expressed in percentage. The bonding interaction between manganese and TCNE occurs through the σ-type orbital, so our main interest is focused on the chemical indices of the number 213. Large Q and U values of the orbital number 213 show that spin density on manganese atom exists and the electron localization is significant. The Y value shows instability in chemical bonds. The smaller diradical character (56%) shows the slight stability of the orbital 213.

4. Conclusions

We discussed on the magnetic character of a manganese porphyrin dimer which is a reduced model of 5,10,15,20 tetrakis(4-bromophenyl)porphyrinatomanganese(III)tetracyanoethenide, ([MnTBrPP][TCNE]). The original one-dimensional chain molecules were converted into two manganese porphyrin and one TCNE. Ab initio calculations were performed to estimate the electronic structure and effective exchange integrals. Our model successfully reproduced the antiferromagnetic interactions and showed ferrimagnetic character. From the viewpoint of natural orbital analysis and its occupation number, the interaction between manganese and TCNE was through the σ-type orbitals.

Acknowledgments

This work has been supported by Grants-in-Aid for Scientific Research on Priority Areas (Nos. 16750049 and 14204061) from Ministry of Education, Culture, Sports, Science and Technology, Japan and by the financial support for the 21 Century COE program entitled "the Creation of Integrated EcoChemistry" in Osaka University.

References

[1] A. Bohm, C. Vazquez, R.S. McLean, J.C. Calabrese, S.E. Kalm, J.L. Manson, A.J. Epstein, J.S. Miller, Inorg. Chem 35 (1996) 3083.
[2] D.K. Rittenberg, A.M. Arif, J.S. Miller, J. Chem. Soc., Dalton. Trans (2000) 3939.
[3] W. Hibbs, D.K. Rittenberg, K. Sugiura, B.M. Burkhart, B.G. Morin, A.M. Arif, L. Liable-Sands, A.L. Rheingold, M. Sundralingam, A.J. Epstein, J.S. Miller, Inorg. Chem. 40 (2001) 1915.
[4] D.K. Rittenberg, J.S. Miller, Inorg. Chem 38 (1999) 4838.
[5] Y. Kitagawa, T. Soda, Y. Shigeta, S. Yamanaka, Y. Yoshioka, K. Yamaguchi, Int. J. Quant. Chem. 84 (2001) 592.
[6] M.J. Frisch, G.W. Trucks, H.B. Schlegel, G.E. Scuseria, M.A. Robb, J.R. Cheeseman, V.G. Zakrzewski, J.A. Montgomery Jr., R.E. Stratmann, J.C. Burant, S. Dapprich, J.M. Millam, A.D. Daniels, K.N. Kudin, M.C. Strain, O. Farkas, J. Tomasi, V. Barone, M. Cossi, R. Cammi, B. Mennucci, C. Pomelli, C. Adamo, S. Clifford, J. Ochterski, G.A. Petersson, P.Y. Ayala, Q. Cui, K. Morokuma, D.K. Malick, A.D. Rabuck, K. Raghavachari, J.B. Foresman, J. Cioslowski, J.V. Ortiz, B.B. Stefanov, G. Liu, A. Liashenko, P. Piskorz, I. Komaromi, R. Gompert, R.L. Martin, D.J. Fox, T. Keith, M.A. Al-Laham, C.Y. Peng, A. Nanayakkara, C. Gonzalez, M. Challacombe, P.M.W. Gill, B. Johnson, W. Chen, M.W. Wong, J.L. Andres, M. Head-Gordon,

E.S. Replogle, J.A. Pople, GAUSSIAN 98, Gaussian, Inc., Pittsburgh, PA, 1998.
[7] R.G. Parr, W. Yang, Density Functional Theory of Atoms and Molecules, Oxford University Press, 1989.
[8] S.H. Vosko, L. Wilk, M. Nusair, Can. J. Phys. 58 (1980) 1200.
[9] C. Lee, W. Wang, R.G. Parr, Phys. Rev. B 37 (1988) 785.
[10] Y. Kitagawa, T. Soda, Y. Shigeta, S. Yamanaka, Y. Yoshioka, K. Yamaguchi, Int. J. Quant. Chem. 84 (2001) 592.
[11] H. Tatewaki, S. Huzinaga, J. Chem. Phys. 71 (1979) 4339.
[12] M. Nishino, Y. Yoshioka, K. Yamaguchi, K. Mashima, K. Tani, A. Nakamura, J. Phys. Chem. A 101 (1997) 705.
[13] K. Yamaguchi, in: R. Carto, M. Klobukoeski (Eds.), Self-Consistent Field Theory and Applications, Elsevier, Amsterdam, 1990, p. 727.
[14] C.E. Shannon, Bell Syst. Tech. J. 27 (1948) 379.
[15] J.C. Ramirez, C. Soriano, R.O. Esquivel, R.P. Sagar, M. Ho, V.H. Smith Jr., Phys. Rev. A 56 (1997) 4477.
[16] Y. Kitagawa, T. Kawakami, K. Yamaguchi, Mol. Phys. 100 (2002) 1829.
[17] K. Yamaguhi, T. Fueno, Chem. Phys. 19 (1977) 35.
[18] K. Koizumi, M. Shoji, Y. Nishiyama, Y. Maruno, Y. Kitagawa, K. Soda, S. Yamanaka, M. Okumura, K. Yamaguchi, Int. J. Quant. Chem. 100 (2004) 943.

sometimes called the counterintuitive pulse method. However, this method has some attractive advantages on the formation of the pulse shape. Namely, it has very flexible conditions for the laser parameters such as amplitude, frequency, pulse width, and so on. Due to the robustness with respect to the laser parameters, we have already applied the STIRAP method [17–19] to the control of proton motion in some molecular systems with the hydrogen bond and the laser control of *cis–trans* isomerization reaction, and have showed that the STIRAP method is very effective and experimentally promising to the quantum control of molecular systems by laser pulses.

The ground state of molecules is usually a spin-singlet state ($|\mathbf{S}| = 0$), where up and down spins are in pairs, and in the exited state there appears the spin-triplet state ($|\mathbf{S}| = 1$) with two parallel spins. In the light absorption process in molecule, the singlet–triplet transition is generally forbidden by the spin selection rule. That is, the direct transition from the singlet ground state to a triplet excited state is not allowed by absorbing one photon. It is, however, well known that singlet and triplet states could be mixed due to the spin–orbit interaction in an excited state of molecules [20,21]. This spin–orbit coupling causes the intersystem crossing of the molecular excited states in the intramolecular relaxation process, and plays a very important role in the radiationless transition from a singlet state to a triplet state.

In this study, we pay attention to the role of the spin–orbit interaction in the light absorption process, and use this coupling to produce efficiently the triplet state from the singlet state. By the STIRAP simulation with the spin-mixed intermediate state, we simulate the complete transfer from a singlet ground state to a triplet excited state. This paper is organized as follows. In Section 2, we briefly summarize the electronic state calculation of Cl_2 molecule by taking into account the spin–orbit coupling. In Section 3, some numerical results of the STIRAP simulations for the control of singlet–triplet transition are shown, and Section 4 gives the concluding remarks.

2. Electronic state calculation of Cl_2 molecule

Let us briefly consider the origin of the spin–orbit interaction. In molecule, the electron with the spin angular momentum (**s**) and the electric charge (−e) moves around the atomic nucleus with the charge (+e). It could be considered that the atomic nucleus rotates around the electron with radius r and frequency v from the other point of view. Then the magnetic field and the electric current induced by the moving atomic nucleus at the position of the electron become $\mathbf{B} = \frac{\mu_0 I}{2r}\mathbf{n}$ and $I = e\frac{v}{2\pi r}$, respectively. Therefore

$$\mathbf{B} = \frac{\mu_0}{2r}\cdot\frac{ev}{2\pi r}\mathbf{n} = \frac{\mu_0}{4\pi m r^3}\mathbf{l}, \tag{1}$$

where **l** and **n** mean the angular momentum operator and its unit vector, respectively. This magnetic field interacts with the magnetic moment ($\boldsymbol{\mu}$) induced from the electron spin angular momentum (**s**), and this interaction energy is given by

$$H_{\mathrm{so}} = -\boldsymbol{\mu}\cdot\mathbf{B} = \left(\frac{\mu_{\mathrm{B}}\mu_0 e}{2\pi m r^3 \hbar}\right)(\mathbf{l}\cdot\mathbf{s}). \tag{2}$$

This Hamiltonian (H_{so}) is called a spin–orbit interaction.

Total Hamiltonian (H_{m}) of the molecular system is composed of the electronic Hamiltonian (H_0) without the spin operator and the spin–orbit interaction Hamiltonian (H_{so}). The eigenstates of H_0 are simultaneously the eigenstate of the spin operator (**s**), but the eigenstates of the total Hamiltonian (H_{m}) are no longer the spin eigenstate, namely , the spin–orbit interaction generates the spin-mixed states as the eigenstates of H_{m}.

The transition between states with a different spin multiplicity such as the singlet–triplet transition is generally forbidden by the spin selection rule. However, the spin–orbit interaction breaks this selection rule, for this interaction can mix the states with the different spin multiplicity. Therefore, an electronic state of a triplet state could have the character of a singlet state, and we could utilize this spin-mixed states to achieve the singlet–triplet transition in molecules.

Here, we have calculated the electronic state of Cl_2 molecule with MCSCF/6-31G method by GAMESS software package, taking into account the spin–orbit interaction. Using HF optimized geometry, we have calculated singlet and triplet states by configuration interaction (CI) method and singlet–triplet mixed states by spin–orbit configuration interaction (SOCI). From above calculations, we have evaluated the energy level of these states, the matrix elements of the spin–orbit coupling between singlet and triplet states, and the transition dipole moment between these states, which are shown in Tables 1 and 2, respectively. The energy level diagram is depicted in Fig. 1. We have found that the singlet excited states $\{|S_1\rangle, |S_2\rangle\}$ and $\{|S_3\rangle, |S_4\rangle\}$ are degenerate, respectively. The triplet states $\{|T_1\rangle, |T_2\rangle\}$ and $\{|T_3\rangle, |T_4\rangle\}$ are also degenerate. These degeneracies come from the symmetry of the x and y axis perpendicular to the molecular axis. We could similarly find out a lot of the degenerate state in the singlet–triplet mixed states.

3. STIRAP simulation

First let us briefly explain the STIRAP method in three-level system. The STIRAP method uses two laser pulses to achieve a complete population transition from

Table 1
The energy level of the Hamiltonian (a) singlet and triplet states by CI (b) spin-mixed states by SOCI (c) the matrix elements of the spin orbit coupling (cm^{-1})

State		S_0		S_1, S_2		S_3, S_4		T_1, T_2		T_3, T_4
(a)										
E (a.u.)		−918.884979		−918.732137		−918.641852		−918.75853		−918.65183
State	1	2, 3	4, 5	6, 7	8, 9	10, 11	12, 13	14	15	16, 17
(b)										
E (a.u.)	−918.885003	−918.759909	−918.758601	−918.75715	−918.732066	−918.653045	−918.651975	−918.650615	−918.65059	−918.641707
E (cm^{-1})	0	27455.4534	27742.6135	28061.0031	33566.4653	50909.7769	51144.5692	51443.1732	51448.5515	53398.2775
	T_1, 0	T_2, −1	T_2, 0	T_2, 1	T_3, −1	T_3, 0	T_3, 1	T_4, −1	T_4, 0	T_4, 1
(c)										
S_0					−262.9994i		262.9994i	−262.9994		−262.9994
S_1	−296.9617i		−50.0824i							
S_2	50.0824i		−296.9617i							
S_3						158.1758i			214.1702i	
S_4						−214.1702i			158.1758i	
T_1, −1		302.7748i								
T_1, 1				−302.7748i						
T_3, −1								−266.6982i		
T_3, 1										266.6982i

Table 2
Matrix elements of the transition dipole moment (a.u.) (a) × (b) z-direction

			4		5		8		9		15
(a)											
1			0.0273		−0.00004		0.05220 + 0.00038i		0.00627 − 0.00114i		
4											0.00003
8											0.00053
9											0.00006
	6	7	10	11	12	13	14	15	16	17	
(b)											
1	−0.002	0.00763									
2			0.02477 + 0.76999i	0.00866 + 0.00014i							
3			−0.00042 − 0.00865i	0.77039							
4					−0.05377 + 0.01856i	0.76545 − 0.00081i			0.05606 − 0.00139i	0.02454 + 0.00363i	
5					−0.67906 − 0.35327i	−0.03918 − 0.04124i			−0.00336 − 0.02457i	−0.00199 + 0.05604i	
6							0.62312 + 0.41112i	0.19048			
7							0.15900 + 0.10490i	−0.74648			
8					−0.00450 + 0.00330i	0.02973 − 0.00018i			−0.50618 + 0.02172i	−0.29342 − 0.05148i	
9					0.02575 − 01487i	0.00555 + 0.00058i			−0.27444 − 0.11589i	0.41349 + 0.29278i	

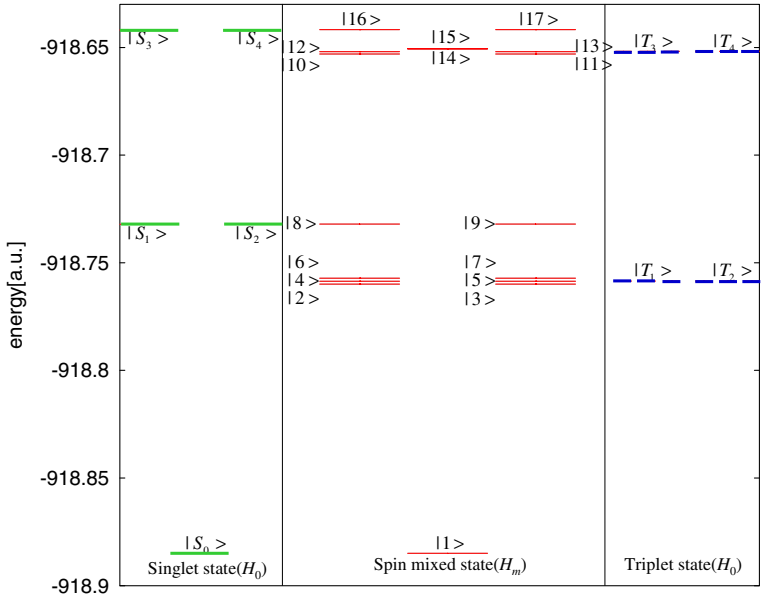


Fig. 1. Schematical energy level diagram. The right and left parts in singlet and triplet states mean the energy of the molecular Hamiltonian without spin–orbit interaction H_0, and the center part indicates the energy levels of the total molecular Hamiltonian H_m.

an initially populated state to a target state via an intermediate state. The first irradiated pulse called Stokes pulse makes a coherence between the intermediate and target states, then the second pump pulse corresponding to the transition between the initial and intermediate states induces the complete population transfer from the initial state to the target state without the population of the intermediate state. The overlap of the two pulses should be sufficiently large, and the pulse area is also sufficiently larger than the π pulse.

The interaction of the laser field and the molecular system is described by the time-dependent Schrödinger equation. Total Hamiltonian of the system is described $H = H_m + V(t)$, where H_m is the unperturbed molecular Hamiltonian and $V(t)$ means the interaction energy of electrons with the external electric field, and is explicitly described as $V(t) = -\boldsymbol{\mu} \cdot \mathbf{E}(t)$, where $\boldsymbol{\mu}$ and $\mathbf{E}(t)$ mean the electric dipole moment and the external electric field, respectively. In our simulation, the pulse shape of the electric field is assumed to be a gaussian shape. The wavefunction of the time-dependent Schrödinger equation is described as $|\Psi(t)\rangle = \sum C_n(t)|n\rangle$ by the superposition of the eigenfunction $|n\rangle$ of H_m. The expansion coefficient $C_n(t)$ is the probability amplitude of finding the eigenstate $|n\rangle$, and the corresponding probability density is given by $P_n(t) = |C_n(t)|^2$. The Schrödinger equation for the expansion coefficients becomes

$$i\hbar \frac{d\mathbf{C}(t)}{dt} = V(t)\mathbf{C}(t), \tag{3}$$

where $\mathbf{C}(t)$ means the set of the expansion coefficient, and $V(t)$ is the interaction operator of the electric field and the molecular system in the interaction picture. The matrix elements of the perturbation operator is given by

$$V_{mn}(t) = -\sum_n \langle m|\mu|n\rangle E(t) \exp\left(-\frac{i\omega_{mn}t}{\hbar}\right), \tag{4}$$

where $\langle m|\mu|n\rangle$ is the transition dipole moment between the states $|m\rangle$ and $|n\rangle$, ω_{mn} is the energy difference between two states $|m\rangle$ and $|n\rangle$.

In the simulation of the singlet–triplet transition, judging from the data of spin–orbit coupling and transition dipole moment, we can find out four reaction pathways from the singlet ground state to the triplet excited state. These four pathways are schematically shown in Fig. 2. In reaction pathways (a) and (b), we first adopt the π pulse to generate the singlet 1st excited state from the singlet ground state, and then we apply the STIRAP method to the achievement of the complete singlet–triplet transition, where the spin-mixed intermediate state is utilized. The difference of the cases (a) and (b) comes from the direction of the dipole moment, i.e., the x or y component of the dipole moment. On the other hand, reaction pathways (c) and (d) use only the STIRAP method to induce the transition from the singlet ground state to the triplet excited state. The difference between cases (c) and (d) is also due to the direction of the dipole moment.

Figs. 3(1) and (2) show the population dynamics of the reaction pathways (a) and (c), respectively. The reaction pathway (a) corresponds effectively to the transition $\{|S_0\rangle \rightarrow |T_1\rangle\}$, because the initial state $|1\rangle$ equals eventually to $|S_0\rangle$, and the main component of the target state $|4\rangle$ is $|T_1\rangle$. The π pulse ω_1 is resonant with the transition from state $|1\rangle$ to $|8\rangle$. The pump pulse ω_2 and the Stokes

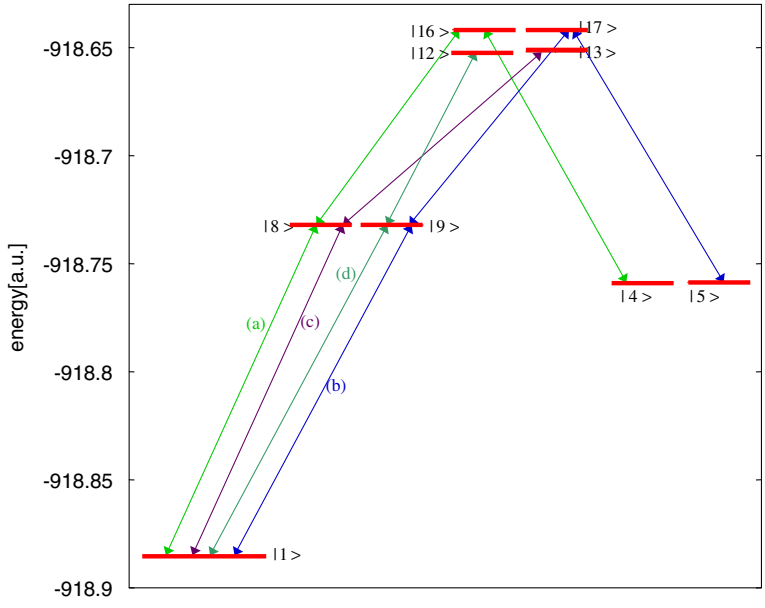


Fig. 2. Four reaction pathways. Cases (a) and (b) utilize the π pulse and STIRAP pulse sequence to generate the transition from the singlet ground state to the lowest triplet state. Cases (c) and (d) adopt only the STIRAP method to induce the transition to the 2nd highest triplet state.

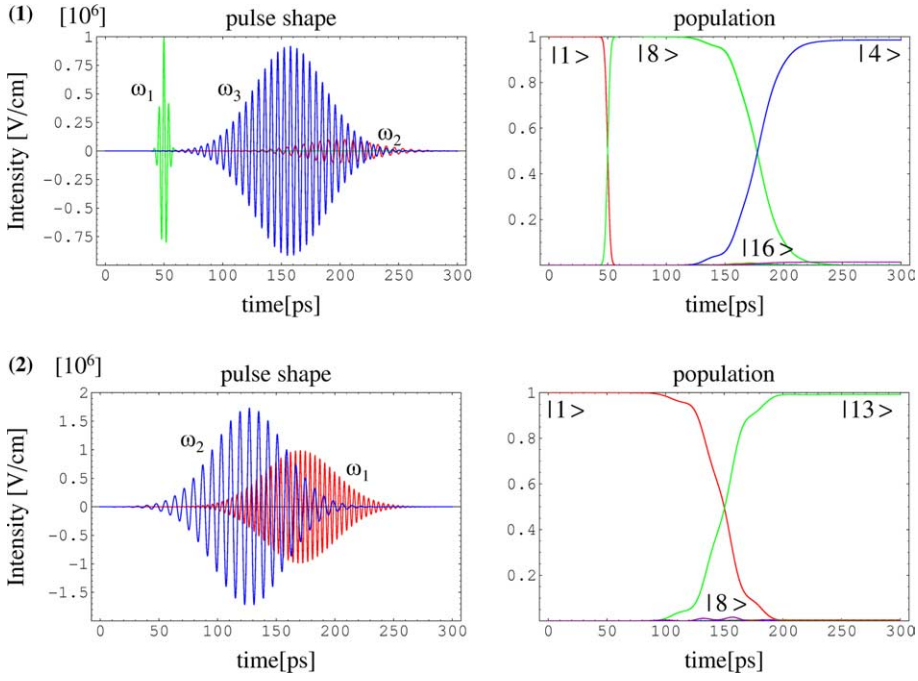


Fig. 3. Time evolution of the field intensity and population: (1) and (2) correspond to two reaction pathways (a) and (c), respectively.

pulse ω_3 are resonant with the transition from the state $|8\rangle$ to $|16\rangle$, and the transition from the state $|16\rangle$ to $|4\rangle$, respectively. The laser frequency, Rabi frequency, the field intensity, and the temporal center of the laser are shown in Table 3(1), respectively. The pulse width and the pulse area are set as $\sigma = 42.9$ ps and $A = 10\pi$, respectively. The numerical results of the STIRAP simulation shown in Fig. 3(1) show that the final product yield of the $|T_1\rangle$ is 98.5%, so we could realize the complete transfer from $|S_0\rangle$ to $|T_1\rangle$. Next, we consider the population dynamics for third reaction pathway (c) $\{|S_0\rangle \rightarrow |T_3\rangle\}$, where the target state $|12\rangle$ includes significantly the state $|T_3\rangle$. In this case, we could directly apply the STIRAP method to the population transition from the singlet ground state to the triplet excited state. The pump pulse ω_1 and the Stokes pulse ω_2 are resonant with the transition from the state $|1\rangle$ to $|9\rangle$, and the transition from the state $|9\rangle$ to $|12\rangle$, respectively. The laser

Table 3
Laser parameters of STIRAP simulation in (1) $\{|S_0\rangle \rightarrow |T_1\rangle\}$ (2) $\{|S_0\rangle \rightarrow |T_3\rangle\}$ pathway

	Frequency (cm^{-1})	Rabi frequency (a.u.)	Intensity (W/cm^2)	Temporal center (ps)
(1)				
π-Pulse (ω_1)	33566.5	1.0×10^{-5}	1.29175×10^{9}	50.0
Pump (ω_2)	19831.8	1.0×10^{-5}	1.3713×10^{7}	200.0
Stokes (ω_3)	25655.7	1.0×10^{-5}	1.11936×10^{9}	157.1
(2)				
Pump (ω_1)	33566.5	1.0×10^{-5}	1.29175×10^{9}	170.0
Stokes (ω_2)	17578.1	1.0×10^{-5}	3.98233×10^{9}	127.1

parameters and the result are also shown in Table 3(2) and Fig. 3(2), respectively. The values of the pulse width and area are the same as in the previous simulation. The final product yield of the $|T_3\rangle$ is 99.3% in this case. The results of the reaction pathway (b) $\{|S_0\rangle \rightarrow |T_2\rangle\}$ and (d) $\{|S_0\rangle \rightarrow |T_4\rangle\}$ are almost the same as the cases (a) and (c), respectively, so that we here omit these results.

4. Concluding remarks

We have performed the STIRAP simulation of the singlet–triplet transition in Cl_2 molecule by taking into account the spin–orbit coupling, and have found that the two-step sequential model of π pulse and the STIRAP methods using the spin-mixed intermediate state makes it possible to achieve a highly effective transition from the singlet ground state to the lowest triplet excited state.

We have calculated the spin-mixed excited state of Cl_2 molecule by using GAMESS software package, and have found four reaction pathways from the singlet ground state to the triplet excited state by investigating numerical data of the spin–orbit coupling and transition dipole moment. In cases (a) and (b), π pulse is first applied to generate the singlet 1st excited state, and then STIRAP method realizes the effective transition to the triplet lowest state. On the other hand, cases (c) and (d) show the transition from the singlet ground state to the triplet 2nd excited state only by the STIRAP method. In both cases, we could also induce the transition to the lowest triplet state by applying the π pulse method.

In this simulation, we have found that, in order to realize the transition from the singlet stable ground state to the lowest triplet state, we need to the π pulse in addition to the STIRAP pulse sequence. We had already made a STIRAP simulation of the four-level system with three laser pulses [16]. Thus, we could apply the four-level STIRAP method to this problem, and might obtain almost the same results as ones in this simulation.

In anyway, from the simplicity and the robustness of the STIRAP method with respect to the laser parameters, we could expect the more applications of this method to various molecular systems. The lowest triplet state has generally a long lifetime, so that such a molecular system with the STIRAP method could be a candidate of the molecular device in future.

Acknowledgment

H.N. is grateful for a financial support of the Ministry of Education, Science and Culture of Japan (Research Nos. 15550010 and 16032204).

References

[1] D.J. Tannor, S.A. Rice, J. Chem. Phys. 83 (1985) 5013.
[2] D.J. Tannor, R. Kosloff, S.A. Rice, J. Chem. Phys. 85 (1985) 5805.
[3] S. Shi, A. Woody, H. Rabitz, J. Chem. Phys. 88 (1988) 6870.
[4] W. Zhu, J. Botina, H. Rabitz, J. Chem. Phys. 108 (1998) 1953.
[5] N. Došlić, O. Kühn, J. Manz, K. Sundermann, J. Phys. Chem. A 102 (1998) 9645.
[6] M. Sugawara, Y. Fujimura, J. Chem. Phys. 100 (1994) 5646.
[7] Y. Fujimura, L. Gonazalez, K. Hoki, J. Manz, Y. Ohtsuki, Chem. Phys. Lett. 306 (1999) 1.
[8] M.V. Korolkov, G.K. Paramonov, Phys. Rev. A 57 (1998) 4998.
[9] N. Došlić, O. Kühn, J. Manz, Ber. Bunsenges. Phys. Chem. 102 (1998) 292.
[10] J.E. Combariza, B. Just, J. Manz, G.K. Paramonov, J. Phys. Chem. 95 (1991) 10351.
[11] S. Chelkowski, A.D. Bandrauk, P.B. Corkum, Phys. Rev. Lett. 65 (1990) 2355.
[12] S. Chelkowski, A.D. Bandrauk, J. Chem. Phys. 99 (1993) 4279.
[13] J.R. Kuklinski, U. Gaubatz, F.T. Hioe, K. Bergmann, Phys. Rev. 40 (1989) 6741.
[14] G. He, A. Kuhn, S. Schiemann, K. Bergmann, J. Opt. Soc. Am. B 7 (1990) 1960.
[15] K. Bergmann, H. Theuer, B.W. Shore, Rev. Mod. Phys. 70 (1998) 1003.
[16] Y. Ohta, H. Kizu, A. Yamada, T. Yoshimoto, K. Nishikawa, Int. J. Quantum Chem. 75 (1999) 511.
[17] Y. Ohta, T. Yoshimoto, K. Nishikawa, Chem. Phys. Lett. 316 (2000) 551.
[18] Y. Ohta, T. Bando, T. Toshimoto, K. Nishi, H. Nagao, K. Nishikawa, J. Phys. Chem. A 105 (2001) 8031.
[19] K. Nishikawa, Y. Ohta, T. Yoshimoto, T. Saito, K. Nishi, H. Nagao, J. Mol. Struct. 615 (2002) 13.
[20] S.D. Peyerimhoff, R.J. Buenker, Chem. Phys. 57 (1981) 279.
[21] D.M. Fedorov, M.S. Gordon, J. Chem. Phys. 112 (2000) 5611.

*2.1.1. General synthetic method for $[M_2A(L)_2(NO_3)_2]\cdot n(sol)$ (**1**–**6**)*

To a methanolic solution (200 ml) of H_2L (124 mg, 0.5 mmol) and triethylamine (101 mg, 1.0 mmol) was added a mixture of $M(NO_3)_2\cdot mH_2O$ (M = Cu, Ni, Co; 0.5 mmol) and $A(NO_3)_2$ (A = Pb, Ba; 0.25 mmol) in hot methanol (200 ml) including a small amount of water, and the mixture was heated for several minutes. The resulting solution was allowed to stand for several days to give single crystals (**1′**–**6′**) which are suitable for X-ray structure analysis. They were collected by suction filtration and dried in vacuo to obtain compounds **1**–**6** which were used for physical measurements.

$[Cu_2Pb(L)_2(NO_3)_2]$ (**1**). Green crystals. *Anal*. Calc. for $C_{26}H_{22}Cu_2N_4O_{14}Pb$:C, 32.91; H, 2.34; N, 5.91. Found: C, 32.61; H, 2.35; N, 5.83%. IR (KBr disk): $\nu = 1594$, 1579, 1517, 1449, 1385 cm^{-1}.

$[Ni_2Pb(L)_2(NO_3)_2]\cdot 5H_2O$ (**2**). Green crystals. *Anal*. Calc. for $C_{26}H_{32}N_4Ni_2O_{19}Pb$: C, 30.34; H, 3.13; N, 5.44. Found: C, 30.11; H, 3.26; N, 5.42%. IR (KBr disk): $\nu = 1600$, 1581, 1515, 1453, 1385 cm^{-1}.

$[Co_2Pb(L)_2(NO_3)_2]\cdot 4H_2O$ (**3**). Red crystals. *Anal*. Calc. for $C_{26}H_{30}Co_2N_4O_{18}Pb$: C, 30.87; H, 2.99; N, 5.54. Found: C, 30.44; H, 3.18; N, 5.53%. IR (KBr disk): $\nu = 1596$, 1579, 1516, 1455, 1385 cm^{-1}.

$[Cu_2Ba(L)_2(NO_3)_2]\cdot 2H_2O$ (**4**). Green crystals. *Anal*. Calc. for $C_{26}H_{26}BaCu_2N_4O_{16}$: C, 34.13; H, 2.86; N, 6.12. Found: C, 34.63; H, 2.95; N, 6.07%. IR (KBr disk): $\nu = 1595$, 1581, 1519, 1452, 1385 cm^{-1}.

$[Ni_2Ba(L)_2(NO_3)_2]\cdot 4H_2O$ (**5**). Green crystals. *Anal*. Calc. for $C_{29}H_{30}BaN_4Ni_2O_{18}$: C, 33.18; H, 3.21; N, 5.95. Found: C, 32.96; H, 3.28; N, 5.93%. IR (KBr disk): $\nu = 1602$, 1580, 1519, 1451, 1385 cm^{-1}.

$[Co_2Ba(L)_2(NO_3)_2]\cdot 4H_2O$ (**6**). Red crystals. *Anal*. Calc. for $C_{26}H_{30}BaCo_2N_4O_{18}$: C, 33.16; H, 3.21; N, 5.95. Found: C, 33.40; H, 3.27; N, 5.80%. IR (KBr disk): $\nu = 1602$, 1579, 1516, 1450, 1385 cm^{-1}.

2.2. X-ray crystallography

Data were collected at −90 °C on a Rigaku/MSC Mercury CCD diffractometer with graphite-monochromated Mo Kα radiation ($\lambda = 0.71070$ Å). The maximum 2θ value was 55.0°. A total of 1240 oscillation images were collected on five sweeps setting. Absorption correction was applied and the data were corrected for Lorentz and polarization effects.

Crystal data for $[Cu_2Pb(L)_2(NO_3)_2(MeOH)_2]$ (**1′**): $C_{28}H_{28}Cu_2N_4O_{16}Pb$, FW = 1010.84, green block, monoclinic, space group $P2_1/c$ (#14), $a = 11.128(2)$, $b = 14.443(1)$, $c = 11.411(2)$ Å, $\beta = 115.563(5)°$, $V = 1654.5$ $Å^3$, $Z = 2$, $D_c = 2.029$ g cm^{-3}, μ(Mo Kα) = 64.39 cm^{-1}, $R = 0.053$, $Rw = 0.102$.

Crystal data for $[Ni_2Pb(L)_2(NO_3)_2(MeOH)_2(H_2O)_2]$ (**2′**): $C_{30}H_{42}N_4Ni_2O_{20}Pb$, FW = 1103.28, green platelets, triclinic, space group $P\bar{1}$ (#2), $a = 9.825(2)$, $b = 10.222(2)$, $c = 11.811(2)$ Å, $\alpha = 74.33(1)°$, $\beta = 81.28(1)°$, $\gamma = 57.674(7)°$, $V = 965.1$ $Å^3$, $Z = 1$, $D_c = 1.898$ g m^{-3}, μ(Mo Kα) = 54.10 cm^{-1}, $R = 0.070$, $Rw = 0.095$.

Crystal data for $[Co_2Pb(L)_2(NO_3)(MeOH)_4](NO_3)\cdot MeOH$ (**3′**): $C_{31}H_{39}Co_2N_4O_{19}$ Pb, FW = 1096.73, orange platelets, triclinic, space group $P\bar{1}$ (#2), $a = 9.267(3)$, $b = 14.308(5)$, $c = 14.856(5)$ Å, $\alpha = 91.660(6)°$, $\beta = 90.306(5)°$, $\gamma = 94.612(5)°$, $V = 1962.5$ $Å^3$, $Z = 2$, $D_c = 1.856$ g cm^{-3}, μ(Mo Kα) = 52.05 cm^{-1}, $R = 0.075$, $Rw = 0.130$.

Crystal data for $[Cu_2Ba(L)_2(NO_3)_2(MeOH)_2]\cdot MeOH$ (**4′**): $C_{28}H_{30}BaCu_2N_4O_{16}$, FW = 942.98, green platelets, triclinic, space group $P1$ (#1), $a = 9.283(1)$, $b = 9.784(2)$, $c = 11.067(2)$ Å, $\alpha = 113.176(3)°$, $\beta = 92.615(3)°$, $\gamma = 115.443(3)°$, $V = 806.1$ $Å^3$, $Z = 1$, $D_c = 1.942$ g cm^{-3}, μ(Mo Kα) = 25.98 cm^{-1}, $R = 0.057$, $Rw = 0.106$.

Crystal data for $[Ni_2Ba(L)_2(NO_3)_2(MeOH)_2(H_2O)_3]\cdot MeOH$ (**5′**): $C_{29}H_{39}BaN_4Ni_2O_{20}$, FW = 1018.37, green prisms, triclinic, space group $P\bar{1}$ (#2), $a = 10.562(2)$, $b = 11.240(2)$, $c = 17.500(4)$ Å, $\alpha = 78.995(8)°$, $\beta = 74.975(7)°$, $\gamma = 70.573(7)°$, $V = 1879.0$ $Å^3$, $Z = 2$, $D_c = 1.799$ g cm^{-3}, μ(Mo Kα) = 21.14 cm^{-1}, $R = 0.087$, $Rw = 0.205$.

Crystal data for $[Co_2Ba(L)_2(NO_3)_2(MeOH)_2(H_2O)_2]\cdot MeOH$ (**6′**): $C_{29}H_{32}BaCo_2N_4O_{19}$, F. W. = 995.78, orange blocks, triclinic, space group $P\bar{1}$ (#2), $a = 9.97(5)$, $b = 14.141(8)$, $c = 14.113(7)$ Å, $\alpha = 79.25(2)°$, $\beta = 74.21(1)°$, $\gamma = 85.08(2)°$, $V = 1884.8$ $Å^3$, $Z = 2$, $D_c = 1.754$ g cm^{-3}, μ(Mo Kα) = 19.76 cm^{-1}, $R = 0.121$, $Rw = 0.246$.

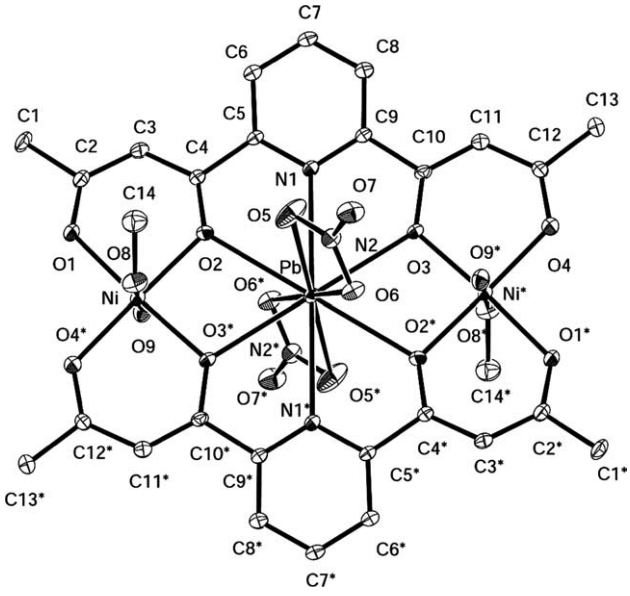


Fig. 1. An ORTEP drawing of $[Ni_2Pb(L)_2(NO_3)_2(MeOH)_2(H_2O)_2]$ (**2′**).

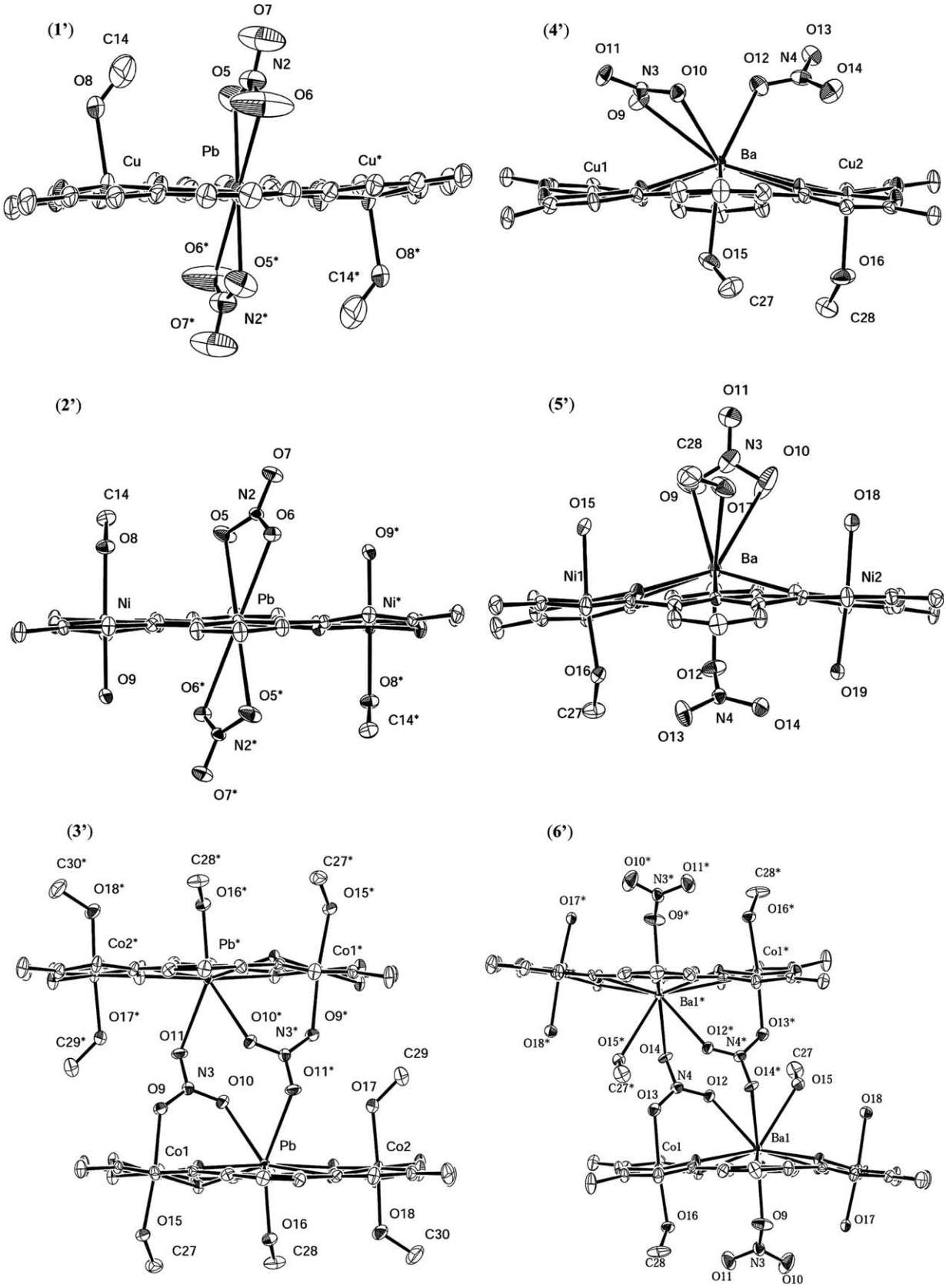


Fig. 2. Side views of ORTEP drawing of $[Cu_2Pb(L)_2(NO_3)_2(MeOH)_2]$ (**1**′), $[Ni_2Pb(L)_2(NO_3)_2(MeOH)_2(H_2O)_2]$ (**2**′), $\{[Co_2Pb(L)_2(NO_3)(MeOH)_4](NO_3)\cdot(MeOH)\}_2$ (**3**′), $[Cu_2Ba(L)_2(NO_3)_2(MeOH)_2]\cdot MeOH$ (**4**′), $[Ni_2Ba(L)_2(NO_3)_2(MeOH)_2(H_2O)_3]\cdot MeOH$ (**5**′) and $\{[Co_2Ba(L)_2(NO_3)_2(MeOH)_2(H_2O)_2]\cdot(MeOH)\}_2$ (**6**′).

Table 1
Average M–O, A–O and A–N distances, and the deviation of A atom from the central N_2O_4 least-squares plane

Complexes	1′	2′	3′	4′	5′	6′
M	Cu	Ni	Co	Cu	Ni	Co
A	Pb	Pb	Pb	Ba	Ba	Ba
M–O (Å)	1.983	2.038	2.071	1.975	2.039	2.078
A–O (Å)	2.683	2.719	2.668	2.843	2.762	2.798
A–N (Å)	2.718	2.789	2.787	2.945	2.957	2.902
Deviation (Å)	0	0	0.281	0.810	0.709	0.592

3. Results and discussion

3.1. Crystal structures

X-ray crystallography for **1′**–**6′** reveals that two ligands and two M(II) ions form a 16-membered metallaazacrown-like structure and one A(II) ion is located in the cavity. An ORTEP drawing for **2′** with atom numbering scheme is shown in Fig. 1.

The structure of **2′** contains a planer $Ni_2Pb(L)_2$. The asymmetric unit consists of the half of $[Ni_2Pb(L)_2(NO_3)_2(MeOH)_2(H_2O)_2]$, and Pb ion locates on an inversion center. Two Ni atoms in the 1,3-diketone sites have an octahedral geometry together with water and methanol molecules. The Pb atom in the 2,6-diacylpyridine site has a 10-coordinate geometry together with oxygen atoms of nitrate ions. The intrametallic Ni···Ni* and Ni···Pb separations are 7.452 and 3.726 Å, respectively. The Ni–O2–Pb and Ni–O3–Pb angles are 104.97° and 106.22°, respectively. The O_4 plane and the N_2O_4 plane form a dihedral angle of 3.51°. Each Ni deviates from the least-squares plane of O_4 by 0.014 Å whereas the Pb locates on the least-square plane of N_2O_4.

Side views of ORTEP drawings for **1′**–**6′** are shown in Fig. 2. In all the M(II)Pb(II)M(II) complexes (**1′**–**3′**) the trinuclear core forms a near coplane. Average M–O, A–O and A–N distances and deviation of A atom from the central N_2O_4 plane for **1′**–**6′** are listed in Table 1. The Pb of **1′** and **2′** shows no displacement from the least-squares plane defined by two 2,6-diacylpyridine moieties whereas the Pb of **3′** is 0.281 Å displaced for the least-squares plane. The side views of the M(II)-Ba(II)M(II) complexes (**4′**–**6′**) clearly indicate non-planar trinuclear core, effected by a large displacement of Ba (0.592–0.81 Å) from the least-squares plane. Obviously Pb(II) with a moderate ionic radius (1.32 Å) can reside within the central cavity formed by two 2,6-diacylpyridine moieties whereas Ba(II) with a large ionic radius (1.50 Å) cannot reside within the cavity. It is also found that Co(II)A(II)Co(II) complexes (**3′** and **6′**) assume a dimeric structure bridged by nitrate ions. It appears that Co(II) with ionic radius (0.88 Å) larger than the ionic radii of Ni(II) (0.84 Å) allows the dimerization of the trinuclear units in **3′** and **6′**. Such dimerization must be difficult in the Cu(II)A(II)Cu(II) complexes because of the Jahn-Teller of Cu(II) ion.

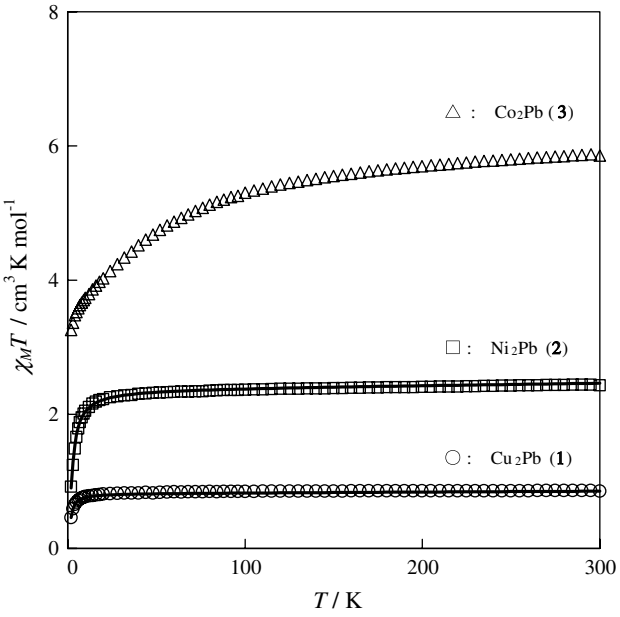


Fig. 3. Plots of $\chi_M T$ vs. T for **1** (○), **2** (□) and **3** (△). The solid lines show best-fitting of the data as described in the text.

3.2. Magnetic property

Magnetic susceptibilities for **1**–**6** were measured in the temperature range of 2–300 K under an applied field of 500 G. The $\chi_M T$ versus T plots for **1**–**3** and **4**–**6** are given in Figs. 3 and 4, respectively. The results suggest

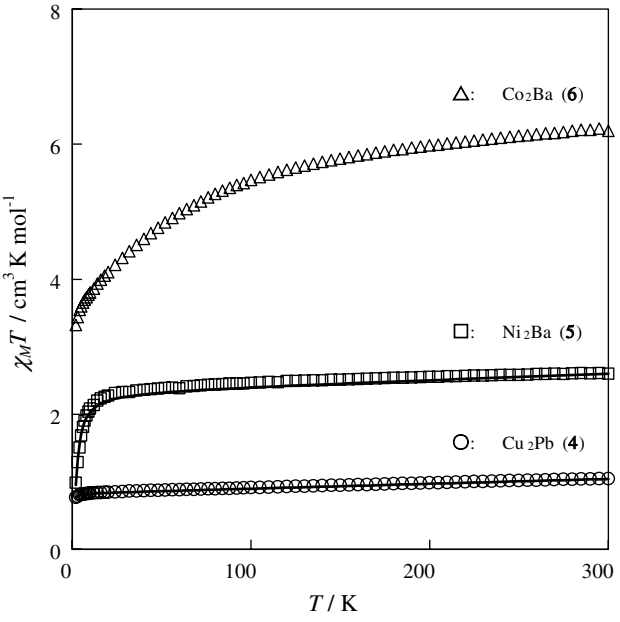


Fig. 4. Plots of $\chi_M T$ vs. T for **4** (○), **5** (□) and **6** (△). The solid lines show best-fitting of the data as described in the text.

that a weak antiferromagnetic interaction operates between the terminal M(II) ions in all the compounds. In the case of **1** and **4**, magnetic analyses were made based on the Bleaney–Bowers equation to obtain the best-fit parameters of $J = -0.98\ \mathrm{cm}^{-1}$ and $g = 2.09$ for **1** and $J = -0.19\ \mathrm{cm}^{-1}$ and $g = 2.10$ for **4**. Similarly, magnetic analyses for **2** and **5** were carried out based on the isotropic Heisenberg model to obtain the best-fit parameters of $J = -0.72\ \mathrm{cm}^{-1}$ and $g = 2.18$ for **2** and $J = -0.67\ \mathrm{cm}^{-1}$ and $g = 2.16$ for **5**. On the other hand, the magnetic behavior of **3** and **6** could not be reproduced by the isotropic Heisenberg model probably because of an orbital contribution of high-spin Co(II) ion. A similar antiferromagnetic interaction has also been observed between the terminal M(II) ions of the M(II)–Ln(III)–M(II) analogous with a diamagnetic Ln ion [13,14].

4. Conclusion

A series of trinuclear compounds, $[M_2A(L)_2(NO_3)_2]\cdot n(\mathrm{sol})$, have been synthesized using 2,6-bis(acetoacetyl)pyridine (H_2L) and their structures and magnetic properties have been characterized. The trinuclear structure comprises a metallaazacrown-like structure derived by two M(II) ions and two L^{2-} ligands with a large Pb(II) or Ba(II) cation in the central cavity. All the compounds show a weak antiferromagnetic interaction between the terminal M(II) ions through Pb(II) or Ba(II) ion.

Together with the previous results of the Cu_2Ln complexes [13,14], the M_2L_2 metallaazacrown accommodate divalent and trivalent metal ions with a wide range of ionic radius from Lu(III) (1.17 Å) to Ba(II) (1.50 Å), affording linear M(II)A(II)M(II) complexes of different combinations of metal ions.

5. Supplementary material

Crystallographic data for **1′**–**6′** has been deposited at the Cambridge Crystallographic Data Centre as the publication citation and deposition numbers CCDC 251924–251929 (**1′**–**6′**). Copies of the data can be obtained free of charge on application to CCDC, 12 Union Road, Cambridge CB2 1EZ, UK, fax: (+44)1223 336 033, e-mail: deposit@ccdc.cam.ac.uk or on the web http://www.ccdc.cam.ac.uk.

Acknowledgments

This work was supported by a Grant-in-Aid for Scientific Research Program (No. 13640561) from the Ministry of Education and Technology of Japan and Precursory Research for Embryonic Science and Technology (PRESTO), JST, Japan.

References

[1] O. Kahn, Molecular magnetism, VCH, New York, 1993.
[2] K. Ito, M. Kinoshita, Molecular Magnetism, Kodansha, Tokyo, 2000.
[3] J.S. Miller, M. Drillon, Magnetism: Molecules to Materials, Wiley-VCH, Weinheim, 2001.
[4] H.S. Nalwa, Handbook of Advanced Electronic and Photonic Materials and Devices, Academic Press, Sandiego, 2001.
[5] J.M. Lehn, Supramolecular Chemistry, VCH, Weinheim, Germany, 1995.
[6] V.L. Pecoraro, A.J. Stemmler, B.R. Gibney, J.J. Bodwin, H. Wang, J.W. Kampf, A. Barwinski, Prog. Inorg. Chem. 45 (1997) 83.
[7] R. Sessoli, H.-L. Tsai, A.R. Schake, S. Wang, J.B. Vincent, K. Folting, D. Gatteschi, G. Christou, D.N. Hendrickson, J. Am. Chem. Soc. 115 (1993) 1804.
[8] H. Oshio, N. Hoshino, T. Ito, J. Am. Chem. Soc. 122 (2000) 12602.
[9] G.S. Hannan, D. Volkmer, U.S. Schubert, J.-M. Lehn, G. Baum, D. Fenske, Angew. Chem. Int. Ed. 36 (1997) 1842.
[10] L. Zhao, Z. Xu, L.K. Thompson, S.L. Heath, D.O. Miller, M. Ohba, Angew. Chem. Int. Ed. 39 (2000) 3114.
[11] K.L. Taft, C.D. Delfs, G.C. Papaefthymiou, S. Foner, D. Gatteschi, S.J. Lippard, J. Am. Chem. Soc. 116 (1994) 823.
[12] F.K. Larsen, E.J.L. McInnes, H.E. Mkami, J. Overgaard, S. Piligkos, G. Rajaraman, E. Rentschler, A.A. Smith, G.M. Smith, V. Boote, M. Jennings, G.A. Timco, R.E.P. Winpenny, Angew. Chem. Int. Ed. 42 (2003) 101.
[13] T. Shiga, M. Ohba, H. Ōkawa, Inorg. Chem Commun. 6 (2003) 15.
[14] T. Shiga, M. Ohba, H. Ōkawa, Inorg. Chem. 43 (2004) 4435.
[15] D.E. Fenton, J.R. Tate, U. Casellato, S. Tamburini, P.A. Vigato, M. Vidali, Inorg. Chim. Acta 83 (1983) 23.
[16] R.W. Saalfrank, N. Low, S. Trummer, G.M. Sheldrick, M. Teichert, D. Stalke, Eur. J. Inorg. Chem. 559 (1998).

the three pairs in the hexagon have strong AF interaction of $J \sim -800$ K, the magnetic properties of the V15 cluster at low temperature are determined only by the three V^{4+} spins on the triangle. The energy scheme at low temperature is given by the ground state of $S = 1/2$ and the excited state of $S = 3/2$ which lies ~3.8 K above [10]. By the application of an external magnetic field, the ground state can be changed from two $S = 1/2$ doubly degenerate states to a $S = 3/2$ state. Magnetization measurements at low temperature clearly exhibit below ~0.5 K the magnetization step at a critical field $H_c \sim 2.8$ T where the two $S = 1/2$ doubly degenerate ground state changes to $S = 3/2$ ground state [11].

In this paper, we have carried out proton nuclear magnetic resonance (NMR) measurements at low temperature in order to shed light from a microscopic point of view on the static and dynamical properties of the V^{4+} spins ($S = 1/2$) on the triangle with the different ground states. In addition, we pay our attention to magnetic properties at the level crossing field $H_c \sim 2.8$ T. In Section 2, we present the experimental results of ^{1}H-NMR spectrum, proton spin–lattice relaxation and spin–spin relaxation rates. In Section 3.1, hyperfine fields at the proton sites are derived. The dynamical properties of the V^{4+} spins are discussed based on an analysis of the relaxation data in Section 3.2. In Section 3.3, we analyze relaxation data to elucidate magnetic properties at the level crossing field in the V15 cluster. Finally, we give a summary of the paper in Section 4.

2. Experimental

Polycrystalline samples of $(K_6[V_{15}As_6O_{42}(H_2O)]8\text{-}H_2O)$ were prepared as described in [12]. The temperature dependence of magnetic susceptibility measured in the samples agrees with the one reported previously [6,8]. The ^{1}H-NMR measurements were carried out utilizing a phase-coherent spin echo pulse spectrometer in the magnetic field range 0.24–8.2 T above 1.5 K. The ^{1}H-NMR spectra were obtained by sweeping the external magnetic field at constant frequency, while the spin echo intensity was averaged using a boxcar integrator. The nuclear spin–lattice relaxation time T_1 was measured by the saturation method with the frequency tuned at the highest peak position in ^{1}H-NMR spectrum. The nuclear magnetization recovery was found to be nonexponential in most measurements, which is due to the existence of protons with inequivalent spatial locations. Such a non exponential behavior in ^{1}H-NMR in the V15 was already reported by Procissi et al. [13]. T_1 values were determined from the initial slope of the recovery behavior, which corresponds to a weighted average relaxation rate of the nonequivalent protons [14]. The nuclear spin–spin relaxation time T_2 was determined by spin–echo decay curve.

2.1. ^{1}H-NMR Spectra

Fig. 1 shows several ^{1}H-NMR spectra at different frequencies measured at $T = 1.5$ K. The observed ^{1}H-NMR spectrum is narrow and its full-width of half amplitude (FWHA) is about 30 Oe below ~2 T and slightly increases with increasing external magnetic field. The FWHA and its magnetic field dependence up to ~5 T at $T = 1.5$ K are in agreement with the result reported previously [13]. However, when the magnetic field is increased above 5 T, the spectrum changes drastically from a single line to a structured spectrum where several peaks can be identified as shown in Fig. 1. Clearly at least 4 peaks (P1–P4) are apparent in the spectrum at high magnetic field (i.e., above ~6 T). The inset shows the H_0 dependence (i.e., resonance frequency dependence) at 1.5 K of $\Delta H = H_0 - H_i$, where H_i is the magnetic field at each peak (P_i). The fact that the absolute shift for each peak is almost field independent above ~6 T indicates that the shift arises from a spontaneous static internal field at the proton sites from a frozen V^{4+} spins configuration on the triangle. The internal field at each proton site is estimated to be 140, ~0, −108 and 335 Oe for P1, P2, P3 and P4, respectively.

2.2. Proton spin–lattice relaxation time T_1 and spin–spin relaxation time T_2

Fig. 2 shows the temperature dependence of $1/T_1$ measured at various external magnetic fields. At low magnetic field (i.e., below ~0.5 T), $1/T_1$ does not depend

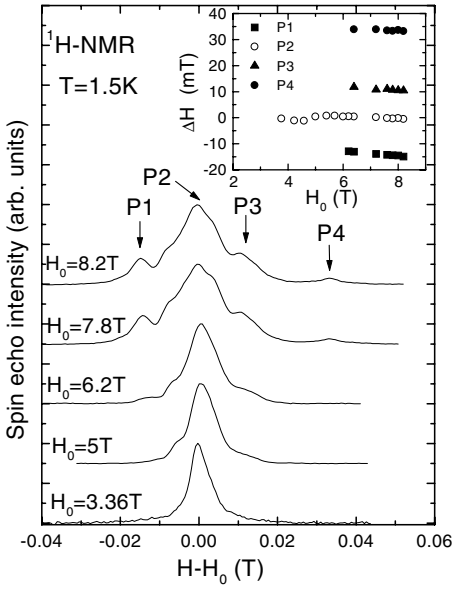


Fig. 1. ^{1}H-NMR spectra in the V15 powder sample at $T = 1.5$ K with different resonance frequencies. The horizontal axis for each spectrum is shifted by the corresponding Lamor field H_0. The inset shows the H_0 dependence of $\Delta H = H_0 - H_i$, where H_i is the magnetic field at each peak (P_i).

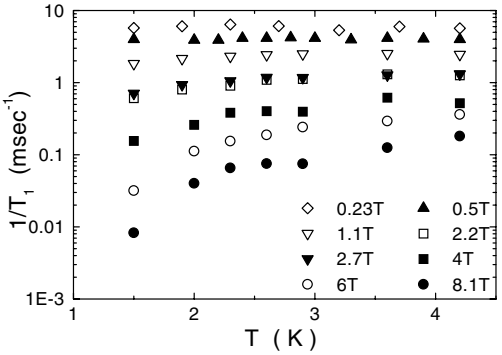


Fig. 2. Temperature dependence of ^1H–$1/T_1$ at different fields.

on temperature. On the other hand, for magnetic fields above 1 T, $1/T_1$ decreases with decreasing temperature at a rate which increases with increasing magnetic field. The external magnetic field dependence of $1/T_1$ at $T = 1.5$ and 4.2 K is plotted in Fig. 3. With increasing magnetic field, $1/T_1$ decreases gradually and shows a peak around $H = 2.7$ T for both temperatures as shown in the figure. A similar behavior was reported by Yoneda et al. [14] in a region of $H = 0.34$–3.3 T. The small but clear peak in $1/T_1$ is observed around $H \sim 2.7$ T which is very close to the reported critical magnetic field $H_c \sim 2.8$ T where the ground state changes from $S = 1/2$ to 3/2. Thus we consider that the enhancements of $1/T_1$ around 2.7 T is due to the level crossing between $S = 1/2$ and 3/2 states.

Fig. 4 shows the magnetic field dependence of $1/T_2$ at $T = 1.5$ and 4.2 K. With increasing magnetic field, $1/T_2$ increases and shows a dip around the level crossing critical field of 2.7 T for both temperatures. Interestingly, $1/T_2$ at $T = 1.5$ K exhibits a broad peak around 6 T, which is contrast to the monotonic decrease of $1/T_1$ with increasing magnetic field as shown in Fig. 3.

In Fig. 5 we report the temperature dependence of $1/T_2$ at several magnetic fields. The behavior of $1/T_2$ changes from being almost T-independent below 1 T

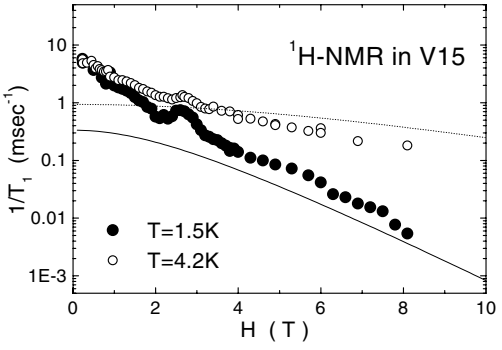


Fig. 3. The external magnetic field dependence of ^1H–$1/T_1$ measured at $T = 1.5$ and $T = 4.2$ K. The solid and broken lines are the calculated curves for $T = 1.5$ and 4.2 K, respectively, with a set of parameters discussed in the text.

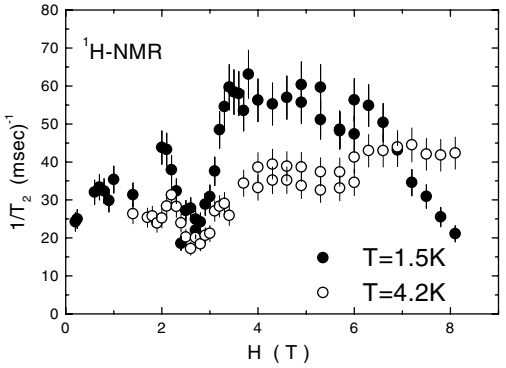


Fig. 4. Magnetic field dependence of ^1H–$1/T_2$. •, $T = 1.5$ K; ○, $T = 4.2$ K.

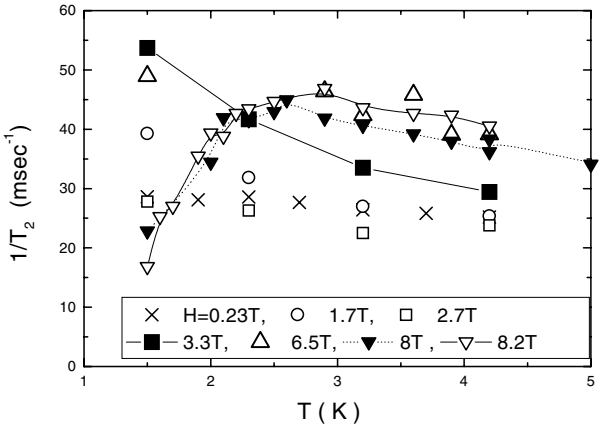


Fig. 5. Temperature dependence of $1/T_2$ at different fields. The solid and dotted lines are guides to the eye.

to an increase by lowering temperature in the field range $H = 1$–6 T. and a behavior with a broad maximum at 2.6 K for a field of 8 T. This is in sharp contrast to the temperature dependence of $1/T_1$ at the same magnetic field region. It is noted that $1/T_2$ around $H \sim 2.7$ T is almost temperature independent, which is considered to be originated from the level crossing between $S = 1/2$ and 3/2 states.

3. Discussion

3.1. Hyperfine fields at proton sites and spin freezing

As shown in Fig. 1, we have observed static internal fields at proton sites at low temperature. In general, there are two possibilities for the origin of the hyperfine field at proton sites, that is, dipolar fields and contact hyperfine fields from the V^{4+} spins. In the case of powder sample, the dipolar fields yield a broadening (and/or shoulder) of the line but no net shift, while the net shift of the line can be produced by the contact hyperfine fields due to the overlap of the s electron wave function

at the proton site with the d electron (V^{4+}) wave function. In the V15 cluster ($K_6[V_{15}As_6O_{42}(H_2O)]8H_2O$), two classes of protons can be mainly classified, that is, eight solvent waters between the clusters and one H_2O molecule inside the core of the cluster. Thus the almost unshifted line (P2) originates from the protons which are coupled to V^{4+} spins with dipolar interaction only, corresponding to the protons in the solvent water between the clusters. On the other hand, the shifted lines (P1, P3 and P4) can be ascribed to the protons in the H_2O molecule inside the core coupled by isotropic hyperfine interaction to the V^{4+} spins. Our experimental results suggest that there are several (at least 3) protons with different contact hyperfine fields, although there is only one H_2O molecule inside the core of the cluster. This implies that the H_2O molecule is located in more than one stable position.

The observation of static hyperfine fields at nuclear sites depends on the fluctuating frequency of the magnetization (spins). Whenever the fluctuating frequency of the magnetization is much smaller than the NMR frequency ($\sim 10^{7-8}$ Hz), one can observe static hyperfine fields at nucleus sites, while the hyperfine fields are time averaged to zero when the fluctuating frequency is higher than NMR frequency. The observation of the static internal fields at proton sites clearly indicates that fluctuating frequency of the V^{4+} spins on the triangle is less than NMR frequency at low temperature, which provides the direct evidence of the spin freezing in the system by the application of the external magnetic field.

Such spin freezing at low temperature is observed in other large spin magnetic molecules like Mn12-ac and Fe8 which have relatively large energy barriers ($\sim$60 K for Mn12 and $\sim$25 K for Fe8) for the reorientation of the spins. On the contrary, the V15 cluster has no energy barrier for the spin rotation. As was pointed out previously in our papers [15–17], fluctuating frequency of the spins is determined by not the energy barrier but transition probability between the ground state and first excited magnetic sublevel. Our experimental results suggest the transition probability between ground state and first excited states is small in the V15 cluster at low temperature under high magnetic field. As will be discussed in next section, such small transition probabilities at high magnetic field are originated from the spin–phonon interaction alone, which is characteristic of isolated magnetic clusters whose intermolecular interaction such as dipolar interactions are negligibly small.

3.2. Very slow fluctuations of V^{4+} spins and spin–phonon interaction

Let us discuss spin dynamics of V^{4+} spins on the triangle based on an analysis of the $1/T_1$ and $1/T_2$ data. The relaxation rates are related to the electron spin–spin correlation function. With an assumption of a simple exponential form of the correlation function $\langle h_\perp(t)h_\perp(0)\rangle = \langle h_\perp^2\rangle \exp(-t/\tau_c)$, where τ_c is correlation time of the fluctuating hyperfine field at proton sites and $\langle h_\perp^2\rangle$ is the average square of the transverse components of the effective hyperfine field due to the interaction of the protons with the local moments of the V^{4+} ions, the nuclear spin–lattice relaxation rate is given as $1/T_1 = \gamma_N^2\langle h_\perp^2\rangle\tau_c/(1+(\omega_N\tau_c)^2)$ [18,19]. Here ω_N is proton Lamor frequency and γ_N is the nuclear gyromagnetic ratio.

Regarding the nuclear spin–spin relaxation rate $1/T_2$, two main contributions to $1/T_2$ are generally present. The first is temperature and magnetic field independent and is due to nuclear dipole–dipole interaction among the ^{1}H nuclei ($(1/T_2)_{dip}$) [18,19]. The second is a temperature (and H) dependent contribution which relates to the correlation time τ_c. With an assumption of weak collision [18,19], the contribution can be expressed as $1/T_2 = \gamma_N^2\langle h_z^2\rangle\tau_c$ when $\gamma_N h_z\tau_c$ is smaller than unity. Here h_z is the z-component of the effective hyperfine fields at proton sites fluctuating very slowly of the order of $\gamma_N h_z$. On the other hand, as discussed below, when $\gamma_N h_z\tau_c > 1$ corresponding to a situation for strong collision, $1/T_2$ can be expected to be proportional to $1/\tau_c$. In any case, the experimentally observed $1/T_2$ originates mainly from the second contribution as can be inferred from the fact that it is T and H dependent and that the first contribution $(1/T_2)_{dip}$ can be estimated to be less than 1 $(ms)^{-1}$ [20].

In the case of $\omega_N\tau_c \ll 1$ (fast motion limit), both $1/T_1$ and $1/T_2$ is proportional to τ_c. Then $1/T_1$ and $1/T_2$ should have the same temperature dependence. On the other hand, if $\omega_N\tau_c \gg 1$ (slow motion limit) and $\gamma_N h_z\tau_c < 1$, $1/T_1 \sim 1/\tau_c$ has an inverse behavior in comparison with $1/T_2$. As shown before, in a region of H = 1–6 T, $1/T_1$ and $1/T_2$ show the opposite temperature and magnetic field dependences. Thus our experimental results can be explained simply by assuming that the correlation time of the hyperfine field fluctuations becomes slower than the Lamor period although remaining faster than the precession time along the local field, i.e., $\omega_N\tau_c > 1$ and $\gamma_N h_z\tau_c < 1$. The increases of $1/T_2$ and decreases of $1/T_1$ with increasing magnetic field and decreasing temperature are reasonably understood as due to an increase of τ_c, which corresponds to slowing of the fluctuations of the V^{4+} spins.

In order to analyze the $1/T_1$ data more quantitatively, we adopt a model in terms of spin–phonon interaction, which seems to explain both the T and H dependences of $1/T_1$ in Mn12 [16,17,21] and Fe8 [15]. In this model, it is assumed that thermal fluctuations of the magnetization among the different quantum number m sublevels of the total spin S state due to spin–phonon interaction give rise to the transverse components of the time-dependent hyperfine field $h_\perp(t)$ at the nuclear sites via the hyperfine interaction between the nuclei and local

electronic spins. In this case, $(1/T_1)_{\text{s–ph}}$ originated from the spin–phonon interaction is given by

$$(1/T_1)_{\text{s–ph}} = \frac{1}{2}\gamma_N^2 \int \langle h_\perp(t)h_\perp(0)\rangle \exp(i\omega_N t)\, dt = \frac{A}{Z}\sum_m \frac{\tau_m \exp\left(-\frac{E_m}{k_B T}\right)}{1+\omega_N^2\tau_m^2}, \quad (1)$$

where τ_m is the life time broadening of the magnetic mth sublevels originating from the spin–phonon interactions. Z is the partition function and A is a parameter related to the hyperfine coupling constants. The life-time τ_m for each individual m state is determined by $1/\tau_m = P_{m\to m+1} + P_{m\to m-1}$. The transition probabilities due to the spin phonon interactions [22] can be expressed by $P_{m\to m+1} = C\Delta^3/\{\exp(\Delta/k_BT)-1\}$ and $P_{m\to m-1} = C\Delta^3/\{1-\exp(-\Delta/k_BT)\}$ and C is the spin–phonon coupling constant and Δ is energy difference between m and $m \pm 1$ sublevels. In the case of the V15 cluster, there are two total spin states, that is, $S = 1/2$ and 3/2 so that $1/T_1$ can be expressed by sum of the two contributions due to the two $S = 1/2$ and 3/2 states as

$$(1/T_1)_{\text{s–ph}} = (B_{1/2}(1/T_1)_{\text{s–ph}}^{S=1/2} + B_{3/2}(1/T_1)_{\text{s–ph}}^{S=3/2})/Z = \frac{B_{1/2}A}{Z}\sum_{m=-1/2}^{1/2}\frac{\tau_m \exp(-E_m/k_BT)}{1+(\omega_N\tau_m)^2} + \frac{B_{3/2}A}{Z}\sum_{m=-3/2}^{3/2}\frac{\tau_m \exp(-E_m/k_BT)}{1+(\omega_N\tau_m)^2}, \quad (2)$$

where $B_{1/2}$ and $B_{3/2}$ is the Boltzmann factor for the two states of $S = 1/2$ and 3/2, respectively, including the two fold degeneracy for the $S = 1/2$ states. The solid and broken lines in Fig. 3 show the calculated results for $T = 1.5$ and 4.2 K, respectively, with a set of parameters of $C = 2.4\times10^4$ (Hz/K^3) and $A = 4.0\times10^{14}$ (rad/s)^2, which reasonably reproduce both H and T-dependences of $1/T_1$ above the level crossing field $H_c \sim 2.7$ T. This indicates that spin dynamics in the system at low temperature is governed by the spin–phonon interaction above H_c where the ground state of the cluster is $S = 3/2$. On the other hand, the "spin–phonon interaction" model can not reproduce the experimental results below H_c, especially below 1 T, where the ground state is formed by two $S = 1/2$ doubly degenerate states. In this low field region the spin dynamics of the V15 cluster must be governed by a mechanism different than the spin–phonon interaction.

Next we consider the observation of a broad peak in the field dependence of $1/T_2$ around 5 T at $T = 1.5$ K (see Fig. 4). It is known that $1/T_2$ estimated by spin–echo decay curve exhibits a peak ($1/T_2 \sim \gamma_N h_z$) when $\gamma_N h_z \tau_c \sim 1$ in the slow motion limit [23,24]. This corresponds to a cross over between weak collision regime ($\gamma_N h_z \tau_c \ll 1$) and strong collision regime ($\gamma_N h_z \tau_c \gg 1$). It is obvious that τ_c above ~6 T is much longer than the reciprocal of NMR frequency because of the observation of the static internal fields at proton sites as shown in the ^{1}H-NMR spectrum. In addition, the $1/T_1$ at $T = 1.5$ K decreases monotonically with increasing magnetic field across 6 T. These results indicate the gradual shortening of $1/\tau_c$ with increasing the magnetic field. Thus the peak of $1/T_2$ around 6 T at 1.5 K can be attributed to the cross over from weak collision to strong collision regime with increasing the magnetic field. This indicates that $\gamma_N h_z \tau_c$ becomes unity around 6 T where $1/\tau_c$ ($=\gamma_N h_z/2\pi$) is estimated to be $\sim 60\times10^3$ (s^{-1}). The value of $1/\tau_c$ is in good agreement with $1/\tau \sim 60\times10^3$ (1/s) for the ground state magnetic level ($m = -3/2$) in the $S = 3/2$ states at $H = 6$ T using the relation of $1/\tau = C\Delta^3/\{\exp(\Delta/k_BT)-1\}$ with the same value of C used in the analysis of $1/T_1$ data. If the correlation time at $T = 1.5$ K becomes longer by the application of the magnetic field, one can expect that with increasing temperature τ_c becomes shorter and $\gamma_N h_z \tau_c$ approaches unity thus generating a peak of $1/T_2$ as a function of temperature for high magnetic fields. This is indeed observed around 2.6 K at $H = 8$ T as shown in Fig. 5. Therefore the peak of $1/T_2$ as a function of the magnetic field is a direct evidence of the very gradual slowing down of V^{4+} spin fluctuations following the application of the magnetic field.

It should be noted that the above expression of $1/T_2$ is valid only for weak collision regime so that it can not be used for $H > 6$ T at low temperature where the strong collision regime is realized. To clarify the situation, we estimate tentatively the H-dependence of τ_c at $T = 1.5$ K from the $1/T_1$ and $1/T_2$ data, assuming $1/T_1 \sim 1/\omega_N^2\tau_{T_1}$ and $1/T_2 \sim \tau_{T_2}$, respectively. Fig. 6 shows the estimated H-dependences of both $1/\tau_{T_1}$ and $1/\tau_{T_2}$ which are normalized to the value obtained at $H = 2.7$ T for

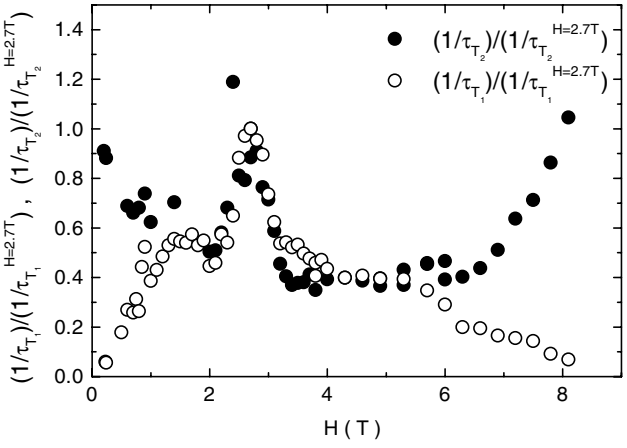


Fig. 6. External magnetic field dependence of $1/\tau_{T_1}$ and $1/\tau_{T_2}$ at $T = 1.5$ K from a relation of $1/T_1 \sim 1/\omega_L^2\tau_{T_1}$ and $1/T_2 \sim \tau_{T_2}$, respectively. Note each value is normalized by a value obtained at $H = 2.7$ T.

each. The two set of data coincide rather well in the field range $H = 1$–6 T, while for at $H > 6$ T one finds the opposite H-dependence for the two quantities. These results are consistent with the assumption that the relation $1/T_2 \sim \tau$ breaks down for $H > 6$ T. As pointed out by Goto et al. [25] for the analysis of $1/T_2$ in Mn12, $1/T_2$ is proportional to $1/\tau_c$ in the strong collision regime. In fact, $1/T_1$ and $1/T_2$ data above $H > 6$ T can be explained qualitatively by their idea. This confirms again the cross-over from the weak collision and strong collision regime around $H = 6$ T as a function of H at $T = 1.5$ K.

It is noted that $1/\tau_{T_1}$ has a different H-dependence from that of $1/\tau_{T_2}$ at low field below ~1 T. In order to check whether the difference originates from our assumption of $1/T_1 \sim 1/\omega_N^2\tau_{T_1}$, we estimated H-dependence of τ_{T_1} using a relation of $1/T_1 \sim \tau_{T_1}/(1+\omega_N^2\tau_{T_1}^2)$ without taking any assumption of the slow motion or the fast motion limit. However, we could not find any reasonable H-dependence of τ_{T_1} to resolve the crucial difference of the H-dependence between the $1/\tau_{T_1}$ and $1/\tau_{T_2}$. This suggests that our simple formula for $1/T_1$ (Eq. (2)) is not applicable for the low magnetic field below $H \sim 1$ T. As shown in Fig. 3, both H- and T-dependences of $1/T_1$ below H_c, especially below 1 T, can not be explained at all by the model in terms of the spin–phonon interaction. This implies the presence of an additional contribution to $1/T_1$, becoming dominant with decreasing magnetic field. It is interesting to point out that both $1/T_1$ and $1/T_2$ are almost independent of temperature at low magnetic field, as shown in Figs. 2 and 4. Similar temperature independent $1/T_1$ at $H = 0.34$ T was reported by Yoneda et al. [14] and they have pointed out a predominance of relaxation process due to level crossings at $H \sim 0$. Alternative possibility is due to quantum effects which originate from $S = 1/2$ triangular lattice of three V^{4+} ions. According to Kawamura [26], the ground state of triangular spins has twofold degenerate according to the two chiralities (different spin configurations) due to the frustration effects. In this sense, two $S = 1/2$ doubly degenerate states might be considered as the two chiralities in the V15 cluster. Since the fluctuations between two chiral states with different spin structures would give rise to a local field fluctuation at proton sites, this could be a relaxation mechanism. In contrast, such a fluctuation would not influence the magnetization measurements because both chiral states have the same $S = 1/2$ states macroscopically. It would be very interesting if the T-independent $1/T_1$ were due indeed to the quantum fluctuation, although we can not establish this for sure from the present data. Further experiments at low temperature below 1 K using a dilution refrigerator will give us information to elucidate the origin of peculiar behavior of $1/T_1$ at low magnetic field. Such measurements are now in progress.

3.3. Level crossing between $S = 1/2$ and $S = 3/2$ at $H_c \sim 2.7$ T

Following our consideration described above, the observations of a peak in $1/T_1$ and a dip in $1/T_2$ as a function of the magnetic field around the level crossing field $H_c \sim 2.7$ T are understood naturally by the idea of slow motion limit. This indicates clearly that the fluctuating frequency of V^{4+} spins in the triangle is less than the NMR frequency at the level crossing field around $H_c \sim 2.7$ T.

The enhancement of $1/T_1$ due to level crossings were reported in other magnetic molecules such as antiferromagnetic rings Fe10 [27,28] and Fe6(Li) [27,29]. In both cases, $1/T_1$ shows a peak at level crossing field as a function of the magnetic field at constant temperature. The H-dependence of $1/T_1$ around crossing fields are well fitted by a phenomenological model [29] in which $1/T_1$ is expressed by $1/T_1 = A\Gamma/(\Gamma^2 + (\omega_L - \Delta(H))^2)$. A is the same parameter as in Eq. (1) which relates to the hyperfine coupling constants, Γ is a temperature dependent damping factor associated with level broadening and $\Delta(H)$ is magnetic field dependent energy difference between the ground and first exited states. Near the level crossing field $\Delta(H)$ can be expressed by $\Delta(H) = \{g\mu_B(H_c - H)^2 + \Delta^2\}^{1/2}$, where Δ is an energy gap at level crossing field. It is noted that Γ affects only the magnitude of $1/T_1$ when Γ is small, while the width of $1/T_1$ peak is determined by the gap Δ.

Using the same expression, we analyze the $1/T_1$ in the V15 cluster at level crossing field. Before doing the fitting, we subtract first from the experimental data the spin–phonon contribution $(1/T_1)_{s-ph}$. The magnetic field dependence of $1/T(_1)_{LC} = (1/T_1) - 1/T(_1)_{s-ph}$ at $T = 1.5$ K is shown in Fig. 7. The FWHA of the $(1/T_1)_{LC}$ peak is ~0.6 T at $T = 1.5$ K. There are several possible origins for the width of the $1/T_1$ peak in our

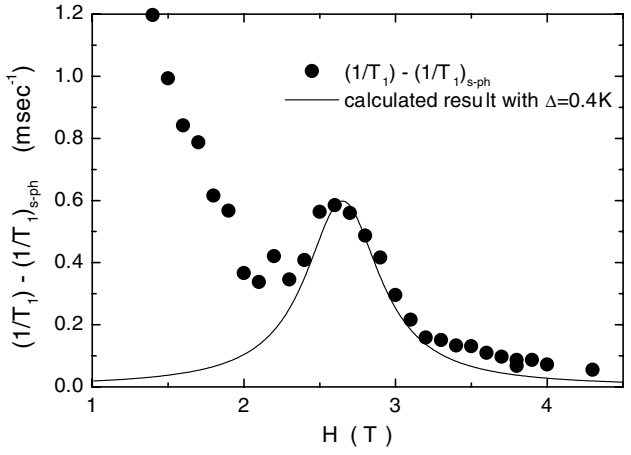


Fig. 7. External field dependence of $(1/T_1)_{LC} = (1/T_1) - (1/T_1)_{s-ph}$. The solid is a calculated curve with $\Delta = 0.4$ K with a set of parameters described in the text.

powder sample. The anisotropy of the electronic g-factor ($g_\perp = 1.953$, $g_\parallel = 1.981$) [30] produces a distribution of the level crossing field in the powder sample. This effect, however, is estimated to be about 0.07 T which is too small to explain the width. The intercluster dipolar and/or hyperfine field distributions (about 0.001 and 0.04 T, respectively [11]) can not account for the FWHA. In addition, the contribution of the thermal broadening to the width should be small because the FWHA at $T = 4.2$ K is a little bit smaller than that at $T = 1.5$ as shown in Fig. 3. On the other hand, the width can be simply explained if we assume the existence of the gap (Δ). The solid line in the figure is best fit to the data with a set of parameters: $\Gamma = 6.3 \times 10^8$ (1/s), $\Delta = 0.40$ K and $H_c = 2.65$ T using the same coupling constant of $A = 4.0 \times 10^{14}$ (rad/s)^2 as in the previous section. The width of $1/T_1$ peak suggests the existence of a gap at the level crossing field, namely of a level anticrossing in the V15 cluster. It should be emphasized that the measurements of $1/T_1$ around the level crossing field will be very useful to elucidate the structure of the magnetic level at H_c.

A gap at the level crossing field requires an interaction which mixes the $S = 1/2$ and $S = 3/2$ states. One possible interaction to be considered is the Dzyaloshinski–Moriya (DM) interaction. The DM interaction is allowed by a symmetry in the V15 cluster [31]. The width of the magnetization step at the level crossing field ~2.8 T measured at $T = 0.1$ K in a single crystal was reported to be ~0.7 T, which was explained by taking the DM interaction into considerations [11]. Recent theoretical calculations using the degenerate perturbation theory also reproduced the width of the magnetization step by including the DM interaction [32]. Thus we consider that the DM interaction play an important role to produce the level anticrossing in the V15 cluster.

Since the measurements were performed in a powder sample the level crossing field is expected to have a distribution of values due to the distributions of the angle between the magnetic field and DM vector axis in the powder sample. The magnitude of the gap $\Delta = 0.4$ K estimated here must be regarded just as a order of the magnitude. In order to make a more quantitative discussion of the structure of the magnetic level at H_c in the V15 cluster, detailed measurements on a single crystal are needed.

4. Summary

We have investigated the spin dynamics in the V15 cluster at low temperature by proton NMR measurements. The observation of the static internal fields at proton sites clearly indicates spin freezing at low temperature. The temperature and magnetic field dependences of T_1 and T_2 indicate very slow spin fluctuations of V^{4+} spin on the triangle less than the NMR frequency (10^{7-8} Hz) at low temperature. The fluctuating frequency becomes smaller and smaller by the application of a magnetic field. At the critical field $H_c \sim 2.7$ T for level crossing between the $S = 1/2$ and $S = 3/2$ states, an enhancement of $1/T_1$ is observed whereby the fluctuating frequency of the V^{4+} spins is revealed to be less than NMR frequency at the level crossing field. The width of the $1/T_1$ peak at the level crossing field suggest the existence of level anticrossing in the V15 cluster.

Both the H- and T-dependences of $1/T_1$ are well explained by a model in terms of the spin–phonon interaction above H_c where the ground state of the cluster is $S = 3/2$. On the other hand, the T_1 data can not be explained by the model in the low magnetic field region where the ground state is two $S = 1/2$ doubly degenerate states, suggesting an existence of another contribution to $1/T_1$. Temperature independent $1/T_1$ and $1/T_2$ at low magnetic field might be originated from the level crossing at $H \sim 0$ and/or quantum fluctuations, which is related to peculiarities of $S = 1/2$ triangle configuration in the V15 cluster.

Acknowledgements

The authors thank Prof. F. Borsa and Dr. A. Lascialfari for fruitful discussions and critical reading of the manuscript. The present work was in part supported by a Grand-in-Aid for Science Research from the Ministry of Education, Science, Sports, and Culture of Japan.

References

[1] J.R. Friedman, M.P. Sarachik, J. Tejada, R. Ziolo, Phys. Rev. Lett. 76 (1996) 3830.
[2] L. Thomas, F. Lionti, R. Ballou, D. Gatteschi, R. Sessoli, B. Barbara, Nature (London) 383 (1996) 145.
[3] C. Sangregorio, T. Ohm, C. Paulsen, R. Sessoli, D. Gatteschi, Phys. Rev. Lett. 78 (1997) 4645.
[4] W. Wernsdorfer, R. Sessoli, Science 284 (1999) 133.
[5] A. Gatteschi, L. Pardi, A.L. Barra, A. Müller, J. Döring, Nature (London) 354 (1991) 463.
[6] A.L. Barra, D. Gatteschi, L. Pardi, A. Müller, J. Döring, J. Am. Chem. Soc. 114 (1992) 8509.
[7] D. Gatteschi, L. Pardi, A.L. Barra, A. Müller, Mol. Eng. 3 (1993) 157.
[8] G. Chaboussantl, R. Basler, A. Sieber, S.T. Ochsenbein, A. Desmedt, R.E. Lechner, M.T.F. Telling, P. Kögerler, A. Müller, H.-U. Güdel, Europhys. Lett. 59 (2002) 291.
[9] I. Chiorescu, W. Wernsdorfer, A. Müller, H. Bögge, B. Barbara, Phys. Rev. Lett. 84 (2000) 3454.
[10] V.V. Dobrovitski, M.I. Katsnelson, B.N. Harmon, Phys. Rev. Lett. 84 (2000) 3458.
[11] I. Chiorescu, W. Wernsdorfer, B. Barbara, A. Müller, H. Bögge, J. Magn. Magn. Mater. 221 (2000) 103.
[12] J. Choi, L.A.W. Sanderson, J.L. Musfeldt, A. Ellern, P. Kögerler, Phys. Rev. B. 68 (2003) 064412.

[13] D. Procissi, B.J. Suh, J.K. Jung, P. Kögerler, R. Vincent, F. Borsa, J. Appl. Phys. 93 (2003) 7810.
[14] H. Yoneda, T. Goto, Y. Fujii, B. Barbara, A. Müller, Physica B 329–333 (2003) 1176.
[15] Y. Furukawa, K. Kumagai, A. Lascialfari, S. Aldrovandi, F. Borsa, R. Sessoli, D. Gatteschi, Phys. Rev. B 64 (2001) 094439.
[16] Y. Furukawa, K. Watanabe, K. Kumagai, F. Borsa, T. Sasaki, N. Kobayashi, D. Gatteschi, Phys. Rev. B. 67 (2003) 064426.
[17] Y. Furukawa, K. Watanabe, K. Kumagai, Z.H. Jang, A. Lascialfari, F. Borsa, D. Gatteschi, Phys. Rev. B 62 (2000) 14246.
[18] A. Abragam, Principles of Nuclear Magnetism, Clarendon Press, Oxford, 1961.
[19] C.P. Slichter, Principles of Magnetic Resonance, Springer-Verlag, Berlin, 1989.
[20] Y. Furukawa et al. Temperature independent $(1/T_2)_{dip}$ of proton is $\sim$1 ms^{-1} in the Fe8 cluster in which the number of the protons is much more than that in the V15 cluster (unpublished).
[21] A. Lascialfari, Z.H. Jang, F. Borsa, P. Carretta, D. Gatteschi, Phys. Rev. Lett. 81 (1998) 3773.
[22] J. Villan, F.H. Boutron, R. Sessoli, A. Rettori, Europhys. Lett. 27 (1994) 159.
[23] M. Takigawa, G. Saito, J. Phys. Soc. Jpn. 55 (1986) 1233.
[24] S. Fujiyama, M. Takigawa, S. Horii, Phys. Rev. Lett. 90 (2003) 147004.
[25] T. Goto, T. Koshiba, T. Kubo, K. Awaga, Phys. Rev. B 67 (2003) 104408.
[26] H. Kawamura, J. Phys.: Condens. Matter 10 (1998) 4707.
[27] A. Lascialfari, F. Borsa, M.-H. Julien, E. Micotti, Y. Furukawa, Z.H. Jang, A. Cornia, D. Gatteschi, M. Horvatic, J. Van Slageren, J. Magn. Magn. Mater. 272–276 (2004) 1042.
[28] M.-H. Julien, Z.H. Jang, A. Lascialfari, F. Borsa, M. Horvatic, A. Caneschi, D. Gatteschi, Phys. Rev. Lett. 83 (1999) 227.
[29] M. Affronte, A. Cornia, A. Lascialfari, F. Borsa, D. Gatteschi, J. Hinderer, M. Horvatic, A.G.M. Jansen, M.-H. Julien, Phys. Rev. Lett. 88 (2002) 167201.
[30] S. Vongtragool, B. Gorshunov, A.A. Mukhin, J. van Slageren, M. Dressel, A. Müller, Phys. Chem. Chem. Phys. 5 (2003) 2778.
[31] S. Miyashita, N. Nagaosa, Prog. Theor. Phys. 106 (2001) 533.
[32] N.P. Konstantinidis, D. Coffey, Phys. Rev. B 66 (2002) 174426.

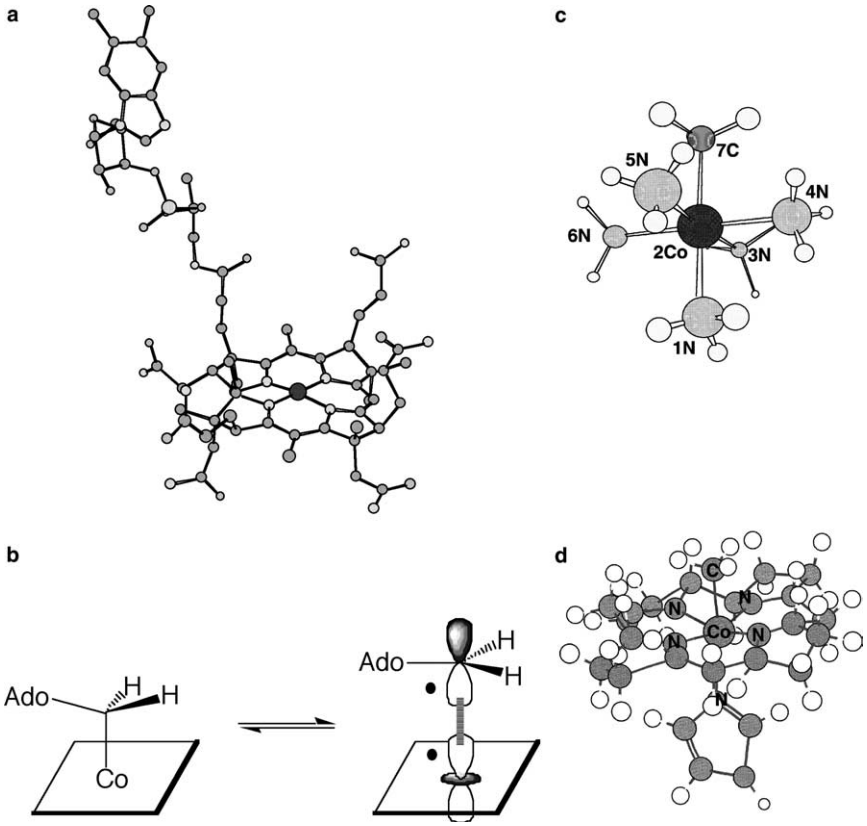


Fig. 1. (a) The structure of active site in cobalamin. (b) Co–C bond breaking on the active site of cobalamin. (c) Small model structure of active site of cobalamin (model **1**). (d) Realistic model structure of active site in cobalamin (model **2**).

2. Formulations

Hubbard Hamiltonian is determined by transfer integral (t_{ij}) and on-site Coulomb repulsion (U) as follows,

$$H = -\sum_{\langle i,j\rangle}\sum_{\sigma} t_{ij}c^{+}_{i\sigma}c_{j\sigma} + U\sum_{i=1}^{N} n_{i\uparrow}n_{i\downarrow}, \tag{1}$$

where $c^{+}_{\sigma i}$ and $c_{\sigma i}$ are creation and annihilation operators for spin σ on the site i, respectively [2]. $n_i\uparrow$ and $n_i\downarrow$ are number operators for up and down spins, respectively. For the application to the metal (M) and non-metal (X) bonding (M–X bond), let us define molecular orbitals (MOs) using atomic orbitals (AOs). If atomic orbital of metal (M) and non-metal (X) are described as χ_M and χ_X, respectively, symmetry adapted (SA) bonding and anti-bonding orbitals are defined as [2–5]

$$\phi = \cos\theta\chi_M + \sin\theta\chi_X, \tag{2a}$$
$$\phi^* = -\sin\theta\chi_M + \cos\theta\chi_X, \tag{2b}$$

where ϕ is bonding and ϕ^* is anti-bonding orbitals, respectively, as illustrated in Fig. 2(a) [2]. In the broken-symmetry method, α and β orbitals are expressed by mixture of bonding and anti-bonding symmetry-adapted (SA) orbitals as follows [2–5],

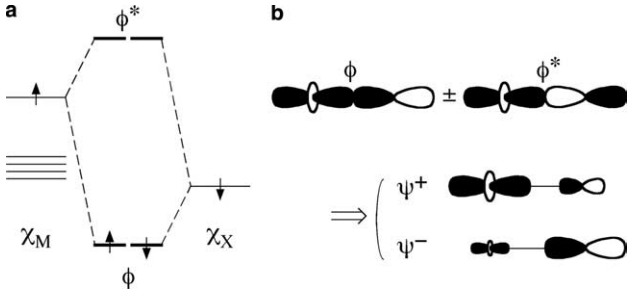


Fig. 2. (a) Spin adapted (SA) bonding (ϕ) and anti-bonding (ϕ^*) orbitals expressed using atomic orbitals of metal (χ_M) and ligand (χ_X). (b) Occupied α (ψ^+) and β (ψ^-) orbitals in broken symmetry method.

$$\psi^+ = \cos\omega\phi + \sin\omega\phi^*, \tag{3a}$$
$$\psi^- = \cos\omega\phi - \sin\omega\phi^* \quad \left(0 \leqslant \omega \leqslant \frac{\pi}{4}\right), \tag{3b}$$

as illustrated in Fig. 2(b) [2]. The wavefunction of the system is expressed by using BS wavefunctions as follows,

$$|\psi_0\rangle = |\psi^+\psi^-\rangle. \tag{4}$$

Because Hamiltonian of the system is defined as

$$\widehat{\mathbf{H}}_0 = \widehat{\mathbf{H}} + \widehat{\mathbf{G}}, \tag{5}$$

by using 1-electron Hamiltonian (**H**) and 2-electron Hamiltonian (**G**), total energies of the system becomes

$$E^{\text{total}} = \langle\psi^+\psi^-|\widehat{\mathbf{H}}_0|\psi^+\psi^-\rangle = \langle\psi^+\psi^-|\widehat{\mathbf{H}}|\psi^+\psi^-\rangle + \langle\psi^+\psi^-|\widehat{\mathbf{G}}|\psi^+\psi^-\rangle. \quad (6)$$

Because ψ^+ and ψ^- are expressed using χ_M and χ_X as follows,

$$\psi^+ = \cos\omega(\cos\theta\chi_M + \sin\theta\chi_X) + \sin\omega(-\sin\theta\chi_M + \cos\theta\chi_X) = \cos(\omega+\theta)\chi_M + \sin(\omega+\theta)\chi_X \quad (7a)$$

$$\psi^- = \cos\omega(\cos\theta\chi_M + \sin\theta\chi_X) - \sin\omega(-\sin\theta\chi_M + \cos\theta\chi_X) = \cos(\omega-\theta)\chi_M + \sin(\theta-\omega)\chi_X, \quad (7b)$$

the energies of α and β electrons of one-electron part become

$$\langle\psi^+|\widehat{\mathbf{H}}|\psi^+\rangle = \langle\cos(\omega+\theta)\chi_M + \sin(\omega+\theta)\chi_X|\widehat{\mathbf{H}}| \times \cos(\omega+\theta)\chi_M + \sin(\omega+\theta)\chi_X\rangle = \cos^2(\omega+\theta)\varepsilon_M + \sin^2(\omega+\theta)\varepsilon_X + \sin(2\omega+2\theta)\beta \quad (8a)$$

$$\langle\psi^-|\widehat{\mathbf{H}}|\psi^-\rangle = \langle\cos(\omega-\theta)\chi_M + \sin(\theta-\omega)\chi_X|\widehat{\mathbf{H}}| \times \cos(\omega-\theta)\chi_M + \sin(\theta-\omega)\chi_X\rangle = \cos^2(\omega-\theta)\varepsilon_M + \sin^2(\theta-\omega)\varepsilon_X + \sin(2\theta-2\omega)\beta, \quad (8b)$$

respectively. In Eqs. (8a) and (8b), $\langle\chi_M|\widehat{\mathbf{H}}|\chi_M\rangle = \varepsilon_M$, $\langle\chi_X|\widehat{\mathbf{H}}|\chi_X\rangle = \varepsilon_X$ and $\langle\chi_M|\widehat{\mathbf{H}}|\chi_X\rangle = \beta$.

While, in the two-electron part, only Coulomb repulsion is effective.

$$(\psi^+)^2 = \cos^2(\omega+\theta)\chi_M^2 + \sin(2\omega+2\theta)\chi_M\chi_X + \sin^2(\theta+\omega)\chi_X^2, \quad (9a)$$

$$(\psi^-)^2 = \cos^2(\omega-\theta)\chi_M^2 + \sin(2\theta-2\omega)\chi_M\chi_X + \sin^2(\theta-\omega)\chi_X^2. \quad (9b)$$

By ignoring overlap ($\langle\chi_v(1)|\chi_v(1)\rangle = 0$) and applying an approximation ($\langle(\chi_M)^2|\widehat{\mathbf{G}}|(\chi_X)^2\rangle = 0$), energy of two electron part becomes

$$\begin{aligned}\langle(\psi^+)^2|\widehat{\mathbf{G}}|(\psi^-)^2\rangle &= \cos^2(\omega+\theta)\cos^2\langle(\chi_M)^2|\widehat{\mathbf{G}}|(\chi_M)^2\rangle + \sin^2(\theta+\omega)\sin^2(\theta-\omega)\langle(\chi_X)^2|\widehat{\mathbf{G}}|(\chi_X)^2\rangle \\ &= \cos^2(\omega+\theta)\cos^2(\omega-\theta)U_M + \sin^2(\theta+\omega)\sin^2(\theta-\omega)U_X, \end{aligned} \quad (10)$$

where $\langle(\chi_M)^2|\widehat{\mathbf{G}}|(\chi_M)^2\rangle = U_M$ and $\langle(\chi_X)^2|\widehat{\mathbf{G}}|(\chi_X)^2\rangle = U_X$, respectively. From the results, total energy becomes

$$\begin{aligned}\langle\widehat{\mathbf{H}}_0\rangle = \langle\widehat{\mathbf{H}}\rangle + \langle\widehat{\mathbf{G}}\rangle &= \cos^2(\omega+\theta)\varepsilon_M + \sin^2(\omega+\theta)\varepsilon_X + \sin(2\omega+2\theta)\beta + \cos^2(\omega-\theta)\varepsilon_M + \sin^2(\theta-\omega)\varepsilon_X + \sin(2\theta-2\omega)\beta \\ &\quad + \cos^2(\omega+\theta)\cos^2(\omega-\theta)U_M + \sin^2(\theta+\omega)\sin^2(\theta-\omega)U_X \\ &= 2\varepsilon_M - \{\sin^2(\theta+\omega) + \sin^2(\theta-\omega)\}(\varepsilon_M - \varepsilon_X) + \sin(2\omega+2\theta)\beta + \sin(2\theta-2\omega)\beta \\ &\quad + \cos^2(\omega+\theta)\cos^2(\omega-\theta)U, \end{aligned} \quad (11)$$

where we introduce the assumption as $U_M = U$, $U_X = 0$. The assumption means that on-site Coulomb repulsion on ligand sites is negligible. The energy is renormalized as follows;

$$\begin{aligned}\mathbf{E} &\equiv \frac{E - 2\varepsilon_M}{U} \\ &= \{\sin^2(\theta+\omega) + \sin^2(\theta-\omega)\}y - \frac{1}{2}\{\sin(2\omega+2\theta)\beta + \sin(2\theta-2\omega)\beta\}x + \cos^2(\omega+\theta)\cos^2(\omega-\theta). \end{aligned} \quad (12)$$

Here, we define the parameters x and y as follows,

$$\begin{cases} y = \dfrac{-\Delta\varepsilon}{U} = \dfrac{-(\varepsilon_M - \varepsilon_X)}{U}, & \text{(a)} \\ x = \dfrac{-2\beta}{U}. & \text{(b)} \end{cases} \quad (13)$$

The parameter x means an index for covalent bond (M–X), while y means an index for charge transfer (M^+–X^- or M^-–X^+). Next, we variationally obtain functions of x and y by regarding the total energy as a function of parameters ω and θ as follows,

$$\begin{aligned}\frac{\partial\mathbf{E}}{\partial\omega} &= \{2\sin(2\omega+2\theta) + 2\sin(2\omega-2\theta)\}\frac{y}{2} + 2x\sin2\theta\sin2\omega - \sin(2\omega+2\theta)\left\{\frac{1+\cos(2\omega-2\theta)}{2}\right\} - \left\{\frac{1+\cos(2\omega+2\theta)}{2}\right\}\sin(2\omega-2\theta) \\ &= 2y\cos2\theta\sin2\omega + 2x\sin2\theta\sin2\omega - \sin2\omega\cos2\theta - \frac{1}{2}\sin4\omega \end{aligned} \quad (14)$$

$$\begin{aligned}\frac{\partial\mathbf{E}}{\partial\theta} &= \{2\sin(2\omega+2\theta) - 2\sin(2\omega-2\theta)\}\frac{y}{2} - 2x\cos2\theta\cos2\omega - \sin(2\omega+2\theta)\left\{\frac{1+\cos(2\omega-2\theta)}{2}\right\} + \left\{\frac{1+\cos(2\omega+2\theta)}{2}\right\}\sin(2\omega-2\theta) \\ &= 2y\sin2\theta\cos2\omega + 2x\cos2\theta\cos2\omega - \sin2\theta\cos2\omega - \frac{1}{2}\sin4\theta \end{aligned} \quad (15)$$

Then total energy becomes

$$\mathbf{E} = \{2 - \cos(2\omega+2\theta) - \cos(2\omega-2\theta)\}\frac{y}{2} - x\sin2\theta\cos2\omega + \left\{\frac{1+\cos(2\omega+2\theta)}{2}\right\}\left\{\frac{1+\cos(2\omega-2\theta)}{2}\right\}, \quad (16)$$

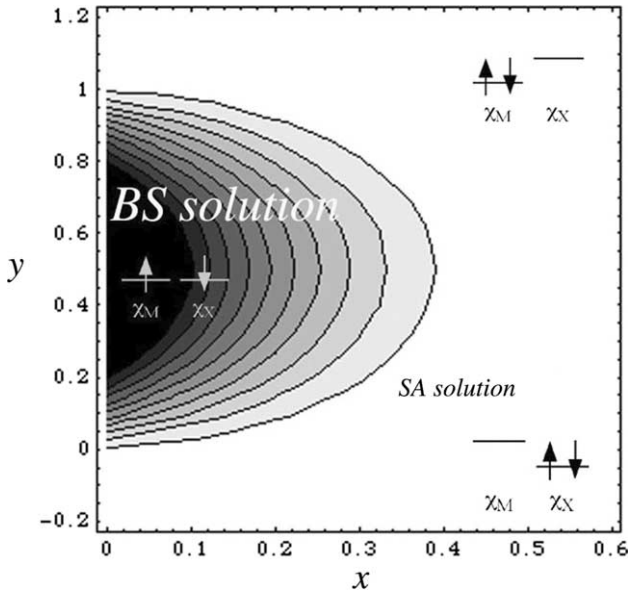


Fig. 3. Calculated phase diagram. In the dark area, BS solution (M·–X·) is more stable than SA solution. In upper white area ($y > 0.5$) is expressing M^-–X^+ and lower white area ($y < 0.5$) expresses M^+–X^-.

and we obtain energy function $E(x,y)$, which satisfies the conditions as follows,

$$\begin{cases} \dfrac{\partial \mathbf{E}}{\partial \theta} = 0 \rightarrow 2y\cos 2\theta \sin 2\omega + 2x \sin 2\theta \sin 2\omega \\ \qquad - \cos 2\theta \sin 2\omega - \frac{1}{2}\sin 4\omega = 0, \qquad \text{(a)} \\ \dfrac{\partial \mathbf{E}}{\partial \varpi} = 0 \rightarrow 2y\sin 2\theta \cos 2\omega + 2x \cos 2\theta \cos 2\omega \\ \qquad - \sin 2\theta \cos 2\omega - \frac{1}{2}\sin 4\theta = 0. \qquad \text{(b)} \end{cases} \tag{17}$$

This is an expression of total energy in terms of SA and BS methods. By solving Eqs. $(17)_{a,b}$ with ω and θ, and substituting them for Eq. (16), then we can obtain a function $E(x,y)$. By subtracting RHF energy (in case of $\omega = 0$) from UHF energy (in case of $\omega \neq 0$), we can obtain potential surface that is depicted in Fig. 3. In the dark area, BS solution is more stable than SA solution. In upper white area ($y > 0.5$), electron is transferred from ligand to metal, while lower white area ($y < 0.5$) electron is transferred from metal to ligand.

3. Calculations

We applied above formulations to the cobalamin system, in which single bond between adenosyl group and cobalt ions dissociate homolyticaly, forming radical pairs [1]. UB3LYP calculations were carried out to elucidate dissociation nature such as potential curves, charge densities and so on.

4. Computational details

Atomic coordinations of complexes were taken from date of X-ray crystal structure analysis of methylmalonyl-CoAMutase (PDB code: 4REQ [6]) that was available in the Protein Data Bank (PDB). We constructed two types of model structures. One is small model (model **1**) and another is realistic model (model **2**) as illustrated in Fig. 1(c) and (d), respectively. In case of the small model complex (model **1**), calculations were performed by the use of Tatewaki-Huzinaga MIDI (533(21)/53(21)/(41)) basis set for Co atoms, 6-31 + G* basis set for ligand atoms. On the other hand, calculations were performed by the use of Tatewaki-Huzinaga MIDI (533(21)/53(21)/(41)) basis set for Co atoms, 6-31G basis set for ligand atoms in case of the realistic model complex (model **2**). All calculation was carried out using UB3LYP [7], which is an unrestricted hybrid density functional theory (UHDFT), on GAUSSIAN98 [8].

5. Calculated results and discussion

The potential curve of small model (model **1**) complex is depicted in Fig. 4(a). From the figure, we could not find any bond formation because there is no minimum in the curve. This result suggests that Corrin ring is necessary to bond formation. The Mulliken charge densities on nitrogens are depicted in Fig. 4(b). Mulliken charges on nitrogen are slightly positive, although formal charges of nitrogens are neutral. It is showing that small model could not reproduce chemical environment of the active site. In the case of model **2**, there is a minimum around $r_{M-X} = 2.1$ Å and a stabilization energy is about 0.85 eV. In contrast with small model, charge densities on nitrogens are negative. Especially charge density on axial nitrogen (N5) is largest, while ones of small model in almost zero. Although Mulliken charges are not adequate for quantitative discussions, this result strongly suggests that axial nitrogen (N5) plays important role in the reactions of cobalamin. Natural orbital analysis was carried as illustrated in Fig. 5. There is an interaction between Co–C bond and corrin ring in case of realistic model, while there is not in case of small model. This result also supports that corrin ring is essential for the Co–C bond formation. From the occupation numbers of natural orbital, instability in Co–C chemical bond (y_i) is estimated using an equation as follows [2],

$$y_i = \frac{n_i^2 - 4n_i + 4}{n_i^2 - 2n_i + 2}, \tag{18}$$

where n_i is occupation number of natural orbital. The calculated y_i values were plotted in Fig. 6. The y_i values show that bond instability (radical dissociation) occurs at about 2.1 Å. In other words, BS solutions are stable

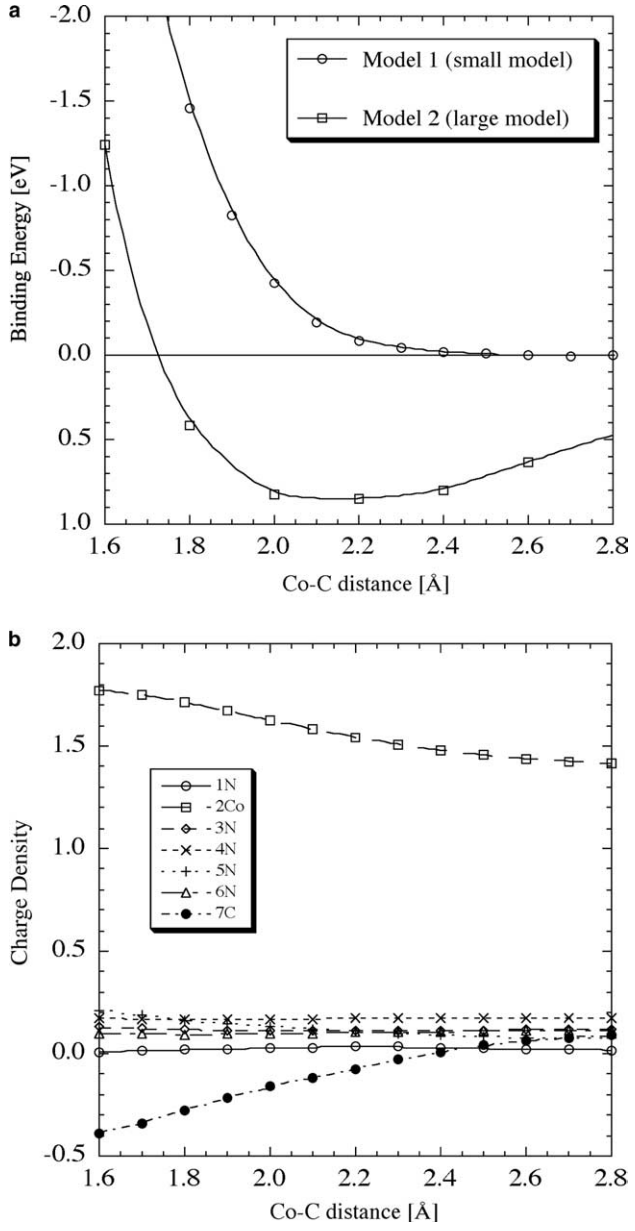


Fig. 4. (a) Calculated potential curve of Co–C bond on small model (model **1**) and realistic model (model **2**). (b) Calculated Mulliken charge densities on model **1**.

where Co–C distances are longer than 2.1 Å. Therefore the potential minimum of Co–C bond belongs to the SA region, showing that Co–C bond is covalent bond. The potential minimum, however, located the boundary between SA solution and BS solution.

The transfer integral (t) and on-site Coulomb repulsion energy on metal ion (U) in Hubbered Hamiltonian were estimating by fitting the parameter using the equation [2],

$$J = \frac{1}{4}\left(\Delta\varepsilon + U - \sqrt{(\Delta\varepsilon + U)^2 + 16t^2}\right), \tag{19}$$

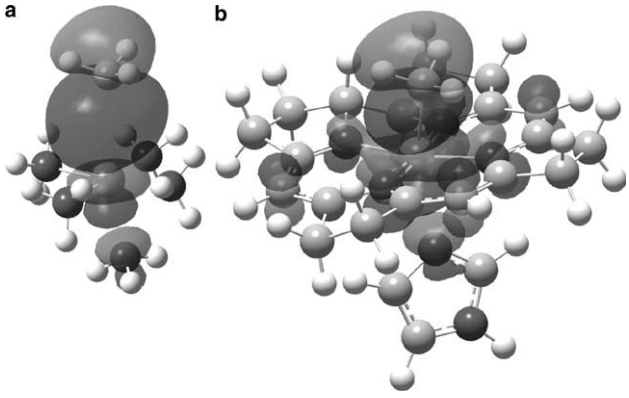


Fig. 5. Calculated natural orbitals (NOs) of small model (model **1**) (a) and realistic model (model **2**) (b), respectively.

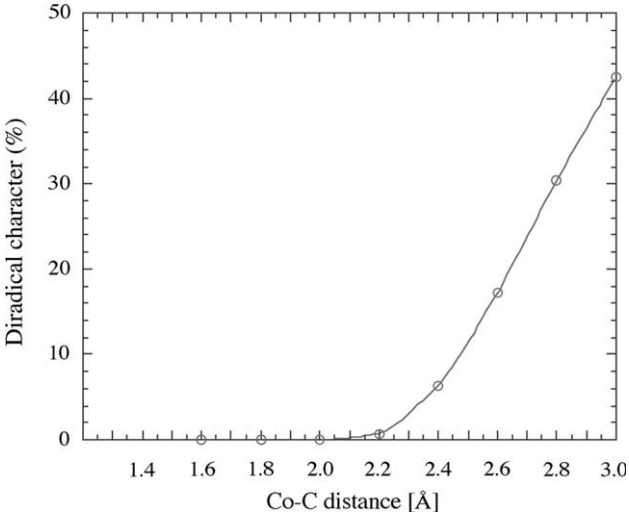


Fig. 6. Calculated instabilities in Co–C bond (y_i) by Eq. (18) using occupation number of natural orbital.

where J is effective exchange integrals, $\Delta\varepsilon$ is an energy gap between α-HOMO and β-HOMO. The J value is calculated by [4,5]

$$J = \frac{E^{\mathrm{LS}} - E^{\mathrm{HS}}}{\langle S^2\rangle_{\mathrm{HS}} - \langle S^2\rangle_{\mathrm{LS}}}. \tag{20}$$

The estimated values are $U = 1.29$ eV and $t = 1.07$ eV. From the estimated t and U, x and y values were also estimated as $x = 1.5$ and $y = 0.1$. By plotting the estimated x and y values in Fig. 3, it becomes obvious that the calculated x value is too large. There are several assumptions such as on-site Coulomb repulsion could be negligible. Those assumptions seem to influence on the overestimation. In addition, this result is suggesting that UB3LYP calculation overestimated the stability of anti-ferromagnetic coupling that have been reported previous paper [9–11]. MEDF approach seems

effective to the analyses of bond breaking in the system [9–11].

6. Conclusion

In this paper, we formulated the M–X bond formation and its dissociation analytically to obtain phase diagram. By estimating x (covalent bond parameter) and y (ionic parameter) values, we could discuss the nature of M–X bond using the phase diagram. The electronic structure of cobalamin, which involves Co–C bond, was calculated by using UB3LYP method. Those calculations revealed that corrin ring was essential for the Co–C bond. Co–C bond in the active site was covalent bond but potential minimum was on a bifurcation point between BS and SA. The covalent bond parameter (x) and ionic parameter (y) were estimated by using calculated J, t and U values. The estimated x was overestimated, suggesting that more appropriate approximation must be needed. On the other hand, Freindorf et al. [12] proposed the elongation (and/or shrinkage) mechanism of Co–N_{axial} bond by using QM/MM calculation results. In the paper, they summarized that elongation of Co–N_{axial} bond makes the radical formation easy. In this study, the Co–N_{axial} bond-length was constant although the Co–C bond-length was only variable. To analyze the phase diagram qualitatively, Co–N_{axial} bond-length also should be considered.

Acknowledgment

This work has been supported by a Grant-in-Aid for Scientific Research on Priority Areas (Nos. 16750049 and 14204061) from Ministry of Education, Culture, Sports, Science and Technology, Japan.

References

[1] A. Messerschmidt, R. Huber, T. Poulos, K. Wieghardt (Eds.), Handbook of Metaloprotains, John Wiley & Sons Ltd., West Sussex, England, 2001.
[2] K. Yamaguchi, T. Kawakami, Y. Takano, Y. Kitagawa, Y. Yamashita, H. Fujita, Int. J. Quant. Chem. 90 (2002) 370.
[3] K. Takatsuka, T. Fueno, K. Yamaguchi, Theoret. Chem. Acta 48 (1978) 175.
[4] T. Kawakami, S. Yamanaka, S. Yamada, W. Mori, K. Yamaguchi, in: Turnbull M.M., T. Sugimoto, L.K. Thompson (Eds.), Molecular-based Magnetic Materials, Theory, Technique and Applications, ACS Symposium Series, vol. 644, American Chemical Society, Washington, DC, 1996, p. 30.
[5] K. Yamaguchi, in: R. Carbeó, M. Klobukowski (Eds.), Self-consistent Field, Theory and Applications, Studies in Physical and Theoretical Chemistry, vol. 70, Elsevier, Amsterdam, 1990, p. 727.
[6] F. Mancia, P.R. Evans, Structure 6 (1998) 711.
[7] A.D. Becke, J. Chem. Phys. 98 (1993) 5648.
[8] M.J. Frisch, G.W. Trucks, H.B. Schlegel, G.E. Scuseria, M.A. Robb, J.R. Cheeseman, V.G. Zakrzewski, J.A. Montgomery Jr., R.E. Stratmann, J.C. Burant, S. Dapprich, J.M. Millam, A.D. Daniels, K.N. Kudin, M.C. Strain, O. Farkas, J. Tomasi, V. Barone, M. Cossi, R. Cammi, B. Mennucci, C. Pomelli, C. Adamo, S. Clifford, J. Ochterski, G.A. Petersson, P.Y. Ayala, Q. Cui, K. Morokuma, N. Rega, P. Salvador, J.J. Dannenberg, D.K. Malick, A.D. Rabuck, K. Raghavachari, J.B. Foresman, J. Cioslowski, J.V. Ortiz, A.G. Baboul, B.B. Stefanov, G. Liu, A. Liashenko, P. Piskorz, I. Komaromi, R. Gomperts, R.L. Martin, D.J. Fox, T. Keith, M.A. Al-Laham, C.Y. Peng, A. Nanayakkara, M. Challacombe, P.M.W. Gill, B. Johnson, W. Chen, M.W. Wong, J.L. Andres, C. Gonzalez, M. Head-Gordon, E.S. Replogle, J.A. Pople, GAUSSIAN98, Gaussian, Inc., Pittsburgh, PA, 2002.
[9] Y. Kitagawa, T. Kawakami, K. Yamaguchi, Mol. Phys. 100 (2002) 1829.
[10] Y. Kitagawa, T. Soda, Y. Shigeta, S. Yamanaka, Y. Yoshioka, K. Yamaguchi, Int. J. Quant. Chem. 84 (2001) 592.
[11] T. Soda, Y. Kitagawa, T. Onishi, Y. Takano, Y. Shigeta, H. Nagao, Y. Yoshioka, K. Yamaguchi, Chem. Phys. Lett. 319 (2000) 223.
[12] M. Freindorf, P.M. Kozlowski, J. Am. Chem. Soc. 126 (2004) 1928.

inner nickel(II) ions were considered to be low spin states ($S = 0$) [10]. However, more details about their electronic structures need to be elucidated. In addition, potentials of these complexes for molecular devices are also interesting issue in the scientific field of coordination chemistry.

In this study, we focused on the magnetic interactions in aligned $Ni(II)_5$ and $Ni(II)_7$ complexes, i.e. $[Ni_5(tpda)_4Cl_2]$ (**1**) and $[Ni_7(teptra)_4Cl_2]$ (**2**), respectively as illustrated in Fig. 1. Their electronic structures were calculated by unrestricted hybrid density functional theory (UHDFT) method, and the magnetic couplings were discussed by using effective exchange integrals (J_{ab}) values. Natural orbitals (NO) and their occupation numbers were analyzed in order to elucidate the mechanism of anti-ferromagnetic interactions. In comparison with those results, we elucidated the effects of bridge-ligands, axial-ligands and a chain length. Finally, the possibility of these complexes for the magnetic electron conductor (or semi-conductor) was discussed theoretically by estimating J_{ab} value of an electron-doped model.

2. Theoretical background

2.1. Effective exchange integrals (J_{ab})

The magnetic properties of transition metal complexes were usually investigated by the use of the Heisenberg–Dirac–van Vleck spin Hamiltonian. For example, the effective exchange interaction between localized spins in binuclear transition metal complexes is described by the total spin form of the spin-coupling Hamiltonian [11–15]

$$H = -2\sum J_{ab}\mathbf{S_a}\cdot\mathbf{S_b}, \tag{1}$$

where J_{ab} is the orbital-averaged effective exchange integral between the metal 'a' and 'b' with total spin operators $\mathbf{S_a}$ and $\mathbf{S_b}$. J_{ab} can be experimentally determined by magnetic susceptibility. Recent development in computational quantum chemistry enabled us to perform large ab initio calculations of J_{ab} values by using broken-symmetry (BS) approach such as UHF or UDFT [14,15]. The BS approach can be performed at a low computing cost. In singlet biradicals and low-spin species, however, it suffers from the spin contamination of high-spin states, leading to spin-projection procedures. Our group proposed spin projection scheme as follows:

$$J_{ab} = \frac{E(\mathrm{LS}) - E(\mathrm{HS})}{\langle S^2\rangle(\mathrm{HS}) - \langle S^2\rangle(\mathrm{LS})}, \tag{2}$$

where $E(X)$ and $\langle S^2\rangle(X)$ denote the total energy and total spin angular momentum for the spin state X, respectively [14,15]. In this paper, the magnetic interactions between Ni(II) ions were discussed using the equation.

2.2. Natural orbital analyses

Usual orbital-correlation diagram, which helps us to understand orbital interactions, is not obtained by the BS calculation because of the DODS approach [16]. In order to clarify the effective exchange interactions in the complexes using expression like the closed-shell MO, we introduced natural orbitals (NOs), which were determined by diagonalizing their first order density matrices as

$$\rho(r, r') = \sum n_i\{\phi_i(r)\}^*\phi_i(r'), \tag{5}$$

where n_i denoted the occupation number of NO ϕ_i [16,17]. If an occupation number of a magnetic orbital is close to 1.0, then two electrons in the orbital are almost localized on each spin site. On the other hand, n_i should be equal to 2.0 if stable chemical bond exists.

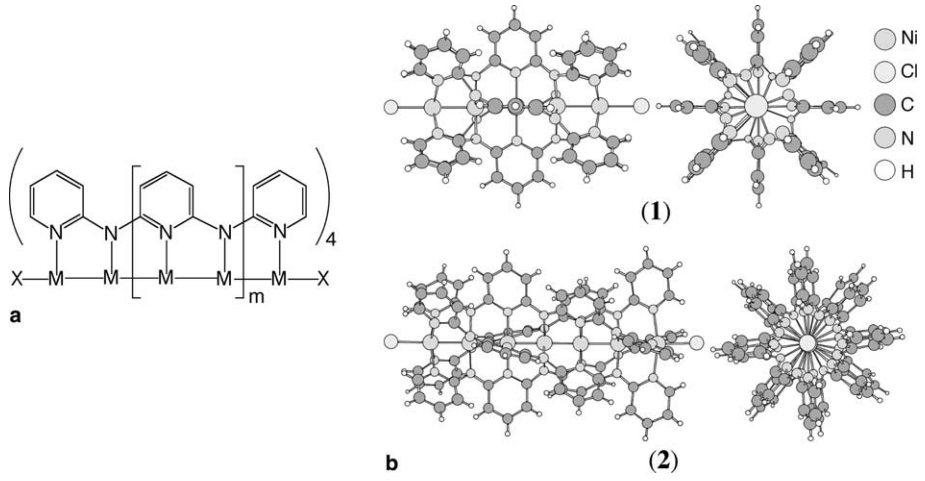


Fig. 1. (a) Illustration of metal chain complexes using oligo-α-pyridylamino ligands. (b) $[Ni_5(tpda)_4Cl_2]$ (**1**) and $[Ni_7(teptra)_4Cl_2]$ (**2**).

In other words, the occupation numbers of the BS method contains an important information to understand the stability in chemical bond.

To assess this instability (diradical character), instability value (y_i) for orbital type i ($i = \sigma$, δ and so on) is introduced here as follows [18]:

$$y_i = 2W_D^2 = \frac{n_i^2 - 4n_i + 4}{n_i^2 - 2n_i + 2}, \quad (9)$$

where n_i and n_i^* are occupation numbers of bonding and anti-bonding NO, respectively and W_D denotes the weight of double excitation for orbital i. If a chemical bond of orbital i is stable, y_i is close to zero. On the other hand, if a chemical bond of orbital i is unstable and spins are localized at metal sites, then y_i is close to unity. Especially, $y_i/2$ is consistent to a weight of the doubly exited configuration in the MCSCF theory.

In this way, metal–metal bond natures and degrees of electron correlation effect, which causes spin-localization are discussed in terms of instabilities in chemical bonds using these indices.

2.3. Computational details

Atomic coordinations of complexes were taken from data of X-ray crystal structure analyses that were available in the Cambridge Structural Database (CSD). Those calculations were performed by the use of Tatewaki-Huzinaga MIDI (533(21)/53(21)/(41)) basis set for Ni atoms, 6-31+G* basis sets for axial ligand atoms and 6-31G basis sets for bridge ligand atoms. All calculation was carried out using GAUSSIAN98 [19].

3. Calculated results

3.1. Effective exchange integrals of $[Ni_5(tpda)_4Cl_2]$ and $[Ni_7(teptra)_4Cl_2]$ complexes

The electronic structures for low spin (singlet) states and high spin states (quintet) of the complexes **1** and **2** were calculated by UB3LYP method [20]. Calculated Mulliken charge densities and spin densities of $[Ni_5(tpda)_4Cl_2]$ (**1**) were summarized in Table 1. Although charge densities on each Ni ion are almost equivalent, spin densities are only appeared on the terminal Ni ions in both cases of high-spin and low-spin state. Calculated Mulliken charge densities and spin densities of $[Ni_7(teptra)_4Cl_2]$ were summarized in Table 2. In this complex, spin densities are also localized on terminal Ni ions. These results are showing that terminal Ni ions are open-shell ($S = 1$) and other inner Ni ions are closed-shell ($S = 0$) structures that are consistent with experimental results. It is showing spin localized structures on the end Ni ions.

Table 1
Calculated charge density and spin densities of $[Ni_5(tpda)_4Cl_2]$ for low spin state (LS) and high spin state (HS)

Atom[a]	Charge density		Spin density	
	LS	HS	LS	HS
Ni1	0.65	0.65	1.58	1.58
Ni2	0.84	0.84	0.12	0.13
Ni3	0.70	0.70	−0.01	0.03
Ni4	0.83	0.83	−0.13	0.15
Ni5	0.64	0.64	−1.57	1.56

[a] Cl–Ni1–Ni2–Ni3–Ni4–Ni5–Cl.

Table 2
Calculated charge density and spin densities of $[Ni_7(teptra)_4Cl_2]$ for low spin state (LS) and high spin state (HS)

Atom[a]	Charge density		Spin density	
	LS	HS	LS	HS
Ni1	0.64	0.64	1.59	1.59
Ni2	0.77	0.77	0.10	0.10
Ni3	0.70	0.70	0.02	0.02
Ni4	0.76	0.76	0.00	0.01
Ni5	0.70	0.70	−0.01	0.01
Ni6	0.79	0.79	−0.10	0.10
Ni7	0.64	0.64	−1.60	1.60

[a] Cl–Ni1–Ni2–Ni3–Ni4–Ni5–Ni6–Ni7–Cl.

The spin densities on open-shell Ni ions of $[Ni_5(tpda)_4Cl_2]$ and $[Ni_7(teptra)_4Cl_2]$ are equivalent, suggesting weak exchange-coupling, which depends on chain length. The effective exchange integrals (J_{ab}) values between spins on terminal Ni ions were calculated by Eq. (2) and they are summarized in Table 3. Total energies and expectation values of the operator $\mathbf{S}^2$ ($\langle S^2 \rangle$) used in the equation are also summarized in the table. Experimental week anti-ferromagnetic couplings are reproduced by UB3LYP calculations well. Both experimental and calculated results indicate that J_{ab} value decreases against an increase of chain length. On the other hand, from computational view point, this result is showing that it is possible to reproduce small J_{ab} values well in such large complexes by unrestricted DFT calculations.

3.2. Natural orbital analyses

Natural orbitals (NOs) and their occupation numbers by UB3LYP method were analyzed in order to elucidate the mechanism of anti-ferromagnetic interactions. The magnetic orbitals are σ type and δ type orbitals (σ orbital and δ orbital, respectively) as illustrated in Fig. 2. In the complexes, σ orbitals were delocalized to axial ligand, while δ orbitals were not. In other words, the character of axial ligands conspicuously appears in the σ orbitals in terms of magnetic property. As a consequence, a dependence upon axial ligands in J_{ab} values that are reported in the references stems from the change

Table 3
Calculated and experimental effective exchange integrals (J_{ab})[a] for $[Ni_5(tpda)_4Cl_2]$ and $[Ni_7(teptra)_4Cl_2]$

Complex	Low-spin state		High-spin state		J_{ab} (calc.)	J_{ab} (expt.)
	Total energy	$\langle S^2\rangle$	Total energy	$\langle S^2\rangle$		
$[Ni_5(tpda)_4Cl_2]$	−11866.2713346	2.2847	−11866.2711053	6.2900	−12.6	−8.3
$[Ni_7(teptra)_4Cl_2]$	−16089.8500892	2.2636	−16089.8499729	6.2551	−6.4	−3.8
$[Ni_5(tpda)_4Cl_2]^{2-}$	−11866.2186237	2.3763	−11866.2179093	6.3368	−39.6	

Theoretical J_{ab} values were calculated by Eq. (2) using total energies[b] and $\langle S^2\rangle$ values of low-spin state and high-spin state summarized together in the table.
[a] In cm^{-1}.
[b] In atomic unit.

of σ orbitals. The δ orbitals have spiral structure that reflects the spiral structure of bridge ligands. This result indicated that the structure of bridge ligands strongly affected shape of δ orbitals because overlaps between atomic orbitals of each Ni ions in δ bonds are small.

Occupation numbers and instability values (y) of magnetic orbitals were summarized in Table 4. Occupation numbers of magnetic orbitals were almost unity, showing that spins were almost localized Ni(II) ions of the both ends. And y values were almost 100%, indicating that direct exchange coupling between spins on the Ni ions is quite small. It means that weak anti-ferromagnetic coupling mainly derived from interactions through bridge ligands. In other words, decrease of exchange-coupling in $[Ni_7(teptra)_4Cl_2]$ in comparison with $[Ni_5(tpda)_4Cl_2]$ comes from the decrease of exchange interactions through bridge ligands. Ni_7 chain and Ni_5 chain are relatively long, therefore the direct exchange between Ni spins of the both ends seemed to be negligible. However, direct exchange coupling might become domestic, in shorter chain complex such as Ni_3, which has larger anti-ferromagnetic coupling.

3.3. Molecular orbitals and their orbital energies near HOMO–LUMO

Molecular orbitals of $[Ni_5(tpda)_4Cl_2]$ and $[Ni_7(teptra)_4Cl_2]$ near HOMO–LUMO are depicted in Fig. 4. HOMOs of both complexes are σ-orbitals. LUMO of Ni_5 complex **1** consists of π-conjugated orbital of bridge ligands, while LUMO of Ni_7 complex **2** is d-orbital of the Ni ions. Orbital energies of

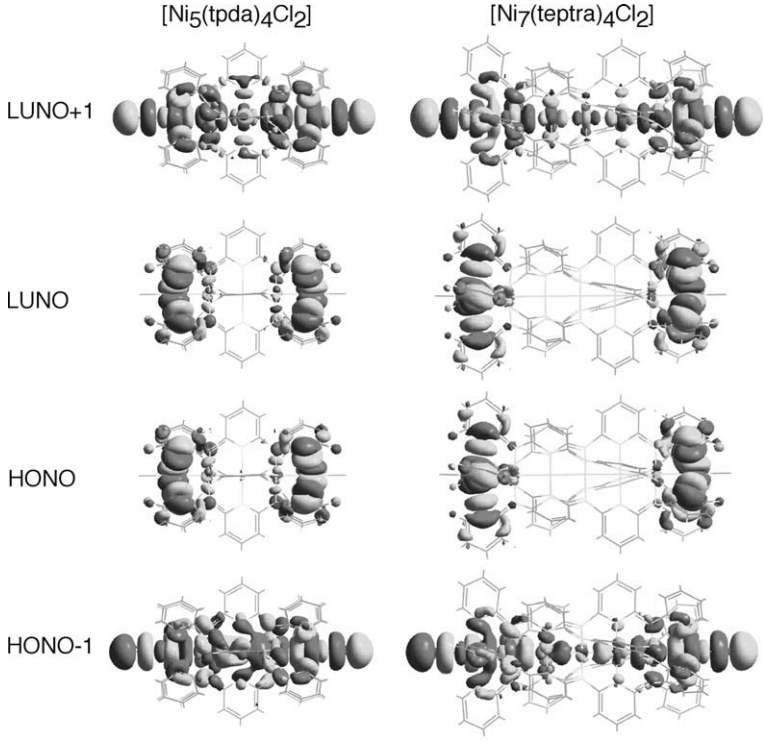


Fig. 2. Natural orbitals of $[Ni_5(tpda)_4Cl_2]$ (**1**) and $[Ni_7(teptra)_4Cl_2]$ (**2**) for low-spin state. Depicted NOs are magnetic orbitals.

Table 4
Occupation numbers and instability values (y)[a] of natural orbitals for $[Ni_5(tpda)_4Cl_2]$ and $[Ni_7(teptra)_4Cl_2]$

Natural orbital	$[Ni_5(tpda)_4Cl_2]$		$[Ni_7(teptra)_4Cl_2]$	
	Occupation no.	y	Occupation no.	y
HONO	1.001	99.8	1.000	100.0
HONO-1	1.078	84.5	1.018	96.4
HONO-2	1.858	1.2	1.894	0.6
HONO-3	1.996	0.0	1.978	0.0
HONO-4	1.997	0.0	1.997	0.0

[a] In %.

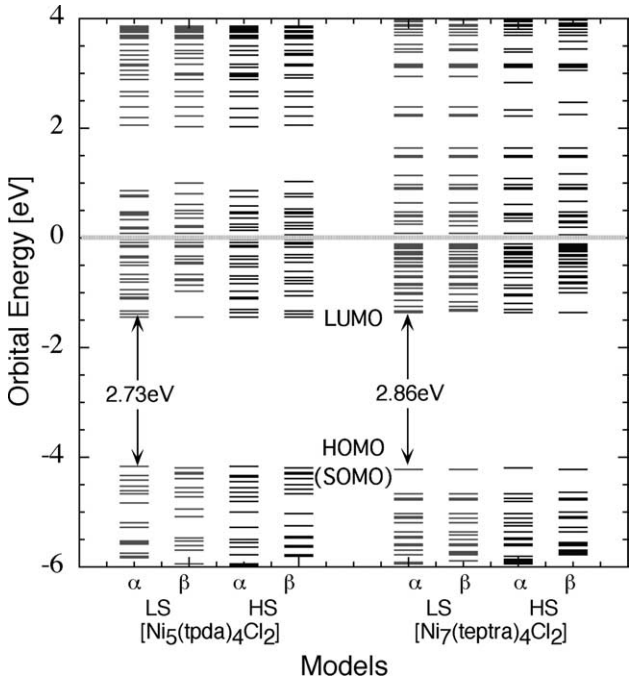


Fig. 3. The α and β orbital energies of $[Ni_5(tpda)_4Cl_2]$ (**1**) and $[Ni_7(teptra)_4Cl_2]$ (**2**) for low-spin state (LS) and high-spin state (HS), respectively. The HOMO–LUMO gaps of them are 2.73 and 2.86 eV, respectively.

$[Ni_5(tpda)_4Cl_2]$ and $[Ni_7(teptra)_4Cl_2]$ obtained by UB3LYP calculations were depicted in Fig. 3. HOMO–LUMO gaps of $[Ni_5$- $(tpda)_4Cl_2]$ and $[Ni_7(teptra)_4Cl_2]$ are 2.73 and 2.86 eV, respectively. These HOMO–LUMO gaps are larger than usual semi-conductors such as Si (1.17 eV) and Ge (0.744 eV) [21]. Interestingly, orbital energies of LUMO and many unoccupied orbitals are negative, showing their high electron affinities. It means electrons are easily doped in the complexes.

3.4. Possibility of magnetic electron conductor using the one-dimensional complexes

The one-dimensional complexes are one of the promising compounds for the magnetic electron conductor [22]. For example, three-terminal devices by using these complexes were proposed as illustrated in Fig. 5(a) [22]. One of the approaches is σ-metal and δ-spin approach as illustrated in Fig. 5(a). In this approach, electrons in σ-orbitals (σ-electron) that have relatively large overlap bear conductivity, while electrons in δ-orbitals (δ-electrons) that act as localized spins bear magnetism. The charge on metal ions, however, changes in a process of charge-doping or electron transfer. It would cause the structural change such as Peierls transition, leading the change in magnetic interaction. In addition, change in formal charge of Ni(II) ions might cause electronic change such as Motto transition that is a transformation to an insulator. Therefore it seems to be better to dope carrier without change in formal charge on metal ions.

There are two ways to dope carrier for the conductivity, one is hole-dope and another is electron-dope. As mentioned before, the complex **1** has HOMO derived from Ni(II) d-orbitals and LUMO derived from π-conjugated ligand orbitals as illustrated in Fig. 4(a). In this system, if hole is doped, charges of Ni ions are changed. On the other hand, if electron is doped, charge is doped in ligand orbitals. In this case, charges on the Ni ions do not change. Therefore, conductivity might appear without a disorder of magnetic interactions between metal ions in the complex. In case of the complex **2**, however, both HOMO and LUMO derive from metal d-orbitals. Therefore, both hole-dope and electron-dope change charges of Ni ions.

To confirm the idea, we carried out UB3LYP calculations using electron-dope model of $[Ni_5(tpda)_4Cl_2]$, in which LUMO was ligand orbital as illustrated in Fig. 4. In order to hold a number of spins, singlet-paired two-electrons were doped in the complex. Calculated result is summarized in Table 5. The negative J_{ab} value of the neutral model is slightly strengthened in electron-dope model because through-ligand interactions (super-exchange interaction) are enhanced by electron-dope. However, the anti-ferromagnetic coupling is not broken by the electron-dope into the ligand orbitals. By using bridge-ligand which was designed for electron conducting, the system of ligand–metal Ni-spin model seemed to be possible. Tanaka and Shionoya et al. [23–25] reported that the one-dimensional metal

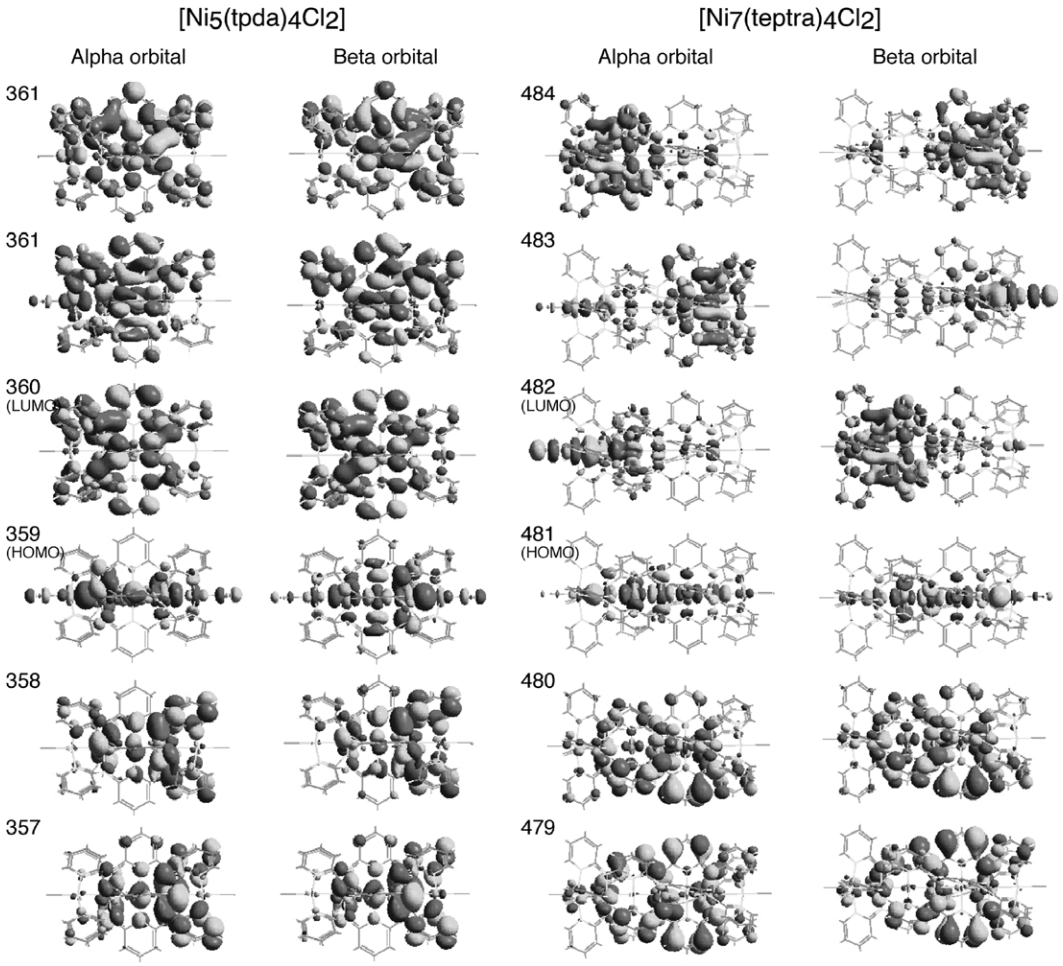


Fig. 4. Molecular orbitals of $[Ni_5(tpda)_4Cl_2]$ (**1**) and $[Ni_7(teptra)_4Cl_2]$ (**2**) for low-spin state around HOMO–LUMO.

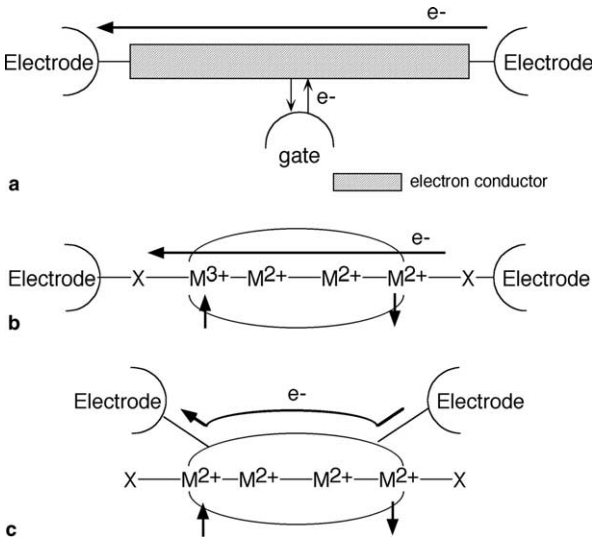


Fig. 5. (a) Illustration of three terminal device in [22]. (b) Illustration of σ-metal, δ-spin model. In this model, electrons in σ-orbitals bear conduction and electrons in δ-orbitals act as spin source. (c) Illustration of ligand–metal, δ-spin model. In this model, electrons doped in bridge-ligands bear conduction and electrons in δ- (or σ-) orbitals act as spin source.

Table 5
Change of J_{ab} by electron-dope

Models	J_{ab} (cm^{-1})
$[Ni_5(tpda)_4Cl_2]$	−12.6 (−8.27)*
$[Ni_5(tpda)_4Cl_2]^{2-}$	−39.6

* Experimental value is in the parenthesis.

complex using DNA as ligand. If DNA-ligands conduct the electron, the complex might be most possible candidate of out strategy.

4. Concluding remarks

In this study, weak anti-ferromagnetic J_{ab} values were reproduced and their mechanism was clarified. Recent development of quantum chemistry and computational method makes it possible to calculate J_{ab} values of large complexes, quantitatively [26–29]. The calculation of J_{ab} value is one of the strategies for the investigations of their electronic structures [30–32].

We also carried out the calculations using electron-doped model complex. From the results, we proposed the possible method for the magnetic electron conductors. The calculations have several weak points that can not be ignored. For example, structure of the complex may change by the electron doping but it is not included in the calculations. Electron conductivity is not also calculated. However, bridge-ligands are usually π-conjugated systems and rigid and high-conducting bridge-ligands will be presented.

Acknowledgement

This work has been supported by a Grant-in-Aid for Scientific Research on Priority Areas (Nos. 16750049 and 14204061) from Ministry of Education, Culture, Sports, Science and Technology, Japan.

References

[1] S.-Y. Lai, T.-W. Lin, Y.-H. Chen, C.-C. Wang, G.-H. Lee, M.-h. Yang, M.-K. Leung, S.-M. Peng, J. Am. Chem. Soc. 121 (1999) 250.
[2] C.-C. Wang, W.-C. Lo, C.-C. Chou, G.-H. Lee, J.-M. Chen, S.-M. Peng, Inorg. Chem. 37 (1998) 4059.
[3] F.A. Cotton, T.R. Felthpuse, Inorg. Chem. 19 (1980) 328.
[4] F.A. Cotton, T.R. Felthpuse, Inorg. Chem. 20 (1981) 600.
[5] F.A. Cotton, X. Feng, P.A. Kibala, M. Matusz, J. Am. Chem. Soc. 110 (1988) 2807.
[6] F.A. Cotton, Y. Kim, T. Ren. Inorg. Chem. 31 (1992) 2723.
[7] F.A. Cotton, Y. Kim, T. Ren, Polyhedron 12 (1993) 607.
[8] J.K. Bera, K.R. Dunbar, Angew Chem. Int. Ed. 41 (2002) 23.
[9] K. Mashima, M. Tanaka, T. Tani, A. Nakamura, S. Takeda, W. Mori, K. Yamaguchi, J. Am. Chem. Soc. 119 (1997) 4307.
[10] S.-M. Peng, C.-C. Wang, Y.-L. Jang, Y.-H. Chen, F.-Y. Li, C.-Y. Mou, M.-K. Leung, J. Magn. Magn. Mater. 209 (2000) 80.
[11] D. Gatteschi, O. Kahn, J.S. Miller, F. Palacio (Eds.), Magnetic Molecular Materials, Kluwer Academic Publishers, Dordrecht, 1991.
[12] O. Kahn (Ed.), Magnetism: a Supermolecular Function, NATO ASI Series C, vol. 484, Kluwer Academic Publishers, Dordrecht, 1996.
[13] E. Coronado, P. Dekhais, D. Gatteschi, J.S. Miller (Eds.), Molecular Magnetism: from Molecular Assemblies to the Devices, NATO ASI Series E, vol. 321, Kluwer Academic Publishers, Dordrecht, 1996.
[14] T. Kawakami, S. Yamanaka, S. Yamada, W. Mori, K. Yamaguchi, in: M.M. Turnbull, T. Sugimoto, L.K. Thompson (Eds.), Molecular-based Magnetic Materials, Theory, Technique and Applications, ACS Symposium Series, vol. 644, American Chemical Society, Washington, DC, 1996, p. 30.
[15] K. Yamaguchi, in: R. Carbeó, M. Klobukowski (Eds.), Self-consistent Field, Theory and Applications, Studies in Physical and Theoretical Chemistry, vol. 70, Elsevier, Amsterdam, 1990, p. 727.
[16] K. Takatsuka, T. Fueno, K. Yamaguchi, Theoret. Chem. Acta 48 (1978) 175.
[17] Y. Takano, Y. Kitagawa, T. Onishi, Y. Yoshioka, K. Yamaguchi, N. Koga, H. Iwamura, J. Am. Chem. Soc. 124 (2002) 450.
[18] K. Yamaguchi, T. Kawakami, Y. Takano, Y. Kitagawa, Y. Yamashita, H. Fujita, Int. J. Quant. Chem. 90 (2002) 370.
[19] M.J. Frisch, G.W. Trucks, H.B. Schlegel, G.E. Scuseria, M.A. Robb, J.R. Cheeseman, V.G. Zakrzewski, J.A. Montgomery Jr., R.E. Stratmann, J.C. Burant, S. Dapprich, J.M. Millam, A.D. Daniels, K.N. Kudin, M.C. Strain, O. Farkas, J. Tomasi, V. Barone, M. Cossi, R. Cammi, B. Mennucci, C. Pomelli, C. Adamo, S. Clifford, J. Ochterski, G.A. Petersson, P.Y. Ayala, Q. Cui, K. Morokuma, N. Rega, P. Salvador, J.J. Dannenberg, D.K. Malick, A.D. Rabuck, K. Raghavachari, J.B. Foresman, J. Cioslowski, J.V. Ortiz, A.G. Baboul, B.B. Stefanov, G. Liu, A. Liashenko, P. Piskorz, I. Komaromi, R. Gomperts, R.L. Martin, D.J. Fox, T. Keith, M.A. Al-Laham, C.Y. Peng, A. Nanayakkara, M. Challacombe, P.M.W. Gill, B. Johnson, W. Chen, M.W. Wong, J.L. Andres, C. Gonzalez, M. Head-Gordon, E.S. Replogle, J.A. Pople, GAUSSIAN98, Gaussian, Inc., Pittsburgh, PA, 2002.
[20] A.D. Becke, J. Chem. Phys. 98 (1993) 5648.
[21] C. Kittel, Introduction to Solid State Physics, John Wiley & Sons, Inc., New York, 1986.
[22] A. Nakamura, N. Ueyama, K. Yamaguchi (Eds.), Organometallic Conjugation, Springer Series in Chemical Physics, vol. 73, Kodansha Ltd./Springer-Verlag, Tokyo/Berlin Heidelberg, New York, 2002.
[23] K. Tanaka, A. Tengeiji, T. Kato, N. Toyama, M. Shionoya, Science 299 (2003) 1212.
[24] K. Tanaka, A. Tengeiji, T. Kato, N. Toyama, M. Shionoya, J. Am. Chem. Soc. 124 (2002) 12494.
[25] (a) K. Tanaka, Y. Yamada, M. Shionoya, J. Am. Chem. Soc. 124 (2002) 8802;
(b) K. Tanaka, M. Shionoya, J. Org. Chem. 64 (1999) 5502.
[26] Y. Kitagawa, S. Nakano, T. Kawakami, K. Mashima, K. Yamaguchi, Polyhedron 22 (2003) 2019.
[27] S. Nakano, Y. Kitagawa, T. Kawakami, K. Yamaguchi, Polyhedron 22 (2003) 2027.
[28] Y. Kitagawa, S. Nakano, T. Kawakami, K. Mashima, K. Tani, K. Yamaguchi, Mol. Cryst. Liq. Cryst. 379 (2002) 525.
[29] Y. Kitagawa, T. Kawakami, Y. Yoshioka, K. Yamaguchi, Polyhedron 20 (2001) 1189.
[30] Y. Kitagawa, T. Kawakami, K. Yamaguchi, Mol. Phys. 100 (2002) 1829.
[31] Y. Kitagawa, T. Soda, Y. Shigeta, S. Yamanaka, Y. Yoshioka, K. Yamaguchi, Int. J. Quant. Chem. 84 (2001) 592.
[32] T. Soda, Y. Kitagawa, T. Onishi, Y. Takano, Y. Shigeta, H. Nagao, Y. Yoshioka, K. Yamaguchi, Chem. Phys. Lett. 319 (2000) 223.

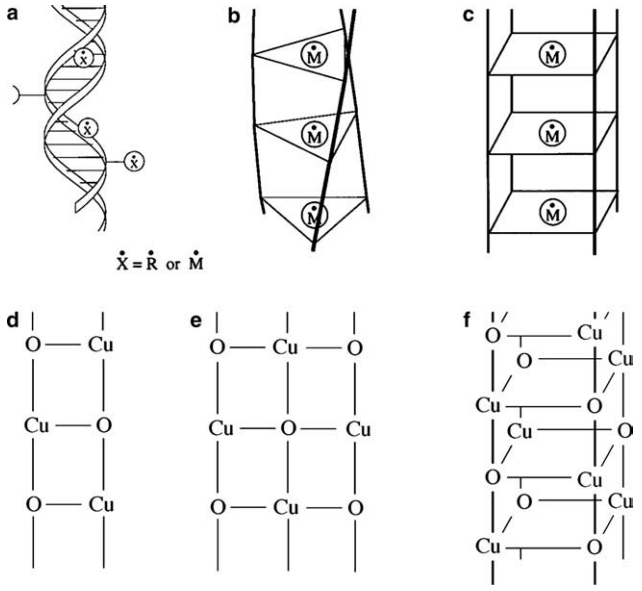


Fig. 1. Structures of double (a), triple (b) and quadruple (c) helices of DNA oligomers with radical groups, as well as single (d), double (e) and quadruple (f) ladders that are respectively analogues of the former three structures.

well as inorganic complexes [66,67]. Fig. 2 illustrates our theoretical efforts toward molecule-based magnetic conductors. Applicability of the field-effect transistor (FET) configuration has been also discussed in relation to the so-called molecular spintronics [64,68].

In order to elucidate electron-donating properties and ionization potentials (IP) of purine and pyridine bases in DNA, we have already performed ab initio MO calculations of guanine (G), adenine (A), thymine (T) and cytosine (C), and their paired oligomers $(GC)_n$ $(AT)_m$ [69–71]. The calculated IP values have been found to become lower and lower for (GG), (GGG) and (GGGG) oligomers, in agreement with experiments [21–34]. The oxidation of these oligomers, however, entails a difficult problem that their reactivities with oxygen, metal ion [71], etc. should be suppressed to obtain stable soft materials for molecular electronics and devices based on DNA. As a continuation of previous works [69–71], we wish to examine three key points theoretically:

(1) structural modification of guanine molecule for the suppression of oxidation damage,
(2) magnetic modification of such guanine derivatives (G) with the introduction of spin sources ($R^{\bullet}$) such as nitroxide and metal complexes,
(3) construction of molecular magnetic conductors and molecular solenoids with G–$R^{\bullet}$ components.

Finally, implications of these computational results will be discussed in the relation to DNA-based magnetic materials.

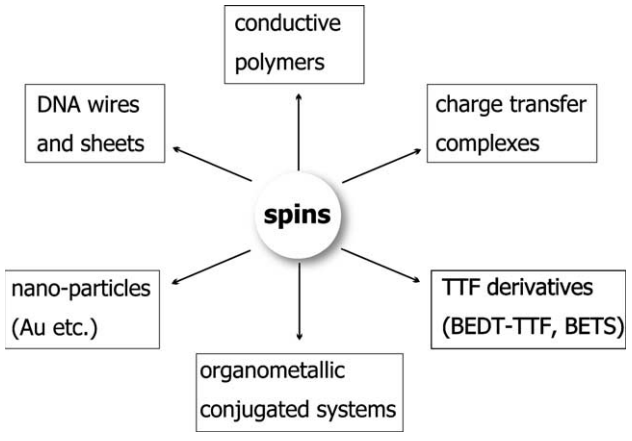


Fig. 2. Schematic diagrams of spin-featured molecular design for organic magnetic conductors.

2. Ab initio computation of effective exchange integrals

2.1. Theoretical models

Band models based on the extended Hückel tight-binding approximation work well for theoretical understanding of many molecular conductors such as TTF-derivatives [72]. Recent experiments, however, have revealed that antiferromagnetic state appears even in organic systems such as phenalenyl dimer [73] because of the strong electron correlation, and resulting Mott insulators that usually entail localized spins. Magnetism is also one of key issues in phenalenyl-derivatives and other related species. Their magnetic properties have been investigated by the Heisenberg-type spin coupling Hamiltonian [74–76]

$$H(\mathrm{HB}) = -\sum_{ab} 2J_{ab}\mathbf{S}_a \cdot \mathbf{S}_b, \quad (1)$$

where J_{ab} is the orbital-averaged effective exchange integral between the ath and bth radical sites with total spin operators $\mathbf{S}_a$ and $\mathbf{S}_b$. Recent development of the ab initio computational techniques has made it possible to calculate the J_{ab} values for phenalenyl derivatives [73]. These methods are classified into two types. One is the spin-symmetry adapted (SA) perturbational and configuration interaction (CI) approach. Use of the SA method is desirable for the quantitative computations of J_{ab} but it is hardly applicable to transition-metal complexes because of the high computational costs. The other is the broken-symmetry (BS) approach [73–76], which is often used for such systems because of their lower computational costs, though the spin contamination problem occurs in the low-spin (LS) state [76].

Broken-symmetry (BS) calculations of J_{ab} for molecule-based magnets have been performed on the basis of different computational schemes such as Eqs. (2a)–(2c).

$$J_{ab}^{(1)} = \frac{^{LS}E(X) - {}^{HS}E(X)}{S_{max}^2}, \tag{2a}$$

$$J_{ab}^{(2)} = \frac{^{LS}E(X) - {}^{HS}E(X)}{S_{max}(S_{max}+1)}, \tag{2b}$$

$$J_{ab}^{(3)} = \frac{^{LS}E(X) - {}^{HS}E(X)}{^{HS}\langle S^2\rangle - {}^{LS}\langle S^2\rangle}, \tag{2c}$$

where $^{Y}E(X)$ and $^{Y}\langle S^2\rangle(X)$ denote, respectively, total energy and total spin angular momentum for the spin state Y by the method X (=UHF, UDFT, etc.). The first scheme $J_{ab}^{(1)}$ has been derived by Noodleman [74], Noodleman and Davidson [75] (ND), while the second scheme $J_{ab}^{(2)}$ has been proposed by ND, Bencini [77] and others. $J_{ab}^{(1)}$ is derived when the overlap of magnetic orbitals is sufficiently small, while $J_{ab}^{(2)}$ is applicable when the overlap is sufficiently large. $J_{ab}^{(3)}$ by our approximate spin projection (AP) procedure [76] is close to $J_{ab}^{(1)}$ by ND if $^{HS}\langle S^2\rangle = S_{max}(S_{max}+1)$ and $^{LS}\langle S^2\rangle S_{max}$, where S_{max} is the spin size for the HS state. $J_{ab}^{(3)}$ becomes equivalent to $J_{ab}^{(2)}$ in the strong overlap region, where $^{LS}\langle S^2\rangle \approx 0$ [76]. Therefore, our scheme [43] involves others [74,75,77] as the strong and weak correlation limits.

As shown previously [78], our AP scheme can be extended to trinuclear, and more larger clusters, though $J_{ab}^{(1)}$ and $J_{ab}^{(2)}$ do not work for them. On the other hand, $J_{ab}^{(4)}$ without spin projection is given for both linear and ring forms by

$$J_{ab}^{(4)} = \frac{^{LS}E(X) - {}^{HS}E(X)}{4(N-1)S_aS_b}, \tag{3}$$

where N is the total spin site number and S_c is the size of spin S_c ($c = a, b$). This equation is applicable to periodic systems involving the same cluster unit cells [79].

2.2. Computational methods

The hybrid-DFT method calculated properties of these derivatives by using B3LYP functional that has Becke's exchange [80] involving the gradient of the density and Vosko, Wilk and Nusair (VWN) [81] correlation functional, and the last term is the correlation correction of Lee, Yang and Parr (LYP) correlation functional [82]. All hybrid density functional (HDFT) calculations were performed by using GAUSSIAN 98 program [83] package.

3. Hubbard, Heisenberg and RKKY models for strong correlation systems

3.1. Model Hamiltonians and electronic properties

In this section we briefly summarize theoretical background for a reduction of ab initio results to model Hamiltonians. Previously, we have examined electronic structures of high-T_C copper oxides using ab initio MO methods [45,84], showing the necessity of N-band models for the systematic descriptions of magnetism, conductivity and superconductivity of the species. Some organometallic and organic systems (isoelectronic to copper oxides) have been also proposed on the basis of the ab initio results [45–48] as shown in Fig. 1. N-band models often reduce to the two-band model, which has been used for the elucidation of Kubo–Inagaki [85,86] mechanism of ferromagnetism and other magnetic states, and Suhl–Kondo mechanism [87,88] and related multi-band models [45–48] for superconductivity.

In previous papers [89,90], the two-band model combined with the temperature Green's function technique has been applied to elucidate phase diagrams of charge density wave (CDW), spin density wave (SDW), singlet superconductivity (SSC), triplet superconductivity (TSC) and ferromagnetism (FM). Instead of the two-band model, Anderson lattice model [91] or Kondo lattice model [92] can be used for the theoretical descriptions of ferromagnetic metals, paramagnetic metals, spin liquid of electron of hole-doped conducting polymers interacting with coordination compounds with spins ($M^{\bullet}$) [93] and the donor (D)–acceptor (A) complexes, where D or A are interacting with the magnetic species ($M^{\bullet}$). The so-called RKKY model [94–96] is used for theoretical description of effective exchange couplings of spins via the spin polarization of conduction electrons. The RKKY model has been employed for theoretical studies of ferromagnetism, antiferromagnetism, helical spin structure and spin glass of organic, organometallic and biomolecular magnetic materials.

3.2. Hubbard models for p–d, π–d and π–R systems

Ab initio calculations of large magnetic clusters in Section 1 are often time-consuming. Therefore, the extended Hubbard Hamiltonian [97–100] can be generally used for p–d, π–d and π–R systems that are insulators because of electron correlation effects

$$H = H_q + H_r + H_{qr}, \tag{4}$$

where H_q denotes the Hamiltonian for (pπ)- or d-electrons, and H_{qr} is the interaction Hamiltonian between them as follows:

$$\begin{aligned} H_q &= \sum_q T_q a_q^{\dagger} a_q + \sum_{qr} U_{qr} a_q^{\dagger} a_q b_r^{\dagger} b_r, \\ H_{qr} &= \sum_{qr} T_{qr}\left(a_q^{\dagger} b_r + b_r^{\dagger} b_q\right), \end{aligned} \tag{5}$$

where $a^{\dagger}$ and $b^{\dagger}$ create electron (or hole) on the qth site and the rth site, respectively (q, r = p, π and d). U_{qq} and U_{qr} (=V) are on-site and inter-site Coulomb repulsions, and T_{qq} (=ε_{qq}) and T_{qr} are orbital energy and transfer

integral between (pπ)- and d(R)-orbitals, respectively. The parameters used in Eq. (5) were estimated from the ab initio results and spectroscopic data as shown previously [45,98–100]. The CT excitation energy (Δ_{qr}) from the donor site to the acceptor vacant orbital is given under the Hubbard model as

$$\Delta_{qr} = (\varepsilon_{rr} - \varepsilon_{qq}) + (U_{rr} - U_{qq}). \tag{6}$$

Therefore, the on-site Coulomb repulsion plays an important role for CT excitation. Then careful examination of these parameters is crucial for rational design of CT complexes near the neutral-ionic transition (see below).

3.3. Heisenberg model

The Hubbard model often reduces to the Heisenberg spin Hamiltonian in the case of strong electron correlation systems. The exact diagonalization (full CI) of singlet and triplet CI matrices of the Hubbard model provide the effective exchange integral in Eq. (1) as

$$E_{\mathrm{CI}}(\text{singlet}) - E_{\mathrm{CI}}(\text{triplet}) = 2J_{dd}. \tag{7}$$

If the effective exchange integral (Eq. (7)) between transition metal ions is weak, it can be approximately given by the perturbation theory as

$$J_{dd} = -\frac{2T_{pd}^4}{\Delta_{pd}}\left\{\frac{1}{\Delta_{pd}^2} + \frac{1}{U_{dd}\Delta_{pd}}\right\}$$

$$= -2(t_{dd})^2\left\{\frac{1}{\Delta_{pd}} + \frac{1}{U_{dd}}\right\}, \tag{8a}$$

$$= \frac{-2(t_{dd})^2}{\Delta_{pd}}\left(t_{dd} = \frac{T_{pd}^2}{\Delta_{pd}}\right). \tag{8b}$$

From Eq. (8a), J_{dd} is sensitive to the magnitude of Δ_{pd} and U_{dd}. Its magnitude increases sharply with the decrease of Δ_{pd} as in the case of copper oxide, and it is approximately given by Eq. (8b). J_{dd} in Eq. (8a) is reduced to the following familiar form if $U_{dd} < \Delta_{pd}$: namely the Mott–Hubbard case.

$$J_{dd} = -\frac{2t_{dd}^2}{U_{dd}}. \tag{9}$$

These situations are similar even for π–R systems in Fig. 2.

3.4. Anderson and Kondo lattice models

As shown in Fig. 1, molecular systems described by multi-band models are our theoretical targets to realize multifunctional materials. Previously, we have used Anderson and Kondo lattice models [45,57,93] for molecular design of doped-magnetic polymers and segregated columns of CT complexes coupled with coordination compounds with spins (M$^{\bullet}$). Very recently, antiferromagnetic and ferromagnetic metal states were discovered for organic-inorganic hybrid systems [101–105]. The Anderson model Hamiltonian for these species is given by

$$H = \sum_{\mathbf{k}\sigma}\varepsilon_{\mathbf{k}}c_{\mathbf{k}\sigma}^{\dagger}c_{\mathbf{k}\sigma} + \sum_{j\sigma}E_{\mathrm{R}}R_{j\sigma}^{\dagger}R_{j\sigma}$$
$$+ U\sum_{i}R_{i\uparrow}^{\dagger}R_{i\uparrow}R_{i\downarrow}^{\dagger}R_{i\downarrow} + T\sum_{i\mathbf{k}\sigma}R_{i\sigma}^{\dagger}c_{\mathbf{k}\sigma} + c_{\mathbf{k}\sigma}^{\dagger}R_{i\sigma}$$
$$= \sum_{\mathbf{k}\sigma}\varepsilon_{\mathbf{k}}c_{\mathbf{k}\sigma}^{\dagger}c_{\mathbf{k}\sigma} + \sum_{j\sigma}E_{\mathrm{R}}R_{\mathbf{k}\sigma}^{\dagger}R_{\mathbf{k}\sigma}$$
$$+ \frac{U}{N}\sum_{\mathbf{k}\mathbf{k}'\mathbf{q}}R_{\mathbf{k}+\mathbf{q}\uparrow}^{\dagger}R_{\mathbf{k}'-\mathbf{q}\downarrow}R_{\mathbf{k}'\downarrow}^{\dagger}R_{\mathbf{k}\uparrow} + T\sum_{\mathbf{k}\sigma}R_{\mathbf{k}\sigma}^{\dagger}c_{\mathbf{k}\sigma} + c_{\mathbf{k}\sigma}^{\dagger}R_{\mathbf{k}\sigma}, \tag{10}$$

where $\varepsilon_{\mathbf{k}}$ is the energy level of conduction electron and U and E_{R} denote the on-site Coulomb repulsion of spin site (R) and SOMO energy level of R, respectively, and T is the interaction matrix element between conduction electron and SOMO electron. The electronic structures of the Anderson lattice model are highly dependent on relative magnitudes of $\varepsilon_{\mathbf{k}}$, E_{R} and U as discussed previously [93]. The so-called Kondo regime [88] is defined as a specific state where the SOMO level (E_{R}) is deeper than the Fermi level (ε_{F}), even if the band width (Γ) of radical electrons is taken into account ($\varepsilon_{\mathrm{F}} - E_{\mathrm{R}} \gg \Gamma$), where $E_{\mathrm{R}} + U - \varepsilon_{\mathrm{F}} \gg \Gamma$ because of the strong on-site repulsion U of radical sites. This implies that subtle balances of the Fermi (HOMO) levels of conducting polymers (or CT complexes) and SOMO levels of coordination compounds, together with U for spin sites are necessary for achievements of Kondo regime. So, we must examine the energy levels of G-spin (R$^{\bullet}$) systems by the ab initio calculations as shown previously [65]. The situation was similar to the case of some TTF-derivatives plus transition metal complexes [45,101–105].

In this situation, spins on the spin sites are alive under chemical doping and physical doping in FET configuration to generate conduction electrons [64,65]. Therefore, several spin-mediated electronic states such as ferromagnetic metal, dense Kondo system, etc. are expected in Kondo regime. Slave boson method, which eliminates the double occupancy of radical states (see [106]), can be used to solve the Anderson lattice model [67] to depict the phase diagram. Some SOMO electrons on radical sites are almost localized in the Kondo regime, only their spin freedom remains, leading to the Kondo lattice model as follows:

$$H_{\mathrm{KM}} = \sum_{\mathbf{k}\sigma}\varepsilon_{\mathbf{k}\sigma}c_{\mathbf{k}\sigma}^{\dagger}c_{\mathbf{k}\sigma} + J_{\mathrm{CM}}\sum_{i}\sigma_i\cdot\mathbf{S}_i, \tag{11}$$

where $\mathbf{S}_i$ means spin localized at radical site i and $\boldsymbol{\sigma}_i$ denotes the spin of conduction electron

$$\mathbf{S}_i = \frac{1}{2}\sum_{\sigma\sigma'}c_{i\sigma}^{\dagger}\tau_{\sigma\sigma'}c_{i\sigma'}, \tag{12}$$

where $\tau = (\tau_x, \tau_y, \tau_z)$ is Pauli spin matrix. The Kondo lattice model has been used for molecular design of organic Kondo and dense Kondo systems, together with π–d conjugated systems [57].

Since localized spin $\langle \mathbf{S}_i \rangle$ at site i induces the local magnetic field $(-J_{\mathrm{CM}}\langle \mathbf{S}_i \rangle)$ on conduction electrons, the spin polarization on site j is given by

$$\langle \mathbf{S}_j^{\alpha} \rangle = -J_{\mathrm{CM}} \sum_{\beta=x,y,z} \chi^{\alpha\beta}(j,i) \langle \mathbf{S}_i^{\beta} \rangle, \tag{13}$$

where $\chi_{ab}(j,i)$ denotes the local magnetic susceptibility. Then the magnetic interaction of localized spin $\langle \mathbf{S}_j^{\alpha} \rangle$ at site j with $\langle \mathbf{S}_j^{\beta} \rangle$ is defined by

$$H_{\mathrm{RKKY}} = -J_{\mathrm{CM}}^2 \sum_{\langle ij \rangle} \sum_{\alpha\beta} \mathbf{S}_j^{\alpha} \chi^{\alpha\beta}(j,i) \mathbf{S}_i^{\beta}, \tag{14a}$$

$$= -\sum_{\langle ij \rangle} 2J_{ij} \mathbf{S}_j \cdot \mathbf{S}_i, \tag{14b}$$

where

$$\frac{1}{2} J_{\mathrm{CM}}^2 \chi^{\alpha\beta}(j,i) = J_{ij} \delta_{\alpha\beta}. \tag{15}$$

Thus the exchange couplings between radical spins via the spin polarization of conduction electrons are described by the RKKY type spin Hamiltonian [94–96]. The RKKY model has been used for molecular design of several magnetic states of magnetic polymers and crystals as shown below.

4. DFT calculations of DNA-radical system

4.1. Molecular design of DNA-based magnetic conductors

We have theoretically examined possible organic, organometallic analogs to copper oxides [45] and magnetic conductors on the basis of both ab initio and Hubbard model calculations as described above. In fact, several strategies are presented; (1) magnetic modification of TTF derivatives [45,57,65], (2) magnetic modification of conducting polymer [53–56], (3) magnetic modification of Ni(dimt) systems [66,67], and (4) construction of organic RVB [45,55]. Past decade, experimental results for the first systems (1) have been reported. Hence, we wish to extend these results to DNA-based magnetic materials.

4.2. Magnetic modifications of DNA wires

We considered some guanine and adenine derivatives introducing radical subtituents, which are depicted in Fig. 3. First, since guanine and adenine are known to be damaged easily upon oxidation, benzene has been introduced into them according to Saito' s studies [52]. The radical substituents have been nitroxides that are rather stable radical groups.

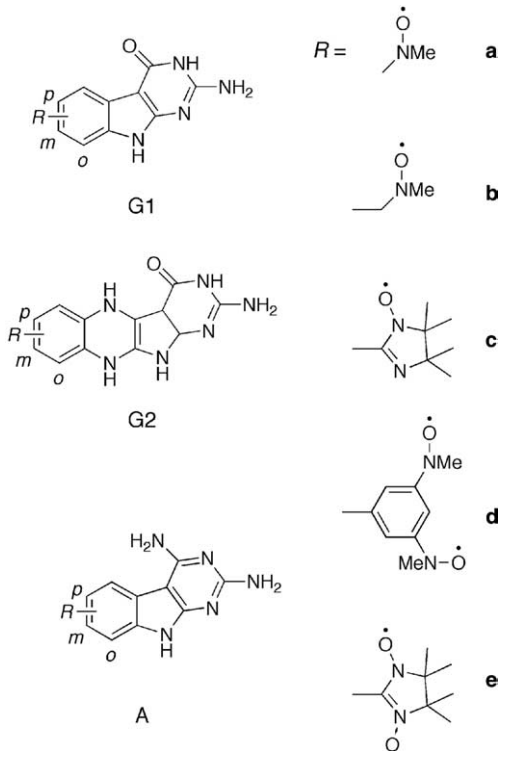


Fig. 3. Molecular structures for guanine and adenine derivatives.

Derivatives ${}_m\mathrm{G1}_a$, ${}_p\mathrm{G1}_a$, ${}_m\mathrm{A1}_a$ and ${}_p\mathrm{A1}_a$ (where the suffices distinguish positions substituted by radical groups) are the simplest models of our magnetic modifications. G2 have dihydrophenazine-like structure that enhances its performance as an electronic donor. ${}_{op}\mathrm{G1}_{aa}$ and $\mathrm{G1}_d$ have the radical group regarded as an almost $S = 1$ spin-site, so that spin moment remains when doped a hole whichever the intramolecular magnetic interaction is ferro or antiferro. $\mathrm{G1}_c$ and $\mathrm{G1}_e$ have iminonitroxide and nitronylnitroxide radicals that are well-known stable radicals. $\mathrm{G1}_b$ is a expansion of $\mathrm{G1}_a$ with methyl group inserted between G1 and the radical. The methyl radical is expected to reduce the intramolecular magnetic interaction.

For the models above, the intramolecular magnetic interactions have been evaluated with hole-doping as well as ionization potentials. These models have been geometry-optimized by using the energy gradient technique based on UB3LYP/6-31G* in the neutral doublet states.

4.3. IP and Js for the models

Summarized in Table 1 are ionization potentials (IP) and intramolecular effective exchange integrals for the guanine and adenine derivatives. IPs are within the energy of ultraviolet (UV). Comparing ${}_m\mathrm{G1}_a$ and ${}_p\mathrm{G1}_a$ (also ${}_m\mathrm{G2}_a$, and ${}_p\mathrm{G2}_a$), IPs are smaller for the *m*-subustituted ones. This is because intramolecular CT occurs more easily for ${}_m\mathrm{G1}_a$ (${}_m\mathrm{G2}_a$) than ${}_p\mathrm{G1}_a$ (${}_p\mathrm{G2}_a$). On the other hand, no difference in IP were found for ${}_m\mathrm{A1}_a$

Table 1
Total energies (a.u.), total angular momentums and effective exchange integrals (cm^{-1}) for guanine and adenine derivatives with radical substituents

Num.	Code	IP/eV	J_1	J_2	J_3
1	${}_pG1_a$	6.316	−5910	−2955	−2905
2	${}_mG1_a$	6.198	−7175	−3588	−3710
3	${}_pA_a$	6.604	−7508	−3754	−3724
4	${}_mA_a$	6.607	−7686	−3843	−3845
5	${}_pG1_b$	6.776	−2370	−1185	−1671
6	${}_pG1_c$	6.722	−2031	−1016	−1386
7	${}_pG2_a$	5.530	−1864	−932	−1456
8	${}_mG2_b$	5.708	−632	−316	−534
9	${}_pG1_d$	6.451	−3542	−1771	−1343
10	${}_{op}G1_a$	6.296	−6074	−3037	−2093
11	${}_pG2_c$	5.710	263	132	260
12	${}_pG2_e$	5.355	285	142	287

and ${}_pA1_a$. The difference in G and A is due to the difference in the inductive effect of carboxyl and ammonia groups. G is negatively inductive, namely it tends to withdraw electrons on the purine site, but A is inclined to provide electrons.

All the models have very strong antiferromagnetic interactions in contrast to phenazine derivatives of the previous study [107,108]. In order to elucidate the origin of these strong antiferromagnetic interactions, we have performed the natural orbital (NO) analyses of the broken-symmetry UB3LYP solutions. Seeing DFT-NOs in Fig. 4(a), it is found that these strong interactions have been orbital overlap effect. Especially for $G1_a$ and $G1_b$, the unpaired electrons on the radical sites were drifted to G and A sites, respectively. In deed, their Mulliken charge densities are $G1^{+0.7}$–$R^{+0.3}$ for instance. Depending on the position of the radical groups, J varies by near 20%. It is found that this variation obeys the McConnell spin-polarization rule because these molecular structures were not far from planar. Since dihydrophenazine-frame of G2 stabilize cationic state of G-site as described above, the effect of orbital overlap reduced and the amplitude of J decreased. By employing stable

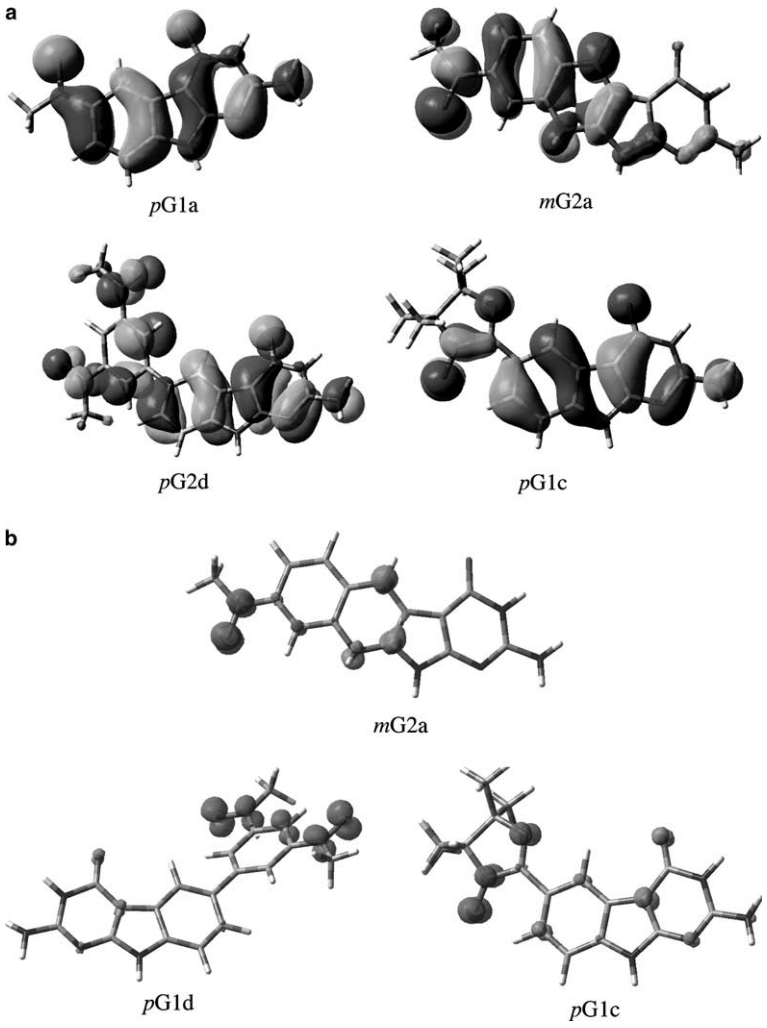


Fig. 4. Natural orbitals (a) and spin density distributions (b) for several guanine derivatives, the contour values of which are 0.0200 and 0.01, respectively.

radicals, antiferromagnetic interaction was weakened by 50% for $G1_c$ than for $G1_a$. By inserting methyl group, $G1_b$ also has 50%-weakened antiferromagnetic interaction than $G1_a$. For ${}_{op}G1_a$ and $G1_d$, ferromagnetic interaction between *N*-methyl nitroxide groups successfully remained and these almost $S = 1$ spin-site interact with G site that has totally $S = 1/2$ in the antiferromagnetic fashion.

Shown in Fig. 4 are spin densities for several models that have clearly spin-polarized ground states. Small spin density was delocalized to guanine site for $G2_a$, which shows intramolecular magnetic interaction is controlled by the delocalization effect. On the other hand, it is found that density of the up- and down-spins distributed alternately along the bonds for ${}_{op}G1_a$ and $G2_d$. Also it is found that spin-polarization is weaker for ${}_{op}G1_a$ than for $G1_d$, which is due to the difference in the way the radicals added. The radicals of ${}_{op}G1_a$ is introduced directly into the protected-G site with the benzene ring, while that of $G1_d$ is separated from the G site by the aryl.

For $G1_c$ and $G2_e$ that are G2 with stable neutral radical, intermolecular ferromagnetic interactions were successfully obtained. It is obvious that large HOMO-(donor)–LUMO(acceptor) gap is needed in deriving the Kondo model for such as G and A derivatives. Success of G2 is arise from its phenazine-like structure.

These models showed strong or very strong intramolecular magnetic interactions when doped a hole. By inserting methyl group or substituting aromatically stable radial, however, the interaction reduces to be moderate value. Their IPs were as large as UV energy. Intermolecular magnetic interaction between G(A)–R through G(A) chain is to be determined in the next works. The following is, however, note worthy. The merit of DNA wires and chains is that using self-organization procedures of G–R sites can easily control these interactions.

5. Discussions and concluding remarks

5.1. Molecular solenoids

The synthesis of chiral magnets is a current topic in molecular magnetism. The DNA wire is one of the helical conducting polymers [10,109,110]. The DNA wire involving guanine site with organic radical in Fig. 1(a) may be paramagnetic before the hole doping in the FET configuration. By the way, after hole (carrier)-doping, moving electrons should entail the intrinsic magnetic field, which can induce the parallel arrangement of organic radical. Thus there is a theoretical possibility to obtain the electronic-field induced molecule-based ferromagnet, the molecular solenoid. In bitro condition we can have telomeric tetramer of guanine as shown in Fig. 1(c). So the tetramer of (G–R) may be formed in the condition: note that $(G–R)_4$ is formally isoelectronic to $(CuO)_4$. To our knowledge, there seems no experimental approach to molecular solenoid based on the DNA wires.

5.2. Organic Kondo and dense Kondo systems and organic ferrimagnets

The effective exchange interaction between doped hole (carrier spin) and localized spin on R is antiferromagnetic. Therefore, we may have organic Kondo and dense Kondo systems if appropriate DNA sheets are constructed like the copper oxide sheets in Fig. 1. To this end, cytosine group should be modified to accept one-electron from G–R group by introducing electron acceptor (A), likely $\{\uparrow R^{\bullet}–G^{\bullet+}(\downarrow)\cdots C–A^{-\bullet}(\uparrow)\}_n$. The organic dense Kondo system may become a precursor of superconductor via electron correlation (EC) effect.

The G site with R may exhibit hydrogen bonding interaction with C-like partner with electron acceptor (A). Therefore, we may construct organic CT complexes, (R–G)(C–A), which are near neutral and ionic transition. So the photo-switching type organic ferrimagnets $(R^{\bullet}–G)(C–A)\leftrightarrow(R^{\bullet}–G^{+\bullet})(C–A^{-\bullet})$ seem feasible if C–A partner is well selected.

5.3. Concluding remarks

Present theoretical results suggest several possibilities of DNA wires, sheets and related materials. One of the key points in our proposal is use of its helicity, together with self-organization. Then organic solenoid is a new target, in addition to conventional magnetic conductors based on the RKKY magnetism.

Acknowledgement

This work has been supported by Grants-in-Aid for Scientific Research (No. 14204061) from the Ministry of Education, Science, Sports, and Culture, Japan.

References

[1] J.D. Watson, F.H.C. Crick, Nature 171 (1953) 737.
[2] M.H.F. Wilkins, A.R. Stokes, H.R. Wilson, Nature 171 (1953) 738.
[3] R.E. Franklin, R.G. Gosling, Nature 171 (1953) 740.
[4] E. Schrödinger, What is Life? Cambridge University Press, 1944.
[5] D. Voet, J.G. Voet, Biochemistry, John Wiley & Sons, Inc, 1995.
[6] P.M. Chaikin, T.C. Lubensky, Principles of Condensed Matter Physics, Cambridge University Press, 1995.
[7] P. Reimann, Phys. Rep. 361 (2002) 57.
[8] D.A. Tomalia, A.M. Naylor, W.A. Goddard III, Angew. Chem. Int. Ed. 29 (1990) 138.
[9] R. Seeman, Angew. Chem. Int. Ed. 35 (1990) 1.

[10] A.E. Friedman, J.-C. Chambron, J.-P. Sauvage, N.J. Turro, J.K. Barton, J. Am. Chem. Soc. 112 (1990) 4960.
[11] L. Zelikovich, L. Libman, A. Shzner, Nature 374 (1995) 790.
[12] C.A. Mirkin, R.L. Lestinger, R.C. Mucic, J.J. Storhoff, Nature 382 (1996) 607.
[13] A.P. Alivisatos, K.P. Johnsson, X. Peng, T.E. Wilson, C.J. Loweth, M.P. Bruchez Jr., P.G. Schulz, Nature 382 (1996) 609.
[14] E. Braun, Y. Eichen, U. Silvan, G.B. Yoseph, Nature 391 (1998) 775.
[15] O.S. Kelly, J.K. Barton, Science 283 (1999) 375.
[16] H.-W. Fink, C. Schonenberger, Nature 398 (1999) 407.
[17] D. Porath, A. Bezryadin, S.d. Vries, C. Dekker, Nature 403 (2000) 635.
[18] L. Cai, H. Tabata, T. Kawai, Appl. Phys. Lett. 77 (2000) 3105.
[19] A.Y. Kasumov, M. Kociak, S. Gueron, B. Reulet, V.T. Volkov, D.V. Klinov, H. Bouchiat, Science 291 (2001) 280.
[20] D.B. Hall, R.E. Holmlin, J.K. Barton, Nature 382 (1996) 731.
[21] S. Priyadarshy, S.M. Risser, D.N. Reratan, J. Phys. Chem. 100 (1996) 17678.
[22] J. Jortner, M. Bixon, T. Langenbacher, M.E. Michel-Beyerle, Proc. Natl. Acad. Sci. USA 95 (1998) 12759.
[23] D. Ly, L. Sanii, G.B. Schuster, J. Am. Chem. Soc. 121 (1999) 9400.
[24] M.W. Grinstaff, Angew. Chem. Int. Ed. 38 (1999) 3629.
[25] G.B. Schuster, Acc. Chem. Res. 33 (2000) 253.
[26] A.A. Voityuk, J. Jortner, M. Bixon, N. Rosch, Chem. Phys. Lett. 324 (2000) 430.
[27] T.T. Williams, D.T. Odom, J.K. Barton, J. Am. Chem. Soc. 122 (2000) 9048.
[28] B. Gisse, Acc. Chem. Res. 33 (2000) 631.
[29] Y.A. Berlin, A.L. Burin, M.A. Ratner, J. Am. Chem. Soc. 123 (2001) 260.
[30] F.D. Lewis, R.L. Lestinger, M.R. Wasielewski, Acc. Chem. Res. 34 (2001) 159.
[31] K. Nakatani, C. Dohno, I. Saito, J. Am. Chem. Soc. 123 (2001) 9681.
[32] K. Kawai, T. Tanaka, S. Tojo, N. Ichiose, T. Majima, J. Am. Chem. Soc. 123 (2001) 12688.
[33] K. Kawai, Y. Wata, M. Hara, S. Tojo, T. Majima, J. Am. Chem. Soc. 124 (2002) 3586.
[34] A. Okamoto, K. Tanaka, I. Saito, J. Am. Chem. Soc. 125 (2003) 5066.
[35] M. Sionoya, E. Kimura, M. Shiro, J. Am. Chem. Soc. 115 (1993) 6730.
[36] K. Tanaka, Y. Yamada, M. Shionoya, J. Am. Chem. Soc. 124 (2002) 8802.
[37] K. Tanaka, A. Tengeniji, T. Kato, N. Toyama, M. Shiro, M. Shionoya, J. Am. Chem. Soc. 124 (2002) 12494.
[38] K. Tanaka, A. Tengeniji, T. Kato, N. Toyama, M. Shionoya, Science 299 (2003) 1212.
[39] A. Okamoto, K. Kanatani, T. Taiji, I. Saito, J. Am. Chem. Soc. 125 (2003) 1172.
[40] I. Saito, T. Nakamura, K. Nakatani, J. Am. Chem. Soc. 122 (2000) 3001.
[41] J.G. Bednort, K.A. Muller, Z. Phys. 64 (1986) 189.
[42] A.P. Kampf, Phys. Rep. 249 (1994) 219.
[43] W. Brenig, Phys. Rep. 251 (1995) 153, and references therein.
[44] M. Imada, A. Fujimori, Y. Tokura, Rev. Mod. Phys. 70 (1998) 1040.
[45] K. Yamaguchi, Int. J. Quant. Chem. 37 (1990) 167.
[46] K. Yamaguchi, Y. Takahara, T. Fueno, K. Nasu, Jpn. J. Appl. Phys. 26 (1987) L1362.
[47] K. Yamaguchi, Y. Takahara, T. Fueno, K. Nasu, Jpn. J. Appl. Phys. 26 (1987) L2037.
[48] K. Yamaguchi, Y. Takahara, T. Fueno, K. Nasu, Jpn. J. Appl. Phys. 27 (1987) L509.
[49] G.C. Hardin, E. Henderson, T. Watson, J.K. Prosser, Biochemistry 30 (1991) 4460.
[50] C. Kang, X. Zhang, R. Ratliff, R. Moyzis, A. Rich, Nature 356 (1992) 126.
[51] O.Y. Fedoroff, M. Salazar, H. Han, V.V. Chemeris, S.M. Kerwin, L.H. Hurley, Biochemistry 37 (1998) 12367.
[52] A. Okamoto, T. Kamei, I. Saito, J. Am. Chem. Soc. 126 (2004) 9458.
[53] K. Yamaguchi, Y. Toyoda, T. Fueno, Kagaku 41 (1986) 585 (in Japanese).
[54] K. Yamaguchi, Y. Toyoda, T. Fueno, Synth. Met. 19 (1987) 81, 87.
[55] K. Yamaguchi, Kinozairyo 10 (1987) 23 (in Japanese).
[56] K. Yamaguchi, M. Nakano, T. Fueno, Kagaku 42 (1987) 583 (in Japanese).
[57] K. Yamaguchi, Y. Takahara, T. Fueno, K. Nakasuji, I. Murata, Jpn. J. Appl. Phys. 27 (1988) 766.
[58] K. Yamaguchi, H. Namimoto, T. Fueno, T. Nogami, Y. Shirota, Chem. Phys. Lett. 166 (1990) 408.
[59] S. Yamanaka et al., Chem. Phys. Lett. 233 (1995) 257.
[60] S. Yamanaka et al., Chem. Phys. Lett. 233 (1995) 88.
[61] K. Yamaguchi, M. Okumura, J. Maki, T. Noro, Chem. Phys. Lett. 207 (1993) 9.
[62] K. Yamaguchi, S. Hayashi, M. Okumura, M. Nakano, W. Mori, Chem. Phys. Lett. 266 (1994) 372.
[63] K. Yamaguchi, M. Okumura, T. Fueno, K. Nakasuji, Synth. Met. 41–43 (1991) 3631.
[64] F. Matsuoka et al., Polyhedron 20 (2001) 1169.
[65] T. Kawakami, T. Taniguchi, S. Nakano, Y. Kitagawa, K. Yamaguchi, Polyhedron 22 (2003) 20511.
[66] M. Fujiwara, T. Matsushita, K. Yamaguchi, T. Fueno, Synth. Met. 41–43 (1996) 3267.
[67] M. Fujiwara, S. Takamizawa, W. Mori, K. Yamaguchi, Mol. Cryst. Liq. Cryst. 279 (1996) 1.
[68] M. Mitani, Y. Takano, Y. Yoshioka, K. Yamaguchi, J. Chem. Phys. 111 (1999) 1309.
[69] I. Saito, T. Nakamura, K. Nakatani, Y. Yoshioka, K. Yamaguchi, H. Sugiyama, J. Am. Chem. Soc. 120 (1998) 12686.
[70] Y. Yoshioka, Y. Kitagawa, Y. Takano, K. Yamaguchi, I. Nakamura, I. Saito, J. Am. Chem. Soc. 121 (1999) 8712.
[71] Y. Yoshioka, H. Kawai, T. Sato, K. Yamaguchi, I. Saito, J. Am. Chem. Soc. 125 (2003) 1968.
[72] T. Mori, Bull. Chem. Soc. Jpn. 71 (1998) 2509.
[73] Y. Takano, T. Taniguchi, H. Isobe, T. Kubo, Y. Morita, K. Yamamoto, K. Nakasuji, T. Takui, K. Yamaguchi, J. Am. Chem. Soc. 124 (2002) 11122.
[74] L. Noodleman, J. Chem. Phys. 74 (1981) 5737.
[75] L. Noodleman, E.R. Davidson, Chem. Phys. 109 (1986) 131.
[76] K. Yamaguchi, Y. Takahara, T. Fueno, in: V.H. Smith et al. (Eds.), Applied Quantum Chemistry, D. Reidel, 1986, p. 155.
[77] A. Bencini, F. Totti, C.A. Daul, K. Doclo, P. Fantucci, V. Barone, Inorg. Chem. 36 (1997) 5022.
[78] T. Kawakami, S. Yamanaka, Y. Takano, Y. Yoshioka, K. Yamaguchi, Bull. Chem. Soc. Jpn. 71 (1998) 2097.
[79] M. Mitani, H. Mori, Y. Takano, D. Yamaki, Y. Yoshioka, K. Yamaguchi, J. Chem. Phys. 113 (2000) 4035, and references therein.
[80] A.D. Becke, Phys. Rev. A38 (1998) 3098.
[81] S.H. Vosko, L. Wilk, M. Nusair, Can. J. Phys. 58 (1980) 1200.
[82] C. Lee, W. Yang, R.G. Parr, Phys. Rev. B37 (1988) 785.
[83] M.J. Frisch, G.W. Trucks, H.B. Schlegel, P.M.W. Gill, B.G. Johnson, M.A. Robb, J.R. Cheeseman, T.A. Keith, G.A. Petersson, J.A. Montgomery, K. Raghavachari, M.A. Al-Laham, V.G. Zakrzewski, J.V. Oritiz, J.B. Foresman, J. Cioslowski, B.B. Stefanov, A. Nanayakkara, M. Challacombe, C.Y. Peng, P.Y. Ayala, W. Chen, M.W. Wong, J.L. Baker, J.P. Stewart, M. Head-Gordon, C. Gonzalez, J.A. Pople, GAUSSIAN 98, Gaussian, Inc., Pittsburgh, PA, 1995.

[84] T. Onishi, Y. Takano, Y. Kitagawa, T. Kawakami, Y. Yoshioka, K. Yamaguchi, Polyhedron 20 (2001) 1177.
[85] S. Inagaki, R. Kubo, Int. J. Magnetism 4 (1973) 139.
[86] S. Inagaki, J. Phys. Soc. Jpn. 39 (1975) 596.
[87] H. Suhl, B.T. Matthias, L.R. Walker, Phys. Rev. Lett. 3 (1959) 552.
[88] J. Kondo, Prog. Theoret. Phys. 29 (1963) 1.
[89] H. Nagao, M. Nishino, Y. Yoshioka, K. Yamaguchi, Int. J. Quant. Chem. 65 (1997) 947.
[90] H. Nagao, M. Mitani, M. Nishino, Y. Shigeta, Y. Yoshioka, K. Yamaguchi, Int. J. Quant. Chem. 75 (1999) 549.
[91] P.W. Anderson, Phys. Rev. 124 (1961) 41.
[92] J. Kondo, Progr. Theoret. Phys. 32 (1964) 37.
[93] K. Yamaguchi, Y. Kitagawa, T. Onishi, H. Isobe, T. Kawakami, H. Nagao, S. Takamizawa, Coord. Chem. Rev. 226 (2002) 235.
[94] M.A. Ruderman, C. Kittel, Phys. Rev. 96 (1954) 99.
[95] T. Kasuya, Progr. Theoret. Phys. 16 (1956) 45.
[96] K. Yoshida, Phys. Rev. 106 (1957) 893.
[97] J. Hubbard, Proc. Roy. Soc. (London) A276 (1963) 238.
[98] K. Yamaguchi, M. Nakano, H. Namimoto, T. Fueno, Jpn. J. Appl. Phys. 27 (1988) L1835.
[99] K. Yamaguchi, M. Nakano, H. Namimoto, T. Fueno, Jpn. J. Appl. Phys. 27 (1989) L479.
[100] K. Yamaguchi, M. Nakano, H. Namimoto, T. Fueno, Jpn. J. Appl. Phys. 28 (1989) L672.
[101] H. Kobayashi, H. Tomita, T. Naito, A. Kobayashi, F. Sakai, T. Watanabe, P. Cassoux, J. Am. Chem. Soc. 118 (1996) 368.
[102] H. Akutsu, K. Kato, E. Ojima, H. Kobayashi, H. Tanaka, A. Kobayashi, Phys. Rev. B58 (1998) 9294.
[103] H. Tanaka, A. Kobayashi, A. Sato, H. Akutsu, H. Kobayashi, J. Am. Chem. Soc. 121 (1999) 760.
[104] A. Sato et al., Phys. Rev. B61 (2000) 111.
[105] H. Kobayashi, A. Kobayashi, P. Cassoux, Chem. Soc. Rev. 29 (2000) 325.
[106] N. Nagaosa, P.A. Lee, Phys. Rev. 64 (1990) 2450.
[107] T. Taniguchi, S. Nakano, T. Kawakami, K. Yamaguchi, Synth. Met. 137 (2003) 1261.
[108] T. Taniguchi, S. Nakano, T. Kawakami, K. Yamaguchi, Polyhedron 22 (2003) 2039.
[109] Y. Kishimoto, M. Itou, T. Miyatake, T. Ikariya, R. Noyori, Macromolecules 282 (1998) 1683.
[110] T. Aoki, Y. Kobayashi, T. Kanko, E. Oikawa, Y. Yamamura, Y. Fujita, M. Teraguchi, R. Nomura, T. Masuda, Macromolecules 354 (1999) 56.

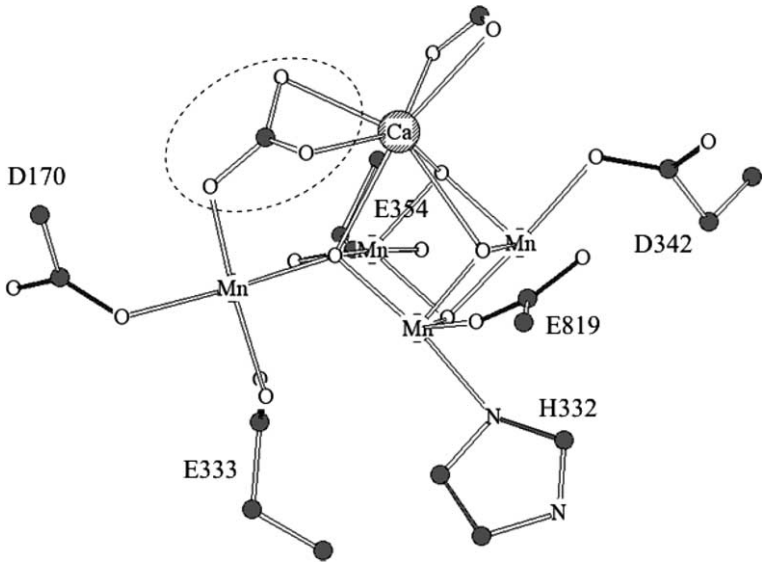
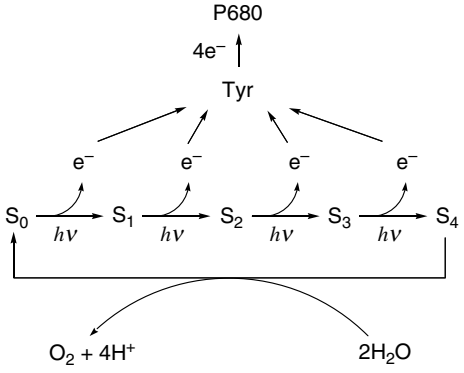


Fig. 1. X-ray structure of the oxygen evolution center (OEC) in PS II [1].



Scheme 1.

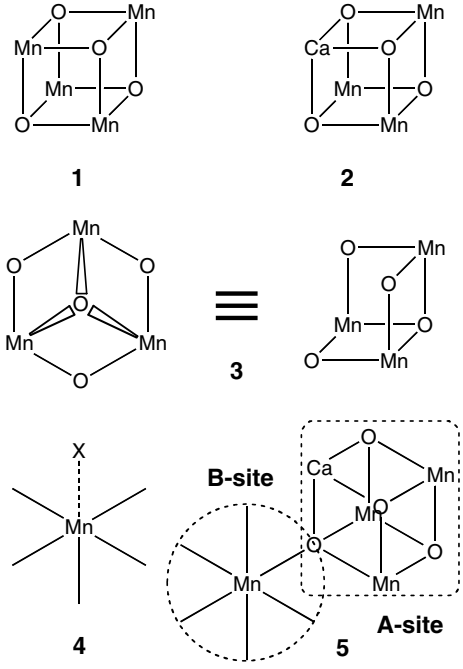


Fig. 2. Core structures of manganese clusters (**1**–**5**) in OEC of PS II.

already been published to elucidate them on the basis of accumulated results. Although cubane structure Mn_4O_4 (**1**) in Fig. 2 has been proposed in these reviews as an active site of OEC, **1** is largely different from cubane-like calcium manganese cluster $CaMn_3O_4$ (**2**) in Fig. 2. Therefore, possible reaction mechanisms of OEC based on **2** might be quite different from those on **1**. The Mn_2 dimer coupled model (so-called Klein model) [7,12,13] $(Mn_2O_2)O(Mn_2O_2)$ (**6**), is also different from **2** as shown in Fig. 3. The butterfly model (Mn_4O_2) (**7**) and cubane model (Mn_4O_3Cl) (**8**) by Hendrickson and Christou and their synthesized model complexes (**7**, **8**) have different molecular structures from **2** (see Fig. 3), though trinuclear Mn complexes Mn_3O and Mn_3O_4 (**3**) in Fig. 2 are used as precursors of **8** [14,15]. The spin frustration problem in distorted cubane $Mn(IV)Mn(III)_3$ is also discussed on the experimental ground [15].

Several theoretical studies on the Mn complexes have been carried out to elucidate the electronic structures of Mn OEC. The LCAO Xα calculation of the tetranuclear manganese complex $Mn(IV)Mn(III)_3Cl_7(O_2CCCH_3)_3]^{3-}$ (**9**), a cubane complex, has been carried out to elucidate its electronic and spin states in relation to the model cluster (**8**). The calculated high-spin ($S = 9/2$) ground state for **9** has been in agreement with the experiment [16]. Blomberg et al. [17] have performed a density functional theory (DFT) study on hydrogen abstraction from manganese-coordinated water by a tyrosyl radical ($Tyr_{Z^{\bullet}}$), proposing a radical mechanism for oxygen evolution

$$4Tyr_{Z^{\bullet}} + 2H_2O \rightarrow 4Tyr_Z + O_2 \quad (2)$$

However, several view points for possible roles of $Tyr_{Z^{\bullet}}$ have been presented on the experimental grounds [3–11].

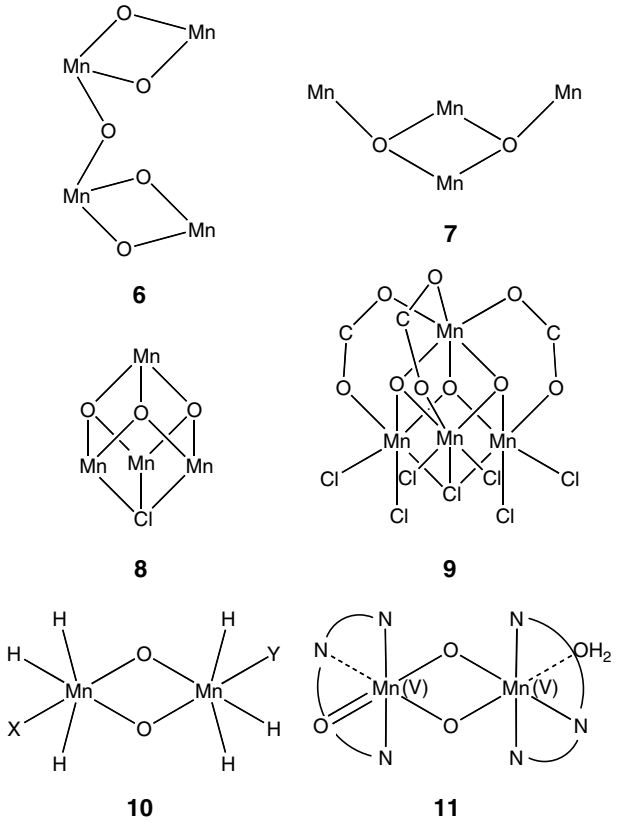


Fig. 3. Molecular structures of manganese model clusters (**6**–**11**) for OEC.

The X-ray structure by Ferreira et al. [1] have denied the possibility of the process in Eq. (2) for OEC. Belinskii [18] has carried out the theoretical studies on the mixed-valence $Mn(III)_3Mn(IV)$ and $Mn(IV)_3Mn(III)$ clusters on the basis of the quantum Heisenberg models, assuming trapezoid, butterfly, bent, T-type and distorted tetrahedron structures, which are different from **2** and **5**. Possible ground spin states for these five structures have been elucidated, changing effective exchange interactions between manganese ions.

We have examined possible spin structures of tetranuclear (**1**) [19] and trinuclear (**3**) [20] manganese clusters in Fig. 2 on the basis of the spin vector model [21]. The strong spin frustration [15] in **3** has provided non-collinear spin structures such as triangular spin structure in Fig. 4, on the assumption of the experimentally determined effective exchange integrals (J_{ij}). The J_{ij} values for the binuclear manganese complexes [22,23] have been calculated using the hybrid DFT method to elucidate the mechanisms for effective exchange interactions between Mn ions [24]

$$J_{ij} = \frac{^{LS}E(\mathbf{X}) - {}^{HS}E(\mathbf{X})}{^{HS}\langle\widehat{S}^2\rangle(\mathbf{X}) - {}^{LS}\langle\widehat{S}^2\rangle(\mathbf{X})}, \tag{3}$$

where $^{Y}E(\mathbf{X})$ and $^{Y}\langle\widehat{S}^2\rangle(\mathbf{X})$ are the total energy and total angular momentum for the state Y (=LS; the lowest spin state, HS; the highest spin state) by the method **X** (=UHF, UMPn, UDFT, etc.). It was shown that the sign

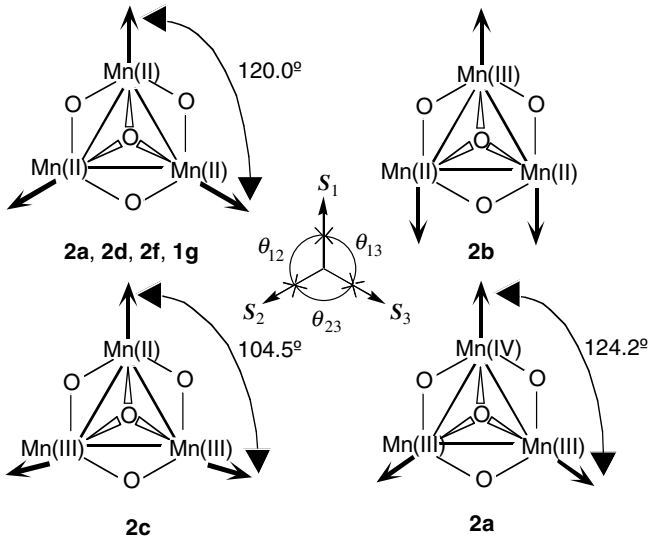


Fig. 4. Schematic illustrations of classical spin structures of the ground state of $CaMn_3O_4$ (**2**).

of J_{ij} is negative because of the greater stability of LS than HS, and the magnitude of J_{ij} values is variable with the oxidation numbers of Mn ion. The calculated J_{ij} values have been consistent with the experiments available. Very recently, Yamanaka et al. [25] have performed the DFT calculation of cubane-type $Mn(II)_4$ cluster (**1**) using the general spin orbitals (GSO), namely, two component spinor.

$$\varphi = \varphi^{+}\alpha + \varphi^{-}\beta, \tag{4}$$

where φ^{+} and φ^{-} denote the up- and down-spin components, respectively. The GSO-DFT calculation by the GSO-X program package [26] has exhibited the 3-dimensional (3D) T_d-type spin densities responsible for spin frustration. This is consistent with the conclusion by the spin vector model, namely, classical Heisenberg model [21]. The negative J_{ij}-value calculated for **1** by GSO DFT has been consistent with the experiment [25] that **1** has the LS ground state.

The variations of charge and spin populations of manganese oxo (MnO) bonds with the oxidation number of Mn ion were also examined by the UHF method. It was concluded that the nature of oxygen atom in the manganese oxo bond (X=O in **4**) varies from nucleophilic to electrophilic with the change of formal charge of Mn from low (II) to high (V) valent. The oxygen atom in the Mn(V)O core exhibited the radical character responsible for the radical reactivity for water [24,27].

As a first step toward theoretical approaches to water oxidation in OEC, Isobe et al. [27] have performed the DFT calculation of the model compound $XH_3Mn(IV)$-$O_2Mn(IV)H_3Y$ (X, Y = O, H) (**10**) for the Limburg compound $[(terpy)(H_2O)Mn(\mu\text{-}O)_2Mn(terpy)(H_2O)]^{3+}$ (**11**) [28] as shown in Fig. 3. It was found that electron correlation plays a crucial role to determine the nature of manganese–oxygen bonds in **8**. Diradical or nonradical

mechanism is found to be feasible for the oxygen atom transfer from water to high-valent manganese–oxo bond Mn(V)═O in **10**. The environmental effects such as solvent are considered to play an important role for control of the mechanism. As a continuation of previous work [24–27], we here perform theoretical studies on manganese clusters (**2**–**5**) in OEC. The electronic structures of these species are investigated from the view point of magnetic interactions. Implications of the calculated results are discussed in relation to possible mechanisms of oxygen evolution in OEC. Our previous [22–27] and present calculations conclude that Mn(V)═O (**4**) plays a crucial role in both native and artificial OEC systems.

2. Theoretical backgrounds and computational results

The construction of possible theoretical models for manganese clusters in OEC is a first step for understanding the mechanism of water oxidation in PS II. Here, we assume that the trinuclear manganese cluster (**3**) in Fig. 2 plays an important role as the electron buffer (pool) group, whereas the mono-nuclear manganese ion (**4**) and calcium ion in **2** are reaction sites for oxygen evolution in OEC. Then, we here investigate two fragments **2** and **4** in the composite cluster **5** in Fig. 2. As previously [20,21], both classical and quantum Heisenberg models are first applied to **2** and **5**. Next, the GSO Hartree–Fock (HF) calculation of **2** is conducted to confirm theoretical conclusions by the HB models. In this paper, we do not touch important roles of photo-excitation of P680 and related proton-electron transfer reactions via tyrosine to control of oxidation states of **5** [3–11].

2.1. Heisenberg model for 2

Possible spin structures of **2**, which is referred to as the A-site of **5**, are investigated by both classical and quantum HB models. Since calcium ion (Ca^{2+}) is non-magnetic, the HB Hamiltonian of **2** is equivalent to that of trinuclear manganese cluster (**3**) [20] in Fig. 2 as

$$H_A = -2J_{12}\boldsymbol{S}_1\cdot\boldsymbol{S}_2 - 2J_{23}\boldsymbol{S}_2\cdot\boldsymbol{S}_3 - 2J_{31}\boldsymbol{S}_3\cdot\boldsymbol{S}_1, \quad (5)$$

where J_{ij} is the effective exchange integral between manganese ions i and j, and $\boldsymbol{S}_i$ denotes the spin operator for manganese ion i. According to our previous hybrid DFT results for binuclear manganese complexes [22,23], the J_{ij} values of Mn(X)–Mn(Y) pairs are simply assumed to be −1, −50, −100, −150 and −200 (cm^{-1}) for Mn(II)–Mn(II), Mn(II)–Mn(III), Mn(III)–Mn(III), Mn(III)–Mn(IV) and Mn(IV)–Mn(IV), respectively. These assumed values are also consistent with the observations [7–11].

If spin operators in Eq. (5) are regarded as classical spin vectors, the Heisenberg Hamiltonian in Eq. (5) is converted as

$$H_A^C = -2J_{12}S_1S_2\cos\theta_{12} - 2J_{23}S_2S_3\cos\theta_{23} - 2J_{31}S_3S_1\cos\theta_{31}, \quad (6)$$

where θ_{ij} is the angle between spin vectors i and j as illustrated in Fig. 4. The sizes (S_i) of spins are taken to be 5/2, 4/2, 3/2 and 2/2 for Mn(II), Mn(III), Mn(IV) and Mn(V), respectively, assuming the high spin state of each manganese ion. The spin structures of **2** by the classical HB model are summarized in Table 1. The ground spin structures of **2** are triangular ($\theta_{12}=\theta_{13}=120°$) and/or noncollinear ($\theta_{12}$, $\theta_{13}\neq 0°$ (parallel) or 180° (antiparallel)) except for **2b** as shown in Fig. 4. Thus, the spin frustration effects are very important for the low-spin (LS) states of **2** like **3**. This implies that the low-spin ground states of **2** are not available by the conventional DFT model which can describe parallel or antiparallel (axial) spin alignments like **2b**. It is noteworthy that the S_z component of $\boldsymbol{S}_2$ and $\boldsymbol{S}_3$ is −2/2 instead of −4/4 in **2a** as illustrated in Fig. 4, and total S_z becomes zero ($S_z=(4-2-2)/2=0$) (see also Fig. 6 below). On the other hand, the S_x component is $+(-)2\sqrt{3}/2$ for $\boldsymbol{S}_2$ ($\boldsymbol{S}_3$) and total S_x becomes also zero. In order to obtain the S_x component, general spin orbitals (GSO) given by Eq. (4) are essential in the case of molecular orbital calculations as shown previously [20,25,26]. The noncollinear spin structure is nothing but the classical presentation of singlet-type spin correlation, $K=\langle\boldsymbol{S}_i\cdot\boldsymbol{S}_j\rangle<0$, between Mn spins [20].

Since the classical HB model predicts the noncollinear spin structures, the exact diagonalization of the quantum HB Hamiltonian given by Eq (5) is desirable to elucidate the ground spin states of **2**. For example, Fig. 5 shows the energy levels calculated for trinuclear manganese cluster Mn(II)Mn(III)$_2$ (**2c**) by the exact diagonalization method. The ground (G) and first-excited (FE) states are quintet ($S_A(G)=3/2$) and doublet ($S_A(FE)=1/2$), respectively. It is noteworthy that axial spin vector model (**2c$_a$**) in Fig. 6 predicts the higher spin state: $S=(4+4-5)/2=3/2$. However, the local spin structure between $\boldsymbol{S}_2$ and $\boldsymbol{S}_3$ is ferromagnetic (F) in **2c$_a$** like **2b**, though all the spin pairs are antiferromagnetic (AF) in the case of **2c** as illustrated in Fig. 6. The discrimination between **2c$_a$** and **2c** by spectroscopic methods is an interesting problem. The ground and first excited states of **2** by the method are summarized in Table 1. The low-spin states become the ground states of **2** except for **2b**, for which the axial spin vector model is

Table 1
Spin structures of manganese clusters ($CaMn_3O_4$) by classical and quantum Heisenberg models

Type	Valence[a]	$S_A(G)$[b]	$S_A(FE)$[b]	Spin structure
2a	(II, II, II)	1/2	3/2	Triangular ($\theta_{12}=\theta_{13}=120°$)
2b	(II, II, III)	6/2	4/2	Axial ($\theta_{12}=\theta_{13}=180°$)
2c	(II, III, III)	3/2	1/2	Helical ($\theta_{12}=\theta_{13}=104.5°$)
2d	(III, III, III)	0/2	2/2	Triangular ($\theta_{12}=\theta_{13}=120°$)
2e	(III, III, IV)	1/2	3/2	Helical ($\theta_{12}=\theta_{13}=124.2°$)
2f	(III, IV, IV)	0/2	2/2	Helical ($\theta_{12}=\theta_{13}=120°$)
2g	(IV, IV, IV)	1/2	3/2	Triangular ($\theta_{12}=\theta_{13}=120°$)

[a] $S=5/2$, 4/2, 3/2 and 2/2 for Mn (II), Mn(III), Mn(IV) and Mn(V), respectively.
[b] Spin quantum numbers of the ground (G) and first excited (FE) states.

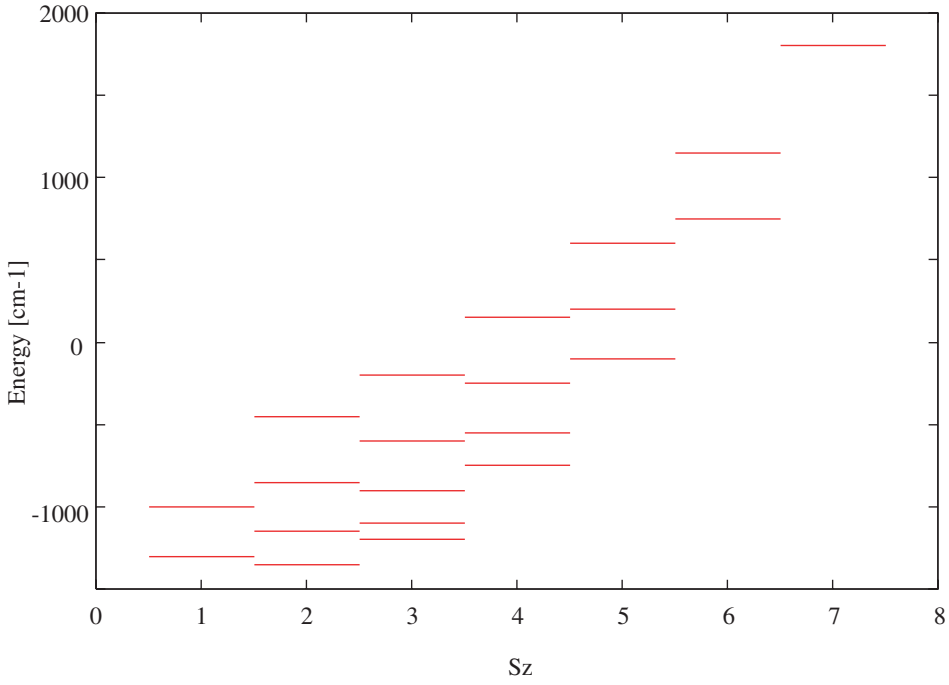


Fig. 5. Energy levels calculated for trinuclear manganese cluster $Mn(II)_2Mn(III)$ (**2c**) by the exact diagonalization method of the Heisenberg model.

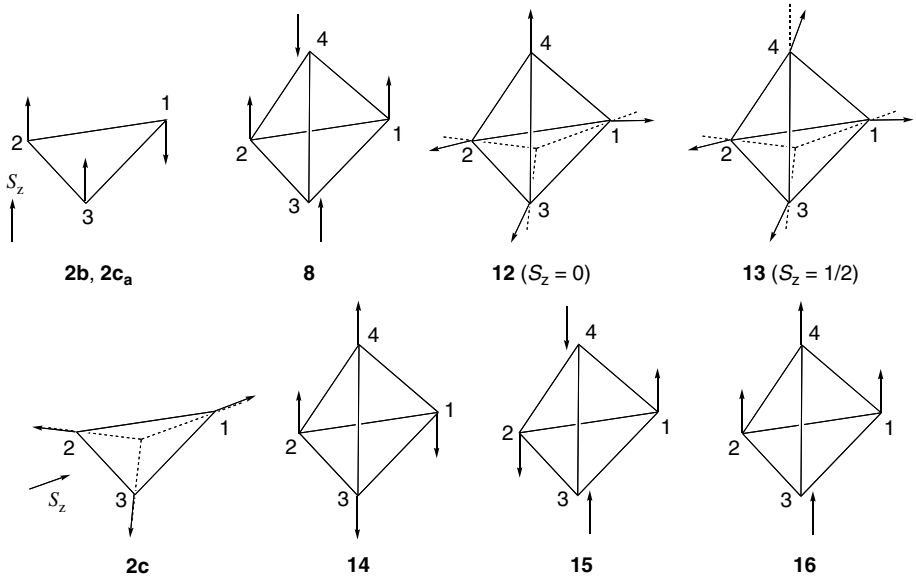


Fig. 6. Axial and general spin structures of tri-(**2**) and tetra-(**8**,**12**,**13**,**14**,**15**,**16**) manganese clusters. The Mn_4 denotes the Mn ion at the B-site.

applicable: $S_A(G) = (5 + 5 - 4)/2 = 6/2$. The relatively low-spin (LS) ground states of **2** are consistent with the ESR experiments for the native manganese clusters in OEC [3–11], though synthetic model clusters often have the relatively high-spin (HS) ground states such as $S = 9/2$ for **9** [14,15].

2.2. Heisenberg model for 5

Here, we have employed the cyclic trinuclear (A)–mononuclear (B) Mn_4 model for **5** to elucidate its spin structure. The total spin Hamiltonian H_T for **5** composed of **2** and **4** are therefore given by

$$H_T = -2J_{AB}\boldsymbol{S}_A \cdot \boldsymbol{S}_B, \tag{7}$$

where $\boldsymbol{S}_A$ denotes the total spin operator of the cluster **2** (A-site): $\boldsymbol{S}_A = \boldsymbol{S}_1 + \boldsymbol{S}_2 + \boldsymbol{S}_3$, and $\boldsymbol{S}_B$ is the spin operator for the manganese ion **4** (B-site) in Fig. 2. Here, we assume the antiferromagnetic exchange interaction ($J_{AB} < 0$) between A and B sites. The oxidation states of **4** are changed from Mn(II) ($S_B = 5/2$) to Mn(V) ($S_B = 2/2$) through Mn(III) ($S_B = 4/2$) and Mn(IV) ($S_B = 3/2$). Both classical

Table 2
Spin states of total manganese clusters ($CaMn_4O_4$) by Heisenberg model

Type	A	S_A(G)	S_{A+B}(G)[a]				Spin structure
			(S_B)[b]	5/2	4/2	3/2	2/2	
5a	**2a**, **2e**, **2g**	1/2		0/2	1/2	0/2	1/2	Helical
5b	**2b**	6/2		(1/2)	(2/2)	(3/2)	(4/2)	Axial[c]
5c	**2c**	3/2		0/2	1/2	0/2	1/2	Helical
5d	**2d**, **2f**	0/2		1/2	0/2	1/2	0/2	Helical

[a] Spin quantum number of the total manganese clusters (A + B). The ground spin structure by the axial spin model is given in the parentheses.
[b] Variations of valence states of the B-site (Mn (X); X = II, III, IV and V).
[c] Axial spin structure is the ground state.

and quantum HB models are applied to **5**. The ground spin states and spin structures of **5** are summarized in Table 2. The low-spin (LS) states such as singlet ($S_{A+B} = 0/2$) and doublet ($S_{A+B} = 1/2$) are predicted by the quantum HB model, though relatively high-spin (HS) states become the ground states by the axial spin vector model as shown in parentheses in Table 2. On the other hand, the LS states of **5** are expressed by the noncollinear spin structures **12** and **13** under the general spin vector model as shown in Fig. 6, in accord with our previous work [20].

The above conclusions are derived from the isotropic spin Hamiltonian in Eq. (7). The ESR experiments have shown that the anisotropic terms (see Eq. (10) below) are not negligible for the Mn oxide clusters [7]. This implies that the Ising model is also worthy of consideration for **5**. The low-spin states of **5** can be constructed by using the axial spin vector models where $\theta_{ij} = 0°$ or 180° in Eq. (6). We assume that the oxidation state of Mn at the B-site is variable from divalent (II) to pentavalent (V), and each manganese ions in A and B sites are high-spin. Table 3 summarizes possible spin states of **5**, which are obtained by the spin coupling between A and B sites. The total singlet and doublet spin-coupled states are feasible by appropriate combinations of axial spins (see for example **14** and **15** in Fig. 6). Then these are also candidates of $\mathbf{S}_i$ sites in OEC. However, it is noteworthy that the local HS (parallel) couplings appear in **14** and **15** in contrast to **12** and **13** where all the spin couplings are antiparallel (LS).

2.3. GSO-HF calculations

In order to confirm the preceding results by the HB model, the generalized Hartree–Fock calculations [22] by the use of general spin orbitals (GSO) in Eq. (4) are performed for the simplest model **2a**, namely, $CaMn(II)_3O_4$ cluster. The MIDI basis sets for M, O and Ca by Tatewaki and Hujinaga [29] have been used for GSO HF calculations. The X-ray structure [1] for **2** in **5** of OEC in PS II is used even for **2a** in the ab initio GSO calculation. Fig. 7 shows the molecular structure, Löwdin charge density, spin density and 3D plot of spin density of **2a** by GSO-HF. The Mn–O bond lengths of the $Mn_1Mn_2Mn_3O_8$ core are short (~1.8 Å), showing the strong bonding nature. While the Ca–O bond lengths of $CaO_5O_6O_7$ core are relatively long (~2.5 Å). The Mn–O bond lengths of the $Mn_2Mn_3Mn_BO_6$ core are about 1.9 Å. The charge density of O_5 and O_6 is about −0.81, and it is 0.71 for Mn_2. The charge and spin populations are unsymmetrical because of the distorted cubane structure. The 3D plot of spin density shows the triangular spin structure, in accord with the classical HB model. Judging from the results in Table 1, similar results are also expected for other oxidation states of **2**, together with **5**. The magnitude of local spin ($S = 5/2$) of Mn(II) ion is largely quenched by the anti-ferromagnetic exchange couplings in **2**(**3**) in the LS state. However, the naked cluster (**2a**) is too simple to discuss chemical reactivity of **5**. Effects of ligand coordination and other environmental effects should be examined for further discussions. For example, axial spin states in Table 3 are obtained by the spin-unrestricted HF (UHF) method based on the different-orbitals-for-different-spins (DODS) approximation. Detailed results of the GSO-HF, UHF and UDFT calculations will be published elsewhere.

Table 3
Spin structures of **5** obtained by the axial spin vector model

Type	A	S_B			
		5/2	4/2	3/2	2/2
5e	**2a**	0/2	1/2	2/2	3/2
5f	**2b**, **2d**	1/2	0/2	1/2	2/2
5g	**2c**, **2e**	0/2	1/2	0/2	1/2
5h	**2f**	1/2	0/2	1/2	0/2
5i	**2g**	2/2	1/2	0/2	1/2

3. Possible mechanisms of oxygen evolution

3.1. Possible electronic structures of OEC

The HB and GSO-HF calculations have provided the ground spin structures of **2** and **5** as summarized in Tables 1–3. These theoretical results are utilized to elucidate possible electronic structures of the OEC complex in PS II, in combination with available experimental results [3–11]. As shown in Fig. 1, there are six carboxyl anion ligands and four oxygen dianion around the Mn_4Ca core (**2**) in OEC. Therefore, the formal charges of the active sites are −1, 0 and 1 for the [Ca(II)Mn(III)$_3$Mn(II)], [Ca(II)Mn(III)$_4$] and [Ca(II)Mn(IV)$_2$Mn(III)] cores, respectively. Experimentally, the first and third cores have been regarded as the zeroth step ($\mathbf{S}_0$) of the water-oxidation cycle in Scheme 1. On the other hand, the second core with the neutral charge is responsible for the S_1 stage. However, if chloride anion is participated even in the S_0 state, the [Ca(II)Mn(IV)$_2$Mn(III)Mn(II)Cl] core becomes neutral. Therefore, we have two different starting oxidation states; [Ca(II)Mn(III)$_3$Mn(II)] and [Ca(II)Mn(IV)$_2$Mn(III), Mn(II)], for the S_0-state. The key point is that the Mn ion at the B-site is divalent in both starting points. Both noncollinear and collinear (axial) spin vector models are feasible for **5** from Tables 1–3. The former model provides

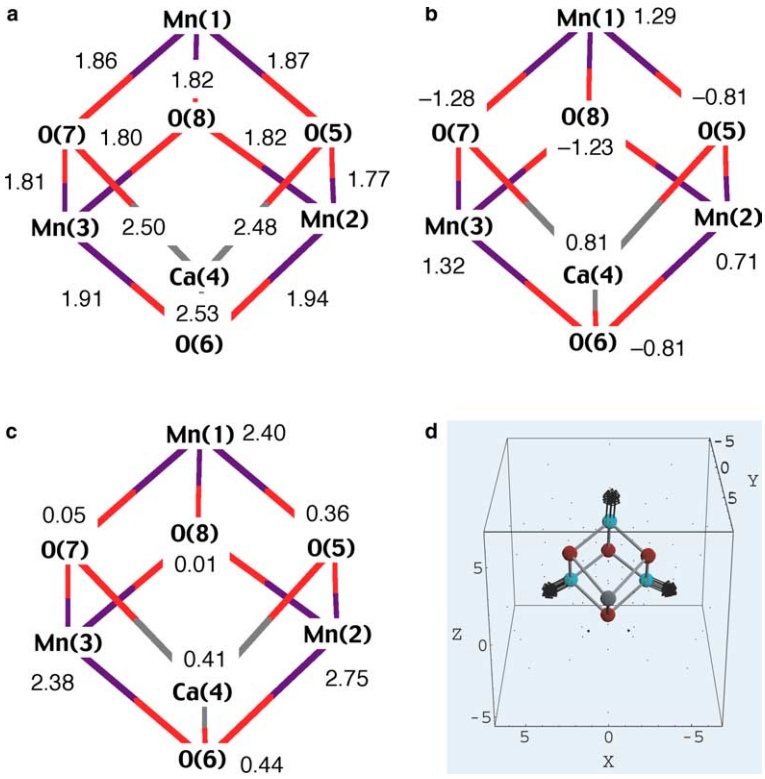


Fig. 7. Molecular structure, Löwdin charge and spin densities and 3D plots of spin density of $CaMn(II)_3O_4$ (**2a**) by GSO-HF.

Table 4
Possible electronic and spin structures of manganese calcium clusters ($CaMn_4O_4$) by noncollinear spin vector models

Type	A ($S^z_A(\mathbf{G})$)	B($S^z_B(\mathbf{G})$)	A + B ($S^z_{A+B}(\mathbf{G})$)
S_0	$CaMn_3$(III, III, III) (0/2)	Mn(II) (1/2)	$CaMn_4$(III, III, III, II) (1/2)
S_1	$CaMn_3$(III, III, III) (0/2)	Mn(III) (0/2)	$CaMn_4$(III, III, III, III) (0/2)
S_2	$CaMn_3$(III, III, IV) (1/2)	Mn(III) (0/2)	$CaMn_4$(III, III, IV, III) (1/2)
S_3	$CaMn_3$(III, III, IV) (1/2)	Mn(IV) (1/2)	$CaMn_4$(III, III, IV, IV) (0/2)
S_{4a}	$CaMn_3$(III, IV, IV) (0/2)	Mn(IV) (1/2)	$CaMn_4$(III, IV, IV, IV) (1/2)
S_{4b}	$CaMn_3$(IV, IV, IV) (1/2)	Mn(III) (0/2)	$CaMn_4$(IV, IV, IV, III) (1/2)
S_{4c}	$CaMn_3$(III, III, IV) (1/2)	Mn(V) (0/2)	$CaMn_4$(III, III, IV, V) (1/2)

the distorted T_d-like spin structure **12** ($S_z = 0$) for the S_0, S_2 and S_4-stages and **13** ($S_z = 1/2$) for the S_1 and S_3-stages, respectively. All the spin coupling pairs are antiferromagnetic in these structures, in conformity with antiferromagnetic exchange interactions. On the other hand, the axial spin vector model concludes the axial spin structure **14** for the S_0, S_1, S_3 and S_{4c} stages and **15** for the S_2, S_{4a}, S_{4b} and S_{4d} stages, respectively. The electronic and spin structures of **5** by these analyses are summarized in Tables 4 and 5.

The so-called S_2-state of **5** is predicted to be doublet ($S_{A+B}(G) = 1/2$), in accord with the ESR experiment [12], while the higher spin state ($S_{A+B} = 5/2$ or 3/2) often assumed for the so-called multiline spectra is the excited

Table 5
Possible electronic and spin structures of manganese calcium clusters ($CaMn_4O_4$) by the axial spin vector models

State	(S_1, S_2, S_3, S_B)	(S_{A+B})
S_0	(−4/2, 4/2, −4/2, 5/2)	(1/2)
	(−3/2, 3/2, −4/2, 5/2)	(1/2)
S_1	(−4/2, 4/2, −4/2, 4/2)	(0/2)
	(−3/2, 3/2, −4/2, 4/2)	(0/2)
S_2	(4/2, −4/2, 4/2, −3/2)	(1/2)
	(3/2, −3/2, 4/2, −3/2)	(1/2)
S_3	(−4/2, 4/2, −3/2, 3/2)	(0/2)
	(−3/2, 3/2, −3/2, 3/2)	(0/2)
S_{4a}	(4/2, −3/2, 3/2, −3/2)	(1/2)
S_{4b}	(4/2, −4/2, 3/2, −2/2)	(1/2)
S_{4c}	(−3/2, 3/2, −3/2, 4/2)	(1/2)
S_{4d}	(3/2, −3/2, 3/2, −2/2)	(1/2)

state. These conclusions are independent on the starting oxidation states, together with the collinear and noncollinear spin models (see Tables 4 and 5). The S_0-state is predicted to be doublet, being consistent with the ESR experiment [30]. On the other hand, the S_1- and S_3-states are singlet in our model calculations. Experimentally, the thermally excited triplet state can be detected for both states [31,32]. The observed singlet–triplet energy gaps are 1.5 and 2.5 K for the S_1- [31] and S_3-[32] states, respectively. Our theoretical results are in consistent with the experiments [3–11]. Three possible electronic structures are concluded for the final state S_4 in the Kok cycle (see Scheme 1) [2] as shown in Tables 4 and 5 if the S_0 state is assumed to be [Ca(II)Mn(III)$_3$Mn(II)]. On the other hand, the S_{4d} structure is available from the other starting S_0 state. These are closely related to the mechanisms of water oxidation in OEC as discussed below.

3.2. A new mechanism for oxygen evolution

The computational results in Tables 4 and 5 enable us to propose a possible mechanism of oxygen evolution in the OEC system as illustrated in Fig. 8. The manganese ion at the B-site in the S_0-state is divalent (Mn(II)), while the A-site is regarded as the Mn(III)$_3$ or Mn(III)Mn(II)$_2$ cluster. The B-site becomes trivalent, Mn(III), followed by the coordination of OH anion in the S_1-state. This is consistent with various experiments. However, we cannot touch the mechanism of photo-induced proton and electron transfers in P680 and related species (see Scheme 1). The electron buffer group (A-site) is further one-electron oxidized in the S_2-state. The Mn(IV) ion close to histidine (His) (see Fig. 1) may extract one electron from His, to afford Mn(III)$_3$ His$^{+\cdot}$ or Mn(III)Mn(IV)$_3$ His$^{+\cdot}$. In fact, this possibility has been proposed on the experimental ground [3–11]. The manganese ion in the B-site is oxidized to be tetravalent, Mn(IV), in the S_3-state. Therefore, chloride anion would play an important role to suppress the reactivity of Mn(IV) in the B-site, which may extract one electron from surrounding coordination ligands (L) in Fig. 1

$$\mathrm{Mn(IV)} + \mathrm{L} \rightarrow \mathrm{Mn(III)L^{+\cdot}} \quad (8a)$$

$$\mathrm{ClMn(IV)} + \mathrm{L} \rightarrow \mathrm{ClMn(III)L^{+\cdot}} \quad (8b)$$

This is also compatible with available experiments [3–11]. However, we cannot explain the tyrosyl radical mechanism in Eq. (2) discussed by Blomberg et al. [17]. The X-ray results by Ferreira et al. [1] is not consistent with their proposal. Detailed theoretical and experimental studies are necessary for further discussion on the role of tyrosyl radical in OEC.

Experimentally, the electronic structure of the final state S_4 is unknown because of very short lifetime. Theoretically, three possible electronic structures are conceivable as shown in Tables 4 and 5, and Fig. 8 if the initial state of S_0 is regarded as Mn(III)$_3$Mn(II). While, only S_{4d} state, Mn(IV)$_3$Mn(V), in Table 5 is available if

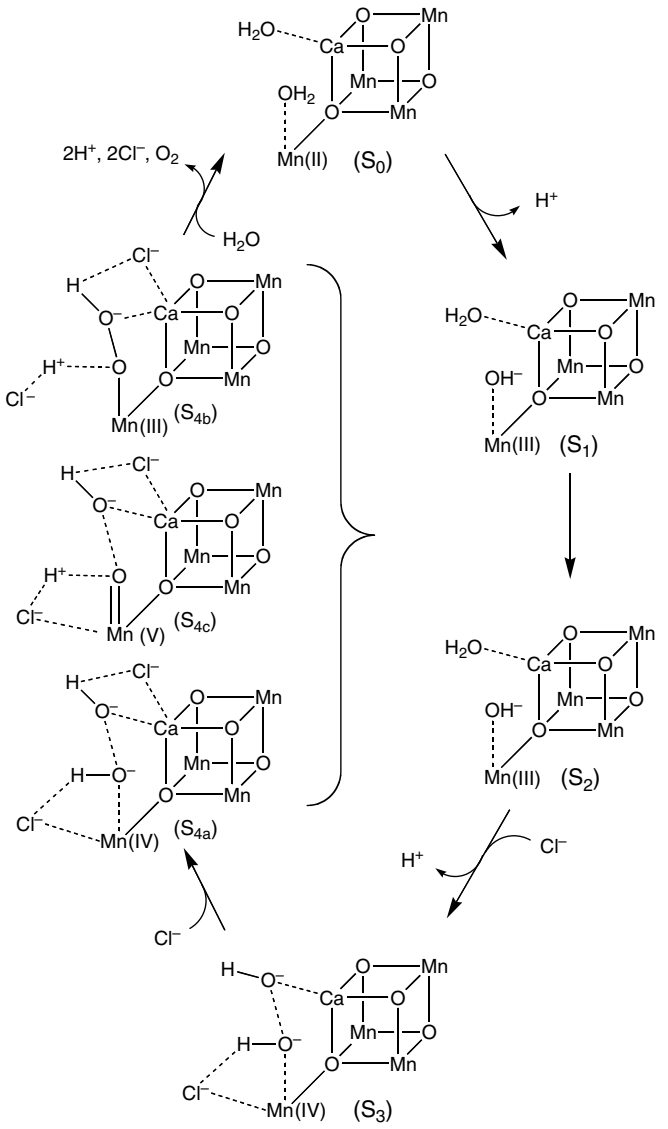


Fig. 8. Schematic illustration of possible mechanisms of oxygen evolution in the OEC system.

S_0 is considered to be Mn(IV)$_2$Mn(III)Mn(II). The dioxygen bridge $(OH^-)_2$ may be formed between the Mn(IV) and Ca(II) ions in the S_{4a} model, where chloride anions play an important role for stabilization of the reaction site. The manganese oxo Mn(V)=O bond may be formed if the deprotonation of hydroxide anion is induced by the participation of chloride anion in the S_{4c} state in Table 4 and S_{4d} state in Table 5. Our previous ab initio calculations [24] have indicated that the high-valent manganese oxo Mn(V)=O bond in S_{4c} exhibits electrophilic behavior [27]. Then it can undergo the electrophilic addition with the other hydroxide anion to generate the hydroperoxide anion inserted between Mn(V) and Ca(II) ions in the S_{4b} state. The chloride anion-assisted deprotonation of HOO^- may generate molecular oxygen–manganese complex Mn(II)O_2, which can evolve O_2 at the final stage of water oxidation in OEC: $S_4 \rightarrow S_0$ as illustrated in Fig. 8.

The key point of our proposal is the participation of calcium ion [33] for formation of the oxygen–oxygen bridge with the manganese ion, which is a crucial step for the O_2 evolution.

3.3. Importance of the Mn(V)=O bond

Past two decades [23–27,34], Yamaguchi et al. elucidated electronic structures and spin states of transition-metal oxides on the basis of ab initio broken-symmetry (BS) (UHF UDFT, GHF and GDFT) calculations followed by the approximate spin projection. It was found that the oxygen atom in the metal-oxo species MO (M = Cr, Mn, Fe) exhibits the nucleophilic character M^+O^- in the case of the lower-valent stage of M^+; M(II) and Mn(III). For example, the Mn(III) ion forms an ionic bond with hydroxide anion, $[Mn(III)–OH]^{2+}$, as shown in Fig. 8. On the other hand, the oxygen atom in the high-valent metal-oxo species such as Mn(V)=O may have singlet or triplet oxygen atom (O) character, showing an electrophilic property to many substrates, for example:

$$Mn(V) = O + {}^{-}OH \rightarrow Mn(IV) - OOH \quad (9a)$$

$$Mn(V) = O + H\text{-}OH \rightarrow Mn(IV) - OH + {}^{\bullet}OH \quad (9b)$$

$$Mn(V) = O + H\text{-}OH \rightarrow Mn(III) + HOOH \quad (9c)$$

The reaction (9a) may be operative in the S_{4b} stage in Scheme 1 to generate the O–O bond. The hydrogen abstraction from water by Mn(V)=O is also conceivable from our theoretical view point.

Isobe et al. [27] have performed the DFT calculations of the model compound (**10**) for the Limburg compound (**11**). They have found that the metal–oxo bonds (Mn(V)=O) in **10** show the diradical character ·Mn–O·, and therefore the oxygen atom in Mn(V)=O in **11** may undergo electrophilic reactions with substrates in Eq. (9). Several evidence [30] suggest that chloride anion plays an important role for oxygen evolution in Limburg reaction systems like native OEC in Fig. 8.

Koizumi et al. [35] have carried out the DFT calculations of dimer of manganese-oxo (MnO) porphyrin (PO) synthesized and characterized by Naruta's group [36]. They have investigated variations of the electronic structures of POMn(X)=O with the change of oxidation number (X) of the Mn ion. It was found that the Mn(V)=O bond in Naruta's oxygen evolution system has the oxygen-diradical character, which may entail the oxygen-atom radical coupling as follows:

$$(POMn(V) = O)_2 \rightarrow POMn(IV)–O–O–Mn(IV)PO \rightarrow (POMn(III))_2 + O_2 \quad (9d)$$

Thus, our theoretical studies on native OEC and artificial OEC [27,28] systems have revealed the crucial role of the high-valent Mn(V)=O bonds as illustrated in Fig. 9. Further theoretical studies on Mn(X)=O in many manganese complexes are interesting for rational design of effective catalysts for oxygen evolution from water.

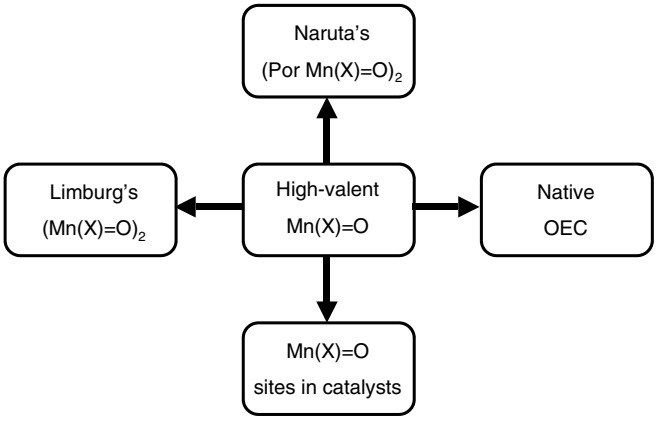


Fig. 9. High-valent Mn-O species generated in several reaction fields.

4. Discussion and concluding remarks

4.1. ESR experiments

There are many ESR studies on manganese oxide clusters [37–41] and tyrosyl radical in OEC. In addition to the Heisenberg Hamitonians in Eqs. (5) and (7), several terms must be included for analysis of the ESR spectra

$$H_{\text{total}} = H_{\text{exch}} + H_0, \quad (10a)$$

where

$$H_{\text{exch}} = -2\sum J_{ij}\boldsymbol{S}_i \cdot \boldsymbol{S}_j, \quad (10b)$$

$$H_0 = \sum \beta \boldsymbol{S}_i \cdot \boldsymbol{g}_j \cdot \boldsymbol{H}_0 + \sum \boldsymbol{S}_i \cdot \boldsymbol{A}_i \cdot \boldsymbol{I}_i + \sum \boldsymbol{S}_i \cdot \boldsymbol{D}_i \cdot \boldsymbol{S}_i + \sum \boldsymbol{S}_i \cdot \boldsymbol{D}_{ij} \cdot \boldsymbol{S}_j. \quad (10c)$$

The first to fourth terms in Eq. (10c) denote the Zeeman, hyperfine, anisotropic and dipole–dipole interactions, respectively. Recently, theoretical calculations of the anisotropic [42,43] and dipole–dipole [44] terms have been performed on the basis of the DFT and hybrid DFT schems. The spin Hamiltonian in Eq. (10c) may be reduced to the following Hamiltonian

$$H_0 = g\beta \boldsymbol{H}_0 \cdot \boldsymbol{S}_{A+B} + A\boldsymbol{I} \cdot \boldsymbol{S}_{A+B} + D[S_z^2 - S_{A+B}(S_{A+B}+1)] + E[S_x^2 - S_y^2], \quad (11)$$

where D and E represent the axial and rhombic zero-field splitting parameters, respectively [42,43].

Goodson et al [45] have reported that the effective exchange integrals in Eq. (10b) are -87, $-140 \sim -151$ and $-87 \sim -144\ \text{cm}^{-1}$ for the $Mn(III)O_2Mn(III)$, $Mn(III)O_2Mn(IV)$ and $Mn(IV)O_2Mn(IV)$ clusters. Our calculated results [22,23] are consistent with these observed values. These parameters are also parallel to those in this paper. The ESR experiments [37–41] have revealed the hyperfine terms in Eq (10c). However, detailed discussions on them are out of concern in this paper. They are calculated in our other papers.

4.2. Relations to other theories

Very recently [46], Lundberg and Siegbahn have performed the UB3LYP calculations of the low-spin (LS) and high-spin (HS) states of the $Mn(IV)_3Mn(III)$ model complex for OEC. It was found that the total energy of the LS state with axial spin structure (**14** or **15** in Fig. 6) is 17 kcal/mol higher than the HS state with parallel spin structure (**16** in Fig. 6), strongly indicating that the HS state is the ground state of the cubane-type structure of the tetranuclear Mn complex. Although the artificial complex (**9**) is certainly high-spin [14,15], the native Mn core of OEC is doublet or singlet by the EPR experiments [31,32]. Our GSO DFT calculations of **1** [25] and **2** indicate that the LS state is more stable than the HS state. Generally, the spin densities of the II, III, IV and V oxidation states of Mn ions in the HS state are about 5, 4, 3 and 2, respectively, and the spin density of oxygen sites is often −1 because of the very strong spin polarization effect by the Mn ions. The UB3LYP results of the HS states by Lundberg and Siegbahn [46] are consistent with this general tendency. On the other hand, the spin densities of the Mn(X) ions become largely reduced in the LS state by GSO DFT as illustrated in Fig. 7. The spin densities on the oxygen atoms are positive (see Fig. 7(c)), showing the spin delocalization effect. This implies that nonradical electrophilic reaction of the high-valent Mn(V)=O with water [27] is feasible in the LS state instead of the radical reaction in the HS state [46]. Further theoretical investigations of the transition structures by GSO DFT are necessary for elucidation the mechanism of oxygen evolution in OEC [47,48].

4.3. Concluding remarks

Theoretical studies on the electronic and spin structures of manganese clusters, **1**, **2**, **3**, **4** and **5**, in Fig. 2 have been carried out on the basis of the Heisenberg models followed by the ab initio molecular orbital calculation by the use of general spin orbitals (GSO). The computational results, together with available experiments, enable us to confirm a high-valent manganese-oxo (Mn(V)=O) model [27,35] for oxygen evolution from water in OEC of PS II as illustrated in Fig. 9. This model is consistent with the present theoretical studies on the basis of recently presented X-ray structure of OEC [1], together with previous theoretical results [24,27,35] for model complexes by Limburg [28] and Naruta [36]. It is also in agreement with the Mn(V)-oxo model for oxygen evolution in OEC by Baber and Iwata [47,48] proposed on the experimental grounds. However, detailed theoretical studies on the surrounding coordination sphere are necessary for further refinements of the model.

Acknowledgement

This work has been supported by a Grant-in-Aid for Scientific Research on Priority Areas (No. 14204061) by the Ministry of Education, Science, Culture and Sports.

References

[1] K.N. Ferreira, T.M. Iversion, K. Maghlaoui, J. Barber, S. Iwata, Science 303 (2004) 1831.
[2] B. Kok, B. Forbush, M. McGloin, Photochem. Photobiol. 11 (1970) 457.
[3] G.C. Dismulces, Photochem. Photobiol. 43 (1986) 99.
[4] G. Renger, Angew. Chem., Int. Ed. 26 (1987) 643.
[5] V.L. Pecoraro, Photochem. Photobiol. 48 (1988) 249.
[6] R.J. Debus, Biochimi. Biophys. Acta 1102 (1992) 269.
[7] V.K. Yachandra, K. Sauer, M.P. Klein, Chem. Rev. 96 (1996) 2927.
[8] G.C. Dismulces, Chem. Rev. 96 (1996) 2909.
[9] W. Ruttinger, G.C. Dismulces, Chem. Rev. 97 (1997) 1.
[10] J. Stubbe, W.A.v.d. Donk, Chem. Rev. 98 (1998) 705.
[11] M. Yagi, M. Kaneko, Chem. Rev. 101 (2001) 21.
[12] V.K. Yachandra, V.J. DeRose, M.J. Latimer, I. Mukerji, K. Sauer, M.P. Klein, Science 260 (1993) 675.
[13] C. Philouze, G. Blondin, J.-J. Gired, J. Guilhem, C. Pascard, D. Lexa, J. Am. Chem. Soc. 116 (1994) 8557.
[14] J.B. Vincent, C. Christmas, H.R. Chang, Q. Li, P.D.W. Boyd, J.C. Huffman, D.N. Hendrickson, G. Christou, J. Am. Chem. Soc. 111 (1989) 2086.
[15] N. Hendrickson, G. Christou, E.A. Schmitt, E. Libby, J.S. Bashkin, S. Wang, H.L. Tsai, J.B. Vincent, P.D.W. Boyd, J.C. Huffman, K. Folting, Q. Li, W.E. Streib, J. Am. Chem. Soc. 114 (1992) 2455.
[16] E.A. Schmitt, L. Noodleman, E.J. Baerends, D.N. Hendrickson, J. Am. Chem. Soc. 114 (1992) 6109.
[17] M.R.A. Blomberg, P.E.M. Siegbahn, S. Styring, G.T. Babcock, B. Åkermark, P. Korall, J. Am. Chem. Soc. 119 (1997) 8285.
[18] B.I. Belinskii, Chem. Phys. 179 (1994) 1.
[19] Y. Yoshioka et al., Bull. Chem. Soc. Jpn 78 (2001) 1231.
[20] K. Yamaguchi, S. Yamanaka, M. Nishino, Y. Takano, Y. Kitagawa, H. Nagao, Y. Yoshioka, Theoret. Chem. Acc. 102 (1999) 328.
[21] K. Yamaguchi, Chem. Phys. Lett. 30 (1975) 288.
[22] T. Soda, Y. Kitagawa, T. Onishi, Y. Takano, Y. Shigeta, H. Nagao, Y. Yoshioka, K. Yamaguchi, Chem. Phys. Lett. 319 (2000) 223.
[23] T. Soda, Y. Kitagawa, T. Onishi, Y. Takano, Y. Yoshioka, K. Yamaguchi, Mol. Cryst. Liq. Cryst. 343 (2000) 157.
[24] K. Yamaguchi, Y. Takahara, T. Fueno, Appl. Quant. Chem. (V.H. Smith et al., Reidel, 1986) 155.
[25] S. Yamanaka, R. Takeda, K. Yamaguchi, Polyhedron 22 (2003) 2013.
[26] S. Yamanaka, K. Yamaguchi, Bull. Chem. Soc. Jpn. 77 (2004) 1269.
[27] H. Isobe, T. Soda, Y. Kitagawa, Y. Takano, T. Kawakami, Y. Yoshioka, K. Yamaguchi, Int. J. Quant. Chem. 85 (2001) 34.
[28] J. Limburg, J.S. Vrettos, L.M. Liable-Sands, A.L. Rheingold, R.H. Crabtree, G.W. Brudvig, Science 283 (1999) 1524.
[29] H. Tatewaki, S. Huzinaga, J. Chem. Phys. 71 (1979) 4339.
[30] J. Messinger, J.H.A. Nugent, M.C. Evans, Biochemistry 36 (1977) 11055.
[31] S.L. Dexheimer, M.P. Klein, J. Am. Chem. Soc. 114 (1992) 2841.
[32] T. Mtsukawa, H. Mino, D. Yoneda, A. Kawamori, Biochemistry 38 (1999) 4072.
[33] A. Onoda, Y. Yamada, Y. Nakayama, K. Takahashi, H. Adachi, T. Okamura, A. Nakamura, H. Yamamoto, N. Ueyama, D. Vypracht-icky, Y. Okamoto, Inorg. Chem. 43 (2004) 4447.
[34] Y. Takahara, K. Yamaguchi, T. Fueno, Chem. Phys. lett. 158 (1989) 95.
[35] K. Koizumi, M. Shoji, Y. Nishiyama, Y. Maruno, Y. Kitagawa, T. Soda, S. Yamanaka, M. Okumura, K. Yamaguchi, Int. J. Quant. Chem. 100 (2004) 943.
[36] Y. Naruta, M. Sasayama, K. Ichihara, J. Mol. Catal A 117 (1997) 115.
[37] M. Kusunoki, Chem. Phys. Lett. 197 (1992) 108.

[38] J. Bonvoisin, G. Blondin, J.-J. Girerd, J.L. Zimmermann, Biophys. J. 61 (1992) 1076.
[39] M. Zheng, G.C. Dismukes, Inorg. Chem. 35 (1996) 3307.
[40] Y. Feyziyev, B.J.v. Rotterdam, G. Berat, S. Styring, Chem. Phys. 294 (2003) 415.
[41] P. Alia et al., Chem. Rev. 294 (2003) 459.
[42] J. Kortas, M.R. Pederson, T. Baruah, N. Bernstein, C.S. Helling, Polyhedron 22 (2003) 1871.
[43] R. Takeda, S. Mitsuo, S. Yamanaka, K. Yamaguchi, Polyhedron 24 (2005) 2238.
[44] M. Shoji, T. Hamamoto, K. Koizmumi, H. Isobe, Y. Kitagawa, Y. Takano, S. Yamanaka, M. Okumara, K. Yamaguchi, Polyhedron 24 (2005) 2701.
[45] P.A. Goodson, A.R. Oki, J. Glerup, D.J. Hodgson, J. Am. Chem. Soc. 112 (1990) 6248.
[46] M. Lundberg, P.E.M. Siegbahn, Phys. Chem. Chem. Phys. 6 (2004) 4772.
[47] J. Barber, K. Ferreira, K. Maghlaoui, S. Iwata, Phys. Chem. Chem. Phys. 6 (2004) 4737.
[48] S. Iwata, J. Baber, Curr. Opin. Struct. Bio. 14 (2004) 447.

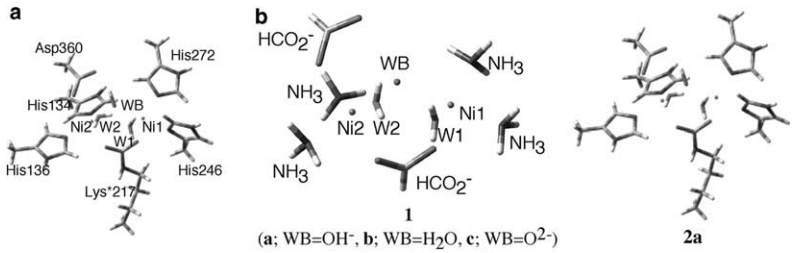


Fig. 1. (a) X-ray crystal structure of active site in *K. aerogenus* (PDB code: 1FWJ) and (b) small model of active site. Model **1a** (WB = OH^-) is depicted here. Realistic model of active site of OH^- bridge model (**2a**).

magnetic coupling between Ni ions. Three possibilities of bridging WB, i.e., H_2O, OH^- and O^{2-} were examined by calculations of their J_{ab} values using the unrestricted hybrid density functional theory (UHDFT) method. First, we constructed the simplest model as illustrated in Fig. 1(b). Next, we carried out theoretical calculations using more realistic models and larger basis sets to obtain more reliable results. Natural orbitals and their occupation numbers were analyzed to explain the antiferromagnetic interactions and elucidate the character of the active site of urease. From the results, we discussed the chemical species of WB. Finally, we proposed one of the theoretical approaches for the active sites of metalloproteins in terms of magnetic interactions.

2. Theoretical background

2.1. Effective exchange integrals (J_{ab})

The magnetic properties of transition metal complexes were usually investigated by the use of the Heisenberg–Dirac–van Vleck spin Hamiltonian. For example, the effective exchange interaction between localized spins in binuclear transition metal complexes is described by the total spin form of the spin-coupling Hamiltonian [7–9]

$$H = -2\sum J_{ab} S_a \cdot S_b, \tag{1}$$

where J_{ab} is the orbital-averaged effective exchange integral between the metal a and b with total spin operators S_a and S_b. J_{ab} can be experimentally determined by magnetic susceptibility. Recent development in computational quantum chemistry enabled us to perform large ab initio calculations of J_{ab} values using broken-symmetry (BS) approach such as UHF or UDFT [10,11]. The BS approach can be performed at a low computing cost. In singlet biradicals and low-spin species, however, it suffers from the spin contamination of high-spin states, leading to spin-projection procedures. Our group proposed spin projection scheme as follows;

$$J_{ab} = \frac{E(\mathrm{LS}) - E(\mathrm{HS})}{\langle S^2\rangle(\mathrm{HS}) - \langle S^2\rangle(\mathrm{LS})}, \tag{2}$$

where $E(X)$ and $\langle S^2\rangle(X)$ denote the total energy and total spin angular momentum for the spin state X, respectively [10,11]. In this paper, the magnetic interactions between Ni(II) ions were discussed using the equation.

3. Natural orbital analyses

Usual orbital-correlation diagram, which helps us to understand orbital interactions, is not obtained by the BS calculation because of the DODS approach [12]. In order to clarify the effective exchange interactions in the complexes using expression like the closed-shell MO, we introduced natural orbitals (NOs), which were determined by diagonalizing their first order density matrices as

$$\rho(r, r') = \sum n_i \{\phi_i(r)\}^* \phi_i(r'), \tag{5}$$

where n_i denoted the occupation number of NO ϕ_i [12,13]. If an occupation number of a magnetic orbital is close to 1.0, then two electrons in the orbital are almost localized on each spin site. On the other hand, n_i should be equal to 2.0 if stable chemical bond exists. In other words, the occupation numbers of the BS method contains an important information to understand the stability in chemical bond.

To assess this instability (diradical character), instability value (y_i) for orbital type i ($i = \sigma$, δ and so on.) is introduced here as follows [14]:

$$y_i = 2W_D = \frac{n_i^2 - 4n_i + 4}{n_i^2 - 2n_i + 2}, \tag{9}$$

where n_i and n_i^* are occupation numbers of bonding and anti-bonding NO, respectively and W_D denotes the weight of double excitation for orbital i. If a chemical bond of orbital i is stable, y_i is close to zero. On the other hand, if a chemical bond of orbital i is unstable and spins are localized at metal sites, then y_i is close to unity. Especially, $y_i/2$ is consistent to a weight of the doubly exited configuration in the MCSCF theory [14].

In this way, metal–metal bond natures and degrees of electron correlation effect, which causes spin-localization are discussed in terms of instabilities in chemical bonds using these indices.

4. Computational details

Atomic coordinations of complexes were taken from data of X-ray crystal structure analysis of *Klebsiella aerogenus* (PDB code: 1FWJ) that was available in the Protein Data Bank (PDB). We constructed two types of model structure in size, one is small model and another is realistic model. In case of the small model complex, calculations were performed by the use of Tatewaki–Huzinaga MINI (5333/533/5) basis set for Ni atoms, STO-3G basis set for ligand atoms. In these models, combinations of WB, W1 and W2 are **1a** (OH^-, H_2O, OH^-), **1b** (H_2O, OH^-, OH^-), and **1c** (O^{2-}, H_2O, H_2O), respectively. On the other hand, calculations were performed by the use of Tatewaki–Huzinaga MIDI (533(21)/53(21)/(41)) basis set for Ni atoms, 4-31G basis set for ligand atoms in case of the realistic model complex. In this realistic model, both W1 and W2 are H_2Os. All calculation was carried out using GAUSSIAN-98 [15].

5. Results and discussion

5.1. Calculated results using small model of urease

First, the electronic structure of active site in urease was examined using smallest models **1a**, **1b** and **1c** as illustrated in Fig. 1(b). The singlet states ($S = 0$) and quintet states ($S = 2$) were computed by UB3LYP method [16] to calculated the effective exchange integrals (J_{ab}). However we could not obtain appropriate electronic states of oxo-bridge model **1c**. Suárez et al. [6] reported that oxo-bridge model was unstable and oxygen of oxy-bridge drew hydrogen from W3, which existed around W1 and W2. Our calculated results are consistent with their results. The result is suggesting that there is little possibility of the oxo-bridge. So, we focused on **1a** and **1b** models.

Table 1
Calculated Mulliken charge densities and spin densities of **1a**, **1b** and **2a** for low-spin state (LS) and high-spin state (HS)

WB	Atom	Charge density		Spin density	
		LS	HS	LS	HS
1a	Ni1	1.269	1.271	1.733	1.741
	Ni2	1.233	1.233	−1.707	1.706
	O(WB)	−0.612	−0.613	−0.050	0.162
1b	Ni1	1.311	1.311	1.744	1.747
	Ni2	1.245	1.245	−1.722	1.721
	O(WB)	−0.119	−0.119	−0.023	0.061
2a	Ni1	0.819	0.821	1.735	1.755
	Ni2	0.866	0.866	−1.747	1.751
	O(WB)	−0.835	−0.836	0.029	0.146

Calculated Mulliken charge densities and spin densities of **1a** and **1b** were summarized in Table 1. Charge densities on Ni ions, especially Ni1, of **1a** are smaller than ones of **1b** because of negative charges on WB oxygen. However a difference in changes on Ni2 between **1a** and **1b** is very small. In other words, electron density on Ni1 is susceptible to the WB in comparison with Ni2. While spin densities on Ni1 and Ni2 of **1a** and **1b** are comparable, respectively.

The effective exchange integrals (J_{ab}) values between spins on terminal Ni ions were calculated by Eq. (2) as summarized in Table 2. Total energies and expectation values of the operator $\hat{S}^2$ ($\langle \hat{S}^2 \rangle$) used in the equation are also summarized in the table. UB3LYP calculations reproduced experimental week anti-ferromagnetic coupling [5]. An order of absolute values of J_{ab} is as follows,

$$|J_{ab}(\mathbf{1a})| > |J_{ab}(\text{expt.})| > |J_{ab}(\mathbf{1b})|.$$

Experimental value is middle between J_{ab}(**1a**) and J_{ab}(**1a**). From the result, it is difficult to decide which model is more reliable.

Natural orbitals of **1a** and **1b** are depicted in Fig. 2 and their occupation numbers are summarized in Table 3. The highest occupied NO (HONO) and lowest unoccupied NO (LUNO) of **1a** are showing interactions through formic acid (through-FA). HONO-1 and LUNO+1 orbitals are indicating interactions through OH^- (through-OH^-). The y values are close to 100%, showing localized spin structure on the both Ni ions. The relation of the y values is

$$y(\text{through-FA}) > y(\text{through-OH}^-).$$

On the other hand, HONO and LUNO of **1b** are through-H_2O interactions and HONO-1 and LUNO+1

Table 2
Calculated total energies[a], $\langle S^2 \rangle$ values and effective exchange integrals (J_{ab})[b] for **1a**, **1b** and **2a**

Model	Low spin state		High spin state		J_{ab}
	Total energy	$\langle S^2 \rangle$	Total energy	$\langle S^2 \rangle$	
1a	−3848.44572772	1.9946	−3848.44552018	6.0051	−11.4
1b	−3848.81240645	2.0024	−3848.81235961	6.0043	−2.6
2a	−4933.76187872	1.9951	−4933.76157408	6.0066	−16.7
Experiment[c]					−6.3

J_{ab} values were calculated by Eq. (2) in the text.
[a] In atomic unit.
[b] In cm^{-1}.
[c] Experimental value was taken from [4].

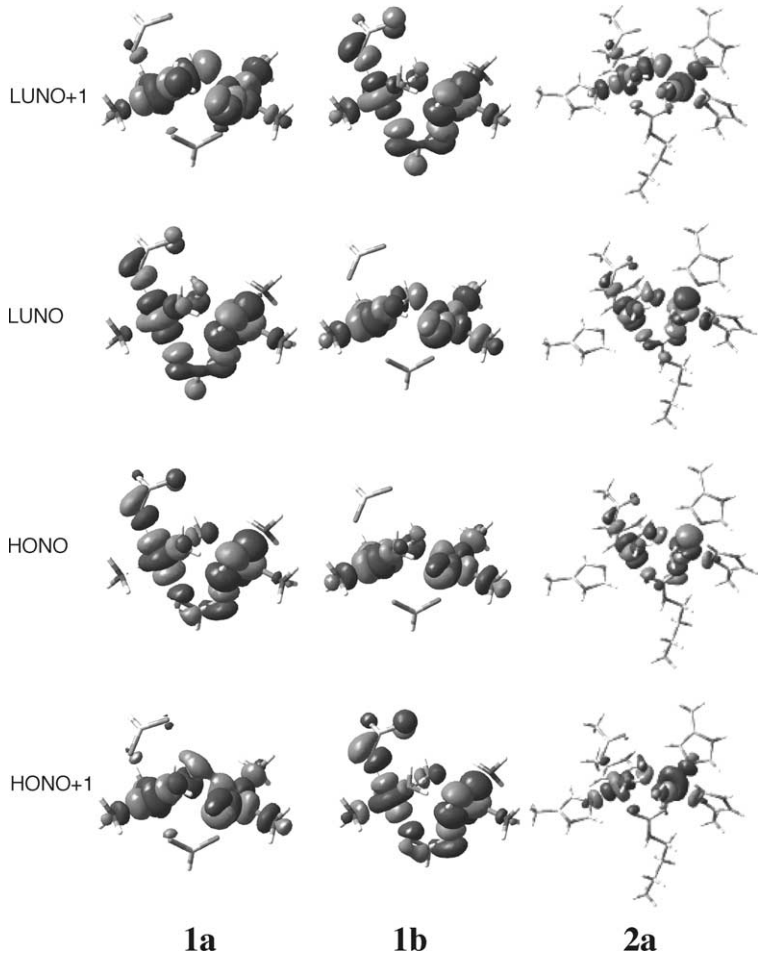


Fig. 2. Natural orbitals of **1a** (WB = OH^-), **1b** (WB = H_2O) and **2a** (WB = OH^-). Depicted NOs are magnetic orbitals.

Table 3
Occupation numbers and instability values[a] of natural orbitals for **1a**, **1b** and **2a**

Orbital	**1a**		**1b**		**2a**	
	Occupation numbers	y	Occupation numbers	y	Occupation numbers	y
HONO	1.0217	95.7	1.0256	94.9	1.0236	95.3
HONO-1	1.0988	86.3	1.0355	92.9	1.1027	79.7

HONO and HONO-1 in the table are magnetic orbitals.
[a] In %.

orbitals are through-FA interaction. And the relation of the y values is

$$y(\text{through-}H_2O) > y(\text{through-FA}).$$

This means that anti-ferromagnetic interactions through hydroxide are stronger than ones of through formic acid but through-water interaction is weaker than ones of through-FA. Accordingly, the strength of anti-ferromagnetic couplings are

$$OH^- > \text{ formic acid } > \text{water}.$$

It is explained by charge delocalization, which helps super-exchange interaction. The negatively charged hydroxide bears stronger super-exchange interactions.

6. Calculated results using large model of urease

To clarify the details about electronic structure of active site in urease, UB3LYP calculations are carried out using more realistic model and larger basis set. The hydroxide bridging model (**2a**) and oxo-bridging model (**2b**) are examined. The model structure of **2a** is illustrated in Fig. 1. Calculated charge densities and spin densities are summarized in Table 1. Spin densities on Ni ions of **2a** are almost equivalent to ones of **1a**, while charge densities are decreased. From the result, it is found that a degree of spin localization is not so much affected by ligands realities in case of **2a**. Natural orbitals of **2a** are depicted in Fig. 2. The magnetic orbitals

of **2a** are similar to ones of **1a**. NOs tend to localize around Ni ions except for bridge-FA, WB and Asp360. This is a reason of small difference between **1a** and **2b** in spin densities on Ni ions. Occupation numbers and calculated y values are summarized in Table 3. The y value of HONO-1 (through-OH^- interaction) decreases in comparison with one of **1a**. Because HONO-1 expresses anti-ferromagnetic interaction through-OH^-, it is expected that anti-ferromagnetic interaction is enlarged. Actually, calculated J_{ab} of **2a** is larger than **1a**, as summarized in Table 2. Calculated effective exchange integrals (J_{ab}) is larger than experimental value. In these calculations, geometry of hydrogen of OH^- is only optimized. It is reported that hydrogen bond plays important role for the reaction in the system [6]. Therefore position of hydrogen atoms around Ni ions must be optimized to carry out quantitative calculations.

We could not appropriate electronic structure of oxo-bridging model (**2b**). An electron on Ni1 is transferred to the Asp360 as a result of iterative self consistent field (SCF) calculation. Suárez et al. [6] reported that one hydrogen atom of bridge H_2O was drawn by Asp360 on model-**2b** after the structural optimization. Consequently, Ni1–H_2O–Ni2 became Ni1–OH^-–Ni2. So, our calculations are also consistent with their results. Interestingly, NOs exhibiting through-FA interaction are delocalized WB and Asp360 in all models. Especially, the NOs distribute on hydrogen of WB. This orbital seemed to be associated with the hydrogen subtraction.

7. Concluding remarks

The electronic structure of active site in urease and chemical species of bridge oxygen, i.e., WB was examined by theoretical calculations in terms of magnetic interactions between Ni(II) ions. In case of small model complexes, experimental weak anti-ferromagnetic interaction was reproduced by WB ligand of H_2O and OH^-. However we could not obtain appropriate electronic state by using H_2O ligand in case of realistic model complexes. Therefore it is concluded that hydroxide is the most possible candidate for the WB ligand. On the other hand, Day et al. [17] reported that there was no evidence for exchange coupling between the two Ni ions. We have to investigate their electronic states and magnetic interactions carefully. Because J_{ab} value is a quantity, which is very sensitive to electronic structure as mentioned before. There are not so much such physical properties that we can use, so J_{ab} value is one of the important crews for the investigation of electronic structure in the metalloprotein. Recent development of quantum chemistry and computational method makes it possible to calculate J_{ab} values quantitatively [18–20]. If there are some candidate of chemical species, position of hydrogens and so on, quantum chemical calculations are powerful way to elucidate them. The calculation of J_{ab} value is one of the strategies for the investigations of active sites in metalloproteins.

Acknowledgement

This work has been supported by a Grant-in-Aid for Scientific Research on Priority Areas (Nos. 16750049 and 14204061) from Ministry of Education, Culture, Sports, Science and Technology, Japan.

References

[1] A. Messerschmidt, R. Huber, T. Poulos, K. Wieghardt (Eds.), Handbook of Metalloproteins, John Wiley & Sons, Ltd., West Sussex, England, 2001.
[2] M.A. Pearson, L.O. Michel, P.R. Housinger, P.A. Karplus, Biochemistry 36 (1997) 8164.
[3] E. Jabri, M.B. Carr, R.P. Hausinger, P.A. Karplus, Science 268 (1995) 998.
[4] S. Benini, W.R. Rypniewski, K.S. Wilson, S. Miletti, S. Ciurli, S. Mangani, Structure 7 (1999) 205.
[5] P.A. Clark, D.E. Wilcox, Inorg. Chem. 28 (1989) 1326.
[6] D. Suárez, N. Díaz, K.M. Merz Jr., J. Am. Chem. Soc. 125 (2003) 15324.
[7] D. Gatteschi, O. Kahn, J.S. Miller, F. Palacio (Eds.), Magnetic Molecular Materials, Kluwer Academic Publishers, Dordrecht, 1991.
[8] O. Kahn (Ed.), Magnetism: a Supermolecular Function; NATO ASI Series C, vol. 484, Kluwer Academic Publishers, Dordrecht, 1996.
[9] E. Coronado, P. Dekhais, D. Gatteschi, J.S. Miller (Eds.), Molecular Magnetism: from Molecular Assemblies to the Devices; NATO ASI Series E, vol. 321, Kluwer Academic Publishers, Dordrecht, 1996.
[10] T. Kawakami, S. Yamanaka, S. Yamada, W. Mori, K. Yamaguchi, in: M.M. Turnbull, T. Sugimoto, L.K. Thompson (Eds.), Molecular-based Magnetic Materials, Theory, Technique and Applications, ACS Symposium Series, 644, American Chemical Society, Washington, DC, 1996, p. 30.
[11] K. Yamaguchi, in: R. Carbó, M. Klobukowski (Eds.), Self-consistent Field, Theory and Applications, Studies in Physical and Theoretical Chemistry, vol. 70, Elsevier, Amsterdam, Oxford, New Tork, Tokyo, 1990, p. 727.
[12] K. Takatsuka, T. Fueno, K. Yamaguchi, Theoret. Chem. Acta 48 (1978) 175.
[13] Y. Takano, Y. Kitagawa, T. Onishi, Y. Yoshioka, K. Yamaguchi, N. Koga, H. Iwamura, J. Am. Chem. Soc. 124 (2002) 450.
[14] K. Yamaguchi, T. Kawakami, Y. Takano, Y. Kitagawa, Y. Yamashita, H. Fujita, Int. J. Quant. Chem. 90 (2002) 370.
[15] M.J. Frisch, G.W. Trucks, H.B. Schlegel, G.E. Scuseria, M.A. Robb, J.R. Cheeseman, V.G. Zakrzewski, J.A. Montgomery Jr., R.E. Stratmann, J.C. Burant, S. Dapprich, J.M. Millam, A.D. Daniels, K.N. Kudin, M.C. Strain, O. Farkas, J. Tomasi, V. Barone, M. Cossi, R. Cammi, B. Mennucci, C. Pomelli, C. Adamo, S. Clifford, J. Ochterski, G.A. Petersson, P.Y. Ayala, Q. Cui, K. Morokuma, N. Rega, P. Salvador, J.J. Dannenberg, D.K. Malick, A.D. Rabuck, K. Raghavachari, J.B. Foresman, J. Cioslowski, J.V. Ortiz, A.G. Baboul, B.B. Stefanov, G. Liu, A. Liashenko, P. Piskorz, I. Komaromi, R. Gomperts, R.L. Martin, D.J. Fox, T. Keith, M.A. Al-Laham, C.Y. Peng, A.

Nanayakkara, M. Challacombe, P.M.W. Gill, B. Johnson, W. Chen, M.W. Wong, J.L. Andres, C. Gonzalez, M. Head-Gordon, E.S. Replogle, J.A. Pople, GAUSSIAN-98, Gaussian, Inc., Pittsburgh, PA, 2002.
[16] A.D. Becke, J. Chem. Phys. 98 (1993) 5648.
[17] E.P. Day, J. Peterson, M.S. Sendova, M.J. Todd, R.P. Hausinger, Inorg. Chem. 32 (1993) 634.
[18] Y. Kitagawa, T. Kawakami, K. Yamaguchi, Mol. Phys. 100 (2002) 1829.
[19] Y. Kitagawa, T. Soda, Y. Shigeta, S. Yamanaka, Y. Yoshioka, K. Yamaguchi, Int. J. Quant. Chem. 84 (2001) 592.
[20] T. Soda, Y. Kitagawa, T. Onishi, Y. Takano, Y. Shigeta, H. Nagao, Y. Yoshioka, K. Yamaguchi, Chem. Phys. Lett. 319 (2000) 223.

phases and new phase transitions different to the usual AFM and FM systems [9]. Indeed, the peculiar critical exponent values are observed for phase transitions of triangular lattice compounds such as VBr_2, VCl_2, $CsMnBr_3$ [10–12].

The relation between magnetism and superconductivity has also been attracted much attention in relation to the high T_c superconductivity of La_2CuO_4 from the viewpoint of the pre-existing entangled spin pairs in a RVB phase [7,8]. In such a context, $Na_{0.35}Co_2O_4$-$(H_2O)_{1.3}$ is an interesting compound in the points that (i) it has a equilateral triangular lattice of spin sources and that (ii) it is recently reported to exhibit the superconductivity [13]. The fundamental electronic properties such as magnetism and superconductivity are thought to be originated from the Co_2O_4 layers having 2-D hexagonal structure. It is also noteworthy that the electronic doping to this layer, which is regulated by Na ions and H_2O, could become the chemical pressure to determine the electronic phase of Co_2O_4. Previously, Yamaguchi and co-workers [14–18] examined the possible mechanism of high-T_c superconductivity on the hypothesis that the cooperative mechanism of electron-phonon, electron correlation, and multiband effects. From the *J*-model used in these previous studies, the magnetic interactions between Co ions play essential role in the superconductivity of this compound. Although the electronic properties of $Na_xCo_2O_4(H_2O)_y$ are determined by its *x*- and *y*-values, the theoretical study on the fundamental magnetic features of Co_2O_4 might provide the important information. As for an ab initio approach applicable for the spin-frustrated systems, we developed the general spin orbital (GSO) version of density functional theory (DFT) and successfully applied for the various classes of non-collinear molecular magnetism [18–23]. Thus, in this study, we start to examine the spin structure of the cluster model for triangular Co_2O_4 layers by ab initio general spin orbital (GSO) density functional theory (DFT) [24] computations. For the purpose, the new calculational scheme of the effective exchange integrals based on spin correlation functional values, which can be applied for the homogenous spin-frustrated systems in general, is presented. The computational *J* values are used to estimate T_c via the previously proposed *J*-model [14–18].

2. Theoretical background

2.1. General spin orbital version of DFT

In this section, we briefly describe the theoretical background of GSO-DFT approach used in our study.

The most essential feature of GSO-DFT is that the fundamental variable is not usual α and β spin densities, $\rho_\alpha(\mathbf{r})$, $\rho_\beta(\mathbf{r})$, but the 2×2 spin density matrix

$$\rho(\mathbf{r}) = \begin{pmatrix} \rho_{\alpha\alpha}(\mathbf{r}) & \rho_{\alpha\beta}(\mathbf{r}) \\ \rho_{\beta\alpha}(\mathbf{r}) & \rho_{\beta\beta}(\mathbf{r}) \end{pmatrix} = n(\mathbf{r}) + \sum_m^{x,y,z} \rho_m(\mathbf{r}). \tag{1}$$

Minimization of KS energy functional is implemented over all non-interacting N-representable spin density matrices such that [24]

$$E_{KS} = \min_{\mathrm{Tr}\rho(\mathbf{r})=N} \left\{ T_S[\rho(\mathbf{r})] + \int d\mathbf{r} \mathrm{Tr} V_{\mathrm{eff}}(\mathbf{r})\rho(\mathbf{r}) \right\}. \tag{2}$$

Here, $T_S[\rho(\mathbf{r})]$ is the non-interacting KS kinetic energy functional involving the effective potential, which we denote $V_{\mathrm{eff}}(\mathbf{r})$. By introducing an exchange-correlation (XC) functional $E_{XC}[\rho(\mathbf{r})]$, the set of coupled equations for KS orbitals that construct a KS single-determinant wavefunction,

$$\sum_{\sigma_2} \left[\delta_{\sigma_1\sigma_2} \left\{ -\frac{\nabla_i^2}{2} + \int d\mathbf{r}' \frac{n(\mathbf{r}')}{|\mathbf{r}-\mathbf{r}'|} \right\} + \frac{\delta E_{XC}}{\delta \rho_{\sigma_2\sigma_1}}(\mathbf{r}) + V_{\mathrm{ext}}^{\sigma_1\sigma_2}(\mathbf{r}) \right] \psi_i^{\sigma_2}(\mathbf{r}) = \varepsilon_i \psi_i^{\sigma_1}(\mathbf{r}), \tag{3}$$

can be obtained. Here, σ_i ($i = 1,2$) is a spin variable (α or β).

In order to make full use of the non-collinearity of this extension of DFT, the GSO version of XC functional of the localized spin density approximation (LSDA) [18–23,25] expressed by

$$E_{XC}^{\text{GSO-LSDA}}[\rho_+, \rho_-] = \int d\mathbf{r}(\rho_+(\mathbf{r}) + \rho_-(\mathbf{r}))\varepsilon(\rho_+(\mathbf{r}), \rho_-(\mathbf{r})) \tag{4}$$

with the localized up (ρ_+) and down (ρ_-) spin densities,

$$\rho_\pm(\mathbf{r}) = n(\mathbf{r}) \pm |\mathrm{Tr}\vec{\sigma}\rho(\mathbf{r})|/2, \tag{5}$$

must be employed, where $\vec{\sigma}$ is the vector of Pauli matrices. The dependency of $\rho_\pm(\mathbf{r})$, so of the XC functional, on the off-diagonal terms of spin density matrices, $\rho(\mathbf{r})$, makes the KS equations to be coupled equations like Eq. (3). In the case of usual collinear magnetic systems, the equation and XC functional is reduced to that of the standard spin-unrestricted DFT (UDFT).

It is well recognized that the LSDA fails to describe the strongly correlated systems just as Na_xCoO_2-$(H_2O)_y$. We here cover the weak point of LSDA by hybridizing with generalized gradient approximation (GGA) and Hartree–Fock (HF) methods. The GSO version of GGA or hybrid XC functional can be straightforwardly derived by a similar manner of LSDA. We examined the familiar exchange-correlation functionals of three classes: (i) Hartree–Fock (HF), (ii) Becke88 [26] + LYP [27] (BLYP) as a gradient-corrected approximation, and (iii) B3LYP [28] as a hybrid approximation. All GSO-DFT computations are of the linear combination of gaussian type orbitals where MINI basis sets [29] are employed.

2.2. An estimation scheme of J value for homogeneous triangular lattices

In previous study of molecular magnetism, we use the equation

$$J = \frac{E^{\mathrm{HS}}_{\mathrm{GSO\text{-}DFT}} - E^{\mathrm{LS}}_{\mathrm{GSO\text{-}DFT}}}{\langle \hat{S}^2 \rangle^{\mathrm{HS}}_{\mathrm{GSO\text{-}DFT}} - \langle \hat{S}^2 \rangle^{\mathrm{LS}}_{\mathrm{GSO\text{-}DFT}}} \tag{6}$$

in order to estimate J value by using ab initio GSO-DFT computational results. However, this J scheme based on $\langle \hat{S}^2 \rangle$ required the addition complicated correction terms to the denominator in order to apply for the general systems. We use, in this study, the alternative and simple estimation scheme based on spin correlation functions. To derive the formula, we need to take two assumptions: (i) all of nearest interactions are equivalent each other and (ii) the non-nearest neighbor interactions are small enough to neglect. We then note that the expectation values of Heisenberg model for any arbitrary spin state (X), are given by

$$E^{X}_{\mathrm{HB}} = -2JN\langle \hat{S}_i \cdot \hat{S}_{i+1} \rangle^{X}. \tag{7}$$

Here, N is the number of the nearest neighbor spin pairs in the systems. By mapping the GSO-DFT computational results into Eq. (7), the J value can be determined by

$$J = \frac{E^{\mathrm{HS}}_{\mathrm{GSO\text{-}DFT}} - E^{\mathrm{LS}}_{\mathrm{GSO\text{-}DFT}}}{2N\left\{ \langle \hat{S}_i \cdot \hat{S}_{i+1} \rangle^{\mathrm{HS}}_{\mathrm{GSO\text{-}DFT}} - \langle \hat{S}_i \cdot \hat{S}_{i+1} \rangle^{\mathrm{LS}}_{\mathrm{GSO\text{-}DFT}} \right\}}. \tag{8}$$

Note that spin correlation function between nearest neighbor sites, i and $i+1$, are equivalent for all i by our assumption, (i). Thus, for the case of the triangular lattice, this estimation equation works with the HSDW solutions of GSO-DFT, but not with the AFM solutions of the usual UDFT, since the UDFT provides distinct (AFM and FM coupled) spin correlation functions for n.n. pairs of spin-frustrated systems.

As compared with the previous scheme given in Eq. (6), there are two superior points in that of Eq. (8). First, if we focus our attention on the local two sites, we note that the spin delocalization effect can be taken into account by Eq. (8). That is to say, $\langle \hat{S}^2_i \rangle^{\mathrm{HS}} = \langle \hat{S}^2_i \rangle^{\mathrm{LS}}$, which is a assumption to derive Eq. (6) from the Heisenberg model, does not always hold since the $\langle \hat{S}^2_i \rangle^{\mathrm{LS}}$ shrinks in general, due to spin delocalized effect. The details of such considerations on diradical systems were described in the previous paper [30], while we shall examine the more general case elsewhere. Here, we would like to emphasize another improved point of this scheme that Eq. (8) can be utilized for any homogeneous spin systems with no modification, while the system-dependent revision is required for Eq. (6) to apply a large homogeneous spin systems. Here, by the term, "homogeneous spin systems", we mean the systems which satisfy the above two assumptions (i) and (ii). Many examples such as, Kagome lattice, the icosidodecahedral magnetic cluster, $Mo_{72}Fe_{30}$, as well as the hypothetical clusters-and-lattices are listed in [18]. Note that the CoO_2 layer of the target compounds in this study, which constitutes of three hexagonal sheets is also one of such "homogenous" spin systems.

2.3. Computational results

The $Na_xCoO_2(H_2O)_y$ ($x = 0.35$, $y = 1.3$) compound consists of three layers as illustrated in Fig. 1(A). The CoO_2 layer is responsible for the electronic and magnetic properties while Na and H_2O layers are thought to regulate the hole-doping rate into the CoO_2 layer. This CoO_2 layer further divided into a Co layer and two O layers, which form sandwiched structure as shown in Fig. 1(A). All of Co and O layers have the hexagonal structure within the plane. From the fact that the distance between two distinct Co layers along the c-axis is larger than 10 Å with intercalating by Na and H_2O layers, this system can be considered as an isolated two-dimensional spin frustrated systems. As shown in Fig. 1(B), the local environment surrounding Co^{4+} ion that is the spin source of this compounds, is trigonally distorted octahedral field consisting of six O^{2-} ions. Thus, an elementary picture of electronic structure for an individual Co is explained as follows. In the octahedral field, five d-orbitals are split into e_{1g} and t_{1g} ones. Due to the trigonal distortion of O_h field, the latter is further divided into A_{1g} and E_g orbitals, with the slight hybridization between e_{1g} and E_g, as shown in the right side of Fig. 1(C). Therefore, the local spins on Co ions has A_{1g} character, which is the singly occupied state of Co^{4+} ion.

The structural parameters used in our ab initio computation are those reported by Takada et al.: $a = b = 2.8230$ Å are intra-layer lattice constants for both of Cos and Os layers, $c = 19.6207$ Å for the c-axis perpendicular to those layers. The Os layer is on 0.0451c (0.88494 Å) to Co layer along the c-axis. The modeled clusters we here examine are illustrated in Fig. 2. A most fundamental unit, which exhibit spin-frustration and preserve the local distorted O_h field for Co^{4+} ion, is $Co_3{}^{4+}O_{2-}{}^{13}$ in Fig. 2(A). However, to avoid

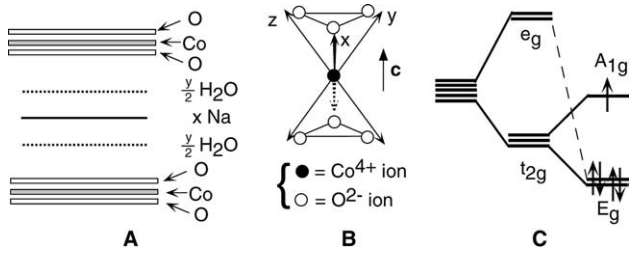


Fig. 1. (A) The layered structure of $Na_xCo_2O_4(H_2O)_y$. (B) The local environment of Co^{4+} ion. (C) Energy splitting of 3d orbitals of Co^{4+} ion due to the ligand field.

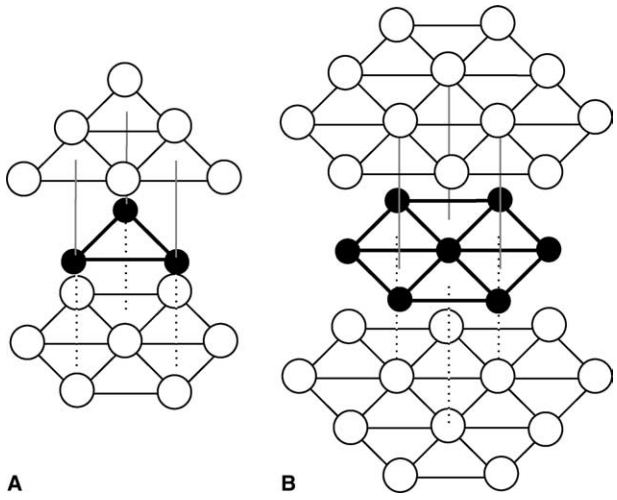


Fig. 2. Model clusters preserved the distorted O_h field for Co^{4+} ions. (A) A triangular unit, $Co_{4+}{}^{3}(2e^{-})_{13}$. (B) A hexagonal unit, $Co_{4+}{}^{7}(2e^{-})_{24}$. Here, white spheres represented oxygen anions, but are replaced point charges 2^{e-} in the actual computation.

the convergence problem of KS-DFT computation due to excess electrons, we replace oxygen anions, O^{2-}, by classical point charges, $2e^{-}$. We also examined a hexagonal unit in Fig. 2(B) with similar replacement oxygens by point charges.

Fig. 3 shows the diagonal part of spin density of ground spin states of those clusters, of $Co_{4+}{}^{3}$ and $Co_{4+}{}^{7}$, $\vec{\rho}_s(\mathbf{r}) = \sum_\mu \vec{P}_{\mu\mu}\chi_\mu(\mathbf{r})^2$, where $\vec{P}$ are spin density matrix vector and $\{\chi_\mu\}$ is the basis set, respectively. Note that the global spin axis is arbitrary, so to be easy to see, we choose the global spin axis for $\vec{\rho}_s(\mathbf{r})$ aligning within the Co planes. We can see that those stable spin structures are obviously helical spin density wave (HSDW) that is localized on the Co atoms due to the d-character of open-shell electrons. Indeed, for all of HSDW solutions obtained using GSO computations, the spin correlation functional values are calculated to be nearly -0.125, which are corresponds to those of classical spin solutions aligned with a relative $\pi/3$ orientation. By using Eq. (8) with those spin correlation values, we estimated the J values. Those results are listed in Table 1, being much smaller than the estimated value from the Curie temperature of $Na_{0.5}CoO_2$, $-56\ cm^{-1}$ [31]. Previously, Yamaguchi and co-workers proposed for the high T_c superconductivity of the layered copper oxides, that the strong superexchange interactions induced the spin-mediated superconductivity and that the transition temperature can be estimated by using the effective exchange integral value, J, via the relation,

$$T_c = CJ, \tag{9}$$

where C is a proportional constant, of which an explicit expression depends on a theoretical model [14–18]. We here listed calculated T_c values by using Eq. (9) in Table 1, all of which are quite smaller than the experimental value. Obviously those differences on the J and T_c values are partially due to an approximation oxygen anions as point charges in this initial work, which imply neglecting of the superexchange interactions.

In order to estimate the effect of superexchange interactions, we implement the comparative computations of J values between the dinuclear Co^{4+} ions, of which interatomic distance is fixed to be 2.823 in accordance with the above GSO-DFT computations: (i) with two bridged oxygen anions and other 8 point charges and (ii) with 10 point charges, both of which anions and point charges form the O_h field for two Co^{4+} ions. It is obvious that the ratio of J(i) and J(ii), i.e., J(i)/J(ii) is roughly close to the ratio of superexchange + direct and direct-only exchange interactions. The computational results of J(i)/J(ii) are, 1240.6, 165.0, and, 181.6, respectively, for HF, BLYP, and B3LYP methods. The simple scaling to J values leads to J(GHF) = −3980, J(BLYP) = −645, and J(B3LYP) = −479.4 (unit: cm^{-1}) of $Co_{4+}{}^{3}$ and J(GHF) = −6774, J(BLYP) = −2706, and J(B3LYP) = −1949 (unit: cm^{-1}) of $Co_{4+}{}^{7}$, all of which overestimate the experimental AFM interaction. Indeed, Zhang et al. [32] added the artificial uniform positive background to balance the itinerant electrons to describe band gaps of CoO_2 layer in LSDA and LSDA + U bands calculations. Thus, we speculate that the actual

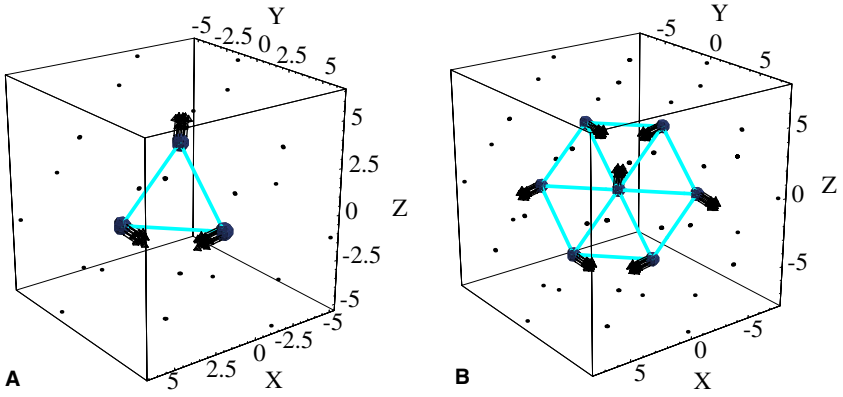


Fig. 3. Three-dimensional Löwdin spin population plots of stable GSO-B3LYP solutions for (A) $Co_{4+}{}^{3}$ and (B) $Co_{4+}{}^{3}$.

Table 1
The effective exchange integral (J) values of $Co_{4+}{}^{3}(2e^{-})_{13}$ and $Co_{4+}{}^{7}(2e^{-})_{24}$ clusters by ab initio GSO methods

	$Co_{4+}{}^{3}(2e^{-})_{13}$		$Co_{4+}{}^{7}(2e^{-})_{24}$	
	J (cm^{-1})[a]	T_c (K)[b]	J (cm^{-1})[a]	T_c (K)[b]
GHF	−3.21	0.46	−5.46	0.79
GSO-BLYP	−3.91	0.56	−16.4	2.35
GSO-B3LYP	−2.64	0.38	−10.7	1.54

T_c values estimated via J-model are also listed.
[a] The estimation value of J of $Na_{0.5}CoO_2(H_2O)_{1.3}$ is 56 cm^{-1} ([31]).
[b] The experimental value of T_c of $Na_{0.35}CoO_2(H_2O)_{1.3}$ is 5 K ([13]).

magnetic interactions of the results of the compromise between superexchange interactions and those suppression by the Na^+ and H_2O environments and required some artifice in ab initio computations.

2.4. Discussion and concluding remarks

In order to treat the homogeneous spin frustrated systems, we present the new scheme for J values connected with GSO-DFT computational results. We apply this scheme for the model clusters of $Na_xCoO_2(H_2O)_y$ ($x = 0.35$, $y = 1.3$). For both of triangular and hexagonal clusters of Co_n ($n = 3.7$) plus point charges, we found that the HSDW solutions are the ground spin states, being consistent with classical spin vector models. However, as for the quantitative aspects, due to an approximation oxygen anions as point charges in this initial work, which imply neglecting of the superexchange interactions, we obtained the considerably small J values as compared to experimental ones. On the other hand, introducing of the effects of bare oxygen anions leads to convergence problems or overestimation of J values, which implies that the some device are required to regulate the amount of the itinerant electrons.

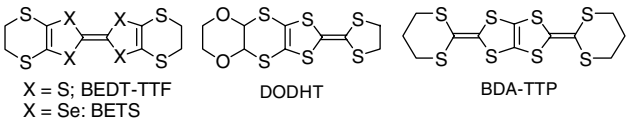
Finally, we would like to emphasize that, although the GSO-DFT provides the classical spin picture, the estimated J value using Eq. (8) is of the spin-corrected, in other words, of the quantum spin state. Thus, the GSO-DFT with the J scheme will work for almost all of spin-frustrated systems, which are not only classical states, but also quantum spin states like the RVB phase.

Acknowledgments

This work has been supported by the Ministry of Education, Science, Sports and Culture, through a Grant-in-Aid for IT program. The authors acknowledge Dr. H. Nagao for his helpful discussions.

References

[1] K. Yoshida, Theory of Magnetism, Springer, 1996.
[2] M. Mekata, K. Adachi, J. Phys. Soc. Jpn. 44 (1978) 806.
[3] K. Awaga, T. Okuno, M. Yamaguchi, M. Hasegatwa, T. Inabe, Y. Maruyama, N. Wada, Phys. Rev. B 49 (1994) 3975.
[4] M. Tamura, R. Kato, J. Phys. Condens. Matter 14 (2002) L729.
[5] A. Yoshimori, J. Phys. Soc. Jpn. 14 (1959) 807.
[6] T. Nagamiya, Solid State Phys. 20 (1967) 305.
[7] P.W. Anderson, Mater. Res. Bull. 8 (1975) 153.
[8] P.W. Anderson, Science 235 (1987) 1196.
[9] S. Miyashita, H. Shiba, J. Phys. Soc. Jpn. 53 (1984) 1145.
[10] K. Takeda, N. Uryu, K. Ubukoshi, K. Hirakawa, J. Phys. Soc. Jpn. 55 (1986) 727.
[11] H. Kadowaki, K. Ubukoshi, K. Hirakawa, J.L. Martizez, G. Shirane, J. Phys. Soc. Jpn. 56 (1987) 4027.
[12] H. Kadowaki, S.M. Shapiro, T. Inami, Y. Ajiro, J. Phys. Soc. Jpn. 57 (1988) 2640.
[13] K. Takada, H. Sakurai, E. Takayama-Muromachi, F. Izumi, R.A. Dilanian, T. Sasald, Nature 422 (2003) 53.
[14] K. Yamaguchi, Int. J. Quantum Chem. 37 (1990) 167.
[15] H. Nagao, M. Nishino, Y. Yoshioka, K. Yamaguchi, Int. J. Quantum Chem. 65 (1997) 947.
[16] H. Nagao, M. Nishino, Y. Shigeta, Y. Yoshioka, K. Yamaguchi, J. Chem. Phys. 113 (2000) 11237.
[17] K. Yamaguchi, D. Yamaki, Y. Kitagawa, M. Takahata, T. Kawakami, T. Ohsaku, H. Nagao, Int. J. Quantum Chem. 92 (2003) 47.
[18] S. Yamanaka, D. Yamaki, R. Takeda, H. Nagao, K. Yamaguchi, Int. J. Quantum Chem. 100 (2004) 1179.
[19] S. Yamanaka, D. Yamaki, Y. Shigeta, H. Nagao, Y. Yoshioka, N. Suzuki, K. Yamaguchi, Int. J. Quantum Chem. 80 (2000) 664.
[20] S. Yamanaka, R. Takeda, K. Yamaguchi, Polyhedron 22 (2003) 2013.
[21] S. Yamanaka, T. Ohsaku, D. Yamaki, K. Yamaguchi, Int. J. Quantum Chem. 91 (2003) 376.
[22] S. Yamanaka, R. Takeda, T. Kawakami, K. Nakata, T. Sakuma, T. Takada, K. Yamaguchi, J. Magn. Magn. Mater. 272–276S (2004) E255.
[23] S. Yamanaka, K. Yamaguchi, Bull. Chem. Soc. Jpn. 77 (2004) 1269.
[24] R.G. Parr, W. Yang, Density-Functional Theory of Atoms and Molecules, Oxford University Press, 1989.
[25] U. von Barth, L. Hedin, J. Phys. C: Solid State Phys. 5 (1972) 1629.
[26] A. Becke, Phys. Rev. A 38 (1988) 3098.
[27] C. Lee, W. Yang, R.G. Parr, Phys. Rev. B 37 (1988) 785.
[28] A. Becke, J. Chem. Phys. 98 (1993) 5648.
[29] S. Hujinaga, Gaussian Basis Sets for Molecular Calculations, Elsevier, Amsterdam, 1984.
[30] Y. Kitagawa, S. Yamanaka, R. Takeda, M. Shoji, K. Koizumi, Y. Nishiyama, Y. Maruno, T. Kawakami, M. Okumura, K. Yamaguchi, Int. J. Quantum Chem. 100 (2004) 927.
[31] G. Baskaran, cond-mat/0303649.
[32] P. Zhang, W. Luo, V.H. Crespi, M.L. Cohen, S.G. Louie, Phys. Rev. B 70 (2004) 085108.



2. Experimental

2.1. Synthesis

DODHT was synthesized according to the method reported previously [3,4]. $(DODHT)_2FeCl_4$ was prepared by electrocrystallization at a constant current of 0.2 μA in *m*-dichlorobenzene with 5% acetone at 5 °C. Concentration of DODHT and $TEA \cdot FeCl_4$ were 0.044 and 0.28 mM, respectively.

2.2. Electrical conductivity

Temperature dependence of resistance was measured for a single crystal of $(DODHT)_2FeCl_4$ by the four-probe dc method using gold wire contacted to the crystal by carbon paste.

2.3. X-ray crystallography

Crystal data for $(DODHT)_2FeCl_4$: $C_{20}H_{20}S_{12}O_4{-}FeCl_4$, FW = 906.8; black plate, triclinic, space group $P\bar{1}$, $a = 5.6701(9)$, $b = 16.247(3)$, $c = 19.185(3)$ Å, $\alpha = 106.720(3)$, $\beta = 93.527(3)$, $\gamma = 94.698(3)°$, $V = 1654.0(5)$ Å^3, $Z = 2$, $R = 0.0337$, $R_w = 0.0899$. CCDC-258294 containing the supplementary crystallographic data for $(DODHT)_2FeCl_4$ can be obtained free of charge via www.ccdc.cam.ac.uk/conts/retrieving.html or from the Cambridge Crystallographic Data Centre, 12 Union Road, Cambridge CB21EZ, UK; fax +44 1223 336033; or deposit@ccdc.cam.ac.uk.

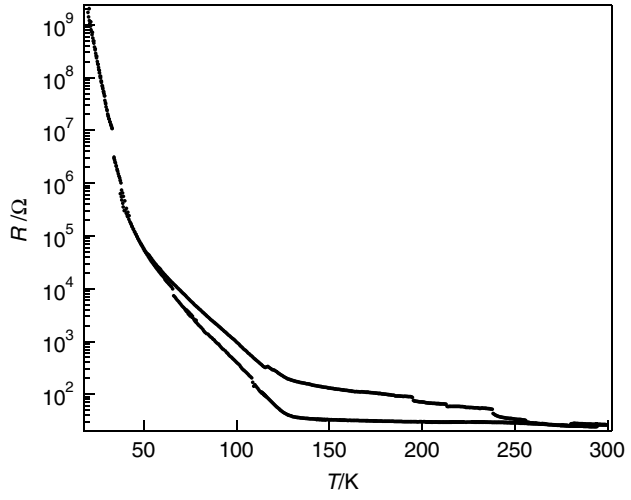


Fig. 1. Temperature dependence of resistence of $(DODHT)_2FeCl_4$.

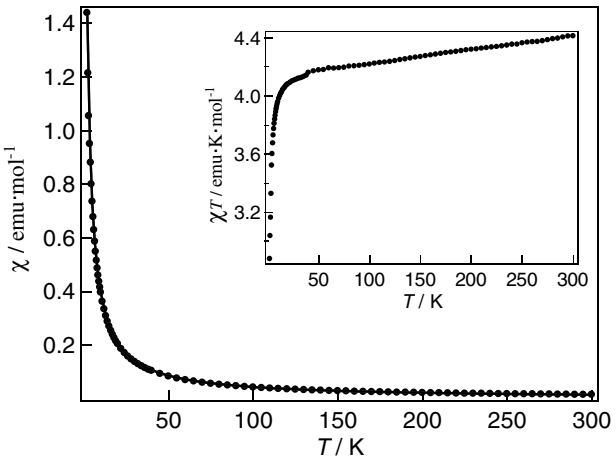


Fig. 2. Temperature dependence of magnetic susceptibility of $(DODHT)_2FeCl_4$. The solid line is a fit by Curie–Weiss law. Inset: $\chi_m T$ vs. temperature plot.

3. Results and discussion

3.1. Electrical and magnetic properties

Fig. 1 shows the resistance of $(DODHT)_2FeCl_4$ as a function of temperature. The electrical conductivity at room temperature was 7.5 S cm^{-1}. As seen in Fig. 1, the temperature dependence of resistance was extremely weak or almost independent of temperature from room temperature to 130 K. Below 130 K, the resistance increased rapidly and turned to be an insulator. The activation energy below 80 K was 32 meV.

In order to investigate magnetism, especially interaction between the conduction electron and the localized magnetic moment on Fe^{3+} ion, so-called π–d interaction, temperature dependence of the magnetic susceptibility of this salt was measured by using a SQUID magnetometer at 10,000 Oe from 300 to 2 K (Fig. 2). The susceptibility was well reproduced by the Curie–Weiss law over the whole temperature range, and the Curie constant and Weiss temperature are 4.39 emu K mol^{-1} and −1.1 K, respectively. The fitted value of Curie constant is almost same to the spin-only value of 4.38 emu K mol^{-1} calculated for a high-spin Fe^{3+} ion ($S = 5/2$, $g = 2.0$), thus the measured magnetization was dominated by the local moment of the Fe in $FeCl_4^-$ anion. Inset of Fig. 2 shows $\chi_m T$ versus temperature plot. The $\chi_m T$ value decreased gradually from 300 K to ca. 30 K, and decreased rapidly at low temperature, which indicates the weak antiferromagnetic interaction exists. The magnetic behavior is well reproduced by the Curie–Weiss law through whole temperature range indicating that the interaction of $\theta = -1.1$ K exists from

room temperature to 2 K. In both plots, there is no anomaly at around 130 K, where the transition from the semiconductor or semimetal to the insulator occurred. This result suggests the π–d interaction in $(DODHT)_2FeCl_4$ is not existing or extremely weak.

3.2. Crystal structure

Fig. 3 shows the crystal structure of $(DODHT)_2FeCl_4$ consisting of one $FeCl_4^-$ anion and two crystallographically independent DODHT molecules as the asymmetric unit. The conducting donor layer of DODHT and the insulating layer of $FeCl_4^-$ anions are arranged alternately along the *b*-axis. In the donor layer, the donor arrangement belongs to the β″-type, similarly to those of superconducting salts, $(DODHT)_2X$ (X = PF_6, AsF_6 and $BF_4 \cdot H_2O$). Donor molecules are stacked along the [1 0 1] direction with a fourfold period in a head-to-tail manner and dimerized with interplanar distances of $d_1 = 3.66$, $d_2 = 3.60$ and $d_3 = 3.99$ Å (Fig. 3(a)). There are several intermolecular S···S contacts shorter than the sum of the van der Waals radii (3.70 Å) between stacks, whereas no S···S contact is observed within a stack. These structural characteristics are seen in the DODHT salt with the same tetrahedral anion, $(DODHT)_2BF_4 \cdot H_2O$, however, interplanar distances of $(DODHT)_2BF_4 \cdot H_2O$ are slightly smaller (3.57, 3.85 and 3.81 Å) than those of $FeCl_4$ salt. Contrarily, intermolecular sulfur contacts along molecular side-by-side direction are shorter in $FeCl_4$ salt (3.368–3.620 Å) than in BF_4 salt (3.414–3.647 Å). As a result, the system of $FeCl_4$ salt is more one-dimensional along molecular side-by-side direction than that of BF_4 salt.

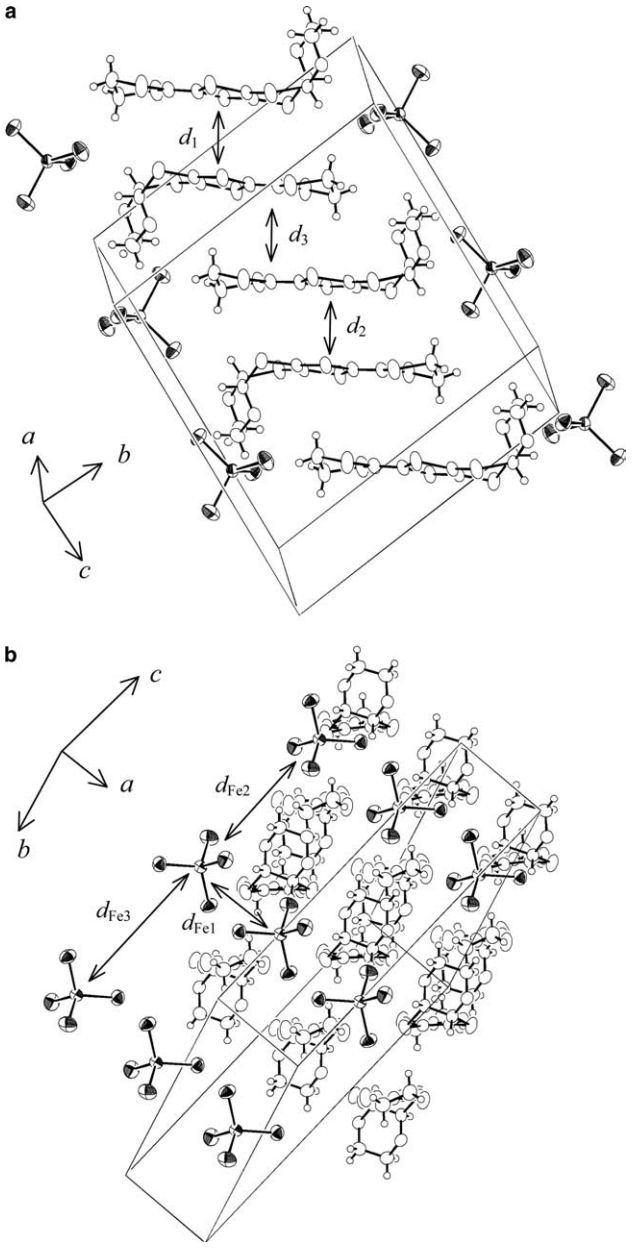


Fig. 3. Crystal structure of $(DODHT)_2FeCl_4$. (a) intermolecular distance: $d_1 = 3.66$, $d_2 = 3.60$, $d_3 = 3.99$ Å. (b) Viewed along donor long axis with $FeCl_4$ anions. Interatomic distance between Fe ions: $d_{Fe1} = 5.607$, $d_{Fe2} = 9.685$, $d_{Fe3} = 9.501$ Å.

In the insulating layer formed by $FeCl_4^-$ anions, interatomic distances between Fe ions are $d_{Fe1} = 5.607$ along *a*-axis, and $d_{Fe2} = 9.685$ and $d_{Fe3} = 9.501$ Å along *c*-axis, respectively (Fig. 3(b)). These distances are rather long to consider the direct interaction between Fe ions. Furthermore, there is no contact between the Cl atoms of the $FeCl_4^-$ anion and DODHT. These facts are consistent with the result of magnetic measurement; long range order of the magnetic moment of Fe ions was not observed and there was no anomaly at the temperature where the transition to the insulator occurred in the temperature dependence measurement of electrical resistance.

4. Conclusion

An electrical conducting radical salt comprising of π-reduced organic donor, DODHT, and an inorganic magnetic anion, $FeCl_4^-$, has newly prepared, and its crystal structure, electrical and magnetic properties were investigated. From the crystal structure, intermolecular interaction between DODHT and $FeCl_4^-$ anions dose not seem to exist, which supports the results of the electrical and the magnetic measurements. Transition temperature from semiconductor or semimetal to insulator of $(DODHT)_2FeCl_4$ is much lower than those observed for superconducting salt, $(DODHT)_2X$ (X = PF_6, AsF_6 and $BF_4 \cdot H_2O$), at ambient pressure. The nature of insulating state of the DODHT superconductors has recently been revealed to be a charge-ordered insulating state with alternating antiferromagnetic chain. Therefore, it is important to investigate the insulating state of $FeCl_4$ salt. Furthermore, since $(DODHT)_2X$ (X = PF_6, AsF_6 and $BF_4 \cdot H_2O$) exhibited superconducting

transition under pressure, the electrical property under pressure of $FeCl_4$ salt must be examined. Further work on this issue is ongoing.

Acknowledgments

This work was partly supported by a Grant-in-Aid for Scientific Research on Priority Areas of Molecular Conductors (No. 15073102) from the Ministry of Education, Science, Sports, and Culture, Japan, and a Grant-in-Aid for Scientific Research (C) (15550127) from JSPS.

References

[1] H. Fujiwara, E. Fujiwara, Y. Nakazawa, B.Z. Narymbetov, K. Kato, H. Kobayashi, A. Kobayashi, M. Tokumoto, P. Cassoux, J. Am. Chem. Soc. 123 (2001) 306.
[2] S. Uji, H. Shinagawa, T. Terashima, T. Yakabe, Y. Terai, M. Tokumoto, A. Kobayshi, H. Tanaka, H. Kobayshi, Nature 410 (2001) 908.
[3] H. Nishiakwa, T. Morimoto, T. Kodama, I. Ikemoto, K. Kikuchi, J. Yamada, H. Yoshino, K. Murata, J. Am. Chem. Soc. 124 (2002) 730.
[4] H. Nishikawa, A. Machida, T. Morimoto, K. Kikuchi, T. Kodama, I. Ikemoto, J. Yamada, H. Yoshino, K. Murata, Chem. Commun. 494 (2003).
[5] E.S. Choi, D. Graf, J.S. Brooks, J. Yamada, M. Tokumoto, J. Phys. IV France 114 (2004) 297.

*b**-axis. Obviously, magnetic torque enables us much more precise determination of both the orientation of the AF easy axis and the value of the spin-flop field. However, its sensitivity is not sufficient for the study of much smaller mixed crystals $(BETS)_2Fe_{1-x}Ga_x$-$Cl_{4-y}Br_y$.

In this paper we will report the measurements of spin-flop transitions in antiferromagnetic organic molecular conductor λ-$(BETS)_2FeCl_4$, using a commercial self-sensing piezoresistive micro-cantilever for atomic force microscopy (AFM) developed by Seiko Instruments Inc. [5]. Ohmichi and Osada [6] reported that this AFM cantilever can be utilized as a sensitive torque magnetometer under pulsed high magnetic fields up to 38 T. Recently, we used it as a sensitive torque magnetometer under steady magnetic fields up to 45 T and succeeded in observation of the de Haas–van Alphen oscillations in a single-component molecular conductor [Ni(tmdt)$_2$] for the first time [7]. Since the magnetic torque is proportional to the magnetic field, its sensitivity decreases under low magnetic fields, where spin-flop transition usually occurs. So far, nobody tried to apply this AFM cantilever to the study of spin-flop transition in antiferromagnets. We have succeeded, for the first time, in observation of spin-flop transitions of tiny single crystals including λ-$(BETS)_2FeCl_4$ as small as less than 1 μg.

2. Experimental

In this study we used a commercial self-sensing piezoresistive micro-cantilever developed by Seiko Instruments Inc. for AFM [5].

Fig. 1 shows the AFM cantilever (left) with a sample mounted and a reference lever (right). A tiny single crystal ($55 \times 20 \times 300$ μm, 0.8 μg) of λ-$(BETS)_2FeCl_4$ is mounted at the end of the beam, on the opposite side of the AFM tip. A reference lever (right) without AFM tip is incorporated on the same platform. This monolithic construction is advantageous for precise measurement, since the background signal originating from the temperature and magnetic field dependence of the piezoresistance of cantilevers can be canceled out, using a Wheatstone bridge circuit. The bridge circuit is fully balanced at zero field, and the deviation (out of balance) signal is measured as a function of applied magnetic field using a Lock-in Amplifier (SR830) operating at a low frequency. The reference output signal of the Lock-in Amplifier was used as a current source fed to the bridge circuit.

The AFM cantilever with a sample was attached to a uniaxial rotator, so that the orientation of the crystal to the magnetic field can be changed precisely.

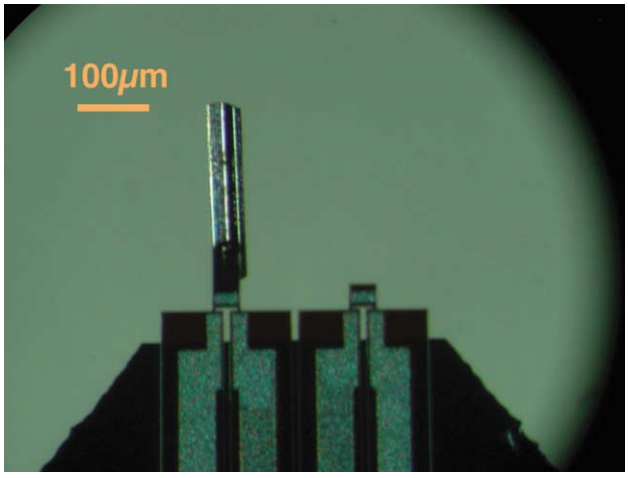


Fig. 1. Piezoresistive AFM cantilever with a sample mounted (left) and a reference lever (right). A tiny single crystal ($55 \times 20 \times 300$ μm, 0.8 μg) of λ-$(BETS)_2FeCl_4$ is glued to the back of AFM tip with epoxy.

3. Results and discussion

Fig. 2 shows the magnetic torque curves of a single crystal of λ-$(BETS)_2FeCl_4$ at 0.5 K in the magnetic field direction with the angle tilted from the *c*- to *b**- axis. For the angle of 30.0° a very sharp structure appears at $H = 1.2$ T, resulting from the spin-flop (SF) transition

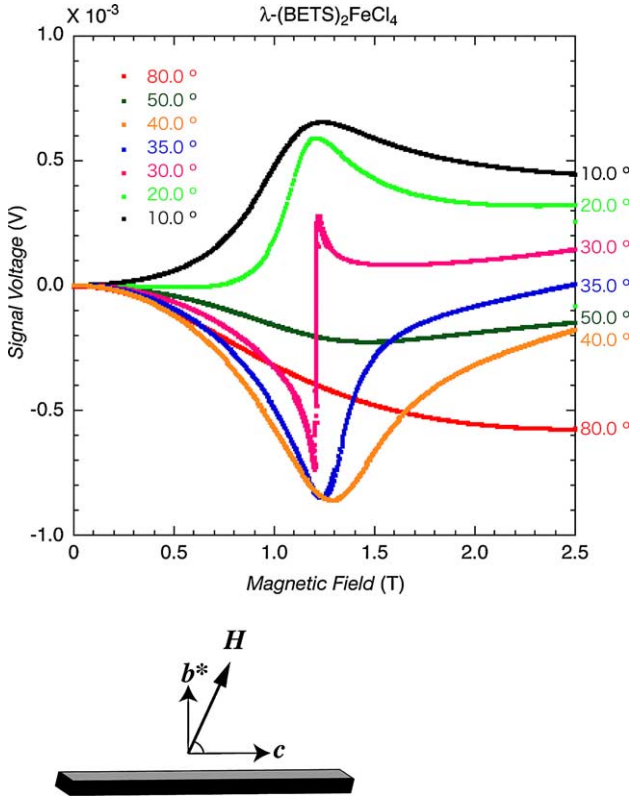


Fig. 2. Magnetic torque curves of a single crystal of λ-$(BETS)_2FeCl_4$ at 0.5 K.

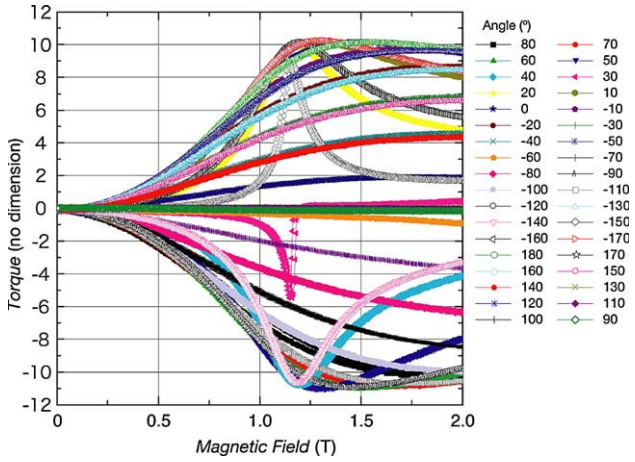


Fig. 3. Magnetic torque curves of a single crystal λ-$(BETS)_2FeCl_4$ at 2 K.

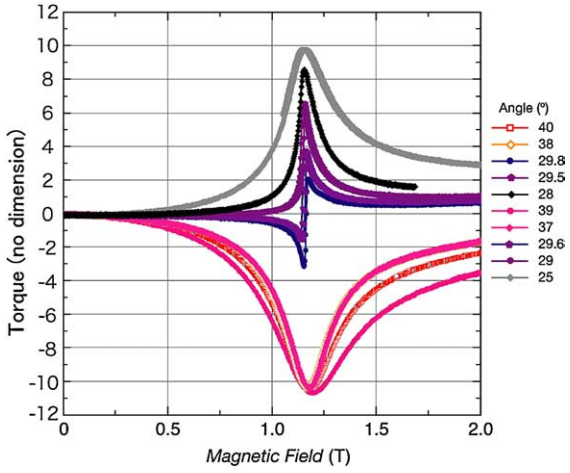


Fig. 4. Magnetic torque curves of a single crystal of λ-$(BETS)_2FeCl_4$ at 2 K.

between the AF in low magnetic field and the canted AF (CAF) in high magnetic field. Tilted from the angle, the structure at the SF transition becomes broader. For the angle of 50° and 80°, the SF transition does not occur and changes to the gradual spin rotation.

The overall results are consistent with the capacitive magnetic torque study on relatively large single crystals (>30 μg) reported by Sasaki et al. [4]. The only difference is that we can now measure considerably smaller crystals.

Fig. 3 shows the magnetic torque curves of a single crystal of λ-$(BETS)_2FeCl_4$ at 2.0 K in the magnetic field direction with the angle tilted from the *c*- to *b**-axis. The sample was rotated fully for the angle of 0° to ±180°. A very sharp structure due to SF transition was observed only at about 30° and a less sharp one near −150°. Fig. 4 shows the magnetic torque curves of a single crystal of λ-$(BETS)_2FeCl_4$ at 2.0 K when the magnetic field was applied in directions close to the easy axis. Near 30°, a very small change in the angle (even less than 1°) caused a drastic change in the magnetic torque curve. Moreover, the sign or polarity changes from positive to negative, or vice versa, when the magnetic field is tilted across the AF easy axis, which enable us a precise determination of the easy axis of antiferromagnets.

Akutsu et al. [8] studied mixed crystals of λ-$(BETS)_2FeBr_xCl_{4-x}$ using SQUID magnetometer. The anisotropy of the magnetic susceptibility was measured by using the oriented (//c) thin needle crystals put in thin quartz capillaries (0.7 mm ϕ). They found that the direction of AF easy axis of λ-$(BETS)_2FeBr_xCl_{4-x}$ is varied according to the Br content (x). Around x = 0.3–0.5, the direction of the easy axis of the AF spin structure changed from parallel to the *c*-axis ($x < 0.2$) to perpendicular to it ($x > 0.6$), suggesting that the direction of AF easy axis is varied according to the magnitude of π–d coupling. Obviously, we need a measurement using a single crystal. As already explained, a torque magnetometry is useful for precise determination of the easy axis as well as the spin-flop field. However, lack of sensitivity of capacitive type cantilever has hindered such measurements so far. It is now necessary to reexamine the direction of AF easy axis of λ-$(BETS)_2FeBr_xCl_{4-x}$ in order to study the effect of π–d coupling more systematically. Measurements on single crystals of λ-$(BETS)_2FeBr_xCl_{4-x}$ are now in progress, and the results will be published separately.

References

[1] H. Kobayashi, A. Kobayashi, P. Cassoux, Chem. Soc. Rev. 29 (2000) 325.
[2] A. Kobayashi, T. Udagawa, H. Tomita, T. Naito, H. Kobayashi, Chem. Lett. 1993 (1993) 2179.
[3] M. Tokumoto, T. Naito, H. Kobayashi, A. Kobayashi, V.N. Laukhin, L. Brossard, P. Cassoux, Synth. Met. 86 (1997) 2161.
[4] T. Sasaki, H. Uozaki, S. Endo, N. Toyota, Synth. Met. 120 (2001) 759.
[5] H. Takahashi, K. Ando, Y. Shirakawabe, Ultramicroscopy 91 (2002) 63.
[6] E. Ohmichi, T. Osada, Rev. Sci. Instrum. 73 (2002) 3022.
[7] H. Tanaka, M. Tokumoto, S. Ishibashi, D. Graf, E.S. Choi, J.S. Brooks, S. Yasuzuka, Y. Okano, H. Kobayashi, A. Kobayashi, J. Am. Chem. Soc. 126 (2004) 10518.
[8] H. Akutsu, K. Kato, E. Ojima, H. Kobayashi, H. Tanaka, A. Kobayashi, P. Cassoux, Phys. Rev. B 58 (1998) 9294.

2. Experimental

The acidic **H0**H, **H1**H, **H2**H, **H3**H, and **M2**H were prepared by the condensation reaction of TEMPOCOOH with HO_3SNH_2, $HO_3SCH_2NH_2$, $HO_3SCH_2CH_2NH_2$, $HO_3SCH_2CH_2CH_2NH_2$, and $HO_3SCH_2CH_2NH(CH_3)$, respectively, in the presence of dicyclohexylcarbodiimide (DCC) and dimethylaminopyridine (DMAP) in 30 mL of CH_2Cl_2 at room temperature with stirring over a few days. Metathesis with $PPh_4 \cdot Br$ yielded their PPh_4 salts, as orange crystals (34–48% yields). TTF (**1**) (tetrathiafulvalene) salts of **H1**, **H2**, and **M2** were prepared by metathesis of $(TTF)_3(BF_4)_2$ and the corresponding PPh_4 salts in acetonitrile for **H1** and acetone for **H2** and **M2**. The TMTSF (**2**) (tetramethyltetraselenafulvalene) and BEDT-TTF salts of **H1** were prepared by electrocrystallization in PhCl + 5% of acetone with the corresponding donor and the PPh_4 salt of **H1**. The materials were characterized by X-ray analysis. They were measured using a Quantum CCD area detector on a Rigaku AFC-7R diffractometer or a Rigaku AFC-5R 4-circle diffractometer, at room temperature. All calculations were carried out using teXsan for Windows version 1.06 and CRYSTALS version 12. Electrical resistivity measurements were done by the conventional four probe method. The magnetic susceptibility measurements using polycrystalline samples were measured with a Quantum Design MPMS5SH magnetometer, from 2 to 300 K.

3. Results and discussion

3.1. PPh_4 salt

The crystal data of five PPh_4 salts are listed in Table 1. All anions form dimers with hydrogen bonds between an oxygen atom of the sulfonate group and N–H or N–CH_3 of the nearest anion. For example, the structure of the **H3** dimer in $PPh_4 \cdot$ **H3** is shown in Fig. 1.

The intradimer $O_{TEMPO}\cdots O_{TEMPO}$ distances are in the range of 14.2–17.5 Å, indicating no magnetic interaction via this interdimer route. Furthermore, the nearest $O_{TEMPO}\cdots O_{TEMPO}$ distances for the **H0**, **H1**, **H2**, **H3**, and **M2** salts are 6.36(1), 8.709(9), 7.16(1), 6.594(6), and 6.229(5) Å, respectively, which are too long to allow any significant magnetic interactions because each dimer is surrounded by the relatively large PPh_4 cations. Actually, the temperature-dependent magnetic susceptibilities have Curie–Weiss behaviours with small Weiss constants ($C/\theta = 0.336/0.01$, 0.391/0.01, 0.337/−1.01, 0.381/−0.02, and 0.387 emu K mol^{-1}/−1.14 K, respectively). In addition, there

Table 1
Crystallographic data of PPh_4 salts

Compound	(PPh_4)(**H0**) · H_2O	(PPh_4)(**H1**) · acetone	(PPh_4)(**H2**)	(PPh_4)(**H3**)	(PPh_4)(**M2**)
Formula	$C_{34}H_{40}N_2O_6PS$	$C_{38}H_{46}N_2O_6PS$	$C_{36}H_{42}N_2O_5PS$	$C_{37}H_{44}N_2O_5PS$	$C_{37}H_{44}N_2O_5PS$
Formula weight	635.73	689.83	645.77	659.80	659.81
Crystal system	triclinic	triclinic	triclinic	triclinic	triclinic
Space group	$P\bar{1}$	$P\bar{1}$	$P\bar{1}$	$P\bar{1}$	$P\bar{1}$
Diffractometer	Rigaku AFC5R	Rigaku AFC5R	Rigaku AFC5R	Rigaku AFC5R	Rigaku AFC5R
a (Å)	15.668(3)	12.616(6)	14.643(3)	11.939(4)	11.782(1)
b (Å)	16.507(6)	14.156(6)	18.006(4)	13.910(2)	13.3553(9)
c (Å)	14.369(4)	11.397(5)	13.706(3)	11.295(1)	11.527(1)
α (°)	109.67(3)	111.64(3)	108.71(2)	95.70(1)	91.307(7)
β (°)	109.33(2)	101.96(4)	97.50(2)	100.24(2)	99.093(9)
γ (°)	83.49(3)	77.70(4)	84.05(2)	74.39(2)	76.336(7)
V (Å^3)	3302(2)	1830(2)	3386(1)	1775.2(7)	1740.1(3)
Z	4	2	4	2	2
T (K)	306	298	301	301	295
μ(Mo Kα) (mm^{-1})	0.1927	0.1793	0.1870	0.1798	0.184
Crystal size (mm^3)	0.5 × 0.5 × 0.08	0.5 × 0.4 × 0.1	0.4 × 0.4 × 0.35	0.5 × 0.3 × 0.15	0.5 × 0.5 × 0.5
θ_{max} (°)	55.0	55.0	55.0	55.0	55.0
Data total	15716	8808	16170	8539	8380
Data unique	15189	8428	15561	8150	7990
Data used	4440 ($I > 3\sigma(I)$)	2582 ($I > 2\sigma(I)$)	5498 ($I > 2\sigma(I)$)	5325 ($I > 2\sigma(I)$)	5161 ($I > 3\sigma(I)$)
Transmission factors	0.908–1.000 (PSI[a])	0.939–1.000 (PSI[a])	0.030–0.040 (DIF[b])	0.947–1.000 (PSI[a])	0.925–1.000 (PSI[a])
R_{int}	0.0505	0.0669	0.0548	0.0203	0.0130
No. of parameters	793	433	811	415	488
R	0.068	0.068	0.067	0.054	0.067
R_w	0.071	0.050	0.068	0.069	0.050
Goodness-of-fit (S)	2.000	1.650	1.980	1.820	1.201
$\Delta\rho_{max}/\Delta\rho_{min}$ (e$^-$ Å^{-3})	0.358/−0.423	0.293/−0.306	0.492/−0.362	0.450/−0.443	0.32/−0.63

[a] PSI scan.
[b] DIFABS (N. Walker, D. Stuart. Acta Cryst. A 39 (1983) 158–166).

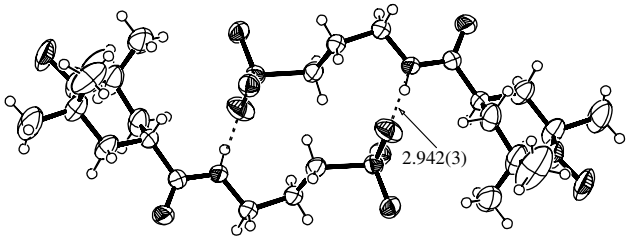


Fig. 1. Hydrogen-bonded dimer of TEMPO-CONH$(CH_2)_3SO_3^-$ in $PPh_4 \cdot$ **H3**. Dashed lines indicate N–H···O–S hydrogen bonds.

is positional disorder of the TEMPO part in $PPh_4 \cdot$ **H3** and the TEMPO atoms apart from O, N, and C of methine were refined over two possible positions. It appears to be due to a rotational disorder along the O–N···C axis.

3.2. TTF salts

The crystal data of three TTF salts are shown in Table 2. The general description of all the crystal structures is as follows. The ratio of TTF to anion is 1:1, indicating that each TTF is a monocation. Each TTF forms a face-to-face dimer and so appears to form a spin singlet. The details of the each crystal structure together with the physical properties are described in the following individual sections.

3.2.1. (TTF)(*H1*) · $2H_2O$

The crystal structure of (TTF)(**H1**) · $2H_2O$ is shown in Fig. 2. There are one TTF cation, one anion and two water molecules in the asymmetric unit. The TTF cations form dimers with many short S···S contacts (see Fig. 2). The dimer interacts with adjacent ones with only a weak S···S contact (see Fig. 2), suggesting that the conduction pathway is very poor. Actually, the room-temperature electrical resistivity of 8×10^6 Ω cm was observed.

There is not shorter contact than the sum of van der Waals radii between the TEMPO parts, although the observed $O_{TEMPO}\cdots O_{TEMPO}$ contact of 4.581(5) Å is magnetically somewhat short. Furthermore, there are short contacts between S or C atoms of TTF and the spin centre O atom of TEMPO (see Fig. 2). Thus, the TEMPO radicals seem to form a spin dimer via the TTF dimer (TEMPO···TTF···TTF···TEMPO). The temperature dependence of magnetic susceptibility is shown in Fig. 3. It can be fitted by a Singlet–Triplet model with $C = 0.330$ emu K mol^{-1} and $J = 5.7$ K. The spin interaction between the TEMPO radicals appears to be mediated through the direct O···O contact and/or via the TTF dimer.

3.2.2. (TTF)(*H2*) · H_2O

Each TTF dimer is surrounded by the relatively large **H2** anions, indicating no conduction pathway through

Table 2
Crystallographic data of TTF (**1**), TMTSF (**2**), and BEDT-TTF (**3**) salts

Compound	(**1**)(**H1**) · $2H_2O$	(**1**)(**H2**) · H_2O	(**1**)(**M2**)$(H_2O)_{0.50}$	(**2**)(**H1**) · $2H_2O$ · PhCl	(**3**)$_5$(**H1**)$_2$ · $6H_2O$
Formula	$C_{17}H_{28}N_2O_7S_5$	$C_{18}H_{28}N_2O_6S_5$	$C_{19}H_{29}N_2O_{5.5}S_5$	$C_{27}H_{41}N_2O_7SClSe_4$	$C_{72}H_{92}N_4O_{16}S_{42}$
Formula weight	532.75	528.76	533.92	888.98	2616.06
Crystal system	triclinic	triclinic	monoclinic	triclinic	triclinic
Space group	$P\bar{1}$	$P\bar{1}$	$P2_1/n$	$P\bar{1}$	$P\bar{1}$
Diffractometer	Quantum CCD	Quantum CCD	Quantum CCD	Quantum CCD	Quantum CCD
a (Å)	8.063(1)	8.673(5)	8.025(8)	7.2219(2)	14.200(3)
b (Å)	11.389(3)	12.197(4)	34.361(7)	13.297(1)	17.189(3)
c (Å)	14.078(2)	12.872(4)	9.3275(9)	18.124(3)	22.005(3)
α (°)	99.104(6)	75.76(2)	90.0	87.514(3)	95.327(4)
β (°)	97.356(2)	89.315(8)	105.373(2)	88.237(2)	94.0213(9)
γ (°)	103.164(2)	70.285(5)	90.0	85.659(1)	95.888(1)
V (Å^3)	1224.8(4)	1238.7(9)	2480(3)	1733.1(2)	5302(1)
Z	2	2	4	2	2
T (K)	303	298	297	301	306
μ(Mo Kα) (mm^{-1})	0.513	0.504	0.502	4.4149	0.8984
Crystal size (mm^3)	$0.5 \times 0.25 \times 0.01$	$0.45 \times 0.2 \times 0.05$	$0.5 \times 0.05 \times 0.02$	$0.47 \times 0.03 \times 0.03$	$0.8 \times 0.15 \times 0.01$
θ_{max} (°)	55.0	55.0	55.0	55.0	55.0
Data total	10431	6253	15855	15077	47305
Data unique	4684	3197	4966	7088	21832
Data used	3516 ($I > 3\sigma(I)$)	1823 ($I > 3\sigma(I)$)	1819 ($I > 3\sigma(I)$)	3868 ($I > 3\sigma(I)$)	9863 ($I > 5\sigma(I)$)
Transmission factors	0.680–1.075 (EMP[a])	0.178–63.9 (EMP[a])	0.250–3.724 (EMP[a])	0.469–1.256 (EMP[a])	0.420–1.154 (EMP[a])
R_{int}	0.029	0.124	0.184	0.060	0.064
No. of parameters	280	280	327	386	1207
R	0.065	0.195	0.133	0.101	0.127
R_w	0.062	0.135	0.062	0.101	0.125
Goodness-of-fit (S)	1.096	1.149	1.233	4.670	8.890
$\Delta\rho_{max}/\Delta\rho_{min}$ (e$^-$ Å^{-3})	0.27/−0.26	0.72/−0.62	0.65/−0.72	1.595/−1.237	1.630/−0.916

[a] Empirical method.

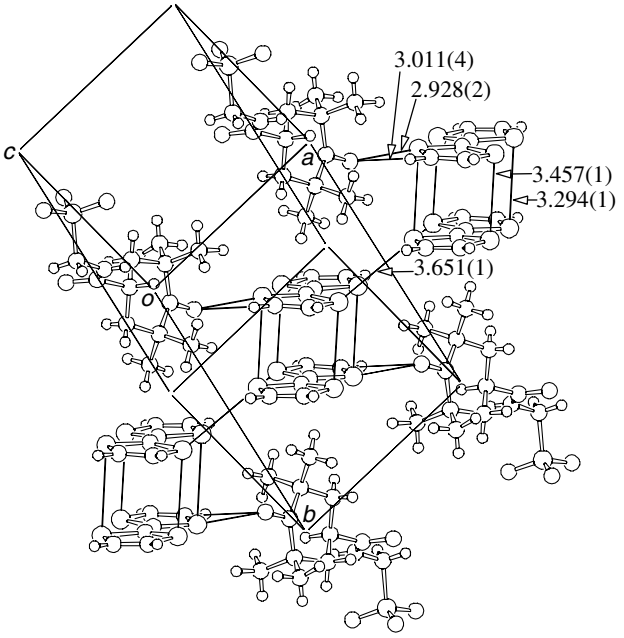


Fig. 2. Crystal structure of (TTF)(**H1**) · $2H_2O$. The water molecules are omitted for clarity. Short contacts are also indicated as solid lines.

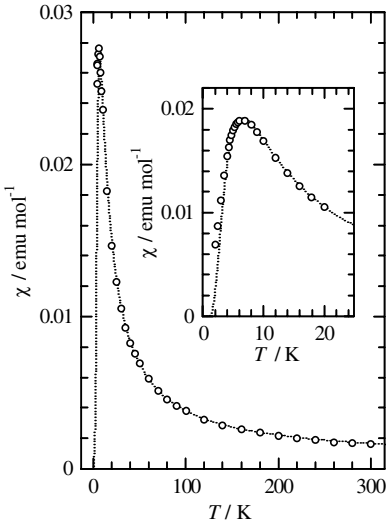


Fig. 3. Temperature-dependent magnetic susceptibility of (TTF)(**H1**) · $2H_2O$ from 2 to 300 K. The inset shows the magnetic susceptibility of another measurement in the low-temperature region.

the crystal. As observed in (TTF)(**H1**) · $2H_2O$, (TTF)(**H2**) · H_2O has a short contact between an S atom of TTF and an O atom of TEMPO, as shown in Fig. 4. However, the distance is 0.2 Å longer than in the **H1** salt. The magnetic susceptibility data fitted the Curie–Weiss model with a Curie constant of 0.384 emu K mol^{-1}, and a Weiss constant of −0.09 K, indicating that the spin interaction is very weak.

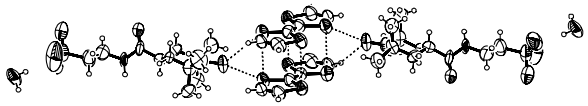


Fig. 4. Structure of TEMPO···TTF···TTF···TEMPO. Dashed lines indicate short S···S (<3.70 Å) and S···O (<3.35 Å) contacts.

3.2.3. (TTF)(**M2**) · 0.50H_2O

The crystal structure is shown in Fig. 5. In the crystal, TTF cations form a stair-like stack with two alternating kinds of overlaps: (i) between two TTF moieties with no lateral shift; (ii) between halves of dithiole rings only, as shown in Fig. 6. There are many short S···S contacts in the case of (i), whilst there is only a short S···S contact in (ii) (see Fig. 6). Moreover, no short contacts between the columns are observed (see Fig. 6). These results indicate that the crystal is not so conductive.

There are no short contacts between TEMPO and TTF as observed in the previously described TTF salts, although direct interaction between TEMPOs are observed (Fig. 7). The spin centre of the TEMPO moiety interacts with a methyl group of another TEMPO moiety (>N–O···H_3C–), giving a 1D magnetic network

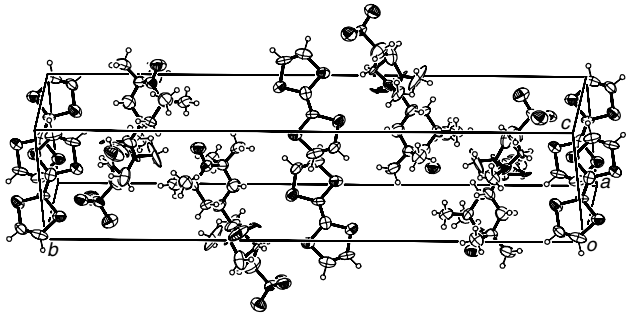


Fig. 5. Crystal structure of (TTF)(**M2**) · 0.50H_2O.

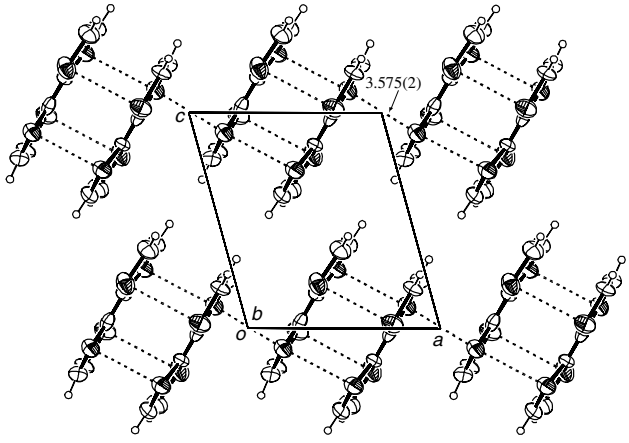


Fig. 6. Donor arrangement in (TTF)(**M2**) · 0.50H_2O. Dashed lines indicate short S···S contacts (<3.70 Å).

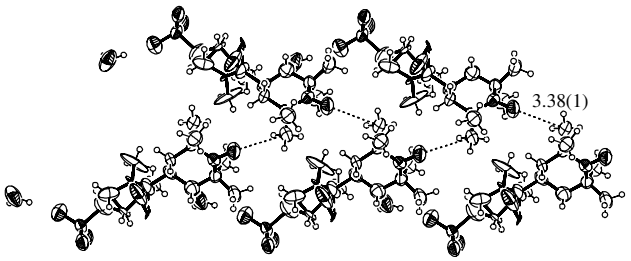


Fig. 7. Magnetic network of the anions in (TTF)(**M2**) · 0.50H_2O. Dashed lines indicate the short C···O (>N–O···H_3C–) contact.

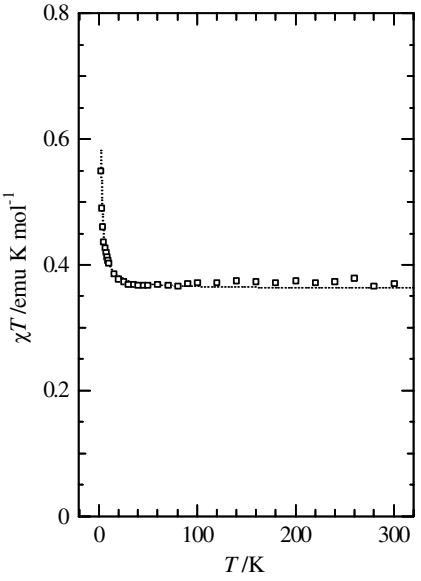


Fig. 8. $\chi T/T$ plot of (TTF)**M2** · 0.50H_2O.The dashed line is calculated on the basis of a 1D ferromagnetic Heisenberg model.

along the *n*-axis (see Fig. 7). According to McConnell's theory [24], the contact can mediate the ferromagnetic interaction. The temperature dependence of magnetic susceptibility is actually explained by the 1D ferromagnetic Heisenberg model with $C = 0.362$ emu K mol^{-1} and $\theta = 0.55$ K (Fig. 8). In addition, there is positional disorder of the O atom of the carbonyl group, the methylamino group, and the adjacent methylene group, and these atoms were refined over two positions. The position of the incorporated water molecule is partially occupied, to be 0.50.

3.3. TMTSF and BEDT-TTF salts

Only the anion **H1** has thus far provided crystalline TMTSF and BEDT-TTF salts. For the TMTSF salt, we reported the crystal structure only and not any physical properties, because we obtained the crystals as very thin needles and only have much less than 1 mg at present.

3.3.1. (TMTSF)(*H1*) · 2H_2O · PhCl

The crystal structure is shown in Fig. 9. One TMTSF, one anion, two H_2O, and one PhCl are independent. TMTSF forms a dimer about the centre of symmetry. The dimer stacks along the *a*-axis to form 1D conducting column. Between the columns, there are no side-by-side interactions because each column is surrounded by the anions and the incorporated molecules. Usually, a CT salt containing the 1D stack consisting of a dimerized donor having a charge of +1 is a band insulator. So the TMTSF salt appears to be a band insulator and the donor part is non-magnetic.

There are no short contacts not only between TMTSF and TEMPO but also between TEMPOs, indicating that no magnetic interaction is likely between spins on the TEMPO moieties. In addition, we adopted a rigid model for the incorporated PhCl in the refinement procedure because of its rotational disorder, and there is positional disorder of the TEMPO moiety, which is similarly observed in PPh_4 · **H3**.

3.3.2. α-(BEDT-TTF)$_5$(*H1*)$_2$ · 6H_2O

The crystal structure is shown in Fig. 10. There are two centrosymmetric pentamers of BEDT-TTF, four anions, and 12 water molecules in the unit cell. A formal charge of +2/5 on each BEDT-TTF and +2 on each pentamer are calculated. The pentamers interact with each other to form an α-type 2D conducting sheet (Fig. 11). The structures of two independent pentamers together with the TEMPO anions, the O atoms of which are in contact with the terminal ethylene groups of BEDT-TTF, are shown in Fig. 12. The BEDT-TTF molecules B, C, E, and F are almost planar, which is typical for cations. In contrast, molecules A and D are not planar, as is the case for neutral BEDT-TTF. These results suggest that the positive charge is unequally distributed over the BEDT-TTF molecules. Thus the system has charge disproportionation, suggesting poor conductivity. The temperature-dependent electrical resistivity is semiconductive with $\rho_{RT} = 9 \times 10^3$ Ω cm and $E_a = 0.4$ eV.

The short contacts between BEDT-TTF and TEMPO, as shown in Fig. 12, are not so important for

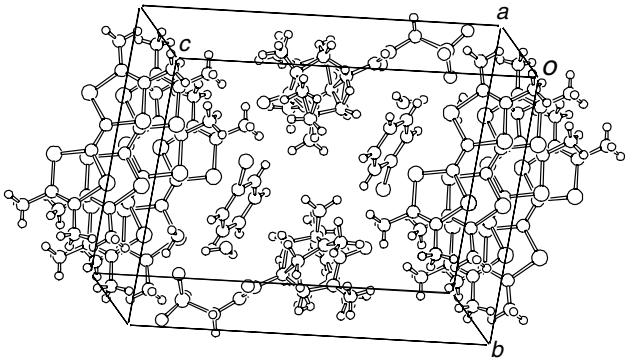


Fig. 9. Crystal structure of (TMTSF)(**H1**) · 2H_2O · PhCl.

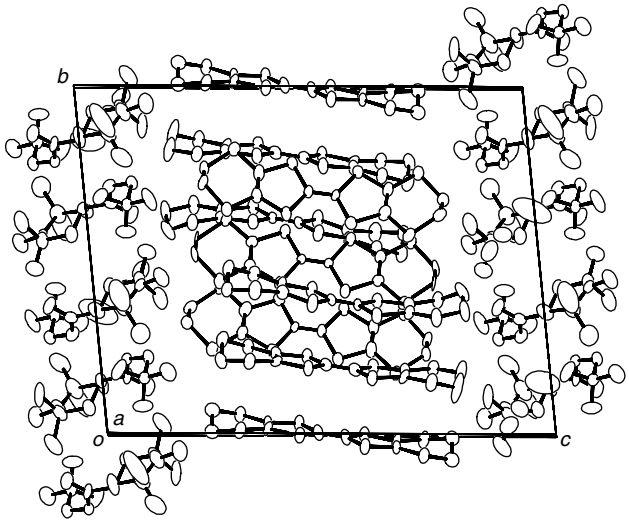


Fig. 10. Crystal structure of α-(BEDT-TTF)$_5$(**H1**)$_2 \cdot 6H_2O$.

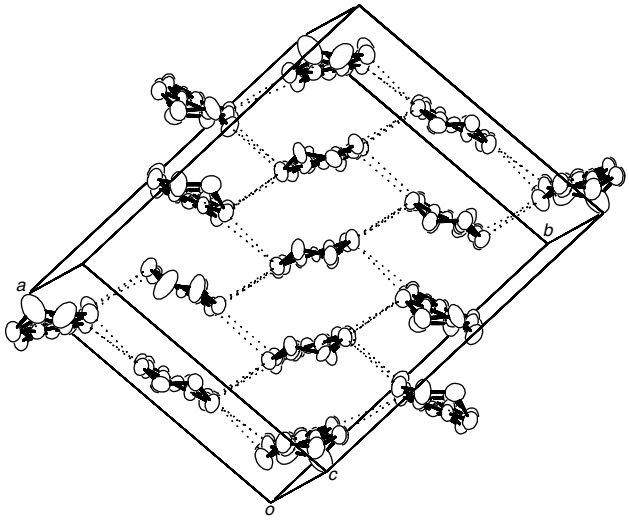


Fig. 11. Donor packing motif in α-(BEDT-TTF)$_5$(**H1**)$_2 \cdot 6H_2O$. Dashed lines indicate short S···S contacts (<3.7 Å).

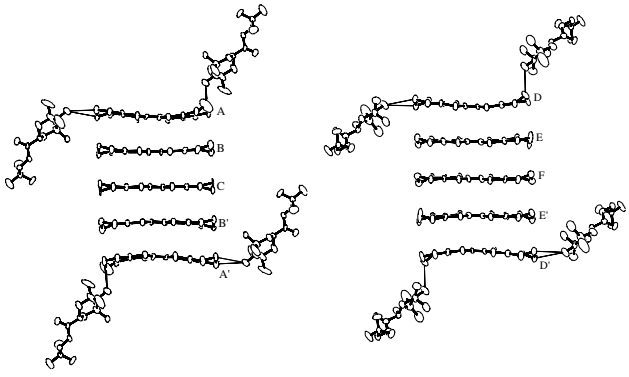


Fig. 12. Structures of the two independent BEDT-TTF pentamers together with the close TEMPO anions.

magnetic interactions because there are no electrons on the terminal ethylene groups. Furthermore, no short contacts between TEMPOs are observed (O···O ≫ 7 Å), which compounds the magnetic isolation of the TEMPO parts. The $\chi T - T$ graph is shown in Fig. 13 where χ is the magnetic susceptibility per a half of the asymmetric unit [(BEDT-TTF)$_{2.5}$ (**H1**) $\cdot 3H_2O$]. The dashed grid lines indicate the degree of spin concentration. The figure indicates that there are two spins at room temperature. As mentioned above, a BEDT-TTF pentamer has an average charge of +2 so that it is possible that a half of a pentamer has one spin (two spins per pentamer). Thus, the observed two spins at room temperature appear to be from a TEMPO molecule and a half of a BEDT-TTF pentamer. The spin concentration gradually decreases with decreasing temperature and reaches to approximately 1.0 at 2 K. To explain the magnetic behaviour, we assumed that the two spins on the BEDT-TTF pentamer interacts with each other in a Singlet–Triplet (S–T) model. On the other hand, the magnetic susceptibility of the spins on a TEMPO molecule were assumed to obey a Curie–Weiss (C–W) model, since they were crystallographically isolated from the other spins, as mentioned above. The magnetic susceptibility is then well explained by the 1:1 combination of a S–T and a C–W model with $J_{S-T} = -41$ K and $\theta_{C-W} = -0.3$ K, as shown in Fig. 14. The fact that the π electrons are not itinerant but localized on the BEDT-TTF pentamer is consistent with the relatively poor conductivity of this 2D-type BEDT-TTF salt.

In conclusion, we have found new TTF-, TMTSF-, and BEDT-TTF-based CT salts that include organic magnetic anions consisting of the TEMPO radical and sulfonates. The relationships between the crystal structures and physical properties are well characterized,

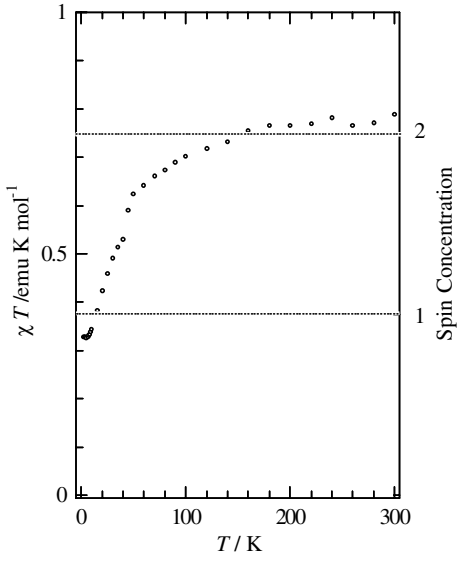


Fig. 13. $\chi T - T$ graph of α-(BEDT-TTF)$_5$(**H1**)$_2 \cdot 5H_2O$, where the χ is the magnetic susceptibility per (BEDT-TTF)$_{2.5}$(**H1**)$_2 \cdot 3H_2O$.

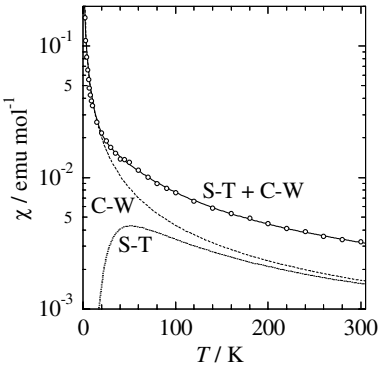


Fig. 14. Temperature dependence of magnetic susceptibility of α-(BEDT-TTF)$_5$(**H1**)$_2 \cdot 6H_2O$. Solid line is calculated on the basis of a 1:1 combination of a Singlet–Triplet and Curie–Weiss models.

but the interplay between π and localized electrons has not provided any new physical phenomena. The previously reported CT salts showing interesting physical properties [1–4], were found to be high conducting. Therefore, further experiments to obtain highly conductive CT complexes is in progress.

4. Supplementary material

Full crystallographic data (CCDC 258012 for (PPh_4)(**H0**) $\cdot H_2O$, CCDC 258013 for (PPh_4)(**H1**) $\cdot$ acetone, CCDC 258014 for (PPh_4)(**H2**), CCDC 258015 for (PPh_4)(**H3**), CCDC 258016 for (PPh_4)(**M2**), CCDC 258017 for (TTF)(**H1**) $\cdot 2H_2O$, CCDC 258018 for (TTF)(**H2**) $\cdot H_2O$, CCDC 258019 for (TTF)(**M2**) $(H_2O)_{0.50}$, CCDC 258020 for (TMTSF)(**H1**) $\cdot 2H_2O \cdot$ PhCl, CCDC 258021 for (BEDT-TTF)$_5$ (**H1**)$_2 \cdot 6H_2O$) have been deposited at the Cambridge Crystallographic Database Centre and are available on request from the Director CCDC, 12 Union Road, Cambridge, CB21EZ, UK (fax: +44 1223 336 033; e-mail: deposit@ccdc.cam.ac.uk or http://www.ccdc.cam.ac.uk).

Acknowledgement

We thank Dr. Scott S. Turner of Exeter University, UK for helpful discussion. This work has been supported by a Grant-in-Aid for Scientific Research (No. 14740330) from Japan Society for the Promotion of Science.

References

[1] M. Kurmoo, A.W. Graham, P. Day, S.J. Coles, M.B. Hursthouse, J.L. Caulfield, J. Singleton, F.L. Pratt, W. Hayes, L. Ducasse, P. Guionneau, J. Am. Chem. Soc. 117 (1995) 12209.
[2] E. Coronado, J.R. Galán-Mascarós, C.J. Gómez-García, V. Laukhin, Nature 408 (2000) 447.
[3] H. Kobayashi, A. Kobayashi, P. Cassoux, Chem. Soc. Rev. 29 (2000) 325.
[4] S. Uji, H. Shinagawa, T. Terashima, T. Yakabe, Y. Terai, M. Tokumoto, A. Kobayashi, H. Tanaka, H. Kobayashi, Nature 410 (2001) 908.
[5] T. Sugano, T. Fukasaka, M. Kinoshita, Synth. Met. 41–43 (1991) 3281.
[6] H. Fujiwara, H. Kobayashi, Chem. Commun. (1999) 2417.
[7] H. Fujiwara, E. Fujiwara, H. Kobayashi, Chem. Lett. (2002) 1048.
[8] H. Fujiwara, H.-J. Lee, H. Kobayashi, E. Fujiwara, A. Kobayashi, Chem. Lett. 32 (2003) 482.
[9] J. Nakazaki, M.M. Matsushita, A. Izuoka, T. Sugawara, Tetrahedron Lett. 40 (1999) 5027.
[10] J. Nakazaki, Y. Ishikawa, A. Izuoka, T. Sugawara, Y. Kawada, Chem. Phys. Lett. 319 (2000) 385.
[11] T. Sugimoto, S. Yamaga, M. Nakai, K. Ohmori, M. Tsujii, H. Nakatsuji, H. Hosoito, Chem. Lett. (1993) 1361.
[12] G. Harada, T. Jin, A. Izuoka, M.M. Matsushita, T. Sugawara, Tetrahedron Lett. 44 (2003) 4415.
[13] E. Fujiwara, A. Kobayashi, H. Fujiwara, T. Sugimoto, H. Kobayashi, Chem. Lett. 33 (2004) 964.
[14] K.A. Hutchison, G. Srdanov, R. Menon, J.-C.P. Gabriel, B. Knight, F. Wudl, J. Am. Chem. Soc. 118 (1996) 13081.
[15] S. Nakatsuji, H. Anzai, J. Mater. Chem. 7 (1997) 2161.
[16] Y. Nakamura, N. Koga, H. Iwamura, Chem. Lett. (1991) 69.
[17] K. Mukai, S. Jinno, Y. Shimobe, N. Azuma, Y. Hosokoshi, K. Inoue, M. Taniguchi, Y. Misaki, K. Tanaka, Polyhedron 20 (2001) 1537.
[18] S. Aonuma, H. Casellas, C. Faulmann, B. Garreau de Bonneval, I. Malfant, P. Cassoux, P.G. Lacroix, Y. Hosokoshi, K. Inoue, J. Mater. Chem. 11 (2001) 337.
[19] H. Akutsu, J. Yamada, S. Nakatsuji, Chem. Lett. (2001) 208.
[20] H. Akutsu, J. Yamada, S. Nakatsuji, Synth. Met. 120 (2001) 871.
[21] H. Akutsu, J. Yamada, S. Nakatsuji, Acta Cryst. C 59 (2003) o433.
[22] H. Akutsu, J. Yamada, S. Nakatsuji, Acta Cryst. E 59 (2003) o1141.
[23] H. Akutsu, J. Yamada, S. Nakatsuji, Chem. Lett. 32 (2003) 1118.
[24] H.M. McConnell, J. Chem. Phys. 39 (1963) 1910.

2. Experimental

Preparation of crystals of $GdB_{18}Si_5$ which were measured in this work were carried out in the following way. First of all, GdB_6 powder was prepared by the borothermal reduction method of rare earth oxide under vacuum using BN crucibles:

$$Gd_2O_3 + 15B \rightarrow 2GdB_6 + 3BO \quad (1)$$

The Si flux method was used to obtain crystals, with a starting composition of Gd:B:Si of around 1:20:100 in molar ratio. The desired amounts of boron and silicon were added to GdB_6. The mixture was heated to a temperature of around 1923 K for 10 h, then cooled to 1573 K at a rate of 50 K/h, after which the heat was switched off and the crucible cooled to room temperature. The excess silicon was removed by a mixture of hydrofluoric acid and nitric acid to obtain crystals of $GdB_{18}Si_5$. Pieces of crystals were broken off and crushed into powder which was then measured with a high resolution powder X-ray diffractometer (Rigaku Co., RINT2000) with Cu Kα radiation which confirmed the single phase of the samples.

The structure of $GdB_{18}Si_5$ is rhombohedral (space group *R3m*) with lattice constants of $a = b = 10.07$ Å, $c = 16.45$ Å. Views of the structure are depicted in Fig. 1. The structure of rare earth boron-rich icosahedral compounds can basically be understood in that the boron icosahedra form a particular arrangement with rare earth atoms occupying sites in spaces among the icoasahedra. In the case of $GdB_{18}Si_5$, in the shortest metal–metal spacing, the gadolinium sites form a zigzag chain along the [1 1 0] axis with a separation of 5.04 Å. The [0 0 1] alignment of the crystals was

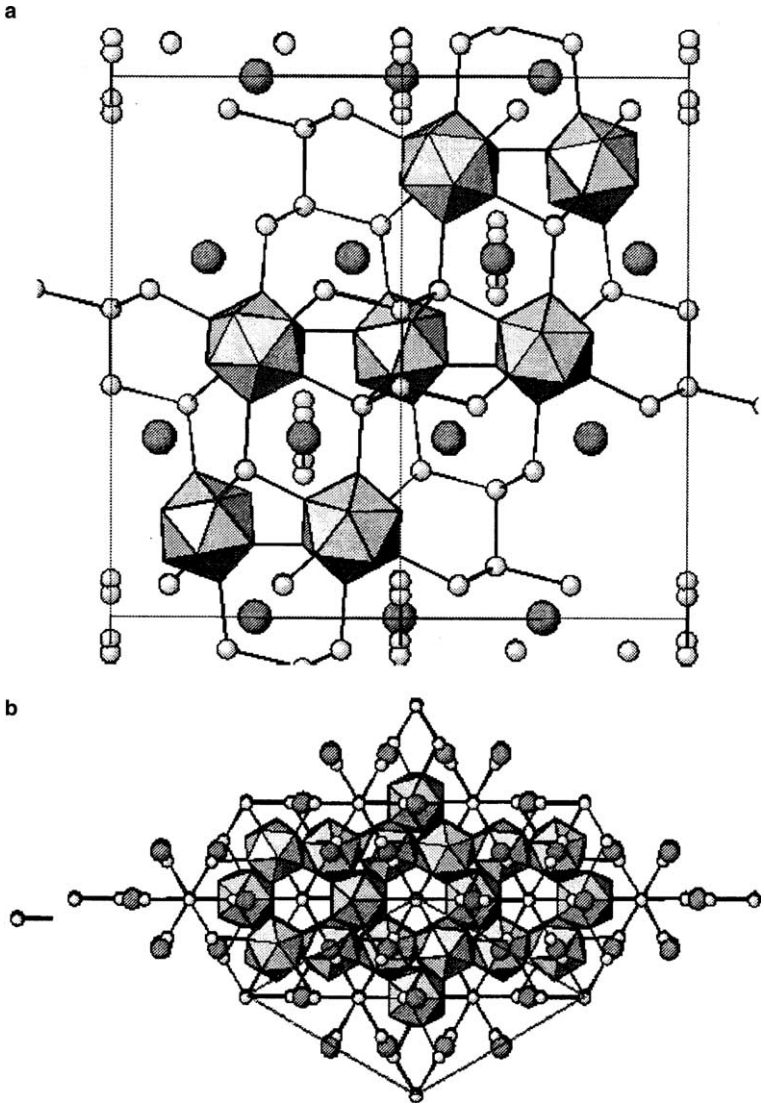


Fig. 1. Crystal structure of $GdB_{18}Si_5$, projected onto the (a) [1 1 0] plane and (b) [0 0 1] plane. The polyhedrons are B_{12} icosahedra, small gray circles indicate silicon atoms, and the large black circles indicate gadolinium atoms.

successfully determined with the [0 0 1] plane forming large faces, however, we could not assign the explicit in-plane alignment of the crystals by Laue photography techniques. Such difficulty has been noticed for other boron-rich systems like $MgAlB_{14}$ and TbB_{50}-type compounds [13] and is generally attributed to the complicated structure and weakness of reflection of boron-rich compounds. However, in the case of the $GdB_{18}Si_5$ crystals, it appears that there are multigrains within the in-plane alignment which are aligned in different directions in-plane (whereas these grains are uniformly ordered along the [0 0 1] direction with the [0 0 1] plane forming orderly). This is indicated from magnetic measurements where the susceptibility below T_N did not differ largely despite incrementally rotating the magnetic field direction in-plane, i.e., the spins are antiferromagnetically aligned in-plane in a certain direction [11] but due to the multigrains aligned in different directions in-plane, the observed susceptibility is a sum of parallel and also perpendicular susceptibility components. Despite not being able to resolve the particular in-plane alignment of a single crystal piece, the in-plane measurements carried out in this work are still important because they obviously contain a component of the parallel susceptibility and reflect its behavior under magnetic field.

Magnetic susceptibility was measured by using a Quantum Design MPMS-XL SQUID magnetometer from 1.8 to 300 K, with fields up to 70 kG. The magnetization was measured with the magnetic field applied along the [0 0 1] *c*-axis and in-plane.

3. Results and discussion

3.1. Magnetic field applied along the c-axis

The temperature dependence of the magnetic susceptibility with the field applied along [0 0 1] for various fields is plotted in Fig. 2. The *c*-axis is perpendicular to the direction the spins are aligned [11] and accordingly little temperature dependence of the *c*-axis susceptibility is observed below the transition temperature. As is typical for antiferromagnetic transitions, the transition temperature shifts to lower temperatures as the magnetic field is increased. We define T_N as the intercept of the lower and higher temperature region extrapolations. The magnetic phase diagram is plotted in Fig. 3. The magnitude of the magnetic field corresponds well with the temperature scale observed here.

The magnetization curve at 1.8 K with field applied along the *c*-axis is shown in Fig. 4. The magnetization increases linearly as the field is increased until it reaches a critical field H_C around 15 kG (as can be estimated from Fig. 3) after which the magnetization rapidly saturates to reach the full moment expected for the $^8S_{7/2}$ ground state of Gd^{3+}.

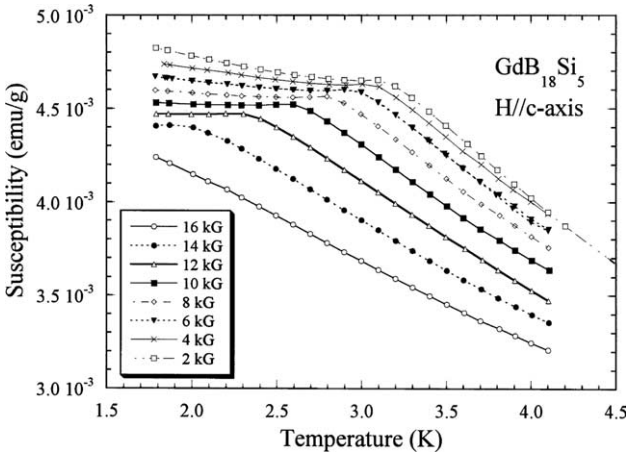


Fig. 2. Temperature dependence of the *c*-axis magnetic susceptibility of $GdB_{18}Si_5$ for 16 kG (open circles), 14 kG (closed circles), 12 kG (open triangles), 10 kG (closed squares), 8 kG (open diamonds), 6 kG (closed triangles), 4 kG (crosses), and 2 kG (open squares). The lines are guides to the eye.

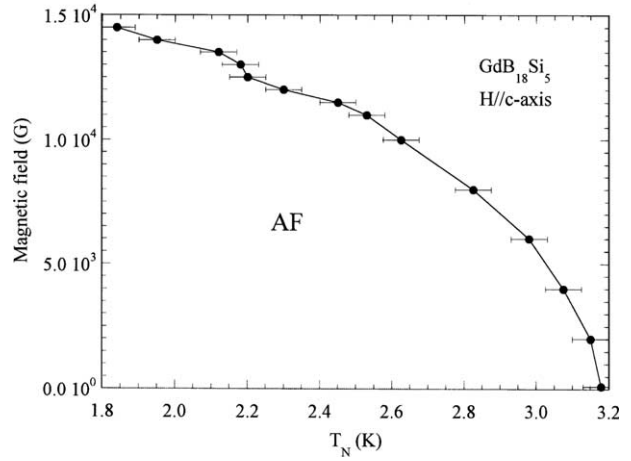


Fig. 3. Magnetic phase diagram of $GdB_{18}Si_5$ with the field applied along the *c*-axis. AF indicates the antiferromagnetic phase. The line is a guide to the eye.

3.2. Magnetic field applied in-plane

As noted in Section 2, the crystals of $GdB_{18}Si_5$ appeared to be composed of multigrains which were not uniformly aligned along a particular direction in the in-plane direction (whereas the alignment of these grains along the *c*-axis was uniformly very good owing to large crystal planes of [0 0 1]). Due to the various alignment of the multigrains leading to a summation of both parallel and perpendicular components, a rotation of the magnetic field within the in-plane

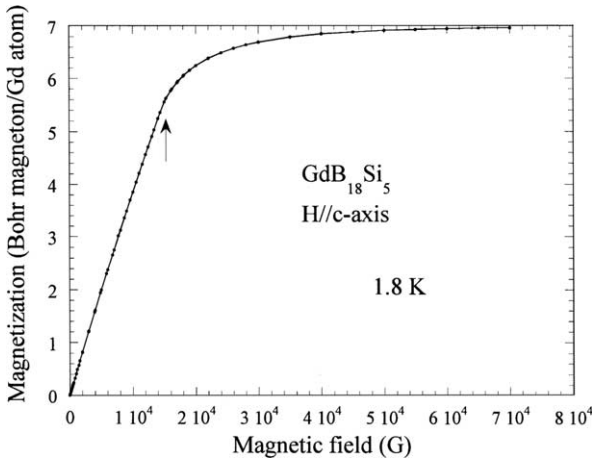


Fig. 4. Magnetization curve of $GdB_{18}Si_5$ with the field applied along the *c*-axis at 1.8 K. The arrow indicates the critical field of 15 kG. The line is a guide to the eye.

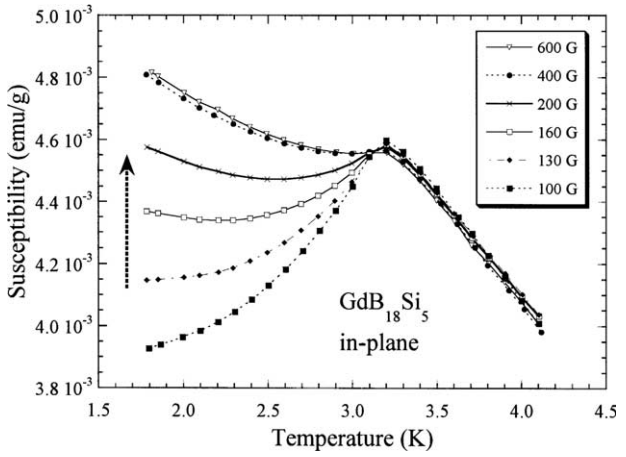


Fig. 6. Temperature dependence of the magnetic susceptibility of $GdB_{18}Si_5$ with field applied in-plane for 600 G (open triangles), 400 G (closed circles), 200 G (crosses), 160 G (open squares), 130 G (closed triangles), and 100 G (closed squares). The lines are guides to the eye.

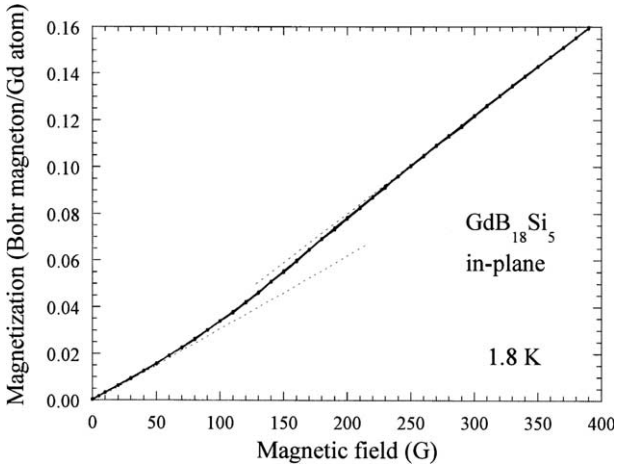


Fig. 5. Low field magnetization curve of $GdB_{18}Si_5$ with the field applied in-plane at 1.8 K. The arrow indicates the critical field of 15 kG. Both field increasing and decreasing data points are plotted together.

direction did not cause a large difference in observed susceptibility. Therefore, although it was not possible to directly measure only the parallel susceptibility, the in-plane measurement was carried out by fixing the magnetic field in a certain direction of the crystal perpendicular to [0 0 1] and varying the magnitude. Since the measured susceptibility can be observed to obviously contain a component of the parallel susceptibility, this gives a measure of the parallel susceptibility behavior under magnetic field.

First of all, the magnetization curve of the in-plane magnetization at low fields is shown in Fig. 5. An interesting dependence at low fields is observed. As field is increased above 50 G the magnetization shows an upper curvature and shifts to a larger regime above 300 G. This behavior can be seen more clearly in the temperature dependence of in-plane susceptibility given for various fields in Fig. 6. The susceptibility above 300 G is similar to the perpendicular (*c*-axis) susceptibility. It appears that a reorientation of the spin direction, a spin flip is achieved at these low fields. We do not think this is a spurious result since the sample is rigidly fixed and the movement of the sample at such low fields (and with this small susceptibility difference) is extremely unlikely. Furthermore, after measurements, the sample was always checked and the physical orientation observed not to have altered at all. The magnetization curve shown in Fig. 5 was measured with a maximum magnetic field of 1 kG (not shown) and there was no hysteresis.

To summarize, the results indicate that a very low field dependence of the parallel susceptibility exists in the $GdB_{18}Si_5$ system with a reorientation of the spin-axis appearing to occur below 300 G. The unusual points of this behavior of the in-plane susceptibility (the parallel susceptibility) are the gradual nature of the shift to higher magnetization and the low field dependence. The origin of this behavior is likely due to the round spin of the gadolinium ions, but the actual observation of a spin flip at such low magnetic fields is rare.

Obtaining more information on the explicit magnetic ordering of $GdB_{18}Si_5$ is desirable. Neutron scattering is a powerful technique to investigate the magnetic structure, but due to the extremely large cross sections of both natural boron and gadolinium this is impossible for the as-prepared samples. We have previously succeeded in synthesizing extremely ^{11}B isotopic pure samples of the even more boron-rich $TbB_{44}Si_2$ sample and carried out neutron diffraction measurements [14]. The procurement of isotope gadolinium is presently being investigated. We are also considering alternate methods using hot neutrons.

4. Conclusions

The magnetic field dependence of the antiferromagnetic transition in the rare earth B_{12} icosahedral cluster compound $GdB_{18}Si_5$ was investigated. Below $T_N = 3.2$ the spins are antiferromagnetically aligned in-plane, perpendicular to the *c*-axis. The magnetic phase diagram was determined with the magnetic field applied along the *c*-axis. Typical dependence of an antiferromagnetic system was observed, with T_N shifting to lower temperatures as field is increased. The magnitude of magnetic field corresponds well to the temperature scale. Rapid saturation to the full moment value for $^8S_{7/2}$ of Gd^{3+} was observed in the magnetization curve above a critical field. An interesting dependence at low magnetic fields was observed when the field was varied in-plane, with a reorientation of the spin-axis appearing to occur at fields below 300 G. The dependence at very low magnetic fields is likely due to the round spin of the gadolinium ion, but such a spin flip actually being observed at these low fields is rare. The observed behavior merits further investigation of the detailed magnetic structure of this compound which is the only system in the rare earth boron icosahedral cluster compounds where three dimensional long range order has been observed, and interestingly has a relatively low partial occupancy of the gadolinium sites.

References

[1] J.S. Miller, M. Drillon (Eds.), Magnetism: Molecules to Materials II, Wiley-VCH, New York, 2001.
[2] R. Boca, Theoretical Foundations of Molecular Magnetism, Elsevier Science, Amsterdam, 1999.
[3] T. Mori, A. Leithe-Jasper, J. Appl. Phys. 93 (2003) 7664.
[4] T. Mori, T. Tanaka, J. Phys. Soc. Jpn. 68 (1999) 2033.
[5] T. Mori, J. Appl. Phys. 95 (2004) 7204.
[6] T. Mori, A. Leithe-Jasper, Phys. Rev. B 66 (2002) 214419.
[7] T. Mori, H. Mamiya, Phys. Rev. B 68 (2003) 214422.
[8] V. Babizhetskyy, J. Roger, S. Deputier, R. Guerin, R. Jardin, J. Bauer, K. Hiebl, C. Jardin, J.V. Saillard, J.F. Halet, Angew. Chem. 116 (2004) 2013.
[9] R. Jardin, F. Weitzer, J. Bauer, K. Hiebl, J. Alloys Comp. 359 (2003) 35.
[10] J.R. Salvador, D. Bilc, S.D. Mahanti, M.G. Kanatzidis, Angew. Chem. 114 (2002) 872.
[11] T. Mori, F. Zhang, J. Phys.: Condens. Matter 14 (2002) 11831.
[12] T. Mori, T. Tanaka, Mat. Res. Bull. 36 (2001) 2463.
[13] T. Mori, T. Tanaka, IEEE Trans. Mag. 37 (2001) 2144.
[14] T. Mori, F. Izumi, Y. Ishii, J. Alloys Comp. 374 (2004) 105.

situation arises due to the possibility that the compounds exhibiting the effect of spin canting derived from chirality to spin structure are much clearer than that of ferro- or ferrimagnets. However, since the effects of chirality on physical properties are poorly understood, theoretically and experimentally, it is quite difficult to identify the experimental results obtained as it. Thus, it is necessary to study achiral compound with similar structure to equivalent chiral compound and make a comparative study between them. The present report describes the synthesizes, crystal structures and magnetic properties of two-dimensional chiral and achiral layered compounds with magnetic ordering, $[Cr(CN)_6][Mn(R)\text{-pnH(DMF)}] \cdot (2H_2O)$ (**1**) and $[Cr(CN)_6][Mn(racemi)\text{-pnH(DMF)}] \cdot (2H_2O)$ (**2**); (pn = 1,2-diaminopropane).

2. Experimental

All chemicals were obtained from Aldrich, Tokyo Kasei or Nacalai Taesuque, and used without purifications. The measurements of temperature and field dependence of the magnetization of the complex were performed on Quantum Design MPMX-XL SQUID operating in the temperature range 2–300 K and an applied field up to 5 T.

3. Preparations of $[Cr(CN)_6][Mn(R)\text{-pnH(DMF)}] \cdot (2H_2O)$ (1) and $[Cr(CN)_6][Mn(racemi)\text{-pnH(DMF)}] \cdot (2H_2O)$ (2)

The syntheses were carried out in the grove box under argon atmosphere, because manganese ion is air sensitive in the KOH solution. Green block-like crystals of **1** were obtained by slow diffusion of $MnCl_2 \cdot 4H_2O$ (5.1 mmol), (*R*)-1,2-diaminopropane dihydrochloride ((*R*)-pn · 2HCl, 6.8 mmol), and KOH (6.8 mmol) in a H_2O/*N*,*N*-dimethylformamide mixture (1:1) into $K_3[Cr(CN)_6]$ (1.5 mmol) in a H_2O/EtOH (1:1) mixture for several weeks. Achiral compound **2** was also obtained as green block-like crystals with racemic pn under the same experimental condition as in **1**.

4. X-ray crystal structure analyses

A single crystals of **1** and **2** were glused on the top of a glass fiber. Data were collected at room temperature on a Brucker SMART APEX CCD area detector with ω scan mode. The diffractometer employs graphite monochromated Mo Kα radiation (0.7107 Å). The data were corrected for Lorentz and polarization effects. The absorption correction was based on symmetry equivalent reflections using the SADABS programs. The structures were solved by direct method and refined by full-matrix least squares against F^2 of all data, using SHELXTL software. All non-hydrogen atoms of **1** and **2** were refined anisotropically. Hydrogen atoms of **1**, except for the water hydrogen atoms, were placed in calculated positions but not refined. The hydrogen atoms of terminal amino group of pn as well as the water hydrogen atoms in **2** were not placed due to the disorder of nitrogen.

Crystal data for (*R*)-isomer **1**: $C_{12}H_{22}N_9O_3Cr_1Mn_1$, M_w = 447.30, orthorhombic, $P2_12_12_1$, a = 7.662(2) Å, b = 14.581(4) Å, c = 19.747(6) Å, V = 2206.2(11) Å^3, T = 293 K, Z = 4, ρ_{calc} = 1.347 g cm^{-3}, μ(Mo Kα) = 1.093 mm^{-1}, R_1 = 0.0440 for 2919 data ($I > 2\sigma(I)$), wR_2 = 0.1245 for 3190 unique data (R_{int} = 0.0254).

Crystal data for **2**: $C_{12}H_{22}N_9O_3Cr_1Mn_1$, M_w = 447.30, orthorhombic, *Pnma*, a = 14.5459(8) Å, b = 7.6509(8) Å, c = 19.723(2) Å, V = 2194.9(4) Å^3, T = 293 K, Z = 4, ρ_{calc} = 1.354 g cm^{-3}, μ(Mo Kα) = 1.098 mm^{-1}, R_1 = 0.0556 for 3975 data ($I > 2\sigma(I)$), wR_2 = 0.1675 for 2418 unique data (R_{int} = 0.0267).

5. Results and discussion

X-ray crystal structure analysis (Fig. 1) of the (*R*)-isomer revealed that compound **1** consists of two-dimensional bimetallic sheets, a situation similar to that of the 2D chiral ferrimagnet $[Cr(CN)_6][Mn(S)\text{-pnH}(H_2O)] \cdot (H_2O)$ with Tc = 38 K [3c]. Each $[Cr(CN)_6]^{3-}$ ion utilizes four cyanide moieties in order to form bridges to four adjacent Mn^{2+} ions within the *ab* plane. The nearest and next nearest neighbor Cr–Mn distances through cyanide bridges within the *ab* plane are 5.366(1) and 5.409(1) Å, respectively, which are nearly identical to those distances in $[Cr(CN)_6][Mn(S)\text{-pnH}(H_2O)] \cdot (H_2O)$. In addition to Mn^{2+} and $[Cr(CN)_6]^{3-}$ ions (one of each), an asymmetric unit in this crystal contains a single molecule each of mono-protonated (*R*)-diaminopropane ((*R*)-pnH) and DMF and two water molecules. An octahedron around the Mn^{2+} ion is completed by coordination of the primary amino group of (*R*)-pnH and the DMF molecules (Mn–O and Mn–N separations are 2.181(3) and 2.323(4) Å, respectively), which separate adjacent bimetallic sheets along the *c*-axis. The two water molecules in **1** occupy gaps between two-dimensional sheets. The shortest and the second shortest inter-sheet metal separations are observed between the homo-metallic atoms (Cr–Cr and Mn–Mn distances are 7.3114(1) and 7.5424(2) Å, respectively). On the other hand, the shortest inter-sheet Mn–Cr separation is 9.2963(7) Å. This observation suggests that this inter-sheet separation is small enough to allow a magnetic interaction between bimetallic sheets in compound **1** and the contact between atoms with the same number of spins is expected to lead an intersheet antiferromagnetic interaction. In the 2D chiral ferrimagnet

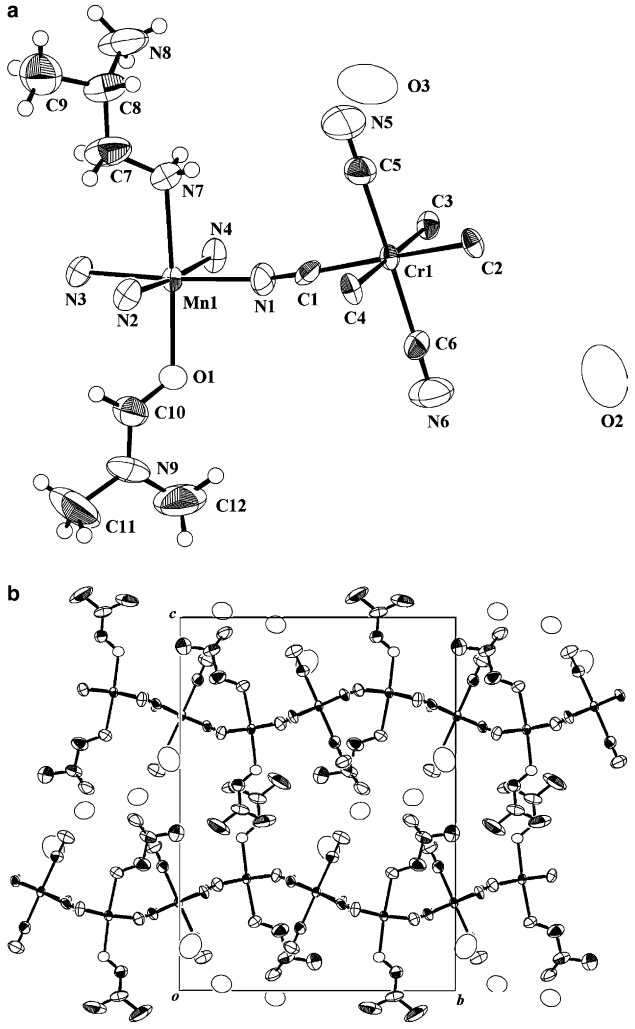


Fig. 1. (a) ORTEP drawing of an asymmetric unit of $[Cr(CN)_6]$-$[Mn(R)$-pnH(DMF)$] \cdot (2H_2O)$ (**1**) with 50% probability level. (b) Crystal structure of $[Cr(CN)_6][Mn(R)$-pnH(DMF)$] \cdot (2H_2O)$ (**1**). Views of the enantiopure layer along the *ab*-plane. Hydrogen atoms are omitted for clarity.

$[Cr(CN)_6][Mn(S)$-pnH$(H_2O)] \cdot (H_2O)$, the inter-sheet homo-metallic separation is beyond 8 Å, while the shortest inter-sheet metal separation between the Cr and the Mn atoms is 7.3105(4) Å. This is probably advantageous to the ferromagnetic interaction between 2D sheets from the point of view of a magnetic dipole interaction [3c].

X-ray crystal structure analysis (Fig. 2) of achiral compound revealed that compound **2** also consists of similar two-dimensional bimetallic sheet to that of chiral compound **1**. The bond distances within the bimetallic sheet in compound **2** are almost the same bond distances as those of compound **1**. The nearest and next nearest neighbor Cr–Mn distances through cyanide bridges within the *ab*-plane are 5.3582(6) and 5.3906(6) Å. However, the inter-sheet separations in compound **2** are quite longer than those in compound **1**. Even shortest metal–metal separation in compound **2** is beyond 8 Å (Mn–Mn, Cr–Cr and Cr–Mn distances are 8.7958(11), 10.5710(8) and 9.278(1) Å, respectively). In such a case, probably, the magnetic interaction between bimetallic sheets is negligible and weak magnetic dipole–dipole interaction is expected to be operative.

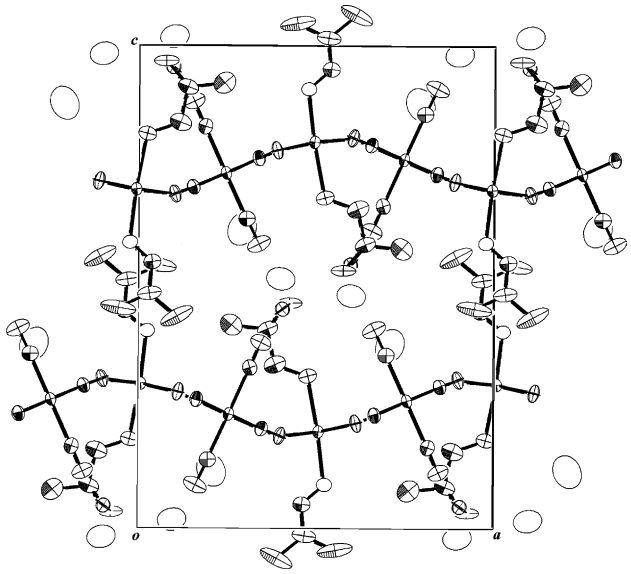


Fig. 2. Crystal structure of $[Cr(CN)_6][Mn(racemi)$-pnH(DMF)$] \cdot (2H_2O)$ (**2**). Views of the bimetallic layer along the *ab*-plane. Hydrogen atoms are omitted for clarity.

The magnetic behavior of polycrystalline samples of compound **1** at 5000 G is presented in Fig. 3 in the form of $\chi_{mol}T$ versus T and effective magnetic moment versus $1/T$ plots. The $\chi_{mol}T$ value, which is 4.92 cm^3 K/mol (6.28 μ_B) at room temperature, decreases with decreasing temperature to a minimum value of 3.53 cm^3 K mol^{-1} (5.31 μ_B) at 82 K. Upon further cooling, the $\chi_{mol}T$ value increases to a maximum value of 36.19 cm^3 K mol^{-1} (17.02 μ_B) at 27 K; subsequently, the $\chi_{mol}T$ value decreases below 27 K. The $1/\chi_{mol}$ versus T plot in the range from 300–120 K obeys Curie–Weiss law with a

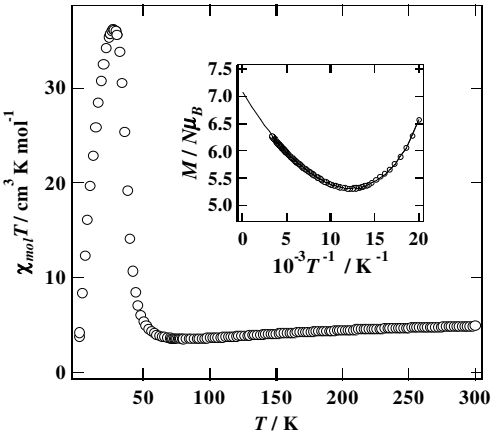


Fig. 3. $\chi_{mol}T$ versus T plot at 5000 G of $[Cr(CN)_6][Mn(R)$-pnH-(DMF)$] \cdot (2H_2O)$ (**1**). Inset: plot of effective magnetic moment versus $1/T$.

Weiss temperature $\theta = -73.5$ K. This finding indicates that antiferromagnetic interaction operates between nearest neighbor Cr^{3+} and Mn^{2+} ions through cyanide bridges. The abrupt increase in the $\chi_{mol}T$ value around 30 K suggests the onset of three-dimensional magnetic ordering. The extrapolated effective magnetic moment value is 7.07 μ_B, which corresponds to the theoretical spin-only value of non-coupled paramagnetic high spin in the high temperature limit (Fig. 3, inset). The $\chi_{mol}T$ versus T plot at 5000 G of compound **2** also display similar behavior to that of compound **1**.

Low-field magnetization measurements of polycrystalline samples of compound **1** at an applied field of 5 G in the temperature range of 1.8–100 K were performed to confirm long range magnetic ordering around 30 K (Fig. 4). Both the zero field-cooled magnetization (ZFCM) and the field-cooled magnetization (FCM) curves display abrupt increases in M below 40 K, which reach a maximum at 28.5 K, followed by a decline below this temperature. Thus, the magnetic phase transition temperature T_N of 28.5 K was determined.

The magnetization versus field (M–H) plot of polycrystalline samples at 2 K exhibits a sigmoid curve in **1**, which is typical of a metamagnet. This result is attributable to a spin-flip transition based on intersheet antiferromagnetic coupling (Fig. 5). The saturation magnetization, $M_S = 2\ \mu_B$, agrees closely with the theoretical value of antiferromagnetic coupling between Cr^{3+} and Mn^{2+} ions (5/2 − 3/2 = 2/2).

On the other hand, both low-field and field dependent magnetization curves of polycrystalline samples in compound **2** show different behaviors from those in compound **1** (Fig. 6). Both the zero field-cooled magnetization (ZFCM) and the field-cooled magnetization (FCM) curves display a long range ferrimagnetic ordering below 28 K. The magnetization versus field (M–H) plot increases sharply with applied field to show the theoretical saturation magnetization value, $M_S = 2\ \mu_B$, of antiferromagnetic coupling between Cr^{3+} and Mn^{2+} ions (Fig. 6, inset).

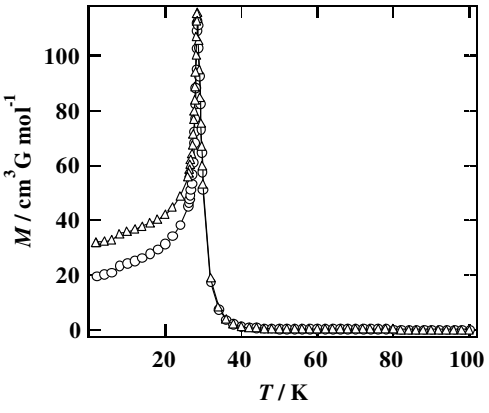


Fig. 4. Temperature dependence of magnetization of $[Cr(CN)_6]$-$[Mn(R)$-pnH(DMF)$] \cdot (2H_2O)$ (**1**). The FC (△) and ZFC (○) magnetizations at 5 G are shown.

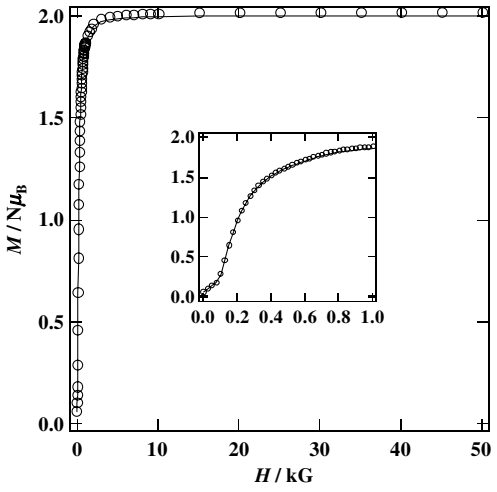


Fig. 5. Field dependence of $[Cr(CN)_6][Mn(R)$-pnH(DMF)$] \cdot (2H_2O)$ (**1**) at 2 K. Inset: the enlarged view in the lower field region.

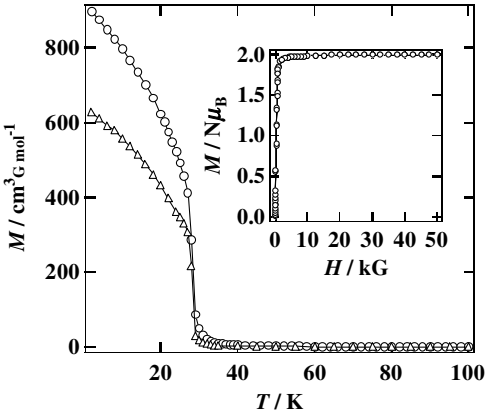


Fig. 6. Temperature dependence of magnetization of $[Cr(CN)_6]$-$[Mn(racemi)$-pnH(DMF)$] \cdot (2H_2O)$ (**2**). The FC (○) and ZFC (△) magnetizations at 5 G are shown. Inset: field dependence of $[Cr(CN)_6]$-$[Mn(racemi)$-pnH(DMF)$] \cdot (2H_2O)$ (**2**) at 2 K.

In conclusion, we successfully constructed the novel chiral and achiral bimetallic compounds $[Cr^{III}(CN)_6]$-$[Mn^{II}(R)$-pnH(DMF)$] \cdot (2H_2O)$ (**1**) and $[Cr^{III}(CN)_6]$-$[Mn^{II}(racemi)$-pnH(DMF)$] \cdot (2H_2O)$ (**2**), respectively. The sharp peak in Fig. 4 and the noticeable escalation of the magnetization at very low fields in the inset of Fig. 5 clearly demonstrate that **1** is a metamagnet with T_N of 28.5 K, on the other hands, Fig. 6 demonstrates that **2** is just a ferrimagnet with T_c of 28 K. These magnetisms are attributed to the slight difference of intersheet arrangement and orientation between compounds **1** and **2**, which phenomena are often observed in the two-dimensional cyanide bridging system [4]. Compound **1** among chiral cyanide-bridged systems is the first example exhibiting antiferromagnetic order and shows very interesting magnetic behavior at low

temperature. Neither the ZFCM nor the FCM of **1** drops to zero below T_N, a quality that is distinct from that of an ordinary metamagnet. This finding suggests that all magnetic moments do not wholly cancel one another between all spins in **1**. The possibilities exist that the magnetic moments in the ground state are canted by the electronic dipole field or by D–M (Dzyalonshisky–Moriya) interaction due to the chiral structure. Magnetization measurements, μSR and neutron diffraction of a single crystal will lead to characterization of the details of chiral spin structure in **1**. Moreover, the study of achiral spin structure in compound **2** as well as compound **1** will be also needed for the purpose of verifying the effect of chirality on spin structure. The experiments are in progress.

Acknowledgement

This work is supported by a Grant-in-Aid for Scientific Research (B) (No. 15340124) from the Ministry of Education, Science, Sports and Culture.

Appendix A. Supplementary data

Crystallographic data have been deposited at Cambridge Crystallographic Data Centre as Supplementary Publication No. CCDC 223745 for compound **1** and CCDC 239941 for compound **2**. Copies of this information may be obtained free charge from The Director, 12 Union Road, Cambridge, CB2 1EZ, UK (fax: +44-1223-336033; e-mail: deposit@ccdc.cam.ac.uk or www: http://www.ccdc.cam.ac.uk). Supplementary data associated with this article can be found, in the online version, at doi:10.1016/j.poly.2005.03.159.

References

[1] (a) G. Wagniere, A. Mejer, Chem. Phys. Lett. 110 (1984) 546;
(b) G.L.J.A. Rikken, E. Raupach, Nature 390 (1997) 493.
[2] (a) H. Kumagai, K. Inoue, Angew. Chem., Int. Ed. Engl. 38 (1999) 1601;
(b) H. Kumagai, A.S. Markosyan, K. Inoue, Mol. Cryst. Liq. Cryst. 40 (2000) 97;
(c) E. Coronado, J.R. Galan-Mascaros, C.J. Gómez-García, J.M. Martinez-Agugo, Inorg. Chem. 40 (2001) 113;
(d) R. Andrés, M. Bissard, M. Gruselle, C. Train, J. Vaissermann, B. Malézieux, J.-P. Jamet, M. Verdaguer, Inorg. Chem. 40 (2001) 4633;
(e) B. Malézieux, R. Andrés, M. Bissard, M. Gruselle, C. Train, P. Herson, L.L. Troitskaya, V.I. Sokolov, S.T. Ovsenko, T.V. Demeschik, N.S. Ovanesyan, I.A. Mamed'yarova, J. Organomet. Chem. 637–639 (2001) 182;
(f) D. Armentano, G.D. Munno, F. Lloret, A.V. Palii, M. Julve, Inorg. Chem. 41 (2002) 2007;
(g) M. Minguet, D. Luneau, E. Lhotel, V. Villar, C. Palusen, D.B. Amabilino, J. Veciana, Angew. Chem. Int. Ed. 40 (2002) 586.
[3] (a) K. Inoue, H. Imai, P.S. Ghalasasi, K. Kikuchi, M. Ohba, H. Ōkawa, J.V. Yakhmi, Angew. Chem. Int. Ed. 48 (2001) 4242;
(b) E. Coronado, C.J. Gómez García, A. Nuez, F.M. Romero, E. Rusanov, H. Stoeckill-Evans, Inorg. Chem. 41 (2002) 4615;
(c) K. Inoue, K. Kikuchi, M. Ohba, H. Ōkawa, Angew. Chem. Int. Ed. 42 (2003) 4810;
(d) H. Imai, K. Inoue, Kohichi Kikuchi, Yusuke Yoshida, Mitsuhiro Ito, Tetsuya Sunahara, Satoru Onaka, Angew. Chem. Int. Ed. 43 (2004) 5618.
[4] (a) M. Ohba, H. Ōkawa, N. Fukita, Y. Hashimoto, J. Am. Chem. Soc. 119 (1997) 1011;
(b) R. Podgajny, T. Kozeniak, M. Balanda, T. Wasiutynski, W. Errington, T.J. Kemp, N.W. Alcock, B. Sieklucka, Chem. Commun. (2002) 1138;
(c) S. Ohkoshi, Y. Arimoto, T. Hozumi, H. Seino, Y. Mizobe, K. Hashimoto, Chem. Commun. (2003) 2772.

negative θ value of about 85 K, and the effective magnetic moment per ion was found to be about 4.4 μ_B.

It is known that Co_3O_4 bulk crystal exhibits antiferromagnetism, with a T_N of 33 K [5].

Recently, we reported a magnetic study of Co_3O_4 nanoparticles 2 or 3 nm in size [6]. No Néel temperature could be observed at 33 K, and transition temperatures between 7.5 and 12.0 K were found instead. Ferromagnetic behavior with slight hysteresis below the transition temperature T_t was observed, and a effective magnetic moment per ion expected at 4.14 μ_B was estimated to be much larger, 8.12 μ_B.

In this paper, magnetization measurements were performed in order to clarify the size dependence of the magnetic properties of Co_3O_4 nanoparticles ranging from 3 to 30 nm in size.

2. Experiment

The Co_3O_4 particle surrounded by an amorphous SiO_2 network precursor was chemically precipitated by mixing a cobalt chloride ($CoCl_2 \cdot 6H_2O$) aqueous solution and a sodium metasilicate nonahydrate ($Na_2SiO_3 \cdot 9H_2O$) aqueous solution. A cobalt chloride ($CoCl_2 \cdot 6H_2O$) aqueous solution mixed with a sodium hydroxide (NaOH) aqueous solution without a metasilicate nonahydrate was also prepared. The resulting pink-colored precipitates were washed several times with distilled water and dried at about 350 K. The obtained glassy solids were crushed into a powder and calcined between 573 and 1023 K in air. The particle sizes were controlled through the annealing temperatures and the concentration of the silicates. The varied mole ratios of Co/Si in the samples were 1, 1.5, 2, and a sample without Si was also prepared. Particle sizes between 3 and 30 nm were obtained.

X-ray powder diffraction patterns were obtained by room temperature Cu Kα radiation. Magnetization was measured by VSM and SQUID magnetometer under a ±50 kOe magnetic field, at temperatures from 2 to 300 K.

3. Results and discussion

3.1. X-ray analysis

Fig. 1 shows the X-ray powder diffraction patterns of samples with particle sizes of 3, 9.7, 12 nm and bulk crystal.

The X-ray diffraction patterns of the prepared particles indicate the formation of the spinel phase of Co_3O_4, without any observable traces of either cobalt hydroxides ($Co(OH)_2$) or cobalt monoxide (CoO). The broad peak at around 25° for the 3 nm particles is associated with the amorphous SiO_2. The lattice constants were found to be between 0.808 and 0.817 nm, depending on the particle size. Using the Scherrer equation, the particle sizes were roughly estimated at between 3 and 30 nm. These sizes are in good agreement with the TEM image given in Fig. 2. The relationship between lattice constants and particle sizes were summarized in Fig. 3.

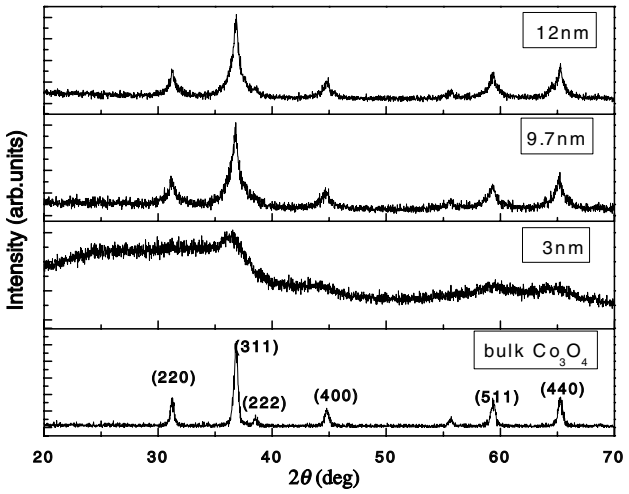


Fig. 1. X-ray powder diffraction patterns of the Co_3O_4 nanoparticles with diameters of 12, 9.7, 3 nm, and of Co_3O_4 bulk crystal.

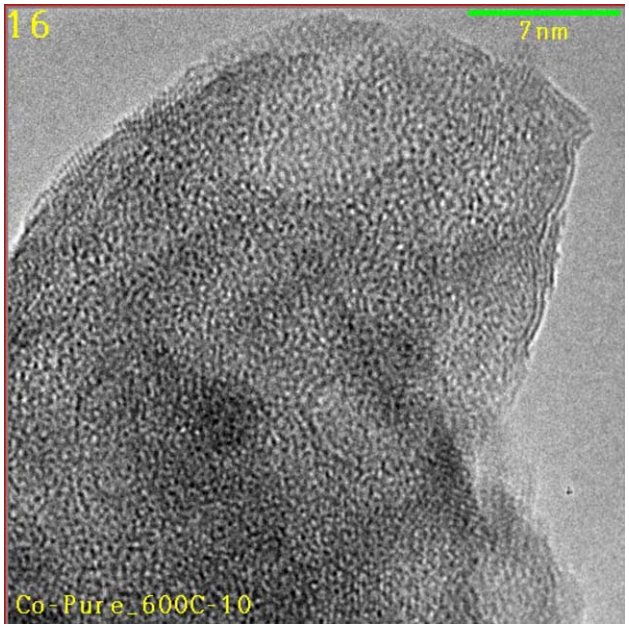


Fig. 2. TEM image of sample no. 1. The scale bar in the picture is 7 nm.

3.2. Magnetization measurements

The temperature dependence of the magnetization in under field-cooled (FC) and zero-field-cooled (ZFC)

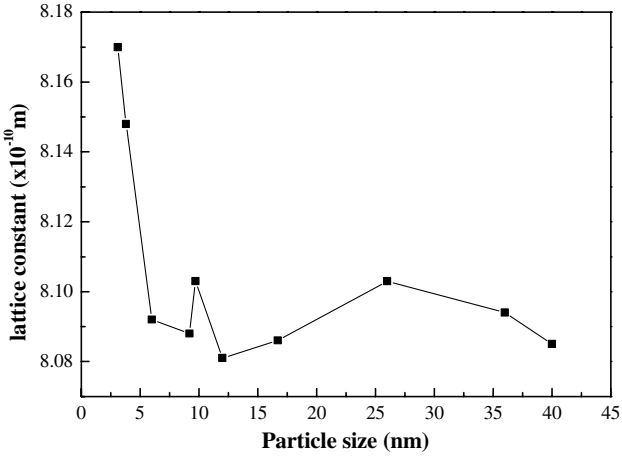


Fig. 3. Dependence of the lattice constant on particle size.

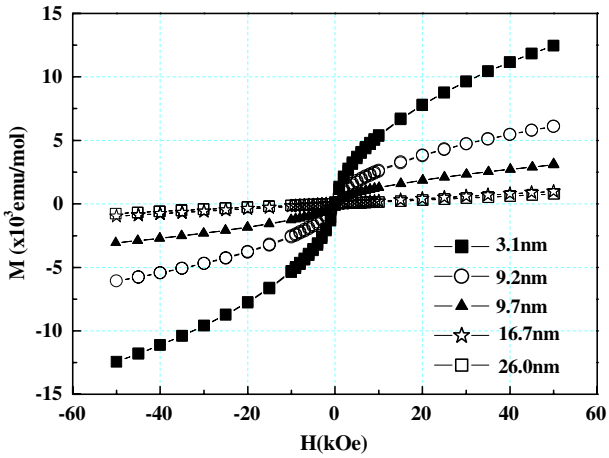


Fig. 5. Magnetization curves for various particle sizes at 5 K.

conditions was examined for all samples. All of these particles could be considered to form a single domain, ordered antiferromagnetically below T_N = 33 K. Fig. 4 shows the M–T curves of both FC and ZFC for the samples 3.1 and 9.2 nm in size. T_N could not be observed at around 33 K; however, the FC and ZFC curves were strongly bifurcated at 12 K for the 3.1-nm sample and at 4 K for the 9.2-nm sample. This bifurcated temperature of FC and ZFC was defined as the blocking temperature T_b. Above 50 K, the plot of χ^{-1} versus T is linear, indicating that the magnetization obeys the Curie–Weiss law, with a negative θ value of about 34 K for the 9.2-nm sample and 48 K for the 3.1-nm sample.

The magnetization curves were measured at temperatures from 5 to 300 K under a ±50-kOe field. The M–H curves for various particle sizes at a temperature of 5 K are given in Fig. 5. It is obvious that the magnetization increases as the particle size decreases, and that it behaves ferromagnetically. Coercivity was observed in the 3.1-nm sample as 110 Oe, and in the 9.2-nm as 150 Oe.

Magnetizations far above T_b were paramagnetic, just above T_b were superparamagnetic forming a magnetization curve. Below T_b ferromagnetic behavior with slight hysteresis was observed and this could be explained by uncompensated surface spins of the Co_3O_4 nanoparticle.

The effective magnetic moment per ion μ_{eff} could be estimated for all the samples from the χ–T plot, and are summarized as a function of particle size in Fig. 6. The saturation magnetization values M_s are also indicated. It is remarkable that both M_s and μ_{eff} increased dramatically below the particle size of about 10 nm. The value of the effective magnetic moment μ_{eff} per ion for the 3.1-nm particle was estimated to be 8.12 μ_B, and this estimation was twice as large as expected (4.14 μ_B). Because uncompensated surface spins behave superparamagnetically, the total magnetic spins became easy to order, and as a result magnetizaion increased.

Co_3O_4 has a normal spinel structure with antiferromagnetic exchange between ions occupying the tetrahedral A sites and the octahedral B sites. The Co^{3+} ions have no moment at the B sites, while the Co^{2+} ions at the A sites have a permanent moment of 3.25 μ_B, as found in neutron diffraction experiments [7]. However, the large effective magnetic moment μ_{eff} estimated from the inverse susceptibility of 8.12 μ_B could not be explained only on the basis of the Co^{2+} ion. Normally, Co^{3+} ions have no magnetic moment because of the large crystal field splitting of the 3d orbitals by the octahedral cubic field. In a small particle system, it is thought that Co^{3+} ions owe their magnetic moment to the defect of oxygen as well as the distortion of the crystal symmetry, though they normally exhibit no magnetic moment. An expansion of the lattice constant according to the downsizing of the particle, shown in Fig. 3, suggests an alteration of the geometry of the spinel structure.

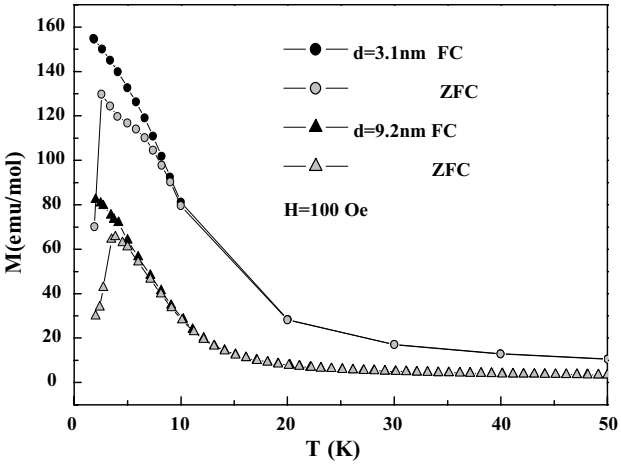


Fig. 4. Temperature dependence of FC (open marks) and ZFC (closed marks) magnetization for each particle size.

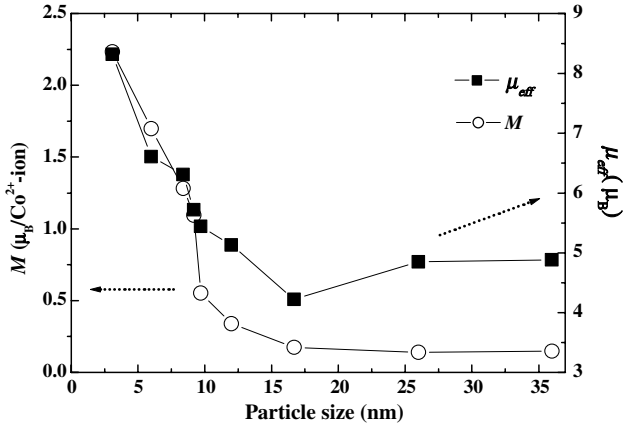


Fig. 6. Dependence of the saturation magnetization and effective magnetic moment on particle size.

4. Conclusion

The Co_3O_4 particles with an average size ranging from 3 to 30 nm were prepared and their magnetic properties depending on particle sizes were reported. Both M_s and T_b increased dramatically below the particle size of about 10 nm. Because uncompensated surface spins behave superparamagnetically, the total magnetic spins became easy to order. The value of the effective magnetic moment μ_{eff} per ion for the 3.1-nm particle was estimated to be 8.12 μ_B, and this estimation was twice as large as expected. This could be also thought that Co^{3+} ions owe their magnetic moment to the defect of oxygen as well as the distortion of the crystal symmetry in a small particle system.

Acknowledgments

The authors thank Ms. K. Yabuta, Mr. S. Konuma and Mr. M. Uzaki for producing the TEM images, and Ms. Y. Itoh for her chemical analysis of the Co-O nanoparticles. The useful discussion with Prof. Y. Kimishima is also appreciated. This study was partially supported by a Grant-in-Aid for Scientific Research offered by the Japan Society for the Promotion of Science (C) (2) (No. 15510089).

References

[1] R.H. Kodama, Salah A. Makhlouf, A.E. Berkowitz, Phys. Rev. Lett. 79 (1997) 1393.
[2] Yuko Ichiyanagi, Naoto Wakabayashi, Junichiro Yamazaki, Saori Yamada, Yoshihide Kimishima, Eriko Komatsu, Hiroyuki Tajima, Physica B 329–333 (2003) 862.
[3] C.F.J. Flipse, C.B. Rouwelaar, F.M.F. de Groot, Eur. Phys. J. D 9 (1999) 479.
[4] Salah A. Makhlouf, J. Magn. Magn. Mater. 246 (2002) 184.
[5] Michi Sato, Shigemi Kohiki, Yuko Hayakawa, Yuko Sonoda, Tomohiro Babasaki, Hiroyuki Deguchi, Masanori Mitome, J. Appl. Phys. 88-5 (2000) 2771.
[6] Y. Ichiyanagi, Y. Kimishima, S. Yamada, J. Magn. Magn. Mater. 272–276 (Suppl. 1) (2004) E1245.
[7] W.L. Roth, J. Phys. Chem. Solids 25 (1964) 1.

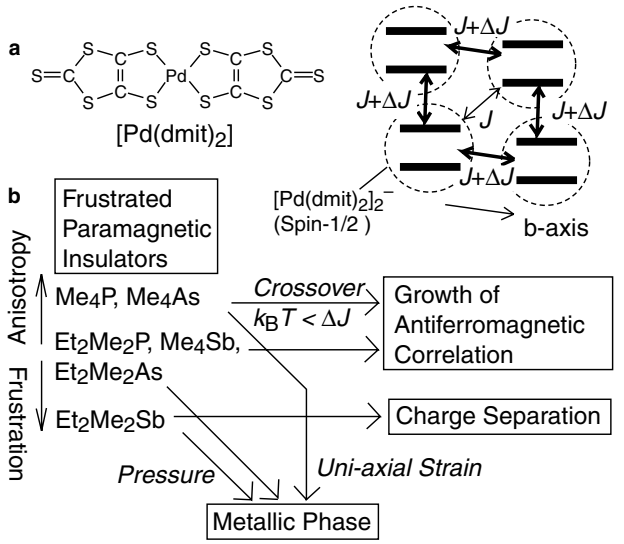


Fig. 1. (a) Schematic display of the anisotropic triangular lattice structure in the $[Pd(dmit)_2]$ salt and the definition of the isosceles model. (b) Classification of the changes of spin states of subjected in this paper. Cation dependence is also indicated.

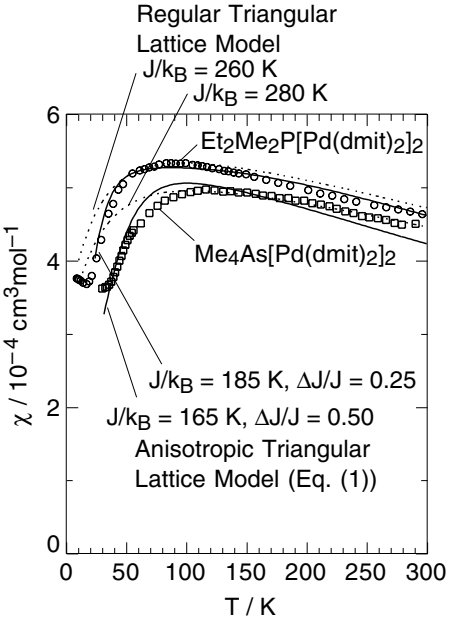


Fig. 2. Temperature dependence of χ of the Me_4As and Et_2Me_2P salts, as compared with the values calculated using the regular triangular lattice model (broken curves) and the phenomenological model for anisotropic triangular lattice (solid curves) with the indicated parameters.

broken symmetry for example. This is the main origin of unorthodox physical behavior of the frustrated systems.

The stability of the metallic state is ruled by the competition between the cost by the intradimer electron repulsion, U_{dimer}, and the kinetic energy gain corresponding to the bandwidth, W. If U_{dimer}/W is sufficiently large, the spin-localized AF state attains more stability by the exchange couplings, J, so that the system becomes insulating. The frustration in the insulating state eliminates the exchange energy gain and provides higher entropy, by suppressing the spin correlation. Thus the frustration operates to stabilize the metallic state relatively. Therefore, the metallic state can appear by a small increase in W, when the system is close to the completely frustrated regular triangular lattice. This tendency is in fact observed in the $[Pd(dmit)_2]$ series [4–6]. For instance, the Me_4P and Me_4As salts, which have the most anisotropic lattice, cannot be metallic under hydrostatic pressure, whereas the Et_2Me_2P and Me_4Sb salts, which are closer to the regular triangular arrangement, readily become metallic under pressure lower than 1 GPa.

At ambient pressure, U_{dimer}/W remains large enough to preclude the metallic state in these salts. As shown in Fig. 2, the temperature dependence of magnetic susceptibility (χ) of these salts can be well explained by the spin-1/2 Heisenberg triangular antiferromagnet model [7], particularly above the temperature where a round maximum of χ appears (T_{max}). The most significant feature of the frustrated spin system, from an experimental viewpoint, is that T_{max} is much lower than the mean-field Weiss temperature θ, estimated from the Curie–Weiss-like high-temperature χ tail [7,8]. In a system without frustration, $T_{max} \approx \theta$ is usually expected, because T_{max} is a measure of the temperature below which the AF correlation grows beyond the lattice spacing. The frustration prevents the AF correlation from growing so as to keep the system "paramagnetic" (or a spin liquid) down to considerably low temperature, which explains the low T_{max}.

As temperature decreases below T_{max} the χ behavior gradually deviates from the regular triangular model. There appears a steep decrease of χ, like in a spin-gapped system, until χ turns to be rather flat at the Néel point [9,10]. The steep decrease of χ indicates a rapid growth of the AF correlation. There should be a crossover from the frustrated paramagnetic state to an antiferromagnetically correlated one, by which the frustration is released. The crossover temperature, as well as the Néel temperature (T_N), shifts to higher, as the lattice deviates from the regular triangular lattice depending on the cation. This magneto-structural correlation indicates that the crossover originates from the lattice anisotropy. As shown in Fig. 1(a), the $[Pd(dmit)_2]$ salts can be modeled as the isosceles system interpolating between the square lattice ($\Delta J \gg J$) and the triangular lattice ($\Delta J = 0$), where ΔJ is the deviation from the regular triangular lattice.

According to theoretical calculations [11,12], the spin excitation spectra of the interpolating system has dip minima leading to long-wavelength AF correlation, and short-wavelength weak dispersion lies approxi-

mately ΔJ above the minimum, which explains the high-temperature paramagnetic behavior due to the frustration. Therefore, ΔJ plays like the spin gap separating the long-wavelength spin-wave excitations predominant at low temperatures and the short-wavelength magnon excitations significant at high temperatures. If this is the case, the frustration is released by the AF correlation growing at low temperatures, $T < \Delta J/k_B T$. Our aim is to describe the temperature dependence of χ, on the basis of this picture. We have proposed an interpolating formula [13]

$$\chi(T) = [z_{tri} J \chi_{tri}(k_B T/J) f(T, \Delta J) + z_{sq} \Delta J \chi_{sq}(k_B T/\Delta J)] / [f(T, \Delta J) + 1](z_{tri} J + z_{sq} \Delta J), \quad (1)$$

where χ_{tri} and χ_{sq} stand for the χ of the triangular lattice (J-lattice) and that of the square lattice (ΔJ-lattice), respectively, $f(T, \Delta J) = 1/[\exp(\Delta J/k_B T) - 1]$ denotes the Bose distribution, and $z_{tri} = 6$ and $z_{sq} = 4$ are the numbers of the neighboring sites. The long- and short-wavelength contributions are approximated by χ_{sq} and χ_{tri}, respectively, in this phenomenology. This explains the observed crossover behavior, as indicated in Fig. 2. The crossover has a characteristic temperature, $T \approx \Delta J/k_B$ which is related to the structural features. In these cases, the frustration is released by the growth of the square-lattice-like AF correlation due to the deviation from the regular triangular lattice.

From the viewpoint of molecular magnetism, it is worth noting that even a small size model of a frustrated spin system exhibits some features showing relevance to the frustration-release crossover. Appearance of a common feature for the small model and the infinite lattice is suggested by the short correlation-length in the frustrated state. The key feature is the energy structure having low-lying antiferromagnetically correlated states and the short-range excitations with weak dispersion. The weak dispersion implies a considerably isolated spin distribution. Let us consider here, for example, the minimal model, i.e., a three-spin Heisenberg model on an isosceles triangle (Fig. 3). At $\Delta J = 0$ (the regular triangle), doubly degenerate $S = 1/2$ states are the lowest. This degeneracy means the complete frustration. As ΔJ increases, one of the $S = 1/2$ levels shifts lower, while the other remains not shifted. There is an energy separation of ΔJ between them. The lower state has antiferromagnetically correlating spin distribution over the triangle, suggesting relevance to the long-range correlation, while the other one has an isolated spin on the center. This is in fact analogous to the excitation spectra considered for the isosceles triangular lattice. It is noteworthy that this low-energy structure is dominated only by the distortion parameter ΔJ, not by J.

The AF correlation grows exponentially like in a square lattice AF below the crossover temperature, so as to spread over large area. This causes another cross-

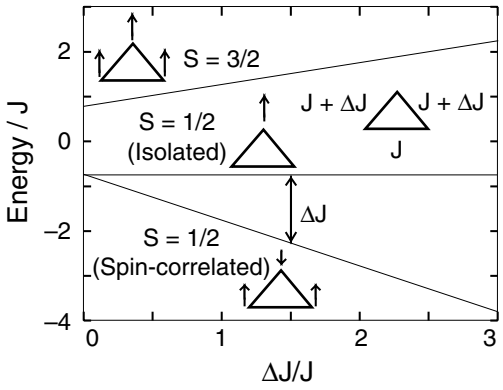


Fig. 3. Energy diagram of a three-spin Heisenberg model on an isosceles triangle as a function of the anisotropy, ΔJ. The spin distributions, being independent of ΔJ, are also depicted.

over to a three-dimensional long-range ordered state, assisted by weak interlayer couplings [13]. The observed Néel temperatures correspond to this dimensional crossover.

Finally, we briefly mention the valence state of a peculiar case, the Et_2Me_2Sb salt, which is closest to the regular triangular lattice. This salt undergoes a first-order phase transition at 70 K. The low-temperature phase is non-magnetic (Fig. 4(a)) and has two types of dimers. Clearly the spin frustration is released by this transition. We have attributed this transition to the charge separation (disproportionation),

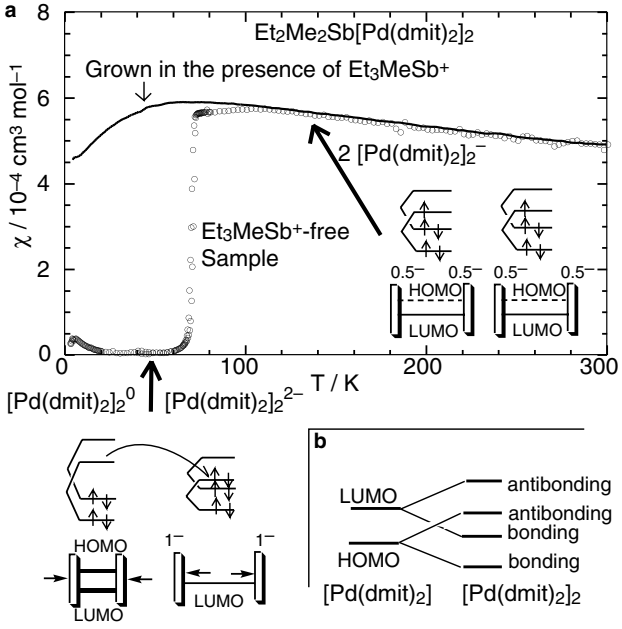


Fig. 4. (a) Temperature dependence of χ of the two types of the Et_2Me_2Sb salt samples. The electronic structures of the dimers above and below the 70 K phase transition are displayed. (b) Energy diagram for the dimerization of $[Pd(dmit)_2]$ to explain the HOMO–LUMO interchange.

$2[Pd(dmit)_2]_2^- \rightarrow [Pd(dmit)_2]_2^0 + [Pd(dmit)_2]_2^{2-}$, accompanied by electron pairing on half of the dimers [14]. The key factor to understand this transition is the unique two-level structure of the $[Pd(dmit)_2]_2$ dimer. The anti-bonding level of the HOMO's and the bonding level of LUMOs interchange due to strong dimerization (Fig. 4(b)) [15,16]. For this reason, the neutral dimer $[Pd(dmit)_2]_2^0$ possesses considerable stability owing to the double-bonding [14]. We have shown, that the energy gain of the double-bonding can compensate the cost for electron pairing on another dimer, by model calculations assuming variation of dimerization for the different dimers [14]. The Et_2Me_2Sb salt is so close to the regular triangle lattice that it cannot release the frustration by growing AF correlation. However, this salt changes the electron occupancy in the two-level structure, so as to escape from the frustration and to achieve a stable non-magnetic ground state. We have noticed a strong impurity effect on this transition. When the crystals are grown in the presence of Et_3MeSb^+ cations, the non-magnetic state is easily broken to let the frustrated paramagnetic state survive down to low temperature, though the content of Et_3MeSb^+ in the crystals is quite small (Fig. 4(a)). The origin of this impurity effect stabilizing the frustrated state is still an open question.

Acknowledgments

This work is supported by Grants-in-Aid for Scientific Research (Nos. 15550135 and 16GS0219) from the Ministry of Education, Culture, Sports, Science and Technology, Japan.

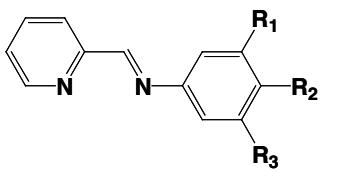
References

[1] M. Tamura, R. Kato, J. Phys.: Condens. Matter 14 (2002) L729.
[2] Y. Shimizu, K. Miyagawa, K. Kanoda, M. Maesato, G. Saito, Phys. Rev. Lett. 91 (2003) 107001.
[3] S. Bramwell, S.G. Carling, C.J. Harding, K.D.M. Harris, B.M. Kariuki, L. Nixon, P. Parkin, J. Phys.: Condens. Matter 8 (1996) L123.
[4] R. Kato, N. Tajima, M. Tamura, J.-I. Yamaura, Phys. Rev. B 66 (2002) 020508(R).
[5] R. Kato, A. Tajima, N. Tajima, A. Nakao, M. Tamura, J. Phys. IV France 114 (2004) 411.
[6] M. Tamura, R. Kato, J. Phys. Soc. Jpn. 73 (2004) 3108.
[7] N. Elstner, R.R.P. Singh, A.P. Young, Phys. Rev. Lett. 71 (1993) 1629.
[8] N. Elstner, R.R.P. Singh, A.P. Young, J. Appl. Phys. 75 (1994) 5943.
[9] T. Nakamura, T. Takahashi, S. Aonuma, R. Kato, J. Mater. Chem. 11 (2001) 2159.
[10] S. Ohira, M. Tamura, R. Kato, I. Watanabe, M. Iwasaki, J. Phys. IV France 114 (2004) 355.
[11] Z. Weihong, R.H. McKenzie, R.R.P. Singh, Phys. Rev. B 59 (1999) 14367.
[12] J. Merino, R.H. McKenzie, J.B. Marston, C.H. Chung, J. Phys.: Condens. Matter 11 (1999) 2965.
[13] M. Tamura, R. Kato, J. Phys. IV France 114 (2004) 383.
[14] M. Tamura, R. Kato, Chem. Phys. Lett. 387 (2004) 448.
[15] E. Canadell, I.E.-I. Rachidi, S. Ravy, J.-P. Pouget, L. Brossard, J.P. Legnos, J. Phys. (France) 50 (1989) 2967.
[16] H. Tajima, T. Naito, M. Tamura, A. Kobayashi, H. Kuroda, R. Kato, H. Kobayashi, R.A. Clark, A.E. Underhill, Solid State Commun. 79 (1991) 337.

temperature or of pressure. When the magnitude of the intermolecular interactions overcomes the threshold value, the spin-crossover phenomenon undergoes co-operativity. In such a case, the spin transition between the low-spin and high-spin states is not only very abrupt, but also occurs with a hysteresis effect [7]. The design of molecules exhibiting bistability is one of the main challenges in molecular material science in order to utilise them for information processing and information storage [8]. Furthermore the design of spin-crossover compounds with multi-function, supramolecular structure and porous materials, has been noted because of leading specific magnetic or optical properties [9,10]. For some iron(II) spin-crossover (high-spin ($S = 2$) ↔ low-spin ($S = 0$)) compounds, light-induced low-spin → high-spin conversion can be observed by green light illumination into a d–d or MLCT (metal-to-ligand charge transfer) absorption band at temperatures well bellow the thermal transition temperature. A mechanism for this phenomenon, denoted as "light-induced excited spin state trapping" (LIESST), has been proposed [11,12]. The development of novel compounds exhibiting LIESST is one of the main challenges in this field [7,13,14]. The LIESST compounds can be used as optical switching molecular devices, and various functional materials including the optical switches can be constructed.

Here we focused on the spin-crossover iron(II) compounds in order to control liquid crystals not only by temperature but also magnetic field and photo-illumination. The spin-crossover iron(II) compounds exhibit spin conversion between diamagnetism ($S = 0$) and paramagnetism ($S = 2$), and the LIESST effect. The design of metallomesogens containing spin-crossover iron(II) center stimulates producing unexpected advanced materials by combining spin-crossover and LIESST with liquid-crystal properties [15].

The iron(II) compounds $[Fe(1C16\text{-}L)_2(NCS)_2]$ (**1**) $[Fe(2C16\text{-}L)_2(NCS)_2]$ (**2**) and $[Fe(3C16\text{-}L)_2(NCS)_2]$ (**3**) were designed in order to construct a spin-crossover and LIESST material with liquid-crystal properties, where 1C16-L, 2C16-L and 3C16-L are Schiff-base bidentate ligands derived from the condensation of 4-hexadecyloxyaniline, 3,4-bis(hexadecyloxy)aniline and 3,4,5-tris(hexadecyloxy)aniline with pyridine-2-carboxyaldehyde (Fig. 1). Because the iron(II) compound *cis*-bis(thiocyanato)-bis [*N*-(2-pyridylmethylene)aniline]iron (II) exhibits spin-crossover and LIESST effect, the ligand of the complex was modified as Schiff-base ligand with elongated substituents [16].



1C16-L: $R_2 = OC_{16}H_{33}$, R_1, R_3 = H
2C16-L: R_1, $R_2 = OC_{16}H_{33}$, R_3 = H
3C16-L: R_1, R_2, $R_3 = OC_{16}H_{33}$

Fig. 1. Structure of the ligands.

2. Experimental

2.1. Preparations of the ligands [17,18]

2.1.1. Preparation of 1,2-didodecyloxybenzene (*2C16*)

Catechol (1.1 g, 10 mmol), K_2CO_3 (3.45 g, 25 mmol), 1-bromohexadecane (7.63 g, 25 mmol), and KI (0.1 g, 0.60 mmol), were mixed in DMF (50 ml). The mixture was stirred at 80 °C for one day. After cooling to room temperature, the mixture was poured into ice/water. The white precipitation was filtrated and washed with acetone; yield: 4.72 g (85%); white needle. ^{1}H NMR ($CDCl_3$): $\delta = 6.90$ (s, 4H), 3.96 (t, $J = 6.5$ Hz, 4H), 1.86–1.26 (m, 56H), 0.88 (t, $J = 6.4$ Hz, 6H). 1,2,3-Tris(hexadecyloxy) benzene (**3C16**) was prepared same as **2C16**; yield: 6.50 g (81%); white solid. ^{1}H NMR ($CDCl_3$): $\delta = 6.90$ (t, $J = 8.3$ Hz, 1H), 6.53 (d, $J = 8.3$ Hz, 2H), 3.96 (t, $J = 6.5$ Hz, 4H), 3.94 (t, $J = 6.7$ Hz, 2H), 1.86–1.26 (m, 84H), 0.88 (t, $J = 6.7$ Hz, 9H).

2.1.2. Preparation of p-nitrohydroxybenzene (*1C16-NO_2*)

p-Nitrohydroxybenzene (1.39 g, 10 mmol), 1-bromohexadecane (4.58 g, 15 mmol), and KI (0.1 g, 0.60 mmol), were mixed in DMF (50 ml). The mixture was stirred vigorously at 80 °C for one day. After cooling to room temperature, the mixture was poured into ice/water. The pale yellow precipitation was filtrated and recrystallized from acetone; yield: 3.5 g (96%); pale yellow needle. ^{1}H NMR ($CDCl_3$): $\delta = 8.20$ (d, $J = 9.5$, 2H), 6.95 (d, $J = 9.5$, 2H), 4.04 (t, $J = 6.5$, 2H), 1.86–1.26 (m, 28H), 0.88 (t, $J = 7.0$, 3H).

2.1.3. Preparation of 1-nitro-3,4-didodecyloxybenzene (*2C16-NO_2*)

To a suspension of silica gel (2.0 g) in $CHCl_3$ (30 ml) were added conc. HNO_3 (30 ml) and then a solution of **2C16** (4.00 g, 7.2 mmol) in $CHCl_3$. The mixture was stirred for 30 min. and the silica gel was removed by filtration. The orange filtrate was washed with H_2O and was concentrated to 15 ml. The product was precipitated by addition of MeOH; yield: 4.2 g (97%); pale yellow solid. ^{1}H NMR ($CDCl_3$): $\delta = 7.84$ (dd, $J = 2.8$, 9.0 Hz, 1H), 7.69 (d, $J = 2.5$ Hz, 1H), 6.84 (dd, $J = 3.0$, 9.0 Hz, 1H), 4.04 (d, $J = 6.5$ Hz, 4H), 1.86–1.26 (m, 56H), 0.88 (t, $J = 6.4$ Hz, 6H). 3,4,5-Tris(hexadecyloxy)nitrobenzene (**3C16-NO_2**) was prepared same as **2C16-NO_2**; yield: 3.64 g (86%); pale yellow solid. ^{1}H NMR ($CDCl_3$)

δ = 7.47 (s, 2H), 4.05 (m, 6H), 1.86–1.26 (m, 84H), 0.88 (t, J = 6.9 Hz, 9H).

2.1.4. Preparation of 4-n-hexadecyloxyaniline (*1C16-NH$_2$*)

A mixture of **1C16-NO$_2$** (2.0 g, 5.5 mmol) and palladium (0.10 g, 10% on carbon) was added to 50 ml absolute EtOH in a 200 ml two-necked round bottomed flask. A solution of hydrazine monohydrate (2.64 g, 44 mmol) diluted with 40 ml of absolute EtOH was slowly added to the flask and the reaction mixture was refluxed for 24 h. The reaction was followed by TLC. The reaction mixture was filtered while is hot to remove insoluble solid. The filtrate was cooled in room temperature. The crude product was recrystallized from EtOH; yield: 1.58 g (86%); white solid. ^{1}H NMR ($CDCl_3$): δ = 6.75 (dd, J = 6.5, 2.5 Hz, 2H), 6.65 (dd, J = 6.5, 2.5 Hz, 2H), 3.89 (t, J = 7.0 Hz, 2H), 1.86–1.26 (m, 28H), 0.88 (t, J = 7.0 Hz, 3H). *Anal.* Calc. for $C_{22}H_{39}NO \cdot 0.75H_2O$: C, 76.13; H, 11.76; N, 4.04. Found: C, 76.35; H, 11.74; N, 3.87%. 1-Amino-3,4-didodecyloxybenzene (**2C16-NH$_2$**) and 3,4,5-tris(hexadecyloxy)aniline (**3C16-NH$_2$**) were prepared same as **1C16-NH$_2$**. For **2C16-NH$_2$**; yield: 1.60 g (84%); white solid. ^{1}H NMR ($CDCl_3$): δ = 6.71 (d, J = 8.3 Hz, 1H), 6.28 (d, J = 2.5 Hz, 1H), 6.19 (dd, J = 2.6, 8.2 Hz, 1H), 3.89 (t, J = 6.5 Hz, 4H), 3.40 (s, 2H), 1.84–1.22 (m, 56H), 0.88 (t, J = 6.9 Hz, 6H). *Anal.* Calc. for $C_{38}H_{71}NO_2$: C, 79.52; H, 12.47; N, 2.44. Found: C, 79.37; H, 12.40; N, 2.52%. For **3C16-NH$_2$**, yield: 1.80 g (94%); white solid. ^{1}H NMR ($CDCl_3$): δ = 6.03 (s, 2H), 3.91 (t, J = 6.5 Hz, 4H), 3.85 (t, J = 6.6 Hz, 2H), 1.86–1.26 (m, 84H), 0.88 (t, J = 6.9 Hz, 9H). *Anal.* Calc. for $C_{54}H_{103}NO_3 \cdot 0.5EtOH$: C, 78.88; H, 12.75; N, 1.67. Found: C, 78.76; H, 12.53; N, 1.89%.

2.1.5. Preparation of 4-hexadecyloxy-N-(2-pyridinylmethylene)-benzenamine (*1C16-L*)

1C16-NH$_2$ (500 mg, 1.5 mmol) and pyridine-2-carboxyaldehyde (160 mg, 1.5 mmol) were mixed in 100 ml of $CHCl_3$. The mixed solution was refluxed for 3 h. The solution was concentrated to 10 ml, the product was precipitated by addition of MeOH, filtered, washed MeOH and dried; yield: 539 mg (85%); yellow solid. ^{1}H NMR ($CDCl_3$): δ = 8.70 (d, J = 4.0 Hz, 1H), 8.63 (s, 1H), 8.20 (d, J = 8.0 Hz 1H), 7.81 (td, J = 7.5 Hz, 1.5 Hz, 1H), 7.35 (m, 3H), 6.95 (dd, J = 6.5, 2.0 Hz, 2H), 3.98 (t, J = 6.5 Hz, 2H), 1.86–1.26 (m, 28 H), 0.88 (t, J = 7.0 Hz, 3H).

Selected FT-IR data (ν/cm^{-1}) using KBr disk: 3064, 2847, 1625, 1579, 1503, 1464, 1246, 836. 3,4-bis-hexadecyloxy-*N*-(pyridinylmethylene)-benzenamine (**2C16-L**) and 3,4,5-tris(hexadecyloxy)-*N*-(pyridinylmethylene)-benzenamine (**3C16-L**) were prepared same as **1C16-L**. For **2C16-L**; yield: 462 mg (80%); yellow solid. ^{1}H NMR ($CDCl_3$): δ = 8.71 (d, J = 5.8 Hz, 1H), 8.64 (s, 1H), 8.20 (d, J = 8.0 Hz, 1H), 7.81 (td, J = 7.5 Hz, 1.5 Hz, 1H), 7.36 (ddd, J = 7.5, 4.5, 0.75 Hz, 1H), 6.97 (d, J = 1.8 Hz, 1H), 6.92 (d, J = 2.5 Hz, 1H), 6.91 (s, 1H), 4.04 (t, J = 6.8 Hz, 2H), 4.03 (t, J = 6.8 Hz, 2H), 1.84–1.22 (m, 56H), 0.88 (t, J = 7.0 Hz, 6H). Selected FT-IR data (ν/cm^{-1}) using KBr disk: 2918, 2849, 1512, 1467, 1265, 1232, 1125. For **3C16-L**; yield: 750 mg (75%); yellow solid. ^{1}H NMR ($CDCl_3$): δ = 8.71 (d, 1H), 8.62 (s, 1H), 8.18 (d, 1 H), 7.81 (td, J = 7.5 Hz, 1.5 Hz, 1H), 7.37 (ddd, J = 7.5, 5.0, 1.5 Hz, 1H), 6.58 (s, 2H), 4.00 (t, J = 6.5 Hz, 4H), 3.97 (t, J = 6.6 Hz, 2H), 1.86–1.26 (m, 84H), 0.88 (t, J = 6.9 Hz, 9H). Selected FT-IR data (ν/cm^{-1}) using KBr disk: 2917, 1583, 1504, 1469, 1432, 1125.

2.2. Preparation of the iron(II) compounds

2.2.1. Preparation of [Fe(1C16-L)$_2$(NCS)$_2$] (*1*)

To a mixture solution of $FeCl_2 \cdot 4H_2O$ (70 mg, 0.35 mmol) and KNCS (69 mg, 0.71 mmol) in $CHCl_3$/MeOH (10 cm^3) was added $CHCl_3$/MeOH solution (20 cm^3) of **1C16-L** (300 mg, 0.71 mmol). The reaction mixture was stirred for a few minutes. The resulted dark green precipitate was collected by filtration and dried in vacuo. Yield: 259 mg (72%). *Anal.* Calc. for $C_{58}H_{84}Fe_1O_2S_2 \cdot 1.5H_2O$: C, 66.70; H, 8.39; N, 8.05; Fe, 5.35. Found: C, 66.97; H, 8.13; N, 8.05; Fe, 5.23%. Selected FT-IR data (ν/cm^{-1}) using KBr disk: 2919, 2850, 2065, 1598, 1505, 1251, 831. [Fe(2C16-L)$_2$(NCS)$_2$] (**2**) and [Fe(3C16-L)$_2$(NCS)$_2$] (**3**) were prepared same as **1**. For **2**; yield: 291 mg (86%). *Anal.* Calc. for $C_{90}H_{148}N_6O_4S_2 \cdot 0.5CHCl_3$: C, 67.57; H, 9.29; N, 5.20; Fe, 3.45. Found: C, 67.46; H, 9.33; N, 5.20; Fe, 3.14%. Selected FT-IR data (ν/cm^{-1}) using KBr disk: 2918, 2850, 2061, 1594, 1513, 1469, 1263, 1133. For **3**; yield: 259 mg (72%). *Anal.* Calc. for $C_{58}H_{84}Fe_1O_2S_2 \cdot 1.5H_2O$: C, 66.70; H, 8.39; N, 8.05; Fe, 5.35. Found: C, 66.97; H, 8.13; N, 8.05; Fe, 5.23. Selected FT-IR data (ν/cm^{-1}) using KBr disk: 2919, 2850, 2065, 1598, 1505, 1251, 831.

2.3. Measurements

Elemental analyses of carbon, hydrogen, and nitrogen were carried out at The Service Center of Elemental Analyses of Kyushu University. Metal analyses were done on a Shimadzu AA-625-11 Atomic Absorption/Flame Emission Spectrometer.

Infrared spectra were measured using KBr disk with a JASCO FT-IR-410.

^{1}H NMR were measured on a Bruker AVANCE SERIES DPX 400 instrument operating at 400 MHz (using the deuterated solvent as the lock and the residual solvent or tetramethylsilane as the internal reference).

Magnetic susceptibilities of ground samples were measured on a Quantum Design MPMS-5S. Samples were put into a gelatin capsule, mounted inside the

straw, and then fixed to the end of the sample transport rod. Illumination experiment was done with using an Hg–Xe lamp ($\lambda = 550$ nm, 1.5 mW/cm^2) as a light source. The light passing through IR and green filters was guided via an optical fiber into the SQUID magnetometer. The sample was placed on the edge of the optical fiber.

The Mössbauer spectra (isomer shift versus metallic iron at room temperature) were measured using a Wissel MVT-1000 Mössbauer spectrometer with a ^{57}Co/Rh source in the transmission mode. All isomer shifts are given relative to α-Fe at room temperature. The measurements at low temperature were performed with a closed-cycle helium refrigerator cryostat (Iwatani Co., Ltd.).

Differential Scanning Calorimetry (DSC) thermal analysis was carried out on a SHIMADZU DSC50 differential scanning calorimeter.

X-Ray powder diffraction (XRD) studies were performed on a Rigaku X-ray diffractometer RAD-2A with a 2.0 kW Cu Kα X-ray.

Optical polarized microscopy was carried out on a Nippon Chemical Industrial corporation polarization microscope OPTICAL POL with a Yanagimoto factory MODEL MP-J3 micro melting point meter.

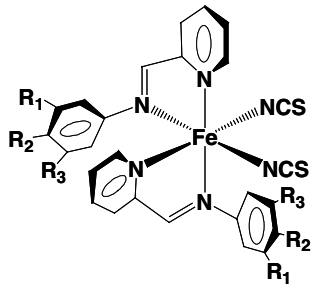
3. Results and discussion

3.1. Structure of the compounds

Single crystals of the compounds **1**–**3** were not synthesized, therefore geometry optimization for the compounds were performed by computer simulation. Létard et al. [19] reported that a iron atom was surrounded by six nitrogen atoms belonging to two NCS^- groups in *cis* positions and two bidentate ligands. Because the iron(II) compound *cis*-bis(thiocyanato)-bis[*N*-(2-pyridylmethylene)aniline]iron(II) exhibits spin-crossover and LIESST effect, the ligand of the complex was modified as Schiff-base ligand with elongated substituents (Fig. 2) [16]. In consideration of the structure of the spin-crossover iron(II) compounds, that of the compounds **1**–**3** have been optimized. The resulted geometry structure has been shown in Fig. 3. A twisted-structure or starfish-like geometry have been proposed for the molecular structures of **1**–**3**.

3.2. Differential scanning calorimetry (DSC)

Phase transition enthalpies were measured by carrying out DSC thermal analysis for the compounds **1**–**3**. The DSC curves of **1**–**3** are shown in Fig. 4. Two peaks were observed for **1** at 365 and 445 K. The DSC peak at 365 K ($\Delta H = 65.9$ kJ mol^{-1}) to a crystal–mesophase transition, and that at 445 K ($\Delta H = 27.7$ kJ mol^{-1}) is assigned to a mesophase–liquid transition. Two peaks were observed for **2** at 363 and 407 K. The first peak at 363 K ($\Delta H = 92.3$ kJ mol^{-1}) to a crystal–mesophase transition, and the second peak at 407 K ($\Delta H = 13.5$ kJ mol^{-1}) is assigned to a mesophase–liquid transition. Two peaks were observed for **3** at 345 and 400 K. The first peak at 345 K $\Delta H = 78.3$ kJ mol^{-1} to a crystal–mesophase transition, and the second peak at 400 K ($\Delta H = 14.7$ kJ mol^{-1}) is assigned to a mesophase–liquid transition. The compounds **1**–**3** exhibit two endothermic peaks in the heating cycles. A large peak at low temperature is assigned to the solid-to-mesophase transition, and a small peak at high temperature, assigned to mesophase-to-liquid transition. DCS were measured in the temperature range from crystal to liquid crystal on the warming and cooling mode reversibly. On cooling, the transition temperatures from mesophase to crystal for the compounds **1**–**3** are 332, 330 and 325 K, respectively. Free ligands, **1C16-L**, **2C16-L** and **3C16-L**, exhibit only one peak, being assigned solid-to-liquid transition.



1: $R_2 = OC_{16}H_{33}$, R_1, R_3 = H
2: R_1, $R_2 = OC_{16}H_{33}$, R_3 = H
3: R_1, R_2, $R_3 = OC_{16}H_{33}$

Fig. 2. Chemical structure of the compounds **1**–**3**.

3.3. Polarizing optical microscopy (POM)

The mesophase was studied by hot-stage polarized optical microscopy (POM), and the texture of liquid-crystal state was observed by optical microscopy. The compounds **1**–**3** are solid state at room temperature. Being heated on the stage of the optical microscope under polarized light, the compounds exhibited mesomorphism. On heating, the compounds undergo a transition from the solid to birefringent viscous fluid, and exhibited a characteristic mosaic texture. When the compounds were cooled from the isotropic liquid to room temperature, the same mosaic texture as before heating was observed. An example of the texture under crossed polarizers for **3** is shown in Fig. 5. The identification of the phase of the liquid-crystal state based on the texture observed by optical microscopy has been not possible.

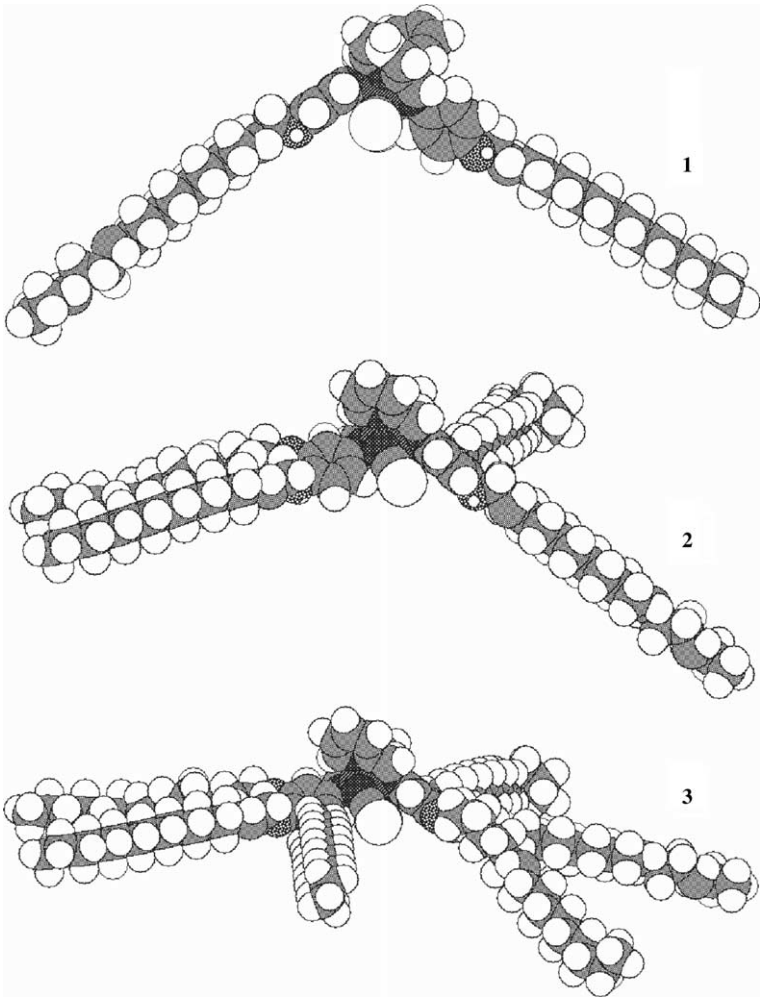


Fig. 3. Computer simulation of the molecular structure of the compounds **1**–**3**.

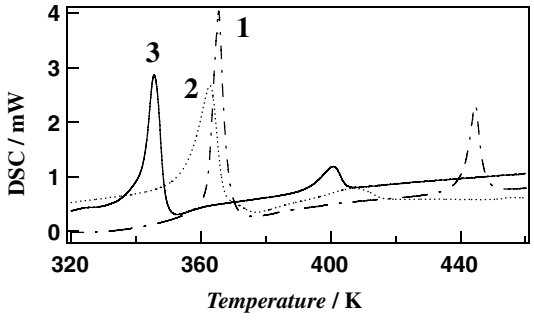


Fig. 4. DSC of the compounds **1**–**3**.

3.4. Powder X-ray diffractions

Temperature-dependent X-ray diffraction measurements were carried out to confirm this mesophase. Fig. 6 shows the powder X-ray diffraction patterns of the crystal and mesophase states for the compound **3** observed in the temperature range from 300 to 380 K. A sharp reflection in the small-angle ($2\theta = 4.1°$) with *d*-spacing of 21.4 Å was detected at 300 and 325 K. This *d*-spacing may correspond to the length of elongated substituents ($l = 21.4$ Å). At 345 K, the peak of $2\theta = 4.1°$ disappeared and a new peak appeared at $2\theta = 2.7°$ ($d = 32.7$ Å). The peak of $2\theta = 21.5°$ ($d = 4.1$ Å) observed below 325 K becomes broad at the same time. The formation of the mesophase is completed at 345 K in accordance with the result observed DSC.

3.5. Magnetic properties

The spin-crossover phenomenon between the high-spin and low-spin states for the compounds **1**–**3** were followed by measurements of the molar magnetic susceptibility χ_M and Mössbauer spectra as a function of temperature. The $\chi_M T$ versus T plots for **1**–**3** are given in Fig. 7.

The $\chi_M T$ value for **1** was 3.04 cm^3 K mol^{-1} at 50 K, and was 3.10 cm^3 K mol^{-1} at 150 K. The $\chi_M T$ values are nearly constant in the temperature range from 50 to 380 K. Spin-crossover phenomenon was not observed,

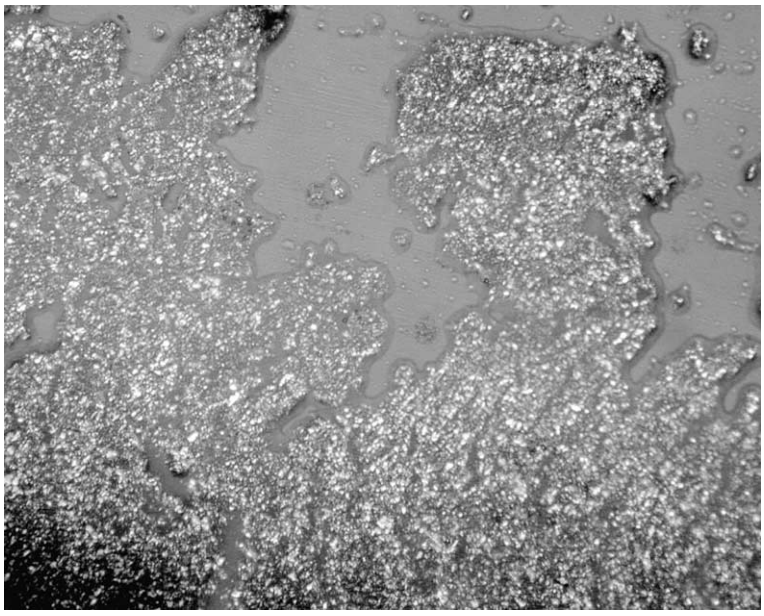


Fig. 5. Texture of the compound **3** under crossed polarizers at 380 K.

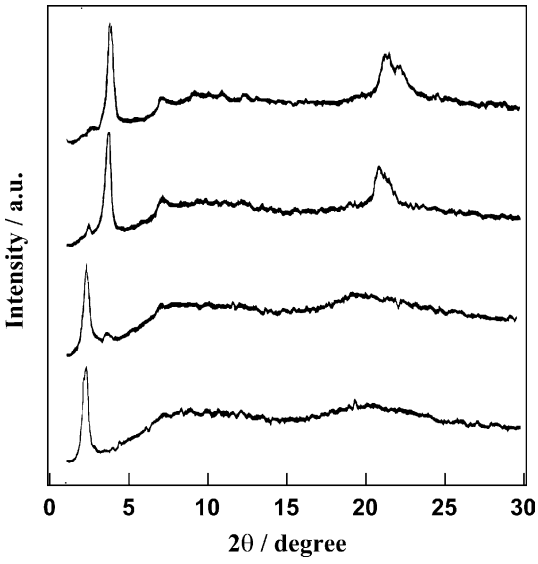


Fig. 6. Temperature dependence of powder XRD pattern of the compound **3**.

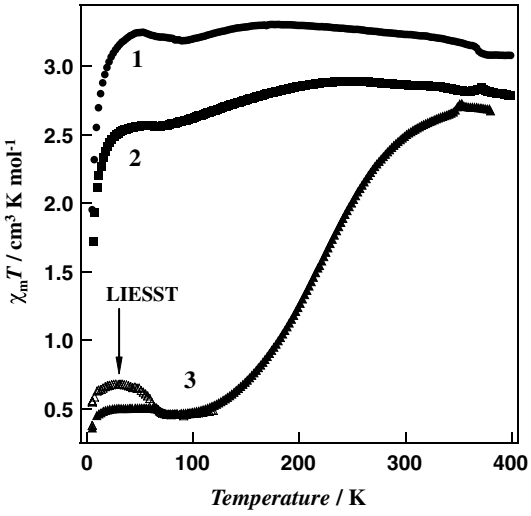


Fig. 7. $\chi_M T$ vs. T plots for the compounds **1**–**3**. $\chi_M T$ vs. T plots for LIESST experiment were recorded in the warming mode (△).

and the compound **1** was in high-spin state ($S = 2$). It is thought that the decrease of $\chi_M T$ value below 50 K is due to zero-field splitting. A decrease of $\chi_M T$ value was observed at 365 K. The temperature is in accordance with the crystal to mesophase transition temperature in the DSC data. The decrease may be explained as molecular orientation due to the mesophase transition.

The $\chi_M T$ value for **2** was 2.56 $cm^3\,K\,mol^{-1}$ at 65 K, and slightly increased with increasing temperature to 2.89 $cm^3\,K\,mol^{-1}$ at 245 K. An incomplete gradual spin-crossover phenomenon was observed. As well as **1**, an increase of $\chi_M T$ value was observed at 370 K. The temperature is in accordance with the crystal to mesophase transition temperature in the DSC data. The increase may be explained as molecular orientation due to the mesophase transition.

The $\chi_M T$ value for the compound **3** is equal to 0.47 $cm^3\,K\,mol^{-1}$ below 100 K, which shows that about 15% of the iron(II) ions remain in the high-spin state. On warming, the $\chi_M T$ values were almost constant from 5 to 100 K, then gradually increased at around spin transition temperature $T_{1/2} = 217$ K. The $\chi_M T$ value at 345 K was ca. 2.73 $cm^3\,K\,mol^{-1}$, showing that the spin transition from the low-spin to the high-spin state is induced. The Mössbauer spectra measured in the temperature range between 5 and 300 K support the existence

of iron(II) in the high-spin and low-spin states and the occurrence of spin-crossover behavior. Mössbauer spectrum at 80 K reveals two doublet peaks, one is a narrow quadrupole-split doublet (quadrupole-splitting ΔQ = 0.57 mm s^{-1}, isomer shift δ = 0.48 mm s^{-1}) representing the low-spin state, and another is a wide doublet (ΔQ = 3.06 mm s^{-1}, δ = 1.13) representing the high-spin state. Mössbauer parameters at 300 K are ΔQ = 0.50 mm s^{-1}, δ = 0.13 mm s^{-1} for low-spin state, and ΔQ = 2.35 mm s^{-1}, δ = 0.93 mm s^{-1} for high-spin state. The $\chi_M T$ value at 300 K is higher than that calculated from the Mössbauer data, suggesting that the recoilless fraction of the high-spin species is smaller than that of the low-spin species near the temperature at which the crystal phase turns to the mesophase. A increase of $\chi_M T$ value associated with the crystal–liquid crystal phase transition was observed at 350 K. The jump indicates the crystal–liquid crystal phase transition may be due to liquid crystal alignment.

3.6. LIESST effect

When the samples for the compound **3** were illuminated at 5 K for 1 h, the $\chi_M T$ value was increased (Fig. 7). The change in the $\chi_M T$ value persisted for many hours, even after the illumination was stopped. This suggests that the transition from the low-spin state to the high-spin state can be induced by illumination. The relaxation temperature of the LIESST effect is defined as T (LIESST) [20], the temperature dependence of $\chi_M T$ after illumination shows that the $\chi_M T$ value decreases with the increase in temperature and that the thermal relaxation to the ground state occurs. The T (LIESST) is 60 K, the compound **3** can exhibit photoswitching below 60 K. About 10% high-spin fraction were induced by illumination.

4. Conclusion

The iron(II) compounds **1**–**3** with long alkyl chains have been synthesized, properties of these compounds were characterized. The compounds **1**–**3** exhibited liquid-crystal property that was confirmed from the results of DSC, XRD diffractions, and texture of under crossed polarizers. The compound **1** was in the high-spin state. On the other hand, The compounds **2** and **3** exhibited spin-crossover phenomena. Furthermore the compound **3** exhibited LIESST effect, i.e., three physical properties, spin-crossover, LIESST effect and liquid-crystal properties, can coexist in a single compound for **3**. Geometrical flexibility in the molecules is very important in order to achieve co-occurrence of various physical properties in the functional molecular-based materials. We believe that our approach, i.e., the co-occurrence of spin-crossover, LIESST and liquid-crystal properties, can be widely applied, not only in the design of LIESST compounds with liquid-crystal properties but also in the design of a variety of optically switchable molecular compounds.

Acknowledgements

This work was supported by Tokuyama Foundation, Ogasawara Foundation and the Research and Education Grant-in-Aid of IEI-J.

References

[1] K. Binnemans, Y.G. Galyametdinov, R.V. Deun, D.W. Bruce, S.R. Collinson, A.P. Polishchuk, I. Bikchantaev, W. Haase, A.V. Prosvirin, L. Tinchurina, I. Litvinov, A. Gubajdullin, A. Rakhmatullin, K. Uytterhoeven, L.V. Meervelt, J. Am. Chem. Soc. 122 (2000) 4335.
[2] K. Ohta, N. Yamaguchi, I. Yamamoto, J. Mater. Chem. 8 (1998) 2637.
[3] R. Werner, K. Falk, S. Ostrovsky, W. Haase, Macromol. Chem. Phys. 202 (2001) 2813.
[4] C. Piechocki, J. Simon, A. Skoulios, D. Guillon, P. Weber, J. Am. Chem. Soc. 104 (1982) 5245.
[5] A.M. Giround-Godquin, J.C. Marchon, J. Phys. Lett. 45 (1984) L681.
[6] Y. Galyametdinov, V. Ksenofontov, A. Prosvirin, I. Ovchinnikov, G. Ivanova, P. Gütlich, W. Haase, Angew. Chem., Int. Ed. Engl. 40 (2001) 4269.
[7] S. Hayami, Z. Gu, M. Shiro, Y. Einaga, A. Fujishima, O. Sato, J. Am. Chem. Soc. 122 (2000) 7126.
[8] O. Kahn, C.J. Martinez, Science 279 (1998) 44.
[9] J.A. Real, E. Andrés, M.C. Muñoz, M. Julve, T. Granier, A. Bousseksou, F. Varret, Science 268 (1995) 265.
[10] G.J. Halder, C.J. Kepert, B. Moubaraki, K.S. Murray, J.D. Cashion, Science 298 (2002) 1762.
[11] S. Decurtins, P. Gütlich, C.P. Köhler, H. Spiering, A. Hauser, Chem. Phys. Lett. 105 (1984) 1.
[12] P. Gütlich, A. Hauser, H. Spiering, Angew. Chem., Int. Ed. Engl. 33 (1994) 2024.
[13] J-F. Létard, J.A. Real, N. Moliner, A.B. Gaspar, L. Capes, O. Cador, O. Kahn, J. Am. Chem. Soc. 121 (1999) 10630.
[14] S. Hayami, Z. Gu, Y. Einaga, Y. Kobayasi, Y. Ishikawa, Y. Yamada, A. Fujishima, O. Sato, Inorg. Chem. 40 (2001) 3240.
[15] S. Hayami, K. Danjobara, K. Inoue, Y. Ogawa, N. Matsumoto, Y. Maeda, Adv. Mater. 16 (2004) 869.
[16] V. Ksenofontov, G. Levchenko, H. Spiering, P. Gutlich, J.-F. Letard, Y. Bouhedja, O. Kahn, Chem. Phys. Lett. 294 (1998) 545.
[17] A. Markus, S. Mathias, Synthesis 15 (2001) 2234.
[18] K.L. Chung, C. Chung-Hsiung, T. Chun-Hsien, J. Chem. Mater. 8 (1998) 599.
[19] J-F. Létard, P. Guionneau, L. Rabardel, J.A.K. Howard, A.E. Goeta, D. Chasseau, O. Kahn, Inorg. Chem. 37 (1998) 4432.
[20] J.-F. Létard, L. Capes, G. Chastanet, N. Moliner, S. Létard J.-A. Real, O. Kahn, Chem. Phys. Lett. 313 (1999) 115.

between spin centers [8]. To overcome these problems, we have focused on a kind of aromatic *N*-oxyl, 2,2-diphenyl-1,2-dihydroquinoline-*N*-oxyl (DPQN) originally synthesized by Colonna et al. (Chart 1) [9].

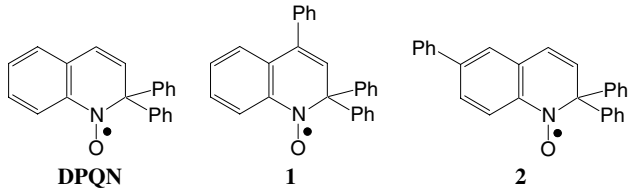
Because DPQN has a characteristic fused structure, the N–O spin center is involved in conjugation with the adjacent aryl group. DPQN is fairly stable due to the two bulky phenyl rings at the 2-position. The diphenyl substituents and the fused coplanar structure could synergistically contribute to the prevention of the direct close contact between the N–O moieties. In addition, the magnetically effective multipoint close contacts between the spin sites are also expected for the DPQN derivatives. Though the synthesis and crystal structure of DPQN have already been reported [9,10], its magnetic property in the solid state has not been reported. Previously, we reported the paramagnetic behavior for DPQN [11]. In the crystal, DPQN has no appropriate close contacts between the spin sites. In the present study, novel aromatic *N*-oxyl derivatives, 2,2,4-triphenyl-1,2-dihydroquinoline-*N*-oxyl (**1**), and its positional isomer, 2,2,6-triphenyl-1,2-dihydroquinoline-*N*-oxyl (**2**), were synthesized, and their crystal structures and magnetic properties were studied.

2. Results and discussion

2.1. Synthesis

The synthetic routes for **1** and **2** are described in Scheme. **1** was obtained via a 4-step synthesis. First, 2,4-diphenylquinoline **3** was derived from commercially available 2-aminobenzophenone according to the literature [12]. The oxidation of the nitrogen atom of the quinoline ring by *m*-chloroperbenzoic acid (*m*-CPBA) gave the *N*-oxide compound **4**. The subsequent reaction with phenylmagnesium bromide, followed by air oxidation in chloroform gave the dark red-colored solid of **1**, see Scheme 1.

Its positional isomer **2** was obtained via a 7-step synthesis. The quinoline skeleton was synthesized according to the reported methods [13,14]. The introduction of a phenyl group at the 6-position was performed via the nickel(0)-catalyzed cross-coupling reaction of **5** with phenylmagnesium bromide. The following procedure, similar to that of **1**, gave the dark red-colored solid of **2**. Interestingly, two types of solids (**2-α**, **2-β**) were obtained due to the polymorphism. They exhibited different melting points (**2-α**: 204–206 °C, **2-β**: 158–160 °C) and showed different vibration modes for the N–O sites (**2-α**: 1368 cm^{-1}, **2-β**: 1375 cm^{-1}).



DPQN **1** **2**

Chart 1.

In the ESR measurements in toluene solutions, both **1** and **2** exhibited a complex pattern due to the presence of many magnetically non-equivalent aromatic nuclei. A computer simulation of the spectra of **1** and **2** gave small a_N values of 1.01 and 0.97 mT, respectively. Generally, the dialkyl *N*-oxyl radicals exhibit hfccs of ca. 1.4–1.5 mT for the *N*-oxyl nitrogen, and these values indicate that the spin density is localized on the N–O group. The observed small a_N values for **1** and **2** confirmed the delocalization of the unpaired electron over the π-conjugation systems.

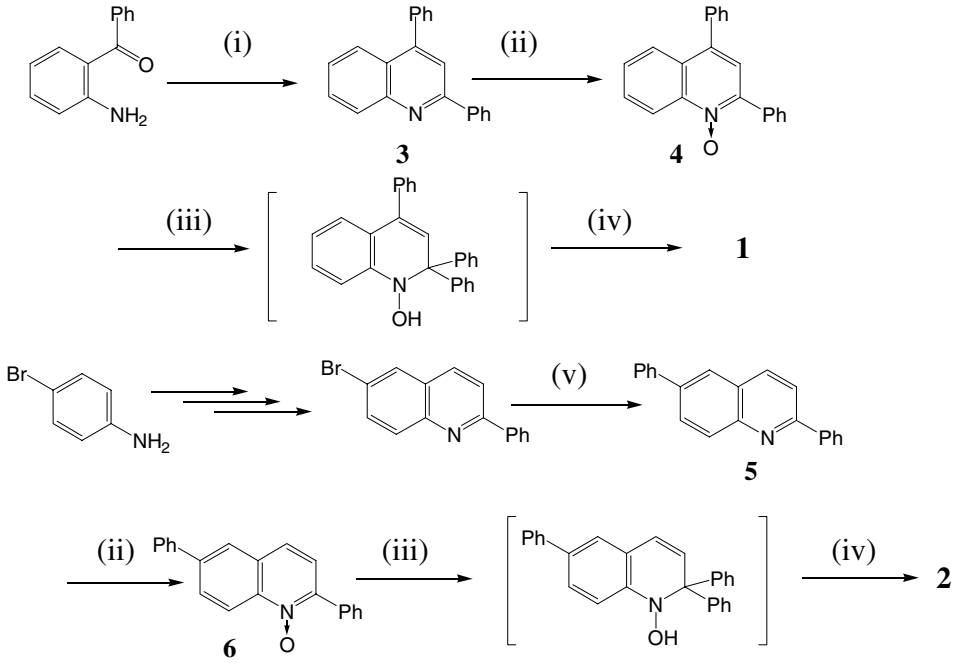
2.2. X-ray crystallographic analysis

The single crystal of **1** suitable for X-ray analysis was obtained from an ethanol solution by cooling. The single crystal of **2** was obtained by slow evaporation of the mixed solvent of dichloromethane/*n*-hexane = 1/1 and found to be **2-α**.[1] Their ORTEP drawings and the crystallographic parameters are summarized in Fig. 1 and Table 1, respectively. As seen in Fig. 1, the dihedral angles between the N–O group and the adjacent aromatic rings are very small due to the characteristic fused structure (**1**: 8.02°, **2-α**: 8.08°), which could increase the spin density over the aromatic rings [15,16]. The dihedral angles between the substituted phenyl ring and quinoline ring are 86.6° (4-position) and 32.4° (6-position) for **1** and **2-α**, respectively. In the case of **1**, a steric effect between the phenyl ring at 4-position and hydrogen atom at the 5-position would increase the dihedral angle between the phenyl ring and quinoline rings to 86.6°. In contrast, **2** has a reduced dihedral angle of 32.4° between the phenyl ring at the 6-position and the quinoline ring. In the crystals of **1** and **2**, close contacts between the N–O spin centers were not observed.

2.3. DFT calculation

In order to estimate the spatial distribution of SOMO and the spin density, we performed the molecular orbital calculations based on the density functional theory (DFT) using the coordinates obtained by X-ray analysis. The popular unrestricted B3LYP hybrid functional [17,18] with the standard split valence 6-31G(d) basis set was used for the computation using the GAUSSIAN 03 program package [19]. The calculated spin densities are

[1] Crystallographic data of **1** and **2-α** in CIF format are available at CCDC. Deposition numbers of **1** and **2-α** are 259384 and 259385, respectively.



Scheme 1. Reagents and conditions: (i) acetophenone, H_2SO_4; (ii) *m*-CPBA in $CHCl_3$; (iii) PhMgBr in THF; (iv) ox. in $CHCl_3$; (v) PhMgBr, Ni(dppp) in THF.

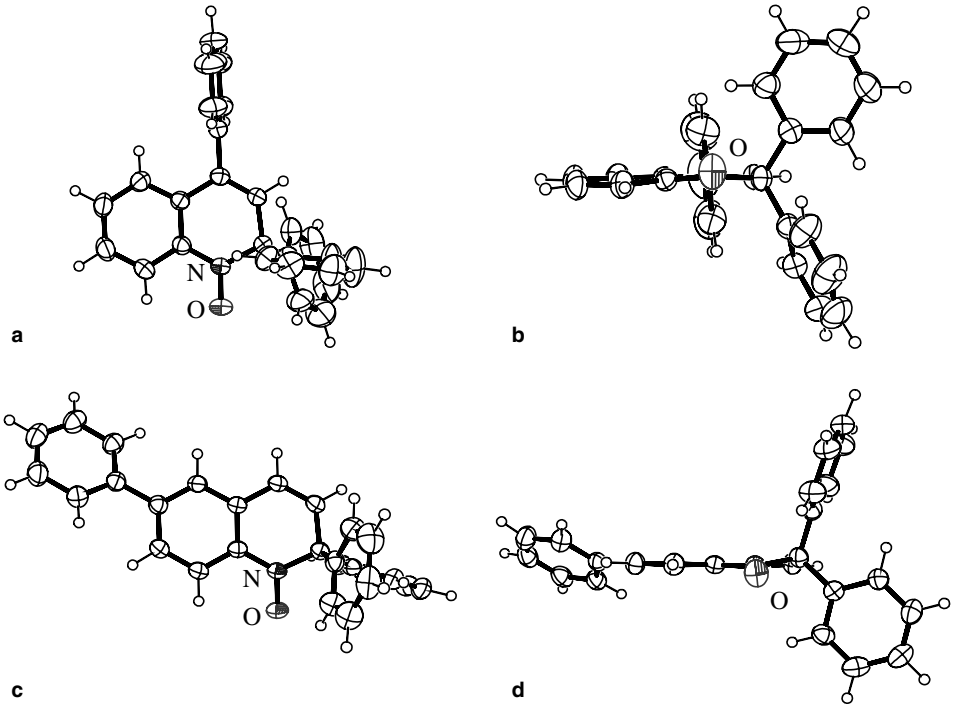


Fig. 1. ORTEP drawing of the molecules of **1** and **2**-α. (a, b) Top view and side view for **1**, respectively. (c, d) Top view and side view for **2**-α, respectively.

summarized in Table 2. The calculated SOMOs and spin density distributions for **1** and **2**-α are shown in Fig. 2. In contrast to the SOMOs of the alkyl *N*-oxyl radicals those of **1** and **2**-α are delocalized over the aromatic rings.

2.4. Solid-state magnetic measurements

Figs. 3 and 4 show the temperature dependence of $\chi_m T$ and $\chi_m{}^{-1}$ for **1** and **2**, respectively. As seen in

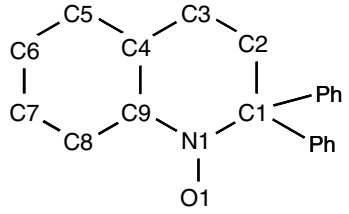
Table 1
Crystallographic parameters of **1** and **2-α**

	1	**2-α**
Crystal system	triclinic	orthorhombic
Formula	$C_{27}H_{20}NO$	$C_{27}H_{20}NO$
Space group	$P\bar{1}$	*Pbca*
a (Å)	10.620(2)	19.914(3)
b (Å)	11.416(1)	14.185(2)
c (Å)	8.886(1)	13.950(2)
α (°)	91.65(1)	90
β (°)	112.30(1)	90
γ (°)	90.51(1)	90
V (Å^3)	996.2(2)	3940.4(9)
Z	2	8
D (g cm^{-3})	1.248	1.262
R [$I > 2\sigma(I)$]	0.042	0.041
R_w (all data)	0.131	0.117
S	1.016	0.998

Fig. 3, the $\chi_m T$ value of **1** decreased below 50 K, exhibiting an intermolecular antiferromagnetic interaction. This behavior was analyzed using the Bleaney–Bowers equation for a dimer model (Eq. (1)) [20]. The best-fit parameters were a correction factor of $f = 0.86$ and a singlet–triplet energy gap of $2J = -4$ cm^{-1}. In the case of **2**, the obtained two phases exhibited different magnetic behaviors. The $\chi_m T$ value of **2-α** was virtually constant above 20 K (Fig. 4(a)), suggesting that **2-α** has a nearly isolated doublet state in the crystal. In contrast, the $\chi_m T$ value of **2-β** increased as the temperature decreased and reached a maximum around 2 K (Fig. 4(b)), indicating the existence of an intermolecular ferromagnetic interaction. The observed magnetic interaction of **2-β** was preliminary analyzed using a dimer model. The best-fit parameter was a singlet–triplet energy gap of $2J = +2.5$ cm^{-1}.

$$\chi_m = f \frac{N_A g^2 \beta^2}{k_B T[3 + \exp(-2J/k_B T)]}. \quad (1)$$

Table 2
Calculated spin density distribution of **1** and **2-α**[a]



	1	**2-α**
N1	0.338585	0.341582
O1	0.479721	0.483192
C1	−0.021546	−0.023167
C2	0.055771	0.018624
C3	−0.040535	−0.040442
C4	0.129841	0.116659
C5	−0.074570	−0.070289
C6	0.143765	0.121826
C7	−0.076439	−0.074005
C8	0.146322	0.134241
C9	−0.118594	−0.111342

[a] UB3LYP/6-31G(d).

2.5. Magneto-structural correlation

In the crystal of **2-α**, the nearest O···O distance is 7.33 Å and there is no effective contact for intermolecular magnetic interactions, supporting the observed isolated doublet state of **2-α**. The N–O sites of **1** are also separated and its nearest O···O distance is 6.50 Å. There seems to be almost no direct interaction between the N–O sites [21]. However, **1** has a short contact with the adjacent molecule through the H(8) atom (Fig. 5). The DFT calculation for **1** gave a relatively large negative spin density for the H(8) atom. Therefore, the observed antiferromagnetic interaction for **1** could be qualitatively interpreted by McConnell's theorem [7].

3. Conclusions

Two aromatic *N*-oxyl radicals bearing the quinoline skeleton, 2,2,4-triphenyl-1,2-dihydroquinoline-*N*-oxyl (**1**) and 2,2,6-triphenyl-1,2-dihydroquinoline-*N*-oxyl (**2**), were newly synthesized. They were isolated as solids, indicating their high stability. The ESR measurements and DFT calculations for **1** and **2** revealed the delocalization of the unpaired electron in the π-conjugation system. Based on the SQUID measurement, **1** exhibited a weak antiferromagnetic interaction in its crystal. The negatively spin-polarized hydrogen atoms probably play a role in the magnetic interaction. In the case of **2**, two types of solids were obtained due to polymorphism. The α-phase of **2** showed a paramagnetic behavior; however, the β-phase of **2** exhibited a ferromagnetic interaction. The observed ferromagnetic interaction was analyzed by a dimer model, and a singlet–triplet gap was estimated to be $2J = +2.5$ cm^{-1}. Further investigations on the magneto-structural correlation of **2-β** are now in progress.

4. Experimental

4.1. Magnetic measurements

The magnetic properties of the microcrystalline sample radicals were measured by a Quantum Design MPMS-5 SQUID susceptometer at the field strength

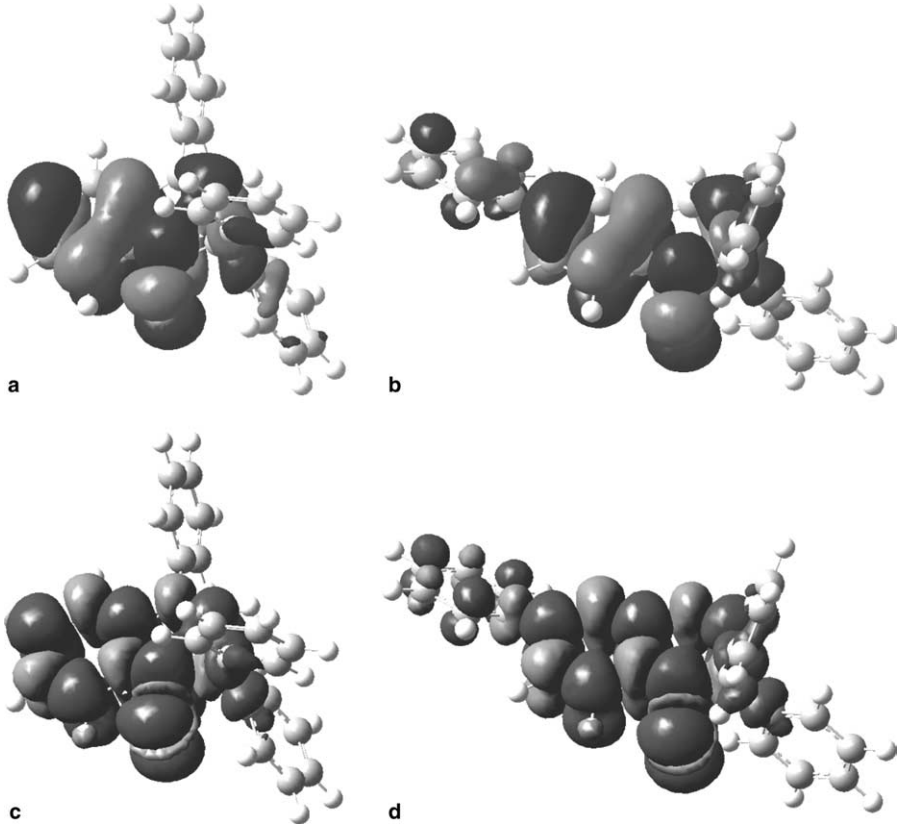


Fig. 2. SOMOs (a, b) and spin density distribution (c, d) for **1** and **2**-α, respectively. The positive spin densities are shown in dark gray and the negative ones are in pale gray.

of 0.5 T. In addition to the correction of the diamagnetic contribution from the sample holder, the diamagnetic contribution from the sample was estimated using the Pacault method (2.41×10^{-4} emu/mol for **1** and **2**) [22].

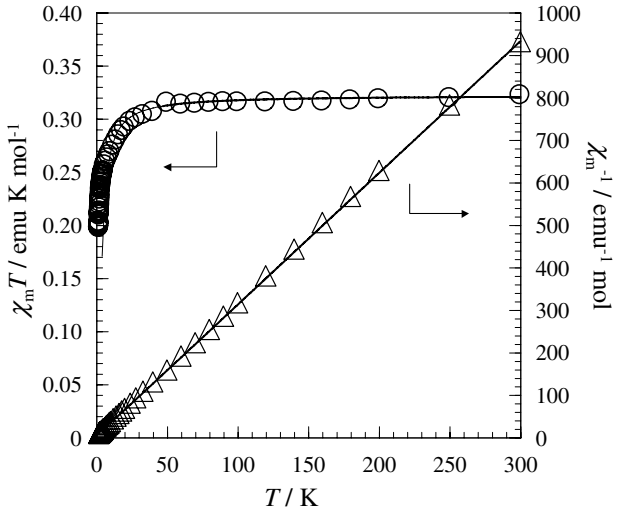


Fig. 3. Temperature dependence of $\chi_m T$ and $\chi_m{}^{-1}$ for **1**. Solid lines correspond to calculated curves ($2J = -4$ cm^{-1}).

4.2. X-ray diffraction analysis

The single crystals were mounted on a glass fiber and measured using a Rigaku four-circle AFC-7R diffractometer with graphite monochromated Mo Kα radiation ($\lambda = 0.71073$ Å). The structure was solved by a direct method [23] and refined by SHELXL-97 [24] with the program system teXsan [25].

4.3. Synthesis

The infrared spectra were recorded using an FT/IR-4000 spectrometer (Jasco Co. Japan). The ^{1}H NMR spectra were measured using a JNM-LA 300 spectrometer (JEOL Co., Japan). Chemical shifts were expressed in parts per million downfield from Me_4Si as the internal standard. Elemental analyses were performed at the Central Laboratory of the Faculty of Science and Technology, Keio University. Tetrahydrofuran was refluxed over and distilled from $LiAlH_4$. All other commercially available reagents were used without further purification, unless otherwise stated. 6-Bromoquinoline was synthesized according to the literature [13,14].

4.3.1. 2,4-Diphenylquinoline (*3*)

In 300 ml round-bottom flask, 2-aminobenzophenone (5.0 g, 25 mmol) and acetophenone (3.0 ml, 25 mmol)

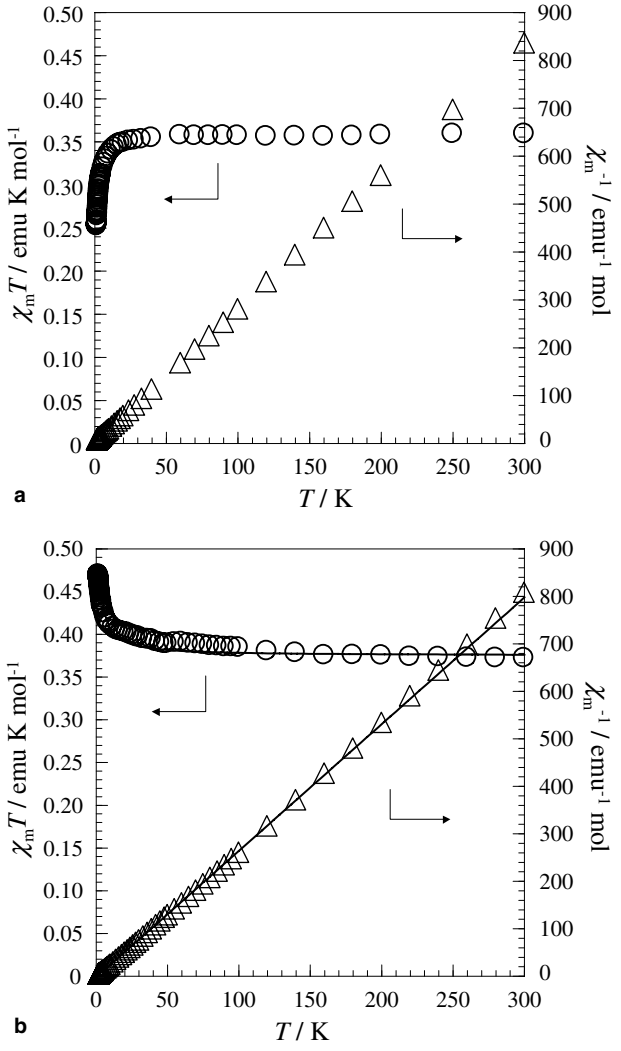


Fig. 4. Temperature dependence of $\chi_m T$ and χ_m^{-1} for **2-α** (a) and **2-β** (b). Solid lines correspond to calculated curves ($2J = +2.5$ cm^{-1}).

were dissolved in acetic acid (100 ml). Sulfuric acid was added to this solution (0.25 ml). The flask contents were refluxed for 18 h. After cooling to room temperature, the solution was neutralized with aqueous ammonia. The resulting solution was extracted with chloroform and the organic layer was dried over $NaHCO_3$ and evaporated to dryness. This crude residue was purified by column chromatography on silica gel eluting with chloroform. The yellow band was collected and evaporated to dryness, giving a yellow solid. Yield: 3.1 g, 44%. M.p.: 115–118 °C. ^{1}H NMR (300 MHz, acetone-d_6): δ 8.41–8.37 (2H, m), 8.20 (1H, d), 8.02 (1H, s), 7.92 (1H, d), 7.80 (1H, t), 7.68–7.48 (9H, m). FAB-MS (3-NBA), Calc. for $C_{21}H_{15}N$: 281.1, Found: 281 $[M]^+$. *Anal.* Calc. for $C_{21}H_{15}N$: C, 89.65; H, 5.37; N, 4.98. Found: C, 89.65; H, 5.26; N, 4.93%.

*4.3.2. 2,4-Diphenylquinoline-N-oxide (**4**)*

A chloroform solution of 1.5 g of *m*-CPBA was gradually added to an ice-cooled, stirred solution of **3** (1.4 g, 5.3 mmol) in chloroform (100 ml). The stirring was continued overnight at room temperature and then basified with a KOH aqueous solution. The organic layer was washed several times with water and dried over Na_2SO_4. After evaporation of the solvent, the residue was purified by column chromatography on silica gel eluting with EtOAc/*n*-hexane = 1/1. Subsequent removal of the solvent gave the yellow solid of **4**. Yield: 1.3 g, 83%. M.p.: 177–180 °C. FAB-MS (3-NBA, *m*/*z*). Calc. for $C_{21}H_{15}NO$: 297.1, Found: 298 $[M + H]^+$. ^{1}H NMR (300 MHz, acetone-d_6): δ 8.88 (1H, d), 8.19–8.15 (2H, m), 7.99 (1H, d), 7.88 (1H, t), 7.75–7.47 (10H, m). IR (KBr pellet): 1216 cm^{-1} (N–O). *Anal.* Calc. for $C_{21}H_{15}NO$: C, 84.82; H, 5.08; N, 4.71. Found: C, 84.40; H, 5.00; N, 4.60%.

*4.3.3. 2,2,4-Triphenyl-1,2-dihydorquinoline-N-oxyl (**1**)*

To a solution of **4** (2.6 g, 8.7 mmol) in 100 ml of dry tetrahydrofuran was added the phenylmagnesium bromide THF solution (17.5 ml, 17.5 mmol) with stirring in a nitrogen atmosphere. After 1 h, the mixture was treated with NH_4Cl aq. and extracted with $CHCl_3$. The organic layer was washed with water and dried over Na_2SO_4. After removal of the solvent, the residue was purified by column chromatography on silica gel eluting with ethyl acetate/*n*-hexane = 1/2. Subsequent recrystallization from ethanol gave the microcrystalline red solid of **1**. Yield: 500 mg, 15%. M.p.: 156–159 °C. IR (KBr pellet): 1382 cm^{-1} (N–O). *Anal.* Calc. for $C_{27}H_{20}NO$:

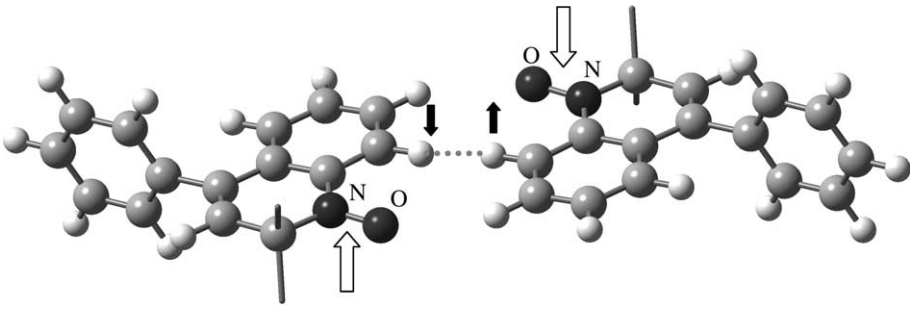


Fig. 5. Qualitative representation of plausible exchange pathway for the dimer of **1**. Phenyl rings at the 2-position are omitted for clarity.

C, 86.60; H, 5.38; N, 3.74. Found: C, 86.38; H, 5.13; N, 3.68%.

4.3.4. 2,6-Diphenylquinoline (**5**)

In a three-necked flask equipped with a reflux condenser, 6-bromo-2-phenylquinoline (1.0 g, 3.5 mmol) and [1,3-bis(diphenylphosphino)propane]nickel(II) chloride (7.9 mg, 0.015 mmol) were dissolved in dry tetrahydrofuran under a nitrogen atmosphere. The phenylmagnesium bromide THF solution (4.4 ml, 4.4 mmol) was then gradually added to the solution. The resulting solution was stirred for 20 min at room temperature and refluxed for 20 h. After cooling, the solution was neutralized to pH 7 with diluted HCl aq. and extracted with diethyl ether. The organic layer was washed with $NaHCO_3$ aq. and then with water several times. The organic layer was separated and dried over Na_2SO_4 and evaporated to dryness. This crude product was purified by column chromatography on silica gel eluting with chloroform/*n*-hexane = 1/3. Subsequent removal of the solvent gave the white solid of **5**. Yield: 0.66 g, 65%. M.p: 206–208 °C. ^{1}H NMR (300 MHz, $CDCl_3$), δ 8.23–8.29 (m, 2H), 8.19 (dd, 2H), 7.99–8.02 (m, 2H), 7.91 (d, 1H), 7.75 (dd, 2H), 7.38–7.57 (m, 6H). *Anal*. Calc. for $C_{21}H_{15}N$: C, 89.65; H, 5.37; N, 4.98. Found: C, 89.21; H, 5.37; N, 4.89%.

4.3.5. 2,6-Diphenylquinoline-N-oxide (**6**)

This compound was synthesized in the same manner as **4** using 140 mg of **5** (0.5 mmol) and 180 mg of *m*-CPBA in a chloroform solution. The desired compound was purified by column chromatography on silica gel eluting with EtOAc/chloroform = 3/1. Subsequent removal of the solvent gave the pale yellow solid. Yield: 140 mg, 96%. M.p.: 242–244 °C. ^{1}H NMR (300 MHz, $CDCl_3$), δ 8.90–8.94 (m, 1H), 7.99–8.06 (m, 3H), 7.82 (d, 1H), 7.74 (d, 2H), 7.42–7.57 (m, 8H). IR (KBr pellet): 1348 cm^{-1} (N–O). *Anal*. Calc. for $C_{21}H_{15}NO$: C, 83.56; H, 5.18; N, 4.64; O, 6.63. Found: C, 83.79; H, 4.66; N, 4.70%.

4.3.6. 2,2,6-Triphenyl-1,2-dihydroquinoline-N-oxyl (**2**)

This compound was synthesized under the condition similar to **1** using 140 mg of **6** (0.47 mmol) and 1 ml of phenylmagnesium bromide THF solution (1 mmol). The obtained crude product was purified by column chromatography on silica gel eluting with chloroform/*n*-hexane = 2/1 followed by recrystallization to give the dark red solid of **2**. Yield: 71% (**2-α**), 53% (**2-β**). M.p., **2-α**: 204–206 °C, **2-β**: 158–160 °C. IR (KBr pellet), **2-α**: 1368 cm^{-1} (N–O), **2-β**: 1375 cm^{-1} (N–O). *Anal*. Calc. for $C_{27}H_{20}NO$: C, 86.60; H, 5.38; N, 3.74. Found for **2-α**: C, 86.17; H, 5.14; N, 3.60%. Found for **2-β**: C, 86.39, H, 5.48; N, 3.53%.

Acknowledgments

This work was supported in part by a Grant-in-Aid for Scientific Research (B) 15310094, and Exploratory Research 116651070. Financial support from the Keio Gijuku Academic Development Funds is also acknowledged. M.Y. gratefully acknowledges the grant-in-aid for the 21st Century COE program "KEIO Life Conjugate Chemistry" from the Ministry of Education, Culture, Sports, Science, and Technology, Japan.

References

[1] J. Veciana, C. Rovira, D.B. Amabilino, Supramolecular Engineering of Synthetic Metallic Materials, Kluwer Academic Publishers, Dordrecht, 1998.
[2] P.M. Lahti, Magnetic Properties of Organic Materials, Marcel Dekker, New York, 1999.
[3] N. Yoshioka, M. Irisawa, Y. Mochizuki, T. Kato, H. Inoue, S. Ohba, Chem. Lett. (1997) 251.
[4] H. Nagashima, H. Inoue, N. Yoshioka, J. Phys. Chem. B 108 (2004) 6144.
[5] H. Nagashima, N. Hashimoto, H. Inoue, N. Yoshioka, New J. Chem. 27 (2003) 805.
[6] H. Nagashima, S. Fujita, H. Inoue, N. Yoshioka, Cryst. Growth Des. 4 (2004) 19.
[7] H.M. McConnell, J. Chem. Phys. 39 (1963) 1910.
[8] V. Ovcharenko, Synthetic Chemistry of Stable Nitroxide Radical, CRC Press, Boca Raton, FL, 2000.
[9] C. Berti, M. Colonna, L. Greti, L. Marchetti, Tetrahedron 32 (1976) 2147.
[10] R. Benassi, F. Taddei, L. Greci, G.D. Andreetti, G. Bocelli, P. Sgarabotto, J. Chem. Soc., Perkin II (1980) 786.
[11] M. Yao, H. Inoue, N. Yoshioka, Chem. Phys. Lett. 402 (2005) 11.
[12] Y. Imai, T. Kato, M. Kurihara, J.K. Stille, J. Poly. Sci., Poly. Chem. Ed. 13 (1975) 2233.
[13] J.A. Castellano, J.E. Goldmacher, L.A. Barton, J.S. Kane, J. Org. Chem. 33 (1968) 3501.
[14] A. Penttila, H.M. Fales, J. Am. Chem. Soc. 88 (1966) 2328.
[15] U. Schatzschneider, E. Rentschler, J. Mol. Struct. (Theochem.) 638 (2003) 163.
[16] H. Oka, T. Tamura, Y. Miura, Y. Teki, J. Mater. Chem. 9 (1999) 1227.
[17] A.D. Becke, Phys. Rev. A 38 (1988) 3098.
[18] C. Lee, W. Yang, R.G. Parr, Phys. Rev. B 37 (1988) 785.
[19] M.J. Frisch et al., GAUSSIAN 03, Revision B.04, Gaussian, Inc., Pittsburgh, PA, 2003.
[20] B. Bleaney, K.D. Bowers, Proc. R. Soc. London, Ser. A 214 (1952) 451.
[21] S. Yamanaka, T. Kawakami, H. Nagao, K. Yamaguchi, Chem. Phys. Lett. 231 (1994) 25.
[22] K.-H. Hellwege, A.M. Hellwege, Landolt-Börnstein New Series, II/16, Springer, Berlin, 1984, p. 4.
[23] A. Altomare, M.C. Burla, M. Camalli, M. Cascarano, C. Giacovazzo, A. Guagliardi, G. Polidori, J. Appl. Crystallogr. 27 (1994) 435.
[24] G.M. Sheldrich, SHELXL-97: Program for the Refinement of Crystal Structure, University of Göttingen, Göttingen, Germany, 1997.
[25] teXsan Single-Crystal Structure Analysis Software, Version 1.11, MSC, The Woodlands, TX (Rigaku, Tokyo, Japan).

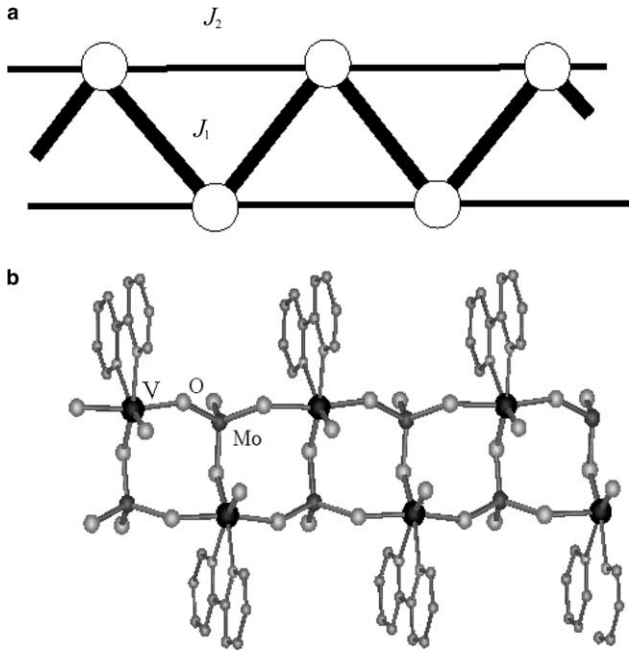


Fig. 1. (a) Schematic diagram for the zigzag spin chain. Open circles represent $S = 1/2$. (b) Crystal structure of [VO(μ_3-MoO_4)(2,2′-bpy)]. H atoms are not shown for clarity.

description in [7]. V_2O_5, V_2O_3, $Na_2MoO_4 \cdot 2H_2O$, MoO_3, 2,2′-bipyridine in the molar ratio of 1:1:2:2:4 in 8 ml water was heated in teflon-lined autoclave for 48 h at 473 K. V_2O_3 was made from V_2O_5, reduced under H_2 gas flow at 1173 K. All measurements were carried out on powder samples. Quality of the specimen was checked by powder-X ray diffraction method. The magnetic susceptibility $\chi(T)$ was measured using the Quantum Design PPMS (physical properties measurements system) in the temperature range between 2.0 and 280 K in an applied field of 0.1 T. The high field magnetization curve was measured at 4.2 K up to about 35 T using an induction method in a pulsed magnetic field.

3. Results

Filled circles in Fig. 2 show the temperature dependence of $\chi(T)$. Very small and broad maximum is observed at around 230 K. $\chi(T)$ increased as decreasing temperature. In the temperature range between 280 and 30 K, $\chi(T)$ approximately followed Curie–Weiss law with Weiss temperature of about −40 K, which indicates that dominant interaction is antiferromagnetic.

Thick line in Fig. 3 shows the magnetization curve M of [VO(μ_3-MoO_4)(2,2′-bpy)] measured at 4.2 K. M increases almost linearly as increasing the magnetic field. No spin gap is observed in the magnetization process, suggesting that the ground state is in the gapless phase with $j < j_c$ An expected saturation magnetization for

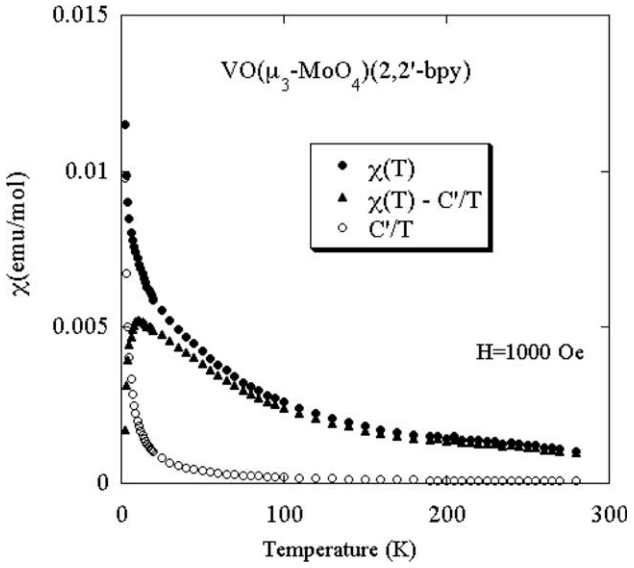


Fig. 2. Temperature dependence of $\chi(T)$ for [VO(μ_3-MoO_4)(2,2′-bpy)] (filled circles). Open circles are Curie contribution C'/T from magnetic impurities with Curie constant C'. Closed triangles are $\chi(T) - C'/T$.

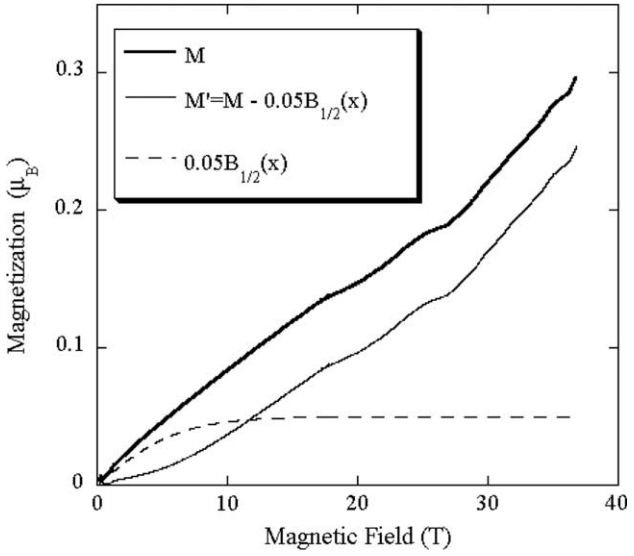


Fig. 3. High field magnetization M of [VO(μ_3-MoO_4)(2,2′-bpy)] at 4.2 K (thick line). Dotted line is Brillouin function for $S = 1/2$ with 5% spin concentration where $x = \mu_B H/k_B T$. Thin line is $M' = M - 0.05B_{1/2}(x)$.

V^{4+} ($S = 1/2$) is about $g\mu_B S \approx 1\ \mu_B$, where μ_B is Bohr mageneton and g is Lande's g-factor. M does not saturate even at 35 T, which suggests that large antiferromagnetic interactions between V^{4+} ions are present in this material.

4. Discussion

It is well known that $\chi(T)$ of 1D antiferromagnet has broad peak at the temperature corresponding to the

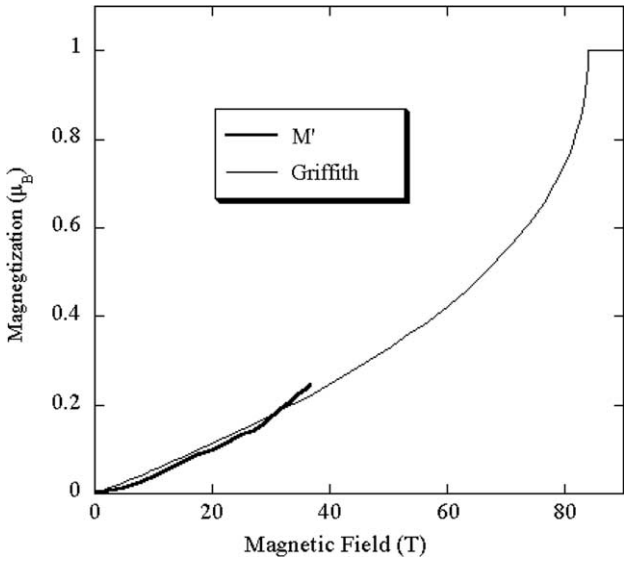


Fig. 4. Comparison of the bulk part magnetization M' of [VO(μ_3-MoO_4)(2,2′-bpy)] with the theoretical curve for $S = 1/2$ 1D HAF calculated at $T = 0$ with the saturation field 84 T.

magnetic exchange interaction, as a reflection of a short range magnetic ordering. Our $\chi(T)$ of [VO(μ_3-MoO_4)-(2,2′-bpy)] does not show such a peak, although the crystal structure is 1D-like and the presence of magnetic interaction is suggested by the magnetization curve. A Curie contribution from small amount of magnetic impurities may mask the low temperature part of $\chi(T)$ to prevent the observation of the broad peak. It is rather difficult to estimate a concentration n of the magnetic impurities from $\chi(T)$ data. Instead, we try to determine n using the magnetization data. The magnetic impurities manifest themselves as a Brillouin function curve $B_s(x)$ where $x = \mu_B H/k_B T$, S is magnitude of spin, H is magnetic field and k_B is Boltzmann constant. Since $B_s(\mu_B H/k_B T)$ saturates easily in higher field, it is sometimes not so difficult to separate the impurities part from bulk part of the magnetization curve. The low field (<5 T) part of the magnetization curve of [VO(μ_3-MoO_4)(2,2′-bpy)] is well fitted by 0.05 $B_{1/2}(x)$ as shown in dotted curve in Fig. 3. The value of n is thus determined to be 0.05 if magnetic impurities have $S = 1/2$. M' in Fig. 3 indicates the bulk part of M after subtraction of the impurity part 0.05 $B_{1/2}(x)$. Let us analyze M' to estimate a saturation field H_s. The magnetization curve for the zigzag chain has been calculated [8]. According to [8], the magnetization curve for the zigzag spin chain is almost independent on the interaction ratio j if $j < j_c$ as far as the magnetic field is lower than about 3 quarters of H_s. Since our M' is far from saturation, it is safe to compare M' with a theoretical curve for 1D HAF without nnn interaction, which was calculated by Griffith [9]. Fig. 4 is the fitting result of M' with the theoretical curve at $T = 0$ using $H_s = 84$ T. A relation between H_s and J_1 is given by an expression $H_s = 2J_1 k_B/g\mu_B$ for $j < j_c$ [10], with which we can estimate a value of J_1/k_B to be about 56 K assuming $g = 2$.

Next, we would like to discuss $\chi(T)$ data. The concentration n of the impurities have estimated to be 0.05 from the magnetization. The Curie constant C' of the magnetic impurities is given as $C' = ng^2\mu_B^2 S(S+1)/3k_B = 0.019$ assuming $S = 1/2$ and $g = 2$.

Filled triangles and open circles in Fig. 2 show a bulk part of the magnetic susceptibility ($\chi_{bulk}(T) = \chi(T) - C'/T$) and C'/T, respectively. At around 11 K, there appears a maximum in $\chi_{bulk}(T)$, which resembles the broad peak at T_{max} often observed in 1D HAF. In case of the 1D HAF without J_2, $k_B T_{max}/J_1 \approx 0.641$ [11]. For [VO(μ_3-MoO_4)(2,2′-bpy)], the ratio $k_B T_{max}/J_1$ between $T_{max} = 11$ K and $J_1/k_B = 56$ K is about $0.2 < 0.641$. We have calculated the temperature dependence of susceptibility of the zigzag spin model for several values of j using the exact diagonalization method for a finite spin chain with N spins up to $N = 10$ [3]. This calculation shows that T_{max} decreases as increasing j, or increasing the spin frustration effect. The observed result that $k_B T_{max}/J_1$ is smaller than the expected value for the 1D HAF without J_2 thus indicates there are non-zero J_2 in [VO(μ_3-MoO_4)(2,2′-bpy)]. In our tentative calculation, N was so small that quantitative comparison between the experimental result and the calculation is difficult.

In summary, $\chi(T)$ and high field magnetization up to 35 T on the model compound for $S = 1/2$ zigzag antiferromagnetic system, [VO(μ_3-MoO_4)(2,2′-bpy)] were measured and reported. No spin gap was observed in the magnetization curve measured at 4.2 K. The magnetization curve was compared with theoretical curve to estimate the nearest-neighbor exchange interaction J_1 to be 56 K. The intrinsic magnetic susceptibility had maximum at around $T_{max} = 11$ K. A ratio T_{max}/J_1 was found to be much less than that expected for one-dimensional antiferromagnet without frustrating next-nearest-neighbor interaction. This result is discussed in terms of the spin frustration.

Acknowledgment

This work is supported by Grant-in-Aid for Scientific Research on Priority Area (B) (No. 13130204; ''Field-Induced New Quantum Phenomena in Magnetic System'') from the Ministry of Education, Culture, Sports, Science and Technology of Japan.

References

[1] F.D.M. Haldane, Phys. Rev. B 25 (1982) 4925.
[2] K. Okamoto, K. Nomura, Phys. Lett. A 169 (1992) 433.

[3] H. Kikuchi, H. Nagasawa, Y. Ajiro, T. Asano, T. Goto, Physica B 284–288 (2000) 1631.
[4] M. Hagiwara, Y. Narumi, K. Kindo, N. Maeshima, K. Okunishi, T. Sakai, M. Takahashi, Physica B 294–295 (2001) 83.
[5] Y. Hosokoshi, K. Katoh, K. Inoue, T. Goto, J. Phys. Soc. Jpn. 68 (1999) 2910.
[6] A.A. Belik, M. Azuma, M. Takano, Inorg. Chem. 42 (2003) 8572.
[7] M.I. Khan, S. Giri, S. Ayesh, R.J. Doedens, Inorg. Chem. Commun. 7 (2002) 721.
[8] K. Okunishi, Y. Hieida, Y. Akutsu, Phys. Rev. B 60 (1999) R6953.
[9] R.B. Griffith, Phys. Rev. 133 (1964) A768.
[10] T. Tonegawa, I. Harada, Physica B155 (1989) 379.
[11] J.C. Bonner, M.E. Fisher, Phys. Rev. 135 (1964) A640.

percolation model. Systematic studies on macroscopic effects of the disordered magnetic structures (fragmentation of magnetic domain) on magnetic and magneto-optical properties will give insight into the control of these physical properties. We report magnetic properties and Faraday ellipticity spectra of the trimetallic solid solutions, $\{[Ni(1,1\text{-dmen})_2]_2[Fe_{(1-x)}Co_x(CN)_6]\}tfs \cdot nH_2O$ ($x = 0.0$, 0.12, 0.23, 0.35, 0.47, 0.54, 0.57, 0.64, 0.72, 0.81, 1.0; 1,1-dmen = 1,1-dimethylethylenediamine, tfs^- = trifluoromethanesulfonate ion) which have a two-dimensional grid structure.

2. Experimental

2.1. Synthesis

All reagents were purchased and used without further purification. Trimetallic solid solutions, $\{[Ni(1,1\text{-dmen})_2]_2[Fe_{(1-x)}Co_x(CN)_6]\}tfs \cdot nH_2O$ ($x = 0.0$, 0.12, 0.23, 0.35, 0.47, 0.54, 0.57, 0.64, 0.72, 0.81, 1.0), were prepared as plate-like crystals by the reaction of mixture of $K_3[Fe(CN)_6]$ and $K_3[Co(CN)_6]$ in each mixing ratio (a total of 0.5 mmol), $[Ni(1,1\text{-dmen})_3]Cl_2$ (1 mmol) and small excess of Natfs (4 mmol) in water [6]. Color of the crystals changes from dark brown to purple with increasing x value. All compounds were efflorescent. Elemental analyses of carbon, hydrogen, and nitrogen were obtained at the Service Center for Elemental Analysis at Kyushu University. The ratios of Fe:Co (x) were determined by Rigaku ZSX-100s X-ray florescence spectrometer.

2.2. X-ray crystallography

X-ray diffraction data were collected at −30 °C on Rigaku Mercury CCD diffractmeter with graphite-monochromated Mo Kα radiation ($\lambda = 0.71070$ Å). Because of the efflorescent nature, single crystals were sealed in a glass capillary. The maximum 2θ value is 55.0°. A total of 1240 oscillation images were collected on five sweep setting. Crystallographic data for compounds ($x = 0.0$ and 1.0) have been deposited with the Cambridge Crystallographic Data Centre (CCDC-189360 and CCDC-189361).

2.3. Magnetic susceptibility measurements

DC and AC magnetic susceptibility data were collected by using a Quantum Design MPMS-5XL SQUID magnetometer in the temperatures range 2–300 K (under applied field of 500 G). Data were corrected for the magnetization of the sample holder and capsule used. Diamagnetic corrections for the constituting atoms were made using Pascal's constants.

2.4. Faraday spectrum

The Faraday spectra were measured on a JASCO J-820 circular dichroism spectrometer using KBr disks in the range of 200–800 nm under 200 G. KBr disks containing ca. 1% of sample were prepared by applying a pressure of 8000 kg/cm^2.

3. Results and discussion

3.1. IR spectrum

IR spectrum (on KBr disk) of FeNi assembly ($x = 0.0$) shows two ν(C≡N) bands at 2144 and 2113 cm^{-1}. The IR band at 2144 cm^{-1} is attributed to the bridging cyanide groups. Also, CoNi assembly ($x = 1.0$) shows two ν(C≡N) bands at 2157 and 2126 cm^{-1}. The other compounds with $x = 0.12$–0.81 show several ν(C≡N) bands whose intensities correspond to x value.

3.2. Crystal structures

X-ray crystallographic results revealed that all compounds form same structure in the same space group ($P2_1/n$). The asymmetric unit consists of one $[M(CN)_6]^{3-}$, one tfs^-, one $[Ni(1,1\text{-dmen})_2]^{2+}$ (Ni3), two $[Ni(1,1\text{-dmen})_2]^{2+}$ moieties (Ni1 and Ni2) and several water molecules. In these solutions, $[Fe(CN)_6]^{3-}$ and $[Co(CN)_6]^{3-}$ units were not distinguished independently and were treated as average unit, $[M(CN)_6]^{3-}$. The $[M(CN)_6]^{3-}$ ion coordinates to four adjacent $[Ni(1,1\text{-dmen})_2]^{2+}$ units with its four cyano nitrogens in a plane. In the lattice, they form a two-dimensional grid structure extended by M–CN–Ni linkages (Fig. 1). Each tfs^- ion locates at the center of the square cavity in the grid and the oxygen atoms of sulfonyl group form hydrogen bonds with amino protons of 1,1-dmen. The lattice water molecules locate between the layers. Average M–CN–Ni distances, d, are listed in Table 1. The d values slightly decrease with increase of x value, whereas, the intersheet distances do not change almostly.

These crystallographic results suggest that these crystals are not mixture of FeNi and CoNi assemblies and $[Fe(CN)_6]^{3-}$ and $[Co(CN)_6]^{3-}$ units statistically disperse in the two-dimensional grid structure.

3.3. Magnetic properties

Magnetic susceptibility measurements were performed in the temperature range of 2–300 K.

χ_M versus T plots of compounds with $x < 0.64$ show an abrupt increase below 10 K, suggesting a ferromagnetic ordering over the lattice (Fig. 2). The saturation magneti-

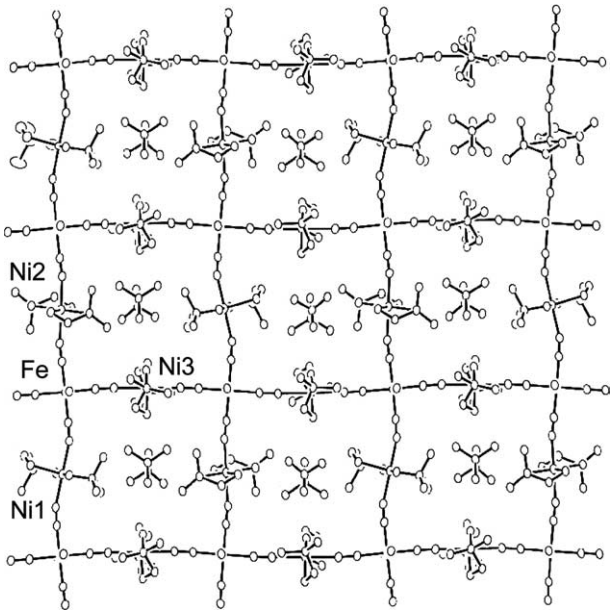


Fig. 1. Two-dimensional grid structure of FeNi assembly ($x = 0.0$).

Table 1
Average M–CN–Ni distance d, and T_c of solid solutions

x	d (Å)	T_c (K)
0.00	10.359	8.9
0.12	10.344	8.3
0.23	10.323	7.0
0.35	10.300	5.4
0.47	10.296	3.6
0.54	10.292	3.0
0.57	10.285	2.4
0.64	10.288	
0.72	10.276	
0.81	10.272	
1.00	10.266	

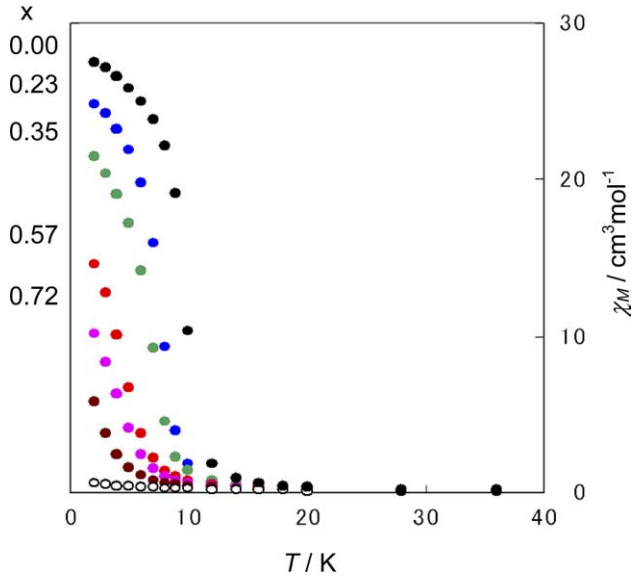


Fig. 2. Temperature dependences of magnetic susceptibility χ_M of solid solutions ($x = 0.0$–1.0).

zation value for $x = 0.0$ is 4.96 $N\beta$ at 5 T, which agrees with the expected value for ferromagnetically coupled one low-spin Fe^{III} ($S = 1/2$) and two Ni^{II} ($S = 1$) ions. The ferromagnetic interaction is explained by strict orthogonality of the magnetic orbitals of the adjacent Fe^{III} and Ni^{II} ions. The saturation value decreases down to 4.02 $N\beta$ with increasing x value. The phase transition temperature (T_c) was confirmed by weak field magnetic studies and AC susceptibility measurements. Compounds with $x > 0.64$ show no magnetic phase transition above 2 K. The phase transition temperature, T_c, decreases and the shapes of χ' versus T and χ'' versus T plots sharpens with increase of x value (Fig. 3).

These results also suggest the statistical dispersion of $[Co(CN)_6]^{3-}$ into the 2-D grid sheet and fragmentation of $Fe^{III}Ni^{II}$ magnetic domain structure by diamagnetic Co^{III} ions. Critical point for vanishing the spontaneous magnetization was estimated at $x = 0.76$ by linear extrapolation. On the other hand, theoretical critical value for 2-D bond percolation model is 0.5. The increase of critical value can be explained that the paramagnetic Ni(II) ions always exist in the 2-D grid independent of x values. Assembly with $x = 0.64$ shows a frequency

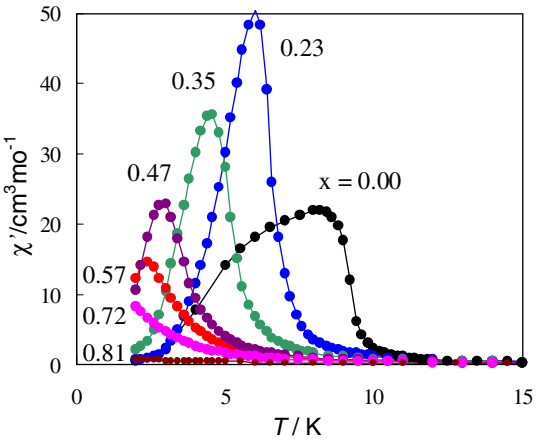


Fig. 3. χ' vs. T plots of solid solutions ($x = 0.0$–1.0).

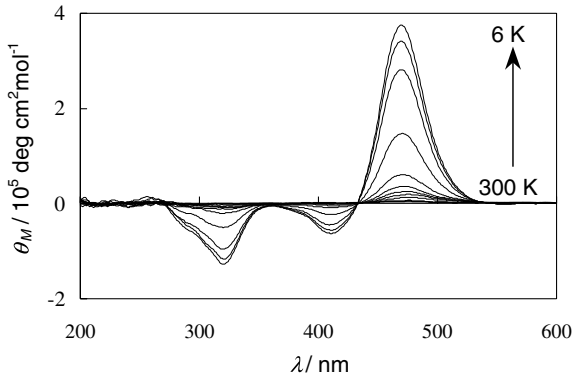


Fig. 4. Temperature dependence of Faraday ellipticity spectra of FeNi assembly ($x = 0.0$) under the external magnetic field of 200 G.

dependence in ac susceptibility. This behavior can be regarded as magnetically disordered state, spin-glass, originated from reduction of magnetic cluster size, though its magnetic relaxation behavior was not completely simulated by theoretical equation.

3.4. Magneto-optical properties

Temperature dependence of MCD spectra for compound with $x = 0.0$ under 200 G is given in Fig. 4. With decreasing temperature the molar Faraday ellipticity θ_M values around 470, 407 and 318 nm are enhanced. Especially, the θ_M value at 470 nm increased more than 100 times after magnetic phase transition. These results indicate that the MCD around 470 nm is associated with the ligand-to-metal charge transfer (LMCT: $^2T_{1u}$ (σ t_{1u}) $\rightarrow$ $^2T_{2g}$ (Fe t_{2g})) band of Fe–CN [18]. The θ_M versus T plots show a sharp increase at 9 K ($\approx T_c$), and this behavior is in harmony with χ_M versus T plots. The large enhancement in the Faraday ellipticity evidently arises from the ferromagnetic ordering over the lattice. The d-d transition bands of Fe(III) and Ni(II) show negligible contribution for θ_M, because the intensity of Laporte-forbidden d-d transition is quite weaker than that of Laporte-allowed LMCT band.

Faraday ellipticity remarkably decrease with the increase of x value (Fig. 5). The reasons of the decrease are explained as follows:

1. Decrease of magnetization value due to the increase of diamagnetic ratio and the fragmentation of magnetic domain.
2. Decrease of LMCT band of Fe–CN having large absorption coefficient.

The maximum value of Faraday ellipticity of CoNi assembly ($x = 1.0$) is less than 1/10 000 of FeNi assembly ($x = 0.0$), because it is a paramagnet and its LMCT is very weak.

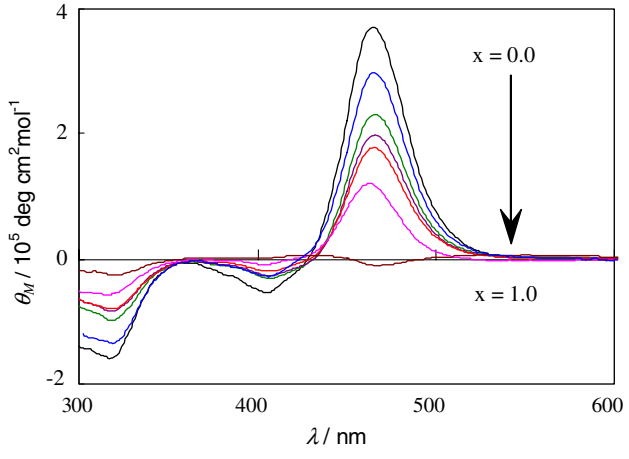


Fig. 5. Faraday ellipticity spectra of solid solution ($x = 0.0$–1.0).

4. Conclusion

Eleven $Fe_{(1-x)}^{III}Co_x^{III}Ni^{II}$ solid solutions, $\{[Ni(1,1\text{-dmen})_2]_2[Fe_{(1-x)}Co_x(CN)_6]\}tfs \cdot nH_2O$, have been prepared as crystals and evaluated their magnetic and magneto-optical properties systematically. They formed same two-dimensional grid sheet structure with statistical dispersion of $[Fe(CN)_6]^{3-}$ and $[Co(CN)_6]^{3-}$ units. Magnetic phase transition temperature T_c and molar Faraday ellipticity θ_M values decrease with increasing x value because of the fragmentation of magnetic domain by diamagnetic Co^{III} ions. Construction of magnetically disordered states in ordered crystal structures and modulation of magneto-optical properties were achieved by insertion of diamagnetic $[Co(CN)_6]^{3-}$ unit into $Fe^{III}Ni^{II}$ ferromagnetic framework. Compounds with large x value ($x > 0.64$) potentially show spin-glass or quantum magnet-like behavior based on nano-sized-domains generated by the fragmentation. Studies on magnetic and magneto-optical properties of the trimetallic compounds are under way together with related compounds.

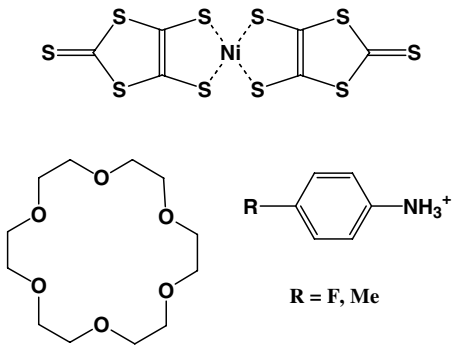
Acknowledgements

This work was supported by a Grant-in-Aid for Scientific Researches from the Ministry of Education, Culture, Sports, Science and Technology, Japan (No. 16655021) and by and Precursory Research for Embryonic Science and Technology (PRESTO), JST.

References

[1] O. Kahn, Molecular Magnetism, VCH, New York, 1993.
[2] K. Ito, M. Kinoshita, Molecular Magnetism, Kodansha, Tokyo, 2000.
[3] M. Verdaguer, A. Bleuzen, V. Marvaud, J. Vaissermann, M. Seuleiman, C. Desplanches, A. Scuiller, C. Train, R. Garde, G. Gelly, C. Lomenech, I. Rosenman, P. Veillet, C. Cartier, F. Villain, Coord. Chem. Rev. 190 (1999) 1023, and references therein.
[4] M. Ohba, H. Ōkawa, Coord. Chem. Rev. 198 (2000) 313, and references therein.
[5] M. Ohba, N. Usuki, N. Fukita, H. Ōkawa, Inorg. Chem. 37 (1998) 3349.
[6] M. Ohba, H. Ōkawa, T. Ito, A. Ohto, J. Chem. Soc., Chem. Commun. 15 (1995) 1545.
[7] M. Ohba, H. Ōkawa, N. Fukita, Y. Hashimoto, J. Am. Chem. Soc. 119 (1997) 1011.
[8] H. Ōkawa, M. Ohba, Bull. Chem. Soc. Jpn. 75 (2002) 1191.
[9] M. Ohba, N. Usuki, N. Fukita, H. Ōkawa, Angew. Chem., Int. Ed. 38 (1999) 1795.
[10] N. Usuki, M. Ohba, H. Ōkawa, Bull. Chem. Soc. Jpn. 75 (2002) 1693.
[11] M. Ohba, T. Iwamoto, H. Ōkawa, Chem. Lett. (2002) 1046.
[12] S. Sugano, N. Kojima, Magneto-optics, Springer, Berlin, 2000.
[13] O. Sato, T. Iyoda, A. Fujishima, K. Hashimoto, Science 271 (1996) 49.

[14] S. Ohkoshi, K. Hashimoto, Chem. Phys. Lett. 349 (2001) 371.
[15] K. Ikeda, S. Ohkoshi, K. Hashimoto, J. Appl. Phys. 93 (2003) 1371.
[16] S. Ohkoshi, M. Mizuno, G. Hung, K. Hashimoto, J. Phys. Chem. B 104 (2000) 9365.
[17] R. Andrés, M. Brissard, M. Gruselle, C. Train, J. Vaissermann, B. Malézieux, J.P. Jamet, M. Verdaguer, Inorg. Chem. 40 (2001) 4633.
[18] P.N. Schatz, A.J. McCaffery, W. Suetaka, G.N. Henning, A.B. Ritchie, P.J. Stephens, J. Chem. Phys. 45 (1966) 722.



Scheme 1.

comparison with the spin-ladder salt of (anilinium)([18]crown-6)[Ni(dmit)$_2$] (**C**). The slight change of supramolecular cation caused a large change in magnetic properties (see Scheme 1).

2. Experimental

Single crystals of **A** and **B** were prepared by a slow diffusion method in acetonitrile. Crystallographic data were collected by a Rigaku Raxis-Rapid diffractometer using Mo Kα (λ = 0.71073 Å) radiation from a graphite monochromator. The space groups of salts **A** and **B** were $P\bar{1}$. Cell parameters of salt **A**: a = 13.489(2) Å, b = 12.642(2) Å, c = 10.893(1) Å, α = 77.213(5)°, β = 75.079(3)°, γ = 80.564(4)°, V = 1739.1(3) Å^3, salt **B**: a = 13.4729(9) Å, b = 12.6900(7) Å, c = 11.2143(5) Å, α = 75.331(1)°, β = 74.668(2)°, γ = 82.044(2)°, V = 1783.6(2) Å^3. The temperature dependent magnetic susceptibility was measured using a Quantum Design MPMS-XL SQUID magnetometer for polycrystalline samples. Static magnetic susceptibilities were measured in an applied magnetic field of 1 T for all samples.

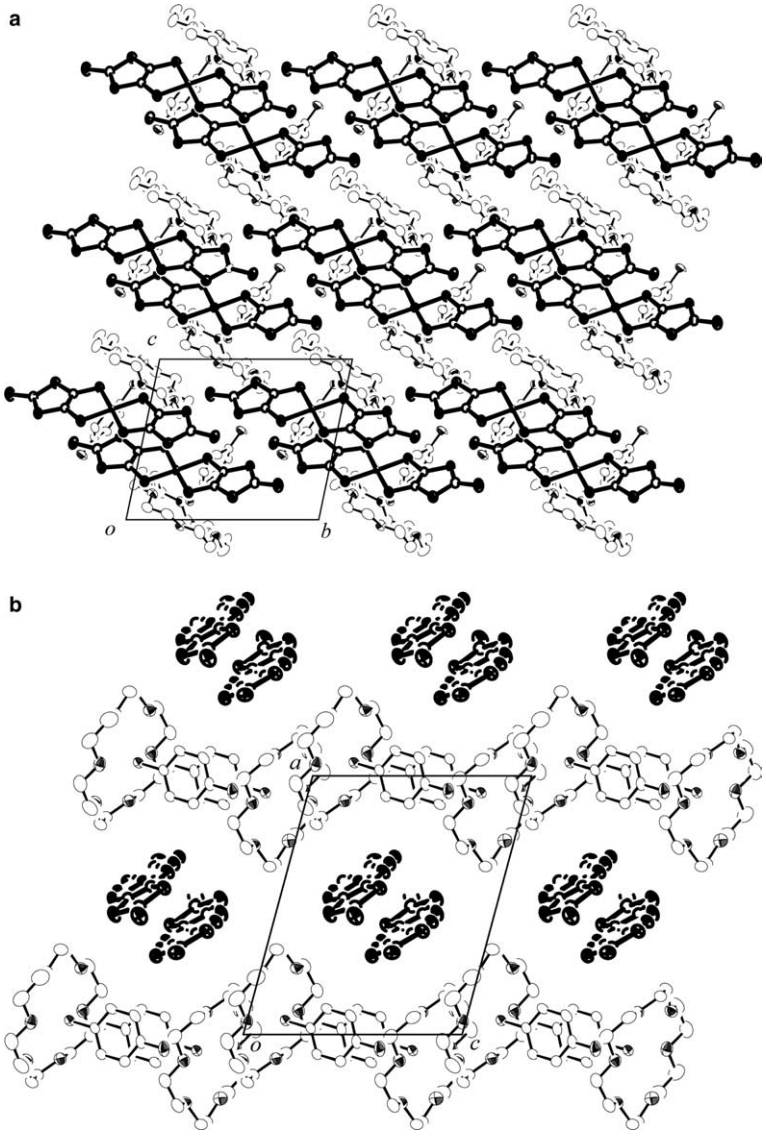


Fig. 1. Crystal structure of (4-fluoroanilinium)([18]crown-6)[Ni(dmit)$_2$] (**A**) viewed along the (a) a- and (b) b-axis.

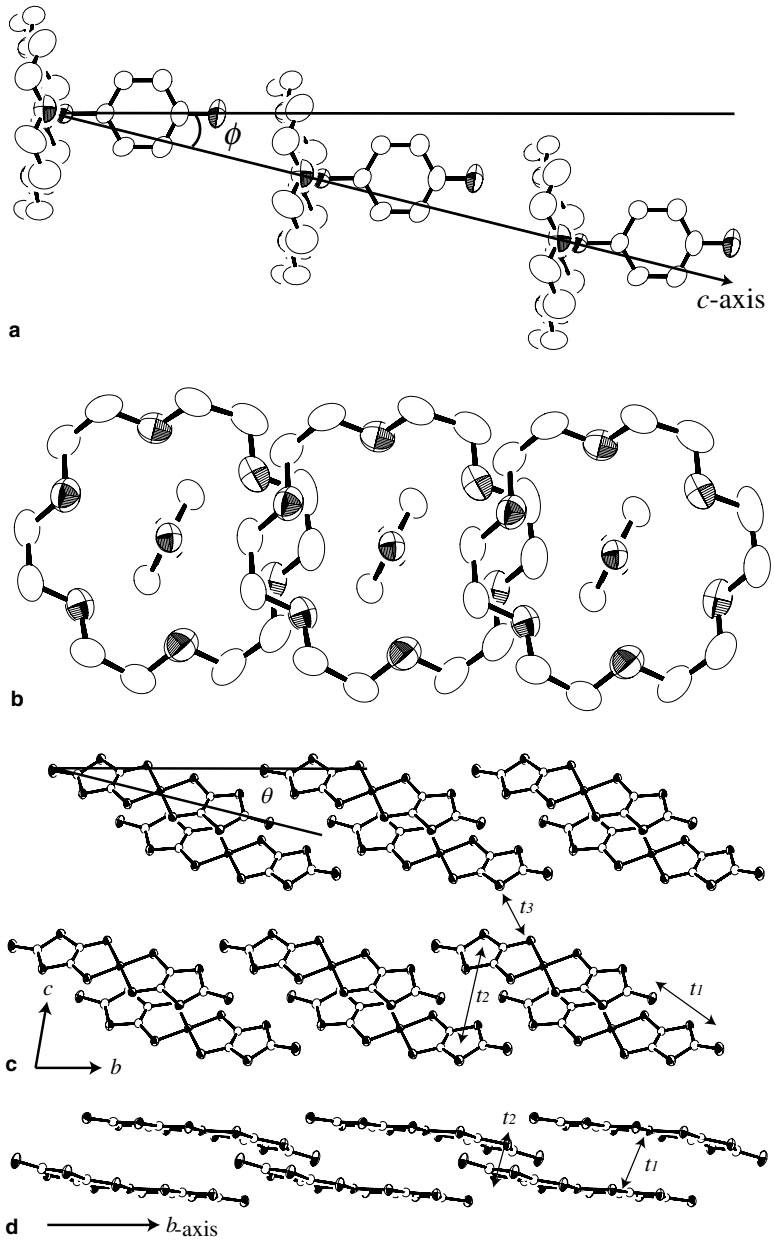


Fig. 2. Supramolecular cation structure of the salt **A** viewed along the (a) *b*- and *c*-axis. One-dimensional arrangement of $[Ni(dmit)_2]^-$ π-dimers in the salt **A** viewed along the (c) *a*- and (d) *c*-axis.

3. Results and discussion

Fig. 1 shows the crystal structure of salt **A**, which was isomorphous to that of salt **B**. In both salts, ammonium moiety of 4-fluoro- and 4-methyl-anilinium cations was completely included into the cavity of [18]crown-6 by hydrogen bonding (N–H···O). The hydrogen bonding lengths between nitrogen atom of ammonium unit and oxygen atom of crown ether were 2.884(7)–2.958(9) and 2.80(1)–2.99(1) Å in salt **A** and **B**, respectively, which are in the range of ordinary N–H···O length (2.87 Å) [13]. The arrangements of supramolecules are shown in Fig. 2(a) and (b). Each cation was regularly stacked along the *c*-axis, which formed cation layer within the *bc*-plane. The cation layers were separated by the $[Ni(dmit)_2]^-$ anion layers along the *a*-axis.

Fig. 2(c) and (d) show the $[Ni(dmit)_2]^-$ arrangements and intermolecular interactions modes between $[Ni(dmit)_2]^-$ anions. The $[Ni(dmit)_2]^-$ molecules formed the π-dimer, which arranged along the *b*-axis. The absolute magnitude of intermolecular interactions were evaluated from the transfer integrals between $[Ni(dmit)_2]^-$ molecules by using extended Hückel molecular orbital calculations [14]. The most effective interactions in the salts **A** and **B** were observed as the intradimer interaction of $t_{A1} = 80.7$ and $t_{B1} = 82.9$ meV, respectively. The

interdimer interactions along the *b*-axis of salts **A** and **B** were $t_{A2} = 17.3$ and $t_{B2} = 13.3$ meV, respectively, while the interchain interactions along the *c*-axis were observed as $t_{A3} = 8.7$ and $t_{B3} = 18.9$ meV, respectively. Since the magnetic exchange interaction (J) is proportional to the square of transfer integral (t^2), the ratio between the intradimer and interdimer magnetic exchange interactions (J_{intra}/J_{inter}) of salts **A** and **B** were estimated as 22 and 19, respectively. Large magnetic anisotropies of the J_{intra} and J_{inter} values suggest that the magnetic behaviour is governed by that of π-dimer of $[Ni(dmit)_2]^-$.

Fig. 3 shows the temperature dependent magnetic susceptibilities of salts **A** and **B**. Curie impurities of 3.93×10^{-3} and 2.01×10^{-3} emu K mol^{-1} for salts **A** and **B**, respectively, have been subtracted. The temperature dependent magnetic susceptibilities of salts **A** and **B** showed a broad maximum around 100 and 115 K, respectively. These magnetic behaviours have been typically observed in materials with the magnetic ground state of spin singlet. Since the crystal structures of salts **A** and **B** suggested that the π-dimer structure govern the magnetic behaviour, the singlet–triplet thermal excitation model,

$$\chi = \frac{C}{T}\frac{4\exp(-2J/k_BT)}{1+3\exp(-2J/k_BT)},$$

was applied for fitting the magnetic susceptibilities of salts **A** and **B**. Fixed Curie constants (C) of 0.394 emu K mol^{-1} ($g = 2.0500$) was employed the fitting [5,6]. The intradimer magnetic exchange energy ($2J/k_B$) of salts **A** and **B** were estimated to be −160 and −170 K, respectively, from the fitting. Similar $2J/k_B$ values of salts **A** and **B** consistent with the magnitude of the calculated intradimer transfer integrals ($t_{A1} = 80.7$ and $t_{B1} = 82.9$ meV).

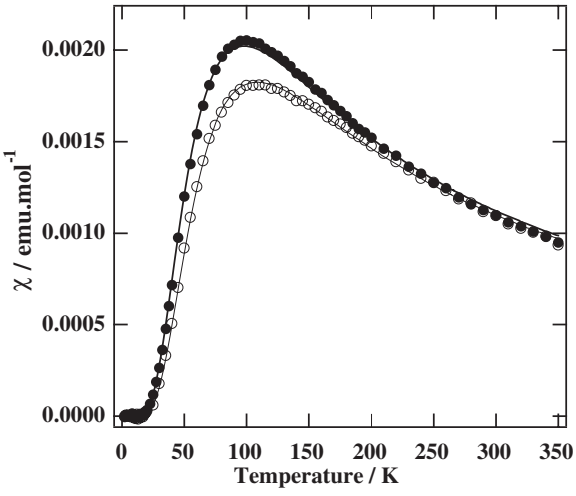


Fig. 3. Temperature dependent molar magnetic susceptibilities of the salts **A** (●) and **B** (○). The solid curves are a fit of the singlet–triplet thermal excitation model (see text).

The crystal structures of salt **A** and **B** are slightly different from the salt **C**, in which the anilinium moiety in supramolecular cation has no substitute at *para* position. However, the magnetic behaviours are large different to each other. The structural parameter of the angle (ϕ) between the C–N bond of anilinium cation and the *c*-axis is a good measure of the structural change in cation arrangement (see Fig. 2(a)). The magnitude of ϕ for salts **A** and **B** were 30.3° and 28.6°, respectively, while the angle ϕ for spin-ladder salt **C** ($\phi = 5.22°$) was much smaller than those of salts **A** and **B**.

The substitution of fluorine atom and methyl group expands the supramolecular cation structure, which caused the distorted stacking of supramolecular cation along the *c*-axis advantage as for the dense packing of cations. The cation arrangements in the *bc*-plane affected the $[Ni(dmit)_2]^-$ arrangement to form isolated dimers rather than dimer chains observed in the salt **C**. As a result, the angles between the long axis of $[Ni(dmit)_2]^-$ and the *b*-axis (θ) of salts **A** and **B** become 24.5° and 24.6°, respectively, which is much large than that of salt **C**. The large angle of θ distorted the stacking of $[Ni(dmit)_2]^-$ molecules along the *b*-axis preventing the interdimer interactions in salts **A** and **B** along ladder-leg direction, which is one of the most important interactions for spin ladder structure.

4. Summary

In conclusion, two supramolecular cations of (4-fluoroanilinium)([18]crown-6) and (4-methylanilinium)([18]crown-6) were introduced into the magnetic $[Ni(dmit)_2]^-$ salts. Basic $[Ni(dmit)_2]^-$ arrangement within the crystals was π-dimer, which arranged along the *b*-axis. The formations of magnetically isolated π-dimer were confirmed by temperature dependent magnetic susceptibility and calculations of intermolecular transfer integrals.

Acknowledgements

The authors thank Dr. K. Ichimura and Professor K. Nomura for the use of SQUID magnetometer. S.N. thanks for supporting from the research fellowship of the Japan Society for the Promotion of Science (JSPS) for young scientists. X.M.R gives thanks to JSPS for financial support.

References

[1] H.S. Nalwa (Ed.), Handbook of Organic Conductive Molecules and Polymers, vol. 1, Wiley, New York, 1997.

[2] P. Cassoux, L. Valade, H. Kobayashi, A. Kobayashi, R.A. Clark, A.E. Underhill, Cood. Chem. Rev. 110 (1991) 115.
[3] P. Cassoux, Cood. Chem. Rev. 186 (1999) 213.
[4] E. Canadell, Cood. Chem. Rev. 186 (1999) 629.
[5] S. Nishihara, T. Akutagawa, T. Hasegawa, T. Nakamura, Chem. Commun. (2002) 408.
[6] S. Nishihara, T. Akutagawa, T. Hasegawa, T. Nakamura, S. Fujiyama, T. Nakamura, J. Solid State Chem. 168 (2002) 661.
[7] S. Nishihara, T. Akutagawa, T. Hasegawa, T. Nakamura, S. Fujiyama, T. Nakamura, Synth. Met. 137 (2003) 1279.
[8] T. Akutagawa, S. Nishihara, N. Takamatsu, T. Hasegawa, T. Nakamura, T. Inabe, J. Phys. Chem. B 104 (2000) 5871.
[9] S. Nishihara, T. Akutagawa, T. Hasegawa, T. Nakamura, Inorg. Chem. 42 (2003) 2480.
[10] T. Akutagawa, T. Hasegawa, T. Nakamura, T. Inabe, J. Am. Chem. Soc. 124 (2002) 8903.
[11] T. Akutagawa, A. Hashimoto, S. Nishihara, T. Hasegawa, T. Nakamura, J. Phys. Chem. B 107 (2003) 66.
[12] T. Akutagawa, A. Hashimoto, S. Nishihara, T. Hasegawa, T. Nakamura, J. Supramol. Chem. 2 (2002) 175.
[13] G.C. Pimentel, A.L. McClellan, The Hydrogen Bonds, Freemann, San Francisco, 1960.
[14] T. Mori, A. Kobayashi, Y. Sasaki, H. Kobayashi, G. Saito, H. Inokuchi, Bull. Chem. Soc. Jpn. 57 (1984) 627.

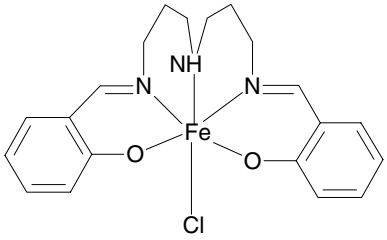


Fig. 1. Structure of the [Fe(^{5}L)Cl] precursor.

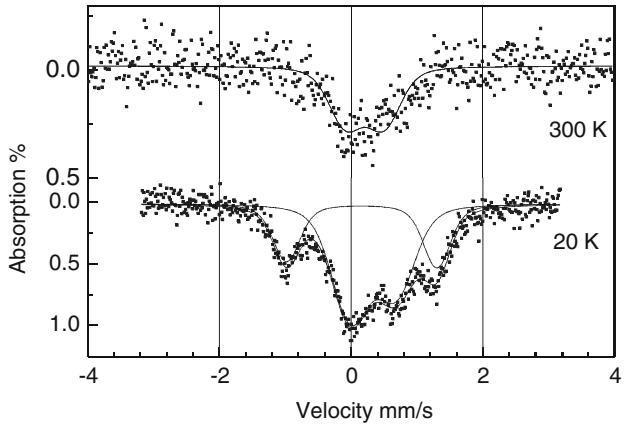


Fig. 2. Mössbauer spectra of the nonanuclear complex [Mo^{IV}{(CN)-$Fe^{III}(^5L)$}$_8$]Cl_4 at 300 and 20 K.

The Mössbauer parameters of Co-star and the Mo-star in comparison with the mononuclear precursor clearly indicate coordination. Apparently the Mo-star deviates much stronger in isomer shift and quadrupol splitting than the Co-star. This is attributed to the sterical possibilities in the heptanuclear and nonanuclear structure.

The hepta- and nonanuclear star-complexes have been characterized by IR spectrum. No evidence for a splitting of the characteristic C–N stretching vibration band indicates a highly symmetric coordination sphere around the central Co(III) and Mo(IV) metal centers, i.e., either all or no cyanides are bridged. The shift of the CN-band from 2200 to 2129 cm^{-1} indicate a bridge. This confirms the conclusion indicated by Mössbauer spectroscopy.

At 20 K in both Co- and Mo-star in addition to the Fe(III) in the high-spin state a second doublet appears which is characteristic for an Fe(III) in the low-spin state [16].

This indicates that in the heptanuclear complex [Co^{III}{(CN)$Fe^{III}(^5L)$}$_6$]Cl_3 clearly a thermally induced transition between an HS to LS state exists. The area fraction of the respective doublets A(Fe^{III}-high-spin):A(Fe^{III}-low-spin) is 65.7:34.3. For the nonanuclear complex [Mo^{IV}{(CN)$Fe^{III}(^5L)$}$_8$]Cl_4 clearly this indicates a thermally induced transition between a high-spin and low-spin state. The area fraction of the respective doublets A(Fe^{III}-high-spin):A(Fe^{III}-low-spin) is 68:32.

In both cases, several Fe(III) centers exhibit electronic switching. This enables us to talk about a multiple electronic transition. This is the first example for electronic switching in a hepta- and nonanuclear complex compound.

Magnetic investigations are in progress and will further resolve the switching in our stars. The difficulties in the evaluation of the magnetic properties, such as coupling, in pure high-spin compounds usually rises, at least exponentially, with the number of spin centers in the molecule. Now the hepta- and nonanuclear-stars exhibit on top of the usual high-spin problems they change to different total high-spin states as a function of temperature.

The technological transfer from the molecular switchability in mononuclear spin transition to multinuclear systems has been achieved. The hepta- and nonanuclear star-shaped compounds open a new dimension and new synergism will be on our road.

2. Experimental

2.1. Ligand $^5LH_2$ and precursor [Fe(^{5}L)Cl]

Ligand $^5LH_2$ and precursor [Fe(^{5}L)Cl] are prepared as described in the literature [10]. The powder was characterized by its IR spectrum and mass spectrum (m/z: 393.1; FeL^+). The precursor $K_4[Mo(CN)_8]\cdot 2H_2O$ was prepared in analogy to Furman and Miller [15]. Yield

Table 1
Mössbauer parameters of the heptanuclear complex [Co^{III}{(CN)$Fe^{III}(^5L)$}$_6$]Cl_3 and nonanuclear complex [Mo^{IV}{(CN)$Fe^{III}(^5L)$}$_8$]Cl_4 at 300 and 20 K

Temperature (K)	Fe(III) HS state			Fe(III) LS state		
	δ (mm/s)	Δ (mm/s)	Fraction (%)	δ (mm/s)	Δ (mm/s)	Fraction (%)
[(^{5}3,3-LFeNC)$_8$Mo]Cl_4						
300	0.208	0.58	100			
20	0.337	0.695	68	0.161	2.283	32
[(^{5}3,3-LFeNC)$_6$Co]Cl_3						
300	0.278	0.775	100			
20	0.356	0.7	65.7	0.267	2.47	34.3

(after double recrystallization): 18.3% rel. to Mo (3.2 g; 6.4 mmol). *Anal*. Calc. for $C_8H_4K_4MoN_8O_2$: C, 19.31; N, 22.60; H, 0.80. Found: C, 19.25; N, 23.15; H, 1.08%. IR(KBr): $\nu(cm^{-1}) = 3400–3600\ cm^{-1}$ (water), 2050–2200 cm^{-1} (C≡N, val.; splitted), 1617 cm^{-1} (water), 496 cm^{-1} (Mo–C, val.).

2.2. Heptanuclear complex $[Co^{III}\{(CN)Fe^{III}(^5L)\}_6]Cl_3$

Heptanuclear complex $[Co^{III}\{(CN)Fe^{III}(^5L)\}_6]Cl_3$ is prepared in analogy to the literature [10]. Yield: 380 mg = 0.012 mmol, 85% based on Co. Elemental *Anal*. Calc. for $C_{126}H_{138}Cl_3CoFe_6N_{24}O_{12}$: C, 56.45; N, 12.54; H, 5.19. Experimental: C, 49.88; N, 11.35; H, 6.17%. IR (KBr): $\nu(cm^{-1}) = 3422\ cm^{-1}$ (N–H, val.), 2930 cm^{-1} (CH_2, val.), 2142 cm^{-1} (C≡N, val.), 1625 cm^{-1} (C=N, val.), 1600–1500 cm^{-1} (aromat. C=C, val.), 760–750 cm^{-1} (C–H, o. o. p.).

2.3. Nonanuclear complex $[Mo^{IV}\{(CN)Fe^{III}(^5L)\}_8]Cl_4$

Nonanuclear complex $[Mo^{IV}\{(CN)Fe^{III}(^5L)\}_8]Cl_4$ is prepared in analogy to the literature [10]. Yield 35% rel. to Mo. *Anal*. Calc.: $C_{168}H_{184}Cl_4Fe_8MoN_{32}O_{16}$: C, 56.18; N, 12.48; H, 5.16. Found: C, 51.43; N, 13.37; H, 5.73%. Note that low carbon content is commonly observed and based on incomplete decomposition to CO_2 due to formation of very stable metal carbides. This is supported by mass spectroscopy: FD MS $m/z = 393.8$ (59.96%, $[^5$3,3-LFe$]^+$); MALDI TOF $m/z = 392.9$ (95%, $[^5$3,3-LFe$]^+$). IR (KBr): $\nu(cm^{-1}) = 3420\ cm^{-1}$ (N–H, val.), 2925 cm^{-1} (CH_2, val.), 2129 cm^{-1} (C=N, val.; single), 1628 cm^{-1} (C=N, val.), 1600–1500 cm^{-1} (aromat. C=C, val.), 760–750 cm^{-1} (C–H, o. o. p.).

2.4. Mössbauer spectroscopy

Mössbauer spectroscopy is performed in a conventional spectrometer in scanning the Mössbauer spectra at 20 K and room temperature (^{57}Co/Rh source kept at room temperature; isomeric shifts are relative to the source).

Acknowledgments

This work was partly funded by the DFG (RE-1627/1-2), the "Fonds der chemischen Industrie", the University of Mainz "Forschungsfond" and the "Material-Wissenschaftliches Forschungs-Zentrum" (MWFZ).

Appendix A. Supplementary data

Supplementary data associated with this article can be found, in the online version at doi:10.1016/j.poly.2005.03.168. These data can be obtained from the CCDC, 12 Union Road, Cambridge CB2 1EZ, UK, fax: +44 1223 336033, e-mail: deposit@ccdc.cam.ac.uk.

References

[1] J.K. McCusker, E.A. Schmitt, D.N. Hendrickson, in: D. Gatteschi, O. Kahn, J.S. Miller, F. Palacio (Eds.), Magnetic Molecular Materials, NATO ASI Series, vol. 198, Kluwer, Dordrecht, 1991, p. 297.
[2] O. Kahn, Molecular Magnetism, VCH, New York, 1993.
[3] D. Gatteschi, in: E. Coronado, P. Delhaes, D. Gatteschi, J.S. Miller (Eds.), Molecular Magnetism: From Molecular Assemblies to the Devices, NATO ASI Series, vol. 321, Kluwer, Dordrecht, 1996, pp. 141–289.
[4] A. Bencini, C. Benelli, A. Caneschi, A. Dei, D. Gatteschi, Inorg. Chem. 25 (1986) 572.
[5] A. Caneschi, D. Gateschi, R. Sessoli, J. Am. Chem. Soc. 113 (1991) 5873.
[6] V. Gadet, M. Bujoli-Doeuff, L. Force, M. Verdaguer, K. ElMalkhi, A. Deroy, J.P. Besse, C. Chappert, P. Veillet, J.P. Renard, P. Beauvillain, in: D. Gatteschi, O. Kahn, J.S. Miller, F. Palacio (Eds.), Magnetic Molecular Materials, NATO ASI Series, vol. 198, Kluwer, Dordrecht, 1991, p. 281.
[7] J. Cano, E. Ruiz, S. Alvarez, M. Verdaguer, Comments Inorg. Chem. 20 (1998) 27.
[8] M. Verdaguer, A. Bleuzen, V. Marvaud, J. Vaissermann, F. Tournilhac, C. Train, R. Ouahes, R. Garde, F. Fabrizi de Biani, C. Desplanches, A. Scuiller, in: G. Ondrejovič, A. Sirota (Eds.), Coordination Chemistry at the Turn of the Century, Slovak Technical University Press, Bratislava, 1999, p. 67.
[9] A. Scuiller, Ph.D. Thesis, University of P. and M. Curie, Paris, 1999.
[10] M. Gembický, R. Boča, F. Renz, Inorg. Chem. Commun. 3 (2000) 662.
[11] N. Matsumoto, S. Ohta, C. Yoshimura, A. Ohyoshi, S. Kohata, H. Okawa, Y. Maeda, J. Chem. Soc., Dalton Trans. (1985) 2575.
[12] A. Ohyoshi, J. Honbo, N. Matsumoto, S. Ohta, S. Sakamoto, Bull. Chem. Soc. Jpn. 59 (1986) 1611.
[13] S. Ohta, C. Yoshimura, N. Matsumoto, H. Okawa, A. Ohyoshi, Bull. Chem. Soc. Jpn. 59 (1986) 155.
[14] R. Boča, Y. Fukuda, M. Gembický, R. Herchel, R. Jaroščiak, W. Linert, F. Renz, J. Yuzurihara, Chem. Phys. Lett. 325 (2000) 411.
[15] N.H. Furman, C.O. Miller, Inorganic Synthesis vol. III (1950) 160.
[16] P. Gütlich, J. Ensling, in: R.I. Solomon, A.B.P. Lever (Eds.), Inorganic Electronic Structure and Spectroscopy, vol. I, Wiley, New York, 1999, p. 161.

After the discovery of light induced excited spin state trapping (LIESST) [15], a number of investigations of the metastable photo-excited HS states have been studied. There the relaxation curves of HS fraction show a typical sigmoidal shape, associated with "self-accelerated" relaxation [16–18]. A dynamical mean-field treatment [21,22] of Wajnflasz and Pick [19,20] with the Arrhenius transition probability reproduced well this behavior, which gives the microscopic origin of the Hauser's formula [16–18].

Relaxation curve of the HS fraction from the photo-excited HS states with the two-step relaxation was observed recently [6]. The first fast relaxation and next slow relaxation, which cannot be explained by the mean-field (MF) theory. We reproduced this two-step relaxation by a Monte Carlo (MC) method [23].

In this paper, we present the equilibrium properties with a variety of two-step phase transition and the non-equilibrium properties with the two-step relaxation of the HS fraction using a MC method.

2. Models and methods

We consider the model introduced by Bousseksou et al. [8], which is an extension of the Wajnflasz and Pick (WP) [19–22,24] model to the case of the two-equivalent sublattices coupled 'antiferromagnetically'

$$\hat{H} = -J^{AA}\sum_{\langle i\in A, j\in A\rangle} S_i^A S_j^A - J^{BB}\sum_{\langle i\in B, j\in B\rangle} S_i^B S_j^B - J^{AB}\sum_{\langle i\in A, j\in B\rangle} S_i^A S_j^B + \Delta\sum_i \left(S_i^A + S_i^B\right),$$
$$S_i = \underbrace{-1,\ldots,-1}_{u},\ \underbrace{1,\ldots 1}_{r}, \tag{1}$$

where the states $S = -1$ and 1 denote the LS and HS states, respectively. J^{AA} and J^{BB} are the 'ferromagnetic' ($J^{AA} > 0$, $J^{BB} > 0$) intrasublattice interactions and J^{AB} is the AF ($J^{AB} < 0$) intersublattice interaction.

The potential energy of the LS and HS states is shown schematically in Fig. 1(a). The degeneracy u and r for the LS and HS state comes from the angular momentum, the spin momentum, the molecular vibration and the phonon degrees of freedom. The parameter Δ is the ligand-field energy. Here, we assume that Δ is the same for the two sublattices. The 'NaCl' lattice structure (fcc) for the two sublattices A and B is considered (Fig. 1(b)). Thus, the coordination numbers between and within sublattices are given by $z_{AB} = 6$ for A–B bonds and $z_{AA} = z_{BB} = z = 12$ for A–A and B–B bonds.

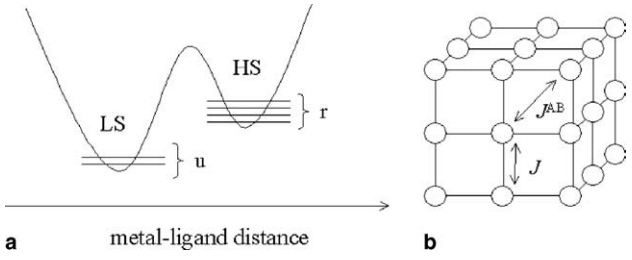


Fig. 1. (a) Schematic diagram of the potential energy of the LS and HS states. The degeneracy of LS state and HS state is taken into account. The axis denotes metal–ligand distance. (b) The model (fcc lattice) with coupling $J(>0)$ and $J^{AB}(<0)$.

We consider the case of equivalent sublattices, then we take $J^{AA} = J^{BB} = J$. Using a temperature dependent field, this model can be expressed formally as follows [21,22]:

$$\hat{H} = -J\sum_{\langle i\in A, j\in A\rangle} S_i^A S_j^A - J\sum_{\langle i\in B, j\in B\rangle} S_i^B S_j^B - J^{AB}\sum_{\langle i\in A, j\in B\rangle} S_i^A S_j^B + \left(\Delta - \frac{\ln g}{2\beta}\right)\sum_i \left(S_i^A + S_i^B\right),$$
$$\text{with } g = \frac{r}{u}, \quad \beta = \frac{1}{k_B T}, \tag{2}$$

where the degeneracy effect is renormalized into the parameter g. The degeneracy ratio g increases up to 100–1000 and becomes temperature-dependent [21,22]. However, for simplicity, we take $g = 100$. The parameter Δ is set as $\Delta = 400$ K, which gives a realistic order of magnitude for the transition temperature.

In order to study the dynamical properties of the system, we use the general master equation

$$\frac{d}{dt}P(S_1\cdots S_k\cdots S_N, t) = -\frac{1}{\tau}\sum_k\sum_{S_k\neq S_k'} W_k(S_k\to S_k')P(S_1\cdots S_k\cdots S_N, t) + \frac{1}{\tau}\sum_k\sum_{S_k\neq S_k'} W_k(S_k'\to S_k)P(S_1\cdots S_k'\cdots S_N, t), \tag{3}$$

where $P(S_1\cdots S_k\cdots S_N, t)$ is the probability of the state $\{S_1\cdots S_k\cdots S_N\}$ at time t and $W_k(S_k\to S_k')$ is the transition probability at the kth site.

We adopt the Arrhenius dynamics, which is suitable to describe experimental data for the relaxation process from the HS state [21,22]. The transition probability is given by

$$\frac{1}{\tau}W_k(S_k\to S_k') = \frac{1}{2\tau_0}\exp(-\beta(E_0 + S_k y)), \tag{4}$$

where S_k is one of the states (± 1) and S_k' is the other state ($S_k' \neq S_k$) and $y = J\sum_A S^A + J^{AB}\sum_B S^B - \Delta + \frac{\ln g}{2\beta}$. Here, E_0 denotes an intramolecular energy barrier, and τ_0 is a quantity related to the time scale. We take $\tau_0 = 1$.

The system has two intrinsic order parameters. One is the fraction of HS molecules defined by

$$f_{HS} = \frac{m_F + 1}{2}. \tag{5}$$

Here, we define the quantity $m_F = \frac{m_A + m_B}{2}$, where the magnetization $m_A = \frac{1}{N}\sum_{i\in A}\langle S_i^A\rangle$ and $m_B = \frac{1}{N}\sum_{i\in B}\langle S_i^B\rangle$ are

the net 'magnetization' per site in the sublattices A and B, respectively. N is the number of all A and B sites, and $\langle\cdots\rangle$ denotes the thermodynamical average. The magnetization m_{F} expresses the degree of 'ferromagnetic' order (i.e., HS–HS, or LS–LS) and f_{HS} takes a value between 0 and 1. The other order parameter is given by

$$m_{\mathrm{AF}} = \frac{m_{\mathrm{A}} - m_{\mathrm{B}}}{2}. \tag{6}$$

This order parameter expresses the degree of the 'antiferromagnetic' (i.e., LS–HS or HS–LS) order.

3. Static and dynamical properties

Two-step phase transitions by the MC method are shown in Fig. 2. The temperature dependence of the HS fraction is shown in Fig. 2(a) and the temperature dependence of AF order parameter is shown in Fig. 2(b). Here, 10 000–50 000 MC steps are taken as waiting time to make the system reach the equilibrium state, and then we perform 10 000–50 000 MC steps for measuring the thermodynamical quantities (f_{HS}). The parameter J^{AB} is set as $J^{\mathrm{AB}} = -12$ K and J is changed as $J =$ 40 K (○), 16 K (◇), and 12 K (×).

The system size is $L^3 = 20^3$. In the low temperatures the system is in the LS phase (all down state) as depicted in Fig. 2 (c)-(I). As the temperature is increased, a transition occurs and f_{HS} reaches the value $f_{\mathrm{HS}} = 1/2$. Then a plateau region appears and the other transition occurs leading to the HS phase (Fig. 2(c)-(III)). This plateau region shows the presence of the phase of the AF order as depicted in Fig. 2(c)-(II). Here, we find three typical two-step transitions: (i) first-order transition at the lower transition temperature and first-order transition at the higher transition temperature as the case $J = 40$ K; (ii) first-order transition at the lower transition temperature and gradual transition at the higher transition temperature as the case $J = 16$ K; (iii) gradual transition at the lower transition temperature and gradual transition at the higher transition temperature as the case $J = 12$ K.

In the following, we discuss the condition of these three cases [6,23]. We define T_{C} as the critical temperature of 3D fcc Ising model, which is given by $T_{\mathrm{C}} = 9.79524\,J$ [25]. Here, we also define T_{C1} and T_{C2} as

$$T_{\mathrm{C1}} = \frac{2\Delta - 2z_{\mathrm{AB}}|J_{\mathrm{A}}|}{k_{\mathrm{B}} \ln g} \quad \text{and}$$
$$T_{\mathrm{C2}} = \frac{2\Delta + 2z_{\mathrm{AB}}|J_{\mathrm{AB}}|}{k_{\mathrm{B}} \ln g}. \tag{7}$$

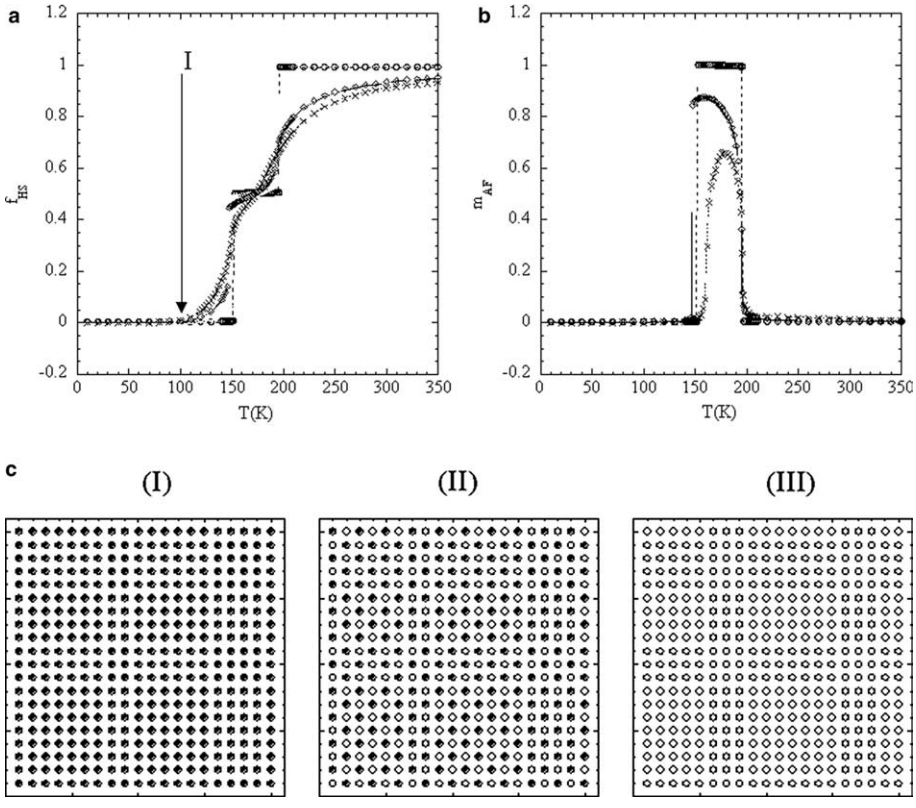


Fig. 2. (a) Temperature dependence of f_{HS} of two-step transitions. $J^{\mathrm{AB}} = -12$ K. $J = 40$ K (○), 16 K (◇), and 12 K (×). The point I is the initial point of the relaxation dynamics. (b) Temperature dependence of the m_{AF} of two-step transitions. (c) Ordered states on the x–y (or y–z) plane of the lattice. (I) LS phase, (II) AF phase, and (III) HS phase.

The temperatures T_{C1} and T_{C2} correspond to the transition temperatures of sharp double first-order transitions [6,23]. Which type of transition occurs depends on values of T_C, T_{C1} and T_{C2}.

When $T_{C1} < T_{C2} < T_C$, first-order transition occurs twice. When $T_{C1} < T_C < T_{C2}$, a first-order transition occurs at T_{C1}, while a gradual transition occurs around T_{C2}. When $T_C < T_{C1} < T_{C2}$, two successive gradual transitions occur.

Next, we study the relaxation dynamics from the HS phase. We investigate the case of $J = 40$ K, in which a strong metastable AF phase exists in the low-temperature region near the lower transition temperature. We take the saturated HS state ($f_{HS} = 1$) at $T = 105$ K as the initial state depicted by I in Fig. 2(a) and observe the relaxation to the LS state.

Relaxation curves of the two order parameters f_{HS} and m_{AF} are observed, respectively, in Fig. 3(a) and (b). The bold line is the average relaxation curve obtained by sampling of 10 independent processes with different sequences of random numbers. We found that the relaxation process consists of two distinct regimes. Fast relaxation with a sigmoidal (convex) shape takes place from the saturated HS fraction ($f_{HS} = 1$) to half of it ($f_{HS} \simeq 0.5$), and slow concave relaxation to the LS phase ($f_{HS} = 0$) follows. The former relaxation with a sigmoidal shape occurs from the HS to AF state and this is due to the Arrhenius dynamics. On the other hand the latter relaxation is that from the AF to LS state. Because the AF state is a strong metastable state, this relaxation is governed by the nucleation process [23].

From the view point of the most probable path (MPP) on the mean-filed free energy, a potential barrier exists between the AF and LS states as we found in the contour diagram before [23]. There the relaxation from the metastable AF phase to LS phase depends on the energy barrier height and temperature. When the thermal fluctuation overcomes this potential energy barrier, relaxation to the LS state occurs.

In Fig. 3(c), an example of nucleation of the LS state in the AF phase is shown. The nucleation process occurs stochastically and the time of the jump is distributed widely as the Poisson process [26]. As a result, the sample-averaged relaxation shows an exponential (concave) relaxation. This shape agrees with the experimental result very well [6]. The mean field theory [6] does not reproduce concave relaxation but convex relaxation where the thermal fluctuation is not taken into account. The introduction of short-range correlations by different analytical methods [27] leads to obtain long tail behavior [28,29] In Fig. 3(a), the thin lines are examples of relaxation with different sequences of random numbers. The upper thin solid line shows a case where the state stays long in the metastable AF state. Here, the concave relaxation curve is observed, which is similar to that obtained by the mean-filed results. On the other hand, the AF state lives in a very short period in the case of the lower thin line.

4. Summary and discussion

We have investigated the static and dynamical properties of the two-step spin-crossover compounds. Using an extended WP-model which consists of two-equivalent sublattices with an intra- ('ferro') interaction and an inter- ('antiferro') sublattice interaction, we present several types of two-step transitions. It was found with this model that basically there exists three types of two-step transitions. In the first case, a first-order transition occurs twice. In the second case, a first-order transition occurs at the lower transition temperature and a gradual transition occurs at the higher transition temperature. In the third case two successive gradual transitions occur. The condition for three types of the two-step transition was also given.

We have studied the relaxation from the fully saturated HS state, which simulates the relaxation from the photo excited saturated high spin state. It was found that the relaxation of the HS fraction consists of two parts. First, fast relation from the HS to AF state occurs. A sigmoidal shape is reproduced in the initial stage

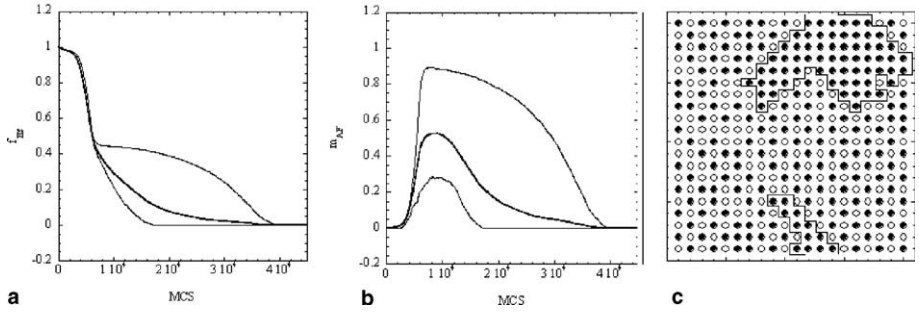


Fig. 3. (a) Relaxation of f_{HS} at $T = 105$ K. The bold line is the average of 10 samples. Thin solid lines are examples of one randon number sequence. (b) Relaxation of m_{AF} at $T = 105$ K. The bold line is the average of 10 samples. Thin solid lines are examples of one randon number sequence. (c) Droplet of the LS state (•) in the AF phase.

of the relaxation, which is typical in relaxations of spin-crossover compounds in experiments. This sigmoidal shape is due to the Arrhenius transition probability in the Monte Carlo simulation as has been pointed out in the mean-field theory [6].

Following the fast relaxation, the slow relaxation from the AF to LS state occurs. When a droplet of the LS state grows in the AF phase and the size of the droplet becomes over the critical droplet, nucleation occurs, which is a stochastic process. If the nucleation rate is low, the stochastic single-nucleation process appears where the AF state relaxes to the LS state suddenly as a Poisson process. On the other hand, if the nucleation rate is high the system shows the multi-nucleation (Avrami) relaxation. They give concave slow relaxation as the average process. This two-step relaxation, i.e., fast sigmoidal and slow exponential relaxation, agree with that found in the experiments [6] very well.

We discussed here the dynamics only focusing on the relaxation from the HS state. Elucidation of various dynamical aspects by photoinduced phenomena [30,31] would be an important problem in the future. In the case of simple spin models as the present treatment, the stable state relaxes rather fast through the local nucleation. More realistic treatment of the elasticity would be a key to investigate a large scale separation of the phases which was observed in the experiment [32].

References

[1] E. König, Struct. Bond. 76 (1991) 51.
[2] P. Gütlich, A. Hauser, H. Spiering, Angew. Chem. 106 (1994) 2109.
[3] P. Gütlich, A. Hauser, H. Spiering, Angew. Chem., Int. Ed. Engl. 33 (1994) 2024, and references therein.
[4] C.P. Köhler, R. Jakobi, E. Meissner, L. Wiehl, H. Spiering, P. Gütlich, J. Phys. Chem. Solids 51 (1990) 239.
[5] R. Jakobi, H. Spiering, P. Gütlich, J. Phys. Chem. Solids 53 (1992) 267.
[6] K. Boukheddaden, J. Linares, E. Codjovi, F. Varret., V. Niel, J.A. Real, J. Appl. Phys. 93 (2003) 1.
[7] J.A. Real, H. Bolvin, A. Bousseksou, A. Dworkin, O. Kahn, F. Varret, J. Zarembowitch, J. Am. Chem. Soc. 114 (1992) 4650.
[8] A. Bousseksou, F. Varret, J. Nasser, J. Phys. I 3 (1993) 1463.
[9] J.A. Real, J. Castro, A. Bousseksou, M. Verdaguer, R. Burriel, M. Castro, J. Linares, F. Varret, Inorg. Chem. 36 (1997) 455.
[10] H. Köppen, E.W. Müller, C.P. Köhler, H. Spiering, E. Meissner, P. Gütlich, Chem. Phys. Lett. 91 (1982) 348.
[11] V. Petrouleas, J.P. Tuchagues, Chem. Phys. Lett. 135 (1987) 21.
[12] D. Boinnard, A. Bousseksou, A. Dworkin, J.M. Savariault, F. Varret, J.P. Tuchagues, Inorg. Chem. 33 (1994) 271.
[13] A. Bousseksou, J. Nasser, J. Linares, K. Boukheddaden, F. Varret, J. Phys. I 2 (1992) 1381.
[14] A. Bousseksou, J. Nasser, F. Varret, J. Magn. Magn. Mater. 140 (1995) 1511.
[15] S. Decurtins, P. Gütlich, C.P. Köhler, H. Spiering, A. Hauser, Chem. Phys. Lett. 1 (1984) 139.
[16] A. Hauser, Coord. Chem. Rev. 11 (1991) 275.
[17] A. Hauser, P. Gütlich, H. Spiering, Inorg. Chem. 25 (1986) 4345.
[18] A. Hauser, J. Chem. Phys. 94 (1991) 2741.
[19] J. Wajnflasz, R. Pick, J. Phys. Status Solidi 40 (1970) 537.
[20] J. Wajnflasz, R. Pick, J. Phys. (Paris). Colloq 32 (1971) C1.
[21] K. Boukheddaden, I. Shteto, B. Hôo, F. Varret, Phys. Rev. B 62 (2000) 14796.
[22] K. Boukheddaden, I. Shteto, B. Hôo, F. Varret, Phys. Rev. B (2000) 14806.
[23] M. Nishino, K. Boukheddaden, S. Miyashita, F. Varret., Phys. Rev. B 68 (2003) 224402.
[24] M. Nishino, S. Miyashita, K. Boukheddaden, J. Chem. Phys. 118 (2003) 4594.
[25] C. Domb, M.S. Green (Eds.), Phase Transition and Critical Phenomena, vol. 3.
[26] P.A. Rikvold, H. Tomita, S. Miyashita, S.W. Sides, Phys. Rev. E 49 (1994) 5080, and references therein.
[27] H. Mamada, S. Takano, J. Phys. Soc. Jpn. 25 (1968) 675.
[28] K. Boukheddaden, F. Varret, S. Salunke, J. Linares, E. Codjovi, Phase Transit. 75 (2002) 733.
[29] B. Hôo, K. Boukheddaden, F. Varret, Eur. Phys. J. B 17 (2000) 449.
[30] M. Nishino, K. Yamaguchi, S. Miyashita, Phys. Rev. B 58 (1998) 9303.
[31] M. Nishino, S. Miyashita, Phys. Rev. B 63 (2001) 174404.
[32] Y. Ogawa, S. Koshihara, K. Koshino, T. Ogawa, C. Urano, H. Takagi, Phys. Rev. Lett. 84 (2000) 3181.

approximation were revealed by accurate measurements on spin transition solids, resulting in a moderate increase of the quantum yield along the photo-excitation process [9–11]. In case of direct competition between opposite photo-excitation processes, light-induced bistability was even observed [11]. However such a non-linear effect will be discarded here, because of the prominent role of the non-linear relaxation;

(ii) the high-spin (HS) towards low-spin (LS) relaxation is a cooperative process [12,13], highly non-linear, leading to typical sigmoidal relaxation curves; the "self-accelerated" character of the relaxation is explained in terms of an internal pressure which is built-up by the depopulation of the metastable HS state, which lowers the E_{HL} barrier energy;

(iii) the thermal effects generated by irradiation are discarded in the present approach.

The assumption of a linear dependence of the barrier energy on the population of the metastable state leads to simple mean-field expressions of the HS → LS cooperative relaxation rate (noted H → L in the following). The present expressions of the H → L and L → H relaxation rates refer to the properties of isolated molecules, obtained when the effects of HS and LS neighbouring molecules cancel each other. The are, respectively, written:

$$k_{HL}(T,n) = k_{HL}(T,1/2)\exp[-\alpha(n-1/2)], \quad (1)$$

$$k_{LH}(T,n) = k_{LH}(T,1/2)\exp[+\alpha(n-1/2)], \quad (2)$$

where $n = n_{HS}$ is the population of the metastable state. The ± signs in the exponential factors result from opposite variations of the E_{HL} and E_{LH} barrier energies driven by the internal pressure effect. The self-acceleration parameter α is associated with steric interactions in the solid. In the thermal activation regime, according to both experiments [14], mean-field [12] and microscopic [15] models, it is written:

$$\alpha = 2zJ/k_BT \quad (3)$$

with z the number of interacting neighbours, and J the intermolecular interaction parameter. Accordingly, the relaxation rates are written:

$$k_{HL}(T,n) = k_\infty \exp(-E_{HL}/k_BT)\exp[-\alpha(n-1/2)], \quad (4)$$

$$k_{LH}(T,n) = gk_\infty \exp(-E_{LH}/k_BT)\exp[+\alpha(n-1/2)] \quad (5)$$

with $g = g_{HS}/g_{LS}$ the "effective" degeneracy ratio of the states, accounting for both electronic and vibrational effects [16].

2. The master equation

In all situations the combination of photo-excitation and relaxation processes governs the evolution of the system. This combination is expressed through the so-called *master equation*, i.e., the evolution equation written in terms of transition rates. The mean-field macroscopic form for a two-state system follows:

$$\begin{aligned} dn/dt = {} & [1-n(t)][I_{LH}\eta_{LH}\sigma_{LH} + k_{LH}(T,n)] \\ & - n(t)[I_{HL}\eta_{HL}\sigma_{HL} + k_{HL}(T,n)], \end{aligned} \quad (6)$$

where $I_{LH}\eta_{LH}\sigma_{LH}$, $I_{HL}\eta_{HL}\sigma_{HL}$ are the photo-excitation terms accounting for light intensities, quantum yields and absorption cross sections. For convenience, we define optical rates in similarity with relaxation rates, and we also use specific notations for the thermal and optical contributions to the master equation:

$$dn/dt = F(n) = F^{therm}(n) + F^{opt}(n), \quad \text{with}$$

$$F^{therm}(n) = [1-n(t)]k_{LH}^{therm}(T,n) - n(t)k_{HL}^{therm}(T,n),$$

$$F^{opt}(n) = [1-n(t)]k_{LH}^{opt} - n(t)k_{HL}^{opt}.$$

It is worth mentioning that the master equation can be used beyond the mean-field approach. In microscopic models, a set of N coupled equations for N microscopic variables has to be solved, see [15] for Ising-like systems.

The master equation provides the description of all static and dynamic properties of the switcheable system: (i) the thermal equilibrium which spontaneously occurs in the dark (including thermal hysteresis), (ii) the low-temperature photo-stationary states (including the light-induced instability and subsequent light-induced hystereses), (iii) intensity thresholds in the case of steady irradiation processes and (iv) temporal evolution for steady and transient thermal and irradiation processes.

3. Master equation approach of the spontaneous spin equilibrium

It is easily shown [15] that the MFMME approach is formally equivalent to the mean-field Ising-like model [17–19] and to the regular solution model in the Bragg approximation [20]. The correspondence relations are $\ln g = \Delta S/R$ and $E_{HS} - E_{HL} = \Delta = \Delta H/R$, where ΔS, ΔH are the molar entropy and enthalpy changes upon L → H spin conversion. The static and photo-stationary processes obey the simple condition $F(n) = 0$, i.e.,

$$F^{therm}(n) = -F^{opt}(n). \quad (7)$$

In the dark Eq. (7) has to be set to zero and leads to the so-called "detailed balance equation"

$$(1-n_{equ})k_{LH}^{therm} = n_{equ}k_{HL}^{therm}, \quad (8)$$

which correlates the ratios of equilibrium populations and of relaxation rates. Straightforward transformation of Eq. (8) leads to

$$\begin{aligned} n_{equ}/(1-n_{equ}) &= k_{LH}^{therm}/k_{HL}^{therm} \\ &= g\exp[-(E_{LH}-E_{HL})/k_BT] \\ &\quad \times \exp[2\alpha(n_{equ}-1/2)], \end{aligned} \quad (9)$$

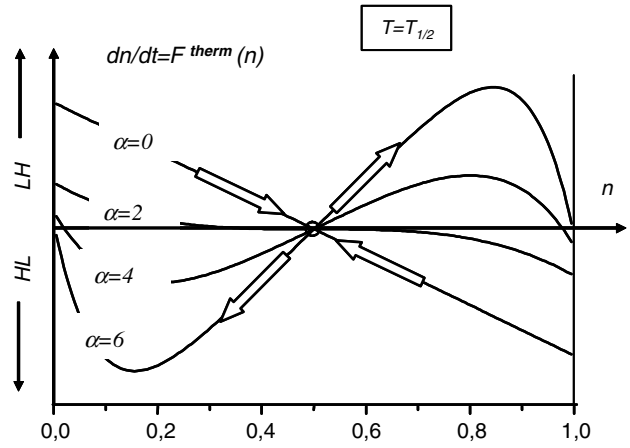


Fig. 1. Spin equilibrium in the dark, in the static MFMME approach: graphical resolution at equilibrium temperature, leading to the instability condition $\alpha > 2$.

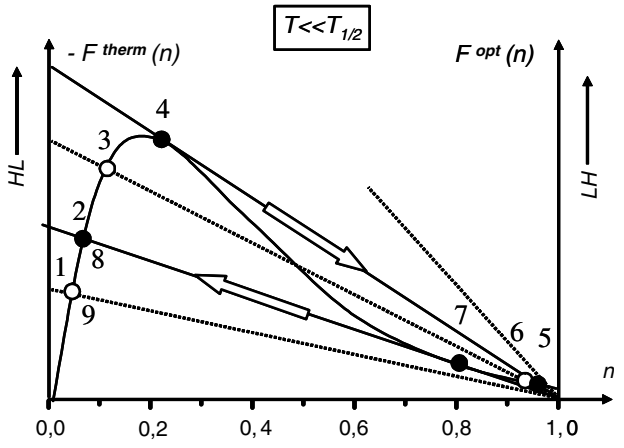


Fig. 2. Light-induced instability in the static MFMME approach, at constant temperature. Straight lines stand for optical terms, at different intensities (slope $-k_{\mathrm{LH}}^{\mathrm{opt}}$). The light-induced optical hysteresis (LIOH) loop is generated along the isothermal sequence $1 \rightarrow 9$. The threshold situations ($\alpha > 4$) are indicated by open arrows.

which becomes at equilibrium temperature $T_{1/2}$ (defined as the spin states equipopulation):

$$T_{1/2} = (E_{\mathrm{LH}} - E_{\mathrm{HL}})/k_{\mathrm{B}} \ln g. \tag{10}$$

Eq. (10) is exactly the mean-field Ising result. We show in Fig. 1 the graphical investigation of the stability of the solution $n = 1/2$ at $T_{1/2}$ using the MFMME approach, as follows:

$$\begin{aligned} \mathrm{d}n/\mathrm{d}t|_{T=T_{1/2}} &= F^{\mathrm{therm}}(n)|_{T=T_{1/2}} \\ &= \{(1-n)\exp[\alpha(n-1/2)] \\ &\quad -n\exp[-\alpha(n-1/2)]\} k_{\mathrm{HL}}(T_{1/2}, 1/2), \end{aligned} \tag{11}$$

which by the way is an odd function of n, centred at $n = 1/2$, represented in Fig. 1. The sense of the spontaneous evolution at the vicinity of $n = 1/2$ is inferred from the sign of the slope of $F(n)$, which is expressed as follows:

$$\mathrm{d}F^{\mathrm{therm}}(n)/\mathrm{d}n|_{n=1/2, T=T1/2} = (\alpha - 2) k_{\mathrm{HL}}(T_{1/2}, 1/2) \tag{12}$$

Instability occurs for a positive slope, leading to the instability condition $\alpha > 2$, equivalent to the mean-field Ising-like result: $zJ > k_{\mathrm{B}} T_{1/2}$.

4. Light-induced instability at low temperature

The low-temperature situation has been already described in [1]. The L → H relaxation can be neglected, as easily seen from Eq. (8). Considering only the L → H optical term, the photo-stationary state Eq. (7) takes the simple form:

$$\begin{aligned} (1-n) k_{\mathrm{LH}}^{\mathrm{opt}} &= (1-n) I_{\mathrm{LH}} \eta_{\mathrm{LH}} \sigma_{\mathrm{LH}} \\ &= n k_{\infty} \exp(-E_{\mathrm{HL}}/k_{\mathrm{B}}T) \exp[-\alpha(n-1/2)], \end{aligned} \tag{13}$$

which provides analytical expressions for $T(n, I)$ and $I(T, n)$ but not for $n(T, I)$. The phase diagram of the photo-stationary states in (T, n, I) space was therefore described analytically. For brevity we refer to [21]; see also [1,22] for light-induced optical hysteresis (LIOH). It is worth noting that the threshold value $\alpha = 4$ for the light-induced instability is twice larger than that derived in Section 3 for the spontaneous instability at $T_{1/2}$. We show in Fig. 2 the graphical determination of the photo-stationary states, in a case which fulfils the instability condition $\alpha > 4$. The solutions are given by the intersects between the curve associated with the relaxation terms, $-F^{\mathrm{therm}}(n)$, and the straight line associated with the photo-excitation term $F^{\mathrm{opt}}(n)$. The slope of the straight line is proportional to the irradiation intensity.

The analytical expression of the light-induced equilibrium temperature (at $n = 1/2$) will be useful here. It is straightforwardly derived from Eq. (13) (after [23]):

$$T_{1/2}^{*} = E_{\mathrm{HL}}/k_{\mathrm{B}} \ln(k_{\infty}/k_{\mathrm{LH}}^{\mathrm{opt}}). \tag{14}$$

Eq. (14) univocally correlates the light-induced equilibrium temperature $T_{1/2}^{*}$ and the photo-excitation rate $k_{\mathrm{LH}}^{\mathrm{opt}}$. The use of the reduced value $k_{\mathrm{LH}}^{\mathrm{opt}}/k_{\infty}$ will be very useful for the quantitative analysis of the experimental results, since it by-passes the difficult estimations of the quantum yield and optical absorption effects in the sample.

5. Photo-switching in the spontaneous thermal hysteresis

We now focus on the switching processes performed at the thermal equilibrium temperature, but the method could be applied at any temperature in the thermal loop.

In Fig. 3 we show the graphical resolution of the photo-stationary states at equilibrium temperature, following Eq. (7). The threshold situations obey the specific condition $\mathrm{d}F^{\mathrm{therm}}/\mathrm{d}n = -\mathrm{d}F^{\mathrm{opt}}/\mathrm{d}n$, leading to the characteristic conditions for intensity thresholds:

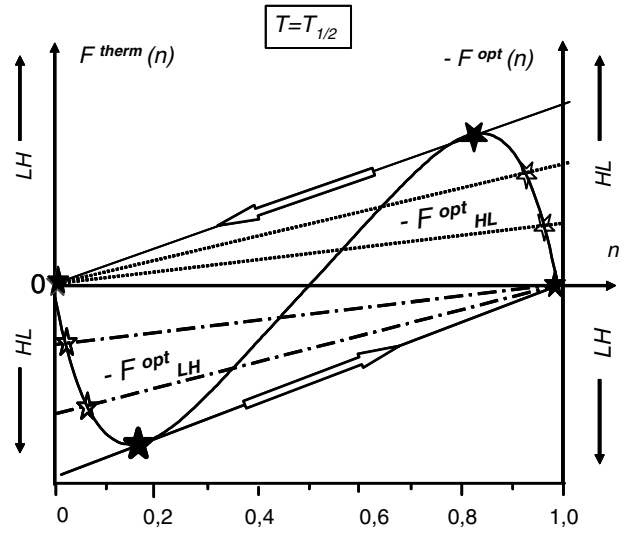


Fig. 3. The static MFMME approach to the intensity thresholds in the thermal hysteresis loop, at equilibrium temperature, for the L → H (bottom) and H → L (top) photo-processes. Straight lines correspond to optical terms. The threshold situations are indicated by open arrows.

$$F(n) = 0, \quad \mathrm{d}F(n)/\mathrm{d}n = 0. \tag{15}$$

The set of coupled non-linear Eq. (15) has no analytical solution and has to be solved numerically. The symmetry properties of Fig. 3 result in an interesting property: the equality of threshold values for L → H and H → L optical rates at $T = T_{1/2}$; of course the intensity values are expected to differ, owing to the different quantum yields and cross sections for the opposite processes.

6. Reversible photo-switching by combination of opposite optical rates

The MFMME approach provides a simple illustration to the case of combined L → H and H → L photo-processes, proposed in [3] for explaining the opposite effects induced by irradiation using the same wavelength at different temperatures: L → H for $T > T_{1/2}$, H → L for $T < T_{1/2}$. Indeed, the mean-field description possesses the essential ingredients of the Domino effect [24,25]: cooperativity and metastability of the initial state. Therefore the MFMME is capable of providing a qualitative approach to the problem. In Fig. 4 we show the graphical determination of the photo-stationary states, in the case of equal (for simplicity) optical rates of the opposite processes, at temperatures above and below $T_{1/2}$, within the hysteresis loop. The optical term in case of opposite processes, $F^{\mathrm{opt}}(n) = (1-n)k_{\mathrm{LH}}^{\mathrm{opt}} - nk_{\mathrm{LH}}^{\mathrm{opt}}$, is represented by a linear function which intersects the n-axis at a value which depends on the ratio between the opposite rates, $n_{\mathrm{equ}}^{\mathrm{opt}} = k_{\mathrm{LH}}^{\mathrm{opt}}/(k_{\mathrm{LH}}^{\mathrm{opt}} + k_{\mathrm{HL}}^{\mathrm{opt}})$, which obviously belongs to the $[0,1]$ interval. It can be clearly seen from this figure that the same irradiation will drive the light-induced thermal

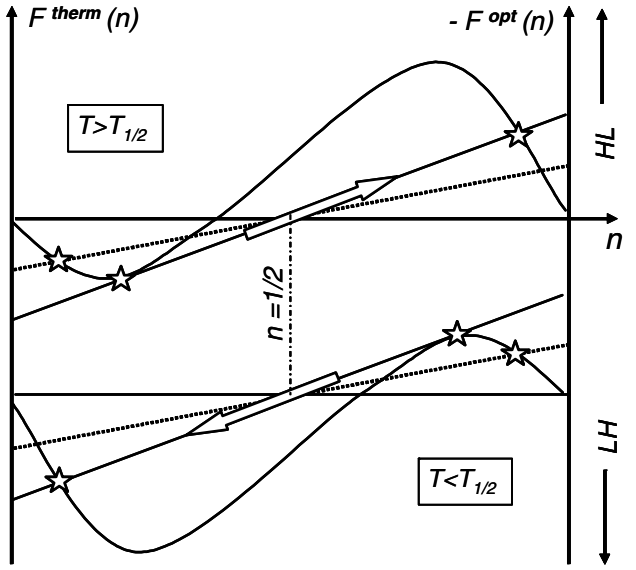


Fig. 4. The competition between optical and relaxation rates, within the thermal hysteresis loop, in the case of combined L → H, H → L photo-processes. The straight lines stand for photo-excitation at different intensities. The threshold situations are indicated by open arrows.

equilibrium towards the HS state for $T > T_{1/2}$, and towards the LS state for $T < T_{1/2}$.

7. Kinetic photo-switching in the spontaneous thermal hysteresis

The MFMME enables to calculate the time dependence of the HS and LS populations. In Fig. 5 we show computed $n(t)$ curves for different intensities above the

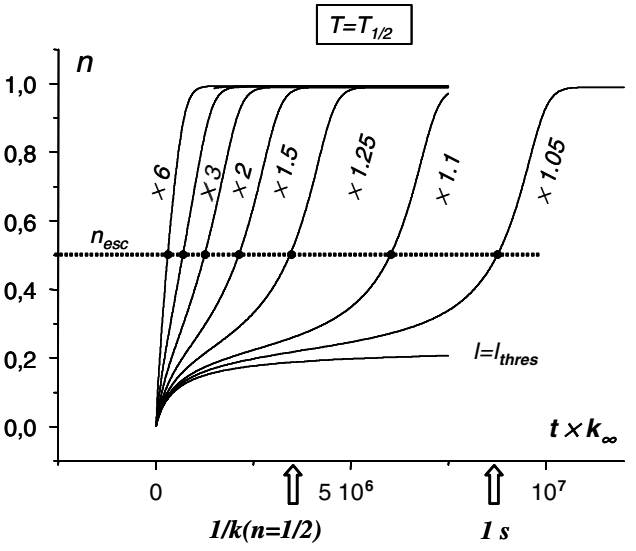


Fig. 5. The $n(t)$ dependence at the equilibrium temperature, for different intensities, and the corresponding escape times $t_{1/2}$, computed using parameter values determined in Section 8.

threshold value, at $T_{1/2}$. Beyond $n = 1/2$, the system can spontaneously decay towards the metastable macroscopic HS state, i.e., irradiation can be switched off. In other words, $n = 1/2$ and $t(n = 1/2) = t_{1/2}$ can be named, respectively, *escape population* and *escape time* of the system from the macroscopic metastable LS state. Similar calculations can be performed at different temperatures, then leading to different values of $t(I, n = n_{esc}(T)) = t_{esc}(T, I)$. The $n_{esc}(T)$ values belong to the instable branch of the spontaneous equilibrium in the thermal hysteresis range and can be easily derived from static calculations.

The plot of the computed relationship between intensity and escape time is presented in Fig. 6 (left scale). A useful interpretation of this plot can be made in terms of a *kinetic intensity threshold*, i.e., the minimum intensity $I^{kin}_{thres.}(t_{irrad.})$ needed to switch the system, for a given irradiation time $t_{irrad.}$. The crucial physical quantity, from application viewpoint, is the *energy threshold* $E_{thres.}(t_{irrad.}) = I^{kin}_{thres.}(t_{irrad.}) \times t_{irrad.}$, which we also plotted in Fig. 6 (right scale); the observed quasi-linear dependence $E_{thres.}(t_{irrad.})$ illustrates the increasing effect of relaxation which proceeds at a quasi-constant rate during the first stage of the switching process.

We now briefly discuss the switching processes induced by pulsed irradiation. A priori short irradiation times have to be preferred, the duration of which should typically compare to the inverse relaxation rates, $1/k_{HL}(T_{1/2}, n = 1/2) = 1/k_{LH}(T_{1/2}, n = 1/2) = 340$ ms with the parameter values used in the present work.

The Energy threshold expected at the limit of very short pulses is irrespective of the relaxation effects. The limiting value of the effective yield of the switching process, i.e., the ratio transformed molecules/absorbed photons then results from the simple balance between the total population created by irradiation and the escape population [2]. It is expressed by the ratio $\eta^{eff}_{LH} = \eta_{LH}/n_{esc.}$ (intrinsic quantum yield/ escape population). The value $2\eta_{LH}$ is then expected at $T_{1/2}$, and should sizably increase on approaching the HS edge of the thermal hysteresis loop. Of course the theoretical value of the escape population value is highly model dependent, and should be drastically lowered in presence of an efficient Domino effect.

8. Experimental data and discussion

We now describe the experimental data recorded for the photomagnetic Prussian Blue Analogue by the Versailles group on $Na_{0.32}Co[Fe(CN)_6]_{0.74}\cdot 3.4H_2O$, synthesized by the Tokyo group, here denoted compound (**1**). In a previous report we analysed the magnetic data recorded during the relaxation process of the metastable state obtained by thermal quenching of the high-temperature phase [26]. Selected relaxation curves are shown in Fig. 7.

The quantitative analysis of the data is briefly reported here (after [26]): calorimetric measurements provided a direct estimate of the degeneracy ratio (Section 3); the measured $\Delta S = 60(10)$ J K^{-1} mol^{-1}, led to $\ln g = \Delta S/R = 7(1)$; the width and location of the thermal hysteresis loop were used to determine the static parameter values: $\Delta = 1600(300)$ K, $zJ \sim 310$ K; subsequent analysis of the self-accelerated relaxation curves, according to Eqs. (4) and (5), with the fixed value $zJ = 310$ K led to the dynamic parameter values: $E_H(n = 1/2) = 3420$ K, $k_\infty \sim 8 \times 10^6$ s^{-1} [26]; a good fit was obtained by introducing a Gaussian distribution of barrier energies ($\sigma_E = 185$ K), associated with the various local environments due to non-stoichiometry of the compound; chemical inhomogeneities at the macroscopic scale were assigned to be responsible for the bent shape of the thermal hysteresis loop.

We now report reflectivity data, see Fig. 8, which actually provide the first experimental example of

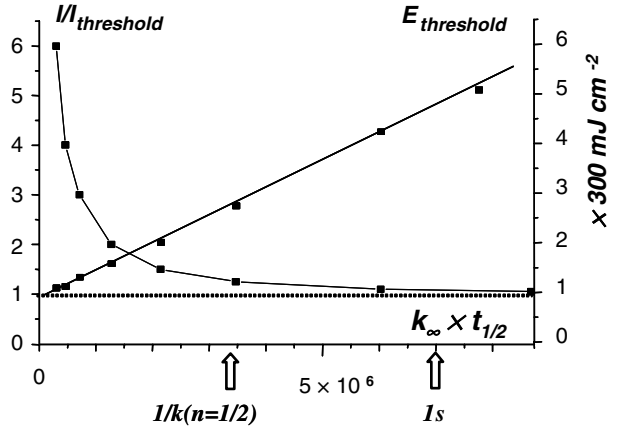


Fig. 6. Computed dependence of the kinetic intensity threshold (left scale) and energy threshold (right scale) with the irradiation time. Parameter values are those of Fig. 5.

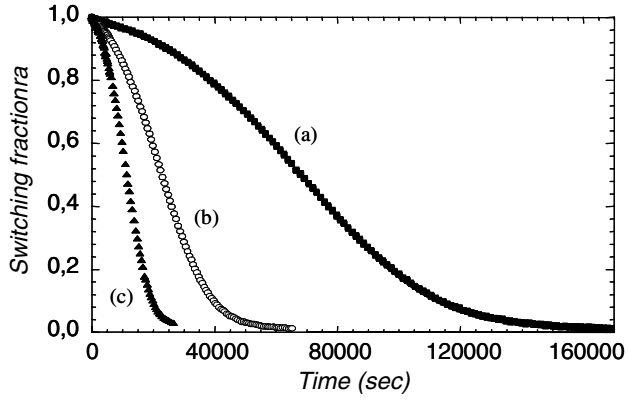


Fig. 7. The relaxation of the thermally quenched state of **1** at several temperatures, (a) 130 K, (b) 135 K, (c) 140 K, after [26]. The sigmoidal character of the curves evidences the self-accelerated relaxation.

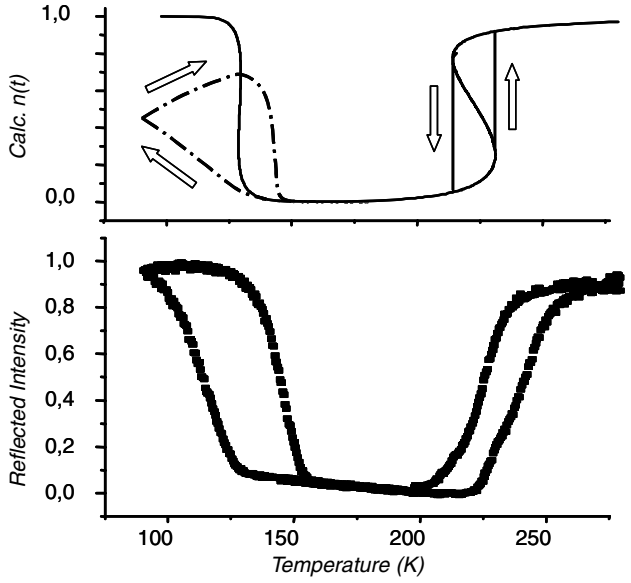


Fig. 8. The spontaneous (right) and light-induced (left) thermal hystereses of **1** recorded by optical reflectivity at 700 nm, 5 mW cm^{-2}. Top figure shows MFMME computed curves: photo-stationary states (full line); kinetic treatment (dotted line).

light-induced thermal hysteresis (LITH) in the cobalt hexacyanoferrate series. Reflectivity measurements have been preferred to magnetic measurements, because they limit the effects of optical absorption through the sample, see [10] for example. However the quantitative character of these reflectivity data, even after the usual Kubelka–Munk treatment remains questionable, mostly because diffusion cannot be correctly accounted for, due to the experimental set-up using quasi-specular reflection. We shall therefore resume the quantitative data from Fig. 8 to the approximate values of the switching temperatures of the TH and LITH loops.

The light-induced equilibrium temperature, according to Eq. (14), is univocally related to the optical rate in reduced units. The experimental value $T^{*}_{1/2} \sim 130$ K yields $k^{\mathrm{opt}}_{\mathrm{LH}}/k_{\infty} \sim 3.8 \times 10^{12}$, a value which specifically refers to the experimental conditions and sample used for the Versailles LITH experiments (see for example [5,10,27,28]). We reported in Fig. 8 (top) several curves computed through the MFMME approach. The static parameter values, $\Delta = 1617$ K, $zJ = 305$ K have been slightly adjusted in order to better fit the reflectivity data. The computed quasi-static LITH loop (full line) is narrow, due to the self-acceleration factor value, $\alpha(130\ \mathrm{K}) = 2zJ/k_{\mathrm{B}}T = 2 \times (305/130) \cong 4.7$, which is not in large excess to the threshold value $\alpha = 4$. The computed loop accounting for the experimental kinetics (sweeping rate 0.1 K/min, dotted line) better compares to the experimental switching temperatures. However some obvious differences remain, e.g., the uncompleted saturation of the system at the turning point (90 K).

The properties of the photo-induced transition obviously differ from those expected from the thermal transition, in the present case. Literature data relevant to the comparison between LITH and TH are yet scarce [14,29,30]. They exclusively dealt with spin transition compounds, and so far indicated a good agreement to the correlation between the widths of the LITH and TH loops. A tentative explanation for this striking discrepancy observed here might be the difference recently reported between the thermally quenched and photo-excited states [31]. Therefore we plan to measure the relaxation curves of the photo-excited state of **1**, after properly solving the conflicting requirements of accurate measurements and low optical absorption. Further effects might be responsible for the bent shape of the LITH curve, again the distribution of chemical composition at the microscopic and macroscopic scales, but also the irradiation intensity distribution which is inherent to the optical absorption process [26].

Straightforward calculations following the strategy described in Section 5 give for the present system, at the equilibrium temperature of 231 K, a photo-excitation rate threshold value 600 times larger than the one used for the LITH experiment. It immediately follows, in the approximation of linear photo-excitation, that the corresponding intensity should be 600 times larger, i.e., $\sim$3 W cm^{-2}. Such a large specific intensity is expected to induce an excessive warming up of the sample. Therefore transient photo-excitations, such as those provided by one-shot laser pulses [2–4], were obviously needed. Actually, the energy threshold values calculated according to Section 5 $\sim$300 mJ cm^{-2}, are far too large with respect to the experimental values, $\sim$15 mJ cm^{-2}. Such a discrepancy finally supports the previous reports of anomalously large values of the effective quantum yield [2,3], i.e., the occurrence of a sizeable Domino effect, and strongly motivates us for further treatments of the master equation beyond the mean-field approximation (see, e.g. [32]). Also, the non-linear character of the photo-excitation terms [10,11] may sizeably contribute to the instability of the system under irradiation, and therefore requires quantitative experimental investigations on the tracks of [9].

Acknowledgements

Acknowledgements are due to the CNRS PICS French–Japanese exchange program and to Profs. H. Cailleau and S. Koshihara for useful discussions.

References

[1] A. Desaix, O. Roubeau, J. Jeftic, J.G. Haasnoot, K. Boukheddaden, E. Codjovi, J. Linares, M. Nogues, F. Varret, Eur. Phys. J. B 6 (1998) 183.
[2] N. Shimamoto, S. Ohkoshi, O. Sato, K. Hashimoto, Chem. Lett. 4 (2002) 486.

[3] H.W. Liu, K. Matsuda, Z.Z. Gu, K. Takahashi, A.L. Cui, R. Nakajima, A. Fujishima, O. Sato, Phys. Rev. Lett. 90 (2003) 167403.
[4] E. Freysz, S. Montant, S. Létard, J.F. Létard, Chem. Phys. Lett. 394 (2004) 318.
[5] F. Varret, M. Nogues, A. Goujon, in: J. Miller, M. Drillon (Eds.), Magnetism: Molecules to Materials, vol. 2, Wiley WCH, 2001, pp. 257–291.
[6] F. Varret, A. Bleuzen, K. Boukheddaden, A. Bousseksou, E. Codjovi, C. Enachescu, A. Goujon, J. Linares, N. Menendez, M. Verdaguer, Pure Appl. Chem. 74 (2002) 2093.
[7] P. Gütlich, Y. Garcia, T. Woike, Coord. Chem. Rev. 219–221 (2001) 839.
[8] A. Hauser, Comments Inorg. Chem. 17 (1995) 17.
[9] C. Enachescu, U. Oetliker, A. Hauser, J. Phys. Chem. A 37 (2002) 9540.
[10] F. Varret, K. Boukheddaden, E. Codjovi, C. Enachescu, J. Linarès, in: P. Gütlich, H. Goodwin (Eds.), Topics in Current Chemistry, vol. 2, Spin Crossover in Transition Metal Compounds, 2004 pp. 199–229.
[11] C. Enachescu, H. Constant, E. Codjovi, J. Linares, K. Boukheddaden, F. Varret, J. Phys. Chem. Solids 62 (2001) 1409.
[12] A. Hauser, P. Gutlich, H. Spiering, Inorg. Chem. 25 (1986) 4245.
[13] A. Hauser, J. Jeftic, H. Romstedt, R. Hinek, H. Spiering, Coord. Chem. Rev. 190–192 (1999) 471.
[14] C. Enachescu, J. Linares, F. Varret, J. Phys.: Condens. Matter 13 (2001) 2481.
[15] K. Boukheddaden, I. Shteto, B. Hôo, F. Varret, Phys. Rev. B 62 (2000) 14796.
[16] A. Bousseksou, H. Constant-Machado, F. Varret, J. Phys. I 5 (1995) 747.
[17] S. Doniach, J. Chem. Phys. 68 (1978) 11.
[18] J. Wanjflasz, R. Pick, J. Phys. Coll. 32 (1971) C1-91.
[19] A. Bousseksou, J. Nasser, J. Linares, K. Boukheddaden, F. Varret, J. Phys. I 2 (1992) 1381.
[20] C.P. Slichter, H.G. Drickamer, J. Chem. Phys. 52 (1972) 2142.
[21] F. Varret, K. Boukheddaden, J. Jeftic, O. Roubeau, in: ICMM'98 (Seignosse, France, Sept. 1998), Proceedings, Mol. Cryst. Liq. Cryst. 335 (1999) 561.
[22] X.J. Liu, Y. Morimoto, T. Kawamoto, A. Nakamoto, N. Kojima, Phys. Rev. B 67 (2003) 012102.
[23] K. Boukheddaden, I. Shteto, B. Hôo, F. Varret, Phys. Rev. B. 62 (2000) 14806.
[24] S. Koshihara, Y. Tokura, K. Takeda, T. Koda, Phys. Rev. Lett. 68 (1992) 1148.
[25] K. Koshino, T. Ogawa, J. Phys. Soc. Jpn. 67 (1998) 2174.
[26] S. Gawali-Salunke, F. Varret, I. Maurin, M. Malarova, C. Enachescu, K. Boukheddaden, E. Codjovi, H. Tokoro, S. Ohkoshi, K. Hashimoto, J. Phys. Chem. B 109 (2005) 8251.
[27] E. Codjovi, W. Morscheidt, J. Jeftic, J. Linares, M. Nogues, A. Goujon, O. Roubeau, H. Constant-Machado, A. Desaix, A. Bousseksou, M. Verdaguer, F.Varret, in: ICMM'98 (Seignosse, France), J. Mol. Cryst. Liq. Cryst 335 (1999) 1295–1304.
[28] A. Goujon, F. Varret, V. Escax, A. Bleuzen, M. Verdaguer, in: ICMM'2000 (San-Antonio, Sept 2000), Proceedings, Polyhedron 20 (2001) 1339–1345.
[29] G. Chastanet, Ph.D. Thesis, University of Bordeaux, 2002
[30] C. Enachescu, Ph.D. Thesis, University of Versailles, 2003.
[31] M. Hanawa, Y. Moritomo, A. Kuriki, J. Tateishi, K. Kato, M. Takata, M. Sakata, J. Phys. Soc. Jpn. 72 (2003) 987.
[32] B. Hôo, K. Boukheddaden, F. Varret, Eur. Phys. J. B 17 (2000) 449.

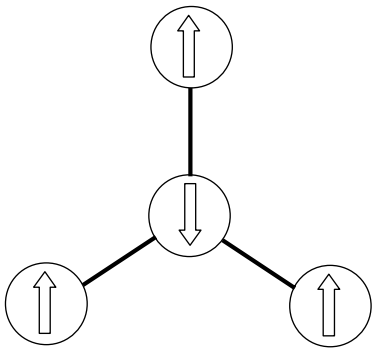
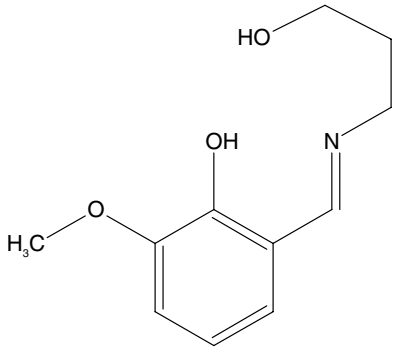


Fig. 1. Spin rationalisation for the $S = 5$ ground state of Fe_4 propellers.



Scheme 1. Schiff-base ligand, L, formed by condensing *o*-vanillin with 3-amino-1-propanol.

$thme^{3-}$ ligands to give $Fe_4(thme)_2(dpm)_6$ [7]. Here we report the synthesis, characterisation and magnetic behaviour of a compound containing similar Fe_4O_6 core but using a different ligand system (Scheme 1) and also a related dinuclear complex with pentacoordinate iron centres with coordination geometries similar to those for two of the Fe(III) centres in the tetranuclear complex.

2. Experimental

The reagents, $FeCl_2 \cdot 4H_2O$ (Fluka), triethylamine (Riedel-de-Haën), *o*-vanillin (Lancaster), aminopropanol (Fluka) and methanol, were used without further purification.

2.1. Synthesis and characterisation

2.1.1. $[Fe_2(vap)_2Cl_2]$ (**1**)

A methanolic solution containing *o*-vanillin (1 mmol, 152 mg) and 3-amino-1-propanol (1 mmol, 75 mg) stirred for 20 min was added to a methanolic solution of $FeCl_2 \cdot 4H_2O$ (1 mmol, 198 mg). Dark brown crystalline rods formed after 1 d. Yield: 180 mg/ 60%. *Anal*. Calc. $C_{22}H_{26}Fe_2N_2O_6Cl_2$: C, 44.25; H, 4.39; N, 4.70. Found: C, 44.02; H, 4.45; N, 4.61%. Infra-red (cm^{-1}): 2926 (m), 2867 (m), 2828 (m), 1610 (s), 1556 (m), 1469 (m), 1450 (m), 1440 (m), 1315 (m), 1253 (m), 1224 (m), 1054 (m), 736 (m), 560 (m), 515 (m), 434 (w).

2.1.2. $[Fe_4(vap)_4(CH_3O)_2Cl_2]$ (**2**)

The procedure for **1** was repeated with the addition of triethylamine (1 mmol, 101 mg) to the ligand solution. Dark brown crystalline prisms of **2** formed after standing for 1 d. Yield: 176 mg/ 59%. *Anal*. Calc. $C_{46}H_{58}Fe_4N_4O_{14}Cl_2$: C, 46.61; H, 4.73; N, 4.73. Found: C, 45.13; H, 4.83; N, 4.65%. Infra-red (cm^{-1}): 2923 (m), 2862 (m), 2830 (w), 1623 (s), 1599 (w), 1552 (w), 1470 (m), 1440 (m), 1313 (m), 1246 (m), 1223 (m), 1050 (m), 735 (m), 496 (m), 433 (w).

2.2. Determination of crystal structure

Data for **1** and **2** were measured on Bruker SMART Apex and Stoe IPDS area detector diffractometers, respectively, using graphite-monochromated Mo-Kα radiation ($\lambda = 0.71073$ Å). The structures were solved by direct methods and refined by full-matrix least-squares against F^2 for all data, using the SHELXTL software package [8]. All non-H atoms were refined anisotropically; H-atoms were either fully refined isotropically (**1**) or placed in calculated positions (**2**).

Crystal data and details of the data collection and structural refinement are summarised in Table 1. Crystallographic data (excluding structure factors) for the structures in this paper have been deposited with the Cambridge Crystallographic Data Centre as supplementary publication nos. CCDC 256909 and 256910. Copies of the data can be obtained, free of charge, on application to CCDC, 12 Union Road, Cambridge CB2 1EZ, UK: http://www.ccdc.cam.ac.uk/perl/catreq/catreq.cgi, e-mail: data_request@ccdc.cam.ac.uk, or fax: +44 1223 336033.

2.3. Magnetic properties

Magnetic measurements were performed using a Quantum Design SQUID MPMS-XL susceptometer. Measurements were performed on a polycrystalline sample of 9.2 mg (**1**) and 10.7 mg (**2**) in the range 1.8–300 K using a 0.1 T field. The magnetic data were corrected for the diamagnetic contribution calculated from Pascal's constants [9].

3. Results and discussion

3.1. Description of the structure

The structure of the dinuclear complex **1** is shown in Fig. 2. In the centrosymmetric complex, the $(vap)^{2-}$

Table 1
Crystal data

Compound	1	2
Formula	$C_{22}H_{26}Cl_2Fe_2N_2O_6$	$C_{46}H_{58}Cl_2Fe_4N_4O_{14}$
Formula weight	597.05	1185.26
Crystal system	monoclinic	monoclinic
Space group	$P2_1/n$	$P2_1/c$
Unit cell dimensions		
a (Å)	8.2430(9)	14.6501(8)
b (Å)	15.5150(17)	14.3068(9)
c (Å)	10.3961(12)	25.0288(16)
β (°)	111.924(2)	102.593(7)
V (Å)^3	1233.4(2)	5119.7(5)
Z	2	4
T (K)	100	200
$F(0\,0\,0)$	612	2448
D_c (Mg m^{-3})	1.608	1.538
μ(Mo-Kα) (mm^{-1})	1.433	1.282
Data measured	5483	33043
Unique data	2651	10000
R_{int}	0.0341	0.0627
Data with $I \geqslant 2\sigma(I)$	2081	4755
$2\theta_{max}$ (°)	55.8	52.0
Completeness to $2\theta = 50°$ (%)	99.5	99.9
wR_2 (all data)	0.0978	0.0907
S (All data)	0.996	0.990
R_1 [$I \geqslant 2\sigma(I)$]	0.0373	0.0455
Parameters	206	639
Biggest difference peak/hole (e Å^{-3})	+0.445/−0.493	+0.653/−0.322

ligands each chelate a ferric cation Fe(1) through the imine nitrogen and the deprotonated propanol and phenol oxygens, resulting in a *mer* geometry for the coordinated ligand. Each of the propanol oxygens also bridges to the other iron centre. This results in two equivalent and nearly symmetric alkoxy bridges with an Fe(1)···Fe(1′) separation of 3.1495(7) Å. The coordination environment about Fe(1) is completed by a chloride ligand Cl(1). The geometry can best be described as square-pyramidal with Cl(1) in the axial position. Fe(1) is displaced by 0.553 Å out of the O_3N plane towards Cl(1), with the Cl–Fe–O and Cl–Fe–N angles all in the range 100.96–110.12°.

The nearest atom to Fe(1) *trans* to Cl(1) is a methoxy hydrogen at 3.711 Å from Fe(1). There are no significant π–π stacking interactions. The closest intermolecular contacts are from C(4), the carbon atom of the imino group, to O(2) (3.450 Å) and O(3) (3.329 Å) of the molecule at $x - 1/2$, $-y + 3/2$, $z - 1/2$.

The structure of the tetranuclear complex **2** is shown in Fig. 3, with selected geometric parameters listed in Table 2. The central iron Fe(1) is bridged to three further iron atoms, via pairs of alkoxy bridges. Unlike in the previously reported examples, the three sets of bridges are not equivalent, The peripheral iron Fe(2) has an octahedral geometry with the two $(vap)^{2-}$ ligands *mer*-chelated, such that the two propanol oxygens are *cis* to each other. These two oxygens form bridges between Fe(2) and the central Fe(1). The two other peripheral irons, Fe(3) and Fe(4), are penta-coordinated with a distorted square-based pyramidal geometry. For both there is a single $(vap)^{2-}$ ligand occupying three sites of the base of the iron, an axial chloride ligand and a bridging methoxy ligand bridging to the central Fe(1). A

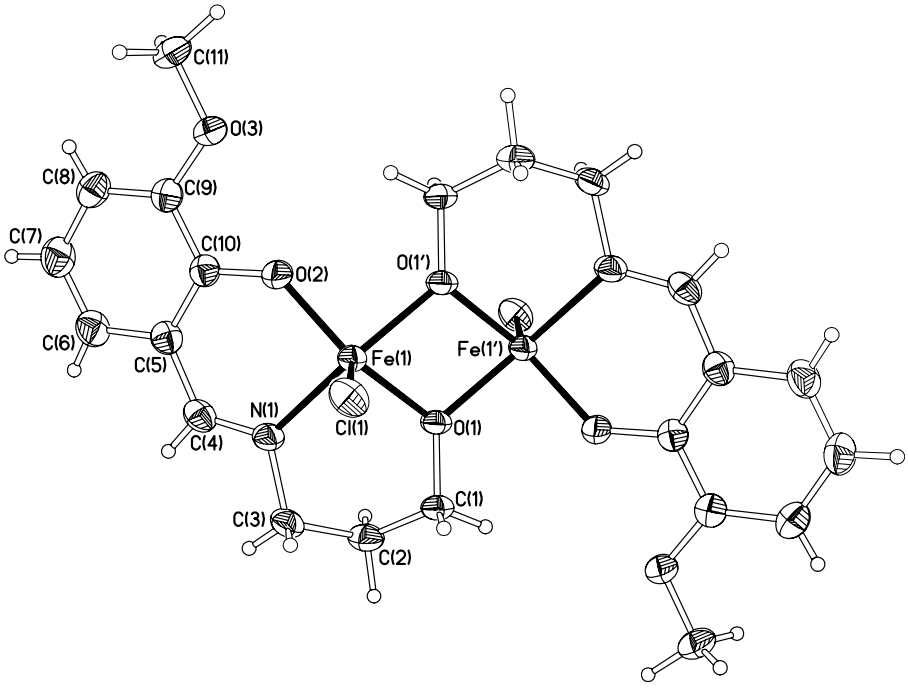


Fig. 2. Structure of $[Fe_2(vap)_2Cl_2]$ (**1**), with 50% thermal ellipsoids. Selected bond distances and angles: Fe(1)–O(1)1.9750(18), Fe(1)–O(1′) 1.9889(17), Fe(1)–N(1) 2.106(2), Fe(1)–O(2) 1.8847(18), Fe(1)–Cl(1) 2.2416(8) Å and Fe(1)–O(1)–Fe(1′) 105.23(8)°.

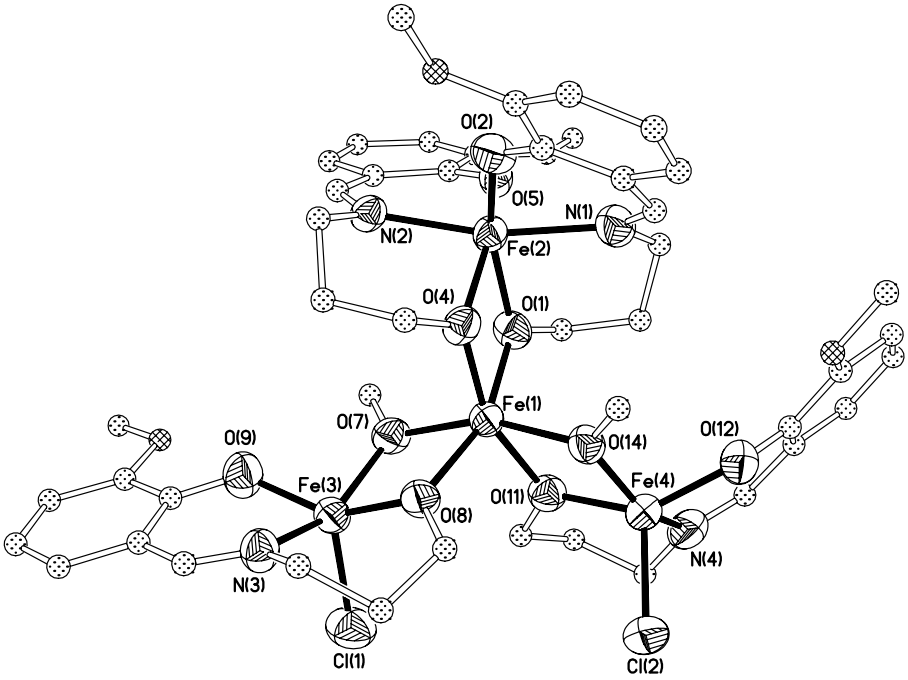


Fig. 3. Structure of $[Fe_4(vap)_4(\mu\text{-}OMe)_2Cl_2]$ (**2**). For clarity, hydrogen atoms and the minor disorder components of C(25) and C(26) have been omitted, and only the Fe and coordinating atoms are shown as 50% thermal ellipsoids and labelled.

Table 2
Selected bond lengths (Å) and angles (°) for **2**

Fe(1)–O(1)	1.975(3)	Fe(1)–O(1)–Fe(2)	107.13(14)
Fe(2)–O(1)	2.008(3)		
Fe(1)–O(4)	1.985(3)	Fe(1)–O(4)–Fe(2)	106.03(14)
Fe(2)–O(4)	2.026(3)		
Fe(1)–O(7)	2.014(3)	Fe(1)–O(7)–Fe(3)	105.40(15)
Fe(3)–O(7)	1.942(3)		
Fe(1)–O(8)	2.025(3)	Fe(1)–O(8)–Fe(3)	104.59(14)
Fe(3)–O(8)	1.952(3)		
Fe(1)–O(11)	2.051(3)	Fe(1)–O(11)–Fe(4)	104.34(14)
Fe(4)–O(11)	1.948(3)		
Fe(1)–O(14)	2.003(3)	Fe(1)–O(14)–Fe(4)	106.26(14)
Fe(4)–O(14)	1.946(3)		
Fe(3)–Cl(1)	2.2266(15)		
Fe(4)–Cl(2)	2.2328(15)		

further bridge to Fe(1) is provided by the deprotonated propanol oxygen of the ligand. The coordination geometries around Fe(3) and Fe(4) are very similar to that observed about Fe(1) in complex **1**. Whilst the two bridges between Fe(1) and Fe(2), involving O(1) and O(4), are essentially symmetrical, the other four bridges are unsymmetrical. In each case the Fe(1)–O distance is significantly longer (by 0.052–0.098 Å) than the corresponding ones to the pentacoordinate Fe(3) and Fe(4). Also the Fe–O–Fe angle for the methoxy bridge is slightly larger than that for the corresponding propanol bridge. The small differences in geometries within the three linkages is most clearly shown in the Fe···Fe separations: 3.2043(9) Å for Fe(1)–Fe(2), compared to 3.1468(8) and 3.1591(10) Å for Fe(1)–Fe(3) and Fe(1)–Fe(4), respectively. The bonding situation for Fe(3) and Fe(4) is the same as that seen for Fe(1) in the asymmetric unit of compound **1**, i.e., square-pyramidal with an axial chloride and an O_3N coordination set in the square base.

The clusters of Gatteschi, Saalfrank and Mallah contain exclusively hexacoordinate Fe(III) centres with D_{3d} molecular symmetry which is crystallographically imposed only for the $Fe_4(thme)_2(dpm)_6$ cluster of Gatteschi. For **2**, the cluster is on a general position with the idealised symmetry reduced to C_2. Nevertheless the geometry of the central $\{Fe_4(\mu\text{-}OR)_6\}$ core in **2** does not deviate greatly from D_{3d} symmetry.

3.2. Magnetic behaviour

Magnetic susceptibility measurements have been performed for compounds **1** and **2**, from 300 to 1.8 K at 0.1 T. For **1**, χT decreases gradually from 4.98 to 0.05 $cm^3\,K\,mol^{-1}$ between 300 and 1.8 K indicating dominant antiferromagnetic interaction between Fe(III) $S = 5/2$ magnetic centres (Fig. S1, Supplementary Data). The dinuclear nature of **1** is clear from the structural analysis and no efficient magnetic pathway has been identified between dinuclear complexes. Therefore, **1** can be seen as a isolated dimer of Fe(III) and magnetic measurements can be modelled in terms of a simple Heisenberg model of $S = 5/2$ dimer with the Hamiltonian $H = -2JS_{Fe_1}S_{Fe_2}$ [10]. The best set of parameters obtained with this model is $g = 2.08$ and $J/k_B = -27.6$ K.

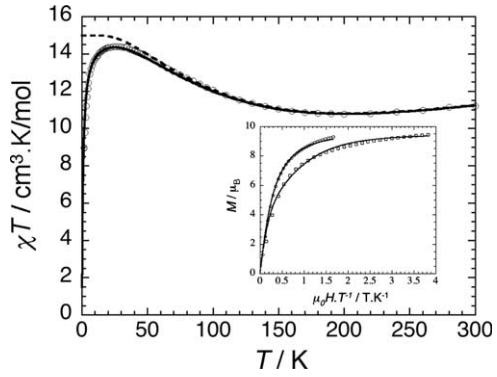


Fig. 4. Temperature dependence of the χT product for **2** at 0.1 T. Solid and dotted lines are the best fit obtained with the Heisenberg $S = 5/2$ tetramer model with and without inter-tetramer interactions (see text). Inset: Reduced magnetisation plot (M vs. H/T) including data at 1.83 and 4.2 K between 0 and 7 T. The solid line is the best fit obtained considering only the $S = 5$ ground state and its anisotropy D (see text).

For **2**, the χT product slightly decreases from 11.3 $cm^3\,K\,mol^{-1}$ at 300 K to 10.8 $cm^3\,K\,mol^{-1}$ at 200 K where it reaches a rounded minimum (Fig. 4). At lower temperature, χT increases and attains a maximum of 14.4 $cm^3\,K\,mol^{-1}$ at 24 K. Below this temperature, the χT decreases down to 8.9 $cm^3\,K\,mol^{-1}$ at 1.83 K.

This complicated thermal behaviour is typical of what has been seen for this type of Fe_4 compounds [3,7] where the antiferromagnetic interaction between the central Fe(III) and peripheral Fe(III) leads to an $S = 5$ ground state. Therefore the magnetic susceptibility of **2** was modelled using the following Heisenberg Hamiltonian $H = -2J(S_{Fe_1} \cdot (S_{Fe_2} + S_{Fe_3} + S_{Fe_4}))$ and the MAGPACK program for numerical simulation [11,12]. The best set of parameters obtained: $g = 2.0$ and $J/k_B = -21.0$ K only reproduces the experimental data down to 60 K. Therefore inter-tetramer interactions have been introduced in the frame of the mean-field approximation, using the following definition [10,13] of the susceptibility:

$$\chi = \frac{\chi_{tetramer}}{1 - \frac{2zJ'}{Ng^2\mu_B^2}\chi_{tetramer}}$$

and yielding a new set of parameters: $g = 2.0$, $J/k_B = -21.0$ K and $zJ/k_B = -0.05$ K giving a fit in excellent agreement with the experimental results (Fig. 4). The value of J thus obtained compares well with other values in the literature for similar compounds as well as for the dimer **1** (see Table 3).

The final decrease of the χT versus T plot can also be qualitatively reproduced by introducing a zero-field splitting term, D, in excess of −4 K for each Fe(III), which, however, is not physically acceptable. Nevertheless, there is no doubt that this low temperature behaviour, which is well simulated by the inter-tetramer interactions, also includes a contribution from the anisotropy of the system (D) as observed in related systems [3,7]. This term can be evaluated using reduced magnetisation plots (M versus H/T), assuming that only the $S = 5$ ground state is populated below 5 K and neglecting inter-tetramer interactions. In the case of $Fe_4(thme)_2(dpm)_6$ the value thus obtained of −0.6 K was confirmed using high-field EPR measurements [7]. Using this method on compound **2** we obtain a D value of −0.45(5) K (inset Fig. 4), falling in the range of those reported for this type of Fe_4 complex (see Table 3).

Comparing **2** with the Fe_4 propeller compounds in the literature reveals that the bonding is similar with significant distortion of the central Fe coordination environment (see Tables 2 and 3). Thus, as for the other Fe_4 complexes, the anisotropy and $S = 5$ ground state should lead to SMM behaviour. Such behaviour was not observed for **2** above 1.83 K using ac measurements with frequencies up to 1500 Hz. Therefore microSQUID measurements were performed (Fig. 5). Rather surprisingly these show no evidence of hysteresis even down to 0.04 K posing the question, "What makes a single molecule magnet?"

A careful examination of the detailed bonding situation does not provide any obvious answer. Although for $Fe_4(thme)_2(dpm)_6$ it was suggested that the bite angles for the central Fe are responsible for the enhanced SMM behaviour [7], here the corresponding angles should be even more favourable. Whereas in the case of $Fe_4(thme)_2(dpm)_6$ D_{3d} symmetry is crystallographically imposed, for the SMMs $Fe_4(CH_3O)_6(dpm)_6$ and $Fe_4(thme)_2(C_3H_7OH)_6Cl_6$ [14], as for compound **2**, this is not the case. The effect of trigonal compression and rotation on the magnetic anisotropy of an FeO_6 chro-

Table 3
Structural and magnetic parameters for **1** and **2** and analogues of **2**

	$Fe_2(vap)_2Cl_2$ (**1**)	$Fe_4(vap)_4(CH_3O)_2Cl_2$ (**2**)	$Fe_4(CH_3O)_6(dpm)_6$	$Fe_4(thme)_2(dpm)_6$	$Fe_4(thme)_2(C_3H_7OH)_6Cl_6$
Reference	this work	this work	[3]	[7]	[6]
Fe–O–Fe (°)	105.23	104.59–107.13	104.2–104.4	102.9	105.0–105.2
Fe...Fe (Å)	3.150	3.147–3.204	3.146–3.133	3.086	3.157–3.158
θ (°)		57.4	57.3	54.1	54.4
φ (°)		36.1	41.8	29.2	25.5
g	2.08	2.00	1.97	2.00	1.98
J/k_B (K)	−27.6	−21.0	−15.2	−11.9	−20.6
D/k_B (K)		−0.45	−0.3	−0.6	−0.46

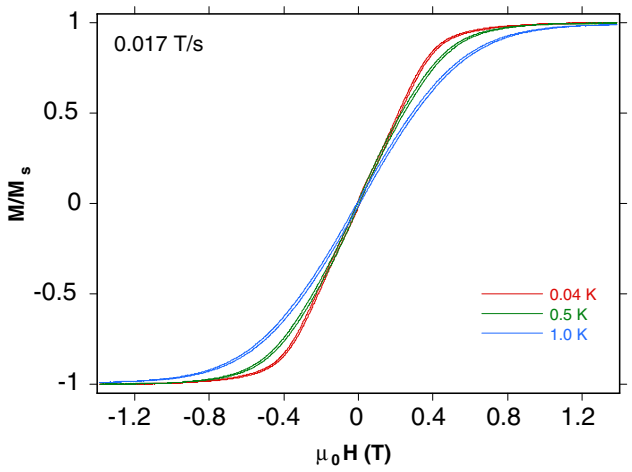


Fig. 5. MicroSQUID measurements on **2** down to 0.04 K.

mophore such as that found at the centre of these complexes and its effect on SMM behaviour has been discussed previously [7,15,16]. The two types of distortion are defined by the angles θ and φ, whose values are 57.74° and 60° respectively for a regular octahedron. Angular overlap model calculations show that trigonal compression, quantified by the angle θ, leads to a positive single ion D value and rotation of an octahedral face about the threefold axis, quantified by φ, favours a negative D value [15]. Comparing the parameters for all four compounds again leads to the conclusion that there is no reason why compound **2** should not show SMM behaviour. For example, compound **2** has a larger extent of trigonal rotation ($\varphi = 36.1°$) than $Fe_4(CH_3O)_6(dpm)_6$ ($\varphi = 41.8°$) for essentially the same extent of trigonal compression ($\theta = 57.4°$ and 57.3°, respectively). In fact, the only significant difference in the structure of **2** is the presence of the two five coordinate peripheral irons. Does this fact somehow abolish the SMM behaviour? One possibility is that for compound **2** there is a large transverse anisotropy (E term) which is allowed by symmetry in this case. A similar situation where a Ni_4 cluster with a negative D term fails to show SMM behaviour has been observed and found to be the result of a large E term [17]. This could be checked using, for example, high-field EPR experiments.

4. Conclusion

The new Fe_4 propeller compound, $Fe_4(vap)_4(CH_3O)_2Cl_2$, has structural features expected to give rise to SMM behaviour, as has been observed for similar compounds of this type. In addition, the magnetic susceptibility measurements are also in line with those of such compounds. Surprisingly, we find no evidence for SMM behaviour. The reasons why such effects are not present are currently unclear, but might be the result of transverse zero-field splitting terms. This proposal will be investigated in future studies, perhaps answering the question, "What makes a single molecule magnet?"

Acknowledgement

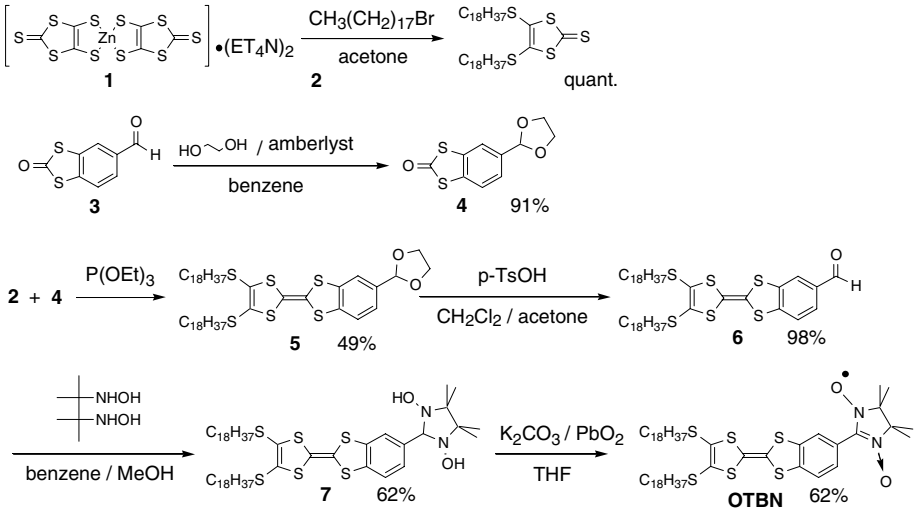
This work was supported by the CNRS, the University of Bordeaux I and the Conseil Regional d'Aquitaine (R.C.), the D.F.G. (SPP 1137, J. S. and N.T.M.; Center for Functional Nanostructures, J.T.) and QuEMolNa (MRTN-CT 2003-504880, I.J.H). The authors are also grateful to J. Modesto Clemente-Juan for teaching and providing the MAGPACK package and to Talal Mallah for supplying the CIF file for $Fe_4(thme)_2(C_3H_7OH)_6Cl_6$.

Appendix A. Supplementary data

Supplementary data associated with this article can be found, in the online version, at doi:10.1016/j.poly.2005.03.015.

References

[1] R. Sessoli, H.L. Tsai, A.R. Schake, S. Wang, J.B. Vincent, K. Folting, D. Gatteschi, G. Christou, D.N. Hendrickson, J. Am. Chem. Soc. 115 (1993) 1804.
[2] R. Sessoli, D. Gatteschi, A. Caneschi, M.A. Novak, Nature 365 (1993) 141.
[3] A.L. Barra, A. Caneschi, A. Cornia, F. Fabrizi de Biani, D. Gatteschi, C. Sangregorio, R. Sessoli, L. Sorace, J. Am. Chem. Soc. 121 (1999) 5302.
[4] R.W. Saalfrank, I. Bernt, M.M. Chowdry, F. Hampel, G.B.M. Vaughan, Chem. Eur. J. 7 (2001) 2765.
[5] H. Rupp, R.W. Saalfrank, Personal communication.
[6] M. Moragues-Cánovas, É. Rivière, L. Ricard, C. Paulsen, W. Wernsdorfer, G. Rajaraman, E.K. Brechin, T. Mallah, Adv. Mater. 16 (2004) 1101.
[7] A. Cornia, A.C. Fabretti, P. Garrisi, C. Mortalò, D. Bonacchi, D. Gatteschi, R. Sessoli, L. Sorace, W. Wernsdorfer, A.-L. Barra, Angew. Chem. Int. Ed. 43 (2004) 1136.
[8] G.M. Sheldrick, SHELXTL 5.1, 6300 Enterprise Lane, Madison, WI 53719-1173, USA, 1997.
[9] E.A. Boudreaux, L.N. Mulay, Theory and Applications of Molecular Paramagnetism, John Wiley & Sons, 1976.
[10] C.J. O'Connor, Prog. Inorg. Chem. 29 (1982) 203.
[11] J.J. Borrás-Almenar, J.M. Clemente-Juan, E. Coronado, B.S. Tsukerblat, Inorg. Chem. 38 (1999) 6081.
[12] J.J. Borrás-Almenar, J.M. Clemente-Juan, E. Coronado, B.S. Tsukerblat, J. Comput. Chem. 22 (2001) 985.
[13] B.E. Myers, L. Berger, S. Friedberg, J. Appl. Phys. 40 (1969) 1149.
[14] T. Mallah, Personal communication.
[15] D. Gatteschi, L. Sorace, J. Solid State Chem. 159 (2001) 253.
[16] E.L. Muetterties, L.J. Guggenberger, J. Am. Chem. Soc. 96 (1974) 1748.
[17] A. Sieber, C. Boskovic, R. Bircher, O. Waldmann, S.T. Ochsenbein, H.U. Güdel, N. Kirchner, J. van Slageren, W. Wernsdorfer, A. Neels, H. Stoeckli-Evans, S. Janssen, F. Juranyi, H. Mutka, Inorg. Chem., accepted.



Scheme 1. Synthesis of **OTBN**.

A zinc chelate of 1,3-dithiol-2-thione [4] (**1**) was reacted with *n*-bromooctadecane to afford 4,5-bis(octadecylthio)-1,3-dithiol-2-thione (**2**). On the other hand, 5-formyl-benzo-1,3-dithiol-2-one (**3**) was converted to an acetal derivative, 5-[1,3-dioxolan-2-yl]-benzo-1,3-dithiol-2-one (**4**), to protect the formyl moiety in the following coupling reaction [5]. A cross-coupling reaction between 4,5-bis(octadecylthio)-1,3-dithiol-2-thione (**2**) and acetal derivative (**4**) was conducted in triethylphosphite to obtain benzo-TTF derivative (**5**). After deprotecting the acetal unit, the resulted formyl derivative (**6**) was reacted with 2,3-dimethyl-2,3-bishydroxyaminobutane to obtain cyclic-bishydroxylamine (**7**) as a radical precursor. The final product, **OTBN**, was obtained as brown powders by the oxidation of precursor **7** with PbO_2 in a reasonable yield.

OTBN showed IR absorption peaks around 3010–2740 and 1470–1350 cm^{-1}; the former bands were assigned to the C–H stretching modes of long alkyl chains and the latter were assigned to N–O and C–N stretching modes of the nitronyl nitroxide group, respectively. The ESR spectrum of **OTBN** in benzene solution showed five lines ($g = 2.0061$, $a_N = 0.75$ mT) which were assigned to the nitronyl nitroxide group. The cyclic voltammogram of **OTBN** in a benzonitrile solution in the presence of 0.1 M tetrabuthylammonium perchlorate as an electrolyte showed three reversible redox waves at 0.64, 0.90 and 0.98 V versus Ag|AgCl. Judging from the redox potentials of **5** (0.60 and 0.95 V versus Ag|AgCl) and phenyl nitronyl nitroxide (**PhNN**) (0.86 V versus Ag|AgCl), the first and the third redox potentials of **OTBN** are assigned to the oxidation potentials of the donor unit, and the second oxidation potential of **OTBN** is assigned to the oxidation potential of the radical unit, respectively. Since **OTBN** can be regarded as a good electronic donor molecule, judged from the first oxidation potential, localized spin on the radical moiety will be intact during the hole injection by application of the gate voltage in the FET measurement.

3. Optical and magnetic properties of powder and film samples of OTBN

A THF solution of **OTBN** shows green color and its UV spectrum is characterized by the presence of bands at 235–330 and 530–770 nm as shown in Fig. 1(a). The former band can be assigned to the donor unit and the latter to the radical, indicating that the electronic structure of **OTBN** consists of the donor and radical units. Differential scanning calorimetric measurement of **OTBN** exhibited an endothermic peak at 54 °C in the temperature increasing process and an exothermic peak at 44 °C in the cooling process. When a color change of the sample was observed under an optical microscope on a hot plate, being sandwiched by a pair of glass plates, it was found that brownish powders changed to green liquid in the heating process, accompanied by the decrease of the absorption peak at 500 nm as shown in Fig. 1(b). The green liquid changed to an uniform brown film with cooling the sample, exhibiting a good fabricating ability of the sample. This color change of **OTBN** from brown to green may be interpreted as follows. Since the **OTBN** molecules are ordered at least locally in a thin film, an intermolecular coupling of transition dipole moments shifts the absorption to the longer wavelength, causing the increase of the intensity of absorption at 500 nm. On the other hand, the absorption at 500 nm decreases at higher temperature than 54 °C, presumably because the orientation of donor radicals becomes disordered in the fused state, diminishing

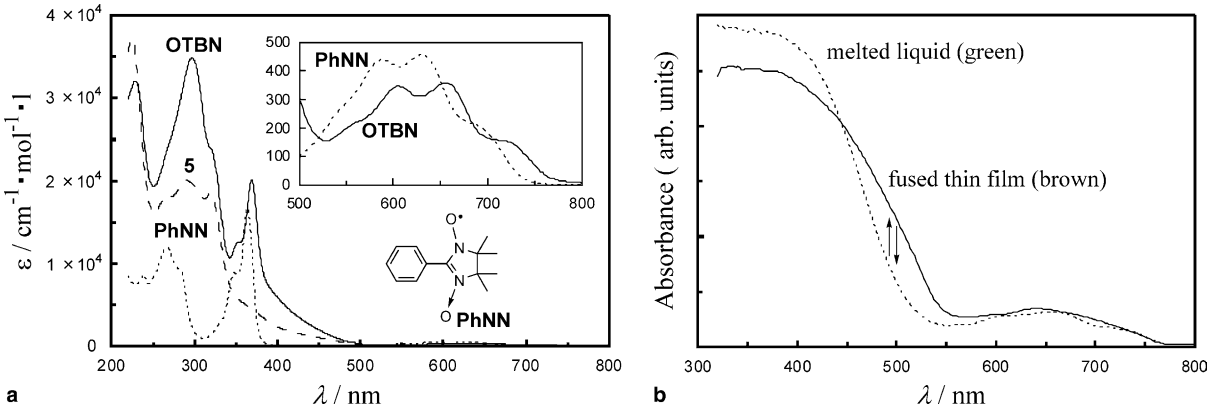


Fig. 1. (a) UV spectra of **OTBN** and reference compounds (**5** and **PhNN**) in THF solution. (b) UV spectra of a fused solid (solid line) and a melted liquid (dotted line) of **OTBN** fabricated between a pair of Pyrex glass.

the excitonic coupling. Since the extinction of the polarized light was not observed on the fused sample, a long range ordering of the molecular alignment is not achieved in the solid. The absorption spectra of the film before and after the melting is practically the same, suggesting that the donor radical is not deactivated in the melting–freezing cycles. Incidentally, the color of the sample turned to orange when the sample was heated above 65 °C. This means that the radical unit is decomposed, leaving the donor unit intact.

The magnetic susceptibility of the powdered and the fused samples of **OTBN** was measured by a SQUID magnetometer. The temperature dependence of the χT values of both samples are shown in Fig. 2. The both traces are practically the same and the χT values increase at lower temperatures, indicating the presence of the ferromagnetic intermolecular interaction. These traces were simulated using the Curie–Weiss law; Curie constants and Weiss constants of both samples were evaluated to be 0.385 emu K mol^{-1} and +0.47 K for the as-grown powder, and 0.385 emu K mol^{-1} and +0.45 K for the fused film, respectively. These ferromagnetic intermolecular interactions may be originated from the alignment of nitronyl nitroxide. The ferromagnetic

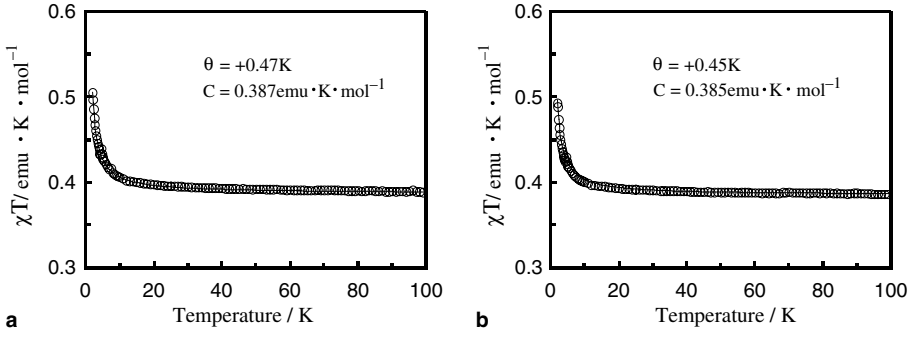


Fig. 2. Temperature dependence of magnetic susceptibility of **OBTN**: (a) the as-grown-powder obtained from a THF solution; (b) the film obtained by melting–freezing process.

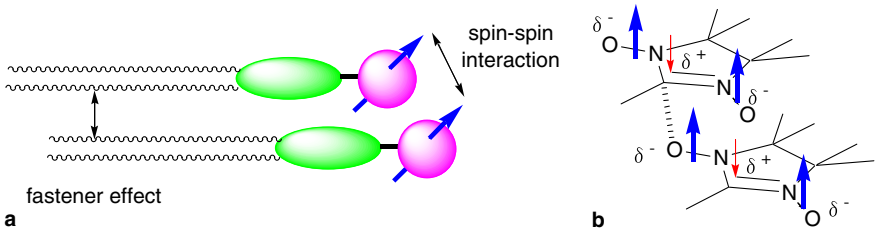


Fig. 3. The schematic illustration of the pausible alignment of **OBTN** to show intermolecular ferromagnetic interaction: (a) molecular derived from the fastener-effect between the alkyl chains; (b) intermolecular ferromagnetic spin alignment between nitronyl nitroxides of neighboring molecules on the basis of McConnell type I mechanism.

alignment of NN must be achieved by the dispersion force of long alkyl chains (Fig. 3). The fact that the ferromagnetic interaction remains constant before and after melting the powdered sample suggests that the local molecular alignment is preserved during the melting–freezing cycles.

4. Construction and measurement of FET device using organic donor, acceptor, and donor radical

In an organic FET device, the change of the passing current in an organic layer between drain and source electrodes is detected as a function of the gate voltage. Fig. 4 shows a bottom-contact type FET device in which the n-doped silicon wafer and a SiO_2 layer are utilized as the gate electrode and the insulating layer, respectively. Source and drain electrodes are prepared on the insulating layer by deposition of gold. An organic film is fabricated between the drain and source electrodes on the insulating layer by a sublimation, spin-coating, or casting method. Fig. 4(b) shows the FET substrate equipped with interdigited electrodes, each facing electrodes of which operate as a pair of drain and source electrodes. Since organic materials generally show high resistivity, interdigited electrodes with a narrow gap are required to explore the conducting property of organic materials. Consequently, interdigited electrodes with a gap of 20, 10, 5, and 2 μm are used in the current study.

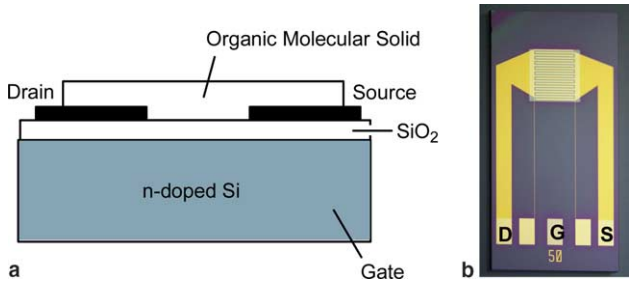


Fig. 4. (a) Geometry of a bottom-contact type organic FET device. (b) A substrate for fabricating the organic field-effect transistor having interdigited electrodes as a of drain and source electrodes. The area of the interdigited electrodes is 2×2 mm.

4.1. FET characteristics of *TTF*, *TCNQ*

Fabrication of a film of an organic molecule is usually performed by a casting method for polymers or sublimation for small molecules. However, we found that a cast film obtained from a solution of a crystalline sample exhibits clear FET characteristics, using interdigited electrodes with a small gap. The obtained results on a typical organic donor or acceptor (**TTF**, **TCNQ**) are shown in Fig. 5. When the negative gate voltage was applied to a cast film sample of **TTF** through the insulating layer, the current between drain and source electrodes (I_{DS}) increased by p-doping of organic layer, exhibiting a distinct FET characteristic. In contrast, the cast film sample of **TCNQ** exhibits a FET characteristic when the positive gate voltage is applied [6]. Incidentally, such FET characteristics were detected when the electrodes with a smaller gap of 2 or 5 μm are used, but not by electrodes with larger gaps, such as 10 or 20 μm. These results suggest that even small crystals obtained by the casting method can bridge over the electrodes with narrow gaps. Accordingly, this method is useful for exploring the conductivity of organic molecules which afford small size crystals.

4.2. FET characteristics of TTC_{18}-TTF

If tight packing of donor units is achieved in a neutral assembly, it is expected to manifest good FET characteristics. In this respect, it is interesting to examine the FET characteristic of **TTC$_{18}$-TTF** in which octadecyl chains

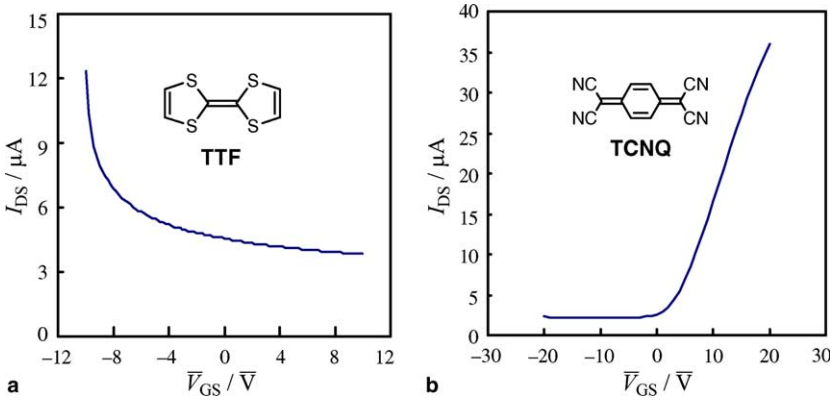


Fig. 5. FET characteristics of typical donor and acceptor exhibited on the interdigited drain source electrodes with a gap of 5 μm. The thickness of an insulating layer (SiO_2) is 180 nm: (a) FET characteristics of **TTF** with the drain–source voltage (V_{DS}) of 1 V; (b) FET characteristics of **TCNQ** with the drain–source voltage (V_{DS}) of 10 V.

are introduced to the bis(ethylenedithio)-TTF skeleton. It has been reported that the neutral crystal of **TTC_{18}-TTF** shows high conductivity due to the fastener-effect of long alkyl chains [7]. Accordingly, a film sample of **TTC_{18}-TTF** was formed on the substrate with 2 μm gap interdigited electrodes and the FET characteristic of **TTC_{18}-TTF** was measured.

Fig. 6 shows the FET characteristic of a cast film of **TTC_{18}-TTF** which was formed by evaporating a dichloromethane solution of **TTC_{18}-TTF**. The ON/OFF ratio turned out to be 10:1, and it increased up to 215:1 when the melting–freezing cycle was performed, taking an advantage of the low melting point of **TTC_{18}-TTF** (92 °C) [8]. The above results suggest that the introduction of long alkyl chains is effective for constructing a FET device from the aspect of the fabrication of donor units.

4.3. FET characteristics of *OTBN*

Since **OTBN** carries long alkyl chains as **TTC_{18}-TTF**, it is expected to provide a thin film by a melting–freezing method. The FET measurement was performed on the **OTBN** film prepared by the melting–freezing method. The FET characteristic of the **OTBN** film is shown in Fig. 7. Although the ON/OFF ratio is small, the drain current is changed by changing the gate voltage. From the *I–V* dependence between the drain and the source, the mobility in the **OTBN** film was evaluated to be 5×10^{-9} cm^2 V^{-1} S^{-1} according to Eq. (1)

$$\mu = \frac{\partial I_{DS}}{\partial V_{GS}} \left(\frac{L}{C_1 \cdot W \cdot V_{DS}} \right), \tag{1}$$

where L is the gap length, C_i is the capacitance per area and W is the gap width. The mobility of the sample may be increased by optimizing the condition of the film-formation. Incidentally, the small ON/OFF ratio may be partly derived from the pre-doping of the sample.

Since the interaction between the localized spin of the donor unit and conduction electrons which run along the donor stack is small, if any, it is indispensable to measure the conductance at cryogenic temperatures to detect the magneto-resistance effect. Although the FET measurement was performed at 4.2 K, no I_{DS} was detected at all even when a high gate voltage ($V_G = -50$ V,

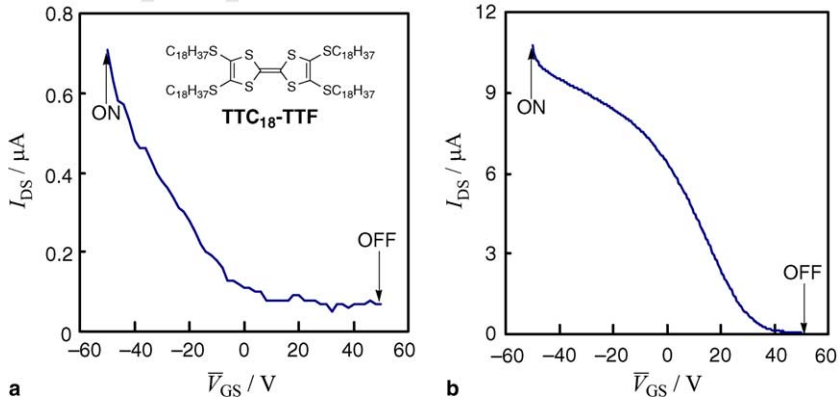


Fig. 6. FET characteristics of **TTC_{18}-TTF** exhibited on an interdigited drain source electrodes with a gap of 2 mm; the thickness of the insulating (SiO_2) was 180 nm. The voltage between drain and source (V_{DS}) was 10 V in both cases. (a) FET characteristics of a cast film of **TTC_{18}-TTF** from a solution of dichloromethane. ON/OFF ratio of I_{DS} between V_G of −50 and 50 V was 10:1. (b) FET characteristics of a film sample of **TTC_{18}-TTF** fabricated by the melting–freezing method. ON/OFF ratio of I_{DS} between $\bar{V}_{GS}$ of −50 and 50 V was 215:1.

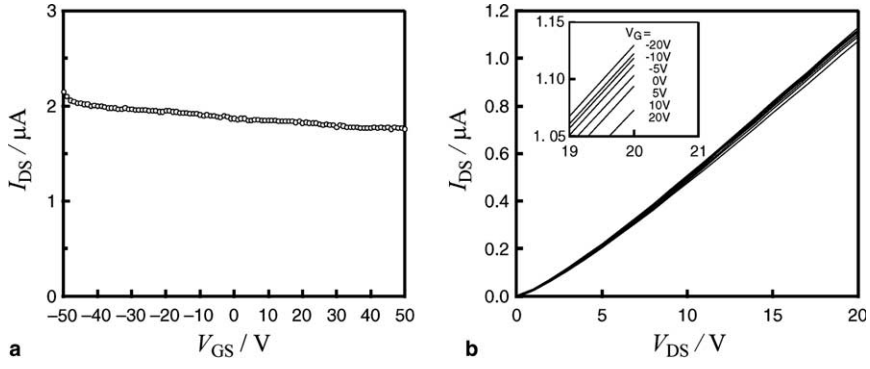


Fig. 7. FET characteristic of **OBTN** measured by the interdigited drain and source electrodes with a gap of 2 μm; the thickness of the insulating layer (SiO_2) is 195 nm. (a) Increase of I_{DS} with the decrease of gate voltage ($\bar{V}_{GS}$) from +50 to −50 V for $V_{DS} = 30$ V. (b) Change of *I–V* characteristics by variation of $\bar{V}_{GS}$.

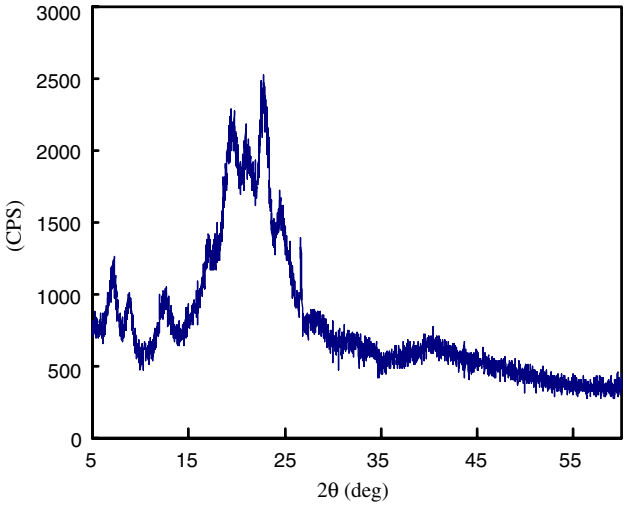


Fig. 8. Thin film X-ray diffraction pattern of **OBTN**.

$V_{DS} = 100$ V) was applied. This means that the hole-mobility was suppressed considerably at cryogenic temperatures.

The thin layer X-ray diffraction experiment was performed on the **OTBN** film. Observation of the diffraction peaks indicated the ordering of donor radicals in the film, but the peak-width of the diffraction was substantially broadened as shown in Fig. 8. The crystallite size of the sample was estimated to be about 10 nm on the basis of the analysis of the broad peak-width by Scherrer formula (Eq. (2)) [9].

$$\text{Crystal size (Å)} = \frac{0.9\lambda}{\beta \cos\theta}, \tag{2}$$

where λ is the wavelength, β is the half-width and 2θ is the Bragg angle. This means that about 10–20 molecules are aligned locally in the sample. This size of the crystalline is too small to interconnect the 2 μm gap of the interdigited electrodes. Judging from the above result, the electron hopping between crystallites is suppressed entirely at cryogenic temperature, although the inter-crystallites electron hopping occurs appreciably at room temperature. If the fabrication process is improved and the crystallite size is enlarged sufficiently, the FET characteristics of **OTBN** at low temperature may be detected.

5. Summary

A bottom-contact type FET device with interdigited electrodes as a pair of drain and source electrodes was constructed, and the FET characteristics of cast films of **TTF**, **TCNQ**, and **TTC$_{18}$-TTF** were observed. The FET characteristics of a donor radical of **OTBN** was also observed, although the hole mobility in the organic layer was very small. However, the FET effect was not observed at lower temperatures presumably due to the suppression of the inter-crystallite hopping of electrons. It would be extremely interesting to observe the FET characteristics of donor radicals at lower temperatures in order to examine the interaction between an organic localized spin and conduction electrons [10].

Acknowledgment

Authors thanks to Dr. Inaba and Dr. Sasaki of Rigaku Denki Corporation for thin layer X-ray diffraction measurement. This work was supported by Grant-in-Aid for Scientific Research on Priority Areas "Application of Molecular Spins" (Area No. 769, Proposal No. 15087101) from Ministry of Education, Culture, Sports Science and Technology (MEXT).

References

[1] (a) F. Garnier, Chem. Phys. 227 (1998) 253;
(b) G. Horowits, Adv. Mater. 10 (1998) 365;
(c) H.E. Katz, Z. Bao, J. Phys. Chem. B 104 (2000) 671.
[2] (a) J. Nakazaki, Y. Ishikawa, A. Izuoka, T. Sugawara, Y. Kawada, Chem. Phys. Lett. 319 (2000) 385;
(b) J. Nakazaki, M.M. Matsushita, A. Izuoka, T. Sugawara, Tetrahedron Lett. 40 (1999) 5027;
(c) R. Kumai, M.M. Matushita, A. Izuoka, T. Sugawara, J. Am. Chem. Soc. 116 (1994) 4523.
[3] J.G. Laquindanum, H.E. Kats, A.J. Lovinger, J. Am. Chem. Soc. 120 (1998) 664.
[4] G. Steimrcke, H. Sieler, R. Kirmse, E. Hoyer, Phosphorus Sulfur 7 (1979) 49.
[5] Y. Ishikawa, T. Miyamoto, A. Yoshida, Y. Kawada, J. Nakazaki, A. Izuoka, T. Sugawara, Tetrahedron Lett. 40 (1999) 8819.
[6] A.R. Brown, D.M. de Leeuw, E.J. Lous, E.E. Havinga, Synth. Met. 66 (1994) 257.
[7] (a) H. Inokuchi, G. Saito, P. Wu, K. Seki, T. Tang, T. Mori, K. Imaeda, T. Enoki, Y. Higuchi, Chem. Lett. (1986) 1263;
(b) K. Imaeda, T. Enoki, Z. Shi, P. Wu, N. Okada, H. Yamochi, G. Saito, H. Inokuchi, Bull. Chem. Soc. Jpn. 60 (1987) 3163.
[8] Z. Shi, T. Enoki, K. Imaeda, K. Seki, P. Wu, H. Inokuchi, G. Saito, J. Phys. Chem. 92 (1988) 5044.
[9] P. Scherrer, Cöttinger Nachr. (1918) v68.
[10] T. Sugawara, J. Nakazaki, M.M. Matsushita, Nanotechnology Toward the Organic Photonics, in: H. Sasabe (Ed.), GooTech, 2002, pp. 41–67.

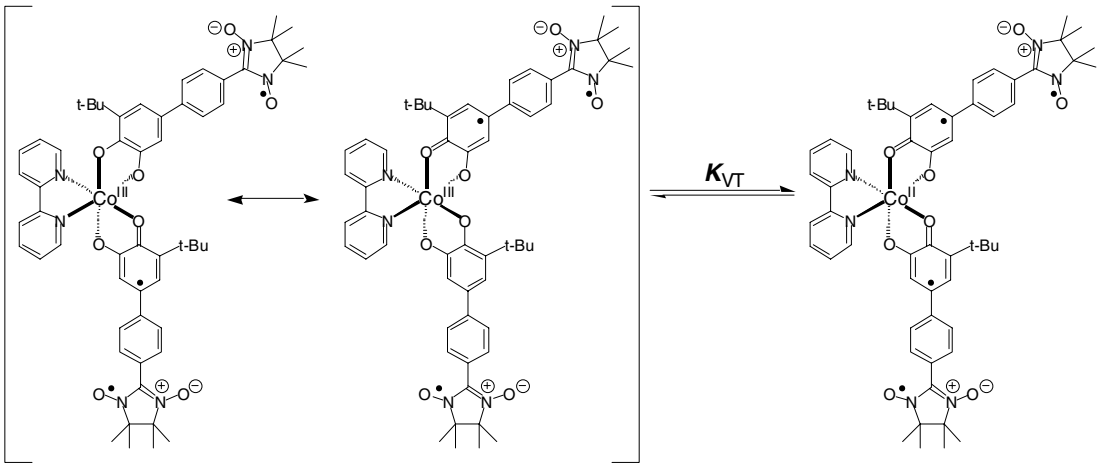


Fig. 1. Mixed-valency and valence tautomerism inherent to complex **1**.

The valence tautomeric equilibrium was studied using variable temperature infrared spectroscopy of amorphous films cast from methylene chloride by measuring the intensity of the intervalence charge transfer band characteristic of the Co^{III} form [3,33]. Representative spectra are shown in Fig. 2, and normalized intensity vs. temperature data are shown in Fig. 3.

The data in Fig. 3 were fit according to the equation [33]:

$$x_{Co^{III}} = 1/[\exp(\Delta H^{\circ}/RT - \Delta S^{\circ}/R) + 1]$$

where $x_{Co^{III}}$ is the mole fraction of the cobalt(III) form of the valence tautomer. The results of the fit are $\Delta H^{\circ} = 9.2$ kcal mol^{-1} and $\Delta S^{\circ} = +22$ cal K^{-1} mol^{-1}. These thermodynamic parameters are slightly smaller than those reported by Pierpont for Co(bpy)(3,5-DBSQ)(3,5-DBCat) valence tautomer [25], and are in line with the redox potential differences [18] between 3,5-di-*tert*-butylorthoquinone and our phenylnitronylnitroxide–orthoquinone [32].

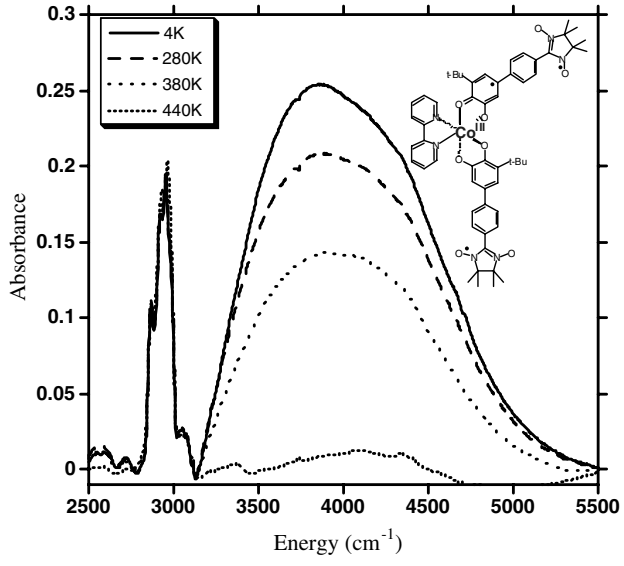


Fig. 2. Intervalence charge transfer (IVCT) band of **1** recorded on a film cast from methylene chloride. Bottom to top: 440–4 K.

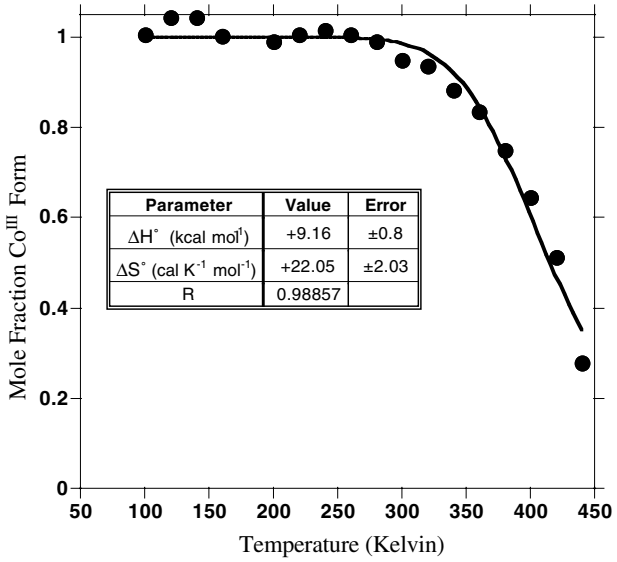


Fig. 3. Mole fraction of Co^{III}-form of **1** (from IVCT band) as a function of temperature. Data were fit according to equation in text.

As mentioned previously, the Co^{III} form of **1** might exhibit double exchange. This contribution to the stabilization of high-spin ground states is the result of the "single-site" semiquinone–nitronylnitroxide ferromagnetic exchange coupling and intramolecular electron transfer between the mixed-valent catecholate and semiquinone dyad. However, the Co^{III} forms of all known valence tautomers are vibronically trapped at low temperature such that catecholate and semiquinone bond lengths are readily distinguished [33]. This indicates that the mixed-valency in the crystalline state is in the Class I to early Class II limit within the Robin and Day scheme [27]. Although the catecholate and semiquinone moieties

are vibronically trapped at low-temperatures in the solid state, and do not show evidence for an appreciable thermal rate of electron exchange between the two sites, this does not preclude electron delocalization. In fact, this represents and interesting case where the off-diagonal electronic coupling matrix element, H_{ab}, is large enough to mix the SQ and CAT wavefunctions, but not large enough to reduce the thermal barrier, E_{th}, for facile thermal electron transfer between the two sites. The intense intervalence charge transfer (IT) transition shown in Fig. 2 provides key evidence for this system being classified in the Class II limit. Assuming simple harmonic potential surfaces and a small H_{ab}, the energy of this IVCT transition can be used to place an upper limit on the thermal barrier for electron transfer between vibronically trapped SQ and CAT sites. Since $E_{th} = E_{IT}/4$ in this limit, the barrier for electron exchange is $\sim$1000 cm^{-1}, which agrees with the valence trapping observed in the X-ray structures of Co^{III} valence tautomers [33]. Typically, a detailed analysis of the IVCT bandshape as a function of temperature is required to determine the degree of wavefunction mixing (electron delocalization) between the mixed valent sites in the Class II limit. We present here an introduction to a method that utilizes radical pendants as reporters of electron delocalization between mixed valent SQ and NN donors in the Co^{III} form of valence tautomeric **1**.

It is common for valence tautomers to display thermodynamic parameters for the valence tautomeric transition that are highly dependent on the matrix environment of the molecule. Thus, solution, polymer film, thin film and crystalline samples all display different entropic and enthalpic contributions to the relative stabilization of the Co^{II} and Co^{III} forms [33]. The magnetic data for a polycrystalline sample of **1** are shown in Fig. 4. The effective magnetic moment decreases from 3.35 μ_B at 350 K to 3.20 μ_B at 175 K. This decrease is indicative of the expected $Co^{II} \rightarrow Co^{III}$ conversion as the temperature is lowered, consistent with the valence tautomeric equilibrium. The magnetic data differ from the infrared results in that more of the Co^{II} form is observed in the latter experiments. The μ_{eff} value at $\sim$200 K is that anticipated for uncoupled $S_a = 1$ and $S_b = 1/2$ spins. Intramolecular exchange interactions in SQ–Ph–NN have been shown to be ferromagnetic, yielding a triplet ground state with $\boldsymbol{J} \sim 100$ cm^{-1} [34]. Thus, S_a represents the spin of the SQ–Ph–NN ligand and S_b that of CAT–Ph–NN. At temperatures below $\sim$150 K, μ_{eff} begins to increase. This is indicative of ferromagnetic *interligand* exchange interactions being operative. Below ca. 30 K, μ_{eff} decreases rapidly due to antiferromagnetic intermolecular interactions, common to nitronylnitroxide radicals [4]. The μ_{eff} data were fit to a field-independent triplet–doublet exchange model according to $\boldsymbol{H} = -2\boldsymbol{J}S_aS_b$ and incorporating intermolecular interactions via a mean-field approximation. The best-fit to the data is presented in Fig. 4, and the relevant spin–Hamiltonian parameters determined are $g = 2.00$ (fixed), $J = +4.7$ cm^{-1}, and $zJ' = -0.6$ cm^{-1}, with the inclusion of a small diamagnetic term.

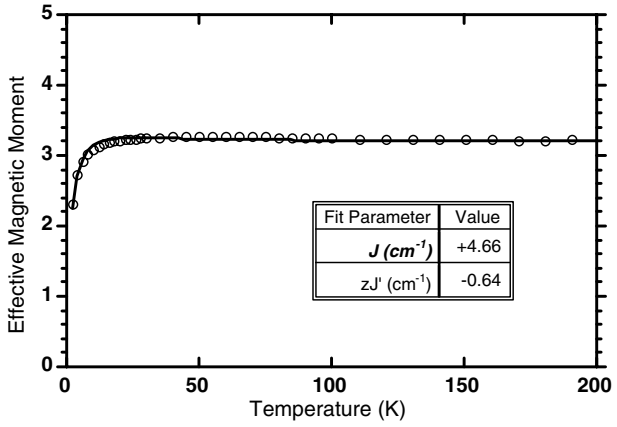


Fig. 4. Effective magnetic moment (B.M) of **1** as a function of temperature between 2 and 200 K.

The presence of interligand exchange is somewhat unanticipated, as the superexchange interactions must occur through a diamagnetic Co^{III} ion, and diamagnetic CAT–Ph. The shortest through-bond superexchange pathway incorporates 11 bonds, including two metal–ligand bonds. It would be remarkable if this represented a superexchange pathway capable of promoting "long-range" ferromagnetic exchange between the SQ–Ph–NN ligand and the NN of CAT–Ph–NN. The appearance of the intense IVCT band provides a key clue as to how to explain this apparent paradox. The intensity of an IVCT band, I_{IT}, is proportional to the square of the overlap intergral between the two molecular orbitals (primarily CAT and SQ in origin) involved in the one-electron promotion. This overlap relates directly to the mixing between SQ–Co^{III}–CAT and CAT–Co^{III}–SQ potential surfaces mediated by H_{ab} in the Robin and Day Class II scheme. This requires electron delocalization between the formal SQ and CAT ligand fragments. Thus, partial delocalization of the SQ unpaired electron onto the CAT moiety provides a convenient way to explain the presence of the intense IT band and ferromagnetic exchange coupling between S_a and S_b. Future work will serve to quantify this mixing, relate it to H_{ab}, and correlate the magnitude of the interligand ferromagnetic exchange with the nature of the interligand IVCT band.

Acknowledgements

D.A.S. acknowledges the National Science Foundation (CHE-0345263; CHE-0091247 SQUID Magnetometer) for financial support, and thanks the Camille and Henry Dreyfus Foundation for a Camille Dreyfus Tea-

cher-Scholar Award. M.L.K. acknowledges the Petroleum Research Fund ACS PRF 38086-AC3 for financial support of this work.

References

[1] D.M. Adams, D.N. Hendrickson, J. Am. Chem. Soc. 118 (1996) 11515.
[2] D.M. Adams, B. Li, J.D. Simon, D.N. Hendrickson, Angew. Chem., Int. Ed. Engl. 34 (1995) 1481.
[3] D.M. Adams, L. Noodleman, D.N. Hendrickson, Inorg. Chem. 36 (1997) 3966.
[4] D.B. Amabilino, J. Veciana, Nitroxide-based organic magnets, in: J.S. Miller, M. Drillon (Eds.), Magnetism: Molecules to Materials II: Molecule-based Materials, Wiley-VCH, New York, 2001, p. 1.
[5] P.W. Anderson, H. Hasegawa, Phys. Rev. 100 (1955) 675.
[6] A. Bencini, A. Caneschi, C. Carbonera, A. Dei, D. Gatteschi, R. Righini, C. Sangregorio, J. Van Slageren, J. Mol. Struct. 656 (2003) 141.
[7] C. Benelli, D. Gatteschi, Chem. Rev. 102 (2002) 2369.
[8] J.J. Borrás-Almenar, J.M. Clemente, E. Coronado, A.V. Palii, B.S. Tsukerblat, Mol. Cryst. Liq. Cryst. Sci. Technol. Sect., A-Mol. Cryst. Liq. Cryst. 306 (1997) 209.
[9] J.J. Borrás-Almenar, J.M. Clemente, E. Coronado, A.V. Palii, B.S. Tsukerblat, R. Georges, J. Chem. Phys. 105 (1996) 6892.
[10] J.J. Borrás-Almenar, E. Coronado, R. Georges, A.V. Palii, B.S. Tsukerblat, Chem. Phys. Lett. 249 (1996) 7.
[11] J.J. Borrás-Almenar, E. Coronado, H.M. Kishinevsky, B.S. Tsukerblat, Chem. Phys. Lett. 217 (1994) 525.
[12] J.J. Borrás-Almenar, E. Coronado, A.V. Palii, B.S. Tsukerblat, R. Georges, Chem. Phys. 226 (1998) 231.
[13] J.J. Borrás-Almenar, E. Coronado, B.S. Tsukerblat, Chem. Phys. 177 (1993) 1.
[14] J.J. Borrás-Almenar, E. Coronado, B.S. Tsukerblat, A.V. Palii, A.V. Babich, J. Struct. Chem. 35 (1994) 454.
[15] O. Cador, F. Chabre, A. Dei, C. Sangregorio, J. Van Slageren, M.G.F. Vaz, Inorg. Chem. 42 (2003) 6432.
[16] O. Cador, A. Dei, C. Sangregorio, Chem. Commun. (2004) 652.
[17] C. Carbonera, A. Dei, J.F. Letard, C. Sangregorio, L. Sorace, Angew. Chem., Int. Ed. 43 (2004) 3136.
[18] A. Dei, Inorg. Chem. 32 (1993) 5730.
[19] J.J. Girerd, V. Papaefthymiou, K.K. Surerus, E. Munck, Pure Appl. Chem. 61 (1989) 805.
[20] J.B. Goodenough, Phys. Rev. 100 (1955) 564.
[21] P. Gütlich, A. Dei, Angew. Chem., Int. Ed. Engl. 37 (1997) 2734.
[22] O.-S. Jung, D.H. Jo, Y.-L. Lee, B.J. Conklin, C.G. Pierpont, Inorg. Chem. 37 (1997) 19.
[23] O.-S. Jung, C.G. Pierpont, J. Am. Chem. Soc. 116 (1994) 2229.
[24] C.G. Pierpont, Coord. Chem. Rev. 216 (2001) 99.
[25] C.G. Pierpont, O.-S. Jung, Inorg. Chem. 34 (1995) 4281.
[26] I. Ratera, D. Ruiz-Molina, F. Renz, J. Ensling, K. Wurst, C. Rovira, P. Gutlich, J. Veciana, J. Am. Chem. Soc. 125 (2003) 1462.
[27] M.B. Robin, P. Day, Adv. Inorg. Radiochem. 10 (1967) 247.
[28] Ruiz-D. Molina, J. Veciana, K. Wurst, D.N. Hendrickson, C. Rovira, Inorg. Chem. 39 (2000) 617.
[29] O. Sato, S. Hayami, Z. Gu, K. Seki, R. Nakajima, A. Fujishima, Chem. Lett. (2001) 874.
[30] O. Sato, S. Hayami, Z.Z. Gu, K. Seki, R. Nakajima, A. Fujishima, Chem. Lett. 9 (2001) 874.
[31] Y. Shimazaki, F. Tani, K. Fukui, Y. Naruta, O. Yamauchi, J. Am. Chem. Soc. 125 (2003) 10512.
[32] D.A. Shultz, Our quinone is more easily reduced than 3,5-di-*tert*-butylorthoquinone by ca. 140 mV, consistent with the greater ΔH° (unpublished results).
[33] D.A. Shultz, Valence tautomerism in dioxolene complexes of cobalt, in: J.S. Miller, M. Drillon (Eds.), Magnetism: Molecules to Materials II: Molecule-based Materials, Wiley-VCH, New York, 2001, pp. 281–306.
[34] D.A. Shultz, K.E. Vostrikova, S.H. Bodnar, H.J. Koo, M.H. Whangbo, M.L. Kirk, E.C. Depperman, J.W. Kampf, J. Am. Chem. Soc. 125 (2003) 1607.
[35] A. Yamaguchi, K. Awaga, J. Mater. Chem. 11 (2001) 2142.
[36] T. Yokoyama, K. Okamoto, K. Nagai, T. Ohta, S. Hayami, Z.Z. Gu, R. Nakajima, O. Sato, Chem. Phys. Lett. (2001).

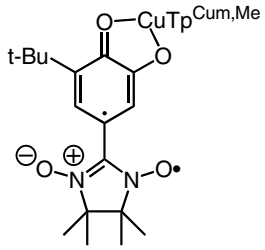


Fig. 1. Structure of (**NNSQ**)CuTp^{Cum,Me}.

where k is a two-electron exchange integral describing the self-repulsion of the overlap density, H_{ab} is the electronic coupling matrix element between orbitals a and b, and U is the single site Coulomb repulsion integral. Since H_{ab} is proportional to the overlap integral, $\langle a|b\rangle$, [4] ferromagnetic coupling is favored when the magnetic orbitals are either strictly or accidentally orthogonal. Under these conditions, $\langle a|b\rangle = 0$ and J reduces to $2k$. For organic biradicals, analysis of intramolecular exchange coupling is simplified by the fact that, within the active electron approximation [3], typically only two magnetic orbitals, a and b, are involved. In such cases, J simply reduces to (2)[2]

$$J = J_{\mathrm{F}} + J_{\mathrm{AF}} = 2k_{ab} - \frac{4H_{ab}^2}{U}. \tag{2}$$

When organic bi- and polyradicals possess orthogonal SOMOs the electronic coupling matrix element, H_{11}, is zero. The presence of a large overlap density, $\rho(i)$ [3], results in an appreciable value for the two-electron exchange integral, k, and a ferromagnetic interaction results [3]

$$k = \int_{\mathrm{space}} \rho(1)\rho(2) r_{12}^{-1}\, \mathrm{d}\tau. \tag{3}$$

This model has been particularly useful for understanding the exchange interaction in non-disjoint [5] symmetric- and non-disjoint unsymmetrical biradicals [2,6–10].

Herein, we use a valence bond configuration interaction (VBCI) model to explain the electronic origin of strong ferromagnetic exchange coupling in an organic biradical ligand. To our knowledge, this is the first time that the VBCI model has been used to examine ferromagnetic exchange interactions in an organic biradical. Moreover, the electronic origin of the high spin ground state is supported by the appearance of an intramolecular charge transfer (ILCT) transition in the biradical ligand **NNSQ**, where **NN** is nitronyl nitroxide and **SQ** is 5-*tert*-butyl-semiquinone (Fig. 1). The VBCI model has been used to understand excited state contributions to the ground state intramolecular exchange interaction, J, in multinuclear transition metal systems [11–19]. Thus, our use of a VBCI model in donor–acceptor biradicals (vide infra) links exchange coupling studies of inorganic systems with their organic counterparts, and provides a connection between heretofore unrelated systems.

[2] Within the active-electron approximation, the intramolecular exchange interaction, J, is expressed as a sum over all antiferromagnetic and ferromagnetic pathways, see [3].

2. Experimental

2.1. Electronic absorption spectroscopy

Electronic absorption spectra were collected using a double beam Hitachi U-3501 UV–Vis–NIR spectrophotometer capable of scanning the wavelength region between 185 and 3200 nm. Wavelength calibration was done against the deuterium 656.10 nm line. Background corrections were accomplished by first scanning neat solvent over the relevant wavelength range in the spectroscopic cell to be used for sample. Room temperature (300 K) spectra were collected in CH_2Cl_2 at 2.0 nm resolution in a single-beam configuration using masked spectrosil quartz cells.

2.2. Electron paramagnetic resonance (EPR) spectroscopy

Frozen glass EPR spectra were measured at X-band (~9.3 GHz) using a Bruker EMX spectrometer. Low temperature EPR measurements were performed using 2-methyl tetrahydrofuran as a glassing agent, and the temperature was held at 4 K in an Oxford liquid helium flow cryostat. Calculation of the $g_{\|}$ and $g_{\perp}$ $\Delta m_{\mathrm{s}} = \pm 1$ EPR line positions were performed using closed form expressions for the eigenvalues of an $S_{\mathrm{T}} = 3/2$ system with the magnetic field oriented parallel and perpendicular to the molecular z-axis.

2.3. Magnetic circular dichroism (MCD) spectroscopy

Low temperature MCD spectra were collected on a system consisting of a Jasco J600 CD spectropolarimeter employing Hamamatsu photomultiplier tubes of either S-1 or S-20 response, an Oxford Instruments SM4000-7T superconducting magneto-optical cryostat (0–7 T, 1.4–300 K), and an ITC503 Oxford Instruments temperature controller. The spectrometer was calibrated for circular dichroism intensity with camphorsulfonic acid and the wavelength was calibrated using Nd-doped glass. All spectra were collected at 2.0 nm resolution at a temperature of 5 K in an applied magnetic field of 7 T. Samples were prepared for low temperature (5 K) MCD spectrosocopy by dissolving the complex in toluene and polystyrene, then casting thin polymer films. The polystyrene films were then housed in a custom designed sample cell. Depolarization of the incident radiation by the sample

was determined by comparing the intrinsic circular dichroism of a standard Ni(+)-tartrate solution positioned in front of and then in back of each sample.

3. Results and analysis

3.1. Electronic absorption spectroscopy

The room temperature electronic absorption spectrum of (**NNSQ**)CuTp^{Cum,Me} is presented in Fig. 2. Relevant band maxima occur at ~11 000 ($\varepsilon \sim 625\ M^{-1}\ cm^{-1}$), ~18 000 ($\varepsilon \sim 1875\ M^{-1}\ cm^{-1}$), 24 500 ($\varepsilon \sim 13\,500\ M^{-1}\ cm^{-1}$), and 29 000 cm^{-1} ($\varepsilon \sim 13\,000\ M^{-1}\ cm^{-1}$). The ~24 500 cm^{-1} band is not present in absorption spectra of the constituent **SQ** and **NN** chromophores found in (**SQ**)ZnTp^{Cum,Me} and the aryl nitronyl nitroxide, Ph–**NN**. This behavior is consistent with the presence of an intraligand ILCT charge transfer transition from the donor (**SQ**) fragment to the acceptor (**NN**) fragment.

3.2. Magnetic circular dichroism spectroscopy

The low temperature MCD data for (**NNSQ**)-CuTp^{Cum,Me} is also presented in Fig. 2 for direct comparison with the electronic absorption spectrum. There are two types of maxima found in the MCD spectrum of (**NNSQ**)CuTp^{Cum,Me}, and these either correspond with, or do not correspond with, the observed absorption maxima. The bulk of the MCD intensity is negative, indicative of a large degree of out-of-state spin–orbit mixing between the excited states and the ground state wavefunction. This type of mixing is also responsible for zero-field splitting of the ground spin state (vide infra). Finally, the MCD features in the ILCT region possesses comparatively low intensity and indicate that very little orbital angular momentum arising from the paramagnetic Cu(II) center is mixed into the excited state responsible for the 29 000 cm^{-1} transition. This provides further support that the 29 000 cm^{-1} band is an ILCT transition.

3.3. Electron paramagnetic resonance spectroscopy

The 5 K X-band frozen glass EPR spectrum of (**NNSQ**)CuTp^{Cum,Me} is presented in Fig. 3, and is typical of an $S_T = 3/2$ ground state. Resonances centered at ~1770, and ~3380 G are typical of $S_T = 3/2$ centers with $D > h\nu$ and represent transitions from molecules oriented perpendicular (xy) and parallel (z) the applied magnetic field direction. A small rhombic anisotropy is evident on the low-field, perpendicular resonance. Additional weak resonances are observed at higher magnetic fields (~5650 and ~6900 G).

Analysis of the EPR spectrum of (**NNSQ**)CuTp^{Cum,Me} is accomplished by constructing resonance line positions as a function of the axial zero-field parameter, D, within an $|S_T = 3/2, m_s\rangle$ basis (Fig. 4). The appropriate spin-Hamiltonian is

$$H = g_{\|}\beta H \cdot \hat{S}_z + g_{\perp}\beta H \cdot \hat{S}_x + D[\hat{S}_z^2 - S_T(S_T+1)/3]. \quad (4)$$

Manual adjustment of the g-values and the axial zero-field splitting parameter, D, were used to generate an appropriate simulation of the resonant line positions, and this analysis yielded a value of $|D| \sim 0.5\ cm^{-1}$ for (**NNSQ**)CuTp^{Cum,Me}.

3.4. The valence bond configuration interaction (VBCI) Model

For organic biradicals, the intramolecular exchange coupling is often described within the active electron approximation [3], where only two magnetic orbitals are involved. Alternatively, the exchange interaction in heterospin biradicals of the donor–acceptor type [20–33] may be described by a VBCI model. The biradical ligand **NNSQ** is a donor–acceptor molecule that has been shown to possess a strong intramolecular ferromagnetic

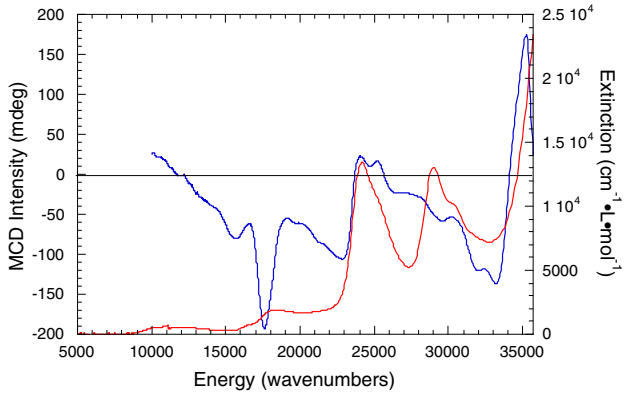


Fig. 2. 5 K MCD, 300 K Absorption overlay. MCD spectra were collected as polystyrene thin films and absorption spectra were recorded in CH_2Cl_2.

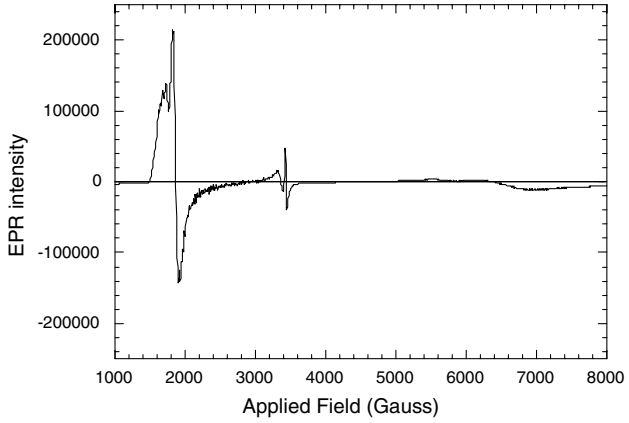


Fig. 3. 5 K X-band EPR spectrum of (**NNSQ**)CuTp^{Cum,Me}. EPR spectra were collected as a 2-methyl tetrahydrofuran glass.

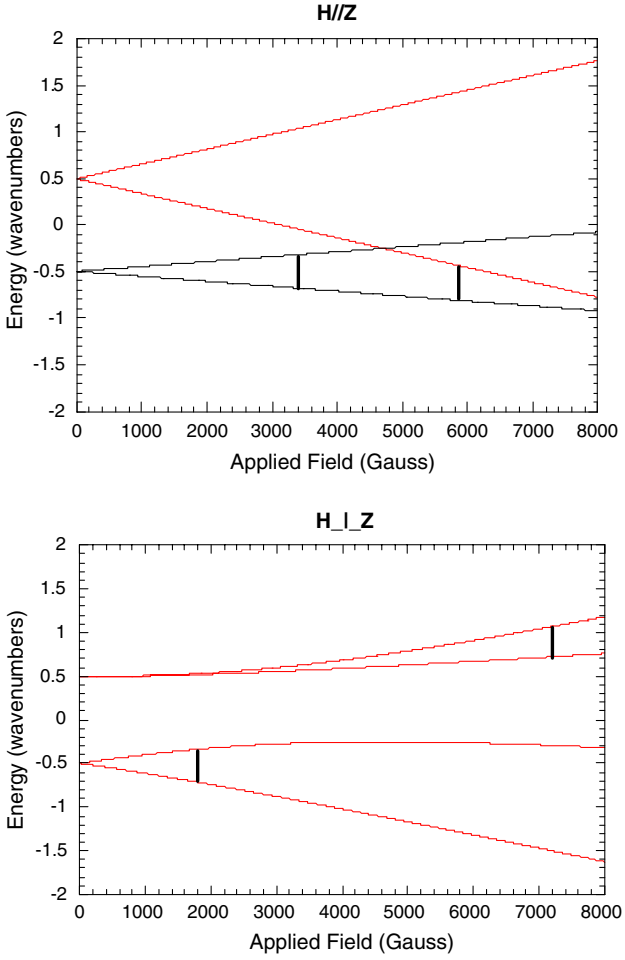


Fig. 4. X-band resonant line positions (vertical lines) calculated for an $S_T = 3/2$ center with $|D| = 0.5$. Two EPR resonances are anticipated with this D value for molecules oriented in the parallel and perpendicular directions relative to the applied magnetic field.

exchange interaction [22,34]. An orbital and state energy diagram for (**NNSQ**)ZnTp^{Cum,Me} is presented in Fig. 5 using **NN** and **SQ** fragment orbitals as initial basis functions. Since the **NN** and **SQ** SOMO fragments are orthogonal, the electronic coupling matrix element,

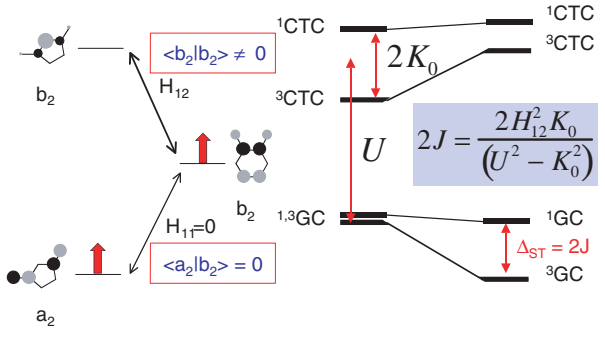


Fig. 5. Frontier orbitals and configurations for the **NNSQ** biradical ligand. Symmetry labels are for idealized C_{2v} symmetry of the donor (**SQ**) and acceptor (**NN**) fragments.

H_{11}, is zero and the singlet (^{1}GC) and triplet (^{3}GC) ground configurations are degenerate in first-order. Therefore, within the active electron approximation, J_{NN-SQ}, $= 0$ is predicted since both H_{11} and k_{11} are zero. The predicted exchange interaction is in stark contrast to what is observed experimentally for this and related donor–acceptor biradicals [24,35]. The intraligand exchange interaction in (**NNSQ**)CuTp^{Cum,Me} was previously shown to be strongly ferromagnetic with an upper limit estimated to be $J_{NN-SQ} \approx +550\ cm^{-1}$. To understand the electronic origin of this strong ferromagnetic exchange interaction, we must proceed beyond the active electron approximation and include virtual orbitals.

According to Fig. 5 a **SQ** $\rightarrow$ **NN** charge transfer (ILCT) transition is anticipated since $H_{12} \neq 0$. Thus, electronic absorption spectroscopy should be a sensitive probe of H_{12}, with the intensity of the ILCT transition being proportional to the square of the electronic coupling matrix element ($I_{ILCT} \propto {H_{12}}^2$). The electronic absorption spectrum in Fig. 2 reveals the presence of an ILCT transition in (**NNSQ**)CuTp^{Cum,Me} that is not present in the constituent chromophores and can be tentatively assigned as a **SQ** $\pi \rightarrow$ **NN** π^* ILCT transition. The extent to which the $a_2^1 b_2^1$ ^{3}CT configuration mixes into the ^{3}GC $a_2^1 b_2^1$ ground configuration will result in an energetic stabilization of ^{3}GC and a high-spin triplet ground state.

To determine the magnitude of the ^{3}GC state stabilization relative to the ^{1}GC state in non-disjoint biradicals, a perturbative expression has be derived within this simple three orbital model. According to this model, the ground state singlet–triplet gap, $2J$, is

$$2J = \frac{2H_{12}^2 K_0}{U^2 - K_0^2}, \tag{5}$$

where K_0 is a single-site exchange integral that splits the $a_2^1 b_2^1$ singlet and triplet excited state configurations (Hund's rule). Eq. (5) shows that the ferromagnetic interaction is maximized in heterospin biradicals when (1) the electronic coupling matrix element that connects one monomer fragment SOMO and the other monomer fragment LUMO is maximized, (2) the single-site exchange integral is large, and (3) the intramolecular ILCT energy ($U - K_0$) is low. Thus, these represent key design criteria for the synthesis of donor–acceptor heterospin biradicals with high-spin ground states.

4. Discussion

A key connection may be made between the VBCI model and the origin of ferromagnetic interactions in the active electron approximation. The magnitude of H_{12} is proportional to the $\langle \mathbf{SQ}(b_2)|\mathbf{NN}(b_2)\rangle$ overlap

integral, which describes the degree of mixing between these two orbitals. This orbital mixing results in some **NN**(b_2) orbital character being mixed into the **SQ**(b_2) SOMO. In the active electron approximation, the SOMO–SOMO overlap is still zero, but there is significant overlap *density* between atomic orbitals localized on the NN fragments of the two SOMO's [3]. This results from the admixture of the **NN** b_2 LUMO into the **SQ** b_2 SOMO, and yields a key relationship between the origins of the ferromagnetic exchange interaction within the VBCI and active electron approximations for heterospin biradicals

$$\frac{H_{12}^2 K_0}{U^2 - K_0^2} = \int_{\text{space}} \rho(1)\rho(2) r_{12}^{-1}\, \mathrm{d}\tau. \tag{6}$$

It is of interest to note that (**NNSQ**)CuTp$^{\text{Cum,Me}}$ possesses a sizable axial anisotropy, $|D|$, of $\sim 0.5\ \text{cm}^{-1}$. This is relatively remarkable for a spin quartet complex that is formed from three different $S_i = 1/2$ spin carriers (Cu(II), **NN**, and **SQ**), two of which possess no appreciable orbital angular momentum. A large value of $|D|$ has also been observed by Gatteschi and coworkers in a Cu–semiquinone complex [36]. A large uniaxial anisotropy is important in the design of single-molecule magnets that possess high blocking temperatures. Thus, the **SQNN** ligand fragment may represent a key design element in the construction of new hybrid organic/inorganic single-molecule magnets.

In summary, utilization of a VBCI model as applied to organic biradicals provides key design criteria for the synthesis of new high-spin organic and hybrid metal–organic molecular materials, which can be monitored conveniently by optical spectroscopies. Stabilization of the zero-field split ^{3}GC is strongly dependent on the magnitude of the electronic coupling matrix element, H_{12}, that describes the efficiency of electron transfer from the **SQ** donor to the **NN** acceptor. Future work will detail the preparation of new donor–bridge–acceptor biradicals dyads, their spectroscopic and magnetic characterization, accurate evaluation of H_{ab}, and the relationship of H_{ab} to the nature of the bridge fragment in D–bridge–A heterospin biradicals.

Acknowledgment

D.A.S. acknowledges the National Science Foundation (CHE-9910076; CHE-0091247 SQUID Magnetometer) for financial support, and thanks the Camille and Henry Dreyfus Foundation for a Camille Dreyfus Teacher-Scholar Award. M.L.K. acknowledges the National Institutes of Health GM-057378 and the Petroleum Research Fund ACS PRF 38086-AC3 for financial support.

References

[1] J.S. Miller, M. Drillon, Magnetism: Molecules to Materials II: Molecule-based Materials, Wiley-VCH, New York, 2001, p. 489.
[2] P.M. Lahti, Magnetic Properties of Organic Materials, Marcel Dekker, New York, 1999.
[3] O. Kahn, Molecular Magnetism, VCH, New York, 1993.
[4] M. Wolfsberg, L. Helmholtz, J. Chem. Phys. 20 (1952) 837.
[5] W.T. Borden, E.R. Davidson, J. Am. Chem. Soc. 99 (1977) 4587.
[6] D.A. Dougherty, Acc. Chem. Res. 24 (1991) 88.
[7] K. Itoh, M. Kinoshita, Molecular Magnetism, New Magnetic Materials, Gordon and Breach, Amsterdam, 2000, p. 347.
[8] A. Rajca, Chem. Rev. 94 (1994) 871.
[9] D.A. Shultz, G.T. Farmer, J. Org. Chem. 63 (1998) 6254.
[10] Y. Liao, C. Xie, P.M. Lahti, R.T. Weber, J. Jiang, D.P. Barr, J. Org. Chem. 64 (1999) 5176.
[11] F. Tuczek, E.I. Solomon, J. Am. Chem. Soc 116 (1994) 6916.
[12] C.A. Brown, G.J. Remar, R.L. Musselman, E.I. Solomon, Inorg. Chem. 34 (1995) 688.
[13] I. Vonseggern, F. Tuczek, W. Bensch, Inorg. Chem. 34 (1995) 5530.
[14] E. Pidcock, H.V. Obias, M. Abe, H.C. Liang, K.D. Karlin, E.I. Solomon, J. Am. Chem. Soc. 121 (1999) 1299.
[15] H. Weihe, H.U. Gudel, H. Toftlund, Inorg. Chem. 39 (2000) 1351.
[16] H. Weihe, H.U. Gudel, Comments Inorg. Chem. 22 (2000) 75.
[17] F. Tuczek, E.I. Solomon, Coord. Chem. Rev. 219 (2001) 1075.
[18] W. Wu, L.C. Song, Z.X. Cao, Q. Zhang, S. Shaik, J. Phys. Chem. A 106 (2002) 2721.
[19] P. Kennepohl, E.I. Solomon, Inorg. Chem. 42 (2003) 679.
[20] R. Kumai, M.M. Matsushita, A. Izuoka, T. Sugawara, J. Am. Chem. Soc. 116 (1994) 4523.
[21] D.A. Shultz, A.K. Boal, Mol. Cryst. Liq. Cryst. 272 (1995) 75.
[22] D.A. Shultz, S.H. Bodnar, K.E. Vostrikova, J.W. Kampf, Inorg. Chem. 39 (2000) 6091.
[23] D. Shultz, K. Vostrikova, S. Bodnar, H. Koo, M. Whangbo, M. Kirk, E. Depperman, J. Kampf, J. Am. Chem. Soc. 125 (2003) 1607.
[24] D.A. Shultz, Polyhedron 22 (2003) 2423.
[25] H. Sakurai, R. Kumai, A. Izuoka, T. Sugawara, Chem. Lett. (1996) 879.
[26] K. Inoue, H. Iwamura, Angew. Chem., Int. Ed. Engl. 34 (1995) 927.
[27] K. Ishiguro, M. Ozaki, N. Sekine, Y. Sawaki, J. Am. Chem. Soc. 119 (1997) 3625.
[28] P.M. Lahti, B. Esat, R. Walton, J. Am. Chem. Soc. 120 (1998) 5122.
[29] Y. Hosokoshi, K. Takizawa, H. Nakano, T. Goto, M. Takahashi, K. Inoue, J. Magn. Magn. Mater. 177 (1998) 634.
[30] M. Tanaka, K. Matsuda, T. Itoh, H. Iwamura, J. Am. Chem. Soc. 120 (1998) 7168.
[31] P.M. Lahti, B. Esat, Y. Liao, P. Serwinski, J. Lan, R. Walton, Polyhedron 20 (2001) 1647.
[32] Q. Fu, Y.Q. Qiu, L. Cui, L.L. Chen, J.C. Ma, Acta Chim. Sin. 60 (2002) 1789.
[33] Y. Morita, J. Kawai, K. Fukui, S. Nakazawa, K. Sato, D. Shiomi, T. Takui, K. Nakasuji, Synth. Met. 137 (2003) 1211.
[34] E. Depperman, S.H. Bodnar, K.E. Vostrikova, D.A. Shultz, M.L. Kirk, J. Am. Chem. Soc. 123 (2001) 3133.
[35] D.A. Shultz, K.E. Vostrikova, S.H. Bodnar, H.J. Koo, M.H. Whangbo, M.L. Kirk, E.C. Depperman, J.W. Kampf, J. Am. Chem. Soc. 125 (2003) 1607.
[36] A. Dei, D. Gatteschi, L. Pardi, A.L. Barra, L.C. Brunel, Chem. Phys. Lett. 175 (1990) 589.

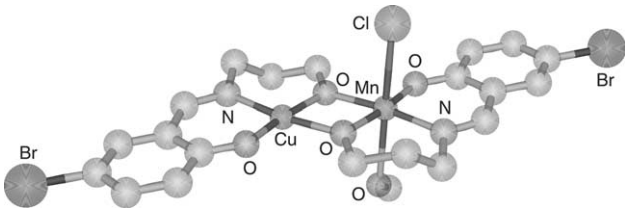


Fig. 1. Molecular structure of $Mn^{III}Cu^{II}(5\text{-Br-sap})_2Cl(MeOH)$. The axial positions of the Mn^{3+} ion are occupied by chloride ion and oxygen, and these positions exhibit Jahn–Teller elongation.

15 K. Hysteresis of magnetization is observed below ~0.5 K by SQUID magnetometer with the slow sweep (<0.1 T/min) of the external field, and the blocking temperature T_B is suggested to be approximately 0.5 K from the AC-susceptibility measurements [1].

NMR has been a powerful tool to study molecular magnets from a microscopic viewpoint. In this paper, we present the experimental results of ^1H and ^{55}Mn NMR of the MnCu cluster in the temperature range down to 0.4 K.

2. Experiments

A single crystal of MnCu cluster was used for our experiments. The magnetic field was always applied along *c*-axis, which is the magnetic easy axis of the crystal. We used a conventional pulsed NMR method and the NMR spectrum was recorded by measuring the intensity of the spin-echo, while sweeping the value of the applied field. The experiments at very low temperatures down to 0.4 K were performed with liquid ^3He.

3. Experimental results and discussion

Fig. 2 shows ^1H NMR spectra observed at several temperatures with the operating frequency of 128.1 MHz. It should be found that the spectrum has several peaks which are widely shifted below about 3 K. This fact suggests that the static magnetic moment is stabilized rapidly with decreasing temperature even above the blocking temperature $T_B \sim 0.5$ K. Then, in this temperature region, one can expect that NMR of Mn nuclei is possible under zero or small external field due to the static and strong hyperfine field caused from the magnetic moment of Mn^{3+}. In fact, we found ^{55}Mn NMR signal of MnCu cluster below about 1.5 K under the applied field around 2 T. Fig. 3 shows ^{55}Mn NMR spectra recorded by sweeping the field applied along the easy axis at $T \sim 1.2$ K. Note that, for Mn_{12} cluster magnets, ^{55}Mn NMR signal has not been detected above the blocking temperature. As shown in Fig. 3, each peak shifted toward higher field as the frequency was reduced. This fact is adequate for the quadrupole-split ^{55}Mn

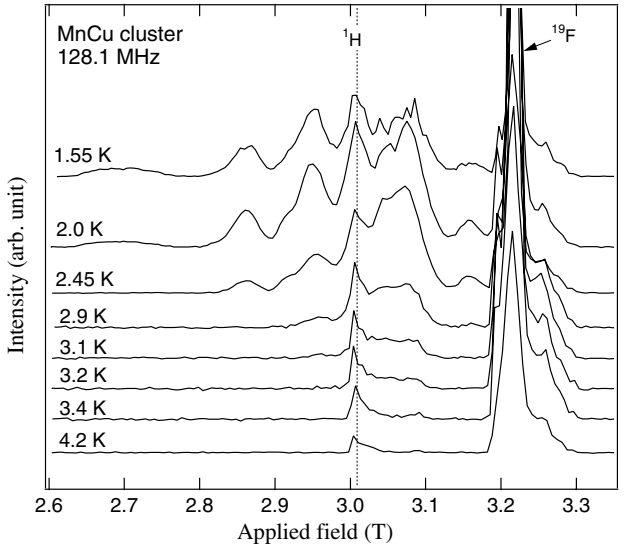


Fig. 2. ^1H NMR spectra observed at several temperatures with the operating frequency of 128.1 MHz. The dotted line shows the zero shift position of ^1H. The spectrum has several peaks and they are widely shifted below about 3 K. ^{19}F was contained in a sample holder, which yields the higher field peaks.

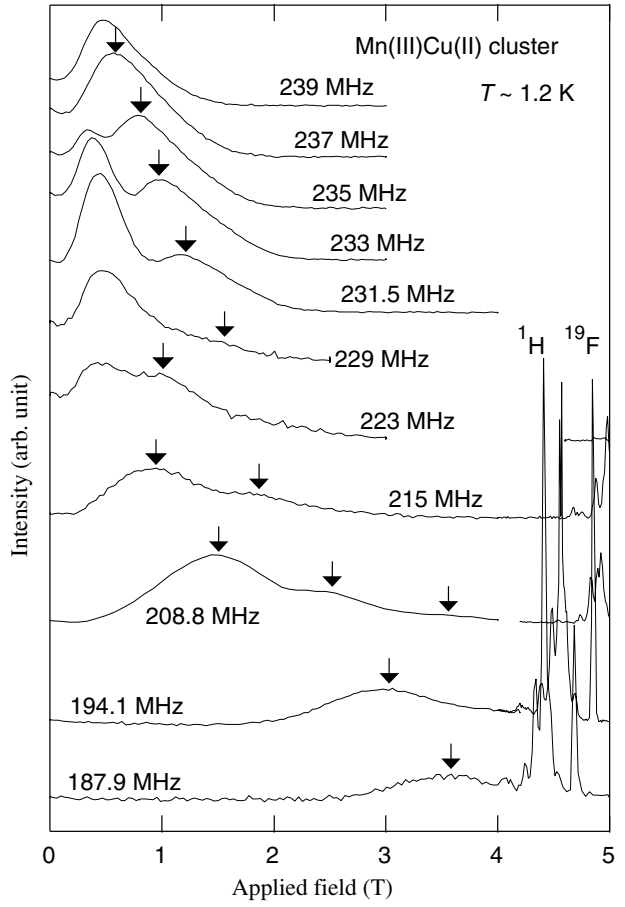


Fig. 3. Field-sweep ^{55}Mn NMR spectra obtained at ~1.2 K at several values of the operating frequency. The magnetic field is applied along the *c*-axis. The arrows indicate ^{55}Mn resonance peaks.

NMR ($I = 5/2$) of Mn^{3+} ions whose moments are nearly parallel to the external field, as discussed below. Because the nuclear spin–spin relaxation time T_2 became very short as the field was decreased, NMR signal was strongly damped near zero field. Then, non-essential peaks appeared around 0.4 T. From these results, we obtain the frequency–field diagram of ^{55}Mn NMR peaks as shown in Fig. 4. Three resonance lines from fivefold quadrupole-split lines for ^{55}Mn nuclei ($I = 5/2$) are clearly observed, and each line shifts as,

$$\nu_i(H) = \nu_i(0) - \frac{^{55}\gamma}{2\pi}H, \tag{2}$$

where $^{55}\gamma/2\pi = 10.55$ MHz/T is the gyromagnetic ratio of ^{55}Mn, except for the non-essential peaks around 0.4 T marked as crosses (+). Then, we found the quadrupole-split of ^{55}Mn to be 9.3 MHz. Because the outside lines arising from the transitions I_z: $\pm 3/2 \leftrightarrow \pm 5/2$ have small intensity as compared to the central three lines, we believe that the center of the observed three lines corresponds to the central transition I_z: $1/2 \leftrightarrow -1/2$. Therefore, the central resonance line at zero field will appear at $\nu_0 = 234$ MHz which correspond to the hyperfine field of $H_N = \nu_0/^{55}\gamma = 22.3$ T. This value of the central resonance line is much smaller than those for Mn^{3+} sites in Mn12Ac, 279.4 and 364.4 MHz [2].

Generally, the magnetic hyperfine field $\boldsymbol{H}_N$ caused at nuclear position consists of the Fermi-contact term $\boldsymbol{H}_F$, dipolar term $\boldsymbol{H}_d$ and orbital term $\boldsymbol{H}_l$, resulting from the corresponding components of the magnetic hyperfine interactions. The Fermi-contact term, which is attributed to the core polarization of inner s electron caused by 3d-electron spins, is dominant in magnitude among the three terms, and opposite in direction to the electronic magnetic moment. Therefore, the above results

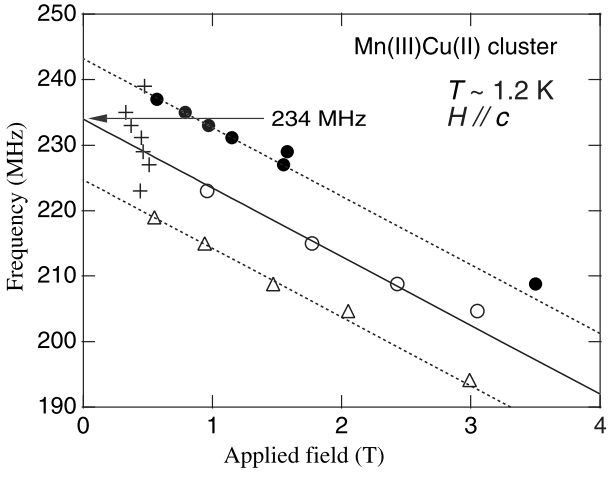


Fig. 4. Frequency–field diagram of ^{55}Mn NMR peaks on the basis of the observed spectra shown in Fig. 3. The non-essential peaks around 0.4 T are marked as crosses (+). The solid and the dotted lines show the field dependences of the central and the next to the central resonance lines of ^{55}Mn nuclei ($I = 5/2$), respectively. The central resonance frequency at zero external field is estimated to be 234 MHz.

that each line shifts as in Eq. (2) are natural when the magnetic moment is directed nearly parallel to the external field. For an orbital doublet ion such as Mn^{3+}, the hyperfine field is rather complicated as compared to orbital singlet ion such as Mn^{2+}, Mn^{4+}, etc., because the electronic ground-state wave function is anisotropic due to Jahn–Teller effect, which causes a considerable amount of the dipolar hyperfine field. The contribution of the dipolar term to the total hyperfine field depends on the angle θ between the magnetic moment and the tetragonal axis of the crystal field. Here, we neglect the orbital term because it is much smaller than other terms for most cases [2].

After all, the value of the magnetic hyperfine field H_N is expressed in terms of isotropic term H_F and anisotropic one H_d as,

$$H_N = H_F + \tfrac{1}{2}(3\cos^2\theta - 1)H_d. \tag{3}$$

It should be noted here that H_F is negative (opposite to the electronic magnetic moment) and H_d is positive, then H_N is negative because $|H_F| > H_d$ normally. In fact, our results suggest the negative value of H_N as shown in Fig. 4. Therefore, the absolute value of the hyperfine field H_N is smallest in case of $\theta = 0°$, namely, the electronic magnetic moment is parallel to the tetragonal axis. Then, let us discuss the absolute value of H_N from now on.

For Mn12Ac, the values of H_F and H_d have been obtained by taking into account the reduction of the local magnetic moments on the manganese ions, which yields the reduction of these values as compared to the values for free manganese ions [2]. For the first approximation, if we use here the values of H_F and H_d for Mn^{3+} in Mn12Ac, we obtain $|H_N| = 25.5$ T for $\theta = 0°$ from Eq. (3). This value is a little larger than our result, 22.3 T. Our results infer that the local moment on Mn^{3+} in MnCu cluster is similarly (or more) reduced as compared to the cases of Mn12 clusters. The followings should be noted: If $\theta = 0°$, which means the magnetic moment is tilted from the crystal c axis by approximately $\pm 20°$, the frequency–field diagram shown in Fig. 4 should be modified to $\nu_i(H) = \nu_i(0) - {}^{55}\gamma H/2\pi \times \cos 20°$. Even though the magnetic moment is tilted, the obtained results of $\nu_i(H)$ shows still in fairly good agreement within the experimental error. In order to clarify the direction of the magnetic moment, the detailed experiments are necessary.

Here, we also present the preliminary results at much lower temperatures. As the temperature was lowered, the spin-echo intensity increased and T_2 became longer, then we can measure the NMR spectrum near zero field. Fig. 5 shows the spectrum recorded at 0.4 K with the sweep rate of 0.4 T/min from the negative to the positive values of the field, which means the reversal of the field crossing the zero field. The hysteresis of the spectrum was observed in ± 0.4 T around zero field. As shown in

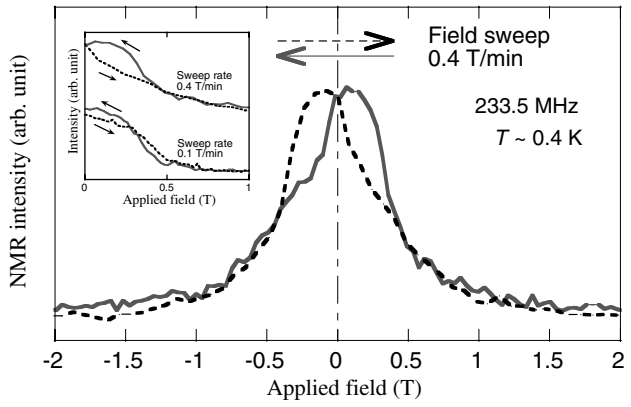


Fig. 5. Field-sweep spectrum obtained at 0.4 K which shows a hysteresis clearly around zero field. The field is increased from −3 to +3 T crossing the zero field for the gray line; the field is swept oppositely for the dashed line, by the same sweep rate of 0.4 T/min. Inset: Comparison between the different values of the sweep rate. The faster the field is swept, the wider the hysteresis becomes.

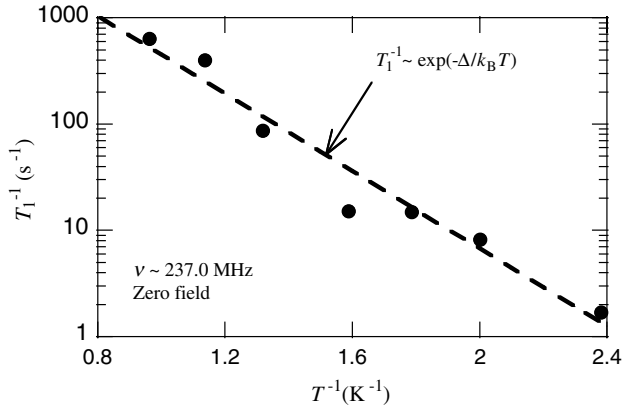


Fig. 6. The nuclear spin-lattice relaxation rate T_1^{-1} of ^{55}Mn vs. inverse temperature $1/T$ under zero external field. T_1^{-1} shows the activation type behavior, $T_1^{-1} \sim \exp(-\Delta/k_B)$ with $\Delta/k_B = 4.2$ K.

the inset, it was also found that the faster the field was swept the wider the hysteresis became. These behaviors are to be attributed to the slow relaxation of the electronic magnetization. Such a hysteresis of NMR spectrum related to the magnetization reversal was clearly shown in Mn12Ac [7].

The temperature dependence of the nuclear spin-lattice relaxation rate T_1^{-1} of ^{55}Mn under zero external field is shown in Fig. 6. The activation type behavior, $T_1^{-1} \sim \exp(-\Delta/k_B)$, was obtained with $\Delta/k_B = 4.2$ K. If we assume that Δ is associated with the energy gap between $S_z = \pm 5/2$ and $\pm 3/2$, Δ/k_B is $4D/k_B \simeq 10$ K. Since our data are rather scattered to date, we will perform further measurements. One may consider that such an activation type behavior of T_1^{-1} suggests no magnetic long-range order down to 0.4 K, because normally T_1^{-1} shows divergent behavior around ordering temperature due to the critical slowing down. However, we should be careful to distinguish by ^{55}Mn NMR the critical slowing down from the slowing down of the reversal probability of the magnetization of each molecule. The further experiments and the detailed discussions will appear elsewhere.

Acknowledgement

This work was partially supported by the Grant-in-Aid for Young Scientists (B), No. 14740207, and by the Grant-in-Aid for Scientific Research on Priority Area (B) on "Field-Induced New Quantum Phenomena in Magnetic Systems" from the Ministry of Education, Culture, Sports, Science and Technology of Japan.

References

[1] H. Oshio, M. Nihei, A. Yoshida, H. Nojiri, M. Nakano, A. Yamaguchi, Y. Karaki, H. Ishimoto, Chem. Eur. J. 11 (2005) 843.
[2] T. Kubo, T. Goto, T. Koshiba, K. Takeda, K. Awaga, Phys. Rev. B 65 (2002) 224425.
[3] T. Goto et al., Phys. Rev. B 67 (2003) 104408.
[4] S. Yamamoto, T. Nakanishi, Phys. Rev. Lett. 89 (2002) 157603.
[5] Y. Furukawa et al., Phys. Rev. B 69 (2004) 014405.
[6] H. Nojiri, et al., private communication.
[7] T. Kubo et al., Physica B 294–295 (2001) 310.

2. Experimental

2.1. Materials and measurements

All reagents and materials used for synthesis were reagent grade and used without further purification.

IR spectra were recorded with KBr pellets on a Brucker EQUINOX 55 FT-spectrometer. ^{1}H, ^{13}C, ^{31}PNMR spectra were taken on an AM-500 spectrometer operating at 500 MHZ, using DMF as solvent.

2.2. Synthesis

The crystal used for X-ray diffraction experiment was obtained as follow: 0.8 g of $Na_2WO_4 \cdot 2H_2O$ and 0.5 g of Na_3PO_4 were dissolved in 30 ml CH_3OH, adjusting its pH to 3.0 with hydrochloric acid, 0.1 g DB18C6 was added, stirring about 20 h, the solution was filtered, the residue was dried at room temperature, then transferred into a Teflon-Steel autoclave inside programmable electric furnace reactor with 20 ml CH_3CN as solvent. Solvothermal reaction lasted for 20 h at 423.15 K, then cooled to room temperature naturally. Yellow prism suitable for single crystal X-ray diffraction experiment was obtained. *Anal*. Calc. C, 19.10; H, 1.97; N, 1.01. Found: C, 19.12; H, 1.94; N, 1.01%. Selected bond lengths and angles are listed in Table 3.

Table 1
Crystallographic data for $[Na(DB18C6)(CH_3CN)]_3[\alpha\text{-}PW_{12}O_{40}]$

Empirical formula	$C_{66}H_{81}N_3Na_3O_{58}PW_{12}$
Formula weight	4150.48
Temperature (K)	293(2)
λ (Mo Kα) Å	0.71073
Crystal system	trigonal
Space group	R^{-3}
Unit cell dimensions	
a (Å)	23.905(3)
b (Å)	23.905(3)
c (Å)	14.686(3)
γ (°)	120
Volume (Å^3)	7268(2)
Z	3
D_{calc} (mg m^{-3})	2.845
Absorption coefficient (mm^{-1})	14.310
F(000)	5694
Crystal shape/crystal color	yellow
Crystal size (mm)	$0.30 \times 0.20 \times 0.15$
θ Range for data collection (°)	2.41–25.06
Index ranges	$-28 \leqslant h \leqslant 28$, $-28 \leqslant k \leqslant 28$, $-17 \leqslant l \leqslant 17$
Reflections collected [R_{int}]	13959/2984 [0.1320]
Reflections observed [$I > 2\sigma$ (I)]	2606
Data/restraints/parameters	2984/1/432
Goodness-of-fit on F^2	0.986
Final R indices [$I > 2\sigma(I)$]	$R_1 = 0.0437$, $wR_2 = 0.0832$
R indices (all data)	$R_1 = 0.0518$, $wR_2 = 0.0859$
Largest differences in peak and hole (e A^{-3})	1.465 and −1.451

2.3. X-ray crystallography

Yellow crystal measuring $0.30 \times 0.20 \times 0.15$ mm, $[Na(DB18C6)(CH_3CN)]_3$ [α-$PW_{12}O_{40}$] was obtained by solvothermal reaction method. At 293 K, the crystal data is collected by Rigaku RAXIS RAPID IP equipped with graphite monochromated Mo Kα radiation. The procedure for data reduction was carried out by SAINT PLUS, and the structure was solved by direct method and refined by use of SHELEX 97. Crystallography data are summarized in Table 1.

3. Results and discussion

3.1. IR spectra

The IR spectra of title compounds exhibit four characteristic asymmetric vibrations, resulting from the heteropolyanions with the α-Keggin structure. Comparing the IR spectra with that of α-$H_3PW_{12}O_{40}$ [15], the peaks belong to the W=Ot bonds shifts from 982 to 981 cm^{-1}, and the W–Ob and W–Oc bonds shift from 890 810 to 895 815 cm^{-1} (Ot = terminal oxygen, Ob = bridged oxygen of tow octahedral sharing a corner, Oc = bridged oxygen sharing an edge); the P–O bonds appear at nearly identical frequencies ($\nu_{(P-O)}$ = 1079 cm^{-1}) to that found for α-$H_3PW_{12}O_{40}$. This shows that polyanions retain the basic α-Keggin structure, yet a little distortion for the coordination influence, and that is in consistent with the result of single crystal X-ray diffraction experiment. Characteristic vibrations of DB18C6, α-$H_3PW_{12}O_{40}$ and the title compound are listed in Table 2. Features at 2937, 1506, 1455, 1254, and 1218 cm^{-1} are characteristic

Table 2
The IR spectra of the title complex, DB18C6 and α-$H_3PW_{12}O_{40}$ (cm^{-1})

	$\nu_{C=C}$	ν_{Ar-O-R}	ν_{R-O-R}	$\nu_{as(X-Oa)}$	$\nu_{as(M-Od)}$	$\nu_{as(M-Ob)}$	$\nu_{as(M-Oc)}$
Complex	1506.53	1254.80 1218.16	1128.57	1079.95	981.12	895.56	815.82
DB18C6	1508.75	1255.55	1130.74 1049.47				
α-$Na_3PW_{12}O_4$				1081	995	900	805

Table 3
Selected bond lengths (Å) and angles (°)

W(1)–O(1)	1.691(15)	W(4)–O(5)	1.900(16)
W(1)–O(4)	1.869(14)	W(4)–O(8)#2	1.964(14)
W(1)–O(4)#1	1.901(13)	W(4)–O(12)	2.500(12)
W(1)–O(2)	1.929(13)	P(1)–O(12)#1	1.490(12)
W(1)–O(3)	1.943(13)	P(1)–O(12)	1.490(12)
W(1)–O(14)	2.436(12)	P(1)–O(12)#2	1.490(12)
W(2)–O(13)	1.655(19)	P(1)–O(14)	1.54(2)
W(2)–O(3)	1.851(13)	Na(1)–O(1)	2.323(18)
W(2)–O(11)#1	1.885(17)	Na(1)–N(1)	2.39(3)
W(2)–O(5)	1.916(16)	O(4)–W(1)#2	1.901(13)
W(2)–O(6)	1.946(15)	O(7)–W(3)#1	1.946(17)
W(2)–O(12)#1	2.464(12)	O(8)–W(4)#1	1.964(14)
W(3)–O(9)	1.723(15)	O(11)–W(2)#2	1.885(17)
W(3)–O(7)	1.865(17)	O(12)–W(3)#2	2.377(12)
W(3)–O(8)	1.890(17)	O(12)–W(2)#2	2.464(12)
W(3)–O(6)	1.915(16)	O(14)–W(1)#1	2.436(12)
W(3)–O(7)#2	1.946(17)	O(14)–W(1)#2	2.436(12)
W(3)–O(12)#1	2.377(12)	W(4)–O(11)	1.875(15)
W(4)–O(10)	1.682(17)	W(4)–O(2)	1.869(13)
O(1)–W(1)–O(4)	103.2(7)	O(12)–P(1)–O(14)	111.1(6)
O(1)–W(1)–O(4)#1	105.4(7)	O(12)#2–P(1)–O(14)	111.1(6)
O(4)–W(1)–O(4)#1	87.1(8)	O(1)–Na(1)–N(1)	170.5(10)
O(1)–W(1)–O(2)	100.9(7)	O(1)–Na(1)–O(17)	81.7(6)
O(4)–W(1)–O(2)	87.9(6)	N(1)–Na(1)–O(17)	93.7(9)
O(4)#1–W(1)–O(2)	153.8(6)	O(1)–Na(1)–O(20)	78.9(6)
O(1)–W(1)–O(3)	101.9(7)	N(1)–Na(1)–O(20)	106.4(9)
O(4)–W(1)–O(3)	154.7(6)	O(17)–Na(1)–O(20)	159.7(6)
O(4)#1–W(1)–O(3)	89.6(6)	O(1)–Na(1)–O(15)	106.8(7)
O(2)–W(1)–O(3)	84.0(6)	N(1)–Na(1)–O(15)	82.7(10)
O(1)–W(1)–O(14)	173.3(7)	O(17)–Na(1)–O(15)	120.6(7)
O(4)–W(1)–O(14)	71.4(5)	O(20)–Na(1)–O(15)	60.7(6)
O(4)#1–W(1)–O(14)	70.9(5)	O(1)–Na(1)–O(16)	84.9(6)
O(12)#1–P(1)–O(12)	107.8(7)	O(12)#1–P(1)–O(14)	111.1(6)
O(12)–P(1)–O(12)#2	107.8(7)	O(12)#1–P(1)–O(12)#2	107.8(7)
N(1)–Na(1)–O(16)	100.6(10)	N(1)–Na(1)–O(17)	93.7(9)
N(1)–Na(1)–O(20)	106.4(9)	N(1)–Na(1)–O(15)	82.7(10)
N(1)–Na(1)–O(18)	83.3(10)	N(1)–Na(1)–O(19)	88.9(10)
C(21)–N(1)–Na(1)	174(3)	P(1)–O(14)–W(1)	126.3(10)

of dibenzo-18-crown-6. In comparison with the free dibenzo-18-crown-6 molecule, ν(C–O) of the compounds shifts from 1231 to 1218 cm^{-1}, which illustrating the crown ether are coordinated to sodium ions.

3.2. NMR spectra

The ^{1}H NMR spectrum contains four sharp signals in a relative ratio 1:1:2:2 (6.91, 6.80, 4.08 and 3.85 ppm) assigned to the aromatic and alky^{l} H atoms of dibenzo-18-crown-6 and a peak at 2.02 ppm related to the H atom of CH_3CN. Six resonances (149.33, 122.49, 112.92, 70.62, 68.90 and 2.00) are exhibited in ^{13}C NMR spectrum, which associated with three aromatic and two alkyl C atoms of DB18C6 and the C atom of $–CH_3$, respectively. The ^{13}C resonance (119.27 ppm) bonded to N atom in CH_3CN has been clarified by gUMBC spectrum (see Fig. 1), which is too weak to be observed in ^{13}C NMR spectrum due to its too low relaxation rate. The ^{31}P chemical shift of title complex is 15.49 ppm in solid state while is 12.75 ppm in DMF solution, showing that a little downfield shift took place on going from solid state to solution.

3.3. Crystal structure

The super molecular complex, shown in Fig. 2, contains an $[\alpha\text{-}PW_{12}O_{40}]^{3-}$ anion and three $[Na(DB18C6)(CH_3CN)]^{+}$ units. $[\alpha\text{-}PW_{12}O_{40}]^{3-}$ reported by Keggin in 1933 shows overall Td symmetry and is based on a central PO_4 tetrahedron surrounded by 12 WO_6 octahedrons arranged in four groups of three edge-shared octahedron W_3O_{13}. The W_3O_{13} triplet linked by shared corners to each other and to central PO_4 tetrahedron [8]. As depicted in Fig. 2, each of sodium cations is located in the cavity of dibenzo-18-crown-6 (DB18C6) with six Na–O bonds and associated with the terminal O atoms of $[\alpha\text{-}PW_{12}O_{40}]^{3-}$ and the N atom of CH_3CN from two sides of the distorted DB18C6 plane. The three terminal O atoms linked with sodium ion are from a single W_3O_{13} triplet of the α-Keggin tungstophosphate anion. The complex $[Na(DB18C6)(CH_3CN)]_3[\alpha\text{-}PW_{12}O_{40}]$, is a neutral and discrete molecule, which is packed in the crystal via van der waals forces seen in Fig. 3.

The three sodium cations are identical in coordination environment and space sphere and the three sodium crown cation units were associated with a single W_3O_{13} triplet by tree Na–O–W bonds. Due to steric hindrance $[Na(DB18C6)(CH_3CN)]_3[\alpha\text{-}PW_{12}O_{40}]$ forms discrete molecule other than polymer. Noritaka et al. has reported the synthesis an structure of $[(CH_3)N_4Na_2H][\alpha\text{-}PW_{12}O_{40}]$, which forms extended three-dimensional structure [16]. Structure of such crown ether-polyoxometalates compounds depend on the coordination interactions between the Na^{+} ions and the terminal oxygen atoms of the α-Keggin anion and the Van der Waals force among organic components.

Organic–inorganic hybrid compounds including heteropolyanions and crown ether reported usually use heteropolyanions as precursor [5,14,6], in which organic and inorganic moieties were connected by electronic interaction or covalent bonds. In our work, $NaWO_4 \cdot 2H_2O$ instead of polyanions was used. It is all known that the structure of polyoxometalates is sensitive to PH, so, we adjusted PH in range of 1–4 with hydrochloric acid, the same compounds was obtained. As usual, it is difficult to assigning the position of C atom connected with N atom by multi-bonds in ^{13}C spectrum because the intensity of ^{13}C resonance of the C atom is too weak to be observed due to its too low relaxation rate, but it has been determined easily by gUMBC spectrum in our paper.

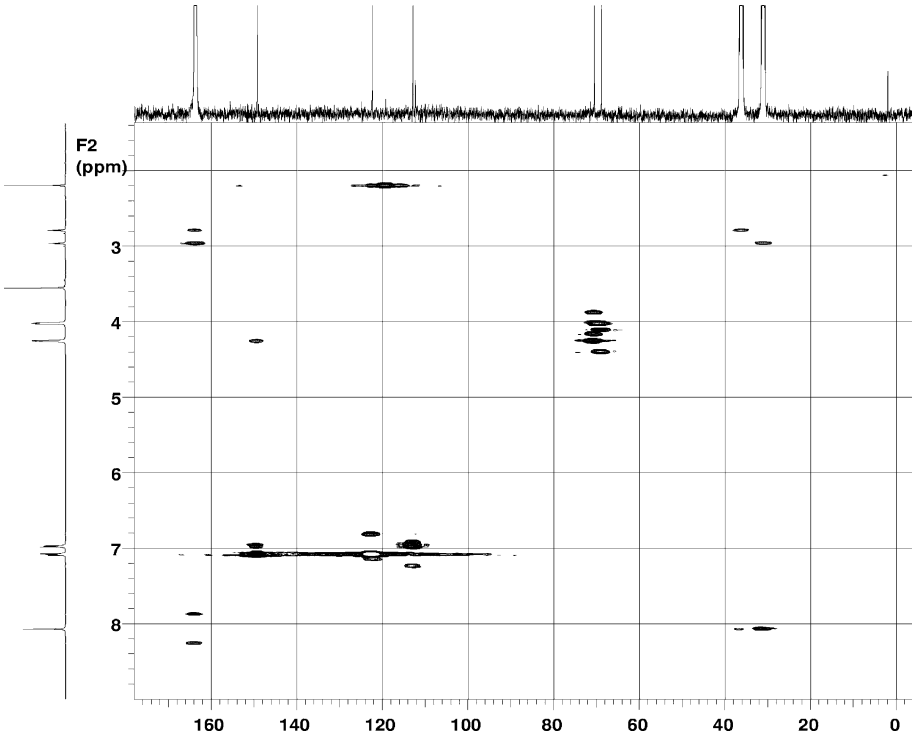


Fig. 1. gUMBC spectrum of title complex.

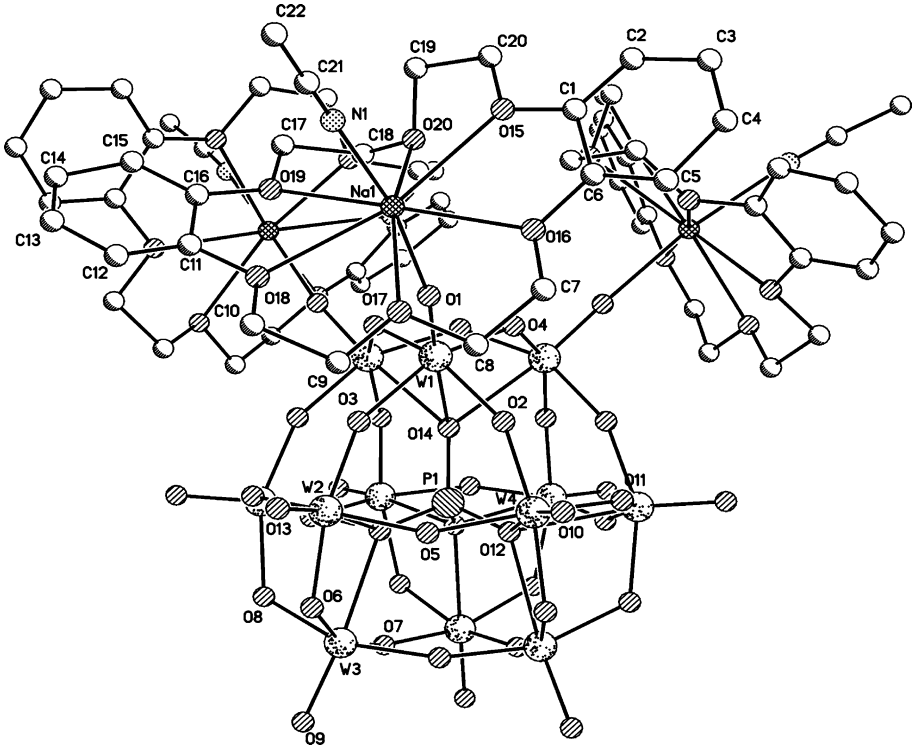


Fig. 2. Structure of $[Na(DB18C6)(CH_3CN)]_3[\alpha\text{-}PW_{12}O_{40}]$.

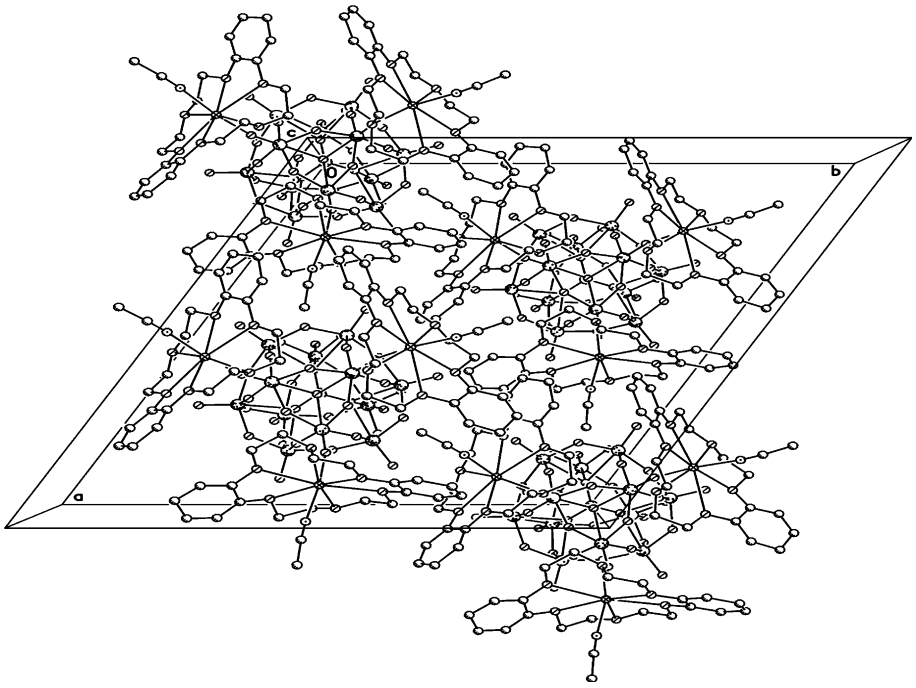


Fig. 3. Packing diagram of $[Na(DB18C6)(CH_3CN)]_3[\alpha\text{-}PW_{12}O_{40}]$ in unit cell.

Acknowledgements

We gratefully acknowledge the financial support of the Natural National Science Foundation (20271034) and Beijing Natural Science Foundation (2012005), which made this work possible.

References

[1] O. Nagano, Y. Sasaki, Acta Crystallogr. B 35 (1979) 2387.
[2] R. Neier, C. Trojanowski, R. mattes, J. Chem. Soc., Dalton Trans. (1995) 2521.
[3] W.S. You, E.B. Wang, H. Zhang, L. Xu, Y.B. Wang, J. Mol. Struct. 554 (2000) 141.
[4] W.S. You, E.B. Wang, Q.L. He, L. Xu, J. Mol. Struct. 524 (2000) 133.
[5] X.M. Lu, R. Zhong, S.C. Liu, Y. Liu, Polyhedron 16 (1997) 3865.
[6] X.M. Lu, H.J. Zhu, S.C. Liu, Chin. Chem. Lett. 5 (1994) 67.
[7] X.M. Lu, X.L. Jin, S.C. Liu, Chem. J. Uni9v. 17 (1996) 1173.
[8] M.T. Pope, Heterpoly and Isopoly Oxometalats, Springer-Verlag, Berlin, 1983.
[9] M.T. Pope, A. Mûller, Angew. Chem., Int. Ed. Engl. 30 (1991) 34.
[10] M. Pope, A. Mûller (Eds.), Polyoxometalates: from Platonic Solids to Anti-retroviral Activity, Kluwer, Dordrecht, The Netherlands, 2001.
[11] C. Hill (Ed.), Polyoxometalates, Chem. Rev., vol. 98, 1998.
[12] M.T. Pope, A. Mûller (Eds.), Polyoxometalate Chemistry: from Topology via Self-assembly to Application, Kluwer, Dordrecht, The Netherlands, 2001.
[13] T. Yamase, M.T. Pope, A. Mûller (Eds.), Polyoxometalate Chemistry for Nano-composite Design, Kluwer, Dordrecht, The Netherlands, 2002.
[14] E.B. Wang, Y. Xu, Y.G. Li, L. Xu, C.W. Hu, Inorg. Chem. 40 (2001) 5468.
[15] J.M. Lehn, Angew. Chem., Int. Ed. Engl. 27 (1998) 89.
[16] N. Honma, K. Kusaka, T. Ozeki, Chem. Commun. (2002) 2896.

2. Experimental

2.1. Compound preparations

All manipulations were performed under aerobic conditions using materials and solvents as received.

2.1.1. $[Mn_{11}O_2(OH)_2(nmpd)(pdmH)_5(pdm)_5Cl_6]\cdot 4MeCN$ (1)

Treatment of a solution of $MnCl_2\cdot 4H_2O$ (0.75 mmol, 0.15 g), $pdmH_2$ (2.5 mmol, 0.34 g) and $nmpdH_2$ (0.75 mmol, 0.10 g) in a mixture of MeCN/MeOH (35 mL/5 mL) with one equivalent of NMe_4OH (0.25 mmol, 0.10 mL) results in the formation of a dark brown solution. This was allowed to stand undisturbed for two days, and during this time large, needle-shaped brown crystals slowly crystallized of a material identified by crystallography as $[Mn^{III}_7Mn^{II}_4O_2(OH)_2(nmpd)(pdmH)_5(pdm)_5Cl_6]\cdot 4MeCN$ ($\mathbf{1}\cdot 4MeCN$). These crystals were isolated by filtration in 64% yield. *Anal*. Calc. for dried (**1**): C, 38.17; H, 4.45; N, 5.44. Found: C, 38.29; H, 4.68; N, 5.69%.

2.1.2. $[Mn_{25}O_{18}(OH)_2(N_3)_{12}(pdm)_6(pdmH)_6]Cl_2\cdot 12MeCN$ (2)

A stirred, pale brown slurry of $MnCl_2\cdot 4H_2O$ (0.75 mmol, 0.15 g), $pdmH_2$ (2.5 mmol, 0.34 g) and NaN_3 (2.5 mmol, 0.16 g) in MeCN/MeOH (20 mL/10 mL) was treated with NMe_4OH (0.25 mmol, 0.10 mL). This resulted in a dark brown solution, which was allowed to stand undisturbed for a few weeks during which time $[Mn^{IV}Mn^{III}_{18}Mn^{II}_6O_{18}(OH)_2(N_3)_{12}(pdm)_6(pdmH)_6]Cl_2\cdot 12MeCN$ ($\mathbf{2}\cdot 12MeCN$) slowly crystallized. The black crystals were isolated in ~30% yield. *Anal*. Calc. for dried (**2**): C, 25.72; H, 2.36; N, 17.14. Found: C, 26.01; H, 2.68; N, 17.15%.

3. Results and discussion

3.1. Structural description of $[Mn_{11}O_2(OH)_2(nmpd)(pdmH)_5(pdm)_5Cl_6]\cdot 4MeCN$ ($\mathbf{1}\cdot 4MeCN$)

A labeled ORTEP plot and the central core of **1** are presented in Figs. 1 and 2, respectively. Complex $\mathbf{1}\cdot 4MeCN$ crystallizes in the monoclinic space group $P2_1/c$ with the asymmetric unit consisting of the cluster and four molecules of acetonitrile. The cluster is trapped-valence $Mn^{III}_7Mn^{II}_4$ and has an unusual undecanuclear cage structure, with seven central manganese ions (Mn3, Mn4, Mn5, Mn6, Mn7, Mn8, Mn9) held together by two μ_4-O atoms (O13, O8). Two dinuclear Mn^{III}–Mn^{II} units (Mn2–Mn1, Mn10–Mn11) are linked to each end of the Mn_7 core via μ_3-alkoxide oxygen atoms (O4, O18) provided by pdm ligands. Furthermore, two hydroxide ions (O5, O17) and alkoxide

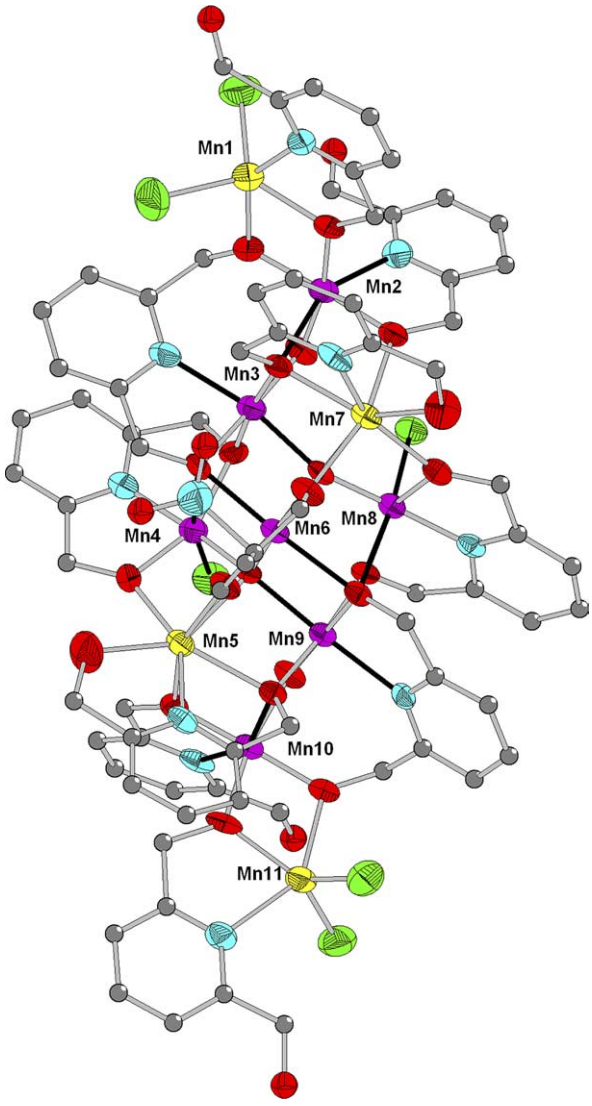


Fig. 1. ORTEP representation at the 50% probability level of complex **1**. All H atoms have been removed for clarity. Color code: purple, Mn^{III}; yellow, Mn^{II}; pale green, Cl; red, O; blue, N; gray, C.

oxygen atoms (O1, O2, O3, O7, O9, O10, O11, O12, O13, O15, O16, O19, O21, O22) from pdm and nmpd ligands provide additional bridges between the Mn ions. The coordination spheres of the Mn ions are completed by N atoms from pdm groups and six terminal Cl^- ions. The hydroxide oxygen atoms (O5 and O17), as well as the uncoordinated oxygen atoms (O25, O26, O27 and O28) are protonated, as confirmed by bond valence sum calculations; their H atoms were included in calculated, idealized positions and were refined riding on their parent atoms.

Inspection of the bond distances and bond valence sum calculations reveal that the Mn(2), Mn(3), Mn(4), Mn(6), Mn(8), Mn(9) and Mn(10) are in oxidation state Mn^{III} while the remainder of the metal ions are Mn^{II} (Figs. 1 and 2). All Mn^{III} centers display Jahn–Teller (JT) distortions as expected for high spin d^4 ions in near

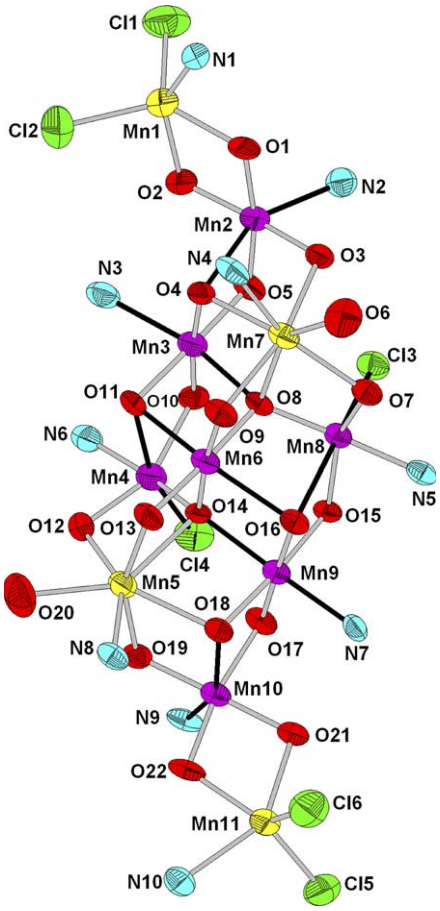


Fig. 2. Labeled ORTEP representation of the central core of complex **1**. JT axes are indicated as solid black bonds.

octahedral geometry. These take the form of axial elongations, and the JT axes are indicated as solid black bonds in Figs. 1 and 2. A close look at the crystal packing reveals no evidence of intermolecular hydrogen bonding interactions between molecules; however, intermolecular pi-stacking interactions involving the phenyl rings of pdm^{2-} ligands from neighboring Mn_{11} clusters are observed.

3.2. Structural description of $[Mn_{25}O_{18}(OH)_2(N_3)_{12}(pdm)_6(pdmH)_6]Cl_2 \cdot 12MeCN$ (**2**)

Complex **2** crystallizes in the triclinic space group $P\bar{1}$. The Mn_{25} cation lies on an inversion center and has a barrel-like structure (Fig. 3). Inspection of the structural features reveals twelve μ_4-O^{2-}, six μ_3-O^{2-} and two μ_3-OH^- ions holding the core together, as well as chelating/bridging pdm^{2-}/$pdmH^-$, and both terminal and bridging N_3^- groups. The metal oxidation states and the protonation levels of O^{2-}, OH^-, pdm^{2-} and $pdmH^-$ O atoms were established by Mn and O bond valence sum calculations, inspection of metric parameters, and detection of Mn^{III} JT elongation axes. The core of the cation may be dissected into five parallel layers of three types with an **ABCBA** arrangement (Fig. 4). Layer **A** is a Mn^{II}_3 triangular unit (Mn1, Mn2, Mn4) with a capping μ_3-OH^- ion; layer **B** is a Mn^{III}_6 triangle (Mn3, Mn5, Mn6, Mn7, Mn8, Mn9) that can be described as three corner sharing Mn^{III} triangles; and layer **C** consists of a Mn^{III}_6 hexagon (Mn11, Mn12, Mn13, Mn11a, Mn12a, Mn13a) in the center

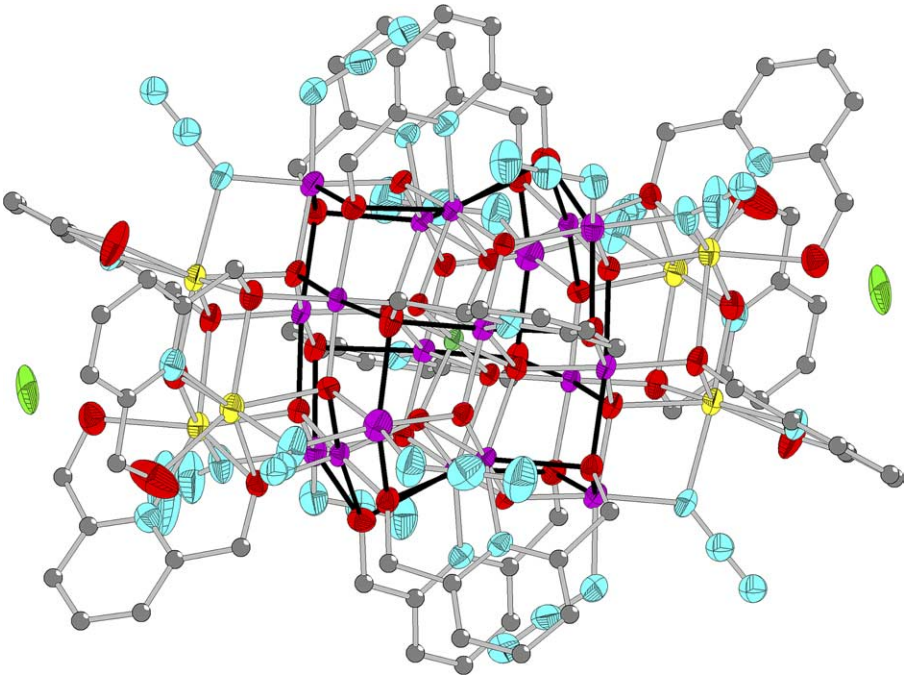


Fig. 3. ORTEP representation at the 50% probability level of the centrosymmetric complex **2**. H atoms have been removed for clarity. Color code: green, Mn^{IV}; purple, Mn^{III}; yellow, Mn^{II}; pale green, Cl; red, O; blue, N; gray, C.

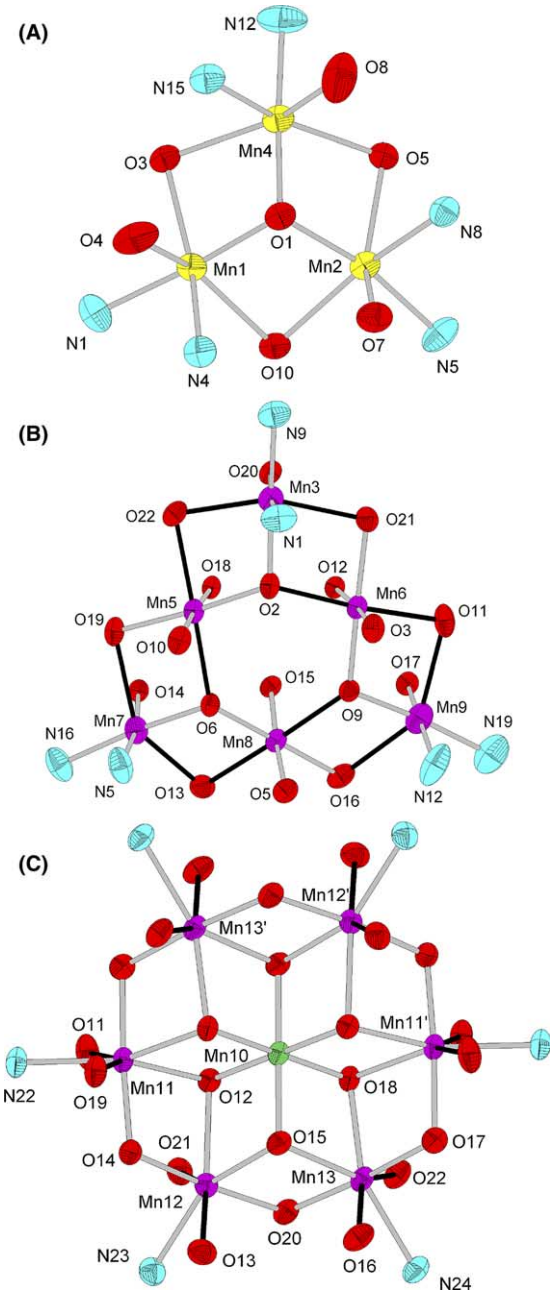


Fig. 4. Three types of constituent layers of the centrosymmetric complex **2**, color coded for clarity. Atom color code: green, Mn^{IV}; purple, Mn^{III}; yellow, Mn^{II}; red, O; blue, N. JT axes are indicated as solid black bonds.

of which is held the Mn^{IV} ion (Mn10) by the bridging O^{2-} ions. Layer **C** is reminiscent of the well known Anderson-type structure seen in some Mn complexes [20]. Each layer is linked to its neighboring layers by a combination of oxide, alkoxide and/or azide bridging groups. The outer coordination shell is occupied by pdm^{2-}, $pdmH^{-}$ and terminal azide ligands (Fig. 3). In addition, inspection of the crystal packing reveals no evidence of intermolecular hydrogen-bonding interactions between molecules.

3.3. Magnetochemistry

3.3.1. DC Magnetic susceptibility

The magnetic properties of **1** and **2** were investigated by solid state magnetic susceptibility (χ_M) measurements in the 5.0–300 K range in a DC field of 1000 Oe (0.1 Tesla); the resulting data are shown in Figs. 5 and 6, respectively, as $\chi_M T$ versus T plots. For complex **1**, the $\chi_M T$ value increases steadily from 40.2 $cm^3\,K\,mol^{-1}$ at 300 K to a maximum of 48.3 $cm^3\,K\,mol^{-1}$ at 25 K, before dropping rapidly to 40.2 $cm^3\,K\,mol^{-1}$ at 5 K. For complex **2**, the $\chi_M T$ value steadily increases from 88.4 $cm^3\,K\,mol^{-1}$ at 300 K to a maximum of 310 $cm^3\,K\,mol^{-1}$ at 15 K, before

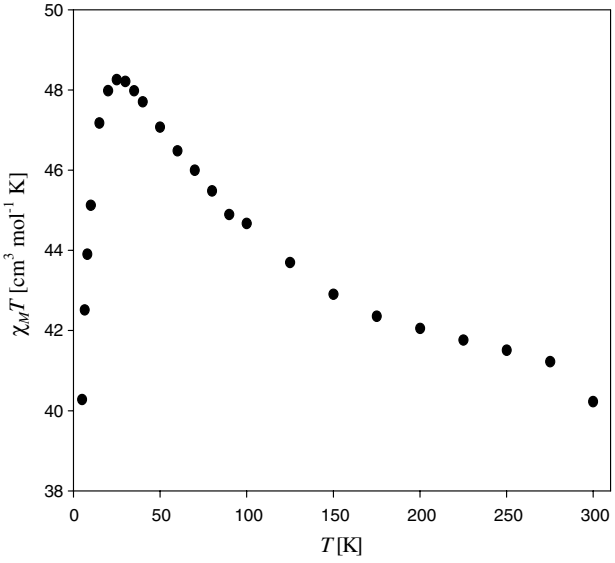


Fig. 5. Plot of $\chi_M T$ vs. T for complex **1** at 1 kG.

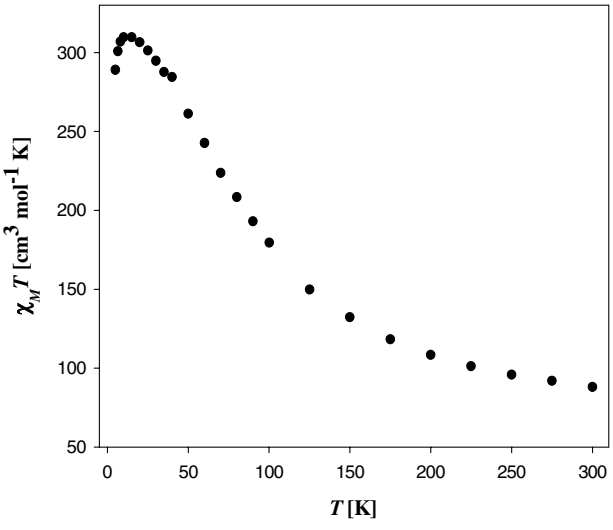


Fig. 6. Plot of $\chi_M T$ vs. T for complex **2** at 1 kG.

dropping to 289 cm^3 K mol^{-1} at 5.0 K. In each case the data suggest a very large ground state spin value. The final decrease of the $\chi_M T$ at the lowest temperatures is likely due to Zeeman effects and weak intermolecular exchange interactions. The 25 K peak value for complex **1** suggests an $S = 10$ spin ground state value, whereas the 15 K peak value for the Mn_{25} cation suggests either an $S = 49/2$ or 51/2 state, whose spin-only ($g = 2$) values would be 337.8 and 312.4 cm^3 K mol^{-1}, respectively.

In order to identify the ground states, magnetization (M) data in the 1.8–4.0 K and 0.1–7 T ranges were collected and fit by matrix diagonalization to a model that assumes only the ground state is populated, includes axial zero-field splitting ($D\hat{S}_z^2$) and Zeeman interactions, and incorporates a full powder average.

For complex **1**, we could not get an acceptable fit under any reasonable conditions, and we attribute this to the population of low-lying excited states, even at these low temperatures. For complex **2**, we used only low fields ($\leqslant$8 kG) to avoid problems associated with M_S levels from excited states with higher S values crossing with the ground state, which would lead to an erroneously high value for the ground state S. The fitting (solid lines in Fig. 7) of the magnetization data gave $S = 51/2$, $D = -0.021(1)$ cm^{-1}, and $g = 1.87(1)$. The fits for $S = 49/2$ and 53/2 were only slightly inferior, and on the basis of the magnetization fits alone, we therefore conclude that the ground state spin of **2** is $S = 51/2 \pm 1$.

An $S = 51/2$ ground state and negative D value suggested that **2** might have a sufficient barrier to magnetization relaxation to be an SMM. The upper limit to this barrier is given by $(S^2 - 1/4)|D|$ for a half-integer spin, or only 14.3 cm^{-1} for **2**, but the actual (or effective) barrier will be significantly less due to QTM through the barrier.

3.3.2. AC Magnetic susceptibility

AC susceptibility measurements were carried out on both samples in the 1.8–10 K temperature range to obtain reliable ground state spin values and assess whether the complexes might be SMMs. For complex **1**, no out-of-phase signal was observed whereas for complex **2** the presence of a frequency-dependent signal was observed below 3 K. The latter suggests **2** might be an SMM. The in-phase data extrapolated to 0 K indicate spin ground states of $S = 10$ and $S = 51/2$ for complexes **1** and **2**, respectively.

3.3.3. Single crystal magnetic measurements

The confirmation of possible SMM behavior requires the observation of hysteresis loops. Single crystals of **1** and **2** were therefore investigated using a micro-SQUID [21], and the obtained M versus applied DC field sweeps are shown in Figs. 8 and 9, respectively. Hysteresis loops, the diagnostic property of a magnet, were observed below ~0.7 K, their coercivities increasing with decreasing temperature, as expected for the superparamagnet-like properties of a SMM. The loops do not exhibit the step-like features indicative of QTM, but it is possible that steps are present but smeared out by broadening effects from dipolar and transverse fields, low-lying excited states, and/or a distribution of molecular environments. The low temperature at which both complexes are SMMs is clearly due to a small D value, which is consistent with the nearly perpendicular disposition of the Mn^{III} JT axes, the primary source of the molecular anisotropy.

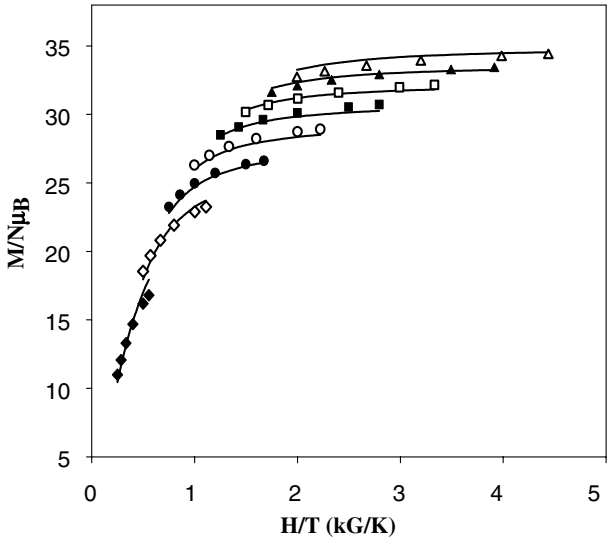


Fig. 7. Plot of reduced magnetization ($M/N\mu_B$) vs. H/T for **2** at 8 (△), 7 (▲), 6 (□), 5 (■), 4 (○), 3 (●), 2 (◇) and 1 (◆) kG. The solid lines are the fit; see the text for the fitting parameters.

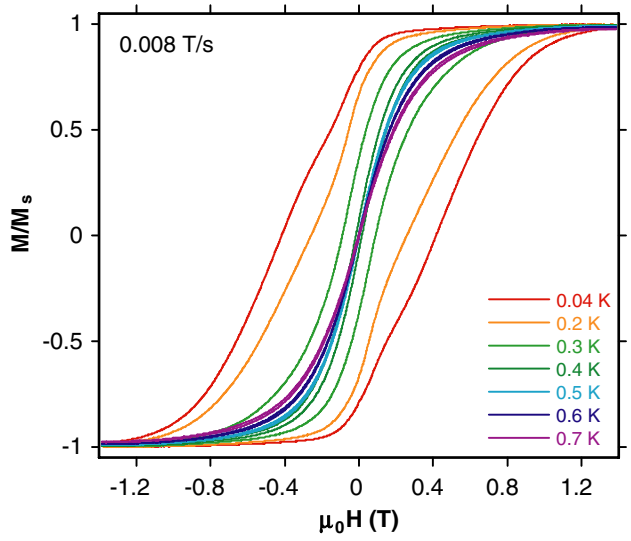


Fig. 8. Magnetization (M) vs. field ($\mu_0 H$) hysteresis loops for single crystals of **1** at the indicated temperatures.

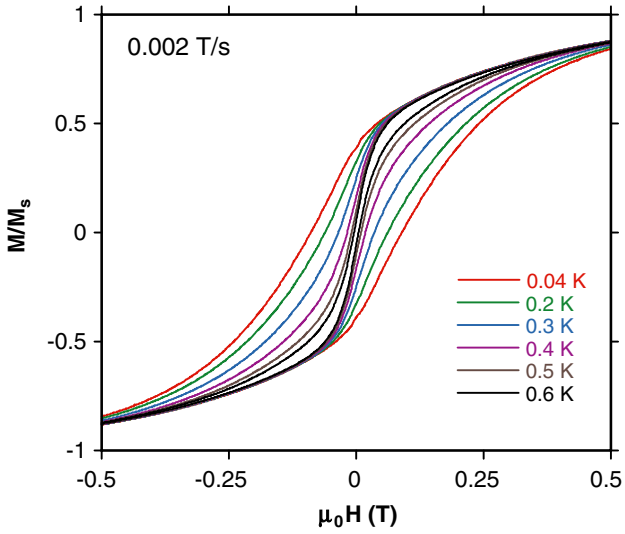


Fig. 9. Magnetization (M) vs. field ($\mu_0 H$) hysteresis loops for single crystals of **2** at the indicated temperatures.

4. Conclusions

A mixed chelate strategy has been used to synthesize two new SMMs $[Mn_{11}O_2(OH)_2(nmpd)(pdmH)_5(pdm)_5Cl_6]\cdot 4MeCN$ (**1**) and $[Mn_{25}O_{18}(OH)_2(N_3)_{12}(pdm)_6(pdmH)_6]Cl_2\cdot 12MeCN$ (**2**). Complexes **1** and **2** have novel core topologies containing seven Mn^{III} and four Mn^{II} ions for the former complex and one Mn^{IV}, eighteen Mn^{III} and six Mn^{II} ions for the latter. Both complexes are amongst the largest spin and size SMMs reported to date. Complex **2**, in addition to being the largest mixed-valent $Mn^{II}/Mn^{III}/Mn^{IV}$ cluster and the largest spin SMM to date, also has the largest spin ($S = 51/2$) for any molecular species, the same as that suggested for the cyano-bridged $Mn^{II}{}_9Mn^{V}{}_6$ complex [22].

5. Supplementary material

Crystallographic data have been deposited with Cambridge Crystallographic Data Centre, CCDC Nos. 238515 and 266403. Copies of this information may be obtained from The Director, CCDC, 12 Union Road, Cambridge, CB2 1EZ, UK (fax: +44 1233 336033; e-mail: deposit@ccdc.cam.ac.uk or www.ccdc.cam.ac.uk).

Acknowledgment

This work was supported by the National Science Foundation.

References

[1] G. Christou, D. Gatteschi, D.N. Hendrickson, R. Sessoli, MRS Bull. 25 (2000) 66, and references therein.
[2] R. Sessoli, H. Tsai, A.R. Schake, S. Wang, J.B. Vincent, K. Folting, D. Gatteschi, G. Christou, D.N. Hendrickson, J. Am. Chem. Soc. 115 (1993) 1804.
[3] E.K. Brechin, J. Yoo, M. Nakano, J.C. Huffman, D.N. Hendrickson, G. Christou, Chem. Commun. (1999) 783.
[4] J. Yoo, E.K. Brechin, A. Yamaguchi, M. Nakano, J.C. Huffman, A.L. Maniero, L.-C. Brunel, K. Awaga, H. Ishimoto, G. Christou, D.N. Hendrickson, Inorg. Chem. 39 (2000) 3615.
[5] M. Soler, W. Wernsdorfer, K. Folting, M. Pink, G. Christou, J. Am. Chem. Soc. 126 (2004) 2156.
[6] W. Wernsdorfer, N. Aliaga-Alcalde, D.N. Hendrickson, G. Christou, Nature 416 (2002) 406.
[7] D. Price, S. Batten, B. Moubaraki, K. Murray, Chem. Commun. (2002) 762.
[8] E.K. Brechin, C. Boskovic, W. Wernsdorfer, J. Yoo, A. Yamaguchi, C. Sanudo, T. Concolino, A. Rheingold, H. Ishimoto, D.N. Hendrickson, G. Christou, J. Am. Chem. Soc. 124 (2002) 9710.
[9] C. Boskovic, W. Wernsdorfer, K. Folting, J.C. Huffman, D.N. Hendrickson, G. Christou, Inorg. Chem. 41 (2002) 5107.
[10] N.E. Chakov, K.A. Abboud, L.N. Zakharov, A.L. Rheingold, D.N. Hendrickson, G. Christou, Polyhedron 22 (2003) 1759.
[11] J.T. Brockman, K.A. Abboud, D.N. Hendrickson, G. Christou, Polyhedron 22 (2003) 1765.
[12] M. Soler, W. Wernsdorfer, K.A. Abboud, J.C. Huffman, E.R. Davidson, D.N. Hendrickson, G. Christou, J. Am. Chem. Soc. 125 (2003) 3576.
[13] M. Soler, W. Wernsdorfer, K.A. Abboud, D.N. Hendrickson, G. Christou, Polyhedron 22 (2003) 1777.
[14] A. Morello, O.N. Bakharev, H.B. Brom, L.J. de Jongh, Polyhedron 22 (2003) 1745.
[15] E. Brechin, M. Soler, G. Christou, M. Helliwell, S. Teat, W. Wernsdorfer, Chem. Commun. (2003) 1276.
[16] C.J. Milios, C.P. Raptopoulou, A. Terzis, F. Lloret, R. Vicente, S.P. Perlepes, A. Escuer, Angew. Chem. Int. Ed. 43 (2004) 210.
[17] M. Murugesu, J. Raftery, W. Wernsdorfer, G. Christou, E.K. Brechin, Inorg. Chem. 43 (2004) 4203.
[18] M. Murugesu, W. Wernsdorfer, K.A. Abboud, G. Christou, Angew. Chem. Int. Ed. 44 (2005) 792.
[19] E.C. Sañudo, W. Wernsdorfer, K.A. Abboud, G. Christou, Inorg. Chem. 43 (2004) 4137.
[20] B. Pilawa, M.T. Kelemen, S. Wanka, A. Geisselmann, A.L. Barra, Europhys. Lett. 43 (1998) 7.
[21] W. Wernsdorfer, Adv. Chem. Phys. 118 (2001) 99.
[22] J. Larionova, M. Gross, M. Pilkington, H. Andres, H. Stoeckli-Evans, H. Gudel, S. Decurtins, Angew. Chem. Int. Ed. 39 (2000) 1605.

Available online at www.sciencedirect.com
SCIENCE DIRECT®
Polyhedron 24 (2005) 2900
POLYHEDRON
www.elsevier.com/locate/poly

Reports on experimental demonstrations: Or molecular magnetism is attractive! ☆

In the following section, three contributions are presented at the ICMM'04 Conference in Tsukuba as experimental demonstrations. The opportunity for such Demo's at an ICMM was offered for the first time by the organizers of the Tsukuba meeting. The basic idea behind these presentations is that molecular magnetism is growing as a scientific discipline and it appears important to now present it to the students and to the general public in an attractive manner.

Chemistry and physics in molecular magnetism can give rise to beautiful, attractive, visually spectacular demonstrations: bright colours, colour changes, shiny crystals, laboratory experiments, and new magnetism-based equipment and devices, as shown by the presenters of the Demo's session in Tsukuba. Beyond the necessity for scientists to develop citizen awareness and to present complex results in a simple manner, it is hoped that such attractive demonstrations that put emphasis on visually spectacular aspects of the discipline can help to attract the most curious and talented students towards our domain.

In Tsukuba, the demonstrations were presented in a place dedicated to this purpose and were accompanied by posters, computer presentations, and video-projections.

The ICMM International Scientific Committee has decided to continue the Demo experience at the ICMM'06 Conference on Vancouver Island in August 2006. We hope that the publication in *Polyhedron* of these three pioneering contributions will encourage the participants of this next ICMM meeting to prepare a large number of even more attractive presentations, which would allow us to gather together a significant volume of didactic documents to be widely used in our universities to demonstrate that, indeed, molecular magnetism is attractive!

M. Verdaguer
Chimie Inorganique et Matériaux Moléculaires
Unité CNRS 7071, Université Pierre et Marie Curie
4 Place Jussieu, 75252 Paris
Cedex 05, France
E-mail address: miv@ccr.jussieu.fr

M. Matsushita
Department of Basic Science
Graduate School of Arts and Sciences
The University of Tokyo, 3-8-1 Komaba
Meguro, Tokyo 153-8902, Japan
E-mail address: michio@pentacle.c.u-tokyo.ac.jp

Available online 19 October 2005

☆ ®L. Thompson, St. John, Canada.

0277-5387/$ - see front matter © 2005 Elsevier Ltd. All rights reserved.
doi:10.1016/j.poly.2005.04.018

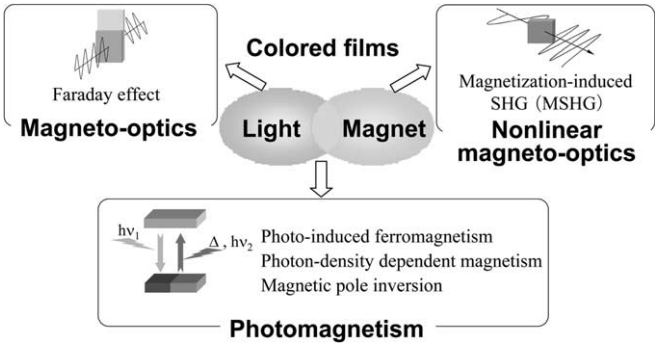


Fig. 1. Magneto-optical phenomenon in colored magnetic films.

ing process. Nafion® 117 membrane (2 cm × 4 cm) is immersed in an aqueous solution of $M^{II}Cl_2$ (10 mM) for 24 h. This membrane is put in an aqueous solution of $K_3[Cr^{III}(CN)_6]$ (10 mM) for 24 h, to deposit Prussian blue analogs on both sides of Nafion film. To remove M^{II} ions from Nafion membrane, these films are dipped into an aqueous solution of KCl (1 M) for 20 min and it is rinsed with distilled water and dried under air. Elemental analyses determined by an inductively coupled plasma (ICP) show that the ratio of M^{II} to Cr^{III} of these films are 3:2. The prepared films shows various colors, i.e., pink (M = Co), yellowish green (M = Ni), and green (M = Cu) (Fig. 2(a)). The CN stretching frequencies in the IR spectra of these films at 2178 cm^{-1} (M = Co), 2176 cm^{-1} (M = Ni), and 2171 cm^{-1} (M = Cu) correspond to those of powder-type of samples prepared by mixing $M^{II}Cl_2$ and $K_3[Cr^{III}(CN)_6]$ aqueous solutions [1,12,13]. Their thicknesses determined by a laser profile micrometer are 320 nm (M = Co), 350 nm (M = Ni), and 400 nm (M = Cu).

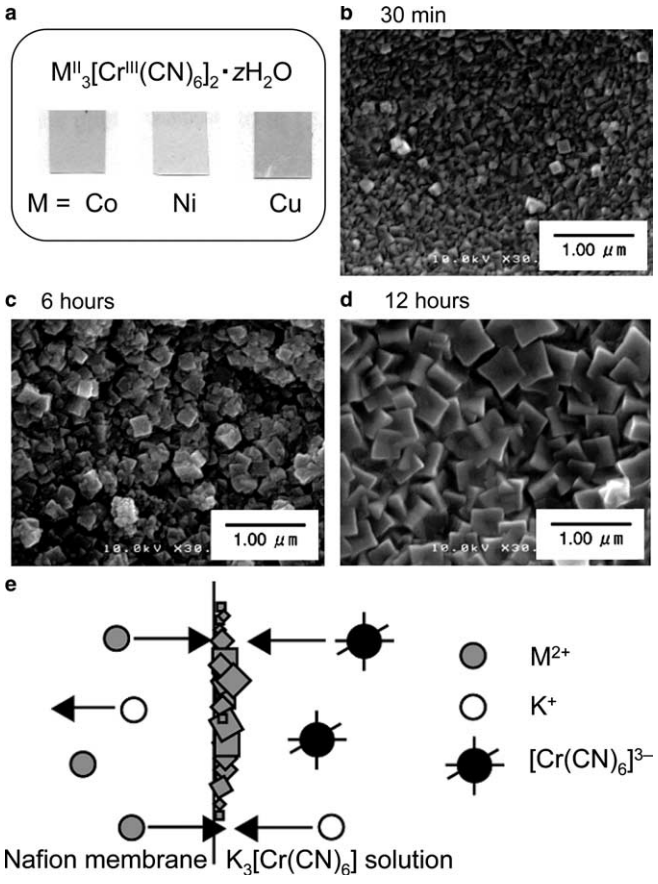


Fig. 2. The photographs for $M^{II}_3[Cr^{III}(CN)_6]_2 \cdot zH_2O$ films (a) and SEM images of the growth process for $Cu^{II}_3[Cr^{III}(CN)_6]_2 \cdot zH_2O$ film; (b) 30 min, (c) 6 h, and (d) 12 h. (e) Schematic illustration of the growth process.

Scanning electron microscopy (SEM) images show that the sizes of the crystals are 150 ± 50 nm (M = Co), 80 ± 20 nm (M = Ni), and 300 ± 100 nm (M = Cu). Fig. 2 shows the growth process of the $Cu^{II}_3[Cr^{III}(CN)_6]_2 \cdot zH_2O$ film. After 30 min, the size of deposited crystals is c.a. 100 nm (Fig. 2(b)). After that, the cubic-type of crystals are observed and the crystal size grows up to c.a. 300 nm (Fig. 2(c) and (d)). In Fig. 2(e), the growth process of the $M^{II}_3[Cr^{III}(CN)_6]_2 \cdot zH_2O$ film is schematically described. When a Nafion membrane containing M^{II} ion is dipped into a $K_3[Cr^{III}(CN)_6]$ solution, M^{II} ion coordinates to $[Cr^{III}(CN)_6]^{3-}$ ion depending on the diffusion rate of M^{II} ions in Nafion membrane, to form $M^{II}_3[Cr^{III}(CN)_6]_2 \cdot zH_2O$ microcrystallines on the surface of membrane.

The field-cooled magnetization versus temperature plots for the films in an external magnetic field (B_0) of 10 G showed T_c of 28 K (M = Co), 70 K (M = Ni), and 70 K (M = Cu). These T_c values almost correspond to reported values of powder-type samples, i.e., T_c = 30 K (M = Co) [1,12], 72 K (M = Ni) [1,13,14], 66 K (M = Cu) [1,14].

3. Electrochemical synthesis of Prussian blue analog-based magnetic films

The thin films composed of $(Fe^{II}_xCr^{II}_{1-x})_3[Cr^{III}(CN)_6]_2 \cdot 15H_2O$ are prepared by reducing aqueous solutions containing three compounds simultaneously, $K_3[Cr(CN)_6]$, $CrCl_3$ and $FeCl_3$, where the mixing ratio x_{mix} (=Fe^{III}/(Fe^{III}+Cr^{III})) is controlled. When we keep the reduction potential at −0.84 V versus saturated calomel electrode and load electrical capacity of 600 mC, insoluble polynuclear metal cyanides thin films with a thickness of c.a. 2 μm are thus deposited on an electrode surface as thin films. The elemental analyses show that the experimentally obtained x values depend on the x_{mix} values of metal ions in the prepared solutions, e.g., $x = 0.04$ ($x_{mix} = 0.05$), $x = 0.08$ ($x_{mix} = 0.10$), $x = 0.11$ ($x_{mix} = 0.13$), $x = 0.13$ ($x_{mix} = 0.15$), $x = 0.20$ ($x_{mix} = 0.20$), $x = 0.31$ ($x_{mix} = 0.30$), and $x = 0.42$ ($x_{mix} = 0.40$). The X-ray powder diffraction patterns for all the films are consistent with the face-centered cubic structure. The lattice constants increase successively from 10.39 to 10.62 Å with increasing x. Moreover, the CN stretching frequencies in the IR spectra for the films decrease continuously from 2189 to 2161 cm^{-1}. The colors of obtained $(Fe^{II}_xCr^{II}_{1-x})_3[Cr^{III}(CN)_6]_2 \cdot 15H_2O$ transparent films change depending on x. For example, the film for $x = 0$ is colorless, that for $x = 0.20$ is violet, that for $x = 0.42$ is red, and that for $x = 1$ is orange

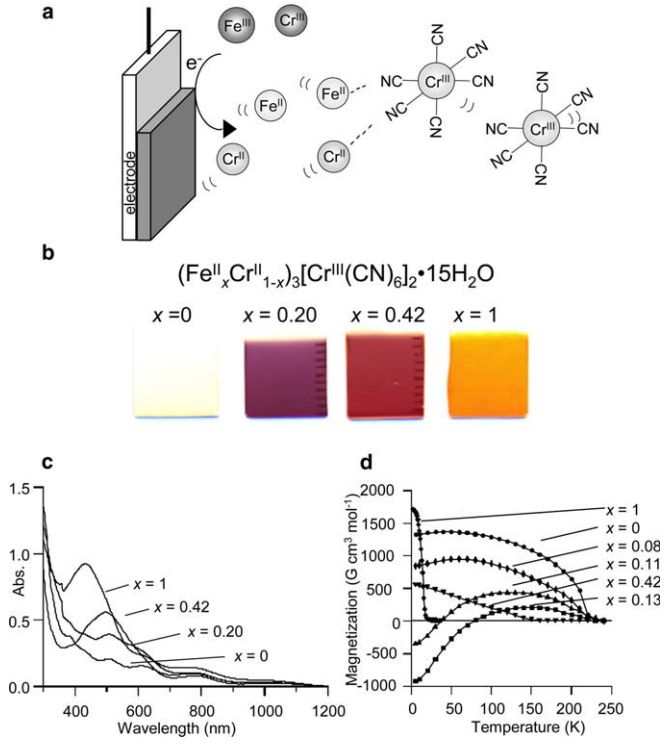


Fig. 3. (a) Schematic diagram illustrating electrochemical synthesis of magnetic thin films. (b) The photographs of obtained transparent and colored $(Fe^{II}_xCr^{II}_{1-x})_3[Cr^{III}(CN)_6]_2 \cdot 15H_2O$ films. (c) UV–Vis spectra of those films. (d) Magnetization vs. temperature curves ($B_0 = 10$ G).

(Fig. 3(b)). This color change is due to the shift of the intervalence transfer (IT) band of Fe^{II} and Cr^{III} in the visible region [15], e.g., $\lambda_{max} = 434$ nm ($x = 1$); 496 nm ($x = 0.42$); 506 nm ($x = 0.20$); 510 and 610 nm ($x = 0$) (Fig. 3(c)). It is known that the wavelength of IT band depends on magnitudes of the vibronic coupling with asymmetrical distortion of each coordination sphere of metal ions and the intensity is proportional to the square of transfer integrals. Therefore, in a series of $(Fe^{II}_xCr^{II}_{1-x})_3[Cr^{III}(CN)_6]_2 \cdot 15H_2O$ films, magnitudes of vibronic coupling parameters and transfer integrals are supposed to be continuously changed from those of Fe^{II}–Cr^{III} to those of Cr^{II}–Cr^{III} with decreasing x. In fact, frequencies of CN stretching and lattice constants continuously shift, indicating that distance between metal ions of $(Fe^{II}_xCr^{II}_{1-x})_3[Cr^{III}(CN)_6]_2 \cdot 15H_2O$ are averaged values of the distance of Fe^{II}–Cr^{III} and Cr^{II}–Cr^{III} as a function of x.

Magnetic susceptibility and magnetization of obtained thin films depend strongly on the x values. The saturation magnetizations (M_s) vary in a systematic fashion as a function of x. Minimum values of the M_s are found with the film of x value close to 0.11. This is because parallel spins (Cr^{III} and Fe^{II}) and anti-parallel spins (Cr^{II}) can be partially or even completely canceled, depending on the x. In addition, the magnetization versus temperature curves below T_c exhibit various types of behavior depending on x ($B_0 = 10$ G) (Fig. 3(d)). Particularly, those compounds in which x are 0.11–0.15 exhibited negative values of magnetization below particular temperatures (compensation temperatures, T_{comp}). The observed T_{comp} of 110 K for $x = 0.15$ is the highest value among molecule-based magnets. This phenomenon is observed because the positive magnetization due to the Cr^{II} sublattice and the negative magnetizations due to the Fe^{II} and Cr^{III} sublattices have different temperature dependences.

4. Magneto-optical effects

Magneto-optical effects are based on the interaction between light and magnetism. Faraday effect, which is one of the magneto-optical effects, is observed when linear polarized light propagates through magnetically ordered materials. Previously, we have observed the Faraday effect of $K^{I}_{0.62}V^{II}_{0.98}V^{III}_{1.02}[Cr^{III}(CN)_6]_{1.88} \cdot 13H_2O$ film with a high T_c of 310 K (Fig. 4) [6]. Here, we show magneto-optical effects of the films of $M^{II}_3[Cr^{III}(CN)_6]_2 \cdot zH_2O$ on Nafion membrane in the ferromagnetic region measured using magneto-optical meter. The Faraday ellipticity (F.E.) spectra for films at 7 K in $B_0 = 500$ G after the application of 1 T are shown in Fig. 5. For M = Co, the dispersive peak is observed around 470 nm with intensity of ± 80 deg cm^{-1} (Fig. 5(a)). For M = Ni, there exist two broad peaks with intensities of 200 and -200 deg cm^{-1} around 440 and 610 nm, respectively (Fig. 5(b)). For M = Cu, a negative peak with intensity of -210 deg cm^{-1} is observed around 550 nm (Fig. 5(c)). From the simulation of F.E. spectra based on the Faraday spectral analysis, the observed F.E. spectra are assigned to the following. For M = Co, the dispersive peak around 470 nm is due to $^4T_{1g} \rightarrow {}^4T_{1g}$ transition on octahedrally coordinated Co^{II} ion. For M = Ni, the peaks around 440 and 610 nm are due to $^3A_{2g} \rightarrow {}^3T_{1g}$ (^3P) and $^3A_{2g} \rightarrow {}^3T_{1g}$ (^3F) on Ni^{II} ion, respectively. For M = Cu, the peak around 550 nm is due to the sum of transitions $^2B_{1g} \rightarrow {}^2E_g$ (556 nm), $^2B_{1g} \rightarrow {}^2B_{2g}$ (625 nm), and $^2B_{1g} \rightarrow {}^2A_{1g}$ (710 nm) on Cu^{II} ion.

5. Nonlinear magneto-optical effects

Let us focus our attention on nonlinear optical effects in molecule-based magnets. Recently, second harmonic

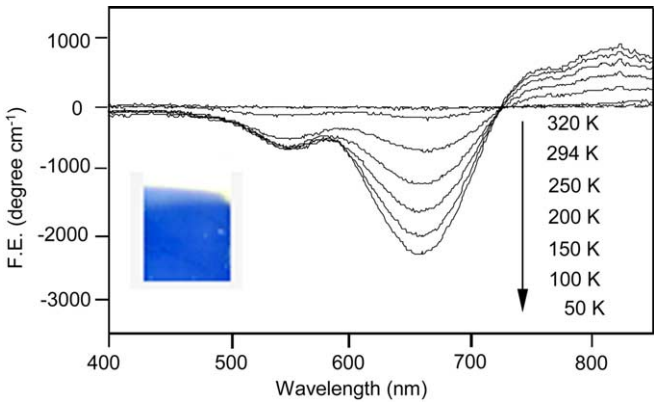


Fig. 4. Faraday ellipticity (F.E.) spectra for $(K^{I}_{0.62}V^{II}_{0.98}V^{III}_{1.02})[Cr^{III}(CN)_6]_2 \cdot 13H_2O$ film ($T_c = 310$ K).

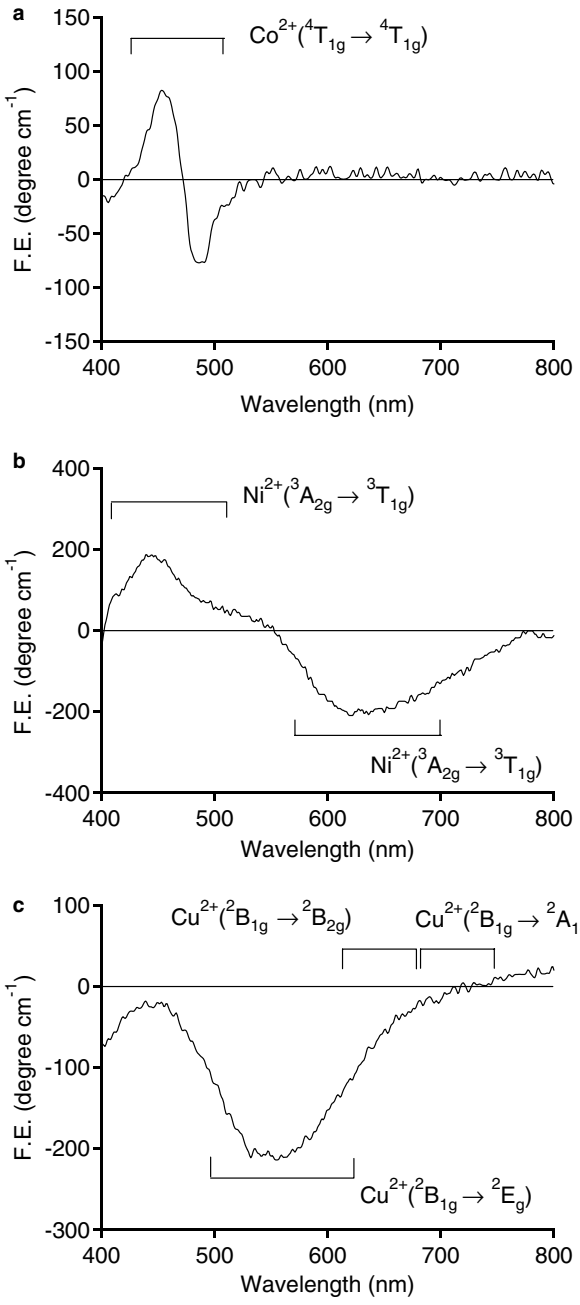


Fig. 5. Faraday ellipticity (F.E.) spectra for $M_3^{II}[Cr^{III}(CN)_6]_2 \cdot zH_2O$ films at 7 K under 500 G after the application of 1 T: (a) M = Co; (b) Ni; (c) Cu.

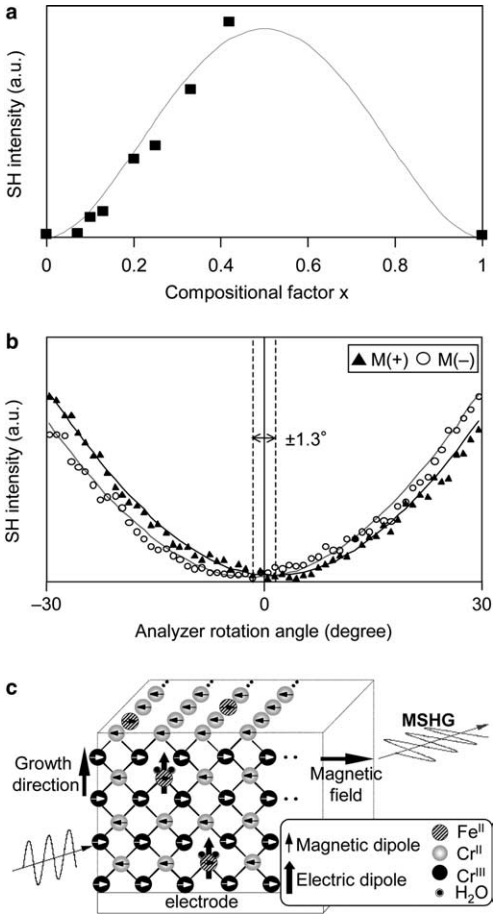


Fig. 6. (a) The SH intensity of Pin-Pout polarization combination vs. x in the film of $(Fe_x^{II}Cr_{1-x}^{II})_3[Cr^{III}(CN)_6]_2 \cdot 15H_2O$ (the incident angle: 45°). (b) The SH intensity vs. the analyzer angle in the film for $x = 0.31$ in an applied magnetic field of 10 kOe at 50 K. The analyzer angle of 0° corresponds to the direction of s-polarized SH radiation. (c) Schematic structure of the ternary metal Prussian blue analog film involving both electric and magnetic dipoles.

generation (SHG) from the surface of magnetic materials, the so-called magnetization-induced SHG (MSHG), is being actively investigated. This new optical phenomenon is useful for observing surface magnetism because the rotation angle of this effect is much larger than that of the linear Kerr effect. In contrast, SHG arising from bulk magnetic materials has been observed in a limited number of cases to date. This is because most conventional ferromagnetic materials have a centrosymmetric structure, and hence, SHG from their bulk is forbidden in the electricdipole approximation. However, electrochemically synthesized $(Fe_x^{II}Cr_{1-x}^{II})_3[Cr^{III}(CN)_6]_2 \cdot 15H_2O$ $(0 < x \leqslant 0.42)$ magnetic films exhibit strong SHG from their bulk (Fig. 6(a)) [10,11]. This SH activity is induced by the preferred orientation of the noncentrosymmetric monoclinic structure. In this system, the electric-dipole moment contributing to SHG is the CN–Fe^{II}–OH_2 site. The magnetic effect on the polarization of SH radiation using a film with $x = 0.31$ are measured. Although the second harmonic (SH) wave does not rotate in the presence of an external magnetic field at 300 K, rotation of the SH wave is observed at 50 K below T_c (Fig. 6(b)). Moreover, reversing the applied magnetic field inverts the rotational direction. The rotation angle of the SH wave is approximately 1.3°, which is much larger than the Faraday rotation angle of 0.079° at 50 K in an applied magnetic field of 10 kOe. The magnetic linear term of $\chi_{ijkL}^{magn(1)}$ explains this SH rotation because reversing the magnetic field inverts the rotational direction. The optical symmetry of the present films in the paramagnetic region is $C_{\infty v}$ because of the out-of-plane orientation of the polycrystals with a C_2 space group. Below T_c, the $\chi_{ijkL}^{magn(1)}$ term is added to the SH susceptibility, and hence, SH wave rotates.

6. Conclusion

In summary, we have prepared transparent colored magnetic thin films composed of Prussian blue analogs by an ion-exchange and an electrochemical method. These films made it possible to observe their Faraday spectra in the visible region. Colored magnetic films have the potential to allow us to develop new types of magneto-optical devices such as opto-magnetic memory devices by selecting specific types of laser color. In addition, the transmitted MSHG in colored magnetic film will give us the possibility of a new optics due to the interaction between electric polarization and magnetic polarizations.

Acknowledgments

We thank Prof. M. Verdagure, Dr. M.M. Matsushita, and Prof. N. Kojima. The present research is supported in part by a Grant for 21st Century COE Program "*Human-Friendly Materials based on Chemistry*" and a Grand-in-Aid for Scientific Research from the Ministry of Education, Culture, Sports, Science, and Technology of Japan.

References

[1] M. Verdaguer, A. Bleuzen, C. Train, R. Garde, F. Fabrizi de Biani, C. Desplanches, Philos. Trans. R. Soc. London, Ser. A 357 (1999) 2959.
[2] T. Mallah, S. Thiébaut, M. Verdaguer, P. Veillet, Science 262 (1993) 1554.
[3] S. Ferlay, T. Mallah, R. Ouahés, P. Veillet, M. Verdaguer, Nature 378 (1995) 701.
[4] S.M. Holmes, G.S. Girolami, J. Am. Chem. Soc. 121 (1999) 5593.
[5] Ø. Hatlevik, W.E. Buschmann, J. Zhang, J.L. Manson, J.S. Miller, Adv. Mater. 11 (1999) 914.
[6] S. Ohkoshi, M. Mizuno, G.J. Hung, K. Hashimoto, J. Phys. Chem. B 104 (2000) 9365.
[7] S. Ohkoshi, A. Fujishima, K. Hashimoto, J. Am. Chem. Soc. 120 (1998) 5349.
[8] M. Mizuno, S. Ohkoshi, K. Hashimoto, Adv. Mater. 12 (2000) 1955.
[9] M. Tozawa, S. Ohkoshi, N. Kojima, K. Hashimoto, Chem. Commun. (2003) 1204.
[10] K. Ikeda, S. Ohkoshi, K. Hashimoto, Chem. Phys. Lett. 349 (2001) 371.
[11] K. Ikeda, S. Ohkoshi, K. Hashimoto, J. Appl. Phys. 93 (2003) 1371.
[12] S. Ohkoshi, K. Hashimoto, Chem. Phys. Lett. 314 (1999) 210.
[13] S. Ohkoshi, T. Iyoda, A. Fujishima, K. Hashimoto, Phys. Rev. B 56 (1997) 11642.
[14] M. Verdaguer, T. Mallah, V. Gadet, I. Castro, C. Hélary, S. Thiébaut, P. Veillet, Conf. Coord. Chem. 14 (1993) 19.
[15] S. Ohkoshi, Y. Einaga, A. Fujishima, K. Hashimoto, J. Electroanal. Chem. 473 (1999) 245.

spectacular. Prussian blue precipitate is not dangerous and can be discarded. It is also possible to destroy it using hypochlorite under a hood.

3. "Attracted" Prussian blue analogue

A few tens of milligrams of powder of the room-temperature magnet **1**, [VCr], are placed in a glass tube under argon. The tube is placed on an overhead projector, perfectly horizontal. When a powerful permanent magnet is approached, the part containing the molecule-based magnet is attracted by the permanent magnet (translation or rotation of the tube). Do the experiment again, approaching the magnet from another side. It is also possible to attract the powder when displacing slowly the magnet along the tube. The synthesis of [VCr], **1**, can be found in [1,2,7].

4. "Oscillating magnet" device

The principle of the device is shown in Fig. 1(a) and a photograph is given in Fig. 1(b).

A few milligrams of [VCr], **1** are sealed in a glass vessel under argon and suspended at the bottom of a pendulum [vertical, position (2) in absence of permanent magnet]. It is then cycled between its two magnetic states: the 3D-ordered ferrimagnetic state, when $T < T_C$, and the paramagnetic one, when $T > T_C$. The three steps are: (i) the room temperature magnet [VCr] is cold ($T < T_C$, ferrimagnetic state). It is attracted (→) by the permanent magnet and deviates from the vertical direction towards position (1). The light beam is focused at this position (1), just above the permanent magnet and heats the sample, the temperature of which increases; (ii) when $T > T_C$, the hot [VCr] magnet is in the paramagnetic state. It is no more attracted strongly and moves away from the magnet (←) under the influence of its own weight. It is then air-cooled and its temperature decreases; (iii) when $T < T_C$, the cold [VCr] magnet is attracted again by the permanent magnet (→) and come back to position (1). The system is ready for a new oscillation. The period of the oscillations, the nature of the movement (periodic, (dis)continuous, chaotic, etc.) can be modified by playing on the parameters of the system: amount of sample, length of the pendulum, position of the permanent magnet, focus of the beam, power of the lamp, etc. In the device presented, all the parameters can be tuned at will.

The demonstration can be used to illustrate what is a "Curie temperature", T_C: paramagnetic disorder above

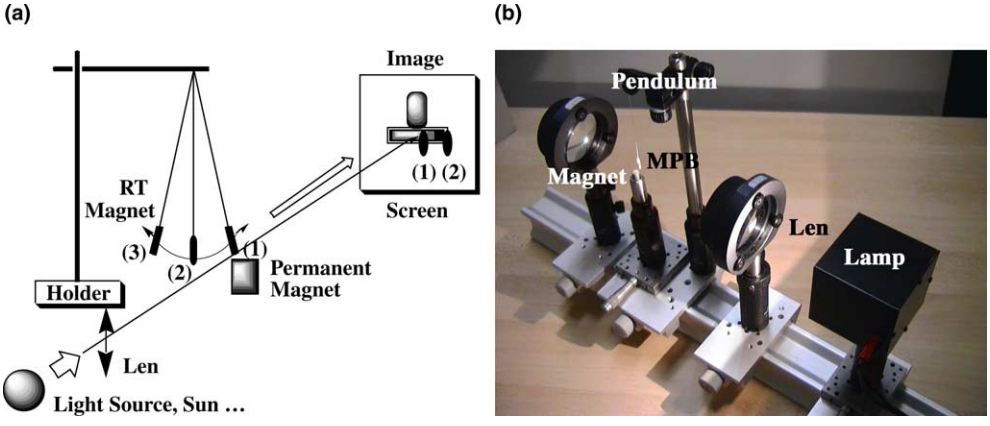


Fig. 1. (a) Principle of an "oscillating" magnet; (b) experimental device.

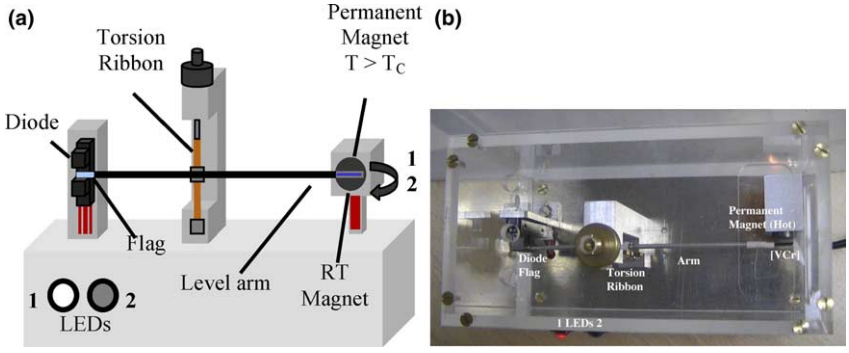


Fig. 2. (a) Scheme of the magnetic switch device; (b) photograph.

T_C (no attraction) and long range magnetic order below T_C (attraction). T_C is the temperature when the thermal quantum kT is close to the interaction J between the magnetic neighbours. The demonstrator is an example of a thermodynamical machine working between two energy baths with close temperatures (light and shadow) allowing the conversion of light into mechanical energy, free of charge!

A first account of the device was proposed in [8]. A different form of the same experiment "flying magnet" is presented in [6].

5. Magnetic switch and thermal probe device

The scheme of the device is shown in Fig. 2(a) and a photograph is given in Fig. 2(b). The device consists of diamagnetic horizontal arm (aluminum tube) coupled to a vertical torsion ribbon. The [VCr] magnet sealed in a glass vessel under argon is fixed at one end of the arm.

Close to this side of the arm, a permanent magnet is fixed and heated by a microresistance to a temperature $T > T_C$; the temperature is tunable. A thin metallic plate used as a flag is fixed at the opposite end of the arm. When the arm rotates, it moves in front of a photodiode and triggers the switching on/off of two warning LEDs (1 and 2). The device can be considered as a magnetic switch or a thermal probe: the [VCr] magnet can take two positions (1 and 2): when $T_{[VCr]} < T_C$, it is attracted (1) by the permanent magnet and a red LED, 1, is switched on. When in contact with the hot permanent magnet the [VCr] temperature increases; when $T_{[VCr]} > T_C$, it is repelled (2) by the mechanical couple applied to the arm by the torsion ribbon. The green LED, 2, is switched on. These demonstrations were presented in front of many audiences and science festivals. They revealed quite effective to demonstrate concepts in physics (Curie temperature) or in chemistry (Lewis acid–base chemistry, chemistry is beautiful, molecular magnetic materials can find their way to applications). Other demonstrators are being prepared [9]. Indeed, room temperature magnetic Prussian blues are attractive!

References

[1] S. Ferlay, T. Mallah, R. Ouahès, P. Veillet, M. Verdaguer, Nature 378 (1995) 701.
[2] S.M. Holmes, G.S. Girolami, J. Am. Chem. Soc. 121 (1999) 5593.
[3] M. Verdaguer, Polyhedron 20 (2001) 1115.
[4] M. Verdaguer, Actualit Chim. (Juin) (2001) 9.
[5] M. Verdaguer, A. Bleuzen, V. Marvaud, J. Vaissermann, M. Seuleiman, C. Desplanches, A. Scuiller, C. Train, R. Garde, G. Gelly, C. Lomenech, I. Rosenman, P. Veillet, C. Cartier dit Moulin, F. Villain, Coord. Chem. Rev. 192 (1999) 1023.
[6] M. Verdaguer, G. Girolami, in: J.S. Miller, M. Drillon (Eds.), Magnetoscience: molecules to materials, vol. V, Wiley, New York, 2004, pp. 283–346.
[7] R. Garde, F. Villain, M. Verdaguer, J. Am. Chem. Soc. 124 (2002) 10531.
[8] M. Verdaguer, T. Mallah, S. Ferlay, V. Gadet, C. Hlary, C. Auberger, R. Ouahès, J. Vaissermann, P. Veillet, in: G. Ondrejovic, A. Sirota (Eds.), Current Trends in Coordination Chemistry, Slovak Technical University Press, Bratislava, 1995, pp. 291–296.
[9] G. Keller, N. Galvez, F. Villain, unpublished work.

by sulfonic acid group) behaves as counter anion as well as transparent substrate. Here, we demonstrate the spin crossover phenomenon for [Fe(II)(H-trz)$_3$]-Nafion.

2. Preparation

2.1. Nafion

Nafion, which was developed by DuPont Company as an ion-exchange resin in 1960s, is used for many industrial applications due to its mechanical strength, chemical stability and permselectivity [8]. Nafion is composed of a polytetrafluoroethylene backbone with perfluorinated ether side chains terminated by sulfonic acid groups as shown in Fig. 1. In the case of Nafion N117, $x = 6$, $y = 1$, $m = 1$, the pendant $-SO_3H$ groups in the perfluorinated ionomer are known to form clusters of 40 Å diameter separated by a distance of 50 Å and interconnected through channels of 10 Å when they are swollen in water [9].

2.2. Preparation of [Fe(R-trz)$_3$]-Nafion (R = H, NH$_2$)

The spin crossover complex film [Fe(R-trz)$_3$]-Nafion, was prepared as follows [10]. The acid form of Nafion was immersed in an aqueous solution of $FeSO_4$. The mobile anions (SO_4^-) were more or less completely excluded from the polymer matrix because their electrical negative charge was identical to that of the ion-exchange group (a sulfonic acid; $-SO_3^-$) in the polymer matrix. After being immersed in the solution for 2 h, the film was rinsed in methanol, then it was immersed in a methanol solution of R-trz at 330 K (Fig. 2). One hour later, the film was picked up and washed with methanol, then dried under a nitrogen atmosphere.

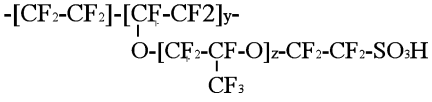


Fig. 1. Molecular formula of Nafion 117: $x = 6$, $y = 1$, $z = 1$.

3. Physical properties and demonstration

3.1. Structure analysis

In order to prove that the one-dimensional Fe(II) chain structure [Fe(R-trz)$_3$]$_n$, is formed on Nafion film, the Fe K-edge EXAFS spectra were measured [10] in the conventional transmission mode at BL-10B in the Photon Factory (operation energy of 2.5 GeV and stored current of 400–200 mA) in the Institute of Materials Structure Science, Tsukuba. A water-cooled Si(3 1 1) channel-cut crystal was employed as a monochromator.

As shown in Fig. 3, a noticeable feature is the existence of peak around 7 Å. In the case of EXAFS spectra for isolated complexes, any distinct peak does not appear in this range. However, in the case that Fe atoms are arranged in a straight chain, the multiple scattering is generally enhanced [11], which causes the appearance of peak appears at long radius region. The peak at about 7 Å corresponds to the Fe–Fe–Fe multiple scattering, which proves the existence of straight one-dimensional Fe chain structure such as [Fe(Htrz)$_2$(trz)](BF$_4$) [12].

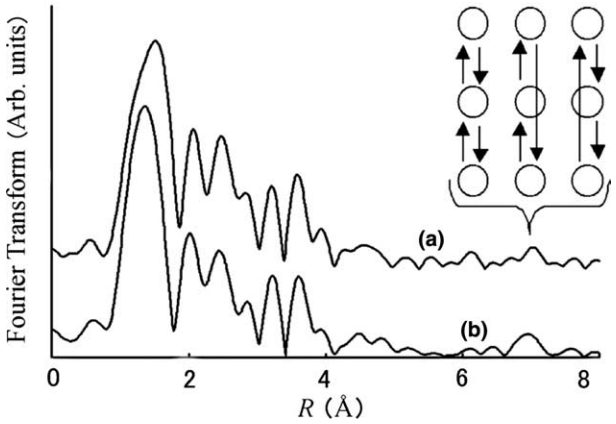


Fig. 3. Fourier transforms of Fe K-edge EXAFS oscillation function $k^3\chi(k)$ for (a) [Fe(H-trz)$_3$]-Nafion and (b) [Fe(NH$_2$-trz)$_3$]-Nafion [10]. Inset shows the multiple scattering from the next nearest neighbor Fe–Fe–Fe shell which is responsible for the EXAFS spectrum at about 7 Å.

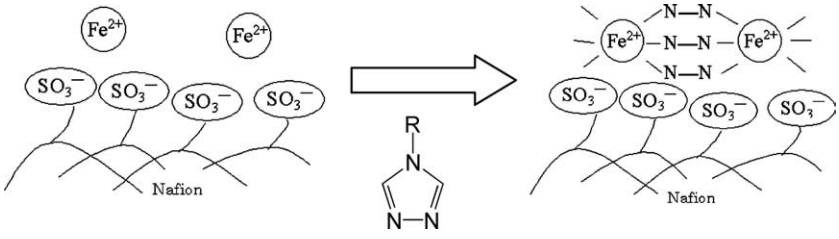


Fig. 2. Schematic preparation process of [Fe(R-trz)$_3$]-Nafion. N–N represents 4-R-trz.

3.2. Magnetic properties

The magnetic behavior of [Fe(H-trz)$_3$]-Nafion is shown in Fig. 4, where the spin transition takes place at about 260 K and finishes at about 320 K. The thermal hysteresis width is estimated at 3 K. In connection with the thermal hysteresis width of the spin transition for [Fe(R-trz)$_3$] complexes, the following should be noted. In the case of [Fe(NH$_2$-trz)$_3$](C$_n$H$_{2n+1}$SO$_3$)$_2 \cdot 2$H$_2$O [7], the hysteresis width of the spin transition decreases from 19 to 6 K, with increasing the length of counter anion from $n = 1$ to $n = 9$. For the complexes of $n > 5$, the hysteresis width is almost the same value of 6 K, which is attributed to the intra-chain interaction in [Fe(NH$_2$-trz)$_3$]$_n$. Therefore, it is considered that the hysteresis width ($\Delta T = 3$ K) of the spin transition for [Fe(H-trz)$_3$]-Nafion film is attributed to the cooperative effect due to the intra-chain interaction in [Fe(H-trz)$_3$]$_n$.

Fig. 4 also indicates the residual paramagnetic fraction below 200 K, which is attributed to the high spin state of Fe(II). In the case of the high spin state (^{5}T$_{2g}$) of Fe(II), ESR signal cannot be observed around 200 K because of rapid spin–lattice relaxation. On the other hand, the high spin state of Fe(III) can be observed even at room temperature. In fact, an ESR signal of [Fe(H-trz)$_3$]-Nafion appears below 10 K. The line profile of ESR is typical of the high spin state of Fe(II).

The residual high spin fraction of Fe(II) is probably attributed to the terminal Fe(II) site in the oligomer of [Fe(H-trz)$_3$]$_n$ on Nafion film. In the Fe(II) trimer complex [Fe$_3$(Et-trz)$_6$(H$_2$O)$_6$](CF$_3$SO$_3$)$_6$ [13], the central Fe(II) site undergoes the LS–HS transition at about 200 K, while the spin state of the terminal Fe(II) sites is the HS state between 2 and 300 K.

From the analysis of the EXAFS spectra and the magnetic susceptibility, it is obvious that the polymeric [Fe(H-trz)$_3$]$_n$ is formed in Nafion film, which is shown in Fig. 5.

Now, we demonstrate the spin transition of transparent spin crossover complex film [Fe(H-trz)$_3$]-Nafion, as thermo-chromism, which is shown in Fig. 6. The color of [Fe(H-trz)$_3$]-Nafion is colorless at room temperature. However, its color becomes purple with decreasing temperature, reflecting the spin crossover phenomenon. Note that the colors of the HS state ($t_{2g}^4\ e_g^2$, $S = 2$) and the LS state (t_{2g}^6, $S = 0$) of [Fe^{II}(R-trz)$_3$]X$_2 \cdot n$H$_2$O (R = H, NH$_2$; X = ClO$_4$, etc.), are colorless and purple, respectively. In fact, the absorption spectrum of [Fe(H-trz)$_3$]-Nafion shows two broad bands at 18 500 and 24 500 cm^{-1} corresponding to the ^{1}A$_{1g} \rightarrow {}^1$T$_{1g}$ and ^{1}A$_{1g} \rightarrow {}^1$T$_{2g}$ transitions, respectively, in the LS state ($S = 0$), while it shows a broad band at 12 500 cm^{-1}

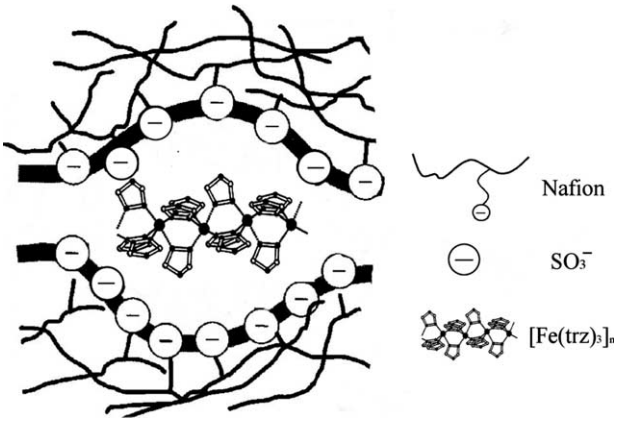


Fig. 5. Schematical representation of the oligomer of [Fe(Htrz)$_3$]$_n$ embedded in Nafion film.

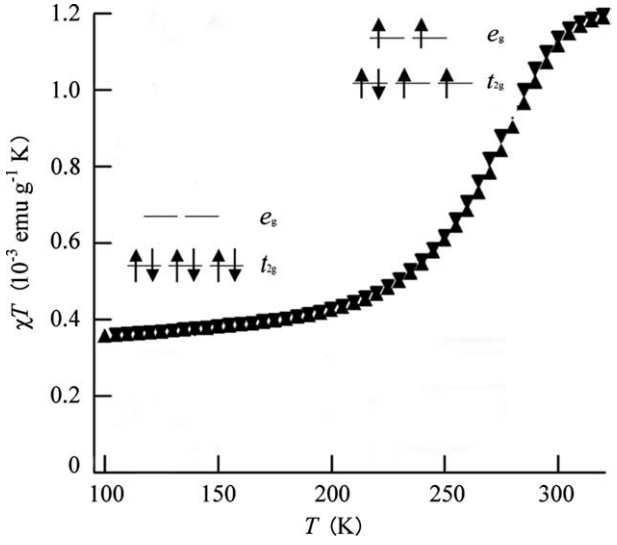


Fig. 4. χT as a function of temperature for [Fe(H-trz)$_3$]-Nafion in cooling mode (▼) and heating mode (▲).

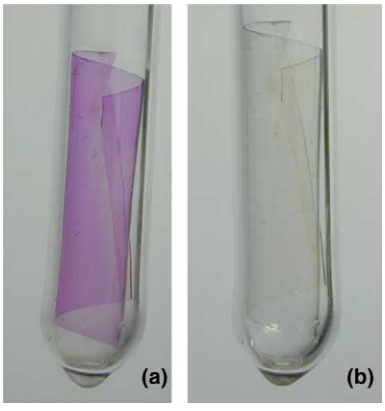


Fig. 6. Demonstration of the thermochromism due to the spin crossover phenomenon for [Fe(H-trz)$_3$]-Nafion, (a) purple in the low-spin state ($T = 77$ K) and (b) colorless in the high-spin state ($T = 300$ K).

corresponding to the $^5T_{2g} \rightarrow {}^5E_g$ transition in the HS state ($S = 2$).

3.3. LIESST

Fig. 7 shows the photoinduced transmission change $\Delta T/T$ ($E_{probe} = 2.54$ eV) at 4.2 K: open circles, closed circles, and triangles represent the data obtained at the power density of $P = 450$, 250, and 40 mW/cm^2, respectively [14]. The photo-irradiation at $E_{ex} = 2.41$ eV, which selectively excites the LS state, is expected to induce the spin state transition. At $P = 450$ mW/cm^2, the $\Delta T/T$ value steeply increases under photo-irradiation, and reached ~7%. This transmission change corresponds to the photo-induced HS fraction of 70%. This photoinduced $\Delta T/T$ signal decreases to ~5% at $P \sim 200$ mW/cm^2, and disappears at 40 mW/cm^2. Fig. 7 shows the P-dependence of the $\Delta T/T$, and a threshold value is found at ~60 mW/cm^2, as indicated by downward arrow. Such a threshold behavior may be ascribed to the critical nucleation of the photo-generated HS clusters. Fig. 7(c) shows the temperature dependence of the photoinduced $\Delta T/T$ value at $P = 350$ mW/cm^2. With the increase of temperature, the $\Delta T/T$ value decreases at 80 K, then disappears above 150 K. We observed no trace of the photoinduced LS–HS transition when we excited the film at 1.55 eV (800 mW/cm^2) and at 4.2 K. This characteristic temperature dependence and photon energy dependence rule out the conventional thermal effect as the origin of the photoinduced LS–HS transition.

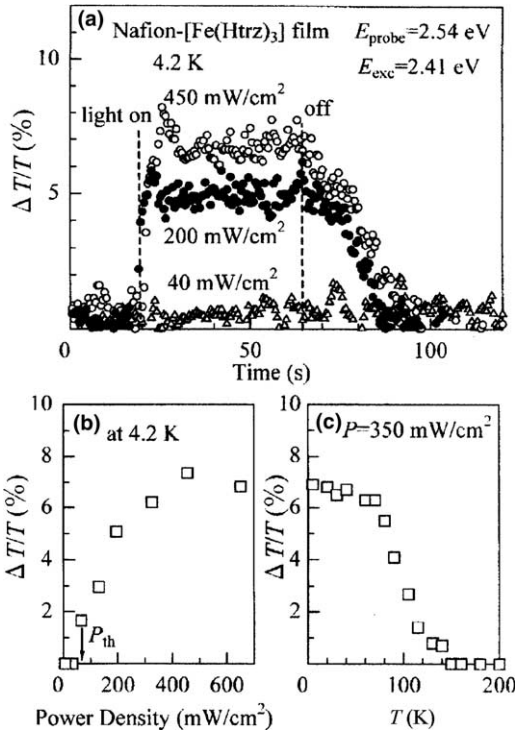


Fig. 7. (a) Temporal evolution of the transmission change $\Delta T/T$ of [Fe(H-trz)$_3$]-Nafion film at 4.2 K during and after photoirradiation at various irradiation power densities P [14]. (b) P-dependence of the $\Delta T/T$ value at 4.2 K. The downward arrow indicates a threshold value Pth of the power density. (c) Temperature dependence of the $\Delta T/T$ value under photoirradiation of $P \sim 350$ mW/cm^2.

4. Conclusion

We have succeeded in synthesizing the transparent [Fe(H-trz)$_3$] complex film by using ion-exchange film (Nafion) as counter anion, which shows the spin crossover phenomenon at about 260 K. In our preparation process, it is possible to prepare the homogeneous [Fe(R-trz)$_3$] complex film of 300 mm × 300 mm. From the analysis of Fe K-edge EXAFS spectra, we could prove the existence of one-dimensional Fe chain structure [Fe(H-trz)$_3$]$_n$, on Nafion film. Moreover, the LIESST effect was observed for [Fe(H-trz)$_3$]-Nafion at 4.2 K. The development of transparent [Fe(H-trz)$_3$]-Nafion film will open a large field of photonic molecular devices based on spin crossover phenomenon.

Acknowledgment

This work was supported by a Grant-in Aid for Scientific Research from the Ministry of Education, Science, Sports and Culture, Japan.

References

[1] S. Decurtins, P. Gütlich, C.P. Köhler, H. Spiering, A. Hauser, Chem. Phys. Lett. 105 (1984) 1.
[2] A. Hauser, Chem. Phys. Lett. 124 (1986) 543.
[3] A. Hauser, J. Chem. Phys. 94 (1991) 2741.
[4] J. Kröber, E. Codjovi, O. Kahn, F. Grolière, C. Jay, J. Am. Chem. Soc. 115 (1993) 9810.
[5] O. Kahn, C. Jay Martinez, Science 279 (1998) 44.
[6] S. Toyazaki, M. Nakanishi, T. Komatsu, N. Kojima, D. Matsumura, T. Yokoyama, Synth. Met. 121 (2001) 1794.
[7] N. Kojima, S. Toyazaki, M. Itoi, Y. Ono, W. Aoki, Y. Kobayashi, M. Seto, T. Yokoyama, Mol. Cryst. Liq. Cryst. 376 (2002) 567.
[8] C. Heitner-Wirguin, J. Membrane Sci. 120 (1996) 1.
[9] T.D. Gierke, G.E. Munn, F.C. Wilson, J. Polym. Sci. 19 (1981) 1687.
[10] A. Nakamoto, Y. Ono, N. Kojima, D. Matsumura, T. Yokoyama, Chem. Lett. 32 (2003) 336.
[11] A. Stern, in: D.C. Koning Sberger, R. Prins (Eds.), X-ray Absorption, Wiley, New York, 1988 (Chapter 1).
[12] A. Michalowicz, J. Moscovici, B. Ducourant, D. Cracco, O. Kahn, Chem. Mater. 7 (1995) 1833.
[13] G. Vos, R.A.G. De Graaff, J.G. Haasnoot, A.M. Van der Kraan, P. De Vaal, J. Reedijk, Inorg. Chem. 23 (1984) 2905.
[14] X.J. Liu, Y. Moritomo, A. Nakamura, T. Hirao, S. Toyazaki, N. Kojima, J. Phys. Soc. Jpn. 70 (2001) 2521.

The syntheses and structural characterization of $[Zn(NCS)_2(4\text{-PDS})]_n$, $[Fe(NCS)_2(4\text{-PDS})_2 \cdot 4H_2O]_n$ and $\{[Co(4\text{-PDS})_2][Cl]_2 \cdot 2CH_3OH\}_n$ form the subject of this report.

2. Experimental

2.1. General procedures

All manipulations were carried out under an atmosphere of dry, oxygen-free nitrogen using Schlenk techniques, unless otherwise noted. Solvents were dried and deoxygenated by refluxing over the appropriate reagents before use. Methanol was purified by distillation from magnesium. IR spectra were recorded on a Bio-Rad FTs-7 spectrometer. Elemental analyses were obtained from a PE 2400 series II CHNS/O analyzer, Perkin–Elmer CHN-2400 analyzer or HERAEUS VaruoEL analyzer.

2.2. Starting materials

The complexes $Zn(NO_3)_2 \cdot 6H_2O$, $CoCl_2 \cdot 6H_2O$, $FeSO_4 \cdot 7H_2O$ and NH_4SCN were used as obtained from commercial sources without further purification. The reagent 4-PDS (4-PDS = 4,4′-dipyridyldisulfide) was purchased from Aldrich.

2.3. Preparation of $[Zn(NCS)_2(4\text{-PDS})]_n$

$Zn(NO_3)_2 \cdot 6H_2O$ (0.19 g, 1 mmol), NH_4SCN (0.15 g, 2 mmol) and 4-PDS (0.22 g, 1 mmol) were placed in a flask containing 10 mL CH_3OH. The mixture was stirred at room temperature for 0.5 h to yield a white precipitate. The white solid was filtered off, washed with CH_3OH and then dried under vacuum. Yield: 0.29 g (72%). *Anal.* Calc. for $C_{12}H_8ZnN_4S_2$: C, 35.84; H, 1.99; N, 13.94. Found: C, 35.48; H, 1.96; N, 14.02%. IR (KBr disk): 3077(m), 2074(m), 1593(s), 1540(s), 1486(m), 1424(m), 1324(m), 1223(m), 1102(m), 1063 (m), 1028(m), 991(s), 964(s), 822(m), 718(m), 500(m). Colourless crystals suitable for X-ray diffraction were grown by slow diffusion of layered CH_3OH and H_2O solutions over three days.

2.4. Preparation of $[Fe(NCS)_2(4\text{-PDS})_2 \cdot 4H_2O]_n$

$FeSO_4 \cdot 7H_2O$ (0.40 g, 1.0 mmol), NH_4SCN (0.15 g, 2.0 mmol) and 4-PDS (0.44 g, 2.0 mmol) were placed

Table 1
Crystal data for **1**–**3**

Formula	$C_{12}H_8N_4S_4Zn$	$C_{22}H_{20}FeN_6O_4S_6$	$C_{22}H_{24}N_4O_2S_4Cl_2Co$
Fw	401.83	680.65	634.52
Crystal system	monoclinic	orthorhombic	triclinic
Space group	*Cc*	*Ccc2*	$P\bar{1}$
a (Å)	15.717(3)	14.065(3)	8.848(1)
b (Å)	9.922(2)	20.322(4)	8.931(1)
c (Å)	11.047(2)	10.965(1)	9.341 (1)
α (°)	90	90	67.868(2)
β (°)	101.348(4)	90	84.765(2)
γ (°)	90	90	75.732(2)
V (Å^3)	1689.1(6)	3134(1)	662.8(1)
Z	4	4	1
d_{calc} (g/cm^3)	1.580	1.443	1.590
Crystal size (mm)	$0.40 \times 0.20 \times 0.10$	$0.80 \times 0.50 \times 0.20$	$0.20 \times 0.20 \times 0.06$
μ(Mo Kα) (mm^{-1})	1.944	0.918	1.193
Range (2θ) for data collection (°)	$4.88 \leqslant 2\theta \leqslant 50.18$	$4.00 \leqslant 2\theta \leqslant 50.08$	$4.70 \leqslant 2\theta \leqslant 50.10$
Temperature (°C)	25	25	25
Limiting indices	$-18 \leqslant h \leqslant 18, -11 \leqslant k \leqslant 8, -13 \leqslant l \leqslant 13$	$-16 \leqslant h \leqslant 16, -12 \leqslant k \leqslant 24, -13 \leqslant l \leqslant 12$	$-10 \leqslant h \leqslant 9, -10 \leqslant k \leqslant 6, 11 \leqslant l \leqslant 10$
Independent reflections [R_{int}]	4106 [0.0168]	2734 [0.0374]	2294 [0.0175]
Refinement method	full-matrix least-squares on F^2	full-matrix least-squares on F^2	full-matrix least-squares on F^2
Data/restraints/parameters	2734/2/190	2734/1/186	2294/0/208
Quality-of-fit indicator[c]	1.025	1.043	1.057
Final R indices [$I > 2\sigma(I)$][a,b]	$R_1 = 0.0312$, $wR_2 = 0.0581$	$R_1 = 0.0517$, $wR_2 = 0.1064$	$R_1 = 0.0355$, $wR_2 = 0.0681$
R indices (all data)	$R_1 = 0.0411$, $wR_2 = 0.0615$	$R_1 = 0.0706$, $wR_2 = 0.1149$	$R_1 = 0.0498$, $wR_2 = 0.0724$
Largest differences in peak and hole (e Å^3)	0.355 and −0.280	0.590 and −0.236	0.541 and −0.279

[a] $R_1 = \sum \| F_o | - | F_c \| / \sum | F_o |$.

[b] $wR_2 = [\sum w(F_o^2 - F_c^2)^2 / \sum w(F_o^2)^2]^{1/2}$. $w = 1/[\sigma^2(F_o^2) + (ap)^2 + (bp)]$, $p = [\max(F_o^2 \text{ or } 0) + 2(F_c^2)]/3$. $a = 0.1874$, $b = 0.0000$ for **1**; $a = 0.000$, $b = 0.9054$ for **2**; $a = 0.0268$, $b = 5.5388$ for **3**.

[c] Quality-of-fit $= [\sum w(|F_o^2| - |F_c^2|)^2 / N_{observed} - N_{parameters}]^{1/2}$.

in a flask containing 10 mL CH_3OH. The mixture was stirred at room temperature for 0.5 h to yield a brown precipitate. The brown solid was filtered off, washed with CH_3OH and then dried under vacuum. Yield: 0.46 g (68%). *Anal*. Calc. for $C_{22}H_{20}FeN_6O_4S_6$: C, 47.44; H, 3.72; N, 14.75. Found: C, 47.24; H, 3.70; N, 14.55%. IR (KBr disk): 3118(m), 2065(m), 1582(m), 1544(s), 1408(m), 1096(m), 979(s), 809(m), 710(m), 618(m), 493(m). Brown crystals suitable for X-ray diffraction were grown by slow diffusion of layered CH_3OH and H_2O solutions over three days.

2.5. Preparation of $\{[Co(4\text{-}PDS)_2][Cl]_2 \cdot 2CH_3OH\}_n$

$CoCl_2 \cdot 6H_2O$ (0.29 g, 1.0 mmol) and 4-PDS (0.44 g, 2.0 mmol) were placed in a flask containing 10 mL CH_3OH. The mixture was stirred at room temperature for 0.5 h to yield a blue precipitate. The blue solid was

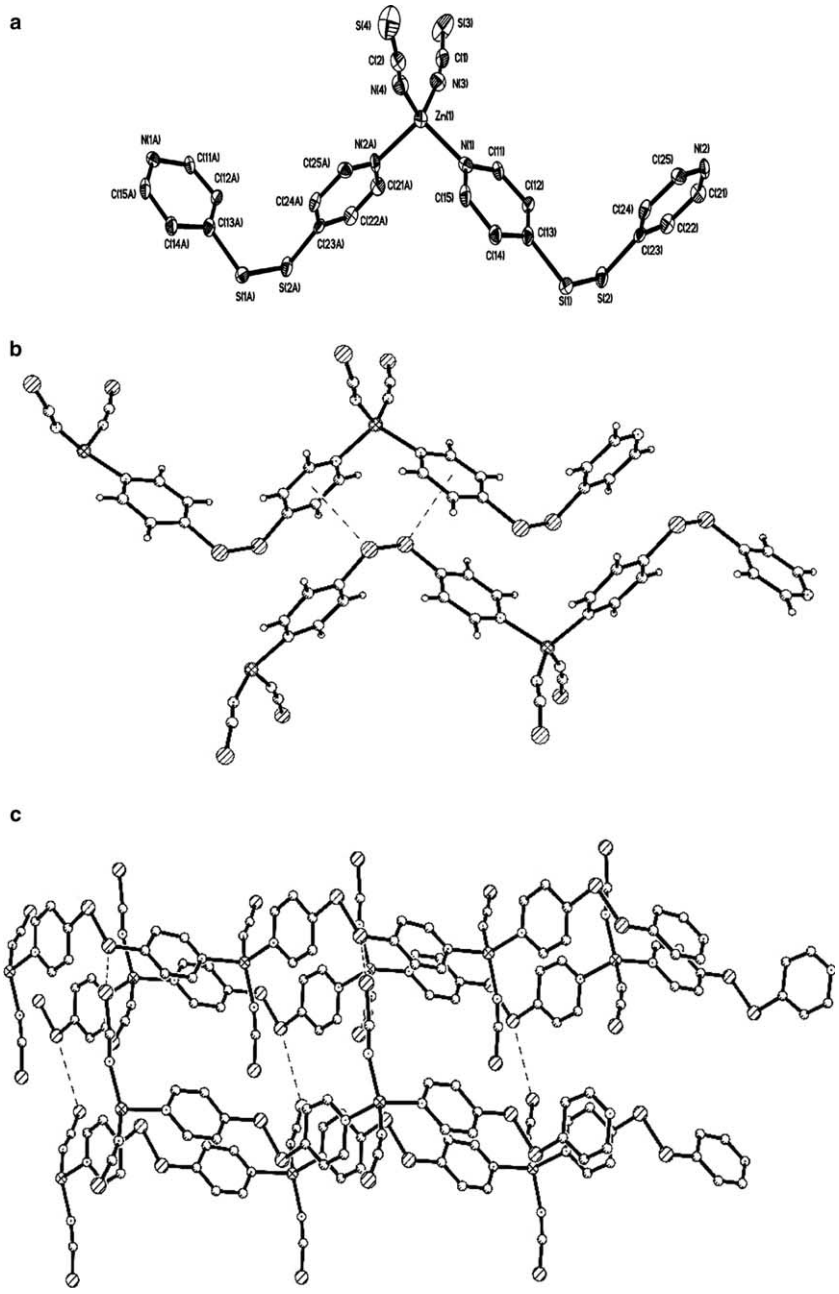


Fig. 1. (a) An ORTEP diagram of the local coordination of Zn in **1**. (b) An ORTEP diagram showing the infinite one-dimensional zigzag chains, showing the short distances between the sulfur atoms of the 4-PDS ligands and the centers of the pyridyl rings. (c) Packing diagram of **1**, showing the NCS···S–S(4-PDS) interactions among the chains.

filtered off, washed with CH_3OH and then dried under vacuum. Yield: 0.39 g (62%). *Anal.* Calc. for $C_{22}H_{24}N_4O_2S_4Cl_2Co$: C, 41.64; H, 3.81; N, 8.83. Found: C, 41.42; H, 3.71; N, 8.61%. IR (KBr disk): 3060(br), 1581(m), 1543(m), 1477(m), 1314(s), 1212(m), 1098(s), 1059(m), 991(s), 804(m), 771(m), 496(s). Blue crystals suitable for X-ray diffraction were grown by slow diffusion of layered CH_3OH and H_2O solutions over three days.

3. X-ray crystallography

The diffraction data of **1**–**3** were collected on a Siemens CCD diffractometer, which was equipped with graphite-monochromated Mo Kα (Kα = 0.71073 Å) radiation. Data reduction was carried out by standard methods with the use of well-established computational procedures [7].

The structures were solved and refined by full-matrix least-squares methods [8]. Basic information pertaining to crystal parameters and structure refinement is summarized in Table 1.

4. Results and discussion

4.1. Syntheses

The reactions of $Zn(NO_3)_2 \cdot 6H_2O$ and $FeSO_4 \cdot 7H_2O$ with 4-PDS (4-PDS = 4,4′-dipyridyldisulfide) and NH_4SCN in CH_3OH afforded the complexes $[Zn(NCS)_2(4\text{-PDS})]_n$ (**1**) and $[Fe(NCS)_2(4\text{-PDS})_2 \cdot 4H_2O]_n$ (**2**), respectively. Complex **3**, $\{[Co(4\text{-PDS})_2][Cl]_2 \cdot 2CH_3OH\}_n$, was prepared by the reaction of $CoCl_2 \cdot 6H_2O$ with 4-PDS in CH_3OH.

4.2. Structure of $[Zn(NCS)_2(4\text{-PDS})]_n$ (1)

Fig. 1(a) shows the local coordination of the Zn(II) metal center, and selected bond distances and angles are listed in Table 2. The single crystal X-ray structure shows that **1** is a coordination polymer consisting of $Zn(4\text{-PDS})(SCN)_2$, which forms one-dimensional zigzag chains (Fig. 1(b)). The distorted tetrahedral Zn(II) metal center is achieved by means of two bridging 4-PDS ligands and two terminal N-bonded NCS^- anions. The distances of the Zn–N bonds (2.007(9) and 2.054(8) Å) to the 4-PDS ligands are significantly longer than those to the NCS^- groups, which are 1.92(1) and 1.93(3) Å. The two independent NCS^- groups are almost linear with the same N–C–S angle of 173 (1)°, while the two Zn–N–C bond angles are significantly different at 170(1)° and 162(1)°, to N(3) and N(4), respectively. The Zn···Zn distance in the molecular chain is 5.561 Å. It is noted that short distances between the sulfur atoms of the 4-PDS ligands and center of the pyridyl rings, 3.501 and 3.508 Å, are observed between the chains.

Table 2
Selected bond distances (Å) and angles (°) for **1**–**3**

1	
Distances	
Zn(1)–N(3)	1.92(1)
Zn(1)–N(1)	2.007(9)
Zn(1)–N(4)	1.93(1)
Zn(1)–N(2)#1	2.054(8)
Angles	
N(3)–Zn(1)–N(4)	120.9(1)
N(4)–Zn(1)–N(1)	107.4(4)
N(4)–Zn(1)–N(2)#1	104.2(4)
N(3)–C(1)–S(3)	173(1)
N(3)–Zn(1)–N(1)	107.8(4)
N(3)–Zn(1)–N(2)#1	107.7(4)
N(1)–Zn(1)–N(2)#1	108.2(1)
N(4)–C(2)–S(4)	173(1)
2	
Distances	
Fe(1)–N(3)	2.072(4)
Fe(1)–N(1)	2.249(5)
Fe(1)–N(2)#2	2.234(5)
Angles	
N(3)–Fe(1)–N(3)#1	179.9(3)
N(2)#2–Fe(1)–N(2)#3	90.3(3)
N(3)–Fe(1)–N(1)	86.9(1)
N(2)#2–Fe(1)–N(1)	89.2(1)
N(1)–Fe(1)–N(1)#1	91.9(2)
N(3)–Fe(1)–N(2)#2	92.9(2)
N(3)–Fe(1)–N(2)#3	87.0(2)
N(3)#1–Fe(1)–N(1)	93.1 (1)
N(2)#3–Fe(1)–N(1)	173.9(2)
N(3)–C(3)–S(3)	164.2(8)
3	
Co(1)–N(2)#2	2.061(3)
Co(1)–N(1)	2.054(2)
Angles	
N(1)–Co(1)–N(2)#2	91.6(1)
N(1)–Co(1)–N(2)#3	88.4(1)

Symmetry transformations used to generate equivalent atoms: **1**: #1 $x, y, z-1$; #2 $x, y, z+1$, **2**: #1 $-x+1/2, -y+1/2, z$; #2 $x, y, z-1$; #3 $-x+1/2, -y+1/2, z-1$; #4 $x, y, z+1$, **3**: #1 $-x+1, -y+3, -z+1$; #2 $-x+1, -y+2, -z+2$; #3 $x, y+1, z-1$; #4 $x, y-1, z+1$.

4.3. Structure of $[Fe(NCS)_2(4\text{-PDS})_2 \cdot 4H_2O]_n$

Fig. 2(a) shows the local coordination of the Fe(II) metal center, and selected bond distances and angles are listed in Table 2. The single crystal X-ray structure shows that **2** is a coordination polymer consisting of Fe(4-PDS)(SCN), which forms one-dimensional metallocycles (Fig. 2(b)). The distorted octahedral Fe(II) metal center is achieved by means of four bridging

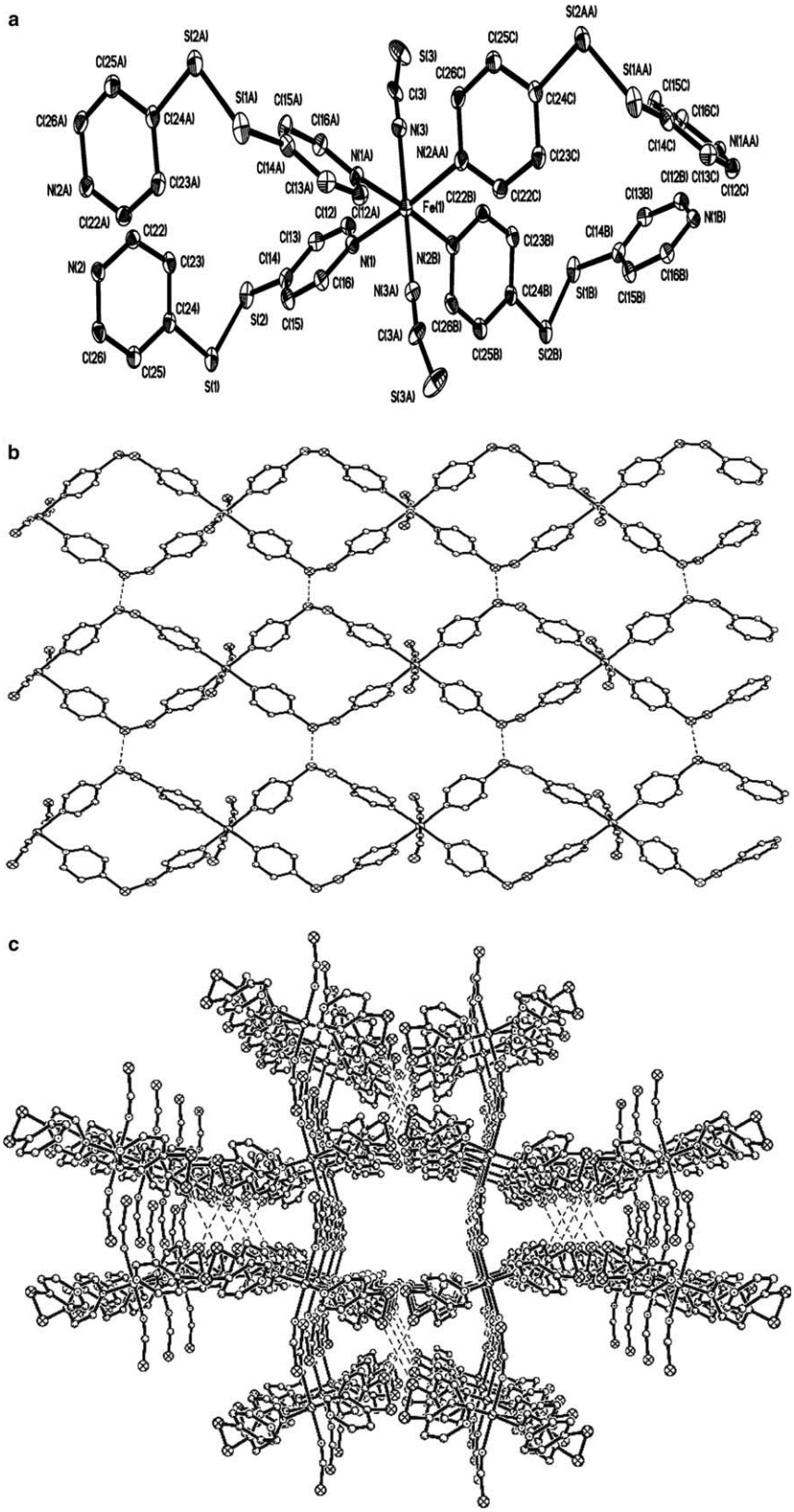


Fig. 2. (a) An ORTEP diagram of the local coordination of Fe in **2**. (b) An ORTEP diagram showing the infinite one-dimensional channel-type chains which are linked by the (4-PDS)S–S···S–S(4-PDS) interactions. (c) An ORTEP diagram showing the 2-D sheets penetrating into each other through S···S interactions, forming d–d cavities that are occupied by the water molecules. The hydrogen atoms and water molecules are removed for clarity.

4-PDS ligands and two *trans* N-bonded NCS^- anions. The Fe–N bond lengths involving the NCS^- groups, 2.072(4) Å are shorter than those involving the 4-PDS ligands, which are 2.249(5) and 2.234(5) Å for N(1) and N(2)#2, respectively. The C(3)–N(3)–Fe(1) bond angle is 169.0(5)°, while the N–C–S bond angles is 164.2 (8)°. The adjacent iron atoms are bridged by 4-PDS ligands to form 22-membered macrocyclic building units. The Fe ··· Fe distance (10.956 Å) in the molecular chain of **2** is longer than that found in a similar one-dimensional channel-type chain complex $[Fe(NCS)_2(bpa)_2]_n$ (bpa = 1,2-bis(4-pyridyl)-ethane) [9], which is 9.995(3) Å, indicating that the bpa ligand, which contains a $-CH_2-CH_2-$ group, is more flexible than the 4-PDS ligand.

One of the remarkable features in complexes **1** and **2** is that weak S···S interactions interlink the molecular chains. In complex **1**, weak S···S (3.64 Å) interactions are formed between adjacent chains through the sulfur atoms of the thiocyanato groups and the sulfur atoms of 4-PDS molecules (Fig. 1(c)). In complex **2**, the S···S weak interactions (3.52 Å), which interlink the one-dimensional metallocycles into 2-D sheets, are formed between adjacent chains through the sulfur atoms of 4-PDS ligands. In fact, the 2-D sheets interpenetrate each other through the S···S interactions, forming a unique 3-D structure with large cavities that are occupied by the water molecules (Fig. 2(c)). The S···S distances of complexes **1** and **2**, which are 3.64 and 3.52 Å, respectively, are shorter than twice the van der Waals radius of sulfur (3.7 Å). S···S interactions have been observed in several compounds, such as $[4,4'\text{-bipyH}_2][M(NCS)_4]$ ($M = Mn^{2+}$, Co^{2+} or Zn^{2+}; 4,4′-bipy = 4,4′-bipyridine) [10], Cu_2Cl_4L (L = 2,5-bis(2-pyridylmethylsufanylmethyl)pyrazine) [11] and $[Hg_2(C_5H_4S_5)_2Cl_4]_n$($C_5H_4S_5$ = 4,5-ethylenedithio-1,3-dithiole- 2-thione) [12]. However, although several complexes containing 4-PDS ligands are known (Table 3, vide infra), only one complex $[Ag(4\text{-PDS}) \cdot NO_3 \cdot (CH_3CN)_{0.5}]$ was reported to show insignificant S···S interactions (3.73 Å) between the chains.

4.4. Structure of $\{[Co(4\text{-PDS})_2][Cl]_2 \cdot 2CH_3OH\}_n$

Fig. 3(a) shows the local coordination of the Co(II) metal center, and selected bond distances and angles are listed in Table 2. The single crystal X-ray structure shows that **3** is a coordination polymer consisting of Co(4-PDS), which forms one-dimensional metallocycles (Fig. 3(b)). The distorted square planar Co(II) metal center is achieved by means of four bridging 4-PDS ligands. The two independent Co–N bond lengths are 2.054(2) and 2.061(3) Å. The adjacent cobalt atoms are bridged by 4-PDS ligands to form 1-D chains based on the 22-membered macrocyclic building units. The Co···Co distance in the molecular chain is 10.207 Å.

Table 3
S–S distances (Å) and C–S–S–C torsion angles (°) for some reported complexes containing 4-PDS ligands

Complex	S–S	C–S–S–C	Reference
1	2.028(1)	91.2	this work
2	2.026(1)	80.9	this work
3	2.031(3)	91.5	this work
$[Ag(4\text{-PDS})_2 \cdot PF_6]$	2.028(2)	91.4(2)	[17]
$[Ag(4\text{-PDS})_2 \cdot ClO_4]$	2.033(1)	89.7(1)	[17]
$[Ag(4\text{-PDS})_2 \cdot OTs]$	1.984(6)	95.5(8)	[17]
$[Ag(4\text{-PDS})_2 \cdot NO_3 \cdot (CH_3CN)_{0.5}]$	2.022(4)	83.8(6)	[17]
[4-PDS · Cu(hfac)]	2.029(2)	88.1(2)	[18]
[4-PDS · Mn(hfac)]	2.031(5)	91.6(6)	[18]
trans-$\{[RuCl(pdma)_2\}_2$-(μ-(4-PDS))$[I_3]_2\}$	2.029(6)	86.6	[19]
$[Zn_7(\mu_4\text{-}O_2)(CH_3CO_2)_{10}$-(μ-(4-PDS))$]_n$	2.021(7)	61.8(5)	[20]
$[Cd(4\text{-PDS})_2(H_2O)_2] \cdot 2NO_3 \cdot 2EtOH \cdot 2H_2O$	2.033(2)	90	[21]

Interestingly, the non-coordinated chloride ions, occupying the axial positions of the square planar metal centers, interact with the Co metal atoms through weak Co···Cl (2.916 Å) bonding. Each chloride atom also interacts with four phenyl hydrogen atoms of the 4-PDS ligands and the hydroxyl hydrogen atoms of the methanol molecules through C–H···Cl (H···Cl = 2.561, 2.638, 2.657 and 2.584 and ∠C–H···Cl = 134.5°, 132.3°, 129.2° and 135.8°; H···Cl = 2.055 Å and ∠O–H···Cl = 174.7°, respectively), hydrogen bonds (Fig. 3(c)). The oxygen atoms of the methanol molecules also interact with the sulfur atoms (S···O = 3.209) of the adjacent chains to form a 2-D network (Fig. 3(d)). Weak C–H···Cl hydrogen bonds have been observed in many compounds, such as CuCl(Pyz) [13], $CdCl_2$(Pyz) [14] and Cu_2Cl_2(Pyz) [15] and have been well established [16]. In this complex, no S···S weak interaction was found, presumably due to the formation of the C–H···Cl hydrogen bonds and the packing of the CH_3OH solvent molecules.

4.5. Conformation of the 4-PDS ligands

Table 3 shows the S–S distances and C–S–S–C torsion angles for some reported complexes containing 4-PDS ligands. The S–S bond distances are 2.208(1), 2.026(1) and 2.031(3) Å, while the S–C–C–S torsion angles are 91.2°, 80.9° and 91.5° for complexes **1**–**3**, respectively. These values are comparable to those in the other reported complexes. The 4-PDS ligand has been reported to show axial chirality, i.e., the *P* and *M*-forms of an optical antipode [17]. Based on Mochida's definition, each 1-D chain in complex **1** is chiral and is represented by either –*M*-(M)-*M*-(M)-*M*- or *P*-(M)-*P*-(M)-*P*-. The complex consists of a 1:1 ratio of *P* and *M*-chains, and is thus achiral. Complexes **2** and **3** can be envisioned as double-strand one dimensional coordination polymers. In **2**, each strand adopts either

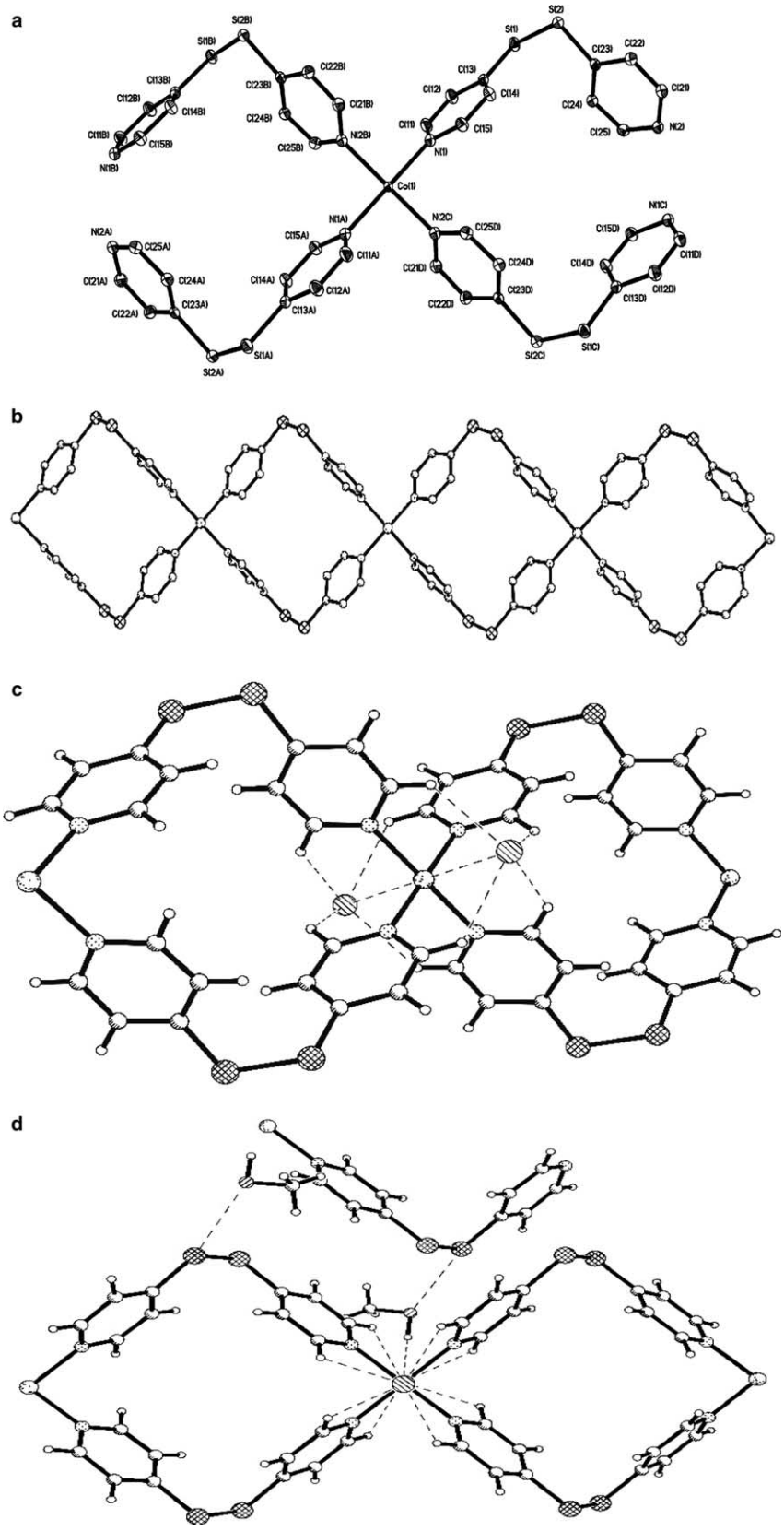


Fig. 3. (a) An ORTEP diagram of the local coordination of Co in **3**. (b) An ORTEP diagram showing the infinite one-dimensional channel-type chains. (c) An ORTEP diagram showing the interactions among the chloride atoms and the cobalt metal centers, where the O–H···Cl and S···O interactions to the methanol molecules are omitted for clarity. (d) A view looking down the Cl–Co–Cl axis, showing the O–H···Cl and S···O interactions between the chains.

P or *M* configurations, forming enantiomeric pairs, while each strand in complex **3** adopts the alternating P-(M)-M-(M)-P achiral conformation.

Acknowledgements

The researchers thank the Nanya Institute of Technology and the National Science Council of the Republic of China for support.

Appendix A. Supplementary data

Crystallographic data (excluding structure factors) for the structures in this paper has been deposited with the Cambridge Crystallographic Data Centre as supplementary publication number CCDC 216195–216197. Copies of the data can be obtained, free of charge, on application to CCDC, 12 Union Road, Cambridge CB2 1EZ, UK [fax: +44(0)-1223-336033 or e-mail: deposit@ccdc.cam.ac.uk] or www.ccdc.cam.ac.uk. Supplementary data associated with this article can be found, in the online version, at doi:10.1016/j.poly.2004.09.034.

References

[1] (a) R. Robson, B.E. Abrahams, S.R. Batten, R.W. Gable, B.F. Hoskins, J. Lieu, Supramolecular Architecture, ACS Publications, Washington, DC, 1992;
(b) H. Gudbjartson, K. Biradha, K.M. Poirier, M.J. Zaworotko, J. Am. Chem. Soc. 121 (1999) 2599;
(c) S.-I. Noro, R. Kitauta, M. Kondo, S. Kitagawa, T. Ishii, H. Matauzaka, M. Yamashita, J. Am. Chem. Soc. 124 (2002) 2568;
(d) C. Janiak, J. Chem. Soc., Dalton Trans. (2003) 2781;
(e) S. Kitagawa, S. Masaoka, Coord. Chem. Rev. 246 (2003) 73;
(f) S.R. Batten, K.S. Murray, Coord. Chem. Rev. 246 (2003) 103;
(g) S.L. James, Chem. Soc. Rev. 32 (2003) 276.

[2] (a) E. Bakalbassis, C. Tsipis, A. Bozopoulos, W. Dreissig, H. Hartl, J. Mrozinski, Inorg. Chim. Acta 186 (1991) 113;
(b) J. Cano, G.D. Munno, J.L. Sanz, R. Ruiz, F. Lioret, J. Faus, M. Julve, J. Chem. Soc., Dalton Trans. (1994) 3465;
(c) R.H. Groeneman, L.R. Macgillvrey, J.L. Atwood, Inorg. Chem. 38 (1999) 208;
(d) L. Deakin, A.M. Arif, J.S. Miller, Inorg. Chem. 38 (1999) 5272;
(e) Y. Suenaga, T. Kuroda-Sowa, M. Maekawa, M. Munakata, Polyhedron 18 (1998) 191;
(f) M.-L. Tong, X.-M. Chen, S.W. Ng, Inorg. Chem. Commun. 3 (2000) 436;
(g) C. Richardson, P.J. Steel, Inorg. Chem. Commun. 1 (1998) 260;
(h) M.-L. Tong, X.-M. Chen, B.-H. Ye, S.W. Na, Inorg. Chem. 37 (1998) 5278.

[3] (a) E. Bakalbassis, P. Bergerat, O. Kahn, S. Jeannin, Y. Jeannin, Y. Dromzee, M. Guillot, Inorg. Chem. 31 (1992) 625;
(b) C.S. Hong, Y. Do, Inorg. Chem. 36 (1997) 5684;
(c) G.K.H. Shimizu, G.D. Enright, C.I. Ratciffe, J.A. Ripmeester, Chem. Commun. (1999) 461;
(d) L. Carlucci, G. Ciani, D.M. Proserpio, Chem. Commun. (1999) 449.

[4] (a) H.J. Choi, M.P. Suh, Inorg. Chem. 38 (1999) 6309;
(b) H.-K. Fun, S.S.S. Raj, R.-G. Xiong, J.-L. Zuo, Z. Yu, X.-Z. You, J. Chem. Soc., Dalton Trans. (1999) 1915;
(c) Y. Suenaga, T. Kamiya, T. Kuroda-Sowa, M. Maekawa, M. Munakata, Inorg. Chim. Acta 308 (2000) 17;
(d) W.-M. Bu, L. Ye, Y.-G. Fan, Inorg. Chem. Commun. 3 (2000) 194;
(e) X.-H. Bu, K. Biradha, T. Yamaguchi, M. Nishimura, T. Ito, K. Tanaka, M. Shionoya, Chem. Commun. (2000) 1953;
(f) L. Carlucci, G. Ciani, D.M. Proserpio, A. Sironi, Angew. Chem. Int. Ed. Engl. 34 (1995) 1895.

[5] (a) C.-W. Su, C.-P. Wu, J.-D. Chen, L.-S. Liou, J.-C. Wang, Inorg. Chem. Commun. 5 (2002) 215;
(b) S.-H. Liu, J.-D. Chen, L.-S. Liou, J.-C. Wang, Inorg. Chem. 40 (2001) 6499;
(c) Y.-F. Hsu, J.-D. Chen, Eur. J. Inorg. Chem. 7 (2004) 1488.

[6] M.-C. Suen, T.-C. Keng, J.-C. Wang, Polyhedron 21 (2002) 270.

[7] SMART/SAINT V5.10, Software for CCD Detector System, Bruker AXS, Inc., Madison, WI, USA, 1998.

[8] G.M. Sheldrick, SHELXTL PLUS, Release 4.1′, Siemens Analytical X-ray Instruments Inc., Karlsruche, Germany, 1991.

[9] M.L. Hemandez, M.G. Barandika, M.K. Urtiaga, R. Cortes, L. Lezama, M.I. Arriortua, T.J. Roio, J. Chem. Soc., Dalton Trans. (1999) 1401.

[10] H.-J. Chen, L.-Z. Zhang, Z.-G. Cai, G. Yang, X.-M. Chen, J. Chem. Soc., Dalton Trans. (2000) 2463.

[11] P.L. Caradoc-Davies, D.H. Gregory, L.R. Hanton, J.M. Turnbull, J. Chem. Soc., Dalton Trans. (2002) 1574.

[12] Q.-H. Wang, D.-L. Long, J.-S. Huang, Polyhedron 17 (1998) 3665.

[13] I. Unamuno, J.M. Guterrez-Zorrilla, A. Luque, P. Roman, L. Lezama, R. Calvo, T. Rojo, Inorg. Chem. 37 (1998) 6452.

[14] R.D. Balley, W.T. Pennington, Polyhedron 16 (1997) 417.

[15] S. Kawata, S. Kitagawa, H. Kumagai, S. Iwabuchi, M. Katada, Inorg. Chim. Acta. 267 (1998) 14.

[16] G.R. Desiraju, Acc. Chem. Res. 29 (1996) 441.

[17] R. Horikoshi, T. Mochida, N. Maki, S. Yamada, H. Moriyama, J. Chem., Dalton Trans. (2002) 28.

[18] R. Horikoshi, T. Mochida, H. Moriyama, Inorg. Chem. 40 (2001) 2430.

[19] B.J. Coe, S. Hayat, R.L. Beddoes, M. Helliwell, J.C. Jeffery, S.R. Batten, P.S. White, J. Chem. Soc., Dalton Trans. (1997) 591.

[20] M.T. Ng, T.C. Deivaraj, J.J. Vittal, Inorg. Chim. Acta 348 (2003) 173.

[21] M. Kondo, M. Shimamura, S.-I. Noro, Y. Kimura, K. Uemura, S. Kitagawa, J. Solid. State. Chem. 152 (2000) 113.

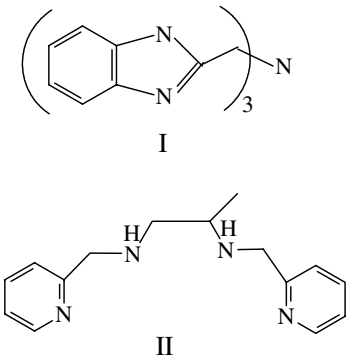


Chart 1.

the structural characterization of organic ligands, solvent system, temperature, pH of the solution, ratio of metal to ligand and counter ions [9–15]. An alteration in any of these factors often results in new complexes with different structural topologies and functions.

Herein, we report the reaction of the tripodal ligand tris(2-benzimidazolylmethyl)amine (ntb) (**I**, Chart 1) with copper chloride and ferric chloride, resulting in the formation of the complexes $[Cu(ntb)Cl]_2[CuCl_4]\cdot 2H_2O$ (**1**) and $[Fe(ntb)Cl_2]Cl\cdot 3H_2O$ (**2**). Each ntb ligand possesses three NH groups that are potential hydrogen-bond donors [16]. In both the complexes, the interaction between cations and anions via bifurcated (N–H···O) and (N–H···Cl) hydrogen-bonds provide extended networks. Well-defined hexagonal channels have also been identified in the assembly of the iron complex. Thus, the present study would serve as an elegant example of the use of different counter ions to effect supramolecular change of a cationic complex.

Of specific relevance to the above, we note that octahedral complexes of tetradentate ligands with reactive sites in a *cis* configuration affords an additional feature in that the *cis* orientation is ideal for coordination/insertion polymerization [17]. There has been a scarcity of information on the structural features of complexes derived from the Fe(bispicpn) moiety (bispicpn = *N*,*N*′-*bis*(2-pyridylmethyl)-1,2-propanediamine, **II**) (Chart 1) [18] and, thereby, the present study has been extended to establish proper synthetic strategies that could lead to any well-defined structural analogue. It may be noted that though the ligands ntb and bispicpn are structurally different, they belong to the N_4 system and form hexacoordinated molecules having the same counter anion (Cl^-). The notable distinguishing feature is that they lead to different extended frameworks.

Paskaly et al. [19] had successfully utilized the N_4 tripodal ligands bis(*N*-methylimidazole-2-yl)(picolyl)-amine and bis(picolyl)(*N*-methylimidazole-2-yl)amine in the synthesis of Fe-containing functional models of catechol dioxygenases. Examples with copper complexes showing such activity are not abundant. The crystal structure and catecholase like activity of a mononuclear complex $[Cu(EDTB)]^{2+}$ (EDTB = *N*,*N*,*N*′,*N*′-tetrakis (2′-benzimidazolylmethyl)-1,2-ethanediamine) have been reported very recently [20]. Therefore, it is a reasonable strategy to explore whether the new complexes derived from ntb and bispicpn with copper and iron can catalyze the oxidation of substituted catechols. The oxidizing activity of these complexes with 3,5-di-*tert*-butylcatechol have been studied in DMF. The copper complex (**1**) actually exhibits (very weak) catecholase activity, whereas the two iron complexes **2** and **3** show very weak dioxygenase activity. The catechol dioxygenase activity of **2** is, however, slightly higher than that of **3**.

2. Experimental

2.1. Materials

All materials used were of reagent grade. *o*-Phenylenediamine, nitrilotriacetic acid, pyridine-2-carboxaldehyde, copper chloride dihydrate, anhydrous ferric chloride and ferric chloride hexahydrate were of analytical reagent grade (Aldrich) and used without further purification. 1,2-Diaminopropane and ethylene glycol were distilled prior to the reaction. All other chemicals, e.g., MeOH, acetonitrile were of reagent grade. Distilled water was used throughout.

2.2. Physical measurements

Microanalysis (CHN) was performed in a Perkin–Elmer 240C elemental analyzer. IR spectra were obtained on a Nicolet MAGNA-IR 750 spectrometer with samples prepared as KBr pellets. Spectral and kinetic measurements were performed in an UV–Vis spectrophotometer (UV-2100, Shimadzu, Japan) equipped with thermostated cell compartments. Cyclic voltammetry was performed at a platinum electrode using an EG&G PARC electrochemical analysis system (Model 250/5/0) in DMF under dry nitrogen atmosphere in conventional three electrode configurations with a scan rate of 0.05 V s^{-1}. Oxygenated products were isolated by preparative TLC and column chromatography using 1:10 v/v of EtOAc and pet ether. NMR spectra were recorded with a Bruker AC 300 apparatus using $SiMe_4$ (δ_0) as an internal standard. DSC was recorded on a Perkin–Elmer DSC 7 instrument.

2.3. Preparation of the ligands

2.3.1. Tris(2-benzimidazolylmethyl)amine (ntb)

This has been synthesized following the procedure reported by Oki et al. [21].

2.3.2. N,N′-bis(2-pyridylmethyl)-1,2-propanediamine(bispicpn)

The ligand was synthesized by a modification of the previously reported method of Michelsen et al. [22]. Pure 1,2-diaminopropane (25 mmol, 2.15 cm^3) was allowed to react with pyridine-2-carboxaldehyde (50 mmol, 4.75 cm^3) in absolute ethanol (30 cm^3) by refluxing the mixture for 10 min. To this solution sodium borohydride (0.066 mmol, 2.5 g) was added in small portions over a period of 3 h. The solution was left overnight and warmed to boiling for 1 h. To the resulting solution hydrochloric acid (7.5 cm^3, 12 M) was added and when the gas evolution had ceased, the solution was made alkaline with a NaOH solution (10 cm^3, 5 M). Precipitated sodium borate was filtered off and the volume of the filtrate was reduced by evaporation under reduced pressure. The remaining solution was extracted with $CHCl_3$. The crude product of *N*,*N*′-bis(2-pyridylmethyl)-1,2-propanediamine were obtained as a viscous liquid by evaporation of the $CHCl_3$ solution (Yield: 66%).

2.4. Preparation of the complexes

2.4.1. [Cu(ntb)Cl]$_2$[CuCl$_4$] · 2H$_2$O (1)

To a 10 cm^3 acetonitrile solution of copper chloride dihydrate (0.85 g, 0.5 mmol) was added an acetonitrile (20 cm^3) solution of ntb (0.204 g, 0.5 mmol) and stirred. A clear green solution was thereby formed which was filtered to remove any suspended materials. The solution was kept in air and after 2 days prismatic pale brown crystals of **1** were formed. It was filtered and washed first by the mother liquor followed by diethyl ether and dried in air (Yield: 75% based on Cu). *Anal.* Calc. for $[Cu(ntb)Cl]_2[CuCl_4]\cdot 2H_2O$ ($Cu_3C_{48}H_{46}N_{14}O_2Cl_6$) ($F_w = 2445.13$): C, 23.56; H, 1.88; N, 8.02. Found: C, 23.12; H, 1.78; N, 7.97%. UV–Vis (MeOH) [$\lambda_{max}(\varepsilon)$]: 366 nm (630 M^{-1} cm^{-1}), 758 nm (154 M^{-1} cm^{-1}). IR (KBr pellet): 3063–3415 cm^{-1} (for H-bonded water molecules), 744 cm^{-1} (for out-of-plane bending vibrations of the *o*-disubstituted phenyl rings of the ntb ligand).

2.4.2. [Fe(ntb)Cl$_2$]Cl · 3H$_2$O (2)

To an acetonitrile (10 cm^3) solution containing ferric chloride hexahydrate (0.135 g, 0.5 mmol) was added an acetonitrile solution (20 cm^3) of ntb (0.204 g, 0.5 mmol) and the resulting solution was kept at room temperature for 3 h to give bright red needle shaped crystals upon slow evaporation of the solvent. The crystals were then filtered and washed first by the mother liquor followed by diethyl ether and dried in air (Yield: 78% based on Fe). *Anal.* Calc. for $[Fe^{III}(ntb)Cl_2]Cl\cdot 3H_2O$ ($FeC_{24}H_{27}N_7O_3Cl_3$) ($F_w = 623.73$): C, 46.17; H, 4.33; N, 15.71. Found: C, 46.05; H, 4.45; N, 15.54%. UV–Vis (MeOH) [$\lambda_{max}(\varepsilon)$]: 255 nm (6500 M^{-1} cm^{-1}), 280 nm (8200 M^{-1} cm^{-1}), IR (KBr pellet): 3045–3446 cm^{-1} (for H-bonded water molecules), 747 cm^{-1} (for out-of-plane bending vibrations of the *o*-disubstituted phenyl rings of the ntb ligand).

2.4.3. [Fe(bispicpn)Cl$_2$]Cl (3)

To a 10 cm^3 acetonitrile solution containing anhydrous ferric chloride (0.081 g, 0.5 mmol) was added an acetonitrile solution (20 cm^3) of bispicpn (0.13g, 0.5 mmol) and the resulting solution was left standing at room temperature. After 3–4 h orange-yellow crystals were isolated (Yield: 88% based on Fe). *Anal.* Calc. for [Fe(bispicpn)Cl$_2$]Cl ($FeC_{15}H_{19}N_4Cl_3$) ($F_w = 417.54$): C, 43.11; H, 4.55; N, 13.41. Found: C, 43.21; H, 4.46; N, 13.29%. [$\lambda_{max}(\varepsilon)$]: 598 nm (97 M^{-1} cm^{-1}), 494 nm (134 M^{-1} cm^{-1}), 453 nm (181 M^{-1} cm^{-1}).

2.5. Crystal structure determination and structural refinements of complexes 1, 2 and 3

Crystal data and other experimental details for **1**, **2** and **3** are reported in Table 1. The diffraction experiments concerning **1** and **2** were carried out on a Bruker SMART CCD area-detector diffractometer at 200 K. No crystal decay was observed, so that no time-decay correction was needed. The collected frames were processed with the software SAINT [23], and an empirical absorption correction was applied (SADABS) [24] to the collected reflections. The calculations were performed using the Personal Structure Determination Package [25] and the physical constants tabulated therein [26]. The structures were solved by direct methods (SHELXS) [27] and refined by full-matrix least-squares using all reflections and minimising the function $\sum w(F_o^2 - kF_c^2)^2$ (refinement on F^2). Anisotropic thermal factors were refined for all the non-hydrogen atoms. The hydrogen atoms of the water molecules were detected in the final Fourier maps and not refined. The remaining hydrogen atoms were placed in their ideal positions (C–H or N–H = 0.97 Å) with the thermal parameter *B* 1.10 times that of the atom to which they are attached, and not refined. In the final Fourier maps the maximum residuals were 0.90(13) e $Å^{-3}$ at 0.87 Å from Cl(1) and 0.85(25) e $Å^{-3}$ at 0.94 Å from Cl(1) for **1** and **2**, respectively.

A single crystal of the complex **3** was collected and mounted on an automatic Bruker P4 diffractometer equipped with graphite monochromated Mo Kα radiation ($\lambda = 0.71073$ Å). Unit cell dimensions and intensity data were measured at 296 K. The structure was solved by direct methods, refined by full-matrix least-squares based on F^2 with anisotropic thermal parameters for non-hydrogen atoms using Bruker SHELXTL (data reduction), SHELXS [28] (structure solution) and SHELXL [29] (structure refinement). The hydrogen atoms were included in structure factor calculations in their idealized positions.

Table 1
Crystallographic information for **1**–**3**

Complex	$C_{48}H_{46}Cl_6Cu_3N_{14}O_2$	$C_{24}H_{27}Cl_3FeN_7O_3$	$C_{15}H_{19}Cl_3FeN_4$
Formula weight	1254.33	623.73	417.54
Crystal system	monoclinic	triclinic	monoclinic
Space group	$C2/c$	$P\bar{1}$	$P2_1/c$
a (Å)	20.420(2)	9.662(1)	15.0357(7)
b (Å)	18.036(2)	11.394(1)	7.4426(3)
c (Å)	14.587(1)	13.698(1)	16.7214(8)
α (°)	90	88.23(1)	90
β (°)	103.08(1)	73.20(1)	106.577(10)
γ (°)	90	73.01(1)	90
V (Å^3)	5232.9(9)	1378.3(2)	1793.43(14)
Z	4	2	4
D_{calc} (g cm^{-3})	1.592	1.503	1.546
μ(Mo Kα) (mm^{-1})	1.574	0.878	1.291
F(000)	2548	642	856
T (K)	200(2)	200(2)	103(2)
λ(Mo Kα)	0.71073	0.71073	0.71073
Maximum and minimum θ range (°)	3.0–27.0	3.0–26.0	2.5–28.3
Total data, unique data	42858, 7926	17907, 6088	14017, 4353
R_{int}	0.0287	0.0874	0.034
Final R indices (R_1, wR_2)[a]	0.050, 0.088	0.095, 0.127	0.0462, 0.1249
Goodness-of-fit[b]	1.196	0.952	1.134

[a] $R_1 = [\sum(|F_o^2 - kF_c^2|)/\sum F_o^2]$, $wR_2 = [\sum w/(F_o^2 - kF_c^2)^2/\sum w(F_o^2)^2]^{1/2}$.
[b] $[w(F_o^2 - kF_c^2)^2/(N_o - N_v)]^{1/2}$, where $w = 4F_o^2/\sigma(F_o^2)^2$, $\sigma(F_o^2) = [\sigma^2(F_o^2) + (pF_o^2)^2]^{1/2}$, N_o is the number of observations, N_v the number of variables, and $p = 0.04$ for **1** and 0.03 for **2**.

3. Results and discussion

3.1. Crystal structure of $[Cu(ntb)Cl]_2[CuCl_4] \cdot 2H_2O$ (*1*)

An ORTEP drawing of the complex with the atom labelling scheme is shown in Fig. 1. The selected bond distances and angles are given in Table 2. The unit cell consists of eight $[Cu(ntb)Cl]^+$ cations, four $CuCl_4^{2-}$ anions and eight water molecules as solvent of crystallization. Copper atoms in the cation and the anion differ in their geometry. In the cation, the geometry of the central copper atom is intermediate between square-pyramidal and trigonal bipyramidal in which two N atoms of the benzimidazole and the amine N atom occupy the equatorial positions, and one of the nitrogen atoms from benzimidazole occupies the axial position. The remaining site of the equatorial plane is occupied by a Cl^- ion. Addison et al. [30] had proposed and defined an angular structural parameter as an index of trigonality in five coordinated systems. By this standard, the coordination geometry of $[Cu(ntb)Cl]^+$ in the solid state is described as being 28% ($\tau = 0.28$) along the pathway of distortion from square-pyramidal towards trigonal bipyramidal. A recent report by Wu et al. [31] on the structural aspect of $[Cu(ntb)(H_2O)](ClO_4)_2 \cdot C_6H_7NO \cdot H_2O$ described the coordination geometry of copper as distorted trigonal bipyramidal with approximate site symmetry $C3$. The geometry of the central metal ion in the anionic part is a distorted tetrahedron occupied by four Cl^- atoms. The $Cu–N_{amine}$ distance in the cation is 2.2440(15) Å and the average distance of equatorial $Cu–N_{benzimidazole}$ is 1.966 Å. The distance between the copper and axial nitrogen is 2.1264(15) Å. These bond distances compare well with previously reported compounds of a similar type [32]. Wu et al. [31] reported the Cu–N(amine) bond distance as 2.096(3) Å. In the $CuCl_4^{2-}$ moiety, the average Cu–Cl bond length is 2.2433 Å. This unit along with two water molecules participate in hydrogen bonding interactions with the benzimidazole nitrogens, generating a 3D architecture (Fig. 2). The four chloride ions of the $CuCl_4^{2-}$ unit provide two different types of H-bonding interactions. Two chloride ions form H bonds with benzimidazole N–H, while the other two are involved in bifurcated H-bonding with a water molecule and benzimidazole N–H to form a 3D framework. The distance between the two Cu centers of the $[Cu(ntb)Cl]^+$ units is 9.643 Å while the Cu atoms of $[Cu(ntb)Cl]^+$ and $CuCl_4^{2-}$ units are 7.0393 Å apart.

3.2. Crystal structure of $[Fe(ntb)Cl_2]Cl \cdot 3H_2O$ (*2*)

An ORTEP drawing of the complex with the atom labelling scheme is shown in Fig. 3. The selected bond distances and angles are given in Table 3. The molecule consists of the cation $[Fe(ntb)Cl_2]^+$ and the anion Cl^- with three solvated water molecules. The central Fe(III) ion displays a distorted octahedral environment, the ligating atoms being two chlorine and four nitrogen

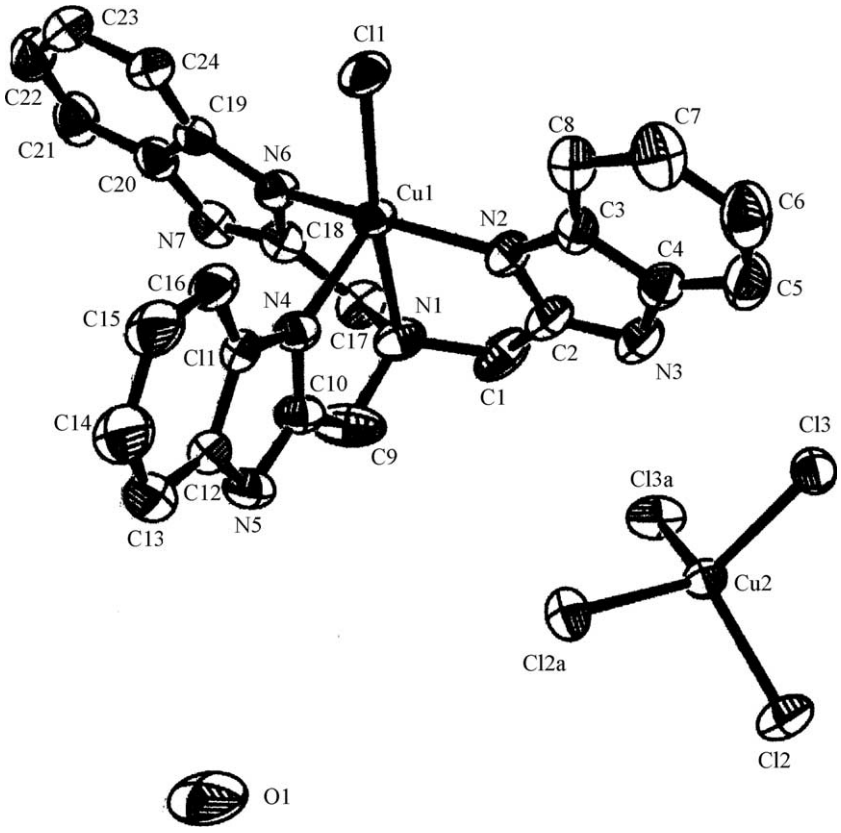


Fig. 1. ORTEP diagram of complex **1**. Hydrogen atoms are omitted for clarity. Ellipsoids are drawn at the 50% probability level.

atoms from the ntb ligand. The *cis* orientation of the two chlorine atoms is indicated by the Cl(1)–Fe–Cl(2) bond angle of 96.8(1)°, comparable to that observed for other *cis*-dichloro species [33]. The equatorial plane is defined by N(2), N(4), N(6) and Cl(2). An apical nitrogen N(1) and another chloride Cl(1) occupy the axial positions. The N-Fe–N *cis* bond angle, imposed by the rigid heterocyclic rings of ntb deviate significantly from 90°, the largest deviation being in the N1–Fe–N2 angle (73.9(1)°). The Fe–Cl(1) and Fe–Cl(2) bond distances of 2.212(1) and 2.350(1) Å, respectively, are in accord with those found in related structures [33]. The average bond distance between the Fe(III) ion and the equatorial

Table 2
Selected bond distances (Å) and angles (°) for complex **1**

Cu1–Cl1	2.279(6)	Cu1–N1	2.244(1)
Cu1–N2	1.969(1)	Cu1–N4	1.962(1)
Cu1–N6	2.126(1)	Cu2–Cl2	2.256(6)
Cu2–Cl3	2.230(5)		
Cl1–Cu1–N1	170.44(4)	Cl1–Cu1–N2	97.18(5)
Cl1–Cu1–N4	97.95(5)	Cl1–Cu1–N6	108.89(4)
N1–Cu1–N2	80.69(6)	N1–Cu1–N4	80.80(6)
N1–Cu1–N6	80.67(5)	N2–Cu1–N4	153.60(6)
N2–Cu1–N6	98.94(6)	N4–Cu1–N6	96.45(6)
Cl3–Cu2–Cl3_a	128.53(2)		
Cl2_a–Cu2–Cl3_a	101.85(2)	Cl2–Cu2–Cl2_a	126.87(3)
Cl2–Cu2–Cl3_a	100.54(2)	Cl2–Cu2–Cl3	101.85(2)
Cl2_a–Cu2–Cl3	100.54(2)		

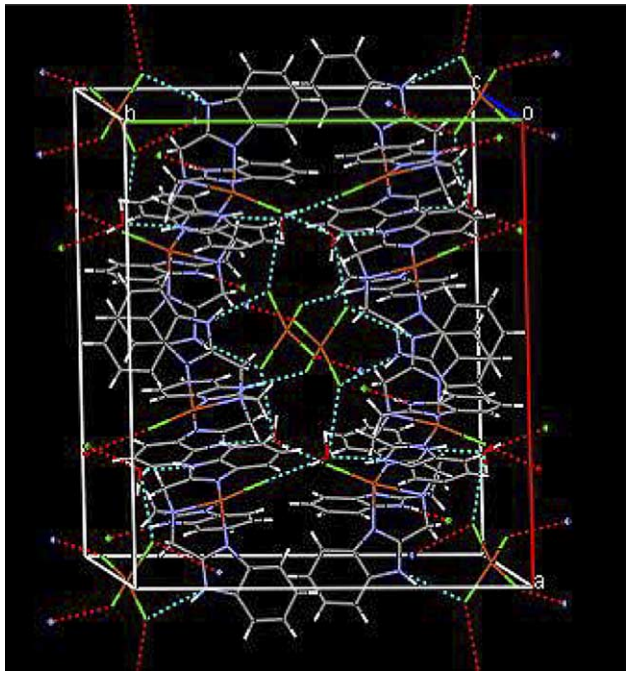


Fig. 2. Crystal packing diagram of complex **1**.

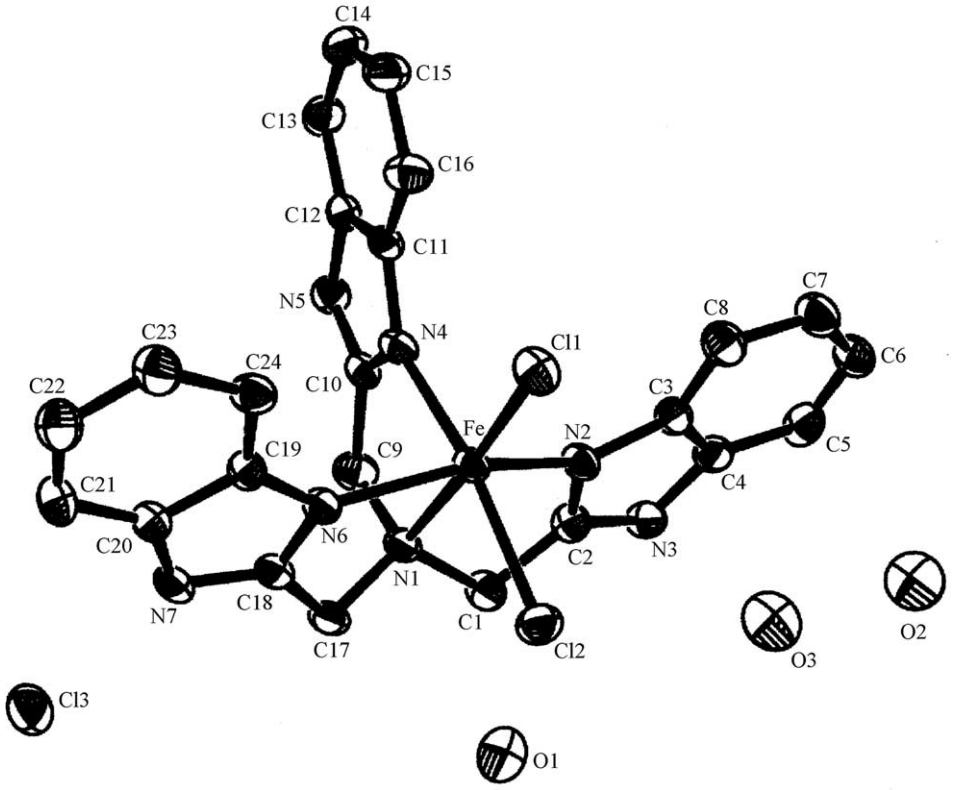


Fig. 3. ORTEP diagram of complex **2**. Hydrogen atoms are omitted for clarity. Ellipsoids are drawn at the 50% probability level.

Table 3
Selected bond distances (Å) and angles (°) for complex **2**

Fe–Cl1	2.212(1)	Fe–Cl2	2.350(1)
Fe–N1	2.363(2)	Fe–N2	2.079(3)
Fe–N4	2.122(2)	Fe–N6	2.082(3)
Cl1–Fe–Cl2	96.8(1)	Cl1–Fe–N1	175.2(1)
Cl1–Fe–N2	105.5(1)	Cl1–Fe–N4	97.8(1)
Cl1–Fe–N6	105.8(1)	Cl2–Fe–N1	88.0(1)
Cl2–Fe–N2	87.8(1)	Cl2–Fe–N4	165.4(1)
Cl2–Fe–N6	92.0(1)	N1–Fe–N2	73.9(1)
N1–Fe–N4	77.4(1)	N1–Fe–N6	74.6(1)
N2–Fe–N4	87.9(1)	N2–Fe–N6	148.5(1)
N4–Fe–N6	84.4(1)		

nitrogen atoms is 2.123 Å, which is much shorter than the axial bond length of 2.363(2) Å, as expected [33].

3.3. Description of the hexagonal channel

There are several interesting features apparent from crystal packing diagram of complex **2** (Fig. 4). Intermolecular H-bonding affords a six-membered channel comprising of four water molecules and two Cl^- ions (Figs. 5(a) and (b)). The volume of the channel is 315.1 $Å^3$ which is 22.9% of the unit cell 1378.3 $Å^3$ [34]. The volume is calculated by neglecting the presence of water molecules and chlorine atoms for simplification. If the calculation is repeated by keeping water molecules and chlorine atoms, there is still a space of 39.6 $Å^3$ which is 2.9% that of the unit cell volume. The magnitude is smaller than a hydrogen bonded H_2O-molecule (40 $Å^3$) and thus the fourth water molecule cannot be seen in the unit cell. The space-filling model for the compound shows a nice projection of the vacant cavities occupied by the guest water molecules and the chlorine counter anions. A notable feature apparent from the view is that the packing forms a helical propagation along the diagonal of the crystallographic axes *b* and *c* (Fig. 6) [34]. Calculations done for the diagonal lengths of the hexagonal channel show an average value of 6.080 Å (Fig. 5(b)) [35].

3.4. Crystal structure of [Fe(bispicpn)Cl_2]Cl (**3**)

An ORTEP drawing of the complex with the atom labelling scheme is shown in Fig. 7. The selected bond distances and angles are given in Table 4. The structure consists of a $[Fe^{III}(bispicpn)Cl_2]^+$ cation and a Cl^- counter ion. The geometry of the central metal ion is a distorted octahedron in which the equatorial positions are occupied by N1A, N1B, N2B and Cl1 whereas N2A and Cl2 occupy the axial positions. The *cis*-dichloro arrangement of the two chlorine atoms is confirmed by the Cl1–Fe–Cl2 angle of 101.07°. The average

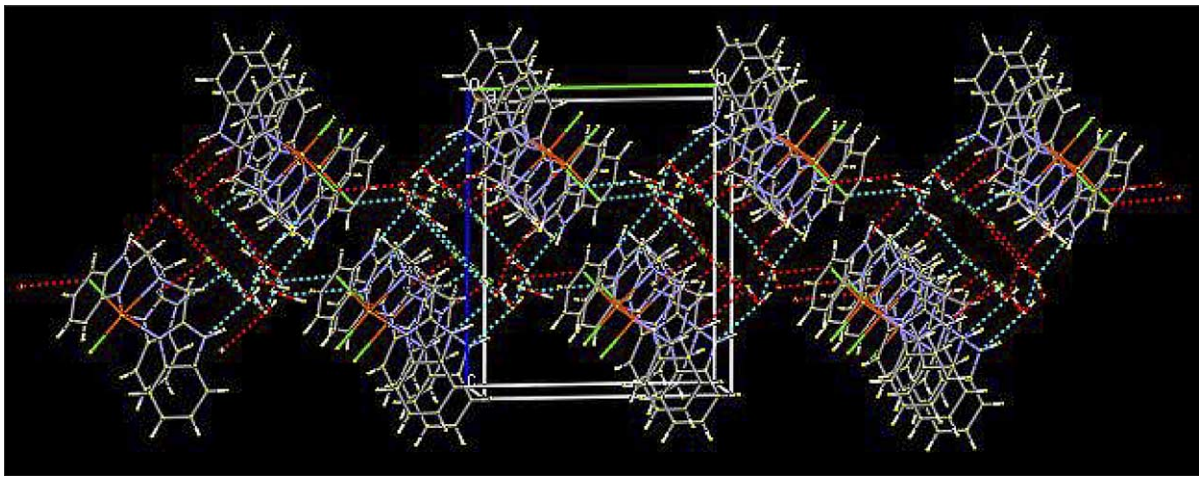


Fig. 4. Crystal packing diagram of complex **2** in the *ab*-plane.

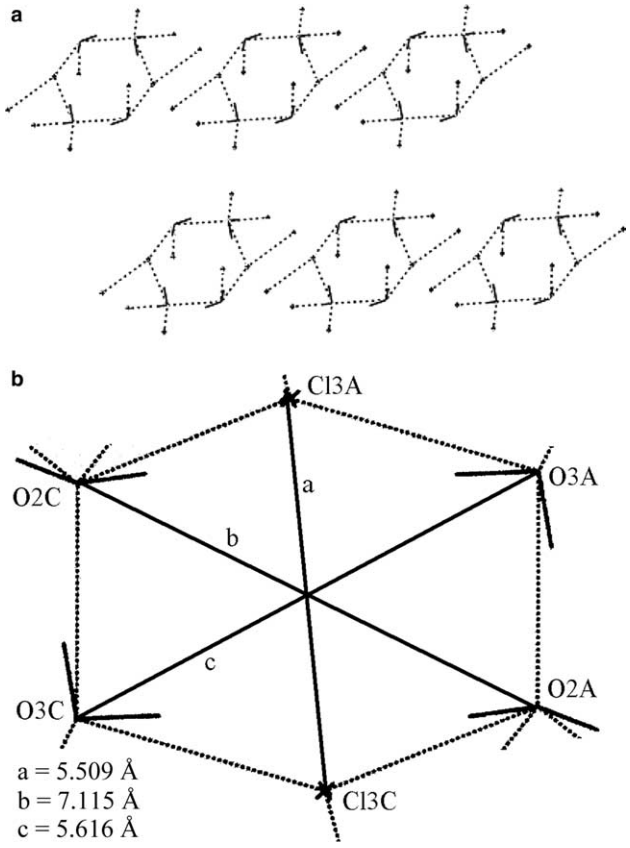


Fig. 5. Hexagonal pores in the crystal packing of complex **2**.

equatorial Fe(III)–nitrogen bond length is 2.170 Å, which is comparable to that observed for other Fe(III)–Schiff base complexes [36]. The axial Fe–N_{amine} distance is 2.166(3) Å. The axial and equatorial Fe(III)–Cl distances are 2.2887(9) and 2.2962(8) Å, respectively, as expected for high-spin Fe(III) complexes [36,37]. The mononuclear fragments are bound together via H-bonding utilizing the chloride counter ion and amine hydrogens, forming a 1D chain as depicted in Fig. 8.

4. Electrochemical studies

The cyclic voltammograms of the complexes **1**–**3** are shown in Fig. 9. The redox potentials are summarized in Table 5. Complex **1** exhibits two reversible one-electron redox couples with $E_{1/2}$ at +0.530 and −0.031 V versus Fc/Fc^{+}. These are in good agreement with those reported by Su et al. [32]. The corresponding redox couples may be shown as follows:

$$[Cu(ntb)Cl]^{1+} \rightleftharpoons [Cu(ntb)Cl]^{0} \rightleftharpoons [Cu(ntb)Cl]^{1-}$$

It is also evident that the $CuCl_4^{2-}$ unit does not undergo electron transfer in the available potential range. The irreversible couple observed at +1.0 V could be assigned to the oxidation of the ntb ligand.

The cyclic voltammogram of complex **2** displays a quasi-reversible Fe(III)/Fe(II) redox reaction occurring at $E_{1/2} = +0.23$ V, which is similar to that observed previously [33]. Another irreversible oxidation at +1.1 V, similar to that observed for complex **1**, was attributed to the oxidation of the benzimidazole rings.

The nature of the cyclic voltammogram of **3** is qualitatively similar to that of **2**. The reversible Fe(III)/Fe(II) redox couple occurs with $E_{1/2} = +0.115$ V and the irreversible oxidation of the bispicpn ligand occurs at +1.014 V [36].

5. Catalytic activity for oxidation of 3,5-di-*tert*-butylcatechol

We have examined the catalytic activity of complexes **1**–**3** for oxidation of 3,5-di-*tert*-butylcatechol (3,

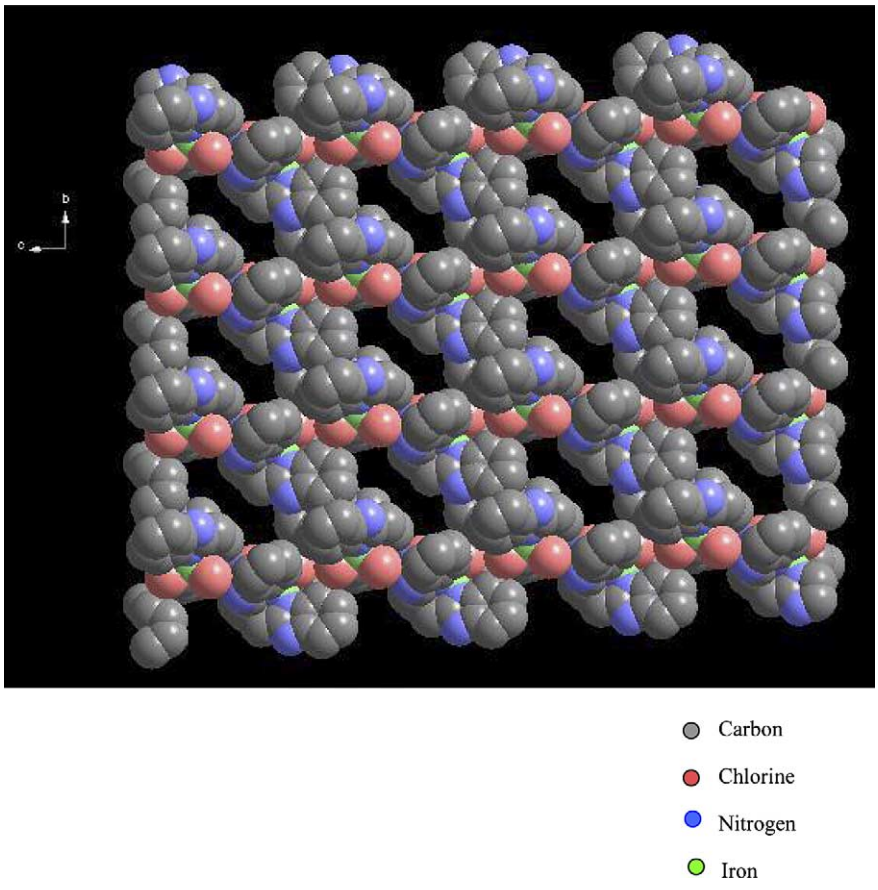


Fig. 6. Space-filling model of the hexagonal pores of complex **2**.

5-DTBC) by O_2 in air saturated DMF solution at 20 °C. The reactivity studies were performed in DMF solution because of the good solubility of the complexes as well as of the substrate and of its products. Kinetic measurements were made for all of the complexes in DMF at 20 °C. For this purpose 10^{-4} mol dm^{-3} solutions of the complexes in DMF were treated with 10^{-3} mol dm^{-3} 3,5-di-*tert*-butylcatechol

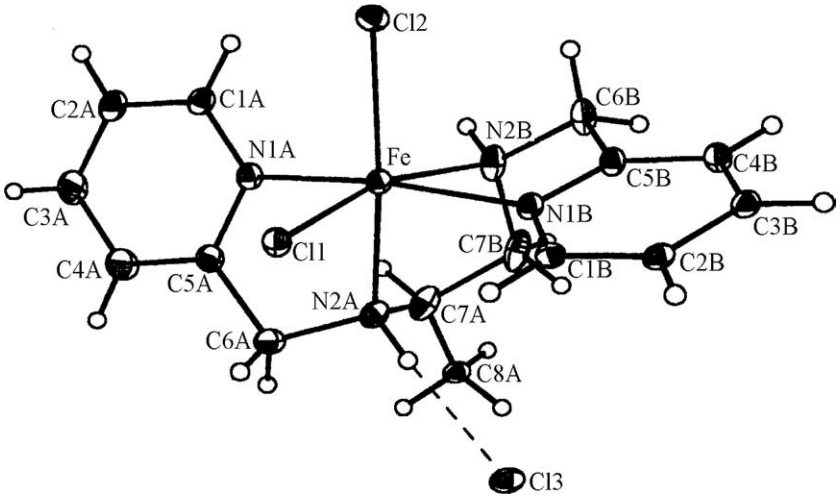
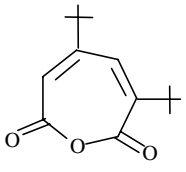


Fig. 7. ORTEP diagram of complex **3**. Hydrogen atoms are omitted for clarity. Ellipsoids are drawn at the 50% probability level.

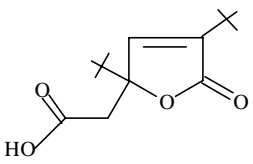
Table 4
Selected bond distances (Å) and angles (°) for complex **3**

Fe–N1B	2.157(2)	Fe–N2A	2.165(3)
Fe–N1A	2.172(2)	Fe–N2B	2.184(2)
Fe–Cl2	2.288(4)	Fe–Cl1	2.296(2)
N1B–Fe–N2A	96.00(9)	N1B–Fe–N1A	169.19(9)
N2A–Fe–N1A	74.55(9)	N1B–Fe–N2B	74.66(9)
N2A–Fe–N2B	79.08(11)	N1A–Fe–N2B	98.03(9)
N1B–Fe–Cl2	95.98(7)	N2A–Fe–Cl2	161.88(7)
N1A–Fe–Cl2	92.06(7)	N2B–Fe–Cl2	91.07(9)
N1B–Fe–Cl1	92.95(6)	N2A–Fe–Cl1	91.83(7)
N1A–Fe–Cl1	92.58(7)	N2B–Fe–Cl1	163.59(8)
Cl2–Fe–Cl1	101.07(3)		

in the presence of air. Reaction of the complexes with 3,5-di-*tert*-butylcatechol yields a solution whose spectra are significantly different from that of the complexes. In the solution the peak at 366 nm, which is due to the π(benzimidazole) $\rightarrow$ Cu(II) LMCT transitions, vanishes [38]. Simultaneously, a band at exactly 400 nm appears that is indicative of the oxidation from 3,5-di-*tert*-butylcatechol to 3,5-di-*tert*-butyl-*o*-quinone [39]. The course of the reaction was followed at 400 nm at regular time intervals. The trace of the reaction is shown in Fig. 10. The iron complexes all react with 3,5-di-*tert*-butylcatechol in presence of dioxygen to yield products due to the oxidative cleavage of the catechol ring. NMR techniques were used to identify the products of the oxidative cleavage. They afford intradiol cleavage products in a major yield that is consistent with the trend noted earlier [40]. The two main products isolated from the reaction mixture are 3,5-di-*tert*-butyl-1-oxacyclohepta-3,5-diene-2,7-dione and 3,5-di-*tert*-butyl-5-(carboxymethyl)-2-furanone [40] as shown here:



Ia



Ib

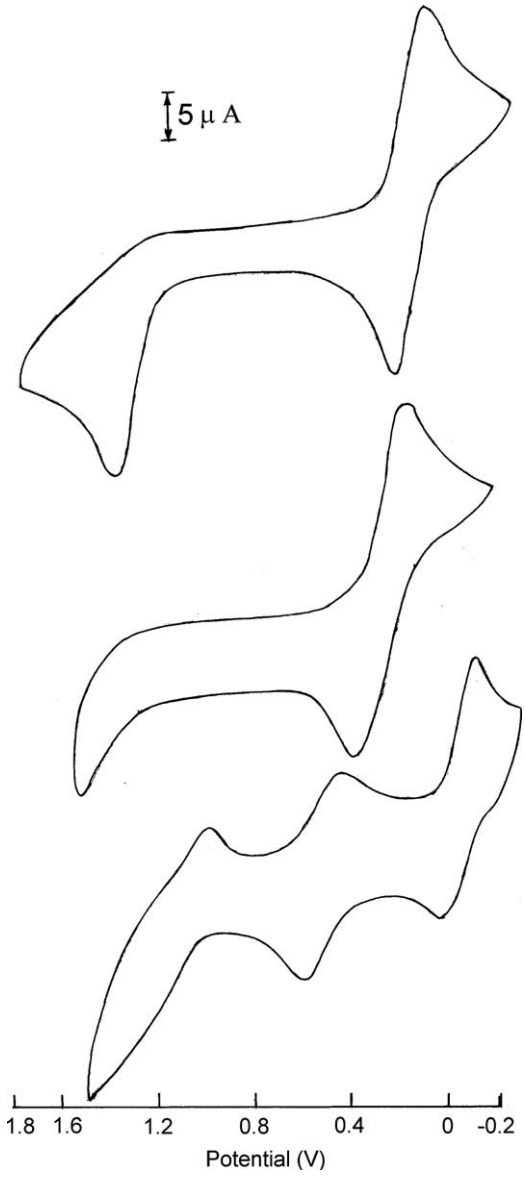


Fig. 9. Cyclic voltammograms (scan rate 50 mV s^{-1}) of complexes **1**, **2** and **3** in DMF at a platinum electrode with ferrocene as an internal standard and TEAP as supporting electrolyte.

In the presence of an excess of substituted catechol, the pseudo-first-order constants were deduced from simulations and the second-order

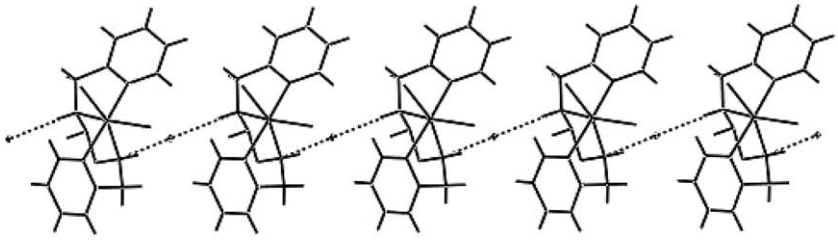


Fig. 8. 1D chain formed by complex **3**.

Table 5
Cyclic voltammetric results for complexes **1**, **2** and **3** at 298 K

Complex	E_1 (V)			E_2 (V)		
	E_{pa} (V)	E_{pc} (V)	$E_{1/2}$ (V)	E_{pa} (V)	E_{pc} (V)	$E_{1/2}$ (V)
1	0.035	−0.097	−0.031	0.605	0.45	0.53
2	0.330	0.133	0.231			
3	0.164	0.067	0.115			

constants (Table 6) were calculated assuming $[O_2] = 4.86 \times 10^{-3}$ M in DMF at 20 °C by using the following equation [40b]:

$$k_{O_2} = k_{obs}/[O_2].$$

Inspection of the data reveals that complex **2** shows enhanced catalytic activity in comparison to that of **3**. The latter reacts approximately four times slower than **2**. Such enhancement in rates is well documented in recent reports [41]. A correlation between the rate of oxidation and the $E_{1/2}$ values of the two iron complexes can be established. The easier the metal complex is reduced, the higher is its catalytic activity. Complex **2** is found to have the higher catalytic activity regarding oxidation of 3,5-di-*tert*-butylcatechol as it is more easily reducible than **3**.

Table 6
Comparison of the kinetic parameters for complexes **1**, **2** and **3**

Complex	k_{obs} (M^{-1} s^{-1})	Yield of products (%)
$[Cu(ntb)Cl]_2[CuCl_4] \cdot 2H_2O$	4.1	3,5-Ditertiary butylquinone (95%)
$[Fe(ntb)Cl_2]Cl \cdot 3H_2O$	3.4×10^{-2}	Ia, Ib (55%, 40%)
$[Fe(bispicpn)Cl_2]Cl$	9.032×10^{-3}	Ia, Ib (67%, 34%)

Kinetic conditions: $[3,5\text{-di-}tert\text{-butylcatechol}] = 1 \times 10^{-3}$ M, $[Complex] = 1 \times 10^{-4}$ M, $T = 20$ °C. The second-order rate constants of the reaction were calculated by using the equation $k_{O_2} = k_{obs}/[O_2]$. The solubility of O_2 in DMF at 20 °C is 4.86×10^{-3} M. The k_{obs} values are the average of three determinations which differ by ±5%.

6. Thermal studies

To investigate the thermal stability of complexes **1** and **2**, we performed Differential Scanning Calorimetry (DSC). In the temperature range 50–100 °C, a single endothermic peak could be observed at 82 °C with $\Delta H = -70.7$ J g^{-1} for complex **1**. For complex **2**, the experiment was performed in the temperature range 70–110 °C. The endothermic peak appears at 99.9 °C having $\Delta H = -164.8$ J g^{-1}. These are related to the loss of hydrogen bonded water molecules in both the complexes.

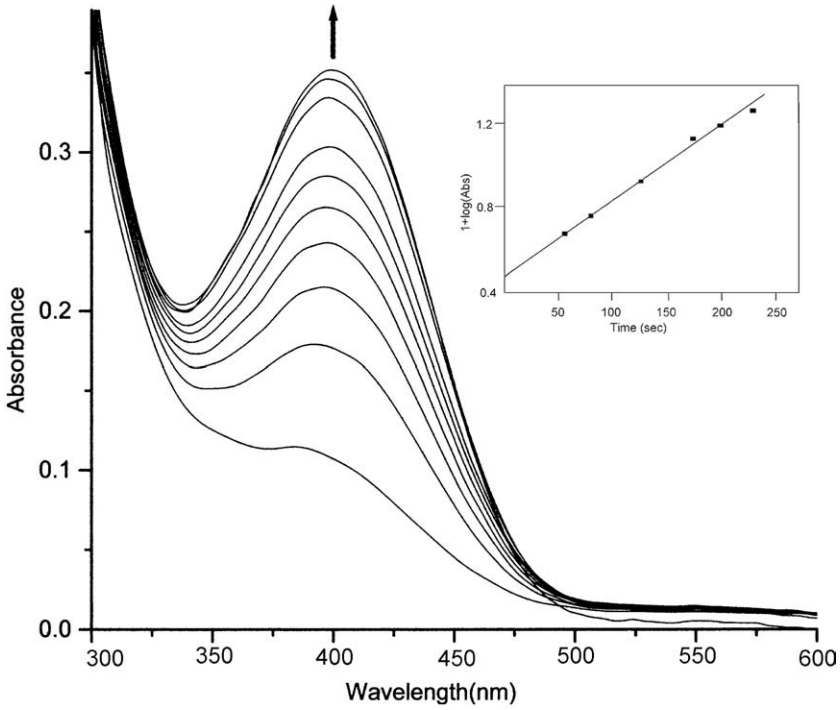


Fig. 10. Progress of the reaction of $[Cu(ntb)Cl]_2[CuCl_4] \cdot 2H_2O$ with O_2 in DMF solution. The appearance of the *o*-quinone band at 400 nm was monitored. Conditions: $[3,5\text{-di-}tert\text{-butylcatechol}] = 1 \times 10^{-3}$ M, $[Complex] = 1 \times 10^{-4}$ M, Temperature = 20 °C. Inset: Plot of $[1 + \log(Abs)]$ vs. time for the reaction of $[Cu(ntb)Cl]_2[CuCl_4] \cdot 2H_2O$ with O_2 at 20 °C in DMF solution at 400 nm.

Acknowledgements

S.G. and P.R. thank the Council of Scientific and Industrial Research, India for the award of research fellowships. Thanks are due to Dr. M.K. Saha, Department of Chemistry, University of Houston, USA for discussions on some aspects of the crystallographic results.

Appendix A. Supplementary data

Full details of the crystal structure analyses of **1**, **2** and **3** have been deposited with the Cambridge Crystallographic Data Centre (CCDC Nos. 244434, 244435 and 244437, respectively). Copies may be obtained free of charge on application to The Director, CCDC, 12 Union Road, Cambridge CB2 1EZ, UK [fax (int. code): +44 1223 336 033, e-mail: deposit@ccdc.cam.ac.uk]. Supplementary data associated with this article can be found, in the online version at doi:10.1016/j.poly.2005.06.020.

References

[1] (a) A.D. Burrows, C.-W. Chan, M.M. Chowdhry, J.E. McGardy, D.M.P. Mingos, Chem. Soc. Rev. 24 (1995) 329;
(b) O.M. Yaghi, H. Li, T.L. Groy, J. Am. Chem. Soc. 118 (1996) 9096;
(c) W.A. Herrmann, N.W. Huber, O. Runte, Angew. Chem., Int. Ed. Engl. 34 (1995) 2187.

[2] (a) J.-M. Lehn, Angew. Chem., Int. Ed. Engl. 27 (1988) 89;
(b) J.-M. Lehn, Supramolecular Chemistry: Concepts and Perspectives, VCH, New York, 1995;
(c) J.W. Steed, J.L. Atwood, Supramolecular Chemistry, Wiley, New York, 2000;
(d) F. Vögtle, Supramolecular Chemistry, Wiley, Chichester, 1991.

[3] (a) V.G. Albano, M.C. Aragoni, M. Arca, C. Castellari, F. Demartin, F.A. Devillanova, F. Isaia, V. Lippolis, L. Loddo, G. Verani, Chem. Commun. (2002) 1170;
(b) T. Suzuki, H. Fujii, T. Miyashi, Y. Yamashita, J. Org. Chem. 57 (1992) 6744;
(c) B.N. Figgis, E.S. Kucharski, M. Vrtis, J. Am. Chem. Soc. 115 (1993) 176;
(d) P.D. Beer, P.A. Gale, Angew. Chem. 113 (2001) 502.

[4] (a) S. Reddy, D.C. Craig, G.R. Desiraju, J. Chem. Soc., Chem. Commun. (1995) 339;
(b) V. Madhu, S.K. Das, Polyhedron 23 (2004) 1235;
(c) R. Wang, M.C. Hong, J. Luo, F. Jiang, L. Han, Z. Lin, R. Cao, Inorg. Chim. Acta 357 (2004) 103.

[5] (a) G.A. Jeffrey, W. Saenger, Hydrogen Bonding in Biological Structures, Springer, Berlin, 1991;
(b) G.R. Desiraju, Chem. Commun. (1997) 1475;
(c) G.M. Whitesides, E.E. Simanek, J.P. Mathias, C.T. Seto, D.N. Chin, M. Mammen, D.M. Gordan, Acc. Chem. Res. 28 (1995) 37.

[6] (a) B. Moulton, M.J. Zaworotko, Chem. Rev. 101 (2001) 1629;
(b) D.L. Caulder, K.N. Raymond, Acc. Chem. Res. 32 (1999) 975;
(c) D. Braga, F. Grepioni, G.R. Desiraju, Chem. Rev. 98 (1998) 1375.

[7] (a) E. Breuning, U. Ziener, J.-M. Lehn, E. Wegelius, K. Rissanen, Eur. J. Inorg. Chem. (2001) 1515;
(b) T.J. Prior, M.J. Rosseinsky, Chem. Commun. (2001) 495;
(c) W. Lu, M.C.W. Chan, K.K. Cheung, C.-M. Che, Organometallics 20 (2001) 2477.

[8] (a) M. Edgar, R. Mitchell, A.M.Z. Slawin, P. Lightfoot, P.A. Wright, Chem. Eur. J. 7 (2001) 5168;
(b) L. Carlucci, G. Ciani, D.M. Proserpio, A. Sironi, J. Chem. Soc., Dalton Trans. (1997) 1801;
(c) C.B. Aakeröy, A.M. Beatty, D.S. Leinen, K.R. Lorimer, Chem. Commun. (2000) 935.

[9] (a) A.N. Khlobystov, A.J. Blake, N.R. Champness, D.A. Lemenovskii, A.G. Majouga, N.V. Zyk, M. Schröder, Coord. Chem. Rev. 222 (2001) 155;
(b) O.S. Jung, Y.J. Kim, Y.A. Lee, J.K. Park, H.K. Chae, J. Am. Chem. Soc. 122 (2000) 9921.

[10] M. Maekawa, H. Konaka, Y. Suenaga, T. Kuroda-Sowa, M. Munakata, J. Chem. Soc., Dalton Trans. (2000) 4160.

[11] (a) R.H. Wang, M.C. Hong, W.P. Su, Y.C. Liang, R. Cao, Y.J. Zhao, J.B. Weng, Inorg. Chim. Acta 323 (2001) 139;
(b) M. Scherer, D.L. Caulder, D.W. Johnson, K.N. Raymond, Angew. Chem. Int. Ed. 38 (1999) 1587.

[12] (a) B.J.S. Johnson, R.C. Schroden, C. Zhu, A. Stein, Inorg. Chem. 40 (2001) 5972;
(b) A.J. Blake, N.R. Champness, P.A. Cooke, J.E.B. Nicolson, Chem. Commun. (2000) 665.

[13] (a) J. Makarevi, M. Joki, B. Peri, V. Tomii, B. Koji-Prodi, M. Žinić, Chem. Eur. J. (2001) 3328;
(b) L. Pan, E.B. Woodlock, X. Wang, K.C. Lam, A.L. Rheingold, Chem. Commun. (2001) 1762.

[14] K.S. Min, M.P. Suh, J. Am. Chem. Soc 122 (2000) 6834.

[15] O.S. Jung, S.H. Park, K.M. Kim, H.G. Jang, Inorg. Chem. 37 (1998) 5781.

[16] C.-Y. Su, B.-S. Kang, H.-Q. Liu, Q.-G. Wang, T.C.W. Mak, Chem. Commun. (1998) 1551.

[17] H. Toftlaund, E. Pedersen, S. Yde-Andersen, Acta Chem. Scand. A 38 (1984) 693.

[18] P.A. Goodson, J. Glerup, D.J. Hodgson, K. Michelsen, H. Weihe, Inorg. Chem. 30 (1991) 4909.

[19] M. Paskaly, M. Duda, A. Rompel, B.H. Sift, W. M-Klaucke, B. Krebs, Inorg. Chim. Acta 291 (1991) 289.

[20] Z.-F. Chen, Z.-R. Liao, D.-F. Li, W.-K. Li, X.-G. Meng, J. Inorg. Biochem. 98 (2004) 1315.

[21] A.R. Oki, P.K. Bommarreddy, H.M. Zhang, N. Hosmane, Inorg. Chim. Acta 231 (1995) 109.

[22] (a) K. Michelsen, K.M. Nielsen, Acta Chem. Scand. A 34 (1980) 755;
(b) H.R. Fischer, D.J. Hodgson, K. Michelsen, E. Pedersen, Inorg. Chim. Acta 88 (1984) 143.

[23] SAINT Reference manual, Siemens Energy and Automation, Madison, WI, 1994–1996.

[24] G.M. Sheldrick, SADABS: Empirical Absorption Correction Program, University of Göttingen, Göttingen, Germany, 1997.

[25] B.A. Frenz, Comput. Phys. 2 (1988) 42.

[26] Crystallographic Computing 5, Oxford University Press, Oxford, UK, 1991 (Chapter 11).

[27] G.M. Sheldrick, SHELXS-86: Program for the Solution of Crystal Structures, University of Göttingen, Göttingen, Germany, 1985.

[28] G.M. Sheldrick, SHELXS-97, Acta Crystallogr., Sect. A 46 (1990) 467.

[29] G.M. Sheldrick, SHELXL-97: Program for Crystal Structure Refinement, University of Göttingen, Göttingen, Germany, 1997.

[30] A.W. Addison, T.N. Rao, J. Reedijk, J. van Rijn, G.C. Verschoor, J. Chem. Soc., Dalton Trans. (1984) 1349.

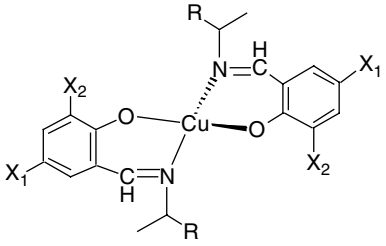
[31] H. Wu, Y. Li, Y. Gao, Acta. Crystallogr., Sect. E 60 (2004) m277.

[32] C.-Y. Su, B.-S. Kang, T.-B. Wen, Y.-X. Tong, X.-P. Yang, C. Zhang, H.-Q. Liu, J. Sun, Polyhedron 18 (1999) 1577.
[33] B. Kwak, K.W. Cho, M. Pyo, M.S. Lah, Inorg. Chim. Acta 290 (1999) 21.
[34] A.L. Spek, PLATON: Molecular Geometry Program, University of Utrecht, The Netherlands, 1999.
[35] G. Mezai, P. Baran, R.G. Raptis, Angew. Chem. Int. Ed. 43 (2004) 574.
[36] N. Shaikh, S. Goswami, A. Panja, X.-Y. Wang, S. Gao, R.J. Butcher, P. Banerjee, Inorg. Chem. 43 (2004) 5908.
[37] I.A. Setyawati, S.J. Rettig, C. Orvig, Can. J. Chem. 77 (1999) 2033.
[38] F. Zippel, F. Ahlers, R. Werner, W. Haase, H.-F. Nolting, B. Krebs, Inorg. Chem. 35 (1996) 3409.
[39] (a) P. Gentschev, N. Möller, B. Krebs, Inorg. Chim. Acta 300–302 (2000) 442;
(b) N. Shaikh, A. Panja, P. Banerjee, M. Ali, Transition Met. Chem. 28 (2003) 871;
(c) C-T. Yang, M. Vetrichelvan, X. Yang, B. Moubaraki, K.S. Murray, J.J. Vittal, J. Chem. Soc., Dalton Trans. (2004) 113.
[40] (a) H.G. Jang, D.D. Cox, L. Que Jr., J. Am. Chem. Soc. 113 (1991) 9200;
(b) M. Velusamy, R. Mayilmurugan, M. Palaniandavar, Inorg. Chem. 43 (2004) 6284.
[41] (a) M. Merkel, F.K. Müller, B. Krebs, Inorg. Chim. Acta 337 (2002) 308;
(b) R. Viswanathan, M. Palaniandavar, T. Balasubramanian, T.P. Muthiah, Inorg. Chem. 37 (1997) 2943.

temperature [20]. (2) Photo-switching of characteristic properties of molecular compounds, for instance chiral molecular recognition, spin crossover and conformational conversion, can be available in contrast to other inorganic solid compounds such as Prussian blue analogues.

In this context, flexible transition metal complexes are suitable as a component of such photo-switching materials. Classically, some Cu(II) or Ni(II) complexes incorporating Schiff base ligands [21] have been known to exhibit flexibility from a square planar to a tetrahedral coordination environment by introduction of various substituents, and show structural phase transitions by heating [22–30]. Especially, Ni(II) complexes exhibit not only flexibility of the coordination environment [31–38] but also interesting magnetic behavior; diamagnetic square planar complexes change into paramagnetic tetrahedral complexes when a complex adopts such coordination geometries in the solid state, or when one is dissolved in solution, so called *solution paramagnetism* [39–41].

Herein, we report structural features, electronic properties, thermally-induced structural phase transition and absorption spectra depending on the solvent for ten Cu(II) complexes with 3,5-halogen-substituted Schiff base ligands (Scheme 1). Crystal structures of two new complexes, bis(*N*-*R*-1-phenylethyl- and *N*-*R*,*S*-2-butyl-5-bromosalicydenaminato-κ^2N,O)copper(II), are also described. Furthermore, we successfully observed a spectral change of d–d and π–π* bands of the complex caused by *cis–trans* photoisomerization of 4-hydroxyazobenzene (4HAZ) for an organic/inorganic system involving bis-(*N*-*R*-1-phenylethyl-3,5-dichlorosalicydenaminato-κ^2N,O)copper-(II) and 4HAZ in chloroform solution.



	R	X_1	X_2
1	C_6H_5	Cl	Cl
2	C_6H_5	Br	Br
3	C_6H_5	H	Cl
4	C_6H_5	H	Br
5	C_2H_5	Cl	Cl
6	C_2H_5	Br	Br
7	C_2H_5	H	Cl
8	C_2H_5	H	Br
9	CH_3	H	Cl
10	CH_3	H	Br

Scheme 1. Molecular structures of **1**–**10**.

2. Experimental

2.1. Materials

Chemicals of the highest commercial grade available (Aldrich and Wako) were used as received without further purification.

2.2. Physical measurements

Elemental analyses (C, H, N) were carried out on an Elementar Vario EL analyser at Keio University. Infrared spectra were recorded using Nujol mulls on a BIORAD FTS-60A spectrophotometer in the range 4000–400 cm^{-1} at 298 K. Thermal analysis was performed on a SHIMADZU DSC-60 differential scanning calorimeter (DSC), where the heating rate was 10 K min^{-1} in the range of 313–673 K. Diffuse reflectance spectra were measured on a JASCO V-560 spectrophotometer equipped with an integrating sphere in the range 850–220 nm at 298 K. Absorption spectra were measured on a JASCO V-560 spectrophotometer in the range 900–200 nm at 298 K. Magnetic susceptibility was measured with a Sherwood Scientific magnetic susceptibility balance at 298 K. Magnetic data were corrected for the magnetization of diamagnetic contributions, which were estimated from Pascal constants. The magnetic properties were investigated with a Quantum Design MPMS-5S superconducting quantum interference device magnetometer (SQUID) at an applied field of 5000 Oe in a temperature range 5–250 K. Semi-empirical molecular orbital calculations were performed with the program ZINDO [42,43] in the CAChe software package based on the crystal structures determined.

2.3. Syntheses of complexes

2.3.1. Bis(*N*-*R*-1-phenylethyl-3,5-dichlorosalicydenaminato)copper(II) (*1*)

To a methanol solution (150 cm^3) of copper(II) acetate (0.91 g, 5.00 mmol), 3,5-dichlorosalicylaldehyde (1.91 g, 10.0 mmol), and *R*-1-phenylethylamine (1.21 g, 10.0 mmol) were added and stirred at 45 °C for 2 h. The resulting brown precipitates were collected by filtration and recrystallized from acetone/methanol. Yield 64.8%. *Anal*. Calc. for $C_{30}H_{24}N_2Cl_4CuO_2$: C, 55.44; H, 3.72; N, 2.31. Found: C, 55.37; H, 3.98; N, 4.09%. IR (KBr) $\nu_{C=N}$ 1623 cm^{-1}, ν_{Cu-N} 445 cm^{-1}, ν_{Cu-O} 419 cm^{-1}, m.p. 483 K (decomposition). Magnetic moment $\mu_{eff}/\mu_{BM} = 1.73$ at 298 K.

2.3.2. Bis(*N*-*R*,*S*-1-phenylethyl-3,5-dibromoosalicydenaminato)copper(II) (*2*)

The same procedure as for **1** afforded the condensation of 3,5-dibromosalicylaldehyde (2.80 g, 10.0 mmol) and *racemic* 1-phenylethylamine (1.21 g, 10.0 mmol).

Yield 74.5%. *Anal*. Calc. for $C_{30}H_{24}Br_4CuN_2O_2$: C, 43.64; H, 2.92; N, 3.38. Found: C, 43.77; H, 2.72; N, 3.25%. IR (KBr) $\nu_{C=N}$ 1617 cm^{-1}, ν_{Cu-N} 444 cm^{-1}, ν_{Cu-O} 424 cm^{-1}, m.p. 478 K (decomposition). Magnetic moment $\mu_{eff}/\mu_{BM} = 1.47$ at 298 K.

2.3.3. Bis(N-R,S-1-phenylethyl-5-chlorosalicydenaminato)copper(II) (3)

The same procedure as for **1** afforded the condensation of 5-chlorosalicylaldehyde (1.57 g, 10.0 mmol) and *racemic* 1-phenylethylamine (1.21 g, 10.0 mmol). Yield 49.6%. *Anal*. Calc. for $C_{30}H_{26}Cl_2CuN_2O_2$: C, 62.02; H, 4.51; N, 4.82. Found: C, 62.07; H, 4.29; N, 4.70%. IR (KBr) $\nu_{C=N}$ 1621 cm^{-1}, ν_{Cu-N} 465 cm^{-1}, ν_{Cu-O} 419 cm^{-1}, m.p. 474 K (decomposition). Magnetic moment $\mu_{eff}/\mu_{BM} = 1.66$ at 298 K.

2.3.4. Bis(N-R-1-phenylethyl-5-bromosalicydenaminato)copper(II) (4)

The same procedure as for **1** afforded the condensation of 5-bromosalicylaldehyde (2.01 g, 10.0 mmol) and *R*-1-phenylethylamine (1.21 g, 10.0 mmol). Yield 24.4%. *Anal*. Calc. for $C_{30}H_{26}Br_2CuN_2O_2$: C, 53.79; H, 3.91; N, 4.18. Found: C, 53.60; H, 3.69; N, 4.11%. IR (KBr) $\nu_{C=N}$ 1620 cm^{-1}, ν_{Cu-N} 463 cm^{-1}, ν_{Cu-O} 418 cm^{-1}, m.p. 469 K (decomposition). Magnetic moment $\mu_{eff}/\mu_{BM} = 1.91$ at 298 K. Brown plate-like single crystals suitable for X-ray crystallography were grown from the filtrate over a period of a few days at 298 K.

2.3.5. Bis(N-S-2-butyl-3,5-dichlorosalicydenaminato)copper(II) (5)

The similar procedure as for **1** afforded the condensation of 3,5-dichlorosalicylaldehyde (0.96 g, 5.00 mmol) and *S*-2-butylamine (0.37 g, 5.00 mmol). Yield 25.8%. *Anal*. Calc. for $C_{22}H_{24}Cl_4CuN_2O_2$: C, 47.71; H, 4.37; N, 5.06. Found: C, 47.76; H, 3.94; N, 5.09%. IR (KBr) $\nu_{C=N}$ 1622 cm^{-1}, ν_{Cu-N} 447 cm^{-1}, ν_{Cu-O} 419 cm^{-1}, m.p. 484 K (decomposition). Magnetic moment $\mu_{eff}/\mu_{BM} = 1.53$ at 298 K.

2.3.6. Bis(N-R,S-2-butyl-3,5-dibromosalicydenaminato)copper(II) (6)

The similar procedure as for **1** afforded the condensation of 3,5-dibromosalicylaldehyde (1.40 g, 5.00 mmol) and racemic 2-butylamine (0.37 g, 5.00 mmol). Yield 26.9%. *Anal*. Calc. for $C_{22}H_{24}Br_4CuN_2O_2$: C, 36.12; H, 3.31; N, 3.83. Found: C, 36.50; H, 2.97; N, 3.84%. IR (KBr) $\nu_{C=N}$ 1620 cm^{-1}, ν_{Cu-N} 446 cm^{-1}, ν_{Cu-O} 420 cm^{-1}, m.p. 459 K (decomposition). Magnetic moment $\mu_{eff}/\mu_{BM} = 1.48$ at 298 K.

2.3.7. Bis(N-R,S-2-butyl-5-chlorosalicydenaminato)copper(II) (7)

The similar procedure as for **1** afforded the condensation of 5-chlorosalicylaldehyde (0.78 g, 5.00 mmol) and racemic 2-butylamine (0.37 g, 5.00 mmol). Yield 46.4%. *Anal*. Calc. for $C_{22}H_{26}Cl_2CuN_2O_2$: C, 54.49; H, 4.40; N, 5.78. Found: C, 54.46; H, 4.53; N, 5.72%. IR (KBr) $\nu_{C=N}$ 1618 cm^{-1}, ν_{Cu-N} 459 cm^{-1}, ν_{Cu-O} 436 cm^{-1}, m.p. 475 K (decomposition). Magnetic moment $\mu_{eff}/\mu_{BM} = 1.55$ at 298 K.

2.3.8. Bis(N-R,S-2-butyl-5-bromosalicydenaminato)copper(II) (8)

The similar procedure as for **1** afforded the condensation of 5-bromosalicylaldehyde (1.01 g, 5.00 mmol) and racemic 2-butylamine (0.37 g, 5.00 mmol). Yield 49.7%. *Anal*. Calc. for $C_{22}H_{26}Br_2CuN_2O_2$: C, 46.05; H, 4.57; N, 4.88. Found: C, 46.10; H, 4.84; N, 4.81%. IR (KBr) $\nu_{C=N}$ 1616 cm^{-1}, ν_{Cu-N} 459 cm^{-1}, ν_{Cu-O} 426 cm^{-1}, m.p. 473 K (decomposition). Magnetic moment $\mu_{eff}/\mu_{BM} = 1.69$ at 298 K. Brown plate-like single crystals suitable for X-ray crystallography were grown from the filtrate over a period of a few days at 298 K.

2.3.9. Bis(N-2-propyl-5-chlorosalicydenaminato)copper(II) (9)

The same procedure as for **1** afforded the condensation of 5-chlorosalicylaldehyde (1.57 g, 10.0 mmol) and 2-propylamine (0.59 g, 10.0 mmol). Yield 50.9%. *Anal*. Calc. for $C_{20}H_{22}Cl_2CuN_2O_2$: C, 52.58; H, 4.85; N, 6.13. Found: C, 52.39; H, 5.16; N, 6.21%. IR (KBr) $\nu_{C=N}$ 1626 cm^{-1},

Table 1
Crystallographic data for **4** and **8**

	4	**8**
Formula	$C_{30}H_{26}Br_2CuN_2O_2$	$C_{22}H_{26}Br_2CuN_2O_2$
Molecular weight	669.88	573.80
Crystal system	monoclinic	monoclinic
Space group	*C*2 (#5)	*C*2/*c* (#15)
a (Å)	17.662(5)	21.816(9)
b (Å)	8.557(3)	10.577(3)
c (Å)	9.522(2)	10.362(2)
β (°)	102.28(2)	96.61(3)
V (Å^3)	1406.2(7)	2375.1(13)
Z	2	4
D_{calc} (g cm^{-3})	1.582	1.605
F(0 0 0)	670.0	730.0
μ (mm^{-1})	3.647	4.304
Crystal size (mm)	$0.50 \times 0.30 \times 0.20$	$0.68 \times 0.68 \times 0.30$
Total unique reflections	1724	2733
Observed reflections ($I > 2\sigma(I)$)	1230	1171
No. of refined parameters	169	132
R,[a] R_w,[b] S	0.0294, 0.0826, 1.028	0.0498, 0.2062, 1.100
Frack parameter	−0.03(2)	
Minimum and maximum residual densities (e/Å^3)	0.37, −0.37	−0.47, 0.48

[a] $R = \sum\|F_o| - |F_c\|/\sum|F_o|$.

[b] $R_w = (\sum w(|F_o| - |F_c|)^2/\sum w|F_o|^2)^{1/2}$, $w = 1/(\sigma^2(F_o) + (0.0286P)^2 + 1.2163P)$ for **4**, $w = 1/(\sigma^2(F_o) + (0.1P)^2)$ for **8**, where $P = (F_o^2 + 2F_c^2)/3$.

ν_{Cu-N} 453 cm^{-1}, ν_{Cu-O} 432 cm^{-1}, m.p. 469 K (decomposition). Magnetic moment $\mu_{eff}/\mu_{BM} = 1.55$ at 298 K.

2.3.10. Bis(N-2-propyl-5-bromosalicydenaminato) copper(II) (**10**)

The same procedure as for **1** afforded the condensation of 5-bromosalicylaldehyde (2.01 g, 10.0 mmol) and 2-propylamine (0.59 g, 10.0 mmol). Yield 54.1%. *Anal.* Calc. for $C_{20}H_{22}Br_2CuN_2O_2$: C, 44.01; H, 4.06; N, 5.13. Found: C, 44.01; H, 4.28; N, 5.05%. IR (KBr) $\nu_{C=N}$ 1624 cm^{-1}, ν_{Cu-N} 451 cm^{-1}, ν_{Cu-O} 429 cm^{-1}, m.p. 481 K (decomposition). Magnetic moment $\mu_{eff}/\mu_{BM} = 1.54$ at 298 K.

2.4. X-ray crystallography

Intensity data of **4** and **8** were collected on a Rigaku AFC-7R four-circle diffractometer at 297 K using graphite-monochromated Mo Kα radiation ($\lambda =$ 0.71073 Å). The structures were solved by direct methods using SIR92 [44] and expanded by Fourier techniques. The structures were refined on F^2 anisotropically for non-hydrogen atoms by full-matrix least-squares methods with SHLEXL97 [45] on a teXsan program package [46]. Empirical absorption corrections were applied based on ψ scans. No significant decay in the intensity of three standard reflections was observed throughout the data collection. The hydrogen atoms were located at geometrically calculated position with C–H = 0.950 Å and refined isotropically. All the non-hydrogen atoms were refined anisotropically. Crystallographic data for **4** and **8** are summarized in Table 1. The crystal structures of **1** [30] and **5** [29] have been already reported elsewhere.

3. Results and discussion

3.1. Description of the structure of *4*

The molecular structure of **4** is depicted in Fig. 1, and selected bond distances and angles of **4** are given in Table 2. Complex **4** adopts a compressed tetrahedral *trans*-[CuN_2O_2] coordination environment, which is ascribed to bulky 1-phenylethyl moieties of the ligands.

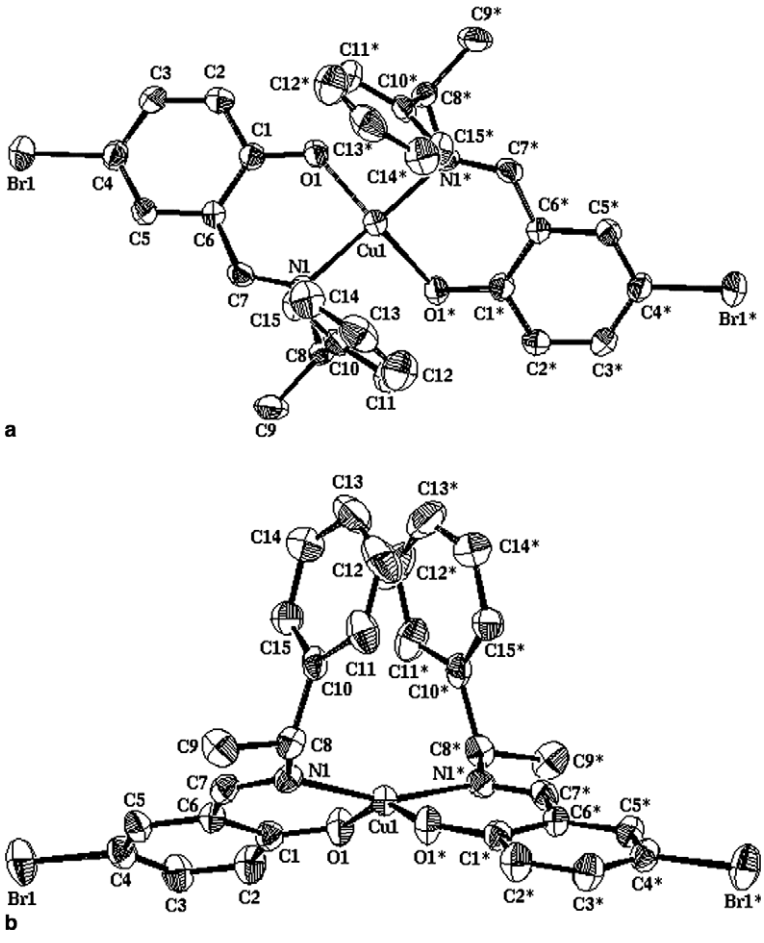


Fig. 1. The molecular structure of **4** showing the atom-labelling scheme (a) top view and (b) side view. Displacement ellipsoids are drawn at the 30% probability level. H atoms are omitted for clarity.

Table 2
Selected geometric parameters (Å, °) for **4**

Cu1–O1	1.890(4)
Cu1–N1	1.972(4)
N1–C7	1.296(6)
C6–C7	1.423(8)
O1–C1	1.319(1)
N1–C8	1.449(7)
C8–C9	1.511(9)
C8–C10	1.514(9)
O1–Cu1–O1*	151.7(3)
N1–Cu1–N1*	159.4(2)
O1–Cu1–N1*	92.0(2)
O1–Cu1–N1	93.0(2)
Cu1–O1–C1	129.2(4)
Cu1–N1–C7	124.0(4)
Cu1–N1–C8	116.5(3)
C7–N1–C8	119.4(4)
O1–C1–C2	119.0(5)
O1–C1–C6	122.7(5)
N1–C7–C6	127.0(5)
N1–C8–C9	115.2(4)
N1–C8–C10	108.6(4)
C9–C8–C10	111.0(5)

Atoms marked with *'s are expanded by the symmetry operation $(-x-1, y, -z-2)$.

The *trans*-N1–Cu1–N1* and *trans*-O1–Cu1–O1* bond angles are 159.4(2)° and 151.7(3)°, respectively, whereas the *cis*-N1–Cu1–O1 and *cis*-N1*–Cu1–O1 bond angles are 93.0(2)° and 92.0(2)°, respectively. The Cu1–N1 and Cu1–O1 bond distances are 1.890(4) and 1.972(4) Å, respectively, and the C7=N1 imine bond length is 1.296(6) Å. There are no remarkable bond distances and angles for analogous compressed tetrahedral complexes [27,30]. The central Cu(II) ion is located at the center of symmetry along the C_2 axis. Since only *R*-enantiomers of 1-phenylethylamine were used for the preparations, the absolute configuration was found to be $\Delta(R,R)$ for the examined crystal of **4**. As for the related bis[(*N*-*R*-1-phenylethyl)(3- or 5-halogen-)salicylideneaminato]M(II) complexes, 3,5-Cl-substituted Cu(II) complex (**1**) of $\Delta(R,R)$ absolute configuration was reported with Cu–N = 1.984(4) Å, Cu–O = 1.890(3) Å, *trans*-N–Cu–N = 144.7(2)° and *trans*-O–Cu–O = 150.9 (1)° [30]. Unsubstituted Cu(II) [27], 3-EtO Cu(II) [30] and 3-Cl Zn(II) complexes [47] were reported to be $\Lambda(R,R)$ absolute configuration. The pendant *R*-1-phenylethylamine groups of the ligands are on the same side of the salicydenaminato plane, and the dihedral angle between the C1/C2/C3/C4/C5/C6 mean plane and the C10/C11/C12/C13/C14 mean planes is 89.5(3)°. Intramolecular and intermolecular hydrogen bonds could not be detectable within van der Waals radii [48], crystal packing as well as chiral molecular recognition of **4** are dominated only by weak van der Waals forces during preparation or crystallization.

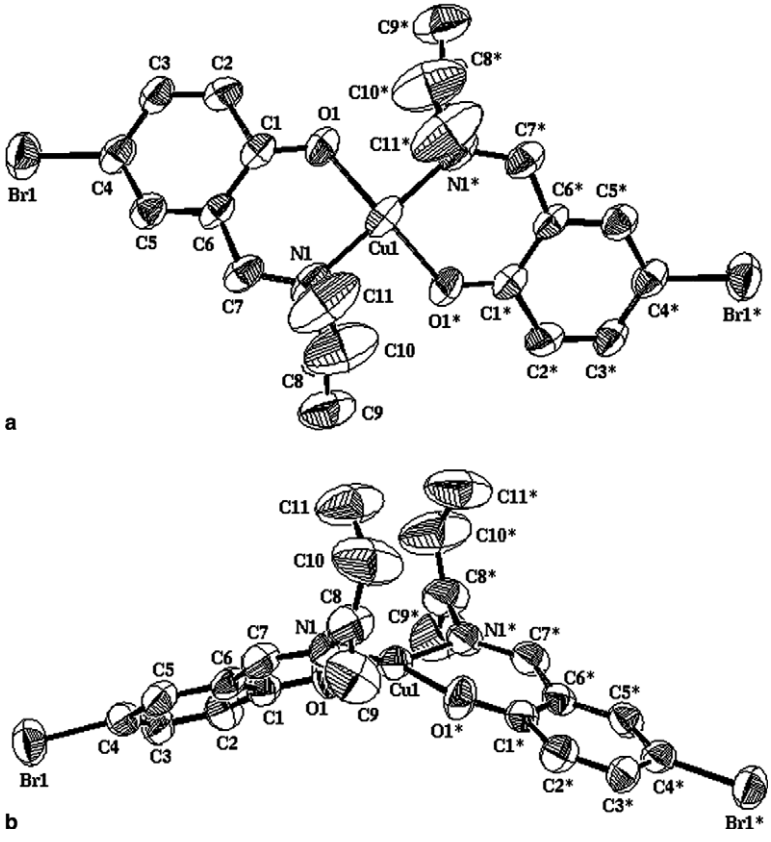


Fig. 2. The molecular structure of **8** showing the atom-labelling scheme (a) top view and (b) side view. Displacement ellipsoids are drawn at the 30% probability level. H atoms are omitted for clarity.

3.2. Description of structure of **8**

The molecular structure of **8** is depicted in Fig. 2, and selected bond distances and angles of **8** are given in Table 3. Complex **8** adopts a compressed tetrahedral *trans*-[CuN_2O_2] coordination geometry similar to **4**. This structural feature suggests that steric hindrance of the ethyl groups is sufficiently effective for distortion of the coordination environment when electron-withdrawing Br-groups are introduced. The central Cu(II) ion is on the center of symmetry. The *trans*-N1–Cu1–N1* and *trans*-O1–Cu1–O1* bond angles are 157.9(3)° and 151.0(3)°, respectively, whereas the *cis*-N1–Cu1–O1 and *cis*-N1*–Cu1–O1 bond angles are 93.3(2)° and 92.2(2)°, respectively. The Cu1–N1 and Cu1–O1 bond distances are 1.966(6) and 1.865(4) Å, respectively, and the C7=N1 imine bond length is 1.339(9) Å. The degree of distortion from square planar towards tetrahedral environment of **8** is larger than that of **4**, which leads to elongate both Cu–N and Cu–O coordination bonds of **8**. The other geometric parameters in the Schiff base ligands do not deviate significantly from the corresponding common values. Selected geometrical parameters of **5** were reported to be Cu–N = 1.969(4) and 1.971(4) Å, Cu–O = 1.886(3) and 1.892(3) Å, *trans*-N–Cu–N = 158.4(2)° and *trans*-O–Cu–O = 158.7(1)° [29]. Both sides of the 2-butyl pendant groups are on the apical side of the umbrella molecular plane. Intramolecular and intermolecular hydrogen bonds are not detectable within van der Waals radii [48] for **8**.

Table 3
Selected geometric parameters (Å, °) for **8**

Cu1–O1	1.865(4)
Cu1–N1	1.966(6)
N1–C7	1.339(9)
C6–C7	1.447(7)
O1–C1	1.284(8)
N1–C8	1.506(9)
C8–C9	1.43(1)
C8–C11	1.29(2)
O1–Cu1–O1*	151.0(3)
N1–Cu1–N1*	157.9(3)
O1–Cu1–N1*	92.2(2)
O1–Cu1–N1	93.3(2)
Cu1–O1–C1	129.1(4)
Cu1–N1–C7	124.1(4)
u1–N1–C8	120.6(6)
C7–N1–C8	115.2(7)
O1–C1–C2	120.3(6)
O1–C1–C6	123.9(5)
N1–C7–C6	124.1(6)
N1–C8–C9	115.0(8)
N1–C8–C10	114.4(8)
C9–C8–C10	130.5(9)

Atoms marked with *'s are expanded by the symmetry operation $(-x-1, y, -z-1/2)$.

3.3. IR spectroscopy

In general, the IR spectra of the analogous free protonated ligands show an imine C=N band around 1635 cm^{-1}, and the disappearance of a C=O peak around 1700 cm^{-1} is indicative of a condensation reaction giving Schiff base ligands [49]. The IR spectra of all the complexes **1**–**10** show the imine C=N bands around 1620 cm^{-1}, and it is found that the C=N bands of the Cu(II) complexes are shifted by about 10 cm^{-1} to the lower energy regions compared to the free protonated ligands [50]. In addition, the Cu–N and Cu–O vibrations are found around 450 and 420 cm^{-1}, respectively. These spectral characteristics are due to the coordination of the imine nitrogens to the metal ions [51]. These peaks are in agreement with related complexes, regardless of the degree of distortion of the *trans*-[CuN_2O_2] coordination environment. The IR spectra are not sensitive to distortion of coordination environment for the present complexes.

3.4. Diffuse reflectance electronic spectroscopy and magnetic properties

The diffuse reflectance electronic spectra of **1**–**10** were recorded at room temperature, and the overall spectral features are similar to that of analogous complexes. The small differences of the spectral features can be classified into five patterns: (i) **1** and **2**, with 1-phenylethylamine moieties and 3,5-substituents, show a broad d–d band in the region 17 000–19 000 cm^{-1} and a strong continuous band in the higher energy region over 22 000 cm^{-1}; (ii) **3** and **4**, with 1-phenylethylamine moieties and 5-substituents, show a broad d–d band in the region 16 000–19 000 cm^{-1} and a strong continuous band in the higher energy region over 23 000 cm^{-1}; (iii) **5** and **6**, with 2-butylamine moieties and 3,5-substituents, show a strong d–d band around 15 000 cm^{-1} and a strong continuous band in the higher energy region over 23 000 cm^{-1}; (iv) **7** and **8**, with 2-butylamine moieties and 5-substituents, show a broad d–d band in the region 16 000–19 000 cm^{-1} and a strong continuous band in the higher energy region over 22 000 cm^{-1}; (v) **9** and **10**, with 2-propylamine moieties and 3,5-substituents, show a strong d–d band around 14 000 cm^{-1} and a continuous band in the higher energy region over 22 000 cm^{-1}. In this way, d–d bands are more sensitive to coordination geometries and electron-withdrawing groups of the ligands than π–π* bands in the case of solid state spectra. Generally, tetrahedral complexes show a d–d band at lower energies, which shift to higher energies on moving from tetrahedral to square planar environments [52]. Apparently, the number of halogen substituents (only 5- or both 3- and 5-) is more effective than the kind of halogen (Cl or Br) substituents. The absence of pendant π-conjugated phenyl

groups in the Schiff base ligands results in the π–π* region.

Theoretically, for Cu(II) complexes (effective symmetry C_{2v} point group) of the ^2D state three transitions, $^2A_1(d_{z^2}) \leftarrow {}^2A_1(d_{x^2-y^2})$, $^2B_1(d_{zx}) \leftarrow {}^2A_1(d_{x^2-y^2})$ and $^2B_2(d_{yz}) \leftarrow {}^2A_1(d_{x^2-y^2})$, are allowed, and a broad d–d band is their convolution. A strong band in the UV region is due to an overlap of the π–π* transition [47,53] and phenolate O atoms of the ligand to Cu(II) metal charge transfer transition. These transitions are related not only to *trans*-[CuN_2O_2] coordination geometries but also the net atomic charge on the coordinating atoms (O and N) of the ligands.

The effective magnetic moments (μ_{eff}) of mononuclear Cu(II) complexes **1**–**10** at 298 K are in the range from ca. 1.4 to 1.9 B.M., which is reasonable compared to the theoretical spin-only value of 1.73 B.M. for $S = 1/2$ systems with a single unpaired electron sited in an essentially $d_{x^2-y^2}$ orbital, the ^2D state. In contrast to the electronic spectra, the effective magnetic moment is not sensitive to distortion of the *trans*-[CuN_2O_2] coordination environment for the present complexes. In order to confirm that there is little or no intermolecular antiferromagnetic coupling, we also investigated variable-temperature (5–250 K) magnetic susceptibility behavior for **1**, whose crystal structure has been determined. Complex **1** obeys the Curie–Weiss law approximately, that is the χ_M^{-1} versus T plot is a linear graph. Thus, in the absence of X-ray structural proof, except for **1**, **4**, **5** and **8**, the effective magnetic moments demonstrate the nature of the mononuclear complexes.

Table 4
Temperature (K) of the phase transition and decomposition by DSC for **1**–**10**

	Phase transition	Decomposition
1	419	556
2	484	547
3	474	547
4	412	542
5	396	557
6	410	532
7	412	548
8	400	544
9	444	542
10	446	554

3.5. Structural phase transition

It has been investigated that the analogous Cu(II) and Ni(II) complexes exhibit a thermally-induced structural phase transition by heating regardless of the coordination geometries (square planar or tetrahedral) at room temperature [21,37]. The temperature of the structural phase transition (endothermic peaks) and decomposition (exothermic peaks) in the DSC curves for **1**–**10** are summarized in Table 4. In analogy with the related Cu(II) complexes [21], the structural phase transition may be ascribed to a transformation from a low temperature phase (compressed tetrahedral) into a high temperature phase (close to right tetrahedral). The relationship between the transition temperature and chemical structures is unclear still. Because of the lability of the compounds, we could not carry out quantitative measurements. The structural phase transition seems to be irreversible for **1**–**10**.

Furthermore, we have examined the possibility of a photo-induced structural phase transition of microcrystalline samples for **1**–**10** with IR spectroscopy in the solid state at room temperature. After irradiation of UV or visible light for 5 min at room temperature, no spectral changes could be detected for **1**–**10**. On the other hand, certain thermochromic Cu(II) complexes also exhibited photochromism in the solid state at low temperature [7,10]. Thus, at least, the present experimental facts support the stability of the Cu(II) complexes against UV or visible light at room temperature.

3.6. Calculation

A summary of the results of ZINDO calculations for **1**, **4**, **5** and **8**, whose crystal structures are known, is listed in Table 5. The dipole moment of the overall molecules were evaluated to be 6.029, 5.033, 4.166 and 4.215 D for **1**, **4**, **5** and **8**, respectively. It can be expected that both introduction of 3,5-halogen substituents and deviation from square molecules as well as breaking

Table 5
Summary of the results of ZINDO calculations for **1**, **4**, **5** and **8**

	1	4	5	8
Heat of formation (kJ mol^{-1})	325.2	295.9	255.4	251.8
Dipole moment (D)	6.029	5.033	4.166	4.215
HOMO–LUMO gap (eV)	8.20	8.09	7.88	7.77
Formal charge Cu	0.196	0.250	0.204	0.200
N	−0.129	−0.084	−0.143	−0.156
O	−0.456	−0.433	−0.483	−0.463
Calculated predominant π–π* transitions (cm^{-1})	32700	33100	31200	29700
	45700	36100	34400	32900
	51300	48300	45700	44400

molecular symmetry lead to an increase of the magnitude of dipole moment. The numbers and kinds of 3,5-halogen substituents are invariable factors for a given molecule, whereas distortion of the overall molecular structure can induce polarity depending on the molecular conformation. Thus, the dipole moment can interact between the complexes and the surrounding species in solution.

The formal charges on the Cu(II) ions are 0.196, 0.250, 0.204 and 0.200 for **1**, **4**, **5** and **8**, respectively. On the other hand, the averaged values on the coordination N atoms are −0.129, −0.084, −0.143 and −0.156, and O atoms are −0.456, −0.433, −0.483 and −0.463 for **1**, **4**, **5**, and **8**, respectively. As indicated for these values, tetrahedral distortion of the coordination environment plays a role in distribution of charge from the coordination atoms to the metal ions through coordination bonds. Although these electronic features are advantageous for charge transfer transitions, it is difficult to estimate their contribution in electronic spectra. Further, π–π* bands consist of several components in the UV regions as calculations exhibit even for the X-ray structures.

3.7. Electronic absorption spectroscopy in various solvents

Fig. 3 shows the electronic absorption spectra and CD spectra of **1** in 0.1 mmol dm^{-3} chloroform solution at 298 K. The reason why **1** is employed for the following investigation and discussion is that **1** displays the largest dipole moment in the solid state and incorporates chiral ligands whose CD spectrum is detectable. Additionally, bulky 1-phenylethyl moieties and electron-withdrawing 3,5-Cl-substituents may enhance the flexibility of **1**. The absorption spectrum of **1** exhibits a broad d–d band in the region 16000–20000 cm^{-1} and a strong π–π* band in the region 24000–28000 cm^{-1}. The corresponding CD spectrum of **1** shows a positive peak around 15000 cm^{-1} and a negative peak around 18000 cm^{-1} in the d–d region, and a negative peak around 23000 cm^{-1} and a positive peak around 25000 cm^{-1} in the π–π* region. The d–d band can be ascribed to convolution of three allowed transitions, $^2A_1(d_{x^2-y^2}) \rightarrow {}^2A_1(d_{z^2})$, $^2A_1(d_{x^2-y^2}) \rightarrow {}^2B_1(d_{xz})$, $^2A_1(d_{x^2-y^2}) \rightarrow {}^2B_2(d_{yz})$, in C_{2v} symmetry. The sign of the CD peaks seems to be reasonable with respect to the Δ(*R*,*R*) absolute configuration of **1**. The change of coordination geometry of **1** and conformation of its ligands in solution may attribute to the difference between absorption spectra and diffuse reflectance spectra.

The electronic absorption spectra were also recorded for **1**–**10** in various solvents, *N*,*N*′-dimethylformamide (DMF) ($\mu = 3.82$; $\varepsilon = 36.710$; $n_D^{20} = 1.428$), acetone ($\mu = 3.11$; $\varepsilon = 20.700$; $n_D^{20} = 1.356$), methanol ($\mu = 2.97$; $\varepsilon = 32.630$; $n_D^{20} = 1.326$), chloroform ($\mu = 1.11$; $\varepsilon = 4.806$; $n_D^{20} = 1.444$) and toluene ($\mu = 0.37$; $\varepsilon = 2.438$; $n_D^{20} = 1.494$) (the figures in parentheses denote dipole moment, μ(D), dielectric constant, ε, and refractive index, n_D^{20}) [15]. The predominant peaks of π–π* bands (ν cm^{-1} and log ε dm^3 mol^{-1} cm^{-1}) are shown in Table 6. The results show that the π–π* bands are sensitive to the physical properties of the solvents for **1**–**10**. However, the shifts of the d–d band, depending on solvents or concentrations (1, 0.1, and 0.01 mmol dm^{-3}), are relatively small for **1**–**10**. Therefore, we can conclude that the changes of polarity of the solvent lead to structural changes of the complexes associated with conformation of the π-conjugated pendant groups of the Schiff base ligands.

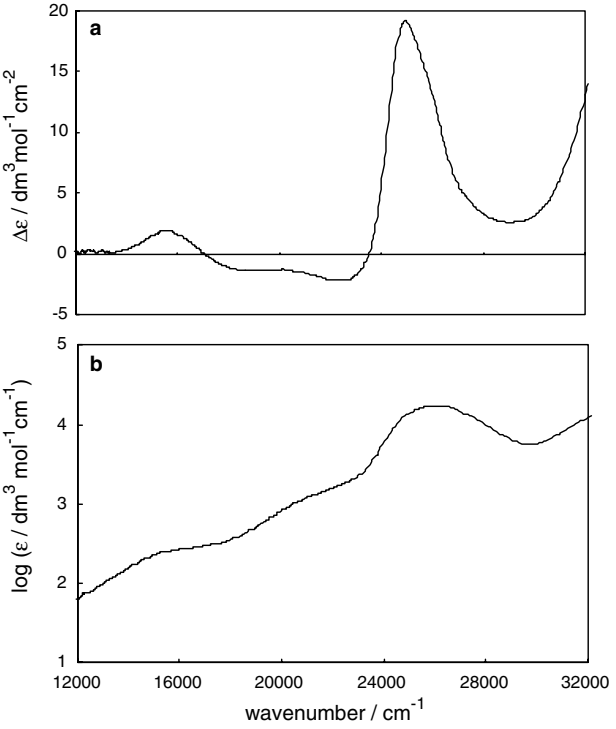


Fig. 3. The electronic (a) CD and (b) absorption spectra of **1** in 0.1 $mmol^{-1}$ dm^3 $CHCl_3$ solution at 298 K.

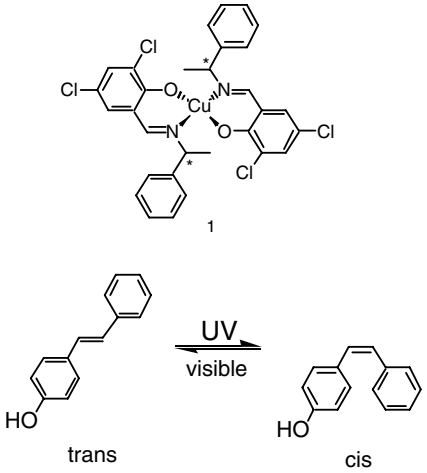
In an attempt to produce *solvatochromism induced by a photochromic solute*, we have measured the absorption spectra of a 0.1 mmol dm^{-3} chloroform solution of **1** containing equimolar 4-hydroxyazobenzene (4HAZ) (Scheme 2). It is well known that irradiation with UV and visible light results in reversible photoisomerization of 4HAZ to the *cis* forms (μ = ca. 3 D) and the *trans* forms (μ = almost 0 D). For a solution of only 4HAZ (Fig. 4(a)), irradiation with UV and visible light for 5 min, which is enough time to saturate the photoisomerization reaction, to the solution results in reversible spectral changes of the π–π* band of 4HAZ around 29000 cm^{-1}. On the other hand, for a solution containing 4HAZ and **1**, very slight and relatively large spectral changes could be observed at ca. 23000 cm^{-1} and ca. 31000 cm^{-1}. Taking into account the absorption spectrum

Table 6
Predominant π–π* peaks (ν(cm^{-1}); log ε ($dm^3\ mol^{-1}\ cm^{-1}$)) of the absorption spectra 0.1 mmol dm^{-3} in various solvents at 298 K for **1**–**10**

	DMF	Acetone	Methanol	Chloroform	Toluene
1	26 530(4.10)	26 460(4.05)	26 460(4.04)	26 180(4.23)	26 110(4.12)
			33 220(3.96)	33 000(4.20)^{sh}	
2	26 530(4.00)	26 460(4.06)	26 390(3.70)	26 180(3.84)	26 110(4.22)
			33 220(3.64)^{sh}	33 000(3.82)^{sh}	
3	26 390(4.05)	26 390(4.25)	26 460(4.03)	26 180(4.12)	26 040(4.21)
			32 680(3.93)	32 570(4.06)	
4	26 460(4.03)	26 390(4.05)	26 460(3.95)	26 180(4.10)	26 110(4.23)
			32 680(3.89)	32 570(4.08)	
5	26 670(4.24)	26 600(4.28)	26 530(4.17)	26 320(4.10)	26 250(4.10)
			33 000(4.13)^{sh}	33 220(4.09)	
6	26 600(3.65)	26 600(4.00)	26 600(3.96)	26 320(4.09)	26 250(4.11)
			33 220(3.97)^{sh}	32 260(4.06)	
7	26 600(4.23)	26 530(4.25)	26 670(4.06)	26 320(4.09)	26 520(4.11)
	32 150(4.18)		32 260(4.01)	32 260(4.06)	
8	26 600(4.08)	26 600(4.12)	26 670(4.09)	26 320(3.94)	26 110(4.45)
	32 150(4.05)		32 360(4.08)	32 260(3.95)	
9	26 670(4.18)	26 670(3.91)	26 740(4.10)	26 390(4.00)	26 300(4.17)
			32 570(4.08)	32 360(4.00)	
10	26 740(4.09)	26 670(3.93)	26 810(4.11)	26 460(4.00)	26 250(4.12)
			32 790(4.17)^{sh}	32 360(4.04)	

The figures marked with ^{sh} denotes a shoulder, and the remaining ones are bands.

of only **1** (Fig. 3(b)), the former band and the latter band are ascribed to d–d and π–π* bands of **1**. The spectral change caused by the photoisomerization of 4HAZ may be ascribed mainly to a conformational change of the pendant 1-phenylethylamine moiety of the ligands (Fig. 4(b)). The possibility of supramolecular helical structures of 4HAZ induced by **1** as chiral dopants in the solution can be denied, because the spectral changes are detected not by CD spectra but by absorption spectra. The fact that solvatochromic behavior mainly affects the π–π* bands, as indicated in Table 6, and the magnitude of the difference of dipole moment photoisomerization of 4HAZ may support this interpretation. Although the other complexes also exhibit spectral shifts depending on the solvent, we could not observe photoisomerization caused by 4HAZ. The appropriate pendant 1-phenylethylamine moiety and molecular flexibility enhanced by electron-withdrawing substituents are necessary for the complex served for this experiment.



Scheme 2. Molecular structure of **1** and *cis–trans* photoisomerization of 4HAZ.

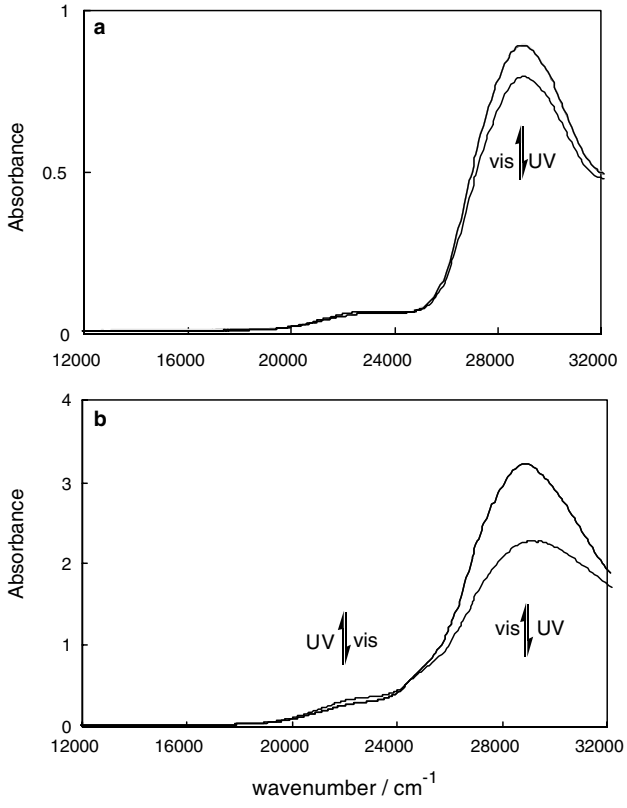


Fig. 4. The absorption spectra of (a) only 4HAZ and (b) 4HAZ and **1** in 0.1 $mmol^{-1}\ dm^3$ $CHCl_3$ solution at 298 K before and after UV or visible light irradiation for 5 min.

4. Concluding remarks

Crystal structures of two new Cu(II) complexes and systematical comparisons of structural features, thermodynamical behavior and electronic or optical properties have been reported for a series of ten related Cu(II) complexes incorporating 3,5-halogen-substituted Schiff base ligands. The pronounced solvatochromic behavior of the absorption spectra can be detected in the π–π* bands rather than the d–d bands for **1**–**10**. As for a chloroform solution of **1**, which has the largest dipole moment in the solid state among **1**–**10** and chiral ligands, and containing equimolar 4HAZ, we have examined solvatochromism of **1** induced by the photochromic solute. Irradiation of light resulted in spectral changes in the π–π* regions and little difference in the d–d regions. Further studies to apply to other nano-structured supramolecular systems of complexes and homogeneous chiral catalysts of transition metal complexes [54] without photochromic functional groups in ligands are underway.

5. Supplementary materials

Crystallographic data for the structural analyses are deposited with the Cambridge Crystallographic Data Centre, CCDC with deposition numbers 265611 and 265612 for **4** and **8**, respectively. Copies of this information can be obtained from the Cambridge Crystallographic Data Centre, 12 Union Road, Cambridge CB2 1EZ, UK (fax: +44-1223-336033; e-mail: deposit@ccdc.cam.ac.uk or www: http://www.ccdc.cam.ac.uk).

Acknowledgements

This work was supported by Grant-in-Aid for the 21st Century COE program 'KEIO Life Conjugate Chemistry' from the Ministry of Education, Culture, Sports, Science and Technology, Japan. The authors thank Professor Yohru Yamada and Dr. Taketo Ikeno (Keio University) for the use of the DSC apparatus, Professor Hidenari Inoue (keio University) for the use of the CD spectrometer and Professor Katsuya Inoue (Institute for Molecular Science) for the use of the SQUID instrument.

References

[1] O. Sato, Acc. Chem. Rev. 36 (2003) 692.
[2] O. Sato, S. Hayami, Y. Einaga, Z.-Z. Gu, Bull. Chem. Soc. Jpn. 76 (2003) 443.
[3] S. Kume, M. Kurihara, H. Nishihara, Chem. Commun. (2001) 1656.
[4] D. Pucci, A. Bellusci, A. Crispini, M. Ghedini, M. La Deda, Inorg. Chim. Acta 357 (2004) 495.
[5] P. Gutlich, Y. Garcia, H.A. Goodwin, Chem. Soc. Rev. 29 (2000) 419.
[6] P. Gutlich, Y. Garcia, T. Woike, Coord. Chem. Rev. 219–221 (2001) 839.
[7] K. Takahashi, R. Nakajima, Z.-Z. Gu, H. Yoshiki, A. Fujishima, O. Sato, Chem. Commun. (2002) 1578.
[8] O. Sato, T. Iyoda, A. Fujishima, K. Hashimoto, Science 272 (1996) 704.
[9] T. Murahashi, Y. Higuchi, T. Katoh, H. Kurosawa, J. Am. Chem. Soc. 124 (2002) 14288.
[10] B. Narayanan, M.M. Bhadbhade, J. Coord. Chem. 46 (1998) 115.
[11] I. Grenthe, P. Paoletti, M. Sandstrom, S. Glikberg, Inorg. Chem. 28 (1979) 2687.
[12] M.J. Riley, D. Neill, P.V. Bernhardt, K.A. Byriel, C.H.L. Kennard, Inorg. Chem. 37 (1998) 3635.
[13] K.L. Bray, H.G. Drickamer, E.A. Schmitt, D.N. Hendrickson, J. Am. Chem. Soc. 111 (1989) 2849.
[14] J. Burgess, S. Maguire, A. McGranaghan, S.A. Parsons, B. Nowicka, A. Samotus, Trans. Met. Chem. 23 (1998) 615.
[15] I. Veroni, A. Rontoyianni, C.A. Mitsopoulou, J. Chem. Soc., Dalton Trans. (2003) 255.
[16] M.M. Bhadbhade, D. Srinivas, Inorg. Chem. 32 (1993) 5458.
[17] M. Boiocchi, L. Fabbrizzi, F. Foti, M. Vazquez, J. Chem. Soc., Dalton Trans. (2004) 2616.
[18] M. Kato, A. Omura, A. Toshikawa, S. Kishi, Y. Sugimoto, Angew. Chem. Int. Ed. 41 (2002) 3183.
[19] E.J. Fernandez, J.M. Lopez-de-Luzuriaga, M. Monge, M.E. Olmos, J. Perez, A. Laguna, A.A. Mohamed, H.P. Fackler Jr., J. Am. Chem. Soc. 125 (2003) 2022.
[20] R. Mikami, M. Taguchi, K. Yamada, K. Suzuki, O. Sato, Y. Einaga, Angew. Chem. Int. Ed. 43 (2004) 6135.
[21] S. Yamada, Coord. Chem. Rev. 190–192 (1999) 537, and references therein.
[22] J.M. Fernandez, O.L. Ruiz-Tamirez, R.A. Toscano, N. Macias-Ruvalcaba, M. Aguilar-Martinez, Trans. Met. Chem. 25 (2000) 517.
[23] A. Castineiras, W. Hiller, J. Strahle, J. Romero, R. Bastida, A. Sousa, Acta Crystallogr. C46 (1990) 770.
[24] T.P. Cheeseman, D. Hall, T.N. Waters, Nature 205 (1965) 494.
[25] P.L. Orioli, L. Sacconi, J. Am. Chem. Soc. 88 (1966) 277.
[26] H. Nozaki, H. Takaya, S. Moriuti, R. Noyori, Tetrahedron 24 (1968) 3655.
[27] G.-P. Li, Q.-C. Yang, Y.-Q. Tang, Y.-D. Guan, Z.-H. Shang, Acta Chim. Sinica 45 (1987) 421.
[28] H. Okawa, M. Nakamura, S. Kida, Inorg. Chim. Acta 120 (1986) 185.
[29] T. Akitsu, Y. Einaga, Acta Crystallogr. E60 (2004) m1605.
[30] T. Akitsu, Y. Einaga, Acta Crystallogr. C60 (2004) m640.
[31] R.L. Braun, E.C. Lingagelter, Acta Cryst. 21 (1966) 546.
[32] K. Ravikumar, S.S. Rajan, V. Rajaram, S.K. Ramalingam, S. Natarajin, Z. fur Krist. 175 (1986) 117.
[33] V. Manriquez, J. Vargas, J. Costamagna, H.G. von Schnering, K. Peters, Acta Cryst. C46 (1990) 772.
[34] M.R. Fox, E.C. Lingafelter, P.L. Orioli, L. Sacconi, Nature 197 (1963) 1104.
[35] M.R. Fox, L. Orioli, L. Sacconi, Acta Cryst. 17 (1964) 1159.
[36] R.L. Braun, E.C. Lingagelter, Acta Cryst. 22 (1967) 780.
[37] N. Arai, M. Sorai, S. Seki, Bull. Chem. Soc. Jpn. 45 (1972) 2398.
[38] T. Ashida, S. Iwata, T. Yamane, M. Kakudo, A. Takeuchi, S. Yamada, Bull. Chem. Soc. Jpn. 49 (1976) 3502.
[39] J.B. Willis, D.P. Mellor, J. Am. Chem. Soc. 69 (1947) 1237.
[40] L. Sacconi, P. Paoletti, M. Ciampolini, J. Am. Chem. Soc. 85 (1963) 411.
[41] H. Hoss, H. Elias, Inorg. Chem. 32 (1993) 317.

[42] M.C. Zerner, G.H. Lowe, R.F. Kirchner, U.T. Mueller-Westerhoff, J. Am. Chem. Soc. 102 (1980) 589.
[43] J.D. Head, M.C. Zerner, Chem. Phys. Lett. 131 (1986) 359.
[44] A. Altomare, G. Cascarano, C. Giacovazzo, A. Guagliardi, M.C. Brurla, G. Polidori, M. Camalli, J. Appl. Cryst. 27 (1994) 435.
[45] G.M. Sheldrick, SHELXL97, Program for the Refinement of Crystal Structures, University of Gottingen, Germany, 1997.
[46] Molecular Structure Corporation. TEXSAN. Version 1.11., MSC, 9009 New Trails Drive, The Woodlands, TX 77381-5209, USA, 2001.
[47] C. Evans, D. Luneau, J. Chem. Soc., Dalton. Trans. (2002) 83.
[48] A. Bondi, J. Phys. Chem. 68 (1964) 441.
[49] K.R. Krishnapriya, M. Kandaswamy, Polyhedron 24 (2005) 113.
[50] G. Das, R. Shukala, S. Mandal, R. Singh, P.K. Bharadwaj, J.V. Singh, K.H. Whitmire, Inorg. Chem. 36 (1997) 323.
[51] F.M. Ashmawy, R.M. Issa, S.A. Amer, C.A. McAuliffe, R.V. Parish, J. Chem. Soc., Dalton. Trans. (1987) 2009.
[52] P.C. Chia, D.P. Freyberg, G.M. Mockler, E. Sinn, Inorg. Chem. 16 (1977) 254.
[53] H. Sakiyama, H. Okawa, N. Matsumoto, S. Kida, J. Chem. Soc., Dalton. Trans. (1990) 2935.
[54] M. Kettunen, A.S. Abu-Surrah, H.M. Abdel-Halim, T. Repo, M. Leskela, M. Laine, I. Mutikainen, M. Ahlgren, Polyhedron 23 (2004) 1649.

1. Introduction

Complexes containing 1,1-dithiolato ligands have been used as fungicides, pesticides, vulcanization accelerators, flotation agents, lubricant additives and in deposition of ZnS or CdS thin films by metal organic chemical vapor deposition [1]. 1,1-Dithiolate ligands have recently attracted much attention mainly because of the interesting photophysical properties derived from their extensive electron delocalization onto all of the ligand atoms [2]. Indeed, the increasing renewed attention paid nowadays to these species arises from their high stability, solvatochromic behavior, room-temperature luminescence in solution [3] and their status as excellent candidates for applications such as photocatalysis [4]. A lot of work is currently taking place to find how the excited-state properties can be altered in a predictable manner through systematic ligand modification [4a]. In addition the variable coordination modes of 1,1-dithiolate ligands to metals make the structural studies more interesting [5]. The 1,1-dithiolate ligands have also been used to stabilize unusually high oxidation states [6] or to facilitate the syntheses of clusters [5,7], and to the syntheses of inorganic–organic hybrid materials, which have a potential in various applications such as electrical conductivity, magnetism [8], ion exchange, separation and catalysis [9].

Previously we reported the synthesis and spectroscopic investigation of some mixed-ligand nickel(II) and copper(II) chelates containing diamine or phosphine and 1,1-dithiolate ligands [10]. The results of these studies indicated that their spectroscopic properties and magnetic behavior strongly depend upon structural details of both the diamine or phosphine and the dithiolate ligands. In this work we describe the synthesis and structural characterization of: (a) nickel(II) and copper(II) complexes containing 1,1-disubstituted-2,2-ethylene-dithiolates; (b) a series of neutral ternary nickel(II) chelates with *N*-donor, *N*-acceptor, cross-conjugated nitrogenous bases and 1,1-dithiolate; and (c) the fascinating sulfur-rich dithiole ligand. Further the structures of (2,2′-bipyridine)(1-cyano-1-phenyl-2,2-ethylenedithiolato) nickel(II) [Ni(bipy)CPD], tetrabutylammonium(1-cyano-1-chlorophenyl-2,2-ethylenedithiolate)copper(II) ($(n\text{-}Bu_4N)_2[Cu(CCPD)_2]$) and the novel 5-amino-4(4-chlorophenyl)-[1,2] dithiole-3-thione ligand (ACDT) were elucidated by X-ray diffraction studies. To the best of our knowledge, this is the first X-ray study of a nickel(II) complex with a 1,1-dithiolate having molecular interactions in the solid state, and the first 1-cyano-1-chlorophenyl-2,2-ethylenedithiolato complex of any metal, and the second X-ray analysis for copper(II) complexes [21a] with 1,1-dithiolate ligands.

2. Experimental

2.1. Reagents

The nitrogenous bases, enR, *N*,*N*′-diphenyl-1,2-diaminoethane (PhenPh), *N*,*N*′-dibenzyl-1,2-diaminoethane (BenB), *cis*-1,2-diaminocyclohexane (C × NN), 2-(aminomethyl)pyridine (ampy), 2,2′-bipyridine (bipy) and 2,2′-dipyridylamine (dipyamH) were purchased from Aldrich. The nitriles, malononitrile ($NCCH_2CN$), ethyl cyanoacetate ($NCCH_2COOC_2H_5$), cyanoacetamide ($NCCH_2CONH_2$) chlorobenzyl cyanide ($NCCH_2C_6H_4Cl$), benzyl cyanide ($NCCH_2C_6H_5$), tetrabutylammonium bromide ($n\text{-}Bu_4NBr$) and tetraethylammonium bromide (Et_4NBr) were procured from Merck. Copper(II) chloride dehydrate, $CuCl_2 \cdot 2H_2O$, nickel(II) chloride hexahydrate, $NiCl_2 \cdot 6H_2O$ and sodium hydride (NaH, as 55% suspension) were procured from Fluka. The dithiolate ligand salts disodium 1-cyano-1-chlorophenyl-2,2-ethylenedithiloate dehydrate ($Na_2CCPD \cdot 2H_2O$), disodium 1-cyano-1-phenyl-2,2-ethylenedithiolate dihydrate ($Na_2CPD \cdot 2H_2O$), disodium 1,1-dicyano-2,2-ethylenedithiolate trihydrate ($Na(i\text{-}MNT) \cdot 3H_2O$), dipotassium 1-cyano-1-carboethoxy-2,2-ethylenedithiolate hydrate ($K_2CED \cdot H_2O$) and dipotassium 1-cyano-1-carbamyl-2,2-ethylenedithiolate dehydrate ($K_2CCED \cdot 2H_2O$) were prepared by the literature procedures [11,12].

2.1.1. Synthesis of homoleptic nickel(II) and copper(II) chelates

The new chelates $[R_4N]_2[M(S_2C{=}C(CN)Y)_2]$ (Y = Cl-ph, ph, COOEt, $CONH_2$) were prepared according to the following general method.

To a methanolic solution (ca. 100 cm^3) containing 4 mmol of the appropriate 1,1-dithiolate salt, 4 mmol of tetrabutylammonium bromide ($n\text{-}Bu_4NBr$) or tetraethylammonium bromide (Et_4NBr) were added. Upon dissolution, the mixture was filtered slowly into a conical flask containing 2 mmol metal chloride dissolved in 20 cm^3 of methanol while stirring. Water was added dropwise under continuous stirring to the reaction mixture. To complete the reaction, stirring was continued for about 1 h. The resultant precipitate was separated by filtration, washed several times with water and dried in air. The complex was purified by dissolving it in acetone, filtering and reprecipitating it by addition of water, then separating by filtration.

2.1.2. Synthesis of 5-amino-4(4-chlorophenyl)-[1,2] dithiole-3-thione

Yellow crystals of the new dithiol ligand (ACDT) of appropriate dimensions suitable for X-ray diffraction analysis were obtained from a slow evaporation of a

water solution of the ligand $Na_2CCPD \cdot 2H_2O$ and lanthanum chloride heptahydrate ($LaCl_3 \cdot 7H_2O$).

2.1.3. Synthesis of mixed-ligand nickel(II) chelates

The new compounds [Ni(enR) $S_2C{=}C(CN)Y$] (Y = CN,Ph, COOEt, $CONH_2$) were prepared according to the following general method.

To a methanolic solution (~40 cm^3) containing 5 mmol of the nitrogenous base, enR, an equimolar amount of the 1,1-dithiolate salt was added. Upon dissolution the mixture was transferred dropwise to a 100 ml conical flask containing 5 mmol $NiCl_2 \cdot 6H_2O$ dissolved in ~20 cm^3 of methanol while stirring continuously. To complete the reaction the stirring was continued for 1 h and then was left undisturbed for a while. The resultant precipitate was separated by filtration and transferred to a beaker. Mixing with water and subsequent filtration ensured removal of unreacted reagents and inorganic salts. The solid product was washed several times with water and finally with a small volume of cold methanol, and then air dried.

2.2. Physical measurements and determinations

Elemental analyses, melting points, molar conductivities in nitromethane, magnetic susceptibility measurements, infrared and electronic spectra were determined as described before [10c]. The compounds prepared, their elemental analyses and some other data are listed in Tables 1 and 2.

2.3. X-ray single crystal structure determination of $(n\text{-}Bu_4N)_2[Cu(CCPD)_2]$, [Ni(bipy)CPD] and ACDT

The data were collected using a STOE Imaging plate diffraction system (IPDS) equipped with Mo Kα radiation. The structure solution was performed with SHELXS-97 [13] and structure refinement was done against F^2 using SHELXL-97 [14]. All non-hydrogen atoms were refined using anisotropic displacement parameters. The hydrogen atoms were positioned with idealized geometries ($d_{C-H} = 0.95$ Å), and refined with fixed isotropic displacement parameters according to the riding

Table 1
Elemental analyses and physicochemical data of some $(R_4N)_2[M(S_2C{=}C(CN)Y)_2]$ (M = Ni(II), Cu(II)) chelates

	Compound	Color	Yield (%)	M.p.[a] (°C)	M_w	C%	H%	N%	Λ_M (S cm^2 mol^{-1})
1	$(n\text{-}Bu_4N)_2$ [Ni(CCPD)$_2$]	light green	85	191–193	995.00	60.5 (60.35)[b]	8.2 (8.10)	5.5 (5.63)	164
2	$(n\text{-}Bu_4N)_2$ [Ni(CPD)$_2$]	deep green	75	176–178	926.21	65.2 (64.84)	9.10 (8.92)	5.92 (6.05)	155
3	$(n\text{-}Bu_4N)_2$ [Ni(CED)$_2$]	brown	80	81–83	918.14	57.4 (57.56)	9.05 (9.00)	6.00 (6.10)	152
4	$(n\text{-}Bu_4N)_2$ [Ni(CCED)$_2$]	green-yellow	78	220–222	860.06	55.6 (55.86)	8.75 (8.91)	9.86 (9.77)	168
5	$(n\text{-}Bu_4N)_2$ [Cu(CCPD)$_2$]	yellow	90	110–112	999.86	60.1 (60.06)	7.9 (8.07)	5.5 (5.60)	170
6	$(n\text{-}Bu_4N)_2$ [Cu(CPD)$_2$]	brown-green	87	78–82	931.04	64.3 (64.50)	8.80 (8.88)	5.90 (6.02)	153
7	$(Et_4N)_2$ [Cu(CED)$_2$]	brown-red	91	145–148	698.54	47.9 (48.14)	7.00 (7.22)	7.87 (8.02)	154
8	$(n\text{-}Bu_4N)_2$ [Cu(CCED)$_2$]	light brown	93	140–143	864.89	55.7 (55.55)	8.67 (8.86)	9.58 (9.72)	160

CED = 1-cyano-1-carboethoxy-2,2-ethylenedithiolate.
CPD = 1-cyano-1-phenyl-2,2-ethylenedithiolate.
CCED = 1-cyano-1-carboamido-2,2-ethylenedithiolate.
[a] Decomposition.
[b] Calculated values in parentheses.

Table 2
Elemental analyses and physicochemical data of some [Ni(enR)($S_2C{=}C(CN)Y$)] chelates

	Compound	Color	Yield (%)	M.p.[a] (C°)	M_r	C%	H%	N%	μ_{eff} (m_B)
1	[Ni(dipyamH)*i*-MNT]	deep brown	90	271–275	370.10	45.2 (45.43)[b]	2.44 (2.45)	18.8 (18.92)	diam
2	[Ni(bipy)CPD]	deep red-brown	83	280–284	406.15	55.8 (56.19)	3.18 (3.23)	10.5 (10.35)	1.71
3	[Ni(C × NN)CPD]	brown-green	76	245–248	364.18	49.9 (49.47)	5.31 (5.26)	11.7 (11.54)	2.19
4	[Ni(dipyamH)CPD]	deep green	77	340–345	421.19	54.3 (54.18)	3.28 (3.35)	13.4 (13.30)	1.82
5	[(Ni(BenB)CED]	light brown	80	231–235	486.30	53.3 (54.34)	5.17 (5.18)	8.67 (8.64)	diam
6	[Ni(C × NN)CED]	orange	74	288–292	360.14	39.8 (40.02)	5.09 (5.32)	11.5 (11.67)	2.52
7	[Ni(PhenPh)CED]	brown	68	257–260	458.25	51.9 (52.42)	4.58 (4.63)	9.26 (9.17)	diam
8	[Ni(ampy)CED]	light brown	80	294–296	354.09	40.5 (40.70)	3.74 (3.70)	12.0 (11.87)	diam
9	[Ni(bipy)CED]	deep red	76	304–306	402.14	47.6 (47.79)	3.19 (3.26)	10.5 (10.45)	diam
10	[Ni(dipyamH)CED]	light brown	75	308–312	417.16	41.9 (42.07)	3.29 (3.38)	13.3 (13.43)	diam
11	[Ni(dipyamH)CCED]	light brown	60	315–318	388.12	43.0 (43.32)	2.73 (2.86)	17.9 (18.05)	diam

i-MNT = 1,1-dicyano-2,2-ethylenedithiolate.
[a] Decomposition.
[b] Calculated values in parentheses.

Table 3
Selected crystal data and experimental details for the structural study of ACDT (**1**), (n-$Bu_4N)_2$[Cu(CCPD)$_2$] (**2**) and [Ni(bipy)CPD] (**3**)

	1	**2**	**3**
Formula	$C_9H_6NClS_3$	$[Cu(C_9H_4NS_2Cl)_2]\cdot 2C_{16}H_{36}N$	$NiC_{19}H_{13}N_3S_2$
MW (g mol^{-1})	259.78	999.86	406.15
Crystal system	triclinic	triclinic	monoclinic
Space group	$P\bar{1}$	$P\bar{1}$	$P2_1/n$
a (Å)	7.3401(6)	9.523(1)	6.9292(5)
b (Å)	13.476(2)	9.908(1)	13.090(1)
c (Å)	16.189(2)	15.830(1)	18.667(2)
α (°)	86.59(1)	83.99 (1)	90.00
β (°)	89.74(1)	72.91(1)	94.61(1)
γ (°)	89.84(1)	71.93(1)	90.00
V (Å^3)	1598.5(2)	1357.2(2)	1687.7(2)
Temperature (K)	170	170	170
Z	6	1	4
D_{calc} (g cm^{-3})	1.619	1.223	1.598
F(000)	792	535	832
2θ Range (°)	3–56	3–56	3–50
$h/k/l$ Ranges	−9/9	−12/12	−8/6
	−17/17	−13/13	−13/15
	−21/21	−20/20	−22/22
μ (Mo Kα) (mm^{-1})	0.9	0.69	1.40
Measured reflections	14939	19675	8807
R_{int}	0.0357	0.0245	0.0825
Independent refl.	7582	5895	2974
Reflections with $I > 2\sigma(I)$	6365	5362	2011
Parameters	380	277	226
R_1 [$I > 2\sigma$(I)]	0.0339	0.0445	0.0404
wR_2 [all data]	0.0936	0.1198	0.0902
Goodness-of-fit	1.018	1.060	0.945
Residual electron density (e Å^{-3})	0.33/−0.44	1.59/−1.20	0.40/−0.51

model [$U_{iso} = 1.2 \times U_{eq}$(C)]. A special feature of the refinement is that in (n-$Bu_4N)_2$[Cu(CCPD)$_2$] some carbon atoms of the 6-membered aromatic ring which is attached to the chloro atom and the chloro atom itself shows some disordering. However, no reasonable split models were found. Selected crystal data and results of the structure refinement as well as bond lengths and angles are found in Tables 3, 8, 9 and 10.

3. Results and discussion

The simultaneous reaction of nickel(II) or copper(II) with 1,1-dithiolato anions $(S_2C{=}C(CN)Y)^{2-}$ and tetrabutylammonium bromide (n-Bu_4NBr) or tetraethylammonium bromide (Et_4NBr) in a 1:2:2 molar ratio, respectively, produces compounds corresponding to the general formulas $[R_4N]_2[M(S_2C{=}C(CN)Y)_2]$, (R = n-Bu, Et, M = Ni(II), Cu(II), Y = phCl (CCPD), ph (CPD), COOEt (CED), $CONH_2$-(CCED)). The new chelates are insoluble in water and soluble in organic solvents. The copper(II) complexes are paramagnetic with magnetic moments, μ_{eff}, in the range 1.65–1.82 m_B and the nickel(II) complexes are diamagnetic. Their electrical conductance values in nitromethane (Table 1) and their solid state magnetic susceptibilities indicate 2:1 type electrolytes, mononuclear compounds.

The concurrent reaction of nickel with equimolar quantities of nitrogenous bases, enR, and the 1,1-dithiolato anions, $(S_2C{=}C(CN)Y)^{2-}$, affords neutral mixed-ligand compounds corresponding to the general formula [Ni(enR)S_2C=C(CN)Y] (Y = CN, Ph, COOEt, $CONH_2$). The compounds are almost insoluble in methanol, ethanol and acetone while their solubility in dimethylformamide (DMF) and dimethylsulfoxide (DMSO) is considerable. Their low electrical conductance values ($\Lambda_m \approx 15$ S cm^2 mol^{-1}) in DMF and their solid state magnetic susceptibility indicate neutral, mononuclear diamagnetic compounds and only the compounds of the [Ni(enR)CPD] series were found to be paramagnetic with magnetic moments, μ_{eff}, in the range 1.7 to 2.3 m_B. This behavior in the solid state merits some comments. It is well known that nickel(II) has a tendency to achieve coordination numbers exceeding four by accepting ligands in the vacant coordination sites, or by aggregation of the parent compounds [10b,15]. Ligands with sulfur donor atoms may instigate intermolecular interactions of the type M–S···M, provided that the arrangement of the monomers in the unit cell permits such interactions. For instance, the molecules in the unit cell of [Ni(bipy)CPD] are arranged

in pairs as shown in Fig. 1(a). Each pair of molecules form two weak intermolecular Ni···S bond interactions at a distance of 3.617 Å (Fig. 1(b)). According to the classic paper by Bondi [16], the sum of the van der Waals radii of nickel and sulfur is 3.4 Å. There is wide agreement that this is an underestimation [17,18]. The Paramagnetism of solid [Ni(bipy)CPD] suggests the same arrangement of the monomers and long range interactions, not uncommon in compounds with dithiolato ligands [18–22]. This notion is supported by the change in the magnetic behavior of [Ni(bipy)CPD], observed when magnetic susceptibility measurements were performed in solutions. This compound is sufficiently soluble in acetone permitting the determination of χ_{mol} by Evans' method. The propensity towards aggregation in the [Ni(enR)CPD] complexes is probably due to the residual Lewis acidity of the nickel atoms as well as the basicity of the sulfur atoms. Further information

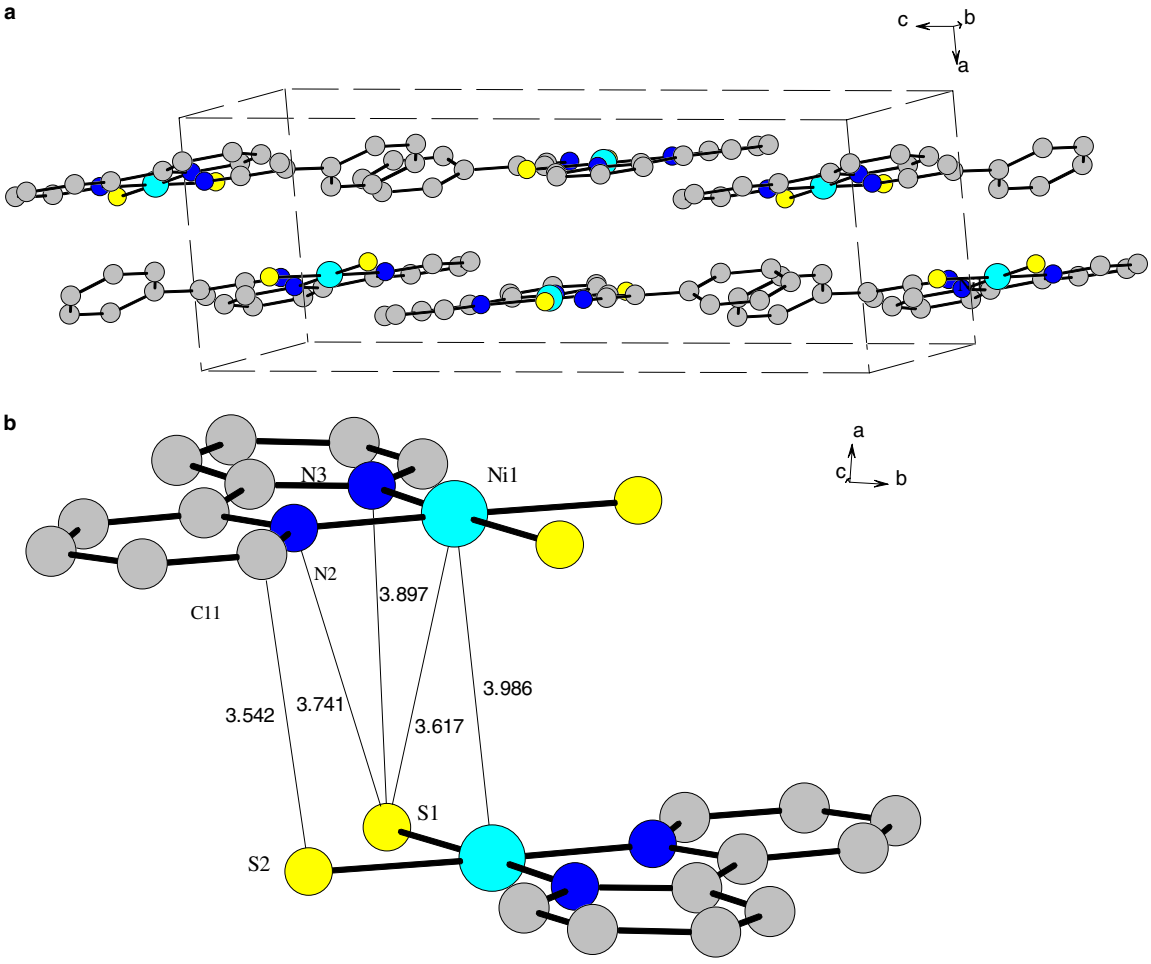


Fig. 1. (a) The arrangement of the molecules in the unit cell of [Ni(bipy)CPD]. (b) A pair of molecules showing the intermolecular distances.

Table 4
Wavenumbers of characteristic bands in the IR spectra of some $(R_4N)_2[M(S_2C{=}C(CN)Y)_2]$ (M = Ni, Cu) chelates

	Compound	ν(C≡N)	ν(C=O)	ν(C=CS$_2$)	ν_{as}(CSS)	ν_s (CSS)	ν(Ni–S)
1	$(n\text{-}Bu_4N)_2[Ni(CCPD)_2]$	$2179_{(vs)}$		$1389_{(s)}$	$905_{(m)}$	$880_{(m)}$	$390_{(m)}$
2	$(n\text{-}Bu_4N)_2[Ni(CPD)_2]$	$2180_{(vs)}$		$1427_{(vs)}$	$905_{(s)}$	$882_{(m)}$	$391_{(m)}$, $376_{(s)}$
3	$(n\text{-}Bu_4N)_2[Ni(CED)_2]$	$2188_{(s)}$	$1673_{(vs)}$	$1395_{(vs)}$	$920_{(s)}$		$383_{(w)}$, $340_{(vw)}$
4	$(n\text{-}Bu_4N)_2[Ni(CCED)_2]$	$2188_{(s)}$	$1640_{(vs)}$	$1425_{(vs)}$	$910_{(m)}$	$878_{(m)}$	$387_{(m)}$
5	$(n\text{-}Bu_4N)_2[Cu(CCPD)_2]$	$2185_{(vs)}$		$1411_{(vs)}$	$907_{(m)}$	$876_{(s)}$	$368_{(m)}$
6	$(n\text{-}Bu_4N)_2[Cu(CPD)_2]$	$2178_{(vs)}$		$1418_{(vs)}$	$910_{(sh)}$	$890_{(s)}$	$410_{(m)}$, $335_{(w)}$
7	$(Et_4N)_2[Cu(CED)_2]$	$2195_{(vs)}$	$1660_{(sh)}$,$1678_{(vs)}$	$1390_{(sh)}$	$928_{(s)}$	$907_{(s)}$	$335_{(m)}$
8	$(n\text{-}Bu_4N)_2[Cu(CCED)_2]$	$2192_{(vs)}$	$1640_{(vs)}$	$1421_{(vs)}$	$918_{(s)}$	$872_{(s)}$	$350_{(m)}$

vs, very strong; s, strong; m, medium; w, weak; vw, very weak; sh, shoulder; br, broad.

on the mode of interaction of the ligands and the structure of the compounds under consideration were obtained from their IR and the electronic excitation spectra.

3.1. Infrared spectra

The infrared spectra of the complexes have been interpreted in the light of earlier investigations [1a,10]. The dianion of the 1,1-dithiol contains the C═CS_2, C≡N and Y (Y = CN, Ph, phCl, COOEt, $CONH_2$) functional groups. The absorptions due to the multiple bond in each group are immediately distinguishable and identified with the very strong bands observed in specific regions of the spectrum. For instance, in K_2S_2C═C(CN)$CONH_2$ the ν(C≡N) and ν(C═O) bands appear at 2172 and 1646 cm^{-1}, respectively, while the ν(C═CS_2) band absorbs at 1340 cm^{-1}. Upon chelation

Table 5
Wavenumbers of the characteristic bands in the IR spectra of some mixed-ligand nickel(II) chelates, [Ni(enR)(S_2C═C(CN)Y]

	Compound	ν(N–H)	(C≡N)	ν(C═O)	ν(C═CS_2)	ν_{as}(CS_2)	ν_s(CS_2)	ν(Ni–N)	ν(Ni–S)
1	[Ni(dipyamH)*i*-MNT]	$3295_{(s)}$, $3250_{(m)}$, $3200_{(s)}$, $3140_{(s)}$	$2206_{(vs)}$		$1387_{(vs)}$	$944_{(m)}$	$901_{(s)}$	$470_{(m)}$	$390_{(m)}$
2	[Ni(bipy)CPD]		$2197_{(vs)}$		$1438_{(vs)}$	$903_{(m)}$		$488_{(w)}$	$405_{(w)}$
3	[Ni(C × NN)CPD]	$3360_{(s)}$, $3270_{(s)}$	$2192_{(vs)}$		$1435_{(vs)}$	$900_{(s,br)}$		$483_{(m)}$	$393_{(m)}$
4	[Ni(dipyamH)CPD]	$3310_{(s)}$, $3240_{(m)}$, $3210_{(s)}$, $3140_{(m)}$	$2192_{(vs)}$		$1438_{(vs)}$	$908_{(vs)}$		$495_{(w)}$	$393_{(w)}$
5	[Ni(BenB)CED]	$3190_{(s)}$, $3170_{(sh)}$	$2206_{(s)}$	$1683_{(vs)}$	$1416_{(sh)}$	$920_{(s,br)}$		$458_{(m)}$	$343_{(w)}$
6	[Ni(C × NN)CED]	$3360_{(s)}$, $3255_{(s)}$	$2222_{(s)}$	$1673_{(vs)}$	$1395_{(sh)}$	$930_{(s,br)}$		$498_{(m)}$	$388_{(m)}$
7	[Ni(PhenPh)CED]	$3180_{(s)}$	$2212_{(s)}$	$1655_{(vs)}$	$1423_{(vs,br)}$	$932_{(s)}$		$518_{(m)}$	$380_{(m)}$
8	Ni(ampy)CED]	$3300_{(s)}$, $3210_{(sh)}$	$2195_{(vs)}$	$1688_{(vs)}$	$1419_{(sh)}$	$926_{(s)}$	$916_{(sh)}$	$488_{(m)}$	$343_{(m)}$
9	[Ni(biby)CED]		$2214_{(s)}$	$1686_{(vs)}$	$1423_{(sh)}$	$928_{(s)}$	$918_{(sh)}$	$483_{(w)}$	$348_{(w)}$
10	[Ni(dipyamH)CED]	$3310_{(s)}$, $3250_{(m)}$, $3210_{(s)}$, $3150_{(m)}$	$2202_{(vs)}$	$1656_{(vs)}$	$1421_{(sh)}$	$933_{(s)}$	$921_{(sh)}$	$483_{(w)}$	$378_{(w)}$
11	[Ni(dipyamH)CCED]	$3300_{(s)}$, $3250_{(m)}$, $3200_{(s)}$, $3140_{(m)}$	$2210_{(vs)}$	$1643_{(vs)}$	$1418_{(vs)}$	$918_{(m)}$	$896_{(m)}$	$478_{(w)}$	$392_{(m)}$

vs, very strong; s, strong; m, medium; w, weak; vw, very weak; sh, shoulder; br, broad.

Table 6
Ligand field excitation bands in the electronic absorption spectra of some $(R_4N)_2$[M(S_2C═C(CN)$Y)_2$] (M = Ni, Cu) chelates

	Compound	Ligand field bands ($\tilde{\nu}$ (μm^{-1}))		
		Nujol	CH_2Cl_2	Pyridine
1	(*n*-$Bu_4N)_2$[Ni(CCPD)$_2$]	1.57	1.58 (95)[a]	1.58 (98)
2	(*n*-$Bu_4N)_2$[Ni(CPD)$_2$]	1.645	1.647 (250)	1.642 (210)
3	(*n*-$Bu_4N)_2$[Ni(CED)$_2$]	$1.66_{(sh)}$[b]	$1.64_{(sh)}$ (150)	$1.65_{(sh)}$ (160)
4	(*n*-$Bu_4N)_2$[Ni(CCED)$_2$]	1.580	1.590 (116)	16.00 (110)
5	(*n*-$Bu_4N)_2$[Cu(CCPD)$_2$]	$1.56_{(sh)}$	$1.56_{(sh)}$ (450)	$1.56_{(sh)}$ (455)
6	(*n*-$Bu_4N)_2$[Cu(CPD)$_2$]	$1.63_{(sh)}$	$1.63_{(sh)}$ (710)	1.650 (674)
7	$(Et_4N)_2$[Cu(CED)$_2$]	$1.60_{(sh)}$	$1.61_{(sh)}$ (670)	$1.61_{(sh)}$ (510)
8	(*n*-$Bu_4N)_2$[Cu(CCED)$_2$]	$1.55_{(sh)}$	$1.56_{(sh)}$ (650)	$1.56_{(sh)}$ (560)

[a] Values of the molar extinction coefficient.
[b] sh, shoulder.

Table 7
Ligand field excitation bands in the electronic absorption spectra of some mixed-ligand nickel(II) chelates, [Ni(enR)(S_2C═C(CN)Y]

	Compound	Ligand field bands ($\tilde{\nu}$ (μm^{-1}))			
		Nujol	DMSO	Pyridine	
1	[Ni(dipyamH)*i*-MNT]	$1.77_{(sh)}$[b]	1.567 (47)[a]	$1.60_{(sh)}$ (50)	1.113 (17)
2	[Ni(bipy)CPD]	$1.72_{(sh)}$	$1.54_{(sh)}$ (44)		
3	[Ni(C × NN)CPD]	$1.55_{(sh)}$	$1.66_{(sh)}$ (93)		
4	[Ni(dipyamH)CPD]	$1.76_{(sh)}$	1.767 (137)	$1.76_{(sh)}$ (125)	
5	[Ni(BenB)CED]	$1.75_{(sh)}$	$1.75_{(sh)}$ (68)		
6	[Ni(C × NN)CED]	$1.55_{(sh)}$	$1.61_{(sh)}$ (66)		
7	[Ni(PhenPh)CED]	$1.64_{(sh)}$	$1.59_{(sh)}$ (65)		
8	[Ni(ampy)CED]	$1.77_{(sh)}$	$1.80_{(sh)}$ (90)		
9	[Ni(bipy)CED]	$1.72_{(sh)}$	$1.72_{(sh)}$ (130)		
10	[Ni(dipyamH)CED]	$1.87_{(sh)}$	$1.77_{(sh)}$ (140)	$1.76_{(sh)}$ (180)	
11	[Ni(dipyamH)CCED]	$1.80_{(sh)}$	$1.61_{(sh)}$ (60)	$1.59_{(sh)}$ (55)	1.119 (16)

[a] sh, shoulder.
[b] Values of the molar extinction coefficient.

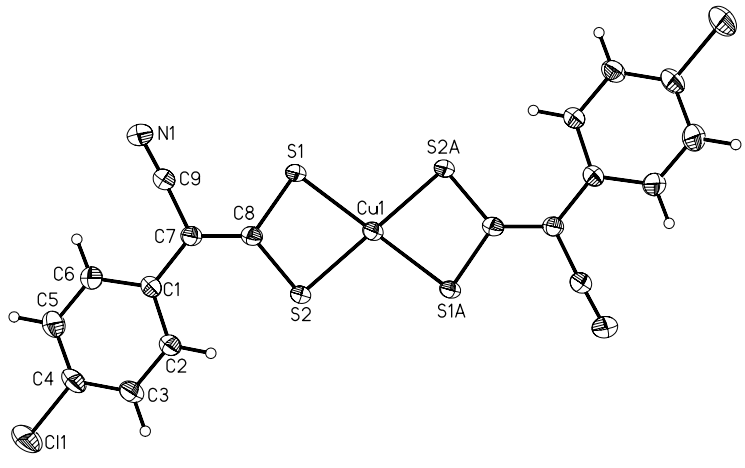


Fig. 2. Structure of $[Cu(CCPD)_2]^{2-}$, in the crystal with thermal ellipsoids at the 50% probability level.

of the dianions these bands are strongly shifted to higher wavenumbers (Tables 4 and 5) since in these planar ligands the extensive π-conjugated system permits a drift of electron density towards the sulfur atoms that results in a shortening of the C≡N, C=O and C=C bonds. The exact frequency of each band is influenced not only by the groups present in the 1,1-dithiolato dianion, but also by the donor strength of the chelated nitrogenous base. Actually, the frequency of the *ν*(C=O) vibration in the chelates [Ni(PhenPh)CED], [Ni(dipyam)CED], and in the complexes of the dithiolate CCED coincides with that of the corresponding free 1,1-dithiolato dianion, probably because of the enhanced double bond character of the bond between the carbonylic carbon atom and the oxygen and nitrogen atoms of the OEt and NH_2 groups. The asymmetric and symmetric stretching vibrations of the $=CS_2$ group generally appear in the 945–900 and the 920–870 cm^{-1} regions, respectively. The stretching vibration of the M–S bond is observed at 370(±30) cm^{-1}.

The absorptions occurring in the region ~3300 to 3200 cm^{-1} are due to the N–H stretching vibrations of partially substituted 1,2-diamines and are shifted to wavenumbers lower than those encountered in the free 1,2-diamines [23]. These shifts and the band near 490(±30) cm^{-1} suggest that the nitrogenous bases chelate, as expected. Bidentate coordination and chelation

Table 8
Selected bond lengths (Å) and bond angles (°) of $(n\text{-}Bu_4N)_2[Cu(CCPD)_2]$

Bond lengths (Å)	
Cu(1)–S(2A)	2.195(1)
Cu(1)–S(1A)	2.213(1)
Cl(1)–C(4)	1.752(2)
S(2)–C(8)	1.743(2)
C(1)–C(7)	1.479(3)
C(7)–C(9)	1.437(3)
Cu(1)–S(2)	2.195(1)
Cu(1)–S(1)	2.213(1)
S(1)–C(8)	1.755(2)
N(1)–C(9)	1.154(3)
C(7)–C(8)	1.378(3)
Bond angles (°)	
S(2A)–Cu(1)–S(1A)	78.39(2)
S(2A)–Cu(1)–S(1)	101.61(2)
C(8)–S(1)–Cu(1)	87.6(1)
C(6)–C(1)–C(7)	120.4(2)
C(4)–C(3)–C(2)	119.9(2)
C(3)–C(4)–Cl(1)	119.5(2)
C(8)–C(7)–C(9)	116.0(2)
C(9)–C(7)–C(1)	115.4(2)
C(7)–C(8)–S(1)	124.6(2)
N(1)–C(9)–C(7)	177.5(2)
S(2)–Cu(1)–S(1A)	101.61(2)
S(2)–Cu(1)–S(1)	78.39(2)
C(8)–S(2)–Cu(1)	88.5(1)
C(2)–C(1)–C(7)	123.2(2)
C(3)–C(4)–C(5)	120.3(2)
C(5)–C(4)–Cl(1)	120.2(2)
C(8)–C(7)–C(1)	128.6(2)
C(7)–C(8)–S(2)	129.8(2)
S(2)–C(8)–S(1)	105.5(1)

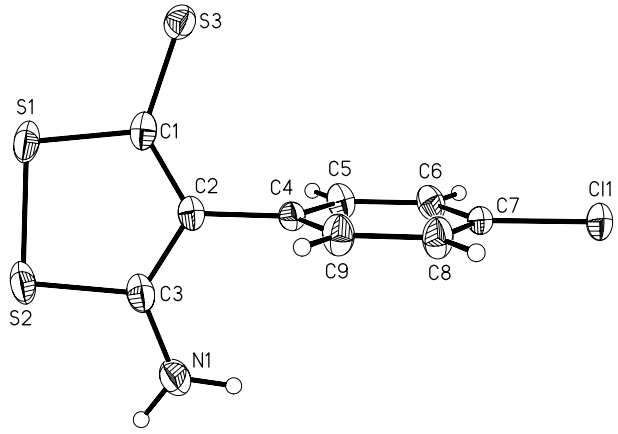


Fig. 3. Structure of ACDT in the crystal with thermal ellipsoids at the 50% probability level.

of the dianion of the 1,1-dithiol suggest the band at 370(±30) cm^{-1} and the bands due to the asymmetric and symmetric vibrations of the $=CS_2$ fragment (Tables 4, 5).

3.2. Electronic excitation spectra

The electronic excitation spectra of the chelates were studied in the visible and the near-infrared region, in the solid state and in solution employing solvents with very different donor ability. Because of the low solubility of the majority of the mixed-ligand complexes, polar solvents with appreciable donor strength were used to obtain the solution spectra. The most interesting feature of these spectra is the band in the region 1.55–1.66 μm^{-1} and for mixed-ligand complexes 1.55–1.87 μm^{-1} (Tables 6 and 7), which may be ascribed to a ligand field (LF) transition for reasons of intensity and energetic considerations.

The energy of the LF band of the homoleptic complexes depends slightly on the nature of dithiolate ligands. The dithiolate ligand field strength (CCPD ∼ CCED < CED ∼ CPD) is related to the ability of their substituents Y to resist electron drift towards the sulfur atoms. The LF band of the complexes has almost the same energy, both in their solid state spectra and those employing solvents with different donor ability (CH_2Cl_2, DMSO, CH_3CN and pyridine). This is probably due to the nucleophilic interaction of the polar solvent molecules with the ligand, leaving the metal unaffected.

In the solid state spectra of the mixed-ligand chelates, the change in the excitation energy may be accounted for by taking into consideration the influence of the substituents Y on the strength of the ligand field (LF) in the chelates [Ni(dipyamH)S_2C=C(CN)Y]. In the diamagnetic compounds of the dianions *i*-MNT, CCED and CED, the LF excitation energy reflects the ability of the Y group to resist electron delocalization towards their sulfur atoms (*i*-MNT ⩾ CCED > CED). The low LF excitation energy of [Ni(dipyamH)CPD] is not consistent with the above explanation since the electron withdrawing ability of the phenyl group is rather restricted. However, the magnetic behavior of the [Ni(enR)CPD] chelates is at variance with the behavior of the other nickel(II) chelates and suggests intermolecular interactions, presumably along the z axis, that change the symmetry of the field in which the nickel(II)

Table 9
Selected bond lengths (Å) and bond angles (°) of ACDT with e.s.d.s in parentheses

Bond lengths (Å)	
S(1)–C(1)	1.737(2)
S(2)–C(3)	1.748(2)
Cl(1)–C(7)	1.747(2)
C(1)–C(2)	1.404(3)
C(2)–C(4)	1.491(2)
S(1)–S(2)	2.070(1)
S(3)–C(1)	1.688(2)
N(1)–C(3)	1.338(3)
C(2)–C(3)	1.396(2)
Bond angles (°)	
C(1)–S(1)–S(2)	96.8(1)
C(2)–C(1)–S(3)	130.9(2)
S(3)–C(1)–S(1)	114.0(1)
C(3)–C(2)–C(4)	120.9(2)
N(1)–C(3)–C(2)	125.1(2)
C(2)–C(3)–S(2)	117.5(2)
C(5)–C(4)–C(2)	120.8(2)
C(8)–C(7)–Cl(1)	119.0(2)
C(3)–S(2)–S(1)	93.6(1)
C(2)–C(1)–S(1)	115.1(2)
C(3)–C(2)–C(1)	116.9(2)
C(1)–C(2)–C(4)	122.1(2)
N(1)–C(3)–S(2)	117.4(2)
C(9)–C(4)–C(2)	120.1(2)
C(6)–C(7)–Cl(1)	119.5(2)

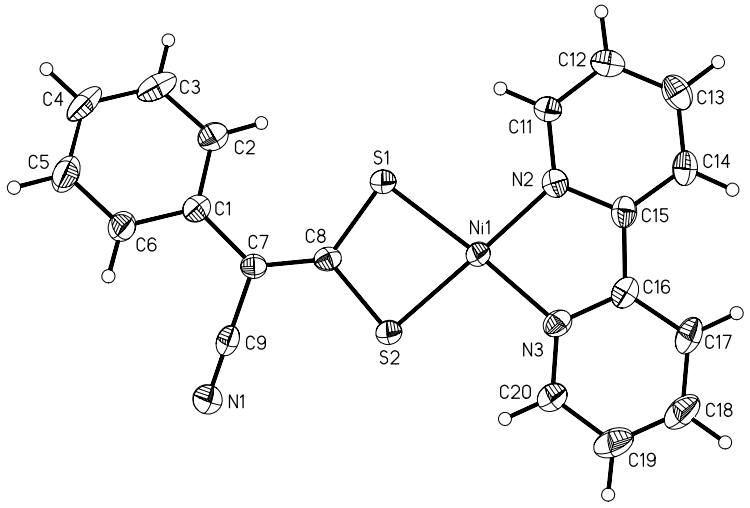


Fig. 4. Structure of [Ni(bipy)CPD] in the crystal with thermal ellipsoids at the 50% probability level.

exists. The existence of axial donor-acceptor interactions is supported by the red shift of the LF band of the other [Ni(dipyamH)(S_2C=C(CN)Y)] chelates when the absorption spectra are obtained in solvents of enhanced donicity and the appearance of an additional band at $\sim$1.1 μm^{-1}, when employing pyridine as solvent. In the case of the compound [Ni(dipyam)CPD] the energy of the LF excitation remains unaltered upon dissolution in DMSO or pyridine. This suggests that the axial S···Ni···S interactions that are eliminated upon dissolution are compensated by the nickel–solvent interactions.

The strength of the field applied by the nitrogenous base is nicely mirrored in the energy of the LF bands in the [Ni(enR)CED] chelates. The weak donating ability of dipyamH does not contribute significantly to the electron density on the nickel atom thus permitting coordination of strong polar molecules, i.e. pyridine or DMSO. On the other hand, the powerful electron donor C × NN upon ligation increases the electron population on the sulfur atoms. Consequently, the intermolecular axial interactions are enhanced while the energy of the transitions within the *d* manifold diminishes. The intermolecular interactions explain the magnetic behavior of the [Ni(enR)S_2C=(CN)Y] chelates and the blue shift observed upon dissolution when the axial interactions are disrupted. In the case of compounds with nitrogenous bases possessing intermediate donor ability, such as bipy and BenB, the energy of the LF transition is the same in solution and in the solid state. Proof that the NiN_2S_2 chromophore is planar was acquired from the X-ray structure determination of [Ni(bipy)CPD].

3.2.1. Description of the structure of $(n\text{-}Bu_4N)_2$-[Cu(CCPD)$_2$]

The structure of the anion is shown in Fig. 2, while selected bond lengths and angles are given in Table 8. There are three molecules per unit cell. The copper atom lies on a crystallographic center of symmetry which requires the CuS_4 unit to be strictly planar. This plane forms a small dihedral angle (1.35°) with the best plane through the S_2C=C–CN fragment of the CCPD ligand. This conformation has been observed in many sulfur chelates which contain a planar MS_4 group [24,6c]. The plane of the phenyl ring makes an angle of 8.87° with the CuS_4 plane. The average Cu–S bond length (2.204 Å) in the present structure is shorter by $\sim$0.099 Å to that reported [21a] for the only other four-coordinated, S-bonded Cu(II) complex with a 1,1-dithiolate chelate, (2.303 Å) in $[Bu_4N]_2$[Cu(*i*-MNT)$_2$], which most probably accounts for the different ability of the ph-Cl and C≡N groups of the dithiolate ligands to resist the electron delocalization towards the sulfur atoms. A distorted square planar coordination environment around the copper ion is evident in the S–Cu–S angles, 78.39(2)° and 101.61(2)°, respectively. There is no intermolecular Cu–S or Cu–Cu interaction in the solid state, with the shortest distances being 10.366 and 9.523 Å, respectively. This feature might be a result of the electronic effects and the unit cell packing caused by the bulky quaternary ammonium cations which occupy much of the space and prevent any intermolecular Cu–S or Cu–Cu interaction [21a].

3.2.2. Description of the structure of ACDT

A thermal ellipsoid drawing of the novel sulfur-rich ligand is presented in Fig. 3. The selected bond lengths

Table 10
Selected bond lengths (Å) and angles (°) for [Ni(bipy)CPD] (e.s.d.s are given in parentheses)

Bond lengths (Å)	
Ni(1)–N(2)	1.915(3)
Ni(1)–S(2)	2.173(2)
S(1)–C(8)	1.741(4)
N(1)–C(9)	1.149(5)
C(7)–C(8)	1.367(6)
N(2)–C(11)	1.362(5)
C(15)–C(16)	1.464(6)
N(3)–C(16)	1.351(6)
Ni(1)–N(3)	1.923(3)
Ni(1)–S(1)	2.188(2)
S(2)–C(8)	1.750(3)
C(1)–C(7)	1.486(5)
C(7)–C(9)	1.442(6)
N(2)–C(15)	1.364(5)
N(3)–C(20)	1.346(5)
C(16)–C(17)	1.392(5)
Bond angles (°)	
N(2)–Ni(1)–N(3)	83.4(2)
N(3)–Ni(1)–S(2)	98.0(2)
N(3)–Ni(1)–S(1)	176.2(2)
C(8)–S(1)–Ni(1)	88.8(2)
C(6)–C(1)–C(7)	119.6(4)
C(8)–C(7)–C(9)	115.1(3)
C(9)–C(7)–C(1)	115.8(4)
C(7)–C(8)–S(2)	124.5(3)
N(1)–C(9)–C(7)	179.0(5)
C(11)–N(2)–Ni(1)	126.9(3)
C(15)–N(2)–Ni(1)	114.9(3)
N(2)–C(15)–C(16)	112.9(4)
C(20)–N(3)–C(16)	118.8(3)
C(16)–N(3)–Ni(1)	114.4(2)
N(3)–C(16)–C(15)	114.2(3)
N(2)–Ni(1)–S(2)	178.5(2)
N(2)–Ni(1)–S(1)	100.4(1)
S(2)–Ni(1)–S(1)	78.2(1)
C(8)–S(2)–Ni(1)	89.0(2)
C(2)–C(1)–C(7)	122.7(4)
C(8)–C(7)–C(1)	129.2(3)
C(7)–C(8)–S(1)	131.5(3)
S(1)–C(8)–S(2)	104.0(2)
C(11)–N(2)–C(15)	118.1(4)
N(2)–C(15)–C(14)	121.9(4)
N(2)–C(11)–C(12)	121.7(4)
C(14)–C(15)–C(16)	125.2(4)
C(20)–N(3)–Ni(1)	126.7(3)
N(3)–C(16)–C(17)	121.4(4)
N(3)–C(20)–C(19)	122.2(5)

Table 11
Experimental average bond lengths (Å) of some [Ni(enR)S_2C=C(CN)Y] chelates

	Compound	Average bond distance (Å)				Ref.
		⟨S_2C=C⟩	⟨C–S⟩	⟨Ni–S⟩	⟨Ni–N⟩	
1	[Ni(Et_2en)*i*-MNT]	1.384(3)	1.716(3)	2.199(8)	1.955(2)	[10a]
2	[Ni(Et_2en)CPD]	1.367(3)	1.741(3)	2.179(1)	1.965(2)	[28]
3	[Ni(bipy)CPD]	1.367(6)	1.746(3)	2.181(2)	1.919(3)	this work
4	[Ni(Me_4en)CPD]	1.366(5)	1.733(3)	2.178(1)	1.974(3)	[28]

and angles are given in Table 9. There are three crystallographically independent molecules in the asymmetric unit which differ in the torsion angles between both rings. Three carbon atoms link with two sulfur atoms forming a five-membered ring. The observed C–S distances are smaller than expected for a C–S single bond (1.82 Å) [25]. The exocyclic S3–Cl bond length is 1.688(2) Å which is longer than the corresponding distance of 1.661(8) Å in dmit ligand [4b] but shorter than the distance found in another dmit ligand [18a]. The S–S bond distance, 2.070(1) Å, is within the normal range (2.007(3)–2.396(3) Å) found for sulfur-rich dithiolate metal complexes [21a]. The C1–C2 bond length, 1.404(3) Å, is similar to the corresponding bond distances in salts of the *i*-MNT ligand [26]. All observed intramolecular bond lengths in the sulfur ring indicate delocalization of the π-electron system.

3.2.3. Description of the structure of [Ni(bipy)CPD]

In the unit cell there are six nickel atoms (Fig. 1(a)). In the immediate vicinity of each nickel atom exist two sulfur and, at shorter distance, two nitrogen atoms (Fig. 4). The sulfur atoms of the dianion of 1,1-dithiol form a bite angle of 78.2(1)° while the bite angle of the 2,2′-bipyridine is 83.4(2)° and reaffirm that the bidentate ligands chelate. Intramolecular bond distances and angles are given in Table 10. The nitrogen atoms are in the plane defined by nickel and the sulfur atoms. In the same plane lie the atoms of the ethene group and the cyano group. The phenyl group, however, forms a dihedral angle of 17.5° with the plane of the NiN_2S_2 chromophore probably because of steric and electronic effects. The S_2C=C–CN fragment of the ligand (CPD) assumes a planar conformation and the bond distances indicate extensive π-conjugation. Actually the C(8)–C(7) distance is characteristic of a bond localized between two C(sp^2) atoms [27], whilst the lengths of the intervening C(7)–C(9) bond and the terminal N≡C bond suggest delocalization. The mean deviation of the 2,2′-bipyridine from planarity is 0.0281 Å, and the torsion angle of the two ring with the chelation ring ($NiN_2C_{15}C_{16}N_3$) is 0.5°.

It is of interest to compare the average lengths of the characteristic bonds in [Ni(bipy)CPD] and the reported chelates [Ni(Et_2en)*i*-MNT] [10a], [Ni(Et_2en)CPD] and [Ni(Me_4en)CPD] [28]. In these compounds the S_2C=C, C–S, Ni–S and Ni–N bond lengths (Table 11) suggest that an electron drift from the X and Y substituent groups of the 1,1-dithiolato ligands towards the sulfur atoms takes place and becomes more intense in the case of the CPD chelate. Consequently, the intensity of the nickel–nitrogen interaction diminishes.

4. Supplementary material

Crystallographic data have been deposited with the Cambridge Crystallographic Data Centre, CCDC Nos. 236938–236940 for compounds ACDT, (n-Bu_4N)$_2$[Cu(CCPD)$_2$], [Ni(bipy)CPD], respectively. Copies of the data can be obtained free of charge on application to The Director, CCDC, 12 Union Road, Cambridge, CB2 1EZ, UK, fax: +44 1223 366 033, e-mail: deposit@ccdc.ac.uk or on the web www: http://www.ccdc.cam.ac.uk.

Acknowledgments

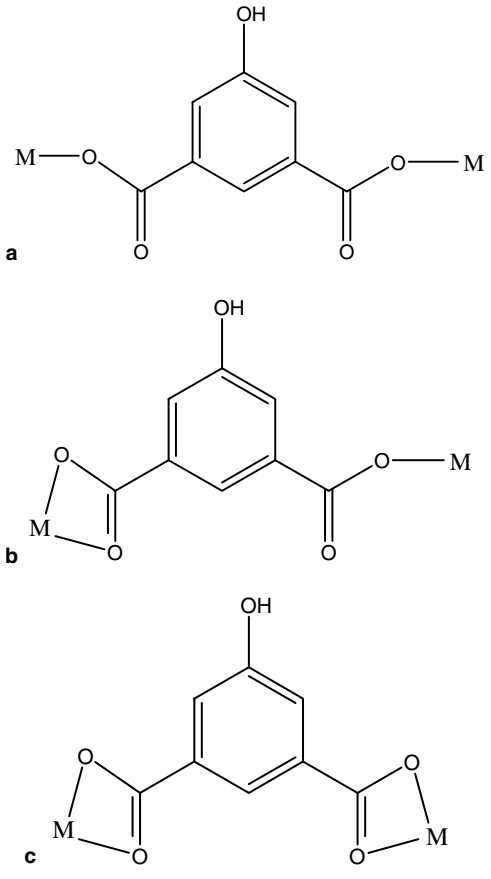
The efforts and cooperation of Professor Dr. Wolfgang Bensch, The Director of the Institute of Inorganic Chemistry, Christain–Albrechts University of Kiel in Germany, are highly appreciated and acknowledged. We are also very grateful for Dr. Christian Näther and Inke Jeß from the University of Kiel for the structure determination of ACDT, (n-Bu_4N)$_2$[Cu(CCPD)$_2$] and [Ni(bipy)CPD].

References

[1] (a) D. Coucouvanis, Prog. Inorg. Chem. 11 (1970) 233;
(b) D. Coucouvanis, Prog. Inorg. Chem. 26 (1979) 301;
(c) R. Burns, F.P. McCullough, C.A. McAuliffe, Adv. Inorg. Chem. 23 (1980) 211;
(d) P.J. Nieuwenhuizen, S. Tima, J.G. Haasnoot, A.L. Spek, J. Reedijk, Chem.-Eur. J. 3 (1997) 1846;
(e) P.J. Nieuwenhuizen, A.W. Ehlers, J.G. Haasnoot, S.R. Janse, J. Reedijk, E.J. Baerends, J. Am. Chem. Soc. 121 (1999) 163;
(f) L. Hart, P. O'Brien, S.R.P. Silva, J.R. Walsh, I.M. Watson, J. Cryst. Growth 167 (1996) 133;
(g) P. O'Brien, J.R. Walsh, I.M. Watson, M. Motevalli, L. Henriksen, J. Chem. Soc., Dalton Trans. (1996) 2491;
(h) R.D. Pike, H. Cui, R. Kershaw, K. Dwight, A. Wold, T.N. Blanton, A.A. Wernberg, J.H. Gysling, Thin Solid Films 224 (1993) 221.

[2] (a) J. Sandström, I. Wennerbeck, Acta Chem. Scand. 24 (1970) 1191;
(b) F.P. Colonna, G. Distefana, J. Sandström, U. Sjöstrand, J. Chem. Soc., Perkin Trans. 2 (1978) 279;
(c) D. Smith, P.J. Taylor, J. Chem. Soc., Perkin Trans. 2 (1979) 1376;
(d) K. Mohanalingam, M. Nethaji, P.K. Das, J. Mol. Struct. 378 (1996) 177;
(e) A. Islam, H. Sugihahara, K. Hara, L.P. Singh, R. Katoh, M. Yanagida, Y. Takahashi, S. Murata, H. Arakawa, J. Photochem. Photobiol. A: Chem. 145 (2001) 135;
(f) J. Vicente, M.T. Chicote, S. Huertas, P.G. Jones, Inorg. Chem. 42 (2003) 4268.
[3] (a) M. Hong, R. Cao, H. Kawaguchi, K. Tatsumi, Inorg. Chem. 41 (2002) 4824;
(b) J.A. Zuleta, M.S. Burberry, R. Eisenberg, Coord. Chem. Rev. 97 (1990) 47;
(c) J.M. Bevilacqua, J.A. Zuleta, R. Eisenberg, Inorg. Chem. 32 (1993) 3689;
(d) J.M. Bevilacqua, R. Eisenberg, Inorg. Chem. 33 (1994) 1886.
[4] (a) W. Paw, S.D. Cummings, M.A. Mansour, W.B. Connick, D.K. Geiger, R. Eisenberg, Coord. Chem. Rev. 171 (1998) 125;
(b) D.Y. Noh, E.M. Seo, H.J. Lee, H.Y. Jang, M.G. Choi, Y.H. Kim, J. Hong, Polyhedron 20 (2001) 1939.
[5] (a) C.W. Liu, B.J. Liaw, J.C. Wang, T.C. Keng, Inorg. Chem. 39 (2000) 1329;
(b) C.W. Liu, C. McNeal, J.P. Fackler Jr., J. Cluster Sci. 7 (1996) 395;
(c) W.P. Su, M.C. Hong, R. Cao, J.T. Chen, D.X. Wu, H.Q. Liu, J.X. Lu, Inorg. Chim. Acta 267 (1998) 313;
(d) F.J. Hollander, D. Coucouvanis, J. Am. Chem. Soc. 96 (1974) 5646;
(e) F.J. Hollander, D. Coucouvanis, J. Am. Chem. Soc. 99 (1977) 6268;
(f) L.E. McCandlish, E.C. Bissel, D. Coucouvanis, J.P. Fackler Jr., K. Knox, J. Am. Chem. Soc. 90 (1968) 7357;
(g) P.J.M.W.L. Birker, G.G. Verschoor, J. Chem. Soc., Chem. Commun. (1981) 322.
[6] (a) F.J. Hollander, R. Pedelty, D. Coucouvanis, J. Am. Chem. Soc. 96 (1974) 4032;
(b) F.J. Hollander, M.L. Caffery, D. Coucouvanis, J. Am. Chem. Soc. 96 (1974) 4682;
(c) D. Coucouvanis, F.J. Hollander, M.L. Caffery, Inorg. Chem. 15 (1976) 1853.
[7] (a) M.C. Hong, W.P. Su, R. Cao, F.L. Jiang, H.Q. Liu, J.X. Lu, Inorg. Chem. Acta 274 (1998) 229;
(b) H. Dietrich, W. Storck, G. Manecke, J. Chem. Soc., Chem. Commun. (1982) 1036;
(c) M.T. Garland, J.F. Halet, J.Y. Saillard, Inorg. Chem. 40 (2001) 3342.
[8] (a) W. Su, M. Hong, J. Weng, Y. Liang, Y. Zhao, R. Cao, Z. Zhou, A.S.C. Chan, Inorg. Chim. Acta 331 (2002) 8;
(b) D.B. Mitzi, S. Wang, C.A. Field, C.A. Chess, A.M. Guloy, Science 267 (1995) 1473;
(c) S. Wang, D.B. Mitzi, C.A. Field, A. Guloy, J. Am. Chem. Soc. 117 (1995) 5297;
(d) N. Matsumoto, Y. Sunatsuki, H. Miyasaka, Y. Hashimoto, D. Luneau, J.P. Tuchagues, Angew. Chem. Int. Ed. 38 (1999) 171;
(e) S. Triki, J.S. Pala, M. Decoster, P. Molinie, L. Toupet, Angew. Chem. Int. Ed. 38 (1999) 113;
(f) J.S. Miller, A.J. Epstain, Chem. Commun. (1998) 1319;
(g) W.E. Buschmann, A.M. Arit, J.S. Miller, Angew. Chem. Int. Ed. 37 (1998) 781.
[9] (a) O.M. Yaghi, H. Li, J. Am. Chem. Soc. 118 (1996) 295;
(b) D. Venkataraman, G.B. Gardner, S. Lee, J.S. Moore, J. Am. Chem. Soc. 117 (1995) 11600;
(c) L. Carlucci, G. Ciani, D.M. Proserpio, A. Soroni, J. Am. Chem. Soc. 117 (1995) 4562;
(d) B.F. Hoskins, R. Robson, J. Am. Chem. Soc. 112 (1990) 1546.
[10] (a) H.H. Alkam, A. Hatzidimitriou, C.C. Hadjikostas, C. Tsiamis, Inorg. Chim. Acta 256 (1997) 41;
(b) C.C. Hadjikosta, H. Alkam, P.D. Akrivos, E.S. Raper, J.R. Creighton, Inorg. Chim. Acta 271 (1998) 195;
(c) C.C. Hadjikostas, H.H. Alkam, C.A. Bolos, P.C. Christidis, Polyhedron 20 (2001) 395.
[11] W.R. Hatchard, J. Org. Chem. 29 (1964) 660.
[12] K.A. Jensen, L. Henriksen, Acta Chem. Scand. 22 (1968) 1107.
[13] G.M. Sheldrick, Acta Crystallogr., Sect. A 46 (1990) 467.
[14] G.M. Sheldrick, SHELXL-97, Program for the Refinement of Crystal Structures, University of Göttingen, Göttingen, Germany, 1997.
[15] (a) F.A. Cotton, G. Wilkinson, Advanced Inorganic Chemistry, 5th ed., John Wiley and Sons, New York, 1988;
(b) F.A. Cotton, G. Wilkinson (Eds.), Comprehensive Coordination Chemistry, vol. 5, Pergamon Press, Oxford, 1987.
[16] A. Bondi, J. Phys. Chem. 68 (1964) 441.
[17] (a) D.S. Brown, A.G. Massey, D.A. Wickens, Acta Crystallogr., Sect. B 34 (1978) 1695;
(b) E.R.T. Tiekink, J. Organomet. Chem. 303 (1986) C53;
(c) S.S. Batsanov, J. Mol. Struct. (THEOCHEM) 468 (1999) 151;
(d) J.S. Casas, M.S. Garcia-Tasende, J. Sordo, Coord. Chem. Rev. 193–195 (1999) 283.
[18] (a) C.S. Lai, E.R.T. Tiekink, Cryst. Eng. Commun. 5 (44) (2003) 253;
(b) J.S. Casas, E.E. Castellano, J. Ellena, I. Haiduc, A. Sanchez, R.F. Semeniuc, J. Sordo, Inorg. Chim. Acta 329 (2003) 71;
(c) M.K. Singh, Indian J. Chem. 30 A (1991) 1070.
[19] (a) R.K. Brown, T.J. Bergendahl, J.S. Wood, J.H. Waters, Inorg. Chim. Acta 68 (1983) 79;
(b) M.J. Cox, E.R.T. Tiekink, Z. Kristallogr. 214 (1999) 571;
(c) J.S. Casac, A. Castineiras, A. Sanchez, J. Sordo, E.M. Vazquez-Lopez, J. Organomet. Chem. 468 (1994) 1.
[20] (a) M. Bonamico, G. Dessy, A. Mugnoli, A. Vaciago, L. Zambonelli, Acta. Crystallogr. 19 (1985) 886;
(b) M.J. Cox, E.R.T. Tiekink, Z. Kristallogr. 214 (1999) 486;
(c) E.R.T. Tiekink, Cryst. Eng. Commun. 5 (2003) 101;
(d) M.J. Cox, E.R.T. Tiekink, Rev. Inorg. Chem. 17 (1997) 1.
[21] (a) C.W. Liu, R.J. Staples, J.P. Fackler, Coord. Chem. Rev. 174 (1998) 147;
(b) C.S. Lai, E.R.T. Tiekink, Acta Crystallogr., Sect. E 58 (2002) m674;
(c) C.S. Lai, E.R.T. Tiekink, Appl. Organomet. Chem. 17 (2003) 194.
[22] (a) W.E. van Zyl, J.M. López-de-Luzuriaga, J.P. Fackler Jr., J. Mol. Struct. 516 (2000) 99;
(b) J. Zukerman-Schpector, E.M. Vazquez-Lopez, A. Sanchez, J.S. Casas, J. Sordo, J. Organomet. Chem. 405 (1991) 67;
(c) E.M. Vazquez-Lopez, A. Castineiras, A. Sanchez, J.S. Casas, J. Sordo, J. Crystallogr. Spectrosc. Res. 22 (1992) 403.
[23] E. Sacher, Spectrochim. Acta, Part A 43 (1987) 747.
[24] (a) D. Coucouvanis, N.C. Baenziger, S.M. Johnson, Inorg. Chem. 13 (1974) 1191;
(b) R.H. Holm, M.J. O'Conner, Prog. Inorg. Chem. 14 (1972) 241;
(c) D. Coucouvanis, N.C. Baenziger, S.M. Johnson, J. Am. Chem. Soc 95 (1973) 3875.
[25] M. Dräger, Z. Anorg. Allg. Chem. 428 (1977) 243.
[26] (a) H.-U. Hummel, Acta Crystallogr. C41 (1985) 1591;
(b) H.-U. Hummel, Acta Crystallogr. C43 (1987) 41.
[27] A.J. Finney, M.A. Hitchman, C.L. Raston, G.L. Rowbottom, A.H. White, Aust. J. Chem. 34 (1981) 2159.
[28] H.H. Alkam, Ph.D. Thesis, Inorganic Chemistry, Aristotle University of Thessaloniki, 1996.

it can adopt different conformations to take part in coordination [21–24]. (2) The aim of combining OH-H_2BDC into the reaction system is to simplify the control and modulation of the final results, because the deprotonated carboxylate groups, which possess rich coordination modes (Scheme 1), may act as anionic groups and afford neutral metal-organic frameworks. (3) The hydroxyl group (–OH) can provide hydrogen bonding interactions with other groups and further stabilize the structures. On the other hand, the architectures from mixed ligands of bpp and di- or poly-carboxylate ligands, to our knowledge, are still rare to date [20,25,26], although some metal-organic frameworks from the direct assembly of bpp and metal ions have been investigated [22–24]. Herein, we wish to report the syntheses and characterizations of three interpenetrated coordination polymers, $\{[Co(bpp)(OH\text{-}BDC)]\cdot H_2O\}_n$ (**1**), $[Ni(bpp)_{1.5}(H_2O)(OH\text{-}BDC)]_n$ (**2**) and $\{[Cd(bpp)(H_2O)(OH\text{-}BDC)]\cdot 2H_2O\}_n$ (**3**), assembly from bpp, OH-H_2BDC with Co^{II}, Ni^{II} and Cd^{II} ions, respectively. All of the three compounds display interpenetrated structures. Exo-bidentate bpp in **1** and **3** adopts a TG conformation, while bpp in **2** acts as a terminal and exo-bidentate ligand with TT and TG conformations, respectively.



Scheme 1. The coordination modes of OH-BDC in compounds **1**–**3**.

2. Experimental

2.1. Materials and physical measures

1,3-bis(4-pyridyl)propane and 5-hydroxyisophthalic acid were purchased from Aldrich and used without further purification, all the other reagents were commercially available and used as purchased. Thermal analyses were performed using a TGA/SDTA851 instrument with a heating rate of 15 °C/min in a nitrogen stream. IR spectra as KBr disks were recorded on a Magna 750 FT–IR spectrophotometer. Elementary analyses were carried out by the elementary analysis group of this institute on an Elementary Vario ELIII analyzer.

2.2. Syntheses of the compounds

2.2.1. Preparation of $\{[Co(bpp)(OH\text{-}BDC)]\cdot H_2O\}_n$ (**1**)

A mixture of $Co(NO_3)_2\cdot 6H_2O$ (0.058 g, 0.20 mmol), 5-hydroxyisophthalic acid (0.032 g, 0.20 mmol), 1,3-bis(4-pyridyl)propane (0.040 g, 0.20 mmol) and NaOH (0.016 g, 0.40 mmol) in distilled water (18 mL) was sealed in a 25 mL stainless reactor with a Teflon liner and heated to 165 °C for 96 h. After cooling to room temperature over 24 h, cube-shaped red crystals of **1** were obtained. Yield: 41%. Elementary *Anal*. Calc. for $C_{21}H_{20}CoN_2O_6$ (455.32): C, 55.40; H, 4.43; N, 6.15. Found: C, 55.38; H, 4.51; N, 6.11%. IR (KBr, cm^{-1}): 3400 (m), 2927 (w), 1615 (s), 1575 (vs), 1401 (vs), 1373 (s), 1276 (s), 1018 (m), 785 (s), 723 (s), 519 (m).

2.2.2. Preparation of $[Ni(bpp)_{1.5}(H_2O)(OH\text{-}BDC)]_n$ (**2**)

A mixture of $Ni(NO_3)_2\cdot 6H_2O$ (0.073 g, 0.25 mmol), 5-hydroxyisophthalic acid (0.045 g, 0.25 mmol), 1,3-bis(4-pyridyl)propane (0.050 g, 0.25 mmol) and NaOH (0.020 g, 0.50 mmol) in distilled water (18 mL) was sealed in a 25 mL stainless reactor with a Teflon liner and heated to 170 °C for 96 h. After cooling to room temperature over 24 h, block green crystals of **2** were obtained. Yield: 64%. Elementary *Anal*. Calc. for $C_{27.5}H_{27}NiN_3O_6$ (554.23): C, 59.60; H, 4.91; N, 7.58. Found: C, 59.62; H, 5.02; N, 7.49%. IR (KBr, cm^{-1}): 3354 (w), 1616 (s), 1562 (vs), 1452 (s), 1412 (vs), 1357 (vs), 1277 (m), 1068 (m), 800 (s), 727 (s), 523 (m).

2.2.3. Preparation of $\{[Cd(bpp)(H_2O)(OH\text{-}BDC)]\cdot 2H_2O\}_n$ (**3**)

A mixture of $Cd(NO_3)_2\cdot 4H_2O$ (0.077g, 0.25 mmol), 5-hydroxyisophthalic acid (0.045 g, 0.25 mmol), 1,3-bis(4-pyridyl)propane (0.050 g, 0.25 mmol) and NaOH (0.020 g, 0.50 mmol) in distilled water (18 mL) was sealed in a 25 mL stainless reactor with a Teflon liner and heated to 170 °C for 96 h. After cooling to room

temperature over 24 h, block yellow crystals of **3** were obtained. Yield: 45%. Elementary *Anal.* Calc. for $C_{21}H_{24}CdN_2O_8$ (544.82): C, 46.30; H, 4.44; N, 5.14. Found: C, 46.31; H, 4.39; N, 5.18%. IR (KBr, cm^{-1}): 3385 (w), 1616 (s), 1554 (vs), 1427 (s), 1377 (vs), 1277 (m), 1227 (m), 1016 (m), 978 (w), 779 (s), 737 (s), 575 (m).

2.2.4. X-ray crystallographic study

Measurement of **1** was conducted on a Rigaku Mercury CCD diffractometer with graphite monochromated Mo Kα radiation ($\lambda = 0.71073$ Å). Reflections (14335) were collected at −100 °C, of which 4327 reflections were unique [27]. Intensity data for **2** and **3** were measured on a Siemens Smart CCD diffractometer with graphite-monochromated Mo Kα radiation ($\lambda =$ 0.71073 Å) at room temperature, the empirical absorption corrections were applied by using the SADABS program [28]. The structures for **1**–**3** were solved by direct methods [29] and refined on F^2 by full-matrix least-squares using the SHELXL-97 program package [30]. The positions of H atoms were generated geometrically (C–H bond fixed at 0.96 Å), assigned isotropic thermal parameters and allowed to ride on their parent carbon atoms before the final cycle of refinement. For **2**, the carbon atom (C15) is handled as disordered at two positions each with an occupancy of 50%. Crystal data and structure determination summaries for **1**–**3** are summarized in Table 1, selected bonds and angles in Table 2.

3. Results and discussion

3.1. Syntheses and characterizations

Compounds **1**–**3** were synthesized through the hydrothermal reactions of bpp, OH-H_2BDC with Co^{II}, Ni^{II} and Cd^{II} salts, respectively. Similar to the previous reports by us and some other groups, the –OH group of HO-H_2BDC is not involved in coordination to the transition metal ions and only serves as a donor for hydrogen bonds to stabilize the structures of **1**–**3** (see below), however, the –OH group as an electron-donating group may influence the self-assembly process although the reaction mechanism still remains unclear, because the expected results were not obtained when using *m*-isophthalic acid (H_2BDC) instead of HO-H_2BDC under the same hydrothermal condition. The IR spectra of the three compounds exhibit strong characteristic vibrational bands of the carboxylate groups. For **1**, the characteristic bands of the carboxylate groups are shown at 1575 cm^{-1} for the antisymmetric stretching band and

Table 1
Crystallographic data for compounds **1**–**3**

	1	**2**	**3**
Empirical formula	$C_{21}H_{20}CoN_2O_6$	$C_{27.5}H_{27}N_3NiO_6$	$C_{21}H_{24}CdN_2O_8$
Formula weight	455.32	554.23	544.82
T (K)	173(2)	293(2)	293(2)
Wavelength (Å)	0.71073	0.71073	0.71073
Crystal system	monoclinic	monoclinic	monoclinic
Space group	$P2_1/n$	$P2_1/n$	$C2/c$
a (Å)	10.96(5)	10.1547(2)	16.6695(11)
b (Å)	10.90(3)	17.8222(5)	17.1742(11)
c (Å)	16.29(5)	14.2077(3)	19.0262(12)
β (°)	103.806(14)	91.89	108.028(1)
V (Å^3)	1891(11)	2569.91(10)	5179.5(6)
Z	4	4	8
D_{calc} (Mg m^{-3})	1.599	1.432	1.397
Absorption coefficient (mm^{-1})	0.952	0.803	0.886
F(000)	940	1156	2208
Crystal size (mm)	0.15 × 0.10 × 0.05	0.32 × 0.26 × 0.18	0.48 × 0.28 × 0.20
θ Range for data collection (°)	2.03–27.48	1.83–25.08	3.15–25.02
Index ranges	$-14 \leqslant h \leqslant 14$, $-14 \leqslant k \leqslant 14$, $-21 \leqslant l \leqslant 14$	$-12 \leqslant h \leqslant 11$, $-10 \leqslant k \leqslant 21$, $-16 \leqslant l \leqslant 11$	$-7 \leqslant h \leqslant 19$, $-20 \leqslant k \leqslant 17$, $-22 \leqslant l \leqslant 20$
Reflections collected	14335	7633	7460
Refinement method	full-matrix least-squares on F^2	full-matrix least-squares on F^2	full-matrix least-squares on F^2
Data [$I > 2\sigma(I)$]/parameters	3447/279	3937/347	3295/298
Goodness-of-fit on F^2	1.131	1.115	1.325
R_1 indices ($I > 2\sigma(I)$)[a]	0.0563	0.0432	0.0587
wR_2 indices ($I > 2\sigma(I)$)[b]	0.1131	0.0980	0.1704
Largest difference peak and hole (e Å^{-3})	0.651 and −0.641	0.296 and −0.299	0.922 and −0.452

[a] $R_1 = \sum\|F_o| - |F_c\|/\sum|F_o|$.
[b] $wR_2 = [\sum w(F_o^2 - F_c^2)^2/\sum w(F_o^2)^2]^{1/2}$.

Table 2
Selected bond lengths (Å) and angles (°) of compounds **1**–**3**

Compound ***1***	
Co–O(1)	1.986(4)
Co–O(3B)	1.978(6)
Co–N(2A)	2.047(4)
Co–N(1)	2.048(9)
O(3B)–Co–O(1)	100.2(2)
O(3B)–Co–N(2A)	118.0(2)
O(1)–Co–N(2A)	110.8(2)
O(3B)–Co–N(1)	112.1(3)
O(1)–Co–N(1)	100.0(2)
N(2A)–Co–N(1)	113.3(1)
Compound ***2***	
Ni–O(1)	2.139(2)
Ni–O(4B)	2.033(2)
Ni–N(1)	2.103(3)
Ni–O(2)	2.115(2)
Ni–OW	2.066(2)
Ni–N(2)	2.105(3)
O(4B)–Ni–OW	94.1(8)
O(4B)–Ni–N(1)	91.4(9)
OW–Ni–N(1)	93.7(1)
O(4B)–Ni–N(2)	87.6(9)
OW–Ni–N(2)	88.6(9)
N(1)–Ni–N(2)	177.6(1)
O(4B)–Ni–O(2)	162.8(8)
OW–Ni–O(2)	102.4(8)
N(1)–Ni–O(2)	92.4(9)
N(2)–Ni–O(2)	87.9(9)
O(4B)–Ni–O(1)	100.9(8)
OW–Ni–O(1)	163.5(8)
N(1)–Ni–O(1)	92.7(9)
N(2)–Ni–O(1)	85.4(9)
O(2)–Ni–O(1)	62.2(7)
Compound ***3***	
Cd–O(4A)	2.284(5)
Cd–N(2B)	2.324(6)
Cd–N(1)	2.341(5)
Cd–O(1)	2.355(5)
Cd–OW1	2.379(6)
Cd–O(2)	2.516(5)
Cd–O(3A)	2.614(5)
O(4A)–Cd–N(2B)	86.4(2)
O(4A)–Cd–N(1)	98.1(2)
N(2B)–Cd–N(1)	96.4(2)
O(4A)–Cd–O(1)	135.5(2)
N(2B)–Cd–O(1)	138.0(2)
N(1)–Cd–O(1)	83.1(2)
O(4A)–Cd–OW1	84.8(2)
N(2B)–Cd–OW1	95.0(2)
N(1)–Cd–OW1	168.5(2)
O(1)–Cd–OW1	87.0(2)
O(4A)–Cd–O(2)	163.3(2)
N(2B)–Cd–O(2)	85.4(2)
N(1)–Cd–O(2)	97.2(2)
O(1)–Cd–O(2)	53.4(2)
OW1–Cd–O(2)	81.5(2)
O(4A)–Cd–O(3A)	52.1(2)
N(2B)–Cd–O(3A)	137.6(2)
N(1)–Cd–O(3A)	83.7(2)
O(1)–Cd–O(3A)	84.2(2)
OW1–Cd–O(3A)	89.4(2)
O(2)–Cd–O(3A)	136.8(2)

Symmetry code: for **1** (A) $x+1/2, -y+5/2, z-1/2$; (B) $x+1/2, -y+3/2, z+1/2$. **2** (B) $x+1, y, z$. **3** (A) $x, -y+1, z-1/2$; (B) $x-1/2, y+1/2, z$.

1401 cm^{-1} for the symmetric stretching band. The separation (Δ) between $\nu_{asym}(CO_2)$ and $\nu_{sym}(CO_2)$ is 174 cm^{-1}. For **2**, one antisymmetric stretching band (1562 cm^{-1}) and two symmetric stretching bands (1412 and 1357 cm^{-1}) are exhibited, the Δ values are 150 and 205 cm^{-1}, respectively. For **3**, the typical antisymmetric and symmetric stretching bands of carboxylate groups are at 1564 and 1387 cm^{-1}, with a Δ value ca. 177 cm^{-1}. The results are consistent with the different coordination modes of the carboxylate groups in the three compounds, one coordination mode in **1** and **3**, two coordination modes in **2** (Scheme 1) [31].

To study the stability of the three compounds, thermogravimetric analyses (TGA) were performed on polycrystalline samples in nitrogen atmosphere. For **1**, the weight loss of 4.08% from 160 to 279 °C is equivalent to the loss of one free water molecule per formula unit (ca. 3.96%), indicating the presence of hydrogen bonding interactions. After 317 °C, the decomposition of the framework starts. For **2**, the thermogravimetric analysis shows that there is no weight loss up to 360 °C, where the entirely decomposition of **2** starts. For **3**, the weight loss of 6.78% (calculated: 6.61%) from 45 to 134 °C, is attributed to the loss of two free water molecules per formula unit. Complete decomposition of the framework starts after 415 °C.

3.1.1. Crystal structure of compound *1*

Single-crystal X-ray diffraction analysis reveals that **1** is a fourfold interpenetrated *adamantanoid* structure. As shown in Fig. 1, each Co^{II} center is in a distorted tetrahedral geometry, which is seldom displayed in cobalt-carboxylate compounds [32]. Two nitrogen atoms from different bpp ligands and two monodentate carboxylate oxygen atoms from different OH-BDC ligands coordinate to the metal center. The average distances of Co–N and Co–O are 1.986(4) and 2.048(1) Å, respectively. OH-BDC acts as a bis-monodentate ligand to link the Co^{II} centers (Scheme 1(a)). The hydroxyl group (–OH) does not take part in coordination, but it is involved in a

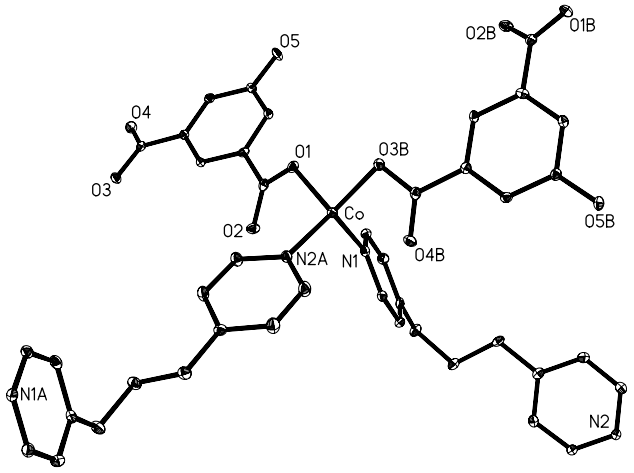


Fig. 1. ORTEP drawing of the coordination environment around Co^{II} in **1** with the thermal ellipsoids at the 30% probability level.

strong hydrogen bonding interaction with a free water molecule (O5–H···OW, 2.692 Å), which is consistent with the result of the TGA. Bpp in a TG conformation bridges the Co^{II} centers, the dihedral angle between the two pyridine rings is 80.6°. Thus, ten Co^{II} centers are connected by twelve bridging ligands, namely six bpp and six OH-BDC, generating a *adamantanoid* cage, which is further extended into a three-dimensional structure (Fig. 2). The separations of the adjacent Co···Co atoms bridged by bpp and OH–BDC are 12.657 and 9.711 Å, respectively. The long spacers between coordination sites result in large cavities within the *adamantanoid* cages. In order to minimize the big void cavities and stabilize the framework by nature, the potential voids are effectively filled via mutual interpenetration of three independent equivalent frameworks, generating a fourfold interpenetrated *adamantanoid* architecture (Fig. 3). Free water molecules are accommodated inside the framework and further shrink the void spaces. Another isomorphous complex, $\{[Zn(bpp)(OH\text{-}BDC)](H_2O)\}_n$, has been obtained and published by us in another report [26].

3.1.2. Crystal structure of compound **2**

Compound **2** is a polythreaded structure constructed through interpenetration of long arms of neutral one-dimensional molecular ladders. As shown in Fig. 4, each Ni^{II} center is in a highly distorted octahedral coordination geometry. Four oxygen atoms from one water molecule, one mono- and one chelating carboxylate groups of different OH-BDC ligands comprise the equatorial plane. Two nitrogen atoms from different conformational bpp ligands occupy the axial positions with the N1–Ni–N2 bond angle being 177.6(1)°. The deviation of the Ni^{II} center from the O_4 equatorial mean plane of the octahedron toward the apical nitrogen atom is 0.232 Å. The Ni–N and Ni–O bond distances are all within the normal ranges. OH-BDC behaves as a bridge through its mono- and chelating carboxylate groups to link different metal centers (Scheme 1(b)). Likewise, the hydroxyl group (–OH) does not participate in coordination, it is involved in a hydrogen bonding interaction with the coordinated water molecule [OW–H···O5^{i} 2.803 Å, (i) $x + 1/2$, $-y + 1/2$, $z + 1/2$].

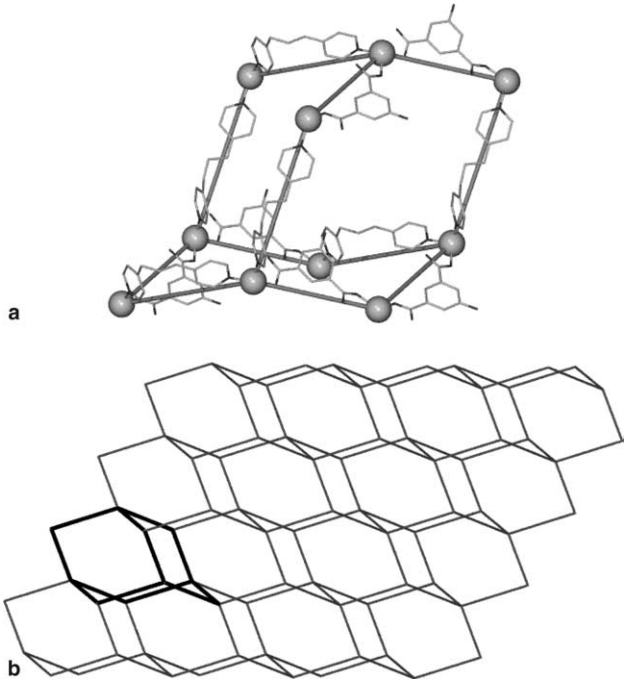


Fig. 2. (a) View of a single *adamantanoid* cage. (b) Perspective view of the three-dimensional *adamantanoid* structure in **1**. For clarity only the Co^{II} centers are shown, with the bonds representing the bridging ligands.

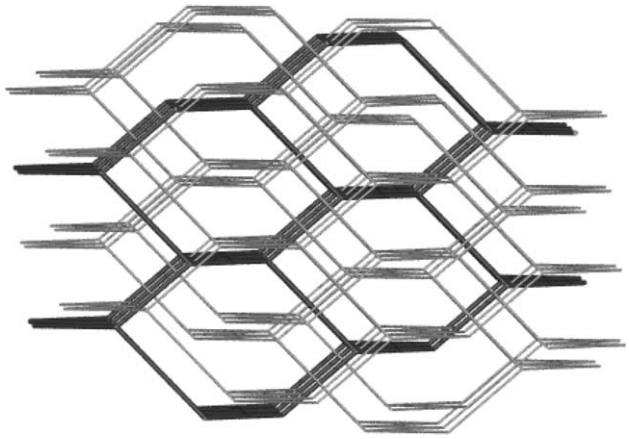


Fig. 3. Perspective view of the fourfold interpenetrated *adamantanoid* network in **1** with bridging ligands and water molecules omitted for clarity.

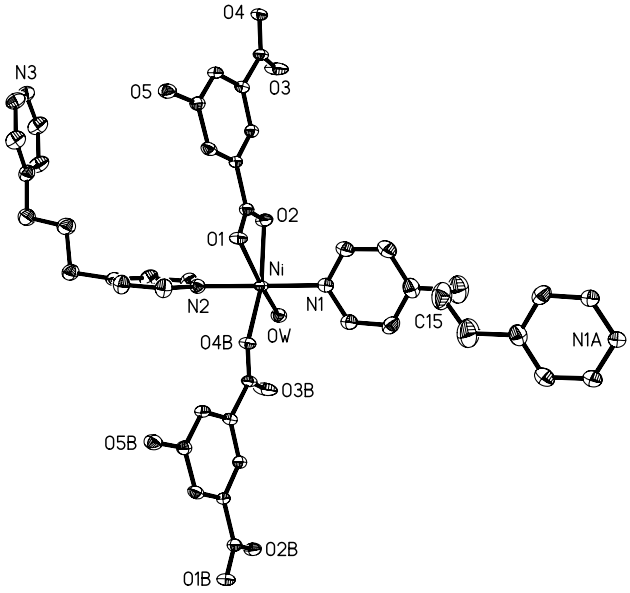


Fig. 4. ORTEP drawing of the coordination environment around Ni^{II} in **2** with the thermal ellipsoids at the 30% probability level.

The most interesting feature of this structure is that there are two types of conformational bpp ligands with different coordination modes [22]. One with the two pyridyl rings being parallel adopts a TG conformation through bridging two Ni^{II} centers. The other possesses a TT conformation and serves as a terminal ligand, the dihedral angle between the two pyridyl rings is 79.6°. As shown in Fig. 5, the TG conformational bpp ligand and OH-BDC engage neighboring Ni^{II} centers into a one-dimensional neutral molecular ladder containing $[Ni_4(bpp)_2(OH\text{-}BDC)_2]$ rectangles (14.023×10.155 Å^2). The TT conformational bpp ligand behaves as a lateral arm of the ladder through its one pyridyl ring coordinating to a Ni^{II} center, which prevents the formation of an extended motif. It is noteworthy that due to the absence of large solvent or guest molecules to fill the void space in the molecular ladder during assembly process, the terminal TT conformational bpp as long arms are threaded into $[Ni_4(bpp)_2(OH\text{-}BDC)_2]$ rectangles of an adjacent molecular ladder. Each rectangle is oppositely penetrated by two lateral arms from different molecular ladders, but there are no $\pi\cdots\pi$ interactions between the two mutual parallel and stagger pyridyl rings (Fig. 6). Such penetration not only effectively fills into the void space of the rectangles, but also results in a polythreaded polymeric structure. The hydrogen bonding interactions between coordinated water molecules and uncoordinated carboxylate oxygen atoms of OH-BDC [OW–H$\cdots$O3^{ii} 2.589 Å; symmetry code: (ii) $x+1, y, z$] as well as the above-mentioned between the coordinated water molecules and hydroxyl groups of OH-BDC further stabilize the whole structural framework. Although some polythreaded architectures from molecular ladders with both inner rungs and lateral arms have been reported [33–35], the structural motif constructed by bpp with different conformations and a dicarboxylate ligand is still unprecedented.

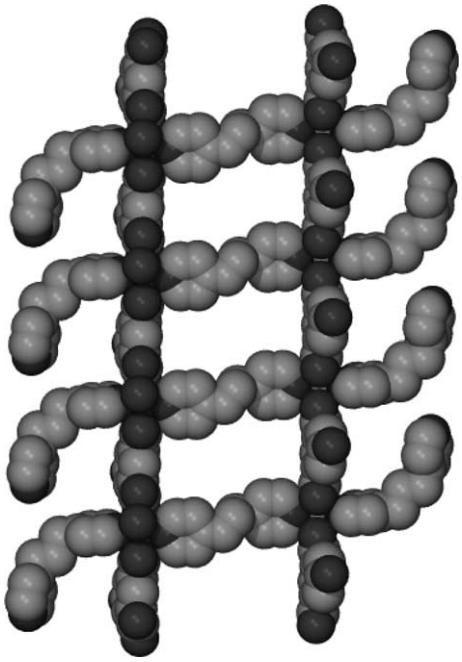


Fig. 5. Space-filling representation of a one-dimensional neutral molecular ladder with long arms.

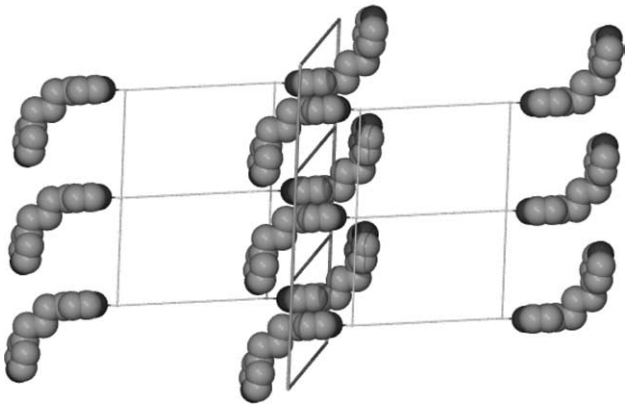


Fig. 6. Perspective view of the polythreaded polymeric structure in **2**, with the bonds representing OH-BDC and exo-bidentate bpp.

3.1.3. Crystal structure of compound *3*

Compound **3** is a twofold interpenetrated three-dimensional framework with free water molecules as space fillers. As shown in Fig. 7, each Cd^{II} center is in a distorted pentagonal bipyramidal geometry. Two chelating carboxylate groups from different OH-BDC ligands and one pyridyl nitrogen atom from a bpp ligand comprise the equatorial basal plane, one water molecule and one pyridyl nitrogen atom from the other bpp ligand occupy the apical sites [OW1–Cd–N1 168.5(2)°]. The Cd^{II} center is displaced about 0.221 Å

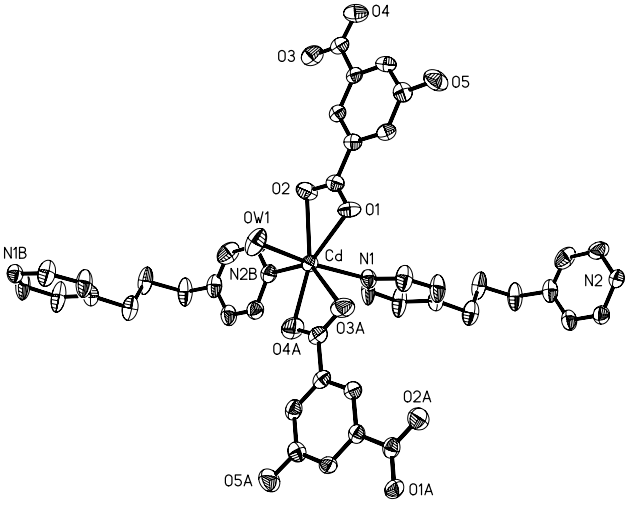


Fig. 7. ORTEP drawing of the coordination environment around Cd^{II} in **3** with the thermal ellipsoids at the 30% probability level.

from the equatorial plane towards the axial donor atom. The Cd–O and Cd–N bond distances are in the range 2.284(5)–2.614(5) Å and 2.324(6)–2.341(5) Å, respectively. Different from **1** and **2**, OH-BDC acts as a chelating bis-bidentate ligand (Scheme 1(c)) and bridges different Cd^{II} centers to give rise to a one-dimensional metal-carboxylate chain (Fig. 8). Exo-bidentate bpp adopts a TG conformation with the dihedral angle between two pyridyl rings being 79.4°, which is similar to that in **1**. Thus bpp links the adjacent one-dimensional chain into a three-dimensional framework with large channels (Fig. 9). The Cd···Cd distances bridged by bpp and OH-BDC are 11.967 and 10.117 Å, respectively. In order to shrink the void space and stabilize the final product, the three-dimensional network is interpenetrated into itself to generate an interwining network (Fig. 10). Free water molecules are accommodated in the residual empties and further stabilize the structural framework through extensive hydrogen bonding interactions between coordinated water molecules and carboxylate oxygen atoms of OH-BDC [OW1–H···O1^{i} 2.679 Å, (i) $-x+1, -y+1, -z+1$], between coordinated water molecules and free water molecules [OW1–H···OW3^{ii} 2.856 Å, (ii) $-x+1, y, -z+3/2$], between free water molecules and carboxylate oxygen atoms of OH-BDC [OW2–H···O2^{ii} 2.900 Å], between free water molecules and free water molecules [OW4–H···OW5 2.116 Å], as well as between hydroxyl groups of OH-BDC and free water molecules [O5–H···OW5 2.700 Å].

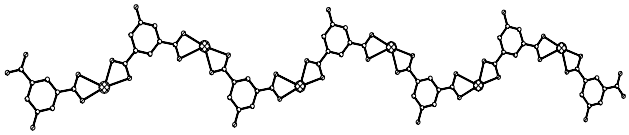


Fig. 8. View of a one-dimensional metal-carboxylate chain.

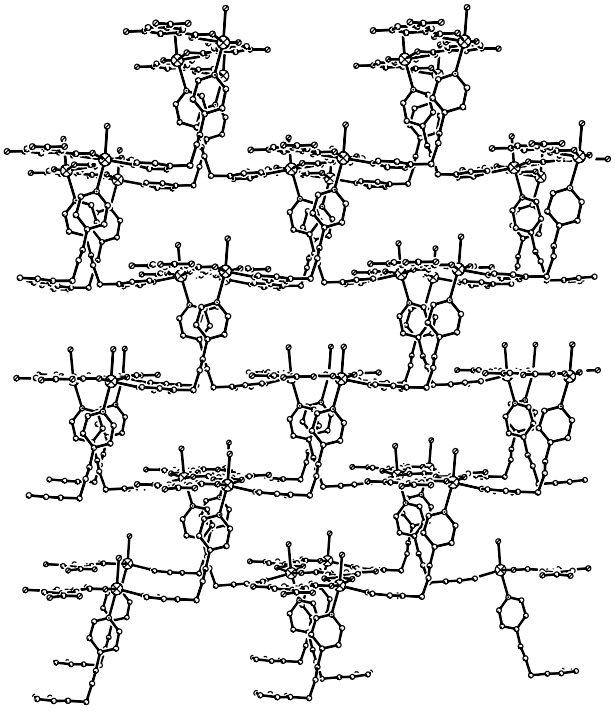


Fig. 9. Perspective view of the three-dimensional network possessing large channels along the *c*-axis in **3**.

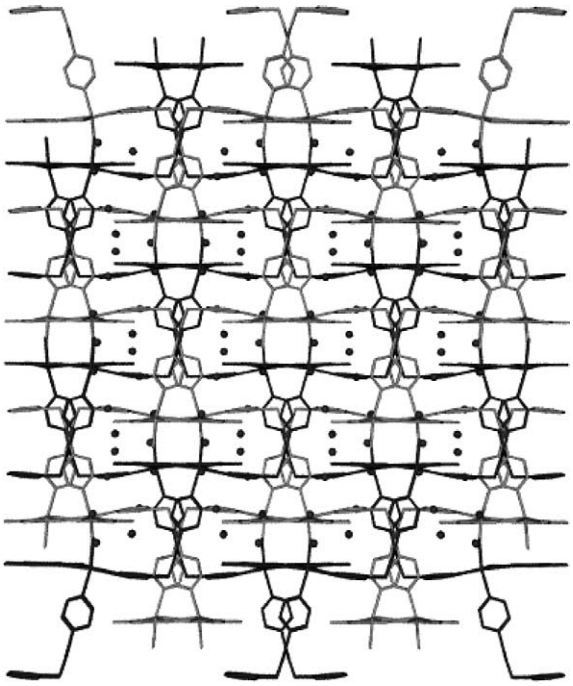


Fig. 10. Perspective view of the twofold interpenetrated three-dimensional network with free water molecules along the *c*-axis in **3**.

4. Conclusions

The hydrothermal reactions of 1,3-bis(4-pyridyl)propane (bpp), 5-hydroxyisophthalic acid (OH-H_2BDC) and different metal salts produced three interpenetrated or polythreaded coordination polymers. The long flexible bpp adopts different conformations to link the metal ions. Owing to the existence of large voids from long metal–metal distances bridged by bpp and OH-BDC, all of the three compounds exhibit interpenetrated structures. This research also demonstrated that the presence of anionic groups (carboxylate groups) can simplify the design and construction of the compounds.

5. Supplementary data

Crystallographic data (excluding structure factors) for the structures in this paper have been deposited in the Cambridge Crystallographic Data Center as

supplementary publication, CCDC Nos. 240643–240645 for complexes **1**–**3**, respectively. Copies of the data can be obtained free of charge on application to CCDC, 12 Union Road, Cambridge CB2 1EZ, UK (fax: (internet) +44 1223 336 033; e-mail: deposit@ccdc.cam.ac.uk). or www at http://www.ccdc.cam.ac.uk].

Acknowledgements

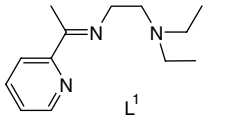
The authors thank the financial support from the National Natural Science Foundation of China (90206040, 20325106, 20333070), the Natural Science Foundation of Fujian Province (B982003), and the ''One-hundred Talent'' Project from CAS.

References

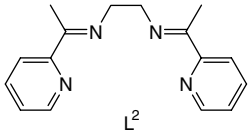
[1] R. Robson, B.F. Abrahams, S.R. Batten, R.W. Gable, B.F. Hoskins, J. Liu, Supramolecular Architecture, American Chemical Society, Washington, DC, 1992, p. 256.
[2] M. Moulton, L.P. Wu, T. Kuroda-Sowa, Adv. Inorg. Chem. 46 (1999) 173.
[3] M.J. Zaworotko, Chem. Soc. Rev. (1994) 283.
[4] O.R. Evans, W.B. Lin, Acc. Chem. Res. 35 (2002) 511.
[5] K. Biradha, M. Fujita, Chem. Commun. (2002) 1866.
[6] M. Kondo, T. Joshitomi, K. Seki, H. Matsuzaka, S. Kitagawa, Angew. Chem. Int. Ed. Engl. 36 (1997) 1844.
[7] K.N. Power, T.L. Hennigar, M.J. Zaworotko, New J. Chem. (1998) 177.
[8] S.R. Batten, R. Robson, Angew. Chem. Int. Ed. 37 (1998) 1460.
[9] X.L. Wang, C. Qin, E.B. Wang, L. Xu, Z.M. Su, C.W. Hu, Angew. Chem. Int. Ed. 43 (2004) 5036.
[10] F.A. Almeida Paz, Y.Z. Khimyak, A.D. Bond, J. Rocha, J. Klinowski, Eur. J. Inorg. Chem. (2002) 2823.
[11] A.J. Blake, N.R. Champness, S.S.M. Chung, W.S. Li, M. Schröder, Chem. Commun. (1997) 1005.
[12] D. Hagrman, R.P. Hammond, R. Haushalter, J. Zubieta, Chem. Mater. 10 (1998) 2091.
[13] S.R. Batten, A.R. Harris, P. Jensen, K.S. Murray, A. Ziebell, J. Chem. Soc., Dalton Tran. (2000) 3829.
[14] J.M. Knaust, S. Lopez, S.W. Keller, Inorg. Chim. Acta 324 (2002) 81.
[15] L. Carlucci, G. Ciani, D.M. Proserpio, S. Rizzato, Chem. Commun. (2000) 1319.
[16] C.V. Krishnamohan Sharma, R.D. Rogers, Chem. Commun. (1999) 83.
[17] M. John Plater, M.R.S.J. Foreman, R.A. Howie, J.M.S. Skakle, Inorg. Chim. Acta 318 (2000) 175.
[18] V. Niel, M.C. Muòoz, A.B. Gaspar, A. Galet, G. Levchenko, J.A. Real, Chem. Eur. J. 8 (2002) 2446.
[19] J.Y. Lu, A.M. Babb, Inorg. Chem. 40 (2001) 3261.
[20] J. Luo, M. Hong, R. Wang, R. Cao, L. Han, Z. Lin, Eur. J. Inorg. Chem. (2003) 2705.
[21] S.R. Batten, J.C. Jeffery, M.D. Ward, Inorg. Chim. Acta 292 (1999) 231.
[22] M.V. Marinho, M.I. Yoshida, K.J. Guedes, K. Krambrock, A.J. Bortoluzzi, M. Hörner, F.C. Machado, W.M. Teles, Inorg. Chem. 43 (2004) 1539.
[23] L. Carlucci, G. Ciani, M. Moret, D.M. Proserpio, S. Rizzato, Angew. Chem. Int. Ed. 39 (2000) 1506.
[24] M.J. Plater, M.R.S.J. Foreman, T. Gelbrich, M.B. Hursthouse, J. Chem. Soc., Dalton Trans. (2000) 1995.
[25] Z.Y. Fu, S.M. Hu, J.C. Dai, J.J. Zhang, X.T. Wu, Eur. J. Inorg. Chem. (2003) 2670.
[26] X.J. Li, R. Cao, D.F. Sun, W.H. Bi, Y.Q. Wang, X. Li, M.C. Hong, Cryst. Growth Des. 4 (2004) 775.
[27] Crystalclear: ver 1.36; Molecular Structure Corporation; Rigaku, MSC/SSI, 491, South Orem Blvd, Orem, UT84058, 2001.
[28] G.M. Sheldrick, SADABS, Program for Empirical Absorption Correction of Area Detector Data, University of Göttingen, Göttingen, 1996.
[29] G.M. Sheldrick, SHELXS 97, Program for Crystal Structure Solution, University of Göttingen, Göttingen, 1997.
[30] G.M. Sheldrick, SHELXS 97, Program for Crystal Structure Refinement, University of Göttingen, Göttingen, 1997.
[31] H.X. Zhang, B.S. Kang, A.W. Xu, Z.N. Chen, Z.Y. Zhou, A.S.C. Chan, K.B. Yu, C. Ren, J. Chem. Soc., Dalton Trans. (2001) 2559.
[32] E. Lee, Y. Kim, D.Y. Jung, Inorg. Chem. 41 (2002) 501.
[33] M.L. Tong, H.J. Chen, X.M. Chen, Inorg. Chem. 39 (2000) 2235.
[34] M.A. Withersby, A.J. Blake, N.R. Champness, P. Hubberstey, W.S. Li, M. Schröder, Angew. Chem. Int. Ed. 36 (1997) 2627.
[35] O.S. Jung, S.H. Park, K.M. Kim, H.G. Jang, Inorg. Chem. 37 (1998) 5781.

cadmium–terephthalate systems either monodentate or chelating bidentate terminal ligands have been used [26,27]. Only one compound has been reported with a tetradentate terminal ligand and the resulting compound is mononuclear [30]. No compound with a tridentate blocking ligand is reported to date. Schiff base type ligands are easily prepared, highly variable and offer a good control on the metal coordination sphere by occupying a square plane of an octahedron or trigonal plane of a trigonal biypramid and leaving the axial bonding sites free for the desired extended coordination [31,32].

In this paper, we report the synthesis of two complexes of cadmium terephthalate using a tridentate (L^1) and a tetradentate (L^2) terminal Schiff base type ligand by the conventional solution method and their crystal structure analyses.



L^1



L^2

2. Experimental

2.1. Materials and physical measurements

Commercially available solvents, 2-acetyl-pyridine, *N*,*N*′-diethylethylenediamine, ethylenediamine, cadmium acetate dihydrate and sodium terephthalate were used without further purification. Elemental analyses were carried out using a Perkin–Elmer 240C elemental analyzer. IR spectra were recorded in KBr (4500–500 cm^{-1}) using a Perkin–Elmer R XI FT-IR spectrophotometer. The thermal analyses (TG-DTA) were carried out on a Mettler Toledo TGA/SDTA 851 thermal analyser in a dynamic atmosphere of dinitrogen (flow rate: 30 $cm^3\ min^{-1}$). The sample was heated in an alumina crucible.

2.2. Preparations

2.2.1. (*E*)-N^1,N^1-diethyl-N^2-(1-(pyridin-2-yl)-ethylidene)-ethane-1,2-diamine (L^1)

N,*N*′-diethylethylenediamine (1.74 g, 15 mmol) and 2-acetylpyridine (1.815 g, 15 mmol) in a 1:1 molar ratio were refluxed in 30 mL of dry methanol for 4 h. The resulting solution was evaporated under reduced pressure to obtain a yellow semi-solid mass. The mass was then extracted thrice (3 × 10 mL) with *n*-hexane which on slow evaporation gave a pale yellow product. Yield: 2.792 g (85%). *Anal*. Calc. for $C_{13}H_{21}N_3$: C, 71.23; H, 9.58; N, 19.17. Found: C, 71.10; H, 9.75; N, 19.02%. IR (ν/cm^{-1}): 1648 ($\nu_{C=N}$).

2.2.2. *N*,*N*′-bis-(1-pyridin-2-yl-ethylidene)-ethane-1,2-diamine (L^2)

This ligand was prepared by a procedure similar to that for L^1, by starting with ethylenediamine (0.9 g, 15 mmol) and 2-acetyl-pyridine (3.639 g, 30 mmol) in a 1:2 molar ratio to obtain a yellow liquid. Light yellow microcrystals were obtained by recrystallization from *n*-hexane. Yield: 90%. *Anal*. Calc. for $C_{16}H_{18}N_4$: C, 72.22; H, 6.75; N, 21.09. Found: C, 72.05; H, 6.88; N, 21.01%. IR (ν/cm^{-1}): 1681 ($\nu_{C=N}$).

2.2.3. Catena-poly[bis{(μ-terephthalato-$\kappa^4O^1,O^{1\prime}:O^4,O^{4\prime}$)-((*E*)-$N^1$,$N^1$-diethyl-$N^2$-(1-(pyridin-2-yl)ethylidene)-ethane-1,2-diamine)-cadmium (II)}nonahydrate], $_\infty^1\{[Cd_2(\mu\text{-}O_2C\text{-}C_6H_4\text{-}CO_2)_2\{2\text{-}C_5H_4N\text{-}C(CH_3)=N\text{-}CH_2CH_2\text{-}N(C_2H_5)_2\}_2]\cdot 9H_2O\}$ (**1**)

A methanolic solution of $Cd(OAc)_2\cdot 2H_2O$ (0.532 g, 2 mmol) and a hot methanolic solution (10 ml) of ligand L^1 (0.438 g, 2 mmol) were added to an aqueous solution of sodium terephthalate (0.42 g, 2 mmol) with constant stirring. The resulting solution was filtered and the filtrate allowed to stand at room temperature for two days to yield colorless plate-like crystals. Yield: 1.976 g (87%). *Anal*. Calc. for $C_{42}H_{68}Cd_2N_6O_{17}$: C, 43.72; H, 5.94; N, 7.28. Found: C, 43.54; H, 5.65; N, 7.36%. IR (ν/cm^{-1}): 3410 (br, ν_{H_2O}), 1572 and 1398 (ν_{CO_2}), 1653 ($\nu_{C=N}$).

2.2.4. [Di-aqua-bis{*N*,*N*′-bis-(1-pyridin-2-yl-ethylidene)-ethane-1,2- diamine}(μ-terephthalato-$\kappa^4O^1,O^{1\prime}:O^4,O^{4\prime}$)-di-cadmium(II)]-terephthalate decahydrate, [{$Cd(H_2O)$-{2-C_5H_4N-$C(CH_3)$=*N*-CH_2CH_2-*N*=$C(CH_3)$-C_5H_4N-2}}$_2$(μ-O_2C-C_6H_4-CO_2)](O_2C-C_6H_4-CO_2)·$10H_2O$ (**2**)

The title compound was prepared by a similar procedure as for **1** using ligand L^2 (0.532 g, 2 mmol) to give colorless crystals. Yield: 1.106 g (85%). *Anal*. Calc. for $C_{24}H_{34}CdN_4O_{10}$: C, 44.24; H, 5.26; N, 8.61. Found: C, 44.30; H, 5.11; N, 8.75%. IR (ν/cm^{-1}): 3410 (br, ν_{H_2O}), 1570 and 1381 (ν_{CO_2}), 1654 ($\nu_{C=N}$).

2.3. X-ray crystallography

Diffraction data was collected at $T = 293(2)$ K for **1** and at $T = 227(2)$ K for **2** by the ω-scan method with Mo Kα radiation ($\lambda = 0.71073$ Å) and the use of a graphite monochromator on a Bruker AXS CCD diffractometer. Data collection and cell refinement were done with SMART [33], data reduction with SAINT [33]. An experimental absorption correction was performed with SADABS [34]. The structure was solved by direct

methods (SHELXS-97) [35]; refinement was done by full-matrix least-squares on F^2 using the SHELXL-97 program suite [35]. All non-hydrogen positions were found and refined with anisotropic temperature factors. In **1** and **2** the hydrogen atoms were calculated with appropriate riding models (AFIX 43 for aromatic hydrogens on pyridine and terephthalate, AFIX 23 for CH_2, AFIX 33 for CH_3) and $U_{eq(H)} = 1.2\ U_{eq(C)}$ for CH and CH_2 and $U_{eq(H)} = 1.5\ U_{eq(C)}$ for CH_3. In **1** the hydrogen atoms on the oxygen atoms of water of crystallization (nine disordered oxygen atoms per formula unit) were neither found nor calculated. In **2** the hydrogen atoms on the aqua ligand and solvent water molecules were found and refined with $U_{eq(H)} = 1.5\ U_{eq(O)}$. In **1** and **2** the five and six strongest peaks, respectively, of the residual electron density are in the near vicinity (within 1.0 Å) of the cadmium atom. Graphics were computed with DIAMOND [36]. Supramolecular interactions (hydrogen bonds, C–H $\cdots\pi$ contacts) were calculated with PLATON for windows [37–39]. For complex **1** the quality of the overall crystallographic refinement is not too good, due to encorporated and disordered water of crystallization. The water of crystallization (nine H_2O per formula unit) is not discussed further nor included in the figures below for reasons of clarity. The metal–ligand moiety could be clearly refined, however. Crystal data are listed in Table 1 and bond angles in Tables 2 and 3 for complexes **1** and **2**, respectively.

3. Results and discussions

3.1. IR spectra

For complexes **1** and **2** strong absorption bands appear at 1572 and 1570 cm^{-1} for the asymmetric stretching and 1398 and 1381 cm^{-1} for the symmetric stretching of the carboxylate groups, respectively. The binding modes of the carboxylate ligands can be accessed on the basis of the difference (Δ) between the asymmetric stretching ν_a (CO_2^-) and symmetric stretching ν_s (CO_2^-) [40]. The Δ value for **1** is 174 cm^{-1} and for

Table 1
Crystal data for complexes **1** and **2**

Complex	**1**	**2**
Formula	$C_{42}H_{50}Cd_2N_6O_{17}$[a]	$C_{24}H_{34}CdN_4O_{10}$
M (g mol^{-1})	1135.70[a]	650.95
Crystal size (mm)	0.26 × 0.14 × 0.06	0.19 × 0.14 × 0.09
θ Range (°)	2.18–26.10	1.77–28.86
h,k,l range	−25,25; −17,17; −23,22	−15,14; −16,16; −16,16
Crystal system	monoclinic	triclinic
Space group	$P2_1/c$	$P\bar{1}$
a (Å)	20.668(7)	11.522(2)
b (Å)	14.172(5)	12.089(2)
c (Å)	18.985(6)	12.567(2)
α (°)	90.00	108.139(3)
β (°)	106.121(5)	94.999(3)
γ (°)	90.00	117.517(3)
V (Å^3)	5342(3)	1418.7(5)
Z	4	2
D_{calc} (g cm^{-3})	1.412	1.524
$F(000)$	2304[a]	668
μ (mm^{-1})	0.864	0.829
Max/minimum transmission	0.9500/0.8065	0.9291/0.8584
Reflections collected	41 335	13 011
Independent reflections (R_{int})	10 571 (0.0801)	6691 (0.0190)
Observed reflections [$I > 2\sigma(I)$]	5668	5448
Parameters refined	615	388
Maximum/minimum $\Delta\rho$[b] (e Å^{-3})	1.048/−0.808	1.280/−0.724
R_1/wR_2[c] [$I > 2\sigma(I)$]	0.0610, 0.1492	0.0334, 0.0670
R_1/wR_2[c] (all data)	0.1385, 0.2020	0.0449, 0.0715
Goodness-of-fit on F^2[d]	1.030	1.082
Weight scheme w; a/b[e]	0.0961/0.1243	0.0311/0.0000

[a] Hydrogen atoms on the oxygen atoms of the water of crystallization (nine disordered oxygen atoms per formula unit) were neither found nor calculated and, hence, are not included in the chemical formula, molar mass M or in $F(000)$.
[b] Largest difference peak and hole.
[c] $R_1 = [\sum(||F_o| - |F_c||)/\sum|F_o|]$; $wR_2 = [\sum[w(F_o^2 - F_c^2)^2]/\sum[w(F_o^2)^2]]^{1/2}$.
[d] Goodness-of-fit = $[\sum[w(F_o^2 - F_c^2)^2]/(n-p)]^{1/2}$.
[e] $w = 1/[\sigma^2(F_o^2) + (aP)^2 + bP]$, where $P = (\max(F_o^2 \text{ or } 0) + 2F_c^2)/3$.

Table 2
Selected distances (Å) and angles (°) for **1**

Cd1–O2	2.255(5)
Cd1–N2	2.276(6)
Cd1–O6	2.280(6)
Cd1–N1	2.358(7)
Cd1–N3	2.373(7)
Cd1–O1	2.622(6)
Cd1–O5	2.653(6)
Cd2–O8[4]	2.253(6)
Cd2–N5	2.286(7)
Cd2–O3	2.331(6)
Cd2–N4	2.377(7)
Cd2–N6	2.430(7)
Cd2–O4	2.508(6)
Cd2–O7[4]	2.638(8)
O2–Cd1–N2	133.1(2)
O2–Cd1–O6	92.6(2)
N2–Cd1–O6	129.7(2)
O2–Cd1–N1	94.0(2)
N2–Cd1–N1	69.9(2)
O6–Cd1–N1	90.7(2)
O2–Cd1–N3	109.5(3)
N2–Cd1–N3	76.4(2)
O6–Cd1–N3	111.3(3)
N1–Cd1–N3	146.2(2)
O2–Cd1–O1	52.3(2)
N2–Cd1–O1	81.5(2)
O6–Cd1–O1	143.3(2)
N1–Cd1–O1	82.7(2)
N3–Cd1–O1	92.7(2)
N3–Cd1–O1	92.7(2)
O2–Cd1–O5	143.8(2)
N2–Cd1–O5	82.1(2)
O6–Cd1–O5	51.5(2)
N1–Cd1–O5	91.3(2)
N3–Cd1–O5	83.8(2)
O1–Cd1–O5	163.6(2)
O8[4]–Cd2–N5	131.5(3)
O8[4]–Cd2–O3	84.21(3)
N5–Cd2–O3	144.0(3)
O8[4]–Cd2–N4	116.7(3)
N5–Cd2–N4	69.5(3)
O3–Cd2–N4	91.3(2)
O8[4]–Cd2–N6	93.1(3)
N5–Cd2–N6	73.6(3)
O3–Cd2–N6	115.3(3)
N4–Cd2–N6	142.4(2)
O8[4]–Cd2–O4	132.7(3)
N5–Cd2–O4	94.2(3)
O3–Cd2–O4	53.4(2)
N4–Cd2–O4	87.3(2)
N6–Cd2–O4	88.3(2)
O8[4]–Cd2–O7[4]	49.7(2)
N5–Cd2–O7[4]	84.7(3)
O3–Cd2–O7[4]	126.1(3)
N4–Cd2–O7[4]	87.8(3)
N6–Cd2–O7[4]	95.9(4)
O4–Cd2–O7[4]	175.1(3)

Symmetry transformations: [4] $= x-2, -y+3/2, z-1/2$.

Table 3
Selected distances (Å) and angles (°) for **2**

Cd–O10	2.254(2)
Cd–N3	2.368(2)
Cd–N2	2.373(2)
Cd–N4	2.391(2)
Cd–N1	2.402(2)
Cd–O1	2.4318(16)
Cd–O2	2.4579(16)
O10–Cd–N3	107.98(9)
O10–Cd–N2	94.28(9)
N3–Cd–N2	70.96(7)
O10–Cd–N4	84.36(7)
N3–Cd–N4	67.84(7)
N3–Cd–N4	136.01(7)
O10–Cd–N1	82.88(8)
N3–Cd–N1	138.30(7)
N2–Cd–N1	68.10(7)
N4–Cd–N1	153.63(8)
O10–Cd–O1	113.05(10)
N2–Cd–O1	136.20(6)
N4–Cd–O1	82.36(6)
N1–Cd–O1	81.57(6)
O10–Cd–O2	164.95(9)
N3–Cd–O2	86.83(7)
N2–Cd–O2	93.15(6)
N4–Cd–O2	99.25(6)
N1–Cd–O2	87.79(6)
O1–Cd–O2	53.58(5)

2 is 189 cm^{-1}. The separation is consistent with binding modes as found in the structural analysis. The broad band in the region of 3410 cm^{-1} for both complexes could be assigned to the stretching vibration of the water molecules involved in hydrogen bonding. The imine (C═N) vibration appears at 1653 and 1654 cm^{-1} for complexes **1** and **2**, respectively.

3.2. Description of the structures

Compound **1** is a 1D polymeric zig-zag chain. Two crystallographically different cadmium centers (Cd1 and Cd2 along with their ligands) alternate along the chain (Fig. 1).

Each cadmium atom is coordinated by three nitrogen donors from the tridentate chelating (neutral) (*E*)-N^1, N^1-diethyl-N^2-(1-(pyridin-2-yl)ethylidene)ethane-1,2-diamine ligand and four oxygen donors from two bis-bidentate bridging (crystallographically different)

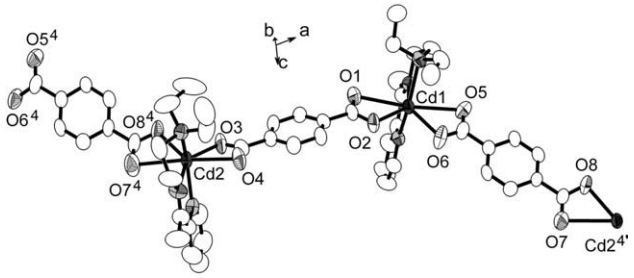


Fig. 1. Short chain segment of **1** with the two different cadmium centers. Symmetry transformations: [4] $= x-2, -y+3/2, z-1/2$; [4′] $= x-1, -y+3/2, z+1/2$.

terephthalate ligands. The coordination environment around cadmium can be described as a distorted trigonal bipyramid (Figs. 2 and 3). The repeat unit along the chain encompasses four cadmium centers (Fig. 4).

There is no element of helicity along the chain propagation axis. The chains do not run along the 2_1-crystallographic axes (parallel to the *b*-axis) but perpendicular to the *b*-axis. All chains are parallel to each other (Fig. 5). Neighbouring chains can be thought of as stacked in planes coplanar with the *ac*-plane. Along the *b*-axis these "planes" are shifted with respect to each other (Fig. 5). The space in-between neighbouring chains – visible in the space-filling representation in Fig. 5 – is filled by water molecules of crystallization (nine H_2O molecules per formula unit). The water arrangement cannot be discussed in more detail because neither could a certain disorder of the oxygen atoms be clearly resolved nor the hydrogen atoms be determined. There are no π–π interactions discernable in the interchain packing in **1**. The shortest centroid-centroid contact for two almost parallel aromatic rings (interplanar angle 8.9°) is found between the pyridyl moieties on the two different Cd1 and Cd2 centers in adjacent chains (symmetry relation $-x$, $-1/2+y$, $1/2-z$ or $-x$, $1/2+y$, $1/2-z$). The centroid–centroid contact of 5.36 Å together with the "slip angle" between the centroid–centroid vector and the normal to the plane of ~50° excludes any meaningful π-overlap (see below) [14h].

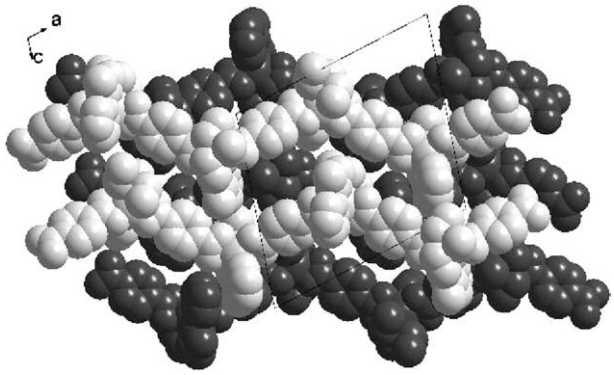


Fig. 5. Packing diagram for the parallel chains (space-filling representation) in **1** with the unit-cell outline included. Chains in different "planes" are differentiated by dark and light grey shading.

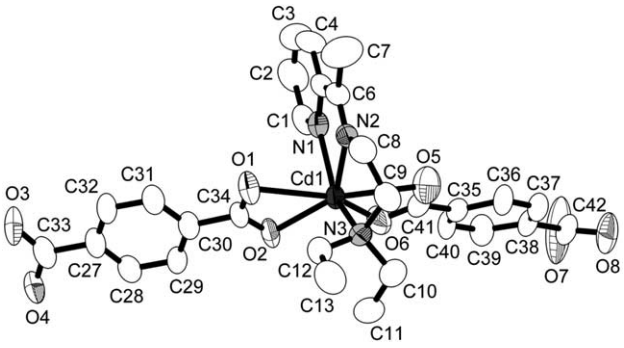


Fig. 2. Coordination environment around Cd1 in **1**; 50% thermal ellipsoids. Symmetry transformation: $^4 = x-2, -y+3/2, z-1/2$.

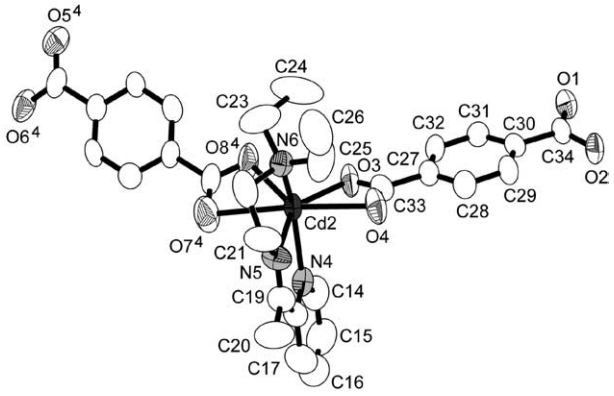


Fig. 3. Coordination environment around Cd2 in **1**; 50% thermal ellipsoids. Symmetry transformation: $^4 = x-2, -y+3/2, z-1/2$.

With respect to the Cd-terephthalate zigzag chain structure in **1**, similar chains with bis-bidentate benzene-1,4-dicarboxylate (bdc) bridges are found in $_\infty{}^1[Cd(\mu\text{-bdc})(NH_3)_2]$ [26] and $_\infty{}^1\{[Cd(\mu\text{-bdc})(H_2O)_3]\cdot 4H_2O\}$, both with an interchain hydrogen-bonding network [41], or in $_\infty{}^3\{[Ph_3PCH_2Ph][Cd(\mu\text{-bdc})Cl]\cdot 2H_2O\}$ as part of a 3D framework with bridging chloro ligands [27d]. Other terephthalato-bridged cadmium coordination polymers contain tetrakis-monodentate ligands in $_\infty{}^3[Cd(\mu_4\text{-bdc})_{1/2}Cl(1,10\text{-phen})]$ [27c] or bis-tridentate terephthalato ligands in $_\infty{}^3[Cd(\mu_4\text{-bdc})(\text{pyridine})]$

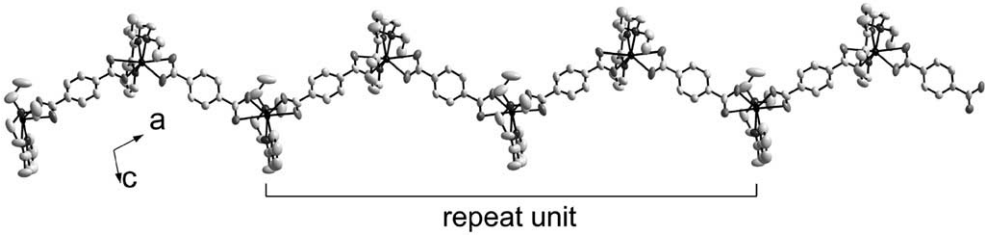


Fig. 4. Longer chain segment of **1** showing the repeat unit of four cadmium centers.

[27a], bridging between four cadmium ions as part of a 3D framework. Noteworthy, the last two structures have been obtained through hydrothermal reactions of 1,4-dicyanobenzene by its slow hydrolysis into terephthalic acid.

Compound **2** consists of centrosymmetric dinuclear (''dimeric'') and cationic complexes with each of the two (symmetry related) cadmium atoms being coordinated by the tetradentate chelating *N*,*N*′-bis-(1-pyridin-2-yl-ethylidene)-ethane-1,2-diamine ligand and an aqua ligand (Fig. 6). The terephthalato ligand bridges between the two cadmium atoms utilizing all of its four oxygen donor atoms. Both of the two carboxylate oxygen atoms coordinate to a cadmium atom with equal Cd–O bond lengths to give a four-membered chelate ring. Thus, each cadmium atom is coordinated by four nitrogen and three oxygen donors in what could be described as a distorted pentagonal bipyramid. The atoms O10–Cd–O2, which form the largest angle (165°) around Cd, present the axis of the bipyramid. The distorted pentagonal plane is formed by Cd–N1–N2–N3–N4–O1 (the largest deviation from that plane is 0.66 Å). From the plane formed by the nitrogen chelating ligand with the metal (Cd–N1–N2–N3–N4), the largest deviation would be 0.21 Å and the axis Cd–O1 would form an angle of 39.4° with that plane. The center of the bridging terephthalate ligand is also a center of inversion which renders the two halves of the dinuclear complex symmetry equivalent.

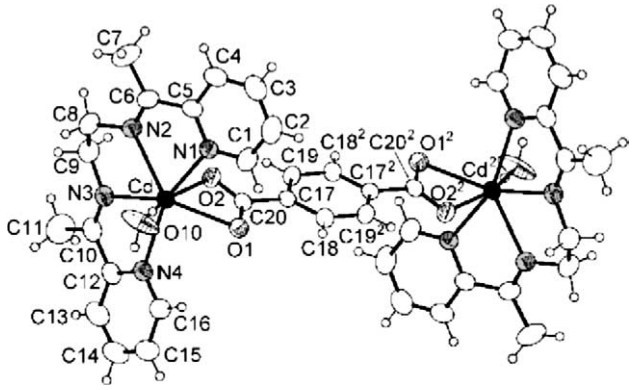


Fig. 6. Molecular structure of the centrosymmetric cationic dinuclear complex of **2**; 50% thermal ellipsoids. Symmetry transformation: $^{2} = -x+1, -y+2, -z$.

The dinuclear complex still has a single positive charge which is balanced by a ''free'', that is, hydrogen-bonded terephthalate anion. The dinuclear complexes form layers parallel to the *ac*-plane of the crystal lattice (Fig. 7). In between, that is sandwiched by the complex layers, are the terephthalate anions together with the water molecules of crystallization. The hydrogen-bonding network, where the aqua ligand and the carboxylate oxygen atoms of the bridging terephthalato ligand also participate, is shown in Fig. 7. Details of the hydrogen-bonding interactions are listed in Table 4.

The intermolecular packing between the complexes of **2**, within the layers formed parallel to the *ac*-plane, shows a rather strong π-stacking interaction [14h] between the parallel (because they are symmetry related) pyridyl planes of N4–C12–C13–C14–C15–C16 with a slip angle of 20.3°, a vertical displacement between the

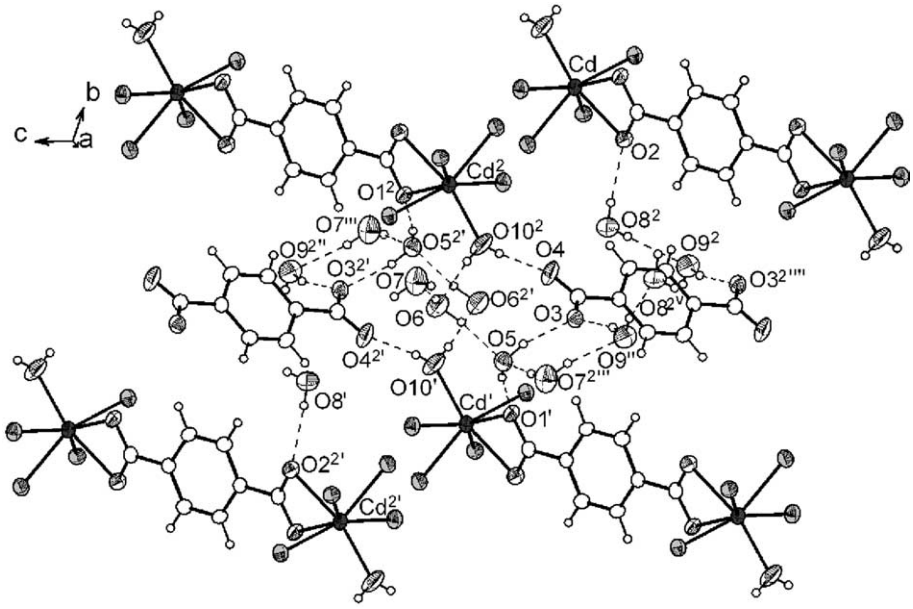


Fig. 7. Hydrogen bonding interaction in **2**. For clarity only the nitrogen atoms of the chelate ligand are shown; 40% thermal ellipsoids; symmetry transformations: $' = x, y-1, z$; $'' = x, y-1, z-1$; $''' = x-1, y, z$; $^{2} = -x+1, -y+2, -z+1$; $^{2'} = -x+1, -y+1, -z+1$; $^{2''} = -x+1, -y+2, -z+2$; $^{2'''} = -x+2, -y+1, -z+1$; $^{2''''} = -x+1, -y+1, -z$; $^{2v} = -x+2, -y+2, -z+1$.

Table 4
Hydrogen bonding interactions in **2**

D–H ⋯ O	D–H (Å)	H ⋯ O (Å)	D ⋯ O (Å)	D–H ⋯ O (°)
O5–H5A ⋯ O3	0.87(3)	1.85(3)	2.700(3)	166(3)
O5–H5B ⋯ O1′	0.87(3)	1.97(4)	2.835(3)	170(3)
O6–H6A ⋯ O7	0.90(4)	1.94(4)	2.813(4)	164(4)
O6–H6B ⋯ O5	0.93(4)	1.88(4)	2.774(3)	161(4)
O7‴–H7D ⋯ O9$^{2''}$	0.84(4)	2.14(4)	2.947(4)	159(4)
O7–H7E ⋯ O5$^{2'''}$	0.83(4)	2.03(4)	2.855(3)	172(4)
O8–H8C ⋯ O2^{2}	0.78(4)	2.05(4)	2.830(3)	175(4)
O8–H8D ⋯ O9	0.71(3)	2.12(3)	2.809(4)	166(5)
O9″–H9C ⋯ O3	0.87(4)	1.87(4)	2.708(3)	163(4)
O9″–H9D ⋯ O8^{2v}	0.72(4)	2.09(4)	2.792(3)	163(5)
O10–H10A ⋯ O4^{2}	0.78(4)	1.88(4)	2.648(3)	166(5)
O10–H10B ⋯ O6^{2}	0.78(4)	1.96(4)	2.736(3)	173(5)

D, donor, H, hydrogen bond acceptor; symmetry relations: $' = x, y-1, z$; $'' = x, y-1, z-1$; $''' = x-1, y, z$; $^{2} = -x+1, -y+2, -z+1$; $^{2''} = -x+1, -y+2, -z+2$; $^{2'''} = -x+2, -y+1, -z+1$; $^{2v} = -x+2, -y+2, -z+1$.

ring centroids of 1.3 Å, a centroid separation of 3.76 Å and an interplanar separation of 3.53 Å. In comparison the pyridyl planes of N1-C1-C2-C3-C4-C5 exhibit no π-interaction because of their very large slip angle of 37.5°, despite an interplanar distance of 3.60 Å. The symmetry related pyridyl planes of N1 have a vertical displacement between the ring centroids of 2.75 Å (centroid separation 4.53 Å) [14h,42–47]. π-Interactions with rather long centroid–centroid distances >3.9 Å, large slip angles (>30°) and vertical displacements (>2.0 Å) between the ring centroids are very weak to negligible.

To the best of our knowledge, among the plethora of terephthalate bridged architectures compound **2** is only the second example where one dicarboxylate ligand joins the metal centers through coordination bonds while a second dicarboxylate anion connects through H-bonds. Here, the terephthalate anions have both a discrete coordination and a H-bonding role in the supramolecular framework construction. The other example is $[\{Zn(tmtsc)(OH_2)\}_2(\mu\text{-terephthalate})](terephthalate)\cdot 2H_2O$ [tmtsc = 1,1,4-trimethylthiosemicarbazide] [48]. Also, a copper complex, $[Cu_2(2,2'\text{-bipy})_4(\mu\text{-terephthalate})](terephthalate)$ is known where one terephthalate links the Cu-centers and the second one balances the charge as a free anion [49].

3.3. Thermal analysis

The simultaneous TG-DTA curves of complex **1** reveal that upon heating it starts to lose water molecules at 30 °C and the dehydration continues up to 80 °C (Fig. 8). The observed weight loss (13.0%) is slightly lower than the calculated one (14.1%, corresponding to nine water molecules of crystallization per formula unit) because the loss of water molecules starts at room temperature and during drying of the sample some of the water molecules are lost. The crystalline sample

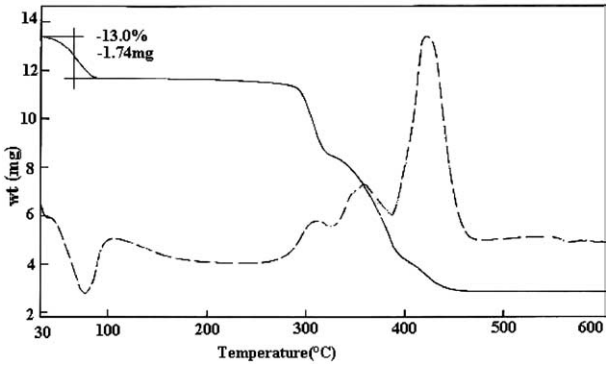


Fig. 8. The TG (——-) and DTA (-----) curves of compound **1** (heating rate: 5 °C/min).

turns into amorphous powders upon removal of water molecules. The dehydrated species is stable up to 260 °C and does not re-absorb any water on exposure to humid atmosphere suggesting that the framework integrity breaks down once the water molecules are lost. Compound **2** starts to lose its water molecules ca. 30 °C and both the crystalline and coordinated water are lost completely at 80 °C in a single step. The observed percentage of weight loss of a freshly prepared sample (16.5%) corresponds to the loss of six water molecules (per reduced formula unit, calc: 16.6%). However, on keeping the sample at room temperature the water molecules are lost gradually and consequently the percentage of water loss may not correspond to the molecular formulae if the sample is not freshly prepared. The anhydrous species is stable up to 240 °C. Here also reabsorption of water molecules does not take place on exposure of the anhydrous species to open air.

4. Conclusion

Herein, we reported two cadmium(II) complexes of terephthalate having nitrogen containing tridentate and tetradentate Schiff-base blocking ligands. Compound **1**, with a tridentate ligand, is a 1D polymeric chain whereas compound **2** with tetradentate ligand is a very rare type of dinuclear complex. In both complexes the water of crystallization is involved in a strong H-bonding network. In complex **2** the intemolecular packing is controlled by typical π-stacking interactions between pyridyl planes.

Acknowledgements

This work was supported by the University Grants Commission (UGC) (Fellowship for S. Banerjee, Sanction No. UGC/548/jr. Fellow Sc 2001/2002), the

Deutsche Forschungsgemeinschaft (Grant Ja466/10-1,-2) and the Fonds der Chemischen Industrie.

Appendix A. Supplementary data

Crystallographic data have been deposited at the Cambridge Crystallographic Data Centre as Supplementary Publication No. CCDC 267613 (compound **1**), 267614 (compound **2**). Copies of the data can be obtained free of charge on application to CCDC, 12 Union Road, Cambridge CB2 1EZ, UK (fax: 44 1223 336033; e-mail: deposit@ccdc.cam.ac.uk). Supplementary data associated with this article can be found, in the online version, at doi:10.1016/j.poly.2005.06.038.

References

[1] Review C. Janiak, Dalton Trans. (2003) 2781.
[2] C. Janiak, Angew. Chem. Int. Ed. 36 (1997) 1431.
[3] S.L. James, Chem. Soc. Rev. 32 (2003) 276.
[4] Review, porous coordination polymers: M. Eddaoudi, J. Kim, D. Vodak, A. Sudik, J. Wachter, M. O'Keeffe, O.M. Yaghi, PNAS 99 (2002) 4900.
[5] Review, luminescent coordination polymers: S.-L. Zheng, X.-M. Chen, Aust. J. Chem. 57 (2004) 703.
[6] Reviews, magnetic (nanoporous) coordination polymers: D. Maspoch, D. Ruiz-Molina, J. Veciana, J. Mater. Chem. 14 (2004) 2713.
[7] S.R. Batten, K.S. Murray, Coord. Chem. Rev. 246 (2003) 103.
[8] Review, polycatenated, polythreaded coordination polymers: L. Carlucci, G. Ciani, D. Proserpio, Coord. Chem. Rev. 246 (2003) 247.
[9] (a) M. Eddaoudi, D.B. Moler, H. Li, B. Chen, T.M. Reineke, M. O'Keeffe, O.M. Yaghi, Acc. Chem. Res. 34 (2001) 319;
(b) O.M. Yaghi, H. Li, C. Davis, D. Richardson, T.L. Groy, Acc. Chem. Res. 31 (1998) 474;
(c) T.M. Reineke, M. Eddaoudi, M. O'Keeffe, O.M. Yaghi, Angew. Chem. Int. Ed. 38 (1999) 2590;
(d) H. Li, M. Eddaoudi, M. O'Keeffe, O.M. Yaghi, Nature (London) 402 (1999) 276;
(e) O.R. Evans, Z. Wang, R.G. Xiong, B.M. Foxman, W. Lin, Inorg. Chem. 38 (1999) 2969;
(f) L. Pan, X. Huang, J. Li, Y. Wu, N. Zheng, Angew. Chem. Int. Ed. 39 (2000) 527;
(g) C. Janiak, T.G. Scharmann, P. Albrecht, F. Marlow, R. Macdonald, J. Am. Chem. Soc. 118 (1996) 6307.
[10] C. Janiak, H. Hemling, J. Chem. Soc., Dalton Trans. (1994) 2947.
[11] C. Janiak, T.G. Scharmann, H. Hemling, D. Lentz, J. Pickardt, Chem. Ber. 128 (1995) 235.
[12] C. Janiak, T.G. Scharmann, K.-W. Brzezinka, P. Reich, Chem. Ber. 128 (1995) 323.
[13] (a) D. Braga, Chem Commun. (2003) 2751;
(b) A.M. Beatty, Coord. Chem. Rev. 246 (2003) 131;
(c) L. Brammer, J.C.M. Rivas, R. Atencio, S. Fang, F.C. Pigge, J. Chem. Soc., Dalton Trans. (2000) 3855;
(d) T.J. Burchell, D.J. Eisler, M.C. Jennings, R.J. Puddephatt, Chem. Commun. (2003) 2228;
(e) Z. Qin, M.C. Jennings, R.J. Puddephat, Inorg. Chem. 41 (2002) 5174;
(f) S. Muthu, J.H.K. Yip, J.J. Vittal, J. Chem. Soc. Dalton Trans. (2001) 3577;
(g) S. Muthu, J.H.K. Yip, J.J. Vittal, J. Chem. Soc., Dalton Trans. (2002) 4561;
(h) L. Schauer, E. Matwey, F.W. Fowler, J.W. Lauher, J. Am. Chem. Soc. 119 (1997) 10245.
[14] (a) O.M. Yaghi, H. Li, T.L. Groy, J. Am. Chem. Soc. 118 (1996) 9096;
(b) C.B. Aakeroy, A.M. Beatty, D.S. Leinen, Angew. Chem., Int. Ed. 38 (1999) 1815;
(c) C.B. Aakeroy, A.M. Beatty, B.A. Helfrich, J. Chem. Soc., Dalton Trans. (1998) 1943;
(d) A.D. Burrows, D.M.P. Mingos, A.J.P. White, D.J. Williams, Chem. Commun. (1996) 97;
(e) K.A. Hirsch, S.R. Wilsen, J.S. Moore, Chem. Eur. J. 3 (1997) 765;
(f) M. Nishio, M. Airohito, Y. Umezawa, The CH/π interation, Wiley–VCH, New York, 1998;
(g) M-.L.Tong, B.H. Ye, J-.W. Cai, X-.M. Chen, S.W. Ng, Inorg. Chem. 37 (1998) 2645;
(h) C. Janiak, J. Chem Soc., Dalton Trans. (2000) 3885;
(i) G. Yang, H.-G. Zhu, B.-H. Liang, X.-M. Chen, J. Chem. Soc., Dalton. Trans. (2001) 580.
[15] Recent examples for Cd(II) compounds: C. Hu, Q. Li, U. Englert, Cryst. Eng. Commun. 5 (2003) 519.
[16] B. Chand, U. Ray, G. Mostafa, T.-H. Lu, C. Sinha, Polyhedron 23 (2004) 1669.
[17] J. Granifo, M.T. Garland, R. Baggio, Inorg. Chem. Commun. 7 (2004) 77.
[18] C. Janiak, L. Uehlin, H.-P. Wu, P. Klüfers, H. Piotrowski, T.G. Scharmann, J. Chem. Soc., Dalton Trans. (1999) 3121.
[19] H.-P. Wu, C. Janiak, G. Rheinwald, H. Lang, J. Chem. Soc., Dalton Trans. (1999) 183.
[20] H.-P. Wu, C. Janiak, L. Uehlin, P. Klüfers, P. Mayer, Chem. Commun. (1998) 2637.
[21] (a) M.L-. Tong, X.-M. Chen, X.-L. Yu, T.C.W. Mak, J. Chem. Soc, Dalton Trans. (1998) 5;
(b) L.R .Macgillicray, R.H. Groeneman, J.L. Atwood, J. Am. Chem. Soc. 120 (1998) 2676;
(c) P. Lightfoot, A. Snedden, J. Chem. Soc., Dalton Trans. (1999) 3549;
(d) P.J. Hagrman, D. Hagrman, J. Zubieta, Angew. Chem., Int. Ed. 38 (1999) 2639;
(e) M.L-. Tong., H.-J. Chen, X.-M. Chen, Inorg. Chem. 39 (2000) 2235;
(f) M.L-. Tong, J.-W. Cai, X.-L. Yu, X.-M. Chen, S.W. Ng, T.C.W. Mak, Aust. J. Chem. 51 (1998) 637;
(g) M.L-. Tong, S.-L. Zheng, X.-M. Chen, Chem. Comm. (1999) 561;
(h) M.L-. Tong, X.-M. Chen, B.-H. Ye, L.-N. Ji, Angew Chem., Int. Ed. 38 (1999) 2237;
(i) M.L-. Tong, H.K. Lee, X.-M. Chen, R.B. Huang, T.C.W. Mak, J. Chem. Soc., Dalton Trans. (1999) 3657;
(j) M.L-. Tong, S.-L. Zheng, X.-M. Chen, Polyhedron. 19 (2002) 1809;
(k) M.L-. Tong, X.-M. Chen, S.W. Ng, Inorg. Chem. Commun. 3 (2002) 436;
(l) Brian D. Wagner, G.J. Mc Manus, Brian Moulton, Michael J. Zaworotko, Chem Comm. (2002) 2176.
[22] (a) P.J. Hagrman, D. Hagrman, J. Zubieta, Angew. Chem., Int. Ed. 38 (1999) 2638;
(b) L. Carlucci, G. Ciani, D. Proserpio, A. Sironi, J. Am. Chem. Soc. 117 (1995) 4562;
(c) O.M. Yaghi, G. Li, H. Li, Nature (London) 378 (1995) 703;
(d) S. Subramanian, M.J. Zaworotko, Angew. Chem., Int. Ed. 34 (1995) 2127;
(e) M.A.S. Goher, F.A. Mautner, M.A.M. Abu-Youssef, A.K. Hafez, A.M.-A. Badr, J. Chem. Soc., Dalton Trans. (2002) 3309;
(f) M.A.S. Goher, F.A. Mautner, M.A.M. Abu-Youssef, A.K. Hafez, A.M.-A. Badr, J. Chem. Soc., Dalton Trans. (2002) 3309.

[23] (a) J. Canno, G. Demunno, J.L. Sanz, R. Ruiz, J. Faus, F. Lloret, M. Julve, A. Caneshi, J. Chem. Soc., Dalton Trans. (1997) 1915;
(b) E.J. Bakalbassis, J. Mrozaski, C.A. Tsipis, Inorg. Chem. 25 (1986) 3684;
(c) M. Verdaguer, J. Gouteron, S. Jeannin, Y. Jeannin, O. Kahn, Inorg. Chem. 23 (1984) 4291;
(d) K.S. Burger, P. Chaudhuri, K. Wieghardt, B. Nuber, Chem. Eur. J. 1 (1995) 583;
(e) P. Chaudhuri, K. Oder, K. Wieghardt, S. Gehring, W. Haase, B. Nuber, J. Weiss, J. Am.Chem. Soc. 110 (1988) 3657.

[24] (a) C.E. Xanthopoulos, M.P. Sigala, G.A. Katsoulos, C.A. Tsipis, A. Terzis, M. Mentzafos, Inorg. Chem. 32 (1993) 5433;
(b) E.G. Bakalbassis, A.P. Bozpoulos, J. Mrozinski, P.J. Rentzeperis, C.A. Tsipis, Inorg. Chem. 27 (1988) 529;
(c) E.G. Bakalbassis, P. Bergerat, O. Kahn, S. Jeannin, Y. Jeannin, Y. Dromzee, M. Guillot, Inorg. Chem. 31 (1992) 625.

[25] C.S. Hong, S.K. Son, Y.S. Lee, M.J. Jun, Y. Do, Inorg. Chem. 38 (1999) 5602.

[26] B. Paul, B. Zimmermann, K.M. Fromm, C. Janiak, Z. Anorg. Allg. Chem. 630 (2004) 1650.

[27] (a) H.-K. Fun, S.S.S. Raj, R.-G. Xiong, J.-L. Zuo, Z. Yu, X.-Z. You, J. Chem. Soc., Dalton Trans. (1999) 1915;
(b) J. Tao, M.-L. Tong, X.-M. Chen, J. Chem. Soc., Dalton Trans. (2000) 3669;
(c) D. Sun, R. Cao, Y. Liang, Q. Shi, W. Su, M. Hong, J. Chem. Soc., Dalton Trans. (2001) 2335;
(d) J.-C. Dai, X.-T. Wu, Z.-Y. Fu, S.-M. Hu, W.-X. Du, C.-P. Cui, L.-M. Wu, H.-H. Zhang, R.-Q. Sun, Chem. Commun. (2002) 12;
(e) S. Banerjee, M.G.B. Drew, A. Ghosh, Polyhedron 22 (2003) 2933;
(f) X. Shi, G. Zhu, Q. Fang, G. Wu, G. Tian, R. Wang, D. Zhang, M. Xue, S. Qiu, Eur. J. Inorg. Chem. (2004) 185.

[28] S. Banerjee, B. Wu, P.-G. Lassahn, C. Janiak, A. Ghosh, Inorg. Chim. Acta 358 (2005) 535.

[29] S. Banerjee, A. Ghosh, B. Wu, P.-G. Lassahn, C. Janiak, Polyhedron 24 (2005) 593.

[30] K.-Y. Choi, M. Suh, J. Kim, G.-H. Choo, I.-H. Suh, S.W. Ng, Main Group Met. Chem. 24 (2001) 119.

[31] R.-Q. Fan, D.-S. Zhu, Y. Mu, G.-H. Li, Y.-L. Yang, Q. Su, S.-H. Feng, Eur. J. Inorg. Chem. (2004) 4891.

[32] Y.-B. Dong, M.D. Smith, H.-C. zur Loye, Inorg. Chem. 39 (2000) 4927.

[33] SMART, Data Collection Program for the CCD Area-Detector System; SAINT, Data Reduction and Frame Integration Program for the CCD Area-Detector System. Bruker Analytical X-ray Systems, Madison, Wisconsin, USA, 1997.

[34] G. Sheldrick, Program SADABS: Area-detector Absorption Correction, University of Göttingen, Germany, 1996.

[35] G.M. Sheldrick, SHELXS-97, SHELXL-97, Programs for Crystal Structure Analysis, University of Göttingen, Germany, 1997.

[36] DIAMOND 2.1e for Windows. Crystal Impact Gbr, Bonn, Germany; http://www.crystalimpact.com/diamond.

[37] A.L. Spek, Acta Crystallogr. A46 (1990) C34.

[38] A.L. Spek, PLATON Version 29-11-98.

[39] L.J. Farrugia, Windows implementation, University of Glasgow, 1998.

[40] K. Nagamoto, Infrared and Raman Spectra of Inorganic and Coordination Compounds. Part B: Applications in Coordination, Organometallic and Bioinorganic Chemistry, fifth ed., Wiley, New York, 1997, p. 59.

[41] O.A. Michaelides, D. Tsaousis, S. Skoulika, C.P. Raptopoulou, A. Terzis, Acta Crystallogr. B. 54 (1998) 657.

[42] π-interactions between pyridyl-type ligands for comparison: K. Abu-Shandi, H. Winkler, H. Paulsen, R. Glaum, B. Wu, C. Janiak, Z. Anorg. Allg. Chem. 631 (2005) 2534.

[43] X.-J. Yang, F. Drepper, B. Wu, W.-H. Sun, W. Haehnel, C. Janiak, Dalton Trans. (2005) 256.

[44] C. Zhang, C. Janiak, Z. Anorg. Allg. Chem. 627 (2001) 1972.

[45] C. Zhang, C. Janiak, J. Chem. Crystallogr. 31 (2001) 29.

[46] C. Janiak, S. Deblon, H.-P. Wu, M.J. Kolm, P. Klüfers, H. Piotrowski, P. Mayer, Eur. J. Inorg. Chem. (1999) 1507.

[47] (a) Recent π-interactions: C. Zhang, G. Rheinwald, V. Lozan, B. Wu, P.-G. Lassahn, H. Lang, C. Janiak, Z. Anorg. Allg. Chem. 628 (2002) 1259;
(b) E. Craven, E. Mutlu, D. Lundberg, S. Temizdemir, S. Dechert, H. Brombacher, C. Janiak, Polyhedron 21 (2002) 553;
(c) C. Zhang, C. Janiak, H. Brombacher, Z. Naturforsch. B 56 (2001) 1205.

[48] A.D. Burrows, R.W. Harrington, M.F. Mahon, S.J. Teat, Eur. J. Inorg. Chem. (2003) 776.

[49] W. Huang, D. Hu, S. Gou,, H. Qian, H.-K. Fun, S.S.S. Raj, Q. Meng, J. Mol. Struct. 649 (2003) 269.

proton nuclear magnetic resonance (^{1}H NMR), carbon nuclear magnetic resonance (^{13}C NMR), single-crystal X-ray diffraction, elemental analysis and infrared spectroscopy (IR). The Cu(II) and Ni(II) complexes have been isolated and their characterization has been carried out by means of elemental analysis, IR, UV–Vis–NIR diffuse reflectance, X-ray diffraction and magnetic susceptibility measurement, and in addition the copper complex has been characterized through EPR spectroscopy.

2. Experimental

2.1. General procedures

All chemicals were of reagent grade and used without any further purification. 2-Acetyl-2-thiazoline was synthesized according to the method described by Doornbos and Peer [20]. Chemical analyses of carbon, hydrogen, nitrogen and sulfur were performed by microanalytical methods using a Leco CHNS-932 microanalyser. IR spectra were recorded on a Perkin–Elmer FT-IR 1720 spectrophotometer, from KBr pellets in the 4000–370 cm^{-1} range and on a Perkin–Elmer FT-IR 1700X spectrophotometer, from polyethylene pellets in the 500–150 cm^{-1} range. Electronic spectra in a solution of the ligand were measured on a Shimadzu UV-3101 PC using a 10 mm quartz cell. The UV–Vis–NIR reflectance spectra for each complex in the 200–1200 nm range was registered from a pellet of the sample, using a Shimadzu UV-3101 PC spectrophotometer and $BaSO_4$ as a reference. Magnetic measurement was made at room temperature on a magnetometer with a pendulum MANICS DSM8, equipped with a helium continuous-flow cryostat and an electromagnetometer DRUSCH EAF 16 UE. Data were corrected for temperature-independent paramagnetism and diamagnetic contributions, which were estimated from the Pascal constants. The EPR spectrum was recorded at room temperature on a BRUKER ESM-300 spectrometer using X band microwave frequencies. ^{1}H and ^{13}C NMR spectra were obtained with a Bruker AM 400 instrument at 400 and 100 MHz, respectively, in DMSO using Me_4Si as the internal standard.

2.2. Synthesis of 2-acetyl-2-thiazoline semicarbazone (ATsc)

To a solution containing 2-acetyl-2-thiazoline (1.00 g, 0.008 mol) and potassium acetate (1.55 g, 0.016 mmol) in 10 mL ethanol 50%, was added a solution of semicarbazide hydrochloride (0,87 g, 0.008 mmol) in 30 mL ethanol 50%, and the resulting solution was heated to reflux for 7 h. Then the solution was cooled and a white powder appeared (1.41 g, 97%). This solid was recrystallized from methanol, yielding prismatic crystals, of considerable size (ca. 0.6 mm), suitable for X-ray diffraction.

^{1}H NMR (DMSO): δ 9.92 (s, 1H, NH), 4.3 (t, $J = 8.3$ Hz, 2H, CH_2–N), 3.22 (t, $J = 8.3$ Hz, 2H, CH_2–S), 2.10 (s, 3H, CH_3); ^{13}C NMR (DMSO): δ 168.53 C(1), 156.23 C(6), 141.04 C(4), 65.10 C(2), 31.79 C(3), 13.04 C(5). *Anal.* Calc. for $C_6H_{10}N_4SO$: C, 38.70; H, 5.41; N, 30.09; S, 17.21. Found: C, 38.68; H, 5.75; N, 29.72; S, 16.99%. UV–Vis (MeOH): λ_{max}, nm; (ε, L mol^{-1} cm^{-1}) 266 (30 090).

2.3. Preparation of [$CuCl_2$(ATsc)]

This complex was prepared by reacting a methanol solution (2 mL) of $CuCl_2 \cdot 2H_2O$ (93 mg, 0.51 mmol) with a methanol solution (40 mL) of ATsc (100 mg, 0.51 mmol). The resulting solution was allowed to evaporate slowly at room temperature. After a day, green prismatic crystals of considerable size (ca. 0.5 mm) were isolated from the solution (173 mg, 73%). The crystals were separated by filtration, washed with cold ether and air-dried. *Anal.* Calc. for $C_6H_{10}Cl_2CuN_4OS$: C, 22.47; H, 3.14; N, 17.47; S, 10.00. Found: C, 22.69; H, 3.41; N, 17.40; S, 9.61%.

2.4. Preparation of [$Ni(ATsc)_2$]$(NO_3)_2 \cdot H_2O$

This complex was prepared by reacting a methanol solution (2 mL) of $Ni(NO_3)_2 \cdot 6H_2O$ (155 mg, 0.51 mmol) with a methanol solution (40 mL) of ATsc (100 mg, 0.51 mmol). The resulting solution was allowed to evaporate slowly at room temperature. After several weeks, dark green prismatic crystals of considerable size (ca. 0.4 mm) were isolated from the solution (72 mg, 47%). The crystals were separated by filtration, washed with cold ether and air-dried. *Anal.* Calc. for $C_{12}H_{22}N_{10}NiO_9S_2$: C, 25.15; H, 3.87; N, 24.44; S, 11.19. Found: C, 24.81; H, 4.10; N, 24.07; S, 10.87%.

2.5. Crystal structure determinations

Experimental details of the crystal structure determinations, including crystal data, data collection, structure determination and refinement parameters for ATsc, [$CuCl_2$(ATsc)] and [$Ni(ATsc)_2$]$(NO_3)_2 \cdot H_2O$, are listed in Table 1. X-ray diffraction measurements were performed using a Bruker SMART CCD diffractometer. The first fifty frames were measured at the end of the data collection to monitor instrument and crystal stability. Absorption corrections were applied using the program SADABS. The structures were solved by direct methods and subsequent Fourier differences using the WINGX package [21] and refined by full-matrix least-squares on F^2, assuming anisotropic displacement parameters for non-hydrogen atoms. The hydrogen atoms on ATsc were obtained from a difference Fourier synthesis and refined without any constrains, excepting hydrogen atoms of methyl group which were calculated

Table 1
Crystal data, data collection and refinement details for ATsc, $[CuCl_2(ATsc)]$ and $[Ni(ATsc)_2](NO_3)_2 \cdot H_2O$

Complex	ATsc	$[CuCl_2(ATsc)]$	$[Ni(ATsc)_2](NO_3)_2 \cdot H_2O$
Crystal shape	prism	prism	prism
Colour	colourless	green	dark green
Size (mm)	$0.63 \times 0.29 \times 0.25$	$0.50 \times 0.29 \times 0.11$	$0.43 \times 0.29 \times 0.26$
Chemical formula	$C_6H_{10}N_4OS$	$C_6H_{11}Cl_2CuN_4OS$	$C_{12}H_{22}NiN_{10}O_9S_2$
Formula weight	186.2	320.7	573.2
Crystal system	triclinic	orthorhombic	monoclinic
Space group	$P\bar{1}$	$Pna2_1$	$C2/c$
Unit cell dimensions			
a (Å)	7.082(1)	14.808(1)	19.073(1)
b (Å)	7.734(1)	6.508(1)	14.621(1)
c (Å)	8.558(1)	12.176(1)	17.672(1)
α (°)	93.587(1)		
β (°)	109.861(1)		106.361(1)
γ (°)	95.814(1)		
Cell volume (Å^3)	436.3(1)	1173.4(1)	4728.5(4)
Z	2	4	8
T (K)	298	298	298
D_{calc} (g cm^{-3})	1.418	1.821	1.610
μ (mm^{-1})	0.329	2.473	1.061
$F(000)$	196	648	2367
Diffractometer	Bruker SMART CCD	Bruker SMART CCD	Bruker SMART CCD
Radiation	Mo Kα ($\lambda = 0.71073$ Å)	Mo Kα ($\lambda = 0.71073$ Å)	Mo Kα ($\lambda = 0.71073$ Å)
Collection method	ϕ–ω	ϕ–ω	ϕ–ω
2θ Range (°)	5.1–56.5	5.5–56.6	3.6–56.7
Index ranges	$-9 \leqslant h \leqslant 9$, $-10 \leqslant k \leqslant 10$, $-11 \leqslant l \leqslant 11$	$-19 \leqslant h \leqslant 19$, $-6 \leqslant k \leqslant 8$, $-15 \leqslant l \leqslant 15$	$-24 \leqslant h \leqslant 25$, $-19 \leqslant k \leqslant 18$, $-23 \leqslant l \leqslant 23$
Independent reflections	1970	2606	5572
Completeness to θ_{max} (%)	91.1	93.4	94.2
Observed reflections	1873[$F > 4.0\ \sigma(F)$]	2506 [$F > 4.0\ \sigma(F)$]	4797 [$F > 4.0\ \sigma(F)$]
Refinement method	full-matrix least-squares on F^2	full-matrix least-squares on F^2	full-matrix least-squares on F^2
Absorption correction	empirical	empirical	empirical
Maximum/minimum transmission	0.922/0.819	0.773/0.371	0.770/0.658
Number of refined parameters	138	137	309
R [$F > 4.0\sigma(F)$][a]	0.039	0.024	0.044
wR [$F > 4.0\sigma(F)$][b]	0.112	0.057	0.122
Goodness-of-fit (GOF)[c]	1.077	1.032	1.037
ρ_{max} and ρ_{min} (e Å^{-3})	0.258 and −0.32	0.332 and −0.232	0.593 and −0.433

[a] $R = \sum \| F_o | - | F_c \| / \sum | F_o |$.
[b] $R = \{\sum [w(F_o^2 - F_c^2)^2] / \sum [w(F_o^2)^2]\}^{1/2}$.
[c] $\mathrm{GOF} = \{\sum [w(F_o^2 - F_c^2)^2] / (N_{rflns} - N_{params})\}^{1/2}$.

in ideal positions. In the complexes, all hydrogen atoms attached to carbon and nitrogen atoms were positioned geometrically, with U_{iso} values derived from U_{eq} values of the corresponding carbon and nitrogen atoms. In the nickel complex, the hydrogen atoms of the water molecule were ignored. Diagrams were generated using ORTEP3 for Windows [22].

3. Results and discussion

3.1. Description of the structures

An ORTEP diagram of the molecular structure of ATsc is shown in Fig. 1. Bond lengths, angles and hydrogen-bond parameters are listed in Table 2.

In the S–C(1)–N(1)–C(2)–C(3) ring, the short endocyclic C=N bond [C(1)–N(1) = 1.266(2) Å] is accompanied by a high N–C–S angle [N(1)–C(1)–S = 118.2(1)°] and a relatively long S^{II}–C(sp^2) bond [S–C(1) = 1.770(1) Å], which is characteristic of a thiazoline ring

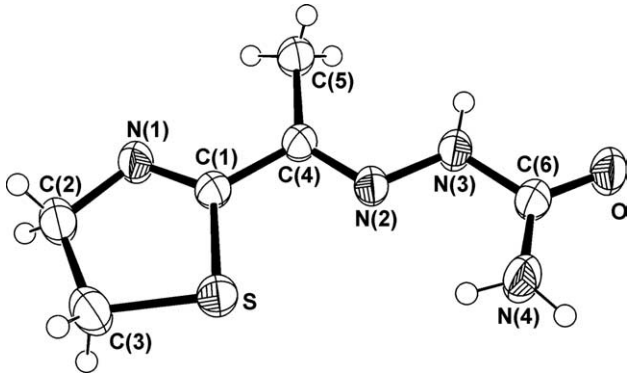


Fig. 1. Crystal structure of ATsc, showing the atom-numbering scheme. The thermal ellipsoids are plotted at the 40% probability level.

Table 2
Bond lengths (Å), angles (°) and hydrogen-bond parameters for ATsc

S–C(1)	1.770(1)	S–C(3)	1.804(2)
C(1)–N(1)	1.266(2)	C(1)–C(4)	1.474(2)
C(4)–N(2)	1.282(2)	C(4)–C(5)	1.493(2)
N(2)–N(3)	1.362(2)	N(1)–C(2)	1.466(2)
C(2)–C(3)	1.524(3)	O–C(6)	1.228(2)
N(3)–C(6)	1.375(2)	N(4)–C(6)	1.324(2)
C(1)–S–C(3)	90.2(1)	N(1)–C(1)–C(4)	123.6(1)
N(1)–C(1)–S	118.2(1)	C(4)–C(1)–S	118.1(1)
N(2)–C(4)–C(1)	112.9(1)	N(2)–C(4)–C(5)	127.6(1)
C(1)–C(4)–C(5)	119.5(1)	C(4)–N(2)–N(3)	119.6(1)
C(1)–N(1)–C(2)	112.6(1)	C(2)–C(3)–S	106.7(1)
N(1)–C(2)–C(3)	111.6(1)	N(2)–N(3)–C(6)	118.0(1)
O–C(6)–N(4)	123.5(2)	O–C(6)–N(3)	119.9(1)
N(4)–C(6)–N(3)	116.6(1)		
D–H···A	Position of A	D···A (Å)	D–H···A (°)
N(3)–H(3C)···O	$-x-1, -y, -z$	2.858(2)	173(2)
N(4)–H(4A)···N(1)	$x, y, z-1$	2.982(2)	158(3)

[23]. It is known that the imino tautomers can exist as two geometric isomers, *syn* (*Z*) and *anti* (*E*), but in this crystal, only the *E* isomers have been observed.

The thiazoline ring shows a conformation near to envelope with the C(3) atom deviating 0.139 Å above the plane formed by S, C(1), N(1) and C(2). This geometry is proved by the puckering parameters $Q = 0.090$ Å and $\phi = 135.5°$, calculated according to Cremer and Pople [24]. As was to be expected, the semicarbazone group C(4)–N(2)–N(3)–C(6)–O–N(4) is essentially planar with maximum least square plane deviations for N(3) [0.032 Å].

The molecular units of ATsc are linked by hydrogen bonds in a one dimensional chain parallel to the *c*-direction, in which carbonyl oxygen atom and thiazolinic N(1) nitrogen atom act as acceptors of hydrogen, whereas the aminic nitrogen atoms of the semicarbazone group, N(3) and N(4), act as donors. A diagram showing the hydrogen-bonds is given in Fig. 2.

The molecular structure of $[CuCl_2(ATsc)]$ with the atomic labelling is shown in Fig. 3. Selected bond lengths, angles and hydrogen-bond parameters are given in Table 3.

The copper(II) complex is five-coordinate, defining a square-pyramidal coordination polyhedron. The shape of the polyhedron has been quantified following two methods reported in the bibliography [25,26] and the results are summarized in Table 4. Both Δ and τ parameters assign a slightly distorted square pyramid for the coordination environment. The equatorial positions are occupied by a chloro ligand [Cu–Cl(2) = 2.223(1) Å], one carbonyl oxygen atom [Cu–O = 2.036(2) Å], one thiazolinic nitrogen atom [Cu–N(1) = 1.999(2) Å] and one iminic nitrogen atom [Cu–N(2) = 1.983(2) Å]. The

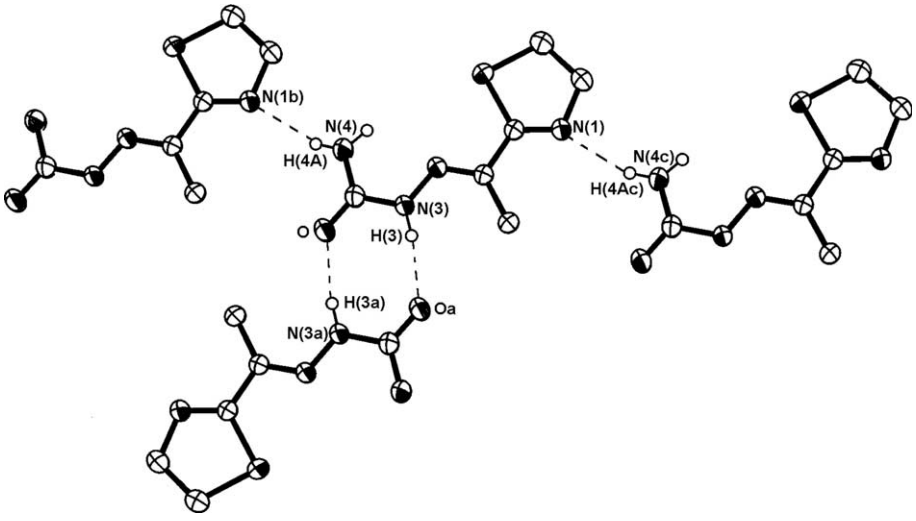


Fig. 2. View of the hydrogen bond network of ATsc.

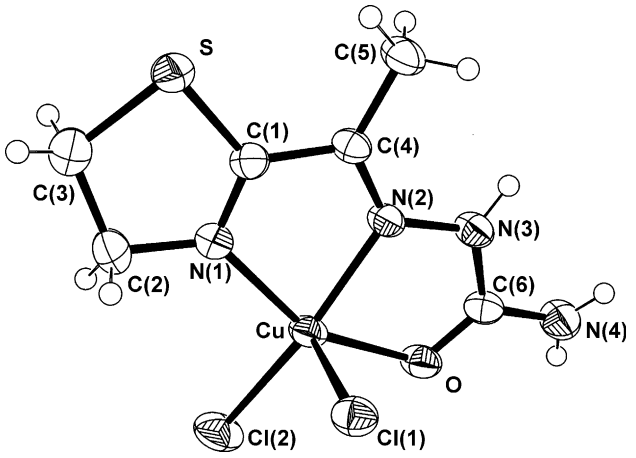


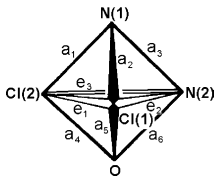
Fig. 3. Molecular structure of [$CuCl_2$(ATsc)], showing the atom-numbering scheme. The thermal ellipsoids are drawn at the 40% probability level.

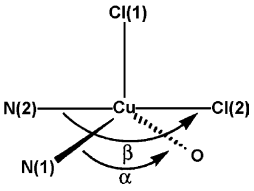
axial position is occupied by the Cl(1) ligand at a distance of 2.500(1) Å from the copper atom. The Cl(1)–metal–basal ligand angles vary from the ideal value for a square pyramid (90°) and they range between 101.8(1)° [Cl(1)–Cu–Cl(2)] and 95.1(1)° [N(2)–Cu–Cl(1)]. Likewise, the basal ligand–metal–basal ligand angles differ from the ideal value of 90°, varying between 100.5(1)° [N(1)–Cu–Cl(2)] and 77.5(1)° [N(2)–Cu–O].

The Cu–Cl basal bond distance is similar to the average value [2.259(43) Å] calculated using the data of 25 square pyramidal copper(II) complexes with an Cl_2N_2O environment, obtained with the CONQUEST software [27] from the Cambridge Structural Database (CSD) [28]. In the same way, the Cu–Cl axial bond distance is comparable to the mean value 2.540(92) Å obtained from 17 complexes collected in the CSD using the data of crystal structures of square pyramidal copper(II) complexes with the chromophore group $CuCl_2N_2O$. Likewise, the Cu–O_{ketone} and Cu–N_{imine} distances are comparable to the mean

Table 4
Quantification of the geometry of the copper(II) polyhedra

Geometrical parameters		Square-based pyramid	[$CuCl_2$-(ATsc)]	Trigonal bipyramid
Dihedral angle[a]	δa1	119.8	116.6	101.5
	δa2	75.7	77.6	101.5
	δa3	119.8	116.1	101.5
	δa4	119.8	116.7	101.5
	δa5	75.7	76.9	101.5
	δa6	119.8	116.1	101.5
	δe1	75.7	89.7	53.1
	δe2	75.7	68.0	53.1
	δe3	0.0	1.37	53.1
	Δ	1.00	0.90	0.00
Angle[b]	α	180.0	163.0	180.0
	β	180.0	153.0	120.0
	τ	0.00	0.17	1.00





[a] Dihedral angles defined following Muetterties and Guggenberger [26].

[b] α and β are the greatest angles around the metal ion. The relative trigonality of the polyhedron $\tau = (\alpha - \beta)/60$ [25].

Table 3
Selected bond lengths (Å), angles (°) and hydrogen-bond parameters for [$CuCl_2$(ATsc)]

Cu–Cl(1)	2.500(1)	Cu–Cl(2)	2.223(1)
Cu–N(1)	1.999(2)	Cu–N(2)	1.983(2)
Cu–O	2.036(2)	C(1)–N(1)	1.285(3)
C(1)–C(4)	1.477(3)	N(2)–N(3)	1.360(3)
N(2)–C(4)	1.277(3)	C(6)–O	1.247(3)
C(6)–N(3)	1.374(3)		
Cl(1)–Cu–Cl(2)	101.8(1)	Cl(1)–Cu–O	96.8(1)
Cl(2)–Cu–O	98.4(1)	N(2)–Cu–O	77.5(1)
N(1)–Cu–O	153.0(1)	N(1)–Cu–N(2)	78.8(1)
N(1)–Cu–Cl(1)	98.0(1)	N(1)–Cu–Cl(2)	100.5(1)
N(2)–Cu–Cl(1)	95.1(1)	N(2)–Cu–Cl(2)	163.0(1)
C(6)–O–Cu	113.8(2)	C(2)–N(1)–Cu	132.4(2)
C(4)–N(2)–Cu	119.1(2)	N(3)–N(2)–Cu	115.3(1)
C(1)–N(1)–Cu	113.3(2)	O–C(6)–N(3)	120.2(2)
C(4)–N(2)–N(3)	125.6(2)	N(2)–C(4)–C(1)	110.0(2)
N(1)–C(1)–C(4)	118.5(2)	N(2)–N(3)–C(6)	111.9(2)

D–H···A	Position of A	D···A (Å)	D–H···A (°)
N(3)–H(3)···Cl(1)	$-x+1/2$, $y-1/2$, $z+1/2$	3.204(2)	141
N(4)–H(4B)···Cl(2)	$-x+1/2$, $y-1/2$, $z+1/2$	3.316(2)	153
N(4)–H(4A)···Cl(1)	x, $y-1$, z	3.300(2)	168

values 2.044(140) and 1.967(54) Å, respectively, found using the data of 12 copper(II) complexes bonded to a semicarbazone moiety obtained from the CSD. Finally, the Cu–$N_{thiazoline}$ bond length is similar to the calculated average value [1.952(38) Å] collected for 12 copper(II) complexes in the CSD.

The five-membered chelate ring Cu–N(1)–C(1)–C(4)–N(2) is essentially planar with maximum mean plane deviation for N(2) (0.040 Å). On the contrary, the chelate ring Cu–N(2)–N(3)–C(6)–O presents a conformation near to half-chair [$q = 0.130$ Å; $\phi = 13.5°$] [24], with Cu and N(2) deviating −0.168 and 0.082 Å, respectively, from the plane formed by N(3), C(6) and O.

For the thiazoline ring, the puckering parameters $q = 0.202$ Å, $\phi = -41.8°$ [26] indicate a conformation near to envelope with the C(3) atom deviating 0.316 Å above the mean plane formed by S, C(1), N(1) and C(2).

Finally, the crystal structure presents a two-dimensional hydrogen-bond network perpendicular to the a-axis in which chloro ligands Cl(1) and Cl(2) act as acceptors of hydrogen, whereas nitrogen atoms N(3) and N(4) act as donors. A diagram showing this network is given in Fig. 4.

The X-ray study of the nickel(II) complex revealed that the crystals are made up of monoclinic unit cells, each containing eight $[Ni(ATsc)_2]^{2+}$ cations, sixteen nitrate anions and eight water molecules held together by hydrogen bonds. The overall view and labelling of the atoms of complex cation are displayed in Fig. 5. Table 5 lists the selected bond lengths, angles and hydrogen-bond parameters.

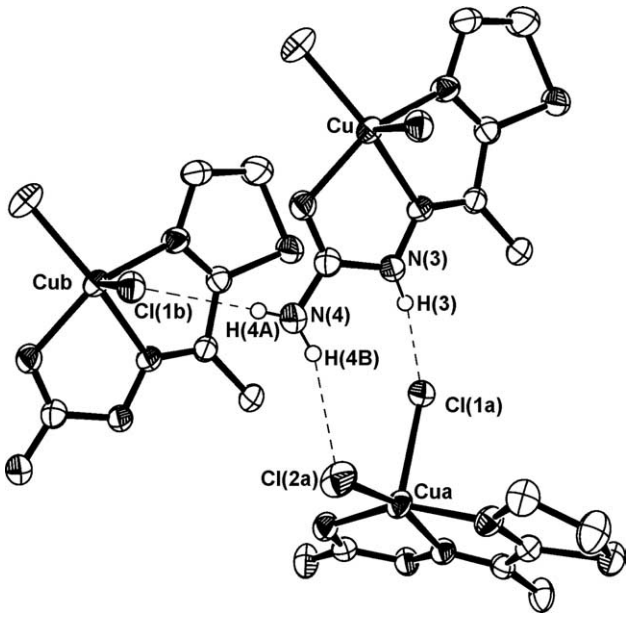


Fig. 4. View of the hydrogen bonds of $[CuCl_2(ATsc)]$.

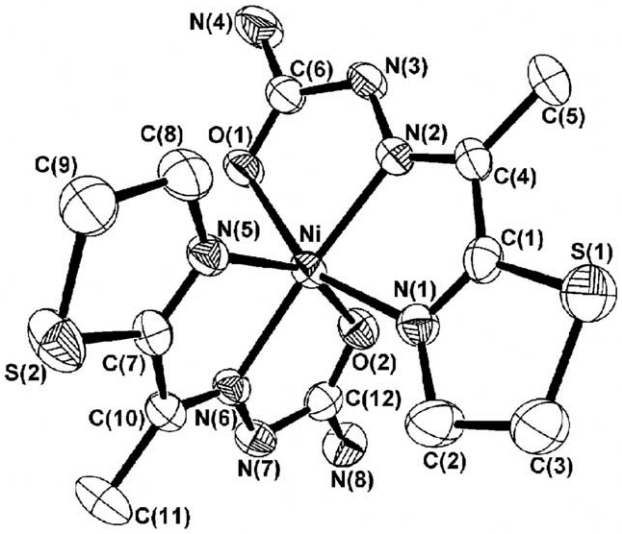


Fig. 5. Molecular structure of cation complex $[Ni(ATsc)_2]^{2+}$, showing the atom-numbering scheme. The thermal ellipsoids are drawn at the 40% probability level.

The complex cation possesses approximately a non-crystallographic C_2 symmetry, with the twofold axis placed at the bisector of the O(1)–Ni–O(2) angle.

The environment around the nickel(II) atom may be described as a distorted octahedral geometry with the ligand–metal–ligand bite angles varying between 76.9(1)° [N(2)–Ni–O(1)] and 107.5(1)° [N(2)–Ni–O(2)]. The metallic atom is coordinated by two carbonyl oxygen atoms [av. Ni–O = 2.103 Å], two thiazolinic nitrogen atoms [av. Ni–N = 2.073 Å] and two iminic nitrogen atoms [av. Ni–N = 2.010 Å].

The Ni–O_{ketone} and Ni–N_{imine} bond lengths have been compared with the mean value calculated with the data of 5 nickel(II) complexes bonded to a semicarbazone moiety obtained from the CSD. Thus, these bond lengths are in good agreement with the mean value of 2.107(35) Å for the Ni–O_{ketone} distance and 1.993(35) Å for the Ni–N_{iminne} distance Finally, the Ni–$N_{thiazoline}$ bond lengths are closer to that found in $[Ni(PyTT)_2(H_2O)_2]Cl_2 \cdot 2H_2O$ (2.061(2) Å) [29], but somewhat longer than that observed in $[Ni(TzHy)_2(H_2O)_2]Cl_2 \cdot 3H_2O$ (2.027(3) Å) [30].

The five-membered chelate rings are essentially planar. The maximum deviation in relation to the corresponding mean plane are produced for N(2) (0.007 Å) [chelate ring Ni–O(1)–C(6)–N(3)–N(2)], N(1) (0.046 Å) [chelate ring Ni–N(2)–C(4)–C(1)–N(1)], N(6) (0.012 Å) [chelate ring Ni–O(2)–C(12)–N(7)–N(6)] and C(7) (0.027 Å) [chelate ring Ni–N(6)–C(10)–C(7)–N(5)].

The thiazoline ring S(1)–C(1)–N(1)–C(2)–C(3) is essentially planar with maximum mean plane deviation for C(3) (0.069 Å). However, the other thiazoline ring S(2)–C(7)–N(5)–C(8)–C(9) shows a conformation near to envelope [$q = 0.096$ Å and $\phi = 134.6°$] [24] with the

Table 5
Selected bond lengths (Å), angles (°) and hydrogen-bond parameters for $[Ni(ATsc)_2](NO_3)_2 \cdot H_2O$

Ni–N(1)	2.075(2)	Ni–N(5)	2.070(2)
Ni–N(2)	2.003(2)	Ni–N(6)	2.017(2)
Ni–O(1)	2.107(2)	Ni–O(2)	2.099(2)
C(1)–N(1)	1.272(3)	N(6)–C(10)	1.281(3)
N(6)–N(7)	1.346(3)	O(2)–C(12)	1.249(3)
N(2)–C(4)	1.277(3)	N(2)–N(3)	1.351(3)
O(1)–C(6)	1.246(3)	N(5)–C(7)	1.271(3)
N(7)–C(12)	1.378(3)	C(7)–C(10)	1.486(4)
N(3)–C(6)	1.374(3)	C(1)–C(4)	1.486(3)
N(1)–Ni–O(1)	154.3(1)	N(1)–Ni–O(2)	92.6(1)
N(1)–Ni–N(2)	77.9(1)	N(1)–Ni–N(5)	92.7(1)
N(1)–Ni–N(6)	103.0(1)	N(2)–Ni–O(1)	76.9(1)
N(2)–Ni–O(2)	107.5(1)	N(2)–Ni–N(5)	97.9(1)
N(2)–Ni–N(6)	175.5(1)	N(5)–Ni–O(1)	95.4(1)
N(5)–Ni–O(2)	154.6(1)	N(5)–Ni–N(6)	77.6(1)
N(6)–Ni–O(1)	102.6(1)	N(6)–Ni–O(2)	77.0(1)
O(1)–Ni–O(2)	90.6(1)	C(1)–N(1)–Ni	111.8(2)
C(10)–N(6)–Ni	119.7(2)	C(10)–N(6)–N(7)	124.8(2)
N(7)–N(6)–Ni	115.5(1)	C(12)–O(2)–Ni	113.2(2)
C(4)–N(2)–N(3)	124.2(2)	C(4)–N(2)–Ni	119.8(2)
N(3)–N(2)–Ni	115.9(1)	C(6)–O(1)–Ni	112.8(2)
C(7)–N(5)–Ni	112.6(2)	N(1)–C(1)–C(4)	120.0(2)
N(6)–N(7)–C(12)	114.2(2)	O(2)–C(12)–N(7)	120.2(2)
N(5)–C(7)–C(10)	119.9(2)	N(2)–N(3)–C(6)	113.7(2)
O(1)–C(6)–N(3)	120.5(2)	N(6)–C(10)–C(7)	110.1(2)
N(2)–C(4)–C(1)	110.1(2)		

D–H···A	Position of A	D···A (Å)	D–H···A (°)
N(8)–H(8A)··· O(6)	x, y, z	2.809(3)	150
N(8)–H(8B)··· O(4)	$-x+1/2, -y+1/2+2, -z$	2.897 (3)	149
N(7)–H(7)··· O(5)	$-x+1/2, -y+1/2+2, -z$	2.789(3)	166
N(4)–H(4A)··· O(3)	$x, -y+2, z-1/2$	2.969(4)	165
N(4)–H(4B)··· O(1W)	$x+1/2, y-1/2, z$	2.841(4)	151
N(3)–H(3)··· O(6)	$-x+1/2, -y+1/2+1, -z$	2.864(3)	134
N(3)–H(3)··· O(2)	$-x+1/2, -y+1/2+1, -z$	3.018(3)	140

apex at C(9). This atom is 0.144 Å out of the mean plane formed by S(2), C(7), N(5) and C(8).

The crystal structure is stabilized by a network of hydrogen-bonds, which forms chains along the [110] direction, in which nitrogen atoms N(3), N(4), N(7) and N(8) act as hydrogen donors, the oxygen atoms of nitrate ions and the crystallisation water molecule act as acceptors.

Finally, it should be pointed out that the main difference in both complexes with respect to the structure of free ATsc is due to the different degree of rotation of the thiazoline ring around the C(1)–C(4) [or C(7)–C(10)] bond, which permits the coordination through thiazoline nitrogen atoms [torsion angle S–C(1)–C(4)–N(2) = 177.7° in $[CuCl_2(ATsc)]$; S(1)–C(1)–C(4)–N(2) = −179.3° and S(2)–C(7)–C(10)–N(6) = −177.0° in $[Ni(ATsc)_2](NO_3)_2 \cdot H_2O$; 4.4° in ATsc]. Similarly, the formation of the complexes requires rotation around the C(6)–N(3) [or C(12)–N(7)] bond, which permits the coordination through the carbonyl oxygen atoms [N(2)–N(3)–C(6)–O = −3.7° in $[CuCl_2(ATsc)]$; N(2)–N(3)–C(6)–O(1) = −0.9° and N(6)–N(7)–C(12)–O(2) = −1.0° in $[Ni(ATsc)_2](NO_3)_2 \cdot H_2O$; 177.5° in ATsc].

3.2. IR spectra

The IR spectrum of ATsc in the 4000–370 cm^{-1} region shows the presence of bands due to the thiazoline ring vibration at 1584 (W_1), 1007 (W_2), 925 (W_3), 762 (W_4), 724 (W_5), 682 (W_6), 592 (W_8), 530 (W_7) and 430 (Γ_1) cm^{-1} [29,31,32]. Moreover, the bands registered at 1685 and 1584 cm^{-1}can be assigned to [ν(C=O)] and [ν(C=N)] vibrations respectively [33,34].

The IR spectra of complexes in the 4000–370 cm^{-1} region show the presence of bands due to ring vibrations as in show in Table 6. Other relevant bands are registered at 1667 [ν(C=O)] and 1651 cm^{-1} [ν(C=N)] for $[CuCl_2(ATsc)]$ and at 1671 [ν(C=O)] and 1645 cm^{-1} [ν(C=N)] for $[Ni(ATsc)_2](NO_3)_2 \cdot H_2O$.

In the low-frequency range, five bands assignable to metal–ligand stretching vibrations are observed for $[CuCl_2(ATsc)]$ spectra and three bands for $[Ni(ATsc)_2](NO_3)_2 \cdot H_2O$ spectra. Thus, in the Cu(II) spectrum the

Table 6
Infrared bands (cm^{-1}) assigned to ring vibrations of ATsc, [$CuCl_2$-(ATsc)] and [$Ni(ATsc)_2$]$(NO_3)_2 \cdot H_2O$

Assignment	ATsc	[$CuCl_2$(ATsc)]	[$Ni(ATsc)_2$]$(NO_3)_2 \cdot H_2O$
Thiazoline			
W_1	1584 (vs)	1651 (vs)	1645 (s)
W_2	1007 (s)	1002 (m)	1005 (w)
W_3	925 (m)	854 (w)	827 (w)
W_4	762 (m)	763 (w)	784 (vw)
W_5	724 (m)	702 (m)	697 (m)
W_6	682 (m)	636 (m)	625 (m)
W_8	592 (m)	589 (m)	577 (m)
W_7	530 (m)	545 (m)	542 (w)
Γ_1	430 (m)	420 (w)	422 (w)

Abbreviations: (s) strong; (m) medium; (w) weak; (v) very.

band at 363 cm^{-1} corresponds to a $\nu(Cu–O_{ketone})$ vibration, in accord with the literature data for this type of bond [33]. The band at 338 $cm^{-1}$is assigned to one ν(Cu–Cl) vibration [35] and the band at 321 cm^{-1} could include the $\nu(Cu–N_{imino})$ vibration [36] and the other ν(Cu–Cl) vibration [35]. The band at 228 cm^{-1} is attributed to $\nu(Cu–N_{thiazoline})$ [36]. Finally, the Ni(II) spectrum shows a first band at 361 cm^{-1}, corresponding to a $\nu(Ni–O_{ketone})$ vibration [33], a second band at 332 cm^{-1} is assigned to the $\nu(Ni–N_{imino})$ vibration [37–39] and the last band can be attributed to a $\nu(Ni–N_{thiazoline})$ vibration [29,31], according to the consulted bibliography.

3.3. Electronic spectra

The reflectance spectrum of the copper complex consists of a broad d–d asymmetric band centred at 12470 cm^{-1}. Presumably all four d–d transitions ($^2A[(d_{x^2-y^2})^1] \rightarrow {}^2A[(d_{z^2})^1], {}^2A[(d_{xy})^1], {}^2A[(d_{xz})^1], {}^2A[(d_{yz})^1]$) of the square-pyramidal geometry [40] are responsible for this band. Likewise, the spectrum shows a strong absorption at 32260 cm^{-1} (309 nm) which may be associated with a charge transfer band.

The electronic spectrum of the nickel complex shows one intense band at 32680 cm^{-1}(360 nm), which is assigned to a charge transfer band. Moreover, the spectrum exhibits bands at 11494, 12658 (sh) and 16835 cm^{-1}, all of which were of low intensity. These bands may be assigned as: $\nu_1[{}^3A_{2g}(F) \rightarrow {}^3T_{2g}(F)]$ (11494 cm^{-1}), $^3A_{2g}(F) \rightarrow {}^1E_g(D)$ (12658 cm^{-1}) and $\nu_2[{}^3A_{2g}(F) \rightarrow {}^3T_{1g}(F)]$ (16835 cm^{-1}) transitions, in an idealized O_h symmetry. The position of the observed d–d transitions permits the calculation of the ligand field parameters, $10Dq$ and B, using the following known relationships [41]:

$$\nu_1[{}^3A_{2g}(F) \rightarrow {}^3T_{2g}(F)] = 10Dq,$$
$$\nu_2[{}^3A_{2g}(F) \rightarrow {}^3T_{1g}(F)] = (1/2)(15B + 30Dq) - (1/2)[(15B - 10Dq)^2 + 12B \cdot 10Dq]^{1/2}.$$

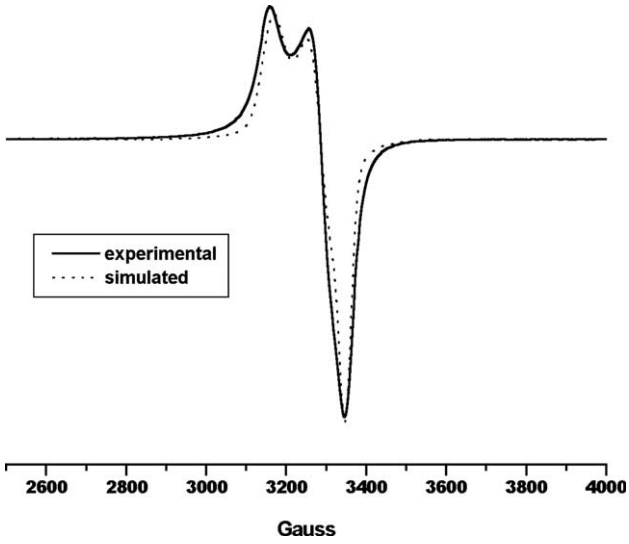


Fig. 6. Experimental and simulated polycrystalline EPR spectrum of [$CuCl_2$(ATsc)].

The calculated values of the ligand field parameters $10Dq = 11494$ cm^{-1} and $B = 568$ cm^{-1} are consistent with the presence of a chromophore group [$Ni^{II}N_4O_2$] [29,42].

3.4. Magnetic susceptibility and EPR spectra

The observed molar magnetic susceptibility for the copper complex was corrected for diamagnetism and temperature-independent paramagnetism to provide the fully corrected magnetic moment at room temperature ($\mu = 2.01$ BM). This value is in the range 1.9–2.2 BM, which allows the exclusion of metal–metal interactions, supporting a monomeric structural formulation for this compound [43].

Fig. 6 shows the EPR spectrum of the polycrystalline copper(II) complex at X-band microwave frequencies.

The EPR value was obtained by simulation [44]. The EPR spectrum is rhombic with g parameters $g_1 = 2.09$; $g_2 = 2.12$ and $g_3 = 2.21$. The value for the R parameter [$R = (g_2 - g_1)/(g_3 - g_2)$] is 0.33, i.e., lower than 1, thus indicating that the unpaired electron is located in a $d_{x^2-y^2}$ orbital [45] associated with a square-pyramidal stereochemistry, in good agreement with the crystallographic results [46].

The corrected magnetic moment measured for the nickel complex was $\mu = 3.31$ BM, which can be related to an octahedral environment [42].

4. Supplementary material

CCDC 271095, 271096 and 271097 corresponding to ATsc, [$CuCl_2$(ATsc)] and [$Ni(ATsc)_2$]$(NO_3)_2 \cdot H_2O$ contain the supplementary crystallographic data for this

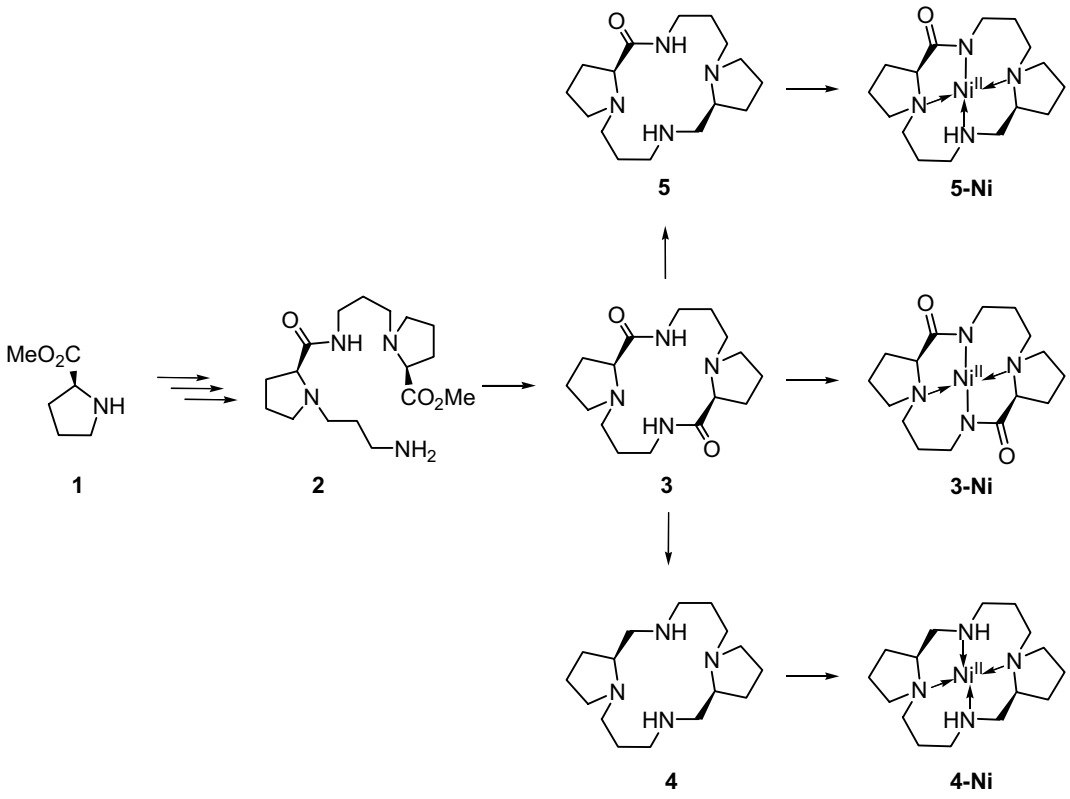
paper. These data can be obtained free of charge via www.ccdc.cam.ac.uk/conts/retrieving.html (or from the CCDC, 12 Union Road, Cambridge CB2 1EZ, UK; fax: +44 1223 336033; e-mail: deposit@ccdc.cam.ac.uk).

Acknowledgements

We thank the Junta de Extremadura (Consejería de Educación, Ciencia y Tecnología) and the FEDER [Projects 2PR02A098 and 2PR04A011] for financial support. M.A. Maldonado-Rogado thanks the Spanish Ministerio de Ciencia y Tecnología and E. Viñuelas-Zahínos thanks the Junta de Extremadura (Consejería de Educación, Ciencia y Tecnología) and the FEDER for their Ph.D. fellowships.

References

[1] N.Z. Kenezevic, V.M. Leovac, V.S. Jevtovic, S. Grguric-Sipka, T.J. Sabo, Inorg. Chem. Commun. 6 (2003) 561.
[2] P. Yogeeswari, D. Sriram, V. Veena, R. Kavya, K. Rakhra, J.V. Ragavendran, S. Mehta, R. Thirumurugan, J.P. Stables, Biomed. Pharmacother. 59 (2005) 51.
[3] J.R. Dimmock, R.N. Puthucode, J.M. Smith, M. Hetherington, J.W. Quail, U. Pugazhenthi, T. Lechler, J.P. Stables, J. Med. Chem. 39 (1996) 3984.
[4] J.R. Dimmock, S.N. Pandeya, J.W. Quail, U. Pugazhenthi, T.M. Allen, G.Y. Kao, J. Balzarini, E. Declercq, Eur. J. Med. Chem. 30 (1995) 303.
[5] J.R. Dimmock, K.K. Sidhu, S.D. Tumber, S.K. Basran, M. Chen, J.W. Quail, J. Yang, I. Rozas, D.F. Weaver, Eur. J. Med. Chem. 30 (1995) 287.
[6] G. Ibrahim, G.M. Bouet, I.H. Hall, M.A. Kahn, J. Inorg. Biochem. 81 (2000) 29.
[7] L. Otero, P. Noblia, D. Gambino, H. Cerecetto, M. Gonzalez, J.A. Ellena, O.E. Piro, Inorg. Chim. Acta 344 (2003) 85.
[8] A. Para, S. Karolczyk-Kostuch, Carbohyd. Polym. 48 (2002) 55.
[9] H. Cerecetto, R. Di-Maio, G. Ibarruri, G. Seoane, A. Denicola, G. Peluffo, C. Quijano, M. Paulino, Il Farmaco 53 (1998) 89.
[10] S.N. Pandeya, V. Mishra, P.N. Singh, D.C. Rupainwar, Pharmacol. Res. 37 (1998) 17.
[11] M.C. Miller III, C.N. Stineman, J.R. Vance, D.X. West, I.H. Hall, Anticancer Res. 18 (1998) 4131.
[12] N.C. Kasuga, K. Sekino, C. Koumo, N. Shimada, M. Ishikawa, K. Nomiya, J. Inorg. Biochem. 84 (2001) 55.
[13] P.F. Lee, C.T. Yang, D. Fan, J.J. Vittal, J.D. Ranford, Polyhedron 22 (2003) 2781.
[14] J. Patole, S. Dutta, S. Padhey, E. Sinn, Inorg. Chim. Acta 318 (2001) 207.
[15] K.H. Reddy, P.S. Reddy, P.R. Babu, J. Inorg. Biochem. 77 (1999) 169.
[16] J.C. Magna, J. Vargas, R. Latorse, A. Alvarado, G. Mena, Coord. Chem. Rev. 119 (1992) 67.
[17] C.G. Bonde, N.J. Gaikwad, Bioorg. Med. Chem. 12 (2004) 2151.
[18] S.H. Kim, H. Son, G. Nam, D.Y. Chi, J.H. Kim, Bioorg. Med. Chem. Lett. 10 (2000) 1143.
[19] L.M. Cañedo, J.A. de la Fuente, C. Gesto, M.J. Ferreiro, C. Jimenez, R. Riguera, Tetrahedron Lett. 40 (1999) 6841.
[20] T. Doornbos, H.G. Peer, Recl. Trav. Chim. Pays-Bas. 91 (1972) 711.
[21] L.J. Farrugia, J. Appl. Crystallogr. 32 (1999) 837.
[22] L.J. Farrugia, J. Appl. Crystallogr. 30 (1997) 565.
[23] C. Cohen-Addad, Acta Crystallogr., Sect. B 38 (1982) 1753.
[24] D. Cremer, J.A. Pople, J. Am. Chem. Soc. 97 (1975) 1354.
[25] A.W. Addison, T.N. Rao, J. Reedijk, J. van Rijn, G.C. Verschoor, J. Chem. Soc., Dalton Trans. (1984) 1349.
[26] E.L. Muetterties, L.J. Guggenberger, J. Am. Chem. Soc. 96 (1974) 1748.
[27] F.H. Allen, Acta Crystallogr., Sect. B 58 (2002) 380.
[28] I.J. Bruno, J.C. Cole, P.R. Edington, M. Kessler, C.F. Macrae, P. McCabe, J. Pearson, R. Taylor, Acta Crystallogr., Sect. B 58 (2002) 389.
[29] A. Bernalte-García, F.J. García-Barros, F.J. Higes-Rolando, F. Luna-Giles, Polyhedron 18 (1999) 2907.
[30] A. Bernalte-García, M.A. Díaz-Díez, F.J. García-Barros, F.J. Higes-Rolando, A.M. Pizarro-Galán, J. Romero-Garzón, C. Valenzuela-Calahorro, Polyhedron 15 (1996) 1691.
[31] A. Bernalte-García, F.J. García-Barros, F.J. Higes-Rolando, A.M. Pizarro-Galán, C. Valenzuela-Calahorro, Thermochim. Acta 339 (1999) 95.
[32] G. Mille, J.L. Meyer, J. Chouteau, J. Mol. Struct. 50 (1978) 247.
[33] G. Ibrahim, M.A. Khan, P. Richomme, O. Benali-Baitich, G. Bouet, Polyhedron 16 (1997) 3455.
[34] R.T. Conley, in: Espectroscopía Infrarroja, Alhambra, Madrid, 1979.
[35] J.R. Ferraro, Low-frequency Vibrations of Inorganic and Coordination Compounds, Plenum Press, New York, 1971.
[36] F.J. Barros-García, A. Bernalte-García, F.J. Higes-Rolando, F. Luna-Giles, M.A. Maldonado-Rogado, E. Viñuelas-Zahínos, Inorg. Chim. Acta 357 (2004) 3574.
[37] B. Singh, R.N. Singh, R.C. Aggarwal, Polyhedron 4 (1985) 401.
[38] M. Shakir, S.P. Varkey, F. Firdaus, P.S. Hamed, Polyhedron 13 (1994) 2319.
[39] M.M. Mostafa, M.A. Khattab, K.M. Ibrahim, Polyhedron 2 (1983) 583.
[40] B.J. Hathaway, in: G. Wilkinson (Ed.), Late Transitions Elements, vol. 5, Pergamon Press, Oxford, 1987, p. 674.
[41] D.K. Rastogi, K.C. Sharma, S.K. Dua, M.P. Teotia, J. Inorg. Nucl. Chem. 37 (1975) 685.
[42] L. Sacconi, F. Mani, A. Bencini, in: G. Wilkinson (Ed.), Comprehensive Coordination Chemistry, Late Transitions Elements, vol. 5, Pergamon Press, Oxford, 1987, p. 51.
[43] B.J. Hathaway, in: G. Wilkinson (Ed.), Comprehensive Coordination Chemistry, Late Transitions Elements, 5, Pergamon Press, Oxford, 1987, p. 656.
[44] WINEPR-Simfonia. 1.25, Bruker Analytik, Kalsruhe, 1994–1996.
[45] B.J. Hathaway, J. Chem. Soc., Dalton Trans. (1972) 1196.
[46] J. Garcia-Tojal, L. Lezama, J.L. Pizarro, M. Insausti, M.I. Arriortua, T. Rojo, Polyhedron 18 (1999) 3703.



Scheme 1.

dioxocyclam **3**. A few simple transformations of L-proline ester **1** led to the aminoester **2** which underwent a cyclization reaction yielding dioxocyclam **3** (Scheme 1). We examined different macrocyclization conditions such as basic catalysis or high-pressure technique and found that the best results were obtained when sodium methoxide as the base and methanol as the solvent were applied (82% yield). Having prepared the macrocyclic compound we decided to transform it into the poliamino analogue **4**. The reduction with the $BH_3 \cdot Me_2S$ complex led to the cyclam derivative **4** in a good yield (75%). By carrying out the reaction under more gentle conditions we were able to reduce only one amide group and obtain monooxocyclam **5** in 57% yield.

All cyclam derivatives **3**–**5** easily form complexes with transition metals. Amide ligands **3** and **5** upon addition of nickel acetate into their methanol solutions undergo deprotonation on the amide groups, thus forming complexes: $[Ni^{2+}(\mathbf{3}^{2-})]$ (denoted as **3-Ni**) and $[Ni^{2+}(\mathbf{5}^{-})](Cl^{-})$ (denoted as **5-Ni**). In the case of the reduced all-amine ligand **4**, a complex of the stochiometry $[Ni^{2+}(\mathbf{4})(AcO^{-})(H_2O)]Cl^{-}$ (denoted as **4-Ni**) is formed.

The X-ray structure of the complex **3-Ni** is illustrated in Fig. 1. The two amide hydrogen atoms have been removed during the complexation process, forming a neutral complex. Nickel is four-coordinated and its coordination geometry can be described as tetrahedrally distorted square planar. The tetrahedral twist, defined as the deviation of atoms from the least-square plane through the nitrogen atoms is ± 0.28 Å with the nickel ion positioned 0.05 Å beyond the plane. The Ni–N bonding distances are characteristic for a low-spin complex (Table 1) [12]. Bonding distances to the deprotonated amide nitrogens are shorter by ca. 0.06 Å than those to amine nitrogen atoms. The five-membered chelate rings formed by Ni1–N1–C1–C2–N2 (and Ni1–N1′–C1′–C2′–N2′) are almost planar, while the 6-membered rings exhibit chair-like conformations. Although the planar coordination geometry of nickel is highly distorted, the mutual position of the chelate rings resembles the *trans*-I (*R*,*S*,*R*,*S*) conformation in the notation approved for the parent cyclam system [13]. Previously, it has been shown that for square-planar nickel complexes of simple cyclams the most stable form is the *trans*-III conformation (and in many cases the only one observed) [14]. However, for some substituted cyclams, the *trans*-I conformation, observed also by us, has also been reported as a minor component [15]. The important feature of this complex from the catalytic point of view is that both proline rings are positioned on the same side of the macrocycle, which shields one side of the metal center completely and leaves the other one exposed.

In the case of the monoreduced ligand **5**, during the reaction with nickel (II) acetate, one amide group is

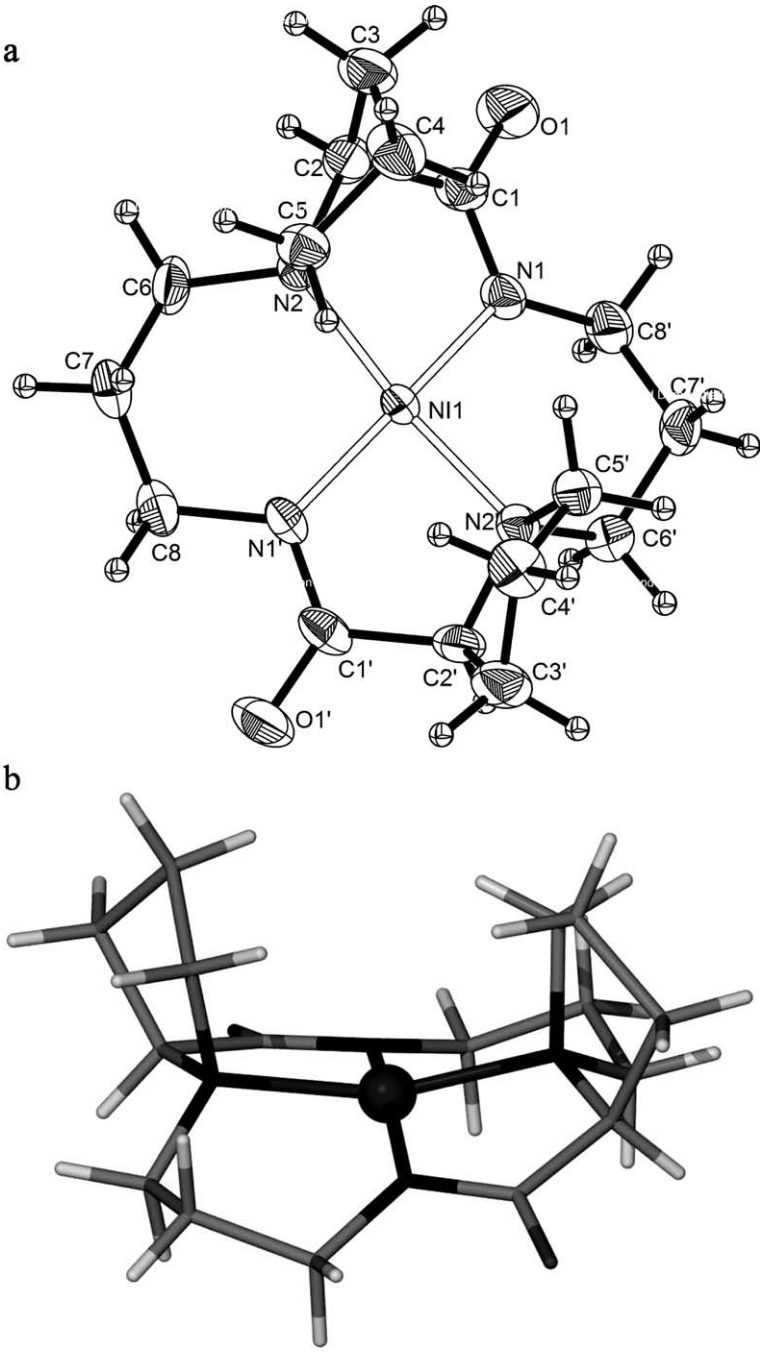


Fig. 1. X-ray structure of **3-Ni**: $[Ni^{2+}(\mathbf{3}^{2-})]\cdot H_2O$. (a) ORTEP presentation in the plane of the macroring. (b) Stick presentation in the plane perpendicular to the macroring.

deprotonated while all the amino groups form coordination bonds. During re-crystallization of the complex from CH_2Cl_2 the acetate counterion exchanges with chloride to give a complex of the stoichiometry $[Ni^{2+}(\mathbf{5}^{-})](Cl^{-})\cdot(H_2O)_2$ (denoted as **5-Ni**) as proven by micro- and X-ray analysis (the ability of carboxylates to exchange with chloride from chlorinated solvents has been observed by us many times during other independent experiments). X-ray analysis shows that the nickel coordination geometry for **5-Ni** is square planar, highly tetrahedrally twisted, with Ni–N distances characteristic for a low-spin complex (Table 1). The distortion from square planar geometry is ± 0.26 Å with the nickel ion positioned 0.02 Å beyond the plane. Again two proline rings shield effectively only one side of the macrocycle, while the other side is exposed. It is interesting to note that the Cl^{-} counterion remains far from the cationic center. The chloride is hydrogen bonded with the amine hydrogen and two water molecules, while the exposed

Table 1
Selected Ni-heteroatom distances

Compound	Distance	(Å)
3-Ni		
	Ni1–N1	1.879(4)
	Ni1–N1′	1.882(4)
	Ni1–N2	1.952(4)
	Ni1–N2′	1.944(4)
4-Ni	Ni1–N1, Ni2–N3	2.104(6), 2.098(6)
	Ni1–N1′, Ni2–N3′	2.115(6), 2.105(6)
	Ni1–N2, Ni2–N4′	2.170(7), 2.185(6)
	Ni1–N2′, Ni2–N4	2.171(7), 2.185(7)
	Ni1–O1, Ni2–O4	2.074(5), 2.078(6)
	Ni1–O3, Ni2–O6	2.113(5), 2.124(5)
5-Ni	Ni1–N1	1.870(4)
	Ni1–N8	1.938(4)
	Ni1–N11	1.954(3)
	Ni1–N4	1.956(3)

side of the macrocycle interacts with the neighboring macrocycle (see Fig. 2).

A completely different coordination environment is observed for the interaction of the reduced, all-amine ligand **4** with nickel (II). The complex stoichiometry, proved by microanalysis, was found to be $\mathbf{4}\cdot Ni^{2+}\cdot 2AcO^{-}$. However, again upon crystallization from CH_2Cl_2 one of the acetate counterions underwent exchange and the stoichiometry found by X-ray analysis is $[Ni^{2+}(\mathbf{4})(AcO^{-})(H_2O)]Cl^{-}$ (denoted as **4-Ni**). In the crystal of **4-Ni** (Fig. 3) two independent molecules are observed, however, both of them have identical conformations and coordination geometries. The nickel cation resides in a six-coordinate octahedral environment interacting with four amine nitrogen atoms, an acetate anion and a water molecule. Such an octahedral coordination is the most common for high-spin complexes (92% of all high-spin complexes) [12]. Indeed, the Ni–N bonding distances are also in agreement with that conclusion (Table 1). The conformation of the macrocycle, in the notation approved for cyclams, is *cis*-V (*R*,*R*,*R*,*R*). For octahedral complexes of *N*-substituted ligands the most common conformation is *trans*-III (52% of all octahedral complexes) [15], however, as observed by us, the *cis*-V conformation is the second most common (39%).

It has been suggested that a *cis*-V conformation of cyclam complexes is crucial for biological activity. In vivo, bislactam based biologically active anti-HIV agents, are believed to interact with a receptor's carboxylate side chains and the presence of carboxylate anions induces a *cis*-V conformation of the complex in the active site [16]. It has also been postulated recently that acetate promotes a *cis*-V conformation for a cyclam–Zn complex [17]. Our structure can be considered as an additional crystallographic hint for the hypothesis that such a conformation might be acetate-driven.

2.1. Conformational changes during complexation

In the preceding communication [11], we have presented the structures of the free ligands **3** and **5**. It is noteworthy that in both cases amide groups were perpendicular to the mean plane of the macrorings, and the carbonyl oxygen atoms were pointing to the same side. Proline rings for the free ligands were in the plane of the macrorings. During complexation the macrocycles rearranged considerably. The carbonyl oxygen atoms are now parallel to the mean plane of the macrorings and the proline rings are perpendicular.

3. Conclusions

We have reported the synthesis and the structures of nickel (II) complexes of chiral cyclams originating from L-proline. X-ray structure analyses indicate that for the complexes, contrary to the free ligands, the chiral proline rings shield only one side of the molecule, the other side remaining exposed. Thus, for future modifications, the structures suggest that substitution at the lower part of the macrocycle (opposite to the proline rings) should be made.

4. Experimental

4.1. General remarks

X-ray measurements were performed using a MACH-3 diffractometer (Enraf-Nonius) in the Institute of Organic Chemistry, Polish Academy of Sciences. The structures were solved and refined using the programs SHELXS-97 (Sheldrick, 1990) and SHELXL-97 (Sheldrick, 1997) respectively. The program X-SEED was used as an interface to the SHELX programs, and to prepare the figures [18]. Cyclam derivatives were prepared according to previously described procedures [11].

4.2. Synthesis

3-Ni: Equimolar amounts of dioxocyclam **3** and nickel (II) acetate were dissolved in methanol and heated up to reflux with stirring. The complex formation was manifested by a color change from green into dark red and acetic acid secretion. The methanol was removed under vacuo to give a red oil which was crystallised from diethyl ether.

Dark red crystals; m.p. 247 °C; $[\alpha]_D^{20} = -294$ ($c = 0.0468$ in MeOH); ^{1}H NMR (500 MHz, $CDCl_3$, 30 °C, TMS): $\delta = 4.79$–4.73 (m, 2H), 3.30–3.23 (m, 4H), 2.99 (dt, 2H, $J_1 = 14.1$ Hz, $J_2 = 4.0$Hz), 2.78–2.70 (m, 2H), 2.28–2.21 (m, 2H), 2.19–2.21 (m, 2H), 2.07–1.95 (m, 4H), 1.93–1.82 (m, 4H), 1.64–1.57 (m,

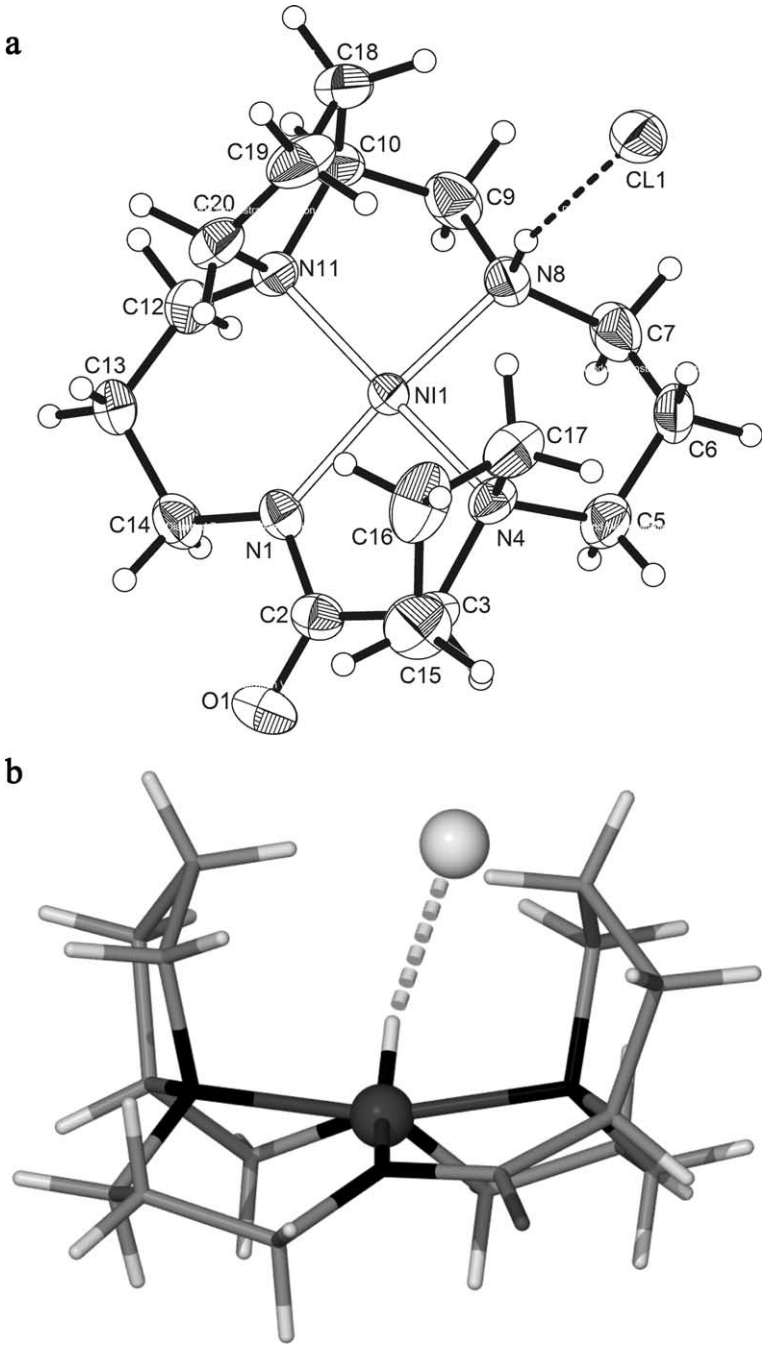


Fig. 2. X-ray structure of **5-Ni**: $[Ni^{2+}(\mathbf{5}^{-})](Cl^{-}) \cdot 2H_2O$. (a) ORTEP presentation in the plane of the macroring. (b) Stick presentation in the plane perpendicular to the macroring.

2H), 1.49–1.39 (m, 2H); ^{13}C NMR (125 MHz, $CDCl_3$, 30 °C, TMS): $\delta = 178.6$, 74.4, 57.3, 55.7, 40.4, 26.5, 24.8, 21.2; IR (KBr): $v = 3442$, 3382, 2937, 2848, 1573, 1420 cm^{-1}; UV/Vis (EtOH): $\lambda_{max}(\varepsilon) = 570$ (80), 480 (180), 210 (15200), 240 nm (15600 l cm^{-1} mol^{-1}); MS HR (LSIMS): *m*/*z* calcd for $C_{16}H_{27}N_4O_2Ni$ $(M + H^+)$ 364.14092, found 364.13833. *Anal.* Calc. for $C_{16}H_{28}N_4O_3Ni_1Cl_1$ $(\mathbf{3}^{2-} \cdot Ni^{2+} \cdot H_2O)$ C, 50.16; H, 7.37; N, 14.62. Found: C, 49.96; H, 7.25; N, 14.44%.

Crystal data for **3-Ni**: $C_{16}H_{28}N_4NiO_3$, $[Ni^{2+} \cdot (\mathbf{3}^{2-})] \cdot H_2O$, $M = 383.13$, $0.28 \times 0.07 \times 0.07$ mm^3, monoclinic, space group $P2_1$ (No. 4), $a = 9.5629(4)$ Å, $b = 7.9621(3)$ Å, $c = 11.7585(6)$ Å, $\beta = 110.896(4)°$, $V = 836.42(6)$ $Å^3$, $Z = 2$, $D_c = 1.521$ g/cm^3, $F_{000} = 408$, Cu Kα radiation, $\lambda = 1.54178$ Å, $T = 293(2)$ K, $2\theta_{max} = 148.2°$, 1772 reflections collected, 1673 unique ($R_{int} = 0.0483$). Final GoF = 0.987, $R_1 = 0.0474$, $wR_2 = 0.1182$, *R* indices based on 1659 reflections with

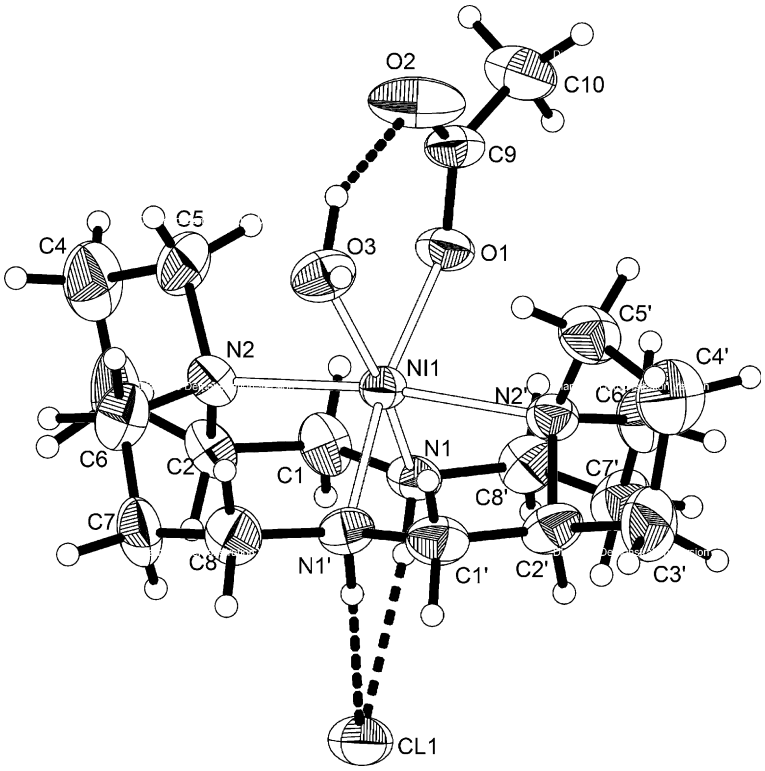


Fig. 3. X-ray structure of **4-Ni**: $[Ni^{2+}(\mathbf{4})(AcO^-)(H_2O)]Cl^-$. ORTEP presentation in the plane perpendicular to the macroring.

$I > 2\sigma(I)$ (refinement on F^2), 226 parameters, 1 restraint. Lp and absorption corrections applied, $\mu = 1.870\ mm^{-1}$. Absolute structure parameter = 0.03(5).

4-Ni: Mixing of equimolar solutions of ligand and $Ni(CH_3COO)_2$ in methanol results in an abrupt color change from green into blue. The solvent was removed by vacuum and the complex was purified by crystallization from the methanol/diethyl ether mixture for analytical purposes and from CH_2Cl_2/penthane for X-ray analysis.

Blue crystals; m.p. 246 °C (decomp.); $[\alpha]_D^{20} = -117$ ($c = 0.216$ in MeOH); ^1H NMR (200 MHz, $CDCl_3$, 23 °C, TMS): very broad signals at: 16.0, 13.6, 1.6, −3.4, −4.8, −16.8, −28.5 ppm; IR (KBr): $\nu = 3360$, 3161, 2958, 2856, 1565, 1407 cm^{-1}; UV/Vis (EtOH): $\lambda_{max}(\varepsilon) = 580$ (30), 363 (50), 210 nm (8800 $l\,cm^{-1}\,mol^{-1}$); MS HR (LSIMS): Calcd for $C_{18}H_{35}N_4O_2Ni$ ($M + AcO^-$) 397.21135, found 397.21728; *Anal.* Calc. for $C_{20}H_{38}N_4O_4Ni_1$ ($\mathbf{4} \cdot Ni^{2+} \cdot 2AcO–$) C, 52.54; H, 8.38; N, 12.25. Found: C, 52.22; H, 8.47; N, 12.06%.

Crystal data for **4-Ni**: X-ray quality crystals were grown from CH_2Cl_2/penthane, $C_{18}H_{37}Cl_1N_4Ni_1O_3$, $[Ni^{2+}(\mathbf{4})(AcO^-)(H_2O)]Cl^-$, $M = 451.68$, monoclinic, space group $P2_1$ (No. 4), $a = 11.450(2)$ Å, $b = 12.269(2)$ Å, $c = 15.807(3)$ Å, $\beta = 99.40(3)°$, $V = 2190.8(7)$ Å^3, $Z = 4$, $D_c = 1.369\ g/cm^3$, $F(000) = 968$, Cu Kα radiation, $\lambda = 1.54178$ Å, $T = 293(2)$ K, $2\theta_{max} = 148.4°$, 4916 reflections collected, 4680 unique ($R_{int} = 0.0486$). Final GoF = 1.188, $R_1 = 0.0717$, $wR_2 = 0.1715$, R indices based on 3994 reflections with $I > 2\sigma(I)$ (refinement on F^2), 504 parameters, 5 restraints. Lp and absorption corrections applied, $\mu = 2.601\ mm^{-1}$. Absolute structure parameter = −0.04(4).

5-Ni: Mixing of equimolar solutions of ligand and $Ni(CH_3COO)_2$ in methanol results in an abrupt color change from green into light red. The mixture was heated up to reflux with stirring, then the solvent was removed by vacuum and the complex was purified by crystallization from CH_2Cl_2/penthane.

Red crystals; m.p. 263 °C; $[\alpha]_D^{20} = -510$ ($c = 0.238$ in MeOH); ^1H NMR (500 MHz, CD_3OD, 30 °C): $\delta =$ 4.17 (dd, 1H, $J_1 = 4.4$ Hz, $J_2 = 7.3$ Hz, $J_3 =$ 11.7Hz), 4.09–4.02 (m, 1H), 3.69 (dt, 1H, $J_1 = 2.3$ Hz, $J_2 = 12.8$ Hz), 3.21–2.94 (m, 6H), 2.85–2.77 (m, 2H), 2.75–2.66 (m, 2H), 2.64–2.54 (m, 2H), 2.39 (dt, 1H, $J_1 = 5.4$ Hz, $J_2 = 11.3$Hz), 2.33–2.04 (m, 7H), 1.99–1.87 (m, 2H), 1.83–1.71 (m, 3H); ^{13}C NMR (125 MHz, CD_3OD, 30 °C): $\delta = 75.0$, 70.1, 65.4, 60.0, 58.7, 58.2, 55.3, 49.4, 38.0, 29.4, 26.9, 25.8, 24.6, 24.4, 24.2; IR (KBr): $\nu = 3434$, 3206, 3071, 2938, 1591, 1445, 1305 cm^{-1}; UV/Vis (EtOH): $\lambda_{max}(\varepsilon) = 472$ (180), 227 nm (19 000 $l\,cm^{-1}\,mol^{-1}$); MS HR (LSIMS): calcd for $C_{16}H_{29}N_4ONi$ (M^+) 351.16948, found 351.17089. *Anal.* Calc. for $C_{16}H_{34}N_4O_3Ni_1Cl_1$ ($\mathbf{5}^- \cdot Ni^{2+} \cdot Cl^- \cdot 2H_2O$) C, 45.26; H, 8.07; N, 13.19. Found: C, 45.43; H, 7.90; N, 13.37%.

Crystal data for **5-Ni**: X-ray quality crystals were grown from CH_2Cl_2/penthane, $C_{16}H_{33}ClN_4NiO_3$, $[Ni^{2+}(\mathbf{5}^-)](Cl^-)(H_2O)_2$,$M = 423.62$, orthorhombic, space group $P2_12_12_1$ (No. 19), $a = 7.8102(2)$ Å, $b = 13.2168(8)$ Å, $c = 18.2920(10)$ Å, $V = 1888.21(16)$ Å^3, $Z = 4$, $D_c = 1.490$ g/cm^3, $F(0\,0\,0) = 904$, Mo Kα radiation, $\lambda = 0.71073$ Å, $T = 293(2)$ K, $2\theta_{max} = 52.7°$, 3859 reflections collected, 3837 unique ($R_{int} = 0.0000$). Final GoF = 1.025, $R_1 = 0.0399$, $wR_2 = 0.0850$, R indices based on 3212 reflections with $I > 2\sigma(I)$ (refinement on F^2), 227 parameters, 0 restraints. Lp and absorption corrections applied, $\mu = 1.192$ mm^{-1}. Absolute structure parameter = −0.007(17).

5. Supplementary information

Crystallographic data (excluding structure factors) for the structures discussed in this paper have been deposited with the Cambridge Crystallographic Data Centre as supplementary publication numbers CCDC-140571-3. Copies of the data can be obtained, free of charge, on application to CCDC, 12 Union Road, Cambridge CB2 1EZ, UK [fax: +44(0)-1223-336033 or e-mail: deposit@ccdc.cam.ac.uk].

References

[1] (a) T. Ito, M. Kato, M. Yamashita, H. Ito, J. Coord. Chem. 15 (1986) 29–52;
(b) S. Bhappacharya, R. Mukhrjee, A. Chakravorty, Inorg. Chem. 25 (1986) 3448–3452;
(c) G.A. Melson, Coordination Chemistry of Macrocyclic Compounds, Plenum Press, New York, 1979.

[2] J. van Alphen, Rec. Trav. Chim. 56 (1937) 343–350.

[3] D.H. Busch, Acc. Chem. Res. 11 (1978) 392–400.

[4] P. Jacquinot, P.C. Hauser, Electroanalysis 15 (2003) 1437–1444.

[5] (a) E. De Clerq, N. Yamamoto, R. Pauwels, M. Baba, D. Schols, H. Nakashima, J. Balzarini, Z. Debyser, B.A. Murrer, D. Schwartz, D. Thornton, G. Bridger, S. Fricker, G. Henson, M. Abrams, D. Picker, Proc. Natl. Acad. Sci. USA 89 (1992) 5286–5290;
(b) J.R. Morphy, D. Parker, T. Alexander, A. Bains, A.F. Carne, M.A.W. Eaton, A. Harrison, A. Millican, A. Phipps, S.K. Rhind, R. Titmas, D.J. Wheaterby, J. Chem. Soc., Chem. Commun. (1988) 156–158;
(c) X. Sun, M. Wuest, G.R. Weisman, E.H. Wong, D.P. Reed, C.A. Boswell, R. Motekaitis, A.E. Martell, M.J. Welch, C.J. Anderson, J. Med. Chem. 45 (2002) 469–477.

[6] (a) S. Amin, J.R. Morrow, C.H. Lake, M.R. Churchill, Angew. Chem. Int. Ed. Engl. 33 (1994) 773–775;
(b) S. Zhu, W. Chen, H. Lin, X. Yin, F. Kou, M. Lin, Y. Chen, Polyhedron 16 (1997) 3285–3291.

[7] (a) J.F. Kinneary, T.R. Wagler, C.J. Burrows, Tetrahedron Lett. 2 (1988) 877–880;
(b) W. Nam, R. Ho, J.S. Valentine, J. Am. Chem. Soc. 113 (1991) 7052–7054;
(c) W. Nam, H.J. Kim, S.J. Kim, R. Ho, J.S. Valentine, Inorg. Chem. 35 (1996) 1045–1049;
(d) T.R. Wagler, C.J. Burrows, Tetrahedron Lett. 29 (1988) 5091–5094;
(e) T.R. Wagler, Y. Fang, C.J. Burrows, J. Org. Chem. 54 (1989) 1584–1589;
(f) T. Hubin, J.M. McCormick, S.R. Collinson, M. Buchalova, Ch.M. Perkins, N.W. Alcock, P.K. Kahol, A. Raghunathan, D.H. Bush, J. Am. Chem. Soc. 122 (2002) 2512–2522.

[8] Y. Kashiwagi, C. Kikuchi, F. Kurashima, J. Anzai, J. Organomet. Chem. 662 (2002) 9–13.

[9] P. Tascedda, E. Dunãch, J. Chem. Soc. Chem. Commun. (1995) 43–44.

[10] (a) S. Olivero, J.C. Clinet, E. Dunãch, Tetrahedron Lett. 36 (1995) 4429–4432;
(b) S. Olivero, J.-P. Rolland, E. Dunach, Organometallics 17 (1998) 3747–3753;
(c) A.P. Esteves, D.M. Goken, L.J. Klein, M.A. Lemos, M.J. Medeiros, D.G. Peters, J. Org. Chem. 68 (2003) 1024–1029.

[11] (a) M. Achmatowicz, J. Jurczak, Tetrahedron Lett. 41 (2000) 5967–5970;
(b) M. Achmatowicz, J. Jurczak, Tetrahedron: Asymmetry 12 (2001) 111–119.

[12] M.A. Donnelly, M. Zimmer, Inorg. Chem. 38 (1999) 1650–1658.

[13] B. Bosnich, C.K. Poon, M.L. Tobe, Inorg. Chem. 4 (1965) 1109–1112.

[14] X. Liang, P.J. Sadler, Chem. Soc. Rev. 33 (2004) 246–266.

[15] P.J. Connolly, E.J. Billo, Inorg. Chem. 26 (1987) 3224–3226.

[16] L.O. Gerlach, R.T. Skerlj, G.J. Bridger, T. Schwartz, J. Biol. Chem. 276 (2001) 14153–14160.

[17] X.Y. Liang, J.A. Parkinson, M. Weishaupl, R.O. Gould, S.J. Paisey, H.S. Park, T.M. Hunter, C.A. Blindauer, S. Parsons, P.J. Sadler, J. Am. Chem. Soc. 124 (2002) 9105–9112.

[18] L.J. Barbour, J. Supramol. Chem. 1 (2001) 189–191.

2. Experimental

2.1. Materials and methods

All operations were carried out in air at room temperature. The starting materials $[Et_4N]_2[MS_4]$ (M = Mo, W) were prepared according to the literature procedures [7], and the compound $CuSBu^t$ was prepared by treating $Cu(NO_3)_2 \cdot 3H_2O$ with $HSBu^t$ in ethanol. Other chemicals were obtained from commercial sources and used as received.

Infrared spectra were recorded on a Nicolet Magna 750 FT-IR spectrophotometer as KBr pellets. Electronic spectra were recorded on a Lambda 35 spectrophotometer in MeCN solution between 600 and 200 nm. Cyclic voltammograms were performed on a microcomputer-based electrochemical analyzer LK-98A. The measurements were conducted in a DMF solution under nitrogen atmosphere with Bu_4NClO_4 as supporting electrolyte. Elemental analyses were performed in the Elemental Analysis Laboratories at our institute.

2.2. Synthesis of $[Et_4N]_4[\{MS_4Cu_2(\mu\text{-}SBu^t)\}_4]$ (**1**, M = Mo; **2**, M = W)

An MeCN solution (15 mL) of $[Et_4N]_2[MoS_4]$ (0.24 g, 0.5 mmol) and $CuSBu^t$ (0.15 g, 1.0 mmol) was stirred at room temperature for 0.5 h and then filtered, ^{i}PrOH (15 mL) was added to the resulting filtrate slowly and the solution was allowed to stand in air for several days to afford **1** as brown crystals. Yield (0.21 g, 74%). Yellow crystals of **2** (0.28 g, 85%) were obtained by a similar way as for **1** except $[Et_4N]_2[WS_4]$ (0.29 g, 0.5 mmol)was used instead of $[Et_4N]_2[MoS_4]$. Recrystallization by vapor diffusion of ^{i}PrOH into a DMF solution of **2** afforded crystals suitable for X-ray diffraction. *Anal.* Calc. for **1**: C, 25.26; H, 5.09; N, 2.46. Found: C, 25.42; H, 4.78; N, 2.45%. *Anal.* Calc. for **2**: C, 21.88; H, 4.41; N, 2.13. Found: C, 22.01; H, 4.11; N, 2.08%. IR (KBr pellet, cm^{-1}) for **1**: ν(Mo–S): 465 (s); for **2**: ν(W–S): 451 (s). UV–Vis (MeCN) λ_{max}/nm (ε_{max}/M^{-1} cm^{-1}) for **1**: 491 (17200), 311 (67500), 262 (55900), 248 (55400); for **2**: 408 (20400), 289 (80400), 235 (54900).

2.3. Synthesis of $\{[Et_4N]_2[MS_4Cu_2(SSS)]\}_n$ (**3**, M = Mo; **4**, M = W)

A DMF solution (10 mL) of $[Et_4N]_2[MoS_4]$ (0.24 g, 0.5 mmol) and CuCl (0.10 g, 1.0 mmol) was stirred for 0.5 h. To this brown suspension was added K_2SSS (0.23 g, 1.0 mmol) and the brown precipitate gradually dissolved. After further stirring for 3.0 h, the resultant solution was filtered. Brown crystals of **3** (0.22 g) were isolated by vapor diffusion of ^{i}PrOH into the filtrate in a 60% yield. Cluster **4** was synthesized in a similar way as for **3** except that $[Et_4N]_2[WS_4]$ (0.29 g, 0.5 mmol) was used instead of $[Et_4N]_2[MoS_4]$ in a 56% yield. *Anal.* Calc. for **3**: C, 28.46; H, 5.27; N, 7.38. Found: C, 28.35; H, 5.06; N, 7.35%. *Anal.* Calc. for **4**: C, 25.50; H, 4.72; N, 6.61. Found: C, 25.43; H, 4.45; N, 6.60%. IR (KBr pellet, cm^{-1}) for **3**: ν(Mo–S): 467 (s); for **4:** ν(W–S): 453 (s). UV–Vis (MeCN) λ_{max}/nm (ε_{max}/M^{-1} cm^{-1}) for **3**: 505 (6100) (sh), 342 (10300), 290 (8900); for **4**: 422 (6500), 310 (10900).

Table 1
Crystallographic data for complexes **2** and **4**

	2	**4**
Empirical formula	$C_{48}H_{116}Cu_8N_4S_{20}W_4$	$C_{18}H_{40}Cu_2N_4S_7W$
Formula weight	2634.37	827.73
Crystal system	monoclinic	monoclinic
Space group	$P2_1/c$	$C2/c$
a (Å)	9.845(1)	28.870(3)
b (Å)	16.223(1)	11.842(1)
c (Å)	28.095(2)	22.676(3)
β (°)	94.501(4)	125.842(4)
V (Å^3)	4473.2(5)	6284(1)
Z	2	8
ρ_{calc} (g cm^{-3})	1.956	1.792
μ (mm^{-1})	7.475	5.473
$F(000)$	2560	3360
Number of reflections measured/unique	19991/6985	18877/5512
Number of reflections $[I > 2\sigma(I)]$	5352	4844
R_{int}	0.0562	0.0301
R_1, wR_2 $[I > 2\sigma(I)]$[a,b]	0.0648, 0.1141	0.0509, 0.1192
Goodness-of-fit on F^2	1.142	1.123

[a] $R_1 = \sum||F_o| - |F_c||/\sum|F_o|$.
[b] $wR_2 = [\sum w(F_o^2 - F_c^2)^2/\sum w(F_o^2)^2]^{0.5}$.

2.4. Structure determinations

The crystallographic data for **2** and **4** are listed in Table 1. Intensity data were collected at room temperature on a Rigaku Mercury CCD area-detector diffractometer with a graphite monochromator utilizing Mo Kα radiation ($\lambda = 0.71073$ Å). The structures were solved by direct methods [8a] and refined on F^2 by full-matrix least-squares using the SHELXL-97 program package [8b]. All non-hydrogen atoms were refined anisotropically. The organic hydrogen atoms were generated geometrically (C–H 0.96 Å).

3. Results and discussion

3.1. Synthesis

Treatment of $[Et_4N]_2[MS_4]$ (M = Mo, W) with 2 equiv. of $CuSBu^t$ in acetonitrile leads to the formation of two molecular squares **1** and **2**. The formation of **1** and **2** was unexpected since the reactions of $[MS_4]^{2-}$ (M = Mo, W) with CuL normally give rise to linear cluster compounds, e.g. $[LCuMS_4CuL]^{2-}$ (L = CN, SCN,

Cl) [9–11]. Clusters **1** and **2** are the first examples where four $CuMS_4Cu$ fragments are linked by thiolato ligands to form a square structural configuration. By using bidentate bis-thiolato ligands, clusters with different structural types can be obtained. Thus treatment of polymeric anions $[MS_4(CuCl)_2]^{2-}$ (M = Mo, W, prepared in situ by the reaction of $[Et_4N]_2[MS_4]$ with 2 equiv. of CuCl in DMF) with K_2SSS (SSS = 1,3,4-thiadiazole-2,5-dithiolate) yields **3** and **4**, which are helical chain polymers. While polymeric linear chains of Mo(W)/Cu/S clusters are common, **3** and **4** appear to be the first polymeric helical chains in the Mo(W)/Cu/S system reported.

3.2. Infrared and UV–Vis spectra

The IR spectra of **1**–**4** show the typical absorptions for the W–S stretching vibrations in the range of 400–520 cm^{-1}, as reported for many other Mo(W)/Cu/S clusters [12]. The spectra of **1**–**4** each exhibits a single sharp band in this region indicates symmetrical coordination around the MS_4^{2-} core [13]. As a general trend for the Mo(W)–S stretching vibration, an obvious red-shift occurs when the number of coordinated hetero-metal atoms increased [14]. Moreover, for isostructural clusters, the Mo–S vibration bands are displayed a little to higher frequency than those of their corresponding W–S bonds [15]. For **3** and **4**, strong peaks arising from coordinated 1,3,4-thiadiazole-2,5-dithiolato ligands also appear at 1182, 1171, 1041 and 999 cm^{-1} [16].

The electronic spectra of **1**–**4** are dominated by three absorptions in the 235–505 nm range that are attributable to ligand-to-metal charge transfer transitions of the $[MS_4]^{2-}$ (M = Mo, W) moieties [17]. Compared with $[Et_4N][MoS_4]$, the longest wavelength absorptions of **1** (505 nm) are red-shifted due to the coordination of CuL units to the central MoS_4^{2-} core [18]. The electronic spectra of the W clusters are similar in profile, wavelength, and intensity of the absorption bands to that found in $(NH_4)_2WS_4$.

3.3. Cyclic voltammetry

The redox properties of clusters **1**–**4** in DMF solution have been studied by cyclic voltammetry. Compared to the studies of the clusters with MOS_3Cu_n (M = Mo, W; $n = 2, 3$) fragments, the reduction behavior of the clusters with MS_4 (M = Mo, W) is not so rich and has been rarely studied [18,19]. The cyclic voltammograms data of **1**–**4** and some relative compounds have been shown in Table 2. The waves ranging from 0.59 to 0.84 V are attributed to the irreversible oxidation of copper (I). The $E_{2(red)}$–$E_{5(red)}$ cathodic waves are associated with the irreversible reduction of M^{IV} (M = Mo, W).

3.4. Description of the crystal structure of $[Et_4N]_4[\{WS_4Cu_2(\mu\text{-}SBu^t)\}_4]$ (2)

The molecular structure of **2** is shown in Fig. 1 and selected bond lengths and angles are listed in Table 3. The 12 metals together with four sulfur atoms from $\{SBu^t\}^-$ ligands are nearly coplanar with the mean deviation of 0.07 Å. The configuration of twelve metal atoms and four S atoms of the thiolato ligands can be approximately described as a square, in which the S atoms form the corners of the square with the Cu–S–Cu angles being 85.9(1)° and 88.1(1)°. In each side of the

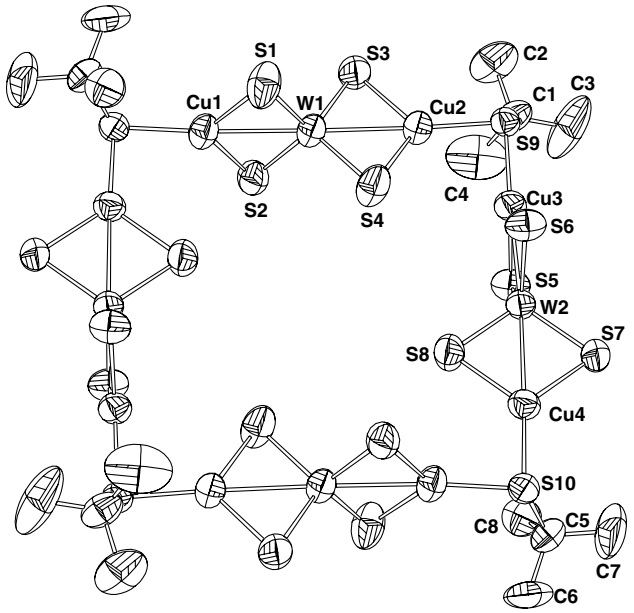


Fig. 1. Structure and labeling of the $[\{WS_4Cu_2(\mu\text{-}SBu^t)\}_4]^{4-}$ anion of **2** (50% probability displacement ellipsoids). The hydrogen atoms are omitted for clarity.

Table 2
Cyclic voltammograms data (*E*/*V*)

Compound	$E_{1(ox)}$	$E_{2(red)}$	$E_{3(red)}$	$E_{4(red)}$	$E_{5(red)}$	References
$[Et_4N]_4[I_6Cu_4MoS_4]$	0.56	0.43		−0.69	−1.41	[19]
$[Et_4N]_4[I_6Cu_4WS_4]$	0.56	0.42		−0.75		[19]
$[Et_4N]_4[\{MoS_4Cu_2(\mu\text{-}SBu^t)\}_4]$ (**1**)	0.59	0.16		−0.66		this work
$[Et_4N]_4[\{WS_4Cu_2(\mu\text{-}SBu^t)\}_4]$ (**2**)	0.66	0.14	−0.20	−0.64	−0.82	this work
$\{[Et_4N]_2[MoS_4Cu_2(SSS)]\}_n$ (**3**)	0.84	0.14		−0.61	−0.11	this work
$\{[Et_4N]_2[WS_4Cu_2(SSS)]\}_n$ (**4**)	0.76	0.17	−0.52	−0.77	−1.1	this work

Table 3
Selected bond lengths (Å) and angles (°) for **2**

W(1)–Cu(1)	2.651(2)
W(1)–Cu(2)	2.653(2)
W(2)–Cu(3)	2.644(2)
W(2)–Cu(4)	2.638(2)
W(1)–S(1)	2.210(4)
W(1)–S(2)	2.207(4)
W(1)–S(3)	2.203(4)
W(1)–S(4)	2.207(4)
Cu(1)–S(1)	2.225(4)
Cu(1)–S(2)	2.242(4)
Cu(1)–S(10)^{i}	2.193(3)
Cu(2)–S(9)	2.201(3)
Cu(2)–S(4)	2.232(4)
Cu(2)–S(3)	2.233(4)
Cu(3)–S(5)	2.219(4)
Cu(3)–S(6)	2.244(4)
Cu(3)–S(9)	2.182(3)
Cu(4)–S(7)	2.225(4)
Cu(4)–S(8)	2.220(4)
Cu(4)–S(10)	2.204(3)
Cu(2)–Cu(3)	2.985(2)
Cu(1)–Cu(4)^{i}	3.058(2)
Cu(1)–W(1)–Cu(2)	177.67(5)
Cu(4)–W(2)–Cu(3)	176.08(5)
S(3)–W(1)–S(2)	110.2(2)
S(3)–W(1)–S(4)	107.5(1)
S(2)–W(1)–S(4)	110.3(2)
S(3)–W(1)–S(1)	109.9(2)
S(2)–W(1)–S(1)	107.6(1)
S(4)–W(1)–S(1)	111.4(2)
S(5)–W(2)–S(6)	107.8(1)
S(5)–W(2)–S(7)	110.4(2)
S(5)–W(2)–S(8)	110.5(1)
S(6)–W(2)–S(8)	109.1(2)
S(6)–W(2)–S(7)	111.6(1)
S(8)–W(2)–S(7)	107.5(1)
S(1)–Cu(1)–S(2)	105.8(1)
S(4)–Cu(2)–S(3)	105.6(2)
S(5)–Cu(3)–S(6)	105.4(1)
S(8)–Cu(4)–S(7)	106.2(1)
W(1)–Cu(1)–S(10)^{i}	170.3(1)
W(1)–Cu(2)–S(9)	177.8(1)
W(2)–Cu(3)–S(9)	173.4(1)
W(2)–Cu(4)–S(10)	176.9(1)

Symmetry transformations used to generate equivalent atoms: (i) $x+1, -y, -z+1$.

square, the (Bu^t)SCuS$_2$WS$_2$CuS(Bu^t) fragment is nearly linear, with the average Cu–W–Cu and S(Bu^t)–Cu–W angles being 176.88° and 174.60°, respectively. Each W atom of the structure is at the center of an essentially tetrahedral WS$_4$ unit in which the W–S bond lengths are almost equal. The WS$_4$ unit acts as a bidentate ligand to coordinate Cu atoms with the W–Cu bond lengths varying from 2.638(2) to 2.653(2) Å. These lie towards the shortest end of the reported range of W–Cu bond distances (2.621–2.784 Å) [20], indicating significant interactions between these heteronuclear metal atoms. In addition, weak interactions between adjacent Cu atoms are also found in the cluster [Cu(2)–Cu(3): 2.985(2); Cu(1)–Cu(4)^{i}: 3.058(2) Å]. All the Cu atoms are in an approximately trigonal environment with the sum of the S–Cu–S angles for each Cu ranging from 359.35° to 359.92°.

3.5. Description of the crystal structure of $\{[Et_4N]_2[WS_4Cu_2(SSS)]\}_n$ (**4**)

Cluster **4** contains linear CuS$_2$WS$_2$Cu fragments that are linked by bridging SSS^{2-} ligands to form a polymeric chain. An ORTEP drawing of a portion of the anion is shown in Fig. 2 and the important bond lengths and angles are listed in Table 4. The configuration of the polymeric anion can be viewed as a helical chain that propagates along the crystallographic *b* axis. For clarity, a simplified diagram with only metal atoms is given in Fig. 3. It is seen that the polymeric anion forms a helical chain with a pitch (length per turn) of 11.84 Å. Although many polymeric chains of Mo(W)/Cu/S clusters with other bridging ligands such as SCN$^-$ or halogen ligands have been reported, species with a helical configuration like **4** have not been previously observed. Each repeated CuS$_2$WS$_2$Cu unit involves short Cu–W distances [2.647(1) and 2.652(1) Å] and an approximately linear

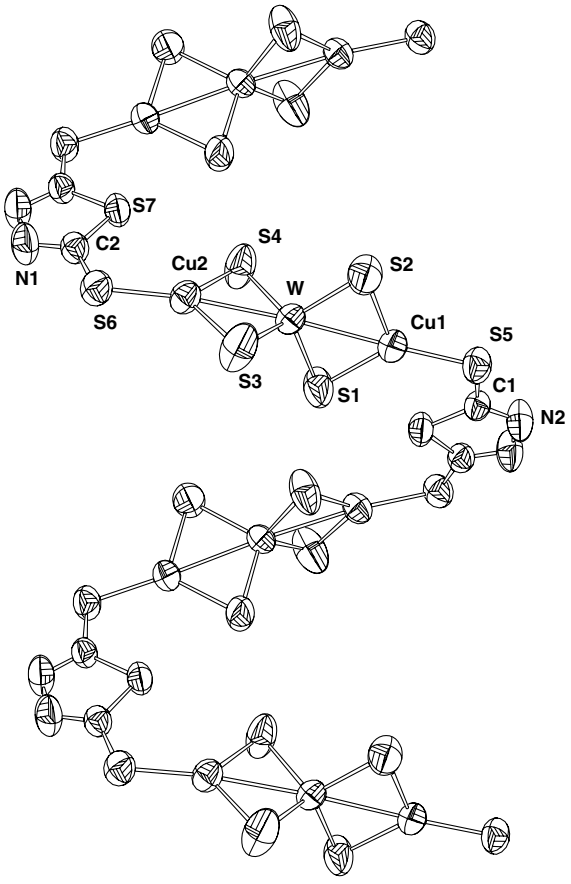


Fig. 2. Structure and labeling of a portion of the anion of **4**. Thermal ellipsoids are drawn at the 50% probability level.

Table 4
Selected bond lengths (Å) and angles (°) for **4**

W–Cu(1)	2.647(1)
W–Cu(2)	2.652(1)
W–S(1)	2.189(3)
W–S(4)	2.191(2)
W–S(3)	2.195(3)
W–S(2)	2.221(3)
Cu(1)–S(1)	2.216(3)
Cu(1)–S(2)	2.224(3)
Cu(1)–S(5)	2.183(2)
Cu(2)–S(3)	2.219(3)
Cu(2)–S(4)	2.217(3)
Cu(2)–S(6)	2.184(2)
S(1)–W–S(2)	107.1(1)
S(1)–W–S(3)	110.8(2)
S(1)–W–S(4)	109.8(1)
S(3)–W–S(2)	111.8(1)
S(4)–W–S(2)	110.6(1)
S(4)–W–S(3)	106.9(1)
S(1)–Cu(1)–S(2)	106.0(1)
S(5)–Cu(1)–S(1)	130.0(1)
S(5)–Cu(1)–S(2)	124.0(1)
S(4)–Cu(2)–S(3)	105.1(1)
S(6)–Cu(2)–S(3)	124.2(1)
S(6)–Cu(2)–S(4)	130.6(1)

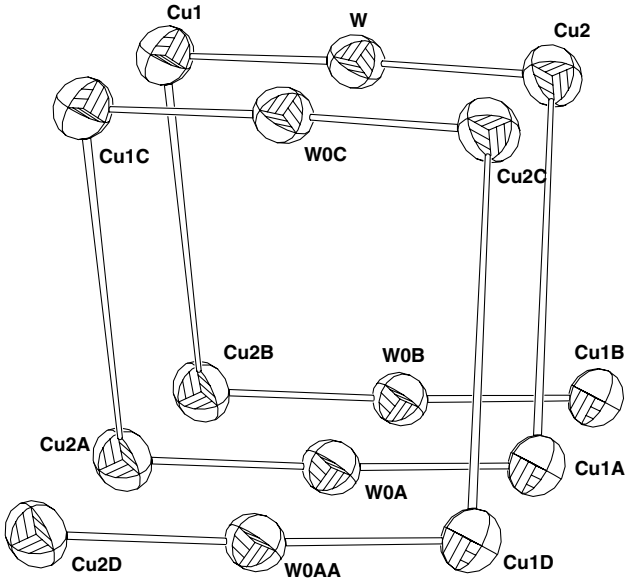


Fig. 3. Simplified diagram of the anionic helical chain of **4** (only metal atoms have been showed for clarity).

Cu–W–Cu array [176.20(3)°], as previously observed in the discrete complex anion of $[Ph_4P]_2[ClCuS_2WS_2CuCl]$ [11]. The tungsten atoms have an essentially tetrahedral geometry while the copper atoms adopt approximately trigonal planar geometries. For each SSS^{2-} ligand, the ring system and the thiolato sulfur atoms and two adjacent WS_2Cu planes are almost coplanar. Besides, all the sulphur atoms of SSS^{2-} ligands point to the center of the helix and the neighboring thiadiazoles are oriented in opposite directions along the chain.

4. Conclusion

By using linear CuS_2MS_2Cu (M = Mo, W) subunits as building blocks and thiolato ligands as linkers, we have successfully constructed four new Mo(W)/Cu/S clusters. With the monodentate SBu^{t-} ligand, molecular squares **1** and **2** have been isolated, respectively. However, with the bidentate bis-thiolato SSS^{2-} ligand, two helical chain polymers **3** and **4** were obtained. The correct choices of subunits and linkers appear critical for the construction of clusters with certain shapes. It should, therefore, be possible to make molecular squares with larger cavities or with other cluster geometries by choosing other Mo(W)/Cu/S building blocks and thiolato ligands.

Acknowledgements

We thank State Key Laboratory of Structural Chemistry, Fujian Institute of Research on the Structure of Matter, Chinese Academy of Sciences (CAS), the Ministry of Science and Technology of China (001CB108906) and the National Science Foundation of China (20333070) for financial support.

Appendix A. Supplementary data

Crystallographic data, excluding structure factors, have been deposited at the Cambridge Crystallographic Data center, CCDC Reference Nos. 254603 (**2**) and 254606 (**4**). Copies of this information may be obtained free of charge from the Director, CCDC, 12 Union Road, Cambridge, CB2 1EZ, UK (fax: +44 1223 336 033; email: deposit@ccdc.cam.ac.cn or www.ccdc.cam.ac.uk). Supplementary data associated with this article can be found, in the online version, at doi:10.1016/j.poly.2005.06.031.

References

[1] (a) B. Kesanli, W.B. Lin, Coord. Chem. Rev. 246 (2003) 305;
(b) M. Fujita, Chem. Soc. Rev. 27 (1998) 417;
(c) F.A. Cotton, C. Lin, C.A. Murillo, Acc. Chem. Rev. 34 (2001) 759;
(d) O.M. Yaghi, H. Li, C. Davis, D. Richardson, T.L. Groy, Acc. Chem. Rev. 31 (1998) 474;
(e) S.R. Seidel, P.J. Stang, Acc. Chem. Rev. 35 (2002) 972;
(f) B.J. Holliday, C.A. Mirkin, Angew. Chem., Int. Ed. 40 (2001) 2022;
(g) M.J. Zaworotko, Angew. Chem., Int. Ed. 39 (2000) 3052;

(h) S. Melanger, J.T. Hupp, Angew. Chem. Int. Ed. 35 (1999) 2222.
[2] (a) A. Müller, W. Hellmann, Spectrochim. Acta A 41 (1985) 359;
(b) J.P. Lang, J.G. Li, S.A. Bao, X.Q. Xin, Polyhedron 12 (1993) 801;
(c) Q. Huang, X.T. Wu, T.L. Sheng, Q.M. Wang, Acta Crystallogr. C 52 (1996) 29;
(d) Q. Huang, X.T. Wu, T.L. Sheng, Q.M. Wang, Acta Crystallogr. C 52 (1996) 795;
(e) Q. Huang, X.T. Wu, J.X. Lu, Inorg. Chem. 35 (1996) 7445;
(f) Q. Huang, X.T. Wu, S.T. Sheng, Q.M. Wang, Inorg. Chem. 34 (1995) 4931;
(g) Q. Huang, X.T. Wu, J.X. Lu, Chem. Commun. (1997) 703;
(h) Q. Huang, X.T. Wu, Q.M. Wang, T.L. Sheng, J.X. Lu, Angew. Chem., Int. Ed. Engl. 35 (1996) 868.
[3] L. Chen, X.T. Wu, X.C. Gao, W.J. Zhang, P. Lin, J. Chem. Soc., Dalton Trans. (1999) 4303.
[4] J.P. Lang, Q.F. Xu, Z.N. Chen, B.F. Abrahams, J. Am. Chem. Soc. 125 (2003) 12682.
[5] J.P. Lang, K. Tatsumi, Inorg. Chem. 37 (1998) 160.
[6] Q.F. Zhang, Y.Y. Niu, W.H. Leung, Y.L. Song, I.D. Williams, X.Q. Xin, Chem. Commun. (2001) 1126.
[7] J.W. McDonald, G.D. Friesen, L.D. Rosenhein, W.E. Newton, Inorg. Chim. Acta 72 (1983) 205.
[8] (a) G.M. Sheldrick, SHELXS-97 Program for X-ray Crystal Structure Solution, University of Göttingen, Germany, 1997;
(b) G.M. Sheldrick, SHELXL-97 Program for X-ray Crystal Structure Refinement, University of Göttingen, Germany, 1997.
[9] S.F. Gheller, T.W. Hambley, J.R. Rodgers, R.T.C. Brownlee, M.J. O'Connor, M.R. Snow, A.G. Wedd, Inorg. Chem. 23 (1984) 2519.
[10] C. Potvin, J.M. Manoli, F. Sécheresse, S. Marzak, Inorg. Chem. 26 (1987) 4370.
[11] F. Sécheresse, M. Salis, C. Potvin, J.M. Manoli, Inorg. Chim. Acta 114 (1986) L19.
[12] A. Müller, E. Diemann, R. Jostes, H. Bögge, Angew. Chem., Int. Ed. Engl. 20 (1981) 934.
[13] G. Alonso, G. Berhault, R.R. Chianlli, Inorg. Chim. Acta 316 (2001) 105.
[14] A. Müller, W. Jaegermann, W. Hellman, J. Mol. Struct. 100 (1983) 559.
[15] J. Guo, T.L. Sheng, W.J. Zhang, X.T. Wu, P. Lin, Q.M. Wang, J.X. Lu, Inorg. Chem. 37 (1998) 3689.
[16] P. Mura, B.G. Olby, S.D. Robinson, Inorg. Chim. Acta 97 (1985) 45.
[17] F. Sécheresse, F. Robert, S. Marzak, J.M. Manoli, C. Potvin, Inorg. Chim. Acta 182 (1991) 221.
[18] H.W. Hou, X.Q. Xin, S. Shi, Coord. Chem. Rev. 153 (1996) 25.
[19] J.P. Lang, W.Y. Zhou, X.Q. Xin, K.B. Yu, J. Coord. Chem. 30 (1993) 173.
[20] Q. Huang, X.T. Wu, Q.M. Wang, T.L. Sheng, J.X. Lu, Inorg. Chem. 35 (1996) 893.

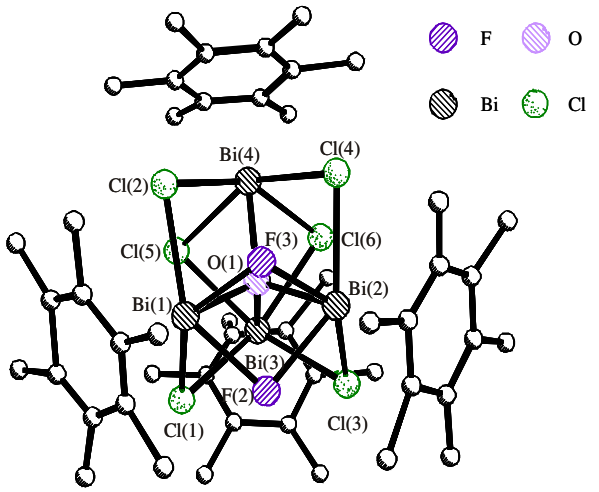


Fig. 1. The crystal structure of the $\{[Bi_4OF_2Cl_6](C_6Me_6)_4\}^{2+}$ cation.

found that the $[Bi_5][AsF_6]_3$ salt has sufficient solubility in SO_2 for the [17] metathesis reaction, replacing the $[AsF_6]^-$ anion (0.110 nm^3 [18]) by the larger $[Al(OC(CF_3)_3)_4]^-$ anion (0.758 nm^3 [19]). The estimated lattice energy of the $[Bi_5][Al(OC(CF_3)_3)_4]_3$ of 1571 kJ/mol is about 900 kJ/mol lower than that of the $[Bi_5][AsF_6]_3$ 2467 kJ/mol[1] and is therefore comparable in energy to those of the SO_2 soluble salts containing homopolyatomic cations of group 16, e.g., $U_{POT}([S_4][AsF_6]_2) = 1557$ kJ/mol, $U_{POT}([Se_4][AsF_6]_2) = 1544$ kJ/mol, $[Te_4][AsF_6]_2$, 1518 kJ/mol.[1]

2. Results and discussion

2.1. Reaction of $[Bi_5][AsF_6]_3$ and $Li[Al(OC(CF_3)_3)_4]$ in SO_2

The reaction of SO_2 soluble $Li[Al(OC(CF_3)_3)_4]$ and $NO[SbF_6]$ [17] gave the insoluble $Li[SbF_6]$ (s) and $NO[Al(OC(CF_3)_3)_4]$. In contrast the corresponding reaction of $Li[Al(OC(CF_3)_3)_4]$ and excess of the weakly soluble $[Bi_5][AsF_6]_3$ afforded insoluble $Li[AsF_6]$ and the reaction product $[Bi_x][Al(OC(CF_3)_3)_4]_3$ (**1**), x close to 4.33 according to the elemental analysis (Eq. (1)), contaminated with 10% of starting material $Li[Al(OC(CF_3)_3)_4]$, determined by quantitative ^7Li NMR

$$3Li[Al(OC(CF_3)_3)_4] + [Bi_5][AsF_6]_3 \xrightarrow{SO_2,r.t.} [Bi_x][Al(OC(CF_3)_3)_4]_3 + 3Li[AsF_6](s) \quad (1)$$

The bismuth containing product is very soluble in SO_2 and contains $[Al(OC(CF_3)_3)_4]^-$ anion [^{19}F, ^{27}Al NMR] showing that the anion has remained a spectator anion. The UV–Vis spectrum contained the band maxima (Table 1, column 2, actual spectra see S.I.) at 405, 450, 523 nm (Table 1) and 347 nm (shoulder) close to those of $[Bi_5]^{3+}$, $[Bi_8]^{2+}$ and probably $[Bi_9]^{5+}$ cations (Table 1) (a full interpretation of the UV spectra of $[Bi_5]^{3+}$, $[Bi_8]^{2+}$, $[Bi_9]^{5+}$ is given in [20]). The digital Gaussian deconvolution of the UV–Vis spectrum yielded the relative intensities of the bands allowing to calculate the molar absorptivities 5.1×10^3 (409 nm), 4.6×10^3 (453 nm), 3.1×10^3 (517 nm), 1×10^2 (804 nm), which are in agreement with the literature data for the $[Bi_5]^{3+}$ or $[Bi_8]^{2+}$ [24,7b,26]. Resolved bands arising from the presence of $[Bi]^+$ cation were not detected, however, a better fit of the calculated curve was obtained by postulating a weak band of $[Bi]^+$ 677 nm superimposed upon the more intense $[Bi_5]^{3+}$ (or $[Bi_8]^{2+}$) absorptions

$$3[Bi_5]^{3+} \overset{SO_2,r.t.}{\rightleftarrows} [Bi_8]^{2+} + 7[Bi]^+$$
$$2[Bi_5]^{3+} \rightleftarrows [Bi_9]^{5+} + [Bi]^+ \quad (2)$$

Thus, the SO_2 solution of the reaction product contained a mixture $[Bi_5]^{3+}$, $[Bi_8]^{2+}$, $[Bi_9]^{5+}$ and the $[Bi]^+$. The given cations could be generated by Eqs. (2) from the $[Bi_5]^{3+}$. We note that $[Sb_8][GaCl_4]$ was isolated from solutions of $SbCl_3$ in the Ga–$GaCl_3$–benzene system [21], whereas previously $[Bi_5]^{3+}$ and $[Bi]^+$ have been observed in Bi–$GaCl_3$–benzene solutions [7] and a products suggested to be $[M_5][GaCl_4]_3$ (M = Sb, Bi) were isolated from the MCl_3–Ga–$GaCl_3$ molten salt systems [4c].

The major IR absorption bands of the reaction products are due to the nonafluorobutoxide ligands. The bands at 832, 864 cm^{-1}, which are not observed in the spectrum of $Li[Al(OC(CF_3)_3)_4]$ have been assigned [22] to the Al–O vibrations of **1**. Energies of these bands are close to those of $Li[Al(OC(CF_3)_3)_4]$ (S.I., Section 2) with differences ca. 10 cm^{-1}. Thus, the local geometry around the Al atom in **1** is distorted and lower symmetry than tetrahedral, much like that in the $Li[Al(OC(CF_3)_3)_4]$, as the bismuth cation could have strong Bi–F and Bi–O contacts reminiscent of those of $[Li]^+$ in $Li[Al(OC(CF_3)_3)_4]$[2] [23].

2.2. Reaction of $[Bi_5][AsF_6]_3$ with $Li[Al(OC(CF_3)_3)_4]$ and C_6Me_6 in CH_2Cl_2

The metathesis reaction of $[Bi_5][AsF_6]_3$ and $Li[Al(OC(CF_3)_3)_4]$ in the presence of C_6Me_6 in CH_2Cl_2 yields dark brown, $Li[Al(OC(CF_3)_3)_4]$ free, highly soluble regularly

[1] Lattice energies have been calculated using the volume-based equation given in [18]. Volume of $[Bi_5]^{3+}$ 0.143 nm^3 was obtained by subtracting the three volumes of $[AlCl_4]^-$ anion 0.156 nm^3 from the molecular volume of the $[Bi_5][AlCl_4]_3$ 0.611 nm^3 [4b]. Volume of the $[AsF_6]$ was taken from [18], lattice energies of $[M_4][AsF_6]_2$ M = S, Se, Te were taken from [18].

[2] $[Li]^+$ in the $Li[Al(OC(CF_3)_2Ph)_4]$ [23a] and $Li[Al(OC(CF_3)_3)_4]$ [23b] is coordinated to the 2 oxygen and 4 fluorine atoms of the ligand, lowering the local symmetry around aluminium atom from T_d to C_{2v}.

Table 1
UV–Vis bands (nm) found in this study for product of interaction of $[Bi_5][AsF_6]_3$ and $Li[Al(OC(CF_3)_3)_4]$ in SO_2 (A), and for compound **4** in DCE – dichloroethane compared with the literature data on cationic bismuth clusters

A in SO_2	**4** in DCE	$[Bi_5]^{3+}$ in H_2SO_4 [4d]	$[Bi_5]^{3+}$ in NaCl–$AlCl_3$ [24]	$[Bi]^+$ in NaCl–$AlCl_3$ [24,25]	$[Bi]^+$ in $GaCl_3$–NaCl [7b]	$[Bi_8]^{2+}$ in Bi–$GaCl_3$ (175 °C) [7b]	$[Bi_8]^{2+}$ in $AlCl_3$–NaCl (250 °C) [26]	$[Bi_9]^{5+}$ in MeBzImCl/$AlCl_3$ melt [20]
347 [0.71] (9.4×10^3)	348 (8.7×10^3)	362 (2.39×10^3)	345[b]				350 (1.2×10^3)	
						387 [1.00]		
409 [0.38] (5.1×10^3)	407 (6.7×10^3)	425 (1.5×10^3)	390 (6.5×10^3)					
	447 (4.8×10^3)					440 [0.76]		
452 [0.34] (4.6×10^3)	468[a] (4×10^3)	460[b]	455 (3×10^3)				450 (0.62×10^3)	450 (s)[e]
517 [0.23] (3.1×10^3)	522 (3×10^3)	525 (0.29×10^3)	540 (1.5×10^3)			530 [0.36]	530 (0.4×10^3)	
	591[a] [0.24]			585 (3.2×10^2)	587 (7×10^2)			
	651[a] [0.10]			657 (1.2×10^2)				
				694 (1.0×10^2)	675 (3×10^2)			
677[a] [0.09]				730 (0.9×10^2)	691 (3×10^2)			750 (w)
804[c] [0.07] (1×10^2)	770 (8×10^2)	720 (1.1×10^2)	770 (3.0×10^2)	900 (ca. 5)	920 (ca. 10)			830 (w)
[d]	875[c] (4×10^2)	821 (1.8×10^2)	875 (5.0×10^2)					

Absorption maxima are given in nm with molar absorptivities in brackets and relative intensities in square brackets.
[a] Band maxima is not resolved and obtained only by Gaussian deconvolution.
[b] Observed in the reflectance spectrum.
[c] Very broad signal.
[d] Instrumental cut off at 820 nm.
[e] Relative intensities and molar absorptivities are not given.

shaped crystals, which did not diffract X-rays. The reaction product is interpreted as a salt containing the $[Bi_5]^{3+}$ cation, e.g., $[Bi_5(C_6Me_6)_4][Al(OC(CF_3)_3)_4]_3$ (**2**) based on the elemental analysis (Eq. (3))

$$3Li[Al(OC(CF_3)_3)_4] + [Bi_5][AsF_6]_3 + 4C_6Me_6 \xrightarrow[+5\,^\circ C]{CH_2Cl_2} [Bi_5(C_6Me_6)_4][Al(OC(CF_3)_3)_4]_3 + 3Li[AsF_6] \quad (3)$$

2

The UV–Vis spectrum (Table 1, spectrum is shown in the S.I. Figs. 8 and 9) of **2** in $C_2H_4Cl_2$ was consistent with $[Bi_5]^{3+}$, $[Bi_8]^{2+}$, $[Bi_9]^{5+}$ cations in solution as well as $[Bi]^+$. Reported band maxima of $[Bi_5]^{3+}$ and $[Bi_8]^{2+}$ and that at 450 nm for the $[Bi_9]^{5+}$ are close to each other, hence these cations might be in equilibrium with **2** (Eq. (2)) in $C_2H_4Cl_2$. The molar absorptivities of $[Bi_5]^{3+}$ in **2** are in the same range but higher, as those of $[Bi_5]^{3+}$ in NaCl–$AlCl_3$ melts, strongly supporting our assignment of the bands to $[Bi_5]^{3+}$ and the presence of $[Bi]^+$, $[Bi_8]^{2+}$ and probably $[Bi_9]^{5+}$.

The IR absorption bands of C_6Me_6 in **2** are slightly shifted from those of C_6Me_6 (Tables 2 and 3), implying weak interaction between the bismuth cation and C_6Me_6. In addition, the IR spectrum contains only one Al–O band 832 cm^{-1} in the range 800–900 cm^{-1} [22] consistent with T_d site symmetry around the aluminium atom and very weak cation–anion interaction in **2**.

2.3. Evidence for $[Bi_4OF_2Cl_6(C_6Me_6)_4][Al(OC(CF_3)_3)_4]_2 \cdot C_6Me_6$

Crystals of **2** $\{[Bi_5(C_6Me_6)_4][Al(OC(CF_3)_3)_4]_3\}$ were deposited from the reaction mixture during a period of 1–6 days. For the next 10 days, crystals of **2** were contaminated with yellow crystals assigned to **3** and $[C_6Me_6H][Al(OC(CF_3)_3)_4]$[3] and after an additional 5 days only yellow and orange crystals of **3**, $[C_6Me_6H][Al(OC(CF_3)_3)_4]$ and colourless crystals[4] were obtained.

We propose that the homopolyatomic cations generated in the metathesis reaction in CH_2Cl_2 are very chem-

[3] Yellow crystals **4** refined in *C*1, $a = 9.825$, $b = 20.046$, $c = 21.148$, $\alpha \approx \beta \approx \gamma \approx 90°$, $Z = 2$ to the *R* factor close to 25% and was consistent with the presence of $[Al(OC(CF_3)_3)_4]^-$ and $\{C_6Me_6\}$ or ($[C_6Me_6H]^+$) moieties. Problem of disordering $-C(CF_3)_3$ groups in the anion precluded further refinement. It could be $Li[Al(OC(CF_3)_3)_4] \cdot C_6Me_6$ or $[C_6Me_6H][Al(OC(CF_3)_3)_4]$. A ^7Li resonance was not observed at r.t. and low temperature for the solution of yellow reaction product, hence $[C_6Me_6H][Al(OC(CF_3)_3)_4]$ formulation seems to be more feasible, additional IR evidence of $[C_6Me_6H]^+$ is described in Section 4.

[4] Colourless crystals that deposits from solution in a period of 1 month at −24 °C refined in *C*1, $a = 14.330(2)$, $b = 18.114(3)$, $c = 22.492(4)$, $\alpha = 84.252(2)$, $\beta = 72.851(2)$, $\gamma = 82.616(2)$, $Z = 4$ to the *R* factor close to 20%. The proposed structure obtained at this point of refinement consistent of $[Al(OC(CF_3)_3)_4]^-$ and $[Al_7O_4F_{14}]^-$ and/or $[Al_7O_3F_{15}]$ moieties. Problem of disordering $-C(CF_3)_3$ groups in the anion precluded further refinement.

Table 2
Raman of **2**, bands of $[Al(OC(CF_3)_3)_4]^-$ anion (assignment see [17,22b,22c]) are omitted for clarity

Observed band	Literature data	Assignment
108 (sh)	103 (sh)	$\nu_6(E'')[Bi_5]^{3+}$
119 (s)	119	lattice mode, also observed previously for anion and C_6Me_6
138 (sh)	142 (sh)	$\nu_1(A_1')[Bi_5]^{3+}$
336 (w)	343(w)	CH_3 motion
380(w)	378 (w)	CH_3 motion perpendicular to the plane of benzene skeleton
450 (m)	450 (m)	deformation mode of benzene skeleton
554 (s)	553 (s)	breathing, benzene skeleton
1294 (vs)	1295 (m)	ν(C–CH_3)
1373 (w)	1364 (m)	δCH_3 symmetry
1396 (m)	1385 (m)	δCH_3 degenerate
1418 (w)	1438[a]	δCH_3 degenerate
1495 (m)	1462[a]	δCH_3 degenerate
1581 (b, w)	1583 (w)	ν(C=C)
2875 (sh)	2939 (vs)	ν(C–H)
2924 (b, vs)	2985 (vs)	ν(C–H)

Assignment for $[Bi_5]^{2+}$ [4d,7b], C_6Me_6 [46].
[a] Observed at low temperature in crystalline hexamethylbenzene [46a].

Table 3
Observed IR bands of C_6Me_6 in **2**, **3** · C_6Me_6, **4** and assignment [47]

2	**3**	**4**	C_6Me_6	Assignment
		682		
793	780		796	out of plane ring bending mode
		889		
1018	1022		998	in plane CH_3 rocking
1062	1069	1061	1057	out of plane CH_3 rocking
1074		1071		
	1102			
		1596		$[C_6Me_6H]^{+a}$

[a] Band at 1590 cm^{-1} is one of the characteristic benzoid C=C skeletal stretching modes of the carbocation [48].

ically active and abstract oxygen and fluorine from the nonafluorobutoxide ligand of the $[Al(OC(CF_3)_3)_4]^-$ anion and chlorine from the CH_2Cl_2 (see S.I. for a detailed discussion). Abstraction of oxygen and fluorine from the $[Al(OC(CF_3)_3)_4]^-$ was observed previously by degradation of phosphorus iodine cations[5] [27]. Bismuth alkoxides $Bi(OR_f)_3$ $R_f = (C_6H_2(CF_3)_3)$ [28,29] decomposed with C–F activation. C–Cl activation by electrophilic metal centers followed by the chlorine transfer to the metal have been observed for a wide range of metals [30] (e.g., for $CHCl_3$ by the rhodium complex $LRh(CO)_2$ L = tris(3,5-dimethyl,4-chloropyrazolyl)borate [30a]).

The salt **3** · C_6Me_6 (Fig. 1) is the first example of a 1:2 salt of the bulky polyfluoroalkoxyaluminate anion, the first example of a discrete oxygen-centered tetrahedral arrangement of group 15, and a rare example of a Bi(III) fluoride complex [31,32]. Four-coordinate oxygen centers have been reported in bismuth alkoxide clusters having complex oligomeric structures (i.e., $Bi_4(\mu_4\text{-}O)(\mu\text{-}OR)_6\{\mu_3\text{-}OBi(\mu\text{-}OR)_3\}_2(C_6H_5CH_3)$) [33] as well as for main group [34,35], d-block [36,37] and f-block [38,39] metal complexes. The structure of **3** · C_6Me_6 was obtained from crystals of poor quality, albeit many unsuccessful attempts made to improve their quality. However, the connectivity in $[Bi_4OF_2Cl_6]^{2+}$ has been established and the data clearly show the presence of C_6Me_6 and the $[Al(OC(CF_3)_3)_4]^-$ anion. The quality of the X-ray structure does not allow unambiguous assignment of the bridging light atoms as oxygen or fluorine within the $Bi_4X_2Cl_4Y$ core and the atom type assignment has been made based on chemical arguments – bond valence theory, ESR and NMR data. The sum of four Bi–O(1) contacts is 2.17 v.u. and consistent with a valence of 2 for oxygen, while four Bi–(F1) contacts would give 1.64 v.u.[6] [40] for fluorine, strongly supporting the assignment of the central atom as oxygen. In addition, a Bi_4F_5 would result in a mixed oxidation state for bismuth and 1 unpaired electron for the dication. However, an ESR signal was not detected for the solid sample, as well as a solution of **3** · C_6Me_6. The same method was applied to assign F2 and F3. The sum of two Bi–F(2), Bi–F(3) contacts is 0.71 and 0.67 v.u., while two Bi–O(2) and Bi–O(3) contacts would give 0.97 and 0.95 v.u., hence bridging atoms are most likely fluorine. In addition, the fluorine NMR spectrum of the freshly prepared SO_2 solution of **3** · C_6Me_6 at −70 °C shows major ^{19}F and ^{27}Al NMR resonances of the $[Al(OC(CF_3)_3)_4]^-$ anion and a minor singlet resonance at −220.5 ppm in the ^{19}F NMR attributed to the fluorine atoms in the $[Bi_4OF_2Cl_6]^{2+}$ cation.

The dication contains four bismuth atoms at the apex of an oxygen centered distorted tetrahedron, linked across the edges by bridging halogen atoms (Figs. 2 and 3). The Bi1–F–Bi2 and Bi(1,2)–Cl–Bi(3,4) angles in **3** are close to 90° within 2° and the Bi3–Cl–Bi4 angles are 83.0(4)° and 85.0(4)°. Also, the estimated Bi4–Bi3 distance is 3.602(1) Å, shorter than the Bi1–Bi2 and Bi3–Bi4 contacts 3.93(±0.04) Å. Each bismuth atom is capped by a weakly bound η^6 C_6Me_6 ring[7] [41,42]

[5] The proposed [27a,27b] decomposition mechanism of the salt of $[P_2I_3]^+$ involved the formation of a tight ion pair $[P_2I_3]^+[Al(OC(CF_3)_3)_4]^-$ followed by liberation of $[P_2I_3][OC(CF_3)_3]$ and the very strong Lewis acid $Al(OC(CF_3)_3)_3$ which abstract fluorine from the $[OC(CF_3)_3]$ and react with the $[Al(OC(CF_3)_3)_4]^-$ forming dimeric anion $[(OC(CF_3)_3)_3Al(\mu\text{-}F)Al(OC(CF_3)_3)_3]^-$. The phosphorus iodine cation abstract oxygen from the $[OC(CF_3)_3]$ forming P_2O_3, P_4, C_4F_8. The final products of decomposition were $[P_2I_3][(OC(CF_3)_3)_3Al(\mu\text{-}F)Al(OC(CF_3)_3)_3]$, phosphorus oxide, phosphorus alkoxide, P_4 and fluorocarbon species.

[6] Values used: Bi(+3)–F(−1) $R_o = 1.99$, $B = 0.37$, Bi(+3)–O(−2) $R_o = 2.094$, $B = 0.37$, Bi(+3)–Cl(−1) $R_o = 2.48$, $B = 0.37$.

[7] The separation distances between Bi(1) and C(301)–C(306) aromatic ring 2.69 Å, Bi(2) and C(101)–C(106) aromatic ring 2.67 Å, Bi(3) and C(401)–C(406) aromatic ring 2.75 Å, Bi(4) and C(201)–C(206) aromatic ring 2.61 Å.

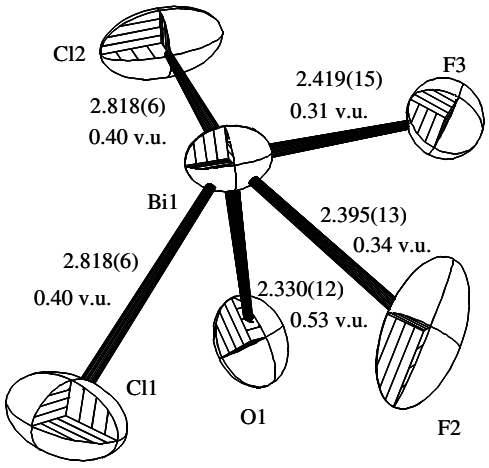


Fig. 2. Environment of the Bi(1) atom in **3**, neighbouring bismuth atom and C_6Me_6 molecules are omitted for clarity.

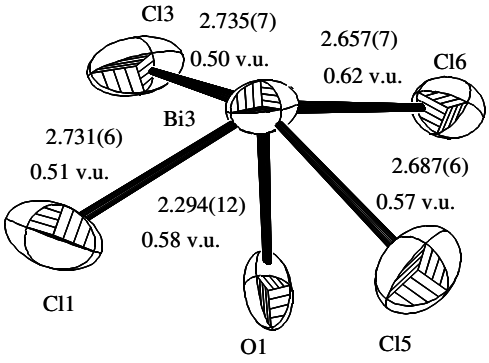


Fig. 3. Environment of the Bi(3) atom in **3**, neighbouring bismuth atom and C_6Me_6 molecules are omitted for clarity.

approximately perpendicular to the corresponding Bi–O bond as illustrated in Fig. 1. The bismuth halogen dication core may be formally regarded as constructed from one $[BiF_2]^+$ moiety, three $[BiCl_2]^+$ units, and $[O]^{2-}$ which donates electron density to the four bismuth atoms with the sum of the Bi–O valency units calculated at 2.14(2) v.u.[6] [40].

In VESPR terms [43], the first coordination around Bi1 and Bi2 can be described as $AX_2X'_2YE$ (X = Cl, X′ = F, Y = O, E = lone pair) and that of Bi3 and Bi4 as AX_4YE illustrated for Bi1 and Bi3 in Figs. 2 and 3, respectively, which include bond distances and valence units. The corresponding figures for Bi2 and Bi4 are included in the Supplemental materials. All the F–Bi–F, F–Bi–Cl, Cl–Bi–Cl, O–Bi–F and O–Bi–Cl angles in **3** are in the range 72.3–76.4°. The sum of the valence units around Bi3 is 2.78 v.u. (Bi1 is 1.98 v.u., Bi2 2.05 v.u., Bi4 2.66 v.u.), the remaining Bi valence units are derived from the donation of electrons from the C_6Me_6 ring to the positively charged bismuth in to the second coordination sphere of bismuth.

We have estimated the lattice energy $U_{POT}([Bi_4OF_2Cl_6(C_6Me_6)_4][Al(OC(CF_3)_3)_4]_2)$ as 912 kJ/mol[8] [44]. This is significantly larger than that of 1:1 salt with the same anion, $U_{POT}(Li[Al(OC(CF_3)_3)_4])$ 361 kJ/mol [19], but smaller than the 1:2 salts $U_{POT}(Ca[NO_3]_2)$ 2209 kJ/mol and $U_{POT}(MgI_2)$ 1944 kJ/mol [18 (Table 2)]. Therefore, the higher solubility of $\mathbf{3}\cdot C_6Me_6$ in SO_2 compared with the poor solubility of $Ca(NO_3)_2$ and MgI_2 may arise from the smaller lattice energy of 1:2 salts with the large anion.

The X-ray microanalysis confirms that $\mathbf{3}\cdot C_6Me_6$ contains Bi and Cl, as well as Al, F, C and O (S.I.). The EI-MS shows $[C_6Me_6^+]$ and as well as fluorocarbon cations derived from $[Al(OC(CF_3)_3)_4]^-$ on decomposition of $\mathbf{3}\cdot C_6Me_6$. The IR spectrum of $\mathbf{3}\cdot C_6Me_6$ contains very strong absorption bands of the perfluorinated ligand of the anion. One Al–O band of the $[Al(OC(CF_3)_3)_4]^-$ anion was detected at 833 cm^{-1} consistent with an almost tetrahedral symmetry at the aluminium center. The observed absorption bands of the C_6Me_6 in $\mathbf{3}\cdot C_6Me_6$ (Table 3) are shifted slightly higher in energy, relative to the band for free C_6Me_6 [47], due to coordination to the $[Bi_4OF_2Cl_6]^{2+}$ cation. For comparison, the Ln(III) complexes $[LnCl_2(C_6Me_6)][AlCl_4]_3$ Ln = Nd, Sm, Gd, Yb exhibit the out of plane mode at 770–780 cm^{-1} and $\nu(CH_3)$ vibrations at 1010–1030 cm^{-1} [45], close to those of **3**.

3. Conclusions

Evidence is presented that we have prepared the SO_2, CH_2Cl_2 and $C_2H_4Cl_2$ soluble salts $[Bi_x][Al(OC(CF_3)_3)_4]$ (**1**) and $[Bi_5(C_6Me_6)_4][Al(OC(CF_3)_3)_4]_3$ (**2**), in a moderate yields by the metathesis reaction between $[Bi_5][AsF_6]_3$ and $Li[Al(OC(CF_3)_3)_4]$ in SO_2 solution and in a solution of CH_2Cl_2 that contained C_6Me_6. This implies that the metathesis reaction in the presence of appropriate donor ligand (arene) in SO_2 and CH_2Cl_2 may generate several of the related salts containing bismuth polyatomic cations. The UV–Vis of solutions of **1** in SO_2 and **2** in $C_2H_4Cl_2$ were consistent with the presence of $[Bi_5]^{3+}$, $[Bi_8]^{2+}$, $[Bi_9]^{5+}$ and $[Bi]^+$.

The bismuth homopolyatomic cations were shown to be chemically reactive and the novel 1:2 salt $[Bi_4OF_2Cl_6(C_6Me_6)_4][Al(OC(CF_3)_3)_4]_2\cdot C_6Me_6$ containing the bismuth cluster cation $[Bi_4OF_2Cl_6]^{2+}$ was isolated from a solution of **2** in CH_2Cl_2. Formation of $[Bi_4OF_2Cl_6]^{2+}$ may be regarded as a self assembly of bismuth halide and oxohalide moieties, however, it is difficult to assess

[8] The volume of the C_6Me_6 ($V_m = 0.252$ nm^3) [44] was subtracted from the volume of $\mathbf{3}\cdot C_6Me_6$ ($V_m = 3.402$ nm^3), obtained from crystallographic data in order to provide the volume of **3** ($V_m = 3.150$ nm^3). The obtained volume was used for calculation of U_{POT}(**3**) using Eq. (3) [18] and parameters $\alpha = 133.5$, $\beta = 60.9$.

the features that governed the $[Bi_4OF_2Cl_6]$ stoichiometry by decomposition of the bismuth homopolyatomic cations under the prevailing experimental conditions. We propose that the process involved fluorine and oxygen transfer from the nonafluorobutoxide ligand and chlorine transfer from the CH_2Cl_2 and conclude that the bulky anion facilitates the formation of a discrete oxygen-centered fluorine- and chlorine-bridged bismuth cluster in a complex with hexamethylbenzene.

4. Experimental

4.1. General remarks

All operations were performed using standard Schlenk line techniques under a purified nitrogen atmosphere. Solid reagents and crystals were manipulated in a Vacuum Atmospheres Dri-Lab equipped with a Dri-Train (HE-493) and 1 kg of 3 Å molecular sieves contained in an internal circulating drying unit. Reactions in SO_2 were carried out in a jointless, single apparatus fitted with Teflon in glass Rotoflo valves (HP 6K) and consisting of two thick walled bulbs ($V = 50$ ml) linked by a glass tube incorporating a sintered fine-porosity glass frit. The compounds $[Bi_5][AsF_6]_3 \cdot SO_2$ and $Li[Al(OC(CF_3)_3)_4]$ were prepared by the literature methods [23a,4d] and the identity of $[Bi_5][AsF_6]_3 \cdot SO_2$ was supported by IR. The IR spectrum of $Li[Al(OC(CF_3)_3)_4]$ included in the S.I. has not been previously reported. Sulfur dioxide was dried over P_2O_5 and distilled prior to use. CH_2Cl_2 and $CDCl_3$ were dried over CaH_2 and degassed. NMR spectra were recorded using Varian 400 NMR spectrometer. Proton and ^{13}C chemical shifts are reported in δ units downfield from Me_4Si with the solvent as the reference signal. $CClF_3$ was used as a reference for ^{19}F spectra and aqueous solutions of $AlCl_3$ and $Li[ClO_4]$ were used as a references in ^{27}Al and ^{7}Li NMR spectra, respectively. NMR samples were prepared in 10 and 5 mm thick walled NMR tubes fitted with J. Young valves. Mass spectra were recorded using a KRATOS ms 50 TC mass spectrometer equipped with the EI source, 30 ev. by the direct inlet method from samples sealed in dried glass m.p.t. tubes. FT-IR spectra (resolution 1 cm^{-1}, 128 scans) were recorded using a Thermo Nicolet spectrometer (Nexus 470 FT-IR). FT-Raman spectra were obtained from neat samples, sealed under nitrogen atmosphere in glass capillaries, using Bruker RFS 100 FT-Raman spectrometer incorporating a Nd:YAG laser (emission wavelength: 1.06 μm; maximum output laser power: 80 mW), 1000 scans, resolution 4 cm^{-1}. We attempted to record FT-Raman spectra of all species; however, the coloured samples **1** and **3** showed fluorescence, compound **2** gave a Raman spectrum with a low signal-to-noise ratio. The UV–Vis spectrum of **1** in SO_2 was measured using HP-8452A diode array spectrophotometer, at room temperature, 300–820 nm range, 14 mg of solid containing 90% **1** and 10% $Li[Al(OC(CF_3)_3)_4]$ in (6 g, 4.11 ml) of SO_2 0.1 cm cell. The compound **2** were measured using a Cary 5E UV–Vis–NIR spectrometer, at room temperature, in 0.2 cm cells. Two spectra, one containing data collected from 3000 to 400 nm and one from 800 to 300 nm were measured using 23.5 mg of sample **2** and 3.8636 g of $C_2H_4Cl_2$. Melting points were measured in sealed capillary tubes under nitrogen and are not corrected. X-ray microanalysis was performed with a JEOL JSM-6400 SEM, equipped with an Edax Genesis X-ray micro analyser. Operating conditions: vacuum close to 10^{-6} Torr, accelerating voltage 15 kV, probe current 1.5 nA, spectra collection time 60 s. Samples were coated with carbon, using an Edwards vacuum evaporator. Elemental analysis was carried out by Galbraith Laboratories, Inc.

Table 4
Crystallographic data of the X-ray diffraction studies of $\mathbf{3} \cdot C_6Me_6$

	$\mathbf{3} \cdot C_6Me_6$
Formula	$C_{92}H_{90}Al_2Bi_4Cl_6F_{75}O_8$
Molecular formula	$[Bi_4OF_2Cl_6(C_6Me_6)_4]$ $[Al(OC(CF_3)_3)_4]_2 \cdot C_6Me$
M_r	3848.22
Temperature (K)	198(1)
Radiation used (λ [Å])	Mo Kα (0.71073)
Crystal description	orange, needle
Crystal size (mm)	$0.1 \times 0.1 \times 0.5$
Crystal system	orthorhombic
Space group	$P2_12_12_1$
a (Å)	15.8671(10)
b (Å)	25.8211(18)
c (Å)	33.209(2)
α (°)	90
β (°)	90
γ (°)	90
V (Å^3)	13605.8(16)
Z	4
$F(000)$	7360
ρ_{calc} (g cm^{-3})	1.879
μ (mm^{-1})	5.437
Total reflections	94818
Unique reflections	30455
R_{int}	0.1001
Scan range Θ (°)	1.2–27.50
Completeness to Θ_{max} (%)	99.2
Index ranges	$-20 \leqslant h \leqslant 20$; $-32 \leqslant k \leqslant 33$; $-42 \leqslant l \leqslant 39$
Data/restrains/parameters	30455/125/712
R_1, wR_2 [$I > 2\sigma(I)$]	0.0858, 0.2289
R_1, wR_2 (all data)	0.2036, 0.2622
Goodness-of-fit on F^2	1.009
Maximum/minimum electron density (e Å^{-3})	3.016 and −1.425
Minimum/maximum transmission ratio	0.860

$wR_2 = (\sum[w(F_o^2 - F_c^2)^2]/\sum[F_o^4])^{1/2}$, $R_1 = \sum||F_o| - |F_c||/\sum|F_o|$, weight $= 1/[\sigma^2(F_o^2) + (0.0745 * P)^2]$; where $P = (\max(F_o^2, 0) + 2 * F_c^2)/3$.

4.2. Preparation of salts **1**

A dried two bulbed (50 ml) vessel equipped with Teflon in glass with Rotoflo valves (HP 6K), was charged with the $Li[Al(OC(CF_3)_3)_4]$ (0.8 g, 0.8 mmol) and $[Bi_5][AsF_6]_3 \cdot SO_2$ (2.7 g, 1.6 mmol). SO_2 (15 ml) was condensed onto the mixture of reagents at −196 °C. The resulting mixture was rigorously stirred at r.t. for 5 days. A dark brown solution was filtered from 2.6 g of yellow insoluble solid and SO_2 was removed under dynamic vacuum to give a brown solid. Yield: 0.9 g, 70% based on the Eq. (1). The relative amount of $Li[Al(OC(CF_3)_3)_4]$ in the reaction product was established as 10% by measuring the intensity of the ^{7}Li NMR resonance relative to that in the spectrum of a solution of $Li[Al(OC(CF_3)_3)_4]$ in SO_2 at a known concentration. **1** could be a mixture of individual compounds. Result of elemental analysis could be interpreted based on the model 90% of $[Bi_5(SO_2)_3][Al(OC(CF_3)_3)_4]_3$ and 10% of $Li[Al(OC(CF_3)_3)_4]$ or alternatively $[Bi_{4.33}][Al(OC(CF_3)_3)_4]_3$ and 10% of $Li[Al(OC(CF_3)_3)_4]$: Calc. C, 14.49; Bi, 22.73; F, 51.65. Found: C, 14.24; Bi, 21.41; F, 51.73%. EI-MS (30 eV, heating r.t. −170 °C): *m/z* (%) = 706 (1) [An^+–$C_3F_{11}O$], 691 (1) [An^+–$C(CF_3)_3$–3F], 504 (30) [An^+–$C(CF_3)_3$–$3CF_3$–2F], 489 (10) [An^+–L–$C_3F_{10}O$], 371 (2) [An^+–2L–CF_3–3F], 302 (4) [An^+–2L–$2CF_3$–3F], 287 (12) [An^+–$2C(CF_3)_3$–$3CF_3$–2F], 64 (25) [SO_2^+], An = $[Al(OC(CF_3)_3)_4]$, L = $OC(CF_3)_3$, non-volatile solid residue left, calculated theoretical isotopes distribution matched that experimentally observed for all peaks. ^{27}Al NMR (104.2 MHz, SO_2, r.t.), δ_{Al} (ppm) = 32.5 (s, $[Al(OC\text{-}(CF_3)_3)_4]^-$). ^{19}F NMR (376.3 MHz, SO_2, r.t.), δ_F (ppm) = −72.4; −74.1 decomposition products of $[Al(OC(CF_3)_3)_4]^-$, −74.9 (s, $[Al(OC(CF_3)_3)_4]^-$); IR (KBr, cm^{-1}, Nujol): 1377 (s), 1364 (m), 1355 (s), 1299 (s), 1273 (s), 1247 (s), 1215 (s), 1173 (s), 1120 (m), 972 (vs), 892 (w), 864 (w), 841 (m), 832 (m), 798 (m), 781 (w), 770 (w), 760 (w), 755 (w), 744 (w), 726 (vs), 620 (w), 580 (m), 571 (m), 561 (m), 550 (w), 537 (s), 480 (m), 450 (m), 397 (w).

Note: The metathesis reaction between the poorly SO_2 soluble $[Bi_5][AsF_6]_3$ and 2,3 equivalents of highly soluble $Li[Al(OC(CF_3)_3)_4]$ in SO_2 followed by removal of the insoluble products afforded a mixture of $[Bi_x][Al(OC(CF_3)_3)_4]$ and $Li[Al(OC(CF_3)_3)_4]$ (IR, ^{7}Li NMR, EI-MS), with the $Li[Al(OC(CF_3)_3)_4]$ as the major product.

4.3. Preparation of $[Bi_5(C_6Me_6)_4][Al(OC(CF_3)_3)_4]_3$ (**2**)

A mixture of $Li[Al(OC(CF_3)_3)_4]$ (1.87 g, 1.9 mmol), $[Bi_5][AsF_6]_3$ (3.1 g, 1.9 mmol) and C_6Me_6 (0.6 g, 3.8 mmol) in a 100 ml Schlenk flask was stirred in CH_2Cl_2 (40 ml) for 4 h. The dark brown solution was filtered and concentrated to approximately 4 ml and held at −24 °C for 2 days. The dark brown (almost black) crystals that formed were separated by filtration. The next crop of the crystalline dark brown solid was obtained from the supernatant solution by crystallization at −24 °C for 2 days. Yield of $[Bi_5(C_6Me_6)_4][Al(OC\text{-}(CF_3)_3)_4]_3$ (1.64 g, 55% based the $Li[Al(OC(CF_3)_3)_4]$). $C_{96}H_{72}F_{108}O_{12}Al_3Bi_5$: Calc. C, 25.07; H, 1.56; F, 44.66; Al, 1.76; Bi, 22.74. Found: C, 24.84; H, 2.01; F, 43.80; Al, 1.26; Bi, 23.91%. 184–186 °C decomposition. EI-MS (30 eV, heating r.t. −170 °C): *m/z* (%) = 197 (5) [$L^+ - 2F$], 167 (17) [$L^+ - CF_3$], 162 (100) [$C_6Me_6^+$], 147 (12) [$L^+ - CF_4$], 97 (15) [$L^+ - C_2F_3O$], L = $OC(CF_3)_3$. A non-volatile solid residue remained. ^{27}Al NMR (104.2 MHz, SO_2, r.t.); δ_{Al} (ppm) = 31.6. ^{19}F NMR (376.3 MHz, SO_2, r.t.), δ_F (ppm) = −75.9 (s); ^{13}C NMR (100.6 MHz, SO_2, r.t.), δ_C (ppm) = 16.5 (C_6Me_6), 121.7 (q, $C(CF_3)_3$, J = 291 Hz), 134.3 (C_6Me_6); ^{1}H NMR (400 MHz, SO_2, r.t.), δ_H (ppm) = 5.2 (s), 4.7 (s), 3.3 (s), 3.1(s), 2.8 (s), 2.6 (s, C_6Me_6 in complex, major signal, relative intensity 85%), 2.5 (s), 2.1 (s), 2.0 (s). The 5.2–2.7 and 2.1–2.0 ppm minor resonances are assigned to the products of oxidation of C_6Me_6, see Supplemental materials, relative intensity is measured relative to all resonances in spectrum; IR of **2** (KBr, cm^{-1}, Nujol): 1301 (vs), 1276 (vs), 1241 (vs), 1216 (vs), 1165 (s), 1135 (m), 1074 (w, C_6Me_6, Table 5), 1062 (w, C_6Me_6), 1018 (vw, C_6Me_6), 973 (vs), 832 (m, Al–O), 793 (w, C_6Me_6), 755 (w), 728 (vs), 571 (w), 561 (m), 537 (m), 447 (m).

Note: keeping the supernatant solution longer than 5 days at −24 °C lead to formation of yellow crystals **3**, **4** and a grey powder Bi (X-ray elemental microanalysis).

4.4. Isolation of $[Bi_4OF_2Cl_6(C_6Me_6)_4]$-$[Al(OC(CF_3)_3)_4]_2 \cdot C_6Me_6$ **3** $\cdot C_6Me_6$: and $[C_6Me_6H][Al(OC(CF_3)_3)_4]$ (**4**)

A mixture of $Li[Al(OC(CF_3)_3)_4]$ (1.5 g, 1.5 mmol), $[Bi_5][AsF_6]_3$ (0.86 g, 0.5 mmol) and C_6Me_6 (0.4 g, 2.5 mmol) in CH_2Cl_2 (40 ml) was stirred for 4 h in a 100 ml Schlenk flask. The dark brown solution was filtered and concentrated to approximately 10 ml and left at −24 °C for 2 weeks. Yellow crystals, a red-brown solid and a grey powder (Bi, X-ray elemental microanalysis) deposited. The solution was filtered and concentrated to 2–3 ml and held at −24 °C for 3 weeks. Orange crystals (yellow as a powder) formed and were separated manually (0.45 g) from the reaction products. The resulting crystals were a mixture of **3** $\cdot C_6Me_6$, **4** (yellow)[3] and colourless crystals,[4] the presence of the $[C_6Me_6H]^+$ cation was confirmed by IR. Result of elemental analysis was interpreted based on the model 75% of **3** $\cdot C_6Me_6$ and 25% of **4**: Calc. C, 28.93; H, 2.17; F, 42.88. Found: C, 30.31; H, 2.16; F, 42.89%.

Compound $[Bi_4OF_2Cl_6(C_6Me_6)_4][Al(OC(CF_3)_3)_4]_2 \cdot C_6Me_6$ **3** · C_6Me_6: EI-MS (30 eV, heating r.t. −170 °C): *m/z* (%) = 679 (4) [An^+–$C(CF_3)_3$–CF_3], 477 (20) [An^+–L–$C(CF_3)_3$–2F], 461 (10) [An^+–2L–2F], 447 (2), [An^+–$2C(CF_3)_3$–C_2F_4], 443 (10) [An^+–L–$C(CF_3)_3$–CF_3], 162 (100) [$C_6Me_6^+$], non-volatile black solid residue remained; ^{19}F NMR (376.3 MHz, $CDCl_3$, r.t.), δ_F (ppm) = −74.1 (s), −75.3 (s); ^1H NMR (400 MHz, $CDCl_3$, r.t.), δ_H (ppm) = 3.8 (s), 2.3 (s). The compound was very poorly soluble in $CDCl_3$, initially dissolved in SO_2 followed by the deposition of a solid over 10–30 min. NMR spectra were measured for the freshly prepared clear SO_2 solution at low temperature. ^{19}F NMR (376.3 MHz, SO_2, −70 °C), δ_F (ppm) = −73.9 (s), −75.0 (s), −75.5 (s), −195.1 (s, Al–F), −220.6 (s, Bi–F); ^1H NMR (400 MHz, SO_2, −70 °C), δ_H (ppm) = 7.4 ($\Delta\omega_{1/2}$ 91 Hz), 4.9 ($\Delta\omega_{1/2}$ 13 Hz, 2H, $C_6Me_5H_2OC(CF_3)_3$), 4.56 (s, $\Delta\omega_{1/2}$ 1.3 Hz, 2H, $(C_6Me_6)_2CH_2$), 3.20 ($\Delta\omega_{1/2}$ 3 Hz, weak), 3.13 ($\Delta\omega_{1/2}$ 3 Hz, 3H, C_6Me_5-$CH_2OC(CF_3)_3$), 3.05 ($\Delta\omega_{1/2}$ 3 Hz, 3H, $(C_6Me_6)_2CH_2$), 2.95 ($\Delta\omega_{1/2}$ 3 Hz, 6H, $C_6Me_5CH_2OC(CF_3)_3$), 2.86 ($\Delta\omega_{1/2}$ 3 Hz, 6H, $(C_6Me_6)_2CH_2$), 2.64 ($\Delta\omega_{1/2}$ 3 Hz, 6H, $C_6Me_5CH_2OC(CF_3)_3$), 2.58 ($\Delta\omega_{1/2}$ 3 Hz, 6H, $(C_6Me_6)_2$-CH_2), 2.40 ($\Delta\omega_{1/2}$ 9 Hz), 1.85 ($\Delta\omega_{1/2}$ 3 Hz, weak), 1.76 ($\Delta\omega_{1/2}$ 3 Hz C_6Me_6 or $[C_6Me_6H]^+$), 0.47–0.35 (aliphatic protons). ^{27}Al NMR (104.2 MHz, CH_2Cl_2, r.t.); δ_{Al} (ppm) = 31.6 (s). IR (KBr, cm^{-1}, Nujol): 1593 (w), 1300 (vs), 1277 (vs), 1251 (vs), 1240 (vs), 1218 (vs), 1165 (s), 1102 (w, C_6Me_6), 1069 (w, C_6Me_6), 1022 (w, C_6Me_6), 973 (vs), 831 (m), 780 (sh, C_6Me_6), 728 (w), 623 (w, Al–F*), 610 (w, Al–F*), 569 (w), 560 (m), 537 (m), 447 (m), * impurity of aluminium fluoride complexes resulted by degradation of $[Al(OC(CF_3)_3)_4]^-$.

Compound $[C_6Me_6H][Al(OC(CF_3)_3)_4]$ (**4**): EI-MS (30 eV, heating r.t. −170 °C): *m/z* (%) = 850 (5) [An^+–C_2F_4O], 675 (8) [An^+–L–3F], 536 (1) [An^+–L–$2CF_3$–3F], 478 (10) [An^+–2L–F], 477 (20) [An^+–L–$C(CF_3)_3$–2F], 461 (10) [An^+–2L–2F], 447 (2), [An^+–$2C(CF_3)_3$–C_2F_4], 445 (10) [An^+–L–$C(CF_3)_3$–CF_3], 443 (10) [An^+–L–$C(CF_3)_3$–CF_3], 441 (10) [An^+–2L–3F], 162 (100) [$C_6Me_6^+$]; NMR spectra of **4** are similar to that of **3** since the yellow crystals are a mixture of both compounds. IR (KBr, cm^{-1}, Nujol): 3300 (br), 1596 (m, $[C_6Me_6H]^+$), 1301 (vs), 1276 (vs), 1251 (vs), 1240 (vs), 1217 (vs), 1165 (s), 1071 (w, $[C_6Me_6H]^+$), 1061 (w, $[C_6Me_6H]^+$), 973 (vs), 889 (w, $[C_6Me_6H]^+$), 831 (m), 756 (w), 728 (w), 682 (w, $[C_6Me_6H]^+$), 571 (w), 560 (w), 537 (w), 447 (m). Absorption band at 1590 cm^{-1} is one of the characteristic benzoid C=C skeletal stretching modes of the carbocations [48].

4.5. Crystal growth and X-ray crystallography

Crystals of **3** · C_6Me_6 were grown from a saturated supernatant solution in CH_2Cl_2 at −24 °C. Single crystals were coated with Paratone-N oil, mounted using a glass fibre and frozen in the cold nitrogen stream of the goniometer. A hemisphere of data was collected on a Bruker AXS P4/SMART 1000 diffractometer using ω and θ scans with a scan width of 0.3° and 30 s exposure times. The detector distance was 5 cm. The data were reduced (SAINT) [49] and corrected for absorption (SADABS) [50]. The structure was solved by direct methods and refined by full-matrix least squares on F^2 (SHELXTL) [51] (Table 4). The compound was a racemic mixture. Anisotropic refinement was employed for all Bi, Cl and Al atoms and F2–F3, O1–O9 and C1–C8. All other atoms were refined isotropically. Hydrogen atoms were included in calculated positions and refined using a riding model. Hexamethylbenzene molecules were restraint to equal distances within the ring and between the methyl groups. CF_3 groups were refined as regular tetrahedra with fixed bond distances of 1.32 Å. The isotropic thermal parameter for C72 was fixed. Refinement was non-convergent and anisotropic refinement lead to many non-positive definites.

Acknowledgement

Acknowledgement is made to NSERC (Canada) and PRF(Canada) for financial support and Neil Buford, Heather Phillips (Dallhouse University) for attempts to measure FT-Raman spectra, Dr. Dr. Kathryn E. Preuss, for measuring of UV–Vis spectra in dichloroethane.

Appendix A. Supplementary data

Crystallographic data (excluding structure factors) for the structures in this paper have been deposited with the Cambridge Crystallographic Data Center as Supplementary Publication No. CCDC 250743. Copies of the data can be obtained, free of charge, on application to CCDC, 12 Union Road, Cambridge CB2 1EZ, UK (fax: +44 1223 336033; e-mail: deposit@ccdc.cam.ac.ukor http://www.ccdc.cam.ac.uk). X-ray microanalysis of reaction products, NMR Reactions in situ and NMR investigation of oxidation of C_6Me_6, IR spectrum of $Li[Al(OC(CF_3)_3)_4]$ 350–4000 cm^{-1}, UV–Vis spectra 300–800 and 400–1100 cm^{-1}, structure **3** · C_6Me_6, details of discussion. Supplementary data associated with this article can be found, in the online version, at doi:10.1016/j.poly.2005.06.032.

References

[1] (a) J.D. Corbett, Prog. Inorg. Chem. 21 (1976) 129 (references therein);
(b) A.N. Kutznetsov, A.V. Shevel'kov, S.I. Troyanov, B.A. Popovkin, Russ. J. Inorg. Chem. 41 (1996) 920, translated from Zh. Neorg. Khim. 41 (1996) 958;

(c) A.N. Kuznetsov, A.V. Shevel'kov, B.A. Popovkin, Russ. J. Coord. Chem. 24 (1998) 861, translated from Koord. Khim. 24 (1998) 919;
(d) J. Beck, T. Hilbert, Eur. J. Inorg. Chem. (2004) 2019.
[2] H. Kalpen, W. Hönle, M. Somer, U. Schwarz, K. Peters, H.G. von Schnering, R. Blachnik, Z. Anorg. Allg. Chem. 624 (1998) 1137.
[3] (a) M. Ruck, Z. Anorg. Allg. Chem. 624 (1998) 521;
(b) M. Ruck, Angew. Chem. Int. Ed. 40 (2001) 1182;
(c) B.A. Popovkin, L. Bengtsson-Kloo, Russ. Chem. Bull. 52 (2003) 2100.
[4] (a) J.D. Corbett, Inorg. Chem. 7 (1968) 198;
(b) B. Krebs, M. Mummert, C. Brendel, J. Less-Common Met. 116 (1986) 159;
(c) S. Ulvenlund, K. Stahl, L.A. Bengtsson-Kloo, Inorg. Chem. 35 (1996) 223;
(d) R.C. Burns, R.J. Gillespie, W.-C. Luk, Inorg. Chem. 17 (1978) 3596.
[5] (a) J. Beck, C.J. Brendel, L. Bengtsson-Kloo, B. Krebs, M. Mummert, A. Stankowski, S. Ulvenlund, Chem. Ber. 129 (1996) 1219;
(b) B. Krebs, M. Hucke, C. Brendel, Angew. Chem. 94 (1982) 453;
(c) B. Krebs, M. Hucke, C. Brendel, Angew. Chem., Int. Ed. Engl. 21 (1982) 445.
[6] (a) A. Hershaft, J.D. Corbett, J. Chem. Phys. 36 (1961) 551;
(b) A. Hershaft, J.D. Corbett, Inorg. Chem. 2 (1963) 979;
(c) R.M. Friedman, J.D. Corbett, Inorg. Chim. Acta 7 (1973) 525;
(d) R.M. Friedman, J.D. Corbett, Inorg. Chem. 12 (1973) 1134;
(e) H. von Benda, A. Simon, W. Bauhofer, Z. Anorg. Allg. Chem. 438 (1978) 53.
[7] (a) A.N. Kuznetsov, B.A. Popovkin, W. Henderson, M.J. Taylor, L. Bengtsson-Kloo, Dalton Trans. (2000) 1777;
(b) S. Ulvenlund, L. Bengtsson-Kloo, K. Stahl, J. Chem. Soc., Faraday Trans. 91 (1995) 4223;
(c) S. Ulvenlund, A. Wheatley, L. Bengtsson-Kloo, Chem. Commun. (1995) 59, solution of $[Bi_5]^{3+}$ polycation in benzene have very dark red (brown) color.
[8] N. Burford, J. Passmore, J.C.P. Sanders, in: J.F. Liebman, A. Greenburg (Eds.), The Preparation, Structure and Energetics of the Homopolyatomic Cations of Groups 16 and 17, From Atoms to Polymers, Isoelectronic Analogies, V.C.H. Publishers, Florida, 1989, p. 53.
[9] (a) M.P. Murchie, J.P. Johnson, J. Passmore, G.W. Sutherland, M. Tajik, T.K. Whidden, P.S. White, F. Grein, Inorg. Chem. 31 (1992) 274;
(b) W.A.S. Nandana, J. Passmore, P.S. White, C.-M. Wong, Inorg. Chem. 29 (1990) 3529;
(c) J. Passmore, G.W. Sutherland, P.S. White, Chem. Commun. (1980) 330;
(d) J. Passmore, M. Tajik, P.S. White, Chem. Commun. (1986) 225;
(e) S. Brownridge, T.S. Cameron, H. Du, C. Knapp, R. Köppe, J. Passmore, J.M. Rautianinen, H. Schnöckel, Inorg. Chem. 44 (2005) 1660.
[10] (a) S. Brownridge, T.S. Cameron, J. Passmore, G. Schatte, T.C. Way, Dalton Trans. (1996) 2552;
(b) P.D. Boyle, T.S. Cameron, J. Passmore, G. Schatte, G.W. Sutherland, J. Fluorine Chem. 71 (1995) 217.
[11] (a) M.P. Murchie, J. Passmore, C.-M. Wong, Inorg. Synth. 27 (1990) 332;
(b) J. Passmore, G.W. Sutherland, T.K. Whidden, P.S. White, C.-M. Wong, Can. J. Chem. 63 (1985) 1209;
(c) J. Passmore, G.W. Sutherland, P.S. White, Inorg. Chem. 21 (1982) 2717;
(d) J. Passmore, G.W. Sutherland, P. Taylor, T.K. Whidden, P.S. White, Inorg. Chem. 20 (1981) 3839;
(e) J. Passmore, G.W. Sutherland, P.S. White, Chem. Commun. (1979) 901.
[12] (a) S. Brownridge, L. Calhoun, R.S. Laitinen, J. Passmore, J. Pietikainen, J. Saunders, Phosphorus Sulfur Silicon Relat. Elem. 168 (2001) 105;
(b) W.A.S. Nandana, J. Passmore, P.S. White, C.-M. Wong, Inorg. Chem. 28 (1989) 3320;
(c) J. Passmore, P.S. White, C.-M. Wong, Chem. Commun. (1985) 1178.
[13] (a) A. Berces, G.D. Enright, G.E. McLaurin, J.R. Morton, K.F. Preston, J. Passmore, D.J. Wood, Mag. Res. Chem. 37 (1999) 353;
(b) P.D. Boyle, T.S. Cameron, A. Decken, J. Passmore, D.J. Wood, Phosphorus Sulfur Silicon 124–125 (1997) 549;
(c) T.S. Cameron, A. Decken, M. Fang, S. Parsons, J. Passmore, D.J. Wood, Chem. Commun. (1999) 1801.
[14] (a) P.D. Boyle, S. Parsons, J. Passmore, D.J. Wood, Chem. Commun. (1993) 199;
(b) P.D. Boyle, J. Passmore, D.J. Wood, Phosphorus Sulfur Silicon 93–94 (1994) 227;
(c) G.D. Enright, J. Morton, J. Passmore, K.F. Preston, C. Thompson, D.J. Wood, Chem. Commun. (1996) 967.
[15] T.S. Cameron, R.C. Haddon, S.M. Mattar, S. Parsons, J. Passmore, A.P. Ramirez, Inorg. Chem. 31 (1992) 2274.
[16] T.S. Cameron, R.C. Haddon, S.M. Mattar, S. Parsons, J. Passmore, A.P. Ramirez, Dalton Trans. (1992) 1563.
[17] A. Decken, H.D.B. Jenkins, G.B. Nikiforov, J. Passmore, Dalton Trans. (2004) 2496.
[18] H.D.B. Jenkins, H.K. Roobottom, J. Passmore, L. Glasser, Inorg. Chem. 38 (1999) 3609.
[19] I. Krossing, H. Brands, R. Feuerhake, S. Koenig, J. Fluorine Chem. 112 (2001) 83.
[20] G. Day, R. Glaser, N. Shimomura, A. Takamuku, K. Ichikawa, Chem. Eur. J. 6 (2000) 1078.
[21] M. Lindsjö, A. Fischer, L. Kloo, Angew. Chem. Int. Ed. 43 (2004) 2540.
[22] (a) A. Adolf, M. Gonsior, I. Krossing, J. Am. Chem. Soc. 124 (2002) 7111;
(b) I. Krossing, Dalton Trans. (2002) 500;
(c) I. Krossing, Chem. Eur. J. 7 (2001) 490.
[23] (a) T.J. Barbarich, S.T. Handy, S.M. Miller, O.P. Anderson, P.A. Grieco, S.H. Strauss, Organometallics 15 (1996) 3776;
(b) I. Krossing, Private communication.
[24] N.J. Bjerrum, C.K. Boston, G.P. Smith, Inorg. Chem. 6 (1967) 1162.
[25] N.J. Bjerrum, H.L. Davis, Inorg. Chem. 6 (1967) 1603.
[26] N.J. Bjerrum, G.P. Smith, Inorg. Chem. 6 (1967) 1968.
[27] (a) M. Gonsior, I. Krossing, L. Müller, I. Raabe, M. Jansen, L. van Wullen, Chem. Eur. J. 8 (2002) 4475;
(b) I. Krossing, I. Raabe, Angew. Chem. Int. Ed. 43 (2004) 2066.
[28] K.H. Whitmire, H.W. Roesky, S. Brooker, G.M. Sheldrick, J. Organomet. Chem. 402 (1991) C4.
[29] C.M. Jones, M.D. Burkart, R.E. Bachman, D.L. Serra, S.-J. Hwu, K.H. Whitmire, Inorg. Chem. 32 (1993) 5136.
[30] (a) T.A. Emmanuelle, F. Malbosc, E.B. Michel, D.B. Jean-Claude, P. Kalck, J. Organomet. Chem. 689 (2004) 1763;
(b) T.S. Lobana, K. Isobe, H. Kitayama, T. Nishioka, I. Kinoshita, Angew. Chem. Int. Ed. 43 (2004) 213;
(c) A.H. Klahn, M. Carreno, F. Godoy, B. Oelckers, A. Pizarro, A. Toro, A. Reyes, J. Coord. Chem. 54 (2001) 379;
(d) K. Ferre, G. Poignant, L. Toupet, V. Guerchais, J. Organomet. Chem. 629 (2001) 9;
(e) A. Zapf, M. Beller, Chem. Eur. J. 7 (2001) 2908;
(f) A.H. Klahn, A. Toro, B. Oelckers, G.E. Buono-Core, V. Manriquez, O. Wittke, Organometallics 19 (2000) 2580;
(g) P. Machnitzki, O. Stelzer, W.S. Sheldrick, C. Landgrafe, J. Organomet. Chem. 554 (1998) 207;

(h) L. Cronin, C.L. Higgitt, R. Karch, R.N. Perutz, Organometallics 16 (1997) 4920;
(i) J.L. Kiplinger, T.G. Richmond, Polyhedron 16 (1997) 409;
(j) U.R. Aulwurm, F. Knoch, H. Kisch, Z. Naturforsch. 51(B) (1996) 1555;
(k) D. Rondon, J. Delbeau, X.D. He, S. Saboetienne, B. Caudret, Dalton Trans. 13 (1994) 1895;
(l) J.M. Valk, R. Vanbelzen, J. Boersma, A.L. Spek, G. Vankoten, Dalton Trans. 15 (1994) 2293.
[31] S. Chitsaz, K. Harms, B. Neumuller, K. Dehnicke, Z. Anorg. Allg. Chem. 625 (1999) 939.
[32] B. Aurivillius, C.-I. Lindblom, Acta Chem. Scand. 18 (1964) 1554.
[33] (a) C.N. Jones, M.D. Burkart, K.H. Whitmire, Chem. Commun. (1992) 1638;
(b) K.H. Whitmire, S. Hoppe, O. Sydora, J.L. Jolas, C.M. Jones, Inorg. Chem. 39 (2000) 85.
[34] A.E.H. Wheatley, Chem. Soc. Rev. 30 (2001) 265.
[35] N.C. Mösch-Zanetti, M. Ferbinteanu, J. Magull, Eur. J. Inorg. Chem. (2002) 950.
[36] (a) H.W. Roesky, I. Haiduc, N.S. Hosmane, Chem. Rev. 103 (2003) 2579;
(b) G. Bai, H.W. Roesky, J. Li, T. Labahn, F. Cimpoesu, J. Magull, Organometallics 22 (2003) 3034.
[37] M. Bera, W.T. Wong, G. Aromi, J. Ribas, D. Ray, Inorg. Chem. 43 (2004) 4787.
[38] (a) W.J. Evans, T.P.H. Sollberger, J. Am. Chem. Soc. 110 (1988) 1841;
(b) K. Yunlu, P.S. Gradeff, N. Edelstein, W. Kot, G. Shalimoff, W.E. Streib, B.A. Vaartstra, K.G. Caulton, Inorg. Chem. 30 (1991) 2317;
(c) S. Kraut, J. Magull, U. Schaller, M. Karl, K. Harms, K. Dehnicke, Z. Anorg. Allg. Chem. 624 (1998) 1193;
(d) A.W.-H. Lam, W.-T. Wong, G. Wen, X.-X. Zhang, S. Gao, New J. Chem. 25 (2001) 531;
(e) O.I. Shchegolikhina, Y.A. Pozdniakova, S.V. Lindeman, A.A. Zhdanov, R. Psaro, R. Ugo, G. Gavioli, R. Battisuzzi, M. Borsari, T. Rüffer, C. Zhcchi, G. Pályi, J. Organomet. Chem. 514 (1996) 29.
[39] J. Wang, S. Li, C. Zheng, N.S. Hosmane, J.A. Maguire, H.W. Roesky, C.C. Cummins, W. Kaim, Organometallics 22 (2003) 4390.
[40] (a) I.D. Brown, in: M. O'Keefe, A. Navrotsky (Eds.), Structure and Bonding in Crystals, Academic Press, London, 1981;
(b) I.D. Brown, D. Altermatt, Acta Crystallogr. B41 (1985) 244;
(c) N.E. Brese, M. O'Keefe, Acta Crystallogr. B47 (1991) 192.
[41] W. Frank, J. Weber, E. Fuchs, Angew. Chem., Int. Ed. Engl. 26 (1987) 74.
[42] W. Frank, J. Weber, E. Fuchs, Angew. Chem. 99 (1987) 68.
[43] (a) J.F. Sawyer, R.J. Gillespie, Prog. Inorg. Chem. 34 (1986) 65;
(b) R.G. Gillespie, I. Hargittai, The VSEPR Model of Molecular Geometry, Allyn and Bacon, a division of Simon and Schuster Inc., Boston, 1991.
[44] L.O. Brockway, J.M. Robertson, J. Chem. Soc. (1939) 1324.
[45] H.Z. Liang, Q. Shen, J.W. Guan, J. Organomet. Chem. 474 (1994) 113.
[46] (a) A. Ron, I.J. Hyams, Chem. Phys. Lett. 17 (1972) 557;
(b) J.W. Murray, D.H. Andrews, J. Chem. Phys. 2 (1934) 119;
(c) A. Giriando, C. Pecile, Chem. Phys. Lett. 20 (1973) 467;
(d) S.D. Woodruff, R. Kopelman, J. Cryst. Mol. Struct. 7 (1977) 29.
[47] (a) J. Mann, H.W. Thompson, Proc. Roy. Soc. (Lond.) A211 (1952) 168;
(b) R.C. Leech, D.B. Powell, N. Shepard, Spectrochim. Acta 22 (1965) 1;
(c) G. Durocher, J. Chem. Phys. 66 (1969) 988;
(d) B. Ware, K. Williamson, J.P. Devlin, J. Phys. Chem. 72 (1968) 3970;
(e) S.D. Woodruff, R. Kopelman, J. Cryst. Mol. Struct. 7 (1977) 29;
(f)SDBSWeb: http://www.aist.go.jp/RIODB/SDBS/ (access date 18.06.2004).
[48] G.A. Olah, P. von R. SchleyerCarbonium Ions, vol. 4, Wiley-Interscience, Toronto, 1973, p. 1507.
[49] SAINT 6.02, Bruker AXS, Inc., Madison, WI, USA, 1997–1999.
[50] George Sheldrick, SADABS, Bruker AXS, Inc., Madison,WI, USA, 1999.
[51] George Sheldrick, SHELXTL 5.1, Bruker AXS, Inc., Madison, WI, USA, 1997.

known LiPc is isostructural (on a molecular level) with MgPc, yet is deficient by one electron, so may be an appropriate p-dopant for MgPc. The aluminum phthalocyanine radical, AlPc, on the other hand, would be an isostructural n-dopant for the normal-valent phthalocyanines.

Because most unfunctionalized phthalocyanine complexes have extremely low solubilities in organic solvents, we have examined 2,3,9,10,16,17,23,24-octa(pentoxy)phthalocyanines (denoted Pc*, Fig. 1). Octa(alkoxy)phthalocyanines are discotic liquid crystals over various temperature ranges, depending upon the alkoxy group [10]; the free base of the octapentoxy derivative is a normal crystalline phase up to 121 °C [11].

There is one previous report of the synthesis of a monolithium octa(alkoxy)phthalocyanine [12] and its electrical and magnetic properties were investigated [13]. However, other monolithium octa(alkoxy)phthalocyanines synthesized by the reported method were contaminated by the corresponding free-base phthalocyanine [12]. We report improved syntheses of both Li_2Pc* and LiPc* that are presumably applicable to any octa(alkoxy)phthalocyanine.

All known aluminum phthalocyanines have an axial substituent such as chloride or an alkoxide on the aluminum, such that the oxidation state of the phthalocyanine ring is the usual −2. A few ring-substituted chloroaluminum and alkoxyaluminum phthalocyanines have been reported [14]. No aluminum phthalocyanine radicals have been previously isolated. There is a published report of the in situ chemical reduction of several metal phthalocyanine complexes (including ClAlPc) and their UV–visible spectroscopy, but none of these reduced species were isolated or studied by other methods [15]. The reduction of the photoexcited triplet state of ClAlPc by aromatic amines and the decay of the resulting radical has been studied spectroscopically [16]. Reduction of a related phthalocyanine complex, chloroindium tetra(*tert*-butyl)phthalocyanine, leads to an In–In bonded dimer [17]. Herein we report the first isolation and characterization of an aluminum phthalocyanine radical, AlPc*, where the oxidation state of the phthalocyanine ring is −3.

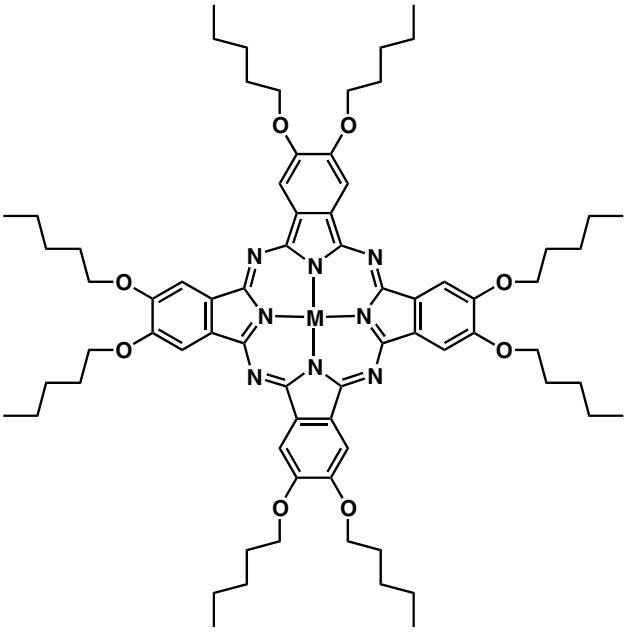


Fig. 1. Octa(pentoxy)phthalocyanine, MPc*. M = H_2, Li_2, Mg, AlCl, Li, or Al.

2. Experimental

2.1. General procedures and materials

Reactions involving metal phthalocyanines were carried out under a nitrogen atmosphere using glove box and Schlenk line techniques. Tetrahydrofuran was distilled from purple sodium/benzophenone. Heptane, toluene and benzene were distilled from sodium/benzophenone with added tetraglyme. Hydroquinone was recrystallized from toluene/ethyl acetate. The reagent 1,2-dicyano-4,5-dipentoxybenzene was synthesized by literature procedures [18,19]. Ferrocenium hexafluorophosphate, $[Cp_2Fe][PF_6]$, was synthesized by the oxidation of ferrocene with sulfuric acid followed by precipitation from aqueous solution with NH_4PF_6 and recrystallization from acetone/ether [20]. All other chemicals were reagent grade and used as received. ^1H and ^{13}C NMR spectra were recorded on a Varian Mercury 300 NMR spectrometer using solvent residual as internal standard. UV–Vis spectra were recorded on a Varian Cary 100 spectrophotometer. ESR spectra were obtained on a Bruker ER200 X-band spectrometer with 0.10 G modulation. Cyclic voltammetry and solid-state conductivity measurements were performed under an inert atmosphere with an EG&G/PAR 263A potentiostat as described previously [9]. Cyclic voltammetry was performed in THF solution with 0.10 M $[NBu_4][PF_6]$ supporting electrolyte, and all electrochemical potentials are relative to internal ferrocene$^{0/+}$ at 0 V. Measurements of solution-phase magnetic susceptibility by the Evans method were performed as described previously [9]. Pressed-pellet electrical conductivity was determined as described previously [9].

2.2. H_2Pc*

Hydroquinone (0.552 g, 5.02 mmol) and 1,2-dicyano-4,5-dipentoxybenzene (5.18 g, 17.3 mmol) were sealed in a Teflon-lined steel bomb and heated to 200 °C for 20 h. The crude product was stirred twice with 150 mL portions of hot ethanol for 30 min and filtered. The dark

green insoluble residue was dissolved in CH_2Cl_2 and filtered through silica gel. The filtrate was concentrated and the product precipitated from CH_2Cl_2/ethanol as a green powder (3.76 g, 72.5%). ^{1}H NMR (C_6D_6): −3.62 (s, 2H), 1.15 (t, 24H, $J = 7.2$ Hz), 1.51–1.63 (m, 16H), 1.63–1.76 (m, 16H), 2.01–2.16 (m, 16H), 4.07 (br, 16H), 8.31 (s, 8H). ^{13}C NMR ($CDCl_3$): 14.22, 22.92, 28.84, 29.69, 69.63, 105.21, 129.66, 147.54, 151.47. UV–Vis in THF; nm, ε (L mol^{-1} cm^{-1}): 698, 3.3×10^5; 660, 2.7×10^5; 644, 1.1×10^5; 598, 6.0×10^4; 426, 7.7×10^4; 348, 1.8×10^5; 295, 1.3×10^5.

2.3. Li_2Pc*

THF (150 mL) was vacuum transferred to a mixture of H_2Pc* (2.164 g, 1.798 mmol) and lithium bis(trimethylsilyl)amide (0.661 g, 3.96 mmol). The reaction mixture was stirred at 22 °C for 2 h and at reflux for 18 h. Volatiles were removed under reduced pressure. The solid was dissolved in a heptane/THF mixture, precipitated by partial evaporation of the solvent, and isolated by filtration to yield a green powder (1.860 g, 85%). ^{1}H NMR (THF-d_8, 22 °C): 1.03 (t, 24H, $J = 6.9$ Hz), 1.47–1.61 (m, 16H), 1.63–1.74 (m, 16H), 1.96–2.08 (m, 16H), 4.46 (t, 16H, $J = 6.3$ Hz), 8.88 (s, 8H). ^{13}C NMR (THF-d_8, 55 °C): 14.45, 23.46, 29.58, 30.56, 70.75, 108.11, 135.89, 151.63, 155.35. UV–Vis in THF; nm, ε (L mol^{-1} cm^{-1}): 661, 2.7×10^5; 631, 3.9×10^4; 598, 4.0×10^4; 357, 1.1×10^5; 282, 6.2×10^4. *Anal.* calc. for $C_{72}H_{96}N_8O_8Li_2$: C, 71.15; H, 7.96; N, 9.22. Found: C, 71.27; H, 7.90; N, 9.25%.

2.4. $LiPc$*

THF (40 mL) was vacuum transferred to a mixture of Li_2Pc* (448 mg, 0.368 mmol) and $[Cp_2Fe][PF_6]$ (122 mg, 0.368 mmol). The solution was stirred at 22 °C for 12 h. Black solid precipitated. The reaction mixture was further refluxed for 18 h. When cooled to 22 °C the product precipitated and it was isolated by filtration and washed with THF. The dark black-green solid was purified by dissolving in hot THF and precipitation at 22 °C. Yield: 385 mg, 87%. ^{1}H NMR (C_6D_6): 0.97 (t, 24H, $J =$ 7.2 Hz), 1.27–1.44 (br, 32H), 1.66–1.84 (br, 16H), 2.80–4.80 (br, 16H). ^{13}C NMR (C_6D_6): 14.25, 22.99, 28.75, 29.82. HRMS (EI) calc. for $C_{72}H_{96}O_8N_8Li$ (M^+) 1207.7511. Found: 1207.7548. UV–Vis in THF; nm, ε (L mol^{-1} cm^{-1}): 785, 1.9×10^4; 699, 1.7×10^4; 661, 1.5×10^4; 506, 6.8×10^4; 418, 4.3×10^4; 342, 1.0×10^5; 284, 8.3×10^4.

2.5. $MgPc$*

THF (70 mL) was vacuum transferred into a flask containing Li_2Pc* (350 mg, 0.288 mmol) and $MgCl_2$ (28 mg, 0.294 mmol). The reaction mixture was stirred at reflux for 12 h. The solvent was removed under reduced pressure and the residue was dissolved in toluene and filtered to remove LiCl. The product was dissolved in a THF/heptane mixture and precipitated by evaporation of some of the solvent to give a deep green solid. Yield: 315 mg, 89%. ^{1}H NMR (C_6D_6): 0.96 (t, 24H, $J = 6.9$ Hz), 1.1–1.3 (m, 32H), 1.40 (m, 16H), 3.54 (br s, 16H), 8.45 (s, 8H). ^{13}C NMR (C_6D_6): 14.75, 23.29, 28.85, 29.63, 70.15, 107.08, 133.77, 150.84, 153.82. UV–Vis in THF; nm, ε (L mol^{-1} cm^{-1}): 673, 3.2×10^5; 644, 3.9×10^4; 609, 4.1×10^4; 409, 1.1×10^4; 363, 6.3×10^4; 347, 8.0×10^4; 289, 5.7×10^4. *Anal.* calc. for $C_{72}H_{96}N_8O_8Mg$: C, 70.54; H, 7.89; N, 9.14. Found: C, 70.97; H, 8.22; N, 9.16%.

2.6. $ClAlPc$*

THF (50 mL) was vacuum transferred into a flask containing Li_2Pc* (1.00 g, 0.831 mmol) and $AlCl_3$ (121 mg, 0.914 mmol). The reaction mixture was stirred at 22 °C for 24 h and at reflux for another 24 h. The solvent was removed under reduced pressure and the product dried under vacuum at 80 °C for 3 h. The dark green solid residue was dissolved in hot toluene and filtered to remove the LiCl. Toluene was removed under reduced pressure. Crystallization from heptane/benzene (reflux to 22 °C) gave the product as dark green solid, which was held under vacuum at 80 °C for 2 h. Yield: 0.910 g, 87%. Alternatively, ClAlPc* can be prepared by the reaction of H_2Pc* and diethylaluminum chloride in CH_2Cl_2, similar to a reported preparation of chloroaluminum tetraphenylporphyrin [21]. ^{1}H NMR (THF-d_8 + DMSO-d_6): 1.08 (t, 24H, $J = 7.8$ Hz), 1.53–1.68 (m, 16H), 1.72–1.83 (m, 16H), 2.06–2.19 (m, 16H), 4.67 (t, 16H, $J = 6.3$ Hz), 9.11 (s, 8H). ^{13}C NMR (THF-d_8 + DMSO-d_6, 55 °C): 14.54, 23.46, 29.48, 30.34, 70.79, 107.65, 132.57, 142.68, 153.62. UV–Vis in THF; nm, ε (L mol^{-1} cm^{-1}): 684, 9.1×10^4; 656, 1.4×10^4; 616, 1.3×10^4; 430, 9.2×10^3; 368, 3.8×10^4; 298, 1.5×10^4.

2.7. $AlPc$*

THF (70 mL) was vacuum transferred into a flask containing ClAlPc* (360 mg, 0.285 mmol) and Na/Hg (8.4 mg, 0.365 mmol Na in 840 mg Hg). The mixture was stirred for 4 h at 22 °C, yielding a purple solution. Volatiles were removed under vacuum, 70 mL toluene was added, and the mixture was filtered. Toluene was removed under vacuum and 60 mL THF and 20 mL heptane were added to dissolve the residue. Evaporation of the solution under vacuum to 10 mL yielded a red-purple precipitate, which was collected by filtration and dried under vacuum for 4 h. Yield: 280 mg, 80%. ^{1}H NMR (C_6D_6): 0.40 (br s, 24H), 0.58 (br s, 32H), 3.5 (br s, 16H), 9.4 (br s, 16H). UV–Vis in THF; nm,

ε (L mol^{-1} cm^{-1}) (contains some oxidized species): 682, 2.2×10^4; 660, 2.1×10^4; 614, 3.8×10^4; 584, 4.8×10^4; 563, 2.5×10^4; 542, 1.7×10^4; 397, 3.5×10^4; 338, 4.3×10^4; 285, 3.6×10^4. *Anal.* calc. for $C_{72}H_{96}N_8O_8Al$: C, 70.39; H, 7.88; N, 9.12. Found: C, 70.14; H, 7.98; N, 9.05%.

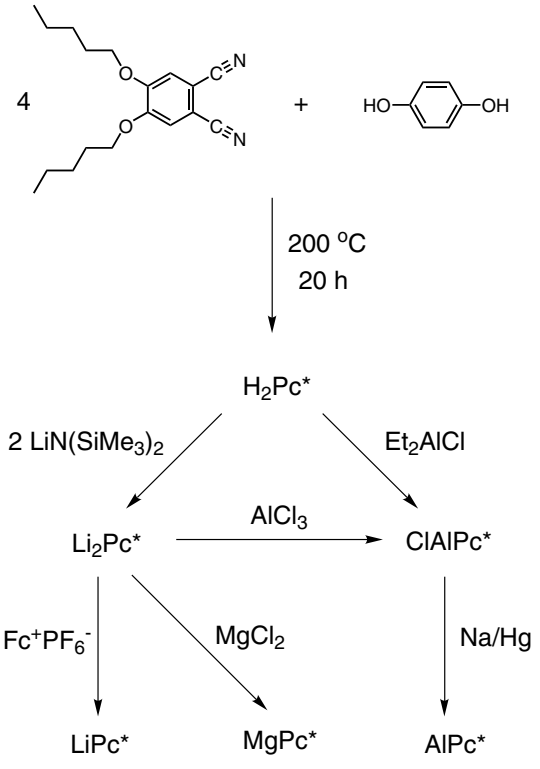
2.8. Co-crystallization of AlPc* and H_2Pc*

AlPc* (20 mg, 0.016 mmol) and H_2Pc* (174 mg, 0.144 mmol) were dissolved in THF (12 mL) and heptane (8 mL) to give a green solution. The solution was slowly concentrated to 6 mL to give a green precipitate. The precipitate was collected by filtration and dried under vacuum for 2 h to yield 174 mg cocrystals.

3. Results and discussion

3.1. Synthesis

The reactions used in the preparation of our phthalocyanine complexes are summarized in Scheme 1. A few 2,3,9,10,16,17,23,24-octa(alkoxy)phthalocyanine derivatives have been synthesized before [19]. We found it most convenient to synthesize free-base octa(pentoxy)phthalocyanine (H_2Pc*, Fig. 1) by a route analogous to one previously reported for the high-purity synthesis of the free base of unfunctionalized phthalocyanine (H_2Pc) [4] and phthalocyanine polymers [22]. The appropriate dicyanobenzene, 1,2-dicyano-4,5-dipentoxybenzene, was reduced by hydroquinone in a Teflon-lined vessel at 200 °C to yield H_2Pc*. It has been noted that standard preparations of metallophthalocyanines result in impurities that are very difficult to separate from the desired MPc and these impurities can have significant effects on the electrical properties of molecular crystals of the phthalocyanines [4]. In contrast, synthesis of H_2Pc by hydroquinone reduction of 1,2-dicyanobenzene and subsequent metalation of H_2Pc results in very pure MPc. The method therefore seemed like the best route to high-purity MPc*. In addition, synthesis of H_2Pc* by the hydroquinone reaction results in higher yields than previously reported methods and does not require chromatographic purification.



Scheme 1. Synthesis of free-base octa(pentoxy)phthalocyanine and several metal complexes.

The dilithium derivative Li_2Pc* was obtained by deprotonation of H_2Pc* with $LiN(SiMe_3)_2$ (similar reactions have been used in the preparation of alkali metal porphyrins [23]). As in the reported syntheses of monolithium porphyrins radicals [24], oxidation of Li_2Pc* with one equivalent of ferrocenium hexafluorophosphate yields the monolithium phthalocyanine radical LiPc*. As noted in Section 1, this route is a distinct improvement over the reported electrochemical synthesis [12].

The standard synthesis of ClAlPc entails the reaction of 1,2-dicyanobenzene with $AlCl_3$ in quinoline [25], but the analogous reaction of 1,2-dicyano-4,5-dipentoxybenzene with $AlCl_3$ was unsuccessful. We found that either the reaction of Li_2Pc* with $AlCl_3$ or the reaction of H_2Pc* with Et_2AlCl gives ClAlPc* cleanly. Reduction of ClAlPc* with one equivalent of sodium amalgam in THF yields the very air-sensitive AlPc*. The radical AlPc* is indefinitely stable at room temperature in the solid state or solution, as long as it is not exposed to air.

3.2. Spectroscopy

3.2.1. NMR

Of the diamagnetic compounds studied, H_2Pc*, MgPc*, and Li_2Pc* have normal ^{1}H NMR spectra. For example, the ^{1}H NMR spectrum of H_2Pc* displays the expected five resonances of the pentyl groups, an aromatic resonance at 8.31 ppm, and the upfield N–H resonance at −3.62 ppm. The final diamagnetic compound examined, ClAlPc*, exhibits extra, broad resonances in its ^{1}H NMR spectrum in THF-d_8. If a few drops of DMSO-d_6 is added to the THF-d_8 solution, the ^{1}H NMR spectrum appears normal, possibly because Cl-bridged aggregates are broken up by the coordination of DMSO to the aluminum.

The ^{13}C NMR spectrum of Li_2Pc* in THF-d_8 at 22 °C has several more than the expected nine reso-

nances. When Li_2Pc^* in THF-d_8 was warmed to 55 °C, the ^{13}C NMR spectrum collapsed to nine sharp resonances. It is possible that there is some aggregation of the Li_2Pc^* in solution at 22 °C that causes the splitting of resonances, a phenomenon that has been observed previously [26], and may involve the formation of ion pairs of the type $[Li(THF)_4]_m[Li_{2n-m}Pc^*_n]$ [23].

For the two paramagnetic species, LiPc* and AlPc*, only some of the possible NMR resonances are observed. The ^1H NMR spectrum of LiPc* displays all five of the pentyl resonances but none for the ring protons; in the ^{13}C NMR spectrum, resonances from only the four outermost carbons of the pentyl groups could be observed. We were unable to observe a ^{13}C NMR spectrum of AlPc* in C_6D_6. Its ^1H NMR spectrum is unusual, with the resonances for the methyl groups and the outer two methylenes of the pentyl groups shifted upfield to about 0.5 ppm. The other methylenes are seen at 3.5 and 9.4 ppm. No resonance for the ring protons was observed. A possible explanation for the unusual chemical shifts of the methyl group and outer methylenes of AlPc* (a phenomenon not observed in LiPc*) is that the Lewis acidic aluminum centers form dative bonds with the oxygens of the pentoxy groups on other molecules. For example, a dimeric structure could form in which a molecule forms an $O \rightarrow Al$ bond with another molecule and a $Al \leftarrow O$ bond with the same partner. The configurations formed by these dative interactions would place the pentoxy groups in close proximity to another molecule's ring system, affecting the chemical shift of the aliphatic protons. If a solution of AlPc* in C_6D_6 is treated with I_2, a ^1H NMR spectrum very similar to that of ClAlPc* is observed, indicating that the radical has been oxidized back to the closed-shell species IAlPc*.

3.2.2. ESR

Both LiPc* and AlPc* display strong ESR signals as dilute solutions in benzene. In neither case could the hyperfine coupling to individual nuclei be distinguished, and instead one broad absorption was observed. In each molecule there is hyperfine coupling to two sets of four equivalent nitrogen atoms and one set of eight equivalent hydrogen atoms, in addition to coupling to lithium and aluminum, respectively. It is therefore not surprising that the individual hyperfine couplings cannot be resolved. Similar single-line ESR spectra have been observed for LiPc [6] and monolithium octa(dodecyloxy)phthalocyanine [13]. The *g*-value of LiPc* is 2.0003 (measured relative to external $TCNE^-$ at $g = 2.00278$ [27]) and the peak-to-peak width is 6.0 G. The *g*-value of AlPc* is 2.0010 and the peak-to-peak width is 5.0 G.

3.2.3. UV–Vis

Phthalocyanines with peripheral substituents have a strong tendency to form loosely associated dimers, trimers, and larger aggregates in solution, and the visible spectra of the aggregates can differ significantly from that of the monomers [2]. All of our UV–Vis spectra were obtained from very dilute solutions (10^{-5}–10^{-4} M) in THF, and appear to be consistent with monomeric species. A thorough study of the aggregation of an octa(alkoxy)phthalocyanine free base in dodecane solution and the effect of aggregation on the visible spectrum of the compound has been published [28], and the published spectrum of a monomeric species agrees very well with our spectrum of H_2Pc^* in THF.

UV–Vis spectra of Li_2Pc^* and LiPc* are similar to those of their respective unsubstituted phthalocyanines Li_2Pc and LiPc [6]. Li_2Pc^* has a Q band at 661 nm, a Soret band at 357 nm, and an N band at 282 nm. When Li_2Pc^* is oxidized to LiPc*, the Q band shifts to significantly higher energy at 506 nm, while the Soret band and N band are relatively unperturbed at 342 nm and 284 nm, respectively. The Q band is due to a HOMO–LUMO transition. Oxidation of Li_2Pc^* to LiPc* converts the HOMO to a singly occupied molecular orbital (SOMO) and the shift in the Q band is due to the fact that the transition no longer involves the unpairing of two electrons in the same orbital [29]. The Soret and N bands shift little because they are due to transitions from lower-energy MOs to the LUMO. New bands appear in the spectrum of LiPc* because of the existence of new transitions to the SOMO. A full analysis of the UV–Vis spectra of ring-oxidized and ring-reduced phthalocyanine complexes has been published [29].

The spectrum of ClAlPc* has a Q band at 684 nm and a Soret band at 368 nm, similar to published values for ClAlPc [29]. With the very low concentrations used to obtain UV–Vis spectra, it was not possible to obtain a clean spectrum of the AlPc* radical without oxidation; a detailed interpretation of the AlPc* spectrum was therefore not attempted.

3.3. Solution-phase magnetic susceptibility

The Evans method [30] was used to determine the magnetic moment of LiPc* and AlPc* in C_6D_6 solution. The assumption of similar volume diamagnetic susceptibilities for the analytes and C_6D_6 allowed the use of a previously described equation [9,31]:

$$\mu_{\text{eff}} = 0.0437\sqrt{\frac{\Delta f \cdot T}{M}}, \tag{1}$$

where μ_{eff} is the effective magnetic moment in Bohr magnetons (μ_B), Δf is the shift in frequency of the analyte solution resonance versus that of the neat reference (in ppm), T is the temperature in Kelvins, and M is the molarity of the solution of analyte. Eq. (1) gives the paramagnetic susceptibility directly, with no diamagnetic correction necessary. A 0.0374 M solution of AlPc* at 20 °C led to a shift of 0.198 ppm in the

C_6D_5H resonance, implying a magnetic moment of 1.72 μ_B, very close to the theoretical value of 1.73 μ_B for one unpaired electron.

The solution-phase magnetic susceptibility of LiPc* is much lower than would be expected for one unpaired electron per molecule. Solutions of LiPc* in C_6D_6 of concentration 0.0215, 0.0291, and 0.0385 M at 21 °C caused shifts of 0.013, 0.018, and 0.023 ppm, respectively, in the C_6D_5H resonance. All of these measurements imply a concentration of molecules with an unpaired spin of about a factor of nine lower than the actual concentration of LiPc*. Aggregation of LiPc* in solution with spin-pairing of the molecules within the aggregates could explain the lower-than-expected paramagnetism. An average aggregate size of about five molecules would account for the observed shift, under the assumption that odd-number-of-molecule aggregates have one unpaired spin and even-number-of-molecule aggregates are diamagnetic. It is surprising that the magnetic moment is attenuated by the same factor in C_6D_6 solutions of different concentrations. A 0.0326 M solution of LiPc* in $CDCl_3$ displayed no paramagnetic shift compared to the reference solution at 21 °C, but when heated to 55 °C exhibited a shift of 0.014 ppm. The behavior in $CDCl_3$ is consistent with dimers or higher aggregates that partly dissociate to monomers at higher temperature.

3.4. Solid-state conductivity

As noted in Section 1, two known phthalocyanine radicals, LiPc and $LuPc_2$, are electrical conductors. We therefore investigated the solid-state conductivity of LiPc* and AlPc*. Polycrystalline samples were pressed between two freshly cleaned copper contacts. Because these were two-point measurements, we measured a series of sample masses for each substance to examine the influence of contact resistance. The cross-sectional area of the pressed pellets in our apparatus is constant, so the thickness of the sample, and therefore its measured resistance, will increase in direct proportion to the sample mass if the contact resistance is not significant. Current was measured as a function of applied potential from 0 to +3 V to −3 to 0 V. Measurements for LiPc* and AlPc* are shown in Fig. 2. For both materials an approximately linear increase in resistance with sample mass was observed.

The resistance of each LiPc* sample was calculated from the slope of its current–voltage plot. If a density of 1.0 g/cm^3 is assumed for LiPc*, its conductivity can be calculated; the average value is $8 \times 10^{-11}\ \Omega^{-1}\ cm^{-1}$. That is significantly lower than the value for single-crystal (unfunctionalized) LiPc, $2 \times 10^{-3}\ \Omega^{-1}\ cm^{-1}$ [7]. LiPc* presumably crystallizes in the columnar structure of similarly functionalized phthalocyanines [11], and electrical transport occurs almost exclusively along the

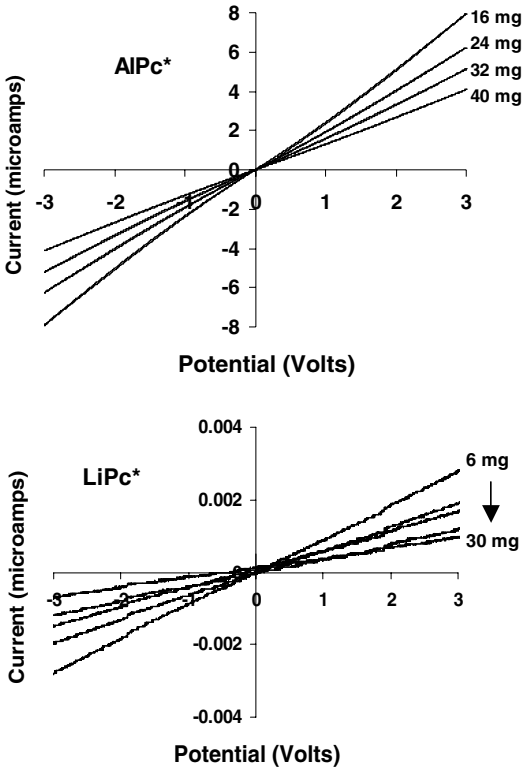


Fig. 2. Current vs. potential measurements for pressed pellets of AlPc* and LiPc*. Samples of mass 16, 24, 32, and 40 mg of AlPc* were examined, and samples of mass 6, 12, 18, 24, and 30 mg of LiPc* were examined.

columns [13]. Polycrystalline LiPc* might then be pictured as bundles of insulated wires in a mixture of random orientations, and it is not surprising that its bulk conductivity is much lower than single-crystalline LiPc.

The data from polycrystalline AlPc* were treated in the same manner as that from LiPc*. The conductivity in this case was $5 \times 10^{-7}\ \Omega^{-1}\ cm^{-1}$, almost four orders of magnitude greater than that of LiPc*. If AlPc is more conductive than LiPc by the same factor, the single-crystal conductivity of AlPc would be $12\ \Omega^{-1}\ cm^{-1}$, which is quite high for a single-component material. That theoretical conductivity can be compared to that of the most conductive single-component molecular conductor, which is $400\ \Omega^{-1}\ cm^{-1}$ [32]. Investigations into the synthesis and crystallization of the parent AlPc are currently under way.

The electrical conductivity of a material can be described by

$$\sigma = ne\mu, \tag{2}$$

where n is the concentration of free carriers (electrons or holes), e is the electron charge, and μ is the mobility of the carriers. The generation of intrinsic carriers in a molecular material occurs through a thermally activated charge transfer from one neutral molecule, M, to another:

$$MM \rightleftharpoons M^+M^- \tag{3}$$

The activation energy for this process, E_a (in eV), is given approximately by the difference between the oxidation and reduction potentials of M ($\Delta E_{1/2}$, in V) times the electron charge. The concentration of carriers is exponentially related to E_a [13]:

$$n = n_0 \exp\left(\frac{-E_a}{2k_B T}\right), \quad (4)$$

where n_0 is the concentration of M in the crystal. So, at a given temperature, the conductivity of a molecular material is determined by E_a and the carrier mobilities. If LiPc* and AlPc* have similar carrier mobilities, their relative conductivities will be determined solely by their values of E_a, or approximately by $\Delta E_{1/2}$ for the two molecules. The $\Delta E_{1/2}$ of LiPc* can only be estimated because its oxidation is irreversible. The separation between the oxidative waves of LiPc*$^-$ and LiPc* is 0.77 V, so that was used as the estimate of $\Delta E_{1/2}$. (The $\Delta E_{1/2}$ of LiPc was reported to be a similar 0.83 V [6].) The $\Delta E_{1/2}$ of AlPc* is 0.66 V (see below and Table 1). If these values are used for E_a in Eq. (4), one finds that the conductivity of AlPc* should be about one order of magnitude larger than LiPc*. So imperfect agreement is found with the experimental values, but the redox potentials do correctly predict that AlPc* is a better conductor than LiPc*.

Another explanation for the large difference in conductivity between LiPc* and AlPc* could be that their packing in the solid state is significantly different. Octa(alkoxy)phthalocyanines generally pack as stacked disks, but dative bonding between oxygen on one AlPc* molecule with the aluminum on another could lead to a very different solid state structure. If that is the case, carrier mobilities in LiPc* and AlPc* could be quite different, and that could account for their widely different conductivity.

3.5. Electrochemistry

Solution-phase measurements of electrochemical redox potentials provide an estimate of the electronic energy levels of molecules in a molecular crystal. We have examined the electrochemistry of LiPc* and AlPc* to determine their viability as p- and n-dopants, respectively, for normal-valent phthalocyanines such as MgPc* and H_2Pc*. Table 1 lists the redox potentials of H_2Pc*, MgPc*, LiPc*, and AlPc* obtained by cyclic voltammetry in THF (referenced to the ferrocene$^{+/0}$ couple at 0 V). From these values the approximate energy level diagrams of MgPc* and H_2Pc* doped with AlPc* and LiPc* shown in Fig. 3 can be constructed. Interestingly, the donor level of AlPc* in MgPc* is about 0.5 eV from the conduction band edge, while the acceptor level of LiPc* in MgPc* is a similar distance of about 0.6 eV from the valence band edge. H_2Pc* is more easily reduced than MgPc*; the donor level of AlPc* in H_2Pc* is only 0.3 eV from the conduction band edge. The system of H_2Pc* doped with AlPc* therefore presents the best possibility of observing electrical doping.

Table 1
Oxidation and reduction potentials of LiPc*, MgPc*, H_2Pc*, and AlPc* in THF vs. ferrocene$^{+/0}$ at 0 V

	MPc*$^{(0/-)}$	MPc*$^{(+/0)}$
Li	−0.54	~0.23 (irr)
Mg	−1.61	0.08
H_2	−1.40	~0.3 (irr)
Al	−1.77	−1.11

The oxidation of LiPc* is irreversible and the oxidation of H_2Pc* is quasi-reversible.

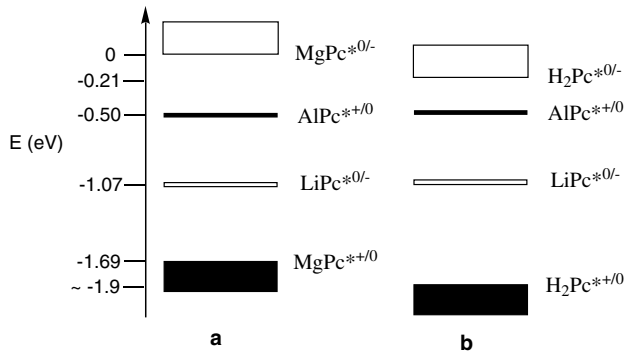


Fig. 3. (a) Relative energy levels of the donor AlPc*, acceptor LiPc*, and the valence and conduction bands of MgPc*. (b) Relative energy levels of the donor AlPc*, acceptor LiPc*, and the valence and conduction bands of H_2Pc*. All are derived from solution-phase electrochemical measurements.

3.6. Doping of H_2Pc* with AlPc*

We anticipated that the cocrystallization of two isostructural phthalocyanines would be straightforward. Previous studies of octakis((dodecyloxy)methyl)phthalocyanine found that solid solutions of the free-base and copper complex were easily prepared by recrystallization of a mixture of the compounds from hexane [33]. Co-precipitation of a 1:9 mixture of AlPc* and H_2Pc* from a heptane-THF mixture yielded a dark green powder. Examination of the powder under a microscope showed no signs of phase separation of the green H_2Pc* and blue AlPc*. There was no significant difference in the powder X-ray diffraction patterns of H_2Pc* and H_2Pc*doped with AlPc*, indicating that the crystal structure of H_2Pc* was maintained with the AlPc* dopant present. A sample of the cocrystallized material was pressed into a pellet and tested for electrical conductivity, but none was detected. Thus it appears that an isostructural n-dopant with a donor level within ~0.3 eV of the host conduction band is not significantly ionized at room temperature.

4. Conclusions

Several octa(pentoxy)phthalocyanine complexes have been synthesized by improved methods and the first synthesis of an aluminum phthalocyanine radical, AlPc*, was presented. Solid-state LiPc* is an electrical conductor with a pressed-pellet conductivity of $8 \times 10^{-11}\ \Omega^{-1}\ cm^{-1}$, while solid AlPc* is a significantly better conductor with a conductivity of $5 \times 10^{-7}\ \Omega^{-1}\ cm^{-1}$. Solution-phase electrochemical measurements indicate that in H_2Pc* doped with AlPc* the donor level of AlPc* lies ~0.3 eV from the conduction band edge of H_2Pc*, but the doped material does not have significant electrical conductivity at room temperature. Electrical doping by isostructural n-dopants will require dopants with donor levels that are very near or even above the conduction band edge of the host molecular semiconductor.

Acknowledgments

This work was supported by NSF Grant CHE-0133068 and Research Corporation Grant RI0697.

Appendix A. Supplementary data

Supplementary data (^{1}H NMR spectra) are available online. Supplementary data associated with this article can be found, in the online version, at doi:10.1016/j.poly.2005.06.021.

References

[1] (a) N.B. McKeown, Phthalocyanine Materials, Cambridge University Press, Cambridge, 1998;
(b) K.M. Kadish, K.M. Smith, R. Guilard (Eds.), The Porphyrin Handbook, vols. 1–10, Academic Press, San Diego, 2000.
[2] C.C. Leznoff, A.B.P. Lever (Eds.), Phthalocyanines: Properties and Applications, vols. 1–4, VCH Publishers, Inc., New York, 1989.
[3] C.J. Schramm, R.P. Scaringe, D.R. Stojakovic, B.M. Hoffman, J.A. Ibers, T.J. Marks, J. Am. Chem. Soc. 102 (1980) 6702.
[4] J.A. Thompson, K. Murata, D.C. Miller, J.L. Stanton, W.E. Broderick, B.M. Hoffman, J.A. Ibers, Inorg. Chem. 32 (1993) 3546.
[5] (a) H. Homborg, W. Kalz, Z. Naturforsch. B 33 (1978) 1067;
(b) H. Sugimoto, M. Mori, H. Masuda, T. Taga, Chem. Commun. (1986) 962;
(c) M. Brinkmann, P. Turek, J.-J. Andre, J. Mater. Chem. 8 (1998) 675.
[6] P. Turek, J.J. Andre, A. Giraudeau, J. Simon, Chem. Phys. Lett. 134 (1987) 471.
[7] P. Turek, P. Petit, J.J. Andre, J. Simon, R. Even, B. Boudjema, G. Guillaud, M. Maitrot, J. Am. Chem. Soc. 109 (1987) 5119.
[8] T. Inabe, H. Tajima, Chem. Rev. 104 (2004) 5503.
[9] T.P. Vaid, A.K. Lytton-Jean, B.C. Barnes, Chem. Mater. 15 (2003) 4292.
[10] J.F. Van der Pol, E. Neeleman, J.W. Zwikker, R.J.M. Nolte, W. Drenth, J. Aerts, R. Visser, S.J. Picken, Liq. Cryst. 6 (1989) 577.
[11] P.G. Schouten, J.M. Warman, M.P. de Haas, C.F. van Nostrum, G.H. Gelinck, R.J.M. Nolte, M.J. Copyn, J.W. Zwikker, M.K. Engel, M. Hanack, Y.H. Chang, W.T. Ford, J. Am. Chem. Soc. 116 (1994) 6880.
[12] M.A. Petit, T. Thami, C. Sirlin, D. Lelievre, New J. Chem. 15 (1991) 71.
[13] Z. Belarbi, C. Sirlin, J. Simon, J.J. Andre, J. Phys. Chem. 93 (1989) 8105.
[14] B.D. Rihter, M.E. Kenney, W.E. Ford, M.A.J. Rodgers, J. Am. Chem. Soc. 112 (1990) 8064.
[15] D.W. Clack, J.R. Yandle, Inorg. Chem. 11 (1972) 1738.
[16] T. Ohno, S. Kato, A. Yamada, T. Tanno, J. Phys. Chem. 87 (1983) 775.
[17] Y. Chen, M. Barthel, M. Seiler, L.R. Subramanian, H. Bertagnolli, M. Hanack, Angew. Chem. Int. Ed. 41 (2002) 3239.
[18] K. Binnemans, J. Sleven, S. De Feyter, F.C. De Schryver, B. Donnio, D. Guillon, Chem. Mater. 15 (2003) 3930.
[19] (a) M. Hanack, A. Gul, A. Hirsch, B.K. Mandal, L.R. Subramanian, E. Witke, Mol. Cryst. Liq. Cryst. 187 (1990) 365;
(b) K. Ohta, L. Jacquemin, C. Sirlin, L. Bosio, J. Simon, New J. Chem. 12 (1988) 751.
[20] D.N. Hendrickson, Y.S. Sohn, H.B. Gray, Inorg. Chem. 10 (1971) 1559.
[21] K. Shimasaki, T. Aida, S. Inoue, Macromolecules 20 (1987) 3076.
[22] A.W. Snow, J.R. Griffith, N.P. Marullo, Macromolecules 17 (1984) 1614.
[23] J. Arnold, D.Y. Dawson, C.G. Hoffman, J. Am. Chem. Soc. 115 (1993) 2707.
[24] A. Gebauer, D.Y. Dawson, J. Arnold, J. Chem. Soc., Dalton Trans. (2000) 111.
[25] J.P. Linsky, T.R. Paul, R.S. Nohr, M.E. Kenney, Inorg. Chem. 19 (1980) 3131.
[26] (a) C. Piechocki, J. Simon, Nouveau J. Chim. 9 (1985) 159;
(b) C. Piechocki, J. Simon, J. Chem. Soc., Chem. Commun. (1985) 259;
(c) G.J. Clarkson, N.B. McKeown, K.E. Treacher, J. Chem. Soc., Perkin Trans. 1 (1995) 1817.
[27] M.T. Watts, M.L. Lu, R.C. Chen, M.P. Eastman, J. Phys. Chem. 77 (1973) 2959.
[28] W.J. Schutte, M. Sluyters-Rehbach, J.H. Sluyters, J. Phys. Chem. 97 (1993) 6069.
[29] P.C. Minor, M. Gouterman, A.B.P. Lever, Inorg. Chem. 24 (1985) 1894.
[30] D.F. Evans, J. Chem. Soc. (1959) 2003.
[31] D.F. Evans, T.A. James, J. Chem. Soc., Dalton Trans. (1979) 723.
[32] H. Tanaka, Y. Okano, H. Kobayashi, W. Suzuki, A. Kobayashi, Science 291 (2001) 285.
[33] J.J. Andre, M. Bernard, C. Piechocki, J. Simon, J. Phys. Chem. 90 (1986) 1327.

reagents were commercially available and were used without further purification.

2.1. Synthesis

A mixture of $[(C_6H_6)RuCl_2]_2$ (0.25 g; 5×10^{-4} mol) and 7,8-benzoquinoline (0.2 g; $\sim 1 \times 10^{-3}$ mol) or 8-hydroxyquinoline (0.25 g; 1.7×10^{-3} mol) in methanol (100 cm^{-3}) was refluxed for 4 h, cooled and filtered. The crystals suitable for X-ray crystal analysis are obtained by slow evaporation of the reaction mixture.

2.1.1. *[(C6H6)RuCl(C13H8N)] (1)*

Yield 79%. IR (KBr): 3067 (ν_{CH}), 3048 (ν_{CH}), 1618 (ν_{ring}), 1567 (ν_{CN}), 1447 ($\nu_{C=C}$), 1408 ($\nu_{ring} + \nu_{CH}$), 1323 (δ_{CH}), 1105 (δ_{CH}), 837 (γ_{CH}), 530 (ν_{Ru-N}). UV–VIS (CH_2Cl_2, λ nm ($\log \varepsilon$)): 381.6 (2.37), 291.2 (2.78), 220.4 (3.24), 215.8 (3.27). ^1H NMR: ($CDCl_3$, ppm) 9.55 (d, H1), 8.47 (d, H10), 8.19 (d, H3), 7.79 (d, H6), 7.76 (d, H5), 7.59 (m, H2; H8), 7.45 (m, H9), 5.59 (s, C_6H_6). ^{13}C NMR ($CDCl_3$, ppm): 176.3 (C19), 152.8 (C7), 136.6 (C14), 135.8 (C18), 134.7 (C15), 134.3 (C9), 129.8 (C13), 129.5 (C10), 127.3 (C17), 122.9 (C12), 121.4 (C8), 121.3 (C16), 86.6 (C_6H_6) *Anal*. Calc. for: C, 63.76; H, 4.28; Cl, 7.53; N, 2.97; Ru, 21.46. Found: C, 63.73; H, 4.25; N, 2.95%.

2.1.2. *[Ru(C9H6NO)3] · CH3OH (2)*

Yield 82%. IR (KBr): 3053 (ν_{CH}), 1566 (ν_{CN}), 1497 (ν_{ring}), 1457 ($\nu_{C=C}$), 1373 ($\nu_{ring} + \nu_{CH}$), 1315 (δ_{CH}), 1105 ($\nu_{CO} + \delta_{CH}$), 823 (γ_{CH}), 742 (ν_{Ru-O}), 525, 411 ($\nu_{Ru-O} + \nu_{Ru-N}$). UV–VIS (CH_2Cl_2, λ nm ($\log \varepsilon$)): 700.2 (1.99), 499.6 (sh), 433.4 (2.39), 252.0 (3.28), 223.8 (3.21). *Anal*. Calc. for: C, 60.78; H, 3.40; N, 7.88; O, 9.00; Ru, 18.94. Found: C, 60.743; H, 3.37; N, 7.90%.

2.2. Physical measurements

Infrared spectra were recorded on a Nicolet Magna 560 spectrophotometer in the spectral range 4000–400 cm^{-1} with the sample in the form of KBr pellet. Electronic spectra were measured on a Lab Alliance UV–VIS 8500 spectrophotometer in the range of 800–280 nm in deoxygenated dichloromethane solution. Elemental analyses (C, H, N) were performed on a Perkin–Elmer CHN-2400 analyzer. The ^1H and ^{13}C NMR spectra were obtained at room temperature in $CDCl_3$ using INOVA 300 spectrometer.

The magnetic measurements of the powdered samples was measured over the temperature range 1.8–300 K using a Quantum Design SQUID – based MPMSXL-5-type magnetometer. The superconducting magnet was generally operated at a field strength ranging from 0 to 5 T measurements. Measurements sample of compounds were made at magnetic field 0.5 T. The SQUID magnetometer was calibrated with the palladium rod sample. Corrections are based on subtracting the sample – holder signal and contribution χ_D estimated from the Pascal constants and equal -288×10^{-6} cm^3 mol^{-1}. The t.i.p. per Ru^{3+} center was assumed to be 115×10^{-6} cm^3 mol^{-1}. The effective magnetic moment was calculated from the equation, $\mu_{eff} = 2.83(\chi_M T)^{1/2}$(BM).

EPR spectra were recorded at room temperature and 77 K on a Bruker ESP 300 spectrometer operating at X-band equipped with an ER 035M Bruker NMR gaussmeter and HP 5350B Hewlett-Packard microwave frequency counter. The spectrum at 4.5 K temperature was measured with a X-band Radioplan SE/X 2543 Spectrometer.

2.3. DFT calculations

GAUSSIAN-03 program [24] was used in the calculations. The geometry optimisation was carried out with the DFT method with the use of B3LYP functional [25,26]. The electronic spectrum was calculated using the TDDFT method [17].

The calculation was performed using the DZVP basis set [27] with *f* functions with exponents 1.94722036 and 0.748930908 on ruthenium atom, and polarization functions to all other atoms: 6–31g(2d,p) – chlorine, 6–31g** – carbon, nitrogen and 6–31g(d,p) on hydrogen atoms.

2.4. Crystal structures determination and refinement

An orange prism crystal of 1 and black prism crystal of 2 were mounted in turn on a KM-4-CCD automatic diffractometer equipped with a CCD detector, and used for data collection. X-ray intensity data were collected with graphite monochromated Mo Kα radiation ($\lambda = 0.71073$ Å) at temperature of 288.0(2) K for complex **1** and 293.0(2) K for **2**, with ω scan mode. A 6 and 4 s exposure times were used respectively and all Ewald sphere reflections were collected up to $2\theta = 50$. The unit cell parameters were determined from least-squares refinement of the setting angles of 13997 and 13489 strongest reflections for complex **1** and **2**, respectively. Details concerning crystal data and refinement are given in Table 1. Examination of two reference frames monitored after each 20 frames measured showed respectively −12.3% and 37.2% loss of the intensity. During the data reduction, the above decay correction coefficient was taken into account. Lorentz, polarization, and numerical absorption [28] corrections were applied. The structures were solved by Patterson method. All the non-hydrogen atoms were refined anisotropically using full-matrix, least-squares technique on F^2. All the hydrogen atoms were found from difference Fourier synthesis after four cycles of anisotropic refinement, and refined as "riding" on the adjacent atom with individual isotropic temperature factor equal 1.2 times the value of equivalent temperature factor of the parent

Table 1
Crystal data and structure refinement details of complexes **1** and **2**

Empirical formula	$C_{19}H_{14}ClNRu$	$C_{28}H_{22}N_3O_4Ru$
Formula weight	392.83	565.56
Temperature (K)	288(2)	293(2)
Crystal system	orthorhombic	monoclinic
Space group	*Pbca*	$P2_1/n$
Unit cell dimensions		
a (Å)	10.9200(4)	10.9491(4)
b (Å)	12.7855(5)	13.2612(6)
c (Å)	21.8142(7)	17.0027(8)
α (°)	90	90
β (°)	90	98.654(3)
γ (°)	90	90
Volume (Å^3)	3045.65(19)	2440.65(18)
Z	8	4
Calculated density (Mg m^3)	1.713	1.539
Absorption coefficient (mm^{-1})	1.199	0.683
$F(000)$	1568	1148
Crystal dimensions (mm)	$0.64 \times 0.55 \times 0.49$	$0.412 \times 0.376 \times 0.379$
θ Range for data collection (°)	3.69–25.14	3.30–25.11
Index ranges	$-13 \leqslant h \leqslant 13$	$-13 \leqslant h \leqslant 13$
	$-15 \leqslant k \leqslant 12$	$-15 \leqslant k \leqslant 15$
	$-25 \leqslant l \leqslant 26$	$-20 \leqslant l \leqslant 19$
Reflections collected	29 967	24 676
Independent reflections	2706 [$R_{(int)} = 0.0391$]	4358 [$R_{(int)} = 0.0210$]
Data/restraints/parameters	2706/0/199	4358/0/348
Goodness-of-fit on F^2	1.145	1.082
Final R indices [$I > 2\sigma(I)$]	$R_1 = 0.0299$	$R_1 = 0.0249$
	$wR_2 = 0.0725$	$wR_2 = 0.0579$
R indices (all data)	$R_1 = 0.0302$	$R_1 = 0.0257$
	$wR_2 = 0.0727$	$wR_2 = 0.0585$
Largest different peak and hole (e Å^{-3})	0.529 and −0.874	0.632 and −0.511

atom SHELXS-97 [29], SHELXL-97 [30] and SHELXTL [31] programs were used for all the calculations. Atomic scattering factors were those incorporated in the computer programs.

3. Results and discussion

The reactions of the ruthenium(II) benzene complex $[(C_6H_6)RuCl_2]_2$ with 7,8-benzoquinoline and 8-hydroxyquinoline have been performed. Refluxing the complex $[(C_6H_6)RuCl_2]_2$ with an excess of 7,8-benzoquinoline in methanol leads to the half-sandwich $[(C_6H_6)RuCl(C_{13}H_8N)]$ (**1**) complex in good yield. When the 8-hydroxyquinoline ligand was used in the reaction the analogous product was not occurred. In this case the ruthenium(II) was oxidized to Ru(III) and the $[Ru(C_9H_6NO)_3]$ (**2**) complex was isolated. The elemental analyses of the complexes are in good agreement with their formulation. The IR spectra of the complexes are consistent with its molecular structures. The bands of C=C and C=N stretching modes are observed at 1447, 1457 cm^{-1} and 1567, 1566 cm^{-1} for complexes **1** and **2**, respectively. The ν_{Ru-N} frequencies are visible at 530 cm^{-1} for complex **1** and with ν_{Ru-O} at 525, 411 cm^{-1} for complex **2**.

In the ^{1}H NMR spectrum of compound **1** the protons of C_6H_6 ligand appears as a singlet at 5.95 ppm. The other signals are attributed to the 7,8-benzoquinoline ligand (details are given in Section 2). The ^{13}C NMR spectrum of this complex display singlet at 86.6 ppm corresponds to the co-ordinated η^6-C_6H_6 ligand and set of signals attributed to benzoquinoline ligand. The C(19) resonance appears as a triplet shifted to 176.3 ppm what confirms the structure of the complex.

3.1. Crystal structures

The $[(C_6H_6)RuCl(C_{13}H_8N)]$ complex crystallises in the orthorhombic space group *Pbca*. The molecular structure of the compound is shown in Fig. 1. The selected bond lengths and angles are listed in Table 2. The ruthenium atom is π-bonded to the benzene ring with an average Ru–C distance of 2.200(4) Å (range 2.142(4)–2.273(3) Å) whereas the distance between the ruthenium atom and the centroid of the ring is 1.701 Å and is consistent with those reported for the other Ru(II) η^6-arene complexes [3d,32,33]. The ruthenium atom is also directly co-ordinated to nitrogen atom of benzoquinoline ligand with a distance of 2.100(2) Å to N atom and to carbon atom with a distance of 2.068(3) Å. The Ru–Cl bond length is 2.4204(7) Å. The angle of the

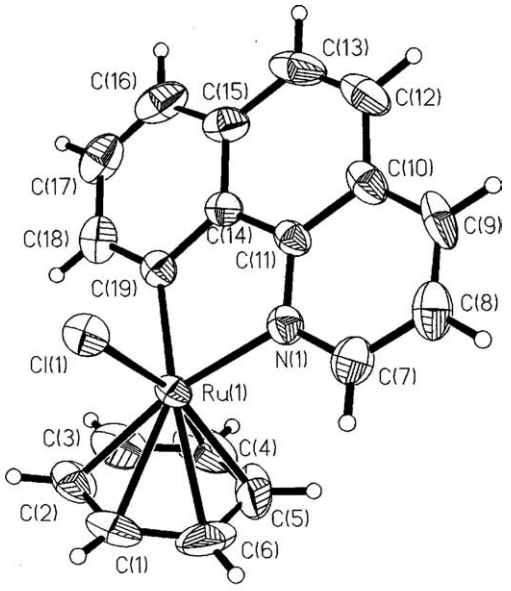


Fig. 1. ORTEP drawing of $[(C_6H_6)RuCl(C_{13}H_8N)]$ with 50% probability thermal ellipsoids.

Table 2
Selected bond lengths [Å] and angles [°] for $[(C_6H_6)RuCl(C_{13}H_8N)]$

	Experimental	Calculated
Bond lengths (Å)		
Ru(1)–C(19)	2.068(3)	2.069
Ru(1)–N(1)	2.100(2)	2.140
Ru(1)–Cl(1)	2.4204(7)	2.428
Ru(1)–C(1)	2.246(3)	2.354
Ru(1)–C(2)	2.205(3)	2.249
Ru(1)–C(3)	2.177(3)	2.235
Ru(1)–C(4)	2.157(4)	2.236
Ru(1)–C(5)	2.142(4)	2.229
Ru(1)–C(6)	2.273(3)	2.376
Bond angles (°)		
C(19)–Ru(1)–N(1)	79.06(10)	78.54
C(19)–Ru(1)–Cl(1)	86.80(7)	86.92
C(19)–Ru(1)–C(6)	164.34(15)	159.14
C(19)–Ru(1)–C(4)	95.40(16)	95.61
C(19)–Ru(1)–C(2)	112.32(12)	117.06
N(1)–Ru(1)–Cl(1)	85.54(7)	85.44
N(1)–Ru(1)–C(2)	168.27(12)	164.33
N(1)–Ru(1)–C(4)	111.58(15)	115.84
N(1)–Ru(1)–C(6)	103.31(12)	102.11
C(2)–Ru(1)–Cl(1)	97.58(9)	93.50
C(4)–Ru(1)–Cl(1)	162.86(14)	158.68
C(6)–Ru(1)–Cl(1)	108.77(14)	113.94
C(2)–Ru(1)–C(6)	64.97(14)	64.04
C(2)–Ru(1)–C(4)	65.83(15)	66.47
C(4)–Ru(1)–C(6)	69.22(18)	65.08

chelating ligand (C(19)–Ru–(N1) 79.06(10)° and the angles between benzoquinoline and chlorine ligands (85.54(7)° (N(1)–Ru–(Cl1), 86.80(7)° (C(19)–Ru–(Cl1)) are close to those observed in the ruthenium arene compounds [34a,34b,34c]. In the structure exist three intramolecular weak hydrogen bonds [44–46] C(2)–H(2)···Cl(1#$-x,-y,-z$), C(4)–H(4)Cl(1#$-x+0.5,y+0.5,z$) and C(13)–H(13)Cl(1#$-x,y+0.5,-z+0.5$) (D···A distances 3.529(4), 3.676(4) and 3.645(3) Å, D–H···A angles 136.3°, 161.7° and 148.1°, respectively). In this way an infinite three-dimensional hydrogen-bonded net is created.

The complex **2** $[Ru(C_9H_6NO)_3]\cdot CH_3OH$ crystallizes in the monoclinic space group $P21/n$. The methanol molecule is approximately 1:1 disordered over two positions. The molecular structure of the compound is shown in Fig. 2. The selected bond lengths and angles are listed in Table 3. The complex adopts a distorted octahedral type of geometry. The maximum distortion is visible in angles between O(1)–Ru(1)–O(21) and N(21)–Ru(1)–O(21) 170.78° and 80.29°, respectively. The Ru–N and Ru–O bond lengths and the angles are comparable with literature values [41–43]. The two intermolecular hydrogen bond [44–46] linking the OH group of methanol and oxygen from hydroxyquinoline ligand O(99A)–H(99O)···O(1) (D···A distance 2.791(6) Å, D–H···A angle 157.7°), C(23)–H(23)···O(99A)(1#$-x+1/2,\ y-1/2,-z+1/2$) (D···A distance 3.231(10) Å, D–H···A angle 134.9°) are observed. In this way an infinite one-dimensional hydrogen-bonded chain along *b*-axis is created. I addition in the structure exists one intramolecular weak hydrogen bond between quinoline C(26)–H(26) and O(21#$-x+3/2,\ y-1/2,-z+1/2$) (D···A distance 3.330(3) Å, D–H···A angle 150.8°).

3.2. Geometry and electronic structure

The optimised geometry parameters for the complex **1** are given in Table 2. The optimised bond distances and angles agree well with the experimental values. The largest differences were found for the ruthenium–benzene carbons distances. The calculated Ru–benzene distance is 1.781 Å.

The formal charge of ruthenium is +2 in this complex. The calculated charge on the ruthenium atom, obtained from natural population analysis, is close 0.665. The population of the d_{xy}, d_{xz}, d_{yz}, $d_{x^2-y^2}$ and d_{z^2} orbitals of the central atom is following 0.933, 1.686, 1.636, 1.764 and 1.032, respectively. This is a result of charge donation from chloride ion and 7,8-benzoquinoline ligand. The charge on the chloride ligand is higher than −1 (−0.551); the charge on 7,8-benzoquinoline nitrogen atom is negative and amounts to −0.419 and on the donor C(19) is close to zero with negative sign (−0.0823). The HOMO–LUMO gap is 3.51 eV.

In Fig. 3 the molecular orbital diagram of complex **1** is presented with the several contours of molecular orbitals (HOMO – Fig. 3(a), LUMO – Fig. 3(b)). The HOMO, HOMO − 1 and HOMO − 3 orbitals are d ruthenium type with the admixture of π chlorine orbitals. The HOMO − 2 is π chlorine orbital. The combinations of π chlorine and d metal orbitals create the

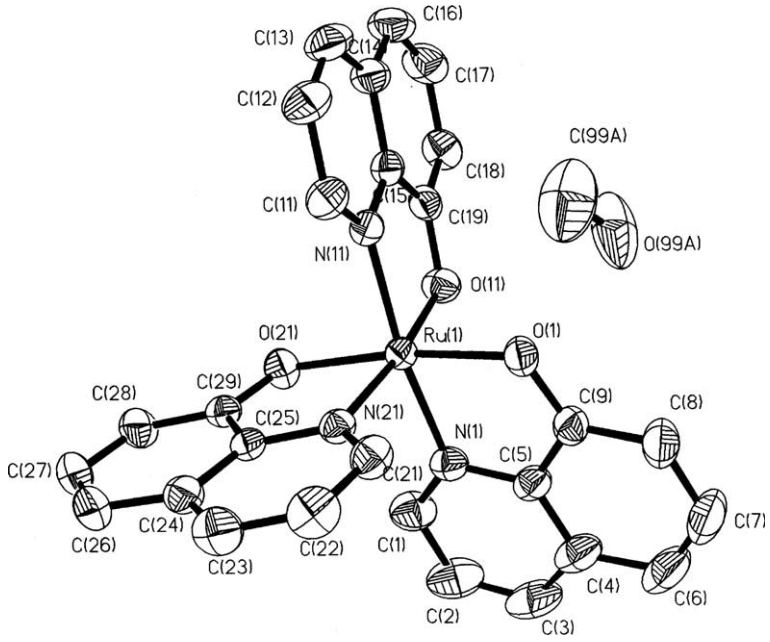


Fig. 2. ORTEP drawing of $[Ru(C_9H_6NO)_3]\cdot CH_3OH$ with 50% probability displacement ellipsoids. Hydrogen atoms were omitted for clarity.

Table 3
Selected bond lengths [Å] and angles [°] for $[Ru(C_9H_6NO)_3]$

	Experimental	Calculated
Bond lengths (Å)		
Ru(1)–N(1)	2.0527(17)	2.0879
Ru(1)–N(11)	2.0685(17)	2.1108
Ru(1)–N(21)	2.0742(16)	2.1236
Ru(1)–O(1)	2.0068(14)	2.0267
Ru(1)–O(11)	1.9932(14)	2.0060
Ru(1)–O(21)	2.0392(14)	2.0715
Bond angles (°)		
N(11)–Ru(1)–N(1)	171.85(7)	170.11
N(11)–Ru(1)–N(21)	95.23(6)	94.97
N(1)–Ru(1)–N(21)	91.84(6)	94.10
N(1)–Ru(1)–O(11)	91.19(6)	90.22
O(1)–Ru(1)–N(11)	93.75(6)	94.98
N(1)–Ru(1)–O(21)	93.64(6)	93.45
N(1)–Ru(1)–O(1)	81.99(6)	80.93
N(21)–Ru(1)–O(1)	91.70(6)	90.88
N(21)–Ru(1)–O(21)	80.29(6)	81.23
N(21)–Ru(1)–O(11)	172.31(6)	172.17
N(11)–Ru(1)–O(11)	82.30(6)	81.23
N(11)–Ru(1)–O(21)	91.53(6)	92.22
O(1)–Ru(1)–O(21)	170.78(6)	167.67
O(1)–Ru(1)–O(11)	95.73(6)	96.26
O(21)–Ru(1)–O(11)	92.47(6)	94.73

HOMO − 5 and HOMO − 6 molecular orbitals of the complex. HOMO − 7 and HOMO − 8 are the σ chlorine orbital. The 7,8-benzoquinoline ligand has a significant contribution in the HOMO − 4 and HOMO − 9, HOMO − 10 molecular orbitals. The lone pair of benzoquinoline nitrogen atoms is visible in HOMO − 10.

The bonding between benzene and ruthenium is formed by the two π orbitals of e_{1g} symmetry (π_2 and π_3) and the empty d orbitals of the metal atom (donation from benzene to ruthenium). The resulting bonding orbitals are HOMO − 12 and HOMO − 13, the antibonding are LUMO + 1 and LUMO + 3. In the back-donation (metal to ligand) the occupied $d_{x^2-y^2}$ and d_{xz} metal orbitals and empty π_4^*, π_5^* benzene orbitals participate (HOMO − 1, HOMO and LUMO + 4, LUMO + 6). The LUMO and LUMO + 2 molecular orbitals are composed of benzoquinoline rings. The ruthenium d orbitals hold shares in LUMO + 5. The σ chlorine orbitals participate in the LUMO + 1 and LUMO + 4 molecular orbitals.

The optimised geometry parameters for the complex **2** are given in Table 3. The complex is paramagnetic and the geometry was optimised for low and high spin state. The calculated energy of triplet state is lower about 4.5 kcal/mol. The predicted bond lengths and angles are in agreement with the values based upon the X-ray crystal structure data. The largest differences were found for the Ru(1)–N(21) distance (∼0.05 Å) and for O(1)–Ru(1)–O(21) angle (3.11°). In the investigated complex are 135 α and 134 β occupied molecular orbitals. Among the occupied MOs of the complex the largest numbers constitute orbitals of the 8-hydroxyquinoline ligand which are not relevant for the discussion. The energy and character of upper valence molecular orbitals are given in Table 4. The d_{yz}, d_{xy}, d_{zx} orbitals of ruthenium are visible in the MO-s HOMO, HOMO − 3 and HOMO − 4 with α spin and in the HOMO, HOMO − 2 and HOMO − 4 with β spin. The molecular orbitals are mixed with the π orbitals of the 8-hydroxyquinoline ligands but the α HOMO − 3 and β HOMO − 2 MO have predominately d character. The d_{z^2} and $d_{x^2-y^2}$ orbitals are visible in LUMO + 10 and LUMO + 11 MO orbitals with α spin and in the LUMO + 12, LUMO + 13 – β spin with an antibonding

admixture of the nitrogen and oxygen orbitals of ($L + 10,12$) and π ($L + 11,13$) character. Some admixture of ruthenium d orbitals play role in the LUMO and LUMO + 2 MO with β spin.

3.3. Electronic spectrum

The spin-allowed, singlet transitions were calculated with the TDDFT method. The experimental spectrum of the complex **1** shows bands at 381.6, 291.2, 220.4, 215.8 nm. The measured (solid line) and calculated (doted line) electronic spectra are shown in Fig. 4. Each calculated transition in Fig. 4 was represented by a gaussian function with the height equal to the oscillator strength and width equal to 0.05.

With the use of the TDDFT method 90, electronic transitions were calculated for $[(C_6H_6)RuCl(C_{13}H_8N)]$ using the DZVP with *f* functions basis set on ruthenium atom (dotted line in Fig. 4). The calculated spectra are in good agreement with the experimental one.

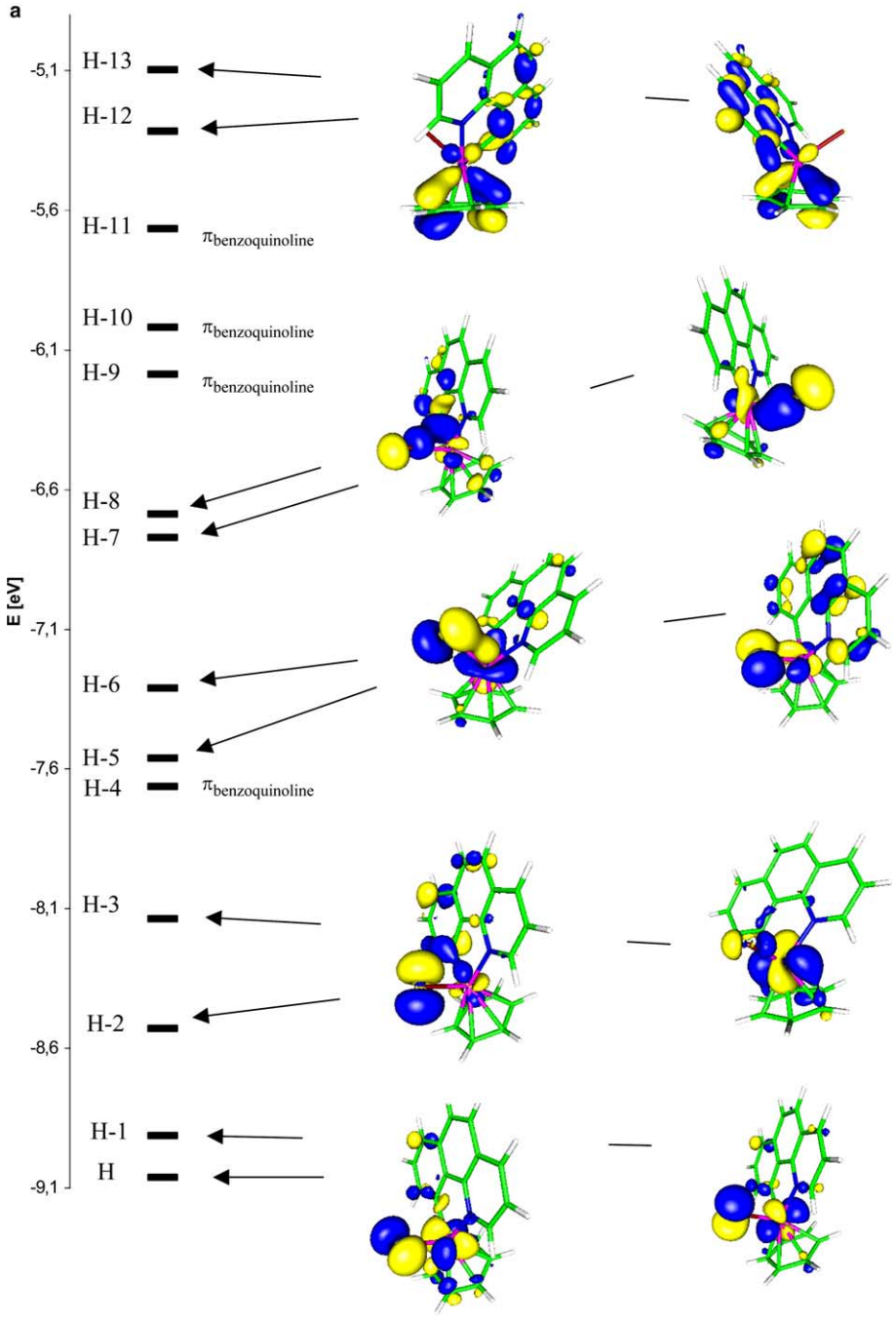


Fig. 3. The molecular orbital diagram (a) HOMO (b) LUMO orbitals of $[(C_6H_6)RuCl(C_{13}H_8N)]$.

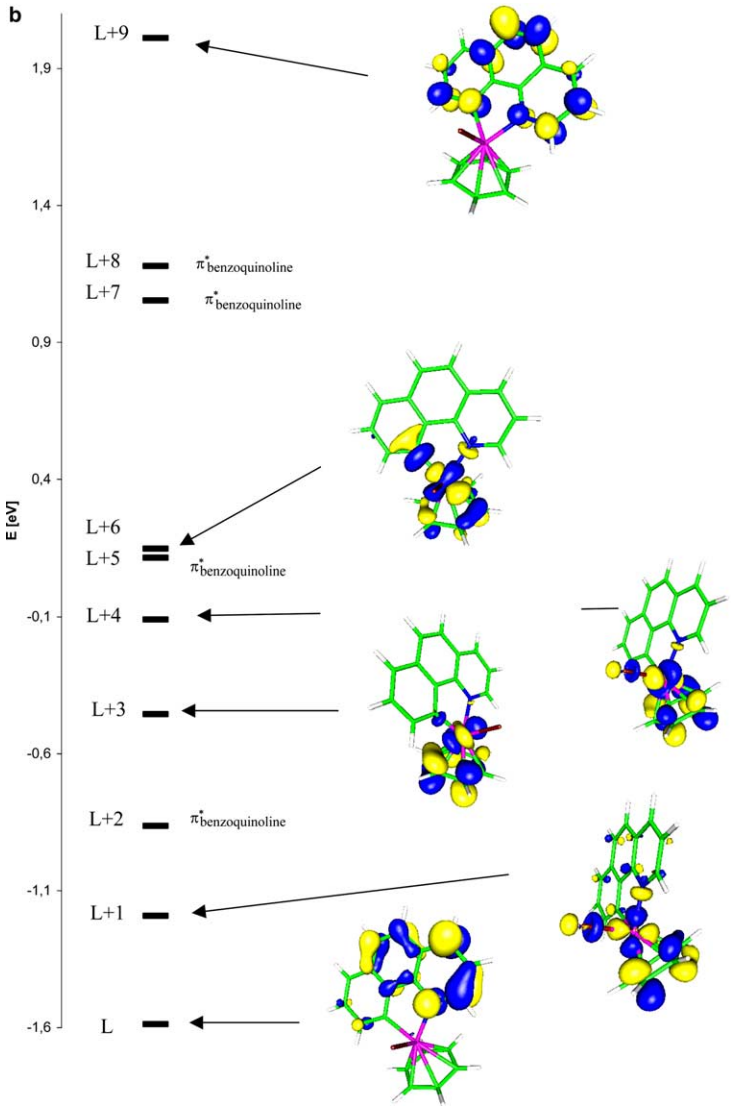


Fig. 3 (*continued*)

The first experimental band at 381.6 nm consists of $d \rightarrow d$ (LF) and $d \rightarrow \pi^*_{bq}$ (MLCT) transitions. The next band at 291.2 nm is consisted from intra- and interligand transitions $\pi_{Cl} \rightarrow \pi^*_{bq}, \pi_{Cl} \rightarrow \pi^*_{benz}, \pi_{bq} \rightarrow \pi^*_{bq}$ with the admixture of $d \rightarrow \pi^*_{benz}$ transition. The LMCT ($d \rightarrow \pi^*_{benz}$) transition is visible in the band at 220.4 nm. The $\pi_{benz} \rightarrow d$ transition has a contribution in the band at 215.8 nm with the interligand CT ($\pi_{bq} \rightarrow \pi^*_{benz}, \pi_{Cl} \rightarrow \pi^*_{benz}, \pi_{Cl} \rightarrow \pi^*_{bq}$) excitations.

The 7,8-benzoquinoline ligand has a significant influence on the spectrum. The transitions with this ligand (MLCT, LMCT, LLCT) occur in the whole spectrum of the complex.

The UV–VIS spectrum of complex with 8-hydroxyquinoline (**2**) was predicted by TDDFT method and the 200 electronic transitions are calculated. The experimental and calculated electronic spectra of $[Ru(C_9H_6NO)_3]$ are presented in Fig. 5. Each calculated transition in Fig. 4 was represented by a gaussian function with the height equal to the oscillator strength and width equal to 0.05. The UV–VIS spectrum of $[Ru(C_9H_6NO)_3]$ was calculated only to 290 nm, so the shortest wavelength experimental bands are not assigned to the calculated transitions.

The UV–VIS spectrum of the complex displayed broad band with maximum at 700.2 nm (14 281 cm^{-1}) resulted from d–d transitions and assigned to $^2T_{2g} \rightarrow {}^4T_{1g}$. In the range of this band was calculated the transition assigned to $^2T_{2g} \rightarrow {}^4T_{2g}$ at 628.7 nm (15 905 cm^{-1}). The shoulder at 499.6 nm (20 016 cm^{-1}) of the next unsymmetrical bands with maximum at 433.4 nm (23 073 cm^{-1}) has been attributed to $^2T_{2g} \rightarrow {}^2A_{1g}$, $^2T_{1g}$ transitions. In the band were calculated the MLCT ($d \rightarrow \pi^*_{quin}$) and LMCT ($\pi_{quin} \rightarrow d$) transitions.

Table 4
The energy and character of upper valence MO of $[Ru(C_9H_6NO)_3]$

MO	α spin		β spin	
	E (eV)	Character	*E* (eV)	Character
HOMO − 10	−7.74	π_{quOH}	−7.90	π_{quOH}
HOMO − 9	−7.50	π_{quOH}	−7.79	π_{quOH}
HOMO − 8	−7.35	π_{quOH}	−7.56	π_{quOH}
HOMO − 7	−7.20	π_{quOH}	−7.45	π_{quOH}
HOMO − 6	−6.93	π_{quOH}	−7.16	π_{quOH}
HOMO − 5	−6.78	π_{quOH}	−6.62	$d_{zx} + \pi_{quOH}$
HOMO − 4	−6.75	$d_{zx} + \pi_{quOH}$	−6.49	d_{yz}
HOMO − 3	−6.38	d_{xy}	−6.22	d_{xz}
HOMO − 2	−5.75	π_{quOH}	−6.09	d_{yz}
HOMO − 1	−5.62	π_{quOH}	−5.60	π_{quOH}
HOMO	−5.33	$d_{yz} + \pi_{quOH}$	−5.31	$d_{yz} + \pi_{quOH}$
LUMO	−3.86	π^*_{quOH}	−4.02	π^*_{quOH}
LUMO + 1	−3.37	π^*_{quOH}	−3.23	π^*_{quOH}
LUMO + 2	−3.23	π^*_{quOH}	−3.21	$d_{yz} + \pi_{quOH}$
LUMO + 3	−2.94	π^*_{quOH}	−3.09	π^*_{quOH}
LUMO + 4	−2.56	π^*_{quOH}	−2.88	π^*_{quOH}
LUMO + 5	−2.15	π^*_{quOH}	−2.49	π^*_{quOH}
LUMO + 6	−1.80	π^*_{quOH}	−2.10	π^*_{quOH}
LUMO + 7	−1.77	π^*_{quOH}	−1.95	π^*_{quOH}
LUMO + 8	−1.24	π^*_{quOH}	−1.73	π^*_{quOH}
LUMO + 9	−0.93	π^*_{quOH}	−0.97	π^*_{quOH}
LUMO + 10	−0.72	$d_{z^2} + \sigma^*_O$	−0.86	π^*_{quOH}
LUMO + 11	−0.60	$d_{x^2-y^2}$	−0.68	$\pi^*_{quOH} + \pi^*_O$
LUMO + 12	−0.40	$\pi^*_{quOH} + \sigma^*_O$	−0.32	d_{z^2}
LUMO + 13	0.31	π^*_{quOH}	−0.09	$d_{x^2-y^2} + \pi^*_O$

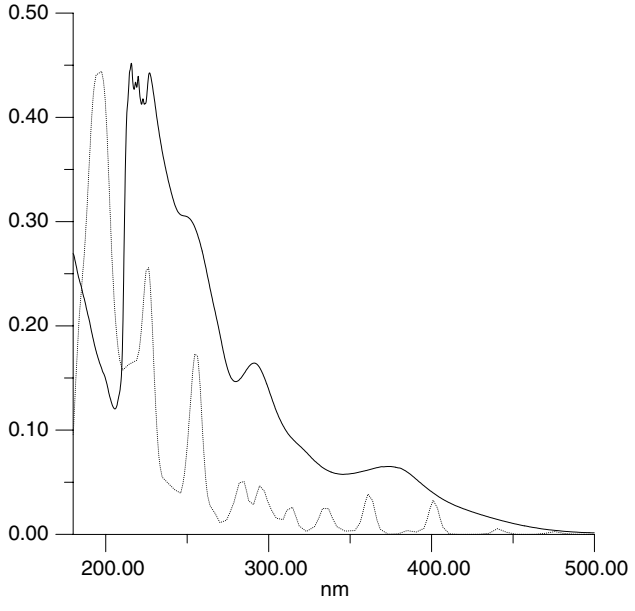


Fig. 4. UV–VIS spectrum of $[(C_6H_6)RuCl(C_{13}H_8N)]$ (solid line – experimental; doted line – calculated).

3.4. Magnetic properties

The magnetic susceptibilities of solid complex $[Ru(C_9H_6NO)_3]\cdot CH_3OH$ was determined over the temperature range 1.8–300 K. Plots of reciprocal magnetic

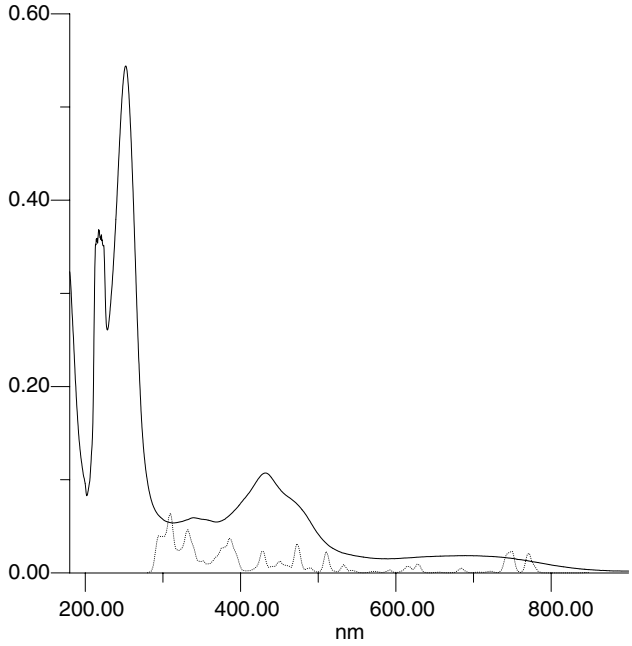


Fig. 5. UV–VIS spectrum of $[Ru(C_9H_6NO)_3]$ (solid line – experimental; doted line – calculated).

susceptibility χ_M and $\chi_M T$ product versus temperature are given in Fig. 6. The value $\chi_M T$ of at 300 K equals 0.441 $cm^3\,mol^{-1}\,K$ (1.87 B.M.). The value of $\chi_M T$ product decreases only slightly with temperature lowering. In the low-temperature range (below 50 K), a more evident decrease of the value of $\chi_M T$ is observed with continuous decrease of the temperature to 0.202 $cm^3\,mol^{-1}\,K$ (1.25 B.M.) at 1.8 K. The decrease of the value $\chi_M T$ in the low-temperature range is caused by occurrence of antiferromagnetic interactions between Ru(III) ions.

On such situation the magnetic data was fitted using the simplest susceptibility equation with a molecular field correction [47]:

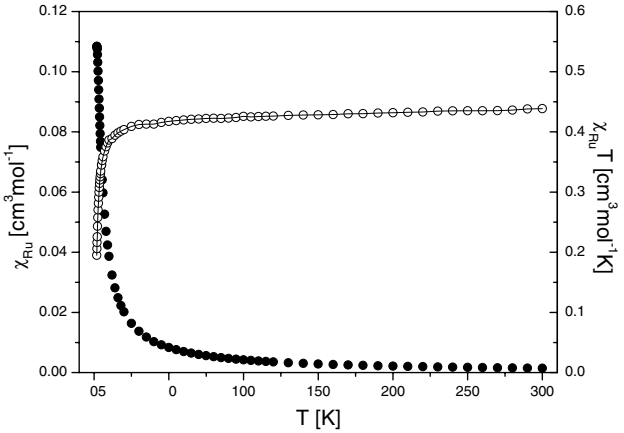


Fig. 6. Plots of the magnetic data for complex $[Ru(C_9H_6NO)_3]\cdot CH_3OH$ experimental χ_M(●) vs. *T* and $\chi_M T$ (○) vs. *T*. The solid line are the calculated curves.

Table 5
EPR data of $[Ru(C_9H_6NO)_3]\cdot CH_3OH$

Temperature T (K)	δ_{Hpp}[a] (Gs)	Spectroscopic splitting factor g_{iso}	hv (GHz)
293	542	2.074	9.769166
77	487	2.148	9.579125
4.5	463	2.156	9.253920

[a] Peak to peak linewidth.

$$\chi_M = \frac{N\beta^2 g^2}{3kT} S(S+1),$$

$$\chi_M^e = \frac{\chi_M}{1 - \frac{2zJ'}{N\beta^2 g^2}\cdot \chi_M},$$

where N is the Avogadro's number, g – the spectroscopic splitting factor, β – the Bohr magneton, k – the Boltzmann constant and zJ' – intermolecular exchange parameter. The best fit parameters are $g = 2.15$, $zJ' = -2.12\ cm^{-1}$ and agreement factor $R = 3.01 \times 10^{-3}$.

The values Curie and Weiss constants determined from the relation $1/\chi_M T = f(T)$ over temperature range 50–300 K are equal to $0.442\ cm^3\ mol^{-1}$ and -3.9 K, respectively. A negative value of Weiss constant suggests the antiferromagnetic coupling of the ruthenium centers in the crystal lattice.

EPR spectrum of $[Ru(C_9H_6NO)_3]\cdot CH_3OH$ complex for the whole temperature range 4.5–293 K indicates single isotropic line only characteristic for Ru^{3+} magnetic center with spin equal to 1/2 (Table 5).

4. Supplementary material

More details of the crystal structure determinations have been deposited with the Cambridge Crystallographic Data Centre with the deposition number: CCDC 266801 for complex **1** and CCDC 266800 for **2**.

Acknowledgements

Crystallographic part was financed by funds allocated by the Ministry of Scientific Research and Information Technology to the Institute of General and Ecological Chemistry, Technical University of Łódź. The GAUSSIAN-03 calculations were carried out in the Wrocław Centre for Networking and Supercomputing, WCSS, Wrocław, Poland under calculational grant No. 51/96.

References

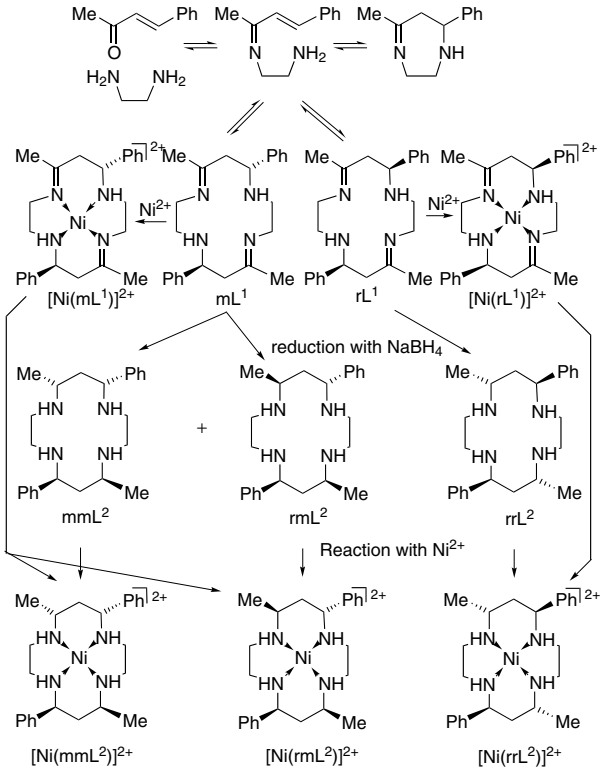
[1] (a) H. Le Bozec, D. Touchard, P.H. Dixneuf, Adv. Organomet. Chem. 29 (1989) 163;
(b) R.M. Moriarty, U.S. Gill, Y.-Y. Ku, J. Organomet. Chem. 350 (1988) 157;
(c) R. Noyori, S. Hashiguchi, Acc. Chem. Res. 30 (1997) 97;
(d) M.A. Bennett, in: E.W. Abel, F.G.A. Stone, G. Wilkinson (Eds.), Comprehensive Organometallic Chemistry II, vol. 7, Pergamon Press, Oxford, 1995;
(e) M.A. Bennett, Coord. Chem. Rev. 166 (1997) 225.
[2] G. Winkhaus, H. Singer, J. Organomet. Chem. 7 (1967) 487.
[3] (a) I. de los Rios, M.J. Tenerio, M.A.J. Tenorio, M.C. Puerta, P. Valerga, J. Organomet. Chem. 525 (1996) 57;
(b) A. Schlüter, K. Bieber, W.S. Sheldrick, Inorg. Chim. Acta 340 (2002) 35;
(c) Y. Chen, M. Valentini, P.S. Pregosin, A. Albinati, Inorg. Chim. Acta 327 (2002) 4;
(d) A. Singh, N. Singh, D.S. Pandey, J. Organomet. Chem. 642 (2002) 48.
[4] (a) B. de Clercq, F. Verpoort, J. Mol. Catal. A: Chemical 180 (2002) 67;
(b) A. Kathó, D. Carmona, F. Viguri, C.D. Remacha, J. Kovács, F. Joó, L.A. Oro, J. Organomet. Chem. 593–594 (2000) 299;
(c) K. Mashima, K. Kusano, N. Sato, Y. Matsumura, K. Nozaki, H. Kumobayashi, N. Sayo, Y. Hori, T. Ishizaki, S. Akutagawa, H. Takaya, J. Org. Chem. 59 (1994) 3064;
(d) S. Hashiguchi, A. Fujii, J. Takehara, T. Ikariya, R. Noyori, J. Am. Chem. Soc. 117 (1995) 7562;
(e) A. Fujii, S. Hashiguchi, N. Uematsu, T. Ikariya, R. Noyori, J. Am. Chem. Soc. 118 (1996) 2521;
(f) A.W. Stumpf, E. Saive, A. Demonceau, A.F. Noels, J. Chem. Soc. Chem. Commun. (1995) 1127.
[5] (a) C.S. Allardyce, P.J. Dyson, D.J. Ellis, S.L. Heath, Chem. Commun. (2001) 1396;
(b) H. Chen, J.A. Parkinson, S. Parsons, R.A. Coxall, R.O. Gould, P.J. Sadler, J. Am. Chem. Soc. 124 (2002) 3064;
(c) R.E. Aird, J. Cummings, A.A. Ritchie, M. Muir, R.E. Morris, H. Chen, P.J. Sadler, D.I. Jodrell, Br. J. Cancer 86 (2002) 1652;
(d) R.E. Morris, R.E. Aird, P. Del, S. Murdoch, H. Chen, J. Cummings, N.D. Hughes, S. Parsons, A. Parkin, G. Boyd, D.I. Jodrell, P.J. Sadler, J. Med. Chem. 44 (2001) 3616.
[6] S. Trofimenko, Chem. Rev. 93 (1993) 943.
[7] R. Mukherjee, Coord. Chem. Rev. 203 (2000) 151.
[8] G. La Monica, G.A. Ardizzoia, Prog. Inorg. Chem. 46 (1997) 151.
[9] A.P. Sadimenko, S.S. Basson, Coord. Chem. Rev. 147 (1996) 247.
[10] A.A. Batista, I.S. Thorburn, B.R. James, S.J. Rettig, R.G. Ball, in: Proceedings of the Sixth International Symposium on Homogeneous Catalysis, Vancouver, Canada, 1988, P-123.
[11] P.C. Hohenberg, W. Kohn, L.J. Sham, Adv. Quant. Chem. 21 (1990) 7.
[12] W. Kohn, A.D. Becke, R.G. Parr, J. Phys. Chem. 100 (1996) 12974.
[13] R.G. Parr, W. Yang, Ann. Rev. Phys. Chem. 46 (1995) 701.
[14] E.J. Baerends, O.V. Gritsenko, J. Phys. Chem. A 101 (1997) 5383.
[15] T. Ziegler, Chem. Rev. 91 (1991) 651.
[16] M.E. Casida, in: D.P. Chong (Ed.), Recent Advances in Density Functional Methods, vol. 1, World Scientific, Singapore, 1995.
[17] M.E. Casida, in: J.M. Seminario (Ed.), Recent Developments and Applications of Modern Density Functional Theory, Theoretical and Computational Chemistry, vol. 4, Elsevier, Amsterdam, 1996, p. 391.
[18] M.E. Casida, C. Jamorski, K.C. Casida, D.R. Salahub, J. Chem. Phys. 108 (1998) 4439.
[19] M.E. Casida, C. Jamorski, K.C. Casida, D.R. Salahub, J. Chem. Phys. 108 (1998) 4439.
[20] C. Adamo, V. Barone, Theor. Chem. Acta 105 (2000) 169.
[21] S.J.A. van Gisbergen, J.A. Groeneveld, A. Rosa, J.G. Snijders, E.J. Baerends, J. Phys. Chem. A 103 (1999) 6835.

[22] A. Rosa, E.J. Baerends, S.J.A. van Gisbergen, E. van Lenthe, J.A. Groeneveld, J.G. Snijders, J. Am. Chem. Soc. 121 (1999) 10356.
[23] M.A. Bennett, T.-N. Huang, T.W. Matheson, A.K. Smith, Inorg. Synth. 21 (1982) 74.
[24] M.J. Frisch, G.W. Trucks, H.B. Schlegel, G.E. Scuseria, M.A. Robb, J.R. Cheeseman, J.A. Montgomery Jr., T. Vreven, K.N. Kudin, J.C. Burant, J.M. Millam, S.S. Iyengar, J. Tomasi, V. Barone, B. Mennucci, M. Cossi, G. Scalmani, N. Rega, G.A. Petersson, H. Nakatsuji, M. Hada, M. Ehara, K. Toyota, R. Fukuda, J. Hasegawa, M. Ishida, T. Nakajima, Y. Honda, O. Kitao, H. Nakai, M. Klene, X. Li, J.E. Knox, H.P. Hratchian, J.B. Cross, C. Adamo, J. Jaramillo, R. Gomperts, R.E. Stratmann, O. Yazyev, A.J. Austin, R. Cammi, C. Pomelli, J.W. Ochterski, P.Y. Ayala, K. Morokuma, G.A. Voth, P. Salvador, J.J. Dannenberg, V.G. Zakrzewski, S. Dapprich, A.D. Daniels, M.C. Strain, O. Farkas, D.K. Malick, A.D. Rabuck, K. Raghavachari, J.B. Foresman, J.V. Ortiz, Q. Cui, A.G. Baboul, S. Clifford, J. Cioslowski, B.B. Stefanov, G. Liu, A. Liashenko, P. Piskorz, I. Komaromi, R.L. Martin, D.J. Fox, T. Keith, M.A. Al-Laham, C.Y. Peng, A. Nanayakkara, M. Challacombe, P.M.W. Gill, B. Johnson, W. Chen, M.W. Wong, C. Gonzalez, J.A. Pople, GAUSSIAN-03, Revision B.03, Gaussian, Inc., Pittsburgh, PA, 2003.
[25] A.D. Becke, J. Chem. Phys. 98 (1993) 5648.
[26] C. Lee, W. Yang, R.G. Parr, Phys. Rev. B 37 (1988) 785.
[27] K. Eichkorn, F. Weigend, O. Treutler, R. Ahlrichs, Theor. Chim. Acc. 97 (1997) 119.
[28] A.D. Becke, J. Chem. Phys. 98 (1993) 5648.
[29] G.M. Sheldrick, Acta Cryst. A 46 (1990) 467.
[30] G.M. Sheldrick, SHELXL-97. Program for the Solution and Refinement of Crystal Structures, University of Göttingen, Germany, 1997.
[31] G.M. Sheldrick, SHELXTL: release 4.1 for Siemens Crystallographic Research Systems, 1990.
[32] U. Beck, W. Hummel, H.B. Burgi, A. Ludi, Organometallics 6 (1993) 20.
[33] F.B. McCormick, D.D. Cox, W.B. Gleason, Organometallics 12 (1993) 610.
[34] (a) R. Tribo, J. Pons, R. Yanez, J.F. Piniella, A. Alvarez-Larena, J. Ros, Inorg. Chem. Commun. 3 (2000) 545;
(b) M. Jahncke, A. Neels, H. Stoeckli-Evans, G. Süss-Fink, J. Organomet. Chem. 561 (1998) 227;
(c) H. Kurosawa, H. Asano, Y. Miyaki, Inorg. Chim. Acta 270 (1998) 87.
[41] T. Hirano, M. Kuroda, N. Takeda, M. Hayashi, M. Mukaida, T. Oi, H. Nagao, J. Chem. Soc., Dalton Trans. (2002) 2158.
[42] K. Kobayashi, H. Ohtsu, T. Wada, T. Kato, K. Tanaka, J. Am. Chem. Soc. 125 (2003) 6729.
[43] H. Wang, T. Hagihara, H. Ikezawa, H. Tomizawa, E. Miki, Inorg. Chim. Acta 299 (2000) 80.
[44] G.R. Desiraju, T. Steiner, The Weak Hydrogen Bond in Structural Chemistry and Biology, Oxford University Press, Oxford, 1999.
[45] G.A. Jeffrey, W. Saenger, Hydrogen Bonding in Biological Structures, Springer Verlag, Berlin, 1994.
[46] R. Taylor, O. Kennard, J. Am. Chem. Soc. 104 (1982) 5063–5070.
[47] J.S. Smart, Effective Field Theories of Magnetism, W.B. Saunders Comp, Philadelphia and London, 1966.

reaction of ethane-1,2-diamine with benzylidene acetone [1,2] crystallises as the *meso*-isomer mL^1. In polar solvents L^1 is present as an equilibrium mixture of, among other compounds, the *meso*-, mL^1, and *rac*-, rL^1, isomers. Reduction of L^1 by using $NaBH_4$ in ethanol yields three isomers of 5,12-dimethyl-7,14-diphenyl-1,4,8,11-tetraazacyclotetradecane, in ca. 83, 15 and <1% yields, respectively [2,3], see the Scheme 1. The major (83%) product is the 5*RS*,7*RS*,12*SR*,14*SR*, *meso–meso*-isomer, mmL^2, formed by reduction of mL^1 [4]. The second (15%) product is the 5*RS*,7*RS*,12*RS*,14*RS*, *rac–rac*-isomer, rrL^2, formed by reduction of the rL^1 present in solutions of mL^1 in polar solvents. The third isomer is now shown to have the 5*SR*,7*RS*,12*SR*,14*SR*, *rac–meso*-configuration, rmL^2, also formed by reduction of mL^1.

The reaction of mL^1 with nickel(II) perchlorate in alcohols yields mixtures of the *meso*- and *rac*-isomeric macrocycle compounds $[Ni(mL^1)](ClO_4)_2$ and $[Ni(rL^1)](ClO_4)_2$, in proportions depending on reaction conditions. Procedures for separating these isomers have been described [5] and the structure of $[Ni(rL^1)](ClO_4)_2$ reported [6].

Reduction of the imine functions of $[Ni(mL^1)](ClO_4)_2$ by using $NaBH_4$ in acetonitrile/methanol yields the isomeric cyclic amine cations $[Ni(mmL^2)]^{2+}$ and $[Ni(rmL^2)]^{2+}$ in ca. 8:1 mol ratio [7], while similar reduction of $[Ni(rL^2)]^{2+}$ forms the cation $[Ni(rrL^2)]^{2+}$ [8]. The isomeric nickel(II) cations are also formed by reaction with nickel(II) of the isomeric amines formed by reduction of ethanol solutions of mL^1.



Scheme 1. Showing the preparation of the isomeric $[Ni(L^2)]^{2+}$ cations.

1.2. Stereochemistry of coordinated 5,12-dimethyl-7,14-diphenyl-1,4,8,11-tetraazacyclotetradecane isomers

Compounds of mmL^2 with cobalt(III) [9], rhodium(III) [9] and nickel(II) [7] have been described. Structures have been reported for mmL^2 [4] and compounds with the 1*RS*,4*RS*,5*SR*,7*SR*,8*SR*,11*SR*,12*RS*,14*RS* configuration: *trans*-β-$[Ni(mmL^2)(NO_2\text{-}N)_2]$ [7], *trans*-β-$[Cu(mmL^2)(NO_3)_2]$ [10] and *trans*-β-$[Cu(mmL^2)(NCB(Ph)_3)_2]$ [11].

Most nickel(II) compounds of mmL^2 have the macrocycle in planar coordination with the *N*-configuration 1*R*,4*R*,8*S*,11*S* (III [12], labelled as β), as $S = 1$ (singlet ground state) salts, e.g., β-$[Ni(mmL^2)](ClO_4)_2$, or as $S = 3$ (triplet ground state) *trans*-di-ligand octahedral compounds *trans*-β-$[Ni(mmL^2)X_2]$. Relatively unstable compounds with chelates α-$[Ni(mmL^2)(A)]ClO_4$ (A = $acac^-$ = pentane-2,4-dionato and $1/2C_2O_4^{2-}$) were prepared. The structure of the $acac^-$ compound shows the macrocycle in folded coordination with *N*-configuration V [7]. Reaction of the $acac^-$ compound with acid yields the metastable $S = 1$ square-planar compound δ-$[Ni(mmL^2)](ClO_4)_2$, shown to have the *N*-configuration II with overall configuration 1*RS*,4*RS*,5*SR*,7*SR*,8*SR*,11*RS*,12*RS*,14*RS*. This is stable as the solid and in acid solution, but in neutral or basic solution readily reverts to the stable β-configuration [7].

In contrast, most compounds of rrL^2 with nickel(II) have the macrocycle in folded coordination with *N*-configuration 1*R*,4*R*,8*R*,11*R* (V, labelled α) with two *cis* additional ligands, or a chelate, completing octahedral coordination; the structure of *cis*-α-$[Ni(rrL^2)(acac)]ClO_4$ was reported [8]. In perchloric acid this forms the cation *cis*-α-$[Ni(rrL^2)(H_2O)_2]^{2+}$ with the same configuration. In basic solution this isomerises to form the $S = 1$ square planar γ-$[Ni(rrL^2)]^{2+}$ cation with the *N*-configuration 1*R*,4*S*,8*R*,11*S* (I, labelled as γ); the structure of γ-$[Ni(rrL^2)][ZnCl_4] \cdot MeNO_2$ was reported [8]. This cation is stable as solid perchlorate and tetrachlorozincate salts. Solutions of the perchlorate salt are stable, but in the presence of anions of better coordinating ability the cation isomerises to the α-configuration, with formation of chelate or *cis*-dianionato species.

In this communication preparations of compounds of $[Ni(rmL^2)]^{2+}$ are described. Molecular mechanics calculations [7] suggested that the square planar cation $[Ni(rmL^2)]^{2+}$ would have similar strain energies for configuration III (1*S*,4*S*,5*S*,7*R*,8*R*,11*R*,12*S*,14*S*, with one methyl substituent axially oriented and the other equatorially oriented) and for configuration II (1*S*,4*R*,5*S*,7*R*,8*R*,11*R*,12*S*,14*S*, with one six-membered chelate ring in a twist-boat conformation, for which all substituents are equatorially oriented). An X-ray

structural characterisation of *cis*-α-[Ni(mmL^2)(acac)]-ClO_4 enables comparison with the mmL^2 [7] and rrL^2 [8] isomeric compounds.

2. Results

2.1. Reduction of $[Ni(mL^1)](ClO_4)_2$

The imine groups of $[Ni(mL^1)](ClO_4)_2$ are rapidly reduced by using $NaBH_4$ in acetonitrile plus a protic solvent (water, or one of the lower alcohols, with the highest yield obtained using 1:1 acetonitrile:methanol). The major product crystallises as *trans*-β-[Ni(mmL^2)-$(MeCN)_2](ClO_4)_2$, with the *meso–meso* isomer of the macrocycle (ca. 83% yield) [7]. Sparingly soluble blue-violet *cis*-α-[Ni(rmL^2)(acac)]ClO_4 precipitates in ca. 13% yield when pentane-2,4-dione and base are added to the filtrate. Alternatively, if the filtrate is acidified with dilute perchloric acid and allowed to evaporate then orange β-$[Ni(rmL^2)](ClO_4)_2 \cdot 0.5H_2O$ crystallises.

2.2. Reduction of mL^1

The isomer of 5,12-dimethyl-7,14-diphenyl-1,4,8,11-tetraazacyclotetradecane which was isolated in <1% yield from the reduction of mL^1 by $NaBH_4$ in ethanol [3] reacted with nickel(II) thiocyanate in ethanol to yield a purple solution from which blue-violet crystals of *trans*-β-$[Ni(rmL^2)(NCS)_2]$ were isolated, see 5.1. Other compounds were prepared from this *trans*-β-[Ni(rmL^2)$(NCS)_2]$ after removal of the NCS^- by reaction with silver perchlorate, or by use of ion exchangers, but these were all identical to, and more easily prepared from, the $[Ni(rmL^2)]^{2+}$ compounds obtained by reduction of $[Ni(mL^1)](ClO_4)_2$.

2.3. Compounds of $[Ni(rmL^2)]^{2+}$

Blue-violet *cis*-α-$[Ni(rmL^2)(H_2O)_2](ClO_4)_2$ crystallises when *cis*-α-[Ni(rmL^2)(acac)]ClO_4 is acidified with perchloric acid. This forms a blue-violet solution in water (in which it is sparingly soluble), but an orange coloured solution in methanol, acetone or nitromethane, indicating the formation of $S = 1$ square-planar nickel(II) cations. The di-aqua compound crystallises from these solutions on evaporation, indicating retention of configuration.

The *cis*-α-$[Ni(rmL^2)(H_2O)_2]^{2+}$ cation persists in acid solution, but slowly in neutral solution, rapidly in basic solution, isomerises irreversibly to the stable orange $S = 1$ square-planar cation β-$[Ni(rmL^2)]^{2+}$. Orange β-$[Ni(rmL^2)](ClO_4)_2$ crystallises from poorly coordinating solvents; the purple adduct *trans*-β-[Ni(rmL^2)-$(MeCN)_2](ClO_4)_2$ crystallises from acetonitrile and blue-violet adducts crystallise from DMF/propan-2-ol or DMSO/propan-2-ol. These are all similar to, but much more soluble than their $[Ni(mmL^2)]^{2+}$ analogues [7]. The facile separation of the $[Ni(rmL^2)]^{2+}$ and $[Ni(mmL^2)]^{2+}$ isomers (see 5.2) is facilitated by the greater solubility in acetonitrile/methanol of *trans*-β-$[Ni(rmL^2)(MeCN)_2](ClO_4)_2$ than the mmL^2 isomeric compound.

Treatment of a solution in methanol of *cis*-α-[Ni(rmL^2)(acac)]ClO_4 with HCl or HBr results in the formation of hydrated blue compounds, which do not contain perchlorate, probably hydrates of the *cis*-dihalido compounds. In basic or neutral solution these halide compounds isomerise to form blue-violet β-*trans*-dihalido compounds, which are also formed from β-$[Ni(rmL^2)(HCO_3)_2]$ (below) and HCl or HBr. Compounds *trans*-β-$[Ni(rmL^2)X_2]$, $X^- = NO_2^-$, NCS^- and HCO_3^-, are formed by reaction of β-$[Ni(rmL^2)](ClO_4)_2$ with a salt of the appropriate anion X^- in methanol/water, or from β-$[Ni(rmL^2)(HCO_3)_2]$ and the appropriate acid HX. Reaction of β-$[Ni(rmL^2)](ClO_4)_2$ with oxalate forms *trans*-μ-oxalato-β-$[Ni(rmL^2)(C_2O_4)] \cdot H_2O$, while reaction of *cis*-α-[Ni(rmL^2)(acac)]ClO_4 with oxalic acid forms the chelate compound *cis*-α-$[\{Ni(rmL^2)\}_2$-$(C_2O_4)](ClO_4)_2$, which isomerises to the *trans*-form in base (as also observed for the $[Ni(mmL^2)]^{2+}$ analogue [7]). Compounds of the potentially chelating anions $NO_3^-, NO_2^-, MeCO_2^-$ and HCO_3^- were isolated only as *trans*-unidentate coordinated β-isomer compounds (again as for their $[Ni(mmL^2)]^{2+}$ analogues, and unlike $[Ni(rrL^2)]^{2+}$ for which these anions coordinate as chelates). Addition of a solution containing $[Ni(CN)_4]^{2-}$ to a solution of $[Ni(rmL^2)]^{2+}$ resulted in the precipitation of sparingly soluble $[\{Ni(rmL^2)\}\{Ni(CN)_4\}] \cdot H_2O$. This has *ν*(CN) bands in the IR similar to those of the mL^2 and rrL^2 analogues, and of other compounds with $\{$-Ni(L)-NC-Ni(CN)$_2$-CN-$\}_n$ chain polymeric structures [13–16].

3. Structural studies

3.1. 1SR,4SR,5SR,7RS,8RS,11RS,12SR,14SR-(5,12-Dimethyl-7,14-diphenyl-1,4,8,11-tetraazacyclotetradecane $\kappa^4N^1,N^4,N^8,N^{11}$)nickel(II) perchlorate hemi-hydrate, β-$[Ni(rmL^2)](ClO_4)_2 \cdot 0.5H_2O$

The structure of a crystal of orange coloured $[Ni(rmL^2)](ClO_4)_2$ grown from acetone/water was determined by X-ray diffraction, to establish the *N*-configuration present, see Table 1 for details.

The structure was solved and refined in space group $P2_1$, with no imposed symmetry. The structure shows disorder, though the macrocylic cation was well resolved, showing the nickel(II) ion in square-planar coordination by the four nitrogen atoms of the macrocycle with the chiral nitrogen centres in configuration (III, β).

Table 1
Crystallographic data[a,b]

Compound	$[Ni(rmL^2)](ClO_4)_2 \cdot 0.5H_2O$	$[Ni(rmL^2)(acac)]ClO_4$
Formula	$C_{24}H_{37}Cl_2N_4NiO_{8.5}$	$C_{29}H_{43}ClN_4NiO_6$
M_r	647.19	637.85
Symmetry/space group	monoclinic, $P2_1$	monoclinic, $P2_1/c$
a (Å)	8.9359(2)	10.0727(1)
b (Å)	15.4003(5)	15.7028(2)
c (Å)	10.8598(3)	19.1247(2)
β (°)	103.339(1)	90.142(1)
Cell volume (Å^3), Z	1454.16(7), 2	3024.94(6), 4
T (K)	200(2)	150(2)
Colour	orange	Blue-violet
Crystal size (mm)	$0.20 \times 0.18 \times 0.16$	$0.38 \times 0.36 \times 0.30$
T_{min}, T_{max}[c]	0.840, 0.869	0.757, 0.800
Reflections (cell)	3808	8192
T (K)	200(2)	150(2)
h_{min}, h_{max}	−10, 10	−12, 12
k_{min}, k_{max}	0, 18	0, 19
l_{min}, l_{max}	0, 12	0, 23
θ_{min}, θ_{max} (°)	1.93, 25.07	1.68, 25.8
Reflections[d] (ref), R_{int}	2664, 0.036	5796, 0.0314
Reflections (gt)[e]	1818	5028
R_1 (all), R_1 (gt)[e]	0.077, 0.048[f]	0.047, 0.040
wR_2 (ref), wR_2 (gt)[e]	0.143, 0.122	0.111, 0.104

[a] Crystallographic data files have been deposited with the Cambridge Crystallographic Data Centre.
[b] Diffraction data was collected using a Siemens CCD diffractometer in ω scan mode, using graphite monochromaticized Mo Kα radiation (λ 0.71073 Å).
[c] Semi-empirical absorption corrections were made using the ψ-scan method [18].
[d] Structures were solved and refined on F^2 using SHELXS-97 and SHELXL-97 [19]. Anisotropic thermal parameters were used for all non-H atoms, with H-atoms in calculated positions and riding.
[e] Data with $F^2 > 2\sigma(F^2)$.
[f] Flack parameter [20] = −0.06(5).

The five-membered chelate rings have gauche conformations with the $\delta\lambda$ configuration and the six-membered rings have chair conformations.

For configuration III in planar coordination the anticipated structure would have both phenyl substituents equatorially oriented and one methyl substituent equatorially and the other axially oriented. The structure found for the perchlorate salt has both phenyl substituents equatorially oriented, but both methyl substituents have half-occupancy of equatorially and axially oriented sites, resulting in a disordered racemate.

The disorder of the methyl groups was modelled with equatorial sites C51A and C12B, and axial sites C51B, and C12A. Site occupancy factors (sof) refined as free variables were within 3σ of the 0.5 values required for chiral balance. Refinement of models with either one of C51A and C12B or C51B and C12A removed from the calculations led to increases in R-values, with large residual peaks at the "omitted" site. Axial or equatorial orientation of the methyl substituents would be expected to cause differences in ring conformation, and superposition of these conformational variants may account for the relatively large adp values observed for many of the atoms.

The results could also be interpreted with disorder of two cations, one with both methyl groups equatorial and the other with both groups axial. However, these would represent different configurations of the macrocycle, $[Ni(mmL^2)]^{2+}$ for the di-equatorial form, and an as yet unobserved isomer for the di-axial arrangement, which is improbable.

The perchlorate ions are located axially with respect to the square-planar nickel(II) cation, with Ni–O11 and Ni–O21 ca. 2.9 Å, indicating only weak interactions. Disorder of these ions was modelled with trigonal bipyramidal arrangements, with three full occupancy "equatorial" oxygen sites, and partial occupancy "axial" oxygen sites. Short Cl–$O_{equatorial}$ distances but long Cl–O_{axial} distances, together with bond angles ca. 90° for O_{axial}–Cl–$O_{equatorial}$ and ca. 120° for $O_{equatorial}$–Cl–$O_{equatorial}$ suggest the presence of two half-occupancy tetrahedral ions, sharing three "equatorial" oxygen sites. A persistent residual peak near oxygen atom site O14 was assigned as a fractional occupancy water oxygen atom site, O1, with O1–O14 = 1.45(1) Å (so sites O1 and O14 cannot be occupied simultaneously). The chlorine site Cl1 could be split into sites Cl1 and Cl1A, separated by 0.39(1) Å. Refinement of sof of the chlorine and oxygen sites indicated that the equatorial sites O11, O12 and O13 have full occupancy, but sof of the two chlorine sites, the axial oxygen sites and of water O1 were all within 3σ of 0.5, so the sof were fixed at 0.5 for final refinement.

The perchlorate ion including Cl2 has a similar trigonal bypyramidal arrangement that was similarly modelled, except that the chlorine site was not successfully split and there was no resolvable residual water oxygen peak associated with this perchlorate ion. Refinement of sof indicated full occupancy for the "equatorial" sites O21, O22 and O23 and occupancies for the "axial" sites O24 of 0.68(3) and for O25 of 0.32(3).

Hydrogen atoms bound to C5, C12 and O1 were not modelled. Large adp values for Cl and O atoms, and residual peaks near these atoms, indicate that this model only approximates the disorder present for the perchlorate ions.

All NH groups form H-bonds with perchlorate oxygen atoms, N11 with the alternative partial occupancy water oxygen atom O1 and perchlorate oxygen atom O15. See the legend to Fig. 1 for significant dimensions.

As the structure is pseudo-centrosymmetrical it was also refined in space group $P2_1/c$, for which the asymmetric unit consists of half the cation and one perchlorate ion. The dimensions for the cation in this solution were not significantly altered, with half-occupancy axial and equatorially oriented methyl substituent sites present. The single perchlorate ion and water sites of

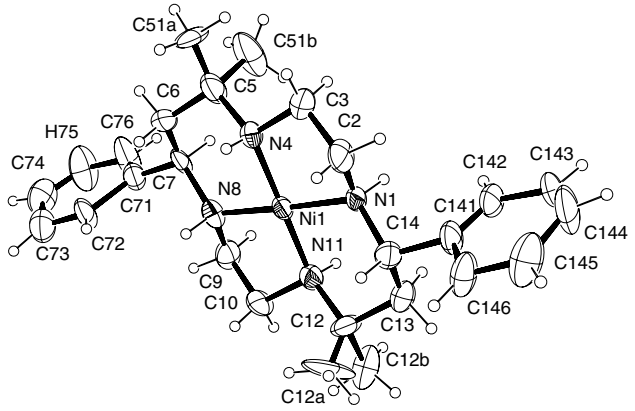


Fig. 1. The cation of *trans*-β-[Ni(rmL^2)(ClO$_4$)$_2$]·1/2H$_2$O, drawn [17] with displacement ellipsoids at the 30% confidence level, with hydrogen atoms as circles of arbitrary radius. Note the half-occupancy axial and equatorial sites for the methyl substituents. Distances within the coordination sphere are Ni–N1 = 1.96, Ni–N4 = 1.96, Ni–N8 = 1.95, Ni–N11 = 1.93, Ni–O11 = 2.92 and Ni–O21 = 2.88 Å, s.u. = 0.01 Å, with angles N1–Ni–N4 = 85.9(4), N1–Ni–N8 = 177.6(6), Ni–Ni–N11 = 94.1(4), N4–Ni–N8 = 92.7(4), N4–Ni–N11 = 179.8(6) and O11–Ni–O21 = 178.5(5)°. Angles N–Ni–O11 and N–Ni–O21 were in the range 84–95°. The N$_4$ group shows tetrahedral displacements of ±0.012(7) Å, with the Ni displaced from the N$_4$ plane by 0.015(8) Å. Displacement of ring atoms from the N$_4$ plane are: C2 −0.39, C3 0.34, C5 0.69, C6 0.32, C7 0.69, C9 0.37, C10 −0.36, C12 −0.83, C13 −0.36, C14 −0.80 Å (s.u. 0.02 Å). The NH groups, perchlorate and water oxygen atoms are linked by N–H···O hydrogen bonding {H–O, N–O/Å, N–H···O/°}: N1–H1···O13 [2.24, 3.102(2), 157]; N4–H4···O24 [2.13, 3.02(2), 148]; N8–H8···O21 [2.11, 3.01(2), 164]; N11–H11···O14 [2.21, 3.05(2), 155] and N11–H11···O1 [2.16, 3.03(2), 161].

$P2_1/c$ were averages of the two $P2_1$ solution sites. The R factors for this solution were $R_1 = 0.066$ [$>2\sigma(I)$], 0.961 (all data), cf. 0.046 and 0.076 for the solution in $P2_1/c$.

3.2. *cis-1SR,4SR,5SR,7RS,8SR,11SR,12SR,14SR-(5,12-Dimethyl-7,14-diphenyl-1,4,8,11-tetraazacyclotetradecane $\kappa^4N^1,N^4,N^8,N^{11}$)(pentane-2,4-dionato κ^2O,O')-nickel(II) perchlorate, cis-α-[Ni(rmL^2)(acac)]ClO$_4$*

The structure of a crystal of lavender coloured *cis*-α-[Ni(rmL^2)(acac)]ClO$_4$ grown from acetone/water was determined by X-ray diffractometry, see Table 1 for details.

The nickel(II) ion is in octahedral coordination by the tetradentate macrocycle rmL^2, folded adjacent to the phenyl substituents (N1–Ni–N8 fold-line), and chelate pentane-2,4-dionate, see Fig. 2. Both six-membered chelate rings have chair conformations; the ring including Ni,N4,N8 has both substituents equatorially oriented, the ring including Ni,N1,N11 has the methyl substituent equatorially oriented and the phenyl substituent axially oriented. This phenyl ring is approximately parallel with the O$_2$C$_3$ plane of the acac$^-$ chelate (inclination of these planes 5.2°, separation ca. 4.4 Å).

The perchlorate ion lies in the cleft in the folded macrocycle opposite the acac$^-$ chelate, with very weak hydrogen bonds between perchlorate oxygen atoms and the fold-line N–H groups N1–H1···O3 {N–O, H–O/Å,

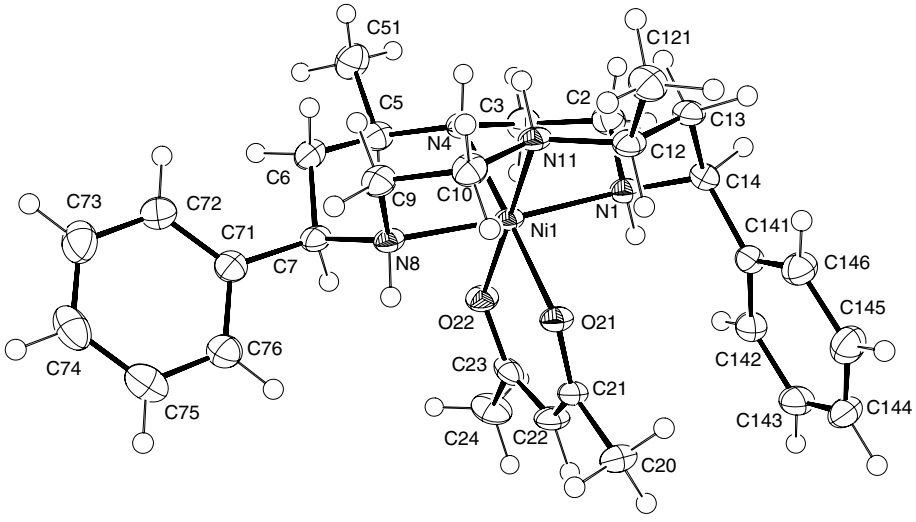


Fig. 2. The cation of *cis*-α-[Ni(rmL^2)(acac)]ClO$_4$, drawn as for Fig. 1 (except for the displacement ellipsoids which are at the 50% confidence level). Significant bond lengths are: Ni–N1 = 2.107(2), Ni–N4 = 2.125(2), Ni–N8 = 2.082(2), Ni–N11 = 2.126(2), Ni–O21 = 2.028(1), Ni–O22 = 2.028(1), O21–C21 = 1.267(3), O22–C23 = 1.264(3), C21–C20 = 1.509(3), C21–C22 = 1.399(3), C23–C22 = 1.390(3) and C23–C24) = 1.515(3) Å. Significant bond angles are: N1–Ni–N4 = 84.70(6), N8–Ni–N4 = 92.99(6), N8–Ni–N11 = 84.47(6), N1–Ni–N11 = 93.17(6), N4–Ni–N11 = 98.16(6), N1–Ni–N8 = 176.45(6), O21–Ni–N1 = 94.64(6), O21–Ni–N4 = 175.98(6), O21–Ni–N8 = 87.85(6), O21–Ni–N11 = 85.83(6), O21–Ni–N4 = 175.98(6), O22–Ni–N1 = 90.71(6), O22–Ni–N11 = 174.71(6), O22–Ni–N4 = 85.77(6), O22–Ni–N8 = 91.81(6), O22–Ni–N11 = 174.71(6) and O21–Ni–O22 = 90.27(6)°. Displacements (Å, s.u < 0.005 Å) from relevant chelate N–Ni–N planes: C2 0.13, C3 −0.56 (gauche); C5 0.77, C51 0.51, C6 0.47, C7 0.86, C71 0.92 (chair, with substituents C51 and C71 equatorial); C9 0.19, C10 −0.50 (gauche); C12 0.87, C121 0.90, C13 0.38, C14 0.33, C141 2.22 (chair, with C121 equatorial and C141 axial). The O$_2$C$_3$ group of the acac$^-$ ligand is approximately coplanar (mean deviation from plane 0.023 Å), with the Ni 0.29 Å from this plane. Intra-cyclic torsion angles, commencing with C14–N1–C2–C3, are: −165.8°, 56.0°, 175.3°, 169.4°, −65.4°, 70.6°, 68.2°, −165.9°, 55.7°, −169.0°, 178.9°, −77.4°, 67.4°, 77.9°.

N–H···O/°} [3.133(5), 2.30, 149]; N8–H8···O1 [3.058(5), 2.61, 162] and to the non-fold-line N–H groups of another cation N4–H4···O4^{i} [3.095(5), 2.25, 151]; N11–H11···O2^{i} [3.279(5), 2.39, 159], symmetry operation i = $-x$, $y + 1/2$, $-z + 1/2$.

3.3. Comparison of isomeric $[Ni(L^2)(acac)]^+$ cations.

The structures of the three isomeric compounds [Ni(L^2)(acac)]ClO$_4$, L^2 = rrL^2 [8], mmL^2 [7], and rmL^2 [this work] have now been determined. These are similar, but with significant structural differences. The mean Ni–N and Ni–O distances for the compounds are similar: *cis*-[Ni(rmL^2)(acac)]ClO$_4$ 2.110(3) and 2.028(1); *cis*-[Ni(rrL^2)(acac)]ClO$_4$ 2.114(6) and 2.019(4) and *cis*-[Ni(mmL^2)(acac)]ClO$_4$ 2.121(6) and 2.042(3) Å, respectively. The Ni atom lies in the C_3O_2 plane of the acac$^-$ chelate for the twofold-symmetric rrL^2 compound, while it is displaced from this plane by 0.11 and 0.29 Å, respectively, for the rmL^2 and mmL^2 compounds. The arrangement of anion and cation is generally similar for the three isomeric compounds, with the perchlorate ion lying in the cleft in the folded macrocycle opposite the acac$^-$ chelate and weakly hydrogen bonded to the non-fold-line NH groups, and to the fold-line N–H groups of another cation to generate a network. For *cis*-[Ni(rmL^2)(acac)]ClO$_4$ the perchlorate oxygen atoms are well resolved with no indication of disorder, while the perchlorate ion is rotationally disordered for the other two compounds.

The cations *cis*-[Ni(mmL^2)(acac)]$^+$ and centrosymmetrical *cis*-[Ni(rrL^2)(acac)]$^+$ both have the macrocycle folded along N^4–Ni–N^{11}, adjacent to the methyl substituents, while *cis*-[Ni(rmL^2)(acac)]$^+$ is folded along N^1–Ni–N^8, adjacent to the phenyl substituents, see Fig. 3. In principle all three isomers could fold either way. For *cis*-[Ni(rrL^2)(acac)]$^+$ the least strained forms of the two possible folding modes have different chiral arrangements; the observed N^4–Ni–N^{11} folded form has the same chirality for the four carbon and four nitrogen asymmetric centres, while the N^1–Ni–N^8 folded form would require the nitrogen and carbon centres to have opposite chiralities. This cation has all substituents equatorially oriented on chair conformation six-membered chelate rings for both folding modes. For *cis*-[Ni(rmL^2)(acac)]$^+$ the two possible folding arrangements have different chiralities (the observed N^1–Ni–N^8 folding, 1*R*,4*S*,5*S*,7*R*(axial),8*S*,11*S*,12*S*,14*S* and N^4–Ni–N^{11} folding, 1*R*,4*R*,5*R*,7*S*(axial),8*R*,11*R*,12*R*, 14*R*) both with one phenyl substituent axially oriented for chair conformation six-membered chelate rings. Adoption of an asymmetric boat conformation for the chelate ring would orient this phenyl group pseudo-equatorially, but apparently the increased strain energy for the unfavourable conformation is greater than the gain from the more favourable substituent orientation. For *cis*-[Ni(mmL^2)(acac)]$^+$ both folding modes have the same chiralities, with both substituents on one chair conformation six-membered chelate ring axially oriented. This chelate ring can adopt one of two asymmetric boat conformations, which orient one of the substituents pseudo-equatorially, the other pseudo-axially. The observed structure has N^4–Ni–N^{11} folding with an asymmetric boat conformation with the phenyl substituent pseudo-equatorially and the methyl substituent pseudo-axially oriented. In this case the strain energy reduction from more favourable substituent orientation is greater than the increase from the unfavourable ring conformation.

4. Discussion

The cation [Ni(rmL^2)]$^{2+}$ predominantly forms compounds in planar coordination, with nitrogen configuration

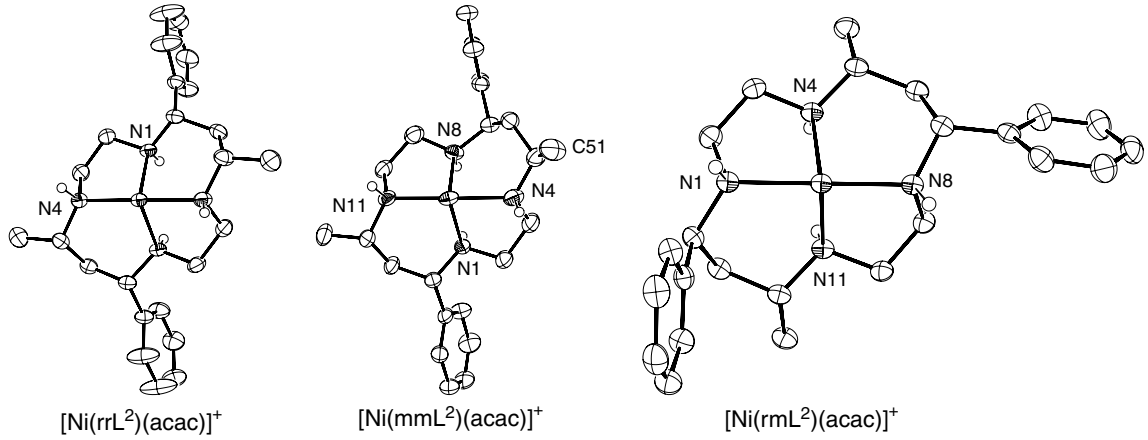


Fig. 3. The cations of the three isomeric [Ni(L^2)(acac)]ClO$_4$ salts, drawn as for Fig. 2, but omitting the pentane-2,4-dionate chelate and H-C atoms, shown from similar perspectives (approximately that of the perchlorate counter-ion). Note the N4–Ni–N11 fold line for [Ni(rrL^2)(acac)]$^+$ and [Ni(mmL^2)(acac)]$^+$ but the N1–Ni–N8 fold line for [Ni(rmL^2)(acac)]$^+$. All substituents are equatorially oriented for [Ni(rrL^2)(acac)]$^+$, one methyl group axially oriented for [Ni(mmL^2)(acac)]$^+$ and one phenyl group axially oriented for [Ni(rmL^2)(acac)]$^+$.

III, in $S = 3$, *trans*-di-ligand or $S = 1$ square planar geometries. The only stable folded coordination, configuration V, compound observed is $S = 3$ [Ni(rmL^2)(acac)]ClO$_4$, though metastable *cis*-α-[Ni(rmL^2)(H$_2$O)$_2$](ClO$_4$)$_2$, –[Ni(rmL^2)Cl$_2$], –[Ni(rmL^2)Br$_2$] and –[{Ni(rmL^2)}$_2$(C$_2$O$_4$)](ClO$_4$)$_2$ have been prepared. The coordination geometry of rmL^2 is thus more similar to that of the mmL^2, rather than the rrL^2, isomer. The differences in properties of these isomeric amines arise from the differing strain energies largely caused by equatorial or axial orientation of the substituents determined by the ligand chirality [7,8]. The cation [Ni(rmL^2)]$^{2+}$ as the perchlorate salt adopts configuration III but rather than a static arrangement with one methyl substituent axially and the other equatorially oriented has a disordered structure with equal occupancies of the two possible arrangements.

5. Experimental

5.1. Preparation of compounds

The perchlorate salts described are not shock-sensitive, and decomposed non-violently when strongly heated. They should still be treated with the caution due to any perchlorate salt.

[Ni(mL^1)](ClO$_4$)$_2$ was prepared and purified from the *C-rac* isomer by crystallisation as the bis(acetontrile) adduct [5]. Any [Ni(rL^1)](ClO$_4$)$_2$ present will reduce to form [Ni(rrL^2)]$^{2+}$ which will contaminate the [Ni(rmL^2)(acac)]ClO$_4$.

The cation [Ni(rmL^2)]$^{2+}$ is very resistant to acid demetallation, so is unaffected by relatively concentrated acid solutions, other than of nitric acid which rapidly oxidises it. The compounds generally have low solubility in water (forming yellow, dissociated solutions), but are often quite soluble in polar organic solvents. The [Ni(rmL^2)]$^{2+}$ compounds in planar coordination are similar to, but generally more soluble than their [Ni(mmL^2)]$^{2+}$ analogues, while compounds in folded coordination are generally similar to their [Ni(rrL^2)]$^{2+}$ counterparts.

5.2. Reduction of 5,12-dimethyl-7,14-diphenyl-1,4,8,11-tetraazacyclotetradeca-4,11-diene

C-meso-(5,12-Dimethyl-7,14-diphenyl-1,4,8,11-tetraazacyclotetradeca-4,11-diene) was reduced in ethanol by using NaBH$_4$ [3]. The mmL^2 isomer was separated as the sparingly soluble hydrochloride salt, and the filtrates made basic and extracted with light petroleum, the extract solution allowed to evaporate, and successive crops of the crystalline rrL^2 amine filtered off. Ultimately crystals with a different habit formed as the more soluble rmL^2 isomer, contaminated with rrL^2, crystallised in <1% yield. Because of the small yield and high solubility this proved difficult to purify by recrystallisation.

5.3. trans-(5SR,7RS,12SR,14SR-5,12-dimethyl-7,14-diphenyl-1,4,8,11-tetraazacyclotetradecane) dithiocyanatonickel(II), trans-β-[Ni(rmL^2)(NCS)$_2$]

Reaction of the crude rmL^2 with nickel(II) thiocyanate in ethanol formed a purple solution from which blue-violet crystals of *trans*-[Ni(rmL^2)(NCS)$_2$] and blue crystals of *cis*-[Ni(rrL^2)(NCS)$_2$] formed. These were repeatedly recrystallised from ethanol until blue-violet crystals, free of the blue material, were obtained. The same product crystallised when NaCNS was added to a solution of β-[Ni(rmL^2)](ClO$_4$)$_2$. *Anal*. Calc. C$_{26}$H$_{38}$N$_6$NiO C, 54.4, H, 6.7, Ni, 10.2. Found: C, 54.6; H, 6.6; Ni, 10.1. Spectra: λ_{max}/nm ν_1(901, 725), ν_2 518; IR ν_{max}/cm^{-1} ν(NH) 3281, 3223, ν(C≡N) 2078vs, 2067sh.

5.4. (5SR,7RS,12SR,14SR-5,12-Dimethyl-7,14-diphenyl-1,4,8,11-tetraazacyclotetradecane)(pentane-2,4-dionato)-nickel(II) perchlorate, cis-α-[Ni(rmL^2)(acac)]ClO$_4$

[Ni(mL^1)](ClO$_4$)$_2$ Purified from the *C-rac* isomer by crystallisation as the bis(acetontrile) adduct, (10 g), was progressively added to a stirred solution of NaBH$_4$ (1.3 g, 1:2 mol proportions) in acetonitrile (25 cm^3) plus methanol (25 cm^3). Effervescence occurred and grey-mauve [Ni(mmL^2)(CH$_3$CN)$_2$](ClO$_4$)$_2$ crystallised, leaving a pale orange coloured solution. After 1 h slight effervescence was observable, indicating the presence of excess BH$_4^-$ (if not a little extra NaBH$_4$ was added). After 2 h, the [Ni(mmL^2)(CH$_3$CN)$_2$](ClO$_4$)$_2$ was filtered off and washed with 1:1 acetonitrile:methanol, retaining the filtrates which contain the rmL^2 compound. The [Ni(mmL^2)(CH$_3$CN)$_2$](ClO$_4$)$_2$ was heated to boiling with 30 cm^3 of the same solvent mixture, then the mixture stirred overnight at ambient temperature. The solid was filtered off and washed as before, retaining the filtrate. The [Ni(mmL^2)(CH$_3$CN)$_2$](ClO$_4$)$_2$ was heated at 80 °C to form the non-solvated compound in ca. 90% yield.

The combined filtrates were boiled, pentane-2,4-dione (2 cm^3) added (care, effervescence may occur if any borohydride remains), followed by hot aqueous ammonia (100 cm^3, 1 mol dm^{-3}) added slowly and the solution then heated near boiling for 30 min. The blue-violet product was filtered from the cold solution and washed with water, sucked dry, then washed with propan-2-ol until the washings were colourless. This was recrystallised from hot acetone/propan-2-ol. Yield: ca. 1.0 g, 10%. *Anal*. Calc. for C$_{29}$H$_{43}$ClN$_4$NiO$_6$: C, 54.6, H, 6.8, Ni, 8.8. Found: C, 54.6, H, 6.7, Ni, 8.7%.

5.5. trans-Di-aqua-(5SR,7RS,12SR,14SR-5,12-dimethyl-7,14-diphenyl-1,4,8,11-tetraazacyclotetradecane)nickel(II) perchlorate hemihydrate, trans-β-[Ni(rmL^2)-(H$_2$O)$_2$](ClO$_4$)$_2$ · 1/2H$_2$O

Perchloric acid (20 cm^3, 0.1 mol dm^{-3}) was added to [Ni(rmL^2)(acac)]ClO$_4$ (1 g) dissolved in acetone (20 cm^3) and the solution allowed to evaporate, when the blue violet *product* crystallised. This was filtered off and recrystallised by dissolving, without heating, in acetone containing a drop of dilute perchloric acid, to form an orange coloured solution. Perchloric, acid (0.1 mol dm^{-1}) was added until just turbid, and the solution allowed to evaporate as before. The blue-violet crystals were filtered off and washed with ethanol. *Anal*. Calc. for $C_{24}H_{37}Cl_2N_4NiO_{8.5}$: C, 44.5; H, 5.8; N, 8.7; Ni, 10.2. Found: C, 44.4; H, 6.1; N, 8.6; Ni, 10.1%. IR spectrum ν_{max}/cm^{-1} *ν*(OH) ca. 3600br, *ν*(NH) 3172s,sp.

5.6. (5SR,7RS,12SR,14SR-5,12-Dimethyl-7,14-diphenyl-1,4,8,11-tetraazacyclotetradecane)nickel(II) perchlorate hemihydrate, [Ni(rmL^2)](ClO$_4$)$_2$ · 1/2H$_2$O

A drop of ethylamine (or methylamine) solution was added to an orange coloured solution of *cis*-α-[Ni(rmL^2)(H$_2$O)$_2$](ClO$_4$)$_2$ in acetone, and the solution boiled. The solution was then acidified with dilute HClO$_4$ and allowed to evaporate, when the orange *product* crystallised. This was recrystallised by evaporation of an acetone/propan-2-ol solution. *Anal*. Calc. for $C_{24}H_{36}Cl_2N_4NiO_8$: C, 45.2, H, 5.7, N, 8.8; Ni, 9.2. Found: C, 44.9, H, 6.7, N, 8.8; Ni, 9.2%. Calc. for hemi-hydrate $C_{24}H_{37}Cl_2N_4NiO_{8.5}$: C, 44.5, H, 5.8, N, 8.7; Ni, 9.1%. IR spectrum ν_{max}/cm^{-1}*ν*(NH) 3172s,sp. Some samples showed weak *ν*(OH) bands. The structural study of a crystal grown from acetone/water confirmed it was a hemi-hydrate.

5.7. cis-Dichloro-(5SR,7RS,12SR,14SR-5,12-dimethyl-7,14-diphenyl-1,4,8,11-tetraazacyclotetradecane)nickel(II) Dihydrate, cis-α-[{Ni(rmL^2)$_2$Cl$_2$] · 2H$_2$O}

Concd. HCl was added drop-wise to an acetone solution of *cis*-α-[Ni(rmL^2)(acac)]ClO$_4$ when the blue *product* crystallised. This was filtered off and washed with water and ethanol. *Anal*. Calc. for $C_{24}H_{38}Cl_2N_4NiO_2$: C, 52.4, H, 7.4, N, 10.3. Found: C, 52.8; H, 7.4; N, 10.3%. Spectra: λ_{max}/nm (MeOH) ν_1 (943, 676), ν_2 541; IR ν_{max}/cm^{-1}; *ν*(NH) 3257m,sp; 3228m,sp.

5.8. cis-Dibromo-(5SR,7RS,12SR,14SR-5,12-dimethyl-7,14-diphenyl-1,4,8,11-tetraazacyclotetradecane)nickel(II) Hemihydrate, cis-α-[{Ni(rmL^2)$_2$Br$_2$] · 1/2H$_2$O}

As for the previous compound, substituting HBr for the HCl, to form the blue *product*. *Anal*. Calc. for $C_{24}H_{36}Cl_2N_4Ni$: C, 56.3, H, 7.5; N, 11.5. Found: C, 56.6; H, 7.7; N, 11.5%. Spectra: λ_{max}/nm (MeOH) ν_1 (943, 676), ν_2 541; IR ν_{max}/cm^{-1}; *ν*(NH) 3257m,sp; 3228m,sp.

5.9. trans-Dichloro-(5SR,7RS,12SR,14SR-5,12-dimethyl-7,14-diphenyl-1,4,8,11-tetraazacyclotetradecane)nickel(II) Dihydrate, trans-β-[Ni(rmL^2)Cl$_2$] · 2H$_2$O

The blue chloro compound was boiled in methanol/water, when the colour changed from blue to blue-violet and the blue violet product crystallised. This was filtered off and washed with water and ethanol. *Anal*. Calc. for $C_{24}H_{40}Cl_2N_4NiO_2$: C, 52.8, H, 7.4, N, 10.3. Found: C, 52.4; H, 7.4; N, 10.2%. Spectra: λ_{max}/nm (MeOH) ν_1 (943, 676), ν_2 541; IR ν_{max}/cm^{-1}; *ν*(NH) 3259m, 3203s.

5.10. trans-Dibromo-(5SR,7RS,12SR,14SR-5,12-dimethyl-7,14-diphenyl-1,4,8,11-tetraazacyclotetradecane)nickel(II) hemihydrate, trans-β-[Ni(rmL^2)Br$_2$] · 1/2H$_2$O

The blue *cis*-dibromo compound was boiled in methanol/water, when the colour changed from blue to blue-violet and the blue violet product crystallised. This was filtered off and washed with water and ethanol. *Anal*. Calc. for $C_{24}H_{37}Br_2N_4NiO_{0.5}$: C, 47.4, H, 6.1, N, 9.2. Found: C, 47.3; H, 6.2; N, 9.2%. Spectra: λ_{max}/nm (MeOH) ν_1 (943, 676), ν_2 541; IR ν_{max}/cm^{-1}; *ν*(NH) 3258m, 3202s.

5.11. trans-(5SR,7RS,12SR,14SR-5,12-Dimethyl-7,14-diphenyl-1,4,8,11-tetraazacyclotetradecane)bis(hydrogen carbonato)nickel(II) hydrate, trans-β-[Ni(rmL^2)-(HCO$_3$)$_2$] · H$_2$O

An aqueous solution of NaHCO$_3$ in small excess was added to an acetone/water solution of [Ni(rmL^2)]-(ClO$_4$)$_2$, when the blue-violet product precipitated. This was filtered off and washed with water and acetone. *Anal*. Calc. for $C_{25}H_{37}N_4NiO_7$: C, 50.1; H, 6.2; N, 9.3. Found: C, 50.3; H, 5.9; N, 9.4%. The IR spectrum shows complex absorption 3600-2600 cm^{-1}, very similar to that shown by the mmL^2 analogue [7]; ν_{max}/cm^{-1} *ν*(OH, NH) 3619m, 3529w, 3418w,br, 3270m, 3058w, 3028w; *ν*C(OH), 2687br, 2647; ν_{as}(HCO$_3^-$) 1610vs,sp; ν_s(HCO$_3^-$) 14105s,sp.

5.12. Other trans-β-[Ni(mmL^2)X$_2$] compounds

Compounds *trans*-β-[Ni(mmL^2)X$_2$] were formed by adding an aqueous solution of a soluble salt of the anion X$^-$, usually of Na$^+$ or Li$^+$, to a methanol solution of β-[Ni(rmL^2)](ClO$_4$)$_2$. Alternatively, an aqueous solution of the acid HX was added to a methanol solution of *trans*-β-[Ni(rmL^2)(HCO$_3$)$_2$]. The methanol was allowed to evaporate when the (usually) blue-violet products

crystallised. The products were filtered off, washed with water and recrystallised from hot methanol/propan-2-ol, unless otherwise specified.

5.13. trans-(5SR,7RS,12SR,14SR-5,12-Dimethyl-7,14-diphenyl-1,4,8,11-tetraazacyclotetradecane)dinitronickel(II), trans-β-[Ni(rmL^2)(NO$_2$)$_2$]

The straw-coloured product crystallised when aqueous $NaNO_2$ was added to an acetone/water solution of [Ni(rmL^2)](ClO$_4$)$_2$. This was filtered off and recrystallised from hot acetonitrile/water. *Anal*. Calc. for $C_{24}H_{36}N_6NiO_4$: C, 54.3; H, 6.8; N, 15.8. Found: C, 54.5; H, 6.9; N, 15.8%. IR spectrum: ν_{max}/cm^{-1} ν(NH) (3202, 31830 s, sp; $\nu_{as}(NO_2^-)$ 1377s,sp, $\nu_s(NO_2^-)$ 1264s,sp.

5.14. trans-bis-Acetato-5SR,7RS,12SR,14SR-5,12-dimethyl-7,14-diphenyl-1,4,8,11-tetraazacyclotetradecane nickel(II) hydrate, trans-β-[Ni(mmL^2)(CH$_3$CO$_2$)$_2$] · H$_2$O

This blue-violet compound was prepared by reaction of the hydrogen carbonato compound with dilute acetic acid and recrystallised from methanol/propan-2-ol. *Anal*. Calc. for $C_{28}H_{42}N_4NiO_4$: C, 60.3; H, 7.6; N, 10.1. Found: C, 60.4; H, 7.7; N, 10.0%. Spectra: λ_{max}/nm (MeOH) ν_1 (1090, 680), ν_2 526 , ν_3 346; IR ν_{max}/cm^{-1} ν(NH) 3246, 3181br, ν_{as}(OCO) 1567vs,br, ν_s(OCO) 1415s.

5.15. μ-Oxalato-bis(5SR,7RS,12SR,14SR-5,12-dimethyl-7,14-diphenyl-1,4,8,11-tetraazacyclotetradecane) oxalato-dinickel(II) perchlorate, cis-μ-C$_2$O$_4$-α-[{Ni(mmL^2)}$_2$-(C$_2$O$_4$)](ClO$_4$)$_2$

Oxalic acid in small excess was added to an acetone solution of [Ni(rmL^2)(acac)]ClO$_4$ in acetone, followed by water. The blue-violet product was filtered, washed with water and then ethanol and recrystallised from acetonitrile/propan-2-ol. *Anal*. Calc. for $C_{25}H_{36}N_4ClNiO_6$: C, 51.5; H, 6.2; N, 9.6. Found: C, 51.2; H, 6.3; N, 9.5%. The compound is stable in acid solution, but in neutral or basic solution slowly converts to the *trans*-β-oxalato compound. IR spectrum ν_{max}/cm^{-1} ν(NH) 3270; ν_{as}(OCO) (1656, 1649, 1644)vs; $\nu_3(ClO_4^-)$ 1084; $\nu_4(ClO_4^-)$ 624.

5.16. catena-μ-Oxalato-(5SR,7RS,12SR,14SR-5,12-dimethyl-7,14-diphenyl-1,4,8,11-tetraazacyclotetradecane) oxalatonickel(II) hydrate, {trans-μ-C$_2$O$_4$-β-[Ni(mmL^2)}$_2$-(C$_2$O$_4$)]$_n$ · nH$_2$O

The μ-oxalato compound was prepared from the perchlorate salt in acetone/water by adding diethyl ammonium oxalate, or by reacting [Ni(rmL^2)(HCO$_3$)$_2$] 1.5H$_2$O with oxalic acid in methanol/water. The insoluble blue-violet *product* was filtered off and washed well with hot water *Anal*. Calc. for $C_{26}H_{38}N_4NiO_5$: C, 57.3; H, 7.0; N, 10.3. Found: C, 57.3; H, 6.6; N, 10.2%. IR spectrum ν_{max}/cm^{-1} ν(OH) 3410; ν(NH) 3227, 3170; ν_{as}(OCO) (1565)vs; ν_s(OCO) 1305.

5.17. Catena-di-μ-cyano-(5SR,7RS,12SR,14SR-5,12-dimethyl-7,14-diphenyl-1,4,8,11-tetraazacyclotetradecane) dinickel(II) Trihydrate trans-μ-CN-α-[{Ni(mmL^2)}-{Ni(CN)$_4$}]$_n$ · 3nH$_2$O

The insoluble blue-violet *product* which precipitated when an aqueous solution of Na$_2$[Ni(CN)$_4$] · 3H$_2$O was added drop-wise to a methanol solution of [Ni(rmL^2)]-(ClO$_4$)$_2$ was filtered off and washed well with water and then methanol. *Anal*. Calc. for $C_{28}H_{42}N_8Ni_2O_3$: C, 51.3; H, 6.4; N, 17.3. Found: C, 51.3; H, 6.3; N, 17.1%. IR spectrum ν_{max}/cm^{-1} ν(OH) 3604; ν(NH) 3443; ν(CN) 2143s, 2127vs; δ(HOH) 1625.

Appendix A. Supplementary data

Crystallographic data has been deposited with the Cambridge Crystallographic Data Centre; [Ni(rmL^2)]-(ClO$_4$)$_2$ · 0.5H$_2$O: CCDC 271481 and [Ni(rmL^2)(acac)]-ClO$_4$: CCDC 271482. Copies may be obtained free of charge from the Director, CDCC, 12 Union Road, Cambridge CBZ 1EZ, UK (fax: +44 1223 336 033; e-mail: deposit@ccdc.cam.ac.uk or www: http://www.ccdc.cam.uk). Supplementary data associated with this article can be found, in the online version, at doi:10.1016/j.poly.2005.06.022.

References

[1] K. Hideg, D. Lloyd, J. Chem. Soc., Sect. C (1971) 3441.
[2] K. Hideg, D. Lloyd, J. Chem. Soc., Chem. Commun. (1970) 929.
[3] D.F. Cook, Ph.D. Thesis, Victoria University of Wellington, 1972.
[4] G. Ferguson, P. Roberts, D. Lloyd, K. Hideg, J. Chem. Soc., Chem. Commun. (1977) 149.
[5] N.F. Curtis, Inorg. Chim. Acta 317 (2001) 27.
[6] N.F. Curtis, D.C. Weatherburn, Acta Crystallogr., Sect. E 58 (2002) 423.
[7] D.F. Cook, N.F. Curtis, C.E.F. Rickard, J.M. Waters, Inorg. Chim. Acta 355 (2003) 1.
[8] D.F. Cook, N.F. Curtis, O.P. Gladkikh, D.C. Weatherburn, Inorg. Chim. Acta 355 (2003) 15.
[9] R.W. Hay, P.M. Gidney, J. Chem. Soc., Dalton Trans. (1976) 974.
[10] D.F. Cook, Inorg. Nucl. Chem. Lett. 12 (1976) 103.
[11] A.Y. Nazarenko, V.K. Bel'skii, N.R. Strel'tsova, Zh. Neorg. Khim. 41 (1996) 1119.
[12] B. Bosnich, C.K. Poon, M.L. Tobe, Inorg. Chem. 4 (1965) 1102.
[13] G.J. Gainsford, N.F. Curtis, Aust. J. Chem. 37 (1984) 1799.
[14] H.Z. Kou, D.Z. Liao, Z.H. Jiang, S.P. Yan, Q.J. Wu, S. Gao, G.L. Wang, Inorg. Chem. Commun. 3 (2000) 151.

[15] S.Z. Zhan, D. Guo, X.Y. Zhang, C.X. Du, Y. Zhu, R.N. Yang, Inorg. Chim. Acta 298 (2000) 57.
[16] Z. Smekal, F. Brezina, Z. Sindelar, R. Klicka, M. Nadvornik, Chem. Zvesti 51 (1997) 95.
[17] L.J. Farrugia, J. Appl. Crystallogr. 30 (1997) 565.
[18] R.H. Blessing, Acta Crystallogr. Sect. A 51 (1995) 33.
[19] G.M. Sheldrick, SHELXS-97 and SHELXL-97: Programs for the Solution and Refinement of Crystal Structures, University of Göttingen, Göttingen , Germany, 1997.
[20] H.D. Flack, Acta Crystallogr., Sect. A 39 (1983) 876.

Recently, we have developed a straightforward synthetic route to the preparation of the new multitopic ligand 2,3-bis(4,5-dimethylthio-1,3-dithiole-2-ylidene) succinonitrile (**L**) [6]. Ag(I) is a soft metal center with a high affinity for soft nitrogen- and sulfur-containing ligands [7]. In principle, the framework of Ag(I) complexes can vary widely as reported in the literature [8]. As a consequence, we have initiated a study of the network topology based on **L** as a function of counterions. Herein, we present structural studies of coordination networks derived from ligand **L** and two different AgX ($X = NO_3^-, CF_3SO_3^-$) salts.

2. Experimental

2.1. Materials and equipment

Unless stated otherwise, all chemicals were purchased from commercial sources and used as received. IR spectra were recorded on a Perkin–Elmer One FT-IR spectrometer. Elemental analyses were performed on an EA 1110 Elemental Analyzer CHNS Carlo Erba Instruments.

2.2. Synthesis of complex $[Ag_2(\mathbf{L})(NO_3)_2]_n$ (1)

The solution of ligand **L** [5] (10 mg, 0.022 mmol) in 5 ml of dichloromethane was added to one side of an H-tube. A saturated solution of $AgNO_3$ in methanol (5 ml) was added to the other side of the H-tube, and the two sides of the H-tube were carefully connected by methanol and left in dark place at room temperature. After one week, yellowish crystals suitable for X-ray analysis were obtained on the wall of the H-tube. Yield: 10.4 mg (60%). *Anal.* Calc. for $C_{14}H_{12}Ag_2N_4O_6S_8$: C, 20.90; H, 1.50; N, 6.96. Found: C, 20.74; H, 1.40; N, 6.67%. IR (cm^{-1}, *v* KBr): 2182, 1508, 1459, 1434, 1332, 1040, 968, 817, 734.

2.3. Synthesis of complex $[Ag_2(\mathbf{L})(CF_3SO_3)_2]_n$ (2)

Following the same procedure as for the preparation of complex **1**, complex **2** has been obtained as yellowish crystals by the slow diffusion between the solution of ligand **L** (13 mg, 0.028 mmol) in 5 ml of dichloromethane and a saturated solution of $AgCF_3SO_3$ in methanol (5 ml). Yield: 13.7 mg (50%). *Anal.* Calc. for $C_{16}H_{12}Ag_2F_6N_2O_6S_{10}$: C, 19.64; H, 1.24; N, 2.86. Found: C, 19.80; H, 1.15; N, 2.77%. IR (cm^{-1}, *v* KBr): 2190, 1523, 1468, 1281, 1197, 1015, 735, 635, 734.

2.4. Crystallography

Intensity measurements for complexes **1** and **2** were collected on a Stoe Imaging Plate Diffractometer System – Stoe and Cie [9], equipped with a one-circle φ goniometer and a graphite-monochromator. Data collection was performed using Mo Kα radiation ($\lambda = 0.71073$). The structures were solved by Direct methods using the programme SHELXS-97 [10]. The refinement and all further calculations were carried out using SHELXL-97 [11].

The hydrogen atoms were included in calculated positions and treated as riding atoms using SHELXL-97 default parameters. All non-hydrogen atoms were refined anisotropically. An absorption correction was applied using DIFABS [12] ($T_{min} = 0.154$, $T_{max} = 0.627$ for **1**; $T_{min} = 0.714$, $T_{max} = 0.722$ for **2**).

Both compounds crystallize in non-centrosymmetric space groups (**1**: $P2_12_12_1$, **2**: $C2$) as racemic twins (**1**: BASF = 0.48(12); **2**: BASF = 0.69(7)). The crystallographic data of the complexes **1** and **2** are collected in Table 1. Selected bond lengths and angles are given in Tables 2 and 3, respectively.

3. Results and discussion

3.1. Structure of complex $[Ag_2(\mathbf{L})(NO_3)_2]_n$ (1)

The compound crystallizes in an orthorhombic space group ($P2_12_12_1$) with a metal to ligand stoichiometry of 2:1. The coordination geometry around the silver ion is a distorted octahedron (Fig. 1) with a NO_3S_2 coordination sphere. Thus, the metal ion is bonded to two sulfur atoms of ligand **L**, one nitrogen atom of a neighboring ligand **L**, two oxygen atoms of a bridging

Table 1
Crystallographic data for the complexes **1** and **2**

	1	**2**
Molecular formula	$C_{14}H_{12}Ag_2N_4O_6S_8$	$C_{16}H_{12}Ag_2F_6N_2O_6S_{10}$
Molecular weight	804.50	978.62
Crystal dimensions (mm)	$0.50 \times 0.10 \times 0.10$	$0.50 \times 0.10 \times 0.10$
Temperature (K)	153(2)	253(2)
Crystal system	orthorhombic	monoclinic
Space group	$P2_12_12$	$C2$
Unit cell dimensions		
a (Å)	14.214(5)	22.395(3)
b (Å)	16.048(5)	5.7611(4)
c (Å)	5.310(5)	11.5488(13)
β (°)	90.000(0)	91.371(14)
U (Å^3)	1211.2(13)	1489.6(3)
Z	2	2
Density calc. (g cm^{-3})	2.206	2.182
Absorption coefficient (mm^{-1})	2.348	2.091
R_{int}	0.0529	0.0429
Measured reflections	6262	5921
Independent reflections	2039	2799
Reflections with $I > \sigma(I)$	1567	1951
R_1 (observed)	0.0823	0.0535
wR_2 (all data)	0.2266	0.1384
Goodness-of-fit	0.996	0.918

Table 2
Selected bond lengths (Å) and angles (°) for **1**

Bond lengths	
S(1)–C(1)	1.748(15)
S(2)–C(3)	1.755(17)
S(3)–Ag(1)	2.756(5)
C(1)–C(4)	1.41(2)
C(4)–C(4)^{i}	1.40(4)
Ag(1)–O(3)	2.577(12)
S(1)–C(2)	1.772(15)
C(2)–C(3)	1.30(2)
S(4)–C(3)	1.735(17)
C(4)–C(5)	1.44(2)
Ag(1)–N(1)^{ii}	2.368(13)
Ag(1)–O(1)	2.604(11)
S(2)–C(1)	1.711(13)
S(3)–C(2)	1.772(18)
S(4)–Ag(1)	2.792(5)
C(5)–N(1)	1.16(2)
Ag(1)–O(2)^{iii}	2.493(16)
Bond angles	
S(1)–C(1)–S(2)	114.3(8)
C(1)–C(4)–C(5)	113.3(16)
S(3)–Ag(1)–S(4)	74.20(14)
S(4)–Ag(1)–N(1)^{ii}	156.3(4)
S(1)–C(1)–C(4)	122.9(11)
C(1)–C(4)–C(4)^{i}	120.7(15)
S(3)–Ag(1)–N(1)^{ii}	84.0(4)
O(2)^{iii} –Ag(1)–N(1)^{ii}	102.3(5)
S(2)–C(1)–C(4)	122.8(12)
C(4)–C(5)–N(1)	179.6(19)
S(4)–Ag(1)–O(2)^{iii}	97.6(3)
N(1)^{ii}–Ag(1)–O(3)	107.6(5)

Symmetry transformations used to generate equivalent atoms: (i) $-x-1, -y-1, z$; (ii) $x-1/2, -y-1/2, -z-1$; (iii) $x, y, z-1$.

nitrate ion in a chelating mode and one oxygen atom of a bridging nitrate ion in a monodentate manner. The average bond distances of Ag–S, Ag–N and Ag–O are 2.774(5), 2.368(13) and 2.558(14) Å, respectively. The greatest deviation from idealized octahedral geometry around the silver ion is observed for the nitrogen and sulfur atoms of ligand, N(1)^{ii}–Ag(1)–S(4) 156.3 (4)° (see Table 2).

Each ligand **L** coordinates four Ag(I) ions, on one side through its sulfur atoms in a chelating mode and on the other side through its nitrogen atoms of the two nitrile groups. Thereby, as illustrated in Fig. 2, an extended coordination network in two dimensions is formed which contains loops of four half **L** molecules and four Ag(I) ions. Furthermore, these 2D networks are interlinked by bridging nitrates through Ag–O–N–O–Ag bonds leading to a Ag···Ag non-bonding distance of 5.31 Å. Overall, due to these bridging NO_3^- anions, a 3D coordination network is generated. Within this network, the shortest S···S distance between the neighboring layers is 5.31 Å, hence significantly longer than the van der Waals radius sum (3.70 Å) [13]. Consequently, the S···S interaction between the neighboring 2D layers is negligible.

Table 3
Selected bond lengths (Å) and angles (°) for **2**

Bond lengths	
S(1)–C(1)	1.722(12)
S(2)–C(3)	1.702(13)
S(4)–C(3)	1.766(11)
Ag(1)–O(1)^{i}	2.419(7)
Ag(1)–O(1)	2.508(8)
Ag(1)–O(2)^{iii}	2.515(7)
S(1)–C(2)	1.772(10)
C(2)–C(3)	1.358(15)
S(3)–Ag(1)	2.581(3)
C(1)–C(4)	1.392(15)
C(4)–C(4)^{ii}	1.461(19)
S(2)–C(1)	1.745(8)
S(3)–C(2)	1.726(11)
S(4)–Ag(1)	2.771(3)
C(4)–C(5)	1.423(16)
C(5)–N(1)	1.117(14)
Bond angles	
S(1)–C(1)–S(2)	114.6(6)
C(1)–C(4)–C(5)	116.5(9)
C(2)–S(3)–Ag(1)	98.7(3)
S(3)–Ag(1)–O(2)^{iii}	90.5(2)
S(3)–Ag(1)–O(1)^{i}	143.5(2)
O(1)–Ag(1)–O(1)^{i}	95.88(18)
S(1)–C(1)–C(4)	122.0(7)
C(1)–C(4)–C(4)^{ii}	121.3(8)
C(3)–S(4)–Ag(1)	95.4(4)
O(1)^{i}–Ag(1)–O(2)^{iii}	77.0(3)
S(4)–Ag(1)–O(1)^{i}	104.2(2)
S(4)–Ag(1)–O(1)	108.0(2)
S(2)–C(1)–C(4)	123.4(9)
C(4)–C(5)–N(1)	178.9(13)
S(3)–Ag(1)–S(4)	76.98(8)
S(3)–Ag(1)–S(4)	76.98(8)
S(3)–Ag(1)–O(1)	118.84(7)

Symmetry transformations used to generate equivalent atoms: (i) $-x-1/2, y+1/2, -z$; (ii) $-x, y, -z+1$; (iii) $x, y+1, z$.

3.2. Structure of complex $[Ag_2(L)(CF_3SO_3)_2]_n$ (2)

In order to evaluate the influence of counterions on the coordination behaviour, $AgCF_3SO_3$ was used instead of $AgNO_3$ in the reaction with **L**, whereby a new complex (**2**) was obtained. On the one hand, $CF_3SO_3^-$

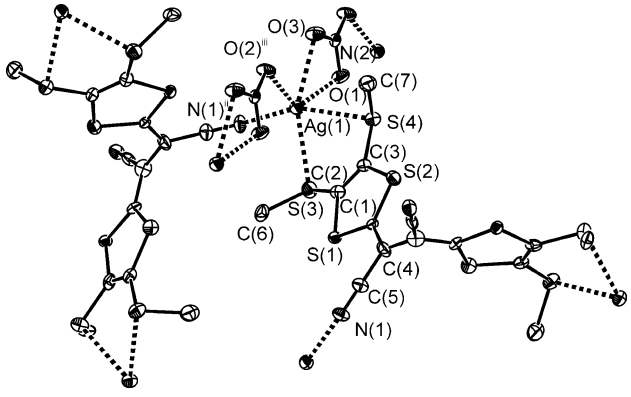


Fig. 1. ORTEP plot (50% probability ellipsoids) showing the Ag(I) coordination sphere of **1**.

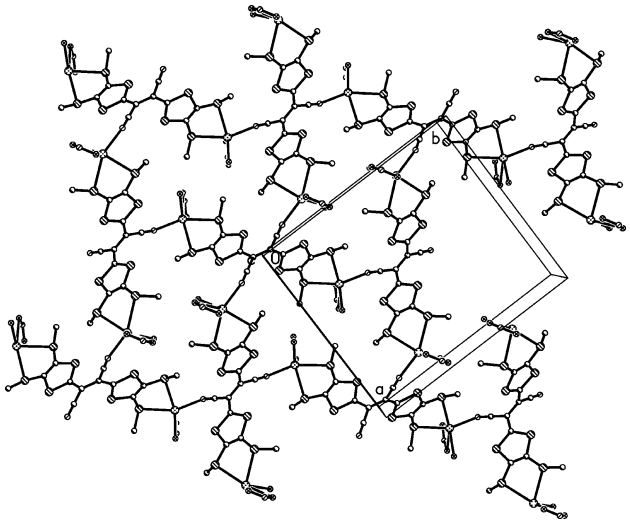


Fig. 2. *ab* projection of the crystal structure of **1**, elucidating the 2D coordination network formed by the $[Ag_2L]$ fragments.

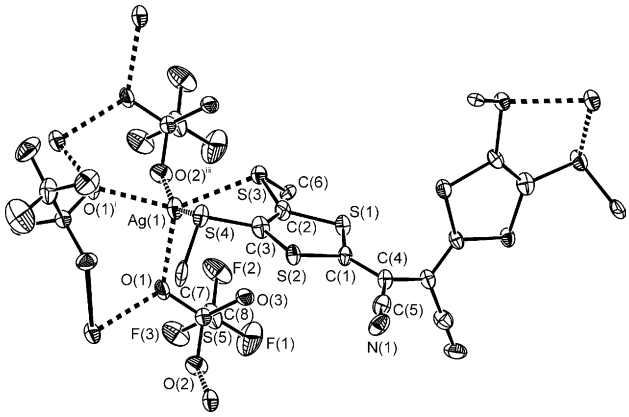


Fig. 3. ORTEP plot (50% probability ellipsoids) showing the Ag(I) coordination sphere of **2**.

is larger than NO_3^-, and on the other hand, its oxygen atoms have a stronger coordination ability than those of NO_3^- [14]. The compound crystallizes in a monoclinic space group (*C*2), again with a metal to ligand stoichiometry of 2:1. Interestingly, as shown in Fig. 3, the silver ions which are bonded to the sulfur atoms of **L** are only bridged by triflate ions and no more coordinated to the nitrogen atoms of the nitrile groups. Specifically, the coordination geometry around the silver ion is distorted square pyramidal with an O_3S_2 coordination sphere. The degree of distortion from the idealized square-pyramidal can be estimated from the geometric parameter τ [15]. If O(1) is chosen as the axial donor atom, α and β are 143.5° and 160.4°, respectively, leading to a τ value of 0.29. The average bond distances of Ag–S and Ag–O are 2.676(3) Å, 2.481(8) Å, respectively (see Table 3), which are distinctly shorter than those of complex **1**.

As illustrated in Fig. 4, **L** adopts a bis-bidentate bonding mode to Ag(I) ions through its sulfur atoms and furthermore, via the bidentate bridging triflate anions, an extended two-dimensional coordination network is formed. Obviously, the nitrile groups of **L** are non-coordinating. The neighboring ligands **L** are parallel to each other with interplanar distances larger than 5.76 Å, indicating that there are no close S···S interactions in **2**, either.

In a systematic investigation of the role of counterions in Ag(I) complexes, it has been concluded that a variety of anions can influence the coordination modes of ligands [16,17]. In the present systems, the NO_3^-

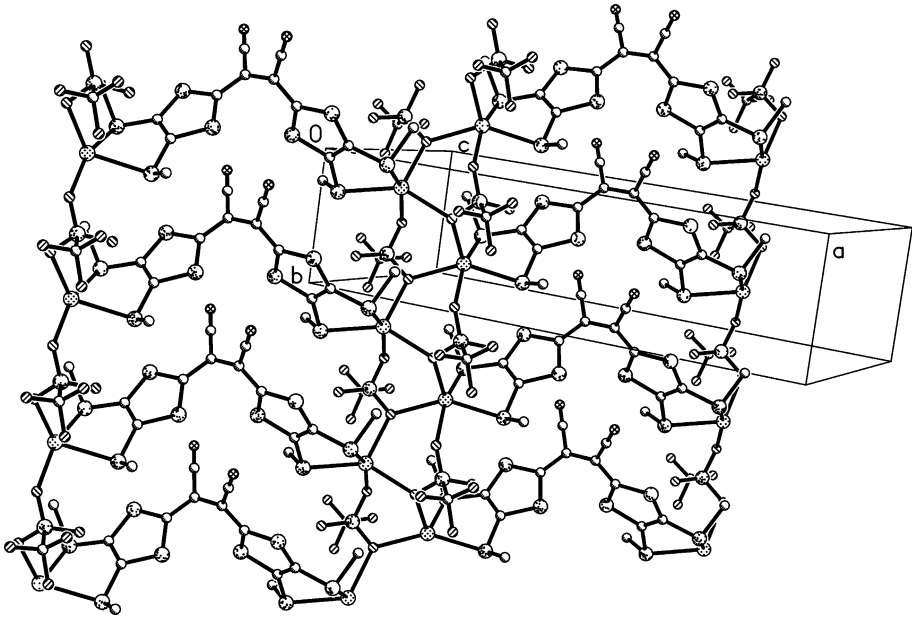


Fig. 4. Perspective view of the undulating 2D coordination network in **2** exhibiting a fragment of one layer.

anion plays a bidentate bridging role in the formation of **1**, so **L** acts as a hexadentate bridging ligand. However, in the case of **2**, the $CF_3SO_3^-$ anion has stronger coordination ability with its oxygen atoms toward Ag(I), thus the ligand **L** takes a bis-bidentate bonding mode with two nitrile groups remaining non-coordinating to Ag(I). In general, the structural differences between **1** and **2** show the profound effect of anions on the framework formation of silver coordination complexes, which nicely reflects their differences in size and coordination strength.

4. Conclusions

In conclusion, in this report we present two new silver complexes **1** and **2** with different structural topologies. In both networks, the bridging of counterions (NO_3^- and $CF_3SO_3^-$) extends the coordination network to 3D and 2D, respectively. The structures, therefore, illustrate how metal coordination assembly in the solid state may be influenced significantly not only by the nature of the counterion, but also by the topicity of the ligand.

Acknowledgement

This work was supported by the SNF programme (Grant No. 200021–100432).

Appendix A. Supplementary data

Crystallographic data for the structures reported in this paper have been deposited with the Cambridge Crystallographic Data Centre, CCDC Nos. 271520 and 271521 for compounds **1** and **2**. Copies of the data can be obtained free of charge on application to CCDC, 12 Union Road, Cambridge CB2 1EZ, UK (fax: +44 1223 336033; e-mail: deposit@ccdc.cam.ac.uk). Supplementary data associated with this article can be found, in the online version, at doi:10.1016/j.poly.2005.06.023.

References

[1] (a) P.J. Stang, B. Olenyuk, Acc. Chem. Res. 30 (1997) 502;
(b) M. Fujita, S.Y. Yu, T. Kusukawa, H. Funaki, K. Ogura, K. Yamaguchi, Angew. Chem. Int. Ed. 37 (1998) 2082;
(c) R. Vilar, D.M.P. Mingos, A.J.P. White, D.J. Williams, Angew. Chem. Int. Ed. 37 (1998) 1258;
(d) M. Scherer, L.D. Caulder, D.W. Johnson, K.N. Raymond, Angew. Chem. Int. Ed. 38 (1999) 1578;
(e) M. Aoyagi, K. Biradha, M. Fujita, J. Am. Chem. Soc. 121 (1999) 7457;
(f) M. Schweiger, S.R. Seidel, M. Schmitz, P.J. Stang, Org. Lett. 2 (2000) 1255;
(g) M. Fujita, K. Umemoto, M. Yoshizawa, N. Fujita, T. Kusukawa, K. Biradha, Chem. Commun. (2001) 509;
(h) S.R. Seidel, P.J. Stang, Acc. Chem. Res. 35 (2002) 972;
(i) A. Hori, A. Akasaka, K. Biradha, S. Sakamoto, K. Yamaguchi, M. Fujita, Angew. Chem. Int. Ed. 41 (2002) 3269;
(j) K.-M. Park, S.-Y. Kim, J. Heo, D. Whang, S. Sakamoto, K. Yamaguchi, K. Kim, J. Am. Chem. Soc. 124 (2002) 2140;
(k) O.V. Dolomanov, A.J. Blake, N.R. Champness, M. Schroeder, C. Wilson, Chem. Commun. (2003) 682;
(l) A. Pop, M.O. Vysotsky, M. Saadioui, V. Boehmer, Chem. Commun. (2003) 1124;
(m) C. Schmuck, Angew. Chem. Int. Ed. 42 (2003) 2448;
(n) C.-Y. Su, Y.-P. Cai, C.-L. Chen, M.D. Smith, W. Kaim, H.-C. zur Loye, J. Am. Chem. Soc. 125 (2003) 8595;
(o) L. Öhrström, K. Larsson, J. Chem. Soc., Dalton Trans. (2004) 347;
(p) O.V. Dolomanov, D.B. Cordes, N.R. Champness, A.J. Blake, L.R. Hanton, G.B. Jameson, M. Schroeder, C. Wilson, Chem. Commun. (2004) 642;
(q) I.M. Müller, D. Möller, Eur. J. Inorg. Chem. 2 (2005) 257.

[2] (a) J.Y. Lu, Coord. Chem. Rev. 246 (2003) 327;
(b) F.M. Tabellion, S.R. Seidel, A.M. Arif, P.J. Stang, J. Am. Chem. Soc. 123 (2001) 7740;
(c) T. Kawano, J. Kuwana, C.-X. Du, I. Ueda, Inorg. Chem. 41 (2002) 4078;
(d) M. Barboiu, G. Vaughan, R. Graff, J.-M. Lehn, J. Am. Chem. Soc. 125 (2003) 10257;
(e) A. Hori, H. Kataoka, T. Okano, S. Sakamoto, K. Yamaguchi, M. Fujita, Chem. Commun. (2003) 182;
(f) T. Yamaguchi, S. Tashiro, M. Tominaga, M. Kawano, T. Ozeki, M. Fujita, J. Am. Chem. Soc. 126 (2004) 10818;
(g) J.C. Chambron, J.P. Collin, V. Heitz, D. Jouvenot, J.M. Kern, P. Mobian, D. Pomeranc, J.P. Sauvage, Eur. J. Org. Chem. 8 (2004) 1627.

[3] (a) C. Janiak, Dalton Trans. (2003) 2781;
(b) S.L. James, Chem. Soc. Rev. 32 (2003) 276;
(c) M. Eddaoudi, J. Kim, D. Vodak, A. Sudik, J. Wachter, M. O'Keeffe, O.M. Yaghi, Proc. Natl. Acad. Sci. USA (PNAS) 99 (2002) 4900;
(d) S.-L. Zheng, X.-M. Chen, Aust. J. Chem. 57 (2004) 703;
(e) D. Maspoch, D. Ruiz-Molina, J. Veciana, J. Mater. Chem. 14 (2004) 2713;
(f) S.R. Batten, K.S. Murray, Coord. Chem. Rev. 246 (2003) 103;
(g) L. Carlucci, G. Ciani, D.M. Proserpio, Coord. Chem. Rev. 246 (2003) 247.

[4] (a) C.-Y. Su, Y.-P. Cai, C.-L. Chen, M.D. Smith, W. Kaim, H.-C. Zur Loye, J. Am. Chem. Soc. 125 (2003) 8595;
(b) R.-Q. Zou, J.-R. Li, Y.-B. Xie, R.-H. Zhang, X.-H. Bu, Cryst. Growth Des. 4 (2004) 79.

[5] (a) R. Vilar, D.M.P. Mingos, A.J.P. White, D.J. Williams, Angew. Chem. Int. Ed. 37 (1998) 1258;
(b) R.D. Schnebeck, E. Freisinger, B. Lippert, Angew. Chem. Int. Ed. 38 (1999) 168;
(c) M. Scherer, D.L. Caulder, D.W. Johnson, K.N. Raymond, Angew. Chem. Int. Ed. 38 (1999) 1587;
(d) X.-H. Bu, W. Chen, W.-F. Hou, M. Du, R.-H. Zhang, F. Brisse, Inorg. Chem. 41 (2002) 3477;
(e) N. Schultheiss, D.R. Powell, E. Bosch, Inorg. Chem. 42 (2003) 8886.

[6] C.Y. Jia, S-X. Liu, A. Neels, S. Decurtins, Synthesis, in press.

[7] (a) I. Ino, J.C. Zhong, M. Munakata, T. Kuroda-Sowa, M. Maekawa, Y. Suenaga, Y. Kitamori, Inorg. Chem. 39 (2000) 4273;
(b) O.M. Yaghi, H. Li, J. Am. Chem. Soc. 118 (1996) 295.

[8] (a) X.-H. Bu, Y.-B. Xie, J.-R. Li, R.-H. Zhang, Inorg. Chem. 42 (2003) 7422;

(b) K.A. Hirsch, S.R. Wilson, J.S. Moore, Inorg. Chem. 36 (1997) 2960.
[9] Stoe, Cie, IPDS Software, Stoe & Cie GmbH, Darmstadt, Germany, 2000.
[10] G.M. Sheldrick, Acta Crystallogr. A 46 (1990) 467.
[11] G. Sheldrick, SHELXL-97 Program for crystal structure refinement, Universität Göttingen, Göttingen, Germany.
[12] A.L. Spek, J. Appl. Cryst. 36 (2003) 7.
[13] S.-X. Liu, A. Neels, H. Stoeckli-Evans, M. Pilkington, J.D. Wallis, S. Decurtins, Polyhedron 23 (2004) 1185.
[14] (a) L. Carlucci, G. Ciani, D.M. Proserpio, A. Sironi, J. Am. Chem. Soc. 117 (1995) 4562;
(b) L. Carlucci, G. Ciani, D.M. Proserpio, A. Sironi, Inorg. Chem. 34 (1995) 5698;
(c) K.A. Hirsch, S.R. Wilson, J.S. Moore, Inorg. Chem. 36 (1997) 2960.
[15] A.W. Addison, T. Nageswara Rao, J. Reedijk, J. van Rijn, G.C. Verschoor, J. Chem. Soc. Dalton Trans. (1984) 1349.
[16] (a) K.A. Hirsch, S.R. Wilson, J.S. Moore, J. Am. Chem. Soc. 119 (1997) 10401;
(b) D. Venkataraman, S. Lee, J.S. Moore, P. Zhang, K.A. Hirsch, G.B. Gardner, A.C. Covey, C.L. Prentice, Chem. Mater. 8 (1996) 2030.
[17] (a) H.-P. Wu, C. Janiak, G. Rheinwald, H. Lang, J. Chem. Soc., Dalton Trans. 2 (1999) 183;
(b) M.A. Withersby, A.J. Blake, N.R. Champness, P. Hubberstey, W.-S. Li, M. Schröder, Angew. Chem. Int. Ed. Engl. 36 (1997) 2327;
(c) C. Janiak, L. Uehlin, H.-P. Wu, P. Klüfers, H. Piotrowski, T.G. Scharmann, J. Chem. Soc., Dalton Trans. 17 (1999) 3121;
(d) F. Bodar-Houillon, T. Humbert, A. Marsura, J.-B. Regnouf de Vains, O. Dusausoy, N. Bouhmaida, N.E. Ghermani, Y. Dusausoy, Inorg. Chem. 34 (1995) 5205.

2. Experimental

2.1. General

All operations were performed using standard Schlenk line and drybox techniques under an inert atmosphere of nitrogen. THF, toluene, and *n*-hexane were dried by standard methods and degassed prior to use. Benzene-d_6 and toluene-d_8 were dried over Na and distilled under argon. $[U(Tp^{Me2})_2I]$ [6], $[U(Tp^{Me2})_2NPh_2]$ [5] and $[U(Tp^{Me2})_2N(SiMe_3)_2]$ [5] were synthesized by reported methods. HOC_6H_2-2,4,6-Me_3 and 3,5-dimethylpyrazole were sublimed prior to use and the corresponding potassium salts were prepared by reacting a small excess of KH with the appropriate reagents in THF. Phenylacetylene was dried over activated molecular sieves and trap-to-trap distilled before use. Me_3SiBr was trap-to-trap distilled before use and Me_3SnCl (Aldrich) was used without further purification. CpH was obtained by cracking of dicyclopentadiene and the sodium salt was prepared by reaction with a stoichiometric amount of sodium metal in THF. ^1H NMR spectra were recorded on Varian INOVA-300 spectrometer and referenced internally using the residual solvent resonances relative to tetramethylsilane (benzene-d_6, 7.15 ppm, toluene-d_8, 2.09 ppm). IR spectra were recorded on a Perkin–Elmer 577 spectrometer. UV–Vis–near-IR spectra were recorded on a Varian Cary 5G spectrophotometer using 1 cm quartz cells. Carbon, hydrogen and nitrogen analyses were performed in-house using a EA110 CE Instruments automatic analyzer.

2.2. Synthesis

2.2.1. $[U(Tp^{Me2})_2(OC_6H_2$-2,4,6-$Me_3)]$ (**1**)

(a) A solution of HOC_6H_2-2,4,6-Me_3 (10 mg, 0.074 mmol) in toluene was slowly added, at room temperature, to a solution of $[U(Tp^{Me2})_2N(SiMe_3)_2]$ (73 mg, 0.074 mmol) in the same solvent. After stirring overnight, the solvent was removed under vacuum. The dark red solid residue was washed with *n*-hexane and dried under vacuum. Yield: 56% (40 mg, 0.041 mmol). Dark red crystals of **1**, suitable for X-ray diffraction, were grown by recrystallization from a THF/hexane solution.

Anal. Calc. for $C_{39}H_{55}N_{12}B_2OU$: C, 48.41; H, 5.73; N, 17.37. Found: C, 49.46; H, 5.51; N, 17.63. IR (Nujol, cm^{-1}): ν(B–H) 2550. UV–Vis–near-IR (in THF, nm): 529, 668, 899. ^1H NMR (C_6D_6, 20 °C): δ: 21.35 (2H, s, 4-*H*), 20.84 (2H, s, 4-*H*), 18.14 (6H, s, CH_3), 15.79 (6H, s, CH_3), 10.02 (3H, br, H_p), 8.47 (6H, br, H_m), 3.34 (6H, s, CH_3), 2.91 (6H, s, CH_3), −2.30 (6H, s, CH_3), −7.71 (6H, s, CH_3), −9.44 (2H, s, 4-*H*), −55.88 (6H, br, H_o).

(b) A solution of $K(OC_6H_2$-2,4,6-$Me_3)$ (29 mg, 0.16 mmol) in THF was slowly added to a solution of $[U(Tp^{Me2})_2I]$ (157 mg, 0.16 mmol) in the same solvent, at room temperature. After stirring overnight, the white precipitate of KI was filtered off and the solution was evaporated to dryness. The dark red solid residue was washed with *n*-hexane and vacuum-dried. Yield: 84% (130 mg, 0.13 mmol).

2.2.2. $[U(Tp^{Me2})_2(dmpz)]$ (**2**)

A solution of K(3,5-Me_2pz) (18 mg, 0.14 mmol) in THF was slowly added to a solution of $[U(Tp^{Me2})_2I]$ (139 mg, 0.14 mmol) in the same solvent, at room temperature. There was immediate formation of an emerald green mixture. After stirring overnight, the mixture was centrifuged to remove the white precipitate of KI and the solvent was removed under vacuum. Crystallization of the residue from a saturated solution of *n*-hexane yielded an emerald green solid with a yield of 54%. (70 mg, 0.075 mmol). Green crystals, suitable for X-ray diffraction analysis, were obtained by slow concentration of a hexane solution. *Anal*. Calc. for $C_{35}H_{51}N_{14}B_2U$: C, 45.32; H, 5.54; N, 21.14. Found: C, 44.54; H, 5.37; N, 20.75. IR (Nujol, cm^{-1}): ν(B–H) 2500. UV–Vis–near-IR (in THF, nm): 566, 643, 682 (sh), 861, 936, 1039(sh), 1145(sh), 1191, 1240, 1274, 1302(sh). ^1H NMR (C_7D_8, 20 °C): δ 29.49 (1H, s, 4-*H* (dmpz)), 6.98 (6H, s, CH_3(dmpz)), 5.0 (6H, vbr, 4-*H*), 0.18 (6H, s, CH_3). ^1H NMR (C_7D_8, −70 °C): δ 38.74 (1H, s, 4-*H* (dmpz)), 12.78 (6H, s, 3-CH_3), 12.35 (2H, s, 4-*H*), 10.62 (6H, s, CH_3(dmpz)), 9.93 (2H, s, 4-*H*), 7.61 (2H, s, 4-*H*), 3.78 (6H, s, 5-CH_3), −1.07 (6H, s, 5-CH_3), −1.81 (6H, s, 5-CH_3), −21.23 (6H, s, 3-CH_3), −49.99 (6H, s, 3-CH_3).

2.2.3. $[U(Tp^{Me2})_2(2$-$SC_5H_4N)]$ (**3**)

Slow addition of a solution of HSC_5H_4N (17 mg, 0.15 mmol) in THF to a solution of $[U(Tp^{Me2})_2N(SiMe_3)_2]$ (148 mg, 0.15 mmol) in the same solvent resulted in a color change from brown to emerald green. Stirring was maintained for 18 h. Removal of the solvent under vacuum gave an emerald green compound that was further washed with hexane. Yield: 69% (96 mg, 0.10 mmol). An analytically pure compound was obtained by concentration of a THF solution. *Anal*. Calc. for $C_{35}H_{48}N_{13}SB_2UOC_4H_8$: C, 46.17; H, 5.56; N, 17.95. Found: C, 46.11; H, 5.28; N, 17.95. IR (Nujol, cm^{-1}): ν(B–H) 2556. UV–Vis–near-IR (in THF, nm): 576, 633, 778, 949, 936, 1053, 1130, 1247, 1281. ^1H NMR (C_6D_6, 20 °C): δ 40.28 (1H, s, SC_5H_4N) 17.77 (1H, t, SC_5H_4N), 16.72 (1H, d, SC_5H_4N), 13.17 (1H, d, SC_5H_4N), 10.71 (1H, s, 4-*H*), 9.17 (1H, s, 4-*H*), 9.02 (1H, s, 4-*H*), 8.38 (1H, s, 4-*H*), 7.97 (3H, s, CH_3), 6.62 (3H, s, CH_3), 3.96 (1H, s, 4-*H*), 3.57 (4H, m, THF), 2.37 (3H, s, CH_3), 2.22 (3H, s, CH_3), 2.09 (1H, s, 4-*H*), 1.40 (4H, m, THF), 1.15 (3H, s, CH_3), −0.77 (3H, s, CH_3), −1.59 (3H, s, CH_3), −1.84 (3H, s, CH_3), −11.31 (3H, s, CH_3), −12.47 (3H, s, CH_3), −25.70 (3H, s, CH_3), −27.06 (3H, s, CH_3).

2.2.4. [U(Tp^{Me2})$_2$(CCPh)] (4)

A mixture of [U(Tp^{Me2})$_2$I] (169 mg, 0.18 mmol) and HC≡CPh (37 μL, 0.36 mmol) in toluene was stirred with sodium amalgam 0.5% (8 mg, 0.36 mmol) at room temperature for 20 h. During this time the colour of the mixture gradually changed from dark purple to dark green. The solution was then separated from Hg and sodium iodide by centrifugation, evaporated to dryness and the resulting dark green residue was washed several times with *n*-hexane. Yield: 41% (69 g, 0.07 mmol). *Anal.* Calc. for $C_{38}H_{49}N_{12}B_2U$: C, 48.89; H, 5.29; N, 18.00. Found: C, 48.64; H, 5.31; N, 17.38. IR (Nujol, cm^{-1}): *ν*(B–H) 2554, *ν*(C≡C) 2049. UV–Vis–near-IR (in toluene, nm): 513, 541, 666, 860, 941, 1066(sh), 1132(sh), 1191, 1255. ^{1}H NMR (C_6D_6, 20 °C): *δ* 20.92 (2H, d, H_o), 13.47 (1H, t, H_p), 10.15 (2H, t, H_m), 7.47 (6H, s, 4-*H*), 0.59 (18H, s, CH_3), −13.64 (18H, s, CH_3).

2.2.5. [U(Tp^{Me2})$_2$Cl] (5)

A solution of Me_3SnCl (38 mg, 0.19 mmol) in THF was slowly added to a solution of [U(Tp^{Me2})$_2$N(SiMe$_3$)$_2$] (158 mg, 0.16 mmol) in the same solvent. The mixture was stirred for 18 h at room temperature, during which time the colour gradually turned from brown to dark blue. After centrifugation the solution was evaporated to dryness. The resulting violet solid was further washed with *n*-hexane and vacuum dried. Yield: 78% (108 mg, 0.12 mmol). *Anal.* Calc. for $C_{30}H_{44}N_{12}B_2ClU$: C, 41.52; H, 5.11; N, 19.37. Found: C, 42.25; H, 5.27; N, 19.50. IR (Nujol, cm^{-1}): *ν*(B–H) 2557. UV–Vis–near-IR (in THF, nm): 578, 634(sh), 820, 938(sh), 1033, 1104, 1192, 1239, 1266. ^{1}H NMR (C_6D_6, 20 °C): *δ*: 9.8 (2H, br, B–*H*), 7.71 (6H, s, 4-*H*), 1.18 (18H, s, CH_3), −14.97 (18H, s, CH_3).

2.2.6. [U(Tp^{Me2})$_2$Br] (6)

Compound **6** was synthesized as described for **5** by using 22 μL (0.17 mmol) of Me_3SiBr and 167 mg (0.17 mmol) of [U(Tp^{Me2})$_2$N(SiMe$_3$)$_2$]. Compound **6** was obtained as a violet solid with a yield of 88% (136 mg, 0.15 mmol). *Anal.* Calc. for $C_{30}H_{44}N_{12}B_2BrU$: C, 39.50; H, 4.86; N, 18.42. Found: C, 39.02; H, 4.69; N, 18.11. IR (Nujol, cm^{-1}): *ν*(B–H) 2556. UV–Vis–near-IR (in THF, nm): 573, 639(sh), 809, 943(sh), 1040, 1114, 1198, 1243, 1269. ^{1}H NMR (C_6D_6, 20 °C): *δ*: 9.3 (2H, vbr, B–*H*), 7.72 (6H, s, 4-*H*), 1.01 (18H, s, CH_3), −14.21 (18H, s, CH_3).

2.2.7. [U(Tp^{Me2})$_2$(Cp)] (7)

A suspension of NaCp (20 mg, 0.23 mmol) in toluene was slowly added to a solution of [U(Tp^{Me2})$_2$I] (222 mg, 0.23 mmol) in the same solvent, at room temperature. There was immediate formation of a dark green mixture. After stirring for 3 h, the mixture was centrifuged to separate the white precipitate of KI. The solvent was removed under vacuum and the resultant dark green solid was washed with *n*-hexane and vacuum dried. Yield: 76% (156 mg, 0.17 mmol). *Anal.* Calc. for $C_{35}H_{49}N_{12}B_2U$: C, 46.84; H, 5.50; N, 18.73. Found: C, 46.95; H, 5.85; N, 18.84. IR (Nujol, cm^{-1}): *ν*(B–H) 2540, 2524 sh, 2360, 2336. UV–Vis–near-IR (in toluene, nm): 560, 598, 632, 661(sh), 732, 793, 937, 1054, 1094, 1116 (sh), 1196, 1263 e 1291 (sh). ^{1}H NMR (C_6D_6, 20 °C): *δ* 19.45 (1H, s, 4-*H*), 10.46 (3H, s, CH_3), 6.83 (1H, s, 4-*H*), 5.98 (3H, s, CH_3), 3.18 (3H, s, CH_3), 3.03 (2H, s, 4-*H*), 0.58 (2H, s, 4-*H*), −1.14 (3H, s, CH_3), −2.24 (6H, s, CH_3), −3.17 (6H, s, CH_3), −3.93 (5H, s, C_5H_5), −6.52 (6H, s, CH_3), −27.89 (6H, s, CH_3).

2.2.8. Thermolysis of [U(Tp^{Me2})$_2$Cp] (7)

[U(Tp^{Me2})$_2$Cp] (200 mg, 0.29 mmol) was placed in a pyrex tube and heated under vacuum at 160 °C for three days. The colour of the green cyclopentadienyl compound changed gradually to brown. During this change, golden and transparent crystals sublimed on the wall of the tube. The crystals were characterized by X-ray diffraction analysis as being [UCp$_3$(dmpz)] (**8**) and 4,8(dihydro)4,8(dipyrazolyl)pyrazabole (**9**), respectively. The structure of **8** was similar to that reported by Raymond [7] for [UCp$_3$(pz)]. Elemental analysis and the NMR spectrum of the brown solid remaining in the bottom of the pyrex tube were consistent with the formulation of the compound as being [U(Tp^{Me2})(dmpz)$_3$] (**10**). *Anal.* Calc. for $C_{30}H_{43}N_{12}BU$: C, 43.91; H, 5.28; N, 20.48. Found: C, 44.79; H, 5.40; N, 19.87. IR (Nujol, cm^{-1}): *ν*(B–H) 2521. UV–Vis–near-IR (in toluene, nm): 488, 529 (sh), 565 (sh), 611 (w), 675, 693, 872 (br), 1067, 1163, 1209(sh).^{1}H NMR (C_6D_6, 20 °C): *δ* 14.48 (3H, 4-*H* (dmpz)), 7.02 (3H, 4-*H*), 2.23 (9H, 5-CH_3), 0.01 (18H, CH_3 (dmpz)), −8.38 (9H, 3-CH_3).

2.3. X-ray crystallographic analysis

Dark red crystals of **1** were grown from a THF solution layered with *n*-hexane. Green crystals of **2** were grown from a concentrated *n*-hexane solution. Dark blue crystals of **5** were obtained from slow diffusion of *n*-pentane into a toluene solution at 4 °C. The crystals were immersed in Nujol and mounted in thin-walled glass capillaries in a nitrogen filled glove-box. Data were collected at room temperature on an Enraf-Nonius CAD4-diffractometer, with graphite-monochromated Mo Kα radiation, using the *ω*–2*θ* scan technique. The data were corrected [8] for Lorentz and polarization effects, for linear decay and empirically for absorption by Ψ scans. Table 1 summarizes the crystallographic data. The structures were solved by Patterson methods [9] and successive difference Fourier techniques, and refined by full-matrix least squares refinement on F^2 using SHELXL-97 [10]. All the non-hydrogen atoms were refined with anisotropic thermal motion parameters, and the contributions of the hydrogen atoms were included at

Table 1
Crystallographic data for complexes **1**, **2** and **5**

Formula	$C_{39}H_{55}B_2N_{12}OU$	$C_{35}H_{51}B_2N_{14}U$	$C_{30}H_{44}B_2N_{12}ClU$
Formula weight	967.60	927.55	867.87
Crystal system	monoclinic	monoclinic	orthorhombic
Space group	$P2_1/n$	$P2_1/c$	$Pc2_1n$
a (Å)	11.713(2)	18.589(7)	10.3682(12)
b (Å)	14.7770(15)	13.558(2)	18.596(4)
c (Å)	25.012(3)	18.703(5)	18.678(3)
β (°)	97.005(15)	118.83(2)	
V (Å^3)	4296.9(9)	4129(2)	3601.2(10)
Z	4	4	4
D_{calc} (g cm^{-3})	1.496	1.492	1.601
Reflections measured	7324	8278	4274
Unique reflections [R_{int}]	6942(0.0968)	8011(0.0479)	4034(0.0546)
Observed [$I > 2\sigma(I)$]	3449	4540	2250
Number of parameters	496	470	415
R_1[a]	0.0913	0.0838	0.0607
wR_2[a]	0.1386	0.1772	0.0985

[a] The values were calculated for data with $I > 2\sigma(I)$.

calculated positions. Atomic scattering factors and anomalous dispersion terms were taken from [9]. The illustrations were made with ORTEP-3 [11].

3. Results and discussion

3.1. Synthesis

Reaction of $[U(Tp^{Me2})_2N(SiMe_3)_2]$ with HOC_6H_2-2,4,6-Me_3, 3,5-dimethylpyrazole (Hdmpz), 2-mercaptopyridine (HSC_5H_4N) or HCCPh resulted in formation of dark red $[U(Tp^{Me2})_2(OC_6H_2$-2,4,6-$Me_3)]$ (**1**), bright-green $[U(Tp^{Me2})_2(dmpz)]$ (**2**) and $[U(Tp^{Me2})_2(SC_5H_4N)]$ (**3**), and green $[U(Tp^{Me2})_2(CCPh)]$ (**4**), mixed with $HN(SiMe_3)_2$ (Eq. (1))

$$[U(Tp^{Me2})_2N(SiMe_3)_2] + HX \rightarrow [U(Tp^{Me2})_2X] + HN(SiMe_3)_2 \quad (1)$$

where X = OC_6H_2-2,4,6-Me_3, **1**; X = dmpz, **2**; X = SC_5H_4N, **3**; X = CCPh, **4**.

The compounds could be also obtained by protonolysis of $[U(Tp^{Me2})_2NPh_2]$ (NMR experiments), with the exception of compound **4**, as addition of HCCPh to the amidouranium compound resulted in recovery of the starting material.

The amine formed in the above reactions was removed by washing the solid products with *n*-hexane. This procedure is satisfactory except for compound **2** that was obtained in low yield due to its high solubility in hexane. It was found more convenient to prepare this compound by simple halide metathesis of $[U(Tp^{Me2})_2I]$ with K(dmpz). The synthesis of **4** by the acid–base reaction proved to be somewhat unreliable and was found to be accompanied by formation of significant amounts of unidentified side products as shown by ^{1}H NMR spectroscopy. The best route for $[U(Tp^{Me2})_2(CCPh)]$ proved to be the one pot reaction of $[U(Tp^{Me2})_2I]$ [6] with HCCPh in the presence of sodium amalgam or simply sodium metal.

The amido precursor, $[U(Tp^{Me2})_2N(SiMe_3)_2]$, also proved to be a convenient starting material for the synthesis of $[U(Tp^{Me2})_2X]$ complexes (X = halide). Reaction with Me_3SnCl or Me_3SiBr in THF, resulted in a gradual colour change from brown to dark blue. After simple workup, $[U(Tp^{Me2})_2Cl]$ (**5**) and $[U(Tp^{Me2})_2Br]$ (**6**) were obtained as violet powders in high yield.

Attempts to make $[U(Tp^{Me2})_2(Cp)]$ by direct reaction of CpH with either $[U(Tp^{Me2})_2N(SiMe_3)_2]$ or $[U(Tp^{Me2})_2(NPh_2)]$ resulted in recovery of the starting material, even after prolonged reaction times. This lack of reactivity was unexpected, since protonolysis of uranium amides by cyclopentadiene has been described as a suitable route for the synthesis of cyclopentadienyl uranium compounds [4b,4c]. As pointed by some authors, the acidity of a ligand increases upon coordination to a Lewis acidic metal center, since the metal can stabilize the negative charge of the conjugate base [12]. Hence, the inertness of $[U(Tp^{Me2})_2N(SiMe_3)_2]$ and $[U(Tp^{Me2})_2NPh_2]$ towards cyclopentadiene could be due to the reduced basicity of the amido ligand when coordinated to the "$[U(Tp^{Me2})_2]$" fragment. Hence, isolation of $[U(Tp^{Me2})_2(Cp)]$ (**7**) was achieved by metathesis of $[U(Tp^{Me2})_2I]$ with stoichiometric amount of NaCp in toluene.

The compounds are soluble in THF and aromatic solvents, but poorly soluble in aliphatic hydrocarbons, except **2** that is highly soluble in *n*-hexane.

The identity of the compounds was established on the basis of elemental analysis, IR, UV–Vis–near IR, and ^{1}H NMR spectroscopies, and by single crystal X-ray diffraction studies. The electronic spectra of the complexes show several weak absorption bands in the near-IR

region, very similar to those found in other uranium(III) polypyrazolylborate compounds [13].

Infrared spectra of compounds **1**–**6** show the usual ν(B–H) stretch in the 2500–2650 cm^{-1} region, characteristic of a tridentate Tp^{Me2} ligand [14]. The IR spectrum of **4** displays a characteristic C≡C triple bond stretching vibration (ν_{CC}) at 2049 cm^{-1}, which is significantly lower than that of free phenylacetylene ($\nu_{CC} = 2110\ cm^{-1}$). Similar decrease in ν_{CC} was observed for other alkynyluranium complexes [15]. In contrast to the above, the infrared spectrum of **7** exhibits two ν(B–H) stretching vibrations, one centered at 2540 with a shoulder at 2524 cm^{-1} and a doublet centered at 2348 cm^{-1}. The positions of these IR bands are indicative of a κ^3- and a κ^2-coordinated Tp^{Me2} ligands [14], as found in its samarium analogue [Sm(κ^3-Tp^{Me2})(κ^2-Tp^{Me2})(Cp)] [16] which exhibits two ν(B–H) stretching vibrations at 2565 and 2448 cm^{-1}. The low frequency associated with the ν(B–H) stretching vibration of the κ^2-Tp^{Me2} ligand is due to the existence of a Sm···HB agostic interaction. However, the difference in frequency of the two coordination modes in the uranium compound is even larger than in the samarium analog, supporting the existence of a stronger U···HB agostic interaction.

The room temperature ^{1}H NMR spectrum of **1** exhibits six Tp^{Me2} methyl and three 4-H singlets, and one set of resonances for the protons of the aryloxide ligand. The spectrum is consistent with a rigid "U(Tp^{Me2})$_2$" fragment and rapidly rotating OAr ligand about the U-OAr bond resulting in an effective C_2 molecular symmetry. The twofold axis renders the two Tp^{Me2} ligands equivalent but within each the three pyrazolyl rings remain chemically different, giving rise to two signals for the Me-3 and Me-5 groups and one for the H-4 proton of each pyrazolyl group. The room temperature ^{1}H NMR spectrum of **3** showed the expected integration and peak multiplicities for the chalcogenolate protons. In addition, the spectrum featured twelve singlets due to the methyl groups and six due to the H-4 protons of the Tp^{Me2} ligands, indicating inequivalence of all six pyrazolyl rings. Thus the observed spectrum is consistent with a non-symmetric C_1 structure, and is very similar to that of the structurally characterized [Sm(Tp^{Me2})$_2$(η^2-2-C_5H_4N)] [17].

The room temperature ^{1}H NMR spectra of compounds **4**–**6** exhibited three resonances in a 3:3:1 ratio assigned to the Tp^{Me2} ligands. Compound **2** showed a similar pattern but with the resonance assigned to the Me-3 moiety of the pyrazolyl rings collapsed in the baseline. The simple spectra, like those of the samarium analogues indicate that the compounds are fluxional on the NMR time scale, the fluxionality being largely determined by the size of the X-ligand [17–19]. Thus, **4**–**6** are fluxional at all accessible temperatures, while cooling a toluene-d_8 solution of **2** resulted in progressive broadening and shifting of the proton resonances associated with the pyrazolylborate ligands. The resonances due to the protons of the dmpz ligand shifted substantially, because of the temperature dependence of the magnetic susceptibility, but suffered minimal line broadening. At −30 °C three resonances due to the Me-3 protons began to emerge, while the resonances due to Me-5 protons and H-4 protons split into three resonances each at −50 °C. By −80 °C the spectrum consisted of six well-resolved resonances assigned to the methyl groups and three assigned to the 4-H methine protons, consistent with a C_2-symmetric structure.

The ^{1}H NMR spectrum of **7** showed a singlet accounting for five protons, in accord with an η^5-Cp igand. The pyrazolylborate ligands gave rise to four sets of resonances in the ratio 2:2:1:1 as already observed for its samarium analogue and in accordance with the structure found in the solid state for the latter compound [16]. Although no solid state structural characterization has been obtained for **7**, its spectroscopic features point unambiguously to a structure similar to that found for the samarium analogue, [Sm(κ^3-Tp^{Me2})(κ^2-Tp^{Me2})(Cp)] [16]. However, despite the similar structures, the result of the thermolysis of **7** differs markedly from that obtained for the samarium compound [16].

When [U(κ^3-Tp^{Me2})(κ^2-Tp^{Me2})(Cp)] was heated under vacuum at 160 °C for three days, two types of crystals (golden and transparent) sublimed on the walls, leaving behind a brown residue on the bottom of the tube. X-ray analysis of the golden crystals revealed that this compound is [UCp$_3$(dmpz)] (**8**) (see SI). Crystallographic investigation of the transparent crystals showed it to be the known 4,8(dihydro)4,8(dipyrazolyl)pyrazabole (**9**)[1] [20]. The brown residue was investigated by ^{1}H NMR spectroscopy. The spectrum displayed one set of resonances with a 3:3:1 intensity ratio, assigned to a Tp^{Me2} ligand, and two resonances in a 1:6 intensity ratio. Elemental analysis and the NMR spectrum were consistent with the formulation [U(Tp^{Me2})(dmpz)$_3$] (**10**). This was further corroborated by comparison of its ^{1}H NMR spectrum with that of an authentic sample obtained by reacting [U(Tp^{Me2})Cl$_3$(THF)] [21] with 3 equiv of K(dmpz). Hence, thermolysis of **7** results in complete oxidation of the uranium centre and redistribution of the ligands.

It is not surprising that the product of oxidation of uranium(III) retains only one coordinated Tp^{Me2} ligand, since the uranium(IV) centre appears not to be able to

[1] The X-ray structure of **9** has been reported ([20]). We have isolated a different crystalline form of the compound. Crystal data for **9** ($C_{20}H_{30}B_2N_8$, fw = 404.14) are as follows: orthorhombic space group *Pcan* with $a = 11.072(2)$ Å, $b = 14.019(2)$ Å, $c = 14.258(2)$ Å, $V = 2213.2(6)$ Å^3, and $Z = 4$; $D_{calc} = 1.213\ g\ cm^{-3}$: A total of 6573 independent reflexions having 2θ (Mo Kα) < 50 were collected on an Enraf-Nonius CAD4-diffractometer. Least-squares refinement of 136 parameters on 1742 absorption corrected reflexions having $I > 2\sigma(I)$ converged at $R(R_w) = 0.0748(0.1845)$.

accommodate two Tp^{Me2} ligands. It has been reported that while the reaction of UCl_4 with one equiv of Tp^{Me2} ligand gives $[U(Tp^{Me2})Cl_3(THF)]$ [21], the reaction with two equiv of Tp^{Me2} results in the formation of $[U(Tp^{Me2})(dmpz)Cl_2]$ and pyrazabole [22]. Furthermore, a recurring feature of the pyrazolylborate ligands, abundantly documented in the chemical literature, is their vulnerability to fragmentation reactions giving pyrazole or pyrazolyl groups [23]. It is likely that during the thermolysis cleavage of a B–N bond occurs with liberation of a transient $dmpz^-$ or dmpzH moiety. However, addition of dmpzH to $[U(Tp^{Me2})_2(Cp)]$ did not lead to any of the oxidation products formed in the thermolysis. The products obtained were $[U(Tp^{Me2})_2(dmpz)]$, due to the acid–base reaction of $[U(Tp^{Me2})_2(Cp)]$ with Hdmpz, pyrazabole and another species that we were not able to characterize.

Although the mechanism is not clear, the products of the thermolysis clearly reflect the accessibility of the +4 oxidation state for uranium. In contrast, thermolysis of the analogous samarium compound, under the same conditions, results in intramolecular C–H activation with formation of $[Sm(\kappa^3\text{-}(Tp^{Me2})\{HB(3,5\text{-}Me_2pz)_2(C_5H_4)\}]$ [16], due to the absence of an oxidative pathway.

3.2. Crystal structures

The molecular structures of compounds **1**, **2** and **5** are shown in Figs. 1–3, respectively. Selected bond distances and angles are given in Table 2. In compounds **1** and **5** the central uranium ion is seven-coordinate by way of two tridentate pyrazolylborates and the oxygen donor of the aryloxide or the chloride ion, in a pentagonal bipyramidal geometry. In compound **2** the uranium is eight-coordinate by six nitrogen atoms of the two tridentate pyrazolylborate ligands and by two others from the pyrazolide ligand. However, due to its small bite, the midpoint of the pyrazolide ligand can be considered as occupying the seventh coordination site of a pentagonal bipyramid. Although the complexes do not have crystallographically imposed symmetry, the molecules are approximately C_2 symmetric.

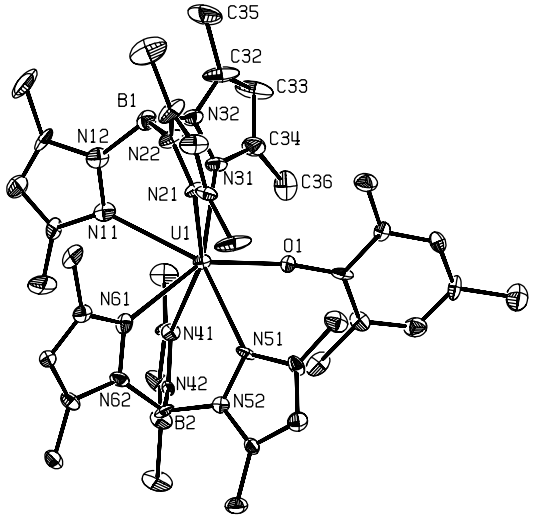


Fig. 1. ORTEP diagram of $[U(Tp^{Me2})_2(OC_6H_2\text{-}2,4,6\text{-}Me_3)]$ using 20% probability ellipsoids.

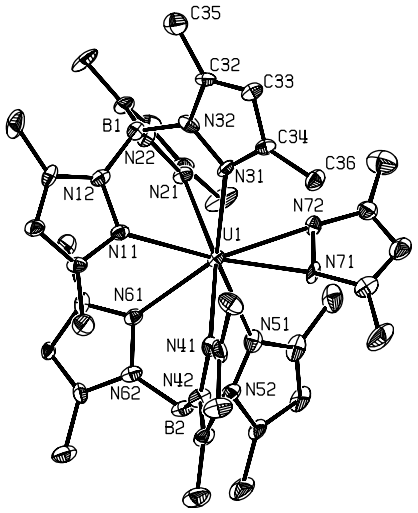


Fig. 2. ORTEP diagram of $[U(Tp^{Me2})_2(dmpz)]$ using 20% probability ellipsoids.

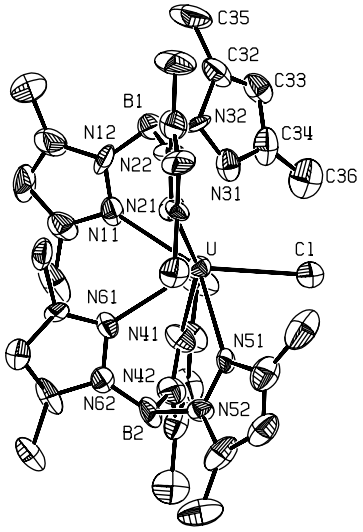


Fig. 3. ORTEP diagram of $[U(Tp^{Me2})_2Cl]$ using 40% probability ellipsoids.

For clarity and ease of comparison the same numbering scheme has been used for all three compounds. The N21 and N41 atoms occupy the apical sites of the pentagonal bipyramid, with the remaining coordinating atoms defining the equatorial plane (rms deviation: 0.1389 for **1**, 0.1924 for **2**, and 0.1946 for **5**). As expected for the less crowded axial sites, the U–N distances are shorter (average 2.544(13) Å in **1**, 2.551(12) Å in **2**, and 2.514(16) Å in **5**) than those in the equatorial girdle (av. 2.677(14) Å in **1**, 2.696(14) Å in **2**, and 2.660(15) Å in **5**). These values compare well with the corresponding

Table 2
Selected bond lengths (Å) and angles (°) for **1**, **2** and **5**

	1	**2**	**5**
Average $(U–N)_{Tpax}$	2.544(13)	2.551(12)	2.514(16)
Average $(U–N)_{Tpeq}$	2.677(14)	2.696(14)	2.660(15)
Range $(U–N)_{Tp}$	2.506(12)–2.697(14)	2.546(12)–2.711(13)	2.500(16)–2.729(15)
U–X	2.159(10)	2.444(11)	2.698(5)
B–U–B	143.7(4)	135.9(4)	142.7(6)
U–O–C	168.2(10)		
N(71)–U–N(72)		32.5 (4)	

distances in $[U(Tp^{Me2})_2(NPh_2)]$ (2.544(6) and 2.66(1) Å) and $[U(Tp^{Me2})_2N(SiMe_3)_2]$ (2.549(5) and 2.73(2) Å) [5]. The somewhat more distorted nature of $[U(Tp^{Me2})_2Cl]$ (**5**), as seen in the wider range of the U–N distances (2.500–2.729 Å) versus 2.506–2.697 Å for **1**, and 2.546–2.711 Å for **2**, can be traced to the less favourable intercalation of the larger, spherical, chloride ion between the pyrazolyl groups N3 and N5 compared with the planar aryloxide and pyrazolide ligands.[2] In fact the structure of $[U(Tp^{Me2})_2I]$ [6], with the very bulky iodide, is severely distorted with one pz ligand side-on bonded to uranium.

The pyrazolylborate ligands in complexes **1**, **2** and **5** are unremarkable, the angles at the boron atoms being essentially tetrahedral. In compound **5** a close contact between C36, the Me-3 carbon of pz ring (N31N32), and the chloride ion can be seen (Cl···C36 is 3.247 Å). Possibly in order to minimize this contact, the U–N31 is very long (2.729 Å). As commonly observed, and also in order to minimize contacts between the methyl groups of the Tp^{Me2} and X ligands, the pyrazolyl rings are twisted about their B–N bonds, with B–N–N–U torsion angles ranging from 2° to 34°. The geometrical requirements of the Tp^{Me2} ligands and the higher coordination number of uranium in complex **1** than in $U(OC_6H_3\text{-}2,6\text{-}^iPr_2)_3$ [24] result in a longer U–O(1) bond length (2.159(10) Å) compared to the corresponding distance of 2.132(8) Å in the latter. The average U–N bond distance of the pyrazolide ligand in complex **2** (2.444(11) Å) compares with the corresponding distance of 2.373(5) Å in the samarium analogue [18], after adjustment for the difference in ionic radii [25]. The U–Cl bond distance of 2.698(5) Å in **5** is the same as those found in the literature for other uranium(III) chlorides [26] and is in accord with those of the analogous lanthanide compounds (samarium, neodymium and lanthanum) [27], taking into account the differences between the ionic radii [25].

[2] The analogous $[U(Tp^{Me2})_2Br]$ appears to be more distorted with U–N distances of 2.45–2.73 Å. Unfortunately poor crystal quality prevented satisfactory structure refinement and hence discussion of the metrical parameters (Y.N. Sun, J. Takats, and V. Day, unpublished results).

4. Conclusions

This work shows that the reactivity of the U–N bond in $[U(Tp^{Me2})_2(NR_2)]$ compounds towards protic substrates and halide source represents a convenient synthetic entry into trivalent organouranium chemistry. Although, in some cases salt metathesis proved to be more suitable. The compounds are structurally similar to the analogous samarium complexes, but the availability of higher oxidation states for uranium leads to a different outcome for the thermolysis of the uranium cyclopentadienyl compound, $[U(Tp^{Me2})_2(Cp)]$.

Acknowledgements

Financial support from Fundação para a Ciência e Tecnologia and Natural Sciences and the Engineering Research Council of Canada is gratefully acknowledged. We thank Yimin Sun, Victor Day and Robert Mc Donald, for providing the available crystal data on $[U(Tp^{Me2})_2Br]$.

Appendix A. Supplementary data

Tables of crystal data, structure solution and refinements, atomic coordinates, bond lengths and angles, and anisotropic thermal parameters for compound **8.** The supplementary crystallographic data for the structurally characterized complexes are: CCDC 266447 (**1**), CCDC 266448 (**2**), CCDC 266449 (**5**) and CCDC 274704 (**8**). These data are available free of charge from The Director, CCDC, 12 Union Road, Cambridge, CB2 1EZ, UK, fax: +44 1223 366 033, e-mail: deposit@ccdc.ac.uk or on the web www: http://www.ccdc.cam.ac.uk. Supplementary data associated with this article can be found, in the online version at doi:10.1016/j.poly.2005.06.025.

References

[1] M. Ephritikhine, J.C. Berthet, Coord. Chem. Rev. 178–180 (1998) 83.
[2] (a) J.L. Stewart, R.A. Andersen, New J. Chem. 19 (1995) 587; (b) A.L. Arduini, J. Takats, Inorg. Chem. 20 (1981) 2480;

(c) J.J. Jamerson, J. Takats, J. Organomet. Chem. 78 (1974) C23;
(d) R.A. Andersen, Inorg. Chem. 18 (1979) 1507.
[3] (a) H. Li, Y. Yao, Q. Shen, L. Weng, Organometallics 21 (2002) 2529;
(b) P.J. Fagan, J.M. Manriquez, S.H. Vollmer, C.S. Day, V.W. Day, T.J. Marks, J. Am. Chem. Soc. 103 (1981) 2206;
(c) A.L. Arduini, J.D. Jamerson, J. Takats, Inorg. Chem. 20 (1981) 2474;
(d) A. Dormond, A. Aaliti, C.J. Moise, Chem. Soc., Chem. Commun. (1985) 1231.
[4] (a) M. Ephritikhine, J.C. Berthet, J. Chem. Soc. Dalton Trans. (1993) 1566;
(b) J.C. Berthet, C. Boisson, M. Lance, J. Vigner, M. Nierlich, M. Ephritikhine, J. Chem. Soc., Dalton Trans. (1993) 3019;
(c) C. Boisson, C.J. Berthet, M. Lance, J. Vigner, M. Nierlich, M. Ephritikhine, J. Chem. Soc., Dalton Trans. (1996) 947;
(d) T.M. Gilbert, R.R. Ryan, A.P. Sattelberger, Organometallics 7 (1988) 2514;
(e) J.C. Berthet, C. Boisson, M. Lance, J. Vigner, M. Nierlich, M. Ephritikhine, J. Chem. Soc., Dalton Trans. (1993) 3027;
(f) C. Boisson, J.C. Berthet, M. Ephritikhine, M. Lance, M. Nierlich, J. Organomet. Chem. 7 (1997) 533;
(g) C. Boisson, J.C. Berthet, M. Lance, M. Nierlich, J. Vigner, M. Ephritikhine, J. Chem. Soc., Chem. Commun. (1995) 543.
[5] M.A. Antunes, G.M. Ferrence, Â. Domingos, R. McDonald, C.J. Burns, J. Takats, N. Marques, Inorg. Chem. 43 (2004) 6640.
[6] Y. Sun, R. McDonald, J. Takats, V.W. Day, T.A. Eberspacher, Inorg. Chem. 33 (1994) 4433.
[7] C.W. Eigenbrot Jr., K.N. Raymond, Inorg. Chem. 20 (1981) 1553, See SI for details of the X-ray crystal structure of **8**.
[8] C.K. Fair, MOLEN; Enraf-Nonius, Delft, The Netherlands, 1990.
[9] G.M. Sheldrick, SHELXL-97: Program for the Solution of Crystal Structure, University of Göttingen, Germany, 1997.
[10] G.M. Sheldrick, SHELXL-97: Program for the Refinement of Crystal Structure, University of Göttingen, Germany, 1997.
[11] L.J. Farrugia (ORTEP-3), J. Appl. Crystallogr. 30 (1997) 565.
[12] (a) R.A. Andersen, J.L. Stewart, New J. Chem. 19 (1995) 587;
(b) P.A. Lay, A.M. Sargeson, B.W. Skelton, A.H. White, J. Am. Chem. Soc. 104 (1982) 6161.
[13] L. Maria, A. Domingos, I. Santos, Inorg. Chem. 42 (2003) 3323.
[14] (a) M. Akita, K. Ohta, Y. Takahashi, S. Hikichi, Y. Moro-oka, Organometallics 16 (1997) 4121;
(b) A. Carvalho, Â. Domingos, P. Gaspar, N. Marques, A. Pires de Matos, I. Santos, Polyhedron 12 (1992) 1481;
(c) Y. Sun, J. Takats, T. Eberspacher, V. Day, Inorg. Chim. Acta 229 (1995) 315.
[15] (a) M. Tsutsui, N. Ely, A. Gebala, Inorg. Chem. 14 (1975) 78;
(b) D. Baudry, A. Dormond, A. Hafid, J. Organomet. Chem. 494 (1995) C22.
[16] I. Lopes, G.Y. Lin, Â. Domingos, R. McDonald, N. Marques, J. Takats, J. Am. Chem. Soc. 117 (1999) 7828.
[17] I. Lopes, A.C. Hillier, S.Y. Liu, Â. Domingos, J. Ascenso, A. Galvão, A. Sella, N. Marques, Inorg. Chem. 40 (2001) 1116.
[18] I. Lopes, B. Monteiro, G. Lin, Â. Domingos, J. Takats, N. Marques, J. Organomet. Chem. 632 (2001) 119.
[19] (a) A.C. Hillier, S.Y. Liu, A. Sella, M.R.J. Elsegood, Inorg. Chem. 19 (2000) 2635;
(b) G.Y. Lin, R. McDonald, J. Takats, Organometallics 19 (2000) 1814.
[20] (a) C. Apostolidis, A. Carvalho, Â. Domingos, B. Kanellakopullos, R. Maier, N. Marques, A. Pires de Matos, J. Rebizant, Polyhedron 18 (1998) 263;
(b) N.W. Alcock, J.F. Sawyer, Acta Crystallogr., Sect. B 30 (1974) 2899.
[21] R.G. Ball, F. Edelmann, J.G. Matisons, J. Takats, N. Marques, J. Marçalo, A. Pires de Matos, K.W. Bagnall, Inorg. Chim. Acta 132 (1987) 137.
[22] N. Marques, J. Marçalo, A. Pires de Matos, K.W. Bagnall, J. Takats, Inorg. Chim. Acta 139 (1987) 79.
[23] N. Marques, A. Sella, J. Takats, Chem. Rev. 102 (2002) 2137.
[24] W.G. Van der Sluys, C.J. Burns, J.C. Huffman, A.P. Sattelberger, J. Am. Chem. Soc. 110 (1988) 5924.
[25] R.D. Shannon, Acta Crystallogr., Sect. A 32 (1976) 751.
[26] (a) A. Zalkin, S.M. Beshouri, Acta Crystallogr., Sect. C 45 (1989) 1219;
(b) A. Zalkin, S.M. Beshouri, Acta Crystallogr., Sect. C 45 (1989) 1080.
[27] (a) X.W. Zhang, G.H. Maunder, S.Y. Liu, T.A. Eberspacher, N. Marques, V.W. Day, A. Sella, J. Takats, Inorg. Chem. 40 (2001) 5106;
(b) J.L. Galler, S. Goodchild, J. Gould, R. McDonald, A. Sella, Polyhedron 23 (2004) 253;
(c) F. Kunrath, O.L. Casagrande Jr., L. Toupet, J.F. Carpentier, Polyhedron (2004) 2437.

of the ligands which could be of help in the design of devices with long-term stability and optimized lifetimes of the near infrared emission [3].

The first step in this direction would be to be able to predict the geometrical structures of Ho(III) complexes at a level of accuracy that could be useful for luminescent devices design, for single-molecule magnets design, and for telecommunications research.

In order to be able to predict geometries of rare earth complexes, we had developed earlier the original Sparkle model [4,5], which we recently largely improved and called Sparkle/AM1 [6]. Until now, Sparkle/AM1 had

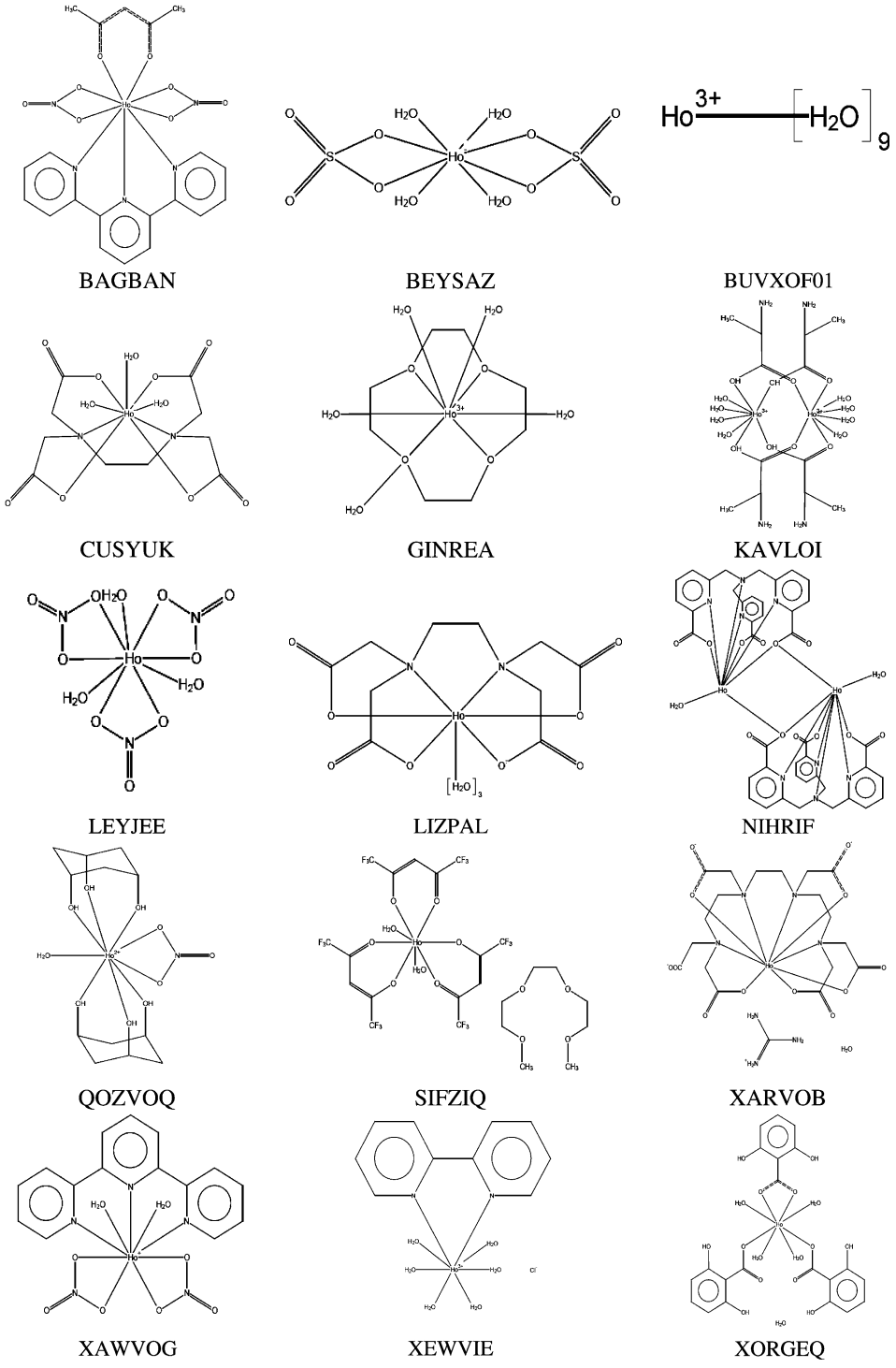


Fig. 1. Schematic two-dimensional representation of the holmium (III) complexes, that constitute the parameterization training set, obtained from the Cambridge Structural Database [7–9].

been only parameterized for Eu(III), Gd(III) and Tb(III) [6]. In the present work, we extend Sparkle/AM1 to Ho(III). The Sparkle/AM1 model replaces the trivalent rare earth ion by a Coulombic charge of $+3e$ superimposed to a repulsive exponential potential of the form $\exp(-\alpha r)$, which accounts for the size of the ion, and uses two Gaussian functions in the core–core repulsion energy term to make it compatible with AM1. That is, Sparkle/AM1 assumes that the rare earth trications behave like simple ions, without any angular steric properties – the angular effects of the f orbitals are assumed to be negligible and are not taken into account. The good agreement between predicted and observed rare earth ion complex structures, as also evidenced below for Ho(III), is a powerful evidence for the effectiveness of this idea.

2. Results and discussion

The Sparkle/AM1 parameterization procedure for Ho(III) is essentially the same as the one described in our previous work on Eu(III), Gd(III) and Tb(III) [6]. Accordingly, we only considered high quality crystallographic structures (R factor $< 5\%$) taken from the "Cambridge Structural Database 2003" (CSD) [7–9]. Ligands important for luminescence and telecommunications research, coordinate to the Ho(III) ion almost exclusively via oxygen or nitrogen atoms, and comprise approximately 75% of all Ho(III) structures available in CSD. As such, we considered all 27 available structures with nitrogen or oxygen as coordinating atoms and classified the various extant ligands into the following types: β-diketone, nitrate, monodentate, bidentate, tridentate and polydentate. We further considered diholmium complexes, where the two Ho(III) ions face each other. From a suitable cluster analysis of all complexes [6], a subset of fifteen different representative structures of Ho(III) complexes was chosen and are presented in Fig. 1.

To find the parameters, we carried out a non-linear minimization of an eight-dimension response function, using a combination of Newton–Raphson and simplex methods, aimed at finding one of its local minima, which ideally should be close enough to the global minimum, if not the global minimum itself, and make chemical sense. The heat of formation of the Ho(III) ion in Sparkle/AM1 was obtained by adding to the heat of atomization of holmium [10], its first three ionization potentials, yielding 1009.6 kcal mol^{-1}. Finally, the atomic mass of Ho(III) was set at 164.9303 amu [10]. The Sparkle/AM1 parameters obtained for Ho(III) are shown in Table 1.

In the validation procedure, we used a set of 12 more complexes, also of high crystallographic quality, for a total of 27 coordination compounds considered, and clustered according to their predominant ligand group as in Table 2.

Table 1
Parameters for the Sparkle/AM1 model for the Ho(III) ion

	Sparkle/AM1 – Ho(III)
GSS	58.0375569983
ALP	3.5558255806
a_1	0.9819487665
b_1	8.9158636523
c_1	1.7513929352
a_2	0.5454296933
b_2	8.6358143694
c_2	3.0176828845

Table 2
Number of holmium (III) complexes in the validation set, classified according to their predominant ligand group

Ligand group number	Ligand type	Number of structures
1	β-Diketone	2
2	Nitrate	4
3	Monodentate	7
4	Bidentate	2
5	Polydentate	9
6	Diholmium	3

As accuracy measure, we used the average unsigned mean error for each complex i, UME_i, defined as

$$UME_i = \frac{1}{n_i}\sum_{j=1}^{n}\left|R_{i,j}^{\mathrm{CSD}} - R_{i,j}^{\mathrm{calc}}\right|, \quad (1)$$

where n_i is the number of ligand atoms directly coordinating the rare earth ion. As for Eu(III), Gd(III) and Tb(III) [6], two cases have been examined: (i) UMEs involving the interatomic distances R_j between the holmium central ion and the atoms of the coordination polyhedron, as well as the interatomic distances R_j between all atoms of the coordination polyhedron, and (ii) $\mathrm{UME}_{(\mathrm{Ho-L})}$s involving only the interatomic distances R_j between the holmium central ion and the atoms of the coordination polyhedron, important in luminescent complex design and to telecommunications research.

Table 3 shows the values of UMEs for all 27 complexes considered and the graphical representations of the UME, and of the $\mathrm{UME}_{(\mathrm{Ho-L})}$s, are shown in parts (a) and (b) of Fig. 2, respectively. Clearly, total UMEs are larger than the $\mathrm{UME}_{(\mathrm{Ho-L})}$s. Indeed, whereas the maximum UME is 0.32 Å, the largest $\mathrm{UME}_{(\mathrm{Ho-L})}$ is only 0.10 Å, indicating that holmium ligand atom distances are more accurately described than the whole coordination polyhedron. And fortunately that is so, because for luminescent complex design, accurate description of distances between the directly coordinating atoms and the central rare earth ion are more important than the whole coordination polyhedron. That is because, to predict the luminescence quantum yield of a rare earth complex, one usually starts by characterizing the interaction

Table 3
Values of the coordination numbers, CNs, and unsigned mean errors, UMEs, for Sparkle/AM1, as compared to the respective experimental crystallographic values, obtained from the Cambridge Structural Database [7–9], for each of the 27 holmium (III) complexes

Structure[a]	CN	UME (Å) sparkle model
BAGBAN [16]	9	0.1265
BEYSAZ [17]	8	0.2511
BUVXOF01 [18]	9	0.1411
CAQFUV [19]	9	0.1423
COZHEE [20]	8	0.1871
CUSYUK [21]	9	0.2729
ECOJEL [22]	9	0.2099
FAGYOC [23]	8	0.1732
GAKYIA [24]	8	0.3215
GINREA [25]	9	0.1573
GODKOZ [26]	9	0.1278
HANCII [27]	9	0.2025
HOESUL02 [28]	9	0.1851
IDOZIK [29]	8	0.1872
KITGOJ [30]	9	0.2171
LEYJEE [31]	9	0.2121
LIZPAL [32]	9	0.2802
NIHRIF [33]	9	0.1281
NUJBAV [34]	9	0.1372
PHPRHO10 [35]	7	0.3130
QOZVOQ [36]	9	0.1791
SIFZIQ [37]	8	0.2786
XARVOB [38]	9	0.1537
XAWVOG [39]	9	0.1425
XEQMEL [40]	7	0.1226
XEWVIE [41]	8	0.2059
XORGEQ [42]	8	0.2137

[a] The structures are identified by their respective codes of reference from the Cambridge Structural Database 2003 [7–9].

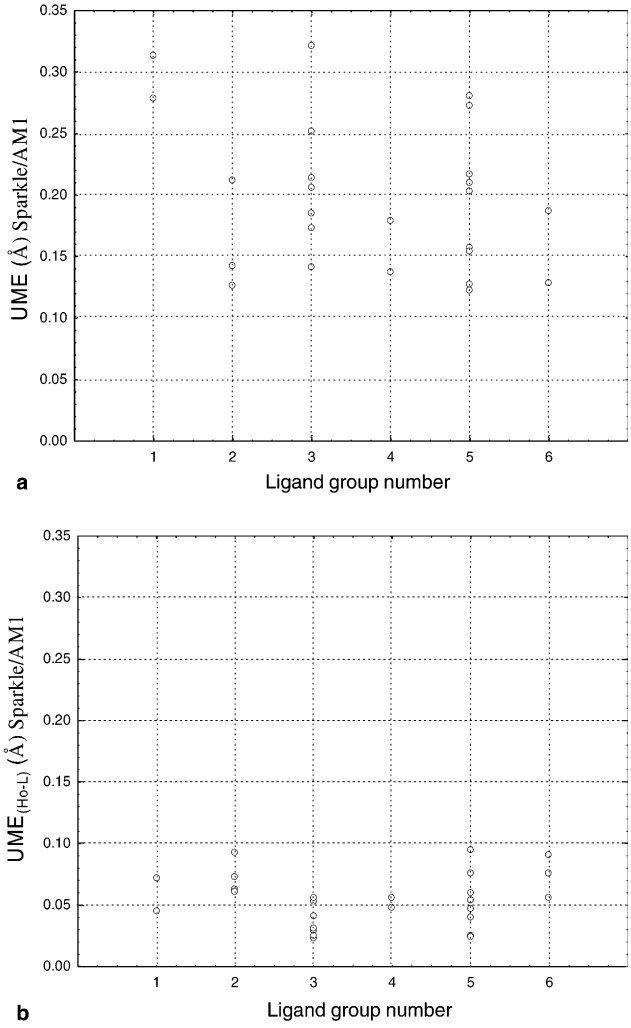


Fig. 2. Unsigned mean errors for each of the 27 holmium (III) complexes, assembled according to the ligand group numbers defined in Table 2. (a) The UMEs and (b) the $UME_{(Ho-L)}$s. The same scale has been used in both to facilitate comparison.

between the ligands and the central ion through the ligand field parameters,, which, within the simple overlap model [11,12], possesses a dependence which goes with the third, the fifth, and even with the seventh power of the ligand–rare earth interatomic distances.

In Table 4, we present Sparkle/AM1 unsigned mean errors for specific types of bond distances, not only for Ho(III) but also for the previously published Eu(III), Gd(III) and Tb(III). Indeed, the same patterns that appeared for the previous ions are reproduced in the case of Ho(III), showing they are all comparable parameterizations. Once again, the very important rare earth ion–ligand atom distances are the most accurately predicted of all interatomic distances.

In a previous paper [6], we performed a series of ab initio effective core potential, ECP, calculations on a set of seven Eu(III) complexes [6] using STO-3G, 3-21G and 6-31G* basis sets, and the average unsigned mean error obtained for all Eu–L and L–L′ distances, where L is a ligand atom directly coordinated to the Eu(III) ion, varied from 0.11 Å for 3-21G to 0.16 Å for 6-31G* ab initio/ECP calculations. The same values

Table 4
Sparkle/AM1 unsigned mean errors for all distances involving the central rare earth ion, Ln, and the ligand atoms of the coordination polyhedron, L, for 96 Eu(III) [6] complexes; 70 Gd(III) [6] complexes; 42 Tb(III) [6] complexes, and all 27 Ho(III) complexes considered

Model	Unsigned mean errors for specific types of distances (Å)					
	Ln–Ln	Ln–O	Ln–N	L–L′	Ln–L and Ln–Ln	Ln–L, Ln–Ln and L–L′
Sparkle/AM1 – Eu [6]	0.1624	0.0848	0.0880	0.2170	0.0900	0.1900
Sparkle/AM1 – Gd [6]	0.1830	0.0600	0.0735	0.2082	0.0658	0.1781
Sparkle/AM1 – Tb [6]	0.2251	0.0754	0.0440	0.2123	0.0746	0.1823
Sparkle/AM1 – Ho	0.2108	0.0555	0.0409	0.2258	0.0547	0.1897

for Eu(III) Sparkle/AM1 for these complexes was 0.11 Å, clearly showing all possess approximately the same geometry prediction accuracy. Moreover, ab initio/ECP calculations on rare earth complexes are so time consuming that, to the best of our knowledge, the largest calculation ever reported on one such complex is our [6] ab initio/6-31G* full geometry optimization of XICHUM (CSD code), a dieuropium complex possessing 134 atoms. While the Sparkle/AM1 full geometry optimization of such complex took only about an hour on an Athlon 1.53 GHz with 1 GB of DDR memory, the 6-31G*/ECP took many months of CPU on the same computer to finally yield a geometry of comparable accuracy.

3. Conclusion

Sparkle/AM1 parameters for Ho(III) are defined here at the same level of quality of the previously introduced Sparkle/AM1 parameters for Eu(III), Gd(III) and Tb(III), and generate geometries of a quality comparable to present day rare earth complex ab initio calculations. Indeed, Sparkle/AM1 geometries may, for example, be used as excellent first guesses of structures of Ho(III) complexes to be further refined in crystallographic structural research, or as a point to proceed with higher level ab initio calculations.

Having obtained the Ho(III) complex optimized geometry, the possibilities that open up for researchers are innumerous. For luminescence research [13], for example, the triplet level of the ligands in their bound conformation can be determined via INDO/CI calculations [14]; the various vibrational frequencies of the complex can be calculated in order to search for high energy vibrations that might quench the luminescence process [15]; and so forth.

Sparkle/AM1 is the only quantum mechanical semiempirical model presently available for the calculation of Ho(III) complexes and may prove useful in molecular design for various applications.

Acknowledgments

We appreciate the financial support from CNPq (Brazilian agency), and also grants from the Instituto do Milênio de Materiais Complexos, FACEPE (Programa Primeiros Projetos) and Construção do Conhecimento por Agrupamento de Dados (CoCADa). We also thank CENAPAD (Centro Nacional de Processamento de Alto Desempenho) at Campinas, Brazil, for having made available to us their computational facilities. Finally, we gratefully acknowledge the Cambridge Crystallographic Data Centre for the Cambridge Structural Database.

Appendix A. Supplementary data

Instructions and examples on how to implement the Ho(III) Sparkle/AM1 model in Mopac93r2. Parts of the codes of subroutines Block.f, Calpar.f and Rotate.f that need to be changed, as well as their modified versions for Ho(III). Examples of Mopac93r2 crystallographic geometry input (.dat) and optimized geometry summary output (.arc) files from Sparkle/AM1 calculations for the Ho(III) complex XEQMEL and for the diholmium complex NIHRIF. Supplementary data associated with this article can be found, in the online version, at doi:10.1016/j.poly.2005.06.027.

References

[1] N. Ishikawa, M. Sugita, W. Wernsdorfer, J. Am. Chem. Soc. 127 (2005) 3650.
[2] J.W. Stouwdam, F.C.J.M. Van Veggel, Nano Lett. 2 (2002) 733.
[3] K.S. Schanze, J.R. Reynolds, J.M. Boncella, B.S. Harrison, T.J. Foley, M. Bouguettaya, T.-S. Kang, Synth. Met. 137 (2003) 1013.
[4] A.V.M. de Andrade, N.B. da Costa Jr., A.M. Simas, G.F. de Sá, Chem. Phys. Lett. 227 (1994) 349.
[5] G.B. Rocha, R.O. Freire, N.B. da Costa Jr., G.F. de Sá, A.M. Simas, Inorg. Chem. 43 (2004) 2346.
[6] R.O. Freire, G.B. Rocha, A.M. Simas, Inorg. Chem. 44 (2005) 3299.
[7] F.H. Allen, Acta Crystallogr. B 58 (2002) 380.
[8] I.J. Bruno, J.C. Cole, P.R. Edgington, M. Kessler, C.F. Macrae, P. McCabe, J. Pearson, R. Taylor, Acta Crystallogr. B 58 (2002) 389.
[9] F.H. Allen, W.D.S. Motherwell, Acta Crystallogr. B 58 (2002) 407.
[10] D.R. Lide (Ed.), Handbook of Chemistry and Physics [CD-ROM], CRC Press, New York, 2002.
[11] O.L. Malta, Chem. Phys. Lett. 87 (1982) 27.
[12] O.L. Malta, Chem. Phys. Lett. 88 (1982) 353.
[13] G.F. de Sá, O.L. Malta, C.D. Donegá, A.M. Simas, R.L. Longo, P.A. Santa-Cruz, E.F. da Silva, Coord. Chem. Rev. 196 (2000) 165.
[14] A.V.M. de Andrade, N.B. da Costa Jr., O.L. Malta, R.L. Longo, A.M. Simas, G.F. de Sá, J. Alloys Compd. 250 (1997) 412.
[15] W.M. Faustino, G.B. Rocha, F.R.G.E. Silva, O.L. Malta, G.F. de Sá, A.M. Simas, J. Mol. Struct. (Theochem) 527 (2000) 245.
[16] Y. Fukuda, A. Nakao, K. Hayashi, J. Chem. Soc., Dalton Trans. 4 (2002) 527.
[17] A. Arhar, L. Golic, V. Jordanovska, J. Siftar, Vestn. Slov. Kem. Drus. (Bull. Slovenian Chem. Soc.) 28 (1981) 311.
[18] C.O.P. Santos, E.E. Castellano, L.C. Machado, G. Vicentini, Inorg. Chim. Acta 110 (1985) 83.
[19] M.G.B. Drew, M.J. Hudson, P.B. Iveson, C. Madic, M.L. Russell, J. Chem. Soc., Dalton Trans. 15 (1999) 2433.
[20] K. Prout, J.M. Marin, C.A. Hutchison Junior, Acta Crystallogr., Sect. C 41 (1985) 201.
[21] L.K. Templeton, D.H. Templeton, A. Zalkin, Acta Crystallogr., Sect. C 41 (1985) 355.
[22] R.S. Dickins, C.S. Love, H. Puschmann, Chem.Commun. 22 (2001) 2308.
[23] O.E. Piro, E.E. Castellano, E.J. Baran, Z. Anorg. Allg. Chem. 628 (2002) 612.
[24] Y. Ohki, Y. Suzuki, T. Takeuchi, A. Ouchi, Bull. Chem. Soc. Jpn. 61 (1988) 393.

[25] R.D. Rogers, A.N. Rollins, M.M. Benning, Inorg. Chem. 27 (1988) 3826.
[26] F. Benetollo, G. Bombieri, S. Aime, M. Botta, Acta Crystallogr., Sect. C 55 (1999) 353.
[27] R.D. Rogers, A.N. Rollins, R.D. Etzenhouser, E.J. Voss, C.B. Bauer, Inorg. Chem. 32 (1993) 3451.
[28] R.E. Gerkin, W.J. Reppart, Acta Crystallogr., Sect. C 40 (1984) 781.
[29] W. Lu, B. Wu, X. Zheng, J. Chem. Cryst. 30 (2000) 777.
[30] R.D. Rogers, R.D. Etzenhouser, J.S. Murdoch, E. Reyes, Inorg. Chem. 30 (1991) 1445.
[31] R.D. Rogers, A.N. Rollins, J. Chem. Cryst. 24 (1994) 321.
[32] N. Sakagami, Y. Yamada, T. Konno, K. Okamoto, Inorg. Chim. Acta 288 (1999) 7.
[33] Y. Bretonniere, M. Mazzanti, J. Pecaut, F.A. Dunand, A.E. Merbach, Inorg. Chem. 40 (2001) 6737.
[34] W. Brzyska, Z. Rzaczynska, W. Ozga, R. Mrozek, T. Glowiak, Pol. J. Chem. 70 (1996) 1008.
[35] A. Zalkin, D.H. Templeton, D.G. Karraker, Inorg. Chem. 8 (1969) 2680.
[36] P. Delangle, C. Husson, C. Lebrun, J. Pecaut, P.J.A. Vottero, Inorg. Chem. 40 (2001) 2953.
[37] S.-J. Kang, Y.S. Jung, Y.S. Sohn, Bull. Korean Chem. Soc. 18 (1997) 266.
[38] A. Mondry, P. Starynowicz, New J. Chem. (Nouv. J. Chim.) 24 (2000) 603.
[39] L.I. Semenova, A.H. White, Aust. J. Chem. 52 (1999) 507.
[40] M. Kanesato, T. Yokoyama, Anal. Sci. 16 (2000) 335.
[41] L.I. Semenova, B.W. Skelton, A.H. White, Aust. J. Chem. 52 (1999) 551.
[42] T. Glowiak, W. Brzyska, A. Kula, Z. Rzaczynska, J. Coord. Chem. 48 (1999) 477.

2. Experimental

All manipulations were carried out in a dry nitrogen atmosphere using Schlenk technique or a glove box. $Ni(NH_3)_6Cl_2$ was obtained from $NiCl_2 \cdot 6H_2O$ (Merck) according to [11]. Dimethylaminoethanol and formic and acetic acids were purchased from Aldrich and dried via prolonged storage on pre-treated granulated molecular sieves. IR spectra were recorded on a Perkin–Elmer IR-1720X spectrometer, using Nujol mulls between KBr plates. UV–Vis spectra were obtained on a Hitachi U 2001 Spectrophotometer for approximately 0.05 M solutions in toluene.

2.1. Preparation of $Ni_6(OH)_2(OR)_8(HCOO)_2(C_7H_8)$ ($R = CH_2CH_2N(CH_3)_2$) (1)

2.1.1. Isolation

The synthesis technique was developed on a basis of the method of $Ni(OR)_2$ ($R = CH(CH_3)CH_2N(CH_3)_2$) synthesis [1]: 0.22 g of sodium (9.56 mmol) was dissolved in a mixture of 1 cm^3 of $HOCH_2CH_2N(CH_3)_2$ and 10 cm^3 toluene and refluxed until clear solution was obtained. 1.03 g of $Ni(NH_3)_6Cl_2$ (4.81 mmol) was added to the cooled yellow solution. The latter was then heated to reflux and maintained at this temperature for 2 h approximately. The NaCl formed was separated by decantation. The solvent was evaporated in vacuo, and the solid compound was dissolved in hot toluene. The resulting solution was left overnight at −15 °C to give a small crop of air-sensitive dark green crystals of compound **1**.

2.1.2. Synthesis

The metathesis reaction and separation of NaCl were carried out exactly as in (a). 0.073 g of HCOOH (1.6 mmol) was added to the cooled solution. The solvent was evaporated in vacuo, and the solid compound was dissolved in hot toluene. The resulting solution was left overnight at −15 °C to give air-sensitive dark green crystals of compound **1**. Yield 0.64 g (65%). IR (cm^{-1}): 3236 (m), 1611, 1277 (w), 1244 (vw), 1169 (vw), 1092 (s), 1027 (m), 954 (m), 892 (vw), 882 (w), 790 (w), 698 (w), 627 (vs), 590 (vs), 482 (m), 451 (m), 420 (w). UV–Vis, λ, nm (ε, $M^{-1}\,cm^{-1}$): 672 (24), 764 (16).

2.2. Isolation of $Ni(CH_3COO)_2(HOR)_2$ ($R = CH_2CH_2N\text{-}(CH_3)_2$) (2)

The experiment analogous to that described above for the preparation of **1**, but using the acetic instead of the formic acid. 0.096 g of CH_3COOH (1.6 mmol) were added to the cooled solution. The solvent was evaporated in vacuo, and the solid compound was re-dissolved in hot toluene. The resulting solution was left overnight at −15 °C to give air-sensitive bluish-green crystals of compound **2**. Yield 0.181 g (64%). IR (cm^{-1}): 1544 (s), 1349 (m), 1333 (m), 1275 (m), 1248 (m), 1182 (m), 1169 (m), 1060 (s), 1028 (s), 951 (m), 914 (m), 880 (s), 784 (m), 665 (vs), 572 (s), 507 (w), 478(m). UV–Vis, λ, nm (ε, $M^{-1}\,cm^{-1}$): 653 (46).

2.3. Preparation of $Ni_6(OH)_2(OR)_8(CH_3COO)_2$ ($R = CH_2CH_2N\text{-}(CH_3)_2$) (3)

The synthesis has been carried out as above but only 0.024 g of CH_3COOH (0.4 mmol) were added to the cooled solution. The solvent was evaporated in vacuo, and the solid compound was re-dissolved in hot toluene. The resulting solution was left overnight at −15 °C to give air-sensitive dark green crystal of compound **1**. Yield 0.434 g (89% in relation to CH_3COOH). IR (cm^{-1}): 3318 (m), 1598 (vs), 1277 (m), 1261 (m), 1245

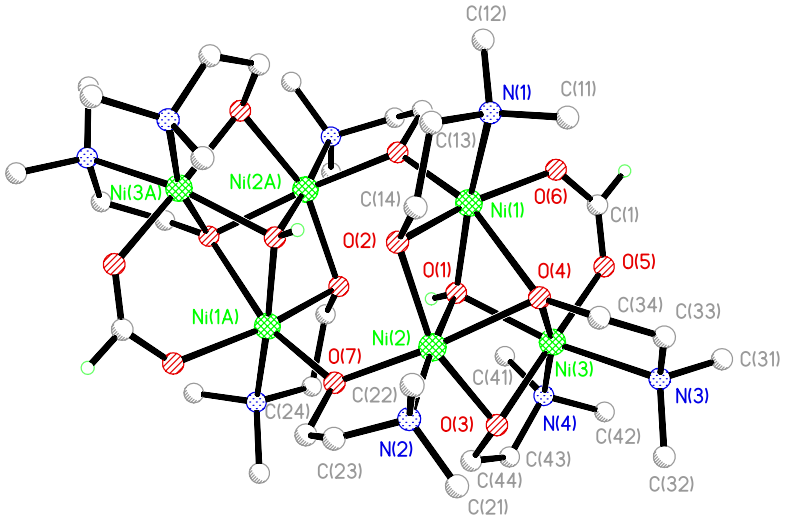


Fig. 1. Molecular structure of $Ni_6(OH)_2(OR^N)_8(HCOO)_2$ ($R = CH_2CH_2N(CH_3)_2$) (**1**).

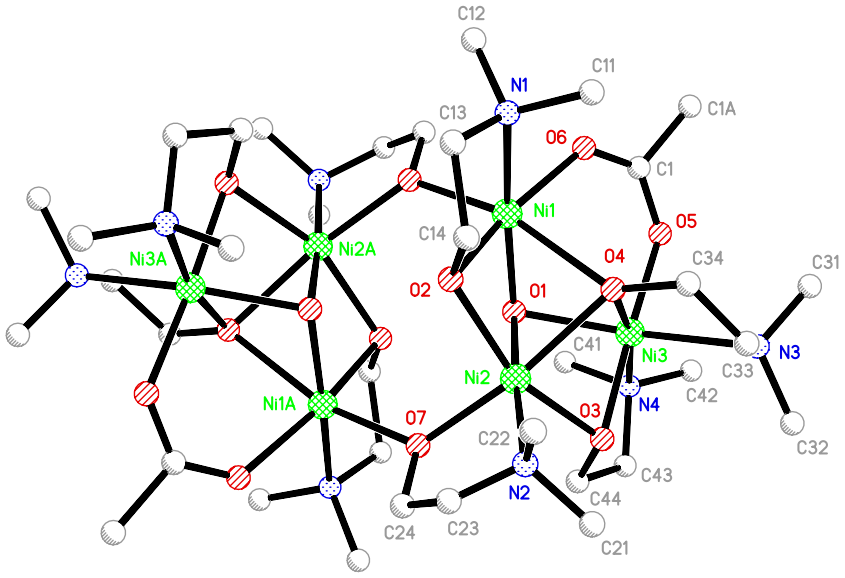


Fig. 2. Molecular structure of $Ni_6(OH)_2(OR^N)_8(CH_3COO)_2$ ($R = CH_2CH_2N\text{-}(CH_3)_2$) (**3**).

(m), 1029 (m), 951 (s), 890 (m), 780 (m), 664 (w), 588 (w), 486 (m), 450 (m), 421 (m). UV–Vis, λ, nm (ε, $M^{-1}\,cm^{-1}$): 670 (38), 760 (22).

2.4. Crystallography

The data collection for all the single crystals of compounds studied was carried out at 22 °C (for details see Table 1). All the structures were solved by standard direct methods. The coordinates of the metal atoms were obtained from the initial solutions and for all other non-hydrogen atoms found in subsequent difference Fourier syntheses. The structures were refined by least squares first in isotropic and then in anisotropic approximations. The coordinates of the hydrogen atoms were calculated geometrically and were included into the final refinement in isotropic approximation for all the compounds. All calculations were performed using the SHELXTL-NT program package [13] on an IBM PC.

Table 1
Crystal data and the diffraction experiments details for compounds **1** and **3**

Chemical formula	$C_{41}H_{92}N_8Ni_6O_{14}$ (**1**)	$C_{36}H_{88}N_8Ni_6O_{14}$ (**3**)
Formula weight	1273.49	1209.40
Crystal system	monoclinic	monoclinic
Space group	*P*2(1)/*n*	*P*2(1)/*n*
μ/mm^{-1}	2.034	2.191
R_1	0.0500	0.0426
wR_2	0.1208	0.0918
a/Å	11.1195(10)	11.1377(19)
b/Å	17.7488(16)	20.002(4)
c/Å	14.4237(13)	11.895(2)
α/°	90	90
β/°	99.428(2)	100.979(13)
γ/°	90	90
V/Å^3	2808.2(4)	2601.4(9)
Z	2	2
Number of independent reflections	3905	3609
Number of observed reflections [$I > 2\sigma(I)$]	2406	2392

3. Results and discussion

The original aim of this work was to investigate the structure of nickel dimethylamino-ethoxide. This compound has even been included into the product list of the Epichem Company, UK, producer of precursors for MOCVD technologies, but its synthesis and properties were never described in literature. We applied a synthetic procedure analogous to that described earlier by us for the preparation of nickel dimethylamino-isopropoxide and discovered unexpectedly formation of a mixture of products: a liquid with the composition (by microanalysis) corresponding to $Ni(OC_2H_4NMe_2)_2$ as a major product and a small amount of crystalline solid. The X-ray single crystal study of the latter showed it to contain formiate ligands. The latter originated apparently from oxidation of the aminoalcohol by the traces of oxygen dissolved in the solvents in strongly basic media formed on dissolution of sodium metal on reflux. Water is the other product in this kind of oxidation processes and the occurrence of hydroxo-ligands in the structure of the modified species is due to its presence. Modification of the reaction mixture with a stoichiometric amount of formic acid strongly improved the yield of the product. The reaction in total can be then represented by the following equation:

$$6\ Ni(OR)_2 + 2H_2O + 2\ HCOOH \xrightarrow[R\ =\ OC_2H_4NMe_2]{} Ni_6(OH)_2(OR)_8(HCOO)_2\ (\mathbf{1}) + 4\ ROH$$

The structure of compound **1** (see Fig. 1, please compare with Fig. 2) is a centrosymmetric hexanuclear aggregate composed of two triangular $Ni_3(\mu_3\text{-}OH)(\mu_3\text{-}OR)$ fragments, consisting of three octahedra, sharing a common edge, defined by the OH–OR vector. The fragments are connected to each other by alkoxobridges. All bidentate alkoxide ligands are coordinated in a μ,η^2-mode, combining the bridging (double or triple one) and a chelating function. The coordination of the nickel atoms is distorted octahedral with the bond lengths falling into the range commonly observed for the nickel aminoalkoxides complexes [11,12]. This structure is bearing two peculiar features. One of them is that the distances between the nickel atoms are rather short (the shortest being 2.8481(12) Å) with the angles in the Ni_3-triangle rather close to each other, which indicates possibility for strong magnetic interactions in this structure. The other unusual feature is that the motive of this structure is in fact very close to that of one of the known structure types for titanium alkoxide carboxylates present, for example, in $Ti_6O_4(OAc)_4(O^iPr)_{12}$ [14] (see Fig. 3). This fact provides one more confirmation for the fact that the structures of metal alkoxides can be derived from packing motives of negatively charged ligands and metal cations [15,16]. Application of bidentate alkoxide ligands in combination with divalent metal cations has already offered a series of molecular structures analogous to those of titanium alkoxides, for example, $Co_4Cl_2(O\text{-}C_2H_4OEt)_6$ [17]. Modification of such systems with carboxylic acids provides access to bigger aggregates again following the same principles in molecular construction.

We sought to confirm the idea about the pronounced stability of the structural types for the alkoxides involving ligands with the same structural requirements and decided to carry out the synthesis of an acetate analogue of **1**. The synthesis employing the stoichiometric

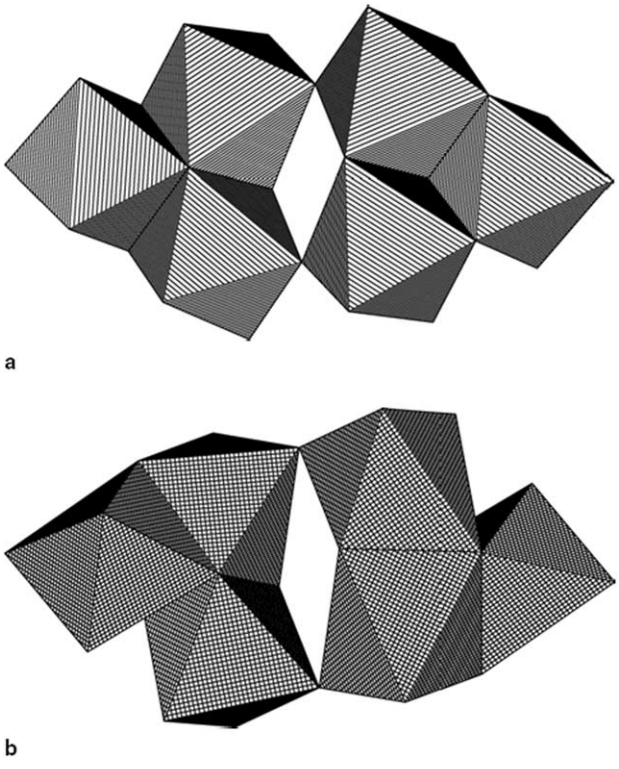


Fig. 3. Comparison of the polyhedral presentations for the structures of (a) $Ti_6O_4(OAc)_4(O^iPr)_{12}$ [14] and (b) compounds **1** and **3**.

Table 2
Selected bond distances (Å) and angles (°) in the structures of **1** and **3**

	1	**3**
Ni(1)–O(1)	1.967(5)	1.978(3)
Ni(1)–O(7)#1	2.032(4)	2.057(3)
Ni(1)–O(2)	2.046(4)	2.058(4)
Ni(1)–O(6)	2.067(5)	2.059(3)
Ni(1)–N(1)	2.155(6)	2.157(4)
Ni(1)–O(4)	2.384(5)	2.286(4)
Ni(1)–Ni(2)	2.8481(12)	2.8387(11)
Ni(2)–O(1)	2.034(4)	2.038(3)
Ni(2)–O(7)	2.040(4)	2.040(3)
Ni(2)–O(3)	2.066(4)	2.091(4)
Ni(2)–O(2)	2.107(4)	2.116(4)
Ni(2)–O(4)	2.156(5)	2.185(4)
Ni(2)–N(2)	2.190(6)	2.192(5)
Ni(2)–Ni(3)	2.7646(12)	2.7714(11)
Ni(3)–O(5)	2.017(5)	2.044(4)
Ni(3)–O(3)	2.018(4)	2.020(4)
Ni(3)–O(4)	2.053(5)	2.038(4)
Ni(3)–O(1)	2.062(4)	2.045(4)
Ni(3)–N(4)	2.152(6)	2.139(5)
Ni(3)–N(3)	2.239(6)	2.275(5)
Ni(3)–Ni(2)–Ni(1)	69.01(3)	68.27(3)
O(1)–Ni(1)–O(7)#1	94.46(18)	92.95(14)
O(1)–Ni(1)–O(2)	86.96(17)	87.50(14)
O(7)#1–Ni(1)–O(2)	97.74(17)	98.13(14)
O(1)–Ni(1)–O(6)	97.7(2)	99.83(16)
O(7)#1–Ni(1)–O(6)	96.50(19)	96.84(15)
O(2)–Ni(1)–O(6)	164.6(2)	162.95(15)
O(1)–Ni(1)–N(1)	167.1(2)	168.75(16)
O(7)#1–Ni(1)–N(1)	96.7(2)	96.07(16)
O(2)–Ni(1)–N(1)	85.3(2)	84.59(16)
O(6)–Ni(1)–N(1)	87.4(2)	85.77(17)
O(1)–Ni(1)–O(4)	68.99(18)	69.79(14)
O(1)–Ni(2)–O(2)	83.66(17)	84.46(13)
O(7)–Ni(2)–O(2)	97.48(17)	96.62(14)
O(3)–Ni(2)–O(2)	159.75(17)	159.54(14)
O(1)–Ni(2)–O(4)	72.78(18)	70.91(14)
O(7)–Ni(2)–O(4)	169.10(18)	167.61(14)
O(3)–Ni(2)–O(4)	80.09(17)	80.93(14)
O(2)–Ni(2)–O(4)	81.14(17)	79.98(14)
O(1)–Ni(2)–N(2)	175.8(2)	175.64(17)
O(5)–Ni(3)–O(3)	174.9(2)	175.31(16)
O(5)–Ni(3)–O(4)	101.3(2)	100.48(15)
O(3)–Ni(3)–O(4)	83.73(19)	82.41(14)
O(5)–Ni(3)–O(1)	96.2(2)	96.98(14)
O(3)–Ni(3)–O(1)	84.10(17)	84.46(13)
O(4)–Ni(3)–O(1)	74.39(18)	73.82(14)
O(5)–Ni(3)–N(4)	90.1(3)	90.44(18)
O(3)–Ni(3)–N(4)	84.8(2)	85.17(18)
O(4)–Ni(3)–N(4)	167.0(2)	169.37(17)
O(1)–Ni(3)–N(4)	98.5(2)	98.91(17)

Symmetry transformations used to generate equivalent atoms: #1 $-x+1, -y, -z+2$.

amounts of acetic acid was, however, not successful offering $Ni(OAc)_2(ROH)$ (**2**) instead of the desired complex. This latter compound possesses apparently rather high thermodynamic stability and is easily separated from the reaction medium by crystallization. We achieved formation of the compound **3**, an acetate analogue of **1** applying a significantly lower amount of the modifying acid. The molecular structure of **3** is very closely analogous to that of **1** (see Fig. 2 and Table 2). The structure type of compounds **1** and **3** is unusual for the homometallic alkoxide derivatives of nickel. The most commonly observed structural element for these compounds is a $Ni_4(\mu_3\text{-}OR)_4$ core with chelating ligands attached in a terminal η^2-mode to the nickel atoms [3], a fragment corresponding to cubic packing of the metal and donor atoms. Application of other bi- and oligodentate ligands such as benzotriazol and benzotriazol oxide resulted in the complexes with more open chain structures [18] or even bigger aggregates involving separate octahedrally coordinated Ni(II) centers connected through the longer ligand fragments [19]. Possibility to obtain a series of analogous alkoxide carboxylates opens a possibility to prepare complexes with related molecular structures involving unsaturated carboxylate ligands that can be transformed into hybrid organic–inorganic magnetic materials via organic polymerization reactions in analogy to the processes described recently for the polymerization of carboxylate complexes of manganese [7].

Acknowledgments

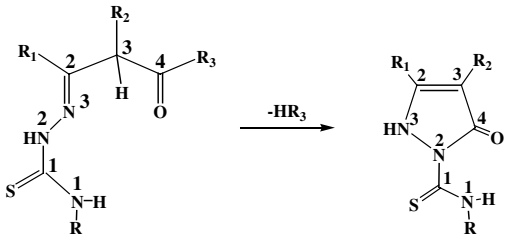
The authors express their gratitude to The Swedish Institute for providing Dr. Ilina with a Guest Researcher Grant for the work at SLU in 2002–2003.

Appendix A. Supplementary data

Supplementary data are available from the CCDC, 12 Union Road, Cambridge CB2 1EZ, UK on request, quoting the deposition numbers CCDC 272517 and 272518 for **1** and **3**, respectively. Supplementary data associated with this article can be found, in the online version at doi:10.1016/j.poly.2005.06.054.

References

[1] J.S. Svensson, C.G. Granqvist, Solar Energy Mater. 16 (1987) 19.
[2] P.M. Forster, A.K. Cheetham, Micropor. Mesopor. Mater. 73 (2004) 57.
[3] E.C. Yang, W. Wernsdorfer, S. Hill, R.S. Edwards, M. Nakano, S. Maccagnano, L.N. Zakharov, A.L. Rheingold, G. Christou, D.N. Hendrickson, Polyhedron 22 (2003) 1727.
[4] J.A. Bertrand, A.P. Ginsberg, R.I. Kaplan, C.E. Kirkwood, R.L. Martin, R.C. Sherwood, Inorg. Chem. 10 (1971) 240.
[5] M.A. Halcrow, J.S. Sun, J.C. Huffman, G. Christou, Inorg. Chem. 34 (1995) 4167.
[6] P.A. Williams, A.C. Jones, J.F. Bickley, A. Steiner, H.O. Davies, T.J. Leedham, S.A. Impey, J. Garcia, S. Allen, A. Rougier, A. Blyr, J. Mater. Chem. 11 (2001) 2329.
[7] F. Palacio, P. Oliete, U. Schubert, I. Mijatovic, N. Husing, H. Peterlik, J. Mater. Chem. 14 (2004) 1873.
[8] N.Y. Turova, E.P. Turevskaya, V.G. Kessler, M.I. Yanovskaya, The Chemistry of Metal Alkoxides, Kluwer Academic Publishers, Boston, 2002.
[9] D.C. Bradley, R.C. Mehrtotra, I.P. Rothwell, A. Singh, Alkoxo and Aryloxo Derivatives of Metals, Academic Press, London, 2001.
[10] C. Sanchez, J. Livage, M. Henry, J. Non-Cryst. Solids 100 (1988) 65.
[11] L.G. Hubert-Pfalzgraf, V.G. Kessler, J. Vaissermann, Polyhedron 16 (1997) 4197.
[12] P. Werndrup, V.G. Kessler, S. Gohil, M. Kritikos, L.G. Hubert-Pfalzgraf, Polyhedron 20 (2001) 2163.
[13] SHELXTL 5.3 Reference Manual, Bruker AXS, 1997.
[14] S. Doeuff, Y. Dromzee, F. Taulelle, C. Sanchez, Inorg. Chem. 28 (1989) 4439.
[15] V.G. Kessler, Chem. Commun. (2003) 1213.
[16] V.G. Kessler, J. Sol–Gel Sci. Technol. 32 (2004) 11.
[17] G.A. Seisenbaeva, M. Kritikos, V.G. Kessler, Polyhedron 22 (2003) 2581.
[18] E. Diamantopoulou, C.P. Raptopoulou, A. Terzis, V. Tangoulis, S.P. Perlepes, Polyhedron 21 (2002) 2117.
[19] V. Tangoulis, C.P. Raptopoulou, A. Terzis, E.G. Bakalbassis, E. Diamantopoulou, S.P. Perlepes, Inorg. Chem. 37 (1998) 3142.



I II

Scheme 1.

I / *II*	R	R_1	R_2	R_3
HTSC[1]/ *HL[1]*	-H	$-\overset{5}{C}H_2\overset{6}{C}H_3$	-H	$-O\overset{7}{C}H_3$
HTSC[2]/ *HL[2]*	-H		-H	$-O\overset{11}{C}H_2\overset{12}{C}H_3$
HTSC[3]/ *HL[3]*	-H	$-\overset{5}{C}H_3$	$-\overset{6}{C}H_2\overset{7}{C}H_3$	$-O\overset{8}{C}H_2\overset{9}{C}H_3$
HTSC[4]/ *HL[4]*	$-\overset{5}{C}H_2\overset{6}{C}H_3$	$-\overset{7}{C}H_3$	-H	$-O\overset{8}{C}H_3$

Scheme 2. Thiosemicarbazone (**I**) and pyrazolone (*II*) ligands.

^{13}C NMR spectra of DMSO solutions were recorded on AMX-300 or AMX-500 spectrometers; chemical shifts are expressed on the δ scale (downfield shifts positive) relative to tetramethylsilane (^{1}H and ^{13}C NMR spectra). All physical measurements were carried out by the RIAIDT services of the University of Santiago de Compostela.

2.2. Materials

Thiosemicarbazide (Merck), N^1-ethylthiosemicarbazide (Merck), methyl propionylacetate (Aldrich), ethyl benzoylacetate (Aldrich), ethyl 2-ethylacetoacetate (Aldrich), methyl acetoacetate (Aldrich) and zinc acetate (Aldrich) were used as received.

2.3. Synthesis of ligands

The synthesis and determination of the physical and analytical properties of HTSC[1], HTSC[2], HL[1] and HL[2] were carried out as described elsewhere (designated in this reference as HTSC[3], HTSC[5], HL[3] and HL[5]) [4].

2.3.1. HTSC[3] (ethyl 2-ethylacetoacetate thiosemicarbazone)

A mixture of ethyl-2-ethylacetoacetate (4.83 mL, 30 mmol) and thiosemicarbazide (2.70 g, 30 mmol) in ethanol (150 mL) was stirred and heated under reflux for 14 h. The solution was allowed to cool down to room temperature and diethyl ether was slowly added until a white solid was obtained. The solid was filtered off and dried under vacuum. M.p. 72 °C. *Anal.* Calc. for $C_9H_{17}N_3O_2S$: C, 46.7; H, 7.4; N, 18.2; S, 13.8. Found: C, 45.6; H, 7.4; N, 18.8; S, 14.8%. MS (electrospray), *m*/*z* (%): 232 (100) $[M+H]^+$. ^{1}H NMR: δ[N(2)H] = 10.07s(1); δ[N(1)H$_2$] = 8.14s(1), 7.47s(1); δ[C(8)H$_2$] = 4.08q(2), δ[C(3)H] = 3.19t(1); δ[C(5)H$_3$] = 1.88s(3); δ[C(6)H$_2$] = 1.68m(2); δ[C(9)H$_3$] = 1.15t(3); δ[C(7)H$_3$] = 0.80t(3). ^{13}C NMR: δ[C(1)] = 179.0; δ[C(4)] = 171.4; δ[C(2)] = 150.0; δ[C(8)] = 60.4; δ[C(3)] = 55.1; δ[C(6)] = 21.9; δ[C(5)] = 14.5; δ[C(9)] = 14.0; δ[C(7)] = 11.7.

2.3.2. HTSC[4] (methyl acetoacetate-^{1}N-ethyl thiosemicarbazone)

A mixture of ^{1}*N*-ethyl-thiosemicarbazide (1.04 g, 9 mmol) and methyl acetoacetate (1 mL, 9 mmol) in ethanol (20 mL) was heated under reflux for 10 min (a longer reaction time afforded the pyrazolone ligand). The resulting solution was concentrated to give an oil, which was stirred with diethyl ether for 24 h to afford a yellow solid. The solid was filtered off and dried under vacuum. M.p. 162 °C. *Anal.* Calc. for $C_8H_{15}N_3O_2S$: C, 44.2; H, 6.9; N, 19.4; S, 14.7. Found: C, 44.3; H, 7.0; N, 19.7; S, 15.1%. MS (electrospray), *m*/*z* (%): 218 (30) $[M+H]^+$. ^{1}H NMR: δ[N(2)H] = 10.02s(1); δ[N(1)H] = 8.22m(1); δ[C(8)H$_3$] = 3.62s(3), δ[C(5)H$_2$] = 3.57m(2); δ[C(3)H$_2$] = 3.46s(2); δ[C(7)H$_3$] = 1.94 s(3); δ[C(6)H$_3$] = 1.09t(3). ^{13}C NMR: δ[C(1)] = 177.7; δ[C(4)] = 170.0; δ[C(2)] = 146.5; δ[C(8)] = 52.2; δ[C(3)] = 44.0; δ[C(5)] = 38.6; δ[C(7)] = 17.0; δ[C(6)] = 14.8.

2.3.3. HL[3] (2,5-dihydro-3-methyl-4-ethyl-5-oxo-1H-pyrazolone-1-carbothioamide)

For the measurement of the ^{1}H and ^{13}C NMR spectra of HL, the 5-pyrazolone ligands were also obtained by cyclization in a basic medium. A 1 M aqueous solution of NaOH was added to a solution of HTSC[3] (0.50 g, 2.26 mmol) in methanol (5 mL) until a pH ca. 8 was reached. The mixture was stirred for 6 h and the resulting white solid was filtered off and dried under vacuum. M.p. 142 °C. *Anal.* Calc. for $C_7H_{11}N_3OS$: C, 45.4; H, 6.0; N, 22.7; S, 17.1. Found: C, 45.3; H, 6.2; N, 22.6; S, 17.1%. MS (electrospray), *m*/*z* (%): 208 (45) $[M+Na]^+$, 186 (95) $[M+H]^+$, 127 (100) $[M+H-(C(S)NH_2)]^+$. ^{1}H NMR: δ[N(3)H] = 11.49s(1); δ[N(1)H$_2$] = 10.38s(1), 9.57s(1); δ[C(5)H$_3$] = 2.15s(3), δ[C(6)H$_2$] = 2.14q(2); δ[C(7)H$_3$] = 0.98t(3). ^{13}C NMR: δ[C(1)] = 175.6; δ[C(4)] = 162.6; δ[C(2)] = 149.5; δ[C(3)] = 104.6; δ[C(6)] = 14.5; δ[C(7)] = 13.7; δ[C(5)] = 10.5.

2.3.4. HL[4] (2,5-dihydro-3-methyl-5-oxo-1H-pyrazolone-^{1}N-ethyl-1-carbothioamide)

This ligand was obtained by treating a solution of HTSC[4] with 1 M NaOH in methanol. The resulting white

solid was filtered off and dried under vacuum. M.p. 187 °C. *Anal*. Calc. for $C_7H_{11}N_3OS$: C, 45.4; H, 5.9; N, 22.7; S, 17.3. Found: C, 45.2; H, 6.0; N, 22.7; S, 17.4%. MS (electrospray), *m*/*z* (%): 208 (40) $[M + Na]^+$, 99 (30) $[M + H - (C(S)NHCH_2CH_3)]^+$. ^{1}H NMR: δ[N(3)H] = 11.39s(1); δ[N(1)H] = 12.05s(1), δ[C(3)H] = 5.18s(1), δ[C(5)H_2] = 3.62m(2); δ[C(7)H_3] = 2.17s(3); δ[C(6)H_3] = 1.17t(3). ^{13}C NMR: δ[C(1)] = 174.8; δ[C(4)] = 163.4; δ[C(2)] = 152.3; δ[C(3)] = 91.4; δ[C(5)] = 39.2; δ[C(6)] = 13.4; δ[C(7)] = 12.0.

2.4. Synthesis of complexes

[ZnL^2] · MeOH was prepared as described previously ([4], in which it was designated as [$ZnL^5{}_2$] · MeOH]) and crystals suitable for X-ray analysis were obtained from the mother liquor.

2.4.1. [$ZnL^1{}_2$(MeOH)]

Crystals of this new complex were isolated from the mother liquor when the synthesis of [$ZnL^1{}_2$] ([$ZnL^3{}_2$] in [4]) was repeated. This product was only used in the X-ray study.

2.4.2. [$ZnL^3{}_2$]

A solution of $HTSC^3$ (0.10 g, 0.43 mmol) in methanol (5 mL) was slowly added to a stirred solution of Zn $(OAc)_2 \cdot H_2O$ (0.05 g, 0.23 mmol) in methanol (5 mL). The mixture was stirred for 6 h and the resulting yellowish crystalline solid was filtered off. This solid contained two different types of crystals (white, *Form I*, and amber, *Form II*) and these were easily separated by hand with the aid of a magnifying glass. *Form I*: M.p. 146 °C. *Anal*. Found: C, 39.1; H, 4.6; N, 19.4; S, 14.6%. *Form II*: M.p. 148 °C. *Anal*. Calc. for $C_{14}H_{18}N_6O_2S_2Zn$: C, 39.1; H, 3.7; N, 19.5; S, 14.9. Found: C, 39.1; H, 4.1; N, 18.8; S, 14.3%.

Both types of crystal showed the same spectroscopic properties. MS (electrospray), *m*/*z*(%): 433 (50) $[M]^+$, 374 (100) $[M + H - (C(S)NH_2)]^+$. ^{1}H NMR: δ[N(1)H_2] = 11.45s(1), 10.23s(1); δ[C(6)H_2] = 2.09m(2); δ[C(5)H_3] = 2.04m(3); δ[C(7)H_2] = 0.97t(3). ^{13}C NMR: δ[C(1)] = 173.7; δ[C(4)] = 164.0; δ[C(2)] = 152.5; δ[C(3)] = 99.3; δ[C(6)] = 14.9; δ[C(5)] = 14.4; δ[C(7)] = 12.7, 12.3.

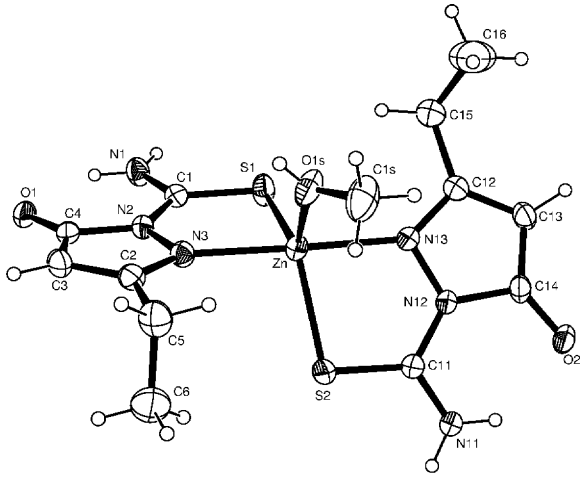
2.4.3. [$ZnL^4{}_2$]

A solution of $HTSC^4$ (0.10 g, 0.46 mmol) in methanol (5 mL) was added dropwise to a solution of $Zn(OAc)_2 \cdot H_2O$ (0.05 g, 0.23 mmol) in methanol (5 mL) and the mixture was heated under reflux and stirred for 6 h. The mixture was allowed to cool down to room temperature. The resulting white crystalline solid was filtered off. M.p. 205 °C. *Anal*. Calc. for $C_{14}H_{20}N_6O_2S_2Zn$: C, 38.8; H, 4.7; N, 19.4; S, 14.8. Found: C, 37.8; H, 4.6;

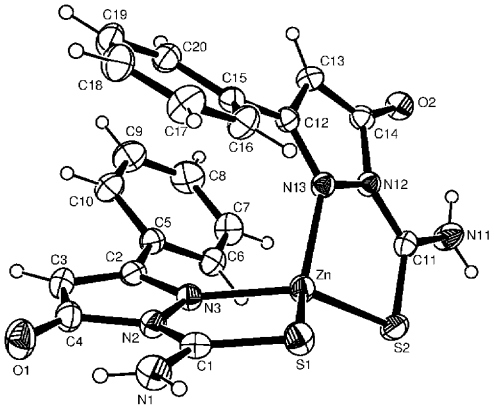
Table 1
Selected crystallographic data for Zn(II) pyrazolonate complexes

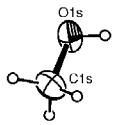
	[$ZnL^1{}_2$(MeOH)]	[$ZnL^2{}_2$] · MeOH	[$ZnL^3{}_2$] (*Form I*)	[$ZnL^3{}_2$] (*Form II*)	[$ZnL^4{}_2$]
Formula	$C_{13}H_{20}N_6O_3S_2Zn$	$C_{21}H_{20}N_6O_3S_2Zn$	$C_{14}H_{20}N_6O_2S_2Zn$	$C_{14}H_{20}N_6O_2S_2Zn$	$C_{14}H_{20}N_6O_2S_2Zn$
M	437.84	533.92	433.85	433.85	433.85
T (K)	293(2)	293(2)	293(2)	293(2)	293(2)
λ (Å)	0.71073	0.71073	0.71073	0.71073	0.71073
Crystal system	monoclinic	monoclinic	orthorhombic	orthorhombic	monoclinic
Space group	$P2_1/n$	$P2_1/c$	$Pna2_1$	*Ibca*	$C2/c$
a (Å)	9.3674(13)	11.1993(13)	9.420(2)	17.505(2)	24.385(2)
b (Å)	17.407(2)	20.759(2)	16.805(4)	21.880(3)	8.7102(8)
c (Å)	11.9457(17)	9.9762(12)	12.225(3)	19.737(3)	8.8322(9)
α (°)	90	90	90	90	90
β (°)	98.517(2)	93.538(2)	90	90	103.785(2)
γ (°)	90	90	90	90	90
V (Å^3)	1926.3(5)	2314.9(5)	1935.3(8)	7559.4(17)	1821.9(3)
Z	4	4	4	16	4
D (cal) Mg/m^3	1.510	1.532	1.489	1.525	1.582
μ (mm^{-1})	1.516	1.277	1.505	1.541	1.598
F(000)	904	1096	896	3584	896
Dimensions (mm)	0.47 × 0.10 × 0.10	0.24 × 0.20 × 0.17	0.45 × 0.23 × 0.07	0.28 × 0.20 × 0.06	0.22 × 0.21 × 0.18
θ Range (°)	2.08–26.41	1.82–28.33	2.06–26.44	1.86–28.96	1.72–26.38
hkl Range	−11, 11; −21, 21; −14, 14	−14, 14; −27, 27; −13, 13	−11, 11;−21, 21; −15, 15	−23, 23; −25, 26; −28, 29	−30, 30; −10, 10; −11, 10
Numbers of measured reflections	16226	21961	16167	35892	7551
Numbers of unique reflections	3942	5621	2084	4777	1861
R_{int}	0.0303	0.0312	0.0636	0.0585	0.0221
R_1 ($I > 2\sigma I$)	0.0305	0.0323	0.0506	0.0466	0.0283
wR_2	0.0765	0.0777	0.1296	0.0923	0.0742
Goodness-of-fit	1.067	1.015	1.063	1.061	1.048

N, 19.3; S, 15.3%. MS (electrospray), *m/z* (%): 433 (45) $[M]^+$. ^{1}H NMR: δ[N(1)H] = 12.59s(1), δ[C(3)H] = 4.84s(1), δ[C(5)H$_2$] = 3.62m(2); δ[C(7)H$_3$] = 2.09s(3); δ[C(6)H$_3$] = 1.18t(3). ^{13}C NMR: δ[C(1)] = 172.9; δ[C(4)] = 165.4; δ[C(2)] = 155.7; δ[C(3)] = 86.8; δ[C(5)] overlaps with DMSO signals; δ[C(6)] = 14.3; δ[C(7)] = 13.7.

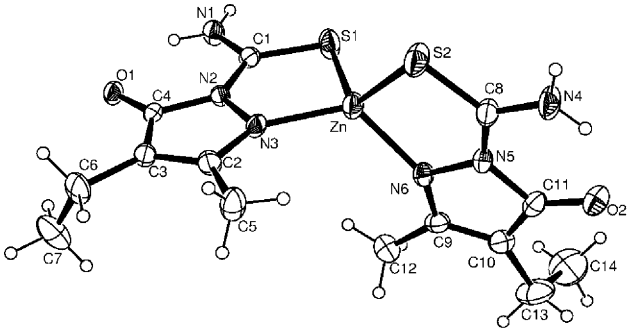


[ZnL$^1_2$(MeOH)]

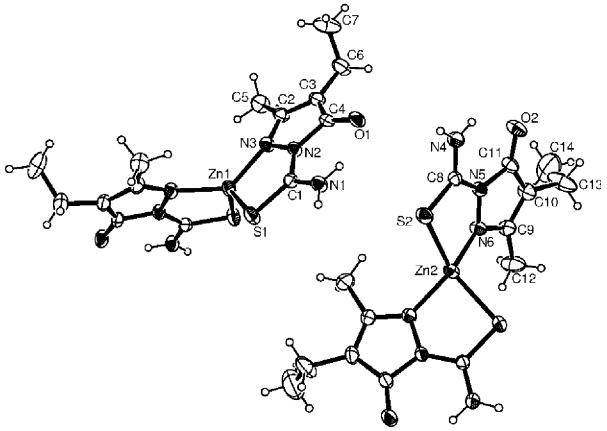




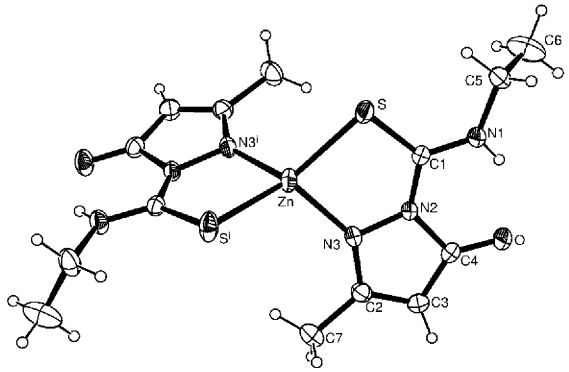
[ZnL$^2_2$]·MeOH



[ZnL$^3_2$] *(Form I)*



[ZnL$^3_2$] *(Form II)*



[ZnL$^4_2$]

Fig. 1. Molecular structure of Zn(II) pyrazolonate complexes. Displacement ellipsoids are drawn at the 30% probability level.

2.5. X-ray crystallography

X-ray data were collected at the RIAIDT services of the University of Santiago de Compostela using a Bruker SMART CCD-1000 diffractometer. Data were corrected for absorption by SADABS [5]. The structures were solved by the Patterson method and refined using SHELX97 [6]. For $[ZnL^3{}_2]$ (*Form I*), the Flack parameter [7] was refined and converged to 0.55(7), which indicated the crystal was racemically twinned. All the H atoms were introduced in calculated positions except H(1) in $[ZnL^4{}_2]$ and H(1S) in $[ZnL^1{}_2(MeOH)]$, which were located in the Fourier difference map and refined isotropically. Molecular graphics were obtained with ORTEP [8], PLATON [9] and MERCURY [10]. Crystal data, experimental details and refinement results are listed in Table 1.

3. Results and discussion

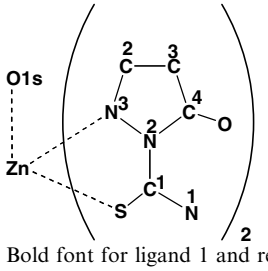
3.1. X-ray crystal structures

The molecular structures of the Zn(II) pyrazolonate complexes are shown in Fig. 1 along with the numbering scheme used. Selected bond lengths and angles are listed in Tables 2 and 3, respectively.

Two polymorphic forms – *Form I* and *Form II* – were isolated for $[ZnL^3{}_2]$ and both of these are orthorhombic, albeit with different cells and space groups. In the *Form I*, the asymmetric unit contains just one complex molecule with crystallographically different ligands. In the *Form II* crystals the asymmetric unit includes two half molecules of the complex. The same situation occurs in $[ZnL^4{}_2]$ but in $[ZnL^2{}_2]\cdot MeOH$ and $[ZnL^1{}_2(MeOH)]$

Table 2
Selected bond distances (Å) in Zn(II) pyrazolonate complexes

Parameter[a]	$[ZnL^1{}_2(MeOH)]$	$[ZnL^2{}_2]\cdot MeOH$	$[ZnL^3{}_2]$ (*Form I*)	$[ZnL^3{}_2]$ (*Form II*)		$[ZnL^4{}_2]$
				Mol. 1	*Mol. 2*	
Zn–N^3	**2.114(2)**[b] 2.108(2)	**1.9832(19)**[b] 2.0110(18)	**1.968(6)**[b] 1.979(7)	1.967(3)	1.993(3)	2.0017(17)
Zn–S	**2.3679(8)** 2.3513(8)	**2.3110(7)** 2.3176(7)	**2.343(2)** 2.315(4)	2.3219(12)	2.3316(12)	2.3137(6)
Zn–O1s	2.043(2)					
S–C^1	**1.698(2)** 1.695(2)	**1.716(3)** 1.707(2)	**1.696(7)** 1.707(9)	1.700(4)	1.704(4)	1.714(2)
O–C^4	**1.285(3)** 1.262(3)	**1.244(3)** 1.272(3)	**1.260(8)** 1.261(10)	1.254(4)	1.249(5)	1.248(3)
N^1–C^1	**1.306(3)** 1.307(3)	**1.305(3)** 1.309(3)	**1.302(10)** 1.323(11)	1.308(4)	1.302(5)	1.309(3)
N^2–C^1	**1.368(3)** 1.366(3)	**1.358(3)** 1.368(3)	**1.364(9)** 1.331(12)	1.366(5)	1.367(4)	1.367(3)
N^2–N^3	**1.386(3)** 1.389(3)	**1.389(3)** 1.385(2)	**1.391(7)** 1.384(9)	1.395(4)	1.396(4)	1.400(2)
N^2–C^4	**1.414(3)** 1.434(3)	**1.446(3)** 1.422(3)	**1.415(9)** 1.427(10)	1.430(5)	1.429(4)	1.433(3)
N^3–C^2	**1.328(3)** 1.330(3)	**1.345(3)** 1.341(3)	**1.342(10)** 1.312(11)	1.337(5)	1.338(5)	1.340(3)
C^2–C^3	**1.397(4)** 1.393(4)	**1.387(3)** 1.389(3)	**1.385(11)** 1.362(12)	1.394(5)	1.386(6)	1.381(3)
C^3–C^4	**1.370(4)** 1.381(4)	**1.394(4)** 1.379(3)	**1.393(10)** 1.379(13)	1.404(6)	1.404(6)	1.392(3)

[a]


[b] Bold font for ligand 1 and regular font for ligand 2.

Table 3
Selected bond angles (°) for Zn(II) pyrazolonate complexes

$[ZnL^1_2(MeOH)]$			
O(1S)–Zn–N(13)	89.77(9)	N(3)–Zn–S(2)	98.26(6)
O(1S)–Zn–N(3)	90.88(9)	O(1S)–Zn–S(1)	119.31(8)
N(13)–Zn–N(3)	177.78(8)	N(13)–Zn–S(1)	95.33(6)
O(1S)–Zn–S(2)	113.92(8)	N(3)–Zn–S(1)	82.50(6)
N(13)–Zn–S(2)	83.41(6)	S(2)–Zn–S(1)	126.75(3)
$[ZnL^2_2]\cdot$ MeOH			
N(3)–Zn–N(13)	104.36(7)	N(3)–Zn–S(2)	133.38(6)
N(3)–Zn–S(1)	88.13(6)	N(13)–Zn–S(2)	86.72(5)
N(13)–Zn–S(1)	129.79(6)	S(1)–Zn–S(2)	119.32(3)
$[ZnL^3_2]$ (*Form I*)			
N(3)–Zn–N(6)	124.5(3)	N(3)–Zn–S(1)	86.75(17)
N(3)–Zn–S(2)	123.6(2)	N(6)–Zn–S(1)	117.6(2)
N(6)–Zn–S(2)	87.7(2)	S(2)–Zn–S(1)	120.54(15)
$[ZnL^3_2]$ (*Form II*)[a]			
N(3)–Zn(1)–N(3)^{i}	133.33(19)	N(6)–Zn(2)–N(6)^{ii}	140.63(19)
N(3)–Zn(1)–S(1)	87.47(9)	N(6)–Zn(2)–S(2)	86.63(9)
N(3)–Zn(1)–S(1)^{i}	113.21(10)	N(6)–Zn(2)–S(2)^{ii}	109.39(10)
S(1)–Zn(1)–S(1)^{i}	127.58(7)	S(2)–Zn(2)–S(2)^{ii}	132.14(7)
$[ZnL^4_2]$[b]			
N(3)–Zn–N(3)^{i}	127.48(10)	N(3)–Zn–S	86.90(5)
N(3)–Zn–S^{i}	113.01(5)	S–Zn–S^{i}	135.26(4)

Symmetry operators: for a (i) $-x+1, -y+1/2, z$; (ii) $-x+3/2, y, -z$; for b (i) $-x, y, -z+1/2$.

the asymmetric unit contains one molecule of complex and one molecule of MeOH. The methanol is not bound to the metal in $[ZnL^2_2]\cdot$ MeOH but in $[ZnL^1_2(MeOH)]$ it occupies one coordination position, thus increasing the coordination number to five.

All five structures contain monodeprotonated N(3), S-coordinated pyrazolones formed by cyclization processes. Deprotonation of the N(3)H group and coordination induce, in all cases, lengthening of the C=S bond {d(C–S) (Å) = 1.6703(15) in HL^3 [11], 1.673(2) in HL^4 [11], 1.663(2) in HL^2 [4] and 1.659(3) in HL^1 [4]} to the thiol form [1.695(2)–1.716(3) Å in the complexes, Table 2], whereas the N(1)–C(1) and N(2)–C(1) bonds become shorter and N(2)–N(3) and N(2)–C(4) either become longer or are not modified.

In $[ZnL^3_2]$ (*Form I*), $[ZnL^3_2]$ (*Form II*), $[ZnL^4_2]$ and $[ZnL^2]\cdot$ MeOH the coordination polyhedron can be described as a very distorted tetrahedron, with the main distortion being the N(3)–Zn–N(6) angle for $[ZnL^3_2]$ (*Form I*), the N(3)–Zn–N(3)^{i} and N(6)–Zn–N(6)^{ii} angles for $[ZnL^3_2]$ (*Form II*), the S–Zn–S^{i} angle for $[ZnL^4_2]$ and the N(3)–Zn–S(2) angle in $[ZnL^2_2]\cdot$ MeOH (see Table 3).

In $[ZnL^1_2(MeOH)]$, the incorporation of the solvent into the coordination sphere increases the coordination number to five and the geometry around the metal is now distorted trigonal bipyramidal ($\tau = 0.85$) [12], with the N(3) and N(13) atoms apical and the main distortions associated with the O(1S)–Zn–S(2) [113.92(8)°] and S(2)–Zn–S(1) [126.75(3)°] bond angles. The additional interaction of the metal with the MeOH induces a lengthening of the Zn–S bonds compared to those in four-coordinate complexes. Similar changes occur when other Zn(II) pyrazolonate complexes incorporate a water molecule into the metal coordination sphere [2]. The Zn–O1s bond distance in $[ZnL^1_2(MeOH)]$ [2.043(2) Å] is similar to the Zn–O(water) bond distance found in these complexes [2.017(4) and 2.092 Å] [4].

Several hydrogen bonding interactions were detected in all of these compounds (see Table 4). These interactions give rise to associations that expand the systems in one ($[ZnL^4_2]$), two {$[ZnL^3_2]$ (*Form II*) and $[ZnL^2_2]\cdot$ MeOH} or three {$[ZnL^3_2]$ (*Form I*) and $[ZnL^1_2(MeOH)]$} directions.

In $[ZnL^4_2]$, the substitution of one hydrogen in the $N(1)H_2$ group by one R group reduces the possibilities for hydrogen bonding with respect to the unsubstituted ligand. Thus, only two bonds are formed; one intramolecular N(1)–H ··· O, which is present in all the compounds, and one intermolecular N(1)–H···O^{i}, which links the molecules in chains (Fig. 2).

In $[ZnL^3_2]$ (*Form II*), in addition to the intramolecular N(1)–H(1A)···O(1) and N(4)–H(4A)···O(2) hydrogen bonds, there are intermolecular hydrogen bonds connecting molecule 1 and molecule 2 (see Table 4 and Figure S3) and this gives rise to a layered lattice that expands along the *ac* plane. Each of these layers is formed by stacking of tubes (or channels) that grow along the *a* axis and are piled up along the *c* axis. Adjacent layers are partially intercalated (although not intertwined) (see Fig. 3).

In $[ZnL^2_2]\cdot$ MeOH (Figure S4), one [N(11)–H(11B) ··· O(2)^{iii}] intermolecular hydrogen bond links molecules in chains parallel to the *c* axis. Each of these chains interacts with two neighbouring chains through MeOH bridges that give rise to – as in the previous complex – a layered network (see Fig. 4).

As mentioned above, the hydrogen bonding in $[ZnL^3_2]$ (*Form I*) and $[ZnL^1_2(MeOH)]$ (Table 4, Figures S5 and S6) results in a 3-D network (Figs. 5 and 6). In $[ZnL^3_2]$ (*Form I*), an N(1)–H(1B)···O(1)^{i} intermolecular hydrogen links molecules to give polymeric chains in the direction of the *a* axis. Furthermore, N(4)–H(4B)···O(1)^{ii} interactions between adjacent chains lead to an infinite three-dimensional network (Fig. 5). In $[ZnL^1_2(MeOH)]$, the O(1S)–H(1S)···O(1)^{iii} interaction associates molecules in dimers. These dimers, which are formed through N(11)–H(11B)···O(1)^{ii} interactions, associate in chains along the *a* axis and these chains, in turn, interact with one another [through N(1)–H(1B)···O(2)^{i} bonds] to give a 3-D network (Fig. 6).

3.2. NMR spectroscopy

The main signals observed in the ^1H and ^{13}C NMR spectra of $[ZnL^1_2(MeOH)]$ and $[ZnL^2]\cdot$ MeOH have

Table 4
Hydrogen bonds (Å, °) in Zn(II) complexes

D–H···A	d(D–H)	d(H···A)	d(D···A)	<(DHA)
$[ZnL^1{}_2 (MeOH)]$[a]				
N(1)–H(1A)···O(1)	0.86	1.99	2.670(3)	135.2
N(1)–H(1B)···O(2)^{i}	0.86	1.96	2.803(3)	165.2
N(11)–H(11A)···O(2)	0.86	2.01	2.682(3)	134.5
N(11)–H(11B)···O(1)^{ii}	0.86	2.14	2.982(3)	167.1
O(1S)–H(1S)···O(1)^{iii}	0.68(3)	1.90(3)	2.582(3)	176(4)
$[ZnL^2{}_2]\cdot MeOH$[b]				
N(1)–H(1A)···O(1)	0.86	1.9575	2.6412	135.58
N(1)–H(1B)···O(1S)^{i}	0.86	1.9361	2.7922	173.44
O(1S)–H(1S)···O(2)^{ii}	0.82	1.9731	2.7680	163.13
N(11)–H(11A)···O(2)	0.86	2.0109	2.6825	134.22
N(11)–H(11B)···O(2)^{iii}	0.86	1.9281	2.7711	166.28
$[ZnL^3{}_2]$ (*Form I*)[c]				
N(1)–H(1A)···O(1)	0.86	1.98	2.658(8)	134.7
N(1)–H(1B)···O(1)^{i}	0.86	1.89	2.747(8)	168.1
N(4)–H(4A)···O(2)	0.86	1.96	2.637(11)	134.4
N(4)–H(4B)···O(1)^{ii}	0.86	2.07	2.919(11)	170.3
$[ZnL^3{}_2]$ (*Form II*)[d]				
N(1)–H(1A)···O(1)	0.86	2.01	2.678(4)	134.1
N(1)–H(1B)···O(2)^{i}	0.86	2.09	2.916(4)	161.1
N(4)–H(4A)···O(2)	0.86	2.01	2.683(4)	133.8
N(4)–H(4B)···O(1)^{ii}	0.86	1.94	2.792(4)	170.0
$[ZnL^4{}_2]$[e]				
N(1)–H(1)···O	0.80(3)	1.97(3)	2.645(3)	142(3)
N(1)–H(1)···O^{i}	0.80(3)	2.50(3)	3.016(2)	123(2)

Symmetry operators: for a (i) $x+1/2, -y+3/2, z-1/2$; (ii)$-x, -y+2, -z$; (iii) $-x+1, -y+2, -z$; for b (i) $x, 1+y, z$; (ii) $1-x, 1-y, 1-z$; (iii) $x, 1, 5-y, -0, 5+z$; for c (i) $x+1/2, -y-1/2, z$; (ii)$-x, -y, z+1/2$; for d (i) $x-1/2, -y, z$; (ii) $x, -y, -z+1/2$; for e (i) $-x+1/2, -y+1/2, -z+1$.

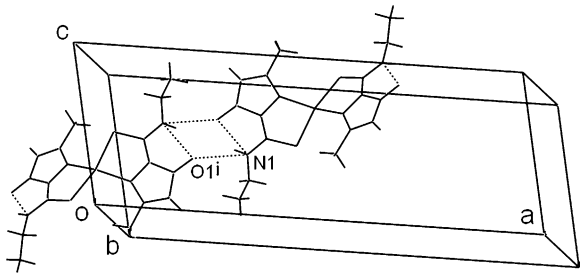


Fig. 2. Chain formed by hydrogen bonding in $[ZnL^4{}_2]$.

been described elsewhere [4] and those of $[ZnL^3{}_2]$ and $[ZnL^4{}_2]$ are given in Section 2 of this work. All signals show changes with respect to those of the free thiosemicarbazones and this is indicative of cyclization and metallation.

Evidence for cyclization is provided by: (a) the disappearance of signals corresponding to the R_3 groups, (b) the absence of the signal corresponding to the proton on C(3) in the ^{1}H NMR spectra and (c) the shielding (about 50 ppm) of the C(3) signal in the ^{13}C NMR spectra.

On the other hand, the absence of the signal corresponding to the N(3)H group in the ^{1}H NMR spectrum of the complexes is consistent with the deprotonation and metallation of the pyrazolone ligand. Furthermore,

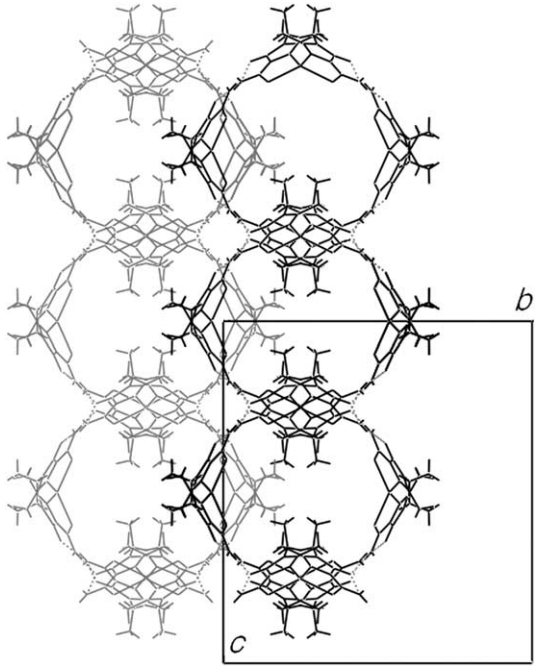


Fig. 3. Layers disposition in $[ZnL^3{}_2]$ (*Form II*) (view parallel to x axis).

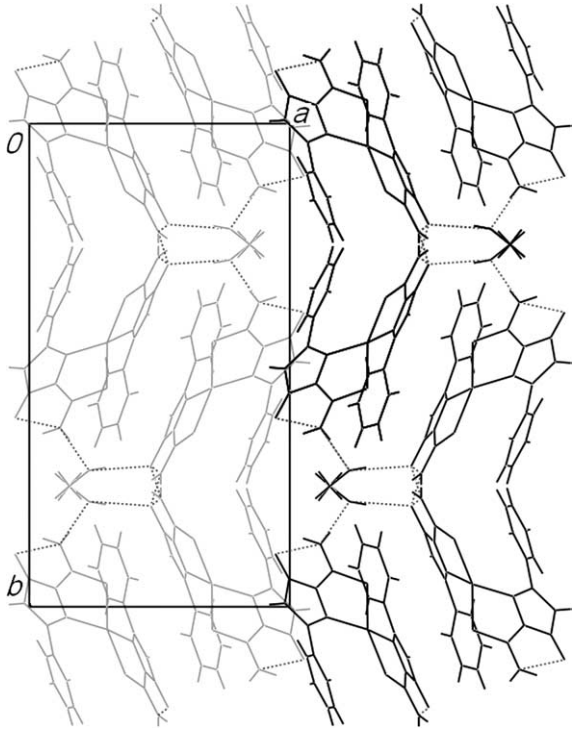


Fig. 4. Layers in $[ZnL^2_2]\cdot$ MeOH (view parallel to z axis).

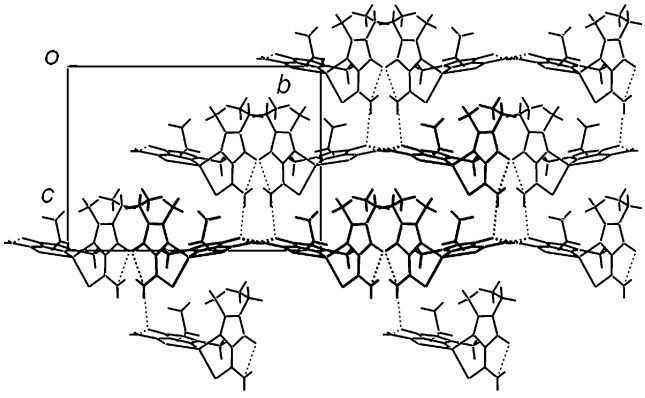


Fig. 5. Three-dimensional network in $[ZnL^3_2]$ (*Form I*) (view parallel to the x axis).

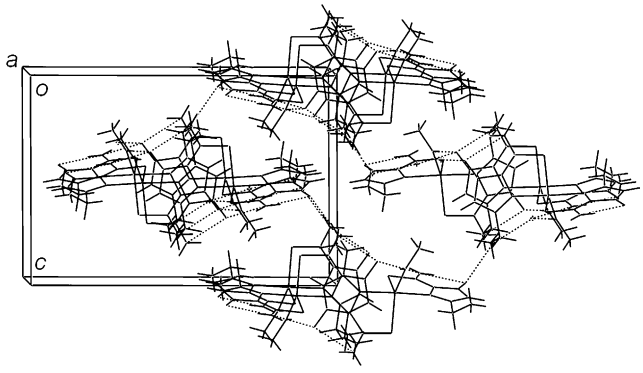


Fig. 6. Three-dimensional network in $[ZnL^1_2(MeOH)]$ (view parallel to the x axis).

the protons of the amine group and the C(2) atom are more deshielded and the C(1) atom slightly more shielded in the complexes than in the free pyrazolones. These changes could be associated with the presence, at least partially, of N(3), S-coordination in DMSO solution.

In summary, zinc(II) acetate is able to induce cyclization under mild conditions of the thiosemicarbazones derived from β-keto esters, possibly with any substituents in the starting molecule. The resulting 5-pyrazolone-1-carbothioamide reacts with the metal to give pyrazolonate complexes with the ligand bound in an N(3), S manner. When the reaction is performed using 1(metal):2(ligand) molar ratio of reactants – as in this work – the 5-pyrazolone loses one proton upon metallation to give molecular complexes that are only associated through hydrogen bonds (for another possibility see [4]).

As the metal retains some residual acidity, it can increase its distorted tetrahedral coordination up to five by interacting with an additional molecule of base, such as a solvent molecule. It is probable that this acidity can be modulated by changing the substituents on the amine group or on the ring, leading to a range of options to obtain five-coordinate complexes. Additional work in this area is currently underway.

Acknowledgment

We thank the Secretaria Xeral de Investigación e Desenvolvemento, Xunta de Galicia, Galicia, Spain, for financial support under Project PGIDT00PX120301PR.

Appendix A. Supplementary data

Additional information on the structure determinations has been deposited at the Cambridge Crystallographic Data Centre (CCDC numbers 67643–267647). Figures S3 to S6 showing hydrogen bonding in compounds $[ZnL^3_2]$ (*Form II*), $[ZnL^2_2]\cdot$MeOH, $[ZnL^3_2]$ (*Form I*) and $[ZnL^1_3]$, respectively. Supplementary data associated with this article can be found, in the online version, at doi:10.1016/j.poly.2005.06.040.

References

[1] J.S. Casas, M.V. Castaño, E.E. Castellano, M.S. García-Tasende, A. Sánchez, M.L. Sanjuán, J. Sordo, Eur. J. Inorg. Chem. (2000) 83.
[2] J.S. Casas, M.V. Castaño, E.E. Castellano, J. Ellena, M.S. García-Tasende, A. Gato, A. Sánchez, L.M. Sanjuán, J. Sordo, Inorg. Chem. 41 (2002) 1550.
[3] R. Carballo, J.S. Casas, E. García-Martínez, G. Pereiras-Gabián, A. Sánchez, J. Sordo, E.M. Vázquez-López, Inorg. Chem. 42 (2003) 6395.

[4] J.S. Casas, M.V. Castaño, M.S. García-Tasende, E. Rodríguez-Castellón, A. Sánchez, L.M. Sanjuán, J. Sordo, Dalton Trans. (2004) 2019.
[5] G.M. Sheldrick, SADABS. Program for Absorption Correction, University of Göttingen, Germany, 1996.
[6] G.M. Sheldrick, SHELX97. An Integrated System for Solving and Refining Crystal Structures from Diffraction Data, University of Göttingen, Germany, 1997.
[7] H.D. Flack, Acta Crystallogr., Sect. A 39 (1983) 876.
[8] J.L. Farrugia, J. Appl. Crystallogr. 30 (1997) 565.
[9] A.L. Spek, PLATON 99, A Multipurpose Crystallographic Tool, University of Utrecht, Utrecht, The Netherlands, 1999.
[10] I.J. Bruno, J.C. Cole, P.R. Edgington, M.K. Kessler, C.F. Macrae, P. McCabe, J. Pearson, R. Taylor, Acta Crystallogr., Sect. B 58 (2002) 876.
[11] J.S. Casas, A. Touceda (unpublished work).
[12] A.W. Addison, T.N. Rao, J. Reedijk, J. van Rijn, G.C. Verschoor, J. Chem. Soc., Dalton Trans. (1984) 1349.

limited to $Hf(OSi^tBuMe_2)_4(Et_2NH)$ [12] and to $Hf(acac)_2(OSi^tBuMe_2)_2$ [15f] although SSP might allow better homogeneity and lower temperature of deposition [16,17].

We wish to report herein the synthesis and characterization of precursors containing both hafnium and silicon, namely $Hf(thd)_2[N(SiMe_3)_2]_2$ (**3**), $Hf(thd)_2(OSiMe_3)_2$ (**4**) and $Hf(thd)_2(OSi^tBuMe_2)_2$ (**5**). Preliminary results of their evaluation for the deposition of $HfSi_xO_y$ films are also reported.

2. Experimental

Syntheses were performed under argon using Schlenk tubes and vacuum line techniques. Solvents were purified by standard methods and stored over molecular sieves. $HfCl_4$, lithium trimethylsilyloxide and lithium bis(trimethylsilyl)amide (Aldrich) were used as received. 2,2,6,6-tetramethyl-3,5-heptanedione (thdH) was dried over molecular sieves. $HfCl_2(thd)_2$ was obtained by improving the reported procedure.[18] FT-IR spectra were recorded with a Perkin–Elmer Paragon 500 Spectrometer as Nujol mulls. ^1H NMR spectra were registered on a Bruker 300 MHz NMR spectrometer. Elemental analyses were done at the Centre de microanalyses du CNRS. TGA experiments were performed under N_2 with a Netzsch-Gerätebau STA 409PC system between 20 and 800 °C using a thermal ramp of 10 °C/min. The spectroscopic data (FT-IR, NMR) are collected in Table 1.

2.1. Synthesis of $Hf(thd)_2Cl_2$ (1) and of $Hf(thd)_3Cl$ (2)

2,2,6,6-tetramethyl-3,5-heptanedione (1.99 g, 10.8 m mol) was added to a suspension $HfCl_4$ (1.73 g, 5.4 mmol) in 15 ml of toluene. Dissolution gave a sligthly yellow solution after 15 min. After refluxing for 16 h and evaporation to dryness, the crude product was washed with petroleum ether (10 ml) giving **1** as a precipitate (2.32 g, 84%). Evaporation of the washings gave **2** (0.1 g, 3%). **1** sublimes at 120–130 °C/2×10^{-4} Torr. *Anal.* Calc. for $C_{22}H_{38}Cl_2HfO_4$: C, 42.90; H, 6.22; Cl, 11.52. Found: C, 43.10; H, 6.34; Cl, 11.07%.

The same procedure applied to 0.97 g of $HfCl_4$ (3 mmol) and 2,2,6,6-tetramethyl-3,5-heptanedione (1.68 g, 9.1 mmol) in 30 ml of toluene, gave after 18 h of reflux and cooling, crystals of **2** (0.8 g, 35%) at −20 °C. **2** sublimes at 130–140 °C/2×10^{-4} Torr. *Anal.* Calc. for $C_{33}H_{57}ClHfO_6$: C, 51.90; H, 7.52; Cl, 4.64. Found: C, 52.05; H, 7.65; Cl, 4.35%.

2.2. Synthesis of $Hf(thd)_2[N(SiMe_3)_2]_2$ (3)

0.72 g (4.2 mmol) of lithium bis(trimethylsilyl)amide were added to $Hf(thd)_2Cl_2$ (1.33 g, 2.1 mmol) in 30 ml

Table 1
IR and NMR data of the various hafnium compounds $Hf(thd)_{4-x}X_x$ (X = Cl, $OSiR_3$, $N(SiMe_3)_2$; $x = 1,2$

Compounds	^1H NMR (ppm, $CDCl_3$)			FT-IR (cm^{-1})	
	CH	^{t}Bu	X	νC–O, νC–C	Hf-X
$Hf(thd)_2Cl_2$ **1**	5.96 (2H)	1.16 (18H)		1607 sh, 1567sh, 1553 sh, 1537 vs, 1511 vs,	644 m, 628 m, 584 w, 508 m, 478 m
$Hf(thd)_2[N(SiMe_3)_2]_2$ **3**	5.86 (2H)	1.10 (36H)	0.02 (Me, 36H)	1574 vs,1542 vs, 1538vs, 1506 vs,	615 s, 487 sh, 484 s
$Hf(thd)_2(OsiMe_3)_2$ **4**	5.85 (5.82) (2H)	1.11 (18H)	0.02 (Me, 18H)	1585 vs, 1574 vs, 1547 vs, 1531 vs, 1509 vs,	621 vs, 610 s, 480 s, 471s
$Hf(thd)_2(OSi^tBuMe_2)_2$ **5**	5.90 (2H)	1.10 (18H)	0.83 (18H, ^{t}Bu) −0.07 (12H, Me)	1609 s,1590 vs, 1565 m, 1561 s, 1540 s, 1509 vs	631 s, 619s, 585 w, 510 s, 476 s
$Hf(thd)_3Cl$ **2**	6.13 (3H)	1.18 (27H)		1590 sh, 1566 vs, 1536 vs, 1513 vs	619 m, 590 w, 498 m, 482 m

of toluene. After refluxing for 18 h, filtration and evaporation to dryness, the crude product was recrystallized in pentane (1.5 g, 72%) at −20 °C. **3** sublimes at 130–140 °C/2×10^{-4} Torr. *Anal.* Calc. for $C_{28}H_{56}HfO_6Si_2$: C, 49.21; H, 8.26. Found: C, 49.55; H, 8.32%. **3** is extremely air sensitive giving a soluble product analyzing as $Hf_2(thd)_4O([N(SiMe_3)_2]_2$.

2.3. Synthesis of $Hf(thd)_2(OSiMe_3)_2$ (4)

0.51 g of lithium trimethylsiloxide (5.2 mmol) was added to $Hf(thd)_2Cl_2$ (1.65 g, 2.6 mmol) in 15 ml of toluene. After refluxing for 3 h and filtration, the filtrate was concentrated. Crystals (1.2 g, 69%) were obtained at −20 °C. **4** sublimes at 130–140 °C/2×10^{-4} Torr. *Anal.* Calc. for $C_{28}H_{56}HfO_6Si_2$: C, 46.49; H, 7.80. Found: C, 46.72; H, 7.95%.

2.4. Synthesis of $Hf(thd)_2[OSi^tBuMe_2]_2$ (5)

0.79 ml of tertbutyldimethylsilanol (5 mmol) were added to $Hf(thd)_2[N(SiMe_3)_2]_2$ (2.12 g, 2.5 mmol) in 20 ml of toluene. After refluxing for 15 h, the solution was evaporated to dryness. The crude product was recrystallized in pentane, giving crystals (1.48 g, 75%) at −20 °C. **5** sublimes at 130–140 °C/2×10^{-4} Torr. The same product was obtained quantitatively by reacting **1** (1 g, 1.6 mmol) with $OHSi^tBuMe_2$ (0.43 g, 3.2 mmol) in 30 ml of toluene. After refluxing for 3 h, the solution was evaporated to dryness. *Anal.* Calc. for $C_{34}H_{68}HfO_6Si_2$: C, 50.57; H, 8.49. Found: C, 50.75; H, 8.65%.

All compounds were soluble in usual organic solvents including aliphatic and aromatic hydrocarbons.

2.5. X-ray structure determination

Suitable crystals of $HfCl(thd)_3$ **2** were obtained as colorless plates from the last crop of crystals of a synthesis of **1** after recrystallization in petroleum ether. Crystals of **5** were obtained in pentane at 0 °C. The crystals were mounted on a Nonius KappaCCD diffractometer equipped with Mo Kα radiation. Accurate cell dimensions were obtained from 262 (**2**) and 72 (**5**) reflections collected at 150 K in the range $2° < \theta < 25°$. Crystallographic data, main collection parameters and refinement features are listed in Table 2. The data were corrected for Lorentz and polarization effects. Computations were performed by using the PC version of CRYSTALS [19]. Scattering factors and corrections for anomalous dispersion were taken from [20]. The structures were solved by direct methods (SIR92) [21] for **2** and SHELX [22] for **5** and refined on F^2 by full-matrix least-squares with anisotropic displacement parameters for all non hydrogen atoms. Hydrogen atoms (except for compound **2**, those on disordered ^{t}Bu groups in a crystallographic mirror) were introduced in calculated positions in the last refinements with an overall isotropic displacement parameter.

Table 2
Crystallographic data and structure refinement

	5	**2**
Empirical formula	$C_{34}H_{68}HfO_6Si_2$	$C_{33}H_{57}ClHfO_6$
Formula weight	1272.52	763.75
Space group	$P2_1/c$	$P2_1/m$
Crystal system	monoclinic	monoclinic
a (Å)	10.854(3)	10.5328(14)
b (Å)	35.606(13)	17.9618(11)
c (Å)	11.781(3)	10.8268(14)
α (°)	90	90
β (°)	107.058(18)	117.31(1)
γ (°)	90	90
V (Å^3)	4352.9(22)	1820.1(4)
Z	4	2
Temperature (K)	150	150
μ (Mo Kα) (mm^{-1})	2.486	2.976
θ Range (°)	3–25	5–25
hkl ranges	−14 to 13, −46 to 46, −14 to 14	−13 to 12, −21 to 23, −10 to 14
Number of reflections collected	55028	13898
Number of unique reflections (R_{int})	8924 (0.02)	4302 (0.03)
Data/restraints/parameters	5586/0/388	3650/0/214
Goodness-of-fit on F^2	0.91	0.99
R_1, wR_2 [$I > 3\sigma(I)$][a]	0.0615, 0.122	0.045, 0.115
R_1, wR_2 (all data)	0.0986, 0.127	0.0544, 0.126
Residual electron density	3.41 and −2.13	1.64 and −2.31

[a] $R_1 = \sum \|F_o - |F_c\| / \sum |F_o|$, $wR_2 = [\sum[w(F_o^2 - F_c^2)^2] / \sum[w(F_o^2)^2]]^{1/2}$.

2.6. CVD experiments

Pulsed liquid-injection MOCVD (PI-MOCVD) was used for preliminary tests of the new compounds for deposition of hafnium silicate films. This technique is based on repetitive injections of microdoses of solutions of a volatile metal-organic precursor, flash evaporation, vapor transport by a carrier gas and decomposition on a hot substrate [23]. Depositions were carried out on Si(1 0 0) substrates at 600–800 °C, using an Ar + O_2 mixture as carrier gas. Solutions of **3**–**5** in toluene (0.05 M) were used as precursor sources. They were injected by microdoses of several micro-litres into an evaporator heated at 250 °C. The crystallization of the films was studied by X-ray diffraction (XRD) with a Bruker D8 diffractometer (Cu Kα radiation). X-ray photoelectron spectroscopy (XPS; RIBER LAS-3000, Mg Kα radiation) was used for composition analysis.

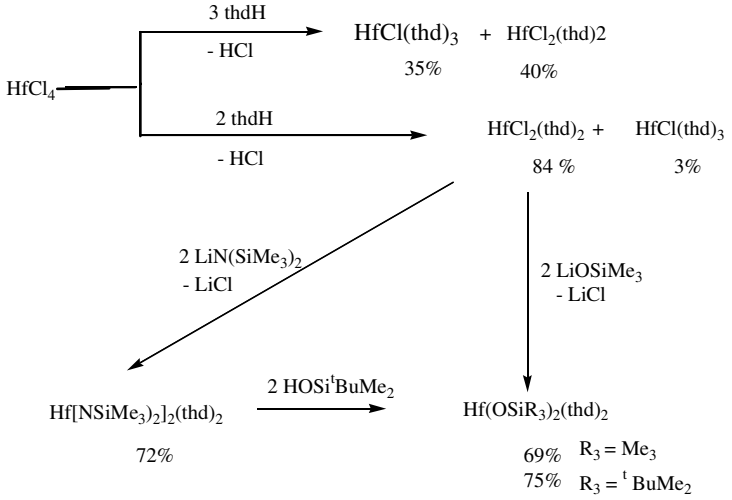
3. Results and discussion

3.1. Synthesis and characterization

The reaction between $HfCl_4$ and thdH (1:2 stoichiometry) afforded after refluxing and work-up a crystalline material **1** analysing as $HfCl_2(thd)_2$. The last crop of crystals corresponded to a more substituted compound $HfCl(thd)_3$ **2**. **2** was obtained in better yields by reacting $HfCl_4$ and thdH in the appropriate stoichiometry, 1:3. Various substitution reactions (Scheme 1) applied to **1** afforded single-source precursors for MOCVD of hafnium silicate namely $Hf[N(SiMe_3)_2](thd)_2$ (**3**), $Hf(OSiMe_3)_2(thd)_2$ (**4**) and $Hf(OSi^tBuMe_2)(thd)_2$ (**5**) in high yields. Surprisingly, the chlorine atoms of $HfCl_2(thd)_2$ were quite labile toward the $OHSi^tBuMe_2$ silanol and **5** could be obtained either by silanolysis of **3** or by reaction between **1** and the silanol, in the absence of any base. The compounds were isolated by crystallization. They were volatile and sublimed in similar conditions [130–140 °C/2×10^{-4} Torr]. The *tert*-butyldimethylsiloxide OSi^tBuMe_2 was selected as siloxide because of the well known ability of the *tert* butyl group to be thermally eliminated as isobutylene [24].

The various compounds were characterized by elemental analyses, FT-IR and ^1H NMR. The spectroscopic data are collected in Table 1. The FT-IR spectra display the characteristics *ν*CO absorption of the β-diketonate ligands. These, as well as the Hf–O vibration in the 650–480 cm^{-1} area were diagnostic for the identification of either the bis or tris-substituted β-diketonates **1** and **2**. The siloxides are also characterized by a strong absorption band at 950 cm^{-1}. The FT-IR spectra confirmed the absence of *ν*OH of NH absorption bands and thus the absence of coordination either by silanol or by an amine as observed for instance for the reaction between $Hf(NMe_2)_4$ and $OHSi^tBuMe_2$ giving $Hf(OSi^tBuMe_2)_4(Me_2NH)$ [15d]. The ^1H NMR spectra confirm the formula of the various compounds. The chemical shifts of the CH groups of the β-diketonate ring are, as well as the FT-IR data, diagnostic for their identification.

The thermal properties of precursors **3**–**5** were studied by TGA under 1 atm of N_2 (Fig. 1) in the 20–800 °C range. **3** leaves 11.5% of residue, the theoretical value for decomposition into HfO_2 being 24.3%. The main process is thus sublimation (∼53%), with part of **3** being decomposed into oxide. In contrast, **4** and **5** sublime to at least ∼90% as shown by the small residues (∼3%). **4** appears as the most volatile under the TGA conditions used. Thus, the thermal stability of the complexes under the TGA conditions used increases along the ranking **3** < **4** < **5.**



Scheme 1. Syntheses of the various derivatives (all reaction in at r.t.).

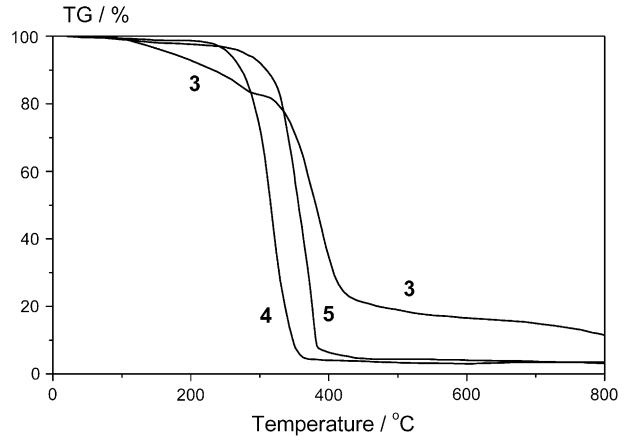


Fig. 1. Thermogravimetric data (N_2, 1 atm) of compounds **3**–**5**.

3.2. Molecular structures of $Hf(thd)_2(OSi^tBuMe_2)_2$ and of $HfCl(thd)_3$

The identity of compound **5** was established by X-ray diffraction studies. $Hf(thd)_2(OSi^tBuMe_2)_2$ corresponds to a monomer as depicted in Fig. 2, the metal being 6-coordinate. The Hf–O bond lengths range from 1.937(7) to 2.170(7) Å, the Hf–O(Si) are as expected shorter (1.951 Å av.) than the Hf–O(thd) ones. The Hf–O–Si angles (169.5° av.) are large. This can be attributed to π-donation of the oxygen lone pairs either into the empty 3d Si orbitals. [25] or into the empty 5d orbitals of hafnium. Indeed, large Hf–O–C bonds are also associated to terminal alkoxide ligands [26]. Hf–O–C angles as large as 175.5° av. have for instance been observed for $HfAl_2(\mu\text{-}OiPr)_2(\mu,\eta^2\text{-}OC_2H_4NMe_2)_2(OiPr)_6$ [27]. The siloxide ligands exert a trans effect and the Hf–O(thd) distances *trans* to the siloxides are noticeably longer (2.168 Å av.) than those *trans* to a β-diketonate (av. 2.078 Å) (Table 3). The coordination polyhedron is distorted as a result of the bulky siloxide in *cis* position (∠O5–Hf–O6 99.6(3)°] and of the small bite angle (78.45° av.) of the β-diketonate ligands.

Hafnium is 7-coordinate in $HfCl(thd)_3$ (Fig. 3, Table 4). The stereochemistry is that of a distorted capped trigonal prism, the molecule having a plane of symmetry through Hf–Cl–O3–C4–C5–C6 and O4–C41–C43–C61–C62. The Hf–Cl bond distance is quite long 2.482(2) Å. The Hf–O(thd) bond lengths are shorter, they display similar values (2.105(5)–2.122(4) Å], their average value being similar to that observed in **5** for hexacoordinated hafnium.

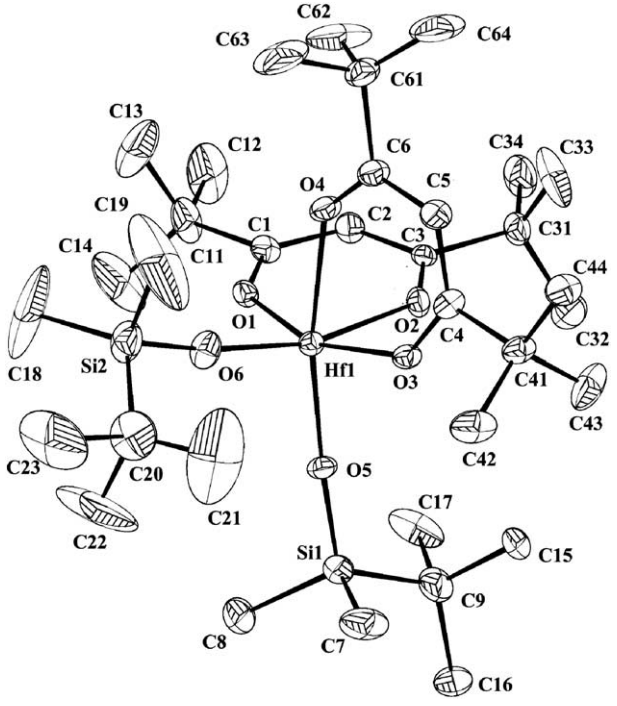


Fig. 2. Molecular structure of $Hf(thd)_2(OSi^tBuMe_2)_2$ showing the atom labeling scheme (ellipsoids at 20% probability).

3.3. $HfSi_xO_y$ films

$HfSi_xO_y$ films were deposited at 600–800 °C. X-ray diffraction $\theta/2\theta$ scans for some $HfSi_xO_y$ films are presented in Fig. 4. Films grown with **3** and **5** were amorphous in all the temperature range, while those deposited with **4** at 800 °C showed some signs of crystallization. XPS was used for the study of composition of the deposited $HfSi_xO_y$ films and of their contamination level. XPS spectra revealed that both Hf and Si were present in all films (Fig. 5). The bulk of the films (studied

Table 3
Selected bond distances and angles of $Hf(thd)_2(OSi^tBuMe_2)_2$

Bond lengths (Å)	
Hf(1)–O(1)	2.070(6)
Hf(1)–O(2)	2.166(6)
Hf(1)–O(3)	2.087(6)
Hf(1)–O(4)	2.170(7)
Hf(1)–O(5)	1.966(7)
Hf(1)–O(6)	1.937(7)
Bond angles (°)	
O(1)–Hf(1)–O(2)	78.0(2)
O(1)–Hf(1)–O(3)	159.7(2)
O(2)–Hf(1)–O(3)	85.3(2)
O(1)–Hf(1)–O(4)	86.8(3)
O(2)–Hf(1)–O(4)	80.0(3)
O(3)–Hf(1)–O(4)	78.9(2)
O(1)–Hf(1)–O(5)	99.5(3)
O(2)–Hf(1)–O(5)	92.9(3)
O(3)–Hf(1)–O(5)	92.7(3)
O(4)–Hf(1)–O(5)	169.4(3)
O(1)–Hf(1)–O(6)	93.3(3)
O(2)–Hf(1)–O(6)	165.9(3)
O(4)–Hf(1)–O(6)	88.5(3)
O(5)–Hf(1)–O(6)	99.6(3)
O(3)–Hf(1)–O(6)	100.6(3)
Hf(1)–O(6)–Si(2)	169.3(6)
Hf(1)–O(5)–Si(1)	169.8(5)

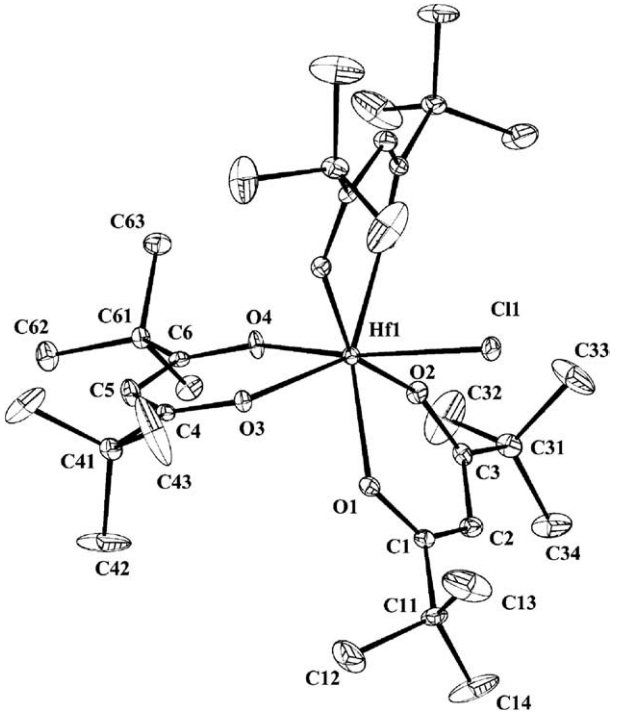


Fig. 3. Molecular structure of $HfCl(thd)_3$ showing the atom labeling scheme (ellipsoids at 20% probability).

Table 4
Selected bond distances and angles of $Hf(thd)_3Cl$

Bond lengths (Å)	
Hf(1)–Cl(2)	2.482(2)
Hf(1)–O(1)	2.122(4)
Hf(1)–O(1)	2.121(4)
Hf(1)–O(2)	2.120(4)
Hf(1)–O(2)	2.121(4)
Hf(1)–O(3)	2.113(5)
Hf(1)–O(4)	2.105(5)
Angles (°)	
Cl(2)–Hf(1)–O(1)	81.9(1)
Cl(2)–Hf(1) – O(1)	82.0(1)
O(1)–Hf(1) – O(1)	125.9(2)
Cl(2)–Hf(1) – O(2)	85.9(1)
O(1)–Hf(1) – O(2)	76.8(1)
O(1)–Hf(1)–O(2)	151.9(2)
Cl(2)–Hf(1)–O(2)	86.0(1)
O(1)–Hf(1)–O(2)	152.0(1)
O(1)–Hf(1)–O(2)	76.7(1)
O(2)–Hf(1)–O(2)	77.2(2)
Cl(2)–Hf(1)–O(3)	122.7(1)
O(1)–Hf(1)–O(3)	73.2(1)
O(1)–Hf(1)–O(3)	73.3(1)
O(2)–Hf(1)–O(3)	133.8(1)
Cl(2)–Hf(1)–O(4)	160.8(1)
O(1)–Hf(1)–O(4)	106.0(1)
O(1)–Hf(1)–O(4)	105.9(1)
O(2)–Hf(1)–O(4)	79.1(1)
O(2)–Hf(1)–O(4)	79.0(2)
O(3)–Hf(1)–O(4)	76.5(2)

after removal of several nanometers thick surface layer by etching with Ar^+ ions) contained high amounts of hafnium with respect to silicon ($Hf/(Hf + Si) = 0.70$–

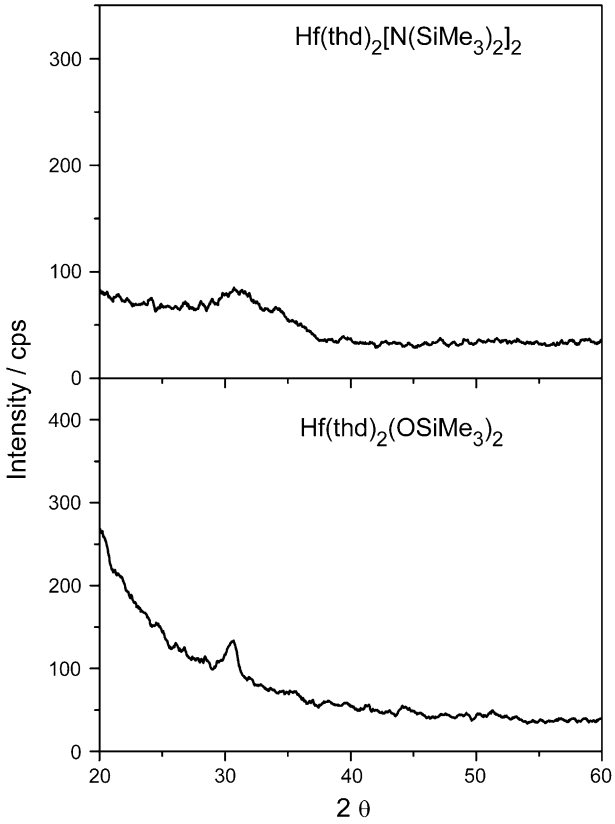


Fig. 4. XRD θ–2θ patterns of some $HfSi_xO_y$ films deposited on silicon and R plane sapphire at 700 °C.

0.85). The bulk of the film was quite pure, the contamination by carbon decreased for higher deposition temperatures and was ~0% after etching for the films issued from 5 for instance). In general, the Si/Hf ratio in the $HfSi_xO_y$ films was significantly lower than in the initial precursor without clear dependence on the temperature of deposition or on the precursor used. Similar observations were reported with $Hf(NEt_2)_4$/^{t} Bu-

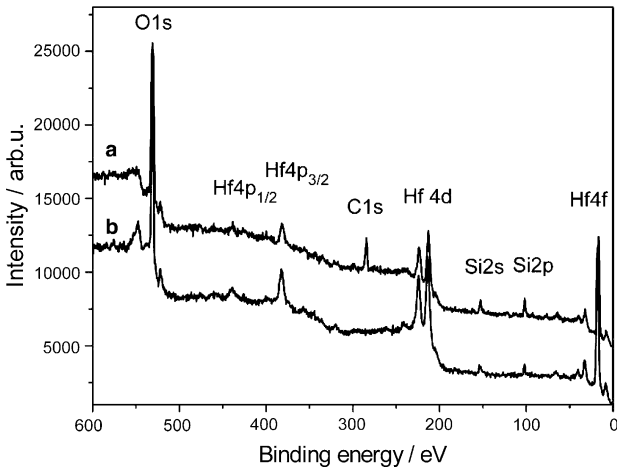


Fig. 5. XPS spectra of a $HfSi_xO_y$ film grown at 700 °C from $Hf(thd)_2(OSi^tBuMe_2)_2$: (a) surface, (b) after 30 min surface cleaning by sputtering with Ar^+ at 1.5 keV.

Me_2SiOH as source [15d]. These results suggest that desorption of Si-containing fragments from the substrate might occur, partial precursor decomposition in the gas phase near the substrate can also play a role. However, our first data allow us to conclude that compounds **3**–**5** are suitable for the incorporation of SiO_2 into HfO_2 films in an amount sufficient for the stabilization of amorphous films. More detailed study of the growth and properties of the $HfSi_xO_y$ films are in progress in order to define the best precursor among compounds **3**–**5** [28].

4. Conclusions

$Hf[N(SiMe_3)_2]_2(thd)_2$ (**3**), $Hf(OSiMe_3)_2(thd)_2$ (**4**), $Hf(OSi^tBuMe_2)_2(thd)_2$ (**5**) were synthesized and characterized by elemental analyses, FT-IR, ^1H NMR and TGA. The molecular structure of **5** is a distorted octahedron with siloxide ligands in *cis* positions despite their steric bulk. The complexes are volatile and were tested as single-source MOCVD precursors for the deposition of hafnium silicate films $HfSi_xO_y$. Amorphous films were grown at 600–800 °C on Si(100). The Si/Si + Hf ratio in the bulk of films varied from 0.15 to 0.30 without clear dependence on the deposition temperature and/or on the precursor. These ratio although far from those in the initial precursors were sufficient for the stabilization of amorphous films.

5. Supplementary material

Crystallographic data (tables of coordinates, of thermal parameters, of bond lengths and angles) have been deposited at the Cambridge Crystallographic Data Base Centre. CCDC Reference Nos. 220717 for $HfCl(thd)_3$ and 220718 for the Si derivative. Copies of this information may be obtained free of charge from The Director, CCDC, 12 Union Road, Cambridge, CB2 1EZ, UK (fax: + 44 1223 336 033; e-mail: deposit@ccdc.cam.ac.uk or www: http://www.ccdc.cam.ac.uk).

Acknowledgements

L.H.P. and S.P. are grateful for financial support by MINEFI (Crolles 2) and Vilnius University, respectively.

References

[1] L. Manchanda, M.D. Morris, M.L. Green, R.B. van Dover, F. Klemens, T.W. Sorsch, P.J. Silverman, G. Wilk, B. Busch, S. Aravamudhan, Microelectr. Eng. 59 (2001) 351.
[2] R.G. Gordon, J. Becker, D. Hausmann, S. Suh, Chem. Mater. 13 (2001) 2463.
[3] J.M. Morais, G.V. Soares, R. Pezzi, K.P. Bastos, M.C.M. Alves, I.J.R. Rotondaro, J.J. Chambers, M.R. Visokay, L. Colombo, Proceedings, Electrochemical Society, 2003, vol. 2002-28 (Physics and Technology of high-k dielectrics I), 179.
[4] S.V. Pasko, L.G. Hubert-Pfalzgraf, A. Abrutis, P. Richard, A. Bartasyte, V. Kazlauskiene, J. Mater. Chem. 14 (2004) 1245.
[5] A. Abrutis, L.G. Hubert-Pfalzgraf, S.V. Pasko, A. Bartasyte, F. Weiss, V. Janickis, J. Cryst. Growth 267 (2004) 529.
[6] S.V. Pasko, A. Abrutis, L.G. Hubert-Pfalzgraf, Mater. Lett. 59 (2005) 261.
[7] A. Baunemann, T. Reiji, R. Becker, M. Winter, R.A. Fischer, P.W.R. Ehrhart, A. Devi, Chem. Commun. (2004) 1610.
[8] S. Mantl, in Neue Materialien für die Informationstechnik, Alternative Gate dielectrics for FET devices, D1, Forschungszentrum Jùlich GmbH, 2001, p. 1–20.
[9] G.D. Wilk, R.M. Wallace, Appl. Phys. Lett. 74 (1999) 2854.
[10] D.A. Neumayer, E. Cartier, J. Appl. Phys. 90 (2001) 1801.
[11] K. Kukli, M. Ritala, M. Leskelä, T. Sajavaara, J. Keinonen, D.C. Gilmer, P.J. Tobin, Mater. Sci. Eng. B 109 (2004) 2.
[12] A.C. Jones, H.C. Aspinall, P.R. Chalker, R.J. Potter, K. Kukli, A. Rathu, M. Ritala, M. Leskela, J. Mater. Chem. 14 (2004) 3101.
[13] B.C. Hendrix, A.S. Borovik, C. Xu, J.F. Roeder, T.H. Baum, M.J. Bevan, M.R. Visokay, J.J. Chambers, A.L.P. Rotondaro, H. Bu, L. Colombo, Appl. Phys. Lett. 80 (2002) 2362.
[14] Y. Ohshita, A. Ogura, M. Ishikawa, A. Hoshino, S. Hiiro, T. Suzuki, H. Machida, Thin Solid Films 416 (2002) 208.
[15] (a) J. Kim, K. Yong, J. Cryst. Growth 263 (2004) 442;
(b) V. Rangarajan, H. Bhandari, T.M. Klein, Thin Solid Films 419 (2002) 1;
(c) P.R. Chalker, A.C. Jones, Proceedings, Electrochemical Society, 2004, 2003-22 (Physics and Technology of High-k gate dielectric II), 73.;
(d) J.L. Roberts, P.A. Marshall, A.C. Jones, P.R. Chalker, J.F. Bickley, P.A. Williams, S. Taylor, L.M. Smith, G.W. Critchlow, M. Schumacher, J. Lindner, J. Mater. Chem. 14 (2004) 391;
(e) L. Zhang, Z. Zhang, S.A. Campbell, W. Gladfelter, J. Mater. Chem. 14 (2004) 3203;
(f) M. Lemberger, A. Paskaleva, S. Zürcher, A.J. Bauer, L. Frey, H. Ryssel, Microel. Reliab. 45 (2005) 819.
[16] L.G. Hubert-Pfalzgraf, Coord. Chem. Rev. 178–80 (1998) 967.
[17] L.G. Hubert-Pfalzgraf, Inorg. Chem. Commun. 6 (2003) 102.
[18] W.W. Zhuang, D.R. Evans, Patent 2002, US 6472337, EP 1308419 (A1).
[19] D.J. Watkin, C.K. Prout, J.R. Carruthers, P.W. Betteridge, Crystals Issue 10, Chemical Crystallography Laboratory, University of Oxford, UK, 1996.
[20] D.T. Cromer (Ed.), International Tables for X-Ray Crystallography, vol. 4, Kynoch Press, Birmingham, UK, 1974.
[21] A. Altomare, G. Cascarano, G. Giacovazzo, A. Guagliardi, M.C. Burla, G. Polidori, M. Camalli, J. Appl. Cryst. 27 (1994) 435.
[22] G.M. Sheldrick, SHELXS86, Program for the solution of crystal structures, Univ. of Göttingen, Germany, 1986.
[23] (a) J.P. Senateur, F. Weiss, O. Thomas, R. Madar, A. Abrutis, Patent 93/08838 PCT FR94/00858 (Europe, USA);
(b) A. Abrutis, V. Plausinaitiene, V. Kubilius, A. Teiserskis, Z. Saltyte, R. Butkute, J.P. Senateur, Thin Solid Films 413 (2002) 32;
(c) J.P. Senateur, C. Dubourdieu, V. Galindo, F. Weiss, A. Abrutis, in: K.-L. Choy (Ed.), Innovative processing of films and nanocrystalline powders, Imperial College Press, London, 2002, p. 71.
[24] S. Zürcher, M. Morstein, N.D. Spencer, M. Lemberger, A. Bauer, Chem. Vap. Dep. 8 (2002) 171.

[25] B. Marciniec, H. Maciejewski, Coord. Chem. Rev. 223 (2001) 301, and ref therein.
[26] D.C. Bradley, R.C. Mehrotra, I.P. Rothwell, A. Singh, Alkoxo and aryloxo derivatives of metals, Academic Press, London, 2001.
[27] L.G. Hubert-Pfalzgraf, S.V. Pasko, N. Touati, A. Abrutis, submitted.
[28] S.V. Pasko, A. Abrutis, L.G. Hubert-Pfalzgraf, V. Kazlauskiene, to be published.

only simple substitution products $[M_3(CO)_{10}(C_4H_4N_2)]$. The Ru and Os analogues have different structures. The Os-derivative has only terminal carbonyl ligands but the Ru analog has three bridging carbonyls [8,9]. However, in both the structures, the two nitrogen atoms of the 1,2-diazine occupy axial positions of two metal atoms. The diimine bridged bis-triosmium pyrazine compound, $[(\mu\text{-H})Os_3(CO)_{10}]_2(pyz)$, and its 1:1 ligand to cluster complex, $[(\mu\text{-H})Os_3(CO)_{10}(pyz)]$ were prepared by reacting $[Os_3(CO)_{10}(MeCN)_2]$ with pyrazine [10]. Very recently Machhado et al. [11] reported that treatment of $[Os_3(CO)_{10}(MeCN)_2]$ with 2,3-bis(2-pyridyl)pyrazine at room temperature gave the cluster $[Os_3(CO)_{10}(C_{14}H_{10}N_4)]$ which contains the chelating ligand coordinated axially through one of the pyridine rings and equatorially through a pyrazine-nitrogen atom. The reaction of the trirhenium cluster $[(\mu\text{-H})_4Re_3(CO)_{10}]^-$ with 1,2-diazine has been reported to give $[(\mu\text{-H})_3Re_3(CO)_{10}(\mu\text{-}\eta^2\text{-}N_2C_4H_3)]^-$ and $[(\mu\text{-H})_2Re_3(CO)_{10}(\mu\text{-}\eta^2\text{-}N_2C_4H_4)]^-$ where the former contains the orthometallated diazine, and the latter shows the ligand bridging through the two nitrogen atoms [12].

We previously reported the synthesis of triosmium clusters of the type $[Os_3(CO)_9(\mu\text{-OH})(\mu\text{-OMeCO})L]$ $\{L = SC(NMe_2)_2, PPh_3, P(OMe)_3\}$ from the reactions of $[Os_3(CO)_{11}L]$ with water in the presence of Me_3NO [13]. With the aim of synthesizing 2:1 cluster to ligand complexes of the type $[\{Os_3(CO)_9(\mu\text{-OH})(\mu\text{-OMeCO})\}_2(pyz)]$ we have investigated the reactions of $[Os_3(CO)_{12}]$ with pyrazine, 2-methylpyrazine, 2,3-dimethylpyrazine, and 2,3,5-trimethylpyrazine and water in the presence of a methanolic solution of Me_3NO. However, our initial objective of linking two triosmium clusters analogous to observation with reactions of pyrazine with $[Os_3(CO)_{10}(MeCN)_2]$ [11] remains unfulfilled. In contrast, the reactions exclusively resulted in 1:1 complexes of the type $[Os_3(CO)_9(\mu\text{-OH})(\mu\text{-OMeCO})L]$ (L = pyrazine, 2-methylpyrazine, 2,3-dimethylpyrazine, and 2,3,5-trimethylpyrazine). The synthetic and characterization details of these clusters as well as the crystal structures of four compounds are described herein.

2. Experimental

All the reactions were performed under a nitrogen atmosphere using standard Schlenk techniques. Solvents were dried and distilled prior to use by standard methods. $[Os_3(CO)_{12}]$ was purchased from Strem. Pyrazine, 2-methylpyrazine, 2,3-dimethyl pyrazine, 2,3,5-trimethylpyrazine, PPh_3, $P(OMe)_3$, ^tBuNC and C_5H_5N were purchased from Aldrich and used as received. Infrared spectra were recorded on a Shimadzu FT-IR 8101 spectrophotometer. ^1H and $^{31}P\{^1H\}$ NMR spectra were recorded on a Varian Unity Plus 400 and a Bruker DPX 400 spectrometers.

2.1. Reaction of $[Os_3(CO)_{12}]$ with pyrazine and water in the presence of Me_3NO/CH_3OH

To a suspension of $[Os_3(CO)_{12}]$ (0.200 g, 0.221 mmol), pyrazine (0.089 g, 1.1 mmol) and water (two drops) in benzene (60 mL), a methanolic solution (5 mL) of Me_3NO (0.043 g, 0.573 mmol) was added dropwise from a dropping funnel for 45 min. The reaction mixture was heated to reflux for 5 h during which time the color changed from yellow to orange. The solvent was removed under reduced pressure and the residue dissolved in a minimum volume of acetone and chromatographed on silica gel TLC plates. Elution with hexane/CH_2Cl_2 (3:2, v/v) gave two bands. The faster moving band was too small for complete characterization. The slower moving band gave $[Os_3(CO)_9(\mu\text{-OH})(\mu\text{-OMeCO})(\eta^1\text{-NCHCHNCHCH-})]$ (**1**) (0.098 g, 45%) as red crystals from benzene (*Anal.* Calc. for $C_{15}H_8N_2O_{12}Os_3$: C, 18.40; H, 0.82; N, 2.86. Found: C, 18.65; H, 0.98; N, 2.92%). IR (ν (CO), CH_2Cl_2): 2091s, 2074w, 2054vs, 1999vs, 1984s, 1921m cm^{-1}, KBr: ν (OH) 3404m, methoxycarbonyl, 1495m cm^{-1}; ^1H NMR (CD_2Cl_2): δ 9.00 (d, 2H, $J = 2.8$ Hz), 8.85 (d, 1H, $J = 2.8$ Hz), 8.78 (d, 1H, $J = 2.8$ Hz), 3.97 (s, 3H), −1.05 (s, 1H); mass spectrum: (m/z) 978 $[M]^+$.

2.2. Reaction of $[Os_3(CO)_{12}]$ with 2-methylpyrazine and water in the presence of Me_3NO/CH_3OH

A similar reaction to that above of $[Os_3(CO)_{12}]$ (0.200 g, 0.221 mmol), 2-methylpyrazine (0.104 g, 1.10 mmol), water (2 drops) and a methanolic solution (5 mL) of Me_3NO (0.043 g, 0.57 mmol) for 7 h followed by similar chromatographic separation afforded $[Os_3(CO)_9(\mu\text{-OH})(\mu\text{-OMeCO})(\eta^1\text{-N=C(CH}_3\text{)CH=NCH=CH—})]$ (**2**) (0.083 g, 38%) as orange crystals recrystallization from benzene at room temperature (*Anal.* Calc. for $C_{16}H_{10}N_2O_{12}Os_3$: C, 19.37; H, 1.02; N, 2.82. Found: C, 19.58; H, 1.25, N, 2.91%). IR (ν (CO), CH_2Cl_2): 2091s, 2053s, 1997vs, 1983s , 1921s cm^{-1}, KBr: ν (OH) 3405m, methoxycarbonyl, 1500m cm^{-1}; ^1H NMR (CD_2Cl_2): δ 8.59 (s, 1H), 8.45 (s, 1H), 8.35 (s, 1H), 3.95 (s, 3H), 2.64 (s, 3H), −1.31 (s, 1H); mass spectrum: (m/z) 992 $[M]^+$.

2.3. Reaction of $[Os_3(CO)_{12}]$ with 2,3-dimethyl pyrazine and water in the presence of Me_3NO/CH_3OH

A similar treatment of $[Os_3(CO)_{12}]$ (0.200 g, 0.221 mmol), 2,3-dimethylpyrazine (0.119 g, 1.10 mmol), water (2 drops) and a methanolic solution (5 mL) of Me_3NO (0.047 g, 0.63 mmol) followed by removal of solvent gave an orange residue which was dissolved in a minimum volume of CH_2Cl_2 and chromatographed by TLC

on silica gel. Elution with hexane/CH_2Cl_2 (2:3, v/v) gave one major and three minor bands. The major band afforded $[Os_3(CO)_9(\mu\text{-}OH)(\mu\text{-}CH_3OCO)\{\eta^1\text{-}N{=}C(CH_3)C(CH_3){=}NCH{=}CH{-}\}]$ (**3**) (0.078 g, 35%) as orange crystals recrystallization from benzene at room temperature (*Anal*. Calc. for $C_{17}H_{12}N_2O_{12}Os_3$: C, 20.28; H, 1.20; N, 2.78. Found: C, 20.42; H, 1.35; N, 2.93%). IR (ν (CO), CH_2Cl_2): 2093s, 2074w, 2054s, 1997vs, 1965s, 1919w, KBr: ν (OH) 3400m, methoxycarbonyl, 1500m cm^{-1}; ^1H NMR (CD_2Cl_2): δ 8.42 (1H), 8.35 (1H), 3.94 (3H), 2.76 (3H), 2.58 (3H), −1.13 (s, 1H); mass spectrum: (*m*/*z*) 1006 $[M]^+$.

2.4. Reaction of $[Os_3(CO)_{12}]$ with 2,3,5-trimethylpyrazine and water in the presence of Me_3NO/MeOH

$[Os_3(CO)_{12}]$ (0.200 g, 0.221 mmol), 2,3,5-trimethylpyrazine (0.135 g, 1.10 mmol), water (2 drops), Me_3NO (0.043 g, 0.57 mmol) in MeOH (5 mL) were reacted as above for 8 h. The solvent was removed under reduced pressure. The residue was dissolved in a minimum volume of acetone and chromatographed on silica gel TLC plates. Elution with hexane/CH_2Cl_2 (3:7, v/v) gave two bands. The first band was was too small for complete characterization. The second band gave $[Os_3(CO)_9(\mu\text{-}OH)(\mu\text{-}CH_3OCO)\{\eta^1\text{-}N{=}C(CH_3)C(CH_3){=}NC(CH_3){=}CH{-}\}]$ (**4**) (0.124 g, 55%) as yellow crystals after recrystallization from benzene at room temperature (*Anal*. Calc. for $C_{18}H_{14}N_2O_{12}Os_3$: C, 21.17; H, 1.38. Found: C, 21.32; H, 1.48%). IR (ν (CO), CH_2Cl_2): 2092s, 2074w, 2054vs, 1997vs, 1983w, 1918m cm^{-1}, KBr: ν (OH) 3420m, methoxycarbonyl, 1488m cm^{-1}; ^1H NMR (CD_2Cl_2): δ 8.23 (s, 1H), 3.94 (s, 3H), 2.88 (s, 3H), 2.62 (s, 3H), 2.51 (s, 3H), −1.19 (s, 1H); mass spectrum: (*m*/*z*) 1020 $[M]^+$.

2.5. Reaction of **1** with PPh_3, $P(OMe)_3$, ^{t}BuNC and pyridine

The reactions of **1** with PPh_3, $P(OMe)_3$, and ^{t}BuNC were carried out with 2 equiv. of the respective ligand. A typical reaction of **1** with PPh_3 was carried as follows: To a dichloromethane solution (20 ml) of **1** (0.051 g, 0.052 mmol) was added PPh_3 (0.027 g, 0.10 mmol) and the reaction mixture was stirred at room temperature for 30 min. Analytical TLC indicated complete consumption of **1**. The solvent was removed under reduced pressure and the residue was chromatographed by TLC on silica gel. Elution with hexane/CH_2Cl_2 (2:1, v/v) gave a single band which afforded $[Os_3(CO)_9(\mu\text{-}OH)(\mu\text{-}CH_3OCO)(PPh_3)]$ (**5**) (0.045 g, 74%) as yellow crystals after recrystallization from hexane/CH_2Cl_2 at −4 °C. IR (ν (CO), CH_2Cl_2): 2087s. 2050vs, 2004vs, 1992s, 1980m, 1932w cm^{-1}; ^1H NMR (CD_2Cl_2): δ 7.41 (m, 15H), 3.58 (s, 3H), 1.93 (d, 1H, $J = 4.8$ Hz); $^{31}P\{^1H\}$ MNR (CD_2Cl_2): δ 21.1 (s). A similar treatment of **1** with PPh_3, $P(OMe)_3$, ^{t}BuNC and pyridine afforded $[Os_3(CO)_9(\mu\text{-}OH)(\mu\text{-}CH_3OCO)\{P(OMe)_3\}]$ (**6**) (85%), IR (ν (CO), CH_2Cl_2): 2088m, 2049vs, 2007s, 1978s, 1960w cm^{-1}; ^1H NMR (CD_2Cl_2): δ 3.90 (s, 3H), 3.75 (d, 9H, $J = 11.8$ Hz), 0.56 (d, 1H, $J = 5.9$ Hz); $^{31}P\{^1H\}$ NMR (CD_2Cl_2) 104.5 (s)), $[Os_3(CO)_9(\mu\text{-}OH)(\mu\text{-}OMeCO)(^t\text{BuNC})]$ (**7**) (89%), IR (ν (CO), CH_2Cl_2): 2177m, 2087s, 2049vs, 2007s, 1978m, 1945w cm^{-1}; ^1H NMR (CD_2Cl_2): δ 3.95 (s, 3H), 1.58 (s, 9H). 0.87 (s, 1H)), and $[Os_3(CO)_9(\mu\text{-}OH)(\mu\text{-}OMeCO)(\eta^1\text{-}NC_5H_5)]$ (**8**) (73%). IR (ν (CO), CH_2Cl_2): 2089m, 2050vs, 2005s, 1994s, 1979m, 1963w cm^{-1}; ^1H NMR (CD_2Cl_2): δ 8.57 (m, 2H), 7.92 (m, 1H), 7.42 (m, 2H), 3.92 (s, 3H), −1.54 (s, 1H).

2.6. Reaction of **2** with PPh_3, $P(OMe)_3$, ^{t}BuNC and pyridine

A similar reaction to that above of **2** with PPh_3, $P(OMe)_3$, ^{t}BuNC and pyridine followed by a similar chromatographic separation gave **5**, **6**, **7** and **8** in 81%, 88%, 75% and 71% yields, respectively.

2.7. Reaction of **3** with PPh_3, $P(OMe)_3$, ^{t}BuNC and pyridine

A similar treatment of **3** with PPh_3, $P(OMe)_3$, ^{t}BuNC and pyridine followed by similar chromatographic separation gave **5**, **6**, **7** and **8** in 79%, 81%, 77% and 79% yields, respectively.

2.8. Reaction of **4** with PPh_3, $P(OMe)_3$, ^{t}BuNC and pyridine

A similar reaction of **4** with PPh_3, $P(OMe)_3$, ^{t}BuNC and pyridine followed by similar chromatographic separation gave **5**, **6**, **7** and **8** in 78%, 73%, 84% and 88% yields, respectively.

2.9. X-ray structure determination of **2**, **3**, **4**, and **8**

Single crystals of **2**–**4** suitable for X-ray diffraction were grown by slow evaporation of benzene solution at room temperature and those of **8** by slow diffusion of hexane into a dichloromethane solution at −4 °C. Crystallographic data were collected at 150 K, on a CAD4 diffractometer using graphite monochromatized Mo Kα radiation ($\lambda = 0.71073$ Å). The unit cell parameters were determined from all observed reflections in a θ-range of 3–10° and refined using the entire data set. The structures were solved by direct methods (SHELXS-97) [14] and refined on F^2 by full matrix least-squares (SHELXL-97) [15] using all unique data. All non-hydrogen atoms were refined anisotropically. The hydrogen atoms were included in calculated positions (riding model) with U_{iso} set at 1.2 times the U_{eq} of the parent atom. Final difference maps did not show any residual electron den-

Table 1
Crystal data and refinement parameters of compounds **2**, **3**, **4** and **8**

	2 · C_6H_6	**3** · C_6H_6	**4**	**8**
Formula weight	1070.97	1084.99	1020.91	977.84
Crystal system	monoclinic,	monoclinic	orthorhombic	monoclinic
Empirical formula	$C_{16}H_{10}N_2O_{12}Os_3 \cdot C_6H_6$	$C_{17}H_{12}N_2O_{12}Os_3 \cdot C_6H_6$	$C_{18}H_{14}N_2O_{12}Os_3$	$C_{16}H_9NO_{12}Os_3$
Space group	$P2_1/n$	$C2/c$	$Pccn$	$P2_1/n$
a (Å)	9.96700(10)	18.5433(6)	18.398(4)	11.5641(4)
b (Å)	23.7924(4)	19.1476(5)	24.332(2)	14.4193(4)
c (Å)	10.5346(2)	18.5059(5)	12.954(3)	13.2005(4)
α (°)	90	90	90	90
β (°)	103.6630(10)	106.060(2)	90	95.947(16)
γ (°)	90	90	90	90
Volume (Å^3)	2427.47(7)	6314.3(3)	5799.0(19)	2189.29(12)
Z	4	8	8	4
D_{calc} (Mg m^{-3})	2.930	2.283	2.339	2.967
Absorption coefficient (mm^{-1})	15.735	12.100	13.167	17.430
$F(000)$	1944	3952	3680	1744
Crystal size (mm)	$0.18 \times 0.15 \times 0.12$	$0.20 \times 0.16 \times 0.15$	$0.22 \times 0.15 \times 0.15$	$0.24 \times 0.16 \times 0.12$
θ Range for data collection (°)	2.17–26.38	1.56–26.62	1.39–26.34	2.10–26.37
Limiting indices	$-12 \leqslant h \leqslant 12$	$-23 \leqslant h \leqslant 23$	$-20 \leqslant h \leqslant 22$	$-14 \leqslant h \leqslant 14$
	$-29 \leqslant k \leqslant 29$	$-23 \leqslant k \leqslant 23$	$-30 \leqslant k \leqslant 30$	$-17 \leqslant k \leqslant 18$
	$-13 \leqslant l \leqslant 13$	$-23 \leqslant l \leqslant 23$	$-14 \leqslant l \leqslant 16$	$-16 \leqslant l \leqslant 16$
Reflections collected	27371	50495	29151	27914
Independent reflections	4952 [$R_{int} = 0.0831$]	6503 [$R_{int} = 0.2974$]	5901 [$R_{int} = 0.0972$]	4472 [$R_{int} = 0.0865$]
Maximum and minimum transmission	0.2539 and 0.1640	0.2640 and 0.1958	0.2427 and 0.1597	0.2288 and 0.1025
Data/restraints/parameters	4952/1/328	6503/1/365	5901/0/321	4472/1/291
Goodness-of-fit on F^2	1.075	1.045	1.065	0.846
Final R indices [$I > 2\sigma(I)$]	$R_1 = 0.0365$,	$R_1 = 0.1041$	$R_1 = 0.0491$,	$R_1 = 0.0389$
	$wR_2 = 0.0920$	$wR_2 = 0.2813$	$wR_2 = 0.1270$	$wR_2 = 0.0985$
R indices (all data)	$R_1 = 0.0432$,	$R_1 = 0.1475$,	$R_1 = 0.1002$,	$R_1 = 0.0525$
	$wR_2 = 0.0960$	$wR_2 = 0.3189$	$wR_2 = 0.1511$	$wR_2 = 0.1084$
Largest difference in peak and hole (e Å^{-3})	1.824 and −2.819	3.931 and −3.661	2.752 and −1.365	1.539 and −1.900

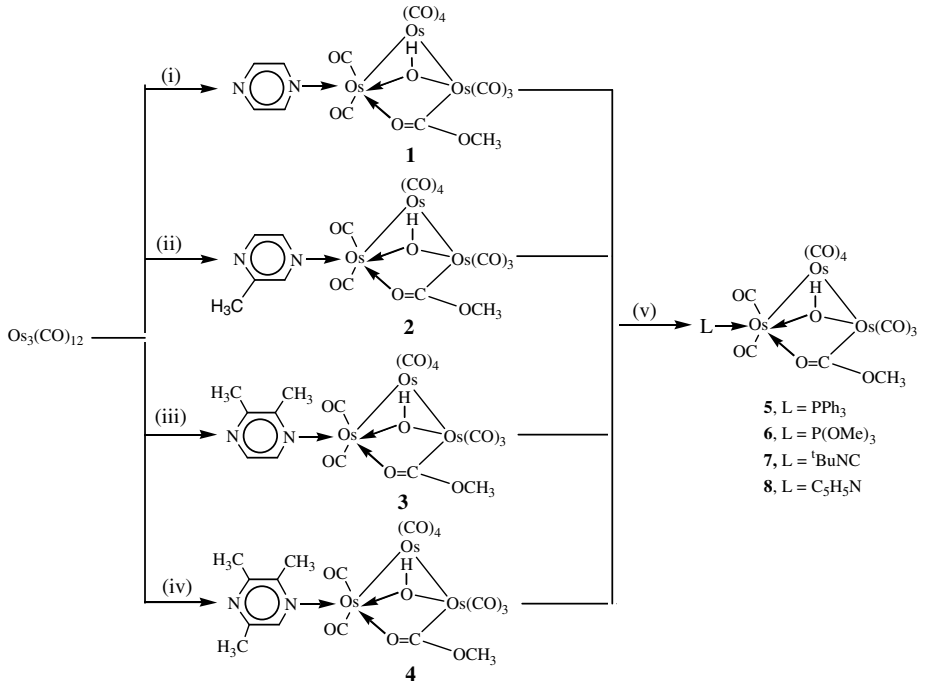
Details in common: X-ray radiation, Mo Kα ($\lambda = 0.71073$ Å), temperature (K) 150(2), refinement method: full-matrix least-squares on F^2.

sity of stereochemical significance. The details of the data collection and structure refinement are given in Table 1.

3. Results and discussion

The reactions of $[Os_3(CO)_{12}]$ with pyrazine, 2-methylpyrazine, 2,3-dimethylpyrazine, and 2,3,5-trimethylpyrazine and water in the presence of a methanolic solution of Me_3NO at 80 °C followed by usual workup and chromatographic separation gave the new compounds $[Os_3(CO)_9[(\mu\text{-OH})(\mu\text{-OMeCO})(\eta^1\text{-NCHCHN-CHCH-})]$ (**1**), $[Os_3(CO)_9(\mu\text{-OH})(\mu\text{-OMeCO})\{\eta^1\text{-N=C-(CH}_3)\text{CH=NCH=CH—}\}]$ (**2**), $[Os_3(CO)_9[(\mu\text{-OH})(\mu\text{-CH}_3\text{OCO})\{\eta^1\text{-N=C(CH}_3)\text{C(CH}_3)\text{=NCH=CH—}\}]$ (**3**), and $[Os_3(CO)_9[(\mu\text{-OH})(\mu\text{-CH}_3\text{OCO})\{\eta^1\text{-N=C(CH}_3)\text{C-(CH}_3)\text{=NC(CH}_3)\text{=CH—}\}]$ (**4**) in 45%, 38%, 35% and 55% yields, respectively. The synthetic details for all the compounds are shown in Scheme 1. The compounds have been characterized by spectroscopic data together with single crystal X-ray diffraction studies for **2**–**4**. Single crystals of **2** were found to exist as discrete molecules in the unit cell with no unusually short inter- or intramolecular contacts.

The solid-state structure of **2**, **3**, and **4** are shown in Figs. 1–3, respectively, crystallographic data are presented in Table 1 and selected bond distances and angles are listed in Table 2. The basic triangular metal skeleton core of **2**–**4** are the same. Each of them contains two Os–Os bonds and a non-bonded separation defined by two osmium atoms Os(1) ⋯ Os(3), nine terminal CO groups, a bridging hydroxy and a bridging methoxycarbonyl (MeOCO) ligand and one substituted pyrazine unit bonded to Os(1) atom though the N(1) atom. Atoms Os (1), Os (2) and Os (3) are ligated by two, four and three CO ligands, respectively. The open edge defined by the atoms Os(1) and Os(3) is mutually bridged by a hydroxy and a methoxycarbonyl ligand. A set of distinctly different metal–metal bonds, {Os(1)–Os(2) = 2.8286 (4) and Os(2)–Os(3) = 2.8744(4) Å for **2**; Os(1)–Os(2) = 2.8259(15) and Os(2)–Os(3) = 2.8805(14) Å for **3**; Os(1)–Os(2) = 2.8166(8) and Os(2)–Os(3) = 2.8631(9) Å for **4**} and non-bonded separation {Os(1) ⋯ Os(3) = 3.359 Å for **2**; Os(1) ⋯ Os(3) = 3.357 Å for **3**; and Os(1) ⋯ Os(3) = 3.375(1) Å for **4**} is comparable with the corresponding distances in $[Os_3(CO)_9(\mu\text{-OH})(\mu\text{-OMeCO})\{\eta^1\text{-SC(N-Me}_2)_2\}]$ {bonding distance = 2.836(1), 2.875 (1), and non-bonded separation = 3.379(1) Å} [13c]. The osmium–oxygen distances involving the asymmetrical



Scheme 1. Reagents and conditions: (i) pyrazine, $Me_3NO/MeOH + H_2O$, C_6H_6, 80 °C, 5 h; (ii) 2-methylpyrazine, $Me_3NO/MeOH + H_2O$, C_6H_6, 80 °C, 7 h; (iii) 2,3-dimethylpyrazine, $Me_3NO/MeOH + H_2O$, C_6H_6, 80 °C, 8 h; (iv) 2,3,5-trimethylpyrazine, $Me_3NO/MeOH + H_2O$, C_6H_6, 80 °C, 8 h; (v) $L' = PPh_3$, $P(OMe)_3$, ^tBuNC, C_5H_5N, CH_2Cl_2, 25 °C.

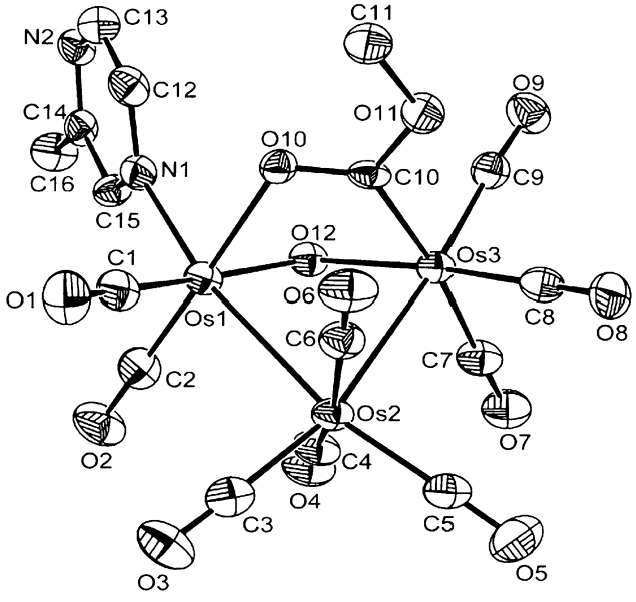


Fig. 1. Molecular structure of $[Os_3(CO)_9(\mu\text{-}OH)(\mu\text{-}OMeCO)\{\eta^1\text{-}N{=}C(CH_3)CH{=}NCH{=}CH{-}\}]$ (**2**) showing the atom-labeling scheme. Thermal ellipsoids are drawn at the 50% probability level.

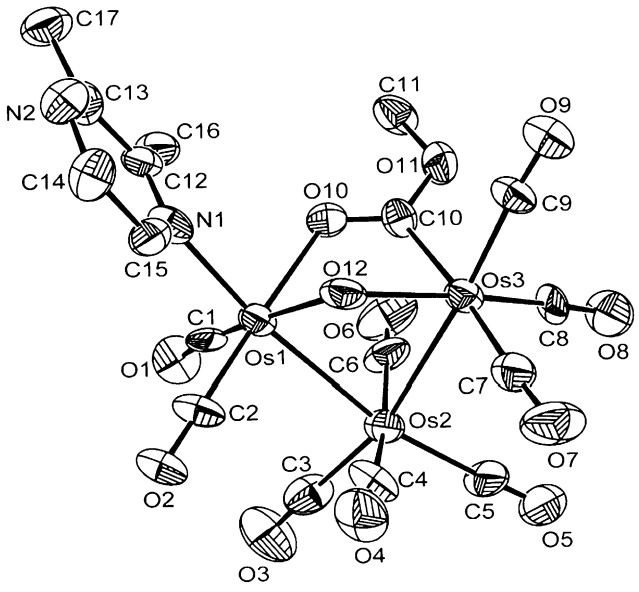


Fig. 2. Molecular structure of $[Os_3(CO)_9(\mu\text{-}OH)(\mu\text{-}CH_3OCO)\{\eta^1\text{-}N{=}C(CH_3)C{-}(CH_3){=}NCH{=}CH{-}\}]$ (**3**) showing the atom-labeling scheme. Thermal ellipsoids are drawn at the 35% probability level.

hydroxy bridge in **2** {Os(1)–O(12) = 2.113(5) and Os(3)–O(12) = 2.142(5) Å} are similar to those of the corresponding distances in **3** {2.17(2) and 2.128(18) Å} and comparable to those found in $[Os_3(CO)_9(\mu\text{-}OH)(\mu\text{-}OMeOCO)\{\eta^1\text{-}SC(NMe_2)_2\}]$ {2.148(8) and 2.084(9) Å} [13c] and $[(\mu\text{-}H)Os_3(CO)_9(\mu\text{-}OH)(PMe_2Ph)]$ {2.135(5) and 2.118(5) Å} [16]. In contrast, the μ-hydroxy ligand symmetrically spans the Os(1)–Os(3) edge in **4** and the Os–O distances {2.134(10) and 2.130(10) Å} are very similar to those found in $[(\mu\text{-}H)Os_3(CO)_{10}(\mu\text{-}OH)]$ {2.136(7) and 2.146(7) Å} [17]. The Os(1)–C(10) bond distance {2.146(5)Å} to methoxycarbonyl bridge in **2** is also similar

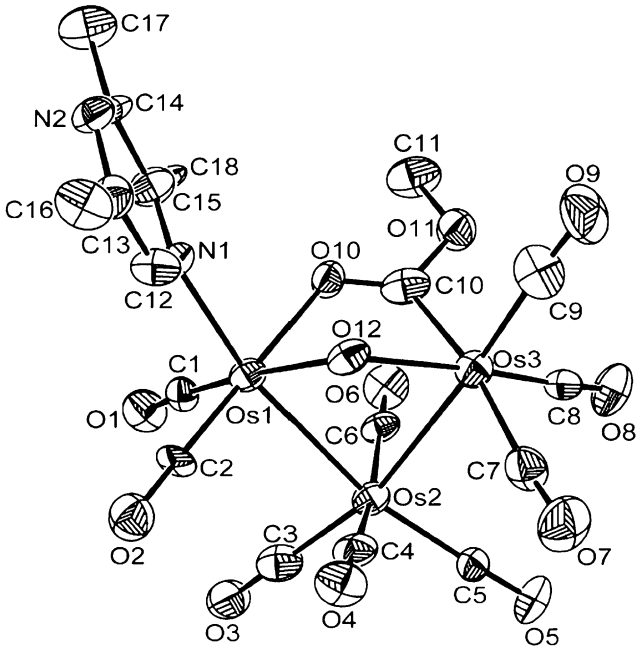


Fig. 3. Molecular structure of $[Os_3(CO)_9(\mu\text{-}OH)(\mu\text{-}CH_3OCO)\{\eta^1\text{-}N{=}C(CH_3)C(CH_3){=}NC(CH_3){=}CH{-}\}]$ (**4**) showing the atom-labeling scheme. Thermal ellipsoids are drawn at the 50% probability level.

to that in **4** {2.137(10) Å} but slightly shorter than that in **3** {2.195(18) Å}. The Os(3)–C(10) bond distance of 2.074(7) Å in **2** is almost equal in magnitude to that of 2.093(16) Å in **4** but substantially shorter than that of 2.13(3) Å in **3**. The 2-methylpyrazine ligand in **2** is coordinated through the *meta* imino nitrogen atom and occupies an equatorial coordination site on Os(1). Similarly, 2,3-dimethylpyrazine and 2,3,5-trimethylpyrazine are also equatorially bound to the Os(1) atom in **3** and **4**, respectively. The η^1-coordinated Os(1)–N(1) bond distance of 2.171(6) Å in **2** is identical to that of 2.217(11) Å in **4**, but somewhat longer than the corresponding distance in **3** {2.23(2) Å} and comparable to that of 2.19(3) in $[(\mu\text{-}H)_4Os_4(CO)_{11}(\eta^1\text{-pyp})]$ (pyp = pyrido[2,3-b]pyrazine) in which the pyp ligand is coordinated through the nitrogen atom of the pyrazole ring [18]. The three acute angles defined by Os(1)–Os(2)–Os(3) in **2**, **3** and **4** are almost equal in magnitude {Os(1)–Os(2)–Os(3) = 72.179(10) for **2**; 72.07(4) for **3** and 72.91(2) for **4**}. Thus, the mode of attachment and disposition of all the ligands in **2** are akin to that of **3** and **4**. The MeOCO ligand is a normal 3 electron donating acyl type bridge that is most probably formed by deprotonation of methanolic OH bond (by NMe_3) followed by attack of CH_3O^- at a coordinated CO ligand. As usual, in each compound, both the bridging MeOCO and OH ligands act as three-electron donor, and the pyrazine derivatives donate two electrons to the cluster which results in a total of 50 valence electrons and the observation of two formal Os–Os bonds in the trinuclear framework is consistent with the electron count.

The spectroscopic data of **2**, **3**, and **5** are consistent with the solid-state structure and are very similar to the spectroscopic data for **1**. The infrared spectra of **1**–**4** in the carbonyl stretching region are very similar to those reported for $[Os_3(CO)_9(\mu\text{-}OH)(\mu\text{-}OMeCO)(PPh_3)]$ [13b], indicating that they have very similar structures.

Table 2
Selected Bond distances (Å) and angles (°) for **2**, **3**, **4**, and **8**

	2	**3**	**4**	**8**
Bond distances				
Os(1)–Os(2)	2.8286(4)	2.8259(15)	2.8166(8)	2.8394(5)
Os(2)–Os(3)	2.8744(4)	2.8805(14)	2.8631(9)	2.8861(6)
Os(1)–Os(3)	3.359	3.357	3.375	3.373
Os(1)–N(1)	2.171(6)	2.23(2)	2.217(11)	2.185(8)
Os(1)–O(12)	2.113(5)	2.17(2)	2.134(10)	2.108(6)
Os(3)–O(12)	2.142(5)	2.128(18)	2.130(10)	2.118(6)
Os(3)–O(10)	2.146(5)	2.195(18)	2.137(10)	2.148(6)
Os(3)–C(10)	2.074(7)	2.13(3)	2.093(16)	2.110(10)
O(10)–C(10)	1.273(8)	1.20(3)	1.194(18)	1.237(12)
Bond angles				
Os(1)–Os(2)–Os(3)	72.179(10)	72.07(4)	72.91(2)	72.186(18)
Os(3)–O(12)–Os(1)	104.3(2)	102.9(8)	104.7(4)	105.9(3)
O(12)–Os(3)–Os(2)	80.41(13)	82.2(5)	80.5(3)	79.92(18)
O(12)–Os(1)–Os(2)	81.98(13)	82.9(5)	81.6(3)	81.21(17)
N(1)–Os(1)–Os(2)	165.83(15)	169.0(6)	166.4(3)	167.5(2)
O(12)–Os(1)–N(1)	84.0(2)	86.3(7)	85.5(4)	88.3(3)
C(10)–O(10)–Os(1)	115.0(4)	116.3(17)	115.8(10)	116.2(6)
C(10)–Os(3)–O(12)	82.5(2)	82.5(8)	81.0(5)	82.1(3)
O(10)–Os(1)–Os(2)	91.16(12)	89.9(5)	88.9(3)	88.81(17)
C(10)–Os(3)–Os(2)	86.12(17)	86.5(7)	84.1(4)	85.0(3)
O(10)–Os(1)–N(1)	84.9(2)	86.6(7)	85.2(4)	83.0(3)
O(12)–Os(1)–O(10)	81.25(17)	80.9(6)	81.1(4)	82.2(3)
O(10)–C(10)–Os(3)	123.4(5)	123.2(19)	125.8(12)	123.7(7)

In addition to the adsorption bands due to terminally coordinated carbonyl ligands, the solid-state infrared spectra of **1**–**4** exhibit absorptions due to the methoxy carbonyl bridge (1500–1488 cm^{-1}) and bridging hydroxyl group (3420–3400 cm^{-1}). The mass spectra of compounds **1**–**4** exhibit a parent peak at *m*/*z* 979, 993, 1007 and 1027, respectively, and fragmentation peaks due to the successive loss of nine carbonyl ligands. In addition to the aromatic proton resonances for the pyrazine ring, the ^1H NMR spectra of **1**–**4** exhibit characteristic resonances for the methyl protons of the methoxy carbonyl ligand (δ 3.97 for **1**; 3.95 for **2**; 3.94 for **3**; 3.94 for **4**) and the hydroxyl proton (δ −1.05 for **1**; −1.31 for **2**; −1.13 for **3**; −1.19 for **4**). It is notable that the resonances of the bridging hydroxyl proton of these complexes are strongly shielded. The strongly shielded resonances for the protons of bridging hydroxy ligands have been observed previously [13,19,20].

We have previously reported that the η^1-tetramethylthiourea ligand in $[Os_3(CO)_9(\mu\text{-}OH)(\mu\text{-}OMeCO)\{\eta^1\text{-}SC(NMe_3)_2\}]$ is labile and could be easily displaced by various two electron donor ligands [13b]. Keeping this in mind, we have investigated the reactions of **1**–**4** with a series of two electron donor ligands. As expected each of the compounds **1**–**4** reacts with L′ at room temperature to give the previously reported compounds $[Os_3(CO)_9(\mu\text{-}OH)(\mu\text{-}OMeCO)(L')]$ {**5**, L′ = PPh_3; **6**, L′ = $P(OMe)_3$; **7**, L′ = ^{t}BuNC; **8**, L′ = C_5H_5N} in high yields (70–90%) as shown in Scheme 1. We have characterized compounds **5**–**8** by a comparison of their spectroscopic data (see Section 2) with those reported [13b] along with a single crystal X-ray diffraction studies for **8**. As described for **2**–**4**, crystals of **8** were found to exist as discrete molecules in the unit cell with no unusually short inter- or intramolecular contacts. The solid-state structure of **8** is depicted in Fig. 4, crystallographic data are presented in Table 1 and selected bond distances and angles are listed in Table 2. The molecule consists of an open cluster of three osmium atoms with two different metal–metal bonds {Os(1)–Os(2) = 2.8394(5) and Os(2)–Os(3) = 2.8861(6) Å} which are comparable with the corresponding distances of 2.875(1) and 2.836(1) Å in $[(\mu\text{-}H)Os_3(CO)_8(\mu_3\text{-}S)(\mu\text{-}OMeCO)\{\eta^1\text{-}SC(NMe_3)_2\}]$ [13c], 2.8286(4) and 2.8744(4) Å in **2**, 2.8259(15) and 2.8805(14) Å in **3** and 2.8166(8) and 2.8631(9) Å in **4**. The open Os(1)–Os(3) edge is simultaneously bridged by the methoxycarbonyl and the hydroxy ligands and the non-bonded distance of 3.373 Å is virtually identical to that of 3.379(1) Å in $[(\mu\text{-}H)Os_3(CO)_8(\mu_3\text{-}S)(\mu\text{-}OMeCO)\{\eta^1\text{-}SC(NMe_3)_2\}]$ [13c], and 3.375 in **4** and slightly longer than that of 3.359 in **2**, and 3.357 in **3**. The μ-hydroxy ligand symmetrically bridges the Os(1)–Os(3) edge and the Os–O distances {2.108(6) and 2.118(6) Å} are comparable to those found in **2**. The disposition of pyridine, two bridging ligands (MeOCO– and –OH) and the nine terminal CO groups are quite similar to that of **2**, **3** and **4**. The Os(3)–O(10) bond distance in the methoxycarbonyl bridge {2.110(10) Å} is slightly shorter than that of 2.13(3) Å in **3** but slightly larger than 2.074(7) Å in **2** and 2.093(16) Å in **4**. The pyridine ligand is coordinated to Os(1) through nitrogen atom N(1) and occupies an equatorial coordination site of Os(1). The Os(1)–N(1) bond distance of 2.185(8) Å is slightly longer than that of 2.14(3) Å in the η^1-coordinated pyridinecarboxyaldehyde ligand in $[(\mu\text{-}H)_4Os_4(CO)_{11}(\eta^1\text{-pya})]$ [18] and comparable to that of 2.171(6) Å in **2** but somewhat shorter than those of 2.23(2) Å in **3** and 2.217(11) Å in **4**. The overall structure of **8** is very similar to those of **2**–**4**, with exception of the pyridine ligand coordinated to Os(1) instead of the pyrazine ligands in **2**–**4**.

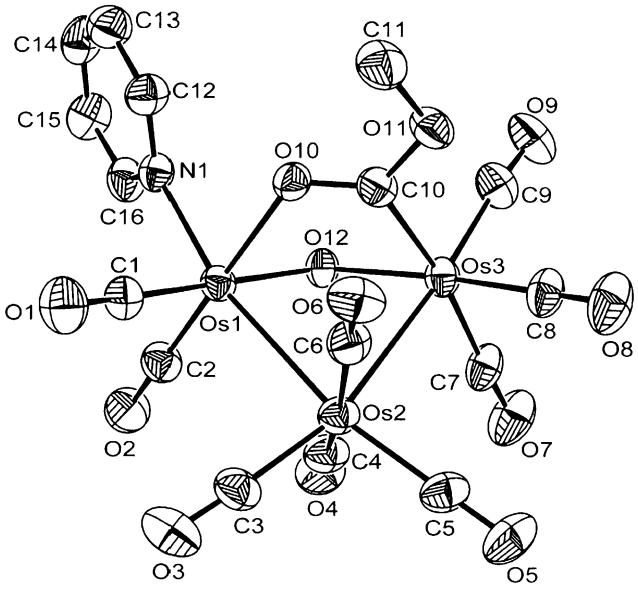


Fig. 4. Molecular structure of $[Os_3(CO)_9(\mu\text{-}OH)(\mu\text{-}OMeCO)(\eta^1\text{-}NC_5H_5)]$ (**8**) showing the atom labeling scheme. Thermal ellipsoids are drawn at the 35% probability level.

4. Conclusions

The present work has provided a facile one-step synthetic route to 50 electron triosmium compounds $[(\mu\text{-}OH)Os_3(CO)_9(\mu\text{-}OMeCO)\{\eta^1\text{-}NCHCHN\text{-}CHCH\text{-}\}]$ (**1**), $[(\mu\text{-}OH)Os_3(CO)_9(\mu\text{-}OMeCO)\{\eta^1\text{-}N{=}C(CH_3)CH{=}NCH{=}CH{-}\}]$ (**2**), $[Os_3(CO)_9[(\mu\text{-}OH)(\mu\text{-}CH_3OCO)\{\eta^1\text{-}N{=}C(CH_3)C(CH_3){=}NCH{=}CH{-}\}]$ (**3**), and $[(\mu\text{-}OH)Os_3(CO)_9(\mu\text{-}CH_3OCO)\{\eta^1\text{-}N{=}C(CH_3)C(CH_3){=}NC(CH_3){=}CH{-}\}]$ (**4**), containing terminal pyrazines, bridging hydroxy and methoxycarbonyl ligands. It is well documented that Me_3NO promotes decarbonylation of metal carbonyls by conversion of a CO ligand into a CO_2 molecule [21]. Thus treatment of $[Os_3(CO)_{12}]$

with pyrazines and water in the presence of a methanolic solution of Me_3NO facilitates the removal of CO as well as the addition of water and the pyrazine ligand to the resulting transient species. The reactions of **1**–**4** with various two electron donor ligands L′ afford the substituted products $[Os_3(CO)_9(\mu\text{-}OH)(\mu\text{-}OMeCO)L']$ (**5**, L′ = PPh_3; **6**, L′ = $P(OMe)_3$; **7**, L′ = ^{t}BuNC; **8**, L′ = C_5H_5N) in high yields, demonstrating that the pyrazine ligands in these complexes are relatively labile. The formation of compound **8** from the reactions of **1**–**4** with pyridine is consistent with the fact that pyridine is a stronger base than diazines (pK_a 0.65 for pyrazine and 5.23 for pyridine). An interesting outcome of these reactions is that compound **8** is inaccessible from the thermal reaction of $[Os_3(CO)_{12}]$ with pyridine, due to the lability of pyridine to orthometallation compared to diazines. The dispositions of the bridging OH and MeOCO ligands and the η^1-coordinated nitrogen heterocyclic ligands in all the compounds are similar.

Acknowledgments

The support of this research by the Ministry of Science and Technology, Government of the Peoples Republic of Bangladesh is gratefully acknowledged. NB acknowledges Sher-e-Bangla Agricultural University for study leave.

Appendix A. Supplementary data

Crystallographic data for the structural analyses have been deposited with the Cambridge Crystallographic Data Centre, CCDC Nos. 270300 for compound **2**, 270301 for compound **3**, 270302 for compound **4**, and 270303 for compound **8**. Copies of this information may be obtained free of charge from The Director, CCDC, 12 Union Road Cambridge, CB2 1EZ, UK, fax: +44 1223 336 033, e-mail: deposit@ccdc.cam.ac.uk or www: http://www.ccdc.cam.ac.uk. Supplementary data associated with this article can be found, in the online version, at doi:10.1016/j.poly.2005.06.045.

References

[1] L. Carlucci, G. Liani, D.M. Proserpie, A. Sironi, J. Am. Chem. Soc. 117 (1995) 4562.
[2] L. Carlucci, G. Ciani, D.M. Proserpio, A. Sironi, Angew. Chem., Int. Ed. Engl. 34 (1995) 1895.
[3] O.M. Yaghi, H. Li, T.L. Groy, Inorg. Chem. 36 (1997) 4292.
[4] A.J. Blake, N.R. Chanpress, A.N. Khlobystov, S. Parsons, M. Schröder, Angew. Chem., Int. Ed. Engl. 39 (2000) 2317.
[5] B.Q. Ma, S. Gao, J. Yi, G.X. Xu, Polyhedron 20 (2001) 1255.
[6] G.A. Foulds, B.F.G. Johnson, J. Lewis, J. Organomet. Chem. 294 (1985) 123.
[7] A.J. Deeming, R. Peters, M.B. Hursthouse, J.D.J. Backer-Dirks, J. Chem. Soc., Dalton Trans. (1982) 787.
[8] G.A. Foulds, B.F.G. Johnson, J. Lewis, J. Organomet. Chem. 296 (1985) 147.
[9] F.A. Cotton, B.E. Hanson, D.J. Jamerson, J. Am. Chem. Soc. 99 (1977) 6588.
[10] R.M. de Souza, F. Martins, E. Stein, J. Organomet. Chem. 559 (1998) 37.
[11] R.A. Machado, M.C. Goite, A.J. Arce, Y. De Sanctis, A.J. Deeming, L. D'Ornelas, D.A. Oliveros, J. Organomet. Chem. 690 (2005) 622.
[12] T. Beringhelli, G. D'Alfonso, D. Maggioni, M. Panigati, P. Mercandelli, A. Sironi, J. Mol. Catal. 204–205 (2003) 361.
[13] (a) N. Begum, Md. I. Hyder, G.M.G. Hossain, S.E. Kabir, S.R. Karmakar, J. Chem. Crystallogr. (in press).;
(b) S.M.T. Abedin, K.A. Azam, M.B. Hursthouse, S.E. Kabir, K.M.A. Malik, R. Miah, H. Vahrenkamp, J. Organomet. Chem. 564 (1998) 133;
(c) K.A. Azam, R. Dilshad, S.E. Kabir, R. Miah, M. Shahiduzzaman, K.I. Hardcastle, E. Rosenberg, M.B. Hursthouse, K.M.A. Malik, J. Cluster. Sci. 7 (1996) 49.
[14] G.M. Sheldrick, Acta Crystallogr., Sect. A 61 (1990) 467.
[15] G.M. Sheldrick, SHELXL-97, Program for Crystal Structure Refinement, University of Göttingen, Germany, 1997.
[16] E.J. Ditzel, M.P. Gomez-Sal, B.F.G. Johnson, J. Lewis, P.R. Raithby, J. Chem. Soc., Dalton Trans. (1987) 1623.
[17] D.W. Knoeppl, J.-H. Chung, S.G. Shore, Acta Crystallogr., Sect. C 51 (1995) 42.
[18] Y.-Y. Chio, W.-T. Wang, J. Organomet. Chem. 573 (1999) 189.
[19] R.D. Adams, B. Qu, Organometallics 19 (2000) 4090.
[20] A.J. Deeming, D.M. Speel, M. Stchedroff, Organometallics 16 (1997) 6004.
[21] J.-K. Shen, Y.-C. Gao, Q.Z. Shi, F. Basolo, Coord. Chem. Rev. 128 (1993) 69.

$Fe_2(CO)_9$ also a mononuclear $Fe(CO)_3$ complex may be isolated in very small yields, in which one of the aromatic carbon carbon bonds shows a side-on coordination to the iron atom [4f]. In addition, treatment of the imine from cinnamaldehyde and *p*-anisidine ends up in the formation of a dinuclear cluster compound with a C–H activated ligand [5].

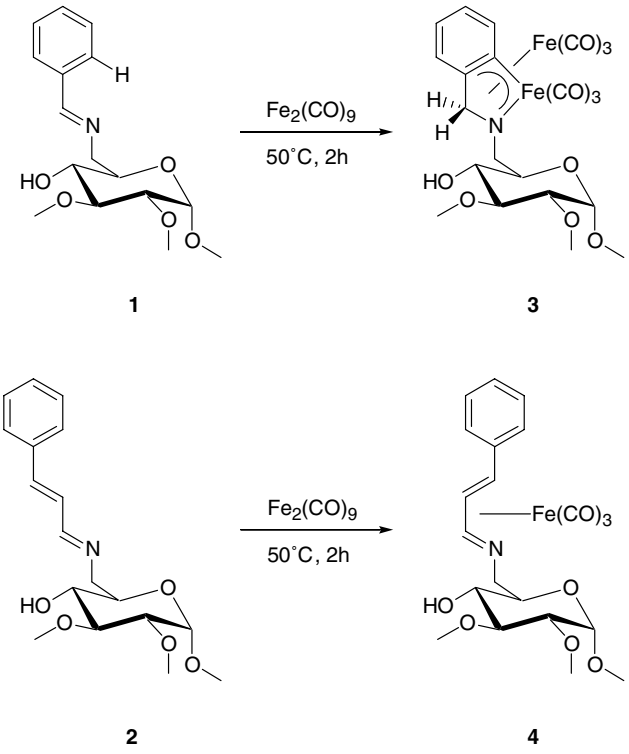
Both kinds of imines may be catalytically activated using $Ru_3(CO)_{12}$ as the precatalyst. Aromatic imines normally react via the formal insertion of an olefin to give alkylated species [6] or via the insertion of CO and ethylene building up a propionyl group [6d,7]. The reaction of β-naphthylimines produces chiral dihydroisoindolone derivatives [7d]. The latter reaction pathway is the typical reaction of acyclic unsaturated imines with CO and ethylene giving chiral dihydropyrrolone derivatives in a selective three component reaction [8]. Recently, we were able to show that the use of chiral 1-azadienes may result in a diastereoselective formation of the new stereogenic center in the dihydropyrrolones in the case of steroidal imines as the substrates [8c].

In this paper, we wish to report the use of carbohydrates and amino acid derivatives as chiral substituents at the nitrogen atoms of α,β-unsaturated imines. The reaction of the corresponding imines with $Fe_2(CO)_9$ will be described.

2. Results and discussion

Scheme 1 shows the formation of mono- and dinuclear iron carbonyl complexes from the reaction of $Fe_2(CO)_9$ with imines derived from 6-amino-6-desoxy-1,2,3-*O*-trimethyl-α-D-glucopyranose. Related imines have recently been used to synthesize chiral copper complexes showing catechol oxidase reactivity [9]. The reaction of 6-amino-6-desoxy-1,2,3-*O*-trimethyl-α-D-glucopyranose with benzaldehyde producing **1** only works if trimethoxymethane is used as the solvent because this acetal readily reacts with water from the condensation reaction, thus shifting the equilibrium towards imine formation. If the reaction time is prolonged the yield of **1** decreases dramatically. In contrast the synthesis of **2** proceeds almost quantitatively at room temperature in ethanol as the solvent.

The reaction of **1** and **2** with $Fe_2(CO)_9$ follows the expected reaction pathways. The benzaldimine **1** reacts via a sequence of C–H activation in *ortho*-position with respect to the exocyclic imine moiety followed by an intramolecular hydrogen transfer reaction towards the former imine carbon atom producing a dinuclear diiron hexacarbonyl compound **3**. Most indicative for this reaction sequence is the observation of a singlet in the proton NMR spectrum at $\delta = 4.13$ ppm representing the methylene group which is produced during the reaction in the place of the former imine carbon atom. The corresponding carbon resonance is found at $\delta = 72.3$ ppm. Both



Scheme 1.

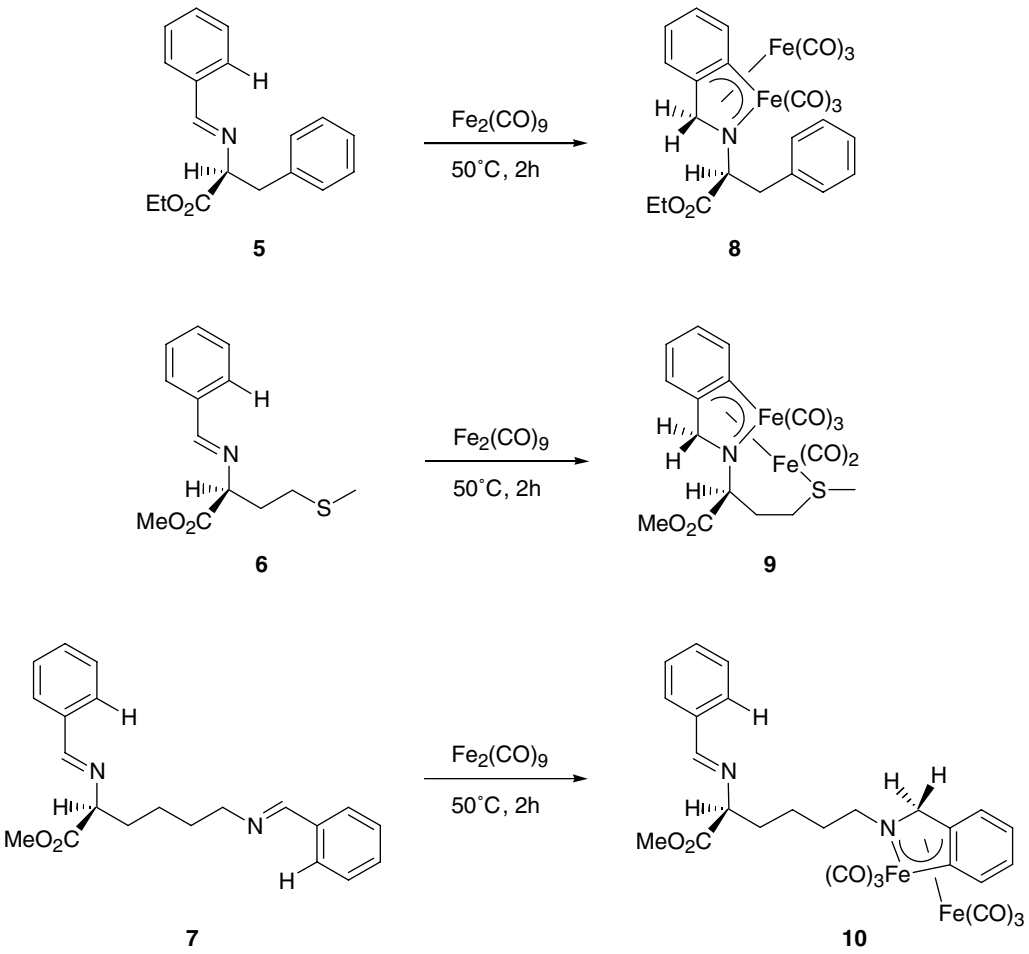
NMR shifts are in the typical range for this kind of iron carbonyl compounds [4]. Although the protons of the methylene group built up during the reaction of **1** with $Fe_2(CO)_9$ as well as the protons of the methylene group of C_6 of the carbohydrate moiety are diastereotopic due to the chiral coordination sphere of the dinuclear $Fe_2(CO)_6$ moiety, only one set of resonances is observed in the NMR spectra of **3** due to the high fluxionality of the iron hexacarbonyl moiety.

The reaction of **2** with $Fe_2(CO)_9$ yields the mononuclear iron carbonyl complex **4**. So in this case, no C–H activation reaction is observed. The NMR spectra are typical for this class of compounds, since the resonances for the hydrogen and carbon atoms of the α,β-unsaturated chain are shifted upfield due to the coordination of the $Fe(CO)_3$ group. In addition, the formation of two diastereomers in a ratio of ≈70:30 is obvious from the splitting of most of the carbon resonances into two seperate signals with very similar chemical shift. Since the 1-azadiene ligand is prochiral, the addition of the iron carbonyl moiety from above or below the plane of the ligand produces an additional element of chirality. Similar observations have been made for quite a number of chiral [(1-azadiene)$Fe(CO)_3$] complexes based on chiral amines, steroidal amines or campher, respectively [5,10]. Up to now only the azadiene complexes derived from imines based on steroidal amines have shown no tendency of epimerization even at elevated temperatures [10j]. In addition, these steroidal imines turned out to react with perfect diastereoselectivities in catalytic

reactions with carbon monoxide and ethylene producing dihydropyrrolones with a new stereogenic center [8c]. So **2** will be a promising candidate to explore the influence of the carbohydrate auxiliary on the diastereoselectivity of catalytic reactions.

Scheme 2 shows the reaction of $Fe_2(CO)_9$ with three different benzylidene amino acid derivatives. All compounds **5**–**7** are easily prepared from the corresponding amino acid ester hydrochlorides and benzaldehyde under basic reaction conditions [11]. Phe–OEt · HCl was prepared from L-Phe and ethanol in the presence of stoichiometric amounts of HCl. It became evident during our investigations of the iron carbonyl complexes of **5** that this esterification led to a complete reacemization of the stereogenic center of the amino acid. So in the synthesis of **6** and **7** enantiomerically pure commercially available amino acid ester hydrochlorides were used. The reaction of L-Lys with benzaldehyde always leads to the diimine **7** no matter which stoichiometry of the reactants is chosen. The L-Met and L-Lys derivatives **6** and **7** were synthesized because of the potential additional donor sites in the side chain of the amino acid. We wanted to explore whether these sulfur and nitrogen donor atoms take part in the coordination of the transition metals in the iron carbonyl complexes used as model compounds for intermediates in the catalytic reactions starting from the same substrates. During catalytic reactions, the additional coordination sites might be helpful to differentiate between diastereomeric intermediates in the catalytic cycle, thus enhancing the overall diastereoselectivity of the reaction.

The dinuclear iron carbonyl compounds **8**–**10** are produced via the same reaction sequence of C–H activation and hydrogen transfer already described for the synthesis of **3**. The NMR spectra of **8** show two sets of signals for the protons of the benzyl group of L-Phe as well as for the protons of the methylene moiety at the former imine carbon atom due to the chiral coordination sphere of the iron atoms. In addition, two resonances representing the carbon monoxide ligands show that in contrast to analogous diiron hexacarbonyl complexes [4] the $Fe(CO)_3$ moieties are not interconverting at room temperature on the NMR time scale. Recrystallization of **8** from a mixture of light petroleum and CH_2Cl_2 at −20 °C produced single crystals suitable for X-ray diffraction. Fig. 1 shows the molecular structure



Scheme 2.

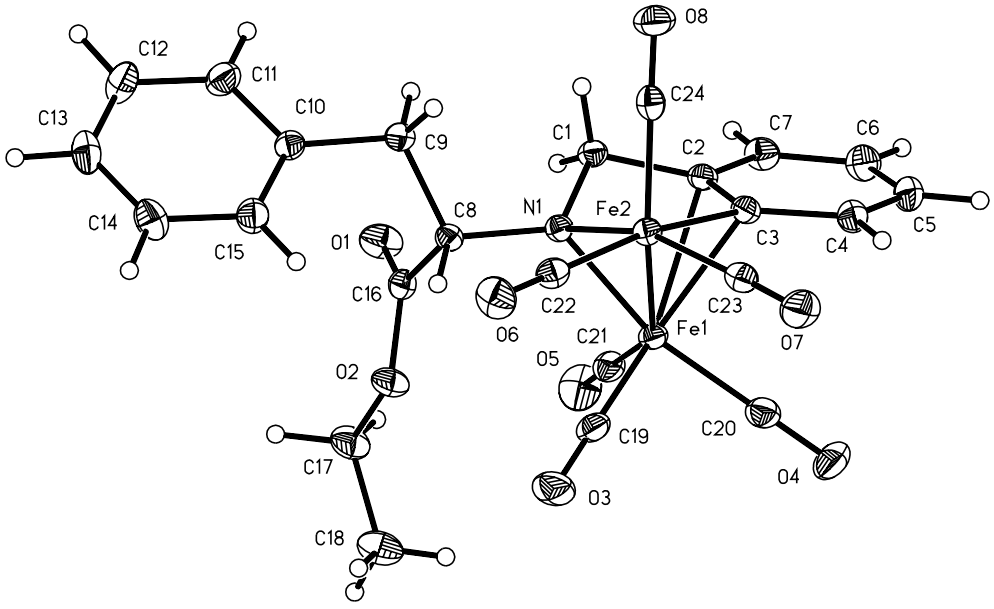


Fig. 1. Molecular structure of **8**. Selected bond lengths [pm] and angles [°]: Fe1–Fe2 245.83(3), Fe1–N1 196.7(1), Fe1–C2 232.9(2), Fe1–C3 217.7(2), Fe2–N1 198.1(2), Fe2–C3 198.7(2), C1–N1 148.2(2), C1–C2 150.7(3), C2–C3 141.5(3), N1–C8 148.4(2), Fe2–Fe1–N1 51.75(4), Fe2–Fe1–C3 50.32(5), Fe2–Fe1–C2 73.44(5), N1–Fe1–C3 74.65(6), N1–Fe1–C2 64.34(6), C2–Fe1–C3 36.40(7), C1–N1–Fe1 99.0(1), N1–Fe2–C3 113.6(1), Fe2–C3–C2 77.66(1), C3–C2–C1 114.7(2), C2–C1–N1 101.4(1), C1–N1–C8 115.1(1), Fe2–N1–C8 120.7(1).

of **8**, crystal data are summarized in Table 1. The crystal structure analysis of **8** clearly indicates the racemization of the amino acid since the compound crystallizes in the non-chiral space group $P\bar{1}$. In Fig. 1, the diastereomer with L-configuration at C8 is shown, but due to the crystallographic center of inversion the corresponding diastereomer with *R*-configuration is also present in the crystal structure. Despite this fact, the molecular structure corresponds very well to those reported for similar iron carbonyl complexes [4]. The C–H activation reaction took place in *ortho*-position with respect to the imine substituent and a new iron carbon bond (Fe2–C3) is established instead. The hydrogen atom is transferred towards the former imine carbon atom (C1) producing a methylene group instead. So a formally six electron donating enylamido ligand is formed coordinating a $Fe_2(CO)_6$ moiety which adopts a slightly distorted saw-horse configuration.

The reaction of $Fe_2(CO)_9$ with **6** also proceeds via the reaction sequence of C–H activation and hydrogen transfer. The most important difference in the molecular structure of **9** (Fig. 2, Table 1) is the coordination of the sulfur atom of the L-Met side-chain towards the apical iron atom of the cluster core. This additional donor site of **6** leads to the formation of another six-membered chelate ring system. The coordination of the enylamido ligand towards the iron carbonyl moieties in **9** is essentially identical to the one described for **8** within experimental errors. **9** crystallizes in the chiral space group $P2_12_12_1$ and thus only the diastereomer exhibiting a L-configuration at C8 is present in the crystal structure

Table 1
Crystal and intensity data for **8** and **9**

	8	**9**
Formula	$C_{24}H_{19}NO_8Fe_2$	$C_{18}H_{17}NO_7SFe_2$
Molecular weight (g mol^{-1})	561.10	503.09
Radiation	Mo Kα	Mo Kα
Monochromator	graphite	graphite
Temperature (K)	183	183
Crystal colour	red	green
Crystal size	$0.10 \times 0.08 \times 0.06$	$0.20 \times 0.12 \times 0.01$
a (Å)	8.4455(2)	8.724(2)
b (Å)	10.9762(2)	15.139(3)
c (Å)	13.8618(2)	15.801(3)
α (°)	70.154(1)	90
β (°)	73.454(1)	90
γ (°)	87.531(1)	90
Volume (Å^3)	1156.57(5)	2087.1(7)
Z	2	4
F(0 0 0)	572	1024
ρ_{calc} (g cm^{-3})	1.611	1.601
Crystal system	triclinic	orthorhombic
Space group	$P\bar{1}$	$P2_12_12_1$
Absorption coefficient (mm^{-1})	1.305	1.529
θ limit (°)	$2.09 < \theta < 27.46$	$1.86 < \theta < 27.47$
Scan mode	ω-scan	ω-scan
Reflections measured	8211	4420
Independent reflections	5270	4420
R_{int}	0.0200	0.0000
Reflections observed ($F_o^2 > 2\sigma(F_o^2)$)	4358	2978
No. of parameters	392	270
Goodness-of-fit	1.011	1.008
R_1	0.0305	0.0550
wR_2	0.0720	0.0882
Final diffraction map electron density peak (e Å^{-3})	0.343	0.366

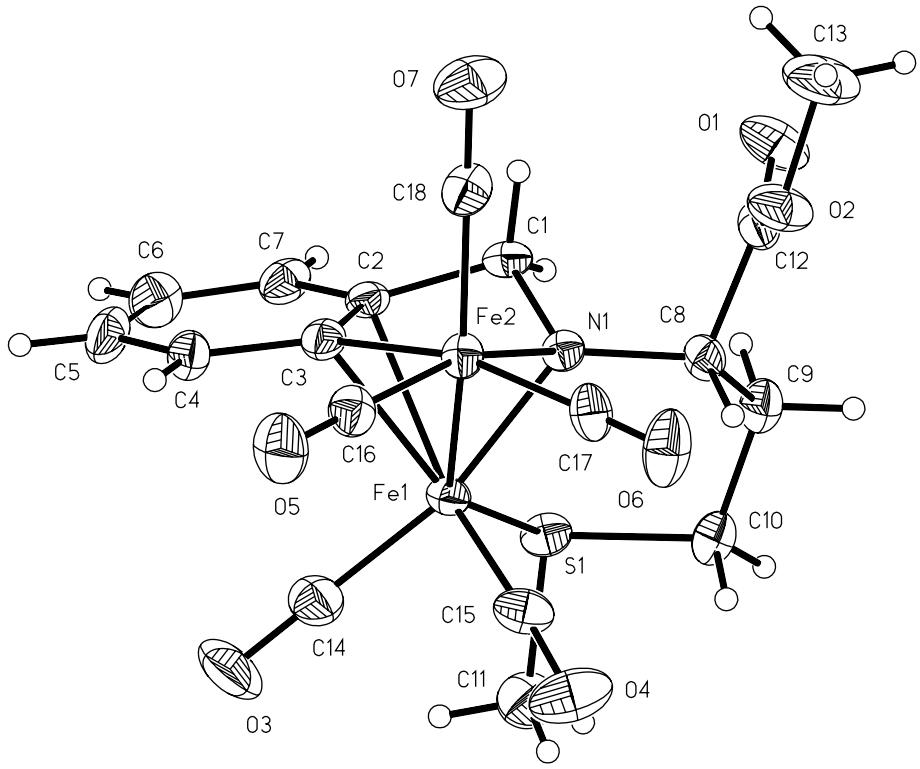


Fig. 2. Molecular structure of **9**. Selected bond lengths [pm] and angles [°]: Fe1–Fe2 246.0(1), Fe1–N1 195.7(4), Fe1–C2 231.0(5), Fe1–C3 218.1(5), Fe2–N1 197.4(4), Fe2–C3 199.5(6), C1–N1 148.2(6), C1–C2 152.2(8), C2–C3 140.1(7), N1–C8 147.8(6), C8–C9 152.9(8), C9–C10 153.5(9), C10–S1 181.2(6), S1–Fe1 226.1(2), Fe2–Fe1–N1 51.6(1), Fe2–Fe1–C3 50.5(2), Fe2–Fe1–C2 73.5(1), N1–Fe1–C3 75.0(2), N1–Fe1–C2 65.0(2), C2–Fe1–C3 36.2(2), C1–N1–Fe1 99.1(3), N1–Fe2–C3 79.0(2), Fe2–C3–C2 113.4(4), C3–C2–C1 114.5(5), C2–C1–N1 100.7(4), C1–N1–C8 113.6(4), Fe2–N1–C8 124.0(3), N1–C8–C9 115.6(4), C9–C9–C10 115.0(5), C9–C10–S1 111.5(4), C10–S1–Fe1 102.5(2), S1–Fe1–Fe2 141.32(5), S1–Fe1–N1 89.88(1), S1–Fe1–C2 94.6(1), S1–Fe1–C3 130.5(2).

(Fig. 2). Nevertheless, the flexibility of the dinuclear iron carbonyl complex is diminished due to additional sulfur coordination. This again leads to the observation of two signals for the carbonyl ligands in the carbon NMR spectrum. In addition, the diastereotopic protons at *C*1 give two dubletts in the proton NMR and the proton at *C*8 gives rise to a dublett of dubletts upon coupling with the diastereotopic protons at *C*9.

The reaction of the diimine **7** with $Fe_2(CO)_9$ also ends up in the formation of a dinuclear iron carbonyl complex **10** as the only product that is obtainable from column chromatography no matter which stoichiometry was chosen. In **10**, only the imine function of the alkylamino side chain of **7** reacted, whereas the imine group attached to the chiral carbon atom of the amino acid remains unreacted. The assignment of the structure is due to the NMR data of **10**. In **7**, the carbon atoms of the imine moieties show resonances at 161.0 and 163.4 ppm, the latter representing the imine function next to the carboxyl group. In the ^{13}C NMR spectrum of **10** only one imine resonance at 163.6 ppm is left indicating that the imine function in α-position with respect to the carboxymethyl moiety did not react. Another hint that the C–H activation reaction took place at the alkylimino group is the downfield shift of the carbon resonance representing the methylene group next to the imine function of the butylimino side-chain. This reactivity may be rationalized by the fact that the nitrogen atom of the imine group of the side-chain is more basic compared to the imine moiety next to the carboxymethyl functional of the former amino acid. This enhanced basicity results in a more efficient coordination of iron carbonyl fragments thus inducing the C–H activation at the observed position. **10** is a highly flexible structure in solution at room temperature as revealed by only one signal representing the terminal carbon monoxide ligands. Corresponding to this finding, there is no diastereotopicity observed for the different methylene groups present in **10**.

In conclusion, we have shown that carbohydrates and amino acid derivatives may be used as chiral auxiliaries in unsaturated imine ligands. The reaction with $Fe_2(CO)_9$ yield the same types of iron carbonyl compounds that we introduced as model systems for catalytic C–H activation reactions before. Catalytic reactions using the same unsaturated imines as substrates exploring the influence of these chiral auxiliaries on the diastereoselectivity of catalytic carbon carbon bond formation reactions are going to be reported in the near future.

3. Experimental

3.1. General

All procedures were carried out under an argon atmosphere in anhydrous, freshly distilled solvents.

Infrared spectra were recorded on a Perkin–Elmer FT-IR System 2000 using 0.2-mm KBr cuvettes. NMR spectra were recorded on a Bruker AC 200 spectrometer (^{1}H: 200 MHz, ^{13}C: 50.32 MHz, $CDCl_3$ as internal standard). Mass spectra were recorded on a Finnigan MAT SSQ 710 instrument. High resolution mass spectra (HRMS) were carried out using a Finnigan MAT 95 XL spectrometer using FAB techniques.

3.2. X-ray crystallographic studies

The structure determinations of **8** and **9** were carried out on an Enraf Nonius Kappa CCD diffractometer, crystal detector distance 29 mm, using graphite monochromated Mo Kα radiation [12]. The crystal was mounted in a stream of cold nitrogen. Data were corrected for Lorentz and polarization effects but not for absorption. The structure was solved by direct methods and refined by full-matrix least squares techniques against F^2 using the programs SHELXS86 and SHELXL97 [13], the molecular illustrations were drawn using the program XP [14]. The crystal and intensity data are given in Table 1.

3.3. Synthesis of *1*

0.750 g (3.390 mmol) 6-amino-6-desoxy-1,2,3-*O*-trimethyl-α-D-glucopyranose and 1.079 g (10.170 mmol) benzaldehyde are refluxed in 5 mL trimethoxymethane for 5 h. Evaporation of all volatile material yields **1** in 98% yield as a pale brown waxlike compound.

MS (CI, H_2O) [*m*/*z* (fragment, rel. intensity in %)]: 310 (MH^+, 54), 292 ($C_{16}H_{22}NO_4^+$, 30), 278 ($C_{15}H_{20}NO_4^+$, 12), 260 ($C_{15}H_{18}NO_3^+$, 2), 229 ($C_{14}H_{15}NO_2^+$, 4), 190 ($C_8H_{16}NO_4^+$, 9), 150 ($C_9H_{12}NO^+$, 13), 123 ($C_8H_{11}O^+$, 95), 107 ($C_7H_7O^+$/$C_4H_{11}O_3^+$, 100), 84 ($C_5H_{10}N^+$, 30), 75 ($C_3H_7O_2^+$, 45); HRMS (ESI in $CHCl_3$/methanol): 310.16464, $C_{16}H_{24}NO_5$ (MH^+), $\Delta = 0.81$ mmu; IR (nujol, 298 K) [cm^{-1}]: 1727–1614 (w, CH=N); ^{1}H NMR ($CDCl_3$, 298 K) [ppm]: 3.04–3.80 (m, 4H, C_2H, C_3H, C_4H, C_5H), 3.37 (s, 3H, OCH_3), 3.48 (s, 3H, OCH_3), 3.61 (s, 3H, OCH_3), 3.80–3.98 (m, 1H, C_6H_2), 4.08 (d, $^3J_{HH} = 12.3$ Hz, 1H, C_6H_2), 4.78 (d, $^3J_{HH} = 3.5$ Hz, 1H, C_1H), 7.09–7.48 (m, 3H, CH_{ar}), 7.62–7.77 (m, 2H, CH_{ar}), 8.29 (s, 1H, CH=N); ^{13}C NMR ($CDCl_3$, 298 K) [ppm]: 54.8 (OCH_3), 58.6 (OCH_3), 60.7 (OCH_3), 61.0 (C_6), 69.3 (C_5), 74.4 (C_3), 82.3 (C_4), 83.0 (C_2), 96.8 (C_1), 128.0 (CH_{ar}), 128.3 (CH_{ar}), 130.4 (CH_{ar}), 136.2 (C_{ar}), 162.8 (CH=N).

3.4. Synthesis of *2*

A 0.750 g (3.390 mmol) sample of 6-amino-6-desoxy-1,2,3-*O*-trimethyl-α-D-glucopyranose is dissolved in 15 mL anhydrous ethanol and 0.448 g (3.390 mmol) cinnamaldehyde are added. After stirring the reaction mixture at room temperature for 20 h, all volatile material is evaporated at slightly elevated temperature. **2** is quantitatively produced as a colourless to pale brown waxlike compound.

MS (CI, H_2O) [*m*/*z* (fragment, rel. intensity in %)]: 336 (MH^+, 100), 304 ($C_{17}H_{22}NO_4^+$, 6), 272 ($C_{16}H_{18}NO_3^+$, 2), 131 ($C_9H_9N^+$, 14), 104 ($C_8H_8^+$, 10); HRMS (ESI in $CHCl_3$/methanol): 336.18132, $C_{18}H_{26}NO_5$ (MH^+), $\Delta = -0{,}22$ mmu; IR (nujol, 298 K) [cm^{-1}]: 1634 (w, CH=N); ^{1}H NMR ($CDCl_3$, 298 K) [ppm]: 3.06–3.96 (m, 6H, C_2H, C_3H, C_4H, C_5H, C_6H_2), 3.38 (s, 3H, OCH_3), 3.46 (s, 3H, OCH_3), 3.63 (s, 3H, OCH_3), 4.79 (d, $^3J_{HH} = 3.4$ Hz, 1H, C_1H), 6.91 (s, 1H, CH), 6.93 (s, 1H, CH), 7.15–7.59 (m, 5H, CH_{ar}), 7.99 (dd, $^3J_{HH} = 4.0$ Hz, $^4J_{HH} = 4{,}0$ Hz, 1H, CH=N); ^{13}C NMR ($CDCl_3$, 298 K) [ppm]: 54.8 (OCH_3), 58.3 (OCH_3), 60.9 (OCH_3), 61.5 (C_6), 70.1 (C_5), 71.8 (C_3), 81.6 (C_4), 83.0 (C_2), 97.3 (C_1), 127.1 (CH_{ar}), 127.6 (CH_{ar}), 128.6 (CH_{ar}), 129.0 (CH), 135.4 (C_{ar}), 142.2 (CH), 164.8 (CH=N).

3.5. Synthesis of *3*

A 0.425 g (1.374 mmol) portion of **1** is stirred together with 0.500 g (1.374 mmol) $Fe_2(CO)_9$ in 35 mL *n*-heptane in a Schlenk tube at 50–60 °C for 2 h. The colour of the suspension turns to dark brown as $Fe_2(CO)_9$ slowly dissolves. All volatile material is evaporated in vacuo. Then, the oily residue is dissolved in 12 ml dichloromethane and chromatographed on silica. Using a mixture of light petroleum (b.p. 40–60 °C) and dichloromethane 20:5 $Fe_3(CO)_{12}$ is eluted as a green band. With a mixture of light petroleum and THF as the eluent **3** is obtained as a deep red band. Yield: 0.322 g (39.8%).

MS (FAB in nba) [*m*/*z* (fragment)]: 590 (MH^+), 561 ($M^+ - CO$), 533 ($M^+ - 2CO$), 505 ($M^+ - 3CO$), 477 ($M^+ - 4CO$), 449 ($M^+ - 5CO$), 421 ($M^+ - 6CO$), 366 ($MH^+ - 6CO - Fe$), 310 ($C_{16}H_{24}NO_5^+$); HRMS (FAB in nba): 590.11628, $C_{22}H_{24}NO_{11}Fe_2$ (MH^+), $\Delta = 0.22$ mmu; IR (nujol, 298 K) [cm^{-1}]: 2063 (s, C=O), 2024 (s, C=O), 1987 (s, br, C=O), 1979 (s, br, C=O), 1959 (sh, s, C=O); ^{1}H NMR ($CDCl_3$, 298 K) [ppm]: 2.43 (d, $^3J_{HH} = 2.6$ Hz, 1H, C_2H), 2.84–3.87 (m, 5H, C_3H, C_4H, C_5H, C_6H_2), 3.36 (s, 3H, OCH_3), 3.46 (s, 3H, OCH_3), 3.60 (s, 3H, OCH_3), 4.13 (s, 2H, CH_2–N), 4.76 (d, $^3J_{HH} = 3{,}4$ Hz, 1H, C_1H), 7,01 (dd, $^3J_{HH} = 7.0$ Hz, $^3J_{HH} = 7.0$ Hz, 1H, CH_{ar}), 7.26 (dd, $^3J_{HH} = 7.0$ Hz, $^3J_{HH} = 7.0$ Hz, 1H, CH_{ar}), 7.51 (d, $^3J_{HH} = 8.0$ Hz, 1H, CH_{ar}), 8.01 (d, $^3J_{HH} = 8.2$ Hz, 1H, CH_{ar}); ^{13}C NMR ($CDCl_3$, 298 K) [ppm]: 56.8 (OCH_3), 58.4 (OCH_3),

61.2 (O*C*H$_3$), 70.4 (*C*$_5$), 72.3 (*C*$_6$, *C*H$_2$–N), 73.7 (*C*$_3$), 81.8 (*C*$_4$), 82.1 (*C*$_2$), 97.8 (*C*$_1$), 121.2 (*C*$_{ar}$), 125.6 (*CH*$_{ar}$), 128.6 (*CH*$_{ar}$), 130.0 (*CH*$_{ar}$), 147.4 (*CH*$_{ar}$), 150.3 (*C*–Fe), 210.8 (*C*O), 210.8 (*C*O).

3.6. Synthesis of **4**

A 0.461 g (1.374 mmol) portion of **2** is stirred together with 0.500 g (1.374 mmol) $Fe_2(CO)_9$ in 35 mL *n*-heptane in a Schlenk tube at 50–60 °C for 2 h. The colour of the suspension turns to an orange to light brown colour as $Fe_2(CO)_9$ slowly dissolves. All volatile material is evaporated in vacuo. Then, the oily residue is dissolved in 12 ml dichloromethane and chromatographed on silica. Using a mixture of light petroleum (b.p. 40–60 °C) and dichloromethane 20:5 $Fe_3(CO)_{12}$ is eluted as a green band. With a mixture of light petroleum and THF as the eluent **4** is obtained as a orange band. Yield: 0.229 g (35.1%).

MS (FAB in nba) [*m*/*z* (fragment)]: 476 (MH^+), 419 ($M^+ - 2CO$), 391 ($M^+ - 3CO$), 336 ($C_{18}H_{26}NO_5^+$); HRMS (FAB in nba): 476.10040, $C_{21}H_{26}NO_8Fe$ (MH^+), $\Delta = 0.38$ mmu; IR (Nujol, 298 K) [cm^{-1}]: 2053 (s, C=O), 1991 (s, C=O), 1974 (s, br, C=O); ^{1}H NMR ($CDCl_3$, 298 K, mixture of two diastereomers) [ppm]: 2.39–3.89 (m, 14H, C*H*, C$_2$*H*, C$_3$*H*, C$_4$*H*, C$_5$*H*, C$_6$*H*$_2$), 3.33 (s, 3H, OC*H*$_3$), 3.39 (s, 3H, OC*H*$_3$), 3.46 (s, 6H, OC*H*$_3$), 3.61 (s, 3H, OC*H*$_3$), 3.63 (s, 3H, OC*H*$_3$), 4.78 (d, $^3J_{HH} = 3.5$ Hz, 1H, C$_1$*H*), 4.81 (d, $^3J_{HH} = 3.4$ Hz, 1H, C$_1$*H*), 5.35–5.58 (m, 2H, C*H*), 6.50 (s, 2H, C*H*=N), 7.01–7.62 (m, 10H, C*H*$_{ar}$); ^{13}C NMR ($CDCl_3$, 298 K, mixture of two diastereomers) [ppm]: 54.8 (OCH_3), 54.9 (OCH_3), 58.3 (OCH_3), 58.4 (OCH_3), 60.5 (*C*$_6$), 60.8 (CH), 61.0 (OCH_3), 61.1 (OCH_3), 61.2 (CH), 70.3 (*C*$_5$), 70.7 (*C*$_5$), 72.0 (*C*$_3$), 72.9 (*C*$_3$), 73.0 (CH), 73.1 (CH), 81.4 (*C*$_4$), 81.7 (*C*$_4$), 82.6 (*C*$_2$), 82.8 (*C*$_2$), 97.0 (*C*$_1$), 97.3 (*C*$_1$), 111.1 (CH=N), 111.6 (CH=N), 126.3 (CH_{ar}), 126.5 (CH_{ar}), 126.6 (CH_{ar}), 128.5 (CH_{ar}), 138.6 (C_{ar}), 138.9 (C_{ar}), 209.1 (br, CO), 210.2 (CO), 215.7 (CO).

3.7. Synthesis of **5**–**7**

A 2-g portion of the corresponding amino acid ester hydrochloride (8.7 mmol L-Phe–OEt · HCl, 9.1 mmol L-Met–OMe · HCl, 8.5 mmol L-Lys-OMe · HCl) is dissolved in 30 mL water and stirred together with an equimolar amount of benzaldehyde and Na_2CO_3 per amino group. This reaction mixture is kept at 40 °C for 1 h and then stirred at room temperature for another 16 h. The solution is then extracted with chloroform (3 × 12 mL) and the collected chloroform layers are dried over $MgSO_4$. Evaporation of chloroform leads to the analytically pure compounds **5**–**7** (Yield: **5**, 1.91 g, 77.9%, white solid; **6**, 1.04 g, 41.4%, pale yellow oil; **7**, 1.87 g, 65.1%, orange oil).

3.7.1. MS and spectroscopical data of **5**

MS (EI) [*m*/*z* (fragment, rel. intensity in %)]: 282 (MH^+, 64), 208 ($M^+ - HCO_2Et$, 74), 190 ($M^+ - C_7H_8$, 100), 117 ($C_8H_7N^+$, 50), 91 ($C_7H_7^+$, 42), 77 ($C_6H_5^+$, 10), 65 ($C_5H_5^+$, 6), 39 ($C_3H_3^+$, 2), 29 ($C_2H_5^+$, 35); HRMS (FAB in nba): 281.35442, $C_{18}H_{19}NO_2$ (M^+), $\Delta = 0.78$ mmu; IR (Nujol, 298 K) [cm^{-1}]: 1740 (vs, C=O), 1643 (s, C=N); ^{1}H NMR ($CDCl_3$, 298 K) [ppm]: 1.24 (t, 3H, $^3J_{HH} = 7.1$ Hz, C*H*$_3$), 3.09–3.42 (m, 2H, C*H*$_2$), 4.10–4.26 (m, 1H, C*H*), 4.17–4.21 (m, 2H, OC*H*$_2$), 7.15–7.71 (m, 10H, C*H*$_{ar}$), 7.94 (s, 1H, C*H*=N); ^{13}C NMR ($CDCl_3$, 298 K) [ppm]: 14.1 (*C*H$_3$), 39.7 (*C*H$_2$), 61.0 (O*C*H$_2$), 74.9 (*C*H), 126.6 (*CH*$_{ar}$), 128.3 (*CH*$_{ar}$), 128.4 (*CH*$_{ar}$), 128.5 (*CH*$_{ar}$), 129.8 (*CH*$_{ar}$), 131.1 (*CH*$_{ar}$), 135.6 (*C*$_{ar}$), 137.4 (*C*$_{ar}$), 163.8 (*C*H=N), 172.1 (*C*=O).

3.7.2. MS and spectroscopical data of **6**

MS (EI) [*m*/*z* (fragment, rel. intensity in %)]: 252 (MH^+, 100), 204 ($M^+ - H_3CSH$, 9), 190 ($MH^+ - C_2H_6S$, 30), 177 ($M^+ - C_3H_7S$), 146 ($C_9H_8NO^+$, 11), 130 ($C_9H_8N^+$, 13), 117 ($C_8H_7N^+$, 44), 90 ($C_7H_6^+$, 10), 77 ($C_6H_5^+$, 6), 61 ($C_2H_6S^+$, 32), 29 ($C_2H_5^+$, 4); HRMS (FAB in nba): 252.10594, $C_{13}H_{18}NO_2S$ (MH^+), $\Delta = -0.11$ mmu; IR (Nujol, 298 K) [cm^{-1}]: 1738 (vs, C=O), 1643 (s, C=N); ^{1}H NMR ($CDCl_3$, 298 K) [ppm]: 2.06 (s, 3H, SC*H*$_3$), 2.21–2.29 (m, 2H, C*H*$_2$), 2.41–2.56 (m, 2H, SC*H*$_2$), 3.71 (s, 3H, OC*H*$_3$), 4.18 (dd, 1H, $^3J_{HH} = 5.5$ Hz, $^3J_{HH} = 7.8$ Hz, C*H*), 7.24–7.46 (m, 3H, C*H*$_{ar}$), 7.71–7.80 (m, 2H, C*H*$_{ar}$), 8.30 (s, 1H, C*H*=N); ^{13}C NMR ($CDCl_3$, 298 K) [ppm]: 15.2 (S*C*H$_3$), 30.3 (*C*H$_2$), 32.0 (S*C*H$_2$), 52.3 (O*C*H$_3$), 71.3 (*C*H), 128.6 (*CH*$_{ar}$), 128.7 (*CH*$_{ar}$), 131.3 (*CH*$_{ar}$), 135.6 (*C*$_{ar}$), 164.4 (*C*H=N), 172.2 (*C*=O).

3.7.3. MS and spectroscopical data of **7**

MS (EI) [*m*/*z* (fragment, rel. intensity in %)]: 337 (M^+, 100), 305 ($MH^+ - CH_3OH$, 3), 277 ($M^+ - HCO_2CH_3$, 12), 231 ($MH^+ - C_7H_8N$, 61), 218 ($MH^+ - C_8H_9N$, 5), 172 ($C_{12}H_{12}N^+$, 48), 160 ($C_{11}H_{12}N^+$, 9), 144 ($C_9H_6NO^+$, 8), 132 ($C_9H_{10}N^+$, 22), 118 ($C_8H_8N^+$, 21), 105 ($C_7H_7N^+$, 87), 91 ($C_7H_7^+$, 52), 77 ($C_6H_5^+$, 43), 65 ($C_5H_5^+$, 5), 51 ($C_4H_3^+$, 12), 29 ($C_2H_5^+$); HRMS (FAB in nba): 337.19127, $C_{21}H_{25}N_2O_2$ (MH^+), $\Delta = 0.33$ mmu; IR (Nujol, 298 K) [cm^{-1}]: 1736 (vs, C=O), 1702 (s, C=N), 1643 (s, C=N); ^{1}H NMR ($CDCl_3$, 298 K) [ppm]: 1.36–1.40 (m, 2H, CH_2), 1.69–1.77 (m, 2H, CH_2), 1.91–2.03 (m, 2H, CH_2), 3.57 (dd, 2H, $^3J_{HH} = 6.9$ Hz, $^3J_{HH} = 6.9$ Hz, NCH_2), 3.70 (s, 3H, OCH_3), 3.98 (dd, $^3J_{HH} = 5.5$ Hz, $^3J_{HH} = 8.1$ Hz, C*H*), 7.24–7.88 (m, 10H, C*H*$_{ar}$), 8.22 (s, 1H, C*H*=N), 8.25 (s, 1H, C*H*=N); ^{13}C NMR ($CDCl_3$, 298 K) [ppm]: 23.6 (*C*H$_2$), 30.4 (*C*H$_2$), 33.1 (*C*H$_2$), 52.2 (O*C*H$_3$), 61.3 (N*C*H$_2$), 73.4 (*C*H), 128.0 (*CH*$_{ar}$), 128.5 (*CH*$_{ar}$), 128.6 (*CH*$_{ar}$), 129.0 (*CH*$_{ar}$),

130.5 (CH_{ar}), 131.1 (CH_{ar}), 135.6 (C_{ar}), 136.2 (C_{ar}), 161.0 (*C*H=N), 163.4 (*C*H=N), 172.7 (*C*=O).

3.8. Synthesis of **8**–**10**

A 500-mg portion of $Fe_2(CO)_9$ (1.374 mmol) is stirred together with an equimolar amount of the corresponding imine of the amino acid esters (387 mg **5**, 345 mg **6**, 463 mg **7**) at 50 °C for 2 h. The colour of the reaction mixture turns to deep red (**8**, **10**) or to dark green (**9**), respectively, as the iron carbonyl slowly dissolves. After the reaction is finished, all volatile material is removed in vacuo, the oily residue is dissolved in dichloromethane and the reaction mixture is chromatographed on silica. The dinuclear iron carbonyl complex **8** is eluted using mixtures of light petroleum (b.p. 40–60 °C) and CH_2Cl_2 1:2 as the eluent, **9** and **10** are obtained using mixtures of light petroleum (b.p. 40–60 °C) and THF 4:1. Yields: **8**, 92 mg (11.9%); **9**, 146 mg (19.4%); **10**, 42 mg (6.0%).

3.8.1. MS and spectroscopical data of **8**

MS (FAB in dmba) [*m*/*z* (fragment, rel. intensity in %)]: 561 (M^+, 2), 533 ($M^+ - CO$, 2), 505 ($M^+ - 2CO$, 27), 477 ($M^+ - 3CO$, 31), 449 ($M^+ - 4CO$, 28), 421 ($M^+ - 5CO$, 72), 393 ($M^+ - 6CO$, 100), 337 ($M^+ - 5CO - Fe$, 36), 281 ($M^+ - 6CO - 2Fe$, 21); HRMS (FAB in nba): 562.10709, $C_{24}H_{20}NO_8Fe_2$ (MH^+), $\Delta = -0.41$ mmu; IR (Nujol, 298 K) [cm^{-1}]: 2116 (w, CO), 2062 (s, CO), 2021 (vs, CO), 1996 (vs, CO), 1978 (vs, CO), 1968 (sh, CO), 1734 (vs, CO_2Et); ^1H NMR (d^8-toluene, 298 K) [ppm]: 0.71 (t, 3H, $^3J_{HH} = 7.1$ Hz, CH_3), 2.75 (dd, 1H, $^2J_{HH} = 12.4$ Hz, $^3J_{HH} = 3.4$ Hz, CH_2), 3.15 (t, 1H, $^3J_{HH} = 12.2$ Hz, C*H*), 3.53 (dd, 1H, $^2J_{HH} = 11.9$ Hz, $^3J_{HH} = 3.4$ Hz, CH_2), 3.67 (d, 1H, $^2J_{HH} = 12.3$ Hz, N–CH_2), 3.83 (q, 2H, $^3J_{HH} = 7.1$ Hz, OCH_2), 4.50 (d, 1H, $^2J_{HH} = 12.3$ Hz, N–CH_2), 6.57 (t, 1H, $^3J_{HH} = 7.4$ Hz, CH_{ar}), 6.77 (t, 1H, $^3J_{HH} = 6.8$ Hz, CH_{ar}), 6.82–7.05 (m, 5H, CH_{ar}), 7.10 (d, 1H $^3J_{HH} = 6.0$ Hz, CH_{ar}), 7.98 (d, 1H, $^3J_{HH} = 8.1$ Hz; CH_{ar}); ^{13}C NMR (d^8-toluene, 298 K) [ppm]: 13.6 (*C*H_3), 40.3 (*C*H_2), 61.0 (O*C*H_2), 66.9 (N*C*H_2), 79.3 (*C*H), 125.6 (C_{ar}), 126.0 (CH_{ar}), 127.1 (CH_{ar}), 128.7 (CH_{ar}), 128.8 (CH_{ar}), 129.0 (CH_{ar}), 130.9 (CH_{ar}), 136.1 (C_{ar}), 145.3 (C_{ar}), 150.9 (CH_{ar}), 170.1 (*C*=O), 210.1 (*C*O), 211.0 (*C*O).

3.8.2. MS and spectroscopical data of **9**

MS (FAB in nba) [*m*/*z* (fragment, rel. intensity in %)]: 503 ($M^+ - CO$, 12), 475 (M^+2 CO, 5), 460 ($M^+ - 2CO -$ Me, 6), 447 ($M^+ - 3CO$, 33), 419 ($M^+ - 4CO$, 11), 391 ($M^+ - 5$ CO, 31), 363 ($M^+ - 6$ CO, 21), 335 ($M^+ - 5CO -$ Fe, 9), 307 ($M^+ - 6CO - Fe$, 100), 289 ($C_{13}H_{17}NO_2S$-$Fe^+ - H_2O$, 62); HRMS (FAB in nba): 504.09321, $C_{18}H_{18}NO_7SFe_2$ (MH^+), $\Delta = 0.19$ mmu; IR (Nujol, 298 K) [cm^{-1}]: 2036 (s, CO), 2000 (vs, br, CO), 1974 (s, CO), 1906 (sh, CO), 1735 (vs, CO_2Et); ^1H NMR ($CDCl_3$, 298 K) [ppm]: 2.02–2.49 (m, 7H, CH_2, SCH_3), 3.18 (dd, 1H, $^3J_{HH} = 11.4$ Hz, $^3J_{HH} = 3.0$ Hz, C*H*), 3.52 (d, 1H, $^2J_{HH} = 11.8$ Hz, N–CH_2), 3.73 (s, 3H, OCH_3), 4.07 (d, 1H, $^2J_{HH} = 11.8$ Hz, N–CH_2), 6.93 (t, 1H, $^3J_{HH} = 6.8$ Hz, CH_{ar}), 7.09 (t, 1H, $^3J_{HH} = 7.3$ Hz, CH_{ar}), 7.32 (d, 1H $^3J_{HH} = 7.7$ Hz, CH_{ar}), 7.92 (d, 1H, $^3J_{HH} = 8.1$ Hz; CH_{ar}); ^{13}C NMR (d^8-toluene, 298 K) [ppm]: 26.5 (S*C*H_3), 27.3 (*C*H_2), 30.3 (*C*H_2), 52.0 (O*C*H_3), 64.4 (N*C*H_2), 72.8 (*C*H), 115.8 (C_{ar}), 124.7 (CH_{ar}), 127.2 (CH_{ar}), 128.7 (CH_{ar}), 129.2 (CH_{ar}), 149.2 (CH_{ar}), 170.5 (*C*=O), 214.8 (*C*O), 215.4 (*C*O).

3.8.3. MS and spectroscopical data of **10**

MS (FAB in dmba) [*m*/*z* (fragment, rel. intensity in %)]: 617 (MH^+, 15), 532 ($M^+ - 3CO$, 39), 504 ($M^+ -$ 4CO, 34), 476 ($M^+ - 5$ CO, 22), 448 ($M^+ - 6CO$, 85), 392 ($M^+ - 6CO - Fe$, 18), 336 ($M^+ - 6CO - 2Fe$, 100); HRMS (FAB in nba): 617.18655, $C_{27}H_{25}N_2O_8Fe_2$ (MH^+), $\Delta = 0.55$ mmu; IR (Nujol, 298 K) [cm^{-1}]: 2061 (s, CO), 2021 (vs, CO), 1978 (vs, br, CO), 1737 (vs, CO_2Et); ^1H NMR ($CDCl_3$, 298 K) [ppm]: 1.24–1.50 (m, 4H, CH_2), 1.85–1.96 (m, 2H, CH_2), 2.71–2.79 (m, 2H, CH_2), 3.70 (s, OCH_3), 3.52–3.56 (m, 3H, NCH_2, C*H*), 6.97 (t, 1H, $^3J_{HH} = 7.2$ Hz, CH_{ar}), 7.22 (t, 1H, $^3J_{HH} = 7.3$ Hz, CH_{ar}), 7.32–7.53 (m, 5H, CH_{ar}), 7.74 (d, 1H, $^3J_{HH} = 7.6$ Hz, CH_{ar}), 7.97 (d, 1H, $^3J_{HH} = 8.1$ Hz, CH_{ar}), 8.23 (s, 1H, C*H*=N); ^{13}C NMR ($CDCl_3$, 298 K) [ppm]: 23.5 (*C*H_2), 30.5 (*C*H_2), 33.0 (*C*H_2), 52.2 (O*C*H_3), 69.1 (*C*H_2), 72.1 (N*C*H_2), 73.2 (*C*H), 122.4 (C_{ar}, CH_{ar}), 125.5 (CH_{ar}), 128.6 (CH_{ar}), 130.1 (CH_{ar}), 131.2 (CH_{ar}), 135.5 (C_{ar}), 147.5 (C_{ar}), 150.0 (CH_{ar}), 163.6 (*C*H=N), 172.3 (*C*=O), 210.7 (*C*O).

Acknowledgements

The authors thank Dr. Michael Gottschaldt, Institute for Organic Chemistry and Macromolecular Chemistry, Friedrich-Schiller-University, Jena, for a sample of 6-amino-6-desoxy-1,2,3-*O*-trimethyl-α-D-glucopyranose.

Appendix A. Supplementary data

Additional material on the structure analyses is available from the Cambridge Crystallographic Data Centre by mentioning the deposition number CCDC-247612 (**8**) or CCDC-247613 (**9**). Supplementary data associated with this article can be found, in the online version at doi:10.1016/j.poly.2005.07.001.

References

[1] (a) B.A. Arndtsen, R.G. Bergman, T.A. Mobely, T.A. Peterson, Accounts Chem. Res. 28 (1995) 154;
(b) G. Dyker, Angew. Chem., Int. Ed. 38 (1999) 1699;

(c) Y. Guari, S. Sabo-Etienne, B. Chaudret, Eur. J. Inorg. Chem. (1999) 1047;
(d) B.M. Trost, D. Toste, A.B. Pinkerton, Chem. Rev. 101 (2001) 2067;
(e) V. Ritleng, C. Sirlin, M. Pfeffer, Chem. Rev. 102 (2002) 1731.

[2] (a) M.I. Bruce, Angew. Chem. 89 (1977) 75;
(b) M. Brookhart, M.L.H. Green, J. Organomet. Chem. 250 (1983) 395;
(c) E.C. Constable, Polyhedron 3 (1984) 1037;
(d) A.E. Ryabov, Chem. Rev. 90 (1990) 403;
(e) J. Dehand, M. Pfeffer, Pure Appl. Chem. 3 (1992) 335;
(f) A.S. Goldman, Nature 366 (1993) 514;
(g) S. Murai, F. Kakiuchi, S. Sekine, Y. Tanaka, A. Kamatani, M. Sonoda, N. Chatani, Pure Appl. Chem. 66 (1994) 1527;
(h) F. Kakiuchi, S. Sekine, Y. Tanaka, A. Kamatani, M. Sonoda, N. Chatani, S. Murai, Bull. Chem. Soc. Jpn. 66 (1995) 62;
(i) B.M. Trost, Angew. Chem. 107 (1995) 285;
(j) A. Sen, Accounts Chem. Res. 31 (1998) 550.

[3] (a) S. Otsuka, T. Yoshida, A. Nakamura, Inorg. Chem. 6 (1967) 20;
(b) M.M. Bagga, W.T. Flannigan, G.R. Knox, P.L. Pauson, F.J. Preston, R.I. Reed, J. Chem. Soc. C (1968) 36;
(c) A. De Cian, R. Weiss, Acta Crystallogr. B28 (1972) 3264;
(d) A.M. Brodie, B.F.G. Johnson, P.L. Josty, J. Lewis, J. Chem. Soc., Dalton Trans. (1972) 2031;
(e) M.F. Semmelhack, C.H. Cheng, J. Organomet. Chem. 393 (1990) 237;
(f) H.-J. Knölker, G. Baum, P. Gonser, Tetrahedron Lett. 36 (1995) 8191;
(g) H.-J. Knölker, H. Goesmann, P. Gonser, Tetrahedron Lett. 37 (1996) 6543;
(h) L.A.P. Kane-Maguire, S.G. Pyne, A.F.H. Siu, B.W. Skelton, J. Aust. Chem. 49 (1996) 673;
(i) W. Imhof, A. Göbel, D. Braga, P. De Leonardis, E. Tedesco, Organometallics 18 (1999) 736;
(j) D. Berger, M. Erdmann, J. Notni, W. Imhof, CrystEngComm. (2000) 4.

[4] (a) P.E. Baikie, O.S. Mills, J. Chem. Soc., Chem. Commun. (1966) 707;
(b) D.L. Wang, W.S. Hwang, L.C. Liang, L.Y. Wang, L. Lee, M.Y. Chiang, Organometallics 16 (1997) 3109;
(c) W. Imhof, J. Organomet. Chem. 533 (1997) 31;
(d) W. Imhof, J. Organomet. Chem. 541 (1997) 109;
(e) W. Imhof, A. Göbel, D. Ohlmann, J. Flemming, H. Fritzsche, J. Organomet. Chem. 584 (1999) 33;
(f) W. Imhof, Organometallics 18 (1999) 4845;
(g) D.L. Wang, W.S. Hwang, L. Lee, M.Y. Chiang, J. Organomet. Chem. 640 (2000) 85;
(h) W. Imhof, A. Göbel, J. Organomet. Chem. 610 (2000) 102;
(i) Y.F. Tzeng, C.Y. Wu, W.S. Hwang, C.H. Hung, J. Organomet. Chem. 687 (2003) 16.

[5] H.-J. Knölker, G. Baum, N. Foitzik, H. Goesmann, G. Ponser, P.G. Jones, H. Röttele, Eur. J. Inorg. Chem. (1998) 993.

[6] (a) F. Kakiuchi, M. Yamauchi, N. Chatani, S. Murai, Chem. Lett. (1996) 111;
(b) F. Kakiuchi, T. Sato, T. Tsujimoto, M. Yamauchi, N. Chatani, S. Murai, Chem. Lett. (1998) 1053;
(c) D. Berger, W. Imhof, J. Mol. Catal. A 165 (2001) 37;
(d) F. Kakiuchi, N. Chatani, Adv. Synth. Catal. 345 (2003) 1077;
(e) D. Dönnecke, J. Wunderle, W. Imhof, J. Organomet. Chem. 689 (2004) 585.

[7] (a) T. Fukuyama, N. Chatani, F. Kakiuchi, S. Murai, J. Org. Chem. 62 (1997) 5647;
(b) C.-H. Jun, C.W. Moon, J.-B. Hong, S.-G. Lim, K.-Y. Chung, Y.-H. Kim, Chem. Eur. J. 8 (2002) 485;
(c) C.-H. Jun, J.-B. Hong, Y.-H. Kim, K.-Y. Chung, Angew. Chem., Int. Ed. 39 (2000) 3440;
(d) D. Berger, W. Imhof, Tetrahedron 56 (2000) 2015;
(e) T. Asaumi, N. Chatani, T. Matsuo, F. Kakiuchi, S. Murai, J. Org. Chem. 68 (2003) 7538.

[8] (a) T. Morimoto, N. Chatani, S. Murai, J. Am. Chem. Soc. 121 (1999) 1758;
(b) D. Berger, W. Imhof, J. Chem. Soc., Chem. Commun. (1999) 1457;
(c) W. Imhof, D. Berger, M. Kötteritzsch, M. Rost, B. Schönecker, Adv. Synth. Catal. 343 (2001) 795;
(d) D. Dönnecke, W. Imhof, Tetrahedron 59 (2003) 8499.

[9] (a) R. Wegner, M. Gottschaldt, H. Görls, E.-G. Jäger, D. Klemm, Chem. Eur. J. 7 (2001) 2143;
(b) R. Wegner, M. Gottschaldt, H. Görls, E.-G. Jäger, D. Klemm, Angew. Chem., Int. Ed. 39 (2000) 595.

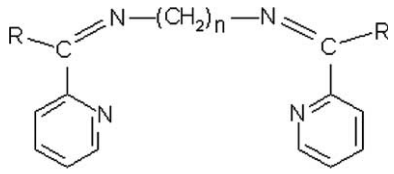
[10] (a) H.-J. Knölker, M. Bauermeister, J.-B. Panek, Chem. Ber. 125 (1992) 2783;
(b) H.-J. Knölker, P. Gonser, Synlett (1992) 517;
(c) H.-J. Knölker, P. Gonser, Synlett (1994) 405;
(d) H.-J. Knölker, H. Hermann, Angew. Chem., Int. Ed. 35 (1996) 341;
(e) H.-J. Knölker, E. Baum, P. Gonser, P.G. Jones, H. Röttele, Organometallics 17 (1998) 3916;
(f) K.G. Morris, S.E. Thomas, J. Chem. Soc., Perkin Trans. (1991) 97;
(g) A.J. Pearson, K. Chang, D.B. McConville, W.J. Youngs, Organometallics 13 (1994) 4;
(h) H.-J. Knölker, G. Baum, P. Gonser, Tetrahedron Lett. 36 (1995) 8191;
(i) F. Maywald, P. Eilbracht, Synlett (1996) 380;
(j) D. Berger, M. Dubs, A. Göbel, W. Imhof, M. Kötteritzsch, M. Rost, B. Schönecker, Tetrahedron – Asymm. 10 (1999) 2983.

[11] R. Grigg, H.Q.N. Gunaratne, J. Kemp, J. Chem. Soc., Perkin Trans. (1984) 41.

[12] (a) COLLECT, Nonius BV, The Netherlands 1998;
(b) Z. Otwinowski, W. Minor, Methods in Enymology, in: C.W. Carter, R.M. Sweet (Eds.), Macromolecular Crystallography Part A, vol. 276, Academic Press, New York, 1997, p. 307.

[13] (a) G. Sheldrick, University of Göttingen, Germany, 1986;
(b) G. Sheldrick, University of Göttingen, Germany, 1997.

[14] XP – Interactive Molecular Graphics, Vers. 4.2, Siemens Analytical Xray Inst. Inc., Madison, WI, 1990.



Scheme 1.

their preparative accessibilities, structural varieties and varied denticities. Self-assembly [3] of a metal ion, blocking ligand and bridging unit is the most important way to make different sets of complexes. With the neutral tetradentate N-donor Schiff bases L [L = *N*,*N*′-(bis(pyridin-2-yl)benzylidene)propane-1,3-diamine-(pbpd) or *N*,*N*′-(bis(pyridin-2-yl)formylidene)butane-1,4-diamine (pfbd)] and using different mole ratios of metal ion:Schiff base:azide, mono-, di- and polynuclear complexes may be produced. A 1:1:2 molar ratio should result in a mononuclear neutral compound $[Cu(L)(N_3)_2]$ and a 1:1:1 ratio should yield dicationic dinuclear $[Cu(L)(N_3)]_2^{2+}$ or polycationic polymer $[Cu(L)(N_3)]_n^{n+}$ compounds. However, with both ratios a pentacoordinated mononuclear cationic complex of the type $[Cu(L)(N_3)]^+$ is afforded. In this work, we report the synthetic details and luminescence, magnetic and some physicochemical properties of these mononuclear complexes of the type [Cu(L)(N$_3$)]X (**1**–**4**) [L = pbpd; X = ClO_4 (**1**); L = pbpd; X = PF_6 (**2**); L = pfbd; X = ClO_4 (**3**); L = pfbd; X = PF_6 (**4**)]. An X-ray crystallographic study has been made for **2** and **3** to define the coordination sphere (Scheme 1).

2. Experimental

2.1. Materials

High purity pyridine-2-carboxaldehyde (Lancester, UK), 2-benzoylpyridine (Lancester, UK), propane-1,3-diamine (Lancester, UK), butane-1,4-diamine (Lancester, UK), copper nitrate tetrahydrate (E. Merck, India), sodium azide (Aldrich, USA) and potassium hexafluorophosphate (Fluka, Germany) were purchased from the respective concerns and were used as received. Copper perchlorate hexahydrate was prepared by treatment of copper carbonate (E. Merck, India) with perchloric acid (E. Merck, India) followed by slow evaporation on a steam-bath, filtration through a fine glass-frit, and preservation in a desiccator containing concentrated sulfuric acid (E. Merck, India) for subsequent use. Purification of solvent (MeOH) and preparation of supporting electrolyte ($[Et_4N][ClO_4]$) for electrochemical work were executed following a published procedure [16]. All other chemicals and solvents were AR grade and were used as received. The synthetic reactions and work-up were done in the open air.

Caution! Perchlorate and azido compounds of metal ions are potentially explosive especially in the presence of organic ligands. Only a small amount of the material should be prepared and it should be handled with care.

2.2. Physical measurements

Elemental analyses (carbon, hydrogen and nitrogen) were performed on a Perkin–Elmer 2400 CHNS/O elemental analyzer. IR spectra (KBr discs, 4000–300 cm^{-1}) were recorded using a JASCO FTIR model 420 spectrometer. Molar conductances were measured using a Systronics conductivity meter where the cell constant was calibrated with 0.01 M KCl solution and dry MeOH was used as the solvent. Ground-state absorption and steady-state fluorescence measurements were made with a JASCO model V-530 UV–Vis spectrophotometer and Hitachi model F-4010 spectrofluorimeter, respectively. Time-resolved fluorescence measurements were carried out using a time-correlated single photon counting (TCSPC) spectrometer, Edinburgh Instruments, model 199; a hydrogen filled coaxial flash lamp with a pulse width of 1.2 ns at FWHM and a Philips XP-2020Q Photomultiplier tube were, respectively, used as the excitation source and the fluorescence detector. Magnetic susceptibilities were measured with a PAR 155 vibrating sample magnetometer. Electrochemical measurements were carried out with the use of a computer controlled EG&G PARC VersaStat model 270 electrochemical instrument using a platinum disk working electrode as described elsewhere [17]. The solutions were IR compensated and the results were collected at 25 °C. The following parameters and relations were used: scan rate (v), 50 mV s^{-1}; formal potential $E^\circ = 0.5(E_{pa} + E_{pc})$, where E_{pa} and E_{pc} are anodic and cathodic peak potentials, respectively; ΔE_p is the peak-to-peak separation. The potentials are referenced to a saturated calomel electrode (SCE) and are uncorrected for junction contributions.

2.3. Preparation of ligands

The Schiff base blockers were prepared following a reported [15] procedure. 2-Benzoyl-pyridine/pyridine-2-carboxaldehyde was condensed with the respective amine in a 2:1 molar ratio. Details are described below.

2.3.1. *N*,*N*′-(bis(pyridin-2-yl)benzylidene)propane-1,3-diamine (pbpd)

Propane-1,3-diamine (0.074 g, 1 mmol) was refluxed with 2-benzoyl pyridine (0.366 g, 2 mmol) in dehydrated alcohol (25 cm^3) for 12 h. The tetradentate ligand was isolated after evaporating the solvent and purified from alcohol. The product is isolated as a brown semi-solid

mass after being dried in vacuo over P_4O_{10} for subsequent use. Yield, 0.425 g (78%). *Anal*. Calc. $C_{27}H_{24}N_4$: C, 80.16; H, 5.98; N, 13.85. Found: C, 80.09; H, 5.92; N, 13.92%. IR: ν(C=N) 1590 cm^{-1}; UV–Vis, λ_{max}: 375 nm.

2.3.2. N,N′-(bis(pyridin-2-yl)formylidene)butane-1,4-diamine (pfbd)

Pyridine-2-carboxaldehyde (0.214 g, 2 mmol) was refluxed with butane-1,4-diamine (0.088 g, 1 mmol) in dehydrated alcohol. After 10 h, the reaction solution was evaporated under reduced pressure to give a gummy mass, which was dried and stored in vacuo over $CaCl_2$ for subsequent use. Yield, 0.242 g (80%). *Anal.* Calc. $C_{16}H_{18}N_4$: C, 72.2; H, 3.0; N, 21.0. Found: C, 72.4; H, 3.1; N, 21.3%. IR: ν(C=N) 1590 cm^{-1}; UV–Vis, λ_{max}: 375 nm.

2.4. Preparation of the complexes

Mononuclear complexes **1**and **3** were prepared from the perchlorate salt of copper(II) using the same mole ratio (1:1:1) of metal, pbpd/pfbd and azide. Complexes **2** and **4** were prepared using a 1:1:1:1 ratio of copper (II) nitrate, pbpd/pfbd, sodium azide and potassium hexafluorophosphate; these were also isolated by metathesis of **1** and **3**, respectively, with potassium hexafluorophosphate. The quality of compound **2** was poor compared to the other complexes. The typical syntheses are described below.

2.4.1. [Cu(pbpd)(N_3)]ClO_4 (**1**)

A methanolic solution (5 ml) of pbpd (0.40 g, 1 mmol) was added dropwise to a solution of $Cu(ClO_4)_2 \cdot 6H_2O$ (0.37 g, 1 mmol) in the same solvent (10 cm^3). NaN_3 (0.065 g, 1 mmol) in warm MeOH (5 cm^3) was added slowly to it. The green solution was filtered and the supernatant liquid was kept in air for slow evaporation. After a few days the desired complex that separated was washed with toluene and dried in vacuo over silica gel indicator. Yield, 0.12 g (70%). *Anal.* Calc. for $C_{27}H_{24}N_7O_4ClCu$ (**1**): C, 53.20; H, 3.97; N, 16.08. Found: C, 53.21; H, 3.95; N, 16.05%. IR (KBr, cm^{-1}): ν(C=N) 1637, 1592; $\nu(ClO_4)$ 1080, 622; $\nu(N_3)$ 2072. Λ_M (MeOH, $\Omega^{-1}\,cm^2\,mol^{-1}$): 130; UV–Vis (MeOH; λ nm): 717, 406. E°_{298}, V (ΔE_p, mV): 0.11 (100).

2.4.2. [Cu(pbpd)(N_3)]PF_6 (**2**)

$Cu(NO_3)_2 \cdot 4H_2O$ (0.24 g, 1 mmol) was dissolved in MeOH (10 cm^3). To this pbpd (0.40 g, 1 mmol) dissolved in same solvent (5 cm^3) was added slowly, followed by NaN_3 (0.065 g, 1 mmol). KPF_6 (0.18 g, 1 mmol) was added at a time. The final solution was filtered, kept for slow evaporation and processed as in **1** to yield pure **2**. Yield, 0.20 g (72%). This was also prepared by metathesis of **1** (0.60 g, 1 mmol) with KPF_6 (0.18 g, 1 mmol) in MeOH–H_2O (2:1) mixture in a better yield 0.34 g (75%). *Anal.* Calc. for $C_{27}H_{24}N_7F_6PCu$ (**2**): C, 49.51; H, 3.69; N, 14.96. Found: C, 49.51; H, 3.66; N, 14.98%. IR (KBr, cm^{-1}): ν(C=N) 1635, 1593; (PF_6) 820, 540; $\nu(N_3)$ 2073. Λ_M (MeOH, $\Omega^{-1}\,cm^2\,mol^{-1}$): 120; UV–Vis (MeOH; λ nm): 718, 404. E°_{298}, V (ΔE_p, mV): 0.11 (100).

2.4.3. [Cu(pfbd)(N_3)]ClO_4 (**3**)

Solid pfbd (0.418 g, 1 mmol) was added pinch by pinch to a solution (10 cm^3) of $Cu(ClO_4)_2 \cdot 6H_2O$ (0.37 g; 1 mmol) in MeOH. To this resulting solution, a methanolic solution of sodium azide (0.065 g, 1 mmol) was added. The mixture was filtered and the supernatant liquid was kept in air for slow evaporation. After 7 days **3** was separated, washed with toluene and dried in vacuo over silica gel indicator. Yield, 0.09 g (70%). *Anal.* Calc. for $C_{16}H_{18}N_7O_4ClCu$ (**3**): C, 40.77; H, 3.85; N, 20.80.Found: C, 40.75; H, 3.86; N, 20.85%. IR (KBr, cm^{-1}): ν(C=N) 1639, 1590; $\nu(ClO_4)$ 1082, 620; $\nu(N_3)$ 2072. Λ_M (MeOH, $\Omega^{-1}\,cm^2\,mol^{-1}$): 120; UV–Vis (MeOH; λ nm): 720, 406. E°_{298}, V (ΔE_p, mV): 0.14 (110).

2.4.4. [Cu(pfbd)(N_3)]PF_6 (**4**)

Complex **4** was prepared using the same procedure and reaction stoichiometry as in **2** except that pfbd instead of pbpd was used as the organic ligand. Yield, 0.16 g (73%).This was also prepared by metathesis of **3** (0.51 g, 1 mmol) with KPF_6 (0.18 g, 1 mmol) in a MeOH–H_2O (2:1) mixture in a higher yield 0.87 g, (80%). *Anal.* Calc. for $C_{16}H_{18}N_7F_6PCu$ (**4**): C, 37.18; H, 3.51; N, 18.97. Found: C, 37.19; H, 3.53; N, 18.95%. IR (KBr, cm^{-1}): ν(C=N) 1637, 1595; $\nu(PF_6)$ 820, 542; $\nu(N_3)$ 2073. Λ_M (MeOH, $\Omega^{-1}\,cm^2\,mol^{-1}$): 130; UV–Vis (MeOH; λ nm): 717, 405. E°_{298}, V (ΔE_p, mV): 0.13 (110).

2.5. X-ray diffraction study

Single crystals of the title complexes were obtained by slow evaporation of a methanolic solution of the reaction mixtures at room temperature (298 K). Suitable colourless crystals were mounted on a Siemens SMART CCD diffractometer equipped with a graphite-monochromator and Mo Kα ($\lambda = 0.71073$ Å) radiation. Diffraction data were measured using the ϕ and ω-scan method. Crystal data, data collection parameters and the results of analyses can be found in Table 1. The intensity data were corrected for Lorentz and polarization effects and an empirical absorption correction was employed using the SAINT [18] and SADABS [19] program for crystals **2**and **3**, respectively. The structures were solved and refined used SHELXTL [20] and the refinement is based on $|F|^2$. All non-hydrogen atoms were refined with anisotropic displacement parameters, whereas hydrogen atoms were placed in calculated positions

Table 1
Crystal data and structure refinement parameters for **2** and **3**

	2	**3**
Empirical formula	$C_{27}H_{24}N_7PF_6Cu$	$C_{16}H_{18}N_7O_4ClCu$
Formula weight	655.04	471.36
Temperature (K)	213(2)	213(2)
Wavelength (Å)	0.71073	0.71073
Crystal system, space group	monoclinic, *Cc*	monoclinic, $P2_1/c$
a (Å)	22.3993(3)	12.1272(4)
b (Å)	12.2380(2)	15.8851(6)
c (Å)	10.3083(1)	10.8302(4)
β (°)	104.707(3)	113.4780(10)
V (Å^3)	2733.16(6)	1913.63(12)
Z	4	4
D_c (Mg m^{-3})	1.592	1.636
μ (mm^{-1})	0.931	1.321
F(000)	1332	964
Crystal size (mm^3)	$0.34 \times 0.32 \times 0.22$	$0.44 \times 0.18 \times 0.14$
θ ranges (°)	2.62–24.77	2.49–28.28
h/*k*/*l*	−26, 25/−14, 14/−12, 11	−9, 16/−16, 21/−14, 10
Reflections collected	6364	11 371
Independent reflections	3330 [$R_{int} = 0.0624$]	4647 [$R_{int} = 0.0516$]
Completeness to theta	99.4% (24.77°)	97.7% (28.29°)
Absorption correction	numerical	numerical
T_{max} and T_{min}	0.8214 and 0.7425	0.8366 and 0.5941
Data/restraints/parameters	3330/2/379	4647/0/262
Goodness-of-fit on F^2	0.984	0.916
Final *R* indices [$I > 2\sigma(I)$]	$R_1 = 0.0643$, $wR_2 = 0.1579$	$R_1 = 0.0469$, $wR_2 = 0.1045$
R indices (all data)	$R_1 = 0.0855$, $wR_2 = 0.1824$	$R_1 = 0.0702$, $wR_2 = 0.1118$
Largest peak and hole (e Å^{-3})	0.657 and −1.365	1.037 and −1.070

where possible and given isotropic *U* values 1.2 times that of the atom to which they are bonded. All crystallographic calculations were conducted with SHELXL-97 [21], ORTEP-3 [22] and PLATON programs [23].

3. Results and discussion

3.1. Synthesis and formulation

The pentacoordinated mononuclear complex $[Cu(pbpd)(N_3)]ClO_4$ (**1**) is initially formed in an MeOH solution containing a 1:1:2 mixture of $Cu(ClO_4)_2 \cdot 6H_2O$, pbpd and NaN_3, a reactant ratio expected to yield a mononuclear species of the composition $[Cu(pbpd)(N_3)_2]_n$. However, microanalyses showed a 1:1:1 ratio of metal, blocking ligand and the pseudohalide, and in the IR spectrum the presence of perchlorate bands was noticed. A reactant ratio corresponding to the product stoichiometry afforded better yields of **1**. In an effort to prepare $[Cu(pbpd)(N_3)_2]$, the starting material was changed to $Cu(NO_3)_2 \cdot 4H_2O$, and a 1:1:2 molar ratio of nitrate salt, ligand and the pseudohalide produced a gummy mass of indefinite composition; however, addition of KPF_6 to the green reaction solution yielded shining microcrystalline powder of **2**. The latter was also obtainable from metathesis of **1** with KPF_6. A change of the ligand from pbpd to pfbd showed similar behaviour and compounds **3** and **4** were isolated. All the four complexes were characterized by elemental analysis, solution electrical conductivity, magnetic susceptibility, IR, UV–Vis, reflectance spectra and electrochemistry. The results are consistent with the proposed mononuclear formulation. The air-stable moisture-insensitive complexes are powders, soluble in a range of common organic solvents such as methanol, ethanol, dichloromethane, acetonitrile, but are insoluble in water. In methanol solutions they behave [24] as 1:1 electrolytes as reflected in their Λ_M values. Room-temperature solid-phase magnetic susceptibility measurements show that the copper (II) complexes have a moment close to the spin-only value ($S = 1/2$), 1.73 BM, expected from discrete and a magnetically non-coupled mononuclear $3d^9$ ion.

In the IR spectra, the point of interest is the band due to azide at ~2070 cm^{-1}. The presence of ionic perchlorate bands at ~1090 and ~620 cm^{-1} and ionic hexafluorophosphate at ~840 and ~540 cm^{-1} is routinely noticed. The ν(C=N) stretching vibrations of the metal bound Schiff bases are seen at ~1635 and ~1590 cm^{-1} [25]. All other characteristic ligand vibrations are seen in the 1600–600 cm^{-1} range. The solutions of **1**–**4** in MeOH are dark green and exhibit absorption in the 400–720 range [**1**: λ, 717, 406 nm; **2**: λ, 718, 404 nm; **3**: λ, 720, 406 nm; **4**: λ, 717, 405 nm]. The transition 700 nm corresponds to a d-d transition of the copper(II) moiety and the band around 400 nm for an intramolecular ($n \rightarrow \pi^*/\pi \rightarrow \pi^*$) charge transfer transition [26].

Reflectance [**1**: λ, 715, 400 nm; **2**: λ, 715, 408 nm; **3**: λ, 716, 404 nm; **4**: λ, 716, 402 nm] in nujol and electronic spectra for each complex in MeOH solutions are akin reflecting similar gross structure and electronic structure in the solid state and in solution of each compound.

3.2. Electrochemistry

The electroactivity of the complexes was studied in MeOH solutions using cyclic voltammetry and coulometry at platinum working electrodes. A one-electron reductive response is observed, presumably due to the electrode reaction shown as follows:

$$[Cu^{II}(L)(N_3)]^{1+} + e \rightarrow [Cu^{I}(L)(N_3)] \quad (1)$$

The electrode process in the CV is reproducible in the potential range 0.08 to −0.08 V with no trace of decomposition as reflected in a smooth cyclic voltammogram. The one-electron stoichiometry of couple 1 was confirmed from the comparison of current height with that of a standard [27] copper(II)–copper (I) couple, since attempted coulometry at potentials more cathodic than E_{pc} gave a continuous coulomb count due to some unidentified side reactions [28]. The similar pattern in electron transfer behaviour of all the complexes at about same potential once again corroborates the closely similar structure of the cationic units.

3.3. X-ray structure

In order to define the coordination sphere conclusively, a single-crystal X-ray diffraction study was made. An ORTEP diagram with the atom numbering scheme of the mononuclear units in **2** and **3** are shown in Figs. 1 and 2. Selected interatomic bond lengths and bond angles are listed in Table 2. The crystal lattice consists of $[Cu(pbpd)(N_3)]^+$ cations and PF_6^- anions for **2** and $[Cu(pfbd)(N_3)]^+$ cations and ClO_4^- anions for **3**. The coordination polyhedron around the metal centre is best described as distorted trigonal bipyramid (tbp) with a CuN_5 chromophore. The coordination includes a tetradentate Schiff base ligated by two pyridine nitrogens (N1, N4) and two imine nitrogens (N2, N3), and one terminal azide nitrogen (N5). The equatorial positions are occupied by one imine nitrogen (N3), one pyridine nitrogen (N1) and the azide nitrogen (N5) while the axial positions are occupied by the remaining imine (N2) and pyridine (N4) nitrogen atoms. The distortion from ideal tbp geometry is due to the asymmetric nature of the Schiff base and the deviations of the defining angles (90degr/120°) formed at the metal centre. The propylinic/butylenic part of the Schiff base N2–C13–C14–C15–N3/N3–C10–C9–C8–C7–N2 is to some extent puckered (Figs. 1 and 2). The equatorial Cu–N distances [2.003(7)–2.121(8) Å] (**2**) and [1.992(2)–2.198(2) Å] (**3**) as well as the bond angles [95.1(3)–134.4(3)°] (**2**) and [101.57(10)–144.53(10) °] (**3**) show significant variations. The axial Cu–N distances [Cu1–N1 1.986(8) Å, Cu1–N3 1.977(8) Å] in **2** and [Cu1–N1 1.997(2) Å, Cu1–N3 1.991(2) Å] in **3** are however close. The three bite angles N4–Cu1–N3, N3–Cu1–N2 and N2–Cu1–N1 are 78.8(3)°, 91.4(3)° and 81.30(3)° in **2** and 79.16(9)°, 96.17(9)° and 81.33(9)° in **3**. The larger bite in N3–Cu1–N2 arises from the six- and seven-membered puckered loop formed from the propylenic and butylenic arm for **2** and **3**, respectively, and it is of a similar value to the non-bite angle [N1–Cu1–N4] 97.35(9)° for complex **3**, but there is significant variation [101.00(3)°] for complex **2**. The axial bond angle N1–

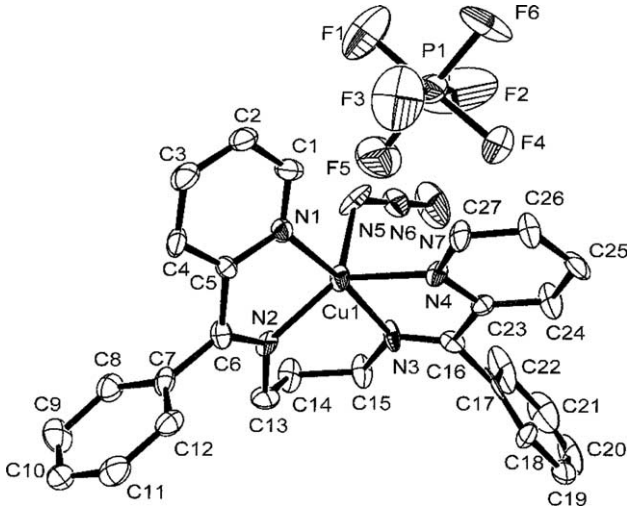


Fig. 1. ORTEP representation of $[Cu(pbpd)(N_3)]PF_6$ (**2**) with the atom labelling scheme and 50% probability ellipsoids for all non-hydrogen atoms.

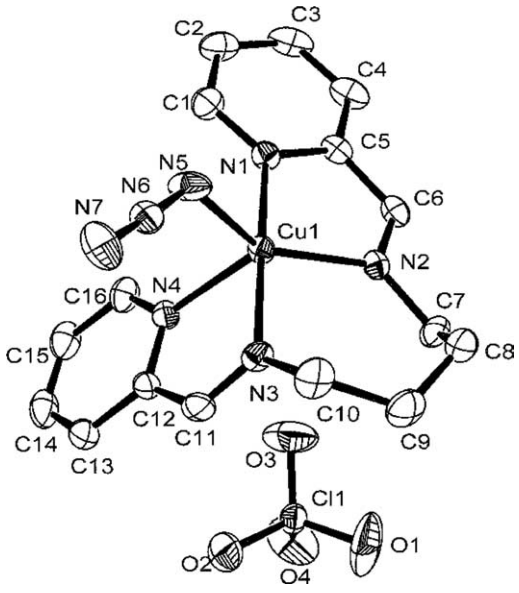


Fig. 2. ORTEP diagram of $[Cu(pfbd)(N_3)]ClO_4$ (**3**) with the atom labelling scheme and 50% probability ellipsoids for all non-hydrogen atoms.

Table 2
Selected bond distances (Å) and angles (°) for **2** and **3**

	2	**3**
Bond distances (Å)		
Cu(1)–N(1)	1.986(8)	1.997(2)
Cu(1)–N(2)	2.003(7)	2.015(2)
Cu(1)–N(3)	1.977(8)	1.991(2)
Cu(1)–N(4)	2.121(8)	2.198(2)
Cu(1)–N(5)	2.074(9)	1.992(2)
N(5)–N(6)	1.198(13)	1.191(3)
N(6)–N(7)	1.124(14)	1.160(3)
Bond angles (°)		
N(5)–Cu(1)–N(4)	95.10(3)	101.57(10)
N(5)–Cu(1)–N(2)	134.40(3)	144.53(10)
N(4)–Cu(1)–N(2)	130.40(3)	113.73(8)
N(2)–Cu(1)–N(l)	81.30(3)	81.33(9)
N(4)–Cu(1)–N(1)	101.00(3)	97.35(9)
N(5)–Cu(1)–N(3)	95.50(3)	93.64(9)
N(4)–Cu(1)–N(3)	78.80(3)	79.16(9)
N(2)–Cu(1)–N(3)	91.40(3)	96.17(9)
N(5)–Cu(1)–N(1)	94.20(3)	91.17(10)
N(3)–Cu(1)–N(1)	170.30(3)	174.54(9)
N(5)–N(6)–N(7)	179.00(13)	177.1(3)

Cu1–N3 [170.3(3)°] (**2**) and [174.54(9)°] (**3**) deviates slightly from the ideal value (180°). The sum (359.9°/359.83°) (**2**/**3**) of the equatorial angles are very close to 360.00°; so the atoms N2, N4, N5 and Cu1 are almost in a same plane. In the terminal azide ligand, the N5–N6 distance 1.198(13) and 1.191(3) Å is longer than the N6–N7 length [1.124(14) and 1.160(3) Å for **2** and **3**, respectively, and the values are very similar to the ones previously reported [29]. The azide is coordinated in a linear fashion as seen from its N5–N6–N7 angle 179.0(13)° and 177.1(3)° for **2** and **3**, respectively.

3.4. Luminescence studies

The spectroscopic data are listed in Table 3. The complexes with pbpd and pfbd feature two intense absorptions at ca. 405 nm which are assigned to intraligand π–π^* transitions. The emission energy of the complexes in MeOH solutions at 298 K is almost same ($\lambda_{max} \approx 475$ nm) and is assignable to intraligand fluorescence [30,31]. The lifetimes of the fluorescence of **1**, **2**, **3** and **4** are 2.63, 2.59, 2.59 and 2.62 ns, respectively. In glassy solutions (MeOH at 77 K) both fluorescence and $^3(\pi$–$\pi^*)$ phosphorescence is observed at 525 nm. In solid state, they show a distinct emission band at 492 nm, differing from their fluorescence spectra in MeOH (Fig. 3).

4. Supplementary data

Crystallographic data for the structural analysis has been deposited with the Cambridge Crystallographic Data Centre No 238521 for **2** and 238522 for **3**. Copies of this information can be obtained free of charge from

Table 3
Photophysical data for **1**–**4**

Sample	Absorption, λ (nm)	Emission, λ (nm)			Lifetime (ns)
		Fluor-escence[a]	Phosph-orescence[b]	Solid state[c]	
Pbpd/pfbd	375	470	525	486	2.58
1	406	475	525	492	2.63
2	404	476	525	492	2.59
3	406	475	525	492	2.59
4	404	475	525	492	2.62

[a] In MeOH at room temperature (298 K).
[b] In MeOH at 77 K.
[c] At room temperature.

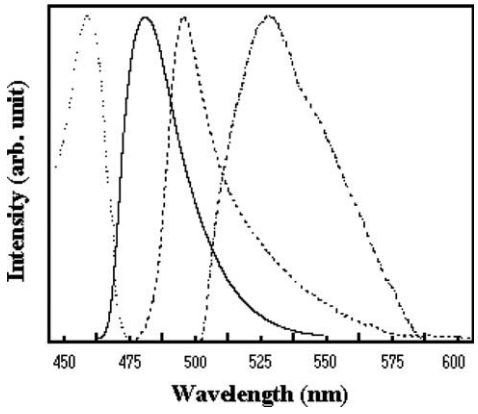


Fig. 3. Emission spectra of **2**: UV in MeOH solution at 298 K (·····), fluorescence (——), phosphorescence in MeOH glassy solution (-·-·-·), solid state at 298 K (– – –).

The Director, CCDC, 12 Union Road, Cambridge, CB2 IEZ, UK (fax: +44 1223 336033; e-mail: deposit@ccdc.cam.ac.uk or www: http://www.ccdc.cam.ac.uk).

Acknowledgement

Financial support from the DST and CSIR, New Delhi, India is gratefully acknowledged.

References

[1] M.J. Zaworotko, Chem. Commun. (2001) 1.
[2] P. Gamez, P. de Hoog, O. Roubeau, M. Lutz, W.L. Driessen, A.L. Spek, J. Reedijk, Chem. Commun. (2002) 1488.
[3] (a) Focus on Self-Assembly, Acc. Chem. Res. 32 (4) (1999) (special issue);
(b) G.F. Swiegers, T.J. Malefestse, Chem. Rev. 100 (2000) 3483;
(c) B.J. Holliday, C.A. Mirkin, Angew. Chem., Int. Ed. 40 (2001) 2022.
[4] (a) O. Kahn, Adv. Inorg. Chem. 43 (1995) 179;
(b) H. Okawa, H. Furatachi, D.E. Fenton, Coord. Chem. Rev. 174 (1998) 51.
[5] (a) S.L. Castro, Z. Sun, C.M. Grant, J.C. Bollinger, D.N. Hendrickson, G. Christou, J. Am. Chem. Soc. 120 (1998) 2365;
(b) A. Escuer, S.B. Kumar, F. Maunter, R. Vicente, Inorg. Chim. Acta 269 (1998) 313;
(c) P. Day, J. Chem. Soc., Dalton Trans. (1997) 701.

[6] S.T. Hyde, B. Ninham, S. Anderson, Z. Blum, T. Landh, K. Larsson, S. Liddin, The Language of Shape, Elsevier, Amsterdam, 1997.
[7] (a) A.M. Golub, H. Kohler, V.V. Skopenko (Eds.), Chemistry of Pseudohalides, Elsevier, Amsterdam, 1986;
(b) C. Blanchet-Boiteux, J.M. Mouesca, J. Am. Chem. Soc. 861 (2000) 122.
[8] (a) D. Bose, S.H. Rahaman, G. Mostafa, R.D.B. Walsh, M.J. Zaworotko, B.K. Ghosh, Polyhedron 23 (2004) 545;
(b) U. Ray, S. Jasimuddin, B.K. Ghosh, M. Monfort, J. Ribas, G. Mostafa, T.-H. Lu, C. Sinha, Eur. J. Inorg. Chem. (2004) 250.
[9] (a) H.-Y. Shen, W.-M. Bu, E.-Q. Gao, D.-Z. Liao, Z.-H. Jiang, S.-P. Yan, G.-L. Wang, Inorg. Chem. 39 (2000) 396;
(b) T.K. Maji, P.S. Mukherjee, G. Mostafa, T. Mallah, J. Cano-Boquera, N. Ray Chaudhuri, Chem. Commun. (2001) 1012.
[10] (a) A. Escuer, M. Font-Bardia, E. Penalba, X. Solans, R. Vicente, Inorg. Chim. Acta 298 (2000) 195;
(b) A. Escuer, M.A.H. Goher, F.A. Mautner, R. Vicente, Inorg. Chem. 39 (2000) 2107.
[11] (a) S. Koner, S. Saha, K.-I. Okamoto, J.-P. Tuchagues, Inorg. Chem. 42 (2003) 4668, and refs therein;
(b) J. Luo, X.-G. Zhou, S. Geo, L.-H. Weng, Z.-H. Shao, C.-M. Zhang, Y.-R. Li, J. Zhang, R.-F. Cai, Polyhedron 23 (2004) 1243.
[12] (a) O. Kahn, Molecular Magnetism, VCH, New York, 1993;
(b) P. Day, A.E. Underhill (Eds.), Metal–Organic and Organic Molecular Magnets, RSC, London, 2000;
(c) J.S. Miller, M. Drillon (Eds.), Magnetism: Molecules to Materials IV, Wiley-VCH, Weinheim, 2003.
[13] (a) K.D. Karlin, J. Zubieta (Eds.), Copper Coordination Chemistry: Bio-chemical and Inorganic Perspectives, Adenine, New York, 1983;
(b) S.J. Lippard, J.M. Berg, Bioinorganic Chemistry, University Science Books, Mill Valley, CA, 1994;
(c) W. Kaim, B. Schwederski, Bioinorganic Chemistry: Inorganic Elements in the Chemistry of Life, Wiley, Chichester, 1994;
(d) D.E. Fenton, Chem. Soc. Rev. 28 (1999) 159.
[14] (a) A.D. Garnovskii, A.L. Nivorozkin, V.L. Minkin, Coord. Chem. Rev. 126 (1993) 1;
(b) V. Alexander, Chem. Rev. 95 (1995) 273;
(c) M.K. Saha, D.K. Dey, B. Samanta, A.J. Edwards, W. Clegg, S. Mitra, J. Chem. Soc., Dalton Trans. (2003) 488;
(d) R. Paschke, S. Liebsch, C. Tschierske, M.A. Oakley, E. Sinn, Inorg. Chem. 42 (2003) 8230.
[15] (a) T.K. Karmakar, S.K. Chandra, J. Ribas, G. Mostafa, T.-H. Lu, B.K. Ghosh, Chem. Commun. (2002) 2364;
(b) J. Banerjee, D. Bose, S.H. Rahaman, M.J. Zaworotko, B.K. Ghosh, Indian J. Chem. 43A (2004) 1119;
(c) C.-M. Liu, R.-G. Xiong, X.-Z. You, Y.-J. Liu, K.-K. Cheung, Polyhedron 15 (1996) 4565;
(d) C.-M. Liu, R.-G. Xiong, X.-Z. You, H.-K. Fun, K. Sivakumar, Polyhedron 16 (1997) 119;
(e) M.S. Ray, R. Bhattacharya, S. Chaudhuri, L. Righi, G. Bocelli, G. Mukhopadhyay, A. Ghosh, Polyhedron 22 (2003) 617.
[16] D.T. Sawyer, J.L. Roberts Jr., Experimental Electrochemistry for Chemists, Wiley, New York, 1974, p. 167.
[17] D. Bose, S.H. Rahaman, J. Banerjee, N.K. Mondal, B.K. Ghosh, Indian J. Chem. 41A (2002) 1374.
[18] G.M. Sheldrick, SAINT, V4, Software Reference Manual Siemens Analytical X-ray Systems, Madison, WI, USA, 1996.
[19] G.M. Sheldrick, SADABS Program for Empirical Absorption Correction of Area Detector Data, University of Gottingen, Germany, 1996.
[20] W. Waratchareeyakul, S. Chantrapromma, H.K. Fun, I.A. Razak, C. Karalai, C. Ponglimanont, Acta Crystallogr., Sect. E 60 (2004) 1964.
[21] G.M. Sheldrick, SHELXL-97, Program for Refinement of Crystal Structures, University of Gottingen, Germany, 1997.
[22] L.J. Farrugia, ORTEP-3, J. Appl. Crystallogr. 30 (1997) 565.
[23] A.L. Spek, PLATON99: Molecular Geometry Program, University of Utrecht, The Netherlands, 1999.
[24] W.J. Geary, Coord. Chem. Rev. 7 (1971) 81.
[25] K. Nakamoto, Infrared and Raman Spectra of Inorganic and Coordination Compounds, Wiley, 1986, p.290.
[26] A.B.P. Lever, Inorganic Electronic Spectroscopy, second ed., Elsevier Science, New York, 1984.
[27] D. Datta, A. Chakravorty, Inorg. Chem. 22 (1983) 1085.
[28] J. Heinze, Angew. Chem., Int. Ed. Engl. 23 (1984) 831.
[29] (a) J. Ribas, M. Monfort, B.K. Ghosh, X. Solans, M. Font-Bardia, Polyhedron 15 (1996) 1091;
(b) J. Ribas, A. Escuer, M. Monfot, R. Vicente, R. Cortes, L. Lezama, T. Rojo, Coord. Chem. Rev. 193 (1999) 102.
[30] K.-Y. Ho, W.-Y. Yu, K.-K. Cheung, C.-M. Che, Chem. Commun. (1998) 2101.
[31] K.-Y. Ho, W.-Y. Yu, K.-K. Cheung, C.-M. Che, J. Chem. Soc., Dalton Trans. (1999) 1581.

Available online at www.sciencedirect.com
SCIENCE DIRECT®
Polyhedron 24 (2005) 3099–3109
POLYHEDRON
www.elsevier.com/locate/poly

Author Index to Volume 24

Aaron Nieto-Álvarez, D., 1054
Abbasi, A.R., 1461
Abboud, K.A., 2350, 2505, 2894
Abe, S., 2676
Abedin, T.S.M., 807
Abrutis, A., 3066
Abu-Youssef, M.A.M., 557, 1829
Achey, R., 2346
Achmatowicz, M., 2981
Adhikary, B., 201
Affronte, M., 2562, 2568, 2573
Afzaal, M., 1101
Agnihotri, P., 1023
Ahlgrén, M., 305
Ahsen, V., 791
Ainai, T., 685
Akbar Ali, M., 383
Akilan, P., 1781
Akita, T., 2321
Akitsu, T., 1869, 2933
Akutagawa, T., 2160, 2844
Akutsu, H., 2126, 2315, 2614, 2796
Al-Humydi, A., 1234
Al-Masri, H.T., 1937
Alam, T.M., 1143
Alberti, M., 639, 1417
Alidori, S., 995
Alikhanyan, A.S., 723
Alkam, H.H., 2944
Allain, M., 327
Almeida, M., 2035
Almeida Paz, F.A., 563
Alvarez, S., 2364
Alves, T.M.d.A., 1153
Amano, T., 2614
Amaral, V.S., 563
Amir, N., 1991
Amirkhanov, V.M., 1007
Amoretti, G., 2459, 2562
Anderson, N., 2284
Anson, C.E., 2864
Antiñolo, A., 1298
Antunes, M.A., 3038
Aoki, T., 2544
Aplincourt, M., 143
Ardavan, A., 2360
Arnaudov, M.G., 1624
Arteaga-Müller, R., 1274
Ashe III, A.J., 1280
Aslanidis, P., 351, 853
Atria, A.M., 501
Atwood, D.A., 865
Augusti, D.V., 1153
Augusti, R., 1153
Avecilla, F., 289
Awaga, K., 2501
Awwadi, F.F., 2153
Azuma, N., 2513
Azuma, Y., 2112

Bacsa, J., 1907
Baek, N.S., 137
Bagherzadeh, M., 1478
Balakrishna, M.S., 475, 1641
Banerjee, D., 1071
Banerjee, P., 771, 2921
Banerjee, S., 593, 2963
Baran, P., 1510
Barbier, J.-P., 143
Barral, M.C., 239
Barreca, D., 521
Barros-García, F.J., 129, 1125, 1764, 1975, 2972
Barszcz, B., 627
Barucci, M., 2568
Baskett, M., 2645
Basu, S., 157
Batista, A.A., 1063
Begum, N., 3074
Beheshti, A., 435
Belapure, A.R., 889
Bellú, S., 501
Belo, D., 2035
Bera, S.K., 343
Bernalte-García, Á., 129, 1125, 1764, 1975
Bernhardt, P.V., 383
Betancourt, P., 511
Bharara, M.S., 865
Bhattacharya, S., 157
Bi, L.-H., 847
Bi, W.-H., 585, 2955
Bian, G.-Q., 2680
Bian, H.-D., 2002
Bilgin, A., 1117
Bin-Salamon, S., 2876
Binyamin, I., 469
Bircher, R., 2455
Blackman, A.G., 1
Bleau, J.E., 463
Blumenfeld, A., 1366
Blundell, S.J., 2108, 2360
Boča, M., 1510, 1913
Boča, R., 1510
Bochmann, M., 151
Bolvin, H., 1033
Bonanno, J.B., 1356
Bondarenko, E.V., 611

doi:10.1016/S0277-5387(05)00717-5

Bontchev, P.R., 1983
Bontchev, R.P., 1983
Booncoon, S., 769
Boro, B.J., 1093
Bose, D., 747, 1755, 1837
Boubekeur, K., 1555
Boudalis, A.K., 711, 1540
Bouet, G.M., 327
Boukheddaden, K., 2852, 2857
Bouwman, E., 41, 979
Boyle, T.J., 1143, 1727
Brasun, J., 1929
Brechin, E.K., 2400, 2443, 2450, 2455, 2573
Bridgewater, B.M., 1356
Brooks, N.R., 435
Brorson, M., 1212
Brown, M.D., 75
Bu, X.-H., 413
Buglyó, P., 837
Bunge, S.D., 1143
Bunton, C.A., 1002
Butcher, R., 2222
Butcher, R.J., 201, 1015, 2921

Cage, B., 2350
Camalli, M., 995
Campagnoli, D., 501
Campello, M.P., 451
Campo, J., 2579
Canary, J.W., 2691
Candini, A., 2562, 2573
Caneschi, A., 2568
Cano, J., 2364
Cantrell, T., 1366
Cao, R., 585, 2955
Cao, X.-Y., 209
Carabel, M., 2043
CarlosChinea, 511
Carmalt, C.J., 463
Carretta, S., 2459, 2562
Carroll, P.J., 391
Casas, J.S., 1196, 3057
Casellas, H., 1549
Castaño, M.V., 3057
Castellano, E.E., 49, 1063
Castiñeiras, A., 1196
Černák, J., 579
Chaboussant, G., 2455
Chaichit, N., 765, 767, 769
Chakov, N.E., 2284, 2346
Chakraborty, J., 771
Chakravarty, A.R., 1922
Chandra, S.K., 343
Chantrapromma, S., 1071
Chattopadhyay, S., 1953
Chattopadhyay, S.K., 201, 1861
Chattopadhyay, T., 1677
Chaudhuri, S., 1015
Chauhan, H.P.S., 89
Chen, B., 2885
Chen, C., 1656
Chen, C.-W., 487
Chen, F., 1656
Chen, J.-D., 539, 1497, 2913
Chen, J.-Z., 173
Chen, T.-M., 189, 881
Chen, X.-D., 1047
Chen, X.-M., 1047
Chen, Y., 2269
Cheng, P., 2002
Cheng, S.-C., 487
Chernega, A.N., 917
Chernyavskaya, A.A., 611
Chiba, M., 2835, 2885
Chikate, R.C., 889, 1689
Chippindale, A.M., 1941
Chong, T.S., 1503
Chowdhury, H., 1755, 1837
Christou, G., 2065, 2284, 2346, 2450, 2505, 2894
Chuburu, F., 143
Chunsheng, L., 1793
Churchill, D.G., 1356
Ciavatta, L., 1878
Cindrić, M., 369, 1717
Cinquantini, A., 1340
Cinti, F., 2568
Ciunik, Z., 1577
Čižmár, E., 2355
Clegg, W., 435
Clérac, R., 2864
Codjovi, E., 2857
Collins, S., 1234
Collison, D., 2443
Conway, S.L.J., 1388
Cook, D.F., 3022
Cornard, J.-P., 1593
Coughlin, E.B., 1347
Couto, M.S.R., 495
Cox, P.J., 351, 853
Craymer, J.F., 1347
Creaven, B.S., 949
Cronin, L., 1651
Cuccoli, A., 2568
Cui, Q., 209
Cumbrera, F.L., 1975
Curtis, N.F., 281, 976, 1606, 3022

da Costa Jr., N.B., 3046
Dalal, N., 2280
Dalal, N.S., 2284, 2346, 2350
Damayanti, M., 909
Dalmázio, I., 1153
Damnatara, K., 767
Dang, D.-B., 1669
Dangleterre, L., 1593
Danjobara, K., 2821
Das, D., 1677
Das, S.K., 1410
Davies, C.J., 2017
Davis, W.L., 1611
Day, P., 2108
de Blas, A., 289
de Carvalho, I.M.M., 65
de Gelder, R., 41, 979
de Sousa Moreira, Í., 65
Déchamps-Olivier, I., 143
Decken, A., 2994
Decurtins, S., 3032
Deguchi, H., 2497, 2501, 2716
del Barco, E., 2284, 2557, 2691, 2695
Delgadillo, A., 1749
Delgado, R., 451
Deng, X., 3004
Deoghoria, S., 343
Depperman, E.C., 2880
Deumal, M., 2368

Dholia, S., 1517
Divanidis, S., 351, 853
Djuran, M.I., 2009
Dobrzyńska, D., 407
Doerrer, L.H., 1388, 1803
Domasevitch, K.V., 917, 1007, 1631
Domingos, Â., 3038
Dong, Z.-C., 295, 571
Dongsheng, Z., 1793
Donnadieu, B., 1033
dos Santos, I.C., 3038
Dracopoulos, V., 619
Dressel, M., 2400
Drew, M.G.B., 1861
Drogo, C., 501
Du, M., 1047
Du, S.-W., 481, 831, 2988
Duczmal, M., 407
Duesler, E.N., 469
Dunbar, K.R., 1907

Eberlin, M.N., 731
Edwards, R.S., 2280
Egan, D.A., 949
Einaga, Y., 1869, 2933
Eisch, J.J., 1325
Eisen, M.S., 1298
El-Kaderi, H.M., 645
Ellena, J., 1063
Erker, G., 1289
Ertem, B., 1117
Escuer, A., 557
Esteban, D., 289
Evangelisti, M., 2562, 2573
Exley, C., 1585

Fajardo, M., 1298
Fan, Z., 1262
Fang, X., 1280
Fawcett, J., 1533, 2017
Felicissimo, M.P., 1063
Felix, A.M., 1093
Feliz, M., 1212
Feng, L., 1262
Ferencová, B., 579
Fernandes, M.A., 958
Fernandez-Alonso, F., 2455
Ferreira, A.G., 1063
Feyerherm, R., 2413
Field, L.M., 2639
Figueira, M.J., 2035
Finke, R.G., 1961
Flynn, E., 1101
Fokin, S., 2094, 2176
Foppa, T., 495
Fregona, D., 521
Freire, R.O., 3046
Frem, R.C.G., 1086
Frye, F., 2355
Fuess, H., 1913
Fujii, Y., 2835, 2885
Fujima, N., 2472
Fujino, M., 2501, 2614
Fujioka, J., 2437
Fujisawa, K., 1991
Fujita, M., 1991
Fujita, W., 2501
Fujiwara, H., 2315
Fujiyoshi, Y., 2737
Fukuda, S., 2680
Fukui, K., 2194, 2200, 2326, 2618
Fun, H.-K., 601, 747, 1071, 1837, 3091
Fursova, E., 2084
Furukawa, Y., 2737
Furuya, T., 2121
Fuyuhiro, A., 2437

Gab Joung, U., 1256
Gallagher, W.M., 1250
Galvez, N., 2906
Gama, V., 2035
Gamez, P., 1549
Gan, X., 469
Ganguly, B., 1023
Gao, S., 823, 1669
García, S., 1079
García-Tasende, M.S., 3057
García-Vázquez, J.A., 2043
Garde, R., 2906
Garribba, E., 799
Garrison, J.C., 1234
Gatteschi, D., 2568
Gehlen, M.H., 65
Geneste, F., 1961
George, P.P., 475
George, R.G., 679
Getova, V.T., 1983
Ghirri, A., 2562, 2573
Gholivand, K., 655
Ghosh, A., 593, 2963
Ghosh, A.C., 3074
Ghosh, B.K., 747, 1525, 1755, 1837, 3091
Ghosh, M., 1677
Ghosh, P.K., 1023
Ghosh, R., 1525, 1755
Ghumaan, S., 333
Gil-bortnowska, R., 1445
Gillitt, N.D., 1002
Girginova, P.I., 563
Głowiak, T., 663
Göbel, A., 3082
Goeta, A.E., 807
Goher, M.A.S., 557
Gök, Y., 1117
Gómez-García, C.J., 2232, 2293
Gómez-Ruiz, S., 1298
Gonzalez-Baró, A.C., 49
González-Prieto, R., 239
Görls, H., 3082
Goswami, S., 2921
Govindaswamy, P., 1710
Green, J.C., 1382
Green, M.L.H., 1388
Grodzicki, A., 663
Grove, H., 807
Grubišić, S., 1701
Gu, K.-C., 173
Gu, W., 2002
Güdel, H.U., 2455
Guérin, C., 1033
Guanghua, L., 1793
Gubina, K.E., 1007
Guillon, E., 143
Guo, J., 927
Gupta, S., 1922

Gürek, A., 791
Gurešić, D.M., 2009

Haddon, R.C., 2076
Hadjikostas, C.C., 2944
Hagen, C.M., 1961
Hamada, I., 2472
Hamamci, S., 693
Hamamoto, T., 2701, 2708, 2758
Hamid, M.H.S.A., 383
Hammud, H.H., 221
Han, L., 2409
Han, L.-M., 759
Han, X.-W., 173
Handa, M., 2658
Handel, H., 143
Harigaya, K., 2491
Harrison, W.T.A., 693
Harrowfield, J., 968, 1569
Harter, A.G., 2346, 2350
Harvey, R.G., 807
Hashimoto, H., 2885
Hashimoto, K., 2857, 2901
Hatanaka, K., 2194
Hatano, M., 2680
Havel, J., 639, 1417
Hay, B.P., 469
Hayami, S., 2821
Hayasaki, S., 2885
Hayes, W., 2108
He, F., 1047
Heeg, M.J., 645
Helliwell, M., 2450
Hendrickson, D.N., 2280, 2557, 2695
Henner, B., 1033
Henriques, R.T., 2035
Herbst, K., 1212
Herrero, S., 239
Hewitt, I.J., 2864
Hey-Hawkins, E., 1340, 1937
Hill, S., 2280, 2284, 2557
Hilton, S.J., 2017
Hirayama, T., 2141
Hiromitsu, I., 2658
Hisatou, H., 2513
Höcher, T., 1340
Hodorowicz, S.A., 627
Holland, G.P., 1143
Holman, K.T., 221
Holmes, S.M., 1845
Hong, C.S., 249
Hong, S.-D., 1269
Horton, P.N., 151
Hoshino, H., 685
Hosokoshi, Y., 2513
Hossain, G.G., 872, 1471, 3074
Howard, J.A.K., 807
Hozumi, T., 2901
Hsu, G.-Y., 487
Hsu, S.-F., 189, 881
Hsu, Y.-F., 2913
Hu, B., 2055
Hu, H.-L., 539, 1497
Hu, S.-M., 831
Hubert-Pfalzgraf, L.G., 1185,3066
Huch, V., 89
Huh, Y.D., 2355
Hundal, G., 1221
Hung, C.-H., 1755
Hure, E., 501
Hursthouse, M.B., 121, 151
Hussain, F., 847
Hyder, M.I., 872, 1471

Ibarra, C., 1002
Ichiyanagi, Y., 2813
Idehara, T., 2835
Ikeda, S., 2901
Ikemoto, I., 2789
Ikorskii, V., 2084, 2094
Ilina, E., 3052
Imai, H., 2808
Imhof, W., 3082
Inoue, H., 2828
Inoue, K., 2112, 2808, 2821
Irie, K., 2716
Irie, M., 2477, 2484
Irwin, L.J., 1314
Isaacman, S., 2691
Isber, S., 221
Ise, T., 2377
Ishida, T., 2584, 2588, 2593
Ishii, A., 1949
Ishimoto, H., 2280
Ishiyama, H., 2599
Isidro, R.M., 2280
Isobe, H., 2701, 2767
Ito, A., 2141
Ito, H., 2544
Ito, T., 2726
Itou, M., 2189
Iuliano, M., 1878
Ivanova, B.B., 1624
Iwahori, F., 2250
Iwamoto, T., 2839
Izakovič, M., 1913

Jabłońska-Wawrzycka, A., 627
Jahan, M., 1682
Janiak, C., 593, 2963
Janicka, A., 1929
Jaworska, M., 267, 359, 419, 701, 1445, 1454, 1893, 3012
Jerschow, A., 2691
Jerzykiewicz, L.B., 407
Jezierska, J., 1425
Jia, C., 3032
Jiang, Q., 1109
Jiang, Z.-H., 2002
Jiansheng, X., 1793
Jiménez, H.R., 1813
Jiménez-Aparicio, R., 239
Jiménez-Cruz, F., 1054
Jin, L.-P., 823
Jin, Q., 549
John, R.P., 601
Jones, L.F., 2443
Jouad, E.M., 327
Judai, K., 2148
Jung, H.Y., 1269
Jung, M.W., 1269
Jurczak, J., 2981
Jwo, T.-Y., 2205

Kabir, S.E., 872, 1471, 3074
Kadam, R.M., 909
Kaim, W., 333
Kaizaki, S., 2437

Kajiyoshi, K., 2464, 2468
Kamatchi, P., 900
Kambe, T., 2464, 2468
Kamenar, B., 369, 1717
Kamigaki, Y., 1798
Kampf, J.W., 1280
Kanamori, K., 1991
Kanan, K.M., 2944
Kandaswamy, M., 113, 900, 1781
Kaneko, T., 2544
Kaneko, W., 2497, 2839
Kapoor, P., 1221
Kapoor, R., 1221
Karagiannidis, P., 351, 853
Karasawa, S., 2102
Kariuki, B.M., 1651
Kasi, R.M., 1347
Kastrissios, D.Th., 619
Kasumov, V.T., 319, 1203, 1821
Kataria, A., 1221
Kato, R., 2817
Kato, T., 2828
Katsuhara, M., 2315
Kavanagh, K., 949
Kawada, Y., 2870
Kawakami, H., 2870
Kawakami, T., 2274, 2382, 2708, 2720, 2745, 2751, 2758, 2778
Kawamoto, T., 2173, 2676
Kawamoto, Y., 1991
Kawata, S., 2437
Keller, G., 2906
Kelly, T.L., 807
Kemp, R.A., 1093, 1739
Kent, A.D., 2284, 2557, 2691, 2695
Kerep, P., 2849
Kessler, V.G., 3052
Keypour, H., 1478
Khan, M.A., 327
Khavryuchenko, A.V., 1631
Khosravi, H., 1682
Kickelbick, G., 1913
Kikuchi, H., 2835
Kikuchi, K., 2315, 2789, 2808
Kim, C.H., 865
Kim, H.K., 137
Kim, J.Y., 968, 1569
Kim, K.M., 249
Kim, M., 1803
Kim, Y., 968, 1569
Kim, Y.-I., 377
Kinoshita, M., 2464, 2468
Kirchner, N., 2400
Kirk, M.L., 2876, 2880
Kirman, C., 2280
Kita, R., 2491, 2533
Kitagawa, H., 2528
Kitagawa, S., 2839
Kitagawa, Y., 2382, 2701, 2708, 2720, 2745, 2751, 2767, 2778, 2784
Kizashi, Y., 2330
Kłak, J., 3012
Klinowski, J., 563
Knickelbein, M.B., 2341
Kobayashi, A., 2793
Kobayashi, H., 2793
Kobayashi, T., 2200, 2326
Kodama, T., 2789
Koga, N., 2102, 2321
Kögerler, P., 1651, 2737
Koikawa, M., 2257
Köksal, F., 319, 1203
Koizumi, K., 2701, 2708, 2720, 2745, 2751, 2767, 2778, 2784
Kojić-Prodić, B., 97
Kojima, N., 2909
Kokado, S., 2491, 2533
Kokozay, V.N., 1425
Kollipara, M.R., 391, 1710
Konaka, H., 2680
Konopińska, D., 443
Kontturi, M., 305
Korber, N., 1565
Kori, K., 89
Kortz, U., 847
Kosaka, W., 2901
Kosugi, K., 2148
Kouka, H., 2870
Koval'chuk, T.V., 611
Kowalik-Jankowska, T., 443
Kozlevčar, B., 1549
Kozłowski, H., 1175
Kreitlow, J., 2413
Krishnapriya, K.R., 113
Kruszynski, R., 267, 359, 419, 701, 1445, 1454, 1893, 3012
Krutošíková, A., 1510
Kubo, T., 2522, 2528, 2885
Kuhns, P., 2346
Kumagai, K., 2737
Kumar, R., 2691
Kumar, R.K., 2876
Kuramitsu, S., 2767
Kuroda-Sowa, T., 2680
Kurup, M.R.P., 601
Kusakabe, K., 2396
Kuzmina, N.P., 723

Labat, G., 3032
Lacerda, S., 451
Lahiri, G.K., 333
Lahti, P.M., 2639, 2645
lal Pratihar, J., 1953
Lampeka, R.D., 1631
Lancaster, S.J., 151
Landee, C.P., 2153, 2222
Lane, S., 2355
Lanfredi, A.M.M., 1599
Langner, E.H.G., 1611
Larionova, J., 1033
Lascialfari, A., 2568
Laskar, I.R., 189, 881
Lassahn, P.-G., 593, 2963
Laurenczy, G., 1961
Laus, G., 533
Lawrence, J., 2280, 2557
Lay, P.A., 1079
Layh, M., 958
Le Baccon, M., 143
Le Goff, X.F., 1033
Lee, C.-J., 487
Lee, G.-H., 157, 215, 2205, 2215
Lee, H., 1269, 1356
Lee, H.-W., 377
Lee, S.-J., 1366
Lee, Y.H., 968, 1569
Lee, Y.-M., 377
Leech, M., 807
Lees, A.M.J., 427
Lees, R.J.E., 1941

Lehtonen, A., 257
Lei, C., 295
Leita, B.A., 2165
Leiva, A.M., 1749
Leng, X.-B., 759
Levason, W., 75, 121
Levina, A., 1079
Li, D.-S., 215
Li, J.-R., 413, 481
Li, L., 1656
Li, X., 2955
Li, X.-J., 2955
Li, Y.-Z., 1669
Li, Z.-H., 481, 2988
Liang, R.-H., 539
Liao, D., 1656
Liao, D.-Z., 2002
Liao, Z.-R., 1617
Lim, L.P., 1503
Lin, J.-N., 1071
Lin, J.G., 2215
Lin, S.-H., 487
Liou, J.-C., 739
Lipetskaya, A.V., 1425
Liu, B., 2889
Liu, G., 2269
Liu, P., 215
Liu, Q., 1656
Liu, Q.-L., 165
Liu, S.-X., 3032
Liu, W.-S., 1160
Liu, X.-J., 2027
Liu, X.-T., 165
Liviotti, E., 2459
Llusar, R., 1212
Lobbia, G.G., 181
Lodowski, P., 701, 1893
Loeb, B., 1749
Loginova, N.V., 611
Long, G.J., 41
Longo, C., 511
Lopez, N., 1907
López-Torres, E., 1435
Lozano-Vila, A.M., 129, 1975
Lu, S.-Z., 823
Lu, T.-H., 343, 739, 1071, 1525
Lu, X., 2889
Luna-Giles, F., 129, 1125, 1764, 1975, 2972
Luneau, D., 1185, 2658
Luzón, J., 2579
Lysenko, A.B., 917

Ma, C., 1656
Ma, C.-L., 1109, 1773
Ma, H.-R., 215
Małecki, J.G., 359, 1445, 3012
Maccato, C., 521
Machura, B., 267, 419, 701, 1454, 1893
Madhu, N.T., 2864
Maeda, T., 2497
Maeda, Y., 2821
Maekawa, M., 2680
Maestro, M.A., 1298
Magnani, N., 2459
Mahon, M., 949
Maiti, N., 1953
Majee, A., 1677
Mak, T.C.W., 940, 1047
Makowski, M., 1929
Maldonado-Rogado, M.A., 1125, 1764, 2972
Malek, K., 1175
Malik, M.A., 1101
Malkerova, I.P., 723
Manassero, M., 2921
Mancilla, T., 1054
Mancini, M., 995
Mao, J.-G., 295, 571
Marotta, E., 97
Marques, N., 3038
Martins, G.T.S., 495
Maruno, Y., 2745, 2778
Maruta, G., 2417, 2424, 2431, 2599, 2607
Maryunina, K., 2094
Masaki, K., 2126
Masci, B., 229
Massera, C., 1599
Masuhara, N., 1798
Mathonière, C., 2413
Mathur, S., 89
Mathur, T., 739
Matković-Čalogović, D., 1717
Matoga, D., 1533
Matsuda, K., 2477, 2484
Matsuda, T., 2901
Matsumoto, N., 685
Matsumoto, T., 2315
Matsuoka, S., 985
Matsushita, K., 2116
Matsushita, M., 2900
Matsushita, M.M., 2263, 2870
Matulková, I., 311
Matuzsná, K., 1913
Maurin, I., 2857
Mauro, A.E., 1086
Mautner, F.A., 557
Mayer-Figge, H., 771, 1624
McCann, M., 949
McInnes, E.J.L., 2573
McIntyre, G.J., 2579
Mehandjiev, D.R., 1983
Mehrotra, R.N., 1167, 1517
Meisel, M.W., 2355
Meléndez-Martínez, J.J., 1975
Mendiola, M.A., 1435
Mendoza, O., 1250
Mendoza-Díaz, G., 777
Meng, Q.-J., 1669, 2160, 2269
Meng, X.-G., 1617
Merola, J.S., 2133
Miah, M.A., 872, 1471, 3074
Micera, G., 799
Midollini, S., 1878
Mihailovic, D., 2173
Miklovič, J., 1510
Mikuriya, M., 2658
Milić, D., 1717
Miller, D.O., 807
Miller, S.A., 1314
Mills, A.M., 41
Milway, V.A., 807
Minacheva, L.Kh., 723
Minamoto, M., 2263
Mirza, A.H., 383
Mishra, D., 201, 1861
Mito, M., 2497, 2501, 2716
Mitsudo, S., 2835

Mitsuo, S., 2238
Mitsutaka, O., 2330
Miura, Y., 985
Miyajima, K., 2341
Miyanaga, T., 685
Miyasaka, H., 2250, 2680
Miyashita, S., 2852
Miyashita, Y., 1991
Miyazaki, E., 2632
Miyazaki, S., 2821
Miyazaki, Y., 985
Miyoshi, S., 2680
Mizoguchi, K., 2173
Mobin, S.M., 475, 1641
Mochida, T., 2189
Moghimi, A., 1682
Mohammed, M., 1234
Mohapatra, M., 909
Moinet, C., 1961
Molina, G., 501
Molinié, P., 1555
Moratal, J.M., 1813
Mori, F., 2588
Mori, H., 2189
Mori, K., 2126
Mori, T., 2315, 2803
Morii, K., 2607
Morita, Y., 2194, 2200, 2326, 2618, 2625, 2632
Moritomo, Y., 2909
Moronta, D., 511
Mosquera, M.E.G., 1274
Mostaanzadeh, H., 655
Mostafa, G., 343, 747, 1837
Motevalli, M., 1101
Motoyama, T., 2112
Moubaraki, B., 2165
Moulton, B., 343
Mozharivskyj, Y.A., 1710
Mukai, K., 2513
Mukherjee, A., 1922
Müller, A.G., 533
Munakata, M., 2680
Muñoz Acevedo, J.C., 501
Murata, H., 2309
Murata, T., 2625
Murray, K.S., 2165
Murugesu, M., 2284, 2894

Nagao, H., 2389, 2550, 2665, 2671, 2726
Nah, M.-K., 137
Nakajima, A., 2341
Nakajima, S., 2185
Nakamoto, A., 2909
Nakamura, A., 2909
Nakamura, T., 2160, 2844
Nakanishi, T., 2732
Nakanishi, Y., 2116
Nakano, H., 2396
Nakano, K., 2437
Nakano, M., 2653
Nakano, Y., 2141
Nakashima, S., 1798
Nakasuji, K., 2194, 2200, 2326, 2522, 2528, 2618, 2625, 2632
Nakata, K., 2250
Nakatsuji, S., 2126, 2614, 2796
Nakazaki, J., 2538
Naresh Kumar, K., 1885
Naskar, S., 201, 1861
Nayak, A., 333
Nečas, M., 1855
Neels, A., 3032
Nejati, K., 1461
Nesterova, O.V., 1425
Nethaji, M., 1133, 1677, 1922
Netto, A.V.G., 1086
Neves, A., 495
Ng, C.H., 1503
Ngai, K.S., 1503
Nguyen, P., 2350
Ni, C.-L., 1669
Ni, Z.-P., 1669
Niclós-Gutiérrez, J., 1968
Nief, F., 549
Niel, V., 807
Nihei, M., 2409, 2885
Niketić, S.R., 1701
Nikiforov, G.B., 2994
Nikolaou, S., 731
Nishi, N., 2148
Nishida, S., 2194, 2200, 2326
Nishide, H., 2309
Nishihara, S., 2160, 2844
Nishijo, J., 2148
Nishikawa, H., 2789
Nishikawa, K., 2665, 2671, 2726
Nishimura, Y., 2625
Nishino, M., 2852
Nishiyama, Y., 2745, 2778
Noble, A., 949
Nogami, T., 2584, 2588, 2593
Nogueira, H.I.S., 563
North, J.M., 2284
Nosova, K., 2084
Notash, B., 1682
Nouri, S.M., 1478
Novak, P., 1717
Novoa, J.J., 2368
Nuida, T., 2901

Oakley, R.T., 2076
O'Brien, P., 1101
Ochsenbein, S.T., 2455
Oda, T., 2472, 2550
Ogawa, Y., 2821
Oh, J.B., 137
Ohara, K., 2513
Ohashi, M., 2528
Ohba, M., 2257, 2497, 2732, 2839
Ohba, T., 2194
Ohkoshi, S., 2857
Ohkoshi, S.-i., 2901
Öhrstrom, L., 557
Okabe, C., 2148
Okabe, E., 2870
Okamoto, K.-i., 1991
Ōkawa, H., 2497, 2732, 2839
Okazawa, A., 2584
Okazawa, K., 2189
Okuda, T., 1798
Okumura, M., 2382, 2701, 2708, 2720, 2745, 2751, 2758, 2778
Oliveira, M.C.B., 495
Olivieri, E., 2568
Olmstead, M.M., 2280
Omerzu, A., 2173
Omondi, B., 958
Önal, A.M., 1821

O'Neill, S.A., 463
Ong, H.K.A., 1503
Onuma, A., 2544
Oomomo, T., 2431
Ortiz, Á.L., 1975
Osetska, O.V., 1631
Oshima, K., 2464, 2468
Oshio, H., 2409, 2789, 2885
Osipovich, N.P., 611
Otero, A., 1298
Otsuka, T., 2793
Ottley, L.A.M., 1727
Ouahès, R., 2906
Ovcharenko, V., 2084, 2094, 2176
Owuor, F.A., 1325
Oyama, M., 2112, 2116, 2121
Özalp-Yaman, Ş., 319, 1821
Ozeki, T., 1949

Padhye, S.B., 889, 1689
Padmanabhan, M., 679
Paim, L.A., 1153
Paine, R.T., 469
Pal, S., 57
Pal, S.K., 2076
Palacio, F., 2579
Panja, A., 2921
Papatheodorou, G.N., 619
Parada, J., 1002
Parajó, Y., 1196
Parajón-Costa, B.S., 49
Pardal, C., 1813
Pardey, A.J., 511
Park, J.-H., 2355
Park, K.-M., 137
Park, Y.-W., 1269
Parkin, G., 1233, 1356
Parkin, I.P., 463
Parkin, S., 865, 1845
Pasca, E., 2568
Pasko, S.V., 3066
Passmore, J., 2994
Pastor, C.J., 1298
Pathak, A., 1221
Patra, S., 333
Patrick, B.O., 2242
Pattanayak, P., 1953
Paul, P., 1023
Pelikán, J., 1510
Pellei, M., 181, 995
Peña-Méndez, E., 1417
Peng, S.-M., 157, 215
Pennington, D.A., 151
Peralta, R.A., 495
Peräniemi, S., 305
Pereira, L.C., 2035
Perlepes, S.P., 1540
Perrotin, P., 1366
Perruchas, S., 1555
Petrusenko, S.R., 1425
Pettinari, C., 181
Petukhov, K., 2284
Pevec, A., 1549
Philip, V., 1133
Phuengphai, P., 769
Piligkos, S., 2450, 2562, 2573
Pini, M.G., 2568
Piro, O.E., 49, 777
Piszczek, P., 663
Platas-Iglesias, C., 289
Platt, A.W.G., 427
Polozov, G.I., 611
Porter III, W.W., 3004
Pótári, N., 837
Potgieter, H., 1968
Pourayoubi, M., 655
Powell, A.K., 2864
Powell, A.V., 1941
Pradeep, C.P., 1410
Prasad, T.K., 1487
Prashar, S., 1298
Prathapachandra Kurup, M.R., 1133
Priego, J.L., 239
Příhoda, J., 1855
Priya, S., 1641
Proniewicz, L.M., 1175
Prosvirin, A., 1907
Pruchnik, F.P., 1577
Psycharis, V., 711
Puranik, V.G., 333
Purcell, W., 1968
Puschmann, H., 281

Qiu, J.-H., 1617

Radanović, D.D., 1701, 2009
Raftery, J., 2443
Rahaman, S.H., 1525, 1755, 1837, 3091
Rajaraman, G., 2450
Rajasekharan, M.V., 1487
Rajewska, A., 443
Ramakrishna, B.L., 2232
Ramesh, R., 1885
Ramsey, C., 2280
Rapko, B.M., 469
Raptopoulou, C.P., 711, 1540
Raspertova, I.V., 1631
Ratnani, R., 121
Rauwald, U., 847
Raveendran, R., 57
Rawson, J.M., 2579
Ray, U.S., 739, 1071
Reed, R.W., 2076
Reedijk, J., 41, 979, 1549, 1599
Rehmann, F.K., 1250
Reibenspies, J.H., 1314
Reicke, M., 847
Reid, G., 75, 121
Ren, X., 2269
Ren, X.M., 2160, 2844
Renz, F., 1913, 2849
Rettori, A., 2568
Reyes, A., 2346
Rezvani, Z., 1461
Rheingold, A.L., 1093, 1739, 1803, 2557
Ricard, L., 549
Richert, M., 663
Rickard, C.E.F., 1606, 3022
Rigotti, G., 777
Risegari, L., 2568
Rizzotto, M., 501, 1079
Robb, M.A., 2368
Robinson, W.T., 976
Rocha, G.B., 3046
Rodriguez, M.A., 1727
Rodríguez-Blas, T., 289

Rogachev, A.Yu., 723
Roh, S.-G., 137
Rohovec, J., 311
Rojas, A.D., 511
Romanenko, G., 2084, 2094, 2176
Romero, J., 2043
Ronconi, L., 521
Roscilde, T., 2568
Roubeau, O., 1599
Rous, A.J., 1250
Rovai, D., 2568
Roy, P., 2921
Royo, P., 1274
Ruiz, E., 1033, 2364
Rumberger, E.M., 2557
Ruschman, C., 1845
Rychlewska, U., 1701, 2009

Sabatini, A., 1878
Safari, N., 1682
Saha, N., 1015
Saha, N.C., 1015
Sailaja, S., 1487
Saini, R., 521
Sakamoto, H., 2173
Sakamoto, M., 2522
Sakashita, H., 985
Sakurai, S., 2901
Sakurai, T., 2665, 2671
Sala, L.F., 1079
Salavati-Niasari, M., 1405
Salehzadeh, S., 1478
Sanakis, Y., 711, 1540
Sánchez, A., 1196, 3057
Sánchez-González, Á., 1196
Sánchez-Nieves, J., 1274
Sanna, D., 799
Santini, C., 181, 995
Santini, P., 2459, 2562
Santos, I., 451
Santos, I.C., 451, 2035
Sañudo, E.C., 2450
Sarkar, B., 333
Sarula, 2889
Sato, K., 2112, 2116, 2121, 2194, 2200, 2326, 2377, 2618
Sawa, H., 2148
Schweda, L., 3082
Scott, C., 511
Scott, T.A., 671
Šedo, O., 639
Seeber, G., 1651
Segawa, H., 2538
Selvaraj, S., 900
Senshu, Y., 2538
Sergienko, V.S., 723
Ševčík, R., 1855
Severino, P.C., 495
Seyedahmadian, M., 1461
Sezer, A., 1203
Shadyro, O.I., 611
Shago, R.F., 1611
Shahin, A.M., 41
Shaik, N.M., 89
Shaikh, N., 2921
Shang, Z.-C., 2027
Shapiro, P.J., 1366
Sharafi, F., 435
Shariatinia, Z., 655
Sharmin, S., 2360
Sheldrick, W.S., 771
Sheryakov, A.A., 611
Shi, Q.-Z., 215
Shi, X., 1325
Shi, Y., 1109
Shiao, H.-A., 2205
Shiba, D., 2513
Shibuya, H., 2828
Shiga, T., 2732
Shimada, T., 2593
Shiomi, D., 2194, 2200, 2326, 2377, 2618
Shirakawa, N., 2405
Shiroishi, H., 2472
Shoji, M., 2382, 2653, 2701, 2708, 2720, 2745, 2751, 2767, 2778, 2784
Shouhua, F., 1793
Shuku, T., 2665, 2671
Shultz, D.A., 2876, 2880
Shvedenkov, Y., 2176
Siaw-Lattey, C., 785
Siddiquee, T.A., 1471
Siebald, H.G.L., 1153
Sieler, J., 917, 1937
Signorella, S., 1079
Sileo, E.E., 777
Sillanpää, R., 257
Silva, N.J.O., 563
Simas, A.M., 3046
Sindal, R.S., 1167
Singh, K.S., 391
Singh, N.R., 909
Singh, O.I., 909
Singh, R.H., 909
Sinha, C., 739, 1071
Skelton, B.W., 181, 1425
Skumryev, V., 1983
Slageren, J.v., 2864
Slebodnick, C., 2133
Smith, J.P., 2165
Soibinet, M., 143
Solan, G.A., 2017
Son, D.Y., 785
Song, L., 831
Song, Y., 1599, 2269
Soni, V., 1167
Sordo, J., 1196, 3057
Sortino, M., 501
Sousa, A., 2043
Sousa-Pedrares, A., 2043
Sóvágó, I., 799
Spagna, R., 995
Špalt, Z., 1417
Spek, A.L., 41
Spencer, M.C., 2133
Sreekanth, A., 601
Stadnicka, K., 627
Stainer, H., 121
Stannard, W., 2017
Stevens, C.L., 2242
Storr, A., 2242
Strekopytov, S., 1585
Strohfeldt, K., 1250
Strukan, N., 369
Stryapan, V.V., 723
Suematsu, T., 2716
Suen, M.-C., 1497, 2913
Sugano, T., 2108, 2360
Sugawara, T., 2263, 2870

Sugimori, K., 2665, 2671, 2726
Sugimoto, T., 2315
Sugiura, K.-i., 2250
Sugiyama, A., 2550, 2665, 2671
Sujandi, , 968
Süllow, S., 2413
Sun, C.-Y., 823
Sun, J., 759, 2055
Sun, Y.-Q., 295
Sun, Y.-X., 2027
Sun, Z.-M., 571
Suni, V., 1133
Suo, Q.-L., 759
Suresh, E., 1023
Süss-Fink, G., 1961
Suzuki, N., 2396
Suzuki, S., 2618
Suzuki, T., 2437, 2491, 2533
Suzuki, Y., 685
Swarts, J.C., 1611
Sweeney, N.J., 1250
Swiatek-Kozlowska, J., 1007, 1929
Szeszel-Fedorowicz, W., 443
Szklarzewicz, J., 1533
Szpoganicz, B., 495
Szumna, A., 2981

Tabbal, M., 221
Tacke, M., 1250
Takada, R., 2309
Takagi, S., 2497, 2501, 2716
Takahashi, S., 2284
Takahata, M., 2653
Takano, Y., 2701
Takats, J., 3038
Takeda, R., 2238, 2708, 2784
Takeda, S., 2417, 2424, 2431, 2599, 2607
Takei, M., 2173
Takeshi, T., 2330
Takui, T., 2112, 2116, 2121, 2194, 2200, 2326, 2377, 2618
Talham, D.R., 2355
Tamura, M., 2405, 2464, 2468, 2817
Tan, M.-Y., 1160
Tan, W.T., 1503
Tanaka, G., 2533
Tanaka, H., 2793
Tanaka, K., 2141, 2658
Tanase, S., 41, 979
Tang, J.-K., 2864
Tang, L.-F., 209
Tang, Y., 1093, 1160, 1739
Tanifuji, N., 2484
Taniguchi, T., 2274, 2382, 2708, 2720, 2758
Taş, E., 319
Tasiopoulos, A.J., 2505
Tatsumi, M., 2112, 2116, 2121
Teat, S.J., 2443
Teki, Y., 2185, 2299, 2337
Teoh, S.G., 1503
Teraguchi, M., 2544
Terenzi, H., 495
Terzis, A., 1540
Tham, F.S., 2076
Thati, B., 949
Thirumavalavan, M., 1781
Thompson, L.K., 807
Thompson, R.C., 2242
Thöne, C., 693
Thuéry, P., 229, 968, 1569
Tian, G.-R., 1773
Tian, L.-J., 2027
Tian, Z.-F., 1669
Timco, G., 2562
Tingting, X., 1793
Titiš, J., 1510
Toichi, T., 2337
Tokii, T., 2257
Tokoro, H., 2857, 2901
Tokumoto, M., 2173, 2793
Toma, H.E., 731
Tomazela, D.M., 731
Tonooka, S., 2396
Torres, M.R., 239
Touati, N., 3066
Touceda, A., 3057
Tournilhac, F., 2906
Trapé, M., 501
Tretyakov, E., 2176
Tribby, L.J., 1143
Trindade, T., 563
Troiani, F., 2562
Trossero, C., 501
Trush, V.A., 1007
Tsai, H.-L., 2205, 2215
Tschan, M.J., 1961
Tuchagues, J.-P., 343, 1540
Turnbull, M.M., 2153
Tušek-Božić, L., 97
Twamley, B., 1366, 2153, 2222, 2232, 2293
Tyree, W.S., 2133

Ueda, A., 2200
Ueda, K., 2491, 2533
Ueda, M., 2189
Urbanos, F.A., 239
Urbina, C., 511
Uriel, S., 1212

Vacca, A., 1878
Vaid, T.P., 3004
Vaissermann, J., 3066
Valko, M., 1913
van Albada, G.A., 979
van Slageren, J., 2400
Várnagy, K., 799
Varret, F., 2852, 2857
Ventura, G., 2568
Venugopalan, P., 1221
Vepsäläinen, J.J., 305
Verdaguer, M., 2900, 2906
Vicent, C., 1212
Vicente, R., 557
Vieille-Petit, L., 1961
Villain, F., 2906
Viñuelas-Zahínos, E., 129, 1125, 1764, 2972
Višnjevac, A., 97
Visser, H.G., 1968
Volkis, V., 1298
Vrdoljak, V., 369, 1717
Vreshch, V.D., 917
Vukićević, M.D., 533
Vukićević, R.D., 533

Wada, K., 2550
Wajda-Hermanowicz, K., 1577
Walsh, M., 949

Wang, G., 2133
Wang, J., 2889
Wang, J.-C., 539, 2913
Wang, K.-M., 539
Wang, W., 1656
Wang, Y.-B., 759, 823
Wang, Y.-H., 2913
Wang, Y.-L., 585, 2955
Wang, Y.-Q., 2955
Wang, Y.-Y., 215
Wang, Z.-M., 1617
Warżajtis, B., 1701, 2009
Washiya, R., 2417
Watanabe, R., 2599
Waters, J.M., 1606, 3022
Watts, R., 75
Webster, M., 121
Wei, H.-H., 487
Wei, K.-J., 165
Wells, B.M., 2153
Wen, H.-R., 671
Wen, L.-L., 1669
Wernsdorfer, W., 2280, 2450, 2505, 2864, 2894
West, D.X., 889
White, A.H., 181
White, P.A.J., 463
Wiesler, K., 1565
Willemin, S., 1033
Willett, R.D., 2222, 2232, 2293
Williams, D.J., 463
Williams, P.A.M., 501
Wilson, A., 2284
Winpenny, R.E.P., 2562
Winter, C.H., 645
Withers, J.R., 1845
Wojtczak, A., 663
Wong, W.-K., 927
Wong, W.-Y., 927
Wu, B., 593
Wu, J.S., 739
Wu, S.-Z., 173
Wu, X.-T., 481, 831, 2988
Wu, X.-W., 173
Wur, C.-S., 2205, 2215
Wurst, K., 533

Xia, S.-Q., 831
XiaoJun, L., 2909
Xie, J.L., 2160
Xie, Y.-B., 413
Xie, Y.-S., 165
Xu, H., 2269

Yagyu, T., 2141
Yamada, J.-i., 2126, 2315, 2614, 2789, 2796
Yamada, K., 2437
Yamada, S., 2813
Yamaguchi, A., 2280
Yamaguchi, K., 2238, 2274, 2382, 2653, 2701, 2708, 2720, 2745, 2751, 2758, 2767, 2778, 2784
Yamamoto, G., 2194
Yamanaka, S., 2238, 2653, 2701, 2708, 2767, 2784
Yamashita, A., 2796
Yamashita, M., 2250, 2680
Yamauchi, O., 2112
Yan, S.-P., 2002
Yánez, J.E., 511
Yang, C.-I., 2205, 2215
Yang, E.-C., 2280, 2695
Yang, G.-M., 2027
Yang, H., 1280
Yano, M., 2112, 2116, 2121
Yanrong, Z., 1793
Yao, M., 2828
Yasin, T., 1262
Yasuda, Y., 2789
Yasutaka, K., 2330
Ye, C., 2889
Ye, J.-H., 759
Yee, G.T., 2133
Yeh, C.-W., 539, 1497, 2913
Yen, T.-Y., 539
Yeoul Lee, B., 1256
Yilmaz, I., 791
Yilmaz, V.T., 693
Yin, Y.-Q., 2055
Ying, E.-B., 397
Ying, M., 1793
Yoneda, K., 2437
Yonezawa, M., 2121
Yoshida, A., 2885
Yoshida, K., 2513
Yoshihiro, M., 2716
Yoshimura, K., 985
Yoshioka, D., 2658
Yoshioka, N., 2828
You, X.-Z., 671
You, Y.S., 249
Youngme, S., 765, 767, 769
Youngs, W.J., 1234
Yu, K.-B., 1160, 1617
Yu, Q., 2002
Yu, Z.-K., 173
Yuetao, Z., 1793

Zacchino, S., 501
Zacharias, P.S., 1410
Žák, Z., 579
Zakharov, L.N., 1093, 1739, 1803, 2557
Zancato, M., 521
Zanello, P., 1340
Zaworotko, M.J., 343
Zhang, H., 785
Zhang, J., 1160, 1185
Zhang, M., 165
Zhang, Q.-F., 1109
Zhang, R.-F., 1773
Zhang, X., 1656
Zhao, H., 1907
Zhao, L., 807
Zhao, X.-L., 940
Zheng, X.-J., 823
Zheng, Y.-Q., 397
Zheng, Z.-Y., 173
Zhou, H.-C., 671
Zhu, B.-H., 2055
Zhu, L., 1617
Zhu, N., 759
Zhu, Z., 2102
Zieliński, T., 2981
Zuber, M., 1577
Zuo, J.-L., 671

Available online at www.sciencedirect.com
SCIENCE DIRECT®
Polyhedron 24 (2005) 3111–3118
POLYHEDRON
www.elsevier.com/locate/poly

Subject Index to Volume 24

Ab initio, 1478
Ab initio calculations, 2579, 2708
Ab initio computation, 1002
Ab initio GSO calculation, 2767
Ab initio MO method, 2382
Acetate, 1425
Acetato bridge, 979
Acetylenediide, 940
Acidic reagents, 3052
Adsorption, 985
AFM cantilever, 2793
AFMR, 2464
Ag cluster, 685
β-alanine, 1503
Alcohol, 1611
Aligned powder, 2346
Alkali and alkaline earth metal ions, 1023
Alkaline earth dications, 121
Alkoxide complexes, 257
Alkoxides, 229
Alkoxo-bridged, 41
Alkyl substituent, 2625
2-Alkylamino azobenzene, 1953
Alkylating cyclization, 343
Alkylhydrides, 1388
Alternating antiferromagnetic chains, 2222
Aluminium, 1585, 1878, 2994
Aluminum cation, 1682
Aluminum phthalocyanine, 3004
AM1, 3046
Amide formation, 837
Amides, 1739, 2981
Amidinium diphenylphosphinate, 927
Amido compounds, 281, 976
Aminals, 968
Amine compounds, 1606
Aminium cationic radical, 2309
Amino acids, 2981, 3082
2-Aminobenzimidazole, 1764
2-Aminoethanethiolate, 865
4-(2-Aminoethyl)morpholine, 1677
4-Amino-2-mercaptopyrimidine, 1109
4-Aminopyridinium tetrachloropalladate(II), 1624
Aminophosphines, 1641
Aminopolycarboxylate complexes, 1701
Aminoxyl, 2593
Ammoniate, 1565
Ammonium salt, 1937
Amorphous, 2321
Amorphous materials, 1461
Amphoteric redox, 2522
Ansa, 1314, 1356
Ansa-metallocene, 1382
Ansa-aluminocene, 1366
Ansa-magnesocene, 1366
Ansa-metallocene, 1388
ansa-Metallocene catalysts, 1269
ansa-Metallocene complexes, 1298
ansa-Metallocenes, 1289
ansa-Zirconocene, 1262
Anthracene, 2544
Anti-cancer drug, 1250
Anti-microbial, 949
Anti-conformation, 958
Antibacterial, 909
Antiferromagnet, 2153, 2793
Antiferromagnetic, 2803
Antiferromagnetic chain, 2232
Antiferromagnetic interaction, 377
Antiferromagnetic phase, 2417
Antiferromagnetics, 2813
Antifungal, 909
Antifungal properties, 501
Antimicrobial activities, 611
Antimonide, 1565
Apda, 1968
Application to functional materials, 2299
Arene complexes, 1798
Arene ligands, 1961
Aromatic *N*-oxyl radical, 2828
Aroylhydrazone, 57
Arsenic, 1417
Arsenic(III), 89
Arsenic clusters, 1417
Arsenic sulfides, 1417
N-Aryl-3,5-Bu^t_2-salicylaldiminepalladium(II) complexes, 319
Arylazoimidazole, 1071
Aryl-substituted, 2017
Ascorbic acid, 1503
Assembled metal complex, 2625
Atomic charges, 1175
ATP–Rh complex, 1577
Azamacrocycles, 3022
Azetidine derivatives, 1569
Azide, 1086, 2002
Azide ligand, 249
Azido complexes, 1829
Azobenzene, 2614
Azobenzenes, 2933
Azoxybenzene, 2614
Azurin, 2665, 2671

Ba(II) complexes, 1487
Barium, 289, 645, 1185
BEDT-TTF, 2126, 2796
7,8-benzoquinoline, 3012
Benzotetrathiafulvalenedithiolate, 671
Benzotriazole, 2443
Beryllium diketonates, 917
BETS, 2382
Bidentate N,N donors, 201
2,2′-Biimidazole, 1196
4,4′-Biimidazole, 2625
Bimetallic chain compound, 2413
Binuclear 5-coordinated copper(II) complex, 377
Binuclear complex, 1983
Binuclear copper complex, 495
Binuclear copper(II) complexes, 900
Binucleating ligands, 900
Biogeochemistry, 1585
Biphosphine oxide, 1063
4,4′-Bipyridine, 940
Bipyridine ligand, 701
Biradicals, 2876
3,5-Bis(2-pyridyl)-pyrazole, 2437
Bis(*N*-alkyl-3,5-Bu^t_2-salicylaldiminato)copper (II) complexes, 1203
2,3-Bis(4,5-dimethylthio-1,3-dithiole-2-ylidene)-succinonitrile, 3032
Bis(diphenylphosphino)methane, 872
1,5-Bis(diphenylphosphino)pentane, 853
Bis(phosphinite), 475
Bis(pyrazinedithiolato)metal complex, 2528
Bis(pyrazol-1-yl)methane, 209
Bis(4-pyridyl)propane, 940
Bis(2-pyridylthio)acetate, 995
Bis(2-thioxo-1,3-dithion-4,5-dithiolato)nickelate compound, 2269
Bismuth(III), 89
Bismuth homopolyatomic cation, 2994
Bisphosphonate, 305
Bistable behavior, 2232
Bistetraazamacrocycles, 143
Blue copper protein, 2665, 2671
Blue phosphorescent, 189
BMXD, 495
Bond cleavage, 1471
Borohydride complexes, 1234
Boron heterocycles, 1280
Boron icosahedra, 2803
Bowl-shaped neutral radical, 2200
Bridging ligand, 940
Bridging water, 2778
Broken symmetry, 2579
Bromination, 2116
Bulk modulus, 2413
Bulky ligands, 1739

doi:10.1016/S0277-5387(05)00718-7

C–F, C–Cl bond activation, 2994
C–H activation, 1234, 1382, 1953, 3082
Cadmium, 627, 847, 865
Cadmium(II), 2955, 2963
Cadmium(II) complex, 1125, 1764
Cadmium complexes, 593
Cage compounds, 295
Calcium, 1656
Calcium (II), 305
Calixarenes, 311
Candida albicans, 949
Car-Parrinello molecular dynamics, 2472
Carbacylamidophosphates, 1007
Carbene, 2321, 2708
Carbohydrates, 3082
Carbon dioxide uptake, 579
Carbon monoxide, 511
Carbonyl dipolar interactions, 1701
Carboxylate complexes, 239
Carboxylates, 2176
Carboxylic acids, 1611, 1727, 2645
Catalysis, 151, 1212
Catalytic activity, 1153, 1885
Catalytic hydrogenation, 319
Catechol, 1143
Catecholate, 2607
Cation–π interactions, 1033
Cd(II), 1829
Ce(IV) complexes, 1487
Centrosymmetric, 1221
Chain complexes, 2658
Charge separation, 2817
Charge-assisted hydrogen bond, 927
Charge-transfer complex, 2337, 2632
Charge-transfer salts, 2315, 2632
Charged high-spin systems, 2116
Charged organic high-spin systems, 2121
Chelate effect, 593
Chelates, 521, 549
Chemical modification, 3052
Chemical nuclease, 495
Chemometrics methods, 1593
Chiral and helical order, 2568
Chiral manganese(IV) complex, 1410
Chirality, 1869, 2808, 2933
Chlorodithiophosphoric acid pyridiniumbetaine, 1855
Chromium, 173, 2808
Chronocoulometry, 1781
cis-Platinum, 1250
Citrate, 1656
Clenbuterol, 1983
Clodronate, 305
Cluster, 2065, 2894
Clusters, 2443
Co(II), 2094
Co(II) complexes, 1071
Co(II) porphyrins, 679
Co(III) complexes, 165
CO_2 reactions, 1093
Co[S_4] core, 585
Cobalamin, 2745
Cobalt, 627, 807, 2017, 2102
Cobalt(II), 2955
Cobalt(III), 1503, 1968
Cobalt–benzoquinone complexes, 2607
Cobalt (III) complex, 1002
Cobalt complexes, 501, 563
Cobalt(II) complexes, 129, 585, 1764
Cobalt(II)/cobalt(III) compounds, 1755
Cobalt(II) pyrazine complex, 221
Coercive force, 2405
Compartmental ligands, 113, 1781
Complex, 427, 1929, 2102
Complex ion stereochemistry, 1569
Complexation, 985
Complexes, 807, 1160, 1185, 1533, 3046
Compressibility, 2413
Conductivity, 671, 2513
Conformation, 539, 1497
π-Conjugated organic spin system, 2299
π-Conjugated polymer, 2309
Conjugated polymer, 2544
Constrained geometry catalyst, 1314
Constrained geometry catalysts, 1793
Constrained-geometry, 1274
Contrast agent, 2691
Coordination, 1641
Coordination chemistry, 1, 2035, 3046
Coordination compounds, 1651
Coordination geometries, 627
Coordination in melts, 619
Coordination modes, 1079
Coordination polymers, 221, 397, 823, 917, 1033, 1086, 1487, 1497, 1907, 2242, 2424, 2913, 2963
Copolymerization, 1269
Copper, 511, 807, 979, 1101, 1185, 1497, 1599, 2043, 2102, 2176, 2189
Copper(II), 949, 1405, 1549, 1651, 1929, 2242
Copper (II) and Nickel (II) complexes, 113
Copper (II) azide, 3091
Copper(II)binuclear complexes, 909
Copper(II)/cadmium(II), 1525
Copper(II) chloride, 2293
Copper(II) complexes, 215, 443, 799, 889, 1913, 2933, 2944, 2972
Copper(II) compounds, 249, 976
Copper(I) halide complexes, 351
Copper halides, 2222
Copper(II) halides, 2153
Corannulene, 2200, 2326
Coronene, 2326
Coumarin, 949
Counterion effect, 3032
Covalency parameters, 889
Cp-surrogates, 1280
Cr(V), 1079
Crossover, 2817
Crown ether, 2844, 2889
Crown ether porphyrin, 1682
Crystal engineering, 917, 2625
Crystal structures, 57, 97, 129, 137, 157, 165, 229, 249, 257, 281, 295, 305, 327, 351, 407, 413, 435, 475, 481, 487, 557, 563, 571, 579, 627, 671, 711, 723, 771, 777, 831, 853, 927, 968, 976, 995, 1023, 1033, 1109, 1125, 1133, 1160, 1196, 1410, 1425, 1435, 1487, 1510, 1555, 1569, 1606, 1617, 1624, 1631, 1641, 1656, 1669, 1717, 1764, 1773, 1869, 1922, 1941, 1975, 1991, 2043, 2055, 2160, 2205, 2222, 2232, 2257, 2269, 2293, 2491, 2513, 2584, 2680, 2732, 2808, 2844, 2889, 2933, 2963, 2972, 2988, 3022, 3032, 3038
CT complex, 2185
CT salt, 2133
Cu(II), 2094
Cu(II) complexes, 165, 968, 1983
Cu(II)–Cu(I) interconversion, 1525
Cu(II) porphyrins, 679
Cu(II)–phenoxyl radical complexes, 1203
Cu(II) thiosemicarbazone complex, 1133
Cubane cluster, 1212
Cuprates, 2035
Curie temperature, 2173
CVD, 463
CVD precursors, 645
Cyanide bridge, 2808
Cyanide networks, 1845
Cyanides, 1533
Cyano-briged metal assemblies, 2901
Cyanocomplex, 579
Cyanometallates, 1033
Cyanoxime complexes, 1175
Cyclams, 2981
Cyclic amine compounds, 281, 976
Cyclic amines, 3022
Cyclic voltammetry, 601, 889, 1212, 1435, 1503, 1611, 1781, 2076, 2112, 2121
Cyclohexane-1,4-diol, 475
Cyclopentadienyl, 1256
Cylindrical or spherical macrocycle, 1117
Cystal structure, 215
Cytotoxic activity, 1196

1D Chains, 343
3d metals complexes, 327
1D systems, 557
2D zigzag sheet, 2528
DC magnetic susceptibility, 2250
Dehydro-peptides, 1929
Dendrimer, 2321
Density functional calculations, 521
Density functional method, 2382
Density functional theory, 2238, 2364, 2720, 2745, 2751, 2778, 2784
Density functional theory calculation, 2194, 2200, 2326, 2618
Deoxy, 2701
DFT, 1033, 1175, 2708
dft, 1382
DFT and TDDFT calculations, 267
DFT calculations, 419, 701, 1250, 1454, 1861, 1893, 2528, 2665, 2671, 2828
Di-2-pyridyl ketone, 1133
Di-Schiff-bases, 593
Dialkyldithiocarbamate derivatives, 89
1,2-Diaminoethane, 2944
Diamond anvil cell, 2497
Diarylethene, 2484
Diazahexatriene, 958
Diazaphenalenyl, 2618
Dibenzo-30-crown-10, 1023
Dicarboxylates, 397
Dicopper(II) complex, 1922
Dicyanamide, 487
4,5-Dicyanobenzene-1,2-dithiolato ligand, 2491
4,5-dicyanobenzene-1,2-dithiolato ligand, 2533
Dihydrobis(thioxotetrazolyl)borato, 585
Diiron, 2701
Diketonate, 3066
Dimeric, 2165
Dimeric lanthanide complex, 137
Dimerization, 2232

Dimers, 2222
Dimetallic ferrimagnet, 2497
Dimethylpyrazine, 2153
πd-interaction, 2315
Dinuclear and tetranuclear silver (I), 693
Dinuclear complexes, 369, 1617, 1651, 2437
(−)-DIOP, 2055
Diorganotin, 1054
Dioxa-diaza macrocycle, 97
Diphenylcarbene, 2708
Diphenylphosphate, 2680
Diphenyltin(IV)complexes of Schiff bases, 383
Diphosphine, 75, 831
Diphosphine ligands, 181
Dipicolinic acid, 49
1,3-Dipolarophil cycloaddition, 1631
Dipole–induced-dipole interactions, 619
Dipropylenetriamine, 1913
2,2′-Dipyridylamine, 747, 1837
4,4′-Dipyridyldisulfide, 2913
Diradical ions, 2108
Dirhodium complex, 1577
Diruthenium compounds, 239
Distortion, 593
Distribution of electron spin density, 2431
Disulfide and diselenide, 475
Dithiadiazolyl radical, 2579
1,6-Dithiapyrene, 2632
Dithiocarbazates, 383
1,1-Dithiolato, 2944
Dithiole, 2944
DNA cleavage, 495
DNA sheets, 2758
DNA wires, 2758
DNA–drug interaction, 495
2-D NMR, 1366
Dopant, 881
Double exchange, 2876
Double-cubane core, 2257
Dynamics, 2852

ECTEOLA–Cellulose, 985
Effective exchange integral, 2274, 2330, 2382
Effective exchange integrals, 2751, 2784
Effective-exchange integral, 2701
Electric conductivity, 2632
Electrical conductivity, 2789
Electrochemical methods, 2116
Electrochemical properties, 157
Electrochemical studies, 900
Electrochemical synthesis, 2043
Electrochemistry, 319, 333, 585, 739, 791, 1071, 1203, 1340, 1611, 1755, 2141
Electrocrystallization, 1555
Electroluminescence, 189, 881
Electron affinity, 2472
Electron paramagnetic resonance, 2284, 2400, 2695, 2880
Electron spin resonance, 2360, 2618
Electron transfer, 2550
Electron transfer stopped-flow method, 2116, 2121
Electronic absorption, 2880
Electronic properties, 679
Electronic spectra, 157, 611
Electronic spin structure, 2194
Electronic-spin structure, 2618
Electrospray ionization, 1153
Electrospray ionization mass spectroscopy, 995
Electrostatic force, 927
Elemental copper, 1425
EPR, 889, 909, 1821, 2350
EPR of copper(II) complexes, 451
EPR Pattern, 1079
EPR spectroscopy, 711, 799, 1540
EPR studies, 679
Erbium complex, 137
ESI mass spectra, 1617
ESI-mass spectrometry, 1503
ESI-MS, 731
ESR, 601, 1101, 1689, 2141, 2173, 2200, 2538, 2716
ESR measurement, 2491
ESR spectroscopy, 2484
ESR study, 2250
Ester tin, 2027
Ethanolamine derivative, 985
Ethylamido (propionylamino) compounds, 281, 976
Ethylene polymerization, 1793
Ethylene/octene copolymer, 1347
Ethylene/styrene copolymer, 1347
Ethylenediamine, 1425
EXAFS, 143, 685, 2909
Exchange coupling, 2094, 2293, 2364, 2876
Exchange integral, 2758
Exchange interaction, 2215, 2538, 2639, 2645
Excited quartet state, 2185, 2337
Excited state quenching, 1749
Excited-state kinetics, 65
Eximer, 881
Experimental demonstrations, 2906
Extended Hückel molecular orbital calculation, 2160
Extraction efficiencies, 311

f electron, 2803
FAB mass spectra, 771
Facial, 189
Fe–CN–Co network, 2355
Fe(III) clusters, 2864
Fe(III)–Co(III), 2849
Fe(III)–Mo(IV), 2849
Fe_{11} complex, 2364
^{57}Fe Mössbauer spectroscopy, 1798
Ferredoxin, 2550
Ferricytochrome *c*-551, 1813
Ferrimagnetism, 2315
Ferrocene, 1611, 1749
Ferrocene derivatives, 533
[3]Ferrocenophanes, 1340
Ferrocenyl group, 2409
Ferrocenylacetylide, 759
1-Ferrocenyl-1-hydroxyiminothialkanes, 533
Ferrocenyl thialkanones, 533
Ferromagnetic exchange, 2880
Ferromagnetic interaction, 2257, 2309
Ferromagnetism, 2148
Ferromagnets, 2293
First-principles molecular dynamics, 2472
Fischer carbene, 173
Five-membered heterocycle, 1855
Fluorenyl, 1314
Fluoride and hexafluorosilicate bridges, 1549
Fluorides, 2443
Fluorinated aryloxide, 1803
Fluorinated carboxylates, 1185
Fluxional, 1366
FMR, 2468
Force-field calculations, 1701
Free radical, 2593
Frustrated spin system, 2396
Frustration, 2817
Fulrene, 1356
Fulvenes, 1250, 1325
Functional groups, 1289
Furan thiosemicarbazone, 327
Furo[3,2-*c*]pyridine complexes, 1510

Generalized ferrimagnetism, 2377
Generalized spin orbital, 2784
Germanium (IV) complex, 2076
Glass-forming, 1461
Gold, 521, 831, 1803
Group 4 metals, 1325

^{1}H and ^{13}C NMR, 3057
H-bond, 221
H-bonding, 1701
Hafnium, 1143, 1298, 3066
Half-sandwich, 1274
Halide bridging copper(II) complex, 377
Halogen-bonding, 2632
Hapticity, 1314
^{3}He, 2405
Heisenberg model, 2389, 2396, 2767
Helical chain polymers, 2988
Helical structures, 785
Hemerythrin, 2701
Hemilabile ligands, 1063
Heptadentate, 1478
Heptanuclear, 2849
Heteroatomic effects, 2618
Heterobimetallic, 1212
Heterocyclic thione complexes, 351
Heterocyclic thiones, 853, 2043
Heterometal complex, 2732
Heterometallic complexes, 917
Heterometallic networks, 1487
Heterometallic polymers, 1425
Heteronuclear metal complex, 2257
Heterospin, 2876
Heterospin biradical, 2880
Heterothiometalates, 831
Hexacyanometalates, 1555
Hexagonal pores, 2921
Hg silylamides, 1093
High pressure, 2413
High spin, 2321
High-spin excited state, 2299
High-spin molecule, 2593, 2849
High-spin polymer, 2544
Histidine analogue, 799
^{1}H NMR, 1968
Hole doping, 2330
Holmium, 3046
Homoleptic phosphine oxide complexes, 121
Hubbard model, 2389, 2665
Hybrid magnetic materials, 3052
Hydrazone, 1125
Hydrazone ligands, 807
Hydrogen bonded 2D network, 771
Hydrogen bonding, 97, 1937, 2645
Hydrogen bonding network, 1410

Hydrogen bonds, 165, 215, 407, 539, 655, 1555, 1922, 2528
Hydrogen carbonato ligand, 281
Hydrogen-bond, 2625
Hydrogen-bonded, 2165
Hydrogen-bonded networks, 2921
Hydrogen/deuterium exchange, 1388
Hydrolysis, 807, 1274
Hydrometallation, 1325
Hydrosilylation, 1298
Hydrothermal synthesis, 295, 571
Hydrotris(pyrazolyl)borate ligands, 3038
Hydroxamic acids, 837
Hydroxy, 3074
α-Hydroxy phosphine oxides, 1641
Hydroxyaluminosilicate, 1585
Hydroxyf1avones, 1593
3-Hydroxypicolinic acid, 563
8-hydroxyquinoline X-ray structure, 3012
Hyperfine coupling, 2607
Hyperfine coupling constant, 2431
Hyperfine coupling of CN ions, 2599
Hyperfine field, 2885
Hysteresis, 2065, 2885, 2894

Imidazole, 1599
Imidazole, 2424
Imidazolidine, 1913
Imidazopyridinium perchlorate, 201
Imido, 151, 1274
Imine compounds, 1606
Iminodiacetate, 771
Iminonitroxide, 2200, 2377
Imino nitroxide, 2176
Impurity, 2676
In situ, 685
Inelastic neutron scattering, 2455
Insertion, 1641
Intensity threshold, 2857
Intermolecular hydrogen-bonding, 865
Internal magnetic field, 2417
Interpenetrated, 2955
Intramolecular, 1388
Intramolecular coordination, 2027
Intramolecular energy transfer, 65
Intramolecular magnetic interaction, 2484
Intramolecular radical–metal interaction, 2112
Ion-exchange film, 2909
Ionic crystals, 2108
Ion metal interaction, 1682
IR, 663, 685, 909, 1175
IR and Raman spectra, 49
Iridium(III) complex, 189
Iron, 41, 807, 2017, 2409, 3082
Iron(II), 2165, 2409
Iron and copper complexes, 2921
Iron (II) complexes, 407
Iron (III) carboxylate chemistry, 1540
Iron oxide cluster, 2472
Iron proteins, 1813
Iron–sulfur clusters, 2550
Ising model, 2676
Isoindolinediimine, 1117
Isostructural doping, 3004
Isotactic polypropylene, 1262
Isoxazolidines, 1631

β-Keggin structure, 1949
Ketones, 533
Kinetics, 1167, 1517, 1781
Kohn–Sham hybrid-DFT, 2274, 2330

Lanthanide, 823, 2588, 3046
Lanthanide complex, 469
Lanthanide ions, 311, 1478
Lanthanide nitrate, 427
Lanthanides, 549, 2341
Lanthanoid, 2588
Laser ablation synthesis, 639, 1417
Laser control, 2726
Lateral macrobicycle, 289
Layer perovskite, 2293
Layered materials, 571, 1701
Lead, 865
LIESST, 2821, 2909
Ligands, 1
Linear chains, 2153
Linear low density polyethylene, 1314
Linkage isomerism, 1677
Liquid crystals, 1461
Lithium-1-azaallyls, 958
Lithium (bis)silylamides, 1739
Lithium phthalocyanine, 3004
LLC-PK, 1250
Local magnetic structures, 2431, 2599
Low-dimensional systems, 2568
Luminescence, 65, 747, 831, 1755, 1837, 1885
Luminescence properties, 1160
Luminescence spectra, 1525, 3091
Lutidinate, 777

Macrobicyclic nickel(II) complexes, 1781
Macrocycles, 451, 3022
Macrocyclic ligands, 2981
Macrocyclic ring size, 1781
Macropolycyclization, 1117
Magnesium (II), 305
Magnetic, 2165
Magnetic anion, 2789
Magnetic anisotropy, 2355, 2455, 2468
Magnetic chains, 2222
Magnetic circular dichroism, 2880
Magnetic cluster, 2472
Magnetic conductors, 2758
Magnetic exchange interactions, 343
Magnetic exchange pathways, 2368
Magnetic interactions, 2102, 2274, 2330, 2584, 2593, 2701, 2720, 2732, 2751, 2778
Magnetic interactions mechanisms, 2579
Magnetic measurements, 143, 2501, 2588
Magnetic order, 2573
Magnetic ordering, 2293
Magnetic properties, 249, 397, 407, 487, 563, 900, 1599, 1656, 1669, 1922, 2002, 2035, 2141, 2160, 2189, 2250, 2269, 2321, 2341, 2364, 2424, 2505, 2614, 2680, 2732, 2808
Magnetic Prussian blues, 2906
Magnetic quantum tunneling, 2205
Magnetic relaxation, 2215
Magnetic resonance imaging, 2691
Magnetic semiconductor, 2513
Magnetic susceptibility, 221, 671, 823, 2153, 2377, 2491, 2716, 2844, 2876, 2880
Magnetic susceptibility simulation, 2368
Magnetic thin film, 2355, 2901
Magnetic torque, 2793
Magnetic torque measurement, 2464
Magnetism, 807, 1510, 1689, 1907, 2108, 2242, 2443, 2450, 2513, 2550, 2817, 2839
Magnetization, 2813
Magnetization curve, 2405
Magnetization tunneling, 2280
Magnetization-induced second harmonic generation, 2901
Magneto-optical effect, 2901
Magneto-optical properties, 2839
Magneto-structural correlation, 2828
Magnetoanisotropy, 2215
Magnetocaloric effect, 2573
Magnetochemical properties, 1983
Magnetochemistry, 557, 711, 1540
Magnetometry, 2695
Maleonitriledithiolate, 1669
Malonates, 1054
Manganese, 557, 1656, 2065, 2102, 2257, 2284, 2400, 2443, 2450, 2455, 2808, 2894
Manganese clusters, 2250, 2767
Manganese polynuclear complexes, 343
Manganese porphyrin, 2720
Manganese(II), 2242
Manganese(II,III), 2084
Manganese(IV), 601
Manganese(II) tetrahedral, 739
Manganese(II)-pseudohalides, 747
Many-band system, 2389
Mass spectrometry, 521
Mass-spectrometry studies, 723
Master equation approach, 2653
Mechanism, 1167, 1517
MEM–$[TCNQ]_2$, 2716
13-Membered macrocycle, 1405
2-(−)-Menthoxycarbonylethyltin, 2027
2-Mercaptopyridine, 995
2-Mercaptopyrimidine, 1109
Mercury complexes, 671
Meridional, 189
Met, 2701
Metal complexes, 75, 487, 1435, 1631
Metal diphosphonates, 571
Metal halide complexes, 539
Metal-induced cyclization, 3057
Metal–ligand bond formation, 2745
Metal–metal bonds, 239
Metal phosphonates, 295
Metallaazacrown, 2732
Metallocenes, 1234, 1256, 1325, 1356, 1793, 2133
Metallomesogen, 2821
Metalloporphyrin, 1682
Metalloprotein, 1813
Metamagnetism, 2133
Methoxycarbonyl, 3074
m-(Methoxy)phenyl nitronyl nitroxide, 2368
Methylaluminoxane, 151
Methylamido (acetylamino, acetamido) compounds, 281
Methylamido (acetylamino) compounds, 976
Michael addition, 173
Micro-scale ring, 2533
Mixed ligand, 57, 1101
Mixed ligand complexes, 723
Mixed metal cluster, 759, 2055
Mixed-metal species, 1949

Mixed valence, 1749
Mixed-valence, 2215
Mixed-valent complexes, 2658
Mn(II), 2094
Mn complex, 2413
Mn_{12} complex, 2680
$Mn^{III}Cu^{II}$(5-Br-sap)$_2$Cl(MeOH), 2885
^{55}Mn NMR, 2346
Mn_6R_6, 2396
Mo(W)/Cu/S clusters, 2988
MOCVD, 3066
MOD, 1185
Model compounds, 41
Models of blue copper proteins, 889
Molecular AF ring, 2562
Molecular cluster, 2382
Molecular conductor, 2789
Molecular design, 2112
Molecular magnetic nanoclusters, 2573
Molecular magnetism, 1651, 2326, 2382, 2844
Molecular magnets, 2084, 2396, 2568, 2885
Molecular mechanics calculation, 1023
Molecular nanomagnets, 2459
Molecular precursors, 3052
Molecular semiconductor, 3004
Molecular square, 2988
Molecular structure, 759
Molecule-based magnet, 2148, 2377, 2497
Molecule-based magnetism, 2368, 2828
Molecule-based material, 2413
Molten salts, 619
Molybdenum, 257, 1033, 1533
Molybdenum(VI) complexes, 369, 1717
Molydbocobaltate (III), 1517
Monocyclic silver alkanethiolates, 481
Monomeric Cu(II) benzodioxotetraazamacrocycle chloro complex, 451
Mononuclear and polynuclear complexes, 1717
Monte Carlo, 2676
Monte Carlo simulations, 2364
Mössbauer, 1689
Mössbauer spectroscopy, 711, 1540
MS, 663
Multinuclear carboxylates, 663
Multi-nuclear complex, 2409
Multiple bonds, 239
Multiple spin transition, 2849

N ligands, 645
2N2O donors, 1885
n-Butyldicyandiamide, 909
N,O ligands, 627, 785
N,S ligands, 2043
N,*N*-bis(carboxymethyl)-β-alaninato(3-) ion, 1968
N,*N*′-chelating ligands, 1710
N,*N*′-Di(2-methoxyphenyl)formamidine, 539
N,*N*,*N*′,*N*′-tetraethylpyridine-2,6-dicarboxamide (O-deap), 1221
N,*N*,*N*′,*N*′-tetraethylpyridine-2,6-dithiocarboxamide (S-dept), 1221
N-(pyrid-2-ylmethylene)-phenyl-amines, 391
Nafion, 2909
Nano-particle, 2417
Nanomagnet, 2280, 2284, 2557, 2695
Nanoscale molecular magnet, 2737
Nanoscopic systems, 2813
Natural orbital, 2701
NBO analysis, 1454
Near-surface spin, 2417
Nematic, 1461
Neo-pentoxide, 1727
Neutral radical, 2076, 2194, 2618
New ligand, 215
Ni(II), 2094
Ni complex, 2413
Ni(II) complexes, 1821, 1991
$[Ni(dmit)_2]^-$, 2844
Ni(dmit)$_2$ complex, 2513
Ni(II) porphyrins, 679
Ni(III) species, 1821
Nickel, 579, 807, 1212, 1803, 2102, 2176, 2257, 2280
Nickel (II) complexes, 1015, 1461, 1869
Nickel (II) nitrite, 1677
Nickel (III) complex, 1669
Nickel alkoxides, 3052
Nickel dithiolate complex, 2232
Nickel(II), 2955
Nickel(II) complex, 585, 1606, 2972
Nickel(II) complexes, 143, 1510, 2944, 3022
Nickel(II) compounds, 281
Nickel(II) thiocyanate, 1221
Nickel(II)/zinc(II)azide, 1837
Nicotinate, 1829
Niobium, 1143, 1274
Niobium nitride, 463
Ni[S_4H_2] core, 585
Nitric oxide, 1533
1-(4′-Nitrobenzyl)-4-aminopyridinium, 1669
Nitrogen donor, 2017
Nitrogen ligands, 785
Nitrogenous base, 2944
Nitrones, 1631
Nitronyl nitroxide, 2084, 2094, 2108, 2141, 2176, 2189, 2880
Nitronyl nitroxide radical, 2250
Nitronyl nitroxides, 2377, 2658
Nitrosyl complexes, 419
Nitroxide, 2477
Nitroxide radicals, 319
Nitroxyl radical, 2102
NMR, 663, 1063, 1577, 1682, 2885, 2889
NMR line-shape analysis, 1366
NMR peak assignment, 1878
NMR spectra, 655
NMR spectroscopy, 311, 1749
Nonanuclear, 2849
Non-bonded interaction, 1109
Non-Kekulé molecule, 2309
Norbornene, 1269
Nuclear magnetic resonance, 2737
Nuclease activity, 1503
Nucleoside, 1079
Nucleotide, 1079

Octabromoporphyrins, 679
Octacyanometalates, 1845
Octacyanomolibudate, 2599
Olefin polymerization, 1314
α-olefins, 1269
Oligoarylamines, 2116, 2121
One-dimensional chain, 2153, 2913
One-dimensional complex, 2751
One-dimensional supermolecular, 215
Open frameworks, 295
Optically active ligand, 1991
Order–disorder, 2350
Organic π-radical and gold cluster hybrid system, 2330
Organic biradicals, 2708
Organic crystals, 2108
Organic ferrimagnet, 2377, 2405, 2468
Organic ferromagnetism, 2173
Organic free radical, 2126, 2796
Organic magnetic conductor, 2126, 2796
Organic neutral radical, 2274
Organic radical, 2360
Organic radical ferromagnet, 2501
Organic superconductor, 2315, 2382
Organic synthesis, 2112
Organometallic sandwich complexes, 2341
Organotin(IV), 209
Organotin(IV), 995
Orthopalladation, 1953
Oxalate, 2002
Oxalato, 1101
Oxidation of iodide ion, 1517
Oxidative cleavage, 927
Oxidizing activity, 2921
Oximes, 533
Oxo-bridge compounds, 49
Oxophenalenoxyl, 2194
Oxovanadium complex, 2491, 2533
Oxovanadium(IV) complexes, 837
Oxy, 2701
Oxygen evolution, 2767

P ligands, 1340
P–N bond cleavage, 1641
γ-*p*-NPNN, 2464
p-NPNN, 2405
Palladium, 2189
Palladium(II), 1086
Palladium(II) and platinum(II), 771
Paramagnetic NMR, 1813
Pb(II) chloride melts, 619
Pb(II) complexation, 1593
Pd(II) complexes, 1991
Pd(II)–phenoxyl radicals, 319
[Pd(dmit)$_2$], 2817
PED, 1175
Pendent-arm macrocycles, 968
Pentamethylcyclopentadienyl, 391, 1710
Periodic condition, 2382
Permanganate, 2505
Peroxychromate, 2350
pH-Potentiometry, 799, 837
Phase transitions, 2232, 2568
Phenalenone, 2076
Phenalenyl, 2522
Phenanthroline, 1002
Phenolate ligands, 257
Phenoxide, 1803
Phenoxyl, 2544
2-Phenylbenzothiazole, 881
Phenylcarbene, 2708
4-Phenylpyridine, 2437
5-Phenyl-1,3,4-oxadiazole-2-thiol, 1773
Phosphato complexes, 1878
Phosphido, 1471
Phosphine oxide, 427, 469
Phosphinido, 1471
Phosphonates, 549

Phosphoramidate, 655
Phosphorylic ligands, 1007
Photo-functionality, 2614
Photochromism, 2477, 2484
Photoinduced anisotropy, 2355
Photoinduced magnetism, 2355
Photoinduced phase transition, 2676, 2857
Photo-induced spin alignment, 2185, 2299, 2337
Photoluminescence, 189, 881
Photophysical properties, 137
Photophysical property, 823
Photo-responsive, 2321
Photoswitching, 2477
Photosynthesis II, 2767
Phthalocyanines, 791, 1117
Piano-stool catalysts, 1347
Picoline, 1445
Planar waveguide amplifiers, 137
Platinum, 1803
Platinum(II)-complex, 881
Platinum (III) complex, 1669
^{31}P NMR spectroscopy, 1878
β-*p*-NPNN, 2468
Polarizable continuum model, 2671
Polyamines, 968
Poly(aryleneethynylene), 2544
Poly(phenylenevinylene), 2309
Poly(4-vinylpyridine), 511
Polyaza ligand, 495
Polycyanide complexes, 2599
Polymer, 1599
Polymeric network, 435
Polymerization, 151, 1234, 1256, 1298
Polymorph, 1047
Polymorphism, 1487, 2828
Polynuclear, 369, 823, 979
Polynuclear complexes, 731, 1991, 2409
Polynuclear transition metal complexes, 2364
Polyoxometalate, 847, 1949
Polypeptides, 2550
Polyphenol oxidase activities, 1617
Polyradical, 2544
Polytungatate, 2889
Porphyrin dimer, 2538
Preparation, 1829
Pressure, 2716
Pressure effects, 2497, 2501
Proctolin analogues, 443
1,3-Propanediaminetetraacetato complexes, 2009
Propylene, 1269
Protonation, 97
Prussian blue, 2676
Prussian blue analogs, 2901
Prussian blue film, 2355
Pseudo-halide bridges, 343
Pseudomonas aeruginosa, 1813
Pt(II) complexes, 1991
Pt(IV) complexes, 1196
Pyrazine, 267, 2153, 3074
Pyrazine (bridging ligand), 1533
Pyrazolato ligands, 645
Pyrazole, 41, 173, 359, 1086, 1893
5-Pyrazolones, 3057
Pyridine, 209
Pyridine-2-carboxaldehyde, 391, 1710
2-Pyridinecarboxaldehyde N-oxide, 1913
Pyridinedicarboxylates, 777, 2242
Pyridine dicarboxylic acid, 49
Pyridine-2,6-dicarboxylic acid, 229
2,6-Pyridinediylbis(2-pyridinyl)methanone, 1047
Pyridine *N*-oxide, 469
2-Pyridineethanol, 693
2-Pyridinepropanol, 693
Pyridone, 2189
4-Pyridyl, 1497
Pyridyl-azo-imidazoles, 739
Pyridyl dithioether, 413
Pyrimidine, 1913
Pyrrolyl, 1356

Quantum computation, 2562
Quantum computing, 2695
Quantum tunneling, 2284
Quantum tunneling of magnetization, 2557
Quantum tunneling of magnetization, 2695
Quantum tunneling of the magnetization, 2459
Quasi-linear trinuclear iron(III) complex, 1047
Quasi-two-dimensional film, 2355
2-Quinolinecarboxaldehyde Schiff bases of *S*-alkyl- and *S*-aryldithiocarbazates, 383
Quinones, 889, 1689

Radical, 3004
Radical cation, 2538
Radical cation salts, 1555
Raman, 1175
Raman spectroscopy, 619
Rare earth, 1160, 3046
Rare earth borides, 2803
Rare earth metal, 2588
Reaction mechanism, 2767
Reactions of coordinated ligands, 1606
Reactivity of amidouranium complexes, 3038
Redox, 333
Redox potentials, 1885
Redox properties, 57, 889, 1689
Redox reaction, 1517
Reductive aggregation, 2505
Reductive dimerization, 1325
Relative stability of four-membered and five-membered chelate rings, 1861
Relaxation, 2691
Review, 1
Rhenium(III) complexes, 701
Rhenium imido complexes, 1454
Rhenium nitrosyl complexes, 267
Rhenium oxo complexes, 1893
Rhodium and iridium complexes, 1710
Rhodium and iridium tris-picolinate complexes, 157
Riboside, 1079
Ring closure, 1289
Rrhenium, 419
Ru and Co, 2055
Ru(II) complexes, 65
Ru–Sn complexes, 1153
Ru–Sn–Fe complexes, 1153
Ruthenium, 391, 1063, 1445, 1961
Ruthenium(II), 57
Ruthenium arene complexes, 3012
Ruthenium(II) carbonyl complexes, 1885
Ruthenium clusters, 731
Ruthenium(II) complexes, 201, 1749
Ruthenium(II,III) complexes, 2658
Ruthenium polypyridines, 731
Ruthenium nitrosyl complexes, 359
Ruthenium–tetrazine, 333
Ruthenium(II) thiosemicarbazone complexes, 1861

S=1/2, 2350
S ligands, 521, 2035
S mixing, 2459
Saccharinate, 693
Salicylaldehyde oxime, 711
Salicylaldimine, 1461
Salt-bridge, 2550
Sandwich-type structure, 847
Saturation moment, 2405
Schiff base chelator, 1525
Schiff base ligand, 2257
Schiff bases, 343, 1461, 1478, 1755, 1821, 1869, 1913, 1922, 2933, 2963, 3091
Scorpionate ligands, 181
Second harmonic generation, 2901
Selenium, 639
Selenium disulfide, 639
Self-assemblies, 413, 785, 1086, 2758
Semicarbazone, 2972
Semiquinonate, 2607
Semiquinone, 2880
Seven-coordinate Cd(II)-1,3-pdta complex, 2009
Short non-bonding contact, 2522
Sigmatropic rearrangements, 1366
Silicate, 3066
Silicic acid, 1585
Silicon (IV) complex, 2076
Silver, 181, 2043
Silver (I), 3032
Silver (I) compounds, 481
Silver complexes, 435
Silver sol, 611
Silver(I), 949
Silver(I) complexes, 413, 611, 853, 940
Silylamide, 3066
Silyloxide, 3066
Single crystal, 2346
Single crystal XRD, 847
Single-crystal X-ray analysis, 2250
Single-molecule magnets, 2065, 2205, 2215, 2238, 2280, 2284, 2346, 2400, 2455, 2505, 2557, 2680, 2691, 2695, 2864, 2880, 2894
Single-site titanium catalyst, 1347
Singlet biradical, 2522
Small HOMO–LUMO gap, 2522
SMM, 2450
Sn(IV) complexes, 1054
Sodiumtetrachloropalladate, 1953
Solid solutions, 2094, 2839
Solid-state ^{111}Cd NMR, 777
Solid-state ^{13}C NMR, 2431, 2599
Solid-state high-resolution deuterium NMR, 2417
Solid-state high-resolution multi-nuclear NMR, 2607
Solid-state high-resolution NMR, 2424
Solid-state ^{2}H NMR, 2431
Solid-state IR-LD analysis, 1624
Solid-state wide line deuterium NMR, 2417
Solution equilibria, 1878
Solvatochromism, 239, 1869, 1913, 2933

Solvent-controlled hydrolysis and solvolysis, 1047
Solvothermal synthesis, 1941
Sonogashira coupling, 2121
Sparkle model, 3046
Speciation, 1878
Specific heat, 2573
Specific heat measurements, 2568
Spectra, 333, 1829
Spectral studies, 1410
Spectroelectrochemistry, 791, 1821
Spectroscopic characterization, 511
Spectroscopic studies, 327, 443, 1015
Spectroscopy, 97, 319, 1054, 1203
Spin coupler, 2484
Spin crossover, 2330
Spin density distribution, 2326, 2424
Spin diverse, 2876
Spin dynamics, 2653
Spin fluctuations, 2607
Spin frustration, 2784, 2835
Spin ladder, 2269
Spin-crossover, 2165, 2437, 2821, 2852
Spin-crossover complex film, 2909
Spin-flop transition, 2793
Spin–orbit coupling, 2238
Spin–orbit interaction, 2726
Spin-Peierls substance, 2716
Spin-phonon coupling, 2653
Spin–spin dipolar coupling, 2708
Spin-polarization, 2593
Spin polarization exchange, 2639
Spin-polarized molecular wire, 2263
Spin relaxation, 2341
Spin transition, 1813, 2094, 2857
Spin waves, 2568
Spiro compound, 2584
Spiro-biphenalenyl, 2274
SQUID, 2528
SQUID measurement, 2828
Stability constants, 443, 451, 627, 837, 1593
Stable open-shell systems, 2116
Stable organic radical, 2326
Stable radical, 2614
π-Stacking, 2639
Stacking interactions, 1577
Static disorder, 1125
Step-like hysteresis loop, 2205
Steric effect, 1773
Sterically hindered diphenols, 611
Stern-Gerlach experiments, 2341
Stibine, 419
STIRAP, 2726
Strontium, 645
Structural change, 2148
Structures, 333, 427, 807, 1093, 1101, 1185, 1533, 1739, 1913, 1983, 2165, 3066
Substituent effect, 2538
Substituted 2,2′-biimidazoles, 1196
Substituted diamines, 1101
Substituted reaction, 759
Sucrose complex, 1002
Sulfadrugs metal complexes, 501
Sulfathiazole, 501
Sulfido ligands, 872
Sulfonate, 1937
Sulfur, 639, 1417
Sulphur, 1212
Superparamagnet, 2280, 2557, 2691, 2695
Superparamagnetics, 2813
Supin susceptibility, 2389
Supramolecular assembly, 940, 2625
Supramolecular cation, 2844
Supramolecular chemistry, 785, 1086
Supramolecular helices, 1922
Supramolecular polymer, 1549
Supramolecular structures, 165
Supramolecular synthon, 1837
Supramolecular systems, 65
Synthesis, 201, 333, 1015, 1093, 1101, 1611, 1739

Tandem mass spectrometry, 1153
Tantalum, 1143
Tantalum nitride, 463
TCNE, 2720
TDAE-C60, 2173
TDDFT method, 359, 1445, 3012
Temperature effect, 1262
Template effect, 1117
Template synthesis, 289, 1405
TEMPO, 2126, 2796
TEMPO radical, 2614
Ten-coordinated lanthanum complexes, 723
Terephthalate, 2963
Terphenyl, 1798
tert-Butylnitroxides, 2639, 2645
Tetra-2-pyridylpyrazine, 487
Tetraamine, 1
Tetracyanoethylene, 1907
Tetradentate, 2017
Tetramethylenediamine, 1101
Tetranaphthylporphyrins, 679
Tetranuclear complex, 2257
Tetranuclear manganese complex, 2215
Tetrathiafulvalene, 1555
Tetrathiometalates, 435
Tetrathiomolybdate, 481, 2988
Tetrathiotungstate, 481, 2988
Tetratolylporphyrins, 679
TGA, 663
Theoretical, 1033
Theoretical calculations, 2368
Theoretical investigation of ESR spectrum, 2491
Thermal behaviors, 723
Thermal studies, 771
Thiazine, 129, 1764, 1975
Thiazolidine, 129, 1975
Thiazoline, 129, 1125, 2972
Thin films, 1727, 2533
Thioantimonate, 1941
Thiocyanate, 289, 2002, 2913
Thione, 2944
Thione complexes, 435
Thiosemicarbazide, 1855
Thiosemicarbazones, 369, 601, 889, 1133, 1689, 1717, 3057
Three-dimensional supermolecular, 215
Time-resolved ESR, 2185, 2299, 2337
Tin(IV) complexes, 383
Tin enolates, 1054
Tin-119 NMR, 995
Titanium, 151, 1143, 1256, 1298, 1356, 1793
Titanium(IV), 663
Titanocene, 1250, 1356
TOF mass spectrometry, 639, 1417
Toluene-3,4-dithiol, 89
π-Topology, 2299
trans-1,2-Bis(diphenylphosphino)ethene, 853
trans-1,2-Bis(diphenylphosphino)ethene complexes, 351
Transient ionic species, 1153
Transition metal, 397, 1117
Transition metal acetylide, 2148
Transition metal complexes, 1689, 2189
Transition temperature, 2497, 2501
Triarylamine, 2112
Triazine, 1435
Triazole, 181
1,2,2-Tricyanoethanolate, 1907
Tridentate, 2017
Tridentate chelate, 469
Tridentate ligands, 1717
Tridentate nitrogen ligand, 2409
Triethylenetetramine, 1913
Trifluoroacetates, 1185
Trifluoroacetic acid, 2528
Trigonal prism, 593
Trinuclear clusters, 1961
Trinuclear complex, 2732
Trinuclear oxo-centered Fe(III) complexes, 711
Triorganotin(IV), 1773
Triosmium clusters, 3074
Tripdal, 427
Triphenylamine, 2141
Triphenylphosphine, 872
Triplet biradical, 2522, 2538
Tripodal, 1
Tripodal ligands, 1160, 1478, 2450
Triruthenium clusters, 872, 1471
Tungsten, 173
Tungsten complexes, 435
Tungstoarsenate, 847
Tunsten, 1388
Two-dimensional molecular magnet, 2160
Two-phase solvent extraction, 1023
Two-step, 2852

Uniaxial strain, 2173
Uranium(III) complexes, 3038
Uranyl ion, 229
Urease, 2778
UV- and ^{1}H NMR data, 1624
UV spectrum, 2112
UV–Vis, 1682
UV–Vis spectroscopy, 1593, 2200
UV–visible spectroscopy, 143

Valence bond configuration interaction, 2880
Valence tautomer, 2876
Valence tautomerism, 2607
Vanadate, 985
Vanadium(V), 49, 837
Variable temperature NMR, 2194
Verdazyl radical, 2513
Vertical detachment energy, 2472
Vinylmethylene, 2708

^{183}W and ^{111}Cd NMR, 847
W/Ag/S polymer, 481
Water absorption, 2148
Water gas shift reaction, 511
Water-induced ferromagnetism, 2148

Water-soluble organometallics, 1961
Weak interactions, 413
Weakly coordinating anion, 2994

X-ray, 739, 1101, 3082
X-ray analysis, 2084
X-ray crystal and molecular structure, 2076
X-ray crystal structure analysis, 1949, 2194
X-ray crystal structures, 181, 289, 369, 549, 1540, 1701, 2009, 2027, 2632
X-ray crystallography, 469, 655, 1015, 1565, 2126, 2796, 3057
X-ray crystallography diffraction, 1109
X-ray data, 1983
X-ray diffraction, 1007, 1533, 1941, 2955, 2981, 1054
X-ray photoelectron spectroscopy, 521
X-ray powder diffractometry, 1975
X-ray single crystal diffraction, 1549
X-ray structures, 49, 75, 201, 209, 267, 359, 397, 419, 539, 663, 701, 747, 872, 949, 958, 1063, 1071, 1445, 1454, 1471, 1525, 1755, 1798, 1829, 1893, 2894, 3074, 3091
X-rays, 601
XANES, 143

Zeolite, 685
Zero-field splitting, 1510, 2238
Zero-field splitting parameters, 2708
Ziegler–Natta polymerization, 1280
Zigzag chain, 2835
Zinc, 579, 627, 791
Zinc(II) complexes, 1975
Zintl anion, 1565
Zirconium, 1143, 1256, 1289, 1298
Zirconium alkoxides, 1727
Zirconium(IV) complexes, 1280
Zirconium oxide, 1727
Zirconocene, 1269
Zn silylamides, 1093
Zn(II), 1829
Zn(II) complexes, 3057

POLYHEDRON

The International Journal for Inorganic and Organometallic Chemistry

Executive Editors

The Americas
G. Christou
Department of Chemistry, University of Florida,
Gainesville, FL 32611-7200, USA
E-mail: christou@chem.ufl.edu

Rest of the world
C.E. Housecroft
Department of Chemistry, University of Basel,
Spitalstrasse 51, CH-4056 Basel, Switzerland
E-mail: poly-chemie@unibas.ch

Associate Regional Editor for China
T.C.W. Mak
Department of Chemistry, University Science Centre,
The Chinese University of Hong Kong,
Shatin NT, Hong Kong, People's Republic of China
E-mail: tcwmak@cuhk.edu.hk

Polyhedron Reports
Editor
G. Christou *(Gainesville, FL, USA)*

Symposia-in-print
Editor
G. Parkin *(New York, NY, USA)*

Editorial Board
N.Y. Barba-Behrens *(Mexico, DF, Mexico)*
A.G. Blackman *(Dunedin, New Zealand)*
D.C. Bradley *(London, UK)*
D. Braga *(Bologna, Italy)*
A. Brodie *(Palmerston North, New Zealand)*
A. Castiñeiras *(Santiago de Compostela, Spain)*
M.H. Chisholm *(Columbus, OH, USA)*
E.C. Constable *(Basel, Switzerland)*
E. Coronado *(Valencia, Spain)*
L. Cronin *(Glasgow, UK)*
W.J. Evans *(Irvine, CA, USA)*
M. Fujita *(Tokyo, Japan)*
L.H. Gade *(Heidelberg, Germany)*
C.D. Garner *(Nottingham, UK)*
L. Hubert-Pfalzgraf *(Villeurbanne, France)*
M.B. Hursthouse *(Southampton, UK)*
T. Kiss *(Szeged, Hungary)*
P.P. Power *(Davis, CA, USA)*
T.B. Rauchfuss *(Urbana, IL, USA)*
J. Reedijk *(Leiden, The Netherlands)*
A.L. Rheingold *(Newark, DE, USA)*
A.M.Z. Slawin *(Fife, UK)*
F.G.A. Stone *(Waco, TX, USA)*
A.G. Sykes *(Newcastle upon Tyne, UK)*
L.K. Thompson *(St John's, NF, Canada)*
M.D. Ward *(Sheffield, UK)*
R.E.P. Winpenny *(Manchester, UK)*
M. Zaworotko *(Tampa, FL, USA)*

Aims and Scope

Polyhedron will publish original, fundamental, experimental and theoretical work of the highest quality in all the major areas of inorganic chemistry. These include synthetic chemistry, coordination chemistry, organometallic chemistry, bioinorganic chemistry, and solid-state and materials chemistry. Papers should be complete pieces of work, and the inclusion of results from spectroscopic and/or physical techniques is encouraged. Papers merely reporting the preparation and X-ray structural characterization of only a single compound will not be considered appropriate unless the compound and its structure are particularly interesting.

Similarly, papers concerned solely with stability constants determined by potentiometric titration data unsupported by other e.g. spectroscopic techniques will not be acceptable nor will solvent extraction data unless supported by other data of interest to inorganic chemists. Unnecessary fragmentation of work is not acceptable.

In addition Polyhedron publishes specially commissioned review articles (Polyhedron Reports) and collections of original research papers (Polyhedron Symposia-in-Print) of appropriate timeliness.

Publication Information: Polyhedron (ISSN 0277-5387). For 2005, volume 24 is scheduled for publication. Subscription prices are available upon request from the Publisher or from the Regional Sales Office nearest you or from this journal's website (http://www.elsevier.com/locate/poly). Further information is available on this journal and other Elsevier products through Elsevier's website (http://www.elsevier.com). Subscriptions are accepted on a prepaid basis only and are entered on a calendar year basis. Issues are sent by standard mail (surface within Europe, air delivery outside Europe). Priority rates are available upon request. Claims for missing issues should be made within six months of the date of dispatch.

Orders, Claims and Journal Enquiries

(no manuscript enquiries)
Please contact the Customer Support Department at the Regional Sales Office nearest you:

Orlando
Elsevier
Customer Service Department
6277 Sea Harbor Drive
Orlando, FL 32887-4800
USA
Tel.: (877) 8397126 or (800) 6542452 [toll free numbers for US customers];
(+1) (407) 3454020 or
(+1) (407) 3454000 [customers outside US]
Fax: (+1) (407) 3631354 or
(+1) (407) 3639661
E-mail: usjcs@elsevier.com or elspcs@elsevier.com

Amsterdam
Elsevier
Customer Service Department
P.O. Box 211
1000 AE Amsterdam
The Netherlands
Tel.: (+31) 20-485-3757
Fax: (+31) 20-485-3432
E-mail: nlinfo-f@elsevier.com

Tokyo
Elsevier K.K.
Customer Service Department
4F Higashi-Azabu, 1-Chome Bldg
1-9-15 Higashi-Azabu
Minato-ku, Tokyo 106-0044
Japan
Tel.: (+81) 3-5561-5037
Fax: (+81) 3-5561-5047
E-mail: jp.info@elsevier.com

Singapore
Elsevier
Customer Service Department
3 Killiney Road
#08-01 Winsland House 1
Singapore 239519
Tel.: (+65) 6349-0222
Fax: (+65) 6733-1510
E-mail: asiainfo@elsevier.com

USA mailing notice: *Polyhedron* (ISSN 0277-5387) is published triweekly by Elsevier Ltd. (P.O. Box 211, 1000 AE Amsterdam, The Netherlands). Annual subscription price in the USA US$ 7049.00 (valid in North, Central and South America), including air speed delivery. Periodical postage rate is paid at Jamaica, NY 11431.
USA POSTMASTER: Send change of address to *Polyhedron*, Elsevier, 6277 Sea Harbor Drive, Orlando, FL 32887-4800.
AIRFREIGHT AND MAILING in the USA by Publications Expediting Inc., 200 Meacham Avenue, Elmont, NY 11003.

Advertising Information

Advertising orders and enquiries can be sent to: **South America:** Mr Tino DeCarlo, The Advertising Department, Elsevier Inc., 360 Park Avenue South, New York, NY 10010-1710, USA; tel.: (+1) (212) 633 3815; fax: (+1) (212) 633 3820; e-mail: t.decarlo@elsevier.com. **Europe, USA, Canada and ROW:** Miss Katrina Barton, Commercial Sales, Elsevier, 84 Theobald's Road, London, WCIX 8RR, UK; phone: (+44) (0) 20 7611 4117; fax: (+44) (0) 20 7611 4463; e-mail: commercialsales@elsevier.com

POLYHEDRON

The International Journal for Inorganic and Organometallic Chemistry

Executive Editors

The Americas
G. Christou
Department of Chemistry, University of Florida,
Gainesville, FL 32611-7200, USA
E-mail: christou@chem.ufl.edu

Rest of the world
C.E. Housecroft
Department of Chemistry, University of Basel,
Spitalstrasse 51, CH-4056 Basel, Switzerland
E-mail: poly-chemie@unibas.ch

Associate Regional Editor for China
T.C.W. Mak
Department of Chemistry, University Science Centre,
The Chinese University of Hong Kong,
Shatin NT, Hong Kong, People's Republic of China
E-mail: tcwmak@cuhk.edu.hk

Polyhedron Reports
Editor
G. Christou *(Gainesville, FL, USA)*

Symposia-in-print
Editor
G. Parkin *(New York, NY, USA)*

Editorial Board

N.Y. Barba-Behrens *(Mexico, DF, Mexico)*
A.G. Blackman *(Dunedin, New Zealand)*
D.C. Bradley *(London, UK)*
D. Braga *(Bologna, Italy)*
A. Brodie *(Palmerston North, New Zealand)*
A. Castiñeiras *(Santiago de Compostela, Spain)*
M.H. Chisholm *(Columbus, OH, USA)*
E.C. Constable *(Basel, Switzerland)*
E. Coronado *(Valencia, Spain)*
L. Cronin *(Glasgow, UK)*
W.J. Evans *(Irvine, CA, USA)*
M. Fujita *(Tokyo, Japan)*
L.H. Gade *(Heidelberg, Germany)*
C.D. Garner *(Nottingham, UK)*
L. Hubert-Pfalzgraf *(Villeurbanne, France)*
M.B. Hursthouse *(Southampton, UK)*
T. Kiss *(Szeged, Hungary)*
P.P. Power *(Davis, CA, USA)*
T.B. Rauchfuss *(Urbana, IL, USA)*
J. Reedijk *(Leiden, The Netherlands)*
A.L. Rheingold *(Newark, DE, USA)*
A.M.Z. Slawin *(Fife, UK)*
F.G.A. Stone *(Waco, TX, USA)*
A.G. Sykes *(Newcastle upon Tyne, UK)*
L.K. Thompson *(St John's, NF, Canada)*
M.D. Ward *(Sheffield, UK)*
R.E.P. Winpenny *(Manchester, UK)*
M. Zaworotko *(Tampa, FL, USA)*

Aims and Scope

Polyhedron will publish original, fundamental, experimental and theoretical work of the highest quality in all the major areas of inorganic chemistry. These include synthetic chemistry, coordination chemistry, organometallic chemistry, bioinorganic chemistry, and solid-state and materials chemistry. Papers should be complete pieces of work, and the inclusion of results from spectroscopic and/or physical techniques is encouraged. Papers merely reporting the preparation and X-ray structural characterization of only a single compound will not be considered appropriate unless the compound and its structure are particularly interesting.

Similarly, papers concerned solely with stability constants determined by potentiometric titration data unsupported by other e.g. spectroscopic techniques will not be acceptable nor will solvent extraction data unless supported by other data of interest to inorganic chemists. Unnecessary fragmentation of work is not acceptable.

In addition Polyhedron publishes specially commissioned review articles (Polyhedron Reports) and collections of original research papers (Polyhedron Symposia-in-Print) of appropriate timeliness.

Publication Information: Polyhedron (ISSN 0277-5387). For 2005, volume 24 is scheduled for publication. Subscription prices are available upon request from the Publisher or from the Regional Sales Office nearest you or from this journal's website (http://www.elsevier.com/locate/poly). Further information is available on this journal and other Elsevier products through Elsevier's website (http://www.elsevier.com). Subscriptions are accepted on a prepaid basis only and are entered on a calendar year basis. Issues are sent by standard mail (surface within Europe, air delivery outside Europe). Priority rates are available upon request. Claims for missing issues should be made within six months of the date of dispatch.

Orders, Claims and Journal Enquiries

(no manuscript enquiries)

Please contact the Customer Support Department at the Regional Sales Office nearest you:

Orlando
Elsevier
Customer Service Department
6277 Sea Harbor Drive
Orlando, FL 32887-4800
USA
Tel.: (877) 8397126 or (800) 6542452 [toll free numbers for US customers];
(+1) (407) 3454020 or
(+1) (407) 3454000 [customers outside US]
Fax: (+1) (407) 3631354 or
(+1) (407) 3639661
E-mail: usjcs@elsevier.com or elspcs@elsevier.com

Amsterdam
Elsevier
Customer Service Department
P.O. Box 211
1000 AE Amsterdam
The Netherlands
Tel.: (+31) 20-485-3757
Fax: (+31) 20-485-3432
E-mail: nlinfo-f@elsevier.com

Tokyo
Elsevier K.K.
Customer Service Department
4F Higashi-Azabu, 1-Chome Bldg
1-9-15 Higashi-Azabu
Minato-ku, Tokyo 106-0044
Japan
Tel.: (+81) 3-5561-5037
Fax: (+81) 3-5561-5047
E-mail: jp.info@elsevier.com

Singapore
Elsevier
Customer Service Department
3 Killiney Road
#08-01 Winsland House 1
Singapore 239519
Tel.: (+65) 6349-0222
Fax: (+65) 6733-1510
E-mail: asiainfo@elsevier.com

USA mailing notice: *Polyhedron* (ISSN 0277-5387) is published triweekly by Elsevier Ltd. (P.O. Box 211, 1000 AE Amsterdam, The Netherlands). Annual subscription price in the USA US$ 7049.00 (valid in North, Central and South America), including air speed delivery. Periodical postage rate is paid at Jamaica, NY 11431.
USA POSTMASTER: Send change of address to *Polyhedron*, Elsevier, 6277 Sea Harbor Drive, Orlando, FL 32887-4800.
AIRFREIGHT AND MAILING in the USA by Publications Expediting Inc., 200 Meacham Avenue, Elmont, NY 11003.

Advertising Information

Advertising orders and enquiries can be sent to: **South America:** Mr Tino DeCarlo, The Advertising Department, Elsevier Inc., 360 Park Avenue South, New York, NY 10010-1710, USA; tel.: (+1) (212) 633 3815; fax: (+1) (212) 633 3820; e-mail: t.decarlo@elsevier.com. **Europe, USA, Canada and ROW:** Miss Katrina Barton, Commercial Sales, Elsevier, 84 Theobald's Road, London, WCIX 8RR, UK; phone: (+44) (0) 20 7611 4117; fax: (+44) (0) 20 7611 4463; e-mail: commercialsales@elsevier.com

POLYHEDRON

The International Journal for Inorganic and Organometallic Chemistry

Executive Editors

The Americas
G. Christou
Department of Chemistry, University of Florida,
Gainesville, FL 32611-7200, USA
E-mail: christou@chem.ufl.edu

Rest of the world
C.E. Housecroft
Department of Chemistry, University of Basel,
Spitalstrasse 51, CH-4056 Basel, Switzerland
E-mail: poly-chemie@unibas.ch

Associate Regional Editor for China
T.C.W. Mak
Department of Chemistry, University Science Centre,
The Chinese University of Hong Kong,
Shatin NT, Hong Kong, People's Republic of China
E-mail: tcwmak@cuhk.edu.hk

Polyhedron Reports
Editor
G. Christou *(Gainesville, FL, USA)*

Symposia-in-print
Editor
G. Parkin *(New York, NY, USA)*

Editorial Board

N.Y. Barba-Behrens *(Mexico, DF, Mexico)*
A.G. Blackman *(Dunedin, New Zealand)*
D.C. Bradley *(London, UK)*
D. Braga *(Bologna, Italy)*
A. Brodie *(Palmerston North, New Zealand)*
A. Castiñeiras *(Santiago de Compostela, Spain)*
M.H. Chisholm *(Columbus, OH, USA)*
E.C. Constable *(Basel, Switzerland)*
E. Coronado *(Valencia, Spain)*
W.J. Evans *(Irvine, CA, USA)*
M. Fujita *(Tokyo, Japan)*
L.H. Gade *(Heidelberg, Germany)*
C.D. Garner *(Nottingham, UK)*
L. Hubert-Pfalzgraf *(Villeurbanne, France)*
M.B. Hursthouse *(Southampton, UK)*
T. Kiss *(Szeged, Hungary)*
P.P. Power *(Davis, CA, USA)*
T.B. Rauchfuss *(Urbana, IL, USA)*
J. Reedijk *(Leiden, The Netherlands)*
A.L. Rheingold *(Newark, DE, USA)*
F.G.A. Stone *(Waco, TX, USA)*
A.G. Sykes *(Newcastle upon Tyne, UK)*
L.K. Thompson *(St John's, NF, Canada)*
M.D. Ward *(Sheffield, UK)*
R.E.P. Winpenny *(Manchester, UK)*
M. Zaworotko *(Tampa, FL, USA)*

Aims and Scope

Polyhedron will publish original, fundamental, experimental and theoretical work of the highest quality in all the major areas of inorganic chemistry. These include synthetic chemistry, coordination chemistry, organometallic chemistry, bioinorganic chemistry, and solid-state and materials chemistry. Papers should be complete pieces of work, and the inclusion of results from spectroscopic and/or physical techniques is encouraged. Papers merely reporting the preparation and X-ray structural characterization of only a single compound will not be considered appropriate unless the compound and its structure are particularly interesting.

Similarly, papers concerned solely with stability constants determined by potentiometric titration data unsupported by other e.g. spectroscopic techniques will not be acceptable nor will solvent extraction data unless supported by other data of interest to inorganic chemists. Unnecessary fragmentation of work is not acceptable.

In addition Polyhedron publishes specially commissioned review articles (Polyhedron Reports) and collections of original research papers (Polyhedron Symposia-in-Print) of appropriate timeliness.

Publication Information: Polyhedron (ISSN 0277-5387). For 2005, volume 24 is scheduled for publication. Subscription prices are available upon request from the Publisher or from the Regional Sales Office nearest you or from this journal's website (http://www.elsevier.com/locate/poly). Further information is available on this journal and other Elsevier products through Elsevier's website (http://www.elsevier.com). Subscriptions are accepted on a prepaid basis only and are entered on a calendar year basis. Issues are sent by standard mail (surface within Europe, air delivery outside Europe). Priority rates are available upon request. Claims for missing issues should be made within six months of the date of dispatch.

Orders, Claims and Journal Enquiries

(no manuscript enquiries)

Please contact the Customer Support Department at the Regional Sales Office nearest you:

Orlando
Elsevier
Customer Service Department
6277 Sea Harbor Drive
Orlando, FL 32887-4800
USA
Tel.: (877) 8397126 or (800) 6542452 [toll free numbers for US customers];
(+1) (407) 3454020 or
(+1) (407) 3454000 [customers outside US]
Fax: (+1) (407) 3631354 or
(+1) (407) 3639661
E-mail: usjcs@elsevier.com or elspcs@elsevier.com

Amsterdam
Elsevier
Customer Service Department
P.O. Box 211
1000 AE Amsterdam
The Netherlands
Tel.: (+31) 20-485-3757
Fax: (+31) 20-485-3432
E-mail: nlinfo-f@elsevier.com

Tokyo
Elsevier K.K.
Customer Service Department
4F Higashi-Azabu, 1-Chome Bldg
1-9-15 Higashi-Azabu
Minato-ku, Tokyo 106-0044
Japan
Tel.: (+81) 3-5561-5037
Fax: (+81) 3-5561-5047
E-mail: jp.info@elsevier.com

Singapore
Elsevier
Customer Service Department
3 Killiney Road
#08-01 Winsland House 1
Singapore 239519
Tel.: (+65) 6349-0222
Fax: (+65) 6733-1510
E-mail: asiainfo@elsevier.com

USA mailing notice: *Polyhedron* (ISSN 0277-5387) is published triweekly by Elsevier Ltd. (P.O. Box 211, 1000 AE Amsterdam, The Netherlands). Annual subscription price in the USA US$ 7049.00 (valid in North, Central and South America), including air speed delivery. Periodical postage rate is paid at Jamaica, NY 11431.
USA POSTMASTER: Send change of address to *Polyhedron*, Elsevier, 6277 Sea Harbor Drive, Orlando, FL 32887-4800.
AIRFREIGHT AND MAILING in the USA by Publications Expediting Inc., 200 Meacham Avenue, Elmont, NY 11003.

Advertising Information

Advertising orders and enquiries can be sent to: **South America:** Mr Tino DeCarlo, The Advertising Department, Elsevier Inc., 360 Park Avenue South, New York, NY 10010-1710, USA; tel.: (+1) (212) 633 3815; fax: (+1) (212) 633 3820; e-mail: t.decarlo@elsevier.com. **Europe, USA, Canada and ROW:** Miss Katrina Barton, Commercial Sales, Elsevier, 84 Theobald's Road, London, WCIX 8RR, UK; phone: (+44) (0) 20 7611 4117; fax: (+44) (0) 20 7611 4463; e-mail: commercialsales@elsevier.com

POLYHEDRON

The International Journal for Inorganic and Organometallic Chemistry

Executive Editors

The Americas
G. Christou
Department of Chemistry, University of Florida,
Gainesville, FL 32611-7200, USA
E-mail: christou@chem.ufl.edu

Rest of the world
C.E. Housecroft
Department of Chemistry, University of Basel,
Spitalstrasse 51, CH-4056 Basel, Switzerland
E-mail: poly-chemie@unibas.ch

Associate Regional Editor for China
T.C.W. Mak
Department of Chemistry, University Science Centre,
The Chinese University of Hong Kong,
Shatin NT, Hong Kong, People's Republic of China
E-mail: tcwmak@cuhk.edu.hk

Polyhedron Reports
Editor
G. Christou *(Gainesville, FL, USA)*

Symposia-in-print
Editor
G. Parkin *(New York, NY, USA)*

Editorial Board

N.Y. Barba-Behrens *(Mexico, DF, Mexico)*
A.G. Blackman *(Dunedin, New Zealand)*
D.C. Bradley *(London, UK)*
D. Braga *(Bologna, Italy)*
A. Brodie *(Palmerston North, New Zealand)*
A. Castiñeiras *(Santiago de Compostela, Spain)*
M.H. Chisholm *(Columbus, OH, USA)*
E.C. Constable *(Basel, Switzerland)*
E. Coronado *(Valencia, Spain)*
W.J. Evans *(Irvine, CA, USA)*
M. Fujita *(Tokyo, Japan)*
L.H. Gade *(Heidelberg, Germany)*
C.D. Garner *(Nottingham, UK)*
L. Hubert-Pfalzgraf *(Villeurbanne, France)*
M.B. Hursthouse *(Southampton, UK)*
T. Kiss *(Szeged, Hungary)*
P.P. Power *(Davis, CA, USA)*
T.B. Rauchfuss *(Urbana, IL, USA)*
J. Reedijk *(Leiden, The Netherlands)*
A.L. Rheingold *(Newark, DE, USA)*
F.G.A. Stone *(Waco, TX, USA)*
A.G. Sykes *(Newcastle upon Tyne, UK)*
L.K. Thompson *(St John's, NF, Canada)*
M.D. Ward *(Sheffield, UK)*
R.E.P. Winpenny *(Manchester, UK)*
M. Zaworotko *(Tampa, FL, USA)*

Aims and Scope

Polyhedron will publish original, fundamental, experimental and theoretical work of the highest quality in all the major areas of inorganic chemistry. These include synthetic chemistry, coordination chemistry, organometallic chemistry, bioinorganic chemistry, and solid-state and materials chemistry. Papers should be complete pieces of work, and the inclusion of results from spectroscopic and/or physical techniques is encouraged. Papers merely reporting the preparation and X-ray structural characterization of only a single compound will not be considered appropriate unless the compound and its structure are particularly interesting.
Similarly, papers concerned solely with stability constants determined by potentiometric titration data unsupported by other e.g. spectroscopic techniques will not be acceptable nor will solvent extraction data unless supported by other data of interest to inorganic chemists. Unnecessary fragmentation of work is not acceptable.
In addition Polyhedron publishes specially commissioned review articles (Polyhedron Reports) and collections of original research papers (Polyhedron Symposia-in-Print) of appropriate timeliness.

Publication Information: Polyhedron (ISSN 0277-5387). For 2005, volume 24 is scheduled for publication. Subscription prices are available upon request from the Publisher or from the Regional Sales Office nearest you or from this journal's website (http://www.elsevier.com/locate/poly). Further information is available on this journal and other Elsevier products through Elsevier's website (http://www.elsevier.com). Subscriptions are accepted on a prepaid basis only and are entered on a calendar year basis. Issues are sent by standard mail (surface within Europe, air delivery outside Europe). Priority rates are available upon request. Claims for missing issues should be made within six months of the date of dispatch.

Orders, Claims and Journal Enquiries

(no manuscript enquiries)
Please contact the Customer Support Department at the Regional Sales Office nearest you:

Orlando
Elsevier
Customer Service Department
6277 Sea Harbor Drive
Orlando, FL 32887-4800
USA
Tel.: (877) 8397126 or (800) 6542452 [toll free numbers for US customers];
(+1) (407) 3454020 or
(+1) (407) 3454000 [customers outside US]
Fax: (+1) (407) 3631354 or
(+1) (407) 3639661
E-mail: usjcs@elsevier.com or elspcs@elsevier.com

Amsterdam
Elsevier
Customer Service Department
P.O. Box 211
1000 AE Amsterdam
The Netherlands
Tel.: (+31) 20-485-3757
Fax: (+31) 20-485-3432
E-mail: nlinfo-f@elsevier.com

Tokyo
Elsevier K.K.
Customer Service Department
4F Higashi-Azabu, 1-Chome Bldg
1-9-15 Higashi-Azabu
Minato-ku, Tokyo 106-0044
Japan
Tel.: (+81) 3-5561-5037
Fax: (+81) 3-5561-5047
E-mail: jp.info@elsevier.com

Singapore
Elsevier
Customer Service Department
3 Killiney Road
#08-01 Winsland House 1
Singapore 239519
Tel.: (+65) 6349-0222
Fax: (+65) 6733-1510
E-mail: asiainfo@elsevier.com

USA mailing notice: *Polyhedron* (ISSN 0277-5387) is published triweekly by Elsevier Ltd. (P.O. Box 211, 1000 AE Amsterdam, The Netherlands). Annual subscription price in the USA US$ 7049.00 (valid in North, Central and South America), including air speed delivery. Periodical postage rate is paid at Jamaica, NY 11431.
USA POSTMASTER: Send change of address to *Polyhedron*, Elsevier, 6277 Sea Harbor Drive, Orlando, FL 32887-4800.
AIRFREIGHT AND MAILING in the USA by Publications Expediting Inc., 200 Meacham Avenue, Elmont, NY 11003.

Advertising Information

Advertising orders and enquiries can be sent to: **South America:** Mr Tino DeCarlo, The Advertising Department, Elsevier Inc., 360 Park Avenue South, New York, NY 10010-1710, USA; tel.: (+1) (212) 633 3815; fax: (+1) (212) 633 3820; e-mail: t.decarlo@elsevier.com. **Europe, USA, Canada and ROW:** Miss Katrina Barton, Commercial Sales, Elsevier, 84 Theobald's Road, London, WCIX 8RR, UK; phone: (+44) (0) 20 7611 4117; fax: (+44) (0) 20 7611 4463; e-mail: commercialsales@elsevier.com

Instructions to Authors

The instructions can also be found on the World Wide Web: http://www.elsevier.com/locate/poly

General

Polyhedron publishes full length papers, commissioned reports and symposia-in-print. All contributions should conform to the Aims and Scope of the journal. All contributions shall be rigorously refereed.
Papers – should be substantial, completed pieces of original research in inorganic and organometallic chemistry which have special significance, general interest and which, in addition are presented clearly and concisely.
Reports – are specially commissioned critical reports reviewing research results of topical importance. Reports will be commissioned by the Editorial Board from recognized authorities in the appropriate fields.
Symposia-in-Print – are collections of original research papers brought together to cover timely areas of inorganic and organometallic chemistry. For each, a Symposium Editor will invite authors active in the field to submit papers.

Submission of contributions

Authors should select the name of the appropriate Regional Editorial Office from the dropdown menu:
Papers from the Americas: G. Christou
Papers from China: T.C.W. Mak
Papers from the Rest of the world: C.E. Housecroft
Papers from Australia: any of the Editors
Polyhedron Reports: G. Christou
Symposia-in-Print: G. Parkin
Alternatively, contributions may be submitted in hardcopy, in triplicate.

Crystallographic data

Crystallographic data need to be validated and deposited (usually by sending a CIF file to deposit@ccdc.cam.ac.uk prior to submission).

Electronic submission

We accept most word processing formats, but Word, WordPerfect or LaTeX is preferred.
Submission of both regular and special issue articles to this journal proceeds totally on-line via the journal's submission website http://ees.elsevier.com/poly. At the submission website you will be guided stepwise through the creation and uploading of the various files. Once the uploading is done, our system automatically generates an electronic (PDF) proof, which is then used for reviewing. All correspondence, including notification of the Editor's decision and requests for revisions, will be by e-mail. Every paper must be accompanied by a letter from the senior author, stating that he/she is submitting the paper for publication in Polyhedron. In the letter, possible reviewers may be suggested.

Manuscript preparation

Language. Articles must be written in good English. For information about language editing services, please contact authorsupport@elsevier.com who will be happy to deal with any questions.
Manuscripts should be prepared with numbered lines, wide margins and double spacing throughout, i.e. also for abstracts, footnotes and references.
Corresponding author. Clearly indicate who is willing to handle correspondence at all stages of refereeing and publication, also post publication. Ensure that telephone and fax numbers (with country and area code) are provided in addition to the e-mail address and the complete postal address. This corresponding author should be clearly indicated by an asterisk.
Please note that the Contents contain Pictograms and Synopses. The authors are therefore asked to provide a drawing or reaction scheme of restricted size illustrating their work and a short synopsis of maximum 50 words.
Every contribution should include a concise, informative *Abstract* and a maximum of six *Keywords*. Equations, tables and legends should be numbered consecutively and separately throughout the paper. The presentation of tables, graphs and formulae should be kept to an absolute minimum, and where possible the results from a series of investigations should be in table form or as a graph. The same data should not be presented in both tables and figures or given in the Discussion as well as the Experimental section.
Illustrations. Graphics and photographs should not be embedded in the text of the manuscript. They should be uploaded separately in a form suitable for reproduction. A detailed guide on electronic artwork is available on our website: http://authors.elsevier.com/artwork. Authors may now submit colour pictures and other supplementary material along with their paper. If, together with the accepted article, usable colour figures are submitted then Elsevier will ensure, at no additional charge, that these figures will appear in colour on the web (e.g., ScienceDirect and other sites) regardless of whether or not these illustrations are reproduced in colour in the printed version. Figure captions should always be listed on a separate page.
References should be numbered consecutively throughout the text, and should be collected together in a reference list, at the end of the paper. Journal abbreviations should normally conform to the ''Chemical Abstracts Service Source Index''.

Nomenclature

All nomenclature should be consistent, clear and unambiguous, and should conform to the rules established by IUPAC. The following IUPAC publications should be consulted: Nomenclature of Inorganic Chemistry and Nomenclature of Organic Chemistry.

Copyright

Upon acceptance of an article, authors will be asked to transfer copyright (for more information on copyright see http://authors.elsevier.com). This transfer will ensure the widest possible dissemination of information. A letter will be sent to the corresponding Author confirming receipt of the manuscript. A form facilitating transfer of copyright will be provided. If excerpts from other copyrighted works are included, the Author(s) must obtain written permission from the copyright owners and credit the source(s) in the article. Elsevier has preprinted forms for use by authors in these cases: contact Elsevier's Rights Department, Oxford, UK, phone: (+44) 1865 843830, fax: (+44) 1865 853333, e-mail: permissions@elsevier.com. Requests may also be completed on-line via the Elsevier homepage (http://www.elsevier.com/locate/permissions).

Proofs

One set of page proofs in PDF format will be sent by e-mail to the corresponding Author, to be checked for typesetting/editing. No changes in, or additions to, the accepted (and subsequently edited) manuscript will be allowed at this stage. Proofreading is solely your responsibility. Elsevier will do everything possible to get your article corrected and published as quickly and accurately as possible. In order to do this we need your help. When you receive the (PDF) proof of your article for correction, it is important to ensure that all of your corrections are sent back to us in one communication. Subsequent corrections will not be possible, so please ensure your first sending is complete. Note that this does not mean you have any less time to make your corrections, just that only one set of corrections will be accepted.

Reprints

Authors are provided with twenty-five reprints free of charge. Additional reprints can be ordered. The order form containing price quotations will be sent to the authors together with a copyright transfer form upon acceptance of the manuscript.

There are no page charges

Author enquiries

For enquiries relating to the submission of articles (including electronic submission where available) please visit Elsevier's Author Gateway at http://authors.elsevier.com. The Author Gateway also provides the faculty to track accepted articles and set up e-mail alerts to inform you of when an article's status has changed as well as detailed artwork guidelines, copyright information, frequently asked questions and more. Contact details for questions arising after acceptance of an article, especially those relating to proofs, are provided after registration of an article for publication.

POLYHEDRON

The International Journal for Inorganic and Organometallic Chemistry

Executive Editors

The Americas
G. Christou
Department of Chemistry, University of Florida,
Gainesville, FL 32611-7200, USA
E-mail: christou@chem.ufl.edu

Rest of the world
C.E. Housecroft
Department of Chemistry, University of Basel,
Spitalstrasse 51, CH-4056 Basel, Switzerland
E-mail: poly-chemie@unibas.ch

Associate Regional Editor for China
T.C.W. Mak
Department of Chemistry, University Science Centre,
The Chinese University of Hong Kong,
Shatin NT, Hong Kong, People's Republic of China
E-mail: tcwmak@cuhk.edu.hk

Polyhedron Reports
Editor
G. Christou *(Gainesville, FL, USA)*

Symposia-in-print
Editor
G. Parkin *(New York, NY, USA)*

Editorial Board
N.Y. Barba-Behrens *(Mexico, DF, Mexico)*
A.G. Blackman *(Dunedin, New Zealand)*
D.C. Bradley *(London, UK)*
D. Braga *(Bologna, Italy)*
A. Brodie *(Palmerston North, New Zealand)*
A. Castiñeiras *(Santiago de Compostela, Spain)*
M.H. Chisholm *(Columbus, OH, USA)*
E.C. Constable *(Basel, Switzerland)*
E. Coronado *(Valencia, Spain)*
W.J. Evans *(Irvine, CA, USA)*
M. Fujita *(Tokyo, Japan)*
L.H. Gade *(Heidelberg, Germany)*
C.D. Garner *(Nottingham, UK)*
L. Hubert-Pfalzgraf *(Villeurbanne, France)*
M.B. Hursthouse *(Southampton, UK)*
T. Kiss *(Szeged, Hungary)*
P.P. Power *(Davis, CA, USA)*
T.B. Rauchfuss *(Urbana, IL, USA)*
J. Reedijk *(Leiden, The Netherlands)*
A.L. Rheingold *(Newark, DE, USA)*
F.G.A. Stone *(Waco, TX, USA)*
A.G. Sykes *(Newcastle upon Tyne, UK)*
L.K. Thompson *(St John's, NF, Canada)*
M.D. Ward *(Sheffield, UK)*
R.E.P. Winpenny *(Manchester, UK)*
M. Zaworotko *(Tampa, FL, USA)*

Aims and Scope

Polyhedron will publish original, fundamental, experimental and theoretical work of the highest quality in all the major areas of inorganic chemistry. These include synthetic chemistry, coordination chemistry, organometallic chemistry, bioinorganic chemistry, and solid-state and materials chemistry. Papers should be complete pieces of work, and the inclusion of results from spectroscopic and/or physical techniques is encouraged. Papers merely reporting the preparation and X-ray structural characterization of only a single compound will not be considered appropriate unless the compound and its structure are particularly interesting.
Similarly, papers concerned solely with stability constants determined by potentiometric titration data unsupported by other e.g. spectroscopic techniques will not be acceptable nor will solvent extraction data unless supported by other data of interest to inorganic chemists. Unnecessary fragmentation of work is not acceptable.
In addition Polyhedron publishes specially commissioned review articles (Polyhedron Reports) and collections of original research papers (Polyhedron Symposia-in-Print) of appropriate timeliness.

Publication Information: Polyhedron (ISSN 0277-5387). For 2005, volume 24 is scheduled for publication. Subscription prices are available upon request from the Publisher or from the Regional Sales Office nearest you or from this journal's website (http://www.elsevier.com/locate/poly). Further information is available on this journal and other Elsevier products through Elsevier's website (http://www.elsevier.com). Subscriptions are accepted on a prepaid basis only and are entered on a calendar year basis. Issues are sent by standard mail (surface within Europe, air delivery outside Europe). Priority rates are available upon request. Claims for missing issues should be made within six months of the date of dispatch.

Orders, Claims and Journal Enquiries

(no manuscript enquiries)
Please contact the Customer Support Department at the Regional Sales Office nearest you:

Orlando
Elsevier
Customer Service Department
6277 Sea Harbor Drive
Orlando, FL 32887-4800
USA
Tel.: (877) 8397126 or (800) 6542452 [toll free numbers for US customers];
(+1) (407) 3454020 or
(+1) (407) 3454000 [customers outside US]
Fax: (+1) (407) 3631354 or
(+1) (407) 3639661
E-mail: usjcs@elsevier.com or elspcs@elsevier.com

Amsterdam
Elsevier
Customer Service Department
P.O. Box 211
1000 AE Amsterdam
The Netherlands
Tel.: (+31) 20-485-3757
Fax: (+31) 20-485-3432
E-mail: nlinfo-f@elsevier.com

Tokyo
Elsevier K.K.
Customer Service Department
4F Higashi-Azabu, 1-Chome Bldg
1-9-15 Higashi-Azabu
Minato-ku, Tokyo 106-0044
Japan
Tel.: (+81) 3-5561-5037
Fax: (+81) 3-5561-5047
E-mail: jp.info@elsevier.com

Singapore
Elsevier
Customer Service Department
3 Killiney Road
#08-01 Winsland House 1
Singapore 239519
Tel.: (+65) 6349-0222
Fax: (+65) 6733-1510
E-mail: asiainfo@elsevier.com

USA mailing notice: *Polyhedron* (ISSN 0277-5387) is published triweekly by Elsevier Ltd. (P.O. Box 211, 1000 AE Amsterdam, The Netherlands). Annual subscription price in the USA US$ 7049.00 (valid in North, Central and South America), including air speed delivery. Periodical postage rate is paid at Jamaica, NY 11431.
USA POSTMASTER: Send change of address to *Polyhedron*, Elsevier, 6277 Sea Harbor Drive, Orlando, FL 32887-4800.
AIRFREIGHT AND MAILING in the USA by Publications Expediting Inc., 200 Meacham Avenue, Elmont, NY 11003.

Advertising Information

Advertising orders and enquiries can be sent to: **South America:** Mr Tino DeCarlo, The Advertising Department, Elsevier Inc., 360 Park Avenue South, New York, NY 10010-1710, USA; tel.: (+1) (212) 633 3815; fax: (+1) (212) 633 3820; e-mail: t.decarlo@elsevier.com. **Europe, USA, Canada and ROW:** Miss Katrina Barton, Commercial Sales, Elsevier, 84 Theobald's Road, London, WCIX 8RR, UK; phone: (+44) (0) 20 7611 4117; fax: (+44) (0) 20 7611 4463; e-mail: commercialsales@elsevier.com

POLYHEDRON

The International Journal for Inorganic and Organometallic Chemistry

Executive Editors

The Americas
G. Christou
Department of Chemistry, University of Florida,
Gainesville, FL 32611-7200, USA
E-mail: christou@chem.ufl.edu

Rest of the world
C.E. Housecroft
Department of Chemistry, University of Basel,
Spitalstrasse 51, CH-4056 Basel, Switzerland
E-mail: poly-chemie@unibas.ch

Associate Regional Editor for China
T.C.W. Mak
Department of Chemistry, University Science Centre,
The Chinese University of Hong Kong,
Shatin NT, Hong Kong, People's Republic of China
E-mail: tcwmak@cuhk.edu.hk

Polyhedron Reports
Editor
G. Christou *(Gainesville, FL, USA)*

Symposia-in-print
Editor
G. Parkin *(New York, NY, USA)*

Editorial Board
N.Y. Barba-Behrens *(Mexico, DF, Mexico)*
A.G. Blackman *(Dunedin, New Zealand)*
D.C. Bradley *(London, UK)*
D. Braga *(Bologna, Italy)*
A. Brodie *(Palmerston North, New Zealand)*
A. Castiñeiras *(Santiago de Compostela, Spain)*
M.H. Chisholm *(Columbus, OH, USA)*
E.C. Constable *(Basel, Switzerland)*
E. Coronado *(Valencia, Spain)*
W.J. Evans *(Irvine, CA, USA)*
M. Fujita *(Tokyo, Japan)*
L.H. Gade *(Heidelberg, Germany)*
C.D. Garner *(Nottingham, UK)*
L. Hubert-Pfalzgraf *(Villeurbanne, France)*
M.B. Hursthouse *(Southampton, UK)*
T. Kiss *(Szeged, Hungary)*
P.P. Power *(Davis, CA, USA)*
T.B. Rauchfuss *(Urbana, IL, USA)*
J. Reedijk *(Leiden, The Netherlands)*
A.L. Rheingold *(Newark, DE, USA)*
F.G.A. Stone *(Waco, TX, USA)*
A.G. Sykes *(Newcastle upon Tyne, UK)*
L.K. Thompson *(St John's, NF, Canada)*
M.D. Ward *(Sheffield, UK)*
R.E.P. Winpenny *(Manchester, UK)*
M. Zaworotko *(Tampa, FL, USA)*

Aims and Scope

Polyhedron will publish original, fundamental, experimental and theoretical work of the highest quality in all the major areas of inorganic chemistry. These include synthetic chemistry, coordination chemistry, organometallic chemistry, bioinorganic chemistry, and solid-state and materials chemistry. Papers should be complete pieces of work, and the inclusion of results from spectroscopic and/or physical techniques is encouraged. Papers merely reporting the preparation and X-ray structural characterization of only a single compound will not be considered appropriate unless the compound and its structure are particularly interesting.

Similarly, papers concerned solely with stability constants determined by potentiometric titration data unsupported by other e.g. spectroscopic techniques will not be acceptable nor will solvent extraction data unless supported by other data of interest to inorganic chemists. Unnecessary fragmentation of work is not acceptable.

In addition Polyhedron publishes specially commissioned review articles (Polyhedron Reports) and collections of original research papers (Polyhedron Symposia-in-Print) of appropriate timeliness.

Publication Information: Polyhedron (ISSN 0277-5387). For 2005, volume 24 is scheduled for publication. Subscription prices are available upon request from the Publisher or from the Regional Sales Office nearest you or from this journal's website (http://www.elsevier.com/locate/poly). Further information is available on this journal and other Elsevier products through Elsevier's website (http://www.elsevier.com). Subscriptions are accepted on a prepaid basis only and are entered on a calendar year basis. Issues are sent by standard mail (surface within Europe, air delivery outside Europe). Priority rates are available upon request. Claims for missing issues should be made within six months of the date of dispatch.

Orders, Claims and Journal Enquiries

(no manuscript enquiries)

Please contact the Customer Support Department at the Regional Sales Office nearest you:

Orlando
Elsevier
Customer Service Department
6277 Sea Harbor Drive
Orlando, FL 32887-4800
USA
Tel.: (877) 8397126 or (800) 6542452 [toll free numbers for US customers];
(+1) (407) 3454020 or
(+1) (407) 3454000 [customers outside US]
Fax: (+1) (407) 3631354 or
(+1) (407) 3639661
E-mail: usjcs@elsevier.com or elspcs@elsevier.com

Amsterdam
Elsevier
Customer Service Department
P.O. Box 211
1000 AE Amsterdam
The Netherlands
Tel.: (+31) 20-485-3757
Fax: (+31) 20-485-3432
E-mail: nlinfo-f@elsevier.com

Tokyo
Elsevier K.K.
Customer Service Department
4F Higashi-Azabu, 1-Chome Bldg
1-9-15 Higashi-Azabu
Minato-ku, Tokyo 106-0044
Japan
Tel.: (+81) 3-5561-5037
Fax: (+81) 3-5561-5047
E-mail: jp.info@elsevier.com

Singapore
Elsevier
Customer Service Department
3 Killiney Road
#08-01 Winsland House 1
Singapore 239519
Tel.: (+65) 6349-0222
Fax: (+65) 6733-1510
E-mail: asiainfo@elsevier.com

USA mailing notice: *Polyhedron* (ISSN 0277-5387) is published triweekly by Elsevier Ltd. (P.O. Box 211, 1000 AE Amsterdam, The Netherlands). Annual subscription price in the USA US$ 7049.00 (valid in North, Central and South America), including air speed delivery. Periodical postage rate is paid at Jamaica, NY 11431.
USA POSTMASTER: Send change of address to *Polyhedron*, Elsevier, 6277 Sea Harbor Drive, Orlando, FL 32887-4800.
AIRFREIGHT AND MAILING in the USA by Publications Expediting Inc., 200 Meacham Avenue, Elmont, NY 11003.

Advertising Information

Advertising orders and enquiries can be sent to: **South America:** Mr Tino DeCarlo, The Advertising Department, Elsevier Inc., 360 Park Avenue South, New York, NY 10010-1710, USA; tel.: (+1) (212) 633 3815; fax: (+1) (212) 633 3820; e-mail: t.decarlo@elsevier.com. **Europe, USA, Canada and ROW:** Miss Katrina Barton, Commercial Sales, Elsevier, 84 Theobald's Road, London, WCIX 8RR, UK; phone: (+44) (0) 20 7611 4117; fax: (+44) (0) 20 7611 4463; e-mail: commercialsales@elsevier.com

POLYHEDRON

The International Journal for Inorganic and Organometallic Chemistry

Executive Editors

The Americas
G. Christou
Department of Chemistry, University of Florida,
Gainesville, FL 32611-7200, USA
E-mail: christou@chem.ufl.edu

Rest of the world
C.E. Housecroft
Department of Chemistry, University of Basel,
Spitalstrasse 51, CH-4056 Basel, Switzerland
E-mail: poly-chemie@unibas.ch

Associate Regional Editor for China
T.C.W. Mak
Department of Chemistry, University Science Centre,
The Chinese University of Hong Kong,
Shatin NT, Hong Kong, People's Republic of China
E-mail: tcwmak@cuhk.edu.hk

Polyhedron Reports
Editor
G. Christou *(Gainesville, FL, USA)*

Symposia-in-print
Editor
G. Parkin *(New York, NY, USA)*

Editorial Board

N.Y. Barba-Behrens *(Mexico, DF, Mexico)*
A.G. Blackman *(Dunedin, New Zealand)*
D.C. Bradley *(London, UK)*
D. Braga *(Bologna, Italy)*
A. Brodie *(Palmerston North, New Zealand)*
A. Castiñeiras *(Santiago de Compostela, Spain)*
M.H. Chisholm *(Columbus, OH, USA)*
E.C. Constable *(Basel, Switzerland)*
E. Coronado *(Valencia, Spain)*
W.J. Evans *(Irvine, CA, USA)*
M. Fujita *(Tokyo, Japan)*
L.H. Gade *(Heidelberg, Germany)*
C.D. Garner *(Nottingham, UK)*
L. Hubert-Pfalzgraf *(Villeurbanne, France)*
M.B. Hursthouse *(Southampton, UK)*
T. Kiss *(Szeged, Hungary)*
P.P. Power *(Davis, CA, USA)*
T.B. Rauchfuss *(Urbana, IL, USA)*
J. Reedijk *(Leiden, The Netherlands)*
A.L. Rheingold *(Newark, DE, USA)*
F.G.A. Stone *(Waco, TX, USA)*
A.G. Sykes *(Newcastle upon Tyne, UK)*
L.K. Thompson *(St John's, NF, Canada)*
M.D. Ward *(Sheffield, UK)*
R.E.P. Winpenny *(Manchester, UK)*
M. Zaworotko *(Tampa, FL, USA)*

Aims and Scope

Polyhedron will publish original, fundamental, experimental and theoretical work of the highest quality in all the major areas of inorganic chemistry. These include synthetic chemistry, coordination chemistry, organometallic chemistry, bioinorganic chemistry, and solid-state and materials chemistry. Papers should be complete pieces of work, and the inclusion of results from spectroscopic and/or physical techniques is encouraged. Papers merely reporting the preparation and X-ray structural characterization of only a single compound will not be considered appropriate unless the compound and its structure are particularly interesting.

Similarly, papers concerned solely with stability constants determined by potentiometric titration data unsupported by other e.g. spectroscopic techniques will not be acceptable nor will solvent extraction data unless supported by other data of interest to inorganic chemists. Unnecessary fragmentation of work is not acceptable.

In addition Polyhedron publishes specially commissioned review articles (Polyhedron Reports) and collections of original research papers (Polyhedron Symposia-in-Print) of appropriate timeliness.

Publication Information: Polyhedron (ISSN 0277-5387). For 2005, volume 24 is scheduled for publication. Subscription prices are available upon request from the Publisher or from the Regional Sales Office nearest you or from this journal's website (http://www.elsevier.com/locate/poly). Further information is available on this journal and other Elsevier products through Elsevier's website (http://www.elsevier.com). Subscriptions are accepted on a prepaid basis only and are entered on a calendar year basis. Issues are sent by standard mail (surface within Europe, air delivery outside Europe). Priority rates are available upon request. Claims for missing issues should be made within six months of the date of dispatch.

Orders, Claims and Journal Enquiries

(no manuscript enquiries)

Please contact the Customer Support Department at the Regional Sales Office nearest you:

Orlando
Elsevier
Customer Service Department
6277 Sea Harbor Drive
Orlando, FL 32887-4800
USA
Tel.: (877) 8397126 or (800) 6542452 [toll free numbers for US customers];
(+1) (407) 3454020 or
(+1) (407) 3454000 [customers outside US]
Fax: (+1) (407) 3631354 or
(+1) (407) 3639661
E-mail: usjcs@elsevier.com or elspcs@elsevier.com

Amsterdam
Elsevier
Customer Service Department
P.O. Box 211
1000 AE Amsterdam
The Netherlands
Tel.: (+31) 20-485-3757
Fax: (+31) 20-485-3432
E-mail: nlinfo-f@elsevier.com

Tokyo
Elsevier K.K.
Customer Service Department
4F Higashi-Azabu, 1-Chome Bldg
1-9-15 Higashi-Azabu
Minato-ku, Tokyo 106-0044
Japan
Tel.: (+81) 3-5561-5037
Fax: (+81) 3-5561-5047
E-mail: jp.info@elsevier.com

Singapore
Elsevier
Customer Service Department
3 Killiney Road
#08-01 Winsland House 1
Singapore 239519
Tel.: (+65) 6349-0222
Fax: (+65) 6733-1510
E-mail: asiainfo@elsevier.com

USA mailing notice: *Polyhedron* (ISSN 0277-5387) is published triweekly by Elsevier Ltd. (P.O. Box 211, 1000 AE Amsterdam, The Netherlands). Annual subscription price in the USA US$ 7049.00 (valid in North, Central and South America), including air speed delivery. Periodical postage rate is paid at Jamaica, NY 11431.
USA POSTMASTER: Send change of address to *Polyhedron*, Elsevier, 6277 Sea Harbor Drive, Orlando, FL 32887-4800.
AIRFREIGHT AND MAILING in the USA by Publications Expediting Inc., 200 Meacham Avenue, Elmont, NY 11003.

Advertising Information

Advertising orders and enquiries can be sent to: **South America:** Mr Tino DeCarlo, The Advertising Department, Elsevier Inc., 360 Park Avenue South, New York, NY 10010-1710, USA; tel.: (+1) (212) 633 3815; fax: (+1) (212) 633 3820; e-mail: t.decarlo@elsevier.com. **Europe, USA, Canada and ROW:** Miss Katrina Barton, Commercial Sales, Elsevier, 84 Theobald's Road, London, WCIX 8RR, UK; phone: (+44) (0) 20 7611 4117; fax: (+44) (0) 20 7611 4463; e-mail: commercialsales@elsevier.com

POLYHEDRON

The International Journal for Inorganic and Organometallic Chemistry

Executive Editors

The Americas
G. Christou
Department of Chemistry, University of Florida,
Gainesville, FL 32611-7200, USA
E-mail: christou@chem.ufl.edu

Rest of the world
C.E. Housecroft
Department of Chemistry, University of Basel,
Spitalstrasse 51, CH-4056 Basel, Switzerland
E-mail: poly-chemie@unibas.ch

Associate Regional Editor for China
T.C.W. Mak
Department of Chemistry, University Science Centre,
The Chinese University of Hong Kong,
Shatin NT, Hong Kong, People's Republic of China
E-mail: tcwmak@cuhk.edu.hk

Polyhedron Reports
Editor
G. Christou *(Gainesville, FL, USA)*

Symposia-in-print
Editor
G. Parkin *(New York, NY, USA)*

Editorial Board
N.Y. Barba-Behrens *(Mexico, DF, Mexico)*
A.G. Blackman *(Dunedin, New Zealand)*
D.C. Bradley *(London, UK)*
D. Braga *(Bologna, Italy)*
A. Brodie *(Palmerston North, New Zealand)*
A. Castiñeiras *(Santiago de Compostela, Spain)*
M.H. Chisholm *(Columbus, OH, USA)*
E.C. Constable *(Basel, Switzerland)*
E. Coronado *(Valencia, Spain)*
W.J. Evans *(Irvine, CA, USA)*
M. Fujita *(Tokyo, Japan)*
L.H. Gade *(Heidelberg, Germany)*
C.D. Garner *(Nottingham, UK)*
L. Hubert-Pfalzgraf *(Villeurbanne, France)*
M.B. Hursthouse *(Southampton, UK)*
T. Kiss *(Szeged, Hungary)*
P.P. Power *(Davis, CA, USA)*
T.B. Rauchfuss *(Urbana, IL, USA)*
J. Reedijk *(Leiden, The Netherlands)*
A.L. Rheingold *(Newark, DE, USA)*
F.G.A. Stone *(Waco, TX, USA)*
A.G. Sykes *(Newcastle upon Tyne, UK)*
L.K. Thompson *(St John's, NF, Canada)*
M.D. Ward *(Sheffield, UK)*
R.E.P. Winpenny *(Manchester, UK)*
M. Zaworotko *(Tampa, FL, USA)*

Aims and Scope

Polyhedron will publish original, fundamental, experimental and theoretical work of the highest quality in all the major areas of inorganic chemistry. These include synthetic chemistry, coordination chemistry, organometallic chemistry, bioinorganic chemistry, and solid-state and materials chemistry. Papers should be complete pieces of work, and the inclusion of results from spectroscopic and/or physical techniques is encouraged. Papers merely reporting the preparation and X-ray structural characterization of only a single compound will not be considered appropriate unless the compound and its structure are particularly interesting.

Similarly, papers concerned solely with stability constants determined by potentiometric titration data unsupported by other e.g. spectroscopic techniques will not be acceptable nor will solvent extraction data unless supported by other data of interest to inorganic chemists. Unnecessary fragmentation of work is not acceptable.

In addition Polyhedron publishes specially commissioned review articles (Polyhedron Reports) and collections of original research papers (Polyhedron Symposia-in-Print) of appropriate timeliness.

Publication Information: Polyhedron (ISSN 0277-5387). For 2005, volume 24 is scheduled for publication. Subscription prices are available upon request from the Publisher or from the Regional Sales Office nearest you or from this journal's website (http://www.elsevier.com/locate/poly). Further information is available on this journal and other Elsevier products through Elsevier's website (http://www.elsevier.com). Subscriptions are accepted on a prepaid basis only and are entered on a calendar year basis. Issues are sent by standard mail (surface within Europe, air delivery outside Europe). Priority rates are available upon request. Claims for missing issues should be made within six months of the date of dispatch.

Orders, Claims and Journal Enquiries

(no manuscript enquiries)

Please contact the Customer Support Department at the Regional Sales Office nearest you:

Orlando
Elsevier
Customer Service Department
6277 Sea Harbor Drive
Orlando, FL 32887-4800
USA
Tel.: (877) 8397126 or (800) 6542452 [toll free numbers for US customers];
(+1) (407) 3454020 or
(+1) (407) 3454000 [customers outside US]
Fax: (+1) (407) 3631354 or
(+1) (407) 3639661
E-mail: usjcs@elsevier.com or elspcs@elsevier.com

Amsterdam
Elsevier
Customer Service Department
P.O. Box 211
1000 AE Amsterdam
The Netherlands
Tel.: (+31) 20-485-3757
Fax: (+31) 20-485-3432
E-mail: nlinfo-f@elsevier.com

Tokyo
Elsevier K.K.
Customer Service Department
4F Higashi-Azabu, 1-Chome Bldg
1-9-15 Higashi-Azabu
Minato-ku, Tokyo 106-0044
Japan
Tel.: (+81) 3-5561-5037
Fax: (+81) 3-5561-5047
E-mail: jp.info@elsevier.com

Singapore
Elsevier
Customer Service Department
3 Killiney Road
#08-01 Winsland House 1
Singapore 239519
Tel.: (+65) 6349-0222
Fax: (+65) 6733-1510
E-mail: asiainfo@elsevier.com

USA mailing notice: *Polyhedron* (ISSN 0277-5387) is published triweekly by Elsevier Ltd. (P.O. Box 211, 1000 AE Amsterdam, The Netherlands). Annual subscription price in the USA US$ 7049.00 (valid in North, Central and South America), including air speed delivery. Periodical postage rate is paid at Jamaica, NY 11431.
USA POSTMASTER: Send change of address to *Polyhedron*, Elsevier, 6277 Sea Harbor Drive, Orlando, FL 32887-4800.
AIRFREIGHT AND MAILING in the USA by Publications Expediting Inc., 200 Meacham Avenue, Elmont, NY 11003.

Advertising Information

Advertising orders and enquiries can be sent to: **South America:** Mr Tino DeCarlo, The Advertising Department, Elsevier Inc., 360 Park Avenue South, New York, NY 10010-1710, USA; tel.: (+1) (212) 633 3815; fax: (+1) (212) 633 3820; e-mail: t.decarlo@elsevier.com. **Europe, USA, Canada and ROW:** Miss Katrina Barton, Commercial Sales, Elsevier, 84 Theobald's Road, London, WCIX 8RR, UK; phone: (+44) (0) 20 7611 4117; fax: (+44) (0) 20 7611 4463; e-mail: commercialsales@elsevier.com

POLYHEDRON

The International Journal for Inorganic and Organometallic Chemistry

Executive Editors

The Americas
G. Christou
Department of Chemistry, University of Florida,
Gainesville, FL 32611-7200, USA
E-mail: christou@chem.ufl.edu

Rest of the world
C.E. Housecroft
Department of Chemistry, University of Basel,
Spitalstrasse 51, CH-4056 Basel, Switzerland
E-mail: poly-chemie@unibas.ch

Associate Regional Editor for China
T.C.W. Mak
Department of Chemistry, University Science Centre,
The Chinese University of Hong Kong,
Shatin NT, Hong Kong, People's Republic of China
E-mail: tcwmak@cuhk.edu.hk

Polyhedron Reports
Editor
G. Christou *(Gainesville, FL, USA)*

Symposia-in-print
Editor
G. Parkin *(New York, NY, USA)*

Editorial Board
N.Y. Barba-Behrens *(Mexico, DF, Mexico)*
A.G. Blackman *(Dunedin, New Zealand)*
D.C. Bradley *(London, UK)*
D. Braga *(Bologna, Italy)*
A. Brodie *(Palmerston North, New Zealand)*
A. Castiñeiras *(Santiago de Compostela, Spain)*
M.H. Chisholm *(Columbus, OH, USA)*
E.C. Constable *(Basel, Switzerland)*
E. Coronado *(Valencia, Spain)*
W.J. Evans *(Irvine, CA, USA)*
M. Fujita *(Tokyo, Japan)*
L.H. Gade *(Heidelberg, Germany)*
C.D. Garner *(Nottingham, UK)*
L. Hubert-Pfalzgraf *(Villeurbanne, France)*
M.B. Hursthouse *(Southampton, UK)*
T. Kiss *(Szeged, Hungary)*
P.P. Power *(Davis, CA, USA)*
T.B. Rauchfuss *(Urbana, IL, USA)*
J. Reedijk *(Leiden, The Netherlands)*
A.L. Rheingold *(Newark, DE, USA)*
F.G.A. Stone *(Waco, TX, USA)*
A.G. Sykes *(Newcastle upon Tyne, UK)*
L.K. Thompson *(St John's, NF, Canada)*
M.D. Ward *(Sheffield, UK)*
R.E.P. Winpenny *(Manchester, UK)*
M. Zaworotko *(Tampa, FL, USA)*

Aims and Scope

Polyhedron will publish original, fundamental, experimental and theoretical work of the highest quality in all the major areas of inorganic chemistry. These include synthetic chemistry, coordination chemistry, organometallic chemistry, bioinorganic chemistry, and solid-state and materials chemistry. Papers should be complete pieces of work, and the inclusion of results from spectroscopic and/or physical techniques is encouraged. Papers merely reporting the preparation and X-ray structural characterization of only a single compound will not be considered appropriate unless the compound and its structure are particularly interesting.

Similarly, papers concerned solely with stability constants determined by potentiometric titration data unsupported by other e.g. spectroscopic techniques will not be acceptable nor will solvent extraction data unless supported by other data of interest to inorganic chemists. Unnecessary fragmentation of work is not acceptable.

In addition Polyhedron publishes specially commissioned review articles (Polyhedron Reports) and collections of original research papers (Polyhedron Symposia-in-Print) of appropriate timeliness.

Publication Information: Polyhedron (ISSN 0277-5387). For 2005, volume 24 is scheduled for publication. Subscription prices are available upon request from the Publisher or from the Regional Sales Office nearest you or from this journal's website (http://www.elsevier.com/locate/poly). Further information is available on this journal and other Elsevier products through Elsevier's website (http://www.elsevier.com). Subscriptions are accepted on a prepaid basis only and are entered on a calendar year basis. Issues are sent by standard mail (surface within Europe, air delivery outside Europe). Priority rates are available upon request. Claims for missing issues should be made within six months of the date of dispatch.

Orders, Claims and Journal Enquiries

(no manuscript enquiries)

Please contact the Customer Support Department at the Regional Sales Office nearest you:

Orlando
Elsevier
Customer Service Department
6277 Sea Harbor Drive
Orlando, FL 32887-4800
USA
Tel.: (877) 8397126 or (800) 6542452 [toll free numbers for US customers];
(+1) (407) 3454020 or
(+1) (407) 3454000 [customers outside US]
Fax: (+1) (407) 3631354 or
(+1) (407) 3639661
E-mail: usjcs@elsevier.com or elspcs@elsevier.com

Amsterdam
Elsevier
Customer Service Department
P.O. Box 211
1000 AE Amsterdam
The Netherlands
Tel.: (+31) 20-485-3757
Fax: (+31) 20-485-3432
E-mail: nlinfo-f@elsevier.com

Tokyo
Elsevier K.K.
Customer Service Department
4F Higashi-Azabu, 1-Chome Bldg
1-9-15 Higashi-Azabu
Minato-ku, Tokyo 106-0044
Japan
Tel.: (+81) 3-5561-5037
Fax: (+81) 3-5561-5047
E-mail: jp.info@elsevier.com

Singapore
Elsevier
Customer Service Department
3 Killiney Road
#08-01 Winsland House 1
Singapore 239519
Tel.: (+65) 6349-0222
Fax: (+65) 6733-1510
E-mail: asiainfo@elsevier.com

USA mailing notice: *Polyhedron* (ISSN 0277-5387) is published triweekly by Elsevier Ltd. (P.O. Box 211, 1000 AE Amsterdam, The Netherlands). Annual subscription price in the USA US$ 7049.00 (valid in North, Central and South America), including air speed delivery. Periodical postage rate is paid at Jamaica, NY 11431.
USA POSTMASTER: Send change of address to *Polyhedron*, Elsevier, 6277 Sea Harbor Drive, Orlando, FL 32887-4800.
AIRFREIGHT AND MAILING in the USA by Publications Expediting Inc., 200 Meacham Avenue, Elmont, NY 11003.

Advertising Information

Advertising orders and enquiries can be sent to: **South America:** Mr Tino DeCarlo, The Advertising Department, Elsevier Inc., 360 Park Avenue South, New York, NY 10010-1710, USA; tel.: (+1) (212) 633 3815; fax: (+1) (212) 633 3820; e-mail: t.decarlo@elsevier.com. **Europe, USA, Canada and ROW:** Miss Katrina Barton, Commercial Sales, Elsevier, 84 Theobald's Road, London, WCIX 8RR, UK; phone: (+44) (0) 20 7611 4117; fax: (+44) (0) 20 7611 4463; e-mail: commercialsales@elsevier.com

POLYHEDRON

The International Journal for Inorganic and Organometallic Chemistry

Executive Editors

The Americas
G. Christou
Department of Chemistry, University of Florida,
Gainesville, FL 32611-7200, USA
E-mail: christou@chem.ufl.edu

Rest of the world
C.E. Housecroft
Department of Chemistry, University of Basel,
Spitalstrasse 51, CH-4056 Basel, Switzerland
E-mail: poly-chemie@unibas.ch

Associate Regional Editor for China
T.C.W. Mak
Department of Chemistry, University Science Centre,
The Chinese University of Hong Kong,
Shatin NT, Hong Kong, People's Republic of China
E-mail: tcwmak@cuhk.edu.hk

Polyhedron Reports
Editor
G. Christou *(Gainesville, FL, USA)*

Symposia-in-print
Editor
G. Parkin *(New York, NY, USA)*

Editorial Board
N.Y. Barba-Behrens *(Mexico, DF, Mexico)*
A.G. Blackman *(Dunedin, New Zealand)*
D.C. Bradley *(London, UK)*
D. Braga *(Bologna, Italy)*
A. Brodie *(Palmerston North, New Zealand)*
A. Castiñeiras *(Santiago de Compostela, Spain)*
M.H. Chisholm *(Columbus, OH, USA)*
E.C. Constable *(Basel, Switzerland)*
E. Coronado *(Valencia, Spain)*
W.J. Evans *(Irvine, CA, USA)*
M. Fujita *(Tokyo, Japan)*
L.H. Gade *(Heidelberg, Germany)*
C.D. Garner *(Nottingham, UK)*
L. Hubert-Pfalzgraf *(Villeurbanne, France)*
M.B. Hursthouse *(Southampton, UK)*
T. Kiss *(Szeged, Hungary)*
P.P. Power *(Davis, CA, USA)*
T.B. Rauchfuss *(Urbana, IL, USA)*
J. Reedijk *(Leiden, The Netherlands)*
A.L. Rheingold *(Newark, DE, USA)*
F.G.A. Stone *(Waco, TX, USA)*
A.G. Sykes *(Newcastle upon Tyne, UK)*
L.K. Thompson *(St John's, NF, Canada)*
M.D. Ward *(Sheffield, UK)*
R.E.P. Winpenny *(Manchester, UK)*
M. Zaworotko *(Tampa, FL, USA)*

Aims and Scope

Polyhedron will publish original, fundamental, experimental and theoretical work of the highest quality in all the major areas of inorganic chemistry. These include synthetic chemistry, coordination chemistry, organometallic chemistry, bioinorganic chemistry, and solid-state and materials chemistry. Papers should be complete pieces of work, and the inclusion of results from spectroscopic and/or physical techniques is encouraged. Papers merely reporting the preparation and X-ray structural characterization of only a single compound will not be considered appropriate unless the compound and its structure are particularly interesting.

Similarly, papers concerned solely with stability constants determined by potentiometric titration data unsupported by other e.g. spectroscopic techniques will not be acceptable nor will solvent extraction data unless supported by other data of interest to inorganic chemists. Unnecessary fragmentation of work is not acceptable.

In addition Polyhedron publishes specially commissioned review articles (Polyhedron Reports) and collections of original research papers (Polyhedron Symposia-in-Print) of appropriate timeliness.

Publication Information: Polyhedron (ISSN 0277-5387). For 2005, volume 24 is scheduled for publication. Subscription prices are available upon request from the Publisher or from the Regional Sales Office nearest you or from this journal's website (http://www.elsevier.com/locate/poly). Further information is available on this journal and other Elsevier products through Elsevier's website (http://www.elsevier.com). Subscriptions are accepted on a prepaid basis only and are entered on a calendar year basis. Issues are sent by standard mail (surface within Europe, air delivery outside Europe). Priority rates are available upon request. Claims for missing issues should be made within six months of the date of dispatch.

Orders, Claims and Journal Enquiries

(no manuscript enquiries)

Please contact the Customer Support Department at the Regional Sales Office nearest you:

Orlando
Elsevier
Customer Service Department
6277 Sea Harbor Drive
Orlando, FL 32887-4800
USA
Tel.: (877) 8397126 or (800) 6542452 [toll free numbers for US customers];
(+1) (407) 3454020 or
(+1) (407) 3454000 [customers outside US]
Fax: (+1) (407) 3631354 or
(+1) (407) 3639661
E-mail: usjcs@elsevier.com or elspcs@elsevier.com

Amsterdam
Elsevier
Customer Service Department
P.O. Box 211
1000 AE Amsterdam
The Netherlands
Tel.: (+31) 20-485-3757
Fax: (+31) 20-485-3432
E-mail: nlinfo-f@elsevier.com

Tokyo
Elsevier K.K.
Customer Service Department
4F Higashi-Azabu, 1-Chome Bldg
1-9-15 Higashi-Azabu
Minato-ku, Tokyo 106-0044
Japan
Tel.: (+81) 3-5561-5037
Fax: (+81) 3-5561-5047
E-mail: jp.info@elsevier.com

Singapore
Elsevier
Customer Service Department
3 Killiney Road
#08-01 Winsland House 1
Singapore 239519
Tel.: (+65) 6349-0222
Fax: (+65) 6733-1510
E-mail: asiainfo@elsevier.com

USA mailing notice: *Polyhedron* (ISSN 0277-5387) is published triweekly by Elsevier Ltd. (P.O. Box 211, 1000 AE Amsterdam, The Netherlands). Annual subscription price in the USA US$ 7049.00 (valid in North, Central and South America), including air speed delivery. Periodical postage rate is paid at Jamaica, NY 11431.
USA POSTMASTER: Send change of address to *Polyhedron*, Elsevier, 6277 Sea Harbor Drive, Orlando, FL 32887-4800.
AIRFREIGHT AND MAILING in the USA by Publications Expediting Inc., 200 Meacham Avenue, Elmont, NY 11003.

Advertising Information

Advertising orders and enquiries can be sent to: **South America:** Mr Tino DeCarlo, The Advertising Department, Elsevier Inc., 360 Park Avenue South, New York, NY 10010-1710, USA; tel.: (+1) (212) 633 3815; fax: (+1) (212) 633 3820; e-mail: t.decarlo@elsevier.com. **Europe, USA, Canada and ROW:** Miss Katrina Barton, Commercial Sales, Elsevier, 84 Theobald's Road, London, WCIX 8RR, UK; phone: (+44) (0) 20 7611 4117; fax: (+44) (0) 20 7611 4463; e-mail: commercialsales@elsevier.com

POLYHEDRON

The International Journal for Inorganic and Organometallic Chemistry

Executive Editors

The Americas
G. Christou
Department of Chemistry, University of Florida,
Gainesville, FL 32611-7200, USA
E-mail: christou@chem.ufl.edu

Rest of the world
C.E. Housecroft
Department of Chemistry, University of Basel,
Spitalstrasse 51, CH-4056 Basel, Switzerland
E-mail: poly-chemie@unibas.ch

Associate Regional Editor for China
T.C.W. Mak
Department of Chemistry, University Science Centre,
The Chinese University of Hong Kong,
Shatin NT, Hong Kong, People's Republic of China
E-mail: tcwmak@cuhk.edu.hk

Polyhedron Reports
Editor
G. Christou *(Gainesville, FL, USA)*

Symposia-in-print
Editor
G. Parkin *(New York, NY, USA)*

Editorial Board
N.Y. Barba-Behrens *(Mexico, DF, Mexico)*
A.G. Blackman *(Dunedin, New Zealand)*
D.C. Bradley *(London, UK)*
D. Braga *(Bologna, Italy)*
A. Brodie *(Palmerston North, New Zealand)*
A. Castiñeiras *(Santiago de Compostela, Spain)*
M.H. Chisholm *(Columbus, OH, USA)*
E.C. Constable *(Basel, Switzerland)*
E. Coronado *(Valencia, Spain)*
W.J. Evans *(Irvine, CA, USA)*
M. Fujita *(Tokyo, Japan)*
L.H. Gade *(Heidelberg, Germany)*
C.D. Garner *(Nottingham, UK)*
L. Hubert-Pfalzgraf *(Villeurbanne, France)*
M.B. Hursthouse *(Southampton, UK)*
T. Kiss *(Szeged, Hungary)*
P.P. Power *(Davis, CA, USA)*
T.B. Rauchfuss *(Urbana, IL, USA)*
J. Reedijk *(Leiden, The Netherlands)*
A.L. Rheingold *(Newark, DE, USA)*
F.G.A. Stone *(Waco, TX, USA)*
A.G. Sykes *(Newcastle upon Tyne, UK)*
L.K. Thompson *(St John's, NF, Canada)*
M.D. Ward *(Sheffield, UK)*
R.E.P. Winpenny *(Manchester, UK)*
M. Zaworotko *(Tampa, FL, USA)*

Aims and Scope

Polyhedron will publish original, fundamental, experimental and theoretical work of the highest quality in all the major areas of inorganic chemistry. These include synthetic chemistry, coordination chemistry, organometallic chemistry, bioinorganic chemistry, and solid-state and materials chemistry. Papers should be complete pieces of work, and the inclusion of results from spectroscopic and/or physical techniques is encouraged. Papers merely reporting the preparation and X-ray structural characterization of only a single compound will not be considered appropriate unless the compound and its structure are particularly interesting.

Similarly, papers concerned solely with stability constants determined by potentiometric titration data unsupported by other e.g. spectroscopic techniques will not be acceptable nor will solvent extraction data unless supported by other data of interest to inorganic chemists. Unnecessary fragmentation of work is not acceptable.

In addition Polyhedron publishes specially commissioned review articles (Polyhedron Reports) and collections of original research papers (Polyhedron Symposia-in-Print) of appropriate timeliness.

Publication Information: Polyhedron (ISSN 0277-5387). For 2005, volume 24 is scheduled for publication. Subscription prices are available upon request from the Publisher or from the Regional Sales Office nearest you or from this journal's website (http://www.elsevier.com/locate/poly). Further information is available on this journal and other Elsevier products through Elsevier's website (http://www.elsevier.com). Subscriptions are accepted on a prepaid basis only and are entered on a calendar year basis. Issues are sent by standard mail (surface within Europe, air delivery outside Europe). Priority rates are available upon request. Claims for missing issues should be made within six months of the date of dispatch.

Orders, Claims and Journal Enquiries

(no manuscript enquiries)

Please contact the Customer Support Department at the Regional Sales Office nearest you:

Orlando
Elsevier
Customer Service Department
6277 Sea Harbor Drive
Orlando
FL 32887-4800
USA
Tel.: 877-8397126 or 800-6542452
[Toll free numbers for US customers];
(+1) 407-3454020 or (+1) 407-3454000
[customers outside US]
Fax: (+1) 407-3631354
or (+1) 407-3639661
E-mail: usjcs@elsevier.com
or elspcs@elsevier.com

Amsterdam
Elsevier
Customer Service Department
P.O. Box 211
1000 AE Amsterdam
The Netherlands
Tel.: (+31) 20-485-3757
Fax: (+31) 20-485-3432
E-mail: nlinfo-f@elsevier.com

Tokyo
Elsevier K.K.
Customer Service Department
4F Higashi-Azabu, 1-Chome Bldg
1-9-15 Higashi-Azabu
Minato-ku, Tokyo 106-0044
Japan
Tel.: (+81) 3-5561-5037
Fax: (+81) 3-5561-5047
E-mail: jp.info@elsevier.com

Singapore
Elsevier
Customer Service Department
3 Killiney Road
#08-01 Winsland House 1
Singapore 239519
Tel.: (+65) 6349-0222
Fax: (+65) 6733-1510
E-mail: asiainfo@elsevier.com

USA mailing notice: *Polyhedron* (ISSN 0277-5387) is published triweekly by Elsevier Ltd. (P.O. Box 211, 1000 AE Amsterdam, The Netherlands). Annual subscription price in the USA US$ 7049.00 (valid in North, Central and South America), including air speed delivery. Periodical postage rate is paid at Jamaica, NY 11431.
USA POSTMASTER: Send change of address to *Polyhedron*, Elsevier, 6277 Sea Harbor Drive, Orlando, FL 32887-4800.
AIRFREIGHT AND MAILING in the USA by Publications Expediting Inc., 200 Meacham Avenue, Elmont, NY 11003.

Advertising Information

Advertising orders and enquiries can be sent to: **South America:** Mr Tino DeCarlo, The Advertising Department, Elsevier Inc., 360 Park Avenue South, New York, NY 10010-1710, USA; tel.: (+1) (212) 633 3815; fax: (+1) (212) 633 3820; e-mail: t.decarlo@elsevier.com. **Europe, USA, Canada and ROW:** Miss Katrina Barton, Commercial Sales, Elsevier, 84 Theobald's Road, London, WCIX 8RR, UK; phone: (+44) (0) 20 7611 4117; fax: (+44) (0) 20 7611 4463; e-mail: commercialsales@elsevier.com

POLYHEDRON

The International Journal for Inorganic and Organometallic Chemistry

Executive Editors

The Americas
G. Christou
Department of Chemistry, University of Florida,
Gainesville, FL 32611-7200, USA
E-mail: christou@chem.ufl.edu

Rest of the world
C.E. Housecroft
Department of Chemistry, University of Basel,
Spitalstrasse 51, CH-4056 Basel, Switzerland
E-mail: poly-chemie@unibas.ch

Associate Regional Editor for China
T.C.W. Mak
Department of Chemistry, University Science Centre,
The Chinese University of Hong Kong,
Shatin NT, Hong Kong, People's Republic of China
E-mail: tcwmak@cuhk.edu.hk

Polyhedron Reports
Editor
G. Christou *(Gainesville, FL, USA)*

Symposia-in-print
Editor
G. Parkin *(New York, NY, USA)*

Editorial Board
N.Y. Barba-Behrens *(Mexico, DF, Mexico)*
A.G. Blackman *(Dunedin, New Zealand)*
D.C. Bradley *(London, UK)*
D. Braga *(Bologna, Italy)*
A. Brodie *(Palmerston North, New Zealand)*
A. Castiñeiras *(Santiago de Compostela, Spain)*
M.H. Chisholm *(Columbus, OH, USA)*
E.C. Constable *(Basel, Switzerland)*
E. Coronado *(Valencia, Spain)*
W.J. Evans *(Irvine, CA, USA)*
M. Fujita *(Tokyo, Japan)*
L.H. Gade *(Heidelberg, Germany)*
C.D. Garner *(Nottingham, UK)*
L. Hubert-Pfalzgraf *(Villeurbanne, France)*
M.B. Hursthouse *(Southampton, UK)*
T. Kiss *(Szeged, Hungary)*
P.P. Power *(Davis, CA, USA)*
T.B. Rauchfuss *(Urbana, IL, USA)*
J. Reedijk *(Leiden, The Netherlands)*
A.L. Rheingold *(Newark, DE, USA)*
F.G.A. Stone *(Waco, TX, USA)*
A.G. Sykes *(Newcastle upon Tyne, UK)*
L.K. Thompson *(St John's, NF, Canada)*
M.D. Ward *(Sheffield, UK)*
R.E.P. Winpenny *(Manchester, UK)*
M. Zaworotko *(Tampa, FL, USA)*

Aims and Scope

Polyhedron will publish original, fundamental, experimental and theoretical work of the highest quality in all the major areas of inorganic chemistry. These include synthetic chemistry, coordination chemistry, organometallic chemistry, bioinorganic chemistry, and solid-state and materials chemistry. Papers should be complete pieces of work, and the inclusion of results from spectroscopic and/or physical techniques is encouraged. Papers merely reporting the preparation and X-ray structural characterization of only a single compound will not be considered appropriate unless the compound and its structure are particularly interesting.

Similarly, papers concerned solely with stability constants determined by potentiometric titration data unsupported by other e.g. spectroscopic techniques will not be acceptable nor will solvent extraction data unless supported by other data of interest to inorganic chemists. Unnecessary fragmentation of work is not acceptable.

In addition Polyhedron publishes specially commissioned review articles (Polyhedron Reports) and collections of original research papers (Polyhedron Symposia-in-Print) of appropriate timeliness.

Publication Information: Polyhedron (ISSN 0277-5387). For 2005, volume 24 is scheduled for publication. Subscription prices are available upon request from the Publisher or from the Regional Sales Office nearest you or from this journal's website (http://www.elsevier.com/locate/poly). Further information is available on this journal and other Elsevier products through Elsevier's website (http://www.elsevier.com). Subscriptions are accepted on a prepaid basis only and are entered on a calendar year basis. Issues are sent by standard mail (surface within Europe, air delivery outside Europe). Priority rates are available upon request. Claims for missing issues should be made within six months of the date of dispatch.

Orders, Claims and Journal Enquiries

(no manuscript enquiries)
Please contact the Customer Support Department at the Regional Sales Office nearest you:

Orlando
Elsevier
Customer Service Department
6277 Sea Harbor Drive
Orlando
FL 32887-4800
USA
Tel.: (+1) 877-8397126
[Toll free number for US customers], or
(+1) 407-3454020
[customers outside US]
Fax: (+1) 407-3631354
E-mail: usjcs@elsevier.com

Amsterdam
Elsevier
Customer Service Department
P.O. Box 211
1000 AE Amsterdam
The Netherlands
Tel.: (+31) 20-485-3757
Fax: (+31) 20-485-3432
E-mail: nlinfo-f@elsevier.com

Tokyo
Elsevier K.K.
Customer Service Department
4F Higashi-Azabu, 1-Chome Bldg
1-9-15 Higashi-Azabu
Minato-ku, Tokyo 106-0044
Japan
Tel.: (+81) 3-5561-5037
Fax: (+81) 3-5561-5047
E-mail: jp.info@elsevier.com

Singapore
Elsevier
Customer Service Department
3 Killiney Road
#08-01 Winsland House 1
Singapore 239519
Tel.: (+65) 6349-0222
Fax: (+65) 6733-1510
E-mail: asiainfo@elsevier.com

USA mailing notice: *Polyhedron* (ISSN 0277-5387) is published triweekly by Elsevier Ltd. (P.O. Box 211, 1000 AE Amsterdam, The Netherlands). Annual subscription price in the USA US$ 7049.00 (valid in North, Central and South America), including air speed delivery. Periodical postage rate is paid at Jamaica, NY 11431.
USA POSTMASTER: Send address changes to *Polyhedron*, Publications Expediting Inc., 200 Meacham Avenue, Elmont, NY 11003.
AIRFREIGHT AND MAILING in the USA by Publications Expediting Inc., 200 Meacham Avenue, Elmont, NY 11003.

Advertising Information

Advertising orders and enquiries can be sent to: **South America:** Mr Tino DeCarlo, The Advertising Department, Elsevier Inc., 360 Park Avenue South, New York, NY 10010-1710, USA; tel.: (+1) (212) 633 3815; fax: (+1) (212) 633 3820; e-mail: t.decarlo@elsevier.com. **Europe, USA, Canada and ROW:** Miss Katrina Barton, Commercial Sales, Elsevier, 84 Theobald's Road, London, WCIX 8RR, UK; phone: (+44) (0) 20 7611 4117; fax: (+44) (0) 20 7611 4463; e-mail: commercialsales@elsevier.com

POLYHEDRON

The International Journal for Inorganic and Organometallic Chemistry

Executive Editors

The Americas
G. Christou
Department of Chemistry, University of Florida,
Gainesville, FL 32611-7200, USA
E-mail: christou@chem.ufl.edu

Rest of the world
C.E. Housecroft
Department of Chemistry, University of Basel,
Spitalstrasse 51, CH-4056 Basel, Switzerland
E-mail: poly-chemie@unibas.ch

Associate Regional Editor for China
T.C.W. Mak
Department of Chemistry, University Science Centre,
The Chinese University of Hong Kong,
Shatin NT, Hong Kong, People's Republic of China
E-mail: tcwmak@cuhk.edu.hk

Polyhedron Reports
Editor
G. Christou *(Gainesville, FL, USA)*

Symposia-in-print
Editor
G. Parkin *(New York, NY, USA)*

Editorial Board
N.Y. Barba-Behrens *(Mexico, DF, Mexico)*
A.G. Blackman *(Dunedin, New Zealand)*
D.C. Bradley *(London, UK)*
D. Braga *(Bologna, Italy)*
A. Brodie *(Palmerston North, New Zealand)*
A. Castiñeiras *(Santiago de Compostela, Spain)*
M.H. Chisholm *(Columbus, OH, USA)*
E.C. Constable *(Basel, Switzerland)*
E. Coronado *(Valencia, Spain)*
W.J. Evans *(Irvine, CA, USA)*
M. Fujita *(Tokyo, Japan)*
L.H. Gade *(Heidelberg, Germany)*
C.D. Garner *(Nottingham, UK)*
L. Hubert-Pfalzgraf *(Villeurbanne, France)*
M.B. Hursthouse *(Southampton, UK)*
T. Kiss *(Szeged, Hungary)*
P.P. Power *(Davis, CA, USA)*
T.B. Rauchfuss *(Urbana, IL, USA)*
J. Reedijk *(Leiden, The Netherlands)*
A.L. Rheingold *(Newark, DE, USA)*
F.G.A. Stone *(Waco, TX, USA)*
A.G. Sykes *(Newcastle upon Tyne, UK)*
L.K. Thompson *(St John's, NF, Canada)*
M.D. Ward *(Sheffield, UK)*
R.E.P. Winpenny *(Manchester, UK)*
M. Zaworotko *(Tampa, FL, USA)*

Aims and Scope

Polyhedron will publish original, fundamental, experimental and theoretical work of the highest quality in all the major areas of inorganic chemistry. These include synthetic chemistry, coordination chemistry, organometallic chemistry, bioinorganic chemistry, and solid-state and materials chemistry. Papers should be complete pieces of work, and the inclusion of results from spectroscopic and/or physical techniques is encouraged. Papers merely reporting the preparation and X-ray structural characterization of only a single compound will not be considered appropriate unless the compound and its structure are particularly interesting.
Similarly, papers concerned solely with stability constants determined by potentiometric titration data unsupported by other e.g. spectroscopic techniques will not be acceptable nor will solvent extraction data unless supported by other data of interest to inorganic chemists. Unnecessary fragmentation of work is not acceptable.
In addition Polyhedron publishes specially commissioned review articles (Polyhedron Reports) and collections of original research papers (Polyhedron Symposia-in-Print) of appropriate timeliness.

Publication Information: Polyhedron (ISSN 0277-5387). For 2005, volume 24 is scheduled for publication. Subscription prices are available upon request from the Publisher or from the Regional Sales Office nearest you or from this journal's website (http://www.elsevier.com/locate/poly). Further information is available on this journal and other Elsevier products through Elsevier's website (http://www.elsevier.com). Subscriptions are accepted on a prepaid basis only and are entered on a calendar year basis. Issues are sent by standard mail (surface within Europe, air delivery outside Europe). Priority rates are available upon request. Claims for missing issues should be made within six months of the date of dispatch.

Orders, Claims and Journal Enquiries

(no manuscript enquiries)
Please contact the Customer Support Department at the Regional Sales Office nearest you:

Orlando
Elsevier
Customer Service Department
6277 Sea Harbor Drive
Orlando
FL 32887-4800
USA
Tel.: (+1) 877-8397126
[Toll free number for US customers], or
(+1) 407-3454020
[customers outside US]
Fax: (+1) 407-3631354
E-mail: usjcs@elsevier.com

Amsterdam
Elsevier
Customer Service Department
P.O. Box 211
1000 AE Amsterdam
The Netherlands
Tel.: (+31) 20-485-3757
Fax: (+31) 20-485-3432
E-mail: nlinfo-f@elsevier.com

Tokyo
Elsevier K.K.
Customer Service Department
4F Higashi-Azabu, 1-Chome Bldg
1-9-15 Higashi-Azabu
Minato-ku, Tokyo 106-0044
Japan
Tel.: (+81) 3-5561-5037
Fax: (+81) 3-5561-5047
E-mail: jp.info@elsevier.com

Singapore
Elsevier
Customer Service Department
3 Killiney Road
#08-01 Winsland House 1
Singapore 239519
Tel.: (+65) 6349-0222
Fax: (+65) 6733-1510
E-mail: asiainfo@elsevier.com

USA mailing notice: *Polyhedron* (ISSN 0277-5387) is published triweekly by Elsevier Ltd. (P.O. Box 211, 1000 AE Amsterdam, The Netherlands). Annual subscription price in the USA US$ 7049.00 (valid in North, Central and South America), including air speed delivery. Periodical postage rate is paid at Jamaica, NY 11431.
USA POSTMASTER: Send address changes to *Polyhedron*, Publications Expediting Inc., 200 Meacham Avenue, Elmont, NY 11003.
AIRFREIGHT AND MAILING in the USA by Publications Expediting Inc., 200 Meacham Avenue, Elmont, NY 11003.

Advertising Information

Advertising orders and enquiries can be sent to: **South America:** Mr Tino DeCarlo, The Advertising Department, Elsevier Inc., 360 Park Avenue South, New York, NY 10010-1710, USA; tel.: (+1) (212) 633 3815; fax: (+1) (212) 633 3820; e-mail: t.decarlo@elsevier.com. **Europe, USA, Canada and ROW:** Miss Katrina Barton, Commercial Sales, Elsevier, 84 Theobald's Road, London, WCIX 8RR, UK; phone: (+44) (0) 20 7611 4117; fax: (+44) (0) 20 7611 4463; e-mail: commercialsales@elsevier.com

POLYHEDRON

The International Journal for Inorganic and Organometallic Chemistry

Executive Editors

The Americas
G. Christou
Department of Chemistry, University of Florida,
Gainesville, FL 32611-7200, USA
E-mail: christou@chem.ufl.edu

Rest of the world
C.E. Housecroft
Department of Chemistry, University of Basel,
Spitalstrasse 51, CH-4056 Basel, Switzerland
E-mail: poly-chemie@unibas.ch

Associate Regional Editor for China
T.C.W. Mak
Department of Chemistry, University Science Centre,
The Chinese University of Hong Kong,
Shatin NT, Hong Kong, People's Republic of China
E-mail: tcwmak@cuhk.edu.hk

Polyhedron Reports
Editor
G. Christou *(Gainesville, FL, USA)*

Symposia-in-print
Editor
G. Parkin *(New York, NY, USA)*

Editorial Board
N.Y. Barba-Behrens *(Mexico, DF, Mexico)*
A.G. Blackman *(Dunedin, New Zealand)*
D.C. Bradley *(London, UK)*
D. Braga *(Bologna, Italy)*
A. Brodie *(Palmerston North, New Zealand)*
A. Castiñeiras *(Santiago de Compostela, Spain)*
M.H. Chisholm *(Columbus, OH, USA)*
E.C. Constable *(Basel, Switzerland)*
E. Coronado *(Valencia, Spain)*
W.J. Evans *(Irvine, CA, USA)*
M. Fujita *(Tokyo, Japan)*
L.H. Gade *(Heidelberg, Germany)*
C.D. Garner *(Nottingham, UK)*
L. Hubert-Pfalzgraf *(Villeurbanne, France)*
M.B. Hursthouse *(Southampton, UK)*
T. Kiss *(Szeged, Hungary)*
P.P. Power *(Davis, CA, USA)*
T.B. Rauchfuss *(Urbana, IL, USA)*
J. Reedijk *(Leiden, The Netherlands)*
A.L. Rheingold *(Newark, DE, USA)*
F.G.A. Stone *(Waco, TX, USA)*
A.G. Sykes *(Newcastle upon Tyne, UK)*
L.K. Thompson *(St John's, NF, Canada)*
M.D. Ward *(Sheffield, UK)*
R.E.P. Winpenny *(Manchester, UK)*
M. Zaworotko *(Tampa, FL, USA)*

Aims and Scope

Polyhedron will publish original, fundamental, experimental and theoretical work of the highest quality in all the major areas of inorganic chemistry. These include synthetic chemistry, coordination chemistry, organometallic chemistry, bioinorganic chemistry, and solid-state and materials chemistry. Papers should be complete pieces of work, and the inclusion of results from spectroscopic and/or physical techniques is encouraged. Papers merely reporting the preparation and X-ray structural characterization of only a single compound will not be considered appropriate unless the compound and its structure are particularly interesting.

Similarly, papers concerned solely with stability constants determined by potentiometric titration data unsupported by other e.g. spectroscopic techniques will not be acceptable nor will solvent extraction data unless supported by other data of interest to inorganic chemists. Unnecessary fragmentation of work is not acceptable.

In addition Polyhedron publishes specially commissioned review articles (Polyhedron Reports) and collections of original research papers (Polyhedron Symposia-in-Print) of appropriate timeliness.

Publication Information: Polyhedron (ISSN 0277-5387). For 2005, volume 24 is scheduled for publication. Subscription prices are available upon request from the Publisher or from the Regional Sales Office nearest you or from this journal's website (http://www.elsevier.com/locate/poly). Further information is available on this journal and other Elsevier products through Elsevier's website (http://www.elsevier.com). Subscriptions are accepted on a prepaid basis only and are entered on a calendar year basis. Issues are sent by standard mail (surface within Europe, air delivery outside Europe). Priority rates are available upon request. Claims for missing issues should be made within six months of the date of dispatch.

Orders, Claims and Journal Enquiries

(no manuscript enquiries)

Please contact the Customer Support Department at the Regional Sales Office nearest you:

Orlando
Elsevier
Customer Service Department
6277 Sea Harbor Drive
Orlando
FL 32887-4800
USA
Tel.: (+1) 877-8397126
[Toll free number for US customers], or
(+1) 407-3454020
[customers outside US]
Fax: (+1) 407-3631354
E-mail: usjcs@elsevier.com

Amsterdam
Elsevier
Customer Service Department
P.O. Box 211
1000 AE Amsterdam
The Netherlands
Tel.: (+31) 20-485-3757
Fax: (+31) 20-485-3432
E-mail: nlinfo-f@elsevier.com

Tokyo
Elsevier K.K.
Customer Service Department
4F Higashi-Azabu, 1-Chome Bldg
1-9-15 Higashi-Azabu
Minato-ku, Tokyo 106-0044
Japan
Tel.: (+81) 3-5561-5037
Fax: (+81) 3-5561-5047
E-mail: jp.info@elsevier.com

Singapore
Elsevier
Customer Service Department
3 Killiney Road
#08-01 Winsland House 1
Singapore 239519
Tel.: (+65) 6349-0222
Fax: (+65) 6733-1510
E-mail: asiainfo@elsevier.com

USA mailing notice: *Polyhedron* (ISSN 0277-5387) is published triweekly by Elsevier Ltd. (P.O. Box 211, 1000 AE Amsterdam, The Netherlands). Annual subscription price in the USA US$ 7049.00 (valid in North, Central and South America), including air speed delivery. Periodical postage rate is paid at Jamaica, NY 11431.
USA POSTMASTER: Send address changes to *Polyhedron*, Publications Expediting Inc., 200 Meacham Avenue, Elmont, NY 11003.
AIRFREIGHT AND MAILING in the USA by Publications Expediting Inc., 200 Meacham Avenue, Elmont, NY 11003.

Advertising Information

Advertising orders and enquiries can be sent to: **South America:** Mr Tino DeCarlo, The Advertising Department, Elsevier Inc., 360 Park Avenue South, New York, NY 10010-1710, USA; tel.: (+1) (212) 633 3815; fax: (+1) (212) 633 3820; e-mail: t.decarlo@elsevier.com. **Europe, USA, Canada and ROW:** Miss Katrina Barton, Commercial Sales, Elsevier, 84 Theobald's Road, London, WCIX 8RR, UK; phone: (+44) (0) 20 7611 4117; fax: (+44) (0) 20 7611 4463; e-mail: commercialsales@elsevier.com

VALIDATION AND DEPOSITION OF CRYSTALLOGRAPHIC DATA

Information and Instructions to Authors of Papers Containing or Comprising Crystal Structures Determinations

1. ***Policy*** Polyhedron will accept for publication papers containing or comprising the results of crystal structure determinations which will be of interest to inorganic chemists. Papers reporting only crystallographic results must relate to work of novelty or special significance to inorganic chemistry, which must be emphasized.

2. ***Submission of papers***. The following procedures should be followed:

   a) **Prior** to the submission of the manuscript, the author(s) should **validate and deposit files in Crystallographic Information File (CIF) format.**
   Validation should occur before deposition via the "checkCIF" service developed by the International Union of Crystallography (IUCr) available at http://checkcif.iucr.org. Authors are strongly recommended to take advantage of this service and submit manuscripts accompanied by an IUCr validation report to help the referees reviewing the manuscript.
   Authors deposit with the relevant Data Centre the data corresponding to each structure to be reported in the intended publication.
   Data for **metal organic** structures, i.e. those which contain organic carbon in **any** of the species present in the structure (including metal carbonyls) should be sent to the Cambridge Crystallographic Data Centre (CCDC) by e-mail (address: deposit@ccdc.cam.ac.uk) preferably in CIF format. A checklist of data items to be included in the deposition can be obtained from the CCDC Home Page on the Worldwide Web (http://www.ccdc.cam.ac.uk/) or by e-mail (to fileserv@ccdc.cam.ac.uk) with the one line message **sendme checklist**.
   Data for **inorganic** compounds should be sent to Fachinformationszentrum Karlsruhe (FIZ) by e-mail (address: crysdata@FIZ-Karlsruhe.de) by FTP (please contact FIZ if you choose this option) or on disk. No hard copy submissions will be accepted.
   The Data Centres will provide, within a day or two of submission, deposition codes for each data set, which should be quoted in suitable form in the manuscript submitted to the Journal. The deposited data will be accessed by the Journal and checked as part of the refereeing process.

   b) When the paper is submitted to the Journal, the following guidelines should be adhered to:

   - The **Title** should contain reference to the presence in the paper of X-ray crystallographic results.
   - The **Abstract** should **not** contain crystal data, but should include a concise statement of the main features of the structural results.
   - The **Experimental** results must be presented in a concise format. In general, authors should not include a detailed text description of data collection, crystal structure solution and refinement, especially if these followed standard procedures and no difficulties were met. Reference to a previous paper containing a more detailed experimental description can be given if relevant. However, if any parts of the structure analysis were unusual, and affected the presentation and/or accuracy of the results, then these should be discussed. The following crystallographic data should be given, all contained in a paragraph (if one structure reported) or Table (two or more structures).

   i) Color, habit and size of crystals used, and behavior of compound under ambient conditions if not mentioned elsewhere in the paper.
   ii) Chemical formula. This should correspond to the complete chemical unit encompassing crystallographic symmetry (e.g. a centrosymmetric dimer should be included in full form). The use of fractional coefficients (e.g. $0.5H_2O$) should be used only if the unit has partial occupancy of its site. Formulae should be presented in a way that molecules, ionic fragments, solvate molecules etc. are separately identified.

iii) Unit cell parameters with esd's, and X-ray wavelength used.
iv) Crystal system, space group and number of complete chemical unit (see ii) per cell.
v) Type of diffractometer used and method of data collection; total number of data collected, excluding any intensity controls, number unique, R_{int} value, number observed (with cut-off parameter) and completeness of data to suitable 2θ or sin θ/γ limit; use or otherwise of absorption correction.
vi) Final results. Give values of R, R_w (and their definitions) and number of parameters. Indicate form of refinement (F or F^2) and treatment of hydrogens.

Note that easily derived parameters (F_{wt}, $F(000)$, μ, D_x) should not be given unless required in discussion of other data (e.g. number of solvent molecules, etc.).

- **Discussion of the structure.** This must include a clear, labelled diagram of the structure (molecule, complex ion or unit cell contents if the structure is polymeric) and a list of relevant geometry parameters – interatomic distances, interbond angles, torsion angles etc. Data for geometrically less important parts of the structure, such as ligand sub groups (phenyl rings, alkyl groups etc.) should not be given. Packing diagrams of crystal structures of "molecular" compounds should not be given unless there are chemically important intermolecular interactions.

3. ***Supplementary data.*** It is not necessary to submit copies of the Supplementary Data with the manuscript. However, authors are recommended to submit with the manuscript, as supplementary sheets, not for publication, any further information which they feel may aid the refereeing process, particularly if any of the usual quality-of-structure indicators point to problems in the analysis.

POLYHEDRON

The International Journal for Inorganic and Organometallic Chemistry

Executive Editors

The Americas
G. Christou
Department of Chemistry, University of Florida,
Gainesville, FL 32611-7200, USA
E-mail: christou@chem.ufl.edu

Rest of the world
C.E. Housecroft
Department of Chemistry, University of Basel,
Spitalstrasse 51, CH-4056 Basel, Switzerland
E-mail: poly-chemie@unibas.ch

Associate Regional Editor for China
T.C.W. Mak
Department of Chemistry, University Science Centre,
The Chinese University of Hong Kong,
Shatin NT, Hong Kong, People's Republic of China
E-mail: tcwmak@cuhk.edu.hk

Polyhedron Reports
Editor
G. Christou *(Gainesville, FL, USA)*

Symposia-in-print
Editor
G. Parkin *(New York, NY, USA)*

Editorial Board

N.Y. Barba-Behrens *(Mexico, DF, Mexico)*
A. Blackman *(Dunedin, New Zealand)*
D.C. Bradley *(London, UK)*
D. Braga *(Bologna, Italy)*
A. Brodie *(Palmerston North, New Zealand)*
A. Castiñeiras *(Santiago de Compostela, Spain)*
M.H. Chisholm *(Columbus, OH, USA)*
E.C. Constable *(Basel, Switzerland)*
E. Coronado *(Valencia, Spain)*
W.J. Evans *(Irvine, CA, USA)*
M. Fujita *(Tokyo, Japan)*
L.H. Gade *(Heidelberg, Germany)*
C.D. Garner *(Nottingham, UK)*
L. Hubert-Pfalzgraf *(Villeurbanne, France)*
M.B. Hursthouse *(Southampton, UK)*
T. Kiss *(Szeged, Hungary)*
P.P. Power *(Davis, CA, USA)*
T.B. Rauchfuss *(Urbana, IL, USA)*
J. Reedijk *(Leiden, The Netherlands)*
A.L. Rheingold *(Newark, DE, USA)*
F.G.A. Stone *(Waco, TX, USA)*
A.G. Sykes *(Newcastle upon Tyne, UK)*
L.K. Thompson *(St John's, NF, Canada)*
M.D. Ward *(Sheffield, UK)*
R.E.P. Winpenny *(Manchester, UK)*

Aims and Scope

Polyhedron will publish original, fundamental, experimental and theoretical work of the highest quality in all the major areas of inorganic chemistry. These include synthetic chemistry, coordination chemistry, organometallic chemistry, bioinorganic chemistry, and solid-state and materials chemistry. Papers should be complete pieces of work, and the inclusion of results from spectroscopic and/or physical techniques is encouraged. Papers merely reporting the preparation and X-ray structural characterization of only a single compound will not be considered appropriate unless the compound and its structure are particularly interesting.
Similarly, papers concerned solely with stability constants determined by potentiometric titration data unsupported by other e.g. spectroscopic techniques will not be acceptable nor will solvent extraction data unless supported by other data of interest to inorganic chemists. Unnecessary fragmentation of work is not acceptable.
In addition Polyhedron publishes specially commissioned review articles (Polyhedron Reports) and collections of original research papers (Polyhedron Symposia-in-Print) of appropriate timeliness.

Publication Information: Polyhedron (ISSN 0277-5387). For 2005, volume 24 is scheduled for publication. Subscription prices are available upon request from the Publisher or from the Regional Sales Office nearest you or from this journal's website (http://www.elsevier.com/locate/poly). Further information is available on this journal and other Elsevier products through Elsevier's website (http://www.elsevier.com). Subscriptions are accepted on a prepaid basis only and are entered on a calendar year basis. Issues are sent by standard mail (surface within Europe, air delivery outside Europe). Priority rates are available upon request. Claims for missing issues should be made within six months of the date of dispatch.

Orders, Claims and Journal Enquiries

(no manuscript enquiries)
Please contact the Customer Support Department at the Regional Sales Office nearest you:

Orlando
Elsevier
Customer Service Department
6277 Sea Harbor Drive
Orlando
FL 32887-4800
USA
Tel.: (+1) 877-8397126
[Toll free number for US customers], or
(+1) 407-3454020
[customers outside US]
Fax: (+1) 407-3631354
E-mail: usjcs@elsevier.com

Amsterdam
Elsevier
Customer Service Department
P.O. Box 211
1000 AE Amsterdam
The Netherlands
Tel.: (+31) 20-485-3757
Fax: (+31) 20-485-3432
E-mail: nlinfo-f@elsevier.com

Tokyo
Elsevier K.K.
Customer Service Department
4F Higashi-Azabu, 1-Chome Bldg
1-9-15 Higashi-Azabu
Minato-ku, Tokyo 106-0044
Japan
Tel.: (+81) 3-5561-5037
Fax: (+81) 3-5561-5047
E-mail: jp.info@elsevier.com

Singapore
Elsevier
Customer Service Department
3 Killiney Road
#08-01 Winsland House 1
Singapore 239519
Tel.: (+65) 6349-0222
Fax: (+65) 6733-1510
E-mail: asiainfo@elsevier.com

USA mailing notice: *Polyhedron* (ISSN 0277-5387) is published triweekly by Elsevier Ltd. (P.O. Box 211, 1000 AE Amsterdam, The Netherlands). Annual subscription price in the USA US$ 7049.00 (valid in North, Central and South America), including air speed delivery. Periodical postage rate is paid at Jamaica, NY 11431.
USA POSTMASTER: Send address changes to *Polyhedron*, Publications Expediting Inc., 200 Meacham Avenue, Elmont, NY 11003.
AIRFREIGHT AND MAILING in the USA by Publications Expediting Inc., 200 Meacham Avenue, Elmont, NY 11003.

Advertising Information

Advertising orders and enquiries can be sent to: **South America:** Mr Tino DeCarlo, The Advertising Department, Elsevier Inc., 360 Park Avenue South, New York, NY 10010-1710, USA; tel.: (+1) (212) 633 3815; fax: (+1) (212) 633 3820; e-mail: t.decarlo@elsevier.com. **Europe, USA, Canada and ROW:** Miss Katrina Barton, Commercial Sales, Elsevier, 84 Theobald's Road, London, WCIX 8RR, UK; phone: (+44) (0) 20 7611 4117; fax: (+44) (0) 20 7611 4463; e-mail: commercialsales@elsevier.com

POLYHEDRON

The International Journal for Inorganic and Organometallic Chemistry

Executive Editors

The Americas
G. Christou
Department of Chemistry, University of Florida,
Gainesville, FL 32611-7200, USA
E-mail: christou@chem.ufl.edu

Rest of the world
C.E. Housecroft
Department of Chemistry, University of Basel,
Spitalstrasse 51, CH-4056 Basel, Switzerland
E-mail: poly-chemie@unibas.ch

Associate Regional Editor for China
T.C.W. Mak
Department of Chemistry, University Science Centre,
The Chinese University of Hong Kong,
Shatin NT, Hong Kong, People's Republic of China
E-mail: tcwmak@cuhk.edu.hk

Polyhedron Reports
Editor
G. Christou *(Gainesville, FL, USA)*

Symposia-in-print
Editor
G. Parkin *(New York, NY, USA)*

Editorial Board
N.Y. Barba-Behrens *(Mexico, DF, Mexico)*
A. Blackman *(Dunedin, New Zealand)*
D.C. Bradley *(London, UK)*
D. Braga *(Bologna, Italy)*
A. Brodie *(Palmerston North, New Zealand)*
A. Castiñeiras *(Santiago de Compostela, Spain)*
M.H. Chisholm *(Columbus, OH, USA)*
E.C. Constable *(Basel, Switzerland)*
E. Coronado *(Valencia, Spain)*
W.J. Evans *(Irvine, CA, USA)*
M. Fujita *(Tokyo, Japan)*
L.H. Gade *(Heidelberg, Germany)*
C.D. Garner *(Nottingham, UK)*
L. Hubert-Pfalzgraf *(Villeurbanne, France)*
M.B. Hursthouse *(Southampton, UK)*
T. Kiss *(Szeged, Hungary)*
P.P. Power *(Davis, CA, USA)*
T.B. Rauchfuss *(Urbana, IL, USA)*
J. Reedijk *(Leiden, The Netherlands)*
A.L. Rheingold *(Newark, DE, USA)*
F.G.A. Stone *(Waco, TX, USA)*
A.G. Sykes *(Newcastle upon Tyne, UK)*
L.K. Thompson *(St John's, NF, Canada)*
M.D. Ward *(Sheffield, UK)*
R.E.P. Winpenny *(Manchester, UK)*

Aims and Scope

Polyhedron will publish original, fundamental, experimental and theoretical work of the highest quality in all the major areas of inorganic chemistry. These include synthetic chemistry, coordination chemistry, organometallic chemistry, bioinorganic chemistry, and solid-state and materials chemistry. Papers should be complete pieces of work, and the inclusion of results from spectroscopic and/or physical techniques is encouraged. Papers merely reporting the preparation and X-ray structural characterization of only a single compound will not be considered appropriate unless the compound and its structure are particularly interesting.
Similarly, papers concerned solely with stability constants determined by potentiometric titration data unsupported by other e.g. spectroscopic techniques will not be acceptable nor will solvent extraction data unless supported by other data of interest to inorganic chemists. Unnecessary fragmentation of work is not acceptable.
In addition Polyhedron publishes specially commissioned review articles (Polyhedron Reports) and collections of original research papers (Polyhedron Symposia-in-Print) of appropriate timeliness.

Publication Information: Polyhedron (ISSN 0277-5387). For 2005, volume 24 is scheduled for publication. Subscription prices are available upon request from the Publisher or from the Regional Sales Office nearest you or from this journal's website (http://www.elsevier.com/locate/poly). Further information is available on this journal and other Elsevier products through Elsevier's website (http://www.elsevier.com). Subscriptions are accepted on a prepaid basis only and are entered on a calendar year basis. Issues are sent by standard mail (surface within Europe, air delivery outside Europe). Priority rates are available upon request. Claims for missing issues should be made within six months of the date of dispatch.

Orders, Claims and Journal Enquiries

(no manuscript enquiries)
Please contact the Customer Support Department at the Regional Sales Office nearest you:

Orlando
Elsevier
Customer Service Department
6277 Sea Harbor Drive
Orlando
FL 32887-4800
USA
Tel.: (+1) 877-8397126
[Toll free number for US customers], or
(+1) 407-3454020
[customers outside US]
Fax: (+1) 407-3631354
E-mail: usjcs@elsevier.com

Amsterdam
Elsevier
Customer Service Department
P.O. Box 211
1000 AE Amsterdam
The Netherlands
Tel.: (+31) 20-485-3757
Fax: (+31) 20-485-3432
E-mail: nlinfo-f@elsevier.com

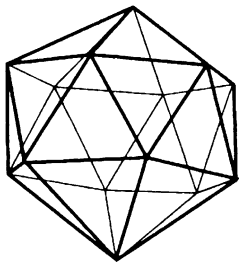
Tokyo
Elsevier K.K.
Customer Service Department
4F Higashi-Azabu, 1-Chome Bldg
1-9-15 Higashi-Azabu
Minato-ku, Tokyo 106-0044
Japan
Tel.: (+81) 3-5561-5037
Fax: (+81) 3-5561-5047
E-mail: jp.info@elsevier.com

Singapore
Elsevier
Customer Service Department
3 Killiney Road
#08-01 Winsland House 1
Singapore 239519
Tel.: (+65) 6349-0222
Fax: (+65) 6733-1510
E-mail: asiainfo@elsevier.com

USA mailing notice: *Polyhedron* (ISSN 0277-5387) is published triweekly by Elsevier Ltd. (P.O. Box 211, 1000 AE Amsterdam, The Netherlands). Annual subscription price in the USA US$ 7049.00 (valid in North, Central and South America), including air speed delivery. Periodical postage rate is paid at Jamaica, NY 11431.
USA POSTMASTER: Send address changes to *Polyhedron*, Publications Expediting Inc., 200 Meacham Avenue, Elmont, NY 11003.
AIRFREIGHT AND MAILING in the USA by Publications Expediting Inc., 200 Meacham Avenue, Elmont, NY 11003.

Advertising Information

Advertising orders and enquiries can be sent to: **South America:** Mr Tino DeCarlo, The Advertising Department, Elsevier Inc., 360 Park Avenue South, New York, NY 10010-1710, USA; tel.: (+1) (212) 633 3815; fax: (+1) (212) 633 3820; e-mail: t.decarlo@elsevier.com. **Europe, USA, Canada and ROW:** Miss Katrina Barton, Commercial Sales, Elsevier, 84 Theobald's Road, London, WCIX 8RR, UK; phone: (+44) (0) 20 7611 4117; fax: (+44) (0) 20 7611 4463; e-mail: commercialsales@elsevier.com



POLYHEDRON

The International Journal for Inorganic and Organometallic Chemistry

Founding Editor: **Sir Geoffrey Wilkinson**✠

Executive Editors

The Americas

G. Christou
Department of Chemistry, University of Florida, Gainesville, FL 32611-7200, USA
E-mail: christou@chem.ufl.edu

Rest of the world

C.E. Housecroft
Department of Chemistry, University of Basel, Spitalstrasse 51, CH-4056 Basel, Switzerland
E-mail: poly-chemie@unibas.ch

Associate Regional Editor for China

T.C.W. Mak
Department of Chemistry, University Science Centre, The Chinese University of Hong Kong, Shatin NT, Hong Kong, People's Republic of China
E-mail: tcwmak@cuhk.hk

Polyhedron Reports

G. Christou
Department of Chemistry, University of Florida, Gainesville, FL 32611-7200, USA
E-mail: christou@chem.ufl.edu

Symposia-in-print

G. Parkin
Department of Chemistry (Box 3115), Columbia University, 3000 Broadway, New York, NY 10027, USA
E-mail: parkin@chem.columbia.edu

Editorial Board

N.Y. Barba-Behrens *(Mexico, DF, Mexico)*
A. Blackman *(Dunedin, New Zealand)*
D.C. Bradley *(London, UK)*
D. Braga *(Bologna, Italy)*
A. Brodie *(Palmerston North, New Zealand)*
A. Castiñeiras *(Santiago de Compostela, Spain)*
M.H. Chisholm *(Columbus, OH, USA)*
E.C. Constable *(Basel, Switzerland)*
E. Coronado *(Valencia, Spain)*
W.J. Evans *(Irvine, CA, USA)*
M. Fujita *(Tokyo, Japan)*
L.H. Gade *(Heidelberg, Germany)*
C.D. Garner *(Nottingham, UK)*
J.F. Harrod *(Montreal, Que., Canada)*
L. Hubert-Pfalzgraf *(Villeurbanne, France)*
M.B. Hursthouse *(Southampton, UK)*
T. Kiss *(Szeged, Hungary)*
P.P. Power *(Davis, CA, USA)*
T.B. Rauchfuss *(Urbana, IL, USA)*
J. Reedijk *(Leiden, The Netherlands)*
A.L. Rheingold *(La Jolla, CA, USA)*
F.G.A. Stone *(Waco, TX, USA)*
A.G. Sykes *(Newcastle upon Tyne, UK)*
L.K. Thompson *(St John's, NF, Canada)*
M.D. Ward *(Bristol, UK)*
R.E.P. Winpenny *(Manchester, UK)*



ELSEVIER

Amsterdam — Boston — Jena — London — New York — Oxford — Paris — Philadelphia — San Diego — St Louis

Available online at www.sciencedirect.com
SCIENCE DIRECT®
Polyhedron 24, issue 18, 8 December 2005
POLYHEDRON
www.elsevier.com/locate/poly

Contents

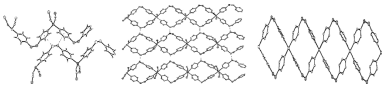
Papers

Maw-Cherng Suen, Yuen-Hua Wang, Yi-Fen Hsu, Chun-Wei Yeh, Jhy-Der Chen, Ju-Chun Wang

Polyhedron 24 (2005) 2913

Syntheses and structural characterization of transition metal(II) coordination polymers containing 4,4′-dipyridyldisulfide

The synthesis and structures of three new coordination polymers, $Zn(NCS)_2(4\text{-PDS})]_n$-(4-PDS = 4,4′-dipyridyldisulfide) (**1**), $[Fe(NCS)_2$-$(4\text{-PDS})_2 \cdot 4H_2O]_n$ (**2**), and $\{[Co(4\text{-PDS})_2]$-$[Cl]_2 \cdot 2CH_3OH\}_n$ (**3**), are reported. Complex **1** exibits 1-D zigzag-chains, while complexes **2** and **3** shows 1-D channel chains structures.

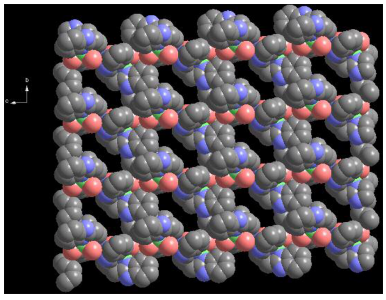


Anangamohan Panja, Sanchita Goswami, Nizamuddin Shaikh, Partha Roy, Mario Manassero, Ray J. Butcher, Pradyot Banerjee

Polyhedron 24 (2005) 2921

Synthesis and X-ray crystallographic characterization of copper and iron complexes with tetradentate-N_4 ligands: Reactivity towards catechol oxidation

The synthesis and structural characterization of new copper and iron complexes $[Cu(ntb)Cl]_2$-$[CuCl_4] \cdot 2H_2O$ (**1**), $[Fe(ntb)Cl_2]Cl \cdot 3H_2O$ (**2**) and $[Fe(bispicpn)Cl_2]Cl$ (**3**) with tetradentate N-ligands, ntb (ntb = tris(2-benzimidazolylmethyl)amine) and bispicpn (bispicpn = *N*,*N*′-bis(2-pyridylmethyl)-1,2-propanediamine) are reported. Detailed structural analysis revealed 3D, 2D and 1D networks. The packing diagram of **2** shows interesting hexagonal pores. Oxidation reactions of 3,5-di-*tert*-butylcatechol by oxygen were performed with these complexes; the copper complex exhibits catechol oxidase like activity while the two iron complexes show catechol dioxygenase like activity.

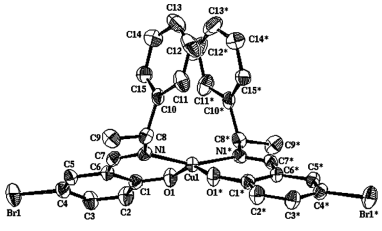


Takashiro Akitsu, Yasuaki Einaga

Polyhedron 24 (2005) 2933

Syntheses, crystal structures and electronic properties of a series of copper(II) complexes with 3,5-halogen-substituted Schiff base ligands and their solutions

We have systematically compared structures, electronic properties, structural phase transitions and absorption spectra depending on solvents for ten Cu(II) complexes incorporating 3,5-halogen-substituted Schiff base ligands. We could observe spectral changes in the π–$\pi*$ region of a complex in chloroform solution of the complex and 4-hydroxyazobenzene caused by its *cis*–*trans* photoisomerization.

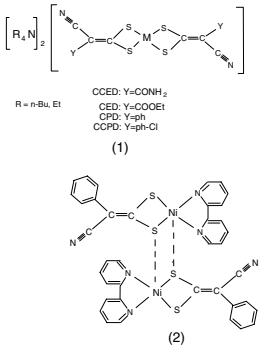


Hussein H. Alkam, Khalid M. Kanan, Christos C. Hadjikostas

Polyhedron 24 (2005) 2944

Syntheses and characterization of some homoleptic (1,1-dithiolato)copper(II) and nickel(II) complexes, and mixed-ligand (1,1-dithiolato)-nickel(II) chelates containing nitrogenous bases. Crystal structures of tetrabutylammonium(1-cyano-1-chlorophenyl-2,2-ethylenedithiolato)copper(II), [(2,2′-bipyridine)(1-cyano-1-phenyl-2,2-ethylenedithiolato)nickel(II)], and 5-amino-4-(4-chlorophenyl)-[1,2]dithiole-3-thione

A series of divalent nickel and copper complexes $[R_4N]_2[M(S_2C{=}C(CN)Y)_2]$ (**1**), and a series of mixed-ligand nickel(II) chelates $[Ni(enR)S_2C{=}C(CN)Y]$ have been prepared and characterized. The crystal structures of three compounds have been determined. The molecules of the complex [Ni(bipy)CPD] are arranged in pairs, each pair forms two weak intermolecular Ni···S bond interactions (**2**).

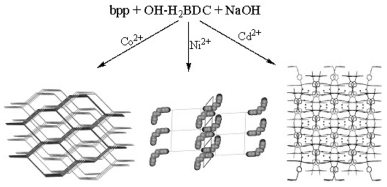


Xiao-Ju Li, Rong Cao, Wen-Hua Bi, Yan-Qin Wang, Yu-Ling Wang, Xing Li

Polyhedron 24 (2005) 2955

Three interpenetrated frameworks constructed by long flexible *N*,*N*′-bipyridyl and dicarboxylate ligands

The hydrothermal reactions of 1,3-bis(4-pyridyl)propane (bpp), 5-hydroxyisophthalic acid ($OH\text{-}H_2BDC$) and different metal ions gave rise to three coordination polymers, $\{[Co(bpp)(OH\text{-}BDC)]\cdot H_2O\}_n$ (**1**) $[Ni(bpp)_{1.5}(H_2O)(OH\text{-}BDC)]_n$ (**2**) and $\{[Cd(bpp)(H_2O)(OH\text{-}BDC)]\cdot 2H_2O\}_n$ (**3**). The long flexible bpp ligands adopt different conformations to take part in coordination in the three compounds.

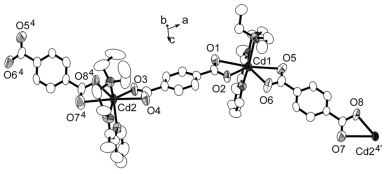


Suparna Banerjee, Paul-G. Lassahn, Christoph Janiak, Ashutosh Ghosh

Polyhedron 24 (2005) 2963

Supramolecular architecture of cadmium(II)–terephthalate complexes having a tridentate or tetradentate Schiff base as blocking coligand

Two new cadmium(II)–terephthalate complexes, one with the tridentate ligand N^1,N^1-diethyl-N^2-(1-(pyridin-2-yl)ethylidene)ethane-1,2-diamine and other with the tetradentate ligand *N*,*N*′-bis-(1-pyridin-2-yl-ethylidene)-ethane-1,2-diamine, have been synthesized. The compound having the tridentate ligand is a 1D polymeric chain whereas the compound with the tetradentate ligand is a very rare type of dinuclear complex.

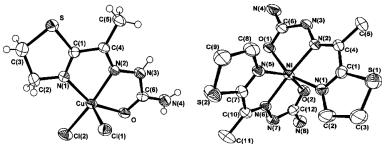


F.J. Barros-García, F. Luna-Giles, M.A. Maldonado-Rogado, E. Viñuelas-Zahínos

Polyhedron 24 (2005) 2972

Ligation properties of 2-acetyl-2-thiazoline semicarbazone (ATsc): Isolation, spectroscopic and X-ray study of ATsc and its Cu(II) and Ni(II) complexes

A new Schiff base ligand 2-acetyl-2-thiazoline semicarbazone (ATsc) and its copper(II) and nickel(II) complexes were synthesized and characterized by physical measurements. The X-ray crystal structures of ATsc, its copper complex and its nickel complex have also been determined. The geometry around the metallic atoms can be described as a distorted square-pyramid for the copper complex and as a distorted octahedron for the nickel complex.

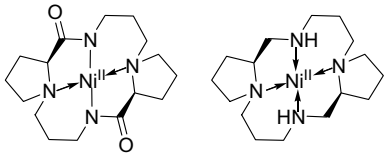


Agnieszka Szumna, Michał Achmatowicz, Tomasz Zieliński, Janusz Jurczak

Polyhedron 24 (2005) 2981

Structural studies of new chiral nickel (II) complexes of cyclams: The influence of a systematically varied number of amide groups

The nickel (II) complexes of the chiral cyclam and its mono- and dioxo derivatives show different complexation modes as proved by the X-ray analysis.

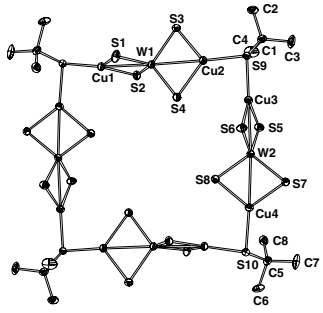


Zhi-Hua Li, Shao-Wu Du, Xin-Tao Wu

Polyhedron 24 (2005) 2988

Assembly of molecular squares and helical chain polymers of Mo(W)/Cu/S clusters using thiolato ligands as linkers

By using linear CuS_2WS_2Cu fragments as building blocks and monodentate or bidentate thiolato ligands as linkers, two novel molecular squares of Mo(W)/Cu/S clusters $[Et_4N]_4[\{MS_4Cu_2(\mu\text{-}SBu^t)\}_4]$ (**1**, M = Mo; **2**, M = W) and two helical chain polymers $\{[Et_4N]_2[MS_4Cu_2(SSS)]\}_n$ (**3**, M = Mo; **4**, M = W) have been isolated. The structural types of these clusters have not been previously reported in the Mo(W)/Cu/S system.



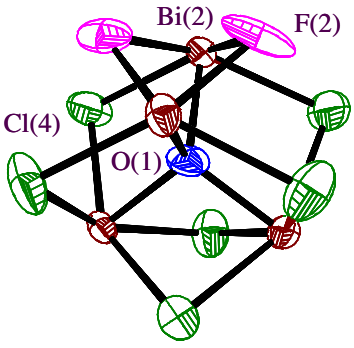
$[Et_4N]_4[\{WS_4Cu_2(\mu\text{-}SBu^t)\}_4]$ **2**

Andreas Decken, Grigori B. Nikiforov, Jack Passmore

Polyhedron 24 (2005) 2994

Evidence for SO_2, $C_2H_4Cl_2$ and CH_2Cl_2 soluble salts of bismuth homopolyatomic cations and $[Bi_4OF_2Cl_6(C_6Me_6)_4][Al(OC(CF_3)_3)_4]_2 \cdot C_6Me_6$, containing the novel $[Bi_4OF_2Cl_6]^{2+}$ cation

Compound $[Bi_4OF_2Cl_6(C_6Me_6)_4][Al(OC(CF_3)_3)_4]_2 \cdot C_6Me_6$ contains the novel $[Bi_4OF_2Cl_6]^{2+}$ cation.

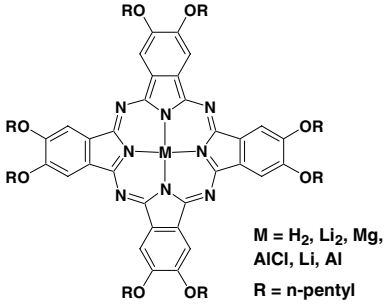


Xiaobin Deng, William W. Porter III, Thomas P. Vaid

Polyhedron 24 (2005) 3004

Aluminum and lithium octa(pentoxy)phthalocyanine radicals

The synthesis and characterization of the aluminum and lithium octa(pentoxy)phthalocyanine radicals, AlPc* and LiPc*, are described. In the solid state LiPc* and AlPc* are electrical conductors with pressed-pellet conductivities of $8 \times 10^{-11\ -1}$ cm^{-1} and $5 \times 10^{-7\ -1}$ cm^{-1}, respectively.

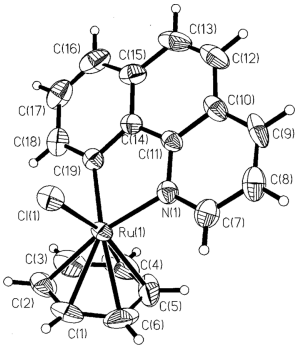


J.G. Małecki, M. Jaworska, R. Kruszynski, J. Kłak

Polyhedron 24 (2005) 3012

Reaction of $[(C_6H_6)RuCl_2]_2$ with 7,8-benzoquinoline and 8-hydroxyquinoline

The reaction of $[(C_6H_6)RuCl_2]_2$ with 7,8-benzoquinoline and 8-hydroxyquinoline in methanol were performed. The obtained complexes have been studied by IR, UV–VIS, ^1H and ^{13}C NMR spectroscopy and X-ray crystallography. The electronic spectra of the obtained compounds have been calculated using the TDDFT method. Magnetic properties of $[Ru(C_9H_6NO)_3] \cdot CH_3OH$ complex suggest the antiferromagnetic coupling of the ruthenium centers in the crystal lattice. EPR spectrum of $[Ru(C_9H_6NO)_3] \cdot CH_3OH$ compound indicates single isotropic line only characteristic for Ru^{3+} with spin equal to 1/2.

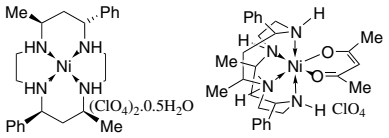


Donald F. Cook, Neil F. Curtis, Clifton E.F. Rickard, Joyce M. Waters

Polyhedron 24 (2005) 3022

Compounds of nickel(II) with 5*SR*,7*RS*,12*SR*,14*SR*-5,12-dimethyl-7,14-diphenyl-1,4,8,11-tetraazacyclotetradecane, rmL^2: The structures of $[Ni(rmL^2)](ClO_4)_2 \cdot 0.5H_2O$ and *cis*-$[Ni(rmL^2)(acac)]ClO_4$

The cyclic tetraamine 5*SR*,7*RS*,12*SR*,14*SR*-5,12-dimethyl-7,14-diphenyl-1,4,8,11-tetraazacyclotetradecane (rmL^2) with nickel(II) mainly forms compounds with the amine planar for $[Ni(rmL^2)]^{2+}$ salts and *trans*-diligand compounds *trans*-$[Ni(rmL^2)L_2]$. Compounds with the amine in folded coordination with *cis* ligands, *cis*-$[Ni(rmL^2)L_2]$, usually metastable with respect to the *trans* form, or with a chelate, as for *cis*-$[Ni(rmL^2)(acac)]ClO_4$ are also formed. Structures of *trans*-$[Ni(rmL^2)](ClO_4)_2 \cdot 1/2H_2O$ with the methyl substituents disordered over axial and equatorial orientations, and *cis*-$[Ni(rmL^2)(acac)]ClO_4$ are reported.

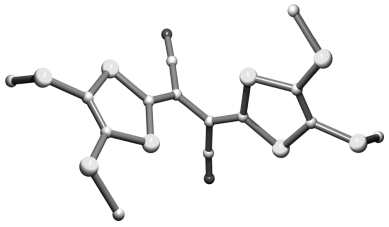


Chunyang Jia, Shi-Xia Liu, Antonia Neels, Gal Labat, Silvio Decurtins

Polyhedron 24 (2005) 3032

Coordination networks of 2,3-bis(4,5-dimethylthio-1,3-dithiole-2-ylidene)succinonitrile with silver salts: A study of network connectivity and topology as a function of counterion

Two new Ag(I) complexes **1** and **2** with a multitopic ligand **L** have been prepared. Their structures illustrate how the metal coordination assembly in the solid state may be influenced significantly not only by the nature of the counterion, but also by the topicity of the ligand.

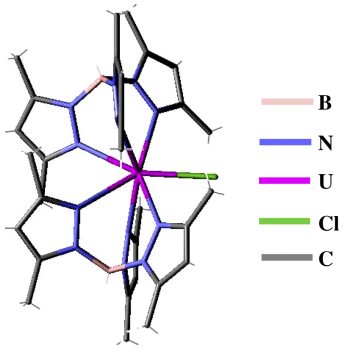


Maria Augusta Antunes, Ângela Domingos, Isabel Cordeiro dos Santos, Noémia Marques, Josef Takats

Polyhedron 24 (2005) 3038

Synthesis and characterization of uranium(III) compounds supported by the hydrotris(3,5-dimethyl-pyrazolyl)borate ligand: Crystal structures of $[U(Tp^{Me2})_2(X)]$ complexes (X = OC_6H_2-2,4,6-Me_3, dmpz, Cl)

A series of $[U(Tp^{Me2})_2(X)]$ complexes has been prepared by reaction of $[U(Tp^{Me2})_2(NR_2)]$ with protic substrates and halide sources and/or metathesis of $[U(Tp^{Me2})_2I]$. The compounds are structurally similar to the analogous samarium complexes, but the availability of higher oxidation states for uranium leads to a different outcome for the thermolysis of $[U(Tp^{Me2})_2Cp]$.

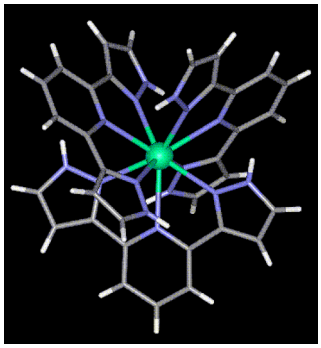


Nivan B. da Costa Jr., Ricardo O. Freire, Gerd B. Rocha, Alfredo M. Simas

Polyhedron 24 (2005) 3046

Sparkle/AM1 modeling of holmium (III) complexes

The sparkle/AM1 model, recently defined for Eu(III), Gd(III) and Tb(III), is now extended to Ho(III). Sparkle/AM1 constitutes the only semiempirical model for the quantum chemical calculation of Ho(III) coordination compounds available, and with geometry prediction accuracies comparable to present day lanthanide complex ab-initio/ECP calculations, while being hundreds of times faster.

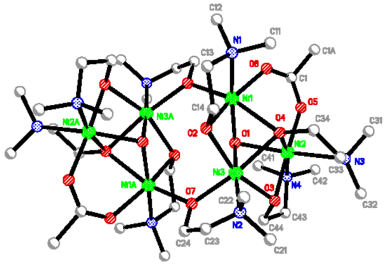


Elena Ilina, Vadim G. Kessler

Polyhedron 24 (2005) 3052

Unexpected structural analogy between early and late 3d transition metal alkoxide carboxylates: Synthesis and single crystal X-ray study of $Ni_6(OH)_2(OR^N)_6(OCOR)_2$, $R^N = C_2H_4NMe_2$, R = H, CH_3

Modification of the liquid $Ni(OR^N)_2$, $R^N = C_2H_4NMe_2$, with carboxylic acids, results in formation of crystalline heteroleptic complexes $Ni_6(OH)_2(OR^N)_6(OCOR)_2$, R = H (**1**), CH_3 (**3**) with the core structure closely analogous to that of hexanuclear titanium (IV) alkoxide carboxylates.

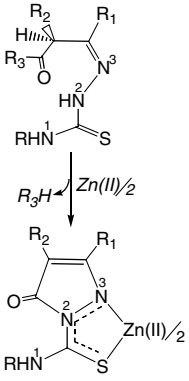


J.S. Casas, M.V. Castaño, M.S. García-Tasende, A. Sánchez, J. Sordo, A. Touceda

Polyhedron 24 (2005) 3057

Zn(II) pyrazolonate complexes obtained by metal-induced cyclization of thiosemicarbazones: Crystal structures and spectroscopic properties

The reaction of zinc(II) with thiosemicarbazones derived from β-keto esters induces the cyclization of the thiosemicarbazone to afford $[ZnL_2]$ and $[ZnL_2(MeOH)]$ complexes, where HL is a pyrazolone ligand. The complexes were studied by X-ray diffraction, which showed that the pyrazolonate ligand binds with the metal through the S and N(3) atoms. The ^1H and ^{13}C NMR spectra of these complexes are also discussed.

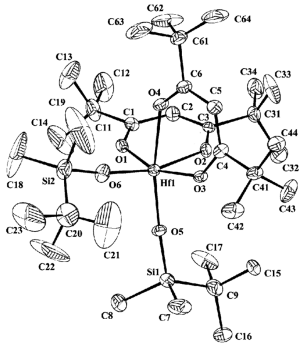


Liliane G. Hubert-Pfalzgraf, Nadia Touati, Sergej V. Pasko, J. Vaissermann, Adulfas Abrutis

Polyhedron 24 (2005) 3066

Synthesis and characterisation of $Hf(thd)_2X_2$ derivatives [X = $N(SiMe_3)_2$, $OSiMe_3$ and OSi^tBuMe_2] as precursors for MOCVD of hafnium silicate films

Volatile hafnium β-diketonato derivatives namely $Hf(thd)_2[N(SiMe_3)_2]_2$ (**3**), $Hf(thd)_2(OSiMe_3)_2$ (**4**) and $Hf(thd)_2(OSi^tBuMe_2)_2$ (**5**) (thd = 2,2,6,6-tetramethyl-3,5-heptanedionate) were synthesized and characterized by FT-IR, ^1H NMR, TGA. and by single-crystal X-ray diffraction for $Hf(thd)_3Cl$ and **5**. These compounds were tested as single-source precursors for the deposition of $HfSi_xO_y$ films by pulsed liquid injection MOCVD on Si(100) and R plane sapphire. The films were characterized by XRD and XPS. The as-deposited at 600–800 °C films were essentially amorphous, Hf-rich, smooth and quite pure with respect to carbon contamination

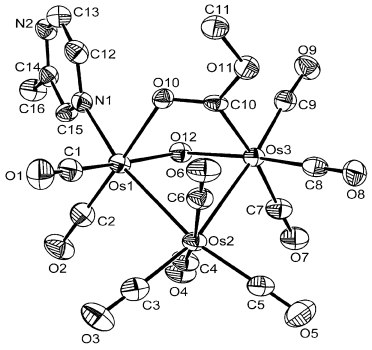


Noorjahan Begum, Amarash C. Ghosh, Shariff E. Kabir, Md. Arzu Miah, G.M. Golzar Hossain

Polyhedron 24 (2005) 3074

Synthesis, structures and reactivity of triosmium clusters containing terminal pyrazines, bridging hydroxy and methoxycarbonyl ligands

Four triosmium carbonyl clusters bearing terminal pyrazines, bridging hydroxy and methoxycarbonyl ligands of general formula $[Os_3(CO)_9(\mu\text{-OH})(\mu\text{-OMeCO})L]$ (**1**, L = pyrazine; **2**, L = 2-methylpyrazine; **3**, L = 2, 3-dimethylpyrazine; **4**, L = 2, 3, 5-trimethylpyrazine) were synthesized by the reactions of $[Os_3(CO)_{12}]$ with the corresponding pyrazine derivatives and water in the presence of a methanolic solution of Me_3NO in moderate yields. The reactions of $[Os_3(CO)_9(\mu\text{-OH})(\mu\text{-OMeCO})L]$ with a series of two electron donor ligands L′ afforded $[Os_3(CO)_9(\mu\text{-OH})(\mu\text{-OMeCO})L']$ (**5**, L′ = PPh_3; **6**, L′ = $P(OMe)_3$; **7**, L′ = ^{t}BuNC; **8**, L′ = C_5H_5N) in high yields.

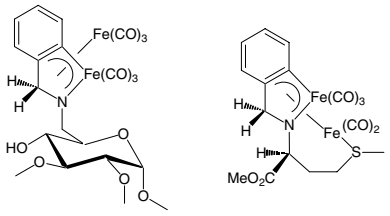


Wolfgang Imhof, Angela Göbel, Linda Schweda, Helmar Görls

Polyhedron 24 (2005) 3082

Synthesis and characterization of chiral iron carbonyl complexes from imine ligands with carbohydrates and amino acids as substituents

Imines derived from 6-amino-6-desoxy-1,2,3-*O*-trimethyl-α-d-glucopyranose or from various amino acid esters react with $Fe_2(CO)_9$ to produce chiral iron carbonyl complexes. The molecular structure of the diiron hexacarbonyl complex of benzylideneamino-l-methionine methyl ester shows that in addition to the α,β-unsaturated imine moiety the sulphur atom of the amino acid side-chain is engaged in binding the metal centres.

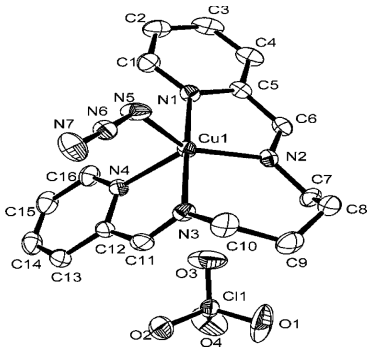


Sk Hafijur Rahaman, Hoong-Kun Fun, Barindra Kumar Ghosh

Polyhedron 24 (2005) 3091

A study on copper(II)-Schiff base-azide coordination complexes: Synthesis, X-ray structure and luminescence properties of $[Cu(L)(N_3)]X$ (L = Schiff bases; X = ClO_4, PF_6)

Two Schiff bases *N*,*N*′-(bis(pyridin-2-yl)benzylidene)propane-1,3-diamine (pbpd) and *N*,*N*′-(bis(pyridin-2-yl)formylidene)butane-1,4-diamine (pfbd) have been used to synthesize four complexes of the type $[Cu(L)(N_3)]X$ (**1**–**4**) [L = pbpd; X = ClO_4 (**1**); L = pbpd; X = PF_6 (**2**); L = pfbd; X = ClO_4 (**3**); L = pfbd; X = PF_6 (**4**)]. Two representative members of the series, **2** and **3**, have been characterized by single crystal X-ray diffraction measurements. They display intraligand $^1(\pi\text{–}\pi)$ fluorescence at room temperature and intraligand $^3(\pi\text{–}\pi)$ phosphorescence in glassy solutions (MeOH at 77 K). Electrochemical electron transfer study reveals Cu^{II}–Cu^{I} reduction in methanolic solutions.



Author Index to Volume 24 3099
Subject Index to Volume 24 3111

The Publisher encourages the submission of articles in electronic form thus saving time and avoiding rekeying errors. For detailed instructions on the preparation of manuscripts and of electronic artwork, consult the Author Gateway for Elsevier at http://authors.elsevier.com

SCIENCE DIRECT®

Full text of this journal is available, on-line from **ScienceDirect**. Visit **www.sciencedirect.com** for more information.

CONTENTS direct

This journal is part of **ContentsDirect,** the ***free*** alerting service which sends tables of contents by e-mail for Elsevier books and journals. You can register for **ContentsDirect** online at: **http://contentsdirect.elsevier.com**

Available online at www.sciencedirect.com
SCIENCE DIRECT®
Polyhedron 24, issue 2, 27 January 2005
POLYHEDRON
www.elsevier.com/locate/poly

Contents

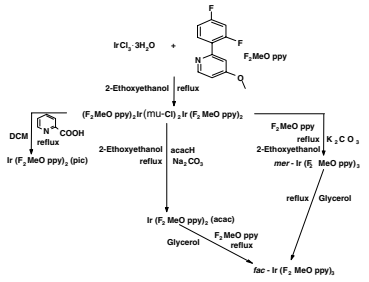
Papers

Inamur R. Laskar, Shih-Feng Hsu, Teng-Ming Chen

Polyhedron 24 (2005) 189

Syntheses, photoluminescence and electroluminescence of some new blue-emitting phosphorescent iridium(III)-based materials

Some blue-emitting iridium(III) based phosphorescent materials were synthesized and their photoluminescence and electroluminescence behaviors were studied. The relative thermodynamic stability of the *mer* versus *fac* isomer was investigated and correlated to their corresponding redox and photoluminescence properties. The fabrication of a device using *m*CP as the host exhibited improved electroluminescence performance.

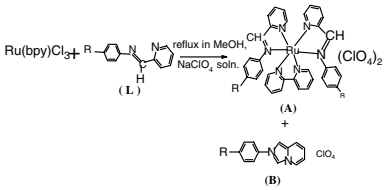


Dipankar Mishra, Subhendu Naskar, Bibhutosh Adhikary, Raymond J. Butcher, Shyamal Kumar Chattopadhyay

Polyhedron 24 (2005) 201

Synthesis, spectroscopic and electrochemical properties of some heteroleptic tris-chelates of ruthenium (II) involving 2,2′-bipyridine (bpy) and *N*-(aryl) pyridine-2-aldimine(L): X-ray crystal structures of $[Ru(bpy)(L_2)_2](ClO_4)_2{\cdot}H_2O$ and 3-*N*(4-tolyl) imidazo [1,5a] pyridinium perchlorate

Reactions of $Ru(bpy)Cl_3$' with *N*-(aryl) pyridine-2-aldimine(L) afford the heteroleptic tris chelate metal complex of the formula $[Ru(bpy)(L)_2](ClO_4)_2{\cdot}H_2O$ (**A**) along with an unusual organic compound, 3-*N*(4-aryl) imidazo [1,5a] pyridinium perchlorate (**B**). One representative member of each has been characterized by X-ray crystallography. All the complexes undergo a quasi-reversible oxidation at ~1.3 to 1.4 V, which may be assigned to a Ru(II) to Ru(III) oxidation. The visible region of the electronic spectra of the complexes consists of a weak transition at ~630 nm and a broad envelope from 600 to 375 nm. 3-*N*(4-Tolyl) imidazo [1,5a] pyridinium perchlorate exhibits luminescence, with a strong emission at ~380 nm.

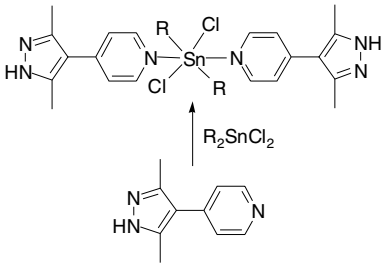


Qian Cui, Xiu-Ying Cao, Liang-Fu Tang

Polyhedron 24 (2005) 209

Diorganotin(IV) derivatives containing the 3,5-dimethyl-4-(4′-pyridyl)pyrazole ligand

The reaction of 3,5-dimethyl-4-(4′-pyridyl)pyrazole with R_2SnCl_2 (R=Ph, Et and *n*-Bu) in a 1:1 ratio yields 2:1 (ligand:tin) adducts, while the reaction of bis[3,5-dimethyl-4-(4′-pyridyl)pyrazol-1-yl]methane with R_2SnCl_2 yields six-coordinate diorganotin linkage coordination polymers.

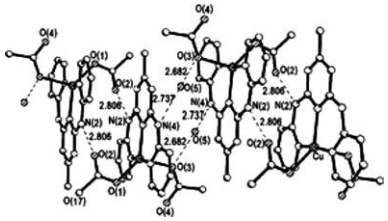


Hai-Rui Ma, Yao-Yu Wang, Ping Liu, Dong-Sheng Li, Qi-Zhen Shi, Gene-Hsiang Lee, Shie-Ming Peng

Polyhedron 24 (2005) 215

Synthesis, characterization and crystal structures of 2,4-di(2-aminopyridine)-6-methypyrimidine (dapmp), $[Cu(dapmp)Cl_2]$ and $[Cu(dapmp)(CH_3COO)_2] \cdot H_2O$

The new ligand dapmp (**1**) and two crystalline polymorphic forms: $[Cu(dapmp)Cl_2]$ (**2**) and $[Cu(dapmp)(CH_3COO)_2] \cdot H_2O$ (**3**), have been synthesized. Single crystal X-ray diffraction showed that (**1**) and (**2**) are each connected by hydrogen bonding to form a one-dimensional supermolecular compound, and (**3**) is connected by hydrogen bonding to form a three-dimensional supermolecular compound.

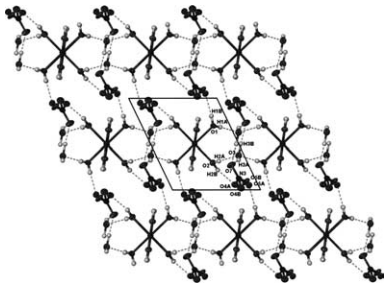


K. Travis Holman, Hassan H. Hammud, Samih Isber, Malek Tabbal

Polyhedron 24 (2005) 221

One-dimensional coordination polymer $[Co(H_2O)_4(pyz)](NO_3)_2 \cdot 2H_2O$ (pyz=pyrazine) with intra- and inter-chain H-bonds: structure, electronic spectral studies and magnetic properties

Complex (**1**) $[Co(H_2O)_4(pyrazine)](NO_3)_2 \cdot 2H_2O$ forms a one-dimensional coordination polymer along the crystallographic *b*-axis. Hydrogen-bonding between chains forms a two-dimensional network in the *ac*-plane. The solvent effect on the electronic spectra of pyrazine and pyrazine cobalt complex **1** has been investigated. The magnetic susceptibility of **1** versus temperature data showed a strong antiferromagnetic coupling between Co ions.

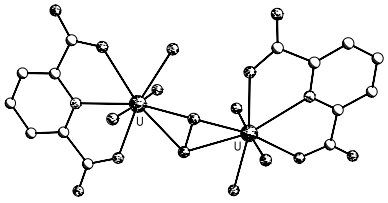


Bernardo Masci, Pierre Thuéry

Polyhedron 24 (2005) 229

Uranyl complexes with the pyridine-2,6-dicarboxylato ligand: new dinuclear species with μ-η^2,η^2-peroxide, μ_2-hydroxide or μ_2-methoxide bridges

New dinuclear uranyl complexes are formed with pyridine-2,6-dicarboxylic acid in the presence of tertiary amines. The two uranyl ions, each of them bound to the nitrogen and two carboxylate groups of the ligand, are bridged by μ-$\eta\eta^2$-peroxide, μ_2-hydroxide or μ_2-methoxide ions. The latter case is the first example of uranyl-bridging methoxide ions to be crystallographically characterized.

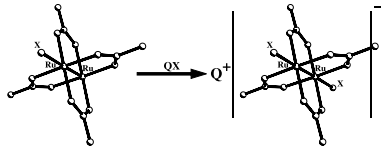


M.C. Barral, R. González-Prieto, S. Herrero, R. Jiménez-Aparicio, J.L. Priego, M.R. Torres, F.A. Urbanos

Polyhedron 24 (2005) 239

Anionic dihalotetraacetatodiruthenium(II,III) compounds

The synthesis and characterization of $Q[Ru_2Cl_2(\mu\text{-}O_2CMe)_4]$ [Q=NEt_4 (**1**), PPh_4 (**2**)], $Q[Ru_2Br_2(\mu\text{-}O_2CMe)_4]$ [Q=NEt_4 (**3**), PPh_4 (**4**), K (**5**)] and $Q[Ru_2I_2(\mu\text{-}O_2CMe)_4]$ [Q=NEt_4 (**6**), PPh_4 (**7**)] are described. The structure of **1**–**3**, **5** and **7** were determined by the single crystal X-ray diffraction method. The electronic properties of all compounds are also explored. Their solvatochromism is less accentuated than the corresponding monohalo derivatives.

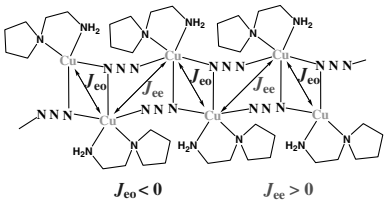


Young Sin You, Chang Seop Hong, Kwan Mook Kim

Polyhedron 24 (2005) 249

Azido-bridged Cu(II) compounds with asymmetric end-to-end and end-on binding modes: magnetic assignments using a spin dimer model

Dinuclear $[Cu(aepi)(N_3)_2]_2$ (**1**) [aepi=1-(2-aminoethyl)piperidine] and 1D chain $[Cu(aepy)(N_3)_2]_n$ (**2**) [aepy=1-(2-aminoethyl)pyrrolidine] have been prepared and characterized by means of X-ray analysis and magnetic measurements. For **1**, the Cu(II) centers are doubly bridged by end-on (EO) azido units in a basal–apical fashion. The molecular structure of **2** features magnetic centers that are linked by μ-1,1,3 azido groups, forming a 1D chain with alternating EO and end-to-end (EE) azido bridging patterns. Magnetic data for **1** and **2** reveal that ferromagnetic and antiferromagnetic interactions are mediated through EE and EO azido bridges, respectively. These assignments are also confirmed by MO calculations using spin dimer model.

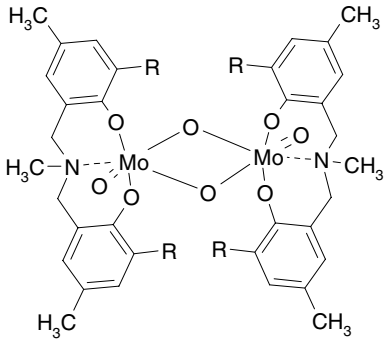


Ari Lehtonen, Reijo Sillanpää

Polyhedron 24 (2005) 257

Dioxomolybdenum(VI) complexes with tri- and tetradentate aminobis(phenolate)s

The reactions of tridentate aminobis(phenol)s with $[MoO_2(acac)_2]$ in methanol lead to the precipitation of monomeric dioxomolybdenum(VI) complexes $[MoO_2(ONO)(MeOH)] \cdot MeOH$. Identical reactions in acetonitrile provide dimeric complexes $[Mo_2O_2(\mu\text{-}O)_2(ONO^R)_2]$. $[MoO_2(acac)_2]$ reacts with tetradentate diaminobis(phenol)s to yield monomeric complexes of type $[MoO_2(ONNO^R)]$. All studied complexes catalyse oxotransfer reactions between DMSO and benzoin or PPh_3.

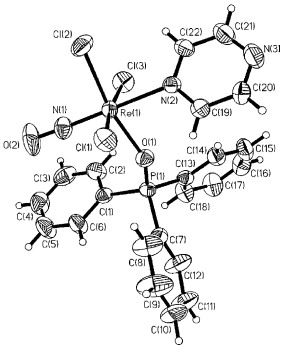


B. Machura, M. Jaworska, R. Kruszynski

Polyhedron 24 (2005) 267

The synthesis, spectroscopic characterisation, crystal and molecular structure of the $[ReCl_3(NO)(OPPh_3)(pyz)]$ complex. DFT calculations for $[ReCl_3(NO)(OPPh_3)(pyz)]$ and $[ReCl_3(NO)(OPPh_3)(PPh_3)]$

The $[ReCl_3(NO)(OPPh_3)(pyz)]$ (**1**) complex has been obtained by two different routes, and characterised by IR, UV–Vis and magnetic measurements. Its crystal and molecular structure has been determined. Theoretical studies of $[ReCl_3(NO)(OPPh_3)(pyz)]$ and the related complex $[ReCl_3(NO)(OPPh_3)(PPh_3)]$ (**2**) have been performed by the DFT method with the aim to investigate their molecular and electronic structures, spectral properties and bonding.

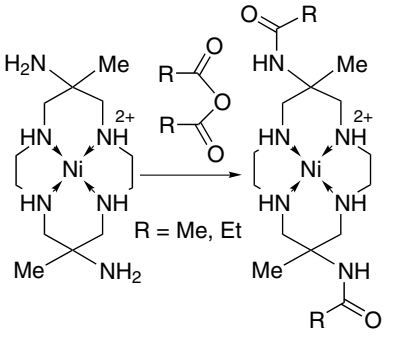


Neil F. Curtis, Horst Puschmann

Polyhedron 24 (2005) 281

Compounds of some alkylamido-substituted cyclic tetraamines with nickel(II); the structure of *trans*-$[Ni(L)(OCO_2H)(OH_2)] \cdot$ *trans*-$[Ni(L)(OH_2)_2]$ $ClO_4 \cdot (HCO_3)_2$, L= *trans*-6,13-dimethyl-6,13-bis(ethylamido)-1,4,8,11-tetraazacyclotetradecane

The amino substituents of (*trans*-6,13-diamino-6,13-dimethyl-1,4,8,11-tetraazacyclotetradecane)nickel(II) are readily acylated by reaction with acetic or propionic anhydrides to form the 6,13-bismethylamido-(acetylamido) or 6,13-bis(propionylamido)-(ethylamido) substituted cations, [Ni(diamme)]or $[Ni(diamet)]^{2+}$.

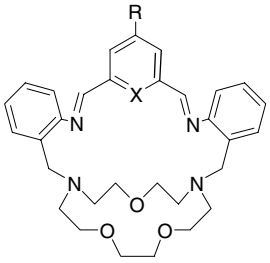


David Esteban, Carlos Platas-Iglesias, Fernando Avecilla, Andrés de Blas, Teresa Rodríguez-Blas

Polyhedron 24 (2005) 289

Barium(II) thiocyanate templating Schiff-base lateral macrobicycles derived from 1,10-diaza-15-crown-5

Herein we discuss the formation of the Schiff-base lateral macrobicycles $\mathbf{L^1}$ and $\mathbf{L^2}$ in the presence of barium thiocyanate, and we describe the X-ray crystal structure of the corresponding barium complex with $\mathbf{L^1}$, comparing it to that previously described for the perchlorate analogue.



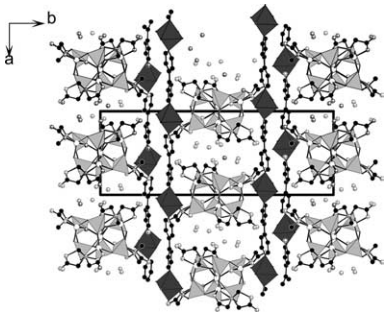
$\mathbf{L^1}$: R = H, X = N
$\mathbf{L^2}$: R = CH_3, X = C-OH

Chong Lei, Jiang-Gao Mao, Yan-Qiong Sun, Zhen-Chao Dong

Polyhedron 24 (2005) 295

Novel inorganic–organic hybrids based on oxo-bridged M_6(M) centered octahedral cage

Three new polyoxometalates, namely, $Cd_9L_6(H_2O)_{12} \cdot 19H_2O$ (**1**) (L=MeN(CH_2-CO_2)(CH_2PO_3)),$\{Zn_7L_6\}\{Ni(bipy)(H_2O)_4\}_2 \cdot 16H_2O$ (**2**) (bipy=4,4-bipyridine) and $[H_3O]$-$\{Zn_7L_6\}\{Ni(H_2O)_2(bipy)_2\}_{1.5} \cdot 12H_2O$ (**3**) are reported. The $[Cd_6(Cd)L_6]$ cages in **1** are interconnected by Cd_2O_2 dimeric units into a 2D layer. The $\{Zn_6(Zn)L_6\}$ clusters in **2** and **3** remain isolated.

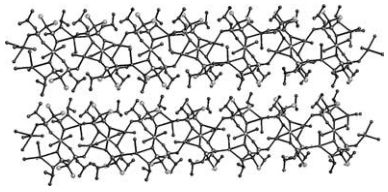


Mervi Kontturi, Sirpa Peräniemi, Jouko J. Vepsäläinen, Markku Ahlgrén

Polyhedron 24 (2005) 305

X-ray diffraction study of bisphosphonate metal complexes: Mg and Ca complexes of (dichloromethylene)bisphosphonic acid *P*,*P*′-diisopropyl ester

Preparation and X-ray structural characterisation of Mg(II) and Ca(II) complexes of *P*,*P*′-diisopropyl(dichloromethylene)bisphosphonate, $[Na_2Mg\{Cl_2C(PO_3iPr)_2\}_2(H_2O)_4]_n$ (**1**) and $[\{Ca_2[Cl_2C(PO_3iPr)_2]_2(EtOH)_2$-$(H_2O)_2\} \cdot H_2O]_2$ (**2**) were carried out. Compound **1** consists of one-dimensional chains along the *c*-direction, and compound **2** is a tetramer; the bisphosphonato ligand acts as chelating and bridging ligand in both compounds.

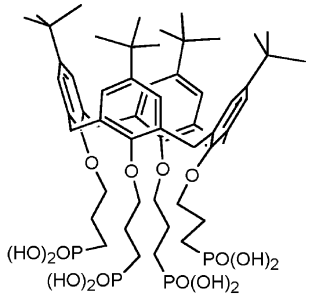


Irena Matulková, Jan Rohovec

Polyhedron 24 (2005) 311

Synthesis, characterization and extraction behaviour of calix[4]arene with four propylene phosphonic acid groups on the lower rim

A new calix[4]arene based ligand bearing four phosphonic acid groups was prepared. The compound was characterized by NMR spectroscopy. The obtained compound proved useful as extractant for certain lanthanide ions (La^{3+}, Eu^{3+}, Yb^{3+}).

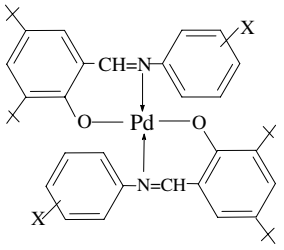


Veli T. Kasumov, Eşref Taş, F. Köksal, Şeniz Özalp-Yaman

Polyhedron 24 (2005) 319

Synthesis, characterization, redox behavior and hydrogenation catalytic activity of bis(*N*-aryl-3, 5-Bu^t_2-salicylaldiminato)palladium(II) complexes

The synthesis, spectroscopic (^{1}H NMR, IR, UV–Vis), electron-transfer properties and catalytic reactivity of new bis(*N*-aryl-3, 5-Bu^t_2-salicylaldiminato)palladium(II) complexes are presented. Introduction of *t*-Bu groups on the salicylic ring increases their catalytic activity towards hydrogenation of nitrobenzene in DMF. The oxidation of the complexes with $(NH_4)_2Ce(NO_3)_6$ generates Pd(II)-phenoxyl radical complexes and nitroxide radicals.



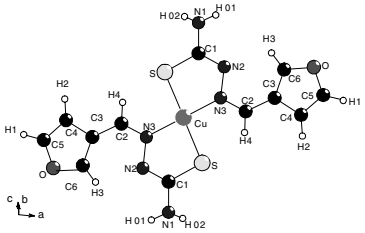
X = H, 2-F, 4-F, 2-Cl, 4-Cl
2-Br, 4-Br, 2-CH_3, 4-CH_3,
2-OCH_3, 4-OCH_3, 4-t-Bu,
5,6-benzo

El Mostapha Jouad, Magali Allain, Mustayeen A. Khan, Gilles M. Bouet

Polyhedron 24 (2005) 327

Structural and spectral studies of nickel(II), copper(II) and cadmium(II) complexes of 3-furaldehyde thiosemicarbazone

The synthesis and characterisation of Ni(II), Cu(II) and Cd(II) complexes of 3-furaldehyde thiosemicarbazone (3FTSC) are reported. The crystal structure of the complex $[Cu(3FTSC)_2]$ is described. In Cu(II) and Ni(II) complexes, the metal ion is coordinated through the S and the N-azomethine atoms while in the Cd(II) complexes the coordination occurs through sulphur and furanic oxygen atoms.



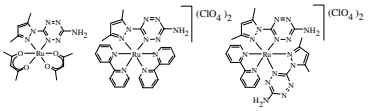
Perspective view of $[Cu(3FTSC)_2]$.

Animesh Nayak, Srikanta Patra, Biprajit Sarkar, Sandeep Ghumaan, Vedavati G. Puranik, Wolfgang Kaim, Goutam Kumar Lahiri

Polyhedron 24 (2005) 333

Tetrazine derived mononuclear $Ru^{II}(acac)_2(L)$ (**1**), $[Ru^{II}(bpy)_2(L)](ClO_4)_2$ (**2**) and $[Ru^{II}(bpy)(L)_2](ClO_4)_2$ (**3**) (L=3-amino-6-(3,5-dimethylpyrazol-1-yl)-1,2,4,5-tetrazine, acac= acetylacetonate, bpy=2,2′-bipyridine): syntheses, structures, spectra and redox properties

Tetrazine derived rather uncommon mononuclear ruthenium complexes **1**, **2** and **3** were prepared. The free tetrazine based ligand exists as a dimeric entity in the solid state via hydrogen bonding interactions with water molecules present in the lattice. **1** Exhibits unusually strong bonds especially from Ruto tetrazine-N (1.913(2) Å).



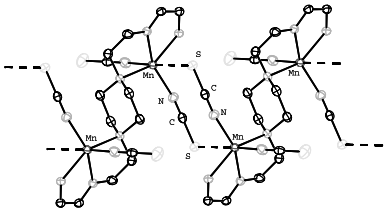
1 **2** **3**

Soma Deoghoria, Sujit K. Bera, Brian Moulton, Michael J. Zaworotko, Jean-Pierre Tuchagues, Golam Mostafa, Tian-Huey Lu, Swapan K. Chandra

Polyhedron 24 (2005) 343

Synthesis, crystal structure, and magnetic properties of binuclear Mn^{III}-azido and 1D polymeric Mn^{II}-$\mu_{1,3}$-thiocyanato novel species based on a neutral hexadentate Schiff base

The binuclear manganese(II) units of this novel 1D chain are bridged via two $\mu_{1,3}$-NCS anions. In spite of the quite long Mn···S distance (3.084 Å), weak intermolecular antiferromagnetic interactions (J=−1.5 cm^{-1}) are transmitted by the $\mu_{1,3}$-NCS bridges between pairs of Mnions located at 6.2 Å of each other.

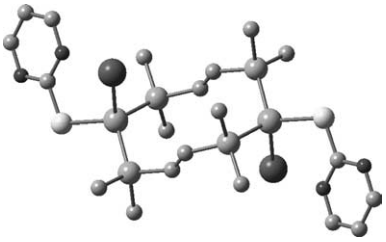


S. Divanidis, P.J. Cox, P. Karagiannidis, P. Aslanidis

Polyhedron 24 (2005) 351

Linking thione-ligated copper(I) centres with *trans*-1,2-bis(diphenylphosphino)ethene (*trans*-dppen): crystal structures of the pyrimidine-2-thione derivatives [CuBr(μ_2-*trans*-dppen)(pymtH)]$_2$ and [CuI(μ_2-*trans*-dppen)(pymtH)]$_2$

The behaviour of the diphos ligand *trans*-1,2-bis (diphenylphosphino)ethene (*trans*-dppen) towards coordination of CuX [X=Br, I] in the presence of several heterocyclic thione ligands has been investigated. The diphos ligand adopts the doubly-bridging coordination mode whereby the thiones are terminally bound through the exocyclic sulfur atom, leading to the formation of homobimetallic complexes of type [CuX(μ_2-*trans*-dppen)L]$_2$. The crystal structures of two examples of the novel complexes have been characterized by X-ray crystallography.

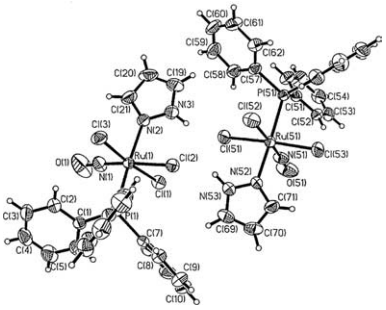


J.G. Maecki, M. Jaworska, R. Kruszynski

Polyhedron 24 (2005) 359

Synthesis, molecular, crystal and electronic structure of [$RuCl_3$(NO)(PPh_3)(HPz)]

New ruthenium nitrosyl complex [$RuCl_3$(NO)(PPh_3)(HPz)] has been obtained in the reaction of [$RuCl_3$(NO)(PPh_3)$_2$] with pyrazole. The complex has been characterized by IR and UV–Vis spectroscopy. The X-ray structure of the compound has been determined. The geometric parameters and UV–Vis spectrum of investigated complex have been examined using the density functional theory method.

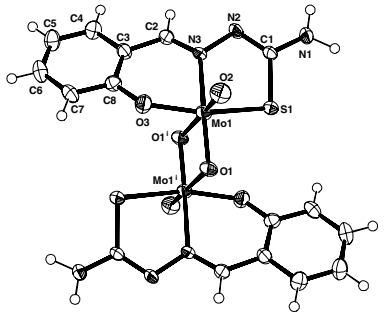


Marina Cindrić, Višnja Vrdoljak, Neven Strukan, Boris Kamenar

Polyhedron 24 (2005) 369

Synthesis and characterization of some mono- and dinuclear molybdenum(VI) thiosemicarbazonato complexes

Mononuclear [MoO_2{C_6H_4(O)CH:NNC(S)NH_2}(D)] and [MoO_2{C_6H_4(O)CH:NNHC(S)NH}(CH_3OH)]·CH_3OH·1/2D and dinuclear [MoO_2{C_6H_4(O)CH:NNC(S)NH_2}(D)]$_2$ molybdenum (VI) complexes have been prepared by the reaction of [$MoO_2(C_5H_7O_2)_2$] [$C_5H_7O_2$=acetylacetonate ion] with salicylaldehyde thiosemicarbazone (C_6H_4(OH)CH:NNC(SH)NH_2) and Lewis base (D) [e.g., pyridine, γ-picoline or 4,4′-bipyridine] in dry methanol. All complexes have been characterized by means of chemical analyses, IR spectroscopy, thermogravimetric analyses and some of them by X-ray crystallography.

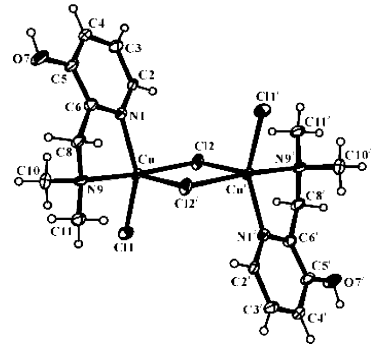


Yong-Min Lee, Hong-Woo Lee, Young-Inn Kim

Polyhedron 24 (2005) 377

Structural and magnetic characterization of copper(II) halide complexes with 2-(dimethylaminomethyl)-3-hydroxypyridine

Dimeric complexes, bis[dihalo(2-dimethylaminomethyl-3-hydroxypyridine)-copper(II)], [Cu(dmamhp)X_2]$_2$, were prepared and the geometry around the copper(II) center in the dimeric unit is a distorted trigonal bipyramid. The magnetic susceptibility data indicates that there are antiferromagnetic interactions between the copper(II) ions.



The Publisher encourages the submission of articles in electronic form thus saving time and avoiding rekeying errors. For detailed instructions on the preparation of manuscripts and of electronic artwork, consult the Author Gateway for Elsevier at http://authors.elsevier.com

SCIENCE DIRECT™

Full text of this journal is available, on-line from **ScienceDirect**. Visit **www.sciencedirect.com** for more information.

CONTENTS Direct This journal is part of **ContentsDirect**, the *free* alerting service which sends tables of contents by e-mail for Elsevier books and journals. You can register for **ContentsDirect** online at: **www. elsevier.com/locate/contentsdirect**

Available online at www.sciencedirect.com
SCIENCE DIRECT®
Polyhedron 24, issue 6, 21 April 2005
POLYHEDRON
www.elsevier.com/locate/poly

Contents

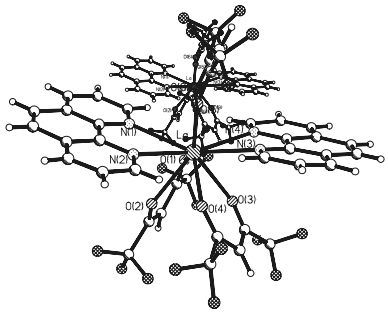
Papers

A.Yu. Rogachev, L.Kh. Minacheva, V.S. Sergienko, I.P. Malkerova, A.S. Alikhanyan, V.V. Stryapan, N.P. Kuzmina

Polyhedron 24 (2005) 723

Synthesis, crystal structure and thermal behaviour of $[La(hfa)_3(Phen)_2]$ (hfa=hexafluoroacetylacetonate, Phen=*o*-phenanthroline)

The mixed ligand complex $[La(hfa)_3Phen_2]$ was obtained by interaction of $La(hfa)_3$ and Phen, and its composition does not depend on the stoichiometry of the reagents. This compounds consists of mononuclear molecules with the coordination number being 10. Thermal behavior and composition of the vapor phase have been studied by thermal analysis and mass-spectrometry using a Knudsen cell.

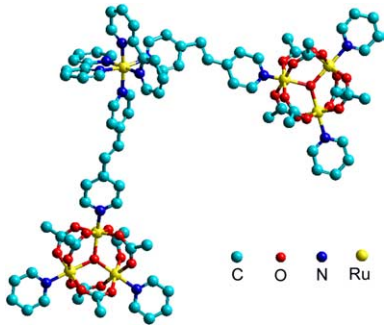


Henrique E. Toma, Sofia Nikolaou, Marcos N. Eberlin, Daniela M. Tomazela

Polyhedron 24 (2005) 731

Synthesis, properties and gas phase collision-induced dissociation of the heptanuclear doubly bridged complex $[Ru(bpy)_2(BPE)_2\{Ru_3O(CH_3COO)_6(py)_2\}_2](PF_6)_4$

The electronic coupling in the heptanuclear complex containing two triangular $[Ru_3O]$ clusters attached to a ruthenium polypyridine center, is strong enough to quench its luminescence and the *cis–trans* photoisomerization of the bridging *trans*-1,2-*bis*(4-pyridyl)ethylene (BPE) ligand.

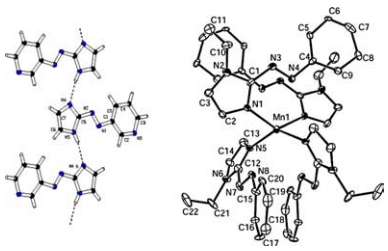


T. Mathur, U.S. Ray, J.-C. Liou, J.S. Wu, T.-H. Lu, C. Sinha

Polyhedron 24 (2005) 739

Manganese(II) complexes of pyridyl-azoimidazoles. Single crystal X-ray structures of 3′-PyaiH and $[Mn(3'\text{-PyaiEt})_4](ClO_4)_2$ (3′-PyaiH = 2-(3′-pyridylazo)imidazole; 3′-PyaiEt = 1-ethyl-2-(3′-pyridylazo)imidazole)

The X-ray structure of 2-[(3′-Pyridyl)azo]imidazole (3′-PyaiH) shows a hydrogen bonded 1D chain. 1-Alkyl-2-[(3′-pyridyl)azo]imidazole (3′-PyaiR′) gives tetrahedral $[Mn(3'\text{-PyaiR}')_4](ClO_4)_2$. The structure has been confirmed by an X-ray study in one case. Azido and thiocyanato complexes, $[Mn(3'\text{-PyaiR}')_2(X)_2]$ (X = N_3, NCS) are also described.

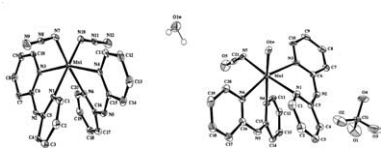


Doyel Bose, Golam Mostafa, Hoong-Kun Fun, Barindra K. Ghosh

Polyhedron 24 (2005) 747

The Mn(II)-2,2′-dipyridylamine-pseudohalide system: Synthesis, crystal structure and luminescence behaviour of $[Mn(dpa)_2(X)_2]\cdot H_2O$ and $[Mn(dpa)_2(X)(OH_2)]ClO_4$ (dpa = 2,2′-dipyridylamine; $X = N_3^-$, NCO^-)

Four mononuclear complexes of the type $[Mn(dpa)_2(X)_2]\cdot H_2O$ (dpa=2,2′-dipyridylamine; $X = N_3^-$, **1**; X = NCO, **2**) and $[Mn(dpa)_2(X)(OH_2)]ClO_4$ ($X = N_3^-$, **3**; $X = NCO^-$, **4**) were synthesized using single-pot reactions of manganese(II) salt, dpa and X in 1:2:2 and 1:2:1 molar ratios, respectively. The compounds have been characterized by X-ray crystallography, microanalytical, physicochemical, spectroscopic and magnetic results. Supramolecular 2D sheet structures are obtained, arising from N–H···N, O–H···N, N–H···O and O–H···O weak intermolecular forces. All thecomplexes display high-energyintraligand $^1(\pi-\pi*)$ fluroscence and intraligand $^3(\pi-\pi*)$ phosphorescence in glassy solutions (DMF at 77 K).

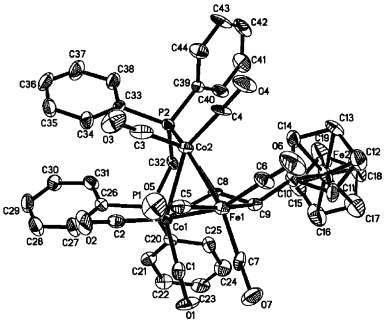


Li-Min Han, Quan-Ling Suo, Yi-Bing Wang, Jie-Hui Ye, Ning Zhu, Xue-Bing Leng, Jie Sun

Polyhedron 24 (2005) 759

Ligand substitution reaction in the parent cluster $(\mu_3\text{-FcCHC})FeCo_2(CO)_9$ and structural characterization of its CO substituted derivatives

The new substituted derivatives $(\mu_3\text{-FcCHC})FeCo_2(CO)_7$dppm (Fc = $C_5H_5FeC_5H_4$, ferrocenyl; dppm = $Ph_2PCH_2PPh_2$) (**1**), $(\mu_3\text{-FcCHC})FeCo_2(CO)_8L$ [L = PPh_3 (**2**); $AsPh_3$ (**3**)] have been synthesized by facile substitution reactions. The molecular structures and electrochemical properties of **1**, **2** and **3** were investigated by single crystal X-ray analysis and cyclic voltammetry, respectively.



Corrigendum to: "Coordination geometries in bis(di-2-pyridylamine)copper(II) complexes. Crystal structures and spectroscopic properties of $[CuL_2(H_2O)_2](S_4O_6)$, $[CuL_2(CF_3SO_3)_2]$ and $[CuL_2(SO_4)]_2[CuL_2(H_2O)_2](PF_6)_2\cdot 2H_2O$ (L = di-2-pyridylamine)" [Polyhedron 21 (2002) 247–253] 765

Corrigendum to: "The coordination chemistry of dinitrato-di-2-pyridylamine copper(II). Crystal structures of catena-poly[[(di-2-pyridylamine)(nitrato-*O*,*O*′)copper(II)]-μ-nitrato-*O*:*O*′] and bis(nitrato-*O*,*O*′)(di-2-pyridylamine)copper(II) dihydrate" [Polyhedron 21 (2002) 943–950] 767

Corrigendum to: "The crystal structure and electronic properties of a *cis*-distorted octahedral CuN_4O_2 chromophore: $[Cu(dpyam)_2(OXO)]^+$, OXO = ONO^-, O_2CH^- and ONO^-" [Polyhedron 23 (2004) 1685–1694] 769

The Publisher encourages the submission of articles in electronic form thus saving time and avoiding rekeying errors. For detailed instructions on the preparation of manuscripts and of electronic artwork, consult the Author Gateway for Elsevier at http://authors.elsevier.com

SCIENCE DIRECT™

Full text of this journal is available, on-line from **ScienceDirect**. Visit **www.sciencedirect.com** for more information.

CONTENTS Direct

This journal is part of **ContentsDirect**, the *free* alerting service which sends tables of contents by e-mail for Elsevier books and journals. You can register for **ContentsDirect** online at: **www. elsevier.com/locate/contentsdirect**

Available online at www.sciencedirect.com
SCIENCE DIRECT®
Polyhedron 24, issue 7, 12 May 2005
POLYHEDRON
www.elsevier.com/locate/poly

Contents

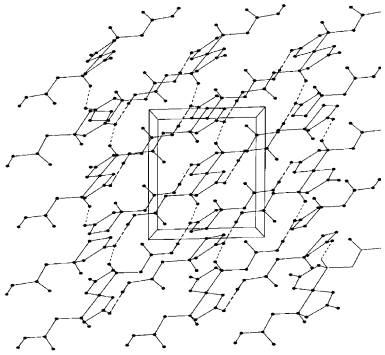
Papers

Jishnunil Chakraborty, Heike Mayer-Figge, William S. Sheldrick, Pradyot Banerjee

Polyhedron 24 (2005) 771

Self-assembly of $[M(Hida)_2]$ ($Hida^-$=iminodiacetate; M=Pd and Pt) in a 2D supramolecular network via extensive hydrogen bonded interactions: Synthesis, X-ray crystal structure, spectroscopic and thermal studies

Reaction of the typically tridentate iminodiacetate ligand (N,O,O′) with M=Pd(II) and Pt(II) results in the self-assembly of $[M(Hida)_2]$ showing 2D supramolecular network via extensive intermolecular hydrogen bonding.

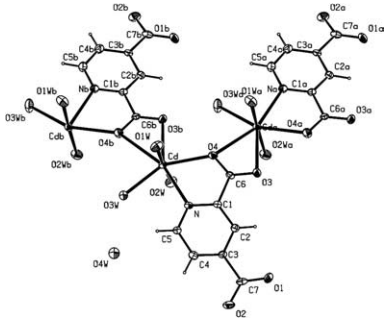


Guillermo Mendoza-Díaz, Graciela Rigotti, Oscar E. Piro, Elsa E. Sileo

Polyhedron 24 (2005) 777

Solid-state ^{111}Cd NMR studies on cadmium(II)-2,*x*-pyridinedicarboxylates. Crystal structure of 2,4-pyridinedicarboxylato triaqua cadmium(II) hemihydrate: $[Cd(II)(2,4\text{-}pydc)(H_2O)_3]\cdot 1/2H_2O$

This paper reports the synthesis and characterisation by solid-stateCd NMR of cadmium 2,*x*-pyridine-dicarboxylates. ^{111}Cd NMR chemical shift is sensitive to the relative position of both carboxylates. The crystal and molecular structure of the seven-coordinated cadmium complex, $[Cd(2,4\text{-}pyridinedicarboxylato)(H_2O)_3]\cdot 1/2H_2O$ is reported. This structure helps in the understanding of how to correlatate coordination and geometry with ^{111}Cd chemical shifts. Anisotropy data is reported.

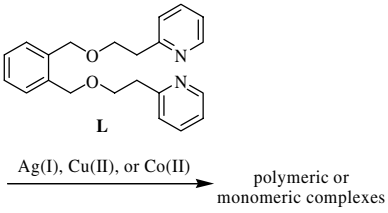


Christiana Siaw-Lattey, Hongming Zhang, David Y. Son

Polyhedron 24 (2005) 785

Synthesis and characterization of a versatile bis(pyridylether) ligand and its complexes with Ag(I), Cu(II) and Co(II)

Ligand **L** reacts with $AgNO_3$ to give a polymer, with $Cu(ClO_4)_2$ to give a bridged dinuclear complex, and with $Co(NCS)_2$ to give a monomeric octahedral complex.



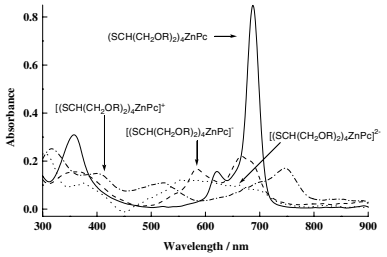
Elsevier Ltd.

Ismail Yilmaz, Ayşegül Gürek, Vefa Ahsen

Polyhedron 24 (2005) 791

Synthesis, electrochemical, and spectroelectrochemical properties of tetrakis(13, 17-dioxa nonacosane-15-sulphanyl)phthalocyaninato zinc(II)

Tetrakis(13,17-dioxa nonacosane-15-sulphanyl) phthalocyaninato zinc(II), ZnPc(SCH(CH_2-$OR)_2)_4$, where R=$C_{12}H_{25}$, was synthesised and investigated electrochemically and spectroelectrochemically in dichloromethane. The well-defined UV–Vis spectra of the electro-reduced and electro-oxidised species of the complex obtained by applied potentials in a thin-layer cell provide a good evaluation of spectral changes. The former shows dimeric formation of the mono-cationic species, while the latter gives characteristic spectral changes corresponding to mono- and di-anionic species of zinc phthalocyanines.

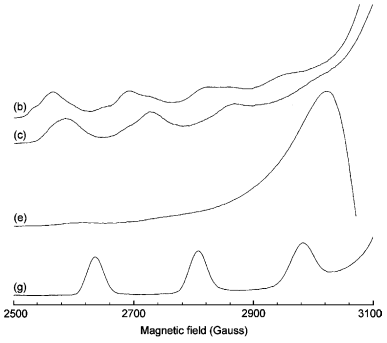


K. Várnagy, E. Garribba, D. Sanna, I. Sóvágó, G. Micera

Polyhedron 24 (2005) 799

Potentiometric and spectroscopic studies on copper(II) complexes of non-proteinogenic histidine analogues

The amino and carboxylate functions are the main binding sites of all non-proteinogenic histidine analogues. The interaction of aromatic triazolyl and pyridyl nitrogen atoms with copper(II) ions is detected in polynuclear and mononuclear complexes, respectively. ^{63}Cu(II)–Triaz-Ala system at 1:2 metal-to-ligand molar ratio and different pH values (b) 2.24 (c) 3.03; (e) 4.00; (g) 10.27.

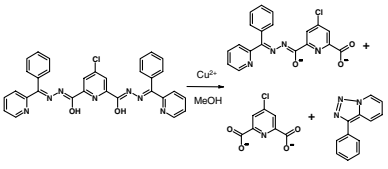


Timothy L. Kelly, Victoria A. Milway, Hilde Grove, Virginie Niel, Tareque S.M. Abedin, Laurence K. Thompson, Liang Zhao, Rosemary G. Harvey, David O. Miller, Michael Leech, Andrés E. Goeta, Judith A.K. Howard

Polyhedron 24 (2005) 807

Complexes derived from hydrolytically 'unstable' hydrazone ligands – Some unexpected products

Solvolytically unstable hydrazone ligands produce unexpected products when reacted with certain transition metal ions in solvents containing water, which often are only revealed from X-ray crystallographic studies. Several examples are highlighted, and their structural and magnetic properties are examined.

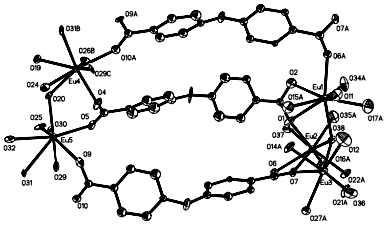


Yi-Bo Wang, Chang-Yan Sun, Xiang-Jun Zheng, Song Gao, Shao-Zhe Lu, Lin-Pei Jin

Polyhedron 24 (2005) 823

Synthesis and characterization of new polynuclear lanthanide coordination polymers with 4,4′-oxybis(benzoic acid)

Three new polynuclear lanthanide coordination polymers $[Ln_5(\mu_3\text{-OH})(oba)_7(H_2O)_2]_n \cdot 0.5nH_2O$ (Ln=Eu (**1**), Ho (**2**)) and $[Yb_6(oba)_9(H_2O)]_n$ (**3**) (H_2oba=4,4′-oxybis (benzoic acid)), were prepared by hydrothermal reactions and characterized by single crystal X-ray diffraction. They show complicated three-dimensional structures based on building blocks of polynuclear lanthanide species.

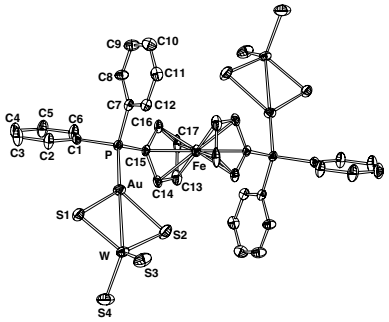


Li Song, Sheng-Qing Xia, Sheng-Min Hu, Shao-Wu Du, Xin-Tao Wu

Polyhedron 24 (2005) 831

Syntheses, crystal structures and characterization of a series of heterothiometallic gold(I) complexes containing bridging diphosphine ligands

A series of tetranuclear heterothiometallic clusters $[Et_4N]_2[(MS_4)_2Au_2(dppe)]$ (**1**: M=Mo; **2**: M=W), $[PPh_4]_2[(MoOS_3)_2Au_2(dppe)]$ (**3**), $[Et_4N]_2[(WOS_3)_2Au_2(dppe)]$ (**4**), $[Et_4N]_2[(MS_4)_2Au_2(dppf)]$ (**5**: M=Mo; **6**: M=W) and $[Et_4N]_2[(MOS_3)_2Au_2(dppf)]$ (**7**: M=Mo; **8**: M=W) have been synthesized. In the molecular structures of **2**, **4** and **6**, the two linear M/Au/S units are linked via bidentate phosphines, dppe or dppf. These clusters all exhibit room-temperature luminescence in the solid state.



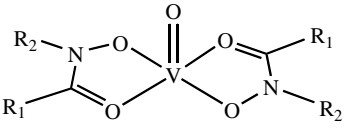
$[(WS_4)_2Au_2(dppf)]^{2-}$ anion of **6**

Péter Buglyó, Norbert Pótári

Polyhedron 24 (2005) 837

Study of the interaction between oxovanadium(IV) and hydroxamic acids

Mono- and dihydroxamic acids were found to be able to oxidise oxovanadium(IV) at pH ~ 5 according to the following equation: $2VO(R_1CON(R_2)O)_2 + R_1CON(R_2)OH + H_2O = 2[VO_2(R_1CON(R_2)O)_2]^- + 2H^+ + R_1CON(R_2)H$ (R_1: CH_3, C_6H_5; R_2: H, CH_3).

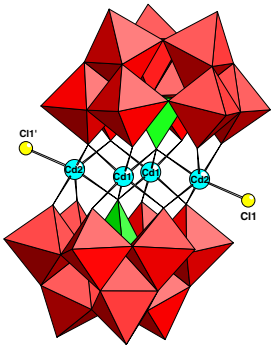


Firasat Hussain, Li-Hua Bi, Urs Rauwald, Markus Reicke, Ulrich Kortz

Polyhedron 24 (2005) 847

Structure and solution properties of the cadmium(II)-substituted tungstoarsenate $[Cd_4Cl_2(B\text{-}\alpha\text{-}AsW_9O_{34})_2]^{12-}$

We report on the synthesis and structure of the cadmium(II)-substituted tungstoarsenate $[Cd_4Cl_2(B\text{-}\alpha\text{-}AsW_9O_{34})_2]^{12-}$ (**1**). Polyanion **1** consists of two lacunary $[B\text{-}\alpha\text{-}AsW_9O_{34}]^{9-}$ Keggin moieties linked via a rhomblike $(Cd_4O_{14}Cl_2)$ group leading to a sandwich-type structure. Interestingly, the two external Cd atoms have a terminal Cl ligand, but the derivative with terminal water ligands, $[Cd_4(H_2O)_2(B\text{-}\alpha\text{-}AsW_9O_{34})_2]$(**2**), can also be prepared as shown by ^{183}W and ^{111}Cd solution NMR.

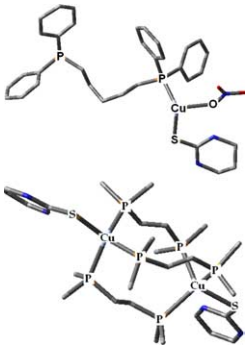


P. Aslanidis, S. Divanidis, P.J. Cox, P. Karagiannidis

Polyhedron 24 (2005) 853

Polymer and cage-type structures in silver(I) complexes with heterocyclic thiones and bridging diphosphine ligands. Crystal structures of $[Ag(\mu\text{-dpppent})(tHpymtH)(ONO_2)]_n$ and $[Ag_2(\mu\text{-}trans\text{-dppen})_3(pymtH)_2](NO_3)_2 \cdot CH_3CN$

The behaviour of the diphos ligands 1,5-bis-(diphenylphosphino)pentane (dppent) and *trans*-1,2-bis(diphenylphosphino)ethene (*trans*-dppen) towards coordination of Ag(I) nitrate in the presence of several heterocyclic thione ligands has been investigated. Both diphosphines adobt the doubly-bridging coordination mode, however, dependent on the nature of the diphos ligand, two types of products have been obtained for the tetrahedraly coordinated metal, namely polymer in the case of the longer chained dppent and triply bridged dimer for the short bite *trans*-dppen. The crystal structure of one representative for each of these two types have been characterized by X-ray crystallography.



The Publisher encourages the submission of articles in electronic form thus saving time and avoiding rekeying errors. For detailed instructions on the preparation of manuscripts and of electronic artwork, consult the Author Gateway for Elsevier at http://authors.elsevier.com



Full text of this journal is available, on-line from **ScienceDirect**. Visit **www.sciencedirect.com** for more information.



This journal is part of **ContentsDirect**, the *free* alerting service which sends tables of contents by e-mail for Elsevier books and journals. You can register for **ContentsDirect** online at: **www. elsevier.com/locate/contentsdirect**

Available online at www.sciencedirect.com
SCIENCE DIRECT®
Polyhedron 24, issue 4, 10 March 2005
POLYHEDRON
www.elsevier.com/locate/poly

Contents

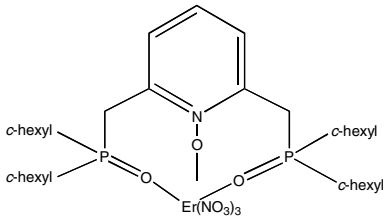
Papers

Xinmin Gan, Brian M. Rapko, Eileen N. Duesler, Iris Binyamin, Robert T. Paine, Benjamin P. Hay

Polyhedron 24 (2005) 469

The synthesis and lanthanide coordination chemistry of 2,6-bis[(dicyclohexyl)phosphino-methyl]pyridine *N*,*P*,*P*′-trioxide

The title pyridine *N*-oxide ligand and its pyridine precursor were prepared and characterized by spectroscopic methods. The coordination chemistry was examined with $Er(NO_3)_3$, and the 1:1 complex of the pyridine *N*-oxide ligand, $Er(L)(NO_3)_3 \cdot Me_2CO$, was isolated and structurally characterized by X-ray diffraction methods. The complex contains a nine coordinate Er(III) ion bonded to a tridentate ligand and three bidentate nitrate ions.

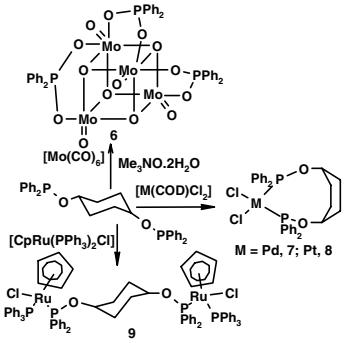


Maravanji S. Balakrishna, P.P. George, Shaikh M. Mobin

Polyhedron 24 (2005) 475

A new diphosphinite derived from cyclohexane-1,4-diol: oxidation reactions, metal complexes, P–O bond cleavage and X-ray crystal structures of $Ph_2P(E)O(C_6H_{10})OP(E)Ph_2$ (E = S, Se)

The synthesis, derivatization and transition metal complexes of $Ph_2PO(C_6H_{10})OPPh_2$ (**1**) are presented. The reaction of **1** with $Mo(CO)_6$ in the presence of $TMNO \cdot 2H_2O$ gives a cubane-shaped tetranuclear molybdenum(V) complex, $[Mo_4O_4(\mu^3\text{-}O)_4(\mu\text{-}O_2\text{-}PPh_2)_4]$ (**6**) due to water assisted cleavage of P–O bonds.

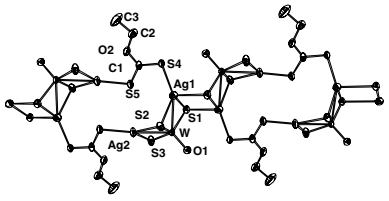


Jian-Rong Li, Zhi-Hua Li, Shao-Wu Du, Xin-Tao Wu

Polyhedron 24 (2005) 481

Syntheses, structures and characterization of heterobimetallic compounds $[Et_4N]_2[(MS_4)Ag_8(SBu^t)_8]$(M = W, Mo) and $\{[Et_4N][WOS_3Ag_2(S_2COEt)]\}_n$

Three new M/Ag/S heterobimetallic compounds $[Et_4N]_2[(MS_4)Ag_8(SBu^t)_8]$ (**1a**, M = W; **1b**, M = Mo) and $\{[Et_4N][WOS_3Ag_2(S_2COEt)]\}_n$ (**2**) have been prepared from the reactions of $[MO_nS_{4-n}]^{2-}$(M = W, Mo; n = 0–1) with $AgSBu^t$ or AgS_2COEt. Compound **1a** contains a $[WS_4]^{2-}$ dianion encapsulated in a neutral octanuclear $(AgSBu^t)_8$ cage via weak Ag···S(WS_4) interactions. Compound **2** is the first W/Ag/S polymer with bidentate thiolato linkages.



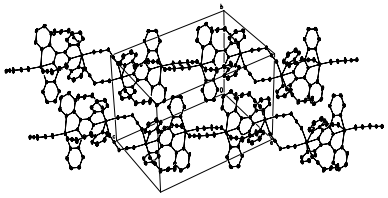
$\{[Et_4N][WOS_3Ag_2(S_2COEt)]\}_n$ **2**

Guang-Yuan Hsu, Chin-Wang Chen, Sung-Chung Cheng, Shin-Huang Lin, Ho-Hsiang Wei, Chin-Jhin Lee

Polyhedron 24 (2005) 487

Structure and magnetic properties of one-dimensional metal complexes constructed from alternating dicyanamide linked through binuclear metal tetra-2-pyridylpyrazine sub-units

The first syntheses and structures of alternating 1-D dicyanamide linked binuclear metal complexes with the ligand tetra-2-pyridylpyrazine (tppz), $[Co(tppz)](dca)_4]$ (**1**), $[Ni_2(tppz)(dca)_4]C_2H_5OH$ (**2**) and $[Cu_2(tppz)(dca)(Cl)_2](dca) \cdot H_2O$ (**3**), have been reported. Temperature dependence of magnetic measu-rements show weak antiferromagnetic couplings in all cases.

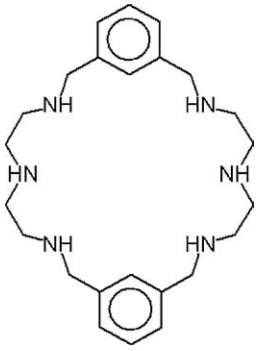


M.C.B. Oliveira, M.S.R. Couto, P.C. Severino, T. Foppa, G.T.S. Martins, B. Szpoganicz, R.A. Peralta, A. Neves, H. Terenzi

Polyhedron 24 (2005) 495

Nucleic acid cleavage by a Cu(II) polyaza macrocyclic complex

In this paper, we describe the activity of the $[Cu_2BMXD]$ complex as a nucleic acid cleav-age agent. The rate constant for the DNA backbone cleavage reaction was estimated to be $4.67 \times 10^{-2}\ h^{-1}$ at 50 °C, pH 7.0. We demonstrate that the DNA cleavage reaction promoted by this complex may occur via an oxidative pathway. This study establishes $[Cu_2BMXD]$ as a novel artificial nuclease.

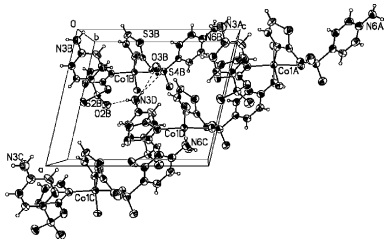


Sebastián Bellú, Estela Hure, Marcela Trapé, Claudia Trossero, Gabriel Molina, Claudia Drogo, Patricia A.M. Williams, Ana María Atria, Juan Carlos Muñoz Acevedo, Susana Zacchino, Maximilano Sortino, Darío Campagnoli, Marcela Rizzotto

Polyhedron 24 (2005) 501

Synthesis, structure and antifungal properties of Co(II)–sulfathiazolate complexes

The reaction between sulfathiazole and cobalt(II) leads to a pink solid, $[Co^{II}(ST)_2(H_2O)_4]$ (**1**), and transforms into red crystals of $[Co^{II}(ST)_2(H_2O)_3]_n$ (**2**) (ST = sulfathiazolate). The Co(II) ion exhibits an octahedral environment in both compounds. Differences between them were noted in the IR spectra in the region corresponding to signals of the amine group. Antifungal properties of (**1**) were evaluated.

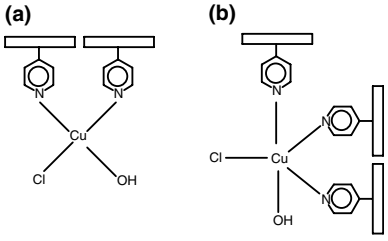


Alvaro J. Pardey, Alcides D. Rojas, Jorge E. Yánez, Paulino Betancourt, Carlos Scott, Carlos Chinea, Caribay Urbina, Delfin Moronta, Clementina Longo

Polyhedron 24 (2005) 511

Spectroscopic characterization of coordination complexes based on dichlorocopper(II) and poly(4-vinylpyridine): Application in catalysis

In this work, the formation of transition metal complexes (**a** and **b**) between $CuCl_2 \cdot 2H_2O$ and poly(4-vinylpyridine)/divinylbenzene(2%) polymeric matrix is described. The SEM/EDX, UV–vis/DR, EPR, FT-IR, XPS, DTA-TGA and DSC techniques suggest the coordination of the nitrogen atom of pyridine groups of the organic polymer to the Cu(II) center. These complexes act as catalyst precursors for the water gas shift reaction as well as the reduction of nitrobenzene to aniline and azobenzene.

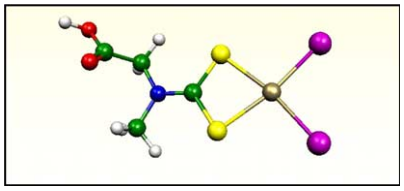


Luca Ronconi, Chiara Maccato, Davide Barreca, Roberta Saini, Mirella Zancato, Dolores Fregona

Polyhedron 24 (2005) 521

Gold(III) dithiocarbamate derivatives of *N*-methylglycine: An experimental and theoretical investigation

The synthesis and characterization of the gold(III) complexes $[(HSDT)AuX_2]$ and $[(HSDT)_2Au]X$ (X = Cl, Br; HSDT = sarcosinedithiocarbamate) are reported. In the discussed compounds coordination takes place through the sulfur atoms in a square-planar geometry around the gold(III) metal center. The complex $[(HSDT)_3Au]$ has also been synthesized and a structural hypothesis is discussed on the basis of experimental results.

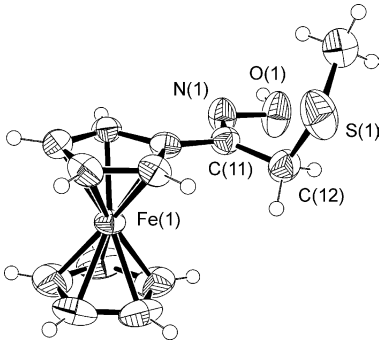


Mirjana D. Vukićević, Klaus Wurst, Adrian G. Müller, Gerhard Laus, Rastko D. Vukićević

Polyhedron 24 (2005) 533

Syntheses and crystal structures of (*E*)/(*Z*)-isomers of 1-ferrocenyl-1-hydroxyimino-3-thiabutane and 1-ferrocenyl-1-hydroxyimino-4-thiapentane

Four new potential bidentate ligands – oximes of ferrocenyl ketones containing sulfur in their side chains [(*E*)-, and (*Z*)-η^5-C_5H_5)Fe(η^5-C_5H_4)–C(NOH)–$(CH_2)_n$–SCH_3, n = 1 or 2] – were synthesised and characterised by spectral data. Single crystal X-ray structure determinations of these compounds are also reported.

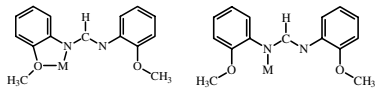


Chun-Wei Yeh, Hui-Ling Hu, Rung-Hua Liang, Kai-Ming Wang, Ting-Yi Yen, Jhy-Der Chen, Ju-Chun Wang

Polyhedron 24 (2005) 539

Synthesis and structural characterization of metal halide complexes containing *N*,*N*′-di(2-methoxyphenyl)formamidine (*o*-HDMophF)

The reactions of *N*,*N*′-di(2-methoxyphenyl)-formamidine (*o*-HDMophF) with transi-tion metal-halide complexes afforded $CuCl_2 \cdot$ (*o*-HD-MophF), (**1**), $[CoX_4][o\text{-}H_2DMophF]_2$ (X = Cl, **2**; Br, **3**) and $MCl_2(o\text{-}HDMophF)_2$ (M = Cd, **4**; Ni, **5;** Mn, **6**; Pd, **7**). The neutral *o*-HDMophF ligands in complexes **4**–**6** and **7** are coordinated to the metal centers in new bidentate and monodentate fashions, respectively. The neutral *o*-HDMophF compound in **1** adopts the *s-trans-anti-s-trans*-conformation, while those in complexes **4**–**6** and **7** adopt the *s-trans-anti-s-trans*- and *s-cis-anti-s-trans*-conformations, respectively. The $o\text{-}H_2DMophF^+$ cations of complexes **2** and **3** adopt the *s-cis-syn-anti-s-trans* and *s-trans-anti-anti-s-trans* conformations.

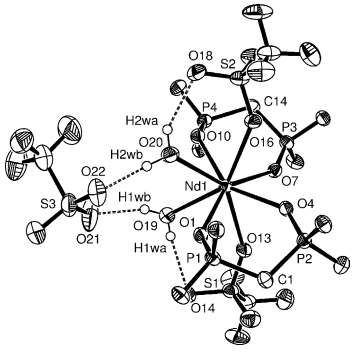


QiongHua Jin, Louis Ricard, François Nief

Polyhedron 24 (2005) 549

Lanthanide complexes with a chelating methylenediphosphonate

Reaction of lanthanide (Ln) triflates with tetrakis(*O-iso*propyl)methylenediphosphonate (L) in a 2:1 ratio afforded $[Ln(L)_2(OTf)_2(O\text{-}H_2)_2](OTf)$. In the crystal structure (Ln = Nd), the 8-coordinated metal atom is chelated by the phosphoryl groups of the two phosphonate ligands, and only bonded to two monodentate triflates. This is in contrast with $[Ln(L)_2(NO_3)_2](CH_3CN)_2$ (Ln = Ce, Pr, Nd) where all nitrates are bonded and bidentate. When the L:Ln ratio was increased to 4:1, $[Ln(L)_4](OTf)_3(CH_3CN)_3$ was obtained (Ln = La), in which the triflates are no longer bonded to the metal.

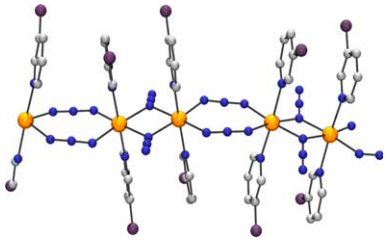


Morsy A.M. Abu-Youssef, Albert Escuer, Ramon Vicente, Franz A. Mautner, L. Öhrstrom, Mohamed A.S. Goher

Polyhedron 24 (2005) 557

New homogeneous and alternating Mn(II)-azido 1D systems

Two new examples of 1D Mn^{2+}/azido systems with different topologies have been characterised. Susceptibility measurements show one AF homogeneous and one alternating AF/F systems for which magnetic data were correlated with previous models.

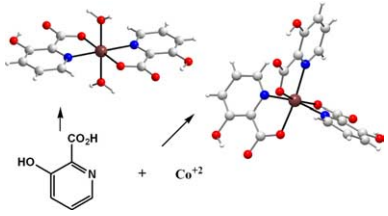


Penka I. Girginova, Filipe A. Almeida Paz, Helena I.S. Nogueira, Nuno J.O. Silva, Vítor S. Amaral, Jacek Klinowski, Tito Trindade

Polyhedron 24 (2005) 563

Synthesis, characterisation and magnetic properties of cobalt (II) complexes with 3-hydroxypicolinic acid (HpicOH): $[Co(picOH)_2(H_2O)_2]$ and *mer*-$[N(CH_3)_4][Co(picOH)_3] \cdot H_2O$

Two complexes with Co^{2+} and 3-hydroxypicolinic acid, $[Co(picOH)_2(H_2O)_2]$ and *mer*-$[N(CH_3)_4][Co(picOH)_3] \cdot H_2O$, have been synthesised and characterised using single-crystal X-ray diffraction, elemental analysis, infrared spectroscopy, and thermoanalytical measurements. The magnetic behaviour of these two materials was also investigated.



The Publisher encourages the submission of articles in electronic form thus saving time and avoiding rekeying errors. For detailed instructions on the preparation of manuscripts and of electronic artwork, consult the Author Gateway for Elsevier at http://authors.elsevier.com

SCIENCE DIRECT™

Full text of this journal is available, on-line from **ScienceDirect**. Visit **www.sciencedirect.com** for more information.

CONTENTS direct This journal is part of **ContentsDirect**, the *free* alerting service which sends tables of contents by e-mail for Elsevier books and journals. You can register for **ContentsDirect** online at: **www.elsevier.com/locate/contentsdirect**

Available online at www.sciencedirect.com
SCIENCE DIRECT®
Polyhedron 24, issue 3, 17 February 2005
POLYHEDRON
www.elsevier.com/locate/poly

Contents

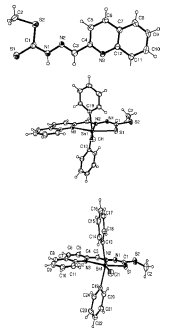
Papers

Mohammad Akbar Ali, A.H. Mirza, Malai Haniti S.A. Hamid, Paul V. Bernhardt

Polyhedron 24 (2005) 383

Diphenyltin(IV) complexes of the 2-quinolinecarboxaldehyde Schiff bases of *S*-methyl- and *S*-benzyldithiocarbazate (Hqaldsme and Hqaldsbz): X-ray crystal structures of Hqaldsme and two conformers of its diphenyltin(IV) complex

The complexes, $Sn(NNS)Ph_2Cl$ (NNS= anionic forms of the 2-quinolinecarboxaldehyde Schiff bases of *S*-methyl- and *S*-benzyldithiocarbazate) have been prepared and characterized. The structures of the free ligand, Hqaldsme and its diphenyltin(IV) complex, $[Sn(qaldsme)Ph_2Cl]$ have been determined by X-ray diffraction. The complex, $Sn(qaldsme)Ph_2Cl$ crystallizes in two distinctly different conformationally isomeric forms each having the same space group but different lattice parameters. In each polymorph, the tin atom adopts a distorted octahedral geometry.

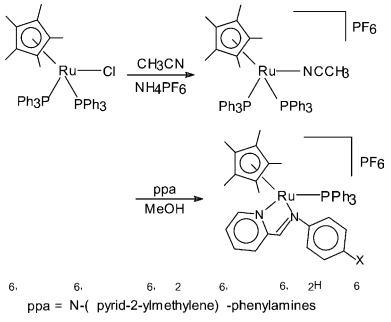


Keisham Sarjit Singh, Patrick J. Carroll, Mohan Rao Kollipara

Polyhedron 24 (2005) 391

Pentamethylcyclopentadienyl ruthenium(II) complexes of *para*-substituted *N*-(pyrid-2-ylmethylene)-phenylamine ligands: syntheses, spectral and structural studies

Pentamethylcyclopentadienyl ruthenium(II) complexes containing *N*,*N*′ donor Schiff base ligands of the formulation $[(\eta^5\text{-}C_5Me_5)\text{-}Ru(PPh_3)(C_5H_4N\text{-}2\text{-}CHN\text{-}C_6H_4\text{-}p\text{-}X)]PF_6$ **[3a]PF$_6$**–**[3f]PF$_6$** (where C_5Me_5=pentamethylcyclopentadienyl, X=H, **[3a]PF$_6$**; Me, **[3b]PF$_6$**; OMe, **[3c]PF$_6$**; NO_2, **[3d]PF$_6$**; Cl, **[3e]PF$_6$**; COOH, **[3f]PF$_6$**) were prepared by reacting the complex $[(\eta^5\text{-}C_5Me_5)Ru(PPh_3)_2(CH_3CN)]PF_6$ with the appropriate ligands (ppa) in methanol.

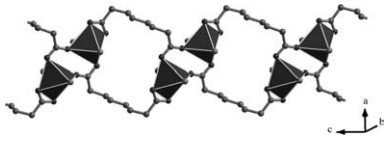


Yue-Qing Zheng, Er-Bo Ying

Polyhedron 24 (2005) 397

New α,ω-dicarboxylate coordination polymers with 4,4′-bipyridine: $Cu(bpy)(C_5H_6O_4)$, $Zn(bpy)(C_5H_6O_4)$, $Zn(bpy)(C_6H_8O_4)$ and $Mn(bpy)(C_8H_{12}O_4) \cdot H_2O$

Metal dimers are co-bridged by 4,4-bipyridine (bpy) and dicarboxylate anions such as glutarate, adipate and suberate anions into (4,4) open layers in $Cu(bpy)(C_5H_6O_4)$ **1**, $Zn(bpy)(C_5H_6O_4)$ **2** and $Mn(bpy)(C_8H_{12}O_4) \cdot H_2O$ **4** as well as into 3D frameworks in $Zn(bpy)(C_6H_8O_4)$ **3**. Twofold interpenetration of 3D frameworks completes the crystal structure of **3**.

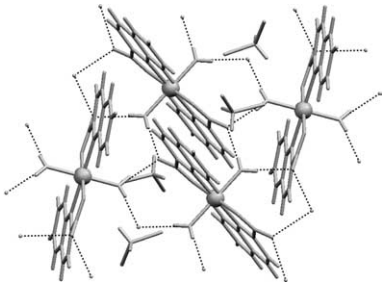


Danuta Dobrzyńska, Lucjan B. Jerzykiewicz, Marek Duczmal

Polyhedron 24 (2005) 407

Synthesis and properties of iron (II) quinoline-2-carboxylates, crystal structure of *trans*-diaquabis(quinoline-2-carboxylato)iron (II) bis(dichloromethane) solvate

Reaction between metallic iron and quinoline-2-carboxylic acid (Hquin-2-c) in dichloromethane yielded the amorphous $Fe(quin\text{-}2\text{-}c)_2$ (**1**). In the presence of a small amount of water, X-ray suitable crystals of $[Fe(quin\text{-}2\text{-}c)_2(H_2O)_2] \cdot 2CH_2Cl_2$ (**2**) were obtained. The structure of **2** is compared with the literature reported $[Fe(quin\text{-}2\text{-}c)_2(H_2O)_2] \cdot 2EtOH\ 2H_2O$ (**3**), a system of strong hydrogen bonds in **2** and **3** create the 2D framework. The spectral and magnetic properties of all compounds are reported.

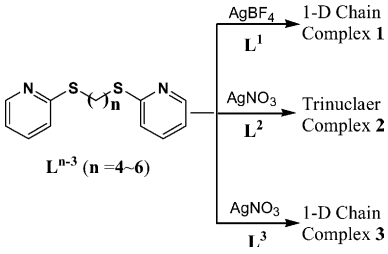


Ya-Bo Xie, Jian-Rong Li, Xian-He Bu

Polyhedron 24 (2005) 413

New silver(I) coordination architectures of pyridyl dithioether ligands with Ag···Ag, Ag···O, Ag···S and C–H···F weak interactions

The syntheses and crystal structures of three new silver(I) complexes with three structurally related flexible pyridyl dithioether bridging ligands are reported. The differences of the ligand spacers remarkably influence the coordination modes of the ligands and result in different structural complexes. Weak interactions play a crucial role in the self-organization of such supramolecular complexes, and stabilize the complex structures in the solid state.

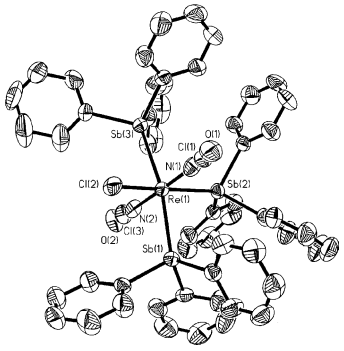


B. Machura, R. Kruszynski, M. Jaworska

Polyhedron 24 (2005) 419

Reactions of $[ReX_5(NO)]^{2-}$ with triphenylstibine. Spectroscopic investigations of $[ReX_2(NO)(SbPh_3)_3]$, X-ray structures of $[ReCl_2(NO)(SbPh_3)_3]$ and $[ReBr_2Cl(SbPh_3)_3]$ and DFT calculations for $[ReCl_2(NO)(SbPh_3)_3]$

New rhenium nitrosyls – $[ReCl_2(NO)(SbPh_3)_3]$ (**1**), $[ReBr_2(NO)(SbPh_3)_3]$ (**2**) – have been obtained in the reactions of $[NBu_4]_2[ReX_5(NO)]$ (X=Cl, Br) with triphenylstibine. The complex $[ReBr_2Cl(SbPh_3)_3]$ (**3**) has been isolated in low yield during slow recrystallization of complex **2** from a mixture of chloroform and ethanol. The stibine rhenium nitrosyls have been characterized by IR and UV–vis spectroscopy. The X-ray structures have been determined for **1** and **3**, and the geometric parameters of **1** have been examined using the density functional theory (DFT) method.

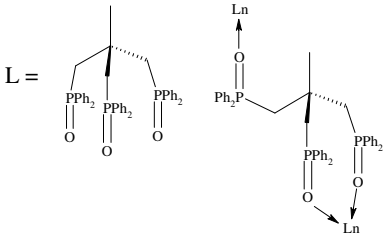


Anthony M.J. Lees, Andrew W.G. Platt

Polyhedron 24 (2005) 427

Preparation and structures of polymeric lanthanide nitrate complexes of $CH_3C[CH_2P(O)Ph_2]_3$

Complexes between lanthanide nitrates and tripodal ligand L lead to the formation of polymeric species in which L acts in a chelating–bridging mode.

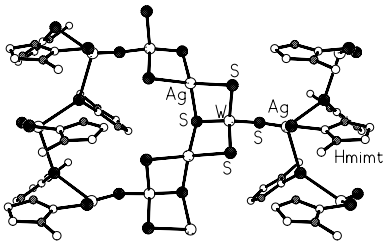


Azizolla Beheshti, William Clegg, Neil R. Brooks, Fatemeh Sharafi

Polyhedron 24 (2005) 435

Synthesis and characterization of the bimetallic polymers $[MS_4Ag_2(Hmimt)_2]_n$ (where M=Mo or W, Hmimt=1-methylimidazoline-2(3H)-thione): crystal structures of $[WS_4Ag_2(Hmimt)_2]_n$ and $[Ag_2I_2(Hmimt)]_n$

The polymeric sheet structure of $[WS_4Ag_2(Hmimt)_2]_n$ is the first example of a complex in which a tetrathiometalate coordinates in a monodentate fashion to another metal. Silver is in two very different coordination environments, one with only $[WS_4]^{2-}$ ligands and the other with both bridging and terminal thione ligands as well as the monodentate $[WS_4]^{2-}$.

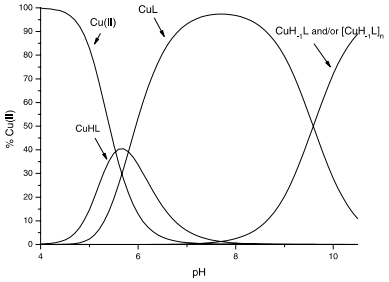


Teresa Kowalik-Jankowska, Anna Rajewska, Wioletta Szeszel-Fedorowicz, Danuta Konopińska

Polyhedron 24 (2005) 443

Bonding of copper(II) ions by proctolin analogues modified in fifth position of the peptide chain

The amine group of the 2,4-diamminobutyric acid (Dab) residue of the proctolin analogue RYLP–Dab, in whole pH range (2.5–10.5) is coordinated to the copper(II) ions, and the deprotonation and coordination of the second amide nitrogen atom to the metal ion is prevented. In solution in wide pH range (5–10.5) the CuL complex with 3N $\{NH_2, N^-_{amide}, CO, NH_{2Dab}\}$ bonding mode is present.

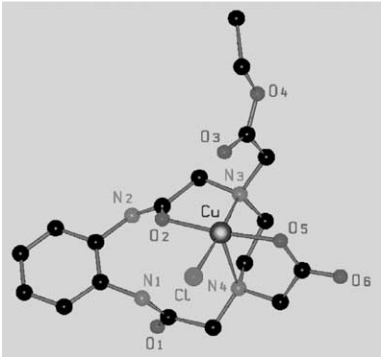


Sara Lacerda, Maria Paula Campello, Isabel C. Santos, Isabel Santos, Rita Delgado

Polyhedron 24 (2005) 451

A *N*,*N*′-diacetate benzodioxotetraazamacrocycle and its transition metal complexes

The 2,9-dioxo-1,4,7,10-tetraazabicyclo[1.10.1] hexadeca-1(11),13,15-triene-4,7-diacetic acid (**H_2L1**) reacts with $CuCl_2 \cdot 2H_2O$ leading to the benzodioxochlorocomplex [Cu(**L**′**1**)Cl] (**1**). The stability constants of **H_2L1** with Cu, Ni^{2+}, Zn^{2+}, Cd^{2+} and Pb^{2+} were determined, and the values follow the trend $[Ni(\mathbf{H_{-1}L1})]^-$ > $[Cu(\mathbf{H_{-1}L1})]^-$ ≫ $[Pb(\mathbf{H_{-1}L1})]^-$ > $[Zn(\mathbf{H_{-1}L1})]^-$ > $[Cd(\mathbf{H_{-1}L1})]^-$. The effect of pH on the coordination sphere of the Cu complexes was also studied by spectroscopic measurements.

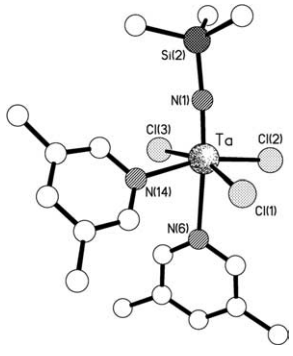


Jenelle E. Bleau, Claire J. Carmalt, Shane A. O'Neill, Ivan P. Parkin, Andrew J.P. White, David J. Williams

Polyhedron 24 (2005) 463

Molecular precursors for the CVD of niobium and tantalum nitride

Low pressure chemical vapour deposition of $[NbCl_3(NSiMe_2Ph)(NH_2SiMe_2Ph)]_2$ and $[TaCl_3(NSiMe_3)(NC_5H_3Me_2\text{-}3,5)_2]$ forms thin films of niobium and tantalum nitride, respectively, at 600°C.



The Publisher encourages the submission of articles in electronic form thus saving time and avoiding rekeying errors. For detailed instructions on the preparation of manuscripts and of electronic artwork, consult the Author Gateway for Elsevier at http://authors.elsevier.com



Full text of this journal is available, on-line from **ScienceDirect**. Visit **www.sciencedirect.com** for more information.



This journal is part of **ContentsDirect**, the *free* alerting service which sends tables of contents by e-mail for Elsevier books and journals. You can register for **ContentsDirect** online at: **www. elsevier.com/locate/contentsdirect**

Available online at www.sciencedirect.com
SCIENCE DIRECT®
Polyhedron 24, issue 14, 3 October 2005
POLYHEDRON
www.elsevier.com/locate/poly

Contents

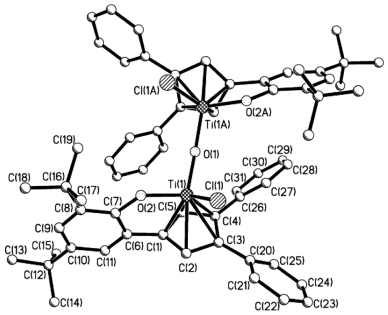
Papers

Zhang Yuetao, Mu Ying, Li Guanghua, Lü Chunsheng, Xiao Tingting, Xu Jiansheng, Zhang Yanrong, Zhu Dongsheng, Feng Shouhua

Polyhedron 24 (2005) 1793

Synthesis, structures, and catalytic properties of dimeric constrained geometry diphenylcyclopentadienyl–phenoxyoxochlorotitanium(IV) complexes

Two dimeric diphenyl cyclopentadienylphenoxyoxochlorotitanium(IV) complexes $\{[\eta^5;\eta^1$-2-(3,4-Ph_2Cp)-4,6-di-^{t}Bu-$C_6H_2O]TiCl\}_2O$ (**3**) and $\{[\eta^5;\eta^1$-2-(3,4-Ph_2Cp)-6-^{t}Bu-$C_6H_3O]TiCl\}_2O$ (**4**) have been synthesized by hydrolysis of the monomeric 2-(3,4-diphenyl-cyclopentadienyl)-4,6-di-*tert*-butyl phenoxytitanium dichloride (**1**) and 2-(3,4-diphenyl-cyclopentadienyl)-6-*tert*-butyl phenoxytitanium dichloride (**2**). The molecular structure of **3** was characterized by spectroscopy and X-ray crystallography. Both of the complexes exhibited high catalytic activities for ethylene polymerization in the presence of $Al(^tBu)_3$ and $Ph_3{}^+B(C_6F_5)_4{}^-$.

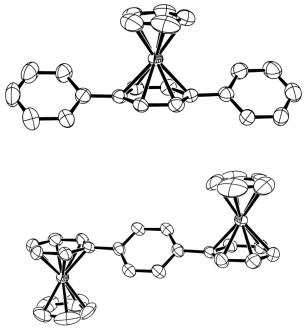


Naoji Masuhara, Yuriko Kamigaki, Satoru Nakashima, Tsutomu Okuda

Polyhedron 24 (2005) 1798

Introduction of $FeCp^+$ to *o*-, *m*-, *p*-terphenyl and the structures of mononuclear and dinuclear complexes

Mononuclear and dinuclear arene complexes of *o*-, *m*-, and *p*-terphenyl were isolated. $FeCp^+$ was introduced to the central benzene in the mononuclear complexes, while they were introduced to the terminal benzenes in the dinuclear complexes.

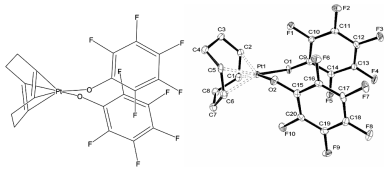


Miki Kim, Lev N. Zakharov, Arnold L. Rheingold, Linda H. Doerrer

Polyhedron 24 (2005) 1803

Synthesis and structural characterization of Groups 10 and 11 mononuclear fluoroaryloxide complexes

A study of the late-transition metal aryloxide complexes $[(Ph_3P)_2Ni(OAr^F)_2]$, $[(Ph_3P)_2Ni(OAr')_2]$, $[(COD)Pt(OAr^F)_2]$, and $[(Ph_3P)Au(OAr^F)]$ is presented which suggests that substantial fluorination of the phenoxide ring facilitates isolation of monodentate aryloxide complexes, versus reduction at the metal center or oligomerization via bridging phenoxides.

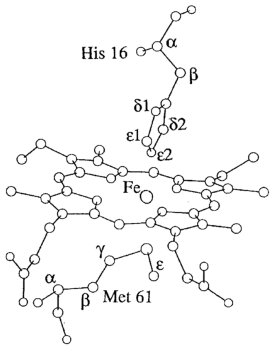


Hermas R. Jiménez, Cristina Pardal, José M. Moratal

Polyhedron 24 (2005) 1813

^{1}H NMR studies of paramagnetic ferricytochrome *c*-551 from *Pseudomonas aeruginosa* at high pH: The role of histidine 16 in the spin transition

The electronic structure of ferricytochrome c-551 from *Pseudomonas aeruginosa* at high pH has been investigated using paramagnetic NMR techniques. The results indicate the existence of a spin transition associated to the deprotonation of histidine-16 axially bound to iron(III), which would trigger the decoordination of the second axial ligand, methionine-61.

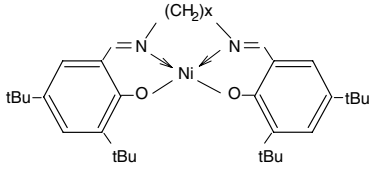


Şeniz Özalp-Yaman, Veli T. Kasumov, Ahmet M. Önal

Polyhedron 24 (2005) 1821

Electrochemistry of nickel(II) complexes with *N*,*N*′-bis(3,5-di-*tert*-butylsalicylidene)-polymethylenediamines

Several *N*,*N*′-polymethylenebis(3,5-di-*tert*-butylsalicylaldiminato)nickel(II) complexes, Ni(L_x) (x = 1–4), have been studied by cyclic voltammetry and in situ UV–Vis spectroscopy in DMF. The first oxidation peak potentials of all the Ni(II) complexes corresponds to the reversible one-electron oxidation process of the metal center, yielding Ni(III) species. The second oxidation peak of the complexes was assigned as the ligand based oxidation, generating a coordinated phenoxy radical species.



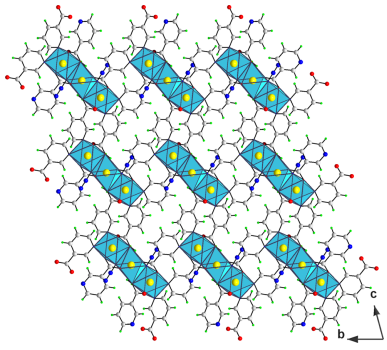
H_2L_x	Ni(L_x)	$(CH_2)_x$
H_2L_1	Ni(L_1)	-$(CH_2)_2CH(CH_3)$-
H_2L_2	Ni(L_2)	-$(CH_2)_2$-
H_2L_3	Ni(L_3)	-$(CH_2)_3$-
H_2L_4	Ni(L_4)	-$(CH_2)_4$-
H_2L_5	Ni(L_5)	-$(CH_2)_5$-
H_2L_6	Ni(L_6)	-$(CH_2)_6$-

Morsy A.M. Abu-Youssef

Polyhedron 24 (2005) 1829

Two new 3D network structures: $[Cd_3(nic)_4(N_3)_2(H_2O)]_n$ and $[Zn(nic)(N_3)]_n$ (nic = nicotinate anion)

Two new metal(II) complexes: $[Cd_3(nic)_4(N_3)_2(H_2O)_2]_n$ and $[Zn(nic)(N_3)]_n$ (nic = nicotinate anion), have been synthesized and found by X-ray crystallography to contain bridging μ-N,O,O′-tridentate nicotinate anions and ($\mu_{1,1}$-N_3) azido ligands.

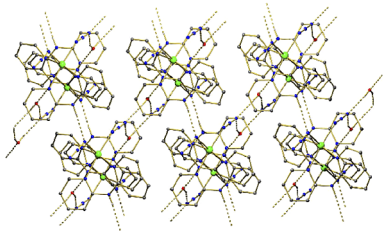


Sk Hafijur Rahaman, Doyel Bose, Habibar Chowdhury, Golam Mostafa, Hoong-Kun Fun, Barindra K. Ghosh

Polyhedron 24 (2005) 1837

Two-dimensional hydrogen bonded sheet structures in nickel(II)- and zinc(II)-2,2′-dipyridylamine-azido complexes

The crystal packing through H-bonds affords infinite two-dimensional (2D) sheets in isomorphous nickel(II)- and zinc(II)-2,2′-dipyridylamine-azido complexes. The pyridyl planes of adjacent sheets are engaged in face-to-face π–π and C–H···π interactions leading to a 3D supramolecular continuum. Both the complexes exhibit high-energy intraligand $^{1}(\pi–\pi^{*})$ fluorescence and intraligand $^{3}(\pi–\pi^{*})$ phosphorescence in glassy solutions (DMF at 77 K).

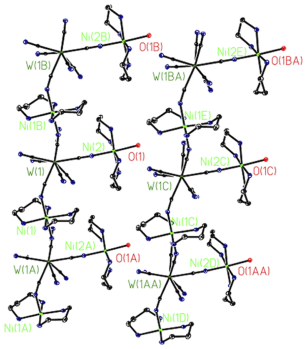


Jeffrey R. Withers, Chad Ruschman, Sean Parkin, Stephen M. Holmes

Polyhedron 24 (2005) 1845

One- and three-dimensional octacyanometalate(IV) networks constructed via a building block approach: {[*trans*-$Ni^{II}(tn)_2(OH_2)$][*trans*-$Ni^{II}(\mu\text{-}NC)_2(tn)_2$][$(\mu\text{-}NC)_3M^{IV}(CN)_5$] · $6H_2O$} (M^{IV} = Mo, W) and $Cs_4[Cu^{II}(OH_2)_4]_2[Cu^{II}(NH_3)]_4[Mo^{IV}(CN)_8]_4 \cdot 2H_2O$

Three octacyanometalate(IV) coordination polymers containing copper(II), nickel(II), 1,3-propanediamine, and ammonia have been prepared. The amine ligands limit the number and directionality of cyano linkages formed between metal centers. Surprisingly, 1- and 3-D structures are obtained instead of the expected 2-D structures.

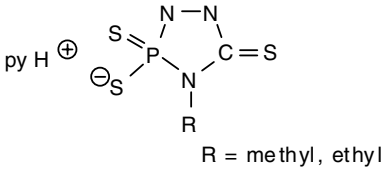


Richard Ševčík, Jiří Příhoda, Marek Nečas

Polyhedron 24 (2005) 1855

On the reactions of chlorodithiophosphoric acid pyridiniumbetaine with polyfunctional nucleophiles. Part III: Reactions with monoalkylderivatives of thiosemicarbazide

Two heterocyclic compounds containing five-membered rings P–N–N–C–N were prepared from chlorodithiophosphoric acid pyridiniumbetaine, py · PS_2Cl, and monosubstituted thiosemicarbazide derivatives $RN(H)C(S)N(H)NH_2$, (R = methyl, ethyl). Both substances were completely characterized by ^{31}P NMR, FT-IR, Raman spectroscopies and their molecular structures were determined by means of X-ray crystallography.

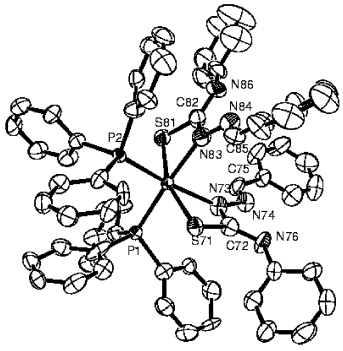


Dipankar Mishra, Subhendu Naskar, Michael G.B. Drew, Shyamal Kumar Chattopadhyay

Polyhedron 24 (2005) 1861

Mononuclear and binuclear ruthenium(II) complexes with 4-(phenyl) thiosemicarbazone of benzaldehyde: A discussion on the relative stabilities of the four-membered and five-membered chelate rings formed by the ligand

Three new ruthenium complexes of formulae *cis*-$[Ru(PPh_3)_2(BzTscbz)_2]$ (**1a**), $[Ru_2(PPh_3)_2(BzTscbz)_4]$ (**1b**) and $[Ru(PPh_3)_2(BzTscHbz)_2](ClO_4)_2$ (**2**) have been synthesized and characterized by various physicochemical methods including X-ray structure determination for **1a** and **1b**. The relative stabilities of the four-membered versus five-membered chelate ring formed by the ligand BzTscbz is discussed on the basis of the experimental results and some semi-empirical as well as DFT calculations.

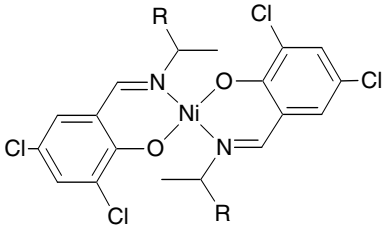


Takashiro Akitsu, Yasuaki Einaga

Polyhedron 24 (2005) 1869

Synthesis, crystal structures and electronic properties of Schiff base nickel (II) complexes: Towards solvatochromism induced by a photochromic solute

We have synthesized and characterized two new nickel (II) complexes, bis(*N*-*R*-1-phenylethyl- or *N*-2-propyl-3,5-dichlorosalicydenaminato)nickel (II), which exhibit a thermally induced structural phase transition and negative solvatochromism. After UV light irradiation, we have successfully observed slight spectral changes in the π–π^* region due to a conformational change of the chiral ligands caused by photochromic solute (4-hydroxyazobenzene) induced solvatochromism.



1 : R = C_6H_5

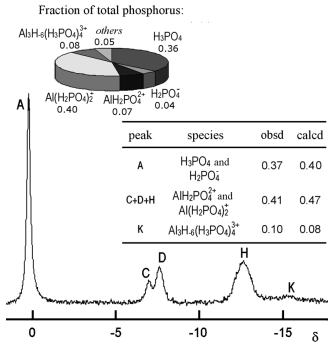
2 : R = CH_3

Liberato Ciavatta, Mauro Iuliano, Stefano Midollini, Antonio Sabatini, Alberto Vacca

Polyhedron 24 (2005) 1878

Phosphorus-31 nuclear magnetic resonance study of aluminium(III) *ortho*-phosphate complexes in aqueous solution

^{31}P NMR spectra have been obtained from a set of aqueous solutions containing $Al(ClO_4)_3$–H_3PO_4–NaH_2PO_4 mixtures. It was assumed that there is slow exchange on the NMR time scale at the aluminium centre. Peaks corresponding to phosphate containing species have been assigned by correlating observed fractional peak areas with fractional complex concentrations calculated using a model previously proposed on the basis of potentiometric titration data. The results provide strong support for the model.



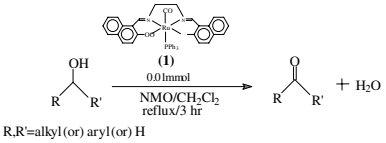
peak	species	obsd	calcd
A	H_3PO_4 and $H_2PO_4^-$	0.37	0.40
C+D+H	$Al(H_2PO_4)_2^+$ and $Al(H_2PO_4)_3^0$	0.41	0.47
K	$Al_3H_4(H_3PO_4)_4^{3+}$	0.10	0.08

K. Naresh Kumar, R. Ramesh

Polyhedron 24 (2005) 1885

Synthesis, luminescent, redox and catalytic properties of Ru(II) carbonyl complexes containing 2N2O donors

Metal complexes of the general formula [Ru(CO)(B)(L)] (where B = PPh_3, $AsPh_3$, py (or) pip; L = dianion of tetradentate Schiff bases) have been synthesized and characterized. All the complexes exhibit luminescence bands in the visible region. Further, the catalytic activity of complex **1** has been found to be high (up to 99%) towards the oxidation of primary and secondary alcohols in the presence of the co-catalyst NMO.

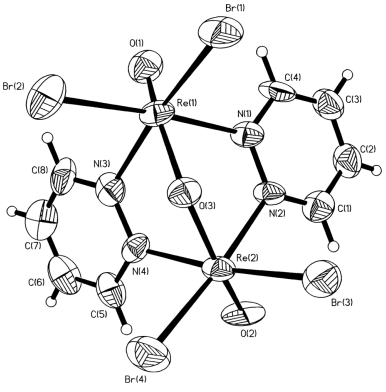


B. Machura, R. Kruszynski, M. Jaworska, P. Lodowski

Polyhedron 24 (2005) 1893

Synthesis, spectroscopic characterization, crystal, molecular and electronic structure of the [{$ReOBr_2(pyz)_2$}$_2$(μ-O)] and [{$ReOBr_2$}$_2$(μ-O)(μ-pyd)$_2$] complexes

The reactions of the complex [$ReBr_3(AsPh_3)$-($OAsPh_3$)] with pyrazine (pyz) and pyridazine (pyd) have been examined and novel dinuclear rhenium oxocomplexes–[{$ReOBr_2(pyz)_2$}$_2$(μ-O)] with a linear ORe–O–ReO backbone (**1**) and [{$ReOBr_2$}$_2$-(μ-O)(μ-pyd)$_2$] with a bent $Re_2O_3^{4+}$ core (**2**) – have been obtained. This paper presents the syntheses, spectroscopic investigations, crystal, molecular and electronic structures for the complexes **1** and **2**. The electronic structures of **1** and **2** have been examined using the density functional theory (DFT) method, and additional information about the binding has been obtained by NBO analysis. The UV–Vis spectra of **1** and **2** have been interpreted on the basis of the results of time-dependent DFT (TDDFT) calculations.



The Publisher encourages the submission of articles in electronic form thus saving time and avoiding rekeying errors. For detailed instructions on the preparation of manuscripts and of electronic artwork, consult the Author Gateway for Elsevier at http://authors.elsevier.com

SCIENCE DIRECT™

Full text of this journal is available, on-line from **ScienceDirect**. Visit **www.sciencedirect.com** for more information.

CONTENTS Direct

This journal is part of **ContentsDirect**, the *free* alerting service which sends tables of contents by e-mail for Elsevier books and journals. You can register for **ContentsDirect** online at: **www. elsevier.com/locate/contentsdirect**

Available online at www.sciencedirect.com
SCIENCE DIRECT®
Polyhedron 24, issue 11, 4 August 2005
POLYHEDRON
www.elsevier.com/locate/poly

Contents

Foreword: Symposia-In-Print, number 27, Ansa metallocenes and related compounds 1233

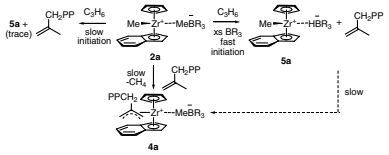
Papers

Abdulaziz Al-Humydi, Jered C. Garrison, Muqtar Mohammed, Wiley J. Youngs, Scott Collins

Polyhedron 24 (2005) 1234

Propene polymerization using *ansa*-metallocenium ions: Catalyst deactivation processes during monomer consumption and molecular structures of the products formed

Ion-pair **2a** is more reactive towards initial monomer insertion in the presence of excess borane and the product of chain transfer is borohydride complex **5a**. Both this complex and ion-pair **2a** are reactive towards the unsaturated oligomers formed, slowly forming oligomeric π-allyl complexes **4a** via a C−H activation reaction.

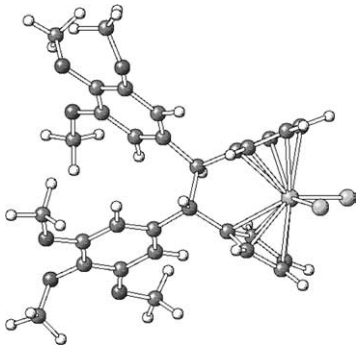


Franz-Josef K. Rehmann, Andrew J. Rous, Oscar Mendoza, Nigel J. Sweeney, Katja Strohfeldt, William M. Gallagher, Matthias Tacke

Polyhedron 24 (2005) 1250

A trimethoxyphenyl substituted *ansa*-titanocene: A possible anti-cancer drug

The water soluble *ansa*-titanocene [1,2-di-(cyclopentadienyl)-1,2-di-(3′,4′,5′-trimethoxyphenyl)-ethanediyl] titanium dichloride is a possible anti-cancer drug and was synthesised starting from 6-(3′,4′,5′-trimethoxyphenyl) fulvene. Herein, we present the synthesis and calculated structures of the fulvene and the titanocene followed by MTT-based cytotoxicity tests on pig kidney carcinoma (LLC-PK) cells.

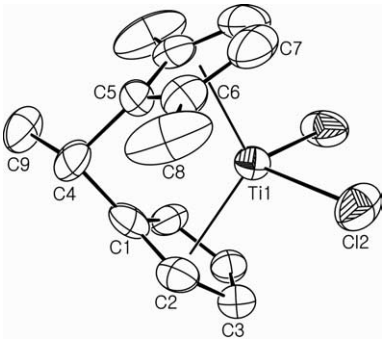


Ui Gab Joung, Bun Yeoul Lee

Polyhedron 24 (2005) 1256

Ethylene and ethylene/1-hexene (co)polymerizations with 2,5-dimethylcyclopentadienyl *ansa*-titanocene and zirconocene complexes

C1-bridged titanocene complexes, [R(H)C-(η^5-C_5H_4)(η^5-2,5-$Me_2C_5H_2$)]$TiCl_2$ have been prepared. The titanocene complexes activated with MAO show much higher activities than the corresponding *ansa*-zirconocene complex [Me(H)C(η^5-C_5H_4)(η^5-2,5-$Me_2C_5H_2$)]$ZrCl_2$ in ethylene polymerization and the molecular weights of the obtained polymers are significantly higher (M_w, ~800000).



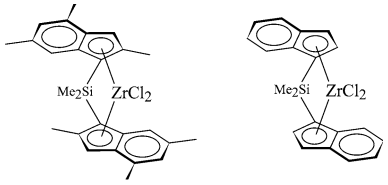
Elsevier Ltd.

Tariq Yasin, Zhiqiang Fan, Linxian Feng

Polyhedron 24 (2005) 1262

Effect of temperature on the isospecific propylene polymerization catalyzed by *rac*-dimethylsilylbis(2,4,6-trimethyl-1-indenyl)zirconium dichloride/methyl aluminoxane

The novel zirconocene *rac*-dimethylsilyl-bis(2,4,6-trimethyl-1-indenyl)zirconium dichloride (**1**) showed higher stability at elevated temperature than *rac*-dimethylsilyl-bis(indenyl)zirconium dichloride (**2**) when used as catalyst for isopecific polymerization of propylene. **1**/MAO is also more stereospecific and regiospecific than **2**/MAO.



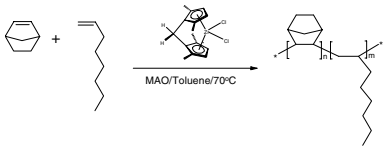
1 **2**

Hye Young Jung, Sung-Don Hong, Min Whan Jung, Hyosun Lee, Young-Whan Park

Polyhedron 24 (2005) 1269

Norbornene copolymerization with α-olefins using methylene-bridged *ansa*-zirconocene

Copolymers of α-olefins such as 1-hexene and 1-octene with norbornene by *ansa*-zirconocene were prepared with moderate activity. Effects of monomer feed ratio on the glass transition temperature, monomer incorporation ratio in the copolymer and molecular weight of the polymers were investigated.

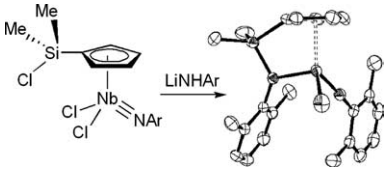


Rocío Arteaga-Müller, Javier Sánchez-Nieves, Pascual Royo, Marta E.G. Mosquera

Polyhedron 24 (2005) 1274

Aryl-imido niobium complexes with chlorosilyl and aryl-η-amidosilyl cyclopentadienyl ligands: X-ray structure of the constrained-geometry compound [Nb(η^5-$C_5H_4SiMe_2$-η^1-NAr)(NAr)Cl] (Ar=2,6-$Me_2C_6H_3$)

Aryl imido niobium compounds with chlorosilyl cyclopentadienyl ligands react with H_2O and LiNHAr giving dinuclear compounds with Si–O–Si bridges and mononuclear constrained geometry compounds, respectively.

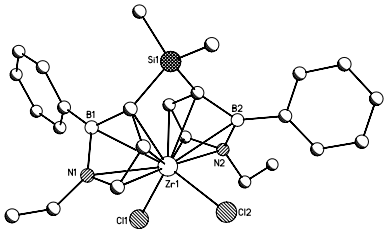


Hong Yang, Xiangdong Fang, Jeff W. Kampf, Arthur J. Ashe III

Polyhedron 24 (2005) 1280

Bridged 1,2-azaborolyl zirconium complexes: Heterocyclic analogs of the *ansa*-zirconocene olefin polymerization catalysts

An efficient synthesis of (η^5-1,2-azaborolyl)-zirconium(IV) dichlorides has been developed. The structure of Me_2Si-bridged-(1,2-azaborolyl) complexes closely resemble those of the corresponding *ansa*-zirconocenes. On activation with excess methylaluminoxane both bridged and non-bridged complexes form highly active catalysts for the polymerization of ethylene.

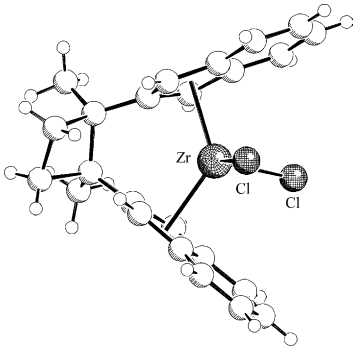


Gerhard Erker

Polyhedron 24 (2005) 1289

Building bridges: *ansa*-Metallocene construction by carbon–carbon coupling reactions at preformed Group 4 bent metallocene frameworks

A number of methods by which various functional groups that are attached at the Cp-rings of Group 4 bent metallocenes can be intramolecularly coupled to yield *ansa*-metallocenes are presented and discussed. These methods include pathways of metallacyclopentane formation from Cp-alkenyl moieties, olefin metathesis reactions between α-olefins attached at the Cp-ligands, photochemically induced [2+2]cycloadditions of substituted vinyl groups and *Lewis* acid- or *Brønsted* acid-catalyzed *Mannich*-type condensation reactions between 1-aminoethenyl functional groups at the bent metallocene framework.

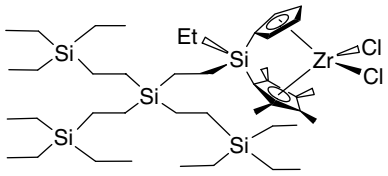


Santiago Gómez-Ruiz, Sanjiv Prashar, Mariano Fajardo, Antonio Antiñolo, Antonio Otero, Miguel A. Maestro, Victoria Volkis, Moris S. Eisen, César J. Pastor

Polyhedron 24 (2005) 1298

Synthesis, hydrosilylation reactivity and catalytic properties of group 4 *ansa*-metallocene complexes

The synthesis and characterization of *ansa*-metallocene complexes with a Si–H bond are described. The modification of the *ansa*-ligand framework in these complexes by hydrosilylation and the catalytic activity of the *ansa*-zirconocene derivatives in the polymerization of ethylene are reported.

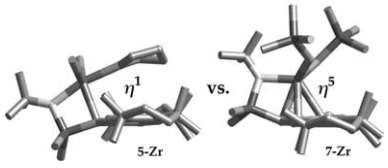


Levi J. Irwin, Joseph H. Reibenspies, Stephen A. Miller

Polyhedron 24 (2005) 1314

Synthesis and characterization of sterically expanded *ansa*-η^1-fluorenyl-amido complexes

Variable solid-state hapticity is observed in sterically expanded zirconium and hafnium fluorenyl-amido complexes of the type $Me_2Si(\eta^n\text{-}C_{29}H_{36})(\eta^1\text{-}N\text{-}^t\text{Bu})MX_2 \cdot L_m$. When the X ligands are small, ethereal adducts with η^1 coordination are observed. When the X ligands are large, ether-free η^5 species are found.

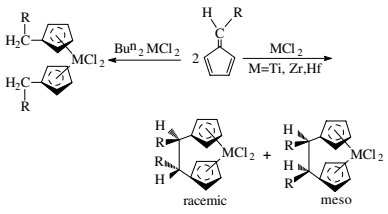


John J. Eisch, Fredrick A. Owuor, Xian Shi

Polyhedron 24 (2005) 1325

New syntheses of *ansa*-metallocenes or unbridged substituted metallocenes by the respective reductive dimerization of fulvenes with Group 4 metal divalent halides or with Group 4 metal dichloride dihydrides

Two unprecedented, high-yielding syntheses of Group 4 metallocenes have been discovered: (1) reaction of MCl_2 with 6-substituted fulvenes to produce substituted ethylene-bis(cyclopentadienyl)metal dichlorides; and (2) reaction of $Bu^n{}_2MCl_2$ with 6-substituted fulvenes by transfer-hydrometallation to yield bis(substituted cyclopentadienyl)metal dichlorides. Reaction mechanistic models based on the reductive dimerization of ketones or imines are invoked in explaining the stereochemistry of *ansa*-metallocene formation.

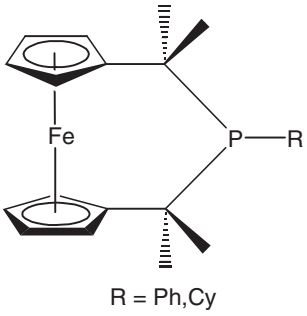


Thomas Höcher, Arnaldo Cinquantini, Piero Zanello, Evamarie Hey-Hawkins

Polyhedron 24 (2005) 1340

Novel [3]ferrocenophanes: Syntheses, redox properties and molecular structures of $[Fe\{(\eta^5\text{-}C_5H_4)CMe_2\}_2PR]$ (R=Ph, Cy)

The [3]ferrocenophanes $[Fe\{(\eta^5\text{-}C_5H_4)CMe_2\}_2PR]$ [R=Ph, Cy] were obtained from $Li[\{(C_5H_4)CMe_2\}PR]$ and $FeCl_2$ and characterised spectroscopically (^1H, ^{13}C, ^{31}P, IR, MS), and by crystal structure determination. Electrochemical investigation on $[Fe\{(\eta^5\text{-}C_5H_4)CMe_2\}_2PPh]$ shows a reversible one-electron oxidation in CH_2Cl_2 solution.

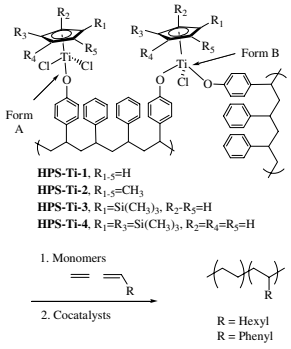


Jeanette F. Craymer, Rajeswari M. Kasi, E. Bryan Coughlin

Polyhedron 24 (2005) 1347

Copolymerizations of ethylene and α-olefins with supported piano-stool catalysts

Piano-stool catalysts ($CpTiCl_3$, and related analogues) were covalently bound to a poly(styrene-*r*-4-hydroxystyrene) copolymer, affording macroligated catalysts. Through copolymerization of α-olefins and ethylene, the effects that the macroligand and substituents on the cyclopentadienyl ring have on various polymer properties were investigated.

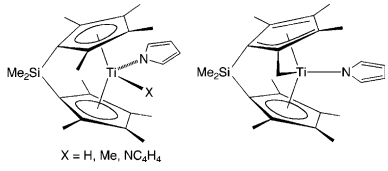


Hyosun Lee, Jeffrey B. Bonanno, Brian M. Bridgewater, David G. Churchill, Gerard Parkin

Polyhedron 24 (2005) 1356

Ansa-titanocene pyrrolyl complexes: The synthesis and structural characterization of $[Me_2Si(C_5Me_4)_2]Ti(NC_4H_4)X$ (X=H, Me, Cl and NC_4H_4) and $[Me_2Si(C_5Me_4)(C_5Me_3\text{-}CH_2)]Ti(NC_4H_4)$

A series of titanium–pyrrolyl compounds, namely $[Me_2Si(C_5Me_4)_2]Ti(NC_4H_4)X$ (X=H, Me, Cl, NC_4H_4) and $[Me_2Si(C_5Me_4)(C_5Me_3\text{-}CH_2)]Ti(NC_4H_4)$ has been synthesized and structurally characterized by X-ray diffraction. Analysis of the $TiNC_4H_4$ bond lengths in these complexes indicates that pyrrolyl does not, by comparison to dialkylamido, act as an efficient π-donor ligand.

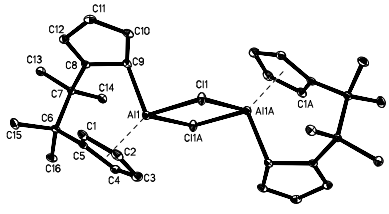


Pamela J. Shapiro, Suh-Jane Lee, Philippe Perrotin, Timothy Cantrell, Alexander Blumenfeld, Brendan Twamley

Polyhedron 24 (2005) 1366

The first example of an *ansa*-bis(cyclopentadienyl)aluminum compound. X-ray crystallographic characterization of $[Me_4C_2\text{-}(C_5H_4)_2Al\text{-}\mu\text{-}Cl]_2$ and its monomeric THF and *t*-BuNC adducts. NMR spectroscopic characterization of the structures and fluxional behavior of these compounds in solution

The *ansa*-aluminocene compound $[Me_4C_2\text{-}(C_5H_4)_2Al\text{-}\mu\text{-}Cl]_2$ and its Lewis base adducts $[Me_4C_2(\eta^5\text{-}C_5H_4)_2Al(L)]$ (L=THF, *t*-BuNC) were prepared and their X-ray crystal structures were determined. The solution structures and fluxional rearrangement of these compounds were characterized using a combination of 1-D and 2-D NMR spectroscopic methods.

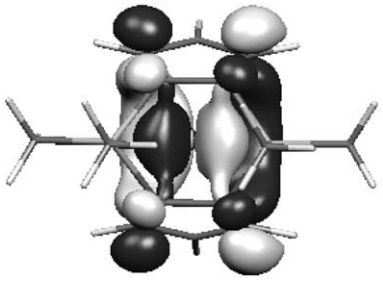


Jennifer C. Green

Polyhedron 24 (2005) 1382

Tuning the gap: Doubly Si-bridged *ansa*-tungstenocene, a proposed intermediate for C–H activation

The doubly Si-bridged *ansa*-tungstenocene, $[W(\eta^5\text{-}C_5H_3)_2(SiMe_2)_2]$ is calculated to have singlet and triplet states of comparable energy, therefore, on an SCF energy surface there is no barrier to formation of a sigma complex with methane, and formation of a methyl hydride is exo-energetic by −125 kJ mol^{-1}.

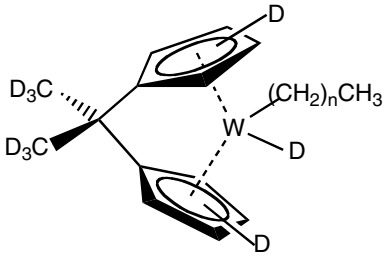


Malcolm L.H. Green, Stephen L.J. Conway, Linda H. Doerrer

Polyhedron 24 (2005) 1388

Hydrogen/deuterium exchange in alkyl-hydride derivatives of *ansa*-tungstenocene compounds

The higher deuterated *n*-alkyl hydrides $[W\{(\eta\text{-}C_5H_4)CMe_2(\eta\text{-}C_5H_4)\}(R)H](R=\{(CH_2)_n\text{-}CH_3\}$, n=1–4) and $[W\{(\eta\text{-}C_5H_4)CMe_2(\eta\text{-}C_5H_4)\}\{CD_2CD_3\}H]$ undergo hydrogen/deuterium exchange processes under thermal conditions and in every case of all the possible alkyl hydrogens of the alkyl groups R only H/D exchange with the α-CH_2 methylene hydrogens was observed.



The Publisher encourages the submission of articles in electronic form thus saving time and avoiding rekeying errors. For detailed instructions on the preparation of manuscripts and of electronic artwork, consult the Author Gateway for Elsevier at http://authors.elsevier.com

SCIENCE DIRECT™

Full text of this journal is available, on-line from **ScienceDirect**. Visit **www.sciencedirect.com** for more information.

CONTENTS Direct This journal is part of **ContentsDirect**, the *free* alerting service which sends tables of contents by e-mail for Elsevier books and journals. You can register for **ContentsDirect** online at: **www. elsevier.com/locate/contentsdirect**

Available online at www.sciencedirect.com
SCIENCE DIRECT®
Polyhedron 24, issue 10, 14 July 2005
POLYHEDRON
www.elsevier.com/locate/poly

Contents

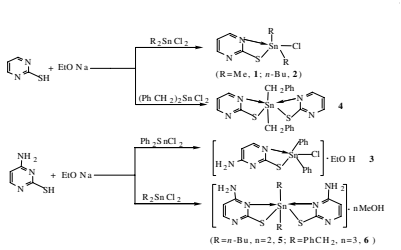
Papers

Chun-Lin Ma, Yang Shi, Qing-Fu Zhang, Qin Jiang

Polyhedron 24 (2005) 1109

Syntheses, characterization and crystal structures of diorganotin compounds with 2-mercaptopyrimidine and 4-amino-2-mercaptopyrimidine

Six diorganotin compounds with 4-amino-2-mercaptopyrimidine (HSapym) and 2-mercaptopyrimidine (HSpym) of the type, $[R_2SnCl_mL_n] \cdot Y$ (when $n = m = 1$: L = Spym, R = CH_3, Y = 0, **1**; R = Bu, Y = 0, **2**; L = Sapym, R = Ph, Y = EtOH, **3**; when $n = 2$, $m = 0$: L = Spym, R = $PhCH_2$, Y = 0, **4**; L = Sapym, R = Bu, Y = 2MeOH, **5**; R = $PhCH_2$, Y = 3MeOH, **6**) have been synthesized. All the compounds **1**–**6** have been characterized by elemental, ^1H NMR spectroscopy and X-ray crystallography diffraction analyses.

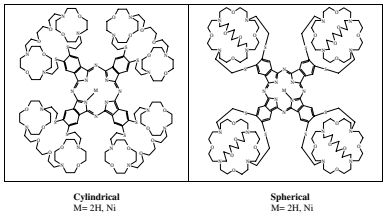


Ahmet Bilgin, Beytullah Ertem, Yaşar Gök

Polyhedron 24 (2005) 1117

Synthesis and characterization of new metal-free and metallophthalocyanines containing spherical or cylindrical macrotricyclic moieties

Cylindrical or spherical macropolycyclic group substituted metal-free and Ni(II) phthalocyanines have been synthesized from the corresponding phthalonitrile derivatives. The new compounds have been characterized by physical and spectroscopic techniques.

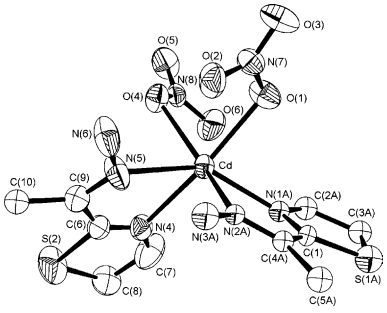


F.J. Barros-García, A. Bernalte-García, F. Luna-Giles, M.A. Maldonado-Rogado, E. Viñuelas-Zahínos

Polyhedron 24 (2005) 1125

Preparation, characterization and X-ray structure determinations of the 2-acetyl-2-thiazoline schiff base of hydrazine (ATH) and its cadmium(II) complex $[Cd(NO_3)_2(ATH)_2]$

Synthesis and characterization of a thiazoline and hydrazone derivative ligand and its Cd(II) complex. The cadmium complex was obtained through the reaction of 2-acetyl-2-thiazoline hydrazone (ATH) with $Cd(NO_3)_2 \cdot 4H_2O$. The complex and the ligand were characterized by single crystal X-ray diffraction, elemental analysis and spectroscopic measurements. The complex presents a distorted octahedral geometry around the cadmium(II) ion.

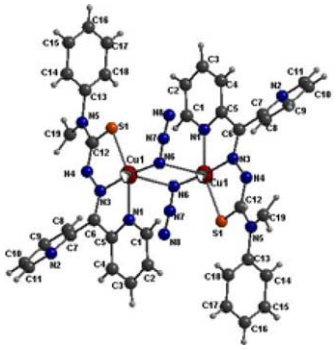


Varughese Philip, V. Suni, Maliyeckal R. Prathapachandra Kurup, Munirathinam Nethaji

Polyhedron 24 (2005) 1133

Novel binuclear copper(II) complexes of di-2-pyridyl ketone *N*(4)-methyl, *N*(4)-phenylthiosemicarbazone: Structural and spectral investigations

Four binuclear complexes $[Cu(dptsc)Cl]_2 \cdot 3H_2O$, $[Cu(dptsc)Br]_2$, $[Cu(dptsc)(\mu\text{-}N_3)]_2$ and $[Cu(dptsc)(NO_3)]_2 \cdot H_2O$ (where Hdptsc = di-2-pyridyl ketone *N*(4)-methyl, *N*(4)-phenylthiosemicarbazone) have been synthesized and physicochemically characterized. Each Cu(II) atom in the monomeric unit exists in a penta-coordinate environment. The single crystals of $[Cu(dptsc)Br]_2$ and $[Cu(dptsc)(\mu\text{-}N_3)]_2$ are centrosymmetric dimers. A distorted square pyramidal geometry is observed around Cu(II) for both the complexes.

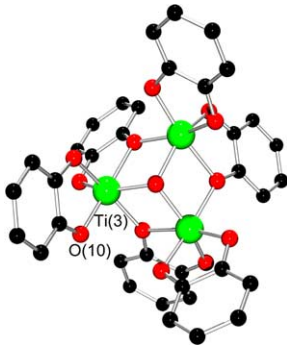


Timothy J. Boyle, Louis J. Tribby, Todd M. Alam, Scott D. Bunge, Gregory P. Holland

Polyhedron 24 (2005) 1143

Catechol derivatives of Group 4 and 5 compounds

Structural modifications of Group 4 and 5 metal alkoxides using catechol ($C_6H_3(OH)_2$-1,3 = cat-H_2) were characterized as $Ti_3(\mu_3\text{-}O)(\mu\text{-cat})_3(cat)(cat\text{-}H)_2$ (**1**, shown), $Zr_4(\mu_4\text{-}O)(\mu\text{-cat})_6(\mu\text{-cat-}H)_2(py)_4$ (**2**), $Hf_4(\mu_4\text{-}O)(\mu\text{-cat})_6(\mu\text{-cat-}H)_2(py)_4$ (**3**), $M(cat)_2(cat\text{-}H)(py)$ (M = Nb (**4**); Ta (**5**)). TGA/DTA data indicated that compound **1** was a reasonable precursor for nanoparticles and used to generate nanoparticles of TiO_2.

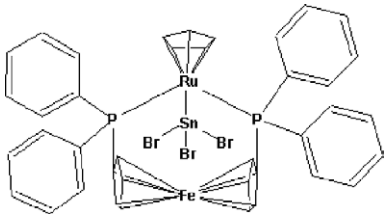


Lilian A. Paim, Daniella V. Augusti, Ilza Dalmázio, Tânia M. de A. Alves, Rodinei Augusti, Helmuth G.L. Siebald

Polyhedron 24 (2005) 1153

Electrospray ionization and tandem mass spectrometry characterization of novel heterotrimetallic $Ru(\eta^5\text{-}C_5H_5)(dppf)SnX_3$ complexes and their heterobimetallic $Ru(\eta^5\text{-}C_5H_5)(dppf)X$ precursors

Electrospray ionization and tandem mass spectrometry were used to characterize some novel heterotrimetallic complexes $Ru(\eta^5\text{-}C_5H_5)(dppf)\text{-}SnX_3$ (**1**) (dppf = diphenylpho-sphine ferrocene; X = Cl, Br) and their heterobimetallic precursors $Ru(\eta^5\text{-}C_5H_5)(dppf)X$ (**2**) (X = Cl, Br, I, N_3). The positive-ion ESI mass spectra of **1** and **2** in acetonitrile solution showed the predominant presence of the $[Ru(^5\text{-}C_5H_5)(dppf)]^+$ cation (**3**) of *m*/*z* 721. In the positive-ion ESI mass spectrum of the complex $Ru(\eta^5\text{-}C_5H_5)(dppf)N_3$ (**2d**), another prominent cation of *m*/*z* 735, $[Ru(\eta^5\text{-}C_5H_5)(dppf)N]^+$ (**4**), was also observed. Its formation was proposed to occur via the oxidation of the ruthenium atom followed by the loss of N_2. Cation **3** was proposed to be the catalytic active species in the single-step conversion of methanol to acetic acid.

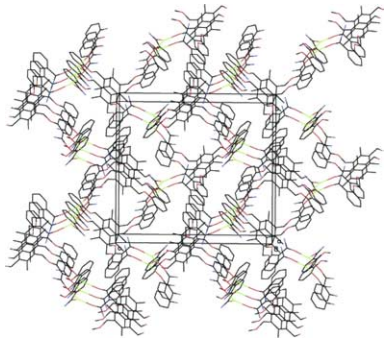


Yu Tang, Jian Zhang, Wei-Sheng Liu, Min-Yu Tan, Kai-Bei Yu

Polyhedron 24 (2005) 1160

Preparation, properties and structure of uncommon (10,3)-a netted rare earth complexes with an amide type tripodal ligand

Solid complexes of rare earth nitrates with a new amide type tripodal ligand **L** have been prepared. The crystal structure of $[Sm(NO_3)_3\mathbf{L}]_n$ shows the first example of a (10,3)-a net directed by RE(III) ions with a tripodal ligand. The luminescence properties of the Eu(III) and Tb(III) complexes were also studied.

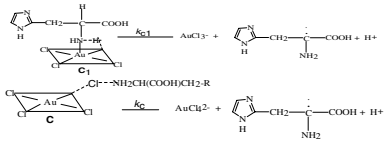


Vimal Soni, R.S. Sindal, Raj N. Mehrotra

Polyhedron 24 (2005) 1167

Kinetics of oxidation of L-histidine by tetrachloroaurate(III) ion in perchloric acid solution

The redox reaction is first order in both $AuCl_4^-$ and histidine. An inner-sphere mechanism is suggested. The rate determining steps in the mechanism are shown. It is shown that the intermediate **C1** decomposes at a rate about 10^3 faster than the rate of decomposition of **C**. It is also shown that the rate of formation of these intermediates (outer-sphere mechanism) cannot be rate determining.

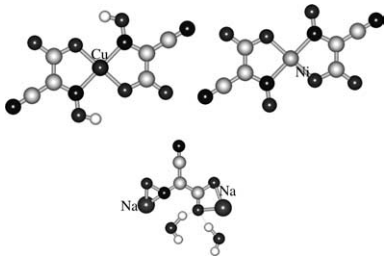


Kamilla Malek, Henryk Kozłowski, Leonard M. Proniewicz

Polyhedron 24 (2005) 1175

Interaction of Na(I), Ni(II) and Cu(II) with 2-cyano-2-(hydroxyimino)acetic acid: Spectroscopic and theoretical studies

Sodium(I), nickel(II) and copper(II) complexes of 2-cyano-2-(hydroxyimino)acetic acid have been characterized by vibrational and EPR spectra based on the DFT calculations. The bidentate ligand with the different protonation state of the oximic group chelates the transition metal ions through the oxime nitrogen and the carboxyl oxygen. However, two sodium ions are bonded to the deprotonated oximic as well as carboxylic groups.

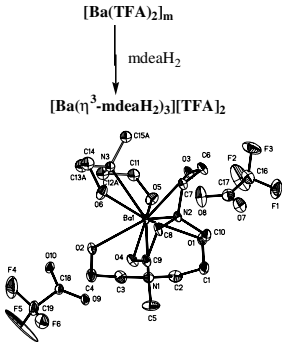


Jianyong Zhang, Liliane G. Hubert-Pfalzgraf, Dominique Luneau

Polyhedron 24 (2005) 1185

Synthesis, characterization and molecular structures of Cu(II) and Ba(II) fluorinated carboxylate complexes

Various routes to Cu(II) and Ba fluorocarboxylate derivatives as possible metal organic deposition (MOD) precursors of high Tc superconductors have been investigated. Reactions between copper(II) trifluoroacetate and functional alcohols such as isopropoxyethanol or dimethylaminoethanol afforded a complex $Cu_2(TFA)_4(OHC_2H_4O^iPr)_2$ or a carboxylatoalkoxide $Cu_4(\mu,\eta^2\text{-}TFA)_4(\mu_3,\eta^2\text{-}OC_2H_4NMe_2)_4$, respectively. The reaction between Ba trifluoroacetate and *N*-methyldiethanolamine ($mdeaH_2$) provided the first example of an ionic Ba TFA derivative

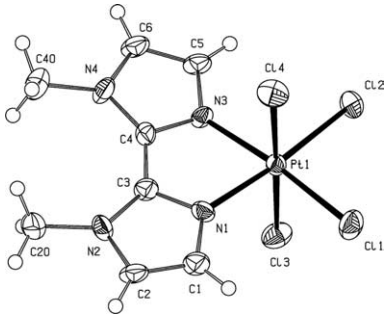


José S. Casas, Alfonso Castiñeiras, Yolanda Parajó, Agustín Sánchez, Ángeles Sánchez-González, José Sordo

Polyhedron 24 (2005) 1196

Synthesis and cytotoxicity of new Pt(IV) complexes of 2,2′-biimidazole and derivatives

Compounds of type $[PtCl_4(LL)]$ [LL = 2,2′-biimidazole (H_2bim), *N*-methyl-2,2′-biimidazole (MeHbim), *N*-hydroxyethyl-2,2′-biimidazole (HOEtHbim), or *N*,*N*′-dimethyl-2,2′-biimidazole (Me_2bim)] were prepared and characterized. The structure of $[PtCl_4(Me_2bim)]$ was determined by X-ray diffractometry. The new compounds were tested for cytotoxicity against the human ovarian cancer cell line A2780 and the cisplatin-resistant line A2780cis. All of them, except the HOEtHbim derivative, circumvent cisplatin-induced resistance.

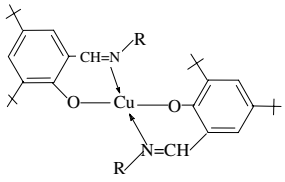


Veli T. Kasumov, Fevzi Köksal, Ali Sezer

Polyhedron 24 (2005) 1203

Synthesis, spectroscopic and redox properties of a novel series of copper(II) complexes of *N*-alkyl-3,5-Bu^t_2-salicylaldimines. Generation of the directly coordinated Cu(II)–phenoxyl radical complexes

The synthesis, spectroscopic (H NMR, IR, UV–Vis, ESR) and electrochemical properties as well as chemical oxidation of new bis(*N*-alkyl-3,5-Bu^t_2-salicylaldiminato)copper (II) complexes are described. Chemical oxidation of the complexes with $(NH_4)_2Ce(NO_3)_6$ as supported by ESR and UV/Vis examination, results in the of generation Cu(II)–phenoxyl radical complexes.



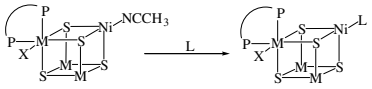
R = CH_3, C_2H_5, n-C_3H_7, n-C_4H_9, iso-C_4H_9, t-C_4H_9, n-C_5H_{11}, t-C_5H_{11}, n-C_6H_{13}, cyclo-C_6H_{12}

Marta Feliz, Rosa Llusar, Santiago Uriel , Cristian Vicent, Michael Brorson, Konrad Herbst

Polyhedron 24 (2005) 1212

Heterobimetallic cuboidal $[Mo_3NiS_4]$ and $[W_3NiS_4]$ cluster diphosphane complexes as molecular models in hydrodesulfurization catalysis

$[M_3NiS_4X_3(diphos)_3(CH_3CN)]^+$ (M = Mo, W; X = Cl, Br; diphos = dmpe, dppe) clusters have been prepared by addition of $[Ni(cod)_2]$ to incomplete cubane-type sulfido clusters-$[M_3S_4X_3(diphos)_3]^+$. The acetonitrile ligand could be substituted by pyridine, tetrahydrothiophene and carbon monoxide in CH_2Cl_2 at room temperature modelling the catalytic sites of heterogeneous Ni–MoS_2 hydrodesulfurization catalysts. All heterobimetallic $[M_3NiS_4]$ clusters reported show two quasireversible oxidation processes, the molybdenum complexes being ca. 0.2 V more difficult to oxidize than the tungsten analogues.

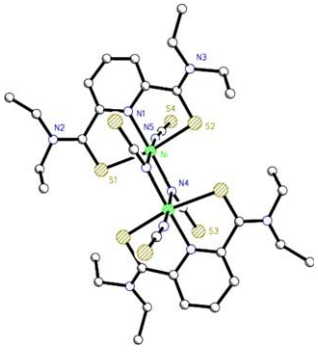


Ramesh Kapoor, Ashok Kataria, Anuradha Pathak, Paloth Venugopalan, Geeta Hundal, Pratibha Kapoor

Polyhedron 24 (2005) 1221

X-ray diffraction, spectral and magnetic studies of the nickel(II) thiocyanate complexes with tridentate 2,6-dithiocarboxamidopyridine *SNS* and 2,6-dicarboxamidopyridine *ONO* ligands: Influence of donor atoms on the coordination geometry of nickel

The unusual structural feature in the complex $[Ni_2(\mu\text{-}NCS)_2(NCS)_2(S\text{-}dept)_2]$ [S-dept = *N*,*N*,*N*′,*N*′- tetraethylpyridine-2,6-dithiocarboxamide] (**1**) is the presence of N-bonding bridging NCS groups between the Ni(II) atoms with the highest asymmetry. The magnetic-exchange interactions between the metal ions are small but significant. The coordination around Ni in the complexes $[Ni(O\text{-}deap)(NCS)_2 \cdot CH_3CN] \cdot CH_3CN$ (**2**) and $[Ni(O\text{-}deap)(NCS)_2 \cdot C_2H_5OH]$ (**3**) [O-deap = *N*, *N*,*N*′,*N*′-tetraethylpyridine-2,6-dicarboxamide] is distorted octahedral with a substantial difference in approach of the two thiocyanate ligands towards the coordination polyhedra. Complexes **2** and **3** show significant differences in their molecular packing.



The Publisher encourages the submission of articles in electronic form thus saving time and avoiding rekeying errors. For detailed instructions on the preparation of manuscripts and of electronic artwork, consult the Author Gateway for Elsevier at http://authors.elsevier.com

SCIENCE DIRECT™

Full text of this journal is available, on-line from **ScienceDirect**. Visit **www.sciencedirect.com** for more information.

CONTENTS Direct

This journal is part of **ContentsDirect**, the *free* alerting service which sends tables of contents by e-mail for Elsevier books and journals. You can register for **ContentsDirect** online at: **www. elsevier.com/locate/contentsdirect**

Available online at www.sciencedirect.com
SCIENCE DIRECT®
Polyhedron 24, issue 9, 28 June 2005
POLYHEDRON
www.elsevier.com/locate/poly

Contents

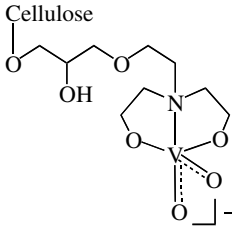
Papers

Yoshinobu Miyazaki, Shiro Matsuoka, Yoshinori Miura, Hirofumi Sakashita, Kazuhisa Yoshimura

Polyhedron 24 (2005) 985

Complexation of vanadium(V) oxoanion with ethanolamine derivatives in solution and in a cross-linked polymer

Vanadate reacts with the functional group of ECTEOLA–Cellulose to form the −1 charged 1:1 (N,O,O)-tridentate complex. In addition to the anion exchange interaction of monovanadates and isopolyvanadates with the protonated functional group, in the alkaline region the adsorbability of vanadium(V) onto ECTEOLA–Cellulose is a consequence of the complexation with the functional group.

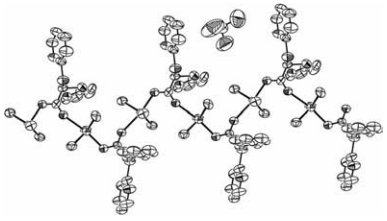


Maura Pellei, Carlo Santini, Marilena Mancini, Simone Alidori, Mercedes Camalli, Riccardo Spagna

Polyhedron 24 (2005) 995

New triorganotin(IV) complexes of a polyfunctional *S,N,O*-ligand

New tri-organotin(IV) derivatives containing the anionic bis(2-pyridylthio)acetate have been synthesized from reaction between SnR_3Cl acceptors and the $Na[(pyS)_2CHCO_2]$ ligand. Crystallisation of the compound $\{[(pyS)_2CHCO_2]Sn(CH_3)_3\}_n$ yielded the complex $\{[(pyS)_2CHCO_2]Sn(CH_3)_3\}_n \cdot CHCl_3$, which has been characterized by X-ray crystallography.

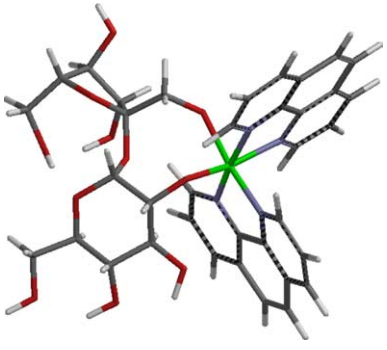


Jose Parada, Carmen Ibarra, Nicholas D. Gillitt, Clifford A. Bunton

Polyhedron 24 (2005) 1002

Sucrose bis(1,10-phenanthroline) cobalt(III). Comparison of semi-empirical and ab initio geometrical optimizations

The title compound (sucrose $Co(phen)_2$) is a dication with the Δ-configuration at Co(III) and ligation through O-2(g) and OH-1(f). Earlier geometrical optimization with semi-empirical PM3(tm) parameters had fitted most of the structural evidence from absorption, CD and NMR spectroscopy, although the site of deprotonation was predicted to be OH-1(f) rather than OH-2(g) as shown by NMR spectroscopy. Both HF and DFT treatments have now been used and they correctly predict deprotonation of OH-2(g), in agreement with experimental data. The earlier PM3(tm) optimization indicated extensive bowing of both phenanthrolines due to steric repulsions, but the ab initio treatments indicate limited bowing which fits the NMR chemical shifts of the phenanthroline hydrogens.



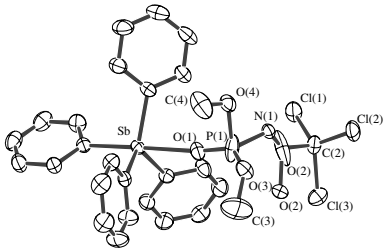
Elsevier Ltd.

Victor A. Trush, Katerina E. Gubina, Vladimir M. Amirkhanov, Jolanta Swiatek-Kozlowska, Konstantin V. Domasevitch

Polyhedron 24 (2005) 1007

Spectroscopic and crystal structure data of the alkali-, thallium (I) and onic-salts of dimethyl-*N*-trichloracetylamidophosphate

This article outlines alkali-, thallium (I) and onic-salts of dimethyl-*N*-trichloracetylamidophosphate [HL]. A brief description of the syntheses and IR and NMR spectroscopic studies of seven carbacylphosphortriamide compounds are given. All synthesized compounds have been structurally characterized. It was determined that the type of metal–ligand interaction in Na[L], Rb[L] and Tl[L] was ionic. IR spectroscopic and X-ray structure analysis of the $[SbPh_4L]$ complex determined the preferable donor center (phosphoryl oxygen atom in the L^-).

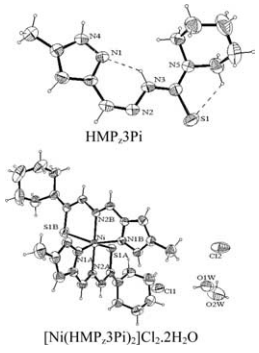


Nitis Chandra Saha, Ray J. Butcher, Siddhartha Chaudhuri, Nityananda Saha

Polyhedron 24 (2005) 1015

Synthesis and spectroscopic characterisation of new nickel (II) complexes with 5-methyl-3-formylpyrazole-3-piperidinylthiosemicarbazone (HMP_z3Pi): X-ray structures of HMP_z3Pi and $[Ni(HMP_z3Pi)_2]Cl_2 \cdot 2H_2O$ with indication for unusual rotation about the azomethine double bond of the free ligand on complexation

The synthesis and spectroscopic characterization of 5-methyl-3-formylpyrazole-3-piperidinylthiosemicarbazone, (HMP_z3Pi) and its nickel (II) complexes, $[Ni(HMP_z3Pi)_2]X_2 \cdot 2H_2O$ (X = Cl, Br, ClO_4, BF_4 and NO_3) have been reported. X-ray crystallography of $[Ni(HMP_z3Pi)_2]Cl_2 \cdot 2H_2O$, as a representative species, has authenticated a NiN_4S_2 octahedral coordination with neutral NNS tridentate function of the primary ligand system with two azomethine nitrogen atoms in *trans*-positions and the pyrazolyl nitrogen atoms and thio-keto sulfurs in *cis*-positions. On comparing the crystal structure of the free ligand, HMP_z3Pi, with that of its Ni(II) complex, $[Ni(HMP_z3Pi)_2]Cl_2 \cdot 2H_2O$, it is observed that an unusual rotation about the azomethine double bond occurs during complex formation. A possible mechanism for this phenomenon has been proposed.

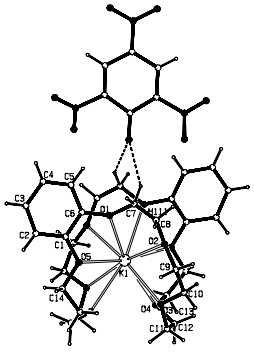


Pragati Agnihotri, E. Suresh, Bishwajit Ganguly, Parimal Paul, Pushpito K. Ghosh

Polyhedron 24 (2005) 1023

Study of the competitive binding of mixed alkali and alkaline earth metal ions with dibenzo-30-crown-10

Selectivity towards Na^+, K^+, Ca^{2+} and Mg^{2+} from their equimolar mixture and also from bittern with DB30C10 and the extraction equilibrium constant for K^+ with the same ligand has been estimated by a two-phase extraction method. Results have been rationalized on the basis of the crystal structure of [K-DB30C10][picrate] and molecular mechanics calculations.

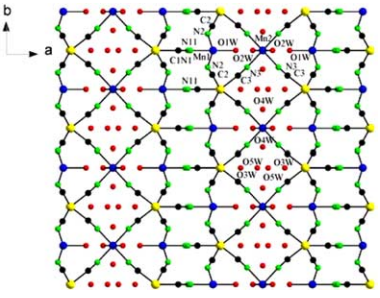


Stéphanie Willemin, Joulia Larionova, Hélène Bolvin, Bruno Donnadieu, Xavier F. Le Goff, Eliseo Ruiz, Christian Guérin, Bernard Henner

Polyhedron 24 (2005) 1033

Cation templation of $Mn^{2+}/[Mo(CN)_7]^{4-}$ system: Formation of pseudo-dimorphs $(NH_4)_2Mn_3(H_2O)_4[Mo(CN)_7]_2 \cdot nH_2O$ (n = 4, 5)

Pseudo-dimorphic phases $(NH_4)_2Mn_3(H_2O)_4[Mo(CN)_7]_2 \cdot nH_2O$ (n = 4 for **2**, n = 5 for **3**) have been obtained by introduction of NH_4^+ into the system $Mn^{2+}/[Mo(CN)_7]^{4-}$. These coordination polymers present similar three-dimensional networks of low symmetry and crystallize in monoclinic system ($C2/c$ space group).

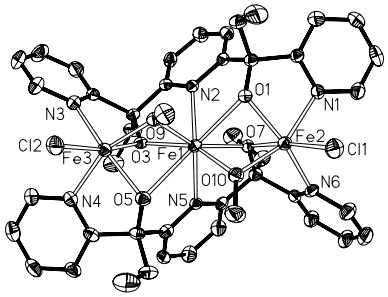


Xu-Dong Chen, Miao Du, Feng He, Xiao-Ming Chen, Thomas C.W. Mak

Polyhedron 24 (2005) 1047

Ligand behavior of 2,6-pyridinediylbis(2-pyridinyl)methanone in solvent-controlled formation of iron(III) complexes: A novel asymmetric quasi-linear trinuclear core containing an eight-coordinate iron center

The crystal structures of two polymorphic forms of 2,6-pyridinediylbis(2-pyridinyl)-methanone (**1**) crystallized from different solvents have been determined by X-ray crystallography. Solvent-controlled reaction between $FeCl_3$ and **1** yielded four crystalline iron(III) complexes exhibiting two structural types: an asymmetric quasi-linear triiron core with a rarely observed eight-coordinate iron(III) center and three mononuclear moieties. Ligand **1** is solvolyzed at both carbonyl groups in the trinuclear complex but hydrolysis/solvolysis occurs at only one carbonyl site in its mononuclear complexes. The variable-temperature magnetic susceptibilities of **2** were also measured.

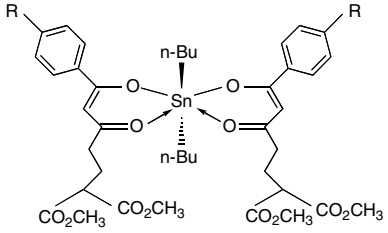


David Aaron Nieto-Álvarez, Federico Jiménez-Cruz, Teresa Mancilla

Polyhedron 24 (2005) 1054

Synthesis and characterization of new di-*n*-butyl[bis{dimethyl-2-(3-oxo-5-phenyl(4-subtituted)penten-5-ato)malonates}]tin(IV): The crystal structure of di-*n*-butyl[bis{dimethyl-2-[5-(4-nitrophenyl)-3-oxo-penten-5-ato]malonate}]tin(IV)

The synthesis and characterization of four new di-*n*-butyl[bis{dimethyl-2-(3-oxo-5-phenyl(4-subtituted)penten-5-ato)malonates}] tin(IV) **2a**–**2d** are reported. Their structures in $CDCl_3$ solution show a distorted octahedral geometry with a *trans* disposition of the *n*-butyl substituents. The ^{119}Sn NMR study at low variable-temperature indicates the presence of *trans anti*- and *syn*-isomers, and solid-state ^{13}C and ^{119}Sn NMR spectra of compound **2d** give also evidence of the isomeric mixture. The X-ray diffraction study of compound **2d** at 168 K shows only the *trans syn*-isomer, where the metal is six-coordinated in a skewed trapezoidal bipyramidal (STB) geometry.



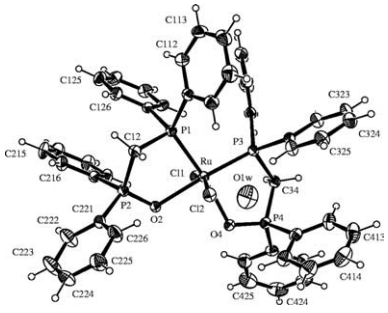
2a-2b

Marcella P. Felicissimo, Alzir A. Batista, Antonio G. Ferreira, Javier Ellena, Eduardo E. Castellano

Polyhedron 24 (2005) 1063

Ruthenium complexes containing the hemilabile ligand $PPh_2(CH_2)P(O)PPh_2$ (dppmO): reactivity towards CO and X-ray molecular structures of *tcc*-$RuCl_2(\eta^2\text{-dppmO})_2$ and *mer*-$RuCl_3(\eta^1,\eta^2\text{-dppmO})_2$

Ruthenium (II) complexes with the *hemilabile* ligand $Ph_2PCH_2P(O)Ph_2$ (dppmO) were obtained and characterized by means of two dimensional analysis ^{31}P–^{31}P gCOSY, ^{13}C–^{1}H HSQC, ^{1}H–^{31}P HMBC IR and cyclic voltammetry. Based on the resulting chemical shifts, coupling constants and correlations between ^{1}H, ^{13}C and ^{31}P spectra it was possible to accurately define the complexes structures. The determination of the crystal structure by X-ray diffraction was obtained for *tcc*-$RuCl_2(\eta^2\text{-dppmO})_2$, and *mer*-$RuCl_3(\eta^1,\eta^2\text{-dppmO})_2$.

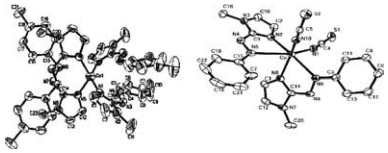


Umasankar Ray, Debasis Banerjee, Suchada Chantrapromma, Hoong-Kun Fun, Jyun-Nan Lin, Tian-Huey Lu, Chittaranjan Sinha

Polyhedron 24 (2005) 1071

Cobalt(II)–azoimidazole complexes: Structures of $[Co(MeaaiMe)_4](ClO_4)_2 \cdot H_2O$ and $[Co(HaaiMe)_2(NCS)_2]$ (MeaaiMe = 1-methyl-2-(*p*-tolylazo)imidazole; HaaiMe = 1-methyl-2-(phenylazo)imidazole)

1-Alkyl-2-(arylazo)imidazole (RaaiR′) coordinates through imidazole-N to Co(II) in a tetrahedral orientation to synthesise $[Co(RaaiR')_4](ClO_4)_2 \cdot H_2O$. The reaction of N_3^- or SCN^- with $[Co(RaaiR')_4](ClO_4)_2 \cdot H_2O$ has synthesized $Co(RaaiR')_2(X)_2$ $(X = N_3^-, SCN^-)$. Representative complexes are characterized by single-crystal X-ray diffraction studies.

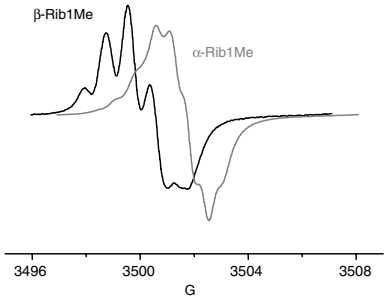


Sandra Signorella, Silvia García, Marcela Rizzotto, Aviva Levina, Peter A. Lay, Luis F. Sala

Polyhedron 24 (2005) 1079

The EPR pattern of Cr^V complexes of D-ribose derivatives

1-Substituted D-ribose derivatives form stable Cr^V bischelates where the ligand is bound to Cr^V through the 2,3-diolato moiety of the furanose ring. Cr^V complexes formed with the α- and β-D-ribose derivatives can be easily identified by EPR spectroscopy.

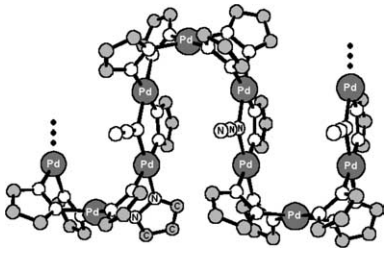


A.V.G. Netto, R.C.G. Frem, A.E. Mauro

Polyhedron 24 (2005) 1086

Low-weight coordination polymers derived from the self-assembly reactions of Pd(II) pyrazolyl compounds and azide ion

This work describes the synthesis of the low-weight Pd(II) coordination polymers $[(N_3)(HL)Pd\{Pd_3(\mu\text{-}N_3)(\mu\text{-}L)_5\}_{10}(\mu\text{-}L)_2Pd(L)(HL)]$ {L = Pz^- (**1**); mPz^- (**2**), IPz^- (**3**)} and $[(N_3)(HPz)Pd\{Pd_6(\mu\text{-}N_3)_2(\mu\text{-}Pz)_5(\mu\text{-}L)_5\}_{10}(\mu\text{-}L)_2Pd(Pz)(HPz)]$ {L = mPz^- (**4**), $dmPz^-$ (**5**); IPz^- (**6**)} {L = pyrazolate (Pz^-), 4-methylpyrazolate (mPz^-), 4-iodopyrazolate (IPz^-), 3,5-dimethylpyrazolate ($dmPz^-$)}. Some structures have been suggested on basis of IR, NMR, UV–VIS and osmometry studies.

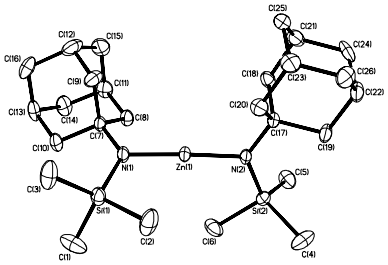


Yongjun Tang, Ana M. Felix, Brian J. Boro, Lev N. Zakharov, Arnold L. Rheingold, Richard A. Kemp

Polyhedron 24 (2005) 1093

Syntheses and X-ray crystal structures of monomeric zinc and mercury bis(silylamides)

Lithium amides $Li[N(SiMe_3)(R)]$ (R = $-SiPh_2{}^tBu$ and adamantyl) have been treated with anhydrous $ZnCl_2$ and $HgBr_2$ to yield the corresponding homoleptic metal silylamides. All complexes are fully characterized and are monomeric as determined by single crystal X-ray crystallography. The adamantyl-containing compounds differ significantly in their solid-state structures. Reactivities of these new compounds with CO_2 are also presented.

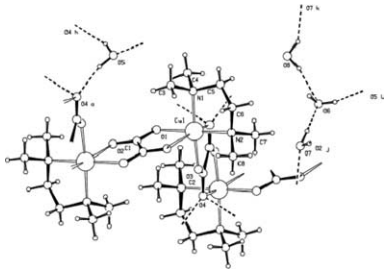


Mohammad Afzaal, Elizabeth Flynn, Mohammad A. Malik, Paul O'Brien, Majid Motevalli

Polyhedron 24 (2005) 1101

Mixed ligand chelates of copper(II) with substituted diamines

Copper complexes with substituted diamines have been synthesized and their X-ray single crystal structures determined.



The Publisher encourages the submission of articles in electronic form thus saving time and avoiding rekeying errors. For detailed instructions on the preparation of manuscripts and of electronic artwork, consult the Author Gateway for Elsevier at http://authors.elsevier.com

SCIENCE DIRECT™

Full text of this journal is available, on-line from **ScienceDirect**. Visit **www.sciencedirect.com** for more information.

CONTENTS Direct

This journal is part of **ContentsDirect**, the *free* alerting service which sends tables of contents by e-mail for Elsevier books and journals. You can register for **ContentsDirect** online at: **www. elsevier.com/locate/contentsdirect**

Available online at www.sciencedirect.com
SCIENCE DIRECT®
Polyhedron 24, issue 8, 2 June 2005
POLYHEDRON
www.elsevier.com/locate/poly

Contents

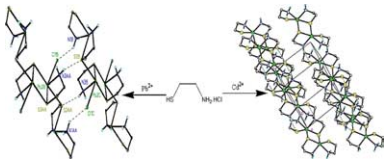
Papers

Mohan S. Bharara, Chong H. Kim, Sean Parkin, David A. Atwood

Polyhedron 24 (2005) 865

Synthesis and X-ray crystal structures of dinuclear hydrogen-bonded cadmium and lead 2-aminoethanethiolates

An in-depth study of dinuclear Cd and Pbcysteamine complexes has been carried out using NMR, IR, mass spectrometry and X-ray crystallography. The intermolecular hydrogen-bonding involving nitrogen, sulfur and counter anion has not been reported for similar dinuclear complexes, except for $[Hg(aet)_2]Cl_2$, previously reported by us. The structures described here should contribute to the understanding of fundamental Cd and Pb-thiolate chemistry of simple as well as complex molecules such as metallothioneins.

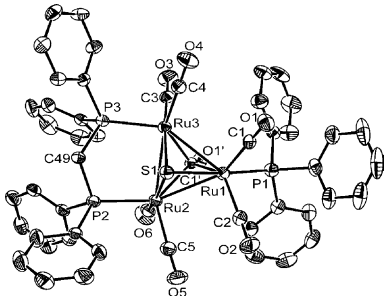


Md. Iqbal Hyder, G.M. Golzar Hossain, Shariff E. Kabir, Md. Arzu Miah

Polyhedron 24 (2005) 872

Triruthenium clusters bearing bridging dppm and capping sulfido ligands: X-ray structures of $[Ru_3(CO)_6(\mu_3\text{-}CO)(\mu_3\text{-}S)(PPh_3)(\mu\text{-}dppm)]$ and $[Ru_3(CO)_6(\mu_3\text{-}S)_2(PPh_3)(\mu\text{-}dppm)]$

Treatment of $[Ru_3(CO)_{10}(\mu\text{-}dppm)]$ (**1**) with PPh_3S at ambient temperature gave $[Ru_3(CO)_7(\mu_3\text{-}CO)(\mu_3\text{-}S)(\mu\text{-}dppm)]$ (**2**) and $[Ru_3(CO)_6(\mu_3\text{-}CO)(\mu_3\text{-}S)(PPh_3)(\mu\text{-}dppm)]$ (**3**). The reaction of $[Ru_3(CO)_7(\mu_3\text{-}S)_2(\mu\text{-}dppm)]$ (**4**) with PPh_3 in the presence of Me_3NO afforded **3**, $[Ru_3(CO)_6(\mu_3\text{-}S)_2(PPh_3)(\mu\text{-}dppm)]$ (**5**) and $[(\mu\text{-}H)_2Ru_3(CO)_7(\mu_3\text{-}S)(\mu\text{-}dppm)]$ (**6**). A similar reaction of $[Ru_3(CO)_7(\mu_3\text{-}S)(\mu_3\text{-}Se)(\mu\text{-}dppm)]$ (**7**) with PPh_3 afforded $[Ru_3(CO)_6(\mu_3\text{-}S)(\mu_3\text{-}Se)(PPh_3)(\mu\text{-}dppm)]$ (**8**). Protonation of **4** and **7** with CF_3COOH gave $[(\mu\text{-}H)Ru_3(CO)_7(\mu_3\text{-}S)_2(\mu\text{-}dppm)]$ (**10**) and $[(\mu\text{-}H)Ru_3(CO)_7(\mu_3\text{-}Se)(\mu_3\text{-}S)(\mu\text{-}dppm)]^+$ (**11**), respectively, isolated as their PF_6 salts.

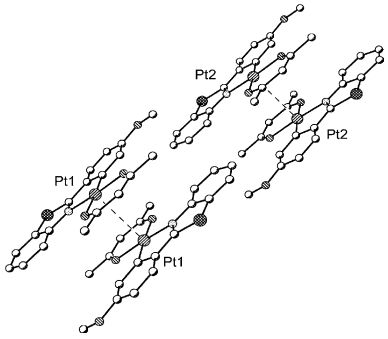


Inamur R. Laskar, Shih-Feng Hsu, Teng-Ming Chen

Polyhedron 24 (2005) 881

Highly efficient orange-emitting OLEDs based on phosphorescent platinum(II) complexes

The syntheses, characterisations, photophysical properties and their applications in organic light emitting devices of a series of 2-phenylbenzothiazolato (bt)/substituted 2-phenylbenzothiazolato (X-bt) platinum(II) based square-planar complexes [(X-bt)-Pt(acac); acac = acetylacetonate; X = unsubstituted, F, OMe and CF_3] are reported.

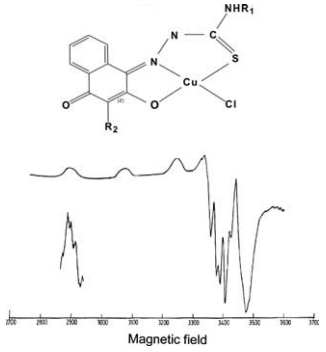


Rajeev C. Chikate, Avadhoot R. Belapure, Subhash B. Padhye, Douglas X. West

Polyhedron 24 (2005) 889

Transition metal quinone–thiosemicarbazone complexes 1: Evaluation of EPR covalency parameters and redox properties of pseudo-square-planar copper(II)–naphthoquinone thiosemicarbazones

EPR studies on pseudo-square-planar copper(II) complexes of naphthoquinone–thiosemicarbazones of the formula [CuLCl] reveal appreciable covalency in the metal–ligand bonding as a consequence of extensive delocalization, while cyclic voltammetric response of these complexes suggests metal-centered redox behavior. There exists a linear relationship between the degree of tetrahedral distortion $f(\alpha)$ with EPR and redox parameters.

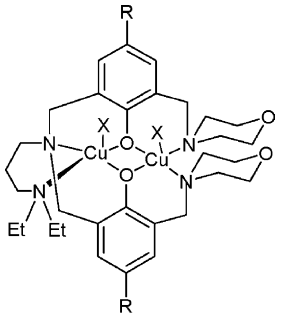


P. Kamatchi, S. Selvaraj, M. Kandaswamy

Polyhedron 24 (2005) 900

Synthesis, magnetic and electrochemical studies of binuclear copper(II) complexes derived from unsymmetrical polydentate ligands

New binuclear copper(II) complexes were prepared using penta and hexadentate ligands and characterized by various spectral studies. Electrochemical and magnetic studies of these complexes were carried out.



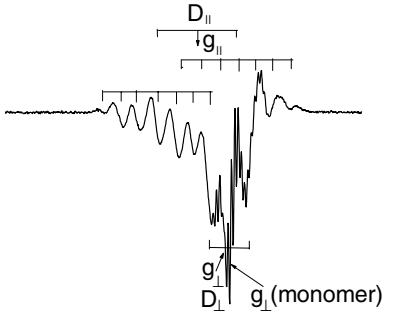
X= ClO_4, Cl, Br

O. Ibopishak Singh, M. Damayanti, N. Rajen Singh, R.K. Hemakumar Singh, Manoj Mohapatra, R.M. Kadam

Polyhedron 24 (2005) 909

Synthesis, EPR and biological activities of bis(1-*n*-butylamidino-*O*-alkylurea)copper(II)-chloride complexes: EPR evidence for binuclear complexes in frozen DMF solution

The EPR spectra of copper(II) complexes of the type $[Cu(1\text{-}Bu^{n}AAUH)_2]Cl_2$, where 1-$Bu^{n}$-AAUH = 1-*n*-butylamidino-*O*-alkylurea, in frozen solutions of DMF showed a signal at *g* ca. 2. In addition to this, a signal at half the resonance field having a well resolved seven-line hyperfine structure was observed, which have been interpreted as arising from $\Delta M_s = \pm 1$ and $\Delta M_s = \pm 2$ transitions. The complexes show growth inhibitory activity against pathogenic fungi and bacteria.

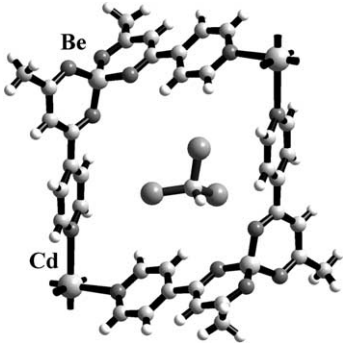


Volodimir D. Vreshch, Andrey B. Lysenko, Alexander N. Chernega, Joachim Sieler, Konstantin V. Domasevitch

Polyhedron 24 (2005) 917

Heterobimetallic Cd(Zn)/Be coordination polymers involving pyridyl functionalized beryllium diketonates

Two-step complexation of pyridyl functionalized diketonate ligands allows preparation of a number of heterobimetallic coordination polymers with alternation of Be and Cd(Zn) metal ions.

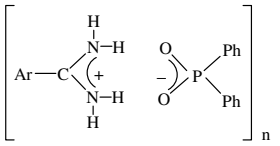


Jianping Guo, Wai-Kwok Wong, Wai-Yeung Wong

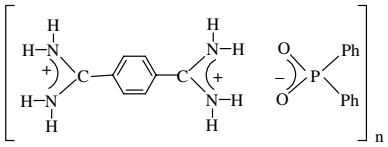
Polyhedron 24 (2005) 927

Synthesis and structural characterization of some arylamidinium diphenylphosphinates: Formation of one-, two- and three-dimensional networks by charge-assisted hydrogen bonds

The preparation, characterization and crystal structures of a series of arylamidinium diphenylphosphinates are described and these ionic salts exist as polymeric networks of various dimensions assembled via charge-assisted hydrogen bonds.



Ar = phenyl, *p*-tolyl, 4-, 3-, 2-pyridyl

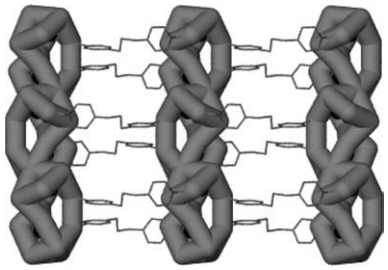


Xiao-Li Zhao, Thomas C.W. Mak

Polyhedron 24 (2005) 940

4,4′-Bipyridine and bis(4-pyridyl)propane as bridging ligands in the supramolecular assembly of silver(I) polyhedra containing embedded acetylenediide

Six new double salts of silver(I) acetylenediide, namely $[Ag_{13}(C_2)_2(CF_3CO_2)_9(bipy)_4(H_2O)_3]$ (**1**), $[Ag_{18}(C_2)_2(C_2F_5CO_2)_{18}(bipyH)_4] \cdot 3H_2O$ (**2**), $[Ag_6(C_2)(CF_3CO_2)_4(bpp)]$ (**3**), $[Ag_6(C_2)(C_2F_5CO_2)_5(bppH)]_n$ (**4**), $[Ag_6(C_2)(CF_3CO_2)_5(bppH)]_n$ (**5**) and $[Ag_{23}(C_2)_4(CF_3CO_2)_{15}(bpp)_6] \cdot H_2O$ (**6**) (bipy = 4,4′-bipyridine, bpp = bis(4-pyridyl)propane), have been shown to exhibit a variety of discrete and higher-dimensional supramolecular architectures.

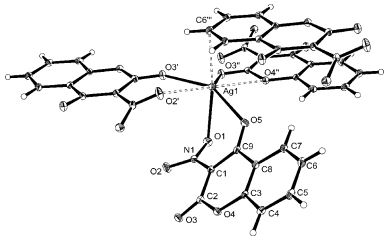


Bernadette S. Creaven, Denise A. Egan, Kevin Kavanagh, Malachy McCann, Mary Mahon, Andy Noble, Bhumika Thati, Maureen Walsh

Polyhedron 24 (2005) 949

Synthesis and antimicrobial activity of copper(II) and silver(I) complexes of hydroxynitrocoumarins: X-ray crystal structures of $[Cu(hnc)_2(H_2O)_2] \cdot 2H_2O$ and [Ag(hnc)] (hncH = 4-hydroxy-3-nitro-2*H*-chromen-2-one)

A series of silver complexes of coumarin-based ligands showed significant anti-microbial activity, particularly against the clinically important methicillin-resistant *Staphylococcus aureus* (MRSA) bacterium and also demonstrated good activity, comparable to that of the commercial fungicides clortrimazole and ketoconazole, against a clinical isolate of the fungal pathogen *Candida albicans*.

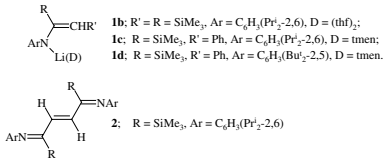


Manuel A. Fernandes, Marcus Layh, Bernard Omondi

Polyhedron 24 (2005) 958

Synthesis and crystal structures of sterically hindered lithium-1-azaallyls and a diazahexatriene

The lithium-1-azaallyl complexes [LiN(Ar)-C(R)CHR′(D)] **1** and the diazahexatriene **2** were obtained in moderate yields from $LiCHR_2$ or LiCH(R)Ph(tmen) and ArNC [Ar = $C_6H_3(Pr^i{}_2\text{-}2,6)$ or $C_6H_3(Bu^t{}_2\text{-}2,5)$]. All compounds were characterized by NMR spectroscopy and single crystal X-ray crystallography. **1b**–**1d** were found to be monomeric in the solid state with **1b** adopting an unusual anti-conformation.



1b; R′ = R = $SiMe_3$, Ar = $C_6H_3(Pr^i{}_2\text{-}2,6)$, D = $(thf)_2$;
1c; R = $SiMe_3$, R′ = Ph, Ar = $C_6H_3(Pr^i{}_2\text{-}2,6)$, D = tmen;
1d; R = $SiMe_3$, R′ = Ph, Ar = $C_6H_3(Bu^t{}_2\text{-}2,5)$, D = tmen.

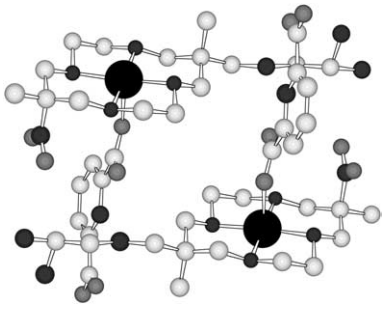
2; R = $SiMe_3$, Ar = $C_6H_3(Pr^i{}_2\text{-}2,6)$

Jack Harrowfield, Jee Young Kim, Yang Kim, Young Hoon Lee, Sujandi, Pierre Thuéry

Polyhedron 24 (2005) 968

Podand hexamines and the synthesis of pendent-arm tetra-azamacrocycles

Coordination of Cu(II) to a podand hexamine enables fcile synthesis of stereoisomeric macrocycles with pendent arms suitable for chelation of an external metal ion outside the macrocycle.

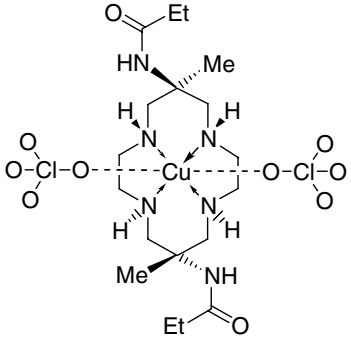


Neil F. Curtis, Ward T. Robinson

Polyhedron 24 (2005) 976

Compounds of some alkylamido-substituted cyclic tetraamines with copper(II): The structure of *di*(perchlorato)*RRSS*(*trans*-(6,13-bis(ethylamido)-6,13-dimethyl-1,4,8,11-tetraazacyclotetradecane)copper(II)

The amino substituents of (*trans*-6,13-diamino-6,13-dimethyl-1, 4, 8,11-tetraazacyclotetradecane)copper(II) are acylated by reaction with acetic or propionic anhydrides to form the 6,13-bismethylamido or bis(ethylamido) substituted cations. Centrosymmetrical *di*(perchlorato-*trans*-6,13-bisethylamido-6,13-dimethyl-1,4,8,11-tetraazacyclotetradecane)copper(II) has copper(II) in square-planar coordination by the endocyclic nitrogen atoms with perchlorate oxygen atoms weakly coordinated axially.

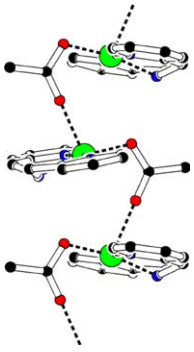


Stefania Tanase, Gerard A. van Albada, René de Gelder, Elisabeth Bouwman, Jan Reedijk

Polyhedron 24 (2005) 979

Crystal structure, magnetic properties and spectroscopic characterization of a rare *syn–anti* acetato-bridged zig-zag chain copper(II) complex

A novel linear-chain copper(II) compound containing *syn–anti* acetato bridges is presented. The compound exhibits a very weak ferromagnetic interaction between the Cu(II) ions with a J value of 0.21 cm^{-1}.



The Publisher encourages the submission of articles in electronic form thus saving time and avoiding rekeying errors. For detailed instructions on the preparation of manuscripts and of electronic artwork, consult the Author Gateway for Elsevier at http://authors.elsevier.com

SCIENCE DIRECT™

Full text of this journal is available, on-line from **ScienceDirect**. Visit **www.sciencedirect.com** for more information.

CONTENTS Direct

This journal is part of **ContentsDirect**, the *free* alerting service which sends tables of contents by e-mail for Elsevier books and journals. You can register for **ContentsDirect** online at: **www. elsevier.com/locate/contentsdirect**

Available online at www.sciencedirect.com
SCIENCE DIRECT®
Polyhedron 24, issue 15, 27 October 2005
POLYHEDRON
www.elsevier.com/locate/poly

Contents

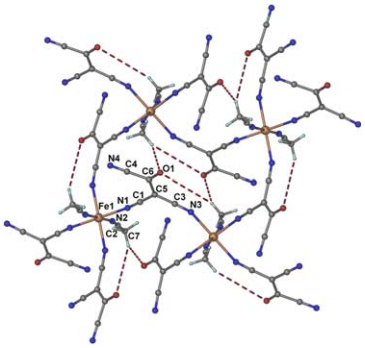
Papers

Hanhua Zhao, John Bacsa, Andrey Prosvirin, Nazario Lopez, Kim R. Dunbar

Polyhedron 24 (2005) 1907

Synthesis, crystal structures and magnetic properties of two new coordination polymers based on the tricyanoethenolate ligand: $\{Fe(C_5N_3O)_2(CH_3CN)_2\}_\infty$ and $\{Co(C_5N_3O)_2(C_4H_4O)_2\}_\infty$

This paper reports two new Fe(II) and Co(II) compounds in which the 1,2,2-tricyanoethanolate ligand coordinates via two of its three nitrile N atoms which leads to the formation of two-dimensional sheets. The metal atoms are in slightly distorted octahedral environments with axially bonded solvent molecules.

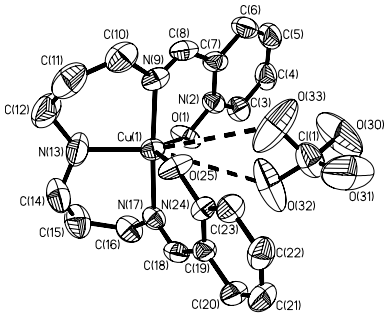


Miroslav Boča, Mário Izakovič, Guido Kickelbick, Marián Valko, Franz Renz, Hartmut Fuess, Katarína Matuzsná

Polyhedron 24 (2005) 1913

Structure of the copper (II) perchlorate complex with Schiff base ligand containing pyridine N-oxide fragments and propylene bridges: Solvatochromic effect

The structure of $[CuL^2](ClO_4)_2$ was solved (L^2 = condensation products of 2-pyridinecarboxaldehyde-N-oxide with dipropylenetriamine). The ligand exists in the form of aliphatic polyamine containing two Schiff bases in contrary to the free form of this ligand with one pyrimidine ring and one Schiff base. Solvatochromic effect on this complex was observed.

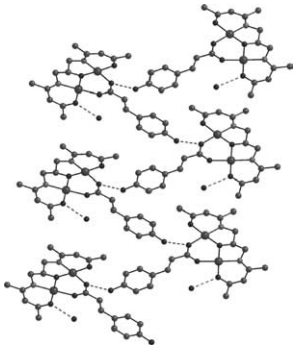


Sunita Gupta, Arindam Mukherjee, Munirathinam Nethaji, Akhil R. Chakravarty

Polyhedron 24 (2005) 1922

Effect of a pentadentate Schiff base on the helical supramolecular structures of (μ-alkoxo)(μ-carboxylato)dicopper(II) complexes

Dicopper(II) complexes $[Cu_2L(O_2CCH{=}CH\text{-}C_6H_4\text{-}p\text{-}OH)(MeOH)] \cdot MeOH$ (**1** · MeOH) and $[Cu_2L(O_2CCH{=}CHC_6H_4\text{-}p\text{-}OH)] \cdot H_2O$ (**2** · H_2O) having a carboxylate ligand with a *p*-hydroxycinnamyl moiety and the pentadentate Schiff base *N*,*N*′-1,3-diyl-bis(acetylacetoneimine)propan-2-ol (H_3L) in its trianionic form, are prepared and structurally characterized by X-ray crystallography. The antiferromagnetically coupled dicopper(II) complexes show hydrogen bonding interactions to form helical supramolecular structures of different conformations.

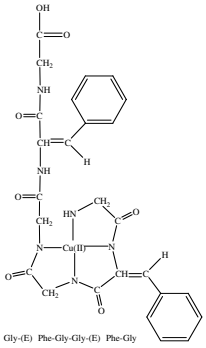


Justyna Brasun, Maciej Makowski, Anna Janicka, Jolanta Swiatek-Kozlowska

Polyhedron 24 (2005) 1929

Influence of the position of two dehydroamino acids residues in the oligopeptide sequence on the binding ability towards Cu(II) ions

The coordination ability towards Cu^{2+} ion of four bis-dehydro-hexa- and pentapeptides was studied by using potentiometry and spectroscopic methods like UV–Vis and EPR. The studied ligands were: Gly–(*Z*)ΔPhe–Gly–(*Z*)ΔPhe–Ala, Gly–(*Z*)ΔPhe–Gly–Gly–(*Z*)ΔPhe–Gly, Gly–(*E*)ΔPhe–Gly–Gly–(*E*)ΔPhe–Gly and Gly–ΔAla–Gly–Gly–ΔAla–Gly.

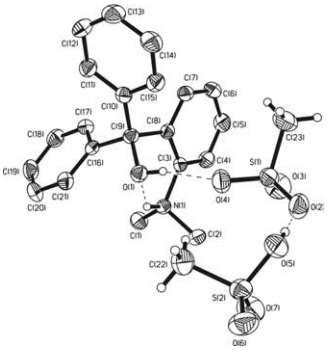


Harbi Tomah Al-Masri, Joachim Sieler, Evamarie Hey-Hawkins

Polyhedron 24 (2005) 1937

Synthesis, characterization and molecular structure of $[1\text{-}HOCPh_2\text{-}2\text{-}NHMe_2C_6H_4]\text{-}[MeSO_3] \cdot MeSO_3H$

$[1\text{-}HOCPh_2\text{-}2\text{-}NHMe_2C_6H_4][MeSO_3] \cdot MeSO_3H$ (**2**) was prepared from $1\text{-}HOCPh_2\text{-}2\text{-}NMe_2C_6H_4$ and methylsulfonic acid and was characterized spectroscopically (NMR, IR) and by crystal structure determination. The latter shows the association of two ions $[1\text{-}HOCPh_2\text{-}2\text{-}NHMe_2C_6H_4]^+$ and $[MeSO_3]^-$ and one molecule $MeSO_3H$ by hydrogen bonding.

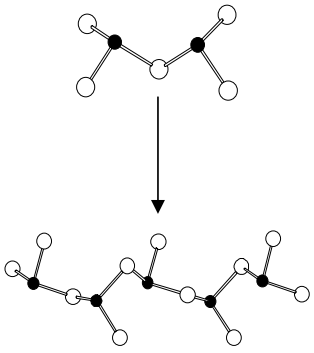


Rachel J.E. Lees, Anthony V. Powell, Ann M. Chippindale

Polyhedron 24 (2005) 1941

The synthesis and characterisation of two new iron thioantimonates: $[Fe(en)_3]_2Sb_2S_5 \cdot 0.55H_2O$ and $[Fe(en)_3]_2Sb_4S_8$

The iron thioantimonates, $[Fe(en)_3]_2Sb_2S_5 \cdot 0.55H_2O$ (**1**) and $[Fe(en)_3]_2Sb_4S_8$ (**2**) have been prepared under solvothermal conditions. Compound **1** contains isolated $Sb_2S_5^{4-}$ anions formed from two corner-sharing SbS_3^{3-} trigonal pyramids, whereas in **2**, repeated corner linking of the same SbS_3^{3-} trigonal pyramids generates SbS_2^- chains.

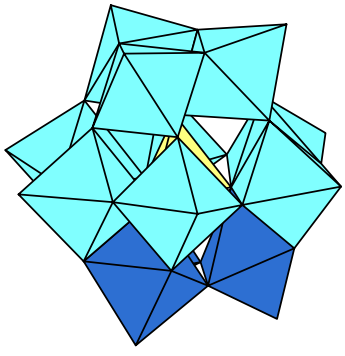


Akihito Ishii, Tomoji Ozeki

Polyhedron 24 (2005) 1949

Crystal structure of a mixed-metal β-Keggin molybdotungstosilicate, $K_4[A\text{-}\beta\text{-}SiMo_3W_9O_{40}] \cdot 9H_2O$

The crystal structure of potassium A-β-trimolybdononatungstosilicate nonahydrate, $K_4[A\text{-}\beta\text{-}SiMo_3W_9O_{40}] \cdot 9H_2O$, have been determined by single crystal X-ray diffraction.

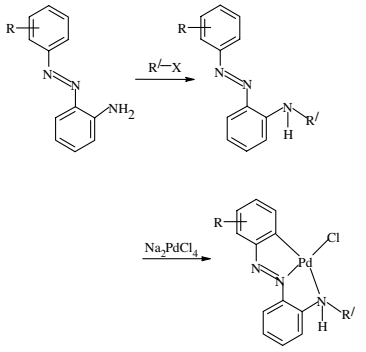


Jahar lal Pratihar, Nilkamal Maiti, Poulami Pattanayak, Surajit Chattopadhyay

Polyhedron 24 (2005) 1953

A strategy of Pd(II) assisted C–H activation in 2-alkylamino azobenzene ligands: Syntheses, characterisation and structure of a new family of orthopalladated complexes

Orthopalladation is a particular method of C–H bond activation, we have described a strategy of orthopalladation in azoamine molecules. Several azoamine molecules have been examined in this regard.

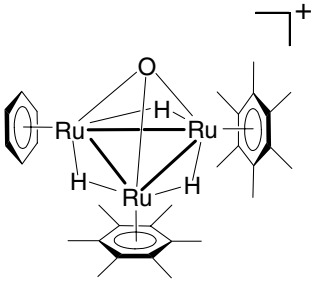


Ludovic Vieille-Petit, Mathieu J.-L. Tschan, Georg Süss-Fink, Gabor Laurenczy, Collin M. Hagen, Richard G. Finke, Florence Geneste, Claude Moinet

Polyhedron 24 (2005) 1961

The water-soluble cluster cation $[H_3Ru_3(C_6H_6)(C_6Me_6)_2(O)]^+$: Improved synthesis, aerobic oxidation, electrochemical properties and ligand exchange studies

The water-soluble trinuclear cluster cation $[H_3Ru_3(C_6H_6)(C_6Me_6)_2(O)]^+$ (**1**) is an efficient catalyst precursor for the hydrogenation of benzene to cyclohexane under biphasic conditions. An improved synthesis of **1** and its chemical properties (aerobic oxidation, electrochemical behaviour and ligand exchange reactions) are reported.



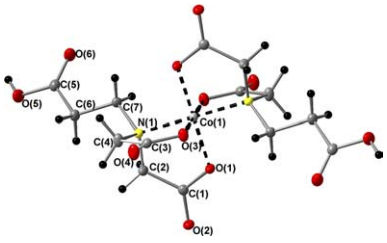
1

Hein Potgieter, Walter Purcell, Hendrik G. Visser, Juan Niclós-Gutiérrez

Polyhedron 24 (2005) 1968

Identification of different Co(III) apda complexes: Crystallisation of $[Co(H_2O)_6] \cdot [Co(Hapda)_2]_2 \cdot H_2O$

Two cobalt(III) complexes with a potentially tridentate ligand, apda was investigated. Crystals of $[Co(H_2O)_6] \cdot [Co(Hapda)_2]_2 \cdot H_2O$ were isolated and studied with X-ray diffraction. The Hapda ligand acts as a tridendate ligand with the longer, pronated β-alaninato arms not bonded. The effective use of ^1H NMR to determine the positioning of the chelate rings of apda is illustrated with a comparative study of the title complex with $[Co(apda)(H_2O)_2]$ where apda acts as a tetradentate ligand.

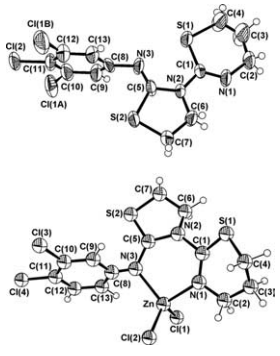


Fernando J. Barros-García, Álvaro Bernalte-García, Francisco L. Cumbrera, Ana M. Lozano-Vila, Francisco Luna-Giles, Juan J. Meléndez-Martínez, Ángel L. Ortiz

Polyhedron 24 (2005) 1975

Synthesis, molecular characterization by infrared spectroscopy, and crystal structure determination by X-ray powder diffractometry of $[ZnCl_2(TdTz)]$ [TdTz = 2-(3,4-dichlorophenyl) imino-N-(2-thiazin-2-yl)thiazolidine]

The title zinc(II) complex was synthesized through the reaction of 2-(3,4-dichlorophenyl)imino-N-(2-thiazin-2-yl)thiazolidine (TdTz) with $ZnCl_2$. The crystal structure of the TdTz organic-ligand was resolved by X-ray single-crystal diffractometry. The zinc(II) complex was first characterized by elemental analysis and infrared spectroscopy, and its crystal structure then resolved by X-ray powder diffractometry using direct-space methods. It was found that the complex adopts a pseudotetrahedral geometry around the zinc(II) ion.

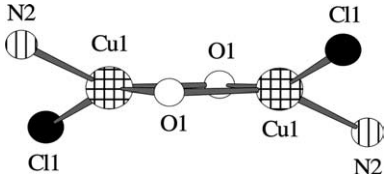


V.T. Getova, R.P. Bontchev, D.R. Mehandjiev, V. Skumryev, P.R. Bontchev

Polyhedron 24 (2005) 1983

Copper(II) complexes with 4-amino-α-(*t*-butylaminomethyl)-3,5-dichlorobenzyl alcohol hydrochloride (Clenbuterol). Crystal structures of the binuclear and mononuclear Cu(II) complexes with Clenbuterol

Two new copper(II) complexes, mono- and binuclear ones, of the aminoalcohol drug Clenbuterol were synthesized and studied by spectral (UV–Vis, IR, EPR), thermogravimetric and magnetochemical methods. Their structures were determined using X-ray diffraction of monocrystals. Solvent molecules are also incorporated in the crystal lattice due to H-bonding with the ligand.

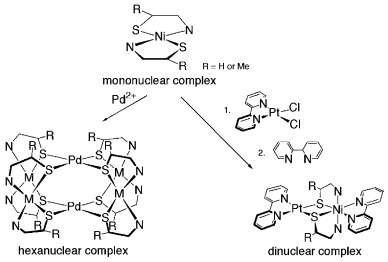


Mitsuharu Fujita, Yoshitaro Miyashita, Nagina Amir, Yoriko Kawamoto, Kan Kanamori, Kiyoshi Fujisawa, Ken-ichi Okamoto

Polyhedron 24 (2005) 1991

Stereoselective formation and properties of mononuclear and polynuclear nickel(II) complexes with 1-amino-2-propanethiolate

Thiolato-type mononuclear and S-bridged polynuclear Ni(II) complexes with 1-amino-2-propanethiolate were newly synthesized. Stereoselective formation based on chirality of the ligand was observed. The spectrochemical properties of these complexes were investigated in comparison with the corresponding complexes with 2-aminoethanethiolate.

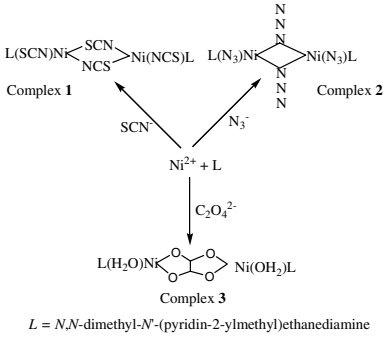


He-Dong Bian, Wen Gu, Qing Yu, Shi-Ping Yan, Dai-Zheng Liao, Zong-Hui Jiang, Peng Cheng

Polyhedron 24 (2005) 2002

Synthesis, crystal structure, and magnetic properties of three nickel(II) complexes with the tridentate ligand *N*,*N*-dimethyl-*N*′-(pyrid-2-ylmethyl)-ethylenediamine

Three dinuclear nickel(II) complexes of the tridentate ligand L (L = *N*,*N*-dimethyl-*N*′-(pyrid-2-ylmethyl)-ethylenediamine) with the bridging ligands of thiocyanate, azide, and oxalate dianion, respectively, have been synthesized, and characterized by X-ray structural analysis, magnetic measurement, IR and UV–Vis–NIR spectra.



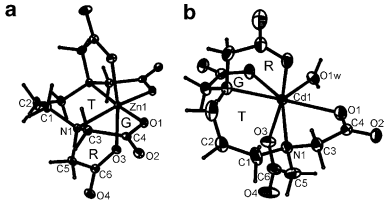
L = *N*,*N*-dimethyl-*N*′-(pyridin-2-ylmethyl)ethanediamine

Urszula Rychlewska, Dejan M. Gurešić, Beata Warżajtis, Dušanka D. Radanović, Miloš I. Djuran

Polyhedron 24 (2005) 2009

Highly selective crystallization of metal(II) ions with 1,3-pdta ligand: Syntheses and crystal structures of the $[Mg(H_2O)_6][Cd(1,3\text{-}pdta)(H_2O)] \cdot 2H_2O$ and two isomorphic $[Zn(1,3\text{-}pdta)]^{2-}$ complexes

X-ray crystallography has been applied to investigate 1,3-pdta complexes of Zn^{2+} and Cd^{2+} ions. The $[Zn(1,3\text{-}pdta)]^{2-}$ (**a**) and $[Cd(1,3\text{-}pdta)(H_2O)]^{2-}$ (**b**) complexes are different in coordination number and geometry, as (**b**) constitutes tzhe first example of transition metal complex with 1,3-pdta ligand that possesses CN equal to 7.

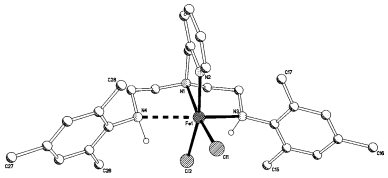


Christopher J. Davies, Stephen J. Hilton, Gregory A. Solan, Wesley Stannard, John Fawcett

Polyhedron 24 (2005) 2017

Functionalised dien ligands of the type $(ArNHCH_2CH_2)_2NR$ [R = Me, (2-C_5H_4N)-CH_2] and their complexes with iron and cobalt halides

The aryl-substituted dien ligand frame has been amenable to functionalisation at the central nitrogen atom allowing access to sterically bulky alkyl- and picolyl-substituted multidentate nitrogen donor ligands; full characterisation of complexes formed from their reactions with iron and cobalt chlorides is reported.

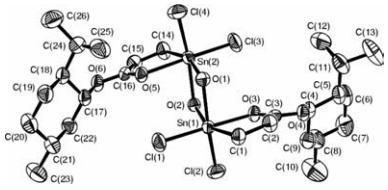


Lai-Jin Tian, Yu-Xi Sun, Xi-Jie Liu, Guo-Ming Yang, Zhi-Cai Shang

Polyhedron 24 (2005) 2027

Synthesis and structural characterization of 2-(−)-menthoxycarbonylethyltin compounds

The title compounds, (−)-MenOCO-$CH_2CH_2SnCl_nPh_{3-n}$ (n = 0, **1**; 1, **2**; 2, **3**; 3, **4**) and [(−)-MenOCOCH$_2$CH$_2$Sn(OH)Cl$_2$]$_2$ · 2(C_2H_5)$_2$O (**5** · 2(C_2H_5)$_2$O) were synthesized and characterized by means of elemental analysis, IR, NMR (^{1}H, ^{13}C and ^{119}Sn) and X-ray crystallography. Compounds **2**–**5** · 2(C_2H_5)$_2$O contain intramolecular carbonyl-to-tin coordination, and the strengths of the interaction between the CO and Sn generally increase in order **1** < **2** < **3** < **4** < **5** · 2(C_2H_5)$_2$O.

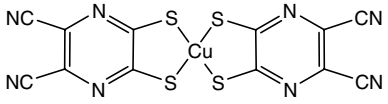


D. Belo, M.J. Figueira, I.C. Santos, V. Gama, L.C. Pereira, R.T. Henriques, M. Almeida

Polyhedron 24 (2005) 2035

Synthesis and characterization of copper complexes with the 2,3-dicyano-5,6-dimercaptopyrazine ligand: Magnetic properties of a ferrocenium salt

Cu(dcdmp)$_2$ was obtained in both dianionic and monoanionic states. The [Fe(Cp*)$_2$]$_2$-[Cu(dcdmp)$_2$] salt presents paramagnetic contributions from both cations and dianions with a large anisotropy and no magnetic ordering down to 1.7 K.



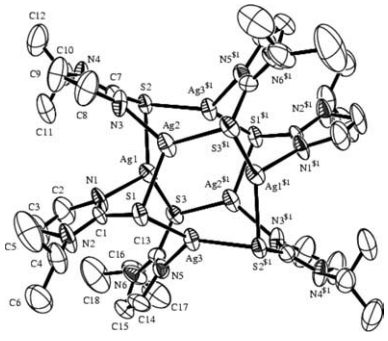
Cu(dcdmp)$_2$

José A. García-Vázquez, Antonio Sousa-Pedrares, Maximiliano Carabel, Jaime Romero, Antonio Sousa

Polyhedron 24 (2005) 2043

Electrochemical synthesis and structural characterization of copper and silver complexes of imidazolidine-2-thione ligands

New multinuclear copper (I) and silver (I) 1-R-imidazolidine-2-thionates of the general formula [Cu(1-RImS)] and [Ag(1-RImS)] (where R = Me, Et, Pr, ^{i}Pr) have been synthesized and characterized. The crystal structures of [Cu(1-EtImS)] (**1**), [Cu(1-PrImS)] (**2**), [Ag(1-PrImS)] (**3**) and [Ag(1-^{i}PrImS)] (**4**) were determined by X-ray diffraction. Compounds (**1**) and (**2**) are tetranuclear and the complexes (**3**) and (**4**) are hexanuclear. In all these compounds each metal atom has a distorted trigonal [MS_2N] environment with each ligand acting as a μ^2-N,S(η^2-S; η^1-N) bidentate S-bridging ligand.

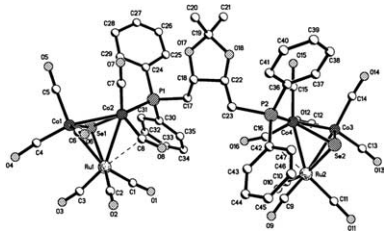


Bao-Hua Zhu, Bin Hu, Yuan-Qi Yin, Jie Sun

Polyhedron 24 (2005) 2055

Synthesis and characterization of new Ru-CoM (M = Co, Mo) mixed-metal linked tetrahedral clusters containing (−)-DIOP and reaction of $[(\mu_3\text{-Se})RuCo_2(CO)_8]_2$((−)-DIOP) with $Na[Mo(CO)_3(\eta^5\text{-}C_5H_4COCH_3)]$

Four mixed-metal Ru–Co linked tetrahedral clusters have been synthesized from reactions of diphosphine compound (−)-DIOP with $[(\mu_3\text{-E})RuCo_2(CO)_9]$ and $[(\mu_3\text{-E})RuCoMo(CO)_8(CpC(O)CH_3)]$ in *n*-hexane or THF at r.t., respectively. The metallic exchange reaction of $[(\mu_3\text{-Se})RuCo_2(CO)_8]_2$((−)-DIOP) with $Na[Mo(CO)_3(\eta^5\text{-}C_5H_4COCH_3)]$ has also been investigated.



The Publisher encourages the submission of articles in electronic form thus saving time and avoiding rekeying errors. For detailed instructions on the preparation of manuscripts and of electronic artwork, consult the Author Gateway for Elsevier at http://authors.elsevier.com

SCIENCE DIRECT®

Full text of this journal is available, on-line from **ScienceDirect**. Visit **www.sciencedirect.com** for more information.

CONTENTS Direct This journal is part of **ContentsDirect**, the *free* alerting service which sends tables of contents by e-mail for Elsevier books and journals. You can register for **ContentsDirect** online at: **www. elsevier.com/locate/contentsdirect**

Available online at www.sciencedirect.com
SCIENCE DIRECT®
Polyhedron 24, issue 13, 15 September 2005
POLYHEDRON
www.elsevier.com/locate/poly

Contents

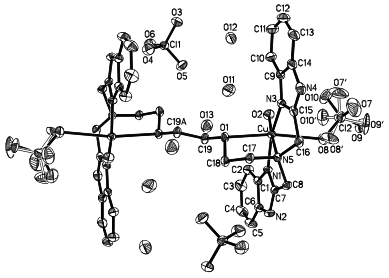
Papers

Jiang-Hua Qiu, Zhan-Ru Liao, Xiang-Gao Meng, Li Zhu, Zhe-Ming Wang, Kai-Bei Yu

Polyhedron 24 (2005) 1617

Crystal structures and polyphenol oxidase activities of dinuclear copper(II) and cobalt(II) complexes with *N*,*N*,*N*′,*N*′-tetrakis (2′-benzimidazolylmethyl)-1,4-diethylene amino glycol ether (EGTB)

Dinuclear copper and cobalt complexes as model compounds for polyphenol oxidase have been synthesized and characterized. Their activities toward pyrogallol and catechol have been studied, and the kinetics obey the Michaelis–Menten equation.

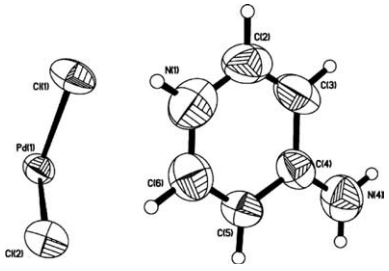


B.B. Ivanova, M.G. Arnaudov, H. Mayer-Figge

Polyhedron 24 (2005) 1624

Molecular spectral analysis and crystal structure of the 4-aminopyridinium tetrachloropalladate(II) complex salt

The distortion of aromatic character and stabilization of imino-form as a result of N_{py} protonation of 4-aminopyridine was proved by conventional and linear-dichroic IR-spectroscopy, UV- and ^{1}H-NMR-data. The structure of the model system 4-aminopyridinium tetrachloropalladate(II) complex salt is determined by single crystal X-ray study. The crystallographic results are compared with the spectroscopic ones.

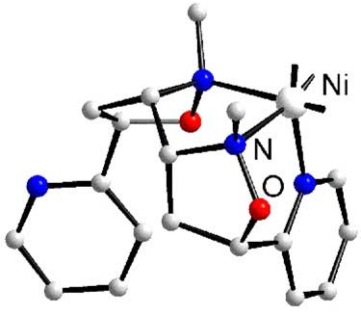


Olga V. Osetska, Ilona V. Raspertova, Aleksey V. Khavryuchenko, Konstantin V. Domasevitch, Rostislav D. Lampeka

Polyhedron 24 (2005) 1631

Coordination preferences of 3,3′-biisoxazolidines: A new kind of conformationally flexible chelating ligand

Substituted conformational flexible 3,3′-biisoxazolidines are a new type of efficient multidentate ligand toward transition metal ions, and in coordination compounds they reveal a variety of chelating modes and adaptability for the demands of the coordination environment.

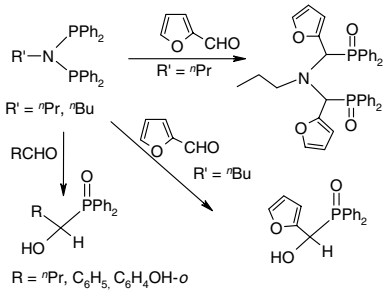


Srinivasan Priya, Maravanji S. Balakrishna, Shaikh M. Mobin

Polyhedron 24 (2005) 1641

Reactions of aminophosphines and aminobis(phosphines) with aldehydes and ketones: Coordination complexes of the resultant aminobis(alkylphosphineoxides) with cobalt, uranium, thorium and gadolinium salts. Crystal and molecular structures of $Ph_2P(O)CH(C_6H_4OH\text{-}o)N(H)Ph$, $Ph_2P(O)CH(OH)C_6H_4OH\text{-}o$ and $Ph_2P(O)N(H)Ph$

The reactions of aminophosphines and aminobis(phosphines) with aldehydes and ketones are described.

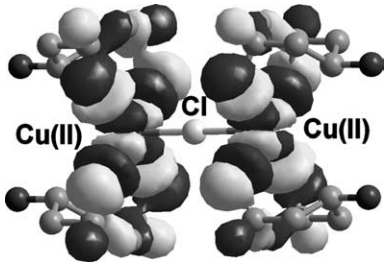


Georg Seeber, Benson M. Kariuki, Leroy Cronin, Paul Kögerler

Polyhedron 24 (2005) 1651

Synthesis, structure and magnetism of a linear Cu–Cl–Cu entity found in $[(Cu(tachH)(tach))_2(\mu\text{-}Cl)]^{5+}$

Two copper(II) complexes of *cis*,*trans*-1,3,5-triaminocyclohexane, formed at pH 11, are interlinked via chloride anions to a dimer featuring a single, linear Cu–Cl–Cu motif. Susceptibility measurements show that the Jahn–Teller-distored copper(II) ions are weakly antiferromagnetically coupled.

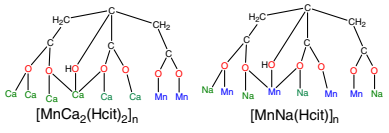


Wenguo Wang, Xiaofeng Zhang, Feng Chen, Chengbing Ma, Changneng Chen, Qiutian Liu, Daizheng Liao, Licun Li

Polyhedron 24 (2005) 1656

Homo- and hetero-metallic manganese citrate complexes: Syntheses, crystal structures and magnetic properties

Mn citrate coordination polymers including Mn/Na and Mn/Ca hetero-bimetal components were synthesized and characterized. The citrate exhibits new coordination modes to connect up to eight or nine metal ions. Weak antiferromagnetic interactions between the Mn(II) sites were correlated to the coordination modes of the carboxylate groups.

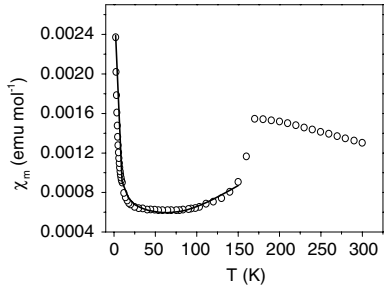


Chun-Lin Ni, Yi-Zhi Li, Dong-Bin Dang, Song Gao, Zhao-Ping Ni, Zheng-Fang Tian, Li-Li Wen, Qing-Jin Meng

Polyhedron 24 (2005) 1669

Syntheses, spectra, crystal structures and magnetic properties of molecular solids based on the $M(mnt)_2^-$ ion (M = Ni, Pt)

Two new ion-pair complexes, [1-(4′-nitrobenzyl)-4-aminopyridinium]-bis(maleonitriledithiolato)nickel ($[NO_2BzPyNH_2][Ni(mnt)_2]$) (**1**) and [1-(4′-nitrobenzyl)-4-aminopyridinium]-bis(maleonitriledithiolato)-platinum ($[NO_2BzPyNH_2][Pt(mnt)_2]$) (**2**) have been characterized structurally and magnetically. An unusual magnetic phase transition around 160 K was observed in **1**, and **2** was diamagnetic.

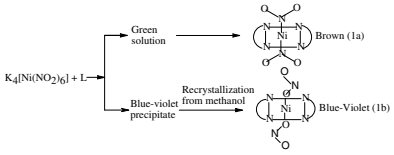


Tanmay Chattopadhyay, Manami Ghosh, Adinath Majee, Munirathinam Nethaji, Debasis Das

Polyhedron 24 (2005) 1677

Linkage isomerism in 4-(2-aminoethyl)-morpholine (L) complexes of nickel (II) nitrite: X-ray single crystal structure of *trans*-[$NiL_2(NO_2)_2$]

The linkage isomers *trans*-[$NiL_2(NO_2)_2$] (brown, **1a**) [L = 4-(2-aminoethyl)morpholine] and *trans*-[$NiL_2(ONO)_2$] (blue-violet, **1b**) are synthesized and characterized.

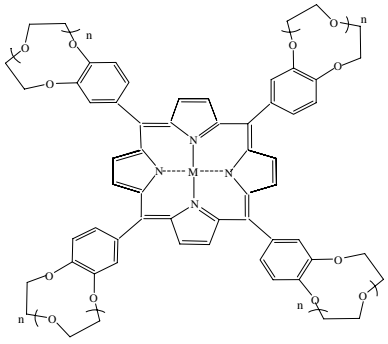


Maryam Jahan, Nasser Safari, Hengameh Khosravi, Abolghasem Moghimi, Behrouz Notash

Polyhedron 24 (2005) 1682

Crown ether-appended porphyrins and metalloporphyrins: Synthesis, characterization and metal ions interaction

Tetrakis(3,4-dimethoxyphenyl)porphyrin (TDMPPH_2), tetrakis(benzo-9-crown-3)porphyrin (TC3PH_2), tetrakis(benzo-12-crown-4)porphyrin (TC4PH_2), and their metallated derivatives have been synthesized and characterized by spectroscopic methods. The interactions of cations with these compounds were studied and have shown that Al^{3+} and Mg^{2+} cations interact with both the porphyrin macrocycles and the crown ether rings.

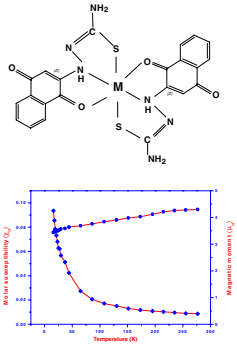


Rajeev C. Chikate, Subhash B. Padhye

Polyhedron 24 (2005) 1689

Transition metal quinone–thiosemicarbazone complexes 2: Magnetism, ESR and redox behavior of iron (II), iron (III), cobalt (II) and copper (II) complexes of 2-thiosemicarbazido-1,4-naphthoquinone

Reactions of naphthoquinone-thiosemicarbazone with Fe(II), Fe(III), Co(II) and Cu(II) yields thionato and thiolato complexes under two different conditions. Magnetic, Mössbauer and EPR measurements reveal unusual magnetic properties for the ferrous and ferric complexes with stabilization of intermediate spin-states, while there exists a significant amount of covalent character in the copper–ligand bonding. These complexes possess metal-centered redox behavior with the iron (III) complexes exhibiting a reversible Fe(III)/Fe(II) redox couple at a fairly positive potential.

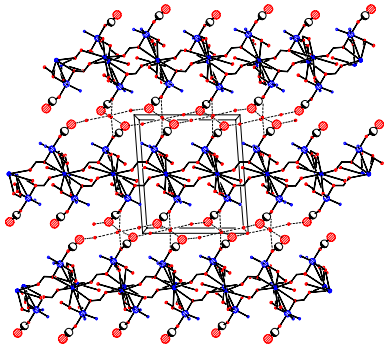


Sonja Grubišić, Svetozar R. Niketić, Dušanka D. Radanović, Urszula Rychlewska, Beata Warżajtis

Polyhedron 24 (2005) 1701

Layered crystal structure of the *trans*(O_5O_6) isomer of potassium (1,3-propanediamine-*N*,*N*′-diacetato-*N*,*N*′-di-3-propionato) cobaltate(III) trihydrate, *trans*(O_5O_6)-K[Co(1,3-pddadp)] · $3H_2O$, stabilized by ionic, hydrogen bond and CO dipolar interactions: Conformational analysis of Co(III) complexes with the 1,3-propanediamine-*N*,*N*′-diacetate-*N*,*N*′-di-3-propionate ligand

The *trans*(O_5O_6) geometry of the K[Co(1,3-pddadp)] · $3H_2O$ complex has been established by X-ray crystallography. Potassium ions and their first coordination sphere form a two-dimensional polymeric layer. Co(III) octahedra are situated above and below this layer. Interactions between the consecutive ionic layers, besides hydrogen bonds, include dipolar carbonyl interactions formed around the centre of symmetry.

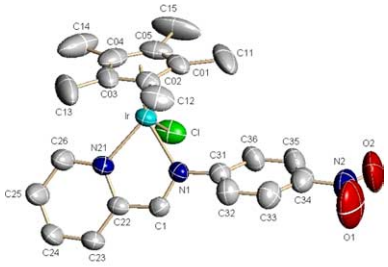


Padavattan Govindaswamy, Yurij A. Mozharivskyj, Mohan Rao Kollipara

Polyhedron 24 (2005) 1710

Syntheses, spectral and structural studies of Schiff base complexes of η^5-pentamethylcyclopentadienyl rhodium and iridium

A series of pentamethylcyclopentadienyl rhodium (III) and iridium (III) Schiff base complexes were synthesized and characterized by spectral studies. The representative compounds were studied by single crystal X-ray diffraction studies.



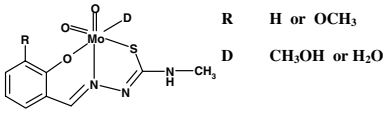
Complex 4e

Višnja Vrdoljak, Marina Cindrić, Dalibor Milić, Dubravka Matković-Čalogović, Predrag Novak, Boris Kamenar

Polyhedron 24 (2005) 1717

Synthesis of five new molybdenum(VI) thiosemicarbazonato complexes. Crystal structures of salicylaldehyde and 3-methoxy-salicylaldehyde 4-methylthiosemicarbazones and their molybdenum(VI) complexes

Polynuclear $[MoO_2\{SalTSC\text{-}4\text{-}Me\}]_n$, $[MoO_2\{VanTSC\text{-}4\text{-}Me\}]_n$ and mononuclear $[MoO_2\{SalTSC\text{-}4\text{-}Me\}(CH_3OH)]$, $[MoO_2\{VanTSC\text{-}4\text{-}Me\}(CH_3OH)]$ and $[MoO_2\{VanTSC\text{-}4\text{-}Me\}(H_2O)] \cdot CH_3CN$ complexes have been prepared by the reaction of $[MoO_2(acac)_2]$ with salicylaldehyde 4-methylthiosemicarbazone or 3-methoxy-salicylaldehyde 4-methylthiosemicarbazone in acetonitrile or in dry methanol.

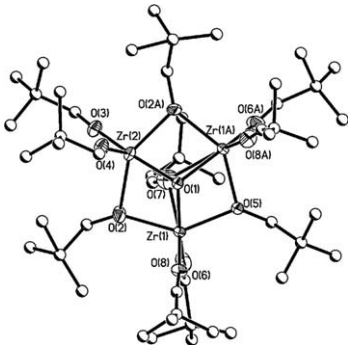


Timothy J. Boyle, Leigh Anna M. Ottley, Mark A. Rodriguez

Polyhedron 24 (2005) 1727

Structurally characterized carboxylic acid modified zirconium alkoxides for the production of zirconium oxide thin films

A series of carboxylic acid (H-ORc) were reacted with $[Zr(\mu\text{-}OPr^i)(OPr^i)_3(H\text{-}OPr^i)]_2$ (**1**) or the novel $Zr_3(\mu_3\text{-}O)(\mu_3\text{-}ONep)(\mu\text{-}ONep)_3(ONep)_6$ (**7**, shown) which yielded the novel family of compounds **2**–**6** (OPr^i) and **8**–**11** (ONep). The highest density thin films of ZrO_2 were found for the larger nuclearity species (**3**).

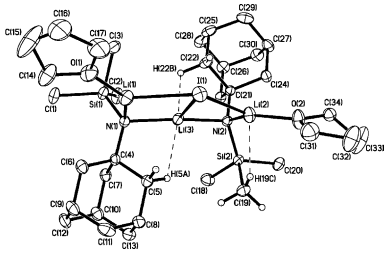


Yongjun Tang, Lev N. Zakharov, Arnold L. Rheingold, Richard A. Kemp

Polyhedron 24 (2005) 1739

Synthesis and structure of lithium amides and solvated derivatives containing bulky bis(silylamide) ligands

Eight new lithium amides, containing various sterically demanding –N[$(SiMe_3)(SiR_3)$] ligands, have been synthesized and structurally characterized in solvated and solvent-free forms. These amides can and have been used in the synthesis of congested metal and main group complexes. Additionally, an unusual trilithium amide with a μ_3-I atom was formed in the reaction between Li[N(adamantyl)$(SiMe_3)$] and CaI_2.

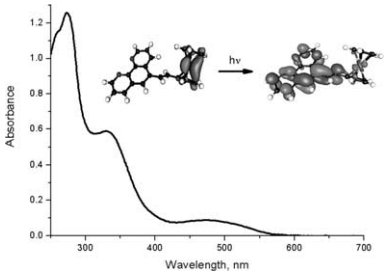


Alvaro Delgadillo, Ana Maria Leiva, Bárbara Loeb

Polyhedron 24 (2005) 1749

Intramolecular excited state quenching: 5-[(*E*)-2-ferrocenylvinyl]-1,10-phenanthroline, a new donor ligand

The 5-[(*E*)-2-ferrocenylvinyl]-1,10-phenanthroline ligand, fcvp, and its corresponding ruthenium complex were synthesized. Ferrocenyl to phenanthroline charge transfer absorption bands were observed in the UV–Vis spectrum. In the ruthenium complex no interaction between the Ru and Fe metal centers was observed in the ground state. In the excited state, the absence of photoluminescence from the Ru center evidences a quenching process, probably of electron transfer nature.

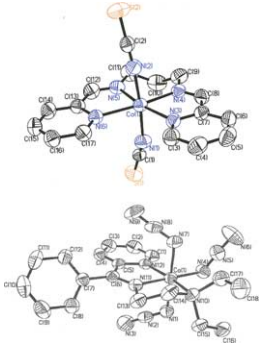


Sk Hafijur Rahaman, Habibar Chowdhury, Doyel Bose, Rajarshi Ghosh, Chen-Hsing Hung, Barindra Kumar Ghosh

Polyhedron 24 (2005) 1755

Synthesis, structure and properties of mononuclear cobalt(II) and cobalt(III) pseudohalide complexes containing N-donor Schiff bases: Synthetic control of metal oxidation levels

Two different sets of hexacoordinated cobalt(II) and cobalt(III) pseudohalide complexes have been prepared in combination with tetra- and tridentate N-donor Schiff bases, respectively. X-ray diffraction measurements of one representative member from each group, viz., *trans*-[Co(pfpd)-$(NCS)_2$] (**1c**) and *mer*-[Co(pbed)$(N_3)_3$] (**2b**) are done to define coordination sphere. All the complexes display intraligand $^1(\pi–\pi^*)$ fluorescence and intraligand $^3(\pi–\pi^*)$ phosphorescence in glassy solutions (MeOH at 77 K).

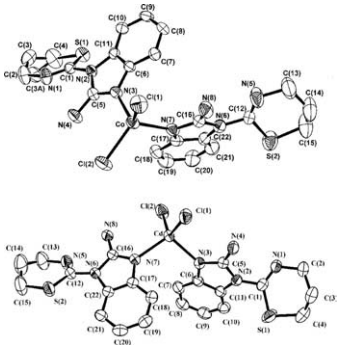


F.J. Barros-García, A. Bernalte-García, F. Luna-Giles, M.A. Maldonado-Rogado, E. Viñuelas-Zahínos

Polyhedron 24 (2005) 1764

Cobalt(II) and cadmium(II) metal complexes of a 2-aminobenzimidazole-thiazine derivative ligand. Synthesis, characterization and X-ray structure determinations

Thiazine/2-aminobenzimidazole derivative ligand *N*-(5,6-dihydro-4H-1,3-thiazin-2-yl)-2-aminobenzimidazole (BzTz) and its cobalt(II) and cadmium(II) complexes were synthesized and characterized by physical measurements. The X-ray crystal structures of BzTz, cobalt and cadmium complexes have also been determined. The geometry around the metallic atoms can be described as a distorted tetrahedron.

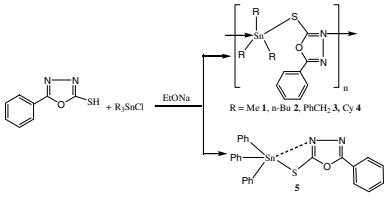


Chun-Lin Ma, Guang-Ru Tian, Ru-Fen Zhang

Polyhedron 24 (2005) 1773

Investigation on steric effect in the coordination of S, N and O donor heterocycle to organotin(IV): Syntheses and crystal structures of triorganotin(IV) derivatives with 5-phenyl-1,3,4-oxadiazole-2-thiol

A series of organotin(IV) complexes with 5-phenyl-1,3,4-oxadiazole-2-thiol of the type $R_3Sn[S(C_8H_5N_2O)]$ (R = Me **1**, *n*-Bu **2**, $PhCH_2$ **3**, Cy **4**, Ph **5**) have been synthesized. Among them, the central tin atoms of complexes **1**–**5** are all five-coordinated with the distorted trigonal bipyramidal geometry. Interestingly, the complexes **1**–**4** exhibit 1D polymeric chains through Sn and N intermolecular interactions.

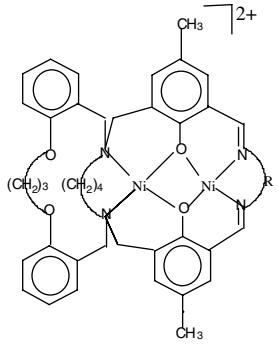


M. Thirumavalavan, P. Akilan, M. Kandaswamy

Polyhedron 24 (2005) 1781

Lateral macrobicyclic compartmental mono and binuclear nickel(II) complexes derived from phenolate ligands: Synthesis, spectral, electrochemical and kinetic studies

Lateral macrobicyclic compartmental mono and binuclear nickel(II) complexes were synthesized. Spectral, electrochemical and kinetic studies were carried out. Cyclic voltammetric studies show quasireversible one electron reduction waves both in cathodic and anodic region. The catalytic activities of the complexes towards hydrolysis of 4-nitrophenyl phosphate increase with macrocyclic ring size. Macrocyclic ring size influences the electrochemical (reduction) and catalytic properties of the complexes.



The Publisher encourages the submission of articles in electronic form thus saving time and avoiding rekeying errors. For detailed instructions on the preparation of manuscripts and of electronic artwork, consult the Author Gateway for Elsevier at http://authors.elsevier.com

SCIENCE DIRECT™

Full text of this journal is available, on-line from **ScienceDirect**. Visit **www.sciencedirect.com** for more information.

CONTENTS Direct This journal is part of **ContentsDirect**, the *free* alerting service which sends tables of contents by e-mail for Elsevier books and journals. You can register for **ContentsDirect** online at: **www. elsevier.com/locate/contentsdirect**

Available online at www.sciencedirect.com
SCIENCE DIRECT®
Polyhedron 24, issue 5, 31 March 2005
POLYHEDRON
www.elsevier.com/locate/poly

Contents

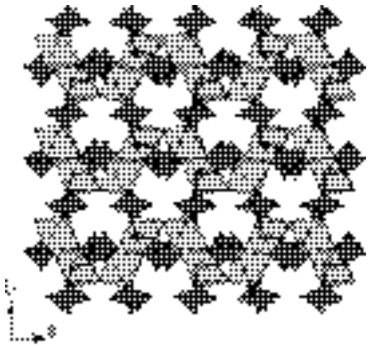
Papers

Zhong-Ming Sun, Jiang-Gao Mao, Zhen-Chao Dong

Polyhedron 24 (2005) 571

Synthesis and structural characterization of three new manganese(II) diphosphonates with layered and double-chain architectures

Hydrothermal reactions of two substituted aminodiphosphonic acids, $C_6H_5CH_2N(CH_2PO_3H_2)_2(H_4L^1)$ and 4-CH_3–$C_6H_4CH_2N(CH_2PO_3H_2)_2(H_4L^2)$, with manganese(II) acetate resulted in three manganese(II) diphosphonates with a layered and double chain structure, namely, $Mn(H_2L^1)$ (**1**), $Mn(H_3L^1)_2$ (**2**) and $Mn_2(H_2L^2)_2(H_2O)$ (**3**). Compounds **1** and **3** are layered with interlayer distances of 12.65 and 16.28 Å, respectively. Compound **2** features 1D double chains along the *c*-axis that are interlinked by strong hydrogen bonds between non-coordinated phosphonate oxygens.

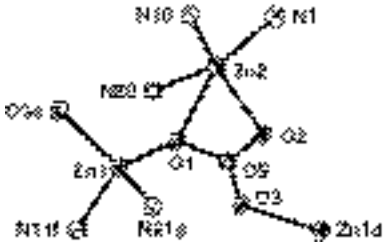


Juraj Černák, Bibiana Ferencová, Zdirad Žák

Polyhedron 24 (2005) 579

First example of atmospheric carbon dioxide uptake by a cyanocomplex: Preparation and structural characterization of $Zn_2(tn)_2(CO_3)Ni(CN)_4{\cdot}H_2O$ (*tn*=1,3-diaminopropane)

Aqueous system Zn(II)-*tn*-$[Ni(CN)_4]^{2-}$ (*tn*=1.3-diaminopropane) in contact with air captured carbon dioxide yielding coordination polymer $Zn_2(tn)_2(CO_3)Ni(CN)_4{\cdot}H_2O$. The carbonato ligand coordinates three zinc atoms by an unusual mode, two by an unidentate and one by a bidentate fashion with one oxygen donor atom forming two ZnO coordination bonds.

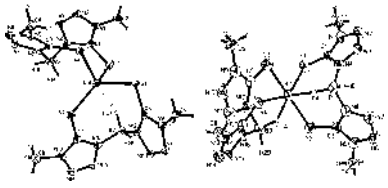


Yu-Ling Wang, Rong Cao, Wen-Hua Bi

Polyhedron 24 (2005) 585

Syntheses and characterizations of Co(II) and Ni(II) complexes of dihydrobis(thioxotetrazolyl)borato with $Co[S_4]$ and $Ni[S_4H_2]$ cores

Two novel complexes $Co(Btt^{Me})_2$ (**1**) and $Ni(Btt^{Me})_2$ (**2**) were synthesized by reaction of the dihydrobis(1-methyl-5-thiotetrazolyl)-borato ligand (Btt^{Me}) with anhydrous $CoCl_2$ and $NiCl_2{\cdot}6H_2O$, respectively. **1** features a central $[CoS_4]$ core with a very weak apical Co···H–B interaction, whereas **2** features a central $[NiS_4H_2]$ core and exhibits relatively strong Ni···H–B interactions.



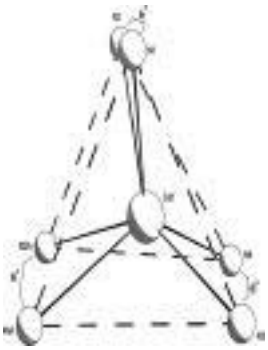
Elsevier Ltd.

Suparna Banerjee, Ashutosh Ghosh, Biao Wu, Paul-Gerhard Lassahn, Christoph Janiak

Polyhedron 24 (2005) 593

Polymethylene spacer regulated structural divergence in cadmium complexes: Unusual trigonal prismatic and severely distorted octahedral coordination

Two neutral tetradentate Schiff base ligands, *N*,*N*′-bis-(1-pyridin-2-yl-ethylidene)-propane-1,3-diamine (L^1) and *N*,*N*′-bis-(1-pyridin-2-yl-ethylidene)-ethane-1,2-diamine (L^2) which differ only in the polymethylene chain $-(CH_2)_3$ and $(CH_2)_2$, respectively, yielded an interesting neutral trigonal prismatic cadmium complex $[Cd(L^1(NCS)_2)]$ and a distorted octahedral complex $[Cd(L^2)(NCS)_2]$.

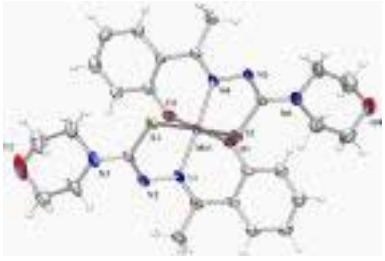


Rohith P. John, Anandram Sreekanth, Maliyeckal R. Prathapachandra Kurup, Hoong-Kun Fun

Polyhedron 24 (2005) 601

Chelating behavior of 2-hydroxyacetophenone *N*(4)-disubstituted thiosemicarbazones: Facile formation of Mn(IV) complexes – X-ray structure, EPR and cyclic voltammetric studies

Facile formation of three manganese(IV) complexes (MnL_2) occur when 2-hydroxyacetophenone *N*(4)-disubstituted thiosemicarbazones (H_2L) were treated with manganese(II) acetate tetrahydrate in ethanol–methanol medium under aerobic condition. The crystal structure of $Mn(L^2)_2{\cdot}0.25H_2O$ reveals an octahedral geometry with a skewed arrangement of the ligand about the metal ion. EPR spectra at 77 K shows a weak $g \approx 4$ signal and a strong sextet at $g \approx 2$ consistent with manganese(IV) with marginally distorted octahedral environment. Cyclic voltammetry in DMSO/dichloromethane show reversible and quasi-reversible peaks corresponding to Mn(IV)/Mn(III) redox couple.

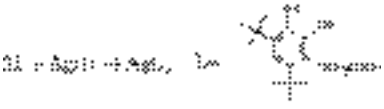


N.V. Loginova, A.A. Chernyavskaya, G.I. Polozov, T.V. Koval'chuk, E.V. Bondarenko, N.P. Osipovich, A.A. Sheryakov, O.I. Shadyro

Polyhedron 24 (2005) 611

Silver(I) interaction and complexation with sterically hindered sulfur-containing diphenol derivatives

The interaction between Ag(I) ions with 3,5-di(*tert*-butyl)-1,2-benzenediol and sulfur-containing derivatives of sterically hindered diphenols was studied. In most cases Ag(I) ions interact with some of these derivatives to give silver sols. 2-[4,6-di(*tert*-butyl)-2,3-dihydroxyphenylsulfanyl]acetic acid (L) does not reduce Ag(I), but forms a complex therewith: The complex was characterized by elemental analysis and various physico-chemical techniques.

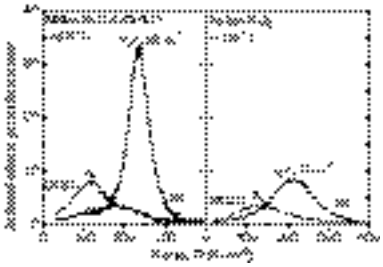


V. Dracopoulos, D.Th. Kastrissios, G.N. Papatheodorou

Polyhedron 24 (2005) 619

Raman spectra and structure of $PbCl_2$–ACl (A=K,Cs) melts

Isotropic and anisotropic Raman spectra of molten mixtures of $PbCl_2$–ACl (A=K,Cs) have been measured up to 680 °C. The relative intensities at different temperatures and compositions indicate the formation of polynuclear Pb coordination polyhedra of the type $Pb_nCl_{3n}^{n-}$ ($n \leqslant 4$). Dipole–induced-dipole interactions appear to be important for these melts.

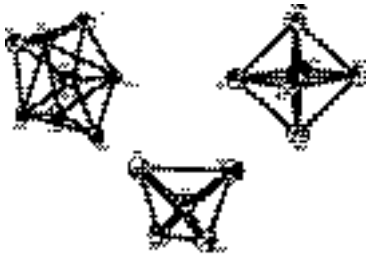


Barbara Barszcz, Stanisław A. Hodorowicz, Katarzyna Stadnicka, Agnieszka Jabłońska-Wawrzycka

Polyhedron 24 (2005) 627

A comparison of the coordination geometries of some 4-methylimidazole-5-carbaldehyde complexes with Zn(II), Cd(II) and Co(II) ions in the solid state and aqueous solution

Reactions of Zn(II), Cd(II) and Co(II) ions with 4-methylimidazole-5-carbaldehyde afforded four novel complexes. The compounds were characterized by X-ray diffraction, establishing tetrahedral, distorted dodecahedral and octahedral coordinating geometries of the Zn(II), Cd(II) and Co(II) metal ions, respectively. In solution, NMR and potentiometric methods have confirmed the preference of the central ions not only to adopt a specific coordination number and geometry of the coordination polyhedra, but also the function of the ligands which can be either monodentate or bidentate.

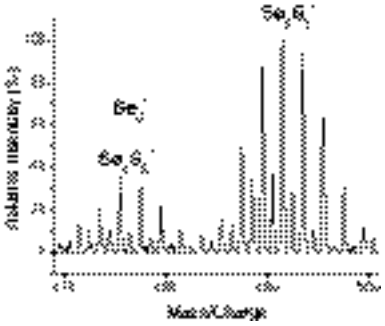


Ondrej Šedo, Milan Alberti, Josef Havel

Polyhedron 24 (2005) 639

Laser ablation synthesis of new binary chalcogen molecules from the selenium–sulfur system

Laser ablation synthesis and simultaneous identification of selenium–sulfur compounds generated from various precursors was studied using a commercial MALDI–TOF mass spectrometric instrumentation. For example, laser ablation of selenium disulfide leads to the formation of at least fifty one compounds. In total, twelve new species and/or clusters are described for the first time.

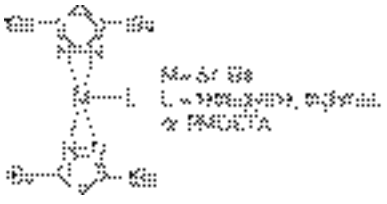


Hani M. El-Kaderi, Mary Jane Heeg, Charles H. Winter

Polyhedron 24 (2005) 645

Synthesis, structure and properties of monomeric strontium and barium complexes containing terminal η^2-3,5-di-*tert*-butylpyrazolato ligands

Treatment of $M(N(SiMe_3)_2)_2(THF)_2$ (M=Sr, Ba) with tetraglyme, triglyme or *N*,*N*′,*N*″,*N*″-pentamethyldiethylenetriamine (PMDETA) followed by 3,5-di-*tert*-butylpyrazole (2 equiv) afforded monomeric complexes of the formula $M(t\mathrm{Bu}_2\mathrm{pz})_2(L)$. These complexes possess monomeric structures with terminal η^2-pyrazolato ligands, and are of relevance to the development of volatile group 2 film growth precursors.

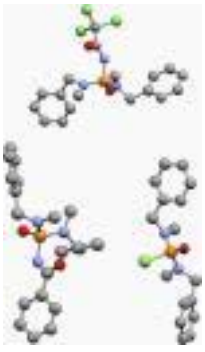


Khodayar Gholivand, Mehrdad Pourayoubi, Zahra Shariatinia, Hossein Mostaanzadeh

Polyhedron 24 (2005) 655

The effect of various substituents on the structural parameters of the P(O)- $[N(CH_3)(CH_2C_6H_5)]_2$ moiety. Syntheses and spectroscopic characterization of some new phosphoramidates, crystal structures of $P(O)(X)[N(CH_3)(CH_2C_6H_5)]_2$, X=$C_6H_5C(O)$NH, Cl and $CCl_3C(O)$NH

Some new phosphoramidates with general formula $P(O)(X)[N(CH_3)(CH_2C_6H_5)]_2$, X=$C_6H_5C(O)$NH (**1**), Cl (**2**), $CCl_3C(O)$NH (**3**), $N(CH_3)_2$ (**4**) and 4-NO_2–C_6H_4NH (**5**) were prepared. The structures of **1** and **3** show centrosymmetric dimmers in crystalline lattice. ^{13}C NMR spectra indicated that $^2J(P,C)_{benzylic} > {}^2J(P,C)_{methyl}$ for these compounds.



P. Piszczek, M. Richert, A. Grodzicki, T. Głowiak, A. Wojtczak

Polyhedron 24 (2005) 663

Synthesis, crystal structures and spectroscopic characterization of $[Ti_8O_8(OOCR)_{16}]$ (where R=Bu^t, CH_2Bu^t, $C(CH_3)_2Et$)

New multinuclear titanium(IV) oxo carboxylates of the general formula $[Ti_8O_8(OOCR)_{16}]$ (where R=Bu^t (**1**), CH_2Bu^t (**2**), $C(CH_3)_2Et$ (**3**)) have been synthesized and characterized by single-crystal X-ray diffraction and spectroscopic techniques. Titanium atoms form oligomeric rings $[Ti_8(\mu_2\text{-}O)_8]$, where each Ti cation is surrounded by six oxygen atoms (two μ_2-oxo and four μ-carboxylato bridges).

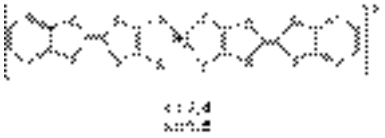


He-Rui Wen, Jing-Lin Zuo, Thomas A. Scott, Hong-Cai Zhou, Xiao-Zeng You

Polyhedron 24 (2005) 671

Synthesis, structure and properties of mercury complexes with a new extended tetrathiafulvalene 4,5-dithiolate ligand

A new extended tetrathiafulvalene dithiolate ligand, benzotetrathiafulvalenedithiolate ($btdt^{2-}$), and mercury complexes based on it have been synthesized and characterized. The crystal structure of $(Me_4N)_2[Hg(btdt)_2]$ is determined. The extending planar conjugation system with phenyl on the ligand framework increases intermolecular reaction and leads to the enhancement of conductivity.

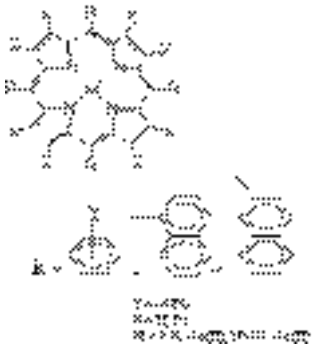


Regimol G. George, M. Padmanabhan

Polyhedron 24 (2005) 679

Studies on cobalt(II), nickel(II) and copper(II) derivatives of some new *meso*-aryl substituted octabromoporphyrins

A series of Co(II), Ni(II) and Cu(II) derivatives of a variety of porphyrins with tolyl (MTxTP) and naphthyl moieties (MNxTP) as *meso*-substituents and their octabromoderivatives (MTxOBP and MNxOBP) by Br-substitution at the eight β-pyrrole positions were synthesised and characterised. The changes observed in their electronic spectra are explained in terms of the energy level re-ordering of the HOMO and LUMO levels due to electron withdrawing Br substituents and the concerted action of eight bulky Br atoms bringing about distortional change on the π-framework, and also due to the mesomeric effect due to *meso*-aryl moieties. The EPR spectra of the Cu(II) derivatives of bromoporphyrins have their spin-Hamiltonian parameters altered when compared to their nonbrominated analogues indicating pronounced electron spin delocalisation on the porphyrinato moiety.

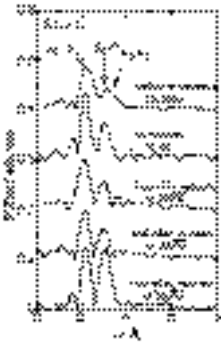


Yushi Suzuki, Naoyuki Matsumoto, Takeshi Ainai, Takafumi Miyanaga, Hideoki Hoshino

Polyhedron 24 (2005) 685

In situ infrared and EXAFS studies of an Ag cluster in zeolite X

The local structures are investigated by EXAFS for the Ag^+–X zeolite up to 300 °C. By evacuation, the coordination number of N_{Ag-O} decreases by removal of water molecules. At 300 °C, N_{Ag-Ag} becomes 2.9, which indicates the stabilization of Ag clusters in the zeolite framework, as shown by IR results.

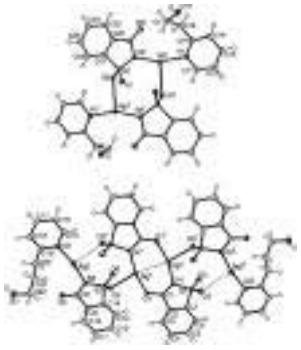


Veysel T. Yilmaz, Sevim Hamamci, William T.A. Harrison, Carsten Thöne

Polyhedron 24 (2005) 693

Di- and tetranuclear silver (I)-saccharinate complexes with 2-pyridineethanol and 2-pyridinepropanol: Syntheses, crystal structures, spectroscopic and thermal analyses of $[Ag_2(sac)_2(pyet)_2]$ and $[Ag_4(sac)_4(pypr)_2]$

Two silver (I) complexes of saccharin with 2-pyridineethanol (pyet) and 2-pyridinepropanol (pypr) are reported. In $[Ag_2(sac)_2(pyet)_2]$, two monomeric $[Ag(sac)_2(pyet)]$ units are doubly bridged by the sulfonyl oxygen atoms of the sac ligands, forming an $[Ag_2(sac)_2(pyet)_2]$ dimer, in which each silver (I) centre is three coordinate with a T-shaped coordination. The tetranuclear complex, $[Ag_4(sac)_4(pypr)_2]$, is achieved by bridging of $[Ag_2(sac)_2]$ with two [Ag(sac)(pypr)] units through the sulfonyl oxygen atoms of the sac ligands. The two silver (I) ions in the centre with a short Ag–Ag bond distance of 2.8480(13)Å exhibit a T-shaped geometry with three sac ligands, while the two terminal silver (I) ions are coordinated by a sac ligand and a pypr ligand in a near linear geometry.

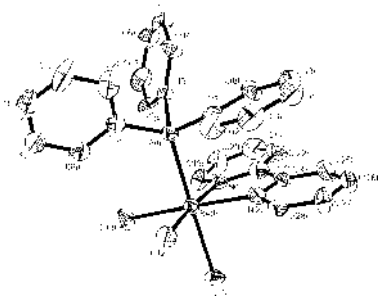


B. Machura, R. Kruszynski, M. Jaworska, Piotr Lodowski

Polyhedron 24 (2005) 701

Crystal, molecular and electronic structure of the $[ReCl_3(bipy)(PPh_3)]$ complex

X-ray structure of the $[ReCl_3(bipy)(PPh_3)]$ complex has been determined and its geometric parameters have been examined using the density-functional theory method. The UV–Vis spectrum of the complex has been discussed on the basis of the electronic transitions of $[ReCl_3(bipy)(PPh_3)]$ calculated with the time-dependent DFT method.

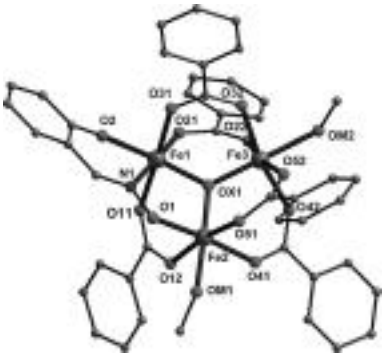


Catherine P. Raptopoulou, Yiannis Sanakis, Athanassios K. Boudalis, Vassilis Psycharis

Polyhedron 24 (2005) 711

Salicylaldoxime (H_2salox) in iron(III) carboxylate chemistry: Synthesis, X-ray crystal structure, spectroscopic characterization and magnetic behavior of trinuclear oxo-centered complexes

Two neutral trinuclear oxo-centered complexes, $[Fe_3(\mu_3\text{-}O)(O_2CPh)_5(salox)L_1L_2]$ (salox = the dianion of salicylaldehyde oxime, $L_1 = L_2 =$ MeOH (**1**), $L_1 =$ EtOH, $L_2 = H_2O$ (**2**)) have been studied by X-ray crystallography, EPR (solid state and frozen solutions) and ^{57}Fe Mössbauer spectroscopies, and their magnetic properties have been explored.



The Publisher encourages the submission of articles in electronic form thus saving time and avoiding rekeying errors. For detailed instructions on the preparation of manuscripts and of electronic artwork, consult the Author Gateway for Elsevier at http://authors.elsevier.com



Full text of this journal is available, on-line from **ScienceDirect**. Visit **www.sciencedirect.com** for more information.



This journal is part of **ContentsDirect**, the *free* alerting service which sends tables of contents by e-mail for Elsevier books and journals. You can register for **ContentsDirect** online at: **www. elsevier.com/locate/contentsdirect**

Available online at www.sciencedirect.com
SCIENCE DIRECT®
Polyhedron 24, issue 12, 25 August 2005
POLYHEDRON
www.elsevier.com/locate/poly

Contents

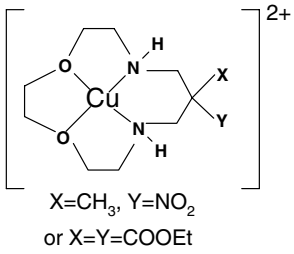
Papers

Masoud Salavati-Niasari

Polyhedron 24 (2005) 1405

Macrocyclic dioxadiaza from the reaction of the (1,8-diamino-3,6-dioxaoctane)copper(II) cation with formaldehyde and the carbon acids nitroethane or diethylmalonate

New square-planar copper(II) complexes of 13-membered diazadioxa macrocyclic ligands have been prepared by the one-pot template reactions of formaldehyde, 1,8-diamino-3,6-dioxaoctane with the carbon acids nitroalkane or diethylmalonate in the presence of the copper(II) ion. The spectra of the complexes show that the two nitrogen and two oxygen atoms are coordinated to the copper(II) ion.

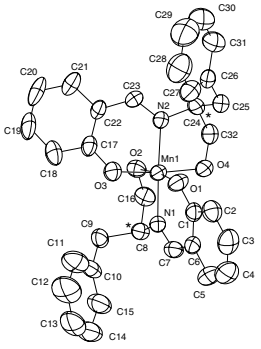


Chullikkattil P. Pradeep, Panthapally S. Zacharias, Samar K. Das

Polyhedron 24 (2005) 1410

Synthesis, structural characterization and properties of an optically active mononuclear Mn(IV) complex

A chiral manganese(IV) complex $[Mn^{IV}L_2] \cdot 2DMF$ was synthesized starting from an enantiopure ligand H_2L and $Mn^{II}(CH_3COO)_2 \cdot 4H_2O$ in MeOH in the presence of air; the title complex has been characterized by elemental analysis and routine spectral studies including single-crystal X-ray structure determination.

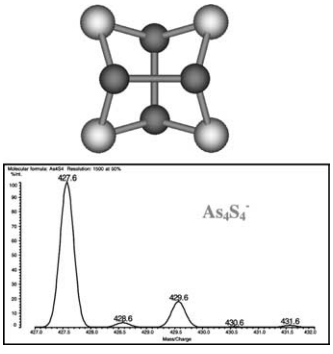


Zbyněk Špalt, Milan Alberti, Eladia Peña-Méndez, Josef Havel

Polyhedron 24 (2005) 1417

Laser ablation generation of arsenic and arsenic sulfide clusters

Laser ablation synthesis and simultaneous identification of arsenic clusters As_n^+ (n = 2–7) and arsenic sulfides generated from As_2S_3, As_2S_5 and/or arsenic-sulfur mixtures was studied using MALDI-TOF mass spectrometry. The following arsenic sulfide ions and/or clusters were generated and identified: AsS, AsS_2, AsS_3, AsS_4, AsS_5, AsS_6, AsS_7, AsS_8, As_2S, As_2S_2, As_2S_3, As_2S_4, As_2S_5, As_2S_6, As_2S_7, As_3S, As_3S_2, As_3S_3, As_3S_4, As_3S_5, As_3S_6, As_3S_7, As_4S_3, As_4S_4. Several of them are described for the first time.



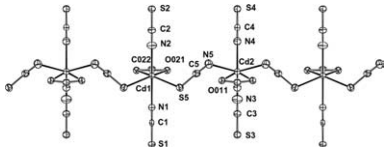
Elsevier Ltd.

Oksana V. Nesterova, Anna V. Lipetskaya, Svitlana R. Petrusenko, Vladimir N. Kokozay, Brian W. Skelton, Julia Jezierska

Polyhedron 24 (2005) 1425

Novel 1D and 2D heterometallic Cu/Cd complexes comprising unique mixed-anion $Cd(\mu\text{-}Cl)(\mu\text{-}O_2CMe)Cl(O_2CMe)^{2-}$, $Cd(\mu\text{-}O_2CMe)_2I(O_2CMe)^{2-}$, $Cd(\mu\text{-}I)(\mu\text{-}O_2CMe)I(O_2CMe)^{2-}$ and $Cd_2(NCS)_6(O_2CMe)_2{}^{2-}$ building blocks: Synthesis from elemental copper, structure and magnetism

Three novel heterometallic Cu/Cd coordination polymers with unique mixed-anion acetate–halide or acetate–thiocyanate building blocks are prepared from elemental copper, and are structurally characterized.

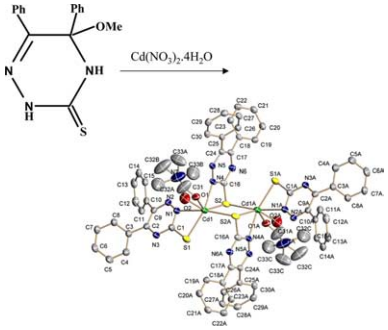


Elena López-Torres, Mª. Antonia Mendiola

Polyhedron 24 (2005) 1435

Complexes of a triazine-3-thione ligand with divalent metals. Crystal structure of $[CdL_2DMF]_2 \cdot 2DMF \cdot 1/4H_2O$

Reactions of 5-methoxy-5,6-diphenyl-4,5-dihydro-2H-[1,2,4]triazine-3-thione LH_2OCH_3 with divalent metal nitrates afforded 1:2 metal/ligand complexes (except for the cobalt complex **4** where the ratio is 1:3), in which the triazine shows a different behaviour depending on the metal structural preferences, acting at least as a NS bidentate ligand.

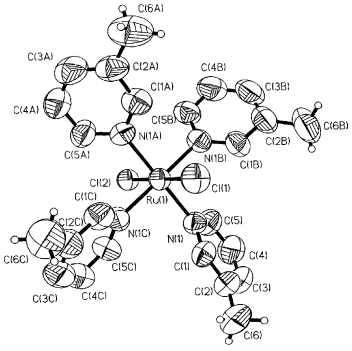


J.G. Maecki, M. Jaworska, R. Kruszynski, R. Gil-bortnowska

Polyhedron 24 (2005) 1445

Synthesis and characterization of $[RuCl_2(picoline)_4]$ complexes: Crystal structure of $[RuCl_2(\beta\text{-pic})_4]$

The reaction of the $[RuCl_2(PPh_3)_3]$ complex with picolines has been examined. New ruthenium(II) complexes – $[RuCl_2(C_6H_7N)_4]$ have been obtained. The crystal structure of the $[RuCl_2(\beta\text{-pic})_4]$ complex has been determined. The electronic spectra of the complexes have been calculated by the TDDFT method.

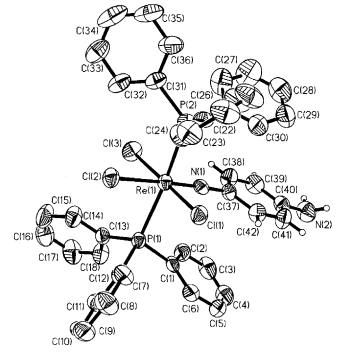


B. Machura, R. Kruszynski, M. Jaworska

Polyhedron 24 (2005) 1454

Reactivity of $[ReOX_3(PPh_3)_2]$ complexes towards 1,4-diaminobenzene: X-ray structure and DFT calculations of the $[Re(4\text{-}NC_6H_4NH_2)Cl_3(PPh_3)_2] \cdot PPh_3$ complex

The reaction of $[ReOX_3(PPh_3)_2]$ (X = Cl and Br) complexes with 1,4-diamnobenzene has been examined and novel imido rhenium complexes – $[Re(4\text{-}NC_6H_4NH_2)X_3(PPh_3)_2]$ – have been obtained. The crystal and molecular structure of $[Re(4\text{-}NC_6H_4NH_2)Cl_3(PPh_3)_2]$ has been determined, and its molecular diagram has been calculated with the density functional theory (DFT) with the use of the B3LYP functional. Additional information about binding in the $[Re(4\text{-}NC_6H_4NH_2)Cl_3(PPh_3)_2]$ complex has been obtained by NBO analysis. The time-dependent DFT method (TDDFT) has been used for calculations of spin-allowed singlet–singlet electronic transitions of $[Re(4\text{-}NC_6H_4NH_2)Cl_3(PPh_3)_2]$, and on this basis the UV–Vis spectrum has been interpreted.

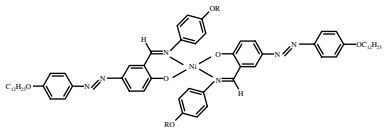


Zolfaghar Rezvani, Amir Reza Abbasi, Kamellia Nejati, Masoud Seyedahmadian

Polyhedron 24 (2005) 1461

Syntheses, characterization and glass-forming properties of new bis[5-((4-^{n}dodecyloxyphenyl)azo)-*N*-(4-^{n}alkoxyphenyl)-salicylaldiminato]nickel (II) complex homologues

A homologue series of bis[5-((4-dodecyloxyphenyl)azo)-*N*-(4-alkoxyphenyl)-salicylaldiminato)]nickel (II) complexes has been synthesized and characterized by NMR, elemental analyses and IR spectroscopy. DSC, X-ray powder diffraction and optical polarizing microscopy studies indicated that the Ni complexes have a resistance to crystallization and give an amorphous glassy state, but after annealing at room temperature for several days transform to an anisotropic glass.

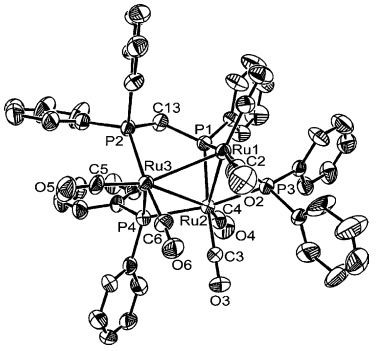


Md. Iqbal Hyder, Shariff E. Kabir, Md. Arzu Miah, Tasneem A. Siddiquee, G.M. Golzar Hossain

Polyhedron 24 (2005) 1471

Reactions of $[Ru_3(CO)_{10}(\mu\text{-dppm})]$ and $[Ru_3(CO)_9\{\mu_3\text{-}\eta^3\text{-}Ph_2PCH_2P(C_6H_4)\}]$ with PPh_2H: X-ray structures of $[(\mu\text{-H})Ru_3(CO)_6(\mu_3\text{-}\eta^2\text{-}PPh_2CH_2PPh)(\mu\text{-}PPh_2)_2]$ and $[Ru_3(CO)_5(\mu\text{-dppm})(\mu\text{-}PPh_2)_2(\mu_3\text{-}PPh)]$

Treatment of $[Ru_3(CO)_{10}(\mu\text{-dppm})]$ (**1**) with PPh_2H in refluxing heptane afforded four triruthenium compounds, $[Ru(CO)_6(\mu\text{-CO})(\mu_3\text{-}CH_2PPh)(\mu\text{-}PPh_2)_2]$ (**3**), $[(\mu\text{-H})Ru_3(CO)_6(\mu_3\text{-}\eta^2\text{-}PPh_2CH_2PPh)(\mu\text{-}PPh_2)_2]$ (**4**) $[(\mu\text{-H})_2Ru_3(CO)_5(\mu\text{-dppm})(\mu_3\text{-}PPh)(\mu\text{-}PPh_2)_2]$ (**5**) and $[(\mu\text{-H})_2Ru_3(CO)_6(\mu\text{-dppm})(\mu\text{-}PPh_2)_2]$ (**6**). Compound **4** can also be prepared in a relatively higher yield from the reaction of $[Ru_3(CO)_9\{\mu_3\text{-}\eta^3\text{-}PPhCH_2P(Ph)(C_6H_4)\}]$ (**7**) with PPh_2H in refluxing THF. The new compounds were characterized by spectroscopic data along with single crystal X-ray diffraction studies on **4** and **5**.

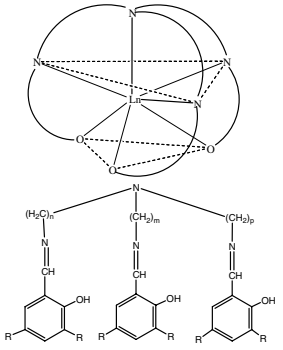


Sadegh Salehzadeh, Seyedeh Mahnaz Nouri, Hassan Keypour, Mojtaba Bagherzadeh

Polyhedron 24 (2005) 1478

Synthesis of gadolinium(III) and samarium(III) complexes of new potentially heptadentate (N_4O_3) tripodal Schiff base ligands, and a theoretical study

The synthesis and characterization of two new potentially heptadentate N_4O_3 tripodal Schiff base ligands H_3L^1 and H_3L^2 are reported. The neutral gadolinium(III) and samarium(III) complexes, [Ln(L)], of these bulky ligands and also a gadolinium(III) complex of a previously known ligand, H_3L^3, were also synthesized and characterized by various spectroscopic methods. The relative capability of these ligands as well as their unsubstituted analogs to encapsulate a lanthanide ion, herein La(III), has been theoretically studied.

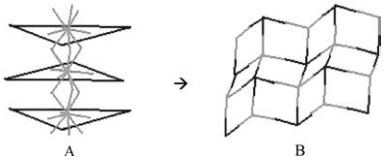


T.K. Prasad, S. Sailaja, M.V. Rajasekharan

Polyhedron 24 (2005) 1487

1-Dimensional and 2-dimensional coordination network structures in the Ba–Ce–dipicH_2 system (dipicH_2 = dipicolinic acid)

Coordination polymers with similar stoichiometries, but very different network structures form in the Ce–Ba–dipicH_2 system depending on the crystallization conditions. $Ba(OH_2)_6Ce(dipic)_3$ (A) is a structural analog of $SrCl_2 \cdot 6H_2O$. At the vertices of the triangles are $Ce(dipic)_3^{2-}$ ions, while a $Ba(H_2O)_9^{2+}$ chain is threaded through the triangles. Its polymorph (B) has a structure analogous to that of PbO. The dark junctions in the net are $Ce(dipic)_3^{2-}$ ions while the lighter junctions represent carboxylate linked $Ba(H_2O)_4^{2+}$ ions.

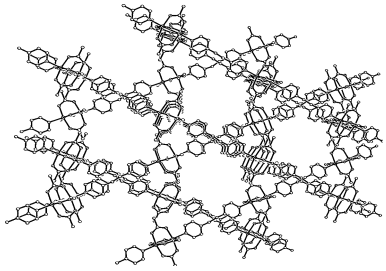


Hui-Ling Hu, Maw-Cherng Suen, Chun-Wei Yeh, Jhy-Der Chen

Polyhedron 24 (2005) 1497

Synthesis and structures of two new copper(II) coordination polymers with pyridyl ligands

The reaction of $Cu(OAc)_2 \cdot H_2O$ with bpa (bpa = 1,2-bis(4-pyridyl)ethane) in CH_3OH afforded the complex $[Cu_2(OAc)_4(bpa) \cdot 2H_2O]_n$ (**1**) while the reaction of $CuSO_4 \cdot 5H_2O$ with bpen (bpen = *trans*-bis(4-pyridyl)ethene) in CH_3OH afforded the complex $[Cu(bpen)(H_2O)_3(SO_4) \cdot 4H_2O]_n$ (**2**). Complexes **1** and **2** form molecular chains which, linking by C–H···π, π–π interactions and hydrogen bondings, line up in layers with each layer crossing the layer beneath to form rhombic channels. Thermal gravimetric analyses and differential scanning calorimetry were carried out to investigate their thermal properties.

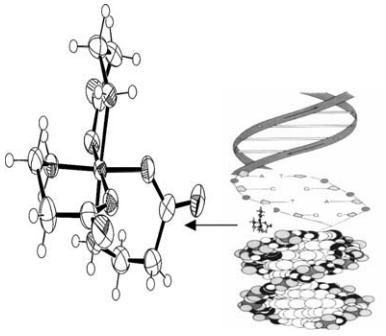


Chew Hee Ng, Han Kiat Alan Ong, Koh Sing Ngai, Wee Tee Tan, Lai Peng Lim, Siang Guan Teoh, Thiam Seong Chong

Polyhedron 24 (2005) 1503

mer-Tris(β-alaninato)cobalt(III): Crystal structure, solution properties and its DNA cleavage in the presence of ascorbic acid

The complex *mer*-[Co(β-ala)$_3$] has been characterized by X-ray crystallography, UV–Vis spectroscopy, electrospray ionization-mass spectroscopy and cyclic voltammetry. The complex alone cannot cleave DNA but can do so in the presence of ascorbic acid.

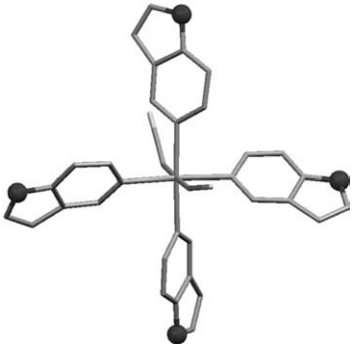


Peter Baran, Miroslav Boča, Roman Boča, Alžbeta Krutošíková, Jozef Miklovič, Juraj Pelikán, Ján Titiš

Polyhedron 24 (2005) 1510

Structural characterization, spectral and magnetic properties of isothiocyanate nickel(II) complexes with furopyridine derivatives

The nickel(II) complexes $[Ni(L^n)_4(NCS)_2]$, where L^1 = furo[3,2-*c*]pyridine, L^2 = 2-methylfuro[3,2-*c*]pyridine, L^3 = 2,3-dimethylfuro [3,2-*c*]pyridine, L^4 = benzo[4,5]furo[3,2-*c*]pyridine and L^5 = isoquinoline, have been prepared and characterized by structural, spectroscopic and magnetic methods. The structures of the all complexes are formed by isolated molecules. The Ni(II) ions are six-coordinate, the equatorial planes are formed by four N-donor heterocycles whereas the isothiocyanate groups coordinate in the axial positions. The magnetism of the complexes exhibits a zero-field splitting, the magnitude of which correlates with the distortion degree of the coordination polyhedra.



Susheela Dholia, Raj N. Mehrotra

Polyhedron 24 (2005) 1517

Estimate of the electron exchange rate constant for the 6-molybdocobaltate(III)/(II) couple from studies on the oxidation with iodide using Marcus theory

Estimate of the electron exchange rate constant for the 6-molybdocobaltate(III)/(II) couple from studies on the oxidation with iodide using Marcus theory. The oxidation of iodide ion by hexahydrogenhexamolybdocobaltate(III) ion in perchloric acid is described by the reactions.

$$[H_6Co^{III}Mo_6O_{24}]^{3-} + H^+ \overset{K}{\rightleftharpoons} [HH_6Co^{III}Mo_6O_{24}]^{2-}$$

$$[H_6Co^{III}Mo_6O_{24}]^{3-} + I^- \xrightarrow{k_4} [H_6Co^{II}Mo_6O_{24}]^{4-} + I^{\bullet}$$

$$[HH_6Co^{III}Mo_6O_{24}]^{2-} + I^- \xrightarrow{k_5} [HH_6Co^{II}Mo_6O_{24}]^{3-} + I^{\bullet}$$

$$I^{\bullet} + I^- \underset{k_{-6}}{\overset{k_6}{\rightleftharpoons}} I_2^{-\bullet}$$

$$[HH_6Co^{III}Mo_6O_{24}]^{2-} + I_2^{-\bullet} \xrightarrow{k_8} I_2 + [HH_6Co^{II}Mo_6O_{24}]^{3-}$$

$$I_2 + I^- \underset{k_{-9}}{\overset{k_9}{\rightleftharpoons}} I_3^-$$

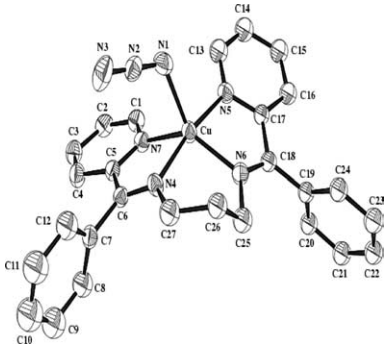
The self-exchange rate constant for the $HCo^{III}Mo_6^{2-}/HCo^{II}Mo_6^{3-}$ couple is estimated from the application of the Marcus theory.

Sk Hafijur Rahaman, Rajarshi Ghosh, Tian-Huey Lu, Barindra K. Ghosh

Polyhedron 24 (2005) 1525

Chelating *N*,*N*′-(bis(pyridin-2-yl)alkylidene)-propane-1,3-diamine pseudohalide copper (II) and cadmium(II) coordination compounds: Synthesis, structure and luminescence properties of $[M(bpap)(X)]ClO_4$ and $[M(bpap)(X)_2]$ [M = Cu, Cd; X = N_3^-, NCS^-]

The chelating ligand, *N*,*N*′-(bis(pyridin-2-yl)-alkylidene)propane-1,3-diamine (bpap) is used to synthesise complexes of type $[Cu(bpap)(N_3/NCS)]ClO_4$ (**1a**–**3b**) and $[Cd(bpap)(N_3/NCS)_2]$ (**4a**–**6b**). Elemental, spectral, electrochemical and other physicochemical results characterize the complexes. The structures of $[Cu(bpbp)(N_3)]ClO_4$ (**3a**) and $[Cd(bpbp)(NCS)_2]$ (**6b**) have been solved using X-ray diffraction. All the complexes display intraligand $^1(\pi-\pi^*)$ fluorescence and intraligand $^3(\pi-\pi^*)$ phosphorescence in glassy solutions (MeOH at 77 K).

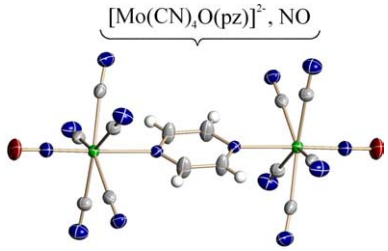


Dariusz Matoga, Janusz Szklarzewicz, John Fawcett

Polyhedron 24 (2005) 1533

Unexpected direct incorporation of NO in the Mo(IV) coordination sphere. X-ray crystal structure of $(PPh_4)_4[\{Mo(CN)_5(NO)\}_2(\mu\text{-pz})] \cdot 2C_2H_5OC_2H_5$

The preparation and characterization of the stable molybdenum cyanonitrosyl dimer, $[\{Mo(CN)_5(NO)\}_2(\mu\text{-pz})]^{4-}$ with bridging pyrazine (pz), is described. The product is formed in anaerobic conditions by direct synthesis from NO and $[Mo(CN)_4O(pz)]^{2-}$ ions as starting materials. The reaction involves unexpected oxo ligand release and NO incorporation. The dimer composition is confirmed by elemental analysis, X-ray crystal structure, ESI-MS spectra as well as UV–Vis, EPR and IR spectroscopy.

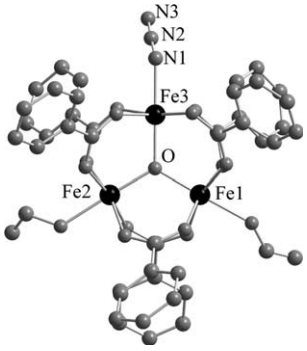


Athanassios K. Boudalis, Yiannis Sanakis, Catherine P. Raptopoulou, Aris Terzis, Jean-Pierre Tuchagues, Spyros P. Perlepes

Polyhedron 24 (2005) 1540

A trinuclear cluster containing the $\{Fe_3(\mu_3\text{-}O)\}^{7+}$ core: Structural, magnetic and spectroscopic (IR, Mössbauer, EPR) studies

The trinuclear "basic iron carboxylato" complex $[Fe_3O(O_2CPh)_6(EtOH)_2(N_3)]$ has been synthesized and characterized structurally, magnetically and spectroscopically by IR, EPR and ^{57}Fe-Mössbauer spectroscopies.

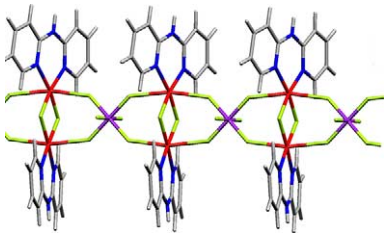


Hélène Casellas, Andrej Pevec, Bojan Kozlevčar, Patrick Gamez, Jan Reedijk

Polyhedron 24 (2005) 1549

An unprecedented $\mu_4\text{-}SiF_6^{2-}$-bridged supramolecular polymer consisting of bis-μ-F^- bridged dinuclear Cu(II) dications

Using thermal conditions a unique supramolecular Cu(II) polymer built up of $[Cu_2(dipyridylamine)_2(\mu\text{-}F)_2]$ motifs repeated infinitely along the (0 1 0) direction via SiF_6^{2-} bridges was synthesised.

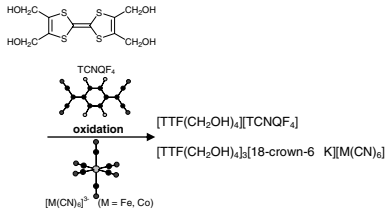


Sandrine Perruchas, Kamal Boubekeur, Philippe Molinié

Polyhedron 24 (2005) 1555

Radical cation salts of $TTF(CH_2OH)_4$ with cyanide anions: Synthesis, crystal structure and magnetic properties of $[TTF(CH_2OH)_4][TCNQF_4]$ and $[TTF(CH_2OH)_4]_3[18\text{-crown-}6 \subset K][M(CN)_6] \cdot DMF$ (M = Fe, Co)

The synthesis, crystal structures and magnetic properties of radical cation salts formulated $[TTF(CH_2OH)_4][TCNQF_4]$ and $[TTF(CH_2OH)_4]_3[18\text{-crown-}6 \subset K][M(CN)_6] \cdot DMF$ (M = Fe, Co) are described. In these salts, associating the tetrakis(hydroxymethyl)tetrathiafulvalene with cyanide anions, the organic molecules are combined in oligomers and strong hydrogen bonds occur between them and the anions.

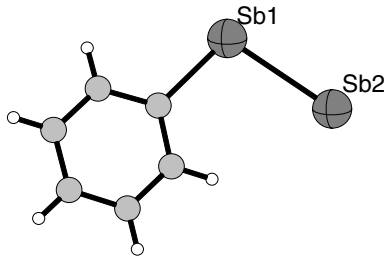


Katharina Wiesler, Nikolaus Korber

Polyhedron 24 (2005) 1565

Synthesis and crystal structure of the phenyl-substituted diantimonide $PhSb_2^{3-}$ in the ammoniate $[Cs_6(PhSb_2)_2] \cdot 11NH_3$

The highly charged diatomic anions Pn_2^{4-} (Pn = P to Bi) of the group 15 elements are known only in solids like Cs_4Sb_2. However, if the overall charge is reduced by introducing a phenyl residue, an anion like $PhSb_2^{3-}$ may be crystallised as a thermally unstable ammoniate. In analogy to the original Zintl chemistry, the compound $[Cs_6(PhSb_2)_2] \cdot 11NH_3$ forms by reducing triphenylantimony with a solution of caesium in liquid ammonia.

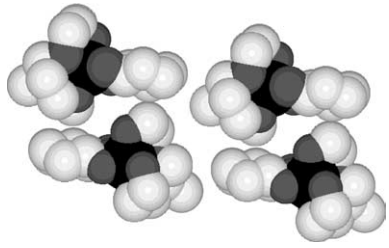


Jack Harrowfield, Jee Young Kim, Yang Kim, Young Hoon Lee, Pierre Thuéry

Polyhedron 24 (2005) 1569

Coordination chemistry of Co(III) complexes of an azetidine-derived quadridentate amine and a related macrocycle

The azetidine ring of a quadridentate ligand is protected from nucleophilic ring-opening by coordination and imparts a rigidity to the ligand which limits the stereoisomerism of its Co(III) complexes, crystal structures of which show evidence for extensive hydrogen-bonding and lipophilic interactions.

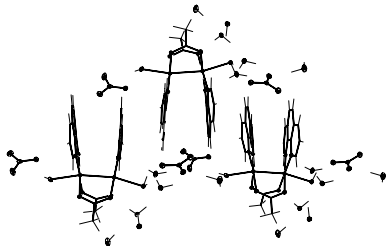


Katarzyna Wajda-Hermanowicz, Florian P. Pruchnik, Marek Zuber, Zbigniew Ciunik

Polyhedron 24 (2005) 1577

Studies of the interaction between adenosine 5′-triphosphate and $[Rh_2(OAc)_2(phen)_2(H_2O)_2](OAc)_2$

ATP interacts with binuclear rhodium (II) complex $[Rh_2(OAc)_2(phen)_2(H_2O)_2](OAc)_2$ by stacking with the phenanthroline ligand. The interaction of Rh(II) complex have been investigated using ^1H, ^{13}C, ^{31}P NMR, ^1H–^{15}N NMR HMBC experiments and UV–VIS difference spectroscopy. NMR and UV–VIS measurements suggest that phosphate residue of ATP does not interact with the positively charged $[Rh_2]^{2+}$ in axial position. In the presence of $[Rh_2(OAc)_2(phen)_2(H_2O)_2](OAc)_2$ in acidic solutions (pD 3.35) deprotonation of N1 nitrogen atom of ATP molecule occurs.

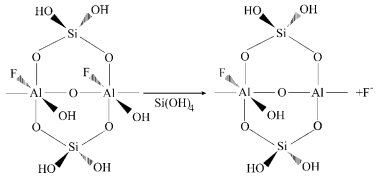


Stanislav Strekopytov, Christopher Exley

Polyhedron 24 (2005) 1585

The formation, precipitation and structural characterisation of hydroxyaluminosilicates formed in the presence of fluoride and phosphate

Hydroxyaluminosilicates (HAS) are important secondary mineral phases formed by the reaction of silicic acid with aluminium. There are two discrete forms of HAS (HAS_A and HAS_B) and we now show the accomodation of fluorine into both forms through its replacement of hydroxyl groups coordinated to octahedral aluminium.

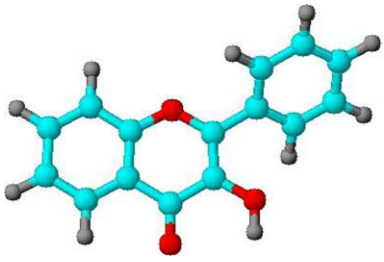


Latitia Dangleterre, Jean-Paul Cornard

Polyhedron 24 (2005) 1593

Interaction of lead (II) chloride with hydroxyflavones in methanol: A spectroscopic study

The interactions between lead (II) ions and 3-hydroxyflavone, 5-hydroxyflavone and 3′,4′-dihydroxyflavone were investigated. The complexes were characterized by electronic absorption spectroscopy combined with chemometrics methods. The stoichiometry composition and stability of complexes have allowed to classify the different sites of chelation of Pb(II) according to their complexing capacity in the following way: catechol > α-hydroxy-carbonyl > β-hydroxy-carbonyl.

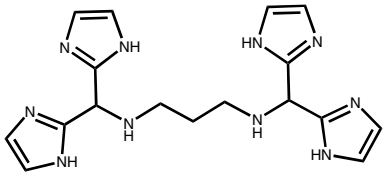


Yufei Song, Chiara Massera, Olivier Roubeau, Anna Maria Manotti Lanfredi, Jan Reedijk

Polyhedron 24 (2005) 1599

Chloro-bridged Cu(II) pairs linked into a 1D coordination polymer through a dinucleating imidazole-based ligand: 3D structure and magnetism

An interesting 1D polynuclear copper(II) complex built from tetranuclear units is reported with the ligand 1,1,7,7-tetrakis(imidazol-2-yl)-2,6-diazaheptane. The tetranuclear building blocks contain both neutral and anionic monodentate imidazole groups. The dehydronated imidazole is strongly hydrogen bonded to a lattice water molecule.

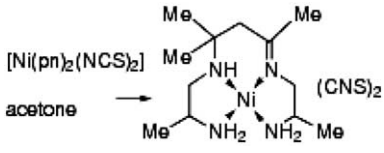


Neil F. Curtis, Clifton E.F. Rickard, Joyce M. Waters

Polyhedron 24 (2005) 1606

The preparation and structure of 2*SR*, 8*SR*, 10*SR*-(5,7,7-trimethyl-4,8-diazaundec-4-ene-2,10-diamine)nickel(II) thiocyanate

Reaction of bis(*rac*-propane-1,2-diamine)-dithiocyanatonickel(II) with acetone yields orange, singlet ground state, (5,7,7-trimethyl-4,8-diazaundec-4-ene-2,10-diamine) nickel(II) thiocyanate, $[C_{14}H_{28}N_4Ni](NCS)_2$-with the Ni in tetrahedrally twisted square-planar coordination by the amine–imine ligand.

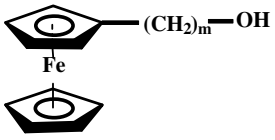


Wade L. Davis, Rebotsamang F. Shago, Ernie H.G. Langner, Jannie C. Swarts

Polyhedron 24 (2005) 1611

Synthesis and electrochemical properties of a series of ferrocene-containing alcohols

Different synthetic methods towards a series of primary ferrocene-containing alcohols with $m = 1$–4 and two secondary alcohols are described. The dependency of formal reduction potentials on chain length has been determined; results are compared to the analogues carboxylic acid series.



The Publisher encourages the submission of articles in electronic form thus saving time and avoiding rekeying errors. For detailed instructions on the preparation of manuscripts and of electronic artwork, consult the Author Gateway for Elsevier at http://authors.elsevier.com

SCIENCE DIRECT™

Full text of this journal is available, on-line from **ScienceDirect**. Visit **www.sciencedirect.com** for more information.

CONTENTS direct This journal is part of **ContentsDirect**, the *free* alerting service which sends tables of contents by e-mail for Elsevier books and journals. You can register for **ContentsDirect** online at: **www. elsevier.com/locate/contentsdirect**

Available online at www.sciencedirect.com
SCIENCE DIRECT®
Polyhedron 24, issue 1, 6 January 2005
POLYHEDRON
www.elsevier.com/locate/poly

Contents

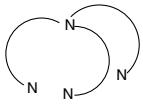
Report

Allan G. Blackman

Polyhedron 24 (2005) 1

The coordination chemistry of tripodal tetraamine ligands

This paper reviews the coordination chemistry of tripodal tetraamine ligands. The different possible arm lengths and N-donor atom types mean that these ligands display a remarkable diversity in their coordination chemistry with both transition metal ions and lanthanide ions, and they are found in chemical species ranging from simple mononuclear metal complexes to heterometallic polynuclear complexes and polymeric metallosupramolecular arrays. Aspects of such chemistry are detailed in this paper.



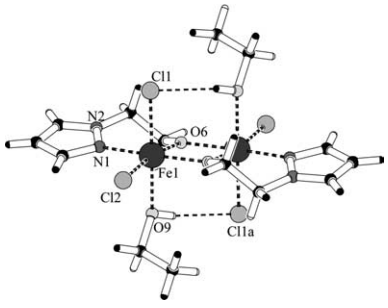
Papers

Stefania Tanase, Elisabeth Bouwman, Gary J. Long, Ahmed M. Shahin, René de Gelder, Allison M. Mills, Anthony L. Spek, Jan Reedijk

Polyhedron 24 (2005) 41

Bis(μ-alkoxo)-bridged dinuclear iron(III) complexes of pyrazole-based ligands as models for iron-oxo proteins

The synthesis, characterization, magnetic properties and the reactivity studies of two new bis(μ-alkoxo)-bridged dinuclear iron(III) complexes, $[Fe(nhep)Cl_2(EtOH)]_2$ and $[Fe(nhed)Cl_2]_2$ are reported. In compound **1**, the iron(III) center has a coordination number of six, with a slightly distorted octahedral geometry. In compound **2**, the bulkier nhed ligand, with methyl groups at the 3- and 5-positions of the pyrazole ring, leads to a coordination number of five at the iron(III) center in a distorted square pyramidal geometry. The magnetic properties of both complexes indicate the presence of fairly weak antiferromagnetic exchange interactions between iron(III) ions.

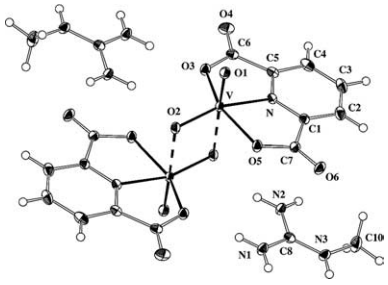


A.C. Gonzalez-Baró, E.E. Castellano, O.E. Piro, Beatriz S. Parajón-Costa

Polyhedron 24 (2005) 49

Synthesis, crystal structure and spectroscopic characterization of a novel bis (oxo-bridged) dinuclear vanadium(V)–dipicolinic acid complex

A new bis(oxo-bridged) binuclear compound of formula $[CH_3NHC(NH_2)_2]_2[V_2O_4(dipic)_2]$ has been synthesized and characterized by single-crystal X-ray diffraction and spectroscopic techniques. The compound sits at a crystallographic inversion center with the pair of V(V) atoms in an edge-sharing distorted octahedral environment. Two methylguanidinium acts as counterions for charge balance.



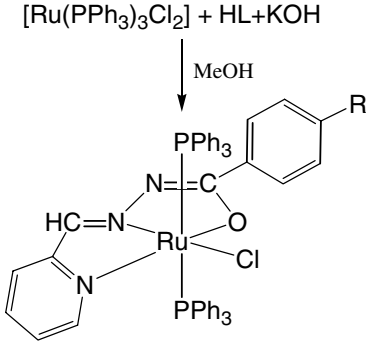
Elsevier Ltd.

Raji Raveendran, Samudranil Pal

Polyhedron 24 (2005) 57

Some *trans*-chlorobis(triphenylphosphine)-ruthenium(II) complexes with N,N,O-donor *N*-(aroyl)-*N*′-(picolinylidene)hydrazines

Syntheses, characterization and physical properties of complexes having the formula *trans*-[RuL(PPh$_3$)$_2$Cl] where L$^-$ represents deprotonated tridentate Schiff bases derived from one mole equivalent each of 2-pyridinecarbaldehyde and aroylhydrazines have been described. The complexes are redox active and display several absorptions in the electronic spectra.

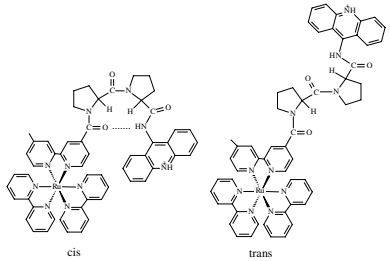


Idalina M.M. de Carvalho, Ícaro de Sousa Moreira, Marcelo H. Gehlen

Polyhedron 24 (2005) 65

Luminescence study of Ru(II) bipyridine–acridine spaced by amide and proline bridges

The photophysical properties of the polypyridyl ruthenium(II) complexes bridged to the acridine chromophore by an amide, one and two prolines were investigated. The inductive effect of the carbonyl group from the bridges cause a decrease in the energy level of the MLCT excited state. The folded structure of the *cis*-[Ru(bpy)$_2$mbpy–(Pro)$_2$acrd] complex confer the fastest rate of T–T energy transfer.

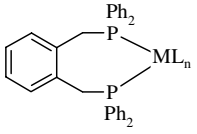


Michael D. Brown, William Levason, Gillian Reid, Rebecca Watts

Polyhedron 24 (2005) 75

Synthesis spectroscopic and structural properties of transition metal complexes of the *o*-xylyl diphosphine *o*-C$_6$H$_4$(CH$_2$PPh$_2$)$_2$

A series of coordination complexes involving the sterically demanding xylyl diphosphine, *o*-C$_6$H$_4$(CH$_2$PPh$_2$)$_2$ (L^1), and metal ions from Groups 9–11 are described together with their spectroscopic and structural properties.

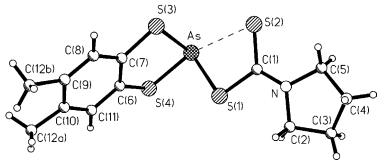


H.P.S. Chauhan, Kavita Kori, Nagulu Meera Shaik, Sanjay Mathur, Volker Huch

Polyhedron 24 (2005) 89

Dialkyldithiocarbamate derivatives of toluene-3,4-dithiolato arsenic(III) and -bismuth(III): synthetic, spectral and single crystal X-ray structural studies

Dialkyldithiocarbamate complexes of the type [C$_6$H$_3$(CH$_3$)S$_2$MS$_2$CNR$_2$] [M=As or Bi] have been synthesized and characterized using physico-chemical and spectral methods. Single crystal X-ray diffraction analyses of toluene-3,4-dithiolatoarsenic(III) dimethyldithiocarbamate and pyrrolidinedithiocarbamate revealed a monodentate chelating mode of the ligand moieties.

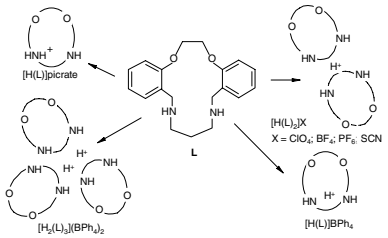


Ljerka Tušek-Božić, Aleksandar Višnjevac, Ester Marotta, Biserka Kojić-Prodić

Polyhedron 24 (2005) 97

The inside and outside protonation of a 15-membered O_2N_2-macrocycle. Synthesis and structural characterization of the protonated ligand salts

The synthesis, isolation and structural characterization of the novel protonated macrocyclic salts of dioxa-diaza macrocycle 5,6,14,15-dibenzo-1,4-dioxa-8,12-diazacyclopentadeca-5,14-diene are described.

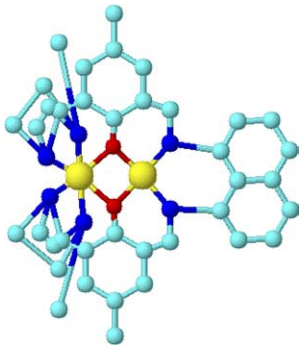


K.R. Krishnapriya, M. Kandaswamy

Polyhedron 24 (2005) 113

Coordination properties of a dicompartmental ligand with tetra- and hexadentate coordination sites towards copper (II) and nickel (II) ions

A new dicompartmental ligand with tetra- and hexadentate coordination sites has been synthesized.The mono- and binuclear Cu(II) and Ni(II) complexes of the ligand have been prepared and characterized by spectral studies.Between the two compartments, the compartment containing azomethine nitrogens has stronger coordination towards the metal ions than the compartment containing piperazine nitrogens.



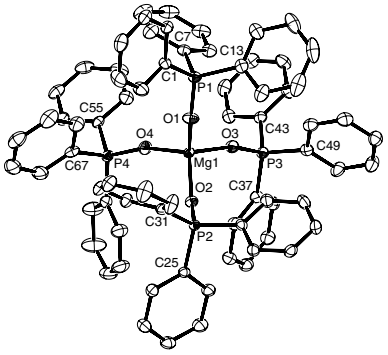
Michael B. Hursthouse, William Levason, Raju Ratnani, Gillian Reid, Holly Stainer, Michael Webster

Polyhedron 24 (2005) 121

Synthesis, spectroscopic and structural properties of an unusual series of homoleptic phosphine oxide complexes of the alkaline earth dications

The reactions of the MCl_2 (M=Mg, Ca, Sr or Ba) with phosphine oxide ligands in the presence of the halide abstractor $SbCl_5$ give a variety of homoleptic phosphine oxide complexes which exhibit a range of coordination numbers and geometries; representative examples are characterised by single crystal X-ray diffraction studies.

$$MCl_2 \xrightarrow[CH_2Cl_2]{SbCl_5/L} [ML_n](SbCl_6)_2$$
$$M = Mg,\ Ca, Sr \text{ or } Ba$$
$$L = OPPh_3, 1/2\ Ph_2P(O)CH_2P(O)Ph_2$$
$$\text{or } 1/2\ o\text{-}C_6H_4(P(O)Ph_2)_2$$

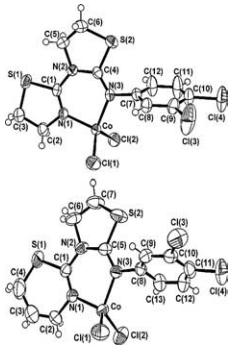


F.J. Barros-García, A. Bernalte-García, A.M. Lozano-Vila, F. Luna-Giles, E. Viñuelas-Zahínos

Polyhedron 24 (2005) 129

Pseudotetrahedral cobalt(II) complexes with thiazoline and thiazine derivative ligands: synthesis and characterization

Two cobalt complexes were obtained through the reaction of 2-(3,4-dichlorophenyl)imino-N-(2-thiazolin-2-yl)thiazolidine (TdTn) with $CoCl_2{\cdot}6H_2O$ and 2-(3,4-dichlorophenyl)imino-N-(2-thiazin-2-yl)thiazolidine (TdTz) with the same metallic salt. Both compounds were characterized by single crystal X-ray diffraction, elemental analysis, spectroscopic and magnetic measurements. Both complexes present a pseudotetrahedral geometry around the cobalt (II) ion.

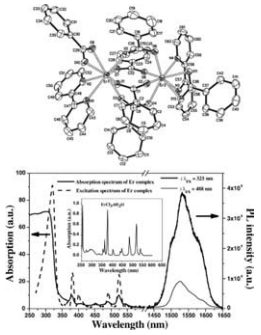


Soo-Gyun Roh, Min-Kook Nah, Jae Buem Oh, Nam Seob Baek, Ki-Min Park, Hwan Kyu Kim

Polyhedron 24 (2005) 137

Synthesis, crystal structure and luminescence properties of a saturated dimeric Er(III)-chelated complex based on benzoate and bipyridine ligands

An Er(III)-chelated complex exhibits a strong intensity NIR emission around 1.53 μm. It can be attributed to an efficient energy transfer between organic ligand and Er ion, since there is a spectral overlap between the emission band of the organic ligands and the absorption bands of the Er ion.

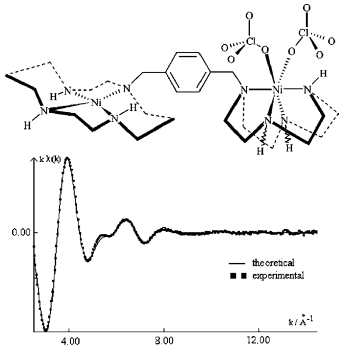


Mathieu Soibinet, Isabelle Déchamps-Olivier, Emmanuel Guillon, Jean-Pierre Barbier, Michel Aplincourt, Françoise Chuburu, Michel Le Baccon, Henri Handel

Polyhedron 24 (2005) 143

Magnetic measurements, UV–Vis spectroscopy, and XAS of dinuclear nickel(II) complexes of bistetraazamacrocycles

The magnetic susceptibility measurements, X-ray absorptions and electronic spectroscopies showed that the six Ni dinuclear compounds with several bis-macrocycles derived from cyclen (1,4,7,10-tetraazacyclododecane) and cyclam (1,4,8,11-tetraazacyclotetradecane) present different geometries, which depend on the macrocyclic cavity and counter-ion used.

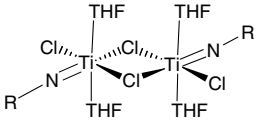


Dale A. Pennington, Peter N. Horton, Michael B. Hursthouse, Manfred Bochmann, Simon J. Lancaster

Polyhedron 24 (2005) 151

Synthesis and catalytic activity of dinuclear imido titanium complexes: the molecular structure of $[Ti(NPh)Cl(\mu\text{-}Cl)(THF)_2]_2$

Reaction of $TiCl_4$ with the reagents $RN(SiMe_3)_2$ in dichloromethane precipitates red to black powders (R=1-adamantyl, phenyl, pentafluorophenyl, 3,5-bis(trifluoromethyl)phenyl), which on treatment with tetrahydrofuran give the new THF adducts $[Ti(NR)Cl(\mu\text{-}Cl)(THF)_2]_2$.

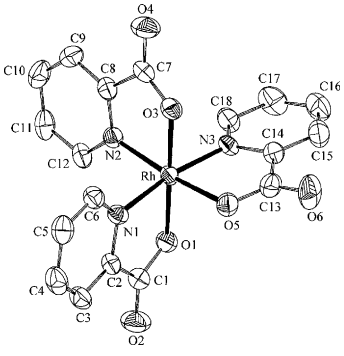


Semanti Basu, Shie-Ming Peng, Gene-Hsiang Lee, Samaresh Bhattacharya

Polyhedron 24 (2005) 157

Synthesis, structure and electrochemical properties of tris-picolinate complexes of rhodium and iridium

Reaction of picolinic acid (Hpic) with rhodium and iridium trichloride affords complexes of type $[M(pic)_3]\cdot H_2O$ (M=Rh, Ir). Structure determination shows that the water of crystallization is hydrogen bonded to the carboxylate fragments of two adjacent $[M(pic)_3]$ molecules and thus acts as a bridge between the individual complex molecules.

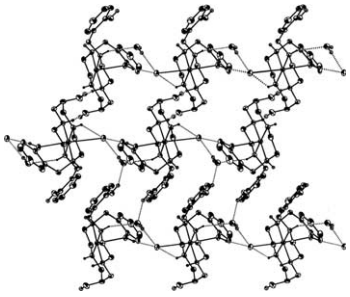


Yong-Shu Xie, Xue-Ting Liu, Min Zhang, Kai-Ju Wei, Qing-Liang Liu

Polyhedron 24 (2005) 165

Supramolecular structures of $Co^{(III)}$ and $Cu^{(II)}$ complexes of a novel alcohol and phenol containing polyamine ligand H_2L (H_2L=*N*,*N*′-bis(2-hydroxybenzyl)-1,3-bis[(2-aminoethyl)amino]-2-propanol)

Octahedrally coordinated Co(III) and Cu(II) complexes of a novel alcohol and phenol containing polyamine ligand H_2L (H_2L=*N*,*N*′-bis(2-hydroxybenzyl)-1,3-bis[(2-aminoethyl)amino]-2-propanol), $[CoL]ClO_4$ (**1**) and $[Cu(H_2L)Cl]ClO_4{\cdot}CH_3OH{\cdot}H_2O$ (**2**) were synthesized, spectroscopically and structurally characterized. **1** and **2** are self-assembled into hydrogen-bonded 1D and 2D supramolecular structures, respectively.

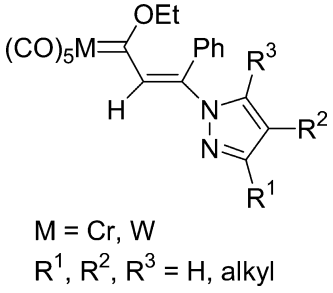


Kai-Chun Gu, Jin-Zhu Chen, Zhao-Yan Zheng, Si-Zhong Wu, Xiao-Wei Wu, Xiu-Wen Han, Zheng-Kun Yu

Polyhedron 24 (2005) 173

Synthesis and structural characterization of (pyrazolyl)alkenyl Fischer carbene complexes of chromium and tungsten

Reactions of 1-alkynyl Fischer carbene complexes $(CO)_5M{=}C(OEt)(C{\equiv}CPh)$ (M= Cr, W) with substituted pyrazoles afforded (pyrazolyl)alkenyl Fischer carbene complexes with an exclusive (*E*)-configuration in mild to excellent yields.

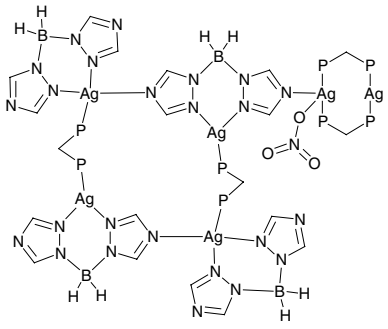


Giancarlo Gioia Lobbia, Maura Pellei, Claudio Pettinari, Carlo Santini, Brian W. Skelton, Allan H. White

Polyhedron 24 (2005) 181

Silver(I) bis(1,2,4-triazolyl)borate complexes containing bidentate phosphine ligands

New silver(I) derivatives containing bidentate phosphine and anionic bis(triazol-1-yl)borate ligands have been prepared from the reaction of $AgNO_3$, $K[H_2B(tz)_2]$ and dppm, dppe or dppf. In $[\{H_2B(tz)_2\}_2Ag_3(dppm)_2(NO_3)_3]$, the silver atom has a $PAgN_3$ environment, utilizing the coordinating capability of one of the additional (exo'-) ring nitrogens not only to complete the four-coordinate array about the silver but, necessarily, to link successive asymmetric units into a single-stranded polymer.



Instructions concerning crystallographic data I

The Publisher encourages the submission of articles in electronic form thus saving time and avoiding rekeying errors. For detailed instructions on the preparation of manuscripts and of electronic artwork, consult the Author Gateway for Elsevier at http://authors.elsevier.com

SCIENCE DIRECT™

Full text of this journal is available, on-line from **ScienceDirect**. Visit **www.sciencedirect.com** for more information.

CONTENTS direct

This journal is part of **ContentsDirect**, the *free* alerting service which sends tables of contents by e-mail for Elsevier books and journals. You can register for **ContentsDirect** online at: **www. elsevier.com/locate/contentsdirect**

Available online at www.sciencedirect.com
SCIENCE DIRECT®
Polyhedron 24, issues 16–17, 17 November 2005
POLYHEDRON
www.elsevier.com/locate/poly

Contents

Preface 2063

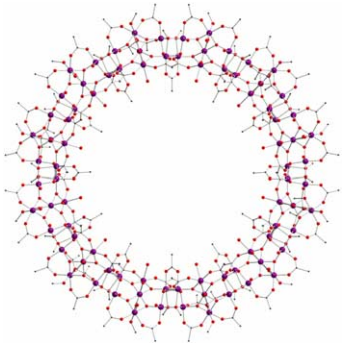
Papers

George Christou

Polyhedron 24 (2005) 2065

Single-molecule magnets: a molecular approach to nanoscale magnetic materials

A brief survey is provided of single-molecule magnets (SMMs), or molecular nanomagnets. The $[Mn_{12}O_{12}(O_2CR)_{16}(H_2O)_4]$ (Mn_{12}; R = various) family of SMMs continues to be the one with the highest blocking temperatures, and the one on which the most detailed studies are being performed within the chemistry and physics communities. For this reason, methods have been developed for their controlled modification in various ways, and these are summarized. In addition, new SMMs continue to be sought to improve knowledge of this phenomenon, and several representative examples of new synthetic procedures and the resulting products are described.

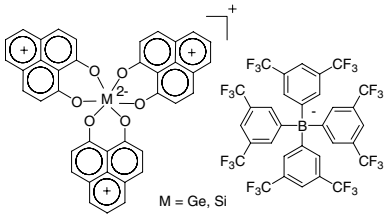


S.K. Pal, F.S. Tham, R.W. Reed, R.T. Oakley, R.C. Haddon

Polyhedron 24 (2005) 2076

Synthesis and characterization of germanium (IV) and silicon (IV) complexes derived from 9-hydroxyphenalenone: X-ray crystal and molecular structure of tris-(9-oxophenalenone)-germanium (IV) and silicon (IV) salts

Two new hexacoordinated germanium and silicon cations containing three phenalenyl units were prepared by reacting 9-hydroxyphenalenone with germanium tetrachloride ($GeCl_4$) and silicon tetrachloride ($SiCl_4$) and characterized by single crystal X-ray diffraction. The cyclic voltammograms show three reversible one-electron reduction steps due to the formation of the radical, anion and dianion as each phenalenyl moiety accepts an electron.

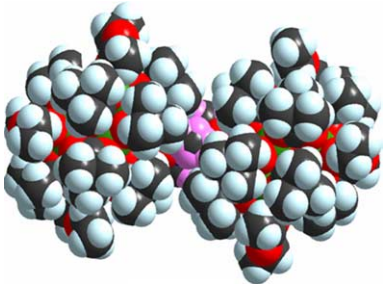


Elena Fursova, Victor Ovcharenko, Ksenia Nosova, Galina Romanenko, Vladimir Ikorskii

Polyhedron 24 (2005) 2084

Heterospin compounds based on the $[Mn_6(O)_2Piv_{10}]$ cluster unit and nitroxides

Synthetic procedures have been developed to prepare heterospin compounds based on the $[Mn_6(O)_2Piv_{10}]$ polymetallic nucleus. The structure of these compounds has been studied. To obtain highly dimensional structures demands structural complementarity of the $[Mn_6(O)_2Piv_{10}]$ and NIT-R nuclei, which is only possible when R = CH_3.

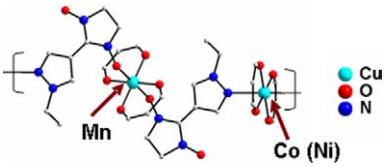


Ksenia Maryunina, Sergey Fokin, Victor Ovcharenko, Galina Romanenko, Vladimir Ikorskii

Polyhedron 24 (2005) 2094

Solid solutions: An efficient way to control the temperature of spin transition in heterospin crystals $M_xCu_{1-x}(hfac)_2L$ (M = Mn, Ni, Co; L = nitronyl nitroxide)

A series of mixed-metal solid solutions $M_xCu_{1-x}(hfac)_2L$ (M = Mn, Ni, and Co) liable to undergo thermally induced spin transitions have been synthesized. The structure and magnetic properties of the compounds have been investigated.

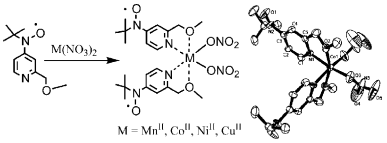


Zhicheng Zhu, Satoru Karasawa, Noboru Koga

Polyhedron 24 (2005) 2102

Crystal structures and magnetic properties of complexes of $M(NO_3)_2$; M = Mn^{II}, Co^{II}, Ni^{II}, and Cu^{II}, with pyridine ligands carrying an aminoxyl radical

Four complexes of $M(NO_3)_2$(**4NOPy-OMe**)$_2$, (**4NOPy-OMe** = 4-(*N-tert*-butyloxylamino)-2-(methoxymethylenyl)pyridine, and M=Mn^{II}, **1**; Co^{II}, **2**; Ni^{II}, **3**; Cu^{II}, **4**), were prepared and fully characterized. The magnetic properties of all complexes were investigated by SQUID magneto/susceptometry.

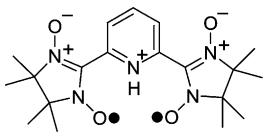


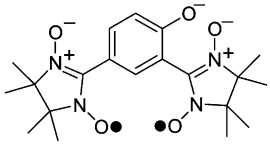
Tadashi Sugano, Stephen J. Blundell, William Hayes, Peter Day

Polyhedron 24 (2005) 2108

Magnetism in organic diradical ion salts based on nitronyl nitroxide

Magnetism in organic diradical ion salts based on (2,4-POBNN)$^{\bullet-}$ and (2,6-PYBNN)$^{\bullet+}$ were investigated by using SQUID magnetometers. The diradical cation salt (2,6-PYBNN)$^{\bullet+}Cl^-$ shows intramolecular ferromagnetic interaction with the exchange coupling constant J/k = +9.0 K and intermolecular antiferromagnetic interaction with the Weiss constant θ = −0.75 K. The intermolecular interaction in the diradical cation salt is about one hundred times as low as that observed in the neutral diradical (2,6-PYBNN)$^{\bullet}$, while the intramolecular interaction is close to that obtained for the neutral radical.



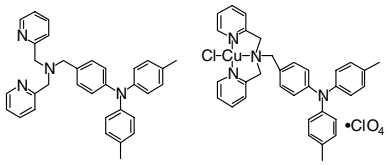


Masafumi Yano, Kazutoshi Inoue, Takeshi Motoyama, Yasuhiro Azuma, Masakazu Tatsumi, Osamu Yamauchi, Munetaka Oyama, Kazunobu Sato, Takeji Takui

Polyhedron 24 (2005) 2112

Synthesis and properties of a triarylamine derivative with a coordination site and its copper (II) complex

A novel ligand with a redox active triarylsamine unit and its copper complex were designed and synthesized. Electrochemical and spectroscopic properties of the complex were examined.

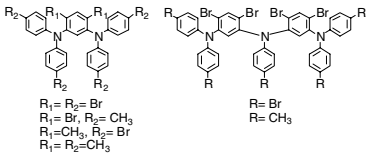


Masafumi Yano, Yasuyuki Nakanishi, Kosuke Matsushita, Masakazu Tatsumi, Munetaka Oyama, Kazunobu Sato, Takeji Takui

Polyhedron 24 (2005) 2116

Organic high-spin systems of oligoarylamines: Properties of tetraaryl-*m*-phenylendiamine oligocations as examined by electron transfer stopped-flow method

Triarylamine-based diamines and triamines were synthesized as precursors of positvely charged high-spin systems. Their electrochemical and spectroscopic prooerties were examined.

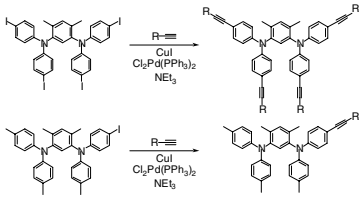


Masafumi Yano, Teruyuki Furuya, Masanori Yonezawa, Masakazu Tatsumi, Munetaka Oyama, Kazunobu Sato, Takeji Takui

Polyhedron 24 (2005) 2121

Synthesis, electrochemical and spectroscopic studies of highly extended tetraaryl-*m*-phenylenediamines as precursors of ground-state triplet dications

Various highly π-extended tetraaryl-1,3-phenylenediamines were synthesized. Their electrochemical and spectroscopic properties were also examined.

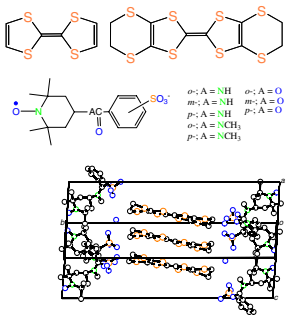


Hiroki Akutsu, Kazuyoshi Masaki, Kenji Mori, Jun-ichi Yamada, Shin'ichi Nakatsuji

Polyhedron 24 (2005) 2126

New organic free radical anions TEMPO–A–CO–(*o*-, *m*-, *p*-)$C_6H_4SO_3^-$(A = NH, NCH_3, O) and their TTF and/or BEDT-TTF salts

We have prepared eight TEMPO-containing anions TEMPO–A–CO–(*n*-)$C_6H_4SO_3^-$ (*n* = *o*, *m*, *p* for A = NH (**N1**, **N2**, **N3**), *n* = *o*, *p* for A = NCH_3 (**M1**, **M3**), and *n* = *o*, *m*, *p* for A = O (**O1**, **O2**, **O3**)) as PPh_4 salts. Metathesis of their salts with $(TTF)_3(BF_4)_2$ gave their TTF salts. Electrocrystallization of BEDT-TTF with $PPh_4 \cdot$ **M1** yielded the α-(BEDT-TTF)$_3$(**M1**)$_2 \cdot 8H_2O$ salt. We report their crystal structures, electrical resistivities, and magnetic properties. The relation between crystal structures and physical properties are discussed.



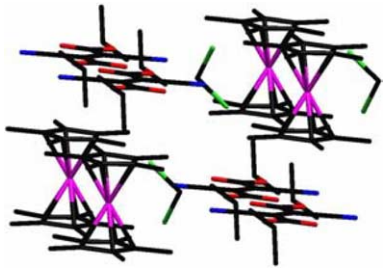
α-(BEDT-TTF)$_3$(TEMPO-N(CH$_3$)CO-*o*-$C_6H_4SO_3$)$_2 \cdot 8H_2O$

William S. Tyree, Carla Slebodnick, Mary C. Spencer, Guangbin Wang, Joseph S. Merola, Gordon T. Yee

Polyhedron 24 (2005) 2133

Structure–property correlations in a family of decamethylmetallocenium charge-transfer salt magnets using dialkyl dicyanofumarates as the one-electron acceptors: Ferromagnetism versus metamagnetism

Charge-transfer salts from the reactions of decamethylmanganocene or decamethylchromocene and di-*n*-propyl dicyanofumarate or di-isopropyl dicyanofumarate have been prepared and characterized. Taken together with previously published compounds, a homologous series has thus been assembled that exhibits a change from ferromagnetism to metamagnetism correlated to a change in crystal structure.

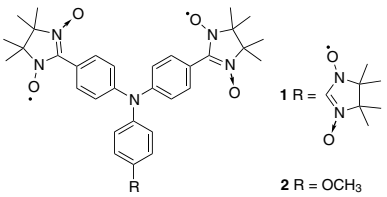


Yoshiaki Nakano, Takuya Yagyu, Takamasa Hirayama, Akihiro Ito, Kazuyoshi Tanaka

Polyhedron 24 (2005) 2141

Synthesis and intramolecular magnetic interaction of triphenylamine derivatives with nitronyl nitroxide radicals

Two triphenylamine derivatives bearing nitronyl nitroxide radicals, **1** and **2**, were synthesized. The weak antiferromagnetic interactions exist between the nitronyl nitroxide moieties in **1** and **2**, and furthermore, those radical groups are oxidized much easier than the central triphenylamine moiety.

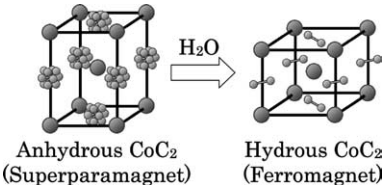


Junichi Nishijo, Kentaroh Kosugi, Hiroshi Sawa, Chie Okabe, Ken Judai, Nobuyuki Nishi

Polyhedron 24 (2005) 2148

Water-induced ferromagnetism in cobalt acetylide CoC_2 nanoparticles

New molecule-based magnet CoC_2 shows water-induced ferromagnetism caused by the orientation ordering of C_2^{2-} molecules. In the anhydrous phase, the orientation of C_2^{2-} is disordered, resulting in the small ferromagnetic domain and superparamagnetism. Once the material absorb the water, the orientation of C_2^{2-} is ordered and the ferromagnetic domains expand, resulting in the ferromagnetic behavior.

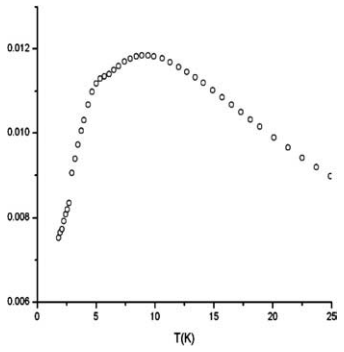


Firas F. Awwadi, Christopher P. Landee, Mark M. Turnbull, Brendan Twamley, Brian M. Wells

Polyhedron 24 (2005) 2153

Low-dimensional quantum magnetic systems: Synthesis, structure and magnetic behavior of (2,5-dimethylpyrazine)copper(II) chloride and synthesis and magnetic behavior of bis(2,6-dimethylpyrazine)copper(II) chloride

(2,5-Dimethylpyrazine)$CuCl_2$ has been prepared and its structure and magnetic behavior determined. The compound crystallizes as chains of $CuCl_2$ units linked by the pyrazine ligand. The chains pack such that each chain has four identical nearest neighbors. The magnetic data support a uniform chain model which crosses directly to three-dimensional behaviour.

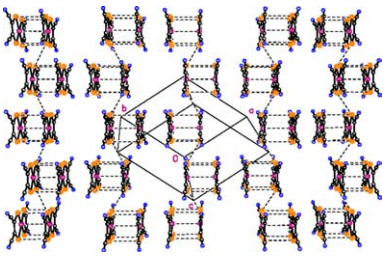


X.M. Ren, S. Nishihara, T. Akutagawa, T. Nakamura, J.L. Xie, Q.J. Meng

Polyhedron 24 (2005) 2160

Two-dimensional molecular magnets based on $[Pt(mnt)_2]^-$ ions: Structures and magnetic properties

A compound consists of [1-(4′-fluorobenzyl)-pyridinium][$Pt(mnt)_2$], and two polymorphisms of its were caused from the solvent molecule, MeCN, incorporating into lattice. The anions of $[Pt(mnt)_2]^-$ in two polymorphs array into different manner of 2D layer, and the neighboring anions in a 2D layer possess AFM interactions.

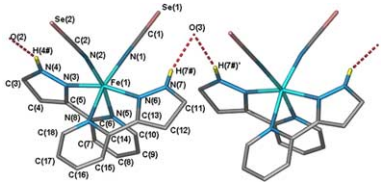


Ben A. Leita, Boujemaa Moubaraki, Keith S. Murray, Jonathan P. Smith

Polyhedron 24 (2005) 2165

Spin-crossover in dimeric hydrogen-bonded iron(II) 2-(pyrazolyl)-pyridine and 2-(imidazolyl)-pyridine complexes

A family of iron(II) *cis*-$[FeL_2(NCX)_2]_2(\mu$-solvate) complexes has been made and structurally characterised, where L is a bidentate pyrazolyl- or imidazolyl-pyridine and X = S, Se. Solvate (water and methanol) molecules hydrogen-bond to NH groups on neighbouring L groups thus forming discrete pseudo-dimeric species, one of which, with X = Se, displays a 'half' spin-crossover. This spin transition is absent upon desolvation.

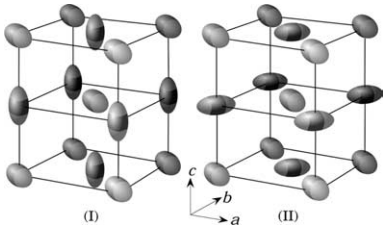


Kenji Mizoguchi, Masato Takei, Hirokazu Sakamoto, Tohru Kawamoto, Madoka Tokumoto, Ales Omerzu, Dragan Mihailovic

Polyhedron 24 (2005) 2173

Uniaxial strain study in purely organic ferromagnet α-TDAE-C_{60} – Mechanism and structure

ESR has been carried out in ferromagnetic α-TDAE-C_{60} under uniaxial strain to study the mechanism and structure of ferromagnetism. Pressure is applied to a single crystal embedded in epoxy resin with a clamp type pressure cell. A preliminary study demonstrates that the uniaxial strain induces a change of the Curie temperature T_C, which depends on the crystal axis where the uniaxial strain applied.

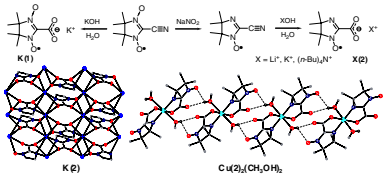


Eugene Tretyakov, Sergey Fokin, Victor Ovcharenko, Galina Romanenko, Yury Shvedenkov

Polyhedron 24 (2005) 2176

A new approach to synthesis of α-nitronyl nitroxide carboxylates. First metal complexes with α-imino nitroxide carboxylate

α-Nitronyl- (**1**) and α-imino nitroxide carboxylates (**2**) were prepared by hydrolysis of the corresponding nitriles. A series of heterospin complexes with **2** were synthesized. For K(**2**), $Cu(\mathbf{2})_2(CH_3OH)_2$, and $Ni(\mathbf{2})_2(py)_2$, crystal and molecular structure has been determined. For $Cu(\mathbf{2})_2$ and $Ni(\mathbf{2})_2$(bipy), cooperative magnetic ordering has been recorded at 16.6 and 4.6 K, respectively.

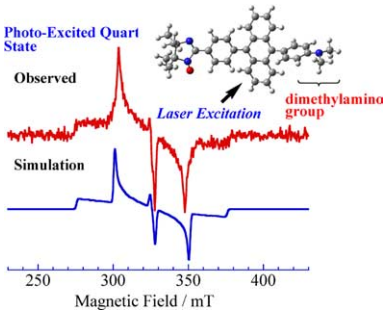


Yoshio Teki, Satoru Nakajima

Polyhedron 24 (2005) 2185

Design, synthesis and electronic states of an iminonitroxide radical with excited quartet high-spin state and photo-induced electron transfer in its CT complex

We report the design, synthesis and electronic state of a π-conjugated stable iminonitroxide radical, **1**, the electron donor property of which is improved by an attachment of dimethylamino group. The photo-excited quartet high-spin state was observed by a time-resolved ESR experiment.

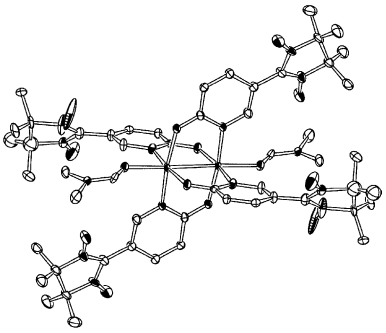


Mikio Ueda, Mamoru Itou, Kazuya Okazawa, Tomoyuki Mochida, Hatsumi Mori

Polyhedron 24 (2005) 2189

Metal complexes with pyridone-based radicals: Preparation and properties of a dinuclear paddle-wheel copper(II) complex and a mononuclear palladium(II) complex

By reaction of a pyridine-based open-shell ligand (**HL**) involving a nitronyl nitroxide moiety with copper(II) and palladium(II) ions, a dinuclear paddle-wheel type complex $[Cu_2(\mathbf{L})_4(DMF)_2]$ (**1**, figure) and a mononuclear complex *trans*-$[PdCl_2(\mathbf{HL})_2]$ (**2**) were prepared. These complexes were characterized structurally and magnetically; the small intramolecular antiferromagnetic interaction in the latter complex may originate from superexchange through the diamagnetic metal center.

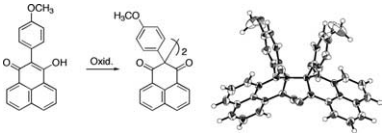


Yasushi Morita, Shinsuke Nishida, Kozo Fukui, Kunio Hatanaka, Tomohiro Ohba, Kazunobu Sato, Daisuke Shiomi, Takeji Takui, Gaku Yamamoto, Kazuhiro Nakasuji

Polyhedron 24 (2005) 2194

2-Aryl substituted 3-oxophenalenoxyl radicals: π-Spin structures and properties evaluated by dimer structure

X-ray crystal structure analysis and variable temperature ^1H NMR study have revealed the dimeric structure of 2-(*p*-methoxyphenyl)-3-oxophenalenoxyl neutral radical. Density functional theory calculations have shown that the kinetic instability of this radical is attributed to the relatively localized nature of the π-spin density distribution, which supports our previous ESR study.

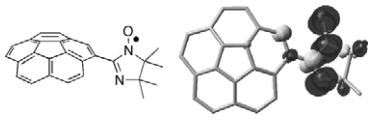


Shinsuke Nishida, Yasushi Morita, Tadahiro Kobayashi, Kozo Fukui, Akira Ueda, Kazunobu Sato, Daisuke Shiomi, Takeji Takui, Kazuhiro Nakasuji

Polyhedron 24 (2005) 2200

Spin delocalization on curved surface π-system: Corannulene with iminonitroxide

Corannulene with iminonitroxide radical has been designed and synthesized as a novel stable bowl-shaped neutral radical. ESR/ENDOR/TRIPLE spectroscopies and density functional theory calculation have shown that appreciable amount of π-spin is delocalized onto the corannulene moiety, although most of the π-spin density is localized on the iminonitroxide moiety.

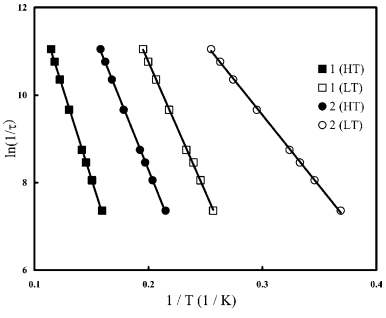


Hui-Lien Tsai, Hong-Ann Shiao, Tyn-Yih Jwo, Chen-I Yang, Ching-Shuei Wur, Gene-Hsiang Lee

Polyhedron 24 (2005) 2205

Single-molecule magnets: $[Mn_{12}O_{12}(O_2CCF_2Cl)_{16}(H_2O)_4]^{0/-}$

The syntheses, X-ray crystal structures and magnetic properties of $[Mn_{12}O_{12}(O_2CCF_2Cl)_{16}(H_2O)_4]$ (**1**) and $[PPh_4][Mn_{12}O_{12}(O_2CCF_2Cl)_{16}(H_2O)_4]$ (**2**) are reported. The results of DC and AC magnetic susceptibility studies are described. Complexes **1** and **2** exhibit two out-of-phase component of the AC magnetic susceptibility with frequency dependent maxima. The anisotropic energies U/k_B are 82.7, 64.8, 56.4 and 32.4 K for complexes **1**(HT), **2**(HT), **1**(LT) and **2**(LT), respectively. Step-like features are seen on hysteresis loops of complex **1**. DC decay relaxation of complex **1** shows quantum tunneling behavior below 2.1 K.

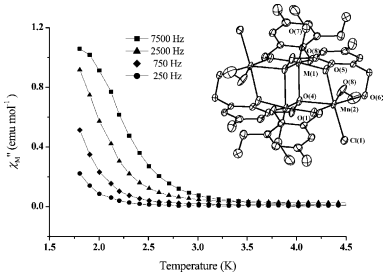


Chen-I Yang, Gene-Hsiang Lee, Ching-Shuei Wur, Jauyn G. Lin, Hui-Lien Tsai

Polyhedron 24 (2005) 2215

Syntheses, structures and single-molecule magnetic behaviors of two dicubane Mn_4 complexes

Two tetranuclear manganese complexes, $[Mn_4(HL)_4(MeOH)_4X_2]$ (X = Cl, Br; H_3L = 2,6-bis(hydroxymethyl)-4-methylphenol), consist of a mixed-valence dicubane structure, which comprises two Mn^{II} and two Mn^{III} ions. Magnetic susceptibilities and magnetization of both complexes indicate that two clusters have an $S = 9$ ground state. The AC frequency-dependent out-of-phase signals susceptibilities were observed in the low temperature range indicating a slow magnetic relaxation.

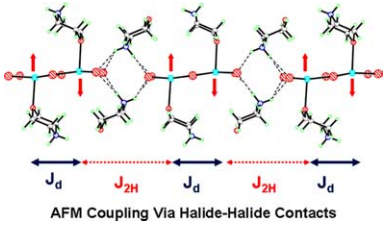


Roger D. Willett, Robert Butcher, Christopher P. Landee, Brendan Twamley

Polyhedron 24 (2005) 2222

Two halide exchange in copper(II) halide dimers: $(Morpholinium)_2Cu_2Cl_xBr_{6-x}$

Hydrogen bonding forces short halide···halide contacts of ~4 Å between otherwise structurally isolated copper(II) dimers in the $(morpholinium)_2Cu_2Cl_xBr_{6-x}$ salts. This contacts provide an efficient magnetic exchange pathway between dimers, so that the systems behave as alternating antiferromagnetic chains. The strength of this halide···halide coupling is approximately seven times as large in the bromide salt as in the chloride salt.

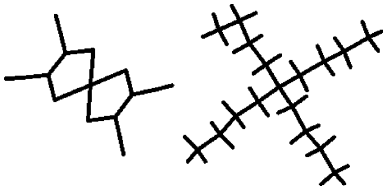


Roger D. Willett, Carlos J. Gómez-García, B.L. Ramakrishna, Brendan Twamley

Polyhedron 24 (2005) 2232

$(NBu_4)Ni(mnt)_2$: A novel bistable high temperature spin-Peierls-like system

The title compound contains novel stacks of antiferromagnetically coupled $[Ni(mnt)_2]^-$ anions. A structural phase transition takes place at 170 K that leads to an increase in the antiferromagnetic interactions, leading to rapid drop in the magnetic susceptibility in the low temperature phase. The phase transition is driven by thermally induced disorder in one arm of the tetrabutylammonium cations. A 7° hysteresis in the phase transition is observed.

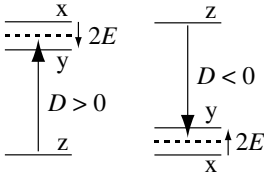


Ryo Takeda, Shoji Mitsuo, Shusuke Yamanaka, Kizashi Yamaguchi

Polyhedron 24 (2005) 2238

Density functional study of zero-field splitting

The zero-field splitting (ZFS) parameters of some basic molecules and a single-molecule magnet [Mn(III)Cu(II)(Br-sap)2Cl(MeOH)] are calculated with the density functional theory (DFT). The DFT is applied to calculating ZFS parameters caused by 1-electron spin-orbit coupling (SOC). The pure DFT methods are in good agreement with the high-precision CI or MCSCF methods.

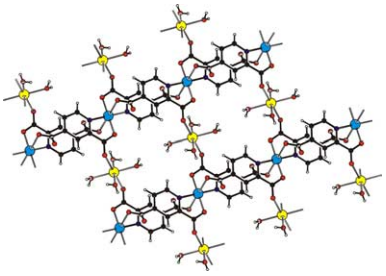


Brian O. Patrick, Cecilia L. Stevens, Alan Storr, Robert C. Thompson

Polyhedron 24 (2005) 2242

Coordination polymers incorporating copper(II) and manganese(II) centers bridged by pyridinedicarboxylate ligands: Structure and magnetism

The heterobimetallic coordination polymers, $[Cu(2,4\text{-pydc})_2Mn(H_2O)_4]_x$ (**1**) and $[Cu(2,5\text{-pydc})_2Mn(H_2O)_2]_x \cdot 4xH_2O$ (**2**), have extended 2-D sheet structures. Ferromagnetic exchange between O–C–O bridged copper and manganese centers dominates the magnetic properties of **1** while the magnetic data for **2** fit well to a model incorporating antiferromagnetic exchange in independent $S = 1/2$ and $S = 5/2$ linear chains.

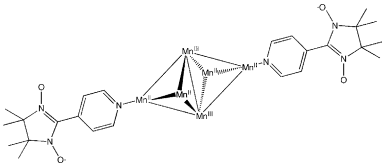


Kazuya Nakata, Hitoshi Miyasaka, Fumiyasu Iwahori, Ken-ichi Sugiura, Masahiro Yamashita

Polyhedron 24 (2005) 2250

A mixed-valence Mn_6 cluster capped by nitronyl nitroxide units

A mixed-valence Mn_6 cluster attached with nitronyl nitroxide radical molecules was synthesized and structurally and magnetically investigated. The compound has a linear array form of [(NNPy)–Mn_6–(PyNN)], where PyNN is 2-(*p*-pyridyl)-4,4,5,5-tetramethylimidazoline-1-oxyl-3-oxide and coordinates to Mn^{II} ion in pyridine-N site. DC susceptibility and ESR measurements revealed that the Mn_6 and NNPy moieties act individually as paramagnetic centers.

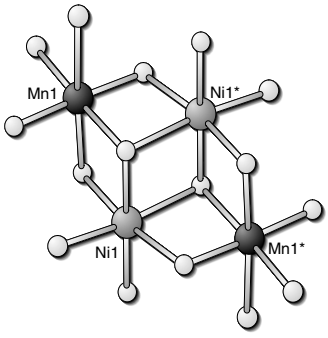


Masayuki Koikawa, Masaaki Ohba, Tadashi Tokii

Polyhedron 24 (2005) 2257

Syntheses, structures, and magnetic properties of tetranuclear Ni_4^{II} and $Ni_2^{II}Mn_2^{III}$ complexes with *ONO* tridentate ligands

Tetranuclear Ni_4^{II} and $Ni_2^{II}Mn_2^{III}$ complexes with a unique defective double-cubane core connected by μ_3-alkoxo bridges of *N*-(2-hydroxymethylphenyl)salicylideneimine have been characterized by X-ray crystal structure analyses and magnetic measurements. Magnetic susceptibility measurements revealed an $S = 6$ ground state of $Ni_2^{II}Mn_2^{III}$ double-cubane.

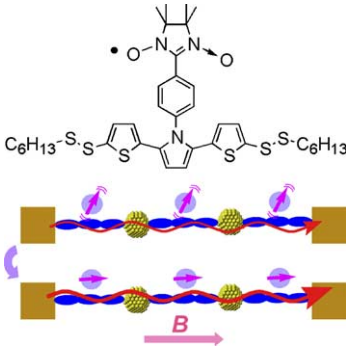


Masaru Minamoto, Michio M. Matsushita, Tadashi Sugawara

Polyhedron 24 (2005) 2263

Construction of a network structure composed of gold nanoparticles and spin-polarized molecular wires and its conducting and magnetic properties

This is the first demonstration of the negative magneto-resistance in the networked gold nano-particles connected with spin-polarized molecular wires. It is a direct proof for the communication between tunneling electrons migrating among nano-particles through the molecular wires and localized spins residing on them.

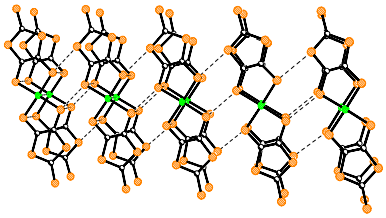


Youcun Chen, Guangxiang Liu, You Song, Heng Xu, Xiaoming Ren, Qingjin Meng

Polyhedron 24 (2005) 2269

Molecular spin ladders self-assembly from $[Ni(dmit)_2]^-$ building blocks: Syntheses, structures and magnetic properties

Two-leg ladder packing structure consisted from the dimers of $[Ni(dmit)_2]^-$ was observed in two ion-pair compounds. The magnetic susceptibilities measured in range of 2–300 K indicated AFM exchange interaction dominatoin both two compounds. A peculiar magnetic transition occurs at ~100 K in compound **1**, and an AFM ordering happens below ~11 K in **2**.

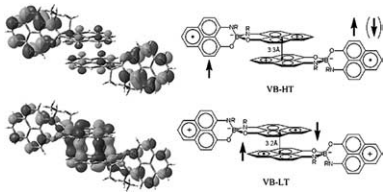


Takeshi Taniguchi, Takashi Kawakami, Kizashi Yamaguchi

Polyhedron 24 (2005) 2274

A theoretical study of electronic structures and intermolecular magnetic interactions for spiro-biphenalenyls

In order to inquire into the mechanism of the change in the magnetism of spiro-biphenalnyls, intermolecular magnetic interaction is investigated in terms of the effective exchange integral of the Heisenberg model for dimeric pairs of diethyl-substituted spiro-biphenalenyl. Variation of the magnetic interaction with respect to temperature is evaluated for X-ray crystallographic structures at several temperature points by Kohn–Sham hybrid-DFT. The intermolecular magnetic interactions were calculated for the π-dimers to be antiferromagnetic at each temperature.

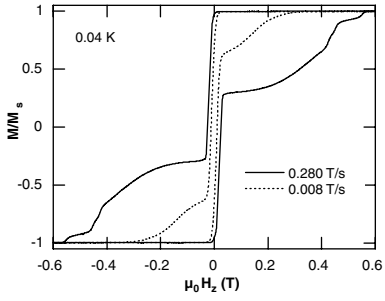


David N. Hendrickson, En-Che Yang, Rose Marie Isidro, Cem Kirman, Jon Lawrence, Rachel S. Edwards, Stephen Hill, Akira Yamaguchi, Hidehiko Ishimoto, Wolfgang Wernsdorfer, Chris Ramsey, Naresh Dalal, Marilyn M. Olmstead

Polyhedron 24 (2005) 2280

Origin of the fast magnetization tunneling in tetranuclear nickel single-molecule magnets

The single-molecule magnet behavior of Ni_4 complexes is characterized by magnetization hysteresis loops. The origin of the fast magnetization tunneling is the result of transverse quartic zero-field interactions (the B_4^4 term in the spin Hamiltonian) as indicated by high-field EPR experiments. The presence of ligand dynamics that become static at low temperatures and are the origin of the splitting of EPR signals observed at low temperature is confirmed by heat capacity and low temperature X-ray crystallography experiments.

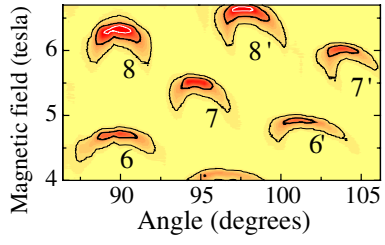


S. Hill, N. Anderson, A. Wilson, S. Takahashi, K. Petukhov, N.E. Chakov, M. Murugesu, J.M. North, E. del Barco, A.D. Kent, N.S. Dalal, G. Christou

Polyhedron 24 (2005) 2284

A comparison between high-symmetry Mn_{12} single-molecule magnets in different ligand/solvent environments

A multi-high-frequency/high-field EPR technique is used to study single crystal samples of three high-symmetry Mn_{12} single-molecule magnets (SMMs): Mn_{12}-Ac, Mn_{12}-BrAc and Mn_{12}-*t*BuAc. The two newer complexes (Mn_{12}-BrAc and Mn_{12}-*t*BuAc) show much sharper EPR peaks, and none of the fine structures seen for the Mn_{12}-Ac complex, thus confirming that the acetic acid solvent significantly influences the properties of this well studied SMM. Indeed, the EPR spectra for Mn_{12}-BrAc and Mn_{12}-*t*BuAc provide spectacular resolution, allowing for unique spectroscopic insights into high-symmetry giant spin SMMs.

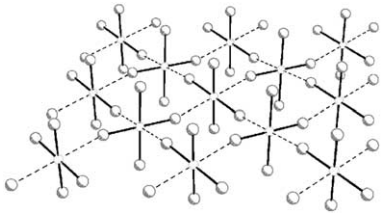


Roger D. Willett, Carlos J. Gómez-García, Brendan Twamley

Polyhedron 24 (2005) 2293

Structure and magnetic properties of $[(R\text{EDA})Cl]_2CuCl_4$ salts: A new series of ferromagnetic layer perovskites

Two new hybrid organic/inorganic layered perovskite systems, based on *N*-substituted ethylenediammonium salts of copper(II) chloride, have been synthesized. The antiferrodistorive arrangement of Jahn–Teller elongated octahedra leads to ferromagnetic intralayer coupling. The compounds undergo three dimensional ferromagnetic long range ordering at ~9 K as revealed by the presence of hysteresis loops in the M versus H data.

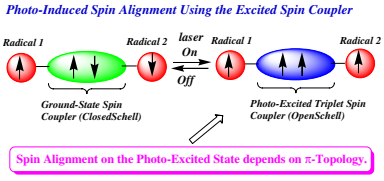


Yoshio Teki

Polyhedron 24 (2005) 2299

Topology and spin alignment utilizing the excited molecular field in π-conjugated organic spin systems

The photo-induced spin alignment and the excited high-spin states of π-conjugated organic spin systems are reviewed. The relationship between the π-topology and spin alignment on the photo-excited states is clarified and the role of the spin polarization and spin delocalization in the spin alignment are revealed.

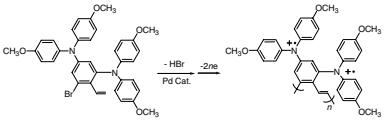


Hidenori Murata, Ryosuke Takada, Hiroyuki Nishide

Polyhedron 24 (2005) 2309

Poly[4,6-bis(bis(4-methoxyphenyl)aminium)-1,2-phenylenevinylene]: A high-spin and durable polyradical

A purely organic and high-spin polyradical molecule was synthesized, along the non-Kekulé- and non-disjoint design of the π-conjugated poly(1,2-phenylenevinylene) backbone pendantly 4,6-substituted with the robust arylaminium radicals. A high-spin ground state with an average $S = 5/2$ for this polyradical was proved by magnetic susceptibility and ESR.

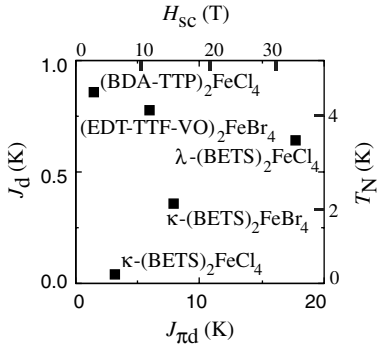


Takehiko Mori, Mao Katsuhara, Hiroki Akutsu, Koichi Kikuchi, Jun-ichi Yamada, Hideki Fujiwara, Takuya Matsumoto, Toyonari Sugimoto

Polyhedron 24 (2005) 2315

Estimation of πd-interactions in magnetic molecular conductors

Calculated J_d and $J_{\pi d}$ values of a new antiferromagnetic superconductor $(BDATTP)_2FeCl_4$ and a semiconducting ferrimagnet $(EDT\text{-}TTF\text{-}VO)_2FeBr_4$ compared with the BETS salts. In the right scale, J_d is converted to T_N and in the upper scale $J_{\pi d}$ is converted to the center field of the field induced superconducting phase.

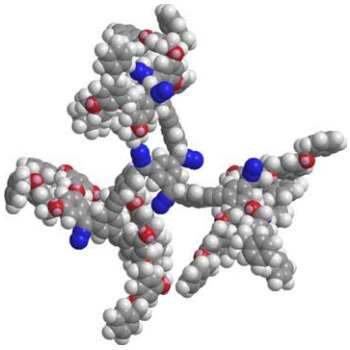


Takeyuki Akita, Noboru Koga

Polyhedron 24 (2005) 2321

Magnetic properties of dendritic polycarbenes substituted by bulky peripheral groups

Three photo-reactive precursors of high-spin organic compounds sterically separated from surroundings by Fréchet-type dendrons, bis{3,5-bis[3′,5′-bis(benzyloxy)benzyloxy]phenyl}diazomethane **1**, bis{3,5-bis{3′,5′-bis[3″,5″-bis(benzyloxy)benzyloxy]bezyloxy}phenyl}diazomethane **2**, and dodecakis[3,5-bis(benzyloxy)benzyloxy]nonakisdiazo compound **3**, were prepared and their magnetic properties after irradiation in their own condensed films were investigated.

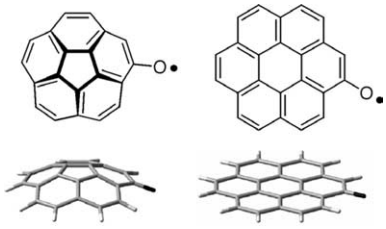


Kozo Fukui, Yasushi Morita, Shinsuke Nishida, Tadahiro Kobayashi, Kazunobu Sato, Daisuke Shiomi, Takeji Takui, Kazuhiro Nakasuji

Polyhedron 24 (2005) 2326

Deflected spin transmission from radical substituent to Corannulene's curved surface: Density functional theory calculations

Density functional theory calculations for a series of corannulene-based neutral π-radicals have revealed the unevenly distributed spin densities on the curved surface as well as the degree of spin delocalizations. Their electronic structures have been discussed in comparison with that of a coronene-based neutral radical with a flat surface structure.

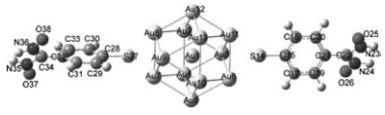


Okumura Mitsutaka, Kitagawa Yasutaka, Taniguchi Takeshi, Yamaguchi Kizashi

Polyhedron 24 (2005) 2330

Theoretical studies of magnetic interaction in organic π-radical and gold cluster hybrid systems

In order to elucidate the magnetic interaction in gold nanoparticles chemisorbed by alkanethiol systems, small gold cluster, such as Au_3 and Au_{13}, and π-radical hybrid model systems were examined using the hybrid DFT method.

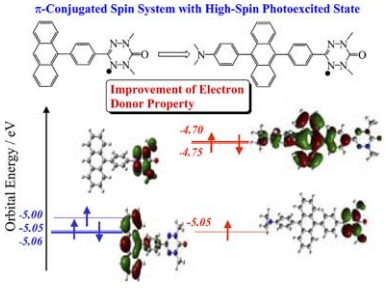


Tetsuya Toichi, Yoshio Teki

Polyhedron 24 (2005) 2337

Design, synthesis and physical property of a π-conjugated photo-excited organic high-spin systems toward the functional material

A design, synthesis and electronic state of a π-conjugated stable verdazyl radical, **1**, are reported, which has a photo-excited quartet high-spin state and the electron donor property is improved by an attachment of dimethylamino group. A CT complex **1**-BQF_4 was also synthesized using **1** as an electron donor.

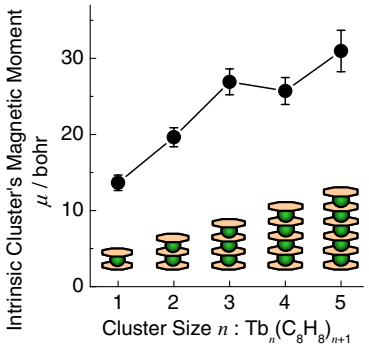


Ken Miyajima, Mark B. Knickelbein, Atsushi Nakajima

Polyhedron 24 (2005) 2341

Magnetic properties of lanthanide organometallic sandwich complexes produced in a molecular beam

The magnetic properties of gas-phase terbium–cyclooctatetraene multi-decker sandwich complexes, $Tb_n(C_8H_8)_{n+1}$, were measured using a Stern-Gerlach type magnetic deflection approach. The drop of the magnetic moment for $Tb_4(C_8H_8)_5$ implies antiferromagnetic interaction of adjacent Tb^{2+} ions at the central portion of the complex.

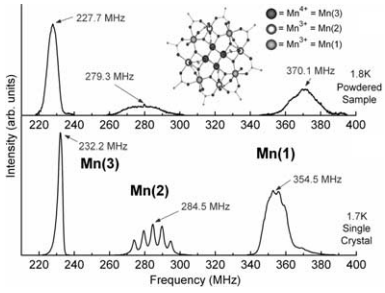


A.G. Harter, N.E. Chakov, R. Achey, A. Reyes, P. Kuhns, G. Christou, N.S. Dalal

Polyhedron 24 (2005) 2346

^{55}Mn NMR spectra of Mn_{12} single-molecule magnets: Single crystal versus aligned powder studies

Zero field ^{55}Mn NMR was performed on Mn_{12}–BrAc as a single crystal and as an aligned powder. The spectrum from the single crystal shows a great increase in resolution and thus provides greater insight into the magnetic structure of these molecules.

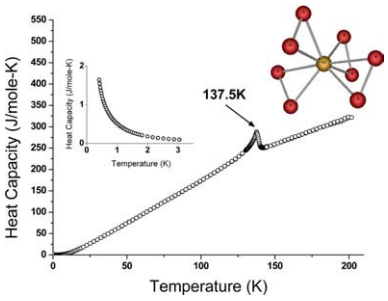


A. Harter, B. Cage, P. Nguyen, K.A. Abboud, N.S. Dalal

Polyhedron 24 (2005) 2350

$(NH_4)_3CrO_8$: A new $S = 1/2$ system exhibiting no magnetic transition down to 0.3 K

We here report the synthesis, crystal structure, and magnetic and thermodynamic characterization of ammonium peroxychromate, $(NH_4)_3CrO_8$, a new compound of Cr(5+), with a $3d_{x^2-y^2}$, $S = 1/2$ ground state, with about 92% molecules devoid of any metal hyperfine interaction. It is the first Cr(5+) compound exhibiting a structural phase transition (at 137.5 K) tentatively assigned to the order–disorder motion of the NH_4^+ ions, but it remains paramagnetic down to 0.3 K. The compound is stable for years if stored in a refrigerator, but it could explode if crushed or subjected to high pressure, or heated to well above room temperature.

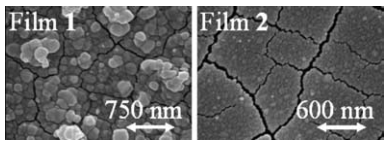


J.-H. Park, F. Frye, S. Lane, E. Čižmár, Y.D. Huh, D.R. Talham, M.W. Meisel

Polyhedron 24 (2005) 2355

Photoinduced magnetic properties of sequentially deposited thin films of $Rb_jCo_k[Fe(CN)_6]_l \cdot nH_2O$

Photoinduced magnetic films of $Rb_jCo_k[Fe(CN)_6]_l \cdot nH_2O$ were generated to have two different surface textures (film **1** and film **2**). Upon irradiation at 5 K with an external magnetic field of 200 G perpendicular to the film surface, the magnetization of film **1** increased, whereas the magnetization of film **2** *decreased*. This contrasting behavior is consistent with a dipolar field model describing the phenomena and is related to the novel anisotropy of the photoinduced magnetism in film **2**, where the photoinduced magnetization increases or decreases depending on the orientation of the film with respect to the external field.

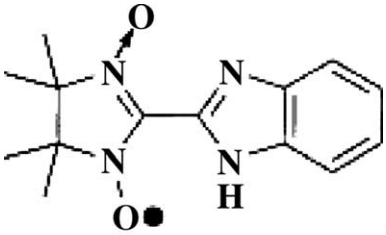


Sonia Sharmin, Stephen J. Blundell, Tadashi Sugano, Arzhang Ardavan

Polyhedron 24 (2005) 2360

Millimetre-wave studies on single crystals of the organic radical 2-benzimidazolyl nitronyl nitroxide

Temperature dependent, angle dependent and frequency dependent millimetre wave spectroscopic studies on single crystals of the organic molecular magnet 2-benzimidazolyl nitronyl nitroxide have been reviewed. The linewidths and resonance fields of the electron spin resonance spectra at low temperatures were particularly observed in detail.



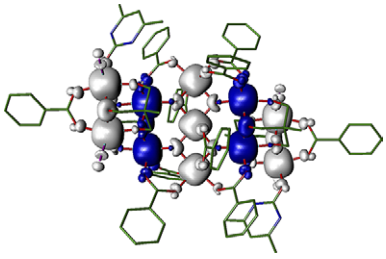
2-BIMNN

Eliseo Ruiz, Joan Cano, Santiago Alvarez

Polyhedron 24 (2005) 2364

An Fe_{11} complex showing single-molecule magnet behavior: Theoretical study using density functional methods and Monte Carlo simulations

An Fe_{11} complex that shows single-molecule magnet behavior has been studied using theoretical methods based on Density Functional Theory combined with Monte Carlo Simulations. Its exchange coupling constants have been calculated and the theoretical magnetic susceptibility is compared with the experimental data. The results obtained extend the conclusions reached previously for other polynuclear Fe(III) complexes with the same bridging ligands, showing similar exchange interactions.

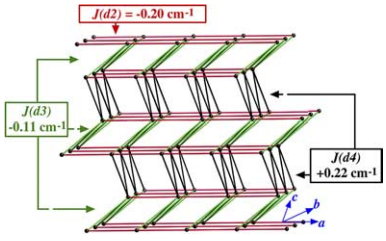


Mercè Deumal, Michael A. Robb, Juan J. Novoa

Polyhedron 24 (2005) 2368

Quantitative analysis of the magnetism of the *meta*-(methoxy)phenyl nitronyl nitroxide crystal: A *bottom–up* analysis of a crystal presenting competing ferro and antiferromagnetic interactions

The magnetic topology of the *m*-(OMe)PhNN crystal consists of bent *bc*-planes defined by FM *J(d3)* and AFM *J(d4)* pair interactions that form a three-dimensional network by means of AFM *J(d2)* exchange interactions. This complex network of competing FM and AFM pathways does not allow a sounding prediction of the macroscopic magnetic susceptibility $\chi(T)$ using qualitative arguments. Our first principles *bottom-up* theoretical procedure numerically computes the χT versus T curve that fully reproduces the experimental shape. Preliminary tests have been carried out in order to uncover the changes needed to modify the dominant AFM behavior of the *m*-(OMe)PhNN crystal into a dominant FM behavior.

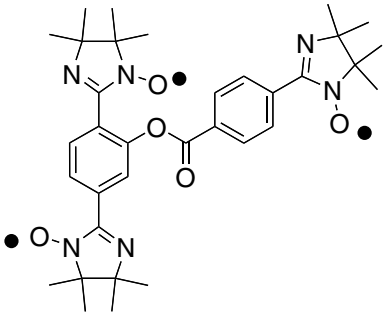


Tomoaki Ise, Daisuke Shiomi, Kazunobu Sato, Takeji Takui

Polyhedron 24 (2005) 2377

Magnetic properties of nitronylnitroxide and iminonitroxide triradicals as model compounds for generalized ferrimagnets

An iminonitroxide triradical (**1**) has been synthesized, in which a ground-state singlet π-biradical and a π-monoradical are united by σ-bonds. The ground state of the molecular assemblage of **1** has been found to be nonmagnetic, which is attributable to an exotic spin alignment predicted in the theory of generalized ferrimagnetism.

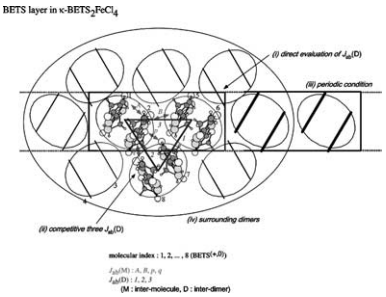


Takashi Kawakami, Takeshi Taniguchi, Mitsuo Shoji, Yasutaka Kitagawa, Mitsutaka Okumura, Kizashi Yamaguchi

Polyhedron 24 (2005) 2382

Theoretical direct evaluation of inter-dimer *J* values in BETS salts

Inter-dimer magnetic interactions ($J_{ab(D)}$) between BETS donors in the κ-$BETS_2FeCl_4$ crystal were studied theoretically by using of ab initio MO and DFT methods. These interaction parameters can describe spin properties. In cluster of four BETS molecules with two holes, more accurate $J_{ab(D)}$ values were evaluated directly, though such $J_{ab(D)}$ values were already evaluated from inter-molecular magnetic interaction ($J_{ab(M)}$) with the approximate equation $J_{ab(D)} = J_{ab(M)}/2$. In cluster of six molecules with three holes, competition of three antiferromagnetic interaction was discussed. Necessity of calculation under periodic condition and for surrounding cluster was introduced.

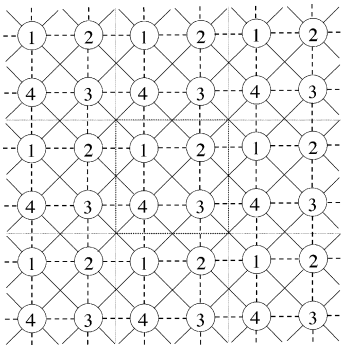


Hidemi Nagao

Polyhedron 24 (2005) 2389

Spin susceptibility in many-band system

We present a two-dimensional 4-sublattice square lattice system, and investigate 4-band effects in magnetism by using spin susceptibility. The spin susceptibility of the sublattice system is calculated. The present results suggest that many-band systems doped with hole have some interesting magnetic properties.

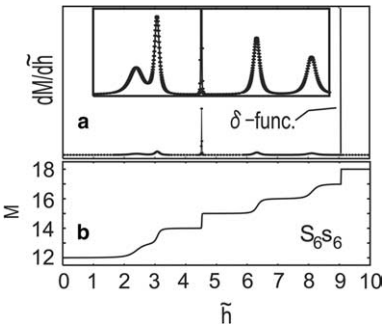


Shun Tonooka, Koichi Kusakabe, Hiroki Nakano, Naoshi Suzuki

Polyhedron 24 (2005) 2396

Size dependence of the magnetic properties in ferrimagnetic rings Mn_xR_x (x = 2–8)

A theoretical calculation shows remarkable size dependence of the magnetization process in the nanoscale ferrimagnetic rings S_xs_x due to the frustration effect. Qualitatively different spin states appear in each molecule. This size dependence can be utilized as a finger print of each molecule.

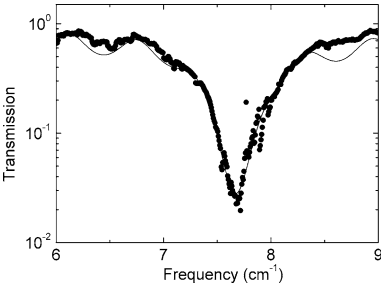


Nadeschda Kirchner, Joris van Slageren, Euan K. Brechin, Martin Dressel

Polyhedron 24 (2005) 2400

Frequency domain magnetic resonance spectroscopy on $[Mn_{12}]^-$ and $[Mn_9]$: Zero-field splittings and lineshape analysis

The zero-field splitting parameters of two non-integer spin single molecule magnets, $[Mn_{12}]^-$ and $[Mn_9]$ were determined using frequency domain magnetic resonance spectroscopy. Interestingly, the resonance line is homogeneously broadened in the case of $[Mn_{12}]^-$.

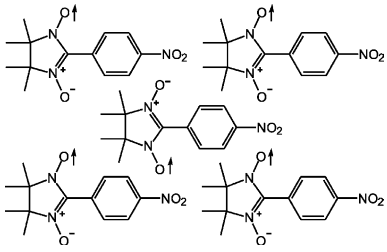


Naoki Shirakawa, Masafumi Tamura

Polyhedron 24 (2005) 2405

Low temperature static magnetization of an organic ferromagnet, β-*p*-NPNN

A ^{3}He refrigerator mountable to a commercial SQUID magnetometer has been used to measure static magnetizations of the first organic ferromagnet, β-*p*-NPNN. The study has revealed that its saturation magnetization is exactly 1 μ_B per molecule unlike the previous study with a dynamical method.

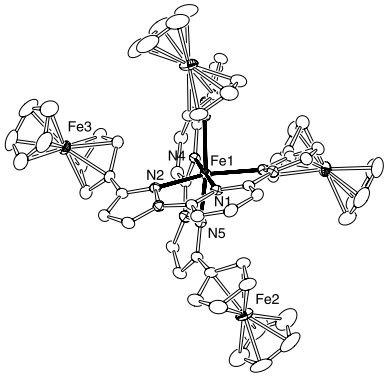


Lingqin Han, Masayuki Nihei, Hiroki Oshio

Polyhedron 24 (2005) 2409

Synthesis, structure and physical properties of an iron(II) complex with four ferrocenyl groups

Novel tridentate ligand with two ferrocenyl groups and its iron(II) complex were synthesized and these structures and physical properties are presented. The central iron(II) ion was coordinated by two tridentate ligands to yield a pentanuclear complex composed of one central ion(II) and four ferrocenyl groups. The redox process of iron(II) complex can be understood by the EC mechanism.

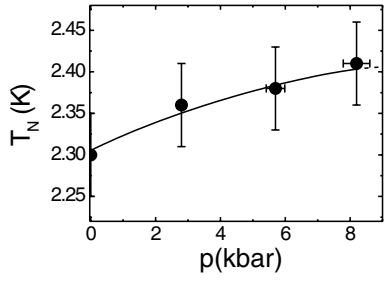


J. Kreitlow, C. Mathonière, R. Feyerherm, S. Süllow

Polyhedron 24 (2005) 2413

Pressure response of the bimetallic chain compound $MnNi(NO_2)_4(en)_2$; en = ethylenediamine

This paper presents the pressure-induced enhancement of the transition temperature in the bimetallic chain compound $MnNi(NO_2)_4(en)_2$.

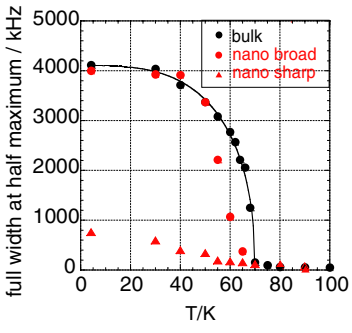


Ryuta Washiya, Goro Maruta, Sadamu Takeda

Polyhedron 24 (2005) 2417

Microscopic study on spin state of nanoparticles of antiferromagnet: ND_4MnF_3

Magnetic behavior of near-surface spins of nano-scale particle was microscopically investigated for antiferromagnetic compound of ND_4MnF_3. It was found that critical behavior of the nano-particles with approaching the Néel temperature is clearly different from the bulk sample, while internal magnetic field of the nano-particles in the low temperature limit is almost the same as that of bulk sample. Near-surface spins of nano-particles in the antiferromagnetic phase were distinguished from the inner spins by wide-line deuterium NMR spectrum.

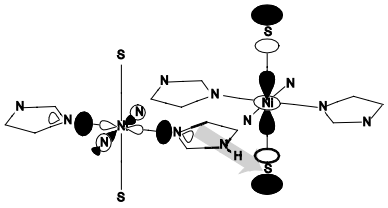


Goro Maruta, Sadamu Takeda

Polyhedron 24 (2005) 2424

Solid-state high-resolution NMR studies on spin density distribution of a ferromagnetic coordination polymer: $Ni(NCS)_2(Him)_2$

We determined hyperfine coupling constants of the imidazole ligand in a ferromagnetic coordination polymer, di-μ-thiocyanatobis-(imidazole)nickel(II), using ^1H-, ^2H-, and ^{13}C-MAS-NMR. An interchain superexchange pathway through N–S hydrogen bond was proposed on the basis of the delocalization of the unpaired electron in $d_{x^2-y^2}$ orbital of Ni(II) ion over the imidazole ligands.

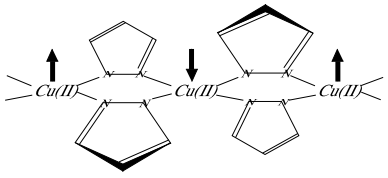


Takayuki Oomomo, Goro Maruta, Sadamu Takeda

Polyhedron 24 (2005) 2431

Magnetic interactions of (μ-pyrazolato)-bridged copper(II) complexes determined by solid-state MAS NMR

Bis-μ-pyrazolato-bridged copper(II) complexes, $[Cu(pz)_2]_n$ and $[Cu_2(pz)_2(NO_3)(H_2O)(phen)_2]NO_3$, were investigated by solid-state high-resolution deuterium and carbon-13 NMR. We found delocalized electron spin on H and C atoms of the bridging ligands. We conclude that the σ-orbital system of the ligand is the dominant magnetic interaction pathway.

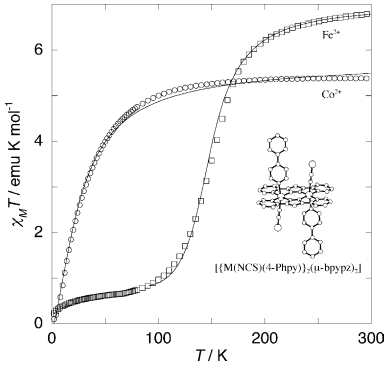


Ko Yoneda, Keisaku Nakano, Junji Fujioka, Koichi Yamada, Takayoshi Suzuki, Akira Fuyuhiro, Satoshi Kawata, Sumio Kaizaki

Polyhedron 24 (2005) 2437

Synthesis, structure and magnetic properties of pyrazolate-bridged dinuclear complexes $[\{M(NCS)(4\text{-Phpy})\}_2(\mu\text{-bpypz})_2]$ (M = Co^{2+} and Fe^{2+})

The dinuclear iron(II) complex $[\{Fe(NCS)(4\text{-Phpy})\}_2(\mu\text{-bpypz})_2]$ displays a single, sharp spin crossover transition between the [HS–HS] and [LS–LS] state with T_c = 150 K while no spin transition occurs in the corresponding cobalt(II) complex.

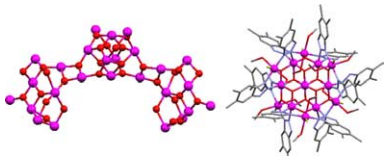


Leigh F. Jones, Jim Raftery, Simon J. Teat, David Collison, Euan K. Brechin

Polyhedron 24 (2005) 2443

Manganese (III) fluoride as a new synthon in Mn cluster chemistry

The syntheses and structures of five new Mn^{3+} clusters are reported, thereby demonstrating the utility of MnF_3 as a new synthon in Mn cluster chemistry.

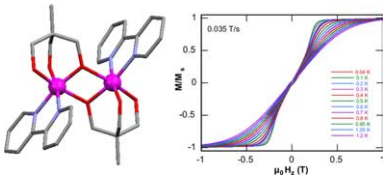


Gopalan Rajaraman, E. Carolina Sañudo, Madeleine Helliwell, Stergios Piligkos, Wolfgang Wernsdorfer, George Christou, Euan K. Brechin

Polyhedron 24 (2005) 2450

Magnetic and theoretical characterization of a ferromagnetic Mn(III) dimer

Magnetic measurements on the dimeric species $[Mn_2(Hthme)_2(bpy)_2](ClO_4)_2$ reveal weak ferromagnetic exchange between the metal centres with $J = +2.13\ cm^{-1}$, $S = 4$, $g = 1.71$ and $D = -0.65\ cm^{-1}$. Single crystal measurements suggest the co-existence of SMM behaviour and strong intermolecular interactions.

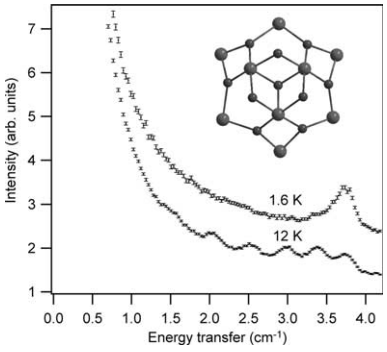


Roland Bircher, Grégory Chaboussant, Stefan T. Ochsenbein, Felix Fernandez-Alonso, Hans U. Güdel, Euan K. Brechin

Polyhedron 24 (2005) 2455

Inelastic neutron scattering study of undeuterated $[Mn_9O_7(OAc)_{11}(thme)(py)_3(H_2O)_2]$

Inelastic neutron scattering spectra of the title compound have been measured at $\lambda = 6.5$ Å and $T = 1.6$ and 12 K, respectively. The peaks observed in this figure enabled accurate determination of the zero field splitting parameters of this single molecule magnet.

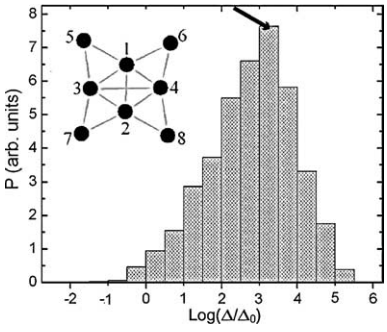


S. Carretta, E. Liviotti, N. Magnani, P. Santini, G. Amoretti

Polyhedron 24 (2005) 2459

Quantum tunneling of the magnetization in molecular nanomagnets: The crucial role of *S* mixing

The role of *S* mixing in the quantum tunneling of the magnetization has been investigated for $[Fe_8O_2(OH)_{12}(tacn)_6]^{8+}$. The effect of *S* mixing on the tunnel splitting Δ is huge and the discrepancy (more than 3 orders of magnitude in the tunneling frequency) between spectroscopic and relaxation measurements can finally be resolved.

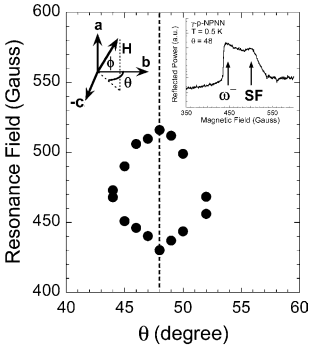


K. Kajiyoshi, T. Kambe, K. Oshima, M. Tamura, M. Kinoshita

Polyhedron 24 (2005) 2464

Antiferromagnetic resonance in quasi-one-dimensional ferromagnet γ-*p*-NPNN

Antiferromagnetic resonance and magnetic torque measurements using piezo-resistive cantilever were performed in the ordered state of γ-phase of *para*-Nitrophenyl Nitronyl Nitroxide below 0.6 K. A spin-flop transition and AF-paramagnetic transition are observed around 470 Gauss and 2100 Gauss at 0.4 K, respectively. The spin-easy axis is almost parallel to the direction to phenyl ring from the ONCNO fragments.

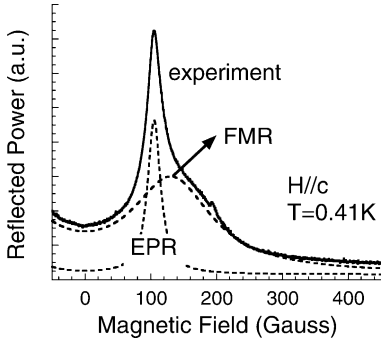


T. Kambe, K. Kajiyoshi, K. Oshima, M. Tamura, M. Kinoshita

Polyhedron 24 (2005) 2468

Ferromagnetic resonance in β-*p*-NPNN at radio-frequency region

FMR were re-investigated at radio-frequency region using spherically molded single crystals of β-*p*-Nitrophenyl Nitronyl Nitroxide. The symmetric FMR signals were clearly observed below 0.8 K for the first time. The resonance field for H//*c* is markedly shifted about 80 Gauss higher than the EPR resonance field. These results clearly indicate the spin-hard axis is parallel to the *c*-axis. The magnetic anisotropy H_K = 61 Gauss using the FMR relation with uniaxial anisotropy are estimated.



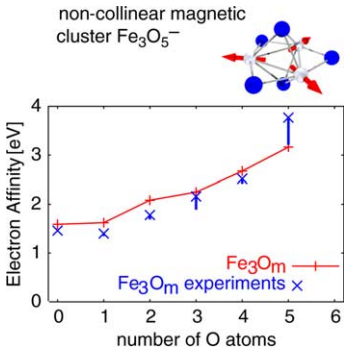
H. Shiroishi, T. Oda, I. Hamada, N. Fujima

Polyhedron 24 (2005) 2472

Structure and magnetism of anion iron oxide clusters, $Fe_nO_m^-$ $(n = 3, 4)$

We have studied structural and magnetic properties in the anion iron oxide clusters, $Fe_3O_m^-$ $(m = 1–5)$ and $Fe_4O_m^-$ $(m = 1–6)$, by means of the first-principles molecular dynamics based on the density functional theory.

The vertical detachment energy was estimated at the ground state geometry of anion clusters. The non-collinear magnetic cluster was stabilized at $Fe_3O_5^-$.

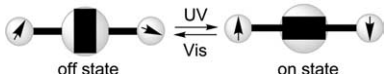


Kenji Matsuda, Masahiro Irie

Polyhedron 24 (2005) 2477

Effective photoswitching of intramolecular magnetic interaction by diarylethene: Backgrounds and applications

Effective photoswitching of intramolecular magnetic interaction by diarylethene is discussed extensively.

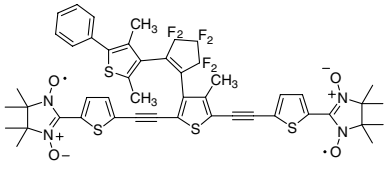


Naoki Tanifuji, Kenji Matsuda, Masahiro Irie

Polyhedron 24 (2005) 2484

Synthesis of a new diarylethene diradical which has extended π-conjugated chains from the 2,5-position of one thiophene ring

This paper describes the synthesis of a new diarylethene having nitronyl nitroxide radicals and discusses its photochemical behavior. Upon irradiation with UV light, photochromic reaction did not take place. Two radicals in the open-ring isomer have the intramolecular exchange interaction $(0.04\ \mathrm{K} < |2J/k_B|)$ and contribution of quinoid structure suppressed photocyclic reaction.

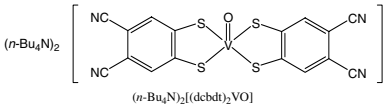


Tomoki Suzuki, Kazumasa Ueda, Ryusuke Kita, Satoshi Kokado, Kikuo Harigaya

Polyhedron 24 (2005) 2491

Synthesis, crystal structure and magnetic property of bis(tetra-*n*-butylammonium) bis(4,5-dicyanobenzene-1,2-dithiolato) oxo-vanadium complex

(n-$Bu_4N)_2[(dcbdt)_2VO]$ (dcbdt = 4,5-dicyanobenzene-1,2-dithiolato), was obtained from the reaction of Na_2dcbdt and vanadium trichloride. The ESR and SQUID measurement showed that the vanadium atom is in the state of V(IV) (S = 1/2) and these magnetic moments interact with each other very weakly antiferromagnetically ($\theta = -0.371$ K).

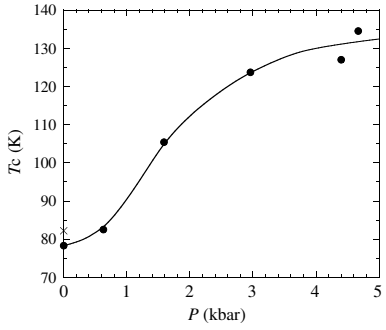


Takuho Maeda, Masaki Mito, Hiroyuki Deguchi, Seishi Takagi, Wakako Kaneko, Masaaki Ohba, Hisashi Ōkawa

Polyhedron 24 (2005) 2497

Pressure effects on a dimetallic ferrimagnet $[Mn(en)]_3[Cr(CN)_6]_2 \cdot 4H_2O$

This paper presents the pressure-induced enhancement of the transition temperature in a dimetallic ferrimagnet $[Mn(en)]_3[Cr(CN)_6]_2 \cdot 4H_2O$, which has an eminent high transition temperature of 69 K in the structurally characterized molecule-based magnet system.

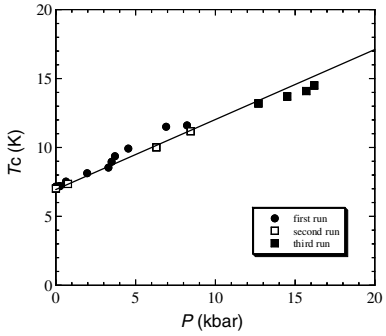


Masaki Mito, Masatsugu Fujino, Hiroyuki Deguchi, Seishi Takagi, Wataru Fujita, Kunio Awaga

Polyhedron 24 (2005) 2501

Pressure effects on an organic radical ferromagnet γ-phase BBDTA · $GaCl_4$

This paper presents the pressure-induced enhancement of the Curie temperature in the ferromagnetic phase of BBDTA · $GaCl_4$.

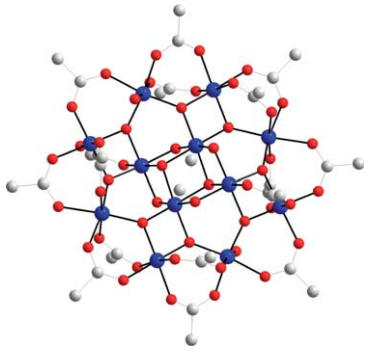


Anastasios J. Tasiopoulos, Wolfgang Wernsdorfer, Khalil A. Abboud, George Christou

Polyhedron 24 (2005) 2505

Two isomeric $[Mn_{12}O_{12}(OMe)_2(O_2CPh)_{16}(H_2O)_2]^{2-}$ single-molecule magnets and a Mn^{III} polymer prepared by a reductive aggregation synthetic route

Two isomeric $[Mn_{12}O_{12}(OMe)_2(O_2CPh)_{16}(H_2O)_2]^{2-}$ complexes (see core structure; blue Mn, red O, gray C) and the polymer $[Mn(OMe)(O_2CPh)_2]_n$ were the first products isolated by a new synthetic procedure in Mn cluster chemistry involving reductive aggregation of permanganate (MnO_4^-) ions in MeOH/benzoic acid. The new Mn_{12} anions are structural variants of the well known $[Mn_{12}]$ family of SMMs and exhibit SMM properties, whereas the polymer is antiferromagnetically coupled with a diamagnetic ground state.

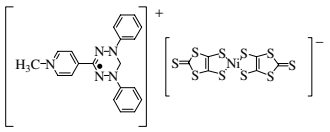


Kazuo Mukai, Daisuke Shiba, Kyohei Mukai, Kenji Yoshida, Hiroyuki Hisatou, Keishi Ohara, Yuko Hosokoshi, Nagao Azuma

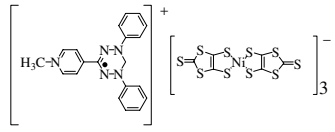
Polyhedron 24 (2005) 2513

Magnetic semiconductors: Molecular materials based on alkyl-pyridinium-substituted verdazyl radical cations and $Ni(dmit)_2$ anion

Five kinds of (1:1) and (1:3) salts of 3-(3- and 4-alkyl-pyridinium)-1,5-diphenylverdazyl (alkyl = ethyl and methyl) radical cations with $Ni(dmit)_2$ anion have been prepared, and found to be new paramagnetic semiconductors.



$[p\text{-MePyDV}]^+[Ni(dmit)_2]^-$



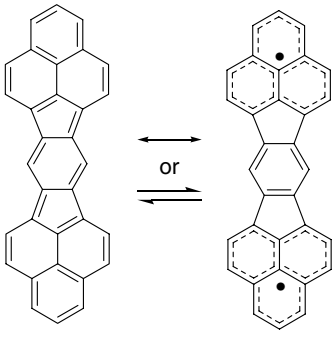
$[p\text{-MePyDV}]^+[Ni(dmit)_2]_3^-$

Takashi Kubo, Maki Sakamoto, Kazuhiro Nakasuji

Polyhedron 24 (2005) 2522

Biradicaloid character of phenalenyl-based aromatic compounds with a small HOMO–LUMO gap

Theoretical and experimental considerations for the biradicaloid character of three phenalenyl-based compounds are described.

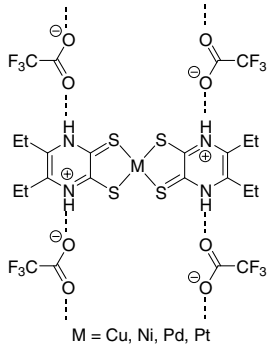


Takashi Kubo, Misako Ohashi, Hiroshi Kitagawa, Kazuhiro Nakasuji

Polyhedron 24 (2005) 2528

Magnetic interaction in 2D sheet structure of bis(1*H*, 4*H*-5,6-diethylpyrazinedithiolato) copper-(II) trifluoroacetate

The synthesis, structural characterization, and magnetic measurement of the protonated bis(pyrazindithiolato) metal complexes are described. The DFT calculation supports the paramagnetic behavior of the Cu complex.

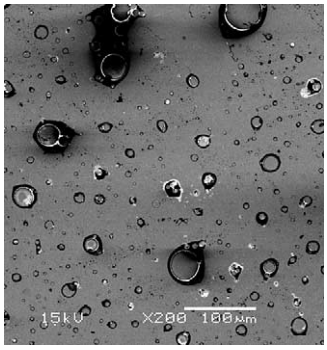


Kazumasa Ueda, Go Tanaka, Tomoki Suzuki, Ryusuke Kita, Satoshi Kokado

Polyhedron 24 (2005) 2533

Physical properties of thin filmed dithiolene vanadium complexes

We have successfully fabricated micro-scale ring structures together with porous, bead, two-dimensional network structures of $(n\text{-}Bu_4N)_2[(dcbdt)_2VO]$, (dcbdt = 4,5-dicyanobenzene-1,2-dithiolato), on several substrates using a simple and easy chemical deposition method under ambient or highly humidified conditions for the first time.

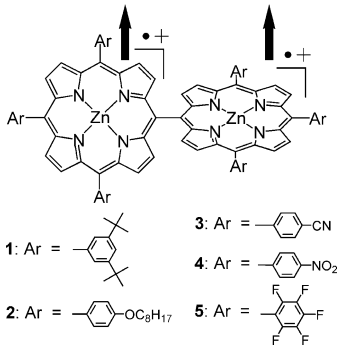


Jotaro Nakazaki, Yutaka Senshu, Hiroshi Segawa

Polyhedron 24 (2005) 2538

Modulative magnetic interaction in π-diradicals of directly *meso*-linked porphyrin dimers

A series of directly *meso*-linked Zn(II) porphyrin dimers were prepared, and properties of their bis(π-radical cation)s were investigated. ESR triplet signal kept almost same intensity at lower temperatures while it changed drastically at higher temperatures. The magnetic interaction was modulated by the electron-donating ability of the *meso*-aryl substituents.

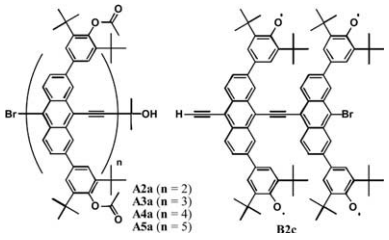


Takashi Kaneko, Akihisa Onuma, Hiroaki Ito, Masahiro Teraguchi, Toshiki Aoki

Polyhedron 24 (2005) 2544

Synthesis and magnetic characterization of monodisperse oligo(9,10-anthryleneethynylene)-based polyradicals with two pendant stable phenoxyls in one anthracene skeleton

Monodisperse oligo(9,10-anthryleneethynylene)s **A2a**–**A5a** were synthesized. The $2J$ (J: spin coupling constant through the dianthrylacetylene unit) value of the dimeric radicals **B2c** ($2J = 34 \pm 1$ cm^{-1}) indicates less steric hindrance between the side chain radicals and the poly(9,10-anthryleneethynylene) backbone.

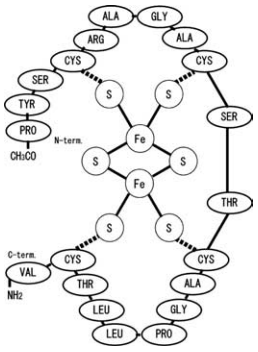


T. Oda, H. Nagao, A. Sugiyama, K. Wada

Polyhedron 24 (2005) 2550

Electronic structure and magnetism at the active site in ferredoxin: Ab initio approach to $(Fe_2S_2)^{2+}$ complex with the 1st peptide shell

The iron–sulfur cluster systems which model an active site of ferredoxine proteins have been studied with using the first priciples electronic structure calculation. We modeled them as a complex of the $(Fe_2S_2)^{2+}$ core and the 1st shell of amino acid residues. The hybridized orbitals consisting of N 2p and C 2p orbitals in the side chain of Arg residue locates just above the HOMO level for the cluster without having the salt bridge.

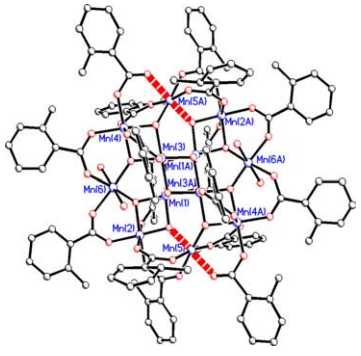


Evan M. Rumberger, Enrique del Barco, Jon Lawrence, Stephen Hill, Andrew D. Kent, Lev N. Zakharov, Arnold L. Rheingold, David N. Hendrickson

Polyhedron 24 (2005) 2557

Fast tunneling Jahn–Teller isomer of the $[Mn_{12}O_{12}(O_2CC_6H_4\text{-}2\text{-}CH_3)_{16}(H_2O)_4] \cdot S$ single-molecule magnet

A single-crystal X-ray structure reveals that the title compound is a new example of a "Jahn-Teller isomer" among Mn_{12} single-molecule magnets. A relatively small activation energy towards magnetization reversal is observed. High-frequency EPR and magnetization measurements have been collected for a single-crystal of this compound.

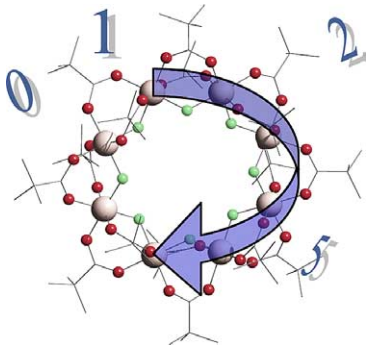


Marco Affronte, Filippo Troiani, Alberto Ghirri, Andrea Candini, Marco Evangelisti, Stefano Carretta, Paolo Santini, Giuseppe Amoretti, Stergios Piligkos, Grigore Timco, Richard E.P. Winpenny

Polyhedron 24 (2005) 2562

AF molecular rings for quantum computation

In this work we show that heterometallic molecular rings with dominant antiferromagnetic exchange coupling between nearest neighbors are suitable electronic spin systems for the implementation of quantum algorithms. One of the main advantage in using molecular clusters is the size of the qubit that will help in the addressing single quantum object. We also underline a further resource of molecular clusters made by their excited states that in a proper computational scheme may constitute an important feature to consider.

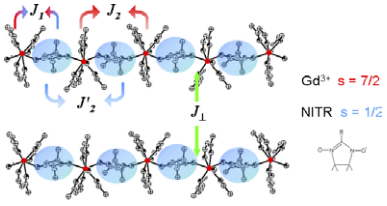


F. Cinti, M. Affronte, A. Lascialfari, M. Barucci, E. Olivieri, E. Pasca, A. Rettori, L. Risegari, G. Ventura, M.G. Pini, A. Cuccoli, T. Roscilde, A. Caneschi, D. Gatteschi, D. Rovai

Polyhedron 24 (2005) 2568

Chiral and helical phase transitions in quasi-1D molecular magnets

We review recent experimental and theoretical data obtained on quasi-one-dimensional molecular magnets Gd(hfac)$_3$NITR. For Gd(hfac)$_3$NITiPr is proposed a chiral order at intermediate temperature and an helical order at lower temperature, while for the compounds Gd(hfac)$_3$NITPh specific heat measurements show the presence of the only three-dimensional (helical order) transition one.

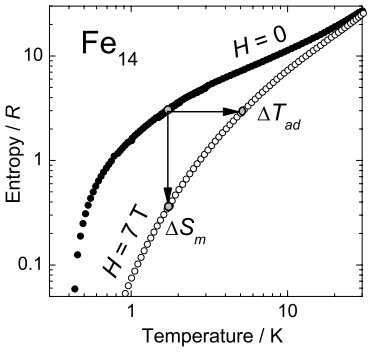


Marco Evangelisti, Andrea Candini, Alberto Ghirri, Marco Affronte, Stergios Piligkos, Euan K. Brechin, Eric J.L. McInnes

Polyhedron 24 (2005) 2573

Molecular nanoclusters as magnetic refrigerants: The case of Fe$_{14}$ with very large spin ground-state

We report on the magnetic and thermal properties of the Fe$_{14}$ molecular nanocluster. We find a huge magnetocaloric response in the temperature range below 10 K. This is to large extent caused by its very large spin ground-state combined with an excess of entropy arising from the admixture of low-lying excited S states. We also show that the high degree of symmetry of the Fe$_{14}$ cluster core, resulting in a very small cluster magnetic anisotropy, enables the occurrence of long-range antiferromagnetic order below T_N = 1.87 K.



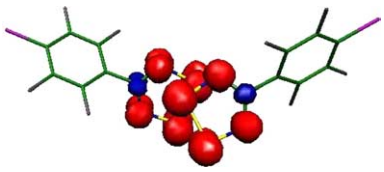
Javier Luzón, Javier Campo, Fernando Palacio, Garry J. McIntyre, Jeremy M. Rawson

Polyhedron 24 (2005) 2579

Ab initio study of the magnetic behavior of four dithiadiazolyl radical compounds

The magnetic interaction mechanisms in four radical crystals, X–C$_6$F$_4$–CNSSN (X = O$_2$N, α-NC, β-NC, Br) have been studied by means of ab initio calculations which has allowed us to explain their different magnetic behaviour.

Following this procedure we have determined the magnitude and the sign of the relevant coupling constants for the radicals. Ordering temperatures determined with our ab initio calculations agree very well with the experimental ones.

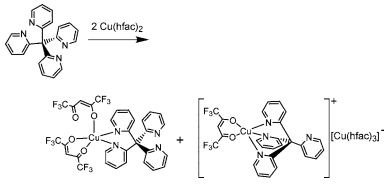


Atsushi Okazawa, Takayuki Ishida, Takashi Nogami

Polyhedron 24 (2005) 2584

Structures and magnetic properties of copper(II) complexes containing tetrakis(2-pyridyl)methane

We attempted to prepare a dinuclear copper(II) complex $[\{Cu(hfac)_2\}_2(py_4C)]$ but we obtained $[Cu(hfac)_2(py_4C)]$ and $[Cu(hfac)_2(py_4C) \cdot Cu(hfac)_3]$. These molecular structures were determined by the X-ray crystal structure analysis.

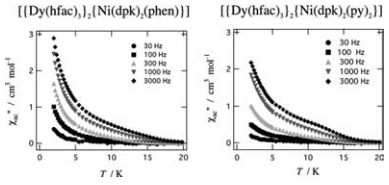


Fumihito Mori, Takayuki Ishida, Takashi Nogami

Polyhedron 24 (2005) 2588

Structure and magnetic properties of 3d–4f heterometallic complexes containing di-2-pyridyl ketoximate: An approach to single-molecule magnets

The N–O groups from di-2-pyridyl ketoxmate bridged the central nickel(II) ion and terminal lanthanide(III) ions, giving a linear trinuclear array (Ln = La, Tb, Dy, Ho, Er). Ac magnetic susceptibility measurements revealed the frequency dependence of out-of-phase ac susceptibility only for the Dy derivatives, which is regarded as an indication of single-molecule magnets.

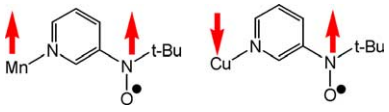


Tomokazu Shimada, Takayuki Ishida, Takashi Nogami

Polyhedron 24 (2005) 2593

Magnetic properties of transition metal complexes with 2,2′-bipyridin-5-yl *t*-butyl nitroxide

Complexes $[Mn^{II}(5bpno)_3(ClO_4)_2]$, $[Mn^{II}(5bpno)(CH_3OH)_2Cl_2]$, $[Cu^{II}(5bpno)_2(ClO_4)_2]$, and $[Cu^{II}(5bpno)Cl_2]$ were prepared, where 5bpno stands for 2,2′-bipyridin-5-yl *t*-butyl nitroxide. Magnetic measurements revealed the presence of ferromagnetic couplings in the Mn complexes, whereas the Cu complexes showed antiferromagnetic couplings.

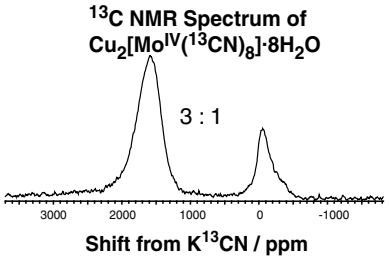


Ryo Watanabe, Hiroki Ishiyama, Goro Maruta, Sadamu Takeda

Polyhedron 24 (2005) 2599

Hyperfine coupling and local structures of octacyanomolibudenum magnetic complexes and related compounds as studied by solid state ^{13}C and ^{2}H NMR

The local magnetic structures of $Cu_2[Mo(CN)_8] \cdot 8H_2O$ (**1**) were investigated. Based on the NMR results for **1** and related octacyanomolibudenum compounds, it is suggested that there are two distinct Cu(II) coordination environments in **1**, namely a square planar and the structure that is largely deformed from the square planar, which may be important for ferromagnetic switching by photoinduced electron transfer from Mo(IV) to Cu(II) ion in a collective manner in the solid state.

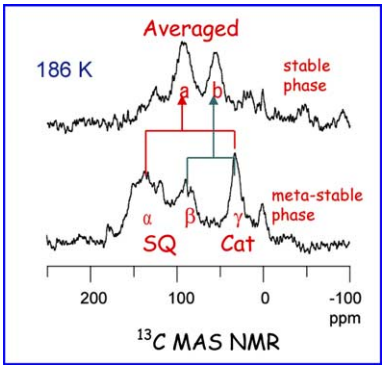


Kunio Morii, Goro Maruta, Sadamu Takeda

Polyhedron 24 (2005) 2607

Solid-state high-resolution NMR studies on spin fluctuation associated with valence tautomerism of metal–benzoquinone system: Cobalt complex in the stable and meta-stable phases

Spin fluctuation associated with valence tautomrtic interconversion was characterized for [Co(3,5-di-*t*-butyl-1,2-benzoquinone)$_2$(2,2′-bipyridine)] · x($C_6H_5CH_3$) in its stable and meta-stable phases by solid-state high-resolution ^{2}H and ^{13}C NMR spectrum. Change of the spin state of the organic radical ligands and of the cobalt ion was detected independently by ^{13}C MAS NMR spectrum of catecholate and semiquinoate ligand, and by ^{2}H MAS NMR spectrum of deuterated bpy-d_{18} ligand, respectively.

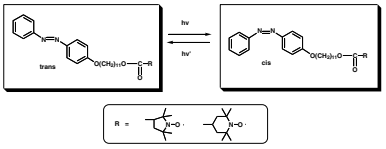


Takamitsu Amano, Masahiro Fujino, Hiroki Akutsu, Jun-ichi Yamada, Shin'ichi Nakatsuji

Polyhedron 24 (2005) 2614

Preparation and properties of aminoxyl radicals having an aromatic core with long alkyl substituents

Among several monoradicals and biradicals having an aromatic core and long alkyl groups prepared, the change of intermolecular magnetic interactions based on isomerization by irradiation was found in a couple of azobenzene derivatives with an aminoxyl radical.

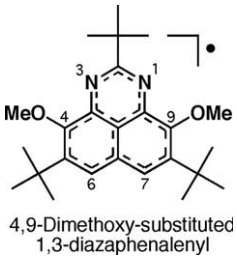


Shuichi Suzuki, Yasushi Morita, Kozo Fukui, Kazunobu Sato, Daisuke Shiomi, Takeji Takui, Kazuhiro Nakasuji

Polyhedron 24 (2005) 2618

Effect of methoxy groups in a 1,3-diazaphenalenyl π-system: Electronic-spin structure of 4,9-dimethoxy-1,3-diazaphenalenyl

A derivative of 4,9-dimethoxy-substituted 1,3-diazaphenalenyl radical has been synthesized and characterized for evaluating the heteroatomic effects on phenalenyl π-system. In comparison with the parent 1,3-diazaphenalenyl radical, it turns out that the title radical significantly undergoes spin redistribution; the spin densities on the 6,7-positions decrease, while those on the 1,3-positions increase.

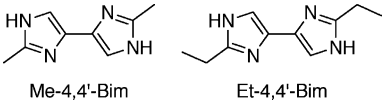


Tsuyoshi Murata, Yasushi Morita, Yoshie Nishimura, Kazuhiro Nakasuji

Polyhedron 24 (2005) 2625

Hydrogen-bonded networks of 2,2′-substituted 4,4′-biimidazoles: New ligands for the assembled metal complexes

The crystal structures of methyl- and ethyl-substituted 4,4′-biimidazole derivatives (Me-4,4′-Bim and Et-4,4′-Bim) were investigated. A simple modification on 4,4′-biimidazole skeleton changes the hydrogen-bonded structures to construct a variety of three-dimensional structures by hydrogen-bonded networks.

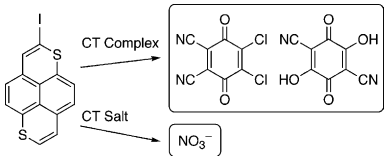


Eigo Miyazaki, Yasushi Morita, Kazuhiro Nakasuji

Polyhedron 24 (2005) 2632

2-Iodo-1,6-dithiapyrene: Syntheses, crystal structures and physical properties of CT complexes and salt

New charge-transfer complexes and salt of 2-iodo-1,6-dithiapyrene (IDTPY) with DDQ, cyananilic acid, nitranilic acid (H_2NRAL), and nitrate were prepared, and their physical properties were investigated by optical and electric conductivity measurements. In the crystals of H_2NRAL complex and nitrate salt, dimeric structures of IDTPY and short I···O contacts were formed.

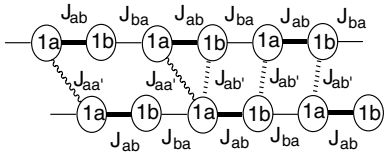


Lora M. Field, Paul M. Lahti

Polyhedron 24 (2005) 2639

Chain versus dimer contacts in crystalline 5-(4-[*N*-*tert*-butyl-*N*-aminoxyl]phenyl)pyrimidine radicals: Choices among competing intermolecular exchange mechanisms

The title compound forms both alternating chains, in-plane dimer, and π-stack dimer contacts between sites of delocalized spin density. Magnetic measurements show that the 50% of molecules that form π-stacked dimers ($\mathbf{J_{a–a'}}$) dominate the exchange behavior at lower temperatures, with the rest of molecules showing essentially paramagnetic behavior.

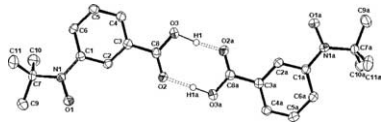


Martha Baskett, Paul M. Lahti

Polyhedron 24 (2005) 2645

Crystallography and magnetism of 3-(*N*-*tert*-butyl-*N*-aminoxyl)benzoic acid

The title compound forms centrosymmetric H-bonded dimers in the solid state, with chains of nitroxide to aryl CH contacts as the major additional packing motif. The magnetic behavior shows overall AFM exchange, with likelihood multiple, weak, competing exchange mechanisms.

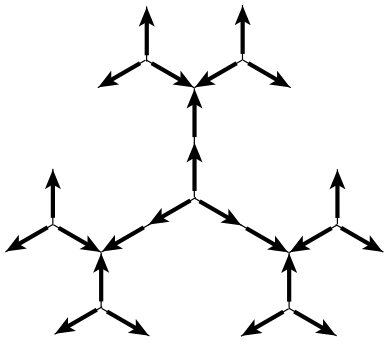


Masahiro Takahata, Mitsuo Shoji, Shusuke Yamanaka, Masayoshi Nakano, Kizashi Yamaguchi

Polyhedron 24 (2005) 2653

Formulation of master equation approach involving spin–phonon coupling: Toward an understanding of spin dynamics in magnetic dendrimers

We investigate a quantum master equation involving spin–phonon coupling in the Markov approximation in order to perform spin dynamics for aggregates which have novel fractal architectures. Such dynamics are important for elucidating the relation between the dynamical magnetic properties and the architectures of spin aggregates.

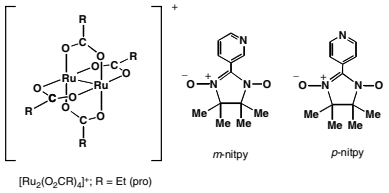


Masahiro Mikuriya, Katsunori Tanaka, Makoto Handa, Ichiro Hiromitsu, Daisuke Yoshioka, Dominique Luneau

Polyhedron 24 (2005) 2658

Adduct complexes of ruthenium(II,III) propionate dimer with pyridyl nitroxides

New mixed-valent(II,III) polymer chain complexes $[Ru_2(pro)_4(m\text{- and }p\text{-nitpy})]_nX_n$ and dimer complexes $[Ru_2(pro)_4(m\text{- and }p\text{-nitpy})_2]X$ (Hpro = propionic acid, X = BF_4 and PF_6) were prepared by the reaction of ruthenium(II,III) propionate with pyridyl nitroxides. The chain and dimer structures were confirmed by X-ray structure analyses of $[Ru_2(pro)_4(m\text{-nitpy})]PF_6$ and $[Ru_2(pro)_4(p\text{-nitpy})_2]BF_4$; the axial sites of Ru(II,III) dimer are occupied by the pyridyl group and one of the two NO groups for the chain complex or by two pyridyl groups, leaving the NO groups uncoordinated for the dimer complex. Ruthenium(II,III) propionate with the pyridyl radicals show that the interaction through the pyridyl group is ferromagnetic when the radical is *p*-nitpy and antiferromagnetic when the radical is *m*-nitpy.

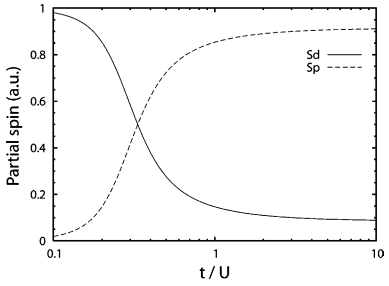


Tomofumi Shuku, Kimikazu Sugimori, Ayumu Sugiyama, Hidemi Nagao, Takeshi Sakurai, Kiyoshi Nishikawa

Polyhedron 24 (2005) 2665

Molecular orbital analysis of active site of oxidized azurin: Dependency of electronic properties on molecular structure

We calculate the potential energy surfaces for distances, angles, and dihedral angles between the copper and 5 surrounding residues. The dependency of the partial charge and spin density on the change of the distance is discussed in relation to electron correlation on d-orbital of the copper ion.

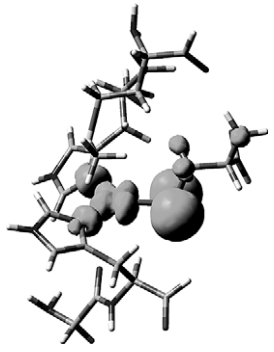


Kimikazu Sugimori, Tomofumi Shuku, Ayumu Sugiyama, Hidemi Nagao, Takeshi Sakurai, Kiyoshi Nishikawa

Polyhedron 24 (2005) 2671

Solvent effects on electronic structure of active site of azurin by polarizable continuum model

We present a cluster model for the active site of oxidized azurin, and investigate the electronic structure by using DFT with polarizable continuum model. The singly occupied molecular orbital and spin density widely distribute around the Cu $3d_{x^2-y^2}$ and S(Cys112) 3p orbitals. The partial spin and charge density on the Cu become larger, when the dielectric constant increases.

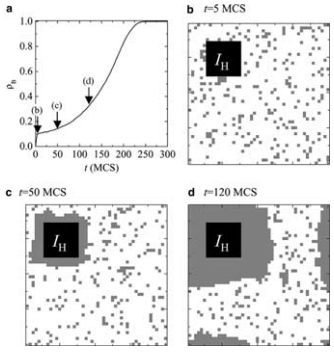


Tohru Kawamoto, Shuji Abe

Polyhedron 24 (2005) 2676

Fixed spin effect on a phase switching of an Ising model under constant excitation: Study for impurity effect on photoinduced spin-state switching in transition metal complexes

We investigated the effect of fixed-spin doping on a phase switching of an Ising model under constant excitation, for studying the impurity effect on the photoinduced spin-state switching of transition metal complexes. The photoinduced switching becomes possible only by weaker excitation when large fixed spin clusters are doped.

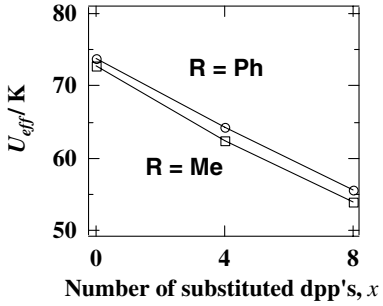


Takayoshi Kuroda-Sowa, Guo-Qing Bian, Masaki Hatano, Hisashi Konaka, Satoshi Fukuda, Shinsuke Miyoshi, Masahiko Maekawa, Megumu Munakata, Hitoshi Miyasaka, Masahiro Yamashita

Polyhedron 24 (2005) 2680

Syntheses, crystal structures and magnetic properties of Mn_{12} single-molecule magnets with diphenylphosphate and their tetraphenylphosphonium salts

Structures and magnetic properties of several Mn_{12} derivatives with partial substitution of diphenylphosphate(dpp), $[Mn_{12}O_{12}(O_2CR)_{16-x}(dpp)_x(H_2O)_y]$, are reported. The increase of the number of dpp ligands resulted in a decrease of the U_{eff} values of these Mn_{12} SMMs, probably due to a decrease of single-ion *D*-values of dpp-coordinated Mn^{III} ions.

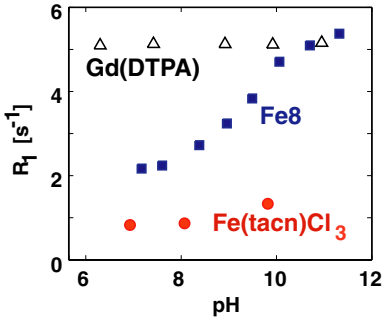


Steven Isaacman, Rajeev Kumar, Enrique del Barco, Andrew D. Kent, James W. Canary, Alexej Jerschow

Polyhedron 24 (2005) 2691

Critical examination of Fe_8 as a contrast agent for magnetic resonance imaging

We examine Fe_8, a small molecule magnet, for its potential use as a contrast agent for magnetic resonance imaging.

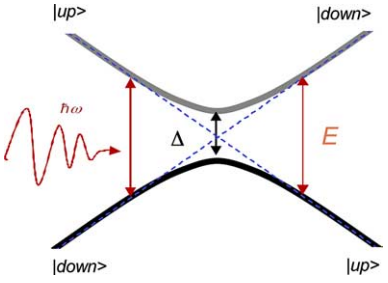


Enrique del Barco, Andrew D. Kent, En-Che Yang, David N. Hendrickson

Polyhedron 24 (2005) 2695

Magnetic and microwave studies of high-spin states of single-molecule magnet Ni_4

The high spin ground state of a single-molecule magnet has been studied in experiments that combine magnetometry with microwave excitation. The results show level repulsion between low-lying states, which indicates the formation of high spin superposition states. Absorption linewidths provide an upper bound of 2 GHz on the decoherence rate of these spin states.

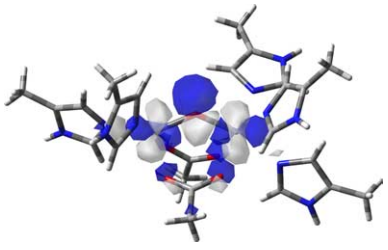


Mitsuo Shoji, Tomohiro Hamamoto, Kenichi Koizumi, Hiroshi Isobe, Yasutaka Kitagawa, Yu Takano, Shusuke Yamanaka, Mitsutaka Okumura, Kizashi Yamaguchi

Polyhedron 24 (2005) 2701

Theoretical study on the magnetic interactions of active site in hemerythrin

The magnetic interactions and electronic structures of active sites in Hemerythrin are investigated by hybrid density-functional theory. Calculated effective-exchange interactions are in good agreement with experimental values. Using natural orbital analysis, their magnetic interaction changes caused by dioxygen binding are discussed.

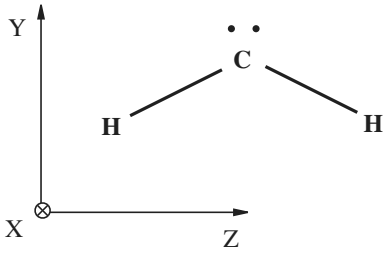


Mitsuo Shoji, Kenichi Koizumi, Tomohiro Hamamoto, Takeshi Taniguchi, Ryo Takeda, Yasutaka Kitagawa, Takashi Kawakami, Mitsutaka Okumura, Shusuke Yamanaka, Kizashi Yamaguchi

Polyhedron 24 (2005) 2708

A theoretical study of zero-field splitting of organic biradicals

Zero-field splitting parameters for typical organic biradicals are calculated by density-functional theory and their spin orbitals and magnetic axes are discussed. These results also indicate the usefulness of our new approach for investigating magnetic properties of organic radicals.

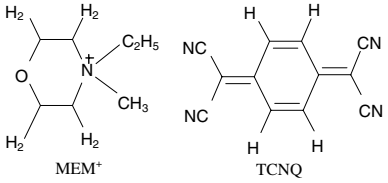


Seishi Takagi, Kunihiko Irie, Tatsuhiro Suematsu, Mitsuru Yoshihiro, Masaki Mito, Hiroyuki Deguchi

Polyhedron 24 (2005) 2716

ESR Spectra of a single crystal under uniaxial pressure for a typical spin-Peierls substance: MEM–$[TCNQ]_2$

Angular and temperature dependence of the ESR spectrum of a single crystal of a salt, MEM-$[TCNQ]_2$, were measured under uniaxial pressure up to 1 kbar by using a handmade pressure cell and a conventional ESR instrument in the temperature range of 1.5–300 K. The ESR spectrum is deformed with increasing pressure and the deformed ESR spectrum significantly depends on the temperature and orientation of the crystal. The ESR spectrum at low temperatures is well separated into three absorptions. One of the absorptions seems to result from free spins and the other two absorptions seem to result from spin-pairs.

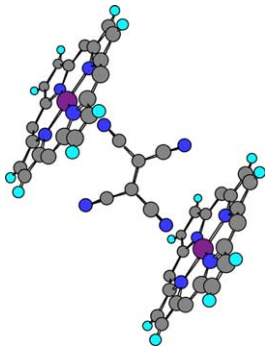


K. Koizumi, M. Shoji, Y. Kitagawa, T. Taniguchi, T. Kawakami, M. Okumura, K. Yamaguchi

Polyhedron 24 (2005) 2720

Theoretical studies on ferrimagnetic behavior of TCNE and manganese porphyrin dimer

The magnetic property of a one-dimensional magnetic chain, 5,10,15,20-tetrakis(4-bromophenyl)porphyrinatomanganese(III)tetracyanoethenide ([MnTBrPP][TCNE]), is investigated by using a model complex and theoretical calculations. Hybrid UDFT (UB3LYP, UB2LYP) and UHF methods are used for the calculation of the model complex and effective exchange integrals (J) values are deduced from the calculated results.

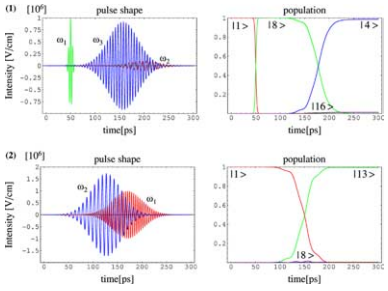


Tomoya Ito, Kimikazu Sugimori, Hidemi Nagao, Kiyoshi Nishikawa

Polyhedron 24 (2005) 2726

Laser control of singlet–triplet transition in molecules

A two-step sequential method with the p pulse and the stimulated Raman adiabatic passage (STIRAP) pulse sequence is applied to the laser control of the singlet–triplet transition in Cl_2 molecule. We find four reaction pathways from the singlet ground state to the triplet excited state by investigating the spin–orbit coupling and the transition dipole moment calculated with gamess software package, and we realize the highly effective singlet–triplet transition by STIRAP method with the spin-mixed intermediate state on picosecond time scale.

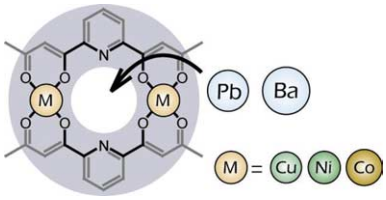


Takuya Shiga, Tatsuaki Nakanishi, Masaaki Ohba, Hisashi Ōkawa

Polyhedron 24 (2005) 2732

Synthesis, structures and magnetic properties of trinuclear M(II)A(II)M(II) complexes (M = Cu, Ni, Co; A = Pb, Ba) derived from 2,6-bis(acetoacetyl)pyridine

A 16-membered metallacrown-like structure derived from two M(II) ions and two 2,6-bis(acetoacetyl)pyridine (H_2L) captures Pb(II) or Ba(II) in the central N_2O_4 site to form M(II)A(II)M(II) trinuclear compounds, $[M_2A(L)_2(NO_3)_2] \cdot n(sol)$ (M = Cu, Ni, Co; A = Pb, Ba; sol = H_2O or MeOH), and their structures and magnetic properties are characterized.

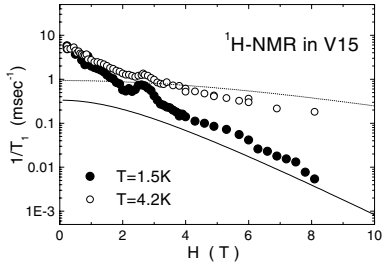


Y. Furukawa, Y. Fujiyoshi, K. Kumagai, P. Kögerler

Polyhedron 24 (2005) 2737

Spin dynamics and level crossing in nanoscale molecular magnet V15 cluster studied by ^{1}H-NMR

We have carried out ^{1}H-NMR to investigate the spin dynamics in a molecular magnet $K_6[V_{15}As_6O_{42}(H_2O)]8H_2O$ (in short, V15). The temperature (T) and magnetic field (H) dependences of ^{1}H-NMR spectrum, $1/T_1$ and $1/T_2$ provide evidence for a gradual slowing of fluctuations of the V^{4+} spins with increasing the magnetic field. The T and H dependence of $1/T_1$ is well explained by the model in terms of spin phonon interaction for $H > 2.7$ T where the ground state of the V15 is $S = 3/2$. On the other hand, the T_1 data can not be reproduced by the model for $H \sim 2.7$ T where the ground state is nearly degenerated $S = 1/2$ states, suggesting the importance of additional contribution to $1/T_1$ due to the peculiarities of the $S = 1/2$ triangle configuration in the V15.

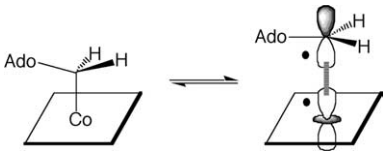


Yusuke Nishiyama, Mitsuo Shoji, Kenichi Koizumi, Yusuke Maruno, Yasutaka Kitagawa, Takashi Kawakami, Mitsutaka Okumura, Kizashi Yamaguchi

Polyhedron 24 (2005) 2745

Theoretical studies on dissociation of metal–carbon bond in Cobalamin: Formulation and calculation

The phase diagram of the metal–ligand (M–X) bond formation was formulated analytically. By using covalent bond parameter and ionic parameter, the chemical bonding and its dissociation nature of M–X bond were discussed. The result was applied to the Co–C bond formation in the active site of cobalamin.

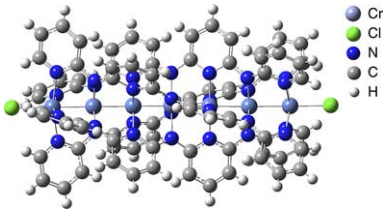


Yasutaka Kitagawa, Mitsuo Shoji, Kenichi Koizumi, Takashi Kawakami, Mitsutaka Okumura, Kizashi Yamaguchi

Polyhedron 24 (2005) 2751

Theoretical studies on magnetic interactions and charge-dope effects in one-dimensional Ni_5 and Ni_7 complexes

The magnetic interactions between Ni(II) ions in $[Ni_5(tpda)_4Cl_2]$ and $[Ni_7(teptra)_4Cl_2]$ were examined by using theoretical calculations. The calculated effective exchange integrals (J_{ab}) reproduced experimental results well. Natural orbitals and their occupation number analyses explained their weak anti-ferromagnetic couplings that depended on their chain length and species of axial ligands.

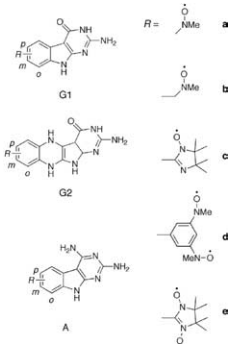


K. Yamaguchi, T. Taniguchi, T. Kawakami, T. Hamamoto, M. Okumura

Polyhedron 24 (2005) 2758

Possibilities of magnetic modifications of DNA wires, sheets and related materials

Guanine and adenine have been modified by radical groups for the design of DNA-based molecular materials. Intermolecular effective exchange integrals have been investigated by the hybrid-DFT method. Possibility of organomagnetic conductors and organic solenoids has been discussed based on this result.

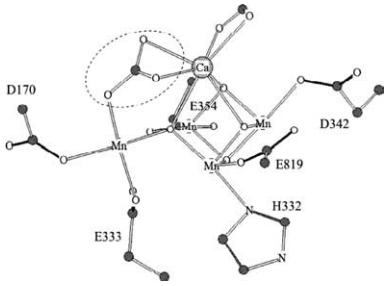


Hiroshi Isobe, Mitsuo Shoji, Kennichi Koizumi, Yasutaka Kitagawa, Shusuke Yamanaka, Seiki Kuramitsu, Kizashi Yamaguchi

Polyhedron 24 (2005) 2767

Electronic and spin structures of manganese clusters in the photosynthesis II system

Electronic and spin structures of manganese clusters, Mn_4O_4 (**1**), $CaMn_3O_4$ (**2**), Mn_3O_4 (**3**), MnX (**4**), and $CaMn_4O_4$ (**5**) are investigated using the classical and quantum Heisenberg models. The calculated results, together with available experiments, enable us to propose possible electronic states (from S_0 to S_4) of tetranuclear manganese cluster **5**, which is the active site of oxygen evolution center (OEC) in the photosynthesis II system. A new reaction scheme for oxygen evolution from water is resulted from both theoretical and experimental results for manganese clusters **1**–**5** in OEC. Implications of computational results are discussed in relation to a key role of the high-valent manganese oxo (Mn(V)=O) species in OEC for oxygen evolution from water.

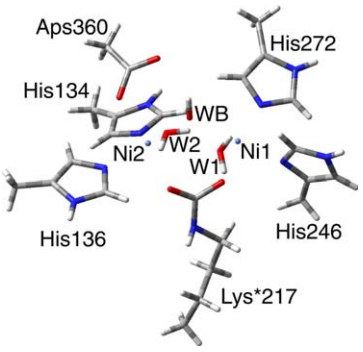


Yusuke Maruno, Mitsuo Shoji, Kenichi Koizumi, Yusuke Nishiyama, Yasutaka Kitagawa, Takashi Kawakami, Mitsutaka Okumura, Kizashi Yamaguchi

Polyhedron 24 (2005) 2778

Theoretical studies on magnetic interactions between Ni(II) ions in urease

The chemical species of bridge oxygen (WB) in active site of urease was examined in terms of a magnetic interaction between Ni(II) ions. For the purpose, the effective exchange integrals (J_{ab}) values between Ni(II) ions were examined by using three candidtes of WB in comparison with experimental results (-6.3 cm^{-1}).

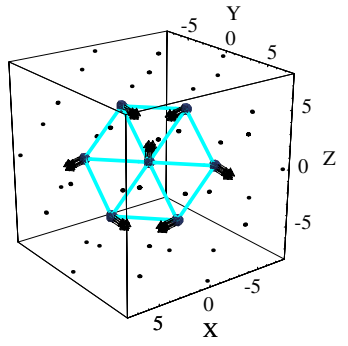


Shusuke Yamanaka, Ryo Takeda, Mitsuo Shoji, Kennichi Koizumi, Yasutaka Kitagawa, Kizashi Yamaguchi

Polyhedron 24 (2005) 2784

Ab initio GSO-DFT study of spin-frustrated transition metal systems

The cluster model of $Na_{0.35}Co_2O_4(H_2O)_{1.3}$ was investigated using ab initio general spin orbital density functional theory. We determined the electronic and magnetic structures of the fundamental triangular and hexagonal parts, Co_nO_x (n = 3.7) of this compound. The effective exchange integral values are computed by employing the new estimation scheme, which is applicable for all of homogeneous spin systems such as triangular and hexagonal systems. The estimation of T_c based on J model is also presented and is discussed in relation to the experimental value.

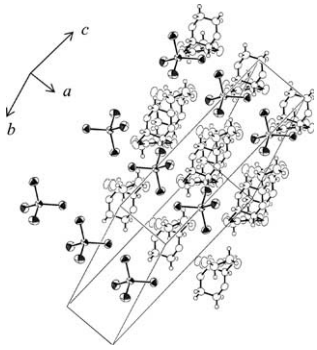


Hiroyuki Nishikawa, Yuri Yasuda, Takeshi Kodama, Koichi Kikuchi, Isao Ikemoto, Jun-ichi Yamada, Hiroki Oshio

Polyhedron 24 (2005) 2789

Crystal structure and physical properties of $(DODHT)_2FeCl_4$

New organic conductor based on DODHT [(1,4-dioxane-2,3-diyldithio)dihydrotetrathiafulvalene] with an inorganic magnetic anion, $FeCl_4^-$, has been synthesized. A clear transition to an insulator was observed at 130 K in the temperature dependence of resistance, but no anomaly was seen in the magnetic susceptibility measured with SQUID in the same temperature range. Crystal structure analysis of $(DODHT)_2FeCl_4$ revealed that the donor arrangement is β″-type similarly to the superconducting DODHT salts, and there is no strong interaction between donor molecules and inorganic anions.

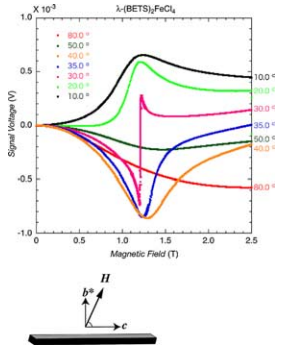


Madoka Tokumoto, Hisashi Tanaka, Takeo Otsuka, Hayao Kobayashi, Akiko Kobayashi

Polyhedron 24 (2005) 2793

Observation of spin-flop transition in antiferromagnetic organic molecular conductors using AFM micro-cantilever

Spin-flop transitions observed by torque magnetometry of a tiny single crystal (less than 1 μg) of antiferromagnetic organic molecular conductor λ-$(BETS)_2FeCl_4$, using an AFM microantilever.

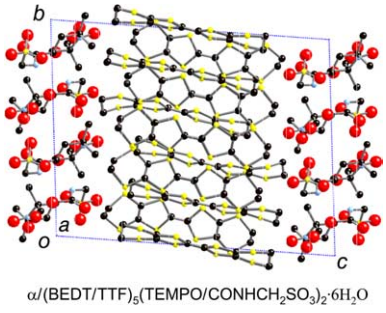


Akiko Yamashita, Hiroki Akutsu, Jun-ichi Yamada, Shin'ichi Nakatsuji

Polyhedron 24 (2005) 2796

New organic magnetic anions TEMPO-$CONA(CH_2)_nSO_3^-$ (n = 0–3 for A = H, n = 2 for A = CH_3) and their TTF, TMTSF, and/or BEDT-TTF salts

Five TEMPO-containing anions TEMPO-$CONA(CH_2)_nSO_3^-$ (**H0**$^-$, A = H, n = 0; **H1**$^-$, A = H, n = 1; **H2**$^-$, A = H, n = 2; **H3**$^-$, A = H, n = 3; **M2**$^-$, A = CH_3, n = 2) have been prepared as PPh_4 salts. So far three TTF salts ((TTF)(**H1**) · $2H_2O$, (TTF)(**H2**) · H_2O, and (TTF)(**M2**) · $0.50H_2O$), one TMTSF salt ((TMTSF)(**H1**) · $2H_2O$ · PhCl), and one BEDT-TTF salt (α-$(BEDT\text{-}TTF)_5$(**H1**)$_2$ · $6H_2O$) have been obtained. Their crystal structures, electrical resistivities, and magnetic properties are reported.

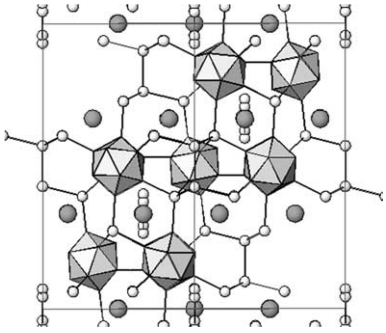


Takao Mori

Polyhedron 24 (2005) 2803

Magnetic field dependence of the rare earth B_{12} icosahedral cluster compound $GdB_{18}Si_5$

$GdB_{18}Si_5$ is the only B_{12} icosahedral system found to have long range magnetic ordering. An interesting dependence at low magnetic fields was observed, with a reorientation of the spin, a spin flip, appearing to occur at fields below 300 G.

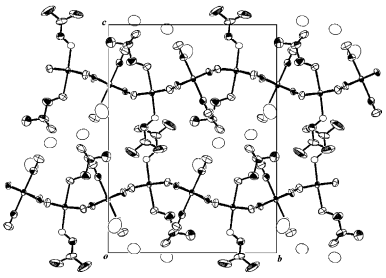


Hiroyuki Imai, Katsuya Inoue, Kohichi Kikuchi

Polyhedron 24 (2005) 2808

Crystal structures and magnetic properties of chiral and achiral cyanide-bridged bimetallic layered compounds

The reaction of $[Cr^{III}(CN)_6]^{3-}$, Mn(II) and diaminopropane (pn) in DMF/EtOH/H_2O affords two bimetallic layered compounds, $[Cr(CN)_6][Mn(R)\text{-pnH(DMF)}] \cdot (2H_2O)$ (**1**) and $[Cr(CN)_6][Mn(racemi)\text{-pnH(DMF)}] \cdot (2H_2O)$ (**2**). They were characterized by single-crystal X-ray diffraction and magnetic susceptibility measurements.

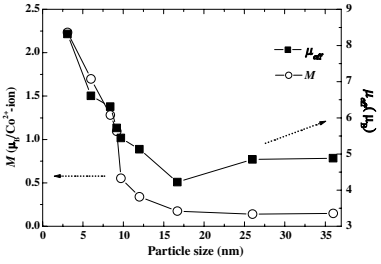


Yuko Ichiyanagi, Saori Yamada

Polyhedron 24 (2005) 2813

The size-dependent magnetic properties of Co_3O_4 nanoparticles

Co_3O_4 nanoparticles were prepared by mixing cobalt chloride($CoCl_2 \cdot 6H_2O$) aqueous solutions with sodium metasilicate nonahydrate ($Na_2SiO_3 \cdot 9H_2O$) aqueous solutions. The diameters of these particles were estimated from the X-ray diffraction patterns as ranging from 3 to 30 nm. The particle sizes were controlled through the annealing conditions and by the Si concentration of the solutions. Magnetization measurements were performed on the various sizes of Co_3O_4 nanoparticles. The blocking temperatures Tb were observed to be between 4 K and 28 K, while the Néel temperature of Co_3O_4 bulk crystal is known to be $T_N = 33$ K. At the blocking temperature, the superparamagnetic spins in the particle are supposed to be blocked against the thermal fluctuation energy. The saturation magnetization M_s increased dramatically for particle sizes below about 10 nm. The calculated effective magnetic moment μ_{eff} for a Co_3O_4 particle of 3 nm was twice as large as that of bulk crystal. These magnetic anomalies, which are dependent on particle size, could be due to the surface spins of the extremely small Co_3O_4 particles.

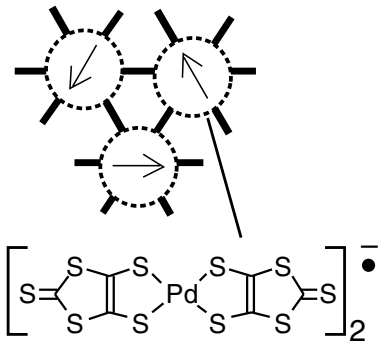


Masafumi Tamura, Reizo Kato

Polyhedron 24 (2005) 2817

Spin-1/2 Heisenberg antiferromagnets on anisotropic triangular lattice, $[Pd(dmit)_2]$ salts – How do they release frustration?

The $[Pd(dmit)_2]$ salts are frustrated antiferromagnets, in which the dimers $[Pd(dmit)_2]_2^-$ form a triangular lattice. Various phenomena related to the release of the frustration can be observed in this system. They are overviewed on the basis of magneto-structural correlation.

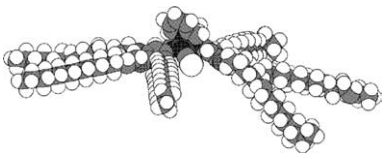


Shinya Hayami, Kazutoshi Danjobara, Soushi Miyazaki, Katsuya Inoue, Yoshihiro Ogawa, Yonezo Maeda

Polyhedron 24 (2005) 2821

Photo-induced spin transition iron(II) compounds with liquid-crystal properties

The iron(II) compounds $[Fe(1C16\text{-}L)_2(NCS)_2]$ (**1**), $[Fe(2C16\text{-}L)_2(NCS)_2]$ (**2**) and $[Fe(3C16\text{-}L)_2(NCS)_2]$ (**3**) were synthesized and the physical properties of the compounds were characterized. The spin-crossover iron(II) compound **3** have exhibited liquid-crystal properties in the temperature range from 345 to 400 K. Therefore the iron(II) compound **3** can undergo spin-crossover, photo-induced spin transition and liquid-crystal properties in a compound.

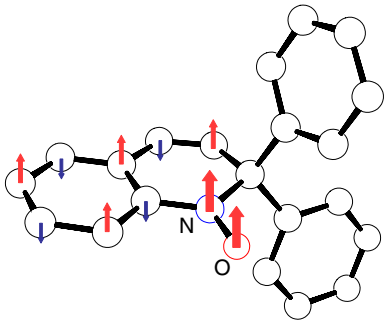


Masaru Yao, Hideki Shibuya, Takashi Kato, Hidenari Inoue, Naoki Yoshioka

Polyhedron 24 (2005) 2828

Synthesis and magnetic properties of 2,2,4- and 2,2,6-triphenyl-1,2-dihydroquinoline-*N*-oxyl derivatives

Two novel aromatic *N*-oxyl radicals based on the quinoline skeleton, 2,2,4-triphenyl-1,2-dihydroquinoline-*N*-oxyl (**1**) and 2,2,6-triphenyl-1,2-dihydroquinoline-*N*-oxyl (**2**) are magnetically characterized. **1** exhibited a weak antiferromagnetic interaction in its crystal. For **2**, two crystalline phases were obtained, and **2-α** exhibited a paramagnetic behavior; however, **2-β** showed a weak ferromagnetic interaction.

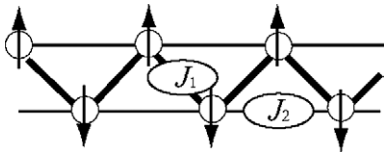


Hikomitsu Kikuchi, Yutaka Fujii, Meiro Chiba, Seitaro Mitsudo, Toshitaka Idehara

Polyhedron 24 (2005) 2835

Magnetic properties of [VO(μ_3-MoO_4)(2,2′-bpy)]: New model compound for $S = 1/2$ zigzag frustrated one-dimensional magnet

The magnetic susceptibility and high field magnetization up to 35 T were measured on $S = 1/2$ zigzag antiferromagnet [VO(μ_3-MoO_4)(2,2′-bpy)]. The magnetization curve was compared with theoretical one to estimate the nearest-neighbor exchange interaction J_1 to be 56 K. The intrinsic magnetic susceptibility had maximum at around $T_{max} = 11$ K. A ratio T_{max}/J_1 was much less than that expected for one-dimensional antiferromagnet without next-nearest-neighbor interaction.

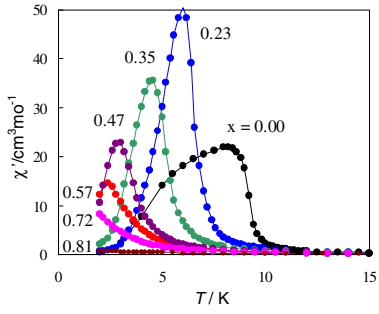


Masaaki Ohba, Takashi Iwamoto, Wakako Kaneko, Susumu Kitagawa, Hisashi Ōkawa

Polyhedron 24 (2005) 2839

Magnetic and magneto-optical properties of two-dimensional cyanide-bridged $Fe_{(1-x)}^{III}$-$Co_x^{III}Ni^{II}$ solid solutions having fragmented magnetic domain

Two-dimensional cyanide-bridged $Fe_{(1-x)}^{III}$ $Co_x^{III}Ni^{II}$ solid solutions, $\{[Ni(1,1\text{-dmen})_2]_2[Fe_{(1-x)}Co_x(CN)_6]\}tfs \cdot nH_2O$ ($x = 0.0$, 0.12, 0.23, 0.35, 0.47, 0.54, 0.57, 0.64, 0.72, 0.81, 1.0; 1,1-dmen = 1,1-dimethylethylenediamine, tfs^- = trifluoromethanesulfonate ion), have been prepared as single crystals and their structures magnetic and magneto-optical properties were characterized. Their ferromagnetic ordering temperature and Faraday ellipticity at ~470 nm associated with the LMCT band of the Fe–CN decrease with increasing x value due to fragmentation of magnetic domain by diamagnetic $[Co(CN)_6]^{3-}$ units.

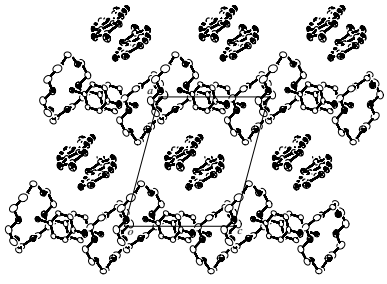


S. Nishihara, X.M. Ren, T. Akutagawa, T. Nakamura

Polyhedron 24 (2005) 2844

Crystal structures and magnetic properties of $[Ni(dmit)_2]^-$ salts including (4-fluoroanilinium)([18]crown-6) and (4-methylanilinium)-([18]crown-6) supramolecular cations

We report the crystal structures and magnetic properties of two new salts; (4-fluoroanilinium)([18]crown-6)[Ni(dmit)$_2$] and (4-methylanilinium)([18]crown-6)[Ni(dmit)$_2$]. Both salts had isomorphous structure of one-dimensional arrangements of $[Ni(dmit)_2]^-$ π-dimer along the *b*-axis. The magnetic ground state of these salts was spin singlet with the intradimer magnetic exchange energy of around −150 K.

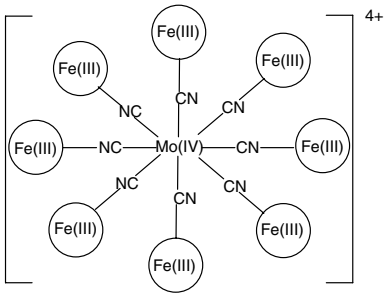


F. Renz, P. Kerep

Polyhedron 24 (2005) 2849

Unprecedented multiple electronic spin transition in hepta- and nonanuclear complex compounds observed by Mössbauer spectroscopy

Synthesis and characterization of the heptanuclear $[Co(III)\{(CN)Fe(III)(^5L)\}_6]Cl_3$ and the nonanuclear $[Mo(IV)\{(CN)Fe(III)\text{-}(^5L)\}_8]Cl_4$ coordination compound with multiple electronic spin transitions between 6 and 30 and 8 and 40 unpaired electrons per star-shaped molecule, while in the heptanuclear $[Fe(II)\{(CN)Fe(III)(^5L)\}_6]Cl_2$ the Fe(III)-centers remain in the high-spin state, i.e. contains 30 unpaired electrons at all temperatures below 300 K.

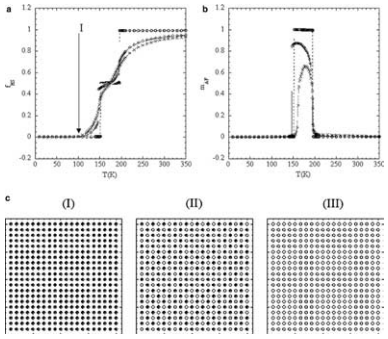


Masamichi Nishino, Kamel Boukheddaden, Seiji Miyashita, François Varret

Polyhedron 24 (2005) 2852

Relaxation dynamics of two-step spin-crossover

We study static and dynamical properties of the two-step spin-crossover solids. A Monte Carlo method with the Arrhenius transition probability is applied to a two-sublattice model with an intrasublattice interaction and an intersublattice interaction. There, an intermediate-temperature 'antiferro' phase, where the sublattices have different states, appears between low-temperature phase (LS phase) and high-temperature phase (HS phase), as observed in the experiments. In particular, we focus on the relaxation from the saturated HS state which is realized by photo excitation. There, two-step relaxation is found: a fast relaxation with sigmoidal shape and following slow relaxation. The former is due to the Arrhenius transition rate and the latter is a result of stochastic relaxation from the metastable antiferro state, which reproduces well the relaxation observed in the experiments.

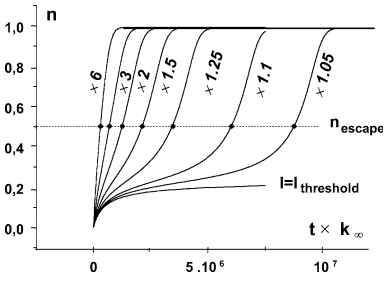


F. Varret, K. Boukheddaden, E. Codjovi, I. Maurin, H. Tokoro, S. Ohkoshi, K. Hashimoto

Polyhedron 24 (2005) 2857

Light-induced thermal hysteresis and intensity thresholds in molecular switcheable solids, by mean-field macroscopic master equation approach: Discussion of the experimental data obtained for Co–Fe Prussian Blue Analogues

Typical application of the mean-field macroscopic master equation of interacting photoswitchable systems: the time dependence of the high-spin fraction, $n(t)$, at equilibrium temperature, for a system initially in the low-spin state, irradiated with intensities above the threshold value. Intersections with the horizontal line provide "escape times" from the initial state.

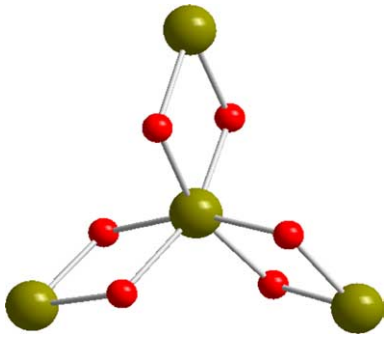


N.T. Madhu, Jin-Kui Tang, Ian J. Hewitt, Rodolphe Clérac, Wolfgang Wernsdorfer, Joris van Slageren, Christopher E. Anson, Annie K. Powell

Polyhedron 24 (2005) 2864

What makes a single molecule magnet?

Recent work in designing and synthesising molecules displaying the phenomenon of "Single Molecule Magnet" (SMM) behaviour has shown how a propeller motif with four paramagnetic metal centres can both stabilise non-zero ground spin states and display slow relaxation of the hysteresis: the signature of an SMM. Having thus identified the structural elements required it should be straightforward to produce new examples and learn how to enhance the SMM characteristics. Here we report on an attempt to do this with the surprising result that a molecule specifically designed to display SMM behaviour proves not to, posing the question as to why this should be.

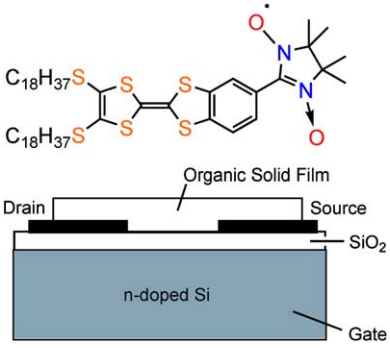


Michio M. Matsushita, Hironori Kawakami, Etsuko Okabe, Hiroto Kouka, Yuzo Kawada, Tadashi Sugawara

Polyhedron 24 (2005) 2870

A field-effect transistor consists of spin-polarized TTF-based donor

TTF-based organic donor molecule bearing stable organic radical moiety and long alkyl chains was synthesized and fabricated into a FET device structure. A fused solid film of the donor radical on the substrate shown by the right figure indicated FET characteristics although the observed hole mobility was very low. This is the first observation of a FET characteristic of an organic radical molecule.

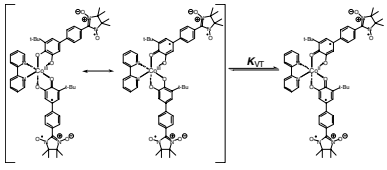


David A. Shultz, R. Krishna Kumar, Sofi Bin-Salamon, Martin L. Kirk

Polyhedron 24 (2005) 2876

Valence tautomerization and exchange coupling in a cobalt–nitronylnitroxide–semiquinone complex

Synthesis and characterization of a novel cobalt valence tautomer comprised of semiquinone-nitronylnitroxide donor–acceptor ligands is presented. Due to the ferromagnetic coupling inherent to the semiquinone-nitronylnitroxide biradical, the Co^{III} form of the valence tautomer may display an additional stabilization of the high-spin ground state resulting from valence delocalization. As such, this would represent a unique example of double exchange in an organic system.

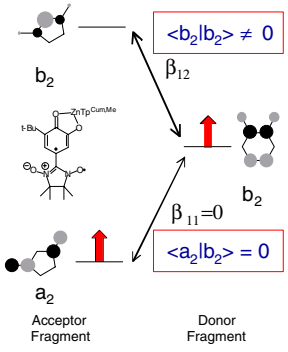


Martin L. Kirk, David A. Shultz, Ezra C. Depperman

Polyhedron 24 (2005) 2880

Beyond the active-electron approximation: Origin of ferromagnetic exchange in donor–acceptor heterospin biradicals

A valence bond configuration interaction (VBCI) model has been employed to describe the origin of strong ferromagnetic exchange coupling in donor–acceptor organic biradicals. This model is useful for using electronic structure theory to study exchange coupling in organic systems, and correlating magnetic exchange parameters with elements of electron transfer theory.

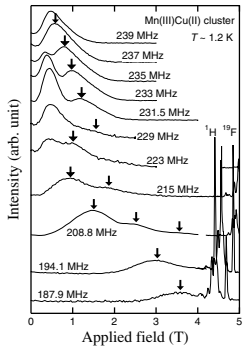


Y. Fujii, S. Hayasaki, H. Hashimoto, M. Chiba, A. Yoshida, M. Nihei, H. Oshio, B. Chen, T. Kubo

Polyhedron 24 (2005) 2885

NMR study of dinuclear molecular magnet $Mn^{III}Cu^{II}$(5-Br-sap)$_2$Cl(MeOH)

^{1}H and ^{55}Mn NMR study of the dinuclear molecular magnet $Mn^{III}Cu^{II}$(5-Br-sap)$_2$Cl(MeOH) has been performed in the temperature range down to 0.4 K. Obtained results suggest that the magnetic moment is stabilized even above the blocking temperature. We also found the hysteresis of the ^{55}Mn NMR spectrum and the activation type behavior of the relaxation rate T_1^{-1} at low temperatures.

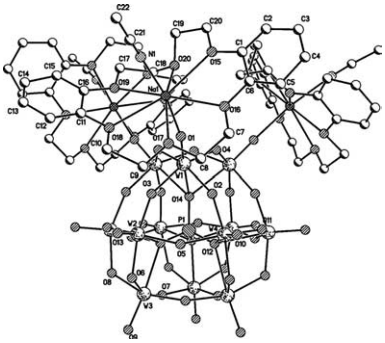


Xiaoming Lu, Bo Liu, Sarula, Jing Wang, Chaohui Ye

Polyhedron 24 (2005) 2889

Synthesis, crystal structure and NMR of $[Na(DB18C6)(CH_3CN)]_3[\alpha\text{-}PW_{12}O_{40}]$

The supra-molecular complex consists of a $[\alpha\text{-}PW_{12}O_{40}]^{3-}$ anion and three $[Na(DB18C6)(CH_3CN)]^{+}$ units in which every sodium ion located in the cavity of DB18C6 and coordinated with a terminal O of $[\alpha\text{-}PW_{12}O_{40}]^{3-}$ and the N atom of CH_3CN. The three terminal O atoms linked with sodium ion are from a single W_3O_3 triplet.

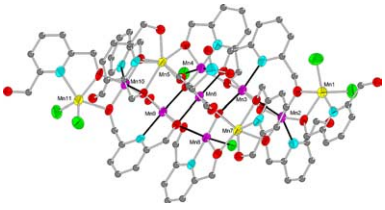


Muralee Murugesu, Wolfgang Wernsdorfer, Khalil A. Abboud, George Christou

Polyhedron 24 (2005) 2894

Single-molecule magnets: synthesis, structures and magnetic properties of Mn_{11} and Mn_{25} clusters

The synthesis and structural characterization of two new manganese complexes $[Mn_{11}O_2(OH)_2(nmpd)(pdmH)_5(pdm)_5Cl_6]\cdot 4MeCN$ (**1**; $Mn^{III}_7Mn^{II}_4$; $nmpdH_2$ = 2-nitro-2-methyl-1, 3-propanediol) and $[Mn_{25}O_{18}(OH)_2(N_3)_{12}(pdm)_6(pdmH)_6]Cl_2\cdot 12MeCN$ (**2**; $Mn^{IV}Mn^{III}_{18}Mn^{II}_6$; $pdmH_2$ = pyridine-2, 6-dimethanol) are presented, together with a study of their magnetic properties.



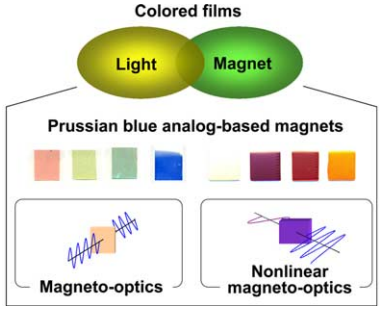
Reports on experimental demonstrations: Or molecular magnetism is attractive! 2900

Tomohiro Nuida, Toshiya Hozumi, Wataru Kosaka, Shunsuke Sakurai, Satoru Ikeda, Tomoyuki Matsuda, Hiroko Tokoro, Kazuhito Hashimoto, Shin-ichi Ohkoshi

Polyhedron 24 (2005) 2901

Colored magnetic films composed of cyano-bridged metal assemblies and magneto-optical functionalities

We show the synthetic procedure of colored magnetic films composed of Prussian blue analog-based magnets and their magneto-optical effects in the visible region. Magnetic thin films of $M^{II}_3[Cr^{III}(CN)_6]_2\cdot zH_2O$ (M = Co, Ni, Cu) are prepared on transparent Nafion membrane by an ion-exchange process and these films exhibit Faraday effect. The film-type of $(Fe^{II}_xCr^{II}_{1-x})_3[Cr^{III}(CN)_6]_2\cdot 15H_2O$ is electrochemically prepared and these films display magnetization-induced second harmonic generation.

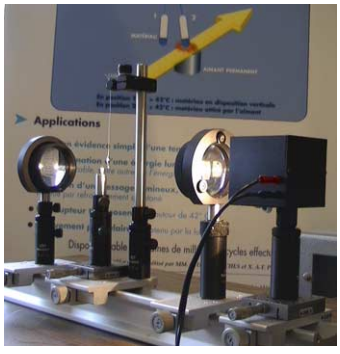


M. Verdaguer, F. Villain, R. Ouahès, N. Galvez, R. Garde, G. Keller, F. Tournilhac

Polyhedron 24 (2005) 2906

Attractive magnetic Prussian blues

Four experimental demonstrations are proposed, which can be presented to large audiences: precipitation of Prussian blue on an overhead; attraction of a room temperature Prussian blue analogue; oscillating magnet, device transforming light in mechanical energy; thermal probe and magnetic switch. The experiments celebrate the 300th anniversary of the discovery of the first coordination compound by its synthesis. They illustrate simply the concept of Curie temperature, the transformation of light into mechanical energy and the use of molecule-based magnets as a thermal probe.

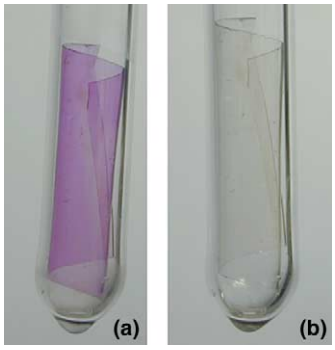


Akio Nakamoto, Norimichi Kojima, Liu XiaoJun, Yutaka Moritomo, Arao Nakamura

Polyhedron 24 (2005) 2909

Demonstration of the thermally induced high spin–low spin transition for a transparent spin crossover complex film [Fe(II)(H-trz)$_3$]-Nafion (trz = triazole)

The spin transition in [Fe^{II}(H-trz)$_3$]-Nafion takes place around room temperature. The color changes from transparent to purple with decreasing temperature.



The Publisher encourages the submission of articles in electronic form thus saving time and avoiding rekeying errors. For detailed instructions on the preparation of manuscripts and of electronic artwork, consult the Author Gateway for Elsevier at http://authors.elsevier.com

SCIENCE DIRECT®

Full text of this journal is available, on-line from **ScienceDirect**. Visit **www.sciencedirect.com** for more information.

CONTENTS direct

This journal is part of **ContentsDirect,** the ***free*** alerting service which sends tables of contents by e-mail for Elsevier books and journals. You can register for **ContentsDirect** online at: **http://contentsdirect.elsevier.com**

Polyhedron Reports

REPORTS EDITOR

G. Christou

Polyhedron Reports are specially commissioned critical reports reviewing research of topical importance. Such articles will be commissioned by the Reports Editor of *Polyhedron* from recognised authorities in the appropriate field. Subject to availability, back issues of *Polyhedron* containing *Polyhedron Reports* may be obtained from the Publisher. Please send enquiries to Elsevier B.V., PO Box 211, 1000 AE, Amsterdam, the Netherlands.

Reports published

No. 1
Carbonylhydrido *tris*(triphenylphosphine)rhodium(I)
1982 **1**(7–8) 569–605 by F.H. Jardine

No. 2
The preparation and properties of metallacyclic compounds of the transition elements
1982 **1**(11–12) 739–777 by S. David Chappell and David J. Cole-Hamilton

No. 3
Mechanisms in the racemization of optically active coordination complexes in the solid state. A review
1983 **2**(4) 233–243 by P. O'Brien

No. 4
The reactions of nucleophiles with complexes of chelating heterocyclic imines; a critical survey
1983 **2**(7) 551–572 by Edwin C. Constable

No. 5
Metal–metal bonds and metal–carbon bonds in the chemistry of molybdenum and tungsten alkoxides
1983 **2**(8) 681–721 by Malcolm H. Chisholm

No. 6
Double bonding between the heavier main-group elements: from reactive intermediates to isolable molecules
1984 **3**(4) 389–432 by Alan H. Cowley

No. 7
Cyclometallated complexes incorporating a heterocyclic donor atom: the interface of coordination chemistry and organometallic chemistry
1984 **3**(9/10) 1037–1057 by Edwin C. Constable

No. 8
Reactions of triosmium clusters with organic compounds
1984 **3**(11) 1175–1225 by Kevin Burgess

No. 9
Chromium(III) and the glucose tolerance factor
1985 **4**(1) 1–14 by J. Barrett, P. O'Brien and J. Pedrosa De Jesus

No. 10
Carbon–hydrogen bond activation in early transition metal systems
1985 **4**(2) 177–200 by Ian P. Rothwell

No. 11
Arene–chromium tricarbonyl complexes: bonding and behaviour
1985 **4**(6) 901–927 by A. Solladié–Cavallo

No. 12
Transition–metal thiocarbonyl complexes: preparative methods, reactivity and thiocarbonyl ligand bonding properties
1985 **4**(11) 1801–1846 by Peter V. Broadhurst

No. 13
The synthesis, structures, bonding and unusual reactivity of sulfido osmium carbonyl cluster compounds
1985 **4**(12) 2003–2025 by Richard D. Adams

No. 14
The preparation and structure of complexes containing simple sulphur–nitrogen ligands
1986 **5**(3) 607–632 by Paul F. Kelly and J. Derek Woollins

No. 15
The structural chemistry of metal thiolate complexes
1986 **5**(5) 1037–1104 by Ian G. Dance

Continued from previous page

Reports published

No. 16
Transition-metal complexes of inorganic sulphur-nitrogen ligands
1986 **5**(11) 1661–1699 by Tristram Chivers and Frank Edelmann

No. 17
Transition-metal aluminohydride complexes
1986 **5**(12) 1897–1917 by Andrew R. Barren and Geoffrey Wilkinson

No. 18
The organometallic chemistry of phosphazenes
1987 **6**(2) 119–157 by Harry R. Allcock, James L. Desorcie and Geoffrey H. Riding

No. 19
Naked phosphorus atoms and units in transition-metal compounds
1987 **6**(3) 151–182 by Massimo Di Vaira, Piero Stoppioni and Maurizio Peruzzini

No. 20
The organometallic chemistry of the lanthanide elements in low oxidation states
1987 **6**(5) 803–835 by William J. Evans

No. 21
Organometallic oxides: the example of trioxo (η^5-pentamethylcyclopentadienyl)rhenium(VII)
1987 **6**(6) 1165–1182 by Wolfgang A. Herrmann, Eberhardt Herdtweck, Martina Flöel, Jürgen Kulpe, Ulrich Küsthardt and Jan Okuda

No. 22
From metallaboranes to transition metal borides: the chemistry of metal-rich metallaborane clusters
1997 **6**(11) 1935–1958 by Catherine E. Housecroft

No. 23
Electron counting in clusters: A view of the concepts
1998 **7**(4) 253–283 by Steven M. Owen

No. 24
Advances in vanadium, niobium and tantalum carbonyls
1988 **7**(18) 1639–1665 by S.C. Srivastava and A.K. Shrimal

No. 25
Homonuclear and heteronuclear oxo-bridged compounds of the transition elements
1989 **8**(3) 219–274 by B.O. West

No. 26
Kinetic deuterium isotope effects in transition metal hydride clusters
1989 **8**(4) 383–405 by E. Rosenberg

No. 27
Bi-phasic and phase transfer catalysis
1989 **8**(4) 407–413 by T.G. Southern

No. 28
Phosphorane iminato complexes of transition metals
1989 **8**(6) 707–726 by K. Dehnicke and J. Strähle

No. 29
Structure, bonding and electron counts in cubane-type clusters having M_4S_4, $M_2M'_2S_4$ and MM'_3S_4 cores
1989 **8**(24) 2843–2882 by S. Harris

No. 30
Electrochemical studies on iron, ruthenium and osmium carbonyl clusters
1990 **9**(4) 455–474 by Simon R. Drake

No. 31
New developments in the organometallic chemistry of calcium, strontium and barium
1990 **9**(11) 1345–1362 by Timothy P. Hanusa

No. 32
Kinetics and mechanisms of CO substitution of metal carbonyls
1990 **9**(13) 1503–1535 by Fred Basolo

No. 33
Synthesis, molecular structures, properties and reactions of halo- and carbonyl(amine)copper(I) complexes
1990 **9**(19) 2319–2351 by K.G. Caulton, G. Davies and E.M. Holt

No. 34
Recent developments in the chemistry of mono- and dinuclear complexes of the macrocyclic dianion, 5,7,12,14-teramethyldibenzo[b,i][1,4,8,11]tetraazacyclotetradecine
1990 **9**(21) 2553–2566 by F.A. Cotton and J. Czuchajowska

No. 35
Coordinatively unsaturated tripalladium and triplatinum clusters: models for reactions on metal surfaces
1990 **9**(23) 2767–2802 by R.J. Puddephan, L. Manojlovic-Muir and K.W. Muir

Continued from previous page

Reports published

No. 36
Homoleptic and related aryls of transition metals
1991 **10**(2) 135–173 by S.U. Koschmieder and G. Wilkinson

No. 37
Ruthenium clusters containing N-donor ligands
1991 **10**(3) 277–322 by M.I. Bruce, M.P. Cifuentes and M.G. Humphrey

No. 38
Aluminium alkoxides, β-diketonates and carboxylates
1991 **10**(17) 1967–1994 by R.C. Mehrotra and A.K. Rai

No. 39
Alkyne rotation on a Rh—Rh bond: an entry to diverse chemistry
1991 **10**(17) 1995–2023 by R.S. Dickson

No. 40
The structures of compounds containing selenium nitrogen, and tellurium–nitrogen bonds
1991 **10**(20/21) 2353–2370 by M. Björgvinsson and H.W. Roesky

No. 41
Reactions of L-ascorbic acid with transition metal complexes
1992 **11**(3) 285–321 by Michael B. Davies

No. 42
Halide ion transfer between main group and transition metal halides as a valuable method for the synthesis of new compounds and catalyst precursors
1992 **11**(7) 715–728 by Piotr Sobota

No. 43
Cyclopentadienylmetal oxides
1992 **11**(14) 1707–1731 by F. Bottomleys

No. 44
Relevance of X-ray structural data to kinetic studies: substitution behaviour of transition metal tetracyano complexes containing oxo or nitrido ligands
1992 **11**(18) 2277–2284 by J.G. Leipoldt, S.S. Basson, A. Roodt and W. Purcell

No. 45
Excited-state acid–base properties of inorganic compounds
1992 **11**(18) 2285–2299 by Johannes G. Vos

No. 46
A thermodynamic scale for oxygen atom transfer reactions
1993 **12**(6) 571–589 by R.H. Holm and James P. Donahue

No. 47
The ligand polyhedral model and its application to the binary carbonyls
1993 **12**(9) 977–990 by Brian F.G. Johnson and Yvonne V. Roberts

No. 48
Lewis base adducts of alane and gallane
1993 **12**(15) 1829–1848 by Cameron Jones, George A. Koutsantonis and Colin L. Raston

No. 49
Stable compounds of the heavier group 14 and 15 elements involving pπ–pπ multiple bonding: an overview of the first decade
1993 **12**(20) 2431–2446 by N.C. Norman

No. 50
The influence of catalyst structure on the dehydro-polymerization of phenylsilane
1994 **13**(15/16) 2231–2243 by Toru Immure and T. Don Tilley

No. 51
Structural systematic in nickel carbonyl cluster anions
1995 **14**(3) 339–365 by Anthony F. Masters and Josephine T. Meyer

No. 52
Multidentate ligands bound via alkyne and group 15 or 16 donor sites
1995 **14**(4) 465–481 by Michael J. Went

No. 53
Chemical vapour deposition of copper from (hfac)CuL compounds
1995 **14**(6) 699–732 by Mark J. Hampden-Smith and Toivo T. Kodas

No. 54
Nickel carbonyl cluster complexes
1995 **14**(7) 829–868 by James K. Beattie, Antinony F. Masters and Josephine T. Meyer

Continued from previous page

Reports published

No. 55
Transition metal butadienyl complexes
1995 **14**(10) 1259–1276 by Brian J. Brisdon and Richard A. Walton

No. 56
Bis(diphenylphosphino)amine and related chemistry
1995 **14**(23/24) 3367–3388 by Pravat Bhattacharyya and J. Derek Woollins

No. 57
Stereochemical aspects of phosphor-1,1-dithiolato metal complexes (dithiophosphates, dithiophosphinates): coordination patterns, molecular structures and supramolecular associations – I
1994 **14**(23/24) 3389–3472 by Ionel Haiduc, D. Bryan Sowerby and Shao-Fang Lu

No. 58
Organotellurium precursors for metal organic chemical vapour deposition (MOCVD) of mercury cadmium telluride (MCT)
1996 **15**(5/6) 745–763 by Harkesh B. Singh and Narasimhan Sudha

No. 59
The chemistry of inorganic and organometallic compounds with adamantane-like structures
1996 **15**(10) 1585–1642 by Jagadese J. Vittal

No. 60
Stereochemical aspects of phosphor-1,1-dithiolato metal complexes: coordination patterns, molecular structures and supramolecular associations in dithio- phosphinates and related compounds
1996 **15**(15) 2469–2521 by Ionel Haiduc and D. Bryan Sowerby

No. 61
Toxic and mutagenic effects of chromium(VI). A review
1996 **15**(21) 3667–3689 by Maria Cieślak-Golonka

No. 62
Ring-opened polymerization (ROP) of strained, ring-titled silicon-bridged [l]ferrocenophanes: synthetic methods and mechanisms
1996 **15**(24) 4311–4329 by Ian Manners

No. 63
Metal–metal bond formation in the oxidative addition to dinuclear gold(I) species. Implications from dinuclear and trinuclear gold chemistry for the oxidative additional process generally
1997 **16**(1) 1–17 by John P. Fackler Jr

No. 64
Applications of electrospray mass spectrometry in organometallic chemistry
1998 **17**(25–26) 4291–4313 by William Henderson, Brian K. Nicholson and Louise J. McCaffrey

No. 65
Recent advances in the chemistry of scandium
1999 **18**(12) 1691–1715 by S.A. Cotton

No. 66
Metal-containing dendritic polymers
1999 **18**(27) 3575–3591 by Fiona J. Stoddart and Thomas Welton

No. 67
Primary alanes and alanates: useful synthetic reagents in aluminium chemistry
2000 **19**(14) 1649–1661 by Rudolph J. Wehmschulte and Philip P. Power

No. 68
The Bioinorganic chemistry of chromium (III)
2001 **20**(1–2) 1–26 by John B. Vincent

No. 69
Recent advances in homogenous catalysis using platinum complexes
2001 **20**(3–4) 151–164 by Matthew L. Clarke

No. 70
Structures of alkali and alkaline earth metal clusters with oxygen donor ligands
2004 **23**(9) 1479–1504 by Katharina M. Fromm and Estelle D. Gueneau

No. 71
The coordination chemistry of tripodal tetraamine ligands
2005 **24**(1) 1–39 by Allan G. Blackman